Energy Research and Power Engineering 2014

Edited by
W.Y. Fan, G.P. Wang, H.D. Liu, Z.J. Xie, Y.P. Chen,
Z.F. Yang and H.C. Wang

TRANS TECH PUBLICATIONS

Energy Research and Power Engineering 2014

Edited by
W.Y. Fan
G.P. Wang
H.D. Liu
Z.J. Xie
Y.P. Chen
Z.F. Yang
H.C. Wang

Energy Research and Power Engineering 2014

Selected, peer reviewed papers from the
2014 International Conference on
Energy Research and Power Engineering
(ERPE'14),
MAY 17-18, 2014, Dalian, China

Edited by

**W.Y. Fan, G.P. Wang, H.D. Liu, Z.J. Xie,
Y.P. Chen, Z.F. Yang and H.C. Wang**

Trans Tech Publications Ltd
Churerstrasse 20
CH-8808 Pfaffikon
Switzerland
http://www.ttp.net

Volumes 986-987 of
Advanced Materials Research *2-part-set*
ISSN print 1022-6680
ISSN cd 1022-6680
ISSN web 1662-8982

Full text available online at *http://www.scientific.net*

***Distributed** worldwide by*

Trans Tech Publications Ltd
Churerstrasse 20
CH-8808 Pfaffikon
Switzerland

Fax: +41 (44) 922 10 33
e-mail: sales@ttp.net

and in the Americas by

Trans Tech Publications Inc.
PO Box 699, May Street
Enfield, NH 03748
USA

Phone: +1 (603) 632-7377
Fax: +1 (603) 632-5611
e-mail: sales-usa@ttp.net

Preface

It is our pleasure to welcome you to the 2014 International Conference on Energy Research and Power Engineering (ERPE'14) in Dalian, China. ERPE’14 is the first conference dedicated to issues related to Advanced Materials Science, Chemical Engineering and Technologies, Power System and Energy Engineering, Its Applications, Environmental Engineering and Resource Development, Industrial, Mechanical and Manufacturing Engineering, Mechatronics, Automation and Control, Computation Methods and Algorithms for Modeling, Simulation and Optimization, Data Mining and Data Processing, Measurement and Instrumentation, Monitoring, Testing, Detection and Identification Technologies, Power and Electric Research, Electronics and Microelectronics, Embedded and Integrated Systems, Communication, Signal and Image Processing, Information Technologies, WEB and Networks Engineering, Information Security and Software Application, Construction Materials, Architecture Science and Civil Engineering, Modern Tendency in Area of Management, Logistics, Economics, Education, Traffic and Urban Engineering.

A major goal and feature of it is to bring academic scientists, engineers, industry researchers together to exchange and share their experiences and research results, and discuss the practical challenges encountered and the solutions adopted.

We hope you will have a technically rewarding experience, and use this occasion to meet old friends and make many new ones. Don’t miss the opportunity to explore in Dalian, China. And don’t forget to take a sample of the many and diverse attractions in the rest of the China.

ERPE’14 promises to be both stimulating and informative with a wonderful array of keynote and invited speakers from all over the world. Delegates will have a wide range of sessions to choose from and will have a difficult decision in deciding which sessions to attend.

We would like to thank the organization staff, the members of the program committees and reviewers. They have worked very hard in reviewing papers and making valuable suggestions for the authors to improve their work. We also would like to express our gratitude to the external reviewers, for providing extra helps in the review process, and the authors for contributing their research result to the conference. Special thanks go to TTP Publisher.

We wish all attendees of the ERPE’14 an enjoyable scientific gathering in Dalian, China. We look forward to seeing all of you next year at the conference.

Organizing Committee

Table of Contents

Chapter 2: Power System and Energy Engineering, its Applications

Chapter 3: Environmental Engineering and Resource Development in Energy Industry

Chapter 4: Design and Research of Components and Mechanisms of Energy Equipment and Installations

Chapter 5: Electrical Machines, Mechatronics, Automation and Control

Chapter 6: Computation Methods and Algorithms for Modeling, Simulation and Optimization

Chapter 7: Measurement and Instrumentation, Monitoring, Testing, Detection and Identification Technologies

Chapter 8: Power and Electric Research, Electronics and Microelectronics, Embedded and Integrated Systems and Applications

Chapter 9: Communication

Chapter 10: Information Technologies

CHAPTER 1:

Semiconductors, Materials and Processing Technologies in Energy and Power Industry

Advanced Materials Research Vols. 986-987 (2014) pp 3-7

doi:10.4028/www.scientific.net/AMR.986-987.3

Z-Transform Implementation of the CFS-PML for Truncating 3D Meta-material FDTD Domains

Yongqing Yue [1,a] , Chunhui Zhu [1,b] and Naixing Feng[1,c]

[1]School of Physics and Mechanical & Electrical Engineering, Xiamen University, Xiamen, 361005, China.

[a] yongqingyue@126.com, [b] zhuchhxd@xmu.edu.cn, [c] fengnaixing@yeah.net

Keywords: perfectly matched layer (PML), meta-material, finite-difference time-domain (FDTD), Z-transform method

Abstract. Efficient Z-transform implementa- tion of the complex frequency-shifted perfectly matched layer (CFS-PML) based on the stretched coordinate PML (SC-PML) formulations and the D-B formulations is proposed for truncating meta-material finite- difference time-domain (FDTD) lattices. In the proposed PML formulations, the Z- transform method is incorporated into the CFS-PML FDTD implementation. The main advantage of the proposed formulations can allow direct FDTD implementation of the Maxwell's equations in the PML regions. A numerical test has been carried out in a three dimensions (3-D) FDTD domain to validate the proposed formulations. It is shown that the proposed formulations with CFS scheme are efficient in holding good absorbing performances.

Introduction

Meta-materials are specifically referred to as a class of artificial materials that have simultaneous negative electric permittivity and magnetic permeability [1] and are also known as left-handed materials (LHMs). In recent years, Meta-materials have been received much attention due to their unusual electromagnetic properties. Meta-materials have been realized by using different models such as the Drude medium and the Lorentzian medium models and so on. Recently, the finite-difference time- domain (FDTD) method [2] has been used successfully in simulating electromagnetic wave propagation in domains that have meta-material properties [3,4,5].

When the FDTD method is used for modelling open region meta-material domains, the abso- rbing boundary conditions (ABCs), such as the stretched coordinate perfectly matched layer (SC-PML), are needed to truncate the computational domain. The SC-PML [6] has been shown to be one of the most effective FDTD ABCs. Recently, different PML formulations have been successfully introduced for truncating meta-material FDTD computati- onal domains [7,8]. In [7,8], the proposed PML formulations have been incorporated into the FDTD implementation of the meta-materials.

In this letter, a novel *Z*-transform algorithm of the CFS -PML is proposed based on SC-PML. Owing to the frequency dependency of the meta-materials, the transformation of the proposed formulations to time domain will lead to convolutions. However, because the convolution in the time domain is just a multiplication in the Z-domain [9], therefore, in the proposed PML formulations, *Z*-transform theory [10] is incorporated into the FDTD implementation of the meta-materials. A numerical test carried out in three dimensional (3-D) domains composed entirely of Lorentzian type meta-material is given to validate the proposed formulations.

Formulation

In 3-D regions, the normalized SC-PML frequency-domain modified Maxwell's curl equations can be written as

$$j\omega \mathrm{D}(\omega)=c_0 \nabla_s \times \mathrm{H}(\omega)\,. \tag{1}$$

$$j\omega \mathrm{B}(\omega)=-c_0 \nabla_s \times \mathrm{E}(\omega)\,. \tag{2}$$

where D and B are given by

$$\mathrm{D}(\omega) = \varepsilon_r(\omega)\mathrm{E}(\omega) . \tag{3}$$

$$\mathrm{B}(\omega) = \mu_r(\omega)\mathrm{H}(\omega) . \tag{4}$$

where c_0 is the speed of light in free space, $\varepsilon_r(\omega)$ and $\mu_r(\omega)$ are, respectively, the relative permittivity and permeability of the meta-materials and the operator ∇_s is expressed as

$$\nabla_s = \hat{x} S_x^{-1} \partial_x + \hat{y} S_y^{-1} \partial_y + \hat{z} S_z^{-1} \partial_z . \tag{5}$$

where $S_\eta, (\eta = x, y, z)$, is the complex stretched coordinate metrics, which was originally proposed [7] to be

$$S_\eta = 1 + \frac{\sigma_\eta}{j\omega\varepsilon_0\varepsilon_r(\omega)} . \tag{6}$$

With the CFS scheme and S_η is defined as

$$S_\eta = \kappa_\eta + \frac{\sigma_\eta}{\alpha_\eta + j\omega\varepsilon_0\varepsilon_r(\omega)} . \tag{7}$$

where σ_η and α_η are assumed to be positive real and κ_η is real and ≥ 1. $\varepsilon_r(\omega)$ is the meta-material permittivity which is assumed to be identical and realized with a Lorentz medium model [3] given by the following expression:

$$\varepsilon_r(\omega) = \mu_r(\omega) = 1 + \frac{\omega_p^2}{\omega_0^2 - \omega^2 + j\omega\Gamma} . \tag{8}$$

where $\mu_r(\omega)$ is the meta-material permeability, ω_p is the plasma frequency, ω_0 is the resonance frequency, and Γ is the absorbtion parameter of the medium.

As an instance, considering the discretization of the z component of (1) in the edges regions, we obtain

$$\frac{(1 - z^{-1})D_z}{c_0\Delta t} = \frac{1}{S_x(z)}\frac{\partial H_y}{\partial x} - \frac{1}{S_y(z)}\frac{\partial H_x}{\partial y} . \tag{9}$$

where Δt is time step and $S_\eta(z)$, $(\eta = x, \text{or } y)$, can be obtained by using the relation $j\omega \rightarrow (2/\Delta t)(1 - z^{-1})/(1 + z^{-1})$ [9].

$$S_\eta(z) = w_\eta \frac{(1 + u_\eta z^{-1} + \theta_\eta z^{-2} + f_\eta z^{-3})}{(1 + v_\eta z^{-1} + \varphi_\eta z^{-2} + \gamma_\eta z^{-3})} . \tag{10}$$

where

$$w_\eta = \frac{a_0\Delta t^3 + a_1\Delta t^2 + a_2\Delta t + a_3}{b_0\Delta t^3 + b_1\Delta t^2 + b_2\Delta t + b_3} .$$

$$u_\eta = \frac{3a_0\Delta t^3 + a_1\Delta t^2 - a_2\Delta t - 3a_3}{a_0\Delta t^3 + a_1\Delta t^2 + a_2\Delta t + a_3} .$$

$$v_\eta = \frac{3b_0\Delta t^3 + b_1\Delta t^2 - b_2\Delta t - 3b_3}{b_0\Delta t^3 + b_1\Delta t^2 + b_2\Delta t + b_3} .$$

$$\theta_\eta = \frac{3a_0\Delta t^3 - a_1\Delta t^2 - a_2\Delta t + 3a_3}{a_0\Delta t^3 + a_1\Delta t^2 + a_2\Delta t + a_3} .$$

$$\varphi_\eta = \frac{3b_0\Delta t^3 - b_1\Delta t^2 - b_2\Delta t + 3b_3}{b_0\Delta t^3 + b_1\Delta t^2 + b_2\Delta t + b_3} .$$

$$f_\eta = \frac{a_0\Delta t^3 - a_1\Delta t^2 + a_2\Delta t - a_3}{a_0\Delta t^3 + a_1\Delta t^2 + a_2\Delta t + a_3}.$$

$$\gamma_\eta = \frac{b_0\Delta t^3 - b_1\Delta t^2 + b_2\Delta t - b_3}{b_0\Delta t^3 + b_1\Delta t^2 + b_2\Delta t + b_3}.$$

where

$a_0 = (\alpha_\eta + \sigma_\eta)\omega_0^2$, $b_0 = \alpha_\eta\omega_0^2$,

$a_1 = (\alpha_\eta + \sigma_\eta)\Gamma + \varepsilon_0(\omega_0^2 + \omega_p^2)$, $b_1 = \alpha_\eta\Gamma + \varepsilon_0(\omega_0^2 + \omega_p^2)$,

$a_2 = \kappa_\eta(\alpha_\eta + \varepsilon_0\Gamma) + \sigma_\eta$, $b_2 = \alpha_\eta + \varepsilon_0\Gamma$,

$a_3 = \kappa_\eta\varepsilon_0$, $b_3 = \varepsilon_0$.

Substituting (10) into (9), we obtain

$$\frac{(1-z^{-1})D_z}{c_0\Delta t} = \frac{1}{w_x}\frac{(1+v_x z^{-1}+\varphi_x z^{-2}+\gamma_x z^{-3})}{(1+u_x z^{-1}+\theta_x z^{-2}+f_x z^{-3})}\frac{\partial H_y}{\partial x} - \frac{1}{w_y}\frac{(1+v_y z^{-1}+\varphi_y z^{-2}+\gamma_y z^{-3})}{(1+u_y z^{-1}+\theta_y z^{-2}+f_y z^{-3})}\frac{\partial H_x}{\partial y}. \quad (11)$$

Introducing two auxiliary variables ϕ_{zx} and ϕ_{zy}

$$\begin{aligned}\phi_{zx} &= \frac{1}{w_x}\frac{1}{(1+u_x z^{-1}+\theta_x z^{-2}+f_x z^{-3})}\frac{\partial H_y}{\partial x} \\ &= -u_x z^{-1}\phi_{zx} - \theta_x z^{-2}\phi_{zx} - f_x z^{-3}\phi_{zx} + \frac{1}{w_x}\frac{\partial H_y}{\partial x}\end{aligned}. \quad (12)$$

$$\begin{aligned}\phi_{zy} &= \frac{1}{w_y}\frac{1}{(1+u_y z^{-1}+\theta_y z^{-2}+f_y z^{-3})}\frac{\partial H_x}{\partial y} \\ &= -u_y z^{-1}\phi_{zy} - \theta_y z^{-2}\phi_{zy} - f_y z^{-3}\phi_{zy} + \frac{1}{w_y}\frac{\partial H_x}{\partial y}\end{aligned}. \quad (13)$$

Considering the time shifting property of the *Z*-transform [9], i.e. if $f^n \overset{z}{\longleftrightarrow} F(z)$ then $f^{n-m} \overset{z}{\longleftrightarrow} z^{-m}F(z)$, (12) – (13) can be written directly in the FDTD form, respectively, as (14) – (15),

$$\phi_{zx}^{n+1} = -u_x\phi_{zx}^n - \theta_x\phi_{zx}^{n-1} - f_x\phi_{zx}^{n-2} + \frac{1}{w_x}\frac{\partial H_y^{n+1/2}}{\partial x}. \quad (14)$$

$$\phi_{zy}^{n+1} = -u_y\phi_{zy}^n - \theta_y\phi_{zy}^{n-1} - f_y\phi_{zy}^{n-2} + \frac{1}{w_y}\frac{\partial H_x^{n+1/2}}{\partial y}. \quad (15)$$

Equation (11) can be written as

$$D_z^{n+1} = D_z^n + c_0\Delta t[(\phi_{zx}^{n+1} + v_x\phi_{zx}^n + \varphi_x\phi_{zx}^{n-1} + \gamma_x\phi_{zx}^{n-2}) - (\phi_{zy}^{n+1} + v_y\phi_{zy}^n + \varphi_y\phi_{zy}^{n-1} + \gamma_y\phi_{zy}^{n-2})]. \quad (16)$$

Finally, E can be obtained from D using (3) (and H from B using (4)), which is available in [10]. A similar method can be used for other regions of the PML.

Numerical Result

To show the validity of the proposed formulations, a numerical test carried out in 3-D FDTD computational domain is provided. A Gaussian pulse, with a central radial frequency equals to $\omega_c = 5.0\times10^9 rad/s$, is excited at the center of 3-D computational domain composed of the meta-material realized with a Lorentz model [3] with the parameters of $\omega_0 = 1.0\times10^9 rad/s$, $\omega_p = 6.9282\times10^9 rad/s$ and Γ=0. With these choices, $\varepsilon_r(\omega)$ and $\mu_r(\omega)$ are equal to –1 at the peak of the incident spectrum ω_c. The size of FDTD computational domain is $50\times50\times50$ grid with the time step Δt = 5.56ps and the

space steps $\Delta x = \Delta y = \Delta z$ =5mm. The meta-material FDTD computational domain is terminated by 8 additional PML layers. Assuming that the origin is at the corner of FDTD grid, a vertically polarized point source locates at (33, 33, 33). The relative reflection error of CFS-PML is first computed over 1200 time iterations for $\kappa_{\max}$ =7, α_η =0.003. This same example is repeated with SC-PML ($\kappa_{\max}$ =11, α_η =0). These optimum parameters are chosen empirically to obtain the lowest reflection. The PML parameters are chosen as PML [8, 2, 0.001%]. The relative reflection error (in decibels) versus time steps is computed at an observation point located at (57, 57, 57) using $R_{dB}(t)=20\log_{10}(|E_z^R(t)-E_z^T(t)|/|E_{z\_\max}^R|)$, where $E_z^T(t)$ is the field computed using the test domain, and $E_z^R(t)$ is the reference field computed by using FDTD computational larger domain truncated by the PML [16, 4, 0.001%].

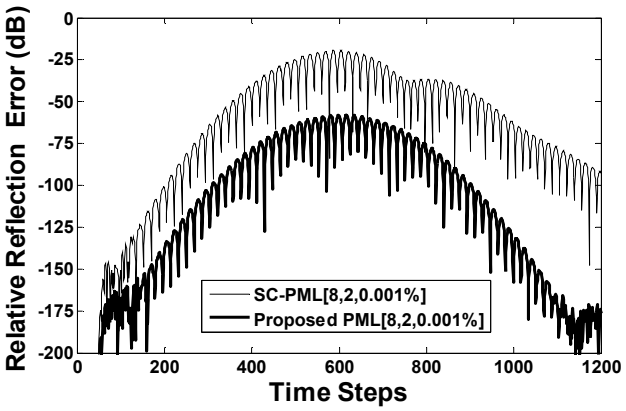

Fig. 1. Relative reflection error versus Time Steps: SC-PML ($\kappa_{\max}$ =11, α_η =0.); Proposed PML ($\kappa_{\max}$ =7, α_η =0.003).

To measure the reflection performance of the proposed PML formulations, Fig.1 shows the relative reflection error of the proposed PML formulations and conventional SC-PML formulations at observation point. The maximum relative errors of the conventional SC-PML and the proposed PML are -20dB and -58dB, respectively. It can be clearly concluded in terms of the maximum relative errors illustrated in Fig.1 that the absorbing performance of the proposed PML formulations has 38dB improvement as compared with the conventional SC-PML formulations. Finally, the reflection performance of the proposed PML formulations as function of frequency is studied. The relative reflection coefficient versus frequency is computed at an observation point located at (57, 57, 57) using $R_{dB}(f)=20\log_{10}(FT\{E_z^R(t)-E_z^T(t)\}\ /FT\{E_z^R(t)\})$. where FT {.} is the Fourier transform operation. Fig.2 shows the relative reflection coefficient for two different PML implementations as well as the frequency spectrum of the incident pulse. The proposed PML formulations hold better absorbing performance than SC-PML over the frequency range of interest, as shown in Fig.2.

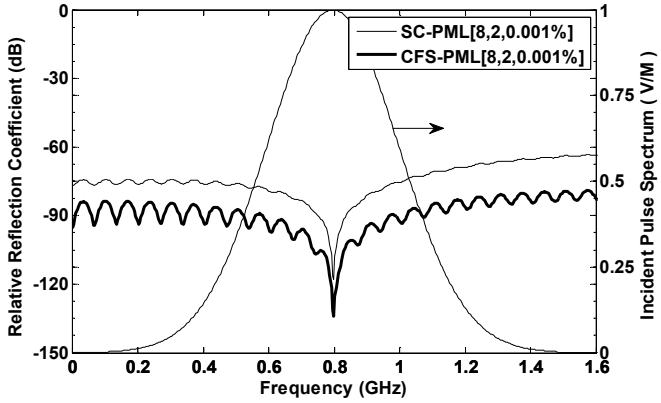

Fig. 2. Relative reflection coefficient versus Frequency: SC-PML ($\kappa_{\max}$ =11, α_η =0.); Proposed PML ($\kappa_{\max}$ =7, α_η =0.003).

Conclusion

The CFS-PML formulations are presented for truncating 3-D meta-material FDTD computati- onal domains. In the proposed CFS-PML formulations, the frequency dependence of the meta-materials has been implemented in the FDTD algorithm by using the *Z*-transform method. A numerical test carried out in 3-D FDTD computational domain shows that the proposed formulation holds comparatively good absorbing performance.

Acknowledgement

These works are financially supported by the Natural Science Foundation of China (NSFC) under Grant 41240029, ZDYZ2012-1-03, 41390453 and 61301008

References

[1] Veselago V G, The electrodynamics of substances with simultaneously negative values of ε and μ[J]. *Sov. Phys. Uspekhi*, 1968, 10(4):509–514.

[2] Taflove A, Hagness S C. Computational electrodynamics[M]. Boston: Artech house, 2000.

[3] Kärkkäinen M K. Numerical study of wave propagation in uniaxially anisotropic Lorentzian backward-wave slabs[J]. *Physical Review E*, 2003, 68(2): 026602.

[4] Prokopidis K P, Zografopoulos D C. Efficient FDTD algorithms for dispersive Drude-critical points media based on bilinear z-transform[J]. *Electronics Letters*, 2013, 49(8): 534-536.

[5] Mukherjee S, Karmakar S, Goswami C, et al.. Electromagnetic wave propagation modeling in Lorentzian DNG metamaterial by auxiliary differential equation based ADI-FDTD[C]. Emerging Technology Trends in Electronics, Communication and Networking, Surat, 2012: 1-4.

[6] Li J, Yang Q, Miao J, et al.. A Novel and Efficient Algorithm of the Uniaxial Perfectly Matched Layer Based on the Z-Transform Method[C]. Control, Automation and Systems Engineering , Auckland , 2011:1-4.

[7] Cummer S A, Perfectly matched layer behavior in negative refractive index materials[J], *IEEE Antennas Wireless Propag*. *Lett,* 2004, 3(1):172–175.

[8] Ramadan O. DSP-PML algorithm for open region DNG meta-material FDTD simulations[J]. *Electronics letters*, 2010, 46(1): 16-18.

[9] Feng N, Li J. Novel and efficient FDTD implementation of higher-order perfectly matched layer based on ADE method[J]. *Journal of Computational Physics*, 2013, 232(1): 318-326.

[10]Feng N X, Li J X, Zhao X M. Efficient FDTD Implementations of the Higher-Order PML Using DSP Techniques for Arbitrary Media[J]. *IEEE Transactions on Antennas and Propagation*, 2013, 61: 2623-2629.

Advanced Materials Research Vols. 986-987 (2014) pp 8-12
© (2014) Trans Tech Publications, Switzerland
doi:10.4028/www.scientific.net/AMR.986-987.8

A Numerical Method for Ge-Profile of Microwave Power Device Based on Si / Si_{1-x}/Si

Shaohua ZHOU[1, a], Qi XIONG[2, b]* and Jiangping ZENG[2, c]

[1]Hunan Engineering and Technology College, Changsha, Hunan, China

[2] Hunan industrial vocational and technical college, Changsha, Hunan, China

[3]University of Hunan, Changsha, Hunan, China

[a]email: zshsa@126.com, [b]email: xq0229@163.com, [c]email: zengjp@hnu.edu.cn

*Corresponding author

Keywords Bipolar; Microwave-power-device; $Si_{1-x}Ge_x$; Numerical-method.

Abstract. A double-mesa hetero-junction bipolar structure of NPN type microwave power device is used. The Si is chosen for emitter and collector, and $Si_{1-x}Ge_x$ alloy is for base. Based on some experiment data, a numerical method is used to get an equation about forbidden band E_g via the variety composition of Ge at 300K using MATLAB, which is more precise than linearization. We also calculate the collector current density J_C via the variety of V_{BE} and the obtained equation is consistent with the experiment result. An optimum Ge composition value was found. It has practical significance for the device design and simulation.

Introduction

With the rapid development of semiconductor material and technology, the microwave power device has grown with higher frequency and larger output power. The design of the microwave power device is transferred from 'doping project' into 'band project'. Thus, heterogeneous form microwave Power Device Based on Si/Si_{1-x}/Si is more appealing with following advantages [1]: higher output power, Si having better performance on conducting heat which improves the overall performance of the device, $Si_{1-x}Ge_x$ alloy used for base area having higher migration rate which improves the microwave performance, and most importantly, the produce process of the device is perfectly compatible to the Si technology which lowers the costs. However, owing to the different Ge constitution, physical parameter and characteristics of $Si_{1-x}Ge_x$ alloy, the feature of device differs with the change of Ge constitution. Linearization method is usually adopted in the emulation towards the forbidden band width of $Si_{1-x}Ge_x$ alloy varying with the x value [2], making the numerical calculation coarser. Through the extraction of the result of the experiment data, we use mathematical methods of interpolation method and fitting method to achieve two better expressions than linear ones. And according to a series of obtained mathematical equations, it can be easily to implement a optimization design and simulation.

Current Density Equation Of Collector Area

As a power device, the fever of the device mainly is concentrated in the collector that we must determine the collector current. The current equation of hetero junction bipolar transistor (HBT) and that of bipolar junction transistor (BJT) differ from each other. In favor of numerical calculation and simulation, make sure in a case of a large current gain to assume that the current density of emission current density and the collector area is equal, namely, JE=JC. Here, we ignore buffer layer parasitic conduction band potential barrier, and thus yielding a current density equation with concise collector area [3]:

$$J_C = J_{C0} \cdot \exp(qV_{BE}/kT) \tag{1}$$

J_{C0} is the collector area saturation current density.

$$J_{C0} = \frac{qD_{n\_SiGe}}{G_{B\_SiGe}} \cdot \frac{(N_C N_V)_{SiGe}}{(N_C N_V)_{Si}} \cdot n^2_{i\_Si} \exp(\Delta E_{Geff}/kT) \tag{2}$$

In the equation (2), D_{n_SiGe} is the minority carrier mobility of SiGe; G_{B_SiGe} is the Gummel number; $(N_CN_V)_{SiGe}$ and $(N_CN_V)_{Si}$ are respectively the conduction band and valence band concentration product of SiGe and Si; n_{iSi} is the intrinsic carrier concentration of Si with its value equal to 1.6×10^{10} c m^{-3}; E_{Geff} is the base forbidden band width change. The parameters above for J_C must be separately obtained.

The Calculation And Determination Of The Parameters Of Model

The determination of base area minority carrier diffusion coefficient

As for SiGe HBT [4]:

$$D_{n\_SiGe} = \frac{D'_n}{1+|E|D'_n/V_T\upsilon_s} \tag{3}$$

$$N_n = \frac{D_{n0}}{1+[N_B(y)/N_m]^m} \tag{4}$$

E is the electric field intensity; υ_s is the saturation drift velocity of the electrons in SiGe and is a number between Si and Ge's saturation drift velocity that decreases gradually with the increase of the components of Ge, and according to its physical properties, we made linear calculation.

$$\upsilon_s = \upsilon_{s\_Si}\cdot(1-x)+\upsilon_{s\_Ge}\cdot x \tag{5}$$

υ_{s_Si} and υ_{s_Ge} are respectively the electronic saturation drift velocity of Si and Ge, the value of which are 8.5×10^{6} and 6×10^{6}. N_B (Y) is the base doping concentration distribution; $N_m=1.14\times10^{4}$c m^{-3} ， m= 0.29.

The number of Gummel number

According to semiconductor physics, the calculating formula for Gummel number is:

$$G_{B\_SiGe} = \int_0^{W_B} N_B(y)\,dy \tag{6}$$

W_B is the base width with base region wide effect decreasing with the increase of the V_{CE}.

Determination of the conduction band and the valence band concentration ratio of SiGe and Si

Although the sensitivity of conduction band and valence band concentration ratio of SiGe and Si towards temperature is very low, the precise value is still hard to be calculated. So the empirical formulas given in the paper [3] are not suitable for parameter simulation calculation to the device. We take advantage of the two groups of data of conduction band and valence band concentration ratio of SiGe and Si presented in the literature.

Use 0.6 (x=0.07), 0.3 (x=0.27) to combine with the conduction band and valence band concentration ratio of Si - Si (x = 0) equaling to 1, and one of Ge-S i (x=1) equaling to 1.3013×10-6 to interpolate. And then through mathematical methods fitting through the comparison, as shown in figure 1, fitting effect of six times is found to be the best.

$$\frac{(N_CN_V)_{SiGe}}{(N_CN_V)_{Si}} = P_1x^6+P_2x^5+P_3x^4+P_4x^3+P_5x^2+P_6x+P_7 \tag{7}$$

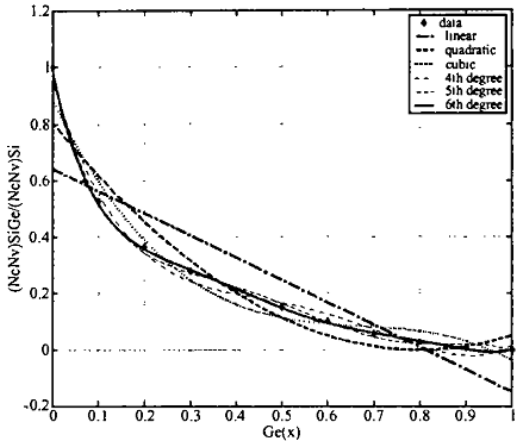

Figure.1 The conduction band and valence band concentration ratio of SiGe and Si along with the change of Ge component

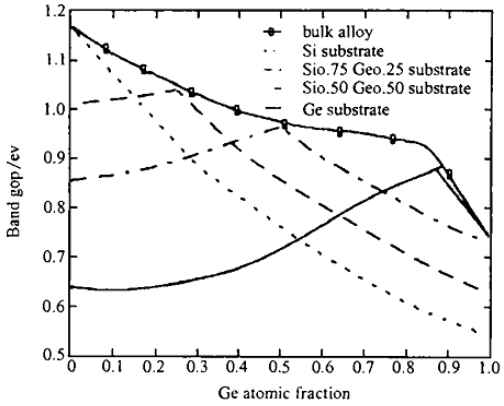

Figure.2 SiGe alloy forbidden band width Eg figure Change with Ge component x experimental data

Therein, P_1=31.374，P_2=109.22，P_3= -150.33，P_4= -103.73，P_5=37.932 ，P_6= -7.674，P_7=1.

SiGe forbidden band width and ΔE_{Geff} calculation mathematical model

The materials forbidden band width must be a precise parameter number in heterojunction devices, for the forbidden band width of Si here with the ready-made data is 1.17eV [5]. Based on reference [3], the SiGe alloy's forbidden band width Eg changes with Ge component which is x in the experimental data graph (as shown in figure 2), a set of data of Si 1-xGex alloy's forbidden band width Eg change with Ge component x can be extracted:

Table.1

x/Ge	0	0.1	0.2	0.3	0.4	0.5	0.6	0.7	0.8
Eg/eV	1.17143	1.10714	1.06786	1.02857	0.99643	0.97500	0.96017	0.95357	0.93929

As the Si and Ge have as much as 4.17% lattice adaptation, the value of Ge component x should be less than 0.4, and the characteristics of the SiGe alloy's band gap structure is similar to the one of Si [6] when x < 0.85, so we took only the value of x to 0.8. , and by using mathematical fitting method of numerical simulation software MATLAB, we get a three fitting equation of Eg and x:

$$E_g(x) = A_1x^3 + A_2x^2 + A_3x + A_4 \quad (0 \le x \le 0.80) \tag{8}$$

Therein, Al, A2, A3 and A4 respectively equal to -0.24652, 0.65423,- 0.65233 and 1.1703. Through the two-dimensional graphic of the fitting, it is obvious that the fitting of three times is better than that of the linear approximation is shown in figure 3 below.

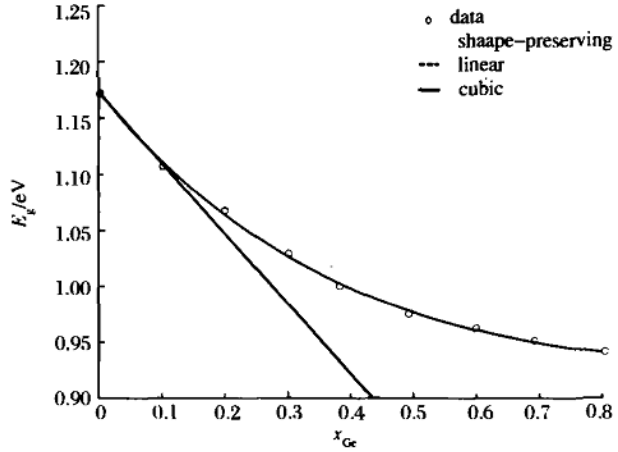

Figure.3 SiGe alloy forbidden band width Eg changes with Ge components fitting

The straight line of what the linearity equation [7] $E_g(x) = 1.17 - 0.63x$ yields is the linear results, while the curve represents the nonlinear fitting result. Linear equation can better reflect the change of Eg(x) when x≤0.2. But when x≥0.2, the error coefficient will be more and more large. At

the following calculation process, the error can reach nearly 0.5 eV. On the contrary, the nonlinear curve can well express the change of the Eg within the whole range.

Due to the base heavy doping, the band is narrowed, and the variation of forbidden band width change ΔE_{g_dop} becomes part of ΔE_{Geff}. According to the empirical formula in literature [3], when the base doping N_B>1018c m-3:

$$\Delta E_{g\text{-}dop} = A + B \cdot \lg\left(\frac{N_B}{10^{18}}\right) \tag{9}$$

A=0.0286 B=0.0274

The variation Ge introduces into the base area of the forbidden band is:

$$\Delta E_{g\text{-}Ge}(x) = 1.17 - E_g(x) \tag{10}$$

So the total variation is:

$$\Delta E_{Geff} = |\Delta E_{g\text{-}Ge}(x)| + |\Delta E_{g\text{-}dop}| \tag{11}$$

Substitute equation (8) (9) (10) into (11), yielding:

$$\Delta E_{Geff} = 0.65233x - 0.65423x^2 + 0.24652x^3 + 0.0286 + 0.0274\lg\left(\frac{N_B}{10^{18}}\right)$$

The Results Of Calculation And Verification

When designing the device, as long as the base area of the doping concentration distribution device and the base components of Ge x as well as the effective width are set, by the above parametric equations can be used to calculate the collector area of the current density of the device (here base extraneous component uniform distribution N_B=2×1019cm-3; ignoring the base region wide change effect; set the base width W_b=20nm and base region Ge components linear distribution x=0～0.4). The Gummel number $G_{B\_SiGe} = W_b N_B$. The field strength of the base area $E = \Delta E_{g\_grade} / q \cdot W_b$. ΔE_{g_grade} is the difference of forbidden band narrow amount caused by Ge constituents between the base on the emitter side and on the collector side. When working on $J_C - V_{BE} - x$ relation, ΔE_{Geff} can be yielded by equation (12) and the conduction band and valence band concentration ratio of SiGe and Si by equation (7). The $J_C - V_{BE} - x$ relationship is shown in Figure 4.

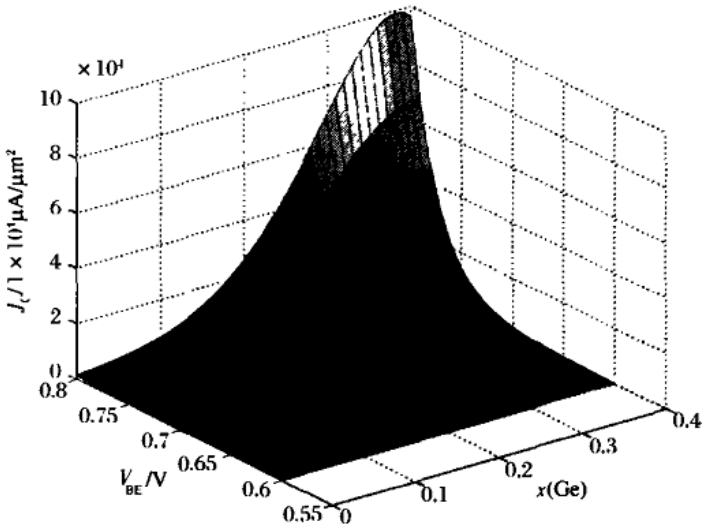

Figure.4 $J_C - V_{BE} - x$ relationship curve

Through numerical simulation, to obtain the maximum J_C when Ge constituents x =0.38. Compared to result of literature [3], [7] and [8], the parameter calculation equation inducing the model results is completely consistent to the numerical method. In addition, previous studies have shown that when Ge constituents have a value between 35% ~ 40%, the base carrier can achieve maximum mobility that verifies the parameter model is accurate and feasible. Conclusion

Based on the analysis of the mechanical theory as the foundation, designed the soccer robot pick the ball institutions optimal design process, found aim function, select design variables and the corresponding optimization algorithm to optimize a complete set of institutions. At last through the test, the final performance parameters of the institution can be achieved. Experiments show that the system has higher accuracy and stability, the new optimize pick the ball have design basic requirements, and achieved good ideal control effect.

Conclusion

According to the experimental parameters, combined with physical characteristics of SiGe alloy, and using numerical simulation software MATLAB, mathematical equations of SiGe alloy's forbidden band width and the conduction band and valence band concentration ratio of SiGe and Si varying with the change of Ge constituents can be determined. And testing and verifying the DC equation of HBT device based on Si/SiGe/Si J_C varying with the change of V_{BE}, to obtain the Ge constituents with maximum current density, confirming the correctness of the equation which has certain guiding role to the design simulation of devices.

Acknowledgment

In this paper, the research was sponsored by the Hunan Department of Education Scientific Research Project(13C198,13C199) and Hunan Scientific and Technological Project(2011FJ4172).

References

[1].Jiang Changling Advances in SiGe semiconductor technology [J]. Journal of semiconductor intelligence, 2000, 4 (3) : 26-31.

[2]Li Chen Chen Peiyi etc. Modulation doped layer in SiGe PMOSFE [J]. The application of microelectronics, 2002, 32 (4) : 249 ~ 252.

[3]Zelilca，Matutinovic - Krsteli ,Venkataraman ,et a1.Base Resistance and Effective Band Gap Reduction in n-p-n Si / S $i_{1-x}Ge_x$ / Si HBT's with Heavy Base Doping[J].IEEE Transactions Electron Device,1996，43 (3) ：457～465.

[4]Huang C H,Abdel-Motaleb I M.A Gummel-Pooh Model for Single and Double Heterojunetion Bipolar Transistors [J].IEEE Bipolar Circuits and Technology Meeting,1989：254～257.

[5], lee Kong Deyi Wei Jinghe. Ultra-thin base region SiGe our HBT current transmission model [J]. Journal of semiconductors, 2000, 2 (1) : 97 ~ 101.

[6]Subramanian S Iyer，Patton G L，Stork J M C．Heterjunction Bipolar Transistors Using Si-Ge Alloys[J]．IEEE Transactions on Electron Device，1999，36(10)：2043～2064 ．

[7] Liu Enke Zhu Bingsheng, Luo Jinsheng. Semiconductor physics [M]. Beijing: national defence industry press.

[8] Dai Xianying Zhang Heming. SiGe our HBT at base area transit under high current density q model [J]. Journal of microelectronics, 2003 (2) : 86 ~ 89.

Advanced Materials Research Vols. 986-987 (2014) pp 13-16

doi:10.4028/www.scientific.net/AMR.986-987.13

Adsorption and separation research of CO_2/CH_4 on modified activated carbon fiber

Qin Yuan[1], Honghong Yi[2,1, a], Xiaolong Tang[2,1], Kai Li[1], Fenrong Li[1], Yundong Li[1]

[1.] College of Environmental Science and Engineering, Kunming University of Science and Technology, Kunming 650093, China

[2.]College of Civil and Environmental Engineering, University of Science and Technology Beijing, Beijing 100083, China

[a] Corresponding Author: yhhtxl@163.com

Key words:Separation; Activated carbon fiber; Carbon dioxide; Methane

Abstract. In this paper, activated carbon fibers were modified by different chemical reagents. The modified adsorbents were used to investigate adsorption and separation performance of CO_2/CH_4 gases mixture, and then it could get the best modified adsorbent. The experimental results show that amine can't great grafting on activated carbon fiber. Compared with blank activated carbon fibers, the adsorption property of CO_2 did not have much influence on the activated carbon fiber modified by amine. However, it can increase the nitrogen functional groups and the specific surface area on the surface of activated carbon fiber that were modified with nitric acid and ammonia. The above two points were conductive to the adsorption and separation of CO_2/CH_4 mixture gases.

Introduction

With increasing seriousness of environmental problems and the lacking of fossil energy, Energy crisis is becoming more and more grievous. How to develop and utilize clean energy to reduce energy consumption and reduce pollution, has become the urgent task today. Therefore many scientific workers are working on clean energy, such as biogas and natural gas, which can replace fossil fuels[1]. However, CO_2 exists in these new energy, and it is directly affected by the combustion efficiency of methane. Therefore, separation CO_2 from CH_4 mixture is very important.

Adsorption separation technology is more and more applied in the separation of CO_2/CH_4. Adsorption separation is a method which using the adsorbent of having stronger ability to remove material[2]. Activated carbon fiber(ACF) has the congenital advantage of benefiting for modification. ACF has developed specific surface area and abundant microporous which contain a series of functional groups[3,4]. So, ACF was used as catalyst carrier is not only beneficial to adsorption and disperse of metal but also itself has adsorption active site. There are study has reported[5]that ACF which was modified by alkaline metal ion is used to removal COS and H_2S , and it was found that modified ACF has promote role for CO_2 adsorption. In addition, organic amine and CO_2 molecular can react to form relatively strong chemical bonds, and amino modification has become a way to increase adsorption selectivity[6,7].

In this experiment, we compared the effect of ACF which was loaded different kinds of chemical reagents applied in adsorption and separation of carbon dioxide and methane. To provide theoretical basis of efficient purification for natural and biogas.

Experiment

Gas and reagent. CO_2 and CH_4 were obtained from Foshan Kodi Gas Chemical industry Co.Ltd. N_2 was obtained from Meisaier Gas company. Adsorbate purities were 99.99%, 99.99% and 99.99% (wt.%) for CO_2 , CH_4, and N_2. Experimental drugs are listed as below: Potassium chloride, Barium chloride, Calcium chloride, Lithium chloride, Ammonium hydroxide(25%～28%), Nitric acidetc (65%)， Ethylene diamine, Triethylamine. These reagents were obtained from Kaimeishente Chemical company and chemical purity level of all experimental drugs are analytically pure.

Experimental process. Kinetics experiment system is described as below. Gases from each cylinder inpour into the mixing tank after go through each flowmeters. The mixing Gases enter into the fixed bed that was placed in Temperature controller to maintain a constant temperature, and then react with adsorbents. Gas chromatographic detector was used as testing instrument. The dynamic adsorption experiments were carried out in a fixed bed reactor using 1.0g of samples at 298K. The volumetric flow rate of the gas was kept at 25mL/min. Concentration for CO_2, CH_4 and N_2 were 15%, 25% and 60%(v%) , respectively.

Adsorption preparation. Firstly, ACF which were washed with distilled water were cut into 1cm × 1cm squares. And then samples were dried at 110 ℃ to remove adsorbed water.

ACF modified by nitric acid: ACF were boiled with nitric acid for 2 hours at 80℃, and then the ACF were washed with distilled water to neutral. Finally, samples were dried at 110 ℃ for 8 hours.

ACF modified by ammonia: Taking a certain amount of ACF into the beaker, and then concentrated ammonia was added into the beaker rapidly with stirring with a glass rod. Finally, putting the adsorbent in adsorption bed quickly.

ACF modified by organic amine: A sample of 1.0g of ACF was placed in a beaker with 100mL solution of ethyl alcohol. Add a certain amount of ethylene diamine into the beaker, and then reflow stirring for 24 hours under the condition of 78℃. Finally, drying at 100 ℃.

ACF modified by metal ion: In this article, impregnation was used in the experiment. A sample of 1.0g of each of the ACF was placed in contact with 17ml of solutions of 0.3mol/L concentrations of metal salts for 30min in Ultrasonic machine. Then he solutions were impregnated on ACF at ambient temperature for 1 hour. Afterwards, impregnated samples were dried at 110℃ to remove adsorbed water. Sequentially, the impregnated samples were calcined at 500℃ for 60min under a N_2(high purity, 99.99%) flow. The samples of the modified ACF were denoted as M-ACFs.

Result and analysis

Screening of activated carbon fiber types. In this study, the polypropylene fine based activated carbon fibers(PAN-ACF) and glue base activated carbon fiber (VACF) were selected to comparative adsorption and separation ability of CO_2/CH_4. The experimental results are shown in Fig.1.

As can be seen from Fig.1, it has not very big difference for adsorption of CO_2 on PAN-ACF and VACF. But VACF is more conductive to adsorption of CO_2. The adsorption capacity of CH_4 on two kinds of substrate has no obvious difference. So, VACF is more conductive to the separation of the mixture gas. VACF is adopted as adsorption material.

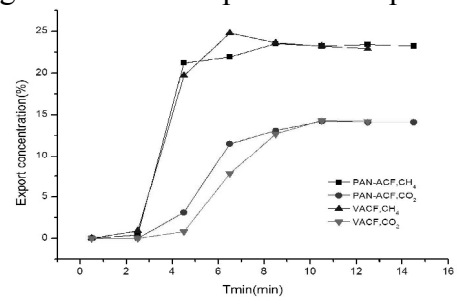

Fig. 1 The breakthrough curve of two kinds of activated carbon fiber(ACF)

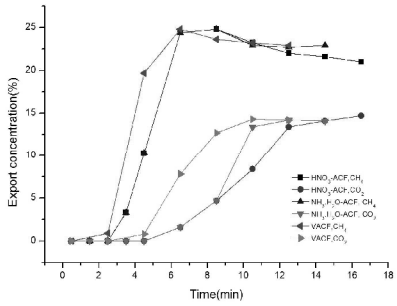

Fig.2 The breakthrough curve of two adsorbents modified by ammonia and nitrate

The study of adsorbent modified by ammonia and nitrate. Adsorption and separation of CO_2/CH_4 on modified adsorbents at 25℃ is shown in Fig.2. The capture capacities and separation factors of carbon dioxide and methane are shown in Tab.1.

Tab.1 The adsorption capacity and the separation factor of CO_2 and CH_4

Adsorbents	Adsorption capacity (mmol/g)		Separation factor α_{CO_2/CH_4}
	CO_2	CH_4	
VACF	1.43	1.37	1.69
HNO_3-ACF	1.58	1.44	1.83
$NH_3.H_2O$-ACFCF	1.54	1.43	1.79

From the Fig.2, it can be seen that adsorption performance of carbon dioxide and methane on ACF that were modified by ammonia and nitrate caused an little higher than that of on blank VACF. Studies have reported that adsorbents which were treated with nitric acid and ammonia could increase nitrogen functional groups on surface[8]. This is benefit for adsorption of CO_2. In addition, from Tab.3, it indicated that adsorption capacity of CO_2 on HNO_3-ACF is better than that of on $NH_3.H_2O$-ACF. This is because that using nitric acid to modify ACF could enlarge pore size and then increase the specific surface area[9]. It also shows that the adsorbing capacity of CH_4 is a little bigger on ACF that were treated with nitric acid than that of on blank ACF. But amplitude of variation is not higher then that of CO_2. Therefore, the separation factor of CO_2/ CH_4 is improved on pretreated ACF. So, the following activated carbon fibers could pretreated with nitric acid.

The study of adsorbent modified by organic amine. The results are shown in Fig.3 and Tab.2.

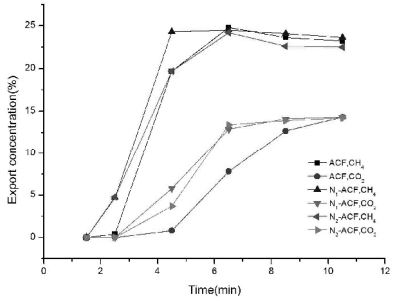

Fig.3 The breakthrough curve of CH_4 and CO_2 on N_1-ACF and N_2-ACF

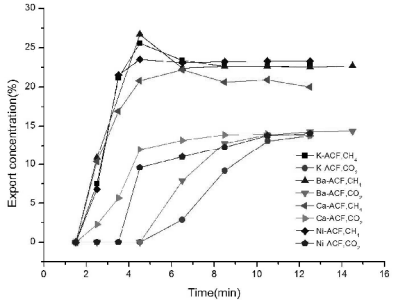

Fig.4 The breakthrough curve of CH_4 and CO_2 on adsorbents modified by metal ions

Tab.2The adsorption capacity and the separation factor of CO_2 and CH_4

adsorbents	adsorption capacity (mmol/g)		separation factor α_{CO_2/CH_4}
	CO_2	CH_4	
VACF	1.43	1.37	1.69
N_1-ACF	1.40	1.34	1.74
N_2-ACF	1.42	1.35	1.75

There are studies have reported that adsorbents modified with organic amine can promote CO_2 adsorption[10,11]. Fig.3 and Tab.2 indicate that ACF were modified by two kinds of organic amine don't promote separation performance of CO_2/CH_4. The reason may be that only a small amount of hydroxyl groups on ACF surface can react with amino functional groups. So, it had a little organic amino functional groups which is conductive to CO_2 adsorption on the surface of ACF. It shows that the method of using organic amine to modify ACF does not apply to separation of mixture.

The study of adsorbent modified by metal ions. Adsorption breakthrough curve of CO_2 and CH_4 on ACF were modified by metal ions as shown in Fig.4 and Tab.3.

Tab. 3 The adsorption capacity and the separation factor of CO_2 and CH_4

Adsorbents	Adsorption capacity (mmol/g)		Separation factor α_{CO_2/CH_4}
	CO_2	CH_4	
K-ACF	1.61	1.30	2.06
Ba-ACF	1.54	1.29	1.99
Ca-ACF	1.42	1.29	1.84
Ni-ACF	1.46	1.31	1.85

As can be seen from the Tab.3, under the same metal loads, the samples for CO_2 adsorption capacity decreased as following: $K^+ > Ba^{2+} > Ni^+ > Ca^{2+}$. Because CO_2 is acidic gas, the introduction of the alkaline earth metal ions and alkaline metal ions would improve the adsorption capacity of CO_2. The more strong of metallic, the more adsorption active site on surface of ACF. So, adsorption performance of CO_2/CH_4 on adsorbent that loaded K ions is stronger than that of on other adsorbents. In addition, Ba^{2+} is divalent metal ions, which has high charge density and polarizability. Its polarization effect is better than other metals. So, Ba^{2+} easily induced deformation of electron cloud of CO_2[12]. Adsorption and separation ability of CO_2/CH_4 on K-ACF is stronger than that of on Ni-ACF and Ca-ACF. To sum up, the adsorption and separation capacity of CO_2/CH_4 on ACF modified with K^+ than that of on adsorbents which were modified with other metal ions.

Conclusion

This article studied that the adsorption and separation properties of CO_2/CH_4 on activated carbon fiber that was modified with different types of chemical reagent. The results show that the activated carbon fibers modified by ammonia and nitrate are good for the separation of CO_2/CH_4 mixture. And loading K ion on adsorbent is more conductive to adsorption and separation of CO_2/CH_4 than loading other metal ions. However, grafting organic amine on activated carbon fiber can not promote the research of adsorption and separation for CO_2 / CH_4. So, it can continue research from two aspects to improve separation capacity of CO_2/CH_4 in the future study. One is adding the amount of nitrogen functional groups on surface of activated carbon fiber. Another is loading different kinds of potassium on activated carbon fiber.

Acknowledgement

The work was supported by The Fundamental Research Funds for the Central Universities (06101046).

References

[1] X.Z. Kong, Adsorption separation and regeneration of gas, Cryog. Eng, 4 (1999) 328-333.
[2] Y. C. Chang，C.C. Lee,H．C.C. Lee，Characterization of microstructure and surface properties of heat-treated PAN-and rayon-based activated carbon fibers, J. Por. Mater., 14 (2007) 227-237.
[3] C．A.Toles，W. E. Marshall, Johns．Surface functional groups on acid-activated nutshell carbons, Carbon, 37 (1999) 1207-1214.
[4]L. Fang, Y.C. Zhang, J.X. Zhou, The study of using activated carbon fiber to removal COS and H_2S from carbon dioxide. Guangzhou, Chem, 33 (2008) 25-31.
[5] X. Xu, X. Zhao, L.Sun, Adsorption separation of carbon dioxide，methane and nitrogen on monoethanol amine modified β-zeolite, J. Nat. Gas Chem., 18 (2009) 167-172.
[6] P. D. Jadhav, R. V. Chatti, R. B.Biniwalem, Monoethanol amine modified zeolite 13X for CO_2 adsorption at different temperatures, Energy Fuels, 21 (2007) 3555-3559.
[7] C. L. Mangun, K. R.Benak, Surface chemistry, pore sizes and adsorption properties of activated carbon fibers and precursors treated with ammonia, Carbon, 39 (2001) 1809-1820.
[8] B. Shen, Y. Zhou, Z. Shi, Research activated carbon fiber pretreatment and SCR catalytic activity, J. Fuel Chem. Technol. , 36 (2008) 376-380.
[9] F. S. Su , G. S.Lu, S. C. Kuo, Adsorption of CO_2 on Amine Y-Type Zeolites, Energy Fuels, 24 (2010) 1441-1448.
[10] C.L. Wu, X.W. Liu, W. Su, SBA-15 modified with DIPA used in the study of separation performance of CO_2/CH_4, Chem. Ind. Nat. Gas, 35 (2010) 42-48.
[11] G. H. Meng, A. M. Li, Q. X. Zhang, Studies on the oxygen-containing functional groups of activated carbon and their effects on the adsorption character, Ion Exch. Adsorpt, 23 (2007) 88-94.
[12] H. K. Song, K. W. Cho, K. H. Lee, Adsorption of carbon dioxide on the chemical modified silica adsorbents, J. Non-Cryst Sol., (1998) 242: 69-80.

Advanced Materials Research Vols. 986-987 (2014) pp 17-20

doi:10.4028/www.scientific.net/AMR.986-987.17

Analyze the effect of Thermal conductivity of Cold insulation materials in cryogenic engineering

Ming LENG[1, b] , Zhaoci LI[1,a] , Jianyuan FENG[2, b] , Guangrang LI[1, b] , Zhaochen LIU[1,b]

[1.] National Engineering Laboratory of Oil and Gas Pipeline Safety Transportation/Beijing Key Laboratory of Urban Oil and Gas Distribution Technology, China University of Petroleum, Beijing, 102249, China;

[2.] Illinois Institute of Technology, Chicago, Illinois, 60616, USA

[a]lizhaoci@cup.edu.cn, [b]lengming123@sina.cn

Keywords: cryogenic engineering; cold insulation materials; thermal conductivity;

Abstract. The pipe heat transfer models were constructed, respectively, to simulate the cryogenic insulated structure, nonlinear partial differential equations was obtained considering the temperature-dependent variation in thermal conductivity of insulation materials. In order to get the temperature profile of insulation layer, Kirchhoff integral method was introduced to process, program, and iteratively calculate the simplified energy equations. The influence of heat-transfer process related to the thermal conductivities of four cold insulators was analyzed. Results indicate that phenolic foam, hydrophobic perlite, and RPUR have superior low-temperature insulation at cryogenic environment, while foam glass has better low-temperature insulation at normal temperature. The thickness of inner cryogenic-insulation layer can be reduced largely by using a multicomponent cold insulator in the discharge pipe of LNG stations, which can save both materials and costs. Meanwhile, it offers a new method to solve variable thermal conductivities.

Introduction

In recent years, with rapid development of LNG stations, there are many new insulation structures of cryogenic pipeline for long distance transportation, and the most popular way to approach the insulation goal economically by accumulative insulation method is though improve the thermal conductivity, water absorptivity, and heat capacity of insulation material. The most often used cryogenic accumulative insulation materials are expanded perlite, foam glass, phenolic foam, aerogels, nitrile rubber and diene foam , polyurethane foam and its upgrade series etc. [1].

Currently, there are two most popular methods to process thermal conductivity of cold insulator: use the average thermal conductivity of the overall period of insulation layer or divide cold insulators into multilayer[2], which use ATCM to calculate the temperature of whole cold insulator, and then find the average thermal conductivity for each layer. These two approaches either have accuracy problem or become too complicated to calculate. To solve this problem, we tried several popular cold insulators as examples to show how to build and calculate the models. The effect of thermal conductivity in cryogenic insulation calculation of pipe is also included in our results.

1 Modeling

1.1 Thermal conductivity of cold insulator

The pipeline cryogenic insulation structures in LNG station usually consists of cold insulate layer, vapor barrier layer and protective layer. As cold insulators continuously booming and updating, water adsorption of material is now significantly low, neglect the vapor barrier layer. The protective layer is constructed by metal foil strip with thickness between 0.25~1mm. Take LNG pipeline as an example, meanly focus on the effect of the varying thermal conductivity in heat transfer calculation, in another

word, only consider the cold insulate layer. The temperature-dependent thermal conductivities of some common cold insulators were figured in literature [2]. Chose some characteristic materials including foam glass, RPUR, phenolic foam, hydrophobic perlite and give simulated profile. The thermal conductivity functions for simulations are summarized in Table 1.

Table 1 Cold insulators thermal conductivity vs. temperature

Cold insulators	λ/(W/m·)	Average λ (W/m·)	Normal temperature λ(W/m·)	Temperature range t/
Foam glass	$-8.611\times10^{-8}t^3-4.535\times10^{-5}t^2-0.007542t-0.3373$	0.055	0.0631	[-163，-100]
	$0.001147e^{-0.02788t}+0.05431e^{0.005647t}$			(-100，40]
	0.0685			(40，60)
RPUR	0.0001148t+0.03082	0.021	0.0211	[-163，-98]
	$-1.656\times10^{-6}t^2-0.0001962t+0.01627$			(-98，-24]
	$-3.357\times10^{-8}t^3+2.871\times10^{-6}t^2+3.594\times10^{-5}t+0.01891$			(-24，50]
Phenolic foam	0.0001084t+0.0344	0.0272	0.0371	[-163,45]
Hydrophobic perlite	0.0001933t+0.06675	0.054	0.0716	[-163，45]

1. Average thermal conductivity λ is determined by the average thermal conductivity between -160 to 25 ;
2. Normal temperature λ is thermal conductivity at 25

1.2 Pipe heat transfer model of cryogenic insulation

Heat transfer problem with cold insulation material involve the Fourier law and energy equation. The energy equation can be approached using general control equation [3]. The cylinder pipe heat transfer can compare with the solution of hot oil transportation pipeline in soil to solve the energy equation with varying thermal conductivity [4, 5], which is required to change coordinate system to simplify equations with average thermal conductivity in temperature range. Establish the following cylinder coordinate as the pipe heat transfer model, shows in fig. 1.

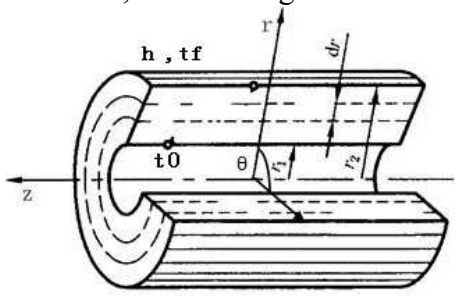

Fig. 1 Pipe model in cylinder coordinate

Because of symmetry, fix one angular θ to discuss heat transfer in roz surface. Similarly, consider the system is steady state and neglect the inner heat source, then can transform this three dimensional question into two dimension. Since λ(T) is a function of T which will make the diffusion term nonlinear, using common method to solve this problem is complicated.

2 Cryogenic insulation calculation and result analysis

In order to eliminate the nonlinear diffusion term in heat transfer equation, cite Kirchhoff integral to define scalar U.

$$U=\frac{1}{\lambda_0}\int_{T_0}^{T}\lambda dT \quad \lambda_0=\lambda\ (T_0 \tag{1}$$

Considering heat convection boundary conditions in pipe model and using Kirchhoff integral scalar U, we can deduce the non-linear equation. Using parameters of discharge pipe in a coastal LNG station to make the result more value in engineering. The outside diameter of pipe is 1016mm, cryogenic insulation layer thickness equal to 230 mm (including metal protective layer and vapor barrier layer etc.), the inner surface of pipe maintain at -160℃, outside surface follows heat convection boundary condition with heat transfer coefficient $h=11.6+7.0v^{0.5}$ W/m$^2\cdot$℃. wind speed v is equal to local highest ten mines wind speed 25m/s, atmosphere temperature t_f is equal to the highest monthly temperature in summer 35℃, and the axis length in x direction of pipe, use unit length 1. Discrete equation with central difference format, and take convergence accuracy of 10^{-3}, though control the step length of Δx, Δt to obtain convergence solution. During tuning program the upper boundary condition have large influence on converge process. When the coefficient $\frac{\Delta t \cdot h}{\lambda_0}$ is smaller, the result can be easier to converge. Similarly, after achieve the converged field U (i, j), it is easy to get the related temperature distribution of each point T (i, j). fig. 2 shows temperature fields of four different cold insulators.

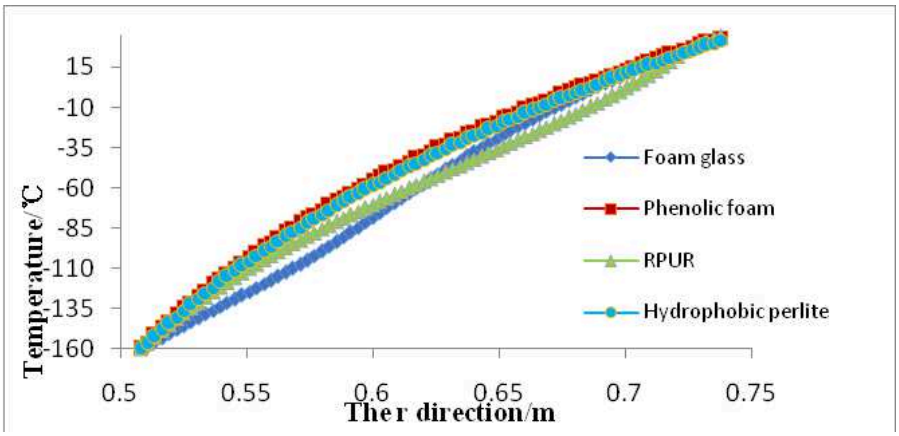

Figure 2 Temperature distribution profiles of insulation materials in radial direction

Under same boundary conditions, phenolic foam and hydrophobic perlite have similar temperature profile between -160~25℃, and they are both convex function. RPUR and foam glass have different convexity around -58℃. Below -58℃, RPUR have greater temperature gradient than foam glass; above -58℃, foam glass have greater temperature gradient than RPUR. In a conclusion, could combine the properties of different cold insulators together. When temperature range is between -160~-58℃, should use RPUR in the inner layer, above -58℃, should chose foam glass. For phenolic foam and hydrophobic perlite have higher temperature in the overall temperature range using either ATCM or VTCM, should consider this in pipe insulation design to efficiently using material. Heat loss and flux of four kinds of cold insulators calculated by three different methods shows in Table 2.

Table 2: Heat loss and heat flux in pipe heat transfer under different thermal conductivity

Cold insulators	ATCM		NTCM		VTCM	
	Heat loss/W	Heat flux/(W/m^2)	Heat loss/W	Heat flux/(W/m^2)	Heat loss/W	Heat flux/(W/m^2)
Foam glass	180.65	38.99	207.13	44.67	179.31	38.67
RPUR	69.15	14.91	69.48	14.98	60.20	12.98
Phenolic foam	89.53	19.31	122.02	26.09	90.72	19.39
Hydrophobic perlite	177.38	38.25	234.88	50.65	179.06	38.62

The outside environment also have great effect to its insulation performance, phenolic foam and hydrophobic perlite shows more obvious difference of convexity in temperature profile, which means heat transfer in pipe is more sensible about thermal conductivity. And especially cryogenic temperature area, these two materials have better insulation property. According to correlated standards [6], the maximum heat flux is 25W/m^2 if we apply the limited-unit-length- heat-loss-method

to design the insulation layer thickness. Under this condition, the LNG discharge pipeline should use phenolic foam and RPUR rather than foam glass and hydrophobic perlite. According to our survey, LNG stations often use the combination of both foam glass and RPUR as their cold insulators. From fig.2, it can be concluded that this method not only takes full advantage of the combined insulation materials' properties in both low and high temperature ranges, but also reduces the cost of insulation materials. Though verification, considering the change of thermal conductivities, the thickness of the combined cold insulators in LNG station can be further optimized. Comparing to the ATCM and VTCM, the NTCM will cause a much higher heat flux of the four materials. Furthermore, this method is too conservative, which will waste materials, and cannot be used in cold insulation verification.

3 Conclusions

The pipe heat transfer models were constructed and simplified to analyze the effects of variable thermal conductivities on cryogenic insulation layers. By applying the Kirchhoff integral factor to solve the nonlinear terms in control equations, the temperature profiles were obtained by programming and iterative calculation, and an innovative way to solve variable thermal conductivity problems was established. All of the four materials have distinct insulation performances in low and high temperature ranges. For cryogenic insulation design, multiple insulation materials can be combined according to their temperature distribution profiles to save materials and reduce costs. Both ATCM and NTCM are too conservative in insulation design and NTCM is not suitable for verification.

Furthermore, when equipment has restrict insulation property requirement and wide operation temperature range, the design of layer thickness and properties verification should consider the variation of thermal conductivities in insulation layers.

Nomenclature

RPUR: Rigid polyurethane foam
ATCM: Average thermal conductivity method
NTCM: Normal temperature thermal conductivity method
VTCM: Variable thermal conductivity method
T_0: Random reference temperature,℃
λ : Thermal conductivity of cold insulators, W/m·℃
λ_0: Thermal conductivity of certain temperature T_0, W/m·℃
Δx: Width of control volume in the x direction, m
Δt: Width of control volume in the t direction, m

References

[1] Guobang CHEN , Peng ZHANG. Cryogenic insulation and heat transfer technology [M]. Beijing: Science Press,China, 2004.

[2] Qiyue JIA, Zhiwei LIU. Structure design of LNG insulation project [J]. Process Equipment & piping, China,2009.6, 46(3): 67~69

[3] Tao W Q. Numerical Heat Transfer (The Second Edition) [M].Xi'an: Xi'an Jiaotong University Press,China,2001.5.

[4] Fuqi HUANG, Jiayou ZHANG, Tanghu LUO.The thermal calculation of underground pipeline[J]. ACTA PETROLEI SINICA, China,1980.1, 1(1): 77~91

[5] Changjun LI, Ziqiang ZENG , Maoze JIANG . Calculation of temperature decrease for oil product during shutdown of heated oil pipeline[J]. YOU QI CHU YUN, China,1991.4, 10(2): 1~11.

[6] Shaowei YIN, Yang YANG, Congtao ZENG. Optimal design of cold-retaining layer for LNG line [J]. Pipeline Technique and Equipment,China, 2011.1, (1): 12~13.

Advanced Materials Research Vols. 986-987 (2014) pp 21-24

doi:10.4028/www.scientific.net/AMR.986-987.21

Application of Hall Effect in Semiconductor Material

Shuai Kang

Zunyi Normal College , 563002, Zunyi, China

Keywords: Hall Effect, Semiconductor characteristics, semiconductor material

Abstract. As the unique properties of semiconductor material, it is made of many semiconductor Hall devices. Semiconductor Hall device has the advantages of simple structure, small volume, long service life, sensitive to magnetic field induction, strong frequency response and large variable voltage output. Hall Effect of semiconductor material is one kind of electromagnetic effects, which has practical significance. It is widely used in measurement technology, electronic technology, automation technology and so on.

Introduction

Semiconductor material has many special properties. It is doping, heat sensitive, photosensitive, rectifying. These characteristics do bring revolutionary, rapid development to science and technology, and also a lot of benefits to our life and work. For example, voice activated switch, light control switch etc. At the same time, magnetoresistive effect, photomagnetic effect, Thomson effect and Hall Effect are also very important special effect is in semiconductor. Especially the Hall Effect, which is a kind of electromagnetic effects, many materials is studied based on it, such as Hall potentiometer, linear Hall sensor. Now Hall Effect has been applied widely in many scientific fields (measurement technology, electronic technology, automation technology and so on). Therefore, Hall Effect of semiconductor materials and its application are discussed in this paper.

Characteristics of semiconductor and semiconductor materials[1-3]

Characteristics of the semiconductor

The resistivity of semiconductor usually is $10^{-5}\Omega.\bullet m \sim 10^{6}\Omega \bullet m$ at room temperature. At the same time, it is doped, heat- sensitive, photosensitive and rectifying.

Doping: Impurities are artificially doped to semiconductor to control the relative conductivity. And its characteristics are also varied with different impurities. For example, when trivalent Boron is doped to pure Silicon crystal to replace silicon atom, P type semiconductor is formed; when pentavalent Phosphorus is doped, N type semiconductor is formed.

Heat sensitive: After doped, a doped semiconductor is formed, in which the density of majority and minority carrier will vary. Since minority carrier is produced by intrinsic excitation, it is sensitive to temperature, and the conductivity decreases with the increase of temperature.

Photosensitive: The resistance of some semiconductor changes with illumination, and greatly reduces under some light, such as laboratory photoelectric switch, daily light controlled switch, etc.
Rectifier: when a positive voltage is applied on a semiconductor, it is conductive; when a negative voltage is applied, it is no longer conductive, i.e. it is selectively conductive, the typical device of which is rectifier tube.

Characteristics of semiconductor materials

After impurities doped in high purity P type and N type semiconductor, they are made to the same silicon piece side by side through corresponding techniques. In the contact area, the electron (or hole) diffuses from higher density to lower density because of density difference. Then, a PN

junction is formed. It has a characteristic of unilateral conductivity because of the diffusion direction. Semiconductor devices with different functions are manufactured using this characteristic, such as diodes, transistors, and so on. In addition, using its photosensitive and heat sensitive, various sensitive elements can be made for information exchange.

Semiconductor has many characteristics, and they are reflected with characteristic parameters, such as forbidden bandwidth, resistivity, non-equilibrium carrier lifetime and mobility. Forbidden bandwidth reflects an excited energy, which excites valence electron from bound state to free state. Conductivity of semiconductor material is represented by carrier mobility. Non-equilibrium carrier lifetime reflects relaxation characteristic of semiconductor materials, transition from non-equilibrium to equilibrium, under the action of external factors. Characteristic parameter of semiconductor is not only an important basis for differing from non semiconductor materials, but also reflects amount difference between different semiconductor materials, even the same material in different states.

Hall Effect of semiconductor materials and application

Hall Effect of semiconductor materials

A semiconductor with current is placed in the magnetic field. Direction x is the direction of the electric field, E_x is the electric field strength, whose direction is perpendicular to magnetic field direction, and along direction z, magnetic induction is B_z. A transverse electric field E_y will be produced in direction y, perpendicular to the direction of electric field and magnetic field, which is called Hall Effect. Hall field E_y, magnetic field strength B_z and current density J_x are in proportional, i.e.

$$E_y = K_H J_x B_z \tag{1}$$

Proportional coefficient K_H is called Hall coefficient.

$$K_H = \frac{E_y}{J_x B_z} \tag{2}$$

Application of Hall Effect of semiconductor materials[4-5]

One of important methods to study semiconductor is through Hall Effect. Using it, carrier density can be determined, then semiconductor type can be judged, and Hall devices can be manufactured.
Now suppose that the sample temperature is uniform, all the carrier velocity is the same. For P type material, when electric field E_x is applied along with the direction +x, hole drift velocity is v_x, current density $J_x = qpv_x$. Under the action of vertical magnetic field B_z, the Lorentz force applied on hole is $q\vec{v}\times\vec{B}$, whose direction is along direction -y, and the value is qv_xB_z. holes deflect to direction -y under Lorentz force, which causes holes accumulated in direction –y. An transverse electric field is produced in direction +y. When action of transverse electric field and Lorentz force cancel each other out, to be stable, Hall field meet following equation.

$$qE_y = qv_xB_z \tag{3}$$

i.e.

$$E_y = v_x B_z = \frac{J_x}{pq} B_z \tag{4}$$

Compared with $K_H = \frac{E_y}{J_x B_z}$

$$R_H = \frac{1}{pq} > 0 \tag{5}$$

It's unit is m^3/C.

The Hall coefficient of N type semiconductor can be got using the same method.

$$R_H = -\frac{1}{nq} < 0 \tag{6}$$

Seen from formula (5) and (6), Hall field of N type and P type are in the opposite direction, through which the conductive type can be judged. Under the corresponding assumption conditions, the Hall coefficient of N type semiconductor is less than zero; on the contrary, the Hall coefficient of P type semiconductor is greater than zero.

Semiconductor Hall device has the advantages of simple structure, small volume and long service life. More importantly, it is sensitive to magnetic field induction, has strong frequency response and large variable voltage output. It is often applied in many fields, such as measurement of semiconductor characteristics, magnetic fluid power generation, electromagnetic nondestructive testing, as well as Hall sensor.

Concerned Hall devices, integrated circuits, components of Hall sensor are made according to the principle of Hall Effect. According to the principle of Hall Effect, certain variables can be measured through controlling other variables. For example, if the current is constant, AC or DC magnetic induction and magnetic field strength can be measured. If the magnitude and direction of magnetic field strength are unchanged, DC or AC voltage and current can be measured.

Hall sensor has a very wide range of applications both in life and industry. The majority of household electrical appliances in life use the Hall sensor, such as drum motor of video tape recorder, tape commutator of sound recorder, and washing machine, which is essential in our life. The speed measurement of its motor is realized through Hall sensors, which detect and control the motor commutation and variable speed.

In industry, the application of Hall sensor is also very extensive. One is the Hall motor, main characteristics of which are relatively stable speed, low noise and long service life. Hall devices detect the relative position change between stator and rotor. The motor uses these signals to change Hall voltage, and then to adjust the drive voltage. This motor is usually applied in DVD player and other electrical appliances production. In the car, Hall devices are widely used, such as automobile brake system ABS and speed detection, because of the advantages of high reliability, good temperature stability, high sensitivity, strong anti magnetic interference ability and so on. At the same time, they are also widely used in the aerospace and military weapons.

In addition, magnetic nondestructive testing of Hall Effect is a common flaw detection method. The steel frame structure of Main Stadium of Beijing Olympic Games, bird nest, has high

requirements for materials. The steel cables for bridge also need material not hurt. There will be a leakage magnetic field in the bug, which can be detected for the high permeability of ferromagnetic materials. This method is reliable, safe, practical, and with high accuracy.

Conclusions

Semiconductor material is a kind of important materials, and Hall Effect is a kind of electromagnetic effect of practical significance. Hall Effect of semiconductor material has been widely developed and applied in many advanced fields.

With the accelerating pace of life, most electronic products cannot be made without semiconductor materials. Based on it, the research and development technology of semiconductor materials will be increasingly high, while more and more semiconductor materials will be developed by Hall Effect. It will have a broad application prospect whether in life or industry.

Acknowledgments

This work is supported by the Science and Technology Foundation of Gui zhou Province under Grant (No. J[2012]2345 and NO. JLKZS[2012]02) and the Special Foundation of Governor of Gui zhou Province for Science and Technology and Education Talents Grant (No. [2012]87) and the Key Project of Education Department of Gui zhou province Grant(No [KY(2013)171]),This work is also supported by the Education Department of Gui zhou Province Talent Innovation Team Grant (NO. [2012]08) and the key discipline of Gui zhou province(NO.[2013]18).

References

[1] Liu En ke, Zhu Bing sheng, Luo Jin sheng et al. Semiconductor Physics (Fourth Edition) [M]. Beijing: National Defence Industry Press, 2011,3:6-21; 270-272; 328-336

[2] Zhao Kai hua, Chen Xi mou. The Electromagnetic(Second Edition)[M]. Beijing: Higher Education Press, 2006,12:150-152

[3] Shi Min.Physics and Technology of Semiconductor Devices (Second Edition) [M]. Su Zhou University Press,.2002.12:127-151

[4]Shi Wen long. The Application of Sensor in the Detection System [J]. Weekly, 2010, 36:176-177

[5]Tang Bing shu; Shen Tinggen. FDTD Numerical Study of Transmission Properties of Two Dimensional Photonic Crystals [J]. Semiconductor Optoelectronics. 2006,1:120-124

Advanced Materials Research Vols. 986-987 (2014) pp 25-29

doi:10.4028/www.scientific.net/AMR.986-987.25

Cloning and Analysis of MeCWINV6 Promoter from Biofuel Plant Cassava (*Manihot esculenta* Crantz)

Jiao LIU[1, a, #], Wenrui XIA[1, 2, b, #], Yanping HU[1, 2, c, #], Yuan YAO[1, d], Shaoping FU[1, e], Ruijun DUAN[1, f], Ruimei LI[1, g], Jianchun GUO[1, h *]

[1]Institute of Tropical Biosciences and Biotechnology, Chinese Academy of Tropical Agricultural Sciences / Key Laboratory of Biology and Genetic Resources of Tropical Crops, Ministry of Agriculture, Haikou 571101, P.R. China

[2]College of Agriculture, Hainan University, Haikou 570228, P.R. China

[a]liujiao@itbb.org.cn, [b]xiawenrui1989@163.com, [c]ziy2013@163.com, [d]yaofaraway1@163.com, [e]fushaoping@itbb.org.cn, [f]duanruijun@itbb.org.cn, [g]liruimei@itbb.org.cn, [h]jianchunguoh@163.com

[#]Jiao LIU, Wenrui XIA and Yanping HU contributed equally to this work

*Corresponding author: Jianchun GUO

Keywords: Cassava; starch accumulation; Cell wall invertase; Promoter; *Cis*-acting elements

Abstract. In order to gain insight into the specific function of the cassava cell wall invertase 6 (*MeCWINV6*), the promoter sequence of *MeCWINV6* gene was cloned using the PCR amplification approach. 118 bp CDS sequence and 1042 bp potential promoter sequence of *MeCWINV6* gene were obtained. PlantCARE analyzed the putative *cis*-elements in silico revealed that these elements can be grouped into five classes: basic transcription elements (CAAT box and TATA box), light responsive elements (ACE, AE-box, ATCT-motif, AT1-motif, Box 4, GAG-motif, GT1-motif and Sp1), phytohormone responsive motifs (GARE-motif, TATC-box, TGACG-motif and TCA-element), defense and stress responsive element (TC-rich repeats and HSE), wounding and pathogen responsive elements (W-box and WUN-motif). This data demonstrate that it might be associated to regulate the cell wall invertase gene function in source-sink relations of cassava starch accumulation and response to internal and environmental stimuli.

Introduction

Cassava (*Manihot esculenta* Crantz) is a widely cultivated tuber crop of the *Euphorbiaceae* family. The starchy storage roots of cassava provide a major calorie source for more than 500 million people in tropical and subtropical regions of Africa, Asia and Latin America [1]. In addition, cassava starch mainly provides raw materials to produce industrial materials and biofuels. Cassava is a typical C3 plant, but has the characteristics of C4 plants photosynthesis. The rate of CO_2 fixation and sucrose synthesis in cassava leaves (source organ) is highest. However, the amount of photosynthate produced by leaves transfers to the roots for strach accumulation is less than 1/5 [2]. So it is meaningful to improve the energy transferring rate from source tissues leaves to sink tissues roots.

In higher plants, sucrose is the major transport form of carbohydrates which synthesized in photosynthetically active source tissues and exported to photosynthetically less active sink tissues via the phloem stream [3]. Cell wall invertases irreversibly hydrolyze sucrose into glucose and fructose, are the key sucrose-metabolizing enzymes transfer photosynthate from leaves to roots [4][5]. They play important roles in phloem unloading during assimilate partitioning by creating a steep sucrose gradient between the phloem and the surrounding sink apoplast to drive phloem unloading, then regulate source-sink relations and promote plant growth [6][7]. The expression of cell wall invertases has been shown to be regulated by a mass of internal and environmental stimuli that affect source-sink relations, including temperature [8], sugar levels [9], light [9], plant hormones, abiotic stress [10], wounding, and pathogen infection [10].

In cassava, the family of cell wall invertases is consisted of six enzymes MeCWINV1-6. In our previous research, we found that the different genes that encode these enzymes exhibit differential expression patterns in the various tissues of cassava at the different growth stages, which implies that each individual isoform has a specific function. In order to gain more insight into the specific function of the *MeCWINV6* gene, we cloned the promoter of *MeCWINV6* gene and analyzed the putative *cis*-elements in silico. Many light response and adversity *cis*-acting elements binding sites were found in the promoter. This will be scientific fundation for researching on the role of cassava invertase in cassava starch accumulation from leaves to roots.

Materials and Methods

Plant material

The cassava cultivar, *Manihot esculenta* SC8 tissue cultured seedlings cultured on MS medium for 45 days, were obtained from the Tropical Crops Genetic Resources Institute, CATAS.

Genomic DNA extraction

The cassava genomic DNA was isolated by the CTAB methods according to the manufacturer's instructions.

Isolation of the *MeCWINV6* promoter region

The 5'-flanking sequence of the cassava cell wall invertase gene *MeCWINV6* was cloned from genomic DNA of the *Manihot esculenta* SC8 tissue cultured seedlings via PCR. The forward primer (5'-AGGATGTGTCCGTTATTGAT-3') was designed according to the predictable 5' UTR region DNA sequences of *MeCWINV6* gene from the Phytozome plant genome database (http://www.phytozome.net/cassava). The reverse primer (5'-TAACCTTGACAGCTTTGACG-3') was designed according to the known coding region sequences of *MeCWINV6* gene (GenBank accession No JX339930) to confirm the product specificity. The PCR reaction (20 μl) contained 1μl genomic DNA, 1 μl primers (10 μM), 0.2 μl *LA* Taq (*TaKaRa*, Dalian, China), 3.2 μl dNTP mixture (2.5 mM), 2 μl 10x buffer and 11.6 μl H_2O. The PCR reaction consisted of 32 cycles of 94 °C, 30 s; 58 °C, 30 s; 72 °C, 2 min. The PCR products were gel-purified and cloned into the pMD19-T vector (*TaKaRa*, Dalian, China) for sequencing (Songon Biotech Ltd, Shanghai, China).

Bioinformatic analysis of the *MeCWINV6* promoter sequences

Analysis of the sequence identity was undertaken using DNAMAN against the known coding region sequences in NCBI GenBank database and the predictable promoter sequences in the Phytozome plant genome database. *Cis*-element search program PlantCARE [11], was used to identify cis-acting elements in the obtained promoter sequence.

Results and Disscusion

PCR-amplified cassava *MeCWINV6* gene promoter regions

According to the predictable DNA sequences of the promoter and the known coding region sequences of *MeCWINV6* gene (GenBank accession No JX339930), we designed the forward primer and reverse primer. The 5'-flanking sequence of *MeCWINV6* gene was cloned from cassava *Manihot esculenta* SC8 genomic DNA using semi-specific PCR method. A special DNA fragment was amplified (Fig. 1).

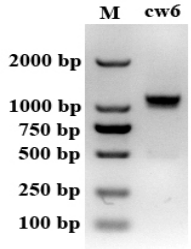

M: DL 2000 marker; cw6: the fragment of *MeCWINV6* promoter

Fig.1. The fragment of *MeCWINV6* promoter PCR amplified

Sequence analysis of promoter regions

Sequencing result showed that a 1160 bp gene fragment was obtained. It consists of 118 bp *MeCWINV6* gene coding region sequence and 1042 bp potential promoter and 5' UTR sequence, as shown in Fig.2. Compared with the predictable promoter sequences in the Phytozome plant genome database and the known coding region sequences of *MeCWINV6* gene, there was 100% sequence identity. Obviously, we isolated *MeCWINV6* gene promoter sequence successfully.

```
   1  AGGATGTGTCCGTTATTGATATGTTATTAACACAAACTGTTGGTAAATAATTTTTACAAC
  61  AGATTTTATTGGTCATTAATCCGTTAATAAATTATTTTATTAACAGATTTTTAATATTCA
 121  CTGATAAAAATTTTTTTTCCTAATGATTGTGAAAATTGTTGTAGTGTAAATTTTTTATTA
 181  TCACTAATATTTTTGACCAACTTAATTTAAATATTTAATTTCATCTGAATTATTAATCTG
 241  TTATTAATAAGTAATATATTTTTTAGAAATTAGTGGTCCCTTGTTTCTTCCAAATTCAGG
 301  TGGTGGCGATGGCCGGAAGGGGAATTCTATATGGTGGTTCACCGGTGGTTGAGCCTGCTA
 361  ATGTTAATGATCTTATTTAATGGCATGAGTGTAATGATATAGTTATAAGAGGTTTAAGGA
 421  GGATGGATATCCTTCATATTAATCGAAATAAATTTAAGAGAGTATTTAATTTAATTAATA
 481  AAATAAAAAATTATTATTCAATTTTTATATTATAATAATTAATTTATTAATTTAAAAAAT
 541  ATATTAAAATATTTCTAAAATTTTAAAAAATTTTCTAATTAATTTTAACCATTAAAATAT
 601  TTTTTATATAAAAAAATAATTAAGAAATTTTTTAAAAATTTAAAAGGGCGATTAATAATT
 661  TTTTTTAAATTATAAAATTTAAATAATAAAATAATTAATGATTAAAATTTTTAATTTTTA
 721  ATTGATAAATATTGAAATTGTTTATAGAATGAAGAAATTTGGAGTTGAAATTCTAATTAA
 781  AAATAAAGGTGAAAAAAGGAAAAAAAAGTTTTAAAAGTTTTTCCTTCAAACAGGAGAAAA
 841  ACTTGCCAAAACAACCGCTAGTAACTAAAGGAGAAAAAAGAGCAAGAGTTATCCACAACT
 901  AATTAAAATTCTAATCTCTCCCGCACACTGTCTCTATAAATCTCACCCTCGCCTCCCGCA
 961  AACTCCTCATTCTCATTATCCCAAACAGATCAACCAGATAAGCCTTCTTCTTCTTCTTCT
1043  TCTTCTTCTTCTCTGTGTTGTCATGGCTGTGTCGAAGTTTCTCGCAGTGTTTGGTTTACT
                          M  A  V  S  K  F  L  A  V  F  G  L  L
1081  CTTAGTTTTCTGCAACAATGGCGTAGAGGGATCTCACAAGATTTACGCTCAGTATCAAAA
       L  L  L  V  F  C  N  N  G  V  E  G  S  H  K  I  Y  A  Q  Y
1141  CGTCAAAGCTGTCAAGGTTA
       Q  N  V  K  A  V  K
```

The initiation codon (ATG) is shown in bold and underlined.

Fig.2. The sequences of *MeCWINV6* promoter

Bioinformatic analysis of promoter *cis*-acting regulatory elements

To study the elements of the *MeCWINV6* gene promoter, the 1042 bp-length potential promoter was analysed using web database PlantCARE [11]. As shown in Table 1, the putative cis-acting regulatory elements can be grouped into five classes: basic transcription elements, light responsive elements, phytohormone responsive motifs, defense and stress responsive element, wounding and pathogen responsive elements. The highly conserved transcriptional regulatory motif TATA box and the universal enhancer element CAAT box were present in the *MeCWINV6* promoter. Light responsive elements ACE, AE-box, ATCT-motif, AT1-motif, Box 4, GAG-motif, GT1-motif and Sp1, which are essential for light-regulated transcriptional activation, were found in the promoter. *Cis*-acting elements responding to phytohormoneswere also revealed in the promoter, such as gibberellins-responsive elements GARE-motif and TATC-box, salicylic acid-responsive element TCA-element and MeJA-responsive elements TGACG-motif and CGTCA-motif. Some potential *cis*-regulatory elements were stress-induced regulatory elements, primarily including defense and stress responsive element TC-rich repeats, heat stress response element HSE, wounding and pathogen responsive elements W-box and WUN-motif. The analysis of *MeCWINV6* promoter *cis*-acting regulatory elements indicates that the *MeCWINV6* promoter is likely functional in situ and *MeCWINV6* gene is expressed in response to the stimuli of light, hormones and abiotic and biotic stresses in the cassava developmental processes.

Conclusion

In this study, we report cloning and characterization of the cassava cell wall invertase gene *MeCWINV6* promoter. 1160 bp fragment contains 118 bp CDS sequence and 1042 bp potential promoter sequence of *MeCWINV6* gene were isolated. A number of *cis*-regulatory elements previously reported to be involved in light responses, phytohormone responses, abiotic and biotic

stress transcription elements were present in the *MeCWINV6* promoter. This is consisted with the function of cell wall invertase in the cassava starch formation, suggesting that it might be associated to regulate the cell wall invertase gene function in source-sink relations of cassava starch accumulation and response to internal and environmental stimuli.

Table 1 Putative *cis*-regulatory motifs identified in the *MeCWINV6* gene promoter

Site Name	Sequence	Position	Function
TATA box	TATA	934(+),903(-),811(-),777(+),742(+)	core promoter element
CAAT box	CAAT	756(-)735(-),730(-),720(-),498(+)	common promoter element
5UTR Py-rich stretch	TTTCTTCTCT	1024(+)	high transcription levels
ACE	AAAACGTTTA	811(-)	light-responsive
AT1-motif	AATTATTTTTATT	481(-)	light-responsive
ATCT-motif	AATCTAATCT	907(+)	light-responsive
Box 4	ATTAAT	74 (+),525(+),473(+),650(+),242(+),577(+)	light-responsive
Sp1	CC(G/A)CCC	951(+)	light-responsive
GAG-motif	AGAGAGT	456(+)	light-responsive
GT1-motif	GGTTAA	584(-)	light-responsive
circadian	CAANNNNATC	109(+)	circadian control
GARE-motif	AAACAGA	56(-),982(+)	gibberellin-responsive
TATC-box	TATCCCA	976 (+)	gibberellin-responsive
CGTCA-motif	CGTCA	70(+)	MeJA-responsive
TGACG-motif	TGACG	70(-)	MeJA-responsive
TCA-element	GAGAAGAATA	1023(-)	salicylic acid-responsiveness
TC-rich	ATTTTCTTCA	749(-)	defense and stress-responsive
HSE	AAAAAATTTC	126(-),565(+),545(+),733(-),166(-),623(+)	heat stress-responsive
W-box	TTGACC	192(+)	wounding and pathogen responsive
WUN-motif	TCATTACGAA	136(-)	wound-responsive
ARE	TGGTTT	663(+)	anaerobic induction
Skn-1_motif	GTCAT	71(+)	endosperm expression

Acknowledgement

This work was supported by the National Basic Research Program of China (973 Program) (2010CB126600); the National Natural Science Foundation of China (31170234, 31371706); the Provincial Natural Science Foundation of Hainan (310081); the Major Technology Project of Hainan (ZDZX2013023-1); the Fundamental Scientific Research Funds for Chinese Academy of Tropical Agricultural Sciences (CATAS-1630052014004); the National Nonprofit Institute Research Grant of CATAS (ITBB130202, ITBB130505); the Earmarked Fund for Modern Agro-industry Technology Research System (CARS-12-hnwwq).

References

[1] Sayre R, Beeching JR, Cahoon EB, Egesi C, Fauquet C, Fellman J, Fregene M, Gruissem W, Mallowa S, Manary M, Maziya-Dixon B, Mbanaso A, Schachtman DP, Siritunga D, Taylor N, Vanderschuren H and Zhang P. The BioCassava plus program: biofortification of cassava for sub-Saharan Africa. Annual Review of Plant Biology, 2011, 62: 251-272.

[2] Ihemere U, Arias-Garzon D, Lawrence S and Sayre R. Genetic modification of cassava for enhanced starch production. Plant Biotechnology Journal, 2006, 4(4): 453-465.

[3] Turgeon R. The sink-source transition in leaves. Annual Review of Plant Physiology and Plant Molecular Biology, 1989, 40: 119-138.

[4] Zhang YL, Zhang AH, Jiang J. Gene expression patterns of invertase gene families and modulation of the inhibitor gene in tomato sucrose metabolism. Genetics and molecular research, 2013, 12(3): 3412-3420.

[5] Chandra A, Jain, R and Solomon S. Complexities of invertases controlling sucrose accumulation and retention in sugarcane. Current Science, 2012, 102(6): 857-866.

[6] Sturm A and Tang GQ. The sucrose-cleaving enzymes of plants are crucial for development, growth and carbon partitioning. Trends in Plant Science, 1999, 4(10): 401-407.

[7] Canam T, Mak SW and Mansfield SD. Spatial and temporal expression profiling of cell wall invertase genes during early development in hybrid poplar. Tree Physiology. 2008, 28(7): 1059-1067.

[8] Ruan YL, Jin Y, Yang YJ, Li GJ and Boyer JS. Sugar input, metabolism, and signaling mediated by invertase: roles in development, yield potential, and response to drought and heat. Molecular Plant, 2010, 3(6): 942-955.

[9] Rabot A, Henry C, Ben Baaziz K, Mortreau E, Azri W, Lothier J, Hamama L, Boummaza R, Leduc N, Pelleschi-Travier S, Le Gourrierec J and Sakr S. Insight into the role of sugars in bud burst under light in the rose. Plant Cell Physiology, 2012, 53(6): 1068-1082.

[10] Tae Kyung Hyun, Anja Hoffmann, Alok K. Sinha and Thomas Roitsch. Tomato mitogen activated protein kinases regulate the expression of extracellular invertase Lin6 in response to stress related stimuli. Functional Plant Biology, 2009, 36(12): 1088-1097.

[11] Lescot M, Déhais P, Thijs G, Marchal K, Moreau Y, Van de Peer Y, Rouzé P and Rombauts S. PlantCARE, a database of plant cis-acting regulatory elements and a portal to tools for in silico analysis of promoter sequences. Nucleic Acids Research. 2002, 30(1): 325-327.

Advanced Materials Research Vols. 986-987 (2014) pp 30-33

doi:10.4028/www.scientific.net/AMR.986-987.30

Co-cracking of bio-oil model compound mixture and ethanol with different blending ratios for bio-gasoline production

Li Zhang[a], Qinjie Cai[b] and Shurong Wang*[c]

State Key Laboratory of Clean Energy Utilization Zhejiang University Hangzhou, China

[a]tension@zju.edu.cn, [b]tccqj2006@zju.edu.cn, [c]srwang@zju.edu.cn

Keywords: Bio-oil; Model compound mixture; Ethanol; Co-cracking; Bio-gasoline

Abstract. Since the composition of crude bio-oil was complex, model compounds were usually used in the study of cracking to simulate the actual bio-oil. However, the cracking of pure model compound mixture generated an inferior oil phase which had a high content of oxygenated byproducts. When ethanol was adopted as the co-reactant, the reactant conversion, yield and quality of oil phase were obviously improved. The conversions of the reactants were 100% and the selectivity of the oil phase was 31.5wt% when the concentration of model compound mixture in the feed reached 30%. Meanwhile, the oil phase also had a superior quality which was entirely composed of aliphatic and aromatic hydrocarbons.

Introduction

The bio-oil from biomass fast pyrolysis, which is regarded as a promising substitute for fossil fuel, is widely studied by researchers. However, crude bio-oil is complex, unstable and corrosive, and it has a low heating value. Therefore, some researchers used catalytic cracking to transform bio-oil to high-quality oil. Williams et al. [1] found that there are mainly two pathways for cracking: the bio-oil was cracked to olefin by zeolite and then the olefin was aromatized, or the oxygenated compounds in bio-oil were deoxygenated to aromatic compounds directly.

Because crude bio-oil had a complex of composition, rich in acids, aldehydes, ketones, alcohols, phenols, esters, ethers and sugars, researchers used model compounds (compounds with typical functional groups) to simplify the cracking reaction, and the proposed reaction mechanism of model compounds could help to understand the cracking pathways of real bio-oil. Gayubo et al. [2,3] carried out a series of cracking experiments of model compounds. The conversions of alcohols were found to be similar to methanol and ethanol, which mainly produced hydrocarbons, and the catalyst coking rate was low. The conversions of ketones and acetic acid mainly involved decarboxylation, decarbonylation, and dehydration to a less extent.

In consideration of the possible influence of oxygen content and unsaturated degree on cracking characteristics, the concept of an effective hydrogen to carbon ratio ($(H/C)_{eff}$) was introduced, as shown in Eq. (1) [4,5]. Mentzel et al. [5] found that the catalysts during the cracking of model compounds with low $(H/C)_{eff}$ ratios were easy to be deactivated.

$$(H/C)_{eff} = \frac{H - 2\cdot O - 3\cdot N - 2\cdot S}{C} \quad (1)$$

The crude bio-oil has a very low $(H/C)_{eff}$ ratio, so the catalyst is easily deactivated by coking during the cracking. Researchers tried to mix the crude bio-oil with compounds with a high $(H/C)_{eff}$ ratio to improve the stability of the cracking process. Ethanol, with a relatively high $(H/C)_{eff}$ ratio of 2, is regarded as a good co-reactant for the cracking of bio-oil, which can effectively improve the yield and quality of the hydrocarbons and extend the lifetime of catalyst. Moreover, compared with the conversion of ethanol to gasoline, the mixture of bio-oil and ethanol is more economical [6].

Hydroxypropanone, cyclopentanone and acetic acid are the typical ketones and carboxylic acids in bio-oil. In the study of co-cracking behavior of the model compound mixture and ethanol, the most suitable ethanol blending amount can be obtained by comparing the reactant conversion and the selectivity and composition of liquid and gaseous products.

Experimental section

Catalyst and materials. The catalyst used was HZSM-5 catalyst (Si/Al=25, purchased from the Catalyst Plant of Nankai University). The catalyst was calcined in the air for the activation at 550 °C for 6 h (the heating rate was 5 °C/h) and then naturally cooled and sieved to 40–60 mesh.

These bio-oil model compounds were mixed according to the component distribution of the bio-oil distilled fraction, and the weight ratio of HPO, CPO and HAc was set as 6:1:5 [7].

Catalytic test. The experimental system was discussed in detail in our previous study [7].The conditions of experiments are presented in Table 1.

Table 1 Conditions of experiments

Reactants	Temperature [°C]	Pressure [MPa]	WHSV [h^{-1}]
100%EtOH	400	2	3
15%HPO+2.5%CPO+12.5%HAc+70%EtOH	400	2	3
25%HPO+4.2%CPO+20.8%HAc+50%EtOH	400	2	3
35%HPO+5.8%CPO+29.2%HAc+30%EtOH	400	2	3
50%HPO+8.3%CPO+41.7%HAc	400	2	3

Results and discussion

Conversion of reactants and Selectivity of liquid products. The influence of EtOH addition on reactant conversion is shown in Fig.1. Ethanol made a contribution to the conversion of model compounds. Only HPO was converted completely during the cracking of pure model compound mixture, while the conversion of CPO and HAc were 89.6% and 80.3%, respectively. When the concentration of model compound mixture decreased to 70% and 50%, the CPO was also converted completely, and the conversion of acetic acid increased to 86.4% and 89.8%, respectively. When the concentration of model compound mixture was 30%, the conversion of all reactants reached 100%.

Fig.2 presents the influence of ethanol addition on liquid product selectivity. The oil phase selectivity was only 18.4wt% during the cracking of pure model compound mixture. The selectivity of oil phase increased with the increasing of ethanol concentration, while the aqueous phase selectivity was opposite. The selectivity of oil phase reached 31.5wt% under the condition of 30% model compound mixture, which was even higher than the oil phase selectivity in the cracking of pure ethanol.

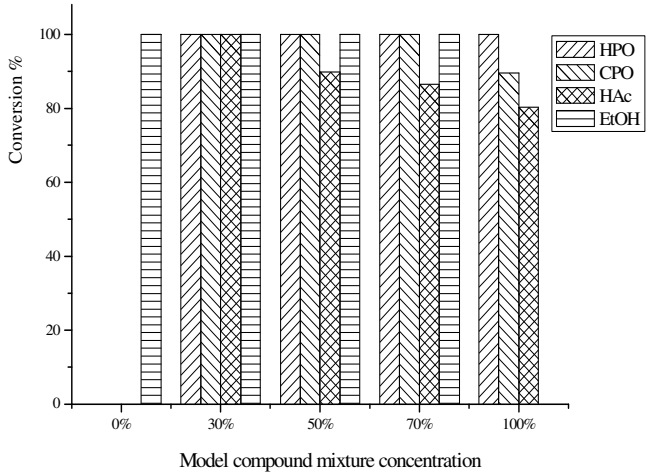

Fig.1. Conversion of reactants

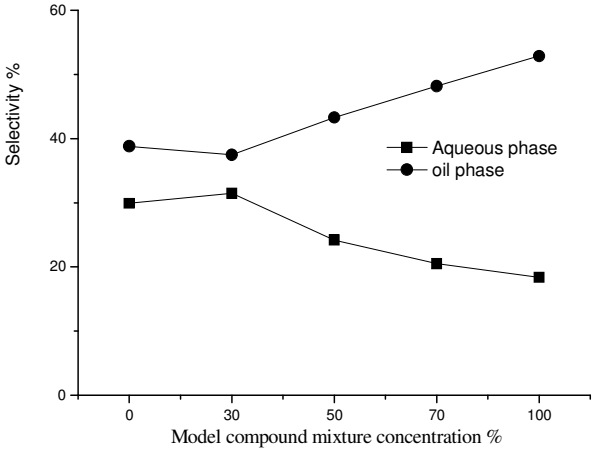

Fig.2. Selectivity of liquid products

Composition of the oil phase. Oil phases were analyzed by GC–MS, and the composition of oil phase under different conditions is presented in Fig.3.

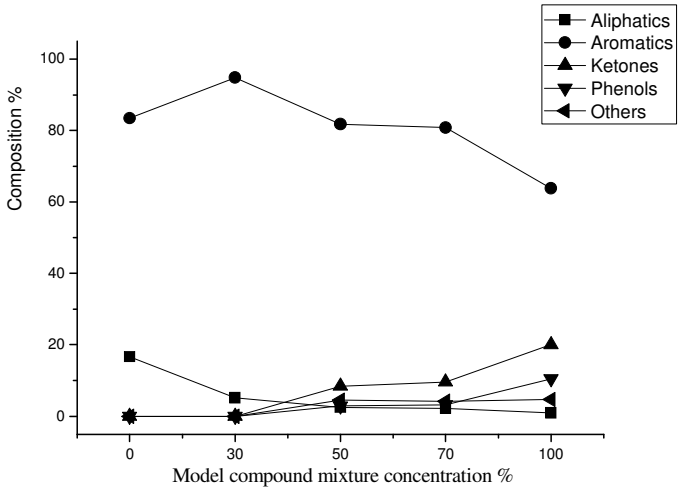

Fig.3. Composition of the oil phases

When the concentration of model compound mixture was 30%, the oil phase was completely composed of hydrocarbons, in which the contents of aliphatic hydrocarbons and aromatic hydrocarbons reached 5.2% and% and 94.8%, respectively. Compared with that from the cracking with higher concentrations of model compound mixture, the quality of this oil phase was much higher. When the model compound concentration was 50%, the contents of aliphatic hydrocarbons and aromatic hydrocarbons were 2.5% and 81.7% respectively, and there were some oxygenated compounds in the oil phase, such as 8.4% ketones and 2.9% phenols. This result showed 50% ethanol could not support the high-efficiency conversion of all the model compounds into hydrocarbons, and a part of model compounds occurred side reactions and formed ketones and phenols. When the model compound mixture concentration reached 70%, the quality of oil phase further declined, the aliphatic and aromatic hydrocarbon contents were 2.2% and 80.8% respectively, with the ketone and phenol contents of 9.6% and 3.2%. Moreover, the contents of ketones and phenols reached 20.0% and 10.5% when cracking pure model compound mixture. The cracking of pure ethanol also generated an oil phase with complete hydrocarbons, but the content of aromatic hydrocarbons was lower than co-cracking of model compound mixture and ethanol, due to the different $(H/C)_{eff}$ ratios in feed. The $(H/C)_{eff}$ ratio of 30% model compound mixture and 70% ethanol was 1.46, so compared with pure ethanol with a high $(H/C)_{eff}$ of 2, it was easier to produce aromatic liquid products ($1 \leq (H/C)_{eff} < 2$) during cracking, which was in agreement with the higher selectivity of oil phase as mentioned before. Therefore, it could be concluded that ethanol could restrain the side reactions of model compounds and thus improve the yield and quality of oil phase.

Composition of vent gas. Table 2 presents the composition of vent gas. The general distribution of gaseous products showed the vent gas under conditions with high oil phase selectivity and quality also had high contents of C_3H_8, which might be released during the aromatization of light olefins into aromatics with high degrees of unsaturation. With the increase of model compound mixture concentration, CO_x was likely to be released because of the carbonyl and carboxyl groups in the model compounds. Since C_2H_4 is regarded as the important intermediate during cracking, its massive release implies that the intensity of aromatization was weaker. The concentrations of C_2H_4 were up to 30.9% and 16.0% under the conditions of 70% and pure model compound mixture.

Table 2 Composition of vent gas under different contents of mixture of model compounds.

Conditions	Relative contents of gaseous products (%)								
	CO	CO_2	CH_4	C_2H_4	C_2H_6	C_3H_6	C_3H_8	C_4H_8	C_4H_{10}
100EtOH	5.1	1.7	5.9	0.6	14.8	0.6	53.6	12.6	5.1
70EtOH	16.4	15.3	1.8	3.4	8.5	1.8	40.5	10.1	2.2
50EtOH	23.9	25.0	2.0	1.4	8.1	1.0	26.8	8.7	3.1
30EtOH	22.3	27.7	1.9	30.9	3.4	2.8	8.7	2.1	0.3
0EtOH	24.8	51.8	1.0	16.0	0.6	0.3	4.2	1.4	0.0

Conclusions

In the co-cracking study of bio-oil model compound mixture and ethanol with different blending ratios, the introduction of ethanol was found to improve the yield and quality of the oil phase. At 400 °C and 2 MPa, when the concentrations of model compound mixture and ethanol in feed were 30% and 70%, the reactants were converted completely and a high selectivity of 31.5wt% for the oil phase was obtained, which was entirely composed of hydrocarbons.

Acknowledgements

The authors are grateful for the financial support from the National Basic Research Program of China (2013CB228101).

References

[1] P.T. Williams, P.A. Horne: Fuel Vol. 74(1995), p. 1839

[2] A.G. Gayubo, A.T. Aguayo, and A. Atutxa: Ind. Eng. Chem. Res. Vol. 43(2004), p. 2610

[3] A.G. Gayubo, A.T. Aguayo, and A. Atutxa: Ind. Eng. Chem. Res. Vol. 43(2004), p. 2619

[4] P.M. Mortensen, J.D. Grunwaldt and P.A. Jensen: Appl. Catal., A Vol. 407(2011), p. 1

[5] U.V. Mentzel, M.S. Holm: Appl. Catal., A Vol. 396(2011), p. 59

[6] S. Wang, Q. Cai and X. Wang: Fuel Process. Technol. Vol. 111(2013), p. 86

[7] S. Wang, Q. Cai and X. Wang: Energy Fuels Vol. 28(2013), p. 115

Advanced Materials Research Vols. 986-987 (2014) pp 34-37

doi:10.4028/www.scientific.net/AMR.986-987.34

Composite electrolyte containing binary ionic liquids and LiDFOB additive on the performance of Graphite anode in Li-ion battery

Zhenfeng Wang[1,a],Xiaoxue Zhang,Cuihua Li,Jianhong Liu,Qianling Zhang

[1]School of Chemistry and Chemical Engineering,Shenzhen University,No.3688,Nanhai District,Shenzhen 518052,China
[a]501323635@qq.com

Keywords: Lithium-ion batteries; Safety; Electrolyte additive; LiDFOB

Abstract: A new composite electrolyte for lithium-ion batteries (LIB_S) was prepared by combining N-methyl-N-propylpyrrolidinium bis(trifluoromethanesulfonyl)imide ($PYR_{13}TFSI$), N-methyl-N-propylpiperidinium bis(trifluoromethanesulfonyl)imide ($PP_{13}TFSI$) and lithium difluoro(oxalate) borate (LiDFOB). Graphite electrode was tested in the LiDFOB-containing electrolyte, exhibiting higher reversible charge/discharge capacity and better cyclic stability. An initial charge capacity of 351.5 $mAh \cdot g^{-1}$ is obtained and a stable capacity of above 332.8 $mAh \cdot g^{-1}$ is retained after 30 cycles. The coulombic efficiency remains high above 99.3%. The outstanding cell performance was associated with the formation of stable solid electrolyte interface (SEI) film on the surface of electrodes derived from LiDFOB.

1. Introduction

LIB_S is considered to be the most promising battery technology in the field of hybrid electric vehicles (HEVs) and electric vehicles (EVs) [1]. However, the thermal runaway of LIBs has caused several severe accidents in HEVs and EVs. The increase in improvement of safety is a key point for commercialization of LIB_S. Recently, ionic liquids (ILs) have been studied as potential safe electrolytes owing to their wide liquid range, a wide electrochemical stability window, negligible volatility, non-flammability, etc [2]. Pyrrolidine (PY) and piperidine (PP)-based ILs attract people′s interest due to their electrochemistry window is higher than 5 V [3]. However Graphite anode is not compatible with this ILs due to the intercalation of the organic cations such as PYR_{13}^+ and PP_{13}^+ between the graphene layers. Another disadvantages of neat ILs are high viscosity and low ionic conductivity lead to poor cyclic stability and rate performance. Several modification methods, such as mixing organic solvents and additives to assist in forming stable solid electrolyte interface (SEI) films [4]. LiDFOB was investigated as an electrolyte additive, with the advantages of both $LiBF_4$ and lithium bisoxalatoborate (LiBOB) and was found to favor a stable SEI film with thinner thickness and much lower interfacial resistance to form on the anodes [5]. In this study, a new composite electrolyte based on ILs with the additive LiDFOB and organic solvents is explored and provided LIB_S with the level of safety. In addition, the effect of LiDFOB on the electrochemical properties of Graphite anode is further investigated.

2. Experimental

2.1 The synthesis of ionic liquids, the preparation of electrolytes and the half cell

The method of preparation is based on a two-step synthesis, N-methyl-N-propylpyrrolidinium bromide($PYR_{13}Br$) was synthesized by heating 1-bromopropane (Alfa Aesar, >99%) with N-methyl pyrrolidinium (Acros, >98%) in ethyl acetate. $PYR_{13}TFSI$ was synthesized by the metathesis reaction of $PYR_{13}Br$ with excess lithium bis(trifluoromethanesulfonyl)imide (LiTFSI, Acros, >99%) in aqueous solution. The resulting $PYR_{13}TFSI$ phase was washed with deionized water until the bromide cannot be detected by 0.1 M $AgNO_3$ solution and then dried in vacuum at 110 ℃ for 48 h to remove the residual water. $PP_{13}TFSI$ was prepared by the same method. The ionic liquid/organic carbonate mixed electrolytes were obtained by adding 0.3 $mol \cdot L^{-1}$LiTFSI and 23 wt% ethylene carbonate (EC) and dimethyl carbonate (DMC)(1:1, w/w) in 70 wt%$PYR_{13}TFSI$/$PP_{13}TFSI$(1:1, v/v) and the additive LiDFOB was added at 0.25 wt%.

The performance of the electrolytes was measured with 2032 type coin cells. The active material, graphite was mixed with carbon black and poly(vinylidene difluoride) (PVDF) at a ratio of 8:1:1 in N-methyl-2-pyrrolidone (NMP). The slurry was casted on Cu foil with a diameter of 14 mm (1.54 cm^2) and dried at 110 ℃ for 12 h under vacuum. All the electrodes were dried in vacuum at 110℃ for at least 12 h prior to use.

2.2 Characterization

Thermogravimetric analysis was carried out using a TA Q50 instrument. The samples were heated from room temperature to 640 ℃ with a heating rate of 5 ℃·min^{-1} using nitrogen as purgegas (40 cm^3·min^{-1}). The charge–discharge experiments of Li/graphite cells were performed galvanostatically at 0.1 C rates in the voltage range of 0.01–2.0 V on battery testers (Land CT2001A). All the potentials throughout the work are in reference to Li/Li^+ couple unless specified otherwise. Cyclic voltammetry (CV) of the cells were measured by electrochemical workstation (14 70E Cell Test System, England) at a scan rate of 0.1 mV·s^{-1} in range of 0.01-2.0 V. The graphite electrode was used as working electrode, and lithium foil as both counter and reference electrode. The morphology of electrode washed with DMC and dried in vacuum was observed with scanning electron microscopy (S-3400N(II), Hitachi Limited).

3. Results and discussion

3.1. Thermal properties

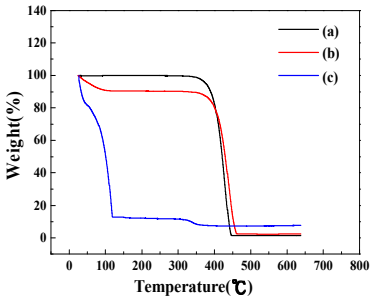

Fig. 1. TGA plots of binary ionic liquid (a), ILs-based electrolyte (b) and of 305 electrolyte (c).

The thermal property of electrolytes is the most important factor for battery safety. Fig. 1 reports the TGA plots of the binary ILs ($PYR_{13}TFSI/PP_{13}TFSI$ (1:1, v/v)), the commercial organic solvent electrolyte (305) and of the ILs-based electrolyte (0.3 M LiTFSI/70 wt%$PYR_{13}TFSI$/ $PP_{13}TFSI$ (1:1, v/v) + 23 wt%EC/DMC (1:1, w/w) + 0.25 wt%LiDFOB). There was almost no weight loss for the binary ionic liquids up to 340 ℃, and less than 0.77 wt% loss was measured at 340 ℃, confirming the high thermal stability of this ILs. In contrast, the weight loss is 17.17% when the 305 electrolyte is heated from 25 to 45 ℃, and 87.3% loss at 120 ℃. When heated from 25 to 120 ℃, ILs-base electrolyte show 9.5% weight losses which is ascribed to the evaporation of organic solvents (EC/DMC), indicating that the evaporation of organic solvents were greedy reduced duo to the intermolecular force among ILs and organic solvents. Another single-step at rather high temperatures of 350–450 ℃, can be attributed to the decomposition of the ILs and the lithium salt (LiTFSI/LiDFOB). This experiment revealed that the high thermal stability of composite electrolyte could be enhanced by adding a certain number of ILs.

3.2. Cyclic voltammetry on Graphite anode

Fig. 2 shows the CV curves of Graphite electrode in 0.3 M LiTFSI/70 wt%$PYR_{13}TFSI/PP_{13}$ TFSI (1:1, v/v) + 23 wt%EC/DMC (1:1, w/w) mixture electrolyte with or without LiDFOB. Fig. 2a show two broad cathodic peak between 0.7 and 0.3 V can be attributed to the intercalation of PP_{13}^+ and PYR_{13}^+ cations into the graphite structure. This process is partially reversible, as there is a small anodic peak detectable at ca. 0.9 V [2]. When LiDFOB was used as an electrolyte additive, the behavior of the graphite electrode was different (Fig. 2b). The irreversible reduction occurred in the

potential region from 1.0 to 0.2 V. In the second and consequent cycles, no electrochemical reduction was visible any more, indicated the irreversible decomposition of LiDFOB in the first cycle and the decomposition is inhibited by the stable interphase film.

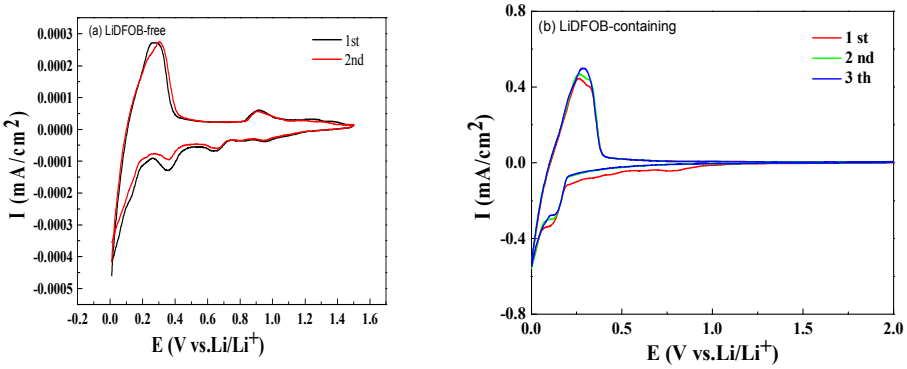

Fig. 2. CV curves of Graphite electrode in two electrolyte. (a) LiDFOB-free and (b) LiDFOB-containing.

3.3. Galvanostatic measurements in Li/Graphite half-cells

The cyclic performances are compared in Fig. 3 for Graphite electrode in 305 electrolyte and 0.3 M LiTFSI/70 wt% $PYR_{13}TFSI/PP_{13}TFSI$ (1:1, v/v) + 23 wt%EC/DMC (1:1, w/w) mixture electrolyte with or without LiDFOB. It is clear from this figure, in the absence of LiDFOB, the cell loses about 38.5% of its initial capacity after 30 cycles. However, in the presence of LiDFOB, the capacity retention was greatly improved to more than 94% after 30 cycles, and the coulombic efficiency is nearly 100%. The results indicate that the addition of LiDFOB to ILs-based electrolyte greatly improves the cyclic stability of the test cells and exhibits excellent performance which can be matched the commercial organic solvent electrolyte (305).

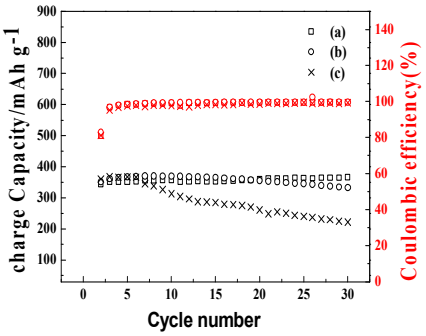

Fig. 3. Cycle performance of Li/Graphite half-cells with three different electrolytes. (a) 305, (b) LiDFOB-containing and (c) LiDFOB-free

3.4 SEM

Fig. 4 shows SEM images of Graphite electrode surfaces after 30 cycles in different electrolytes. The surface morphology of LiDFOB-free electrode is still homogeneous. However, in the present of LiDFOB, the surface of the electrode is covered with the compact film. This show that the addition of LiDFOB can favor stable SEI film to form on the graphite electrode.

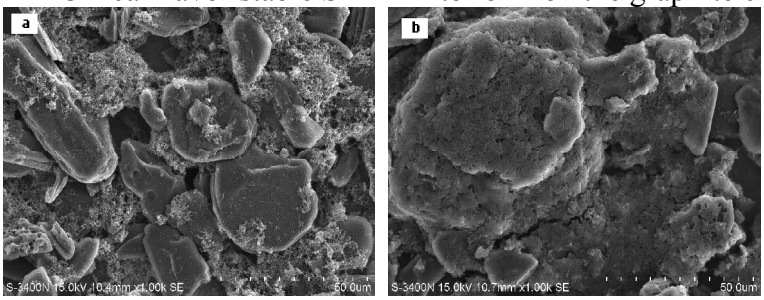

Fig. 4. SEM images of Graphite electrode surface with: (a) LiDFOB-free, (b) LiDFOB-containing mixed electrolytes after 30 cycles.

4. Conclusions

A new electrolyte component was obtained through mixing LiDFOB, $PP_{13}TFSI/PYR_{13}TFSI$ and organic solvents. The results of TGA tests indicate that ILs-based electrolyte exhibits a high thermal stability (up to 340 ℃). Electrochemical measurements demonstrate that the graphite electrode shows good cycling performance in ILs-based electrolyte with LiDFOB. The cell delivers high reversible capacity (332.8 $mAh \cdot g^{-1}$) with coulomb efficiency close to 100% after 30 cycles, due to the addition of LiDFOB can favor stable SEI film to form on the graphite electrode. The film can prevent further co-intercalation and decomposition of PP_{13}^{+} and PYR_{13}^{+} cations. The results suggest that ILs-based electrolytes with LiDFOB could be a promising electrolyte for Graphite anode in terms of high thermal stability and better electrochemical performance.

Acknowledgment

This work was financially supported by Scientific and Technological Research and Development Foundation of Shenzhen City (20120602111424454), 973 National Defense Project (613142020201) and Shenzhen Key Laboratory of Functional Polymer Foundation (FP20130008).

References

[1] Xiang J, Wu F, Chen R, et al. High voltage and safe electrolytes based on ionic liquid and sulfone for lithium-ion batteries[J]. Journal of Power Sources. 233, 115-120(2013).

[2] Reiter J, Nadherna M, Dominko R. Graphite and $LiCo_{1/3}Mn_{1/3}Ni_{1/3}O_2$ electrodes with piperidinium ionic liquid and lithium bis (fluorosulfonyl) imide for Li-ion batteries[J]. Journal of power sources. 205, 402-407(2012).

[3] An Y, Zuo P, Cheng X, et al. The effects of LiBOB additive for stable SEI formation of $PP_{13}TFSI$-organic mixed electrolyte in lithium ion batteries[J]. Electrochimica Acta. 56(13), 4841-4848(2011).

[4] Hu M, Wei J, Xing L, et al. Effect of lithium difluoro (oxalate) borate (LiDFOB) additive on the performance of high-voltage lithium-ion batteries[J]. Journal of Applied Electrochemistry. 42(5), 291-296(2012).

[5] Wu Q, Lu W, Miranda M, et al. Effects of lithium difluoro (oxalate) borate on the performance of Li-rich composite cathode in Li-ion battery[J]. Electrochemistry Communications. 24, 78-81(2012).

Advanced Materials Research Vols. 986-987 (2014) pp 38-41

doi:10.4028/www.scientific.net/AMR.986-987.38

Determination of the Collapse and Transfer Pressure for Monomolecular Layer of Copper (Ⅱ) Phthalocyanine

Lin Zhu[1, a], Yong-Jian Chen[1,a], Feng Xu[1,a], Hai-Ning Cui[1,a,*] and Hai-Shui Wang[2,b]

[1]Department of Optical Information Science and Technology, College of Physics and College of Zhaoqing (526061) , Jilin University, Changchun(130012), P. R. China

[2]School of Chemistry and Chemical Engineering, South China University of Technology

[a]cuihaining2009@126.com

Keywords: Copper Phthalocyanine film, transfer pressure, Monomolecular Layer.

Abstract. Systematic research on monomolecular layer of symmetrically substituted copper (α) phthalocyanine (CuPc) derivatives bas been done. An attention is focused upon final determination of the transfer pressure in an ordered nano assembly film of CuPc by comparing different methods about surface pressure-area (π-A) isotherm, morphology observation and thickness measurement by transmission electron microscopy (TEM) . The present study and improvement methods provide new insight into the choice of transfer pressure for mono molecule layer .

Introduction

Since phthalocyanine (Pc) derivatives have the possibility of application in many aspects such as photoconductor, semiconductor materials, solar cells, gas-sensors, nonlinear optical material and molecular electronic devices, systematic research on their monomolecular layer, nanometer assembly film was attracted to scientists for the past decade[1-2]. In order to understand copper (Ⅱ) phthalocyanine (CuPc) nanometer assembly films and to design new film structure based on CuPc, it is very important to study the transfer pressure by means of Langmuir-Blogdett (LB) technique. In this paper attention is focused upon the determination of the film transfer pressure of CuPc. The selection of optimum transfer pressure of CuPc by comparing different direct and indirect justing methods such as surface pressure-area (π-A) isotherm, the cross-sectional area difference (ΔA) method （ or Compression-Recompression Isotherms ） , transfer ratios result, surface pressure(π))-TEM thickness isotherm and π-volume (Vol.) isotherm in which is involved in morphology observation and thickness measurement, was investigated .

Experiments and Preparation of the film

To improve properties of the ordered film the symmetrically substituted CuPc were synthesized according to the procedures reported by Snow et al [3] and they are shown as in Table 1. Details of the preparation and characterization were described elsewhere [4]. KSV-5000 Langmuir trough (Finland) with a Wilhelmy balance and domestic LB trough were employed for the π-A measurements and the monomolecular layer fabrication.

Discussions and Determination of the transfer pressure

Generally, a π-A isotherm is used for determination of the collapse pressure and transfer pressure. The π-A isotherm of CuPc[bpsp]4 and CuPc[dtpp]4 is shown as in Fig.1. The traditional collapse pressure is generally considered about 60 mNm^{-1} for CuPc[bpsp]4 , and the choice of transfer pressure of LB film is flexible in the range of 30-50 mNm^{-1}. In experiment we derive following just methods from further analysis and value the collapse pressure and transfer pressure.

Table 1. Schematic structure of symmetrically substituted CuPc

CuPc (-O-  -SO_2-  -OCH_2- )$_4$	⟶ CuPc[bpsp]$_4$
CuPc (-$COOCH_2CH_2OCH_3$)$_4$	⟶ CuPc[mec]$_4$
CuPc (-$COOCH_2CH_2OCH_2CH_2CH_2CH_3$)$_4$	⟶ CuPc[bec]$_4$
CuPc (-O-  -C_5H_{11})$_4$	⟶ CuPc[dtpp]$_4$

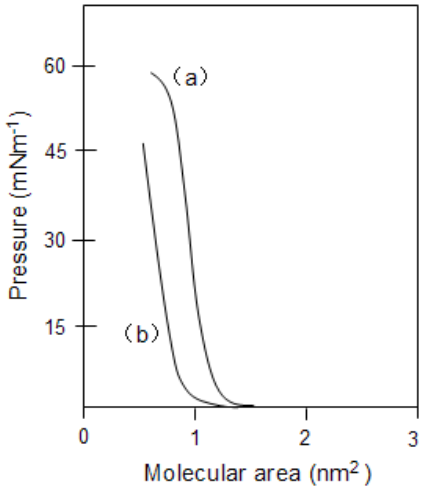

Fig. 1 A normal surface pressure-area (π-A) isotherm of Pc； (a) CuPc[bpsp]4, (b) CuPc[dtpp]4

A cross-sectional area difference (ΔA) method and Transfer ratios

A cross-sectional area difference (Δ A) method, which has relation with hysteresis phenomenon, is to identify the collapse of monolayers at the air-water interface and describe the collapse behavior of monolayer. It can be used to determine a bettter transfer pressure. For examples, two cycle isotherms of CuPc[bpsp]$_4$ were obtained by four sweeps: compression from zero to target pressure--expansion from target pressure to zero-- second compression to target pressure--second expansion to zero pressure, which are shown in Fig. 2. So we can also call it Compression-Recompression Isotherms method. The cross-sectional areas A_f and A_s per molecule at target pressure for first cycle (curve 1) and for second cycle (curve 2) respectively were recorded, and their difference $\Delta A = A_f - A_s$ was calculated. Here "f" stands for the first cycle and "s" for the second cycle. Fig.3 is the bar graph of Δ A versus target pressures. The results show that Δ A is dependent on the target pressure. For target pressures below 40 mNm^{-1}, Δ A is less than 0.01 nm^2 mol^{-1} and almost constant. For target pressure in the range 40-52 mNm^{-1} , Δ A increases gradually. For target pressures higher than 52 mNm^{-1}, A increases drastically. These results indicate that the monolayer structure may have undergone some irrecoverable changes for pressures higher than 40 mNm^{-1}. However, according to the traditional pressure-area isotherm (compression curve of "f" cycle), the Pc monolayer collapses at 52 mNm^{-1} and should be fairly good films in the linear region from 40 mNm^{-1} to 52 mNm^{-1}, We propose that the bar graph of Δ A versus target pressures be more clearly than the traditional pressure-area isotherm in identifying the collapse in this region. This point of view was supported by following transfer ratios results.

Discussion of transfer ratios

As we know, good transfer ratio of the monolayer is the key under the LB film fabrication. Here the measurement of transfer ratio was done and the result shows that it is wrong that the 52 mNm^{-1} in

the first cycle (Fig.1) is considered as the traditional collapse pressure. Transfer ratio of $CuPc[bpsp]_4$ monolayer at different pressures were recorded. The satisfactory transfer ratios are above 0.856 for pressures lower than 30 mNm^{-1}. The transfer ratios is 0.759 for pressures at 40 mNm^{-1} and begin clearly poor. It is because the partial collapse of the monolayer may account for the poor transfer ratios.

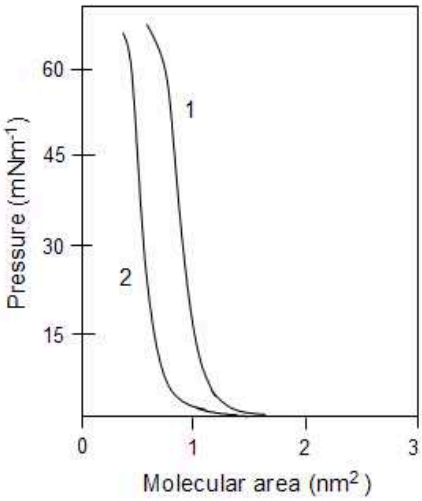

Fig. 2 Two cycle isotherms of $CuPc[bpsp]_4$

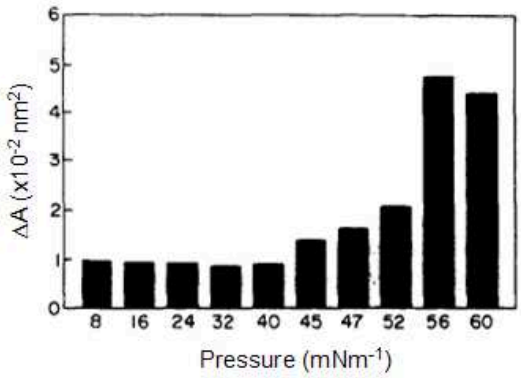

Fig. 3 the bar graph of ΔA versus target pressures for $CuPc[bpsp]_4$

Surface pressure(π)-TEM thickness isotherm and π-Vol. isotherm

The samples for transmission electron microscopy (TEM) were prepared by floating-folding method. Detail of the operation and the thickness measurement was described elsewhere[5-6]. The characterization of CuPc[mec]4, CuPc[bec]4 and CuPc[dtpp]4 in the process of LB film forming has been studied by TEM. Fig. 4 exhibits the relationship curves between surface pressure and monolayer thickness from the TEM measurement. The measured thickness of a monolayer is rather thinner at 10 mNm^{-1} surface pressure and the thickness at 35 mNm^{-1} is far greater than that of low surface pressure in Fig.4. The probable reason is no evident border between the adjacent molecules and between monolayers; that is, some molecules in the monolayer present protrusions and there are multilayer forming at the air-water interface. The molecules on the interlayer present a certain cross-arrangement. Any way, we can conclude the best deposited pressure should be below 25 mNm^{-1} rather than above 25 mNm^{-1} like the traditional transfer pressure from π-A isotherm. This conclusion is agreement with following statement derived from the pioneer work[7-8]. The surface morphology of the LB films obtained at 5, 10, 20, 25 and 35 mNm^{-1} demonstrated that the CuPc film deposited at 5 mNm^{-1} pressure are not composed of domains of a certain size. This is reflected at a low surface pressure, e.g. 10 mNm^{-1} , the floating monolayer is in an expanded 'liquid' phase, and the molecular interval is larger. It is obvious that the surface morphology is not homogeneous, fine and close enough. The CuPc film deposited at 20~25 mNm^{-1} pressure is composed of domains of a certain size which is about 70 nm, possessed a homogeneous surface morphology and is considered as the best molecular arrangement. The CuPc films deposited at 35 mNm^{-1}appears striped protrusions, which apparently is the late collapse condition. Fig. 4 shows that it is wrong that generally the 35 mNm^{-1} is thought the traditional collapse pressure for CuPc[mec]4 , because the pressure 25 mNm^{-1} is turning-point of the change in which collapse of the monolayer begin.

Combined Fig.4 and Fig. 5 (π-A isotherm), another easy figure may be drawn and it can exhibit a relationship of the volume(Vol.) occupied per molecule and the surface pressure (π-Vol. isotherm). It will show that the molecular arrangement is loosely dispersive at a low pressure. The molecules arrange tidiness and the volume occupied per molecule become smaller little by little while the pressure of film is increased.

In addition, CuPc[mec]4 arrangement in LB film is easier to begin collapsing than CuPc[bec]4 , as shown in Fig.4. We can explain as following. Through these two CuPc have the same ether bond (R.O.R), which is of a certain flex, the CuPc[mec]4 's chain is shorter than CuPc[bec]4 's, so the former's ability of tangle, lengthening and shortening is smaller. Of course , the reaction of intermolecule is also smaller than that of CuPc[bec]4 . All above make a part of the CuPc[mec]4 protrusive from the monolayer easily. Hence, CuPc[mec]4 ' s turning point is sharp apparently.

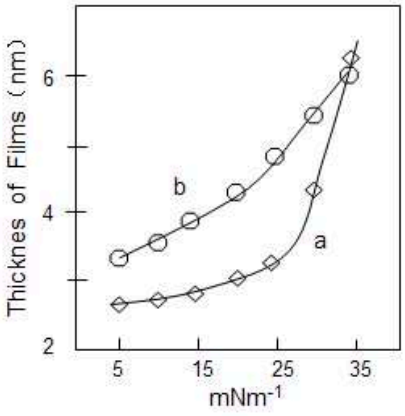

Fig. 4 The relationship of thickness and surface pressure; curve a- CuPc[mec]4, curve b-CuPc[bec]4.

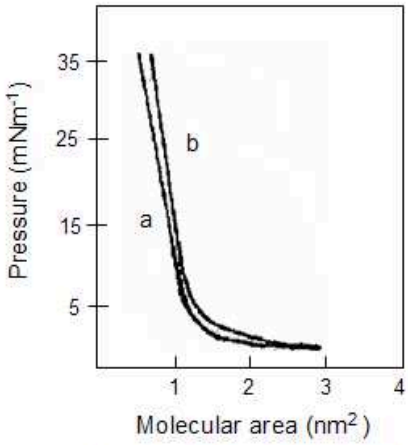

Fig. 5 π-A isotherm of the CuPc on water. curve a- CuPc[mec]4, curve b-CuPc[bec]4

Above results and conclusions were also obtained for samples of other symmetrically and asymmetrically substituted CuPc—CuPc[dtpp]$_4$ and CuPc-n[dtpp]$_3$, et al.

Acknowledgements

Authors would like to thank Prof. S. Q. Xi and Prof. W. Q. Chen (Changchun Institute of Applied Chemistry, China) for their help and support. We acknowledge partial financial supports from Jointly Funded Project (No. 61179055) of Chinese Civil Aviation Authority, National Natural Science Foundation of China, Talent Grant (2013-ZQXY-05） of Educational Commission of Guangdong Province, China and Jilin University Science and Technology Innovation Fund (No. 450060487476).

References

[1] K. P. Gentry and G. Thomas: (2009) Phys. Rev. B , 80:174118

[2] A. Capobianchi, A. M. Paoletti, G. Rossi, G. Zanotti and G. Pennesi: (2009) Sensors and Actuators B: Chemical 142 (1): 159

[3] A. W. Snow and N. L. Jarvis: J. Am. Chem. Soc., 1984, 106, 4706

[4] Y. Zang, W. Q. Chen and Q. Shen: Chem. J.of Chinese Universities, 1993, 11, 1483 and 1995, 11, 547

[5] H. N. Cui, W. Y. Wang and E. L. Zhou: Thin Solid Films, 1992, 214, 238~242

[6] X. G. Zhao, E. L. Zhou: Membrane Separation Science and Technology(China), 1987, 1, 13

[7] X. G. Zhao, E. L.Zhou, S. D. Jin: Chinese J. of Appl. chem., 1992, 9(1), 76-78

[8] A. D. Lu, X. M.Pang, Y. J. Li , D. P. Jiang ,Y. L. Hua, W. Q. Chen and E. L.Zhou:Thin Solid Films, 1991, 196, 323~328

Advanced Materials Research Vols. 986-987 (2014) pp 42-46

doi:10.4028/www.scientific.net/AMR.986-987.42

Determination of the optical constants of Gallium oxide films

Changlong Sun[1], Zhenping Wu[2], Shijie Lu, Zhen Ren, Yuehua An, Daoyou Guo, Xuncai Guo, Xulong Chu, Weihua Tang[3]

(School of Science, Beijing University of Posts and Telecommunications, Beijing 100876 China)

[1]clsun@bupt.edu.cn, [2]zhenpingwu@bupt.edu.cn, [3]whtang@bupt.edu.cn

Keywords: Optical constants, Reflectance spectrum, Transmission spectrum, Ga_2O_3 film

Abstract: Transmission spectrum and reflectance spectrum have long been used to characterize gap semiconductor. Transmission spectrum can be measured very directly, but the influence of substrate absorption is often unavoidable. However, when using the reflectance spectrum measurement, the absorption of thin film, substrate absorption, and coherent interference will make the reflectance spectrum much more complicated. In this paper, Considering the absorption of thin film, substrate absorption, and coherent interference, we use the envelope curves algorithm to achieve the calculation formula of refractive index deduced from the reflectance spectrum. Through the analysis of the reflectance spectrum of Ga_2O_3 film, we achieved thickness of the film, refractive index, extinction and absorption coefficient and dispersion constant.

Introduction

β-Ga_2O_3 exhibits the largest band gap among transparent conductive oxides(TCOs), about 4.8 eV[1]. The research value of wide-band gap semiconductor gallium oxide is growing, how to obtain the optical constants of its thin film easily and accurately is of great significance to its production and application.

For decades, there have been many methods for the determination of optical constants and thickness of thin film. For example, Abeles[2], Thickness interferometry[3], Elliptic polarization measurement method[4], Heterodyne interferometry[5], Phase shifting interferometry[6], Photometric method[7], Reflection spectroscopy[8,9], Transmission spectra method[10], Prism coupling method and so on. However, today the most common approach is spectral analysis. Spectral analysis can provide precision measurement of thickness and refraction of thin film, which is based on the reflectance or transmission spectrum of thin film.

Experimental procedures

1)Experimental details: Gallium oxide (Ga_2O_3) thin films were deposited on Si substrates by radio-frequency magnetron sputtering. The conditions are as follows: the substrate temperature is 750℃; vacuum degree of growth chamber is 9×10^{-5} Pa; sputtering time is two hours. The samples are annealed in oxygen or nitrogen for 1 hour at 900℃. Label the six groups samples with F01, F02, F03(The corresponding proportion of argon and oxygen is 2: 1, 3: 1, 4: 1 respectively, annealing in oxygen) and F11, F12, F13(The corresponding proportion of argon and oxygen is 2: 1, 3: 1, 4: 1 respectively, annealing in nitrogen).

2)Determination of the optical constants of Gallium oxide films

Theoretical model. As show in Fig. 1, consider a thin film with an average thickness d, and a complex refractive index $\tilde{n}_2 = n_2 - jk_2$. The thin film is on an absorbing substrate with a complex refractive index $\tilde{n}_3 = n_3 - jk_3$. The film-substrate system is immersed in air with refractive index n_1=1. The complex amplitude of reflection of reflection from the film-substrate system can be expressed as[11,12]:

$$r = \frac{E_{0r}}{E_{0i}} = \frac{r_{12} + r_{23}e^{-i\delta}}{1 + r_{12}r_{23}e^{-i\delta}} \tag{1}$$

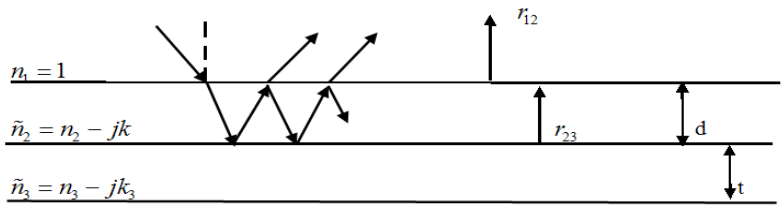

Fig. 1 Reflection on the thin film

Where $\delta = 2\pi\Delta/\lambda = 4\pi\tilde{n}_2 d/\lambda$ is the phase difference term inside the film. r_{12}, r_{23} are the reflectance amplitudes at the interfaces between air-film, and film-substrate.

$$r_{12} = \frac{(\tilde{n}_1 - \tilde{n}_2)}{(\tilde{n}_1 + \tilde{n}_2)} = \frac{1-(n_2 - jk_2)}{1+(n_2 - jk_2)} \tag{2}$$

$$r_{23} = \frac{(\tilde{n}_2 - \tilde{n}_3)}{(\tilde{n}_2 + \tilde{n}_3)} = \frac{(n_2 - jk_2)-(n_3 - jk_3)}{(n_2 - jk_2)+(n_2 - jk_3)} \tag{3}$$

The magnitudes that we can effectively measure are the reflectance R=r r*(r* is the complex conjugate of r). We have, from Eqs.(1) , Eqs.(2) and Eqs.(3),

$$R = \left|\frac{E_{0r}}{E_{0i}}\right|^2 = rr* = \frac{r_{12}^{\ 2} + \alpha^2 + 2r_{12}\alpha\cos(\delta + \phi_{12} - \phi_{23})}{1 + r_{12}^{\ 2}\alpha^2 + 2r_{12}\alpha\cos(\delta - \phi_{12} - \phi_{23})} \tag{4}$$

$\alpha = r_{23}e^{(-4\pi k_2 d/\lambda)}$, $\delta = 4\pi n_2 d/\lambda$, $\phi_{12} = \arctan(\frac{2k_2}{1 - n_2^{\ 2} - k_2^{\ 2}})$, $\phi_{23} = \arctan(\frac{2(n_2 k_3 - n_3 k_2)}{n_2^{\ 2} - n_3^{\ 2} + k_2^{\ 2} - k_3^{\ 2}})$

The condition of maximum or minimum reflectance is $\cos(\delta \pm \phi_{12} - \phi_{23}) = 1$ (5)

Substituting from Eq.(5) in Eq.(4) we get the upper envelope (lower envelope) for maximum (minimum) reflectance R_{max} (R_{min}) such that:

$$R_{max} = \frac{(r_{12} + \alpha)^2}{(1 + r_{12}\alpha)^2} \tag{6}$$

$$R_{min} = \frac{(r_{12} - \alpha)^2}{(1 - r_{12}\alpha)^2} \tag{7}$$

When the thin film absorption is small, namely $\alpha > r_{12}$, from Eqs.(6), (7), [13]

$$r_{12} = \frac{1 - \sqrt{R_{max}R_{min}} - \sqrt{(\sqrt{R_{max}R_{min}} - 1)^2 - (\sqrt{R_{max}} - \sqrt{R_{min}})^2}}{(\sqrt{R_{max}} - \sqrt{R_{min}})} \tag{8}$$

$$\alpha = \frac{1 + \sqrt{R_{max}R_{min}} - \sqrt{(\sqrt{R_{max}R_{min}} + 1)^2 - (\sqrt{R_{max}} + \sqrt{R_{min}})^2}}{(\sqrt{R_{max}} + \sqrt{R_{min}})} \tag{9}$$

Optical constants. Determination of approximate values for the films index

In this paper the absorption of Gallium oxide thin films is small, Therefore, according to the Eqs.(2) and Eqs. (8) we can calculate the refractive index of a thin film. The test results of reflection spectrum of Ga_2O_3 film is showed in Fig. 2.

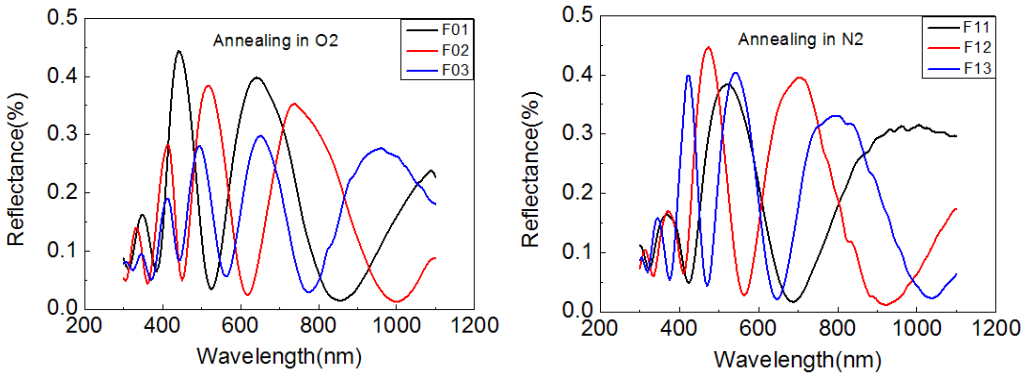

Fig. 2 Measured reflection spectrum for Ga_2O_3 film on Si (111) substrate

Put k_2=0 in Eq. (2) and solving for n_2 to get an approximate initial value for the film refractive index n_{20}: $n_{20} \approx \frac{1+r_{12}}{1-r_{12}}$ $(n_2 > 1)$ (10)

Determination of the film thickness

Using the above-obtained approximate values of n_{20} from Eq.(10), the interference order P can be determined as follows:

$$d_0 = \frac{\lambda_1 \lambda_2}{4(n_2\lambda_1 - n_1\lambda_2)} \tag{11}$$

Film thickness can be given by Eq.(11), where n_1 and n_2 are the refractive index at two adjacent extreme point at λ_1 and λ_2. Using the above-obtained approximate values of n_{20} with the values of $\overline{d}_0$ to get P for each extreme wavelength from the equation:

$$2nd = P\lambda \tag{12}$$

P is rounded to the nearest integer or half-integer. The value of the film thickness(d) is calculated from Eq.(12) for each extreme wavelength. Then the average final value of $\overline{d}$ is calculated for all wavelengths. The film refractive index n is also calculated from Eq.(12) for each wavelength using the obtained values of P and $\overline{d}$.

Determination of the extinction coefficient and absorption coefficient

r_{23} can be determined using Eq.(13) after calculating the real and imaginary parts of the refractive index for the Si substrate alone (n_3, k_3) from its reflectance and transmittance spectra using the method reported in reference[14].

$$r_{23} = [\frac{(n_3 - n_2)^2 + (k_3 - k_2)^2}{(n_2 + n_3)^2 + (k_2 + k_3)^2}]^2 \tag{13}$$

The extinction coefficient(k_2) and absorption coefficient(α_2) of the film can be determined as follows:

$$\ln(\alpha) = -\frac{4\pi k_2 d}{\lambda} + \ln(r_{23}) \quad (\text{where } \alpha_2 = \frac{4\pi k_2}{\lambda} = -\frac{1}{d}\ln(\frac{\alpha}{r_{23}})) \tag{14}$$

Table 1 shows the results of F03, it is obvious that the average approximated film thickness $\overline{d}_0$ is (1287.6±3053)nm(237.1%), while the average final thickness $\overline{d}$ is (1265.9±42.1)nm(3.32%).

Table 1 Calculated optical parameters for the Gallium oxide film on Si substrate

	Rmax	Rmin	n2i	d_0(nm)	Po	P	d(nm)	n2	K2
315	0.1235	0.0817	1.0352		8.4590	8.5	1293.2	1.0574	0.0079
330	0.1280	0.0789	1.0453	2104.8	8.1533	8	1262.8	1.0426	0.0052
360	0.1656	0.0735	1.1163	3745.7	7.9815	8	1289.9	1.1374	0.0047
390	0.2689	0.0691	1.2933	1161.1	8.5357	8.5	1281.6	1.3092	0.0061
435	0.4467	0.0645	1.6458	535	9.7386	9.5	1255.5	1.6321	0.0066

495	0.5050	0.0505	1.8443	4341.1	9.5903	9.5	1274.8	1.8572	0.0049
570	0.4124	0.0105	1.7085	343.17	7.7152	7.5	1251.1	1.6884	0.0047
680	0.3609	0.0226	1.6257	412.1	6.1537	6	1254.8	1.6114	0.0059
845	0.3491	0.2904	1.6605	587.3	5.0581	5	1272.2	1.6686	0.0052
1055	0.0906	0.0641	1.5086	467.2	3.6807	3.5	1223.8	1.4583	0.0079

Result and discussion

Fig.3 shows the refractive index of the six groups samples between 300nm and 1100nm wavelength range, which is close to the refractive index reported[15,16]. In near ultraviolet band(≤400nm), refractive index increases as increasing the wavelength; In visible light region, refractive index first increased and then decreased as increasing the wavelength; In near infrared region (700nm-1100nm), refractive index towards stability. The calculation results of extinction coefficient k_2 is showed in Fig.4, in 300nm-1100nm band Ga_2O_3 film has low light absorption.

Optical energy band gap Eg can not only give the basic absorption edge of film material, but also reflect the energy band structure of film. Band gap and absorption

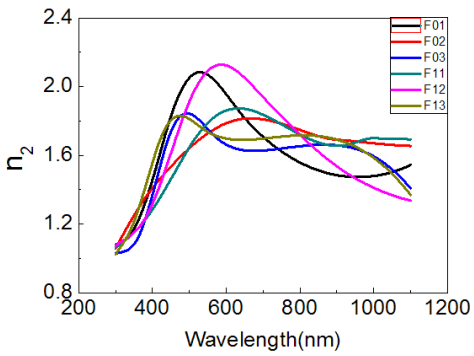

Fig. 3 Refractive index(n)

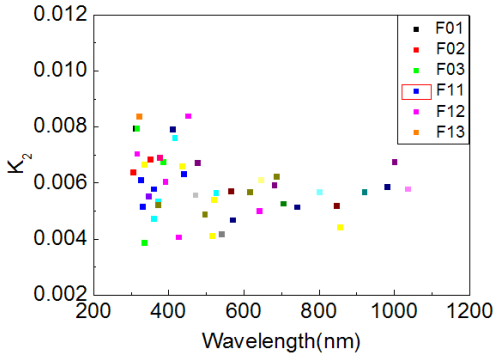

Fig. 4 Extinction co-efficient (k) spectra

coefficient have the following relations[17]: $\alpha hv=A(hv-E_g)^{1/2}$, so energy band gap Eg can be obtained by the relationship diagram $(\alpha hv)^2$ between and hv. Fig.5(left) is the relationship diagram $(\alpha hv)^2$ between and hv, which shows a steep absorption edge in the ultraviolet region.

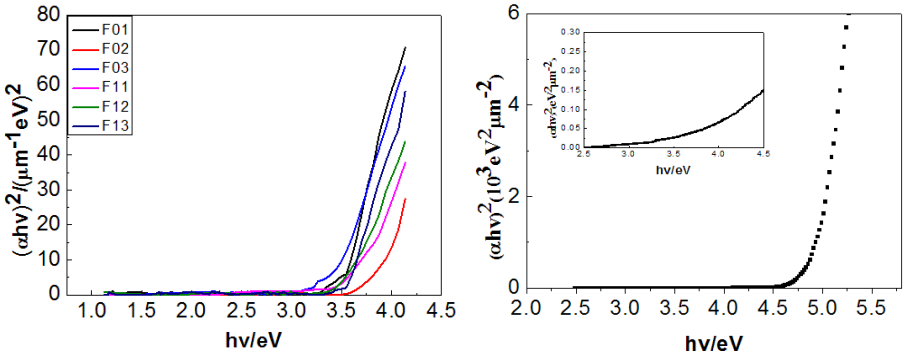

Fig. 5 $(\alpha hv)^2$ versus hv spectrum for the Gallium oxide films on Si (111) substrate

Thin film materials under different generating conditions have different absorption edge. As we can see from Table 2, when the ratio between argon and oxygen is 3:1, absorption edge is minimum, other proportions will appear a certain redshift. Fig.5(right) is the energy band gap diagram (inset in Fig.5(right) is magnification) which is consistent with the experimental data. As we didn't measure the reflectance spectrum in 200nm-300nm band range, so we can not get energy band gap Eg according to Fig.5(left).

Under different conditions, the optical constants and their limit errors were obtained using the method described in this paper. We can see from Table 2 that when the ratio between argon and oxygen is 3:1, the optical performances of film samples are best.

Table 2 Optical constants of Gallium oxide films

Samples	n(λ=632.8 nm)	d(nm)		k	Edge nm
F01	1.87	937.8	69.7	0.0041	370
F02	1.91	1787.1	35.4	0.0025	340
F03	1.64	1265.9	42.1	0.0022	410
F11	1.86	1464.6	21	0.0018	385
F12	2.08	1524.7	33.6	0.0023	365
F13	1.69	1354.8	43.9	0.0017	425

Conclusions

Gallium oxide films were synthesized on silicon substrate by magnetron sputtering. According to the reflectance spectrum, adopting the method described in this article, we calculated the refractive index, extinction coefficient, thickness and energy band gap of Ga_2O_3 film samples fairly accurately in 300nm-1100nm band. By the results of the energy band gap, we know that by adjusting growth conditions of films can realize the control of energy band gap, which is the prerequisite for preparing optoelectronic devices. Our work is useful for continued perfection of characterizing optical properties and guiding the preparation and application of Ga_2O_3 films.

References

[1] Tippins H H 1965 *Phys. Rev.* 140 A316-A319

[2] Yang L Y, Guan W D, Gu Z M 1991 Technology of thin film on Material surface (Beijing: China Communications Press)

[3] Xue Z Q, Wu Q D, Li J 1991 *Physics of thin films* (Beijing: Publishing House of Electronics Industry)(In Chinese)

[4] Jakopic G, papousek W 2000 Appl. Opt. 39 2727-2732

[5] Chiu M, Lee J, Su D 1999 Appl. Opt. 38 4047-4052

[6] Cheng Y Y, James C 1985 Appl. Opt. 24 804-807

[7] Panayotov V, Konstantinov I 1991 Appl. Opt. 30 2795-2800

[8] Trull J, Cojocaru C, Massaneda J, Vilaseca R, Martorell J 2002 Appl. Opt. 41 5172-5178

[9] Ohlidal I, Franta D, Ohlidal M, Navratil K 2001 Appl. Opt. 40 5711-5717

[10] Cisneros J I 1998 Appl. Opt. 37 5262-5270

[11] Ye Y T, Xiao J, Rao J Z 2011 *Optics* (Beijing: Tsinghua University Press) pp171-181(in Chinese)

[12] El-Naggar A M, El-Zaiat S Y, Hassan S M 2009 Opt & Laser Technol 41 334-338

[13] Yang P, Xu Z L, Xu L 2000 Spectroscopy and Spectral Analysis **3** 20

[14] Khashan M A, El-Naggar A M 2000 Opt Commun. 174 445-453

[15] Donmez I, Ozgit-Akgun C, Biyikli N 2013 J. Vac. Sci. Technol A31 01A110

[16] Shan F K, Liu G X, Lee W J, Lee G H, Kim I S 2005 J. Appl. Phys. 98 023504

[17] Mi W, Ma J, Zhu Z, Luan C N, Lv Y, Xiao H D 2012 Journal of Crystal Growth. 354 93-97

Advanced Materials Research Vols. 986-987 (2014) pp 47-50

doi:10.4028/www.scientific.net/AMR.986-987.47

Effect of different radios of two complexes on the structural and optical properties of ZnS thin films

Jin Shang, Huan Ke, Shuwang Duo[a], Tingzhi Liu, Hao Zhang

Jiangxi Key Laboratory of Surface Engineering, Jiangxi Science & Technology Normal University, Nanchang 330013,China

[a]swduo@126.com

Keywords: ZnS films; different radios; optical properties; structure; chemical bath deposition.

Abstract. ZnS thin films were deposited at three different radios of $V(NH_3 \cdot H_2O)/V(N_2H_4)$ on glass substrates by chemical bath deposition (CBD) method without stirring the deposition bath during the deposition process. The structural and optical properties were analyzed by X-ray diffraction (XRD) and UV-VIS spectrophotometer. The results showed that ZnS thin film deposited at the radio of $V(NH_3 \cdot H_2O)/V(N_2H_4)$=15:15 is higher than that of the other two different solutions. With the radio of $V(NH_3 \cdot H_2O)/V(N_2H_4)$ decreasing from 15:5 to 15:15, homogenous precipitation of $Zn(OH)_2$ easily forms in the bath, but ZnS precipitation first become suppressed and then easily forms in solution. It means that the concentration of OH^- ion increases with the volume of N_2H_4 increasing, which accelerates the formation of $Zn(OH)_2$. However, when the volume of N_2H_4 increases to 15mL, relatively high concentration of OH^- ion not only accelerates the formation of $Zn(OH)_2$, but also be used to the hydrolysis of thiourea. The average transmissions of all the ZnS films from three different solutions ($V(NH_3 \cdot H_2O)/V(N_2H_4)$=15:5, 15:10 and 15:15) are greater than 90% for wavelength values in visible region. The direct band gaps range from 3.80 to 4.0eV. The ZnS film deposited for 2.5h with the radio of $V(NH_3 \cdot H_2O)/V(N_2H_4)$=15:15 has the cubic structure only after single deposition.

Introduction

ZnS is a wide, direct band gap, Ⅱ-Ⅵ semiconductor and because of its good transmittance in visible range [1], ZnS materials have been widely used in photoelectric and solar cells area. Various techniques have been employed to prepare ZnS thin films, such as molecular beam epitaxy (MBE) [2], sputtering [3], and chemical bath deposition (CBD) [4-7] and so on. Among these methods, the CBD technique is actually the principal method used in buffer layers deposition of $Cu(In, Ga)Se_2$ (CIGS) solar cells[8] and has demonstrated be the most suitable method for depositing uniform and adherent thin films in a large area.

In recent years, CBD have attracted more and more interest because it does not require vacuum system and other expensive equipments; the low temperature required in CBD process avoids oxidation and corrosion of metallic substrates, furthermore a chemical etching of the surface of the absorber can be done during the CBD process [9]. Over the past two decades, almost all research groups focused on the reaction mechanisms, new complexing agents and different reaction systems. However, few literatures discussed the effect of different radios of two or more complexes on structural and optical properties of ZnS films. In this paper, ZnS thin films had been deposited by CBD method onto glass substrates in alkaline liquor with $NH_3 \cdot H_2O$-N_2H_4 system. The different volume radios of two complexes ($V(NH_3 \cdot H_2O)/V(N_2H_4)$) on optical and structural properties of ZnS thin films were discussed.

Experimental. The concentrations of reactants and the volume radios of $V(NH_3 \cdot H_2O)/V(N_2H_4)$ were given in Table 1. The ZnS thin films were grown on commercial glass substrates ($76 \times 25 \times 1 mm^3$) which were consecutively ultrasonically cleaned with detergent, degreased with acetone, followed by ethanol, and then washed by distilled water. A calculated amount of reagent was added to the deionized water for a final solution of 150mL in a beaker. The cleaned glass slides were immersed vertically in the deposition bath. The bath solutions were maintained at 80℃ for 2 hours or 2.5 hours.

After the deposition, the glass substrates were taken out of the beaker, washed with deionized water and dried with hairdryer.

Table 1 The concentrations (M) of reactants and the volume radios of $V(NH_3 \cdot H_2O)/V(N_2H_4)$

	$Zn(CH_3COO)_2$	$SC(NH_2)_2$	$V(NH_3 \cdot H_2O) : V(N_2H_4)$
Solution A	0.050	0.070	15 : 5
Solution B	0.050	0.070	15 : 10
Solution C	0.050	0.070	15 : 15

Results and discussion. The thicknesses of the ZnS films deposited for 2h and 2.5h were given in Table 2. It is clear from the Table 2 that the ZnS films from solution C were thicker than that from the other solutions with the same deposition time. This result indicates that with the decrease of the volume radios of $V(NH_3 \cdot H_2O)/V(N_2H_4)$, the growth rate of ZnS films increases, in other words, the increasing of the amount of N_2H_4 promotes the formation of heterogeneous ZnS thin films.

Table 2 The thicknesses (nm) of the ZnS films deposited for 2h and 2.5h from different solutions

	Deposited for 2 h	Deposited for 2.5 h
Solution A	76	88
Solution B	71	82
Solution C	80	91

As can be seen from the Fig.1, all the transmissions of ZnS films deposited for 2h and 2.5h from three different solutions were over 90% in visible range. It is noteworthy that the transmittances of ZnS films have shifted towards long wavelengths with the increase of the volume of N_2H_4.

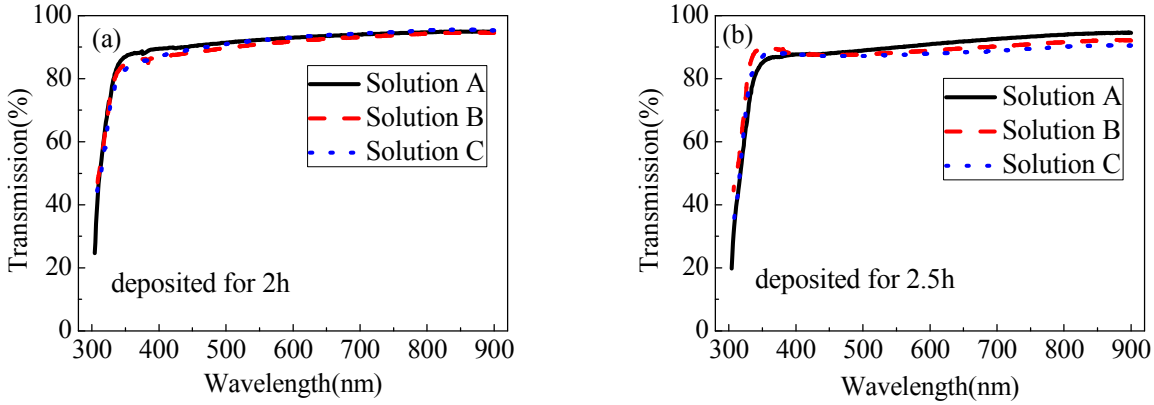

Fig.1 Transmission spectra of ZnS films deposited for different deposition time: (a) deposited for 2h; (b) deposited for 2.5h

For obtaining the optical band gap values of the film, the absorption coefficient (α), which was calculated from the transmittance, was analyzed. From the Beer-Lambert law, we could get the function of absorption coefficient and transmittance as follows: $\alpha = -\ln T/d$ where d is the thickness of the ZnS film. Then, α is used to obtain the following expression for near-edge optical absorption of semiconductors: $(\alpha h\nu)^2 = A(h\nu - E_g)$ where A is a constant, E_g is the separation between the valence and conduction bands. By this equation, the band gap value is determined from the intercept of the straight-line portion of the $(\alpha h\nu)^2$ against the graph on the $h\nu$-axis. Fig.2 shows the plot of $(\alpha h\nu)^2$ versus the incident radiation energy $h\nu$ (eV). The band-gap values of all films are higher than that of bulk ZnS (3.7eV) [10], ranging from 3.8eV to 4.0eV. The E_g values are large and have obviously shifted towards shorter wavelengths due to the quantum size effect of confinement of electrons. It is noteworthy that with the decreasing of the radios of $V(NH_3 \cdot H_2O)/V(N_2H_4)$, band gaps of ZnS thin film first decreased and then increased. This result indicates that when the volume of N_2H_4 increases from 5mL to 10mL, the grain growth of thin film becomes easy, which results in E_g decrease. However, when the volume of N_2H_4 increases to 15mL, the higher concentration of N_2H_4 increases the number of nucleation points on the substrate and decreases the single grain growth rate.

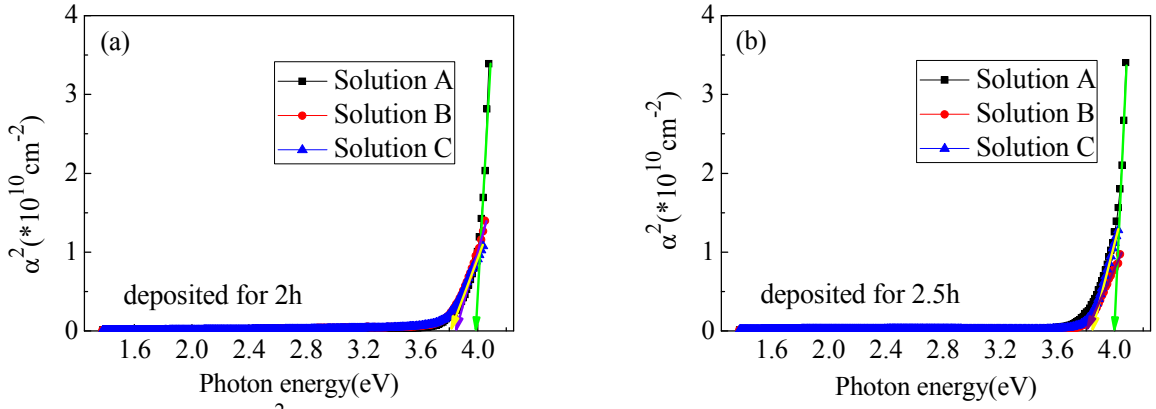

Fig.2 The plots of $(\alpha h\nu)^2$ versus hν of ZnS films deposited for different deposition time: (a) deposited for 2h; (b) deposited for 2.5h

Fig.3(a) shows the XRD patterns of ZnS films deposited for 2.5h from three different solutions. As is showed in Fig.3 (a), the ZnS thin film from solution C has one significant peak at about 2θ=29.16° which can be assigned to the (111) reflection of the sphalerite structure, while the ZnS thin films from the other two solutions have no obvious peaks. It means that the crystallinity of ZnS thin film is improved when the volume of N_2H_4 increases to 15mL, this probably because the ZnS film from solution C is thicker than that from the other two solutions, which agrees well with the figures in Table 2. Fig.3(b) shows the XRD patterns of homogeneous precipitations deposited for 2.5h from three different solutions. As can be seen from the Fig.3(b), the homogeneous precipitations deposited for 2.5h from three different solutions consist of ZnS and $Zn(OH)_2$. With the increase of the volume of N_2H_4, the $Zn(OH)_2$ peaks intensity increases, but the cubic ZnS peaks intensity of (111), (220) and (311) first decreases, and then increases. It means that when the volume of N_2H_4 increases from 5mL to 10mL, the concentration of OH^- ion increases, which accelerates the formation of $Zn(OH)_2$. However, when the volume of N_2H_4 increases to 15mL, relatively high concentration of OH^- ion not only accelerates the formation of $Zn(OH)_2$, but also be used to the hydrolysis of thiourea.

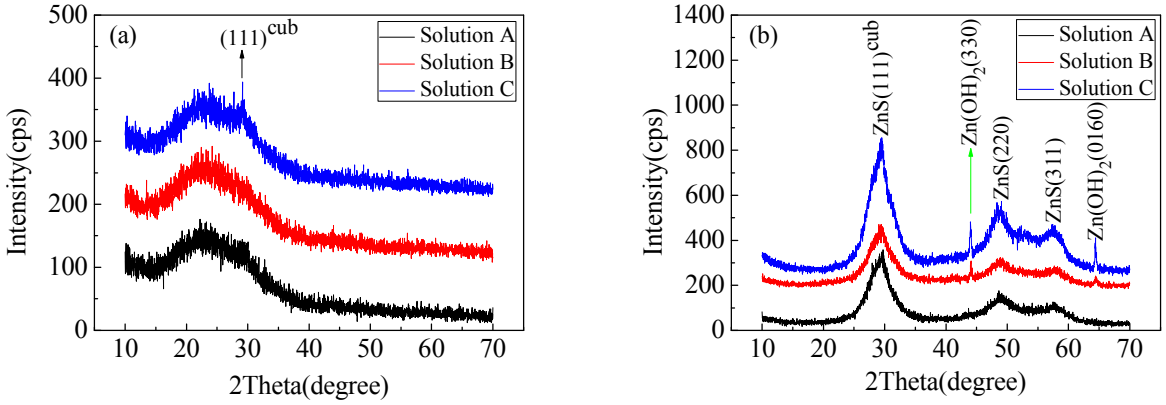

Fig.3 XRD spectrum of the samples deposited for 2.5h from three different solutions and XRD of homogenous precipitations (2.5h) collected from the reaction bath: (a) ZnS thin films; (b) homogenous precipitations

Summary

Comparing with those deposited at the radio of $V(NH_3 \cdot H_2O)/V(N_2H_4)$=15:5 and 15:10, the growth rate of ZnS thin film deposited at the radio of $V(NH_3 \cdot H_2O)/V(N_2H_4)$=15:15 is highest. With the radio of $V(NH_3 \cdot H_2O)/V(N_2H_4)$ decreasing from 15:5 to 15:15, homogenous precipitation of $Zn(OH)_2$ easily forms in the bath, but ZnS precipitation first become suppressed and then easily forms in solution. It means that the concentration of OH^- ion increases with the volume of N_2H_4 increasing, which accelerates the formation of $Zn(OH)_2$. However, when the volume of N_2H_4 increases to 15mL, relatively high concentration of OH^- ion not only accelerates the formation of $Zn(OH)_2$, but also be

used to the hydrolysis of thiourea. The average transmissions of all the ZnS films from three different solutions ($V(NH_3 \cdot H_2O)/V(N_2H_4)$=15:5, 15:10 and 15:15) are greater than 90% for wavelength values in visible region. The direct band gap energy varies from 3.80 to 4.0eV. XRD results show that ZnS film with low thickness deposited for 2.5h at the radio of $V(NH_3 \cdot H_2O)/V(N_2H_4)$=15:15 has the cubic structure only after single deposition, while the ZnS films deposited for 2.5h at the radio of $V(NH_3 \cdot H_2O)/V(N_2H_4)$=15:5 and 15:10 are amorphous.

Acknowledgement

Financial support from the National Natural Science Foundation of China (51363007), the Science Funds of Natural Science Foundation of Jiangxi Province (20132BAB206033), the Project of Jiangxi Youth Scientist (No. 20122BCB23031). and the Project of the Science Funds of Jiangxi Education Office (KJLD13070).

References

[1] J. A. Ruffner, M. D. Himel, V. Mizrahi, G. I. Stegeman, U. Gibson. J. Appl. Opt. Vol. 28,(1989), 5209.

[2] Y. Z. Zhao, S. C. Eou, J. K. Sang. Materials Chemistry and Physics. Vol. 135(2012), 287.

[3] S. M. Salim, A. H. Eid, A. M. Salem and H. M. Abou El-khair. Surf. Interface Anal. Vol. 44(2012), 1214.

[4] J. M. Dona, J. Herrero. Thin Solid Films. Vol. 5(1995), 268.

[5] T. Nakada, M. Mizutani, Y. Hagiwara, A. Kunioka. Solar Energy Materials & Solar Cells. Vol. 67(2001), 255.

[6] Axel Eicke, Thomas Ciba, Dimitrios Hariskos, et al. Surf. Interface Anal. Vol. 45(2013), 1811.

[7] Reiner Klenk, Alexander Steigert, Thorsten Rissom, et al. Prog. Photovolt: Res. Appl. Vol.22 (2014), 161.

[8] J. Herrero, M. T. Guttierez, C. Guillen, J. M. Dona, M. A. Martinez, A. M. Chaparro and R. Bayon. Thin Solid Films. Vol. 361-362(2000) 28.

[9] N. Naghavi, D. Abou-Ras, N. Allsop, N. Barreau, S. Bücheler, A. Ennaoui, C. H. Fischer, C. Guillen, D. Hariskos, J. Herrero, R. Klenk, K. Kushiya, D. Lincot, R. Menner, T. Nakada, C. Platzer-Bjorkman, S. Spiering, A. N. Tiwari, T. Torndahl. Progress photovoltaics, Res. Appl. Vol. 18(2010), 411.

[10] W. Vallejo, C. Quinones, G. Gordillo. Journal of Physics and Chemistry of Solids. Vol. 73(2012), 573.

Advanced Materials Research Vols. 986-987 (2014) pp 51-54

doi:10.4028/www.scientific.net/AMR.986-987.51

Effect of the concentrations of the reactants on electrochemical performance of composite cathode material $LiFePO_4$/C

Xiaoling Ma , Youxiang Zhang

College of Life Science and Chemistry, Wuhan Donghu University,
Wuhan, 430212,China
Email address: 240200025@qq.com

Keywords: cathode material, lithium-ion batteries, $LiFePO_4$/C, concentration.

Abstract: $FePO_4 \cdot 2H_2O$ nanoplates are synthesized by a hydrothermal method, using Fe(III) compound as the iron source and are lithiated to $LiFePO_4$/C by a simple rheological phase mathod. The structure, morphology and electrochemical properties of the $FePO_4 \cdot 2H_2O$ nanoplates and $LiFePO_4$/C composites synthesized by changing the concentration of the reactants were characterized in detail by X-ray(XRD), scanning electron microscope(SEM), high-resolution transmission electron microscope and electrochemical measurement. The $LiFePO_4$/C nanoparticles lithiated from the $FePO_4 \cdot 2H_2O$ nanoplates when there were about 10 mmol Fe^{3+} in 20 ml water solution demonstrates excellent cyclic performance.

Introduction

With high capacity and power, lithium-ion battery has been considered to be one of the beat energy conversion and storage systems [1-2]. The $LiFePO_4$ is an attractive electrode material for the rechargeable lithium-ion batteries due to nontoxicity, environmental friendliness, and low cost. Although $LiFePO_4$ possesses many advantages, it has suffered from poor electronic conductivity and Li-ion diffusion coefficient. To overcome the problem, the $LiFePO_4$ particles are reduced to the nanometre scale to shorten the diffusion length for electrons and lithium ions and increase the effective reaction areas[3].

Herein, we synthesized nanscale $FePO_4 \cdot 2H_2O$ using a hydrothermal method and are lithiated to $LiFePO_4$/C with the same structures by a simple rheological phase method. The $LiFePO_4$/C nanoparticles show excellent electrochemical performance and long-term cyclability as the cathode in lithium-ion battery, with the specific capacities 151mAh/g.

Experimental

The $FePO_4 \cdot 2H_2O$ were synthesized using the same formulas as literature [4]. $FeCl_3$ was dissolved in water to give a 0.05mol/L Fe^{3+} precursor as sample FP-1 and $FeCl_3$ was dissolved in water to give a 0.50mol/L Fe^{3+} precursor as sample FP-2 . In a typical synthesis, The CTAB surfactant was added to distilled water and stirred for 30 min. Then, $FeCl_3$ was added and stirred. After that, H_3PO_4 was dropped to the solution and stirred. Then the solution was aged for 24h in waterbath and dried at 100℃ for 4h.

A simple rheological phase method was employed to synthesize $LiFePO_4$/C composite[5]. The $FePO_4 \cdot 2H_2O$ nanoplates, $LiOH \cdot H_2O$, PEG and appropriate amount of water were mixed, then ground for several to get a rheological. After several time, the rheological body was calcined at 600℃, and then the $LiFePO_4$/C composite was obtained. The composite LFP-1 was using the sample FP-1 precursor as sources for both the Fe and P in the materials. The composite LFP-2 was using the sample FP-2 precursor as sources for both the Fe and P in the materials.

The phase purity of the products was examined by powder X-Ray Diffraction on a Bruker D8 Advance X-ray diffractometer using Cu Kα radiation (λ = 1.54056 Å). The crystal size and morphology of the products were examined with a scanning electron microscope(SEM, QUANTA 200, Holland).

Electrochemical measurements were carried out using two-electrode cells with lithium metal as the counter electrode. The working electrode was fabricated by compressing a mixture of the

$LiFePO_4$/C composite/acetylene black/polyvinylidene fluoride (PVdF) with a weight ratio 65/30/5. The weight of active materials varied between 2.0 and 3.0 mg. The electrolyte was a 1 M $LiPF_6$ in a 1:1 mixture of ethylene carbonate (EC)/diethyl carbonate (DEC) and the separator was Celgard 2500. The cell was assembled in a glove box filled with high purity argon gas. The galvanostatic charge/discharge experiment was performed between 2.0 and 4.4 V at 1C current density with each experiment repeated at least 5 times. The experiments produced reproducible results.

Results and Discussion

The X-ray diffraction (XRD) results for the $LiFePO_4$/C are presented in Figure 1. The diffraction peaks are in good agreement with the standard values for $LiFePO_4$ (JCPDS 81-1173), which shows the high-purity of the as-synthesized samples.

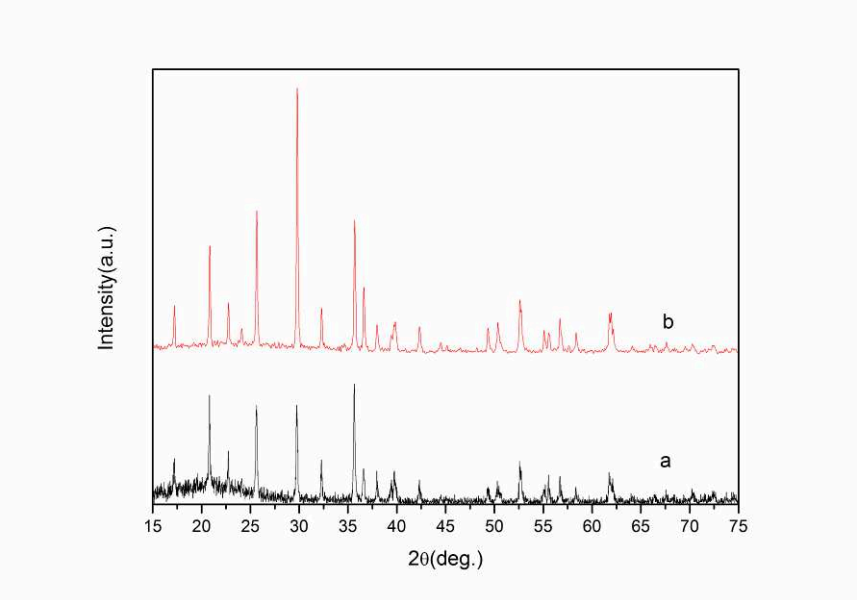

Fig. 1 XRD patterns of the as-synthesized $LiFePO_4$/C. (a) LFP-1 (b)LFP-2

Figure 2 shows the scanning electron microscope (SEM) image of the as-synthesized $LiFePO_4$/C. The nanoparticles are of morphology with very small sizes (30~ 80nm). The measurement is in agreement with the crystallite size deduced from XRD analysis.

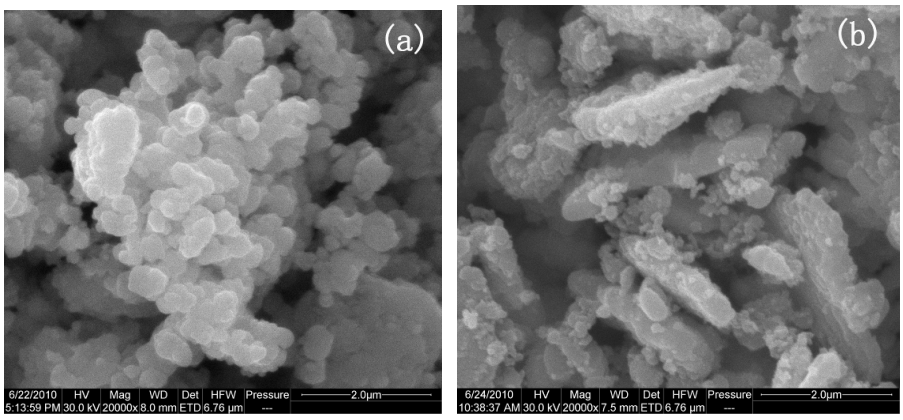

Fig. 2 SEM images of the as-synthesized $LiFePO_4$/C. (a) LFP-1 (b) LFP-2

The discharge-charge cycling of the $LiFePO_4$/C was carried out in the voltage window 2.0 and 4.4 V (vs. Li^+/Li) at a current density of 1C at room temperature. The LFP-1 sample delivers a discharge capacity of 151.3 $mAh \cdot g^{-1}$ and The LFP-2 sample delivers a discharge capacity of 131.5

$mAh \cdot g^{-1}$. Fig. 4 demonstrate that the $LiFePO_4/C$ also exhibit an excellent cycling performance. While the discharge specific capacity of the LFP-1 sample can stabilize at about150 $mAh \cdot g^{-1}$, the discharge specific capacity of the LFP-1 sample can stabilize at about130 $mAh \cdot g^{-1}$ at this current density of 1C.

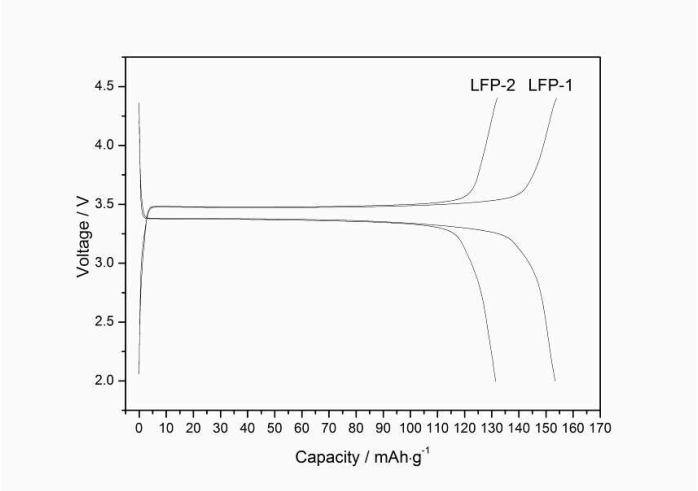

Fig.3 Typical charge-discharge curves at 1C between 2.0-4.4V. (a) LFP-1 (b) LFP-2

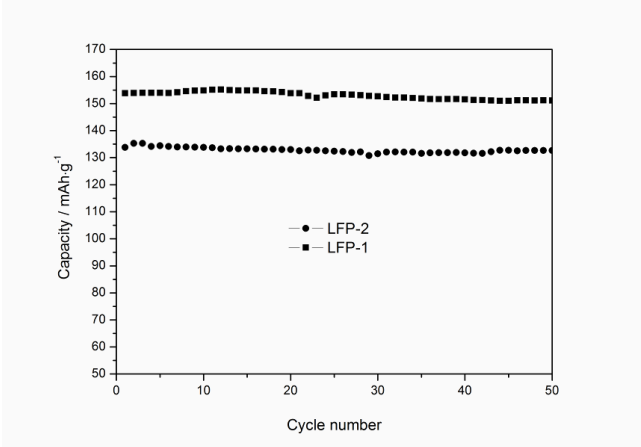

Fig. 4 The discharge capacities of the as-synthesized $LiFePO_4/C$ for the first 50 cycles.

Conclusions

In summary, nanscale $FePO_4 \cdot 2H_2O$ are synthesized using a hydrothermal method and lithiated to $LiFePO_4/C$ by a simple rheological phase method. The sample can deliver a better discharge capacity by changing the concentrations of the reactants. When $FeCl_3$ was dissolved in water to give a 0.05mol/L Fe^{3+} precursor as sample can deliver a better discharge capacity of 151.3 $mAh \cdot g^{-1}$. The nanoscale $LiFePO_4/C$ show excellent electrochemical performance and long-term cyclability.

Acknowledgement

This study was supported by the Youth Foundation of Wuhan Donghu University.

References

[1] S. Zhang, C. Deng, B. L. Fu, S. Y. Yang, L.Ma. Doping effects of magnesium on the electrochemical performance of Li_2FeSiO_4 for lithium ion batteries [J]. Journal of Electroanalytical Chemistry, 2010, 644: 150~154

[2] Li.M. Li, H. J. Guo, X. H Li, Z. X. Wang, W. J. Peng, K. X. Xiang, X. Cao. Effects of roasting temperature and modification on properties of Li_2FeSiO_4/C cathode [J]. Journal of Power Sources, 2009, 189: 45~50

[3] X. B. Huang, X. Li, H. Y. Wang, Z. L. Pan, M. Z. Qu, Z. L. Yu. Synthesis and electrochemical performance of Li_2FeSiO_4/C as cathode material for lithium batteries [J]. Solid Sta te Ionics, 2010, 181: 1451~1455

[4] P. G. Bruce, B. Scrosati. J. M. Tarascon. Nanomaterials for rechargeable lithium batteries [J]. Angewandte Chemie International Edition, 2008, 47: 2930~2946

[5] D. M. Kempaiah, D. Rangappa, I. Honma. Controlled synthesis of nanocrystalline Li_2MnSiO_4 particles for high capacity cathode application i n lithium-ion batteries [J]. Chemical Communications, 2012, 48: 2698~2700

Advanced Materials Research Vols. 986-987 (2014) pp 55-58

doi:10.4028/www.scientific.net/AMR.986-987.55

Effect of UV Radiation on HTV-Silicon Rubber under different humidity

YI Chunfang[1,a], SHI Qian [2,a], LIANG Peisong[2,a]

[1]Guangxi Power Grid Corp, China

[2]School of Electrical and Electronic Engineering, North China Electric Power University, Baoding 071003, China

Project Supported by National Natural Science Foundation of China(51207055), Natural Science Foundation of Hebei Province(E2013502213) and Guangxi Power Grid Corp (K-GX2017-076)

[a]shiqian0911@163.com

Keywords: HTV-silicon rubber; humidity ; UV radiation; aging; FTIR;

Abstract. Along with our country " west-east electricity transmission " project and UHV projects,HTV-silicon rubber has been more and more widely used in the western regions of China,such as xining, Lhasa, hami and other regions, has strong solar radiation, long sunshine time, but the region environment humidity conditions are different. Therefore, it is necessary to study the Effect of UV Radiation on HTV-Silicon Rubber under different humidity. In this paper, the extraction of relative humidity variable, under different humidity conditions,HTV silicone rubber material taken for artificial ultraviolet aging experiment, to explore under different humidity conditions,HTV silicone rubber material's ultraviolet aging properties. Experimental samples of artificial ultraviolet aging experiment taken in static contact angle test, hardness test, fourier transform infrared spectroscopy (FTIR) analysis, then integrate the test data and make theoretical analysis.The experimental results show that both samples hardness are larger, the flexibility are reduced; their both surface static contact angle are decreased, the hydrophobic are part of the loss; their both surface roughness are bigger,and a part of filler is leaked; FTIR of peak area of Si-CH_3 and Si-O-Si keys absorption peak are reduced, shows a portion of the Si-CH_3 and Si-O-Si keys is interrupted into free radicals; UV radiation has a certain influnce on HTV silicone rubber.Humidity variable has two contray sides influence on ultraviolet aging characteristics of HTV silicone rubber material,its process is complicated.

Introduction

Compared with ceramic and glass insulators, HTV-silicon rubber composite insulator has strong resistance ability of pollution flashover, light weight, easy maintenance, etc. Therefore it has been widely used in electric power system [1–3] .In these strong UV radiation region, humidity is different, moisture variables influence on UV aging characteristic of composite insulation materials also has not been studied.In the western region of China, the UV radiation strong, composite insulator aging problem is more not allow to ignore.

Experiment

A. Experimental setup

The average annual sunshine of strong ultraviolet region amount in more than 2500h, but the relative humidity conditions vary widely, such as kunming average relative humidity is 74%, Lhasa dry season average humidity is only 15%. Soset up relative humidity variable two extreme cases are 5% and 80% respectively. Two groups of experiment is carried out .HTV silicone rubber are performed for irradiation ageing. the experiment are for 1000h respectively.1000h later the radiation is about 2015 ~ 3149 MJ/m^2 ,is equivalent to 7 ~ 11 months ultraviolet radiation in strong ultraviolet area.

B. Sample preparation

Take HTV silicone rubber materials cut into 50 mmx50mmx2mm (length x width x thickness) size, each experiment of the samples is 10 pieces, according to the preprocessing of DL/T 810-2002 [10] .

C.Test equipment and measuring instrument

Experiment equipment adopts Beijing Lihui company production of SN-66 xenon lamp aging box.Measuring instrument uses the American kono industrial company in the production of SL200A/B type contact Angle measuring instrument and the analysis software to do the sample surface hydrophobic measurement is shown in Fig.1.This paper adopts the ThermoFisher scientific company in production of Nicolet Is5 type Fourier transform infrared spectrometer, application of total reflection accessories, spectrometer is shown in Fig.2.

Fig.1 Contact angle meter

Fig.2 FTIR instrument

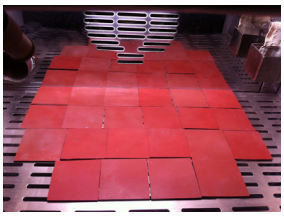

Fig.3 Xenon lamp aging box

D. Experimental scheme

According to the two relative humidity variable set, compared the two groups of HTV silicone rubber sample artificial accelerated ultraviolet aging test, as shown in figure 3, specific test plan is as follows:

Test a: 10 specimens placed in xenon lamp aging test box, set the board temperature is 65^{o} C, the specimen surface temperature of (65±5)^{o} C, relative humidity is 5% (aging experiment box has been modified). In order to ensure the consistency of the test specimen surface irradiance, after every 48h samples position has been adjusted. Take out every 100h two kind of sample each 1 piece of hydrophobic testing, hardness testing, FTIR testing, the total test time of 1000h.

Test b: The preparation of sample has another 10 specimens placed in same conditions set same xenon lamp aging test box, only relative humidity to 80%. In order to ensure the consistency of the test specimen surface irradiance, after every 48h samples position has been adjusted. Take out every 100h two kind of sample each 1 piece of hydrophobic testing, hardness testing, FTIR testing, the total time of 1000h.

Experimental results and discussions

A. Static contact angle

As shown in figure 4, the sample of hydrophobic are lower, but in the early stage of the radiation time under the condition of 80% relative humidity hydrophobic inferior to the sample under the condition of 5% relative humidity of hydrophobic, but with the increase of irradiation time, begin to appear in 300h specimen under the condition of 80% relative humidity of hydrophobic gradually is better than that of the sample under the condition of 5% relative humidity of hydrophobic trend.

B.Hardness change

As shown in figure 5, the hardness of sample are bigger, but the change of the specimen hardness change and hydrophobic have the same trend, turning point at 300h.

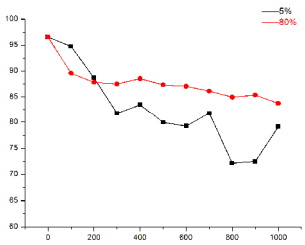

Fig.4 Sample surface static contact angle change

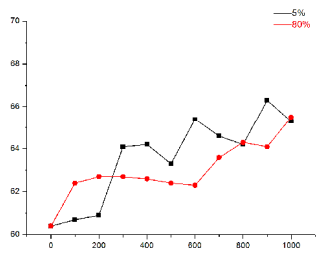

Fig.5 Sample hardness change

C.Infrared spectrum analysis

As shown in Fig. 6 and Fig. 7, Sample groups in peak area is smaller, the early stage of the test of time, relative humidity of 5% of the peak area significantly greater than 80% relative humidity of reactive peak area, but with the increase of irradiation time, relative humidity 5% began to appear in the 600h peak area gradually less than 80% relative humidity of the reactive peak area ofthe trend.

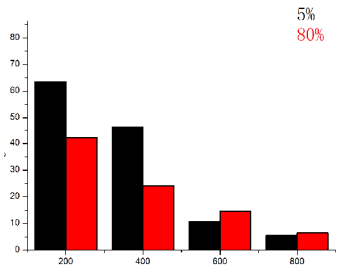

Fig.6 Si-CH_3 peak area percentage

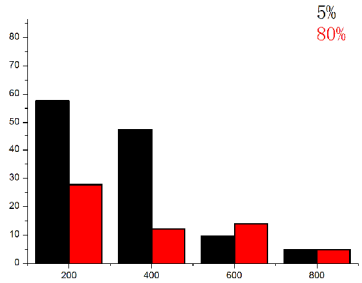

Fig.7 Si-0-Si peak area percentage

Discussions

Water molecules in the ultraviolet aging test of HTV silicone rubber, the two opposite effect:

1) on the one hand under the radiation of ultraviolet light, water molecules involved in ultraviolet aging chemical reactions inside the silicone rubber. Due to the residual catalyst in silicone rubber, silicone rubber inside the inorganic salt content increases, the residue of inorganic salt in addition to the easy absorption of water be affected with damp be affected with damp to lower the resistance to water, also make the silica in the silicone rubber chain rupture, accelerate damage vulcanizates mesh structure, an enormous influence on characteristics of silicon rubber ultraviolet aging.

2) on the other hand, the water molecules will be distributed on the surface of silicone rubber, and the sample is combined with a variety of filler particles precipitate Si particles, and have enough oxygen plays a role of medium, small changes in the molecular structure of silicon rubber outer surface, namely a kind of organic low molecular polymer silica, gradually spread evenly throughout the outer surface, a thin layer of protection, the thin layer will protect silicone rubber is no longer a further by UV light.

Conclusion

The experimental results show that:

a. Both samples hardness are larger, the flexibility are reduced.

b. Their both surface static contact angle are decreased, the hydrophobic are part of the loss.

c. Their both surface roughness are bigger,and a part of filler is leaked.

d. FTIR of peak area of Si-CH_3 and Si-O-Si keys absorption peak are reduced, shows a portion of the Si-CH_3 and Si-O-Si keys is interrupted into free radicals.

e. Humidity variable has two contray sides influence on ultraviolet aging chara-cteristics of HTV silicone rubber material,its process is complicated.

Acknowledgements

This paper was supported by Grant Guangxi Power Grid Corp (K-GX2017-076), No.113 of Natural Research Projects and with the support of Hebei Provincial Key Laboratory of Power Transmission Equipment Security Defense, North China Electric Power University, Baoding, China.

References

[1] QIU Zhi-xian.High Voltage composite insulator and its application [M]. Beijing, China: China Electric Power Press,2006.

[2] FU Guan-jun, Wang Li-ming, Hou Lei,et al. Feasibility of application of composite insulators in ±800kV UHV DC tension strings[J]. Proceedings of the CSEE, 2011, 31(22): 119-125.

[3] J P R eyndery, I P Jandrell, et a1. Review of aging and recovery of silicone rubber Insulation for outdoor use[J]. IEEE Trans Dielectric and Electrical Insulation, 1999,

6(5):620-631.

[4] XU Qi-ying.Experimental study on aging resistance of silicone rubber composite insulators[J].Insulating Materials, 2009, 42(3):49-51.

[5] ZHOU Zhi-min.Development and application of silicone rubber composite insulators[J].Popular Utilization of Electricity,2004, 20(6):20- 22.

Advanced Materials Research Vols. 986-987 (2014) pp 59-62

doi:10.4028/www.scientific.net/AMR.986-987.59

Electro-catalytic Performance of Different Pt/Ag Ratio on H_2O_2 Electro-reduction for Direct $NaBH_4$ - H_2O_2 Fuel Cell

Tingfang YANG[a], Dan ZHENG[b], Zaoxi YU[c]

School of Chemical and Environmental Engineering, Shanghai Institute of Technology, Shanghai, 201418, China

[a]email:1072093383@qq.com, [b]email:zhengdan@sit.edu.cn, [c]email:1181088053@qq.com

Keywords: Pt-Ag ratio; cathode catalysts; hydrogen peroxide; electro-reduction

Abstract. In this paper the different proportional Pt/Ag on XC-72 carbon are studied to serve as the electro-catalysts of H_2O_2 in acid media. All catalysts are prepared by impregnation reduction method and characterized by XRD and TEM. The electrochemical performance tests are examined by cyclic voltammetry (CV) at 25°C and 30°C, respectively. The results suggest that the peak current density increases with increasing the Ag content in Pt-Ag/C. Attributed to the temperature factor, the electro-catalytic activity of all catalysts at 30°C is better than that of 25°C.

Introduction

Direct $NaBH_4$ -H_2O_2fuel cell (DBHFC) is attractive as a new, clean alternative power source for portable electronic devices due to their high energy density, raw materials are easier to store and transport [1] [2] . In DBHFC, sodium borohydride is oxidized at anode based on following reactions of

$$BH_4^- + 8OH^- + 8e^- \rightarrow BO_2^- + 6H_2O \qquad E^0 = -1.24Vvs.SHE \tag{1}$$

Hydrogen peroxide is restored at cathode according to following reactions of

$$4H_2O_2 + 8H^+ + 8e^- \rightarrow 8H_2O \qquad E^0 = 1.77Vvs.SHE \tag{2}$$

Accordingly, the net cell reaction in DBHFC is

$$BH_4^- + 4H_2O_2 \rightarrow BO_2^- + 6H_2O \tag{3}$$

The theoretical fuel cell potential and specific energy of DBHFC are 3.01V and 17.06KWh/kg, respectively

Now, for this type of fuel cell, carbon supported Pt is widely used as cathode catalyst [3-6]. But the limited resources and higher cost of Pt greatly limit the development of DBHFC. Finding a new type of catalyst, which can not only reduce the amount of Pt but also maintain the high catalytic activity to H_2O_2 electro-reduction, is important for promoting the DBHFC technology and commercial process.

Catalyst Ag/C has higher catalytic activity to H_2O_2 electro-reduction [7]. In this paper, we prepare different ratio of Pt/Ag of Pt-Ag/C catalysts by impregnation-reduction method [8-11]. The Pt is 4% and Ag is x% (X=10, 15, 20, 25, 30, 36). In order to examined their electro-catalytic performance, we compared the reductive peak currents of catalysts at temperature25°C and30°C, respectively.

Preparation of electro-catalysts

10% Ag/C catalysts was prepared by impregnation-reduction method. In brief, 90mg XC-72Carbon and 100ml deionized water were ultrasound dispersed for 1h. 15.7 mg $AgNO_3$ and 80 mg sodium citrate, which are mixed in 20ml deionized water, was added to above suspension and ultrasound dispersed 1.5h, the PH was adjusted to alkali with ammonia solution. 10ml (0.1M) $NaBH_4$ was added to that mixture slowly and magnetic stir continually for 1h at room temperature. The mixture solution was separated by vacuum filtration, washed with distilled water, and dried at 80°C for 24h. The 15%, 20%, 25%, 30%, 36%Ag/C catalysts were got with the same procedure above.

There was a same procedure to prepare $Pt_{4\%}$-Ag $_{x\%}$/C(X=10, 15, 20, 25, 30, 36) . In brief, 96mg Ag $_{x\%}$/C(X=10, 15, 20, 25, 30, 36), 100ml deionized water and 0.4ml(0.01g/ml) H_2PtCl_6 were ultrasound dispersed for 1.5h, the PH was adjusted to alkali with ammonia solution, and excessive $NaBH_4$ solution was added in slowly. The sample was stirred continually for 3 h at80-90°C, filtered, washed, dried in vacuum for 24h at constant temperature 80°C. Finally, we got $Pt_{4\%}$-Ag $_{x\%}$/C(X=10, 15, 20, 25, 30, 36)catalysts.

Preparation of working electrode

Generally, our working electrode area is 0.5cm^2 with 2mg/cm^2 loading of catalysts. The method of preparing working electrode is as follows: firstly, a 5mg catalyst sample prepared above and a small amount of 0.5% nafion solution were ultrasonic dispersed a few minutes until a uniform ink-like formed. Secondly, the catalyst ink was coat on one side of the carbon paper, and then was put in a 40°C oven for 30 minutes.

Electrochemical test

The electrochemical performance tests of these six catalysts were examined by CV. The Pt gauze and saturated calomel electrode (SCE) were used as the counter electrode and reference electrode. The working electrode prepared above and the Pt gauze, SCE electrode worked together to complete the circuit in0.5mol/L H_2SO_4 and 0.05mol/L H_2O_2. Before testing, we need pour high purity nitrogen to the solution about 20 minutes to exclude oxygen.

Results and discussion

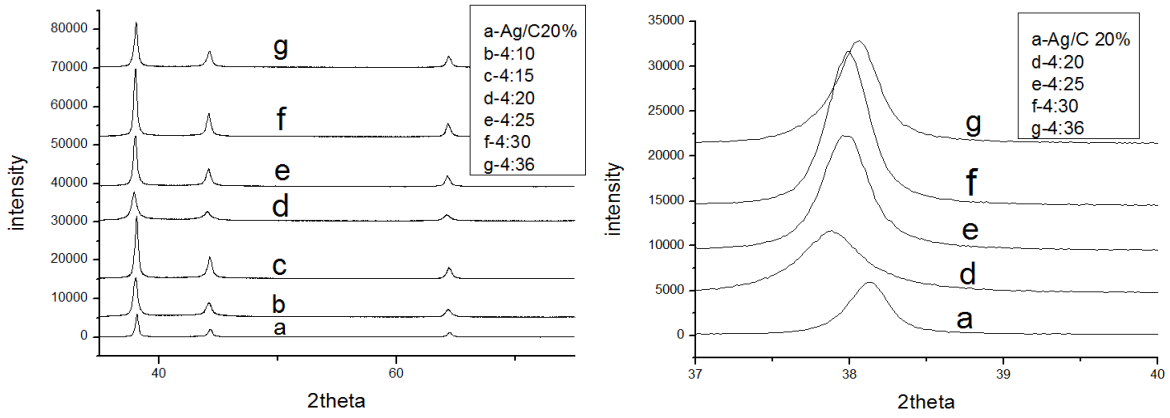

Fig.1. The XRD spectra of six catalysts

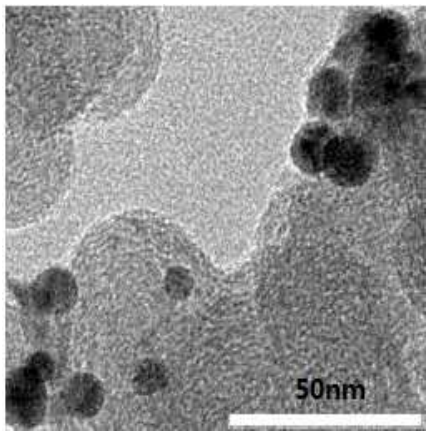

Fig.2.TEM of Pt-Ag/C catalyst

Fig.1 is the XRD spectra of six catalysts. We can know that there is a little change in peak position with the increasing content of Ag in Figure1. The angle of 2θ = 38.1°(111), 44.3°(200),

64.4°(220) are the characteristic peaks of purely metallic Ag particles. In contrast, $Pt_{4\%}$-$Ag_{20\%}$/C showed diffractions at 2θangles significantly lower than that of $Ag_{20\%}$/C, and with the increasing content of Ag, the 2θangles are more higher based on the same content of Pt4%. While the peaks at 2θ value of 38.6°, 44.9°, 65.5°are well matched for (111),(200),(220) planes of Pt, respectively. These observations may suggest that Ag and Pt are all in face-centered cubic structure but they are not fully alloyed [12]. Fig.2 shows us that Ag-Pt particles with diameters from 6 to 14 nm were uniformly dispersed on the support.

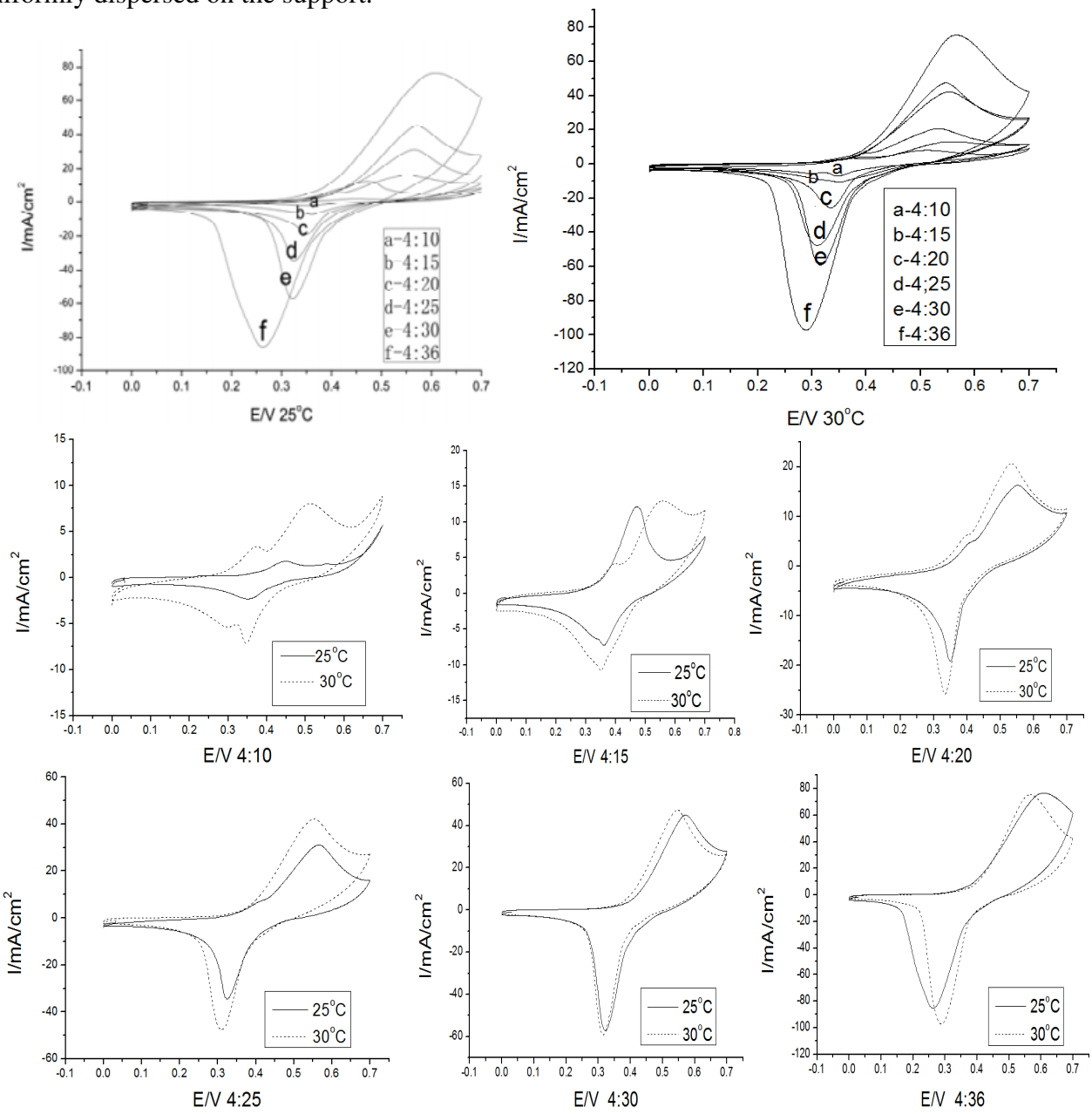

Fig.3. CV of Pt-Ag/C catalysts with different Pt/Ag ratio at 25°Cand30°C in 0.5 M H_2SO_4+0.05M H_2O_2 solution.

The electrochemical performance test results are shown in Fig.3. From Fig.3, we can know that, based on the same proportion of 4% Pt, the peak current densities increases with increasing Ag content both at 25°C and 30°C. At the same time, the six catalysts have the same change trend: the catalytic activities are higher at 30°C than that at 25°C. The data tell us that elevating temperature and increasing the proportion of Ag can contribute to improving the catalytic activity of Pt-Ag/C catalysts.

Conclusions

Six catalysts with different atomic Pt/Ag ratio were prepared by impregnation-reduction method. The XRD results indicate that six catalysts are all in face-centered cubic structure. The average particle size of the Pt-Ag nanoparticles was about 10nm. CV results indicate that elevating temperature and increasing the proportion of Ag are helpful for electrochemical reduction of H_2O_2.

Acknowledgement

We gratefully acknowledge the financial support of this research by National Natural Science Foundation of China (60936003).

Reference

[1] J. Ma, N.A. Choudhury, and Y. Sahai: Renew. Sust. Energ. Rev. 2010(14)183

[2] B.H. Liu and Z.P. Li: J Power Sources Vol. 2009 (187) 291

[3] Yang H, Vogel W, Lamy C. Structure and Electrocatalytic Activity of Carbon-Supported Pt–Ni Alloy Nanoparticles Toward the Oxygen Reduction Reaction. J Phys Chem B, 2004(108) 11024-11034

[4] Paulus U. A, Wokaun A, Scherer G. G. Oxygen reduction on high surface area Pt-based alloy catalysts in comparison to well defined smooth bulk alloy electrodes. Electrochimica Acta. 2002(47)3787-3798

[5] Wang X. H, Huang H, Holmb T. Thermal stabilities of nanoporous metallic electrodes at elevated temperatures. Journal Power Sources. 2008(175)75–81

[6] Choudhury N. A, Raman R. K An alkaline direct borohydride fuel cell with hydrogen peroxide as oxidant. Journal of Power Sources. 2005(143)1-8

[7] Dong Y L, Ling J Y. Progress in H_2O_2-based fuel cell cathode catalyst. Chemical Engineer [J] (in chinese).2011:189(6):1002-1124

[8] Masaharu Tsuji, Mika Hamasaki. Synthesis of Pt–Ag alloy triangular nanoframes by galvanic replacement reactions followed by saturated NaCl treatment in an aqueous solution .Materials Letters 2014 (121) 113–117

[9] Shuping Yu, Qun Lou, Kefei Han. Synthesis and electrocatalytic performance of MWCNT-supported Ag@Pt coreeshell nanoparticles for ORR. International journal of hydrogen energy 2012 (37) 13365-13370

[10] B. Molina Concha. Direct oxidation of sodium borohydride on Pt, Ag and alloyed Pt–Ag electrodes in basic media Part II. Carbon-supported nanoparticles. Electrochimica Acta 2009 (54) 6130–6139

[11] Zhenmeng Peng. Ag–Pt alloy nanoparticles with the compositions in the miscibility gap. Journal of Solid State Chemistry 2008 (181) 1546–1551

[12] Dan Zhao, Yuan-Hao Wang, Bing Yan.Manipulation of Pt - Ag Nanostructures for Advanced Electrocatalyst. J. Phys. Chem. C 2009(113)1242–1250

Advanced Materials Research Vols. 986-987 (2014) pp 63-66

doi:10.4028/www.scientific.net/AMR.986-987.63

Electrodeposition of ZnO thin films on a flexible conductive substrates

He Wang[1], Yong-Jian Chen[1], Feng Xu[1], Hai-Ning Cui[1,a,*], Bernabé Marí[2], Miguel Mollar[2], Rong Wang[1,b,*]

[1]Department of Optical Information Science and Technology, College of Physics and College of Zhaoqing (526061) , Jilin University, Changchun(130012), P. R. China

[2]Departament de Física Aplicada-IDF. Universitat Politècnica de València, Camí de Vera s/n, 46022 València, Spain

[a]cuihaining2009@126.com [b]Wangr@jlu.edu.cn

Keywords: electrodeposition; ZnO films; modified surface of the polymer-PEN; pentagonal flake structure; Energy Dispersive X-ray Spectroscopy (EDX); photoluminescences.

Abstract. Since transparent conducting oxides can be as a buttom layer of complex film electrodes, electrodeposition technique may produce ZnO films depending on variety conditions and modified surface layers of substrates in electrochemical procedures. Here we invested the structure and morphologies of ZnO films by using modified surface of the substrate-ZnO/ITO/polymer-PEN and ZnO doped Ga/ ITO/polymer-PEN.

Introduction

Zinc oxide (ZnO) is one of the most promising materials for the fabrication of optoelectronic devices operating in the blue and ultraviolet (UV) region, owing to a direct wide band gap and a large exciton binding energy. It has been shown that ZnO thin films can be deposited electrochemically and that the films produced are of high structural quality [1]. ZnO layer made by electrodeposition method is for potential application of grade material and semiconductor junction devices. As we know, control of morphology and structures of oxides are of great importance for above applications and their implementation on technological devices. Zinc oxides had be obtained in different structures such as Pentagonal ZnO nanorods, hexagonal ZnO collunms , sheet nano-zinc oxide crystals with a hexagonal, pentagonal, rectangular or an irregular form etc.[2]. Different temperatures, solute and post-annealing for fabrication and characterations of ZnO films were systematically investigated by authors. In this paper, We will focus the structure of ZnO films, especially pentagonal flake structure, relation of morphologies and the surface of substrates.

Experimental Details

In the electrodeposition procedure of ZnO films a three electrode electrochemical cell is needed. It contains a aqueous solution with 5 mM $ZnCl_2$ and 100 mM KCl as supporting electrolyte and dissolved oxygen at 90 ^{0}C [3]. The conducting substrate was set up as a working electrode and was located near the referential cathode at approximately 1cm. A potentio galvanostat was used to keep a constant potential (a variant potential from -0.50 to -0.80 V) during the deposition. During the electrodeposition process four main growth variables- molarity ratios of solution, concentration of the solution, potential and modified surface of substrates have been controlled at a fixed time and temperature. The modified surface layer of one substrate used is high density ZnO film made by reactive magnetron sputtering on ITO/polymer-PEN.

Scanning electron microscopy (SEM) images and quantitative elemental analysis were obtained by a JSM 6300. The content ratio of elements in the film was obtained by means of Energy Dispersive X-ray Spectroscopy (EDX). For structural characterization it has been measured by an high-resolution X-ray diffraction (XRD) in the Θ-2Θ configuration with a copper anticathode (CuKα, 1.54 Å). Optical properties were monitored by transmittance using a Xe lamp and in association with

a 500 mm Yvon–Jobin HR460 spectrophotometer using back-thinned CCD detector optimized for the UV–VIS range. Photoluminescences (PL) measurements were carried out at 6k-300k temperature using a He-Cd Laser as a light source at an excitation wavelength of 325 nm.

Discussion on morphology and structures of ZnO films

Generally electrochemical procedures permit the synthesis of ZnO films on different morphologies depending on the solute, concentrations of the solutions, temperature, PH value, and electrical potential ,etc. Until now， these have been systematically investigated. In order to know that the variant morphologies of synthesised ZnO films depending on the surface of substrate, here the different modified surfaces of substrates has been used in the electrochemical method. We found a regularity of the film growth about the effect of the substrate mainly.

Fig.1 and Fig.2 show some SEM images of these kinds of ZnO films on the substrate-ZnO/ITO/polymer-PEN and ZnO doped Ga/ITO/polymer-PEN respectively. SEM reveals an aggregation of flat pentagonal flake which looks like ZnO quasi-3D structures consisted of quasi-nanowalls. These pentagonal flakes that grew up on the surface of the first basic ZnO layer do not exhibit ordered pattern.All flat pentagonal flake were predominantly normal to the substrate. Up images of Fig 1 are zoom of bottom photos of Fig 1(a)-(d).The thickness of the flakes or walls is approximately 160 nm and one edge size of a pentagonal flake is about 3.16 μm in Fig 1. and Fig.2. In case of Fig.2 above similar micro structure,an aggregation of flat pentagonal flake was not found. This could be deduced that ZnO doped Ga on surface of polymer-PEN did not form good conductive layer and suitable structure of ZnO.

EDS analysis was selected in the photo of SEM and its spectrum is shown in Fig.3. In its spectrum atomic percentage of O and Zn is 59.77% and 23.32% respectively. It indicates that there is larger intrinsic – Zinc vacancy (Vzn, Acceptors). The reason is possibly the initial formation of an hydroxides in the solution, which would slowly dehydrates. In fact zinc hydroxide forms at room temperature by precipitation of Zn^{2+} by OH^- addition [4] , and it means and suggests that the film is $Zn(OH)_2$. This is why finally the zinc oxide film with Vzn forms and grows.

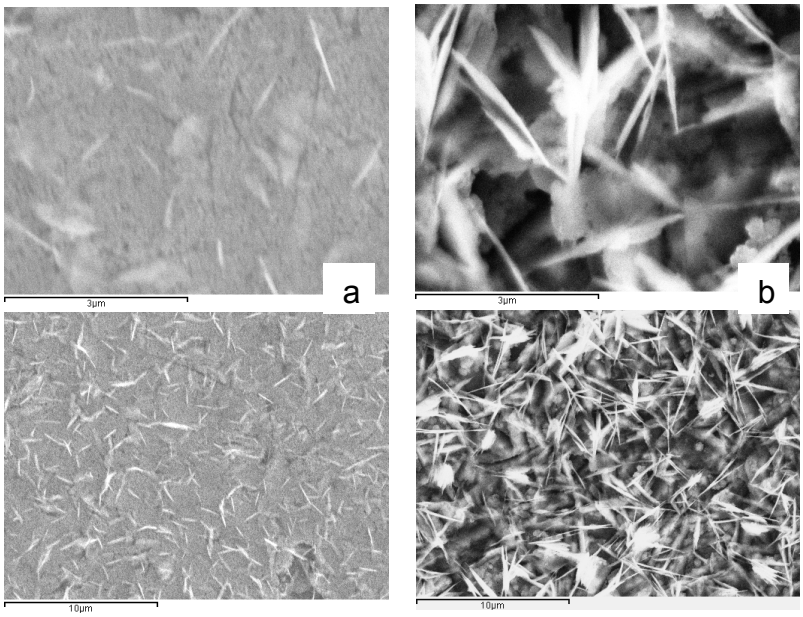

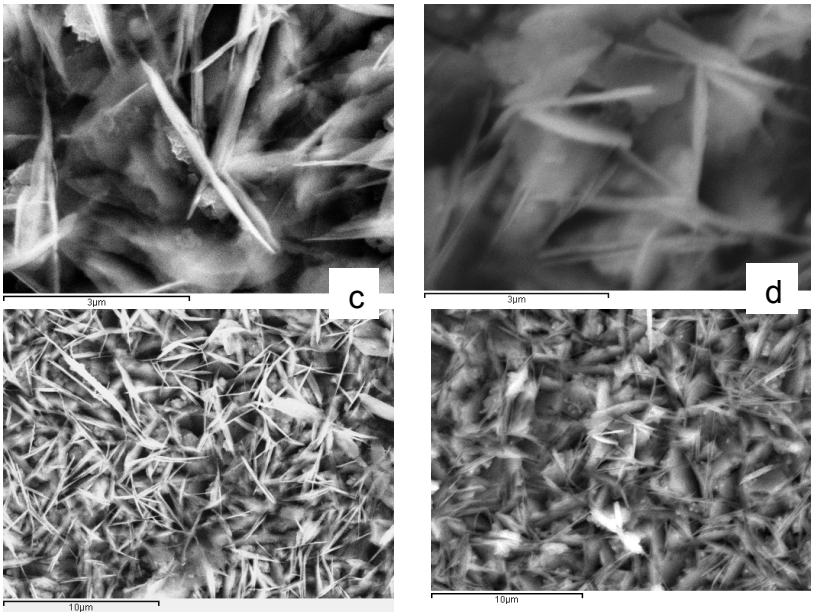

Fig.1 SEM images of ZnO film prepared in different deposition time on ZnO/ITO/polymer-PEN substrates. (a) 130s (Q= -0.1C); (b) 690s (Q=-0.4C); (c) 1500s; (d) 2800s. SEM: x20000 (up, scale : 3 micrometers), × 5000 (buttom, scale : 10 micrometers).

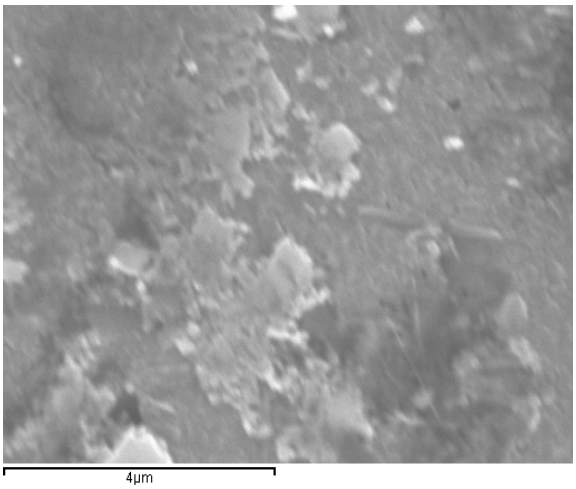

Fig.2 SEM images of ZnO film prepared in 690s (Q=-0.4C) deposition time on ZnO doped Ga/ITO/polymer-PENsubstrates. x15000, scale : 4 micrometers .

Generally it is realized that micro structure of ZnO film is of more functional and PL may gives much information about relation of the structure. There are various models being proposed to explain the complex PL band of ZnO materials. A strong PL emission peak at 370 nm is the intrinsic PL emission of ZnO crystallites due to the near band-edge emission (NBE) . It had mostly been attributed to the radiative transition between electron (in conduction band) and hole (in valence band) recombination process, of course it corresponds to the bound exciton (BE). PL spectra of the ZnO thin films from the temperature of 6 k to 300 k were measured. Two broadening PL emissions at 350-440 nm and 471-770 nm, which belong to broader NBE and deep level emission (DLE) respectively, are observed. Comparing previous results of PL band of ZnO, it is deduced that the broad NBE band shows two components—one band centred around 370 nm (3.351 eV) and another one centred around 420 nm in the range.

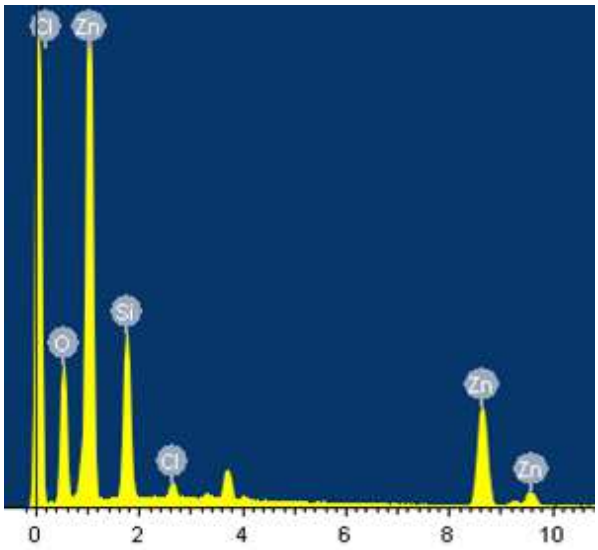

Fig.3 Discussion on morphology and structures of ZnO

Conclusion

The ZnO on modified surfaces of substrates such as ZnO/ITO/polymer-PEN and ZnO doped Ga/ITO/polymer-PEN were prepared by the electrochemical method. We carried out the experiments by adjusting concentration of the solution, potential, substrate and deposition time. The combination of the effect of solution and potential on the growth of the film, the controlled pentagonal flake structure of ZnO is obtained by us.

Acknowledgements

Authors would like to thank Prof. S. Q. Xi and Prof. W. Q. Chen (Changchun Institute of Applied Chemistry, China) for their help and support.We acknowledge partial financial supports from Jointly Funded Project (No. 61179055) of Chinese Civil Aviation Authority and National Natural Science Foundation of China, Talent Grant (2013-ZQXY-05) of Educational Commission of Guangdong Province, China and Jilin University Science and Technology Innovation Fund (No. 450060487476 and No.450060497067).

References

[1] T. Pauport´e, R. Cort`es, M. Froment, B. Beaumont, D. Lincot:Chem. Mater. 14 (2002) 4702.

[2] Z.F Liu, Z.G Jin, J.J Qiu, X.X Liu, W.B Wu and W Li : Semicond. Sci. Technol. 21 No 1 (January 2006) 60-66

[3] M. Tortosa, M. Mollar, B. Marí : Journal of Crystal Growth 304, 97 (2007) 97-102

[4] G.Deroubaix, P.Marcus : Surf.Interf.Anal.18(1992)39.

Advanced Materials Research Vols. 986-987 (2014) pp 67-71
© (2014) Trans Tech Publications, Switzerland
doi:10.4028/www.scientific.net/AMR.986-987.67

Equilibrium analysis on sulfur material in oxyfuel combustion

XIAO Haiping[a], Han Gaoyan[b], Dai Yukun[c], Dong Lin[d]

North China Electric Power University, Beijing 102206, China
[a]xiaohaiping@ncepu.edu.cn,[b]hangaoyan123@126.com,[c]changshoubuyu@163.com,
[d]945024915@qq.com

Keywords: oxyfuel combustion; sulfur; SO_2; SO_3; thermodynamic equilibrium

Abstract: To study migration and transformation of sulfur species in oxyfuel combustion, the study attempts to analyze distribution of sulfur compounds with thermodynamic equilibrium. Results show that sulfur-containing gases predominantly are SO_2 and SO_3, the maximum thermodynamic equilibrium concentration of those in oxyfuel combustion respectively increase by 3.4 and 4.5 times compared with the conventional combustion. Furthermore, SO_2 gas formation rate decreases while SO_3 increases under oxyfuel combustion. Sulfur-containing gases are generally more sensitive to temperature and excess air coefficient. The amount of sulfur compounds significantly increases in oxyfuel combustion.

Introduction

Oxyfuel combustion is one of the promising technologies for capturing CO_2 from power plant. Concentrations of SO_2 and H_2O increase rapidly. Sulfur species change and SO_3 concentration is improved significantly because of flue circulation[1]. Hao Liu et al [2] presents that SO_2 concentration is 6 times for oxyfuel combustion as large as that for traditional combustion and content of H_2O in flue gas varies from 10% to 40%. Daniel Fleig et al[3] indicates that SO_3 concentration in oxyfuel combustion is 4 times as large as that in traditional combustion. Existing forms of sulfur is not only related to the oxygen content in flue gas, but also to temperature and mineral composition of coals.

Measurement for sulfur existing forms is comparatively complicated because of the interference between SO_2 and SO_3[4], whereas thermodynamic equilibrium is proposed as a guidance for analysis. Through thermodynamic equilibrium calculation, the distribution of sulfur species for traditional combustion and oxyfuel combustion are predicted. Rules of sulfur's migration and transformation are revealed.

Computation method

Thermodynamic equilibrium calculation is based on the minimum free energy of Gibbs principle. Amount of sulfur element is set to 1mol in coal sample. Mole fractions of other components will be converted accordingly. The data for components of bituminous coal and the components of bituminous coal ash are shown in Table.1 and Table.2 respectively.

Table.1 Components of bituminous coal[%]

C_{ar}	H_{ar}	O_{ar}	N_{ar}	S_{ar}	M_{ar}	A_{ar}
48.51	2.57	3.78	0.77	0.64	6.78	36.95

Table.2 Components of bituminous coal ash[%]

SiO2	Al_2O_3	Fe_2O_3	CaO	MgO	K_2O	Na_2O	others
60.53	27.23	3.92	0.58	0.99	0.71	0.2	5.84

As for oxyfuel combustion, oxidizing agent consists of circulated flue gas and pure oxygen. In consideration of simplification, flue gas is regarded as theoretical flue gas. In terms of converted mole fractions of all components, the components of theoretical flue gas are deduced by iterative computation in oxyfuel combustion. O2 concentration in oxidizing agent required by the combustion of bituminous coal is set to 29%. Accordingly the compositions of oxidizing agent are presented. Converted mole fractions of all components for bituminous coal and the amount of oxidizing agent for different combustion methods were entered into the software for thermal equilibrium calculation. Components of theoretical flue with wet flue circulation under oxyfuel combustion are shown in Table.3.

Table.3 Components of circulated flue gas[vol%]

O_2	N_2	CO_2	H_2O	SO_2
4.55	3.02	65.27	26.83	0.323

Computational result analysis

Temperature. The objective of present work is to research the impact of temperature on existing forms of sulfur in power station boiler. All initial conditions are as follows: excess air coefficient is 1.2, air pressure is 0.999atm and the range of temperature is from 200˚C to 1800˚C. The results of calculation are presented in Figure.1 and Figure.2.

For oxyfuel combustion in pulverized coal fired boiler, the sulfur-containing gases are predominantly SO_2 and SO_3. The distribution of SO_2 is shown in Figure.1(a). From 487˚C, thermodynamic equilibrium concentration of SO_2 increases rapidly with the raise of temperature. For traditional combustion, the concentration of SO_2 is basically stable around 900˚C, while the concentration of SO_2 is not stable for oxyfuel combustion until the temperature is about 1103˚C and the highest concentration of SO_2 is 0.322%, which is 4.4 times compared with traditional combustion. SO_2 is the predominantly existing form of sulfur at high temperature.

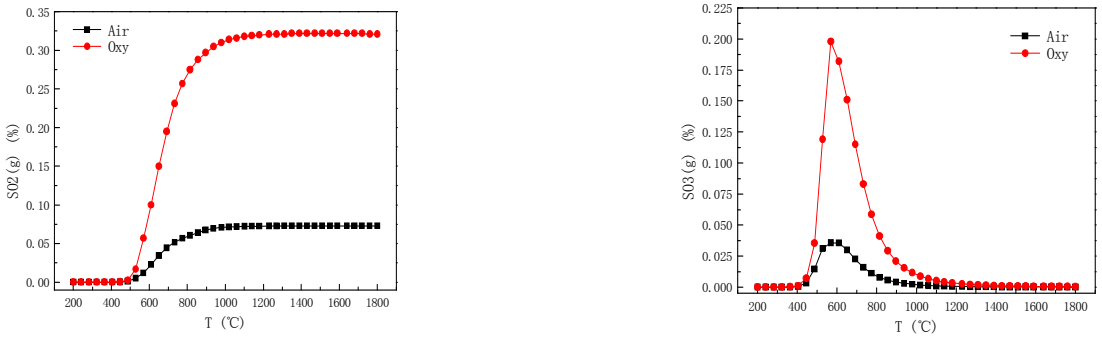

(a)Volume concentration of SO_2 (b)Volume concentration of SO_3

Figure.1 The distribution of sulfur-containing gases

Figure.1(b) indicates the distribution of SO_3 concentration. As the rise of temperature, thermodynamic equilibrium concentration of SO_3 first increases and then declines. SO_3 combines with steam to generate sulfuric acid steam at low temperature. However, SO_2 is more stable than SO_3 at high temperature. For traditional combustion, the concentration of SO_3 reaches a peak of 0.036% at 585˚C, while for oxyfuel combustion, the concentration of SO_3 peaks at 580˚C, which is 0.199% and it is 5.5 times than that of traditional combustion.

Actually, the resistance time of flue gas is pretty short in pulverized coal furnace. The formation rate of SO_3 is small at low temperature while it is big at high temperature. Therefore, the actual

concentration of SO_3 in pulverized coal furnace is near the thermodynamic equilibrium concentration of SO_3 at high temperature, but it is far below the thermodynamic equilibrium concentration of SO_3 at low temperature. D. Fleig [5] estimates the time required by SO_3 in the flue gas to reach 90% of thermodynamic equilibrium concentration of SO_3, when temperature is higher than 1400K, required time within 1 second, and it increases steeply with the fall of temperature, for instance, it requires 20 hours to reach 90% of thermodynamic equilibrium concentration of SO_3 when temperature drops to 800K.

The concentrations of sulfur-containing gases in oxyfuel combustion raise rapidly compared with traditional combustion, two main factors are as follows: one is that the concentration of oxidizing agent is higher than that of traditional combustion, and after air staging N_2 is not fed, which makes the decrease of flue gas. When oxygen concentration of oxidizing agent is 29%, the amount of flue gas decreases 27.3%, which leads to higher concentration of sulfur-containing gases; another reason is that approximately 70% flue gas recycling in oxyfuel combustion, leading to accumulation of moisture and sulfur-containing gases in flue gas, as a result, the concentrations of SO_2 and SO_3 are higher than that of traditional combustion.

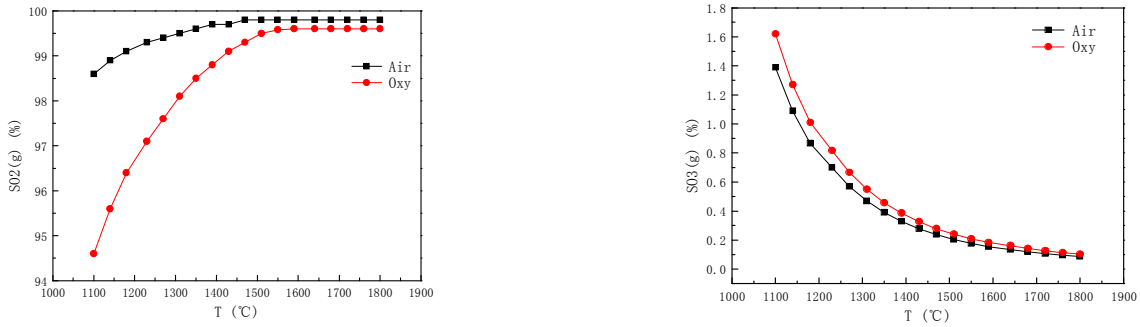

(a)Conversion for S to SO_2 in fuels (b)Conversion rate for SO_2 to SO_3

Figure.2 Conversion rate for existing forms of sulfur.

Figure.2 indicates the relation between temperature and conversion rate of sulfur-containing gases, as the raise of temperature, the formation rate of SO_2 increases with the decrease of conversion rate for SO_2 to SO_3. Compared with traditional combustion, the formation rate of SO_2 is lower and the formation rate of SO_3 is higher in oxyfuel combustion. At the temperature of 1100˚C, formation rate of SO_2 for oxyfuel combustion is only 94.59%, which is 3.9% lower than that of traditional combustion, while in 1550˚C the formation rate of SO_2 for oxyfuel combustion is merely 0.21% lower. At a temperature of 1100˚C conversion rate for SO_2 to SO_3 in oxyfuel combustion is merely 1.63%, 0.25% higher than that of traditional combustion, and at 1550˚C the conversion rate for oxyfuel combustion is only 0.02% higher than traditional combustion. With the same excess air coefficient in thermodynamic equilibrium, the content of O_2 for oxyfuel combustion is higher than that of traditional combustion, which leads to a considerable improvement of SO_3 formation rate. Hence, the ratio of sulfur in the form of sulfates increases, and it results in a decline for the formation rate of SO_2, since it is hard for sulfates existing in high temperature, the formation rate of SO_2 and SO_3 for two combustion methods are closer to each other as temperature rising.

Solid sulfur compounds. Figure.3 shows the solid sulfur compounds in thermodynamic equilibrium for different combustion methods. Sulfates commonly exist below 1000˚C and the amount of sulfates increase as the decline of temperature. As for discussed coal in this paper, aluminum sulfate takes the maximum amount in the oxyfuel combustion, whereas for traditional combustion,

magnesium sulfate has the largest amount. Furthermore, $CaSO_4$ would not form until temperature drops to 1000˚C or below and $MgSO_4$ generates only when temperature is 750˚C or below. Consequently, Ca performs best in sulfur immobilization, Mg comes next. Their ability of sulfur immobilization is better than most other alkali metals. Monckert P etc[7] presents that capture of sulfur happens in convection section of boiler over the range of temperature from 450˚C to 1100˚C, in an agreement with the range of sulfates formation temperature. Thus, during the cooling process of flue gas, gaseous sulfur first reacts with Ca to generate $CaSO_4$, when the content of gaseous sulfur is large enough and also Ca is depleted completely, gaseous sulfur starts to react with Mg to generate $CaSO_4$ when temperature is below 750˚C. Theoretically, as long as the coal contains enough alkali metals, all the sulfur can be immobilized. The concentration of gaseous sulfur increases by a large margin in the oxyfuel combustion, leading to much more powerful sulfation ability in boiler, and Al in the ash is taken and depleted to generate more $Al_2(SO_4)_3$[7].

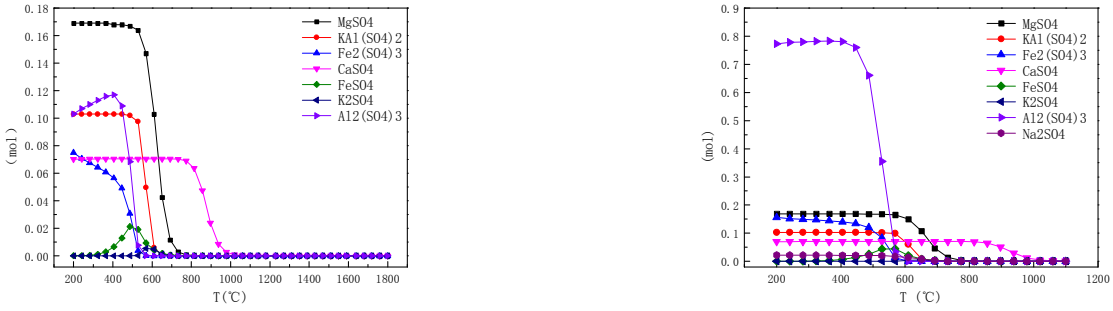

(a)Traditional combustion (b)Oxyfuel combustion

Figure.3 The distribution of solid sulfur compounds.

Excess air coefficient. In order to discuss the impact of excess air coefficient on sulfur existing forms, initial parameters are set as follows: temperature is 1200˚C, air pressure is 0.999atm and excess air coefficient varies from 1.1 to 1.5, and according to the 6% oxygen content, concentrations of sulfur-containing gases are converted.

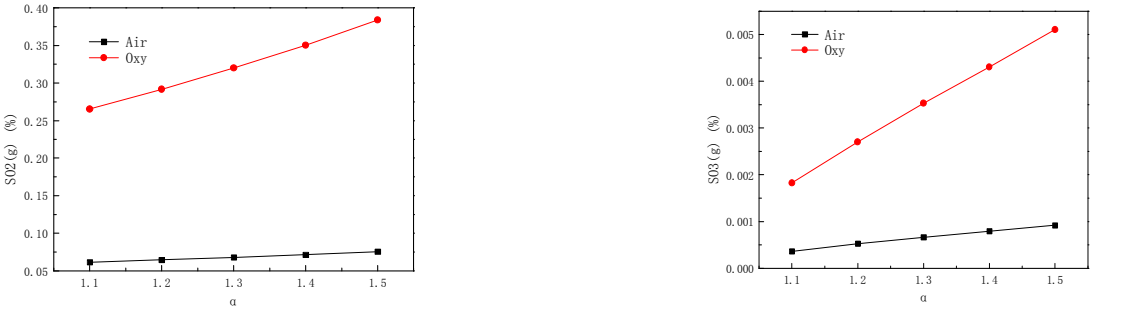

(a)Volume concentration of SO_2 (b)Volume concentration of SO_3

Figure.4 The distribution of SO_2 and SO_3 under different excess air coefficient.

Figure.4 indicates the distribution of SO_2 and SO_3 with different excess air coefficients. The concentrations of SO_2 and SO_3 increase correspondingly as the increase of excess air coefficient, The SO_2 and SO_3 concentrations are more sensitive to excess air coefficient in oxyfuel combustion. When the excessive air coefficient increases 0.1, SO_2 concentration increased by 0.0298%. SO_3 concentration increases by 0.00082% in oxyfuel combustion, while the SO_2 concentration changes only 0.0035%, the SO_3 concentration changes only 0.00014% in traditional combustion. The O_2 concentration increases with the increase of excess air coefficient in traditional combustion, which

promotes the generation of SO_2 and SO_3, however, the increase of excess air coefficient contributes to the increase of O_2 concentration as well as the amount of circulated flue gas in oxyfuel combustion. This leads to the increase of SO_2 brought by circulated flue gas in the boiler, since SO_3 formation is promoted, as the result, the concentration of SO_3 increases.

Conclusion

(1) The main sulfur-containing gases are SO_2 and SO_3. Compared with the traditional combustion, the maximum thermodynamic equilibrium concentration of SO_2 and SO_3 respectively increases by 3.4 and 4.5 times in oxyfuel combustion.

(2)The solid sulfur compounds are primarily alkali metal sulfates in oxidative atmosphere, which exist steadily at low temperature and decompose at high temperature. Ca performs best in sulfur immobilization, Mg comes next. The alkali metal sulfation is stronger in oxyfuel combustion.

(3) The formation rate of SO_2 is lower and SO_3 is higher in oxyfuel combustion than in traditional combustion. In addition, the sulfur-containing gases are generally more sensitive to temperature and excess air coefficient.

Acknowledgments

Project is supported by National Natural Science Foundation of China (51206047) and “the Fundamental Research Funds for the Central Universities”, Which is grateful acknowledged.

Reference

[1] E.Croiset, K.V. Thambimuthu. NO_x and SO_x emissions from O_2/CO_2 recycle coal combustion. fuel, 2001(8): 2117-2121.

[2] Hao Liu, Yingjuan Shao. Predictions of the impurities in the CO_2 stream of an oxy-coal combustion plant. Applied Energy . 2010(87): 3162–3170.

[3] Daniel Fleig, Fredrik Normann, Klas Andersson, etc. The fate of sulphur during oxy-fuel combustion of lignite. Energy Procedia, 2009,1: 383–390.

[4] D. Fleig, E.Vainio, K. Andersson, A. Brink, F. Johnsson, M. Hupa. Evaluation of SO_3 Measurement Techniques in Air and Oxy-Fuel. Energy Fuels, 2012, 26: 5537-5549.

[5] D. Fleig, Experimental and Modeling Studies of Sulfur-Based Reactions in Oxy-Fuel Combustion . Chalmers University of Technology, Göteborg, Sweden 2012.

[6] Monckert P, Dhungel B, Kull R, Maier J. Impact of combustion conditions on emission formation (SO_2, NO_x) and Fly Ash. In: 3rd MEETING of the OXY-FUEL COMBUSTION NETWORK 2008. Yokohama Symposia, Yokohama, Japan: IEA Greenhouse Gas R&D Programme.

[7] Rohan Stanger, Terry Wall. Sulphur impacts during pulverised coal combustion in oxy-fuel technology for carbon capture and storage. Progress in Progress in Energy and Combustion Science 37 (2011) 69-88.

Advanced Materials Research Vols. 986-987 (2014) pp 72-75

doi:10.4028/www.scientific.net/AMR.986-987.72

Experimental Investigation of Chemical Looping Combustion of CO with Fe-based Oxygen Carrier

Qu Li[1], Changfeng Lin[1], Junjiao Zhang[1], Weiliang Cheng[2], Wu Qin[1]

[1.] National Engineering Laboratory for Biomass Power Generation Equipment, North China Electric Power University, Beijing 102206, China
[2.] School of Energy, Power and Mechanical Engineering, North China Electric Power University, Beijing 102206, China

[1.] liqu11222020432@163.com

Keywords: Chemical-looping combustion; Fe-based oxygen carrier; CO; CO_2-enrichment.

Abstract. Reaction activities of Ni-doped and Cu-doped Fe_2O_3 oxygen carriers (OCs) with CO were investigated using thermo gravimetric (TG-DTG).The structures of the prepared OC were characterized by X-ray diffract meter (XRD).TG-DTG investigations indicated that rational Ni and Cu doping could efficiently enhance the reactivity of Fe-base oxygen carrier for oxidizing CO under different conditions. And Fe-based OC doped with 20 wt. % Ni can realize the highest reactivity.

Introduction

Climate system warming caused by the greenhouse gas, especially CO_2 emission is gaining increasing nowadays [1].Chemical-looping combustion (CLC) has been revealed as an efficient and low costly process to achieve easier CO_2 capture [2].Compared with the traditional combustion, the dominating advantage of CLC is that it can achieve high concentration CO_2 only by condensing the exhaust gas without any extra energy penalty. In addition, CLC can minimize formation of NOx [3].

Development of efficient OCs is essential to improve the efficiency of CLC. Generally oxides of iron, nickel, and copper have been selected as the most promising candidates for CLC process [4]. Among them, because of the low cost and environmental compatibility, Fe based OC is considered an attractive option for CLC applications [5].NiO has shown very high reactivity and good performance working at the high temperatures(900-1100℃), except its toxicity [6]. CuO has not received significant attention due to the low melting point of Cu and high cost ,despite its highly reactivity in manifold cycle [7]. Based on the above, Fe-based OCs which introduced inert support Al_2O_3 doped Ni and Cu were studied. This paper focuses mainly on the reaction of Fe_2O_3 OCs with CO by TG-DTG, the structure of the prepared oxygen carriers were characterized by X-ray diffraction (XRD). The study tried to reveal the reaction mechanism of Cu-Fe_2O_3/Al_2O_3 and Ni-Fe_2O_3/Al_2O_3 with CO, and make a preparation for large-scale industrial applications in the future.

Experimental

Preparation of Oxygen Carrier. Fe-based OCs were prepared by the co-precipitation method. A certain amount of the compounds（$FeCl_3$・$6H_2O$, $CuCl_2$・$6H_2O$ or $NiCl_2$・$6H_2O$,NaCl） were dissolved in deionized water, polyethylene glycol (PEG) as dispersant. Then the solution was gradually heated to 120℃. Na_2CO_3 (0.2mol/L) was added to the solution at 120℃.The precipitate was filtered, dried in a vacuum at 50℃ for 6h. To increase the mechanical strength and eliminate the microstructure interference when heating at the TGA, oxygen carrier precursors were at calcined at 800℃ for 2h. Finally five Fe-based OCs were prepared (shown in Table 1).

Characterization of Oxygen Carrier. The solid product components were measured by XRD using Rigaku X-ray diffractometer Company (TTR Ⅲ). From the Fig.1, Fe_2O_3 patterns were very stable and had good crystallization. With the increase of Ni and Cu doped amount, the grain became larger and had higher crystallinity degree.

Table 1 The Fe-based doped Cu and Ni oxygen carrier on different proportions

Sample	Mass rate	Component
FeAl	50%:50%	Fe_2O_3,Al_2O_3
Ni5FeAl	5%:50%:50%	NiO,Fe_2O_3,Al_2O_3
Ni20FeAl	20%:50%:50%	NiO,Fe_2O_3,Al_2O_3
Cu5FeAl	5%:50%:50%	CuO,Fe_2O_3,Al_2O_3
Cu20FeAl	20%:50%:50%	CuO,Fe_2O_3,Al_2O_3

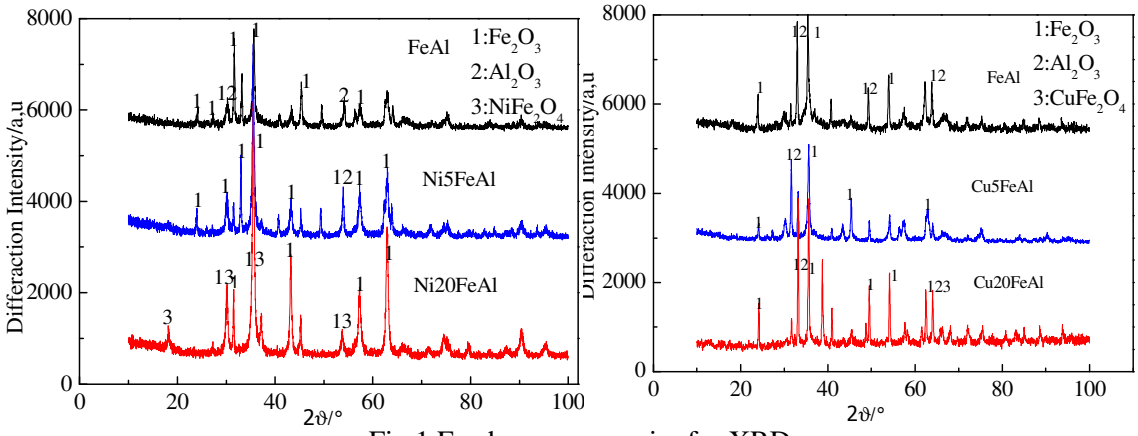

Fig.1 Fresh oxygen carrier for XRD

Experiment method. The reaction of OCs with CO were performed in TGA (STA6000, PerkinElmer Instruments, US). The experiment processes can be described as flows: firstly, N_2 was passed through for 5 min before the experiment to purge air and gas impurities. And approximately 10mg sample were heated from 30℃ to 850℃ in N_2 at 40℃/min at TGA, then CO was introduced and kept 50min at 850℃. After the reduction, oxidizing gas, air was fed for 20 min. The total gas flow rate was fixed at 40ml/min.

The general reactions for the Fe-based oxygen carrier reduction in the fuel-reactor were as following:

$$CO+3Fe_2O_3 \rightarrow 2Fe_3O_4+CO_2,\quad CO+Fe_3O_4 \rightarrow 3FeO+CO_2, CO+FeO \rightarrow Fe+CO_2,$$
$$CO+NiO \rightarrow Ni+CO_2, CO+CuO \rightarrow Cu+CO_2.$$

The conversion x of the oxygen carrier is defined as Eq.1, $$x=\frac{m_{ox}-m(t)}{m_{ox}-m_{re}} \quad (1)$$

where m(t) is the instantaneous mass and the denominator is the maximum oxygen transport between the fully oxidized, m_{ox}, and reduced, m_{re}, oxygen carrier .

Results and Discussion

The conversion rate analysis. In this part, the Fe-based OCs' reaction with CO were carried out in the TGA. The results of weight loss (TG) and the corresponding weight loss rate (DTG) were shown in Fig.2.

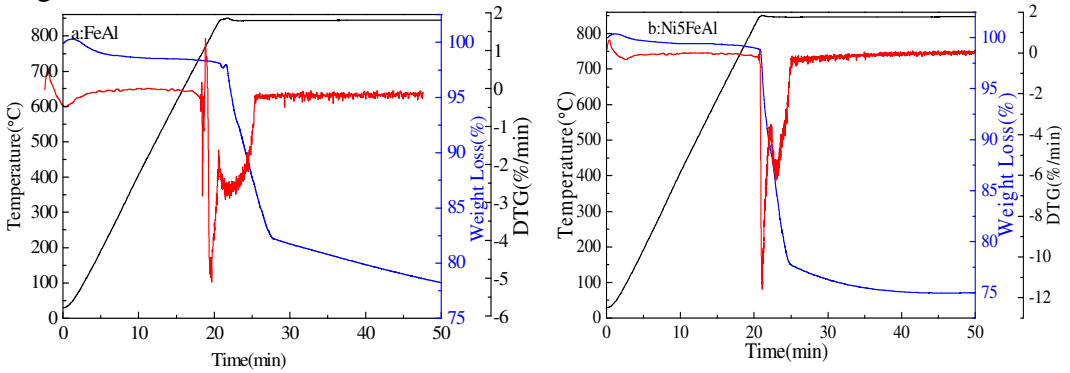

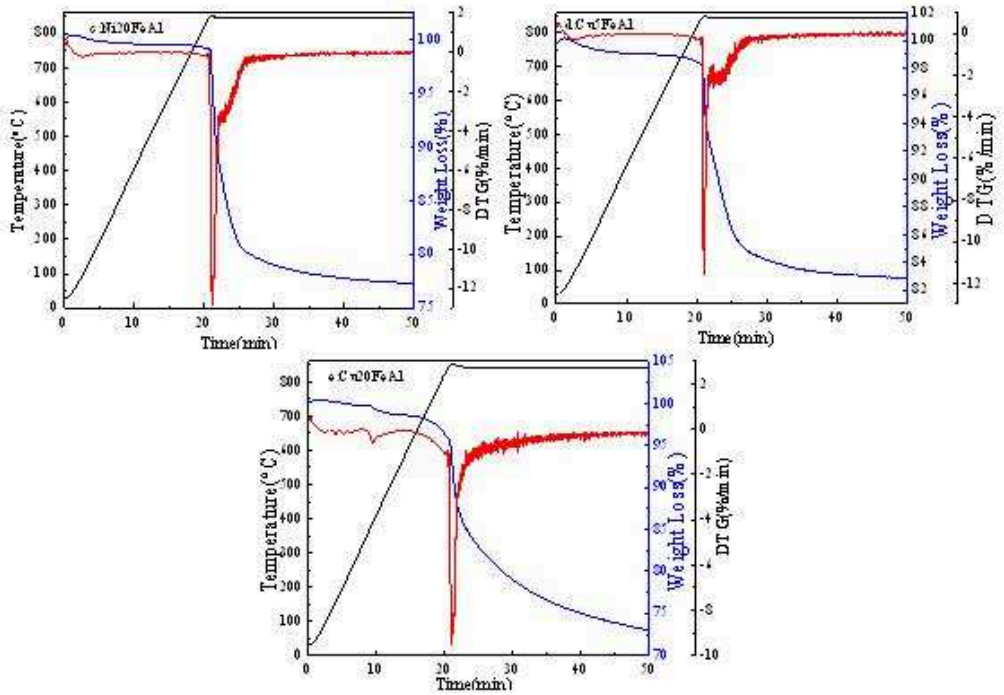

Fig.2 The TG/DTG curves for different oxygen carrier at 850℃ (a) FeAl (b) Ni5FeAl (c)Ni20FeAl (d) Cu5FeAl and (e) Cu20FeAl

From the Fig.2, the total reaction time was held for 50min. The five DTG curves all had sharp weight loss peak at 21min, and weight loss rate were 4.64, 10.2, 11.9, 11.4 and 8.7%/min. It can be concluded that the reaction rate of Ni20FeAl was faster than others, and the second was Cu5FeAl at the beginning reaction. The activity of OCs doped Ni and Cu were higher than Fe_2O_3/Al_2O_3.and the doped amount order was Ni (20 wt. %)> Cu (5 wt. %)> Ni (5 wt. %)> Cu (20 wt. %)> Fe_2O_3. From the TG curve, it can be seen that the reaction rapidly completed in 10min at 850℃. The weight losses were 78.2%, 74.9%, 77.3%, 82.9% and 74.6% corresponding to Fig.2 (a) (b) (c) (d) and (e) at 50min.The curve declined gentle without carbon deposition phenomenon.

The conversion of three oxygen carrier was calculated using Eq.1, shown in Fig.3.The finial conversion was 97.5%, 76.8%, 52.1% in 3min corresponding to 20 wt. % Ni, 20 wt. % Cu and FeAl. It was further confirmed that the Fe-based OC doped 20 wt. % Ni was the best. The images (a) and (b) were at high magnification (5000×). The particles of residues after reaction were much larger than the fresh OC, and the latter was uniformity. It was distinct from the images that there were little agglomeration.

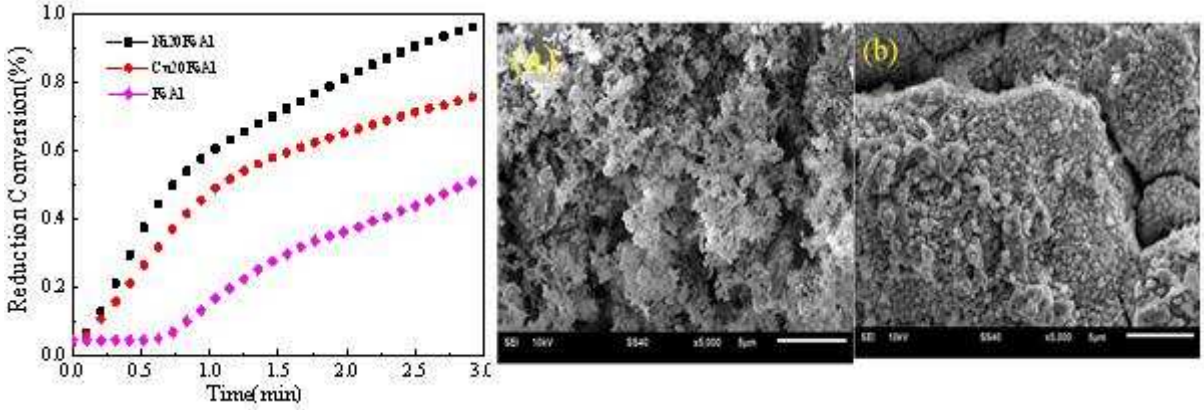

Fig.3 The conversion curves for different oxygen carrier at 850℃ and the SEM images of (a) fresh Ni20FeAl and (b) the mixture after reaction

Conclusion

Reactions between Fe-based OCs with CO were performed in a TGA, and then further investigated by XRD, SEM. It was found that the activity of oxygen carrier doped Ni and Cu were higher than Fe_2O_3/Al_2O_3, and the reactivity order corresponding to doped amount was Ni (20 wt. %) > Cu (5 wt. %)> Ni (5 wt. %)> Cu (20 wt. %)> Fe_2O_3. The final conversion of Ni20FeAl for CLC reached 97.5% and had little agglomeration occurred during CLC of CO.

Acknowledgment

The authors thank the financial support for this work provided by National Natural Science Foundation of China (51206044) and Beijing Municipal Natural Science Foundation (3132017).

References

[1] IPCC. Fourth Assessment Report 2007: synthesis report, IPCC (2007).

[2] H. G. Jin and B. Q. Wang. Principle of cascading utilization of chemical energy: Journal of Engineering Thermo physics, Vol. 25, (2004), p.181.

[3] M. Ishida and H. G, Jin. Industrial and Engineering Chemistry Research, Vol. 35 (1996), p. 2469.

[4] Adánez, J., de Diego, L.F., et al, 2004. Selection of oxygen carriers for chemical-looping combustion. Energy Fuels, Vol.18, (2004), p.371.

[5] Abad A, Adánez J, García-Labiano F, et al. Mapping of the range of operational conditions for Cu-, Fe- and Ni-based oxygen carriers in chemical-looping combustion. Chemical Engineering Science, Vol. 62, (2007), p.533.

[6] Juan Adanez, Alberto Abad and Francisco Garcia-Labiano et al. Progress in Chemical-Looping Combustion and Reforming technologies. Progress in Energy and Combustion Science Vol.38, (2012), p. 215.

[7] E. Jerndal, T. Mattisson, A. Lyngfelt: Chemical Engineering Research and Design. Vol. 84(2006), p. 795.

Advanced Materials Research Vols. 986-987 (2014) pp 76-79

doi:10.4028/www.scientific.net/AMR.986-987.76

Experimental Study on Factors Affecting the Generation of Ferrous Sulfide

Liqun Xiu[1, a], Shuai Liu[2,b], Weidong Yuan[3,c], Chao Mu[4,d] and Di Xu[5,e]

[1] Northeast Petroleum University, China
[2]Daqing Oilfield Limited Company, China
[3]Daqing Oilfield Limited Company, China
[4]Daqing Oilfield Limited Company, China
[5] Northeast Petroleum University, China

[a]996577741@qq.com, [b]772149128@163.com, [c]84523798@qq.com,
[d]muchao120@163.com,[e]987672378@qq.com

Keywords: Ferrous sulfide; corrosion; trial; influencing factors

Abstract. Now steam stimulation gradually become one of the major thermal recovery methods, and hydrogen sulfide appears in the well casing. With the increase of the thermal recovery time and the application of SAGD technology, the number of wells containing hydrogen sulfide increased, and concentration of hydrogen sulfide are also rising,Producing corrosion products - ferrous sulfide. Ferrous sulfide has pyrophoric. When ferrous sulfide in contact with oxygen in the air can cause spontaneous combustion at room temperature. In order to avoid the occurrence of spontaneous combustion of ferrous sulfide we had an in-depth study of the spontaneous combustion of ferrous sulfide. Through laboratory tests we found the following points. At room temperature,sulfurization reaction of H_2S gas and iron oxides occurs more easily in a dry environment. Temperature, H_2S humidity, various iron oxides,have important effects on the generation of iron sulfide.

Introduction

According to statistics, China's annual growth rate of total oil consumption is 4%. Annual growth rate of domestic crude oil was less than 1%. Shortage of crude oil is imported to supplement. However, the sulfur content of imported crude oil is relatively high, especially in the Middle East ,are greater than 1%, up to 3.09%. When processing high sulfur crude oil is not only a threat to the environment making it very difficult to guarantee the quality of products, but also the sulfur can cause spontaneous combustion. So how to prevent and avoid the generation of sulfide become a top priority for crude oil processing, and it is important for the development of oil field.

Experimental Purpose

With the application of a series of mining technology,in the case of the control measures are not taken, the content of hydrogen sulfide in the tank will increase,and the interaction between hydrogen sulfide and tank will also increase. In order to prevent spontaneous combustion of ferrous sulfide in tank, it is necessary to analyze the factors affecting ferrous sulfide.

Several aspects were identified through the experiment. Different H_2S humidity and temperature, different iron oxides and different water content of iron oxides have different effects on iron sulfide formation

Experimental Equipment

（1）H_2S gas bag.（2）Film pump.（3）Cushion airbags.（4）Drying tower.（5）Capillary flow meter.（6）Quartz sample tube.

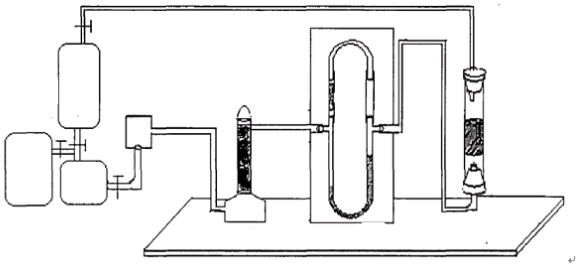

Fig .1 Set-up diagram

Experimental Process

Before the experiment weighed 4g dry iron oxide：Fe_2O_3 and Fe_3O_4. Then weigh 10g of dried iron oxide and add some deionized water making the water content of the iron oxide be 0.5%, 10%, 15%, 20% and 30%. Put them into the quartz sample tube, cover the rubber plug and connect the experimental device.

When the experiment starts, extracting some of the thin film of high-purity nitrogen gas to pump the air out of the system, and then extracting hydrogen sulfide gas. To remove water vapor, hydrogen sulfide gas flows through the airbag cushion into drying tower, Then flows through a capillary flowmeter into the quartz sample tube. The unreacted hydrogen sulfide gas may return to the gas bag.

We set the flow rate of hydrogen sulfide gas to 220mL/min.After completion of the sulfurization reaction when cooled to room temperature for the oxidation reaction experiments, when the air flow is controlled to 220mL/min, the temperature is recorded every minute.

Analysis of experimental results

（1）The temperature change of the product that produced by dried H_2S and Fe_3O_4

When the temperature is 25 ℃, dry hydrogen sulfide gas and dry Fe_3O_4 had vulcanization reaction , the temperature curve of their product was shown in Figure 2.

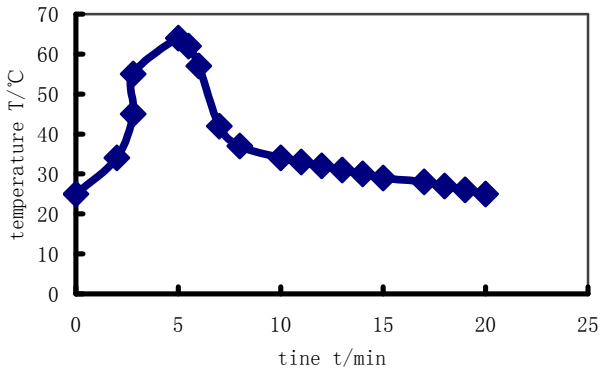

Fig .2 The temperature change of the product produced by dry H_2S and Fe_3O_4

As can be seen from the chart, the reaction temperature rises faster at the beginning stage of the reaction,and the temperature has reached the highest 64℃ in 5 minutes. However, the temperature quickly dropped 5 minutes later. This shows that at room temperature, dry hydrogen sulfide gas and the dry Fe_3O_4 can have sulfurization reaction, and their curing products have high self-ignitability. This also shows that their relatively slow curing reaction rate.

（2）The temperature change of the product produced by dry H_2S and Fe_2O_3 under two temperatures

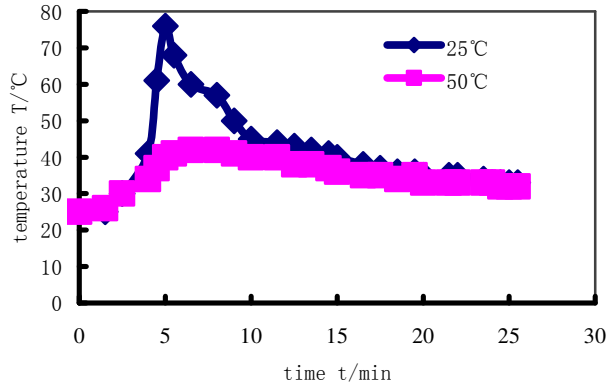

Fig .3 The temperature change of the product produced by dry H_2S and Fe_2O_3

At a temperature of 25 ℃ and 50 ℃ dry hydrogen sulfide gas and dry Fe_2O_3 had vulcanization reaction , the temperature curve of their product was shown in Figure 3. Their oxidation temperature curve is not the same. In the initial oxidation reaction,the temperature of hydrogen sulfide and Fe_2O_3 increased in varying degrees, indicating that it has a high spontaneous combustion. When the curing temperature is 50 ℃, the oxidation temperature is significantly higher than that of the curing temperature of 25 ℃, indicating that it is easier to spontaneous combustion.

At low temperature, dry hydrogen sulfide gas can react with dry Fe_2O_3, and the temperature is rising, which indicates that vulcanized product is high pyrophoric and more dangerous.

（3）The temperature change of the product produced by Fe_2O_3 that has different moisture content

Under anaerobic conditions,make Fe_2O_3 and H_2S have curing reaction.Make sure that Fe_2O_3 has different water content ,and H_2S is saturated humidity. After the end of the curing reaction cool it to room temperature, then some of the humidified air was put in so that oxidation reaction was conducted.

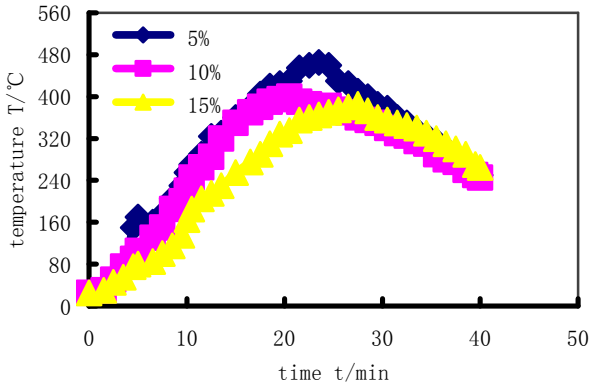

Fig .4 The temperature change of the product produced by Fe_2O_3

From the above chart we can see that the more it has water the more slowly it reaches the maximum temperature,and that the maximum temperature is more and more low.

（4）The temperature change of the product produced by Fe_3O_4 that has different moisture content

When the temperature is 25℃, make sure that the environment is anaerobic. Make Fe_3O_4 and H_2S have curing reaction.Make sure that Fe_3O_4 has different water content ,and H_2S is saturated humidity. After the end of the curing reaction cool it to room temperature, then some of the humidified air was put in so that oxidation reaction was conducted.

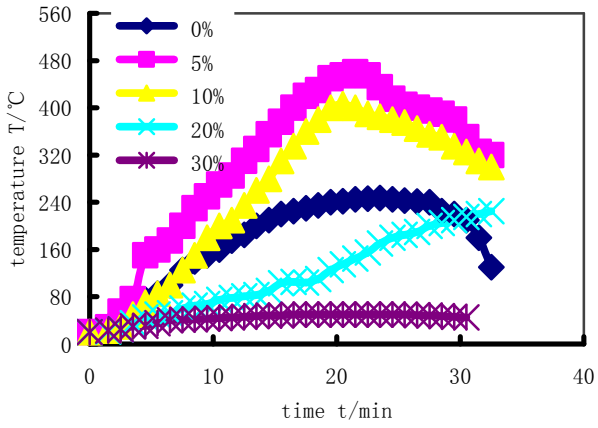

Fig .5 The temperature change of the product produced by Fe_3O_4

The figure shows that the temperature within ten minutes is more than 250℃. When the water content is between 5% and 10%,vulcanized product has a high self-ignitability. When the moisture content of the sample continued to increase, pyrophoric sulfide product decreases. When the moisture content of the sample is 30%, the curing reaction of the product of the oxidation hardly occurs at room temperature.

Summary

（1）At room temperature, sulfurization reaction of dry H_2S gas and iron oxide is more likely to occur. Product of their effects has a high spontaneous combustion.

（2）When the curing temperature increases, spontaneous combustion of vulcanized products are also increasing. Due to the presence of water vapor, H_2S gas increases the spontaneous combustion of products.

（3）Within a certain range ,water can promote the generation of ferrous sulfide However, beyond this range, the curing reaction rate is reduced.

References

[1] Yee H C.Construction of explicit and implicit symmetric TVD scheme and their applications[J]. JcompPhys, 1987, (68): 151-179.

[2] M.Hurchings.A model for the erosion of metals by spherical particles at normal incidence[J].Wear,1981(70):269-281.

[3] Tilly G P.A two stage mechanism of ductile erosion[J].Wear,1973(23):87-96.

[4] Bitter J G.A study of erosion phenomena[J].Wear,1983(6):5-21.

[5] Finnie I .Stevick G R,Ridgely J R.The influence of impingement angle on the erosion of ductile metals by angular abrasive particles[J].Wear,1992(152):91-98.

Advanced Materials Research Vols. 986-987 (2014) pp 80-83

doi:10.4028/www.scientific.net/AMR.986-987.80

FEC-LiTFSI-Pyr_{1A}TFSI ionic liquid electrolyte to improve low temperature performance of lithium-ion batteries

Xiaoxue Zhang[1,a], Zhenfeng Wang, Cuihua Li, Jianhong Liu, Qianling Zhang

[1]School of Chemistry and Chemical Engineering, Shenzhen University, No.3688, Nanhai District, Shenzhen 518052, China

[a]719109703@qq.com

Keywords: electrolyte; Fluoroethylene carbonate; low temperature

Abstract. N-methyl-N-allylpyrrolidinium bis(trifluoromethanesulfonyl)imide ($PYR_{1A}TFSI$) with substantial supercooling behavior is synthesized to develop low temperature electrolyte for lithium-ion batteries. Additive fluoroethylene carbonate (FEC) in LiTFSI/$PYR_{1A}TFSI$/EC/PC/EMC is found that it can reduce the freezing point. $LiFePO_4$/Li coin cells with the FEC-$PYR_{1A}TFSI$ electrolyte exhibit good capacity retention, reversible cycling behavior at low temperatures. The good performance can be attributed to the decrease in the freezing point and the polarization of the composite electrolyte.

1. Introduction

Current Li-ion technology typically employs carbonate-based electrolytes that have a temperature range of approximately -20 to 40 ℃[1]. Energy and capacity of lithium-ion batteries (LIBs) are sharply reduced at -20℃. But at present a usable temperature range of -60 to 60℃ is desirable for the electrolytes on military and space applications[2]. So it's significant for ionic liquids to apply in the research of low temperature performance of lithium-ion batteries in view of its excellent properties. Also it was found that the $LiFePO_4$ electrode, which was cycled in electrolyte containing 2 v% FEC, exhibited higher discharge capacity and better rate performance at low temperature than that without FEC [3]. So in this work, our main target was to synthesize a new ionic liquid and prepare composite electrolytes for lithium-ion batteries at lower temperature, and to characterize the effect of FEC on the capacity of $LiFePO_4$/Li at lower temperatures.

2. Experimental

Ionic liquid $Pyr_{1A}TFSI$ was synthesized according to scheme 1. The freezing point was tested by the DSC (differential scanning calorimeter), scanning from 60℃ to -60℃ at 5℃/min^{-1} [4]. In an argon-filled glove box (water content: <0.1ppm, oxygen content: <0.1ppm), the blank electrolyte with a composition of 0.5mol/L LiTFSI 1:3:7(v%) EC/PC/EMC solution (composite electrolyte I), and the electrolyte with content FEC (2v%) (composite electrolyte II) in above blank solution were prepared[5]. Then the freezing point and viscosity were tested by DSC and rheometer.

$LiFePO_4$/Li coin half-cells were assembled using lithium as the anode, $LiFePO_4$ as the cathode, Celgard polypropylene as the separator and filling with different composite electrolyte I and II [3] . The charge/discharge performance of $LiFePO_4$/Li half cells was evaluated at a constant current density of C/10 rate on a land charge/discharge instrument, China, at -30℃. A high-low temperature test-chamber (TEMI880,China) was used to provide a constant temperature environment for test. And then the $LiFePO_4$/Li half-cells were cycled at room temperatures to check whether they can reach the original and theory capacity. After the low temperature charge/discharge test, the SEM

(scanning electron microscope) test was used to observe the surface morphology of the $LiFePO_4$ electrode. CV(cyclic voltammetry) was carried out on the electrochemical workstation(1470E Cell Test System, Britain) at a scan rate of 0.1 mV/s in range of 2.6-4.2 V. The $LiFePO_4$ electrode was used as working electrode, and lithium foil as both counter and reference electrode.

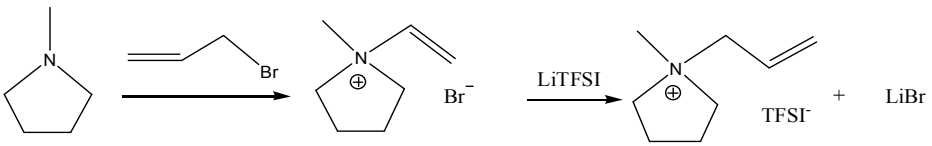

Scheme 1. Scheme of synthesis procedure followed in this work for the preparation of the $ILPyr_{1A}TFSI$.

3. Results and discussion

3.1 The physical properties of the pure $Pyr_{1A}TFSI$ and composite electrolytes

From table.1, the viscosity of the pure $Pyr_{1A}TFSI$ was 0.01898Pa.s which is much higher than the composite electrolytes. It can demonstrate that the addition of the organic and FEC can significant reduced the viscosity and enhance the low temperature performance. According to the DSC, the exothermic peak moves from -8℃ to -13 ℃ when instead free-FEC electrolyte of the FEC one. It proves that FEC can reduce the freezing point and increase the ionic mobility.

Table.1. The consequences of viscosity and DSC in different electrolytes

electrolyte	$Pyr_{1A}TFSI$	Ⅰ	Ⅱ
Viscosity	0.01898Pa.s	5.59E-03Pa.s	6.14E-03Pa.s
Exothermic peak	4.1℃	-8℃	-15℃

3.2 Discharge capacity of $LiFePO_4$/Li half cells at -30℃

The discharge curves of $LiFePO_4$ electrode in the composite electrolyte with and without FEC were shown in Fig.1 at -30℃ in the rate of 0.1C. The capacity of the half cell without FEC was 63.5mAh/g, and the one with FEC was 73.5mAh/g. The capacity retention at -30℃ (155mAh/g related to the capacity at 25℃) are 41% and 47.5%. Compared with the capacity 63.5mAh/g of the free-FEC cell, the FEC-containing cell exhibits higher reversible capacity. So by adding the FEC addition, the low temperature properties can be significant improved. According to the Fig.2, the capacity of each electrolyte half cells can finally return back to about 155mAh/g(the capacity at 25℃) after cycled at -30℃. It certified that the cycles of the half cells at low temperature don't destroy the structure of the whole cells including the electrode, electrolytes and separator.

3.3 The effect of FEC on surface morphology at -30℃

SEM images for $LiFePO_4$ electrode in the composite electrolyte without and with FEC after having cycled at -30℃ was shown on Fig.3.The particles of the $LiFePO_4$ of the FEC-free cells are larger and more inhomogenous, and also the cracks between the particles are broader than FEC-containing cells. The $LiFePO_4$ electrode with FEC show smooth and uniform morphology, which is attributed to the weaker polarization of the electrode due to the formation of the SEI film. These can explain why the FEC can improve the capacity of the half cells at low temperatures.

3.4 The cyclic voltammograms of the half cells

The CV for $LiFePO_4$ electrodes in the 0.5mol/L LiTFSI composite electrolyte with and without FEC at 25℃ were shown on Fig.4. Compared with the electrolyte with FEC (b) which show a sym-

metric peak, similar area and relatively low peak potential differences 0.625V, the electrolyte without FEC(a) display more asymmetric peak and wider peak potential differences. Also the peak intensity of the $LiFePO_4$ electrode in FEC-electrolyte is dramatically higher than the FEC- free one. In conclusion, again it can prove that the addition of the FEC can weak the polarization of the $LiFePO_4$ electrode no matter at room or low temperatures.

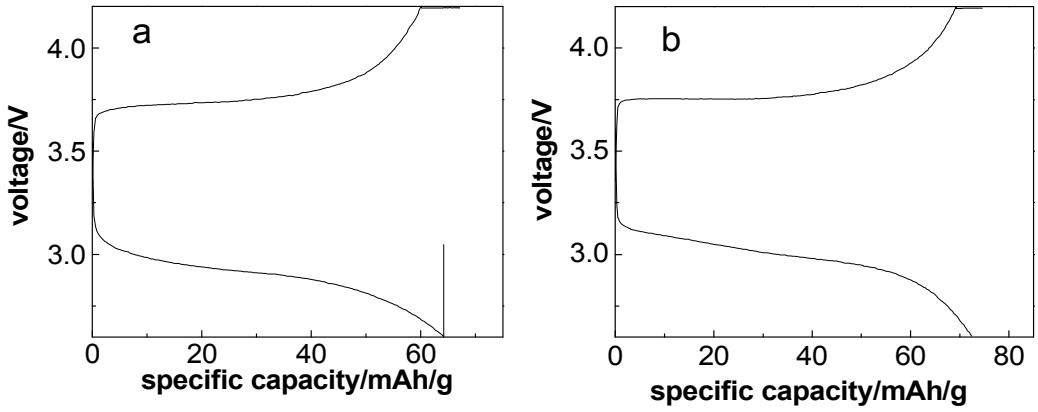

Fig.1. Charge and discharge curve of $LiFePO_4$ electrode in the composite electrolyte without FEC (a) and with FEC (b) at -30

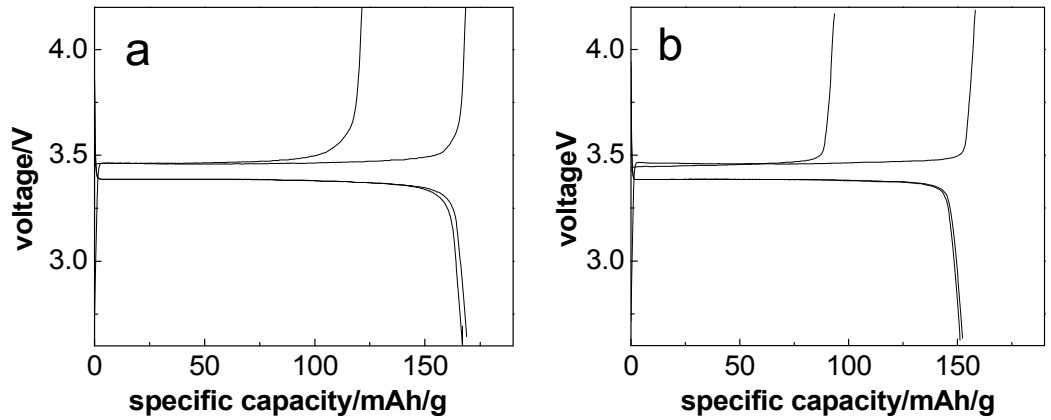

Fig.2. Charge and discharge curve of $LiFePO_4$ electrode in the composite electrolyte without FEC (a) and with FEC (b) at 25 after cycled at -30

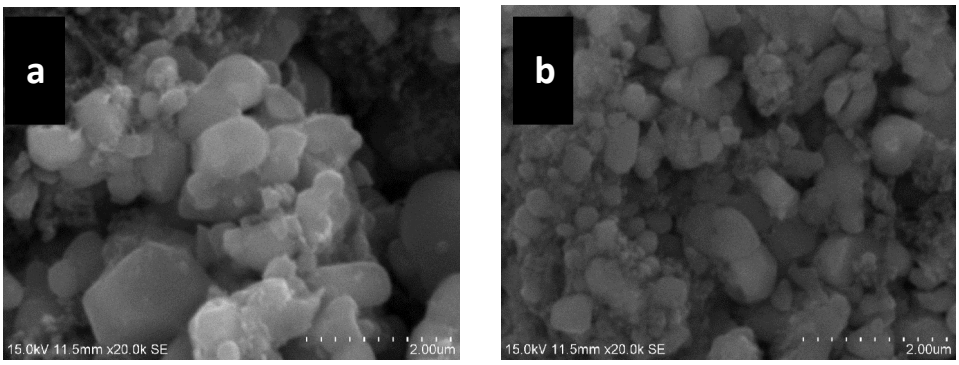

Fig.3. SEM images for $LiFePO_4$ electrode in the composite electrolyte without FEC (a) and with FEC (b) after having cycled at -30

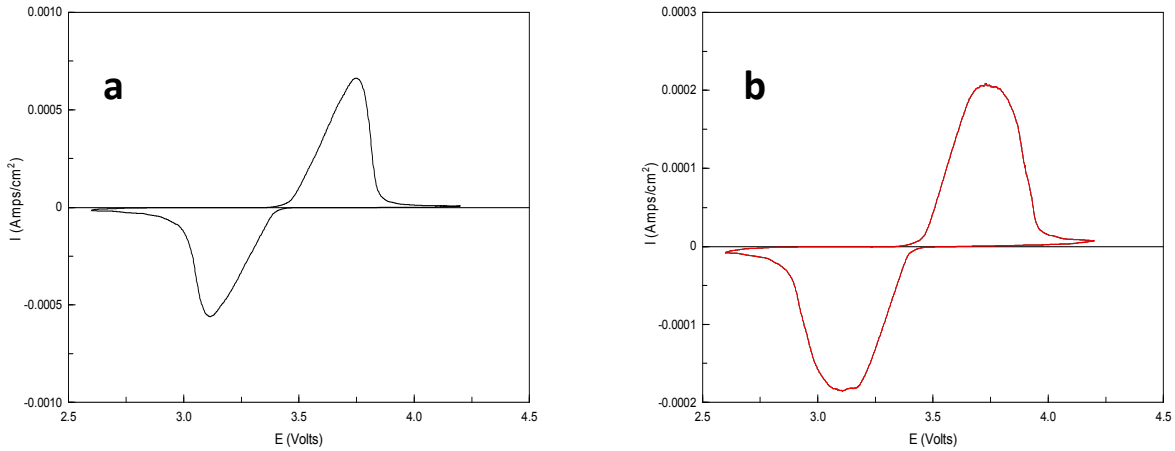

Fig.4. The cyclic voltammograms of $LiFePO_4$ electrode in the composite electrolyte without FEC (a) and with FEC (b) at 25

4. Conclusions

Addition of FEC to LiTFSI/PYR_{1A}TFSI/EC/PC/EMC electrolyte can reduce the freezing point and improve the performance of the composite electrolytes at the low temperature. FEC can dramatically increase the specific capacity at low temperatures and help the $LiFePO_4$ electrode to form more smooth and uniform surface morphology. It's attributed to the weak polarization of the $LiFePO_4$ electrode and excellent electrode/electrolyte interfacial properties. All above results demonstrated that FEC in LiTFSI-Pyr1ATFSI ionic liquid electrolyte can dramatically improve low temperature performance of lithium-ion batteries.

Acknowledgment

This work was financially supported by Scientific and Technological Research and Development Foundation of Shenzhen City (20120602111424454), 973 National Defense Project(613142020201) and Shenzhen Key Laboratory of Functional Polymer Foundation (FP20130008).

References

[1]. K.A.Smith,Electrolytes Containing Fluorinated Ester Co-Solvents for Low-Temperature Li-Ion Cells, ECS Transactions,2008.11(29):p.91-98.

[2]. Mandal, B.K., et al., New low temperature electrolytes with thermal runaway inhibition for lithium-ion rechargeable batteries. Journal of Power Sources, 2006. 162(1): p. 690-695.

[3]. Fernicola, A., et al., LiTFSI-BEPyTFSI as an improved ionic liquid electrolyte for rechargeable lithium batteries. Journal of Power Sources, 2007. 174(1): p. 342-348.

[4]. Li, J., et al., Limiting factors for low-temperature performance of electrolytes in LiFePO4/Li and graphite/Li half cells. Electrochimica Acta, 2012. 59: p. 69-74.

[5]. Liao, L., et al., Fluoroethylene carbonate as electrolyte additive to improve low temperature performance of LiFePO4 electrode. Electrochimica Acta, 2013. 87: p. 466-472.

Advanced Materials Research Vols. 986-987 (2014) pp 84-87

doi:10.4028/www.scientific.net/AMR.986-987.84

Graphene Oxide Prepared via Ultrasonic Assisted Chemical Oxidation Method and Its Fluorescence Property

Yanqun Cui[1], Ze Wu[1], Limin Dong[1,2], Qin Li[1], and Zhidong Han[1,2,a]

[1]College of Materials Science and Engineering, Harbin University of Science and Technology, Harbin, China

[2]Key Laboratory of Engineering Dielectrics and Its Application, Ministry of Education, Harbin University of Science and Technology, Harbin, China

[a] corresponding author: harbinzhidonghan@hrbust.edu.cn

Keywords: Graphene oxide, Ultrasonic, Chemical oxidation, Fluorescence

Abstract. Graphene oxide (GO) was prepared via ultrasonic assisted chemical oxidation method. Contrasting with modified hummers method, GO prepared by ultrasonic assisted chemical oxidation method showed thinner flakes, the interlayer spacing increases. The emission spectra of the GO showed a similar excitation-dependent feature with the strongest peak (552 nm) excited at 477 nm.

Introduction

Graphene is a new type of two-dimensional nano materials which was discovered in 2004[1]. It has rich and novel physical properties because of special single atomic layer structure, thus received great attention and extensive research in the past few years. In the research and application of graphene, it is necessary for effective modification and surface functionalization of graphene to give full play to its excellent properties and improve its processability, therefore GO has emerged as a precursor offering the potential of cost-effective, large-scale production of graphene-based materials[2].

GO is consided as a single-layer of graphite oxide, it is usually produced by the chemical treatment of graphite through oxidation to obtain subsequent dispersion and exfoliation in water or suitable organic solvents[3,4]. In general, GO is usually synthesized by either the Brodie [5], Staudenmaier[6], or Hummers method[7]. All three methods involve oxidation of graphite to several levels. Brodie and Staudenmaier use potassium chlorate ($KClO_3$) with nitric acid (HNO_3) to oxidize graphite, while the Hummers method involves the oxidation treatment of graphite with potassium perman-ganate ($KMnO_4$) and sulfuric acid (H_2SO_4). Graphite salts made by intercalating graphite with strong acids such as H_2SO_4, HNO_3 or $HC1O_4$ have also been used for the subsequent oxidation to GO[8].Hummers method has advantage of simple synthesis, short time, high safety and less pollution to the environment, it has become the most common method used for preparing GO.

In this paper, we prepared GO via ultrasonic assisted chemical oxidation，ultrasonic auxiliary operation started in the medium and high temperature reaction stages of modified hummers method. In the process of preparing, an interesting phenomena of GO with fluorescence luminous performance was found, so we conducted a preliminary research.

Experimental

In this paper, the preparation of GO was divided into three stages. Oxidant potassium permanganate and acid(concentrated sulfuric acid and nitric acid) was added in low temperature reaction stage, oxide intercalated between the layers, temperature was controlled to 0~5 ℃. The second reaction stage started with ultrasonic, the reaction was warmed to 35~38 ℃, at which time deep oxidation was happened, and the graphite layers exfoliation were speed up under the action of ultrasonic. Ultrasonic was continued in high temperature, raise the reaction temperature to 82~85℃, at which time deionized water was added slowly for hydrolysis reaction of interlayer compounds. In order to research the ultrasonic effect in the process of GO preparation，modified hummers method was conducted as a contrast test.

Results and Discussion

Structure analysis. Fig. 1 is the XRD spectra of GO prepared by ultrasonic assisted chemical oxidation and chemical oxidation, respectively. The (001) crystal plane diffraction peak of two samples were both appeared，and diffraction peak of GO prepared by ultrasonic assisted chemical oxidation inclined left. According to the Prague equation $2d\sin\theta=\lambda$, calculations predicted that the interlayer spacing of the material is 7.3Å, larger than 6.9 Å that of GO prepared by chemical oxidation, indicating that ultrasonic contributes to the exfoliation of graphite layers.

FTIR-ATR spectra (Fig. 2) were recorded, and the following functional groups were identified in samples, the peak shape of two samples are in basic agreement. Both of the samples have a wide strong absorption band at 3200~3500cm^{-1}, corresponding to -OH stretching vibrations. In addition, the remaining water molecules also have an effect on the absorption peak. The absorption peaks in the 1735cm^{-1}, 1399cm^{-1}, 1093cm^{-1} belong to C=O, C-O-C, and C-OH stretching vibrations, respectively. The absorption peak of 1618cm^{-1} belongs to the -OH bending vibration of water molecules, indicating that the GO remains water molecules. The existence of a large number of oxygen functional groups indicated that graphite layers were inserted into a large amount of oxygen-containing groups after potassium permanganate and acid treatment.

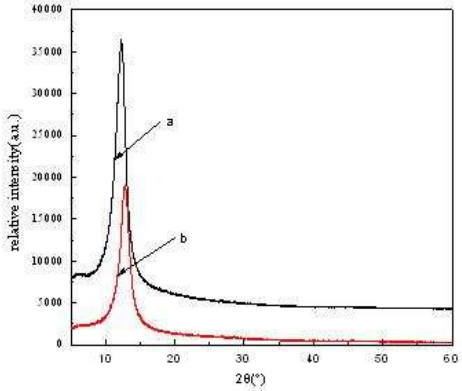

Fig. 1 XRD spectra of GO
a) Ultrasonic assisted chemical oxidation b) Chemical oxidation

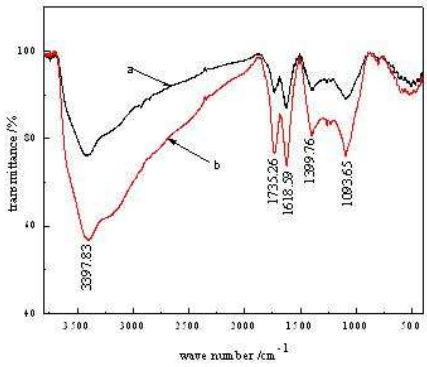

Fig. 2 FTIR-ATR spectra of GO
a) Ultrasonic assisted chemical oxidation b) Chemical oxidation

Morphology analysis. Transmission electron microscopy (TEM) photographs of the products are shown in Fig. 3. It is apparent that GO prepared by ultrasonic assisted chemical oxidation has a different morphology from that by chemical oxidation, the thickness of GO in Fig.3a is obviously thiner than that in Fig.3b, and folding in surface.The appearance is due to the effect of ultrasonic leads to the exfoliation of graphite layers,which is conform with the analysis result of Fig. 1.

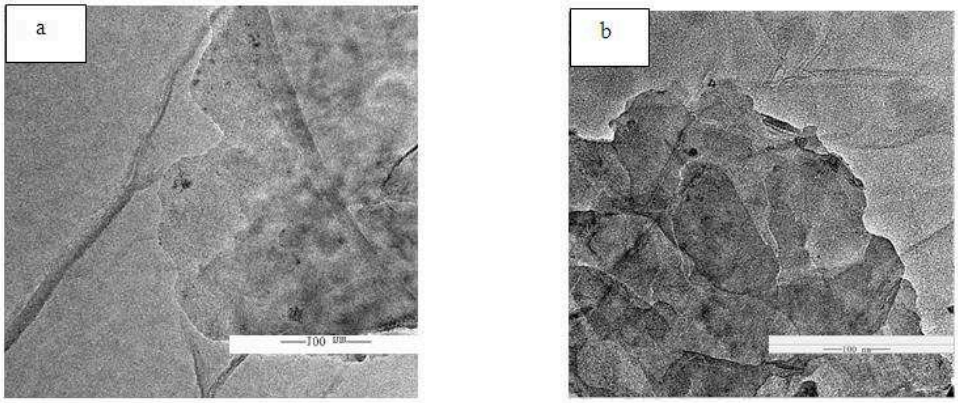

Fig. 3 TEM images of GO
a) Ultrasonic assisted chemical oxidation b) Chemical oxidation

Performance analysis. We have found an interesting phenomena that GO prepared by ultrasonic assisted chemical oxidation performs a certain degree of fluorescence property, thus we carried out a series of fluorescent light spectrum analyses of GO which prepared by two methods. Fig. 4, 5 are PL spectra and normalized PL spectra of GO at different excitation wavelengths. The emission spectra of the GO show a similar excitation-dependent feature with the strongest peak (552 nm,547 nm) excited at 477 nm and 470 nm, respectively. In addition, when the excitation wavelength changed to longer , the PL peak shifts to longer wavelengths at the same time, and its intensity first increased to the maximum(552 nm,547 nm), then decreased. GO prepared by ultrasonic assisted chemical oxidation showed more severe degree of shift. The reason is that oxygen-containing groups of graphite layers increased the number of defects, leading to fracture if external mechanical stress applied, the size of graphite layers then decreased to nanoscale and showed the similar to the quantum confined effect, fluorescence properties was then appeared. This property is closed to the fluorescence property of graphene quantum dots (GQDs)[9]. This may give a helpful advice for synthesis of GQDs.

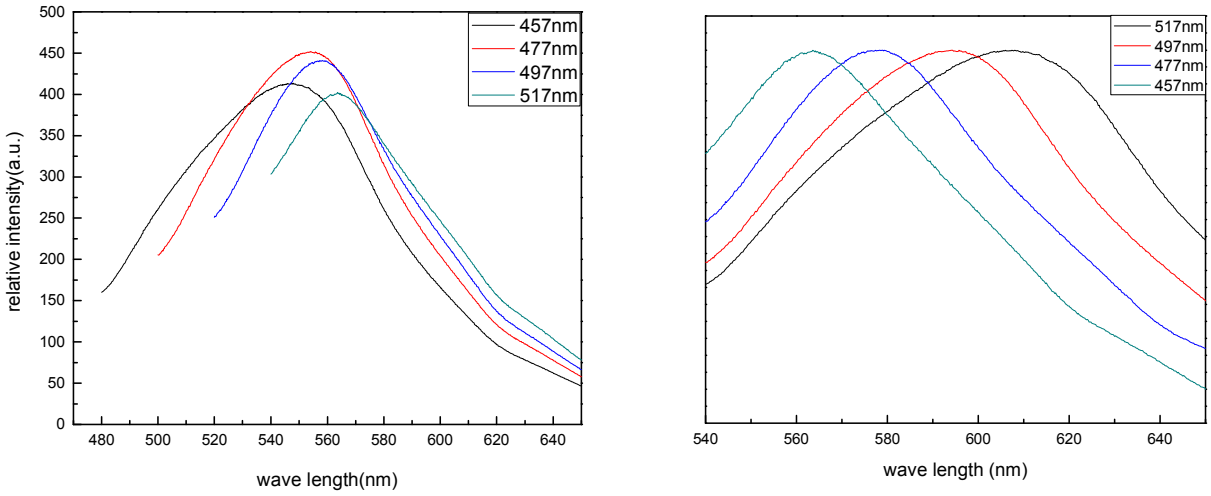

(a) (b)

Fig. 4 PL spectra of the GO prepared by ultrasonic assisted chemical oxidation
a) PL spectra of the GO at different excitation wavelengths b) The normalized PL spectra

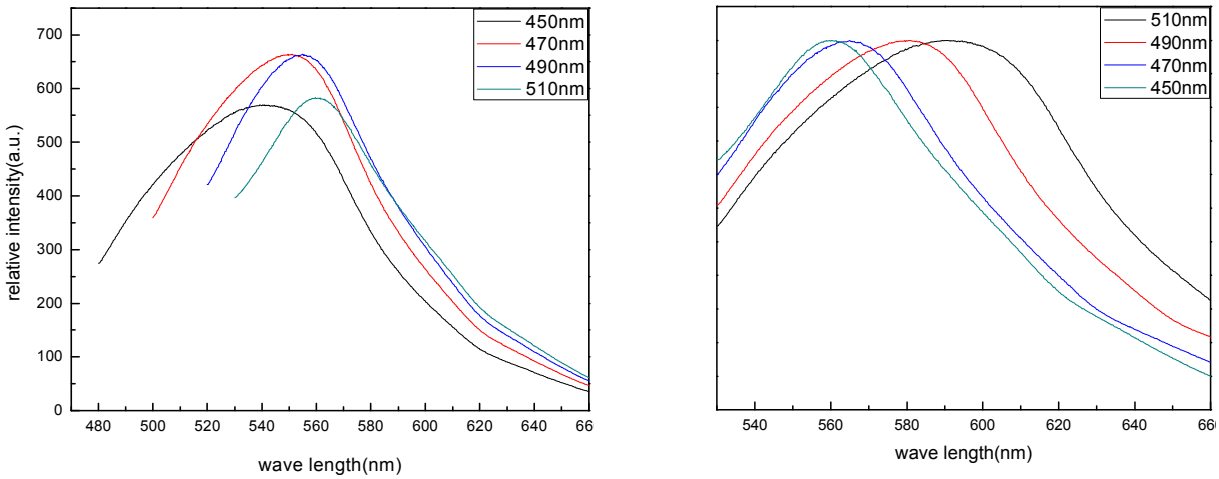

(a) (b)

Fig. 5 PL spectra of the GO prepared by chemical oxidation
a) PL spectra of the GO at different excitation wavelengths b) The normalized PL spectra

Summary

GO prepared by ultrasonic assisted chemical oxidation shows thinner, smaller size. Ultrasound can promote the separation between the graphite layers, increasing the interlayer spacing of graphite. The oxygen containing functional groups of GO which prepared by chemical oxidation produce a number of surface defects. The use of ultrasound provides external stress, which increases the chance of graphene sheet fracture, leading to smaller size. when the size reduces to a certain extent, quantum confinement effect occurs and exhibits fluorescence property.

Acknowledgements

This work was financially supported by program for innovative research team in university of Heilongjiang province (2013TD008).

References

[1] K.S. Novoselov, A.K. Geim, S.V. Morozov, D. Jiang, Y. Zhang, S. V. Dubonos, I. V. Grigorieva, A. A. Firsov. *ElectricField Effect in Atomically Thin Carbon Films [J]*. Sci. 2004, 306: 666-669.
[2] Park S, Ruoff R S. *Chemical methods for the production of graphenes [J]*. Nat. nanotechnol. 2009, 4(4): 217-224.
[3] Stoller M D, Park S, Zhu Y, et al. *Graphene-based ultracapacitors[J]*. Nano letters. 2008, 8(10): 3498-3502.
[4] Dreyer D R, Park S, Bielawski C W, et al. *The chemistry of graphene oxide [J]*. Chemical Society Reviews, 2010, 39(1): 228-240.
[5] Brodie B C. *Sur le poids atomique du graphite [J]*. Ann. Chim. Phys, 1860, 59(1860): 466-472.
[6] Staudenmaier L.Ber.Deut.Chem.Ges.,1898, 31 (2):1481-1487.
[7] W. S. Hummers, R. E. O. Ffeman, J. Am. Chem. Soc. 1958, 80, 1339.
[8] M. Segal, Nat. Nano. 2009, 4, 612.
[9] D. Pan, J. Zhang, Z. Li, et al. *Hydrothermal Route for Cutting Graphene Sheets into Blue-Luminescent Graphene Quantum Dots[J]*. Adv. Mater, 2010, 22(6): 734-738.

Advanced Materials Research Vols. 986-987 (2014) pp 88-91

doi:10.4028/www.scientific.net/AMR.986-987.88

Hydrogen desorption/absorption kinetics of MgH_2 catalyzed with TiO_2

Yan Wang[1, a], Shiwei Wu[2, b], Hao Yu[1, c], Nana Gong[1, d], Zhongqiu Cao[1, e], and Ke Zhang[1, f]

[1] College of Chemistry and Life Science, Shenyang Normal University, Shenyang 110034, China;

[2] Experimental Center, Shenyang Normal University, Shenyang 110034, China.

[a]wangyan11287@sina. com, [b]wswcn1975@163. com, [c]seeyu206@foxmail. com, [d]gladysnana@163.com, [e]caozhongqiu6508@sina. com, [f]Zhangke@synu.edu.cn

Keywords: Magnesium hydride, Hydrogen storage, Kinetics, Mechanical milling

Abstract. We report on the preparation and hydrogen desorption/absorption kinetics of nanocrystalline magnesium hydride (MgH_2) added commercial TiO_2 by high-energy ball milling. The phase and composition of the as-milled powders are characterized by X-ray diffraction(XRD). The results show that the milled sample contained MgH_2 phase, small amount of Mg and various phases of TiO_2 such as tetragonal and orthorhombic structure. The effect of the milling time (10, 20 and 30 h) on the hydrogen desorption property of MgH_2 has been investigated and found that the milling time of 20 h has excellent dehydrogenation properties, which can release 3.3 wt% H_2 within 60 min at 300 ^oC, which indicates that the kinetics of hydrogen desorption of MgH_2-TiO_2 composite has been greatly enhanced compared to the pure MgH_2. Moreover, hydrogen absorption kinetics of the sample milled 20 h has been studied and the hydrogen content is 0.7, 0.8 and 1.2 wt% H_2 at 250, 280 and 300 ^oC within 60 min, respectively.

Introduction

In Magnesium hydride (MgH_2) has been considered as a promising hydrogen storage material due to its high hydrogen capacity (gravimetric 7.6 wt% hydrogen and volumetric 110 kg H_2 m^{-3}) of hydrogen theoretically. And also it is cheap and abundant in the earth's crust[1]. However, MgH_2 is too stable and both dehydrogenation/ absorption kinetics are very slow and require high temperature, which creates a burden for the industrial-scale applications[2, 3]. To overcome these drawbacks, tremendous efforts have been devoted to catalysis[4, 5], alloying[6, 7] and nano-structuring[8, 9] in the past two decades, and signicant progress has been made to enhance the dehydrogenation/ absorption properties, in particular the hydrogen release kinetics.

It is advantageous to manufacturing nanocrystalline powder by high-energy ball milling. The nanocrystalline hydrides synthesized by high-energy ball milling showed very fast absorption and desorption kinetics due to faster diffusion of hydrogen along grain boundaries, as well as the high number of heterogeneous nucleation sites of the hydride on absorption[10]. Moreover, one of the most notable studies is on the addition of transition-metal oxides such as Nb_2O_5[11-15], Cr_2O_3[16, 17], CeO_2[18, 19], La_2O_3[19] and TiO_2[16, 20-22] that have been proven to ameliorate signicantly the hydrogen sorption kinetics of MgH_2. Among them, TiO_2 possesses many interesting characteristics, and has attracted much attention as an important catalyst in several typical hydrogen storage systems. For example, Schober[2] reported that dissolving hydrogen by TiO_2 after dissociation of hydrogen molecules could provide an effective path for hydrogen penetration of TiFe–TiO_2 composite systems. Wang et al.[22] prepared the nanostructured composite Mg–TiO_2 (rutile) by reaction ball milling (RBM). The addition of TiO_2 resulted in a markedly improved hydrogenation performance of Mg, such as rapid kinetics and low working temperature. Jung et al.[21] showed that the kinetics of hydrogen sorption was greatly enhanced by magnesium hydride doped with nano-sized TiO_2.

However, in spite of many researches carried out on the Mg–TiO_2 system, it is hard to enhance hydrogen desorption/ absorption kinetics simultaneously. Motivated by this, we performed a

systematic investigation on the hydrogen desorption/ absorption kinetics of MgH_2 catalyzed with various TiO_2, which was synthesized by the high-energy ball milling method.

Experimental procedures

Synthesis. The starting material MgH_2 (purity of 95%) and TiO_2 (purity of 99.8%) were purchased from Sigma–Aldrich and were used as received. The samples of MgH_2 containing TiO_2 (8 mol%) were prepared by the high-energy ball milling under argon atmosphere for 10, 20 and 30 h at a disc revolution speed of 400 rpm. The weight ratio between the ball and powder is 40:1. All material handing (including weighing and loading) was carried out in a glove box under an inert pure argon (99.999%) atmosphere so as to minimize the contamination effect of oxygen and water on the sample.
Characterization. The Powder X-ray diffraction (XRD) patterns were taken on a D/Max-RB X-ray diffractometer using Cu Kα radiation (λ=1.54178Å) to determine the phase composition of the as-milled powders. The X-ray intensity was measured over a diffraction angle from 20° to 80°. The pressure- composition-temperature (P-C-T) curves for hydrogen absorption and desorption kinetics were determined by using a computer controlled Gas Reaction Controller apparatus (PCTPro 2000).

Results and discussion

XRD analyses. Fig. 1 shows a series of powder X-ray diffraction (XRD) patterns of the pure MgH_2 and as-milled samples obtained at different milling time. It can be seen that the phase composition does not significantly change after ball milling. By inspecting the XRD pattern of MgH_2+TiO_2 mixture at different milling time, the peak intensity ascribed to MgH_2 decreases obviously after ball milling. Especially, when the milling time is 20 h, the peak ascribed to MgH_2 broadens distinctly, and this broadening can be attributed to a reduction in crystallite size and/or amorphization. So, it could conclude that the particle size of MgH_2 is smaller than the size of as-milled samples after 10 and 30 h. The milling finally results in the presence of tetragonal and orthorhombic phase TiO_2 (Joint Committee on Powder Diffraction Standards (JCPDS) No. 65-1119 and 65-2448, respectively).

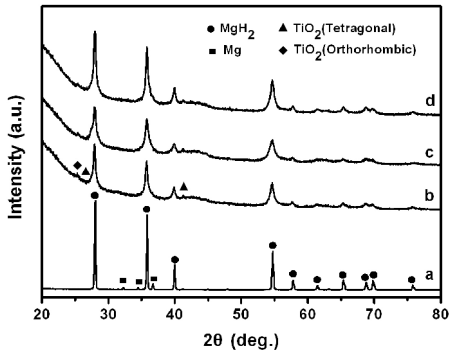

Fig. 1 Powder XRD patterns of pure MgH_2 (a) and MgH_2+TiO_2 mixture as a function of milling time: (b) 0 h, (c) 20 h and (d) 60 h, respectively.

Hydrogen desorption of MgH_2+TiO_2 composite. To determine the hydrogen desorption kinetics of the as-prepared MgH_2+TiO_2 mixture for different milling time of 10, 20, and 30 h, Fig. 2 gives the typical hydrogen desorption curves at 300 °C. It is demonstrated that the sample milled 20 h exhibits much higher kinetics than that of the others. As shown in Fig.2, the sample milled 20 h releases 3.3 wt% H_2 in 60 minutes at 300 °C. In contrast, the sample milled 10 and 30 h release 1.0 and 3.0 wt% H_2 under the same conditions. For prolonged milling (such as 30 h), it should be noted that there is no further enhancement of the dehydrogenation kinetics properties. The reason may be the larger particle sizes compared with the sample milled 20 h. The XRD curve for the dehydrogenated MgH_2+TiO_2 has been showed in Fig. 3, and it can be seen that the final product is composed of TiO_2, Mg and some residual MgO.

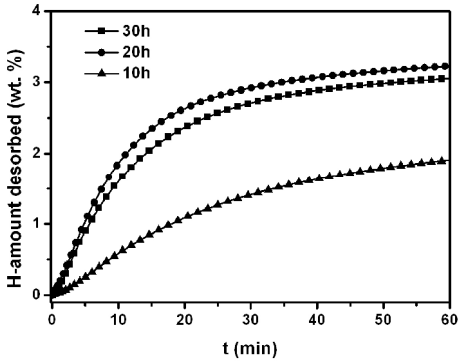

Fig. 2 Dehydrogenation curves of the as-prepared MgH_2+TiO_2 mixture for different milling time of 10, 20, and 30 h at 300 °C.

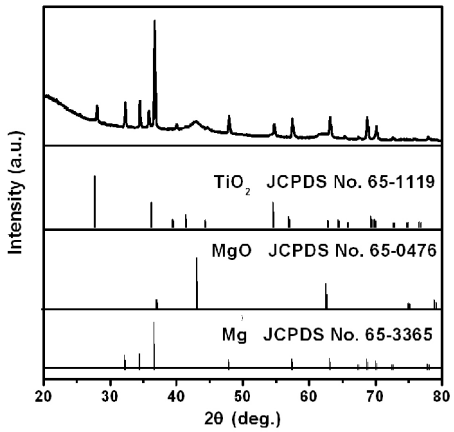

Fig. 3 The XRD curve for the dehydrogenated MgH_2+TiO_2 mixture milled 20 h.

Hydrogen absorption of MgH_2+TiO_2 composite. Besides the improvement in the dehydrogenation kinetics, the hydrogen absorption kinetics of the as-prepared MgH_2+TiO_2 milled 20 h is also shown in Fig.3a for different temperatures of 250, 280 and 300 °C. It can be seen that the sample releases 0.7, 0.8 and 1.2 wt% H_2 in 15 minutes at 250, 280 and 300 °C , respectively, while the pure MgH_2 sample can not release any hydrogen below 300 °C. It can be found that the hydrogen absorption kinetics of MgH_2 is significantly improved by the adding of TiO_2.

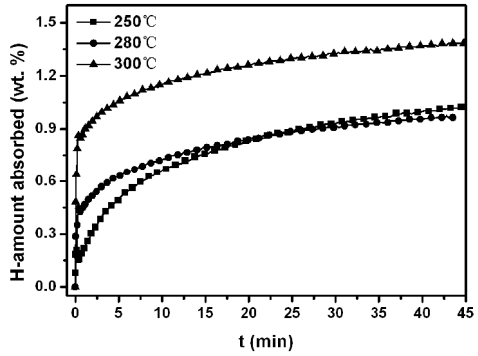

Fig. 4 The hydrogen absorption kinetics of the as-prepared MgH_2+TiO_2 milled 20 h for different temperatures of 250, 280 and 300 °C.

Conclusion

In summary, we have prepared nanocrystalline magnesium hydride (MgH_2) added commercial TiO_2 by high-energy ball milling. The results of XRD tests show that the milled sample contained MgH_2 phase, small amount of Mg and various phases of TiO_2 such as tetragonal and orthorhombic structure. The effect of the milling time (10, 20 and 30 h) on the hydrogen desorption property of MgH_2 has been investigated and found that the milling time of 20 h has excellent dehydrogenation properties,

which can release 3.3 wt% H_2 within 60 min at 300 ^oC, which indicates that the kinetics of hydrogen desorption of MgH_2-TiO_2 composite has been greatly enhanced compared to the pure MgH_2. The final product is composed of TiO_2, Mg and some residual MgO. Moreover, hydrogen absorption kinetics of the sample milled 20 h has been studied and the hydrogen content is 0.7, 0.8 and 1.2 wt% H_2 at 250, 280 and 300 ^oC within 15 min, respectively.

Acknowledgments

This work was supported by Doctoral Scientific Research Fund (054-554401009005) and the Sixth Batch of school education and teaching reform project (JG2012-YB084) of Shenyang Normal University.

References

[1] W.Grochala, and P.P. Edwards: Chemical Reviews, vol. 104 (2004) no. 3, p. 1283-1316.
[2] T. Schober: Journal of the Less Common Metals, vol. 89 (1983) no. 1, p. 63-70.
[3] B. Bogdanović, T.H. Hartwig, and B. Spliethoff: International Journal of Hydrogen Energy, vol. 18 (1993) no. 7, p. 575-589.
[4] Z. Dehouche, J.Goyette, T. K. Bose, et al: Nano Letters, vol. 1 (2001) no. 4, p. 175-178.
[5] P. Adelhelm and P.E. de Jongh: Journal of Materials Chemistry, vol. 21 (2011) no. 8, p. 2417-2427.
[6] A. Zaluska, L. Zaluski and J.O. Ström-Olsen: Journal of Alloys and Compounds, vol. 289 (1999) no. 1–2, p. 197-206.
[7] M. Bououdina, and Z.X. Guo: Journal of Alloys and Compounds, vol. 336 (2002) no. 1–2, p. 222-231.
[8] A. M. Seayad and D.M. Antonelli, Advanced Materials, vol. 16 (2004) no. 9-10, p. 765-777.
[9] K. F. Aguey-Zinsou and J. R. Ares-Fernández: Chemistry of Materials, vol. 20 (2007) no. 2, p. 376-378.
[10] Z. Dehouche, T. Klassen, W. Oelerich, et al: Journal of Alloys and Compounds, vol. 347 (2002) no. 1–2, p. 319-323.
[11] G. Barkhordarian, T. Klassen, and R. Bormann: Journal of Alloys and Compounds, vol. 364 (2004) no. 1-2, p. 242-246.
[12] T. Ma, S. Isobe, Y. M.Wang, et al: The Journal of Physical Chemistry C, vol. 117 (2013) no. 20, p. 10302-10307.
[13] M. O. T. da Conceição, M. C Brum, D. S dos Santos, et al: Journal of Alloys and Compounds, vol. 550 (2013) no. 0, p. 179-184.
[14] M. Porcu, A.K. Petford-Long, and J.M. Sykes: Journal of Alloys and Compounds, vol. 453 (2008) no. 1-2, p. 341-346.
[15] O. Friedrichs, D. Martínez-Martínez, G. Guilera, et al: The Journal of Physical Chemistry C, vol. 111 (2007) no. 28, p. 10700-10706.
[16] D. Rafiud, X. H. Qu, P. Li, et al: The Journal of Physical Chemistry C, vol. 116 (2012) no. 22, p. 11924-11938.
[17] Q. Li, K. D. Xu, K. C. Chou, et al: Intermetallics, vol. 13 (2005) no. 11, p. 1190-1194.
[18] R. K. Singh, T. Sadhasivam, G. Sheeja, et al: International Journal of Hydrogen Energy, vol. 38 (2013) no. 14, p. 6221-6225.
[19] R. Gupta, F. Agresti, S. L. Russo, et al: Journal of Alloys and Compounds, vol. 450 (2008) no. 1-2, p. 310-313.
[20] S. K. Pandey, A. Bhatnagar, R. R. Shahi, et al: Journal of Nanoscience and Nanotechnology, vol. 13 (2013) no. 8, p. 5493-5499.
[21] K. S. Jung, D. H. Kim, E. Y. Lee, et al: Catalysis Today, vol. 120 (2007) no. 3-4, p. 270-275.
[22] P.Wang, A. M. Wang, H. F. Zhang, et al: Journal of Alloys and Compounds, vol. 313 (2000) no. 1–2, p. 218-223.

Advanced Materials Research Vols. 986-987 (2014) pp 92-96

doi:10.4028/www.scientific.net/AMR.986-987.92

Influence of Gas-Gas Heater on wet flue gas desulfuration

Xiao Haiping[a], Dong Lin[b], Han Gaoyan[c] and Ning Xiang [d]

North China Electric Power University, Beijing 102206, China
[a]dr_xiaohaiping@126.com,[b]945024915@qq.com,[c]hangaoyan123@126.com

Keywords: flue gas desulfurization system; gas-gas heater; water balance; flue temperature

Abstract: Material balance calculation was adopted to a wet flue gas desulfurization (WFGD) system for exploring impacts of gas-gas heater (GGH). Effects of GGH on flue and water consumption were analyzed. Results showed that inlet flue temperature of desulfurization tower reduced by 3.4 ℃ at 100% load after installation of GGH. Exhausted gas temperature of system increased by 34.9℃. The heat release of original flue in desulfurization tower reduced by 43.72%. Plume rise height was significantly improved. Water evaporation in desulfurization tower declined by 42.07%.Amount of addendum water reduced by 39.06%, and water vapor carried by flue decreased by 19.78% at the outlet of WFGD. Therefore, operation condition of flue emission is improved and water consumption decreases with GGH.

1. Background

Wet flue gas desulfurization was widely applied in thermal power plant due to mature technology and high desulfurization efficiency. Gas-gas heater(GGH) was the key equipment of WFGD system. The original and net flue gas desulfurized exchanged heat at GGH, original flue gas temperature reduced and net flue gas temperature increased. Since the operation was not standardized and the purge process was unreasonable, heat storage components of GGH was prone to be choked up by scaling, causing the system pressure increased and booster fan stalled when seriously, leading to the entire unit outage finally[1,2]. Therefore, GGH were tend to be canceled in existing WFGD systems. However, the original flue gas temperature and evaporation of process water in desulfurization tower could be reduced with GGH, aiming at water conservation, which has practical significance for thermal power plants in arid regions of the Midwest. Net flue gas discharge temperature was enhanced with GGH, flue gas and acid dew point was reduced as well as flue gas carrying water, smoke plume discharge height was uplifted and corrosion of chimneys was on the decrease together with plaster rain phenomenon[3,4,5]. In this paper, the impact of GGH on important parameters of WFGD was analyzed for a 600MW unit to provide a reference for the optimization of desulfurization system.

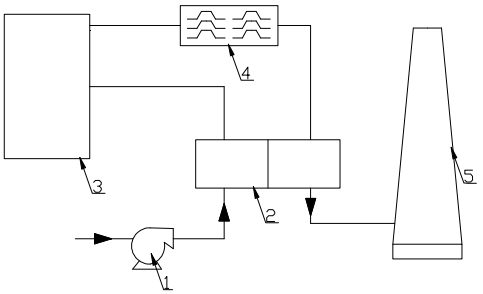

1.Booster fan 2.GGH 3.Wet desulfurization tower 4.Defogger 5.Chimney
Fig.1 Wet flue gas desulfurization with Jet bubble reactor

2. Methods

A WFGD system of 600MW unit was analyzed using a mass balance calculation in desulfurization system, influence of GGH on exhaust gas temperature and water consumption was analyzed. Flue gas balance, energy balance, solid balance, water balance and chlorine balance were included in material balance of WFGD systems as sub-modules[6]. The exhaust gas temperature of desulfurization system was obtained by energy balance calculations, water consumption of system by Water balance calculation, and volume of wastewater was determined by chlorine balancing. First, assuming exit gas temperature of desulfurization tower and GGH exports temperature of net flue gas side, evaporation of water at hypothetical temperature was determined with energy balance calculation. Making the net flue gas water vapor pressure the same as saturated steam at hypothetical temperature by iterative calculation, then hypothetical temperature of GGH was checked. All material balance data of desulfurization system was finally obtained[7]. Calculation for acid dew point was executed with A.G.Okkes acid dew point formula, and plume rise height was calculated with thermal power plant air pollutant emission standards (GB13223-2003) at 100% load, the detailed process see ref[8].

3. Results and analysis

3.1 Effect on flue gas emissions

Energy release of WFGD system major covered heat release of the original flue gas (dry basis), original smoke carrying steam, chemical reactions and oxidation air cooled. Energy balance calculations showed that heat release of the original flue gas (dry basis) accounted 87.3% of the system energy taking into the desulfurization, which was the biggest heat source dragged-in. While after GGH installed, heat release of the original flue gas in desulfurization tower reduced by 43.72% by transmitting heat of 97947.8MJ / h to net flue gas. Simultaneously, heat release of water vapor of absorber in original the flue gas reduced 9149.4MJ / h, accounted 43.57%. Energy absorbing embraced heat process water(maintain the level), gypsum slurry circulating water and limestone slurry assimilated along with heat taking away by evaporation of water. Heat absorption of water evaporation in tower was the largest term, accounted for 94.0% of the total. Calculations showed that heat absorption of water evaporation in desulfurization tower decreased by 41.89% with GGH, corresponding to 101023.9MJ / h. Meanwhile, 5356.6MJ / h for reduction of addendum water heat absorption, accounted by 49.92%, 186.2MJ/h for limestone slurry, equivalently 22.65%. So energy brought into the desulfurization tower and water evaporation heat absorption reduced with GGH.

Tab. 1 Influence of GGH on exhausted gas temperature of WFGD systems [℃]

GGH	GGH imports raw flue gas temperature	Import gas temperature of desulfurization tower	flue gas temperature spray desuperheated	Net flue gas outlet temperature of desulfurization tower	Net gas exports temperature of GGH
with	132	95	47.8	47.6	84.9
without	-	132	51.2	50.8	-

Table 1 showed influence of GGH on flue gas temperature in desulfurization system. Flue gas temperature reduced by about 37 ℃ after the original flue gas flowing through GGH with installation of GGH in desulfurization system. Compared to conditions without GGH, temperature of original flue gas spray desuperheated lowered by 3.4 ℃ and desulfurization reactor outlet flue gas temperature increased by 3.2 ℃ at working conditions installed GGH. In this case, chimney flue temperatures added to 84.9 ℃, and only 50.8℃ for conditions without GGH.

SO2 oxidation rate in flue gas was taken for 1%, dew point and acid dew point of the desulfurization system outlet flue gas were calculated. Chimney flue gas inlet dew point temperature was 46.95 ℃ and acid dew point was 122.39 ℃ without GGH, in the opposite condition, dew point was 41.84 ℃ and acid dew point was 120.67℃, 5.11℃and 1.72℃ respectively lower than the former. The reason was that the saturation temperature of desulfurization system flue gas outlet was reduced with installation of GGH, thereby moisture content of net flue gas was reduced together with dew point temperature. Simultaneously, water vapor partial pressure at the system outlet of the net flue gas was also decreased, so that net flue gas acid dew point temperature dropped. Therefore, GGH will reduce dew point and acid dew point temperature of chimney imports flue gas, thus working environment of backpass improved.

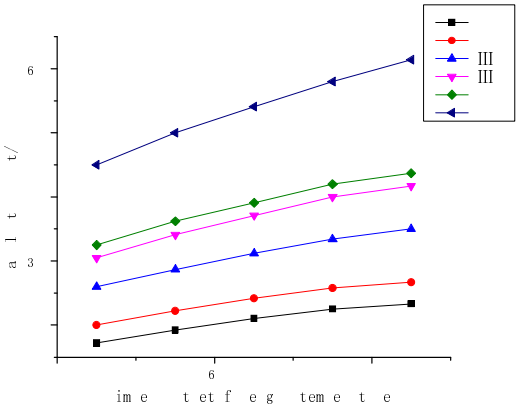

Fig.2 Influence of flue temperature on gas lift height

Plume rise height was calculated taking chimney height as 180m, wind speed at chimney ten meters as 2m/s, and exhaust gas temperature distributed at 45 ~ 85 ℃. Relationship between plume rise height and exhaust gas temperature for different atmospheric stability has shown in Figure 2. Gas lift height increased directly with atmospheric stability, similarly with chimney flue gas outlet temperature. When atmospheric stability was at level V, gas lift height was almost above 450m, which will increase 130m as the flue gas temperature rising from 45 ℃ to 75 ℃, traditional chimney gas lift height can reach to 614m corresponding to exhaust gas temperature. While I level, gas lift height was almost below 250m, which was only 172m as the flue gas temperature was 45 ℃.Different atmospheric stability and flue gas emission temperatures corresponded to 442m gap in plume rise height. Because of low WFGD system exhaust gas temperature, corresponding chimney gas lift height was low, which was less than 200m in the low atmospheric stability, resulting that smoke flowed back to the ground in the vicinity of the power plant and produced gypsum rain phenomena. Moreover, the exhaust gas temperature could be upgraded to 85 ℃ by GGH, and plume rise height was increased, phenomenon above would relieve.

3.2 Impact on the water balance

Desulfurizer water, raw flue gas carrying steam and addendum water (including equipment wash water, cooling water, gas cooling water, desulfurizer prepared water) constituted inflow item of WFGD system water balance. In which raw flue gas carrying steam was major source of system influent water, accounted more than 54% of the total. Effluent items included gypsum carrying water, net smoke carrying steam, net smoke carrying liquid and desulphurization wastewater, in which net smoke carrying steam was the most and accounted more than 95%.

Impact of GGH in WFGD system on water balance has shown in Table 2. Addendum water declined of 39.06%, net smoke carrying steam of 19.78% and desulfurization wastewater reduced by 11.53% with GGH. Decrease of net smoke carrying steam was in favor of alleviating wet flue gas emissions. Known from energy balance calculations, flue gas temperature entering the desulfurization tower reduced 3.4 ℃ and original flue gas heat in desulfurization tower reduced by 43.72% after installation of GGH. Water balance calculations indicated that evaporation in tower decreased from 101.32t / h down to 58.69t / h, reduced by 42.07%. Total evaporation of water in tower reduced with GGH, resulting in decrease of addendum water consumption, while variation in net smoke carrying steam, net smoke carrying liquid and gypsum water was small. Addendum water reduced by GGH, which leading to decrease of chloride ions brought into the desulfurization system, thus desulfurization waste water reduced, therefore desulfurization waste water was closely related to addendum water. In conclusion, energy into the tower reduced by GGH, significantly similar with evaporation of water tower, desulfurization wastewater and net smoke carrying steam, thus the consumption of process water and flue gas humidity were effectively reduced.

Tab.2 Influence of GGH on water balance

GGH	Inflow Item				Effluent Item		
	Original flue carrying steam	Chemical reaction water	Addendum water	Net flue Carrying steam	Net flue Carrying water droplets	Gypsum water	Desulfurization wastewater
with	130.55	0.63	68.36	189.24	0.17	0.41	8.59
without	134.59	0.65	112.18	235.91	0.17	0.42	9.71

4. Conclusion

（1） Because of the presence of GGH, water evaporation heat in absorption tower reduced along with flue gas carrying heat into the absorption tower. Flue gas dew point and acid dew point temperature also reduced as the flue gas absorption tower imports temperature. Therefore, plume rise height raised along with system exhaust gas temperature improving.

（2） Water evaporation in tower and the desulfurization wastewater greatly reduced with GGH, resulting process water consumption and flue gas humidity effectively reduced.

Acknowledgments. Project is supported by National Natural Science Foundation of China (51206047) and “the Fundamental Research Funds for the Central Universities”, Which is grateful acknowledged.

References

[1] XIAO Haiping, ZHANG Qian,SUN Baomin. Analysis on blockage mechanism of Gas-Gas Heater in wet flue gas desulfurization systems[J]. Journal of Chinese Society of Power Engineering, 2011,31(1):53-57.

[2] SUN Zhichun,XIAO Haiping,SUN Baomin. Experimental study on performance optimization of horizontal mist eliminator in Taishan power plant[J]. Journal of Chinese Society of Power Engineering, 2010,30(11):889-894.

[3] ZENG Tinghua,YANG Hua,LISO Yongjin,etal. Wet FGD system commissioning, testing and operation[M].BeiJing: China Electric Power Press, 2008.

[4] ZHONG Yi,GAO Xiang,HUO Wang,etal. Analysis of scaling on Gas-Gas Heater surfacesof wet flue gas desulfurization systems[J]. Journal of Power Engineering, 2008,28(2):275-278.

[5] LV Ming,ZHAO Zhijun,YIN Guoqiang,etal. Achieving water-saving purpose by reducing in-let gas temperatures in wet flue gas desulfurization process[J]. Journal of Chinese Society of Power Engineering, 2010,30(9):695-698.

[6] ZHOU Qulan,XU,Tongmo,HUI Shien. Development and application of China's own wet Flue Gas Desulfurization technique[J]. Journal of Power Engineering, 2006,26(2),261-264.

[7] LI Pengfei,TONG Huiling. Comparison and analysis on the calculation methods of acid dew point of flue gas[J]. Boiler Technology, 2009,40(6):5-8.

[8] YU Qinjian.Study of desulfurization system mass balance[D]. BeiJing, North China Electric Power University, 2013.

Advanced Materials Research Vols. 986-987 (2014) pp 97-100

doi:10.4028/www.scientific.net/AMR.986-987.97

Investigating on the flow distribution of a planar solid oxide fuel cell stack

Huanhuan He[a], Shundong Zhang[b], Qiang Zhang[c], Shichuan Su[*], Bo Wang, Wanli Zhang ,

School of Energy and Power Engineering, Jiangsu University of Science and Technology, Zhenjiang 212003, China.

[a]0840502102@163.com, [b]445697695@qq.com, [c]JackZhang155@163.com

Keyword: Planar solid oxide fuel cell stack, Flow distribution, Investigation, Geometric parameters.

Abstract. In this paper, a realistic 3D numerical model is established to investigate the flow distribution of a 10-cells short planar SOFC stack. The effect of the basic geometric parameters, such as the sub-manifold radii (R_s) and the single channel width (W_{ch}), on the stack flow uniformity is examined. And the results and discusses are presented in this paper. This investigation for the SOFC stack holds great significance for the SOFC stack commercialization.

Introduction

The planar solid oxide fuel cell (SOFC) is regarded as one of the most promising technology for electrical power generation because of its great advantages such as cleaning, high efficiency and easy to manufacture [1, 2]. A typical planar solid oxide fuel cell stack with a co-flow distribution pattern has been reported by Jean [3].

One of the most emergency technology problems in the design of the planar SOFC stack is how to get a better stack performance [4]. Therefore, the aim of this work is investigating the air flow distribution in the SOFC stack and optimizing the flow uniformity as much as possible.

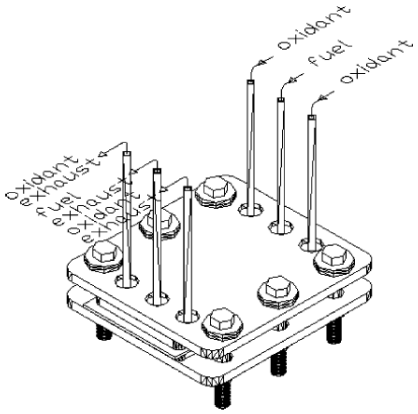

Fig. 1 The planar solid oxide fuel cell stack reported by Jean [3]

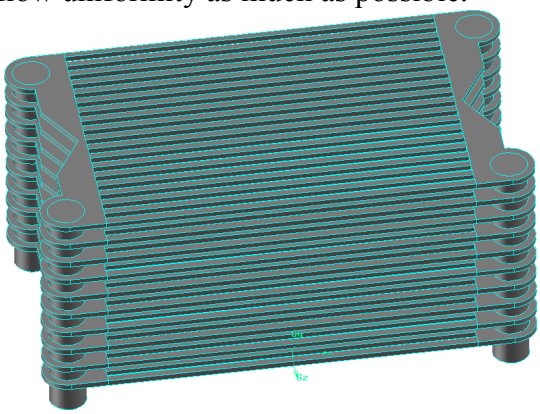

Fig. 2 The 10-cells short planar SOFC stack air flow model

The 3D realistic air flow model and CFD Calculation

This paper establishes a realistic 10-cells short planar SOFC stack air flow model with the MEA areas of 75 mm×100 mm, shown in Fig. 2, and the air flow model in a unit cell is illustrated in Fig. 3.

Commercial software, FLUENT 6.3 based on the finite volume method is adopted in our CFD calculation[5]. The governing equations including the continuity equation, the momentum equation should be calculated in this model [6]. Other relevant parameters are listed in Table 1 [7].

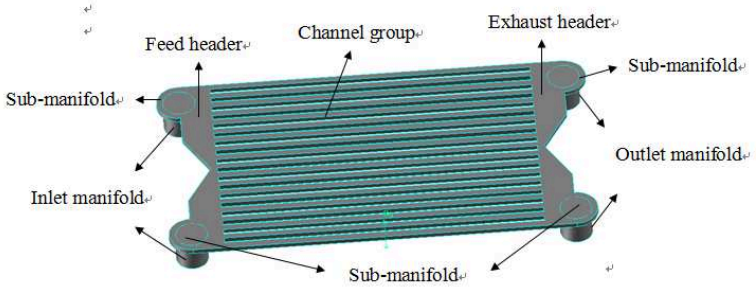

Fig. 3 The air flow model within a unit cell

Table 1. Relevant parameters should be set in FLUENT 6.3

Operation temperature	1073 [K]
Average current density	7000 [A/m2]
Oxygen utilization	0.3
Oxygen mole fraction	0.21
Density of air	0.329[kg/m3]
mole mass of air	0.029 [kg/mol]
Viscosity of air	$4.31\times10\text{-}5\ [\mathrm{kg/(m\cdot s)}]$
Inlet velocity	12.1 [m/s]

The investigation of the sub-manifold radii R_s

Fig.4 compares the flow rates of the 10 unit cells by varying the sub-manifold radii. The stack flow uniformity index U is analyzed and optimized to get better stack performance.

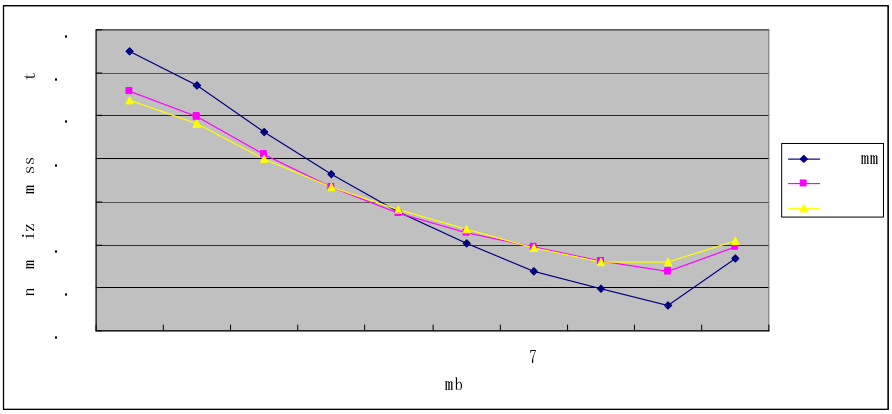

Fig. 4 The stack flow uniformity index when R_s=6 mm, 8 mm, 10 mm.

As can be seen in Fig. 4, for R_s=6 mm, 8 mm, 10 mm, the stack flow uniformity index is calculated to be 0.878, 0.879, 0.93. So the stack flow uniformity index has a certain degree of improvement with the increase of the sub-manifold radius. This may be interpreted that the flow rate can be reduced around the sub-manifold through expanding the sub-manifold radii, which helps to reduce the disorder of the gas flow from the inlet manifold. This interpretation also can be verified by Fig. 5(a-b), from this figure we can know that the 10-th unit cell velocity in the stack with R_s = 8 mm is a little larger than which in the stack with R_s=10 mm.

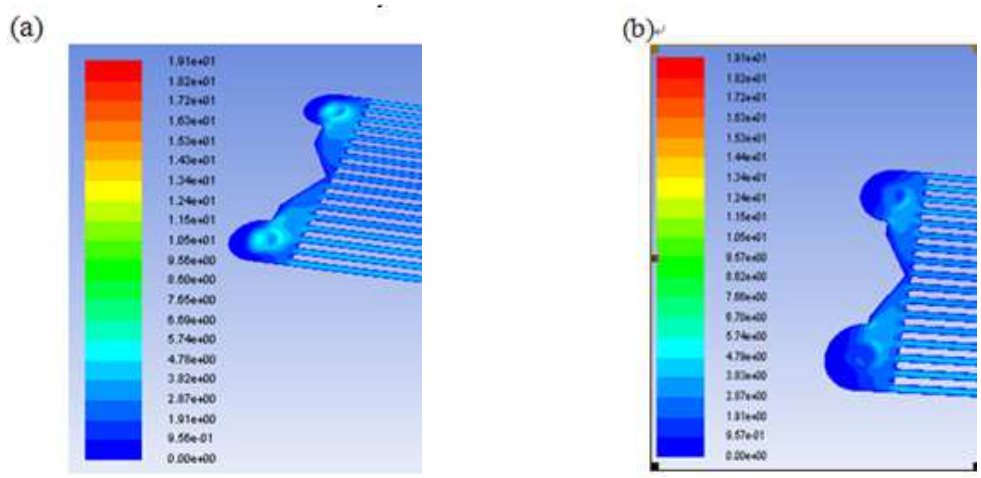

Fig. 5 The velocity diagram around the manifold of the 10-th unit cell (a) the stack with R_s =8 mm; (b) the stack with R_s =10 mm.

The investigation of the single channel width W_{ch}

In this simulation, the total interconnect plane is limited in the region between 73 mm and 75 mm. So the channel number changes along with the single channel width change.

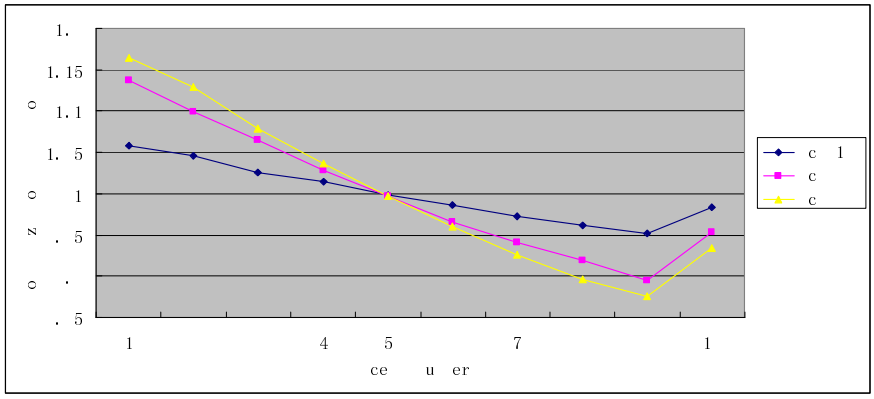

Fig. 6 The stack flow uniformity index for W_{ch} =3 mm, 2 mm and 1mm

A rang of 1mm-3mm is considered for the single channel width in the stack with R_s =8mm to examine the effect of single channel width on the flow distribution. As shown in fig.6, the flow distribution expresses better uniformity when W_{ch} =1 mm.

This phenomenon may be reasonable explained in Fig.7(a-b) , The static pressure drop shown in Fig.7(a) (the static pressure drop is about 300 pa) is much larger than which shown in Fig.7(b) (the static pressure drop is about 100 pa), which leads to better uniformity of the stack with W_{ch} =1 mm.

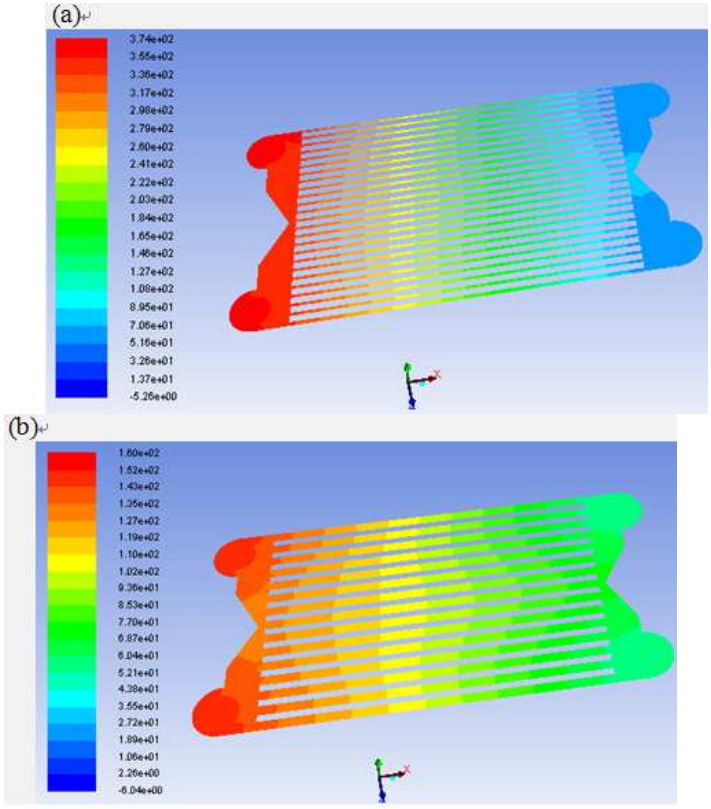

Fig. 7 The static pressure distribution of the 6-th unit cell, (a) the stack with W_{ch}=1 mm, (b) the stack with W_{ch}=3mm.

Conclusion

Realistic 3D 10-cells short planar SOFC stacks are built and investigated through CFD method using the commercial software Gambit and FLUID 6.3. The result shows that increasing the sub-manifold radii properly and decreasing the single channel width can improve the stack performance. However, the improvement of the stack performance through optimizing the channel dimension is under the expense of consuming more materials. All these analytic models and conclusions are useful and robust for the further development and commercialization of the planar SOFC stack.

Reference:

[1] Chen, D., H. He, D. Zhang, H. Wang, and M. Ni. Energies, 2013. **6**(3): p. 1632-1656.
[2] Daifen Chen, Qice Zeng, Huanhuan He, Liang Wei, and Z. Yu1. Advanced Materials Research, 2013. **662**: p. 266-272.
[3] Duquette, J. and A. Petric. Journal of Power Sources, 2004. **137**(1): p. 71-75.
[4] Yokoo, M., Y. Tabata, Y. Yoshida, K. Hayashi, Y. Nozaki, K. Nozawa, and H. Arai. Journal of Power Sources, 2008. **178**(1): p. 59-63.
[5] Lu, L., D. Chen, G. Zhao, X. Ren, and G. Guo. The Journal of Physical Chemistry C, 2010. **114**(43): p. 18435-18438.
[6] Boersma, R.J. and N.M. Sammes. Journal of Power Sources, 1996. **63**(2): p. 215-219.
[7] O'Hayre RP, C.S., Colella W, Prinz FB, *Fuel cell fundamentals*. John Wiley&Sons, 2005: p. 151-4.

Advanced Materials Research Vols. 986-987 (2014) pp 101-105

doi:10.4028/www.scientific.net/AMR.986-987.101

Preparing Sodium Methoxide from Sodium Hydroxide by Reaction Coupling with Separation Processes

Meng Xiong[1,a], Chengxi Wang[2,b] and Dandan Shao[3,c]

[1,2,3]Department of Chemical and Biological Engineering, Zhejiang University,

Hangzhou 310027, China

[a]xiongmeng0205@163.com, [b]wang_cx@zju.edu.cn

Keywords: Sodium methoxide, sodium hyrdoxide, reaction coupling with separation model

Abstract. Preparing sodium methoxide by reacting sodium hydroxide with methanol was investigated. The chemical equilibrium constant was small. Removing water out of the reaction phase could drive the reaction to produce more sodium methoxide. The experiments were carried out at different temperatures and 1 atm in semi-batch reactor by liquid evaporating to remove water. The effects of initial sodium hydroxide concentration and liquid evaporating speed were discussed. A mathematical model coupling reaction with separation processes was built and the predicted results by the model were in good agreement with experiment results. The model provides useful information for industrial simulation.

Introduction

Recent years, sodium methoxide(CH_3ONa) is being extensively investigated as an efficient catalyst for biodiesel production, aiming to lower the reaction temperature, reduce the reaction time and increase biodiesel yields[1]. One method to prepare CH_3ONa is reacting metallic sodium with methanol, because of the high cost of metallic sodium and hydrogen release in the process[2], another preparation method by sodium hydroxide and methanol is more widely used in continuous production. It is usually carried out in a reactive distillation column with large amount of gaseous anhydrous methanol fed into bottom of the column. Gaseous methanol contacts countercurrent with sodium hydroxide-methanol solution, removes water from the reaction phase and increases the production of CH_3ONa [3]. The chemical reaction can be represented as follows:

$$CH_3OH + NaOH \leftrightarrow CH_3ONa + H_2O \quad (1)$$

To reduce energy consumption and improve the product purity, it is of great value to simulate and optimize this reactive distillation process. The purpose of this paper is to conduct experiments to obtain kinetic equation of the reaction. Since the chemical equilibrium constant is small[4], it is difficult to determin the amount of CH_3ONa and H_2O accurately only by homogenenous reaction method. A semi-batch experiment method coupling reaction with seperation processes was employed, removing water by liquid evaporating. The effects of initial NaOH concentration and liquid evaporation speed on the decresing rate of NaOH concentration in reaction phase were investigated. A mathematic model was built to simulate the reaction coupling separation processes.

Experiment

Chemicals. The sodium hydroxide (96.0 mass %), anhydrous methanol (99.5 mass %) and Karl Fischer reagent were purchased from Sinopharm Chemical Reagent Co. Ltd.. The water content in the methanol did not exceed 0.05 mass %. The hydrochloric acid solution (36.0～38.0 mass %) was obtained from Hangzhou Chemical Reagent Co. Ltd..

Experimental procedures. Mixtures consisting of methanol and sodium hydroxide were prepared gravimetrically using analytical balance. For each experiment, appropriate amount of sodium hydroxide-methanol solution with various concentrations of sodium hydroxide was charged

into a three-necked round-bottom flask (500 mL) equipped with a separating funnel, a condenser and a thermometer. The flask was placed in an electric heating tank. When the solution was heated to evaporate, it was set as the start-point of the reaction. The liquid evaporating speed was kept stable by controlling electrical heating power. The vapor was condensed and collected in a conical beaker. Fresh anhydrous methanol liquid was added into the flask continuously through the separating funnel to maintain the liquid level nearly the same. The samples of the liquid mixtures in flask and conical beaker were taken through micro syringe at an interval of about 15 minutes.

Initial concentration of sodium hydroxide in methanol solution was determined by weighing the sodium hydroxide and methanol and varied from (1.25 to 5) mol/L. Sodium hydroxide and methoxide were regarded as nonvolatile components. The total concentration of sodium hydroxide and water in liquid of the flask and the water in liquid of conical beaker could be determined by Karl Fischer titration[5]. The molar fraction of methanol in liquid was close to 1, so the salt effect of sodium hydroxide and sodium methoxide on vapor-liquid equilibrium (VLE) of methanol-water system could be neglected according to literatures[6]. The concentration of water in liquid of the flask could be deduced based on the VLE of methanol-water binary system and the water in vapor could be regarded as equal to the water concentration in the liquid of conical beaker. The total concentration of sodium hydroxide and sodium methoxide in liquid was determined by titration using hydrochloric acid solution, and the concentration of sodium methoxide could be calculated.

Kinetic model

The general reaction rate expression in homogeneous phase can be written as:

$$-r_{NaOH} = k_1 C_{CH_3OH} C_{NaOH} - k_2 C_{CH_3ONa} C_{H_2O}. \quad (2)$$

where r and C represent the reaction rate (calculated based on NaOH concentration) and molar concentration respectively, and k_1, k_2 are the apparent rate constants. The concentration of methanol is great and can be regarded as a constant, so the equation can be simplified as Eq.3. k_1' is a developed apparent rate constant.

$$-r_{NaOH} = k_1' C_{NaOH} - k_2 C_{CH_3ONa} C_{H_2O}. \quad (3)$$

Because the chemical equilibrium constant is very small, the concentration of CH_3ONa and H_2O in homogeneous reaction phase is difficult to be analyzed accurately. By liquid evaporating to remove water, the reaction was driven to the right. The experimental results showed the decreasing rate of NaOH concentration in reaction phase was related to both the reaction rate in reaction phase and the liquid evaporating speed. A mathematic model coupling reaction with separation processes was built and the decreasing rate of NaOH concentration can be written as:

$$-\frac{\mathrm{d}C_{NaOH}}{\mathrm{d}t} = v \cdot (k_1' C_{NaOH} - k_2 C_{CH_3ONa} C_{H_2O}). \quad (4)$$

Where v represents the liquid evaporating speed per unit of liquid volume, t is the reaction time. v can be determined by the amount of condensed liquid collected in conical beaker over a period time. k_1' and k_2 are related to temperature of the reaction phase. The concentrations of NaOH, CH_3ONa and H_2O were determined directly or calculated from the experiment results and regressed to obtain the parameters of the model.

Results and Discussion

Effect of initial concentration of NaOH. In order to study the effect of initial concentration of NaOH, a series of experiments were carried out where the initial NaOH concentration was set at (1.25, 2.25, 3.75, 4.38 and 5.00) mol/L respectively. It is difficult to determine the composition accurately when the initial concentration is too low or more than 5.00 mol/L. Relationship between

the boiling point of the solution and initial concentration of sodium hydroxide is shown in Fig.1. It indicates that the boiling point increases with the rising initial concentration of NaOH, because the salt effect of NaOH and CH_3ONa decreases the saturated vapor pressure of methanol and increases the boiling point of the solution[6,7]. When initial NaOH concentration was held the same, the reaction temperature nearly remains unchanged during the whole process. It can be deduced that NaOH converting to CH_3ONa has little effect on the reaction temperature.

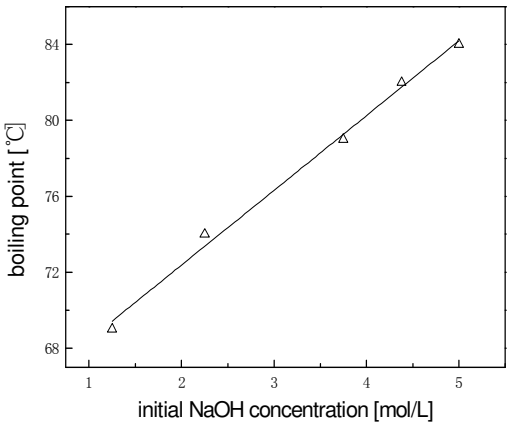

Fig. 1 Effect of initial NaOH concentration on boiling point of methanol solution

When the initial NaOH concentration varied from (1.25 to 5.00) mol/L, the liquid evaporating speed was held the same. The variation of NaOH concentration in reaction phase depending on reaction time is shown in Fig.2, represented as points in different shape. It shows that the increasing of initial NaOH concentration can enhance the decreasing rate of NaOH concentration in reaction phase. The variation of water concentration in reaction phase depending on reaction time is also shown in Fig.3.

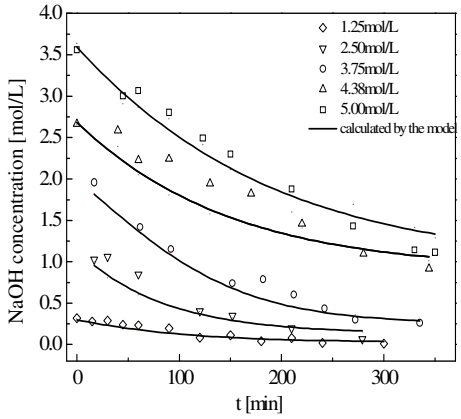

Fig. 2 Variation of NaOH concentration versus reaction time with different initial NaOH concentration

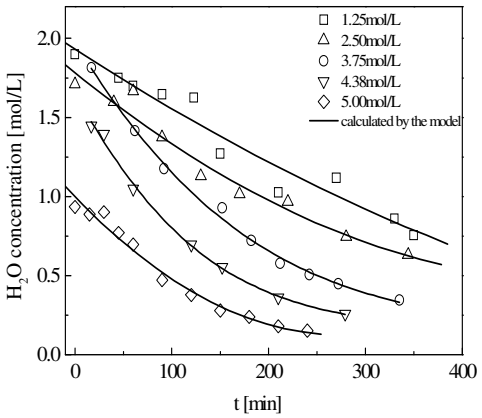

Fig. 3 Variation of H_2O concentration versus reaction time with different initial NaOH concentration

Effect of liquid evaporating speed. The liquid evaporating speed can be changed by controlling the electronic heating power. The experimental results showed that at the same reaction temperature, the decreasing rate of NaOH concentration in reaction phase gets faster with a rising liquid evaporating speed. When the liquid evaporating speed increases, more water can be removed from reaction phase into vapor phase and the reaction is driven to the right. Fig.4 shows the the variation of NaOH concentration in reaction phase depending on reaction time with different liquid evaporating speed, v, in g/(min • L), and the initial NaOH concentration fixed at 3.75 mol/L. The

experimental data is represented as points in different shape. The variation of water concentration in reaction phase depending on reaction time is also shown in Fig.5.

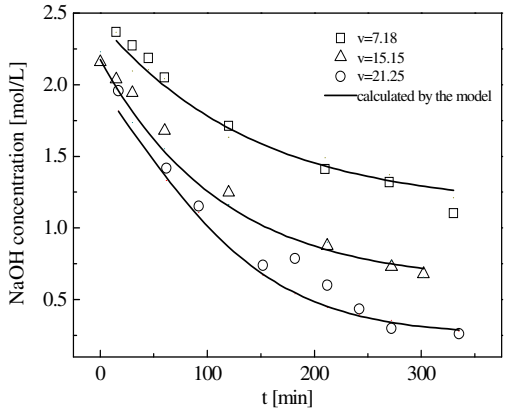

Fig. 4 NaOH concentration versus reaction time with different liquid evaporating speed

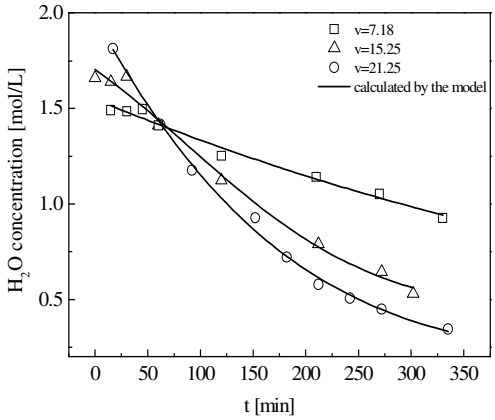

Fig. 5 H_2O concentration versus reaction time with different liquid evaporating speed

Regressed model parameters. The experimental results were fitted with multiple linear regression function to obtain the values of k_1' and k_2 in model (Eq.4) at different temperatures, and the results show that k_1' and k_2 increase with the rising temperature. According to Fig.6 and Fig.7, $\ln k_1'$ and $\ln k_2$ are linearly associated with the reciprocal of temperature.

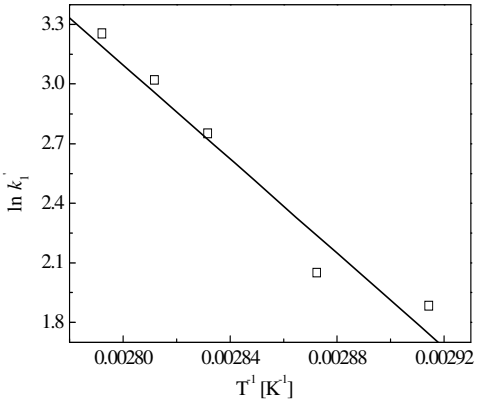

Fig. 6 Relationship between ln k_1' and 1/T

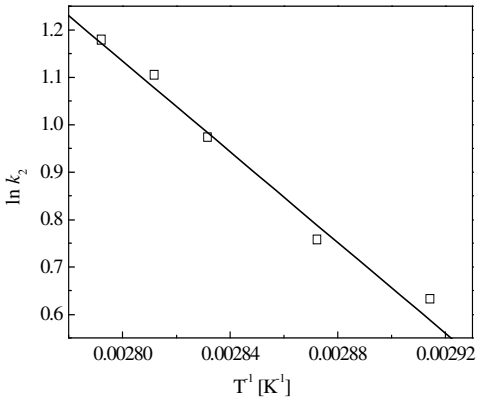

Fig. 7 Relationship between ln k_2 and 1/T

The equations between k_1', k_2 and temperature are as follows:

$$k_1' = 5.59 \times 10^{15} \exp(-\frac{11844.72}{T}). \quad (5)$$

$$k_2 = 2.06 \times 10^{6} \exp(-\frac{4787.67}{T}). \quad (6)$$

The contrasts between the predicted concentrations of sodium hydroxide and water in reaction phase by the mathematic model (Eq.4) and the experimental data are obviously shown in Fig.2, Fig.3, Fig.4 and Fig.5, the predicted results are represented as solid lines. As shown in these figures, the predicted results were in good agreement with the experimetal results. A rigorous statistical analysis was conducted on predicted results by the model and the experimental data[8]. The total sum of squares, regression sum of squares and residual sum of squares were calculated and shown in table 1. The correlation coefficient ρ^2 was found to be 0.95, and variance test value, F, was more than ten times of rejection region, $F_{0.01}$. It was concluded that when the confidence coefficient was set at 99%, the model predicted the experimental data appropriately. The model coupling reaction with separation processes can provide basic information for reactive distillation simulation.

Table 1 Statistical test of the predicted and experimental results

Statistical Index	Computing Method	Value
Experiment point, N	—	64
Independent variables, M	—	5
Total sum of squares, L	$L=\sum_{i=1}^{N}(x_i-\bar{x})^2$	54.82
Regression sum of squares, U	$U=\sum_{i=1}^{N}(\hat{x}_i-\bar{x})^2$	45.84
Residual sum of squares, Q	$Q=\sum_{i=1}^{N}(x_i-\hat{x}_i)^2$	2.75
Correlation coefficient, ρ^2	$\rho^2=1-Q/L$	0.95
Variance test value, F	$F=\frac{U/M}{Q/(N-M-1)}$	193.45
Rejection region, $F_{0.01}$	—	3.34

Conclusions

It has been demonstrated that the boiling point of methanol solution becomes higher as the initial NaOH concentration increases. Rising initial NaOH concentration and liquid evaporating speed can improve the decreasing rate of NaOH concentration in reaction phase and the degree of the reversible reaction. A mathematical model was obtained by regressing the results of experiments coupling reaction with separation processes, and it was found from the model that temperature, concentration of each component and liquid evaporating speed had great effect on the decreasing rate of NaOH concentration in reaction phase. The predicted results were in good agreement with the experimental data. The model could be used for further simulation and process optimization.

References

[1] Y.C.Lin, K.H.Hsu, J.F.Lin. Rapid palm-biodiesel production assisted by a microwave system and sodium methoxide catalyst[J]. Fuel. Vol.115: 306~311 (2014).

[2] X.D.Sun, X.D.Sun and H.B.Zhang. Process for preparing sodium methoxide from sodium metal [J]. Journal of Chemical Production and Technology. Vol.10 (5) : 35~37(2003). (in Chinese)

[3] W.G.Chen. Process for producing solution of sodium methoxide in methanol[J]. Journal of Methanal and Methanol. Vol. 6:7~9(2003). (in Chinese)

[4] B.P.Tarasov, N.G.Vergunova, V.P.Belovodskii, et al. Study of the sodium methoxide sodium hydroxide equilibrium in concentrated solutions of sodium methoxide in methanol[J]. Journal of Applied Chemistry of the USSR. Vol. 59(8Part 2):1655~1658(1986).

[5] A.P.Wang, R.Z.Mao, X.L.Liang, et al. Determination of free alkali in potassium tert-butoxide by Karl-Fischer coulomb titration Method[J]. Chemical Analysis and Meterage. Vol.17 (5):36~38(2008). (in Chinese)

[6] T.F.Sun, K.R.Bullock, A.S.Teja. Correlation and prediction of salt effects on vapor–liquid equilibrium in alcohol–water–salt systems [J]. Fluid Phase Equilibria. Vol.219:257~264(2004).

[7] W.B.Liu, J.J.Wang, T.C.Bai, et al. Isobaric Vapor-liquid equilibrium of methanol-ethanol-water -salt systems[J].Chemical Journal of Chinese University.Vol.12(4):521~524(1992). (in Chinese)

[8] C.X.Wang. Reactive process and kinetic studies on synthesis of guaiacol with catechol and methanol[J].Chemical Reaction Engineering and Technology. Vol.19(3):248~253(2003). (in Chinese)

Advanced Materials Research Vols. 986-987 (2014) pp 106-109

doi:10.4028/www.scientific.net/AMR.986-987.106

Study on the Composite Insulator Material's Characteristics under Artificial Corona Aging Condition

Yi Chunfang[1], Chen Yixin[2], LIANG Peisong[2]

[1.] Guangxi Power Grid Corp, China [2.] North China Electric Power University,

Project Supported by National Natural Science Foundation of China(51207055), Natural Science Foundation of Hebei Province(E2013502213) and Guangxi Power Grid Corp (K-GX2017-076)

Keywords: HTV SIR; Corona; Aging; FTIR; volume resistivity-temperature character

Abstract. The HTV SIR provided the superior hydrophobicity for the composite insulator. But it faces the aging problem more than the inorganics. Corona, as an inevitable influence factor in insulator's operation, its effect to the material could not be ignored. The paper developed a multi needles to plate corona aging equipment, 1000 hours' corona aging to the HTV SIR was done. The duration of corona aging effect was study by FTIR, SEM and volume resistivity-temperature character testing. Three testing methods from the aspect of material's chemical, physical and electrical characters to evaluate the aging effect with time went on. It had good consistency in all three methods for HTV SIR's corona aging evaluation.

Introduction

The superior hydrophobicity and the mobility of hydrophobicity have highly improved the insulator's pollution flashover ability[1]. The high temperature vulcanizing silicone (HTV SIR) provided its excellent ability. Contrast with the porcelain the HTV SIR is the organic material, the aging problem become more serious. The resistance of corona and ozone are one of the twelve performance index for outdoor high voltage polymer insulator, which is recommended by CIGRE Working Group D1.14[2]. And the effect way to study corona's affect is use the artificial corona[3].

The paper developed a multi needles to plate corona aging equipment for HTV SIR's corona aging. The FTIR, SEM[4] and volume resistivity-temperature testing[5] were done after the aging. The comprehensive assessments were done in the aspects of the chemical character, physical character and the electric character.

Testing

2.1 The artificial corona aging testing equipment

The traditional single needle to plate corona aging equipment is with small effect area. And contrast with plate to plate corona aging equipment, the multi needles to plate is easier in control the bloom. Several schemes had been made in electrostatic simulation software. The scheme showed in figure 1 was selected. 12 needles were placed in two concentric annuluses with the diameter of 13.5mm and 27mm. The figure 2 showed the electrostatic simulation results when the gap between needles to plate is 6mm. The experimental circuit was showed in figure 3. The longest corona aging time was set to 1000 hours. 100 hours, 300 hours, 500 hours, 700 hours corona aging samples were selected in order to research the change with the aging time.

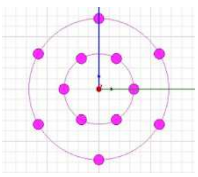

Fig. 1 The needles arranged planform

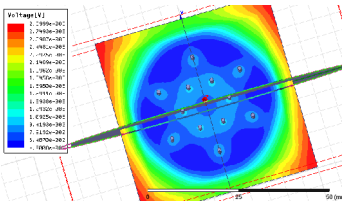

Fig. 2 Simulation of static electric field

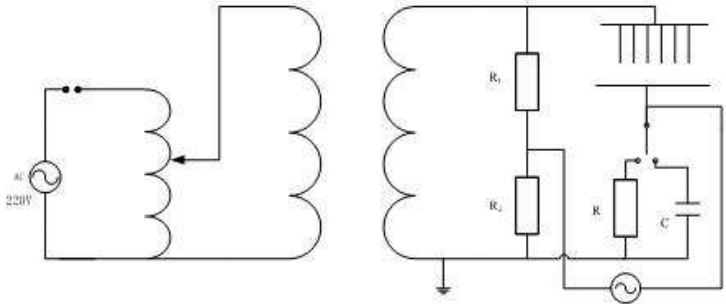

Fig. 3 Testing circuit

2.2 Testing results

The figure 4 showed the samples after different aging time. As corona aging time gain, the surface suffered more. After 100 hours corona effect, the black product come out and the affect area showed a radial effect right under the needles. The inner area was suppressed by outside needles. After 300 hours of corona aging the white product occurred and the black product became deepened.

Fig. 4 Samples after corona aging

Analysis

The material's electric character, physical character and chemical character would change under corona aging. The corona aging effect assessment was done in those three aspects.

3.1 FTIR testing

The FTIR testing was done by Nicolet Is6 Fourier transform infrared spectrometer. Based on FTIR spectrogram, the main chain Si-O-Si and side chain $Si-CH_3$ were selected to do the quantitative analysis. The original surface testing results after corona aging were showed in figure 5. Table 1 listed out the percent of each absorption peak area against the new one's. The absorption peak decreased sharply. The C-H absorption peak diminished to zero. The $Si-CH_3$ and Si-O-Si absorption peak went down largely. After 100 hours aging effect, the three –OH absorption peaks became one widely absorption peak. But as aging time gained, the absorption peak diminished. One thing should be mention was that the original surface showed the Si-O-Si absorption peak moved from $1007.624cm^{-1}$ to $1041.372cm^{-1}$, the second peak $1073.192cm^{-1}$ stayed invariability. The study figured out the absorption peak's shifting due to the long polymer chain break into short chain. After one time's FTIR testing, the product on surface fell off. So we clean the surface with alcohol and then the test to be done again. The figure 6 showed the testing results. The absorption peak compared between new and the cleaned surface had been done in Table 1 too. After cleaned the surface, the Si-O-Si absorption peak shifted to the original position and the area improved. It proved that the corona aging effect the surface more than the inner. The –OH absorption peak diminished after 100 hours' corona aging. The $Si-CH_3$ absorption peak went down slowly. After 500 hours' corona aging, the Si-O-Si absorption peak didn't show an obvious decreased. The area of absorption peak exceed to the new samples. After 700 hours' aging, the Si-O-Si absorption peak went down. Take a close look at absorption peak in $1100\sim1000cm^{-1}$, the low polymer chain in $1073cm^{-1}$ went up. It showed that the long Si-O-Si chain break into small molecule.

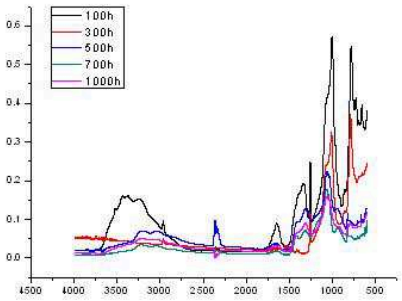

Fig. 5 Original surface's FTIR

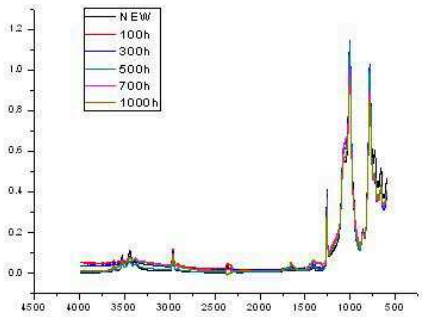

Fig. 6 Cleaned surface's FTIR

Table 1. Percentage of absorption peaks

	Si-O	Si-CH_3	C-H	-OH
100h	61.95%	73.86%	30.98%	352.05%
300h	31.52%	17.71%	16.70%	0.00%
500h	24.62%	23.19%	0.00%	4.86%
700h	22.69%	2.89%	0.00%	8.36%
1kh	18.67%	16.97%	0.00%	28.73%
C 100h	103.36%	95.16%	88.79%	34.20%
C 200h	104.80%	90.15%	83.58%	50.39%
C 300h	102.51%	91.08%	85.29%	49.11%
C 500h	103.63%	81.58%	81.33%	46.49%
C 700h	97.76%	57.77%	62.47%	51.26%
C 1kh	87.09%	69.27%	63.98%	52.29%

3.2 SEM testing

The product came out after corona was removable, so the contrast between original surface and cleaned surface had been done. The image of 500 magnified times were chosen(Figure 7). From the image, the surface of new sample was smooth and compact. As the corona aging time went on, the floccule came out and the floccule's density enhanced. The cleaned surface could not see obvious change in visual(Figure 8). But the image of 500 magnified times showed that as time went on, the hole appeared and became deeper and larger. It showed that the corona had chemical corrosion and mechanical erosion to the material.

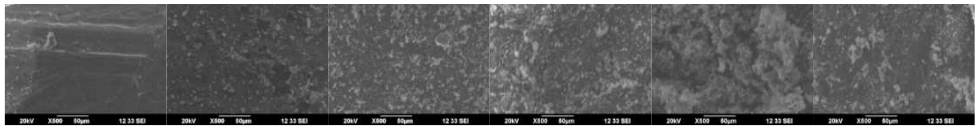

Fig. 7 The original surface

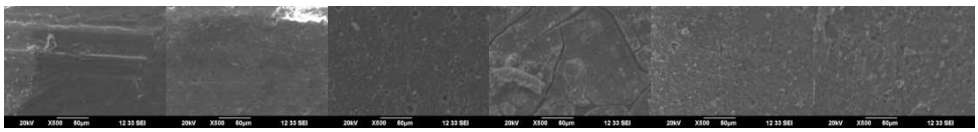

Fig. 8 The cleaned surface

3.3 Volume resistivity-temperature testing

The volume resistivity-temperature testing was done by self-made three electrode testing experiment, Which was made based on paper.

In 293K, the volume resistivity didn't show the law with the corona aging time went by. But once the linear fitting to be done from 293K to 343K, the R-Squared declined as the corona aging time gained. 500 hours and more time's aging effect, the linear had complete broke down. Take a close look at the curve; the linear first broke under temperature from 293K to 313K. The linear in 313K to 343K still kept.

Table 2. The results of volume resistivity-temperature testing

$10^{14}\Omega \cdot cm$	20	30	40	50	60	70
New	3.43	2.66	2.12	1.58	1.08	0.67
100h	2.76	2.52	1.82	1.03	0.57	0.43
300h	3.60	3.07	2.89	2.48	1.67	1.27
500h	3.10	2.85	2.16	2.04	1.33	0.87
700h	6.08	9.87	3.98	3.11	1.48	0.89
1000h	0.85	1.12	1.72	1.31	0.97	0.61

Conclusion

The multi needles to plate corona aging equipment were developed. It would get a more corona aging area and it could be average. One manufacture's HTV SIR was used. 1000 hours' corona aging was done. The duration of corona aging effect was studied by different corona aging samples. The FTIR, which reflected the chemical character, showed that the high polymer chain broke down obvious on surface. It also influenced the inner area but less obvious than the surface. The SEM testing showed that as time went on, the hole appeared and with serious erosion. The crack would appear in the serious condition. The material volume resistivity has a linear correlation with the temperature change in range 293K to 343K. As corona aging time went on, the linearity broken. And the linearity broke first in lower temperature's volume resistivity. It showed that the corona aging influence the material's chemical, physical and electric characters. All of three instruments showed a uniform in reflect the corona aging for the HTV SIR.

References

[1] N. Yoshimura and S. Kumagai. Electrical and Environmental Aging of Silicone Rubber Used in Outdoor Insulation[J]. IEEE Transactions on Dielectrics and Electrical Insulation, Vol. 6 No. 5, October 1999

[2]CIGRE WG D 1.14, "Material properties for non-ceramic outdoor insulation: State of the art", Technical Brochure No. 255, 2004.

[3] H.Hillborg, Loss and Recovery of Hydrophobicity of Polydimethyl-siloxane after Exposure to Electrical Discharges, Ph.D thesis, Department of Polymer Technology, Royal Institute of Technology, Stockholm Sweden, 2001.

[4] Wu Qiye, Zhang Ping, Yang Wenjun, et al. Gaofenzi Wulixue Physics of Polymer[M]. Beijing: Higher Education Press, 2011: 125~128 (in Chinese).

[5] Liang ying, Chen Yixin, Liu Yunpeng. The Development of the Three-Electrode Testing System for the Volume Resistivity of Composite Insulation Materials[C]. Power and Energy Engineering Conference, 2012 Asia-Pacific

Advanced Materials Research Vols. 986-987 (2014) pp 110-113

doi:10.4028/www.scientific.net/AMR.986-987.110

Synthesis and Performance Evaluation of Pour Point Depressants for Lubricating Oil

Zheng Wangang [1,2,a], Wang Shujun [1,2,b,*], Meng Fanbin[1,2,a], Ma Huanqing[1,2,a], Li Yanshan[1,2,a]

[1]State Key Laboratory of Heavy Oil Processing, China University of Petroleum, Beijing 102249, China

[2] College of Science, China University of Petroleum, Beijing 102249, China.

[a] zwg0124@126.com, [*, b] bjwsjbj@sina.com

Keywords: Pour point depressant, Temperature-viscosity curve, Lubricating oil, Copolymer.

Abstract. The paper describes synthesis and evaluation of polymeric additives for improving the flow properties of lubricating oils. The polymer (AAV) was prepared by the free-radical initiated polymerization of methacryl esters (A_{14}) with acrylamide and vinyl acetate. A_{14} and AAV were characterized by infrared spectroscopy (IR). Three lubricating oils were selected as the test oil samples and the effect of solidification point depressant (ΔSP) with different mass fractions and other physicochemical characteristics of the samples with and without AAV added were investigated. In order to analyze the effect of AAV on the viscosity of lubricating oils, viscosity-temperature curves were plotted. The results showed that AAV not only had a good effect on dropping solidifying point for Yanshan lubricating oils, but also had a good effect on dropping viscosity; what's more, other physicochemical characteristics of lubricating oil have little changes before and after AAV added.

Introduction

Lubricating oil has been widely treated with chemical additives (pour point depressants) to improve its flow properties at low temperature. Using flow improvers is often the most economic and effective solution for the lubricating oil flow problems [1]. These additives change the size and shape of wax crystals in such a manner as to allow the oil to remain fluid at lower temperature [2].

Recently, many kinds of polymers have been developed and used as pour point depressant (PPD) to influence the behavior of n-paraffin wax formation [3] [4], such as ethylen-vinyl acetate-propylene polymers[3], styrene-maleic anhydride (methoxypolyethylene glycols) copolymers [5], maleic anhydride-vinyl acetate copolymer amides [6], maleic anhydride-hexadecene-vinyl acetate terpolymers [7], methyl methacrylate-alkyl methacrylate copolymers [8], Poly-acrylic acid derivatives [9], and so on. In recent years, increasing attention has been paid to Methyl acrylate polymers, which not only were used to improving the low temperature flow performance of lubricating oils, but also had effects on temperature-viscosity properties [10].

In the present work, methacryl esters-acrylamide-vinyl acetate copolymer (AAV) was synthesized, and the chemical structures of the polymer prepared were studied by means of IR. Kinematic viscosity, flash point, neutralization number, oxidation stability etc. are the vital properties to affect the abilities of lubricating oil, however, to date, little work has been focused on the research of these characteristics with and without AAV.

Experimental

Materials. Copolymer AAV was synthesized and purified in the laboratory. Methacrylic acid (purity≥99.5%) and Tetradecyl alcohol (A. R.) were provided by Tianjin Guangfu Fine Chemical Research Institute. Acrylamide (A. R.) was obtained from the Tianjin Fuchen Chemical Reagent Company. Vinyl acetate (purity≥99.5%) was obtained from the Fine Chemistry Trial Plant of Nankai

University. Methylenzene (purity≥99%) and Ethanol (A. R.) were provided by the Beijing Chemical Reagent Company.

In the experiment, A, B and C lubricating oils samples were 150SN, 350SN and 500SN, respectively, which obtained from Yanshan Petrochemical Corporation.

Esterification. Methacrylic acid ester was prepared by the reaction of 1.2mol methacrylic acid and 1mol tetradecyl alcohol in a round bottom flask equipped with a Dean-Stark apparatus to remove the water of reaction azeotropica as it was formed. The reaction took place in the presence of toluene (100mL) as solvent, hydroquinone (0.9%, mass fraction) as polymerization inhibitor and paratoluenesulfonic acid (0.8%, mass fraction) as catalyst. After the completion of the reaction, the toluene was removed through distillation at reduced pressure, and the crude product was neutralized using Na_2CO_3 solution and distilled water to remove the catalyst and unreacted acid, then dried over anhydrous $CaCl_2$ for 8h. Eventually, the first monomer was obtained.

Polymerization. The copolymers were prepared by reacting 0.6 mol tetradecyl acrylate with 0.1mol acrylamide and 0.3mol vinyl acetate in toluene solvent using benzoyl peroxide (0.8% by wt) as initiator. The copolymerization was conducted at 75 °C for 4 h with constant stirring and nitrogen atmosphere. Afterward, removing the solvent by reduced pressure distillation, and purifying the copolymer in ethanol and vacuum dried at 50 °C for 12h, then the polymer was prepared.

The process of the reaction is as Fig. 1:

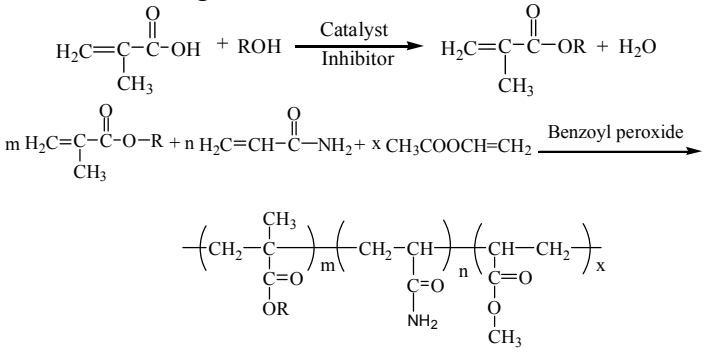

Fig. 1 The process of the reaction

Solidification point measurement. The cold flow performance, solid point depression (ΔSP) of the tested lubricating oils samples were determined according to GB/T 510 standard methods. The solid point depression was determined by SWXK-402D multi-functional tester for petroleum product made in Shanghai Pengpu Refrigeration Corporation. The lubricating oil samples, either containing additive or not, was warmed in a water bath up to (50±2) °C and cooled to (35±5) °C, then transferred to the solidification point tube kept in cooling bath, After each 2 °C interval the tube was taken out and tilted to see the behavior of the oil sample. Until the movement of the sample did not occur, the corresponding temperature was noted as the SP of the samples.

Viscosity measurement. The viscosity measurement was determined according to the national standard GN/T265-1988 "Viscosity petroleum products - Determination of kinematic viscosity and calculation of dynamic viscosity", by American Brookfield company's DV-I+ digital display viscometer. The America Brookfield company production of rotary viscometer is viscosity determination of world standard.

Results and Discussions

Characterization of chemical structures of copolymers and Methacrylic acid ester. The chemical structures of the first monomer and copolymer AAV were studied by means of infrared spectrometry in chloroform solution. MAGNA-IR 560 was used for IR spectral determination. The scanning range was from 4000 to 400 cm^{-1}, the differentiating rate was 0.35cm^{-1}, and the signal-to-noise ratio was 30,000:1.

It can be clearly seen from the Fig. 2(a) that the stretching peaks of the fatty alcohol hydroxyl (3200~3300cm^{-1}) characteristic absorption peak has gone, the stretching peaks of the characteristic -C=O of unsaturated ester is at 1722cm^{-1}, and the absorption peak of the character C-O-C is at 1165cm^{-1}. The results indicated that the A_{14} monomer was obtained.

By comparing Fig. 2(b) with Fig. 2(a), it can be seen that the stretching vibration peak of characteristic C=O of amide are at 1680cm^{-1}, the typical swing absorption peaks of character -CH_2- of long-chain alkyl is at 721cm^{-1}. However, the stretching vibration peak (1640 cm^{-1}) of C=C and in-plane rocking vibration peak (938cm^{-1} and 814cm^{-1}) of =CH_2 has disappeared. The results showed that the copolymer AAV was obtained.

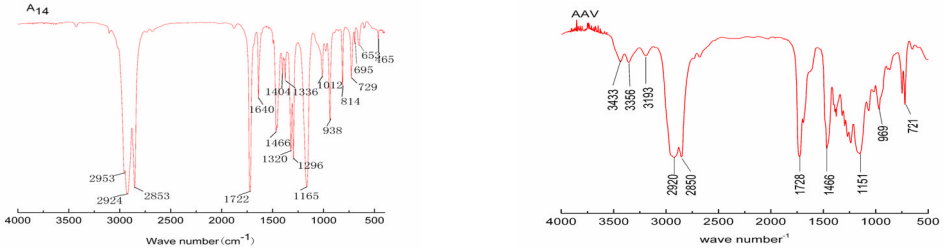

(a) (b)

Fig. 2 FT-IR spectra of A_{14} and AAV: (a) A_{14}; (b) AAV

Evaluation of the cold flow performance. The cold flow performance of the tested lubricating oils was evaluated by the addition of AAV at different dosages. The results were described in Table 1.

Table 1 Influence of different dosage on pour point for different lubricating oil

w (AAV) (%)	Solidification point depression (ΔSP) (°C)		
	A	B	C
0.25	8	8	4
0.50	17	16	13
0.75	30	26	23
1.00	28	29	29
1.25	28	28	26

The mechanism of pour point depression has been well explained [6] [11]. The PPD when present in the lubricating oil, changes the wax crystal sharps from thin extensively interlocking plates to more compact crystals by co-crystallizing with the wax. The performance of the flow improver depends on the total wax content. 150SN, 350SN and 500SN were distinguished by Saybolt viscosity at 40 °C. 150SN, for example, means the Saybolt viscosity is about 150 at 40 °C, so do the 350SN and 500SN. The higher the number, the greater the viscosity, correspondingly, the higher mass fraction of wax will be. According to the figure in the table, the pour point of 150SN could be reduced by 30 °C with 0.75% of the additive, and 350SN and 500SN were reduced by 29 °C, 29 °C with 1% of the additives, respectively. On the basis of this conclusion and theoretical analysis, the pour point of sample A would be dropped easily than B and C, as the wax crystal of A was less.

Comparison of other physicochemical characteristics of the tested oils without and with AAV added. Kinematic viscosity, flash point, neutralization number aniline point, extrinsic feature, density and oxidation stability are the physicochemical characteristics related to the applications of the lubricating oil. To evaluate the effect of AAV copolymer on these physicochemical characteristics, the three base oils were selected as the tested samples. The physicochemical characteristics of the three samples before and after 0.75% (mass fraction) AAV added were furnished in Table 2.

It can be noted from the Table 2 that the kinematic viscosity at low temperature were reduced more than half compared with the samples without AAV. To evaluate the effect of AAV copolymer on the viscosity characteristic, the viscosity-temperature curves of sample A and B with and without AAV had been given as Fig. 3.

The results given in Fig. 3 showed that there were obvious drops in kinematic viscosity from -5 °C to 40 °C. What's more, compared with the blank sample, the viscosity-temperature curve of oil with 0.75% AAV becomes relatively smooth. It can be concluded that AAV additives performs well at the

viscosity-temperature properties. What' more, see Table 2, the flash point of tested oils with AAV added were reduced 2 °C to 3 °C, meaning that the AAV additive raised the vapor pressure of the oil sample. Compared with the flash point, there were no obvious changes in the extrinsic feature, neutralization number, density, aniline point and Oxidation stability.

Table 2 Influence of AAV on the physicochemical characteristics of tested oils

contents	A		B		C	
	Before	After	Before	After	Before	After
-5 °C viscosity (mPa·s)	392.9	263.4	1200	353.9	1288	407.6
40 °C viscosity (mPa·s)	27.3	22.8	71.6	36.5	103.5	61.6
100 °C viscosity (mPa·s)	5.5	5.5	8.4	8.4	11.0	11.1
SP (°C)	-11	-41	-9	-35	-9	-32
Extrinsic feature	hyaline	hyaline	hyaline	hyaline	hyaline	hyaline
Flash point (°C) (Open up)	208	206	236	233	246	244
Neutralization number (mg KOH.g^{-1})	0.01	0.01	0.01	0.01	0.02	0.02
Density (40 °C) (g.cm^{-3})	0.8678	0.8673	0.8782	0.8778	0.8804	0.8798
Aniline point (°C)	101.5	101.2	106. 8	106. 5	110.7	110.6
Oxidation stability (min), (RBOT, 150 °C)	208	209	210	210	159	160

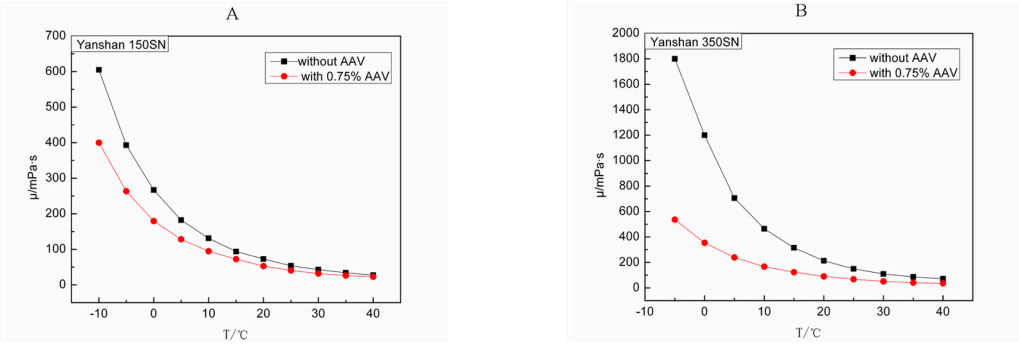

Fig. 3 Viscosity-temperature curve of Sample A and B with and without AAV

Summary

The polymer (AAV) was prepared by polymerization of methacryl esters (A_{14}) with acrylamide and vinyl acetate. When the dosage of improver AAV was 7500 μg/g, the ΔSP of the Sample A, B and C lubricating oils were lowered by 30 °C, 26 °C and 23 °C respectively. The copolymer not only had a good effect on the pour point depressant, but also had a good effect on the viscosity-temperature properties, while the other physicochemical characteristics of lubricating oil can not be significantly changed after AAV added.

References

[1] Y. P. Song, and T. H. Ren: Petroleum Science and Technology, vol. 23 (2005) no.5-6, p. 669-679.
[2] I. M. El-Gamal, and A. M. Al-Sabbagh: Fuel, vol. 75 (1996) no. 6, p. 743-750.
[3] C. J. Wu, J. L. Zhang, W. Li, et al: Fuel, vol. 84 (2005) no. 16, p. 2039-2047.
[4] S. Han, Y. P. Song, T. H. Ren, et al: Energy & Fuel, vol. 23 (2009) no. 5, p. 2576-2580.
[5] S. S. Hou, P. L. Kuo: Polymer, vol. 42 (2001) no. 6, p. 2387-2394.
[6] H. K. Zhang, H. Y. Liu, S. h. Wang: Petroleum Science, vol. 6 (2009) no. 1, p. 82-85.
[7] H. K. Zhang, S. J. Wang, H. Y. Liu, et al: Acta Petrolei Sinica (Petroleum Processing Section), vol. 24 (2008) no. 6, p. 669-674.
[8] R. A. Soldi, A. R. Oliveira, R. V. Barbosa, et al: European Polymer Journal, vol. 43 (2007) no. 8, p. 3671-3678.
[9] C. Y. Jiang, M. Xu, X. L. Xi, et al: Journal of Natural Gas Chemistry, vol. 15 (2006) no. 3, p. 217-222.
[10] L. A. Quinchia, M. A. Delgado: Industrial Crops and Products, vol 37 (2012) no. 1, p. 383-388.
[11] P. S. Hemant, D. P. Bharambe, A. Nagar, et al: Indian Journal of Chemical Technology, vol. 12 (2005) no. 1, p. 55-61.

Advanced Materials Research Vols. 986-987 (2014) pp 114-118

doi:10.4028/www.scientific.net/AMR.986-987.114

The effect of field emission characteristic on partial arc caused by pollutant and water

Dongming Liu[1], Fusheng Guo[1,a] and Wenxia Sima[2]

[1]Yantai Electric Power Bureau, Yantai 264000, China;

[2]State Key Laboratory of Power Equipment & System Security and New Technology, College of Electrical Engineering, Chongqing University, Chongqing 400044, China.

[a]guofs2012@sina.com

Keywords: Insulation, discharge, field emission, partial arc

Abstract. A flat plate model are employed to investigate the development mechanism of the initial electrons along the insulation surface in this paper, and the field emission properties of pollutant (NaCl) and water (H_2O) adsorbed on the copper electrode are studied. The voltage when partial arc occurs is computed and a flat plate experiment is carried out to validate the computing results. Results indicate that pollutant and water have an important impact on the field emission, where pollutant is more significant than water. Meanwhile, the pollutant and water can increase the probability to form the partial arc.

Introduction

The discharge along the polluted surface of insulator is a major problem in power transmission system all the time, and it remains a hot subject in high voltage insulation field and receives much concern [1]. Many methods have been developed to deal with the polluted flashover of insulator, and a great progress has been achieved in engineering application [2-6]. Recently, the basis of selecting the parameters and their characteristics in early models are studied [7], and the calculation model is optimized too. However, there is no perfect model exists.

It is well known that the problem is more severe for HVDC lines where DC insulators are found to collect more pollutants and also flashover more readily than AC units under otherwise identical conditions [8]. Although the early scholars have already discussed some aspects about the mechanism of polluted surface discharge and learned that the pollutant can enhance field emission and aggravate the discharge along the insulation surface [9,10], the discharge reason in a profound physical meaning is still not clear. So it needs to research the discharge from the generation of initial electrons to the formation of partial arc.

In order to analyze the polluted surface discharge mechanism better, in this paper, a flat plate model is employed. The effect of field emission characteristics in dry band caused by pollutant and water are emphatically studied based on the first-principle.Then the voltage when partial arc appeared is computed and an experiment.

Physical model

For actual suspension insulators are difficult to analyze theoretically since they have a complex shape, it is more convenient to use a simpler shape for calculation and experiment. In the paper, a flat glass plate model with size of 60cm×20cm×1cm and two column electrodes with the radius of 5cm are employed, as shown in Fig.1.

Under the humid condition, the pollutant layer on the insulator surface became a conductive film, and the leakage current increased. The area where current density or layer resistance is larger produced more heat and dried much faster. A dry band formed here first, and then it became a high-resistance area without ionic conductivity.

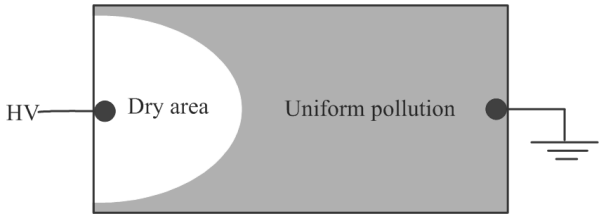

Fig.1 Flat plate model of the polluted insulator

Arc voltage calculation

Although the Malter effect, the defects, and the polarization of dielectric are different in the discharge, they can be equivalent to the field emission. The field emission current density [11] can be expressed as follows:

$$J_f = CE^2 \exp(-\frac{D}{E})$$

$$C = \frac{e^2\Phi_m^2}{2\pi h(\Phi+\Phi_m)\Phi^{1/2}} = \frac{6.16\times10^{-6}}{\Phi_b}\sqrt{\frac{\Phi_m}{\Phi}}$$

$$D = \frac{8\pi}{3h}(2me)^{\frac{1}{2}}\Phi^{\frac{3}{2}} = 6.83\times10^9\Phi^{\frac{3}{2}}$$

$$E = \frac{U}{R}$$

where Φ is the work function of metal; Φ_{m} is the potential band of metal; U is the applied voltage; R is the electrode burr tip curvature radius; and N is the electron density per cubic meter in metal. Thus, the equation J_f can be rewritten:

$$J_f = 6.16\times10^{-6}\frac{1}{\Phi_b}\sqrt{\frac{\Phi_m}{\Phi}}\times(\frac{U}{R})^2\exp(-\frac{6.83\times10^9\Phi^{\frac{3}{2}}R}{U})$$

Based on the equations [12] as follows:

$$r = \sqrt{\frac{I}{14500\pi}}$$

$$I = \pi r^2 J_f$$

the current density acquired when the partial arc occurs can be obtained:

$$J_f = 14500$$

Suppose that the arc is formed by field emission, and the current density of arc equals to the field emission current density. For the copper electrode, Φ=4.65eV, Φ_m=7eV. The surface roughness of the electrode used is R=0.5μm. The voltage calculated is $U\approx$6.01 kV when the partial arc occurs.

Tests and analysis

Tests. A DC high voltage of up to 200 kV is supplied by a cascade rectifying circuit controlled by the thyristor voltage – current feedback system, which ensured a dynamic voltage drop of less than 5% when the load current is 0.5 A. The test power supply meets the requirements commended by the IEEE Standard-4-1995 and IEC 61245 – 1993 [13-14].

The same size specimens mentioned in Section 2 are used. Referring to [14-16], the test procedures in this paper are as follows. Before the tests, all specimens are carefully cleaned. All traces of dirt and grease are removed, and dried naturally. A positive polarity-applied voltage generally results in higher flashover voltage than the negative polarity; therefore, negative DC voltages are introduced in the present paper. Every specimen is subjected to 10 tests; the average value is taken as the trial value.

Analysis.

The Field Emission Characteristics. Three kinds of electrodes were prepared: one clean, one with water, and one with pollutant. The glass surface was kept clean during the preparation of specimens. After the preparation, DC voltage was applied to the specimens and increased until flashover occurs. Fig. 2, 3, and 4 is the microdischarge of different systems before flashover (T_f), respectively.

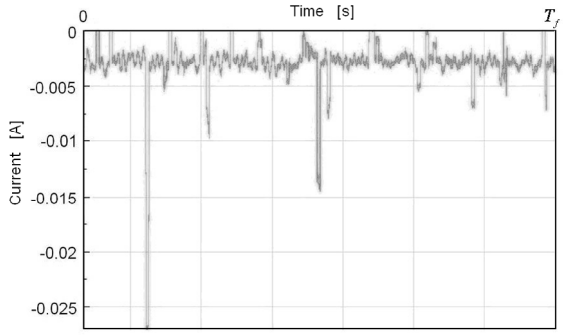

Fig.2 Micro-discharge of clean electrode

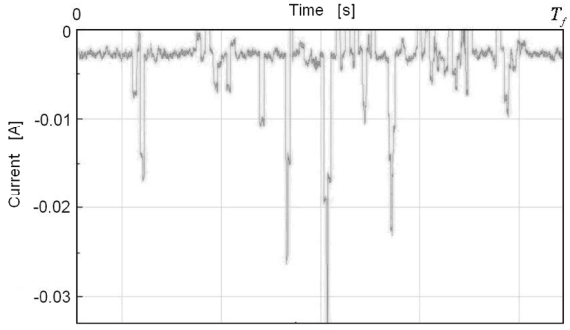

Fig.3 Micro-discharge of electrode with water

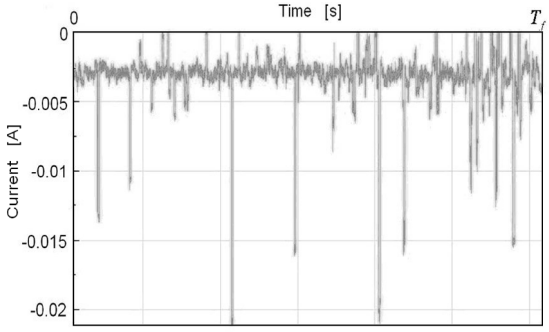

Fig.4 Micro-discharge of electrode with contamination

Figs. 2, 3 and 4 present that pollutant and water can enhance field emission, aggravate the discharge along the insulation surface, and increase the number of micro-discharge pulses. The effect of pollutant is more significant than that of water, which is consistent with the conclusion from molecular simulation. Thus, the existence of pollutant can not only reduce the flashover voltage under wet conditions, but also deeply influence the development of discharge at the beginning of applied voltage.

Table.1 The total current and times of strong discharge under different conditions

	clean	water	pollutant
Total current [A]	0.1043	0.1715	0.2358
Times of strong discharge [I>0.01A]	3	7	10

Table 1 shows the statistics of the total current and the number of strong discharge before flashover. When pollutant and water are present, the total current is 1.6 times and 2.3 times larger than that of the clean electrode, respectively, whereas the number of strong discharge is 2.3 times and 3.3 times

larger than that of the clean electrode, respectively. The effects of water and pollutant not only increase the discharge strength, but also increase the probability to form the partial arc.

Effect on the Partial Arc Voltage. One hour after the aforementioned preparation, the solid-layer method was applied to the pollution layer on the specimens where sodium chloride and kaolin were electric and inert materials, respectively [17]. The equivalent salt deposit density (ESDD, mg/cm^2) has been widely used to characterize the severity of outdoor pollution. In the present work, the authors prepared ESDD of 0.03, 0.05, 0.1, and 0.2 mg/cm^2 in four kinds of pollution grade glass flats. The pollution layer on the flat was wetted completely; in this process, the temperature was controlled to be lower than 35°C.

The relationship between voltage and ESDD is shown in Fig. 5. The blue and red curves indicate that with the increment of ESDD, the critical flashover voltage and the voltage when the partial arc appeared are all reduced exponentially. The voltages reduced 45.95% and 37.62% from clean to the pollution grade of 0.2 mg/cm^2, respectively. The black curve is the theoretical value of the appearance of the partial arc, which is always larger than experiment value when pollutants exist; the more severe the pollution is, the lower the voltage of the partial arc will be. The factors influencing discharge include pollutant particles, ambient temperature, humidity, pressure, and ray irradiation, all of which benefit discharge. The trial value at clean condition is larger than the theoretical value because the air molecule has a barrier, thereby requiring an adsorption effect and a higher voltage to maintain discharge. The green curve is the voltage difference of the critical flashover and the appearance of the partial arc, which is also reduced exponentially with the ESDD. The existence of pollutant not only reduces the critical flashover voltage under wet conditions, but also influences the development of discharge at the beginning of applied voltage deeply.

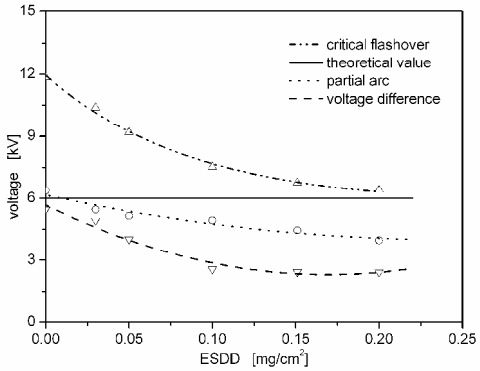

Figure.5 Relationship between voltage and ESDD

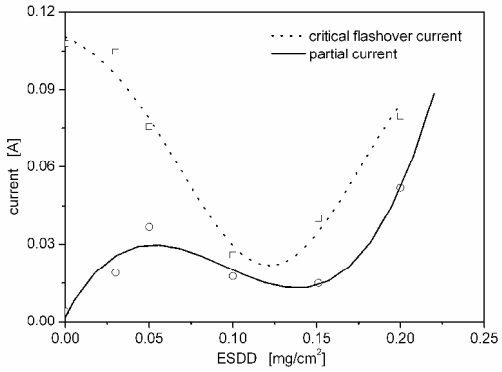

Figure.6 Relationship between the current and ESDD

The critical flashover current and the current when the partial arc appeared are compared in Fig. 6. The black curve indicates that the critical flashover current initially decreases and then increases, and has a parabolic relationship with ESDD. The red curve indicates that the current when the partial arc appeared initially decreases increases, and then increases even further. The main reason for the change in the black curve is that although conductivity is small at a low pollution grade, the high applied voltage can generate a high field that is beneficial to field emission. The residual polluted layer conductivity is high when it is at a high pollution grade. Nearly all the voltage is applied on the dry band, leading to a strong field that is also beneficial to field emission. From the two conditions

above, the current measured is high. The main reason for the change in the red curve is that the air molecule has a barrier and an adsorption effect, resulting in a weak current at clean condition. The curve shows that, up to the moderate pollution grade, the current increases because of the field emission of the pollutant particle at a strong field. When the pollution grade increases, the surface conductivity increases; thus, the voltage distributed on the electrode vicinity produces a low field and weakens the field emission, leading to a low current. The residual polluted layer conductivity is large when it is at a high pollution grade. Nearly all the voltage is applied on the dry band, leading to a strong field that is also beneficial to field emission.

Although the ESDD of a moderate pollution grade ranges from 0.1 to 0.17 mg/cm^2, little difference is found between the critical flashover current and the current when the partial arc appeared. However, the interval between the appearance of the partial arc and the flashover is very short at close quarters; it can be considered as occurring simultaneously, which is consistent with experimental observation.

Conclusion

The voltage when partial arc occurs is computed and a flat plate experiment is carried out to validate the computing results. The results indicate that the pollutant and the water promoted the field emission effectively and the effect of the pollutant is more serious than that of water, which increased the probability to form the partial arc and reduced the critical flashover voltage too.

References

[1] B. Subba Reddy, Udaya Kumar, Journal of Materials Engineering and Performance .20(2011), p.24-30.
[2] Huafeng Su, Zhidong Jia, Zhicheng Guan, IEEE Transactions on Dielectrics and Electrical Insulation 17(2010), p.1635-1640.
[3] Zafer Aydogmus, Mehmet Cebeci, IEEE Transactions on Electrical Insulation 11(2004), p.577-581.
[4] Muhsin Tunay Gencoglu, Mehmet Cebeci, Electric Power Systems Research 78(2008), p.1914-1921.
[5] R. T. Waters, A. Haddad, H. Griffiths, N. Harid and P. Sarkar, IEEE Trans on Dielectrics and Electrical Insulation 17(2010), p.417-421.
[6] S. Venkataraman, R. S. Gorur, IEEE Transactions on Dielectrics and Electrical Insulation 13(2006), p.862-868.
[7] M. EI-A. Slama, A. Beroual, H. Hadi, IEEE Transactions on Electrical Insulation 17(2010), p.1764-1769.
[8] T. C. Cheng, C. Y. Wu, H. Nour, IEEE Transactions on Electrical Insulation 19(1984), p.536-541.
[9] Alston L L, Zoeledziowski S, PROC. IEE, Vol. 110(1963), No. 7, pp. 1260-1266.
[10] Woodson H H, Mcelroy A J, IEEE Transactions on Power Apparatus and Systems 89(1970), p.1858-1862.
[11] J.Reece Roth. Industrial plasma engineering, 1: Principles, IOP publishing Ltd, 1995.
[12] Zhijin Zhang, Ph.D. Thesis, Chongqing University, Chongqing (2007).
[13] IEEE Standard Techniques for High-Voltage Testing, IEEE Std.-4, (1995).
[14] Artificial pollution tests on high-voltage insulators to be used on d. c. systems, IEC Tech. Rep., (1993).
[15] Artificial pollution tests on high-voltage insulators to be used on dc systems, IEC Tech. Rep. GB/T 22707, 2008
[16] CIGRE WG’ S-33.04. Electra, 140 (1992).
[17] Amitesh Maiti, Jan Andzelm, Noppawan Tanpipat, Physical Review Letters 87(2001), 155502.
[18] l Furnace, vol. 31 (2009) no. 2, p. 9-14.

Advanced Materials Research Vols. 986-987 (2014) pp 119-122

doi:10.4028/www.scientific.net/AMR.986-987.119

The Improving Measures Research on the Cycle Life of Lead-acid Batteries for Electric Vehicles

Lu Junmin[1,a], Wang Xiaokan[1,b]

[1]Henan Mechanical and Electrical Vocational College, Xinzheng, 451191, China

[a]wxkbbg@163.com, [b]wangxiaokan@126.com

Keywords: Grid alloys;Mixing Paste and Curing Process;The Negative Additive;The Combination of the Positive and Negative Plates

Abstract. By describing the main affecting factors of the small electric vehicles cycle life for the lead-acid batteries,then studying the main technical measures that how to improve the deep cycle performance of the batteries to prolong its life.When the methods of the combination of grid alloys ,mixing paste and curing process parameters control, the selection of the negative organic additives and the sets mode of the positive and negative plates were used,the battery performance and the cycle life greatly improved and the failure rate decreased.

Introduction

Electric bicycle is a green traffic tool which has already formed the new industry in the recent years. the representative small electric vehicles of the golf carts, sightseeing vehicle and warehouse forklift trucks are rapidly developing, and which cause the market demands of the lead-acid battery continue expanding,so that it was paid well attention to the industry peers.The battery is the key component of electric vehicle,the battery palaced space of the vehicle is limited and the battery energy requirements are higher, so the battery of the small electric vehicles are usually using the pasted positive and negative electrode. The rated voltage is 6V and the rated capacityis170 - 210Ah (5h ratio) of the golf car is the representative products of the battery (hereinafter referred to the power battery). The key indicators of this battery is the deep circulation discharge life which the cycle numbers should be no less than 400 under the condition of 80% DOD, by this way could ensure the actual use life of the battery will more than reach to 1.5-2 years. This paper mainly introduces the main factors which influencing power battery life, and studies the main measures of improving the the deep circulation performance and service life.

The Main Influence Factors of the Power Battery Life

The Corrosion Deformation of the Positive Plate

When the battery is in the long deep discharge cycle,the positive plate will suffer corrosion, grid size will linearly increase, which resulted to ribs and border elongation deformation or fracture even occurs short circuit.Anatomizing the end life battery, the deformation and fracture,the irregular fracture penetration separator plate can be seen on both sides of the plate, the upper plate expansion to the bus and cause cell short-circuit phenomenon.Theory and Practice has proved that grid corrosion and deformation is one of the important causes of deep cycle battery life shortened,so the electrochemical properties of the power battery plate should be smaller corrosion rate and non intergranular corrosion,and also should have the appropriate hardness,strength and creep resistance on the mechanical properties.

The Softening and Shedding of the Positive Active Material

In the charge- discharge cycle, PbO2 and PbSO4 will mutual transform,the volume of the active material will change and increase the change volume with the incasement of the cycle numbers.In the living plate 4BS plays an important role for the electrode plate active material strength,if mixing paste and curing process is out of control, when the 4BS content is lower than 60%,the plate active material intensity will be poor,easy soften and shed, and reduce the use life of the battery.

The Precipitation of the Negative Additive

In fasting charge and overcharge state, the battery temperature reaches above 60℃,the negative electrode plate in the high temperature electrolyte will early precipice because of the soluble of the organic expander.In the battery liquid injection hole the redness electrolyte will obviously be observed.The negative plate in the high temperature of the electrolyte, the organic expansion agent soluble, to the early from the negative precipitation, is observed in , the loss of the organic additive makes the performance of the negative electrode deteriorate.

Research of Prolonging the Cycle Life of the Battery

The Selection of the Grid Alloy

The selection of the deep cycle battery grid alloys have been many reported in the literature,the major combinations were shown in the table 1.

Table 1 The Combination Of Positive And Negative Grid Alloy

Alloy code	The alloy composite of the positive plate	The alloy composite of the negative plate	Water loss
A	$Pb{\cdot}Ca{\cdot}Sn{\cdot}Ai$（four alloy composite）	$Pb{\cdot}Ca{\cdot}Ai$（three alloy composite）	1.2-2.5
B	$Pb{\cdot}Sb$（2-2.5%）$\cdot As{\cdot}Sn{\cdot}Se{\cdot}Cu$（six alloy composite）	$Pb{\cdot}Ca{\cdot}Ai$（three alloy composite）	3.0-5.0
C	$Pb{\cdot}Sb$（2-2.5%）$\cdot As{\cdot}Sn{\cdot}Se{\cdot}Cu$（six alloy composite）	$Pb{\cdot}Sb$（2-2.5%）$\cdot As{\cdot}Sn{\cdot}Se{\cdot}Cu$（six alloy composite）	5.0-7.0

The combination of the above three grid alloy which were the grid material of the power battery, the cycle life of the merits tendency is C> B> A. A kind of combination is generally believed that the use of Pb-Ca positive grid that the active material interface layer of the corrosion resistance of purified large insulating film.To prevent the generation of the purification, the general method is to add the Sn,that is, high Sn and low Ca alloy,so the alloys are used in the positive plate of poor water VRLA battery which the water loss is a minimum and its test data is 1.5-2.5g/Ah.but the mechanical strength,creep resistance and deep charge and discharge performance (no effect in the presence of antimony) of Pb-Ca alloy is still below the Pb-Sb alloy.The small electric vehicle batteries use flooded design that it could regularly pay replenishment and maintenance,so Pb-Sb multi-alloy should be the best selection.B alloy is the best combination which can effectively improve performance while maintaining deep cycle relative reduction of water loss purposes.The alloy components are:

Positive plate alloy : Pb+Sb(1.8-2%)+As(0.1-0.2)+Sn(0.2-0.5)+Se(0.02-0.04)+Cu(0.03-0.04),

Negative plate alloy : Pb+Ca(0.06-0.1)+Ai(0.02-0.04%).

In addition,Pb-Sb alloy contains a certain amount of Cu according to relevant literatures which has an important influence on the size and composition of the alloy grain.If the alloy was aging treated at a temperature,then could obtain the recrystallized grains which without grain crystalline grains,the grain structure would be more favorable to reduce the creep rate.Many test results show that if the six Pb-Sb alloy positive plates heat treatment at temperatures of 80±5℃ for 10-12 hours, and then at room temperature for 3-5 days in a state of natural aging,its have a significant effect for the improvement of the positive plate formation and crack,meanwhile improving the battery life.

Mixing Paste and Curing Process Control

The mixing paste temperature control and raw plate curing conditions have an important role in the life on deep cycle battery life,so it must be given adequate attention.It is well known that the main ingredients of raw plate are 3BS and 4BS.The content of 3BS is high with the thinner skeleton structure ,after curing that the content of β-PbO2 in living material is high and the initial capacity of the battery is good,but the strength of the active material is poor.The 4BS with coarse skeleton structure after curing which could transform into α-PbO2 with high strength, so it plays the role of "reinforced concrete".So we could control the process to improve the content of 4BS and enhance the strength and prolong the service life of the positive plate.Theory analysis and practice research have proved that,the mixing paste temperature has an important influence on the lead paste structure under the same conditions of the positive lead paste formula and acid content.If the positive lead

paste was prepared at the highest temperature 80℃,it would mainly compose of 4BS;If the positive lead paste was prepared at less than 65℃,it would mainly compose of 3BS.When the temperature is 65℃-85℃,the highest temperature was controlled at 65℃, 70℃, 75℃, 80℃, 85℃ were divided into five groups by preparing paste which could adjust by the automatic adding acid device to control acid speed;the smear process could act as the same above process and make the rapid surface after drying and curing.Making up the positive lead paste needing Barton lead powder which must be cured at high temperature,so it could obtain a satisfactory quality.According to the characteristics of the original Barton oxide and curing process,the curing temperature was controlled at 72℃-78℃,the humidity was more than 95%, then using a multi-stage temperature and humidity control to cur the test plate and make it format and dry.The five plates with each assembly of 2 6V190Ah (5h rate) to install in the golf cart battery.The capacity and life test of small electric vehicle lead-acid battery could be carry out by the Japanese industrial standard SBA S 0802-1996 test method.The test data was shown in the table 2(each group of data are the mean values of 2 battery test data).

Table 2 The mixing paste test data at different temperatures

Mixing paste temperature control (℃)	Curing conditions	the appearance and strength of the positive plate	the initial capacity of the battery (%)	the maximum capacity of the battery (%)	cycles
65	Temperature :72 ℃ -78 ℃ ; humidity: ≥95%	If the surface was pale yellow,the strength would be poor.	106.75	118	292
70		If the surface was yellow,the strength would be plain.	97.98	119	373
75		If the surface was yellowish,the strength would be plain.	94.12	107	433
80		If the surface was orange, the strength would be good.	86.86	103	457
85		If the surface was dark orange，the strength would be good.	84.11	94	382

Seen from the table 2,if the maximum temperature of the mixing paste could control at the range of 75℃-80℃,the capacity and cycle life of the battery would better improve.

The Negative Expander Selection

The negative organic additives of the deep cycle discharge battery are not suitable for using alone lignin.The three organic expanders of the deep cycle battery negative plate are lignin,lignin+humic acid and humic acid which stability sequence is humic acid,lignin+humic acid and lignin.If using the humic acid or lignin+humic to replace alone using lignin that could get the better charge acceptance and deep cycle life performance;but it noted that the dosage should be slightly lower the car battery negative organic expanders in order to avoid the excessive expansion of the negative electrode active material plates under the deep cycle state.It should also be appropriately increased the carbon black and barium sulfate content of the negative inorganic additives,generally added 1.2-1.5 times than the organic expanders,by this way can effectively improve the performance of deep cycle batteries.

Improved Methods of Battery Design

The Design Method of Positive Plate More Than Negative Plate

Power batteries are generally run in the low- rate discharge status which mainly be controlled by the positive plate.After dissecting the life test batteries,most of them were the positive grid corrosion caused by an internal short circuit of the deformation of live material softening off, while the negative plate was normal.The improved measure is using the combination of the positive plate more than the negative plate to replace the traditional polar groups of the negative plate more than the positive plate.

Under the same charging and discharging conditions,the positive plates increased, so the relative surface area was increased that the unit area carrying current of positive plate would reduce and the corrosion and deformation of the positive plate would decrease.Take 6V 190Ah (5h rate) golf cart

batteries for an example,if changing the original monomer +9, -10 to +10, -9, that is, the battery pack of the positive plate assembled the negative plate.The performance testing showed that the method has significantly improved the performance, the capacity increased 3-5% in five hours,the cycle life improved 13% , the material consumption only increased 1.2%.

The Improved Method of the Plate Outlines

Power batteries generally use the bag separator plate with the materials of PE+fiberglass or plastic and glass fiber composite,the tight assembly of the positive plate could effectively prevent the short circuit of the battery bottom which caused by the plate living material fall away with the electric vehicle bumping and vibration.The solution of the problem is to use a unequal design of the positive and negative plate.Namely,the positive plate dimensions remain unchanged,the width of the negative plate needs reducing 4-5mm and other dimensions are unchanged,so the positive and negative plates of the assembly monomers make each side maintain a certain distance.Thus even if at both sides of the partition edge cracks that it also could effectively prevent short circuit fault of the polar group side.

The test data of the improved assembly 6V 190Ah battery(5h rate) were shown in the table 3.

Table 3 The Improved Test Data

serial number	Inspection items	Inspection standard	Standard requirements	Unit	The measured data	
					The first group	The second group
1	Capacity	SAE J537-2000	≥100	%	102.4	101.3
2	The large current discharge	SAE J537-2000	≥30	Min	36.23	37.58
3	75A discharge	SAE J537-2000	≥105	Min	117	114
4	The storage characteristics	SAE J537-2000	≥85	%	95.12	91.87
5	life	SAE J537-2000	≥400	times	455	473

Conclusion

（1）The alloy complex of the positive Pb-Sb and the negative Pb-Ca was used appropriate heat treatment,so it helps to improve the deep cycle life of small flooded power battery and could be achieved low maintenance performance.

（2）The mixing paste and curing process at high temperature and high humidity conditions can significantly increase the strength of the positive plate, although the initial capacity of the battery is low, but the cycle life is significantly extended.

（3）The organic additive of the negative uses the high purity lignin+humic acid and humic acid, it is more favorable for deep cycle discharge.

（4）The design method of positive plate more than negative plate and the plate outlines which can effectively improve the battery performance and reduce the failure rate.

References

[1] Hao Xiaohong; Qin Jian Feng; Wang Du; GAO Yun-fang.Analysis of New Energy Storage System Using Factors Lead-Acid Battery Life[J]. Energy Projects, 2012（08）：45-47

[2] Li Wei; Hu Yong.Research on Current Development Momentum and Lead-acid Battery Life. China Manufacturing Information, 2011（04）：53-55

[3] Le Jun; Li Haoping;. Liu Min. Electric Bicycle Study The Relationship Between Life with Symptom VRLA batteries. Battery, 2003（06）：15-18

[4] Lv Yongyao;Lei Zhenyue;Fu Yongzhe.Compare Several VRLA Battery Electric Technology. Ship Electrical Technology,2012（08）:87-90.

[5] Shi Qinfang.Analysis of Lead-Acid Batteries And Lithium Battery Electric Bicycle. analysis. Electric Bicycles, 2011（10）：16-19

Advanced Materials Research Vols. 986-987 (2014) pp 123-126

doi:10.4028/www.scientific.net/AMR.986-987.123

A review of fluorinated proton exchange membrane

Shizhong Chen[1,*], Shiyu Xing[1]

[1] School of transportation and mechanical engineering, Shenyang Jianzhu University, Shenyang, 110168China

*Corresponding author

Key words: PEM; fuel cell; membrane

Abstract: The proton exchange membrane (PEM) plays a key role on performance of PEM fuel cell. This paper reviewed recent developments of perfluorinated and partially fluorinated PEMs for PEM fuel cells.Comparative analysis of various PEM parameters was presented. Perfluorinated sulfonic PEMs with better technology have the issues of complicated preparation process and high cost.Partially fluorinated PEMs have lower price,but performance is not good enough.

Introduction

PEM is the key technical material of fuel cell[1].What's more,it's the heart of the cell,whose performance directly affects the performance of fuel cell operation.Aiming at the characteristics of PEM,this paper reviews the basic properties and research progress.

1 The basic properties of proton exchange membrane

The proton exchange membrane(PEM) is the key part of PEM fuel cell. The PEM includes perflourinated membrane,partially fluorinated membrane,non-fluorinated membrane and composite membrane.The classification of membranes based on materials are shown in Figure1.

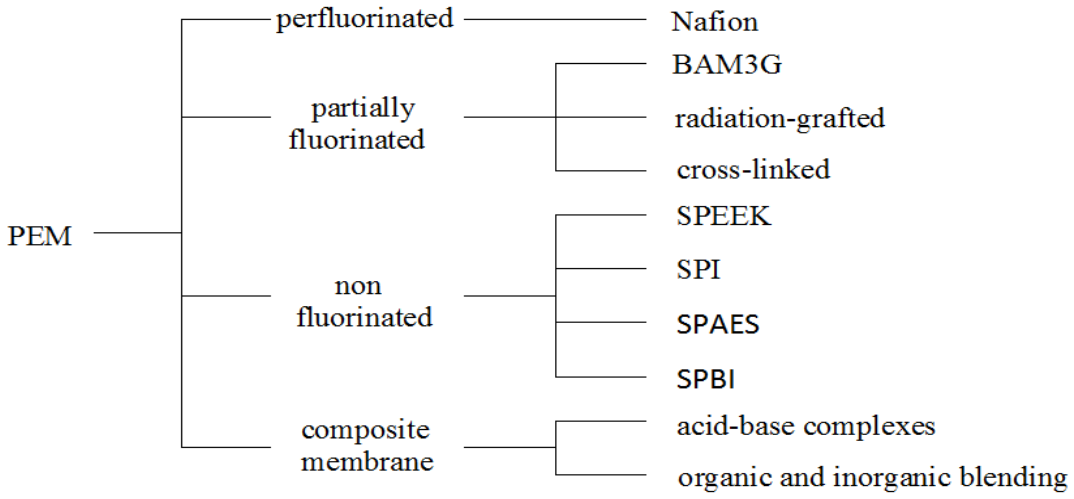

Fig.1 The classification of membranes

The performance of PEM can not only affect cell performance directly,but also be vitally important to reduce the cost and internal resistance of the cell, and improve the energy conversion efficiency[2].Therefore,PEM should meet the following conditions[3]:(1) high proton conductivity,(2) low electron conductivity,(3) low permeability to fuel and oxidant,(4) thermal, chemical, oxidative, and hydrolytic stability,(5) desirable mechanical properties in both the dry and hydrated states,(6) cost, and(7) capability for fabrication into membrane electrode assemblies (MEAs).

In this paper,the perfluorinated membrane and partially fluorinated membrane will be studied in detail.

2 Perfluorinated proton exchange membrane

Perfluorinated sulfonic proton exchange membrane(PFSA) is currently the only widely used proton exchange membrane in PEM fuel cell,and the most representative one is the Nafion membrane which is developed by Dupont in the late 1960s.After that,several other similar proton exchange membranes come into appearance in succession: DuPont's Nafion, Asahi Glass's Flemion, Asahi Chemical's Aciplex, Dow Chemical membrane, etc[4].

At present, DuPont's Nafion is the most widely used membrane both at home and abroad.It shows excellent chemical stability as well as high proton conductivity at moderate temperature and high relative humidity[5].While it also has some shortcomings.As the high temperature will cause the decrease of electrical conductivity and chemical degradation,the preparation is difficult,high cost; the waste is refractory.It may be inclined to methanol leaking when used in methanol fuel cell.

It functions only in a highly hydrated state and therefore it is limited to operation at relatively low temperatures of around 80℃ under ambient pressure in order to maintain a high water content in themembrane[6].The major factors hindering the development of PFSA are higher prices,complex production engineering and high risk.Consequently,their wider applications are limited.To overcome the disadvantages of PFSA, new proton exchange membranes have appeared.

3 Partially fluorinated proton exchange membrane

3.1 Polytrifluorostyrene membrane

Early Polytrifluorostyrene sulfonic acid membrane cannot meet the requirements of the long-term use of fuel cells,because of poor mechanical strength and chemical stability.The most prominent representatives of modified proton exchange membrane is BAM3G membrane developed by Ballad company.The life of BAM3G membrane can be increased, up to 15000h.Cost is also lower than the Nafion membrane and the Dow membrane,that is much more easily accepted[7].Due to the differences in structure, BAM3G has good thermal stability, chemical stability and mechanical strength.What's more prominent is the quality with a lower capacity (EW) and high water content, its performance is better than the Dow and Nafion117 membrane[8].

3.2 Radiation-grafted proton exchange membrane

Radiation-grafted polymer film is synthetized through copolymerization on the selected basal membrane such as polytetrafluoroethylene,polyvinylidene fluoride, copolymerization of tetrafluoroethylene,perfluoropropylene and so on.Then Ion exchange groups will be mixed by sulfonationreaction[9].This technique allows introducing ion conducting (electrolytes) regions directly into polymer films,which have excellent thermal and mechanical properties[10]. Especially, radiation grafting, a powerful method for the introduction of the proton conducting ability into commercial films has been widely utilized to prepare PEM[11].

E.E. Abdel-Hady et al. prepared the membrane in this way.The membranes achieve better water uptake, ion exchange capacity, AC electrical conductivity and tensile strength compared to that of Nafion-112[12].

3.3 Cross-linked membrane

Cross-linking can hinder the mobility of the polymer chains and efficiently enhance the mechanical strength by limiting the high degree of water uptake[13].The cross-linked membranes displayed somewhat lower proton conductivities than the corresponding uncross-linked ones

because of the reduced IECs of the former. Nevertheless, the proton conductivities of the cross-linked membranes were still at reasonably high level.

J. Ren et al. fabricate the cross-linking Am-SPAES/SiO2 hybrid membranes,and the performance of the hybrid membranes containing cross-linking network structure was considerably improved[14].Luo et al. prepare a double cross-linked membrane.The second cross-linking significantly decreased the water uptake of the membrane. The performance of direct methanol fuel cell was slightly improved as compared to Nafion 117 due to its low methanol permeability[15].

3.4 Comparative analysis of various membrane parameters

Through the in-depth study of the proton exchange membrane,all kinds of partially fluorinated and non-fluorinated proton exchange membrane come into being.This paper focuses on the characteristics of perfluorinated and partially fluorinated PEMs.The performance compared with Nafion is shown in the Table1.

It can be seen from Table 1,these partial fluorizated membranes will be superior to the Nafion membrane in the mechanical strength, thermal stability, proton conductivity and methanol permeability,as well as the prices.However, many properties is not optimal due to materials limitations.

Table 1 Performance reference table of partially fluorinated membrane

	BAM3G	Radiation grafted	Crosslinked
Thermal stability	good	good	low
Chemistry stability	good	good	good
Mechanical strength	good	good	enhance
Methanol permeability		low	low
Proton conductivity	improve limited	equal	decreace
Oxidation stability		worse	

4 Conclusion

Perfluorosulfonic acid membranes with better performance have the issues of complicated preparation process and high cost.Besides,the poor alcohol resistance restricts its application. Partially fluorinated proton exchange membranes have been developed,whose performance is better than perfluorinated membranes,and the price is much lower.However,overall performance is not good enough.It is not suitable for wider application.Therefore,it is significant to prepare novel proton exchange membranes to improve the performance of fuel cell.

Acknowledgments

The work is supported by the Liaoning Province Doctor Foundation (No.20121050),Shenyang S&T Plan (NO.F12-277-1-30) and Programfor Liaoning Excellent Talents in University (NO.LJQ201205).

Reference

[1] T.Y.Na,KShao,JZhu,H.Ch.Sun,Zh.G.Liu,Ch.J.Zhao,Zh.Q.Zhang,Ch.M.Lew, G.Zhang: Block sulfonatedpoly(arylene ether ketone) containing flexible side-chain groups for direct methanol fuel cells usage.Journal of Membrane Science,6(2012),p.1-7.

[2] Y.H.Wu,Sh.zh.Chen:Research on proton exchange membrane fuel cell water management. Beijing(2011),Science Press.

[3] Zh.Y.Dou:New synthesis and properties of proton exchange membrane fuel cell research(Jilin University,2011).

[4] P.J.ZapataB.:High throughput study of fuel cell proton exchange Membranes:Poly(vinylidene fluoried)/acrylic polyelectrolyte blends and Nanocomposites with zirconium.Georgia Institute of Technology,(2009),p.122-130.

[5] Y.Zhao,J.Yin:Synthesis and properties of poly(ether etherketone)-block-sulfonated polybutadiene copolymers for PEM Applications.European PolymerJournal, 46(2010),p.592-601.

[6] W.Qian,Y.M.Shang,M.Fang,S.B.Wang,X.F.Xie,J.H.Wang,W.X.Wang,J.Y.Du,Y.W.Wang, Z. Q.Mao:Sulfonated polybenzimidazole/zirconium phosphate composite membranes for high temperature Applications.International Journal of Hydrogen Energy,(2012),p.1-6.

[7] Z.X.Liu,W.Qian,J.W.Guo,J.Zhang,C.Wang,Z.Q.Mao:Materials for proton exchange membrane fuel cell.Progress in chemistry,23(2011),p.487-500.

[8] K.Cheng,Y.Z.Xin,E.K.Wen:Progress in key technologies of proton exchange membrane fuel cell,5(2011),p.16-32.

[9] Y.Q.Wang,H.W.Zhang:Fluorinated Proton-Exchange membranes for fuel cell research. Materials review,19(2005),p. 95-112.

[10] M.Ahmed,M.B.Khan,M.A.Khan,S.S.Alam,M.A.Halim,M.A.H.Khan: Characterization of polyethyleneterephthalate (PET) based proton exchange membranes prepared by UV-radiation-induced graft copolymerization of styrene.Journal of power sources, 196(2011),p.614-619.

[11] Y.S.Joon,J.S.Hae,M.S.Joo,H.S.Jun,C.N.Young:Radiation-grafted proton exchange membranes based on co-grafting from binary monomer mixtures into poly(ethylene-co-tetrafluoroethylene) (ETFE)film.Radiation Physics and Chemistry,81(2012),p.923-936.

[12] E.E.Abdel-Hadya,M.M.El-Toonyb,M.O.Abdel-Hameda:Graftingof glycidyl methacrylate/ styrene onto polyvinyldine fluoridemembranes for proton exchange fuel cell.Electrochimica Acta,103(2013),p.32-37.

[13] S.H.Zhou,D.J.Kim.Cross-linked aryl-sulfonated poly(arylene ether ketone) proton exchangemembranes for fuel cell.Electrochimica Acta,63(2012),p.238-244.

[14] J.N.Ren, S.L.Zhang, Y.Liu,Y. Wang,J.H.Pang ,Q.H.Wang, G.B.Wang.A novel crosslinking organic–inorganic hybrid proton exchange membrane based on sulfonated poly(arylene ether sulfone) with 4-amino-phenyl pendant group for fuel cell application.Journal of Membrane Science,434(2013),p.161-170.

[15] H.Z.Luo,G.Vaivars,M.Mathe:Double cross-linked polyetheretherketone protonexchange membrane for fuel cell.International Journal of Hydrogen Energy,37(2012),p.6148-6152.

Advanced Materials Research Vols. 986-987 (2014) pp 127-130

doi:10.4028/www.scientific.net/AMR.986-987.127

Effects of Drying Process on Lignite Quality

Wenjiao TANG[1, a], Shouyu ZHANG[1, b], Jianxun DONG[2], Xi GUO[1], Aixia DONG[1], Hongjun ZHENG[1], Wenxiang DENG[1], Yanjun DING[3], Junfu LV[3]

[1]School of Energy and Power Engineering, University of Shanghai for Science and Technology, Shanghai 200093, China

[2]CPI Mengdong Energy Group Co, Ltd, Tongliao 028000, Inner Mongolia, China

[3]Department of Thermal Engineering, Tsinghua University, Beijing 100084, China

[a]email: tangwenjiao321@163.com, [b]email: zhangsy-guo@163.com, corresponding author

Keywords: Lignite Dewatering; Coal Quality; Oxygen Adsorption; Spontaneous Combustion

Abstract. The drying experiments of three typical kinds of Inner Mongolia lignite were conducted on a self-designed apparatus. The proximate analyses and oxygen adsorbing capacities of all the samples were analyzed on an industrial analyzer and a coal spontaneous combustion tendency tester. The results show that the treated samples show no apparent changes in their properties compared to the original lignite and no pyrolysis or combustion phenomenon occurs in the drying process. It is also observed that the oxygen adsorbing capacity of the dewatered sample is lower than that of the original lignite. Especially the oxygen adsorbing capacity of the lignite sample undergoing high-temperature drying process decreases significantly. Considering the amount of adsorbed oxygen can reflect the spontaneous combustion tendency of coal to a certain extent, the spontaneous combustion tendency of the treated lignite decreases.

Introduction

China is rich in lignite. Lignite is a kind of cheap fuel, while its utilization is considerable limited for its characteristics. So far, the coal has been mainly used for electricity generation in the pulverized coal boiler of pithead power plants [1][2]. A large amount of dust discharged with flue gas during the direct combustion process, which will cause serious environmental pollution and thermal inefficiency use of lignite. Hence, it is necessary to improve the quality of lignite before application.

At present, the upgrading technologies of coal include washing, drying and topping process. The drying upgrading technology is mainly studied in the work. For the defect of high cost of drying medium in traditional drying technology, high-temperature flue gas drying technology was introduced and the properties of the samples treated under different drying temperature were investigated.

During the drying process, while the moisture content of the lignite decreasing, some small molecular compounds and volatile matters will emit from the coal particles under the high temperature and long residence time. So it is more likely to spontaneous combustion or explosion after the drying process. Generally, the dewatered coal will adsorb oxygen in the air. With oxygen binding interactions, the dewatered coal may generate heat through oxidation reaction. When the accumulation of the heat is enough, the spontaneous combustion will be caused [3][4]. Therefore, it is really useful to study that the changes of the spontaneous combustion characteristics and properties of the coal after the drying process. Moreover, the chromatographic method of fluid oxygen adsorption was applied to determine the spontaneous combustion tendency of the coal [5].

Experimental

Coal samples

Xilingol lignite, Yimin lignite, Datang five rooms lignite before and after drying process were chosen as the samples for the investigation. After the samples were milled, the lignite particle

passing through 80 mesh sieve were placed in weighing bottles for the following experiments. The effects of drying temperature and coal type were investigated in the experiments. The specific conditions for the preparation of the samples were introduced as follows.

(1) Effects of temperature

Table 1
Experimental temperature

	Gas temperature /K	Residence time
High temperature drying process	1073	30s
	973	30s
	873	30s
Low temperature drying process	463	10min
	413	10min

(2) Effects of coal type

The three lignites with the particle size of 3~25mm were selected as the experimental samples. The samples were dried in a simulated flue gas (7% O_2) flow with the rate of 0.5cm/s. The relevant experimental conditions were given in Table 2.

Table 2
Experimental coal type

	Coal type	Gas temperature /K	Residence time
High temperature drying	XLGL	1073	30s
	YM	1073	30s
	DT	1073	30s
Low temperature drying	XLGL	463	10min
	YM	463	10min
	DT	463	10min

Note: XLGL = Xilingol lignite; YM = Yimin lignite; DT = Datang five rooms lignite.

Experimental equipments

The experimental equipment used in this paper is self-designed for the drying process with high temperature flue gas. The structure of self-designed drying apparatus is shown in Figure 1. The bench with the function of temperature programming can be heated up to 1273K. A 5E-MAC III industrial analyzer (Changsha Kaiyuan Instruments Co. Ltd.) and a coal spontaneous combustion tendency analyzer of ZRJ-2000 (Beijing Star Hengtong Technology Co. Ltd.) were used to determine the properties of the lignite samples.

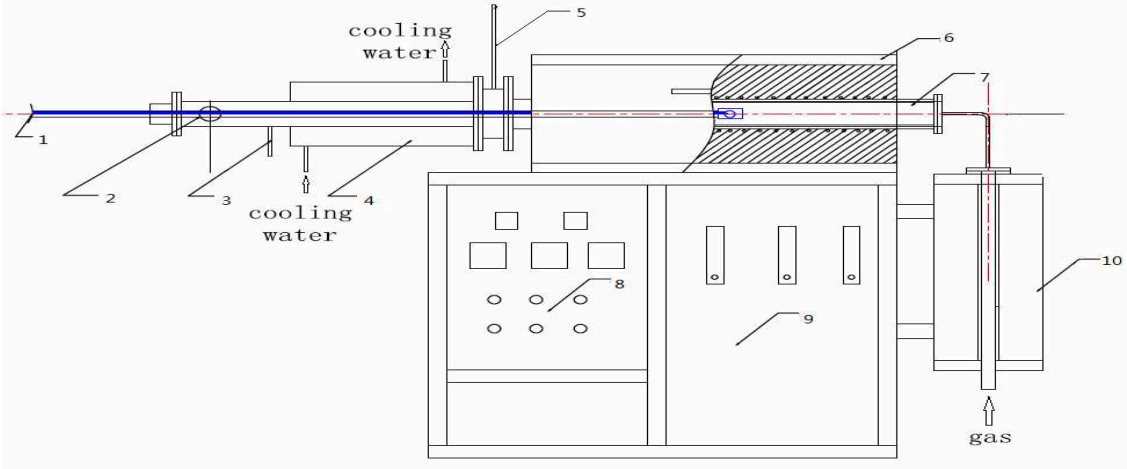

Fig.1. Self-designed drying apparatus

1-push rod with coal loading basket, thermocouples and nitrogen inlet; 2-operating hole; 3-cooling nitrogen inlet; 4-water-cooling jacket; 5-nitrogen outlet; 6-electric heater; 7-dryer; 8-controller; 9-panel with flowmeters; 10-preheater

Experimental procedure

The original lignite with particle size of 3~25mm was selected as the experimental samples. The industrial analyses and oxygen adsorption of the raw coal and the samples obtained on the

self-designed drying apparatus under different drying processes were measured. The Industrial analysis was analyzed according to GB/T212-2008, and the capacity of oxygen adsorption was measured by coal spontaneous combustion tendency tester according to GB/T20104-2006.

Results and Discussion

The results and discussion of Industrial analysis

The results of the industrial analyses of the original and partially dried samples are shown in Table 3. The drying time at high and low temperature is 30 seconds and 10 minutes, respectively.

Table 3
Proximate analysis of samples

Samples	M_t/%		M_t Reducti-	M_{ad} /%		A_d /%		V_{daf} /%		FC_{daf} /%	
	1	2	on/%	1	2	1	2	1	2	1	2
XLGL-413-G	11.67	7.09	39.29	7.16	7.26	11.42	17.81	50.69	51.50	49.31	48.51
XLGL-463-G	12.30	1.18	90.44	7.98	4.23	14.05	21.28	47.17	48.69	52.83	51.31
YM-463-G	31.43	19.65	37.48	6.29	5.67	14.56	16.10	45.34	48.98	54.67	51.02
DT-463-G	26.92	16.22	39.73	4.83	4.45	24.63	19.59	47.53	50.62	52.47	49.39
XLGL-873-G	12.41	5.68	54.21	7.56	6.97	12.97	10.29	49.01	49.03	51.00	50.97
XLGL-973-G	11.30	3.51	68.90	6.95	6.66	17.22	17.25	49.35	49.64	50.65	50.36
XLGL-1073-G	11.91	3.18	73.26	8.23	5.82	16.69	17.14	49.20	48.48	50.81	51.52
YM-1073-G	35.85	6.65	81.46	7.77	6.63	13.97	16.40	50.31	49.47	49.70	50.53
DT-1073-G	25.94	13.63	47.46	6.73	6.31	30.26	21.42	48.86	49.36	51.14	50.64

Note: 1 = before drying; 2 = after drying; M_t = total moisture; 413K, 463K, 873K, 973K, 1073K mean the temperature of drying medium during drying process; ad = air dried basis; d = dried basis; daf = dry ash free; t = total; G = Gas.

Table 3 shows that during low temperature drying process, the total moisture removal at 463K is much greater than at 413K. Moreover, the internal moisture content of the sample dried at 463K decreases obviously. It can infer that the rise in drying temperature may help to remove the moisture from the lignite, especially for the internal moisture. Compared with Xilingol lignite, the moisture removal degree of the other coals is lower under the low-temperature drying conditions, which may be due to the different moisture content of the coals. Therefore it needs different amount of heat to obtain the equal moisture removal degree. The same drying temperature and residence time can provide the equal amount of heat, so the different samples have different moisture removal degrees. For example, the raw coal with higher moisture content shows a lower moisture removal degree.

According to industrial analyzing data of Xilingol lignite before and after drying process, the moisture removal degree of the sample dried at high temperature with the same residence time increase. Compared with the drying process at low temperature, the moisture removal degree of the sample at the high temperature drying process exceeds 50% in only 30 seconds. The result means that the drying process at higher temperature has a better efficiency. In addition, the volatile or ash yields of the samples before and after the drying process change a little and the properties of the coal does not change a lot. Obviously, no pyrolysis or combustion occurs during the high temperature drying process. When dried in the simulated flue gas with 1073K, the moisture removal degree varies for the different lignite samples with different internal and external water content and different pore structures [6][7].

Results and discussions about oxygen adsorption measured

The samples were dried at different temperature. The results are listed in Table 4.

According to the dates shown in Table 4, the original sample has the highest amount of adsorbed oxygen. After a short period of drying at high temperature, the amount of adsorbed oxygen is significantly lower than that treated under low-temperature drying. Obviously, drying temperature has a great impact on the amount of adsorbed oxygen of lignite [8][9]. As the oxygen adsorption can reflect the tendency of spontaneous combustion of coal partly and a higher oxygen adsorption may lead to an easier spontaneous combustion, so the spontaneous combustion tendency of the

lignite decreases after drying. The lignite has the dewatering degree of above 70% in a short time after high-temperature drying process with simulated flue gas as drying media. The oxygen absorption capacity of the dewatered lignite decreases a lot. Therefore, high-temperature drying process with flue gas is suitable for lignite dewatering.

Table 4
Oxygen adsorption of XLGL lignite before and after drying

Samples	Oxygen adsorption cm3/g·Dry coal	Level of spontaneous combustion tendency
XLGL-Raw	0.97	I class (Easy)
XLGL-463-Gas	0.93	I class (Easy)
XLGL-1073-Gas	0.74	I class (Easy)

Note: Easy = easy to spontaneous combustion.

Conclusion

The experimental results demonstrate that the moisture removal degree of the lignite increases with the increasing temperature during the high-temperature drying process. The moisture removal degree of the lignite varies to the kinds of coal. The properties of the lignite before and after drying process change a little and no pyrolysis or combustion reaction occurs during the drying process. Compared with the low-temperature drying process, the high-temperature drying process has a higher efficiency. The dewatered lignite, especially the coal treated after high temperature drying process, has a lower amount of adsorbed oxygen than the raw coal, which means the spontaneous combustion tendency of the dried lignite decreases.

Acknowledgement

In this paper, the research was sponsored by the National science and technology support plan of China (No. 2012BAA04B01).

References

[1] Yuehua Gong. Inner Mongolia coal resources and their utilization [J]. Coal Processing and Comprehensive Utilization, 2005 (6) 17-18.
[2] Jinzhou Qu, Xiuxiang Tao, Jinyan Liu and so on. Research progress on upgrading technology of lignite [J]. Coal Science and Technology, 2011:39 (11):121-125.
[3] Jun Deng, Jingcai Xu, Xiaokun Chen. Perspectives on spontaneous combustion mechanism and prediction theory of coal [J]. Journal of Liaoning Technical University, 2003:22 (4):455-459.
[4] Dunliang He, Jingcai Xu. The relationship of coal surface heat of reaction and pyrophorisity [J]. Safety in Coal Mines, 1990 (6) 31-36.
[5] Zhuang Liang, Jiren Wang. The technology of forecasting and predicting the hidden danger of underground coal spontaneous combustion [J]. Procedia Engineering, 2011 (26) 2301-2305.
[6] Yonggang Zhou, Pei Li, Jianguo Yang and so on. Research on Energy Consumption for Different Moisture Evaporation of Lignite [J]. Proceedings of the CSEE, 2011 (31) 114-118.
[7] Xianchun Li, Jianglong Yu and so on. Experimental study on drying and moisture adsorption characteristics of an Indonesian lignite [J]. Modern Chemical Industry, 2009:2 (9): 5-7.
[8] Yifeng Wu, Mo Chu, Zhibing Chang and so on. Drying Upgrading Affected to Surface Structure of Lignite [J]. Coal Engineering, 2012 (2) 99-101.
[9] Chenggong Sun, Jiashan Wu, Baoqing Li. Surface properties of thermally upgraded low-rank coals and their effect on the rheological behavior of coal water slurry [J]. Energy and Fuel, 1996:24 (2) 174-180.

Advanced Materials Research Vols. 986-987 (2014) pp 131-135

doi:10.4028/www.scientific.net/AMR.986-987.131

Electron Mobility Model for Tensile Strained-Si(101)

Jian'an Wang[1, a], Meng Nan[2], Huiyong Hu[2], Heming Zhang[2]

[1]Sichuan Institute of Solid State Circuits, CETC, Chongqing, 400060, Peoples R China

[2]Key Laboratory for Wide Band-Gap Semiconductor Materials and Devices, School of Microelectronics, Xidian University, Xi'an, 710071, Peoples R China

[a]wja@sisc.com.cn

Keywords: Strain; Electron; Model

Abstract. Nowadays, the strained-Si technology has been used to maintain the momentum of semiconductor scaling due to its enhancement performance result from the higher mobility. In this paper, the influence of ionizing impurity scattering, acoustic phonon scattering and intervalley scattering to strained-Si(101) material is discussed.In addition, a calculation of the electron mobility in Strained-Si(101) material is made using the average momentum relaxation time method described in Ref[1]. The results show that the electron mobility increases gradually for both [001] and [100] orientations while for [010] orientation increases rapidly with the increasing Ge fraction x.[1]

Introduction

Strained-Si technology, expected to set a new technology roadmap for the CMOS industry, is more and more popular due to its enhancement of mobility.Lots of studies have been done about inversion layer of strained-Si MOS[2-5], however, the study of the mobility in strained-Si material is seldom reported which is of great importance.

The structure in this paper is organized as below: In Section Ⅱ, the influence of ionizing impurity scattering, acoustic phonon scattering and intervalley scattering to strained-Si(101) material are discussed. We have also calculated the electron mobility in strained-Si(101) material as a function of strain and orientations using K·P theory and the average momentum relaxation time method described in Ref[1]. In section III, an analysis of variation of the mobility with the increasing Ge fraction x as well as Ni for [001], [100] and [010] orientations is made. The last section gives the summary of this paper.

Calculation Process

The scattering is one of the essential factors that influence the mobility. During the calculation of Electron Mobility for Strained-Si(101), ionizing impurity scattering, acoustic phonon scattering and intervalley scattering are under consideration. Their models are listed below:

$$\frac{1}{\tau_i}=\frac{N_i q^4}{16\pi(2m^*)^{1/2}(\varepsilon_o\varepsilon_{Si})^2E^{3/2}}\ln(\frac{12m^*k_B^2T^2\varepsilon_o\varepsilon}{q^2\hbar^2n_i}) \tag{1}$$

$$\frac{1}{\tau_a}=\frac{m^{*3/2}\Xi^2K_BT(2E)^{1/2}}{\pi\hbar^4c_L} \tag{2}$$

$$\frac{1}{\tau_{in}}=\frac{D_i^2(m^*)^{3/2}Z_f}{2^{1/2}\pi\hbar^3\rho\omega_i}(M_i+\frac{1}{2}\mp\frac{1}{2})(E\pm\hbar\omega_i-\Delta E_{fi})^{1/2} \tag{3}$$

τ_i, τ_a, τ_{in} represents the rate of ionizing impurity scattering, acoustic phonon scattering and intervalley scattering respectively, and by substituting those parameters into the formula (4) could we obtain the scattering rate.

m^*, the density-of-states effective mass of the strained-Si(101), is needed to calculate the scattering rate. We are not going to discuss this parameter in this paper since this work was already done in Ref[6].

The average momentum relaxation time of the scatterings mentioned above is decided according to the method in Ref[1]. As all of the three types scattering exist at any time, the total scattering rate of the strained-Si(101) can be figured out by formula (4).

$$\frac{1}{<\tau>}=\frac{1}{<\tau_i>}+\frac{1}{<\tau_a>}+\frac{1}{<\tau_{in}>} \tag{4}$$

Here, $<\tau_i>$, $<\tau_a>$, $<\tau_{in}>$ are average value of τ_i, τ_a, τ_{in} respectively.

Meanwhile, we use K·P theory to obtain the conduction band E-k relation and the conductivity effective mass m_c of the strained-Si, which can be obtained in Ref[7].

It shows that the conductivity effective mass m_c for [100] and [001] orientations increases with the increasing Ge fraction x, and approximately equals to 0.318 m_0. The conductivity effective mass m_c for [010] orientation decreases with the increasing Ge fraction x, and approximately equals to 0.19 m_0 when x is larger than 0.2.

$$\mu=\frac{q<\tau>}{m_c} \tag{5}$$

By substituting the scattering rate and the conductivity effective mass mentioned above into formula (5), we can obtain electron mobility of the strained-Si(101).

Table 1. Scattering Parameters Used in This Paper

Parameters	Symbols	Units	Value
deformation potential constant	Ξ	(eV)	5.0
longitudinal elastic constant	c_L	(kg/(m.s^2))	1.903×10^{11}
energy difference between initial and final valleys	ΔEfi	(eV)	0.443x(f),0(g)[8,9]
thermodynamics temperature	T	(K)	300
Boltzmann constant	K_B	(J/K)	1.380×10^{-23}
Planck constant divided by 2π	$\hbar$	(J.s)	1.054×10^{-34}
vacuum permittivity	ε_0	(F/m)	8.854×10^{-12}
permittivity of silicon	ε_{Si}	(ε_0)	11.9
density of ionized impurity	N_i	(cm^{-3})	10^{17}
density of electrons in silicon after doping	n_i	(cm^{-3})	10^{17}
electron charge	q	(C)	1.602×10^{-19}
number of final equivalent valleys	Z_f		4(f),0(g)
deformation potential constant for intervalley phonon scattering	D_i		*
intervalley phonon angular frequency	ω_i		*
thermal equibibrium number of optical phonons	M_i		*

*: Ref [10]

Results and Discussions

The calculation results of the rates of ionizing impurity scattering, acoustic phonon scattering and intervalley scattering are given as follows (figure1~figure5), and figure3~figure5 represents f2 type, f3 type and g3 type intervalley scattering respectively. It should be noted that the P in the figures below represents scattering probability, and equals to 1/τ.

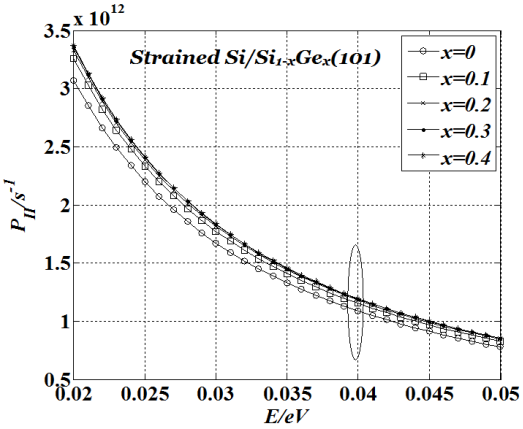

Fig.1 Ionizing impurity scattering probability of the strained- Si(101) versus with E and Ge fraction x.

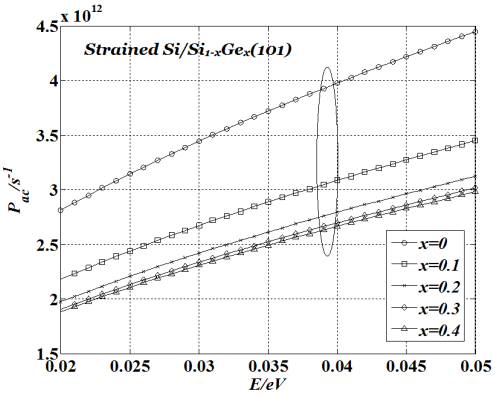

Fig. 2 Acoustic phonon scattering probability of the strained- Si(101) versus with E and Ge fraction x.

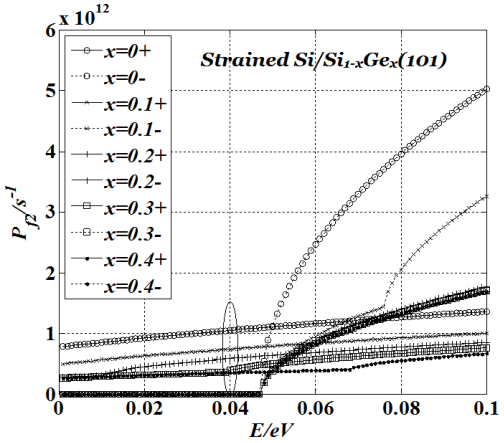

Fig. 3 f2 type intervalley scattering probability of the strained- Si(101) versus with E and Ge fraction x.

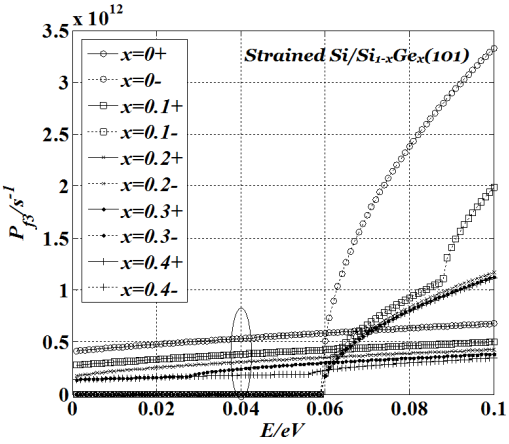

Fig. 4 f3 type intervalley scattering probability of the strained- Si(101) versus with E and Ge fraction x.

It is shown in figure1 that the ionizing impurity scattering probability of the strained-Si(101) decreases with the increasing energy, and increases with the increasing Ge fraction x when the energy is 40meV (the average energy of electron carry). Figure2 shows that the acoustic phonon scattering probability of the strained-Si(101) increases with the increasing energy, and decreases with the increasing Ge fraction x when the energy is 40meV. And from figure3, figure4 and figure5 we can find the intervalley scattering probability of the strained-Si(101) decreases with the increasing Ge fraction x when the energy is 40meV.

The electron mobility for [001], [100] and [010] orientations are showed in figure6 and figure7.It shows in figure6 that electron mobilities for [001]/[100] orientations in strained-Si(101) material versus N_i and Ge fraction x are identical.

According to figure6 and figure7, the electron mobility decreases with the increasing N_i (density of ionized impurity). It should be noted that the electron mobility get a sharp decline when N_i is larger than 10^{16}. This variation can be explained by formula (1) : the ionizing impurity scattering probability is proportional to N_i. The increasing N_i leads to an increasing ionizing impurity scattering probability thus results in a risen of the total scattering rate and a reducement of the mobility.

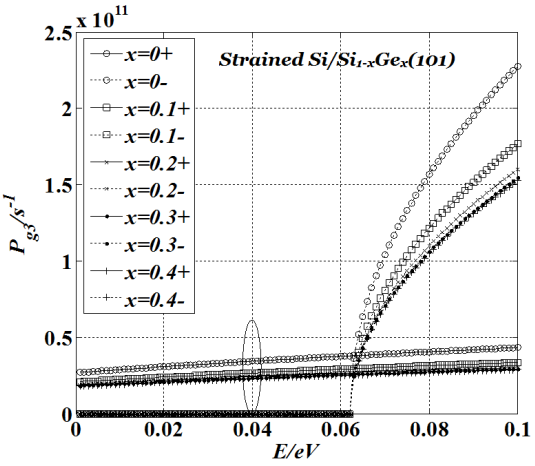

Fig. 5 g3 type intervalley scattering probability of the strained- Si(101) versus with E and Ge fraction x.

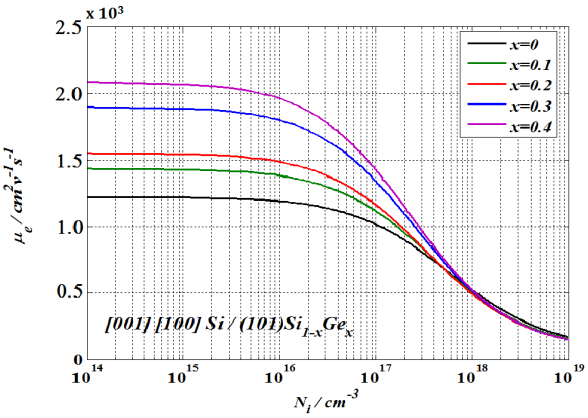

Fig. 6 Electron mobility for [001], [100] orientations in strained-Si(101) material versus Ni and Ge fraction x.

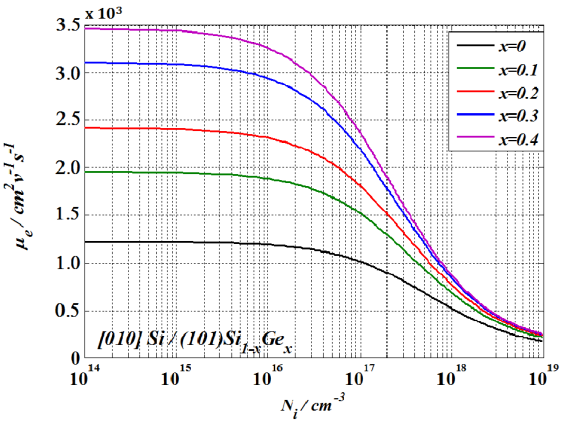

Fig. 7 Electron mobility for [010] orientations in strained-Si(101) material versus Ni and Ge fraction x.

Then we are trying to figure out how the mobility varies with Ge fraction x. For [001] and [100] orientations, the maximum mobility of the Strained-Si is about 1.68 times that of the relaxed Si material. But for [010] orientation, the electron mobility increases much more rapidly compared to other orientations and its maximum value is approximately 2.8 times that of the relaxed Si.

This phenomenon of the electron mobility of the strained-Si(101) material for different orientations can be explained as follows. The conductivity effective mass m_c for [100] and [001] orientations increases with increasing Ge fraction x, and is approximately equals to 0.318 m_0, while the conductivity effective mass m_c for [010] orientation decreases with increasing Ge fraction x, and approximately equals to 0.19 m_0 when x is larger than 0.2. Besides, the tensile strain splits the six-fold degenerate Si conduction band minimum into a two-fold (Δ_2) and a four-fold (Δ_4) degenerate band. For strained-Si(101), the four-fold degenerate band is lower in energy, so electrons prefer to occupy the Δ_4 band. The energy difference ΔE between the Δ_2 and the Δ_4 bands is proportional to the Ge fraction x [11], the Δ_4 population increases and the intervalley scattering decreases with increasing Ge fraction x，as is shown in figure3~figure5. With increasing Ge fraction x, the electron mobility for [001] and [100] orientations increase gradually while the mobility for [010] orientation get a higher increasing rate, because of the suppression of scattering and the reduction of conductivity effective mass.

Summary

In this paper, based on the analysis of the scattering in Strained-Si(101) material, the calculation of the electron mobility in strained-Si(101) material as a function of strain and orientation is made using K·P theory and the average momentum relaxation time method described in Ref[7]. The results show that the electron mobility decreases with N_i. Besides, the electron mobility for [001] and [100] orientations increase gradually with increasing Ge fraction x, while for [010] orientation, the electron mobility increases rapidly with increasing Ge fraction x, and its maximum can reach a value approximately 2.8 times that of the relaxed Si material. This result is valuable and can be used as a reference to the design of strained-Si devices.

References

[1] S.S. Li: Semiconductor Physical Electronics, New York: Springer Press, (2006), p. 185

[2] J.Y. Lin, Y.H. Tang and M.H. Tsai: 2009 Computer Physics Communication, 180 659

[3] A.T. Pham and C. Jungemann: Solid-State Electronics Vol. 52 (2008), p.1437

[4] S.H. Olsen, L. Yan, R. Aquaiby: Strained Si/SiGe MOS Technology: Improving Gate Dielectric Integrity. Microelectron Eng Vol. 86 (2009), p. 218

[5] ,H.Y. Hu, , H.M. Zhang, , X.Y. Dai: Chinese Journal of Semiconductors Vol. 26 (2005), p. 641

[6] J.J. Song and H.M. Zhang: Acta Phys. Sin. Vol. 59 (2010), p. 2064

[7] L.X. Zhao and H.M. Zhang: Model of Electronical Conductivity Effective Mass of Strained Si. Acta Phys. Sin.Vol. 59 (2010)

[8] J.J. Song and H.M. Zhang: Chinese Physics Vol. 16 (2007), p. 3827

[9] J.J. Song and H.M. Zhang: Research & Progress of SSE. Vol. 29 (2009), p. 14

[10] J.Y. Tang and K. Hess: J. Appl. Phys. Vol. 54 (1983), p. 5145

[11] T. Vogelsang, K.R. Hofmann: Appl. Phys. Lett. Vol. 63 (1993), p. 186

[12] J.J. Song, H.M. Zhang, X.Y. Dai, H.Y. Hu and R.X. Xuan: Acta Physica Sinica.Vol. 57 (2008), p. 5918

[13] J.J. Song, H.M. Zhang, X.Y. Dai, H.Y. Hu and R.X. Xuan: Acta Physica Sinica. Vol. 57 (2008), p. 7228

[14] J.J. Song, C. Yang, H.M. Zhang, H.Y. Hu, C.Y Zhou and B. Wang: Science in China, Physics Mechanics and Astronomy Vol. 55 (2012), p. 2033

[15] J.J. Song, H.M. Zhang, H.Y. Hu and Q. Fu: Science in China, Series G: Physics, Mechanics and Astronomy Vol. 52 (2009), p. 546

Advanced Materials Research Vols. 986-987 (2014) pp 136-145

doi:10.4028/www.scientific.net/AMR.986-987.136

On the Mechanism of AC electroosmosis

Chaochao Dong[1, a], Zheyao Wang[2, b]

[1]Tsinghua National Laboratory for Information Science and Technology Institute of Microelectronics, Tsinghua University, Beijing 100084, China

[2]Tsinghua National Laboratory for Information Science and Technology Institute of Microelectronics, Tsinghua University, Beijing 100084, China

[a]email: azure19871229@163.com, [b]email: z.wang@mail.tsinghua.edu.cn

Keywords: AC electroosmosis, double layer capacitor (DLC), electric double layers (EDL)

Abstract. Previously researchers considered ions in electric double layers (EDL) to analyze the phenomenon of alternating current electroosmosis (ACEO). However, they did not give a deep interpretation about the formation mechanism of ACEO and their theories cannot explain some experimentally observed phenomena. In this paper, we propose a physical model to analyze the formation mechanism of ACEO by considering ions both in EDL and in solution. It is found that the ions in solution play an important role in ACEO, and by considering the effect of ions both in EDL and in solution, we can reasonably explain some phenomena, including flow reversal at high frequency (typically 10-100 kHz) and inapplicability of ACEO at high salt concentration (above 30 μM), which existing theories cannot give convincing explanations. We also use Navier-Stokes equation to theoretically analyze the ACEO and it is found that the flow reversal can be predicted by our concepts in certain conditions.

Introduction

Electroosmosis (EO) is the phenomenon of movement of uncharged liquid in a channel charged by an externally applied electric field [1]. EO is inherent to the fact that many solid materials obtain surface charges at the solid-liquid interface when contact with liquids, and an electric field is established to attract the charges in the liquid with the same polarity and repulse the charges with opposite polarity, inducing EDL. The EDL contains high concentration charges with polarity opposite to the surface charges of the solids, enabling a direct current (DC) voltage applied in parallel to the channels to force the ions in the EDL to move and to generate a motion of the bulk fluid by dragging the liquid as a result of the viscosity, so-called DCEO. This EDL model for DCEO, established by Helmholtz and improved by Smoluchowski, has since served as the basis for interpretations of electrokinetic behaviors at liquid-solid interfaces.

Alternating current electroosmosis (ACEO) refers to driving fluids using the principle of EO at AC voltage. As a method to drive microfluids, ACEO only needs very low voltage (several volts) and has no moving parts, thus it can effectively prevent Faradaic reaction and can meet the requirements of limited voltage with the increasingly stringent demand of device size and long lifetime. ACEO has been employed as a potential tool for pumping fluid [1]-[3], mixing liquid [4], and manipulating biomolecules like DNA [5]. Different electrodes have been developed for ACEO, such as symmetry planar electrodes [6][7], asymmetry planar electrodes 0-[10], and three dimensional electrodes [2][3]. The symmetry planar electrodes cannot generate net flow due to that the forces produced on electrodes cancel each other out. However, when AC voltage is applied to an array of asymmetric electrodes, the difference between electrodes will produce asymmetric electric fields and this will impose dissimilar forces on microfluids, finally inducing a unidirectional fluid flow.

Similar to DCEO, ACEO has been interpreted as the action of the electric field on the induced charges in the EDL between the electrolyte and the electrode [6], [7], [10]-[13]. For example, it is believed that electric field normal to electrodes induces the EDL and electric field tangential to the electrodes drives ions in EDL to move [10]. However, this theory cannot account for several

experimental observations such as the flow reversal at high frequency [14][15] and low salt concentration limitation [16].

To address these phenomena, theoretical efforts have been devoted. Storey et al. explained the flow reversal by considering steric effects [14]. They suggested a maximum capacitance near a critical voltage across the EDL which will be influenced by power supply frequency. After the critical frequency, EDL capacitance will fall and narrow electrodes' charging time will decrease, and thus the narrow electrodes have sufficient time to charge and have more time to drive ions in fluid. This eventually causes the flow reversal. However, this explanation did not consider the forces produced by the ions beyond the Debye length [17], which could be important to the pumping mechanisms. Lastochkin et al. studied the influence of Faradaic reaction on fluid flow [18][19]. This effect only happens at low frequency and high power supply voltage, thus it cannot explain the flow reversal which only happens at high frequency. There are also some existing theories about induced-charge electroosmosis (ICEO) [20]-[22], which consider inducing EDL on electrodes by applying outside electric potential and are different from ACEO that electric potential is applied directly on electrodes.

Another inconsistency between ACEO theories and experiments is the unpredictable strong decay of the flow with increasing salt concentration of the solution. The flow effectively vanishes above a bulk salt concentration of above 10 mM salt concentration, so all experiments in the literature have used few electrolytes with concentration of an order lower than most biological solutions, such as very dilute solutions (mostly KCl) or de-ionized water. To address this phenomenon, new explanations of the EDL at large voltages, such as a dramatic increase in the diffuse-layer viscosity upon ion crowding, has been proposed [16].

Understanding the inconsistency between the theory and the experiments is of great importance from both fundamental and practical points of view. However, until now, the theories about ACEO are not convincing enough and cannot explain all the experimentally observed phenomena. In this paper, we put forward our own understandings about ACEO, and try to explain some experimental results using the proposed operation mechanism. Theoretical deduction based on the Navier-Stokes equation and our proposed mechanism is presented to theoretically predict the flow reversal.

Proposed Mechanism of ACEO

With an AC electric field, the ions in solution respond to the charge on the electrode at each half-cycle, retarded by their frictional drag through the medium. The EDL then becomes sensitive to the frequency of the alternating electric field, since electrode charge oscillating faster/slower than the ions can/cannot respond and lead to incomplete/complete formation of the EDL. Considering that ACEO produces flow by charging and discharging the electrodes, which is similar to the charging and discharging process in a double layer capacitor (DLC) [23]-[25], we propose to use the DLC process to analyze ACEO.

Figure. 1 schematically shows the charging process of a DLC. When voltage applies to electrodes in aqueous solution, it will result in the collection of ions near the electrodes and form EDL. The EDL is equivalent to a capacitor of which the distance between the two "plates" is shorter than 1 nm [25], thus DLC has a capacitance thousands of times larger than ordinary plate capacitors that have the same structure but without aqueous solution.

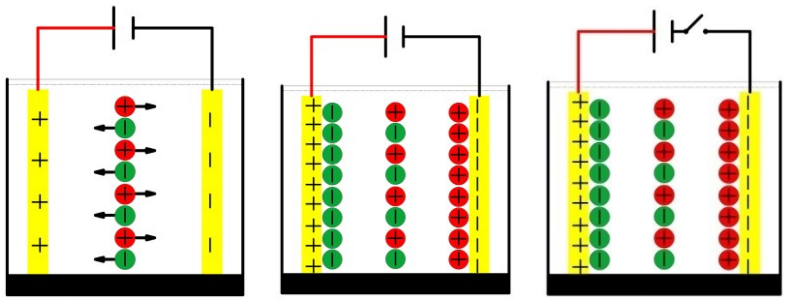

(a) (b) (c)

Figure. 1 Schematic diagram of DLC's charging process (a) start, (b) end, (c) after removing power source. (Red circles represent positive ions and green ones represent negative ions)

If there is no voltage applied to electrodes, there will be no forces exerted on ions in aqueous solution and the ions are uniformly distributed in the solution. At the beginning when applied with voltage, the ions in solution will be forced to move towards the electrodes by the electric potential, as shown in Figure. 1 (a). As long as the supply voltage is smaller than the decomposition voltage of aqueous solution, there will be no faradaic reaction in the contact interface [25].

During this charging process, fluid flow is generated by the dragging force of ions as a result of fluid viscosity. After the DLC is fully charged, there will be no electric field left in aqueous solution because the electric field caused by the DLC electrodes cancels that caused by the EDL, and thus the aqueous solution can be regarded as an equipotential body, as shown in Figure. 1 (b). Therefore, there is no force imposed on the ions in solution and they can move only through inertia, which will stop very quickly under the action of fluid resistance. Thus, only in the charging process there the ions in solution experience driving forces; after EDL is completely formed, there is no force exerted on the ions. After removing the applied voltage, the EDL can sustain a long time, as illustrated in Figure. 1 (c).

Under AC voltage conditions, the DLC has both charging and discharging processes. If the voltage frequency is smaller than the system's relaxation frequency, there will be enough time for the electrodes to be fully charged. On this occasion, the EDL will charge and discharge in the order of Figure. 2 (a)→ (b), (c), (d), (e) → (b), (c), (d), (e) →…. At the beginning there is no EDL originally, and the ions are forced to form the EDL just after the voltage applies. This charging process is identical to Figure. 1. When the electric voltage reverses, the electrodes reverse instantly due to that the charges on the electrodes are neutralized by the power and thus is extremely fast, as shown in Figure. 2 (c). Meanwhile, since there is no enough time for the ions in the EDL to move because of the resistance of solution, the ions in the EDL remain almost their original positions just after the electric voltage reverse, leading to the electric field in the solution to be a superposition of that of the electric voltage and that of the EDL. With the movement of ions in EDL, a new EDL is formed and the ions in the solution reach a new steady-state, as shown in Figure. 2 (d). In this process, ions in EDL move to aqueous solution and ions in aqueous solution move to electrodes simultaneously, and they combine to driving fluids. Therefore, when there is EDL on the electrodes, the charging and discharging process will be in the order of Figure. 2 (b), (c), (d), (e) → (b), (c), (d), (e).

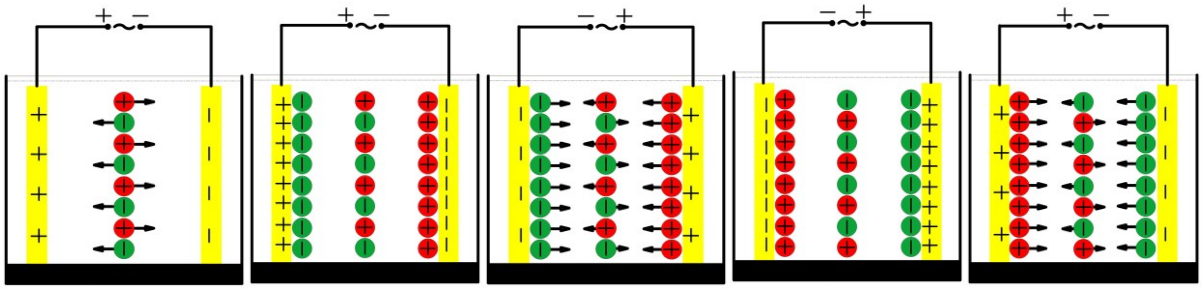

(a) (b) (c) (d) (e)

Figure. 2 (a) electrodes charging begins, no EDL originally, (b) charging ends, EDL completely formed (c) electric potential reverses, (d) EDL discharging and charging ends, (e) electric potential reverses.

As the charging and discharging processes in ACEO are the same as they are in DLC, ACEO can be reasonably explained below using the principle of DLC. In ACEO, if there is no EDL originally, the movement of ions in aqueous solution will be like the charging process of DLC, just as illustrated in Figure. 3(a). The electrodes are separately charged and fringe electric field will be formed in aqueous solution. The electric field forces ions in aqueous solution to move to the electrodes and form EDL. In this process, the movement of ions will drive nearby fluids to move, as shown in Figure. 3(b).

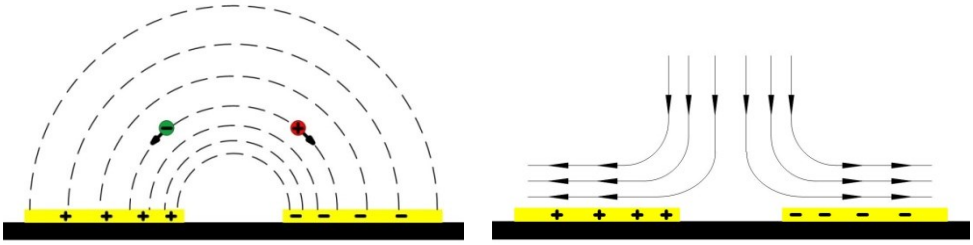

(a) (b)

Figure. 3 The mechanism of ACEO, (a) charging begins without EDL originally (b) fluid streamline

It can be seen that in the proposed mechanism the fluid movement will be affected by ions in both the EDL and in the aqueous solution if there is EDL on electrodes. After the electric potential reverses, electric charges on electrodes is rapidly be neutralized and therefore become opposite instantly. However, ions in EDL and aqueous solution move more slowly correspondingly because they should overcome more resistance in liquid.

There are mainly three kinds of forces exerted on ions in EDL after electric potential reverses. The first force F_e is from the electric field which is produced by the charges on the DLC electrodes. After electric potential reverses, the charges on electrodes will have the same polarity with the ions in nearby EDL, thus the ions in EDL will be exerted with repulsive force. Ions in solution will also suffer this force.

The second force F_i is from the interaction of ions between EDL on relative electrodes. From the analysis above it is clear that if charging time is longer than system's relaxation time, there will be no electric field left in aqueous solution because the electric fields produced by the ions in EDL have the same magnitude but the opposite directions. Immediately after electric potential reverses, electric field produced by ions in EDL will not change as quickly as electric field produced by electric charges on electrodes, leading to the ions in EDL to experience attractive force from the relative EDL. If the DLC has been fully charged, the amount of charges in EDL is far more than ordinary plate capacitors. Thus the electric field produced by the EDL will be much larger than ordinary plate capacitors. This electric field will have a great influence on ions' movement in EDL and it will soon disappear due to the ions' movement in EDL. This force will exert on ions in solution too.

The third force F_{Diff} is from the diffusion of ions in EDL. The ions concentration in EDL is much higher than that in aqueous solution, thus ions in EDL will diffuse from EDL to aqueous solution.

Explanations for experimental results

1. Direction of streamlines

Using existing theories, the streamlines of ACEO are expected to be downwards along the middle of two adjacent electrodes to the electrode surface [7][26]. If the streamline of fluid flow on symmetry electrodes is like this, it can be reasonably inferred that flow direction on asymmetry electrodes is from wide electrodes to nearby narrow electrodes because electric field is stronger nearby the narrow electrodes than the wide electrodes. However, almost all experimental results showed that the flow direction in ACEO on asymmetry electrodes was from the narrow electrode to the nearby wide electrode except at high frequency. Thus the existing theories must have missed something in explaining ACEO fluid flow. Brown et al. revised this defect by introducing a fluidic cycle to reverse the flow direction 0[10]. However, no forces can be found to reverse the fluid flow.

Streamlines of ACEO will be analyzed using our proposed mechanism. The direction of forces imposed on ions in EDL and in soluion of symmetry and asymmetry electrodes are illustrated in Figure. 4. From analysis in section 2, it is clear that the force produced by ions in EDL will be dominant at relatively low frequency. Ions in EDL are forced to move from the electrodes to the gap between the two electrodes. Ions density in EDL and electric charges density on symmetry

electrodes are the same, thus the ions' movement in EDL and solution will have same forces on fluid. When fluids from symmetry electrodes encounter each other in the middle of the gap between electrodes, streamline will be like in Figure 5 (a).

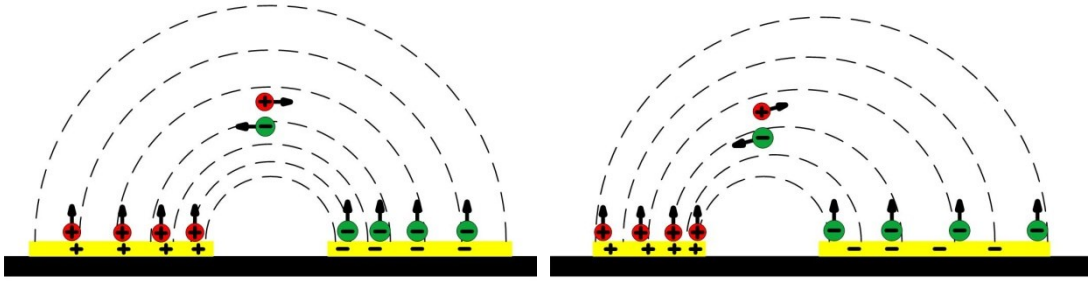

(a) (b)

Figure. 4 Forces exerted on ions in EDL of (a) symmetry and (b) asymmetry electrodes

For asymmetry planar electrodes, ions density in EDL of the narrow electrodes is larger than the wide ones due to the reason that the amount of ions in each electrode is the same if ions in each EDL have the same valence [14]. The larger ions density in EDL will form a stronger electric field after electric potential reverses. Furthermore, electric charges on the narrow electrodes will also produce a greater electric field than wide electrodes due to electric charges' density difference. Therefore the forces on fluid from narrow electrodes will be larger than the ones from wide electrodes, and streamline will be like in Figure. 5 (b).

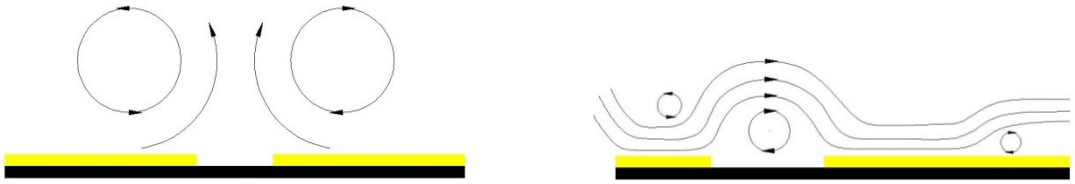

(a) (b)

Figure. 5 Fluid flow streamlines of (a) symmetry electrodes and (b) asymmetry electrodes

2. Flow reversal

Flow reversal at high frequency is the most puzzling phenomenon which the existing theories cannot explain. From the aforementioned analysis, the fluid flow is due to the interaction between the ions in both EDL and in aqueous solution. It is clear that the electrodes of ACEO need a RC time to charge. As long as the charging time is longer than the RC time, i.e., the power supply frequency of ACEO is smaller than the system's relaxation frequency, there will be no electric force exerted on ions in aqueous solution after the EDL have been fully charged. On this occasion, fluid will not be successively driven by ions. With the increase of power supply frequency, though forces exerted on ions do not change, the time during which there is no electric field force on ions will be shorter. Thus the average driving force and thus the fluid velocity will get higher. If the power supply frequency equals to the system's relaxation frequency, the fluid velocity will be the highest.

When the power supply frequency increases further, there will not be enough time to form EDL and the effect of ions in EDL will weaken. This implies that if the charging time is shorter than the RC time, the ion amount in EDL and the contribution of the ions in EDL to pumping will decrease with the increase in frequency. With further increase in the power frequency to a threshold value, the force produced by the ions in EDL will be so weak that the force produced by the ions in aqueous solution becomes dominant. For example, if the frequency of power supply voltage is 100 times of the system's relaxation frequency, i.e., the charging time is 1% of RC time, the amount of ions in EDL will decrease to about 1% of that being completely charged according to the rudimentary charging equation which follows exponential relation with charging time

$$V_t = V[1-\exp(-t/RC)] \quad (1)$$

Considering the analysis in Figure 3, it is clear that the forces produced by ions in solution will have the direction in Figure. 6. In this situation, the resulted force will have the direction from wide electrodes to the nearby narrow electrodes because of the stronger electric field above the narrow electrode than the wide electrode. This change will finally result in flow reversal. The tendency is consistent with the experimental results given in previous report [15].

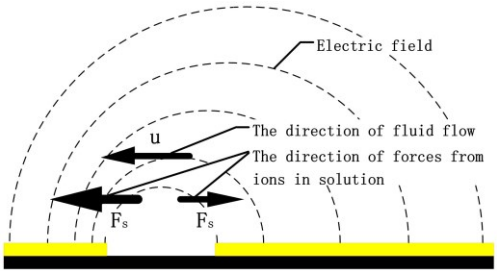

Figure. 6 Flow direction in high frequency (u represents velocity and F_s represents the force produced by ions in solution. The thickness of the arrows represents the magnitude of the force)

3. Flow decay in high concentration solution

The second phenomenon which the existing theories cannot explain is that only low concentration aqueous solution can be driven in ACEO. Experimental results show that fluid flow velocity decreases above 1 mM and if the concentration is above 30 mM it is difficult to observe fluid flow [16]. We try to explain this phenomenon using the proposed ACEO mechanism. As the capacitance of EDL is determined by the product of the capacitor and the applied voltage, the ion density of EDL will not change with the variation in the solution concentration when the electrodes are fully charged, and therefore the force magnitude generated by the ions in the EDL will not vary with solution concentration.

With the increase in the solution concentration, the ions in the solution in the vicinity of the electrodes are sufficient to fully charge the EDL, and it is not necessary for the ions in far solution (the middle of the channel) to move to the electrode surface to charge the EDL. Therefore, the EDL can be fully charged more quickly than in lower concentration because of the avoidance of ion movement through a long distance. This leads to the movement duration and movement distance of the ions in the EDL becomes shorter, so the driving force and the fluid flow arising from the ions in the EDL decrease.

Once the EDL is fully charged, the resultant electric field in the far solution is zero as a result of the superposition of the electric fields caused by the electrode and the opposite electric fields caused by the EDL. Thus, with the continuous increase in the solution concentration, the movement duration of the ions in the far solution, which equals to the duration of EDL establishment in a half cycle, will be shorter and shorter, leading to the ions in solution experience smaller and smaller forces. Finally, the fluid flow vanishes because both the ions in the EDL and the ions in the solution experience zero force.

Theoretical analysis about ACEO and prediction for flow reversal

Navier-Stokes equation is the governing equation for electrokinetics driven fluidics,

$$\rho\frac{\partial\vec{u}}{\partial t}+\rho\vec{u}\cdot\nabla\vec{u}=-\nabla p+\eta\nabla^2\vec{u}+\rho_E\cdot\vec{E} \tag{2}$$

where ρ is the space charge density, u is the fluid flow velocity, p is the pressure, η is the dynamic viscosity of the solution and E is the electric field. The left side of the formula stands for the system's momentum change rate and the right side stands for the resultant of body force and surface force on the boundary. The fluid flow velocity does not change if the voltage and frequency of the power supply remain the same, thus the system's momentum change rate is zero. By considering the adjacent narrow electrode and wide electrode, Eq. (2) can be written as

$$\eta\nabla^2\vec{u}+\rho_E\cdot\vec{E}=0 \tag{1}$$

In ACEO, ions in the EDL and solution will both be driven by electric field. However, the electric field differs with locations. Thus ions in different locations suffer different forces. Specifically, the electric field near the narrow electrodes is larger than that near the wide electrodes, thus ions near the narrow electrodes will suffer a greater force. Though the direction of electric field alternates frequently, the forces produced by ions in EDL and solution will not change, as illustrated in Figure. 7. We only consider the forces along the pipeline direction and use F_{DL} and F_S to represent the forces suffered by ions in EDL and solution, respectively.

From the analysis above it is clear that resultant of ions in EDL and solution has an opposite direction. Eq. (3)can be written as:

$$\eta\nabla^2 u + \rho_{DL} \cdot E_{DL} - \rho_S \cdot E_S = 0 \tag{2}$$

where ρ_{DL} and ρ_s stand for the space charge density of ions in EDL and solution, respectively, and E_{DL} and E_s separately stand for the electric filed suffered by ions in EDL and solution.

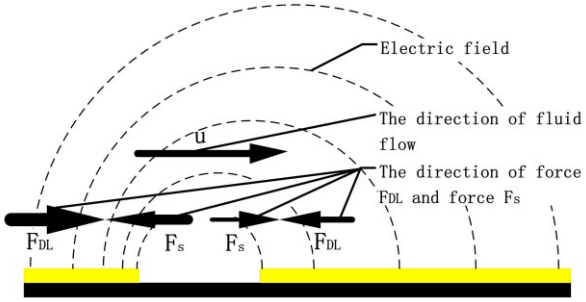

Figure. 7 The direction of forces in ACEO. (The thickness of the arrows represents the magnitude of the force)

At low frequency, there is enough time for the EDL to charge, thus the number of ions in EDL reaches its maximum. This maximum number is determined by the electrode capacitance and the supply voltage. Though the numbers of ions in EDL on adjacent narrow and wide electrode are the same, these ions suffer different electric fields due to the electrode asymmetry. As a result, the resultant produced by ions in EDL will have the direction from narrow electrode to the nearby wide electrode. Resultants suffered by ions in EDL in per unit volume can be deduced from Eq. (1)

$$F_{DL} = \rho_{DL} \cdot E_{DL} = C\tilde{V}[1 - \exp(-\frac{1}{2fRC})] \tag{3}$$

where $C\tilde{V}$ is the maximum space charge density of ions in EDL, f is frequency and RC is the system's relaxation time. EDL can be regard as the average electric field exerted on ions in EDL. In half a power period, $t = 1/2f$, the exponent part stands for the relationship between ion space charge density in EDL and power supply frequency. It shows that ions in EDL will decrease with the frequency's increase (which means the charging time will decrease).

There are both positive and negative ions in the solution, which is different from ions in EDL. It can be assumed that the space charge density of the ions in solution equals to the maximum space charge density of the ions in EDL, and formula can be written as:

$$F_S = \rho_S \cdot E_S = C\tilde{V} \cdot E_{S\max} \cdot \exp(-\frac{t}{RC}) \tag{4}$$

where t stands for time in half a period circle, $E_{S\max}$ can be regard as the maximum average electric field exerted on ions in solution. It can be assumed that space charge density of ions in solution does not change with frequency and time because solution concentration is constant. Formula (1) stands for the relationship between voltage and time on electrode, thus the potential drop in solution can be calculated by subtracting voltage on electrode from power supply voltage.

Then formula (4) can be written as:

$$\eta\nabla^2 u + C\tilde{V}[1 - \exp(-\frac{1}{2fRC})] \cdot E_{DL} - C\tilde{V} E_{S\max} \cdot \exp(-\frac{t}{RC}) = 0 \tag{5}$$

Here it can be assumed that the acting times of ions in EDL and solution are the same. If power supply's half a period is longer than the charging time, it can be assumed that forces suffered by ions in EDL and solution both become zero. Thus we can postulate that when $t > 3RC$, formula (7) becomes:

$$\eta \nabla^2 u = 0 \tag{6}$$

Figure. 8 The dimension and schematic diagram of pipeline

Figure. 8 shows the dimension of the pipeline and b represents half the pipeline height. By integrating formulae (7) and (8) we get:

$$\begin{cases} u = \dfrac{1}{2\eta}\left(b^2 - y^2\right) \cdot \left\{ C\tilde{V}[1 - \exp(-\dfrac{1}{2fRC})] \cdot E_{DL} - C\tilde{V} E_{S\max} \cdot \exp(-\dfrac{t}{RC}) \right\}, t \le 3RC \\ u = 0, t > 3RC \end{cases} \tag{7}$$

The average velocity can be calculated by integrating the velocity in half a period and then dividing the integration by time. When frequency is low, namely $T = \dfrac{1}{2} f > 3RC$, the average velocity is:

$$\begin{aligned} u &= \frac{1}{2\eta}\left(b^2 - y^2\right) C\tilde{V} \cdot \frac{\int_0^{3RC} \left[[1 - \exp(-\frac{1}{2fRC})] \cdot E_{DL} - E_{S\max} \exp(-\frac{t}{RC}) \right] dt + \int_{3RC}^{T} 0 dt}{T} \\ &= \frac{1}{2\eta}\left(b^2 - y^2\right) C\tilde{V} \cdot 2fRC \left\{ 3\left[1 - \exp\left(-\frac{1}{2fRC} \right) \right] \cdot E_{DL} - E_{S\max}\left(1 - e^{-3}\right) \right\}, 0 < 2fRC < \frac{1}{3} \end{aligned} \tag{8}$$

If the frequency is large enough, that is to say $T = \dfrac{1}{2} f \le 3RC$, the integration of the velocity is:

$$\begin{aligned} u &= \frac{1}{2\eta}\left(b^2 - y^2\right) C\tilde{V} \cdot \frac{1}{T} \int_0^T \left[[1 - \exp(-\frac{1}{2fRC})] \cdot E_{DL} - E_{S\max} \exp(-\frac{t}{RC}) \right] dt \\ &= \frac{1}{2\eta}\left(b^2 - y^2\right) C\tilde{V} \cdot \left\{ \left[1 - \exp\left(-\frac{1}{2fRC} \right) \right] \cdot E_{DL} - E_{S\max} \cdot 2fRC \left[1 - \exp\left(-\frac{1}{2fRC} \right) \right] \right\}, 2fRC \ge \frac{1}{3} \end{aligned} \tag{9}$$

In ACEO, if the solution concentration remains unchanged, the RC time will be constant. Thus for the convenience of analysis, let $x = 2fRC$ and $E_{DL} = 2E_{S\max}$. If we do not consider the coefficient of formulae (10) and (11), the two formulas can be rewritten as:

$$\begin{cases} y = x\left\{ 6\left[1 - \exp\left(-\dfrac{1}{x} \right) \right] - \left(1 - e^{-3} \right) \right\}, 0 < x < \dfrac{1}{3} \\ y = 2\left[1 - \exp\left(-\dfrac{1}{x} \right) \right] - x\left[1 - \exp\left(-\dfrac{1}{x} \right) \right], x \ge \dfrac{1}{3} \end{cases} \tag{10}$$

Figure. 9 is the curve drawn using Matlab which shows the relationship between x and y, and it can reveal the relationship between frequency f and velocity u. With the increase in x, y increases but decrease after a specific value. Flow reversal can be observed in this figure. By comparing Figure. 9 with experimental results reported in [15], it is clear that their tendencies are consistent.

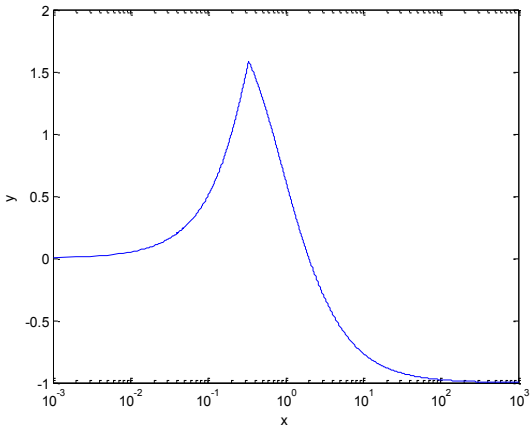

Figure. 9 The changes of y versus x. The flow changes and flow reversal can be observed.

In the simplification above, we let $E_{DL} = 2E_{S\max}$ because ions in EDL suffer a larger average electric field compared with ions in solution. Ions in EDL concentrate on the surface of the electrodes and separately suffer the maximum and minimum electric field, thus the average electric field exerted on ions in EDL will be larger than electric field suffered by ions in solution. The electrodes size and the gap between wide electrodes and narrow electrodes will both influence this ratio.

Conclusion

ACEO is like a DLC and its fluid flow is influenced both by ions in aqueous solution and EDL. In this paper, we first give an introduction about ions movement mechanism in ACEO, and then analyze two kinds of experimental phenomena that the existing theories cannot explain by using our own concepts. Furthermore, we give formulas about fluid flow velocity in section 4 and its calculated velocity tendency is consistent with experimental results. Therefore, it is clear that our understandings can reasonably explain the ACEO phenomena.

Acknowledgement

In this paper, the research was sponsored by the Nature Science Foundation of Henan Province (Project No. 201112400450401) and Youth Fund Project of Luoyang Institute of Science and Technology (Project No. 2010QZ16).

References

[1] Wang X, Cheng C, Wang S and Liu S. Electroosmotic pumps and their applications in microfluidic systems. Microfluid Nanofluid, 2009 (6) 145-162.
[2] John Paul Urbanski, Todd Thorsen, Jeremy A. Levitan and Martin Z. Bazant. Fast ac electro-osmotic micropumps with nonplanar electrodes. Applied Physics Letters, 2006 (89) 143508.
[3] Chien-Chih Huang, Martin Z. Bazant and Todd Thorsen. Ultrafast High-pressure AC Electro-osmotic Pumps for Portable Biomedical Microfluidics. Lab Chip, 2010 (10) 80-85.
[4] Naoki Sasaki, Takehiko Kitamori and Haeng-Boo Kim. AC electroosmotic micromixer for chemical processing in a microchannel. Lab Chip, 2006 (6) 550-554.
[5] Jiong-Rong Du, Yi-Je Juang, Jie-Tang Wu and Hsien-Hung Wei.Long-range and superfast trapping of DNA molecules in an ac electrokinetic funnel. Biomicrofluidics, 2008 (2) 044103.
[6] A Ramos, H Morgan, N G Green and A Castellanos. Ac electrokinetics: a review of forces in microelectrode structures. J. Phys. D: Appl. Phys, 1998 (31) 2338-2353.
[7] A Ramos, H Morgan, N G. Green and A Castellanos. LETTER TO THE EDITOR AC Electric-Field-Induced Fluid Flow in Microelectrodes. Journal of Colloid and Interface Science, 1999 (217) 420-422.

[8] A. B. D. Brown, C. G. Smith and A. R. Rennie. Pumping of water with ac electric fields applied to asymmetric pairs of microelectrodes. Physical Review E, 2000 (63) 016305.
[9] V. Studer, A. Pépin, Y. Chen and A. Ajdari. Fabrication of microfluidic devices for AC electrokinetic fluid pumping. Microelectronic Engineering, 2002 (61-62) 915-920.
[10] A. Ramos, A. González, A. Castellanos, N. G. Green and H. Morgan. Pumping of liquids with ac voltages applied to asymmetric pairs of microelectrodes. Physical Review E, 2003 (67) 056302.
[11] Ajdari A. Pumping liquids using asymmetric electrode arrays. Phys Rev E, 2000 61(1) R45–R48.
[12] Gonzalez A, Ramos A, Green NG, Morgan H and Castellanos A. Fluid flow induced by non-uniform ac electric fields in electrolytes on microelectrodes. II. A linear double-layer analysis. Physical Review E, 2000 (61) 4019–4028.
[13] Bazant MZ and Ben Y. Theoretical prediction of fast 3D AC electro-osmotic pumps. Lab Chip, 2006 (6) 1455–1461.
[14] Brian D. Storey, Lee R. Edwards, Mustafa Sabri Kilic and Martin Z. Bazant. Steric effects on ac electro-osmosis in dilute electrolytes. Physical Review E, 2008 (77) 036317.
[15] Vincent Studer, Anne Pépin, Yong Chen and Armand Ajdari. An integrated AC electrokinetic pump in a microfluidic loop for fast and tunable flow control. Analyst, 2004 (129) 944-949.
[16] Martin Z Bazant, Mustafa Sabri Kilic, Brian D Storey and Armand Ajdari. Nonlinear electrokinetics at large voltages. New Journal of Physics, 2009 (11) 075016.
[17] P. Garcia-Sanchez, A. Ramos, A. Gonzalez, N. G. Green and H. Morgan. Flow reversal in traveling-wave electrokinetics: an analysis of forces due to ionic concentration gradients. Langmuir, 2009 25(9) 4988–4997.
[18] D. Lastochkin, R. H. Zhou, P. Wang, Y. X. Ben and H. C. Chang. Electrokinetic micropump and micromixer design based on ac faradaic polarization Journal of Applied Physics, 2004 (96) 1730-1733.
[19] L. H. Olesen, H. Bruus and A. Ajdari. Ac electrokinetic micropumps: The effect of geometrical confinement, Faradaic current injection, and nonlinear surface capacitance. Physical Review E, 2006 (73) 056313.
[20] Todd M. Squires. Induced-charge electrokinetics: fundamental challenges and opportunities. Lab Chip, 2009 (9) 2477-2483.
[21] Martin Z. Bazant and Todd M. Squires. Induced-Charge Electrokinetic Phenomena: Theory and Microfluidic Applications. Physical Review Letters, 2004 92(6) 066101.
[22] T S Mansuripur, A J Pascall and T M Squires. Asymmetric flows over symmetric surfaces: capacitive coupling in induced-charge electro-osmosis. New Journal of Physics, 2009 (11) 075030.
[23] H. E. Becker 1957 U.S. Patent 2 800 616
[24] John R. Miller, R. A. Outlaw and B. C. Holloway. Graphene Double-Layer Capacitor with ac Line-Filtering Performance Science, 2010 (329) 1637-1639.
[25] B. E. Conway. Electrochemical Supercapacitors: Scientific Fundamentals and Technological Applications, New York: Kluwer Academic/Plenum Publishers,1999.
[26] N. G. Green, A. Ramos, A. González, H. Morgan and A. Castellanos. Fluid flow induced by nonuniform ac electric fields in electrolytes on microelectrodes. III. Observation of streamlines and numerical simulation. Physical Review E, 2002 (66) 026305.

Advanced Materials Research Vols. 986-987 (2014) pp 146-150

doi:10.4028/www.scientific.net/AMR.986-987.146

Research on Viscosity of Watered Fuel Oil prepared by Mechanical Agitation

Lu ZHANG, Yinmin ZHU*, Tie LI, Hongpeng ZHANG

Dalian Maritime University, Dalian, 116026, China

email: ntp@dlmu.edu.cn

Keywords: Viscosity; Watered Fuel Oil; Oil temperature; Water Content; Agitation Speed;

Abstract. Viscosity of Watered fuel oil, which was prepared by a self-made mechanical micro-mixing device, was measured with rotation viscosimeter. The effects of oil temperature, agitation speed and water content on viscosity were investigated in this research. The experimental results showed that: viscosity of watered fuel oil decreases with the increasing of oil temperature between 60-80 ℃ and water contents in 2.0-8.0 %, but increases with the accelerating agitation speed at 1000-1300 r/min.

Introduction

Under the situation of oil resource shortage and serious environment pollutions, the emulsified fuel oil which is due to both economic and environmental advantages has become one of technologies on energy saving and emission reduction with the prospect of application [1].

Viscosity is one of the most important physicochemical characteristics to watered fuel oil. Viscosity could influence watered fuel oil on aspects of transfer, preparation and spray quality. The viscosity of heavy oil is usually high at normal temperature, so it is quite important to understand how to get over the harmful effect from high viscosity oil in the course of watered fuel oil preparing. And it is benefit for improving the produce quality of watered fuel oil preparing by knowing the variation law of viscosity, which could affect the combustion of watered fuel oil [2]. Although there is a key relationship between combustion effects and law of property changes, the researches on influence factors of oil property changes after emulsification were few. Therefore, for making sure watered fuel oil could play a better role in energy saving and emission reduction, this research has studied on the measurement of viscosity influence and effect factors of watered fuel oil, which could provide the theoretical basis and foundation for technology application of watered fuel oil.

Materials and method

Devices used to prepare watered fuel oil

Figure 1 is a self-made device which is used to prepare watered fuel oil. It is made from mechanical micro-mixing central part, metering pump, rotary pump, mixing motor (0-1400 r/min adjustable), water tank, fuel oil tank, watered fuel oil tank and electrical system. The main part is connected to water way and oil way respectively by fast joints. There are three stage zones of mixing inside mechanical micro-mixing central part. The first stage is a cylindrical rotor, the second and third stages are interlocking gear wheels. And the entrance at a micron magnitude width is in the middle of the first and second mixing zones. Rotational speed of gear wheels and entrance width are both adjustable. Fuel oil and water are injected into mechanical micro-mixing central part at about 3 atm (standard atmosphere) and 2 atm, respectively, according to a certain proportion from different angels. Then water-in-oil (W/O) of water droplet size at the micron magnitude is prepared by combined actions which are impulse force, shear stress, friction and surface tension.

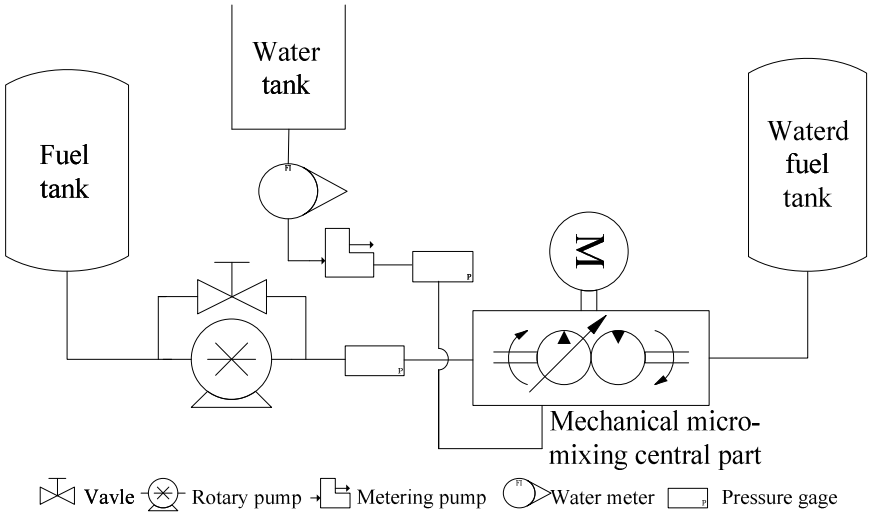

Figure 1 Flow chart of experiment

Parameters control

Watered fuel oil was prepared with mixed fuel oil from oil field and water as raw materials. Fuel oil temperature (T, ℃) in oil tank was controlled by electric heating and temperature transmitter. Agitation speed (v, r/min) was adjusted by changing rotational speed of gear wheels with the frequency transformer. Water content in watered fuel oil was adjusted by accurately controlling flow of water and oil. Sampling point was set at oil outlet of mechanical micro-mixing central part. Then viscosity was measured by using rotation viscosimeter (BROOKFIELD DV-Ⅱ+Pro). We used the thermal constant temperature extraction method to determine water volume in emulsified samples after static separation and to figure out the water content (ρ_w, %).

Results and discussion

The effects of oil temperature on viscosity

Viscosity of heavy fuel oil is high at the normal temperature. Considering the poor fluidity of oil, it needs preheat before been used. Previous studies shows the fuel oil possesses certain fluidity at the oil temperature above 50 ℃, and keeps stability well at the temperature 80 ℃, but the oil and water soon separates once the temperature exceeding 90 ℃. So we chose 60-80 ℃ as the temperature range in this research.

When agitation speeds were 1000, 1100, 1200, 1300 r/min, viscosities of watered fuel oil were measured at different temperatures 50, 60, 70, 80 ℃. As figure 2 showed, the viscosity decreased with the increasing of oil temperature at the same agitation speed. Viscosities of 4 kinds of agitation speed all reached all minimal at temperature 80 ℃, and all maximum at temperature 50 ℃. Then temperature elevated to 70 ℃, the decline of viscosity was certain. When the temperature increased from 70 to 80 ℃, the viscosity decreased significantly, and the average reduce rate was 35.3 %.

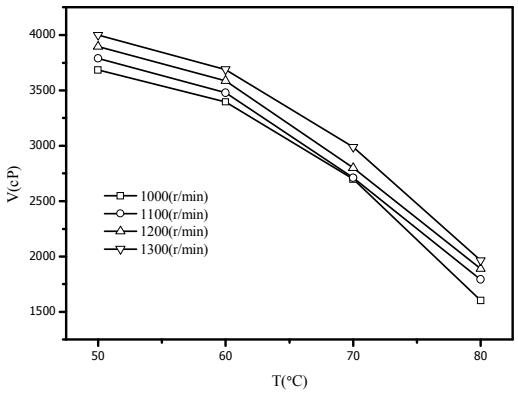

Figure 2 Viscosities of watered fuel oil at different preheating temperatures

The experiment showed, the higher temperature made viscosity of watered fuel oil lower. The reason is that high temperature causes molecules thermal motion strenuous, intermolecular interactions weaken [4], and then agitation resistance reduce, so the viscosity decreased. Fluid viscosity mainly comes from intermolecular interactions. In low temperature conditions, relatively, molecules orderly arrange, regularly move, and then intermolecular interactions are great. When temperature increasing, molecules thermal motion strengthens, next, intermolecular distances increase and inner friction reduces, as the result, viscosity decreases. From the energy point of view, thermal energy transforms into kinetic energy of molecules, and then intermolecular interactions weaken so viscosity decrease. Xiao et al researched on viscosity of emulsified oil, the results were similar with this experiment [2]. From the analysis above, increasing temperature is the effective method to decrease viscosity of watered fuel oil.

The effects of agitation speed on viscosity

Previous studies indicated, if agitation speed was lower than 1000 r/min, emulsification effect of watered fuel oil was bad. The max agitation speed of the device in this research was 1400 r/min, for the sustained and steady agitation, the next experiment chose the range of agitation speed 1000-1300 r/min.

Viscosities of watered fuel oil were measured at different agitation speeds (1000, 1100, 1200, 1300 r/min) when preheating temperatures were 50, 60, 70 and 80 ℃.As shown in figure 3, the viscosity of watered fuel oil increased with the increase of agitation speed at the same temperature. But the increase extent was small; each adding 100 r/min could increase about viscosity 110 cP. When agitation speed was 1000 r/min, viscosities of 4 kinds of temperatures were all minimal and maximum at agitation speeds 1000 and 1300 r/min, respectively. The viscosities increased 7.9-18.4 % as agitation speeds from 1000 r/min to 1300 r/min.

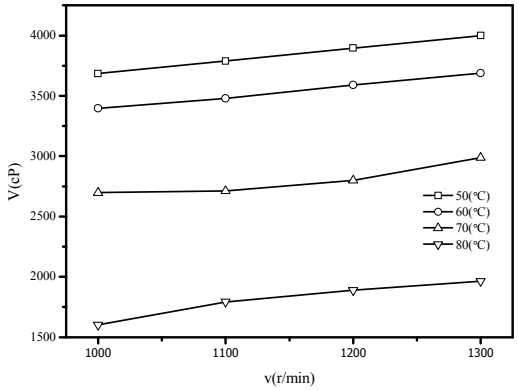

Figure 3 Viscosities of watered fuel oil at different agitation speeds

The experiment results showed, viscosity of watered fuel oil could increase slightly by adding agitation speed from 1000 r/min to 1300 r/min. The main reason is that high agitation speed makes particles of dispersed phase more and smaller, and then the viscosity increased in certain degree. In addition, fluid viscosity comes from fluid inner friction between adjacent fluidity layers. The impulse, shear and friction force can effect from different angels at mechanical agitation, which makes inner layers of watered fuel oil moved by vary speed, as the result, friction produced. High agitation speed causes adjacent fluidity layers speed difference adding, and then viscosity increases. Some researcher provided the same conclude as this experiment that increasing agitation speed could make the viscosity of emulsified oil increase [2] [5]. Though adding agitation speed can increase the viscosity of watered fuel oil, it is benefit to water droplet of dispersed phase smaller [6] [7], and improving combustion effect [8]. Therefore, it needs overall consideration to choose agitation speed in the course of preparing watered fuel oil.

The effects of water content on viscosity

Water content of emulsified oil should control in certain range. Too much water content is not good for stability of watered fuel oil, and could cause dispersed particles big, even oil-water separated. On the contrast, too little water content would limit effect of microexplosion, oil saving and pollution reducing. So the range of water content controlled from 2.0 % to 8.0 %.

Figure 4 showed viscosities of watered fuel oil at vary water content (2.0, 3.5, 5.0, 6.7 and 8.0 %) when oil temperatures were 60, 65, 70, 80 ℃ and agitation speed was 1300 r/min. From figure 4, viscosities of watered fuel oil increased with water content increasing at the same oil temperatures and agitation speed. When water content was 2.0 %, viscosities of watered fuel oil at 4 kinds of temperatures were all minimal. If increasing water content to 8.0 %, viscosities were all maximum. When water content increased from 2.0 % to 5.0 % and temperature was 80 ℃, viscosity increased 4.8 % which was the most.

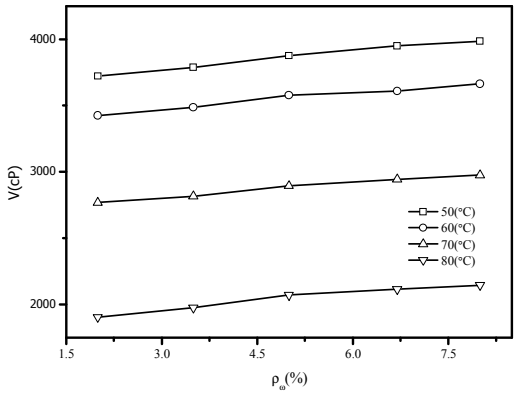

Figure 4 Viscosities of watered heavy oil at different water content

Experiment results indicated, at the range of water content 2.0-8.0 %, the more water content was, and the more viscosity was. Because the effect of water content on viscosity is closely related to the structure of water molecule. A molecule of water is made up of two atoms of hydrogen and one atom of oxygen, and three atoms are formed an isosceles triangle with two hydrogen atoms as the bottom and oxygen atom as the top. Positive and negative charge centre of molecule does not coincide, and dipole moment is quite great with very strong polarity. Because shared electron in H-O sharply deflects the side of O, H that atomic nucleus bared combine closely other atoms of strong electronegativity, short atomic radius and lone electron pair. At a certain external condition, H_2O molecule playing the double roles of the donor and acceptor of hydrogen bonding could form the stable emulsion with fuel oil depending on intermolecular and intramolecular hydrogen bonding. High water content causes much hydrocarbon combination, then increasing viscosity [6].

Conclusion

By preparing watered fuel oil using mechanical micro-mixing method without surfactant, the following conclusions can be made to this research:

(1) Viscosity of watered fuel oil decreased with increasing oil temperature. However, this applies before the oil temperature is too high to cause oil-water separation.

(2) Viscosity of watered fuel oil increased slightly with increasing agitation speed.

(3) Viscosity of watered fuel oil increased with increasing water content.

Acknowledgement

In this paper, the research was supported by ministry of industry and information technology (Project No. [2012]541) & the key scientific and technological projects of Dalian (Project No. 2008E12SF180).

References

[1] Ke Li, Jianchun Jiang, Xiangyu Li. Research progress on emulsified diesel. Biomass Chemical Engineering. 2010; 44(1): 44-50.

[2] Hongfei Xiao, Yunli Deng. A study of the influential factors of emulsified heavy-oil (EHO) viscosity. Journal of Fuel Chemistry and Technology. 2000; 15(3): 61-65.

[3] Yimin Zhu, Tie Li, Xiaojia Tang, Shuang Liu. Oil quality-condition system of a mechanical mixing device for watered fuel oil. CN, 2011200449050. 2011.

[4] Zhongqing Wang. Liquid viscosity and an analysis of the mechanism of viscosity reduction by magnetization. Acta Petrolei sinica. 1995; 16(4): 154-160.

[5] Knudsen Jes C, Øgendal Lars H, Skibsted Leif H. Droplet surface properties and rheology of concentrated oil in water emulsions stabilized by heat-modified β-Lactoglobulin B[J]. Langmuir, 2008, 24(6): 2603-2610.

[6] Lu Zhang, Shuang Liu, Na Li, Ran Yu, Xiaomei Wu, XiaojiaTang, Yinmin Zhu. Research on water droplet size influencing factors in watered fuel oil prepared by mechanical agitation[C]. The third conference on energy and environment technology, Zhangjiajie, China, 2012.

[7] Behrend O, Ax K, Schubert H. Influence of continuous phase viscosity on emulsification by ultrasound[J]. Ultrasonics Sonochemistry, 2000, 7(2): 77-85.

[8] Yunli Deng, Hongfei Xiao. Study of dispersity of emulsified heavy-oil (EHO). Journal of Fuel Chemistry and Technology. 2001; 29(1): 91-94.

Advanced Materials Research Vols. 986-987 (2014) pp 151-155

doi:10.4028/www.scientific.net/AMR.986-987.151

Impacts on water consumption in wet flue gas desulfuration

Xiao Haiping[a], Dong Lin[b], Han Gaoyan[c] and Ning Xiang[d]

North China Electric Power University, Beijing 102206, China
[a]dr_xiaohaiping@126.com,[b]945024915@qq.com,[c]hangaoyan123@126.com

Keywords flue gas desulfurization system water balance water consumption gas-gas heater

Abstract Material balance calculation was adopted to a bubbling desulfurization system of 600MW unit for water-saving measures. Analysis was made on main factors affecting water consumption. Results showed that heat release of desulfurization reaction and water evaporation went up with sulfur content increasing; Free water and bound water in gypsum increased rapidly with calcium improved; When sulfur content enhanced from 0.5% to 3.5%, water evaporation of reactor increased by 28.9% and waste water increased by 7.8%; With inlet flue temperature of WFGD raised from 120℃ to 200℃, waste water increased by 25.3% and evaporation of water increased by 102.35%; Once gas-gas heater (GGH) was installed, heat release of original flue gas decreased by 43.72% and the total water consumption decreased by 39.06%. Therefore, with sulfur content and temperature of inlet flue increasing, water consumption raises. Installation of gas-gas heater(GGH) can effectively reduce water consumption of WFGD system.

1 Background

Sulfur dioxide (SO2), generated mainly from large-scale coal utilization, causing environmental problems such as acid rain when discharged to the atmosphere. Wet flue gas desulfurization system （WFGD）is widely applied in our country with advantages of high desulfurization efficiency, mature technology and low operating cost[1,2]. Large amounts of water was consumed by WFGD, making water conservation urgently required due to shortage of water resources in western dry areas of China.

Study of mass balance has been always basis of desulfurization system design and optimization. Mass balance import and export items of the desulfurization system was calculated, selection of desulfurization system individual devices could be determined and the system design could be further optimized[3,4]. NIE Pengfei et al[5] calculated process water consumption of a 600MW unit WFGD system, conclusion displayed water evaporation inside the absorber occupied total system water consumption by more than 90%, therefore, water-saving measures to reduce inlet flue gas temperature with low-temperature economizer were proposed. The water consumption of calcium-based wet and semi-dry flue gas desulfurization process scheme was compared by Tong Huiling et al[6] Studies have shown that water consumed of semi-dry desulfurization was larger, and the amount of water vapor carried by net flue gas after desulfurization significantly increased with exhaust gas temperature rising. LV Ming et al[7] analyzed variation of water vapor temperature in WFGD system, and found that process water evaporation in absorber effectively reduced by lowering the original flue gas temperature after calculation of water consumption before and after reducing inlet flue gas temperature, thus water consumption in desulfurization system decreased. Water balance is a very important part of material balance in desulfurization system.

A bubbling bed desulfurization system of 600MW unit was analyzed in this paper, calculation table of material balance listed below. Research provided theoretical support for selection and optimization of desulfurization process with analysis of the main factors affecting water consumption.

2 Calculation Method

Material balance of WFGD system consists of flue gas, energy, solid, water and chlorine balance modules. Volume and mass flow of inlet flue dry and wet in desulfurization system were computed by a given coal, energy balance calculation for evaporation of water in desulfurization tower, and solid balance calculation for in or out solid material items, thereby calculation of the energy and water balance partly completed. Wastewater discharge was determined by the chlorine balance in desulfurization system[8,9]. Material balance calculations for a bubble column WFGD systems of 600MW unit was performed with operation at rated load, desulfurization efficiency was 95%, ratio of calcium to sulfur was 1.05, O / S was 2.5 , moisture content of free water for dehydration gypsum was 7%, and rinse water consumption was 0.5t / t gypsum. Other parameters used in the calculation listed in literature[10].At first, outlet flue gas temperature of jet bubbling reactor and GGH net gas side were assumed, the evaporation of water was determined at assuming temperature with energy balance calculations. Next step was checking the assuming temperature of GGH, according to an iterative calculation to make net flue water vapor pressure the same as saturated vapor pressure under the assumption. All material balance data in desulfurization system finally obtained[11].

3 Results and Analysis

3.1 Effects of Sulfur Content

Water balance proceeds of WFGD mainly consist of water vapor carried by original flue and air oxidation, water carried by desulfurizer (dry) and addendum water (equipment wash water and cooling water). Expenses include net flue carrying steam and liquid, gypsum bound water, free water and desulfurization wastewater. In which amount of net flue carrying water vapor depended on evaporation of water in tower[12].

Tab.1 Influence of sulfur content on input and output of water balance

Coal Sulfur Content [%]	Expense of Water Balance[t/h]					Proceeds of Water Balance[t/h]		
	Evapora-tion of water	Net flue liquid	Gypsum free water	Gypsum bound water	Desulfuri-zation wastewater	Chemical reaction water	Gypsum wash water	Addendum water
0.5	58.69	0.16	0.41	1.17	8.59	0.63	2.94	65.45
1	61.57	0.17	0.81	2.33	8.70	1.23	5.77	66.58
1.5	64.41	0.17	1.20	3.50	8.82	1.83	8.59	67.68
2	67.36	0.17	1.60	4.66	8.94	2.42	11.42	68.89
2.5	70.11	0.17	2.00	5.83	9.06	3.02	14.24	69.9
3	72.82	0.17	2.39	7.00	9.17	3.61	17.07	70.86
3.5	75.68	0.17	2.79	8.16	9.29	4.21	19.89	71.98

Effects of different sulfur content on the water balance listed in Table 1. With coal sulfur content increasing, the evaporation of water and desulfurization wastewater increased, gypsum combined and free water increased dramatically. When coal sulfur content added from 0.5% to 3.5%, water evaporated into the flue gas increased by 28.9%, and 7.8% for desulfurization wastewater, free water of plaster increased from 0.41t/h to 2.79t / h, gypsum bound water was from 1.17t/h to 8.16t/h. The rate of increasing was consistent with the magnitude of sulfur content variation. Addition of sulfur content in coal and desulfurizer respectively resulted in elevation of SO2 concentrations in the flue gas and increasing of gypsum carrying water, the desulfurization efficiency was ensured. Increasing of desulfurization reaction heat led to increasing of total water evaporation in tower. Therefore, gypsum carrying water and chemical reaction of water were roughly proportional to

generation of gypsum with increasing of sulfur, increasing of sulphur caused significant increasing of the evaporation of water in flue.

Fluctuations of water consumption were caused by changes of sulfur inevitably, water was mainly consumed by the way of evaporation of water in tower, net flue gas carrying liquid, free and bound water in the gypsum and desulfurization wastewater. When sulfur content changed from 0.5% to 3.5%, the proportion of evaporation of water in tower reduced from 85.03% to 78.76%, and net flue liquid was from 0.23% to 0.18%, desulfurization wastewater from 12.45% to 9.67%. While proportion of free water in plaster rose from 0.59% to 2.90%, 1.70% to 8.49% for bound water. Therefore, evaporation of water accounted the highest for total water consumption, desulfurization wastewater followed. Proportion of evaporation of water, net flue liquid and desulfurization wastewater decreased, gypsum free and bound water increased with sulfur content increasing.

3.2 The impact of import of flue gas temperature

Changing in boiler operation led that import temperature of flue gas changed, sequentially caused affects on desulfurization efficiency and mass balance, in which water consumption was particularly affected. Take desulphurization system without GGH for example, desuperheating water before desulfurization tower and outlet temperature of net flue varied with import flue gas temperature of WFGD varying. Calculations showed import flue gas temperature of FGD increased from 120℃ to 200℃, flue gas temperature would increased by 6.1℃ and reached to 56.2℃ after spray, equally 6℃ for outlet flue temperature of desulfurization tower and made it reached to 55.8℃. Flue temperature spray desuperheated and JBR outlet would rose 0.75 ℃ once average import flue gas temperature elevated by 10℃. Raising the temperature of flue gas in desulfurization tower would inevitably lead to increasing in water consumption.

The impact of import flue gas temperature of desulfurization system on water balance listed in Table 2. When the temperature increased from 120 ℃ to 200 ℃, wastewater in desulfurization system increased by 25.3%. Desuperheating water increased rapidly and growth rate reached to 106.84% as the flue gas temperature increased. Simultaneously, carrying heat increased with flue gas temperature, and total evaporation of water increased by 102.35% in desulfurization tower. Eventually, the process water consumption in desulfurization system increased by 95.29%.

Tab.2 Influnce of Flue Temperature on water consumption

Flue gas temperature [℃]	Wastewater [t/h]	Evaporation water in tower[t/h]	Desuperheating water [t/h]	Process water consumption [t/h]
120	9.36	88.00	84.85	98.50
130	9.65	98.99	95.95	109.78
140	9.94	110.14	107.19	121.22
150	10.23	121.30	118.45	132.68
160	10.53	132.62	129.72	144.30
170	10.83	143.81	141.02	155.79
180	11.13	155.17	152.45	167.44
190	11.42	166.53	163.90	179.11
200	11.73	178.07	175.50	190.95

When the inlet flue gas temperature increased from 120 ℃ to 200 ℃, Desuperheating and total evaporation water had nearly doubled, there is also a small increase for amount of wastewater. Variation of process water consumption mainly based on water evaporation in tower, and desuperheating water was main supplement. Therefore, water balance affected greatly by inlet temperature of the flue gas in desulfurization system. The higher import flue gas temperature, the more energy taken into the desulfurization system, thereby the more water was consumed.

3.3 Impact of GGH

Temperature of inlet and outlet flue gas in desulfurization system would be influenced by GGH, water balance of the system was changed as variation in flue gas carrying heat in desulfurization system. Installation of GGH in desulfurization system caused a series of changes, followed by temperature of inlet and outlet net flue gas, energy balance in desulfurization reactor and water balance. Heat release of the original gas in desulfurization tower decreased by 43.72% with GGH，43.71% for water vapor, 49.92% for heat absorption of addendum water, and 22.65% for limestone slurry. The heat taken away by evaporation of water in desulfurizing reactor reduced by 41.89% with GGH, so that the heat required evaporation of water taking away significantly reduced.

Calculations showed that the original flue gas temperature lowered to 95 ℃ with GGH, and it further reduced to 47.8 ℃ after spray desuperheater. Net flue gas temperature after desulfurization increased to 84.9 ℃ by GGH heat absorption. Without the installation of GGH, original flue gas of 132℃ entered escape system, then decreased to 51.2 ℃ after spray desuperheating, net flue gas temperature out of desulfurization tower reached to 50.8 ℃. Reduction of 37 ℃ for original flue gas and improvement of 26.1 ℃ for exports net flue gas was achieved with GGH.

The total process supplemental water reduced by 39.06%, and desulfurization wastewater volume had a decline of 11.53% with application of GGH. The reason was that GGH reduced the amount of energy carrying into desulfurization reactor with original flue gas, thereby the temperature in desulfurization reactor and the total evaporation of water reduced. There is a certain air leakage coefficient for GGH, resulted in part of the original flue gas leakage into the net flue gas, and amount of water vapor carried by original flue gas decreased. The net flue gas carrying liquid and plaster surface carrying water were changed lightly due to changes in total flow of net flue gas and gypsum production. Total desulfurization wastewater was closely related to addendum water. The increase in total addendum water inevitably led that more chloride ions were taken into the desulfurization system. Total amount of addendum water decreased with GGH, leading to reduction of chloride ions, and amount of desulfurization waste water also reduced. Therefore, the consumption of process water effectively decreased because of water evaporation in desulfurization tower and the desulfurization wastewater significant reduced with GGH.

Conclusion

（1）Heat release of desulfurization reaction in tower and the amount of water evaporated increased directly with sulfur content of coal. Since more calcium was plunged in, free and bound water in gypsum rapidly increased.

（2）Flue gas inlet temperature of desulfurization tower raised with that of desulfurization systems, variation of water consumption was mainly caused by increasing of water evaporation in tower.

（3）Heat release of original flue gas in desulfurization tower decreased with GGH, resulting in decline of water evaporation, which was the main reason for saving water with GGH.

Acknowledgements.

Project is supported by National Natural Science Foundation of China(51206047) and “the Fundamental Research Funds for the Central Universities”, Which is grateful acknowledged.

References

[1] GAFFNEY J S, MARLEY N A. The impacts of combustion emissions on air quality and climate from coal to biofuels and beyond[J].Atmosphere Environment,2009,43(1):23-26.

[2] LUO Yi. China Environment Statistical Yearbook[M].BeiJing: China Environmental Science Press, 2011.

[3] SUN Keyin,ZHONG Qin. FGD system design construction and operation[M].BeiJing: Chemical Industry Press,2005.

[4] WANG Wenlong,MA Chunyuan,HU Mingqiang,etal. Study on utilization radio of desulfurizing agent based on composition analysis of by-products[J].Journal of Power Engineering, 2009,29(12):1143-1147.

[5] NIE Pengfei,WANG Yang,WU Xuemin. Water consumption of wet FGD device for 600 MW units[J]. Thermal Power Generation, 2012, 41(10),35-37.

[6] TONG Huiling,SUN Xuguang,LI Dingkai,etal.Comparison of water consumption between wet and semi-dry lime FGD processes[J].Power System Engineering, 2003, 19(6):1-3.

[7] LV Ming,ZHAO Zhijun,YIN Guoqiang,etal. Achieving water-saving purpose by reducing in-let gas temperatures in wet flue gas desulfurization process[J]. Journal of Chinese Society of Power Engineering, 2010,30(9):695-698.

[8] ZHOU Qulan,XU,Tongmo,HUI Shien. Development and application of China's own wet Flue Gas Desulfurization technique[J]. Journal of Power Engineering, 2006,26(2),261-264.

[9] CHEN Guojin. Research on technology of desulphurizing,dedusting and energy-saving of middle and small-sized coal fired boilers[J]. Journal of Power Engineering, 2003,23(2):2333-2337.

[10] YU Qinjian.Study of desulfurization system mass balance[D]. BeiJing, North China Electric Power University, 2013.

[11] LI Pengfei,TONG Huiling. Comparison and analysis on the calculation methods of acid dew point of flue gas[J]. Boiler Technology, 2009,40(6):5-8.

[12] ZENG Tinghua,YANG Hua,LISO Yongjin,etal. Wet FGD System commissioning, testing and operation[M].BeiJing: China Electric Power Press, 2008

Advanced Materials Research Vols. 986-987 (2014) pp 156-159

doi:10.4028/www.scientific.net/AMR.986-987.156

Color tunability of blue phosphors by changing cations for near-UV InGaN-based light-emitting diode

Yiwen Zhu [a], Fenfen Hu [b], Meili Zhou[c], Ping Cheng [d], Zhengliang Wang [e]

Engineering Research Center of Biopolymer Functional Materials of Yunnan, School of Chemistry and Biotechnology, Yunnan University of Nationalities, Kunming 650500, China

[a] busiyi1012@126.com, [b] 957345499@qq.com, [c] 1132468813@qq.com, [d] 632126722@qq.com, [e] wangzhengliang@foxmail.com

Keywords: Optical materials; Luminescence; Optical properties

Abstract: The serials of blue phosphors, $CaAl_2Si_2O_8$: Eu^{2+} doped with different content Sr^{2+} and Mg^{2+} ions, were prepared by solid-state reaction at high temperature. And their structure and photo-luminescent properties were investigated. In $Ca_{0.96-y}Sr_yAl_2Si_2O_8$: $0.04Eu^{2+}$ (y = 0.10, 0.30, 0.50, 0.70, 0.90) system, for $y \leqq 0.03$, all the compositions crystallize in triclinic structure of $CaAl_2Si_2O_8$, and on further increase of y, the system undergoes a compositionally induced phase transition from triclinic to monoclinic structure. For $Ca_{0.96-y}Mg_yAl_2Si_2O_8$: $0.04Eu^{2+}$ (y = 0.10, 0.30, 0.50, 0.70, 0.90) system, for $z \leqq 0.03$, all the compositions are of triclinic structure of $CaAl_2Si_2O_8$. With the further increase of z, other phase appears. The emission spectra of these phosphors show blue shift with the introduction of Sr^{2+} ions, and red shift with Mg^{2+} ions. The reason may be due to the difference ionic radii of Mg^{2+}, Ca^{2+}, Sr^{2+}. These phosphors show excellent blue emission and broad excitation band in near-UV (ultraviolet) range. They may be potential phosphors for near-UV light-emitting diodes (LEDs).

Introduction

In recent years, the semiconductor white-light-emitting diodes (W-LEDs) attract more and more attention, since they have many advantages, such as high efficiency, energy saving and environmental-friendly characteristics[1,2]. A higher efficiency white LED with an appropriate color temperature and a higher color-rendering index can be obtained by using near-ultraviolet (nr-UV) InGaN-based LED chip coated with blue/green/red tricolor phosphors[3]. The commonly used blue-emitting phosphor for nr-UV InGaN-based white LEDs is $BaMgAl_{10}O_{17}$: Eu^{2+} (BAM: Eu^{2+})[4], which is used as commercial blue phosphor in fluorescent lamps[5]. However the excitation intensity around nr-UV range is weak, so it is interesting to find new blue phosphors with the intense excitation and emission for the near-UV LED chips.

The excitation band of Eu^{2+} in phosphors is a broad band, which is due to the 4*f*- 5*d* transitions. It can exhibit intense emission from violet to red light region in the different hosts with different crystal filed[6,7]. So the excitation and emission bands of Eu^{2+} can be controlled by changing the crystal filed. The different cations with different radii in the host compound would induce some change in the sub-lattice structure around the luminescent center ions[8], hence the crystal filed will be changed, which leads to different photo-luminescent properties.

Recently, $CaAl_2Si_2O_8$ doped with the luminescent centre ion were investigated, and it shows excellent blue emission with broad band in near-UV range, which can match the excitation of the near-UV GaInN chip[9,10]. Anorthite ($CaAl_2Si_2O_8$) in a triclinic crystal system was reported by Angel in 1988[11]. In the crystal lattice, one type of Ca^{2+} ion occupies an octahedral site with six oxygen atoms, and other Ca^{2+} ions occupy three kinds of polyhedral sites with seven coordinated oxygen atoms. Al and Si atoms both occupy tetrahedral sites with four coordinated oxygen atoms.

Ca^{2+}, Sr^{2+} and Mg^{2+} ions are alkaline earth metal ions with the same charge. The sub-lattice structure of $CaAl_2Si_2O_8$ will be changed by replacing part of Ca^{2+} with Sr^{2+} and Mg^{2+}. And the photo-luminescent properties of will be different $CaAl_2Si_2O_8$: Eu^{2+} by introducing Sr^{2+} and Mg^{2+} ions. So in this article, the phosphors $CaAl_2Si_2O_8$: Eu^{2+} doped with different content Sr^{2+} and Mg^{2+} were prepared by solid state reaction and their luminescent properties were investigated.

Experimental

The polycrystalline samples $CaAl_2Si_2O_8$:Eu doped with different content Sr^{2+} and Mg^{2+} were prepared by solid-state technique at high temperature. The stoichiometric mixtures of $CaCO_3$ (A.R. grade), Al_2O_3 (A.R. grade), SiO_2 (A.R. grade), $SrCO_3$ (A.R. grade), MgO (A.R. grade), and Eu_2O_3 (99.99 % purity) were first ground and heated at 1400 ºC in CO atmosphere for 6 h.

The structure of the final products was examined by X-ray powder diffraction (XRD) using Cu K_α radiation on RIGAKU D/max 2200 vpc X-Ray Diffractometer. The excitation and emission spectra were recorded on a JOBIN YVON FL3-21 spectrofluorometer at room temperature and a 450 W xenon lamp was used as excitation source.

Results and discussion

$Ca_{1-x}Al_2Si_2O_8$: xEu^{2+}

The XRD pattern of $Ca_{0.96}Al_2Si_2O_8$:$0.04Eu^{2+}$ is shown in Fig. 1. It is close to the JCPDS card 41-1486 [$CaAl_2Si_2O_8$]. Little other can be found in this pattern. This indicates that the phosphor $Ca_{0.96}Al_2Si_2O_8$:$0.04Eu^{2+}$ shares the similar phase with $CaAl_2Si_2O_8$. The ionic radius of Eu^{2+} (117 pm, CN = 6) is close to that of Ca^{2+} (100 pm, CN = 6), so the little doping of Eu^{2+} does not change the crystal structure, and Eu^{2+} ions occupy the site of Eu^{2+} ions in this crystal lattice.

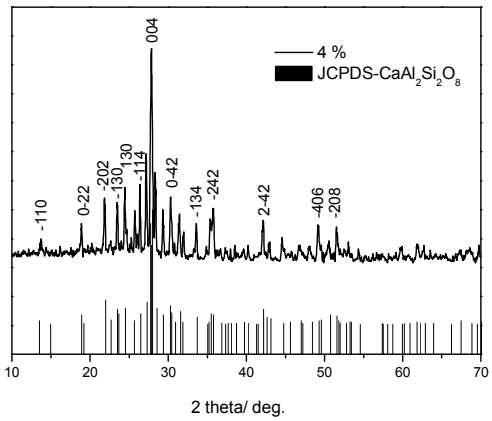

Fig. 1 The XRD pattern of $CaAl_2Si_2O_8$:$0.04Eu^{2+}$

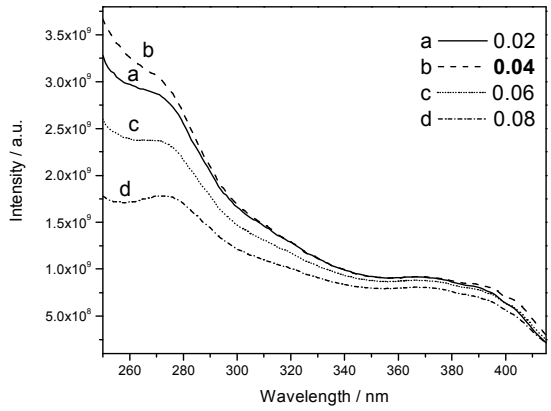

Fig.2 The excitation spectra of $CaAl_2Si_2O_8$: xEu^{2+} by monitoring emission at 435 nm

Fig.2 is the excitation spectra of the phosphors $Ca_{1-x}Al_2Si_2O_8$: xEu^{2+} (x = 0.02, 0.0.04, 0.06 and 0.08) by monitoring emission at 435 nm. The broad excitation band from 250 nm to 415 nm is due to the $4f - 5d$ transitions of Eu^{2+}. The excitation bands from 360 to 400 nm show a flatform, this is useful to find application on near-UV-LED chips. When the content of Eu^{2+} is 0.04, the excitation intensity is the strongest.

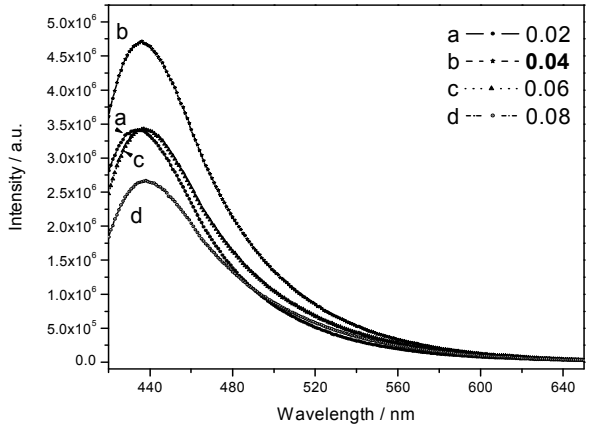

Fig.3 The emission spectra of $CaAl_2Si_2O_8$: xEu^{2+} under 400 nm excitation

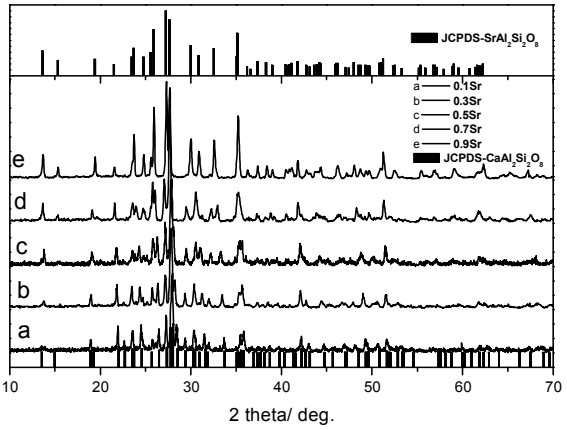

Fig.4 The XRD patterns of $Ca_{0.96-y}Sr_yAl_2Si_2O_8$: $0.04Eu^{2+}$ (y = 0.10, 0.30, 0.50, 0.70, 0.90)

Our aim is to investigate the blue phosphor for near-UV LED chips ($\lambda_{em} \approx 400$ nm), then the emission spectra of $Ca_{1-x}Al_2Si_2O_8$: xEu^{2+} (for x = 0.02, 0.0.04, 0.06 and 0.08) under 400 nm excitation are shown in Fig.3. The broad blue emission is due to the $5d - 4f$ transitions of Eu^{2+}. It is observed that the emission bands of the phosphors show some red shifts with an increase of Eu^{2+} concentration. J. Qiu. et al.[12] had reported that the probability of an energy transfer among Eu^{2+} ions. When the content of Eu^{2+} becomes larger, the distance between Eu^{2+} ions becomes less, and the probability of energy transfer among Eu^{2+} ions is improved. In other words, the energy transfer of Eu^{2+} ions from the higher $5d$ levels to the lower $5d$ levels of Eu^{2+} ions is increased. Hence the $4f - 5d$ transitions of Eu^{2+} show the red shift with higher Eu^{2+} concentration. The sample $Ca_{0.96}Al_2Si_2O_8$: $0.04Eu^{2+}$ shows the strongest emission with appropriate CIE chromaticity coordinates ($x = 0.163$, $y = 0.112$).

$Ca_{0.96-y}Sr_yAl_2Si_2O_8$: $0.04Eu^{2+}$

The serials of samples $Ca_{0.96-y}Sr_yAl_2Si_2O_8$: $0.04Eu^{2+}$ (y = 0.10-0.90) were prepared. As examples, the XRD patterns of $Ca_{0.96-y}Sr_yAl_2Si_2O_8$: $0.04Eu^{2+}$ (y = 0.10, 0.30, 0.50, 0.70, 0.90) are shown in Fig.4. In this system, for $y \leqq 0.03$, all the compositions crystallize in triclinic structure of $CaAl_2Si_2O_8$ and on further increase of y, the system undergoes a compositionally induced phase transition from triclinic to monoclinic structure. The phase transformation is due to the distinct ionic radii between Ca^{2+} (100 pm, CN = 6) and Sr^{2+} (118 pm, CN = 6).

Fig.5 is the excitation spectra of $Ca_{0.96-y}Sr_yAl_2Si_2O_8$: $0.04Eu^{2+}$ (y = 0.10, 0.30, 0.50, 0.90) by monitoring emission at 435 nm. The broad excitation band from 300 nm to 415 nm is due to the $4f - 5d$ transitions of Eu^{2+}. The phosphor $Ca_{0.66}Sr_{0.30}Al_2Si_2O_8$: $0.04Eu^{2+}$ shows the strongest excitation intensity in near-UV range (seeing the inset figure in Fig. 5).

The emission spectra of $Ca_{0.96-y}Sr_yAl_2Si_2O_8$: $0.04Eu^{2+}$ (y = 0.10, 0.30, 0.50, 0.90) are shown in Fig. 6. The emission band shifts to a shorter wavelength with an increase in Sr^{2+} concentration. It is well known that the ionic radius of Sr^{2+} is bigger than that of Ca^{2+}. In the triclinic structure of $CaAl_2Si_2O_8$, the length of the c axis increases by replacing part of the Ca^{2+} by Sr^{2+} ions, the effect of preferential orientation of a d-orbital in the chain direction decreases, so that the Eu^{2+} emission shifts to shorter wavelength[13]. The sample $Ca_{0.96-y}Sr_yAl_2Si_2O_8$: $0.04Eu^{2+}$ shares the intense emission, and its CIE chromaticity coordinates are calculated to be $x = 0.165$, $y = 0.123$.

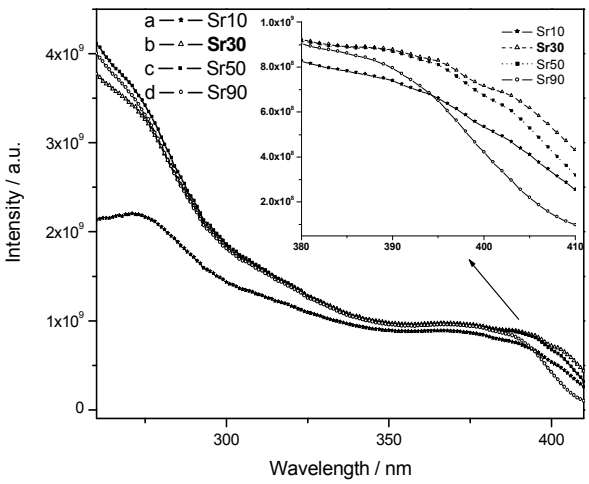

Fig.5 The excitation spectra of $Ca_{0.96-y}Sr_yAl_2Si_2O_8$: $0.04Eu^{2+}$ by monitoring emission at 435 nm

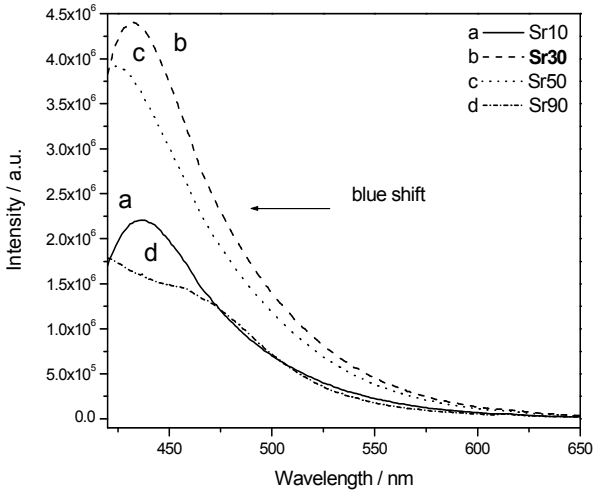

Fig.6 The emission spectra of $Ca_{0.96-y}Sr_yAl_2Si_2O_8$: $0.04Eu^{2+}$ under 400 nm excitation

$Ca_{0.96-z}Mg_zAl_2Si_2O_8$: $0.04Eu^{2+}$

Fig.7 is the excitation spectra of $Ca_{0.96-z}Mg_zAl_2Si_2O_8$: $0.04Eu^{2+}$ (z = 0.10, 0.30, 0.50) by monitoring emission at 435 nm. These three curves share similar sharp. When the z is 0.30, the sample shows the strongest excitation. The emission spectra of are exhibited in Fig.8. The emission band shows red shift with an increase in Mg^{2+} concentration. The reason may be due to the difference between ionic radius of Mg^{2+} and ionic radius of Ca^{2+}. In the triclinic structure of

$CaAl_2Si_2O_8$, the length of the *c* axis increases by replacing part of the Ca^{2+} by Mg^{2+} ions, the effect of preferential orientation of a *d*-orbital in the chain direction increases, so that the Eu^{2+} emission shifts to longer wavelength[13]. The phosphor exhibits the strongest emission with appropriate CIE chromaticity coordinates ($x = 0.166$, $y = 0.125$).

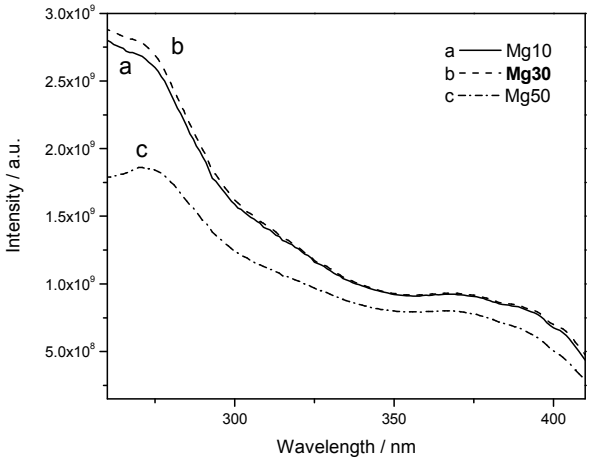

Fig.7 The XRD patterns of $Ca_{0.96-z}Mg_zAl_2Si_2O_8$: $0.04Eu^{2+}$ ($z = 0.10, 0.30, 0.50, 0.70, 1.0$)

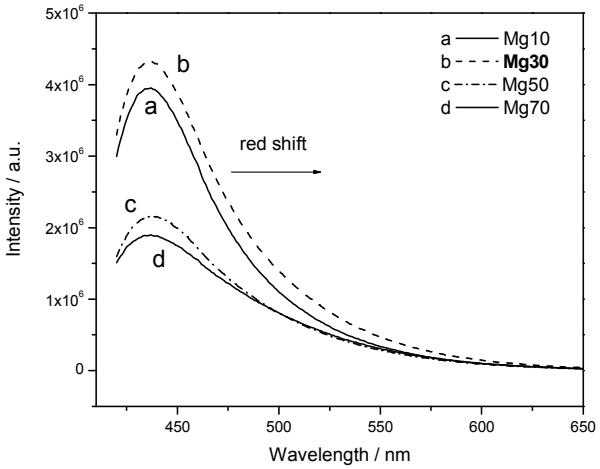

Fig.8 The excitation spectra of $Ca_{0.96-z}Mg_zAl_2Si_2O_8$: $0.04Eu^{2+}$ by monitoring emission at 435 nm

Conclusion

We have prepared blue phosphors, $CaAl_2Si_2O_8$: Eu^{2+} doped with different content Sr^{2+} and Mg^{2+}, and investigated their photo-luminescent properties. The emission spectra show blue shift with the introduction of Sr^{2+}, and red shift with Mg^{2+}. This is due to the ionic radius difference of Ca^{2+}, Sr^{2+} and Mg^{2+}. These phosphors show intense blue emission with broad excitation in near-UV range, which maybe find application in near-UV InGaN-based LED.

Acknowledgements

This work was financially supported by the National Natural Science Foundation of China (21261027)

References

[1] S. Dalmasso, B. Damilano, C. Pernot, A. Dussaigne, D. Byrne, N. Grandjean, M. Leroux and J. Massies, Phys. Stat. Sol. (a). 192 (2002) 139.
[2] J.-H. Yum, S.-Y. Seo, S. Lee and Y.-E. Sung, J. Electrochem. Soc. 150 (2003) H47.
[3] X. Piao, K. Machida, T. Horikawa,H. Hanzawa, J. Electrochem. Soc. 155 (2008) J17
[4] S. Neeraj, N. Kijima, A.K. Cheetham, Chem. Phys. Lett. 387 (2004) 2.
[5] P. Yang, G. Q. Yao, J. H. Lin, Opt. Mater. 26 (2004) 327
[6] Z.C. Wu, J.X Shi, J. Wang, M.L. Gong, Q. Su, J. Solid State Chem. 179 (2006) 2356
[7] H. Wu, X. Zhang, C. Guo, J. Xu, M. Wu, Q. Su, IEEE Photon. Technol. Lett., 17 (2005) 1160.
[8] J. P. M. Van Vliet, G. Blasse, L. H. Brixner, J. Solid State Chem. 76 (1988) 160.
[9] W. J. Yang, L. Luo, T. M. Chen, N. S. Wang, Chem. Mater. 17 (2005) 3883
[10] T. Ohgaki, A. Higashida, K. Soga, A. Yasumori, J. Electrochem. Soc. 154 (2007) J163
[11] Angel, R. J. Am. Mineral. 73 (1988) 1114.
[12] J. Qiu, K. Miura, N. Sugimoto, K. Hirao, J. Non-Cryst. Solids. 213&214 (1997) 266.
[13] S. H. M. Poort, J. W. H. van Krevel, R. Stomphorst, A. P. Vink, G. Blasse, J. Alloys Compd. 241 (1996) 75.

Advanced Materials Research Vols. 986-987 (2014) pp 160-163

doi:10.4028/www.scientific.net/AMR.986-987.160

Metal-semiconductor-metal Ultraviolet Photodiodes Fabricated on Bulk GaN Substrate

Feng Xie[1,2,a], Guofeng Yang[2,3,b], Jun Wang[1,c], Guosheng Wang[1,d], Man Song[1,e], Tanglin Wang[1,f], Haoran Wu[1,g] and Jin Guo[1,h]

[1]China Electronics Technology Group Corporation No.38 Research Institute, Hefei 230088, China

[2]School of Electronic Science and Engineering, Nanjing University, Nanjing 210093, China

[3]School of Science, Jiangnan University, Wuxi 214122, China

[a]fxie@foxmail.com, [b]gfyang@jiangnan.edu.cn, [c]xuanyu2020@163.com, [d]wgs0818@sina.cn, [e]songman1986@163.com, [f]arnoldone@126.com, [g]whr.123@163.com, [h]phenixgj@hotmail.com

Keywords: GaN, metal-semiconductor-metal, photodetector, homoepitaxy

Abstract. We report the demonstration of a GaN-based planar metal-semiconductor-metal (MSM) ultraviolet photodetector (PD). The MSM PD with semitransparent interdigitated Schottky electrodes is fabricated on low-defect-density GaN homoepitaxial layer grown on bulk GaN substrate by metal-organic chemical vapor deposition. The dislocation density of the GaN homo-epilayer characterized by cathodoluminescence mapping technique is ~5×10^{6} cm^{-2}. The PD exhibits a low dark current density of ~4.1×10^{-10} A/cm^{2} and a high UV-to-visible rejection ratio up to 5 orders of magnitude at room temperature under 10 V bias. Even at a high temperature of 425 K, the dark current of the PD at 10 V is still <1×10^{-9} A/cm^{2} with a reasonable UV-to-visible rejection ratio more than 3×10^{4}, indicating that such kind of PDs are suitable for high temperature operation.

Introduction

GaN-based semiconductor material system is one of the best choices for ultraviolet (UV) photon detection due to its wide direct band gap energy, superior radiation hardness and high temperature resistance. Such UV photodetectors (PDs) are important components in a variety of military and commercial applications, such as flame detection, environmental monitoring, chemical/biological agent detection, and space communications [1]. To achieve a high-performance metal-semiconductor-metal (MSM) type UV PDs, it is important to reduce dark current of the device which determines the lowest detectable optical signal strength. Although detailed reverse leakage mechanism of GaN-based Schottky contacts is still under debate, it is well accepted that structural defects, especially dislocations, within GaN epilayer play an important role in determining junction leakage [2]. However, GaN layers grown on foreign substrate like sapphire typically have threading dislocation densities on the order of >10^{8} cm^{-2}, increasing device leakage and resulting in a premature device breakdown. In order to develop a higher signal-to-noise ratio and more reliable GaN-based PD, one should first obtain the availability of a low-dislocation GaN substrate technology.

Recently, significant improvements in material quality and device performance are expected using homoepitaxially grown GaN. With very low impurity and dislocation density, high performance GaN-based light-emitting diodes [3], high electron-mobility transistors [4], and Schottky rectifier [5] on bulk GaN substrate by employing homoepitaxial growth technique is reported. However, in spite of the excellent device performance reference above, there have been limited published reports regarding the UV PDs fabricated on bulk substrates.

In this work, we report the fabrication and characterization of a MSM PD based on low-defect-density homoepitaxial GaN layer. The PD shows low dark current and high UV-to-visible rejection ratio.

Experiment

The freestanding conductive bulk GaN substrate used in this work is prepared by hydride vapor phase epitaxy with a thickness of 320 μm and a room-temperature resistivity of ~0.01 Ω·cm. The device structure is grown by metal-organic chemical vapor deposition with optimized growth conditions, consisting of a 1 μm silicon-doped n^+-GaN (~3×10^{18} cm^{-3}) transition layer and a 3 μm n-GaN active layer (~3×10^{16} cm^{-3}). The homoepitaxial GaN is characterized by using cathodoluminescence (CL) mapping technique, high-resolution x-ray diffraction (XRD) and atomic force microscopy (AFM) respectively. In fabrication of the MSM PDs, standard photolithography and lift-off techniques are used to define the interdigitated Schottky contact electrodes, which are based on semitransparent Ni/Au (5 nm/5 nm) metal stack. The fingers of the contact electrodes are 5 μm wide and 400 μm long with a spacing of 5 μm. Finally, a 200 nm Ti/Au bi-layer is evaporated and patterned to serve as the contact pads. Figure 1 shows a schematic and a topview image of one finishied PD with an effective device area of 400×400 μm^2.

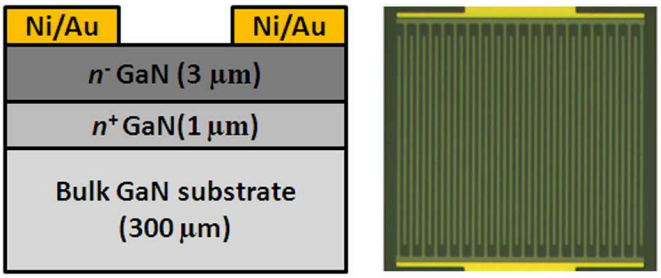

Fig.1 (a) Schematic of the device structure and (b) top wiew image of one fabricated PD with an effective device area of 400×400 μm^2.

Results and discussions

The dislocation density of the device structure on bulk GaN substrate is measured by a CL mapping technique which has been confirmed to be a reliable method to count dislocations in low-defect-density GaN [6]. Figure 2(a) shows a typical panchromatic CL mapping image of the homoepitaxial GaN layer examined over a large surface area, in which each dislocation is represented by a small dark spot resulting from strong local non-radiative recombinations. The dislocation density of the homoepitaxial GaN layer is estimated to be ~5×10^6 cm^{-2} in average, which is about 2-3 orders lower than that of the control sample grown on sapphire substrate (see Fig. 2(b), dislocation density>10^8 cm^{-2}). The corresponding full width at half maximum of the GaN (0002) XRD rocking curve is 80-100 arcsec, which agrees with the low dislocation density determined by CL mapping. The surface roughness of the GaN homo-epilayer measured by AFM over a 5×5 μm^2 area is ~0.5 nm. The above analysis indicates that low-dislocation-density GaN epilayer with reasonable surface morphology has been obtained through the homoepitaxial growth process.

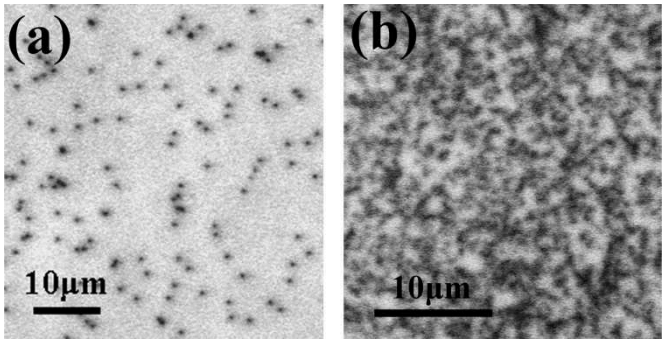

Fig. 2 (a) Typical CL mapping image of homoepitaxial GaN layer grown on bulk GaN substrate. (b) CL mapping image of the control GaN layer grown on sapphire.

The dark and photo-current curves of the MSM PD are shown in Fig. 3, in which the optical power density of the 365 nm UV illumination is ~6.5 μW/mm^2. The PD exhibits a low RT dark current of less than 1 pA at 10 V bias, which can be attributed to the low dislocation density within the homoepitaxial GaN layer. Even at a high temperature of 425 K, the dark current at 10 V is still below 5 pA, suggesting that the device is suitable for high temperature applications. The decrease of photocurrent with increasing temperature can be explained by thermal activation of trapped holes at the semiconductor/metal interface, which will be discussed later. In addition, enhanced recombination loss at high temperature can also reduce the photocurrent.

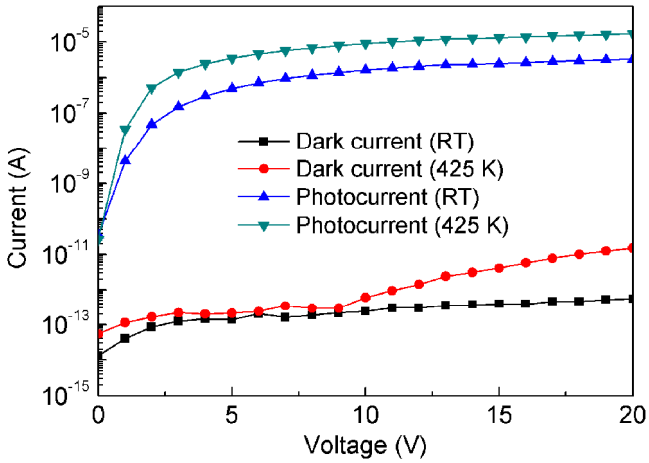

Fig.3 I-V characteristics of the PD measured under dark and under 365 nm light illumination at RT and 425 K, respectively.

Figure 4 show the spectral response characteristics of the PD at RT and at 425 K respectively. A sharp cutoff in the photo-response curves occurs at approximately 365 nm, which corresponds to the bandgap energy of GaN. At 10 V bias, the UV-to-visible rejection ratio of the PD could be as high as 1×10^5 at RT, and is still higher than 3×10^4 even at a high temperature of 425 K. Here, the UV-to-visible rejection ratio is defined as the responsivity measured at 360 nm divided by that measured at 500 nm. It can be seen clearly that the measured responsivity of PD is >1 A/W at 10 V bias, the corresponding PD quantum efficiency could well exceed 100%, indicating that an internal gain mechanism exists within the device.

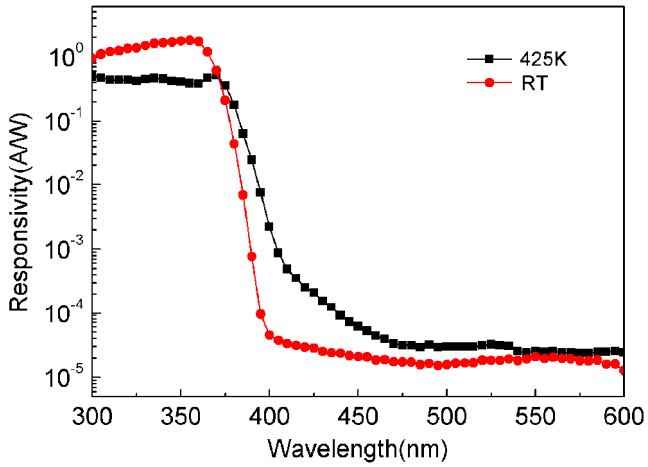

Fig.4 Spectral response of the GaN MSM PD measured at RT and 425K, respectively.

Photocurrent gain has been widely observed in various MSM PDs, which is desirable for applications requiring high responsivity but could limit the detector bandwidth simultaneously. It

seems that the internal gain is not necessarily linked to the crystalline quality of the semiconductor, as it could also present in MSM PDs based on much maturer semiconductors like GaAs [7]. Several theories have been suggested to explain the gain mechanism, such as photoconductive gain, avalanche carrier multiplication, and trapping of photo-carriers at semiconductor/metal interface. In addition, image force lowering of Schottky barrier height should happen more or less in most Schottky-based PDs at high applied bias.

Summary

We have reported the demonstration of a high performance MSM PD fabricated on low-dislocation-density homoepitaxial GaN layer on bulk GaN substrate. The PD exhibits low dark-current and high UV-to-visible rejection ratio both at RT as well as at 425 K, suggesting that the device is suitable for high temperature applications. An internal gain is observed within the PD which is explained by lowering of Schottky barrier due to photo-generated holes trapped at semiconductor/metal interface as well as image-force lowering near the contact edge of cathode electrodes where electric field is particularly high.

Acknowledgement

This work was financially supported by the National Natural Science Foundation of China under Grants (61306089, 61307049, 61307040), the Anhui Provincial Natural Science Foundation under Grants (1408085MF118, 1408085QF113) and the International S&T Cooperation Program of China under Grant (2013DFE13090).

References

[1] M. Razeghi and A. Rogalski: J. Appl. Phys. Vol. 79 (1996), p. 7433.

[2] J. W. P. Hsu, M. J. Manfra, D. V. Lang, S. Richter, S. N. G. Chu, A. M. Sergent, R. N. Kleiman, L. N. Pfeiffer, and R. J. Molnar: Appl. Phys. Lett. Vol. 78 (2001), p. 1685.

[3] X. A. Cao, and S. D. Arthur: Appl. Phys. Lett. Vol. 85 (2010), p. 3971.

[4] K. K. Chu, P. C. Chao, M. T. Pizzella, R. Actis, D. E. Meharry, K. B. Nichols, R. P. Vaudo, X. Xu, J. S. Flynn, J. Dion, and G. R. Brandes: IEEE Electron Device Lett. Vol. 25 (2004), p. 596.

[5] H. Lu, R. Zhang, X. Q. Xiu, Z. L. Xie, and Y. D. Zheng: Appl. Phys. Lett. Vol. 91 (2007), p. 172113.

[6] H. Lu, X. A. Cao, S. F. LeBoeuf, H. C. Hong, E. B. Kaminsky, and S. D. Arthur: J. Cryst. Growth Vol. 291 (2006), p. 82.

[7] J. Burm and L. Eastman: IEEE Photon. Technol. Lett. Vol. 8 (1996), p. 113.

CHAPTER 2:

Power System and Energy Engineering, its Applications

Advanced Materials Research Vols. 986-987 (2014) pp 167-171

doi:10.4028/www.scientific.net/AMR.986-987.167

A Comparative Study on the Effects of Power Supply Patterns in Microgrids for DC Powered Electrical Appliances

Siddharth Narayanan[1,a], Rajagopalan Badrinarayanan[1,b], Lu Zhen[1,c]

[1] Power Engineering Division, School of EEE, Nanyang Technological University, Singapore.

[a]email: siddhart2@e.ntu.edu.sg, [b]email: raja0048@ntu.edu.sg, [c]email: luzhen@ntu.edu.sg

Keywords: Phase-shifting transformer step-down rectifier, Energy storage system, DC microgrid, Electrical appliance, Equivalent efficiency

Abstract. To increase the energy efficiency and reduce the cost, the DC-Microgrids will have a very promising future in the power supply systems. In this paper, two power supply patterns for modern appliances, the central rectifier pattern and the distributed rectifier pattern, are investigated and compared. A concept of equivalent efficiency of diode bridge rectifier for DC-powered appliances is introduced and then it is applied in the model simplification. A Curved-Load model is constructed which is based on the specific efficiency characteristics of diode bridge rectifier in a particular current range and the statistics for appliance's energy consumption as a percentage of the total. Using the Curved-Load model, the comparison of two microgrid system models was conducted with the help of simulations using Ansoft Simplorer 9.0 aiming to examine the conversion efficiency of rectifier patterns.

Introduction

The usage of renewable energy is escalating and more modern electric appliances being pro to DC power supply, and energy storage system such as vanadium-redox flow battery energy storage system [1, 2] is required to couple with the renewable energy resources to remove the intermittent manner. It is high time to reconsider employing DC grids for power distribution [3]. The concept of DC Microgrid is a subset of distributed generation which is still in its nascent stage. Microgrids are brought into picture to improve the reliability and to bring down the dependence on the main grid [4, 5]. DC microgrid is a promising microgrid adaptation which not only offers an effective way to link up renewable resources such as solar PV panels or wind turbines with DC/DC converters, but also increases the overall energy transmission efficiency from AC grid to end-user electrical appliances [6]. With the development of power electronics, many modern domestic electrical appliances are evolving—their inbuilt power supply has transformed from Alternating Current (AC) into Direct Current (DC). As a known fact, the present grid architecture in AC based and for these devices to operate, a converter arrangement is needed for AC/DC conversion. Each of these appliances uses an individual arrangement (usually is a diode bridge rectifier) as a gateway for the power inlet.

Several questions such as the amount of power loss in this power supply pattern or the presence of efficient alternatives for the conventional system arise at this stage. To answer these questions, one of the available ways is to construct the power supply system models for each pattern and then to examine them by means of simulation.

Being one of the prominent electric energy resources for DC microgrids, AC grid supplies the main share of electricity demand in the system. With the great global efforts in the development of next generation alternative energy resources such as the advanced nuclear energy systems discussed in [7-9], it can be expected that the AC power sources will continue to play a key role in the whole energy package in the future. So devising a methodology to efficiently convert the power from AC grid to the consumers in DC microgrid is an important issue for consideration in the construction of DC microgrids [10-12]. The distributed rectifier pattern based power supply scheme in Fig. 1(a) shows the typical power supply structure for modern domestic appliances, which can be called as the distributed rectifier pattern as each appliance has an individual rectifier inside. While the central

rectifier pattern based power supply scheme in Fig. 1(a) is the other model where all of the appliances in the DC microgrid use a single rectifier—the thyristor bridge rectifier in the phase-shifting transformer step-down rectifier. Before implementing the comparison of simulations, firstly it is needed to specify the main blocks as well as their relevant parameter settings in both of the system models.

Both systems are microgrid models with a capacity of 500 KW and connected to a 22 KV transmission line of AC grid by transformers. The phase-shifting transformer (PST) in the DC microgrid system model is nothing more than a conventional transformer with multiple secondary legs and with specific parameter settings. According to the comparison of simulation results (shown in Fig. 1 (b)), the performance of the PST is as good as or better than the performance of its counterpart—the conventional transformer in the AC microgrid system model. So comparing the impact of the two transformers has no significant effect on the comparison of the two rectifier patterns.

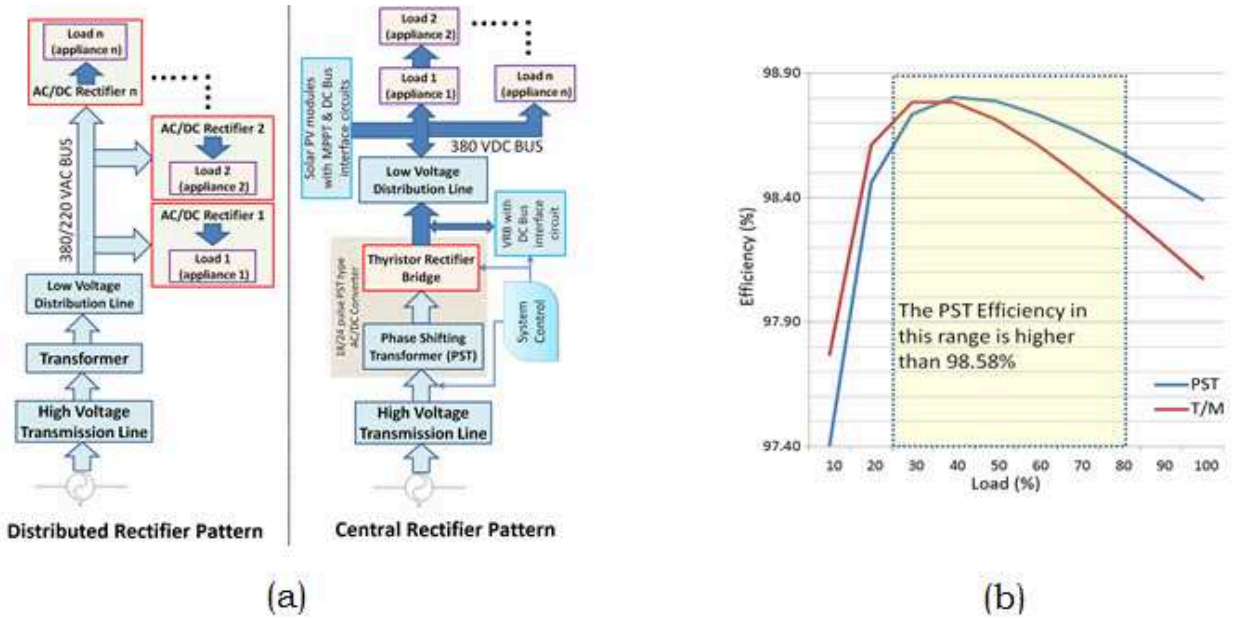

Fig. 1. (a) Block diagram of the two power supply schemes (b) Efficiency comparison between the 2 models

To make the two microgrid system models being comparable, the bus voltage of the DC microgrid is set to 380 VDC, which is equal to the RMS value of the line voltage of the AC microgrid. Therefore the low voltage distribution lines' effects on the comparison of the two rectifier patterns are also omissible. Regarding the other blocks in the DC microgrid, they have no effect on the comparison of the two rectifier patterns too. In fact, the other blocks in the DC microgrid system model are only used in assisting the optimized operation of the DC microgrid. Therefore, it is meaningful to examine the power supply patterns only by comparing the performance of the rectifier stage in the two microgrid system models.

Efficiency analysis of the diode bridge rectifier in modern domestic electrical appliances

There is a plethora of various kinds of electrical appliances in AC microgrid. So it is not practical to construct an AC microgrid system model with specific models for all the electrical appliances. The appliance models can be simplified according to the statistics on all kinds of domestic electrical appliances as well as their relevant load curves. The simplified model is constructed based on the following assumption. Since the aim of the simulation is focused on comparison of the conversion efficiency in the rectifier stage of the two power supply patterns, the model simplification effects on other components in the microgrid system models can be omitted if they satisfy the following conditions:

1. The effect is insignificant on simulation results.

2. The effect is not favorable for the DC microgrid system model (since the aim of the comparison simulation is to examine the advantages of central rectifier pattern).

The concept of equivalent efficiency of diode bridge rectifier will be introduced in the following paragraphs.

A. The efficiency characteristic of diode bridge rectifiers

The efficiency characteristic of a diode bridge rectifier varies with specific parameters. However, the basic efficiency characteristic of diode bridge rectifiers follows the typical efficiency characteristic curve. When the working current is above 10% of the rated current, the efficiency curve is almost a horizontal line; whereas the efficiency is not so good if its working current is below 10% of the rated current, and it even drops down to below 80% when the working current is lower than 1% of the rated current.

Usually, the normal working current of electrical appliances is above 10% of its rated current. Therefore, it is reasonable to use a constant, which equals to the average efficiency in the normal operation range, to represent the efficiency rating of the diode bridge rectifier of the appliance. On the other side, as the standby current and leakage current of the electrical appliances is much below 10% of its rated current, the efficiency of the diode bridge rectifier of the appliance in standby state and off state is very sensitive to the current value.

B. Equivalent efficiency of diode bridge rectifier for appliances

The equivalent efficiency of diode bridge rectifier for specific electrical appliances is used to represent their efficiency in the electrical appliances' model simplification. It is calculated based on the statistics and the specific efficiency characteristic of the diode bridge rectifier in a current range. This includes the rated efficiency, efficiency in standby as well as leakage current loss on average, for that kind of electrical appliances. The procedure for calculation is as follows:

1. Select an appliance for which the efficiency has to be calculated and identify its rated current and voltage. Based on these values, calculate the minimum requirements of the diode bridge parameters that are needed.
2. Look up for the datasheet of the diode that suits the parameter requirements. The diode parameters needed for simulation are obtained from the respective datasheets.
3. Apply the parameters of the diode bridge rectifier in the simulation circuit and extract the efficiency data from the simulation for rated current, standby current and leakage current.
4. Use the weighted average method to calculate the equivalent efficiency of diode rectifier bridge, i.e.

$$EE = AC*\eta_{AC} + SB*\eta_{SB} + LK*\eta_{LK} \quad (1)$$

Where, EE— equivalent efficiency, AC—share of the energy consumption in normal working state, η_{AC}— efficiency in normal working state, SB—share of the energy consumption in standby state, η_{SB}— efficiency in standby state, LK—share of the energy consumption in leakage current state, η_{LK}— efficiency in leakage current state.

C. Overall equivalent efficiency of diode bridge rectifiers of all electrical appliances and Curved-Load model

Further, using the weighted average method, a more accessible model simplification for electrical appliances, Curved-Load model, can be obtained. Firstly, the Curved-Load model actually is the equivalent model for all electrical appliances; therefore its load follows the typical residential (or commercial) load curve, instead of a specific load curve for each electrical appliance type. This is a very useful feature for the simulation. Secondly, the Curved-Load itself can yield a power loss that is proportional to the momentary load value. The proportional coefficient is just the overall equivalent efficiency of diode bridge rectifiers of all electrical appliances, which can be calculated as follows:

$$OEE = \sum EE_I * I_{SHARE} \quad (2)$$

Where, OEE—the overall equivalent efficiency of diode bridge rectifiers of all electrical appliances, EE_I—the equivalent efficiency of the kind of the electrical appliance I, I_{SHARE}—the percentage share of the energy consumption of the kind of the electrical appliances I in total energy

consumption. Again notice that the overall equivalent efficiency is calculated by means of weighted average of energy consumption in a large amount of this kind of electrical appliances, so that the deviation is small enough to omit the effect of the model simplification on energy conversion efficiency calculation.

Comparison of two microgrid system models' simulation and the discussion on the results

The Curved-Load model uses the typical load curve to simulate the process of analysis, which simplifies the computation process and facilitates easier operational methodologies. The two microgrid system models are constructed with the following considerations.

1. All of the models as well as their parameter setting are in the same value or as near as possible.
2. If there is any insignificant effect on examining rectifier patterns in conversion efficiency, the effect should be equitable to both system models, or at least should not favor the DC microgrid system model.
3. The models of electrical appliances are reduced to 6 Curved-Load models in each microgrid system model, whose loads vary according to the pre-setting load curve;

A. Comparisons based on Simulation results

As a model simplification measure, all of the rectifier models do not take the inductance-capacitance loss in account (this measure is equitable to both system models) and the solar PV (mentioned in Fig. 1(a)) is not considered in this model. Table I shows the comparison of transformers and rectifiers used in AC and DC microgrids. The conventional transformer used in the AC grid is denoted as T/M and the phase shifting transformer in DC microgrid is denoted as PST. It can be clearly seen from the table that the results of the transformers in both are comparable. In the rectifier stage efficiency comparison, the DC microgrid using a central PST based thyristor rectifier has an advantage of about 2.67% increase in efficiency.

TABLE I
EFFICIENCY COMPARISON IN TRANSFORMER AND RECTIFIER STAGE

Load	Transformer Efficiency			Rectifier Stage Efficiency		
	T/M	PST	Δ	AC	DC	Δ
10%	97.77%	97.08%	-0.69%	96.74%	99.41%	**2.67%**
20%	98.61%	98.34%	-0.27%	96.74%	99.41%	**2.67%**
30%	98.78%	98.71%	-0.07%	96.74%	99.41%	**2.67%**
40%	98.78%	98.86%	0.08%	96.74%	99.42%	**2.68%**
50%	98.71%	98.90%	0.19%	96.74%	99.42%	**2.68%**
60%	98.61%	98.89%	0.28%	96.74%	99.42%	**2.68%**
70%	98.49%	98.85%	0.36%	96.74%	99.42%	**2.68%**
80%	98.36%	98.81%	0.45%	96.74%	99.42%	**2.68%**
90%	98.22%	98.74%	0.52%	96.74%	99.41%	**2.67%**
100%	98.07%	98.67%	0.60%	96.74%	99.40%	**2.66%**

B. Discussion on the simulation results comparison

1. The comparison of simulation results shows that the central rectifier pattern is comprehensively superiors to the distributed rectifier pattern. For instance, only in rectifier stage, the conversion efficiency improves from 96.74% to 99.41% based on simulation results.
2. The overall equivalent efficiency of diode rectifier bridges for all of electrical appliances would more likely be lower in tropical countries like Singapore. The reason is that there are fewer non-DC powered electrical appliances (such as space heating does not need for Direct Current power supply) in use today at these places. Therefore, the conversion efficiency improvement margin would be even larger.
3. Moreover, the overall equivalent efficiency of the diode rectifier bridges for all the electrical appliances would more likely be lower with more and more DC powered appliances getting popular. This is because the power-output controllability of DC powered electrical appliances is better than that of non-DC powered electrical appliances, DC powered electrical appliances can efficiently work in a wide power-output range.

Conclusion

Introducing the concept of equivalent efficiency of diode bridge rectifier for appliances is a creative idea for model simplification, which allows us to evaluate the two power supply patterns for modern appliances—the central rectifier pattern and the distributed rectifier pattern—in a quantitative manner by means of simulation. Considering the drawbacks in the present scheme, the proposed methodology has a very good scope in reducing the losses. In the proposed method, the AC/DC conversion is centrally done and the need to use separate converter for each DC appliance is avoided. As the percentage of appliances using DC power has an upward slope, the use of DC as the primary supply becomes inevitable and the techniques discussed in this paper are in coherence with the expected future DC grid architecture.

The advantages of the central rectifier pattern over the distributed rectifier pattern are not only limited in the rectifier stage but also profound in all aspects of microgrid development. Especially for green buildings which are equipped with considerable capacity of solar PV modules and other renewable energy sources, its importance would be double.

Acknowledgement

We wish to acknowledge the funding for this project from Nanyang Technological University under the Undergraduate Research Experience on Campus (URECA) programme.

References

[1] Zhongbao Wei, Jiyun Zhao, Maria Skyllas-Kazacos, Binyu Xiong, "Dynamic thermal-hydraulic modeling and stack flow pattern analysis for all-vanadium redox flow battery", Journal of Power Sources, Vol. 260, pp. 89-99 (2014).

[2] Binyu Xiong, Jiyun Zhao, etc., "Thermal Hydraulic Behavior and Efficiency Analysis of an All-Vanadium Redox Flow Battery", Journal of Power Sources, pp. 314-324 (2013).

[3] Garbesi, K., Catalog of DC appliances and power systems. 2012.

[4] Bae, I.-S. and J.-O. Kim, Reliability evaluation of customers in a microgrid. Power Systems, IEEE Transactions on, 2008. 23(3): p. 1416-1422.

[5] Mitra, J. and M.R. Vallem, Determination of Storage Required to Meet Reliability Guarantees on Island-Capable Microgrids With Intermittent Sources. Power Systems, IEEE Transactions on, 2012.

[6] Khodaei, A. and M. Shahidehpour, Microgrid-Based Co-Optimization of Generation and Transmission Planning in Power Systems. Power Systems, IEEE Transactions on, 2013. 28(2): p. 1582 - 1590.

[7] J. Zhao, P. Saha and M. S. Kazimi, "Hot Channel Stability of Supercritical Water-cooled Reactors-I: Steady State and Sliding Pressure Startup," Nuclear Technology, 158, 158-173 (2007).

[8] J. Zhao, P. Saha and M. S. Kazimi, "Hot Channel Stability of Supercritical Water-cooled Reactors-II: Effect of Water Rod Heating and Comparison with BWR Stability," Nuclear Technology, 158, 174-190 (2007).

[9] J. Zhao, P. Saha and M. S. Kazimi, "Core Wide (In-Phase) Stability of Supercritical Water-cooled Reactors-I: Sensitivity to Design and Operating Conditions," Nuclear Technology, 161, 108-123 (2008).

[10] Divshali, P.H., et al., Decentralized cooperative control strategy of microsources for stabilizing autonomous VSC-based microgrids. Power Systems, IEEE Transactions on, 2012. 27(4): p. 1949-1959.

[11] Majumder, R., et al., Power management and power flow control with back-to-back converters in a utility connected microgrid. Power Systems, IEEE Transactions on, 2010. 25(2): p. 821-834.

[12] Roggia, L., et al., Integrated full-bridge-forward DC-DC converter for a residential microgrid application. Power Electronics, IEEE Transactions on, 2013. 28(4): p. 1728-1740.

Advanced Materials Research Vols. 986-987 (2014) pp 172-176

doi:10.4028/www.scientific.net/AMR.986-987.172

A Compound Positioning and Splitting Criterion for Power System Oscillation Center with Predicting Function

Suna Jiang[1,a],Yuxiao Zhou[1,b],Dunwen Song[2,c],Jianhong Hao[1,d], Hong Bin[1,e], Zhaolei Qin[3,f]

[1]School of Electrical & Electronic Engineering, North China Electric Power University, Beijing,102206, China

[2] Power System Department, Electric Power Research Institute, Beijing,100192, China

[3] School of Electrical & Electronic Engineering, North China Electric Power University,Baoding,071003,China

[a]jsn2008@ncepu.edu.cn,[b]403255676@qq.com,[c]yn8800@163.com,

Keywords: power system, oscillation center positioning, $U\cos\varphi$, splitting, compound criterion

Abstract. In this paper, an oscillation center fast positioning method and the criterion $U\cos\phi$ that determines whether a system is out-of-step are combined together to put forward a compound oscillation center positioning and splitting criterion with predicting function. Simulation of a classical numerical example of four-machine system in two regions and an actual example of central China-north China power grid proves that this method can pre-locate lines where oscillation center lies after out-of-step operation of the system when the system is oscillating intensely but still keeps synchronized.

Introduction

With haze problem aggravating, social demand for transporting capacity of new energy power is increasing. Therefore our country speeds up the construction pace of ultra-high voltage and large power grid, and is gradually forming a super large power system interconnected by major regional power grids. Thus, out-of-step oscillation between generator groups and areas has brought unprecedented challenges to the safe operation of power grid. To deal with out-of-step oscillation, we need to locate oscillation center quickly, and even take extreme measures like splitting to avoid blackouts[1][2].

In the early development of accidents, transmission lines and sections where oscillation center will appear must be timely and accurately predicted to block fault zone and narrow the blackout area[3]. Basing on the improved oscillation center positioning method and splitting criterion $U\cos\varphi$, a kind of compound splitting criterion with the function of predicting oscillation center is put forward. It is of great significance for power system security analysis and taking necessary control strategies[4].

Principle and Implementation Method of the Compound Criterion

2.1 Principle

An oscillation center positioning algorithm is shown as Eq. 1 below:

$$\left.\begin{aligned} L_{center}&=0 \quad ,U_2\cos\theta_{12}>U_1 \\ L_{center}&=1 \quad ,U_1\cos\theta_{12}>U_2 \end{aligned}\right\}\theta_{12}\le\theta_{set}$$
$$L_{center}=\frac{P_1R+Q_1X}{I^2(R^2+X^2)},\quad \theta_{12}>\theta_{set} \qquad (1)$$

Where, electric parameters P_1, Q_1, I can be measured by measurement units. R and X is circuit natural parameters, and voltage phase angle difference on both ends is $\theta_{12}=\theta_1-\theta_2$. When these quantities are known, it can accurately locate out-of-step oscillation center when the system is in synchronous oscillation state[5]. Combined with rapid and reliable splitting criterion, we can achieve fast, reliable out-of-step splitting control[6].

Therefore, combining oscillation center positioning algorithm and oscillation center voltage criterion $U\cos\phi$, a compound criterion with predicting function can be constructed. The compound criterion can timely predict the out-of-step runtime oscillation center line, determine the weak section when the system is in synchronous oscillation or subsynchronous resonance(SSR). It provides a valuable reference to take measures to ensure the system operate stably. When the system runs into the state of out-of-step oscillation, the criterion can quickly locate oscillation center line, and judge whether out-of-step center falls in the oscillation center circuit, and provides a best splitting position for the system.

2.2 Implementation of the method

Concrete steps to implement the criterion with predicting function are as follows :

(1) Output the needed electricity parameters：bus voltage amplitude and phase angle, active power and reactive power of transmission line, circuit impedance read from flower file.

(2) Substitute the electric parameters in step one into oscillation center positioning algorithm showed in Eq. 1.Calculate oscillation center position and get the transmission lines where the predicted oscillation center lies.

(3)Judge whether out-of-step center is in the predicted transmission line where oscillation center lies with oscillation center voltage, namely to determine whether the system is in asynchronous state.

2.3 Two-region four-machine example simulation

Fig. 1 is the schematic of the system used for simulation. The simulation system with two similar regions are connected by a weak tie. Each area has two coupling generators, with rated voltage of 20 kV and rated capacity of 900 MVA. Generator parameters in per unit value (under rated voltage and rated capacity) are shown in Table 1.

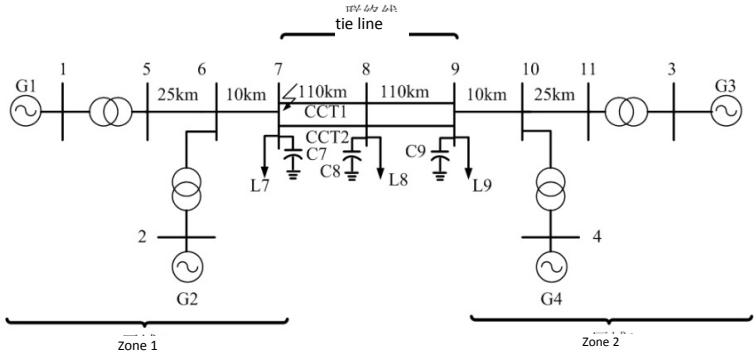

Figure 1. Two-region four-machine system with load on node 8

Table 1. Generator parameters list [p.u]

Symbol	Value	Symbol	Value	Symbol	Value	Symbol	Value
X_d	1.8	X_q	1.7	X_l	0.2	X'_d	0.3
X'_q	0.55	X''_d	0.25	X''_q	0.25	R_a	0.0025
T'_{d0}	8.0	T'_{q0}	4.0	T''_{d0}	0.03	T''_{q0}	0.05
A_{sat}	0.015	B_{sat}	9.6	ψ_{T1}	0.9	H_1	6.5
H_2	6.5	H_3	6.175	H_4	6.175	K_D	0

Under the benchmark of 20/230 kV and 900 MVA, each transformer has the change ratio 1.0, impedance $0+j0.15pu$. Transmission network voltage is rated at 230 kV. Line length is shown in Fig. 2. Circuit parameters in per unit value (capacity benchmark is 100 MVA, voltage benchmark is 230 kV) are as follows:

R_L=0.0001pu/km X_L=0.001pu/km B_C=0.00175pu/km

The generator output values are shown in Table 2.

Table 2. Generator output values

	G 1	G 2	G 3	G 4
Generator active power [MW]	700.0	700.0	712.8	700.0
Generator reactive power [MVar]	145.877	140.307	126.240	85.902

Load and reactive power compensation value as shown in Table 3.

Table 3. Load and reactive power compensation value

	Node7	Node 8	Node 9
active load [MW]	900	100	173
reactive load [MVar]	100	100	100
reactive power compensation [MVar]	200	200	350

In transient simulation, we use the six order model for generators and constant impedance model for load. When the system is in stable operation to 2.9 seconds, CCT1 transmission line of node 7 and 8 occurred three-phase short-circuit fault. CCT1 jumped in 0.1 seconds after fault, and the system eventually entered a state of asynchronous operation. Figure 2-3 and 2-4 are respectively the curves of oscillation center position and $U\cos\phi$ get from node 7.

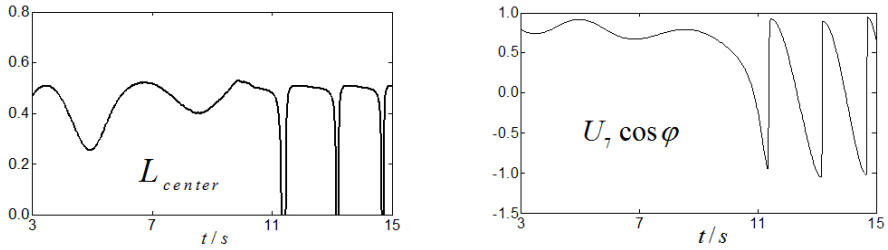

Figure 2. Oscillation center and $U\cos\varphi$ curve of node 7

Fig 2. oscillation center curve shows that before the system entered into asynchronous operation state, the oscillation center positioning method can predict that oscillation center will appear in CCT2 between node 7 and 8 after the system goes into asynchronous operation. Figure 2-4 shows that after the system goes into out-of-step operation, oscillation center appeared on line CCT2. Thus proves that the composite criterion with prediction is accurate and effective. The trajectory of criterion $U\cos\phi$ provides an important basis for splitting at the same time.

Implementation and Application in PSD - BPA Software

3.1 Implementation method in PSD - BPA

In the process of PSD - BPA electromechanical transient simulation, each simulation step contains a large amount of data. these data have important value in the analysis of stability of power grid[7]. After a simulation step, bus voltage, phase angle, active power and reactive power of transmission line, generator output, angle difference and so on are used to locate oscillation center in a system. After oscillation center positioning, judge whether the oscillation center is out of step according to the criterion$U\cos\phi$. Concrete steps are as follows:

(1) Before the start of PSD - BPA transient simulation, establish an underlying database on the basis of flow file and stable file with all transformer and circuit parameters concerned.

(2) Calculate the oscillation center position for all the transmission lines in the network. If the results is between 0~1, and is changing constantly, then the transmission lines is the one where oscillation center lies. Store all the electric parameters of oscillation center lines.

(3) Calculate all the oscillation center lines whose information have been stored according to the criterion $U\cos\phi$, and determine whether the system is out of step.

3.2 Simulation results of implementation in central China-north China power grid

We use central China – north China power grid data in 2012 for simulation.

(1) Fault scenario 1: Three-phase fault on Honggou side of transmission line Honggou-Banqiao, disconnect double circuit line. The position and voltage of Honggou-Banqiao fault oscillation center are shown in Fig.3.

(2)Fault scenario 3: Short-circuit fault in Lang-Bazhou 51 bus. After 4.5 cycles disconnect all lines connected to bus 51 on Lang-Bazhou side. Five cycles later, the other side of all lines connected to bus 51 are disconnected. The position and voltage curve of Lang-Bazhou fault oscillation center are shown in Fig.4.

(3) Fault scenario 2: Three-phase fault on Fengzhen side of transmission line Fengzhen-Wanquan. Disconnect double-circuit line. The position and voltage of Fengzhen-Wanquan fault oscillation center are shown in figure Fig.5.

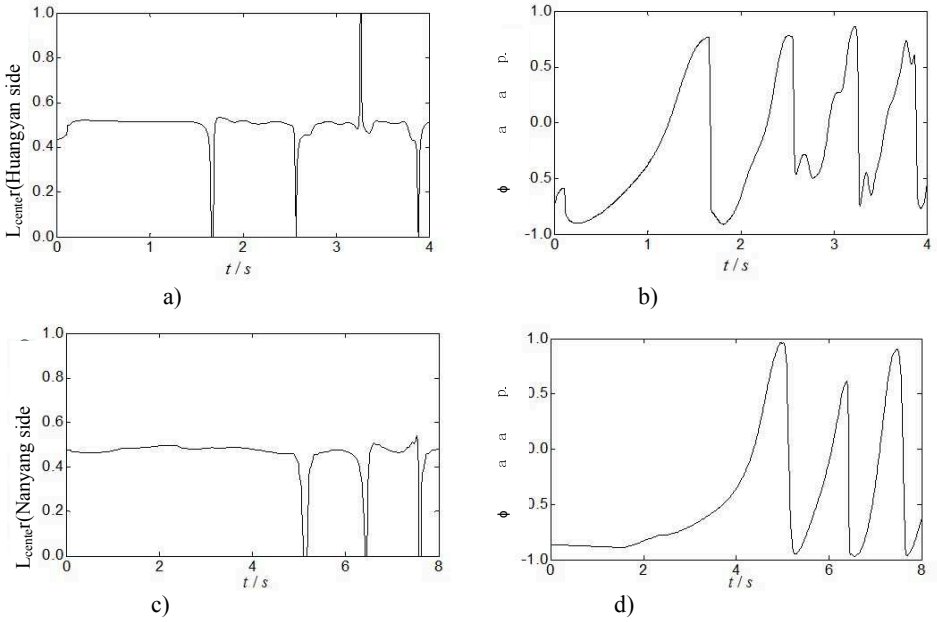

Figure 3. Oscillation center position and voltage curve corresponding to Honggou-Banqiao fault

a) Oscillation center position curve of Huangyan side b) $U\cos\varphi$ curve of Huangyan side

c) Oscillation center position curve of Nanyang side d) $U\cos\varphi$ curve of Nanyang side

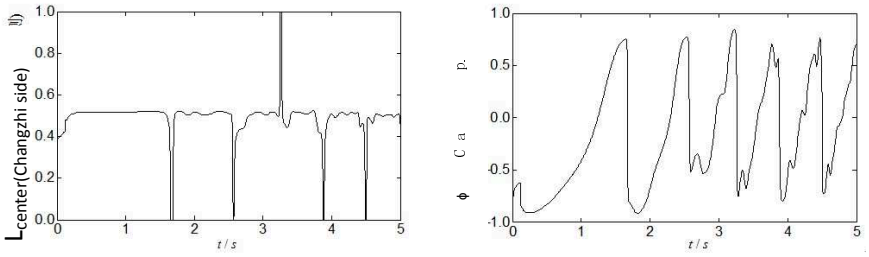

Figure 4. Oscillation center position and voltage curve corresponding to Lang-Bazhou bus 51 fault

a) Oscillation center position curve of Changzhi side b) $U\cos\phi$curve of Changzhi side

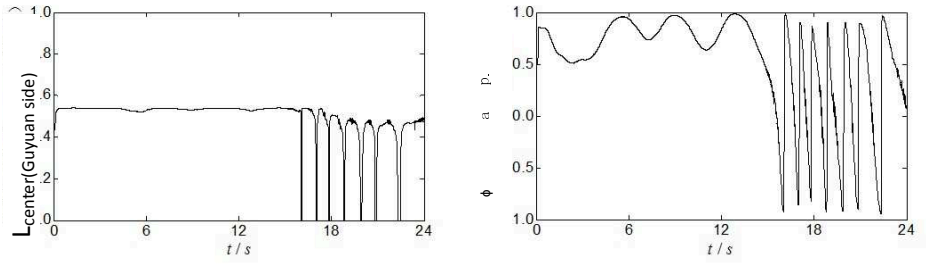

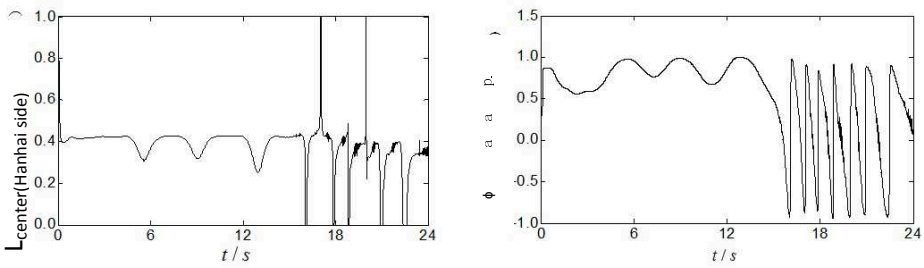

c) d)

Figure 5. Oscillation center position and voltage curve corresponding to Fengzhen-Wanquan fault
a) Oscillation center position curve of Guyuan side b) $U\cos\phi$ curve of Guyuan side
c) Oscillation center position curve of Hanhai side d) $U\cos\phi$ curve of Hanhai side

Results of Fig 3.Fig 4. and Fig 5. are summarized in Table 4.

Table 4. Simulation results

Fault scenario	Predicted location of oscillation center	Actual location of oscillation center
Honggou-Banqiao fault	Huangyan -Wanxian& Nanyang-Jingmen	Huangyan -Wanxian&Nanyang-Jingmen
Lang-Bazhou bus 51 fault	Changzhi- Nanyang	Changzhi- Nanyang
Fengzhen-Wanquan fault	Hanhai-Guyuan&Guyuan -Taiping	Hanhai-Guyuan&Guyuan-Taiping

Table 3-1 shows that in these three fault scenarios, compound criterion with prediction can correctly predict on which line the oscillation center will appear before the system runs out of step. The criterion can also provide a reference for a beat splitting position.

Conclusion

Simulation on two-region four-machine system and central China-north China power grid proves that this method has the ability to predict oscillation center of the line before the system is out-of-step. Compared with traditional splitting criterion, this criterion has the advantage that it can accurately predict transmission lines where oscillation center lies before the system is out-of-step after disturbance. It can also locate weak sections of transmission lines, being an important basis to take measures to improve system stable level. Once timely discover the system is running in poor stability state, take certain measures can reduce the possibility of blackouts causing by system running from poor stability into out-of-step operation state.

References

[1] Chen Shousun, Ni Yixin, Zhang Baolin．Theory and analysis of dynamic power system[M]．Beijing: Tsinghua University Press, 2005(in Chinese)

[2] Pourbeik P, Kundur P S, C W．The Anatomy of a power grid blackout[J]．IEEE Power and Energy Magazine, 2006, 4(5)：22-29

[3]Gao Peng, Wang Jianquan, Zhou Wenping, et al．Study on capturing out-of-step splitting section based on reactive power[J]．Automation of Electric Power Systems, 2005, 29(5)：15-20(in Chinese)

[4] Ni Jingmin, Shen Chen, Li Ying, Tan Wei．An on-line weak-connection identification method for controlled islanding of power system[J]．Proceeding of the CSEE, 2011, 31(4)：24-30(in Chinese)

[5] Li Li．Studies on out-of-step splitting criterion and control scheme based on wide area measurements[D]．Shandong University, 2009(in Chinese)

[6] C.W Taylor, J.M.Haner, L.A.Hill. A new out-of-step relay with rate of change of apparent resistance augmentation[J]．IEEE Tran On Power Apparatus and System, Vol.PAS-102, March 1983：631-639

[7]Hou Junxian, Han Minxiao, Tang Yong, et al．Identification method of electromechanical transient simulation in oscillation center and its application[J]．Proceedings of the CSEE, 2013, 33(13)：1-7(in Chinese)

Advanced Materials Research Vols. 986-987 (2014) pp 177-180

doi:10.4028/www.scientific.net/AMR.986-987.177

A Costal Wave Energy Power Station Equipment

TONG Junjie[1,a]

[1] Guangdong Ocean University of Technology, School of Engineering, Zhanjiang 524006, China

[a]jjtong9311@163.com

Keywords: dual channel, wave energy, costal wave

Abstract. This paper introduced a coastal wave energy power generation and its unique dual channel structure, in which two–way coastal current was transformed into single direction rotation of the impeller. Also according to coastal wave energy characteristics, the paper analyzed relationship between inshore sea water kinetic energy and the wave amplitude away from the coast. In addition, the water velocity and flow area of equipment through power generation equipment are studied.

Introduction

Ocean wave energy is the most widely distributed renewable energy which accounted up to 50%[1,2]. In recent years, wave energy has represented the development of marine energy. Compare to more studies on using of wave energy in deep sea region [3~6], there were few study on using of wave energy in costal region.

Wave energy of deep sea region shows potential energy while costal wave energy shows kinetic energy, which performances two-way flow of sea water. This paper described a costal wave energy power generation equipment of unique dual-channel structure, in which was transformed into single direction rotation of the impeller and stability of the output power was improved. Also this paper analyzed the relationship between inshore sea water kinetic energy and the wave amplitude away from the coast. In addition, the seawater velocity and flow area of equipment through power generation equipment are studied.

1. The dual-channel structure power generation equipment and its working principle

The dual-channel structure power generation equipment developed by the author's research team is composed of transmission, impeller, generators and valves. The structure and its working principle are shown as Figure 1 and Figure 2 respectively.

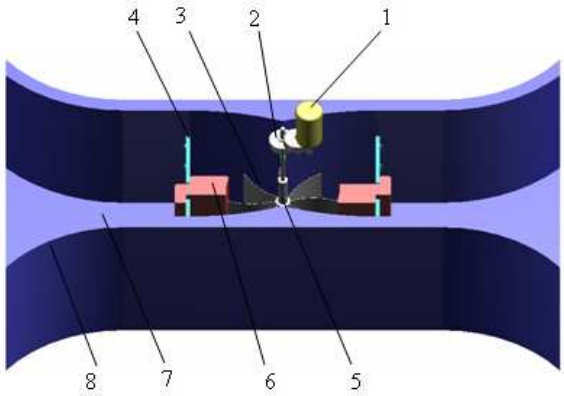

1-generator 2-transmisson 3-impeller 4-valve 5-axle 6-baffle; 7-floor board 8-side board

Fig. 1 The structure of dual channel electric power equipment (removing roof)

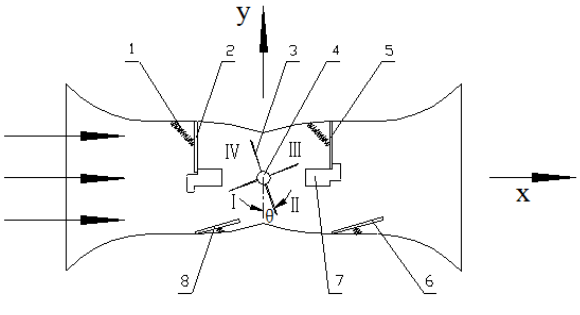

1-reposition spring 2-valve 1 3-blade 4- impeller axle 5-valve 2 6-valve 3 7-baffle 8-valve 4

Fig.2 Dual channel power generation equipment works

As shown in Figure 1, The dual-channel structure power generation equipment is composed of valves, baffles, floor board, side boards, transmission and generators. The combination of valves open or close decides that water flow right or left. Sea water promotes impeller rotation and drive generator running through transmission.

As shown in Figure 2, when sea water flows to right or to left the flow channel is formed as follows:

When sea water flow into the generation equipment from its left inlet, the valve 1 and the valve 2 are closed at the baffle position, simultaneously the valve 3 and the valve 4 are turned right and open. Sea water flow to right and promote impeller rotating counterclockwise.

Similarly when sea water flow into the power generation equipment from its right inlet, the valve 3 and the valve 4 are closed at the baffle position, simultaneously the valve 1 and the valve 2 are turned left and open. Sea water flow to left and promote impeller rotating counterclockwise.

Costal wave energy shows kinetic energy, which performances two-way flow of sea water. The impeller is promoted in the same direction whether sea water flow to left or to right. Thus the instability of energy output is reduced.

The inlet and outlet of the power generation equipment are designed as reduction-shaped which increase energy input.

2. Analysis of costal wave

Costal wave energy shows kinetic energy and costal wave energy is analyzed as follow.

(1)Without considering the effect of wind on the kinetic energy of the inshore water, inshore sea water kinetic energy is mainly transformed by potential energy of wave away from the shore.

(2)The energy loss of wave breaking is ignored.

(3)The kinetic energy loss of inshore sea water is caused mainly from resistance of shore.

(4)Due to little resistance of the sea floor, the kinetic energy of the sea water flow to shore reaches the maximum at the position where a certain distance from shore. The kinetic energy is mainly transformed by the potential energy of the wave away from shore.

(5) The kinetic energy of the sea water flows to the shore is more than the kinetic energy of the sea water reflows from the shore at the certain position that mentioned above as analysis (4).

According to the above analysis, when the power generation equipment is set at the position mentioned as above analysis (4), the kinetic energy will be taken advantage of to the maximum. Based on the above analysis and the Bernoulli equation, the follow equation can be obtained:

$$N = (Z_1 + \frac{p_1}{\gamma} + \frac{\alpha_1 U_1^2}{2g}) = (Z_2 + \frac{p_2}{\gamma} + \frac{\alpha_2 U_2^2}{2g}) + h_{12} \quad (1)$$

Z_1, p_1, U_1 and α_1 represent the wave amplitude, the water pressure, the water velocity and kinetic energy correction factor in the region away from the coast respectively. In contrast, Z2, p2, U2 and α_2 represent the amplitude, pressure, velocity and Kinetic energy correction factor of the water at the position mentioned above as analysis (4) respectively.

N, g, γ and h_{12} are the total pressure, gravitational acceleration, bulk density and resistance loss respectively..

For the dual-channel structure power generation equipment, utilizing the water kinetic energy is near sea surface and the kinetic energy loss is neglected. The equation 1 can be simplified to:

$$H_W = Z_1 - Z_2 = \frac{U_2^2}{2g} \tag{2}$$

The relationship between H_W and U_2 are shown as Fig 3 when the gravitation acceleration g is assumed 9.81m^2/s.

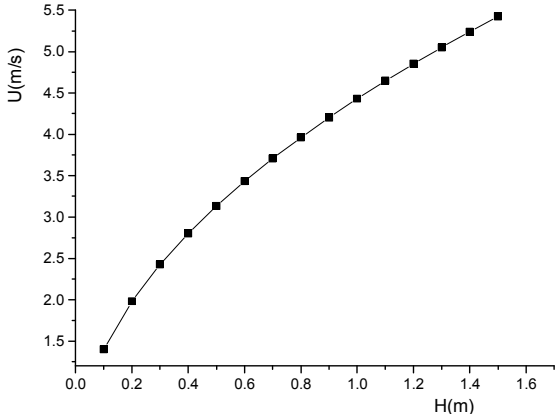

Fig.3 Fluid flow velocity and flow area through the device

As shown in Fig.3, in the process of wave energy transformation in the costal region, when the potential energy of the wave away from the shore increases the velocity of the water at the position mentioned above as analysis (4) increases correspondingly.

3. The seawater flow and flow area of the generation equipment.

When the sea water flow through the generation equipment the follow equation can be obtained based on the Bernoulli equation[7]

$$H_{io} = (Z_i + \frac{p_i}{\gamma} + \frac{\alpha_i U_i^2}{2g}) - (Z_o + \frac{p_o}{\gamma} + \frac{\alpha_o U_o^2}{2g}) \tag{3}$$

Z_i, p_i, U_i and α_i represent the amplitude, the pressure, the velocity and the kinetic energy correction factor of the sea water in the generation equipment inlet respectively. In contrast, Z_i, p_i, U_i and α_i represent the amplitude, the pressure, the velocity and the kinetic energy correction factor of the sea water in the generation equipment inlet respectively.

Due to the structural symmetry and seawater incompressible, the equations can be obtained as follows

$$U=U_i=U_o <= U_2 \tag{4}$$

$$Z_i=Z_o \tag{5}$$

$$H_{io} = \frac{p_i}{\gamma} - \frac{p_o}{\gamma} <= H_w \tag{6}$$

$$P = \gamma\, Q H_{io} \eta \tag{7}$$

Q is the seawater flow; η is the power conversion efficiency for the equipment.

The relationships for seawater velocity U , flow area of equipment and the available pressure head H_{io} are shown as Fig 4.

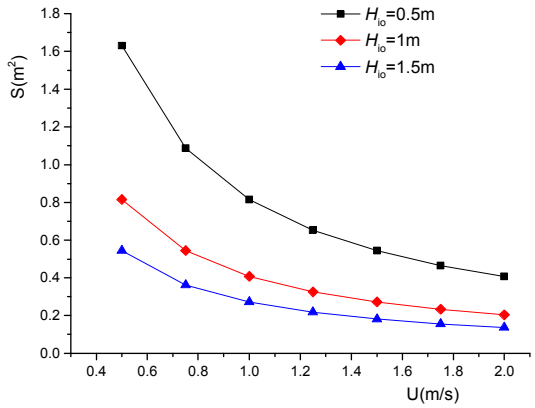

Fig.4 Fluid flow velocity and flow area through the device

4. Conclusions

(1) This paper introduced a coastal wave energy power generation and its unique dual channel structure, in which two–way coastal current was transformed into single direction rotation of the impeller. Thus the instability of energy output is reduced.

(2) The kinetic energy of the sea water flow to shore reaches the maximum at the position where a certain distance from shore. The kinetic energy is mainly transformed by the potential energy of the wave away from shore.

(3)The generation equipment output power W is determined mainly by the available pressure head Hio and seawater flow Q

(4)When generation equipment output power W is kept constant, lower seawater velocity U require larger flow area S that affects device compactness.

(5)In this paper, the costal wave and the dual-channel structure power generation equipment are analyzed without considering effects of wave breaking and wind. Thus effects on costal wave by wave breaking and winding need further research

Acknowledgements

This work was financially supported by the PhD Start-up Fund of Natural Science Foundation of Guangdong Province, China (1209386)

References

[1] Wang Chuankun, Lu Wei. Analysis methods and reserves estimation of ocean resources [M], Beijing：Ocean press, 2009(in Chinese)

[2] Westwood A. Ocean power: Wave and tidal energy review [J]. Refocus, 2004, 5(5): 50-55.

[3]Zhang D, W Lin and Y Lin. Wave energy in China: Current status and perspectives.[J] Renewable Energy, 2009. Volume 34,(Issue 10): p. Pages 2089-2-92.

[4] Lin Jiangbo, Dynamic analysis and emulation of float-type wave power generation boat [D], Qinhuangdao: Yanshan university, 2006. (in Chinese)

[5] Li Shicheng, Experimental investigation on the performance of the oscillating buoy wave power device [D], Dalian university of technology, 2006. (in Chinese)

[6]WNG Lingyu, The structure design and experiment study of an ocean buoy wave power device [D]. Dalian: Dalian university of technology, 2008(in Chinese)

[7] KONG Long. Engineering fluid mechanics(The second edition)[M]. Water power press,1992(in Chinese)

Advanced Materials Research Vols. 986-987 (2014) pp 181-186

doi:10.4028/www.scientific.net/AMR.986-987.181

A Energy Optimization Management Method of the Microgrid Based on Priority Ranking

Qin-Zheng Yu[1, a], Dong-Mei Zhao[1]

[1] North China Electric Power University, Changping District, Beijing 102206, China;

[a]cau_fisch@163.com

Keywords: microgrid; energy optimization management; priority raking; particle swarm optimization

Abstract. Energy optimization management can realize optimal operation of the microgrid, to meet the requirements of economic operation, power supply reliability and environmental benefit, etcetera. Artificial intelligent algorithms are most widely used to solve this problem currently. In order to avoid the weaknesses of intelligent algorithms, this paper puts forward a simple and practical method based on priority ranking. A energy optimization management model of a grid-connected microgrid is established. Using the priority ranking method, optimal operation schemes under different optimization strategies are figured out. The analysis and discussion of optimal operation schemes and the comparison with the optimization result of particle swarm optimization (PSO) indicate that the method based on priority ranking is simple, effective and practical.

Introduction

In order to make full use of the distributed generation (DG), the concept of the microgrid was proposed at the beginning of this century. As an important part of the microgrid research, energy optimization management can realize optimal operation of the microgrid, so as to meet the requirements of economic operation, power supply reliability and environmental benefit, etcetera.

Artificial intelligent optimization algorithms, including genetic algorithms (GA)[1-3], particle swarm optimization (PSO)[4,5], ant colony optimization (ACO)[6,7] and immune algorithm (IA)[8], have been applied in the energy optimization management problem of the microgrid. The algorithms mentioned above are well-adapted to different problems and are able to obtain the global optimum. However, it brings many difficulties, when using intelligent algorithms. Firstly, the optimization results are usually uncertain, and easy to fall into local optimum. Secondly it takes long time to compute. Lastly it is difficult to solve DGs start-stop unit commitment problem, because the number of dimensions is too large.

Therefore, in order to avoid the difficulties caused by intelligent algorithms, this paper proposes a energy optimization management method of the microgrid based on priority ranking, which is simple, effective and practical.

the Energy Optimization Management Model of a Grid-connected Microgrid

Typically, a microgrid is connected with the main grid, and gets frequency and voltage support from the bulk grid. Pointing at a grid-connected microgrid, this paper establishes a energy optimization management model, which contains various types of DGs, and takes a battery as the energy storage. In the interval Δt between two adjacent operation instructions, assumptions are made as following: the load demand, the output power of each DG and battery, the interaction power between the microgrid and the main grid and the electricity price maintain constant.

Objective Function

In this paper, the objective function of this optimization model is the minimum operation cost, considering feul costs, maintenance costs and interaction power costs, as Eq. 1.

$$\min C_{OPE} = \int_0^T \left[\sum_i^N \left[C_{i,t_k}^{fuel} + C_{i,t_k}^{M} \right] + C_{t_k}^{PE} \right] dt = \int_0^T \left[\sum_i^N \left[f^{fuel}\left(P_{i,t_k}\right) + K_i^M P_{i,t_k} \right] + c_{t_k}^{pe} P_{grid,t_k} \Delta t \right] dt \qquad (1)$$

Where T stands for the optimization period, here is 24 hours; t_k stands for a optimal operation time; N stands for the amount of DGs in this system; i is the DG number; C_{OPE} stands for the operation cost; C_{i,t_k}^{fuel} and C_{i,t_k}^{M} stand for the fuel cost and maintenance cost of the i-th DG at time t_k; $C_{t_k}^{PE}$ stands for the interaction power cost at time t_k; P_{i,t_k} and P_{grid,t_k} stand for the output power of the i-th DG and the interaction power at time t_k; $c_{t_k}^{pe}$ stands for the electricity price at time t_k.

Constraint Condition

●Power balance constraint: $\sum_{i}^{N} P_{i,t_k} + P_{bat,t_k} + P_{grid,t_k} - P_{\text{load},t_k} = 0, k = 1, 2, \cdots, num$ (2)

Where $num = T / \Delta t$; P_{bat,t_k} and P_{load,t_k} stand for the charge or discharge power of the battery and the load at time t_k.

●Upper and lower output limit of DGs: $P_{\text{i}}^{\min} \le P_{i,t_k} \le P_{\text{i}}^{\max}$ (3)

Where, $P_{\text{i}}^{\min}$ and $P_{\text{i}}^{\max}$ stand for the minimum and maximum output power of the i-th DG.

●State of charge (SOC) constraint of the battery: $SOC_{\min} \le SOC_{t_k} \le SOC_{\max}$ (4)

Where SOC_{t_k} stands for the SOC of the battery at time t_k; $SOC_{\min}$ and $SOC_{\max}$ stand for the minimum and maximum SOC of the battery.

●The start and end state of SOC constraint in the optimization period: $SOC_{t_1} = SOC_{t_{num}}$ (5)

Considering the involvement of the battery in the optimization process, the SOC in the beginning and in the end should be equal. The battery completes a charge-discharge cycle.

●The charge and discharge power constraint of the battery:

$SOC_{t_k} - P_{bat,t_k} \Delta t / BAT_{cap} = SOC_{t_{k+1}}, k = 1, 2, \cdots, num$ (6)

$P_{bat}^{\min} \le P_{bat,t_k} \le P_{bat}^{\max}$ (7)

Where $P_{bat}^{\min} < 0$ and $P_{bat}^{\max} > 0$ stand for the maximum charge and discharge power; BAT_{cap} stands for the battery capacity.

●Upper and lower limit of the interaction power: $P_{grid}^{\min} \le P_{grid,t_k} \le P_{grid}^{\max}$ (8)

Where $P_{grid}^{\max}$ and $P_{grid}^{\min}$ stand for the minimum and maximum interaction power between the microgrid and the main grid.

Optimization Strategy

As the renewable energy, wind and photovoltaic power are not controllable; produce less pollution, without fuel consumption; cost less operation cost; start to work quickly; changes the output rapidly. Due to the advantages mentioned above, the optimization strategy gives top priority to the use of wind and photovoltaic power; make they work in the maximum power point tracking (MPPT) mode.

And then, according to the main grid whether to involve in the optimization process and the exchange mode of the interaction power between the microgrid and the main grid, the optimization strategies of a grid-connected microgrid can be generally divided into the following 3 types.

Strategy 1: In order to make full use of DGs, firstly DGs are utilized to meet the load demand, and the main grid is taken as a supplement. Interactive power is unidirectional, which means the microgrid can absorb power from the main grid, but can not deliver power to the main grid.

Strategy 2: From the economic point of view, considering the influence of peak-valley electricity price, both the DGs and the main grid take part in optimization process. when the electricity price of the main grid is lower than the power generation cost of DGs, it takes precedence that the microgrid absorbs power from the main grid. The exchange mode of the interaction power is the same with Strategy 1.

Strategy 3: Both the DGs and the main grid take part in optimization process. Interactive power is bidirectional, which means the microgird can not only absorb power from the main grid, but also deliver power to the main grid.

the Energy Management Optimization Method of the Microgrid Based On Priority Ranking

The principle of the priority ranking method is that according to the objective function and optimization strategy on which researchers focus, sort the output of DGs and the main grid in the specified order; when load changes, adjust the state (work or stop) of DGs and arrangements the output of DGs and the main grid, based on the given output priority level. This method includes the following steps:

Step 1: establish a "output of DGs and the main grid-optimization objective" curve

Through the statistical analysis and calculation of the related data, establish a "output of DGs and the main grid-optimization objective" curve. For the energy optimization problem, the optimization objective can be operation cost, environmental benefit, depreciation cost and comprehensive cost etc.

The optimization objective in this paper is operation cost. The operation cost of DGs can be fitted by a quadratic function of output power[9-11], which is similar to a linear function. The operation cost of the main grid is proportional to the electricity price.

Step 2: make the output priority level of DGs and the main grid

According to different optimization strategies, under different load demands, sort the output of DGs and the main grid in a specified order, based on the curve given by Step1.

Step 3: calculate the curve of the net load

The net load represents the load which subtracts the output of wind and photovoltaic power, as $P_{\text{net},t_k} = P_{\text{load},t_k} - P_{\text{PV},t_k} - P_{\text{WT},t_k}$ shows. Where P_{net,t_k}, P_{PV,t_k} and P_{WT,t_k} stand for the net load, the output of wind and photovoltaic power at time t_k.

Step 4: figure out a charge and discharge plan of the battery in the optimization period

In a grid-connected microgrid, the active effect of a battery is that: 1) The battery can be used in peak load shifting to inhibit the fluctuation of the tie line power; 2) The battery can draw energy from the main grid, when load demand is low and electricity is cheap. Contrary, the battery discharges to reduce peak power demand, when electricity is expensive. Therefore, the economic benefit is improved.

When all the constraints of the battery are met, according to the net load curve obtained in Step 3, figure out the output of the battery at each moment, to make the battery complete a charge-discharge cycle in the optimization period and play a role described above.

Step 5: calculate the actual load demand

On the one hand wind and photovoltaic power generate electricity preferentially, on the other hand, a charge and discharge plan of the battery has been determined. Therefore, we can calculate the actual load demand which is met by the DGs and the main gird, as $P_{\text{real\_load},t_k} = P_{\text{load},t_k} - P_{\text{PV},t_k} - P_{\text{WT},t_k} - P_{bat,t_k}$ shows. Where $P_{\text{real\_load,tk}}$ stands for the actual load demand which is met by the DG and the main gird.

Step 6: figure out the optimal operation scheme

According to the optimization objective and strategy, arrangement the output of DGs and the main grid, based on the output priority level given by Step 2 and the actual load demand given by Step 5.

Step 7: fine-tune the optimal operation scheme

Through the above steps, the output of DGs may not satisfy the constraints. It is necessary to fine tune the scheme.

Example Analysis

Example Data

The calculation example of the microgrid considered in this paper consists of Wind Turbine(WT)，Photovoltaic(PV), Diesel Engine(DE), Fuel Cell(FC), Micro-Turbine(MT) and the battery. This microgrid system operates in the grid-connected mode. The prediction power of WT, PV and the load demand in the next day and the electricity price is shown in Fig.1.

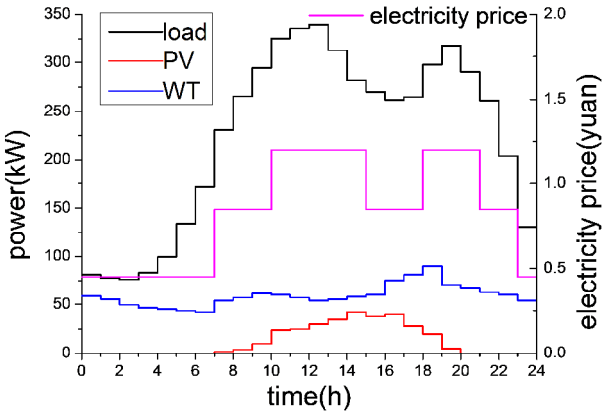

Fig.1 Prediction power and electricity price

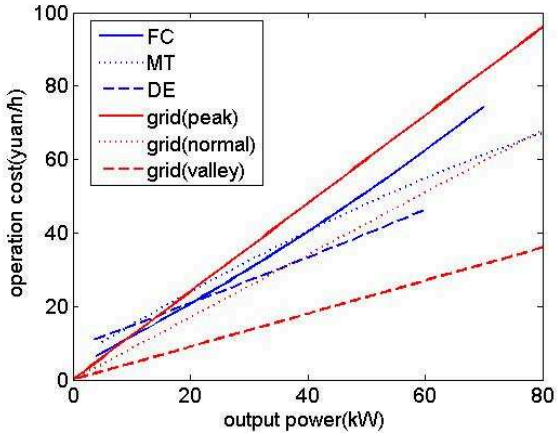

Fig.2 Output-operation cost curve

In this microgrid system, the upper and lower output limit of FC, DE and MT is 4~70kW, 3~60kW and 5~80kW respectively. Fuel costs of DGs can be fitted with a quadratic function. As shown in Fig.2[10,12], in this paper, the fuel and maintenance cost of each DG is taken as a whole (objective, the operation cost) to consider. Fig.2 also shows the operation cost of the main grid. The maximum charge and discharge power of the battery is 40kW, and its capacity is 200kWh. In order to prevent excessive charge and discharge, the operating range of SOC is set to 0.3~0.9pu, and its initial state in a optimization period is set to 0.4pu. The interactive power is limited to ±50kW.

Figure out the Output Priority Level

Through the statistical analysis and calculation of the related data, the "output-operation cost" curve is shown in Fig.2, which provide a sorting information for priority ranking. According to Fig.2, in order to reduce the operation cost to the minimum, Table 1 gives out the priority level of DGs and the main grid, under different optimization strategies and different load demands.

Table 1 The priority level of DGs under different optimization strategies

optimization strategy			the priority level of DGs and the main grid under different load demand					
Strategy 1	load demand [kW, the same below]		0-21	21-60	60-100	100-140	140-210	210-260
	priority level		FC	DE	DE, FC	DE, MT	DE, MT, FC	DE, MT, FC, grid
Strategy 2	peak	load demand	……	69-100	100-140	140-149	149-210	210-260
		priority level	……	DE, FC	DE, MT	DE, MT, grid	DE, MT, FC	DE, MT, FC, grid
	valley	load demand	0-50	50-71	71-110	110-150	150-190	190-260
		priority level	grid	grid, FC	grid, DE	grid, DE, FC	grid, DE, MT	grid, DE, MT, FC
	normal	load demand	0-38	38-60	60-110	110-137	137-190	190-260
		priority level	grid	DE	DE, grid	DE, grid, FC	DE, MT, grid	DE, MT, grid, FC
Strategy 3	peak	load demand	……	140-210		210-260		
		priority level	……	DE, MT, FC(-)		DE, MT, FC, grid		
	valley	load demand	0-50	50-71	71-110	110-150	150-190	190-260
		priority level	grid	grid, FC	grid DE	grid, DE, FC	grid, DE, MT	grid, DE, MT, FC
	normal	load demand	10-60	60-87	87-140	140-190	190-260	
		priority level	DE(-)	DE, grid	DE, MT(-)	DE, MT, grid	DE, MT, grid, FC	

Notes: DE(-), FC(-) and MT(-) mean that DE, FC, MT generate the most power, and deliver the surplus power to the main gird, when the limit of the interaction power is met.

Analysis of the Optimal Operation Scheme

According to the net load curve in Fig.3 and Step 4 of this method described in section 3, the actual load demand curve which is met by DGs and the main grid can be obtained, as Fig.3 shows. The battery charges during 0:00-4:00, when load demand is low, and discharges at peak period 10:00-13:00 and 19:00-20:00.

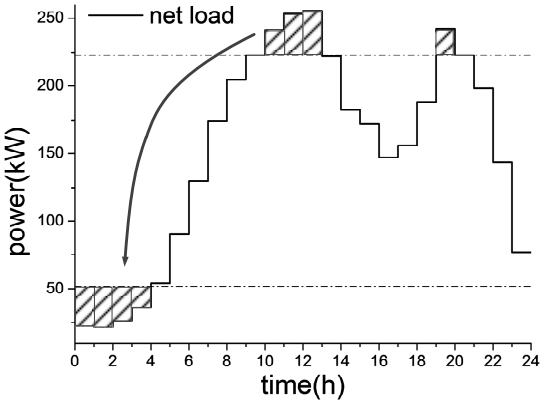

Fig.3 A charge and discharge plan of the battery

Based on the output priority level in Table 1 and the actual load demand in Fig.3, optimal operation schemes under different optimization strategies are figured out, which take the operation coat as the objective, as Fig.4.

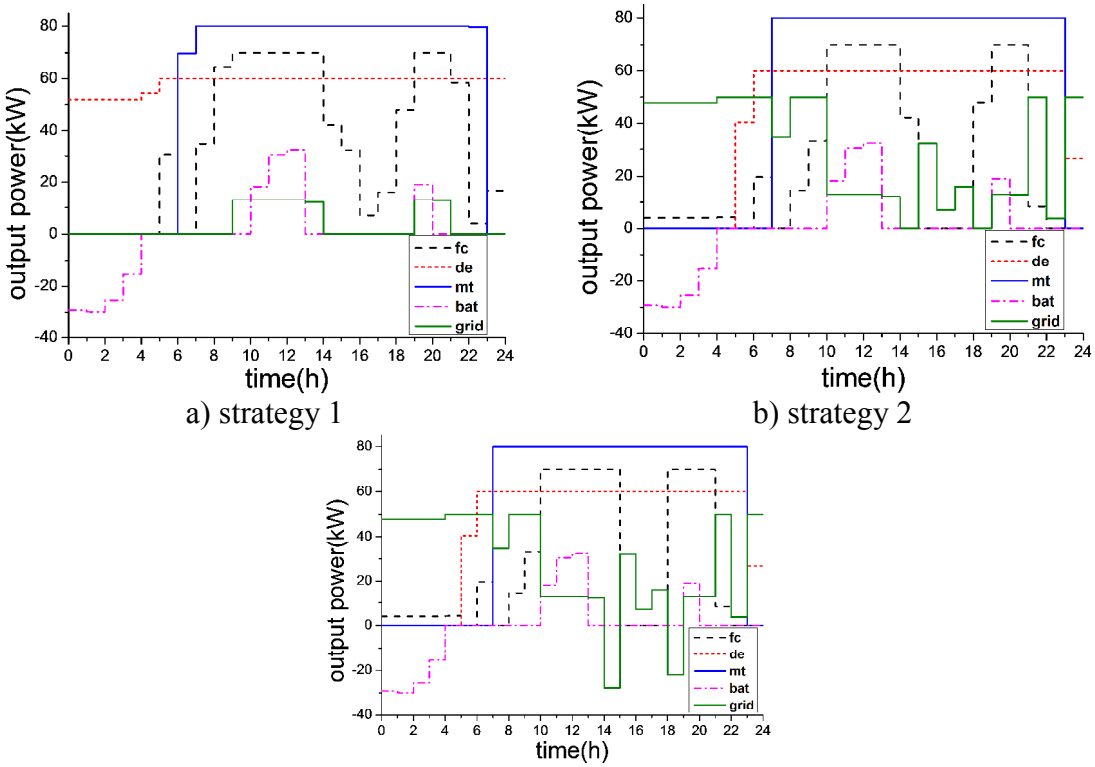

a) strategy 1 b) strategy 2

c) strategy 3

Fig.4 Optimal operation schemes under different optimization strategies

As can be seen from Fig.4: 1)When this microgrid system uses Strategy 1, DGs generate power in the order from the lowest operation cost to the highest. The microgird draws power from the main grid, when all the DGs can not meet the load demand. 2) When using Strategy 2, both the DGs and the main grid take part in optimization process. The DG or the main grid which possesses lower operation cost have priority to generate power. The interactive power is also unidirectional. 3) When using Strategy 3, the DGs deliver power to the main grid to gain profit at peak period. The economic benefits of strategy 1, 2 and 3 are gradually improved, as shown in Table 2.

To verify the optimization accuracy by using the priority ranking method, PSO algorithm is used to calculate the same example. The result of PSO algorithm can be regarded as the global optimum. The optimization results of two methods and the errors are shown in Table 2.

Table 2 The operation cost [yuan]

	The priority ranking method	PSO	error
Strategy 1	3216.00	3216.00	0%
Strategy 2	3049.31	3049.13	<0.1%
Strategy 3	3046.76	3046.53	<0.1%

As can be seen from Table 2: Compared with the intelligent algorithm, the priority ranking method also possesses a high accuracy. The optimization results of two methods have little difference. However the priority ranking method costs less time to compute.

Conclusion

This paper establishes a energy optimization management model of a grid-connected microgrid, which consists of various types of DGs and a battery. Using the priority ranking method, optimal operation schemes under different optimization strategies are obtained. Through the analysis and discussion of the optimization schemes and the comparison with the optimization result of PSO, it indicates that using the priority ranking method can not only guarantee the calculation accuracy, and greatly reduce the computational time, but also avoid the weaknesses, when using intelligent algorithms. Therefore, this energy optimization management method of the microgrid based on priority ranking is simple, effective, easy to use, fast to compute and worthy to be used in engineering practice.

References

[1] CHEN Jie, Yang Xiu, ZHU Lan, et al, *Microgrid multi-objective economic dispatch optimization*, Proceedings of the CSEE, Vol. 22(2013), p. 57-66.
[2] HONG Bo-wen, GUO Li, et al, *Model and method of dynamic multi-objective optimal dispatch for microgrid*, Electric Power Automation Equipment, Vol. 33(2013), p. 100-107.
[3] Lin Wei, CHEN Guang-tang, et al, *Optimal load distribution of microgrid based on improved self-adaptive genetic algorithm*, Power System Protection and Control, Vol. 40(2012), p. 49-55.
[4] CHEN Da-wei, ZHU Gui-ping, *An investigation on iptimal load distribution of microgrids*, Automation of Electric Power Systems, Vol. 34(2010), p. 45-49.
[5] WANG Rui, GU Wei, *Economic and optimal operation of a combined heat ang power microgrid with renewable energy resouces*, Automation of Electric Power Systems, Vol. 35(2011), p. 22-27.
[6] AI Xin, CUI Ming-yong, *Environmental and economic dispatch of microgrid using chaotic ant swarm algorithms*, Journal of North China Electric Power University, Vol. 36(2009), p. 1-6.
[7] Colson C M, Nehrir M H, Wang C. *Ant colony optimization for microgrid multi-objective power management*, Power Systems Conference and Exposition, Seattle, WA(2009) , p.1-7..
[8]WANG Xin-gang, AI Qian, *Multi-objective optimal energy management of microgrid with distributed generation*, Power System Protection and Control, Vol. 37(2009), p. 79-83.
[9]Mohamed F A, Koivo H N, *Online Management of MicroGrid with Battery Storage Using Multiobjective Optimization*, POWERENG2007 International Conference on Power Engineering - Energy and Electrical Drives Proceedings , Setubal, Portugal(2007), p.231-236.
[10]SHI Qing-jun, Research on Optimal Sizing and Optimal Energy Management for Microgrid, Master Thesis, Zhejiang University, 2012.
[11]GUO Jia-huan, Study on Economic Operation Optimization of Microgrid, Master Thesis, North China Electric Power University, 2010.
[12]SHI Qing-jun, GENG Guang-chao, JIANG Quan-yuan, *Real-time optimal energy dispatch of standalone microgrid*, Proceedings of the CSEE, Vol. 32(2012), p. 26-35.

Advanced Materials Research Vols. 986-987 (2014) pp 187-191

doi:10.4028/www.scientific.net/AMR.986-987.187

A Heuristic Analysis Method for the Impact of DGs to Power System Reliability

Bo ZENG[1], Kai WANG[1], Xiangyu Kong[2, a], Yi Zeng[2, b], Qun Yang[2]

[1]Electric Power Research Institute of Guangxi Power Grid Corporation, Nanning, China

[2] Key Laboratory of Smart Grid (Tianjin University), Ministry of Education, Tianjin, 300072, China

[a]email: kongxy06@163.com, [b]email: zengyiroom@163.com,

Keywords: High penetration; Distributed generation; Monte-Carlo method; Reliability analysis

Abstract. With high penetration of distributed generation connected to the grid, distribution system will have some huge impacts, and system reliability calculation models and assessment methods are changing. Based on Monte-Carlo method, a heuristic reliability analysis method for distribution system with distributed generations was proposed in the paper, which focuses on the mode of distributed generation in parallel to system power supply. Functional role of distributed generation in the power distribution system failure and distributed power adapter with load strategies were analyzed in this method. Cases simulation analysis was used to verify its effectiveness.

Introduction

With the use and development of clean and renewable energy, numerous Distributed Generations (DG) are connected to the distribution system, resulting in the changes of traditional distribution network and operation modes. The penetration rate is defined as the ratio of DG system's capacity accounting for the distribution system capacity, which is considered high when it reaches 70% generally [1]. Currently, DG system has formed a high penetration in some area distribution system.

The traditional distribution network is usually supplied radiantly by a single point generation and the model is single-supply as well. When any feeder of the grid falls in a fault, all the loads behind the fault point will lose power. However, with the installation of DG, the distribution system becomes a network with multiple power supply. The loads can avoid losing power in a fault with the help of DGs behind the fault point [2]. As the output of DG (like wind and solar) is uncertain and uncontrollable, in the case of high penetration, reliability evaluation models and methods for distribution system are different from traditional ones, and reliability analysis method also becomes complicated[3].

In [4], the uncertain factors of system components and load parameters are studied, and some impacts for different installation positions on distribution system were given by calculating the range reliability indices before and after the installation of DG. In [5], the authors proposed a reliability analysis strategy based on the Network Equivalent Method of minimum cut set. This strategy can separate distribution system into sections properly, which is suitable for the dividing of distribution system with scattered DG. An island partitioning algorithm was proposed in [6] to divide the distribution system with DG. The algorithm analyzes the reliability according to the power balance features of island operation and different requirements for power reliability. In [7], the authors equaled the DG as a distribution device, and took samples with Monte-Carlo method to analyze the power supply ability of distribution system with DG.

Currently, some results have been achieved in reliability evaluation and distributed generation technique, but the supply turning strategies for DG in a fault and the analysis methods for impact on distribution system reliability need further study. Based on Monte-Carlo Method, a reliability analysis method for distribution system with high penetration of DG was proposed in this paper, which focuses on the mode of DG in parallel to system power supply. Functional role of DG in the distribution system failure and distributed power adapter with load strategies were considered here.

Reliability Analysis of Distribution Network with DG

Operation Modes for DG. Different operation modes for DG have different impacts on the power supply reliability of distribution network system [8], mainly including three cases: 1) DG acts as the standby power for the system; 2) System power acts as the standby power for the DG; and 3) DG supports the load points in parallel to system power.

The distribution system has become a multiple power network and customers can gain power from different power supply. Thus, system power and the DG prepare for each other to improve the reliability of distribution system. However, if the control measures of disintegration are improper, system may face a problem of unsynchronized power islands. Even the stability of system will be affected when it's critical. Considering the efficiency and stability in the distribution system with DG of high penetration, the mode of DG in parallel to system power will be the mainstream [9]. This paper studies the mode of DG in parallel to system power and the same analysis method is also suitable for other modes.

Grouping Strategy for DGs and Loads. There is a circuit breaker on each line and the line is divided into forward region, middle region and backward region in a fault. As the existence of DG, the strategies of breaker tripping and the island operation of DG need to be considered. And the impacts of fault on forward region and backward region may be different, so the loads in forward and backward regions need to be divided into groups differently according to breaker tripping strategy.

Some load can turn to a DG directly without any switch operation after breaker acts. In this way, the forward and backward regions are divided into four groups: same and different groups in forward region, same and different groups in backward region. When there is more than one DG in forward or backward regions, different DGs are allowed to be in more than one same branch-group. Some load points can't turn to any DG for power and they are included in different branch-group with those in the traditional distribution network.

Distributed Power adapter with Load Strategies. In the failure of distribution system, DG carries a part of the loads in forward and backward regions directly or through quick operation. And the strategy is: the DG meets the important load in the same branch-group preferentially, and if some extra power is available, supplies the rest load in the group. If there is still more power, load in the different branch-group from the DG can also be supplied. This is for the decrease of switches operation quantity and power loss.

For backward region, even though a fault occurs, the DG will continue running because of the protection of breaker tripping strategies, so the load points in the same branch-group as DG may not lose power. It depends on the sizing comparison between DG's output and load. If the output of DG is big enough to supply all load points in the same branch-group, they will not lose power, and the extra power can be used to support the load points in different branch-groups. Or, only important load can be meted, and a rank of load points is necessary.

For forward region, when breaker acts to separate a fault, several islands with DG will be formed. The load points and DGs in forward region need to be divided into groups. For some load points, they may not lose power because of the existence of DG, but it depends on the sizing comparison between DG's output and load. If the output of DG is big enough to supply all load points in the same branch-group, they will not lose power. Or, only important load can be meted, and a rank of load points is necessary.

Interruption Indices. The purpose for reliability analysis of distribution system is to obtain the quantifiable indices of reliability. For the analysis of distribution network with DG, this paper selects the *LOLP* (Loss of Load Probability) and *AAID* (Annual Average Interruption Duration) indices.

LOLP presents the probability of load power failure in the distribution system, calculated using:

$$LOLP = \frac{1}{N}\sum_{i=1}^{n} F_{LOLP}\left(\overline{X_i}\right) \tag{1}$$

In the type: N stands for the number of randomly sampled system status; F_{LOLP} stands for possible load-shedding situations when system stays in the status $\overline{X_i}$, defined as:

$$F_{LOLP}\left(\overline{X_i}\right)=\begin{cases}0 & \text{No load-shedding in the state of } \overline{X_i}\\ 1 & \text{Load-sheeding in the state of } \overline{X_i}\end{cases}$$

AAID presents the annual average interruption duration (in hours) observed at a load point in the distribution system, and it is calculated using:

$$AAID=\frac{\sum_{i\in NS} F_{AAID}\left(\overline{X_i}\right)}{NS} \tag{2}$$

In the type, $F_{AAID}\left(\overline{X_i}\right)$ stands for the interruption duration of the observed load point every time the system stays in the sampled state $\overline{X_i}$; *NS* stands for the quantity of loads at that node.

A Heuristic Reliability Analysis Algorithm of Distribution System

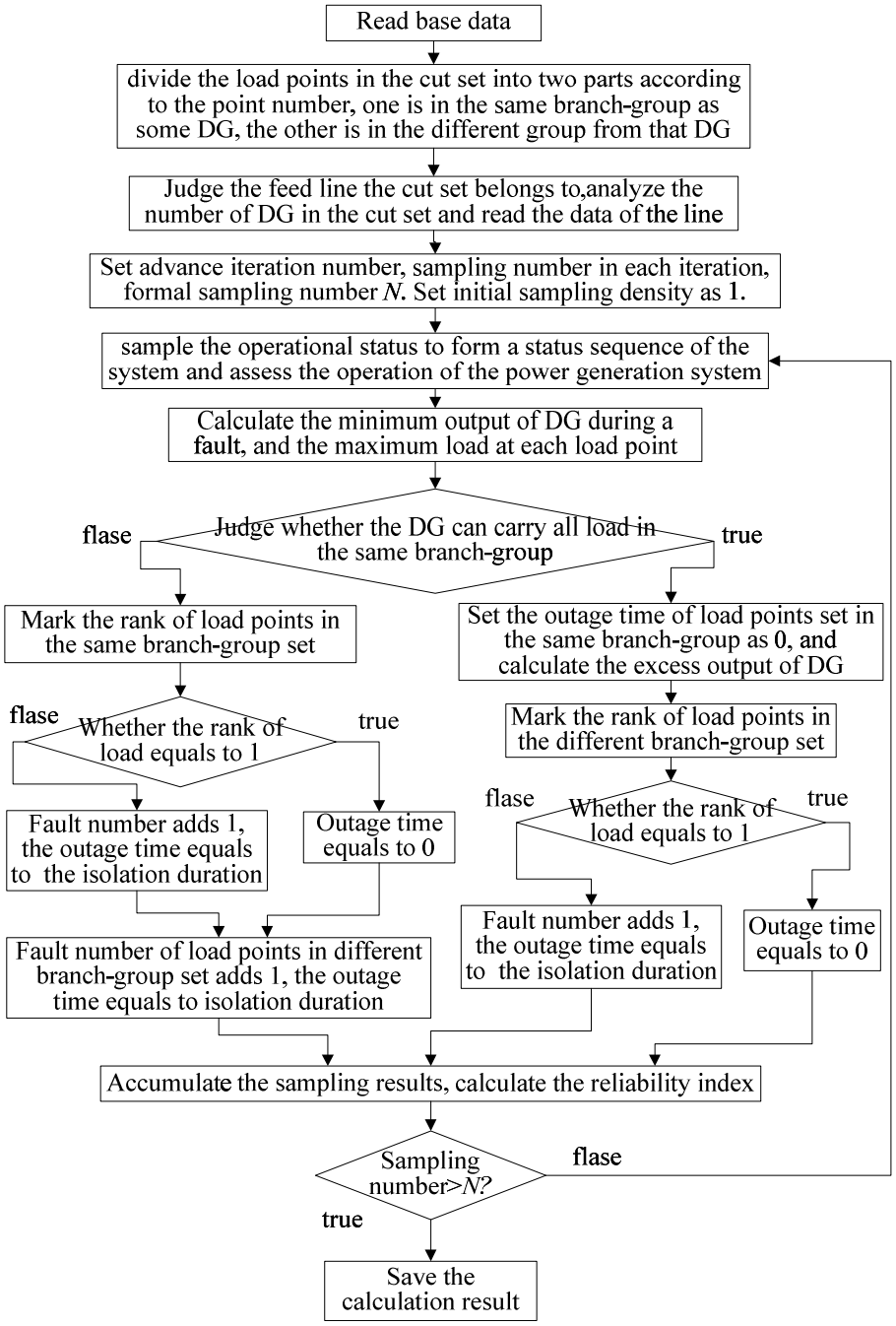

Fig.1 Distribution system reliability analysis flow chart for considering DG

Assumptions. After more and more DGs, like solar and wind, connect to the distribution system, the intermittency and uncontrollability will increase the difficulty of reliability analysis [10]. To simplify the analysis in this paper, switching devices, like breakers, are assumed no misoperations or refusing actions in the premise of computation accuracy. Thus, it is considered that the modes between connection to grid and islands can always transform to each other quickly and successfully.

Algorithm Flow. To analyze a distribution system, different kinds of fault need to be assembled at different nodes and in different timing sequence. The computation will be massive, so the fault status is sampled by Monte-Carlo Method for analysis in this paper.

First, divide the load points in the cut set into two parts according to the point number, one part is the same branch-group as some DG, the other is the different branch-group from that DG. Then, based on the judgment of feeder the cut set belongs to, analyze the quantity of DG in the cut set and read the data of corresponding line. After that, use the Monte-Carlo Method to sample the operational status to form a state sequence of the system and assess the operation of the power generation system. For a fault on the line, analyze the load restoration according to the comparison between the sizing of DG and the amount of planned loads as well as the importance of load in forward and backward regions. Last, get the reliability index of distribution system. The algorithm flow is shown in Fig. 1.

Using this method, the intermittence and uncontrollability of solar and wind due to climate changing need to be considered. In the reliability analysis, the climate factor affects the distribution system reliability a lot. It can be solved by multiplying the device reliability in different time and different climatic situations by a weight coefficient, and the weight coefficient is used to simulate different climatic status also.

Simulations and results

The proposed algorithm is applied on the IEEE-RBTS BUS6 distribution system and its specific parameters can be found in literature [11]. In Fig. 2, two DGs are connected to the buses 22 and 29 with small-capacity power storage devices. In a fault, the loads 14 to 18 and 19 to 23 can be supplied by network that works independently.

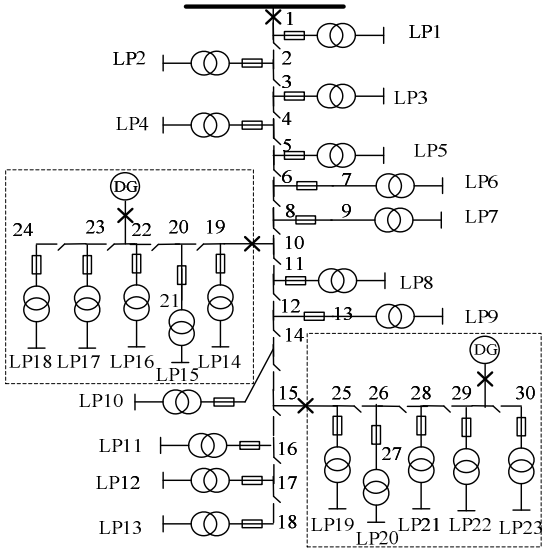

Fig. 2 Case study of IEEE-RBTS BUS6

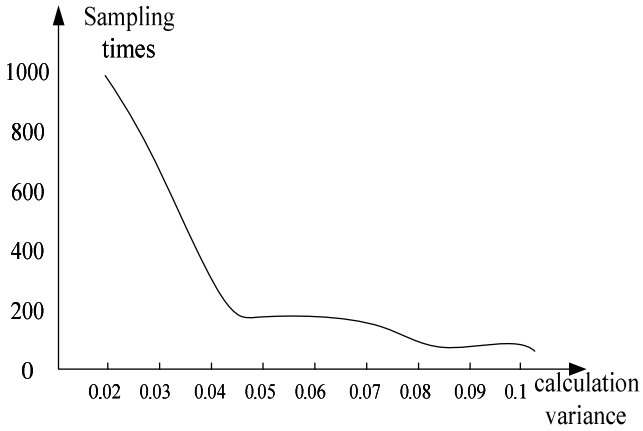

Fig. 3 Sampling occasions curve with Monte Carlo sampling calculation accuracy

Tab. 1 Monte Carlo sampling occasions and assessment results

Sampling times *N*	*LOLP*	Variance of *LOLP*	*AAID* [h]	Variance of *AAID*
200	0.0255	0.0731	4.0261	0.1243
500	0.0262	0.0460	4.1856	0.0611
1000	0.0255	0.0124	4.0197	0.0164
2000	0.0254	0.0103	4.0182	0.0139

The computation example analyzes the convergence and accuracy of this algorithm. Table 1 shows that, with the increase of sampling, the values of *LOLP* and *AAID* respectively converge to 2.54% and 4.01 hours. And the results are of high convergence. By the simulations and analysis, it can be found that the sampling times and accuracy follow inverse relationship as what is seen in Fig.3. In order to make sure the variance of reliability index is small enough, a lot of sampling times are needed.

Although the DG and inverters may increase the probability of system failures due to their own faults, the faults of DG usually don't lead to power interruption of corresponding load. In a fault, as the feeders with DG can work as an island, the probability of power failure on that line becomes lower.

Conclusion

DG has the feature of diversity, intermittent and uncontrollability. What affect the reliability are the type of DG, the modes of connection and control, the climate situation and the automation level of distribution system. For optimal effects, the proposed reliability analysis method for distribution system with DG based on Monte-Carlo Method needs to consider various factors.

Acknowledgement

This work was supported in part by 863 National High Technology Research and Development Program of China (2011AA05A115).

References

[1] Jikeng Lin, Xudong Wang, Ling Qin. Reliability evaluation for the distribution system with distributed generation [J]. European Transactions on Electrical Power, 2011, 21(1): 895-909.

[2] Li Peng, Chen Jijun. Impact of Distributed Generation and Grid Connection on Distribution Networks [J]. Guangdong Electric Power, 2012，25(1): 75-79.

[3] Atwa Yasser M, Saadany E, Ehab F. Reliability evaluation for distribution system with renewable distributed generation during islanded mode of operation [J]. IEEE Transactions on Power Systems, 2009, 24(2): 572-581.

[4] Qian Kejun, Yuan Yu. Study on Impact of Distributed Generation on Distribution System Reliability [J], Power System Technology, 2008.32(11): 74-78.

[5] Qi Yanpeng, Zhang Yan, Yu Jianping, et al. Application of Minimum cut set and Network-equivalent Method in Distribution System Reliability Analysis [J]. Proceedings of the CSU-EPSA, 2011, 23(2):98-104.

[6] Zeng Ming, Wu Jianhong, Wang Jingjing. Impact of intermittent wind distributed generation on the reliability of distribution system [C]. 2010 Asia-Pacific Power and Energy Engineering Conference, March 28, 2010, Chengdu, China.

[7] Yi Xin, Lu Yuping. Islanding Algorithm of Distribution Networks with Distributed Generators [J], Power System Technology, 2006，30(7):50-54.

[8] Wang Yuanshan, Distribution System Reliability research Considering the Impacts of Distributed Generation [D], Tianjin: Tianjin University, School of Electrical Engineering & Automation, 2007.

[9] Xu Shengyou, Chen Minyou, Wade Neal, *et al*. Reliability evaluation of electric power system containing distribution generation [J]. Advanced Materials Research, 2012, (383): 3472-3478.

[10] Xiangyu Kong, Dazhong Fang, Chung T S. Economy and reliability evaluation of generating including wind energy systems[C]. 3rd International Conference on Deregulation and Restructuring and Power Technologies, Apr, 2008, (1): 2653-2657, Nanjing, China.

[11] Billinton R, Kumar S, Chowdhury N, *et al*. A reliability test system for educational purposes: basic data [J]. IEEE Trans. on Power Systems, 1989, 4 (3): 1238-1244.

Advanced Materials Research Vols. 986-987 (2014) pp 192-195

doi:10.4028/www.scientific.net/AMR.986-987.192

A Research on Fixed Series Compensation

QIN Li-jun[1, a], XIONG Chao[2,b]

[1] North China Electric Power University, Beijing 102206 China

[2] North China Electric Power University, Beijing 102206 China

xiongc@163.com

Keywords: fixed series compensation(FSC); power flow control in power systems; loss reduction on grids

Abstract. Series compensation can improve the line efficiency significantly, reduce line loss and raise line voltage obviously. The paper introduces the basic principles of series compensation, and studies the influence of series compensation's installation position on compensation effect, the loss reduction effect of series compensation as well as the influence of series compensation on power flow control.

Introduction

Using series compensation in power systems can reduce line impedance, improve reactive equilibrium, enhance the transmission capacity of electric transmission lines, increase the transient stability limit, and improve the load distribution among parallel lines, so as to reduce the loss of lines, make full use of existing power system resources, and promote electric power development. Adopting the capacitors of series compensation can avoid the heavy investment on new-built lines to some extent, so as to obtain a relatively high input-output ratio. Under the circumstance that it becomes more difficult to get a line corridor at present, series compensation will be widely used further.

The Basic Principles of Series Compensation

Applying Series Compensation to Improve the Transient Stability of System

Improving the transient stability of system is one of main reasons for a power system to add series compensation, and its basic principle is to offset the inductive reactance through the capacitive reactance of series capacitor, so as to improve system stability. The schematic diagram of improve system stability is shown as follows:

Figure 2-1

A Two-machine Power System Where System S1 Transmits Power to System S2 Through Long Distance Transmission Lines

The transmitting power of transmission lines between System S1 and System S2 is:

$$P = \frac{E_1 E_2}{X_1} \sin \delta_{12} \tag{2-1}$$

After the devices of series compensation are installed in those lines, the transmitting power of lines changes to:

$$P = \frac{E_1 E_2}{X_1 - X_c} s\text{in}\,\delta_{12} \tag{2-2}$$

For the given node voltage, the transmitting power is in inverse proportion to the line reactance when the phase angle difference is constant, because series compensation reduce the reactance of compensated lines, so as to improve the stability of lines.

Applying Series Compensation to Raise Line Voltage and Reduce Line Loss

Series compensation also can improve the operating voltage of power systems, and reduce line loss. Its principle is shown as follows:

For the π equivalent circuit of lines:

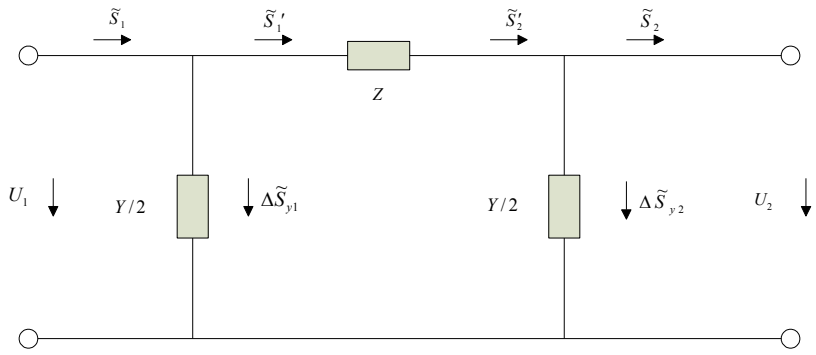

Figure 2-2

The active power loss on the Line Z is

$$\Delta P_z = \frac{P_2'^2 + Q_2'^2}{U_2'^2} R \tag{2-3}$$

The voltage loss is

$$\Delta U = \frac{P_2' R + Q_2' X}{U_2} \tag{2-4}$$

When a series compensation capacitor is added in lines, the inductive reactance of lines will be offset, so its equivalent reactance decreases. Based on the Equation 2-4, it can be found that the voltage loss on lines decreases and the voltage at the terminal of lines raises.

Through analyzing Equation 2-3, it can be found that the active power loss is in inverse proportion to the voltage at the terminal of lines, because the voltage at the terminal of lines goes up, and the active power loss on Line Z goes down with it.

The Control of Series Compensation for Power System Flow

Series compensation controls the flow of power lines through changing the series reactance of transmission lines. The application of series compensation provides people with the approach for optimizing the power flow on specific lines through changing the degree of series compensation, which is also one of considerations when people design series compensation on lines.

We can control power flow through changing the compensation degree of series compensation, so as to minimize the compensation degree of entire system.

See Figure 3-1. Line 1 is an existing line, Line 2 is a new-built line, and the minimum active power loss can be realized through controlling the compensation degree of Line 2.

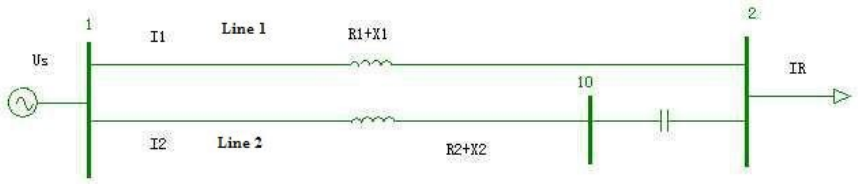

Figure 3-1

The current of two parallel branches is:

$$I_1 = \frac{Z_2}{Z_1 + Z_2} I_R$$
$$I_2 = \frac{Z_1}{Z_1 + Z_2} I_R \tag{3-1}$$

As the function of current at the terminal, the current of Line 1 can be shown as follows:

$$I_1 = \frac{R_2 + jX_2}{(R_1 + R_2) + j(X_1 + X_2)} I_R$$
$$= \frac{[R_2(R_1 + R_2) + X_2(X_1 + X_2)] + j[X_2(R_1 + R_2) - R_2(X_1 + X_2)]}{(R_1 + R_2)^2 + (X_1 + X_2)^2} I_R \tag{3-2}$$

Similarly, the similar result also can be obtained for Line 2.

The total loss of those two lines is:

$$P_L = R_1 I_1^2 + R_2 I_2^2$$
$$= \frac{R_1(R_2^2 + X_2^2) + R_2(R_1^2 + X_1^2)}{(R_1 + R_2)^2 + (X_1 + X_2)^2} I_R^2 \tag{3-3}$$

In order to work out the minimum loss, the equation above is used to take the derivative of Line 2, and then the result is set to zero. The degree of series compensation is not unique, so the reactance is a variable.

$$\frac{dP_L}{dX_L}$$
$$= \frac{2R_1X_2[(R_1 + R_2)^2 + (X_1 + X_2)^2] - 2(X_1 + X_2)[(R_1(R_2^2 + X_2^2) + R_2(R_1^2 + X_1^2)]}{[(R_1 + R_2)^2 + (X_1 + X_2)^2]^2} I_R^2$$
$$= 0 \tag{3-4}$$

The formula is expended and simplified to obtain:

$$\frac{X_2}{R_2} = \frac{X_1}{R_1} \tag{3-5}$$

Therefore, the loss of entire system will be minimum if the two values of impedance are equal, regardless of the resistance of Line 2. Therefore, for the given value, the degree of series compensation can be adjusted to make it match with the original line, so as to guarantee the minimum loss of entire system.

References

[1] CHEN Hang:Steady-state analysis of power systems[M], China Electric Power Press Third Edition

[2] Larry Morgan. James M. Barcus. Satoru Iham. Distribution Series Capacitor with High-energyVaristor Protection[J].IEEE Transactions on Power Delivery. 1993, 8(3)：1413-1419.

[3] S. A. Miske. Considerations for the Application of Series Capacitors to Radial Power Distribution Circuits. IEEE Transactions on Power Delivery,2001, 16(2).

[4] Niu Xiao-rain, Shi Wei. Over-voltage of series compensated EHV transmission lines[J]. High Voltage Apparatus, 1997, 33(6)：6-11.

[5] GB/T 6115. 1-2008 Series capacitors for power systems Part l：General[S].

Advanced Materials Research Vols. 986-987 (2014) pp 196-201

doi:10.4028/www.scientific.net/AMR.986-987.196

A Research Summary on Combined Peaking Load Strategies of Nuclear Power Plant

Tao Zhang[1], Xiaodong Ma[2], Yu Zhu[1], Gang Wang[1], Peng Ye[3]

[1] State Grid Liaoning electric power research institute, Shenyang, 110006, China

[2] Electrical Engineering Department Shenyang University of Technology, Shenyang, 110870, China

[3] Electrical Engineering Department Shenyang Institute of Engineering, Shenyang, 110136, China

Keywords: peak load regulation mode; nuclear power plant(NPP); coordinated operation

Abstract: Based on extensive research, introduced the peak load regulation characteristics and capacity of different nuclear power plant (NPP) in this paper. The running mode of NPP participating in peak load regulation of power system, combined operation tactics of NPP with other peaking power source and synergistic scheduling of an integrated power generation system with wind, photovoltaic, energy storage unit and NPP were summarized, technology development trend of NPP participating in peak load regulation of power system was analyzed and forecasted.

I. Introduction

The power grid urgently needs a new economic and efficient energy to join. Because of wind power, solar power, tidal power and all kinds of new energy have the problem of large-scale power generation and economy, so accelerate the development of nuclear power has become an inevitable choice to solve the problem of China's power supply. According to the national "long-term nuclear power development plan", the new 30-million-kilowatt nuclear power plant, the total installed capacity of nuclear power reach 58 million kilowatts and 30 million kilowatts under construction in 2020. In the future, nuclear power will become a main power supply and will occupy more and more proportion.

In recent years, the rapid growth of China's electric power load and the gradual wideness of peak -valley difference have brought greater pressure to the power network construction and operation. Due to the growth of the proportion of nuclear power in electric network, power system demands for nuclear power participate in power grid peak shaving is growing. Nuclear power can participate peaking operation, nuclear power peaking operation involved in what manner, the balance of power peaking will be what kind of impact has become a problem requires a high degree of concern. While the new energy in the grid and the rapid growth of network capacity, joint operations and coordination between the various power controls has become a key issue in modern grid operation. Nuclear power plants with other power peak load regulating operation for the joint in the system, the coordination of joint store nuclear power generation system scheduling and intelligent control is the future of NPP to participate in the operation of the technology development direction.

Firstly, the various types of nuclear power load characteristics and load capacity of the unit were introduced in this paper. Secondly, the NPP's operation tactics combined with other peaking power source and synergistic scheduling of an integrated power generation system with wind, photovoltaic, energy storage unit and NPP were summarized. Finally, technology development trend of NPP participating in peak load regulation of power system was analyzed and forecasted.

II. The Situation of NPP Peak Load Regulation

Countries around the world especially focus on the peak load regulation of power grid, since the 1970s, the United States, Germany, France, Japan and other countries have implemented load tracking test and practical operation of pressurized water reactor (PWR), boiling water reactor and the improved thermal reactor nuclear power reactor type [1-5]. Pressurized water reactor more than 40 years of daily load tracking operation experience showed that daily or weekly load tracking has

no adverse effect the performance of the fuel, the circuit of the coolant radioactive concentration not rise, verify the reliability and feasibility of daily load-following operation of PWR [6-9].

Foreign peaking running instance was shown in Tab.1.

Tab.1 Foreign peaking running instance

countries	Type of reactor	summary	Output rate of change in a minute
The US	Pressurized water reactor Boiling water reactor	often implement between 50% to 100% load operation of the output range every day	Around 0.25%-1%
French	Pressurized water reactor	often implement between 40% to 100% load operation of the output range every day	Highest 5%， Usually 3%
Germany	Pressurized water reactor Boiling water reactor	often implement between 50% to 100% load operation of the output range every day	5%-10%

Our country existing nuclear power plants are built in the eastern or southern coastal developed areas, near the load center. Because of east and south China power grid capacity great, nuclear power installed capacity for a small proportion, local power shortage perennial, plan to maximize the power plant unit annual utilization hours, take maximum economic benefit of nuclear power construction, also based on the various consideration of nuclear power plant and power grid safe operation, at present, in addition to the first phase of Qinshan, Dayawan and the first phase of Lingao nuclear power plants in the past two years the Spring Festival, National Day and other special load days down load operation to peak load regulation, other nuclear power plants in any heap shape and size, are not to participate in power grid peak load regulation.

However, as the growth of NPP and increase of peak-valley difference, wind, photovoltaic and other renewable energy, electric power system load situation more and more serious, the domestic many units have been conducted on the feasibility study of nuclear power to participate in power grid peak load regulation [10-12], growing demand for nuclear power plants in power grid peak load regulation.

III. Peak Load Regulation Mode of NPP

Once nuclear power are required to participate in peak shaving, Not only for the safe operation of NPP challenges, but also will have great influence on its economy [8], [13,14]. To alleviate the pressure of the system load, nuclear power plants are usually adopting the following three ways to participate in peak load regulation:

(1) Reasonable arrange the refueling outage time

After running a power generation cycle, nuclear power plants will be offline and the new fuel component replaced spent fuel components. During the refueling time, Nuclear power plants refuel overhaul of plant in order to maintain and improve equipment operating characteristics, to ensure the safety stability of the unit in the next cycle operation. Refueling overhaul of the plants in the winter can improve the operation rate of thermal power plants, the corresponding adjustable power ratio and the load capacity of the system. In this way, nuclear power participation in the system peaking makes its economy influence down to the minimum and easily to implement. It is a commonly used of current scheduling winter peak load regulation.

(2) Load following peaking

① Modern pressurized water reactor could be designed for a larger negative temperature coefficient. When the load increases, the core cools down will automatically increase the power, run and maintain the power levels, improve the ability of nuclear track to unit load, reducing the demand for reactor power regulating system, such as accuracy, etc.;

② In response to the transient changes increase unit margin, on the design of unit, load linear change plus or minus 5% plus or minus 10% Pn/min or step change of Pn cases, one, two loop

safety protection device is not action, rely on the automatic adjustment to keep the unit stable operation;

③ The use of advanced control system and improve nuclear track load capacity. Using reactor and coordinated control of the steam turbine unit make a change, in the secondary circuit working condition, and large disturbance in cases such as the main process parameters of smaller, higher safety margin, fully digital instrument control system, which makes nuclear power units to load change of the parameters in the process of quality control is more ideal.

(3) Compression load operation in special day

In the case of system adjustable power supply dwindling, with power system peak-valley difference increasing, the load demand is more and more serious. If NPP can't peak load regulation, it needs to compression load operation to improve the boot capacity of hydropower and thermal power adjustable power supply in special load day, increase the peak load regulation capacity of the system.

IV. Combined Operation Tactics of NPP and Other Power Source

There are various modern power grid, and it is complementarily between the power on operating characteristics. Based on operating characteristics various power supply, considering the security constraints and system operating constraints of various power supply, order to safe and economic operation of the grid, we can combine to determine the power peaking mode of operation and coordinated control strategy through optimization methods.

A. NPP Directly Involved in the Daily Load Peaking Regulation

Modern Nuclear power plant have a excellent load following capability, but considering the safety of nuclear power itself and peaking speed and depth limit of NPP, the PWR nuclear power plant generally take "12-3-6-3" mode of power regulation, as shown in fig.1.

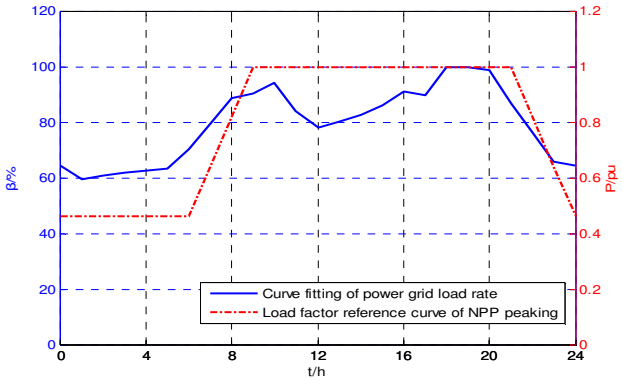

Fig.1 Mode of NPP participating in peak load regulation of power grid

The mode of power regulation of NPP in fig.1 can meet the requirements of peak load following, more in line with the trend of power grid load, the depth and speed of power regulation meet the constraints of NPP, actually it should order to the actual operation of NPP as a reference to determine the depth and speed of peak load regulation.

B. Combined Operation of NPP, Hydropower and Thermal Power

Hydropower, thermal power coordination and joint optimization of operation of nuclear power is a hot issue at home and abroad in recent years. The traditional short-term optimal operation of hydro-thermal model of the joint is usually simple to system operating costs a minimum of the objective function, to determine a certain period of time hydropower, thermal power joint power generation plan of the unit. However, a variety of joint supply planning to introduce nuclear energy structure after it is transformed into a high dimension, nonlinear, multi-constraint multi-objective optimization problem, it consider more factors, system load demand, spinning reserve, the unit output nonlinear characteristics, unit start-stop frequency and duration, flow, output and storage

constraints, the views of experts and decision-makers, and so generally include, It is a large-scale, mixed integer optimization problems.

NPP, hydropower and thermal power combined operation reasonable load distribution shall be: First let's hydropower bring the peak load of the power system, NPP bring the base-load, thermal power balance the load-left, if thermal power does not meet the speed range of the motor group climbing, we will change the power regulation mode of NPP based on thermal power ramp rate and the remaining load characteristics, determine the depth and mode of nuclear power peak load regulation. This will not only avoid abandoned water peaking of hydropower, but also ensures that the thermal power run the optimal regulation.

C. Combined Operation of NPP and New Energy Unit

(1) Combined operation of NPP and Pumped storage power plant

Pumped-storage plant has two major characteristics [15, 16]: Flexibility to switch between power generation and consumption for power system reduces the gap between peaks and troughs and double peaking capacity; the plant starts fast, flexible, reliable and able to respond quickly to changes in network load. It can assume the grid frequency, phase modulation, emergency reserve, black start and so on.

The paper [17] has analyzed the issue of nuclear power and pumped storage plants participating in jointly power peaking. According to the operating characteristics of pumped storage plants, three models of nuclear power and pumped storage power joint peaking were presented: complete tracking mode, three sections of the system tracking mode and incomplete tracking mode. Through simulation analysis proved that nuclear power and pumped storage plants jointly run power peaking can satisfy the requirements, and ensured the safe operation of nuclear power plants with base-load, with high economy.

(2) Combined operation of NPP, wind power, photovoltaic and energy storage unit

Currently, there are many studies on wind power, photovoltaic power generation and energy storage technologies [18-20], unlike conventional power, wind power and photovoltaic power generation has random, volatility and intermittent characteristics. In addition, the technical bottleneck of forecasts, scheduling and control made it different from conventional power in independent source of power generation characteristics and network coordination compared with. When wind power, photovoltaic power generation and other large-scale renewable energy power system access to power system, the traditional plant’s ramp rate often do not meet the requirements of dramatically and power fluctuations of short duration caused by renewable energy. Joint operation of wind, photovoltaic, energy storage plants and NPP can effectively weaken the fluctuations caused by wind power and photovoltaic power generation with alleviated stress of power peaking.

For example, a region’s power system contained nuclear power, wind power, photovoltaic power generation and energy storage power station. The four forms Combined to track grid load. During the day the wind power generating capacity is usually small, and the large amount of photovoltaic power generation. To ensure the operation of photovoltaic full generation power with base-load，the nuclear power should be adjusted according to changes of photovoltaic. When photovoltaic generation in large, the nuclear power will properly reduce operating. Energy storage units store energy in the load trough. Photovoltaic power plants do not generate electricity at night, but wind power is sufficient and volatile. The nuclear power should be adjusted according to changes of wind power. Storage or generation of energy storage power station needs to be based on load conditions.

V. Conclusion

Nuclear power load for optimizing the power structure, speed up the non-fossil energy alternatives to fossil energy has the effect that cannot replace. NPP has larger peak shaving depth and load capacity, can assist to complete the grid load demand. the peak shaving benefits include:

(1) To improve the safety margin of the power system operation and scheduling flexibility, better adapt to all kinds of uncertainty factors;

(2) To reduce the thermal power load pressure; Drop the thermal power key; Bring down the high cost of fuel gas and fuel power generate operation cost;

(3) To improve clean energy such as wind power and photovoltaic power generation access scale and efficiency.

Based on the analyze of all kinds of nuclear power peaking capacity and regulating mode , the NPP's operation with other peaking power source and synergistic scheduling of an integrated power generation system with wind, photovoltaic, energy storage unit were summarized. Provides a reference for future nuclear power peaking. Joint operations and coordination between various power control is to ensure grid security, stability and economic operation.

Acknowledgement

The Science and Technology Program：Nuclear Power Plant Participate in Peak Load Regulation of Power System and Research of Combined Operation with Wind Light and Energy Storage,2014YF-22.

References

[1] Berkovich V M, Gorokhov V F, Tatarnikov V P. Possibility of regulating the capacity of a power system by means of nuclear power plants[J]. Teploenergetika,1974(6):16-19.

[2] Grum A. Design of nuclear power plant with pressurized water reactor for optimum load follow capability[J]. Atomkernenergic Kerntechnik,1986,48(3):138-143.

[3] Levent A H, Altin V. Rule-based fuzzy logic controller for a PWR-type nuclear power plant[J]. IEEE Transactions on Nuclear Science, 1991, 38(2):883-890.

[4] Christenson J M. Application of optimal control theory to a load following pressurized water reactor[J]. Nuclear Technology,1992,100(3):361.

[5] Wu Guo-wei, Tao Jin. Research of Load Follow for Nuclear Power Plant with Pressurized Water Reactors[J]. Nuclear Power Engineering, 1998, 19(5):394-397.

[6] Ge Bin, Wu Yi[J]. A Study on a real-time simulation for the second loop of PWR nuclear power unit[J]. Proceedings of the CSEE, 2002, 22(6):142.145.

[7] Wu Ping, Liu Di-chen, Zhao Jie, et al. Fuzzy adaptive PID control-based load following of pressurized water reactor[J]. Power System technology, 2011, 35(4):76-81.

[8] Zhao Jie, Liu Di-chen, Wu Yao-wen. Modeling of pressurized water reactor nuclear power plant integrated into power system simulation[J]. Proceedings of the CSEE, 2007, 29(31):8-13.

[9] Zhang Xue-cheng, Hu Xue-hao, Zhou Xiu-ming, et al. Development of MID term dynamic simulation program including nuclear power plant model and study of interaction between large nuclear power plant and power system[J]. Power System technology, 1995, 19(2):5-10.

[10] Ma Xi-peng. Discussion on large-scale PWR power plants participating in sufficing peak- load of Grid[J]. Shandong DianLiJiShu, 2007(6):35-40.

[11] Chen Han-xiong, Zheng Yong. Adaptability of large-capacity nuclear power plants accessing Sichuan and Chongqing grids and ability of participating in system peak-load regulation[J]. Electric Power, 2011, 44(3):1-5.

[12] Zheng Xiu-bo, Liu Yun, Sun Jing-qiang. The peak load regulation of nuclear power plant in Guangdong power grid[J]. Electric Power Technology, 2010, 19(13-14):82-85.

[13] Brendan K, John K, Harvey L, et al. Nuclear Generating Stations and Transmission Grid Reliability[C] //2007 39th North American Power Symposium. Las Cruces, USA:Power Engineering Society, 2007:279-287.

[14] Maldonado G I. The performance of North American nuclear power plants during the electric power blackout of August 14, 2003[C]//Nuclear Science Symposium Conference. Rome, Italy:IEEE,2004:4603-4606.

[15] He Yongxiu, Yang Weiwei, Lu Yu, et al. Peak-load regulation and emergency response function of weekly adjusted pumped storage station in Beijing-Tianjin-Tangshan Power Grid[J]. Power System Technology, 2006, 30(19):71-75.

[16] Yang Jingyan, Fu Zhikui. A model and arithmetic for the planning of pumped-storage power plant[J]. Proceedings of the CSEE, 2001, 21(2):33-36.
[17] Zhao Jie, Liu Di-chen, et al. Analysis of Nuclear Power Plant Participating in Peak Load Regulation of Power Grid and Combined Operation With Pumped Storage Power Plant[J]. Proceedings of the CSEE, 2011, 31(7):1-5.
[18] Li Bi-hui, Shen Hong, Tang Yong, et al. Impacts of energy storage capacity configuration of HPWS to active power characteristics and Its Relevant Indices[J]. Power System Technology, 2011, 35(4):123-128.
[19] Wang Hao-huai, Tang Yong, et al. Composition modeling and equivalence of an integrated power generation system of wind, photovoltaic and energy storage unit[J]. Proceedings of the CSEE, 2011, 31(34):1-9.
[20] Liu Xia, Jiang Quan-yuan. An optimal coordination control of hybrid wind/ photovoltaic/ energy storage system[J]. Automation of Electric Power Systems, 2012, 36(14):5-100.

Advanced Materials Research Vols. 986-987 (2014) pp 202-205

doi:10.4028/www.scientific.net/AMR.986-987.202

An Empirical Analysis on Guangdong's FDI, Energy Intensity and Industrialization

Xin-lin Liao

School of Economics and Management, Wuhan University, Wuhan, China

2602882823@qq.com

Keywords: FDI, energy Intensity, industrialization, Guangdong

Abstract. Energy is the base of modern industrial economy. Basing on the data of cities and industries in Guangdong from 2000 to 2013, this paper analyzes the relationship of energy intensity, FDI and industrialization by regression model. The results show that the industrialization levels of the cities in Guangdong are in accordance with their energy consumption and economic conditions, and Guangdong should focus on the development of "win-win" industries which both increasing industrial output and reducing energy efficiency.

Introduction

Guangdong's industrialization has made great progress and its energy industry has also witnessed rapid growth since the reform and opening-up policy was introduced. With the rapid industrialization and urbanization, the high energy-intensive industries has accounted for a big proportion in Guangdong.

Many scholars have given sustained attention to China and Guangdong's energy and industrialization, a brief literature review as follows. He and Zhang(2005) insisted that the main reason for the rise of energy intensity in recent years in China was the rapidly development of industry, especially heavy chemical industry, which leading to massive increase in industry energy consumption[1]. Fisher-Vanden(2006) found that production structure changes was one of the major factors for the decline of energy efficiency in China[2]. Hu and Wang(2006) analyzed the energy efficiencies of 29 administrative regions in China for the period 1995–2002. By the data envelopment analysis (DEA), they tried to find energy input of each region in China, and insisted that the energy efficiency in China would eventually improve [3].

Yu(2007)pointed out that Guangdong was the lowest province of unit GDP energy consumption in China, and the main driving force for the decrease of Guangdong's energy intensity comes from the improvement of industry energy efficiency. He suggested that Guangdong should move on to adjust and optimize the industrial structure, raise the energy-saving technological and improve the industrial energy efficiency [4]. Zhang(2010) employed the panel data of 30 provinces, cities and autonomous regions in China and by the SFA method to compare the energy efficiency, industrial structure and development gap of them from 1990 to 2008. The conclusion was that the energy efficiency of the eastern region is the first, the middle region is the second, and the western region is the third. He insisted that more attention should be paid to optimize the industrial structure [5]. Zhu, Cao and Luo(2013) suggested that the evolution of the industrial structure is one of the important factors to affect energy efficiency, and China economy would rely on extensive and high energy consumption in a long time[6].

Empirical Analysis

Set of Model. The empirical analysis of this paper bases on the panel data of the 21 Guangdong cities' industries from 2000 to 2013. First, I divide the Guangdong 21 cities into four economic regions, named the Pearl River Delta, the east wing, the west wing and the mountain area. Among them, the Pearl River Delta includes Guangzhou, Shenzhen, Zhuhai, Jiangmen, Dongguan, Foshan, Zhongshan, Huizhou and Zhao Qing; the east wing includes Shantou, Shanwei, Chaozhou and

Jieyang; the west wing includes Zhanjiang, Maoming and Yangjiang and the mountain area includes Shaoguan, Heyuan, Meizhou, Qingyuan and Yunfu.

Then I select 36 representative industrial sub-sectors which as follows: universal equipment manufacturing industry, oil and gas mining industry, transportation equipment manufacturing industry, tobacco manufacturing industry, recycling and disposal of waste industry, instrumentation and culture, electrical machinery and equipment manufacturing industry, office equipment manufacturing industry, pharmaceuticals manufacturing industry, garments, shoes, special equipment manufacturing industry, caps manufacturing industry, beverage manufacturing industry, leather, furs, feathers manufacturing industry, food manufacturing industry, handicrafts Manufacturing industry, nonferrous metals mining industry, ferrous metals mining and extraction industry, furniture manufacturing industry, printing and copying industry, sporting articles manufacturing industry, metal products industry, chemical raw materials manufacturing industry, nonmetal mineral mining and extraction industry, plastic products industry, nonferrous metals smelting and rolling processing industry, agro-food processing industry, wood, bamboo, timber processing industry, rubber products industry, chemical fiber manufacturing industry, water processing and supplying industry, hot power producing and supplying industry, papermaking and paper products industry, oil processing, textiles industry, electric power, coking and nuclear fuel processing industry, nonmetal mineral products industry, gas producing and supplying industry, ferrous metals smelting and rolling processing industry.

In terms of analysis method, first is the test and regression of the four economic regions, then to synthetically study the regression results. The data come from the Guangdong Statistical Yearbook, all the analysis will be done with the help of Eviews6.0.

I established a logarithmic model which taking energy intensity as dependent variable, FDI and industrialization index as independent variables.

$$\ln EI_{it} = \alpha_i + \beta_i \ln FDI_{it} + \gamma_i \ln IND_{it} + \delta_i \ln ING_{it} + \varepsilon_{it} \quad (1)$$

Among them, EI, FDI and IND respectively represent the energy intensity, the foreign direct investment and the industrial coefficient, in which the unit GDP energy consumption indicates the EI, the value-added of foreign-funded industrial enterprises above designated size indicates the FDI and the per capita GDP indicates the IND. In addition, I take the industrial structure variable as control variables. The industrial structure represented by the proportion of industrial added value and GDP (ING). The subscript *i* and *t* respectively represent the city and the time, *e* as a random disturbance term.

Type and Test of Model. First is the Hausman test. The Hausman test can be used to determine that, the fixed effect model and random effect model, which should be employed. The Hausman test results show that all the test coefficients of the four regions were less than 0.05 probability, therefore, the null hypothesis were rejected at 5% significance level, so I may conclude that the fixed effects model is better than the random effect model in this paper and the fixed effects model should be adopted. In econometrics and statistics, a fixed effects model is a statistical model that represents the observed quantities in terms of explanatory variables that are treated as if the quantities were non-random. Then with the help of the F test, I can determine which kind of the fixed effect models should be adopted. Take the Pearl River delta as example.

$$F=\frac{(SSE_r - SSE_u)/(N-1)}{SSE_u/(NT-N-1)}=\frac{(16.52565-0.318422)/(9-1)}{0.318422/(9\times 9-9-1)}=452.21 \quad (2)$$

Because $F=452.21 > F_{0.05}(8,71)=2.08$, therefore, reject the null hypothesis, an individual fixed effects model should be established. With the same method, I get the F values (19.76, 275.96 and 83.24) of the other three regions. Such results tell us that all the null hypothesis of the four regions should be refused, and the fixed effects model should be adopted.

The unit root test is the standard method of statistical sequence equilibrium. In order to avoid the negative effects of the unit root test method and its test results, the unit root test of this paper will use three kinds of methods, named LLC, Fisher-ADF and Fisher-PP. The test results of the Pearl River Delta region show that lnEI, lnFDI, lnIND and lnING not reject the null hypothesis of unit root, all of

them are random processes of unit root. Adopting the same method of unit root test to the other three regions, I find the results are same. The result of unit root tests in Table 1. The cointegration test results of the four regions show that their residual series are stable, and reject the null hypothesis of no cointegration relationship.

Table 1 The results of unit root test

Variables	Level value			Variables	Second order differential value		
	LLC test	MW test	PP test		LLC test	MW test	PP test
lnEI	-39.392 (0.000)*	59.094 (0.041)**	88.549 (0.000)*	lnEI	-452.815 (0.000)*	174.410 (0.000)*	172.936 (0.000)*
lnFDI	-0.084 (0.466)	23.343 (0.991)	36.145 (0.724)	lnFDI	-26.371 (0.000)*	144.532 (0.000)*	145.298 (0.000)*
lnIND	-4.286 (0.000)*	22.746 (0.993)	66.492 (0.009)	lnIND	-13.869 (0.000)*	139.714 (0.004)*	150.999 (0.000)*
lnING	-12.823 (0.000)*	111.039 (0.000)*	202.874 (0.000)*	lnING	-14.671 (0.000)*	138.189 (0.000)*	140.918 (0.074)***

Notes: (1) the arentheses values are probability. (2) * ,**,*** denote statistical significance at the 10%, 5% and 1% levels respectively.

Table 2 The regress results of the four regions of Guangdong

Variables	Pearl River Delta	East wing	Variables	West wing	Mountain area
lnIND	-0.812637 (-15.0356) ***	-0.421409 (-1.9153) *	lnIND	-0.589438 (-8.3407) ***	-0.588277 (-5.1495) ***
lnING	0.240806 (4.1135) ***	0.565673 (2.2810) **	lnING	0.669782 (5.0931) ***	0.422002 (4.9089) ***
lnFDI	0.424228 (12.0463) ***	0.150757 (3.2437) *	lnFDI	0.056501 (2.4980) **	0.090955 (1.7204) *
Adj-R2	0.975454	0.820713	Adj-R2	0.944139	0.907125
F	290.0228	16.05321	F	88.88846	0.889554
DW	0.908614	0.959534	DW	1.694560	0.898564

Note: the values in brackets are *t* value.

Regress Results. The regress results of the four regions of Guangdong in Table 2. As shown in Table 2, all the estimated values of all coefficients belong to the state of significant in the level of 1%, 5% or 10%, and the T values pass the test. The fitting is high, and the explanatory ability of the model is strong. In a word, there is the long-term relationship between the variables of the model.

Conclusion

Table 2 shows that, to the four regions in Guangdong, all the regress coefficients of industrialization index variables are negative, what suggesting that their industrialization index were inversely proportional to their energy intensity, and their energy intensity constantly lower with the progress of industrialization. The regress coefficients of the industrial added value proportion and the FDI are positive, what means that the energy intensity would increase with the increase of the proportion and the total volume. The Pearl River Delta region, for example, has the highest industrial index regression coefficient and the lowest industrial added value proportion regression coefficient, which indicating that its energy utilization efficiency is the highest across Guangdong. The regress result tell us that, as the most developed region in Guangdong, the industrial structure of the Pearl River Delta is also the most conducive to reducing energy intensity.

At the same time, the FDI regress coefficient of the Pearl River Delta is the highest, what means that its foreign-funded industrial enterprises above designated size have relied too much on high energy consumption industries and products. According to the regress coefficients of the other three regions, their industrialization levels in accordance with their resource endowment and economic conditions. In the aspect of reducing energy intensity, the Pearl River Delta and the other three regions have theirs relative merits, should learn from each other.

References

[1] J. K. He and X. L. Zhang: Analysis on the Impact of the Structural Changes in the Manufacturing Industry on the Rising of Intensity of GDP Resources and its Trend, Environmental Protection, Vol. 12(2005), p. 37.

[2] K. Fisher-Vanden, G. H. Jefferson and M. Jingkui: Technology development and energy productivity in China, Energy Economics, Vol. 28(2006), p. 690.

[3] J. L. Hu, and S. C. Wang: Total-factor energy efficiency of regions in China, Energy Policy, Vol. 17(2006), p. 3206.

[4] P. G. Yu: Analysis on the Factors of Energy Intensity in China: Take Guangdong as a Case, Academic Research, Vol. 2(2007), p.74.

[5] W. S. Zhang: Energy Efficiency, Industrial Structure and Regional Economic Development in China, Journal of Shanxi Finance and Economics University, Vol. 8(2010), p. 63.

[6] S. Q. Zhu, W. D. Cao and J. Luo: Research on Regional Differences of Mechanism of Energy Efficiency Response to Industrial Restructuring in China, Human Geography, Vol. 28(2013), p. 118.

Advanced Materials Research Vols. 986-987 (2014) pp 206-210

doi:10.4028/www.scientific.net/AMR.986-987.206

An Improved FCM Algorithm Based on Subtractive Clustering for Power Load Classification

Rui Dong[1,a], Mingxiang Huang[2,b]

[1]Department of Electrical Engineering, Zhejiang University, Hangzhou 310027, China;

[2]Department of Electrical Engineering, Zhejiang University, Hangzhou 310027, China.

[a]dong.rui3@163.com, [b]huangmx@zju.edu.cn

Keywords: power load classification; subtractive clustering; fuzzy C-means algorithm(FCM).

Abstract：FCM is used in many power load classification currently, but it also has some shortcomings. This paper give an algorithm based on Subtractive Clustering and improved Fuzzy C-means Clustering (SUB-FCM) to solve this problem. This algorithm use subtractive clustering to initialize the cluster center matrix, solve the random initialization of FCM, and improve the global search ability, avoid falling into local optima. Experimental analysis found this algorithm also could accelerate the convergence speed, and has better clustering results. It can be applied to power load classification effectively.

Introduction

With the deepening of the electric power system reform and the economics of electric power development, the trend of the future is to establish a categorized time-of-use(TOU) power price. It will help to develop the peak shaving capability of the user[1], and optimize the configuration of the electric power resource. Categorized TOU power price means to develop different TOU power price for different load characteristics of power users[2], so it has to classify the load characteristics. The so-called load characteristic classification is merge consolidated load in the same power network which have similar load characteristics into one class. And the key is the choice of load characteristics and the classification method[3].

In the early 1990s, british scholars began to study the load classification problem to develop a reasonable pricing scheme[4].Since then, the study of load

classification method is more and more deeply, and the clustering analysis method occupy the dominant position. Compared with system clustering, K-means clustering algorithm[5], clustering algorithm using the SOM neural network[6], clustering analysis based on ant colony optimization algorithm[7], fuzzy C-means clustering(FCM)[8] introduced a membership function for dividing the data softly. The method can reflect the clustering results more objectively, therefore, it is widely used in electric power load characteristics category. Literature [9] study the real power data classification using FCM and clustering validity function. But FCM is a local search algorithm, it is sensitive to initial value, easy to get the local optimal solution, and the clustering number is difficult to be identified. In order to solve this problem, literature [10] took the hypothesis testing method to determine the clustering number, but this method is very tedious and the calculation speed is very slow. Literature [11] put forward a simulated annealing genetic algorithm based fuzzy C-means (SAGA-FCM) to improve the global search ability, but it still failed to select the initial parameters. Literature [12] proposed an improved algorithm based on differential evolution (DE) adaptive optimization to reduce the dependence on initial value.

In view of this, the paper put forward an improved FCM algorithm based on subtractive clustering (SUB-FCM)[13] to application for load classification under the background of the smart grid. Subtraction clustering provides a new way to solve the problem of the FCM initial value. Find the initial clustering center with subtraction clustering before using FCM, can avoid falling into local optimal solution, improve the clustering speed, and generate a better clustering number automatically.

Algorithm description and improvement strategy

FCM Algorithm. In 1981, Jim Bezdek proposed FCM, the core idea is to determine the extent of each data point belongs to a cluster with membership[14]. Randomly selected a cluster center number first, and then calculate the optimal cluster center by iteration, make the weighted squared error function from each sample to each cluster center in a class reaches a minimum.

FCM divides the n data vectors $x_i(i = 1,2,\dots,n)$ into c fuzzy groups, if sample sets for U, cluster center for V, so the objective function can be expressed as:

$$\min J_m(U,V) = \sum_{k=1}^{n}\sum_{i=1}^{c}(u_{ik})^m (d_{ik})^2 \tag{1}$$

where m is the fuzzy factor which is used to control the degree of sharing between fuzzy classes. u_{ik} is the degree of membership about the kth data in the ith cluster and it satisfied: $d_{ik} = \|x_k - v_i\|$ is the distance about the kth data to the ith cluster center v_i.

Update the iterative center and membership according to the formula (3) and (4) after the end of each iteration process.

$$v_i^{(r+1)} = \frac{\sum_{k=1}^{n}(u_{ik}^{(r)})^m x_k}{\sum_{k=1}^{n}(u_{ik}^{(r)})^m}, \quad u_{ik}^{(r+1)} = \frac{1}{\sum_{j=1}^{c}(d_{ik}^{(r)}/d_{jk}^{(r)})^{\frac{2}{m-1}}} \tag{2}$$

where r is the iterations number; For a given threshold ρ, if $\left|J^{(r+1)} - J^{(r)}\right| < \rho$, then stop the clustering process. Otherwise, continue iterating until the stop condition is met.

Subtractive Clustering Algorithm. Subtractive clustering method put all sample data as the candidate cluster center point, it's more quick and independent. It is a simple linear relationship with the calculation amount and the number of sample data, and has nothing to do with the dimensions of the problem under consideration[13].

Consider the n data points $x_i(i = 1,2,\dots,n)$ in M dimensional space, then the steps[15] are as follows:

(1)Calculate the density of all data points x_i:

$$D_i = \sum_{j}^{n} exp\left[-\frac{\|x_i - x_j\|^2}{(0.5r_a)^2}\right] \tag{3}$$

where r_a is a positive number which defines the point's radius, and the contribution of the data points outside the radius to the density index is very small, take $ra = \frac{1}{2}\min_k\left\{\max_i\left\{\|x_i - x_k\|\right\}\right\}$. Choose the data point with the highest density as the first cluster center, make x_{c1} for the selected points, D_{c1} for its density index.

(2)Fixed the density indicator of each data point according to the kth cluster center:

$$D_i = D_i - D_{ck} exp\left[-\frac{\|x_j - x_{ck}\|^2}{(0.5r_b)^2}\right] \tag{4}$$

where r_b is a positive number, defines a area its density index function reduced significantly. In order to avoid cluster centers are too close, take $r_b = 1.2r_a$.Choose the data point x_{ck+1} with the highest density as a new cluster center.

(3)Exit condition:

$$\frac{D_{ck+1}}{D_{c1}} < \delta \tag{5}$$

if the condition is not hold, then go to step (2). Where $\delta < 1$ is a given parameter that determines the final number of initialized cluster center, smaller δ cause more cluster number.

An Improved FCM Algorithm Based on Subtractive Clustering. Subtractive clustering can select cluster center according to the density index directly. Subtractive clustering and FCM

combines in this paper, use the result of subtractive clustering as the initial cluster center of FCM, ensure that the final result is a global optimal clustering solution.

Using subtractive clustering, the order of the cluster center is determined by the density index, the data point with the higher density will appear earlier, and it will be more likely the reasonable improved initial cluster center. Therefore, when the cluster number is c, just use former cluster center generated by subtractive clustering as the new initial center, thus improve the efficiency of clustering. Flowchart of SUB-FCM is as follows:

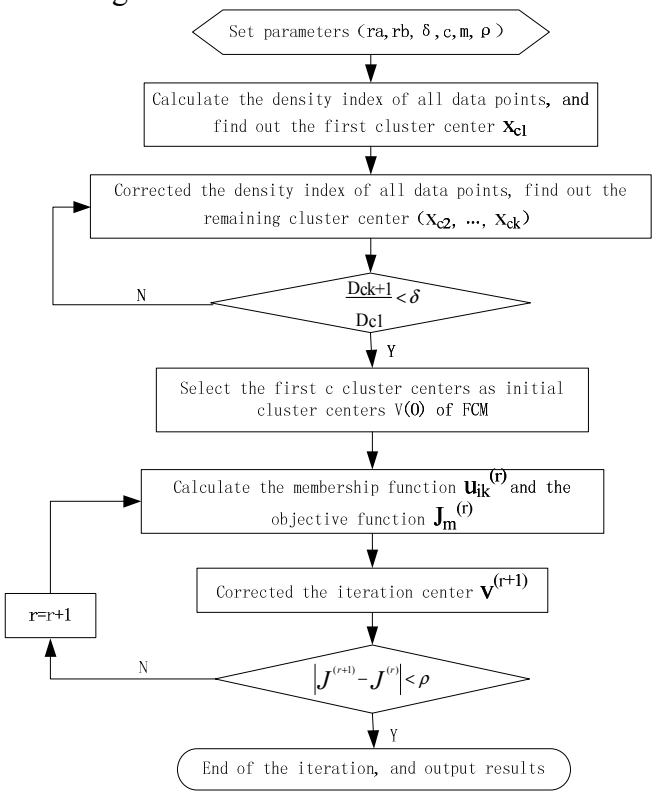

Fig 1. Flowchart of SUB-FCM

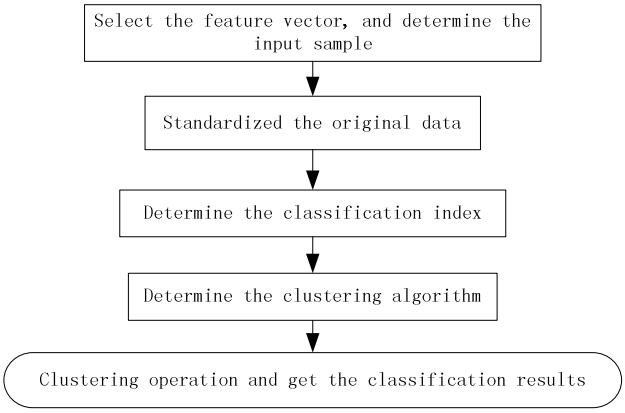

Fig 2. Model of load characteristics classification

Power load classification based on SUB-FCM

Model of Power Load Characteristics Classification. Load characteristics classification is that analysis the same or similar load samples in essentially, it is the basis of the power system planning, peak management, TOU electricity price and load forecasting. Its model is shown as Figure 2.

In order to get a good classification results, the selection of feature vector in the model should be able to reflect the essential characteristics of an object. In engineering practice, generally use run or time feature vector. In addition, raw data should be standardized before clustering calculation, in order to avoid the impact of different units and magnitude of the original data. Generally, range normalization method can be dealed with it. And the main classification indicators are description, comparison and curve. Finally, choose a suitable clustering algorithm to classify.

The Practical Problems of SUB-FCM.

(1) c is the clustering number, namely the cluster validity problem. The optimal clustering number can be determined through effective calculation, to ensure the minimal compactness and the maximum separation.

(2)The determination of other parameters. The selection of the best fuzzy weighted index m is lack of theoretical guidance currently. The larger m lead to more fuzzy result, so the value of m should not be too large. So this paper take $m = 2$, and the neighborhood $r_a = 0.5, r_b = 0.6$ cause the larger r_a, r_b lead to less clustering number. And proportion parameter $\delta = 0.5$, allow the minimum error $\rho = 1e-5$, the maximum iteration number is 100.

Analysis of examples

The paper take consolidated load characteristic data of substations in a grid somewhere to carry out the analysis of examples, and the results were compared with the traditional FCM. The original data from six major industries which are electricity typical users of, and it has been standardized. The optimal clustering number is known as $c = 7$ [11].

Search Strategy Comparison.

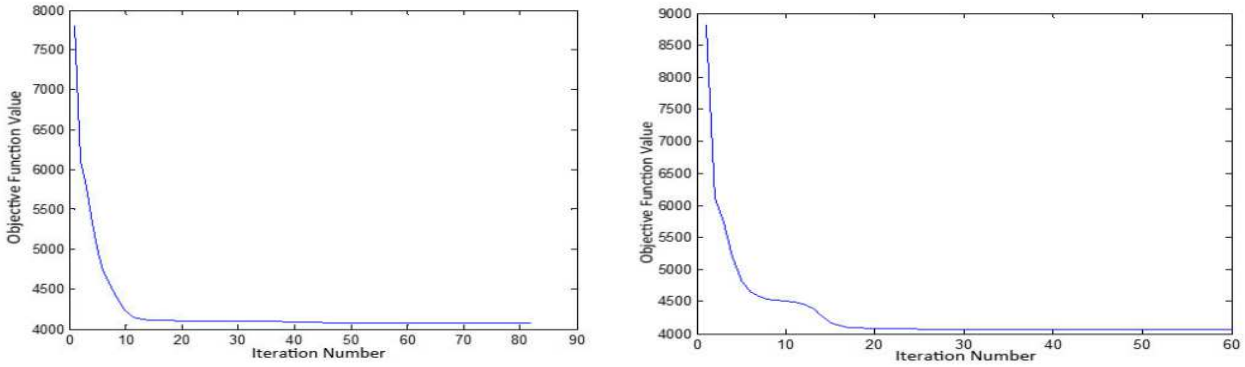

(a)FCM (b)SUB-FCM

Fig 3. Evolution curve of objective function values

Comparing figure 3(a) and (b), it can be seen that the evolution curve of objective function value of the traditional FCM is smoother, it means its easy to fall into local optimal solution. And the evolution curve of SUB-FCM appeared obvious repeated, which can avoid local minimum convergence result effectively.

From the search speed, the FCM have the final result after iteration 83 times, while the SUB-FCM only need 60 times. It shows that SUB-FCM requires less iterations, and can improve the search speed.

In addition, the objective function value of FCM eventually converge to 4098.5162, and the SUB-FCM converge to 4068.3601. The optimal solution of SUB-FCM is less than FCM, shows that the SUB-FCM has better clustering results.

Clustering Effect Comparison. Cluster validity problem is about whether the fuzzy clustering results are reasonable, and now many functions have been proposed for testing the clustering validity. A good classification requires smaller intra-class compactness and larger between-class separability.

Using cluster validity function v_{XB} [17] proposed by Xie and Beni, and v_{FP} [18] proposed by Fan Jiulun which is based on the probability distribution to test the validity of the results. Under the same clustering number, the value of v_{XB} and v_{FP} should as small as possible.

Table 1. Results of validity assessment

Algorithm	v_{XB}	v_{FP}
FCM	0.2991	0.0018
SUB-FCM	0.1551	0.0014

As can be seen from Tab.1, both v_{XB} and v_{FP} of SUB-FCM are smaller than FCM. It means that SUB-FCM is better than FCM in the same clustering number.

Performance Analysis of Algorithms When *c* Changes. Clustering number c has a great influence on the clustering results. Generally, FCM needs to determine the optimal clustering number by validity functions in advance. The optimal clustering number is $c = 7$ in this paper, and SUB-FCM with subtraction clustering determines $c = 17$ automatically.

Analysis the performance of algorithms by comparing the objective function values and iteration numbers under different value of c. Considering the random initialization of FCM, the following experiments using the average of 10 simulation results for FCM.

When the clustering number is close to the optimal clustering number, the result of two algorithms are basically the same in the case of FCM does not fall into local convergence. With the increase of clustering number, the objective function value of SUB-FCM is smaller than FCM, and it shows that SUB-FCM has better results. Cause the optimal clustering number is unknown in most cases, so use SUB-FCM can get the clustering number directly, and better clustering results.

The iteration numbers of SUB-FCM is always less than FCM, no matter how the clustering number changes. When dealing with complex issues and large amount of calculation, SUB-FCM can improve the computing speed effectively.

Epilogue

This paper apply an algorithm based on Subtractive Clustering and improved Fuzzy C-means Clustering (SUB-FCM) to the power load classification. The algorithm use subtractive clustering to find the initial clustering center, and solve the random initialization of FCM effectively. In addition, the experiment shows that the algorithm can avoid falling into local optima, improve the convergence speed, and has better clustering results.

References

[1] GUO Lianzhe, LI Li, TAN Zhongfu, et al. Time-of-use price design models based on fuzzy demand and users' diverse response[J]. East China Electric Power. 2007, 35(5): 11-15.
[2] LUO Ling. Research on categorized time-of-use power price based on fuzzy c-means clustering[D]. Shandong University, 2013.
[3] LI Peiqiang, LI Xinran, CHEN Huihua, et al. The characteristics classification and synthesis of power load based on fuzzy clustering[J]. Proceedings of the CSEE. 2005, 25(24): 73-78.
[4] Birch A P, Ozveren C S, Sapeluk A T. A generic load profiling technique using fuzzy classification[C]. Brighton, UK: Proceedings of Eighth International Conference on Metering and Tariffs for Energy Supply, 1996. 203-207.
[5] LIU Li, WANG Gang, ZHAI Denghui. Application of K-means clustering algorithm in load curve classification[J]. Power System Protection and Control. 2011, 39(23): 65-68, 73.
[6] LI ZHiyong, WU Jingying, WU Weilin, et al. Power customers load profile clustering using the SOM neural network[J]. Automation of Electric Power Systems. 2008(15): 66-70.
[7] SUN Yaming, WANG CHenli, ZHANG ZHisheng, et al. Clustering analysis of power system load series based on ant colony optimization algorithm[J]. Proceeding of the CESS. 2005(18): 40-45.
[8] DUAN Ru, ZHANG Caiqing, LIU Aifang. Application of fuzzy clutering method in classification of electricity customers[J]. Power Demand Side Management. 2005, 7(5): 18-20.
[9] Prahastono I, King D J, Ozveren C S, et al. Electricity load profile classification using fuzzy c-means method[C]. 43rd International Universities Power Engineering Conference, 2008. 1-5.
[10] ZHOU Kaile, YANG SHanlin. An improved fuzzy c-means algorithm for power load characteristics classification[J]. Power System Protection and Control. 2012(22): 58-63.
[11] ZENG Bo, ZHANG Jianhua, DING Lan, et al. An improved adaptive fuzzy c-means algorithm for load characteristics classification[J]. Automation of Electric Power Systems. 2011(12): 42-46.
[12] XIAO chunJing, ZHANG Min. Research on fuzzy clustering based on subtractive clustering and fuzzy c-means[J]. Computer Engineering. 2005(S1): 135-137.
[13] YU Jian, YANG Minshen. Optimality test for generalized FCM and its application to parameter selection[J]. IEEE Transactions on Fuzzy Systems. 2005, 13(1).
[14] YANG Hao, ZHANG Lei, HE Qian, et al. Study of power load classification based on adaptive fuzzy C means[J]. Power System Protection and Control. 2010(16): 111-115.
[15] ZHANG Xun, DENG Huiwen. On the FCM clustering based on subtractive clustering and cluster validity evaluation[J]. Journal of Chongqing Institute of Technology. 2006(05): 59-62.
[16] FAN Jiulun, PEI Jihong, XIE Weixin. Cluster validity based on possibilistic distribution[J]. Acta Electronica Sinica. 1998(04): 113-115.

Advanced Materials Research Vols. 986-987 (2014) pp 211-214

doi:10.4028/www.scientific.net/AMR.986-987.211

AN Research on Energy Management and Cooperation Performance in Eco-industrial Symbiosis Network

Ya-ling Zou [1, a], Chun-fa Li [1, b], Zhan-dong Yao [2, c], Ying-ying Cao [1, d]

[1]School of Management, Tianjin University of Technology, Tianjin 300391，China

[2]Chip Division, Sanan Optoelectronics Co., LTD, Tianjin 300384，China

[a]zyl89521@yeah.net, [b]chunfali@163.com, [c]1015551241@qq.com, [d]caoying868889@163.com

Keywords: Energy Management; Eco-industrial Symbiosis Network; Cooperation Performance; Structural Equation Modeling

Abstract. With the rapid development of economy and technology, enterprises in eco-industrial symbiosis network (EISN) are facing enormous challenges. However, the emergence and development of EISN is closely tied with the energy management in eco-industrial park (EIP). This paper takes institution construction, allocation and new technology of energy management, cooperation performance and long-term cooperation relationship into research and develops a theoretical model of energy management accordingly. We conduct statistical analysis and Structural Equation Modeling using SPSS17.0 and AMOS17.0 based on 241 valid questionnaires from the EISN enterprise managers. The findings indicate institution, allocation and new technology are significantly positively related to cooperation performance, and cooperation performance has positive significant influence on long-term cooperation relationship. Based on the above results, the relative strategies and suggestions of strengthening energy management to enhance cooperation performance are given.

Introduction

At present, to deal with environment pollution, nations around the world are actively promoting Eco-industrial Park (EIP). Eco-industrial symbiosis network (EISN) as the core organization of EIP discards the higher consumption and waste in traditional way, achieves material recycling, reduces the energy consumption and obtains both economic and environmental benefit [1]. Eco-industrial symbiosis network (EISN) is a special organization of industry. It arouses scholars' research interests, and they explain the competitive advantages of EISN from economic, social and environmental aspects[2, 3, 4]. However, the emergence and development of EISN is closely tied with the energy management in eco-industrial park (EIP).

Wang[5] thinks the level of energy management and energy efficiency is important for the development of enterprises. AN[6] puts out that Study on global energy management system by its mode and feature is helpful to accelerate China's energy reform and to optimize laws, policies, and organizations and function division. Taking this as point, we conduct statistical analysis and develop a theoretical model of energy management. Based on the above results, we put forward the relative strategies and suggestions of enhancing energy management to achieve long-term corporation and play full competition advantages of the whole EIP.

Literature References and Empirical Research

The institution construction is the important basis and safeguard to establish the stable cooperation relation[7]. Between the cooperative enterprises establishing the stable restriction and incentives can limit the cooperation into eligible scope and effectively reduce the energy waste, finally achieve the expected performance of cooperation.

To sum up, this paper generates following hypothesis:

H1: The institution construction of energy management has a positive effect on cooperation performance.

The companies in network points conduct energy allocation by information and technology interaction. The more equal allocation in interaction, the better benefit and cooperation companies can get. To sum up, this paper generates following hypothesis:

H2: The allocation of energy management has a positive effect on cooperation performance.

New technology brings new impetus for enterprises, decrease energy consumption, reduce the cost of cooperation and achieve the desired performance. To sum up, this paper generates following hypothesis:

H3: The new technology of energy management has a positive effect on cooperation performance.

Cooperation is a forecast of the future, there is a big uncertainty. Reasonable energy management makes their relations more closely. The more effective energy management is, the less the conflict exists in cooperation and the higher satisfaction it has, finally, the cooperation will be more effective. To sum up, this paper generates following hypothesis:

H4: The cooperation performance has a positive effect on long-term cooperation relationship.

Based on the above, the theoretical model is shown in Figure 1:

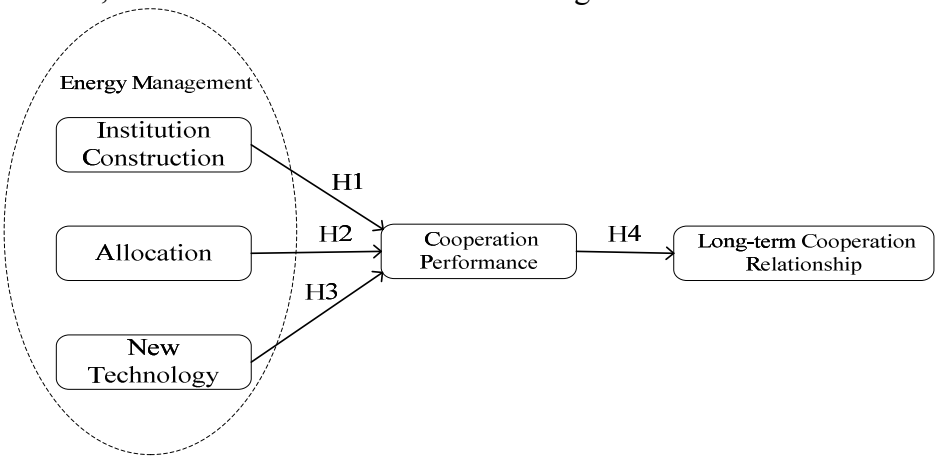

Figure 1 Theoretical Model

This paper uses the questionnaire method and measurement scale should try to come from the improved ones. Finally it has 7 items about institution construction, 9 items about allocation, 5 items about new technology, 4 items about cooperation performance and 4 items about long-term cooperation relationship. It uses Likert-type scale with the score 1 to 5 which represents "perfectly unfitted" to "perfectly fitted". In this paper, the questionnaires get recovered by direct distribution and Email which sends 300 questionnaires and totally retrieve s 172 questionnaires and effective questionnaire returns-ratio is 85.3%. Finally, excluding the incomplete ones, there were 241 valid questionnaires. The sample statistics information of valid questionnaires is shown in Table.1:

Table 1 Sample Statistics Information

	Variable	Frequency /Person	Percentage/%
Gender	Male	116	0.48
	Female	125	0.52
Age	Under 20	0	0
	20-30	99	0.41
	30-40	51	0.21
	40-50	43	0.18
	50-60	48	0.20
	Over 60	0	0
Unit Property	Private Companies	77	0.32
	State-owned Companies	65	0.27
	Colleges	77	0.32
	Other	22	0.09

Cronbach's alpha, exploratory factor analysis and confirmatory factor analysis were performed by SPSS17.0 during the study to test the reliability and validity of the scale, and Cronbach's alpha is shown in Table.2.

Table 2 Cronbach's Alpha

Variable	Number	Cronbach's Alpha
Institution Construction	7	0.819
Allocation	9	0.866
New Technology	5	0.760
Cooperation Performance	4	0.872
Long-term Cooperation Relationship	4	0.755

The analysis showed that every Cronbach's alpha was greater than 0.7, which indicated a higher reliability of the scale, and the reliability could be accepted.

To test the validity of questionnaire, we measured goodness-of-fit of relevant data using AOMS17.0. The relevant indicators, ideal values and acceptable values are shown in Table.3. It can be seen from the table that X^2/df, GFI, AGFI, CFI, NFI, RMSEA and RMR are in an acceptable range, illustrating the higher degree of fitting between the model and data and the better convergence of variables in the model.

Table 3 Fit Results of Validity

	Ideal Level	Acceptable Level	Institution Construction	Allocation	New Technology	Cooperation Performance	Long-term Cooperation Relationship
X^2/df	≤2.00	≤3.00	1.425	1.815	1.850	3.073	1.280
GFI	≥0.90	≥0.80	0.978	0.966	0.982	0.994	0.992
AGFI	≥0.90	≥0.80	0.932	0.903	0.934	0.937	0.960
CFI	≥0.90	≥0.80	0.992	0.977	0.977	0.996	0.999
NFI	≥0.90	≥0.80	0.974	0.952	0.953	0.931	0.994
RMR	≤0.05	≤0.08	0.024	0.025	0.027	0.008	0.015
RMSEA	≤0.05	≤0.08	0.052	0.072	0.073	0.093	0.042

For more in-depth analysis of the relationships between variables in research model, we gave the model further analysis and comparison, and got the model's path coefficients table and the latent variables' path coefficients table by using AMOS software. In this paper, the path coefficients are standardized, and the larger the coefficient is, the more important variable of the path relationship becomes.

Table 4 Path Coefficient between Latent Variable

Path Coefficient	Path coefficient	P value	Result
Institution Construction→Cooperation Performance	0.190	**	H1 Tenable
Allocation→Cooperation Performance	0.336	***	H2 Tenable
New Technology→Cooperation Performance	0.016	***	H3 Tenable
Cooperation Performance→Long-term Cooperation Relationship	0.464	***	H4 Tenable

*p 0.05 ** p 0.01 *** p 0.001

From the Table.4, institution construction, allocation and new technology are significantly positively related to cooperation performance, which means H1, H2 and H3 are tenable. And cooperation performance has positive significant influence on long-term cooperation relationship, which means H4 is H4. However, the path coefficient between new technology and cooperation performance is just 0.016, which indicates that this factor has negligible impact on cooperation performance.

Summary

This paper, from the view point of institution construction, allocation and new technology about energy management, discusses its facilitating roles to promote the cooperation performance in EISN. It can be used as a reference for the management in EISN; in the meantime, we have some experience to following:

(1) Correctly handle the energy management relationship between institution construction, allocation and new technology.

Firstly, institution construction is the basis and assurance in setting up collaboration between EISN companies. But, because of the complex in EISN, too much institution can hinder cooperation activities. Only with the better energy management between allocation and new technology, it can get satisfactory results.

(2) Pay careful attention to energy management, because cooperative relations in EISN is episodic.

The managers in EISN enterprises should do a good job for preventing and eliminating the undesirable energy management that might appear. In a poorly mismanaged energy, it is impossible to produce high quality cooperation performance and long-term cooperation intention between EISN enterprises, and is unlikely to get any success from development. Therefore, the terrible energy management in EISN is the key barrier to interrupt enterprises cooperation activities.

References

[1] Wang Zhaohua. The research on industrial symbiosis network in Eco-industrial Park[D]. Dalian University of Technology, 2002.

[2] Li Chunfa, Li Mengmeng, Wang Qiang, Wang Xiangli. Study on the Relationship of Stakeholders of Eco-industrial Symbiosis Network[J]. Soft Science, 2012, 12(26): 5-9.

[3] Han Shia, Marian Chertowa, Yuyan Song. Developing country experience with eco-industrial parks: a case study of the Tianjin Economic-Technological Development Area in China[J]. Journal of Cleaner Production, 2010, 3(18): 191-199.

[4] Marian R. Chertow. "Uncovering" Industrial Symbiosis[J]. Journal of Industrial Ecology, 2007, 1(11): 11 - 30.

[5] Wang jiamo, Chen Lei, Shi Longyu. Research and Practice on Energy Management of Public Institutions[J]. Standard Science, 2013(9): 89-92.

[6] Haizhong An, Zhong Weiqiong, He Bo, Ding Yinghui. Study on Global Energy Management System[J]. Resources & Industries, 2013, 15(6):1-6.

[7] Leng Junfeng, Ren Shenggang. On the Countermeasures of Institution Construction of RIS of the Central Part[J]. Science Economy Society, 2006, 24(105): 29-32.

Advanced Materials Research Vols. 986-987 (2014) pp 215-218

doi:10.4028/www.scientific.net/AMR.986-987.215

Analysis of Arc Suppression Coil Accident in Fushun Zhongzhai 66kV Substation

Liu Chenyang, Zhang Yunshan, Wang Qinghao, Guan Ling, Zhang Hua, Shan Yi, Liu Guobin, Liu Bo, Li Zhi, Ge Changxin

Fushun Power Supply Company, Liaoning Electric Power Company Limited, State Grid, China,

wts55@126.com

Keywords: insulation breakdown, arc suppression coil, oil chromatography, infrared detection

Abstract. Through the analysis of 66kV arc suppression coil smoke accident in Fushun Zhong Zhai 220kV substation,scientifically pointed out that the accident was due to leave hidden trouble in the process of design and manufacture of cause.This paper introduces the working principle of arc suppression coil and use value, and cites several reasons can cause arc suppression coil accidents.This paper introduces in detail the whole process of hoisting core checks after the accident in Liao Ning Yongtai Transformer Manufacturing Co., Ltd,and carefully check the chromatography test data and the operation report before and after the accident, proveing the results of the analysis of the accident is correct.

Introduction

In the 66kV system,due to large capacitive current ,if the neutral is not grounded,when the single-phase grounding fault happens, will cause throughout the whole system of arc grounding overvoltage, also known as intermittent arc grounding overvoltage.If measures are not taken, will pose a great threat to low insulation equipment and insulation weakness in the system.In the current 66kV systerm,in order to reduce the grounding current,most of the neutral point grounding by arc suppression coil[1-3].

Arc suppression coil is actually a adjustable inductance L ,which is equipped with air gap iron core.Arc suppression coil is connected between the neutral point and the ground.When single-phase grounding happened , the arc suppression coil can produce inductive current offset fault current(or capacitive current).This current can greatly reduce the single-phase grounding current,and it can avoid the arc grounding over voltage [4,5].

The reason of arc suppression coil accident

The arc suppression coil accident has a very close relationship with the faults or abnormal operating condition in the system.When the grid is normal,the voltage effect on arc suppression coil only a low displacement voltage of neutral point.So,only a small current through the arc suppression coil.Only when the single phase to ground fault occurs in the system,or the serious asymmetry,arc suppression coil will generate a larger compensation current.Therefore,arc suppression coil is generally only in the system grounding, disconnection and three-phase asymmetry, a larger current long time through, could have serious internal fault.The reasons of arc suppression coil accident are following:a,resonance overvoltage;b,overcurrent;c,the lack of oil;d,design and manufacturing processes that do not meet the requirements.

The analysis of 66kV arc suppression coil smoke accident in Fushun Zhong Zhai 220kV substation.

(1) The accident survey

On October 22,6:50,the monitoring system display the occurrence of C phase grounding fault.A three-sect currentt protection of Qingliu line of Qingyuan 66kV substation tripped immediately,distance protection and reclosing no action(third segment protection tripped,locking

the reclosing;the phase to phase fault was derived from the single-phase grounding fault through the transition resistance,the large ground transition resistance beyond the scope of protection of the three-step distance relays,the protection device was not acted,after the inspection results show that action was right),the grounding systerm was disappered.Er Daogou 66kV substation,Liu huatie 66kV substation,Gao Jiajie 66kV substation and Xia Jiapu 66kV substation,this four substations in the Qingliu line were power cut.Through inspection ,the equipments in Qingyuan substation were all right.The dispatcher ordered operated the 66 kV Qingliu line.The Qingliu line was operated successfully at 07:02,and the Zhong Zhai substation 66kVsysterm C phase ground signalling was displayed,34 seconds later,the three-sect currentt protection of Qingliu line tripped again.7:04,the light, heavy gas protection signal of Zhong Zhai substation 66kV arc suppression coil was displayed.At 7:30,the Zhong Zhai operation team reported that the arc suppression coil was smoking.7:34,dispatcher ordered power down the 66kV arc suppression coil .

(2) Operation before the accident

Zhong Zhai substation No.2 main transformer was operating ,and leading the Qingyuan substation, Nanzamu substation and Hongtoushan substation etc.19 substations which belonged to Fushun power supply company,3 user substations,3 power plants,the No.1 main transformer backup.Before Failure,the load was 86MW.Through calculation,the Zhongzhai net capacitive current was 85.68 A.When put into use the two arc suppression coils,Zhongzhai used 100A,Qingyuan used 25A.All of them were manual mode, compensation degree was 45.9%.

(3) Returned for hanging core inspection after the accident

The 66kV arc suppression coil smoke accident in Fushun Zhong Zhai 220kV substation was put into operation on May 12, 2010 ,which made by an electric incorporated company,the date was 2008 December.Manufacturing load switch manufactured by Shanghai Huaming Electric Power Equipment Co., Ltd,whose production date wass 2008 November.After the accident,the arc suppression coil was transfered to a repaire shop for hanging core inspection.The damaged condition of arc suppression coil following Figure 1.

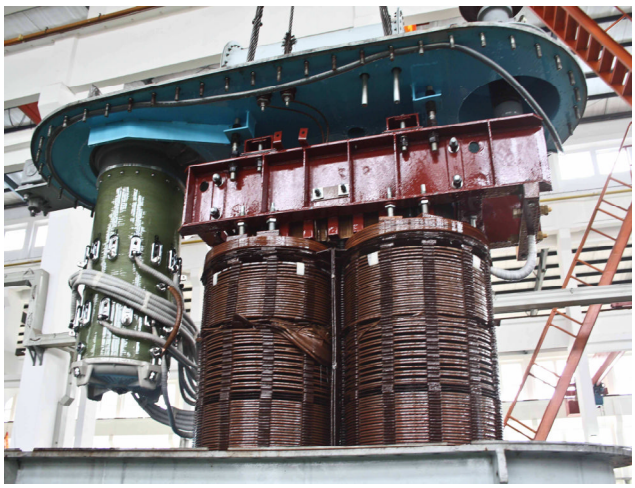

Fig. 1 The core in the middle 22.23.24 layers was twisted seriously

The first, the tail section of core was normal, but in the middle 22.23.24 layers, the core was twisted seriously, the coil plate, meter coil wire and rod insulation was cracked.

On load switch, moving contact discharger he upper portion of the switch along strapping.The contactor and the moving contact of insulation cylinder only has few arc mark,as shown in Fig. 2:

Fig. 2 The contactor in the On-load voltage regulating switch barrel and the switch

Analysis of the causes of the accident

Firstly, let us examine the experimental data before and after the accident, as shown in Table 1.

Table 1 The experimental data of the arc suppression coil

Component Data	Content μl/L							
	H2	CO	CO2	CH4	C2H6	C2H4	C2H2	C1+C2
2010.04.28	20	53	453	4.21	0.22	0.65	0.11	5.19
2011.07.15 oil injection	35	132	1959	3.79	1.15	0.67	0.07	5.68
2012.07.05	14	139	2522	4.02	1.9	1.76	0.79	8.47
2012.07.06 test again	8	125	2270	4.06	1.59	1.64	0.76	8.05
2012.10.22 oil injection	901	501	2044	151.9	3.95	222.3	672.18	1050.33

July 15, 2011.In the later operation, the content of C2H2 was growing. It proved that the discharge phenomena were happened in the arc suppression coil.

Secondly, from these waveforms out of fault wave record instrument, system resonance did not occur when twice grounding, and a smooth transition.

When Zhongzhai 66kV system C-phase was grounded, the displacement - voltage ruled in arc suppression coil was escalated and remained at about 31kV after 5 frequencies. The arc suppression coil can operate fewer 2 hours in this voltage, but the gas protection was acted when only operated 1 minute and 28 seconds. So, it can be sure that insulation of on - load - tap - changing switch. From the experimental data showed in table 1, there would be discharge phenomena once the arc suppression coil launched.

Therefore, the accident was due to the hidden trouble in the process of design, manufacture. when single-phase grounding appears in the system, impulse over voltage generated instantly would cause a voltage oscillations in the winding. With the voltage oscillation, the potential to further expand, internal insulation was further damaged, eventually caused the winding deformation fracture.

The commissioning test and operation requirements

In order to ensure the safe operation of arc suppression coil, it needs to meet the following conditions:

(1) The requirement of experiment technique.

At present, test items as follows: 1) DC resistance of windings and casings; 2) The insulation resistance and the absorption ratio of windings and casings; 3) The dielectric loss tangent of oil immersed type arc suppression coil and casings; 4) Insulation oil test.

Handover testing project should be complete, must increase the following test, if do not have test conditions, it can be appointed manufacturer for test.1) arc suppression coil volt-ampere characteristics. 2) DC leakage current of oil immersed type arc suppression coil and casings.3) AC

withstand voltage test me on DC resistance of windings and casings.4) Impact closing test under rated voltage.

(2) The operation requirements of the unit.

1) The current and voltage of arc suppression coil should be accessed to fault wave record system.

2) Increase the infrared imager on substation professional investment, strengthen the infrared detection technology training, and improve the infrared detection ability of operators

3) If the grounding fault lasts 15 min is not eliminated, related personnel should immediately sent to check the arc suppression coil body, the upper temperature should be normal, there should be no smoke injection phenomena, casing should be no traces of discharge, joints should be no heating phenomenon, and every 20 min check once a. When the oil temperature exceeds 95 ℃, continuous running time exceeds the specified value, should apply to dispatcher on duty for disabling the arc suppression coil.

Conclusion

When procuring arc suppression coil, should choosing the authority of the State Department identified, test and inspection within the period of validity and the arc suppression coil needs experience. For a long time, because of the problem of part manufacturing plant, leading to the design and manufacturing process of product problems. In the anti resonant and anti short circuit ability is poor. The quality problem of the tap-changer also exists. It is because of these problems, which leads to the arc suppression coil smoke occurred, fuel injection, sound abnormal accidents often start in. Because of the manufacturing process of the arc suppression coil needs large amount of manual operation, the process control difficult and larger dispersion. We must send professionals to the manufacturing process of supervision, and the test report and inspection report as the original data file.

Reference

[1] Chen Jiabin. Substation operation and management techniques. China power press, 2004 .

[2] Lei Yugui. Substation maintenance. China Waterpower Press, 2006.

[3] The North Star power network. Function and selection of arc suppression coil. 2008.

[4] State Grid Corporation. 10 ~ 66 kV arc suppression coil plant operation specification.2005.

[5] State Grid Corporation. 10 ~ 66 kV arc suppression coil device technical supervision regulation.

Advanced Materials Research Vols. 986-987 (2014) pp 219-222

doi:10.4028/www.scientific.net/AMR.986-987.219

Analysis of Industrial Structure Optimization based on Energy Saving

Ying-ying CAO[1,a], Ya-ling ZOU[1,b]

[1] School of Management, Tianjin University of Technology, Tianjin300384, China

[a]caoying868889@163.com, [b] zyl89521@yeah.net

Keywords: Energy industry; Industry structure; Energy saving; Optimal path

Abstract. The industrial structure optimization based on energy saving is different from the traditional industrial structure optimization. It relays on the supply and demand of industrial structure. It takes low carbon cycle, energy conservation and environmental protection as guiding principles and maximization of the use of resource and minimization of production from environmental pollution as the goals. Innovation of technology has also be taken as a means to help industry be sustainable, healthy and orderly and to shape an industrial optimization model that economy, society, nature are harmoniously existed. In this paper, we have an analysis of the energy industry structure to point out the shortages of the structure, technology, policy, talent and so on in energy industry. Then based on these shortages we explored the optimal path of industrial structure for energy saving.

Introduction

The rapid development of industry satisfied the material and cultural needs of people. But it follows with the problems of excessive of resource and the growth of natural ecological environment load and so on. And people are becoming pay attention on construction of ecological civilization. In year of 2007, to build ecological civilization has been put forward at the report of the 17th Communist Party Congress. In year of 2008, to promote ecological civilization has been stressed at the 18th Communist Party Congress. As a pattern of economy development, industry structure is the core problem of ecological civilization[1].So we should to find shortages of industry structure in ecological civilization and explore the optimum paths of industrial structure to help save energy.

The shortages existed in the energy industry structure

In traditional industrial structure theory, the process of optimizing the industrial structure is to adjust the supply and needy structure which has influence on the change of industry structure. By doing this we can realize the resource optimal allocation and configuration to promote the rationally and highly development of industry structure[2]. The industrial structure optimization based on energy saving is different from the traditional industrial structure optimization. It not stresses on the quantity growth and quality improvement ,but also stresses on being sustainable, healthy and orderly. It shapes an industrial optimization model that economy, society, nature can existed harmonious by optimizing the structure of industry. It demands structure status and trend of change could comply with the concept of ecological civilization. And the direction of the industrial structure optimization could promote energy conservation, industrial ecology transformation, the self-organizing ability of industrial structure and the sustainable development ability improvement. Nowadays, the industrial structure based on energy saving has much space on optimizing the configuration, technology and policy of industry structure. It has to be adjusted and innovated constantly in to be more rationally, more empirically and more efficient. So the self-organizing ability and sustainability of the industry structure can be improved.

The first, development of traditional energy industry is not harmonious, and it mainly depends on material resources. Industry structure optimization concentrating on promoting energy conservation requires economy, society and environment coordinated developed, maximizing the utilization rate of natural resource and minimizing the damage to environment[3]. From the development of energy industry in our country, first of all, the development of regional economy and energy industry are uncoordinated. The disparity between east and west, north and south are really obviously. The advantages and characteristics of the local energy industry have not be validly used, which have much bad influence in healthy development of the energy industry. Secondly, the economic growth mode of energy industry in China is too extensive, mainly depends on material resources, the rate of configuration and use are low as well as the huge cost during developing of energy industry. However, material resources are scarcely and it will be short when economic development arrives at a certain stage and it also will pose a threat to the long-term development of the energy industry.

The second, traditional energy industry technology innovation level needs to be improved. Because the industrial construction starts late in our country, so there is a big gap on the technical innovation between the developed countries and China[4]. The gap mainly shows in the backward production technology and smaller innovation strength, the lack of pollution control and treatment technology and immature of green energy saving technology. What's more, research level of China's energy industry lags behind, the cooperation with universities, scientific research institutes and other research institutions is insufficient. Industrial technology innovation system that integrating research, development and production has not been formed, this has a big influence on the improvement of the energy industry technology innovation level in China.

Thirdly, the energy industry administrative policy need to be improved. Laws, regulations and economic policies are two main policy tools the government used for optimizing the structure of the relevant industries. The execution of them are mandatory and they are important measures of optimizing the structure of energy industry in our country[5]. However, it ignores the regional differences in the development of energy industry, the characteristics of the regional advantage can not get to play due to the similar regional energy industry policy, this limits the development of the regional energy industry. In addition, today's energy industry policy emphasizes too much performance requirements and performance evaluation on GDP growth and ignores environmental protection and other important factors. However, the environmental protection sells at a discount in the effect of guiding the upgrading of the industry.

The fourth, talents of energy industry are pool and efficient talent introduction and cultivation mechanism has not be formed. For now, the trend of talent proportion of China's high technology and new strategy emerging energy industry is gradually rising, but the amount is still insufficient. Most of the high-quality talents are in traditional energy industries, which has be a bottleneck of in the process of advancing the energy industry structure optimization in our country. What's more, because of the lack of talent introduction and cultivation mechanism, high-level, shortage of talents are still in a state of loss and unable to meet demand of leading industry.

The path of industry structure optimization to facilitate energy saving.

The industry structure optimization based on energy saving must under target of coordinated development of economy, society and environment. It also should be guided by scientific development concept and economic cycle theory, so it can radically solve problems such as high pollution, high consumption but poor efficiency in the model of economic development. What's more, the optimization can explore the energy industry structure of saving resource and environmentally-friendly energy industry structure from aspects such as structural transformation, technology innovation and policy changing.

Transformation of the industry structure optimization to facilitate energy saving. Because of insufficiency in the structure of energy industry, industry structure optimization should pay attention to economy of each region , especially the coordinated development of services and

manufacturing industry in three traditional industry. Industry structure optimization also should strengthen the support on service industry. It should adjusts the first industry according to the principles of re-use and recycling. It should optimize the second industry by principles of low consumption, pollution but high efficiency. It should strengthen the third industry by the principles of raising proportion and added-value. It should introduce the zero industry (i.e., natural resources industry) and high industry (i.e., environmental industry and high technology industry) [6] to the industrial structure, and make it to be the leader industry in industry optimization and upgrading. We also should give full play to the resource advantage, optimize the allocation of resources, adjust the energy structure, reducing the use of traditional energy, increase use new clean energy development and utilization. Furthermore, energy industry should be guided by knowledge resources. It can take advantages of features such as sharing, limitless and green of the knowledge resources to make the energy industry structure changing from relying on material resources to relying on knowledge resources.

Push energy industry technology innovation in all sides. Due to rapid development of modern information technology, energy industry structure should be adjusted to focus on integration between industrialization, informatization and achieving “tri-networks integration” in order to deal with the impact from information industry to traditional industry. Moreover, we should aggressively develop the energy-saving and technology innovation system which is leaded by the group of enterprises, colleges and research institutes. We also should increase the capability of independent innovation of the energy industry, pushing energy industry technology innovation in all sides. On side of production, enterprises can take benefits from the rapid development of modern information technology, and then broaden use of information technology in production. We should upgrade high-tech, environmental protection technology in traditional energy industry, We should eliminate the outdated technology, bring advanced critical equipments from foreign countries and domestic market, motivate enthusiasm of the enterprises to create. So development direction of industry can be leaded from environment-damage to environment-friendly. On side of pollution management and treatment, enterprises should go for energy conservation and emissions reduction. They should take low-carbon cycle production mode as dominate role and develop the low damage and environmentally eco-industry system to improve the efficiency of resource utilization. Enterprises can strengthen the contact with universities and social scientific research institutions, deepen the pollution management research, investing more funding into the energy-saving research and development, and making the pollution management be used in reality. On side of green-energy-saving, enterprises should enhance investment of new strategic industry. They should not only import new technology or upgrade technology, but also need to invest more funds in the research projects.

Complete the policy-guide mechanism to change the policy from enforced to induced. In order to reduce negative influence caused by regional differences and performance requirements, implementation of energy conservation policy should change from been enforced to be induced as the following aspects:

(1) Develop regional characteristic industry based on the local condition. Apply a flexible guiding policy according to the regional characteristics of the environment. Limit haphazard investment and redundant construction.

(2) Improve the assessment of government. Reform the assessment criteria based on GDP, take resource use, energy conservation and emissions reduction, environmental management, development of new energy into the evaluation system. Emphasize the government's environmental responsibility and the important of coordinated development between economic growth and environment protection.

(3) Encourage and cultivate the development of emerging strategic industries. The new strategic industries like new energy industry, green environmental protection industry and bioengineering and pharmaceutical industry, the policy can trend to cultivate by funds and scientific research service.

(4) Legislate ecological compensation mechanism. It requires the enterprises to handle pollution after they developed, and it asks enterprises to take responsibility for the environment management. Otherwise, the negative effects from environment will turn to be a cost onto enterprise.

(5) Improve the enterprises credit evaluation system. Environmental protection behaviors benefit the enterprises, so enterprises should pay attention on environmental protection, clean, energy-saving and emission reduction. At present, our country enterprise credit evaluation system in the pilot stage, the system needs to be improved.

Increase the talent pool of emerging energy industry to promote the formation and nurturing talent introduction mechanism. Integration of talents and industries is an important condition to promote talent agglomeration. Technology innovation and structural adjustment should be dominated by talents. The coordinate relationship of talent, industry and technology innovation can be ensured by the relationship between human, social and environmental, so we can strive to build talent support system to promote energy conservation[7]. Talent strategy development, the first is the construction industry talent base, through industrial projects to attract and gather talent to play a leading role, while focusing on core talent training of existing personnel. Optimize energy industry base supporting measures, provide a good environment for industry professionals. Second, to promote industrial innovation and talent training mode to enterprises, universities, research institutes as the main combination of research. Strengthen cooperation with universities and research institutes to promote use of resources. Take university as the main talent transport platform to meet the talents need of the industrial structure optimization. So enterprises, talents and technological innovation can develop mutual integrated and common developed.

Summary

In this paper, we have an analysis of the energy industry structure to point out the shortages of the structure, technology, policies, talent and so on. Then based on these shortages we explored the optimum paths of industrial structure to help saving energy. First, change the industry structure optimization to promote energy saving. Second, push energy industry technology innovation in all sides. Third, complete the policy-guide mechanism to change the policy from enforced to induced. Forth, increase the talent pool of emerging energy industry to promote the formation and to nurture talent introduction mechanism.

References

[1] Xiao-dong LI. The Ecological Civilization and the Construction of Eco-industrial System in the High-tech Zone [J]. Reformation & Strategy, 2013, 29(1): 90-93.

[2] Dong-shui SU. Industrial Economy [M]. Higher Education Press, 2000.

[3] Korhonen J, Okkonen L, Niutanen V. Industrial ecosystem indicators-direct and indirect effects of integrated waste-and by-product management and energy production[J]. Clean Technologies and Environmental Policy, 2004, 6(3): 162-173.

[4] Jaruwan Chontanawat, Lester C. Hunt, Richard Pierse. Causality between energy consumption and GDP: Evidence from 30 OECD and 78 non-OECD countries [J]. The Journal of Policy Modeling, 2008, 30(2): 209-220.

[5] Bo-qiang LIN. Econometric analysis of China's energy demand [J]. Statistical Research, 2001, 10: 34-39.

[6] Xi-san ZHAO. China's Industrial Restructuring Under the Ecological Civilization [J]. Ecological Economy, 2010, (10): 43-47.

[7] Zi-liang ZHANG. Realize the interaction of talent and industry on how to create a talent and industry "ecosystem"[J]. Chinese Talents, 2007, (5): 26-27.

Advanced Materials Research Vols. 986-987 (2014) pp 223-226

doi:10.4028/www.scientific.net/AMR.986-987.223

Analysis of Key Factors Affecting Double-circuit Transmission Lines Parameters and Transposition Schemes

Cheng Ben, Zhenxing Li [a], Danfeng Xu, Linjuan Wu

College of Electrical Engineering and New Energy, China Three Gorges University, 443002, Yichang, Hubei Province, China

[a]email: lzx2007001@163.com

Keywords: Double-circuit Transmission Lines; Line Parameters; Symmetry

Abstract. Double-circuit transmission lines parameters symmetry would affect the normal operation of the transmission lines and relay protection actions directly. This paper analyzes the impacts of three different phase sequence arrangements on parameters symmetry of conventional un-transposed double-circuit lines, and requirements can be met by the parameters symmetry for double-circuit transmission lines with different types and different length. Took practical engineering requirements into consideration, a simple and admissible suggestion on phase sequence arrangements and the transposition modes is given. The research results provide useful guidance and reference for future designs of double-circuit lines, especially for the compact one.

Introduction

Double-circuit transmission lines parameters would affect the normal operation of the transmission lines and relay protection actions directly [1-2]. Numerous conductors in double-circuit transmission lines make it difficult to achieve complete transposition. Diverse operation conditions, close proximity between each loop, serious electromagnetic and electrostatic coupling would cause severe parameter asymmetry.

Conventional calculation method of the transmission line parameters simplified the circuit model to make it easy for analysis, such as the literature [5] assumed that three-phase conductors transposed completely, literature [6] assumed that the parameters were symmetrical. But these assumptions are not applied in double-circuit transmission lines especially when a conventional method is used to calculate paralleled double-circuit line parameters. As loop-loop distance is greater than phase-phase distance, it ignored coupling effects between positive sequence and negative sequence [7]. While in double-circuit transmission lines, electromagnetism is strong in two lines, coupling effects between positive sequence and negative sequence cannot be ignored.

By analyzing the effects of transposition on double-circuit transmission lines parameters symmetry, this page adopts the appropriate phase sequence arrangement and combines easily realized transposition mode in a practical project to improve double-circuit transmission lines parameters symmetry. It is of great significance for the standardization of the design of transmission lines, and the improvement of the quality of power supply.

Analysis of Key Factors Affecting Double-circuit Transmission Lines Parameters

(1) Double-circuit Transmission Lines Parameters

According to the single circuit parameters calculation method, and the double-circuit transmission lines model shown in Fig.1.

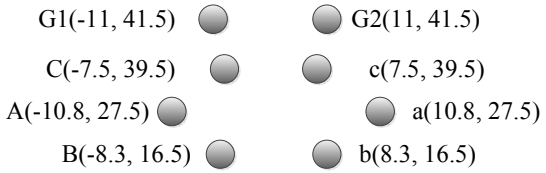

Fig.1. Transmission lines arrangement of 500kV double-circuit

Assuming that the lines do not transpose completely, double-circuit lines parameters can be calculated after the influence of the ground considered. Details can be shown in type (1).

$$\begin{bmatrix} \dot{U}_{\mathrm{IA}} \\ \dot{U}_{\mathrm{IB}} \\ \dot{U}_{\mathrm{IC}} \\ \dot{U}_{\mathrm{IIA}} \\ \dot{U}_{\mathrm{IIB}} \\ \dot{U}_{\mathrm{IIC}} \end{bmatrix} = \begin{bmatrix} Z_{\mathrm{IAIA}} & Z_{\mathrm{IAIB}} & Z_{\mathrm{IAIC}} & Z_{\mathrm{IAIIA}} & Z_{\mathrm{IAIIB}} & Z_{\mathrm{IAIIC}} \\ Z_{\mathrm{IBIA}} & Z_{\mathrm{IBIB}} & Z_{\mathrm{IBIC}} & Z_{\mathrm{IBIIA}} & Z_{\mathrm{IBIIB}} & Z_{\mathrm{IBIIC}} \\ Z_{\mathrm{ICIA}} & Z_{\mathrm{ICIB}} & Z_{\mathrm{ICIC}} & Z_{\mathrm{ICIIA}} & Z_{\mathrm{ICIIB}} & Z_{\mathrm{ICIIC}} \\ Z_{\mathrm{IIAIA}} & Z_{\mathrm{IIAIB}} & Z_{\mathrm{IIAIC}} & Z_{\mathrm{IIAIIA}} & Z_{\mathrm{IIAIIB}} & Z_{\mathrm{IIAIIC}} \\ Z_{\mathrm{IIBIA}} & Z_{\mathrm{IIBIB}} & Z_{\mathrm{IIBIC}} & Z_{\mathrm{IIBIIA}} & Z_{\mathrm{IIBIIB}} & Z_{\mathrm{IIBIIC}} \\ Z_{\mathrm{IICIA}} & Z_{\mathrm{IICIB}} & Z_{\mathrm{IICIC}} & Z_{\mathrm{IICIIA}} & Z_{\mathrm{IICIIB}} & Z_{\mathrm{IICIIC}} \end{bmatrix} \begin{bmatrix} \dot{I}_{\mathrm{IA}} \\ \dot{I}_{\mathrm{IB}} \\ \dot{I}_{\mathrm{IC}} \\ \dot{I}_{\mathrm{IIA}} \\ \dot{I}_{\mathrm{IIB}} \\ \dot{I}_{\mathrm{IIC}} \end{bmatrix} \tag{1}$$

Represented by matrix vector

$$\dot{\boldsymbol{U}}_{\mathrm{I\text{-}II}} = \boldsymbol{Z}\dot{\boldsymbol{I}}_{\mathrm{I\text{-}II}} \tag{2}$$

In order to get each sequence parameters in each line, the two loops of voltage and current phasor are transformed into two groups of symmetrical components, by the sequence component transformation, the following types can be obtained.

$$U_{1201'2'0'} = SZS^{-1}I_{1201'2'0'} = Z_{SD}I_{1201'2'0'} \tag{3}$$

$$Z_{SD} = SZS^{-1} \tag{4}$$

For the lines with completely symmetric parameters, after symmetrical component transformation, each sequence parameters are completely independent. So the circuit parameters symmetry can be represented by the transformed independence of sequence. Thus, this page simultaneously adds positive sequence voltage in two loops, and then calculates sequence current of each loop, according to type (3). If the larger proportion positive sequence current accounts and the smaller proportion negative sequence and zero sequence current accounts then the independence between each sequence are better, that is to say, the symmetry of the circuit parameters is better.

(2) Phase sequence arrangements effects on double-circuit transmission lines parameters

Compared to the compact double-circuit lines, the conventional double-circuit transmission lines phase distance is larger within each loop, the typical arrangement are same phase sequence, inverse phase sequence and heterogeneous sequence arrangement, as shown in Fig.2.

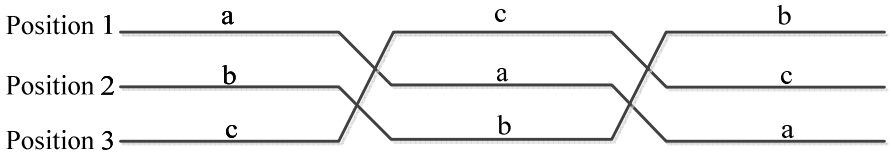

Fig.2. Sketch map of transposition in transmission lines

Here taking Fig.1 for an example, the lines parameters under same phase sequence, inverse phase sequence and heterogeneous sequence arrangements were calculated and analyzed respectively. According to type (3), Z_{SC} the impedance matrix of different kinds of phase sequence arrangements was firstly calculated, then, assuming that 500kV positive sequence line voltage was added up to two loops. Based on type (2), each sequence current under different phase sequence arrangements can be calculated. The results are listed in Table 1.

As it can be seen from Table1, under the same phase sequence, the ratio of the negative sequence current and positive sequence current is 16%, and the ratio of the zero sequence current and positive sequence current is 0.69%.Under inverse phase sequence, the ratio of the negative sequence current and positive sequence current is 3.72%, and the ratio of the zero sequence current and positive sequence current is 1.31%. Under heterogeneous sequence, the ratio of the negative sequence current and positive sequence current is 8.54%, and the ratio of the zero sequence current and positive sequence current is 4.5%.

Table1 Regular double-circuit transmission lines current pharos and amplitude of each sequence

		same phase sequence		inverse phase sequence		heterogeneous sequence	
		I_P/kA	I_M/kA	I_P/kA	I_M/kA	I_P/kA	I_M/kA
Line I	I_1	1.99-j52.831	52.8682	2.7136-59.0878j	59.150	5.4677-57.9503j	58.208
	I_2	7.476+j3.913	8.4391	2.1074+0.6293j	2.1994	4.9711-0.0982j	4.9721
	I_0	0.3599-j0.1314	0.3831	0.6409+0.4388j	0.7767	2.5289+0.5427j	2.5865
Line II	I'_1	1.99-j52.831	52.8682	2.1478-59.1282j	59.167	0.7102-58.401j	58.405
	I'_2	7.476+j3.913	8.4391	1.3337+1.7667j	2.2136	-4.9134+0.3406j	4.9252
	I'_0	0.3599-j0.1314	0.3831	0.0866-0.6813j	0.6868	-2.4596-0.9180j	2.6253

In the table 1: I_P stands for current pharos; I_M stands for current amplitude; I_1 stands for positive sequence current; I_2 stands for negative-sequence current; I_0 stands for zero sequence current.

When the lines are under inverse phase sequence, the ratio of negative sequence current and positive sequence current and the ratio of the zero sequence current and positive sequence current are small. So under this arrangement the symmetry of the line parameters is the best.

A digital simulation model shown in Fig.1 can also be built by PSCAD software, which is used to prove the accuracy of the analysis above. In the simulation, 500 kV line voltages were added in the head of line, three phases was shorted grounding in the terminal. At this time, each phase current waveform of the double-circuit lines under different phase sequence arrangements can be got in Fig.3. By contrast of each sequence current waveform, we can see intuitively when the lines are under inverse phase sequence arrangements, the symmetry of the parameters is the best. The results of the simulation correspond with previous theoretical analysis.

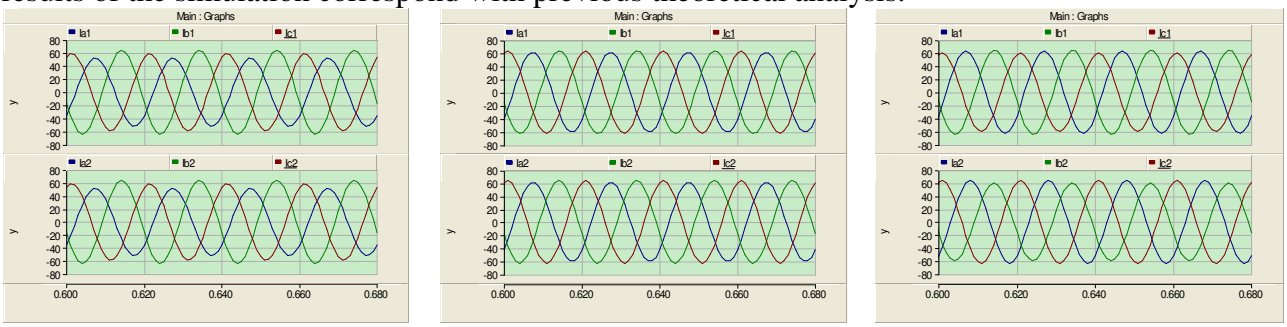

(a) (b) (c)

Fig.3. The contrast of each phase current of conventional double-circuit transmission lines under (a) same phase sequence, (b) inverse phase sequence and (c) heterogeneous sequence

According to the analysis above, for conventional un-transposed double-circuit lines, when two lines are all in operation, different phase sequence arrangements have apparent effects on the parameters symmetry. Among them, using inverse phase sequence the lines parameters symmetry is the best. It should be noted that when one line is not in operation, the case is the same as the single-circuit, different phase sequence arrangements have no effect on parameters symmetry, the lines parameters symmetry mainly depend on its transposition mode. Further analysis and calculation indicate that as the transposition is needed in a long double-circuit transmission lines, inverse phase sequence arrangement should be adopted to coordinate separate transposition of two loops. But after the transposition, each lines arrangement should be guaranteed to still be the inverse phase sequence. By this time, the lines parameters symmetry can be ensured well.

Double-circuit Transmission Lines Phase sequence arrangements and transposition schemes

Combined with previous analysis, this section focus on different type of double-circuit transmission lines under various conditions, and provides phase sequence arrangements and transposition schemes.

1) For short distance conventional un-transposed lines in practical, it is recommend adopting inverse phase sequence arrangement.

2) For long distance conventional un-transposed lines, two lines transpose respectively. After the transposition, inverse phase sequence arrangement is recommend adopting.

3) For the compact double-circuit lines, its parameters symmetry is superior to the conventional double-circuit lines and still be affected by phase sequence arrangements. It is also recommended adopting inverse phase sequence arrangement, and the parameters symmetry can be ensured though the lines without transposition.

Conclusion

This paper analyzes the effects of three different phase sequence arrangements on the parameters symmetry of conventional un-transposed double-circuit lines. Results indicate that different phase sequence arrangements have great influences on the lines parameters symmetry and requirements can be met by the parameters symmetry for double-circuit transmission lines with different types and different length. Combined with practical engineering requirements, a simple and admissible suggestion on phase sequence arrangements and the transposition modes is given. The research results provide useful guidance and reference for future designs of double-circuit lines, especially for the compact one.

Acknowledgement

In this paper, the research was sponsored by the National Natural Science Foundation of China (No.51307097).

References

[1] Huang Weigang. Study on conductor configuration of 500 kV chang-fang compact line. IEEE Trans on PWRD，18(3)：1002-1008，2003.

[2] Wenzel T., Leibfried T. Vacuum Circuit Breakers in Flexible AC Transmission Systems. IEEE Transactions on Power Delivery, 27(1): 236-244, 2012.

[3] Faruque M. O., Yuyan Zhang; Dinavahi V. Detailed Modeling of CIGRE HVDC Benchmark System Using PSCAD/EMTDC and PSB/SIMULINK. IEEE Transactions on Power Delivery, 21(1): 378-387, 2006.

[4] Yining, Z., Jiale S. Phaselet-based Current Differential Protection Scheme Based on Transient Capacitive Current IET Compensation. Generation, Transmission & Distribution, 2(4): 469-477, 2008.

[5] SUN Qiu-qin, WANG Guan, LI Qing-min, ZHANG Yu-jun, XU Di, ZOU Zhen-yu. Calculation and Analysis of the Coupling Effects of the UHV Double - circuit Transmission Lines. High Voltage Engineering.2010.

[6] ZHANG Yao-qiang，ZHANG Tian-guang，WANG Yu-ping，LI Ben-liang，HU Xuan. Research on Electric Unbalance Degree and Conductor Transposition of 1000 kV Double-Circuit Transmission Line on the Same Tower. Power System Technology.2011.

[7] BAN Lian-geng，WANG Xiao-gang，BAI Hong-kun，LIN Ji-ming，MAO Yu-bin，XIANG Zu-tao，WANG Xiao-tong，ZHENG Bin，HAN Bin，LI Xiao-ming. Simulative Analysis of Induced Voltages and Currents Among Multi Circuit 220 kV and 500 kV Transmission Lines on Same Tower. Power System Technology.2012.

Advanced Materials Research Vols. 986-987 (2014) pp 227-230

doi:10.4028/www.scientific.net/AMR.986-987.227

Analysis of Live Working Safety Distance for 750kV Double Circuit Transmission Line in Different Altitude Areas

SUN Hui[1, a], DING Yujian[1, 2, b], XIE Qing[1]

[1]North China Electric Power University (Baoding), Baoding071003, Hebei Province, China;

[2]China Electric Power Research Institute, Haidian District, Beijing 10092, China;

[a]sh_ee126@163.com, [b]hv_cepri@126.com

Keywords: 750kV double circuit transmission line; altitude correction; live working; safety distance; combined gap

Abstract. In order to determine the required live working safety distance for 750kV double circuit transmission line in different altitude areas of China, by using the test data of 750kV double circuit transmission line in the low altitude areas, and combining the common altitude correction methods, the live working safety distances of different altitude correction methods are obtained. By comparing and analyzing the results of different analysis methods, the required minimum approach distances and minimum combined gap distances of live working are recommended under different working conditions in the altitude of 1000m ~ 5000m areas. The results could provide technical reference for 750kV double circuit transmission line in different altitude areas.

Introduction

With the 750kV transmission lines becoming the backbone of the Northwest power grid gradually, on one hand, the layout of 750kV double circuit transmission line could improve the transmission capacity, reduce the line corridor areas; On the other hand, the increasing of 750kV transmission line leads to many transmission lines passing through the high altitude areas, and the altitude of some lines are over 3000m, or even approaching 5000m. Live working has an important significance to guarantee the reliability and security of the transmission lines. Research of live working on 750kV double circuit transmission line in the altitude of less than 3000m areas had been performed by some research institutes, and appropriate standards and guidelines were formulated. But for the areas more than 3000m altitude, there is no corresponding provision.

The best way to study on live working is to carry out the relative live working test in high altitude areas, which could determine the live working safety distance reasonably. Currently, due to the absence of live working test data of high altitude, the analysis combining the test data of low altitude areas with the existing altitude correction methods is also an effective method for the determination of the live working safety distance in high altitude areas.

By using common altitude correction methods, and combining the test data of 750kV double circuit transmission line in the low altitude areas, the required live working minimum approach distances (MAD) of 750kV double circuit transmission line are recommended under different working conditions in the altitude of 1000m ~ 5000m areas.

Analysis of altitude correction factor k_a

For the high altitude correction of air gap discharge voltage, the current domestic and international standards mainly include: GB/T16927.1-2011, IEC 60071-2-1996, DL/T620-1997 and GB311-2012, among these correction methods, the method in GB/T16927.1-2011 is only applicable to the altitude of 2000m and requires the actual atmospheric conditions, which leads not to be considered in the article; the method in GB311-2012 has been adopted the formulas and curves given in IEC60071-2, therefore only the altitude correction methods of IEC 60071-2 and DL/T620-1997 are considered for analysis in this paper.

The recommended formula of altitude correction factor k_a in IEC 60071-2 is:

$$K_a = e^{m(H/8150)}. \quad (1)$$

In the formula, H is the altitude, m

m is the correction factor.

For SI, m is relative to the voltage amplitude, in the article, m is selected as 0.59 by checking the curve in the IEC 60071-2.

Altitude correction method in IEC60071-2 only applies to the altitude of 2000m and lower areas, by extending the application scope to the altitude of 5000m, k_a of different altitude are obtained in Table 1.

Tab. 1 Altitude correction factors k_a according to IEC 60071-2

Altitude(m)	1000	2000	3000	4000	5000
k_a	1.08	1.16	1.24	1.34	1.44

For weather conditions correction method of external insulation discharge voltage in DL/T 620-1997, the meteorological parameters of altitude 0m~3500m given in DL/T 620-1997 are extended to the altitude of 5000m areas firstly, which could be used to calculate k_a of air gap distances ranging between 3.0m and 7.0m according to the altitude correction method recommended in DL/T 620-1997, as are shown in Table 2.

Tab. 2 Altitude correction factors k_a of switching voltage according to DL/T620-1997

k_a		Altitude (m)				
		1000	2000	3000	4000	5000
Gap distance(m)	3	1.10	1.20	1.31	1.46	1.60
	4	1.08	1.17	1.26	1.38	1.49
	5	1.07	1.13	1.20	1.30	1.38
	6	1.05	1.10	1.15	1.22	1.28
	7	1.05	1.10	1.15	1.22	1.28

Analysis of live working safety distance

According to the provisions of *working regulations of power safety*, for a typical 750kV transmission lines, the overvoltage is selected as 1.80p.u..The live working risk ratio can be calculated by formula 2.

$$R_0 = \frac{1}{2}\int_0^{\infty} p_0(U)p_d(U)dU. \quad (2)$$

In the formula, $P_0\ (u)$ is the probability density function of switching over-voltage amplitude;

$P_d\ (U)$ is the air gap breakdown probability distribution function under the condition that the switching over-voltage is U.

The typical live working positions of 750kV double circuit transmission line are in Figure 1.

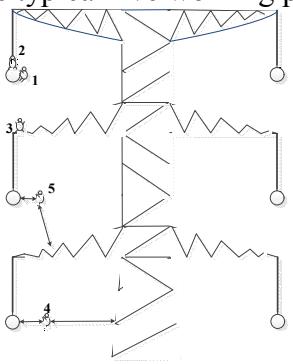

Fig.1 Schematic diagram of live working in different positions

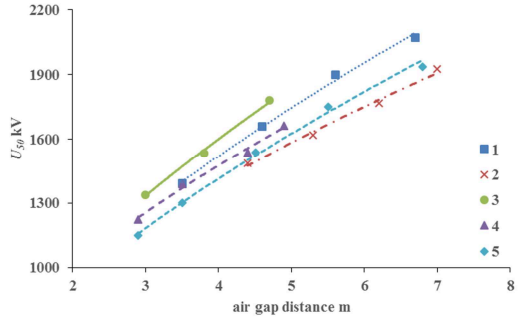

Fig.2 Live working clearance discharge characteristics curves of 750kV double circuit transmission line in different positions

In Figure 1, position 1 represents *equal potential worker to the tower body*, position 2 represents *equal potential worker to the cross arm*, position 3 represents *middle phase cross arm ground potential worker to the upper phase conductor*, Position 4 represents *lower phase conductor- workers - the tower body*, position 5 represents *middle phase conductor - workers - lower phase cross arm*.

Under the standard meteorological conditions, the live working clearance discharge characteristics curves of 750kV double circuit transmission line in different positions are shown in Figure 2.

According to k_a calculated by the methods in IEC60071-2, DL/T620-1997, and combining with the discharge characteristics curves when the worker in different positions of Figure 2, the required MAD are obtained under different working positions and different k_a in the altitude of 1000m ~ 5000m areas. As is shown in Table 4.

Tab.4 The required MAD are obtained under different working positions and different k_a in the altitude of 1000m ~ 5000m areas

Position \ Altitude (m)		0	1000	2000	3000	4000	5000
1	IEC60071-2	3.7	4.1	4.6	5.2	5.8	6.6
	DL/T 620	3.7	4.2	4.6	5.0	5.4	5.8
2	IEC60071-2	4.2	4.8	5.5	6.2	7.1	8.1
	DL/T 620	4.2	4.8	5.3	5.7	6.2	6.6
3	IEC60071-2	3.4	3.8	4.3	4.8	5.4	6.0
	DL/T 620	3.4	3.9	4.3	4.6	5.1	5.4
4	IEC60071-2	3.8	4.4	5.0	5.6	6.4	7.3
	DL/T 620	3.8	4.4	4.8	5.3	5.8	6.1
5	IEC60071-2	4.1	4.6	5.2	5.8	6.6	7.4
	DL/T 620	4.1	4.6	5.0	5.4	5.9	6.3

Remark: the range of human activity is not considered in the table.

As can be seen from Table 4: For the altitude of 1000m ~ 2000m areas, when workers are situated in different positions, the MAD obtained by the two correction methods are almost the same, however, for the altitude of 3000m areas and above, with the altitude increasing, the difference of the results obtained by the two altitude correction methods is getting bigger. At the altitude of 5000m, the results obtained by the IEC60071-2 is 1.04m larger than those of DL/T 620.

In the altitude of 1000m ~ 3000m areas, the calculation results of positions 1 and 4 compared with the provision values in DL/T 1060-2007, as are shown in Figure 3 and Figure 4.

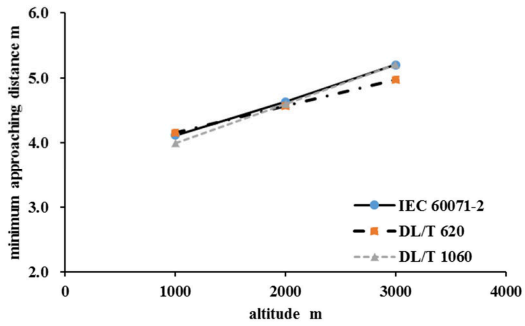

Fig.3 Results comparison of different analysis methods in position 1

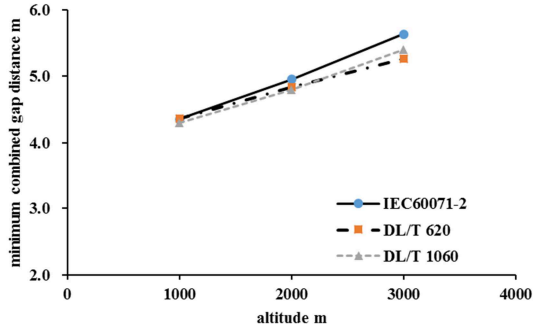

Fig.4 Results comparison of different analysis methods in position 4

As can be seen from Figure 3 and Figure 4, in the altitude of 1000m ~ 3000m areas, when workers are situated in position 1 and position 4, the MAD obtained by three analysis methods are almost consistent, and the difference is not more than 0.2m, therefore, for other working positions, the recommended the MAD obtained by the altitude correction methods have the rationality.

For security consideration, the MAD of different working positions in the altitude of 1000m ~ 5000m areas are recommended by the larger result obtained by the two altitude correction methods, as are shown in Table 5.

Tab.5 Recommended MAD in different working positions at the altitude of 1000m ~ 5000m

Working position	Altitude (m)				
	1000	2000	3000	4000	5000
equal potential worker to the tower body	4.2	4.6	5.2	5.8	6.6
equal potential worker to the cross arm	4.8	5.5	6.2	7.1	8.1
middle phase cross arm ground potential worker to the upper phase conductor	3.9	4.3	4.8	5.4	6.0
lower phase conductor- workers - the tower body	4.4	5.0	5.6	6.4	7.3
middle phase conductor - workers - lower phase cross arm	4.6	5.2	5.8	6.6	7.4

Remark: the range of human activity is not considered in the table.

In addition, the test data of low altitude areas is not under the condition of standard SI wave form (250μs/2500μs), instead, it is under the condition that the front time of the SI wave form is 740μs. The relationship between rod-plate air gap switching impulse breakdown voltage and front time in the literature [7] shows that the breakdown voltage of the air gap will increase when the front time is increasing, so the gap distance values recommended in this paper may be conservative.

Conclusion

1) Based on the test data of 750kV double circuit transmission line in the typical live working positions at low altitude, k_a of 1000m ~ 5000m altitude areas are obtained by two altitude correction methods in IEC60071-2 and DL/T620-1997. For the altitude correction method in IEC60071-2, with the increasing of the altitude, k_a also increase, and the growth rate is even; but for the altitude method in DL/T620-1997, whose k_a is relative to the air gap distance and the altitude, with the increasing of the gap distance, k_a at the same altitude is decreasing, in addition, with the increasing of the altitude, k_a under the same gap distance is also increasing.

2) According to the obtained k_a, and by calculation, comparison and analysis, the MAD of 750kV double circuit transmission line different working positions in the altitude of 1000m ~ 5000m areas are recommended. In general, the MADs in different working positions from the altitude of 1000m to 5000m are increasing, for different working positions, the position which requires the maximum MAD is *equal potential worker to the cross arm*, the position which requires the minimum MAD is *middle phase cross arm ground potential worker to the upper phase conductor*.

3) The results are based on the low altitude live working experimental data of 750kV double circuit transmission line and the altitude correction methods, which could be a reference for 750kV double circuit transmission line live working at high altitude. If the test conditions at high altitude are appropriate, it is recommended to carry out verification tests on 750kV real size tower head at high altitudes.

Acknowledge

Project Supported by National Natural Science Foundation of China (51307060); Colleges and Universities in Hebei Province Science and Technology Research Project (Z2013086); Fundamental Research Funds for the Central Universities (2014MS84).

References

[1] HU Yi，WANG Li-nong，LIU Kai，et a1．Research of live working on 750 kV double circuit AC transmission line [J]． High Voltage Engineering， 2009， 35(2): 373-378．

[2] DL/T 1060-2007 Technical guide for live working in 750kV AC transmission line[S]， 2007．

[3] GB/T 16927．1—2011 High-voltage test techniques Part 1: General definitions and test requirements[S]． 2011．

[4] IEC．IEC 60071-2—1996 Insulation coordination，part 2：Application guide-third edition[S]．1996．

[5] DL/T 620—1997 Overvoltage protection and insulation coordination for AC electrical installations[S]．1997．

[6] Ding Yi-zheng． Live working technology foundation [M]． Beijing， China: China Electric Power Press， 1998．

[7] ZHOU Ze-cun， SHEN Qi-gong． High Voltage Technology [M]． Beijing， China: China Electric Power Press， 2007．

Advanced Materials Research Vols. 986-987 (2014) pp 231-234

doi:10.4028/www.scientific.net/AMR.986-987.231

Analysis of Passive Residual Heat Removal System at Primary Side when Station Blackout Occurs

Jun-teng LIU[1,a], Qi CAI[1,a], Xia-xin CAO[2,b]

[1]Department of Nuclear Science and Engineering, Naval University of Engineering, Wuhan 430033, China

[2]National Key Discipline Laboratory of Nuclear Safety and Simulation Technology, Harbin Engineering University, Harbin 150001, China

[a]email:liujunteng2005@163.com, [b]email:243566324@qq.com

Keywords: Passive Residual Heat Removal System, Station Blackout, RELAP5

Abstract. This paper regarded CNP1000 power plant system as the research object, which is the second-generation half Nuclear Reactor System in our country, and tried to set Westinghouse AP1000 passive residual heat removal system to the primary circuit of CNP1000. Then set up a simulation model based on RELAP5/MOD3.2 program to calculate and analyze the response and operating characteristic of passive residual heat removal system on assumption that Station Blackout occurs. The calculation has the following conclusions: natural circulation was quickly established after accident, which removes core residual heat effectively and keep the core safe. The residual heat can be quickly removed, and during this process the actual temperature was lower than saturation temperature in reactor core.

Introduction

AP1000 is the representative of the third generation nuclear technology, the design and application of its passive safety system are focused on by scholars in many countries. Now, in our country, AP1000 nuclear power plant has been imported by State Nuclear Power Technology Corporation. However, the response of passive residual heat removal system under accident conditions was not known clearly. Based on the familiarity of AP1000 passive residual heat removal system, this paper set the passive system to the primary circuit of CNP1000. Then the simulation model is built by RELAP5/MOD3.2 program to analyze the ability of removing residual heat when Station Blackout Occurs. The conclusions could inform the improvement of the second-generation half Nuclear Reactor System in our country.

System Overview

There are three coolant loops in CNP1000 power plant system, and each coolant loop has one steam generator, one coolant pump, one hot leg and one cold leg. The pressurizer is connected with the hot leg of one coolant loop. By contrast, the AP1000 power plant system only has two coolant loops, and the structure is also different form CNP1000. But the changes of residual heat in reactor core are similar, because these two power plant system have the same output rating. So the study of heat transfer performance of the AP1000 passive residual heat removal system based on the primary circuit of CNP1000 was reasonable.

The AP1000 passive residual heat removal system was drove by natural force, and the valves follow the fail-safe standards. When the power supply lost or the guard signal reached, the valves would be triggered automatically, and then passive residual heat removal system would be put in to operation. The function of passive residual heat removal system is removing residual heat in reactor core by the usage of natural circulation under the design basis accidents. The heat exchanger of this system was made up of C-type tubes and put into the refueling water tank. The schematic diagram of passive residual heat removal system is shown below [1-3].

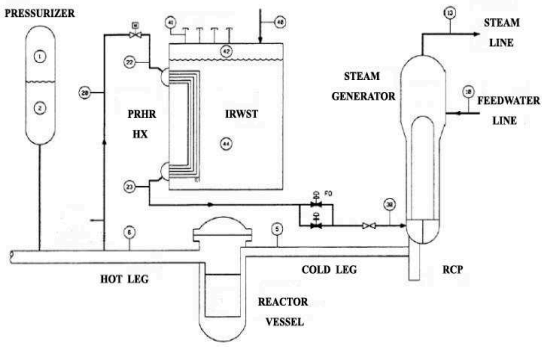

Fig.1. Schematic diagram of passive residual heat removal system

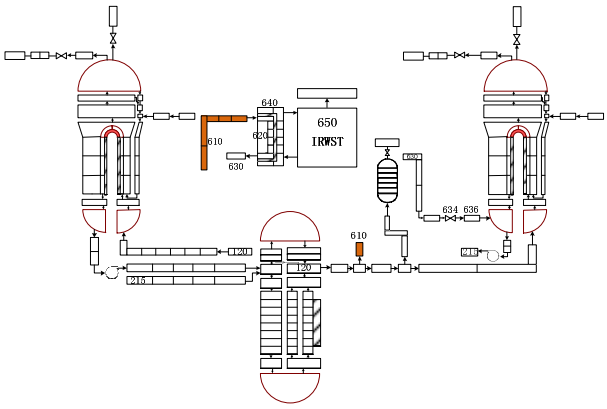

Fig.2. Control volumes of the system

The inlet pipe of the heat exchanger was connected with the hot leg of reactor coolant system. And the outlet pipe was connected with the cold chamber of steam generator's channel head. On the outlet pipe, there was a normally closed valve that would be open when air pressure lost or control signal triggered. These said equipment and pipes construct a loop associated with the pipes of reactor coolant system. When the passive residual heat removal system was put in to operation, the natural circulation would be built, and the residual heat could be removed by the coolant.

System Model

Based on RELAP5/MOD3.2 program, the model of CNP1000 reactor coolant system was built, in which the passive residual heat removal system was used. And then, the transient response of the whole system was analyzed when station blackout occurs. The key equipment include reactor vessel, coolant pipe, pressurizer, reactor coolant pump, steam generator, passive heat exchanger, refueling water tank, the relevant pipe and valves. To simplify the system model, the secondary side pipes of steam generator were set as boundaries, because this main analytical thesis being the transient response of passive residual heat removal system.

After setting the AP1000 passive residual heat removal system to the primary circuit of CNP1000, the graph of control volumes for this whole system is shown below. It should be noted that, to illustrate expediently, the loop on left side in the graph represents the two loops that have no connection with pressurizer in CNP1000 reactor coolant system.

The up-leg of passive residual heat removal system is connected with the hot leg on the main system, through which the coolant flows into the heat exchanger, whose control volume number is 620. Out of the heat exchanger the cooled fluid flows into the cold chamber of steam generator's channel head. On the outlet pipe the control volume, whose number is 634, simulated the normally closed valve that would be open when steam generator level was low. In consideration of the increase in heat transfer by natural convection, control volumes of No.650 and No. 640 were used to simulate this phenomenon [4].

Result of Calculation and Analysis

After station blackout occurred, the low speed signal of reactor coolant pump would close the reactor, and then the turbine would drop out. The feed water of steam generator would be lost, so the pressure and temperature in the secondary side would go up. When the pressure reached the setting value, drain valve would be open and the steam was discharged to air. At this time, steam generator level became lower and lower, finally the normally closed valve on the outlet pipe was tripped to open, and the passive residual heat removal system was put in to operation [5].

Tab.1 shows the design parameters of passive residual heat removal system and refueling water tank respectively [3].

Tab.1. Main design parameters of passive residual heat removal system

Design flow	2.28×10^5 Kg/h
Inlet temperature	570.35K
Outlet temperature	365.95K
Design pressure	17.1 Mpa
Design temperature	616.45K
Number of heat transfer tubes	689
External diameter of heat transfer tubes	0.0017m
Total area of heat transfer tubes	$286.9m^2$
Material of heat transfer tubes	Alloy Inconel 690

Let the system stabilize and introduce station blackout accident in 500 seconds. Then the coolant pumps began to run down, and the main feed water stopped, the low speed signal of reactor coolant pump would close the reactor. At that time, the core power began to decay form the 7 percent of the rated value and the point-reactor model was used to simulate the variety of power. 150 seconds after station blackout occurred, the coolant pumps stopped, and the level of steam generator became lower and lower, finally the passive residual heat removal system was put in to operation by low water level signal of steam generator. The key events after accident were shown in table 2.

Table 2 Key events after accident

Key events	Time(s)
Station blackout	500
Reactor shutdown	504
Pressurizer safety valve open	505
Pressurizer safety valve closed	511
Passive residual heat removal system start	554
Coolant pump stop running	650

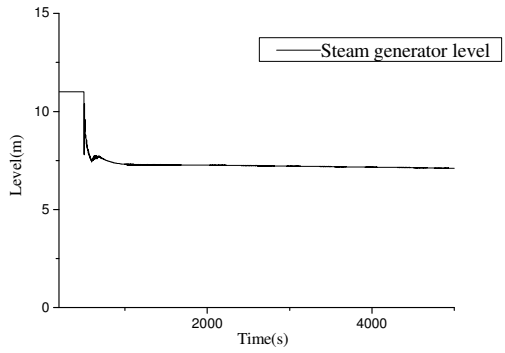

Fig.3. Level of steam generator

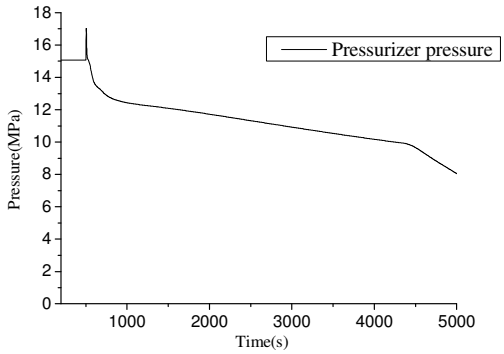

Fig.4. Pressurizer pressure varying with time

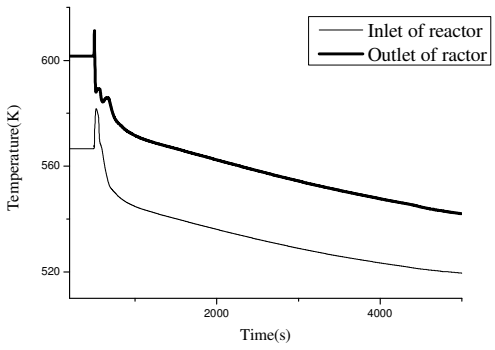

Fig.5. Inlet and outlet temperature of reactor

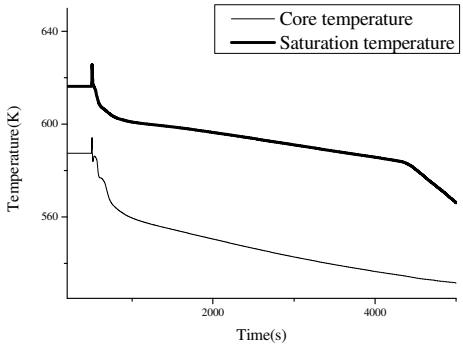

Fig.6. Core's temperature and saturation temperature under corresponding pressure

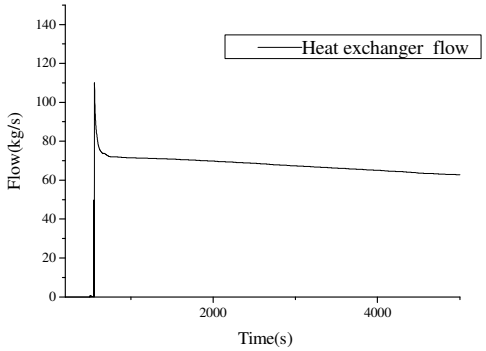

Fig.7. Flow of heat exchanger varying with time

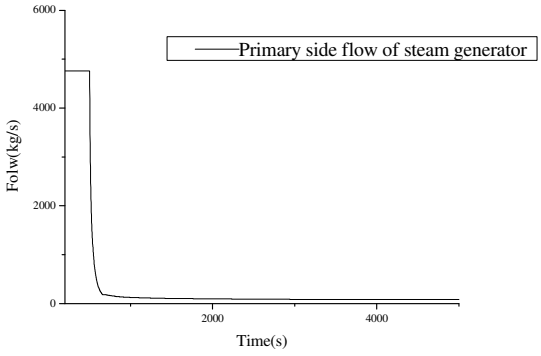

Fig.8. Primary side flow of steam generator

Before the passive residual heat removal system put in to operation, the pressure and temperature of the primary loop increased sharply, and the pressurizer safety valve was triggered to open. However after the normally closed valve became open, the residual heat of the core was quickly removed. The pressure and temperature, shown in Fig.4 and Fig5, dropped considerably. During the whole process, the core temperature was lower than the saturation temperature, shown in Fig.6, and the departure from nucleate boiling (DNB) didn't occur. Because of the gravity head of natural circulation, the coolant flow was about 60 kg/s in the passive residual heat exchanger, shown in Fig.7, and 84 kg/s in the steam generator, shown in Fig.8. It means that the gravity head of natural circulation can remove the core residual heat effectively. When the passive residual heat removal system operated steadily, the steam generator has already lost the function of hot trap. However in the steam generator heat was removed from the secondary side to the primary side. Thus it can be seen that the capacity of passive residual heat removal system can fully meet design requirements.

Calculations show that, at blackout accident, operating passive residual heat removal system can make the temperature and pressure dropped quickly. Setting the Westinghouse AP1000 passive residual heat removal system to the primary circuit of CNP1000 could ensure the security of the whole system when station blackout occurs. Testified by RELAP5 program, this scheme is feasible. After designing the passive residual heat removal system reasonably, the residual heat can be removed effectively and chronically, the core would be safe at blackout accident.

Conclusion

The aim of this paper is to set Westinghouse AP1000 passive residual heat removal system on the primary circuit of CNP1000 and use RELAP5/MOD3.2 program to calculate and analyze the response and operating characteristic of passive residual heat removal system on assumption that Station Blackout occurs. The calculation model could simulate the steady state accurately. And calculations show that, natural circulation was quickly established after accident, and residual heat can be quickly removed, and during this process the actual temperature was lower than the saturation temperature in reactor core.

References

[1] Jin SHEN, Guangming JIANG, Gang TANG. Preliminary study of AP1000 passive safety system [J]. Foreign Nuclear Power, 2006,1:1-6.

[2] Schulz T L. Westinghouse AP1000 advanced passive plant. Nuclear Engineering and Design. 2006(236):1547-1557

[3] Chengge LIN, An Advanced Passive Plant AP1000[M].BEIJING, Atomic Energy Press,2010.

[4] Tianhong YUAN, Lei YU, Chuan WANG. Research on Passive Residual Heat Remove System Under Loss of Power[J].Atomic Energy Science and Technology，2010.

[5] AP1000 European Design Control Document Rev. 1 [R].America: Westing House Electric Company LLC,2009

Advanced Materials Research Vols. 986-987 (2014) pp 235-238

doi:10.4028/www.scientific.net/AMR.986-987.235

Analysis of Wind Field Fan Based on Performance Enhancement Method

Xiaolong Tan[1], Jia Zhou[1], Wenbin Wang[1,a]

[1] Yalong River Hydropower Development Company LTD, Chengdu, 610051, China

[a] email: wangwenbin@ylhdc.com.cn

Keywords: Wind Field, COMSOL Fan, Wind Load Simulation

Abstract: For the simulation of wind turbine, the wind speed is extremely important parameters and indicators to measure the output power of the unit is the wind load. Therefore, in the airflow dynamics and simulation of wind loads before establishing an accurate wind speed model is crucial. At present, the application for wind turbines COMSOL fan, fan blades and wind load simulation field, the extremely important wind speed model is not perfect, most of the research is confined to a single constant wind speed, wind speed virtually ignored the magnitude and direction of change, on changes over time and space at the same time is one of the few studies of wind, so find a way to accurately describe the range of wind speeds, and can be combined well with COMSOL method can greatly improve the aerodynamic performance of wind turbines the overall level of .

Introduction

COMSOL was able to get a very wide range of applications, in addition to highlighting meshing capabilities, rich physical models and advanced algorithm for solving the border issue dynamic variable grid technology, but also has an easy user-defined program secondary development interface[1] . This article is based wind turbine simulation analysis to achieve the specifications in the wind load model and simulation data and theoretical calculations through comparison proved the feasibility and accuracy of the method.

Vertical Wind Shear Model

Wind shear associated with the change of wind speed, wind turbine cycle is the main source of alternating load one[2] . Velocity shear wind speed amplitude model refers to the different spatial positions with changed circumstances, including horizontal shear and vertical shear types, this study is the vertical velocity shear. Reaction vertical wind shear wind profile v (z) is the average wind speed anywhere but highly Z varies as a function, for the standard requirements of the wind turbine wind load performance simulation and load calculations, fan wind profilers meet the following power exponential equation:

$$v(z) = v_{hub}(\frac{z}{z_{hub}})^{a} \quad (1)$$

z_{hub} — Hub height, previously established through the whole wind field model shows that Z_{hub} =80m;

a — Wind profile index is used to determine the surface through the rotor swept when the average wind shear, a= 0.2;

v_{hub} — The average hub height wind speed, vg=10m/s:

z — Height from the ground, is a function of the independent variable.

Each parameter value into equation (1), wind profiler function becomes formula (2):

$$v(z) = 10(\frac{z}{80})^{0.2} \quad (2)$$

As a non-integer, resulting in the COMSOL power exponential function and can not be called directly, this introduces a power series expansion method to simplify the formulas[3] . Elementary

functions in power series expansion binomial series is ideal for wind profiler function unfolds, binomial series as formula (3) below.

$$(1+x)^a = 1+ax+\frac{a(a-1)}{2!}x^2+\cdots+\frac{a(a-1)\cdots(a-n+1)}{n!}x^n+\cdots \quad (3)$$

COMSOL into predefined macro access to the grid coordinates of the center of the height x[l], the wind field model considering the position of the origin of coordinates, of the formula (2) in the independent variables from the original Z represents a height from the ground center height direction with grid coordinates expression m = z = x [1] +80, so that y = m/80, the wind profile function becomes formula (4)[4] :

$$v(z) = 10(1+(y-1))^{0.2} \quad (4)$$

Gust Model

On the standard scale wind turbine, wind turbine design requirements repetition period of N years gust amplitude hub height by the following formula (5) Calculation:

$$V_{gustN} = \beta(\sigma_1 / (1+0.1D/\Lambda_1)) \quad (5)$$

V_{gustN} — amplitude of the gust;

σ_1 — turbulent wind standard deviation of longitudinal component;

Λ_1 — Hub height of the vertical turbulence scale parameter;

D — wind wheel diameter, D=77m；

B — repeat cycle with constant related, β=4.8 for N=l, β=6.4 for N=50.

To repeat the cycle of N = l example, a case study was to select the level of wind turbines Grade I_a, Richard extremes reference to the average wind speed V_{ref} = 50m / s, the average wind speed v_{are} = 10m / s, turbulence intensity characteristic values I_{15} = 0.18, slope parameter a = 2: wheel hub height of 80 meters from the ground, thereby determining the longitudinal turbulence scale parameter Λ_1 = 21m; selection conditions for the average wind speed at hub height V_{hub} = 10m / s, thus calculate the standard deviation σ_1[5] :

$$\sigma_1 = 0.18(15+2\times10)/(2+1)m/s = 2.1m/s \quad (6)$$

Simulation of Aerodynamic Characteristics of Wind Turbines

In the full establishment of the whole wind field model, accurately describe the vertical velocity shear and other wind model, a reasonable set solvers and turbulence models and other parameters correctly determine wind convergence conditions, the fan performance simulation. Primary authentication of the wind speed constant, and the blade is highly integrated speed 13m / s and a vertical gust two tangential velocity of the working conditions of detailed calculations obtained wind pressure, wind velocity and wind loads, such as simulation junctions.

Build wind turbine wind field model for 10m/s, 11.5m/s and 13m/s three kinds of constant wind speed, rotor speed for a variety of conditions of the simulation analysis. Figure 1 is left with the wind speed and wind wheel torque relationship between speed curve is calculated by the formula right out of the wind turbine output power curve. As can be seen from the figure, the wind wheel starts from rest, by the action of wind generated after the initial torque, but speed is zero so that the output power is zero; the torque under the action of the wind wheel begins to accelerate, starts to output power; for different stream wind velocity, wind turbine output power reaches a maximum when they correspond to different optimum speed. For proper operation of the wind turbine, the programmable system will adjust the size of wind rotor speed, making the process of change in wind speed wheel stroke can maximize the output power.

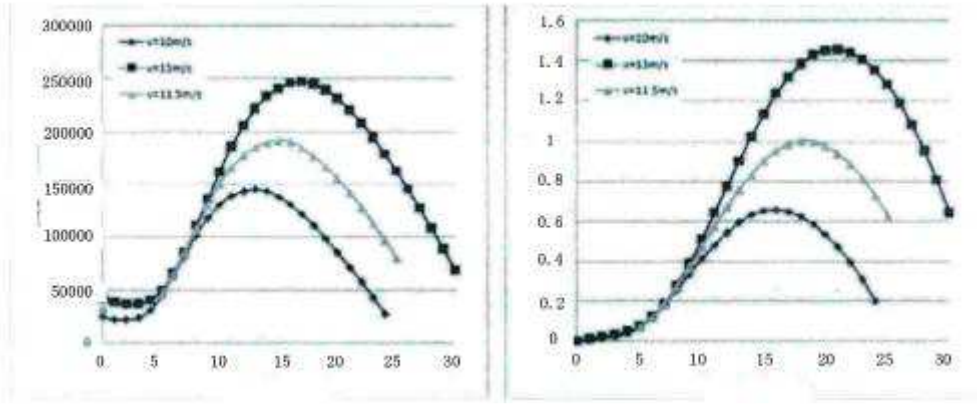

Fig.1 Relationship of torque, speed and power

In the height direction is established at Y =-20m horizontal section, the two wind conditions do not read a lot of time to the cloud static pressure distribution in the cross section shown in Figure 2, where the left is the initialization phase, the right vertical velocity shear conditions.

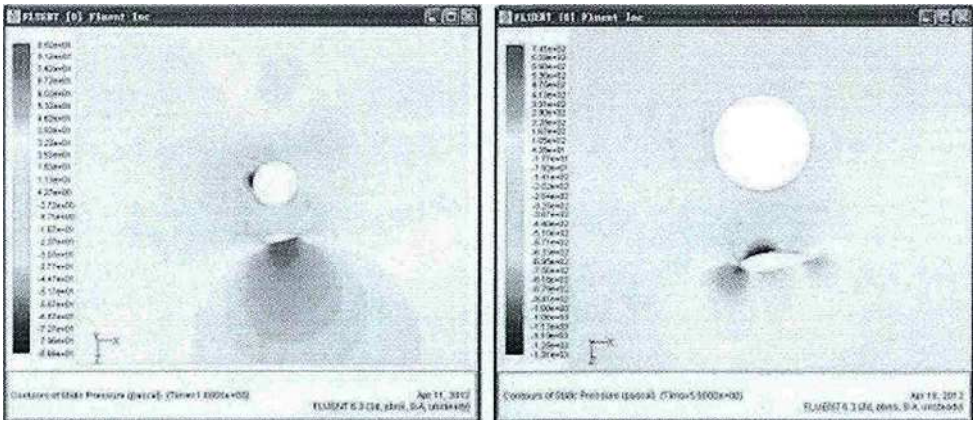

Fig.2 Pressure distribution of initialization and wind shear conditions Y =-20m

Figure 3 is a wind wheel left stationary initialization phase Y =-20m sectional velocity vector in the direction of the velocity windward surface substantially perpendicular to the blade, encounter obstacles to the right and left sides of flow, bypassing the flow of the wind tower field behind the tower between the blade and the blade trailing edge and the rear tower have formed a disaster flow; shear air damper position is right at t = 5.9s time Y =-20m sectional velocity vector cloud, then blade substantially in the tower in front of the wind wheel with 18.6rpm angular velocity in the tower is not formed between the blade cylinder and the swirling disaster, but rather from the leading edge to the rear edge of the air presence in the tower and the blade trailing edge is the same forming a vortex.

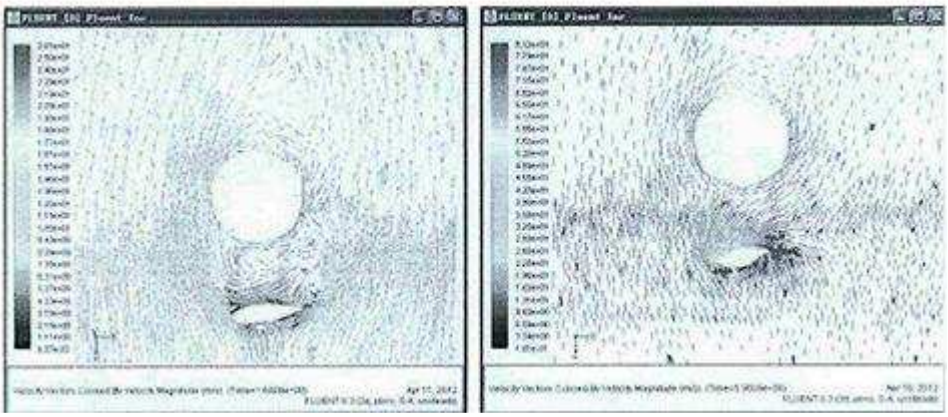

Fig.3 Y =-20m sectional velocity vector

This paper chooses the average wind speed at hub height of 10m/s, the wind wheel speed 18.6rpm, pitch angle of zero degrees vertical wind shear changes and random time-varying wind conditions for wind turbines two global model simulation, the simulation time exceeds a wind wheel rotation cycles, where the tangential wheel power condition shown in Figure 4, the calculated power is 1.32MW, 79.8% of the standard value. Torque coefficient curve shown in Figure 5.

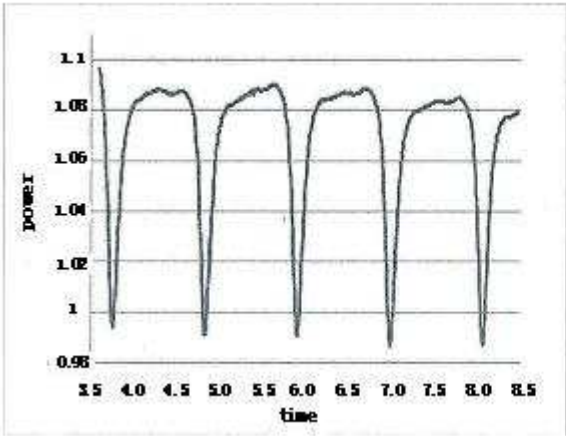

Fig.4 Wind shear conditions of the power curve

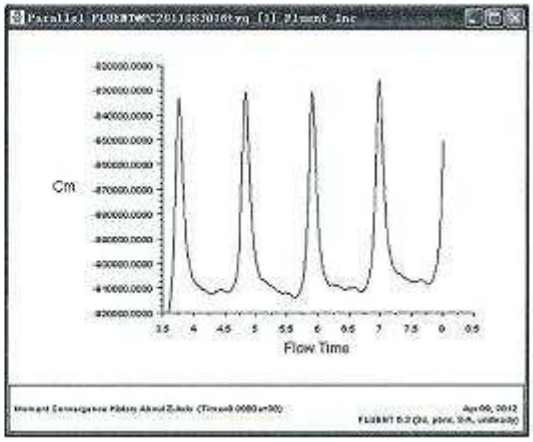

Fig.5 Wind shear conditions of the torque coefficient curve

Conclusion

This chapter of the fan operating characteristics of the simulation results were analyzed, the first step of 0.06s in the premise of the eight working conditions of constant wind power simulation verification, the basic calculation error less than 13%, reducing the simulation time step after the calculation accuracy has greatly improved, 0.02s step error is reduced to 12.3% while, thus proving COMSOL accuracy of the method, and reduces simulation step can further improve the accuracy, on the basis of analysis of the results of the other; through wind pressure and wind velocity of the gas stream with the discussion of the interaction of the blade mechanism was studied; vertical tangential wind conditions change, for example, the calculated torque and the rotor blades with three-time curve of the load, via the torque and power variation found negative effects of tower shadow effect; the particular location during rotation of the blade aerodynamic loads, to give the waving direction and the bending moment in array, and standards were compared limit load.

References

[1] A. Baoumhauer, C. koning. On the Stability of Oscillations of an AeroplaneWing. NACATM 223. 1923

[2] Jing X, Sun X. Discrete vortex simulation on the acousticnon-linearity of an orifice. AIAA Journal. 2000

[3] ZHAO Hongwu, SUN Xiaofeng. Active control of wall a-coustic impedance. AIAA Journal. 1999

[4] Sun Xiaofeng, Jing Xiaodong, Zhao Hongwu. Control lf Blade Flutter by Smart-Casing Treatment. Journal of Propulsion Technology. 2001

[5] So R. M. C, Jadic I, Mignolet M. P. Oncoming Alternating Vortices. Journal Of Fluids And Structures. 1999

Advanced Materials Research Vols. 986-987 (2014) pp 239-242

doi:10.4028/www.scientific.net/AMR.986-987.239

Analysis on capacity of transmission line based on thermal rating

Yang Bo,Wu Kuihua,Wang Yiqun,Yang Shenquan

Economic & Technology Research Institute, State Grid Shandong Electric Power Company, Shandong Jinan 250021

Keywords: Transmission capacity; Static thermal rating; Real-time static thermal rating

Abstract. The rapid growth of power grid load put forward higher requirements on the transmission capacity of line, with the growing tension of line corridors, building new transmission lines is becoming more and more difficult. Therefore, it is of realistic significance to analyze the transmission capacity of existing transmission line and fully tap the existing power grid transmission capacity. On the basis of previous studies, and consulting a large number of references, this paper summarizes and expounds the methods of improving transmission capacity by using the thermal rating analysis, introducing static thermal rating and real-time static thermal rating. Also, this paper verifies applications of the above methods in actual running environment.

1 Introduction

As an important component of power system, transmission line is the carrier of connecting power generation side and power demand side, and its transmission capacity will directly affect the level of the power generation side and electricity side, which have important influence on the development economic and social. Especially the rapid growth of social power load in recent years, how to improve the transmission capacity of power grid has becoming a hot spot of research.

On the issue of improving grid transmission capacity, on one hand, strengthening the construction of power grid and new power transmission and transformation projects, optimizing the existing network structure, to improve the power transmission capacity; on the other hand renovating the existing grid technical to improve the transmission capacity of the existing grid. For the transmission lines in power network, the transmission capacity is determined by the conductor itself limited factors. When current through conductor, temperature of the conductor rises and stress and sag of the conductor increases, which are the main factors of limiting transmission capacity. The transmission capacity of conductor is determined by the temperature of the conductor, tension and sag, which is restrained at first, in practice, temperature is usually used to express uniformly. So methods of improving the transmission capacity of existing transmission grid can mainly considering from two aspects: one method is to improve the conductor operating temperature, without changing the circuit structure to improve the transmission capacity, the permission of the allowed operating temperature is higher, the conveying capacity is greater. The other is based on the operating conditions of a transmission line changing, through real-time online measurement information (such as temperature, light intensity, etc.), through the mathematical model calculation to calculate and determine the real-time operation condition of line, on the basis of meeting the safety running to play the actual transmission capacity of line as much as possible. In the actual operation environment, power grid transmission capacity is mainly affected by transient stability, voltage and the thermal stability the three constraints, with the grid is becoming stronger and stronger, and the application of FACT technology, transient stability and voltage constraints are no longer the main factor of restricting the transmission capacity, thermal stability has gradually become the bottleneck of limiting transmission capacity[1]. Therefore, to develop thermal load capacity of the existing grid has important research value. On the basis of previous studies, this paper summarizes two analysis methods of thermal load capacity of transmission line.

2 Thermal fixed value analysis method

2.1 Static thermal rating of conductor

Static thermal rating is the maximum allowable current carrying value which is calculated according to conductor allowable temperature from the thermal equilibrium equation under stable operation condition. Now many countries and organizations put forward the solving and modeling method of static thermal constant value of transmission lines, of which the more representative is the IEEE standard, CIGRE standard calculation method[2-3]. The calculation basis of these methods are basically the same, all based on the thermal balance equation of the transmission line, which is thermal balance according to the wire in a variety of heating and cooling factors in the process of operation, to calculate the maximum allowable current carrying value, only the factors in the process of calculation is different, but difference between the results is small. Following is the analysis and calculation to the IEEE standard.

When the heat generated by the conductor itself and absorbed from the outside world is equal to the quantity of heat lost to the world, the conductor runs in the thermal equilibrium state. Assume the transmission line is a uniform conductor, the heat balance equation of conductor expressed by the IEEE standards is:

$$q_l + q_s = q_c + q_r \tag{1.1}$$

q_l on behalf of the heat generated by conductor caused by current, and q_s for the heat of conductor absorbed from sun; q_c on behalf of convection heat of conductor, and q_r means the radiation heat of conductors. In CIGRE standard, in addition to the above four factors, the evaporative heat loss and the corona loss are also taken into account, but because of the changes in the quantity of heat balance caused by those is small and has strong randomness, CIGRE standard did not give specific calculation expression.

In the range of allowable operating temperature, the approximate expression of the calorific value caused by conductor current according to IEEE standard is:

$$q_l = I_{ac}^2 R(T_c) \tag{1.2}$$

I_{ac} on behalf of the AC current, $R(T_c)$ is the AC resistance when the temperature of conductor is T_c, and

$$R(T_c) = \left[\frac{R(T_{High}) - R(T_{Low})}{T_{High} - T_{Low}}\right] \cdot (T_c - T_{Low}) + R(T_{Low}),$$

$R(T_{High})$ and $R(T_{Low})$ respectively represent the AC current resistance under the known high temperature T_{High} and low temperature T_{Low}.

For the other three factors in the heat balance equation, the IEEE standard also gives the corresponding calculation method and calculation model, no longer will we say here.

Various factors affecting the transmission line in actual operation are considered in equation (1.1), including heating and cooling factors, and the equation really reflects the relationship between conductor current and temperature in a certain operation environment. Static thermal rating of transmission line is solved according to the heat balance equation through setting conservative boundary conditions (such as high temperature, strong light, small wind speed, etc.). Therefore, the calculated difference between static thermal constant values is relatively large when using different boundary conditions. For example, some nations have their own rules to the allowable operating temperature, Japan and the United States taking the temperature of wire heating allowed is 90℃, Germany, the Netherlands, Switzerland is 80℃. Our country in the original design procedure is 70℃(large span is 90℃) referring to the standard of the former Soviet union, due to restriction of wires allow temperature, the line transport capacity is also limited. In 2010, the latest issued national standard increased the allowing temperature of conductor heating to 80℃, according to the experience, carrying capacity can be increased by 24% - 27% if wire allowing temperature from 70℃ to 80℃. Therefore, the carrying capacity can further increase if we can improve the allowing temperature of wire heating, further improving the transmission capacity of existing grid, namely

without changing conductor structure to increase transmission capacity. In order to improve the transmission capacity of the line, further researches are needed in material of transmission line to improve the allowing temperature of line in the long running time.

Static thermal rating converted the limit of the allowing temperature of conductor to the limit of the allowing current, which is convenient for the use of engineering. But because of its conservative boundary conditions, its real transmission capacity is limited in most time. In order to solve this problem, on the basis of the static thermal rating, some countries and regions began to try to calculate multiple static thermal rating under different conditions, for guiding operation scheduling and control of the system. Such as setting multiple fixed values one year or a day, some places enact normal situation, short-term situation, an emergency of the thermal constant value, etc. By setting different static thermal rating under different condition, line transmission ability can be improved in a certain extent, which is conducive to play real transmission capacity of the line as much as possible [4].

2.2 Real-time static thermal rating of conductor

When designing the line, the setting limit value of the line is a kind of static value, in order to prevent line fault if the transmission capacity more than the allowed conveying capacity, it is assuming the line running on the basis of harsh weather conditions, and determining a conservative static limited capacity. But in the actual operation conditions, such bad weather conditions is rare, so the line can't effectively play its transmission capacity and waste a portion of the resources in the vast majority of cases. Therefore, considering the combination of line heat balance equation, and the line in the actual operating conditions of a variety of circumstances (such as the weather temperature, wind speed, etc.), to consider improving transmission line transmission capacity.

With the continuous development of modern measuring technology, the environment temperature, wind speed, sag, tension, and light and other related measuring technology is mature, making it is possible to determine the load capacity of conductor environment according to the actual measurement, which is the real-time static thermal rating. Davis, in 1977, first put forward the concept of real-time static thermal constant value, is on the basis of the theory of the extension of the SCADA system, which include the meteorological data (sunshine intensity, wind speed, wind direction, environment temperature, etc.) and the conductor temperature. The system has made many times experiments study[5], combined with the thermal equilibrium equation and the actual operation environment parameter data of line, real-time static thermal rating can be further excavated the real transmission capacity of conductor, slows down the demand for construction and expansion of the line, save investment, and improve the reliability of system.

Taking LGJ - 300 overhead line used commonly for example, to demonstrate the theory that based on the actual operating conditions of real-time static thermal constant value can significantly improve the line thermal load ability, combined with the region's environmental parameters, analysis the real-time static thermal constant value of lines, and compared with its static thermal constant value (safety current).

Combining circuit parameters, and through the calculation of the heat balance equation, the static thermal constant value of LGJ - 300 transmission lines (safety current) is 710A. Through collecting meteorological data in the region (sunshine intensity, wind speed, wind direction, environment temperature, etc.), calculate and obtain real-time static thermal rating of the transmission line based on the actual running environment in a few selected time period, as is shown in Fig.1.1.

The selected three moment in Fig.1.1 respectively is on August 8, October 8, and December 28, in which August 8 represents the region appeared typical moment of maximum temperature throughout the year, and December 28th annual minimum temperature for the region of typical moment throughout the year.

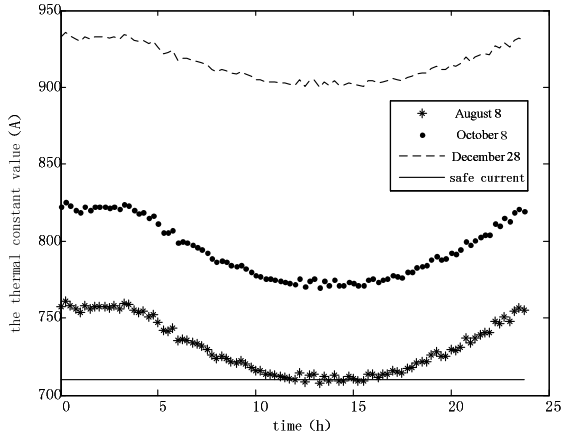

Fig.1.1 Real-time static thermal rating of LGJ - 300 transmission lines (safety current)

According to the curve in Fig.1.1, because August is the highest temperature in the region, so, in August 8, most of the time real-time static thermal constant value are higher than the safety current value, only in the moment 1, 2 PM due to environment temperature reach the highest temperature during the day, it is likely to appear the real-time static thermal constant value is lower than the safety current situation, but as the environment temperature is the extreme maximum temperature in the region; and October 8, the environment temperature is reduced, the current real-time static thermal constant value are higher than the safety current value; By December 28, the environment temperature is far lower than the temperature in August and October, so at this time the real-time static thermal constant value is much higher than current value.

Therefore, the calculated real-time static thermal rating is basically greater than the safety current value, in most of the time even far higher than the safety current value, this can also prove safety current value, namely the setting of static thermal constant is conservative, is not conducive to transmission lines to give full play real load capacity, also verify the analysis method of real-time static thermal constant value can better play to the line of actual transmission capacity.

3 Conclusion

On the basis of precious study, this paper summarized methods of researching and improving the thermal load capacity of transmission line. Combined with the heat balance equation of the transmission line, first elaborated thermal constant value analysis method based on the heat balance equation of transmission line, including static rating and real-time static thermal rating analysis methods. The paper also analyses the application of both in improving the transmission capacity of transmission line combined with the actual running environment.

Reference

[1] Zhang Qiping, Qian Zhiyin. Raise 500 kv transmission line transmission capacity [C]. Proceedings of 2004 China institute of electrical engineering, hainan, 2004
[2] IEEE Standard Board, IEEE Standard for Calculation of Bare Overhead Conductor Temperatures[S]. IEEE P738-1993., Nov. 1993
[3] CIGRE. Thermal Behavior of Overhead Conductors[J]. ELECTRA, 1992, No. 144: 107-125
[4] [4] Qian Zhiyin. the feasibility study on the real-time dynamic expansion of transmission line of [J]. Journal of east China power. 2005(07):18-21
[5] J.K. Raniga, R.K. Rayudu. Dynamic rating of transmission lines-a New Zealand experience [C]. IEEE Power Engineering Society Winter Meeting, 2000, 4(23-27):2403 – 2409

Advanced Materials Research Vols. 986-987 (2014) pp 243-246

doi:10.4028/www.scientific.net/AMR.986-987.243

Analysis on Capacity of Wind Power Integration into Grid Based on Power Balance

Liang Han[1,a], Yonggang Li[1,b]
[1]Department of Electrical Engineering, North China Electric Power University, Baoding 071003, China.
[a]hfhanliang111@126.com

Keywords: Peak regulation; Capacity of wind power; Power balance.

Abstract. Among all the factors influencing the capacity of wind power, peak regulation capability is commonly regarded as one of the most important constraint factors. From the perspective of peak regulation, the maximum peak-load regulating adequacy revised by the wind power characteristic coefficient is the limitation of the capacity of wind power. This paper proposes an assessment system on capacity of wind power integration into grid based on power balance. First of all, this assessment system takes the impact of wind power integration on the reserve capacity of the power system into consideration. Then calculate the reserve capacity based on power generation reliability index. Finally, evaluate the capacity of wind power based on the peak regulation capability of the units during the low load period. This paper analyses the capacity of wind power integration into Liaoning power grid based on power supply characteristics, load characteristics and peak-valley difference, and points out that the phenomenon of the "wind curtailment" is unavoidable. According to the specific situation of wind power limitation, this paper proposes measures to maximize the capacity of wind power.

Introduction

Wind power generation, as a fully-developed renewable energy power generation technology has developed rapidly in China in recent years. While different degrees of phenomenon of the "wind curtailment" appears in different areas, which leads to heat discussions and wide researches on the capacity of wind power integration into power grid. The capacity of wind power integration into power grid is limited and affected by aspects of safe and reliable operation of the power system, such as, the limitation of frequency regulation and peak regulation, the limitation of steady state power flow, the limitation of transient stability and the limitation of reactive power and voltage. Among these limitations, the capacity of peak regulation which has a significant influence on safe and reliable operation of the power system and is widely considered as the key factor to limit the capacity of wind power relates to the economic cost in system operation, the accurate prediction of wind power output and the component ratio and features of power.

[1] and [2] made a detailed research on the characteristics of wind power output in Jiuquan wind power base and concluded that the problem of frequency regulation the system are facing after large scale wind power integration is not obvious due to the complementarity of wind power output within a short time. Peak regulation of the system faces great pressure within a long time because of the correlation of wind power output. Usually the wind power integration into power system in a large scale requires deep spinning reserve of conventional thermal power units or the cold stand-by of hydroelectric unit to deal with the intermittent fluctuations of wind power. A large amount of reserve capacity required for the operation of wind power is the root of great pressure the system are facing after large scale integration of wind power. In order to provide support for the reasonable arrangement of the local wind power planning and scheduling strategy [3-4], based on the wind power clustering effect [5], this paper concludes the capacity of wind power integration into power grid through the analysis on the characteristics of the power supply and the load of Liaoning power grid.

The Assessment System on Capacity of Wind Power

The characteristic indexes on capacity of wind power. Because the capacity of wind power integration into power grid is not directly determined by characteristic indexes of wind power and power grid, they influence and control each other and are indirectly determined by the coordinated operation of large power grid. This paper proposes the characteristic indexes on capacity of wind power from the aspects of wind power characteristics and power grid characteristics.

Characteristic indexes of power grid mainly include the power supply characteristics, structure characteristics, load characteristics and safety reliability. Characteristic indexes of wind power include simultaneity rate, power change rate, peak-shaving capability, power prediction, credible capacity, wind power curtailment ratio and utilization rate of wind energy. Fig.1 shows the assessment system of the capacity of wind power.

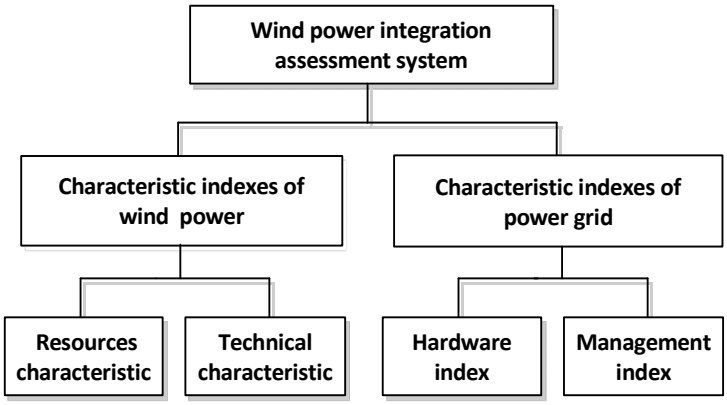

Fig. 1. The hierarchy of wind power integration assessment system

The method of evaluation on wind power integration capacity. The capacity of wind power during the low load period determines the capacity of the wind power integration into power grid. The analysis on power supply and lowest load is the main aspect of the assessment system. Power supply arrangement should consider enough spinning reserve when thermal power units and hydroelectric units are in peak load period, besides, generation power of thermal power units can reduce to the lowest output according to the deep-regulation, and the output of hydroelectric units are able to reduce to zero, but it is better to consider some unit-operating capacity of system. The capacity of wind power during the low load period equals the difference between the lowest load and the lowest output of all units in operation. The capacity during the low load period is converted to the capacity of wind power integration into power grid according to simultaneity rate [6-7].

Evaluation procedures on capacity of wind power integration into grid based on power balance as follows：

1) The overall analysis of power source composition， load characteristics, peak-valley difference, reserve capacity and fluctuation of wind power.

2) Calculate the reserve capacity according to system reliability.

3) Calculate non-dispatchable output, the capacity of heating units, tie line power and the capacity of pumped storage unit P_{pump}.

4) The maximum output $P_{g\,max}$ and the minimum output $P_{g\,min}$ inside the power system as follows

$$P_{g\,max} = P_{load\,max} - P_{tie}. \quad (1)$$

$$P_{g\,min} = P_{load\,min} + P_{pump} - \lambda_1 P_{tie}. \quad (2)$$

Where $P_{load\,max}$ is the peak load, P_{tie} is tie line power, $P_{load\,min}$ is the valley load, λ_1 stands for regulation rate of tie line power.

5) The output of peak regulation unit during peak load period $P_{reg\,max}$ and low load period $P_{reg\,min}$ as follows

$$P_{reg\,max} = P_{load\,max} - P_{con} - \lambda_2 P_{thermal}. \quad (3)$$

$$P_{\text{reg min}} = P_{\text{load min}} - P_{\text{con}} - \lambda_2 P_{\text{thermal}} . \quad (4)$$

Where P_{con} is the non-dispatchable output, λ_2 and $P_{thermal}$ stand for peak regulating rate of heat supply unit and capacity of heat supply unit.

6) The unit-operating capacity of peak regulation unit $P_{commit\ max}$ and the minimum output $P_{commitmin}$ as follows, where γ stands for regulation rate of peak regulation unit.

$$P_{\text{commit max}} = P_{\text{reg max}} + P_{\text{reserve}} . \quad (5)$$

$$P_{\text{commit min}} = \gamma P_{\text{commit max}} . \quad (6)$$

7) The capacity of wind power integration into power grid P_{wind} as follows, where β is simultaneity rate of wind power.

$$P_{\text{wind}} = \frac{P_{\text{reg min}} - P_{\text{commit min}}}{\beta} . \quad (7)$$

Analysis of Power Supply Characteristics and Load Characteristics in Liaoning Power Gird

Table 1 presents the components of power supply in Liaoning by the end of 2012, with thermal power being the major component and heat supply unit taking a relatively large portion. So the peak regulation capacity of power supply is low.

Table 1 The development of power supply and load in Liaoning Province

Category	2007	2008	2009	2010	2011	2012	annual rate of growth [%]
Peak load [MW]	19330	19450	22100	24650	24960	27750	7.50
Installed capacity of power supply [MW]	21310	22010	25550	32275	34004	38070	12.30
Tie line power [MW]	6000	6050	6800	6800	9000	9620	9.44
Installed capacity of wind power [MW]	346.7	833.6	1733.2	3084.4	4023.3	4755.9	68.83

Wind power develops quickly in Liaoning power grid and it has become the second largest power, ranking the fourth in the system of State Grid Corporation. The daily average load of Liaoning power grid in winter, 2012 is presented in figure 2. The maximal difference between peak and valley load is presented in figure 3.

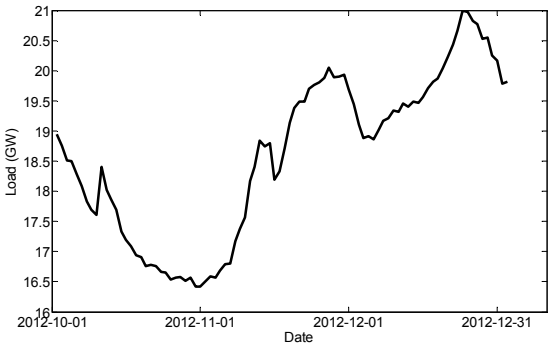

Fig.2 Daily average load of Liaoning power grid in winter

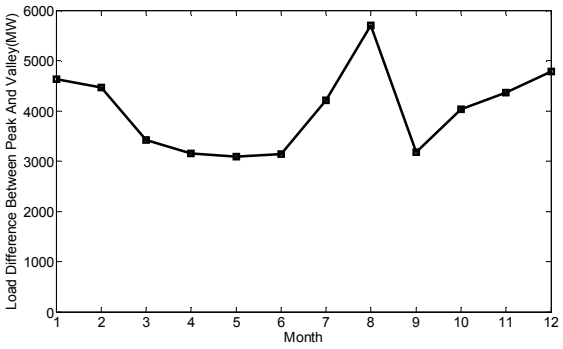

Fig.3 Maximal difference between peak and valley load

The above analysis shows that the peak-valley difference mainly appears in summer and winter which is contradictory with the distribution of wind power output, thus it leads to reverse peak regulation of wind power.

The analysis of wind power capacity in Liaoning power grid

Start-up mode is determined in the mode of winter peak time, spring festival, summer peak time and May 1st every year. Start-up principle is that power supply in peak hours must guarantee enough Spinning reserve capacity, not too much as well. Generation power of thermal power units can reduce to the lowest output according to the deep-regulation, and the output of hydroelectric units are able to reduce to zero.

The following is the illustration of calculation on capacity of wind power integration into power grid by taking winter peak time as an example. Installed capacity is 22129MW, and tie line power is 9600MW. According to statistics of wind power in 2012, the highest load demand in Dec, 24th is 23581MW and the lowest load demand is 18050MW. λ_1 is 0.7, λ_2 is 0.78, γ is 0.6, simultaneity rate is 0.7, and preserve capacity is 764MW.

Through the analysis and calculation, P_{gmax} is 13981MW according to historical data provided by Liaoning power grid. P_{gmin} is 11330MW, $P_{reg\ max}$ and $P_{reg\ min}$ are 12871MW and 10220MW respectively. So the capacity of wind power is 2914MW. The installed capacity of wind power in Liaoning power grid is 4756MW in 2012. So, when the wind power output is larger than the limitation, the phenomenon of "wind curtailment" is unavoidable. Table 2 presents the Generating capacity and wind power curtailment monthly in Liaoning Province.

Table 2 Generating capacity and wind power curtailment monthly in 2012

Category	Jan	Feb	Mar	Apr	May	Jun	Jul	Aug	Sep	Oct	Nov	Dec
Installed capacity of wind power [MW]	4100	4170	4340	4390	4420	4420	4560	4560	4660	4710	4710	4760
Generating capacity [Million KWH]	306	662	783	1100	685	631	535	407	632	770	624	743
Wind power curtailment [Million KWH]	119	200	164	156	19	10	15	31	15	51	198	152
Curtailment proportion [%]	38.89	30.21	20.95	14.18	2.77	1.58	2.80	7.62	2.37	6.62	31.73	20.46
Utilization hours	75	159	186	255	154	142	116	86	135	156	132	156

Summary

The evaluation system of wind power capacity based on system reserve and peak-regulation capacity is proposed in this article. By the overall analysis of power source composition, load characteristic, reserve capacity, tie line power and peak-regulation capacity of thermal power unit, taking Liaoning power grid as an example, the result of evaluation shows that the phenomenon of "wind curtailment" exists in the low load hours during winter heating period.

References

[1] Chuangying Xiao, Ningbo Wang, Kun Ding. System Power Regulation Scheme for Jiuquan Wind Power Base. Proceedings of the CSEE, Vol. 30(10), p. 1-7. (2010).

[2] Chuangying Xiao, Ningbo Wang, Jing Zhi. Power Characteristics of Jiuquan Wind Power Base. Automation of Electric Power Systems, Vol. 34(17), p. 64-67. (2010).

[3] Jilijia Matevosyan. Wind Power Integration in Power Systems with Transmission Bottlenecks. IEEE Trans on Power Systems, Vol. 17(4), p. 1132-1139. (2007)

[4] A Feijoo, J Cidras. Modeling of Wind Farms in the Load Flow Analysis. IEEE Trans on Power Systems, Vol. 15(1), p. 110-115. (2010)

[5] Changling Luo, H. Golestani Far, H. Banakar, Ping-KwanKeung, Boon-Teckoi. Estimation of Wind Penetration as Limited by Frequency Deviation. IEEE Transaction on Energy Conversion, Vol. 22(3), p. 783-791. (2007).

[6] Mohammed El Moursi, Geza Joos, Fellow, IEEE, and Chad Abbey, Student Member, IEEE. A Secondary Voltage Control Strategy for Transmission Level Interconnection of Wind Generation. IEEE Transactions on Power Electronics, Vol. 23(3). (2008)

[7] Hongliang Guan, Haixiang Zhao, Yongning Chi. Requirement for LVRT Capability of Wind Turbine Generator in Power System, Vol. 31(7), p.78-82. (2007)

Advanced Materials Research Vols. 986-987 (2014) pp 247-250

doi:10.4028/www.scientific.net/AMR.986-987.247

Application Research of Gas CCHP System to Hotel Buildings in Shanghai

Gu Qunyin[1,a], Yan Jiachen[1,a], Wu Cuiyu[1,a], Chen Haiyan[1,a], Song Ying[2,b] and Zhao Xiaodan[3,c]

[1]College of Electric Power Engineering, Shanghai Electric Power University, Shanghai, 200090,China

[2]Sichuan Province Electric Power Company Construction Management Center, Chengdu,610021, China

[3]Sichuan Electric Power Construction Company, Chengdu, 610000, China

[a]email: guqy0000@163.com, [b]email:451474004@qq.com, [c]email:715446610@qq.com

Keywords: CCHP; gas engines; gas turbines; economics

Abstract. In this paper, case of hotel in Shanghai was studied, and three kinds of CCHP import solutions are discussed by this algorithm based on real working condition parameters of thermoelectric load. Then, put forward the relative conclusions based on comparison of each scheme and calculation of power supply benefits and heating benefits, from the point of power supply economics and heating economics. So it has certain realistic meaning for the application of CCHP system in city hotel buildings.

Introduction

It is well known that the present energy structure does great harm to our environment, and delayed the implementation of sustainable development. At present, the important issues are Energy Price, the stability of the electric power grid, environmental pollutions and global climate change, and how to save energy and protect the environment have become an imminent. To resolve the above problems, it is necessary to adjust the energy resources structure and the extensive development of clean energy resources including nature gas. As a kind of distributed energy systems, systems of combined cold, heat and power driven nature gas has become a trend in the world. And it can realize the project of the synthetic of saving energy, environment protection, increasing electricity servicing, dealing with the air pollution and enhancing the energy’ s synthetic utilization ratio[1,2].

Due to the special business position, hotel has large demand of power, heating and cooling. CCHP can make full use of waste heat from power generation to supply heating and cooling for users, by using waste heat recovery equipment. In this way, the primary energy utilization ratio of the system can be improved; the comprehensively cascaded utilization of energy can be enhanced[3]. And it can also supply power as energy complementary which increasing the economy income and efficiency of the entire system[4,5].

Overview of the case

The case chosen for this article is a hotel in Shanghai which covers an area of 34,700 m^2, with a total floorage of 59,320 m^2 and 500 guest rooms. Relevant information shows that hotel can be divided into big, medium and small hotel, according to the scale of the hotel (number of guest rooms in the hotel). The big hotel more than 600 guest rooms; small hotel has 300 guest rooms or less; medium hotel has 300 to 600 guest rooms. Therefore, hotel chosen in this case belong to medium-scale hotel. Before importing CCHP, three traditional sets of CJHS-G713 fuel steam boilers in original heating system of hotel. Electricity supplied by 2 sets of 2500kVA transformers. In the winter, The minimum power load is 649.59kW, maximum load is 1791.58kW, The minimum heat

load is $1288.79kW$, maximum load is $3525.15kW$. The minimum cool load is $0kW$, maximum load is $227.679kW$.

CCHP introduction plans

CCHP Introduction Model. A salient feature of Building Cooling Heating Power is multi-energy output, and it is mainly in different heat-electricity proportion. Different output proportion will greatly degrades the efficiency of the system. Combined Cooling Heating and Power system has two traditional operating modes: “fixing power based on heat" and "fixing heat based on power", “fixing power based on heat" is to determine the power output according to the heating load or cooling load[6,7]. However "fixing heat based on power" is to determine the heating output or cooling output according to the power load. Only when ratio of heat to power in actual energy consumption is approximate to that in CCHP system, the CCHP system can get good economic benefits. Capacitance of CCHP system is determined by the annual minimum power demand, and it can ensure grid-connected operation without power injection. Meanwhile, In this model, heat is generated by system much more annual heating demand, and the heat generated by system is 100% utilization, and the system will bring in great economic benefits (contribute a lot to economic profit).so, in this paper, "fixing heat based on power" is selected as the operating mode in CCHP system. Shortage of electric power could be supplied by power grid, and shortage of heating could be solved by supplementary fuel layout. And three $1.46t/h$ of gas turbine boilers are selected as supplementary equipment[8].

Introduction Plans. Considering the constraint of energy-saving potentials, this paper discusses four methods.

The first scheme: Yanmar EP350G gas internal combustion turbines and 0.188T / h HRSG;

The second scheme: Wilson PG475B gas turbine cogeneration units;

The third scheme: Caterpillar 500F/C15 diesel generator sets;

The forth scheme: United Technologies Corporation PureCell-400 fuel cells.

The first scheme. Internal combustion engine generator as one part of power plant, can combined with heat recovery steam generator highly efficient to recover waste heat, to enhances the efficiency of the whole system. Considering the limitation of energy-saving potentials, power load can be supplied by urban power network and gas internal combustion engine, and the Yanmar EP350G internal combustion engine generator set was selected as power plant.

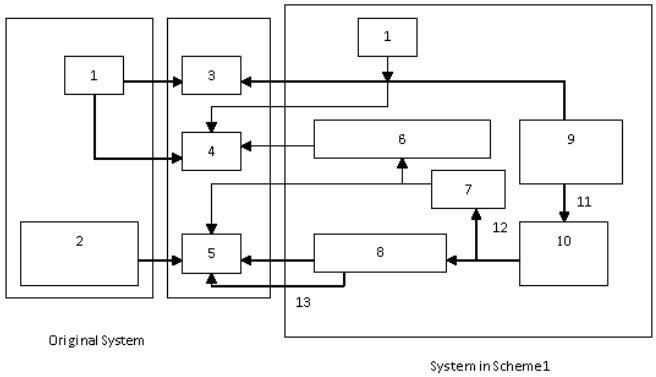

1-Commercial Power; 2-CJHS-G713 Oil-Fired Steam Boiler; 3-Power Supply; 4-Cool Supply; 5-Heat Supply; 6-Lithium Bromide Absorption Refrigerating Machine; 7-Boiler Cylinder; 8-Tubular Gas-Fired Boiler; 9-Gas Engine; 10-Afterheat Steam Evaporator; 11-High-Temperature Flue Gas;12-Steam; 13-Supplemental Combustion

Fig. 1 Flowchart of Yanmar EP350G gas turbine program

As Fig. 1 shows that, power load can be Time-Interval supplied by urban power network and internal combustion engine, the high temperature exhaust gas from the turbine is used to recovery steam generator for steam generation, and connected into gas-distributing cylinder in boiler room, which was combine by three 2t/h one-through gas boiler and one 7T/h old boiler, which can provide with heat for shower, cooking and drying. Shortage of heating could be solved by tubular gas boiler, and cooling can be achieved by the steam lithium bromide absorption chiller.

The second scheme. Gas Turbine suitable to the model of gas turbine and heat driven absorption chiller/ heater, the high temperature exhaust gas from the turbine is fully used to produce heating, and it can increase fuel efficiency. Wilson PG475B gas turbine cogeneration units was selected, for it is a high-efficiency set of solutions designed for CCHP by Wilson, with high reliability and utilization of flue gas for hotels transformation.

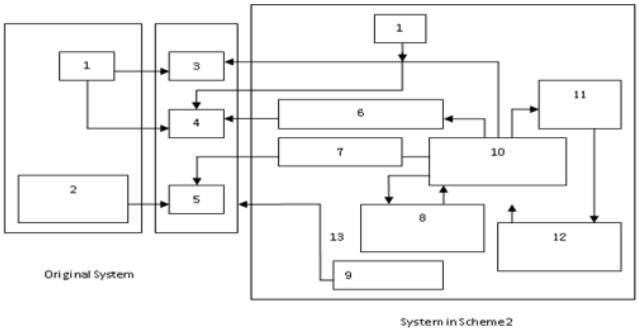

1-Commercial Power; 2-CJHS-G713 Oil-Fired Steam Boiler; 3-Power Supply; 4-Cool Supply; 5-Heat Supply; 6-Lithium Bromide Absorption Refrigerating Machine;7-Waste Gas Heat Recovery Furnace; 8-Inner-Cooling Cooling Water System and Remote Radiator; 9-Tubular Gas-Fired Boiler; 10-Wilson PG475B Gas Turbine; 11-Primary Heat Exchanger; 12-Jacket Cooling Water System and Remote Radiator; 13-Supplemental Combustion

Fig. 2 Flowchart of Wilson PG475B gas turbine cogeneration program

As Fig. 2 shows that, power load can be Time-Interval supplied by urban power network and internal combustion engine. When gas turbine is working, waste gas recovered by Waste Gas Treatment and Heat Recovery Equipment, there is a maneuvering directional valve at the inlet of equipment. The water recovers the heat of cylinder water by the primary heat exchanger and exhaust heat recovery device to further improve the temperature of water.

The third scheme. Today, research on the use of heat of diesel generators plays a less important role than gas turbines and internal combustion engines. In fact, the temperature of the exhaust gas of diesel generators is up to five-six degrees Celsius, with a high energy value in use. Considering the hotel's transformation space limitations and discharge exhaust temperature, the final choice is 500F/C15 Caterpillar diesel generator sets.

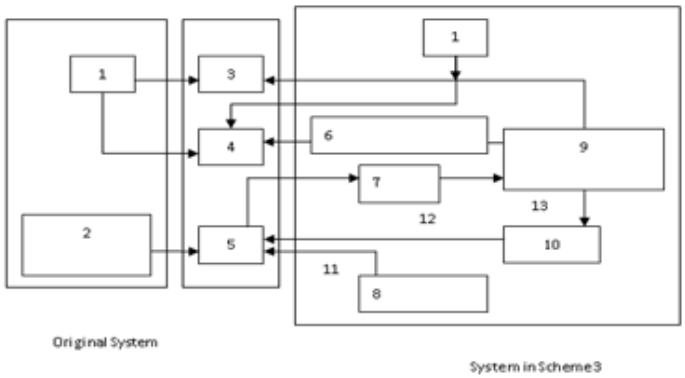

1-Commercial Power; 2-CJHS-G713 Oil-Fired Steam Boiler; 3-Power Supply; 4-Cool Supply; 5-Heat Supply; 6-Exhaust Gas Adsorption Refrigeration System; 7-Feed Water Pump; 8-Tubular Gas-Fired Boiler; 9-Caterpillar 500F/C15 Diesel Generating Set; 10-Cooler; 11-Supplemental Combustion; 12-Hot Water; 13-Exhaust

Fig. 3 Flowchart of Caterpillar 500F/C15 diesel generator program

As fig. 3 shows that, power was supplied by the market and diesel generator together. Diesel generator exhaust gas through a heat exchanger to get hot water, then hot water piped to each user, which can be adsorption refrigeration in the summer and gain heat by directly using hot water in the winter. You can also install a valve for 24-hour hot water supply.

Economy Analysis on Power Supply

The following table shows the price of electricity in Shanghai 2013.

Table 1 Price of electricity in Shanghai 2013(commercial and industrial category)

	Time (Non-Summer)	duration (h)	Price (￥/kWh)
Low valley	22:00-6:00	8	0.350
Peak	8:00-11:00 18:00-21:00	6	1.167
average	6:00-8:00 11:00-18:00 21:00-22:00	10	0.714
	time (Summer)	duration (h)	Price (￥/kWh)
Low valley	22:00-6:00	8	0.285
Peak	8:00-11:00 13:00-15:00 18:00-21:00	8	1.202
average	6:00-8:00 11:00-13:00 15:00-18:00 21:00-22:00	8	0.749

The first scheme. Based on the data obtained recently, we know that the price of natural gas used for the generator in Shanghai is 2.43 Yuan/m^3. The consumption of gas engine of Yanmar EP350G is 90m^3/h. Then we can calculate the cost of power generation is $0.625 Yuan/kWh$.

Program 2. The unit consumption of Wilson PG475B gas turbine cogeneration is 126.2m^3/h. The unit cost of power generation is $0.807 Yuan/kWh$.

Program 3. According to some information, the unit price of diesel is about $7 Yuan/L$. The unit consumption of Caterpillar 500F/C15 diesel generator is $116.5 L/h$, so we can calculate the unit cost of power generation is $2.24 Yuan/kWh$.

Conclusion

Finally, based on the conclusions and experience, following recommendations about the application of Gas CCHP System to Hotel Buildings in Shanghai are given in this paper:

(1) With CCHP, heating benefit is much higher than electrical power benefit, and the former is 4 to 5 times of the latter by calculating;

(2) Gas internal combustion engines and gas turbines will be better choice with higher economy, when selecting CCHP power plant.

(3) When selecting the specific brand and model of the unit, unit generation cost should be focus on, in order to increase the time of power generation as much as possible, and get more heat energy. Then, much more revenue can be derived, for higher market price of steam and the huge demand of heating in the hotel.

(4) If cost of self-electric power generation is not too much exceeding to market price, CCHP system can be used to self-electric power generation. Though power benefit decrease, heating benefit can make up for the loss of power benefit, for increasing of heating benefit.

Reference

[1] Li Fangqin, Wei Dunsong. Thermal Economy Analysis of Natural Gas Co-Generation [J]. Power Engineering. 2004(2), 24(1):57-61

[2] Hu Xiajian, Zhang Xuemei, Cai Luyin. Recent Research Progress of Optimization for Combined Cooling Heating and Power Systems (CCHP) [J]. Energy Research and Management. 2010, 13(2):13-40.

[3] Li Hua, Li Huiqiang, Shuai Xiaogen, Wang Zhixiang. Economic Analysis on Green Energy Project of Cooling-heating-power Supply [N]. Journal of Huazhong University of Science and Technology (Urban Science Edition). 2006(5), 23(2)

[4] Wang Chaoqun, Long Weiding. Economical analyses of combined cooling heating and power: a case study [J]. Hv & Ac.2004, 34(4):38-41

[5] Wang Xiaochun,Kou Jianyu,Shi Yanhui. Technology and Applications of Combined Cooling Heating and Power System [J]. Electric Power Survey & Design. .2010(1):42-45

[6] Wu Guihui. Development of distributed energy in China[J]. Zhejiang Energy Conservation, 2007(4):57-58

[7] Lan Li, Zhang Ling,Gu Dengfeng. Building Cooling,Heat and Power Cogeneration System and Sustainable Development [J]. Gas & Heat, 2006(1):49-57

[8] Weng Yiwu, Weng Shilie, Su Ming. The microturbine distributed energy supply system[J]. China Power, 2003.36(3):136-140

Advanced Materials Research Vols. 986-987 (2014) pp 251-254

doi:10.4028/www.scientific.net/AMR.986-987.251

Benefits Analysis of Energy Tax Reform

Ma Jian Song Yang [a]Ji Liuhe

Shenyang University, Shenyang 110044

[a]yang_wenlin@163.com

Keywords: Energy Tax, Benefit, consumer surplus, producer surplus

Abstract: Sustainable economic growth of a country needs support from energy industry. The limitation and environmental problems caused by energy makes the governments to re-examine their energy strategies. As an important tool for national macro-control, tax policy has an irreplaceable role on the promotion of conventional energy conservation, sustainable use and introduction of new energy sources. More and more theories and practices have proved that the energy tax is beneficial to conservation and utilization of energy. At present, China has yet to levy a special energy tax. There are many problems in energy taxes, so we have to reform our current energy taxes. Evaluation of the effect of the reforms can be judged in many ways. In this article, we will analyze it from a social welfare perspective, trying to build an optimization of the energy tax system in order to achieve social welfare maximization.

Introduction

The limitation and environmental problems caused by energy makes the national governments to re-examine its energy strategy. There are two orientations among countries: the first one is saving energies and committing to the development of energy-saving technologies and energy-efficient products; the second is developing new energies which can replace conventional energy sources. It can lead energy consumption structure to the direction of efficient, clean, renewable, low-carbon direction or carbon nuclear, solar and wind energy. As an important tool for national macro-control, tax policy has an irreplaceable role on the promotion of conventional energy conservation, sustainable use and introduction of new energy sources. More and more theories and practices have proved that the energy tax is beneficial to conservation and utilization of energy. At present, China has yet to levy a special energy tax. There are many problems existing in energy taxes, so we will reform current energy tax.

For the tax system, people want to be able to take into account not only fair but also to efficiency, and achieve the balance between these two and a tax optimal results. However, under the influence of a variety of factors in reality, it is difficult to achieve optimal results. So, in academia, their researches are more about how to make the tax system as close as the optimization. Through analysis of the tax system, the objective of tax system optimization is to reform and adjust itself to maximize its compliance with current environmental conditions and the choice of the parties of economic entities, and then maximize the social welfare. Only setting tax rate scientifically and rationally, guiding the behavior of businesses and consumers, can really achieve the effect of saving energy and protect the environment. In order to achieve the desired results, there must be a scientific and reasonable tax rates. If the interest rate is too high,it will hit some sectors and get opposition. So the tax can not be successfully implemented, and can not achieve the intended effect; but if tax rate is too low, it will not stimulate and guide consumer behavior. Therefore, scientific and reasonable tax rate is very important for its succes, so is energy tax. The significance of this article lies in the attempts to establish an optimization of the energy tax system to achieve the desired goal of social welfare maximization. The following is my analysis of the benefits of energy tax policy.

Differentiated price optimization model based on the objective of maximizing the benefits

According to "Ramsey rule ", for taxing different commodities with minimal loss of economy overall efficiency, the rate of different commodities should inversely relate to its demand elasticity, we should take the optimal tax rate for residents of differentiated tax as Ramsey's solution. Therefore, the implementation of differentiated tax rate based on the consumption amount is in conformity with sub-groups of incomes tax principles. The core idea is to maximize social welfare under the constraints of balanced budgets (to meet the monopoly break-even). Ramsey model takes into account both the producer's costs, and the consumer's willingness to pay. it has been seen as the model which meets the requirements of social welfare and has important guiding significance for the design of differential tax rates.

It's cost function is $C(q)$, The marginal cost is $c(q)$. Diversity of consumer demand can be represented by $\theta \in [\underline{\theta}, \overline{\theta}]$ (it mainly refers to the needs of different consumers in different income level). Assuming parameter θ only relates to income. People'needs increase as the income increase. So, the demand function for each resident can be expressed as follows.

$$q = q(p, \theta) \tag{1}$$

Where, q-- quantity residents use; p-- price, yuan / liter.

The total cost can be expressed as

$$P = F + q(p, \theta) \times p(q, \theta) \tag{2}$$

Where F-- is the fixed part in cost; $p(q, \theta)$-- marginal price related with q, yuan / liter.

The objective of resident differentiated tax rate is the maximization of social welfare, namely, the maximization of consumer and producer surplus and the welfare equilibrium between residents and businesses. The social welfare is maximized at this time.

We we use $q_{\min}$ to represent the minimum amount, $q_{\max}$ to represent the maximum amount. Total consumer surplus is represented by the following formula:

$$CS = \int_{q_{\min}}^{q_{\max}} Q(P(q), p(q), q)dq + \int_{p_{\min}}^{\infty} Q(F, 0, q_{\min})dF \tag{3}$$

Producer surplus is represented by the formula:

$$PS = \int_{q_{\min}}^{q_{\max}} Q(P(q), p(q), q)[p(q) - c(q)]dq + Q(p_{\min}, 0, q_{\min})[P_{\min} - C(q_{\min})] \tag{4}$$

Welfare maximization is represented by the formula

$$\begin{aligned} &\max_{p(q), q_{\min} P_{\min}} \int_{p_{\min}}^{\infty} Q(F, 0, q_{\min})dF + \int_{q_{\min}}^{q_{\max}} Q(P(q), p(q), q)dq \\ &+ \int_{q_{\min}}^{q_{\max}} Q(P(q), p(q), q)[p(q) - C(q)]dq \\ &+ [Q(P_{\min}, 0, q_{\min})[p_{\min} - C(q_{\min})] \end{aligned} \tag{5}$$

We get:

$$\frac{p(q) - c(q)}{p(q)} = -\frac{\alpha}{\varepsilon_p^q(q)} \tag{6}$$

In the above formula, $\varepsilon_p^q(q)$-- Price elasticity of residents'demand. From the formulas' results, the solution depends on the elasticity of demand and the marginal cost of production. The commodities demand functions for different people is different, so is the price strategy .

Calculation model of social welfare under the differentiated price

Using Marshall consumer surplus to calculate the variation of consumer welfare of different residents(based on the income). The definition of consumer surplus variation (CSV) is: the possible money saved for each resident after changing current energy price to hypothesized price. The definition of producer surplus variation (PSV) is: the possible producer loss after change current energy price to hypothesized price. Definition of social change welfare (WV) is: For society as a

whole (general consumers and supply companies), the average income of each individual (or losses). In relative terms, changes in welfare is the average energy consumption of the general population changes apart from changes in consumer surplus and producer surplus.

Consider a typical resident. The type of this resident is θ. the price structure is $p = \{n, p_i\}$, n is the number of grades of differentiated prices residents, pi is the i-th grade marginal price.

This resident's consumer surplus was represented as below

$$U(p,\theta) = \sum_{i-1}^{n-1} \int_{p_i}^{p_i+1} q(p,\theta)dp + \int_{p_n}^{\infty} q(p,\theta)dp \tag{7}$$

Where $q(p_i,\theta)$ is the Marshall linear demand function of each grade.For each price system, the average price in different range is calculated as $(p - \sum_{i-1}^{n-1} b_i p_i)$, which bi is the percentage ith takes in total expenditure.

For current residents price, these ratios can be drawn from the data observation. Residents features θ can be used to calculate the optimal resident price, it is represented by the following formula:

$$P[q(\overline{p},\theta) \le \overline{x}] \Leftrightarrow P[\theta \le \frac{1}{\beta_2}(\overline{x} + \beta_1 \overline{p} - \beta_0)] \tag{8}$$

Where $q(\overline{p},\theta)$ --the current total demand's functional prediction in definition; $\overline{x}$ --upper levels of different intervals.

Reduced consumers surplus of typical residential is represented by the following formula:

$$U(\overline{p},\theta) = \int_{\overline{p}}^{\infty} q(p,\theta)dp \tag{9}$$

Changes in consumer surplus is represented by the following formula:

$$CSV = \int_{p_0}^{p_i} q(p,\theta)dp \tag{10}$$

In the formula, p_0 --Current prices; p_1 --The value of the resident price ladder programs.

The producer surplus obtained by producer who facing residents of type θ and price structure $p = \{m, p_i\}$ is represented by following:

$$PS = (p,\theta) = \sum_{i-1}^{m} [p_i - c(q)]q(p_i,\theta) \tag{11}$$

Where $c(q)$ --marginal cost when the producer's supply is $q(p_i,\theta)$

The remaining production is expressed as the following formula:

$$PS(p,\theta) = q(p_0,\theta)[p - c(q)] \tag{12}$$

The surplus changes in production are expressed as the following formula:

$$PSV = q(p_1,\theta)[p_1 - c(q)] - q(p_0,\theta)[p_0,\theta)[p_0 - c(q)] \tag{13}$$

Finally, the total welfare changes are expressed as the following formula:

$$WV = CSV + PSV \tag{14}$$

Empirical analysis of energy tax reform benefits

Benefit calculation was gotten by setting research objects as a whole, which use empirical distribution that based on subjects and proportion of consumer distributed into different price zone. Here, we take oil tax as research objects calculating the consumer and producer surplus. For products like oil, the amount of each resident use can not be measured like water and electricity. So it can not be taxed based on amount. However, by measuring the oil consumption amount of different income group, we can know what tax rate we should use for different income group. We can subsidize different income group to reflect the differentiated tax rate. Detailed empirical analysis is as follows:

Table 1 Transportation cost effects function and demand function of five grades urban households.

Income Quintile	Consumption demand function
Low income households	$x_1 = 1342.5 / p_1$
Second quintile income households	$x_1 = 1150.15 / p_1$
Middle-income households	$x_1 = 1762.25 / p_1$
Fourth quintile income households	$x_1 = 2647.88 / p_1$
The highest income households	$x_1 = 10875.68 / p_1$

Elasticity of demand was drawn from table1 and get residents differentiated oil program according to formula 6.

Then we can get residents social welfare changes according to Equation 14.

Table 2 Changes in the social welfare of residents

Residents Type	Welfare changes
Low-income	-5.26 -5.26
Middle-income	15.1 15.1
High income	6.35 6.35
Total	16.19 16.19

As can be seen from the results, after implementing differentiated oil price according to the amount consumption, the welfare of the society increased. For low-income residents, changes in oil prices program will reduce social welfare. This is due to we reduced oil price in the frist and second grade in the simulation program. We ensure the needs of low-income residents and improve the consumer surplus. But then, the marginal cost of producer is higher than the price, so the producer surplus was reduced. So for the consumption amount in the first and second grades, they correspond to low income group, the total welfare changes are negative, that means the total welfare was reduced. The last two grades is aimed to middle and high income residents. The simulation price is increasing gradually and even higher than current price, then the consumer surplus decreases, producer surplus increase and social welfare changes turn to positive, that means the total welfare is increasing. Finally, the sum of each group's welfare is the social total welfare,which means the increase of social welfare. Therefore, the differentiated tax rate will lead to the differentiated price which increase the social welfare effectively.

Summary

Through the analysis of the energy tax benefits. We can see that the setting of energy tax should take into account its energy production, consumption characteristics and the level of economic development. Developing differentiated tax rate according to region and time. Meanwhile we can take full advantage of preferential tax policy to subsidize different energy products, producers and consumers to achieve the maximization of social welfare. You can take advantage of tax incentives and subsidies for different energy products, businesses and consumers in order to maximize social welfare.

References

[1] Deng Zhigao. China's energy structure and economic growth. Shanxi Energy and Conservation,1997(1), p.14-28

[2] Fan Gang. China marketization index--the relative progress of the regional markets. Beijing: Economic Science Press,2004, p.40-65

[3] Wu Qiaosheng. Process of industrialization in China's energy consumption changes. China Industrial Economy,2005(4), p. 30-37

[4] Yu Jiang. Resource constraints, structural change and economic growth. Beijing:People's Publishing House,2008, p. 123-156

[5] Guo Kesha. China:Reform Economic Growth and Structural Change. Shanghai:Shanghai People's Publishing House,1996, p. 122-124

[6] Han Wenke.Trend of China's energy consumption structure and the Countermeasures. Beijing: China Planning Press, 2007, p. 13-28

[7] Lin Bo. China's energy needs Econometric Analysis. Statistical Research,2001(10), p. 34-39

Advanced Materials Research Vols. 986-987 (2014) pp 255-258

doi:10.4028/www.scientific.net/AMR.986-987.255

BIPV with On-grid Tariff Policy in China

Rong Guo

RM208, Gaoceng Building,NO.13,Yanta Road,Xian city,Shanxi province,710000China

guorong1114@126.com

Keywords: BIPV; On-grid tariff; Sustainable Development

Abstract. Building integrated photovoltaic (BIPV) is an important direction of the green building. BIPV has developed rapidly in many developed countries and effectively saved resources. It owes to the government's effective promotion policy. The implementation of the on-grid tariff policy is a new stage of BIPV development. BIPV on-grid tariff pricing is a key point of BIPV promotion. Whether on-grid tariff is reasonable and applicable or not will directly affect the implementation effect of BIPV on-grid tariff policy. The current international common standard cost method is used to calculate on-grid tariff. Many countries implement unified on-grid tariff standard in their country, and often ignores the differences between different projects and areas. Based on the average on-grid tariff with standard cost method ,combined with the influence factors of BIPV on-grid tariff this paper build a corresponding on-grid tariff adjustment coefficient system with the current study method. Three methods used to get this goal are given and analyzed in this paper, the Delphi method， fuzzy mathematics method and neural network. This paper uses the Delphi method to build the on-grid tariff adjustment coefficient system model and choose three main factors, annual effective utilization hours, combination mode and PV system capacity, to build the on-gird tariff coefficient adjustment system model. This paper provides a reference basis of BIPV promotion policies and on-grid tariff pricing model for many countries.

GENERAL INSTRUCTION

With the world's growing demand, the contradictions between energy supply and demand further strengthened. The vigorous development of renewable energy can contribute to the world economy to achieve sustainable development. Construction is one of the top three energy consumption industry. Building energy efficiency get more and more national attention. Building energy consumption is almost 1/3 in China's total energy consumption [1]. Construction combined with Renewable energy has become an important development direction of building energy efficiency. Renewable energy sources include solar, wind, geothermal etc. With its advantage of abundance, clean, universality, solar energy has become widely accepted in building energy efficiency.

Solar energy on building applications include BAPV and BIPV. BAPV is Building Attached Photovoltaic, and BIPV is Building Integrated Photovoltaic. BIPV is a new direction of solar system combined with the construction[2]. Now, photovoltaic technology has gradually matured after years' development. The Chinese government has also proposed a series of policies to promote the development of BIPV, but the scale of BIPV is still a very small proportion in Chinese market. BIPV development is still in its infancy in China. To a certain scale, the government needs to formulate incentives policy to increase developer initiative to develop photovoltaic building and increase consumers' awareness of consume BIPV products.

Many foreign countries in promoting BIPV have made an notable achievement, and also accumulated abundant experience. Germany issued the "On-grid Tariff Act." Its effectiveness, scientific and operability was quickly confirmed. Many European countries followed Germany and issued On-grid Tariff policy. They also got a certain success[3].

This article will focus on China status to establish a BIPV average on-grid tariff model. Because there are many factors affect in on-grid tariff, this article will establish a factor regulation system model with Delphi Method on the base of the average on-grid tariff, in order to increase the scientific

tariff calculation and practicality. The model will make the Chinese on-grid tariff more scientific and practical.

THE METHOD OF BIPV ON-GRID TARIFF ADJUSTMENT COEFFICIENT SUSTEM

BIPV average on-grid tariff model

Standard cost method, an important part of management accounting in the West, is a method based on prepared cost criteria, with comparing standard cost with actual cost, accounting and analyzing cost diversity. Calculating on-grid tariff with standard cost method is one of the most scientific tariff calculation methods currently [4]. In this paper the annual sunshine coefficient is Chinese average coefficient and letter "U" stands for the current Chinese BIPV systems' annual generation capacity, and "pe" stands for system efficiency[5]. On these conditions, on-grid tariff calculation mode can be built with this method [6]. Currently generally widely accepted PV tariff calculation model with standard cost method is :

$$P=\left[(1-p_a)\cdot R_e\cdot C+\frac{p_a C}{n}+\sum_{i=1}^{n}\left(1-\frac{i}{n}\right)p_a\cdot C\cdot R_i+\frac{p_0 C}{n}+p_1C_0+p_2C+p_3C\right]\div p_e U$$

p-the PV tariff

Pa-The loan proportion of the initial investment

Re- Annual return rate of capita

C-Initial investment

n- Loan Term

Ri-Annual interest rate

P0-the proportion of fixed asset investment accounted for initial investment

P1-the Operation and maintenance fee rates

C0-Fixed Asset Investment

P2-the Salaries and benefits rates

P3-the Equipment upgrades and overhaul costs rates

Pe-the PV System efficiency

U-Annual generation capacity of PV system

BIPV on-grid tariff adjustment coefficient system model with Delphi method

(1)Choosing experts

Choosing experts is the first step on the Delphi method, Expert decide whether the results is objective and accurate or not with Delphi method .The experts must be familiar with the Chinese BIPV on-grid's characteristics and the basic characteristics of BIPV in each area and the factors of BIPV on-grid tariff. They must have a profound professional theory, rich experience and forecast ability. Their academic viewpoints must be authoritative and representative. They must be interested in Chinese BIPV on-grid tariff adjustment coefficient system model and can attend all along. The expert should include BIPV and related industries economic experts who accord with fore-mentioned conditions, a certain percentage of the professional personnel, management experts, technical experts and senior decision makers. The experts' number is also very important. The number should be appropriate and it can be confirmed based on the expert accords with fore-mentioned conditions. It usually should be at least 9 and not more than 25 people. Too small number it doesn't guarantee the representation of the experts and in this situation the veracity and rationality of the result isn't guaranteed. If the number is too large, the workload is too much and the time is too long and also their opinions are not unified.

(2)Design consultation table

Before design the table, extensively research work should be done, combined with factors which influence the BIPV on-grid tariff, and the main factors can be drew up as comprehensively as possible so that experts can synthetically evaluate and make choice. Consultation table's content must be comprehensive. Each part in the table will be closely linked to BIPV on-grid tariff adjustment goal. These factors must be what experts are familiar with and care about. Many factors have an effect on

BIPV on-grid tariff. Three main factors have been chosen in this paper's consultation table， capacity of， PV systems ,the combination ways of photovoltaic system and building, the effective utilization hours in different area. They are shown in table 1.Then some explanatory notes such as regional background, the meaning of each factor, must be prepared. These materials and consultation table shall be mailed or delivered directly to experts, so that the experts accurately express their evaluation opinions. Experts independently give their evaluation in consult table and write comments, and then send or retrieve on schedule. This process involves on-grid tariff influence factors for determination, consult information, statistical information, information feedback and the second consult and statistics and feedback to consult again.

Table1. Factors' adjustment coefficient.

NO.	1			2			3	
Factors	Annual effective utilization hours			Annual generation			Binding mode	
	1200	1200-1400	1400-	0-0.5U	0.5U-2U	2U-	Attached	Integrated
Adjustment coefficient	$\overline{X}$	$\overline{X}$	$\overline{X}$	$\overline{X}$	$\overline{X}$	$\overline{X}$		
Note	The calculation of national average tariff is based on the annual Effective utilization hours is 1250,the annual generation is U. The binding mode is attached							

(3)Consulting and feedback

The consultation table and the relevant information sent directly to each selected experts. The experts independently give their written opinions without meeting each other and any psychological impact of the situation, and they must send them back in time. This process includes consultation tariff factors , each factor's assessment, consult statistical information collation, feedback and consulting again, and then re-statistics and feedback again. According to the importance degree and the degree of dispersion of expert opinion, the progress can be carried on 2times to 5times.

(4)Statistical processing of the data

After each round of consultation, expert advice will be counted and distinguished correctness. Then they are been quantitative statistics and evaluated by statistical methods and mean ,standard deviation and r variance of he weight of each factor score given by experts are calculated. Finely they are summarized in the corresponding tabular form.

Mean ($\overline{X}$) is the arithmetic mean of the scores given to each factor by experts, and is calculated as:

$$\overline{X} = \frac{X + X + \ldots + X}{n} = \frac{}{n}\sum X$$

Range(R) is the different value of the maximum and minimum. Formula is as follows:

$$R_j = X_{j\max} - X_{\mathrm{jmin}}$$

Standard deviation(σ) represents the extent of expert opinion. Formula is as follows:

$$\sigma_j = \sqrt{\frac{1}{n}\sum_{i=1}^{n}\left(X_{ji} - \overline{X_j}\right)^2}$$

Variance(σ2), standard deviation squared :

$$\sigma_j = \frac{1}{n}\sum\left(X_j - \overline{X_j}\right)$$

Based on mean, range and the standard deviation, you can observe and learn about the trends spread of expert advice in each survey round, to determine whether consultation results is useful. If the next round of consultation activities is needed, the results will be fed back to the experts as valuable reference material of the next round of consultation to get accurate final result. In the next round of consultation, the experts compare their own opinion with other experts advice based on the measured statistics of the last round of the regional factors mean, range and variance, and amend their own opinions appropriately. Then, the mean approaches the final result, and make smaller range and

variance. Thus, the difference advice of experts is less. After several rounds of determination, until the experts give their fixed judgment and evaluate opinions, the results are not change any more.

(5)Determine the results

After several rounds of consultation, the experts' advice is relatively stable. Finely, you can permutate and combine the different values of each factors by statistical methods. There is a power project. The annual effective utilization hours is below 1100.The annual generation is below 0.5U.The binding mode is dependent mode. The project tariff adjustment factor should be $\overline{X} \cdot \overline{X} \cdot \overline{X}$. With this method, BIPV tariff adjustment system table (Table2) can be made.

Table2. Adjustment factor value of BIPV tariff model.

		Annual effective utilization hours			Binding mode
		1200	1200-1400	1400-1600	
Annual effective utilization hours	0.5	$\overline{X}\ \overline{X}\ \overline{X}$	$\overline{X}\ \overline{X}\ \overline{X}$	$\overline{X}\ \overline{X}\ \overline{X}$	Attachment
	0.5-2	$\overline{X}\ \overline{X}\ \overline{X}$	$\overline{X}\ \overline{X}\ \overline{X}$	$\overline{X}\ \overline{X}\ \overline{X}$	
	2	$\overline{X}\ \overline{X}\ \overline{X}$	$\overline{X}\ \overline{X}\ \overline{X}$	$\overline{X}\ \overline{X}\ \overline{X}$	
	0.5	$\overline{X}\ \overline{X}\ \overline{X}$	$\overline{X}\ \overline{X}\ \overline{X}$	$\overline{X}\ \overline{X}\ \overline{X}$	Integrated
	0.5-2	$\overline{X}\ \overline{X}\ \overline{X}$	$\overline{X}\ \overline{X}\ \overline{X}$	$\overline{X}\ \overline{X}\ \overline{X}$	
	2	$\overline{X_1}\,\overline{X_6}\,\overline{X_8}$	$\overline{X}\ \overline{X}\ \overline{X}$	$\overline{X}\ \overline{X}\ \overline{X}$	

SUMMARY

BIPV tariff policy can effectively promote the development of photovoltaic building. Chinese government should perform reasonable BIPV tariff and establish a related policies adjustment systems. Many methods can be used to establish this adjustment system, such as Fuzzy Math, Neural network. When formulating Policy Chinese government can also use these method to establish corresponding policy to promote the development of photovoltaic building .

References

[1] Al-Salaymeh, A., Al-Hamamre, Z., Sharaf, F.,Abdelkader,M.R.: Technical and Economical Assessment of the Utilization of Photovoltaic Systems in Residential Buildings: the Case of Jordan. Energy Conversion and Management 51, 1719–1726 (2010)

[2] Cellura, M., Di Gangi, A., Longo, S., Orioli, A.: Photovoltaic Electricity Scenario Analysis in Urban Contests: an Italian Case Study. Renewable and Sustainable Energy Reviews 16, 2041–2052 (2012)

[3] Y. Mishing, in: Diffusion Processes in Advanced Technological Materials, edtied by D. Gupta Noyes Publications/William Andrew Publising, Norwich, NY (2004), in press.

[4] Suri, M., Huld, T.A., Dunlop, E.D., Ossenbrik, H.A.: Potential of Solar Electricity Generation in the European Union Member States and Candidate Countries. Solar Energy 81, 1295–1305 (2007) CrossRef

[5] Villarini, M., Limiti, M., Abenavoli, R.I.: Overview and Comparison of Global Concentrating Solar Power Incentives Schemes by Means of Computational Models. In: Murgante, B., Gervasi, O., Iglesias, A., Taniar, D., Apduhan, B.O. (eds.) ICCSA 2011, Part IV. LNCS, vol. 6785, pp. 258–269. Springer, Heidelberg (2011) CrossRef

[6] European Photovoltaic Industry Association, http://www.epia.org

Advanced Materials Research Vols. 986-987 (2014) pp 259-262

doi:10.4028/www.scientific.net/AMR.986-987.259

Comprehensive Evaluation of the Offshore Wind Power Project Navigation Safety

Fucai Jiang [a], Yanbin Guo [b], Quandang Ma [c]

School of Navigation, Wuhan University of Technology, Wuhan 430063, China

[a]guoyanbin@whut.edu.cn, [b]hangyuanjfc@163.com, 313246440@qq.com

Keywords: Energy, offshore wind power project, navigation safety, evaluation.

Abstract. This paper introduce the necessity of the construction of offshore wind power projects, analysis of the impact on the marine transport of offshore wind power project after completion, and then use the fuzzy comprehensive evaluation method to carry out a comprehensive assessment of offshore wind power projects, by identifying risk assessment index system, establish model for risk assessment, the final task is use the model to evaluate the navigation safety of an offshore wind power project.

Introduction

Energy is an important material basis for economic and social development; China is rich in offshore wind resources, with conditions development of offshore wind power resources.

When offshore wind power projects are completed which have influence on the navigable waters nearby. Therefore, the use of a safety assessment model for navigation safety of offshore wind farms comprehensive evaluation is very important. This paper used the comprehensive evaluation method for quantitative safety demonstration. By introducing an ample, paper proves the practicality of this model.

Integrated assessment model

Build process assessment model. Navigation safety assessment of offshore wind farm projects is a complex system, influenced by many factors, and the degree of influence are quite different, are the result of decisions directly and accurately measure the difficulty of the problem. Therefore, the mathematical model is more suitable for the method of fuzzy mathematics and analytic hierarchy process combining methods, namely multi-level comprehensive evaluation model, the establishment of multi-level comprehensive evaluation model steps are as follows:

1) Assessment index system established;
2) Each evaluation index weights established;
3) The assessment index membership to determine:
4) Establishment and application of integrated assessment model.

Establishment of evaluation index system. Through expert advice and comprehensive surveys and research scholars in this field, selected assessment evaluation factors can affect the overall response of offshore wind power projects in the navigation safety.

Through seek the opinion of experts, this paper identifies six factors for level indicators and identifies eight factors as two evaluation indicators; according to affiliation assessment criteria and indicators, carried on the lower orders, as shown in Fig.1 form factor set U.

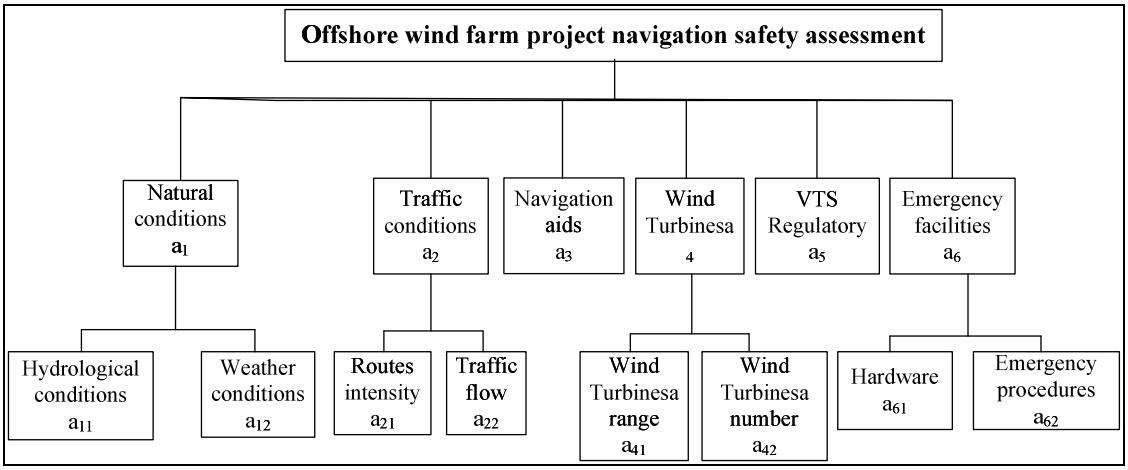

Fig. 1 The hierarchy structure of the evaluation

The evaluation index weights determined. Using questionnaires, investigators including wind farm managers, maritime experts and senior high-grade officers from Maritime Universities. Evaluation of the relative importance given judgment, and these judgments by introducing an appropriate scale (in numerical representation), generates judgment matrix. Details of the assessment index weight *W* in Table 1.

Table 1 The weight of the index

Indicators	α_1	α_2	α_3	α_4	α_5	α_6		
Weights	0.11	0.25	0.18	0.19	0.13	0.14		
Indicators	α_{11}	α_{12}	α_{21}	α_{22}	α_{41}	α_{42}	α_{61}	α_{62}
Weights	0.51	0.49	0.45	0.55	0.59	0.41	0.61	0.39

Determine the degree of membership of each evaluation index. In this paper, the evaluation grade is divided into five levels, that is V = { good, better, fair, poor, worse}, the corresponding value set is F = {5,4,3,2, 1}, As shown in Table 2.

Table.2 The evaluation grade

5	good
4	better
3	fair
2	foor
1	worse

The establishment of multi-level integrated assessment model. Through the above three steps, get the index set offshore wind farm project U {u_1, u_2, u_3, ... u_n}, offshore wind farm project safety assessment set V {v_1, v_2, v_3, ... v_n}, assessment indicators weight W {w_1, w_2, w_3, ... w_n} and evaluation matrix R. Through assessment indicators weight W and evaluation matrix R, we can get matrix B, the equation can be expressed as:

$$B = W \times R$$

For the B anti-blur, he may have a layer of navigation safety evaluation index value or the value of navigation safety assessment. Anti-blur method to calculate the center of gravity of this paper, which is calculated as follows:

$$b = \frac{\sum_{i=1}^{5} b_i \times v_i}{\sum_{i=1}^{5} b_i}$$

Multi-level Comprehensive Evaluation

Expert scores on the index. According to the article，we have established offshore wind farm projects navigation safety evaluation model, there are 20 experts carried out according to the actual situation in this article to establish offshore wind farm project evaluation, this paper summarized the results of the evaluation, the expert appraisal results table below:

Tab. 3 A navigable waters offshore wind farm project security expert appraisal result

Index Name	Select the index number of the appropriate level of the standard(Total 20 people)				
	Good (5)	Better (4)	Fair (3)	Poor (2)	Worse (1)
Hydrological conditions	0	4	5	11	0
Weather conditions	7	11	2	0	0
Routes intensity	0	10	7	3	0
Traffic flow	8	6	6	0	0
Navigation aids	2	6	10	2	0
Wind turbine range	6	11	3	0	0
Wind turbine number	0	4	12	4	0
VTS regulatory	10	8	2	0	0
Hardware	2	15	2	1	0
Emergency procedures	1	9	10	0	0

Single-factor fuzzy comprehensive evaluation. We deal with each results from experts about navigation safety indicators, you can get its single factor evaluation matrix:

(1) For natural conditions A1 and traffic situation A2 single factor evaluation matrix:

$$R_1=\begin{bmatrix} 0 & 0.2 & 0.25 & 0.55 & 0 \\ 0.35 & 0.55 & 0.1 & 0 & 0 \end{bmatrix} \qquad R_2=\begin{bmatrix} 0 & 0.5 & 0.35 & 0.15 & 0 \\ 0.4 & 0.3 & 0.3 & 0 & 0 \end{bmatrix}$$

(2) For wind turbine facilities A4 and emergency facilities A6 single factor evaluation matrix:

$$R_4=\begin{bmatrix} 0.3 & 0.55 & 0.15 & 0 & 0 \\ 0 & 0.2 & 0.6 & 0.2 & 0 \end{bmatrix} \qquad R_6=\begin{bmatrix} 0.1 & 0.75 & 0.1 & 0.05 & 0 \\ 0.05 & 0.45 & 0.5 & 0 & 0 \end{bmatrix}$$

From the above give natural conditions A1, traffic conditions A2, wind turbine facilities A4 and emergency facilities A6 univariate weights, we can get index weights:

$$W_1=(0.51,0.49), W_2=(0.45,0.55)\ , W_4=(0.59,0.41), W_5=(0.61,0.39)$$

We use synthetic operation can get comprehensive evaluation about A1, A2, A4, A6, which is calculated as follows:

$$B_1=W_1.R_1=(0.17,0.37,0.18,0.28,0); \quad B_2=W_2.R_2=(0.22,0.39,0.32,0.067,0)$$

$$B_4=W_4.R_4=(0.18,0.41,0.34,0.82,0); \quad B_6=W_6.R_6=(0.08,0.63,0.26,0.03,0)$$

Multilevel Comprehensive Evaluation. Calculated by the above we get B1, B2, B4 and B6, and A3 and A5 can be obtained by the factor score results:

$$B_3=(0.1,0.3,0.5,0.1,0); \quad B_5=(0.5,0.4,0.1,0,0)$$

We can construct a single-level comprehensive evaluation matrix R based on two factors that determine the result of the judgment:

$$R=\begin{bmatrix} 0.17 & 0.37 & 0.18 & 0.28 & 0 \\ 0.22 & 0.39 & 0.32 & 0.067 & 0 \\ 0.1 & 0.3 & 0.5 & 0.1 & 0 \\ 0.18 & 0.41 & 0.34 & 0.82 & 0 \\ 0.5 & 0.4 & 0.1 & 0 & 0 \\ 0.08 & 0.63 & 0.26 & 0.03 & 0 \end{bmatrix}$$

Right from the above evaluation level weight can be given:

$W = (0.11, 0.25, 0.18, 0.19, 0.13, 0.14)$

So comprehensive evaluation result is:

$B = A \bullet R = (0.202, 0.410\text{v}0.304, 0.226, 0)$

Multi-level fuzzy comprehensive evaluation of the results of the anti. Anti-blur method to calculate the center of gravity of this paper, which is calculated as follows:

$$b = \frac{\sum_{i=1}^{5} b_i \times v_i}{\sum_{i=1}^{5} b_i} = \frac{0.202\times5 + 0.410\times4 + 0.304\times3 + 0.226\times2 + 0\times1}{0.202 + 0.410 + 0.304 + 0.226 + 0} = 3.515$$

It can be seen that the navigable waters of the offshore wind farm project safety evaluation results between "fair" and "better".

Conclusion

Offshore wind power project as a new energy industry, application prospects, but as offshore installations, and its impact on marine transportation cannot be ignored, and therefore its impact on navigation safety research is necessary. The fuzzy comprehensive evaluation method can optimize the siting and design of offshore wind power project, for the construction of wind power projects currently play a certain specifications and guidance.

References

[1] C. Ge, Y.P. He: China Offshore Platform, Vol. 23 (2008) no.6, p.31.
[2] S.B. Xu: The Principle of AHP (Tianjin Press, China 1988).
[3] W.K. Wang: Offshore wind power project navigation risk assessment and security research (MS., Wuhan University of Technology, China 2013).
[4] L.P. Yun: Design, Fuzzy Comprehensive Evaluation of the Wind Farm Site Optimization (MS., North China Electric Power University, China 2008), p.12.
[5] Z.J. Jiang: Fuzzy Math Tutorial (Defense Industry Press, China 2004).
[6] J. Han: Study Selection and Evaluation System Based Supplier of Intelligent Fuzzy Comprehensive Evaluation (MS., Shandong University, China 2006), p.13.
[7] F. Wu: Risk of Developing Offshore Wind Power (MS., Tsinghua University, China 2011), p.16.

Advanced Materials Research Vols. 986-987 (2014) pp 263-266

doi:10.4028/www.scientific.net/AMR.986-987.263

Considering the wire erecting model of transmission grid planning under the market environment

Yang Shenquan[1], Hu Xingwang [2], Zhang Xiaolei [2], Wu Kuihua[1] , Yang Bo[1]

([1.]Economic&Technology Research Institute,State Grid Shandong Electric Power Company ,Jinan,250021,china;[2.] State Grid Shandong Electric Power Company, Jinan 250002, China).

Keywords：transmission planning；the Same Tower；Monte Carlo simulation

Abstract. Electricity market reform has brought new challenges to transmission grid planning, the traditional only considers a future scenarios of transmission grid planning, this method can't meet the actual needs. In this paper, the uncertainty factors of market environment is analyzed, based on the relaxation factor and the way of wiring ,the transmission grid planning model is established. The security not only takes the N-1 breaking cases into account, but also includes the same tower Multiple-loop breaking at the same time. The model is solved using the methods based on Monte Carlo simulation and hierarchical genetic algorithm, ultimately the resulting meets reliability requirements and minimum total cost of transmission planning programmes under the future uncertainty environment. To build the simulation model, simulating the different methods of wiring way impacts on the investment and risk of the grid planning.

0 Introduction

Under the traditional vertical integration system, Transmission grid planning is based on load forecasting and power planning, it usually only considers one of the most likely future scenario, and the N or N-1 static security conditions must be met, so it generally uses penalty function method to deal with the static security constraint requirement, not taking the various kinds of uncertainty factors into account.[1~3] During the course of practice, due to the emergence of uncertainty factors, it may lead to that the mathematically rigorous optimal scheme requires a lot of compensation investment. In addition, the competitive market will cause the cooperation and competition among market participants, and lead to the uncertainty of unit power output changing. The presence of these elements has brought new challenges to the transmission planning. [4]

At present, with the rapid growth of power load, the newly built power plant capacity is bigger and bigger, the number of outgoing circuits also increased accordingly. Construction of ultra-high voltage with multiple-loop towers, due to the less land, saving line corridors and increasing the transmission capacity of per unit area and reducing the overall investment etc, has begun to favor by planning department. [5] While setting up double circuit lines on the same tower reduce the cost of investment , but also improve the security risk of system operation, how to consider the impact is a question which is worthy of study in the early stages of planning. This article puts the wiring way into single-loop and multiple-loop on the same tower, From the perspective of the wiring way, we have the grid planning. In the early stages of planning, we consider multiple-loop wiring on the same tower. The impact of the difference wiring way on the grid investment and operation risk is discussed, can help planners saving investment in the face with the erection of double-loop towers and given the quantitative indicators when the game risk increased, to facilitate decision making.

1 An uncertain power injection vector

The capacity and load of power plant in the future is uncertain, so they are random variables, probability density function we can use probability density function to describe them.

During the planning period, the new capacity of node I generally obey a discrete probability distribution:

$$P_r\{P_{G.i} = P_{G.i}^k\} = p_i^k \quad (k=1, 2,\ldots M) \tag{1}$$

where, $0 \le p_i^k \le 1$, $\sum_{k=1}^{M} p_i^k = 1$。

The active load $P_{D.i}$ of node I generally obey the normal distribution $N(\mu_i, \sigma_i^2)$ where ui is the expected value of the load and σ_i is the standard deviation of the load.

Therefore, the injection power of random vectors is recorded as ξ. According to node i's active injection power $P_i = P_{G.i} - P_{D.i}$ According to the probability distribution function of each the power source and load injected power, We are random sampling Using the monte-carlo simulation method, We can get M injection power vectors $\boldsymbol{P} = \{\xi_1, \xi_2, \xi_3 \ldots \xi_M\}$.

2 the transmission grid planning model

Power source construction and the load increase in the market environment and each generator node power output change due to the bidding behavior of power plant such as the uncertainty factors can be said as the uncertainty of system node active injection power.

Accordingly, we give the optimal the transmission grid planning model which meets the minimum comprehensive cost of the system and the requirements of operation reliability.

$$\min C = \sum_{ij \in NI} U_{ij} I_{ij} L_{ij} + \sum_{ij \in NL} V_{ij} B_{ij} L_{ij} + \alpha Z_1 \tag{2}$$

$$Z_1 = \sum_{k \in M} C_k^s + \sum_{k \in M} C_k^d \tag{3}$$

st.

$$\left.\begin{aligned} &\boldsymbol{B\theta} = \xi_k \\ &\boldsymbol{P}_b = \boldsymbol{B}_b \boldsymbol{q}_b \\ &|\boldsymbol{P}_b| \le \boldsymbol{P}_{b.max} \end{aligned}\right\} \tag{4}$$

$$\left.\begin{aligned} &\boldsymbol{B}_b^l \boldsymbol{\theta}_b^l = \xi_k \\ &\boldsymbol{P}_b^l = \boldsymbol{B}_b^l \boldsymbol{\theta}_b^l \\ &r \le \delta \end{aligned}\right\} \tag{5}$$

$$I_{ij} = \begin{cases} 0 \\ 1 \end{cases}$$

$$0 \le B_{ij} \le B_{ij}^{max}$$

In formula (2) C represents investment construction costs, including line construction costs and expenses of cutting load.

NI, NL respectively represents single loop line and multiple loop lines waiting for the selection; U_i represents unit construction investment cost of the single loop line; I_i represents 0-1 decision variables of line i, line i joins the grid $I_i = 1$,otherwise $I_i = 0$;

B_j represents decision variables of circuit number on the same tower, $B_j \in (0,1,2,3 \ldots n)$, V_j represents unit investment cost of multiple loop lines waiting for the selection,Its value varies with B_j , $V_j \in (V_{j1}, V_{j2}, V_{j3} \ldots V_{jn})$; L_i and L_j represent line length.

Z1 represents minimum load-shedding in the system,Including the N-1 minimum breaking load-shedding under M injection power vectors and the minimum breaking load-shedding of multiple circuit lines on the same tower,Thereinto, C_k^s and C_k^d respectively represents the N-1 breaking load-shedding under the K-th injection power vector and load-shedding of multiple circuit lines cutting load at the same time on the same tower, α represents unit load-shedding punishment costs.

formula (4) is the security constraints to the normal operation;formula (5) is N-1 static security constraint. ξ_k is the K-th injection power vector, $\boldsymbol{B}$ and $\boldsymbol{B}^l$ are the node admittance matrix which

correspond to the non-breaking ways and branch L breaking way, vector θ and θ^{l} are the voltages phase angle under above two mode, P_b and P_b^{l} are the corresponding branch power flow, θ_b and θ_b^{l} are the phase angle difference at both ends of branch, B_b and B_b^{l} are the diagonal matrix consisting of each branch admittance, $P_{b.\max}$ is the heat capacity limitation of branch, δ is the given risk factor threshold.

3 the example simulation

This article uses the "18-node system example in reference 7,Because there is no feasible scheme under the static security of the N-1 criterion, so we make the line transmission capacity limit increase to 3000MW.Its unit investment costs 600,000 yuan/km. Original system node values are the same with reference ,Node 11, 14, 16, 18 are new power source nodes that may appear, the probability distribution function obeys two-point distribution, the load of new added nodes satisfy the normal distribution, specific parameters of the probability distribution function can be found in reference 7.

In this paper, the simulation model was constructed as follows, to validate the proposed model and algorithm in this paper, we simulate the influence of the risk factor, the wiring way and the load-shedding punishment on the transmission grid planning result. As chart 1

Table 1 Simulation model

solution	risk factors	wiring way	punishment of cutting load (ten thousand yuan /MW)
1	δ=0.1	single loop/ multiple loop	8
2	δ=0	single loop/ multiple loop	8
3	δ=0.1	single loop/ multiple loop	80
4	δ=0	single loop/ multiple loop	80

Table 2 The simulation optimization wiring scheme

solutions	planning scheme
1	1-11, 4-16, 5-11, 5-12, 6-14（2）, 7-8, 7-13, 7-15, 8-9（2）, 9-10（2）, 9-16, 10-18, 12-13, 14-15（2）, 16-17（2）, 17-18（2）
2	1-11, 4-7, 4-16（2）, 5-11（2）, 6-14（2）, 7-8, 7-13（2）, 7-15, 8-9（2）, 9-10（2）, 10-18, 11-12（2）, 12-13, 14-15（2）, 16-17（2）, 17-18（2）
3	1-11, 4-16（2）, 5-11, 5-12, 6-13, 6-14（2）, 7-8（2）, 7-13, 7-15, 8-9（2）, 9-10（2）, 9-16（2）, 10-18, 11-12, 12-13, 14-15（2）, 16-17（2）, 17-18（2）
4	1-11, 4-16（2）, 5-11（2）, 5-12, 6-13, 6-14（2）, 7-8（2）, 7-13, 7-15（2）, 8-9（2）, 9-10（2）, 9-16（2）, 10-18, 11-12, 12-13, 14-15（2）, 16-17（2）, 17-18（2）

table 2 the number behind two nodes in parentheses is the increasing number of loop

Table 3 Simulation optimization results

solutions	investment costs of single loop/multi-loop (ten thousand yuan)	investment costs of single loop/multi-loop (ten thousand yuan)	investment costs of single loop/multi-loop (ten thousand yuan)
1	200320/172120	8650/25360	208880/197480
2	229920/187320	0/22240	229920/209596
3	245120/200920	800/121600	245920/322930
4	264160/210440	0/113600	264160/324040

From the comparison between scheme 1 and scheme 2 we can obtain that, in the same way of wiring and cutting load punishment cases, with the decrease of the risk factor δ, planning solution need to meet more operation mode, planning cost also increasing. From table 3 planning results, analyzed and obtained that the investment costs of multi-loop mode significantly lower than the single loop, cutting load is significantly higher than the single loop way. Considering both comprehensive cost, according to different punishment of cutting load, the comprehensive cost difference is bigger, when punishment of cutting load is small, the integrated cost of single loop

mode is bigger, on the contrary, the integrated cost of multi-loop mode is bigger. Therefore, in practice, wiring way can be choose according to the actual situation.

This paper also carried simulation of the punishment of cutting load influence on planning solution. Plan 1, 2, 3 and 4 were compared, in the same risk factor, with the increasing of the punishment of cutting load, the more the expansion of the line number is, the greater the investment cost is, reduced the cutting load.

4 Conclusion

This paper, by using monte-carlo simulation method to deal with the uncertainty of the future market environment, under the condition of risk factor constraints further consider the double-loop tower circuit open or shut down at the same time conditions, transmission grid planning model considering the double-loop towers is established, making the grid planning can consider the erection of double-loop towers at the beginning of the planning, can help planners saving investment in the face with the erection of double-loop towers and given the quantitative indicators when the game risk increased, to facilitate decision making.

The intervention of risk factor constraints, can make the planning scheme on the basis of further meet the requirements of a certain reliability consider the erection of the double-loop circuit tower open and shut down at the same time, making the model solution hierarchy more stronger, the planning scheme can satisfy the requirements of reliability of the global optimal solution.

Using hierarchical genetic algorithm for the grid planning model , through the underlying genetic algorithm can get the optimal solution, on the basis of the optimal solution high genetic algorithm can be well to obtain the global optimal solution. Hierarchical genetic algorithm improved the speed and efficiency of iteration, the example calculation shows that it is an effective method of solving complex grid planning

Reference

[1] Wen Fuquan, Han Zhenxiang. The optimal rules f transmission system based on Tabu search method o. Grid technology, 1997, 21 (5) : 2-7

[2] Chen Genjun, wang lei, Tang Guoqing. The optimal transmission grid expansion planning based on ant colony. Grid technology, 2001, 25 (6) : 21-24

[3] Wu Li, Wu Jie, Zhong Danhong. The application of multi-objective optimization improved genetic algorithm in the power grid planning. Automation of electric power systems, 2000, 24 (12) : 45-48

[4] De La Torre T, Feltes J W.. Deregulation, privatization, and competition: transmission planning under uncertainty. IEEE Trans on Power Systems,1999,14(2):460－465

[5] Zhu Zhonglie. With four towers line fault and transient simulation analysis method. Automation of electric power systems. 2008, 32 (8) : 49-54

[6] Wang Xifan. Optimal planning of power system. Beijing: water conservancy electric power press, 1990.

[7] Ma Changhui. Transmission planning based on the static and dynamic security risk of. Automation of electric power systems. 2006.30 (14) : 10 to 13

Advanced Materials Research Vols. 986-987 (2014) pp 267-270

doi:10.4028/www.scientific.net/AMR.986-987.267

Countermeasure Research on New Energy Automobile Industry Chain Optimization

Donghui WANG[1, a]

[1]Hunan Communication Polytechnic, Changsha 410132,China

[a]DonghuiWang427@yeah.net

Keywords: countermeasure, new energy, automobile industry chain

Abstract. As the international energy supply remains tense, international oil price continues rising and calls for global environmental protection becomes higher, people attach more and more importance to the research and development of new energy automotive technology, and the industrialization development. Rapid industrialization led to heavy pollution, increasing greenhouse gas emission, which makes the development of new energy automobile have practical significance.

Automobile industry is an important mainstay in national economy, its industrial chain is long, correlation degree is high and the consumption pursuing is big. New energy automobile based on the gradual development of low carbon economy is a systemic revolution to the transportation that our society uses and the way of using energy, which will bring to the technical revolution of automobile industry.

1.Brief introduction.

1.1New energy automobile.

New energy automobile refers to other energy automobiles except those automobiles use gasoline and diesel engine, mainly refers to the fuel cell vehicles, hybrid vehicles, pure power cars and solar cars, etc. The development of new energy automobile industry has great importance to sustaining economic growth, expanding domestic demand, optimizing industrial structure, strengthening independent innovation ability and promoting industrial upgrading in the current situation.

1.2New energy automobile industry chain.

New energy automobile industry chain is extended on the basis of traditional automobile industry chain. It adds battery, motor, electric system and automatic transmission parts etc. Battery is the key in new energy automobile industry chain, the most core part.

And among all the new components in the new energy automobiles, battery system accounts for the highest percentage and costs the most. Among the cost composition in pure electric automobiles, power battery is as high as 60%. We can see from the analysis of each link of the traditional automobile industry chain and the new energy automotive industry chain, the new energy automobile industry chain has different characteristics in power source, basic facilities and related professional and technical talents. Facing with the needs of the low carbon economy, prominent energy problem and the trend of the upgrading of the automobile industry, the development of new energy automobile industry chain is extremely urgent. At present, it is all recognized that hybrid car is the most suitable new energy automobile for industrialization with the most mature technology.

2.The structure of new energy automobile industry chain.

Any of the industry chain can be divided into three parts: upstream, midstream and downstream. The new energy automobile industry chain can also be such divided. Upstream mainly includes the purchasing and production of components; midstream mainly includes the manufacturing of all the parts of automobile; downstream mainly includes sales and providing relevant after-sales services.

2.1Key nodes and their mutual relations of new energy automobile industry chain.

We can know from the analysis of new energy automobile industry chain that each node mainly includs whole automobile manufacturers, components manufacturers, sales manufacturers and after-sales service providers.

In recent years, along with the development of the automobile industry, sales profits gradually shift from manufacturing and sales to after-sales service providers. The improvement of the facilities, generality of charging pile and so on are all that needed to strengthen in order to make the after-sales service more perfect. So, with the development of new energy automobile industry chain, its downstream profit will be gradually increased, which will directly decide its future development.

2.2Analysis of main raw material.

Battery resources: in the next few years, our country will focus on the development of pure electric automobile. And the main battery is nickel metal hydride battery and lithium ion power battery.

Motor resources: new energy motor as a source of new energy automobile, auto motor changes electric energy into kinetic energy to drive the car. And if we see from the development of present and the demand in the future, then permanent magnet motor will become the main drive motor.

2.3Analysis of new energy automobile industry chain.

At present, the hybrid technology is relatively mature. It dose not have high requirement to battery and don not reached the requirements of pure electric vehicles, so we see from chart 1 that the nickel metal hydride batteries can meet their requirements. However, hybrid automobile can't solve energy and environmental problem very well due to engine, is only considered as a transition fro traditional automobile industry to new energy automobile industry.

In the next few years, therefore, the key is to strengthen the perfection of pure electric automobile technology and the development of fuel cell. Lithium ion battery mainly contains four parts: the cathode materials, anode materials, electrolytes, other auxiliary materials such as diaphragm and ultra-thin copper foil aluminium foil etc. Positive electrode materials and electrolyte and the diaphragm is the three core kinds of materials, which directly determine the battery safety, capacity, and account for more than 70% of the cost of lithium ion power battery.

kinds	nickel metal hydride battery	Lithium ion battery
Voltage V	1.2	3.7
Weight/energy Wh/Kg	60-80	110-190
Volume/energy Wh/L	150-200	250-500
Specific power W/kg	160-230	400-1300
Cyle life times	500-1000	1000-2000
Self discharge	30-35%	<5%
Harmful substance	no	no

Chart 1: Battery performance comparison

3.Characteristics of new energy automobile industry chain.

3.1Different power source.

New energy automobiles adopt different fuel as their power sources (or use different normal fuel but adopting new on-board power plant). Power control and drive of the vehicles have advanced technology, technical theory and new structure.

New energy automobile mainly includes fuel cell vehicles, hybrid vehicles, pure power cars and solar cars, etc. Hybrid vehicles have no external power supply and the motor assists combustion with starting, acceleration and climbing; or hybrid vehicles have external power supply which drives cars alone when battery has enough electricity and starts the combustion enter into HEV working style. Pure power cars rely on its own battery as their power source which dependents on external power supply to charge.

3.2Different facilities.

For now, there are three kinds of mature technology of electric charging stations: one kind is inserted filling pattern, charging by vehicles staying at the stations for a long time; the second one is changeable battery, changing battery by equipment automatically; the last one is quick filling pattern, recover most of the electricity in several minutes. However, the last one does much damage to the battery, so we mainly adopt the first two for the time being.

3.3More technical talents.

The promotion and application of the new energy automobiles needs a large quantity of professional people. They should have not only experience on the automobile services but also the ability of communication, analysis and learning. Some jobs even have higher requirements such as the motor drive, application of electric material, control technique of automotive motor and the control of hybrid power etc. These jobs need both good foreign language ability and skilled computer operation.

4.Optomization countermeasures.

4.1Gathering parts manufactures.

Enforcing regional gathering of parts manufactures can solve the problem of innovation and accomplish scale effect. Regional government should purchase and directly invest the industry; give them tax subsidy or tax credit; bring in high-technology professions.

4.2Perfection of battery and motor.

The main problem in battery and motor is the technology is not enough advanced and the lack of key technology. So, in the regional innovation system, the key is improving the technology on battery and motor. Regional government should give priority to the self-dependent innovation products and buy innovation products in order to stimulate the their innovation enthusiasm; accomplish motor industry gathering in the region and improving innovation by giving tax preference or tax credit; the key to battery and motor innovation is profession policy and technology policy, government can provide accommodation and welfare to them to accomplish the bringing in professions. Besides these, company should improve their quality of after-sales service.

Summary.

Because of gradual and continuous climbing of the oil price, and the increasing emission of greenhouse and the rising of temperature, and pollution, we implement a new development strategy that is new energy automobile industry chain which is the vehicle developing destination in the future. There are many countermeasures for new energy automobile industry chain optimization, such as give priority to purchasing the innovation product, tax preference, promote technology of battery and motor etc. The development of new energy automobile industry chain has much practical significance.

References.

[1]Chen Yu, New Energy Automobile: Developing Destination of Future Vehicals,2010.

[2]Li Wenhui, The Construction and Research on New Energy Automobile Industry Chain, 2012.

[3]Li Kesong, Development of New Energy Automobile Industry Chain under the Regional Renovatin Angle of View, 2012.

[4]Reng Yuan, Analysis on New Energy Automobile Industry Chain, 2014.

[5]Sun Guodong, The Formation and Stability of Industry Chain, 2007.

Advanced Materials Research Vols. 986-987 (2014) pp 271-278

doi:10.4028/www.scientific.net/AMR.986-987.271

Design and Develop Resources Investigation and Evaluation System of Electric Power DSM

Lefeng CHENG[1, a], Bin ZHOU[2, b], Tao YU[3, c]

[1]Electric Power College, South China University of Technology, Guangzhou, 510640, China

[1]Electric Power College, South China University of Technology, Guangzhou, 510640, China

[1]Electric Power College, South China University of Technology, Guangzhou, 510640, China

[a]email: lefengCheng_ieee@163.com, [b]email: ieee_binzhouscut1@163.com,

[c]email: taoyu_ieee@163.com

Keywords: Demand Side Management; Demand Side Response; Resources Investigation and Evaluation; Energy-saving Potential; Evaluation of Integrated Energy Efficiency; Power Users

Abstract. More and more deep integrated resource planning methods and demand side management (DSM) technologies have been studied and applied in China. Using technological and economic means of DSM, exploiting energy-saving potentialities from demand side, balancing load, easing contradictions of power structure, improving energy utilization rate, etc. have been important tasks in electric power enterprises. Based on this background, the paper designed and developed resources investigation and evaluation system of electric power DSM, which could investigate electricity resources of DSM of China, and implement energy-saving potential evaluation and energy efficiency analysis. From aspects of technology, economy, management, etc. suggestions were proposed for DSM, trying to be more rational and effective to allocate and use electricity resources, seeking satisfaction of power demands to the greatest degree, thus promote sustainable development of electric power enterprises effectively.

Introduction

Electric power is essential element of life in modern society, when economy of China is developing in a high speed, the contradiction is still sharp in power industry, and not solved essentially; resources of power industry are not in reasonable configuration, and energy utilization remains tense [1][2][3][4][5]. Based on this, it is necessary to establish management evaluation indicator system considering the whole process of infrastructure to promote the development of DSM projects and direct the planning for DSM projects management [6], and reference [6] analyzed the key factors of each stage influencing DSM projects with the whole process theory, and proposed an indicator system for DSM projects management evaluation; reference [7] introduced the status of power supply enterprise DSM at the county level, and from the administrative, technical, economic and other aspects, it put forward measures and methods to improve the capacity utilization efficiency of distribution transformers and electricity power factor, reduce line losses, eliminate harmonic to improve power quality, guide the users to change and optimize power consumption, improve the efficiency of electricity end-users, improve economic efficiency of power supply enterprises; in reference [8], it designed the main function modules of DSM decision supporting system, and constructed a DSM decision supporting system of B/S structure according with J2EE architecture, and the system realized ten functions, including energy efficiency assessment, DSM program design, DSM project management, DSM electricity savings analysis, electric load analysis and forecast, peak load shifting management, DSM policy modeling, DSM project comprehensive evaluation, DSM case management and DSM prime data management, this DSM decision supporting system can provide a unified decision sup-porting platform with universal functions for participants in DSM work; and in wind power integration management work in China, the implementation modes of demand side response in the initial stage, transition stage and mature stage of electricity market, are put forward respectively on the background of large-scale wind power integration, aiming to provide an useful reference in China [9].

In this paper, the management technology of DSM was studied, a resources investigation and evaluation system of electric power DSM was designed and developed, which implemented investigation aimed at electricity resources of China, developed electric power projects scientifically and reasonably, configure power resources effectively, etc. thus can greatly improve the electricity utilization rate of users. Especially for the data collection precision of DSM terminal, the methods proposed in reference [10] were adopted, and for hardware design, in reference [11], a validated design method of a power synthesized parameters monitor was presented which includes the user's demand. The design method involves analog signal regulation module, synchronous detection circuit, GPRS communication module, and the corresponding software. The monitor can measure power parameters accurately such as electric power quality, quantity and temperature. The high precision, powerful operation and reliability of monitor can be demonstrated on the experiments. Based on the hardware principle used in reference [11], the hardware was developed in this paper, and its structure scheme was given, the hardware was used to collect data of distribution system of electricity users, and the collected data supplied fundamental electricity utilization information for the upper analysis software.; In this paper, based on the technology and methods of DSM system in smart grid field [12], the resources investigation and evaluation system of electric power DSM was developed to make the power grid corporations have the ability to completely grasp potential energy-saving service opportunities of consumers from each aspect, such as the area, industry, enterprise, and electric equipment, thus will play a significant supporting role in finishing DSM work targets responsibility stipulated by national power grid corporations.

Resources definition of power demand side

The potential electricity-saving resource of power users is called "power demand side resource", which is realize by DSM, including reduced power consumption by improving electricity utilization rate, decreasing electricity demand by changing utilization mode, and the saving electric power and electricity amount through alternative energy, interruptible load of contract agreement, improving the electrical environment, etc. The power demand side resource can be classified permanent and temporary electricity saving resource according to electricity-saving time. Specific contents are shown in Fig.1 below.

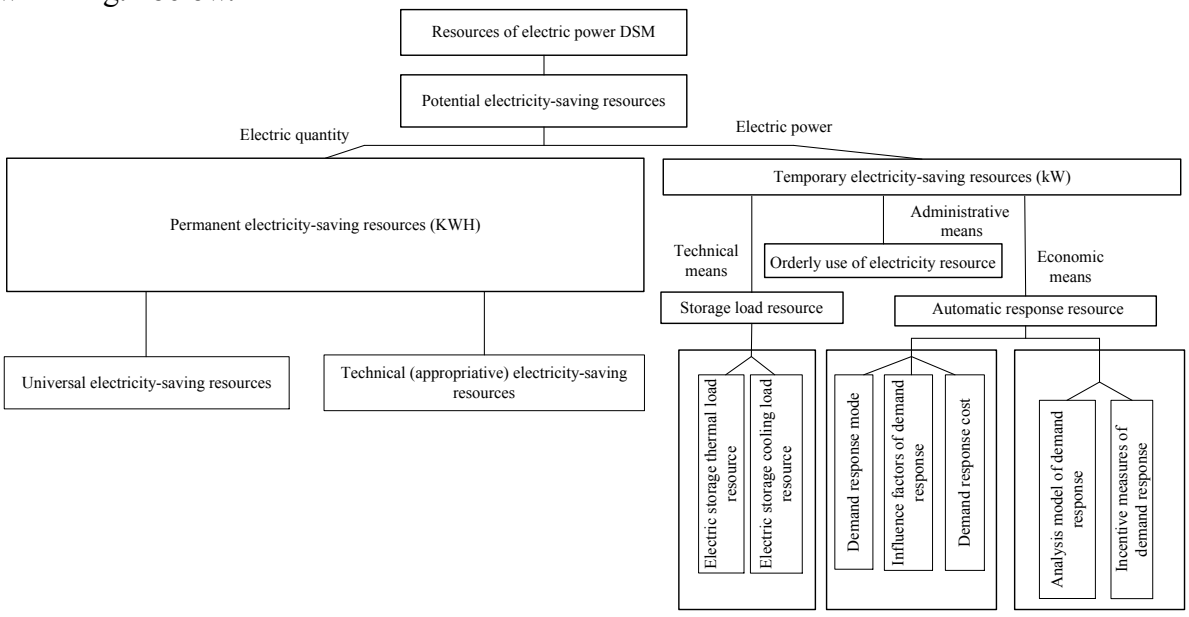

Fig.1 Resource classification of DSM

Hardware subsystem

According to the diagram of hardware subsystem structure which is shown in Fig.2, the hardware configuration of total system is composed of signal sampling unit, signal conditioning

unit, synchronous signal sampling unit, A/D converting unit, DSP core processing unit, CPLD and its peripheral human-computer interaction unit, external interface unit and so on. The device get in the signal of special users' power lines through signal sampling unit, and invert voltages and currents by voltage / current transformer, so as to acquire three-phase voltages, three-phase currents signal of special users' testing lines; then signals are transmitted into signal conditioning unit and in which the signals are treated with filtering and magnifying, A/V converting, sample-and-hold, data buffering and so on, thus these manipulated signals enter into A/D sampling unit with 8 bit analog signal (they are Ua,Ub,Uc,Un,Ia,Ib,Ic,In), during which the DSP core processing unit controls it's A/D converting process.

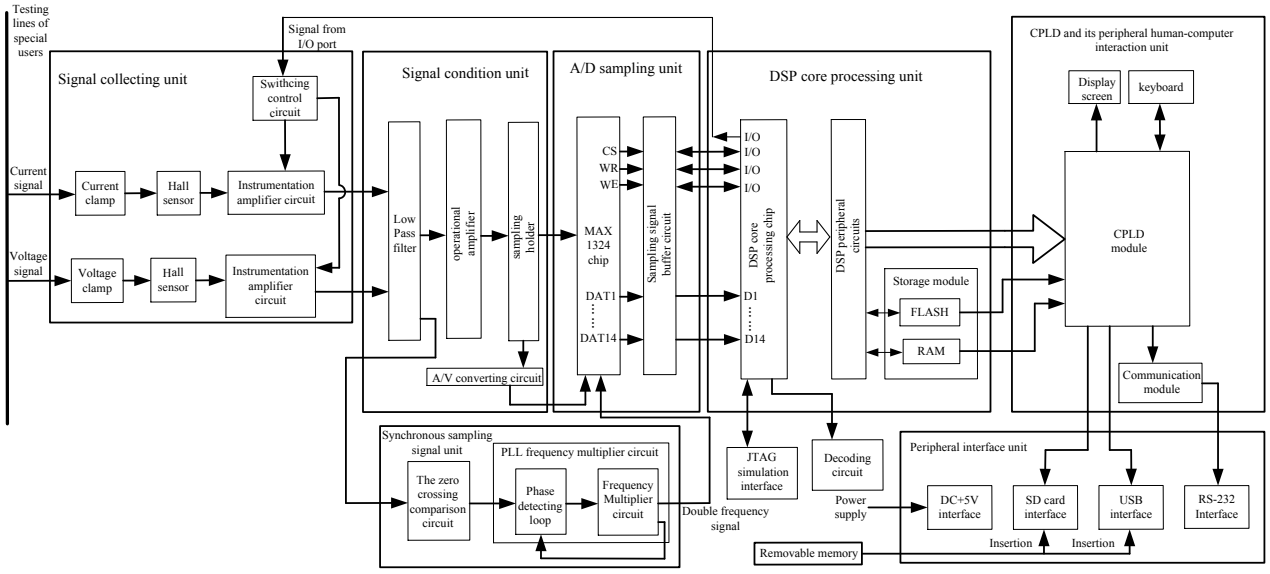

Fig.2 Hardware subsystem principle and structure block diagram

Software subsystem

The software subsystem utilizes building block design, the programs of which uses C++ language, and its main functions are to complete A/D conversion, digital filter, FFT processing, data insert, energy analysis, results display, generate data format file etc. Fig.3 shows the DSP main program chart of energy saving diagnosis operation, DSP main program is core hardware processing program in the detector, and its main functions is data filtering and FFT analyzing; Fig.4 shows Signal sampling and data analysis flow chart, at the end of the figure, through FFT analyzing and other analyzing of DSP, we get the energy consumption data files of users , which conclued various functional parameters detected and recorded by DSP chip and they are very significant for the final generation of users energy-saving audit analysis report. Fig.5 shows the user-friendly and supporting software interface of energy saving diagnosis and analysis, which concludes 6 parts: DSP chip initization, enable interrupt, start samping, sample completed, Data proceess, display results impoert data.

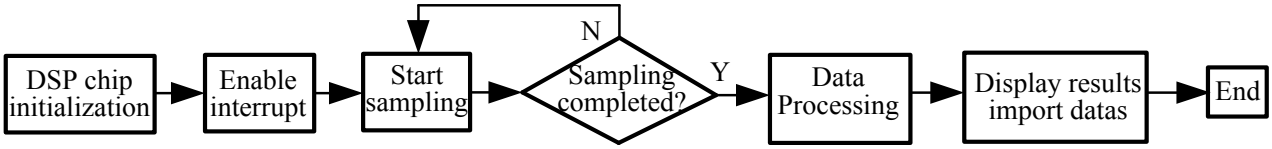

Fig. 3 DSP main program flow chart

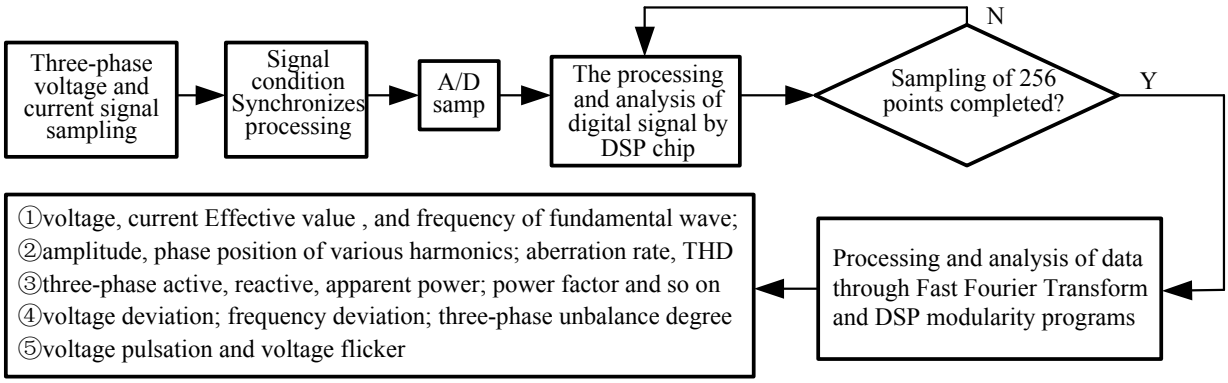

Fig. 4 Signal sampling and data analysis flow chart

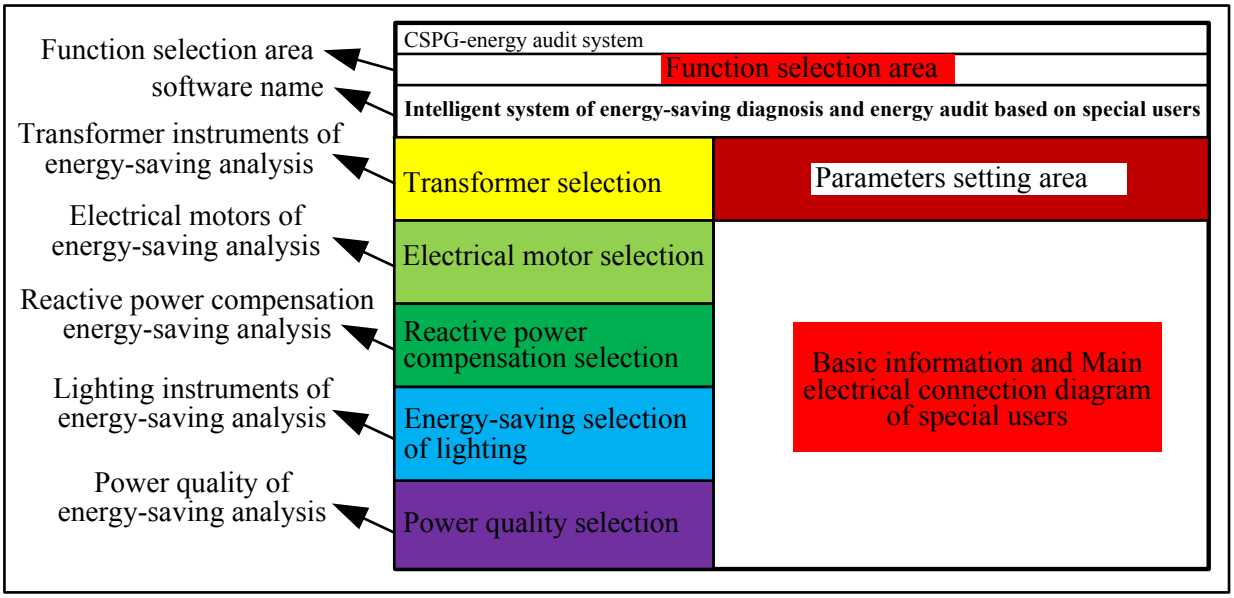

Fig. 5 The software interface of energy saving diagnosis and analysis

Test results

Utilizing the special users' energy saving potential intelligent diagnosis instrument developed in this paper to implement diagnosis and analysis of energy-saving and power quality detection in a medium-size cement factory in Guizhou province. The 35 kV Zhongyin line and Liangyin line as inlet wires of this cement factory, whose voltage reduce to 6 kV through 2 sets of S7-8000/35 main transformers. Among them, the raw mill, coal mill, and cement mill and so on, they use 6kV power source directly, at the same time, a 6 kV regional is transported to the mine substation. The voltage of I segment, II segment 6kV line reduce to 380/220 V through two fractions changed buck, which provides supply for low voltage electrical equipment. The electrical equipment were continuously measured and recorded 24 hours with using of the intelligent diagnosis instrument developed in this paper, and we record the measurement point of the main wiring diagram in detail, which is shown in Fig.6.

（1）Energy-saving diagnosis

1#electromotor (Mill), whose energy efficiency limit value is 94%, doesn't meet the limit value of require according to the GB18613—2012, and only partly operates in the economic operation area. The following table shows the energy-saving diagnosis parameters of 1#electromotor. Overall, this electromotor doesn't operate economically. The energy-saving diagnosis result of 1# electromotor is shown in Tab. 1 below.

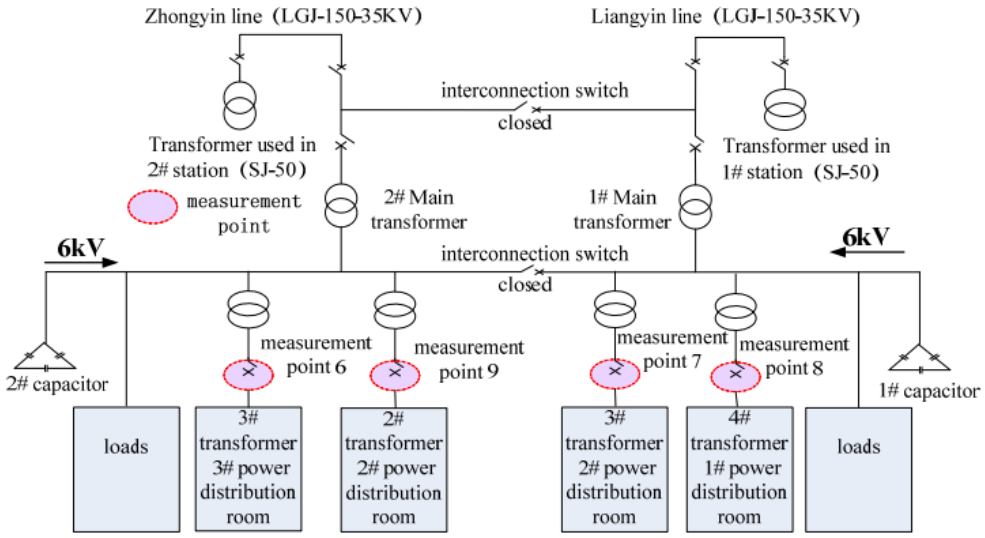

Fig.6 Measuring point of the main wiring diagram

Fig.6 Measuring point of the main wiring diagram

Tab.1 Energy-saving diagnosis result of 1# electromotor

Motor number	Motor name	Rated power (kW)	Average loss (kWh)	Efficiency	Economical probability	Economical running
1#	Mill	1000	66.7577	92.96%	31.83%	No

（2）Energy-saving solutions

Solution 1: using variable-frequency technique. While using the variable-frequency technique, the power saving rate ranges between 30% and 50%, for an electromotor with 1000 kW rated power, thus, its input power is about 11000 kW, so, its energy-saving ability is about 330-550 kW, at the same time, we assume this electromotor runs 7200 hour per year, thus, its energy-saving potential is shown in Tab. 2.

Tab.2 Energy saving potential of 1# electric motor

Annual operating time (h)	7200
Annual savings of electricity	3168000
Equivalent standard coal (t)	1279.87
Equivalent carbon dioxide emissions (t)	3353.26
Energy benefit (ten thousand RMB)	145.73

Solution 2: replacement of high efficiency electromotor. In order to achieve the purpose of energy conservation and loss reduction, it is important to replace those energy-saving motors in high efficiency.

Looking for the least loss motor in the database automatically, which could be a suggestion to choose the motor, meanwhile calculate the energy saving amount as well as the energy saving benefit and investment payback period. We can also customize a motor as a replacement of the motor by ourselves and then judge whether the effect of energy saving is well; moreover we can calculate its energy efficiency at the same time. The below Tab.3 shows the effect of energy saving by replacing energy-saving motors.

Tab.3 Energy saving potential analysis of 1# electric motor under case 2

	Current motor	Proposed motor	Optional motor
Motor type	Y1000-10/1430	YR6302-10	YR1000-12/1430
Power loss under the rated conditions (kW)	67.279	40.171	107.313
Annual energy-saving (kWh)	—	245621.3	More than the current motor
Equivalent standard coal (t)	—	95.19	—

Equivalent CO2 emissions (t)	—	249.4	—
Energy benefit(million RMB)	—	11.84	—
Estimated investment (million .RMB)	—	100	—
Investment recovery period(year)	—	7.5	—

（3）Power quality analysis

Harmonic analysis.Through monitoring power quality of the transformer, the voltage and current measured is respectively made into FFT calculation, then can get 1~25 times of harmonic content and harmonic total content, and which are compared with the national standard. According to GBT24337-2009 " Power Quality Public Power Grid harmonic", we can determine that the voltage, current harmonic content are both in a limited range. Due to harmonics, annual loss is about 82700 kWh, and the specific harmonic waveform is shown in Fig.7.

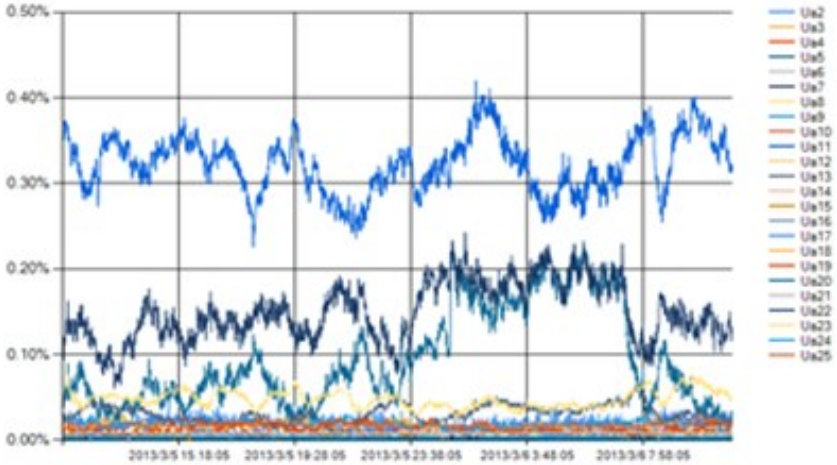

Fig.7 Harmonic analysis

According to the results of harmonic analysis, the software system will produce harmonic control scheme automatically, which shows that we can use the passive power filter (PPF) and active power filter (APF) as scheme. Because of fast response and high controllability of APF, for each times of harmonic, can be compensated effectively, and has adaptive function and is not subject to the system impedance. The use of filter is recommended as APF, which the type can be matched automatically by the software system, and that is APF-100-3L, considering other factors, the users can also choose other types of filter from the database.

（4）three-phase unbalance

The three-phase voltage and current unbalance waveform will be got through the comparision between the three-phase voltage and current monitoring data and its rated value. The average and maximum vlaue of voltage unbalance, current unbalance and power unbalance will be calculated respectively, and then they will be compared with the rated value, among them, the limited value of voltage and current unbalance is both 2, and the calculatino results are shown in Tab.4 below.

Tab.4 Unbalanced calculation

	Voltage unbalance		Current unbalance	
	Average value (%)	Maximum value (%)	Average value (%)	Maximum value (%)
Measurement value	3.797	6.838	0.096	0.177

According to the standard, voltage unbalance exceeds the requirements of limited value. Through calculation, the annual loss due to three-phase unbalance is 1396.57 kWh. The upper software will automatically produce the three-phase unbalance control scheme, that is, use cross phase conversion and other methods to make asymmetric load distribute to each phase reasonably, thus try to keep it in balance; also can choose proper compensation device, to achieve three-phase unbalance compensation. There are two kinds of compensation methods, one is to adopt TSC static

compensation device for compensation, and another is to adpot TSC+TCR mixed type of static compensation device.

（5）Energy efficiency assessement

This paper utilizes analytic hierarchy process to calculate the index weight, firstly, adopt comprehensive understanding of experts for the cement enterprise power efficiency evaluation index importance, after the corresponding mathematical calculation (results retained 3 decimal places), can get the weight of each index are as follows: the total industrial output value 0.991; economic added value 1.844; ten thousand RMB value of energy consumption 1.844; power saveing rate 3.432; each phase power factor 2.795; over load cumulative time 2.795; unqualified voltage cumulative time 5.078; unbalanced current cumulative time 5.078; harmonic content 9.227; electricity loss amount 9.227; reactive power compensation 9.246; transformer 16.014; motor 26.933; lighting device 5.498 (unit: %). Adopt recursive comprehensive evaluation method to make comprehensive energy efficiency evaluation for electricity users, thus can get energy efficiency and total efficiency level of second index. Refer to industry standard, and base on this evaluation results, then aim at the weak link of enterprise efficiency, take effective measures to make scientific energy-saving scheme, thus can fully tap the potential of energy-saving.

Conclusions

This paper aims at the problem of high energy consumption of special users and which is becoming increasingly prominent, the paper designed and developed special users' energy-saving potential online automatic diagnosis intelligent detector and based on DSP2812 and resource investigation and evaluation system of power DSM based on Visual Stidio 2012. The results shows that:

(1) This detector utilizes advanced digital signal processing technology and high accuracy technology, meanwhile, concludes high accuracy, multi channel sampling A/D converter. Through inserting data processed and recorded by detector into the internal energy-saving analysis software, thus, special users obtain the energy consumption data files and energy audit report, which provide reasonable energy-saving measures and suggestions with special users so that improve their potential ability and maximize their energy-saving production;

(2) This detector is of great practical significance in engineering, and is an urgent need for power grid enterprises to implement energy-saving and emission reduction work. Through the actual running test, indicating that the detector has a good performance of diagnosis, thus, this detector can greatly improve the efficiency, the degree of information and automation in electrical energy audit work;

(3) Technically, this detector has higher innovation. If it vigorously promotes in the energy market, the direct economic benefits and social benefits will be very significant;

(4) The resource investigation and evaluation system of power DSM is the system of investigating, evaluating and analyzing resource of DSM, and which is a DSM system of comprehensive data acquisition, storage, analysis and report. The system has friendly interface, complete function, rights management and support for multiple users, thus realize complete analysis and evaluation of DSM from downward and upward, and it can be used to study and can also for actual program of DSM, so as to provide reference for DSM planning;

(5) Through practical engineering application, the DSM resource investigation and evaluation system can achieve data acquisition and management, energy-saving analysis of demand side resource and automation and scientific of DSM decision-making analysis, then will provide convenient information service of actual load analysis work and DSM work, thus can greatly improve the work efficiency.

Acknowledgement

In this paper, the research was sponsored by the National Basic Research Program of China (973 Program) (2013 CB228205), National Science Foundation of China (51177051), and Science and Technology Projects of China Southern Power Grid.

References

[1] Feng Han, Zhuo Wang, Xiaoyi Sun, and so on. Construction and application of power demand side energy efficiency management platform [J].Jilin Electric Power, 2013 41 (4) 4-6, 10.

[2] Junhong Li, Lei Jin, Lu Xue, and so on. Promotion practice of DSM technology [J]. Power Demand Side Management, 2007 9(1) 56-59.

[3] Beibei Wang, Yang Li, Ciwei Gao, and so on. Demand side management outlook under smart grid infrastructure [J]. Automation of Electric Power Systems 2009 33 (20) 17-22.

[4] Jianhong Gao, Baozhi Zang. Demand Side Management under Smart Grid Framework [J]. Journal of Shandong College of Electric Power, 2010 13(2) 64-66.

[5] Naicheng Ge, Liwei Zhuang. Demand Side Response Implementation Methods and Case Analysis [J]. East China Electric Power, 2012 (5) 744-747.

[6] Shengming Quan, Xiaoli Zhu, Song Xue, and so on. Management evaluation indicator system of DSM projects considering the whole process and its application [J].International Journal Hydroelectric Energy, 2012 (9) 180-183.

[7] Miao Zhou. DSM measures and meanings of county-level electric power supply enterprises [J]. Power Demand Side Management, 2011 13(4) 71-72.

[8] Xiandong Tan, Baoguo Shan, Zhaoguang Hu, and so on. Design and development of DSM decision supporting system [J].Power Demand Side Management, 2012 (5) 4-8.

[9] Ming Zeng, Chen Li, Yingjie Chen, and so on. Implementation Mode of Power Demand Side Response to Large-scale Wind Power Integrated Grid in China [J]. East China Electric power, 2012 (3) 363-367.

[10] Gang Li, Yibo Zhou, Baiyuan Qing, and so on. Discussion on Test Method of Electric Demand Side Management Terminal in Guangxi [J].Guangxi Electric Power Technology, 2012 (5) 53-56.

[11] Weiwei Ding, Tianhong Pan, Zhengming Li, and so on. Design of Power Synthesized Parameters Monitor for Power Demand Side [J]. Instrument Technique and Sensor, 2012 (7) 26-28.

[12] Bingbing Wang. Demand Side Management Design Based on LonWorks [J]. Instrument Standardization & Metrology, 2012 (4) 40-43, 48.

Advanced Materials Research Vols. 986-987 (2014) pp 279-285

doi:10.4028/www.scientific.net/AMR.986-987.279

Determination of Photovoltaic and Wind Turbine Capacities in an Islanded Operation Mode with Meteorological Data

C. X. Wu, H. F. Xiao

[1] the School of Electrical Engineering, Zhejiang University, Hangzhou, 310027, Zhejiang Province, China
[2] School of Automation, Hangzhou Dianzi University, Zhejiang Province, China, 310018

Keywords: photovoltaic generation, wind turbine, capacity optimization, meteorological data, reliability, economics

Abstract. Sufficient and economical power supply is important for an islanded operation mode with renewable energy. This paper deals with the problem of optimizing photovoltaic (PV) and wind turbine (WT) capacities from the point of view of power supply reliability as well as economics. Meteorological data is analyzed, and then PV and WT capacities are optimized to supply the load reliably. The optimization is also discussed when the load profile is changes. Short-term power system operation is also analyzed. Several different cities in China with different climate features are simulated.

1. Introduction

Photovoltaic solar energy and wind energy conversion systems have been widely used for electric power supply in isolated locations far from the distribution network. Since solar energy and wind energy fluctuate depending on the climate [1], [2], it is difficult to operate or plan the system. However, solar energy and wind energy are complementary. Solar energy is rich in day time and none at night, but the wind energy may be richer at night time than in the day time. In the long term, solar energy is usually richer in summer than in winter, but wind energy may be richer in winter and spring than in summer. The meteorological feature is also different in different areas.

Some reference studied reliability of hybrid WT/PV systems and explored optimization of economics and reliability of power supply from a hybrid WT/PV system [3],[4]. Many papers focus on stand-alone photovoltaic or wind turbine system. In[5], a new probabilistic model that took into account the random nature of solar irradiance and load is developed. In[6], various solar radiation prediction methods along with hourly mean solar radiation (HMSR) method are compared, it is found that reliability indices, additional load hours (ALH) and additional power (AP) exponentially decrease with an increase in load. Fuel saving is also investigated. A probabilistic technique to evaluate the distribution system reliability utilizing the segmentation concept and a novel constrained Grey predictor technique for wind speed profile estimation is presented in [7]. In[8] an approach to evaluate the contribution of wind power to the load carrying capability of a power generating system is presented in an operating scenario. In [9] the reliability effects on a composite generation and transmission system associated with the addition of large-scale wind energy conversion systems is investigated using the state sampling Monte Carlo simulation technique.

Some research work is concentrated on the PV/WT hybrid system. the solar arrays and the composition of the solar-wind change. System reliability and fuel savings are analyzed in[10]. Several combinations of WT and PV capacity are compared by several reliability indexes in [11]. The probabilistic method is employed to analyze the optimization. These are only several possible kinds of combinations that be considered. In[12], leveled cost of energy and loss of power supply probability are employed to optimize the configuration of solar-wind system, but the optimization is not global optimization, but only different capacity combinations. A hybrid (wind/photovoltaic) system sizing optimization procedure is proposed in[13], but the capacity of PV and WT is in terms of the number of rated power units, the load models are constant or simply different between night time and day time.

Much work has been done to analyze the economic and reliability features of PV/WT hybrid systems, most only discuss the proportion of PV/WT capacity simply changes or when the capacity is the number of per unit capacity. The solar radiation calculated with altitude, solar declination or wind speed simulated with Weibull distribution is not so accurate, especially for solar energy, it is interrelated with radiation intensity and sunshine hours. The load model is often considered as constant.

This paper investigates the least cost installation of PV/WT hybrid system considering the reliability index energy supplied rate (ESR) to the load, and from the economic point of view that PV/WT power is greater than load: additional power (AP) is evaluated after optimization. Practical meteorological data is analyzed and used to evaluate the optimal capacity of PV and WT in the hybrid system. Different cities in China with different climatic features are simulated to test the proposed method.

3. Theoretical Formulation

The power output deduction of solar cell and wind turbine according to the meteorological data is as follows.

A. PV Output

If the peak radiation hour d_i is known, the output energy by installed peak power of PV module can be calculated as equation (1). Peak radiation hour is the hour which the PV cell temperature is $25°C$ and air mass is 1.5 and the sunshine radiation is $1000W/m^2$, its unit is hour.

$$W_{PV} = P_{PV} \times \eta \times d_i \times 10^{-3} \tag{1}$$

Where P_{PV} is installed PV peak power (W). The unit of $W_{PV}(t)$ is kWh. η is efficiency of installed PV which is a total efficiency of PV and other components in PV arrays. η is about 0.6 to 0.9, in this paper η is considered to be 0.75. The peak sunshine hour is converted from sunshine radiation in equation (2)

$$d_i = H \times 0.0116(h) \tag{2}$$

Where H is real sunshine radiation on the earth surface, and 0.0116 is the conversion coefficient between the sunshine radiation and peak sunshine hour, its unit is $h \cdot cm^2/cal$. H is formulated as equation (3) when daily sunshine hour S in meteorological data is known.

$$H = H_L(a + b\frac{S}{S_L}) \tag{3}$$

Where a,b is constant coefficient. S_L is day time hour which is calculated by equation (4). H_L is sunshine radiation passed through atmosphere in sunny day calculated in equation(5).

$$S_L = (2/15)W_S \tag{4}$$

$$H_L = \tau \times H_0 \tag{5}$$

Where W_S is hour angle. H_0 is sunshine radiation outside the atmosphere as equation. W_S and H_0 are calculated with equation (6) and (7). τ is the transmittance coefficient of the atmosphere[14], when the day is clear with sunshine, τ is about 0.4 to 0.8 depending on the atmosphere and some other conditions.

$$W_S = \cos^{-1}(-\tan\Phi \times \tan\delta) \tag{6}$$

$$\begin{aligned} H_0 = (1/\pi) \times G_{SC} \times E_0 \times (&\cos\Phi \times \cos\delta \times \sin W_S \\ &+ (\pi/180) \times \sin\Phi \times \sin\delta \times W_S) \end{aligned} \tag{7}$$

Where Φ is latitude, δ is solar declination. $G_{SC} = 1.367W/m^2$ is the solar constant which is the solar radiation before enters the earth's atmosphere, E_0 is adjusted factor of earth orbit eccentricity.

$$\delta = c_0 - c_1\cos\Gamma + c_2\sin\Gamma - c_3\cos 2\Gamma + c_4\sin 2\Gamma - c_5\cos 3\Gamma + c_6\sin 3\Gamma \quad (8)$$

$$E_0 = e_0 + e_1\cos\Gamma + e_2\sin\Gamma + e_3\cos 2\Gamma + e_4\sin 2\Gamma \quad (9)$$

Where Γ is year angle. $\Gamma = 2\pi(l-1)/L$， l is day number, for example the day number of Jan. 1 is 1. in leap year, L=366， and non-leap year, L=365。

B. WT output

WT power is decided by wind speed. The total energy output by WT during time t is:

$$W_{WT} = \int_0^t P_{(v)}dt \quad (10)$$

Where $P_{(v)}$ is the power output by WT at the wind speed of v. The wind turbine generation can be approximately expressed mathematically as follows:

$$P(v) = \begin{cases} 0 & v < v_{in}, v > v_{out} \\ \dfrac{v - v_{in}}{v_r - v_{in}} P_{WT} & v_{in} \le v \le v_r \\ P_{WT} & v_r < v \le v_{out} \end{cases} \quad (11)$$

Where P_{WT} is rate power of installed wind turbine. v_{in}, v_r, v_{out} are respectively the cut-in speed, the rated speed, the cut-out speed.

The wind speed from national meteorological center is obtained from an anemoscope 10m above the ground. When the type of wind turbine is selected, the wind speed v_0 should be transformed to the height of the hub v. The increase of wind speed with height is known as wind shear. Exponential function is applied to the wind shear transforming in equation (12).

$$v = v_0\left(\frac{Z}{Z_0}\right)^{\alpha} \quad (12)$$

Where Z is the height of the hub, Z_0 is the reference height of anemoscope, α is roughness of the ground; it is 1/7 for the open area.

With equation (11)-(12) daily WT output energy can be computed.

C. Month Average Energy by Hybrid PT/WT System

From section II and part A and B in this section, month average daily peak radiation hour and wind speed can be calculated. If the installed PV module is P_{PV}, the PV output power of ith month can be calculated by equation (13) which is equation (1) multiplied by the day number m_i of month i. If the installed rated WT power is P_{WT}. $P_{(v)i}$ is WT output power(kW) according to the month average daily wind speed v. The WT energy output in a whole day is $24\times P_{(v)i}$, and the month WT output energy is multiplied by the day number of month i: m_i, as equation(14).

$$W_{PVi} = m_i \times P_{PV} \times \eta \times d_i \times 10^{-3}(kW\cdot h) \quad (13)$$

$$W_{WTi} = m_i \times 24 \times P_{(V)i}(kW\cdot h) \quad (14)$$

4. the mathematical model

A. The Indices of Energy Sufficient Rate and Additional Power

Using equation (18) the energy sufficient rate (ESR) of the *ith* month is formulated:

$$ESR_i = \frac{W_{PVi} + W_{WTi}}{E_{Li}} \tag{15}$$

Where ESR_i is monthly energy sufficient rate form January to December W_{PVi} is PV output energy in month i, W_{WTi} is WT output energy in month i, E_{Li} is total load in month i. From the view of economic, AP is expected to be a relatively small value. AP and the rate of additional power (RAP) are defined as equation (16), (17) respectively:

$$AP = \sum_{i=1}^{12} W_{PVi} + \sum_{i=1}^{12} W_{WTi} - \sum_{i=1}^{12} E_{Li} \tag{16}$$

$$RAP = AP / \sum_{i=1}^{12} E_{Li} \tag{17}$$

B. Optimization Model

To find the economist fixed cost capacity of PV and WT, the objective function is:

$$\min(C_{PV} + C_{WT}) \tag{18}$$

Subject to:

$$ESR_i > \lambda (i = 1, 2 \cdots 12) \tag{19}$$

Where C_{PV} is fixed cost of PV, $C_{PV} = P_{PV} \times C_{0PV}$, C_{0PV} is per peak power cost of PV fixed cost. C_{WT} is fixed cost of WT. $C_{WT} = P_{WT} \times C_{0WT}$, C_{0WT} is per unit cost of rated WT power. $ESR_i > \lambda$ means ESR of each month should be greater than threshold. The simple combination searching method is employed to WT/PV capacity optimization.

5. Simulation Result

A. The Simulation Station Information and Load Model

The life of WT and PV array is about 15 to 25 years. In this paper 20 years is assumed as the life time of PV and WT. The fixed cost includes equipment cost, control system cost, transport cost, installation cost etc. In this paper the PV per unit fixed cost is about 25000￥/kW, and the WT per unit fixed cost is about 8000￥/kW. Based on the recent ten years meteorological, several cities are selected to simulate the model. The station information is shown in table 1. In this paper, v_{in} is 3m/s, v_r is 12m/s, v_{out} is 25m/s. the hub is assumed to be 40m. In order to evaluate the long term plan of PV/WT hybrid capacity, two cases of load model is listed in table 2. It is the month average daily load power of every month, with the unit in kW・h.

TABLE 1 STATION INFORMATION

Station number	City name	Latitude(degree)
53399	Zhang Bei	41.15
51463	Wu Lu Mu Qi	43.47
50873	Jia Mu Si	46.49
58467	Ci Xi	30.16

TABLE 2 MONTH AVERAGE DAILY LOAD

Month	1	2	3	4	5	6	7	8	9	10	11	12
Case1	75	60	55	50	45	60	85	95	80	55	60	70
Case 2	50	70	80	90	100	100	100	95	80	55	60	50

B. The Optimization Result by Case 1 Load Model

For the station 53399 when the load model is as case 1. When the ESR of each month is not less than 0.9, the optimization result is 26 kW PV and 15kW WT installed, the least cost is 770,000￥.

The month average daily load is the blue column shown in Fig 1. Since the wind and solar energy is sufficient in April and May while the load is relatively low, more energy exceeds the load level.

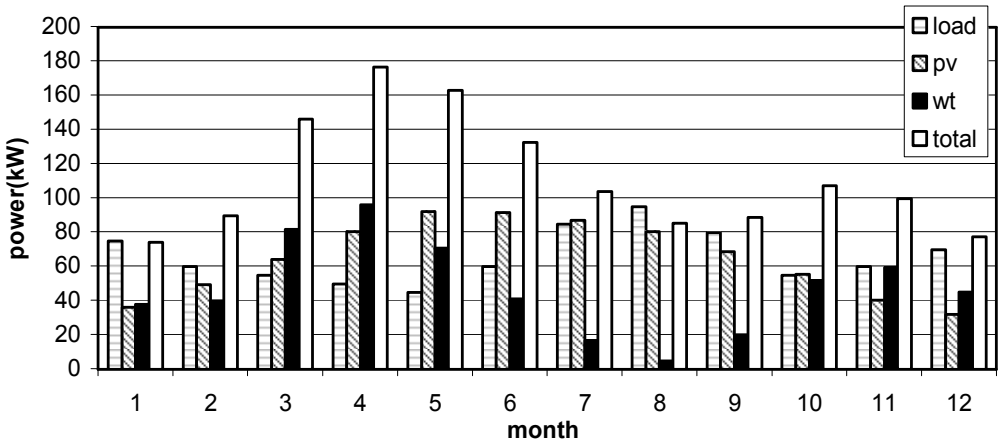

Fig. 1 Optimized power output and load level of case 1 in station 53399

Optimization of other stations with the same load model of case 1 with the constraint ESR of every month no less than 0.9 is shown in table 3. The cost of only PV or WT with the same constraint is also listed to compare with the hybrid system. For the same load model, the optimization result is very different. The proportion of the PV capacity and WT capacity is different and the economic fixed cost is very different from one city to another. Normally the hybrid system is more economical than a single PV or WT. But in the station 51463(Wu Lu Mu Qi city), for the same load level, the optimization result is that PV is the most economic way to satisfy the load. It is attributed that the wind speed is relatively smaller than the solar radiation, especially in January and December, when the month average daily wind speed is less then 3m/s, below the wind turbine cut-in speed.

TABLE 3 OPTIMIZATION RESULT WITH ESR OF EACH MONTH NOT LESS THAN 0.9

Station	Cost or capacity	PV+WT	Only PV	Only WT
Zhang Bei	Total cost(10000)	77	127.5	202.4
	PV capacity(kW)	26	51	0
	WT capacity(kW)	15	0	253
Wu Lu Mu Qi	Total cost(10000)	220	220	It can't be satisfied only by WT
	PV capacity (kW)	88	88	
	WT capacity (kW)	0	0	
Jia Mu Si	Total cost(10000)	77.7	192.5	83.2
	PV capacity (kW)	17	77	0
	WT capacity (kW)	44	0	104
Ci Xi	Total cost(10000)	124.8	127.5	140.8
	PV capacity (kW)	48	51	0
	WT capacity (kW)	6	0	176

For the same load level of case 1, when ESR changes the optimization is different too. As seen from Fig 2, the optimized total cost will increase when the ESR becomes larger in each station, though different places get different optimization results.

C. The Optimization Result Contrast with Case 2 Load Model

When load model of every month changes to case 2, the optimization result is 27 kW PV and 6 kW WT in station 53399, while the fixed cost is 723,000￥. It can be seen that less energy is wasted in such a load level from Fig. 3.

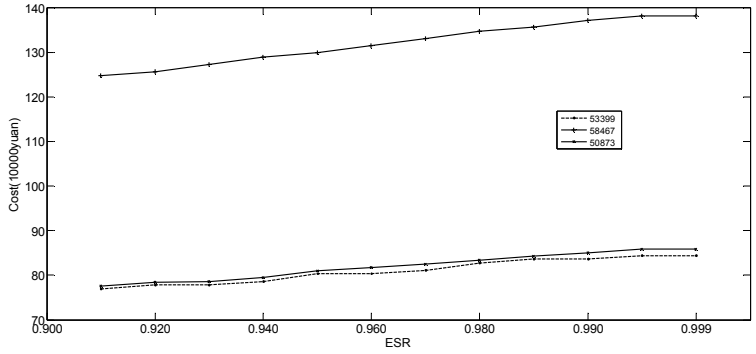

Fig. 2 The economic cost of different ESR

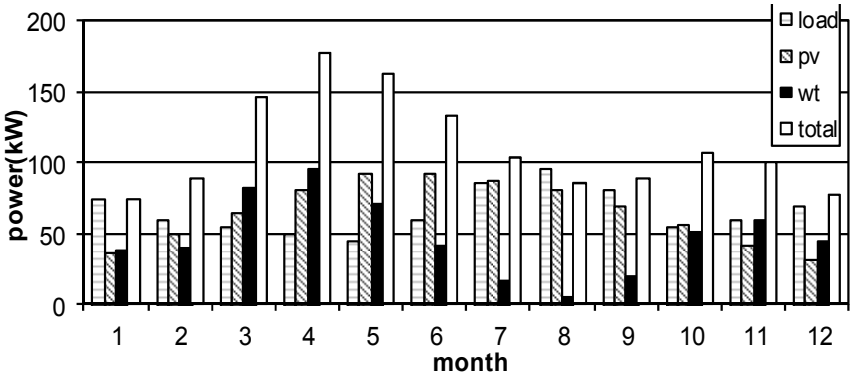

Fig. 3 Case 2 month average daily load level and optimized total output power in station 53399

D. The ESR and RAP evaluated by daily power balance

In this paper, a long term plan of the PV/WT hybrid system is optimized which is logical and meets the power supply sufficient demand in the long term.

Daily output of PV and WT is simulated by optimal installed capacity with load model case 2 with ESR greater than 0.9. Table 4 is the year ESR and RAP from 2001 to 2004 of the stations. Seen from the power supply reliability, each station in each year ESR is about 0.9, while seen from the economic aspect, RAP is about from 50% to 150%. RAP is smallest in station 58674, station 53399 has a relatively larger RAP, and station 50873 has the largest RAP. It is attributed to the proportion of wind turbine capacity in the hybrid system. Proportion of PV/WT in station 58467 is the highest while that in station 50873 is the lowest. Wind energy contributes to the unstable operation of the island system. Solar energy is relatively more stable than wind energy.

TABLE 4 EENS AND RAP IN DIFFERENT YEARS TO DIFFERENT STATIONS

year	53399(PV:26,WT:15)		50873(PV:17,WT:44)		58467(PV:48,WT:6)	
	ESR	RAP	ESR	RAP	ESR	RAP
2001	92.8%	78.96%	80.8%	150.24%	91.84%	60.48%
2002	89.68%	60.72%	79.23%	126.8%	87.76%	48.48%
2003	87.52%	47.04%	72.1%	91.23%	90.88%	60.96%
2004	91.84%	60.7%	73.3%	108.7%	91.12%	61.68%

6. Conclusion and Discussion

This paper proposes the optimization model of PV/WT hybrid system to decide the most economical capacity dispatch between PV and WT. the main attribute is: 1) economic aspect of hybrid PV/WT system is analyzed in many papers, but the best optimization capacity decision is not mentioned. The optimization capacity is obtained in this paper. The optimization model is proven to be feasible with the optimal system that the yearly ESR and RAP are meet the requirement. The optimization method is very simple and the plan capacity could be got fast and easy. 2) the optimization model is based on actual meteorological data, which is more instructive than generate

wind speed or solar radiation by some simulation software. In particular, the solar energy is evaluated by the number of sunshine hours which is more accurate than by astronomical solar radiation. 3) different circumstances are compared during the long term run plan of deciding PV and WT capacity, such as load level change and ESR change.

8. Reference

[1] I. E. Lee, M. L. Sim, F. W. L. Kung and Z. Ghassemlooy, "Statistical analysis and modeling of one-minute global solar irradiance for a tropical country," *2nd International Symposium on Environment-Friendly Energies and Applications (EFEA)*, Northumbria University, 2012, pp. 243-248.

[2] T. Burton, D. Sharpe, N. Jenkins and E. Bossanyi, Wind Energy Handbook, Chichester: John Wiley & Sons Ltd. 2001.

[3] F. O. Hocaoglu, O. N. Gerek, M. Kurban, "A novel hybrid (wind/photovoltaic) system sizing procedure," *Solar Energy*, vol. 83, no. 11, pp. 2019-2028, Dec. 2009.

[4] J. L. Bernal-Agustín and and R. Dufo-Lópeza, "Multi-objective design and control of hybrid systems minimizing costs and unmet load," *Electric Power Systems Research*, vol. 79, no. 1, pp. 170-180 Jan. 2009.

[5] F. J. Ruiz-Rodriguez, J. C. Hernandez and F. Jurado, "Probabilistic load flow for radial distribution networks with photovoltaic generators," IET Renew. Power Gener., vol. 6, no. 2, pp. 110–121, 2012.

[6] R. M. Moharil and P. S. Kulkarni, "Reliability analysis of solar photovoltaic system using hourly mean solar radiation data," *Solar Energy*, vol. 84, no. 4, pp. 691-702, Apr. 2010.

[7] Y. M. Atwa and E. F. El-Saadany, "Reliability evaluation for distributed system with renewable distributed generation during islanded mode of operation," *IEEE Transactions on Power Systems*, vol. 24, no. 2, pp. 572-581, May. 2009.

[8] R. Billinton, Bipul Karki, Rajesh Karki and G. Ramakrishna, "Unit commitment risk analysis of wind integrated power systems," *IEEE Transactions on Power Systems*, vol. 24, no. 2, pp. 930-939, May. 2009.

[9] R. Billinton, Yi Gao and Rajesh Karki, "Composite system adequacy assessment incorporating large-scale wind energy conversion systems considering wind speed correlation," *IEEE Transactions on Power Systems*, vol. 24, no. 3, pp. 1375-1382, Aug. 2009.

[10] Rajesh Karki and Roy Billinton, "Reliability/cost implications of PV and wind energy utilization in small isolated power systems," *IEEE Transactions on Energy Conversion*, vol. 16, no. 4, pp. 368-373, Dec. 2001.

[11] G. Tina, S. Gagliano and S. Raiti, "Hybrid solar/wind power system probabilistic modelling for long-term performance assessment," *Solar Energy*, vol. 80, no. 5, pp. 578-588, May. 2006.

[12] S. Diaf, D. Diaf, M. Belhamel, M. Haddadi, A. Louche, "A methodology for optimal sizing of autonomous hybrid PV wind system," *Energy Policy*, vol. 35, no. 11, pp. 5708-5718, Nov. 2007.

[13] F. O. Hocaoglu, O. N. Gerek, M. Kurban, "A novel hybrid (wind/photovoltaic) system sizing procedure," *Solar Energy*, vol. 83, no. 11, pp. 2019-2028, Dec. 2009.

[14] D. M. Gates, Biophisical Ecological, New York: Spring verlag, 1980.

Advanced Materials Research Vols. 986-987 (2014) pp 286-290

doi:10.4028/www.scientific.net/AMR.986-987.286

Distributed Energy Resource Impacts On FLISR Scheme In Distribution System

Haitao LIU[1, a], Hui YU[1, b], Yiming LU[1], Guangxian LV[1],
Yu CHEN[2], Xinhui ZHANG[2]

[1] China Electric Power Research Institute, Beijing 100192,China

[2]Shandong University of Technology, Zibo 255049, China

[a]email: lhtcn@epri.sgcc.com.cn, [b]email: yuhui3@epri.sgcc.com.cn

Keywords: FLISR, Distributed Generation, Distribution Automation

Abstract. The key distribution automation (DA) application for implementing a self-healing smart distribution network is the fault location isolation and service restoration (FLISR) application. With DGs introduce significantly more variability into distribution system power flows, it has a great impact to FLISR. Based on summarizing the existing FLISR scheme, this paper analyses the influence of fault detection and service restoration with large-scale DGs.

Introduction

One of the important characteristics of the smart grid is its ability to "self-heal". The key distribution automation (DA) application for implementing a self-healing network is the fault location isolation and service restoration (FLISR) application. FLISR creates a switching plan for re-energizing portions of a distribution circuit that have been de-energized as a result of a permanent feeder fault. Once the switching plan is created, FLISR can automatically execute the plan to restore service where possible, usually in less than one minute following the initial fault occurrence.

Around the world, conventional power system is facing the problems of gradual depletion of fossil fuel resources, poor energy efficiency and environmental pollution. These problems have led to a new trend of generating power locally at distribution voltage level by using non-conventional renewable energy sources like natural gas, wind power, solar photovoltaic cells, fuel cells, combined heat and power (CHP) systems etc. This type of power generation is termed as distributed generation (DG) [1].

DGs are connected to the low- or medium-voltage distribution system, where traditionally only consumption has been connected. So distribution lines are from single source to multi-source, which brings to impacts to fault detection and service restoration algorithm[2][3][4]. Based on summarizing the existing FLISR scheme, this paper analyses the influence of fault detection and service restoration with large-scale DGs.

FLISR Application function

The FLISR application function automatically detects that a fault has occurred, locates the fault (between two switches), sends control commands to open the switches that bound the faulty area to isolate the faulty section of the feeder, and then closes other switches (where possible) to restore service to healthy sections of the feeder. The key steps are detailed below:

(1)Fault Detection: FLISR should only operate following a short circuit (fault) on the feeder itself or in the facilities that normally supply the feeder. To meet this requirement, one or more fault detectors are needed to trigger FLISR operation when fault-level currents are detected. Common practice is to use a protective relay intelligent electronic device (IED) in the substation and feeder terminal units (FTUs) on feeder line to determine that a fault occurred in the distribution feeder protection zone and then provide a signal to trigger FLISR operation.

(2)Fault Location: The second step is to determine the "section" of the feeder that contains the fault. FLISR "sections" are portions of the feeder that are bounded by remotely controlled switches. By use the information of FTUs, FLISR algorithm determines what section is faulted. The faulted section is bounded by one FTU that has a fault indication and one or more FTUs that did not "see" the fault.

(3)Fault Isolation: FLISR then sends control commands to open the switches needed to completely isolate the faulty section. It is common practice for FLISR to defer these control actions until the standard automatic reclosing sequence has been completed. This ensures that feeder reconfiguration by FLISR is only performed following a permanent fault (should not reconfigure the feeder if fault is a self-clearing "temporary" fault).

(4)Service Restoration: Once the faulty section of the feeder is isolated, FLISR attempts to restore service to as many "healthy" sections of the feeder as possible via the available sources. Available sources include the normal source of supply to the feeder as well as any available backup sources that are connected to the faulted feeder via normally-open, remotely controlled tie switches that have spare capacity to carry additional load.

FLISR process is as figure 1 below.

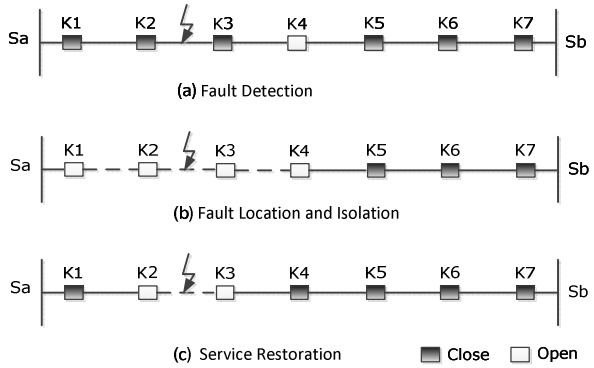

Fig.1 FLISR Process

FLISR Scheme

For each utility, the FLISR implementation process will look a little different, depending on its unique needs. FLISR applications can use either decentralized, substation, or control-center intelligence and that each has advantages and drawbacks.

Local-intelligence Scheme

Local-intelligent schemes are rudimentary applications where automatic functions occur without any communication with other devices. The schemes do sequential reclosing control by using recloser and section switch, realize the fault isolation and restore power. Due to multiple reclosing on permanent fault, it will result in stress to the system, overloads, and additional outages. This local-intelligent scheme is limited in that the breakers will simply trip and close based on breaker position, thus it has many drawbacks. A more intelligent scheme is therefore required.

Centralized Scheme

By the master control center to handle all FTU information to detect faults and fault location, remote control FTU to operate switches to achieve fault isolation and service restoration. The central intelligence remains with the system operator and the DA benefit is basically to reduce the time to manually isolate the faulted section and perform the load transfers. The system operator can utilize various SCADA data inputs from remote devices to make switching decisions in order to reconfigure the system. Reliable communications for the inputs can include open/close status points, current, voltage, and other quantities in order to ensure timely system data is transmitted to the operator. The system operator may also have the tools to make sure that the transfer will not overload the substation or the back-up circuit.

Decentralized Scheme

Distributed intelligence applies communication and software to localized sectionalizing and fault-interrupting devices to provide automated control that can vary from a simple circuit segment

to a region where multiple circuits interconnect numerous substations. While these devices are primarily controlled at the installed location, rather than from a central location, the shared software and communication distribute the data pertaining to the event or condition among the devices to effect the required circuit reconfigurations.

This solution is based on communication between FTUs, to achieve cooperative control, to improve the control response speed. Since the scheme does not depend on the master station, fault isolation and service restoration can be completed within seconds. FTUs needs peer communication network and smart control, so FTU requires a high degree of intelligence and investment is more than the other scheme.

Integrity DG in distribution system

The connection point of an energy source to the grid is usually referred to as the point of connection (PCC)[5]. Its definition depends on the ownership and utility interconnect requirements. Two different possible definitions are shown in Figure 2, where typically the interconnection relay (protection) is installed at the PCC. It will be assumed here that the PCC is the connection point before the interconnection transformer. PCC can be connected directly or as a branch line connected to the feeder line and substation bus.

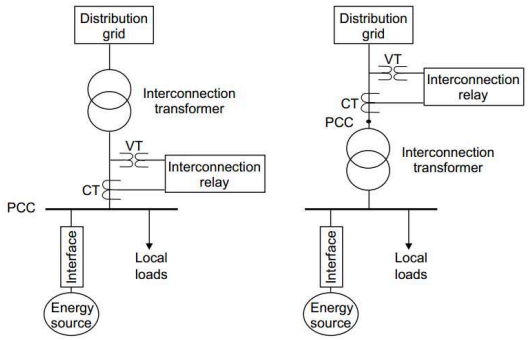

Fig.2 Two possible definitions of PCC

Impacts on Fault Detection, Location and Isolation

Most existing distribution networks were designed for one-directional flow, where power flows from the grid substation to end-users at lower voltages, and were not intended to accommodate distributed generation. Traditionally, distribution networks are designed as passive systems and ring structure but open loop operates. With DG introduces significantly more variability into distribution system power flows, it has a great impact to FLISR.

Bi-directional power flow and changes in network voltage profile caused important impact on the operation of conventional feeder fault detection schemes that are originally designed based on radial network operation assumption. Some impacts are due to an increase in fault current because of the generator. Other impacts occur because the fault current contribution from a generator is too small.

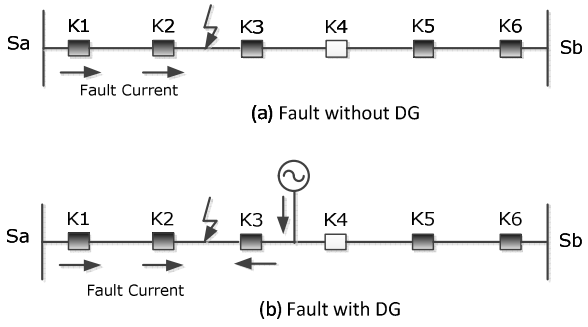

Fig. 3 Impacts on fault current with DGs

The impact of distributed generation on protection strongly depends on the fault current contribution and thus on both the size and type of the interface. Synchronous generators deliver a continuous short-circuit current; induction generators contribute during one or two cycles in case of a three-phase fault and longer in case of a non-symmetrical fault. Units with power electronics interface have none or a very limited contribution to the fault current.

Protection theory of a distribution network, in the vast majority of cases, is based on overcurrent protection. This can be definite-time or inverse-time overcurrent protection. Adding a generator to a distribution feeder will change the fault currents and thus increase the risk of a protection failure.

The following protection failures could occur due to distributed generation:

(1) The fault current contribution from the generator could result in a total fault current exceeding the rating of some equipment.

(2) The presence of a generator along a feeder will reduce the fault current at the start of the feeder, for a fault beyond the generator. When the fault current for a fault at the end of the feeder drops below the overcurrent setting of the relay at the start of the feeder, a failure to operate may occur.

(3) The fault current by the generator, for a fault on another feeder, could result in unwanted opening of the breaker at the start of the feeder.

(4) When using fast reclosing for fuse saving, the coordination between the fuse and the recloser is endangered by the presence of distributed generation along the feeder.

(5) The fault current contribution of some generators is not big enough for the overcurrent protection to detect the fault. A failure to operate could result from this. This is especially a concern for small generators and any generator equipped with a power electronics interface.

(6) The presence of a generator on a distribution feeder could result in the incorrect operation of fault current indicators. These are commonly used in underground cable networks to facilitate the location of the faulted section and to reduce the duration of an interruption of the supply for the customers.

(7) Single-phase reclosing or single-phase fuse clearing can result in ferroresonance conditions with distributed generation. Therefore, fuses and single-phase breakers should be avoided between a three-phase generator and the next upstream three-phase breaker.

For questions listed above, there have been many studies currently in progress to resolve.

Impacts on Service Restoration

Service restoration needs reconfiguration of a power distribution system, that is an operation to alter the topological structure of distribution feeders by changing open/closed status of sectionalizing and tie switches. Configuration management operation involves the restoration of service to as many customers as possible during a restorative state following a fault.

When carrying out the net reconfiguration, the operations that are executed should guarantee that the system satisfies some conditions [9][10][11][12], such as:

(1) The capacity of current of the transformers and lines should be within specified limits;

(2) The voltage drop should stay inside an established margin;

(3) System should continue being radial;

(4) The Number of operations of the equipment show be reduced as much as possible;

(5) Important customers should be given priority;

(6) System must be balanced in the best possible way;

(7) The coordination of the protection must be maintained.

With DGs introduce, systems can increase capacity to restore priority and non-priority load. But the addition of DGs significantly increases circuit reconfiguration algorithm complexity.

Circuit reconfiguration can vary based upon the system need. Reconfigured lines bring about changes in load current, available fault currents, and voltage drop. The new circuit configuration may alter protective device coordination. The load of the new circuit configuration may also exceed the existing trip settings of the protective devices.

Conclusion

The impacts with introduction of generating sources into the distribution system could be positive or negative depending on the system operating condition, distributed generation characteristic, location and sizing. FLISR scheme needs as much as possible to use advantages of DG, to avoid problems that DGs introduced. Whether existing FLISR scheme to meet requirements need to be carefully assess. Implement new FLISR scheme, information model should comply IEC61850/61970/61968 standards.

Acknowledgement

In this paper, the research was sponsored by the State Grid Corporation of China (Project No. PD71-13-037).

References

[1] S. Chowdhury, S. P. Chowdhury, P. Crossley, Microgrids and Active Distribution Networks, The Institution of Engineering and Technology, London, UK, 2009.

[2] P.P. Barker, R.W.D. Mello, Determining the Impact of Distributed Generation on Power Systems. I. Radial Distribution Systems, in IEEE/Power Eng Soc. Summer Meeting, vol 3, 2000, pp 1645-1656.

[3] Y.Mao, K.N.Miu, Switch Placement to Improve System Reliability for Radial Distribution Systems with Distribution Generation, in IEEE Trans. on Power Systems, vol 18, no 4, Nov 2003.

[4] Zhang Chao，Ji Jianren，Xia Xiang．Effect of distributed generation on the feeder protection in distribution network[J]．Relay，2006，34(13)：9-12(in Chinese)．

[5] IEEE, Standard 1547 Interconnecting Distributed Resources with Electric Power Systems, (2009).

[6] Pang Jianye，Xia Xiaobin，Fang Mu．Influence of protection on distribution network in distribution system[J]．Relay，2007，35(11)：5-8(in Chinese)．

[7] Kauhaniemi K，Kumpulainen L．Impact of distributed generation on the protection of distribution networks[C]．Developments in Power System Protection，Hawaii，2004．

[8] L.K Kumpulainen, K.T Kauhaniemi, Analysis of the Impact of Distributed Generation on Automatic Reclosing, Power Systems Conference and Exposition, 2004, IEEE PES, vol. 1, pp. 603-608, 10-13 Oct. 2004.

[9] Yasin, Z.M. ; Rahman, T.K.A., Influence of Distributed Generation on Distribution Network Performance during Network Reconfiguration for Service Restoration Power and Energy Conference, 2006. IEEE PES, pp: 566- 570,2006.

[10] Luan W P，Irving M R，Daniel J S．Genetic algorithm for supply restoration and optimal load shedding in power system distribution networks[J] ．IEE Proceedings of Generation ，Transmission and Distribution，2002，149(2)：145-151．

[11] Xu Yuqin，Zhang Li，Wang Zengping，et al．Algorithm of supply restoration for large area blackout in distribution network with distributed generation[J] ．Transactions of China Electrotechnical Society，2010，25(5)：61-67 (in Chinese)．

[12] Lu Zhigang ，Dong Yuxiang ．Service restoration strategy for distribution system with DGs[J] ．Automation of Electric Power Systems，2007，31(1)：89-92(in Chinese)．

Advanced Materials Research Vols. 986-987 (2014) pp 291-294

doi:10.4028/www.scientific.net/AMR.986-987.291

Doubly-Fed Wind Farm Engineering Aggregation Model Used for Planning

Meng Dai[1, a]

[1]Tsinghua University, Beijing 100084, China;

[a]daimeng83@126.com

Keywords: electrical calculation in wind power integration planning; doubly-fed wind farms; engineered aggregation model

Abstract. Establishing an appropriate aggregation model of wind farm is the first step of the electrical computation in wind power integration planning. This paper first summarizes the technical requirements of wind farm model from the viewpoint of engineering, then proposes an aggregation DFIG model of wind farm. Because of the lack of measured data in the planning stage, the single equivalent model is used in this paper, and be improved by considering the equivalent collection lines model. The accuracy of the aggregation model in different electrical calculation, such as power flow, transient stability and shortcut current simulation, is verified through a sample system in DIgSILENT.

Introduction

The development of wind power is fast in recent years[1, 2], so it's necessary to consider the influence of wind power at the stage of power grid planning. As the detailed model of one wind turbine is already very complex[3], the detailed model of a wind farm consisting of dozens of wind turbines is too complex to be used for the electrical calculation in wind power integration planning. As a result, it's necessary to build an equivalent model of wind farm specially for the wind power integration planning, which can simplify the calculation at the same time of ensuring the accuracy.

The existing equivalent models of wind farm still have their disadvantages when using for planning. The literatures [4, 5] introduce the method of parameter identification to build the equivalent model. This method needs the operating data of the wind farm which can't be gotten at the stage of planning. So the method of parameter identification is unsuitable for planning. The literatures [6, 7] introduce the reduced-order equivalent method to build the wind farm model. This method simplifies the differential equations of the wind turbines so that the model of the wind farm is simplified. However, the wind power integration planning is often carried out in some fixed software such as DIgSILENT and BPA. The model of the wind turbine is fixed in the software. We can't change the turbine's model easily, so the method of reduced-order is not suitable for planning.

To solve the problems mentioned above, this paper build a kind of aggregation model of wind farm, which can be used in existing software directly and simplify the calculation in planning. Then the effectiveness and accuracy of the built aggregation model are checked through building a simulation example.

Technical Requirements to the Aggregation Model Used for the Wind Power Integration Planning.

The calculation process of the wind power integration planning can be described as the fig.1 shows. There are three kinds of calculation in the process of wind power integration planning. They are power flow calculation, transient calculation and short-circuit current calculation. Each of the calculations has its requirements to the wind farm aggregation model.

Power Flow Calculation. It's required to calculate the load of the lines and the bus voltage in power flow calculation. So the wind farm aggregation model is required to give the similar terminal voltage and output active power compared with the detailed model of the wind farm.

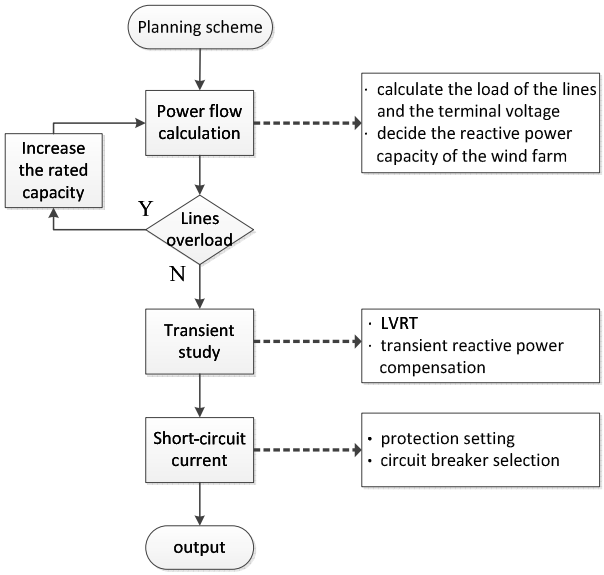

Fig. 1 The process of calculation in wind power integration planning

Transient Calculation. Transient calculation requires the model to give exact transient variables such as the drop value and recovery time.

Short-circuit Current. Short-circuit current calculation requires the model to give the exact peak value of the short-circuit current.

Table 1 Technical requirements to the equivalent model used for planning calculation

calculation	Key requirements
all	Can be used in existing software
Power flow	keep the 35kv terminal
	Give exact terminal voltage
	Give exact output active power
Transient calculation	Exact drop value and recovery time of terminal voltage
	Exact drop value and recovery time of acitive power output
	Exact drop value and recovery time of reactive power output
Short-circuit	The peak value of the short-circuit current

Aggregation Model of the Doubly-Fed Wind Farm

As the doubly-fed wind turbine is the most widely used turbine, this paper takes the doubly-fed wind farm as example to build the aggregation model. The aggregation model of the wind farm consists of two part: the aggregation model of the wind turbines and the aggregation model of the collector lines.

Aggregation Model of the wind turbines. The aggregation model of the wind turbines can be described as follows.

$$S_{eq} = mS \tag{1}$$

$$\begin{cases} X_{m\_eq} = \dfrac{X_m}{m}, X_{s\_eq} = \dfrac{X_s}{m}, X_{r\_eq} = \dfrac{X_r}{m} \\ R_{s\_eq} = \dfrac{R_s}{m}, R_{r\_eq} = \dfrac{R_r}{m} \end{cases} \tag{2}$$

$$\begin{cases} H_{gen\_eq} = mH_{gen}, H_{WTR\_eq} = mH_{WTR} \\ k_{sh\_eq} = mk_{sh}, c_{sh} = mc_{sh} \end{cases} \tag{3}$$

In these equations, S is the capacity of one turbine. m is the number of turbines in the wind farm. Subscript eq represents the equivalent aggregation model. The second equation describes the aggregation of the generator's parameters. X is the reactance and R is the resistance. The third equation describes the aggregation of the shaft. H is the time constant. k is the stiffness coefficient of the shaft.

Aggregation Model of the Collector Lines. There are two kinds of collector lines in wind farms. One of that is called route type. The turbines are linked by collector lines one by one. The aggregation model is as follows.

$$Z_{eq} = \frac{\sum_{i=1}^{n}\left(\sum_{k=1}^{i}\left(Z_k\sum_{j=k}^{n}P_j\right)P_i\right)}{\left(\sum_{i=1}^{n}P_i\right)^2} \tag{4}$$

The other is called radial type. The turbines are linked to one terminal separately. The aggregation model is as follows.

$$Z_{eq} = \frac{\sum_{i=1}^{n}\left(Z_i P_i^2\right)}{\left(\sum_{i=1}^{n}P_i\right)^2} \tag{5}$$

P is the active power output of one turbine. The subscript represents the number of the turbine.

Simulation and Verification

As the software DIgSILENT is the accepted software of electrical calculation with wind power, this paper makes use of DIgSILENT to check the accuracy of the aggregation model. Firstly a wind farm example is built as follows. The aggregation model is built through the method mentioned above.

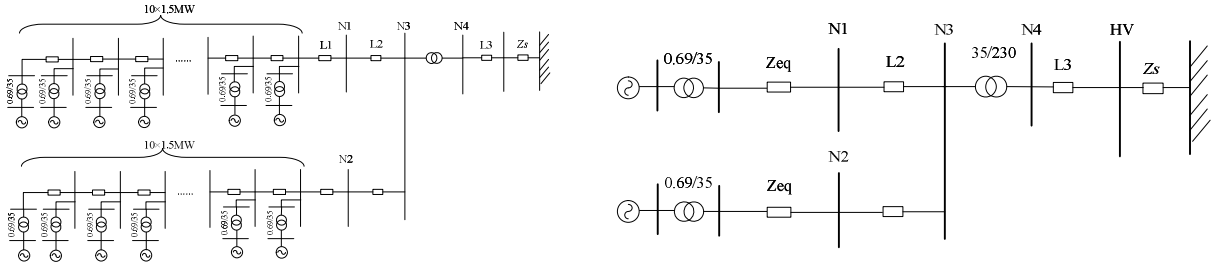

Figure 2 Detailed and aggregation model of the example

Accuracy Check of Power Flow. Calculate the terminal voltage and active power output of the wind farm. The results of the detailed model and the aggregation model are compared as follows.

Table 2 Results of power flow(voltage)

	amplitude/p.u.		Phase angle/°	
	detailed	aggregation	detailed	aggregation
N1	1.02	1.02	25.92	25.91
N3	1.02	1.02	25.54	25.53
N4	1.01	1.01	7.13	7.13
HV	1.01	1.01	6.82	6.83

Table 3 Results of power flow(active power)

	Active power/MW	
line	detailed	aggregation
N1-N3	14.9134	14.9271
N2-N3	14.9134	14.9271
N4-HV	29.4338	29.4610

It is concluded that the power flow results are similar between detailed model and aggregation model. It can be inferred that the equivalent model is suitable for the power flow calculation in planning.

Accuracy Check of Transient Calculation. Firstly the transient fault is set to be three-phase short circuit in the transformer high-voltage bus for 0.2 seconds. The terminal voltage of the wind turbine, the active power and reactive power output of the wind farm are simulated. The results are as fig. 3, fig. 4 and fig. 5 shows.

The key indexes of each figure are analyzed, which is shown in table 4. The transient results are also similar between detailed and aggregation model. It can be inferred that the equivalent model is suitable for the transient calculation in planning.

Accuracy Check of Short-circuit Current Calculation. The short-circuit fault is set the same as that in transient calculation. The short-circuit current is simulated as fig. 6 shows.

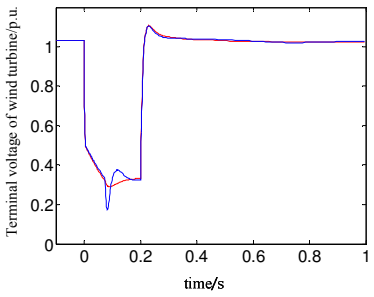

Figure 3 Voltage

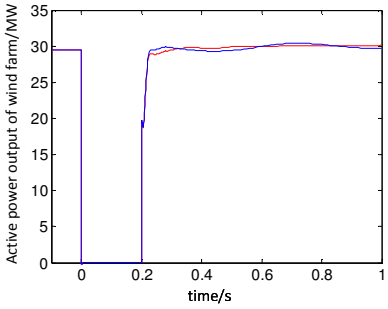

Figure 4 Active power

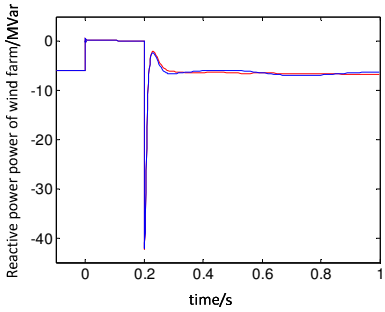

Figure 5 Reactive power

Table 4 Key indexes of the transient simulation

	Drop value		Recovery time/s	
	detailed	aggregation	detailed	aggregation
voltage/p.u.	0.1723	0.2896	0.0127	0.0128
Active power/MW	0.0230	0.0230	0.0210	0.0188
Reactive power/Mvar	-42.2346	-42.2777	0.0173	0.0173

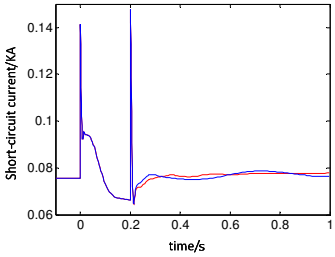

Figure 6 Short-circuit current simulation

It is inferred that the equivalent model is suitable for the short-circuit current calculation in planning.

Summary

This paper concludes the requirements to the wind farm aggregation model of planning. Based on the requirement, a method of building aggregation model is proposed. Then a simulation example is built, which verifies that the proposed aggregation model is suitable for electrical calculation in planning.

References

[1] ZHANG Liying, YE Tinglu, XIN Yaozhong, et al. Problems and measures of power grid accommodating large scale wind power[J]. Proceedings of the CSEE, 2010, 30(25):1-8. (Chinese)

[2] LI Junfeng, et al. 2012 China Wind Power Outlook[M]. Beijing:China Environmental Science Press, 2012 :75-76. (Chinese)

[3] ZHANG Zhaoyan: study on real-time simulation and modeling of VSCF wind turbine group system (master, north china electric power university, china, 2011). P. 1-5

[4] SUN Jian-feng, JIAO Lian-wei, WU Jun-ling, et al. Research on multi-machine dynamic aggregation in wind farm[J]. Power System Technology, 2004, 28(7): 58-61.

[5] CHEN Ying: research on wind farm equivalent modeling based on operation data (master, north china electric power university, china,2012). P. 15-18.

[6] Castro R M G,Ferreira de Jesus J M.A wind park reduced-order model using singular perturbations theory. IEEE Transactions on Energy Convertion,1996,11(4):735-741

[7] Morton A B.Model aggregation of wind farms and other ensemble systems.2007 Australasian Universities Power Engineering Conference, Perth, Western Australia, 2007

Advanced Materials Research Vols. 986-987 (2014) pp 295-298

doi:10.4028/www.scientific.net/AMR.986-987.295

Evaluation of China's energy strategy

WANG Shuai

School of Management, Tianjin University of Technology, Tianjin300384, China

E-mail: ysp08wangshuai@163.com

Keywords: Energy strategy; Evaluation of energy; Sustainable development

Abstract: The energy problem is a matter of human survival and development of a global issue. With the deepening of the new industrialization, energy resources, climate change, environmental problems to human challenge is becoming more and more serious. In the development of China's energy consumption, energy consumption structure and the world in general there are many differences between the consumption structure, rational utilization of domestic coal resources, improve efficiency, promote the reform of energy-using way, will become China's energy industry development in the future be solved the problem. To build China's energy security system is not only the need of China's economic and social development, but also to enhance our voice and influence in the global energy affairs.

Introduction

For a long time, pursuing the growth of GDP has seen as the goal and motivation of national economic development, and the demand and consumption for resources play the center role on the choice of growth model in many countries. Under the domination of development concept, the economy in the pursuit of maximum economic benefits, many countries destroy the resources and environment for the maximum economic benefits without hesitate. As a result, the resource have been weakening, degradation and depletion. Meanwhile, the ecological environment has been wracked[1]. Since the 1990s, sustainable development has gradually become the center goal and guiding principle of national resources and environment policy. Obviously, the traditional energy evaluation already couldn't adapt to the requirements of sustainable development. It have mainly focused on the project level of energy development activity so that often fail to take the influence impact by macroeconomic factors such as political, legal, economy, technology and social cultural on regional energy strategic targets and strategic choice into account. Therefore, the research on the energy strategy evaluation which can reveal the internal mechanism between energy strategy and regional sustainable development has become a necessity.

Different from the traditional energy evaluation, energy strategy evaluation gives policymakers strategic, accumulated, indirect and induced resources environment influence as well as the information of social and economic meaning. The evaluation content tend to be more focused on the economic, social and environmental benefits of resources development and utilization strategy. The essence of energy strategy evaluation is the evaluation of sustainable utilization of energy, one of the major differences is social evaluation, economic evaluation and environmental evaluation are included. Combining the resources and environment problem with the social economy, and give the qualitative, macro conclusions guidance. In the review process, energy strategy evaluation has more uncertainty compared with traditional energy evaluation; on the evaluation methods, energy strategy evaluation has such features: need more data and information, span long time, contains more projects, effect widely files, strong comprehensive and poor accuracy. The difference between the energy strategy evaluation and general energy evaluation can been see in the table 1

Table 1The contrast of Evaluation of energy strategy and Traditional energy strategy evaluation

Compare the projec	Evaluation of energy strategy	Traditional energy strategy evaluation
object	Energy policy and planning	Specific energy development projects
Affect the situation	Indirectly, strategy	directly
Geographical scope	Global and regional	Local and regional
The evaluation conclusion	qualitative	quantitative
Time scale	Early and long-term	In the late
composition	Strategic component	The direction of the project

Energy strategy evaluation system

Energy evaluation refers to through the analysis of the construction project, calculation of the project of various energy consumption structure and consumption, accounting major energy-using equipment utilization of energy, analyzed the effect of all kinds of energy saving measures, the accounting unit of the project products and energy efficiency index and economic index per unit of output, evaluation of the project can use rationality and sophistication of a kind of evaluation method. Key of energy strategy evaluation is through revealing the internal mechanism of interaction between the energy strategy and sustainable development, realize the coordinated development of regional economy and energy[2]. In the process of implement the strategy of regional sustainable development, comprehensive coordination control objects include: energy strategy in human production and all-round development as the center of the first production process again and again; In order to meet the consumer demand of the development of the human existence in material production as the center of the reproduction process; In order to protect the resources sustainable use and ecological environment recovering well into the center of the third reproduction process.Between three types of reproduction process, the first serious lead reproduction process, the second category of serious distortion of the process of reproduction and the lag of the third class reproduction process, caused the energy strategy and collaborative mismatch between regional sustainable development and the main reason leading to the invalid energy strategy, the key point of energy strategy coordinated control[3]. Therefore need to press the following train of thought to strengthen positive interaction between collaborative forces.

1) We should be examined from a strategic height and try to reverse the process of reproduction in three broad categories of disorder and to reverse the process of interaction between In use energy strategy means to control the negative influence of the first and second process of reproduction and bad process at the same time, should establish and strengthen the third reproduction process as soon as possible, efforts to narrow the range of the synergy between three types of process dislocation, gradually form a positive interaction force of synergy, to overcome or the amount in the condition of synergy appear a series of negative effect, increase the efficiency of the energy strategy in collaborative work.

2) The key is to ensure that form a positive interaction between the three types of reproduction process, one is to control the population, improve population quality, promoting scientific and moderate consumption and meet the requirements of the modern civilization life style; 2 it is the second reproduction process must be taken to meet the requirements of the sustainable development of economic growth mode, i.e., according to the efficient and low consumption, less pollution intensive economic growth mode instead of extensive economic growth mode in the past; Three is to establish and implement inventory for energy and flow and its wealth value for scientific metrology and incorporated into the national economic accounting system for the center content of energy accounting system and the system of environmental economic loss compensation; Four is to advocate big coordinating economics under the guidance of multi-dimensional statistical method, and statistical ecology, environment, resource, population, economy, society and multidimensional data and their mutual influence factors, statistical result not only, also the statistical damage, to help people develop continuously to overcome the loss of energy planning.

3) But in the three types of reproduction process under the condition of synthetic together, mutual coordination to form a positive and orderly interaction between them, and create synergy resonance between the three, only constantly in collaborative resonance can also gradually realize the total energy consumption and the relative balance of resources and environment carrying capacity, Mr PRED coordinated development and the social sustainable development strategy. In such a coordination mechanism under the action of energy strategy evaluation is helpful to realize the sustainable use of energy.

China's energy consumption structure is not reasonable

In China's energy consumption structure, coal accounts for absolute advantage, far below the level of developed countries, the proportion of oil and gas is almost 38% lower than the world average (see chart 2). From the point of industry, the total energy consumption in the top five are: black metal smelting and rolling processing industry, chemical raw materials and products manufacturing, non-metallic mineral products supply hot water, electricity, steam production industry, oil processing and coking industry[4]. China's energy consumption structure irrationality is particularly prominent in the world.

Table2 The world's major national energy consumption

Total Energy Consumption in 2012						
Country	Total Energy Consumption (One million tons of oil equivalent)	The proportion of total consumption				
		Natural gas	Oil	Coal	Nuclear power	Hydropower
World	8755.6	28.6	50.8	37.9	10.9	3.5
United States	2243.8	27.4	46.7	26.9	10.2	2.5
Russia	683.5	62.7	25.1	19.5	6.1	3.2
Britain	253.4	38.6	34.9	18.3	12.8	0.5
France	275.9	16.5	40.3	6.3	48.5	3.2
Japan	543.8	14.3	58.6	20.3	17.2	1.8
Germany	342.8	25.6	45.2	24.3	14.3	0.8
Canada	278.2	29.2	38.8	8.6	8.6	1.6
India	305.4	8.6	38.6	57.6	1.3	2.4
South Africa	143.7	-	23.5	78.3	3.4	0.5
Korea	189.7	8.7	56.1	21.6	15.2	0.7
China	783.5	3.6	28.5	70.2	0.8	2.9

China's energy strategy thinking

1)China is a coal power, coal resources to reach 5.57 trillion tons, can support the development of Chinese economy in 100. The world's energy supply is restricted by many factors such as economic, political, China to achieve industrialization must be based on national conditions, make full use of domestic energy resources, carry out clean coal utilization, energy resources structure of disadvantage into advantage in the development of the economy.

2)Healthy and orderly development of the energy industry is closely related to the government's strong support, the Chinese government shall, according to the country and social development needs, constantly improve energy policy, to ensure security of energy supply to the promotion of the competitiveness of the energy companies[5].

3)Facing the intricate international political and economic relations and geopolitical risk threat, to build the safety of China's energy security system, we must vigorously develop the oil and gas trade, through active participation in global trade in oil and gas, enhance the voice.

4) Social and ecological environment must be at the same time as the important measure of the best scheme of energy development and utilization. Regional development is a very comprehensive multi-dimensional concept, is both economic growth and economic structure, including social development and people, and to improve the quality of the ecological environment improvement, from the aspects such as multivariate multilevel progress process, so the scheme of energy

development and utilization and the final selection must be at the same time with length scales, social progress and ecological environment dimension to an equal measure.

Reference

[1] Xiao-dong LI. TheEcological Civilization and the Construction of Eco-industrial Systemin the High-tech Zone [J]. Reformation & Strategy, 2013, 29(1): 90-93.

[2] Clem Tisdell: Globalization and Sustainability: Environmental Kuznets Curve and the WTO, in: Ecological Economics, 2001, (39): 185-196.

[3] Wang Yan-zhong: The puzzling Phenomenon of China’ s High Economic Growth and the Decline of Energy Consumption in the World Economy & China, 2001, (4): 37-41.

[4] Kang wu, Binsheng Li. Energy development in China[J].Energy Policy, 1995, 23 (2):167-178.

[5]Bai J, Perron P. Computation and analysis of multiple structural changmodels[J]. Journal of Applied Econometrics, 2003, 18(1):1-22.

Advanced Materials Research Vols. 986-987 (2014) pp 299-302

doi:10.4028/www.scientific.net/AMR.986-987.299

Experimental Study on Effect of Contamination on Electric Field Distribution of 330kV Composite insulator

Dingjun WEN[1, a], Xiubin ZHANG[1, b], Honggang CHEN[1, c], Feng JIANG[1, d], Yaming SUN[1, e]

[1] Equipment condition assessment center, State Grid Gansu Electric Power Research Institute, Lanzhou 730050, China

[a]email: djwxjtu@163.com, [b]email: xiubin@aa.seu.edu.cn, [c]email: dhgch3476@hotmail.com,

[d]email: power_jiang@21cn.com, [e]email: sunyaming@sina.con

Keywords: 330kV composite insulator; Pollution flashover; Electric field measurement

Abstract. 330kV transmission line in the northwest region of China is much complex while pollution flashover is a major threat to the safe operation of the system. In this paper, experimental study on effect of contamination on electric field distribution of 330kV composite insulator is presented. High voltage test system of 330kV composite insulator is established according to the ratio of 1:1. Surface electric field and potential of the insulator is measured using GDC-100 optical fiber voltage electric field measuring instrument. Potential, electric field distribution of the two kinds of 330kV composite insulator are tested in different environment of clean, dry and uniform pollution layer. The test and simulation result is also compared.

Introduction

They were a lot of work on the line overvoltage and potential distribution of tower insulator at home and abroad based on which design differentiation of line insulation were take, that investment can be saved and flashover can effectively reduce. But research data on the long distance transmission line in high altitude area was scarce. Complete and effective technical measures to prevent insulator flashover of transmission line have not been put forward up to now. There are significant security risks in the operation of transmission line. Because there is a close relationship between transmission line flashover and geographical environment, climatic conditions and pollution, the characteristics of each flashover are not identical. In this paper, effect of contamination on electric field distribution of 330kV composite insulator is studied and compared with simulation result.

The Building of Test Platform

The test was taken in High-voltage test hall of State Grid Gansu Electric Power Research Institute, of which electrical wiring diagram is show in Fig.1. Rated voltage and rated capacity of Test transformer is 1000kV and 2000kVA. During the test, terminal voltage of the insulator is measured by AC capacitor divider. High voltage arm capacitor value of the divider is 458pF while low voltage arm 4581nF. The physical map is show in Fig.2.

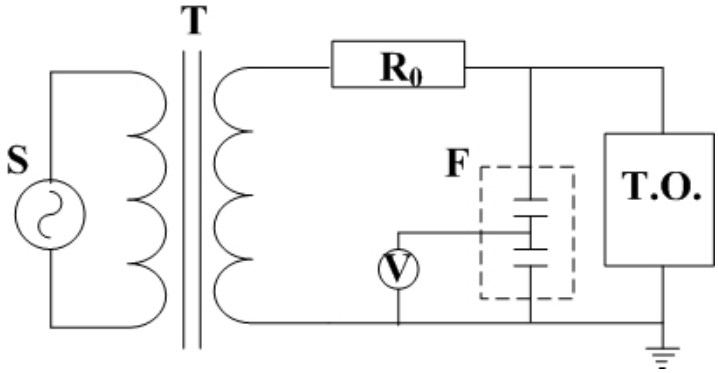

Fig.1. Electrical wiring diagram of the test

Fig.2. Physical map of the test

Arrangement of experimental tower: Simulation tower is built according to the ratio of 1:1. Double split wire is 40m long. Insulator is suspended just agreement with the actual, show in Fig.3.

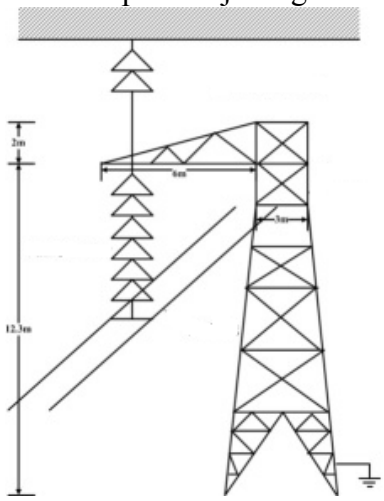

Fig.3. Arrangement of experimental tower

Stain and Humectation of the Insulator

Quantitative brushing method is taken according to GB/T 4585. Stained insulator was suspended in a cool and dry place for 24 hours. Deionized water was sprayed on the surface contamination layer of the insulator evenly. The distance between nozzle and insulator is not less than 1m, so that the spray along the insulator is in uniform. While surface pollution of the insulator layer is fully moisture, the test voltage was added later.

Determine of the test voltage

Tab.1. Total creepage distance and the minimum value of applied voltage of different insulator

	#1 organic composite insulator	#2 organic composite insulator
Total creepage distance(m)	8.42	11.89
The minimum value of applied voltage of different insulator(kV)	5.89	8.32

To avoid serious error caused by heating and drying of dirty layer during the test, voltage on the two end of insulator must to minimize. To eliminate the effect of test voltage on the electric field around the insulator, voltage on the insulator should more than 700V per meter in total creepage distance according to IEC60507. Total creepage distance and the minimum value of applied voltage of different insulator is show in tab.1.

The test results

The electric field distribution of organic composite insulator in clean and dry state: the model of the organic composite insulator in this paper is FXBW-330/100. #1 insulator has 66 sections of sheath. The measured surface electric field intensity of the sheaths in clean and dry environment is show in Tab.3

Tab.3 Measured surface electric field intensity of the sheaths in clean and dry environment

Serial number	Surface electric field(V/cm)	Serial number	Surface electric field(V/cm)
1	104	57	15.4
2	67.8	58	17.3
3	63.8	59	17.3
4	62.2	60	20.1
5	63.3	61	20.3
6	57.2	62	20.3
7	52.5	63	22.5
8	49.9	64	25.3
9	42.5	65	22.2
10	104	66	27.7
Voltage across the insulator string:6.78kV Average electric field intensity of the insulator:24.44V/cm			

The measured surface electric field intensity of the sheaths covered with a homogeneous conducting contamination layer is show in Tab.4.

Tab.4 Measured surface electric field intensity of the sheaths covered with a homogeneous conducting contamination layer

Serial number	Surface electric field(V/cm)	Serial number	Surface electric field(V/cm)
1	17.1	57	15
2	16.7	58	15.0
3	16.5	59	15.1
4	16.1	60	15.0
5	15.7	61	15.0
6	15.1	62	15.3
7	15.1	63	16.1
8	15.0	64	16.5
9	15.0	65	16.3
10	15.1	66	16.9
Voltage across the insulator string:6.78kV Average electric field intensity of the insulator:24.44V/cm			

Comparison of simulation and test

Fig.4 shows the comparison of simulation and test of the organic composite insulator in clean and dry environment, while Fig.5 covered with a homogeneous conducting contamination layer.

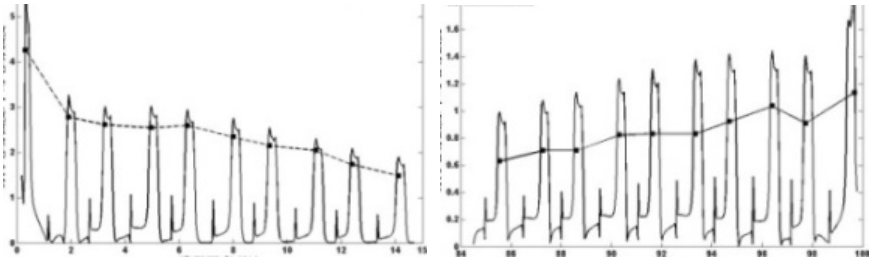

（a）1-10 （b）57-66

Fig.4 Comparison of simulation and test of the organic composite insulator in clean and dry environment

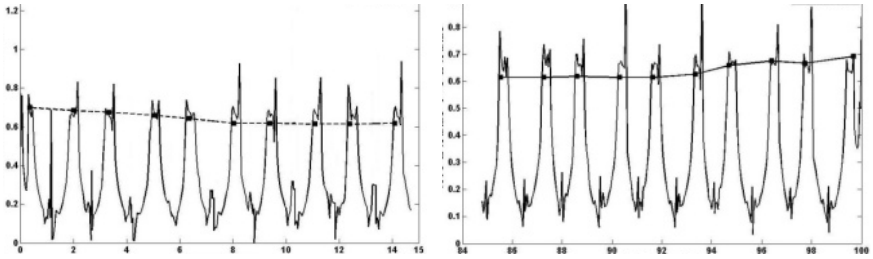

（a）1-10 （b）57-66

Fig.5 Comparison of simulation and test of the organic composite insulator covered with a homogeneous conducting contamination layer

Conclusion

It can be judged from the simulation and test results that in the situation that organic composite insulator covered with a homogeneous conducting contamination layer, there is high normal electric field intensity at the edge of the insulator. With the increase of the conductivity of the pollution layer, normal electric field gradually increases. Corona will appear at the edge of the insulator with the increase of applied voltage. There is high tangential electric field intensity in the sheath of the insulator in the situation that organic composite insulator covered with a homogeneous conducting contamination layer. Partial electric arc will appear in the surface of the sheath near the high end fittings. To improve the anti pollution flashover ability and potential distribution of insulator, the structure must be optimized, hydrophobic must be improved.

References

[1] D.J. Si, H.C. Shu, X.Y. Chen, and J.L. Yu. Study on Characteristics and Identification of Transients on Transmission Lines Caused by Lightning Stroke[J]. Proceeding of the CSEE, Vol. 25 (2005).

[2] C.J. Wang, L.Y. Zhu, S.C. Ji and Q.G. Zhang. Present and Development of Lightning Protection for HV Transmission Lines and Substations[J]. Insulations and Surge Arresters, Vol. 3 (2010).

[3] J.H. Chen, J. Lv, Z.Y. Qian, Y.X. Liu and S.Q. Gu. Differentiation Technology and Strategy of Lightning Protection for Transmission Lines[J]. High Voltage Engineering, Vol. 35 (2009).

[4] X.L. Li, X.G. Yin, R.S. Yu and J.J.He. Calculation of Shielding Failure Flashover Rate for Transmission Line Based on Revised EGM[J]. High Voltage Engineering, Vol.32 (2006).

[5] Z.J. Zhang, W.X. Sima, X.L. Jiang, C.X. Sun and L.C. Shu. Study on the Lightning Protection Performance of Shielding Failure for UHV&EHV Transmission Lines[J]. Proceeding of the CSEE, Vol. 25 (2005).

Advanced Materials Research Vols. 986-987 (2014) pp 303-310

doi:10.4028/www.scientific.net/AMR.986-987.303

Fast Evaluation Method on Thermal Stability Limit of Power Grid Cross-Section

TIAN Chunzheng[1,a], YU Linlin[1,b], HUANG Jinghui[1,c], XIE Yan[2], SHEN Xuhui[3] and ZHANG Xin[3]

[1]State Grid Henan Economic Research Institute, China

[2] School of Electrical and Electronic Engineering, North China Electric Power University, China

[3] China Electric Power Research Institute, China

[a]chunzheng_tian@163.com, [b]fishlin84@163.com, [c]huang_jinghui@163.com

Keywords: thermal stability limit, fast evaluation, DC power flow

Abstract. Enhanced grid structure makes the system thermal stability problems increasingly prominent. The thermal stability of grid section is deduced by use of DC power flow method in typical equivalent system, furthermore, the effect of section N-1 breaking on active power flow in operating equipment is analyzed. Based on the principle of active power flow distribution to meet the impedance proportional relationship, thermal stability limit section assessment methods and processes are presented, which can achieve fast assessment on thermal stability limits and restriction faults. Finally, the summer maximum loads mode of Henan Power Grid in 2014 is taken as example, and the thermal stability limit in northern sections is evaluated. The simulation results prove the feasibility of the proposed method. The research results can provide references for dispatchers and related software developers.

1. Introduction

With the continuous developments of power grid in China, the main power system grid is growing enhanced. In order to promote the reliability and flexibility of operation, the characteristics of main power system grid made up of UHV AC/DC lines are more prominent [1-3]. In the process of development and change of grid structure, the main contradiction and focus of grid stability problems gradually is changed from stability problem in the early development to thermal stability problem limited by power capacity of the device itself [4-8]. Therefore, research of the grid thermal stability problem and its solution, especially thermal stability limit of power grid cross-section has become an inevitable important subject in practical production of power grid.

With respect to the evaluation method on thermal stability limit of power grid cross-section, a lot of research such as linear/quadratic programming method, continuous power flow method, genetic algorithm and monte carlo simulation method has been carried out. These methods are far different from the actual way of adjustment taken by the dispatchers and are not conducive to the popularization and application in actual power grid. In actual calculation work, in order to determine the limiting value and the constraint fault of power grid cross-section thermal stability, offline power flow adjustment for many times combined with transient stability calculation simulation is still used. With the rapid development of power grid, especially the acceleration of UHV grid construction, rapid and profound changes spring up in the external boundaries of the existing 500 kV power grid section. What's more, the evaluation on thermal stability limit of power grid cross-section becomes more frequently as the expansion in transmission capacity and transformation of original lines. The old method, that adjusting power flow many times to approach the limiting value, is behind the actual work needs.

Based on the equivalent system of n AC lines, and the impedance distribution principle of section power flow, combined with the DC power flow model, an evaluation method on thermal stability limit of power grid cross-section is proposed in this paper. The evaluation on thermal stability limit of

power grid cross-section and the accurate selection of constraint fault can be realized through a N-1scan.

For checking the accuracy of the proposed method, the north of Henan Henan Power Grid is taken as an example. Fast evaluation results on thermal stability limit is approached and compared with the results of PSD-BPA time-domain simulation. It is confirmed that the results of fast evaluation method proposed in this article are basically identical with time-domain simulation method. The fast evaluation errors for result are analyzed, and the method of reducing the errors is proposed.

2. Fast evaluation method on thermal stability limit of power grid cross-section

The typical two equivalent system of n AC lines is shown in Fig. 1, where l_i is the nth line, $i \in [1,n]$, x_i is the reactance of the ith line, $\boldsymbol{V_s}$ and $\boldsymbol{V_r}$ are the voltages of buses of sending-end and receiving-end section, δ_{sr} is the voltage phase angle difference of buses of sending-end and receiving-end section. The line resistance and susceptance were ignored. Adopting the method of DC power flow for calculation in order to make the fast evaluation based on the maintenance of the calculation results accuracy.

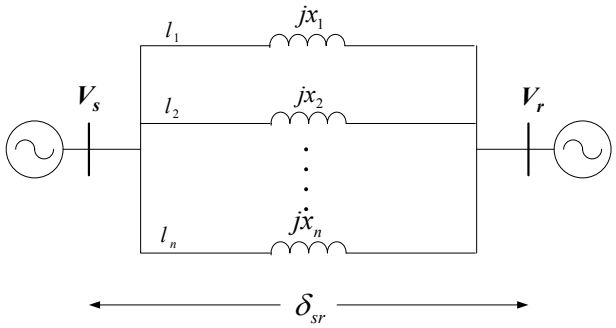

Fig. 1 Two equivalent system with cross-section

When calculating the power of line thermal stability limit, the thermal stability limit current of device is usually converted into current active power flow, and the influence of environment temperature is taken into consideration, as shown below:

$$\begin{aligned} P_t &= \sqrt{3} U I_{\max} \cos\varphi \\ I_{\max} &= K I_s \end{aligned} \tag{1}$$

where $I_{\max}$ is the thermal stability limit current, I_s is the safe current under the environment temperature of 25℃, K is the temperature correction coefficient , the power factor $\cos\varphi$ is usually 0.95, P_t is the power of line thermal stability limit.

The active power flow of two equivalent system can be calculated as Eq. 2

$$\begin{aligned} P_i &= \frac{V_s V_r \sin\delta_{sr}}{x_i} \\ P_\Sigma &= V_s V_r \sin\delta_{sr} \sum_{i=1}^{n} \frac{1}{x_i} \\ i &= 1 \ldots n \end{aligned} \tag{2}$$

As shown in Eq. 2, the power flow is proportional to each reactance of each line, that is $P_{i1} / P_{i2} = x_{i2} / x_{i1}$.

If line l_j is disconnected, the total active power flow of the section will remain unchanged because there is no change in the active power flow supply and demand in the section on both sides of the

system. The active power flow of the line l_j will be transferred to other lines in the section. The active power flow $\bar{P}_{kj}$ of line l_k after line l_j is disconnected is shown in Eq. 3

$$\bar{P}_{kj} = \frac{V_s V_r}{x_k} \sin \bar{\delta}_{srj} \tag{1}$$

Therefore, the active power flow increment of line l_k is shown in Eq. 4

$$\Delta P_{kj} = \bar{P}_{kj} - P_k = \frac{V_s V_r}{x_k} \left(\sin \bar{\delta}_{srj} - \sin \delta_{sr} \right) \tag{2}$$

where P_j is the sum of active power flow increment each line, as shown in Eq. 5

$$P_j = \sum_{k=1}^{n} \Delta P_{kj} = V_s V_r \left(\sin \bar{\delta}_{srj} - \sin \delta_{sr} \right) \sum_{k=1}^{n} \frac{1}{x_k} \tag{3}$$

where $k \neq j$.

According to Eq. 4~ Eq. 5, active power flow transfer ratio η_{kj} of line l_k after line l_j is disconnected, as shown in Eq. 6

$$\eta_{kj} = \frac{\Delta P_{kj}}{P_j} = \frac{\sum_{k=1}^{n} \frac{1}{x_k}}{x_k} \tag{4}$$

$$k \neq j$$

It can be seen that P_j will be transferred to the rest of lines according to the relationship of reactance proportion.

Till then, the definition of active power flow transfer ratio λ_{kj} of line l_k caused by the outage of line l_j can be given as Eq. 7

$$\lambda_{kj} = \frac{\Delta P_{kj}}{P_k} = \frac{\eta_{kj} P_j}{P_k} = \eta_{kj} \frac{x_k}{x_j} \tag{5}$$

λ_{kj} reflects the active power flow influence on line l_k caused by the outage of line l_j. It can be seen in Eq. 7 that λ_{kj} is a determined value associated with the section line parameters. According to Eq. 7, if $k = j$, $\Delta P_{kk} = P_k$ and $\lambda_{kk} = 1.0$.

Based on the meaning of λ_{kj}, the static power flow N-1 can be used in the disconnection simulation in section shown in Fig. 1, so is the transient N- 1. The reason is that steady state power flow of each line in section follows the reactance proportion relationship. Based on the initial power flow, a series of values λ_{kj} can be obtained after a round of disconnection simulation in section shown in Fig. 1, and relevant matrix are defined as follows:

$$\boldsymbol{\lambda} = \begin{bmatrix} 1 & \lambda_{12} & \cdots & \cdots \\ \lambda_{21} & 1 & \cdots & \cdots \\ \vdots & \vdots & \vdots & \vdots \\ \lambda_{k1} & \lambda_{k2} & \cdots & \cdots \\ \vdots & \vdots & \vdots & \vdots \\ \lambda_{n1} & \lambda_{n2} & \cdots & \cdots \end{bmatrix} \tag{6}$$

According to Eq. 7, if the section shown in Fig. 1 is in the thermal stability limit condition, one of the lines l_j will be disconnected, resulting in at least one line l_k reach the thermal stability limit condition. Therefore, active power flow of line l_k before the outage of line l_j can be obtained as follows:

$$\begin{aligned} \lambda_{kj} &= \frac{P_{kt} - P_{kj}}{P_{kj}} \\ P_{kj} &= \frac{P_{kt}}{1+\lambda_{kj}} \qquad k \neq j \end{aligned} \tag{7}$$

where P_{kt} is the power of line thermal stability limit. According to Eq. 8~ Eq. 9, active power flow matrix of section $\boldsymbol{P_T}$ in the thermal stability limit condition can be obtained as shown in Eq. 10

$$\boldsymbol{P_T} = \begin{bmatrix} P_1 & P_{12} & \cdots & \cdots \\ P_{21} & P_2 & \cdots & \cdots \\ \vdots & \vdots & \ddots & \vdots \\ P_{k1} & P_{k2} & \cdots & \cdots \\ \vdots & \vdots & \ddots & \vdots \\ P_{n1} & P_{n2} & \cdots & \cdots \end{bmatrix} \tag{8}$$

where the diagonal elements of the matrix P_j is shown in Eq. 11

$$P_j = \sum_{\substack{k=1 \\ k\neq j}}^{n} \Delta P_{kj} = \sum_{\substack{k=1 \\ k\neq j}}^{n} \left(P_{kt} - P_{kj} \right) \tag{9}$$

Till then, all the elements in matrix P_j are obtained. Corresponding to the j th column of the matrix P_j is the active power flow of each line before the outage of line l_j. The matrix P_j reflects situation of the power flow distribution before the outage of each element. The operation power flow of the section before the outage of line l_j by summing up all the elements in each column in matrix P_j. The minimum of the sums is the thermal stability limit evaluation result $P_{\Sigma t}$ on section as shown in Eq. 12

$$P_{\Sigma t} = \min \left(P_j + \sum_{\substack{k=1 \\ k\neq j}}^{n} P_{kj} \right) \qquad j = 1, \cdots \tag{10}$$

The value j, corresponding to the minimum value in Eq. 12, is the constraint outage fault of the thermal stability limit. Based on the result of evaluation result, fast reaching the thermal stability limit can be realized by operation mode adjustment of power system. The above process of obtaining the thermal stability limit is shown in Fig. 2:

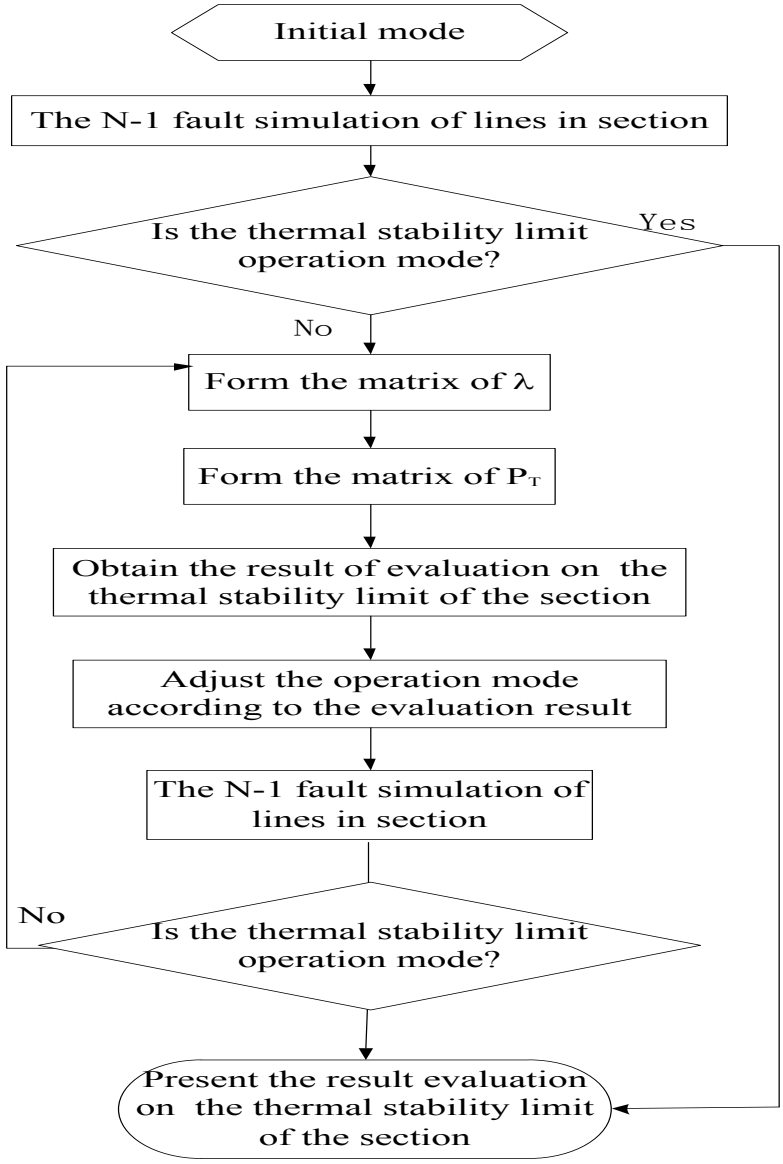

Fig. 2 Evaluation procedure of thermal stability limit in cross-section

In the evaluation process is shown in figure 2, the criteria, by which to determine whether the section is under the thermal stability limit operation mode, is that: whether the steady state power flow after line outage reaches the power of thermal stability limit P_t. Different from the existing offline method that contains times of power flow adjustment, the result of evaluation on the thermal stability limit can be obtained by each round of evaluation with proposed method. And with the target of the result, the operating generation units output can be adjusted, thereby the evaluation on thermal stability limit of power grid cross-section and the constraint fault can be realized.

3. Simulation and verification

Taking the power flow of Henan Power Grid under summer heavy load as an example, evaluate the transmission north section of Henan Power Grid with the method proposed in this article. The structure of the transmission section is shown in Fig. 3, made up of double-circuit lines HH and single-circuit line TC.

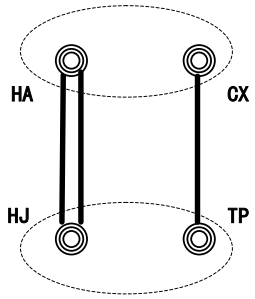

Fig. 3 Primary connection diagram on north cross-section of Henan Power Grid

The initial power flow and the thermal stability limit power flow of north section of Henan Power Grid are shown in Table 1.

Table 1 The initial power flow and the thermal stability limit in north section of Henan Power Grid

	HH I line	HH II line	TC line
initial power flow[MW]	595.8	595.8	644.9
the thermal stability limit[MW]	2056	2056	1655

After a round of Transient N-1fault simulation, the matrixes of λ and P_T can be obtained as shown in Table 2 with method proposed in this article.

Table 2 Evaluation on thermal stability in north cross-section of Henan Power Grid

		HH I line N-1	HH II line N-1	TC N-1
Power flow after outage	HH I line	——	990	918
	HH II line	990	——	918
	TC	850	850	——
Transferred power	HH I line	——	394.2	322.2
	HH II line	394.2	——	322.2
	TC	205.1	205.1	——
λ	HH I line	1	0.662	0.541
	HH II line	0.662	1	0.541
	TC	0.318	0.318	1
The thermal stability limit poewr	HH I line	1218	1237.3	1237.3
	HH II line	1237.3	1218	1334.3
	TC	1255.7	1255.7	1443.2

According to the active power flow results in the thermal stability limit condition shown in Table 2 and the judgment method in Eq. 12, the thermal stability limit of north section of Henan Power Grid is 3711MW, while the constraint fault is N-1 outage of HH lines.

Adjust the operation mode according to the results and after 4 times of adjustments, the north section of Henan Power Grid is adjusted to reach the thermal stability limit. The final result of the thermal stability limit of north section of Henan Power Grid is 3534MW. It can be seen that the result error of the first evaluation is 5%. But after adjusting for several times according to the evaluation results, the error can quickly be reduced and close to the final real results.

The source of the error of this evaluation method includes two aspects: 1) Approximate treatment on voltages of both sides of the system, thinking that the voltages of both sides of the system are 1.0 p.u. when adjusting the operation mode. 2) In practical system, it is often that a certain line first reach the thermal stability limit rather than all the lines in the section. This is the main reason for bigger

error of the thermal stability limit of north section of Henan Power Grid. However, the operation mode can be made to approach the thermal stability limit by adjusting for several times, the error can quickly be reduced.

4. Conclusion

Based on the derivation of section power flow of typical interconnected system, fast evaluation method on thermal stability limit of power grid cross-section is proposed. This paper takes the power flow of Henan Power Grid under summer heavy load as an example. The simulation and verification of the thermal stability limit of north section of Henan Power Grid is made. The following conclusions can be obtained, as follows:

The estimated value of thermal stability limit and the constraint fault can be evaluated at the same time by the proposed method in this paper. According to the evaluation results, the accurate value of thermal stability limit can be determined quickly by power grid operation mode adjustments in few times, which is convenient for dispatchers to analyze.

The errors of the proposed fast evaluation method can be controlled, and can be ignored when the power grid operation mode is approaching the thermal stability limit of cross-section.

The proposed method and process of the fast evaluation can be important references to intelligent simulation software development of power system.

References

[1] LIU Zhen-ya, ZHANG Qi-ping. Study on the Development Mode of National Power Grid of China[J]. Proceedings of CSEE, 2013, 33(7):1-10.

[2] ZHANG Wen-liang, ZHOU Xiao-xin, GUO Jian-bo, et al. Feasibility of ± 1000kV Ultra HVDC in the Power Grid of China[J]. Proceedings of CSEE, 2007, 27(28):1-5.

[3] ZHOU Hao, YU Yu-hong. Discussion on Several Important Problems of developing UHV AC Transmission in China[J]. Power System Technology, 2005, 29(12):1-9.

[4] CHEN Yi, GUO Rui-peng, YE Lin, et al. Calculation model and method for thermal stability control limit to transmission interfaces in power grid[J]. Automation of Electric Power Systems, 2012, 36(17): 20-24(in Chinese).

[5] FANG Da-zhong, WU Ming-bo, LI Chuan-dong, et al. Analysis method of transfer capability of transmission Interfaces under Thermal Stability Constraints[J]. Proceedings of the CPSA, 2007, 19(4): 111-115(in Chinese).

[6] LI Yong, Yao Wen-feng, Yang Liu, et al. Analysis on the Problems of Thermal Stability and Standard-Exceed Short Circuit Current in the CSG Main Grid[J].

[7] Lei Ting, Hu Xiao-fei, HU Shi-jun, et al. Thermal stability control technology in dispatching center based on grid steady-state data[J], Automation of Electric Power Systems, 2013, 37(11):103-106.

[8] LUAN Juan, ZHANG Zhi-gang, KOU Hui-zhen, et al. Research on improving transmission ability of 500kV network[J]. Power System Technology, 2005, 29(19):15-17.

[9] Hamound G. Assessment of available transfer capability of transmission system[J]. IEEE Trans. On Power Systems, 2000,15(1):27-32.

[10] QU Y. , Singh C. Assessment of available transfer capability and margins [J]. IEEE Trans. On Power Systems, 2002,17(2):463-468.

[11] Ejebe G. C. , Tong J. , Waight J. G. , et al. Available transfer capability calculations[J]. IEEE Trans. On Power Systems, 1998, 13(4):1521-1527.

[12] Shaaban M. , Yinxin Ni , WU F. Total transfer capability calculations for competitive power networks using genetic algorithms [A]. IEEE, IEE. Proceedings of International Conference on DRPT [C]. London: Institute of Electrical and Electronics Engineers, 2000.114-118.

[13] Mello Jco, Melo A. C. G. , Granville S. Simultaneous transfer capability assessment by combining interior point methods and monte carlo simulation[J]. IEEE Trans. On Power Systems, 1997, 2(2):736-742.
[14] CHEN Jing，LI Hua-qiang，LIU Hui, Calculation of available transfer capability for AC/DC power systems based on continuation power flow[J]. Power System Protection and Control, 2010, 38(16):1-5.
[15] MA Xiao-ming, FAN Chun-ju, HU Tian-qiang, et al. Calculation of current carrying capacity of overhead transmission line based on thermal stability constraint[J]. Power System Protection and Control, 2012, 40(14):86-91.
[16] TANG Guo-dong, LI Hua-qiang, XIAO Ling, et al. Evaluation of available transfer capability for AC/DC power systems[J]. Power System Protection and Control, 2010, 38(2):12-17.

Advanced Materials Research Vols. 986-987 (2014) pp 311-314

doi:10.4028/www.scientific.net/AMR.986-987.311

Fault-tree Analysis for Power Gird Emergency Logistics System under Large-scale Natural Disaster

Feng YU[1, a], Xiangyang LI[1, b], Guojun YUE[1, c]

[1]School of Management, Harbin Institute of Technology, Harbin City, Heilongjiang Province, China

[a]email: fengyu@hit.edu.cn, [b]email: xiangyangli@hit.edu.cn, [c]email: yuegj@cofco.com

Keywords: Power grid emergency logistics system (PG-ELS); Fault-tree analysis; Interval number

Abstract. Power grid, one of the critical infrastructures, is a vital component of the world's energy supply. Once large-scale natural disaster occurs, it is inevitable to meet unexpected faults on emergency logistic. Fault-tree analysis (FTA) is a risk estimation tool to describe and model causal interactions and logical relationships between undesired events in a system Taking uncertain situation and response failure into consideration, this paper proposed a fault-tree analysis on PG-ELS with fuzzy probabilistic confidence. The most critical failure mode is identified using the ranking method based on interval number.

Introduction

Critical infrastructure such as power grid is national basic support of society and economy. Once large-scale natural disaster occurs, it is bound to generate a large number of emergency logistics demand like the snow disaster in southern China, 2008. As an emerging research issue, emergency logistics management attracts more and more attention [1]. With the frequent occurrence of crisis, the existing emergency logistics system has emerged lots of defects. From the fault-perspective, it is leisured to deal with unexpected events which reduce the vulnerability instead of promoting the reliability for emergency logistics for power grid. FTA has been widely used for providing logical functional relationship among components and subsystems of a system and identifying the root causes of the undesired events in a system failure [2]. Many studies on emergency management focus on the response failure [3,4,5]. In most real applications, the probability of response failure does not assess as exactly as mechanical system. Hideo Tanaka firstly proposed the processing method of uncertain probability based on fuzzy set theory for FTA [6]. Taking into consider imprecise failure probability, many studies has introduced relevant uncertain theory. Unascertained number is employed to represent failure data combined with grey theory [3], intuitionistic fuzzy sets theory is applied to FTA on the emergency shutdown system [7] and also put into use [8].

Unfortunately, only very less paper takes into account the response failure on ELS. In this paper, to complete the FTA of PG-ELS under uncertain situation, interval number is employed to represent the failure rate. The most critical component is found to determine vulnerability and reveal parts where key improvement must be made.

Power grid emergency logistics system (PG-ELS)

Logistics support of power grid is one of the major response activities that deliver commodities such as electrical components, materials, repair equipment from warehouse to the affected area effectively [1]. It is a process that aims to pursue the greatest time benefit and the least loss. Emergency logistics may meet faults which cause delay or breakdown under various constraints.

The most important requirement is to ensure the rapidness of preparation, coordination and transportation. Components of function follow as: 1) Emergency supplies preparation (ESP) means emergency supplies reserve includes warehouses and signed production reserve; 2) Emergency supplies coordination (ESC) refers to content collaborative allocation for delivering power grid materials; 3) Emergency supplies transportation (EST) needs select the optimal or more convenient route without traffic jam or damage.

Fault-tree diagram for PG-ELS

Fault-tree analysis intuitively analyzes potential danger including qualitative description of system failures and quantitative operation. The detailed procedure for constructing the fault-tree can be known from references [1,5]. Prior to the expression of the PG-ELS fault-tree, it is necessary to have an in-depth understanding of the relationship between each section of PG-ELS. In this paper, three assumptions are essential to be clarified: 1) all basic events are independent; 2) all the events only have two states namely occurrence and nonoccurrence; 3) large-scale natural disaster can give rise to the lack of storage that enables production reserve. Thus, the FTA of the PG-ELS is developed in Fig.1, and the description of basic events is listed in Table 1.

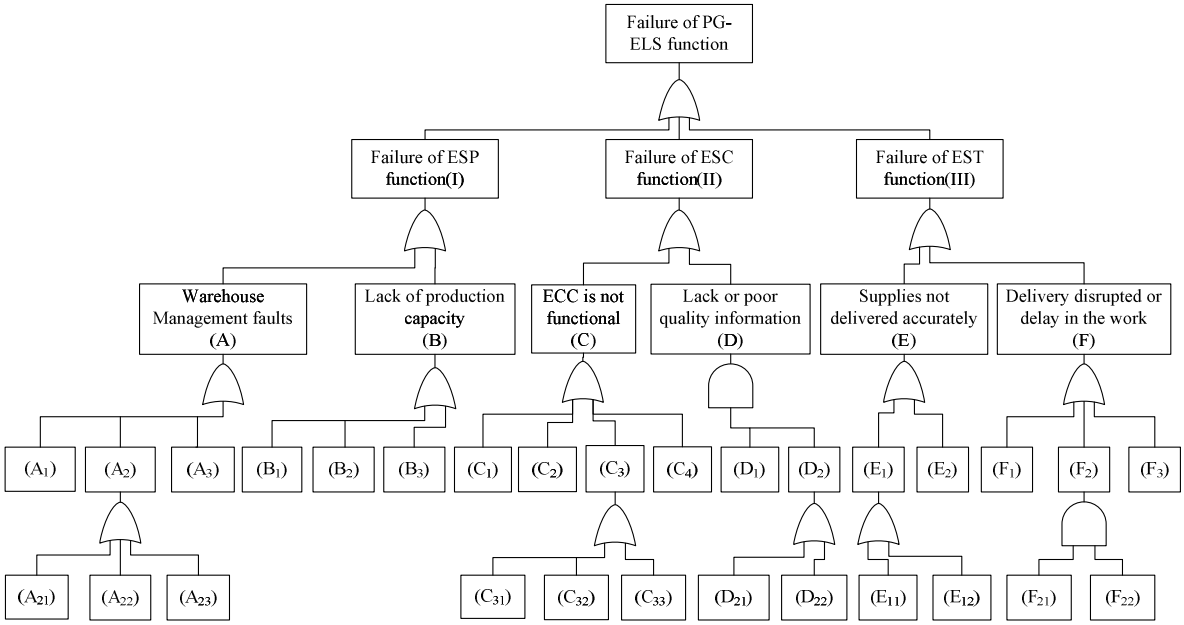

Figure 1 The fault-tree of emergency logistics system (PG-ELS)[1]

Table 1 The descriptions of the basic events of ELS system fault

Code	Details of basic event (BE)	Code	Details of basic event (BE)
A_1	Major supplies damaged or overdue	C_{33}	Communication misunderstand
A_{21}	Inventory records incorrect	C_4	Necessary ECC staff unavailable
A_{22}	No inventory management system	D_1	Loss contact to responders on site
A_{23}	Inventory management system not used	D_{21}	Incident out of sensors detection range
A_3	No resources found in appointed warehouse	D_{22}	Sensors damaged failure
B_1	Time-consuming on production	E_{11}	Command failure on destination
B_2	Workshop damaged by catastrophe	E_{12}	Go to the wrong routes
B_3	Less materials on production	E_2	Ignore some of logistics orders
C_1	Critical facilities disrupted by incident	F_1	Transportation infrastructure damaged
C_2	Operation plans not followed	F_{21}	Most of vehicles damaged by catastrophe
C_{31}	Insufficient capacity of staff	F_{22}	No third party logistics support
C_{32}	Inadequate critical facilities	F_3	Meet traffic jam or accident

After building fault-tree, we must fully understand the PG-ELS under large-scale natural disaster. More importantly, expertise and knowledge on PG-ELS operation should be required to assess the risk of each part. In the fault-tree of PG-ELS, there are 24 basic events(BE) and 22 minimal cut sets. Minimal cut set means the minimal failure set which can make the emergency logistics system failed. It is worth mentioning that there are still some critical faults have not been found out for the uncertain situation, Fig.1 only shows the key faults. On the basis of the fault-tree diagram, the failure probability operation of "and" and "or" is (f_i refers to ith event with probability of p_i):

$$f_1 \cap f_2 \cap \ldots \cap f_i = p_1 \cdot p_2 \cdot \ldots \cdot p_i \quad (1)$$

$$f_1 \cup f_2 \cup \ldots \cup f_i = 1-(1-p_1)(1-p_2)\ldots(1-p_i) \quad (2)$$

[1] A_2: "inventory management system faults"; C_3: "ECC (emergency command center) duties and setup not executed effectively", D_2: "Sensors don't work well", E_1: "Supplies delivered to incorrect location", F_2: "Insufficient transportation vehicles".

Proposed method

In order to express the uncertain situation and fuzzy probability of failure, interval number is used to represent the result. Interval number a is defined as $a=[a^L,a^U]=\{x|a^L\le x\le a^U\}$, if $a^L=a^U$, then a degenerates a crisp number [9], and the arithmetic operations can also see the reference [9]. Let $a=[a^L,a^U]$, and $b=[b^L,b^U]$ be two interval numbers, $l_a=a^U-a^L$, $l_b=b^U-b^L$, $p(a>b)\in[0,1]$ means the possibility degree of a>b, then:

$$p(a>b)=\frac{\min\{l_a+l_b,\max(a^U-b^L,0)\}}{l_a+l_b} \tag{3}$$

The fuzzy sensitivity analysis is therefore applied to identify the weakest part of the PG-ELS. P_{TE} denotes the probability of top event assumed all basic events occur, P_{TEi} represents that P_{TE} is not include the i^{th} probability of basic event. So, the fuzzy importance measure (FIM) is:

$$FIM_i=[\frac{P_{TE}-P_{TEi}}{P_{TE}}]\times 100\% \tag{4}$$

The probability important degree (PID) of event i means the extent of system unreliability changes due to the change of component i, where f_s and f_i represents the unreliability of top event and event i. The PID (I_{Pri}) is:

$$I_{PRi}=\lim_{\Delta fi\to 0}\frac{\Delta f_s}{\Delta f_i}=\frac{\partial f_s}{\partial f_i} \tag{5}$$

Case study

Shenzhen power gird is oversize urban power network with the largest power load density, advanced reliability of power supply and provincial power grid scale in China. In order to analyze the possible key faults emerged on PG-ELS, we need to use the proposed method for risk analysis. The collected data of probabilities are listed in Table 2. The bound and range of value are obtained from local power grid department and emergency office. Especially it is very difficult to estimate failure probability of manual operation failure can be estimated by expert's semantic evaluation.

Table 2 The interval probabilities of each basic event

BE	Prob.	BE	Prob.	BE	Prob.	BE	Prob.
A_1	$[1.2,1.4]\times10^{-2}$	B_2	$[4.5,5.1]\times10^{-3}$	C_{33}	$[4.5,7.2]\times10^{-3}$	E_{12}	$[6.6,7.5]\times10^{-5}$
A_{21}	$[4.5,4.7]\times10^{-3}$	B_3	$[8.8,9.4]\times10^{-3}$	C_4	$[8.4,9.2]\times10^{-5}$	E_2	$[2.5,3.2]\times10^{-3}$
A_{22}	$[8.5,8.6]\times10^{-3}$	C_1	$[3.5,4.2]\times10^{-3}$	D_1	$[3.5,4.2]\times10^{-2}$	F_1	$[2.7,3.1]\times10^{-2}$
A_{23}	$[1.2,1.4]\times10^{-3}$	C_2	$[5.4,6.0]\times10^{-4}$	D_{21}	$[1.5,2.1]\times10^{-3}$	F_{21}	$[5.8,6.4]\times10^{-3}$
A_3	$[2.4,2.6]\times10^{-2}$	C_{31}	$[7.5,7.8]\times10^{-4}$	D_{22}	$[1.4,2.0]\times10^{-2}$	F_{22}	$[1.0,1.4]\times10^{-2}$
B_1	$[3.1,3.9]\times10^{-2}$	C_{32}	$[6.4,7.2]\times10^{-5}$	E_{11}	$[4.8,5.6]\times10^{-4}$	F_3	$[1.8,2.2]\times10^{-2}$

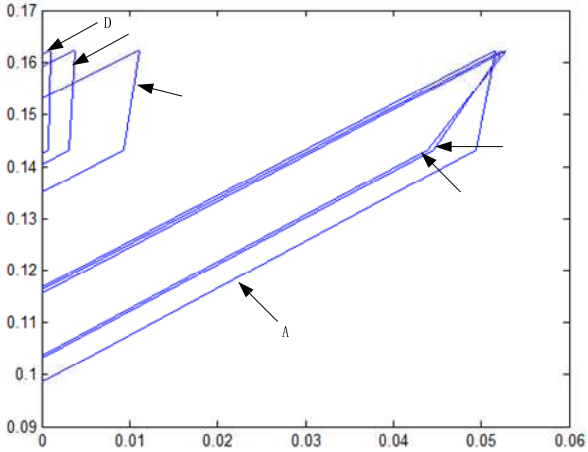

Figure 2 The interval graph of fuzzy sensitivity of event A-F

Firstly, according to Eq.(1)-(2), the probabilities of three parts I, II and III of PG-ELS are [0.0911,0.1019], [0.0102,0.0122], [0.0475, 0.0560]. Furthermore, the top event failure probability is [0.1431,0.1625]. It means that the success rate of PG-ELS is about 85.3 percent under large-scale natural disaster. The P_{TEi}, $FIM_{i\ and}$ I_{PRi} can be calculated by Eq.(4)-(5) shown in Table 3.

According to Eq.(3), the result is $p(FIM_F > FIM_B)=0.5018$, $p(FIM_A > FIM_F)=0.5259$, $p(I_{PRF} > I_{PRB})=0.5040$, $p(I_{PRA} > I_{PRF})=0.5623$ and the upper bound of A is maximal. So, the rank of criticality is A>F≈B>C>E>D. Furthermore, the fuzzy sensitivity interval graph (sensitivity function line represented by interval number) is shown in Fig.2. Obviously, the FIM of A, B, F is higher than C, D, E, and A, B, F all has certainly lots of room for improvement.

Table 3 Probabilities of key faults A-F

Key fault	Lower bound	Upper bound	P_{TEi}	FIM_i	I_{PRi}
A	$4.94x10^{-2}$	$5.17x10^{-2}$	[0.0986,0.1168]	[16.18%,44.65%]	[0.8832,0.9014]
B	$4.39x10^{-2}$	$5.29x10^{-2}$	[0.1038,0.1157]	[16.86%,41.02%]	[0.8843,0.8962]
C	$9.41x10^{-3}$	$1.11x10^{-2}$	[0.1350,0.1531]	[0,19.22%]	[0.8469,0.8650]
D	$7.53x10^{-4}$	$1.09x10^{-3}$	[0.1424,0.1616]	[0,14.05%]	[0.8384,0.8576]
E	$3.05x10^{-3}$	$3.83x10^{-3}$	[0.1405,0.1593]	[0,15.58%]	[0.8407,0.8595]
F	$4.46x10^{-2}$	$5.24x10^{-2}$	[0.1031,0.1162]	[16.55%,41.51%]	[0.8838,0.8969]

Conclusions

In this paper, we obtained expert's knowledge on PG-ELS and integrated the interval number operation on FTA. To identify the key component that is most useful to improve the performance of PG-ELS. The result is that the most critical event is A "warehouse management faults". It also needs to pay attention to B "lack of production capacity" and F "delivery disrupted or delay in the work". Warehouse management should tend to be continuous improvement for avoiding faults.

Acknowledgement

This work is supported by the National Science Foundation of China (NSFC) under the Grant Nos. 91024028, 91024031 and 91324018.

References

[1] Teperi, A., Leppänen, A. Managers' conceptions regarding human factors in air traffic management and in airport operations [J]. Safety Science, 2011, 49(3): 438-449.

[2] Ejlali, A., Miremadi, S.G. FPGA-based Monte Carlo simulation for fault tree analysis [J]. Microelectronics Reliability, 2004, 44(6): 1017-1028.

[3] Discovery Method on Failure Factors of Collaborative Allocation under Power Grid Emergency [A]. Proceedings 2013 International Conference on Collaboration Technologies and Systems [C]. 2013.

[4] Information on http://www.rand.org/publications/permissions.html.

[5] Yang Liu, Zhi-Ping Fan, Yuan Yuan, Hongyan Li. A FTA-based method for risk decision making in emergency response [J]. Computer & Operations Research, 2014, 42: 49-57.

[6] Hideo Tanaka, Fan L T, Lai F S and so on. Fault-tree analysis by fuzzy probability [J]. IEEE Transaction on Reliability 1983, 32(5): 453-457.

[7] Shuen-Ren Cheng, Binshan Lin, Bi-Min Hsu, Ming-Hung Shu. Fault-tree analysis for liquefied natural gas terminal emergency shutdown system [J]. Expert Systems with Applications, 2009, 36(9): 11918-11924.

[8] I.M. Dokas, D.A. Karras, D.C, Panagiotakopoulos. Fault tree analysis and fuzzy expert systems: Early warning and emergency response of landfill operations [J]. Environmental Modeling & Software, 2009, 24(1): 8-25.

[9] Moore R, Lodwick W. Interval analysis and fuzzy set theory [J]. Fuzzy Sets and Systems, 2003, 135(1): 5-9.

Advanced Materials Research Vols. 986-987 (2014) pp 315-321

doi:10.4028/www.scientific.net/AMR.986-987.315

Features and Application Analysis of Advanced Small Nuclear Power Reactors

Wenbin XIONG[1,2,a], Houming ZHANG[3,b], Boping ZHANG[1,c], Huwei LI[1,d], Gang WANG[2,e], Jie ZHU[1,f,*]

[1]Nuclear and radiation safety Center, MEP, Beijing,100082, China

[2]China Institute of Atomic Energy, Beijing, 102413, China

[3]North Regional Office, MEP, Beijing,100191, China

[a]email: xiongwb84@126.com, [b]email: houming.zhang@foxmail.com,
[c]email : zhangboping@foxmail.com, [d]email :alihuwei@163.com, [e]email : w0701g@163.com,
[f,*]Corresponding author, email : jiezi147@126.com

Keywords: SMR, modular, Versatile, NPP

Abstract. In recent years, advanced small nuclear power reactors, namely small modular reactors (SMRs), gained widespread attention. In areas where energy can't be provided by large scale reactors and the nuclear power plants with large scale reactors can't compete with the non-nuclear power plant technology, SMRs, as a versatile distributed integrated energy source, which result in expanding peaceful applications of nuclear energy, have enormous potential. This article describes the characteristics and analyzes prospects and challenges of SMRs.

Introduction

In recent years, advanced small nuclear reactors have attracted worldwide attention. Advanced small nuclear reactors are also called small modular reactors(SMRs, <300MW), which were designed to achieve modular construction, short construction period and passive safety, nuclear proliferation prevention, financial risk reduction and other characteristics[1]. These features encourage and allow many developing countries, with limited budget and grid capacity, to construct nuclear power plants.

Although, compared with large scale reactors, SMRs have higher specific capital cost, but also have economic advantage because of short construction period, quick learning effects[2], multi-module sharing site and infrastructure, simplified design and layout flexibility. In those areas where traditional large scale nuclear power plant can not be deployed, SMR is a option for peaceful use of nuclear energy. It can be expected that, in the future, SMRs would be widely used for urban heating supply, desalination, industrial steam supply and marine resources, and so on.

The characteristics of SMRs

SMRs have became another focus of nuclear engineering research, due to its diversity of functional application. In the future, nuclear energy will inevitably trend towards two directions, large scale nuclear power plants which can supply electrical power more than 1000MW, and SMRs with power less than 300MW. However, compared with large scale nuclear power plants, SMRs have the following features:

(1) Small size. Since smaller "size" of SMRs, compared to the large scale reactors, the total individual unit initial investment was significantly lower than large reactors. So the SMRs' investment cycle is short and with less investment risk. And then, each module can easily be transported by truck or rail to sites, while SMRs' facilities are also greatly simplified, compact plant layout, and more environmental- friendly.

(2) Modular design and construction. Modular design allows multiple units to share some systems, so the number of systems could be reduced. Modules' production and assembly can be carried out in factory, which greatly shorten construction period (24~36 months). And construction cost can also be effectively reduced, while schedule risk can be reduced. Modules can be separated and removed easily, which makes decommissioning work simplified.

"Small" and "modular" are the main characteristics of SMRs. From the sketch of SMRs designed by NuScale and Westinghouse showed in Fig.2, SMRs' characteristics can directly be caught in the picture [3].

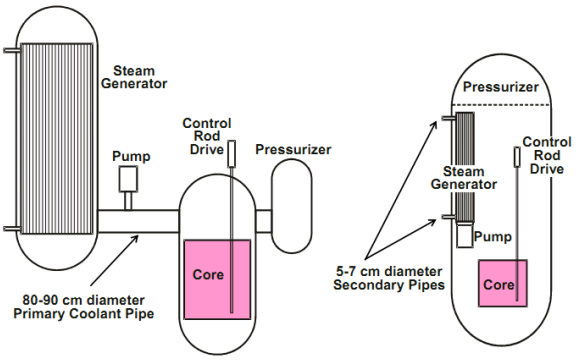

Fig.1 Comparison chart of integration PWR (right) and current (left) PWR

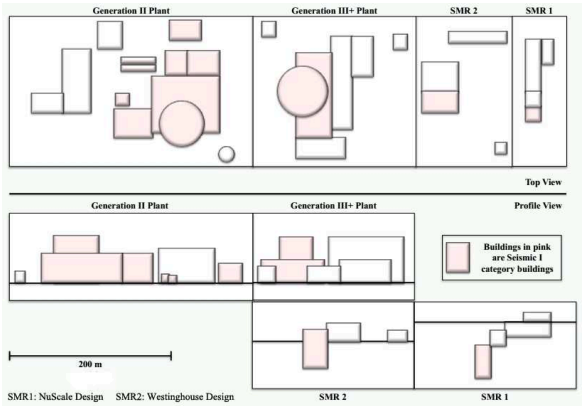

Fig.2 Comparison of the whole plant layout with SMR and large NPP

(3) Low power level, less source items. Due to low power level, SMRs can match grid which with limited power generation capacity. Meanwhile, source terms are less than large scale reactors.

(4) Simplified design to improve safety. Advanced Pressurized Water Reactor type SMRs would arrange primary systems in pressure vessel, use of passive safety systems extensively to minimize numerous pipelines, valves and other equipments. Compared with the current PWRs' loop type reactor systems, integrated small modular pressurized water reactor (iPWR) layout[4], for example, is showed in Fig.1.

(5) Long refueling cycle. Advanced SMRs(except HTR, AHWR) are usually designed as long refueling cycle, and some SMRs can even design as a whole life cycle operation without refueling. So load factor would be large, and fuel transport expense would be low.

(6) Configuration flexibility and easy to increase capacity. More modules can be added as energy demand increases. SMRs can be easily grouped together to form a larger nuclear power plant.

(7) Siting flexibility and adaptability. SMRs can be built in those remote areas where lack of energy, or in those areas with harsh environment. So it needs no long-distance transmission lines so as to avoid energy losses and to save the cost of long-distance transmission facilities.

(8) Versatile. SMRs can be designed to provide heat, supply steam, desalinate water, and product hydrogen, etc.

(9) Nonproliferation. SMRs' reactor module can be designed with lower degree of enrichment of uranium and constructed in underground location. So, it reduces the risk of proliferation.

Meanwhile, Some SMRs could be designed to arrange in a pool, making further improvement safer[5], as shown in Figure 3.

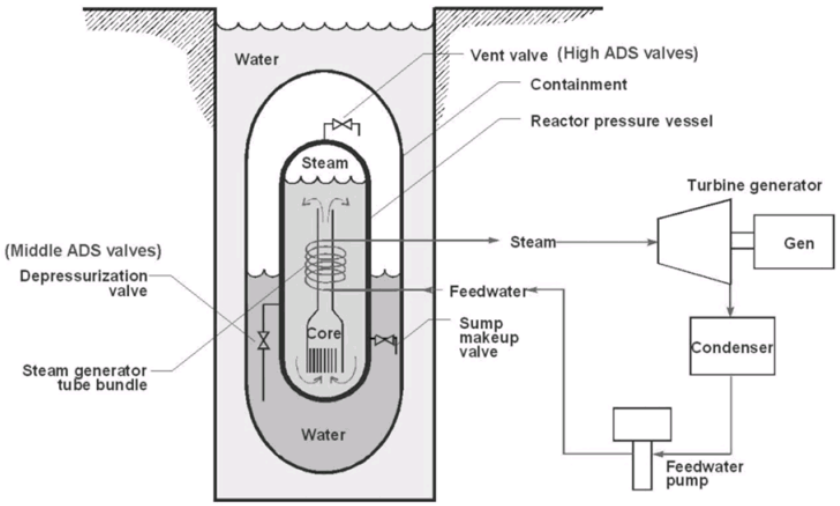

Fig.3 Design concepts of LWR type SMR

International R & D Status of SMRs

SMRs' development can be traced back to 1950s, and was mainly used for military purposes. American Navigant Research's report in June 2013 predicted that there would be 18.2GW of SMRs in operation by 2030[6]. University of Chicago predicts that SMRs would occupy 1/4 nuclear power capacity by 2050. Figure 4 shows Ux Cosulting Company's prediction of international SMRs capacity in the next 25 years[7].

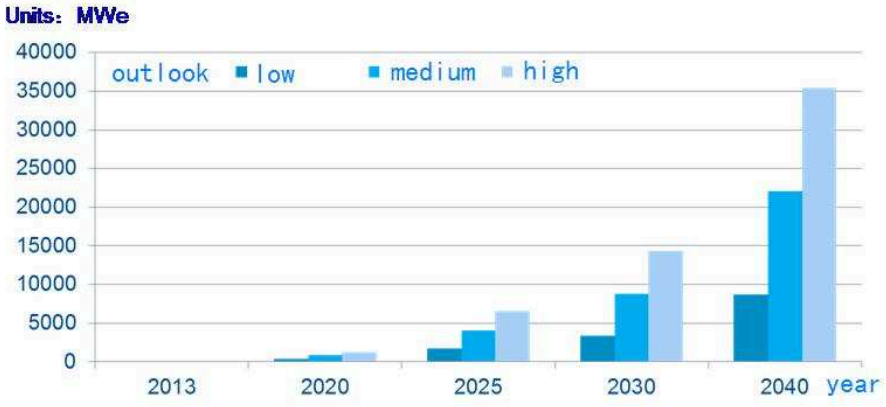

Fig.4 UxC forecasts global SMR's capacity over the next 25 years

Currently, United States, Russia, France, South Korea, Argentina and other countries are motive in the development of advanced commercial SMRs. Table 1 shows the current 22 kinds of SMRs development in brief.

Tab 1 Introduction of foreign advanced SMR development

Name	Type	Designer	P(MWe)	Country	Status
mPower	PWR	Babcock & Wilcox	125	USA	Began pre-application interactions in July 2009. Design certification application expected 3rd quarter of calendar year 2014[8]
NuScale	PWR	NuScale Power	48	USA	Began pre-application interactions in July 2008. Design certification application expected 3rd quarter of calendar year 2015[9]
Westinghouse SMR	PWR	Westinghouse	225	USA	Design certification application date to be determined[10]
SMR-160	PWR	Holtec	160	USA	Design certification application expected 4th quarter of calendar year 2016[11]
GT-MHR	HTR	General Atomics & Rosatom	287	USA	Has completed the concrete conceptual design
HPB	LMR	Hyperion Power Generation	25	USA	Licensing pre-application
PRISM	LMR	GE & Hitachi	311	USA	Under Development
KLT-40S	PWR	OKBM Afrikantov	35	Russia	Under construction
VBER-300	PWR	OKBM Afrikantov	302	Russia	The detailed design Has completed
ABV-6M	PWR	OKBM Afrikantov	8.6	Russia	Part of the design has been licensed
SVBR-100	LMR	AKME(with Rusal & Rosatom)	101.5	Russia	Prototype has used in submarines, commercial reactor has entered the stage

					of detailed design
VVER-300	PWR	OKBM Afrikantov	300	Russia	Conceptual Design Stage
BREST	LMR	NIKIET	300	Russia	Conceptual Design Stage
NP-300	PWR	AREVA	100~300	France	Conceptual Design Stage
Flexblue	PWR	AREVA & EDF & DCNS & CEA	50~250	France	Conceptual Design Stage
ANTARES	HTR	AREVA	285	France	Conceptual Design Stage
4S	LMR	Toshiba	10	Japan	Detailed Design Stage
SMART	PWR	KAERI	100	Korea	Detailed Design Stage
CAREM-25	PWR	CNEA & INVAP	27	Argentina	Under construction , FCD(2014.2.8)
FBNR	PWR	UFRGS	72	Brazil	Conceptual Design Stage
AHWR	HWR	BARC	304	India	Has completed the detailed design, is expected to start in 2015 to construction
PBMR	HTR	ESKOM	165	South Africa	Licensing of a demonstration plant in South Africa is being reconsidered. Agreement with Chinese for cooperation in development[12]

Development of China's SMRs

In present, China National Nuclear Corporation, China General Nuclear Power Group, China Nuclear Engineering and Construction Corporation, China Power Investment Group, the State Nuclear Power Technology Co., Tsinghua University, all have groups working on research and development of SMRs. National Energy Board also launched a national energy application technology research and engineering demonstration project - "small modular reactor demonstration of key technology research and application.". Meanwhile, National Nuclear Safety Administration also started research in regulations and standards, safety requirements for the design. Table 2 summarizes several advanced SMRs design.

Tab 2 Introduction of advanced SMR designs in China

Name	Type	Designer	P(MWe)	Status	Application
ACP100	PWR	CNNC	100	Detailed engineering phase	Land-based NPP & barge-mounted or floating Nuclear power station; supply heating/ electricity/ demineralized water/steam[13]
ACPR100	PWR	CGN	130	Preliminary design phase	Land-based NPP; supply heating/ demineralized water/steam[14]
ACPR50S	PWR	CGN	55	Preliminary design phase	Land-based NPP & barge-mounted or floating Nuclear power station; supply heating/ electricity/ demineralized water/steam[14]
CAP150	PWR	SNPTC	150	Conceptual Design Stage	Land-based NPP & floating Nuclear power station; supply electricity/ demineralized water
HTR-PB	HTR	Tsinghua University & China Hua	212	Under construction	Land-based NPP; can supply heating/electricity/demineralized water, also for Nuclear hydrogen

		Neng Group Corporation			production and refrigeration
NHR200-Ⅰ/Ⅱ	LWR	CNECC & Tsinghua University	200*	The preliminary design have been completed	Type Ⅰ for Urban heating and Thermal-desalination/ Type Ⅱ for providing industrial steam and hybrid desalination with MSF/RO

* Here is thermal power

The prospects and challenges of SMRs

In the areas where energy can not be provided by traditional large nuclear power plants, SMRs have huge potential in peaceful application of nuclear energy. IAEA predicted that in the next 20 years 50% energy consumption would be heat supply (urban district heating, industrial process heating, desalination, etc.). The demand for clean energy will increase rapidly, therefore, various SMRs designs are leading to non-electricity production application modules. So, in the near future SMRs would be designed for heating and industrial steam supply, water desalination, and marine power.

Application Prospects

Domestic Market

According to China's energy development "12th Five-Year Plan"[14], in the future, SMRs' potential onshore application can be seen in Table 3. The potential market for SMRs' offshore application is shown in Table 4.

Tab 3 SMR onshore market prospect of China's future

Potential market	Application	Current market size	Forecast the future size of the market 2015	2020
Distributed electricity market	Distributed generation	3 436 GW	6 400 GW	15 400 GW
Heating market	Industrial steam supply	10.60 Mt/h	13.35 Mt/h	—
	Urban heating	4.7 Gm^2	—	7.4 Gm^2
	CHP	127 GW	250 GW	—
Desalination water market	Desalination	750 kt/d	2 200 kt/d	2 500~3 000 kt/d
	Inland brackish water desalination	2.96 Mt/d	—	—

Tab 4 SMR offshore platform market prospect of China's future

Potential market	Application	Current market size	Forecast the future size of the market
Offshore oil and gas exploration	Energy supply	51.85 Mt/200 units*	60 Mt/231 units*(2015)
		—	150 Mt/579 units*(2030)
Island power supply	Electricity generation	3 122MW	3 835MW(2015)

* represents the number of offshore oil and gas platforms

It concludes that the future applications of SMRs would be in China's western regions where power grid are small, heat supply, water desalination, or used for supplying high temperature steam, marine power and other aspects.

Overseas Market

SMRs commercial operating experience in Russia, Canada, Bulgaria, Hungary, Ukraine, Slovakia and Switzerland and other countries have nearly 500 reactor-years with 18 reactors for heat supply. In Unites States, Japan, Kazakhstan, there are over 100 reactor-years of operating experience of nuclear desalination. Canada, Germany and Switzerland have experienced nuclear supply heating for industry with about 100 reactor-years.

According to the capital investment, national grid capacity, infrastructure and human resources, drinking water needs, as well as other aspects, we can draw SMRs overseas potential market[15], shown in Figure 5:

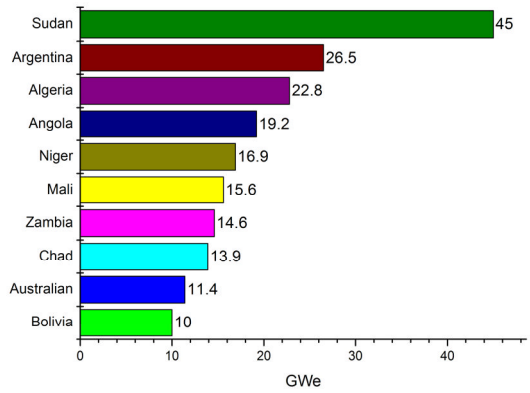

Fig.5 SMR potential overseas markets (potential deployment capacity of the top ten countries)

Challenges of SMR

There will be challenges from the technical aspects and the institutional aspects in development of SMRs.

(1)Integrated design causes SMRs to use some novel technical features and non-standard components. These technical features and components, such as steam generators in pressure vessel and compact containment designs, will make difficult in periodic in-service inspection. Many advanced SMRs are designed to achieve simplify operation and maintenance, while simplifying operation and maintenance requirements will bring challenges to instrumentation reliability,.

(2)Some of SMRs designed as off-site refueling mode. Refueling cycle would be 5 to 30 years. Although the design of fuel burn-up does not exceed the value of the same typical design, in terms of all the advanced reactor technology, the key issue is structural materials. Therefore, materials, structures and components must be Verification and Validation in design.

(3)Some of SMRs are design to be half-buried or buried underground, it causes a problem, the vulnerability of natural flood. So how to eliminate the problem becomes another issue. An if flood accident occurs, emergency activities would be more difficult, because arrive and stay in the deeply buried nuclear reactor module may be more difficult.

(4)SMRs widely adopted passive safety design. The concept of passive safety design is considered as an improvement of overall safety. However, this improvement is based on reduction of the possibility of failures in the active safety system functions, in other words, in some case it also needs highly reliable of active backup systems and I&C systems.

(5)SMRs would be design as multi-modules operating in the same time, so the control room design and operator staffing would be another issue.

(6)Based on a small source term, the SMRs' designs are all referred to simplify off-site emergency planning zone, some designers even declare there are no need of off-site emergency. So, how to simplify the off-site emergency planning zone must be scientific appraised and technical proved. And if SMRs was deployed close to the user, there would be impact on the public acceptability inevitably.

In short, SMRs can extend clean and abundant nuclear power to a wider range of energy demands. The development of SMRs is an effective way to solve the issues of air pollution and carbon dioxide emissions. But the application of SMRs would bring some challenges. Those challenges, which are not only technical but also institutional, must be addressed and demonstrated. The solution of these challenges will determine the application prospect of SMRs.

Conclusion

In present, China over relies on unsustainable fossil energy, while emissions caused the environmental pollution increasingly serious. Development of nuclear energy becomes an effective way to guarantee sufficient energy supply, pollution reduction. In some fields, SMRs have some advantages than large scale nuclear power plants and also have some disadvantages. It provides an option for China's nuclear power development. Therefore, China should be fully prepared for advanced SMRs' application in two aspects:

(1) Safety is the prerequisite for development of SMRs. Strengthen nuclear safety policies, regulations, standards, to build the foundation for safety development of small nuclear power reactors.

(2) R&D organizations and supervision departments should strengthen cooperation to promote safety and economy in the development of SMRs. Strengthen cooperation, not only to optimize the design of advanced small nuclear power reactors, but also to coordinate the safety and economy of SMRs.

Acknowledgement

The author would like to acknowledge the informations and support provided by Professor Tianying Duan from China Institute of Atomic Energy.

References

[1] Ioannis N. Kessides, Vladimir Kuznetsov. Small modular reactor for enhancing energy security in developing countries[J]. Sustainability, 2012 4(8) 1806-1832.

[2] OECD. Current status，technical feasibility and economics of small nuclear reactors[R]. France:NEA.2011.

[3] Ahmed Abdulla, Inês Azevedo, M. Granger Morgan. Elicitation of Expert Assessments of Small Modular Reactor Costs[R]. Pittsburgh: Carnegie Mellon University. 2013.

[4] Daniel T. Ingersoll. An overview of the safety case for small modular reactors. ASME 2011 Small Modular Reactors Symposium[C]. Washington DC: ASME.2011.

[5]Jason R. Casey. High Pressure Condensation Heat Transfer in the Evacuated Containment of a Small Modular Reactor[D]. Corvallis: Oregon State University.2012.

[6] Navigant Research. Worldwide Capacity of Small Modular Reactors Could Surpass 18 Gigawatts by 2030.Available online: http://www.navigantresearch.com/newsroom/worldwide-capacity-of-small-modular-reactors-could-surpass-18-gigawatts-by-2030 (accessed on 10 March 2014).

[7] Ux Consulting. SMR Market Outlook[R]. Roswell:UxC.2013.

[8] NRC. B&W mPower™. Available online:http://www.nrc.gov/reactors/advanced/mpower.html (accessed on 20 March 2014).

[9] NRC. NuScale.Available online:http://www.nrc.gov/reactors/advanced/nuscale.html(accessed on 20 March 2014).

[10] NRC. Westinghouse Small Modular Reactor (SMR). Available online:http://www.nrc.gov/ reactors/advanced/smr.html(accessed on 20 March 2014).

[11] NRC. Holtec SMR-160.Available online:http://www.nrc.gov/reactors/ advanced/holtec.html (accessed on 20 March 2014).

[12] NRC. Pebble Bed Modular Reactor (PBMR). Available online:http://www.nrc.gov /reactors/advanced/pbmr.html(accessed on 20 March 2014).

[13] Danrong Song.Small modular nuclear reactor research and development progress of China National Nuclear Corporation. 2013 Chengdu small nuclear power reactors Forum[C]. Chengdu: CNEA,2013.

[14] Jianlin Guo.Small reactor (ACPR) R&D and market applications.2013 Chengdu small nuclear power reactors Forum[C]. Chengdu: CNEA,2013.

[15] Victor.Current Status, Technical Feasibility and Economics of SMRs in Russia.Available online: http://www.andrew.cmu.edu/user/ayabdull/Victor_RussianSMRs.pdf(accessed on 20 March 2014).

Advanced Materials Research Vols. 986-987 (2014) pp 322-325

doi:10.4028/www.scientific.net/AMR.986-987.322

Grid electricity market bidding model based on Agent

Chao-Chun Ou[3, a], Jia-Qing Zhang[2,b,*] and Xiao-Hua Wang[1, c]

[1] China Nuclear Power Technology Research Institute

Shenzhen, China

[2] China Nuclear Power Technology Research Institute

Shenzhen, China

[3] China Nuclear Power Technology Research Institute

Shenzhen, China

[a] wangxiahua@cgnpc.com.cn, [b] zhangjiaqing@cgnpc.com.cn, [c] ouchaochun@cgnpc.com.cn

* Corresponding author Jia-Qing Zhang

Keywords: grid, power market, price bidding, Agent

Abstract. Grid technology can provide electricity market bidding to achieve the ability to provide large-scale computing. Agent technology has the autonomy, interoperability, and self-learning, can effectively solve the grid resource discovery and management, computing task allocation and scheduling problems, shared grid environment of heterogeneous computing resources. Introduction grid technology related content, Agent technology and proposes a use of Agent technology in the electricity market bidding model grid environment. Bidding able to provide the technology platform the parties a fair trade.

Introduction

With the gradual development of China's market reforms and the deep power, the power industry is gradually moving towards a fair and competitive electricity market in which bidding is a very critical issue. Generation side and user side open market, how to effectively get different regional electricity market generation and user quotes. Implementation mechanism of bidding. Become one of the problems to achieve. Since some services offer a great amount of data and distributed in different locations. Different variety of data representation, the operating system is different, therefore, to achieve efficient access to these data, the need for new technology [1].

To overcome these difficulties, you can take advantage of grid technology, accreditation and to provide users with a user interface through the mesh portal, user-submitted information and a quote; via grid middleware to manage and deal with these pricing information, computing and optimal coordination quotes portfolio, which is based on the user computing tasks can be divided into multiple tasks in parallel, when a larger number of users. Calculation of the local server to bear large, you need to use other computer resources[2]. In a grid environment, the grid middleware can find free computer resources available, assign tasks to the computer is idle, and the results returned to the user.

But to achieve grid technology, there are still many problems, such as heterogeneity, scalability and dynamic adaptability, autonomy and Agent technology, interoperability and ability to learn is an intelligent technology that can better grid computing to solve the problem. Compared with object-based expert system. Agent technology can achieve through self-learning to adapt to environmental changes, can take the initiative to interact with other Agent, more complex problems. If conflict expert systems can be used to ask for coordination among multi-agent to solve. This paper introduces the grid technology, Agent technology, and then discusses the auction model based on functional grid environment under the Multi-Agent technology and the modules and implementation processes.

Grid technology

Grid computing is an integrated environment and resources, computing resources can be fully absorbed and transformed them into a readily available, reliable, standard or economy while computing power. Grid-based problem solving is grid computing [4].

Grid computing is an emerging technology, with grid computing technology. It had nothing to servers, storage systems and networks can be combined together to form a larger system. For the end-user or application, the grid looks like a huge virtual computing systems.

Grid is divided according to a certain hierarchy, where the grid is the most critical core middleware layer, which is responsible for the distribution of resources for effective management, providing efficient, safe, reliable service [5] for the entire grid. Hierarchy shown in Figure 1.

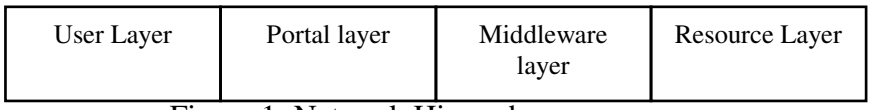

Figure 1: Network Hierarchy

Agent Technology

Was first developed by the Massachusetts Institute of Technology, part of the computer and artificial intelligence areas. Generally, Agent should have knowledge, goals and abilities. Knowledge is the solution of environmental problems and requires a certain Agent at its description by the user, the other Agent (in Multi-Agent System) or to get their own learning; goal is Agent required solutions for problems and tasks; capacity is Agent methodologies and tools can solve the problem.

Usually considered an Agent all or part of the following characteristics:

- Autonomy: Agent able to complete most of its functions in the absence of human intervention or other Agent, to control its internal state.
- Social competence: Agent can actively interact with other Agent or persons, in order to achieve their goals.
- Passive response capabilities: Agent can sense changes in the surrounding environment and the generation of real-time response meantime.
- Active response capabilities: Agent can be based on their own goals and beliefs of activities actively.
- Time Continuity: Agent process is continuous, rather than just the general procedure again on the end of that period.
- Adaptability: Agent can adapt to changes in the environment, which is often achieved through learning mechanism.
- Mobility: Agent can carry data and instructions to move to other environments and where the instruction is executed.

The electricity market bidding

Over the years, we have implemented a national network; vertically integrated factory system is not conducive to the development of the power industry in a market economy situation. Therefore, to introduce competition mechanism in the power industry and achieve a real sense of Changwangfenkai mechanism of bidding. With the deepening of reform and development, the power industry is gradually implementing the electricity market, breaking the monopoly, to a fair and competitive. Due to the existing administrative relationship between power companies and grid companies no longer exist, the formation of equitable economic relations, power companies cannot be issued executive orders to independent generating companies directly. Only be resolved by contract, agreement, "bidding" must be within the maximum range of resources to optimize the configuration of the target, to ensure safe and stable operation of the power grid, based on the minimal cost of purchasing electricity to meet the load demand [6].

Electricity market bidding is more complex , and tariff policy under state control , a variety of factors such as market pattern , the weather changes , the system unit's technical structure and ownership structure, fuel prices, rainfall , environmental standards, power suppliers bidding strategies influence ; single Agent functionality is limited, which requires an appropriate architecture through the multiple Agent tissue to form multi-Agent System (MAs), come together to complete the task of bidding , and the ability of MAS is much larger than a single Agent , not only does it have the resources to share with the general distributed systems , easy expansion , reliability, flexibility, and good real-time performance , and asked each Agent to achieve through coordinated scheduling of resources, management [7] . Agent cooperation between the various task -sharing and solved using a combination of the results of the shared task sharing refers to a complex problem into several sub-problems , each sub-problem solving respectively, by a sub- Agent to solve the problem by the Management Agent is responsible for managing each execution and results of the sub- task processing ; sharing is the result of each individual Agent work together to solve a complex problem , shared results of the Agent to each other by the Agent in charge of coordinating the results of organic integrated to form a complete answer [8] .

Participants in the electricity market transactions, including the generation side and user side, it is the physical basis of the grid, in order to achieve a balance between supply and demand for the dispatch center under the supervision of the management department. Each individual component of the electricity market are subject to the overall coordination of independent autonomy. Therefore, it is suitable for Multi-Agent Systems for problem solving. In the multi-Agent system. Adopt a distributed collection of learning methods, the use of contract negotiations between each network protocol method.

Electricity market bidding system can be divided into three parts, power generation, management section, purchase parts, each realized by the Multi-Agent Systems in a grid environment, the whole system is built on a grid platform in the grid environment bidding resources needed to get the work completed bid selection, management. Such a model can provide electricity for the power generation side and bid fair and square platform more successful scheduling, it can effectively deal with different market environments, offer different regions and rapid processing and computational problem solving large-scale data. The following section describes in detail the function of each part of the model module and bid process.

BIDDING specific model

(1) Web Module

Web module for visitors to provide a unified interface; mainly responsible for user authentication, use the grid to determine the user's permission. Part and the part of the purchase of electricity generation only after certification by the Web interface to manage part of the bids submitted to, and the result is also informed by it, that is, the specific choice of the market for the purchase of electricity generators and suppliers to the user is shielded, users can only wonder if his bid is accepted, but not about this process. Thus avoiding violations speculation and other secret operations occur.

Workflow: power generation companies, the electricity supplier first log in the web interface registration, Web Agent to verify eligibility for certification; After successful authentication, the bids submitted through the Web interface to manage part; management section the results published to the Web interface, and notify the user. Web module certification after registration center, also issued a request to the mobile library, mobile Agent will perform their respective tasks [9].

(2) Grid Environment

In this model, the system is the provision of a grid computing power. Its existence can become an open bidding system that provides computing and data into a regional internal bidding, you can also solve the problem of communication between different regions. In addition, access to different resources, different market environments can bid for market and related management.

Library Mobile Agent: Mobile Agent can move the grid node can autonomously move to a different address space to perform, during the transfer of its execution state is maintained after the transfer to the implementation of the objectives is ongoing; complete computing tasks can be carried needed for code and data as well as running the Agent between different hosts on the grid migration and complete the action. Move into task execution Agent, Mobile Agent and resources to move the query Agent. Mobile Agent responsible for calculating the task execution of specific tasks, assign tasks to carry a given grid node migration step to ask, will return the results to calculate the results of the General Agent. Query Mobile Agent in the registry after certification to the Resource Center to find the resources to meet user needs, and returns the query results to the appropriate Agent; resources to get and Mobile Agent is responsible for providing the resources required to calculate and scheduling (free to acquire, purchase, lease etc.). In order to facilitate the management, these three types of mobile Agent in Mobile Agent library.

Computing centers: the actual computing platform, different nodes in grid environment, in accordance with the principles of low priority and users real-time quote size selection generation bids. Specific computing market clearing price, handling the auction and related issues under different market conditions.

Resource Center: Provides resource sharing, publishing platform, a variety of data required to manage part of the algorithm, knowledge, models, patterns and other resources transactions can get from here. Some of the resources and power generation companies are also required to purchase electricity supplier from the Resource Center.

Summary

Grid technology is to solve large-scale data processing and distributed computing a powerful tool. Agent-based grid technology can better address some of the problems inherent in grid technology, its application to the electricity auction trading, distribution and help solve the problem of heterogeneous multi-regional multi-level electricity market, can quickly for large-scale data processing and computing, the entire bidding process for the realization of an important role.

References

[1] DuZhiYu,LiuPeng. Grid computing [M]. Beijing: Tsinghua University Press, 2008.10.

[2] Zhang Jie, GaoLiang LiQiangGen. Agent technology in advanced manufacturing in [M]. Beijing: Science Press. 2008.10.

[3] FanYuShun, CaoJunWei. Multi-agent systems theory, method and application [M]. Beijing: Tsinghua University Press. 2008.5.

[4] ZhangWei,Shen ShenChen. Preliminary electricity network systems (two) power grid architecture [J]. Automation of Electric Power Systems, 28 (23) :1-5.

[5] ZhangWei,Shen ShenChen. Design and Implementation (c) Preliminary prototype system power grid system [J]. Automation of Electric Power Systems. 28 (24) :5-8.

[6] Chen Yajun, XiaAnBang, Bidding Agent-based trading system, the calculation model [J]. Application Research of Computers, 2010, (10) :257-260.

[7] CaiGuangLin, WeiHua. Grid computing and its preliminary application in power system [J]. Relays, 2008,33 (19) :70-74.

[8] Wang Li, a smart grid software architecture agent technology [J] based. Taiyuan University of Technology, 2011,35 (5) :545-549.

[9] YangDongJu, HuZhengGuo. ZhengWeiChuan. Grid resource management system model hierarchy [J] based. Application Research of Computers, 2012, (10) :257-260.

Advanced Materials Research Vols. 986-987 (2014) pp 326-329

doi:10.4028/www.scientific.net/AMR.986-987.326

GROUNDING METHOD AND PROTECTION OF LOW VOLTAGE MULTIPLE GENERATORS

Guobin[1, a], LiuHui[2,b]

[1]Heping Road No. 146, Langfang City, Hebei Province, China

[2]Heping Road No. 146, Langfang City, Hebei Province, China

[a] cppeguobin@cnpc.com.cn, [b]cppeliuhui@cnpc.com.cn

Keywords: solid grounding, zero-sequenced reactance, grounding-fault protection, restricted grounding fault protection, back-up grounding fault protection

Abstract. This paper focuses on *proper grounding practices* and *grounding fault protection* for low voltage generators in island mode. The paper presents the fundamentals of power system grounding and requirements of IEEE with respect to grounding, the need for low voltage ground fault protection and implement is execution.

The paper outlines the solid grounding method is used and necessary grounding fault protection for multiple generators in low voltage system.

Introduction:

The more than one generator with sharing a common load is rapidly increasing. This system can provide the more reliable electrical power where there is no external power grid. Generators are essential part of the system. The safety of plant personnel and the reliability of the equipment are highly dependent on the type of system grounding selected and the type of grounding-fault protection selected.

In the low voltage system (below 600V or less), the solidly-grounded system is the most common system because it will support three-phase and single-phase loads. However, parallel generators that are directly connected to bus share common loads, care must be taken account into neutral circulating current considering selection of grounding method.

Electrical faults in low voltage system, estimated to be over 90% are grounding fault. Since a grounding fault is a common and potentially dangerous fault for stator windings, it must be detected and tripped as soon as possible. Special attention must be given to generator grounding fault protection.

Grounding system in low voltage network: In offshore oil & gas piping project, the multiple-isolated generator application consists of several units operating in parallel without connection to any electric utility supply system.

The main goals of system grounding are to minimize voltage and thermal stresses on equipment, provide personnel safety, reduce communications system interference, and give assistance in rapid detection and elimination of ground faults.

There are several grounding methods typically used in low voltage power system. These include undergrounded, solid grounded and impedance grounded. Source grounding may be accomplished by the grounding of the generators. However, the solid grounding is common arrangement in case of low voltage generator system.

In solid grounding, grounding conductor is connected to the ground with no intentional added impedance in the circuits. The following advantages and disadvantages of solid grounding are briefly listed.

Advantages:

- The neutral is effectively held at earth potential.
- When there is an earth fault on any phase of the system, transient over-voltage is eliminated. That permits to insulate the equipment for phase voltage. Therefore, there is a saving in the cost of equipment.

- It becomes easier to protect the system from earth faults which frequently occur on the system. When there is an earth fault on any phase of the system, large fault current flows between the fault point and the grounded neutral. This permits the easy operation of earth-fault relay.

Disadvantages:

- Since most of the faults are phase to earth faults, the system has to bear a large number of severe shocks. This causes the system to become unstable.
- The solid grounding results in heavy earth fault currents. Since the fault has to be cleared by the circuit breakers, the heavy earth fault currents may cause the arcing of circuit breaker contacts.
- The increased earth fault current results in greater interference in the neighbouring communication lines.

There are two different practical implementations of solid grounding in multiple generators:

a) Each generator grounded (Fig 1): where all multiple generators must be solidly grounded individually, it prevents circulating 3rd harmonic current. But it has cumulative effect on ground fault current.
b) Each source neutral connected to a common neutral bus, which is then grounded(Fig 2) : Where sources are in close proximity, or where the system is four wire, the common neutral or ground bus should be used. In a four-wire system the sources would not be considered as separately derived. And collecting neutrals and solidly grounding them collectively creates a path for excessive 3^{rd}.

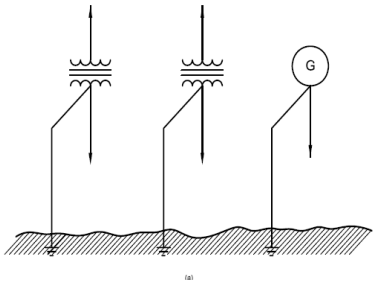

Fig. 1 Solidly grounded individually

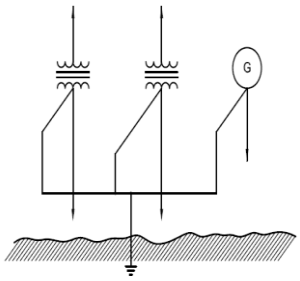

Fig 2 Common neutral bus grounded

In general, it is recommended that source one point grounded (Fig 2) for the generators with two-third pitch winding operated in parallel which have negligible circulating currents.

In order to limit the disadvantages of recommended grounded method, care about selected generator and ground fault protection method shall be taken.

Industrial low voltage generator characteristics: Generator construction will compatible with the common neutral bus grounding.

For generator, the zero-sequenced reactance has the lowest value in comparison to positive-sequence. Thus, the generator will usually have higher initial ground-fault current than a three-phase fault current in case of solid neutral grounding. However, the low voltage generator typically appears to have sufficient bracing for solid grounding.

A generator can develop a significant third-harmonic voltage when loaded. A solidly neutral grounded and lack of external impedance to circulating currents are flow of the third-harmonic current, whose value may approach rated current. However, this third-harmonic voltage will be suppressed for the generator with two-thirds pitch. Thus, generator with two-thirds pitch is best way for most electric loads that require a three phases, four wire system.

The load sharing method is important for multiple generators in parallel. The unbalance load sharing will result in 3th circulating current. Intelligent controller of generator based on digital isochronous sharing are produced to ensure that active and reactive load sharing are balanced properly.

Furthermore, it is best way that multiple generators are the same design (i.e. controller) and pitch (i.e. two-thirds pitch).

Grounding fault protection of generator: Generator is the heart of power system in island mode. The grounding fault is common for generator. It should be noted that the method of grounding fault protection is directly related to the method of system grounding used. In solid grounding, the protection can trip as soon as possible.

Range rated power of low voltage generator is less than 2500KVA. Grounding protection of generator includes the following internal and external ground fault.

- Overcurrent relay with voltage restrained (51 V)
- Stator grounding fault current (51 G)
- Restricted grounding fault (64REF)

In general, the 64REF is not too popular in small low voltage generator protection because sensitive grounding fault protection can be achieved by 51 G. But where large low voltage generator is used as prime power, the 64REF is recommended to provide more sensitive grounding.

The typical scheme of protection relay is shown on Fig 3.

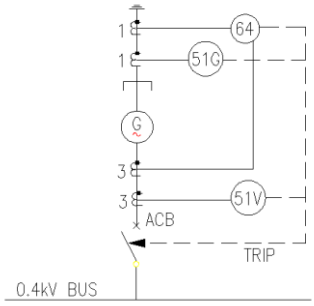

Fig3 Protection device for 64REF

A restricted grounding fault (REF) means the grounding fault from a restricted/localized zone of a circuit. In case of an internal grounding fault within the stator windings, the stator earth fault relay (i.e.64REF) will initiate and disconnect the defective generator to reduce damage. 64REF as "unit protection" applied to star windings of generator. 64REF relay is normally instantaneous operating protection and provided in neutral grounding circuit where current flows only if there is fault only involving ground/earth fault. Hence there is no great need for time discrimination.

64REF responds to only ground fault within the protected zone, while REF does not respond to phase-phase fault either within the protected zone or outside the protected zone.

The star-point connection to ground is provided with a current transformer and a sensitive relay. The Relay (5I G) is of inverse time delay type so that it can be graded as back-up protection to earth fault relays at downstream feeders and consumers. This device is based in a current transformer that surrounds the generator phases and the neutral. This configuration permits to measure the grounding current coming from the generator and the system and in this way, grounding faults are detected. The figure 4 shows the connection of generator.

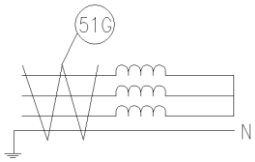

Fig 4 Connection of 51G

A standard overcurrent relay does not have a characteristic that can give a fast enough response once the initial decay has taken place. To overcome this effect the change in terminal voltage at the generator is used to measure the severity of the fault. Voltage Restrained Overcurrent Relay (51 V) as

back-up protection is produced to provide protection for fault outside of the generator zone of protection. Fig 5 show 51V connection via generator terminal connected current transformer.

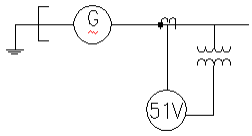

Fig 5 Connection of 51V

Summary. In the paper, the common neutral bus grounding is employed for low voltage multiple generators application. However, compatibility between system and generators shall be considered to ensure reduce the circulating currents at limited level. At the same time, it is important to select proper grounding protection for generator, which can ensure low voltage system is reliable and stable.

References

[1] IEEE142 IEEE Recommend Practices for Grounding of Industrial and Commercial Power

[2] IEEE std C37.102 IEEE Guide For AC Generator Protection

[3] IEEE std C37.101 IEEE Guide For Generator Ground Protection

[4] Dr Jawad Al-Tayie AC Generators with 2/3 rd and 5/6 th Winding Pitch

[5] Alan. L.Sheldrake Handbook of Electrical Engineering (2003)

Advanced Materials Research Vols. 986-987 (2014) pp 330-333

doi:10.4028/www.scientific.net/AMR.986-987.330

Impact of 750kV Transmission Line Series Compensation Capacity on Power Frequency Overvoltage

Dingjun WEN[1, a], Xiubin ZHANG[1, b], Honggang CHEN[1, c], Feng JIANG[1, d], Yaming SUN[1, e]

[1] Equipment condition assessment center, State Grid Gansu Electric Power Research Institute, Lanzhou 730050, China

[a]email: djwxjtu@163.com, [b]email: xiubin@aa.seu.edu.cn, [c]email: dhgch3476@hotmail.com,

[d]email: power_jiang@21cn.com, [e]email: sunyaming@sina.con

Keywords: 750kV Transmission Line; Power Frequency Overvoltage; Series Compensation

Abstract. The overvoltage calculation of 750kV transmission line with series compensation has great significance on the design, insulation coordination and protection of the line. In this paper, a transient model of 750kV power transmission system with series compensation is established. Effects of different capacity on no-load capacitive rise overvoltage, single-phase grounding overvoltage, two-phase grounding overvoltage are calculated. Secondary arc current and recovery voltage of different series compensation capacity in single-phase grounding is also calculated.

Introduction

Series compensation technology is the key to solve the contradiction of urgency and expensive of ultra high voltage long distance power transmission. The installing of series compensation can offset inductive reactance of the line, that transmission distance, power transfer limit and transmission efficiency increases effectively. In addition, subsynchronous oscillation can be suppressed with the application of FACTS in TCSC. Transient component can be effectively damped.

To analysis the impact of series compensation on power frequency overvoltage of 750kV ultra high voltage power system, working conditions of a transmission line with series compensation is calculated and analyzed. Simplified equivalent circuit is show in Fig.1. Centralized compensation is installed in the end of the line. The degree of compensation is 30%,40%,50%,60% and 70%. Short circuit fault occurred in the head, middle and end of the line, 0km, 186km and 372km to B.

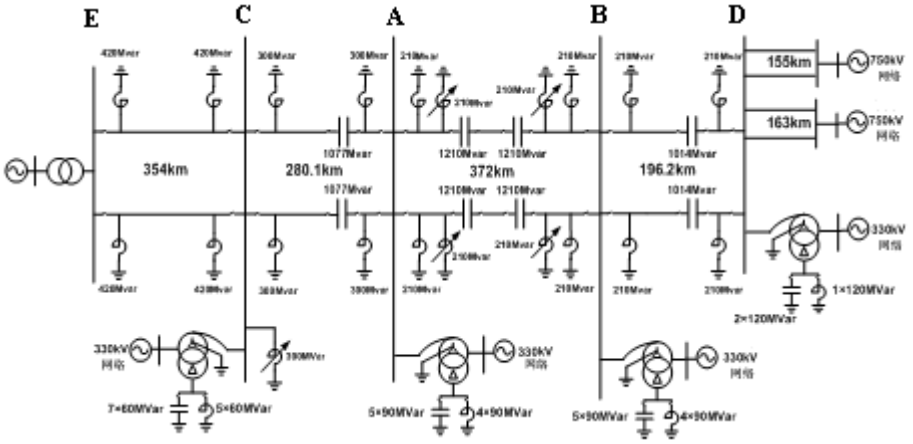

Fig.1. Simplified equivalent circuit

Research Methods

By ATP-EMTP, operation mode and parameters are calculated according to Fig.1. Overvoltage, secondary arc current and recovery voltage is also calculated. Serial number of calculation is show in Tab.1.

During calculation, Ⅱloop is in operation. The degree of compensation vary when Ⅰloop is light load. The value of compensation degree: 30%,40%,50%,60% and 70%. Transmission power of C-A: 3380MVA, B-D:4188MVA.

The reference value of calculation: $1.0 p.u. = 800/\sqrt{3} = 461.89 kV$

Tab.1. Serial number of calculation

Number of Series capacitor	Number
Ⅰloop A side	1#
Ⅰloop B side	2#
Ⅱloop A side	3#
Ⅱloop B side	4#

No-load Capacitive Rise Overvoltage

No load line can be seen as composition of countless series circuit of L and C. In power frequency voltage, the capacitive reactance of the line is far outweighed than inductive reactance. So, each point voltage is higher than the first end of the line. For double loop transmission system, there is a certain relationship between overvoltage amplitude of the end side of no load line and voltage, equivalent impedance of power side and operation of the other loop. Affected by the transmission capacity, equivalent impedance of the supply side depends on the open site.

Take C phase as an example, Tab.2 and Tab.3 is the power frequency overvoltage and the series compensating capacitor of the line when the degree of compensation varies from 30% to 70%.

Tab.2. Power frequency overvoltage of A-B transmission line in different series compensation degree

Node	Compensation degree				
	30%	40%	50%	60%	70%
Midpoint of Ⅰloop C phase	0.961	0.957	0.953	0.949	0.946
Midpoint of Ⅱloop C phase	0.959	0.957	0.955	0.955	0.955
Left of Ⅰloop C phase	0.956	0.952	0.948	0.944	0.941
Left of Ⅱloop C phase	0.949	0.946	0.943	0.940	0.937
Right of Ⅰloop C phase	0.956	0.952	0.948	0.944	0.941
Right of Ⅱloop C phase	0.941	0.940	0.941	0.946	0.958
No load side of Ⅰloop C phase	0.955	0.954	0.953	0.953	0.952

Tab.3. Overvoltage on series capacitor of A-B transmission line in different series compensation degree

Node	Compensation degree				
	30%	40%	50%	60%	70%
C phase of 1# capacitor	0.093	0.093	0.092	0.091	0.091
C phase of 2# capacitor	0.082	0.082	0.082	0.082	0.082
C phase of 3# capacitor	0.424	0.481	0.555	0.658	0.808
C phase of 4# capacitor	0.419	0.473	0.545	0.644	0.789

According to calculation, the variety of A-B transmission compensation degree line from 30% to 70% almost has no effect on the overvoltage of the high voltage bus, but has influence on overvoltage of node on line itself. With the increase of compensation degree, capacitive overvoltage monotone decrease, the maximum reduction is 3.104%. Series compensation capacitor voltage of

Ⅰloop monotone decrease with the increase of compensation degree, the maximum reduction is 3.261%. Series compensation capacitor voltage of Ⅱloop monotone increase with the decrease of compensation degree, the maximum elevation is 90.566%.

Single-phase grounding fault

When transmission line is no load, the voltage of other phase will rise during single-phase grounding fault. Because it is a common that single-phase grounding happen, the analysis of overvoltage of other phase should be take. Since the maximum voltage difference is no more than 1.5% during three single phase failures, one phase could be taken as example.

Tab.4 to Tab.5 is the power frequency overvoltage of each nod and the series compensation device during single phase fault in B phase of Ⅰloop B side when Ⅱloop in normal operation.

Tab.4. Overvoltage of the line when single-phase grounding occurred in B side

Overvoltage of Node	Compensation degree					
	0%	30%	40%	50%	60%	70%
A phase in fault point	1.261	1.246	1.242	1.238	1.234	1.230
B phase in fault point	0.029	0.006	0.006	0.006	0.006	0.006
C phase in fault point	1.169	1.157	1.151	1.150	1.146	1.143

Tab.5. Overvoltage of the line when single-phase grounding occurred in middle

Overvoltage of Node	Compensation degree					
	0%	30%	40%	50%	60%	70%
A phase in fault point	1.246	1.225	1.218	1.212	1.205	1.199
B phase in fault point	0.055	0.055	0.055	0.055	0.055	0.056
C phase in fault point	1.201	1.190	1.184	1.179	1.174	1.170

According to calculation, the variety of A-B transmission compensation degree line from 30% to 70% almost has no effect on the overvoltage of the Ⅱloop, but has influence on overvoltage of node on Ⅰloop itself. With the increase of compensation degree, capacitive overvoltage monotone decrease, the maximum reduction is 3.7%. Series compensation capacitor voltage monotone increase with the increase of compensation degree, the maximum elevation is 95.27%.

Two-phase grounding fault

When transmission line is no load, the voltage of other phase will rise during two-phase grounding fault. Lightning arrestor and fast discharge gap protection is in parallel with series compensation capacitor. When short fault occur, Fast discharge gap discharge after 1ms of the fault.

According to calculation, the influence of compensation degree to node voltage is tiny when the fault happened in the middle of the line. With the increase of the compensation degree, node voltage slight decrease, series compensation capacitor voltage monotone increase with the increase of compensation degree.

Secondary arc current and recovery voltage

Take the grounding resistance as 5Ω, Tab 6 and Tab 7 show the secondary arc current and recovery voltage of the A-B transmission line when single-phase grounding occurred in B side and middle side of the line.

The calculation results show that: the compensation degree of series compensation device has influence on the secondary arc current and recovery voltage in the fault point. With the increase of

compensation degree, secondary arc current and recovery voltage monotone increase. When compensation degree increase from 0% to 70%, secondary arc current add 22.56% , while recovery voltage add 23.74%. In addition, secondary arc current and recovery voltage is much higher when the fault happens in the middle of the A-B transmission line than the fault happens in the end of the line.

Tab.6. Secondary arc current and recovery voltage of the line when single-phase grounding occurred in B side

Node	Compensation degree					
	0%	30%	40%	50%	60%	70%
Secondary arc current in short point (A)	20.239	21.831	22.500	23.236	24.255	25.509
Recovery voltage in short point (kV)	135.338	146.469	151.127	156.257	163.304	171.967

Tab.7. Secondary arc current and recovery voltage of the line when single-phase grounding occurred in middle

Node	Compensation degree					
	0%	30%	40%	50%	60%	70%
Secondary arc current in short point (A)	21.723	23.180	23.801	24.536	25.443	26.624
Recovery voltage in short point (kV)	203.716	218.254	224.394	231.644	240.547	252.081

Conclusion

The variety of A-B transmission series compensation degree from 30% to 70% almost has no effect on the overvoltage of the two buses. It has influence on the overvoltage of node on the line itself. With the increase of the compensation degree, capacitive increase overvoltage monotone decrease. The influence of compensation degree to node voltage is tiny when the fault happened in the middle of the line. The compensation degree of series compensation device has influence on the secondary arc current and recovery voltage in the fault point.

References

[1] P.H. Zhou, M.H. Xiu, D.X. Gu, M. Dai and Y. Lou: *Study on Overvoltage Protection and Insulation Coordination for ±800kV HVDC Transmission System*. Trans High Voltage Engineering, Vol. 32 (2006), China.

[2] Q. Liu, Y.F. Zhang, and Y. Cheng: *Research on Protection Against Lightning Overvoltage on Transformer in a 220kV GIS Substation*. Trans High Voltage Apparatus, Vol. 44 (2008), China.

[3] C.H. Lu, D.Z. Nie: *Discussion on the Insulation Coordination for Lightning Overvoltage*. Trans High Voltage Engineering, Vol. 22 (1996), China.

[4] J. Pei: *Research on Lightning Over-voltage for Transmission Line Based on ATP-EMTP*. Trans Science & Technology Information, Vol.29 (2010), China.

[5] D.J. Si, H.C. Shu, X.Y. Chen, and J.L. Yu: *Study on Characteristics and Identification of Transients on Transmission Lines Caused by Lightning Stroke*. Trans Proceeding of the CSEE, Vol. 25 (2005), China.

[6] C.J. Wang, L.Y. Zhu, S.C. Ji and Q.G. Zhang: *Present and Development of Lightning Protection for HV Transmission Lines and Substations*. Trans Insulations and Surge Arresters, Vol. 3 (2010), China.

Advanced Materials Research Vols. 986-987 (2014) pp 334-338

doi:10.4028/www.scientific.net/AMR.986-987.334

Introduction of the Assessment Model of Nuclear Safety Culture

Jiaxu ZUO[1, b], Xu XU[2], Jianshe CHAI[1], Chunming ZHANG[1], Jianping JING[1, a]

[1]Department of Nuclear and Radiation Safety Research, Nuclear and Radiation Safety Center, MEP, Beijing 100082, China

[2]Liaoning Hongyanhe Nuclear Power Co.,Ltd., Dalian, 116319, China

[a]email: jingjianping@163.com, [b]email: zuojiaxu@chinansc.cn

Keywords: nuclear safety; nuclear safety culture; nuclear safety climate; index system; assessment system

Abstract. The nuclear safety became the more important after the Fukushima accident. The development of nuclear safety culture is one of the most effective methods to improve the safety. Also the assessment shows the level of the nuclear safety culture. The nuclear safety assessment model is described. The assessment model was described from its time and space, and it was also discussed from macro and micro levels. The internal and external environment parameters are considered and the assessment of different levels of safety culture is described. According to established principles of nuclear safety culture, the selection rules of the different levels evaluation indicators of nuclear safety culture are discussed too. And it is pointed that the assessment of nuclear safety culture is a long time project and an integrated system.

Introduction

With the development of the nuclear power, the safety culture was more and more important. After Three Mile Island and Chernobyl, the safety culture of the nuclear power plant (NPP) was widely attention. In 1992, the International Atomic Energy Agency (IAEA) clarified the definition of nuclear safety culture in NO.75-INSAG-4. The safety culture is that assembly of characteristics and attitudes in organizations and individuals which establishes that, as an overriding priority, nuclear plant safety issues receive the attention warranted by their significance [1]. After Fukushima, the safety culture is more and more important with the development of the nuclear power.

The nuclear safety will be extended into the research, development and application of the nuclear technology. And the nuclear safety was also combined with the design, construction and operation of NPP. Also, the nuclear safety is not only an industry security, but also a radiation safety [12]. But the nuclear safety is needed more professional, comprehensive, effective and sustainable to assessment the nuclear safety culture. The nuclear safety culture belongs to management culture. It is a kind of cultural and divided into the spiritual culture, institutional culture, behavior culture and material culture [2-5].The nuclear safety culture covers the human and physical. It is contacted with the ideas, the environment, and behavior patterns.

It is important that to assess the safety culture with the scientific model. From the quantitative assessment, the safety culture levels and weak points will be shown. The development roadmap and trend of the safety culture also will be discussed from the assessment. That information will be provided as reasons to improve the work and regulation. Between the assessment, the model and the index system will be one of the most important steps and the basic of the assessment.

The Assessment of Nuclear Safety Culture

From assessment of nuclear safety culture, the overall situation of nuclear safety culture is shown from the different perspective and levels. The general recognition is clear [6]. The main objectives were to identify specific problems in the nuclear safety culture, and analysis its causes and improvement methods. The improvement and regulation will be guided by analysis results.

The assessment process of the nuclear safety culture must be away from the benefit. And it should be ensure that the assessment results are objective reality. The assessments should be done by the third party position. The successful assessment system of nuclear safety culture should be scientific, comprehensiveness, comparability, feasibility and stability.

The assessment range should be clearly. In assessing steps, the scope should be identified, and the nuclear safety is the mainstay of the scope. As the same time, the nuclear safety-related factors of external environment indirectly impact must be considered, such as the laws and regulations, the government regulation, the industry specifications and the families of employees.

In general, the assessment the safety culture should be in the mature and stable period. This kind of assessment could reflect the real condition of the culture.

The Object of Nuclear Safety Culture Assessment

The safety culture is composed of two general parts. Firstly, it is the necessary framework within an organization and the responsibility of different management level. The second is the attitude of staff at all levels in responding to and benefiting from the framework. Based on the responsibility of different level, the safety culture is component into policy level, managers and individuals. Also the responsibility of different level is made clearly (Fig1) [1].

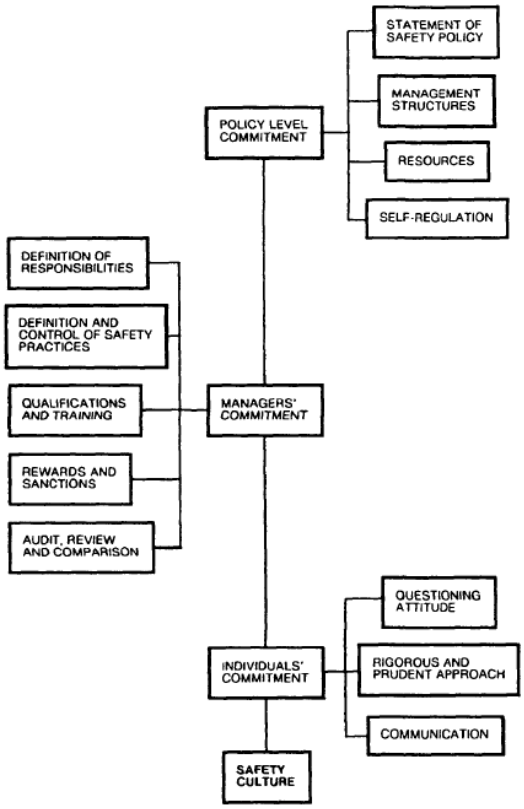

Fig.1. The Levels of Safety Culture

The policy level is the highest level of the system. This level has its permission to utilize the variety of resources and have a decisive influence. The highest level affecting nuclear plant safety is the legislative level, at which the national basis for safety culture is set. When the highest level was assessed, we focused on the emphasis and understanding of the implementation the concepts, mechanisms and measures. The management level is in the middle level of system functions, and connects the policy level and individuals. The assessment of management level should focused on the management, implementation and monitoring. Their knowledge and the implementation of training will also be assessed. The communications with employees are attention too. The individuals are the operational level. Their activities directly affected to nuclear safety level, and they affect and change the nuclear safety status at any time. So the individuals are key factors in state of nuclear safety. The assessment of individuals should focus on the responsibilities, establishment of a long-term mechanism of nuclear safety training and awareness of safety culture.

The Process and Methods of Assessment

Figure 2 shows the nuclear safety culture assessment process [6, 12]. In the really assessment, the process always more than one stage at the same time or staggered. Sometimes, the process is a circulation until get the active results. In general, before the nuclear safety culture assessment, the assessment method has been defined. The most important steps are selection the indicator system and method.

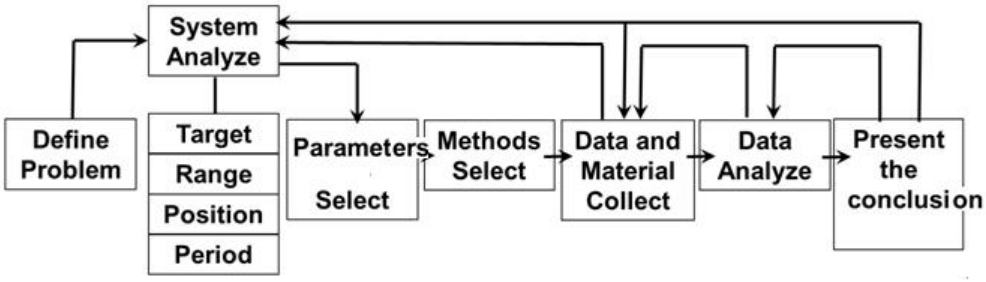

Fig.2. The Steps of Safety Culture Assessment

In the assessment process, a clear target of the assessment will be clearly, and the evaluation criteria are defined base on that target. Secondly, we will collect the quantitative data which is based on the evaluation criteria. Finally, the assessment results will be analysis and compare with the environment and background of the evaluation object to get the suggestion with reference value.

The Nuclear Safety Assessment Model

The main evaluation targets of the assessment model are the policy level, managers and individuals [1, 9], and the model is persistently and stability which are the characteristics of the culture. The external and internal environmental factors of the independent organization are also considered in the assessment index system. Those factors will focus on analysis of external manifestations, such as behaviors, risk perception and pressure.

The SMART standard [7] is the principle to design of evaluation index system of nuclear safety culture. SMART is composed of five initial in the words, and they are specific, measurable, attainable, relevant and trackable.

There are three levels of the index. The first level is designed by considered the external and internal environmental factors. Then, the evaluated objects' level in the system and the functions and roles of the objects will be considered to construct the second-level and third-level indicators. At the same time, there are three key points are considered as the following: the macro-scale and micro-scale factors, the point in time and a particular length of time influence, and the indirect effects of government regulators and employee families

The nuclear safety assessment model and its index system consists two parts. The first part reflects the long-term and relatively stable system of nuclear safety culture, and it includes the macro-scale, a length of time features and the external environmental factors. The second part reflects the atmosphere of the nuclear safety culture in the real time status. And it includes the micro-scale, the point in time and internal working environment [6]. Because of the relation between the factors, the parameters of the nuclear safety culture assessment are divided into four levels, which are the objectives, criteria, indicators and programme.

The detailed assessment model is shown in Table 1.

Table.1. The Assessment Model of Nuclear Safety Culture

Classify		Explain	Substance
Nuclear Safety Culture	macro-scale	Focus on the integrity system and concept culture	(1) The concept culture reflects nuclear safety philosophy, values, safety awareness and attitudes. (2) The institutional culture reflects the commitment, management system and the institution of rewards and punishments.

	Time View: the particular length of time	With persistence, stability and continuity the same as a “video”	(1) Production in the activities process of evaluated object, (2) With the relative stability indicators, (3) The indirectly factors which reflect characteristics.
	Space View: the external environmental	the external environmental and external environmental status relatively stable	(1) The standards and regulations on nuclear safety and the policy; (2) The government’s supervision and management of the nuclear safety; (3) Nuclear safety atmosphere of the industry; (4) The environment of the locale.
Nuclear Safety Atmosphere	micro-scale	the environmental factors and factors of individual cognition and consciousness	(1) To show the nuclear safeguards, nuclear safety supervision and the working environment, and attention on the status of nuclear safety and the internal environmental factors. (2) To show the staffs' risk perceptions, competencies, expertise and pressure of work, those are the factor of the individual awareness of nuclear safety.
	Time View: the point in time	the cognitive within the specific moment, the reflection of real-time status; a "photograph" of evaluation	Time changing with the time, people and environments, the parameters dependence on the state of nuclear safety and the working environment.
	Space View: Internal environment	the internal working environment; the internal working environment state is variable.	(1) The safety and advanced of the equipment and the public order; (2) Compliance with the nuclear safety regulations, and employees wear the safety protective; (3) The conditions of intermittent resting places are supplied for employees in the worksite.

The Selection of Nuclear Safety Culture Assessment Parameters

The parameters should focus on the macro level and micro level, and the particular length of time and the point in time. The internal and external factors should be considered too. The policy level, managers and individuals are the mainly object. The persistence and identity of the system should be included. The external manifestations are the key points to be assessed and analyzed.

For the policy level, the macro level will focus on the values, beliefs and policies of nuclear safety. But the micro levels will take attention on the supports and the implementation of the nuclear safety atmosphere creating [12]. For the managers, the assessment focuses on the supervision, communication and their awareness and attitudes. It is also very important that their knowledge of nuclear safety and the training mechanism of the nuclear safety culture. For the individuals, the long term training mechanism for nuclear safety culture will be the most important.

There are exchanging massages and communication between the system and the external, so the external environmental must be considered. At the same time, the real time of nuclear safety will be directly affected by the internal environmental, so it also must be focused on. Those are measurements of the openness of the system. As the culture’s characteristic, there is persistence, stability and continuity. Therefore, it is considered that the values, beliefs and attitudes are formed for a long time. This is the persistence of the culture.

Summary

The nuclear safety culture is the method and culture of management from top to bottom. The assessment of it should also take top to bottom, and it is an effective and sustainable mechanism for all departments. The policy level, managers and individuals are the mainly object, and the persistence and openness are considered. The assessment will be focused on the external manifestations such as the behaviors, risk perception and working pressure. The parameters can be divided into safety culture and safety atmosphere system. Those influences are considered which are the macro and micro scale, the particular length of time and the point in time, the external and internal environmental.

The assessment of nuclear safety culture is a long time project and need an integrated system. Base on the assessment and analysis, the trend of safety culture's development will be shown and the improved points will be presented.

References

[1] IAEA, International Nuclear Safety Advisory Group, Safety Culture, Safety Series, No. 75-INSAG-4., 1991

[2] Zhou Tao, Lu Dao-gang, Li You-ran, The Nuclear Culture And the Nuclear Power Development, Modern Electric Power [J], 2006 (5) 16-23

[3] Luo Yun, The Purpose Meaning And Scope of Safety Culture, Construction Safety [J], 2002 (10) 10-11

[4] Li Zhi-xian, Yang Man-hong, Impact Mode of Safety Culture on Safety Behavior, CHINA SAFETY SCIENCE JOURNAL [J], 2001, 11 (5) 14-16

[5] Zhang Xian-bao, Exploration and Practice of Safety Culture Construction in Coal Mine Enterprises, CHINA SAFETY SCIENCE JOURNAL [J], 2006, 16 (7) 81-86

[6] Wang Yi-hong, Study on the Assessment System of the Enterprise Safety Culture, Tianjin University, PhD Thesis, 2007

[7] He Yu, Zhang Jin-long, Bao Yu-kun, Design of Nuclear Safety Culture Indicators Based on SMART, Electric Power [J], 2004, 37 (5) 85-87

[8] Mao Hai-feng, Assessment System of the Enterprise Safety Culture, MODERN OCCUPATIONAL SAFETY [J], 2003 (8) 24-25

[9] Li Shao-gang, The Nuclear Safety Culture of AP1000 in Haiyang, CHINA ELECTRIC POWER EDUCATION [J], 2010 (30) 223-225

[10] Chan A, Kwok W, Duffy V, Using AHP for determining priority in a safety management system, Industrial Management Data Systems [J], 2004 (5/6) 430-445

[11] Lu Wei, Tang Yan-zhao, Cultivation of Nuclear safety Culture in Guangdong Nuclear Power Station, Chinese Journal of Nuclear Science and Engineering [J], 2004 (3) 205-230

[12] Chai Jian-she, Theory and Practice of Nuclear Safety Culture, Chemical Industry Press [C], Beijing, 2012.6

Advanced Materials Research Vols. 986-987 (2014) pp 339-344

doi:10.4028/www.scientific.net/AMR.986-987.339

Liaoning Wind Power Integration into Power System Problems Analysis and its Strategies

WANG Gang, ZHAO Qing-song, ZHU Yu, GE Yang-yang, LI Sheng-hui

State Grid Liaoning Electric Power Research Institute, Shenyang, Liaoning, 110006, China

email:hi295@163.com

Keywords: wind energy integration; wind power usage; power peaking; wind energy storage

Abstract. For the actual situation in Liaoning Power Grid, analyzed the problems the wind power interconnection brought. Involving power quality, power fluctuations, power peaking, power delivery and so on. Proposed related coping strategies. Strengthen wind power connection management, plan the power structure scientifically and rationally, carry out multi-channel consumer of wind power actively, improve the security and stability level of the power grid.

Introduction

With energy and environmental issues have become increasingly prominent,in recent years the world are increasing the size of the development and utilization of wind energy. China's wind power installed capacity is in explosive growth in recent years [1]. Since 2005,China's wind power installed capacity to double growth for five consecutive years. 2010,China's total wind power installed capacity surpassed the United States, ranking first in the world. After years of rapid growth, China wind power market is entering a period of steady development.

Due to the volatility of wind power is difficult to accurately prospective, when wind power interconnection reached a certain level, the adverse effects caused to the grid in turn restricts the size of its access to the grid [2, 3]. At present, China's wind power development has become a trend of large-scale access to the grid,in order to take full advantage of the resources of wind farms which have been built,how to improve the performance of network operation of wind power is the key to ensuring the sustainable development of wind power,is currently the key research project [4, 5].

The outstanding problems of grid-connected wind power operation in Liaoning

As of March 2013, the Liaoning power grid wind power capacity grew to 4.959 million kilowatts, compared with 2007's 347,000 kilowatts, an increase of 14.29 times in six years. Although the domestic wind power development slowed down, but the Liaoning power grid wind power will continue to be an annual rate of around one million kilowatts increase. The rapid development of wind power in Liaoning brings power quality, power fluctuations, power peaking, and power sending a series of questions to the grid, posed a great challenge for the safe and stable operation of the grid.

Power structure is irrational,hinder the development of wind power

Liaoning Power Grid primary energy structure can basically be summed up as: more coal, windy, less water, less gas. As of the end of 2012, Liaoning Power Grid thermal power accounted for 80.33% of the total installed capacity,hydropower 7.15%,wind power 12.49%. Because of the special structure of power in Northeast, resulting in insufficient system peaking capacity, a serious impediment to the development of wind power in Liaoning Power Grid.

Liaoning Power Grid is mainly coal-fired thermal power grid, and its hydropower units is less, and no gas, oil and other generators, the grid quickly peaking capacity is relatively weak. Meanwhile, thermal power affecting output due to equipment defects and poor coal quality will always exist, bring enormous pressure to low power peaking. Moreover, Liaoning Power Grid heating units are more, in the winter heating period, they need to determine power generation by heat, which limited adjustable output range. Thus, the winter is the most difficult period of power peaking in Liaoning

Province, coupled with anti-wind power output peaking characteristics presented in the winter, brings more power peaking difficulty.

Wind turbine skill levels uneven, wind power to run in security risk

When the grid fails, the wind turbines tend to protect the unit automatically removed, so that the grid troubleshooting more difficult, may cause the accident to expand and even the grid voltage instability, cause a serious threat to the safe operation of the grid, the problem of low voltage ride through of wind turbine for the current run maximum security risks for wind power [6]. Liaoning Province strengthened wind turbine low voltage ride through capability requirements, most wind turbines have possessed low-voltage ride-through capability. As the national standards set requirements is not very specific for wind turbine response capability in the process of low voltage ride through, lead to the ability of grid-connected wind turbine low voltage ride through showing a large difference. Figure 1 shows the responsiveness of different wind turbines at low voltage ride through:

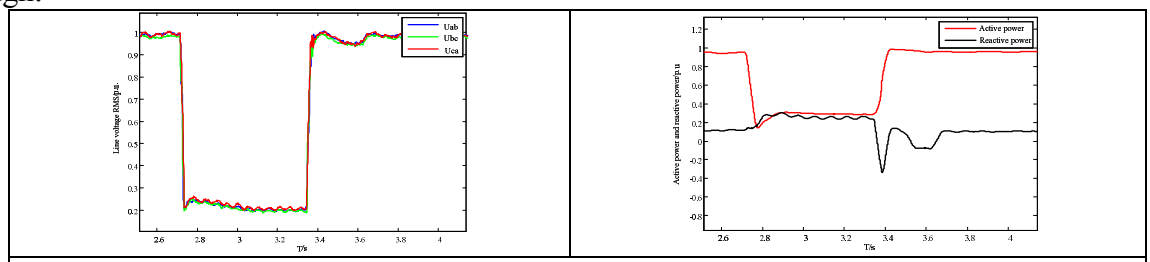

Domestic direct-drive wind turbines (failure process can emit reactive current, active power recovery faster)

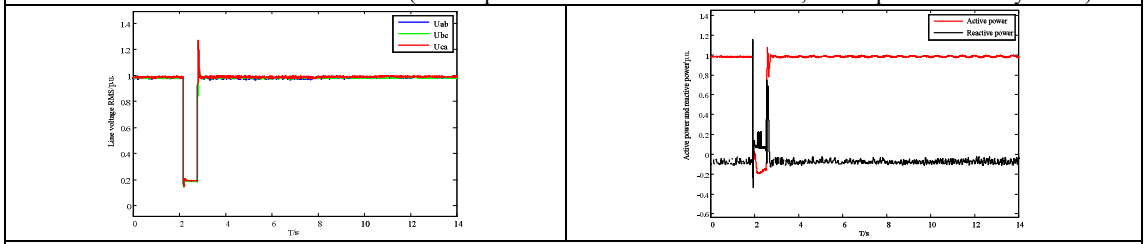

Foreign doubly-fed wind turbine (failure process can emit reactive current, active recovery faster)

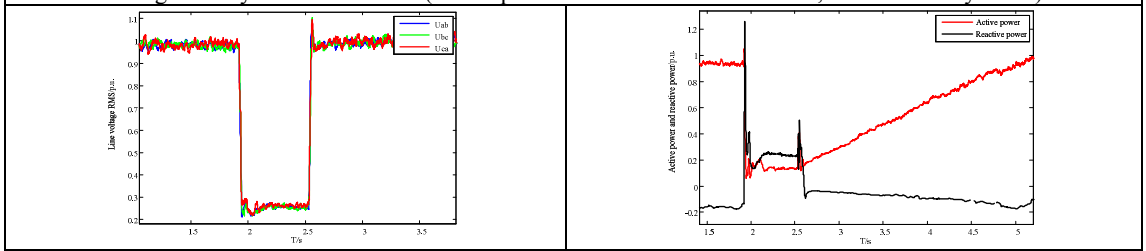

Domestic doubly-fed (1 can emit a certain reactive power, active recovery slower) CRE

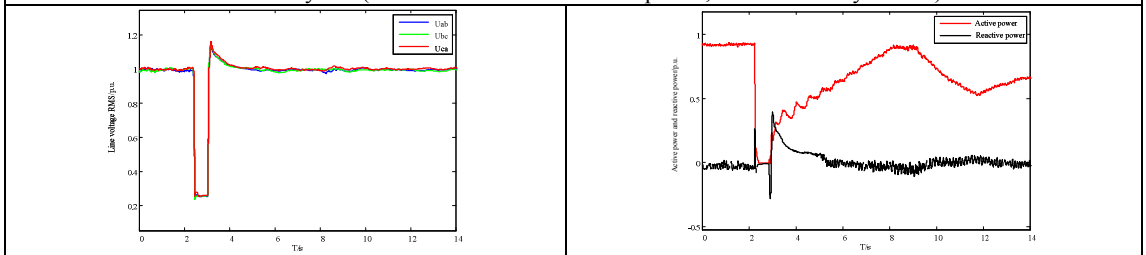

Domestic doubly-fed (2 can transmit a certain reactive power, active power recovery process have greater volatility) Sinovel

Figure 1 Wind Turbine responsiveness at low voltage ride through

It's visible that WTG reactive power and voltage output , power recovery, terminal voltage fluctuations exist big difference at low voltage ride through, which has brought great uncertainty and security risks to the safe operation of the power grid and even the wind farm during power failures.

Wind power Influence grid voltage stability

Wind power with random fluctuations and intermittent inherent properties, so that large-scale wind power connects to grid will affect the stability of the power system. Since the majority of wind farms located in the peripheral grid, power grid construction is relatively weak, more likely to cause the grid voltage stability problems. Liaoning EPRI carried out more than 20 wind farms operating

characteristics and network testing in Liaoning Province, during the test, found that wind farms absorb reactive power from the grid, active power fluctuations exceeding the national standards, voltage fluctuations, these phenomena will all bring great security risks to wind farms and outlets voltage stability. Figure 2 shows wind farms absorb reactive power from the grid and the power change rate during the test.

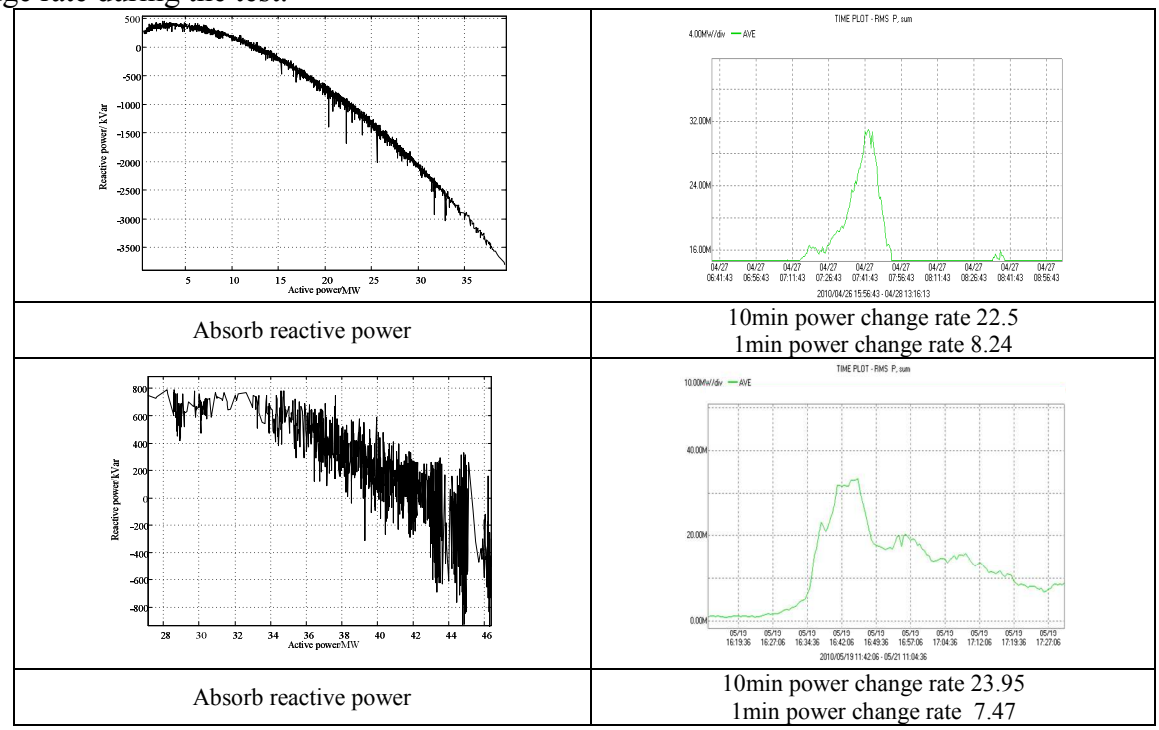

Figure 2 Wind Farm absorb reactive power from the grid and power change rate

Wind power bring critical challenge to power peaking

The power output of wind power is random fluctuations and uncontrollable, the prediction accuracy is poor, large-scale wind power generation connected to the grid make it difficult to formulate generation plan, need to increase system spare capacity, this increases the economic costs of the system operation; It put forward new demands to both the power mode operation plan and system spare capacity, especially thermal power peaking-based Liaoning grid facing enormous issue.

With the rapid development of wind power, wind power usage problem gradually emerged. Beginning in 2010, wind power usage capacity shortage emerged in portion period, wind power abandoned 110 million kWh 2010,which increased to 1.129 billion kWh 2012, an increase of nearly 9.26 times.(2012 abandoned wind power 773 million kWh in the cause of peaking, accounted for 68.47% of total abandon wind power, 356 million kWh in the cause of grid constraint, accounted for 31.53% of total abandon wind power.) Limited power ratio increased from 2.34% in 2010 to 14.33% in 2012. Table 1.1 shows 2007 to 2012 wind power limited power situation in Liaoning power grid.

Table 1 2007 to 2012 wind power limited power and generation situation in Liaoning power grid

Year	2007	2008	2009	2010	2011	2012
Limited power （hundred million kWh）	--	--	--	1.1	5.62	11.29
Limited power generation ratio（%）	--	--	--	2.34	8.51	14.33
Power utilization hours	1388	1764	2025	2033	1934	1761

Liaoning Power Grid the heating period and strong winds period are at the same time, and there is a big difference between peak and off-peak load in winter heating period. Affected by heating, thermal power peaking capacity decreased, absorptive capacity of wind power is serious shortage. Spring, autumn and summer peak and off-peak load difference decreases, and thermal power peaking capacity enhancement, wind power usage capacity has increased significantly. Table 2 shows the month of 2012 wind power generation and wind power abandoned, Figure 3 shows the past three years limited power generation ratio.

Table 2 The month of 2012 wind power generation and wind power abandoned

Month	Jan	Feb	Mar	Apr	May	Jun	Jul	Aug	Sept	Oct	Nov	Dec
Wind power capacity Ten thousand kilowatts	410	417	434	439	442	442	456	456	466	471	471	476
Wind power generation hundred million kWh	3.06	6.62	7.83	11	6.85	6.31	5.35	4.07	6.32	7.7	6.24	7.43
Abandoned wind power hundred million kWh	1.19	2	1.64	1.56	0.19	0.1	0.15	0.31	0.15	0.51	1.98	1.52
Limited power ratio %	38.89	30.21	20.95	14.18	2.77	1.58	2.80	7.62	2.37	6.62	31.73	20.46
Power utilization hours	75	159	186	255	154	142	116	86	135	156	132	156

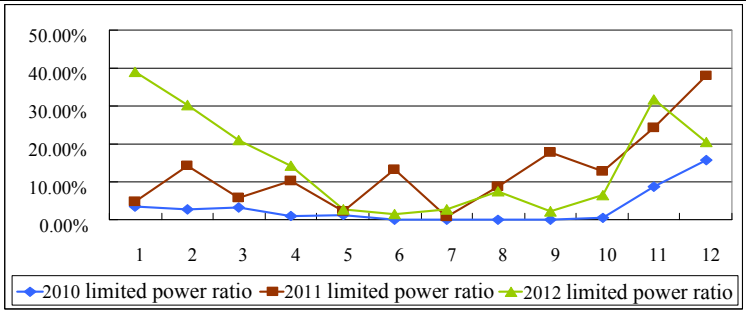

Figure 3 The past three years limited power ratio

According to wind power data analysis of nearly three years, spring and autumn (Mar-May, Oct-Nov) are the windy months, followed by winter (Dec- Feb the following year), summer (Jun-Sept) is minimal. Shortage acceptance of wind power capacity mainly from November to April the following year, 989 million kWh of wind power abandoned, account for 87.5% of total abandon wind power. Monthly wind power limited power ratio more than 10%. Which in addition to April, the rest are heating period, wind power generation power rationing more than 20%. Windy months centralized heating period, resulting in Shortage acceptance of Liaoning grid wind power capacity.

Measures on the impact of Liaoning Power Grid wind energy integration

Strengthen wind power connection management, Improve the technical level of wind energy integration

For the status of wind power manufacturing level of technological uneven, the need to actively promote wind power testing. By grid-connected testing can urge manufacturers to improve their production technology level, so as to ensure that the wind farm grid-connected security. Currently, Liaoning Power Grid has developed a comprehensive wind power detection system, and established a wind energy integration management system with wind power detection as the core, which include wind energy pre-integration technical supervision, wind energy integration security management, wind energy integration testing and evaluation. Ensure the Liaoning Power Grid wind energy integration technology at a high level.

Plan the power structure scientifically and rationally, promote wind power development and its economic intensive use

Northeast power grid is currently facing structure is irrational, the rapid development of wind power, winter heating units' capacity is large and long-running and other problems, thus bring great pressure to power peaking and frequency regulation. In this situation, accelerate the development of the power grid to adjust and optimize the power structure of the Northeast, ensure the safe, economic and stable development of the grid, has become a problem which power regulators, grid operators, power generation companies and research institutions in all aspects are extremely concerned and need to take urgent measures to solve.

Liaoning EPRI carried out a special study on the power structure influence acceptance of wind power capacity, study showed in the 2020 an increase in Liaoning different pumped storage power generation capacity, the amount of wind power abandoned fell to 0.03 percent from 2.07 percent, it can effectively improve the situation of abandoned wind power.

Table 3 Abandoned wind conditions in increased different pumped storage power generation at 2020

Increase Pumped Storage （Ten thousand kW）	0	30	50	60
Abandoned wind power （Ten thousand kW）	13151	4319	976	198
Days of abandoned wind power	80	68	16	10
Abandoned wind power/Wind power generation	2.07%	0.68%	0.15%	0.03%

Excavate thermal power peaking capacity and improve the ability of wind power consumption

Abandoned for wind power operating mode, through the analysis of peaking power technology research at home and abroad, According to the characteristics of the Northeast power grid, determine the technical route of this subject. Under the conditions of other peaking power is difficult for large-scale applications, carry out experimental research of various types of thermal power units operating characteristics at low load, as well as economic research. On the basis of the existing power peaking, proposed technology and policy to improve the ability of in depth peak load cycling of thermal power, As well as various types of units approved recommendations of load under deep cyclic operation. On this basis, use less oil combustion technology to improve the ability of in depth peak load cycling. Use unconventional peaking, develop technology of generating units under deep cyclic operation, and maximize the power grid acceptance of clean energy.

According to the characteristics of the northeast power grid, make full use of large-capacity thermal power characteristics, enhance the ability of in depth peak load cycling, use unconventional peaking, to solve a large number of wind power abandoned. On the ability of in depth peak load, Liaoning EPRI carried out research in the following areas：

1）Experimental study on the minimum stable combustion boiler load

2）Research on coal characteristics effect on peaking capacity of generating units

3）Study on various boiler operating characteristics under low load

4）Determine power generation by heat system technology research

5）Thermal automation adaptability research

6）Experimental research of various types of thermal power the ability of in depth peak load cycling

7）Deep cyclic economy research on generating units

The study results, involve Northeast and Mondon power grid all types of power units, and its range is wide, its technical factors is complicated. Northeast power peaking is extremely difficult at present, and it is often under curtailment operation, wasted a lot of wind power. Improve the thermal power peaking capacity, make full use of wind energy resources is essential, is technically feasible. Use thermal power deep cyclic technology, optimize energy configuration by grid, maximize the use of renewable energy, save Primary energy, and achieve energy conservation. According to calculation, after the realization of the deep cyclic operation, economic, environmental and social benefits are huge. Thermal power deep cyclic technology can greatly improve the power peaking capacity and it can be an effective solution to the problem of wind curtailment. The technology has great value for solving grid acceptance clean energy, energy conservation.

Conduct performance analysis of energy storage systems connected grid, promoting coordinated development of wind energy storage

2011, Liaoning Electric Power Co. declared a national 863 project "key technologies of energy storage system improve the ability of intermittent power connected to the grid research and development", aims to build large-capacity storage system to improve intermittent power connected to the grid method system. Focus on research and development of configure, manage, control and other aspects of technology about energy storage system, to improve the ability of intermittent power

supply connected to the grid, breakthrough Intermittent power scale development bottlenecks in the grid and source coordination.

May 2013, Liaoning EPRI completed energy storage power station performance test acceptance. The next step will be to carry out a series of thematic studies, including storage devices improve power quality and the capacity connected to grid, the role of energy storage device for smooth power output, feasibility of energy storage devices to run in the case of reactive output, the role of energy storage device for improving the wind farm ability of low voltage ride through, energy storage device as a black start power feasibility, energy storage device islanding capability. Use energy storage devices scientifically and rationally.

Develop coordination of a variety of new energy development, develop and utilize of wind power thermal storage technology, promote the application of wind power heating technology in the conditions suitable areas, replace the existing coal-fired boiler heating, local or remote consumptive rich wind power.

Conclusions

Liaoning power grid increasing proportion of wind power, triggering a series of wind power connected to grid issues. Need to strengthen management, implement grid-connected technology requirements strictly, plan the power structure scientifically and rationally, excavate thermal power peaking capacity, improve the capacity of wind power consumptive, while continuing to carry out a variety of new energy coordinated development, develop wind power thermal storage and other new technologies, multi-channel consumptive wind power.

References

[1] Guo Jian. Study on Impact of Grid-connected Wind Turbine & Wind Farm on Power System [J]. The New Energy Power Control Technology；2010 (1)：47~50.

[2] W. Z. Gandhare, G. R. Bhagwatikar. Power pollution due to connected wind electric converter. Proceedings of the 2000 IEEE, international conference on control applications, Anchorage, Alaska, USA, Sep. 25~27, 2000.

[3] Boulaxis N G, Papathanassiou S A, Papadopoulos M P. Wind turbine effect on the voltage profile of distribution networks [J]. Renewable Energy, 2002, 25(3):401~415.

[4] Akhmatov V. Analysis of dynamic behavior of electric power systems with large amount wind power [D]. Technical University of Denmark, 2003.

[5] Chi Yongning, Wang Weisheng, Liu Yanhua, etal. Impact of large scale wind farm integration on power system transient stability [J]. Automation of Electric Power Systems, 2006, 30(15):10-14.

[6] Sun T, Chen Z, Blaabjerg F. Voltage recovery of grid-connected turbines after a short-circuit [C]. Annual Conference of the IEEE Industrial Electronics Society, Virginia, USA, 2003.

Advanced Materials Research Vols. 986-987 (2014) pp 345-348

doi:10.4028/www.scientific.net/AMR.986-987.345

Lightning Impulse Voltage Correction of Power Transmission and Transformation Project Typical Gap

PENG Ying-jie[1, a]，DING Yu-jian[1,2,b]，Lü Fang-cheng[1]

[1]North China Electric Power University，Baoding，Hebei 071000，China

[2]China Electric Power Research Institute，Haidian District，Beijing 10092，China

[a,]pengyingjie2008@163.com, [b]dingyj@epri.sgcc.com.cn

Keywords: power transmission and transformation project, typical gap, lighting impulse, correction

Abstract: External insulation design of UHV power project is important. The lightning impulse (LI) voltage is one of the main factors that determine the air gap distance. Based on existing LI voltage results of power project typical gap, impact of gap structure and distance on LI discharge correction is analyzed. And from a theoretical aspect, existing LI discharge correction methods are summarized. Furthermore, by the use of common correction methods, LI voltage correction factors of rod - plane were calculated and analyzed. Results show no significant impact of gap type or gap distance on LI voltage correction is found out. Average atmospheric conditions are effective when atmospheric parameters method is used for LI voltage correction. DL/T 620, IEC 60060-1 and IEC 60071-2 can be used for LI voltage correction at areas with altitudes of 1000-5000m. While GB311.3-improvement method can be used for LI voltage correction at areas with altitudes blow 4000m.

Introduction

Dielectric strength of air is affected by humidity, temperature and pressure. Thus, during insulation design or test, it is necessary to correct air- gap discharge voltages. From the 1950s to now, scholars has carried out a number of studies about air gap discharge and has made a lot of achievements [1].

LI breakdown voltage is one of the main factors that determine air gap distance. A variety of methods which can be used for power project typical gap LI correction are recommended in current standards [2-5]. While different methods may lead to different results. In this paper, based on the existing LI voltage results of power project typical gap, impact of gap structure and distance on LI discharge correction is analyzed. And from a theoretical aspect, existing LI voltage correction methods are summarized. Furthermore, by use of these methods, LI voltage correction factors of rod - plane were calculated and analyzed.

Influencing Factors of LI Voltage Correction for Power Project Typical Gap

Effect of gap structure on LI voltage correction

To study whether gap structure affects LI voltage correction, gaps of soft bus to architecture column (which can be referred to as "soft bus to ground"), grading ring to architecture column (which can be referred to as "grading ring to ground") and rod-plane are selected as comparison objects.

Test sites of soft bus to ground and grading ring to ground are Wuhan outdoor test site (elevation 23m) and Dawu town, in Qinghai province (elevation 3727m) respectively in reference[6]. The soft bus is two split phase-changing soft bus. The distance of centerline of simulated cross arm to the ground 16m and the distance of soft bus to ground is 12m. By moving hanging point, the distance of bus to architecture column is adjusted and LI discharge test at different gap distances was carried out. Grading ring is lightning arrester grading ring and the distance of it to ground is 5.7m. By moving the insulation pillar air gap distance was adjusted and LI discharge test at different gap distances was carried out. For rod-plane, LI voltage are test results in Dawu town. Italian scholars Paris L and other people gives a relationship formula between LI voltage and rod-plane air gap distance at zero altitude areas [7], which is:

$$U = 537d \quad (1)$$

Where: U is LI discharge voltage , kV; d is the gap distance , m.

LI discharge voltage results of the three gap structure are shown in Figure 1. Soft bus to ground and grading ring to ground LI discharge voltages in Wuhan has been corrected to standard atmospheric conditions at zero altitude .

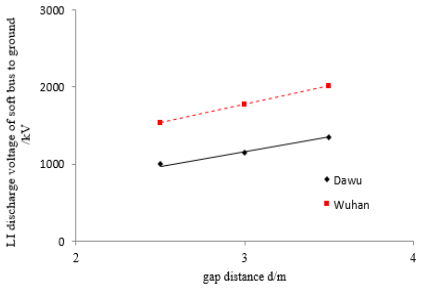

Fig.1(a) LI discharge characteristics of soft bus to ground

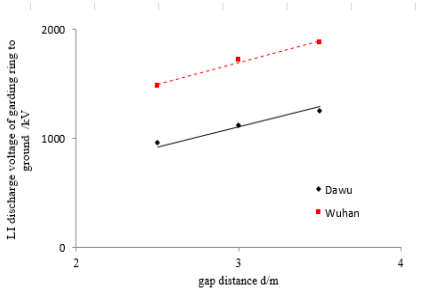

Fig.1(b) LI discharge characteristics of grading ring to ground

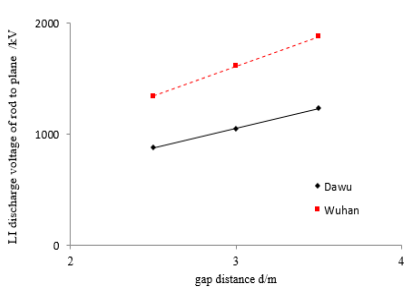

Fig.1(c) LI discharge characteristics of rod - plane

According to above results, LI voltage correction coefficients of different gap structures are obtained, as shown in Table 1.

Table 1 LI voltage correction coefficients of different gap structures

Air gap type	Soft bus to ground	Grading ring to ground	rod - plane
correction coefficients	1.52	1.53	1.53

As can be seen from Table 1, the LI voltage correction coefficients under three types of gaps are 1.53,1.52,1.53. No significant impact of gap type on LI voltage correction is found out.

Effect of gap distance on LI voltage correction

In order to study the effect of gap distance on LI voltage correction, LI voltage correction coefficient with gap distance of 2.5-3.5m and 4.0-8 .0 are compared. LI voltages with gap distance of 2.5-3.5m are rod - plane gap test results in the above chapter while those of 4.0 - 8.0 m are of test results in reference [8]. LI discharge characteristics curve of DC v-shaped string tower head in Tibet and Beijing are shown in Fig.2, where LI discharge voltages in Beijing has been corrected to standard atmospheric conditions at zero altitude.

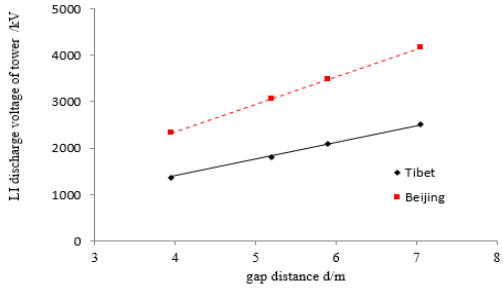

Fig.2 LI discharge characteristics curve of DC v-shaped string tower head

According to LI discharge characteristics curve at zero altitude and high altitude areas, LI discharge characteristics curves at areas with altitudes of 1000m, 2000m, 3000m, 4000m and 5000m can be obtained by linear interpolation, respectively, which is shown in Fig. 3 and Fig.4

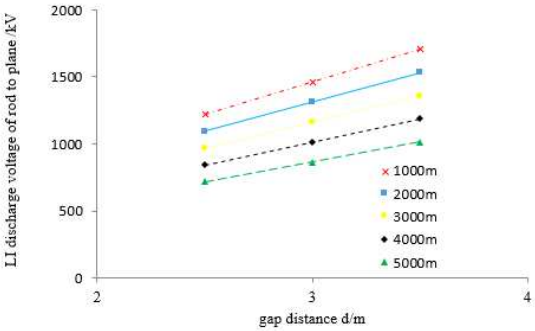

Fig.3 LI voltage of 2.5-3.5m gap distance at different areas

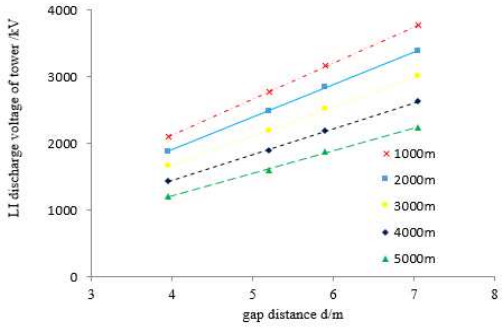

Fig.4 LI voltage of 4.0-8.0m gap distance at different areas

LI voltage correction coefficients of different gap distances are obtained, as shown in Table 2.

Table 2 LI voltage correction coefficients of different gap distances

Air gap / correction coefficients	2.5-3.5m	4.0-8.0m
1000m	1.10	1.11
2000m	1.23	1.24
3000m	1.38	1.39
4000m	1.59	1.60
5000m	1.86	1.89

As can be seen from Table 2, the maximum error of LI voltage correction coefficients of gap distance of 2.5-3.5m and 4.0-8.0m at same altitude is 1.6%. No significant impact of gap type on LI voltage correction is found out.

Analysis of Commonly Used LI Voltage Correction Methods

There are several methods can be referred to correcting LI voltage. According to theory basis, they are classified by atmospheric parameters method and altitude method. Atmospheric parameters method requires the meteorological conditions of project site, which is relatively accurate, but it is often difficult to acquire weather data. As for altitude method, it only need altitude values. This method is simple and practical, but relatively coarse. Because even in the same altitudes, meteorological conditions may still be different.

Atmospheric parameters correction method

In DL/T 620-1997[4], outer insulation discharge voltage correction method is given. The discharge voltage is corrected by the formula (1):

$$K_a = \delta^n / H^n \tag{1}$$

Where: δ is the relative air dentist; H is air humidity correction factor; n is corrected index. For LI voltage, H is decided by $1+0.009(11-h)$. h is absolute air humidity, g/m^3.For LI, n = 1.The Standard also recommend relative air dentist and absolute air humidity values under different altitudes.

In IEC 60060-1 (2010) [3], discharge voltage is corrected by the following formula:

$$U = U_0 \cdot K_t \tag{3}$$

Where: U_0 is the discharge voltage under standard atmospheric conditions, kV; U is the actual discharge voltage, kV; K_t is atmospheric correction factor, which is product of air density correction factor K_1 and air humidity correction factor K_2. K_1 depends on the relative air density δ. That is $K_1 = \delta^m$. As for K_2, it is $K_2 = K^w$.

Where K depends on the type of the test voltage. For LI discharge, formula (4) is used:

$$K = 1 + 0.010(h/\delta - 11) \tag{4}$$

m and W are corrected index , which are decided by parameter g.

Altitude correction method

In IEC 60071-2 (1996), atmospheric correction factor K_a should be calculated as follows [3]:

$$K_a = e^{m(H/8150)} \tag{5}$$

Where: H is the height over sea level, m; m is correction factor. For LI voltage, m = 1.

Based on GB311.1 (1997), Wuhan High Voltage Research Institute proposed a method [5]. Altitude correction factor K_a should be calculated with the following formula (6):

$$K_a = 1/(1.0 - mH/10000) \tag{6}$$

H is the height over sea level, m For LI voltage, m = 1.

Comparison of current LI voltage correction methods

According to test data of rod-plane, LI voltage correction methods, DL/T 620, IEC 60060-1, IEC 60071-2 and GB 311.1-improvement are compared. Because atmospheric parameters are not given at

4000m and 5000m areas in DL/T 620, they are obtained by fitting atmospheric data at areas with altitude from 500m to 3500m. As for IEC 60060-1, atmospheric conditions are obtained by the same approach of DL/T 620. Correction coefficients are shown in Table 3.

Table 3 LI voltage correction coefficients under different methods

Correciton mehtods		Atmospheric paramater mcorrection		Altitude correction		Test result
		DL/T 620	IEC 60060-1	IEC 60071-2	GB311.1-improvement	
1000m	Correction coefficients	1.13	1.13	1.13	1.11	1.10
	Correction errors	2.73%	2.73%	2.73%	0.91%	--
2000m	Correction coefficients	1.28	1.27	1.28	1.25	1.23
	Correction errors	4.07%	3.25%	4.07%	1.63%	--
3000m	Correction coefficients	1.43	1.43	1.44	1.43	1.38
	Correction errors	3.62%	3.62%	4.35%	3.62%	--
4000m	Correction coefficients	1.62	1.63	1.63	1.67	1.59
	Correction errors	1.89%	2.52%	2.52%	5.03%	--
5000m	Correction coefficients	1.86	1.91	1.85	2.00	1.86
	Correction errors	0.00%	2.69%	-0.54%	7.53%	--

At areas with altitudes of from 1000 to 5000m, absolute values of correction error obtained by DL/T 620, IEC 60060-1 and IEC 60071-2 are less than 5%, which means they apply to voltage correction in high altitude areas. Absolute values of correction errors obtained by GB311.1 -improvement are less than 5% at areas with altitudes below 4000m while are more than 5% at areas with altitudes of 4000m or above. When taking average atmospheric conditions at a certain area, atmospheric parameters method give basically the same correction coefficients with experimental results. With comprehensive comparison of the above correction methods for simplicity and accuracy of calculation, method IEC 60071-2 is recommended for engineering design of LI voltage correction.

Summary

By correcting LI voltages of air gaps for soft bus to ground, grading ring to ground, and DC v-shaped tower head and rod-plane at different areas, no significant impact of gap type or gap distance on LI voltage correction is found out. Average atmospheric conditions are effective when atmospheric parameters method is used for LI voltage correction. DL/T 620, IEC 60060-1 and IEC 60071-2 can be used for LI voltage correction at areas with altitudes of 1000-5000m. While GB311.3-improvement method can be used for LI voltage correction at areas with altitudes blow 4000m.

Acknowledge

Project Supported by National Natural Science Foundation of China (51307060); Colleges and Universities in Hebei Province Science and Technology Research Project (Z2013086); Fundamental Research Funds for the Central Universities (2014MS84).

References

[1] Sun Zhaoying，Li Qingfeng，Su Zhiyi，et al．Electric Power，2006，39（10）：47-51．
[2] IEC 60071-2．Third edition，1996-12．
[3] IEC 60060-1. Edition 2.0，2010-09．
[4] DL/T 620-1997. Beijing: China Standardization Press，1998．
[5] Wan Qifa，Chen Yong，Gu Lili，et al．Reliminary Discussion on Altitude Correction Factors for External Insulation in High Altitude[J]．High Voltage Engineering，2003，29(5)：6-6．
[6] Cao Jing．Research on Air-gap Discharge Characteristics and Altitude Correction of High Altitude Converter Station[D]．Wuhan University，2013．
[7] Paris L，Cortina R．Switching and Lightning Impulse Discharge Characteristics of Large Air Gaps and Long Insulator Strings [J]．IEEE Transactions on Power Apparatus and Systems，1968，87(4)：947-957．
[8] Ding Yujian et al．Proceedings of the CSEE，2011，31（34）：156-164．

Advanced Materials Research Vols. 986-987 (2014) pp 349-353

doi:10.4028/www.scientific.net/AMR.986-987.349

Line Vulnerability Assessment on Power Grid Based on Combination Weighing Method

ZENG Xin[1, a], CHEN Yanzhen[2,b] , YANG Qi[3,c],MIAO Miao[2,d] , REN Jianwen[1, e], LI Xuanxuan[2,f]

[1] North China Electric Power University, Baoding 071003, Hebei Province, China

[2] Electric Power Technology Economic Research Institute, Qinghai Electric Power Company, Xining, 810008, China

[3] China Electric Power Research Institute, Haidian District, Beijing ,100192, China
[a]923258144@qq.com, [b]chenyzh@126.com, [c] yangqi@epri.sgcc.com.cn,
[d]mmiao2019@qh.sgcc.com.cn, [e]rjw219@126.com, [f]lxxun2623@qh.sgcc.com.cn

Keywords: entropy weight expert weight cascading failures vulnerability assessment

Abstract. To study the mechanism of cascading failures in a power grid and find out the key vulnerable lines propagating cascading failures, entropy theory and analysis hierarchy process were applied in entropy-weighted fuzzy comprehensive evaluation model, and information of objective data and the subjective opinion of experts were combined in the model to implement effective evaluation and sorting of line vulnerability. The article builds a index system that contains voltage deviation, power flow coefficient and electric betweenness in considering the network structure and real-time running state of the system, and then the lines vulnerability assessment method is proposed .This method can be used to help power grid designers and operators spot the lines prone to black-out. Numerical example results show that the proposed indicators can overcome the deficiency of existing indicators not taking the state of the grid structure and operation into account which proves the assessment method is feasible.

Introduction

In recent years, several large-scale power system blackouts occured domestic and international[1]. Research shows that these blackouts are mostly caused by the initial failure of a chain of accidents[2-3]. Very few of which have long-range connections line play a role in fueling[4-5], if we can identify these key lines and take appropriate measures to protect the control is bound to reduce the probability of cascading failures and thus reduce the likelihood of accidents blackout. Therefore, how to judge these fragile lines, has important theoretical and applied research value.

To the problem of comprehensive evaluation is very important to determine the weighing, values of weights change will directly affect the scientific rationality of the comprehensive evaluation results. some scholars of vulnerability assessment is discussed for transmission lines [5-10], but most of the literature didn't explore the methods of determine the weighing values, only using single subjectively or objectively, such as the literature [6] when determining weights depend entirely on the entropy weight method, the multi-target the relative importance of the order of the target can't reflect, literature [7] when determining weights depend entirely on expert experience, subjectivity is too strong. the existing analysis method of Line vulnerability assessment, many from the angle of the grid structure with the knowledge of the complex network theory to analyze the line vulnerability [5,8-10], not considering the actual power flow operation, evaluation results are likely to appear unreasonable.

1 theory basis of combination weighting evaluation

1.1 entropy weight method

Entropy weight method is a mathematical method to calculate the comprehensive index. According to the size of information of each index is passed to the decision makers to determine its weight, the greater the entropy weight, the smaller the variance of the information provided. With

index can be used to represent different objects to distinguish between degrees of entropy method.To calculate the objective weight steps are as follows:

(1) Develop initial evaluation index matrix；

(2) Positive and dimensionless processing of data.This is a process of various indexes can be converted to relatively unified dimension, divided into the index data type as good cost index and the bigger the better efficiency index. considering indexes for efficiency index was proposed in this paper, formula for its standardization;

(3) The calculation of entropy and entropy weight.

1.2 Analytic Hierarchy Process

Indicators of entropy reflects the objective data of lines, namely the difference degree between the grid lines, do not reflect the index to the importance of the practical problems, expert need to make decisions according to the actual situation own preferences. This article uses the nine expert decision scale method to decision.Steps are as follows:

(1) establish a class hierarchy,put the evaluation target hierarchical.

(2) building judgment matrix, after the construction of the target hierarchy, the subordinate relations between the level indicator is determined, on the same level indicators, two comparison and the comparison results in nine scaling expression [11] .

(3) verify consistency to ensure data reliability, calculated by the judgment matrix elements are being compared relative weight, calculate the combination weight of each element.

1.3 Line vulnerability evaluation index combined weights

Considering the entropy weight method can't reflect the multi-index of target sorting the relative important degree, and the analytic hierarchy process lack of objective basis, which requires the combination of subjective and objective weight, get a set of objective and subjective comprehensive weights, to overcome the disadvantages of the above two methods.

2 Line vulnerability evaluation index

To the problem of the transmission line vulnerability, if the probability of line fault sorting as the total target, influence factors as the criterion, establish the hierarchical structure of the model as shown in figure 1:

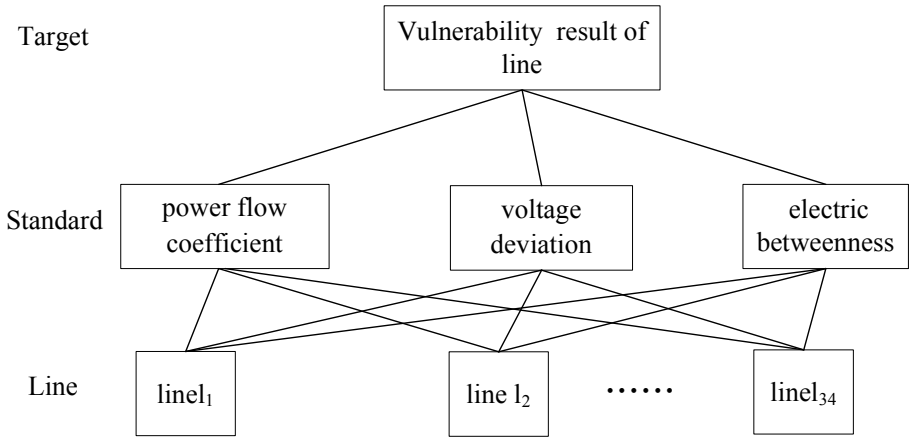

Fig.1 Architecture of AHP

This article selects three kinds of vulnerability assessment index build index set, the index definition is given below:

(1)the electric betweenness of line(m,n) as follow：

$$B_{\mathrm{e}}(m,n)=\sum_{\substack{i \\ \mathrm{j}}}^{\substack{G \\ \mathrm{L}}}\sqrt{\mathrm{W_i}W_j}\left|I^{ij}(m,n)\right| \tag{1}$$

(2)the voltage deviation of node as follow:

$$D_{\mathrm{u}} = \sum_{s \quad S\ 1)} \left| U_{\mathrm{s}} - U_{so} \right| \tag{2}$$

(3) the power flow coefficient of line as follow:

$$C_{\mathrm{i}} = \left| \frac{P_{io}}{S_L} \right| \sum_{j=1}^{L-1} \left| \frac{\Delta F_j}{F_{jo}} \right| \tag{3}$$

3 Power grid vulnerable line evaluation methods

process of vulnerability line identification consider the following factors:

(1) the analytic hierarchy process (AHP) and entropy weight method to the calculation of equal status to participate in the comprehensive weight

(2) a is 0.02, which only consider the voltage offset value greater than or equal to 0.02 per unit. According to section 2 the proposed index by using the method of section 1 figure 2 processes to calculate

4 simulated analysis

This section uses the New England 39 node system as a test system, New England 39 node system [5]have a total of 10 generator, 19 load and 34 lines (regardless of the transformer branch), system wiring diagram is shown in figure 3. PSD – BPA used as simulation calculation tool which developed by The China electric power research institute.

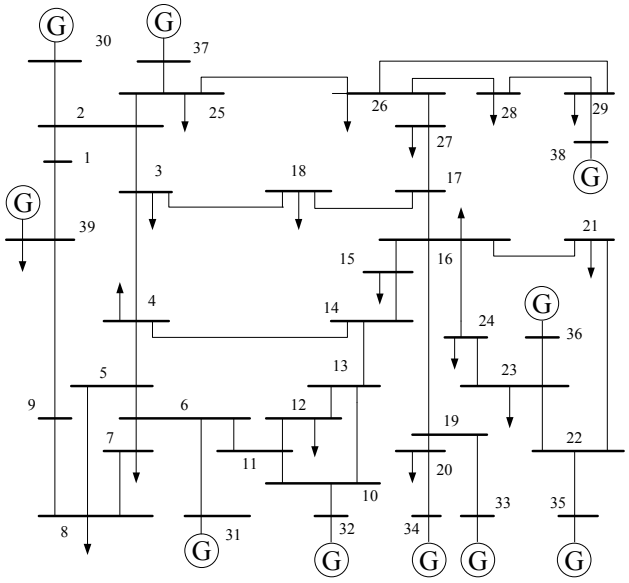

Fig.3 Connection diagram of IEEE 39-bus system

First, after every line fault the vulnerability index are calculated separately, the entropy weight line vulnerability index is obtained, as shown in table 1:

Tab.1 Entropy weights of the indices

indicator type	Power flow coefficient	voltage deviation	electric betweenness
Entropy	0.8059	0.5713	0.9140
Entropy weights	0.2738	0.6048	0.1214

Can be seen from table 1, the relationship between entropy and entropy weight is inversely, the greater the entropy, the entropy weight is smaller. Entropy weight of voltage offset is the largest which shows that important degree is high of the index in the sense of competition compare to power flow coefficient and electrical betweenness.

To build judgment matrix based on nine scaling criterion layer, as shown in table 2:

Tab.2 Judgment matrix

judgment matrix	Power flow coefficient	voltage deviation	electric betweenness
Power flow coefficient	1	2	3
voltage deviation	1/2	1	2
electric betweenness	1/3	1/2	1

Validated by the consistency index, the weight of Power flow coefficient voltage offset and electrical betweenness are: 0.5396, 0.297, 0.1634.

According to network structure to calculate the electrical betweenness, judgment matrix is given by electrical betweenness according to ways provided by table 3, thereby calculating 34 lines index weight of electrical betweenness.

Tab. 3 Expert scoring table of electric betweenness

electric betweenness	0.5-1	1-1.5	1.5-2.0	2.0-2.5	2.5-3.0
Expert score	1	2	3	4	5

Regardless of system with intermittent operation of the power grid, disconnect does not exist any line overload in test system, isolated net running system appear when disconnect the line 16-19, so the line 16-19 is the most vulnerable line The rest of the line comprehensive vulnerability index from big to small order as shown in table 4:

Tab.4 Vulnerability identification result of line

line	Power flow coefficient	rank	voltage deviation	rank	electric betweenness	rank	combination weighting
22-21	3.1	3	14	1	1.135	24	0.183
16-15	1.9	5	8	2	2.08	2	0.114
26-27	1.655	8	5.9	3	1.805	7	0.087
2-3	3.067	4	3.1	6	1.69	9	0.081
10-11	4.43	1	—	/	1.175	22	0.067
25-2	1.727	7	—	/	1.93	5	0.054
10-13	3.3	2	—	/	1.21	21	0.051
29-28	0.229	17	4.5	4	0.75	34	0.045
24-16	0.015	30	4.2	5	1.16	23	0.044
6-7	0.77	14	2.6	7	0.94	26	0.038

Summarize the foregoing analysis and calculation results:

As you can see sorting of lines on fragility , relative to the electrical betweenness, Line vulnerability in maintaining the structural vulnerability identification, take the operating conditions including voltage offset and power flow coefficient into consideration, to make evaluation results more reliable Comprehensive, so as to improve the recognition effect and accuracy, for example, electrical betweenness of Line (22-21) is not high, but through the lines of the deviation of the tidal current and voltage amplification effectively, making it a fragile degrees higher line.

Summary

two aspects of power system vulnerability is considered In this paper: the structure state of vulnerability and running state vulnerability, assessment of structural vulnerability uses the electrical betweenness to judge vulnerability, electrical betweenness is the inherent nature of grid structure to describe the vulnerability degree of power grid, the operation of the power system uses the combination of local and global indicators evaluated the grid vulnerability on the other hand, consideration of the above factors, vulnerability assessment method is proposed on the basis of comprehensive vulnerability index. From the structure vulnerability and the open circuit state balance voltage deviation to evaluate the influence of grid function in the process takes the intermittent power grid-connected operation impact on line vulnerability into consideration. The method can effectively

consider the various factors influencing the system vulnerability, and according to the system operating conditions, adjust the weights of affecting factors.

References

[1] YinYong-hua,Guo Jian-bo,Zhao Jian-jun,et al.Preliminary analysis of large scale blackout in interconnected North American power grid on August 14 and lessons to be drawn[J].Power System Technology,2003,27(10) :8-11.

[2] Tang Baosheng.Blackout in south of London and its lessons[J].Power System Technology,2003,27(11) :1-5(in Chinese) .

[3] Hu Xuehao.Rethinking and enlightenment of large scope blackout in interconnected North American power grid[J] .Power System Technology,2003,27(9) :2-6(in Chinese) .

[4] Ding Ming，Han Pingping.Small-world topological model based vulnerability assessment to large-scale power grid[J] .Proceedings ofthe CSEE,2005,25(supplements) :118-122(in Chinese) .

[5] Cao Yijia,Chen Xiaogang,Sun Ke.Identification of vulnerable lines in power grid based on complex network theory[J] .Electric Power Automation Equipment,2006,26(12) :1-5，31(in Chinese) .

[6] FENG Jing,XIAO Xian-yong,CUI Zhen,et al.Synthetic Risk Assessment of Catastrophic Failures in Power System Based on Entropy Weight Method[J].East China electric power,2012，40(7) :1144-1147.

[7] Zhu Jihong,XuGuoyu.An Application of Analytic hierarchy Process to Automatic Contingency Selection and Ranking[J] .Journal of Chongqing University,1992,15(3)：31-36.

[8] Ni Xiangping,Mei Shengwei,Zhang Xuemin.Transmission lines'vulnerability assessment based on complex network theory[J].Automation of Electric Power Systems,2008,32(4)： 1-5(inChinese) .

[9] Meng Xiangying,Sun jing.Research on the Searching Method of Critical Vulnerable Lines for Cascading Failures Analysis [J] .Modern Electric Power. 2013,30(5) :41-45.

[10] LiuYao-nian,Zhu Xi,Kang Ke-fei,et al.Identification of vulnerable lines in power grid based on the weighted reactance betweenness index[J].Power System Protection and Control， 2011,39(23) :89-93.

[11] Fang Jun,Zhang Yongping,Wei Ping,et al.A new market-based congestion management method-part1:flow-based tradable transmission rights[J].Power System Technology,2001,25(7) :4-8(in Chinese) .

Advanced Materials Research Vols. 986-987 (2014) pp 354-357

doi:10.4028/www.scientific.net/AMR.986-987.354

Medium and Long Term Load Forecasting of Power System Based on Interval Taylor Model Arithmetic

ZHENG Zhijie[1], WANG Shouxiang[2], WANG Yan[1], ZHAO Long[1], Zhang Jie[1]

[1.] Economic & Technology Research Institute, State Grid Shandong Electric Power Company, Shandong Jinan 250021, China

[2.] Key Laboratory of Smart Grid of Ministry of Education, Tianjin University, Tianjin 300072, China

Keywords mid-long term load forecasting; interval arithmetic; Taylor model; Monte Carlo method; reliable computing

Abstract. For long time span, the impact of many factors, uncertainties and other characteristics of mid-long term load forecasting, as well as the over-estimation of interval arithmetic, a mid-long term load forecasting method based on interval Taylor model algorithm was presented. In order to avoid misjudgment of the relationship between variables, reducing over-estimation problem, a global variable named Taylor model ID was presented to identify the independent variables and the dependent variable. The same independent variables construct the interval Taylor model only once. Use Maclaurin formula to derive the interval Taylor model of correlation function formula, and then get a quadratic exponential smoothing method based on interval the Taylor model. The proposed method has been tested on a provincial calculation. The results demonstrated the effectiveness and practical value of the approach by comparing with the results of Monte Carlo simulation and interval method.

Introduction

Power system mid-long term load changes are subject to system operating characteristics, natural conditions, social impact, and many other factors. How to consider these uncertainties and determine their effect on the original data is very critical issue. Over the past few decades, a variety of mathematical methods such as expert systems theory, genetic programming, neural networks and the system dynamics are introduced to load forecasting field[1-6].

For the above analysis, this paper introduces theinterval Taylor model algorithm to deal with the uncertainty in mid-long term load forecasting of power system, uses the Taylor model to describe uncertainty ofparameters, proposes and implements mid-long term load forecastingbased on interval Taylor model algorithm. Finally, examples are given to verify and demonstrate the results.

Interval Taylor model arithmetic

Interval Taylor model arithmetic is a kind of “Reliable Computing” arithmetic. “Reliable Computing” is first designed to avoid errors of floating point algorithm, improve the reliability of calculation results and effectively avoid the uncertainty of calculation caused by uncertainty of the parameters[7-13].

Interval Taylor model algorithm’s principle is using polynomial to represent function approximately, quantitatively estimating the size of the error.

Although the interval Taylor model algorithm is the development of the interval algorithm, , the basic data types are no longer interval number, but the interval Taylor model in interval Taylor model algorithm. An interval Taylor model $_{\alpha,}$ can be represented by the sum of a Taylor polynomial $_{\alpha,}$ and a remainder term $I_{\alpha,f}$ on bounded interval:

$$_{\alpha,} = _{\alpha,} + I_{\alpha,} \tag{1}$$

In the formula， α is the parameter of the Taylor polynomial, including order n, reference point $\vec{x}_0$,domain$[\vec{a},\vec{b}]$. That is：

$$\alpha = (n, \vec{x}_0, [\vec{a},\vec{b}]) \tag{2}$$

$P_{a,f}$ complies with polynomial algorithm, while $I_{\alpha,f}$ and polynomial parts whose order is higher than ncomply with the algorithm of interval arithmetic.

Interval algorithm can't distinguish independent variables from dependent variables. When the same variable appears many times, the interval algorithm regards them as different variables. Interval Taylor model algorithm can reduce over-estimation problem of relative variables, but has some difficulty to distinguish independent variables from dependent variables. If only distinguish by parameter α, it may cause misjudgment.

Therefore, this paper distinguishes the independent variables from dependent variables by setting a global variable—Taylor model ID. The same independent interval variables construct Taylor model only once. New independent variables mainly come from two aspects:

1) The introduction of the new independent interval variables.

2) New interval variables are generated by operation of two or more independent interval variables.

Example of interval Taylor model computing is shown in Table1:

Tab. 1 Example of interval Taylor model computing

item	ID	interval value	Interval Taylor model values	Taylor polynomial coefficients				Remainder Term
				power0	power1	power2	power3	
X	1	[2,4]	[2,4]	3	1	0	0	[0,0]
1/X	1	[0.25,0.5]	[0.25,0.5]	0.3333	-0.1111	0.03704	-0.01235	[0,0.03125]
X+(1/X)	1	[2.25,4.5]	[2.46914,4.30285]	3.3333	0.8889	0.03704	-0.01235	[0,0.03125]
Y	2	[1,7]	[1,7]	4	1	0	0	[0,0]
X+Y	3	[3,11]	[3,11]	7	1	0	0	[0,0]

Quadratic exponential smoothing method based on the interval Taylor model.

2.1Quadratic exponential smoothing method based on the interval Taylor model.

In order to reduce over-estimation problem of interval Taylor model, this paper adopts the deformation formula of quadratic exponential smoothing methoddemonstrated in literature[14].

Single exponential smoothingdeformation formula:

$$S_t^{(1)} = \alpha \sum_{i=0}^{t-1} (1-\alpha)^i x_{t-i} + (1-\alpha)^t S_0^{(1)} \tag{3}$$

Linear intercept deformationpredicting formula:

$$\begin{aligned} \hat{a}_t = & \sum_{i=1}^{t} (2 - i\alpha)(1-\alpha)^{i-1} \alpha x_{t+1-i} \\ & + (2 - t\alpha)(1-\alpha)^t S_0^{(1)} - (1-\alpha)^t S_0^{(2)} \end{aligned} \tag{4}$$

Linear slope deformation predicting formula:

$$\begin{aligned} \hat{b}_t = & \sum_{i=1}^{t} \alpha^2 (1-\alpha)^{(t-i-1)} [1 - (t-i+1)\alpha] x_i \\ & + \alpha(1-t\alpha)(1-\alpha)^{t-1} S_0^{(1)} - \alpha(1-\alpha)^{t-1} S_0^{(2)} \end{aligned} \tag{5}$$

In formula (3)—(5)，interval Taylor model operatorsinclude elementary arithmetic and power function. Arithmetic formula of Taylor model can be found in Literature [11], power function formula derivation can be seen in formula (6)—(7).

Assuming the interval Taylor model of function f is $T_{\alpha,f} = (P_{\alpha,f}, I_{\alpha,f})$.The constant part of function f that depends on $\vec{x}_0$ is recorded as $c_{\alpha,f}$. It is equal to the constant part of the Taylor polynomial $P_{\alpha,f}$, the non-constant part of its rest is recorded as $\bar{f}$.

That is:

$$f(\vec{x}) = c_{\alpha,f} + \bar{f}(\vec{x}) \tag{6}$$

Using Maclaurin formula:

$$\begin{aligned}\left(f(\vec{x})\right)^m &= \left(c_{\alpha,f}+\overline{f}(\vec{x})\right)^m \\ &= c_{\alpha,f}^m\left(1+\frac{\overline{f}(\vec{x})}{c_{\alpha,f}}\right)^m \\ &= c_{\alpha,f}^m\cdot 1+\left\{\frac{m\,\overline{f}(\vec{x})}{c_{\alpha,f}}+\frac{m(m-1)\,\left(\overline{f}(\vec{x})\right)^2}{2!\,c_{\alpha,f}^2}\right. \\ &\qquad \left.+\cdots+\frac{m!\,\left(\overline{f}(\vec{x})\right)^k}{(m-k)!\,k!\,c_{\alpha,f}^k}\right\} \\ &\quad +c_{\alpha,f}^m\cdot\frac{m!\,\left(\overline{f}(\vec{x})\right)^{k+1}}{(m-k-1)!\,(k+1)!\,c_{\alpha,f}^{k+1}} \\ &\quad \cdot\left(1+\theta\cdot\overline{f}(\vec{x})/c_{\alpha,f}\right)^{m-k-1}\end{aligned} \tag{7}$$

Example and Analysis

This paper based on the maximum load data of a province between 1991 and 2009 forecasts the maximum load to 2012.

Assume that the actual value of power load is uncertain, its value is interval number[x_t×0.99, x_t×1.01].

Respectively use Monte Carlo method (simulation times are 500000, random numbers are uniformly distributed within the agv), interval algorithm, and the interval Taylor modelalgorithm to predict power load values of a province covering 1991 ~ 2012.The results are shown in Table 2.

Tab. 2 The load forecasting from 1991 to 2012

year	MC[$\hat{x}_t$]	IA[$\hat{x}_t$]	TM[$\hat{x}_t$]
1991	[5988,6108]	[5988,6108]	[5988,6108]
1992	[6814,7162]	[6685,7296]	[6789,7187]
1993	[7474,7835]	[7122,8197]	[7240,8075]
1994	[8509,8910]	[8088,9333]	[8252,9169]
1995	[8654,9081]	[8205,9543]	[8385,9365]
1996	[9039,9484]	[8553,9978]	[8745,9788]
1997	[10493,10995]	[9963,11525]	[10174,11316]
1998	[11385,11921]	[10808,12507]	[11037,12281]
1999	[11582,12151]	[10970,12780]	[11214,12539]
2000	[13377,14011]	[12700,14693]	[12970,14426]
2001	[13295,13965]	[12590,14688]	[12872,14410]
2002	[14311,15011]	[13545,15786]	[13848,15487]
2003	[17840,18683]	[16995,19527]	[17339,19187]
2004	[18683,19570]	[17760,20523]	[18132,20154]
2005	[21595,22585]	[20537,23653]	[20960,23234]
2006	[25751,26907]	[24544,28122]	[25029,27640]
2007	[27742,29026]	[26404,30407]	[26944,29871]
2008	[31354,32800]	[29824,34343]	[30437,33736]
2009	[30242,31808]	[28650,33442]	[29299,32807]
2010	[39891,41754]	[38056,43610]	[38814,42859]
2011	[44405,47427]	[41534,50315]	[42449,49434]
2012	[48919,53099]	[45012,57020]	[46083,56009]

Note：MC[$\hat{x}_t$]is load prediction using Monte Carlo method, IA[$\hat{x}_t$]is load prediction using interval arithmetic, TM[$\hat{x}_t$]is load prediction using interval Taylor model arithmetic.

Result in Table 2：the load forecasting results using interval Taylor model algorithmcontain the resultsusing Monte Carlo method and are obviously less than the width of results gained from interval algorithm. It shows the effectiveness of the interval Taylormodel algorithm.

Conclusions

The power load forecast especially mid-long term load forecastisaffected by many factors that are uncertain and difficult to be measured accurately by numerical methods.

This paper introduces interval Taylor model algorithm to deal with the uncertainty of data in mid-long term load forecast.A global variable named Taylor model ID is presented to identify the independent variables and the dependent variable, avoiding misjudgment of the relationship between variables. It derives the interval Taylor model of correlation function formula, and then gets a quadratic exponential smoothing method based on interval the Taylor model.

The results demonstrated the effectiveness and practical value of the approach by comparing with the results of Monte Carlo simulation and interval method.

References

[1] KANG Chongqing，XIA Qing，ZHANG Boming．Review of power system load forecasting and its development． Automation of Electric Power Systems， 2004， 28(11)：1-11．

[2] MAO Lifan，YAO Jiangang，JIN Yongshun et al． Theoretical Study of Combination Model for Medium and Long Term Load Forecasting．Proceedings of the CSEE，2010，30(16)：53-59．

[3] JU Ping，LI Jingxia，LU Xiaotao．Genetic programming for power system load forecasting． Automation of Electric Power Systems， 2000， 24(11)：355-38．

[4] JIANG Ping，JU Ping．Medium-term electric load forecasting using artificial neural network． Automation of Electric Power Systems，1995，19(6)： 11-17．

[5] WEI Lingyun，WU Jie，LIU Yongqiang．Long-term electric load forecasting based on system dynamics．Automation of Electric Power Systems，2000，24(16)： 44-47．

[6] QIAN Weihua，YAO Jiangang，LONG Libo et al．Short-term correlation and annual growth based mid-long term load forecasting．Automation of Electric Power Systems，2007，31(11)：59-64．

[7] Berz M，Hoffstatter G．Computation and application of taylor polynomials with interval remainder bounds[J]． Reliable Computing， 1998，4(1)：83-97．

[8] Berz M，Hoffstätter G．Computation and application of taylor polynomials with interval remainder bounds[J]． Reliable Computing， 1998，4(1)：83-97．

[9] Arnold N．Taylor forms - use and limits[J]．Reliable Computing, 2003, 9(1)：43-79．

[10] Makino K，Berz M．Taylor models and other validated functional inclusion methods[J]．International Journal of Pure and Applied Mathematics，2003，4(4)：379-456．

[11] Revol N，Makino K，Berz M．Taylor models and floating-point arithmetic: proof that arithmetic operations are validated in COSY[J]．J．Log．Algebr．Program，2005，64(1)：135-154．

[12] Makino K，Berz M，Kim Y．Range Bounding with Taylor Models – Some Case Studies[J]．WSEAS Trans．on Mathematics，2004，3： 137-145．

[13] WANG Shouxiang，ZHENG Zhijie，WANG Chengshan． Power System Simulation under uncertainty based on interval taylor model arithmetic．Proceedings of the CSEE，2008，28(7)：46-50．

[14] ZHENG Zhijie，LI Lei，ZHAO Lanming．Medium and long term load forecasting considering data uncertainty[J]．Power System Protection and Control，2011，39(7)：123-126,132．

Advanced Materials Research Vols. 986-987 (2014) pp 358-362

doi:10.4028/www.scientific.net/AMR.986-987.358

Method Based on Multi-attribute Decision Making of Receiving-end Power Grid DC Location Selection

Xiao-ming Liu[1], Xin-sheng Niu[1], Yuan Wang[2], Yi-qun Wang[1] ,
Kui-hua Wu[1], Feng Lan[1], Li-sheng Li[1], Tian-bao Zhang[1]

[1]Economic and Technology Research Institute, State Grid Shandong Electric Power Corporation Jinan 250001

[2]State Grid Shandong Electric Power Company Jinan 250001

Keywords: Receiving-end power grid; DC Location selection; Multi-attribute decision making

Abstract. For Receiving-end AC system, DC location selection depends on its role in supporting the DC system and economy. This paper proposes a method based on multi-attribute decision making of receiving-end power grid DC location selection. First, the balance of power DC location selected by region; then select the optimal placement through multi-attribute decision making; finally checked by calculating the feasibility of the selected placement. Zha Lute DC Shandong receiving-end power grid placement choice proved the effectiveness of the proposed method.

Introduction

HVDC transmission has a transmission capacity, low loss, effectively limit the short circuit current, applicable to inter-regional networking features, grid development in China has been more widely used [1-4]. For the receiving-end power grid is concerned, DC location choice for the protection grid security and stability, reduce network losses has very important significance (here's DC location selection refers 500kV HVDC converter station AC bus of choice, the same below).

DC Location selection needs to consider the stability and economy of the grid , a typical Multi-attribute decision making problem. Currently, most of the literature study of AC and DC systems are selected after DC Location interaction , DC Location selection aspects of research literature is not much. [5] proposed a balance of stability and economy of DC Location selection method , consider Effective Short Circuit Ratio (ESCR), the static voltage stability index and active power loss (ΔP) three factors by linear weighting method to select optimal placement . DC Location selection methods described in the literature the following three questions: First, for a DC transmission projects, there is an inherent link between the ESCR and static voltage stability indicators are reflecting the receiving-end power grid voltage DC project support capacity ; Second, the DC Location selection problems in network planning is often balancing selection in the largest regional power shortfall of electricity as DC Location by region, mainly for local load power , and then choose the right node by comparing the technical and economic as DC Location; Third Location not selected to determine its feasibility by the trend, shorts and checked.

In this paper, the power balance is selected by the appropriate DC location, select the ESCR and ΔP two indicators through multi-attribute decision making to select the optimal placement; facts show that the method has certain feasibility and effectiveness.

Method of Receiving-end Power Grid DC Location Selection

location selection. Receiving-end power grid for partitioning power balance, choose the largest power gap partition as DC location selection areas.

Select of location bus. Suppose there are N nodes can share 500kV location selection, specific selection method is as follows.

1) Effective Short Circuit Ratio

The formula for ESCR:

$$ESCR = (S_{ac} - Q_{cN}) / P_{dN} \tag{1}$$

Where:

S_{ac} In other short-circuit capacity of the AC bus station; Q_{cN} Rated voltage, reactive power generated by the equipment; P_{dN} DC rated power delivery.

SCR reaction by the end of the AC system for DC system support capabilities, mainly voltage support capability, for the purposes of HVDC system, based on the theoretical research and practical experience, the strength of the system is divided as follows: ESCR>5 high; ESCR = 3~5 medium; ESCR = 2~3 lower; ESCR<2 low.

For N nodes location areas respectively ESCR calculated the corresponding value.

2) Calculate active power loss

AC active power loss calculation system is:

$$P_{loss} = \sum_{k=1}^{N_k} G_k(i,j)\left[V_i^2 + V_j^2 + 2V_iV_j\cos(\theta_i - \theta_j)\right] \tag{2}$$

Where:

N_k —Number of branches; $G_k(i,j)$ —Branch conductance;

V_i , V_j , θ_i , θ_j —Amplitude and phase angle of each node voltages.

3) Select the target function

Firstly establish DC location selection based on linear weighted objective function and method. Set up two goals $f_i(x)\,(i=1,2)$, corresponding to ESCR and ΔP, ideal placement ESCR corresponding maximum and minimum ΔP. Assuming the weighting coefficients $\omega_i\ (i=1,2)$, the new objective function is:

$$F(x) = \omega_1 f_1(x) + \omega_2 f_2(x) \to \min \tag{3}$$

When the minimum value of the objective function, the nodes corresponding to the optimal location. To determine the appropriate DC location should solve two problems: First, a number of attributes normalized, the second is to find a suitable weighting factor.

4) Normalization process

Since the active power loss ESCR receiving-end communication system and is not an order of magnitude, and in practice the better ESCR hope, reactive power losses as small as possible, direct linear weighting of these indicators is likely to cause an unreasonable result, it is necessary the first of these two indicators normalized.

The larger the system, the more stable though ESCR, but when ESCR to a certain value after its numerical size may in itself is not very important for the stability, and therefore need to introduce thresholds $ESCR_{margin}$, so that the normalization process more reasonable.

Press formula for ESCR and active power loss of these two indicators normalized.

$$\begin{cases} f_1(x) = ESCR' = \max\left\{ \dfrac{ESCR_{\max} - ESCR}{ESCR_{\max} - ESCR_{\min}} , \dfrac{ESCR_{\max} - ESCR_{margin}}{ESCR_{\max} - ESCR_{\min}} \right\} \\ f_2(x) = \Delta P' = \dfrac{\Delta P - \Delta P_{\min}}{\Delta P_{\max} - \Delta P_{\min}} \end{cases} \tag{4}$$

Where:

ESCRmax, ESCRmin—The maximum and minimum ESCR,

Δ pmax, Δ Pmin—Maximum and minimum active power loss.

5) Set the weighting factor

Empowering method using relatively weighting coefficients determined, As shown in Table 1:

Table 1 ESCR and ΔP score sheet

	ESCR	ΔP
ESCR	0.5	1
ΔP	0	0.5

In the table, the first column i and the row j of the i-line attribute value represents the relative importance of the attributes of the first column j, the weighting factor is set as follows.

$$\lambda_{ij} = \begin{cases} 1 & x_i \text{ more important than } x_j \\ 0.5 & x_i \text{ and } x_j \text{ are equally important} \\ 0 & x_j \text{ more important than } x_i \end{cases} \tag{5}$$

Finally, the right weight values were normalized to give a weight different properties as follows:

$$w' = \left[\frac{w_1}{w_1 + w_2}, \quad \frac{w_2}{w_1 + w_2} \right] = [0.75, 0.25] \tag{6}$$

Case Study

Zha Lute DC project in Shandong power grid location selection, for example, to prove the effectiveness of this method. According to the plan, in 2018 Zha Lute HVDC project location Shandong power grid, engineering rated voltage ± 660kV, rated capacity of 8,000,000 kilowatts delivery.

Region Selection. According to the balance of power in 2018, located in the southern region of Shandong Linyi largest active shortfall. This is mainly due to the rapid economic development in recent years, resulting in Linyi region increased demand for electricity, and restrict their energy and environmental factors makes the slow construction of local power, electricity supply and demand is growing. Therefore, considering the placement of Linyi, Shandong Engineering Zha Lute DC area.

Select bus.

1) Calculation of ESCR

Linyi 500kV sites within the region is calculated to give each node ESCR DC location, as shown in Table 2.

Table 2 Each computing node ESCR

Node Name	ESCR
Yi Meng	4.93
Lan Ling	4.79
Zhi Sheng	4.90
Lv Nan	4.60

2) Active power loss calculation

The Zha Lute direct placement on the Linyi region were different 500 kV bus, obtained by calculating the size of active power loss under different circumstances, Shandong province, and the results are shown in Table 3.

Table 3 Shandong Province, the size of the power loss

Node Name	ΔP（MW）
Lan Ling	1512.70
Zhi Sheng	1512.40
Lv Nan	1500.70
Yi Meng	1531.20

3) Normalization process

By normalization, the results shown in Table 4.

Table 4 Results normalized

Node Name	ESCR’	ΔP’
Lan Ling	0.4242	0.3836
Zhi Sheng	0.0909	0.3836
Lv Nan	1.0000	0.0000
Yi Meng	0.0000	1.0000

4) Priority calculation

After addition of the weight coefficient, the value of the objective function is calculated for each node, as shown in Table 5.

Table 5 The objective function values calculated

Node Name	Function value
Zhi Sheng	0.1641
Yi Meng	0.2500
Lan Ling	0.4141
Lv Nan	0.7500

The smaller the value of the objective function, then the higher the DC Location priority. From Table 5, the objective function value of 0.1641 Zhisheng station, the smallest in all the nodes, it should be considered Zha Lute DC Location Zhisheng station to ease the power shortage situation in Linyi region.

location feasibility check. Zha Lute DC project for placement Zhisheng tide stations respectively, short circuit, and stability check. The results show that the trend of a reasonable distribution of the site, each busbar short-circuit current in the circuit breaker are within the current range, there is no stability problems under N-1 fault conditions, the placement by checking feasible.

Conclusion

This paper proposes a method based on multi-attribute decision making of receiving-end power grid DC location selection, can fully consider the power grid stability and economy, Zha Lute DC project by the end of Shandong power grid placement choice proved the effectiveness of this method. In the rapid development of China's current project today, healthy and stable development of the method for DC receiving-end power grid has an important role in guiding.

References

[1] Bai Jia-lin, Zhang Xiao-hu, Chen Chen, Cao Guo-yun. Review of multi-infeed HVDC transmission system s in Yangtze River Delta region and interaction characteristics of AC /DC and DC /DC systems[J]. East China Electric Power, 2009,37(3):1170-1174.

[2] Shao Yao，Tang Yong. Research Survey on Multi-Infeed AC/DC Hybrid Power Systems [J]. Power System Technology, 2009, 33(9): 24-30.

[3] Li Peng, Wu Xiao-chen, Zhang Yao, Jin Xiao-ming. Interaction and Coordination of Modulation Controllers of Multi-infeed HVDC in CSG [J]. Automation of Electric Power Systems, 2007, 31(11): 90-93.

[4] Yang Wei-dong, Xue Yu-sheng, Jing Yong. Influence of DC System’s Control Strategy on The Transient Stability of South China Power Grid [J]. Automation of Electric Power Systems, 20033, 27(9): 57-60.

[5] Wang Kang, Liu Chong-ru,Han Min-xiao, Cai Heng. A Method of Selecting DC Links Termination at AC Locations Considering Stability and Economy at Once[J]. Automation of Electric Power Systems, 2011,35(12):73-78.

Advanced Materials Research Vols. 986-987 (2014) pp 363-366

doi:10.4028/www.scientific.net/AMR.986-987.363

Micro-grid fault transient characteristics and relay protection

Fen-fen Chen[1,a], Shi-wu Xiao[1]

[1] State Key Laboratory of Alternate Electrical Power System with Renewable Energy Sources, North China Electric Power University, Beijing 102206, China

[a]email: dianqichenfenfen@163.com

Keywords micro-grid; relay protection; transient characteristics; control mode

Abstract. Micro grid can minish the impact from fluctuation of distributed generator by control and management system as a new type of power system. But micro-grid also brings disadvantages on power attemperation, function and relay protection. Firstly the inverter's electric model is built and the fault transient is simulated. Inverter interfaced distributed generator shows evident non-linear characteristic for the limits on power and current from control system. In this paper, according to the fault transient simulation results, analysis of the problems faced by the existing relay protection and corresponding solutions is given respectively.

Introduction

Clean energy such as wind power, photovoltaic power generation, as a clean, efficient, easy to get, no energy consumption of renewable energy, has become an important part of smart grid. New energy sources such as wind power, photovoltaic mostly in the form of distributed power supply connected to the electricity grid to facilitate centralized coordination management operation, so the micro grid change arises at the historic moment. Micro-grid is composed of all kinds of DG with various load distributed energy, system capacity generally between a few kW to a few MW, the voltage level is low or medium pressure. The traditional power transmission and distribution have been unified planning, current flow to one side of the distribution network. Because of the micro grid access of distributed power supply, current flow is no longer a one-way [1][2][[3].

Micro-grid allows distribution network rendering multiple power features, making the distribution network does not work based on three-current protection current amplitude. For micro-grid, the bidirectional trend makes micro-grid protection selectivity is difficult to do, interconnection and island operation is facing a large difference of short circuit fault current. Aiming at 10kV voltage level microgrid, including wind power, photovoltaic and turbine power generation system, in parallel operation mode failure cases, the article simulates and analysis transient fault features, to illustrate problems of the micro network relay protection, and put forward ideas.

Micro-grid model and parameters

A micro-grid model builded in PSCAD is shown in Figure 1[4][5][6]. In the model photovoltaic systems, wind power systems and turbine generator systems are rectified by step-up transformer inverter then by 0.4/10kV access to micro-grid, respectively. Micro-grid internal transmission line is a short distance transmission, the length of the transmission line as shown in the figure 1 with resistance of 0.1209 Ω / km and with positive sequence reactance of 0.386Ω/ km.

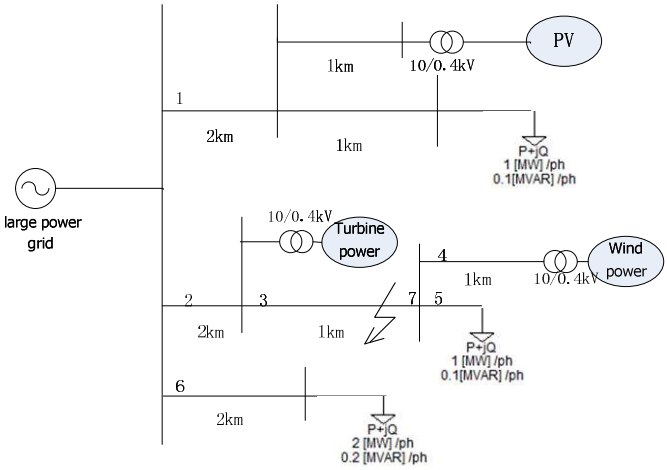

Figure 1 Micro grid model structure

Wind power system inverter adopts constant dc voltage control method, as shown in figure 2. Filter is using RLC filter. PV system inverter control method use fixed DC voltage and the filter circuit use RLC filter. Turbine power generation system inverter side uses PQ control and the control structure is shown in figure 3.

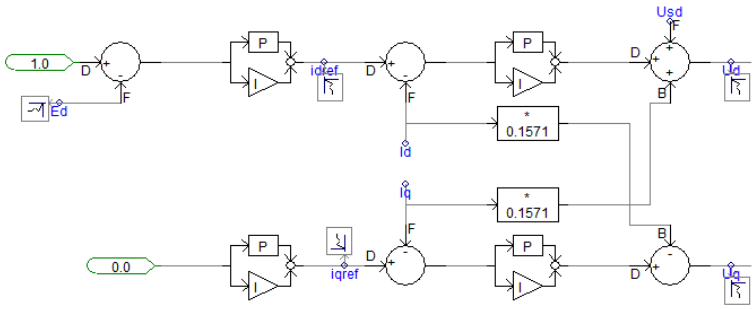

Figure 2 Dc voltage control mode

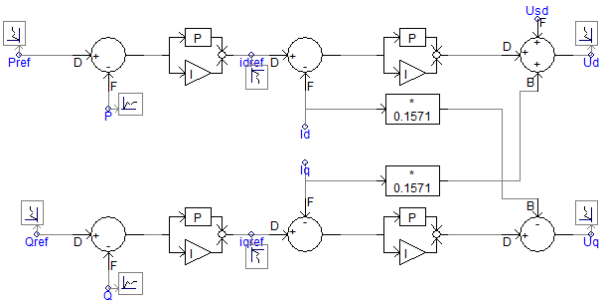

Figure 3 PQ control mode

Micro -grid fault features

In figure 1 fault location in 3.0 s set three phase fault, and the fault for 0.3 s. For power flow direction is by grid outflow for the positive direction. For motor taking out is for the positive direction. Breaker 4 measured power parameters are shown in Figure 4.

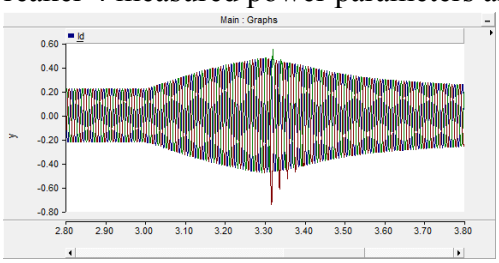

a）current

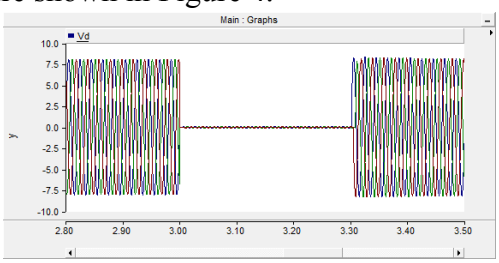

b）voltage

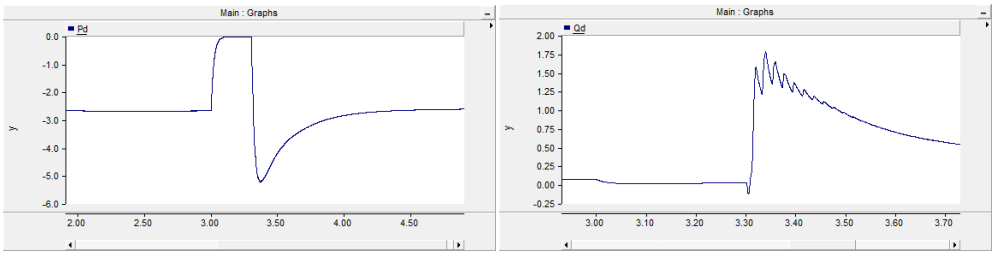

c） active power d） reactive power

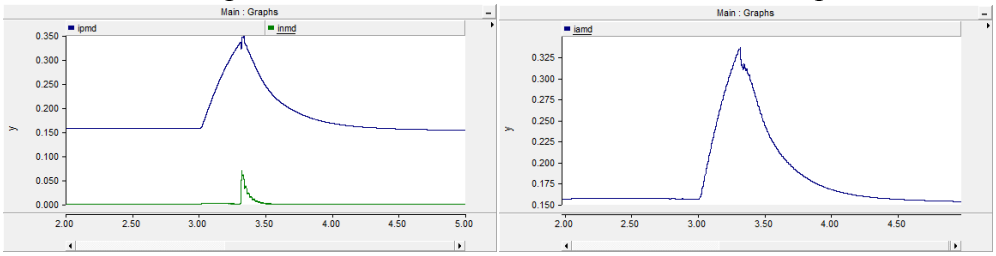

e） Positive sequence and negative sequence current f） A phase current amplitude

Figure 4 Breaker 4 measured parameters

The path of the wind power generation system, although the current increases, the voltage decreases, but the large amount of power flow change, so it will not malfunction. (Overcurrent protection may malfunction, and the following as long as it comes to the direction of current discrimination, over-current protection not apply.)

In the position shown in figure 1 circuit breaker 7 measured parameters is as shown in figure 5.

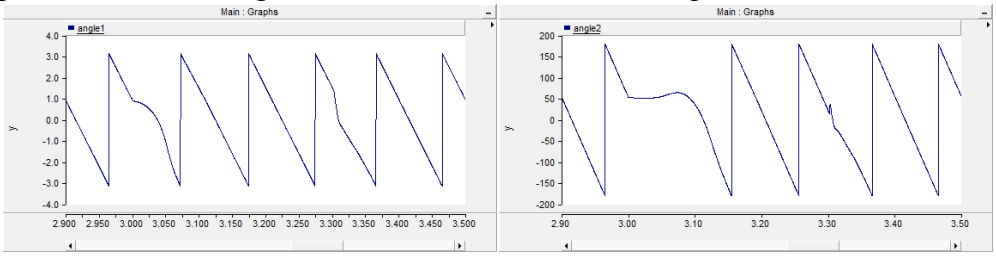

a） current phase Angle at 3 position b） current phase Angle at 7 position

Figure 5 Breaker 7 measured parameters

Close to the power grid side (circuit breaker 3) the phase angle is no more than 4^{o}. Close to the wind power system the phase angle reaches 178^{o}. For the longitudinal differential protection, 180^{o} -178^{o} $=2^{o}$, so the ends of the angle difference is not large. This demonstrates that longitudinal current differential protection can run in the micro grid.

For micro power grid protection strategy

When fault occurs within the micro-grid, only faulty equipment should be removed to ensure the power range minimum; When the primary network failure, The micro network should splitting with the main grid and continue to run in an island state with load; when failure occurs in the micro grid, the relay protection should identify the fault location and remove fault element reliably.

For over-current protection, Micro-grid has distributed power grid access, which makes the distribution network based on the current amplitude of the over-current protection not work properly. Two-way flow make the selective of micro-network protection difficult to achieve selective. Distributed power supply smaller short-circuit current may cause over-current tripping.

For distance protection, distance protection is based on the measured impedance to reflect the distance from the point of failure to protect the installation, and according to the distances to determine the action time. The micro-grid contain distributed power with power electronic devices, which makes the fault current distributed power provided is generally several times the rated current,

so the tradition distance protection can not accurately measure distance in accordance with fault voltage and fault current. The fault current is reduced as provided, distance protection cannot guarantee sensitivity.

For pilot protection, longitudinal protection can be divided into longitudinal differential protection, comparative longitudinal direction and distance protection pilot protection categories. Longitudinal differential protection equipment price is higher, to determine the fault location and movement, but requires simultaneous sampling. Comparative longitudinal direction of protection does not require synchronous sampling, there is literature to be applied to the proposed micro-grid line protection. The longitudinal distance protection problems like distance protection are that the access of the micro-power makes fault impedance measurement deviations.

Conclusions

The article simulates and analysis transient fault features, to illustrate problems of the micro network relay protection. In wind power system, the application of power electronic control device makes the wind power system to provide only 2 ~ 3 times of the rated short circuit current, so the application of relay protection method should be able to meet the characteristics of fault current. Longitudinal current differential protection can run in the micro grid.

References

[1] Jin Qiang. Research on Analysis of Distributed Generation Fault Characteristics and Protection Schemes for Micro-grid [D]. Tianjin: Tianjin University. 2011 . (In Chinese)

[2] Zhang Yu-hai, Wang Xin-chao, Xu Zhi-cheng, Wang Jun-cheng. Analysis of microgrid protection [J]. Power System Protection and Control, 2012, 40(11): 55-60. (In Chinese)

[3] Zhang zong-bao, Yuan Rong-xiang, Zhao Shu-hua, et al. Research on micro-grid protection- a new system [J]. Power System Protection and Control, 2010, 38(18): 204-209. (In Chinese)

[4] Nikkhajoei H, Lasseter R H. Distributed generation interface to the CERTS microgrid [J]. IEEE Transactions on Power Delivery, 2009, 24: 1598-1608.

[5] Lasseter R H. Microgrids and distributed generation[J]. Journal of Energy Engineeriong, 2007, 133(3): 144-149.

[6] Hatziargyriou, Hiroshi Asano, Reza Iracani, et al. Microgrid overview[J]. IEEE Power & Energy Magazine, 2007.

Advanced Materials Research Vols. 986-987 (2014) pp 367-370

doi:10.4028/www.scientific.net/AMR.986-987.367

Modeling and simulation of grid-connected photovoltaic system based on PSCAD

Xiansui Han, Qihui Liu

State Key Laboratory of Alternate Electrical Power System with Renewable Energy Sources, North China Electric Power University, Beijing 102206, China

[a]han_xiansui@163.com, [b]liu_qifeihui@126.com

Keywords: PV plants; MPPT; PSCAD; converter and control system.

Abstract. In order to investigate the impacts of large scale PV power plants on the stability of power system, dynamic PV models are of particular interest to the industry for simulating large-scale power systems. The transient model of large scale grid-connected PV generation system was given based on the model of each component of PV generation system. Response of the model was simulated respectively when the illumination changes. The methods proposed could be applied to the power grid with photovoltaic generation integration.

Introduction

In recent years, as the technology of PV is increasing steadily, large-scale grid-connected PV plants have broad prospects [1] ,However, large-scale PV power stations also exists a large number of technical issues needing to improve and perfect [2]. Considering the random fluctuation power, more issues may also appear in large-scale PV power plants, such as the harmonics, power quality and stability problems. With the increasing penetration of PV power plants, in order to investigate the impacts of large scale PV power plants on the stability of power system, dynamic PV models are of particular interest to the industry for simulating large-scale power system. The model which reflects the inherent mechanism and external mathematical characteristic of PV plants is required [3-6].

Basic composition of MW level PV plants

Large-scale photovoltaic power plants are generally composed of one or more of the basic units shown in Fig.1, where each unit is about 1MW. For example, one 10MW PV plant, it has twenty 500kW basic units. Among them, the large area of PV array component makes the photoelectric conversion and assigns the DC through the convergence device to the inverter part, and then the inverter and the filtering device convert the DC to AC that meets the quality requirements of the grid. In order to reduce the transmission loss, the transformer is required to raise its secondary voltage level (to 10/35kV). The inverter or the first stage integrated DC/DC converter also adjusts the PV output voltage for maximum power point tracing (MPPT).

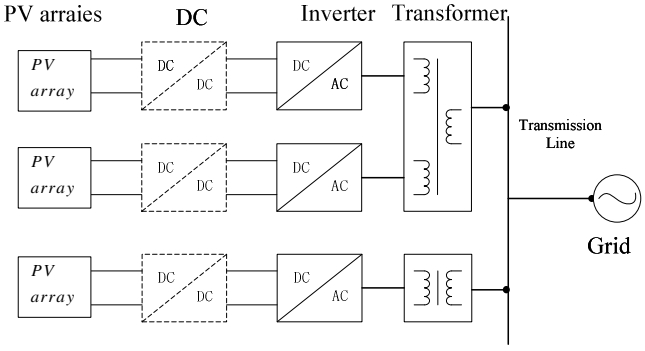

Fig.1 Topology of large-scale PV plants

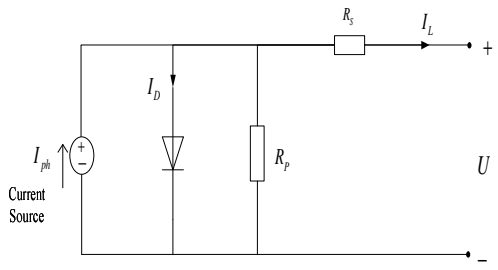

Fig 2 PV cell current-voltage characteristics

Modeling of PV array

Choose the simplification model which is used by project, the input and output characteristics of the photovoltaic battery can be expressed by the following formula:

$$I_L = I_{SC}[1 - C_1(\exp\frac{V}{C_2 V_{OC}} - 1)] \tag{1}$$

Whereby: $$C_1 = (1 - \frac{I_m}{I_{SC}})\exp(-\frac{V_m}{V_{OC}}), C_2 = (\frac{V_m}{V_{OC}} - 1)[\ln((1 - \frac{I_m}{I_{SC}})]^{-1} \tag{2}$$

Note:The four parameter is the test result on the condition of standard cell temperature $T_{ref} = 25^0$ and standard light intensity $S_{ref} = 1000W/m^2$ provided by the PV cell producer, so it must be amended by the actual temperature and light intensity, that is:

$$\Delta T = T - T_{ref}, \Delta S = \frac{S}{S_{ref}} - 1 \tag{3}$$

$$I_{scc} = I_{sc}\frac{S}{S_{STC}}(1 + \alpha\Delta T), I_{mm} = I_m\frac{S}{S_{ref}}(1 + \alpha\Delta T) \tag{4}$$

$$U_{occ} = U_{oc}(1 - \gamma\Delta T)\ln(e + \beta\Delta S), U_{mm} = U_m(1 - \gamma\Delta T)\ln(e + \beta\Delta S)$$

Among it, I_{scc}, U_{occ}, I_{mm}, U_{mm} is the short current, open voltage, peak power current, peak power voltage; T is the cell temperature; S is the light intensity; α, β, γ is the constant coefficient, experience value is $\alpha = 0.0025$; $\beta = 0.5$, $\gamma = 0.0028$.

Maximum Power Point Tracking techniques (MPPT)

It is also noticeable that the P-V curves present a unique maximum power point (MPPT) under given atmospheric conditions. The MPPT varies under different atmospheric conditions, thus I_{PV} or V_{PV} should be adjusted in an adequate way to track the MPP under these varying conditions.

The perturbation and observation method has been widely used because of its simple feedback structure and fewer measured parameters. The schematic diagram perturbation and observation method is shown in Fig. 3. It is based on the following criterion: if the operating voltage of the PV array is perturbed in a given direction and if the power drawn from the PV array increases, this means that the operating point has moved toward the MPP, therefore, the operating voltage must be further perturbed in the same direction. Otherwise, if the power drawn from the PV array decreases, the operating point has moved away from the MPP and, therefore, the direction of the operating voltage perturbation must be reversed.

Modeling of the control strategy for converters

The inverter control, which its aims is to control the active injected into the grid; control the reactive power; control voltage at PCC; control the DC bus voltage; ensure high quality of the injected power; Grid synchronization.

It can be get the converter and the transient mechanical and electrical mode of inner control system，as the fig 4 shown, where u_d ,u_q and i_d , i_q are the d- and q- axis components of the three phase inverter's output voltages and currents respectively; u_{gd} and u_{gq} are the d-and q- axis components of the grid voltage. Then all the AC current variables are all converted to the DC current ones; the active and reactive powers can be decoupled with each other. So, it is beneficial to achieve good close-loop control performance by PI controllers. Use voltage current double closed loop vector control strategy based on two phase synchronization *dq* coordinatesystem to control Photovoltaic Grid-connected generation system.

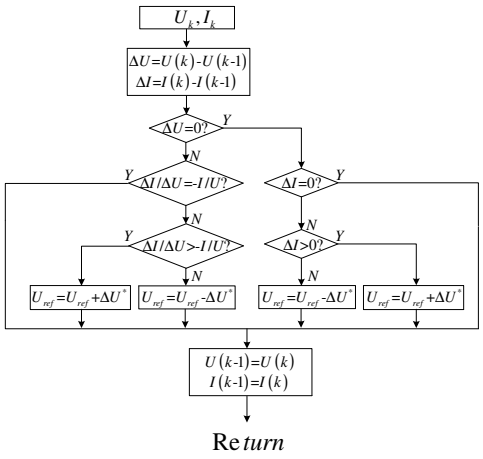

Fig.3 Flow chart perturbation and observation method

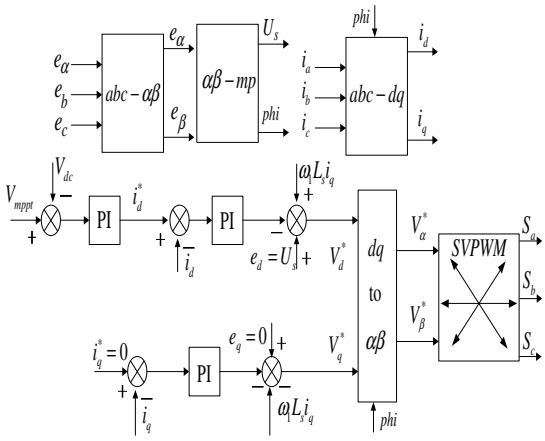

Fig.4 Main circuit of PV converter and control

Case Study

Modeling and simulation of a PV plant

A 10MW photovoltaic power plant is taken as an example for modeling. The PV plant consists of 10 unit structures shown in Fig.1. Each unit is 1MW and consists of two 500kW inverters that are connected to the1.2MVA transformer with two sets of three-phase primary windings. The inverter's output AC voltage is 270V. The three-winding transformer raises the voltage to 10kV, and connected to the terminal of distribution grid. Electromechanical modeling of large-scale grid-connected photovoltaic systems are developed on PSCAD/EMTDC.

Considering that the irradiance is equal to the whole PV array, but varies from 500W/m^2 to 1000W/m^2 at 2s, the power injected to grid, the waveforms of grid current in single inverter, the capacitor voltage and the MPPT voltage, are shown in fig5 respectively. The temperature is 25^{0}C in the simulation. From fig.5, it can be found that the PV plant is under unit power factor operation. The output power and grid current vary with the irradiance. The inverters can track the new maximum power point and maintain stable current output when the irradiance changes.

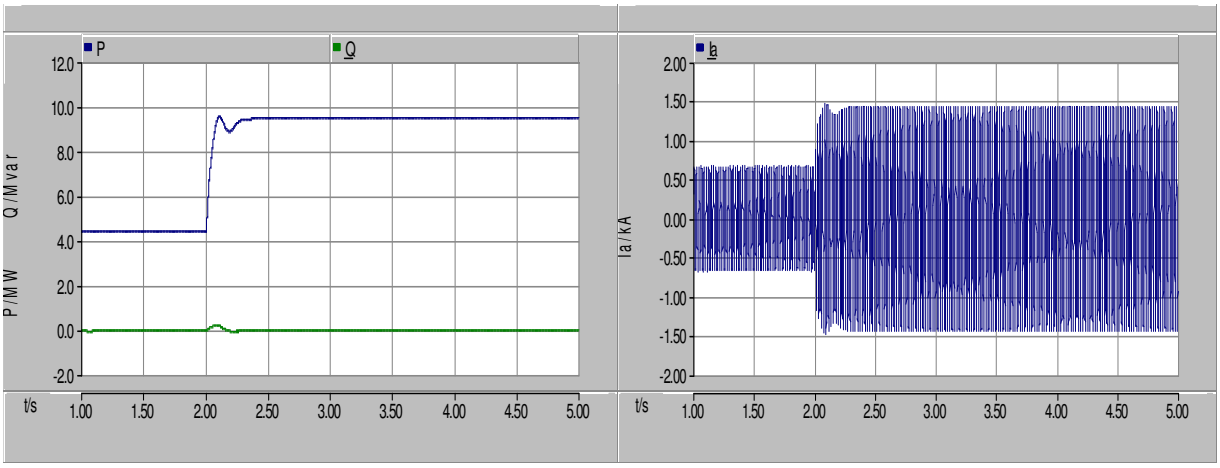

(a)The power injected to grid (b) The grid side current

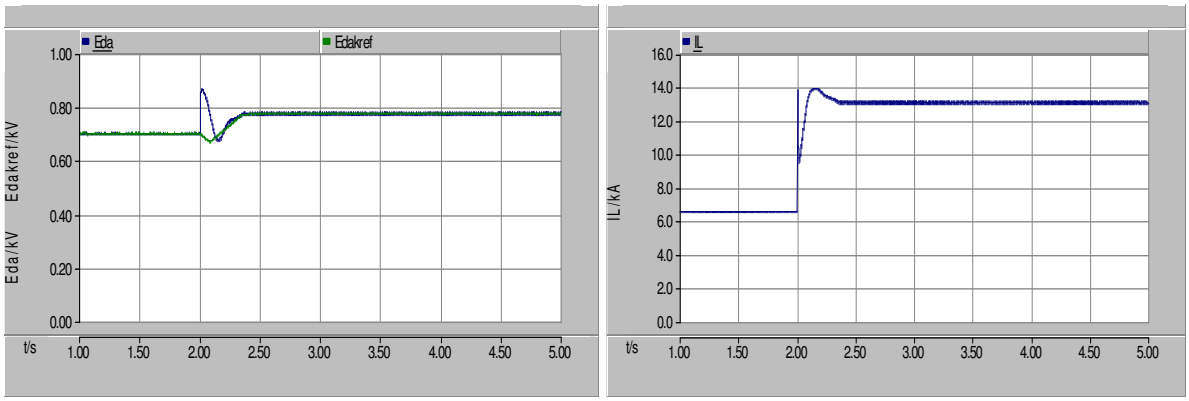

(c)The capacitor voltage and MPPT voltage (d) PV cell current

Fig .5 The output of the PV plant when the irradiance changes

Summary

Based on the composition, inherent characteristic and mechanism of large-scale MW level PV plants, the model of PV array, inverter and its control system , and the grid interface are set up.The operation of a real MW-level PV plant is investigated by simulation in detail. Main results are summarized below:

(1) Large area PV array may have a multi-peak output character, and the proposed overall MPPT strategy is effective;

(2) The provided model represents the operation mechanism of large-scale MW level PV plants and is also suit for further researches, such as the impact of PV plants on the grid;

(3) Simulations validate the modeling. All these work make a foundation to the further research on electromechanical simulation of large-scale photovoltaic system connected in practical power grids.

References

[1] Zhao Z M,Liu J Z,Sun X Y.Overview of Large-scale PV Integration Key Technologies and Its Impact[J].Solar photovoltaic power generation and application.Sciences Press, 2010, 18(6): 47-50

[2] Dou W,Xu Z G,Peng Y C.Current controller optimum design for three-phase photovoltaic grid-connected inverter[J].Transactions of China Electrotechnical Society,2010,25(8):85-90

[3] N. Femia, D. Granozio, G. Petrone, G. Spagnuolo, and M. Vitelli. Optimized One-Cycle Control in Photovoltaic Grid ConnectedApplication[J].Transactions on Aerospace and Electronic Systems, 2002,38(1):262–270.

[4] M. Veerachary, T. Senjyu, and K. Uezato.Voltage-Based Maximum Power Point Tracking Control of PV System[J]. IEEE Transactions on Aerospace and Electronic Systems, 2006,42(3) :954–972

[5] Xu Pengwei, Liu Fei, Liu Bangyin, Duan Shanxu. Analysis,Comparison and Improvement of Several MPPT Methods for PV System[J]. Power Electronics, 2007, 41(5):3-5

[6] XHWu,SKPanda,JXXu.Design of a Plug-In Repetitive Control Scheme for Eliminating Supply-Side Current Harmonics of Three-Phase PWM Boost Rectifiers Under Generalized Supply Voltage Condition[J].IEEE Transactions on Power Electronics,2010,25(7):1800-1810

Advanced Materials Research Vols. 986-987 (2014) pp 371-376

doi:10.4028/www.scientific.net/AMR.986-987.371

MPC based approach for reliable power system energy management with high penetration level of renewable energy resources

Yan Zhang [1, a], Bo Guo [1, a], Tao Zhang [1, 2, a]

[1] College of Information System and Management, National University of Defense Technology, Changsha 410073 China;

[2] State Key Laboratory of High Performance Computing, National University of Defense Technology, Changsha 410073, China.

[a] zy331214534@126.com

Keywords: Battery energy storage system (BESS), model predictive control (MPC), renewable energy resources (RER), optimal control

Abstract. This paper discusses using the battery energy storage system (BESS) to mitigate intermittency and sustain stability of distribution system integrating high penetration level of renewable energy resources (RER). The goal of the control is to have the BESS provide as much smoothing as possible, so that the RER power can be dispatchable in some kind and reliable. The effectiveness of model predictive control (MPC) based approach proposed in this paper have been tested by detail case study, also compared with the day ahead control strategy, load following strategy , and normal situation without energy storage which are usually used before. The result shows that the proposed MPC based approach is more practical, and more robust.

Introduction

Renewable energy resources (RER) such as solar and wind are environment friendly to reduce pollutants produced by conventional fossil power plants, and energy purchasing cost associated with rising fuel price. Many governments such as Germany, France, U.S. and China have recognized the advantages of RER, providing much favorable legislation to incent RER installations [1] and using. In the near future, some places will have a high penetration level of renewable generation, such as California will have 33% of its total electric generation from RER by 2030 [2], Yancheng district of Jiangsu province will have 34% of its total electric generation from RER by 2017, and electricity generation from RER have exceeded the conventional sources in some districts even now [3], [4].

As the penetration level of RER into the grid, it poses new challenges to the electricity market and grid operators, in that RER power outputs are intermittent, which may larger the deviations in frequency and voltage on the grid than before. If there is no suitable control and power management to these intermittent sources with high grid penetration, negative impact to the grid performance will give [5]. Since a large-scale BESS is an expensive option for power system operator, adopting a control strategy for optimal use of the BESS becomes a critical issue. Various studies for sizing and adaptive control of BESS to accommodate RER exist the literature, including BESS sizing problems such as maximizing the price arbitrate and improve renewable energy integration in distribution networks by forward dynamic programming [6], minimizing costs of BESS by stochastic linear programming [7], maximizing the service life-time/ unit cost index of BESS as mixed line programming [8], minimizing cost of an off-grid hybrid PV–Wind–Diesel system by genetic algorithm [9]. Other studies concerning control approaches of BESS not sizing such as using MPC to track battery state of charge (SOC) and to smooth wind power output [10]-[12], a rule-based two-threshold policy BESS charging and discharging control to maximize the benefit in an infinite horizon [13]. This paper focus on the control strategy of BESS to smooth the fluctuation and mitigate intermittency of RER power output, so that the RER may be dispatchable like conventional power plant in some kind. The MPC based control strategy proposed in this paper will be used to control the charge and discharge of BESS to smooth the RER power output as much as possible, and compensate

the forecast errors. This paper will discuss the sizing of BESS for mitigating RER fluctuation and intermittency, also analysis the sensitivity of control algorithm with different forecast errors. Case study results shows that the MPC based control strategy is more effective in smoothing RER fluctuation and more robust to forecast errors, a smaller BESS capacity will achieve the same performance by MPC based control strategy.

The remainder of the paper is organized as follows: Section Ⅱ describes the model used in this paper, Section Ⅲpresents the mathematical models of the strategies, a detail case study and analyses are given in Section Ⅳ, and conclusions are presented in Section Ⅴ.

Modeling and System Configuration

Assuming a distribution system are consisted of a lot of micro-grids, therefore, if every controller of microgrid can mitigate the fluctuation and intermittence automatically and cooperate with the supervisory controller, the power system will be sustain reliability and stability, and the RER will be dispatchable in some kind. The configuration of microgrid as Fig. 1 shows.

A microgrid consists of a local controller, local consumers (e.g. large cooling house), renewable generators (e.g., wind turbine or/and solar) and storage facilities (e.g., BESS), and connected with the external grid.

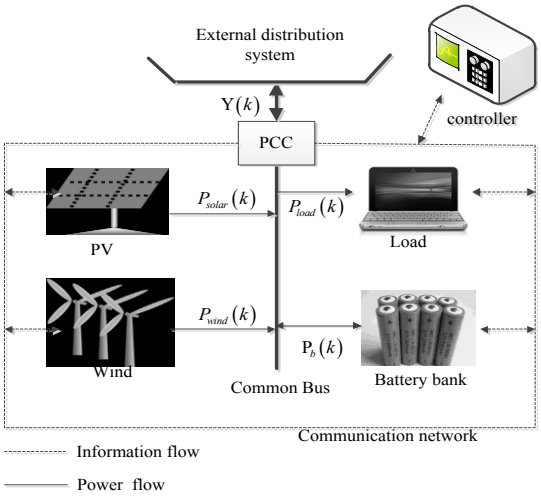

Fig. 1: Microgrid architecture

Fig. 1 precisely shows the interactions between the independent components in microgrid, the power transmitted into BESS at time period k is represented by $P_b(k)$, where $P_b(k) > 0$, indicates that BESS charge energy, which can be from RER or/also from the external grid, and $P_b(k) < 0$ $P_b(k) < 0$ indicates that BESS exports energy to compensate forecast errors or/and smooth the RER power output. Power generated by wind and solar at time period k is represented by $P_{wind}(k)$ and $P_{solar}(k)$ respectively. Load demand at time period k is represented by $P_{load}(k)$. Net power injected into or supplied from the external grid is represented by $Y(k)$, similar to BESS, if $Y(k) > 0$ $Y(k) > 0$, the microgrid transmitted extra energy to the external grid, in the opposite, the external grid transmits energy to the microgrid to keep power balance. The main objective should be reached in this paper and constraints should be met can be formulated as follows:

Objective:

$$Var = \left\{ (1/NM) \sum_{d=1}^{M} \sum_{k=1}^{N} \left[Y(k) - (1/N) \cdot \sum_{i=1}^{N} Y(k) \right]^2 \right\}^{\wedge(1/2)} \quad (1)$$

Where M represents the whole simulation horizon (e.g. one year), and N represents one finite receding horizon (e.g. one day). The main objective is to smooth the power flow in the microgrid and shafting peak power, which resulted in sustaining the microgrid reliable and stable as much as possible and (1) must subject to the following constraints.

Constrains:

(1) Energy balance constraints: The load demand at time interval t should be equal to the energy supplied by RER, BESS and the external electric network over the whole scheduling time range. That is

$$Y(k) = P_{wind}(k) + P_{solar}(k) - P_{load}(k) - \eta P_b(k) \quad (2)$$

(2) BESS operation constraints: The energy stored in BESS and power charged or discharged at any time interval k should be subject to:

$$SOC_{bmin} \le SOC_b(k) \le SOC_{bmax} \quad (3)$$

$$D_{max} \le P_b(k) \le C_{max} \quad (4)$$

$$SOC_b(k) = SOC_b(k-1) + (\eta P_b(k)\Delta t)/Q \quad (5)$$

D_{max} represents the maximum discharge power of BESS, and C_{max} represents the maximum charge power of BESS, they both are constant. $SOC_b(k)$ represents the state of charge at the end of each period, η represents the BESS discharge and charge efficiency, Δt represents the time interval of each period, and Q denotes the capacity of the BESS.

(3) Available RER and load demand constraints. Including each renewable energy generator has its maximum and minimum generation limit, and the energy supplied by them should not excess the limit.

$$0 \le P_{wind}(k) \le P_{wind}max \quad (6)$$

$$0 \le P_{solar}(k) \le P_{solar}max \quad (7)$$

$$0 \le P_{load}(k) \le P_{load}max \quad (8)$$

The utilized RER power is equal to or less than the available RER power. Extra RER energy will be curtailed.

(4) Power grid congestion constraints.

$$0 \le P_{grid}(k) \le P_{grid}max \quad (9)$$

The power transmitted into or from the external electric network cannot excess the limit of the transformer.

BESS Control Strategies

Many new infrastructure and technologies are put into for better integration RER, by taking advantage of the communication network, rich data and information can be sent and received from each component of microgrid in a timely fashion, as shown in Fig. 2. Study results have shown that RER power output (e.g. wind and solar) and load demand can be modeled effectively using autoregressive (AR) processes or machine learning or other methods in short term prediction. As communication network and forecast methods are not the focus of this paper, the communication network and forecast information are assumed to be given.

The operation of BESS is very flexible and behaves very different, which can be operated to as generation, load, or simply standby according the needs of distribution system operator or local operator. How BESS is operated has a major impact on microgrid reliability and economic benefits. In this section, BESS control strategy of day-ahead programming [14], MPC based programming and load following control strategy [15] are presented. Approach for microgrid power fluctuation smoothing of these strategies is discussed.

Strategy 1: MPC based BESS control strategy. MPC is widely used in control community (e.g. transportation network, and power plants unit commitment) to manage systems with high dynamic characteristics and uncertainties, due to its ability to use a prediction of system evolution to establish an updated control response.

MPC based operation control is a real-time strategy, the detail control strategy operated at period k can implemented as follows:

(1) Obtain the actual RER power output and load demand in current period i.

(2) Select a receding optimization horizon N periods (e.g. one day), then use forecast model of RER power output and demand to obtain the most updated information of them for the period $i+1$ to $i+\mathrm{N}$.

(3) Solve the real-time energy shifting problem, formulated as

$$\min\left\{(1/N)\cdot\sum_{k=i+1}^{i+N}\left[\mathrm{Y}(k)-(1/N)\sum_{k=i+1}^{i+N}\mathrm{Y}(k)\right]^2\right\}^{\wedge(1/2)} \tag{10}$$

Subject to constraints (2)-(9), and $k=i+1,i+2,\cdots,i+\mathrm{N}$.

(4) Implement the first period operation of the above optimization problem, which is BESS should be operated at time interval $i+1$.

(5) Update the BESS state, move to the next period and then repeat form 1) to 5) in the whole simulation horizon.

Strategy 2: Day ahead programming strategy. Optimize the BESS operation day-ahead with the day-ahead microgrid state and forecast information of the next day, and then implement the plan in real-time. The objective function is

$$\min\left\{(1/N)\sum_{k=1}^{N}\left[\mathrm{Y}(k)-(1/N)\sum_{i=1}^{N}\mathrm{Y}(k)\right]^2\right\}^{\wedge(1/2)} \tag{11}$$

Subject to constraints (2)-(9), and $k=1,2,\cdots,\mathrm{N}$. The microgrid controller will schedule the BESS operation of the next day, and will operate BESS according to the schedule strictly. To the next day will repeat this algorithm of (11).

Strategy 3: Load following strategy. No forecast information is needed to this strategy; the operation under this strategy is based on real-time microgrid information. In real-time operation, BESS will charge as much as possible unless reaching operation limits if not fully charged and is positive, then inject the surplus energy into the external grid [15]. In the opposite case, BESS will discharge as much as possible unless reaching operation limits if there is enough energy stored in the BESS, if cannot compensate the mismatched energy yet, will absorb additional energy from the external grid.

Case Study and Results

In this section, we will study the performance of mitigating fluctuation of the microgrid of the all above strategies though a series of case, and discussion the relationships referred.

The time interval $\Delta t=1hour$, which means $\mathrm{N}=24$, and $\mathrm{M}=365$ the profiles of RER power output and load demand are extracted from the website of "elia" [16] and simplified the data, and the BESS capacity constraints are soft constraints as in Fig. 3 in order to avoid system infeasibility in case of high forecast errors. BESS charge and discharge bounds are $SOC_{bmax}=2700kwh$, and $SOC_{bmin}=300kwh$ the BESS charge variation bounds $\mathrm{D}_{\max}=-800kw$, $\mathrm{C}_{\max}=800kw$ (merely19.2% of the peak demand power), η=0.95.

Next, Fig. 2 shows the solar power $P_{solar}(k)$ output, wind power $P_{wind}(k)$ output, load demand $P_{load}(k)$, and net generation from top to down, respectively.

For case study, the forecast error is needed. According to the research work on RER forecast and load demand forecast, a simplified real-time net generation forecast error is used instead to represent the forecast errors. This was formulated as follows:

$$Y_{real}(k)=Y_{real}(k)\cdot\left(1+E_{P,max}\cdot R_P\right) \tag{12}$$

Where $Y_{real}(k)$ is the forecast value of net generation power for the microgrid at future period k, $Y_{real}(k)$ is the real-time net generation of microgrid at period k, $E_{P,max}$ is random number with a Gaussian distribution, with mean value 0 and variation 1, R_P is the maximum forecast error percentage for future period k.

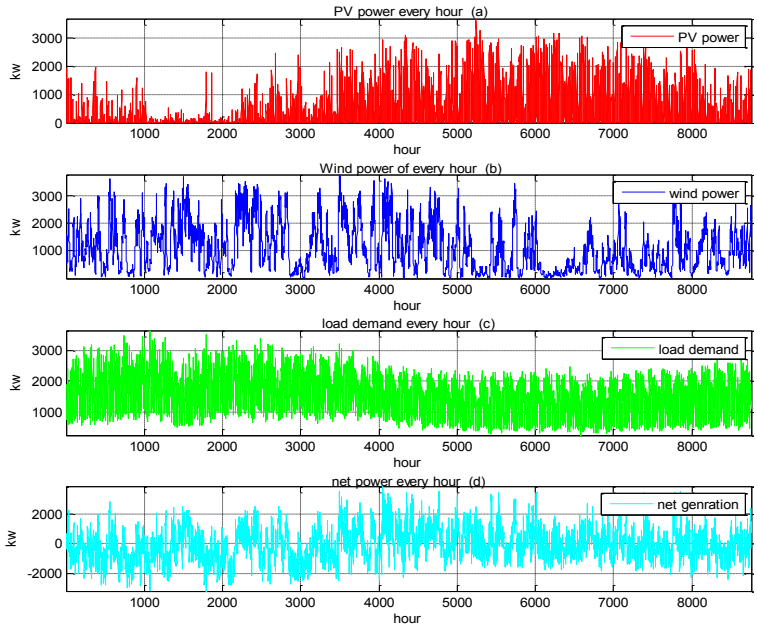

Fig. 2 Power generation and load demand of the grid-connected HES day ahead forecasted

First, for better understanding the performance of each strategy, a simple case with two typical days will be studied first. The performance of all strategies in mitigating fluctuation of the net-generation power flow in microgrid of the two days is shown in table Ⅰ,and Fig. 3.

Table I. Performance of alleviating fluctuation of the net-generation on the whole horizon period (two days)

index	Dispatch strategy			
	Strategy 1	Strategy 2	Strategy 3	Normal situation
Var	526.3576	534.445	623.0287	771.9786

Indicator of *Var* represents the standard deviation power flowed in the common bus of microgrid, which is the main index to evaluate the performance of each strategy in mitigating fluctuation of power flow in microgrid. Indicator of peak power P_{peak} is used to evaluate the performance of each strategy in power leveling in microgrid.

The values of table Ⅰ are obtained from the net generation uncertainty of 15%. From the values in table Ⅰ and two day case results in Fig. 3, we could find that MPC based approach have the best performance in mitigating power fluctuation of microgrid, day-ahead programming cannot deal with forecast errors effectively in real-time. And we could find BESS under load following strategy have no independence, all operation was determined by net generation $Y(k)$ and BESS constraints.

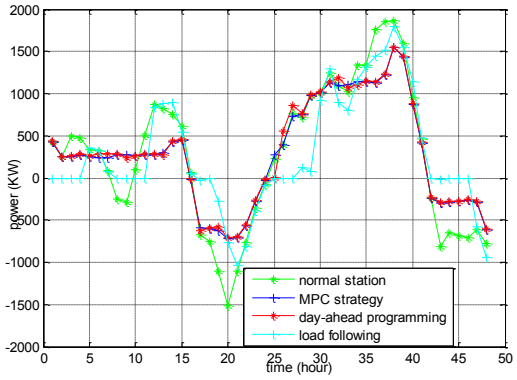

Fig. 3: Performance of alleviating fluctuation of the net-generation about all strategies (two days case)

Next, the impaction of mitigating fluctuation performance of all strategies presented in this paper will be discussed with different forecast error level in whole horizon. The net generation uncertainty of $E_{P,max}$ is assumed 0%, 5%, 10%, 15%, 20%, and 25% respectively. For saving space, we shorted forecast uncertainty as FOU. The results of robust study are shown as follows:

Table Ⅱ. Performance of all the strategies in mitigating fluctuation of RER and progressing power quality of one year

index		Dispatch strategy			
		Strategy 1	Strategy 2	Strategy3	Normal situation
Var	FOU (0%)	412.545	412.545	584.7724	685.5841
	FOU (5%)	410.187	407.005	586.8724	696.2485
	FOU (10%)	416.622	417.037	593.7003	707.9431
	FOU (15%)	424.525	434.191	613.8278	720.0404
	FOU (20%)	445.322	462.445	638.2989	739.655
	FOU (25%)	463.188	503.374	683.8895	751.7926

Table Ⅱ shows the standard deviation of power flowed in microgrid facing 6 different levels of forecast uncertainties.

Discussion and Conclusion

This paper proposes using MPC based approach to control the charge and discharge of BESS for mitigating and smoothing power flow in a microgrid. A detail case study implanted for evaluating the performance of the proposed BESS control strategy and three other strategies, the simulating results show that MPC based BESS control strategy can achieve both more smooth power flow of microgrid and robust performance, which means to cover the same performance of RER power output fluctuation and microgrid power flow the strategy of MPC based approach needs deploy less BESS than the other strategies, namely, more economic.

Future work will be focused on: 1) optimal operation management analysis of grid-connected or isolated microgrid; 2) more sophisticated BESS model to analysis of all the strategies; 3) economic analysis will be included.

References

[1] Kevin Lo: Renewable and Sustainable Energy Reviews. vol 29 (2014), p.508–516.
[2] Information on: http://apps1.eere.energy.gov/states/maps/renewable_portfolio_states.cfm
[3] WANG Shenzhe, GAO Shan, LI Haifeng, LUO Jianyu: Power System Technology, vol.37 (2013), p. 2129-2135.
[4] R. Luna-Rubio, M. Trejo-Perea, D. Vargas-Vazquez, et al: Solar Energy .vol. 86 (2012), p. 1077–1088.
[5] S. O. Geurin, A. K. Barnes, and J. C. Balda: 2012 IEEE PES, 2012, pp. 1-8.
[6] Samuele Grillo, Mattia Marinelli, Stefano Massucco, et al: IEEE TRANSACTION ON SMART GRID, vol. 3(2012) no. 2, p.950-958
[7] S. Dutta and R. Sharma: IEEE PES Conference on Innovative Smart Grid Technologies, Arlington, VA, pp. 1-7, 2012
[8] Q. Li, S.S. Choi, Y. Yuan, D.L. Yao: IEEE Transactions on Sustainable Energy, vol. 2 (2011) no. 2, p. 54-62.
[9] Ghada Merei, Cornelius Berger, Dirk Uwe Sauer: Solar Energy, vol. 97, pp. 460–473, 2013
[10] M. Khalid and A. V. Savkin: Renewable Energy, vol. 35, pp. 1520-1526, 2010.
[11] L. Xie, Y.Z. Gu, A. Eskandari, and M. Ehsani: J. Energy Eng, vol. 138 (2012), pp. 43-53.
[12] Ionela Prodan, Enrico Zio1: 2013 IEEE Workshop on Integration of Stochastic Energy in Power Systems, Romania, 2013, p. 1202-1206.
[13] Ioannis G，Damousis, Minas C.et al: IEEE Transactions on Energy Conversion, vol.19 (2004) no.2, p.352-361.
[14] M. Korpas and A.T. Holen: Energy Conversion, IEEE Transactions on, 21(3) (2006), p. 742-749.
[15] A. Gupta, R.P. Saini, M.P. Sharma: Renewable Energy.Vol.36, pp.466-473. 2011.
[16] Information on: http://www.elia.be/en/about-elia

Advanced Materials Research Vols. 986-987 (2014) pp 377-382

doi:10.4028/www.scientific.net/AMR.986-987.377

Optimal Capacitors Placement of Distribution Systems using 2nd Order Power Loss Sensitivity Analysis and Hierarchical Clustering

Huimin Gao [1, a], Jianmin Zhang [2,b] Chenxi Wu [3,c]

[1] Information engineering School of Hangzhou DianZi University 310018, Zhejiang Province, China

[2]Automation School of Hangzhou DianZi University 310018, Zhejiang Province, China

[3]Automation School of Hangzhou DianZi University 310018, Zhejiang Province, China

[a] huimingao@hdu.edu.cn, [b]zhangjmhzcn@hdu.edu.cn, [c] wuchenxi@hdu.edu.cn

Keywords: second order loss-reactive power sensitivity matrix; sensitivity analysis; hierarchical clustering; location of capacitors; distribution system

Abstract. Heuristic methods by first order sensitivity analysis are often used to determine location of capacitors of distribution power system. The selected nodes by first order sensitivity analysis often have virtual high by first order sensitivities, which could not obtain the optimal results. This paper presents an effective method to optimally determine the location and capacities of capacitors of distribution systems, based on an innovative approach by the second order sensitivity analysis and hierarchical clustering. The approach determines the location by the second order sensitivity analysis. Comparing with the traditional method, the new method considers the nonlinear factor of power flow equation and the impact of the latter selected compensation nodes on the previously selected compensation location. This method is tested on a 28-bus distribution system. Digital simulation results show that the reactive power optimization plan with the proposed method is more economic while maintaining the same level of effectiveness.

Introduction

In the radial distribution systems, capacitors must be installed in order to compensate the reactive power of the loads to reduce energy losses, to improve the voltage magnitude profile. Optimal capacitor placement (OCP) problem as a significant and vital issue has been investigated widely.

Optimal capacitor placement is a mixed integer non-linear programming problem, which consists in determining the optimal locations and sizes. The solution techniques for the OCP problem can be classified into four categories [1]: analytical, numerical programming, heuristic, and artificial intelligence-based (AI-Based).

Analytical methods were based on unrealistic assumptions of a feeder with a constant conductor size and uniform loading [2]. Numerical programming methods require more time than for analytical methods [3]. Heuristic methods pinpoint the sensitive node by sensitivity analysis in that section having the greatest effect on the system loss reduction to decrease the exhaustive search space for large distribution systems [4]. AI methods have demonstrated fine capabilities for capacitor placement, but the computational burden is nevertheless heavy, especially for large distribution systems. And they suffer from the inability to escape local optimal solutions and encounter non-convergence problems which can be troublesome to rectify [5-9].

To overcome this issue, the OCP problem of distribution system can be divided to two problems, first determining the locations of capacitors by heuristic methods and then identifying the sizes of capacitors by AI methods. It can effectively reduce the computation burden and the size of search space to avoid local optimal solutions [10]. So determining the locations of capacitors is important.

Heuristic methods often use sensitivity analysis to calculate static first order sensitivity of power loss to node reactive power under primary distribution system before installing capacitors to select the candidate buses of capacitors [11-13]. In a feeder line maybe there are several nodes with higher sensitivity. However there is one node with really high sensitivity. Other nodes that are near the node

and have high sensitivity may have not real high sensitivity. When the node with real high sensitivity has installed capacitors, other nodes with higher sensitivity have significantly decreased lower sensitivity, which is called virtual high sensitivity node. It is caused by nonlinear of power flow equations. Especial when location of capacitors is much in the whole buses, the nonlinear of power flow equations could not be neglected. Obviously, first order sensitivity analysis ignores the nonlinear of power flow, which could be a big barrier to reach the maximum efficiency. And the numbers of OCP could not be determined by first order sensitivity.

To consider nonlinear of OCP problem, this paper proposes a novel method using dynamic second order power loss sensitivity analysis and hierarchical clustering to select optimal candidate location of capacitors for distribution systems and determine optimal capacities by improved genetic algorithms. Dynamic second order power loss sensitivity analysis and hierarchical clustering can consider nonlinear of OCP problem to avoid virtual high sensitivity node to be selected as candidate nodes. Improved genetic algorithms determine the upper and lower limit by heuristic methods and regulate the sufficiency by hierarchical clustering. Computer program to implement the proposed method is written in C++. Simulations with a 28-node test system are implemented. The test results validate the proposed method.

The contents of the paper are as follows. In Section 2 second section the second order loss-reactive power sensitivity matrix is build. In Section 3 hierarchical cluster for nodes of each distribution feeder is introduced. In Section 4 the method of the optimal candidate location and capacitors using second order loss analysis and hierarchical cluster is proposed. In Section 5 Capacity of capacitors could be determined by improved genetic algorithm. In the last section the simulation results with a 28-node test system are shown.

Second order loss-reactive power sensitivity matrix (SOLPSM) calculation

Suppose there are *n* nodes in a distribution system, then the active power loss is calculated as:

$$P_{\mathrm{L}} = \sum_{i=1}^{n}\sum_{j=1}^{n} U_i U_j (G_{ij}\cos\delta_{ij} + B_{ij}\sin\delta_{ij}\} \tag{1}$$

So, the first order loss-reactive power absolute sensitivity can be calculated using equation (2):

$$\frac{\partial P_{\mathrm{L}}}{\partial \boldsymbol{u}} = (\boldsymbol{J}^{\mathrm{T}})^{-1}\frac{\partial P_{\mathrm{L}}}{\partial \boldsymbol{x}} \tag{2}$$

Where x is voltage variable matrix $\boldsymbol{x} = \begin{bmatrix} \boldsymbol{\delta} \\ \boldsymbol{U} \end{bmatrix}$; u is node input power matrix $\boldsymbol{u} = \begin{bmatrix} \boldsymbol{P} \\ \boldsymbol{Q} \end{bmatrix}$; $\boldsymbol{J}$ is Jacobian matrix.

Because of the nonlinearity of distribution system, the first order loss-reactive power sensitivity has bigger error when there are many reactive power compensation locations.

In this paper, the second loss-reactive power sensitivity is derived in equation (3).

$$\begin{aligned} \frac{\partial^2 P_{\mathrm{L}}}{\partial \mathbf{u}\partial \mathbf{u}} &= \partial\left(\frac{\partial P_{\mathrm{L}}}{\partial \mathbf{x}}\cdot\frac{\partial \mathbf{x}}{\partial \mathbf{u}}\right)/\partial \mathbf{u} \\ &= \frac{\partial P_{\mathrm{L}}}{\partial \mathbf{x}}\cdot\left(-\mathbf{J}^{-1}\cdot\sum_{j=1}^{n}\frac{\partial \mathbf{J}}{\partial x_{\mathrm{j}}}\frac{\partial x_{\mathrm{j}}}{\partial \mathbf{u}}\cdot\mathbf{J}^{-1}\right) + \left(\sum_{j=1}^{n}\frac{\partial^2 P_{\mathrm{L}}}{\partial \mathbf{x}\partial x_{\mathrm{j}}}\frac{\partial x_{\mathrm{j}}}{\partial \mathbf{u}}\right)\cdot\mathbf{J}^{-1} \end{aligned} \tag{3}$$

Second loss-reactive power sensitivity can show the coupling between different reactive power equipment nodes.

According to Taylor series expansion,

$$\Delta P_{\mathrm{L}} = \frac{\partial P_{\mathrm{L}}}{\partial \boldsymbol{u}}\Delta \boldsymbol{u} + \frac{1}{2}\Delta \boldsymbol{u}^{\mathrm{T}}\cdot\frac{\partial^2 P_{\mathrm{L}}}{\partial \boldsymbol{u}\partial \boldsymbol{u}}\cdot\Delta \boldsymbol{u} \tag{4}$$

In equation (4), ΔP_L is called loss-reactive power revised sensitivity when first order sensitivities and second order sensitivity matrices are calculated and $\Delta u \ \Delta u$ is set as the one percent of total reactive power. If $\Delta u \ \Delta u$ equals the node reactive power increment, then the second loss increment of distribution system can be obtained. If the second order items are ignored in equation (4), the first loss increment can be obtained.

$$\Delta P_L = \frac{\partial P_L}{\partial \boldsymbol{u}} \Delta \boldsymbol{u} \tag{5}$$

Hierarchical clustering

Nodes of each distribution feeder are hierarchical cluster in this paper. The main steps are as follows:

1) *n* nodes of each distribution feeder if firstly divided to *n* cluster.
2) Node distance is set as $\frac{\partial^2 P_L}{\partial Q_i \partial Q_j}$, which can reflect node mutual interaction.
3) Find the minimum distance of nodes, and the two nodes is combined to one cluster. Cluster distance is set as minimum distance between nodes in one cluster and nodes in another cluster.
4) When the cluster distance is more than the cluster threshold value, clustering stop. Otherwise turn to (2).

Determination of the optimal candidate locations of capacitors by SOLPSM **and hierarchical clustering**

The candidate locations of capacitors of distribution system can be determined using the second order sensitivity matrix, revised sensitivity and hierarchical clustering. The main steps are as follows:

(1) The first order loss-reactive power sensitivity is calculated by (2).

(2) The second order loss-reactive power sensitivity matrix is calculated by (3).

(3) The candidate nodes set is null at first. Then the unit reactive power increment is added nodes that are not in the candidate nodes set respectively. Finally the revised loss-reactive power sensitivities of the nodes that are not in candidate nodes set are calculated. From equation (3), the revised loss-reactive power sensitivity reflects the mutual effect between nodes and nonlinear factor of distribution system.

(4) By sorting the revised loss-reactive power sensitivities of nodes that are not in reactive power compensation node set, the node with maximum revised loss-reactive power sensitivity can be found. If the node is not the same cluster with the nodes, then the node is added to candidate nodes set. The nodes with virtual high sensitivities can be avoided to be selected by hierarchical clustering.

(5) By exhaustive searching, the trial compensation capacity of the selected node is determined. The capacity is installed in the node, by checking if power loss decrement is more than node investment charge.

If power loss decrement is more than node investment charge, then the selected node is selected in the candidate nodes set and then return to the first step. If not, then exit program. So with the method virtual high sensitivity nodes can be excluded and the number of capacitors can be determined.

Although the trial compensation capacity of nodes when selecting nodes is not the optimal value, they are near optimal value by the method.

(6) Install the trial capacity at the nodes within the candidate node set (except the just selected node), calculate revised sensitivity, and check if it's more than the revised sensitivity of the previously selected node. If true, then take the node out of the candidate nodes set. In doing so, the previously

selected nodes can be taken out if they are not good for power loss when latter selected nodes install relevant reactive power capacity.

(7) Following the procedures of (1)-(6), all optimal candidate nodes can be determined.

Improved genetic algorithms

Capacity of capacitors could be determined by improved genetic algorithm. The improved genetic algorithm proposes some modification to genetic algorithms. The main steps are as follows:

1) Coding. Real coded substring exists for new capacitor locations. Upper and lower limit value are set as the trial compensation capacity when determination of the optimal location of capacitors by SOLPSM and hierarchical clustering in order to reduce search space of genetic algorithm.
2) Selection. Remainder stochastic sampling is the selection scheme used. And by hierarchical clustering the fitness of the strings in the same clustering is adjusted to escape local optimal solutions as far as possible. If the fitness is large then the fitness is adjusted larger.

Case Study

A distribution system with 28 nodes and parameters are shown in reference 14.

Hierarchical clustering results of branches of 28 node system by second order sensitivity matrix are shown in Fig.1.

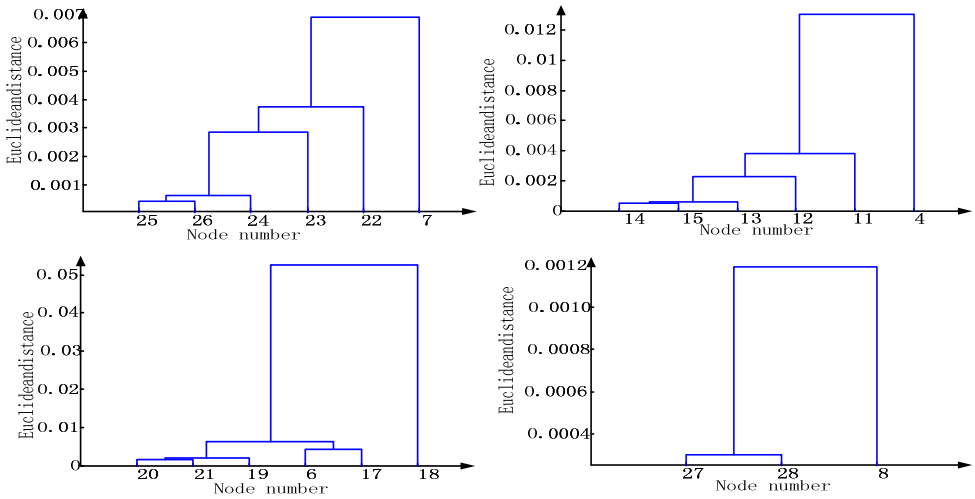

Fig.1 Hierarchical clustering result of branches of 28 node system

From Fig.1, branch {7, 22, 23, 24, 25, 26}have lesser distance than other branches. When the threshold value is set, clusters of each branch would be determined. If the threshold value is set as 0.002, it means that {24, 25, 26} is belong to the same cluster in branch {7, 22, 23, 24, 25, 26}, {13, 14, 15}is belong to the same cluster in branch {4,11,12,13,14,15},{8, 27, 28} is belong to the same cluster in branch {8, 27, 28}.When the candidate nodes are selected by second order revised sensitivity, the nodes in the same cluster are only selected one.

The node selection results by first order sensitivity and second order sensitivity are shown in Table 1.

Table.1 Loss with many locations by different sensitivity analysis method

	Node selection by first order sensitivity	Node selection by second order sensitivity
Reactive power compensation nodes	24,11,28,26,20,8,15	25,28,22,20,14,6,11
Power loss before compensation (kW)	86.48	86.48

Power loss after compensation (kW)	40.51	40.25
Lowest voltage before and after compensation	0.8921/0.9485	0.8921/0.9489
Total benifit rmb）	10.79	10.85
Total compensation capacity (kvar)	630	610

From Table 1, the selected nodes of the reactive power compensation by second order power loss based sensitivity analysis and genetic algorithm are different from the selected nodes of the reactive power compensation by first order power loss based sensitivity analysis. And the power loss decrement and total benefit by second order power loss based sensitivity analysis are more than that by first order power loss based sensitivity analysis. It shows that optimal capacitors replacement method by second order power loss based sensitivity analysis, hierarchical clustering and improved genetic algorithm is valid.

Summary

This paper presents an effective method to optimally determine the location and capacities of capacitors for distribution system, based on an innovative approach by the second order sensitivity analysis, hierarchical clustering and improved genetic algorithm. Comparing with the traditional methods, the new method considers the nonlinear factor of power flow equation and the impact of the latter selected nodes on the previously selected location. This method is tested on a 28-bus distribution system. Digital simulation results show that the capacitors replacement by the proposed method is more economic while maintaining the same level of effectiveness.

Acknowledgement

This work was supported by National Natural Science Funds of China (51307038), Key Science and Technology Project of Zhejiang Province (LZ12E07001)

References

[1] H.N. Ng, A.Y. Chikhani, Classification of capacitor allocation techniques, IEEE Trans. Power Del, 15 (1) (2000) 387–392.

[2] S. Civanlar, J.J. Grainger, Volt/Var control on distribution systems with lateral branches using shunt capacitors and voltage regulators. Part II. The solution method, IEEE Transactions on Power and Application Systems, 104 (1985) 3284–3290.

[3] R. Baldick, F.F. Wu, Efficient integer optimization algorithms for optimal coordination of capacitors and regulators, IEEE Transactions on Power Systems, 5 (1990) 805–812.

[4] M. Chis, M.M.A. Salama, S. Jayaram, Capacitor placement in distribution systems using heuristic search strategies, IEE Proceedings – Generation, Transmission and Distribution, 144 (1997) 225–230.

[5] S.Sundhararajan and A. Pahwa, “Optimal selection of capacitors for radial distribution systems using a genetic algorithm,” IEEE Trans. Power Systems, 9(3)(1994): 1499-1505.

[6] Das B, Kumar P. Artificial neural network based optimal capacitor switching in a distribution systems. Electrical power energy systems, 60(2)(2001)55-62.

[7] C.T. Su, C.S. Lee, Feeder reconfiguration and capacitor setting for loss reduction of distribution systems, Electric Power Systems Research, 58 (2001) 97-102.

[8] M.D. Reddy, V.C.V. Reddy, Optimal capacitor placement using fuzzy and real coded genetic algorithm for maximum savings, J. Theor. Appl. Inf. Technol. (2008) 219-226.

[9] Ahmed R. Abul’ Wafa. Optimal capacitor allocation in radial distribution systems for loss reduction: A two stage method, Electric Power Systems Research, 95 (2013) 168-174

[10] Gang Xu, Qi Zhou, Comprehensive Sensitivity-based reactive power optimization under the hierarchical and regional in transmission network, Environment and Electrical Engineering (EEEIC), 2012 11th International Conference on (2012) 292-297.
[11] B.Mirzaeian Dehkordi,M.Moallem ,S.J.Rezazadeh, O. Amanifar , M.Keivanfard, Optimal capacitor placement and sizing in TABRIZ distribution system using loss sensitivity factors and particle swarm optimization (PSO), Electrical Power Distribution Networks (EPDC), 2012 Proceedings of 17th Conference on (2012) Electrical Power Distribution Networks (EPDC), 2012 Proceedings of 17th Conference on p1-6.
[12] c.P. Ionescu, C. Bulac, M. Eremia, M. Roscia, "Evolutionary techniques, a sensitivity-based approach for handling discrete variables in reactive power planning," Harmonics and quality of power(ICHQP), 2012 IEEE 15th International conference on , (2012)476-480Ionescu, C.F. ; Bulac, C. ; Eremia, M. ; Roscia, M.
[13] Alberto Berizzi,Cristian Bovo, Marco Merlo, Gabriele Callegari, Marco Porcellini,Massimo Pozzi. Second order sensitivities for constrained reactive optimal power flow. Universities Power Engineering conference，(2008)1-7
[14] Das D, Nagl H S, Kothari D P. Novel method for solving radial distribution network. IEE Proc Gener Trans Distrib, 141 (4)(1994) 291-298.

Advanced Materials Research Vols. 986-987 (2014) pp 383-387

doi:10.4028/www.scientific.net/AMR.986-987.383

Optimal Configuration of Dynamic Reactive Power Compensation for Large Petrochemical Enterprise Grid

Li Siyu[1,a], Yang Qi[2,b], Huang Jiadong[1,c], Guo Qingkui[3,d], Yuan Yongyu[3,e], Sun Jianjun[3,f]

[1]School of Electrical and Electronic Engineering, North China Electric Power University, Baoding, Hebei, 071003, China

[2]China Electric Power Research Institute, Haidian District, Beijing, 100192, China

[3]China Petroleum & Chemical Corporation Tianjin Branch, Tianjin, 300271, China

[a]ymdhyk@163.com, [b]yangqi@epri.sgcc.com.cn, [c]huajd5188@sina.com, [d]guoqingkui.tjsh@sinopec.com, [e]yuanyongyu.tjsh@sinopec.com, [f]sunjianjun.tjsh@sinopec.com

Keywords: STATCOM; enterprise grid; configuration strategy; power quality

Abstract. Considering different kind of external grid failures, this paper gives analysis of voltage fluctuation and flicker of large petrochemical enterprise grid. Trajectory-based time-domain dynamic simulation method is used to analyze problems of transient voltage security. A strategy for the application of STATCOM is proposed in order to improving electric power quality. The total loss of motor load of the whole system is counted and buses are sorted according to sensitivity analysis to ascertain installing sites of STATCOM. Then the optimal capacity of STATCOM can be gained by the way of solving linear programming model, which is suitable for transient voltage security under multi-faults. Test simulations show very encouraging result.

Introduction

With the development of power system and constant improvement of the level of industrial automation, power consumers have increasing requirements for electrical power quality and reliability. Recently, some measures have been taken to meet the requirements of power quality. However, it is still an important issue that whether the power grid could maintain its stability while it is disturbed. As a new kind of dynamic reactive power compensation device, STATCOM could be applied to improve system power factor and suppress system voltage fluctuation and flicker.

1. Modeling for Enterprise Grid

Qingdao Petrochemical Enterprises grid is used as an example. This power grid is linked to Haihe 220kV transformer substation of external power grid by two 110kV lines. It is divided into two parts by two 110kV transformer substation and each of them contains seven 35kV transformer substations. Fig. 1 shows the structure of this power grid. The influence of external grid failure should be taken into account in order to give analysis of voltage changes and motor load losses of the power system in this enterprise. Fig. 2 shows the structure of external power grid.

2. Problem of Voltage Stability in Enterprise Grid

2.1 Normal operation mode of external grid

There are two generators in this enterprise grid. Typically only one of them is operational while the other one is closed. A reasonable simulation is established to assess power system reactive voltage level. The analysis shows that all of nodal voltages are within the specified range.

2.2 Enterprise grid voltage perturbation analysis under external grid faults

Despite a certain reactive power reserve has been applied to ensure system voltage stability (generators and low voltage capacitors, etc.), but loss of motor loads will happen under several specified failures of external grid that are shown in Table 1.

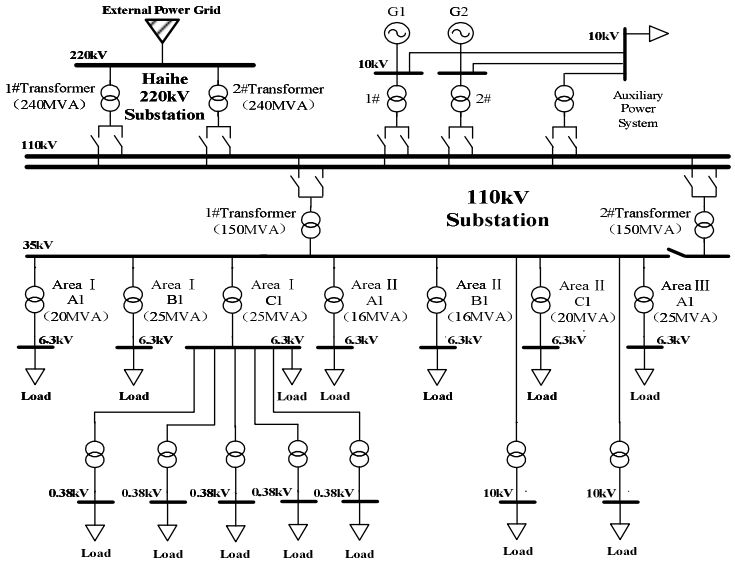

Fig. 1 Structure of Qingdao Petrochemical Enterprises grid

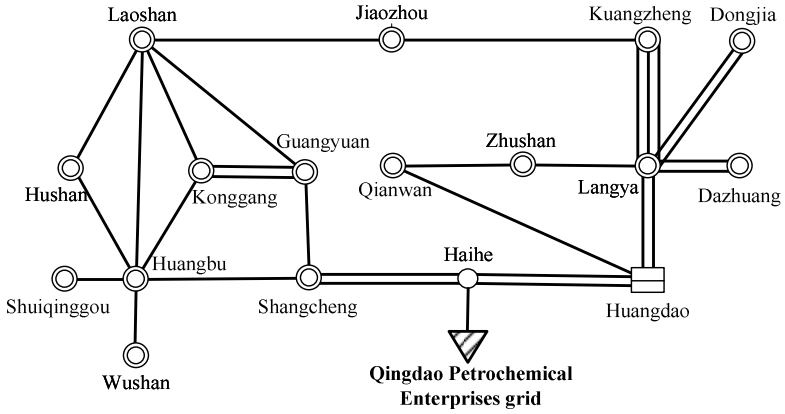

Fig. 2 Structure of external power grid

Tab.1 Loss of motor loads due to corresponding three-phase short-circuit faults

Fault Type	Fault Position	Loss of motor loads[MW]
Line	Haihe～Shangcheng	58.69
	Haihe～Huangdao	58.69
	Shangcheng～Huangbu	41.07
	Shangcheng～Guangyuan	41.07
	Huangdao～Qianwan	58.69
	Qianwan～Zhushan	*7.59
	Guangyuan～Laoshn	*7.59
	Guangyuan～Konggang	*7.59
	Jiaozhou～Kuangzheng	0
	Huangdao～Langya	0
	Laoshan～Hushan	0
Transformer	Haihe Substation 1#Transformer	14.42
Generator	Huangdao G1	65.69
Operation Mode Variation	Low voltage capacitors of Haihe Substation	0
	Load variation near Haihe Substation	0
	Output volatility of Huangdao G3	0

Voltage stability of the enterprise grid will be severely affected by three-phase short-circuit faults on external power lines near Haihe Substation. Bus voltage drops sharply after faults as is shown in Fig.3. The total loss of motor load of the whole system will be a large number.

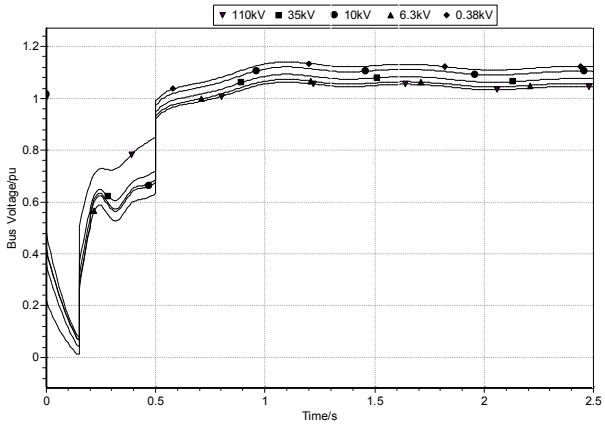

Fig. 3 Bus voltage recovery curve after Haihe~Shangcheng 220kV line fault

3. Analysis on Influences of STATCOM on Voltage Stability of Enterprise Grid

3.1 Comparison between STATCOM and SVC

STATCOM and SVC are two typical type of controllable reactive power generator. STATCOM is more effective and more rapid than SVC regarding to V-I characteristic, V-Q characteristic, transient stability and response time[1-4]. STATCOM's output is adjusted continuously to inject or absorb the reactive current. It can be treated as a shunt-connected synchronous voltage source. Comparison results between SVC and STATCOM is shown in Tab. 2.

Tab.2 Comparison between SVC & STATCOM

Items	SVC	STATCOM
Continuity of control	Discontinuous	Continuous
Control	Phase control	PWM Control
Phase delay (max.)	0.5 ~ 1 cycle	Very few
Low-order harmonics	Much	Small
Installation space	Large.	Small
Size of reactive components	Bigger	Small
Loss	Bigger	Very small
Response speed	Slow	Very fast

3.2 Analysis of allocation position of STATCOM

By the time that the voltage magnitude of system recovers to normal, sensitive buses can be ascertained. Then these sensitive buses are sorted according to sensitivity analysis. Both sensitive buses and region balance of system should be taken into account in order to ascertain installing sites of STATCOM. Based on the above analysis, two schemes of reactive power compensation are proposed that install STATCOM in low-voltage side of the transformer: Concentrated installation scheme (STATCOMs are installed in 35kV low-voltage side of the transformer in 110kV transformer substation.) and Decentralized installation scheme (each 6kV low-voltage side of the transformer in 35kV transformer substation will be installed a STATCOM device.)

3.3 Determination of optimal Capacity of STATCOM

The appropriate capacity of STATCOM should be determined to meet the requirements of voltage regulation which is suitable for transient voltage security under multi-faults. We treat the minimum of total capacity of STATCOM as objective function. By calculating the trajectory sensitivity of the magnitude of bus voltages to the capacity of each STATCOM, the transient voltage security constraints are transformed into linear inequality constraints of the capacity of STATCOM[5,6].

$$\min \sum_{i=1}^{n} S_{ci} \tag{1}$$

$$\text{s.t.} \begin{cases} \sum_{i=1}^{n} \left.\frac{\partial U}{\partial S_{ci}}\right|_{t=t_c+t_{\lim}} (S_{ci} - S_{ci}^{'}) + U_{(t_c+t_{\lim})} \geq U_{\lim} \\ \sum_{i=1}^{n} \left.\frac{\partial U}{\partial S_{ci}}\right|_{t=t_c+t_s} (S_{ci} - S_{ci}^{'}) + U_{(t_c+t_s)} \leq U_s \\ S_{ci\,\min} \leq S_{ci} \leq S_{ci\,\max} \end{cases}$$

The allocation capacity of STATCOM will influence the loss of motor loads. Take the concentrated installation scheme for example. The specific loss in different capacity will be analyzed by iterative calculation as is shown in Table 3. Finally, two 50 Mvar STATCOMs are installed (A total of 100 Mvar). A reasonable simulation experiment by BPA software is established to test and verify the above scheme. Test results show very encouraging result. All motor loads operate normally and no loss will happen after these failures that mentioned in Tab.1.

Tab.3 The specific loss in different capacity of STATCOM

Capacity of STATCOM[Mvar]	Loss of motor loads[MW]
0	51.1
10×2	51.1
20×2	33.48
30×2	32.04
40×2	20.4
45×2	9.77
50×2	0

Similarly, we can determine the optimal capacity of STATCOM of the decentralized installation scheme: each low-voltage side of the transformer in 35kV transformer substation will be assigned a 7 Mvar STATCOM device sequentially.

3.4 Simulation of applying STATCOM to enterprise grid

3.4.1 Determination of allocation position and optimal capacity of STATCOM

The dynamic reactive power response capabilities of reactive power compensation devices during the transient process are utilized to dynamically provide reactive power to the grid to mitigate voltage drop in real time. Fig. 4 shows the comparison curve of bus voltage recovery between concentrated installation scheme and decentralized installation scheme.

As can be seen from Fig. 4, decentralized scheme can help generator improve the reactive power responding speed effectively, consequently the transient voltage can be recovered faster than concentrated scheme.

3.4.2 Comparison on effectiveness between SVC and STATCOM

A comparison on effectiveness between SVC and STATCOM can be made. Take scheme I for example, a selected 35kV bus voltage changes curve with the same capacity of SVC or STATCOM (50×2 Mvar) is shown in Fig. 5. Obviously, the bus has a faster rate of voltage recovery by installing STATCOM than SVC.

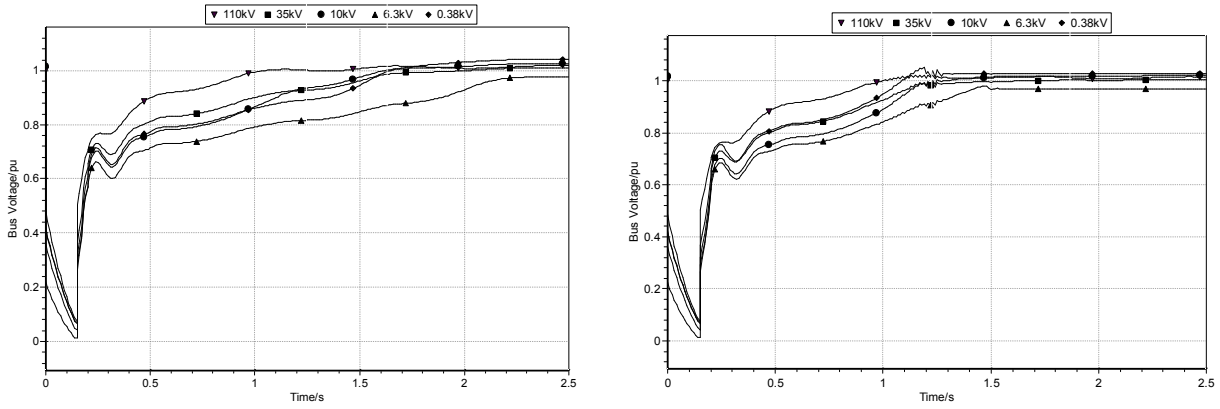

a) concentrated scheme b) decentralized scheme

Fig. 4 Comparison curve of bus voltage recovery between concentrated scheme and decentralized scheme.

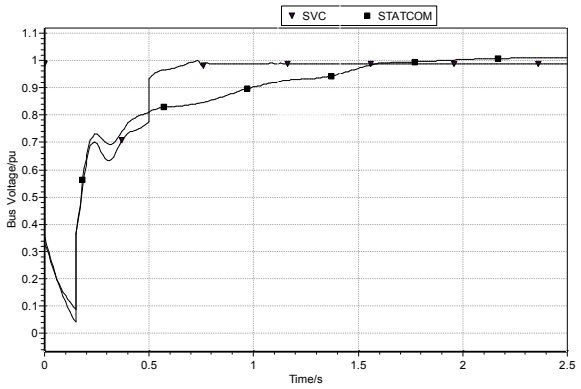

Fig. 5 35kV bus voltage recovery curve with the same installed capacity of SVC or STATCOM

4. Conclusion

STATCOM is a more effective and more rapid compensator than SVC. As a new kind of dynamic reactive power compensation device, STATCOM could be applied to improve system power factor and suppress system voltage fluctuation and flicker. This paper takes a large petrochemical enterprise grid as an example to make simulations of the grid voltage recovery caused by the external faults. A strategy for the application of STATCOM is proposed in order to improving electric power quality. Test simulations show very encouraging result.

References

[1] Liu Wenhua, Liang Xu, Jiang Qirong, et al. Development of ±20 Mvar STATCOM Employing GTO Inverters[J]. Automation of Electric Power Systems, 2000(23)：19-23.

[2] Liu Wenhua, Jiang Qirong, Liang Xu, et al. Overall Design of ±20 Mvar STATCOM[J]. Automation of Electric Power Systems, 2000(23)：14-18.

[3] Song Shan, Chen Jianye. Theory and Prototype Verification of Thyristor Based STATCOM[J]. Automation of Electric Power Systems, 2006, 30 (18)：49-53.

[4] Wang Zhonghong, Shen Fei, Wu Tiezheng, et al. Facts Applications in China and Its Developing Trends [J]. Automation Of Electric Power Systems, 2000, 24(23)：1-5.

[5] Ma Shiying, Yin Yonghua, Tang Yong, et al. Simulation and Evaluation for Short Term and Mid/Long Term Voltage Stability [J]. Power System Technology, 2006, 30(19)：14-20.

[6] Li Haichen, Liu Mingbo, Lin Shunjiang. Selection of STATCOM's Installation Site and Capacity Optimization Considering Transient Voltage Security [J]. Power System Protection and Control, 2011, 39(5)：69-76, 80.

Advanced Materials Research Vols. 986-987 (2014) pp 388-393

doi:10.4028/www.scientific.net/AMR.986-987.388

Optimal Energy Management for Smart Distribution Grid based on Virtual Power Plant

Shao-xin MENG[1,2,a], Hao BAI [3,b], Yuli WANG[2,a]

[1]Wuhan University School of Electrical Engineering, Wuhan, 430072, China

[2]High Voltage Research Institute, China Electric Power Research Institute , Wuhan, 430074,China

[3]School of Electrical & Electronic Engineering, Huazhong University of Science & Technology, Wuhan, 430074, China

[a] email: mengshaoxin@epri.sgcc.com.cn [b] email: baihao@hust.edu.cn

Keywords: Virtual Power Plant; Distributed Generation; Energy management system;Optimal Energy Management;

Abstract. Virtual Power Plant (VPP) technology can take advantage of interactive communication a nd energy management system to optimize and coordinate the control of distributed generation, cont rollable load, energy storage device, so as to integrate them and participate in the energy exchange o f the grid and the quote trading of power market. This paper is devoted to study the energy manage ment system in virtual power plant. Under the day-ahead market， this project puts forward the ma ximum profit model, analyzes the operation condition of various elements in virtual power plant, an d set restrictions for its operation and energy storage; According to the randomness of the energy res ources such as wind and light in actual operation as well as the price in power market, the change of power grid load and electricity demand, and the fluctuations in the retail price of electricity, this pa per adopts the proposed model of optimal allocation to coordinate and optimize the configuration of the elements in virtual power plant.

Introduction

For aggregating Distributed Energy Resources (DER), aims to overcome the capacity limits of single DER and the intermitted natural characteristics of renewable energy sources, the autonomy of distributed generation is emphasized in microgrid that make DGs overcome technical contradictions to coordinate well with power grid[1]. However, the main control target of microgrid is to achieve on-site balance between DGs and customers which is limited by geographical area, the effective utilizing of many areas, large-scale DGs and scale benefits in the electricity market has certain limitations[2] [3]. Virtual power plant provides methods to solve these problems[4] [5].

Virtual power plant (VPP) is collection of distributed generations and flexible loads connected and operated by communication network and advanced power management system[6]. As smooth transition between a conventional distribution network and smart power grid, based on the centralized control of distributed generations and load, intelligent management of power flow is able to be achieved[7] [8].

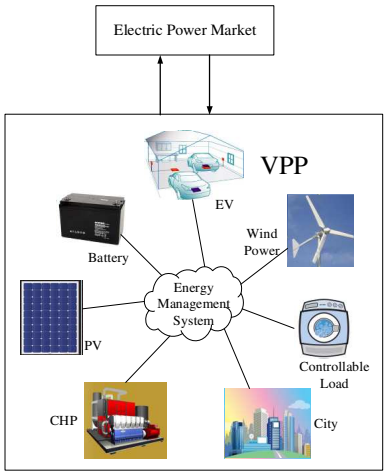

Fig.1. The structure of VPP

In Figure1, this paper sets up a VPP system consists of distributed generations (photovoltaic, wind generators), controllable load, electric vehicles stations, and energy storage units. The VPP emphasizes the external characteristics of power plant, so the implementation of diverse DER aggregation control in VPP is particularly important research content. This main work is to put forward the relevant constraints under maximal profit targets, besides, by solving the optimization algorithm will be solved and determine reasonable DER allocation to ensure the quality of electric and improve power generation efficiency.

Optimal Energy Management

The objective of VPP optimal dispatch in energy and reserve markets is to maximize comprehensive income . It regulate the output power of PV , WTG and other renewable units, exchanges power with the power market, supplies heat and power to resident, charges and discharges power to battery and electric vehicle ,and flexibly controls interruptible load[9]. Based on the above explanation, the objective function of the optimal energy management for the VPP can be expressed as

(1) Objective function:

$$\begin{aligned}\text{profit}=&\sum_{t=1}^{24}\rho_{\mathrm{e},t}\times E_t+\sum_{t=1}^{24}\rho_{\mathrm{r},t}\times R_t+\sum_{t=1}^{24}\rho_{\mathrm{l},t}\times L_t+\sum_{t=1}^{24}\rho_{\mathrm{h},t}\times H_t-\\&\sum_{\substack{t=1\\ i\in S_{DG}}}^{24}\left(C_{DG,i,t}\times P_{DG,i,t}+ST_{i,\mathrm{t}}+SH_{i,t}\right)-\sum_{\substack{t=1\\ i\in S_{CL}}}^{24}\left(C_{\mathrm{IL},i,t}\times IL_{i,t}\right)-\sum_{\substack{t=1\\ i\in S_{CHP}}}^{24}\left(C_{CHP,i,t}\times P_{\mathrm{CHP},i,t}\right)\end{aligned}\tag{1}$$

Where : S_{DG}, S_{CL} , S_{CHP} :sets of distributed generation , controllable load and combined heat and power ; $\rho_{\mathrm{e},t}$, $\rho_{\mathrm{r},t}$, $\rho_{\mathrm{l},t}$, $\rho_{\mathrm{h},t}$:the rate of electricity market, heat energy market,electricity retail to consumer and heat retail to consumer; E_t : bid of VPP to electricity market (positive and negative values indicate purchasing and selling from/to the electricity market respectively ; R_t : bid of VPP to heat energy market ; L_t : sell electricity to consumers , H_t : sell heat to consumers ,

C_{DG} : generation costs of DG units, P_{DG} : generation of DG ;ST : start up cost of DG unit ;SH :shut down cost of DG unit ; C_{IL} : cost of an interruptible consumer to curtail its load : IL the curtailment value of dispatchable load ; C_{CHP} : generation costs of CHP units: IL : heat and electricity generation of CHP ;

(2) Constraints.

A. network security[10]:

$$P_i - P_j = |V_i||V_j||Y_{ij}|\cos(\theta_{ij} + \delta_i - \delta_j) \quad (2)$$

$$Q_i - Q_j = |V_i||V_j||Y_{ij}|\sin(\theta_{ij} + \delta_i - \delta_j) \quad (3)$$

$$V_{min} < V < V_{max} \quad (4)$$

Where $P_i, P_j \ Q_i, Q_j \ V_i, V_j \ \delta_i, \delta_j$:active power,voltage and angle of two terminal in bus ; θ_{ij} : angles of complex Y-bus matrix elements (rad) ; Y_{ij} : magnitude of admittance matrix element ; V_{min}, V_{max} minimum and maximum limits on bus voltages ;

B. DG constraints : The DG constraints include Output capacity limit- Equations (5) ; Ramp limit [6] [11]-Equations (6) to (7) ; Minimum-up and down time constraint [12]-Equations (8) to (9) .

$$P_{DG.min} \le P_{DG} \le P_{DG.max} \quad (5)$$

$$P_{DG,i,t+1} - P_{DG,i,t} \le R_{DG.max} \quad (6)$$

$$P_{DG,i,t-1} - P_{DG,i,t} \le R_{DG.min} \quad (7)$$

$$\left[T_{i,t-1}^{on} - MUT_i\right] \times \left[I_{i,t-1} - I_{i,t}\right] \ge 0 \quad (8)$$

$$\left[T_{i,t-1}^{off} - MDT_i\right] \times \left[I_{i,t-1} - I_{i,t}\right] \ge 0 \quad (9)$$

Where $P_{DG.min}, P_{DG.max}$:minimum and maximum DG capacity limit for active power .

$R_{DG.min}, R_{DG.max}$:ramp-down and ramp-up limit for DG unit

MDT, MUT :minimum down time minimum up time and limit for DG unit

T^{off}, T^{on} :Number of hours for which DG unit has been on/off controllable load constraints :

C. Energy balance: electric balance and heat balance

$$E_t + SE_{dischage} + \sum P_{DG} + \alpha \sum P_{CHP} = SE_{chage} + L_t$$

$$R_t + SH_{dischage} + \beta \sum P_{CHP} = SH_{chage} + H_t \quad (10)$$

Where α, β :the scale factor of electric and heat generation in CHP ; SE, SH : battery to store electricity and boiler to store heat

D. Storage constraints :

$$SE_{min} \le SE \le SE_{max} \quad (11)$$

$$SH_{min} \le SH \le SH_{max} \quad (12)$$

Where SE_{max}, SE_{min} :maximum charge and discharge rate of electrochemical storage ; SH_{max}, SH_{min} :maximum charge and discharge rate of heat storage ;

E. Controllable load constraints :

$$IL \le IL_{max} \quad (13)$$

Where IL_{max} :Upper limit for curtailing on interruptible load.

Examples of application

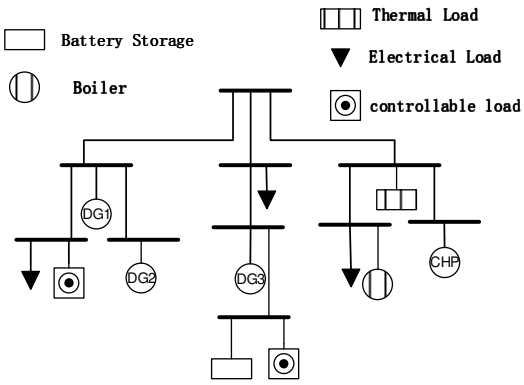

Fig.2. The Case of VPP

The procedure has been tested on different configurations of distribution systems with embedded generation, part of which aggregated into a VPP, and it has demonstrated the ability to give consistent and reliable results in compliance with all the network physical constraints and bounds. In the following, a case study example carried out on the system depicted in Figure. 2 is presented. The DG1 is PV (photovoltaic) power plant, the DG2 is WPP (wind power plant), the DG3 is micro gad turbine.The grid consists of three electical loads ,a thermal load and a conrollable load. The battery to storage electricity and the the boiler to storage heat .The CHP produce electricity and heat , it focus on the heat in case.VPP can buy or sell power from the power market accroting to the electricity price and domestic supply and demand. The details of elements is show as Table .1

Table .1 Maximum and minimum capacity

	Pmin	Pmax
DG1	0	3
DG2	0	4
DG3	0	4
Battery	0.2	2
Boiler	0.2	2
CHP	0	3

The total load of the VPP is according to Figure. 3(a). The price of wholesale energy market and the capacity price of heat market are indicated in Figure. 3(b). The retail price is shown in Figure. 3(c).

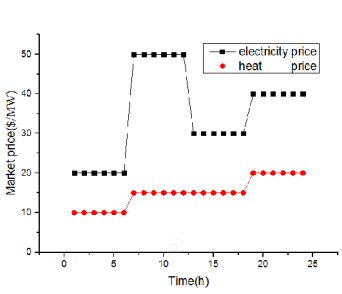

(a) The market price curves

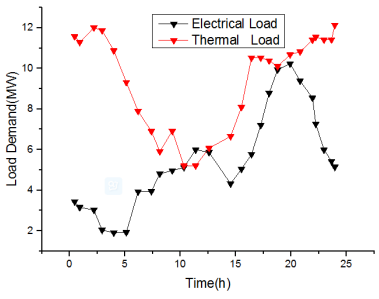

(b) The load curves

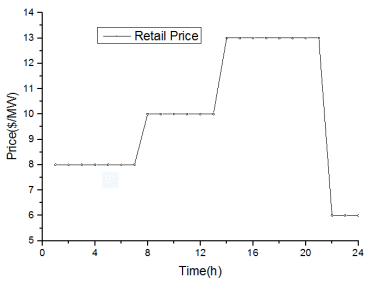

(a) The retail price curves

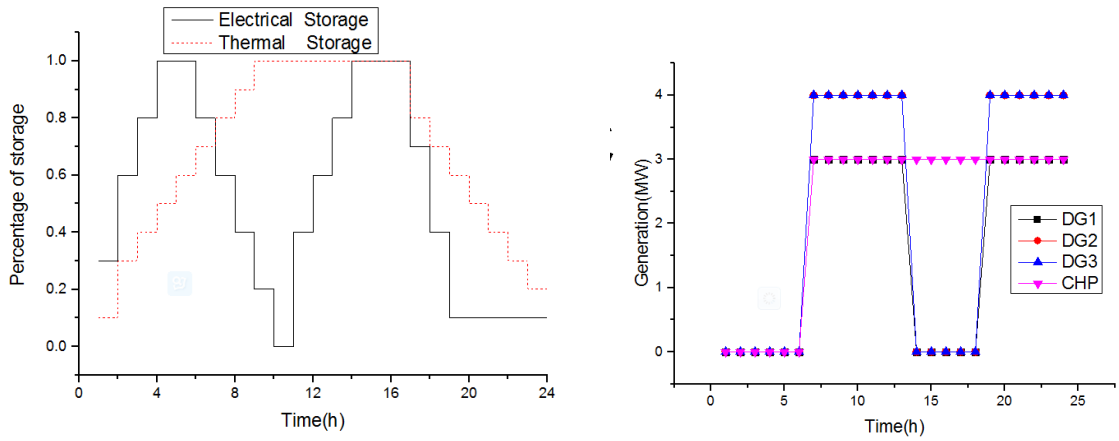

(a) The storage curves (b) The generation curves

Fig.4. The experimental results

It Uses genetic algorithm to solve the optimal control problem in the study case .The results of solving the bidding problem are shown in Fig. 4(a)–(b). In the time period between hours 1 to 6, the prices of electrity and heat maket are lower than the expence of DG,so the VPP tends to buy energy from the market, meanwhile the electrical storage and themal storage begin chage untill the it is fully charged.

During the hours 7 to 11, the prices of electrity is higher than expence of DG, The VPP change consumer role to prodeucer, DG1 ,DG2,DG3 work in max capacity to achive generation as much as possible. The prices of heat is higher than expence of CHP, The CHP produces heat energy which was stored in boiler and sold to market and themal load. The electrical storage begins dischage to gets more economic benefits.

However,the electicity price goes down at 12 :00, VPP turns off expensive units including DG1 and DG3.On the contrary, the thermal price goes up ,so CHP would better not cut production capacity.During the time between the hours 19 and24, the VPP is providing energy for the market and tends to sell its surplus energy to the network.The electrical storage and themal storage begins dischage to meet the load demand.

Conclusion

In this paper,according to the technical and economic constraints, by adopting genetic optimization algorithm, optimal energy management strategy will be designed to maximize the utilization of renewable DER and achieve optimal power flow. The optimal energy management strategy have be simulated and applied in a study case. The experimental results show that the proposed optimization management strategy provides high quality solutions while meets constraints.

References

[1] Mohammadi J, Rahimi-Kian A, Ghazizadeh M S. Joint operation of wind power and flexible load as virtual power plant. In: IEEE, 2011. 1~4

[2] Asmus P. Microgrids, virtual power plants and our distributed energy future. The Electricity Journal, 2010, 23(10): 72~82

[3] Salmani M A, Anzalchi A, Salmani S. Virtual power plant: New solution for managing distributed generations in decentralized power systems. In: IEEE, 2010. 1~6

[4] Mashhour E, Moghaddas-Tafreshi S M. Bidding Strategy of Virtual Power Plant for Participating in Energy and Spinning Reserve Markets&2014;Part II: Numerical Analysis. Power Systems, IEEE Transactions On, 2011, 26(2): 957~964

[5] Mashhour E, Moghaddas-Tafreshi S M. Bidding Strategy of Virtual Power Plant for Participating in Energy and Spinning Reserve Markets&2014;Part I: Problem Formulation. Power Systems, IEEE Transactions On, 2011, 26(2): 949~956

[6] Soltani M, Raoofat M, Rostami M A. Optimal reliable strategy of virtual power plant in energy and frequency control markets. In: IEEE, 2012. 1~6

[7] Yang H, Yi D, Zhao J, et al. distributed optimal dispatch of virtual power plant based on elm transformation. Management, 2014, 10(4): 1297~1318

[8] Peik-Herfeh M, Seifi H, Sheikh-El-Eslami M K. Decision making of a virtual power plant under uncertainties for bidding in a day-ahead market using point estimate method. Electrical Power and Energy Systems, 2013, 44(1): 88~98

[9] Sučić S, Dragičević T, Capuder T, et al. Economic dispatch of virtual power plants in an event-driven service-oriented framework using standards-based communications. Electric Power Systems Research, 2011, 81(12): 2108~2119

[10] Arslan O, Karasan O E. Cost and emission impacts of virtual power plant formation in plug-in hybrid electric vehicle penetrated networks. Energy, 2013, 60: 116~124

[11] Hropko D, Ivanecky J, Turcek J. Optimal dispatch of renewable energy sources included in Virtual power plant using Accelerated particle swarm optimization. In: IEEE, 2012. 196~200

[12] Petersen M, Bendtsen J, Stoustrup J. Optimal Dispatch Strategy for the Agile Virtual Power Plant. In: IEEE, 2012. 288~294

Advanced Materials Research Vols. 986-987 (2014) pp 394-399

doi:10.4028/www.scientific.net/AMR.986-987.394

Optimization of Voltage and Reactive Power in Regional Power Network Based on MCR

Xueyong Xu[1, a], Pan Zhou[2, b], Qizhe Huang[3, c], Chunming Deng[3], Mengmeng Shi[2] and Gang Xue[2]

[1]Equipment Management Department, Guangxi Power Grid Corporation, China

[2] School of Electrical Engineering, Wuhan University, China

[3] Hechi Power Supply Bureau, Guangxi Power Grid Corporation, China

[a]xu_xy@gx.csg.cn, [b]909617978@qq.com, [c] qizhe.huang@189.cn

Keywords: Global reactive optimization, Magnetic control reactor (MCR), Immunity genetic algorithm, Inductive reactive power compensation.

Abstract. Along with the increasing use of cables in power grid and the increasing ration of distributed power sources' synchronization, such as small hydropower's synchronization, increasing the reactive power transmission on the line, make it difficult to achieve the balance of reactive hierarchical partition. Take a certain region's power grid for actual examples, after the installation of magnetic control reactor (MCR), using immune genetic algorithm (IGA) to coordinate the capacity of magnetic control reactor and the existing reactive power resources, the results show that the magnetic control reactor does much good to absorb the system's excessive reactive power and limit the voltage's increasing.

Introduction

Voltage is an important indicator to the characterization of power quality [1-2], and reactive power to ensure that the system power quality, reduce the damage and to maintain system security and stability is crucial. The trend of power system dynamic change and influence each other. In the distributed control mode [3-4], various power plants and the transformer substation all take own bus voltage as the regulative goals, but cannot coordinate each factory from the overall situation angle to stand the reactive power assignment. Therefore, that the introduction of network voltage reactive power optimization [5] coordinates the compensation in the regional power grid between multiple substations and the different voltage rank.

Immune genetic algorithm (IGA) is a recently developed multi-objective heuristic search algorithm [6-7]. IGA treats the solution of the actual problem objective function, the multi-constraint condition and the invasion life body antigen corresponds, while the feasible solution and the antibodies produced by immune system correspond. The size of affinity is measured to the merits of the candidate solution of the problem.

Based on the actual situation of a substation, the reactors and capacitors are paralleled in transformer side for voltage active power compensation. From the perspective of global optimization, established minimum net loss, the qualified node voltage, and the generator reactive power is not overstepped as the augmentation objective function optimization mathematical model. According to the characteristic of voltage reactive power optimization problem and the applicability of the immune genetic algorithm in solving global optimization problems, this article applies the immune genetic algorithm for voltage reactive power optimization system.

The working principle of MCR

Figure 1 is a schematic structure of magnetically controlled reactor (MCR) [8-9]. When the MCR is parallel operation, the two silicon-controlled rectifiers T_1, T_2 both have induced voltage on both ends,

and its size is only about 1% of the power grid voltage. Triggers the break-over silicon-controlled rectifier T_1 and T_2 in turn in the supply voltage plus and minus half period, which can produce a DC control current controlling current $i_1^{'}$ and $i_2^{'}$ in the reactor return route, then causes the reactor work iron core magnetism valve to be at the saturated condition. The size of the MCR output current is related to the size of the DC control current, namely is related to the conduction angle of silicon controlled rectifier.

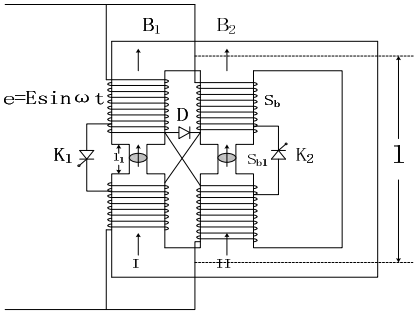

Fig. 1 MCR diagram

Regional power grid perceptual reactive power compensation points and the determination of capacity

From a particular region of the actual grid as an example for analysis, the region grid hydropower proportion is larger, power grid operation mode large changes with the seasons, and voltage level with wet and dry seasons exist different voltage adjustment problems. The optimal allocation of reactive power compensation device is to determine the installation location, equipment type and capacity in order to obtain the maximum economic efficiency and the security benefit under some constraint conditions [10-11].

As follows, the table 1 shows in the area the magnetic control reactor's installation site, voltage rank and capacity size.

Tab.1 Magnetic reactor installed capacity

installation site	voltage rank (kV)	capacity size (MVar)
2	110	30
8	35	10
17	35	10

Mathematical model and algorithm steps

Mathematical model. This paper from the perspective of safety and economy, the optimization goal is to the total net loss of the whole network minimum when each node in the grid voltage is not over limit and generator reactive power output does not exceed the limit values. The objective function is constructed in the form of penalty function, as follows:

$$\begin{cases} \min F = P_{Loss} + \lambda_V \sum \left(\dfrac{V_i - V_{il}}{V_{i\max} - V_{i\min}} \right)^2 + \lambda_Q \sum \left(\dfrac{Q_{Gi} - Q_{Gil}}{Q_{Gi\max} - Q_{Gi\min}} \right)^2 \\ V_{il} = \begin{cases} V_{i\max}, & V_i > V_{i\max} \\ V_i, & V_{i\min} \le V_i \le V_{i\max} \\ V_{i\min}, & V_i < V_{i\min} \end{cases} \\ Q_{Gil} = \begin{cases} Q_{Gi\max}, & Q_{Gi} > Q_{Gi\max} \\ Q_{Gi}, & Q_{Gi\min} \le Q_{Gi} \le Q_{Gi\max} \\ Q_{Gi\min}, & Q_{Gi} < Q_{Gi\min} \end{cases} \end{cases} \tag{1}$$

In the objective function 2nd item and the 3rd item respectively is the penalty item for the system PQ node voltage exceeding the limit and the penalty item for PV node source reactive power output

exceeding the limit. λ_V and λ_Q are the corresponding penalty coefficients, whose value can be determined by the experience and experimental observation.

Equality constraints are the power flow constraints. The inequality constraints take into account the control variable constraints of the system and the state variable constraints. Generator terminal voltage V_{Gi}, the ratio of on-load voltage regulating transformer k_{Ti} and the output of reactive power compensation device Q_{Ci} are the control variables; and the state variable constraints include node voltage and generator reactive power output constraints, as follows:

$$X_{\min} \le X \le X_{\max} \tag{2}$$

Among them, X is the variable.

Algorithm steps. The implementation steps of immune genetic algorithm in reactive power optimization of power system voltage are as follows:

(1) Input the original data. The original data include electrical network parameters and parameters of immune genetic algorithm.

(2) Generate the initial antibody population. Randomly generate initial antibody population in the solution space of voltage reactive power optimization problem, the number of iterations is set to 1.

(3) Power flow calculation. Decode the control variable condition corresponding to each antibody and calculate the power flow, and then obtain system loss, node voltage and PQ node generator reactive power output over-limit condition, and then calculate the objective function value.

(4) Calculate the antibody affinity. Calculate affinity of each antibody in the population, according to the objective function value from power flow calculation.

(5) Calculate the concentration of antibody.

(6) Antibody promotion and inhibition. According to the affinity of antibody and antibody concentration, calculate the immune selection probabilities of antibodies and then based on this probability value, select genes from the parent population to the next generation of antibody.

(7) Produce the new generation of antibody. Carry out a series of genetic crossover and mutation operations to the individuals selected out based on immune selection function, and obtain a new generation of antibody population.

(8) Evolution termination check. Check whether meet the termination conditions of evolution, if so, stop the iteration and output the final result of the optimization; and if not, iterate the number of times to add 1 and go to step (3) to start the next iteration.

Calculation and analysis of optimization of voltage and reactive power in regional power network

Before the calculation of voltage reactive power optimization in local power network, the network parameters on the regional power grid is firstly counted, then the calculation program via IGA is optimized and calculations of voltage and reactive power optimization on global scope for four kinds of typical operation modes, including wet season under heavy load and light load and dry season under heavy load and light load, are made in the region respectively. In both cases of MCR's installation and not, the optimization is calculated and the two results are compared.

Pretreatment of network parameters. As is shown in Figure 2, this is the grid structure diagrams in this region. There are totally 32 nodes, including 8 power source nodes and 5 shunt capacitor compensation nodes. And there are totally 35 branches, including 10 on-load voltage-regulating transformers (including four sets of three winding transformers, 6 double winding transformers).

For the convenience of calculation, the form of per unit value is used to indicate the region's power grid network parameters. In case of conversion, let the base capacity be S_B=100 (MVA), and the base voltage be U_B=U_{av}, besides, convert all of the parameters to the high-pressure side uniformly.

There are 26 Reactive power control variables ,including 8 voltage parameters of power source nodes, 5 compensation susceptance parameters of shunt capacitor compensation nodes,10 transformation ratio parameters of on-load voltage regulating transformers and 3 equivalent

susceptance parameters of Parallel magnetic control reactor nodes. The algorithms of parameter values are set as follows:

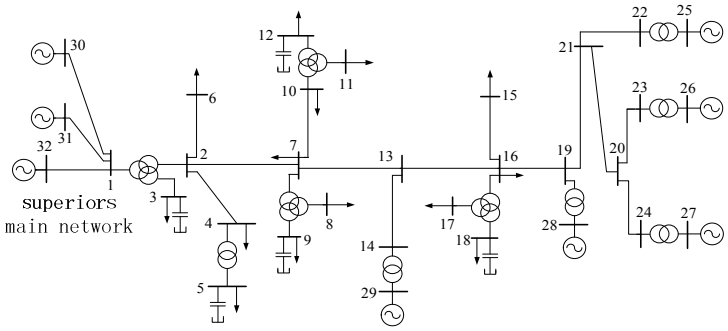

Fig.2 A regional power grid structure diagrams

Let the population size N be 100 and the maximum evolution algebra T be 200,the crossover probability of genes between real and integer section in chromosome Pc1and Pc2 be 0.6, the reality section gene variation probability Pm1 to be 0.15, the integer section gene variation probability Pm2 be 0.15, the objective function coefficient penalty λ_V=6, λ_Q = 4 .

Since the IGA is a global probability random search algorithm, each time of optimization result in optimization calculation varies, for each operation mode, the optimization algorithm are calculated for 20 times, and the results of each optimization are finally counted.

Analysis of loss data. As is shown in figure 3, the loss's comparison diagrams before and after optimization in the 4 kinds of typical operation modes are drawn.

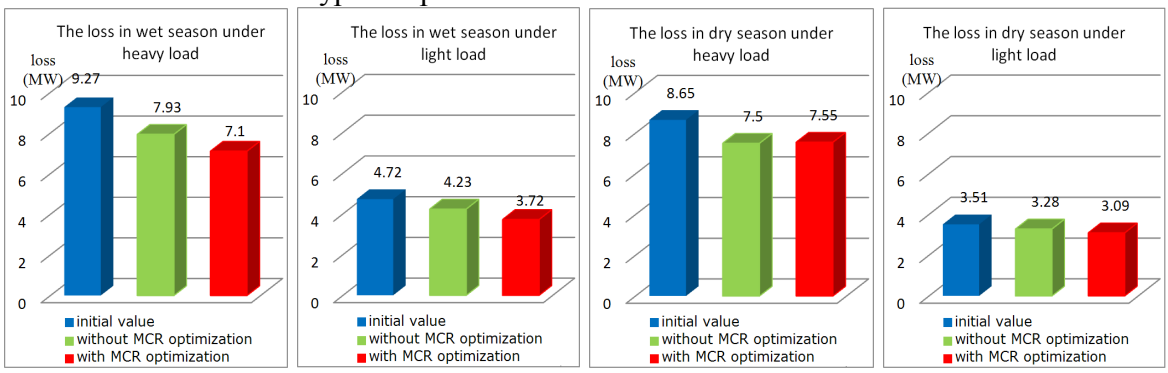

(a) (b) (c) (d)

Fig.3 Before and after optimization Web damage Comparison Chart

From the comparison, it can be seen that the loss after optimization has reduced significantly, the optimized effect is obvious.

(1)During the wet season, the loss has reduced significantly when the magnetic control reactor is added, the effect of the reactor's compensation is obvious.

(2)During the dry season, the loss has reduced when the magnetic control reactor is added, but is higher than the wet season period.

Voltage limiting effect analysis. Figure 4 has shown the voltage distribution curve before and after optimization in the 4 kinds of typical operation modes.

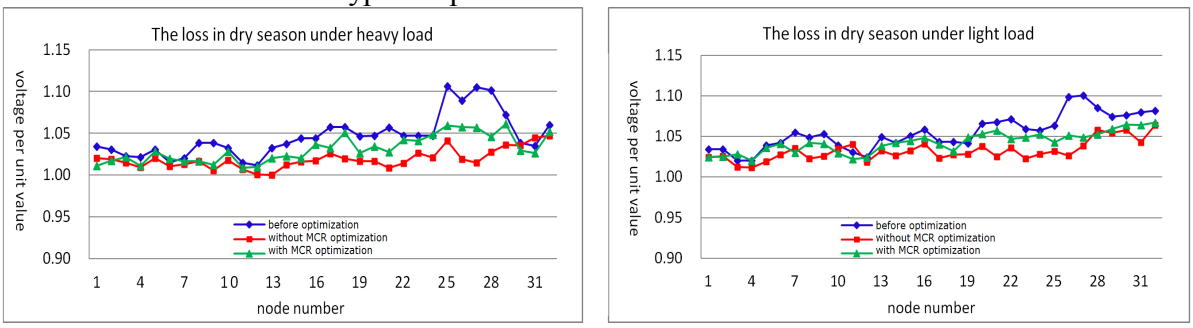

(a) wet season under heavy load (b) wet season under light load

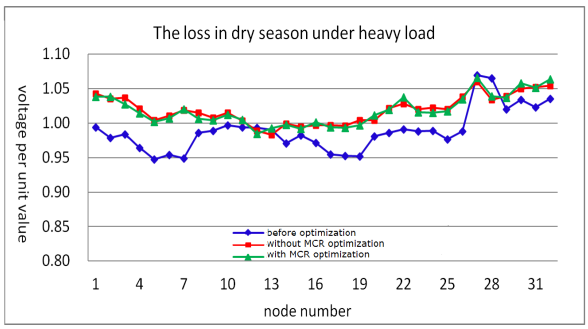

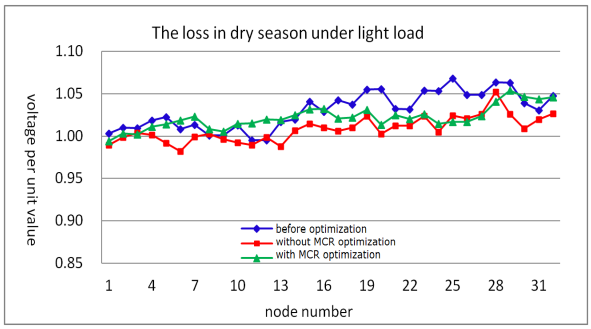

(c) dry season under heavy load (d) dry season under light load

Fig.4 Before and after optimization node voltage distribution

From the picture, it can be concluded that:

(1)During the wet season under heavy load season, it can be seen that MCR has a significant impact on the region's voltage in this operation mode and the effect of voltage limiting is obvious.

(2)During the wet season under light load season, after the use of MCR, the node voltage is limited to the allowed value.

(3)During the dry season under heavy load, the reactive power has small or no surplus, the magnetic control reactor has little affect and even run out of operation.

(4) During the dry season under light load, MCR has a significant impact on the region's voltage in this operation mode and the effect of voltage limiting is obvious.

Reactive power output analysis. Figure 4 indicates the output of reactive power of generator nodes in 4 kinds of typical load conditions before and after optimization.

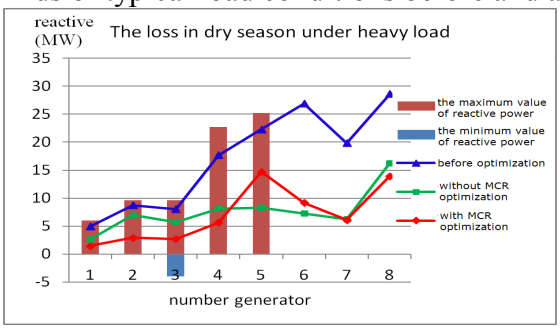

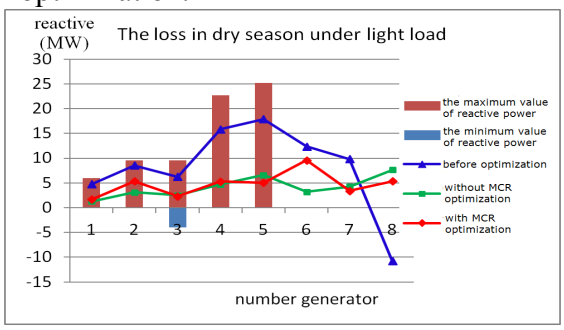

(a) wet season under heavy load (b) wet season under light load

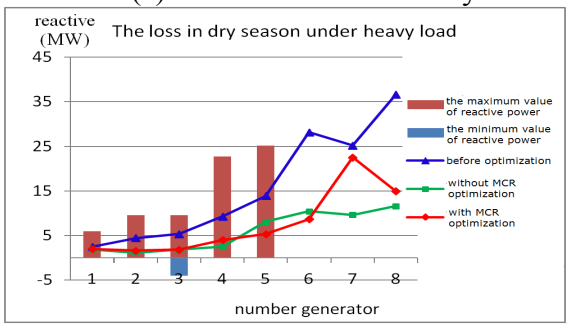

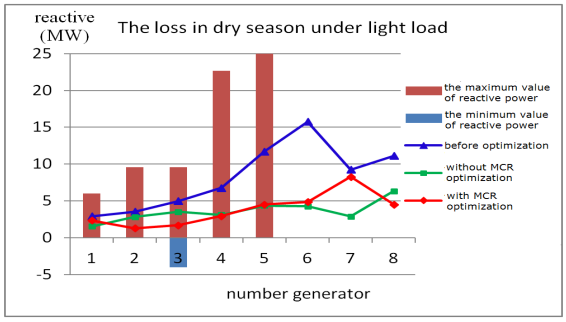

(c) dry season under heavy load (d) dry season under light load

Fig.4 Before and after optimization generator reactive contribution

Comparing the output of generators, it can see that with the shunt capacitors or inactive power compensation of shunt reactor, combined with on-load voltage regulating tap effect on reactive power flow distribution, the output of the reactive power has a different degree of decrease after optimization. Especially during the wet season under light load season, the output of 500kV superior network equivalent power source's reactive power is negative, that is to say, the regional grid network delivers massively reactive power to the system, after the optimization calculation ,the equivalent source node pours smaller reactive power into regional grid network and has avoided the reactive power's traversing between different voltage levels as well as massive long-distance transmission thought lines, thus achieving the balance of the hierarchical partitioning of reactive power, and can also do good to reduce system network loss.

Summaries

Applying IGA optimization program based on MCR, for the four kinds of typical operation modes of the region, and carrying on voltage reactive power optimization within the global scope. The impact of the magnetic control reactor into the regional power network voltage and network losses is analyzed, and then the conclusions are as follows:

(1) Installing magnetic control reactor in the area and with the various existing reactive voltage and reactive power regulation equipment in the area for the regional power grid optimization, the regional power grid reactive power and voltage regulation level can be greatly improved, and the voltage will greatly increase compared with the pass rate.

(2)The reactive power optimization of regional power grid will make relevant hydropower's output of reactive power to be rationalized and reduce the reactive power flow between the various voltage levels, but also reduces the reactive power string action, thus reducing losses and greatly saving power.

References

[1] Ch'i-Hsin Lin, Shin-Yeu Lin. Distributed Optimal Power Flow With Discrete Control Variables of Lager Distributed Power Systems. IEEE Trans. Power Syst., vol.23, no.3, pp. 1383-1392, August 2008.

[2] K. R. C. Mamandur, R. D. Chenoweth. Optimal control of reactive power flow for improvements in voltage profiles and for real power loss minimization. IEEE Transactions on Power Apparatus and Systems, Vol. PAS-I1O, No. 7 July 1981.

[3] WANG Tie-qiang, CHENG Hai-yan, ZHOU Ji-lu, et al. Based on a hierarchical partition coordinate control of the Hebei power grid AVC system design and implementation. Power System Technology, 2008, 32 (S2): 13-18.

[4] CHEN Gang, MAAi-jun, ZHANG Ji-hong, et al. AVC decentralized control mode voltage and reactive power control research. Power System Technology, 2010, 34 (12): 187-192.

[5] Victorovna S N, Victorovich M Y, Victorovna K Y. Optimal compensation of reactive power in distribution nets as means of voltage regulation. Electrical Power Quality and Utilisation. Loda, Poland: IEEE, 2009: 1-6.

[6] WANG Xiu-yun, ZOU Lei, ZHANG Ying-xin, et al. Reactive power optimization of power system based on the improved immune genetic algorithm. Power System Protection and Control, 2010, 38(1): 1-5.

[7] XIONG Hu-gang, CHENG hao-zhong. Multi-objective reactive power optimization based on immune algorithm. Proceedings of the CSEE, 2006, 26 (11): 102-108.

[8] QIAN Jian-hua, CHEN Bai-chao. Based on the magnetic valve-controlled reactor of the reactive power compensation system. Proceedings of the CSU-EPSA, 2003, 15 (2): 66-70.

[9] YU Meng-ze, CHEN Bai-chao CAO Zhi-huang, et al. The 110kV parallel controllable reactor and its application[J]. Automation of Electric Power Systems, 2008, 32 (3): 87-91.

[10] Baran M E, Wu F F. Optimal capacitor placement on radial distribution system. IEEE Transactions on Power Delivery, 1989, 4(1): 725-734.

[11] HUANG Bin, XU Jing, CHENG Min, et al. 220kV and below power carrying capacity of the inductive reactive power compensation [J]. System Technology, 2009, 33 (19): 148-151.

Advanced Materials Research Vols. 986-987 (2014) pp 400-403

doi:10.4028/www.scientific.net/AMR.986-987.400

Optimized Electric Vehicle Charging Pricing Method Using Game Theory

LU Kuan[1],GAO Wenshan [2],LI Jing [3],XUE Wanlei [1],SUN Wenxue[3]

([1.] Shandong Electric Power Company Economy & Technology Research Institution, Jinan 250000, China;

[2.] State Grid Shandong Electric Power Company, Jinan 250001, China

[3.] State Grid Zhangqiu Power Supply Company, Jinan 250001, China)

Keywords: pricing model; electric vehicle; charging price

Abstract. First, behavior models of the station operator and consumer are established considering all the main factors. Second, an optimized EV charging pricing method using Game Theory is introduced based on benefit-cost analysis. The calculation of government subsidies is also proposed in order to reach an equilibrium charging price. Finally, actual data of Hebei is used and results are shown to give supports to local government and charging station operator's decision making.

Introduction

Electric Vehicle Charging mode includes ac slow charging and dc fast charging, both of them are the consumers purchasing the vehicle and the charging stations providing the charging services. Literature [1]discusses promoting the development of electric vehicles should adopt to the market mechanism, like conventional charging station performs commercial time-sharing electricity price, emergency charging stations accords the commercial electricity charge in the rush hour, but do not make a concrete analysis of each specific question of the electricity price. Literature[2] discusses the charge of electricity of the interests of all parties involved, the operators should be considered to ensure that they can recovery cost of the charging station and gain profit, but consumers should consider car consumption costs and the choice of charging ways. Literature [3] considering, because the charge electricity price is a matter of each side with conflicting of interest, the charge electricity price formulation is determined through the game analysis, on the basis of the sensitivity model is set up respectively by the electricity suppliers, station operators and consumers charging tariff, Through analyzing the government, the charging party (composed of power suppliers and charging station operators) and consumers tripartite of static game analysis, concluding that the three parties are acceptable range of floating charge of electricity.

This paper assumes that charging station operators in time-sharing electricity price to buy electricity, then using charge of electricity. Starting from the charge carriers and consumer benefits, and the time value of money, operators and consumers all can realize relative profit for the principle, discussing the charge of electricity of formulation and government subsidies.at last, empirical data of Heibei province is used to calculate the specific subsidies for the electric vehicle charging business.

Benefit model established

1.1 Operators benefit model

Charging station operator efficiency can be represented as follows:

$$Y_1(t) = Q_c \cdot \pi_c - (Q_c \cdot \pi_p / \eta + S_r \quad (1)$$

, of which, Q_c is the charging stations in charge capacity; π_c is the charging for electricity price; π_p is the grid electricity price ; η is the charging efficiency; S_r is the site operation cost respectively.

1.2 Consumers benefit model

Because the economy is the important factors that affect consumers to choose the car type[4] generally, only when the electric car use cost is lower than the traditional fuel cars, consumers

would choose electric cars. As a result, this paper will regard consumers to use electric cars as an investment, using the expense of the electric vehicle is equal to the cash outflows, the cash inflows are expressed as a fuel car use, then establish a consumer relative efficiency model, see type（2）.

$$Y_2(t) = (\Delta C_v + C_f + B_{r,t}) - (B_{s,t} + C_c + B_m) \quad (2)$$

Type: Y_2 is the consumers of relative efficiency; ΔC_v is the fuel cars and electric cars naked car purchase price; C_f is the fuel costs; C_c , B_m is respectively of charging, battery maintenance fee; $B_{r,t}$ is the battery recycling income; $t = 8,16,\cdots$, is effective; $B_{s,t}$ is the battery costs; $t = 0,8,16,\cdots$, is effective.

Charging tariff design

2.1 Based on the charge of electricity of absolute economic benefit index

This paper adopts the method of cost-benefit make charge of electricity, using the economic benefit index shown in table 1 for examining basis. Type（1）and type（2）give the cash inflow and outflow of charging station operators and consumers, above all, the economic benefit index calculation can be performed, and then determine an acceptable charging power for operators and consumers. The specific method is as follows: Bring type (1) and (2) into the calculation formula of each index in the table 1.For both parties of charging electricity price range, the upper is consumers can accept the highest prices, the lower is the minimum charge of electricity for operators.

Tab.1 Table of absolute economic benefit indices

Indicators	Mathematical Expression	Characteristic	Judgment Criteria
NPV	$NPV = \sum_{t=0} (CI - CO)_t (1+i_0)^{-t}$	profitability indicators.	$NPV \geq 0$
IRR	$\sum_{t=0} (CI - CO)_t (1+IRR)^{-t} = 0$	profitability indicators.	$IRR \geq i_0$

Note： i_0 is the benchmark yield, in this paper, taking 5%.

2.2 Analyze the method of the government subsidies

By the analysis of related data, the electric car battery market's supply and demand both sides cannot achieve common profit, therefore needs the government fiscal subsidies, in order to form a benign operation of the market environment. The calculation method of fiscal subsidies is:

First of all, make determine charge level of electricity to consumers' acceptable π_c;

Second, regard which both sides can accept charge of electricity of price difference as government subsidies, let the operator gain profit. Every year the government subsidies are looked as the non-business income [5] CI_{gov} , as type（3）. And converting it to the initial years in accordance with the benchmark yield, to get general government subsidies to project life cycle CI_g , as type（4）.

$$CI_{gov} = \Delta\pi_c \cdot Q_c \quad (3)$$

$$CI_g = \sum_{t=0}^{T} CI_{gov_t} (1+i_0)^{-t} \quad (4)$$

Finally, use type（5）fixing operators cash inflow, then do the calculation method for measuring according to section 2.1, government subsidies for charge of electricity can be obtained.

$$CI = CI_1 + CI_{gov} \quad (5)$$

Empirical Analysis

3.1 Basic Data

This paper bases on a charging station data for empirical analysis in Hebei province.Grid electricity price regards the TOU price in Hebei of the industry and commerce as the criterion, shown in the table 2. according to the probability distribution of the charging time can get

equivalent power tariff of a bus and passenger car equivalent power tariff π_{p2}, π_{p3} are 0.34yuan /kWh and 0.78yuan/kWh respectively.

Tab.2 Time of use power price of Heibei province and probability of different kinds of EV's charging behaviors

Time Frame	Time	Grid electricity price/yuan/*kWh*	Vehicle type	Charging time	Charging probability of each time frame
Time of valley	23:00—7:00	0.32	Bus	10:00-16:30	0.5
Time of plant	7:00—8:30 11:30—18:00	0.80		23:00-5:30	0.5
Time of top	8:30—10:30 18:00—19:00 21:00—23:00	1.28	Car	7:30-17:00 19:00-7:00	0.2 0.7
Peak hour	10:30—11:30 19:00 21:00	1.36		19:00-22:00	0.1

3.2 Calculation of charge electricity price that operators can accept

When the power grid equivalent electricity price is 0.78 yuan/kWh, each index of operators under different charge electricity price are shown in table 3. When all economic indicators of project reach profitable level, charging price just take 2.18 yuan/kWh. That is when $\pi_c \geq$2.18 yuan/kWh, charging station with operators investment can realize profits.

Tab.3 Economic benefit indices analysis of operator

π_c /yuan/*kWh*	T_s / year	T_d /year	*IRR*	*NPV*/ten thousand
2.15	15	>T	4%	-109.9
2.18	14	23	5%	35
2.23	13	21	6%	179.9

3.3 Calculation of charge electricity price of consumers

In order to promote widely use of the electric car, the subsidies of the government are needed to provide. Purchase subsidies of current policy for a car are 60000 yuan, the index calculation is shown in table 4. As you can see, charge electricity price of consumers can accept is 1.14 yuan/kWh.

Tab.4 Dynamic economic analysis of consumer

π_c /yuan/*kWh*	*IRR*	*NPV*/ ten thousand
1.20	5%	-0.02
1.14	6%	0.12
1.10	6%	0.27
0.95	8%	0.56

3.4 Win-win charge electricity price

As we can see, considering the existing purchase subsidy policy of electric car, there is not a win-win charging electricity price range charging station operators and consumers can achieve.

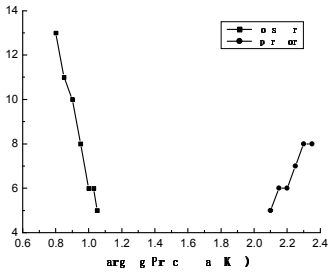

Fig.1 Comparison of IRR between operator and consumer under different charging prices

3.5 Influence of government subsidies on the charge electricity price

By the previous analysis, the role of government subsidies is to make up for the cost loss of the electric car operation and use, and in this case government subsidies of charging station operators should be greater than 1.04 (namely 2.18-1.14) yuan/kWh, when it is taken as 1.1 yuan/kWh, CI_g is $30.357 million, at this time there is a win-win charge electricity price. The influence of government subsidies on the charge electricity price is as shown in figure 2, whose lower limit reduces with the increase of subsidies level.

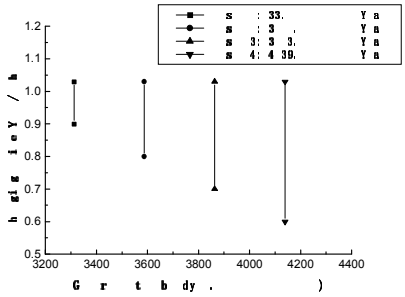

Fig.2 Effect of government subsidies on charging price

Conclusion

This paper concludes that: (1) under the current conditions, building the power tariff and charging station site cost are more higher, we cannot find the acceptable charge of electricity between operators and consumers; (2)after considering time-sharing electricity price and the charging behavior of different models, with the equivalent power tariff of charging stations become low, the operators will enhance the profitability and accept a lower charge of electricity;(3)government subsidies can effectively improve the profitability of charge carriers, it is sure closely related to the calculation of charge of electricity. In this paper, the results of the calculation of concrete examples for subsidies at least 1.04 yuan per kilowatt-hour.

References

[1] Liu Qiang, Wang Chunli. Electric power service of electric automobile based on market environment [J]. Power Demand Side Management，2007，9(1): 45-47.

[2] Chen Xiaofeng, Sun Bing. The influence of electric vehicle development on electric power marketing [J]. Hubei Electric Power，2010，34 (4): 68-70.

[3] Teng Yun, Hu Tianjun, Wei Zhenlin. Analysis on Charge Price of Electric Vehicles [J]. Journal of Transportation Systems Engineering and Information Technology，2008，8(3): 126-130.

[4] Li Z, OUYANG M. A win–win marginal rent analysis for operator and consumer under battery leasing mode in China electric vehicle market [J]. Energy Policy, 2011, 39 (6):3222-3237.

[5] The ministry of finance of the People's Republic of China. Accounting standards for enterprises no. 16 - government subsidies [S]. Beijing, 2006.

Advanced Materials Research Vols. 986-987 (2014) pp 404-411

doi:10.4028/www.scientific.net/AMR.986-987.404

Optimizing the Allocation of the Relay Setting Related to Power grid and Over Frequency Generator Tripping Scheme

YANG Qi[1, a], ZENG Xin[2, b], GUO Qingkui [3,c], YUAN Yongyu[3,d], SUN Jianjun[3,e], REN Jianwen[2, f]

[1] China Electric Power Research Institute, Haidian District, Beijing ,100192, China

[2] North China Electric Power University, Baoding 071003, Hebei Province, China

[3] China Petroleum & Chemical Corporation Tianjin Branch，Tianjin，300271, China

[a]yangqi@epri.sgcc.com.cn, [b]923258144@qq.com, [c]guoqingkui.tjsh@sinopec.com, [d]yuanyongyu.tjsh@sinopec.com,[e]sunjianjun.tjsh@sinopec.com, [f]rjw219@126.com

Keywords: Over frequency generator tripping measure;overspeed protection;islanding operation; optimizing allocation

Abstract. Through the summary of typical accident, the problem between the over speed protection device of thermal power unit steam turbine and over frequency generator tripping measure is analyzed in island operation of sending ends of regional grid. The optimizing allocation principle between over frequency generator tripping measure and over speed protection equipment is put forward. By a variety of program analysis and comparison, the optimizing scheme is given. Finally, the typical models of thermal power unit steam turbine over speed protection are established in software. Based on a practical power system as an example, the whole process of islanding is simulated. Checking the coordination with existing over frequency generator tripping measure and the relay setting related to power network in the islanding operation, the validity and practicability of the optimal scheme and principle are analyzed. With the method, the regional grid will remain safe and stable.

Introduction

In recent years, with large scale renovation and construction of China's power girds, the 500kV grid has been formed. The reliability is greatly improved. With the development of the untying electromagnetic loop network in 500kV/220kV gird, the fault of the local power grid, the local power grid fault, extreme weather, geological disasters and man-made error, all may contribute to the regional power grid islanding operation parting from the main grid. Especially for the sending ends of regional gird, when the power is large, it may result in the frequency rising rapidly. If the control measures are not properly, large area blackout may appear. It will bring great economic loss.

At present, the accident of over frequently often occurs in the sending ends of gird when running in the islanding operation[1-5], such as: Guizhou South grid "7.7" accident, "6.25" accident in Henan power grid and "2.24" accident in Kunming power grid. Although the evolution process and cause of accident are not the same, from the accident analysis and accident simulation, it has been found that over frequency generator tripping measure and OPC, primary frequency modulation function and OPC, even under frequency load shedding and over frequency generator tripping measure mismatch. Especially, when the setting value of OPC is set properly, resulting in the generator repeatedly opened and closed. With the power of large oscillation in the isolated grid, the frequency of the grid gets instability, eventually the whole network gets outage. Finding the characteristics of OPC and identifying the reason of the power oscillation have become research hotspots that many experts and scholars concern on.

In this paper, the typical model and parameters of domestic thermal power unit steam turbine overspeed protection have been collected through the investigation. Combined with the configuration status of the OPC in China, it reveals that there will remain improper between the OPC, over frequency generator tripping measure and under frequency load shedding strategy in the end of regional isolated power grid. By the typical OPC model established in PSD-BPA, and taking actual

area grid for example, the coordination scheme between the over frequency generator tripping measure and OPC is checked. It ensures the regional gird safe and stable.

1 Generator protection related to the grid in the regional gird of high frequency

1.1 High frequency protection of the generator

The generator will result in damage, when it run in high frequency, even resulting in t collapse of the grid. According to the national standard(DL/T 1040-2007《Power Grid Operation Criterion》), the island grid frequency should be control in the area that high frequency protection of generator allowable and frequency limits of the turbine. It is shown in table 1:

In this paper, the typical model and parameters of domestic thermal power unit steam turbine The generator will result in damage, when it run in high frequency, even resulting in t collapse of the grid. According to the national standard(DL/T 1040-2007《Power Grid Operation Criterion》)[6], the island grid frequency should be control in the range that high frequency protection of generator allowable and frequency limits of the turbine. It is shown in table 1:

Tab. 1 Operation time of Turbo-generator allowed when the frequency exception

Frequency range/Hz	The allowable operating time	
	Sum（min）	Single（sec）
51.0～51.5	>30	>30
50.5～51.0	>180	>180
48.5～50.5	inadmissibility	
48.5～48.0	>300	>300
48.0～47.5	>60	>60
47.5～47.0	>10	>20
47.0～46.5	>2	>5

1.2 The over speed protection controller of turbine

The over speed protection controller is an important function module of the steam turbine control system in power plant. It can inhibit the turbine over speed, preventing the emergency protector action leading to excision of steam turbine. Thereby it will short the time that the generators reconnect to the grid. When the generator reaches the fixed value, OPC will turn the adjustment of the corresponding valve in accordance with the establish logic, preventing further increase of speed. When the rotor over speed, OPC will quickly control the regulation system, forcing valve short closed. After certain delay, regulating system recovery control turbine speed, thus it effectively inhibit generator over speed. OPC typical action logic is shown in figure1[7], there are three typical function in the OPC:

(1)103% turbine over speed protection;

(2) 110% turbine over speed protection;

(3) load drop prediction function.

The OPC action is related to the control logic and its setting value. OPC control method is different in different manufacturers. And the OPC operation mode is related to the grid state and the control measures for islanding stability.

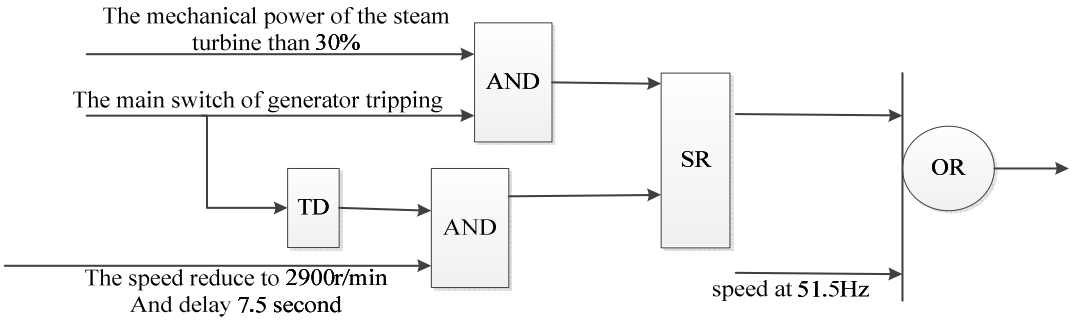

Fig. 1 OPC typical action logic

2 Optimizing scheme of over frequency generator tripping measure and OPC

2.1 Current problems between the over frequency generator tripping measure and OPC

At present, the over frequency generator tripping measure is not matching with the OPC value in the actual grid. When making the over frequency generator tripping measure, the makers mostly consider the coupling relation between the unit commitment, load and transmission power which exits in the island grid. They main ignore the effect of the OPC action to the isolated grid, and the effect to the over frequency generator tripping measure. In the OPC setting process of the power plant, it is completely on the unit itself safe operation, ignoring the interaction between the OPC and grid. The setting values are often selected according to the operation experience and suggestion. Therefore, it causes the mismatch, when the island occurred, OPC will lead to preemptive action or disoperation, and over frequency generator tripping measure will miscut or loss of cutting unit. It will directly lead to the regional power network unstable.

2.2 The principle of optimal allocation

This paper focuses on the relationship between coordination over frequency generator tripping measure and OPC. In order to solve the problem the high frequency in the isolated gird, the basic principles for all levels of measures are shown by definition:

1) To remaining the grid safe and stable, over frequency generator tripping measure of the generators should be set, as the backup measure when the chain measures are reject action.

2) When making the over frequency generator tripping measure, the generator of small capacity should be cut priority, remaining the generator of large the over frequency generator tripping measure capacity in the grid. The method will ensure the efficiency and economy of generators. And one unit should be retained in the plant, avoiding the blackout.

3) The value of the over frequency generator tripping measure is should be set in higher frequency than the OPC value, in order to minimize the isolated network under excess power impact.

4) The coordination scheme between the over frequency generator tripping measure and OPC should ensure that the island frequency can be controlled at a reasonable level, not leading the action of the underfrequency load shedding. And the scheme will avoid loss of cutting units and resulting in high frequency operation state of power grid.

5) The over frequency generator tripping measure should be configured to meet a variety of isolated network operation mode. It should have adaptability that can adapt to large load, small load and other power supply ways.

6） The fixed value of the OPC should be proper that can ensure the island frequency within the reasonable range. If it can not guarantee the island frequency controlled, the value should be set to try to ensure unit own safety.

7) The coordinated scheme should avoid repeated action of OPC and resulting collapse of the isolated grid.

2.3 The optimized allocation scheme

In order to coordinate the over frequency generator tripping measure and OPC scheme in the regional isolated gird, solving the problem of high frequency existed and maintaining stable operation, there are three options.

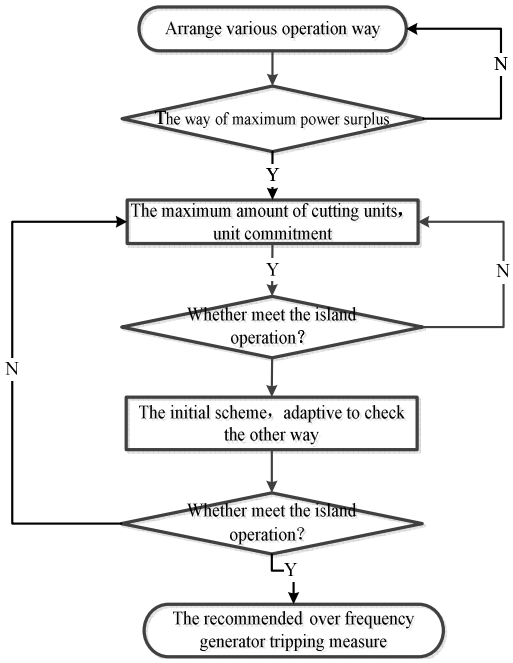

Fig. 2 The flow chart of program one

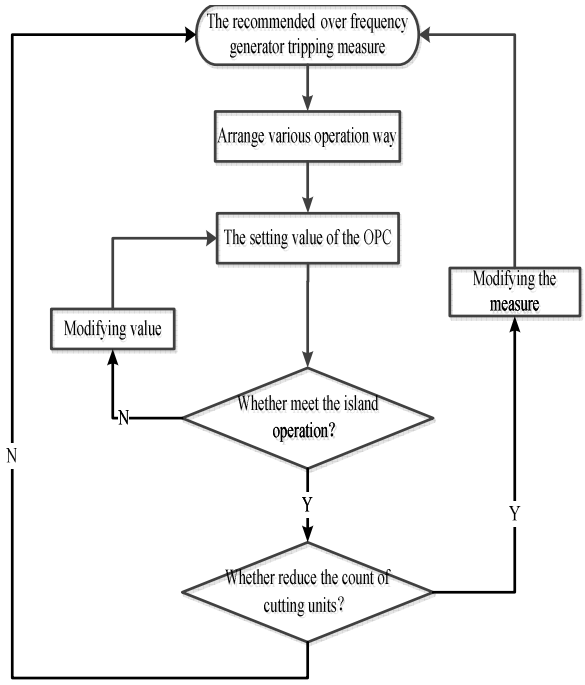

Fig. 3 The flow chart of program three

1) The first plan: the value of the over frequency generator tripping measure is lower than the OPC setting value. The over frequency generator tripping measure act first, controlling the frequency at a reasonable level without the action of the OPC.

2) The Second plan: The OPC setting value is lower than the over frequency generator tripping measure. The OPC scheme acts first, controlling the frequency at a reasonable level without the action of the over frequency generator tripping measure.

3) The Third plan: Considering the optimization of the OPC and he over frequency generator tripping measure，it will be evaluated that the OPC access may reduce the count of cutting units.

3 The analysis of the example

Taking Jiang Zhongzhu grid for example, it mainly consists of three areas: Zhong Shan grid, Zhong Zhu grid and Zhuhai power grid. The installed capacity of the regional grid is 8590MW. And the maximum load is 6635.8MW; it belongs to the typical sending end of the grid.

Through the analysis of the Jiang Zhongzhu grid, taking the waist load way for research, then the rationality of high load way and low load way will be checked.

3.1 The frequency controlling scheme of Jiang Zhongzhu grid at present

From the investigation and analysis on the OPC value and the over frequency generator tripping measure, it can be found as bellow:

1) At present, not all value of the turbine OPC is configured. The OPC principle is different, and its fixed value is also different. The existing OPC scheme is more complex, irregular. Beginning from the 51.0Hz, the generators are divided into six rounds by step of 0.5Hz. Each round of OPC starting value, closing time, and restarting value are not the same.

2) The value of over frequency generator tripping measure is set from the 51.0Hz, divided into five rounds by step of 0.5Hz. The generators' starting values and delay setting of each round are not the same. The capacity of first, second, third, fourth and fifth round are respectively 665,845, 3200,

1900, 700MW. Most of generators are involved in the high frequency controlling, but their starting values and delaying parameters need to check through the actual power network simulation.

3.2 The existing problem in the gird

Taking the waist load way for example, the external lines have the three-phase short circuit accident at the 0.2 second, and at the 0.3 second all the accident is cleared and all the tie lines are disconnected with the external grid. It will lead the Jiang Zhongzhu grid to become isolated network. Without considering the over frequency generator tripping measure and OPC, the frequency of the grid will control in about 50.7Hz, and the highest value is not more than 51.52Hz during the action, depending on the governor itself. The frequency change is shown as follow:

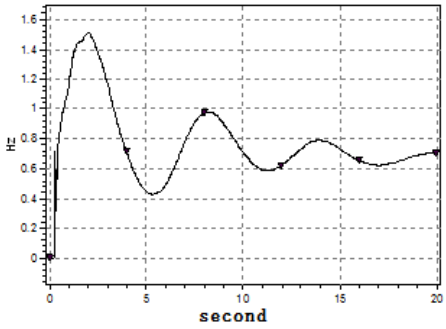

Fig. 4 The frequency curve of the grid (without OPC and over frequency generator tripping measure)

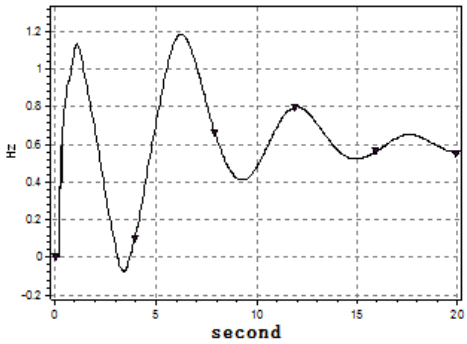

Fig. 5 The frequency curve of the grid (with OPC and over frequency generator tripping measure existing)

Considering the over frequency generator tripping measure and OPC existed, the frequency will be controlled at about 50.6Hz, the highest frequency is about 51.6Hz in the process. The frequency change is shown as follow:

From the table two, it can be seen that a total of 485MW generators are cut in the process. But the frequency of the grid cannot recovery to 50±0.5Hz. More generators need to be cut for eliminating the power surplus. The Heng Men #2 value of the over frequency generator tripping is 51.1Hz, its delay time is 10cycle, and its OPC value is 51.0Hz. So they may act at the same time. In the process, Heng Men #2 generator's OPC acts two times. At the last time, while the OPC closed the valve, Heng Men #2 was cut by the over frequency generator tripping. The over frequency generator tripping cannot act correctly.

Through the above analysis, without considering the OPC and over frequency generator tripping measure, the isolated grid is hard to maintain stability. While considering the OPC and over frequency generator tripping measure, the frequency condition is better, but it still cannot return to a reasonable range. Therefore, the scheme of OPC and over frequency generator tripping measure must be optimized.

Considering the over frequency generator tripping measure and OPC existed, the frequency will be controlled at about 50.6Hz, the highest frequency is about 51.6Hz in the process. The frequency change is shown as follow:

From the table two, it can be seen that a total of 485MW generators are cut in the process. But the frequency of the grid cannot recovery to 50±0.5Hz. More generators need to be cut for eliminating the power surplus. The Heng Men #2 value of the over frequency generator tripping is 51.1Hz, its delay time is 10cycle, and its OPC value is 51.0Hz. So they may act at the same time. In the process, Heng Men #2 generator's OPC acts two times. At the last time, while the OPC closed the valve, Heng Men #2 was cut by the over frequency generator tripping. The over frequency generator tripping cannot act correctly.

Through the above analysis, without considering the OPC and over frequency generator tripping measure, the isolated grid is hard to maintain stability. While considering the OPC and over frequency generator tripping measure, the frequency condition is better, but it still cannot return to a reasonable range. Therefore, the scheme of OPC and over frequency generator tripping measure must be optimized.

Tab. 2 Action of the over frequency generator tripping measure and OPC in the grid

Order	Time(s)	Incident
1	0.26	Zhu Hai#1, #2， ΔMW reaches to the triggering value，OPC triggered, high pressure and medium-pressure valve closed
2	0.54	The speed of the Heng Men #2 reaches 3060r/min (51.0Hz), OPC triggered，high pressure and medium-pressure valve closed
3	1.06	The speed of the Shuang Shui #5, #6 reach 51.1Hz,the generators are cut
4	1.07	The speed of the Nan Lang #4 reaches 51.0Hz,the generatos is cut
5	3.06	The frequency got down to 50 Hz, the OPC of Heng Men #2，Zhu Hai #1 and Zhu Hai#2 are triggered, all of the valve are opened.
6	5.54	The speed of the Heng Men #2 reaches 3060r/min (51.0Hz), OPC triggered，high pressure and medium-pressure valve closed
7	5.99	The speed of the Heng Men #2 reaches 51.1Hz,the generator is cut

3.3The optimized allocation scheme

On the basis of 2.3 chapter, there are three kinds of scheme existing.The analysis process is as follows:

(1) Using scheme 1: depending on the over frequency generator tripping measure entirely, the final configuration as shown in table three:

Tab. 3 The scheme of the over frequency generator tripping measure

Round	Starting Frequency（Hz）	Delay (Cycle)	Unit commitment
1	50.8	10	Heng Men #2,Nang Lang #3,Heng Men #2,Shuang Shui #5
2	50.8	35	Zhu Hai#3
3	51.0	15	Tong Gu#3
4	51.5	15	Nang Lang #1,Heng Men #1,Nang Lang #4
5	51.8	10	Zhu Hai#1,Shuang Shui # 6,Zhu Hai #4,Tong Gu#4
6	52.0	10	Zhu Hai #2,Tong Gu #5
7	52.5	15	Tong Gu #6, Tong Gu #7

(2) Using scheme 2: By changing the OPC value, the valves of some turbine will repeatedly open and close. Because of the fluctuation of output power, the frequency of the grid will lose stability, even getting to oscillation.

(3) Using scheme 3: Considering the output is much lower than the initial state after the OPC action, so the OPC action will help to eliminate some excess power, it will reduce the capacity of the cutting generators and will help the system recovery.

Compared with the scheme1, the frequency will be better in the isolated network by using the OPC configuration set. The excess power will be eliminated by the OPC action.

While sending power in 2000MW to 2600MW, it will reduce a round generator cutting by using optimized scheme. The generator of the third round will not be cut. The frequency of the grid can also remain stability. The final grid frequency will maintained within 50.5Hz.

While sending power in 1200MW to 1300MW, the frequency of the grid will remain at about 50.5Hz, only by governor of generators and the OPC of Zhu Hai #1 \#2. Compared with scheme 1, it will reduce the amount of generator cutting.

The optimized scheme has better adaptability from large load way and small load way checking.

Tab. 4 The optimized scheme of the over frequency generator tripping measure

Round	Starting Frequency（Hz）	Delay (Cycle)	Unit commitment
1	50.8	10	Heng Men #2,Nang Lang #3,Heng Men #2,Shuang Shui #5
2	50.8	35	Zhu Hai#3
3	51.0	15	Tong Gu#3
4	51.2	20	Zhu Hai#2
5	51.5	15	Nang Lang #1,Heng Men #1,Nang Lang #4
6	51.8	10	Zhu Hai#1,Shuang Shui # 6, Zhu Hai #4,Tong Gu#4
7	52.0	10	Tong Gu #5
8	52.5	15	Tong Gu #6, Tong Gu #7

Tab. 5 The optimized scheme of the OPC

Round	Starting Frequency（Hz）	Delay（Cycle）	OPC
1	——	——	Zhu Hai#1, Zhu Hai#2
2	51.0	150	Shuang Shui#5,Heng Men#2
3	51.8	100	Tong Gu#3
4	52.0	25	Zhu Hai#3
5	52.1~52.5	10	Heng Men#1（52.1）,Shuang Shui#6（52.2）,Nan Lang #4(52.3）, Tong Gu#5（52.5）
6	52.6~53.0	15	Nan Lang #2（52.6）, Zhu Hai#4(52.7), Tong Gu#4(53.0)

Summary

Through the investigation of the development of process of OPC, combined with the status of turbine, the typical OPC model has been established. By the typical OPC model established in PSD-BPA, and taking Jiang Zhongzhu grid for example, the over frequency generator tripping measure and OPC scheme is optimized. The reasonable proposals are put forward, and it will ensure the safe and stable of the gird operation. With proper OPC method, it can reduce the amount of generator cutting and improve the restoring of frequency

References

[1] Huang Zongjun,Chao Jian,Li Xingyuan,et al．High frequency phenomenon caused by fault occurred in southern part of Gui Yang power grid and simulation of over speed protection controller [J]．Power System Technology，2007，31(15)：26-32(in Chinese)．

[2] Xu Yanhui, He Renmu, Kong Xiangyun．The effect of overspeed protection control on power system stability[J]．Modern Electric Power，2006，23(6)：6-9 (in Chinese)．

[3] Cai Yunqing, Wang Lei, KipMorison, et a1．Current status and prospect of wide—area protection (dynamic stability control) technologies[J].Power System Technology,2004,28(8): 20—25(in Chinese)．

[4] Chen Xinghua, Luo Xiangdong, Wu Guobing, et al .A machine network coordination scheme of electromagnetic ring rejection for Guang Dong Zhong Zhu power grid[J].Southern power system technology, 2008, 2(3): 56-59（in Chinese).

[5] FU Shuti. Summary on power system security problems on 2004 PES meeting and recommendation for developing defense measures s[J] .Automation of Electric Power Systems, 2005, 29 (8): 124（in Chinese) .

[6] XUE Yusheng. The way from a simple contingency to system wide disaster: lessons from the eastern interconnection blackout in 2003. Automation of Elect ric Power Systems , 2003 , 27 (18) :1-5(in Chinese)．

[7] DAI Yiping , ZHAO Ting , GAO Lin. Research on characteristics of power system primary frequency control operating on power plants. Electric Power, 2006, 39 (11) :37-41(in Chinese)．

Advanced Materials Research Vols. 986-987 (2014) pp 412-418

doi:10.4028/www.scientific.net/AMR.986-987.412

Power Control of Microgrid with Rich Small Hydropower Stations

Yuhui XING[1, a], Guiping ZHU[1], Yonghong XIA[2], Jianbo XIN[2]

[1]Department of Electrical Engineering, Tsinghua University, Beijing, 100084, China

[2]Electric Power Research Institute of Jiangxi Province, Nanchang, 330096, China

[a]email: xyh1990@126.com

Keywords: Small Hydropower Stations; Microgrid; Power Control

Abstract. In China, some remote areas with rich small hydropower stations suffer from a tradeoff between water surplus and off-limit voltage in the grid during wet seasons. The microgrid of new energy sources provides a new way of solving this problem. Under the background of the microgrid proposed in somewhere of Jiangxi Province, this paper firstly carries out simplified model on the actual system. Output models of PV and small hydropower stations are established. Then with Minimizing transmission losses of microgrid system and the amount of all small hydropower abandoned waters as the optimization objective, and considering the output constraints of each micro power source, power balance constraints and voltage constraints. A micro-power output optimization model is established and then solved by improved particle swarm optimization algorithm. By comparing the micro-power output and system line loss before and after the optimization, it verifies that the proposed power control method can prevent the off-limit voltage effectively and reduce transmission losses of the system.

Introductions

Small hydropower stations has become an important part of China's hydropower stations; by 2010, our country has built 45,000 small hydropower stations, with the installed capacity of more than 54 million kW and the annual generating capacity of over 160 billion kWh[1]. However, small hydropower is often built at the end of the distribution network in remote rural areas, concentrated along the river, which output is greatly influenced by climatic season. When the total installed capacity of several small hydropower stations reaches a certain scale, it may have a greater impact on the operation of regional power grid, which may endanger the normal safe operation of the power grid. Especially in small hydropower-rich regions, the output of the small hydropower in wet period is much larger than the load capacity within the area, and most of the small hydropower has no ability to regulate the storage capacity, resulting in prominent voltage out-of-limit problem of the distribution grid [2-3].

In recent years, the rapid development of smart microgrid provides a new way to deal with the problems of microgrid in the area with rich small hydropower stations. Microgrid combines the distributed generation, load and energy storage devices, the control devices together to form an independently controllable power supply system. Smart Microgrid is used to accept the distributed new energy power generation, including small hydropower, and it can realize the optimal allocation of energy, improve the power quality and power consuming efficiency, so as to promote energy conservation and emission reduction. Scholars at home and aboard conducted extensive research [3-7] for the energy management and optimization of operational control of new energy microgrid, proposing a variety of control strategies under different technical objectives and economic objectives. At present, most of the researches for small hydropower operation optimization are in the aspect of voltage quality control. Optimization and improvement of the voltage quality by controlling the online power factor of small hydropower is proposed in [8]; a multi-objective mathematical model on voltage bias, voltage optimization investment and grid loss, etc. are established in [9] and [10], and the voltage optimization control research on the distribution grid with rich small hydropower is conducted by using an improved adaptive genetic algorithm. But currently, there are few researches over the world, working on the optimized control of small hydro-rich new energy Microgrid.

This paper mainly studies the problem of optimization control of new energy microgrid with rich small hydropower stations. Under the premise of meeting the system safe operation constraints, optimize the output of various distributed power supplies, to minimize the total transmission losses of the system and the abandoned water quantity for all small hydropower stations.

Microgrid system with rich small hydropower stations

The examples in this paper are based on a practical microgrid system which is prepared in a county of Jiangxi Province; the microgrid has four small hydropower stations, a small-scale PV power station, and a small amount of residents load. The actual system is simplified into a system with 26 nodes, with the system frequency of 50Hz and the reference voltage of 10kV. The equivalent parameters of each feeder are shown in Figure 1. The total load distribution capacity of the entire system is 1216kVA. Furthermore, the system also has a photovoltaic power generation of 10kW.

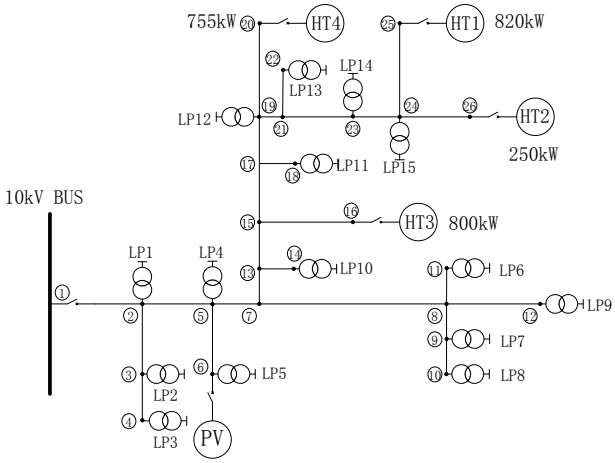

Fig.1.Simplified model of the microgrid with new energy and rich small hydropower stations

The rated power of each small hydropower is shown in Table 1, and the transmission line parameters are shown in Table 2.

Table.1. Rated power of each small hydropower

Power station	Capacity
HT1	820kW
HT2	250kW
HT3	800kW
HT4	755kW

Table.2. Transmission line parameters

Line model / length	Line equivalent resistance (Ω)	Line equivalent reactance (Ω)	Line model / length	Line equivalent resistance (Ω)	Line equivalent reactance (Ω)
1-2	0.05477	0.06793	5-15	0.2089	0.06416
2-3	0.05477	0.06793	5-16	1.306	0.7632
3-4	0.05477	0.06793	16-17	0.7830	0.2404
4-5	1.325	0.5535	6-18	0.1251	0.0384
4-6	0.5145	0.5533	8-19	0.2165	0.0665
6-7	0.5145	0.5533	9-20	0.4930	0.2880
7-8	0.5145	0.5533	9-21	0.7275	0.4251
8-9	0.5145	0.5533	21-22	0.7275	0.4251
9-10	0.1808	0.1056	22-23	0.5928	0.3463
2-11	0.2977	0.1739	22-24	0.3591	0.2080
11-12	0.2977	0.1739	7-25	0.3587	0.2853
3-13	0.2076	0.0638	10-26	0.3323	0.1941
5-14	2.168	0.6288			
5-15	0.2089	0.06416			

In the system, the small hydropower stations are all run-off-river hydropower stations without reservoir regulation ability; during the actual operation, the electricity is generated as much as possible based on the runoff conditions. In wet period, the station is running with full output, while in dry period, limited by the runoff conditions, the generating capacity is low, even sometimes zero.

Local grid companies require that the power factor of small hydropower should be no less than 0.95.

The national standards stipulate that the voltage fluctuations of the line with 10kV should not exceed 7% of the rated voltage. Currently, in the actual operation, in wet period, the output of small hydropower has no any regulation and control; the voltages of five key nodes are detected exceeding the upper limit of the rated value, and the problem of high voltage is very prominent, as shown in Table 3. Therefore, it is quite necessary to control the power of the microgrid with rich small hydropower.

Table.3. The voltage of the key nodes in wet period without optimization

Load rate	Node 2 (p.u.)	Voltage of node 5 (p.u.)	Voltage of node 8 (p.u.)	Voltage of node 15 (p.u.)	Voltage of node 19 (p.u.)
10%	1.095	1.096	1.096	1.112	1.123
40%	1.088	1.09	1.089	1.105	1.115
70%	1.082	1.083	1.082	1.098	1.107

Output power model of micro power supply

Separate output models are built for the photovoltaic module and the small hydropower in the microgrid system with new energy.

The photovoltaic power generation system uses the MPPT control strategies to obtain the largest active power[11]; and the active power of the small-scale photovoltaic power station can be estimated according to the following formula

$$P_{PV} = P_{STC}(\frac{G_T}{G_{T,STC}})[1+\alpha_P(T_c - T_{c,STC})] \quad (1)$$

where, P_{PV} represents the active power of small-scale photovoltaic power station; P_{STC} represents the rated output active power of the photovoltaic array under standard rating conditions, with the actual value of 10kW; G_T represents irradiance intensity; $G_{T,\mathrm{STC}}$ represents the irradiance intensity of the light source under the standard test conditions, with the value of 1000w/m2; α_P represents photovoltaic battery power temperature coefficient and it's related to the types of photovoltaic battery and materials, and in fact, the photovoltaic battery power temperature coefficient α_P of the mainstream polycrystalline silicon photovoltaic battery used in the market is -0.5; $T_{c,\mathrm{STC}}$ represents photovoltaic battery operating temperature under standard test conditions, with the value of 25℃; T_c represents the operating temperature of photovoltaic battery in photovoltaic power generation system. According to local natural conditions, the photovoltaic output power can be calculated according to the Formula (1). During optimization, regard the photovoltaic as "Negative" load for treatment.

For small hydropower stations, the local power grid requires its power factor above 0.95. For simplicity, assuming that all small hydropower stations are running under constant power factor mode and the power factor is always 0.95, then its active power output is the system optimization variable.

Optimized mathematical model of small hydropower output

Take the small hydropower output as an optimization variable and setthe optimal scheduling cycle of the microgrid as 1 h.And take the microgrid composed by the small hydropower, photovoltaic and energy storage devices and the interconnected distribution grid as an infinite power supply, then set the constant voltage at the grid connection point as 10.5kV.

Objective function

The optimization objective of this paper is under the premise of meeting a variety of operating constraints of the system, to

(1) Minimize the line loss of the system

(2) Minimize the abandoned water quantity,that is maximizing the output power of each small hydropower station in the system to achieve a better economic benefit.

Optimization objective function is:

$$\min F = \min C \cdot P_{Loss} + \sum_{i=1}^{N_G} (P_{GNi} - P_{Gi}) \tag{2}$$

Where, F represents the optimization objective which is the composite function of system line loss and small hydropower generating capacity; C represents the weight coefficients of system line loss; P_{Loss} represents the total line loss of system, which is obtained through load flow calculation; N_G represents the total number of small hydropower; P_{Gi} represents the output power of the ith small hydropower station, P_{GNi} represents the rated output power of the ith small hydropower station.

Constraints

Constraints of the system include micro-power output constraints, the system power balance constraints and bus voltage constraints.

(1) Micro-power output constraint:

$$P_{Gi,\min} \le P_{Gi} \le P_{Gi,\max} \tag{3}$$

Where, P_{Gi} represents the output power of the i[th] small hydropower, $P_{Gi,\min}$ represents the lower limit of the output power of the i[th] small hydropower, $P_{Gi,\max}$ represents the upper limit of the output power of the i[th] small hydropower.

(2) System power balance constraint:

$$\sum_{i=1}^{N_G} P_{Gi} + P_{PCC} = \sum_{j=1}^{N_{load}} P_{load} + P_{Loss} \tag{4}$$

Where, N_G represents the total number of small hydropower; P_{Gi} represents the output power of the i[th] small hydropower; P_{PCC} represents the active power that the large power grid inputted to microgrid at the connection point of microgrid; P_{Loss} represents the total line loss of system, which is obtained through load flow calculation.

(3) Constraint of voltage without out-of-limit:

The national standards stipulate that the line voltage of 10kV should not exceed $\pm 7\%$ of the rated voltage, therefore,

$$0.93Un_i \le U_i \le 1.07Un_i \tag{5}$$

Particle Swarm Optimization (PSO)

Particle swarm optimization was put forward by James Kennedy and Russell Eberhart in 1997 for the first time, which belongs to evolutionary algorithms, with advantages such as easy to program, less empirical parameters need to be set and fast to convergence, etc.. In this paper, the particle swarm optimization with inertia weight was used to accelerate the convergence speed [12, 13]

When conducting practical programming, selecting active power of four small hydropower stations $P_{Gi}(i = 1,2,3,4)$ as the optimization variables, therefore, each particle has four dimensions as $[P_{G1}, P_{G2}, P_{G3}, P_{G4}]$. For the constraints given by Formula (3), exterior penalty function method is introduced, to reckon the constraints into the objective function in the form of a penalty term of penalty function, with the value of penalty factor of 100, as shown in Formula (6):

$$\min F'(x)=\begin{cases} F(x)+\sigma\left\{\sum(U_i-1.07U_{ni})^2\right\} & \text{if } U_i>1.07U_{ni} \\ F(x)+\sigma\left\{\sum(U_i-0.93U_{ni})^2\right\} & \text{if } U_i<0.93U_{ni} \\ F(x) & \text{else} \end{cases} \quad (6)$$

Optimization results

According to natural lighting data of the microgrid area, using Formula (1) to calculate the output of small-scale photovoltaic power stations as shown in Figure 2.

Typical daily load factor curve of the microgrid area is shown in Figure 3.

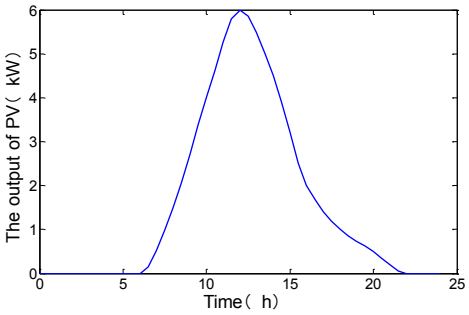

Fig.2. The output power of photovoltaic power generation

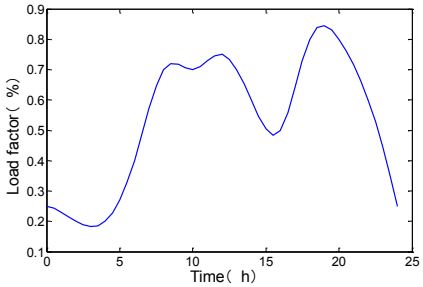

Fig.3. Typical daily load factor curve of the microgrid area

According to the above model and data, using MATLAB to conduct optimal calculations, use MATPOWER flow calculation program and particle swarm optimization, and then the optimized active power output of four small hydropower stations will be obtained, as shown in Figure 4.

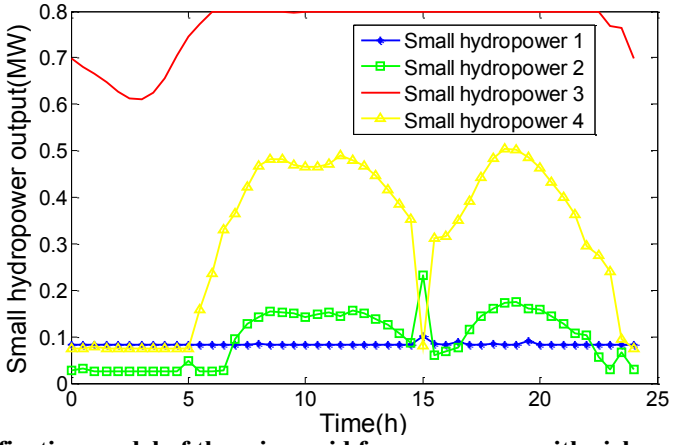

Fig.4. Simplification model of the microgrid for new energy with rich small hydropower

Figure 4 shows that, the output power of small hydropower 3 remains higher after optimization and it keeps in full load at high load; while the output power of small hydropower 1 and small hydropower 2 are significantly restricted. Compared to the system model shown in Figure 1, we can find that, it is because small hydropower 1 and 2 are at the tail end of power grid that their output power give a great impact on the voltage of the tail end of the line. The output must be restricted to prevent bus voltage of microgrid out-of-limit,.

Voltages of each node of small hydropower output before and after optimization are shown in Table 4. It can be seen that the voltage of each node are all qualified after optimization. The comparison of line loss of the system before and after optimization is shown in Table 5; we can see that the system line losses have a significant reduction as well after optimization.

Table.4. Comparison of the voltage of the key nodes before and after optimization.

	Node 2 (p.u.)	Voltage of node 5 (p.u.)	Voltage of node 8 (p.u.)	Voltage of node 15 (p.u.)	Voltage of node 19 (p.u.)
Without optimization	1.092	1.093	1.093	1.109	1.120
After optimization	1.042	1.043	1.043	1.059	1.069

Table.5. The comparison of transmission losses of the system before and after optimization

Time (h)	0	2	4	6	8	10	12
Line losses of the system before optimization (MW)	0.012	0.012	0.009	0.015	0.024	0.027	0.024
Line losses of the system after optimization (MW)	0.072	0.069	0.069	0.063	0.057	0.057	0.057
Time (h)	14	16	18	20	22	24	
Line losses of the system before optimization (MW)	0.024	0.021	0.024	0.024	0.021	0.009	
Line losses of the system after optimization (MW)	0.06	0.063	0.057	0.057	0.06	0.069	

Conclusions

This paper studies the optimization problem of each micro power supply of microgrid with small hydropower. Under the premise of meeting all constraints of system operation, take output power of each small hydropower in microgrid as optimization variables to make transmission losses of the system as small as possible and the abandoned water quantity of small hydropower as little as possible. Take the real system somewhere in Jiangxi as examples, and then adopt particle swarm optimization to conduct numerical simulation. The calculating result verifies the validity of the optimization algorithm mentioned in the paper, and provides a meaningful reference for further study of economic operation of new energy microgrid with small hydropower.

Acknowledgement

In this paper, the research was sponsored by the Technology Project of State Grid Corporation of China (Project No. 52182013000V).

References

[1] Tong Jiandong, Small Hydropower in China [M], China WaterPower Press, 2006: 40-44.
[2] Bai Yaopeng. Study on the Impact of System Operation Grid-accessed Small Hydropower Stations [D], Beijing Jiaotong University, 2010.
[3] Ijumba N M, Jimoh A A, Nkabinde M. Influence of distribution generation on distribution network performance: Africon, 1999 IEEE, Cape Town, 1999[C].1999
[4] Piagi P, Lasseter R H. Autonomous control of microgrids: Power Engineering Society General Meeting, 2006. IEEE, Montreal, Que., 2006[C].2006
[5] Wang Chengshan, Xiao Zhaoxia and Wang Shouxiang, Synthetical Control and Analysis of Microgrid [J], Automation of Electric Power System, 2008(07): 98 - 103.
[6] Yunwei L, Vilathgamuwa D M, Poh C L. Design, analysis, and real-time testing of a controller for multibus microgrid system [J]. Power Electronics, IEEE Transactions on, 2004，19(5)：1195-1204.
[7] Peas Lopes J A, Moreira C L, Madureira A G. Defining control strategies for MicroGrids islanded operation. Power Systems [J], IEEE Transactions on, 2006，21(2)：916-924.
[8] Jinlei H, Yao Z L G, Huifan X. Optimization of Power Factor for Operation of Small Hydro Stations: Power System Technology, 2006. PowerCon 2006. International Conference on, Chongqing, 22-26 Oct. 2006[C]
[9] Liu Yi, Ye Sheng and Peng Xiangang, et al. Voltage Optimal Control Research on Small Hydropower Stations Group in Regional Grid [J]. Power System Protection and Control, 2010 (09): 136 - 140.
[10] Shi Xuntao, Research on Voltage Optimization and Control of Distribution Grid with Small Hydropower [D], South China University of Technology, 2012.

[11] Zhang Liwen, Zhang Juwei and Tian Wei, et al, Technology and Application of Solar Energy Photovoltaic Power Generation [J], Applied Energy Technology, 2010 (03): 4 - 8.
[12] Zeng Jianchao, Jie Jing and Cui Zhihua, Particle Swarm Optimization [M], Science Press, 2004: 19-20.
[13] Ji Zhen, Miao Huilian and Wu Qinghua, Particle Swarm Optimization and Application [M], Science Press, 2009: 17-21.

Advanced Materials Research Vols. 986-987 (2014) pp 419-423

doi:10.4028/www.scientific.net/AMR.986-987.419

Power Distribution System Evaluation in Chemical Industry Park using Subjective and Objective comprehensive Weight method

Zaipeng DUAN[1], Xinming QIAN[1, a], Rujun WANG[2], Yingquan DUO[2]

[1]State Key Laboratory of Explosion Science and Technology, Beijing Institute of Technology, Beijing, 100081, China

[2]China Academy of Safety Science and Technology, Beijing, 100012, China

[a]email: qsemon@bit.edu.cn

Keywords: Chemical Industry Park; Power Supply and Distribution system; Fuzzy Comprehensive Evaluation; Subjective and Objective Comprehensive Weight; AHP; Standard Deviation

Abstract. The plan for power supply and distribution system in the Chemical Industry Park is complex. The evaluation method must be easy and truly show the site conditions in order to maintain the proper function of the system. Thus the fuzzy comprehensive evaluation method was chosen and applied in this paper. As for the weight calculation, Analytic hierarchy process (AHP) was used to compute the subjective weight; on the purpose of avoiding strong effect of subjective factors, the standard deviation for each index was calculated, and then the subjective weight was integrated to build the subjective and objective comprehensive weight model. Lastly fuzzy comprehensive evaluation method was applied into the model for assessing the power supply and distribution system in the Chemical Industry Park.

Introduction

Planning and configuration of the power supply and the distribution system in the chemical industry park is complicated. The topology, load, power source and distribution unit are different from those in high-voltage transmission systems [1]. According to statistics, the percentage of power outage caused by faults of distribution units exceeded 90% [2]. The evaluation method must be easy and truly show the site conditions in order to maintain the proper function of the system. Fuzzy comprehensive evaluation, which integrates the qualitative and quantitative analyses, has been widely used in the areas of engineering technology and management evaluation [3] [4]. The first key point for utilizing this method is the selection of membership function, and the second one is the determination of the index weight [5].

Subjective and Objective Comprehensive Weight

In this paper, the target layer A is set as a single element; the criteria layer B contains p elements; the index layer C contains m elements. Referring to the index weight for the target layer A and the criterion layer B, the importance of each index in the criteria layer is compared using the AHP classical method [3]. The following judgment matrix was built:

$\mathbf{A}$ - $\mathbf{B_i}$	$\mathbf{B}_1$	$\mathbf{B}_2$	…	$\mathbf{B}_p$
$\mathbf{B}_1$	b_{11}	b_{12}	…	b_{1p}
$\mathbf{B}_2$	b_{21}	b_{22}	…	b_{2p}
…	…	…	…	…
$\mathbf{B}_p$	b_{p1}	b_{p2}	…	b_{pp}

The judgment matrix $A-B_i=\left(b_{ij}\right)_{p\times p}$ has the following nature: ① $b_{ij}>0$ ② $b_{ji}=1/b_{ij}$ ③ $b_{ii}=1$ .Among which, b_{ij} is the importance degree for b_i compared to b_j . The rating scale method, 1-9, is generally used[4].

The judgment matrix shows the importance degree between two elements, and the result is ${W_B}^A = \left({w_{B_1}}^A, {w_{B_2}}^A, \cdots, {w_{B_p}}^A \right)$. In order to maintain consistency of importance degree for all elements in a layer, consistence check needs to be performed, and the eigenvalue method is generally used. The calculation method for the weight of index layer-criterion layer ${w_{C_j}}^{B_k} = \left({w_{c_1}}^{B_k}, {w_{c_2}}^{B_k}, \cdots, {w_{c_m}}^{B_k} \right), j \in (1,2,\cdots,m), k \in (1,2,\cdots,p)$ is the same as that for the weight of criterion layer-target layer. It is noted when index C_j and B_k in the index layer are not related, the value of ${w_{C_j}}^{B_k}$ is 0 [5].

The number of p weight between the criterion layer B and the target layer A is ${w_B}^A$. The number of m weight between the index layer C and index B_j in the criterion layer is ${w_{C_j}}^{B_k}$. The sequence for element C in the index layer to the target layer is as follows:

$$ {w_{C_j}}^A = \sum_{j=1}^{m} {w_{B_k}}^A \cdot {w_{C_j}}^{B_k} \tag{1} $$

If n experts evaluate a system including m indexes, the score matrix is F.

$$ F = \begin{bmatrix} F_{11} & F_{12} & \cdots & F_{1m} \\ F_{21} & F_{22} & \cdots & F_{2m} \\ \vdots & \vdots & & \vdots \\ F_{n1} & F_{n2} & \cdots & F_{nm} \end{bmatrix} $$

Expectation μ_j of unified j attribute and standard deviation σ_j are as follows:

$$ \mu_j = \frac{1}{n} \cdot \sum_{i=1}^{n} F_{ij} $$

$$ \sigma_j = \sqrt{\frac{1}{n-1} \cdot \sum_{i=1}^{n} \left(F_{ij} - \mu_j \right)^2} \tag{2} $$

Based on the standard deviation σ_j, its standard deviation weight w_j is calculated as follows:

$$ w_{obj} = \frac{\sigma_j}{\sum_{j=1}^{m} \sigma_j} \tag{3} $$

If ε_j is the subjective and objective index of index j, the subjective and objective comprehensive weight is as follows:

$$ w_j = \frac{\varepsilon_j}{\sum_{j=1}^{m} \varepsilon_j} = \frac{{w_{C_j}}^A \cdot \sigma_j}{\sum_{j=1}^{m} \left({w_{C_j}}^A \cdot \sigma_j \right)} \tag{4} $$

Fuzzy Synthetic Evaluation Model

The factor gather is set to $U = (u_1, u_2, \cdots, u_s)$, and the assessment set is $V = (v_1, v_2, \cdots, v_m)$. If the evaluation result of the i expert among n experts is fuzzified by membership function, then the fuzzy relationship matrix is described as R_i.

Based on the calculations of the subjective and objective comprehensive weight w and the evaluation matrix R_i, the mathematical model for fuzzy comprehensive evaluation is $B = R_i \times w$. The common form of this model in the paper is:

$$ B_i = R_i \cdot w \tag{5} $$

B_i is unified to $\overline{B}_i$, and the comprehensive evaluation result of the i expert is as follows:

$$G_i = \overline{B}_i \cdot V^T \tag{6}$$

Based on the previous sequence, perform the calculations and integrate evaluations of n experts, so the vector $G = [G_1, G_2, \cdots, G_n]$.

Case Analysis

Fig.1 shows the index evaluation system for the power supply and distribution system in a chemical industry park, in which the operating status was evaluated using the fuzzy comprehensive evaluation method.

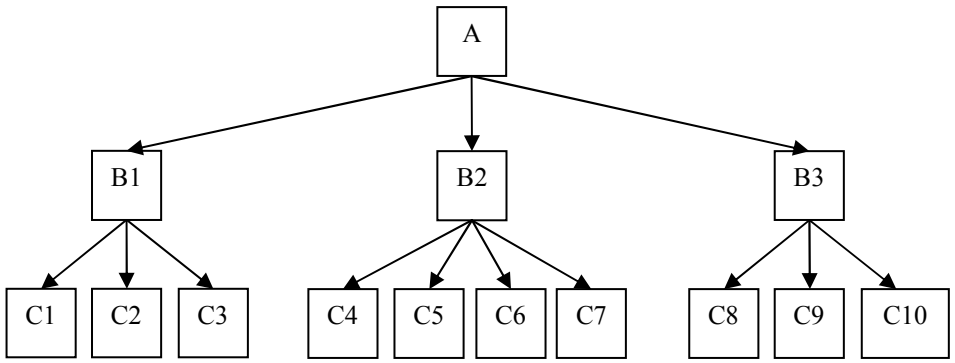

Fig.1. Index Evaluation System for Power Distribution System in Chemical Industry Park

Note: **A: overall performance; B1: economical efficiency;** C1: operating economical efficiency; C2: construction economical efficiency; C3: annual cost; **B2: reliability;** C4: average duration for system power outage; C5: average frequency for system power outage; C6: average system power supply availability; C7: costs of power outage; **B3: coordination;** C8: coordination of power supply capability for medium voltage distribution network; C9: coordination of power supply capability for high voltage distribution network; C10: matching degree of various level power transformation capacity.

The 5 scales conservative trapezoidal membership functions are utilized, as shown in Fig2-1. The score scale is defined as: 50-100, 100-90, optimum; 80-90, suboptimum; 70-80, good; 60-70, worse; 50-60, worst. Eight experts marked 10 indexes, and the result matrix F is shown as follows:

$$F = \begin{bmatrix} 78.0, 78.0, 91.0, 75.0, 93.0, 83.0, 82.0, 85.0, 80.0, 82.0 \\ 70.0, 68.0, 80.0, 73.0, 88.0, 92.0, 75.0, 71.0, 77.0, 77.0 \\ 71.0, 87.0, 87.0, 77.0, 91.0, 87.0, 78.0, 79.0, 78.0, 94.0 \\ 67.0, 83.0, 89.0, 83.0, 89.0, 80.0, 76.0, 77.0, 82.0, 68.0 \\ 65.0, 87.0, 88.0, 79.0, 90.0, 84.0, 77.0, 76.0, 80.0, 81.0 \\ 67.0, 79.0, 89.0, 81.0, 93.0, 90.0, 88.0, 85.0, 87.0, 65.0 \\ 77.0, 91.0, 90.0, 88.0, 89.0, 82.0, 84.0, 77.0, 81.0, 89.0 \\ 78.0, 88.0, 85.0, 76.0, 91.0, 89.0, 84.0, 83.0, 75.0, 84.0 \end{bmatrix}$$

According to the contents of first section, the results are $w_B{}^A = [0.54, 0.30, 0.16]$ and $w_C{}^B = [0.14, 0.29, 0.57, 0.15, 0.50, 0.27, 0.08, 0.12, 0.32, 0.56]$. The subjective and objective comprehensive weight is $w_C{}^A = [0.08, 0.15, 0.31, 0.05, 0.15, 0.08, 0.02, 0.02, 0.05, 0.09]$ according to Eq.1.

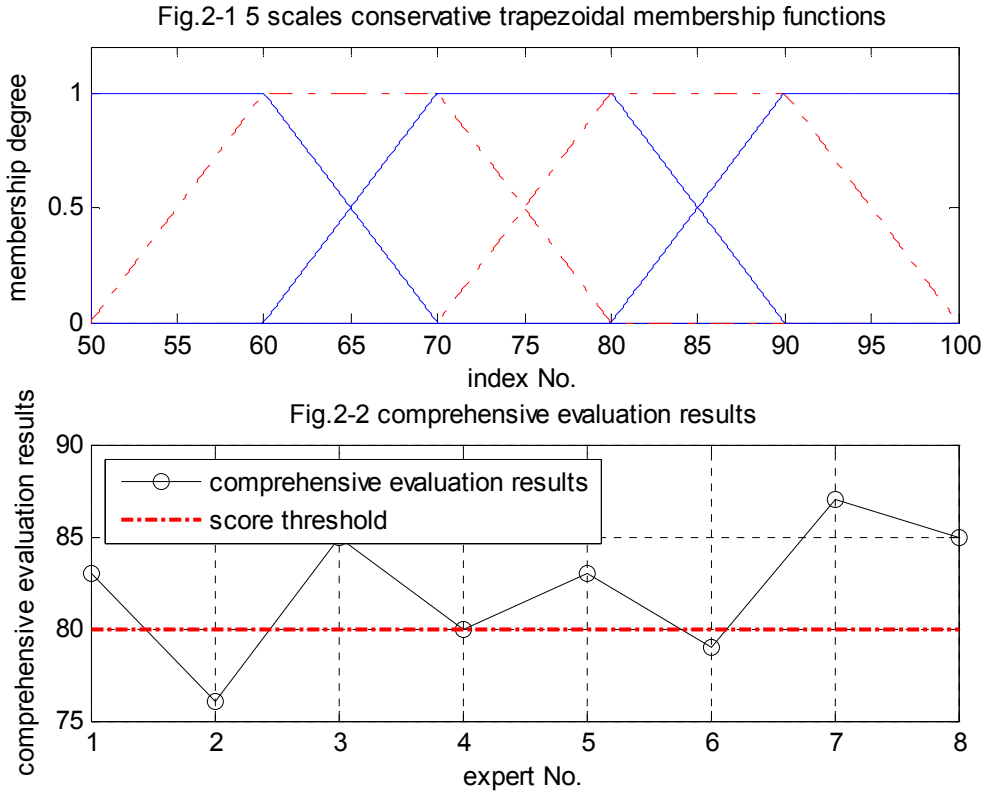

Fig.2. Membership functions and comprehensive evaluation results

The standard deviation for indexes F is $\sigma=[5.34,7.42,3.50,4.87,1.85,4.26,4.66,4.91,3.63,9.83]$, and the standard deviation weight for indexes F is $w_{obj}=[0.11,0.15,0.07,0.10,0.04,0.08,0.09,0.10,0.07,0.20]$, according to the Eq. 2 and Eq. 3; the subjective and comprehensive parameter is $\varepsilon=[0.41,1.14,1.08,0.22,0.27,0.34,0.11,0.10,0.19,0.90]$, according to formula 4; the subjective and objective comprehensive weight is $w=[0.09,0.24,0.23,0.05,0.06,0.07,0.02,0.02,0.04,0.19]$, as shown in Fig. 3.

The assessment $V=(50,65,75,85,95)$. The score threshold in the thesis is 80, and the threshold for number of people is 80%. The vector for eight experts' evaluation scores is $G=[83,76,85,80,83,79,87,85]$ according to formula Eq. 5 and formulae. 6, so 7 people pass the score threshold, as shown in Fig2-2. So the requirements for threshold for number of people is met, which mean the power supply and distribution system in the chemical industry park passes the evaluation.

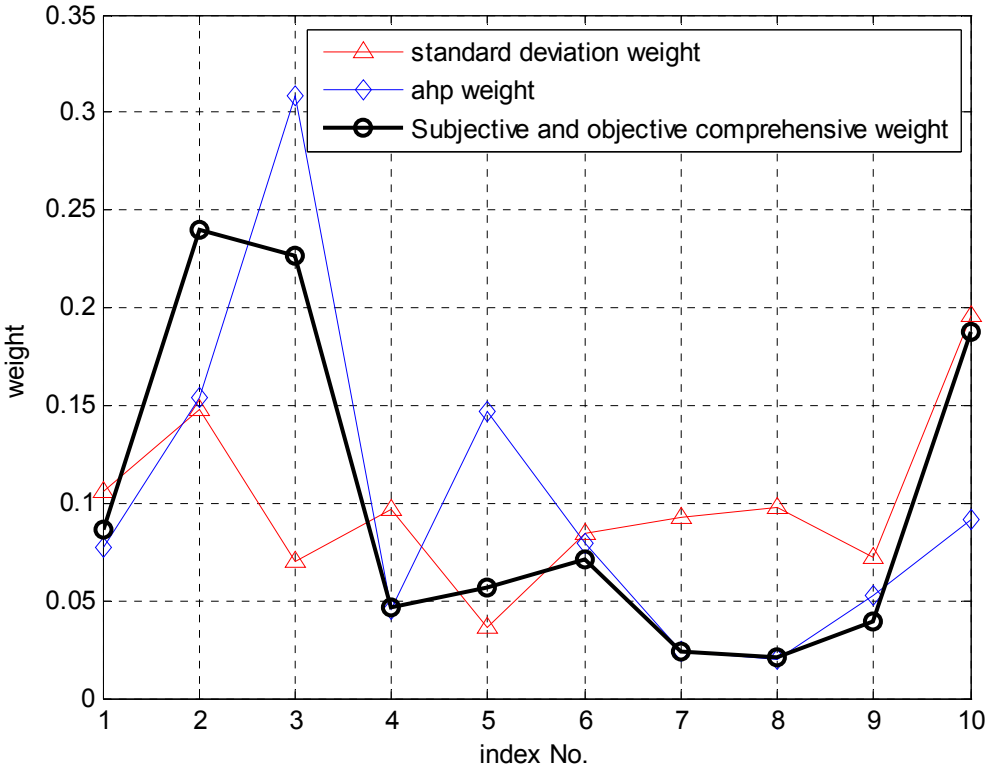

Fig.3. The three weights comparison chart

Conclusion

In this paper, we set the standard deviation weight as the objective weight, which is more constant. AHP weight is set as the subjective weight, which is more volatile. Subjective and objective comprehensive weight is as far as we can see in Fig. 3, which combines the advantages of both standard deviation weight and AHP weight, so that the comprehensive weight is even more moderate. . In the model being assessed, the evaluation result is consistent with the actual situation of the power distribution system.

Acknowledgement

In this paper, the research was sponsored by the Twelfth Five-Year National Science and Technology Support Program of China (Project No. 2012BAK13B01).

References

[1] Fengzhang Luo. Evaluation theory and integrated application for the modern power distribution system [D]. Tianjin University, 2009.

[2] Riehard E Brown. Electric Power Distribution Reliability [M]. New York: Marcel Dekker, 2002.

[3] ZadehL A. Outline of a new approach to the analysis of complex systems and decision processes [J]. IEEE Transactions on Engineering Management, 1990 37 (3) 222-228.

[4] Zhen Zhang and so on. Research on supplier evaluation based on AHP and fuzzy comprehensive evaluation [J]. Northeastern University Journal, 2006 27 (10) 1142-1145.

[5] Juliang Jin and so on. Fuzzy comprehensive evaluation model based on improved analytic hierarchy process [J]. Journal of Hydraulic Engineering, 2004 (3) 65-70.

Advanced Materials Research Vols. 986-987 (2014) pp 424-427

doi:10.4028/www.scientific.net/AMR.986-987.424

Power System Planning by Simulation

Ying WANG[1, 2, a], Liying SUN[3], Mingjiu PAN[3], Yue SHAO[1]

[1]Department of Mechanical and Electrical Engineering, China JiLiang University,Hangzhou, 310018, China

[2]Department of Electrical Engineering, Zhejiang University, Hangzhou, 310027, China

[3]Economic and Technical Research Institute of Zhejiang Electric Power Corporation,Hangzhou, 310008, China

[a]email: sara.wy@163.com

Keywords: Power System Planning, Simulation, Contingency Analysis

Abstract. The objective of power system planning is to meet the requirements of the customers of the power supply bureau in a region. In addition, a good system planning is helpful to the construction, operation and power supply of a power system. Using a simulation tool is much more convenient than relying on experience or the pure analysis in theory for power system planning. In this paper a method of system planning by simulation is discussed through a certain case. Based on the results of experiments, it is shown that this is an efficient way to make a power system plan.

Introduction

Power system planning is not only an important part of the development of economy and society of a region, but also a fundamental basis of the long-term growth of the power system. The objective of power system planning is to meet the need of its users. Moreover, a good system planning is helpful to the construction, operation and power supply of power networks [1].

In order to make a perfect plan, a simple and convenient method is used in this paper. Rather than relying on experience or the pure analysis in theory [2] [3], using a simulation tool may promote power system planning. With the development of power system, it is significant to make power system planning by simulation.

The Design of a power system planning by simulation

The design of a power system planning is as follows. First, initial power flow is to be analyzed to make sure the security situation of a certain power system. Generally the assessment indicators are the bus voltage and line load by the results of simulation. Second, use the contingency analysis function of the simulator to make N-1 fault analysis. Finally the most secure and economical expanding plan is determined on the base of the load added to the original power system.

There are 3 schemes designed according to the given condition of the certain case. By the comparing of both technical and economical aspects, the final program is decided. The calculation formula of the cost is as follows:

The total cost of reconstruction = the additional construction cost – the saving cost after reconstruction.

A simulator named Power World Simulator (PWS) is used. PWS is a kind of visual software of power system [4]. It consists of 5 modules: power flow function, fault analysis, sensitivity analysis, OPF analysis, and malfunction analysis [5] [6].And the modules of power flow function and fault function are used here.

In a word, with the increasing of the load and the complexity of power system, it is significant and practical to use the method of simulation for power system planning.

A case about application on power system planning by simulation

The given conditions are as follows: A large enterprise will build a new plant in the city. To meet the additional load, a new substation served at 69kV will be constructed at this location.

The peak load of the substation is 45MW and 100Mvar. Because the production is very sensitive to blackouts, this new plant requests that at least two separate lines to the new substation are provided. The new substation is required to be large enough to accommodate a 138/69-kV transformer as well.

Now, the goal is to design a new substation on the least cost way. At the same time, it is an opportunity to fix some existing contingency problems. Specifically, the task is to make recommendations for the best transmission system besides reinforce the power system. The secure system operation requires that no lines or transformers are loaded higher than 100% of their ratings and that all bus voltage magnitudes are between 0.95 and 1.08 per unit.

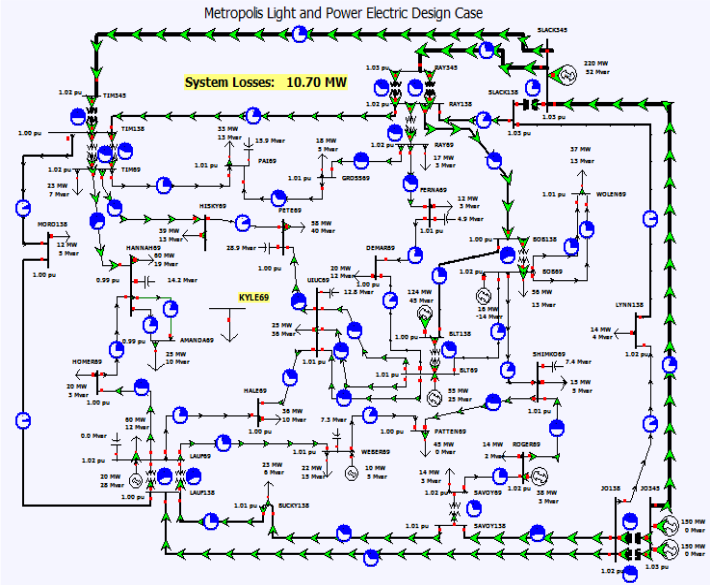

Figure 1 Initial power system of the case

Design procedures are as follows:

(1)Use Power World Simulator to make a one-line draw. Examine the operation situation of power system without new load by demonstrating original power flow. Make sure that all the line flows and bus voltage magnitudes are within certain limits.

(2)Make contingency analysis which means to considerate N-1 fault analysis under any outage of transmission line or transformer.

(3)Use the given parameters and costs of transmission line to determine the least expensive system addition so that the base case and all the contingences results in secure operation points with the new KYLE69 load(in Fig. 1). The definition of the total cost of an addition is equal to the construction cost plus the cost from changes in system losses over in the next five years.

According to the request, build simulating model and make power flow calculation by using PWS. The calculation results are shown in Fig. 1.

It is shown that all the buses and circuits are in good condition in the original power system. None of the electric parameter goes beyond the limits.

Then a contingency analysis on the original power system is conducted. That is N-1 fault analysis. And the results are shown in Fig. 2.

The results shows that although the power flows don't go beyond the limits while the original power system is operating normally, some hided weaknesses can be exposed by contingency analysis simulation.

So the corresponding solution is put forward: some reactive power compensation equipments are used to make voltage regulation according to the phenomenon of low voltage. And the design of the new economic program relates to the security of the power system.

The given conditions are as follows:

Transmission lines (69KV and 138KV): new transmission lines include a fixed cost and a variable cost. The fixed cost is for purchase or installation of the 3-phase circuit breakers, associated relays, and changes to the bus structure in the substation. The variable costs depend on the type of conductor and the length of the line. Transformer (138KV/69KV): Transformer costs include associated circuit breakers, relaying and installation.

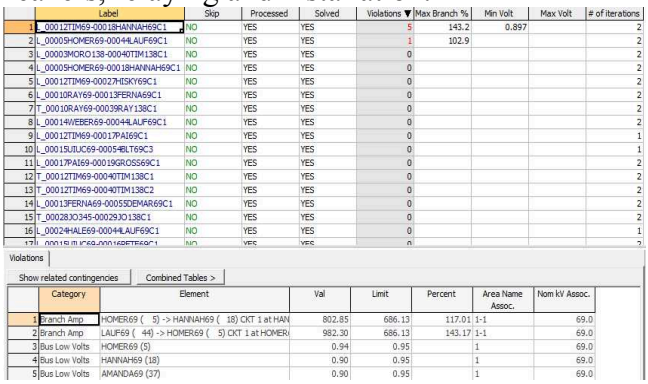

	Label	Skip	Processed	Solved	Violations ▼	Max Branch %	Min Volt	Max Volt	# of iterations
1	L_00012TIM69-00018HANNAH69C1	NO	YES	YES	5	143.2	0.897		2
2	L_00005HOMER69-00044LAUF69C1	NO	YES	YES	1	102.9			2
3	L_00003MORO138-00040TIM138C1	NO	YES	YES	0				2
4	L_00005HOMER69-00018HANNAH69C1	NO	YES	YES	0				2
5	L_00012TIM69-00027HISKY69C1	NO	YES	YES	0				2
6	L_00010RAY69-00013FERNA69C1	NO	YES	YES	0				2
7	T_00010RAY69-00039RAY138C1	NO	YES	YES	0				2
8	L_00014WEBER69-00044LAUF69C1	NO	YES	YES	0				2
9	L_00012TIM69-00017PAI69C1	NO	YES	YES	0				1
10	L_00015UIUC69-00054BLT69C3	NO	YES	YES	0				1
11	L_00017PAI69-00019GROSS69C1	NO	YES	YES	0				2
12	T_00012TIM69-00040TIM138C1	NO	YES	YES	0				2
13	T_00012TIM69-00040TIM138C2	NO	YES	YES	0				2
14	L_00013FERNA69-00055DEMAR69C1	NO	YES	YES	0				2
15	T_00028JO345-00029JO138C1	NO	YES	YES	0				2
16	L_00024HALE69-00044LAUF69C1	NO	YES	YES	0				1
17	L_00015ULUC69-00016PETE69C1	NO	YES	YES	0				2

Violations | Show related contingencies | Combined Tables >

	Category	Element	Val	Limit	Percent	Area Name Assoc.	Nom kV Assoc.
1	Branch Amp	HOMER69 (5) -> HANNAH69 (18) CKT 1 at HAN	802.85	686.13	117.01	1-1	69.0
2	Branch Amp	LAUF69 (44) -> HOMER69 (5) CKT 1 at HOMER	982.30	686.13	143.17	1-1	69.0
3	Bus Low Volts	HOMER69 (5)	0.94	0.95		1	69.0
4	Bus Low Volts	HANNAH69 (18)	0.90	0.95		1	69.0
5	Bus Low Volts	AMANDA69 (37)	0.90	0.95		1	69.0

Figure 2 Results of contingency fault analysis to the initial system

According to the request there are three additional proposals as shown in Fig. 3, 4 and 5 respectively. The project requests that the new load should be provided power by two lines for the reason of reliability.

(1)Proposal 1:select 2 from 7 69-kV buses discretionarily and connecting them to KYLE69.（Fig.3）

(2)Proposal 2: select 2 from 3 138-kV buses discretionarily and connecting them to KYLE69 by 2 138/69kV additional transformers respectively. （Fig.4）

(3)Proposal 3: discretionarily select 1 from 7 69-kV buses connected to KYLE69 right and 1 from 3 138-kV buses connected to KYLE69 by a 138/69kV additional transformer. （Fig.5）

(4)

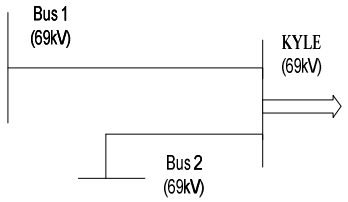

Fig. 3 Diagram for Proposal 1

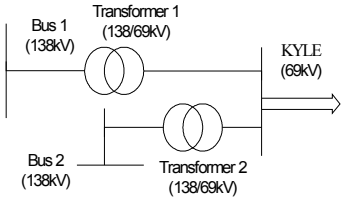

Fig. 4 Diagram for Proposal 2

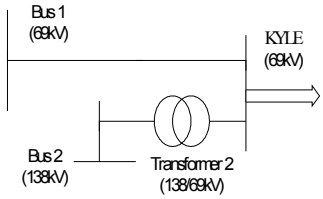

Fig.5 Diagram for Proposal 3

The analysis of the proposals simulation and calculation of new cost is as follows.

Among 3 proposals if proposal 1 is chosen, the power system can't be in normal operation and has more problems in contingency analysis. The initial power system is frailer in the region of additional load. Additional load is much larger than other load in this region. So the power system may be over loaded easily when additional load is connected. What's more, problems of low bus voltage and line overload may become more serious in original power system while N-1 fault happens.

If proposal 2 is chosen, by PWS simulation to the additional load program, power system can be in stable and normal operation. And the problem of contingency can be well solved by a potential transformer. But high cost should be considered.

If proposal 3 is chosen, power system can be in stable operation and normal situation. The problem of contingency can be well solved by an additional transformer. The highest loss is 12MW if MORO138 and AMANDA69 are chosen to be connected to KYLE69.And there is 1.2MW more than the initial loss. But from the total cost of rebuilding comparison, the cost of connecting MORO138 and AMANDA69 to KYLE69 is much lower than any connecting way of the other two.

Test results

The calculation formula of the cost is as follows:

The total cost of rebuilding = the additional building cost – the saving cost after rebuilding

Make the cost calculation of other connection methods in the same way as Table 1.

Three proposals are designed aimed at the request of additional load based on initial power system. Connecting additional load to KYLE 69 may lead to the power system breakdown or malfunctions during N-1 faults according to proposal 1. Proposal 2 and 3 can both meet the request of the project, but proposal 2 has to increase a very large cost for adding another potential transformers. The most economic method is to connect MORO138 and AMANDA69 to KYLE69. The total price of rebuilding is $3610200 which is the lowest. And power system can be in stable and secure operation if N-1 faults happen.

Table 1 Comparison of the cost from several ways of connection

Location	HISKY	AMANDA	PETE	TIM	LAUF	UIUC	HOMER
Addition Cost /$10^4$$	579.52	361.02	559.36	649.11	601.36	628.48	583.00

Conclusion

This paper mainly introduces the application of simulation in power system planning. The power flow analysis and contingency analysis to initial power system are made firstly. And more attention to comparing those proposals in both security and economy aspects after connecting new load is paid. Then the most reasonable method of connection is developed.

The practical result to design power system by simulation is drawn in this paper. With the development of power system, the method of using simulation software to design and plan power system has become the tendency.

Acknowledgement

In this paper, the research was sponsored by the Scientific Research Project of Zhejiang Province Department of Education (Project No. Y201431800) and Project of Priority Course of China JiLiang University (Project No. 130003).

References

[1] Xuefeng WANG. Exploration and Innovation of Regional Urban System Planning: A Review and Analysis on the Urban System Plan of Jiangsu Province [J].China City planning Review, 2012,1.

[2] Henderson,M. Power System Planning Process and Issues[C]. Power & Energy Society General Meeting. PES '09. IEEE, 2009 .1-6.

[3] Peng Jiang. Research on Power Grid Program and Economic Evaluation[J]. East China Electric Power, 2010,38(1)24-26.

[4] Guohui SHEN and so on. Research and Application of Power System Visualization Technology [J].Power System Technology,2009,33(17)31-36.

[5] Qinghong WANG and so on. User Manual for Power World Simulator[M].GXED.2009.

[6] J.Duncan Glover,Mulukutla.S.Sarma. 《Power System Analysis and Design》[M], China Machine Press.2009.

Advanced Materials Research Vols. 986-987 (2014) pp 428-432

doi:10.4028/www.scientific.net/AMR.986-987.428

Quantitative Analysis of the Relationship Between Temperature and Power Load

Jianliang Zhong[1, a], Bei Zhao[1, b], Da Zhang[2, a], Hai Bao[1, c]

[1]State Key Laboratory of Alternate Electrical Power System With Renewable Energy Sources (North China Electric Power University), Changping District, Beijing, 102206, China

[2] State Grid Liaoning Electric Power Company Limited Benxi Electric Power Supply Company, Benxi, Liaoning, 117000, China

[a]email: zhongjl@ncepu.edu.cn, [b]email:alabei@126.com, [c]email: hdbh@vip.sina.com

Keywords: Load; Forecasting; Decision; Tree Step Regression

Abstract. This paper presents the results of a study regarding the relationship between temperature and power load of the electric power system. Weather-influenced load part is picked up from original load series data with the conclusion that the lagged effect of temperature on load is within 12 hours. Furthermore, decision tree and step regression methods are employed to get a group of decision trees and corresponding regression equations which are able to quantitatively describe the relationship between load and temperature. A short-term load forecasting algorithm is then developed and its practical implementation shows this quatitative analysis method could reliably reflect the influence of the temperature changes on the load and effectively improve the accuracy of short-term load forecasting.

Introduction

Short-term load forecasting, defined as the estimation of the load in future day , is an important daily work of power system operation department. The accuracy of load forecasting has a great impact on the economic profit of power generation and distribution companies.

Short-term load forecasting is influenced by many factors such as weather condition and holidays. Among these factors, the weather factors, especially the temperature, are the most important factors on accuracy of short-term load forecasting. So the consideration of weather condition is involved in short-term load forecasting in recent years.

Some methods are developed to deal with weather factors in short-term forecasting:

(1) Simple model for load forecast[1][2]. Single piece of weather information and the load of forecasted day are fitted to get the function relationship between load and weather factor.

(2)Similar days Method[3]. The method obtains the similarity of the day forecasted and days in history via cluster analysis on related factors which have influence on load. The load could be forecasted by weighted processing of the loads of days that are similar to forecasted day.

(3) Artificial neural network[4][5]. The neutral network is trained by adopting history data of weather and load. Then the neutral network approaching of non-linear function between load and related factors such as weather can be obtained.

However, these methods still have some disadvantages. In simple model for load forecasting, the randomness of selecting weather information and the form of function make it difficult for load forecasting. The similar days method takes insufficient consideration of long-term load growth. The artificial neural network method is a black box model and operators could not get the quantitative relationship between load and weather factors. These methods do not analyse load and weather factors quantitatively. For load forecasters, the quantitative relationship between load and weather factors is the basis of accurate forecasting.

In this paper, a new method of load forecasting is proposed. The method classifies the load based on weather and other factors. Progressively regression is then performed to get the relationship between load and weather factors in particular type of load. The method could obtain the quantitative relationship between load and different weather conditions. That helps to improve the

accuracy of load forecasting. Because of the weak influence on load forecasting and the inconvience of quantitative analysis, this paper ignores some weather factors such as barometric pressure and humidity. Only temperature is taken into account in the process of quantitative analysis.

Weather-influenced Load Part

Load series could be decomposed into four parts[6]. The load at moment k is shown as followed:

$$Y(k) = N(k) + W(k) + S(k) + r(k) \quad (1)$$

In the equation(1):*Y(k)* is total load; *N(k)* is base load; *W(k)* is weather-influenced load part; *S(k)* is load of special events; *r(k)* is random load part.

As special events have great impacts on load but not representative, the impact should be declined to the bottom to analyse the influence of weather factors on load. *S(k)* should be removed.

The increase of distance between crest and trough and the increase of base load would lead to the increase of total load. The average growth rate of load at different moment should be calculated before analysing the effect of long-term increase load part. The average growth rate of load is shown as Fig.1:

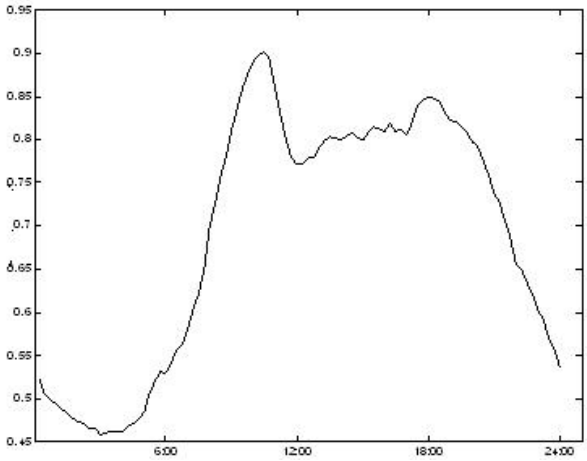

Fig 1 Load growth rate of different moment

The base load, long-term growth load and the load in special events are removed, the load at moment k could be presented as followed equation:

$$Y'(k) = W(k) + r(k) \quad (2)$$

In the equation(2): the definitions of $Y'(k)$, $W(k)$ and $S(k)$ are the same as that in equation(1). Since the random load obeys normal distribution with zero mean and constant variance, the random load would be neglected in the following analysis. This implies the character of load series $Y'(t)$ reflects that of weather-influenced load series $W(t)$.

Analysis of Lagged Effect on Load Caused by Temperature

The effect on load caused by temperature is inevitable because the effect is the response to weather change made by users and the effect is lagged.

As $Y'(t)$ is in day and month periodicity and the data of temperature is also in day periodicity, the article analyses the lagged effect in splited periods.

Because the temperature at close time has the same trend, the conclusion that the load varies with the change of temperature could not be reached. This article obtains the lagged effect of load caused by temperature by calculating the correlation coefficient between load and temperature each moment.

Table 1 Load and temperature correlation coefficient of summer(Jul~Sep)

Hour	0	-3	-6	-9	-12	-15	-18	-21	-24
2	0.80396	0.8373	**0.84293**	0.76385	0.67368	0.82887	0.74447	0.71026	0.62492
5	0.82647	0.78902	**0.82908**	0.82448	0.737	0.64526	0.81179	0.75637	0.71121
8	0.74323	**0.7536**	0.63241	0.69714	0.65406	0.62497	0.58681	0.63689	0.6383
11	**0.73534**	0.73299	0.70838	0.57694	0.64538	0.59809	0.58716	0.56497	0.58905
14	0.71206	**0.74**	0.70869	0.69755	0.58335	0.64504	0.61464	0.61447	0.55144
17	**0.77547**	0.71206	0.77212	0.73256	0.71345	0.61292	0.65919	0.63804	0.62168
20	**0.86054**	0.84034	0.74767	0.8543	0.73968	0.70342	0.61313	0.6722	0.65957
23	0.82968	**0.86091**	0.80964	0.71755	0.84089	0.72736	0.68725	0.59572	0.66643

Table 2 Load and temperature correlation coefficient of winter(Nov~Feb)

hour	0	-3	-6	-9	-12	-15	-18	-21	-24
2	-0.67306	-0.72832	**-0.7526**	-0.73518	-0.68729	-0.7183	-0.73041	-0.71102	-0.71934
5	-0.65084	-0.65981	-0.70872	**-0.7274**	-0.70339	-0.64776	-0.66985	-0.69606	-0.68365
8	-0.56026	-0.56579	-0.59342	-0.60168	**-0.6279**	-0.60901	-0.58852	-0.59375	-0.58583
11	**-0.6571**	-0.60754	-0.59519	-0.63426	-0.62239	-0.65632	-0.65609	-0.64787	-0.64773
14	-0.6479	**-0.6543**	-0.57191	-0.55693	-0.5989	-0.58407	-0.61883	-0.624	-0.61948
17	**-0.6646**	-0.64671	-0.62949	-0.5282	-0.51446	-0.55285	-0.5389	-0.57356	-0.58512
20	**-0.7688**	-0.74943	-0.71027	-0.74081	-0.74176	-0.73301	-0.75273	-0.74952	-0.77229
23	-0.75085	**-0.7621**	-0.73496	-0.70043	-0.74202	-0.74318	-0.73026	-0.75263	-0.74975

The correlation coefficients of the power load temperature are shown in Table 1 and Table 2. The numbers in bold indicate bigger correlation coefficients. The temperature at corresponding moment is considered to have the most impact on power load. The lagged effect of power load after midnight is obvious and the users who work before midnight react to the change of temperature rapidly.

Then the conclusion could be drawn that the lagged effect of temperature on load changes by time but generally the effect is within 12 hours.

Quantitative Analysis of the Impact of Temperature on Power Load

The relationship between weather factors and power load is multi-variable and non-inear It is so complicated that it can not be expressed by simple model. With decision tree, this article analyses the power load at different periods and temperatures before the studied period. Then the tree-constructed relationship between power load and temperature is obtained. Practically, the data of power load is classified by weather factors at the same time. The classified power load changes within a small range of weather. The relationship between the same type of power load and temperature could be considered linear approximately. With the step regression analysis of every type of load and temperature, the model of the temperature effect on power load could be expressed as decision tree with a set of regression equations. The regression equations represent the quantitative relationship between power load and the temperature belongs to the leaf node of decision tree.

Decision tree is one of the main algorithms of data mining and it is a widely used statistical process. The algorithm of decision tree could be simply described as followed optimization problem: the minimum of $p_e(T, F, d)$ could be obtained in limited training example space. In $p_e(T, F, d)$, P_e is total error rate; T is the structure of tree; F is the test property of inner node; d is the decision rule of inner node.

Because of the day periodicity of $Y'(t)$ and the difference of temperature lagged effect on load at different moment, this article gets 24 decision trees by modeling on load at 1 to 24 o'clock.

Based on the analysis, this article chooses the temperature data at 8 o'clock on the forecasted day and the day before as the property parameters of the decision trees. Taking the week periodicity of $Y'(t)$ into account, the article also chooses the type of forecasted day(non-holiday and holiday) as the property parameters. Then there are 17 property parameters in the test property of final decision trees.

Take the load at 14 o'clock as an example and the forming process of decision trees could be described as followed.

The decision tree has 147 nodes including 67 leaf nodes after fully growing. The best tree with minimum cost complexity could be picked up by cross verificating decision tree in the test collection.

Cut the branches of the best tree based on optimal tree scale and the decision tree after cutting branches is shown as Fig.2:

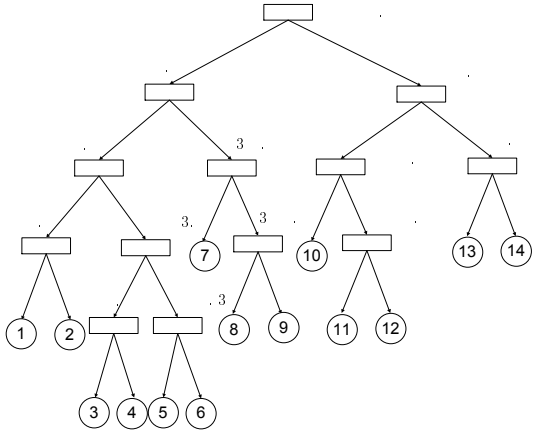

Fig.2 The decision-tree by non-holiday 14 o'clock data

X1 to X16 in Fig.2 are the temperature data at 8 o'clock on the forecasted day and the day before. X17 is the type of forecasted day with the range of 1 to 7 which means Monday to Sunday.

The power loads at 14 o'clock each day could be classified as 14 types which are on behalf of different weather conditions and types of non-holiday. Take the fourteenth leaf node as example and only the nodes which fit the following requirement could be considered as a part of node 14:

1 The temperature at 5 o'clock on forecasted day has to be bigger than 24.15;

2 The forecasted day has to be Saturday or Monday.

3 The load at 20 o'clock the day before has to be more than 24.75 kW • h.

As can be seen, node 14 stands for the condition of holiday with higher temperature which happens in summer especially in July and August. There are 19 data points which could be classified as load type like node 14 in practice data. Similarly, 14 nodes means 14 sets of different types of weather conditions.

After formulating decision trees, this article fits the relationship between weather and load at the same node with stepwise regression. Node 14 is still taken as an example of this process.

The regression equation of node 14 after backward step regression is shown in (3):

$$load = -264.86 + 505.86 * temp(10) \tag{3}$$

The test value F is 19.13, which means the regression effect is good.

In the data of all nodes, the number of rest values is less than two and the notable effect could be ensured at the confidence interval of 95%.

Test Result

To check the correctness of the relationship between weather and power load obtained in the article, the load data from January to August is forecasted by the method developed in this article. The data received by the method is compared with that received by traditional BP neural network and the result is shown as Table 3:

Table3 Comparison of the result with mentioned method and BP method

Month	Day Everage RMSE of Months	
	Method in this article	BP neural network
January	3.06%	3.43%
February	3.29%	4.65%
March	2.95%	3.52%
April	2.37%	2.89%
May	2.54%	2.65%
June	2.62%	2.73%
July	2.96%	3.81%
August	3.43%	4.53%

It could be seen from Table 3 that the method developed in this article is better than traditional BP neural network especially in winter and summer with a large amount of weather-influenced load part. The accuracy of the model gets improved because the quantitative relationship between temperature and power load could reflect the character of weather-influenced load part. The algorithm adopted in this article could avoid the influence of long-term increased load part on the forecasting accuracy in the forecasting process.

Conclusion

The relationship between temperature and load is complicated and nonlinear. It has lagged effect so the quantitative relationship between temperature and load could not be expressed by common functions. However, the quantitative analysis of weather factors and load are the base of accurate load forecasting. This article analyses the power load and weather data recent years. Then the data is classified based on the relationship between load and temperature at different moments with decision tree technique. This article also shows the regression expression about the effect of temperature data on power load. The quantitative relationship between temperature and power load in different weather conditions is then obtained. In addition, the article develops a new short-term load forecasting algorithm. The verification of the new algorithm based on practical system shows that the algorithm could handle different kinds of influence on load and reflects the time-series character of load. The new algorithm helps to improve the accuracy of short-term load forecasting.

References

[1] Palacio, D.R. Simple model for load forecast weather sensitive Electricity Distribution, 2001. Part 1: Contributions[C]. CIRED. 16th International Conference and Exhibition (IEE Conf. Publ No. 482) , Volume: 4 , 18-21 June 2001 Page(s): 3 pp. vol.4.

[2] Sforna M. Searching for the Electric-Load Weather Temperature Function By Using the Group Method of Data Handling. Electric Power Systems Research, 1995:32 (1) 1-9.

[3] Kang Chongqing Cheng Xu Xia Qing shen Yu. A New Unified Approach to Short-Term Load Forecasting Considering Correlated Factors[J]. Automation of Electrical Power Systems, 1999: 23(18) 32-35.

[4] Khotanzad A, Afkhami-Rohani R, Maratukulam D. ANNSTLF-artificial neural network short-term load forecaster generation three[J]. Power Systems, IEEE Transactions on, 1998:13(4): 1413-1422.

[5] Chow T W S, Leung C T. Neural network based short-term load forecasting using weather compensation[J]. Power Systems, IEEE Transactions on, 1996:11(4): 1736-1742.

[6] Hyde O, Hondnett PF. Modelling the effect of weather in short-term electricity load forecasting. MATHEMATICAL ENGINEERING IN INDUSTRY, 1997:6 (2): 155-169.

Advanced Materials Research Vols. 986-987 (2014) pp 433-438

doi:10.4028/www.scientific.net/AMR.986-987.433

Reactive compensation research of HVAC cables for offshore wind farms

Dui Xiaowei, Zhu Guiping

National key laboratory of power system, department of electrical engineering, Tsinghua University, Beijing, 100084

Keywords: HVAC submarine cable; Reactive compensation; Maximum transmission capacity

Abstract. This paper proposes a reactive compensation optimization method for HVAC cables of offshore wind farms, establishing the optimization model of reactive compensation capacity of HVAC submarine cables with cable current-carrying capacity as the main constraints. The maximum transmission power and transmission distance of HVAC submarine cables are calculated, considering the constraints including power factor, line loss and reactive compensation cost. Using minimum average annual cost as the objective function compensation capacity of both cable ends and corresponding average annual cost is obtained are optimized.

Introduction

With the rapid development of wind power industry in our country, China began to explore offshore wind power construction and operation in southeast coastal areas. Compared to the terrestrial environment, offshore wind resource is more abundant and stable, which is suitable for the development of wind power generation. However, offshore wind farms transmit power to onshore grid through HVAC or HVDC submarine cable which is more difficult comparing with power transmission of onshore wind farms. HVAC submarine cable transmission is more suitable for the power transmission of offshore wind farms close to shore. According to domestic and overseas project experience, when the transmission distance is less than 50km, HVAC submarine cable will be more economic. Due to the large unit capacitance of HVAC submarine cable, long-distance power transmission will produce higher charging power, thus affecting transmission capacity of their HVAC submarine cable and leading to a certain of line loss[1]. Therefore, charging power of HVAC submarine cable is one of the key issues to be solved in offshore wind farm. Reactive compensation is the preferred solution for HVAC submarine cable, namely, compensating the charging power of HVAC submarine cable through establishing reactive compensation equipment in wind farms or onshore substation. In recent years, the researches on the reactive compensation problem of HVAC submarine mainly focus on reactive compensation optimization scheme and economics. The literature [2, 3] discusses the differences between single-end and both-end compensation as well as compensation effects of different compensation capacities; the literature [4] compares the economics of reactive compensation scheme and HVDC submarine transmission, drawing a conclusion that reactive compensation is more economical when the transmission distance is less than 50km.

In this paper, a distributed circuit model of HVAC submarine cable is established for researching the relations among transmission capacity, transmission distance and reactive compensation capacity of the HVAC submarine cable. And the differences of compensation effect between compensation at wind farm and compensation at onshore substation are compared, drawing a conclusion that compensation at wind farm can improve the transmission capacity of HVAC submarine cable by balancing current distribution along HVAC submarine cable while compensation at onshore substation cannot. However, better power factor at the grid connection point and less line loss can be achieved by compensation at onshore substation. At the end of the paper, taking the optimal economics within service life of offshore wind farm power transmission system as objective, the reactive compensation capacity of both ends of HVAC submarine cable are optimized, considering the cost of reactive compensation and line losses of the submarine cable.

Optimization results have some reference value for the planning and design of reactive compensation in offshore wind farms.

Theoretical analysis of reactive compensation of HVAC submarine cable

Distributed circuit model of HVAC submarine cable

Represent HVAC submarine cable single-phase model as Π equivalent circuit shown in Figure 1, and its transmission characteristics are as shown in Formula 1.

$$\begin{bmatrix} \dot{U}_1 \\ \dot{I}_1 \end{bmatrix} = \begin{bmatrix} \cosh \gamma l & Z_c \sinh \gamma l \\ \dfrac{\sinh \gamma l}{Z_c} & \cosh \gamma l \end{bmatrix} \begin{bmatrix} \dot{U}_2 \\ \dot{I}_2 \end{bmatrix} \tag{1}$$

Where, γ represents propagation constant, Z_c represents characteristic impedance and l represents line length. Π Equivalent circuit parameters are as follows:

$$Z_{\Pi} = Z_c \sinh \gamma l, Y_{\Pi} = \frac{\cosh \gamma l - 1}{Z_c \sinh \gamma l}$$

To compensate for the capacitor charging power of the HVAC submarine cable, inductive reactive compensation can be installed at both ends. Due to frequent fluctuation in wind farm output power, SVC or STATCOM is usually adopted to guarantee the compensation effect. After the installation of reactive compensation, the HVAC submarine cable single-phase model is shown in Figure 2.

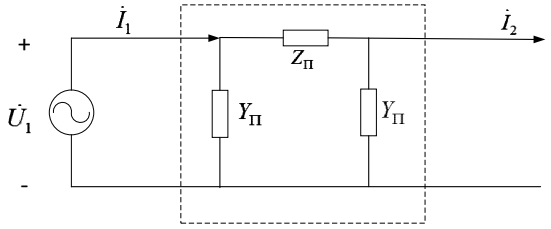

Figure 1 Schematic diagram of HVAC submarine cable model

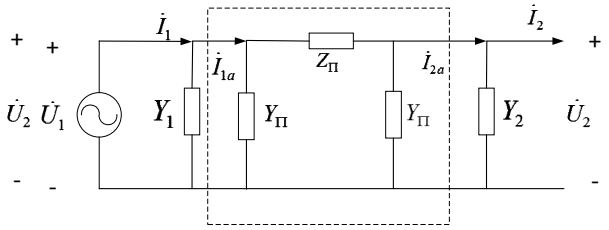

Figure 2 Schematic diagram of HVAC submarine cable reactive compensation model

Where, Y_1 represents the equivalent admittance of offshore end compensation, Y_2 represents the equivalent admittance of onshore substation compensation, in this case its transmission characteristics of its ports is shown in Formula (2):

$$\begin{bmatrix} \dot{U}_1 \\ \dot{I}_1 \end{bmatrix} = \begin{bmatrix} \cosh \gamma l + Z_c Y_2 \sinh \gamma l & Z_c \sinh \gamma l \\ (\dfrac{1}{Z_c} + Z_c Y_1 Y_2) \sinh \gamma l + (Y_1 + Y_2) \cosh \gamma l & \cosh \gamma l + Z_c Y_1 \sinh \gamma l \end{bmatrix} \begin{bmatrix} \dot{U}_2 \\ \dot{I}_2 \end{bmatrix}$$

The maximum transmission power of HVAC submarine cable

The maximum transmission power of HVAC submarine cable is constrained by a variety of conditions, of which the electrical factors mainly include current-carrying capacity and voltage deviation. Excessive current in the cable will raise cable temperature, and thus restricting the transmission capacity of the cable, meanwhile high temperature will have a negative impact on the power transmission security and cable life. Consequently current-carrying capacity is the major factor limiting power transmission capacity of the HVAC submarine cable. The range of allowable voltage deviation shall be determined according to the corresponding standard. In china, the standard *Technical Rule for Connecting Wind Farm to Power System* [5] specifies that the voltage deviation at grid connection point of wind farm should be between -3% and +7% of the nominal voltage. Usually, when the current-carrying capacity constraint is satisfied, the voltage deviation constraint can also be satisfied [1].

The maximum current occurs at either end of HVAC submarine cable, thus the constraints of current-carrying capacity is that the currents just after offshore compensation point and just before onshore compensation point should be below the upper limit of current-carrying capacity.

（1） Calculating the current before onshore end compensation point

Generally the power factor of wind turbine is close to 1, which can be considered that the output current and voltage of wind farm are in same phase. Assuming that the phase angles of $\dot{U}_1$ and $\dot{I}_1$ are both 0, the output voltage $\dot{U}_1$ is 1.05p.u. , and the length l of HVAC submarine cable is known, solve the onshore end current according to Formula (2). As onshore end compensation has no effect on the current distribution along HVAC submarine cable, it can be calculated in accordance with Y2 = 0, therefore

$$\dot{I}_2=\frac{\dot{U}_1-(\dot{I}_1-\dot{U}_1Y_1)Z_c/\tanh\gamma l}{Z_c(\sinh\gamma l-\cosh\gamma l/\tanh\gamma l)}$$

（2） Calculating the current after the offshore end compensation point

The current after the offshore end compensation point can be calculated as:

$$\dot{I}_{1a}=\dot{I}_1-\dot{U}_1Y_1$$

（3）Solving the maximum transmission power

The maximum transmission power of the offshore end equals the maximum output power of wind farm which is calculated as P_1= $3U_1I_1$. According to current-carrying capacity constraints and the foregoing calculation, assuming that the offshore end compensation capacity is Q_a, and the upper limit of current-carrying capacity is I_m, and solve the optimization problem:

$$\max \quad P_1$$

$$\begin{cases} \dot{I}_2=\dfrac{\dot{U}_1-(\dot{I}_1-\dot{U}_1Y_1)Z_c/\tanh\gamma l}{Z_c(\sinh\gamma l-\cosh\gamma l/\tanh\gamma l)} \\ \dot{I}_{1a}=\dot{I}_1-\dot{U}_1Y_1 \\ Y_1=-jQ_a/U_1^2 \\ \left|\dot{I}_2(I_1)\right|\le I_m \\ \left|\dot{I}_{1a}(I_1)\right|\le I_m \\ P_1=3U_1I_1 \end{cases}$$

The onshore end compensation capacity of HVAC submarine cable

Technical Rule for Connecting Wind Farm to Power System stipulates that, for the wind farm connecting to public grid through wind power collection system with 220kV voltage or higher, its inductive reactive compensation equipment should be able to compensate for all the charging power of HVAC submarine cable. Generally the power factor at the outlet of wind turbine is 1, therefore, the power factor of onshore end of the HVAC submarine cable (grid connection point) is also approximately equal to 1, after calculating the offshore end compensation capacity, and the onshore end compensation capacity can be calculated in accordance with the onshore end power factor, namely:

$$Q_b=3\,\mathrm{Im}(U_2I_2)$$

Where, Q_b is the onshore end compensation capacity.

Optimization of HVAC submarine cable reactive compensation

HVAC submarine cable reactive compensation is mainly for improving the transmission capacity, reducing line losses and improving grid power factor; correspondingly, reactive compensation optimization is to maximize transmission capacity, minimize economics and satisfies power factor standards.

As the largest output of wind farm is less than the maximum transmission power of HVAC submarine cable, in the optimization of reactive compensation, it needs to recalculate the economically optimized offshore end compensation capacity. Take offshore end compensation capacity as the independent variable and calculate line loss and reactive compensation cost. Then set the average annual cost as the objective to calculate the required onshore end compensation capacity. The average annual cost proposed in this paper includes economic losses caused by line losses and reactive compensation costs.

（1） Calculation of line loss

Since the onshore end compensation has no impact on the current distribution on HVAC submarine cable, line losses are only related to the offshore end compensation capacity. After calculating the offshore end compensation capacity corresponding to maximum transmission power in accordance with the foregoing method, the economic losses caused by the line losses of HVAC submarine cables are calculated as:

$$C_L = PTp = (P_1 - P_2)Tp$$

Where, C_L represents economic losses of line losses, $\triangle P$ represents loss of active power, T represents converted operation time under maximum power, which is indicated to be the operating time of the wind farm when transmission power is maximized after conversion, and p represents the gird purchase prices.

（2） Annual conversion costs of reactive compensation

Reactive compensation equipment belongs to one-time investment, which should be converted into annual costs within the service life for calculate. For simplicity, this paper share the total cost equally on an annual basis,

$$C_{ca} = C_{ct} / T_L = (kQ_a + Q_b)p_c / T_L$$

Where, C_{ca} represents annual conversion cost of reactive compensation, C_{ct} represents initial total investment cost of compensation equipment, T_L represents design service life of compensation equipment, k represents the offshore cost coefficient, indicating that the unit capacity cost of offshore end compensation equipment is k times of onshore end compensation equipment, p_c represents unit capacity cost of the onshore end compensation equipment.

Considering the constraints of line loss and reactive compensation cost, taking minimum average annual conversion cost of HVAC submarine cable transmission system as the objective, establish reactive compensation optimization model of HVAC submarine cable as follows:

$$\min \quad C$$

$$\begin{cases} Q_b = 3\,\mathrm{Im}(U_2 I_2) \\ Q_a \le Q_{a\max} \\ C_{ca} = (kQ_a + Q_b)p_c / T_L \\ C_L = (P_1 - P_2)Tp \\ C = C_{ca} + C_L \end{cases}$$

Where, $Q_{a\max}$ represents the required offshore end compensation capacity for maximum transmission power when the line length is *l*.

Examples

Use ZS-YJQF41 HVAC submarine cable for calculation example of which main parameters associated with the calculation are shown in Table 1.

Table 1 Main parameters of ZS-YJQF41

Rated voltage (kV)	Capacitance (μF/km)	Inductance (mH/km)	Resistance (Ω/km)	Current-carrying capacity (A)
127/220	0.116	0.437	0.0615	569

Calculate relations between the maximum transmission power and the transmission distance, and the result is shown in Figure 2.

Figure 2 shows that the maximum transmission distance of this model cable is 118km without compensation, and the maximum transmission distance increases to 168km after installing 100MVar compensation at offshore end. It can be seen that the offshore end compensation can increase the transmission distance of HVAC submarine cable. However, excessive compensation capacity will increase current of offshore end, leading to a slight decrease of maximum transmission power of HVAC submarine cable in reason of the limits of offshore end current-carrying capacity constraints. Therefore, the curves in Figure 3 are started from a straight line.

Calculate the offshore end compensation capacity based on the length of HVAC submarine cable to make the HVAC submarine cable reach the maximum transmission power. The relation between the offshore end compensation capacity and the transmission distance is shown in Figure 4.

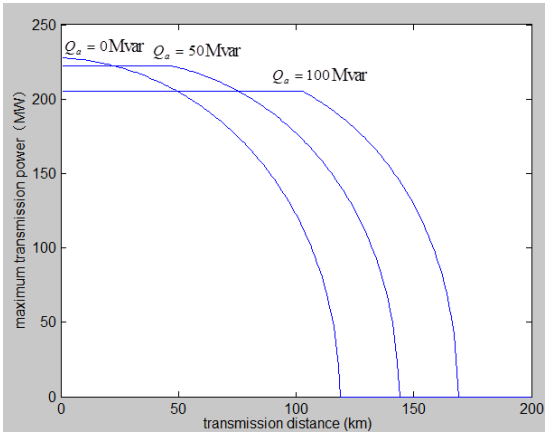

Figure 3 The relations between the maximum transmission power and the transmission distance of HVAC submarine cable

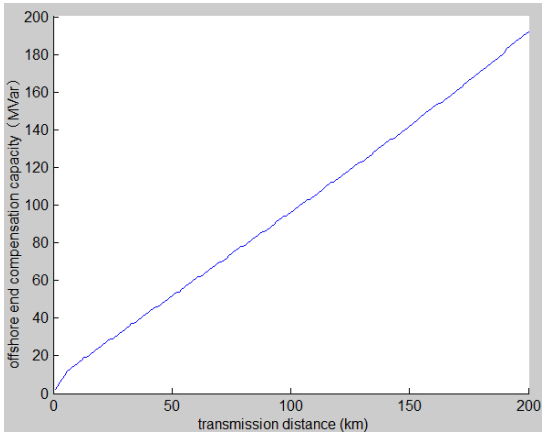

Figure 4 The relations between the offshore end compensation capacity and the transmission distance of the HVAC submarine cable

Figure 4 shows that there is basically a linear proportional relation between the offshore end compensation capacity and the transmission distance. With the increase of the offshore end compensation capacity, the transmission distance will increase accordingly.

The power transmission distance of offshore wind farm is generally less than 50km. Thus take the power transmission distance of $l = 30\text{km}$ and the offshore end transmission power of 100MW to calculate the current distribution and line losses ΔP of the HVAC submarine cable when the offshore end compensation capacity is respectively 0Mvar, 25Mvar and 50Mvar. The results are shown in Figure 5.

Figure 5 shows that, when the compensation capacity is low, the current at the onshore end of the HVAC submarine cable is relative high, and when the compensation capacity is relative high, the current at the offshore end is high. A reasonable compensation should be able to minimize the difference between onshore end and offshore end current magnitude to reach the least line loss.

Optimize the compensation capacity at both end and corresponding average annual conversion cost, using calculating parameters shown in Table 2. Optimization results are shown in Figure 6.

Table 2 Calculating parameters

Unit compensation cost (Yuan/Mvar)	Offshore cost coefficient	Service life (year)	Sales price to network (Yuan/kWh)	Transmission distance (km)	Output power of wind farm (MW)	Onshore end power factor constraint
200,000	1.5	20	0.97	30	100	$\cos\varphi = 1$

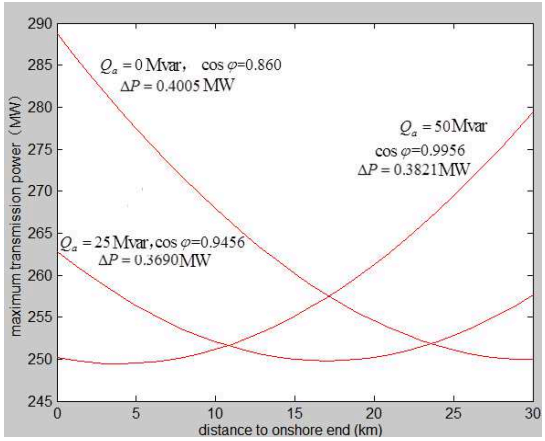

Figure 5 Schematic diagram of current distribution along HVAC submarine cable

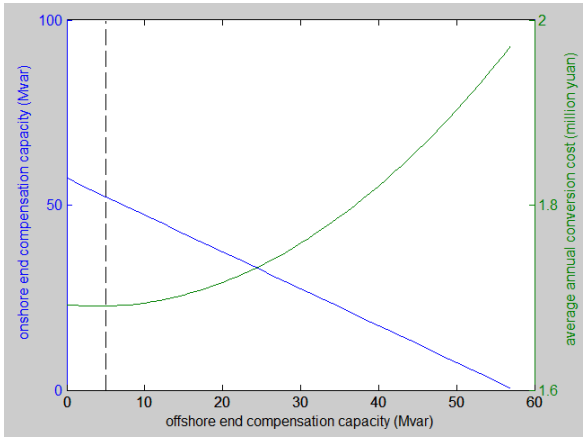

Figure 6 The relations between the compensation capacity of both head end and tail end and average annual conversion cost

When the offshore end compensation capacity is 5Mvar and the onshore end compensation capacity is 52Mvar, the average annual cost is the lowest with 1.691 million Yuan, among which, the conversion cost of reactive compensation equipment is 1.093 million Yuan, the loss caused by line losses is 598,000 Yuan. Obviously, the reactive compensation cost is the main part of the average annual cost, and the economic losses caused by line loss is relatively low, therefore the optimization results tend to reduce the compensation capacity.

Conclusions

In this paper, the reactive compensation of HVAC submarine cable in offshore wind farm has been researched in-depth; the main conclusions are as follows:

（1）The current-carrying capacity constraint is the main factor restraining the power transmission capacity of HVAC submarine cable. This paper deduced the maximum transmission power and the calculation method for the offshore end compensation capacity according to the offshore end and onshore end current-carrying capacity constraints of the HVAC submarine cable.

（2）Considering the factors including requirement of grid connection power factor, line loss of submarine cable and reactive compensation cost, etc., it carries out optimization on both end compensation capacity of HVAC submarine cable taking the minimum value of annual average conversion cost of HVAC submarine cable including reactive compensation equipment as the optimization objective and obtains the economically optimized reactive compensation configuration method.

（3）Through analysis of examples, maximum transmission power and both end compensation capacity have been calculated by using actual cable parameters. From analysis, the offshore end compensation can improve the current distribution, power factor and reduce the line loss of HVAC submarine cable, however, the cost is higher. The onshore end compensation cannot improve the current distribution along HVAC submarine cable, however, it can improve the power factor and reduce line loss with a lower cost comparing with offshore end compensation.

Acknowledgement

In this paper, the research was sponsored by the National Nature Science Foundation of China (Project No. SKLD13M10).

References

[1] N. Barberis Negra, J. Todorovic , T. Ackermann. Loss evaluation of HVAC and HVDC transmission solutions for large offshore wind farms. Electric Power Systems Research, v 76, n 11, p 916-27, July 2006

[2] Zhang Zhengguo, Yu Dan and Xu Ying, et al. Design Research of Reactive Power Compensation of Large Length High-Voltage HVAC Submarine Cable. Power Capacitor & Reactive Power Compensation, 2010, 31 (6):32-38

[3] W. Wiechowski and P. Børre Eriksen. Selected studies on offshore wind farm cable connections - challenges and experience of the Danish TSO. 2008 IEEE Power & Energy Society General Meeting, p 8 pp., July 2008

[4] Gregory F. Reed, Hashim A. Al Hassan, Matthew J. Korytowski .etc. Comparison of HVAC and HVDC solutions for offshore wind farms with a procedure for system economic evaluation. 2013 IEEE Energytech, p7, 2013

[5] GB/T 19963-2011 Technical Rule for Connecting Wind Farm to Power System, 2011

Advanced Materials Research Vols. 986-987 (2014) pp 439-444

doi:10.4028/www.scientific.net/AMR.986-987.439

Reliability Evaluation Research of 10 kV Typical Configuration Feeder based on the FMEA

Li Wenwu[1,a], Zhu Xinchun[1,b], Zhang Cheng[1,c]

[1]College of Electrical Engineering & New Energy, Three Gorges University, Yichang City, Hubei Province,China

[a]liwenwu7508@ctgu.edu.cn, [b]zhuxinchun40331@163.com,[c] zhangch116@163.com

Keywords: FMEA; the different distribution ways; 10 kV radial lines; reliability assessment

Abstract. The 10kV feeder typical configuration is divided into two categories of no standby power and standby power in the paper, and subdivided into different configurations, then we use FMEA to analyze the power supply reliability of 10 kV radial lines under the different configurations, at last we compare and analyze the reliable indexes of the different equipment configuration schemes, such as the reliable rate RS-1, the system average interruption frequency AITC-1 etc. The research results show that space truss structure and switch configuration directly affect the power supply reliability of the distribution network. In the conditions of reserved auto-switch-on device and section switches automatically isolating faults, the power supply reliability rate is the highest, and the average interruption frequency and outage time are the lowest.

Introduction

Distribution power system is in the end of power system, which connects directly to the users. Once the equipment or line fails, it would lead to the interruption of power supply. According to incomplete statistics, more than 80% user power failures are caused by the failures of distribution system, and 10kV feeders are in the end of distribution system, therefore, we urgently need to evaluate reliability of 10kV feeders. A study on reliability of 10 kV typical configuration feeders is conducive to improve the power supply reliability of distribution network, and also has the instruction function to the planning, construction, expansion and reconstruction of power distribution system. Statistics, analysis, evaluation of the reliability indexes and the application of the statistical analysis results have guiding significance to the present system and equipment from the design to manufacture, installation, maintenance and repair [1].

At present, the entire distribution network is as the object of study in the distribution network reliability analysis of domestic and international. The experts set the reliability statistical methods of distribution network fully in detail; developed the software of reliability assessment of distribution system, then established the management mechanism related to distribution system reliability, so that the power supply reliability of the distribution network is researched and managed in China. In other countries, the experts established and perfected the power supply reliability evaluation indexes system, and their research results mainly focused on the reliability evaluation models and algorithms of distribution system.

In this paper, we analyze the reliability of the 10kV feeders in different configuration schemes, basing on the emanate wiring. We combine closely with domestic 10kV feeder typical configuration, and consider mainly that the trunk line installed subsection switches; the first of branch line installed fuses; a standby power supply etc. 10kV feeder has a variety of configuration schemes, and all schemes will be evaluated by using FMEA in the paper. The assessment results will help the electrical technical personnel to choose reasonable configuration schemes, according to the actual situation, which has strong practice and guiding significance.

10kV Feeder Typical Equipment Configuration

We use a typical 10kV domestic emanate feeder as the basis. It is divided into both having standby power and no standby power, and then subdivided into several different configurations. Device configuration classifications are as follows: ① the head of branch lines have not been installed the fuses; ②the head of branch lines have been installed the fuses; ③ the main line has not been installed section switches; ④ the main line has been installed manual section switches; ⑤the main line has been installed automatic section switches; ⑥standby power manual control; ⑦ standby power automatic control. All the cases have been arranged and combined to form different configurations, see table1.

Table1. Line configuration table

Classification / Scheme name			②					
no standby power supply	scheme 1							
	scheme 2							
	scheme 3							
	scheme 4							
Having standby power supply	scheme 5							
	scheme 6							
	scheme 7							
	scheme 8							

The Power Supply Reliability Indexes and FMEA

Common Indexes of Distribution Network Reliability Evaluation. Distribution system reliability indexes include the load point reliability indexes and system reliability indexes [2]. The reliability indexes of system basing on the load point reliability indexes are quantitative assessment of the distribution network reliability level [3].

Load Point Reliability Indexes. Load point reliability indexes include [4]: failure outage rate λ (time / year); the average outage duration r (hours/time); the annual average outage time U (hours / year).

System Reliability Indexes. System reliability indexes are as follows. AITC-1: the average Interruption times of customer, it refers to the power customer average interruption time in the statistical period, unit: time/ household.

AIHC-1: the average interruption hours of Customer, it refers to the customer average interruption hours in the statistical period, unit: hour/ household.

CAIDI: customer average interruption duration index, it refers to the average interruption duration, which the users without electricity endure at per unit of time. The index is a ratio that the sum of users' interruption duration divided by the total interruption times of users in a year.

RS-1: reliability on service in total, it is a ratio that the total hours during the effective power supply time to users divided by the number of hours in statistical period. The general statistical time is one year, which has 8760 hours in non-leap years and 8784 hours in leap year.

ENS: the electricity shortage index, it refers to the electricity shortage provided to users due to component failure in one year, which is the sum that average load power of every load point multiplied by the load point average interruption duration.

AENS: average energy shortage index, it is electricity expectations of relative power losses of each user caused by the insufficient power supply in distribution system [5].

FMEA. The paper uses FMEA to analyze all possible fault events or component failure, and determine the influence of the load point, then list the failure mode and effects analysis table, at last, obtain the reliability indexes basing on the table. FMEA can calculate three kinds of reliability indexes used grid commonly: load point reliability index, system reliability index, and reliability index related to the load and energy, which can reflect the reliability degree to different aspects [6].

When a fault occurs, the circuit breaker and section switch trip, and we look up the fault segment, then the fault section is isolated in order to troubleshoot. When the circuit breakers and switches close, the loads before fault segment restore power by bus. When the rest loads can be transferred to other line, their outage time is equal to operating time of contact switch, or its outage time is equal to the component troubleshooting time.

4 Reliability Analysis Examples under10 kV Typical Configuration Feeder

A 10kV feeder within the scope of substation jurisdiction work as an example in the paper, and its reliability is analyzed by failure effects analysis method under several kinds of typical configuration schemes. We consider that the power failure of repairing, without considering the equipment periodic maintenance test，construction and expansion, effect of user application, external effect factors, ignoring the effect of bad weather, the power shortage and scheduled interruption. All the branches failure and repairs are independent events. Combining switch configuration, network structure, the main factors that influence the reliability of distribution network are concluded.

According to the data of the wiring, equipment and loads provided by a power substation, it is concluded that the data of reliability assessment we need.

1) The loads concentrate at three places, such as load1, load2, load3 and the loads power are 123.5kW, 171kW, 152kW separately.

2) The main component failure rates and repair time

Failure rates and recovery time of circuit breaker, isolating switches, fuses, switches, trunk line and branch lines are based on amounts of data provided by certain substation. The data include operating records, dispatching logs, planned outage applications, records of switch accident trip in five years.

Reliability Analysis of Different Schemes. 1) No standby power

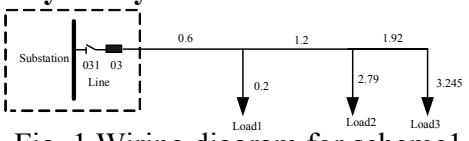

Fig. 1 Wiring diagram for scheme1

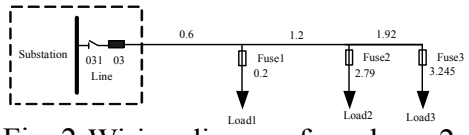

Fig. 2 Wiring diagram for scheme2

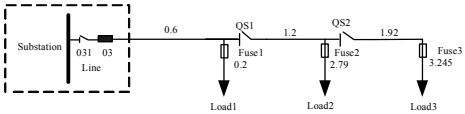

Fig. 3 Wiring diagram for scheme3

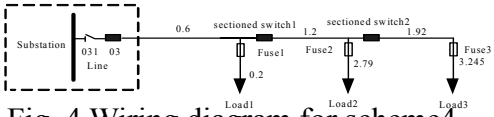

Fig. 4 Wiring diagram for scheme4

Scheme 1: The branch lines have no fuses, the trunk line is not segmented, and no standby power supply, see figure 1. There are not the sectioned switches or disconnector to segment the trunk line in scheme 1. When a trunk line or branch line faults, it will cause the main breaker to trip. There is no breakpoint to isolate system, so it is necessary to exclude each fault before the breaker reclosing. As long as any line encounters fault, it will lead to the all lines outage, each load point has the same failure rate.

Scheme 2: The branch lines have fuses, the trunk line is not segmented, and no standby power supply, see figure 2. The fuses installed in the initial of branch line in scheme2 are a kind of protective measures used usually in the actual power distribution system, namely the branch line protection. T points in each branch line install a fuse, once the branch line faults, the fuse will burn out, so it does not affect other load points and the trunk line.

Scheme 3: The branch lines have fuses, the trunk line is segmented, fault manual isolation, and no standby power supply, see figure 3. The trunk line has been mounted disconnectors in scheme 3. When a fault occurs on the trunk line, the circuit breaker 01 trips, and open disconnector, which can isolate the fault section. The loads in front of fault segment have not been influenced, and their fault outage duration time equals to operation time of disconnector.

Scheme 4: The branch lines have fuses, the trunk line is segmented, fault automatic isolation, and no standby power supply, see figure 4. The disconnectors have been changed into sectioned switches in the trunk line, which can make the load in non faulty line segment be freed from the effect of faulty line segment.

2) Supplied by the standby power

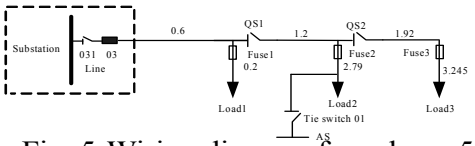

Fig. 5 Wiring diagram for scheme5

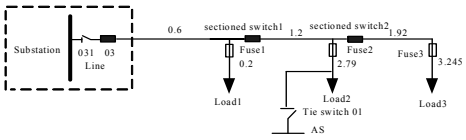

Fig. 6 Wiring diagram for scheme6

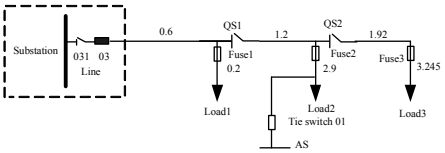

Fig. 7 Wiring diagram for scheme7

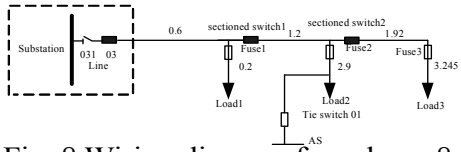

Fig. 8 Wiring diagram for scheme8

Scheme 5: The branch lines have fuses, the trunk line is segmented, fault manual isolation, and a standby power supply (manual control), see figure 5. The standby power connects to the trunk line by the tie switch01, which reduces the power cut off range in scheme 5. When the line that 0.6km long gets a breakdown, load2 and load3 are supplied by standby power. When the line that 1.2km long gets a breakdown, load1 can restore power by main power supply, but load 2, 3 are not supplied by the standby power, and this line section is not charged because of troubleshooting. When the line that 1.92km long gets a breakdown, load1and load2 supplied by the main power, but the load 3 is not supplied until the line has been repaired.

Scheme 6: The branch lines have fuses, the trunk line is segmented, fault automatic isolation, and a standby power supply (manual control), see figure 6. The disconnectors have been changed into sectioned switches in the trunk line, which can make the load in non faulty line segment be freed from the effect of faulty line segment.

Scheme 7: The branch lines have fuses, the trunk line is segmented, fault manual isolation, and a standby power source automatic switch device, see figure 7. Compared with the scheme 6, switching time of standby power decreases, which can reduce the loads' outage time greatly.

Scheme 8: The branch lines have fuses, the trunk line is segmented, fault automatic isolation, and a standby power source automatic switch device, see figure 8. The disconnectors have been changed into sectioned switches in the trunk line.

Reliability Evaluation Procedure and Results Analysis. The calculation steps are as follows:

1) According to the characteristics of FMEA method, the wiring used in distribution network are equivalent, transformers are equivalent to load points.

2) We select the suitable fault criterions, and accord the criterions to analyze all possible failure events, and then determine its impact on the load point, at last list the FMEA table.

3) According to the load reliability indexes in second step and the number of users in the corresponding line, calculate the system reliability indexes related to system.

4) According to the load reliability indexes in second step and the loads data in the corresponding line, calculate the system reliability indexes related to the load and energy [6].

Reliability indexes of the schemes are seen table2.

Table 2. Summary table of system reliability indexes of each scheme

Index / schemes		AITC-1 [Time/ (use year)]	AIHC-1 [(Hour/ (user year)]	CAIDI [Hour/ time]	RS-1	ENS [kWh/ year]	AENS [kWh/ (user year)]
no standby power supply	1	1.641222	2.658944	1.6201	0.999697	1165.636	129.5151
	2	1.413667	2.085667	1.47536	0.999763	922.849	102.5388
	3	1.7803333	2.619	1.4710728	0.9997018	1100.803	122.31144
	4	1.25833	2.16367	1.71947	0.99975	920.797	102.311
a standby power supply	5	1.7803333	1.7583333	0.9876428	0.9997998	729.334	81.037111
	6	1.258333	1.371911	1.09026	0.999844	577.9458	64.2162
	7	1.7803333	1.5113333	0.8489047	0.9998279	622.5445	69.171611
	8	1.25833	1.18091	0.93847	0.99987	494.412	54.9347

The reliability rate RS-1 is the lowest and the wiring is the simplest in scheme1. In scheme8, it has the highest reliability. In scheme2, the reliability is higher than that in scheme 1, because the head of branch lines have been installed the fuses. When any branch line encounters fault, it has no influence on the other loads, which can reduce the scope of fault influence. System average interruption frequency AITC-1 is the same in the scheme3, scheme5 and scheme7. This is to say, system average interruption frequency with radial distribution system installed a backup power is the same as that with single power supply distribution system, which shows that there is no effect on AITC-1 neither the system has standby power supply or not, but the load average interruption duration and the system average outage duration get shortened.

By comparing scheme4 with scheme3, scheme6 with scheme5, scheme8 with scheme7, we can change the disconnector to section switch, so the main breaker in the head of the trunk line does not trip. When any section of line encounters fault, the reliability could improve, because that the section switch isolated fault automatically, and it no longer affects the supply of other loads. Comparing the scheme5 with scheme7, scheme6 with scheme8, we can see that the fault rates of all load point are the same in radial distribution system with standby power, either the standby power supply for manual or automatic, so the average interruption frequency of the system is the same.

In short, the head of branch lines have installed fuses, so the fault line is separated from the trunk line automatically by fuse. When the branch line encounters fault, it does not make the main breaker trip, and does not affect other branches line power supply, so the power outage range reduces [7]. The trunk line has been installed section switches, in the first place, the fault line and the trunk line have been isolated without affecting other loads power supply interruption; in the second place, the non fault line that between the power and the section switch can continue to supply power, which is not affected by the fault line; in the third place, the non fault line that between standby power source point and section switch can restore power by switching operation, which reduces the fault influence scope and the load interruption duration. Through the analysis, standby power can reduce the load average interruption duration, and not affect the failure rate of load, which can reduce the average outage duration AIHC-1 under the unchanged number of users. Thereby BZT is more obvious effect than the manual operation device, which shortens the outage time.

5 Conclusions and Prospect

In the paper, we can see the 8 kinds' schemes in power distribution and their reliability analysis basing on a typical substation 10kV feeder, then we get some conclusions: the reliability of power supply directly affected by device configuration. In scheme1, the reliability is the lowest and the system average interruption duration AIHC-1 is the longest, which due to have not sectioned switches, branch line protection devices and standby power. In scheme8, the reliability is the highest, the system average interruption duration AIHC-1 is the shortest and the ENS is the lowest, which due to the trunk line section, the branch line fuse protection and BZT. Thus it can be seen that sectioned

switch, fuses and standby power play a positive role in the power supply reliability of distribution network.

In order to improve the reliability of power supply, it needs to add sectioned switches, branch line protection devices, the standby power supply and reasonable measures according to the actual situation of power grid. The economic investment question is not considered in the paper, so the problem of economic and reliability coordination is going to be next research direction.

References

[1] Chen Wengao, in: Basis of Distribution System Reliability, edited by Chinese Power Press, Beijing (1998), in press.
[2] Xiao Yangming: Reliability Evaluation and Research of 10kV Distribution Network in Anji County, Beijing North China Electric Power University (2012).
[3] Zhang Lei, in: Study on Distribution Network Reliability Analysis Method Based on Fault Consequences. chapter, 5, View of Science and Technology (2013).
[4] Yao Lixiao, Peng Jingning, Wu Li and Wang Qin, in: Reliability Evaluation of Complex Distribution System, volume 20, chapter, 10, Journal of Xi'an University of Technology (2004).
[5] Guo Yongji, in: Electrical system reliability analysis, edited by Tsing hua University press, Beijing (2003), in press.
[6] Jia Xiaohong: Study of Tengzhou Urban Distribution Network Reliability, Shandong University (2007).
[7] Zou Yinrong, in: Influence Factors of Medium Voltage Distribution Network Power Supply Reliability Analysis, volume 20, Rural Electrification(2003).

Advanced Materials Research Vols. 986-987 (2014) pp 445-448

doi:10.4028/www.scientific.net/AMR.986-987.445

Research and Simulation of Reasonable Distribution of Energy Saving Design Model in Rural Residential

WANG Ying-quan

Sichuan College of Architectural Technology, Sichuan,Deyang 618000,China

KEYWORDS: Residence; Reasonable distribution; Energy saving design

ABSTRACT: In today's society, resources and energy are short. In order to promote our country to build a conservation-oriented society and to achieve sustainable development in the construction industry, the demand for modern residential energy conservation is also growing. Studying and designing of energy-efficient rural residential are one of the key work of energy-saving building. In this paper, the design of residential land use planning, building envelope, outside doors and windows, roof and interior supporting facilities are described for equitable distribution of energy-saving design in rural residential, so as to achieve the design of energy-saving rural residential purposes.

1 Introduction

Currently, the energy shortage has become a constraining bottleneck of China's economic and social development, and building energy consumption accounts for a sizeable proportion of all energy consumption in the country [1-3]. Do best to the work of building energy saving is the key to energy saving [4]. In terms of the construction industry, construction of energy-efficient buildings and reducing building energy consumption have been urgent affairs [5]. The purpose of Building energy efficiency design is through certain building construction practices, choosing the right materials, to achieve the purposes of reducing energy consumption and heat, cold, electricity, fuel and others, but also to guarantee a certain level of comfort. Many energy-saving elements in rural residential, which has great potential, including several aspects of land planning design, building envelope design, external doors and windows design, roof design and interior supporting facilities design.

2 Energy saving design model

2.1 The main content of reasonable distribution of energy saving design in rural residential

Rural residential energy saving design is a systematic project, including planning, design, construction, maintenance and operation management. Its influence factors are complex, to emphasize one aspects separately is very difficult to achieve a comprehensive residential energy saving goals. Rural residential buildings should be arranged in the villages of the best natural conditions and health conditions, and should avoid the pollution of air and water, and bad location, there should be a certain amount of public green space and basic health facilities. Residential orientation has a great impact on its lighting and natural ventilation, so the choice of residential in the "Best orientation" should be based on geographical conditions and climatic conditions. North-south residential arrangement can guarantee residential obtaining adequate sunshine and gables facing the west can effectively avoid exposure to sunlight.

2.2 Achievement of reasonable distribution of lighting energy-saving design in rural residential

In the process of reasonable distribution of energy-saving design in rural residential, the lighting distribution design is a core step, which can select a reasonable lighting modes for reasonable distribution of energy saving design in rural residential. Moreover, the use of rural residential lighting control model can convert the lighting pattern. The procedure describes as follows:

Assuming the rural residential lighting device's voltage parameter is U_j, current sensing coefficient is l, capacitance parameter is d, and lighting duration is T, the following equation can describe the low light illumination model:

$$\begin{cases} U_j = U_l \\ U_l = l \cdot \dfrac{dj_l}{dT} \end{cases} \tag{1}$$

The use of following equation can describe the change of the voltage in process of lighting mode conversion:

$$\Delta U_l^+ = \int_0^{T_1} \frac{U_l}{l} dT = \frac{U_j}{l} T_1 \tag{2}$$

When using a medium brightness lighting mode, the input voltage of the illumination device is cut off, it needed to use the saved voltage to supply power, so it is possible to use the following equation to describe the medium brightness lighting mode.

$$\begin{cases} U_l + U_0 = 0 \\ U_l = l \cdot \dfrac{dj_l}{dT} \end{cases} \tag{3}$$

The use of following equation can describe the change of the voltage in process of lighting mode conversion:

$$\Delta U_l^- = \int_{T_1}^{T_2} \frac{-U_0}{l} dT = \frac{-U_0}{l} \cdot (T_2 - T_1) \tag{4}$$

The following equation can describe high brightness lighting mode:

$$\begin{cases} U_j - U_l = U_0 \\ U_l = l \cdot \dfrac{dj_l}{dT} \end{cases} \tag{5}$$

The following equation can describe the change of the voltage in process of lighting mode conversion:

$$\Delta U_l^- = \int_{T_1}^{T_2} \frac{U_j - U_0}{l} du = \frac{U_j - U_0}{l} (T_2 - T_1) \tag{6}$$

2.3 The evaluation of reasonable distribution of energy saving design methods in rural residential

Using five-point scale to determine the weight function. According to the importance coefficient of each function W_i, it can get the function's average of importance coefficient W, i.e. weights.

$$W = \frac{\sum_{i=1}^{k} W_i}{k} \tag{7}$$

In the equation, K is a function item of participating in evaluation.

The value coefficient is calculated according to the function coefficients and cost coefficients of each program. The equation is $V_i=F_i/C_i$.

Using the data calculated by the equation to get the C to A's comprehensive weight vector that is $N=D^T$.

D=(0.037，0.217，0.097，0.037，0.232，0.046，0.083，0.028，0.129，0.042，0.049，0.036，0.014)

The judgment matrix is $\begin{bmatrix} 1 & 1/3 & 1/5 & 1/7 \\ 3 & 1 & 3/5 & 3/7 \\ 5 & 5/3 & 1 & 5/7 \\ 7 & 7/3 & 7/5 & 1 \end{bmatrix}$, and its eigenvalue of maximum is 4, the consistency ratio CR=0<0.1, passing the one-time test.

Similarly, it can also get the other indicators weights of project X layer to C layer.

$$M=\begin{bmatrix} 0.32 & 0.26 & 0.33 & 0.31 & 0.17 & 0.20 & 0.31 & 0.25 \\ 0.37 & 0.35 & 0.40 & 0.38 & 0.25 & 0.30 & 0.54 & 0.25 \\ 0.26 & 0.30 & 0.20 & 0.23 & 0.33 & 0.30 & 0.08 & 0.25 \\ 0.05 & 0.09 & 0.07 & 0.08 & 0.25 & 0.20 & 0.08 & 0.25 \end{bmatrix} \quad (8)$$

Then it gets:

$$M \times N = \begin{bmatrix} 0.261 & 4 \\ 0.347 & 5 \\ 0.277 & 0 \\ 0.162 & 2 \end{bmatrix} \quad (9)$$

Thus it gets to know that X2's weight is the highest.

3 Calculation and analysis of energy saving effect of reasonable distribution of energy saving design in rural residential

Calculated as shown in Table 1, for example, the effect of rural residential reasonable distribution of energy saving design is analyzed. Through various energy-saving measures, the calculated values and reduction rate of energy consumption can be drawn from the residential reasonable distribution of energy saving, as shown.

In terms of residential reasonable distribution of energy saving, it can also take advantage of the rural ecological advantages, including straw, firewood, making fermentation to produce gas in biogas digester and other energy sources, which can save a lot of coal, electricity and fuel, and improve sanitation in rural areas, as well as can improve manure fertilizer, expanding fertilizer sources, so as to realize recycling of energy, have good economic and social environmental benefits.

Table 1 Calculation and analysis of the effect of residential reasonable distribution of energy saving design

Energy use	Calculation method	Design value /GJ	Standard value /GJ	Energy consumption reduction rate /%
Heating	11.8×0.55×0.9×0.6	3.5	12.8	73
Air condition	2.3×0.8×0.53×0.6	0.55	2.4	77
Aeration	4.6×0.6	2.7	4.7	43
Hot water Supply	23.5×0.5	11.7	24.5	52
lighting	10.4×0.94×0.6	5.87	10.7	45
Household appliances	22.8×0.6	13.7	23.7	42
Other		4.4	4.4	0
Total		44.2	83.2	47

Energy consumption reduction rate = (1 - energy consumption design value of residential energy saving / standard value of energy consumption)

Calculated as shown in Table1, for example, the effect of rural residential reasonable distribution of energy saving design is analyzed. Through various energy-saving measures, the calculated values and reduction rate of energy consumption can be drawn from the residential reasonable distribution of energy saving, as shown.

In terms of residential reasonable distribution of energy saving, it can also take advantage of the rural ecological advantages, including straw, firewood, making fermentation to produce gas in

biogas digester and other energy sources, which can save a lot of coal, electricity and fuel, and improve sanitation in rural areas, as well as can improve manure fertilizer, expanding fertilizer sources, so as to realize recycling of energy, have good economic and social environmental benefits.

4 Conclusion

After 20 years of efforts, China's rural residential energy saving has made tremendous progress, but compared with developed countries, the gap is still large. Developed countries continue to improve building's energy saving level, China must make more efforts to narrow the gap with the developed countries. Due to rural residential energy saving is a comprehensive and systematic project, involving architectural design, building science technology, materials, structure, construction, heating ventilation air conditioning, property management, policies and regulations and other aspects, the reasonable distribution of rural residential energy saving design work need strengthen cooperation and joint effort of each professional department to be well done.

References

[1] Kaoru Kawamoto, Yoshiyuki Shimoda, Minoru Mizunob, Energy saving potential of office equipment power management. Energy and Buildings, 2005, 36.
[2] PedroAlbreeht. AtmosPheric Cormsion resistance of structural steels [J]. Journal of Materials in Civil Engineering, 2003: 236-245.
[3] Hetao Hou, Guoqiang Li, Xaojing Hu. Flexural behaviour of sandwich composite panels used in steel residential House-experimental and theoretical investigations [C]. The 5th International Symposium on Steel Structures, Seoul, Korea, March, 2009: 629-635.
[4] Per Heiselberg. Energy performance of buildings-the European approach to sustainability. In: The International Conference on Asia-European Sustainable Urban Development. Chongqing: Chongqing University Press, 2006: 4-6.
[5] Chris Scheuer, Gregory A. Keoleian, Peter Reppe. Life cycle energy and environmental performance of a new university building: modeling challenges and design implications [J]. Energy and Buildings, 2003(35): 1049-1064.

Advanced Materials Research Vols. 986-987 (2014) pp 449-452

doi:10.4028/www.scientific.net/AMR.986-987.449

Research for smart micro-grid system of optimal operation on the island

Liu Jiaojiao[1, a], Wang Zhijie[1, b], Zhang Zhenhai[1, c] and Ye Yizhi[2, a]

[1]College of Electrical Engineering, Shanghai Dianji University,Shanghai 200240, China;

[2] Shanghai Electric Group CO.LTD Central Academe, Shanghai 200240, China.

[1,a]261945962@qq.com, [1,b] wzisdstu@163.com, [1,c]997048419@qq.com,
[2,a]yeyz@shanghai-electric.com

Keywords: Island, smart micro-grid, renewable energy sources, optimal operation

Abstract. The paper introduces the advantage of the application of new energy generation, and then describes the structure of a smart micro-grid system built on an island which includes wind, solar, tidal-wave energy system. The method of day-ahead optimal operation was applied to smart micro-grid system on the island to minimize the operation cost by using genetic algorithm. Taking actual datum of Shanghai Electric Group's micro-grid for case study, the dynamic economic dispatch is compared with traditional dispatch strategy. The results verify the effectiveness of the dynamic economic.

Introduction

It is difficult for the electricity company to power consumer on the island because most of islands is far from the mainland. There are abundance of wave, solar and wind energy on the island. It is significant to develop smart micro-grid project on the island.

The literature [1] described the tidal power generation projects and scale in South Korea. But the micro-grid did not establish an effective optimal operation model and the generation system was uneconomical. The literature [2] put forward a scheduling model which takes the difference between the beginning and end of the state of charge of battery as objective function. But in actual operation, the state of charge of battery should be consistent, the scheduling was uneconomical. The optimal operation model and strategy of smart-grid on the island has not been established at present. In this paper, according to the characteristics of the micro-grid on the island, the island smart micro-grid was built. All kinds of distributed generation units of each model was established, the various economic performance factors to the micro-grid on the island was fully taken into account, and the generation plan of micro-grid on the island was developed.

Mathematical model of distributed generation units

Tidal-waves generator output power model :

$$P_{wa}(t)=\frac{0.145\rho g}{\pi}\lambda^2 A^2\omega\cos^2(\omega t-\alpha)$$

Where λ=wave length of wave; A=wave height; ω= wave angular speed; ρ = seawater density; g =acceleration of gravity; α =the initial phase Angle of wave.

Photovoltaic cells output power model:

$$P_{PV}=P_{STC}\frac{G_{ING}}{G_{STC}}(1+k(T_c-T_r))$$

Where P_{PV} = The actual output power of photovoltaic cells; G_{ING} = actual solar radiation intensity; G_{STC} = solar radiation intensity in standard test condition; P_{STC} = The maximum output power of photovoltaic cells in standard test condition; k =temperature power coefficient; T_r =photovoltaic cell rated temperature; T_c = photovoltaic cell actual temperature.

$$P_{WT}=\begin{cases}0 & v<v_i \quad or \quad v>v_0\\ k_2v^2+k_1v+k_0 & v_i\le v<v_r\\ P_r & v_r\le v<v_0\end{cases}$$

Wind generator output power model:

Where k_0 , k_1 and k_2 are Wind turbine power curve parameters; v_i =cut-in wind speed of wind generator; v_r =rated wind speed of wind generator; v_0 = cut-out wind speed of wind generator; P_r =rated power of wind generator.

Mathematical model of optimal operation

Objective function. Optimal operation was to minimize operating cost. Objective function of operation cost: $\min M_{ope}=\sum_{i=1}^{24}[C_{OM}(P_{wt-i})+C_{OM}(P_{pv-i})+C_{OM}(P_{gt-i})+C_{OM}(P_{wa-i})]+\sum_{i=1}^{24}(s\cdot P_{gt-i})$

Where $C_{OM}(P_i)=K_{OM}\cdot P_i$; M_{ope} = operating cost of micro-grid; $\min M_{ope}$ = minimum of operating cost; P_{wt-i} = wind generator output power at the time i; P_{pv-i} = PV output power at the time i; P_{gt-i} =gas turbine output power at the time i; P_{wa-i} =tidal-waves generator output power at the time i; s = gas turbine fuel cost in a hour; $C_{OM}(P_i)$ = operation cost of DG; K_{OM} = coefficient of DG operation cost, literature [3] provided coefficient of each DG.

Constraint conditions. The main constraint conditions are described and analyzed as following:

1. Load balance: $P_{pv-i}+P_{wa-i}+P_{bat-i}+P_{gt-i}=P_{load-i}$
2. Gas turbine constraint: $P_{gt-i}>0$
3. Starting SOC must be same with terminal SOC: $SOC_0=SOC_{24}$
4. SOC constraint: $SOC_{\min}\le SOC_i\le SOC_{\max}$

Where $SOC_{\max}$ =maximum of SOC； $SOC_{\min}$ =minimum of SOC. Battery can't over-charging and over-discharging to prolong the lifetime of the battery.

5. Generating capacity constraint: $P_{i\text{-}\min}\le P_i\le P_{i-\max}$

Variables. The output power of tidal-wave generator, wind generator and PV cell can't be Variables. Because their output power are uncontrollable, while, gas turbine output power can be controlled. Gas turbine output power from the first hour to the 24th hour in a day was decided to variables. $P_{gt\text{-}1},P_{gt\text{-}2},\cdots,P_{gt\text{-}i},\cdots,P_{gt-23},P_{gt-24}$

Battery output power from the first hour to the 24th hour in a day also was decided to variables. $P_{bat-1},P_{bat-2},\cdots,P_{bat-i},\cdots,P_{bat-23},P_{bat-24}$

Case study

The island micro-grid system model of Shanghai Electric Group can be seen in Fig.1. It consists of gas turbine system (rated power 7 MW), PV system (rated power 1000 KW), wind generation system (rated power 4 * 1500 KW), tidal waves generation system (rated power 5 MW), battery (rated power 1000 KW) and the load.

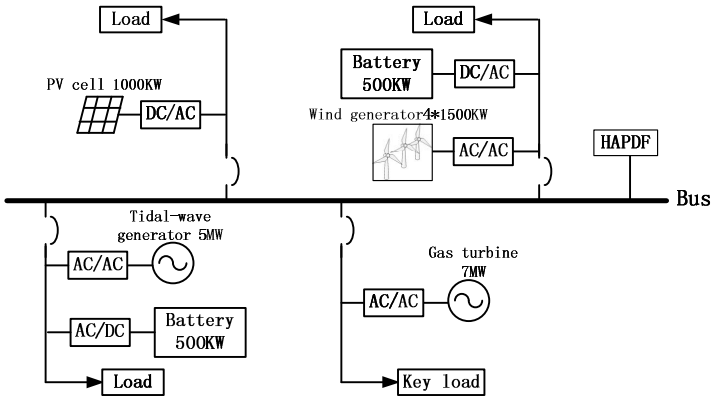

Fig.2. Chat of island micro-grid system model

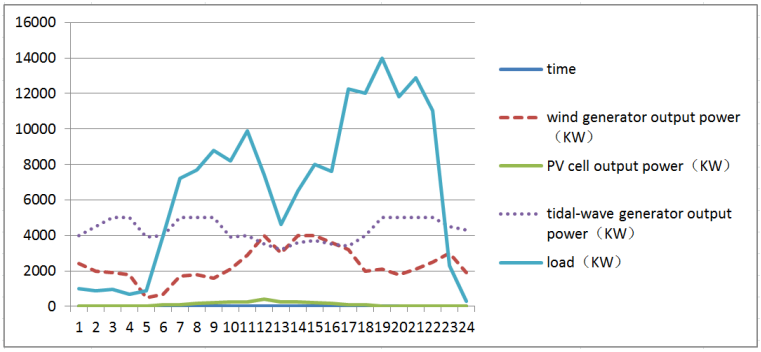

Fig.3. Chat of power prediction

Table.1 Table of DG operation coefficient

Type	Gas turbine	PV	Wind generator	Tidal-wave generator
Operation coefficient KOM RMB/KW• h)	0.0401	0.0096	0.0296	0.0315

Simulation parameters and strategy are limited: Battery initial SOC is 80%; Gas turbine keep running all day and its minimum output power is 100KW; Battery was charged and discharged on the rated voltage. The electricity generated by tidal waves, solar and wind turbine priority supply to load. The redundant electricity is used for battery charging. Battery output power was set 0 and gas turbine output power is 100KW when the battery is full and DG output power can meet load. Optimal operation of micro-grid is a typical multi-variable nonlinear optimization problem and it needs to be solved using genetic algorithm. System is simulated based on MATLAB. The simulation results can been seen in Fig.4. Random operation curve was shown in Fig.5. to comparison.

Simulation results

M_{ope} is 14572 when we apply optimal operation to island micro-grid while M_{ope} is 14972 when we apply random operation to island micro-grid. Operating cost of optimal operation was lower than before.

The battery after optimal operation charge and discharge twice in 24 hours and the gas turbine output power in night and noon from the view of optimal operation curve. When lack of electricity, battery output power first and the insufficient added by the gas turbine. Because the gas turbine operation consume fuel and its operating maintenance cost is too high from the view of objective function. Gas turbine supplied power to load on the optimal operation curve in 20th hour. While, gas turbine supplied power to load and battery on the random operation curve in 20th hour which increase operation cost. Obviously, the random operation is not economic.

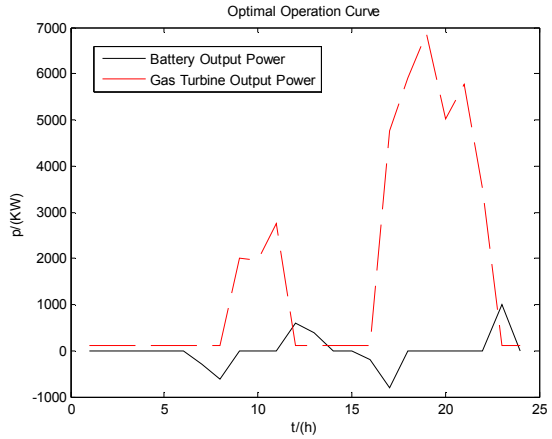

Fig.4. Optimal operation curve

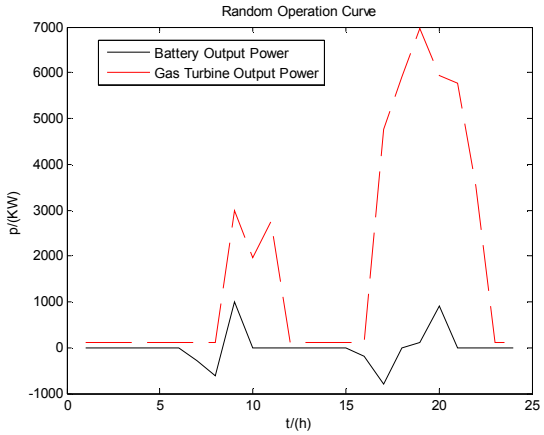

Fig.5. Random operation curve

Conclusion

Optimal operation of Shanghai Electric Group's island micro-grid was planned. It can make its operational cost minimized. Genetic algorithm was used to solve this problem. The results verify the effectiveness of the optimal operation. The paper provided a reference for other island micro-grid's optimal operation.

Acknowledgement

This paper is funded by the Shanghai municipal education commission key projects of scientific research innovation (12ZZ197), Shanghai natural science fund (12 ZR1411600), Shanghai science and technology innovation project (2011 MH065/2011 MH097 MH089/2011/2011 MH099), national natural science foundation of China (11201267) projects.

References

[1] Su lun: Energy Utilization, Vol. 01 (2013) No.1, p. 25-26.
[2] Wang chengshan, Hong bowen, Guo li: Power System Technology, Vol. 37 (2013) No.7, p. 1775-1782.
[3] J.Lee,B.Han, Y,seo: *8th International Conference on Power Electronics-ECCE Asia* (The Shilla Jeju, Korea, May 30-June 3, 2011). Vol.1, p.248-255.
[4] Meibom P, Barth R, Hasche B: IEEE Trans on Power Systems, Vol. 26 (2011) No.3, p. 1367-1379.
[5] Dennis B C, Byron Winn C: Solar Energy, Vol. 4-6 (2011) No.58, p. 165-179.
[6] Xiaoping L, Ming D, Jianghong H: *2nd IEEE International Symposium on Power Electronics for Distributed Generation Systems (PEDG)* (Hefei, China, June 16-18, 2010. Vol.1, p.914-917.
[7] Mohsen Mahoor,Negar Iravani: *2013 Smart Grid Conference (SGC)* (Tehran, Iran, December 17-18, 2013). Vol.1, p.125-129.

Advanced Materials Research Vols. 986-987 (2014) pp 453-458

doi:10.4028/www.scientific.net/AMR.986-987.453

Research on Adaptability Evaluation Contents and Indexes for Large Power Grid Construction

Yanwei CHEN[1, a], Lianguang LIU[2, b]

[1, 2,] North China Electric Power University, Changping District, Beijing, 102206, China

[a]email: yanweichen@csu.edu.cn, [b]email:liulianguang@ncepu.edu.cn

Keywords: Large Power Grid; Adaptability; Evaluation Content; Evaluation Index

Abstract. With the deepening of the electricity market reform and the development of community economy, as well as the increasing of grid scale, researching and establishing the adaptability evaluation theory and method of power grid construction not only is a realistic demand, but also has great influence on improving the evaluation theory system of power grid planning. In this paper, the adaptability evaluation content for large power grid construction consists of the adaptability of the national economy, the energy structure adaptability, grid structure adaptability and the adaptability of technology development. The paper also discusses the constructing theory and practice basis of the evaluation contents, in addition, the evaluation indexes of adaptability are presented in the paper.

Introduction

With the deepening of the electricity market reform and the increasing of the external environment constraints, the coordinated development between the grid and the external environment has become an increasingly important problem [1][2]. Under the new situation of high speed development of social economy, electricity market reform and the connection of national grid, the traditional grid planning thinking which mainly considers the evaluation indexes of security and power grid's economy [3][4][5], little considers the adaptability between grid and the external environment, such as energy resources, social economic development and environmental protection, will make it not coordinated between the development of the grid and power source, social economy. The incoordination has negatively impacted on the development of social economy, therefore, to put forward the evaluation contents and evaluation indexes of power grid construction adaptability, and to build a whole adaptability evaluation theory system is the reality demand. The evaluation content system is put forward for large power grid construction in this paper based on the analysis of the influencing factors of grid, which is shown in figure 1.

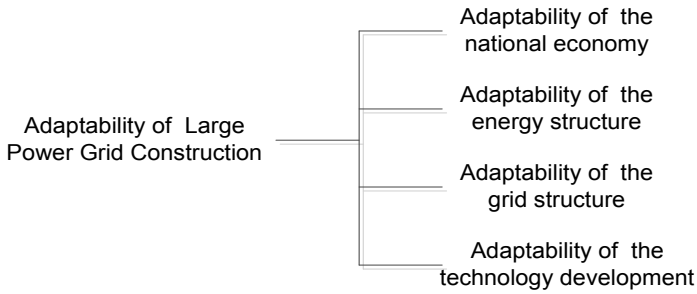

Fig.1. Adaptability evaluation content system for large power grid construction

Construction Foundation of the Evaluation Contents

(1). The need for development of national economy. Electric power industry is the foundation of the national economic construction and development, on one hand, if the development of power grid behind that of load, it will seriously restricts the development of national economy. On the other hand, the development of the national economy also has great impact on the construction of power grid. It was mentioned in literature [6][7] that power demand and national economy has

strong positive correlation, the correlation coefficient of more than 0.98, thus, both of them should develop harmonically to ensure the national economy developing well and healthily. Hence, adaptability of the national economy should be included in the adaptability evaluation system for large power grid construction.

(2). The need for optimizing the distribution of resources. It is known that energy resources and load demand is reverse distribution in China. As is shown in figure 2, power resources are mainly distributed in the west, and the load are mainly distributed in the eastern coast. In order to improve the efficiency of energy utilization, ensure national energy security, we need to build a suitable grid to realize the optimal allocation of power energy across the country [8][9].

Fig.2. Energy resources and load distribution in China

(3). The need for environmental protection, energy saving and emission reduction. With the increasing requirements for environmental protection, environmental protection and energy-saving emission reduction must be considered in the construction of power grid in future. At present, the thermal power accounts for the dominant position in China, and the environmental pollution caused by coal-fired power has become increasingly prominent. Vigorously developing solar, wind and other clean energy sources in the power structure could solve the serious polluted problems. The distribution and development of clean energy such as solar energy, wind energy, plays a very important role in the construction of large power grid.

Consolidated (2) and (3), the adaptability of the energy structure should be included in the adaptability evaluation system of the large-scale power grid.

(4). The need for the development of power grid. According to the characteristics of energy distribution in China and the trend of energy development in future, most of new power plants will be located in western and northern China; on the contrary, the main power load is likely to appear in eastern China, resulting in a further increase of the distance and demand to satisfy with the power transmission of the scale cross-flow. There is needed to build a strong, flexible and adaptive primary network to solve the overload of transmission and excessive levels of short circuit, which caused by the overweight of power flow. Therefore, the adaptability of grid structure is one of the issues which should be considered in the construction of power grid.

In addition, in the history of power grid, science and technology plays a supporting role in the construction of power grid which profoundly influenced by the development of technology. Consequently the construction of large grid needs to adapt with the current science and technology, otherwise there would be not built safe, reliable and flexible power grid. Therefore, the adaptability of technology development is one of the important contents of the adaptability evaluation for large power grids.

Adaptability Evaluation Indexes for Large Power Grid Construction

Evaluation indexes of national economy adaptability

From 1980 to 2050, the growth trend of China's GDP and electricity demand shown in Figure 3 [10], the growth rate trend of GDP is consistent with the electricity that of consumption. In addition, the increasing of power load would affect directly the substation’s capacity in the construction of larger power grid. Thus the adaptability evaluation indexes of the National Economic includes Electricity balance coefficient, the elastic coefficient of electricity production and capacity load ratio, as shown in table 1.

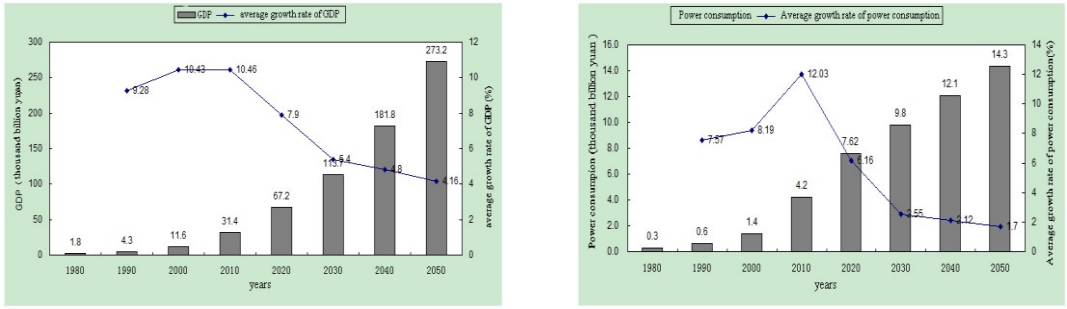

(a) (b)

Fig.3. Change trend of economy, power consumption and their growth rate of China
(a) the change trend of economy and its growth rate
(b) the change trend of power consumption and its growth rate

Among them, the electricity balance coefficient is the ratio of the power supply to power demand, which represents if the electricity supply is adapt to the demand, and if there is an phenomena of overload or supply surplus; the elastic coefficient of electricity production refers to the ratio of the average growth rate of electricity production to the average growth rate of GDP, which represents the adaptation of the speed of power grid construction to the speed of economy development; capacity load ratio is the ratio of the transformer capacity(kVA) to the total load(kW) in the specific region and voltage level, which refers to the matching degree between the capacity and the load of the electrical. Capacity growth rate refers to the ratio of the growth rate of transformer capacity to the growth rate of load in specific voltage level during the development of power grid, which reflect the relationship of relative speed between the average annual growth rate of main transformer capacity and load average annual growth rate, and can reflect the coordination of substation capacity and load growth to a certain extent.

Table 1. Evaluation indexes of national economy adaptability

Level indicators	The adaptability of the national economy			
Secondary indicators	electricity balance coefficient	elastic coefficient of electricity production	capacity load ratio	Capacity growth rate

Evaluation indexes of energy structure adaptability

One of the major consideration contents in constructing a large grid is to achieve the optimal allocation of national resources. According to the national energy development strategy, new energy sources such as wind power and solar energy will be vigorously developed. However, thermal power will still act as the main energy in our country [8], which calls for the optimal allocation of coal to achieve the goal of efficient, clean and optimized utilization of coal resources. Meanwhile, the environmental impact on large power grid construction is mainly that thermal power plant discharges the atmospheric pollutants such as sulfur dioxide. The permissible discharge of environment becomes the constraint of thermal plant construction in cities caused by the differences in environment capacity and the cost variations in environmental management, which leads to a certain impact on the structure of power source in cities [11]]12]. Thus the evaluation indexes of energy structure adaptability are shown in Table 2.

Table 2. Evaluation indexes of energy structure adaptability

Level indicators	The adaptability of energy structure adaptability		
Secondary indicators	permissible discharge of environment	utilization efficiency of coal	ability to accept new energy

Here we need to point out the index that the permissible discharge of environment, which determines the maximum capacity of the region's new power plant, means the maximum limit of pollutant emissions in a regional environment.

It was mentioned in literature [13][14][15] that coal resources in west and north can be used in the middle eastern load area by train or by truck, thus the plants can be built near the load area. Also,

large coal and electricity bases can be built in western and northern areas, and then transit the energy to the middle and eastern areas by UHV. In addition, the evaluation index of the coal utilization efficiency should be considered into the adaptability evaluation index system of power grid and energy structure, for that the optimal allocation in a wide range and the utilization efficiency can not be achieved by rail-based transport of coal.

The ability to accept new energy [16][17] is the installed capacity to admit new energy which means the largest installed capacity to admit new energy when all the sources, including the new energy, keep balance with the load, all the operation power supply are reasonable in peak shaving, and the demand of safe and reliable operation of power grids, under overloaded of transformers and lines is meet.

Evaluation indexes of grid structure adaptability

The grid structure adaptability concludes three aspects of coordinating development between the power grid and power supply, the different levels of voltage, the load and power supply. Among them, the adaptability between the grid structure and power supply can be described as: a grid structure is able to meet the access of the power supply and to transmit electric power. The adaptability of the internal grid mainly means that the different voltage levels can be coordinated and adapted each other. The abilities of power transformation among different voltage levels matched together in order to alleviate the load pressure, which is conducive to the sustainable development of power grid. The adaptability between the grid structure and the load can be manifested that the power grid is able to provide high-quality, reliable electricity for users as much as it can. Meanwhile it can also adapt to the load fluctuation in different periods, specific indicators are shown in Table 3.

Table 3. Evaluation indexes of grid structure adaptability

Level indicators	The adaptability of grid structure adaptability				
Secondary indicators	variable machine ratio	line machine ratio	adaptability of power supply ratio	average losing power ratio	the peak-valley difference of grid withstanding

Variable machine ratio means the ratio between the public step-down substation capacity of any voltage level and the installed capacity of the centralized dispatching power. The line machine ratio means the ratio between the length of transmission line of any voltage level and the installed capacity of the same voltage level. These two ratios reflect the harmonious degree between power grid and power source.

The adaptability among different voltage levels can be reflected by the adaptability of power supply ratio among various voltage levels. The power supply ratio refers to the rate of total real transformer capacities between the upper and lower substations [18].

Power grid interconnection is an important aspect for large power grid construction, and its reliability can be reflected by average losing power ratio. The losing power ratio refers to the ratio of load that can't be transferred and the total load which is provided by the substation, when the substation breaks down. The ratio can reflect the ability to transfer load of the grid, and it also reflects the degree of interconnection and adaptation.

With the rapid growth of air conditioners and other electrical equipment, the peak-valley difference of load is increasing quickly, power grid need to improve the adaptive ability to adapt to the load changing so that it can withstand the peak-valley difference of load in different conditions. The more prominent the peak-valley difference of load that the grid can withstand, means that the stronger the flexibility of the grid, and the stronger the ability of grid to adapt to load fluctuations.

Evaluation indexes of technology development adaptability

The development of large power grid is closely related to the innovation of science and technology, which can improve the proportion of new energy power for optimizing the energy structure, and promote the power energy-saving emission reduction. Furthermore, the power grid will be more reliable and stable strong, and the operation capability of grid will be further enhanced. So the innovation of science and technology closely interrelated the large grid is significant to the

security of national energy and the steady and rapid development of economy. The adaptability evaluation index of technology development is shown in table 4.

Table 4. Evaluation indexes of technology development adaptability

Level indicators	The adaptability of technology development adaptability		
Secondary indicators	permissible discharge of environment	utilization efficiency of coal	ability to accept new energy

Conclusion

1) In the situation of social economy rapid development, conventional energy draining, and interconnection of power grid, improving safety evaluation indexes, Expanding economic evaluation indexes, and proposing adaptability evaluation indexes, are the practical needs for large power grid construction. In adaptability evaluation, we take the adaptability of the national economy, the energy structure adaptability, grid structure adaptability and the adaptability of technology development as the adaptability evaluation contents for large power grid construction. The contents put forward in the paper improve the evaluation contents for large power grid construction.

2) The paper also discusses the constructing theory and practice basis of the evaluation content, and puts forward sixteen evaluation indexes which constitute the adaptability evaluation system for large power grid construction, such as electricity balance coefficient, elastic coefficient of electricity production. In addition, the paper proposes the calculation methods of the indexes.

3) In the field of electric power planning, this paper pays as much attention to the adaptability evaluation for large power grid construction as the economic and safety evaluation. Only a part of indexes have been presented in this paper. Establishing adaptability evaluation theory and evaluation method for the large grid construction is of great academic significance and practical value, more work need to do as the theory and algorithm of the adaptability evaluation for large power grid construction involves many theories, such as energy and electrical power systems, economics and sociology.

References

[1] Liu Zhenya, Zhang Qiping. Study on the Development Mode of State Grid[J]. proceedings of the CSEE, 2013, 33(7): 1-11.

[2] Liu C C, Vittal V. The Strategic Power Infrastructure Defense System[J]. IEEE Control Systems Magzine. 2000,13(8):40-52.

[3] Sun Xin, Liu Zehong, Yin Yonghua, et al. UHV Synchronous Power Network Constitution in China and Its Economic and Safety Analysis[J]. Electric Power Construction, 2007, 28(10): 7-11.

[4] Yin Yonghua, Guo Qiang, Zhang Yunzhou, et al. Scheme Study and Safety Analysis of UHV Synchronous Power Grid Composition[J]. Electric Power Construction, 2007, 28(2): 1-4.

[5] Wang Zhonghong. Economic and Security Analysis of UHV AC System in China[J]. Electric Power Automation Equipment, 2007, 27(10): 1-5.

[6] Chen Yinfeng. Research on the Relationship in Power Demand and Economic Development[D]. Shanghai: shanghai jiaotong university, 2010

[7] Zhao Sihua. Empirical Study of Relationship between Power and Economic Growth of China[D]. Beijing: NCEPU, 2006

[8] Liu Zhenya. Electric Power and Energy in China[M]. Beijing: China Electric Power Press, 2012.

[9] Zhang Yunzhou．Prospects Analysis for Trans-regional Power Resource Allocation[J]．Electric Power, 2004, 37(9)：5-7．

[10] Hu Zhaoguang, Tan Xiandong, Xu Zhaoyuan, et. al. Exploration on Chinese Economic Development and Power Demand[M]. Beijing：China Electric Power Press, 2011

[11] Su Yinbiao, Zhang Yunzhou. Research on the Optimizing Energy Delivery Mode in China[J]. Electric Power, 2007, 40(11)：4-8

[12] Huang Meili. Optimizing the Energy Structure, Improving Environmental Quality [J]. Energe and Environment, 2004, 3：51-52

[13] Pan Jiazhen. Discussion on Coal and Transmission Problems [J]. Power System and Clean Energy, 2011, 27(2)：1-3

[14] Lin Boqiang, Yao Xin. Power Layout Optimization and Energy Integrated Transport System [J]. Economic Research, 2009, 6: 105-115

[15] Ding Wei, Hu Zhaoguang. Comparison Study on Economy of UHV Transmission System[J]. Power System Technology, 2006, 30(19)：7-13

[16] Wei Lei, Jiang Ning, Yu Guangliang, et. al. Research on the Ability to Accept New Energy in Ningxia Eletric Power System[J]. Power System Technology, 2010, 34(11)：176-181

[17] Guo Xiangrong. Thinking about the Ability of Grid to Accept Lager-scale wind power capacity[J]. Guangdong Electric Power , 2011, 24(5): 20-23

[18] Fu Meiping. Research on Coordination Extent Evaluation and Coordination of Transmission Network Planning Method [D]. Zhengzhou：Zhengzhou University, 2010

Advanced Materials Research Vols. 986-987 (2014) pp 459-464

doi:10.4028/www.scientific.net/AMR.986-987.459

Research on characteristics of partial discharge in typical defects of High-voltage XLPE cable

Yu-li WANG[1a], Jian-kang ZHAO[1], Rong XIA[1]

[1]China Electric Power Research Institute,Wuhan 430074, China

[a]email:wangyuli@epri.sgcc.com.cn

Keywords: Power cables, Partial discharges, Defect models, Statistical operators

Abstract. Six models of typical insulation defects are designed and lab-simulated system used for partial discharge (PD) detection of cables and accessories has been constructed to study PD characteristics of internal insulation defects in 110 kV XLPE cable system. By employing CPDM, a kind of on-line PD detector, test data of various models including related PD diagrams are obtained for our research. Based on these characteristic parameters, discharge characteristic analyses of a single PD pulse are presented and statistical operators can be obtained by numerical calculation. The experimental results show that CPDM on-line detecting method is effective for detecting PD signals from internal defects of cable accessories. In addition, there are significant differences in the some statistical parameters (e.g. discharge phase, discharge repetition rate, etc) and characteristic parameters of time-domain PD waveform which can be used as reference points for PD patterns identification in future research.

Introduction

Partial discharge (PD) is the main performance of early cable and its accessories fault. It is not only the main cause of insulation aging, but also the key parameter indexing insulation situation [1]. Power cable failures/defects statistics show that more than 70% cable faults are caused by the accessories under the condition of disregarding the external force damage [2-3]. Moreover, affected by widely distributed of laying path, complex and varied operating conditions, XLPE cable lines are susceptible to external damage, weak product quality, uneven accessory installation quality and other factors, so certain operational risk and danger consist in cable line operation.

Numerous researches on internal partial discharge mechanism, detection methods, discharge characteristics and other aspects of the XLPE cable and its accessories have been paid attentions widespread in the world [4-8]. A lot of study on the typical PD models have been done as well, but these research basically emphasize simulation of metal tip and the air gap defects in a variety of partial discharge test models that doesn't conform to the actual situation and cannot be a true reflection of representative typical defect properties, characteristics and discharge mechanism of cable accessories exposed during the manufacturing, installation, operation process.

For the actual operating cable lines, especially for the cables soaked in the water under the ground, research on detection and analyzes of the potential insulation defects and diagnosis of the insulation healthy level are nearly empty. The insufficiency in relevant experience and data conduce impossibility to reach the requirements of detecting abnormality in advance or fault predicting and promptly maintenance by the operation and maintenance unit. Thus it hinders the development and application of defect detection and diagnosis technique under complicated operation conditions of XLPE cable insulation.

Based on this, we closely combine PD detection and diagnosis technology with the high voltage XLPE cable state detection and maintenance. According to the research on partial discharge detection and diagnosis technology, along with investigation about nationwide high voltage, ultra high voltage cable typical faults and defects especially in the high water level environment, the defective cable and its accessories specimens with various types and different degradation degree were established and simulated in laboratory. Then, time domain waveforms, spectrum distribution, frequency spectrum characteristics of discharge signals are collected to construct PD fingerprinting database for identifying different defects types. It lays a foundation for PD live detection and condition diagnosis of HV cable.

Modeling of typical defects of high voltage XLPE power cable

According to the previous collection of relevant literature, historical data, statistics and analysis of HV cable fault types, probability distribution and fault cause, the weakness of cable insulation and frequently failure location have been summarized. The main technical reasons and key factors of operation failure of high voltage cables have been studied. We discuss the typical defects of cable and its accessories during laying, construction, installation, operation and other links. In order to make the basic research to guide practice, considering the comprehensive representative and defect types of defects, eventually the following 6 types of representative defects were formed which are shown in the following table:

Table 1 Type and Main Physical Parameters of Representative Defects

NO.	Defect Type	Main Physical Parameters	The Images of Defect Models
1	Soaking joint	Cable inside joint was soaked in water for 24h,and water was injected during installation	
2	Incision on cable	Breadth and depth of incision is 10 cm and 2mm.Length of outer shielding lay wound is 5cm;	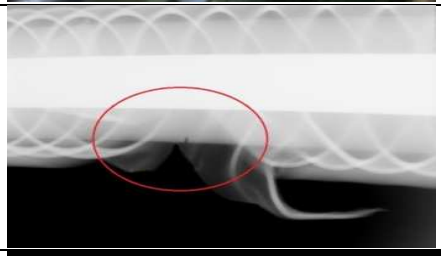
3	Puncture on cable	Diameter and depth of puncture are 3 cm and 4mm.	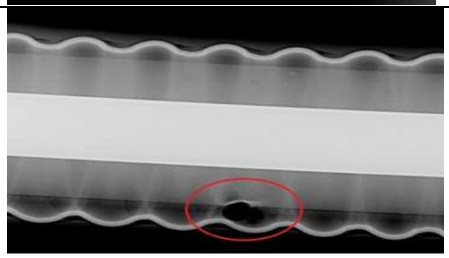
4	Sharp insulation screen on outer semiconductive layer	Two sharps are isosceles triangles which bottom edge is 4mm,height is 1cm, spacing is 8mm.	
5	Conductive grain on the interface of composite insulation	Area of conductive grain is about 5cm×7.5cm	
6	Prefabricated unit offset	Stress cone is 5mm away from standard location.	

Experiments design

The lab-simulated system is composed of 110kV XLPE cable, compound insulation termination, prefabricated joint, water-insulated cable test termination and related auxiliary, according to typical defects in Table 1, adopting CPDM, experiment was conducted to study the performance of PD in the laboratory. Parts of representative spectrum diagrams are given as follows:

Table2 Pulse and frequency spectrum of typical defects

The spectrum of soaking joint defect	The spectrum of incision defect
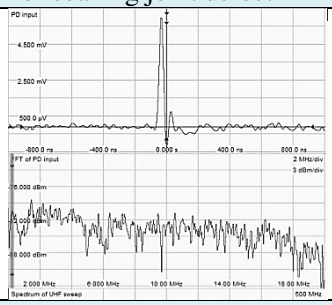	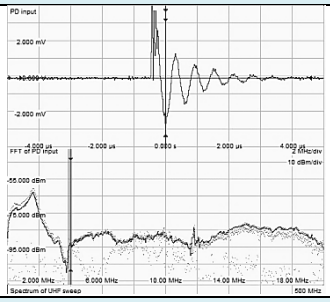
The spectrum of puncture defect	**The spectrum of sharp insulation screen defect**
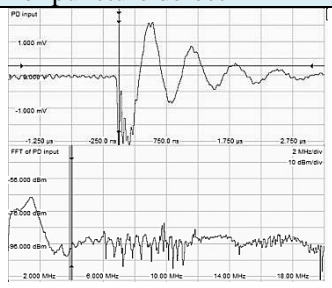	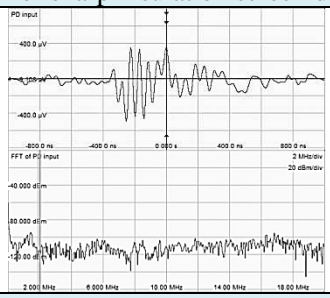
The spectrum of conductive grain defect	**The spectrum of prefabricated unit offset defect**
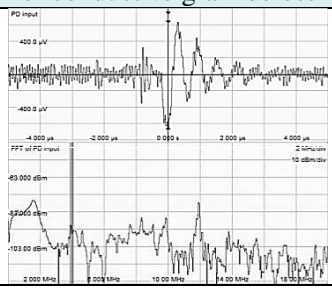	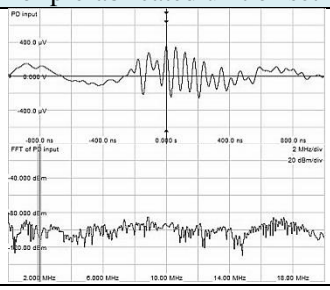

Table3 Q-Φ spectra of typical defects

The spectra of soaking joint defect	The spectra of incision defect	The spectra of puncture defect
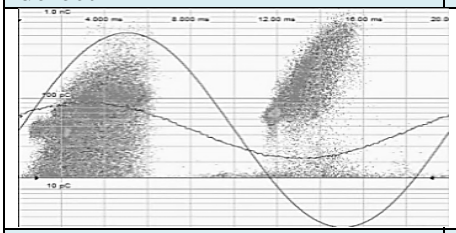	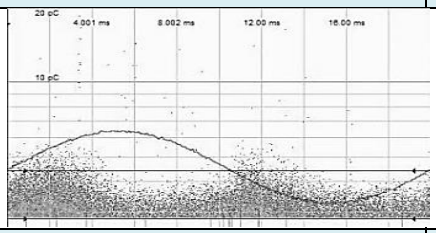	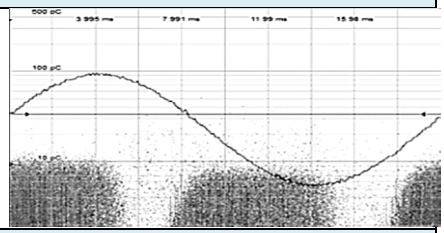
The spectra of sharp insulation screen defect	**The spectra of conductive grain defect**	**The spectra of refabricated unit offset defect**
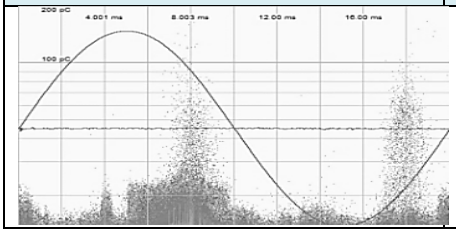	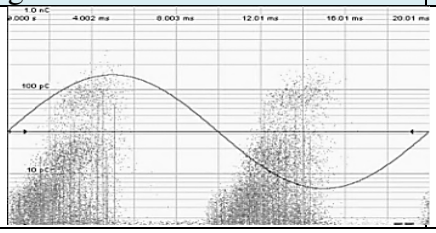	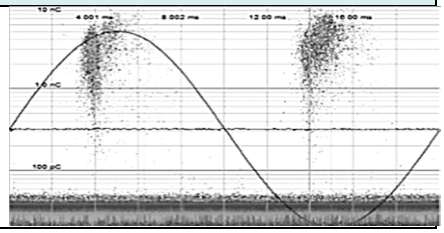

In this section, the characteristic spectrum diagrams of typical defects have been concluded, discharge signals in 6 samples of typical defects were acquired by CPDM in the pure electromagnetic laboratory, typical discharge signal samples were achieved in time domain, frequency domain, and corresponding Q-Φ spectra, it could achieve the obvious differences in the statistics table of various defect characteristics and it is laying foundations on identification database. All these partial discharge data will be discussed in detail later.

Experiments results analysis

Based on the experimental results, it's able to be found that all these partial discharge features are distinct and complex. Various feature extraction methods were extensively applied to pattern recognition and insulation condition diagnosis of partial discharge. However, most of these analysis methods drop or ignore some original partial discharge characteristics in calculating process more or less. In our work, whole natural parameters were collected and statistical estimators are used to compare the PD pulse pattern shapes. These statistical estimators are kurtosis, skewness, Cross Correlation, charge asymmetry; these are defined by the following expressions [9]:

$$S_k = \sum_{i=1}^{N}(x_i - \mu)^3 f(x_i)/[\sigma^3 \sum_{i=1}^{N} f(x_i)] \quad (1)$$

Where

x_i : sample value of the distribution

μ : mean value

N: number of samples

σ:standard deviation

Skewness describes the asymmetry aspect with respect to the normal distribution.

$$K_u = \sum_{i=1}^{N}(x_i - \mu)^4 f(x_i)/[\sigma^4 \sum_{i=1}^{N} f(x_i)] - 3 \quad (2)$$

Kurtosis represents sharpness with respect to the normal distribution.

$$Cc = \frac{\sum_{i=1}^{W} x_i^+ x_i^- - (\sum_{i=1}^{W} x_i^+ \sum_{i=1}^{W} x_i^-)/W}{\sqrt{[\sum_{i=1}^{W}(x_i^+)^2 - \sum_{i=1}^{W}(x_i^+)^2/W][\sum_{i=1}^{W}(x_i^-)^2 - \sum_{i=1}^{W}(x_i^{\pm})^2/W]}} \quad (3)$$

Where

x_i^+ and x_i^- sample value of the distribution at the corresponding phase φ_i and $\varphi_i + \pi$ respectively.

W number of samples of the wave period

Asymmetry represents the charge transfer differences in the positive and negative polarity discharge events; this feature has the following expression:

$$A_{sy} = N_2 \sum_{i=1}^{N_2} x_i^- / N_1 \sum_{i=1}^{N_1} x_i^+ \quad (4)$$

Where

N_1 and N_2 are number of sampling intervals in the positive and negative half-wave period.

Parts of selected representative characteristic parameters are presented in following table.

Table 2 Representative characteristic parameters of various defects

	Soaking joint defect	Cable incision defect	Cable puncture defect	Sharp screen defect	Conductive grain defect	Cutting into main insulation
Phase range of discharge	10º~100º 200º~280º	0 ° ~60 ° 180 ° ~230 °	0º~90º 180º~270º	100º~180º 220º~300º	50º~150º 220º~270º	20º~120º 190º~300º
Phase of peak	92º and 268º	31 ° and 204 °	36 ° and 207 °	89º and 253º	96º and 272º	95º and 266º
Discharge magnitude	982 pC	3.5 pC	12.4 pC	172 pC	102 pC	9 nC
Repetition rate	81 PDs⁄s	48 PDs⁄s	66 PDs⁄s	30 PDs⁄s	32 PDs⁄s	35 PDs⁄s
Rise time	21ns	33ns	227ns	143ns	279ns	18ns

Fall time	36ns	85ns	485n	189ns	364ns	35ns
Skewness	1.021(+) 1.153(-)	0.598(+) 0.526(-)	1.4244(+) 1.5029(-)	-1.717(+) -1.565(-)	1.253(+) 1.463(-)	0.847(+) 0.614(-)
Kurtosis	-0.798(+) 1.02(-)	-0.337(+) -0.382(-)	-0.7411(+) -0.6458(-)	1.266(+) 2.195(-)	0.491(+) 0.422(-)	2.267(+) 2.829(-)
Cross Correlation	0.316	0.905	0.7869	0.95	0.543	0.858
Asymmetry	1.642	1.033	0.807	0.696	0.717	0.914

In the table, rise time and fall time refer to the PD pulse waveform in time domain, phase of peak means the phase of PD maximum point. Besides, Skewness and Kurtosis were calculated in positive and negative semi-cycle respectively.

Conclusion

Based on statistical analysis of power cable faults by the State Grid Corporation, 6 kinds of typical defects have been constructed in the actual 110 kV cable which can effectively reflect the nature of the defects, characteristics and discharge mechanism in the manufacture, installation, operation process.

The analysis of typical defect types of cable and its accessories was conducted in this paper, lab-simulated system was constructed. And, the representative PD characteristics collection of 6 typical cable defects was obtained. All these fingerprint characteristics constitute our PD fingerprint database to conduct PD patterns recognition and troubleshooting. Meanwhile, in view of our research, references to work of PD identification have been proposed as follow:

A. The partial discharge signals are gathered in two clusters, the phase difference is nearly 180 º.
B. The partial discharge pulse repetition rate is higher than 30 n/s.
C. Employing adaptive filtering and anti-interference measures, partial discharge can be clearly distinguished from the noise signals.
D. After eliminate interference, partial discharge should repeat in relative long period.
E. Peaks of partial discharge spectrum may appear in multiple frequency bands
F. In time domain, single partial discharge pulse duration should be ns level.
G. For partial discharge signals, rise time should be less than fall time.

References

[1] Katsumi Uchida, Hideo Tanaka, and Ken'ichi Hirotsu, Study on detection for the defects of XLPE cable lines, IEEE Trans. On Power Delivery, Vol. 1, No. 2, pp663-669 ,April 1996.

[2]Peter H. F. Morshuis, Degradation of solid dielectrics due to internal partial discharge: some thoughts on progress made and where to go now, IEEE trans. on Dielectrics and Electrical Insulation, vol. 12, No. 5, pp905-913 ,Oct. 2005.

[3]. R. Schwarz, T. Judendorfer and M. Muhr, "Review of Partial Discharge Monitoring techniques used in High Voltage Equipment", IEEE Conf. Electr. Insul. Dielectr. Phenomena, pp. 400-403, 2008.

[4]Tozzi M, Cavallini A, Montanari G C, et al. PD detection in extruded power cables: an approximate propagation model [J]. IEEE Transactions on Dielectrics and Electrical Insulation, 2008,15 (3):832-840.

[5]Tian Y, Lewin P L, Pommerenke D, et al. Partial discharge on-line monitoring for HV cable systems using electro-optic modulators[J]. IEEE Transactions on Dielectrics and Electrical Insulation, 11(5), 861-869, 2004.

[6]Tian Y, Lewin P L, Davies A E, el at. Acoustic Emission Techniques for Partial Discharge Detection within Cable Insulation[C] IEE Eighth Int. Conf. on Dielectric Materials, Measurements and Applications., pp503-508, 2000.

[7] E. Gulski, J. J. Smit and F. J. Wester. "PD knowledge rules for insulation condit ion assessment of distribut ion power cables", IEEE. Trans on Diel and EI Ins, Vol. 12, no.2, pp. 223-239. Apr.2005

[8]IEC 60270 Partial discharges measurements[S]. USA: IEC. 2006.

[9] Antonello Rizzi, F. M. F. Mascioli, Francesco Baldini, et al Genetic Optimization of a PD Diagnostic System for Cable Accessories[J] IEEE Trans on power delivery, vol. 24, no. 3, pp.1728-1738, jul. 2009.

Advanced Materials Research Vols. 986-987 (2014) pp 465-469

doi:10.4028/www.scientific.net/AMR.986-987.465

Research on Combined Peak Load Regulation with Hydropower, Thermal Power and Nuclear Power Plants

Gang Wang[1], Xiaodong Ma[2], Chao Wang[1], Peng Ye[3]

[1] State Grid Liaoning Electric Power Research Institute, Shenyang, 110006, China

[2] Electrical Engineering Department Shenyang University of Technology, Shenyang, 110870, China

[3] Electrical Engineering Department Shenyang Institute of Engineering，Shenyang, 110136, China

Keywords: nuclear power plant, combined peak load regulation, operation mode

Abstract: Base on Nuclear Power Plant (NPP) participating in peak load regulation of power grid, this paper studies the operation mode of hydropower, thermal power and NPP in Combined Peak Load Regulation. The optimization model for Peaking depth of NPP was set up. The case based on actual power grid were calculated and analyzed, results of the research show that in combined peak load regulation of hydropower, thermal power and NPP, a reasonable peaking depth of NPP will effectively alleviate the peaking pressure of power grid, avoid start-stop of thermal power and abandoned water of hydropower, while ensuring the hydroelectric generating capacity in the low load periods, and ensure thermal power output smooth, it further reduce the operating costs, verify the effectiveness of the model.

I. Introduction

In recent years, with the increase of the gap between peak load and valley load in power system, proportion of nuclear power in the grid, and grid connection capacity of the new energy such wind and light power, only rely on traditional load such as hydropower, thermal power will not be able to meet the demand of power system load in the future. Grid security, stability and economic operation threatened the power system needs of the nuclear power plant to participate in the growing power peaking. For grid peak shaving and optimization with the nuclear power has a great significance. Hydropower, thermal power and NPP peak load regulating operation for coordination scheduling and the joint will be necessary in order to ensure the healthy development of the future power grid security and effective measures.

Since the 1970s, the United States, Germany, France, Japan and other countries have implemented a PWR/BWR, improved thermal neutron reactors and other nuclear power reactor type load following tests and the actual operation [1-5]. During 40 years , daily load-following operation experience of PWR has shown that there is no adverse effects of daily or weekly load following on fuel performance and radioactive concentration of the coolant will not rise because of load following. The feasibility of PWR and reliability of daily load-following operation were both verified [6-9]. Considering the safety of nuclear power itself and peaking speed and depth limit of NPP, the PWR nuclear power plant generally take "12-3-6-3" mode and maximum 50% of peaking depth participate in peak load regulation of power grid [10].

Based on the NPP involved in the daily load-following operation, research the allocation of output within a day of each period of hydropower, thermal power and NPP in this paper. Through the judgment of nuclear power participates in peaking, determine the operating position of NPP. The method of hydropower, thermal power and NPP load distribution were presented. Analysis and gives the optimization model of NPP peaking at the depth of the load. The validity of the model has been verified by numerical examples

II. Output Assignment of Combined Peak Load Regulation

If NPP need to participate in peak load regulation, hydroelectric, thermal power and NPP need to re-adjust the operation mode, rational distribution of load, ensure peak regulation capacity balance of power system and operation the lowest cost. To achieve peak regulation cost minimization, it

should be based on various types of investment instruments peak regulation order, decision the best combined peak load regulation scheme.

Combined with the literature [11-12], operation cost of hydroelectric, thermal power and NPP is shown in Table 1, NPP peak load regulation cost is less then start-stop of thermal power and abandoned water of hydropower, so we need to invoke NPP peak load regulation capacity first. To avoid start-stop of thermal power and abandoned water of hydropower, we need reasonable arrangements the depth of NPP peak load regulation, the specific optimization method is described in detail in the next section. If still remaining output when invoke maximum peak load regulation of NPP, start-stop of thermal power and abandoned water of hydropower will be considered.

Tab.1 Operation cost of peak load regulation

Peak load Shaving schemes	deep peak regulation	NPP peak regulation	start-stop of thermal power	abandoned water of hydropower
Operation cost (Yuan/MW·h)	40	71	167	250

III. Optimization of NPP Peaking Depth

In combined peak load regulation of hydroelectric, thermal power and NPP, NPP peaking will let it loss of marginal costs and benefits of clean energy, and by the security, economic and other constraints, therefore NPP peaking need to be judged.

Consider only hydropower, thermal power and NPP in power grid, and without start-stop of thermal power and abandoned water of hydropower, power capacity balanced and peak regulation capacity balanced of power grid as follows:

$$\begin{cases} D=P_{H\max}+P_{T\max}+P_{N\max}-P_{L\max}-P_R \\ T=P_{L\min}-P_{T\min}-P_{F\min}-P_{N\max}-P_{R'} \end{cases} \quad (1)$$

Wherein: D is surplus capacity of the power system; T is lowered peak surpluses capacity of the power system; $P_{L\,max}$ and $P_{L\,min}$ are minimum and maximum power load of planned date; $P_{H\,max}$ and $P_{H\ min}$ are planned date the whole system adjustable maximum and minimum output of all conventional hydroelectric generating in load peaks and troughs; $P_{T\,max}$ and $P_{T\,min}$ are planned date the whole system adjustable maximum and minimum output of thermal power in load peaks and troughs; $P_{N\,max}$ is rated output of NPP planned date whole system; P_R and $P_{R'}$ are the positive and negative spinning reserve capacity.

while meeting $D \geq 0$ and $T \geq 0$, NPP don't need to participate in peak load regulation.

In the case of reasonable arrangement of hydroelectric, thermal power output mode, if T <0, means that cut peak load capacity is insufficient when the load trough, NPP need to participate in peak load regulation. Criterion is:

$$P_{L\min} < P_{H\min} + P_{T\min} + P_{N\max} + P_{R'} \quad (2)$$

The average depth of NPP participating in peak load regulation is set up for λ, then NPP output when the load trough is:

$$P_{N\ min}=(1-\lambda)P_{N\ max} \quad (3)$$

After determining need NPP peaking, the depth of the NPP peaking will be optimized base on proportion of hydroelectric, thermal power and NPP and their operating characteristics, in order to achieve the goal of peaking capacity balance and operating costs to a minimum.

Optimized unit output goal is to the lowest operating costs, including coal consumption and peak shaving costs. When established optimization model needs to meet the maximum output peaking of hydropower, thermal power output duration as long as possible and the maximum output rate of nuclear power load trough period. For such general solving multi-objective, multi-objective solving equations can be established, or simply goals into constraints to be solved. The second method was taken to solve it in this paper.

The largest output model of NPP in power grid load trough:

$$J = \max \sum_{t=0}^{6} \sum_{i=1}^{m} P_{Ni\min} \tag{4}$$

Wherein $P_{Ni\min}$ is the *i*-th NPP's output in power grid load trough, the number of NPPs is m.

Formula (4) was subject to system constraints, independent water system constraints, thermal power constraints and NPP safety constraints.

(a) System constraints

To simplify the calculation, where only consider the system peaking capacity balance constraints in low load periods:

$$P_{L\min} - P_{H\min} - P_{T\min} - P_{N\min} - P_{R'} \geq 0 \tag{5}$$

(b) Independent water system constraints

①Daily water balance conditions:

$$\sum_{i=1}^{n} (\mathrm{q}_{it} + \mathrm{w}_{it}) + spl_t = Q_t \tag{6}$$

Total hydropower is n.

②Hydropower output constraints:

$$P_{Hi,\min} \leq P_{Hi,t} \leq P_{Hi,\max} \tag{7}$$

③Hydropower generation flow constraints:

$$Q_{i,\min} \leq Q_{i,t} \leq Q_{i,\max} \tag{8}$$

④Reservoir water level constraints:

$$Z_{i,\min} \leq Z_{i,t} \leq Z_{i,\max} \tag{9}$$

⑤Hydro no abandoned water conditions:

$$K = \max \sum_{t=1}^{T} \sum_{i=1}^{n} N_t^i(\mathrm{Q}_t^i) \tag{10}$$

Where in $\mathrm{N}_t^i(\mathrm{Q}_t^i)$ is the output value by the *i*-th hydropower flow stations in the time *t*, *K* maximum means no abandoned water.

(c) Thermal power constraints

①Thermal power ramp rate constraints:

$$\left| P_{L,t+1} - P_{L,t} \right| \leq S_t \cdot t \tag{11}$$

Where in $S_t = \sum_{i=1}^{z} S_{i,t}, i = 1, 2.....z$, S_t represents a climbing speed thermal power. $S_{i,t}$ is climbing speed of i-th thermal power.

②The minimum period of continuous thermal power output:

$$\begin{cases} \left| \partial P_T \right| = 0, 0 \leq \left| t \right| \leq T_{\min} \\ \left| \partial P_T \right| \geq 0, \left| t \right| > T_{\min} \end{cases} \tag{12}$$

(d) NPP safety constraints

①Nuclear power peaking Constraints:

By the characteristics of its own, NPP can only be tracked by the shape like "12-3-6-3" output mode. In this paper, nuclear power output in accordance with this running.

②NPP peaking depth constraints:

$$\eta_i \leq \eta_{\max} \tag{13}$$

Where in, η_i represents peaking depth of the i-th nuclear power generating units. Its value was determined by the performance requirements of their own nuclear power plants, safety factors and expert advice decisions.

③NPP peaking speed constraints:

$$\rho_{\min} \le \rho_i \le \rho_{\max} \tag{14}$$

ρ_i is the *i*-th NPP's speed of change power.

IV. Example Analysis

Set up a regional power grid containing water, fire and nuclear power peaking three categories. Nuclear power capacity 1280MW and rated at 1090MW accounting for about 10% of the total installed capacity. Hydropower installed capacity of 1700 MW. Thermal power peaking capacity load of 2400 MW. Grid daily load curve shown in Figure 1, according to the power grid, load characteristic and power source structure, list the following 3 kinds of load plan.

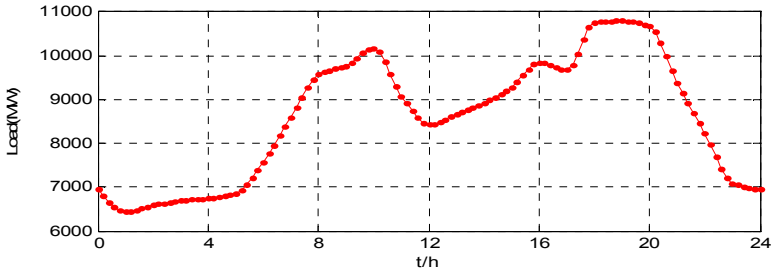

Fig.1 The daily load curve of a grid

Case 1: Hydropower peaking+ thermal power deep peak shaving + NPP peaking with smaller depth. Take NPP peak shaving depth of 20%.

Case 2: Hydropower peaking+ thermal power deep peak shaving + NPP peaking with largest depth. Take NPP peak shaving depth of 50%.

Case 3: Hydropower peaking+ thermal power deep peak shaving + NPP peaking with proper depth. Take NPP shaving depth of 40%.

Assuming that when the depth of the nuclear power peaking take 40%, hydropower peaking its daily output is just equal to the amount of water can be adjusted for maximum power. It can effectively prevent the emergence of disposable water peaking situation. In the low load periods, hydropower output help thermal power climbing and make its output steady, reaching the lowest operating costs of the system. NPP peaking insufficient depth in case 1, will result in low load periods shutting down small thermal power units, even abandoned water peaking. Accordingly, lead to a waste of resources and higher costs peaking. Case 2 NPP peaking depth is too large, did not make full use of the capacity of thermal power peaking resulting increase in coal consumption and waste of nuclear energy, increasing the cost of the peaking. In the case 3, NPP was operated based on "12-3-6-3" output mode. The actual load power curve, the curve of NPP peaking, and equivalent daily load curve are shown in Figure 2.

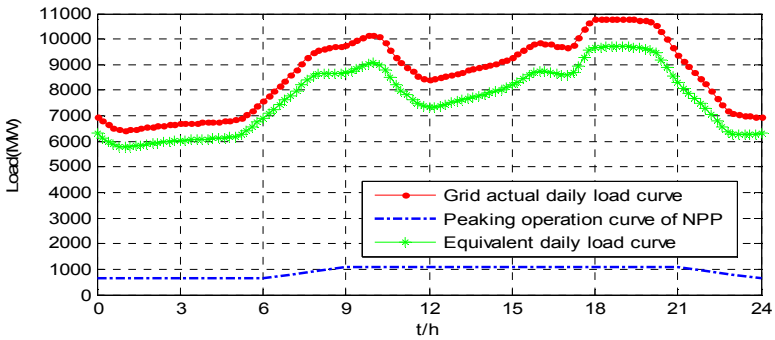

Fig.2 The actual daily load and equivalent daily load

Figure 4 shows that the equivalent daily load compared with the actual date, the trend is consistent. During 6:00-9:00 and 21:00-24:00 when nuclear power output was adjusted, the rate of change is equivalent to the daily load decreases. Occurrence of load peaks and valleys of the same, but the difference between peak load is reduced by 436MW. Therefore, the equivalent daily load

peaking effectively alleviate the pressure of peaking .It more suitable for hydropower and thermal power peaking. By optimizing depth of peaking involved in nuclear power peaking, effectively avoiding start-stop of thermal power and abandoned water of hydropower. Ensuring the smooth thermal power output and decreasing the costs of peaking, it contributes to the security, stability and economy of the power system.

V. Conclusion

In this paper, the combined peaking hydropower, thermal power and nuclear power as a starting point, nuclear with arrangements "12-3-6-3" model participate in hydropower and thermal power peaking. Through the judgment of NPP participation in power peaking, the location of NPP to run were analyzed and determined, then the hydropower, thermal power and NPP load distribution were offered. Optimization model NPP peaking at the depth of the trough load was presented. Obtained by a numerical example, in the united peaking hydropower, thermal power and NPP, NPP peaking take reasonable depth of power will effectively ease the grid pressure. It's effectively avoid start-stop of thermal power and abandoned water of hydropower, while the hydroelectric generating capacity at the time of low load, thus ensuring a smooth thermal power output and reduced the running costs. The validity of the model has been verified.

Acknowledgement

The Science and Technology Program：Nuclear Power Plant Participate in Peak Load Regulation of Power System and Research of Combined Operation with Wind Light and Energy Storage,2014YF-22.

References

[1] Berkovich V M, Gorokhov V F, Tatarnikov V P. Possibility of regulating the capacity of a power system by means of nuclear power plants[J]. Teploenergetika,1974(6):16-19.
[2] Grum A. Design of nuclear power plant with pressurized water reactor for optimum load follow capability[J]. Atomkernenergic Kerntechnik,1986,48(3):138-143.
[3] Levent A H, Altin V. Rule-based fuzzy logic controller for a PWR-type nuclear power plant[J]. IEEE Transactions on Nuclear Science, 1991, 38(2):883-890.
[4] Christenson J M. Application of optimal control theory to a load following pressurized water reactor[J]. Nuclear Technology,1992,100(3):361.
[5] Wu Guo-wei, Tao Jin. Research of Load Follow for Nuclear Power Plant with Pressurized Water Reactors[J]. Nuclear Power Engineering, 1998, 19(5):394-397.
[6] Ge Bin, Wu Yi[J]. A Study on a real-time simulation for the second loop of PWR nuclear power unit[J]. Proceedings of the CSEE, 2002, 22(6):142.145.
[7] Wu Ping, Liu Di-chen, Zhao Jie, et al. Fuzzy adaptive PID control-based load following of pressurized water reactor[J]. Power System technology, 2011, 35(4):76-81.
[8] Zhao Jie, Liu Di-chen, Wu Yao-wen. Modeling of pressurized water reactor nuclear power plant integrated into power system simulation[J]. Proceedings of the CSEE, 2007, 29(31):8-13.
[9] Zhang Xue-cheng, Hu Xue-hao, Zhou Xiu-ming, et al. Development of MID term dynamic simulation program including nuclear power plant model and study of interaction between large nuclear power plant and power system[J]. Power System technology, 1995, 19(2):5-10.
[10]Zhao Jie, Liu Di-chen, et al. Analysis of Nuclear Power Plant Participating in Peak Load Regulation of Power Grid and Combined Operation With Pumped Storage Power Plant[J]. Proceedings of the CSEE, 2011, 31(7):1-5.
[11]Zhao Jie, Liu Di-chen, et al. Operation mode and benefits of nuclear power plant participating in peak load regulation of power system[J]. Power System technology, 2012, 32(12):252-253.
[12]Chen Qi-xin, Kang Chong-qing, Xia Qing. Operation mechanism and peak-load shaving effects of carbon-capture power plant[J]. Proceedings of the CSEE, 2010, 30(7):22-28.

Advanced Materials Research Vols. 986-987 (2014) pp 470-473

doi:10.4028/www.scientific.net/AMR.986-987.470

Research on Economic Security Evaluation of China's Coal Cities based on Neural Network

Haisheng LIU[1, a], Cang CHEN[2, b]

[1] Basic Department, North China Institute of Science and Technology, Sanhe, 065201, China

[2] Dean's Office, North China Institute of Science and Technology, Sanhe, 065201, China

[a]email: liuhs223@126.com, [b]email:Cc9089@163.com

Keywords: PSR model; BP neural network; economic security; coal cities

Abstract. According to the pressure-state-response model, building an evaluation index system, evaluating the level of economic security of 21 coal cities by back propagation (BP) neural network theory and means of MATLAB. The results show that the level of economic security of coal cities in China is not ideal and must be improved. The level of economic security shows regional differences.

Introduction

With the rapid development of China economy, the demand for energy is increasing, while the pollution and damage to the environment is more and more serious. PM2.5 and haze become the focus at one's leisure talk. Whether the city economic development is safe and sustainable have attracted the attention of many researchers. However, most of them are limited to concept of study, selection of indicators, as well as individual city practice research. And for a certain class of city, especially in resource dependent city group (such as coal city), there is not much research. The predatory exploitation of coal resources has a direct relationship with the deteriorating environment, therefore, research on coal city economic security is of great practical significance and important.

To coal cities, the ecological security and sustainability is of vital importance to the economic development. Based on the results of previous studies, using the index system of ecological security of classic international framework of PSR model, using artificial neural network to study China coal city economic security system, we get China coal city economic security evaluation and provide scientific basis for the evaluation and management of city economic security decision.

The western developed countries study on coal city resources cities were relatively early and the theoretical basis are the adjustment of the economic structure theory and the theory of labor market segmentation. The representatives are Bradbury, Hayter, and Barnes. They point out, cyclical mining industry has a strong influence on mining city migration, economic development and community development.

Study on coal city in China lag behind the rapid development the coal city on the whole. Early research mainly focused on industrial development and planning. After 90 years of the last century, research has begun to pay attention to the comprehensive adjustment of industrial structure and sustainable development.

Determine of the Evaluation System and Index

The coal city has not a strict definition so far. Most believe that the coal city is formed and developed as a result of development of local coal resources, and the coal industry occupies an important position in the city industrial structure in the city. This paper studies the coal city with city level dependency: Mines are mainly in the city's urban and suburban areas, and the mining industry is the city's main pillar industry. The total of such cities are 21, respectively is: Datong, Jincheng, Yangquan, Shuozhou, Qitaihe, Hegang, Jixi, Shuangyashan, Zibo, Zaozhuang, Fushun, Huainan, Huaibei, Jiaozuo, Pingdingshan, the new port, Pingxiang, Hebi, Shizuishan, Liupanshui, Tongchuan [1].

Economic security is generalized on economic security, which includes economic, also includes the natural environment, resources, social security. From the concept of speaking, ecological security is economic security. The coal city economic security can be understood that the economic system of the coal city has the ability of facing the threat of recovery, and can make the natural resources in the population, economy, ecological conditions stable, coordinated, orderly and sustainable utilization.

PSR (Pressure-State-Response), namely pressure, state, response, is a common evaluation model of the environmental quality assessment of ecosystem health evaluation sub disciplines which was, originally proposed by the Canadian statistician David J.Rapport and Tony Friend, then developed as framework system on environmental problems by the organization for economic cooperation and development (OECD) and the United Nations Environment Program (UNEP) in later twentieth Century.

On the basis of existing research, system of coal city economic security evaluation index of four level 16 indexes by using the PSR model. See table 1.

Table 1 Coal city economic security evaluation index system

Target layer	Project level	Factor level	Index layer
Comprehensive index of economic security	Pressure on the economic environment	Population pressure	Population density (/km2)
			The natural growth of population rate（‰）
		Resource pressure	The public green area per capita（m2）
			Road area per capita（m2）
			Housing area per capita（m2）
		pressure on the social and economic	Per capita GDP（yuan）
			Every million people have the bus (car)
			Every ten thousand people owned hospital beds
	Economic systems state	Resource state	Green coverage rate in developed area (%)
			Compliance rate of centralized drinking water source water quality (%)
		Environment state	Volume of industrial waste water emissions (ten thousand tons)
			Volume of industrial soot emissions (t)
			Volume of industrial so2 emissions (t)
	Economic system response	Social response	People have a volume of books (book)
		Economic response	Education investment accounted for the proportion of GDP (%)
			The third industry accounted for the proportion of GDP (%)

According to the established evaluation system, the indicators data collected 21 cities. 16 indicators of original data are from China city statistical yearbook 2010 and part of the provincial statistical yearbook [2]. Raw data is slightly.

According to the frame of the assessment index system of city ecological security of the building, according to the following principles for determining the sign of each single index value: (1) where the existing national standards or international standards index, as far as possible the specified flag value.(2) referring to the current situation of foreign has good characteristics of city value.(3) referring to the current situation of domestic city value trend extrapolation, determine the sign value.(4) based on the existing environment and society, economy coordinated development theory, to a flag value quantification.(5) the current statistical data is not very complete, but there is a very important index in the index system, the lack of relevant statistical data index, use similar index instead of [3].

Artificial Neural Network Model

Research on neural network field background work began in late nineteenth Century and early twentieth Century, and its essence is a nonlinear dynamic system, has the strong association, self learning, recognition function, subject to artificial intelligence and systems engineering science. As a large-scale parallel processing of nonlinear dynamic systems, artificial neural networks have been widely used in economic analysis, optimization, forecasting and other fields in recent years, has obtained the good effect of [4].

Method of grading according to various index at home and abroad, the design of a determined coal city economic security classification table, so that to evaluate Chinese coal city from the overall economic security [5]. Specific classification in table 2.

Table2 Coal city economic safety criteria

Each index	Unsafe	Not safe	A security	Very safe
Population density (/km2)	4500	4000.00	3500.00	3000.00
The natural population growth rate （‰）	1	0.90	0.80	0.70
The public green area per capita （m2）	16	17.00	18.00	19.00
Road area per capita（m2）	28	29.00	30.00	31.00
The per capita housing area（m2）	14	15.00	16.00	17.00
Industrial wastewater emissions (tons)	450	400	322	300
Volume of Industrial Soot Emission (ton)	3500	3000	2574	2000
Industrial SO2 emission (ton)	9500	9000	8366	8000
Per capita GDP (yuan)	10000	15000	20000	25000
Every million people have the bus (car)	85	90.00	100.00	110.00
Every million people have hospital beds (Zhang)	85	90.00	92.48	95.00
Coverage rate of the developed area (%)	35	40	45	50
Compliance rate of centralized drinking water source water quality (%)	90	95.00	100.00	100.00
People have a volume of books (Books)	25000	30000.00	35000.00	40000.00
Education investment accounted for the proportion of GDP (%)	5	6	7	8
The third industry accounted for the proportion of GDP (%)	40	45	50	55

Test results

In order to eliminate the dimension of economic security, need to be graded standard coal city. After the network training, it is need to test network. By training the network, test network. The practical simulation output network is shown in table 3.

Table 3 The actual network simulation output

Datong	Jincheng	Yangquan	Suzhou	Qitaihe	Hegang	Jixi
Unsafe	Not safe	Unsafe	Unsafe	Very unsafe	Very unsafe	Very unsafe
Shuangyashan	Zibo	Zaozhuang	Fushun	Huainan	Huaibei	Buxin
Unsafe	Not safe	Not safe	Not safe	Unsafe	Unsafe	Unsafe
Jiaozuo	Pingdingshan	Pingxiang	Hebi	Shizuishan	Liupan	Tongchuan
Not safe	Unsafe	Unsafe	Unsafe	Unsafe	Very unsafe	Unsafe

From the table we can see, on the whole Chinese coal city economic security level is relatively low, this and they serve as resources mining city has the very big relations, and also with the criteria for the selection of the most for the relationship between the excellent city construction indicators. In addition, the economic security level showing geographical features. The two cities of Shandong Province, Anhui Huaibei, Henan Jiaozuo, Liaoning Fushun and Shanxi Tongchuan than any other city in Shanxi province is good, poor, Heilongjiang province is not the most ideal.

Conclusion

Based on the analysis of the city economic security theory as the foundation, we find that city economic security relates to resource, environment, economy, social aspects, reflect these factors should be comprehensive, but not too much. This article take the system of city ecological security assessment index of PSR model, it is still difficult to avoid subjectivity and bias. From the BP network operation result, the overall recognition rate is higher, the selection of network parameters and relationships, between complexity and economic safety evaluation. In addition, although the standard mostly adopts excellent city standard, but the standard itself and the extrapolation process or with certain subjective elements.

Acknowledgement

In this paper, the research was sponsored by the Central Universities Science Foundation (Project No. 3142014127) and Key disciplines Fund Project of North China Institute of Science and Technology (Project No. HKXJZD201402).

References

[1] Zhang wenju. China sustainable development master volume ninth [M]. Beijing: Science Press, 2007

[2] China City Statistical Yearbook 2010[M]. Beijing: Chinese Statistics Press, 2011

[3] Xie hualin,Li bo. The city ecological security evaluation index system and evaluation method [J]. Journal of Beijing Normal University (NATURAL SCIENCE EDITION), 2004 (5): 705-710

[4] Martin T.Hagan, Dai kui etc. Neural network design[M]. Machinery Industry Press, 2002

[5] Gan Xinhua, Shi Yong, Lin Bao. The application of BP neural network Matlab in atmospheric environmental quality assessment based on Anhui chemical industry, 2008.10

Advanced Materials Research Vols. 986-987 (2014) pp 474-478
© (2014) Trans Tech Publications, Switzerland
doi:10.4028/www.scientific.net/AMR.986-987.474

Research on electricity load of three industries and residents' life

Zhichao REN [a], Kaijiang CAO [b]

State Grid Sichuan Power Economic Research Institute, Chengdu, 610094, Sichuan, China

[a]email: 80217831@qq.com, [b]email: 511452698@qq.com

Keywords: Economic structure; Electricity load characteristics; Industries' structure; Three industries and residents' life; Electricity load structure

Abstract. In recent years, strategic adjustment of economic structure is as the main direction of accelerating transformation of economic development mode in Sichuan province of China. Electricity load characteristics and its development trend could reflect industries' structure of Sichuan province. The ways of typical day selection and load curve calculation are discussed. Electricity load of typical trades of three industries and residents' life is analyzed, whose load curves of everyday as well as the four seasons are obtained. As a result, relationship between electricity load structure and industrial structure is get.

Introduction

Electricity load characteristics and its development trend is the base of electricity plans, electricity programs and production operation. Recently, speed of world economic recovery becomes lower obviously, and China is under pressure of economy downlink. Strategic adjustment of economic structure is as the main direction of accelerating transformation of economic development mode in Sichuan. The purpose is to upgrade the level and core competitiveness of industry, and to promote the coordinated development of three industries[1]. Electric power industry, as the barometer of national economy, has great adjustment and dependence for adjustment of industrial structure[2].

Based on previous researchers' work[3-5], historical load-controlled electricity data for large customers was collected, superposed and checked. Electricity load curves for typical trade of three industries and residents' life were obtained in Sichuan. Electricity load characteristics and its law of development were studied. The largest load of three industries was estimated. Structure of power consumption for the whole society was analyzed. Relationship between load structure change and industrial structure adjustment was investigated. As a result, it provides a scientific basis for electricity grid development planning and market development.

Estimation of load curve

(1) Selection of typical day

For different climatic conditions, months corresponding four seasons are different for different places. Normally, the spring, summer, autumn and winter is from March to May, from June to August, from September to November and from December to next February respectively. At present, there is no uniform regulation but mainly three methods for selection of typical day.

Method 1: Daily load curve without abnormal distortion, whose daily load rate is most approaching to average daily load rate of a period (a season or a month), is as the typical day load curve of this period (a season or a month).

① Average daily load curve of working day for this month:

$$L(h)=\frac{1}{N}\sum_{d=1}^{N}L(d,h) \qquad h=0,1,2,3...23 \tag{1}$$

L(h) is average value of working day load curve of this month, in other words, average daily load curve; L(d,h) is load curve of any working day; h are 24 integral points everyday; N is the number of working day for this month.

② Daily load curve L(d,h) of working day for this month, which is most approaching to above average daily load curve L(h), is as the typical day load curve L(d*,h) of this month.

Approaching means that the distance following is smallest:

$$\sum_{h=0}^{23}\left|L(d^*,h)-L(h)\right|^2=\min_{1\le d\le N}\sum_{h=0}^{23}\left|L(d,h)-L(h)\right|^2 \tag{2}$$

Method 2: A fixed working day (e.g. the 3rd working day of 3rd week of a month) of a period (a season or a month) is as typical day.

Method 3: The day of largest load is as typical day.

(2) Calculation of load curve

Firstly is to select typical day according to above method. Secondly is to obtain typical day load curve of large customers for typical trade through load-controlled collection. Thirdly, L_1, which is electricity load curve superposition of large customers, could show the load curve shape of typical trade of this place. The total electricity consumption C_1 of these customers that day could be gained through L_1. Fourthly, daily electricity consumption C equals to electricity consumption of the customers for this month divided by days. Fifthly, M equals to C divided by C_1. That is the proportion of consumption for the customers to that for the typical trade. Finally, typical day load curve is M times of load for all the points L_1.

Investigation of electricity load characteristic

(1) Load characteristic analysis of typical trade for primary industry

Research object for primary industry is irrigation trade, as shown in Figure 1(a). There is no morning peak in spring, where it appears from 6 to 7 o'clock in summer, autumn and winter. The noon peak appears from 11 to 12 o'clock in spring and winter, where it appears from 12 to 13o'clock in summer and autumn. The evening peak appears from 20 to 21 o'clock in spring, where it appears from 21 to 22 o'clock in summer, as well as it appears from 19 to 20 o'clock in autumn and winter.

Typical day load rate is relatively large in summer, and relatively small in autumn. It shows obvious downtrend year by year. The smallest load rate of typical day is relatively large in summer, and relatively small in spring. It shows obvious downtrend year by year. The typical day peak-valley difference rate is relatively large in summer, and relatively small in summer. It shows obvious rising trend year by year.

Research object for secondary industry is chemical fiber trade, as shown in Figure 1(b). The morning peak appears from 5 to 6 o'clock in spring, where it appears from 6 to 7 o'clock in autumn, as well as it appears from 7 to 8 o'clock in summer and winter. The noon peak appears from 14 to 15 o'clock in spring, where it appears from 11 to 12 o'clock in summer, as well as it appears from 10 to 11 o'clock in autumn and winter. The evening peak appears from 21 to 22 o'clock in spring, where it appears from 17 to 18 o'clock in summer, as well as it appears from 18 to 19 o'clock in autumn and winter.

The largest load of typical day for this trade increases year by year. Typical day load rate is relatively large in winter, and relatively small in summer. It shows obvious rising trend year by year. The smallest load rate of typical day is relatively large in winter, and relatively small in spring. It shows obvious rising trend year by year. The typical day peak-valley difference rate is relatively large in spring, and relatively small in winter. It shows obvious downtrend year by year. Affected by the international financial crisis, traditional industries of labor-intensive, as well as great consumption of energy and resources, which were located in eastern China before, were relocated to the west. Because the cost of these traditional industries rose, and production could not be sustained. As a result, some enterprises with high energy consumption develop too fast is some places of Sichuan.

Research object for tertiary industry is hotel and catering trade, as shown in Figure 1(c).There is no morning peak in summer. The morning peak appears from 7 to 8 o'clock in spring, where it appears from 8 to 9 o'clock in autumn, as well as it appears from 6 to 7 o'clock in winter. The noon

peak appears from 11 to 12 o'clock in spring and winter, where it appears from 16 to 17 o'clock in summer, as well as it appears from 12 to 13 o'clock in autumn. The evening peak appears from 20 to 21 o'clock in spring, where it appears from 22 to 23 o'clock in summer, as well as it appears from 21 to 22 o'clock in autumn and winter.

The largest load of typical day for this trade increases year by year. Typical day load rate and the smallest load rate of typical day are both relatively large in summer, and both relatively small in spring. Both of them show obvious rising trend year by year. The typical day peak-valley difference rate is relatively large in spring, and relatively small in summer. It shows obvious downtrend year by year.

(2) Load characteristic of residents' life

Electricity load of resident are mainly composed by basic load and seasonal load. Basic load are mainly consumed by refrigerators, electric cookers and lights. seasonal load are consumed for cooling (including air conditionings and fans, etc) and heating (including air conditionings and heaters).

Residents' life load in Sichuan has obvious seasonal characteristic. Typical day load curve of four seasons for residents' life in Sichuan is as shown in Figure 1(d). There is no morning peak in summer and winter. The morning peak normally appears from 6 to 7 o'clock in spring, where it appears from 7 to 8 o'clock in autumn. The noon peak appears from 11 to 12 o'clock in spring and autumn, where it appears from 15 to 16 o'clock in summer, as well as it appears from 12 to 13 o'clock in winter. The evening peak appears from 18 to 19 o'clock in spring, autumn and winter, where it appears from 22 to 23 o'clock in summer, as well as it appears from 21 to 22 o'clock in summer.

The largest load of typical day for t residents' life increases year by year. Typical day load rate and the smallest load rate of typical day are both relatively large in summer, and both relatively small in autumn. Both of them show obvious downtrend year by year. The typical day peak-valley difference rate is relatively large in winter, and relatively small in summer. It shows obvious rising trend year by year.

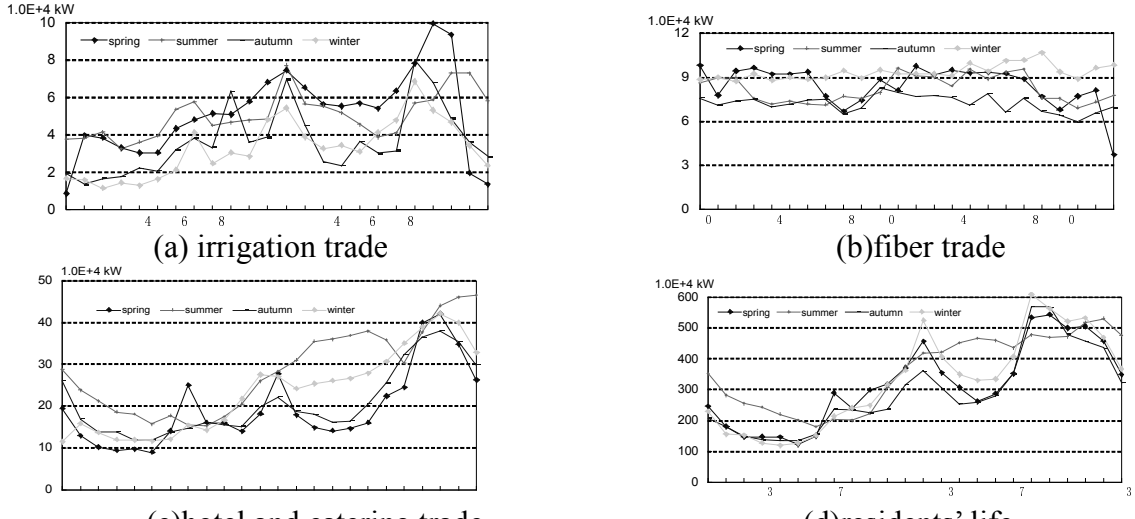

(a) irrigation trade (b)fiber trade

(c)hotel and catering trade (d)residents' life

Fig.1. Typical day load curve of four seasons in Sichuan

Investigation of electricity load structure

(1) Analysis of electricity load structure

Table 1 shown the load structure of three industries in Sichuan from 2010 to 2012.

Proportion of electricity load of primary industry is small. Irrigation is representative trade of electricity consumption trades for primary industry in Sichuan. According to relationship of electricity consumption between primary industry and irrigation, the approximate load curve of primary industry can be obtained. As spring for example, the largest load of primary industry is about 255 thousands kW in Sichuan of 2012, which is reduced by 1.16% compared to last year.

Proportion of electricity load of secondary industry is relatively large. Manufacturing of iron and steel, chlor-alkali, chemical fiber, cement manufacturing, fertilizer manufacturing and phosphorus are representative trades of electricity consumption trades for secondary industry in Sichuan. According to actual electricity consumption of typical large customers, the approximate load curve of secondary industry can be obtained. As spring for example, the largest load of secondary industry is about 21.49 millions kW in Sichuan of 2012, which is only increased by 1.56% compared to last year.

Tab.1. Load structure of three industries in Sichuan from 2010 to 2012

year	Season	date	the largest load of primary industry/1.0E+4kW	the largest load of secondary industry/1.0E+4kW	the largest load of tertiary industry /1.0E+4kW	the largest load of residents' life/1.0E+4kW
2010	spring	4/21	33.0	1718	448	467
	summer	8/18	18.9	1722	431	440
	Autumn	10/20	20.8	1825	390	519
	winter	12/15	24.0	1665	410	472
2011	spring	4/20	25.8	2116	537	515
	summer	8/17	18.7	2214	494	460
	Autumn	10/19	27.5	2110	465	574
	winter	12/21	24.8	2040	467	508
2012	spring	4/18	25.5	2149	578	543
	summer	8/15	21.1	2279	555	531
	Autumn	10/17	25.2	2175	514	571
	winter	12/19	24.9	2157	563	608

Electricity load of tertiary industry develops rapidly. Hotel and catering are representative trade of electricity consumption trades for tertiary industry in Sichuan. In similar way above, the approximate load curve of tertiary industry can be obtained. As spring for example, the largest load of primary industry is about 5.78 millions kW in Sichuan of 2012, which is reduced by 7.64% compared to last year. With fast development of tertiary industry and continuous improved quality of residents' life, compared to years before, increasing rate of load for tertiary industry and residents' life load were rising year by year. To some extent, load rate of the whole electric grid is reduced.

(2) Adjustment of industries' structure and its influence

Since 11th five-year, proportion of three industries in Sichuan adjusts from 20.1:41.5:38.4 in 2005 to 14.4:50.5:35.1 in 2010, 14.2:52.4:33.4 in 2011 and 13.8:52.8:33.4 in 2012 respectively, as shown in Figure 5. Trend of industrial structure in Sichuan is that proportion of primary industry reduced gently, while proportion of secondary industry increased greatly, and proportion of tertiary industry nearly kept the same. The largest load growth of primary and tertiary industry is lower than that of secondary industry. To some extent, development of tertiary industry increased peak-valley difference of load, and it reduced the largest load utilization hours of the whole society.

New industry is adhered in Sichuan. Industry structure will be adjusted in expanding the increment, and mode will be changed in accelerating development. Industrial efficiency would be taken the lead in the nation. A industrialization way of innovation-driven, green and low carbon, high-end trades introduced, open and cooperative, accelerating of progress will be explored.

From the point of secondary industry total to analyze its electricity consumption. In 2012, electricity consumption proportion of secondary industry was about 70.3%. Electricity load proportion of secondary industry was relatively high. Since 11th 5-year, as adjustment of three industries' structure, proportion of secondary industry total to GDP was from 34.2% to 42.0%. Secondary industry total kept fast increasing, and the largest load of secondary industry rose continuously.

From the point of secondary industry structure to analyze its electricity consumption. In 2012, heavy industry total grew by 16.0%, while light industry total grew by 16.4%, and the ratio of heavy industry total to light one is 66.8:33.2. Since 2005, the ratio of heavy industry total to light one present increasing trend. As new industry is being adhered and secondary industry structure is being adjusted in Sichuan, some enterprises with high electricity consumption and heavy pollution

would be suppressed. As a result, its electricity load growth would decrease. Load of new trades (including IT, electronic information, new materials, new energy, etc) would increase steadily year by year.

In 2015, the ratio of three industries total would be from 14.4:50.5:35.1 of 11th five-year adjusted to 10.2:50.8:39. The second industry would continue to be a "locomotive", but its power forward are mainly from innovation and technology upgrading.

Conclusions

(1)There is no morning peak of load in spring for irrigation trade. Typical day load rate is relatively large in summer, and relatively small in autumn. There is nearly no change of load curve of chemical fiber trade in winter. Typical day load rate is relatively large in winter, and relatively small in summer. There is no morning peak in summer for hotel and catering trade. Typical day load rate is relatively large in summer, and relatively small in spring.

(2)There is no morning peak of residents' life load in summer and winter in Sichuan. Typical day load rate and the smallest load rate of typical day are both relatively large in summer, and both relatively small in autumn. Both of them show obvious downtrend year by year. The typical day peak-valley difference rate is relatively large in winter, and relatively small in summer. It shows obvious rising trend year by year.

(3)Proportion of electricity load of primary industry is small in Sichuan. Proportion of secondary industry is relatively large. With fast development of tertiary industry and continuous improved quality of residents' life, to some extent, load rate of the whole electric grid is reduced.

Acknowledgement

In this paper, the research was sponsored by Sichuan electric power company.

References

[1] Sichuan Provincial People's Government. 12th Five-Year Plan of National Economic and Social Development in Sichuan [N]. Sichuan Daily,2011-1-28(1).

[2] Kang Chongqing, Li Shunfu, Xia Qing, etc. Structure Analysis of Electricity Consumers and Its Instruction to Marketing. Automation of Electric Power Systems, 2003,27(14):27-31.

[3] Jiang Fengqing, Zheng Huai, Li Rongmin. Analysis of Electricity Load Structure and Its Characteristic Forecast in Shanghai. Electric Power of East China, 2008,36(9):51-52.

[4] Lu Yan, Tan Jian. Analysis of Electricity Load Structure in Jiangshu. Electric Power of East China, 2007, 35(7):26-29.

[5] Huo Chengjun. Analysis of Power System Load Characteristic. Tianjin: Tianjin university, 2007.

Advanced Materials Research Vols. 986-987 (2014) pp 479-482

doi:10.4028/www.scientific.net/AMR.986-987.479

Research on Energy Logistics Service Quality Management Implications to Sustainable Development

Fang-xu HAN[1,a] , Chun-fa LI[2, b], Qi-qi YANG[3,c]

[1,2,3] School of Management, Tianjin University of Technology, Tianjin 300384, China

E-mail: [a]fangxu_han@163.com, [b]chunfali@163.com, [c]yqq17791@163.com

Keywords: Energy logistics; Sustainable development; Service quality

Abstract: Analyzed about the present situation of energy logistics service quality, and combined with related literature at home and abroad, select “energy logistics tracking information timeliness”, “accuracy of energy logistics tracking information”, ”energy delivery time accuracy”, “energy distribution accuracy “, “energy integrity “, “error handling” six elements as a measure factors of the energy logistics service quality, establish research model. Through questionnaire investigation and quantitative analysis verify this research model. The Conclusions: energy distribution of accuracy have significant positive effects on sustainable development, and influence degree; Energy delivery time accuracy, integrity have significant positive effects on sustainable development, but the impact is relatively small; While energy logistics tracking information timeliness, accuracy and error of energy logistics tracking information treatment had no significant influence to the sustainable development of economy and society. Energy logistics is an important part of the logistics industry, also is an important support of economic society and people's life. Improve the quality of energy logistics service, to play an important role in promoting sustainable development.

Introduction

At present, our country's energy consumption dominant energy products mostly belong to the non-renewable energy, such as coal, oil, natural gas and so on. In terms of the logistics industry, not only to solve the problem of logistics cost, research on logistics service quality to energy saving and sustainable development has the important theory value and practical significance. Energy logistics has a very high requirement about energy geographic distribution, place of origin, off ground, quantity of flow, the timeliness. Strengthen energy logistics service quality is the important way to save energy and to realize the sustainable development.

In recent years, many scholars studied the energy logistics at home and abroad. Energy logistics service system is not a separate system, and it goes with the energy supply chain upstream and downstream production and downstream consumption link closely [1]. With the development of Internet technology and application, the RFID technology, wireless sensor technology gradually in-depth in the energy exploitation and transportation enterprises [2]. E-commerce is booming, especially in the energy and steel areas in our country, but the development is far from imaginary faster and better, which logistics capability is an important reason for the lag [3]. Hei from the point of view of the negative external economic adverse effect on the construction of urban logistics system planning process caused by the West and proposed countermeasures [4]. The energy characteristics of production, circulation and consumption, which determine the effective implementation of energy logistics service, provided energy in all aspects of information sharing must be able to effectively convey and share [5].

With different contents of the study, the paper from the point of view of energy logistics service quality, gives an empirical research about energy development status, which has guiding significance for the development of energy companies, a great significance to achieve sustainable development.

Research model and hypotheses

Logistics is an integral part of the energy transaction process, the paper based on the view of energy companies to explore the impact of logistics service quality to achieving sustainable development, combined with related literature at home and abroad, select “energy logistics tracking information timeliness”, “accuracy of energy logistics tracking information”, ”energy delivery time accuracy”, “energy distribution accuracy “, “energy integrity “, “error handling” six elements as a measure factors of the energy logistics service quality, establish research model(Fig.2.1).

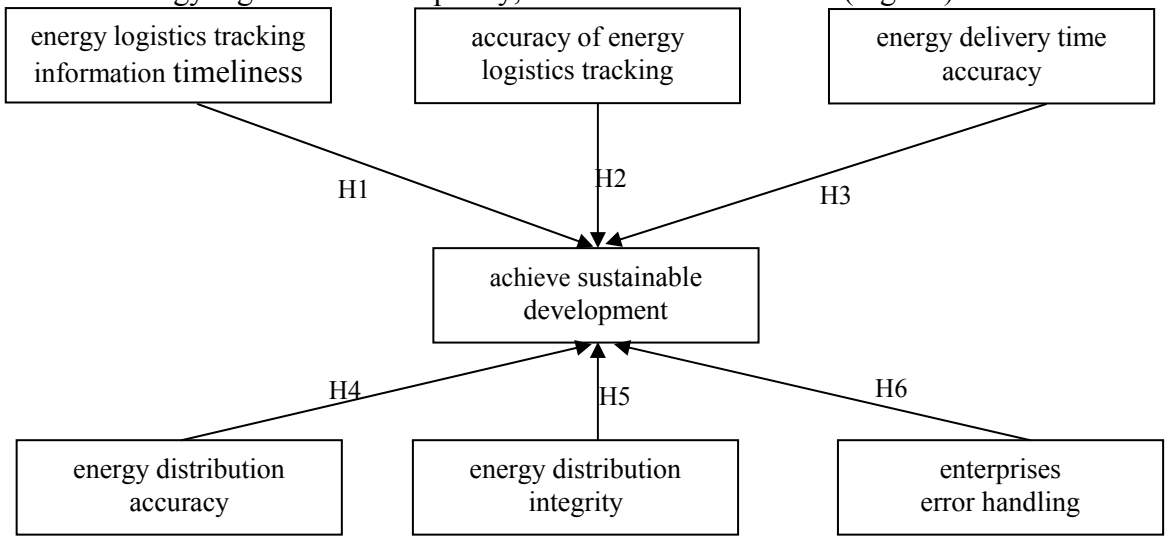

Fig.2.1 Energy logistics service quality impact model for sustainable development

Hypotheses:

H1： Energy logistics tracking information timeliness has a significant positive relationship to sustainable development

H2： Accuracy of energy logistics tracking information has a significant positive relationship to sustainable development

H3： Energy delivery time accuracy has a significant positive relationship to sustainable development

H4： Energy distribution accuracy has a significant positive relationship to sustainable development

H5： Energy integrity has a significant positive relationship to sustainable development

H6： Error handling has a significant positive relationship to sustainable development

Data analysis and hypothesis testing

Reliability and validity analysis

Tab.3.1 Reliability testing of each variable

Variables	Cronbach's a	Index	Cronbach's a of Delete the index
energy logistics tracking information timeliness	0.661	D1	0.910
		D2	0.903
accuracy of energy logistics tracking	0.681	X1	0.903
		X2	0.900
energy delivery time accuracy	0.651	J1	0.904
		J2	0.902
energy distribution accuracy	0.653	Z1	0.900
		Z2	0.902
energy integrity	0.741	W1	0.903
		W2	0.901

error handling	0.672	C1	0.900
		C2	0.903
sustainable development	0.656	P1	0.900
		P2	0.902

Tab.3.2 Validity testing of each variable

Variables	Index	Factor loading quantity	Variable degree of interpretation (%)	KMO	Bartlett Significant probability
energy logistics tracking information timeliness	D1	0.526	74.815	0.600	0.000
	D2	0.692			
accuracy of energy logistics tracking	X1	0.514	75.907	0.550	0.000
	X2	0.861			
energy delivery time accuracy	J1	0.963	74.119	0.634	0.000
	J2	0.585			
energy distribution accuracy	Z1	0.898	74.310	0.684	0.000
	Z2	0.898			
energy integrity	W1	0.615	79.898	0.600	0.000
	W2	0.668			
error handling	C1	0.861	75.682	0.550	0.000
	C2	0.946			
sustainable development	P1	0.867	74.413	0.570	0.000
	P2	0.899			

Hypothesis testing

Tab.3.3 Study variables correlation analysis

independent variables	sustainable developmen(dependent variable)
energy logistics tracking information timeliness	
Pearson correlation	0.342
Statistically significant (two-sided)	0.000
N	215
accuracy of energy logistics tracking	
Pearson correlation	0.413
Statistically significant (two-sided)	0.000
N	215
energy delivery time accuracy	
Pearson correlation	0.525
Statistically significant (two-sided)	0.000
N	215
energy distribution accuracy	
Pearson correlation	0.740
Statistically significant (two-sided)	0.000
N	215
energy integrity	
Pearson correlation	0.627
Statistically significant (two-sided)	0.000
N	215
error handling	
Pearson correlation	0.159
Statistically significant (two-sided)	0.020
N	215

Tab.3.4 The sustainable development of regression coefficient

model	Non-standardized coefficients		standardized coefficients	t	Sig.
	B	Standard error			
(constants)	.017	.197		.088	.930
timeliness	.035	.051	.035	.690	.491
tracking accuracy	.090	.046	.100	1.945	.053
time accuracy	.237	.057	.207	4.185	.000
distribution accuracy	.467	.042	.502	11.040	.000
integrity	.261	.043	.282	6.009	.000
error handling	.091	.038	.112	2.408	.017

Tab.3.5 The sustainable development of regression coefficient adjustment

model	Non-standardized coefficients		standardized coefficients	t	Sig.
	B	Standard error			
(constants)	.051	.185		.274	.000
timeliness	.223	.051	.195	4.400	.000
distribution accuracy	.486	.042	.522	11.439	.000
integrity	.280	.042	.303	6.604	.000

After removing discrepancies variables, get new regression coefficient table, so the impact of logistics service quality to sustainable development of regression equation is as follows:

WY=0.223SJS+0.486SZQ+0.280SWH+0.051.

Summary

Energy is the important guarantee of economic development. Due to large amount of energy flowing, send area wide, need to pay the huge logistics cost, so to strengthen the energy of logistics management, guarantee with minimal logistics cost, meet people's production and living energy demand, is our country national economy and social development of major issues. Through this study, the establishment of public logistics information platform, realize the department and the enterprise information sharing, coordination, improve the quality of energy logistics service, need the cooperation of government and enterprises, finally, achieve economic and social sustainable development.

References

[1] Ya-hui CAO, Energy major logistics gradually awakening [EB/OL]. http://www.un56.com/2010/0303/7247.html, 2010-03-03.

[2] Man CUI, Jian-jun LU, Research of things based on coal enterprise logistics information platform [J]. Coal Technology, 2011, 30(1):243-245.

[3] Fan-jun MENG, Cost savings and green development, growing energy logistics [N]. China Industry News, 2013-9-12 (A02).

[4] Xiu-ling HEI, Analysis of negative external economic problems in the western city planning and construction of the logistics system[J]. Chinese Market, 2011(19):16-17.

[5] Xiu-ling HEI, Strategy research of western energy logistics information management system [J]. Network and Information, 2012, 31(8):362-364.

[6] Gold S, Seuring S. Supply chain and logistics issues of bio-energy production [J]. Journal of Cleaner Production, 2011, 19(1): 32-42.

[7] Frombo F, Minciardi R, Robba M, et al. Planning woody biomass logistics for energy production: A strategic decision model [J]. Biomass and Bioenergy, 2009, 33(3): 372-383.

Advanced Materials Research Vols. 986-987 (2014) pp 483-488
© (2014) Trans Tech Publications, Switzerland
doi:10.4028/www.scientific.net/AMR.986-987.483

Research on flow calculation of wind power integration

Wang yiqun[1],Zhang bo[2],Wu kuihua[1],Yang shenquan[1],Yang bo[1]

[1] Economic & Technology Research Institute, State Grid Shandong Electric Power Company, Shandong Jinan 250021;

[2] School of Electrical Engineering of Shandong University, Jinan Shangdong 250061

Keywords: wind power;flow; reactive; voltage

Abstract. In this paper, the flow calculation problem of wind power connected to the grid was researched and the corresponding models were put forward.According to the relationship between the node voltage and reactive power of wind farms, modified the jacobian matrix.Implement and trend of the expression for calculating and according to the relationship between the node voltage and reactive power of wind farms, to modify the traditional methods of jacobian matrix and axle and consistency.Finally through the IEEE - 14 standard system, to verify this model and algorithm in this paper, satisfactory effect was obtained ,also laid the foundation for the further research.

Introduction

Wind energy is cheap and renewable.The power technology which based on wind has been paid close attention to,and now this technology has made breakthrough progress. Its performance and price more and more towards the good direction. Thus the current wind power has become a way of generating renewable energy with the fastest developing speed in, also very promising[2].

In this paper, with the help of wind turbines involved active and reactive power relations, the flow calculation problem of wind power connected to the grid compared with the traditional power flow calculation is consistent. This model considers characteristics of asynchronous generator itself, the active and are expressed as the function of wind speed, the power characteristic of induction generator can be expressed as a power and voltage and slip function.To correct the traditional wind Jacobian associated node elements, achieve simple and easy, the performance which consistent with traditional power flow calculation was researched.This idea is also convenient to other issues (such as optimal power flow ,control, etc.) processing, also accord with the actual needs.

1.The description of the association between active and reactive power of fan

1.1Active expression of the fan

Generating capacity of wind turbines affected by many factors, primarily wind speed, the blade wind area of wind turbine , etc.Mechanical power generated can be expressed as[3]:

$$P_m = 0.5 C_p \rho S V^3 \qquad (1)$$

In the formula: S is the fan blade swept area, m^2； ρ is the air density, kg/m^3; V is the wind speed, m/s ; C_p is the power coefficient of wind turbine,It is a function of tip speed ratio λ ,Among them, $\lambda = \omega r / V$ ， ω is the angular velocity of the wind wheel, rad/s ； r is wind wheel radius, m .

From the formula (1) we can see,Mechanical power of wind generator and wind area and the three times square wind speed is directly proportional relationship,as long as we know the wind the theoretical power output of wind turbine can be get.

1.2 The association between active and reactive power of fan

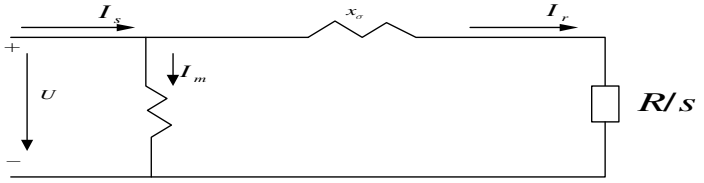

Chart 1 Equivalent circuit of induction generator

The chart 1 is the equivalent circuit of induction generator,where a is the terminal voltage of induction generator. I_s is stator current, I_m is exciting current , I_r is rotor current, x_m is exciting reactance, R is mechanical load equivalent resistance, x_σ is the value of the stator leakage reactance and rotor leakage reactance, s is slip ratio.

Form the chart 1 the electromagnetic power and power factor output by induction generator can be derived as following expression.

$$P_e = \frac{sRU^2}{s^2 x_\sigma^2 + R^2} \tag{2}$$

The power factor is

$$tg\Phi = \frac{R^2 + x_\sigma(x_\sigma + x_m)s^2}{sRx_m} \tag{3}$$

At the same time, asynchronous generator slip ratio can be expressed as:

$$s = \frac{R(U^2 - \sqrt{U^4 - 4x_\sigma^2 p_e^2})}{2p_e x_\sigma^2} \tag{4}$$

Similarly, asynchronous generator output reactive power can be expressed as:

$$Q = \frac{[R^2 + x_\sigma(x_m + x_\sigma)s^2]P_e}{sRx_m} \tag{5}$$

By formula (4) and (5) we can see that the induction generator reactive power has been transformed into a function, and this function has associated with active and voltage, and active power (ignoring losses) is the wind speed function.

Therefore, if the wind speed is determined, we can make use of the formula (1) to obtain the active power output of the wind turbine, and then by means of the formula (4) and (5) of the wind turbines needed to absorb reactive power，and then through the type (4) and (5) get the reactive power which wind turbines need to absorb.

2 The correction of traditional fashion model

Correction equations when solve traditional flow equations can be expressed as [3]:

$$\begin{bmatrix} \Delta P \\ \Delta Q \end{bmatrix} = \begin{bmatrix} H & N \\ L & J \end{bmatrix} \begin{bmatrix} \Delta\theta \\ \Delta V / V \end{bmatrix} \tag{6}$$

According to the association between active and reactive power of fan, when calculating the trend which contains wind power system, we need to modify the traditional flow correction equation.Because the function of wind farm node becomes the node voltage when it injected reactive power,therefore, when the formation of Jacobian need to supplement wind farm nodes inject reactive derivative terms of voltage to modify the Jacobi matrix related items of J .

From the formula (4), (5) and the formula (1), can get：

$$Q_e = \frac{2P_e^2 x_\sigma^2}{r_2(-U^2R+\sqrt{U^4R^2-4P_e^2R^2x_\sigma^2})x_m}\cdot \\ [-R^2-\frac{(-U^2R+\sqrt{U^4R^2-4P_e^2R^2x_\sigma^2})^2(x_\sigma+x_m)}{4P_e^2x_\sigma^3}] \tag{7}$$

Further derivation can get：

$$\frac{\partial Q}{\partial U} = -\frac{x_\sigma+x_m}{Rx_mx_\sigma}(-2UR+\frac{2U^3R^2}{\sqrt{U^4R^2-4P_e^2R^2x_\sigma^2}})- \\ \frac{2P_e^2x_\sigma^2}{Rx_m}[-2UR+2U^3R^2(U^4R^2-4P_e^2R^2x_\sigma^2)^{-\frac{1}{2}}]\cdot \\ (-U^2R+\sqrt{U^4R^2-4P_e^2R^2x_\sigma^2})^{-2}\cdot \\ [-R^2-\frac{x_\sigma+x_m}{4P_e^2x_\sigma^3}(-U^2R+\sqrt{U^4R^2-4P_e^2R^2x_\sigma^2})^2] \tag{8}$$

Visible. in the Jacobi matrix. Simply accumulated in the derivative of wind farm node reactive power to the voltage of it,the remaining elements of the Jacobi matrix unchanged.

3 The calculation of process

On the basis of the last section,The steps of power system load flow calculation and the traditional power flow calculation are consistent,except that the wind farm node into active and inactive calculation,and the modified Jacobi matrix of the nodes corresponding to the wind farm.Specific calculation process shown in Figure 2.

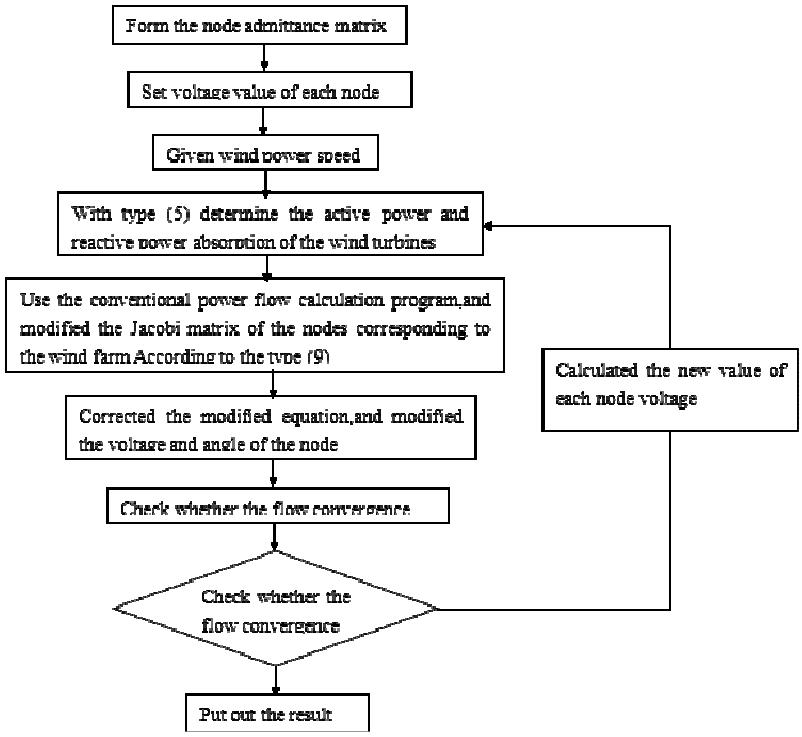

Figure 2.Wind power system flow calculation flow chart

4 An example and its analysis

The background of validation example constructed in this article described as follows: Assuming wind farm connected to the 14 node[2]of IEEE14 system(see Figure 3) through the 110KV line.Transmission impedance of accessible wind power system is:3.14963+j6.23997Ω.The capacity of wind farm is:20 × 800KW,Stator leakage reactance is:0.07620Ω,Rotor resistance is:0.00759+j0.18289Ω.Excitation reactance is:3.44979Ω. The cut-in speed, rated wind speed, excised wind speed of the wind turbine are:3m/s, 14m/s , 25m/s.After access the wind farm.,The load of 14 node increases 16MW based on the original.

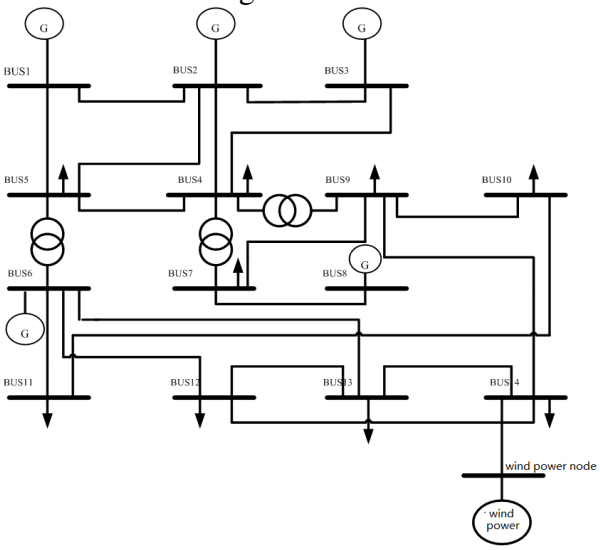

Figure 3.The system diagram of wind farm integrated

Calculated for this case with the proposed model and algorithm, and given analysis .

Table 1 is the result of wind farm node which under different wind speeds, active power, reactive power and voltage node.

Table 1:The active,reactive and node voltage of wind farm node which under different wind speed

Wind speed/m/s	Active power/pu	Reactive power/pu	Node voltage/pu
4	0.01072	-0.028067	1.0027878
6	0.03444	-0.0311064	1.0050965
8	0.0612	-0.0383134	1.0066221
10	0.091	-0.0517204	1.0067961
12	0.12384	-0.0752712	1.0044994
14	0.16	-0.129509	0.99596703

As seen in Table 1,Increasing with the wind speed,the active power output by the wind farm is gradually increased, while the absorption of reactive power also increases gradually, and the node voltage is first increased and then decreased.

When the wind speed reaches 14m/s, wind turbine operation at rated condition,at that time we compare the voltage of the 14 node of system with no wind power.As shown in table 2.

Table 2.The comparison of the ourteen node voltage when wind turbine access and non access

Node number	The model result/p.u	The results missed wind power system/p.u	Percentage deviation
1	1.06	1.0600	0
2	1.045	1.0450	0
3	1.01	1.0100	0
4	1.0192573	1.020652	0.137%
5	1.0211453	1.0220971	0.09%
6	1.07	1.07	0
7	1.0496667	1.0540368	0.39%
8	1.09	1.0900	0
9	1.0306246	1.0392594	0.83%
10	1.0302193	1.0373848	0.69%
11	1.0465128	1.0501854	0.35%
12	1.0533493	1.0558563	0.24%
13	1.0424381	1.0484186	0.57%
14	0.9981851	1.0250826	2.6%

From table 2 we can see,the node voltage amplitude changes in a small range, when the access of wind power,this phenomenon is consistent with the actual requirements, verify the correctness of the model.In the wind power access node,the voltage of the 14 node with maximum deviation. With the active power from wind turbines increaseing, at the same time the need of absorb reactive power also increaseing.As wind power and network.14 nodes need to support the wind turbine provides with reactive,so the node voltage decreases.

Table 3.The comparison of the access point of the voltage and not access point voltage,when wind farm connected to different nodes.

The node number of wind power integration	After accessing the node voltage/pu	Before accessing the node voltage/pu	Percentage deviation
4	1.015567	1.020652	0.50%
5	1.0168799	1.0220971	0.51%
7	1.0444124	1.0540368	0.91%
9	1.027298	1.0392594	1.15%
10	1.0250185	1.0373848	1.19%
11	1.0424299	1.0501854	0.74%
12	1.0562332	1.0558563	0.04%
13	1.0421935	1.0484186	0.59%
14	0.9981851	1.0250826	2.6%

From table 3 we can see. When the wind power access to 9, 10, 14 node, the voltage effect on the access point is larger. When the wind power access to 4, 5, 12, 13 node, has little effect on the access point voltage.This also shows that the connection of nodes 10, 14 with the entire system is weak,and other nodes they connect are not able to provide enough PV nodes which support with reactive,and they are no reactive compensation device.So when these nodes access wind power the effect of voltage on them is larger.

When the wind power access to these nodes of 4, 5, 12, 13 ,voltage has little influence on the access point,this is because these nodes and other nodes in the system is closely related to,on the other hand ,it also because all the nodes which connect with those nodes have PV node,with the increaseing of active output from power wind ,the reactive power absorbed by it will increase,although the access point itself without reactive power compensation device,but it is closely associated with the system, and it is also linked with PV nodes which has the ability to provide reactive power,Thereby ensuring the node voltage is not too much lower.

We can see,wind at different access points, the effect is different from the access point.If the access point is closely associated with the system, or it itself has no power compensation capabilities, it is less affected by wind power access.With the gradual increaseing in wind power capacity, in order to ensure access point voltage is not more limited,we conduct a reasonable choice of the access point and reactive compensation in the access point is very necessary.

5 Conclusion

(1)Throught the association between active and reactive power of fan,based on neglecting the mechanical loss power,we just need to correcte on the traditional trend slightly,flow calculation of wind power can be done.

(2)Computational analysis showed. When access to different nodes of wind power, its influence is different,it has a close relationship with system support conditions of reactive voltage.This idea in this paper provides a good foundation for studying the effect of wind power to power grid.

Wang yiqun(1983-),Male,Jinan Shandong ,Han,Graduate,Research directions ia network planning.
Zhang bo (1963-), Male, Weihai Shandong, Han, professor,Teaching and researching work is mainly engaged in power system operation and control.

Reference

[1]Lei yazhou,Research topics which has relation with wind power grid[J], Power System Automation ,2003, 27 (8):84-89.

[2]Wang weisheng,Shen hong.Power flow calculation method which considers the wind farm node,Journal of north China electric power university,2002，SuP29(5):150-153

[3]Wu yichun Ding ming,Zhang lijun.Power flow calculation with wind farms,Chinese Society for Electrical Engineering,2005，25（4）：36-39.

Advanced Materials Research Vols. 986-987 (2014) pp 489-492

doi:10.4028/www.scientific.net/AMR.986-987.489

Research on New Energy Industrial Upgrading in Tianjin Based on SWOT Analysis

Qi-qi YANG[a], Fang-xu HAN[b]

School of Management, Tianjin University of Technology, Tianjin 300384, China

[a]yqq17791@163.com, [b]fangxu_han@163.com

Keywords: SWOT analysis; new energy; new energy industry; industrial upgrading

Abstract: The development of new energy industry is one of the important breakthroughs to solve energy and environmental issues and fulfill commitment to the international community for China. SWOT analysis was used to study the new energy industrial upgrading in Tianjin in this paper. By analyzing the strengths, weaknesses, opportunities and threats of the development of new energy industry in Tianjin, the current situations and problems were summarized, in order to provide reference for the practice of new energy industrial upgrading in Tianjin.

Introduction

The aggravation of energy crisis and environmental pollution promotes national economy to develop in the direction of environmental protection, low carbon and sustainable development. The new energy industry which takes renewable energy as the core is the innovation point of the world economic growth, and has significance to industrial restructuring and transformation of economic growth mode[1]. Our country has made the development of new energy industry rise to national strategic level.

Concepts of new energy and new energy industry

New energy is directly or indirectly from the sun or the earth's interior heat. It has various forms, in addition to solar energy, wind energy, biomass energy, geothermal energy, nuclear energy and hydropower, biofuels and hydrogen derived from renewable energy involved[2].

New energy industry refers to a low carbon, environmental protection and green industry which has the wide resources endowment, complex technology, less pollution to the environment and sustainable regeneration[3].

SWOT analysis of new energy industrial upgrading in Tianjin

SWOT analysis is a kind of strategic planning research technology, mainly on the strengths, weaknesses, opportunities and threats factors analysis[4]. Summarizing the actuality and existent problem by studying the external and internal factors that influence the development of new energy industry in Tianjin is of great significance.

Strength analysis

Application and industrial development of new energy have become a global consensus.

At present, new energy industry has become an important basis to measure the level of high and new technology development of countries and regions. It's also the strategy for a new round of international competition. Europe and the United States and other developed countries have taken the development of new energy industry as the main means against the financial crisis, and a series of policies to promote its development have rolled out. Major consumption of energy in China is coal and oil, so applying new energy and developing new energy industry are important means to change structure of energy consumption, ensure energy security and achieve sustainable development.

Tianjin has formed a complete new energy industry chain and industry cluster.

Now Tianjin new energy industry has four principal parts: energy storage battery, solar cell, fuel cell and wind power generation. An area of 6.6 km^2 in Binhai High-tech Zone has planned and constructed as the new energy industry base[5]. Nearly 10 large new energy companies such as Haitai group, Lishen Battery, Lantian Power, Jinneng Battery and Bamo Technology are gathered there, and develop a batch of products with strong domestic and international market competitiveness. Both the number and output value of the new energy companies here account for more than half of the city. It has formed the new energy industry cluster with the most complete product categories and highest technical level in China. Lishen company, for example, through independent research and development projects, has formed a scale that annual production capacity is 100 million pieces of lithium ion battery, and become the nation's largest lithium ion power battery production base.

Government provides support in terms of funds, policy and technology.

Tianjin municipal committee and municipal government attach great importance to the development of new energy industry that they have recognized it as one of the key hi-new-tech industries. A number of preferential policies are issued to keep the average growth rate of new energy industry more than 40%. First of all, financial investment has increased. A total of 200 million yuan a year to support new energy enterprises listing, merger, implementing major science and technology industrialization projects, developing the international market, introducing and developing related enterprises, etc.; Second, the management approach has been issued to encourage scientific and technological talents to innovate and carve out. Third, efforts have been made to construct the system of new energy industry science and technology innovation. The municipal committee and municipal government have formed the Binhai institute of new energy industry, the productivity promotion center, the public technology platform of green energy, the national industrialization base of new energy high technology, technology and product innovation centre, and the demonstration center of application of new energy products. Supporting all kinds of innovation platform has speed up the new energy industry transformation of scientific and technological achievements into realistic productivity. A good policy environment has become one of the core competitiveness of Tianjin new energy industry.

New energy products of Tianjin have high market share and huge market prospects.

In recent years, new energy industry of Tianjin has formed a batch of competitive large enterprises. 24 of them earn more than 100 million yuan and 8 enterprises earn more than 1 billion yuan, that guarantee Tianjin the dominance in the national new energy industry, and the market share of wind power equipments, lithium ion batteries and nickel metal hydride batteries among the top. Tianjin new energy industry in market share, market recognition and the future development potential has a strong core competitiveness.

Weakness analysis

The investment in human resources, capital is still inadequate.

With the rapid development of new energy industry and the implementation of related personnel policy and financial support policy in Tianjin, though a batch of high-level innovative talents of science and technology have been introduced and cultivated, and a group of domestic and foreign large-scale new energy enterprises have been attracted, that make the city's new energy industry personnel quantity and investment reach a certain scale, it’s still inadequate in terms of the demand of talents and funds. Compared to Beijing, Shanghai, the pearl river delta and Yangtze river delta region, the income level of professional and technical personnel in Tianjin is obviously on the low side, and the government guidance funds are more limited.

Opportunity analysis

International situation brings opportunities for new energy industrial upgrading.

Currently, the fossil energy consumption accounts for more than 90% of total energy consumption. There is a prominent contradiction between serious environmental pollution and the continued rapid growth in energy demand, which brings a rare opportunity for energy restructuring

and new energy development. In response to environmental pollution, international developed countries generally carried out the "Energy New Deal" to reform the energy industry. There is no exception in China. China invested 522×10^8 dollars for the development of renewable energy in 2011, an increase of 17%, accounting for 58.5% of the total annual investment in developing countries. China announced to join the International Renewable Energy Agency officially in 2013.

The development of low carbon economy speeds up the new energy industrial upgrading.

The energy development and utilization in Chain is faced with energy dwindling, sustained and rapid growth in energy demand and serious environmental pollution. Reportedly, in the first half of 2013, the annual averages of PM2.5 in Beijing, Tianjin and Hebei haven't reached the standard. Moreover, days that air quality exceeds the severe-pollution level in Beijing-Tianjin- Hebei region accounted for 21.2% in June[6]. Represented by wind and solar energy, the new energy is characterized by being abundant, clean and renewable, and meets the requirements for promoting circular economy. It is a significant way to solve the resource shortage and environmental pollution efficiently.

The energy policy in Tianjin is advantageous to the new energy industrial upgrading.

Tianjin is rich in natural resources and the development of new energy industry has begun to take shape. Accompanying with "the twelfth five-year plan of new energy and new materials industry development of Tianjin" rolled out, the government pointed out the direction and priorities of new energy industry development from green battery, wind power, photovoltaic power generation, nuclear power and biomass energy.

Threat analysis

The consumption scope of new energy products is narrow.

The new energy products sales in the domestic market are limited to the development needs of national hard targets and enterprises utilize. Individual consumers lack confidence in it that the personal consumption market of new energy products has not been formed, and domestic new energy and renewable energy account for less than 10%. Chinese new energy products which take foreign countries as the main application market are affected by photovoltaic industry expansion and the financial crisis. Spain and Germany reduced subsidies for solar energy photovoltaic industry, then the European clean energy market was shrinking, the export of new energy products suffered restriction.

New energy enterprises lack of innovation ability.

New energy is a technology-intensive industry, product development and technology innovation are key factors to improve the core competitiveness and ensure the development of new energy industry. In the new energy industry in Tianjin, except the fields of green battery, photovoltaic power generation and wind power develop leadingly, independent technology innovation ability of most new energy industry is weak, which increases the transformation difficulty of new energy technologies into practical products, reduces the reliability and economy of new energy products, and influences the sustainable development and market competitiveness of new energy industry Directly.

The supporting service system of new energy is not vigorous.

The new energy industry is a new industry that has broad prospects for development and good social benefits. It needs not only strong support of national policy, but also the supporting service system. At present, the information on new energy industry development, technological innovation, the mechanisms of talents training, mobility and introduction are not vigorous, and the financing guarantees, technical standards, professional consulting, talents training, mobility and introduction mechanisms that associate with the new energy industry are also not established. To some extent, both of them restrict the development of new energy industries.

Summary

Through the SWOT analysis of new energy industrial upgrading in Tianjin, we find that the biggest strength of new energy industry development is the solid new energy industry base and

strong supports from the government; the biggest weakness is the lack of talents and funds required; the biggest opportunity is the promotion from the development of low carbon economy on new energy industrial upgrading; the biggest threat is the lack of innovation ability and the narrow consumption scope of new energy products. On the whole, the prospects of new energy industry development are very broad, and Tianjin has a unique advantage. However, funds, technology and effective measures are still needed to realize the new energy industrial upgrading.

References

[1] Chao Gao. New Energy: the Next Economic High Ground Developed Countries Take [J]. China's Foreign Trade, 2011 (4): 48-51.

[2] Jingchao Lu. Countermeasures for China's New Energy Industry During the 12th Five Year Plan Period [J]. Theoretical Investigation, 2011 (1):95-98.

[3] Shang Ni. Research on the Development of New Energy Industry Cluster in Tianjin [D]. Tianjin Normal University, 2012.

[4] Mu Yuan, Xiaoguang Zhang, Ming Yang. Application and Innovation of SWOT Analysis in the City Strategic Planning [J]. City Planning Review, 2007, 31(4):53-58.

[5] Xiaofeng Li, Shuangshuang Wang. Identification and Cultivation about the Core Competitiveness of A Regional Strategic Emerging Industries—Take Tianjin's New Energy Industry for Example [J]. Science & Technology Progress and Policy, 2011, 28(11):55-58.

[6] Sha Luo. the Ministry of Environmental Protection: the Annual Averages of PM2.5 in Beijing-Tianjin- Hebei Were Not Standard in the First Half of the Year, the Air Quality is Relatively Poor in Seven Cities Including Hebei [N]. Baoding Evening News, 2013-08-01(B01).

Advanced Materials Research Vols. 986-987 (2014) pp 493-497

doi:10.4028/www.scientific.net/AMR.986-987.493

Research on Power System Stochastic Economic Dispatch Considering Interruptible Load and Wind Power

Xiaoyi MA[1, a], Wei WEI[1, b]

[1] Key Laboratory of Smart Grid of Ministry of Education, Tianjin University, Tianjin 300072 China

[a]email: xiaoyi.0912@163.com, [b]email: weiw@tju.edu.cn

Keywords: Demand Response; Interruptible Load; Economic Dispatch; Fluctuant Wind Power; Monte Carlo; Interior Point Method

Abstract. Interruptible load was an important measure for demand response which can effectively implement the interaction between grid side and demand side. It's also the important feature and component of smart grid. This paper established a stochastic economic dispatch model which brought both interruptible load and stochastic wind generation models into scheduling, and took the active and reactive power constraint of generator, the adjustable capacity constraint of interruptible load and the constraint of branch power flow into account. On the basis of Monte Carlo simulation and modified interior point method, a comprehensive optimization algorithm is proposed to tackle the above stochastic economic dispatch model. The result of IEEE 118-bus system illustrated that the proposed method can effectively curtail system's operational cost and, to some extent, boost grid's adaptability to wind power.

Introduction

Traditional dispatching model in power system which only considers resource in generation side cannot meet requirements for the rapid development of smart-grid. Load can participate in power Economic Dispatch (ED) by advanced technologies based on modern network, which can implement the interaction between information on feed side and demand side. Demand response (DR) regarding Advanced Metering Infrastructure (AMI) as the core is important resource in smart grid [1], which can be divided into two types: Price-based DR and Incentive-based DR. Interruptible load (IL) is a kind of incentive-based DR that plays a crucial role in power dispatching as a virtual power plant, and enhances elasticity of demand.

In paper [2], the comprehensive analysis of characteristics on various kinds of DR is constructed, and put forward that the IL is an available approach that realizes exchange between information and electrical power. Paper [3] summarizes technical structure of five actual smart grid companies in the world, in which load control participate in system regulator including demand side bidding and strategy. Paper [4] regards IL as reserve, and optimizes IL reserve and generation side reserve coordinately based on time-of-use power price. Above research has proved the preferable economic efficiency and feasibility of IL, but it is only treated as a kind of ancillary services, the effect of IL on generation cost and renewable energy is overlooked.

In this paper, an ED model considering both of stochastic wind generation and IL is established. On the basis of Monte Carlo simulation and modified interior point method, the comprehensive optimization algorithm is proposed. Based on a modified IEEE 118-bus system, the numerical results illustrate the effectiveness of the ED method and optimum algorithm.

Interruptible Load Model

The form of IL participating in system dispatch as a kind of interactive resource can be determined through an IL contract between grid companies and IL customers. Ordinarily, consumers declare the interruptible capacity and compensative payment according to the price published by grid companies. The optimal generation scheduling is presented based on the condition of both demand and generation side. Then the contract will be signed which includes the

interruptible capacity, compensation mode and price. Finally, the ultimate compensation can be built up according to the situation which the customers are actually called upon [5].

The specific compensation cost includes two components, capacity cost and an additional activation energy cost which is actually called by grid operator. Capacity compensation is fixed cost in accordance with the contract based on different abilities of maximize interruption capability, it can't be changed whether IL is interrupted or not practically. Energy compensation is generated for the interrupted load after participate in actual operation, the optimal interrupted power is calculated by ED. Compensation cost model within a certain dispatch period of time t is as follows:

$$f_{DR,j}=C_{cap,j}Cap_{DR,j}+C_{power,j}P_{DR,j} \tag{1}$$

Where $f_{DR,j}$ is the total compensation for the jth IL customer, it is composed of both capacity cost and energy cost; $C_{Cap,j}$ and $Cap_{DR,j}$ are the capacity compensation price and the maximum ability (capacity) for the jth customer respectively; $C_{power,j}$ and $P_{DR,j}$ are the jth customer's interruptible price for unit energy and the actual interrupted power, $P_{DR,j}$=0 represents the IL is inactive.

Output Power Model of Wind

The stochastic volatility of wind power can be represented by a probabilistic model. In this paper, a model of wind output in which the actual output power is expressed as the sum of wind power prediction and the deviation value will be utilized as follows [6]:

The deviation of wind power is normal distribution of a given variance within a certain dispatch period of time t:

$$P_{W,\Delta} \sim N(\mu_W, \sigma_W^2) \tag{2}$$

$$\mu_W = 0, \quad \sigma_W = P_{Wy}/\alpha + W_{wind}/\beta \tag{3}$$

Where μ_W and σ_W are the expectation and variance of this distribution respectively; P_{Wy} presents the prediction of wind power at time t; W_{wind} is wind total installed capacity; α and β are calculation parameters of standard deviation; Actual output power of wind at time t is as follows:

$$P_W = P_{Wy} + P_{W,\Delta} \tag{4}$$

In the type: P_W is actual output power. A collection of wind power fluctuations can be obtained through random sampling which can simulate a variety of situations of wind power fluctuation, and then the collection of actual output can be got as follow, where N_M is the total number of samples.

$$\{P_W(1), P_W(2), \cdots, P_W(N_M)\} \tag{5}$$

Stochastic Economic Dispatch Model Considering IL and Wind Power

Taking the IL and wind models into dispatch, optimizing demand side resource and conventional unit output comprehensively, an ED model at time t is set up as follows:

1) Objective function:

$$Minf(P_{G,i}, P_{DR,j}) = Min(\sum_{i=1}^{N_G} f_{G,i} + \sum_{j=1}^{N_{DR}} f_{DR,j}), \quad f_{G,i} = a_i P_{G,i}^2 + b_i P_{G,i} + c_i \tag{6}$$

Where $P_{G,i}$ is the active power of the ith unit; N_G and N_{DR} are the total numbers of generators and IL customers respectively; $f_{G,i}$ is the operation cost function of the ith unit, and a_i, b_i, c_i are it's correlation coefficients.

2) Constraints:

$$\begin{cases} \sum_{i\in k} P_{G,i} + \sum_{m\in k} P_{W,m} - \left(P_{L,k} - \sum_{j\in k} P_{DR,j} \right) - V_k \sum_{l=1}^{N} V_l \left(G_{kl}\cos\theta_{kl} + B_{kl}\sin\theta_{kl} \right) = 0 \\ \sum_{i\in k} Q_{G,i} - \left(Q_{L,k} - \sum_{j\in k} Q_{DR,j} \right) - V_k \sum_{l=1}^{N} V_l \left(G_{kl}\cos\theta_{kl} - B_{kl}\sin\theta_{kl} \right) = 0 \end{cases}, \quad k = 1, 2, \cdots, N \tag{7}$$

Formulation (7) is node power balance constraint. Where $Q_{G,i}$ is the reactive power of the ith unit; $P_{L,k}$ and $Q_{L,k}$ are the active and reactive load of the kth bus; V_k and V_l are the voltage magnitude of

the kth and lth bus; G_{kl} and B_{kl} are used to represent the conductance and susceptance of branch kl; θ_{kl} is the phase angle between bus k and l; N is the system bus numbers. The inequality constraints of the model are as follows:

$$\begin{cases} V_{k.\min} \le V_k \le V_{k.\max} & ,k = 1,2,\cdots,N \\ P_{G,i.\min} \le P_{G,i} \le P_{G,i.\max} & ,i = 1,2,\cdots,N_G \\ Q_{G,i.\min} \le Q_{G,i} \le Q_{G,i.\max} & ,i = 1,2,\cdots,N_G \\ P_{DR,j.\min} \le P_{DR,j} \le P_{DR,j.\max} & ,j = 1,2,\cdots,N_{DR} \\ |L_l| \le |L_{l.\max}| & ,l = 1,2,\cdots,N_L \end{cases} \tag{8}$$

In the type (8): the inequality constraints represent the voltage constraint, the active and reactive power constraint of generator, the adjustable capacity constraint of IL and the power flow constraint of branch successively; Where L_l is the current through the lth branch; N_l is the branch numbers.

In this paper, Monte Carlo method is used to simulate the fluctuation of wind power. On the basis of this, this paper optimizes and calculates the above models through Interior Point method to get the optimal scheduling scheme; The expectation, maximum and standard deviation of the results can be used to evaluate the effectiveness of the method proposed by this paper. The calculation flow charts are as follows:

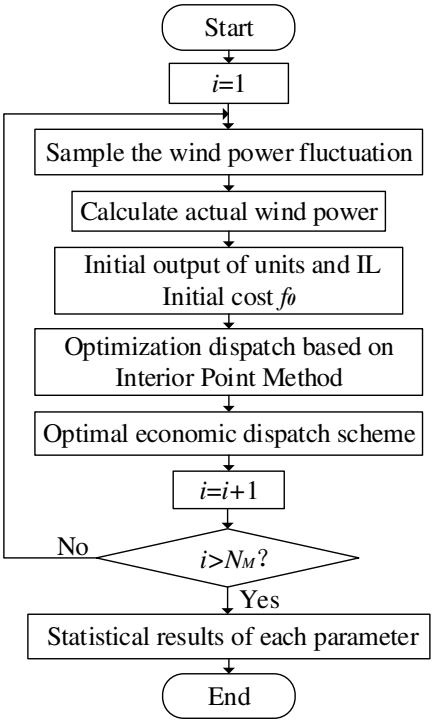

Fig.1. Calculation flow chart

Tab.1. Wind power generation parameters

Wind farm	Bus	Prediction power (MW)	Installed capacity (MW)
1	63	40	100
2	102	60	100
3	117	100	200

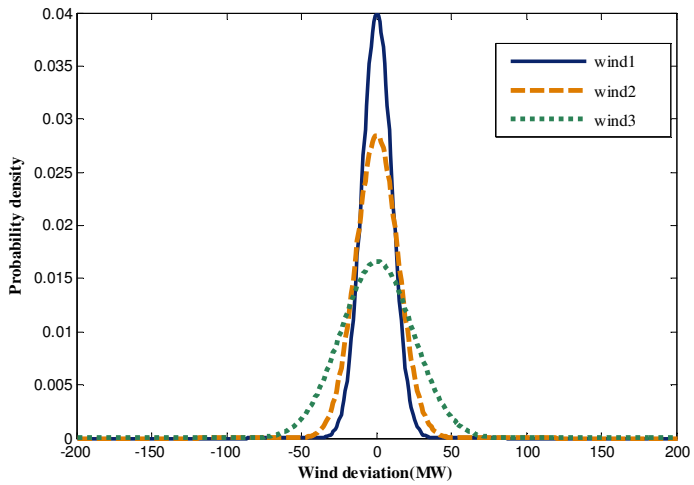

Fig.2. Probability distribution of wind generation deviation

Simulation results

A modified IEEE 118-bus system is used to clarify the proposed stochastic ED method, the system data and unit parameters reference [7]. Three wind farms with total installed capacity of 400MW which account for 10% of the total capacity of system are installed at bus 63, 102 and 117 respectively. The dispatch cycle is set to be 1 hour. The installed capacity and prediction of each wind farm at time t is shown in Table1. Using Monte Carlo method to simulate the fluctuation, the actual fluctuant wind output is obtained, α and β are set to be 5 and 50 respectively [8]. Figure2 demonstrates the probability distribution of wind generation deviation.

To facilitate the presentation, the load is set to basic level (total load is 4000MW) and heavy load level (150% of basic), which describes two scenarios with different load level. 30% of load buses are set to be IL bus, the maximum interruptible capacity is set to 50% of each total active load. Assume that the power factor remains during the process of interruption. The price of IL capacity and interrupt energy can reference [3-4]. Table2 indicates the parameters of each IL.

Tab.2. Interruptible load parameters

IL bus	11	15	18	27	32	34	40	42	49	54	55
Max. capacity (MW)	35	45	30	35	30	30	33	48	44	50	30
Capacity price ($/MW)	0.5	0.8	0.5	0.5	0.5	0.5	0.5	1.3	0.8	1.3	0.5
Energy price ($/MWh)	12.89	14.47	12.89	12.89	12.89	12.89	12.89	17.15	14.47	17.15	12.89
IL bus	56	59	60	62	76	78	80	90	92	112	116
Max. capacity (MW)	42	50	39	39	34	35	50	50	33	34	50
Capacity price ($/MW)	0.8	0.8	0.8	0.8	0.5	0.5	1.3	1.3	0.5	0.5	1.3
Energy price ($/MWh)	14.7	17.15	14.47	14.47	12.89	12.89	17.15	17.15	12.89	12.89	17.15

According to the above settings and the dispatching model in this paper, the simulation results with a wind power sample of 1000 cases are illustrated as follows. Table3 compares optimal results between two scenarios with or without IL participate in generation scheduling. The following conclusions can be obtained:

Tab.3. Comparison of Economic Dispatch results

Scenario	IL	Avg. cost ($)	Max. cost ($)	Actual IL (MW)	Total units Generation(MW)		
					Avg.	Max.	SD
1	No	62835.70	68533.97	_	3994.03	4160.27	78.0287
	Yes	61117.87	65474.03	423.85	3560.95	3634.98	47.4966
2	No	110509.01	117755.81	_	6150.81	6231.67	84.6578
	Yes	105957.19	111762.53	783.20	5343.45	5476.93	52.0627

(1) Both the average and maximum values of the total cost of the optimal dispatch results are effectively reduced after considering IL in two scenarios. In Scenario1, the average cost with IL participate in is 1700$ less than the condition without IL, while the maximum cost decreased much more, around 3000$. It indicated that the ED model considering IL can reduce the generating cost, especially for the maximum cost.

(2) The current through branch30-38 is 1.19kA in Scenario1, approach to its limit 1.26kA. When the load increases, the closely related high-cost units G15, G18 and G19 will give an additional 96.52MW output if IL not participate in. Compared with the model including IL, the increased power is only 57.68MW and the cost of dispatching high-cost units is effectively decreased. The comparison between Scenario1 and 2 shows when the load level is increasing, output of some low-cost units is limited due to the constraints of the transmission capacity and generation capacity, which give rise to an additional generation of some high-cost units in the condition without IL to meet the demand of load, that leads to the decrease of system economic efficiency. The actual interrupt amount of IL in Scenario2 is much more than that in Scenario1, which is part of substitution of high-cost units' generation. The system cost is reduced by 4.5% and the diseconomy caused by the transmission and generation capacity constraints has been improved.

(3) The generators have to change within a certain range to balance the power fluctuation due to wind generation, which make the dispatch scheme present certain randomness. The ensemble volatility in both conditions shown in Table3 presented that with IL, the standard deviation of the generation is much reduced in both of two scenarios. IL shows a more flexible adjustment ability to balance the influence of wind fluctuation than conventional unit. Unit generation fluctuate range can be decreased by dispatching IL. For further clarification of the IL ability to adjust the undulation of single unit, part of the units' maximum changes in generation that may occur during the simulation are shown in Table4.

In Scenario1 without IL, the output of unit G12 changes from 109.78MW to 182.45MW for the influence of wind fluctuation, the maximum possible variation is 73MW. This is improved to

Tab.4. Unit fluctuation in Scenario1

IL	Max. variation of units generation			
	G12	G62	G80	G89
No	72	41	69	54
Yes	26	12	23	16

26MW after considering IL dispatch. It can be perceived that the unit generation changes can be improved much smoother through IL participate.

Conclusion

This paper established a stochastic economic dispatch model which took both interruptible load and stochastic wind generation models into account. This model considered conventional unit output and demand side resource comprehensively, and was constructed with IL interaction and wind power interconnection. The comprehensive optimization algorithm based on Monte Carlo simulation and modified interior point method was used to obtain the optimal scheme. The results demonstrated the proposed method reduced the output of high-cost units and also curtailed system's operational cost. In the meanwhile, it dampened the fluctuation of units' generation due to wind variation, therefore dampened the adverse effects from wind integration, and boosted the security and economy of grid.

Acknowledgement

In this paper, the research was sponsored by the Nature Science Foundation of China (Project No.51337005).

References

[1] Qin Zhang, Xifan Wang, Min Fu, Jianxue Wang. Smart Grid from the Perspective of Demand Response [J]. Automation of Electric Power Systems, 2009 33(17) 49-55.

[2] Jianxue Wang, Xifan Wang, Xian Zhang, Zhende Zhang. Interruptible Load Management in Power Market and Interim System-Part1 Cost-benefit Analysis of Interruptible Load [J]. Electric Power Automation Equipment, 2004 24(5) 15-19.

[3] Grayson Heffner, Charles Goldman, Brendan Kirby, Michael Kintner-Meyer. Loads Providing Ancillary Services: Review of International Experience [R], 2007.

[4] Xiaocong Liu, Beibei Wang, Yang Li, Jianguo Yao, Shengchun Yang. Day-ahead Generation Scheduling Model Considering Demand Side Interaction under Smart Grid Paradigm [J]. Proceedings of the CSEE, 2013 33(1) 30-38.

[5] Jianxue Wang, Xifan Wang, Xiuli Wang. Study on Model of Interruptible Load Contract in Power Market [J]. Proceedings of the CSEE, 2005 25(9) 11-16.

[6] Ronan Doherty, Mark O'Malley. A New Approach to Quantify Reserve Demand in Systems with Significant Installed Wind Capacity [J]. IEEE Transactions on Power Systems, 2005 20(2) 587-595.

[7] Xiao Liu, Xin Ai, Qian Peng. Optimal Dispatch Coordinating Power Generation with Carbon Emission Permit for Wind Farms Integrated Power Grid Considering Demand Response [J]. Power System Technology, 2012 36(1) 213-218.

[8] Francois Bouffard, Francisco D. Stochastic Security for Operations Planning with Significant Wind Power Generation [C]. Power and Energy Society General Meeting-Conversion and Delivery of Electrical Energy in the 21st Century, 2008.

Advanced Materials Research Vols. 986-987 (2014) pp 498-502

doi:10.4028/www.scientific.net/AMR.986-987.498

Research on the Effect of the Integration of Renewable Energy Resources on Economical Operation of Power Grid Based on System Dynamics

XUE Wanlei[1], JIA Shanjie[1], ZENG Ming[2], LU Kuan [1], ZHAO Xin [1], DUAN Kaiyan[2], XU Nan[1]

[1.]Economic&Technology Research Institute, State Grid Shandong Electric Power Company, Jinan 250021

[2.] Research Advisory Center of Energy and Electricity Economics, North China Electric Power University, Beijing 102206

Keywords: renewable energy; system dynamics; economical operation

Abstract. The integration of renewable energy resources(RERs) not only shows significant environmental effect, social effect and economic effect, but also brings many challenges to grid planning and economic operation of power grid. Based on systematic dynamics, from the perspective of changes of cost and benefit of grid enterprises caused by the integration of RERs, the effect of the integration of RERs on economical operation of power grid is studied. Finally, a simulation of effect trend based on empirical data of one province demonstrates the validity of the model proposed in this paper.

Introduction

Because the installed percentage of renewable energy capacity has risen steadily, the influence of which on power grids the economic operation are increasingly highlighted. Renewable energy sources generation technologies such as wind power, photovoltaic power have their own power features, which have brought about great challenges for power grid economic operation after integration of renewable energy [2]. Research on the influence of integration renewable energy source on grid economic operation, especially on electric power loss and the economic dispatch, etc, has great significance on choosing grid economic operation mode scientifically and rationally and improving the management efficiency of the power grid company.

There are some documents that made a research on the influence of integration of renewable energy grid on power grid at present. These research, from different perspective angle, will study the impact of the renewable energy source integration on a segment of power system, but not from other segments such as power generation, transmission and electricity sales to make comprehensive analysis for the influence of the renewable energy source integration on the economic operation of power grids and power grid overall management. Therefore, this paper uses the method of system dynamics, by constructing the grid economic operation system flow chart, from angles of changes of the power grid enterprise operating costs and benefits caused by renewable energy combined to the grid to study the influence of the renewable energy grid integration on the economic operation of power grids, and uses the real data of the province over the next decade to simulate the influence trend of renewable energy grid integration on economic operation of power grids .

Impact analysis of renewable energy grid integration to economic operation of power grids

Renewable energy power generation technology has achieved rapid development in recent years, whose costs have reduced continually, but a large amount of renewable energy access generated a large impact on the structure of the distribution system and power grid economic operation [1]. Mainly manifested in the following two aspects:

(1) Impact on loss of power grid

After access of power distribution network to renewable energy power generation system, the load distribution of whole distribution network will change, which can lead to the increase of network loss, and it depends on factors such as the location of the renewable energy access, the size of access capacity and the network topology structure,etc.

(2) Impact on the line power flow

Because wind power and photovoltaic power generation force are highly affected by the weather and so on, they have intermittent and uncertainty, which will directly result in randomness of system trend, and the traditional trend algorithm will be no longer suitable to use. In addition, the renewable energy grid integration will also produce certain effect on the economic dispatch operation, which main perform difficult power prediction and bad generation electricity planning, bringing about a challenge to the ways of the grid scheduling and real-time monitoring .

And the influence of renewable energy grid integration on power grid enterprise operation cost has following several aspects:

(1) Power generation side. Renewable energy grid integration can share the partial load of the traditional thermal power and hydroelectric generating set , greatly reducing the consumption of fossil fuels, and reducing the operation costs of the power generation side.

(2) Power grid side. Due to characteristics as intermittent, uncertainty, and so on, renewable energy grid integration will affect system stability, reliability and power quality, increasing the power auxiliary service cost such as frequency control, reserve capacity, reactive power and voltage regulation, etc.

(3) Electricity side. Electricity power grid enterprises accepted the renewable energy power generation, at the same time, countries offered certain subsidy for sales power price , to a certain extent, reducing the cost of the power grid enterprise.

Model description

Based on the above analysis of the influence of renewable energy grid integration on economic operation of power grids, this part plans to adopt the system dynamics, to establish system dynamics model of renewable energy grid generation to economic operation of power grids.

In this paper, the model mainly includes three parts: First is the amount of renewable energy power generation; Second is power grid enterprises operating costs; Third is to power grid enterprise benefits.

(1) Amount of renewable energy power generation. It mainly researches the renewable energy electricity gross generation in a given area by the support technological progress and government policies, .

(2) Power grid enterprise running cost. It mainly researches considerance of the cost of line loss and auxiliary service cost that the renewable energy grid-connected power grid enterprise need to bear, on the basis of ensuring grid security operation and quality of power supply level, and meeting the demand of power supply.

(3) Power grid enterprise income. It mainly researches selling electricity income of power grid enterprise in the case of renewable energy grid-connected. Thereinto electricity selling price of renewable energy considered electricity price subsidies of the renewable energy power generation.

Based on the above analysis, this article selects the core index such as the power grid enterprise operation efficiency and renewable energy power generation, and correlation indicators affecting the core indexes. Using system dynamics software vensim, it has combed the qualitative relations between the various indicators, and constructed the grid economic operation system flow diagram, as shown in figure 1:

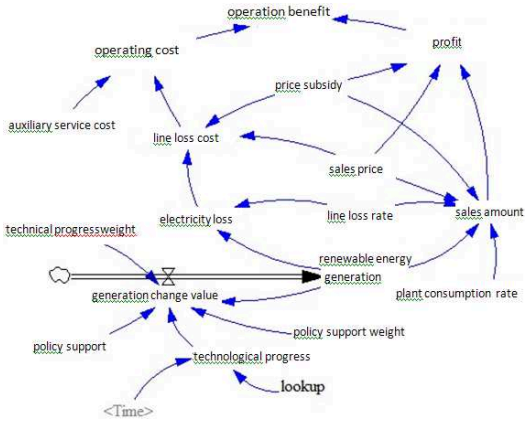

Figure 1 System Flow Chart of Economical Operation of Power Grid

Table 1 Related Factors of Economical Operation of Power Grid and their Meanings

Influence factors	The meaning of the influence factors
Electricity sales amount	Amount of renewable energy power power grid enterprise providing for the end users.
Selling electricity tariff	Renewable energy power generation electricity price electricity power grid enterprise selling to the end users.According to different renewable energy power generation technology, the price is also different , which includes wind power, solar power generating electricity price and biomass power generation electricity price, etc.
Electricity price subsidies	To encourage renewable energy grid-connected power generation, the country provides grid electricity price subsidies for grid companies in its development and promotion period.Power generation technology is different, and there are different electricity price subsidies.
Line loss cost	Loss of the cost value of renewable energy power in the process of transmission .
Auxiliary service cost	It includes three parts such as peaking and frequency modulation and spinning reserve cost renewable energy bringing about due to power generation output volatility and instability.
Amount of power wastage	Loss of electric energy renewable energy generating in the process of transmission of electricity.
Rate of waste	Power losses in the process of transmission accounts for the proportion of the total electricity transmission.

On the basis of building the system flow chart, the relationships between each index of the flow chart are e analyzed quantificationally, and system dynamics equations are presented.

(1)State equation:

$$Q_{renew}(t) = Q_{renew}(0) + \int_0^t q_{renew}(t)dt \tag{1}$$

In the formula,

$Q_{renew}(t)$ ——Renewable energy sources energy production,kWh;

$Q_{renew}(0)$ ——Renewable energy sources initial energy production,kWh;

$q_{renew}(t)$ ——Renewable energy sources power change value,kWh/year。

(2)Rate equation:

$$q_{renew}(t) = \frac{TECH(t)*TECHW(t)+POLICY(t)*POLICYW(t)}{TECHW(t)+POLICYW(t)} * Q_{renew}(t-1) \tag{2}$$

where,

$TECH(t)$ ——Technical progress factor;

$TECHW(t)$ ——Technical progress weight;

$POLICY(t)$ ——Policy support factor;

$POLICYW(t)$ ——Policy support the weight.

(3)Auxiliary equation:

A.Power grid enterprise operation cost

$$C_{grid}(t) = C_{auxi}(t) + C_{loss}(t) \tag{3}$$

$$C_{loss}(t) = Q_{loss}(t) * p_{grid}(t) \tag{4}$$

$$Q_{loss}(t) = Q_{renew}(t) * \vartheta \tag{5}$$

where,

$C_{grid}(t)$——Power grid enterprise operation cost, yuan;

$C_{loss}(t)$——Line loss cost, yuan.

$Q_{loss}(t)$——power wastage, kWh;

ϑ——Rate of waste;

$p_{grid}(t)$——Selling electricity tariff,yuan/kWh。

B.Power grid enterprise income

$$B_{grid}(t) = Q_{grid}(t) * \left(p_{grid}(t) + p_{subs}(t) \right) \tag{6}$$

$$Q_{grid}(t) = Q_{renew}(t) * (1 - \vartheta - \zeta) * \left(\frac{\alpha * p_{subs}(t)}{\beta * p_{grid}(t)} \right) \tag{7}$$

where,

$B_{grid}(t)$——Power grid enterprise income, yuan;

$Q_{grid}(t)$——Power grid enterprise electricity sales amount, yuan;

$p_{subs}(t)$——Subsidy electricity price, yuan/kWh;

α——Subsidy electricity price influence coefficient, shows the effects of subsidy electricity price on electricity sales amount, which is proportional to the electricity sales amount;

β——Selling electricity price influence coefficient, shows the effects of selling electricity price on electricity sales amount, which is inversely proportional to the electricity sales amount.

C.Power grid enterprise operation efficiency

$$E_{grid}(t) = B_{grid}(t) - C_{grid}(t) \tag{8}$$

In the formula, $E_{grid}(t)$ expresses power grid enterprise operation efficiency, yuan.

Examples analysis

This part, taking province renewable energy grid integration as an example, has simulated and run for 10 consecutive years with the time interval for 1 year, simulating and analyzing , the influence of the renewable energy grid integration on economic operation of power grids from 2011 to 2020. (1)To assignment constant in the model, as shown in the table below:

Table 2 Values of parameters in SD model

Variable quantity	Assignment	Unit
Unit length operation and maintenance cost	0.05	Ten million yuan/km
Unit length investment cost	1200	Ten million yuan/km
Unit capacity operation and maintenance cost	50	Million yuan/kvA
Unit capacity investment cost	33	Million yuan/kvA
Renewable energy grid integration proportion	0.07	1
Factor 2	7.5	1

(2) Given the technology continuous advances in renewable energy power generation, interconnection and scheduling aspects, this section will set "technical progress" as function, and its function image is shown in figure 2.

(3) Along with the advance of renewable energy power generation technology, using Vensim software simulates the model, then the operation efficiency of power grid enterprises trend diagram about renewable energy grid (figure 3) can be obtained:

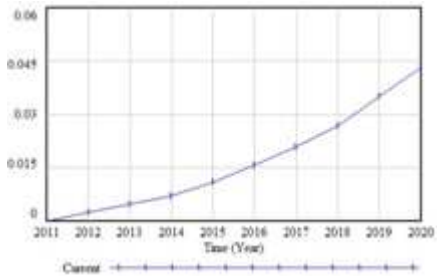

Figure 2 The Graph of Technical Progress Function

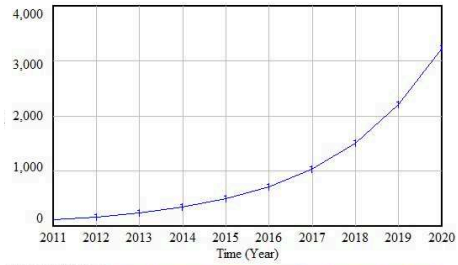

Figure 3 The Simulation Graph of Operation Benefit of Grid Enterprises

From above trend diagram, you can see in the next 10 years, with the development of technology, renewable energy power generation will increase constantly, and power grid enterprises income will gradually be improved, so renewable energy grid integration will promote economic operation of power grid.

Conclusion

This paper uses the method of system dynamics, by constructing the grid economic operation system flow chart, from angles of changes of the power grid enterprise operating costs and benefits caused by renewable energy combined to the grid to study the influence of the renewable energy grid integration on the economic operation of power grids, and uses the real data of the province over the next decade to simulate the influence trend of renewable energy grid integration on economic operation of power grids .Simulation results show that generating capacity will increase continuously with the development of renewable energy power generation technology and a complete set of power transmission technology, and the grid economic operation will get constant optimization, at the same time for the benefit of the power grid enterprise is also increasingly prominent. As a result, from the point of long-term development, the province should continue to increase the intensity of renewable energy, based on technology and management, constantly promote the progress and development of renewable energy grid integration correlation technology, improving the proportion of renewable energy installation, further optimizing economic operation ways of power grid.

Reference

[1] REN Shan,XUE Hui-feng.The Monetary Quantify and Systematic Evaluation of External Benefits of Renewable Electricity[J].Electric Power Technology and Environmental Protection,2010,26(4):7-10.

[2] QIN Xiang-ling.Power Generation Policy and Environmental Benefits Analysis Method of Renewable Energy[D].Beijng,North China Electric Power University,2011.

[3] HAN Dong,YAN Zheng,SONG Yi-qun,et al.Dynamic Assessment Method for Smart Grid Based on System Dynamics[J].Automation of Electric Power Systems,2012,36(3):16-21.

[4] WU Jun,LI Jian-she,ZHOU Jian.Influence of Wind Power Generation Integrating into Power Grid[J].Southern Power System Technology,2010,4(5):48-52.

[5] ZHANG Feng.Influence and Countermeasures of Renewable Power Generation on Power Grid Operation[J].Zhejiang Electric Power,2010,(3):9-11,50.

Advanced Materials Research Vols. 986-987 (2014) pp 503-506

doi:10.4028/www.scientific.net/AMR.986-987.503

Research on Thermal Power Industrial Security Issues Based on Sustainable Energy Development

LI Chunyan[1, a]

[1]China Center for Industrial Security Research, Beijing Jiaotong University, No.3 Shangyuancun, Xizhimenwai, Beijing, China

[a]lichy1973@163.com

Keywords: Energy, Sustainable development, Thermal power, Industrial security, Issues.

Abstract. China is faced with significant challenges in the energy sector such as energy shortage, environmental pollution, greenhouse gas emission, and energy supply in rural areas, which severely restrict its sustainable development. In this paper, the current status and trends of thermal power industrial security issues based on sustainable energy development in China are elaborated. The strategies of sustainable energy in China are brought forward accordingly, such as efficient thermal power industry, green thermal power industry. The corresponding implementations of sustainable energy development in China are expounded as well. In the end, this paper concludes that China must set a step-by-step unified national energy plan to promote the construction of a sustainable energy system, which will be economically, environmentally, and socially viable, and, thus, China would play an important role to promote global sustainable development.

Introduction

Energy has been the life-blood for continuing progress of human civilization. Since the beginning of industrial development around two centuries ago, the global energy consumption has increased by leaps and bounds to accelerate the human living standard [1]. China has been going through a rapid progress of industrialization and urbanization since the 1980s, with an annual gross domestic product (GDP) growth rate of approximately 16 percent from 1980 to 2008, and this fast developing trend is projected to continue in the foreseeable future [2]. To maintain the economic development, a corresponding increase in the primary energy consumption is also expected.

Thermal power industry energy security and sustainable development are closely related in China. Since the reform and opening up in 1978, China's industrial growth rate has remained at around 10%. Based on its GDP, China's economy has multiplied more than eight times, while is illustrated in Fig.1. However, industrial growth is mainly focused on highly energy-intensive industries, which brings the expansion of industrial scale [3]. The energy production has been unable to meet the needs of consumption. China's power shortage has been occurred in 2003, which leads to the shortage of the coal and diesel supply [4]. To solve this problem, a serious challenge to the thermal power industry needs to be faced in China.

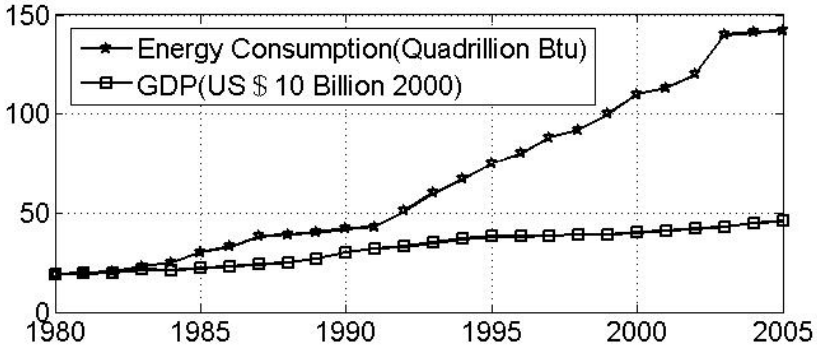

Fig.1. GDP and energy consumption

Economic growth mainly depends on the consumption of energy. China's energy consumption of 1,386 Mtoe (million tons of oil equivalents) ranks second in the world. In the past two decades,

China has been enjoying a 9.7% average annual GDP growth while limiting its annual incensement of energy usage to only 4.6%. This means that its efficiency in energy utilization has improved. Its energy intensity, as defined in terms of energy consumption per dollar of GDP, has gone through a significant 70% reduction. In other words, to produce the same amount of economic output, it is now using only 30% of the energy which had been consumed before.

Current Status of the Thermal Power Industry

Energy industry is an infrastructure sector. China is not only a large energy producing country, but also a large energy consuming country. Sustainable energy resources are most often regarded as including all renewable sources, such as wind power, solar power, biomass, geothermal power, tidal and wave power [5]. It usually also includes technologies that improve energy efficiency. China is the world's most populous nations, the world's fastest economy growth, and one of the world's biggest coal producer and consumer. Coal plays a very important role in the primary energy consumption structure and it will remain for a long time. Energy resource in China is complete in variety, rich in deposits, but uneven in distribution. Among the total electricity generation, mostly is coal-fired. Evidently, power plants will become the biggest coal consumer.

The installed generation capacities of coal, hydro, nuclear, and wind power generation from 2005 to 2008 are tabulated in Table 1. The total installed power generation capacity in China was 517.18 GW in 2005, 622 GW in 2006, 713.29 GW in 2007, and 792.53 GW in 2008 [6], and it will reach about 1600 GW by 2020. Note that coal has been playing a dominant role in the energy mix in China, which is around 75% of the total installed capacity [7]. As can be foreseen, the required coal depletion would be unbearable considering the substantial growth of total installed power generation capacity based on the current energy mix. Therefore, effective changes of energy structure must be made in the future so as to promote China's sustainable development.

Table 1 Installed power generation capacity (2005-2008) in China

Capacity (GW) / Energy	2005	2006	2007	2008
Coal	391.38	484.05	554.42	601.32
Hydro	117.39	128.57	145.26	171.52
Nuclear	6.84	6.85	8.85	9.1
Wind	1.06	1.87	4.03	8.94
Others	0.51	0.66	0.73	1.65
Total	517.18	622	713.29	792.53

As the second largest energy consumer in the world, China has a significant impact on global energy supplies. In the past two decades, China has been enjoying a 9.7% average annual GDP growth while limiting its annual incensement of energy usage to only 4.6% [8]. However, driven by industrialization and urbanization, China requires a dramatic increase of energy supply in the coming decades. The future energy supply would not be sustainable unless significant changes can be made in the power production and consumption patterns. Hence, China's overall energy strategy is striving to shift its coal based energy.

Environmental Problems

China's heavy dependence on coal is the root of its environmental problem. The environmental impacts of coal, from extraction to end use, encompass land disturbance, water usage, groundwater

contamination, and air pollution. Coal contributes to 90% of the total sulfur dioxide (SO_2) emission in the atmosphere, 65% of nitrogen oxides (NO_x) emission, 70% of particulates, and 80% of carbon dioxide (CO_2) emission in China. Oil also contributes to NOx, particulates, and to SO_2 to a lesser extent. All fossil fuels contribute to CO_2 emission.

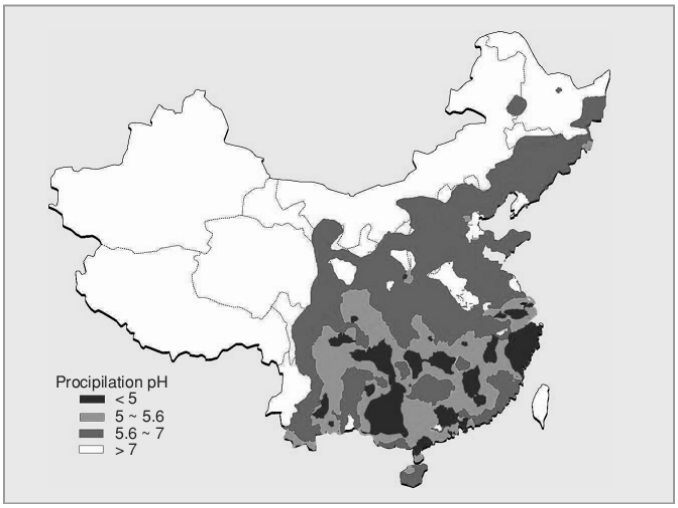

Fig.2. Geographical distribution of the pH value of depositions (2001)

Emissions of SO_2, NOx, and solid particulates have detrimental implications for air quality and health. SO_2 and NOx may travel hundreds of miles, causing acid depositions made from sulfur and nitrogen oxides mixed with rain (acid rain) over a large region. Acid rain results in damage to trees and crops and sometimes extends to the acidification of streams and lakes, resulting in the destruction of aquatic ecosystems. It also leads to the corrosion, erosion, and discoloration of buildings and monuments. In China, the affected area by acid rain has expanded to more than 1,000,000m^2 since the 1990s. Moreover, one-third of China has a pH value of less than 5.6. The graph of the geographical distribution of the pH value of depositions is presented in Fig. 2**.**

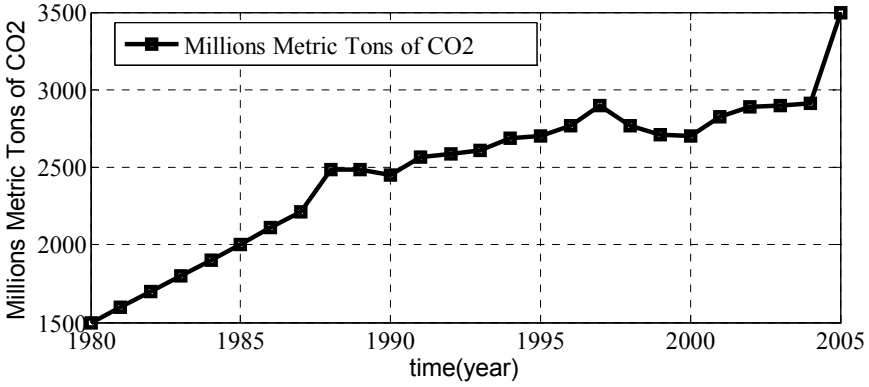

Fig.3. CO_2 emission evolution

Carbon dioxide is the major cause of greenhouse gases that contribute to global climate change. The other major greenhouse gas is methane. These gases have a long residence time. The accumulation of man-made greenhouse gases due to the burning of fossil fuels has occurred since the industrial revolution, and it is believed to have reached the maximum point of the atmosphere's carrying capacity, trapping radiated heat from the sun, and leading to higher long-term atmospheric temperature. The effect of climate change is long term, and it is global. Notably, the CO_2 emission in China has more than doubled in the last 20 years, as shown in Fig. 3. In addition, it ranks second worldwide in CO_2 emission. Fig. 4 compares the total emission of China with that of the United States, Japan, and Germany. On a per capita basis, however, China's CO_2 emission is only 14% of that produced by the United States, 29% of Japan, and 68% of the world average.

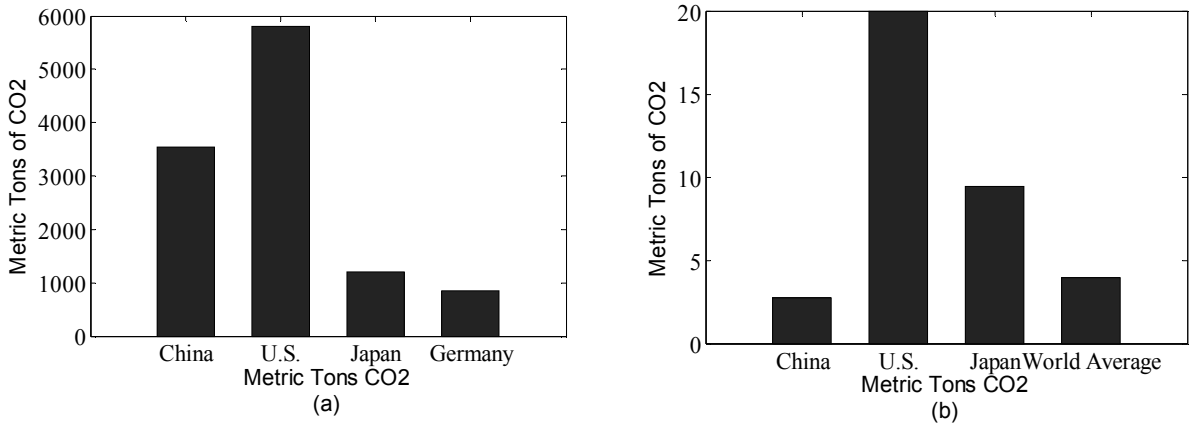

Fig.4. CO_2 emission in 2001: (a) total amount and (b) per capita

In summary, except for oil, China is basically self-sufficient and will remain so in terms of energy supply. It is heavily dependent on coal, and almost every energy and environmental problem China is currently facing, such as large quantity, low efficiency, and high emissions, can be traced back to coal.

Summary

This contribution illustrates China's current status of the energy sustainable development and thermal power industry security issues. Because of the burning of fossil fuels, environmental problems are also discussed in this paper. On all accounts, China must boost renewable energy development rapidly in the future. At the same time, China needs to attach great importance to enhancing energy saving and conservation**,** accelerating nuclear power development, and further promoting the economy.

References

[1] U. Bossel, "On the way to a sustainable energy future," in *27th Int. Telecommunications Conf. (INTELEC)*, Sep. 2005, pp. 659–668.

[2] J. Wen, "Keeping China energized: UNDP support to sustainable energy in China", *Premier of People's Republic of China*, Jun. 2005.

[3] Comprehensive statistical data and materials of electric power industry in (1985–2005) China Electricity Council.

[4] D. Zhou, "Sustainable energy development in China," *Contemporary Int. Relations (CIR)*, vol. 19, no. 2, pp. 1–23, Mar. 2009.

[5] Z. Yang, "Approaches for sustainable development of China's Energy Industry," *Electricity*, vol. 18, no. 3, pp. 16–18, 2007.

[6] Z. Zhang, "Hydropower development strategy and its policy orientation in China," *China Water Resources*, no. 2, pp. 18–21, 2010.

[7] Medium and long-term development plan for renewable energy State Council of China, 2007.

[8] Q. Wang, "China end use energy consumption and energy efficiency," *Energy Conservation and Environment Protection*, no. 4, pp. 11–13, 2009.

Advanced Materials Research Vols. 986-987 (2014) pp 507-511

doi:10.4028/www.scientific.net/AMR.986-987.507

Review of Quick Search for Transmission Section

XIE Yan[1,a], TANG Xiaojun[2,b], REN Jianwen[1,c], TIAN Chunzheng[3], YU Linlin[3] and HUANG Jinghui[3]

[1]School of Electrical and Electronic Engineering, North China Electric Power University, China

[2]China Electric Power Research Institute, China

[3]State Grid Henan Economic Research Institute, China

[a]xieyan1990@hotmail.com, [b]tangxj@epri.sgcc.com.cn, [c]rjw219@126.com

Keywords: power system, transmission section, cascading failure, search algorithm

Abstract. This paper introduces the current research status of quick search for transmission section. Firstly, the definition of transmission section is introduced. Secondly, search algorithm for transmission section is presented. Thirdly, the safety protection measures that can prevent cascading failure are introduced. Finally, outlook on quick search for transmission section is proposed.

1 Introduction

With the enlargement in area and the increase in capacity of the interconnected power system, on the one hand, the use of resources can be rational which can bring considerable economic benefits and social benefits. On the other hand, catastrophic blackout caused by cascading failure can result in disastrous impact upon society and dairy life. According to reports about some blackouts in the world[1~3], in the early stages of the development of blackout, cascading failure often occurs in a set of lines whose safety margin is small but electrical contact is close. This set of lines can be called transmission section. Blackout can be prevented by focusing on monitoring certain transmission section rather than monitoring the entire power grid, which can save more manpower and material resources. Quickness and integrity are two main problems of search for transmission section.

2 Definition of Transmission Section

As with the definition of transmission section, a set of lines whose direction of power flow are the same and electric distance is near, under a certain base power flow, is called transmission section in literature [4]. Two other related definitions are also often involved, namely parallel transmission section and key transmission section. Transmission section with the same power supply area and load area with the overloaded line, under a certain base power flow, is defined as parallel transmission section in literature [4]. Normal transmission section which is closest to transmission limit state under a certain operation mode is defined as key transmission section or vulnerable transmission section of the system in literature [5]. In literature [6], three concepts are proposed. Initial transmission section is defined as minimum cut set of grid. Transmission section is defined as initial transmission section which has the same power flow direction and bigger LODF (line outage distribution factor). Key transmission section is defined as transmission section which has less safety margin but big influence on grid safety. The relationship of those definitions above is shown in Fig. 1.

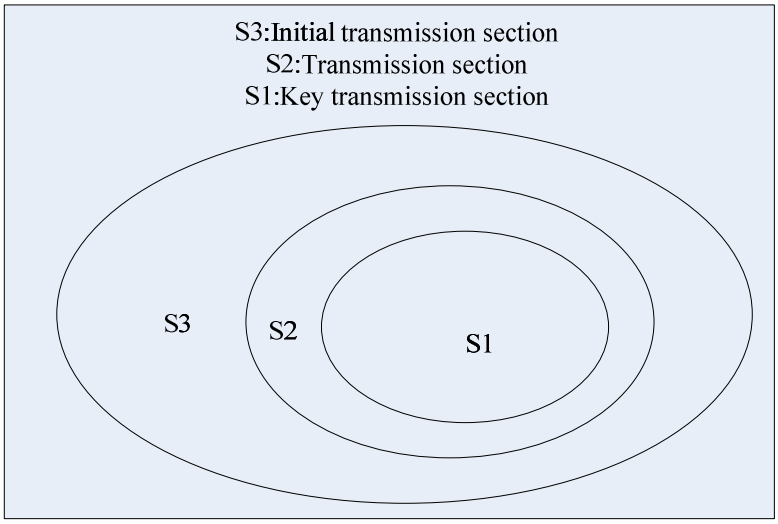

Fig. 1 Relationship of three definitions

In conclusion, there are many definitions of transmission section. But some factors should be taken into consideration such as power flow direction, topological connection and electrical connection.

3 Search Algorithms for Transmission Section

The principle of quick should be followed when search the transmission section, then a certain transmission section can be determined after an accident occurred. So related emergency control measures can be taken in order to prevent the blackout. Many algorithms have been proposed in order to search transmission section quickly.

A quick search algorithm for transmission section based on graph theory is proposed in literature [7]. The essence relationship between search for transmission section and identification of network topology .Firstly, the original network should be simplified. Secondly, the concept of "region" is defined and the system state diagram is established. Finally, parallel transmission section corresponding to an overloaded transmission line can be determined through the calculation of adjacency matrix and path matrix. As partition and simplification of the initial network are only associated with the network topology structure of power system, so the first step can be taken in advance and the second step can be taken periodic. Only the third step should be taken when a transmission line is overloaded. This algorithm is convenient for online real-time control because the calculation is fast. However topological parameters are not taken into considerations and some key transmission lines can't be searched because they are in the "region" which corresponding solution can't be found in literature [7].

A quick search algorithm for transmission section based on minimal basic circuit set is proposed in literature [8]. A conclusion is obtained by qualitative analysis. When an overloaded line is removed, the power of the removed line flows into lines whose direction of power flow is opposite to the overloaded one in the loop calculated by the ring sum of the minimal basic circuit sets. The minimal basic circuit set can be generated online based on graph theory according to network topology structure, physical parameters of component and the power flower distribution. When a transmission line is overloaded, through comparing the directions of lines in the loop that contain the overloaded line, expanding the search scope by the ring sum and calculating the active current distribution coefficient, then the transmission section can be determined. This algorithm has the feature of less amount of calculation which can save real-time analysis time.

A risk value is proposed in literature [9], after the transmission section is determined through graph theory, this risk value can reflect the mutual influence and cumulative effect between accidents. High risk line set can be filtered through comparing the risk value. The scope of lines needed to be analyzed, monitored and controlled in power system can be narrowed. However, this algorithm may have a lot of calculation.

A new search algorithm for transmission section based on K shortest paths is proposed in literature [10]. By analyzing the features of flow transferring caused by overload removal, the conception of flow transferring factor (FTF) is introduced, a new definition of transmission section based on FTF is given. By simplifying the real-time power network into a topology, based on dynamic programming theory, the K shortest paths between the two nodes of the overload line in a subgraph with overload line as its center can be fast found. Finally transmission section suffered greatly from power flow transferring can be determined. The security analysis of the whole system is reduced to the analysis of a transmission section; the workload of further analysis is greatly reduced, so it's very beneficial to avoid cascading failures.

A new search algorithm for transmission section based on deviation path is proposed in literature [11]. After analyzing the features of power flow transferring after switching off overloaded branches, it was pointed out that the branches greatly affected by power flow transferring were concentrated on the range electrically adjacent to the switched off branches. A new algorithm to rapid search lines related to the overloaded branches was given to turn real-time power network into topological graph. The k shortest paths based on deviation path was adopted to rapidly search out the lines greatly affected by power flow transferring, thus the situation of miss-searching of partial branches due to too narrow searching scope under the single path-based search could be avoided and the integrality of transmission section could be ensured. When overload occurred, the affection of overload on the security of the whole power network could be rapidly assessed by means of analyzing the influences of overload trips on lines related to the transmission section. Thus the calculation amount could be greatly reduced and it was favorable to prevent the occurrence of cascading failures.

A fast search algorithm of power flow transfers based on the concept of active power increase factor is proposed in literature [12]. When line outage failure occurs in power system, transmission section can be fast identified through searching transmission lines in upper and lower classes connected to both ends of the outage line by using graph theory and computing their active power increase factors. The transmission section is composed of transmission lines whose active power is increased evidently. According to the proposed concept of active power increase factor, it can be ensured that those lines, whose active power is increased and the directions of power flow is reversed，will not be missed．This algorithm does not need to search for the whole network topology and does not contain any large mass matrix calculation, which ensures online real-time calculation.

In conclusion, there are many algorithms proposed to search transmission section. However, quickness and integrity are two main factors needed to be taken into consideration because they can ensure the requirements of instantaneity and safety. Quickness and integrity are two contradictory factors, how to coordinate them is the key problem of designing algorithm.

4 Safety Protection Measure

The safety protection measure is defined as the measure that needed to be taken in order to avoid cascading failure after an accident occurred.

A new wide area backup protection strategy based on WAMS (Wide Area Measurement System) to identify the flow transfer is proposed in literature [13]. A new concept of flow transfer relativity factor (FTRF) is proposed to estimate the flow distribution after flow transfer occurred, and the strict definition and calculation method are presented. A new concept of PMC (Protection and Monitoring Center) is proposed to identify the power flow transfer by cooperating with the distributed protection device, and the protection device is blocked in order to avoid cascading failures. WAMS is firstly introduced in the protection strategy proposed to identify power flow transfer.

A security correction strategy combined with opposite equal quantity adjustment is proposed to find out the controlling node in literature [14]. When a transmission line is overload, generator output adjustment should be taken to alleviate overload of transmission lines and tie line groups rather than load shedding. Units can be grouped by sensitivity calculation. Each generator with positive sensitivity can be matched with a generator with negative sensitivity. Each group of generators is adjusted with opposite equal quantity in order to obtain a strategy with a balanced active power and minimum adjustment value.

In literature [15], the principal component analysis (PCA) combined importance weight is used to evaluate control nodes' comprehensive capability to alleviate overload on the transmission section, and determine the operation sequence of control nodes. AC power flow calculation is not needed in this strategy because the choice of controlling node and its quantity can ensure that normal branch won't overload and the power flow of overload branch won't arise.

A virtual branch control method is proposed to alleviate the overloaded lines in literature [16]. By adding a virtual branch to the overloaded branch, the original current of the overloaded branch can be reduced to the target level of branch current. The admittance of the virtual branch can be obtained by target shunting coefficient, and then the virtual branch can be replaced by a parameterized virtual power source. The remove of the virtual branch can be turned into injection power increase problem on the two buses of the overloaded lines. Based on sensitivity of the apparent power of the branch with respect to bus injection power, the minimum cost control strategy for overloaded branch can be obtained.

A new power flow tracing algorithm combined with superposition theorem and the principle of proportional distribution is proposed in literature [17]. This algorithm can be applied in emergency control of overloaded lines. Using the proposed algorithm, occupation coefficients of each line by each generator and each load can be calculated. Then the generator output reduction is proportional to the amount of load shedding. Then the overloaded situation can be eliminated under the principle that the amount of shedding load should be as few as possible.

In conclusion, there are many safety protection measures which can avoid cascading failures. Protection device block, generator output adjustment and load shedding are the main measures that need to be taken into consideration. However, how to optimize the sequence of the measures and determine the amount of adjustment or shedding is still worthy studying.

5 Summary and outlook

Different definitions of transmission section are introduced in section 2, and the main factors of transmission section are also summarized.

The typical search algorithms are presented in section 3. The basic problem of quick search for transmission section belongs to the problem of network identification. Therefore, the application of graph theory can effectively solve the problem. The grid topology, power grid real-time power flow (magnitude and direction) can be easily obtained due to the introduction of WAMS technology. Combining with the parameters of each route, the real-time status of the system can be reflected effectively and quickly.

The main safety protection measures are introduced in section 4. The main safety protection measures of transmission section are protection device block, generator output adjustment and load shedding. The sequence and amount of the measures are also determined according to the reference factor (risk coefficient, line outage distribution factor, etc.).

In conclusion, those literatures listed above are some typical analysis methods of quick search for transmission section. However, it is worthy thinking that whether there is a new theory or a better algorithm that can be used to analyze quick search for transmission section.

References

[1] Talukdar S N, Apt J, Ilic M, et al. Cascading failures: survival versus prevention[J]. The Electricity Journal, 2003, 16(9): 25-31.

[2] Liscouski B, Elliot W. Final report on the august 14，2003 blackout in the united states and Canada: Causes and recommendations[J]. A report to US Department of Energy, 2004, 40: 4.

[3] LI Zaihua, BAI Xiaomin, DING Jian, et al. Analysis of the Western Europe Blackout[J]. 2007, 31(1): 1-3.

[4] ZHANG Baohui, YAO Feng, ZHOU Decai, et, al. Study on Security Protection of Transmission section and its key technologies[J]. Proceedings of the CSEE, 2006, 26(21): 1-7.

[5] KOU Yan, Sutdy on Transmission Section of Power System[D]. Shangdong University(2008)

[6] ZHAO Feng, SUN Hongbin, ZHANG Boming, et, al. Electrical Zone Division Based Automatic Discovery of Flowgates[J]. Automation of Electric Power Systems, 2011, 35(5): 42-46.

[7] ZHOU Decai, ZHANG Baohui, YAO Feng, et, al. Fast Search for Transmission Section Based on Graph Theory[J]. Proceedings of the CSEE, 2006, 26(12): 32-38.

[8] CHENG Linyan, ZHANG Baohui, HAO Zhiguo, et, al. Fast Search of Power Flow Transfers Based on Minimal Basic Circuit Set[J]. Automation of Electric Power Systems, 2010, 34(18): 21-16.

[9] NI Hongkun, XU Yuqin, WANG Lijing. Research on Risk Assessment of Power System Parallel Transmission Section[J]. Power System Protection and Control, 2012, 40(9): 93-96.

[10] WANG Zengping, LI Gang, REN Jianwen. A New Search Algorithm for Transmission Section Based on K Shortest Paths[J]. Transactions of China Electrotechnical Society, 2012, 27(4): 193-201.

[11] REN Jianwen, LI Gang, WANG Zengping, et, al. New Algorithm for Searching Tie Lines Based on Deviation Path[J]. Power System Technology, 2012, 36(4): 121-127.

[12] LI Sha, REN Jianwen. Fast Search of Power Flow Transfers Based on Active Power Increase Factor[J]. Power System Technology, 2012, 36(12): 176-181.

[13] XU Huiming, BI Tianshu, HUANG Shaofeng, et, al. WAMS Based Flow Transfer Identification Algorithm[J]. Automation of Electric Power Systems, 2006, 30(14): 14-19.

[14] DENG Youman, LI Hui, ZHANG Boming, et, al. Adjustment of Equal and Opposite Quantities in Pairs for Strategy of Active Power Security Correction of Power systems[J]. Automation of Electric Power Systems, 1999, 23(18): 5-8.

[15] YAO Feng, ZHANG Baohui, ZHOU Decai, et, al. Active Power Security Protection of Transmission Section and Its Fast Algorithm[J]. Proceedings of the CSEE, 2006, 26(13): 31-36.

[16] MIAO Fengxian, BAI Xuefeng, GUO Zhizhong. A Virtual Branch Method for Branch Power Flow Off-limit Analysis[J]. Automation of Electric Power Systems, 2009 (14): 32-36.

[17] REN Jianwen, LI Sha, YAN Minmin, et, al. Emergency Control Strategy for Line Overload Based on Power Flow Tracing Algorithm[J]. Power System Technology, 2013, 37(2): 392-397.

Advanced Materials Research Vols. 986-987 (2014) pp 512-515

doi:10.4028/www.scientific.net/AMR.986-987.512

Risk analysis of grid operational performance influencing factors based on ISM- model

Haitao YUE[a], Xiaobao YU[b], Puyu HE, Haibo LIU, Wenyan LIU, Zhongfu TAN

North China Electric Power University, School of Economics and Management, Beijing, 102206, China

[a]email: 597099718@qq.com, [b]email: yuxiaobao1222@163.com

Keywords: ISM model, risk analysis, grid operational performance

Abstract. The ISM model is applied to the influencing factors risk analysis of grid operational performance. The research constructed multilevel hierarchical structure diagram by the association between various factors and reflected the hierarchical relationship of the index intuitively. Select a large driving force factors as the core influencing factors and develop a risk prediction radar diagram to provide a theoretical basis for grid operational performance improving. A provincial power grid company provides the data for empirical analysis to explore the applicability of the model.

Introduction

Grid Company is a natural monopoly industry. The business scope and the resources allocation of enterprises are controlled strictly by state. The company's business practices should be subordinated to the government's goals and plans; Grid Company is a company with strong scale effect but the sales price is under control, and the economic efficiency and profit margins are largely determined by the state. It belongs to the public utility with public characteristics and undertaken by the public service functions. Its behavioral targets are diverse.

In the process of deepening power system, implementing "separation of generation and transmission, using bidding price", building separation of government functions from enterprise management, fair competition, open and ordered, healthy development of the electricity market system, new situation and tasks bring the new opportunities to the grid enterprises as well as presenting the new challenges and giving a new mission. In this situation, the study of relationship of grid operational performance affecting factors has great significance to improve grid operational efficiency. This research identifies the relationship between grid operational influencing factors by means of Interpretative structure model and indicated the relationship between them by multilevel hierarchical structure visually, thus providing theoretical suggestions for improving the performance of the grid operation.

The establishment of ISM model

Determination of Grid operational performance influencing factors

This model select 32 operational performance related factors by the principle of optimal in accordance with national grid operational analysis model namely: “a strong three excellent” objective programming. Among them, there are eight indicators in the core resources system, such as: total assets (S1), total liabilities (S2), Line length per capita (S3), Total staff (S4), net value of fixed assets (S5), Total income (S6), The proportion of skilled talents(S7), Net income Per capita (S8); Customers market system contains eight indicators: Tariff recovery rate(S9), market share(S10), The average difference between purchase and sale price(S11), Electricity sales(S12), Customer satisfaction rate(S13),Power supply population(S14), CO_2 emission reduction through generating rights trading(S15), Province purchase (sale) electricity contract execution equalization rate(S16); Internal operation system contains eight indicators: Power supply reliability rate(S17), Comprehensive line loss rate(S18), Voltage qualification rate(S19), Loading rate(S20), Inventory

Turnover (S21), Power system failure outage rate (S22), Inventory idle rate (S23), New energy and power generation capacity (S24); Asset-liability ratio(S25), per capita profit (S26), Economic Value Added (S27), Industrial added value (S28), Total owners' equity (S29), ROE (S30), transmission and distribution costs (S31) , network maintenance operation costs (S32).

In order to analyze the impact of these factors and determine the relationship of their mutual influence (influence directionality), ISM model always uses V, A, X, O four symbols to indicate the direction of mutual influences between factors, shown in Table 1. Table 1 is called factor relation binary matrix .V is that the row factor has effects on the column factor; A is that the column factor has effects on row factor; X is that the row and column factors have mutually influence; O is that the two factors have no effects on each other.

Table 1 Relationship chart of the core resource influencing factors

	S1	S2	S3	S4	S5	S6	S7	S8
S1		A	O	A	A	O	A	O
S2			O	O	O	A	A	O
S3				A	A	O	O	O
S4					A	A	O	O
S5						O	O	O
S6							A	O
S7								O
S8								

Table 2 Relationship chart of customer market influencing factors

	S9	S10	S11	S12	S13	S14	S15	S16
S9		A	A	A	A	A	O	A
S10			A	A	A	A	O	A
S11				A	A	A	O	A
S12					A	A	O	A
S13						A	O	A
S14							O	A
S15								O
S16								

Table 3 Relationship chart of internal operational influencing factors

	S17	S18	S19	S20	S21	S22	S23	S24
S17		A	A	O	A	A	O	A
S18			A	O	O	A	O	A
S19				O	O	A	O	A
S20					O	O	O	O
S21						O	A	O
S22							O	A
S23								O
S24								

Table 4 Relationship chart of operational results influencing factors

	S25	S26	S27	S28	S29	S30	S31	S32
S25		O	O	A	O	O	O	O
S26			O	O	A	O	A	O
S27				A	O	O	O	A
S28					O	O	O	A
S29						O	A	O
S30							O	O
S31								O
S32								

The establishment of the adjacency matrix

In order to establish the ISM model systematically, we should set up an adjacency matrix A which expressing the relationship between each factors firstly. The elements of adjacency matrix A can be calculated by converting the corresponding elements in Table 2. The conversion rule is: If a_{ij} is corresponding to V in Table 2, so $a_{ij}=1$,and $a_{ji}=0$;If a_{ij} is corresponding to A in Table 2, so $a_{ij}=0$, and $a_{ji}=1$; If a_{ij} is corresponding to X in Table 2, $a_{ij}=a_{ji}=1$; If a_{ij} is corresponding to O in Table 2, so $a_{ij}=a_{ji}=0$ .Therefore, we can obtain the adjacency matrix A.

$$A_1=\begin{bmatrix}0&1&0&1&1&0&1&0\\0&0&0&0&0&1&1&0\\0&0&0&1&1&0&0&0\\0&0&0&0&1&1&0&0\\0&0&0&0&0&0&0&0\\0&0&0&0&0&0&1&0\\0&0&0&0&0&0&0&0\\0&0&0&0&0&0&0&0\end{bmatrix}\quad A_2=\begin{bmatrix}0&1&1&1&1&1&0&1\\0&0&1&1&1&1&0&1\\0&0&0&1&1&1&0&1\\0&0&0&0&1&1&0&1\\0&0&0&0&0&1&0&1\\0&0&0&0&0&0&0&1\\0&0&0&0&0&0&0&0\\0&0&0&0&0&0&0&0\end{bmatrix}\quad A_3=\begin{bmatrix}0&1&1&0&1&1&0&1\\0&0&1&0&0&1&0&1\\0&0&0&0&0&1&0&1\\0&0&0&0&0&0&0&0\\0&0&0&0&0&0&1&0\\0&0&0&0&0&0&0&1\\0&0&0&0&0&0&0&0\\0&0&0&0&0&0&0&0\end{bmatrix}\quad A_4=\begin{bmatrix}0&0&0&1&0&0&0&0\\0&0&0&0&1&0&1&0\\0&0&0&1&0&0&0&1\\0&0&0&0&0&0&0&1\\0&0&0&0&0&0&1&0\\0&0&0&0&0&0&0&0\\0&0&0&0&0&0&0&0\\0&0&0&0&0&0&0&0\end{bmatrix}$$

Among them, A_1 is for the adjacency matrix of core resource influencing factors relationship, A_2 is for the adjacency matrix of customer market influencing factors relationship, A_3 is for the adjacency matrix of internal operational influencing factors relationship, A_4 is for the adjacency matrix of operational results influencing factors relationship.

The establishment of reachable matrix

Reachable matrix means that using matrix form to describe that after a certain length of path, the level reached between each node in the directed connection diagram. It is calculated as: the Boolean algebra rules. Therefore, each influencing factors' reachable matrix are as below tables:

Table 5 The reachable matrix of core resource influencing factors

	S1	S2	S3	S4	S5	S6	S7	S8	Driving force
S1	1	1	0	1	1	1	1	0	6
S2	0	1	0	0	0	1	1	0	3
S3	0	0	1	1	1	1	1	0	5
S4	0	0	0	1	1	1	1	0	4
S5	0	0	0	0	1	0	0	0	1
S6	0	0	0	0	0	1	1	0	2
S7	0	0	0	0	0	0	1	0	1
S8	0	0	0	0	0	0	0	1	1
dependency	1	2	1	3	4	5	6	1	

Table 6 The reachable matrix of customer market influencing factors

	S9	S10	S11	S12	S13	S14	S15	S16	Driving force
S9	1	1	1	1	1	1	0	1	7
S10	0	1	1	1	1	1	0	1	6
S11	0	0	1	1	1	1	0	1	5
S12	0	0	0	1	1	1	0	1	4
S13	0	0	0	0	1	1	0	1	3
S14	0	0	0	0	0	1	0	1	2
S15	0	0	0	0	0	0	1	0	1
S16	0	0	0	0	0	0	0	1	1
dependency	1	2	3	4	5	6	1	7	

Table 7 The reachable matrix of internal operation influencing factors

	S17	S18	S19	S20	S21	S22	S23	S24	Driving force
S17	1	1	1	1	1	1	0	1	7
S18	0	1	1	1	1	1	0	1	6
S19	0	0	1	1	1	1	0	1	5
S20	0	0	0	1	1	1	0	1	4
S21	0	0	0	0	1	1	0	1	3
S22	0	0	0	0	0	1	0	1	2
S23	0	0	0	0	0	0	1	0	1
S24	0	0	0	0	0	0	0	1	1
dependency	1	2	3	4	5	6	1	7	

Table 8 The reachable matrix of the operational results influencing factors

	S25	S26	S27	S28	S29	S30	S31	S32	Driving force
S25	1	0	0	1	0	0	0	1	3
S26	0	1	0	0	1	0	1	0	3
S27	0	0	1	1	0	0	0	1	3
S28	0	0	0	1	0	0	0	1	2
S29	0	0	0	0	1	0	1	0	2
S30	0	0	0	0	0	1	0	0	1
S31	0	0	0	0	0	0	1	0	1
S32	0	0	0	0	0	0	0	1	1
dependency	1	1	1	3	2	1	3	4	

Reachable matrix reordering

According to the study, the greater the driving force the more the important is. So, this research selected the largest twelve driving force as key factors. And the influencing factors should be reordered according to the extent of driving force to get all the factors Interpretive Structural Modeling. According to the reordering reachable matrix, the factors with same driving force can be considered as the same hierarchical structure factor; then, use arrow to connect the related factors box. We can get the Interpretive Structural Modeling chart shown in Figure 1.

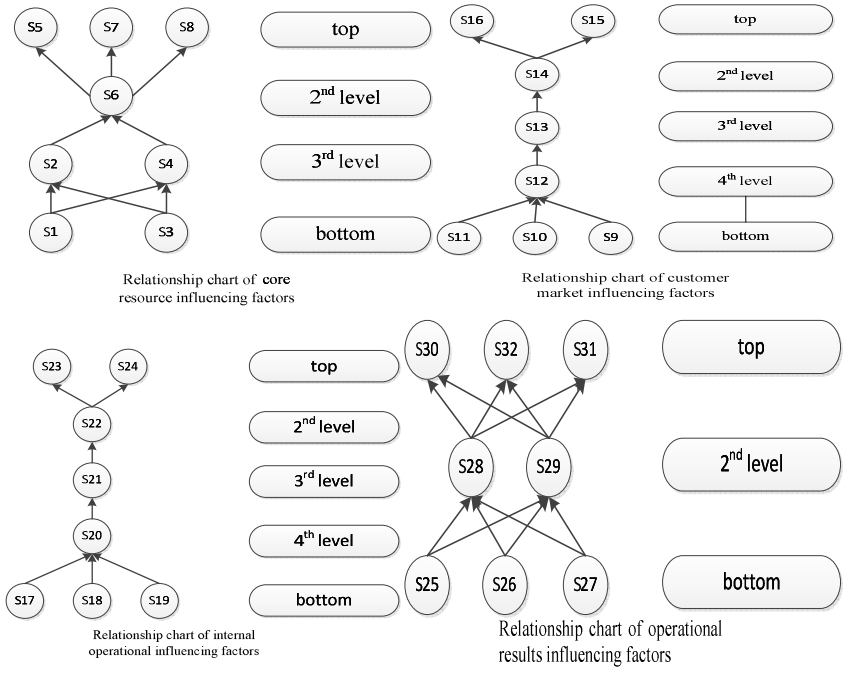

Fig1 All factors Interpretive Structural Modeling chart

Influencing factors classification

We can confirm the biggest driving force factor and the factor at the bottom by Interpretive Structural Modeling chart. The specific selection factor is as follows:

Table 9 Key factors categorized in all kinds of index system

Core resource	Customer market	Internal operation	Operational results
Total assets	Tariff recovery rate	Power supply reliability rate	Asset-liability ratio
Total liabilities	Market share	Comprehensive line loss rate	Per capita profit
Line length per capita	The average difference between purchase and sale price	Voltage qualification rate	Economic Value Added

ISM model analysis

The ISM model established above, the driving force and dependency distribution diagram visually show that the relationship between influencing factors of grid operational performance and their own attributes. The model will contribute to the grid administrator to find out the factors and deal with them.

Through the Interpretive Structural Modeling, we can see that the implementation of the twelve key factors is the largest factor to control the grid operational performance development. Therefore, the project manager should be fully aware of the importance of the grid operational performance development control and focus on the control of strong driving force factor in specific project management. So the grid enterprises can get the excellent results in operational performance.

Conclusions and Suggestions

With the social economic development and social environment changes, the uncertain factors which having effect on the development of power grid enterprises are increasing. In order to reduce the probability of risk occurrence, we need to identify sources of risk of grid operational performance and take detailed analysis. This research confirms 32 main influencing factors which impacting on the grid operational performance through statistical survey. Establish a clear hierarchical structure system and risk transfer chain of grid operational performance risk by ISM model. On this basis, we built a risk analysis model of grid operational performance based on ISM model. This method can effectively improve the prediction level of the grid operational performance risk factors and provide a basis for decisions.

The initial establishment model in this research based on ISM grid operational performance risk analysis model, considering the uncertain risk factors affecting the grid operational performance, should be discussed deeply on the transfer characteristics of risk transfer chain of grid operational performance and the effects in the future.

References

[1] Wu Yunna, Bian Qing. Wind turbine based on ISM model analysis of factors affecting cost control of construction project [J]. Journal of Wuhan University of technology (communications science and Engineering Edition). (2012): 257-261

[2] Liu Min. Power grid Corporation "a strong three-excellent" techno-economic study on the evaluation index system of [D]. Changsha University. 2007.04

[3] Han Jinshan, Tan Zhongfu. General interpretative structural model of power system [J]. Power system automation. (2008): 42-49

[4] Li Ziquan, Guo Xiuying, Li Jingyu. ISM analysis on the factors affecting the cost [J]. Modern economic information. 2012 (2): 290-291

[5] He Yongxiu, Tao Weijun, Yang Weihong, Dai Aiying, Cai Qi, Furong LI. urban power load forecasting based on interpretative structural modeling [J]. Power system automation. (2009): 37-42

[6] Shu Xiaohui, Chen Yifei, Gui Wenlin, Liu Jianping. Application of radar in the listed company finance early warning [J]. Statistics and decision making. 2005.03:34-37

Advanced Materials Research Vols. 986-987 (2014) pp 516-519

doi:10.4028/www.scientific.net/AMR.986-987.516

Safeguard Mechanism Research for Effective Implementation of Energy Tax Policy Reform

Wang Mingyou Song Yang [a]Ji Liuhe

Shenyang University, Shenyang 110044

[a]yang_wenlin@163.com

Keywords: Energy tax, Local government, Tax game analysis

Abstract: Energy tax policy has an irreplaceable role in promoting conventional energy conservation, sustainable use and promotion of new energy sources. But China's current energy taxes still has many problems and needs an energy tax reforms. The effective implementation of the energy tax policy reform must have relevant supporting mechanisms to ensure implementation of the policy. Thus we need analyze the behavioral characteristics and trade-offs involved in policy-related aspects to achieve the establishment of appropriate safeguards.

Introduction

In general, there is long-term equilibrium relationship between energy and economic growth. Sustainable economic growth needs sustainable energy output for support. However, the limited quantity and environmental problems caused by coal, oil, natural gas and other fossil fuels makes the country's governments re-examine their energy strategy. There are two guides in countries energy strategy: the first one is saving energy and committing to the development of energy-saving technologies and products. The second is to develop and utilize new energy as alternatives to conventional energy sources and make energy consumption structure to go to energy consumption structure which makes efficient, clean, renewable, low-carbon or non-carbon nuclear, solar and wind energy. As an important tool for national macro-control, the tax policy has an irreplaceable role in promotion of conventional energy conservation, sustainable use and introduction of new energy sources. More and more theories and practices have proved that the energy tax benefit the conservation and use of energy. At present, China has yet to levy a special energy tax. There are many problems in current energy taxes so we need reform. The effective implementation of the energy tax policy reform must have relevant supporting mechanisms. Thus we need analyze the behavioral characteristics and trade-offs involved in policy-related aspects to achieve the establishment of appropriate safeguards.

Status of the tax allocation structure

After the tax reform, China's tax revenue allocation structure is composed of three parts: central tax, local taxes and shared taxes. Among them, the central taxes include: customs duties, excise duty and VAT levied by the customs, excise duty, central corporate income tax; local banks, foreign banks and non-bank financial corporate income tax; Sales tax, income, profits, and city maintenance and construction tax, vehicle purchase tax paid by the railway sector, the banks head office of insurance company etc. Local tax is a kind of tax managed and used by local government.

These include: sales tax (excluding the sales tax paid by railway sector, the banks head office and insurance companies), local corporate income tax (excluding the above-mentioned local and foreign banks and non-bank financial corporate income tax), personal income tax, urban land use tax, fixed asset investment direction adjustment tax, urban maintenance and construction tax (excluding the parts paid by railway sector, the banks head office and insurance companies), property tax, vehicle tax, stamp duty, slaughter fees, agricultural tax, agricultural tax levied on the income of agricultural specialty (referred to special agricultural product tax), farmland occupation tax, deed tax, land value-added tax. There are three shared taxes: VAT, resources tax and securities transaction tax. Among them, the central share of 75% VAT, the local share of 25%. Resources taxes are divided by

varieties of different resources. Part of the resources taxes are local income. Offshore oil resources are the central income tax. Central and local share 50 percent of securities transaction tax separately. But in fact, share tax also include business tax, corporate income tax and urban maintenance tax(because these three taxes are local fixed income, but local and foreign banks and non-bank financial enterprises income tax, railway departments, bank headquarters, the insurance Corporation and other centralized payment of sales tax, income tax, urban maintenance and construction tax are collected to the central government). In our country, the current value added tax is a shared tax, the local gets 25%.

Taking VAT revenue in 1994, before tax reform, as a base, central will return the parts exceed 30%, so the local get 47.5% directly and indirectly. 1994 tax reform established the basic pattern of the existing central and local fiscal decentralization. Hereafter, the local is constantly adjusting. In 1997,the stamp duty on securities transactions increased from sharing ratio that central and local each get 50% to center share 80%,local 20%. center get 97% local 3% since 2002; income tax change from according to the enterprise subordinate relations such as division of the central and the local income tax to according to the proportional sharing between the central government and local government. After 2003, the share percentage is the central gets 60%, local 40%; export tax rebate from the original central bear all to the central bears 75%,local 25% since 2004. In addition, the intergovernmental transfer payment system also continue getting improved.

Analysis of local governments behavioral characteristics of Chinese-style fiscal decentralization.

Public choice theory holds that people's political behavior and economic behavior is the same, both are dominated by selfish motivation. Everyone participates politics for their own interests, not the good and beauty. It is because that we conceive the person as seeking to maximize their own interests that we need design incentive and restraint systems of human behavior in order to enable people to meet public interest objectives in accordance with the direction of behavior. As a government, it is a complex entity with multiple attributes. Although the government has essentially public nature and it is representing the public interest, in the actual process of operation, the government's behavior is heavily influenced by the will and preferences of the ruler. The ruler is the "economic man" who uses the government as an organization form to pursue and achieve their effectiveness, strive to minimize the cost and get the maximum benefits. In economic aspect, the rulers take maximizing revenue as their goal, trying to improve the efficiency of resource allocation, accelerate economic growth and thereby maximizing revenue. "Economic man" paradigm provides us with unified basis for analyzing the local governments. From the "economic man" perspective to exam local governments, local government has its own characteristics. Essentially they are rational "economic man", they need to maximize their own interests. Their actions do not necessarily represent the public interests in accordance with the needs, but under certain constraints, by rational cost - calculated benefits, decide their own actions. After taking into account the characteristics of the local government itself, The designed tax system which takes local governments as a part of the game has more real operability.

Western theory of fiscal decentralization, generally base on the rational allocation of revenue and expenditure authority and responsibility, thus contributing to all levels of government to provide public goods and services more effectively and achieve social welfare maximization. Especially for local governments, most of theory state that local governments has advantages on information and incentives to provide public goods, thus has a higher efficiency. Different from western fiscal decentralization, China's fiscal decentralization plays a role on incentive local government economic behavior. That decentralization of the central government to local governments property rights means independent interests status of local governments was confirmed by the central government. Local government can pursue their own interests through the central government-approved way. Meanwhile, the local governments as rational economic men have clear expectations--maximize their own interests. The better local economic development, the higher financial revenue, the more money the local governments share. Local governments began to have

"surplus profits", so the interest consciousness of local governments are awakened. Local governments began to seek their own interests. After Decentralization, local government will be more and more like business. Seeking to maximize their own interests becomes its main objective. For local government, reasonable decentralization can make local government clear their rights and responsibilities and improve the efficiency of the use of financial resources. Thus, local governments will compete with each other so that the whole community will achieve welfare maximization.

Game analysis between taxpayers and tax authorities

Design and implementation of specific tax subsidy policies will affect the interests of the tax authorities and consumer behavior choices. Next, we will analyze benefits of tax authorities and taxpayers after imposing energy tax. Tax authorities are subjects who implementing taxes and subsidies provider. consumers are both taxpayers and subsidy beneficiaries. Assuming P is the price of refined oil program, the current price of oil products is P1 .When the size of P in the range of [P-N，P+N] (N is a changing constant, varies with the amount) we can assume consumers do not pay taxes;if P1> P+N and P1; P> P1, we can assume the consumption is low. At this time, the tax department needs to subsidize: when consumers pay taxes, assuming that the tax department after adjusting for the tax effect (P - P 1) (T - t) - C, taxpayer's utility is [(PN)-P] (Tt), namely -N(Tt), reflecting the loss of the tax deduction of subsidies; when tax department subsidies and taxpayers do not pay taxes,the tax department utility is 0-C,which reflects as net loss of subsidies. The taxpayer's utility is 0, so the tax authorities do not need to make tax adjustments.

When tax authorities do not subsidize and taxpayers pay taxes: P 1 will be less than (P - N), the tax department utility is （P1-P）（T-t） which reflects in the net income tax. The taxpayers's utility is [（ PN）-P1]（Tt) which reflects tax net loss; when tax authorities do not subsidize and taxpayers do not pay taxes. Tax department utility is 0, the tax payer's utility is also 0.

Strategy portfolio's payoff matrix of tax authorities and taxpayers is as follows:

		Tax department	
Taxpayer		investigated	Not investigated
	Pay taxes	（P-P1）(T-t)-C，[（P-N)-P] (T-t)	（P1-P)(T-t)，[(P-N)-P1] (T-t)
	Do not pay taxes	-C,0	0,0

First, given a, the expected benefits when tax authorities choose subsidies (θ = 1) and choose not to subsidize (θ=0) the expected benefits :

$$\pi(1,a) = [(P - P_1)(T - t) - C]a + (-C)(1 - a) = (P - P_1)(T - t)a - C \quad (1)$$

$$\pi(0,a) = [(P_1 - P)(T - t)]a + 0 \cdot (1 - a) = (P_1 - P)(T - t)a \quad (2)$$

In the above formula, π represents the expected benefits, a and 1-a is the probability that the taxpayers pay taxes and do not pay taxes, used as weights, and 0≤a≤1. Set equal the expected return of two options, π(1, a) =π(0, a), Optimal probability of tax and non-tax game equilibrium when the taxpayer is taxable $a^* = \frac{C}{2}(P_1 - P)(T - t)a$

When a> a *, the optimal choice of the tax department is to subsidize;
When a <a *, the optimal choice of the tax department is not to subsidize;
When a = a *, the tax department randomly selected subsidies or no subsidies.

Second, given θ, the the expected benefits when taxpayers choose the to pay the tax (a = 1) and choose not to pay taxes (a = 0), respectively,are as follows:

$$\pi(\theta,1) = [(P-N)-P](T-t)\theta + [P-N)-P_1)](T-t)(1-\theta)$$
$$= -N(T-t)\theta + (P-N-P_1)(T-t)(1-\theta)$$
$$= -(P-P_1)(T-t)\theta + (P-N-P_1)(T-t) \quad (3)$$
$$\pi(\theta,0) = 0\cdot(1-a) + 0\cdot a = 0 \quad (4)$$

In the above formula, π represents expected income, θ and 1-θ is subsidized and non-subsidized probability of the tax department, representing weights here, and $0 \le \theta \le 1$. Set equal the expected benefits of the two options, namely π (θ, 1) = π (θ, 0). Optimal probability of tax and non-tax game equilibrium when the tax payer's taxable :

When θ<θ *, the optimal choice for taxpayers is to pay taxes;

When θ>θ *, the optimal choice of the taxpayer is not to pay the tax;

When θ =θ *, the taxpayer may be randomly selected pay the tax or not.

Summary

Summarizes the characteristics of the entire model, we can see that (1) the greater the price change constant N, the smaller tax department subsidies probability θ*. Differences in tax rates affect the motivation of government subsidies decisions, whether subsidize some group or not and the subsidies amount; (2) level of subsidy plays an important role on whether the taxpayer will pay the tax; (3) the price difference (P-P1) or (P1-P) determines the taxpayer's choice. When price differences is large, the probability that the taxpayer will pay taxes is low.The size of the rate difference determine the price difference, thereby setting rate differences has a great influence on consumer consumption amount choice.

When evaluating the effectiveness of the proposed energy tax reform, we must consider the relevant supporting mechanisms to ensure the effectiveness of policy implementation. By analyzing the behavioral characteristics of Chinese-style local government under fiscal decentralization, we propose that there should be a reasonable division of property rights between the central and local government. Forming a benign interaction in the energy tax issues between central government and local government to ensure the motives of energy tax reform. Through building the game model of the tax authorities and the taxpayer (the consumers) game analysis, we know the design of tax rate will affect the revenue of tax authorities, consumption behavior of taxpayers and authorities'subsidies to taxpayers to ensure that the energy tax reform was carried out in the interests of all parties on the balanced basis, so that the reform is running effectively.

References

[1] Deng Zhigao. China's energy structure and economic growth. Shanxi Energy and Conservation,1997(1), p.14-28

[2] Fan Gang. China marketization index--the relative progress of the regional markets. Beijing: Economic Science Press,2004, p.40-65

[3] Wu Qiaosheng. Process of industrialization in China's energy consumption changes. China Industrial Economy,2005(4), p. 30-37

[4] Yu Jiang. Resource constraints, structural change and economic growth. Beijing:People's Publishing House,2008, p. 123-156

[5] Guo Kesha. China:Reform Economic Growth and Structural Change. Shanghai:Shanghai People's Publishing House,1996, p. 122-124

[6] Han Wenke.Trend of China's energy consumption structure and the Countermeasures. Beijing: China Planning Press, 2007, p. 13-28

[7] Lin Bo. China's energy needs Econometric Analysis. Statistical Research,2001(10), p. 34-39

Advanced Materials Research Vols. 986-987 (2014) pp 520-523

doi:10.4028/www.scientific.net/AMR.986-987.520

Short-term Load Forecasting Based on GA-Elman Model

Wenxia YOU[1, a], Junxiao CHANG[1, b], Ziheng ZHOU[1, c], Ji LU[1]

[1]College of Electrical Engineering & New Energy, China Three Gorges University, Yichang, 443002, China

[a]email: You.Wenxia@gmail.com, [b]email:changjx163@163.com, [c]email:henryzhou1st@gmail.com

Keywords: Load Forecasting; Neural Network; Genetic Algorithm; GA-Elman; Error

Abstract. Elman Neural Network is a typical neural-network which shares the characteristics of multiple-layer and dynamic recurrent, and it's more suitable than BP Neural Network when it's applied to forecast the short-term load with periodicity and similarity. To solve the problem that Elman Neural Network lacks learning efficiency, GA-Elman model is established by optimizing the weights and thresholds using Genetic Algorithm. An example is then given to prove the effectiveness of GA-Elman model, using the load data of a certain region. Relative error and MSE have been considered as criterions to analyze the results of load forecasting. By comparing the results calculated by BP, Elman and GA-Elman model, the effectiveness of GA-Elman model is verified, which will improve the accuracy of short-term load forecasting.

Introduction

Electric power can't be stored largely, and its supply and demand should be always in a balance. So load forecasting becomes the fundamental job in power system planning, designing as well as safe, stable operation. To arrange generation plan and solve economic dispatch problems more reasonably, load forecasting (including short-term forecasting) algorithms should be improved.

A great number of theories and methods have been provided, such as Time Series Theory, Fuzzy Theory, and BP Neural Network. Reference [1] forecasts the load by Time Series Theory. Reference [2] and [3] present the utilization of Fuzzy Theory and BP Neural Network respectively.

Elman Neural Network, a typical neural-network which shares the features of multiple-layer and dynamic recurrent, carries out the basic structure of BP Neural Network. By storing the internal states, Elman model gets a dynamic mapping feature, which gets the system ready to different changes [4]. Elman Neural Network, a feedback neural network, has a strong non-linear approach capability at arbitrary precision and the input of it has a time-delay. Traditional Elman model is suitable to predict short-term load with periodicity and similarity, however, slow learning speed, slow arithmetic speed and the local minimum value it often leads to really discourage the prediction accuracy. GA-Elman model which combines Genetic Algorithms and Elman Neural Network is established. GA is used to optimize and determine initial thresholds of the network and weights of each layer. Then the optimized thresholds and weights will be assigned to Elman model. In the end, an example is provided to verify the effectiveness of GA-Elman model.

GA-Elman Model

The decision of weights and thresholds of the network will have great influences on prediction accuracy and training time. With the back propagation of error during learning and training period, Elman model revises the weights and thresholds by Gradient Descent Algorithm. The learning speed of Gradient Descent Algorithm is slow, and it would easily lead to local minimum value.

While Genetic Algorithm shares the features of efficient and heuristic search, parallel computing, great global optimization ability, etc. As a consequence, GA-Elman model which combines GA and Elman Neural Network is established in this paper. Elman model optimized by Genetic Algorithm can help to improve the precision of calculation. Figure 1 shows how this model works.

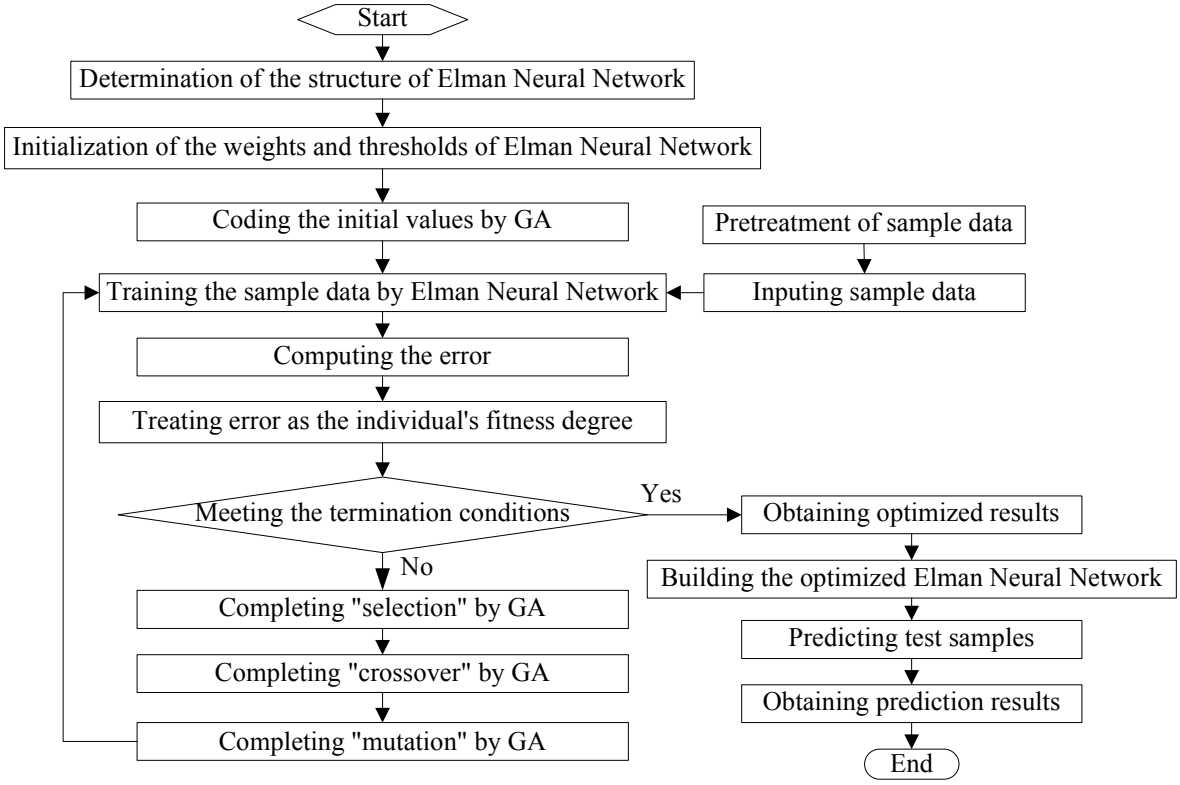

Fig.1. Algorithm flow of GA-Elman Model

In this algorithm, the structure and initial network parameters would be decided in the first place. Then selection operator, crossover operator and mutation operator in Genetic Algorithm are used to optimize the network parameters. In the end, the optimized parameters are made use of to establish a new Elman Neural Network and finish calculation with the test data. There are 5 basic elements to be noted in Genetic Algorithm procedures: parameter coding, determination of initial population, design of fitness degree function, setting of control parameters (preferably refer to population size and probability of genetic manipulation mainly), and design of heredity operation.

Application Principle of GA-Elman Model in Load Forecasting

The short-term load is constantly in a random variation, and it's hard to be described by a function, but the overall load data shows an obvious periodicity and similarity, including the regular pattern in the same hours during different days and the same day during different weeks.

GA-Elman model works well on short-term load forecasting when choosing the input and output variables, network structure as well as Genetic Algorithm parameters correctly. In GA-Elman model, each individual in the population contains all the weights and thresholds of the whole network. Treat the weights and thresholds of each individual as a chromosome, and assign real coding as coding method for chromosomes. The absolute sum of difference value between the output of network and the expected output of sample can be regarded as the fitness degree for individuals. Smaller fitness degree is better, and the probability of being selected for each individual is inversely proportional to the fitness degree of each individual. As a consequence, before selecting an individual, take the reciprocal of its fitness degree first, and randomly select two individuals to pair them up. Then let them share information in intersections which are randomly decided between the two paired individuals. In this way, a new generation is formed. Pick an individual from the new generation, and mutate the chromosome of it, for making the newly-produced individual better.

The terminal conditions for GA-Elman model is that the fitness should be less than a given value, or the difference of the optimal fitness degree between two successive generations should be less than a given value. Then pick out the individual that has the best fitness degree, and get the most optimized weights and thresholds for the Neural Network from it.

GA-Elman model can make fully use of the advantages of both Genetic Algorithm and Elman Neural Network, and it would be a better choice when dealing with short-term load forecasting.

Example Analysis

Pretreatment of Sample Data

The sample load data may be interfered by SCADA and the collected data may become abnormal. As a consequence, in order to improve the precision of load forecasting, effective cleaning needs to be done to the historical load [5]. In this procedure, saturation phenomenon needs to be avoided and the dimensions of different input samples need to be unified. As a result, equation (1) can be used to complete normalized operation for data in input layer, and equation (2) can be used to complete reverse normalized operation for data in output layer.

$$y = \frac{x - x_{\min}}{x_{\max} - x_{\min}} \tag{1}$$

$$x = x_{\min} + (x_{\max} - x_{\min}) * y \tag{2}$$

where $x_{\max}$ and $x_{\min}$ are the largest load value and the smallest load value.

The Selection of Input value

The data which has been used to verify the effectiveness of GA-Elman model is the 24-hour (on the hour) historical load data from Aug. 1st, 2012 to Mar. 31st, 2013 from a certain region. When choosing the input of a neural network, the issues below should be taken into consideration.

a) The load has its periodic peaks and valleys in each day. A great number of references indicate that the load value is relative to the type of date. Let's assume the 7 days in a week as 7 types, and number them as 1, 2, … , 7.
b) Since cumulative effect influences temperature, the load of a day is influenced by the current local weather, and the local weather of the day before that day. The maximum temperature and minimum temperature of these two days are all regarded as the input values for the weather part.
c) The load variation is more dependent on the days more recently, so the load of the day before prediction day is regarded as the input values for the load part.

The Analysis of The Result

Choose a day in the sample data as test day. Then the historical data of the whole 3 months before the test day are regarded as the training sample. After that, build the model according to the method mentioned in this paper. Relative error e and MSE have been considered as criterions to analyze the results of load forecasting [6], the equations (3) and (4) are below.

$$e = \frac{Y - \widetilde{Y}}{Y} \times 100\% \tag{3}$$

$$MSE = \frac{1}{n}\sum_{i=1}^{n}(Y_i - \widetilde{Y}_i)^2 \tag{4}$$

where Y and $\widetilde{Y}$ represent the actual value and predictive value, Y_i and $\widetilde{Y}_i$ are noted as the i-th actual load and predictive load, e and MSE are relative error and mean square error.

Table 1 shows the actual load on the hour of Mar. 20th, 2013. The prediction results as well as their relative errors by BP, Elman and GA-Elman model are also presented in Table 1.

If relative error which is no larger than 3% could be treated as up to standard, we can make the conclusion that less than 50% of the results by BP Neural Network are qualified. Meanwhile, about 63% of the results by Elman Neural Network and 80% of the results by GA-Elman model are eligible. Obtained by calculation, MSE of the results by GA-Elman model is the smallest of these models. Above all, GA-Elman model is better than BP and Elman Neural Network.

Table1. Forecasting results of different forecasting models

Time	Actual Load(MW)	BP Neural Network		Elman Neural Network		GA-Elman Model	
		Forecasting Value (MW)	Relative Error (%)	Forecasting Value (MW)	Relative Error (%)	Forecasting Value (MW)	Relative Error (%)
01:00	976.1319	965.1665	1.123	987.3359	-1.148	951.0330	2.571
02:00	941.8089	927.4463	1.525	918.6887	2.455	948.4902	-0.709
03:00	885.0347	873.6895	1.282	889.6618	-0.523	873.2793	1.328

04:00	898.7438	899.4363	-0.077	887.6666	1.233	899.3912	-0.072
05:00	885.7673	943.8837	-6.561	894.9927	-1.042	849.7409	4.067
06:00	924.3382	918.1597	0.668	902.7332	2.334	907.4790	1.824
07:00	1143.398	1071.481	6.290	1123.980	1.698	1081.978	5.372
08:00	1250.305	1155.278	7.600	1213.213	2.967	1246.856	0.276
09:00	1471.042	1358.034	7.682	1484.240	-0.897	1433.693	2.539
10:00	1535.537	1450.649	5.528	1561.001	-1.658	1587.609	-3.391
11:00	1614.982	1537.780	4.780	1570.526	2.753	1627.990	-0.806
12:00	1534.904	1429.885	6.842	1511.557	1.521	1507.864	1.762
13:00	1449.990	1356.823	6.425	1383.504	4.585	1427.148	1.575
14:00	1447.042	1384.906	4.294	1379.395	4.675	1473.734	-1.845
15:00	1421.754	1316.380	7.412	1489.807	-4.787	1373.309	3.407
16:00	1435.858	1352.031	5.838	1351.930	5.845	1444.702	-0.616
17:00	1517.537	1456.738	4.006	1467.450	3.301	1511.888	0.372
18:00	1526.169	1556.695	-2.002	1522.818	0.220	1560.609	-2.257
19:00	1658.592	1618.333	2.427	1598.748	3.608	1672.742	-0.853
20:00	1617.222	1545.443	4.438	1553.765	3.924	1585.262	1.976
21:00	1555.409	1483.774	4.606	1511.183	2.843	1490.028	4.204
22:00	1377.706	1394.649	-1.230	1343.666	2.471	1387.998	-0.747
23:00	1189.991	1207.266	-1.452	145.297	3.756	1226.375	-3.058
24:00	1097.182	1017.930	7.223	1026.710	6.423	1069.026	2.566

Conclusion

GA-Elman model which combines Genetic Algorithms and Elman Neural Network is established in this paper. The optimized thresholds and weights used in load forecasting really help. In the example showed in part 3, GA-Elman model avoid the local minimum value, and has better accuracy than BP and Elman Neural Network. The example verified the effectiveness of GA-Elman model in short-term load forecasting problems, which may be helpful in power market.

Acknowledgement

In this paper, the research was sponsored by the Science & Technology Research and Development Project of Yichang City (Project No. A09302-35).

References

[1] Li Ni, Jiang Yuechun, Huang Shan, Mao Lifan. Short-Term Load Forecasting Based on ARIMA Transfer Function Model [J]. Power System Technology, 2009, 33(8):93-97.

[2] S.H. Ling, Frank H.F. Leung, H.K. Lam, Peter K.S. Tam. Short-term electric load forecasting based on a neural fuzzy network [J]. IEEE TRANSACTIONS ON INDUSTRIAL ELECTRONICS, 2003, 50(6): 1305-1316.

[3] Li Wei, Sheng Deren, et al. The Application of Double BP Neural Network Combined Forecasting Model in Real-time Data Predicting [J]. Proceeding of the CSEE, 2007, 27(17): 94-97.

[4] Zhang Jianmei, Zhou Buxiang, Lin Nan, et al. Prediction of Mid-long Term Load Based on Gray Elman Neural Networks [J]. Proceeding of the CSU-EPSA, 2013, 25(4): 145-149.

[5] Zhang Xiaoxing, Cheng Qiyun, et al. Dynamic Intelligent Cleaning for Dirty Electric Load Data Based on Data Mining [J]. Automation of Electric Power Systems, 2005, 29(8): 60-64.

[6] Niu Dongxiao, Cao Shuhua, et al. Technology and Application of Power Load Forecasting (Second Edition) [M]. Beijing: China Electric Power Press, 2009.

Advanced Materials Research Vols. 986-987 (2014) pp 524-528

doi:10.4028/www.scientific.net/AMR.986-987.524

Short-Term Wind Power Dynamic Prediction Based on GA-BP Neural Network

KE Ting-jing[a], CHEN Min-you[b], LUO Huan[c]

State Key Laboratory of Power Transmission Equipment & System Security and New Technology, School of Electrical Engineering, Chongqing University, Chongqing 400044, China

[a]Ketingjing@126.com, [b]mchencqu@126.com, [c]yolanda_1989@163.com

Keywords: wind power; dynamic prediction; genetic algorithm; BP neural network

Abstract. This paper proposes a short-term wind power dynamic prediction model based on GA-BP neural network. Different from conventional prediction models, the proposed approach incorporates a prediction error adjusting strategy into neural network based prediction model to realize the function of model parameters self-adjusting, thus increase the prediction accuracy. Genetic algorithm is used to optimize the parameters of BP neural network. The wind power prediction results from different models with and without error adjusting strategy are compared. The comparative results show that the proposed dynamic prediction approach can provide more accurate wind power forecasting.

Introduction

Wind power as one of the most widely available renewable energy resources, has been recognized as the main promising form of clean energy. With the development of mature technology and low cost, wind power has been listed as priority development strategy of the national energy in many countries [1]. However, due to the inherent intermittence and volatility of wind power, it is imperative to accurately predict wind power hours even days ahead to enhance the flexibility of the operation and control of real-time power systems including power and load dispatch. Short-term wind power prediction has attracted a lot of attention in recent years [2-3]; quite a few short-term wind power prediction systems have been successfully developed.

At home and abroad [4], most wind power prediction is using time series method based on the historical data. With the time going by, the operating condition is changing. Without considering weak correlation between the training data and real-time measurement data, the existing training models have not adapted to the present stage forecast work.

This paper proposed a dynamic model for the short-term prediction of GA-BP neural network wind farm output power. Using genetic algorithm to optimize the BP neural network algorithm, the proposed method is able to realize the dynamic prediction of wind power by discriminant function and dynamic adjustment model.

Wind power prediction

Genetic algorithm to optimize the BP neural network

BP neural network , which is a kind of effective self-learning network, has the ability of self-organizing, self-learning and distributed storage and parallel processing of information, therefore BP neural network has been widely used. However, BP neural network uses the root-mean-square error and gradient descent algorithm to realize the correction of the network connection weight, it is inevitable to exist the following problems, such as falling into local minimum value, slow convergence speed, over-fitting and so on[5].

Genetic algorithm (GA) [6] is a kind of intelligent generation process simulation, through the selection, crossover and mutation of genetic process to retain good individual fitness value, eliminate the poor individual fitness value, according to the above conditions for repeated cycle until meeting the convergence condition. Genetic algorithm, which has the characteristics of parallelism, global

optimization, stability and good robustness, is widely used in function optimization, combinatorial optimization and production scheduling, etc.

In order to overcome the shortcoming of the low sensitivity of BP network and the local minimum, the weights and thresholds of BP neural network are optimized by genetic algorithm [6]. Compared with the original BP neural network algorithm, the BP neural network, which is improved by the genetic algorithm, has higher calculation accuracy.

Discriminant error function

Mean absolute error (MAE) [7] is the average of the absolute value of the deviation between all of the individual observations and arithmetical mean. MAE is defined as shown in the following type, the index is able to evaluate the average amplitude of the prediction error.

$$e_{MAE} = \frac{\sum \left| y_i - y_i^{'} \right|}{nP} \tag{1}$$

Where, y_i is the measured data sequence，y'_i is the predicted data sequence n is the number of prediction validation data, P is the rated power of wind farm.

There is no offset problem about the mean absolute error, which can reflect the actual situation of the prediction error. Using MAR as an error discriminant function, this paper dynamically adjusts the model training set.

Wind power dynamic prediction model

Wind power, which is difficult to be predicted, has the characteristics of strong randomness. The research results show that based on the historic data to establish the prediction model, the prediction error will gradually increase with the passage of time. due to the weak correlation between the current data and the training data in the period of modeling, the existing prediction models is not able to track the data, the existing methods is no longer suitable for the prediction work at the present stage. Therefore, a dynamic adjustment strategy, which has higher prediction precision, is proposed in this paper, according to the prediction error, the prediction error adaptively adjusts the model parameters, so the prediction error is improved due to the weak correlation between the training data and real-time measurement data. Dynamic prediction model is shown in figure 1

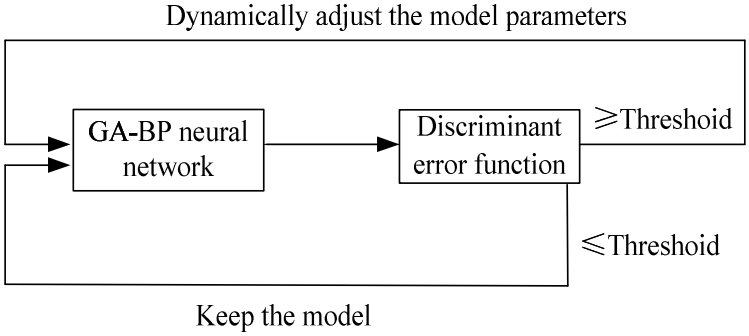

Fig 1. Dynamic prediction model

Wind speed and air temperature are the main influence factors of wind power [8]. The historic data of wind power can be provided by the energy management system of the micro-grid, and the meteorological data can be provided by the supervisory control and data acquisition (SCADA), such as wind speed, temperature, etc. The dynamic prediction model of wind power is shown figure 2.

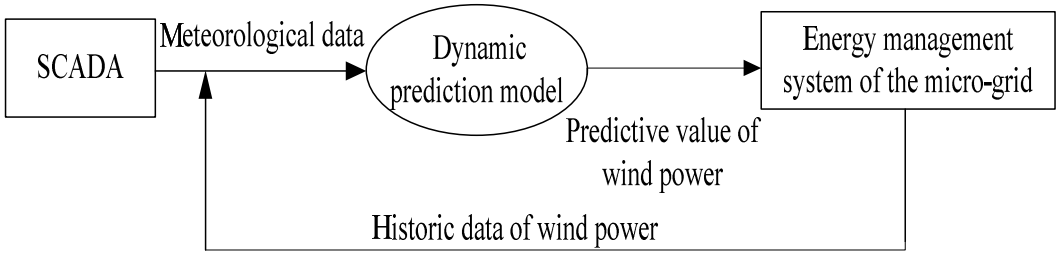

Fig 2. The dynamic prediction model of wind power

The specific steps of the dynamic prediction model of wind farms output power based on GA-BP neural network as follows:

(1) Use the traditional GA-BP neural network to train the model parameters;
(2) Input test sample to predict wind power by the prediction model;
(3) Judge whether the output of the prediction model to achieve the precision threshold by the error discriminant function;
(4) If the prediction error is less than the precision threshold, return to step (2), continue to predict the next data, on the contrary, if the prediction error is larger than the precision threshold, go to step (5);
(5) Using the suitable data as the training set, dynamically adjust the model parameters, repeat step (1) to train the model parameters.

Case study

Data from a month of a wind farm is used for analysis, modeling and prediction in this case, including the actual power and the meteorological data, such as wind speed and temperature, etc. The data sampling period for 10 minutes at a time, rated capacity of the wind turbine is 850kW. Using the 100 groups of data as the training samples and 200 groups of data as the test samples, dynamic model and static model are used to predict short-term output power of wind farm respectively. The root-mean-square error (RMSE) and the relative error (RE) are selected as the error discriminant function in this paper.

The threshold of the discriminat function

When the threshold of MAE is larger than the precision error, the prediction model cannot achieve effective dynamic adjustment and reach to the expected accuracy requirement. When the threshold of MAE is too small, the model will be unnecessary to adjust. In addition, the threshold of the discriminant function has a certain influence on the final prediction accuracy of wind power.

Using the genetic algorithm to optimize the BP neural network model, the prediction result is shown in figure 4. The result of figure 4 shows that most of the MAE of the prediction power by traditional static GA-BP model is less than 0.02, a few time point of the MAE value is too larger; the highest amount to 0.07, the average value is 0.0161 by calculating. On the basis of ensuring the prediction precision, aiming at the least number of the dynamic adjustment, the precision threshold is selected.

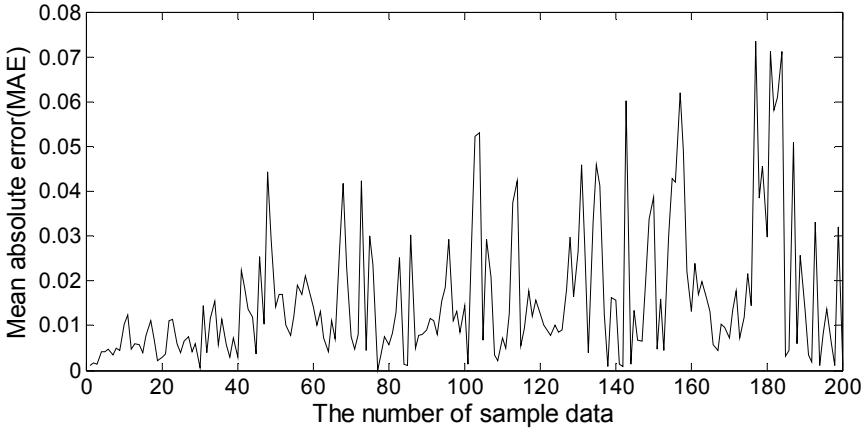

Fig3. The mean absolute error of the static GA-BP neural network output power

Tab.1 The MAE and dynamic adjustment number of the different precision threshold

Precision threshold	MAE%	The number of the dynamic adjustment	Precision threshold	MAE%	The number of the dynamic adjustment
0.01	0.9273	43	0.016	1.154	20
0.011	0.9743	37	0.017	1.179	17
0.012	1.012	33	0.018	1.194	15
0.013	1.074	28	0.019	1.218	13
0.014	1.104	25	0.020	1.249	12
0.015	1.148	22	0.021	1.302	11

The threshold, which gradually increases to 0.021 of the step length of 0.001, is set to 0.010 at first. In order to find the best accuracy threshold, the simulation of this paper uses the dynamic GA-BP neural network model to predict the 200 sets of data. According to table 1,it will be the ideal prediction effect when the Precision threshold is 0.016.

Result analysis

The prediction power of the dynamic and static GA-BP neural network model and the corresponding actual power are shown in figure 4. The mean absolute errors of the dynamic and static model are also shown in figure 4. It can be seen from the figure 5 that the prediction power of the dynamic model is closer to the actual power, compared to the static model, the dynamic model has better prediction effect.

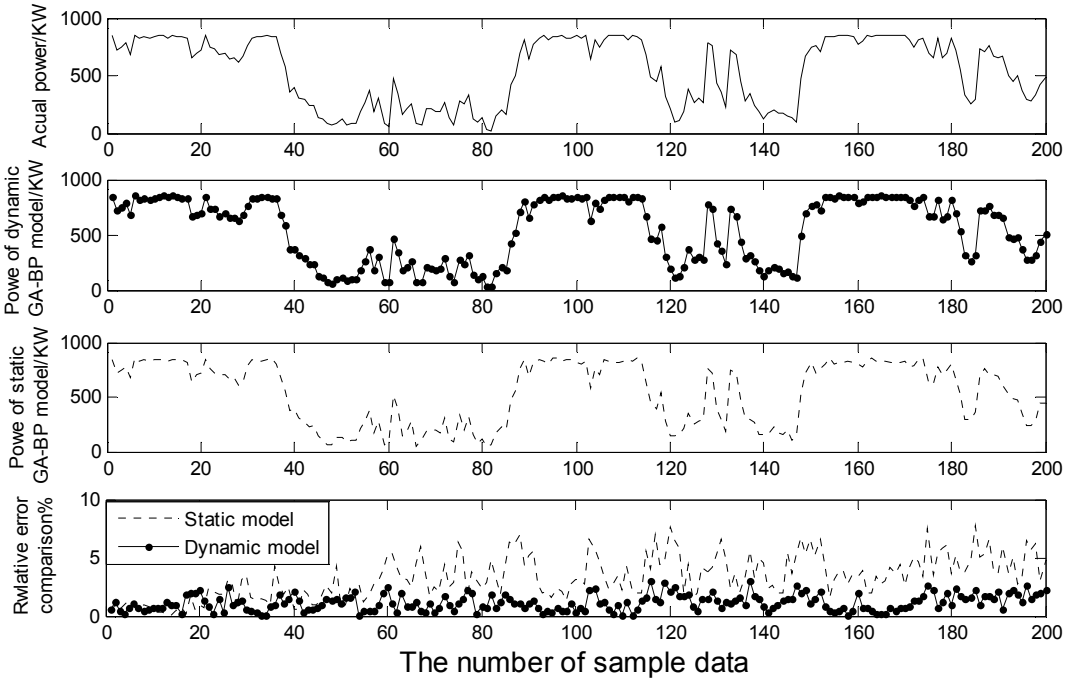

Fig.4 The wind power prediction result

The result of errors is shown in table 2. After using the dynamic model, the mean value and the maximum value of the prediction relative error decline 59.15% and 60.98% respectively. In addition, after introducing the dynamic adjustment strategy, the mean square error of the prediction power declines 57.49%.

Tab.2 The wind power prediction error

	Relative error		Mean square error kW
	Average	Maximum	
Dynamic model	0.0116	0.0302	11.50
Static model	0.0284	0.0774	27.05
Improved situation	59.15%	60.98%	57.49%

In the process of the dynamic model simulation, the dynamic adjustment situations and the prediction time of the each set of sample data need to be recorded. According to the results, the average prediction time of the each set of sample data is 0.0465s without dynamic adjustment, the average prediction time of the each set of sample data is 0.503s with dynamic adjustment. Every 91

minutes the prediction model need to be dynamically adjusted at a once, and the number of the dynamic adjustment is 22, it takes 19.34 in total.

Combined with figure 4 and table 2, it can be seen that the prediction precision of wind power has a considerate improvement after introducing the dynamic adjustment strategy. The dynamic model, which is used for a period of time after completing the each dynamic adjustment, has the characteristic of sustainability. Compared with the time of the prediction sample, the dynamic adjustment time is negligible. Therefore, the dynamic model has a certain practicability.

Conclusion

In view of the traditional static wind power prediction model has a series of problems about the weak correlation between the current data and the training data, a short-term dynamic prediction model of wind farm output power based on the GA-BP neural network is proposed in this paper, according to the mean absolute error, the dynamic prediction model adaptively adjusts model parameters. At first, the best precision threshold of the discriminant function is determined. Then, this paper analyzes the prediction performance before and after introducing the dynamic adjustment strategy. In general, the relative error and root-mean-square error of the dynamic prediction model are greatly improved; the dynamic prediction has higher prediction precision.

References

[1] L. Yongqian, H. Shuang, H. Yongshen. Review on short-term wind power prediction. Modern Electric Powe, Vol. 24 (2007), p. 6.

[2] Kariniotakis G． Next generation short-term forecasting of wind power-overview of the animas project． European Wind Energy Conference，Athens，2006．

[3] Giebel G, Landberg L, Kariniotakis G, et al. State-of-the-art on methods and software tools of short-term prediction of wind energy production． European Wind Energy Conference & Exhibition EWEC，Marid，Spain，2003．

[4] Z. Bo, C. Minyou, N. Wade, R. Li. A prediction model for wind farm power generation based on fuzzy modeling. Proceedings of International Conference on Energy and Environment, vol. 3 (2011), p. 195.

[5] T. Suli, L.Yufeng. Development and application of artificial neural network technology. Computer Development & Applications, Vol. 22 (2009), p. 59.

[6] W. Youxun, W. Zhouqing, W. Wen-ie, et al. Optimization of BP neural network for short-term climate prediction of rainfall amount in flood season based on genetic algorithm. Journal of Anhui Agricultural University, Vol. 40 (2013), p. 299.

[7] X. Man, Q. Ying, L. Zongxiang. Comprehensive evaluation method short-term wind power prediction error. Automation of Electric Power Systems, Vol. 35 (2011), p. 20．

[8] Y. Xiao. A prediction model for wind farms power generation based on fuzzy neural network. Journal of Chongqing University of Technology, Vol. 26 (2012), p. 86.

Advanced Materials Research Vols. 986-987 (2014) pp 529-532

doi:10.4028/www.scientific.net/AMR.986-987.529

Simulation on Multi-objective Wind Power Integration Using Genetic Algorithm with Adaptive Weight

Jie Ren[1,a] ,Jianshe Tian[1,b]

[1] North China Electric Power University, Baoding, Hebei, 071003, China

[a]1024762385@qq.com, [b]tianjs_2521@163.com

Keywords: wind power integration; multi-objective reactive power optimization; genetic algorithm; adaptive weight

Abstract: Aiming at problems which were brought by large-scale wind power integration, and the problem of multi-objective reactive power optimization considering the coexistence of discrete variables and continuous variables, a method of simulation based on genetic algorithm with adaptive weight is brought out. A solving thinking presents that capacitor switching and transformer tap adjusting and other discrete equipments are first, and the action sequence of generator and dynamic reactive power compensation (DRPC) devices and other continuous equipments setting follows, which is presented that optimization problem is decomposed into continuous variable optimization and discrete variable optimization, then they are solved respectively and cross iteration until convergence. In view of the optimization complexity and the coexistence of discrete variables and continuous variables, genetic algorithm with adaptive weight is presented for finding global optimal solution. Case studies show that the proposed thinking and algorithm for solving multi-objective reactive power optimization are reasonable.

Introduction

Wind power is developing at large pace in the need of energy and environmental sustainability nowadays. Large-scale wind power bases of China in plan are gradually carrying out the construction, the areas of wind power integration are most weak in grid, and the base load there is always small, as a result a large number of wind power needs to be transmitted out[1]. And in the process of transmission, the random changes in wind power output will have a great impact on the grid nearby. There might have the risks of Imbalances in the distribution of reactive power and unbalanced voltage fluctuations, and might cause problems such as voltage instability which are more serious[2]. The problem of multi-objective reactive power optimization of wind power integration on optimization of power loss, voltage quality and voltage stability after wind power integration needs to be solved. There are always DRPC devices and other continuous equipments in wind power base, and mechanical capacitors and transformer tap and other discrete devices in the grid nearby, and there are also thermal generator, hydro generator and other conventional generator, so the their terminal bus voltage can be controlled continuously. As a result, the study on multi-objective reactive power optimization of wind power integration with discrete variables and continuous variables has important theoretical and practical significance of engineering.

The difficulty of multi-objective reactive power optimization is the coexistence of discrete and continuous variables and the optimization complexity, the optimization is multi-objective. Much research has been done on this problem. Paper [3] uses the novel quadratic penalty function to handle with discrete variables for Newton optimal power flow. Paper [4] discusses in detail about the theory of penalty function dealing with discrete variables and how to bind to Primal-dual

interior point method directly and presents a new method to solve the problem of reactive power optimization in large-scale power systems with discrete variables. The disadvantage of methods above is that it's hard to achieve to the best optimal solution within an acceptable time. And Modern optimization techniques such as the simulated annealing algorithm, the tabu search method and the genetic algorithm(GA) and other strategies of randomly optimization[5], can guarantee to achieve to the best optimal solution within an acceptable time in principle, and are easy to deal with discrete variables. And among them the genetic algorithm(GA) on reactive power optimization is quite attractive. Though certain achievements have been made on the study of multi-objective reactive power optimization considering the coexistence of discrete variables and continuous variables, more research and investigation should be made to solve the problem better[6].

A method of multi-objective reactive power optimization of wind power integration based on genetic algorithm with adaptive weight is presented. Case studies show that the proposed model, thinking and algorithm are reasonable.

Simulation of Wind Power Integration

Most wind farms in Jiuquan wind power base are connected to the grid via two step-up transformers-0.69kV/35kV, 35kV/330kV, and are sent out vie the long passage: Dunhuang-Jiuquan-Hexi-Wusheng 750kV, such as 1st,2ed,3rd wind farm in Ganxi, 1st,2ed,3rd wind farm in Gandong, 1st,2ed,3rd wind farm in Qiaoxi, 1st,2ed,3rd wind farm in Qiaodong. Every wind farm has the installed capacity of about 200MW. The fluctuant wind power is sent out via the long transmission passage, which will have an impact on the reactive power balance of the passage and will bring the problem of increasing power loss, voltage fluctuation and voltage instability.

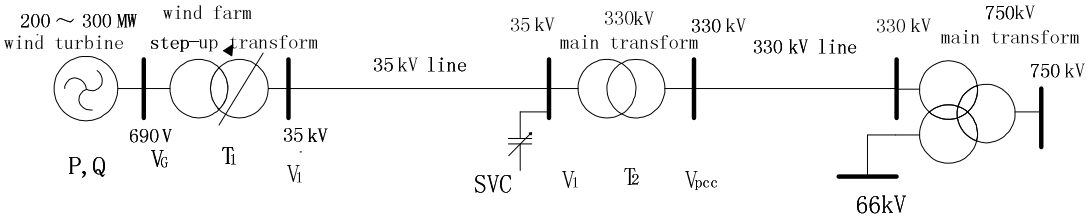

Fig.1 Typical wiring and location of dynamic reactive power compensation diagram

As Fig.1 says, DRPC devices are set at the side of 35kV of the step-up transformer of every wind farm, which are in control of the 330KV bus voltage of the high-voltage side of the step-up transformer. That means the control bus of the DRPC devices is the bus of 330kV[13]. The numbers of DRPC devices are twelve. The capacitive capacity of the DRPC devices of every wind farm in Jiuquan wind power base is 20% of the installed capacity of wind farm, and the inductance capacity is 30% of the capacitive capacity.

The algorithmic routine about this study is written by C++ , and Tab.1 gives out the power loss, voltage quality and load margin before optimization.

Tab.1 VALUE of objectives before optimization

objectives	calculated value(p.u.)
power loss(p-loss)	0.0634
voltage quality(v-quality)	0.01983
load margin(l-margin)	7.28874

Solve the continuous variable optimization and discrete variable optimization respectively, and put into cross iteration until convergence and get the optimal control solution. Tab.2 gives out the coding of continuous variables and discrete variables:

Tab.2 Coding of control variables

	adjustable step	lower (p.u.)	upper (p.u.)	coding length of unit	total length (unit length×device number)
generator	0.01	0.90	1.10	5	5×6=30
DRPC	0.01	0.90	1.10	5	5×12=60
transformer	0.02	0.90	1.10	4	4×4=16
capacitor	0.01	0.00	0.20	5	5×4=20
coding length of continuous variable	90				
coding length of discrete variable	36				

After operation for many times, the better set parameter of searching performance of genetic algorithm is get. The population scale is 60, the selectivity rate is 0.6, the retention rate is 0.05~0.1, the cross rate and mutation rate are given adaptively as mentioned earlier. Tab.3 gives out the information of time consuming and iteration number of genetic solution algorithm.

Tab.3 Statistic for time consuming and iteration number of genetic solution algorithm

time consuming of continuous variable optimization (1time)	12(m)
time consuming of discrete variable optimization (1 time)	10(m)
iteration number	5 times
total time consuming	22×5=110(m)

After 5 times' iteration optimization of discrete variable and continuous variable, and get the optimal solution after convergence, and Tab.4 gives out the optimal solution of control variables:

Tab.4-1 Optimal solution of control variables

generator	terminal bus voltage	substation	transformer tap ratio	substation	capacitor susceptance
Jiure#1	1.04	Dunhuang	1.00	Dunhuang	0.20
Jiure#2	1.04	Jiuquan	1.02	Jiuquan	0.12
Zhangye#1	1.02	Hexi	0.96	Hexi	0.08
Zhangye#2	1.02	Wusheng	0.94	Wusheng	0.06
Jinchang#1	1.08				
Jinchang#2	1.08				

Tab.4-2 Optimal solution of control variables

DRPC	controlled bus voltage	DRPC	controlled bus voltage
Ganxi#1	1.06	**Gandong#1**	1.08
Ganxi#2		**Gandong#2**	
Ganxi#3		**Gandong#3**	
DRPC	**controlled bus voltage**	**DRPC**	**controlled bus voltage**

Qiaoxi#1	1.05	**Qiaodong#1**	1.04
Qiaoxi#2		**Qiaodong#2**	
Qiaoxi#3		**Qiaodong#3**	

Every optimal objectives after optimization has greatly improved comparing with every optimal objectives before optimization, as Tab.5:

Tab.5 VALUE of objective after optimization

objectives	calculated value (p.u.)
power loss(p-loss)	0.0609
voltage quality(v-quality)	0.00645
load margin(l-margin)	7.45082

Conclusion

This paper aims at the problems which were brought by large-scale wind power integration, considering the coexistence of DRPC devices, the terminal bus voltage of conventional generators and other continuous equipments, and the coexistence of mechanical low-voltage compensation devices, adjustable transformer tap ratio and other discrete equipments, and creates the model of multi-objective reactive power optimization of power loss, voltage quality and voltage stability, gives out a thinking of solving model of multi-objective reactive power optimization based on genetic algorithm with adaptive weight. The study gives out the strategy of coordinative optimization of discrete variables and continuous variables, and the operation strategy of the coding of genetic algorithm, cross and variation, and adaptive determined method of multi-objective weight in the process of genetic algorithm, writes an algorithm program using C++, gives the simulation of multi-objective reactive power optimization based on the large-scale wind power base integration in Gansu Jiuquan of China and confirms the certainty of this model.

References

[1] MA Yan-hong, WANG Ning-bo, HE Shi-en, et al. The Current Situation and Prospect for Jiuquan 10GW Wind Power Base[J]. Power System and Clean Energy, 2009,25(11):76-79.

[2] CHI Yong-ning, LIU Yan-hua, WANG Wei-sheng,et al. Study on Impact of Wind Power Integration on Power System[J]. Power System Technology,2007,31(3).

[3] SHI Wei, WEI Hua, BAI Xiao-qing. Reactive Power Optimization in Large-scale Power Systems with Discrete Variables[J]. Electric Power Automation Equipment, 2007, 27(3):41-45.

[4] CHENG Ying, LIU Ming-bo. Reactive-power Optimization of Large-scale Power Systems with Discrete Control Variables[J]. Proceedings of the CSEE, 2002, 22(5):54-60.

[5] Hsiao Y T, Liu C C, Chiang H D, et al. A New Approach for Optimal VAR Sources Planning in Large Scale eElectric Power Systems[J]. IEEE Trans on Power Systems, 1993, 8(3):988-996.

[6] WANG Qin, FANG Ge-fei. Multi-objective Reactive Power Optimization Considering Voltage Stability[J]. Automation of Electric Power Systems, 2001, 23(3):31-34.

Advanced Materials Research Vols. 986-987 (2014) pp 533-536

doi:10.4028/www.scientific.net/AMR.986-987.533

Smart Grid and Its Application

Yuwei Li

School of Electrical & Electronic Engineering,
North China Electric Power University, Beijing 102206, China
E-mail: 1162062263@qq.com

Keywords: Smart grid; Distributed generation; Energy market; Distribution automation

Abstract: Smart grid could meet the electricity demand against the rapid development of economy and society. The idea to implement smart grid is fully in accordance with the energy developing strategy and it will exert far-reaching impact on the adjustment of energy structure, the sustainable development of society as well as low-carbon economy. Currently, smart grid has attracted wide attention around the world and major countries in the world have been carrying out related researches. This paper describes the background and basic concepts of the smart grid, and takes the United States, European Union and China for example to introduce the development characteristics and typical projects. Besides, this paper analyzes and compares the smart grid in U.S., E.U. and China and gives related suggestions on the key issues of the development of smart grid in China.

Introduction

Due to energy crisis and increasing concerns about environment, strict environmental supervision is needed around the world. The proportion of generation based on renewable energy is required to increase in energy policies. In North America, European Union, Japan, Australia and other countries, powerful research groups have been formed to carry out IntelliGrid / self-healing grid (SHG) / modern power/smart grid study[1-3]. These words have similar meaning and “Smart Grid” is more used at present.

Concept of the Smart Grid

Research objects of Smart grid include various aspects of electric power systems such as power generation, transmission, distribution and consumption. Studies on research and development of new power control technology, information technology and management technology, achieves the intelligent communication of information in all aspects of electricity from power generation to consumption, and optimizes systematically the whole process of power production, transmission, distribution and consumption. Represented by developed countries in American and European, the European Commission, U.S. Department of Energy and the various types of power enterprises and organizations have invested considerable manpower, materials and financial resources, trying to make substantial breakthroughs as soon as possible.

However, there is no uniform definition for smart grid. Given studies of smart grid at home and abroad, the definition of smart grid can be considered that: the smart grid is a fully automated power network, where each customer and node have been real-time monitored and it is ensured that information of every point between the power plant to electrical of the client is bidirectional flowing [4-5]. By widely used smart devices, broadband communications and automatic control system integration, it can ensure the real-time of market transactions and seamless connections and real-time interaction among members in the power grid online.

Fig. 1 is schematic diagram of the smart grid operation. It can be seen from the figure that through the trade center smart grid links organically the energy market, control system of transmission system and power distribution system, combined cooling heating and power system (CCHP), distributed generation,

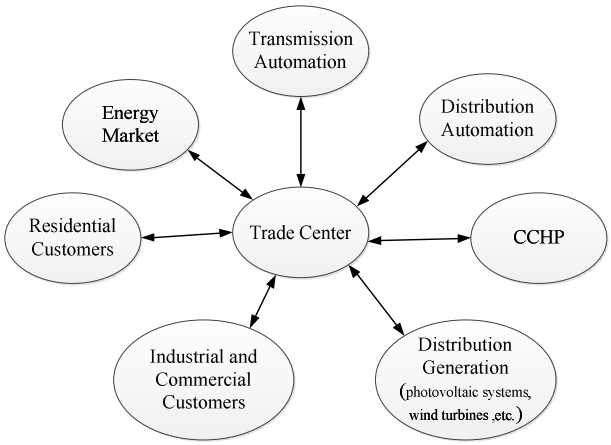

Fig. 1 Sketch map of smart grid operation

industrial and commercial customers, residential customers and so on. In terms of the power system, the smart grid is an intelligent network which is gotten from the combination of the power system and advanced communications and computer technology, power electronics technology, which can predict and self-heal before the system losses control during system failure and has higher flexibility. In terms of customers, power provided by smart grid has greater reliability and security and energy consumption is lower. The smart grid can provide better service with a low cost.

Smart Grid Implementation

(1)The Smart Grid In U.S.

1) Research situation of the smart grid in U.S.

EPRI of U.S. firstly proposed the concept of smart grid in 2001.And the U.S. government proposed planning of "Grid 2030" in February 2003, which officially launched the research and development of smart grid. Subsequently, UCA, SISCO, Lucent, EnerNex, Hypertek and other companies took part in an international scientific cooperation project aiming at studying on the architecture of power system in the future, which was created by the EPRI and run by GE. In the 18 months from early 2003 to 2004, the project firstly completed the IECSA (integrated energy and communication system architecture), followed by an extension study on the architecture of smart grid. Smart Grid of EPRI mainly emphasizes features such as safety, self-healing, coordination, integration, interaction, forecasting, and optimization, etc. In October 2008, a smart grid working group was established in the United States and the working group cooperated with NIST (National Institute of Standards and Technology) and EPRI for smart grid standards development and working on smart grid appliances which were adapted to new smart grid technologies. In 2009, the U.S. government formulated a series of development and implementation plans of smart grid and invested to accelerate the intelligent process of power grid.

2) Smart grid demonstration projects in U.S.

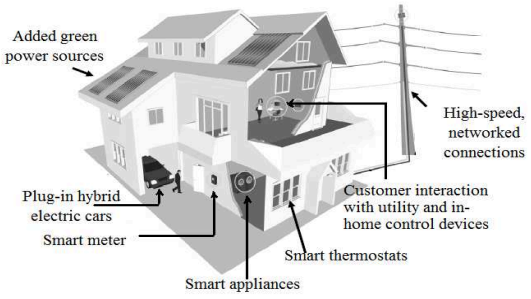

Fig. 2 The smart home

Main functions of smart home are: to achieve two-way communication and interaction with the supply network, priority use of the wind, solar and other clean energy sources intuitively based on real-time information, monitoring and interaction for home by telephone, mobile and remote

networks, management of energy consumption and reduction of energy costs, reasonable distribution of power in substation through the collection of every household's electricity consumption.

Currently, there are other Smart Grid projects in the United States, such as Pacific Northwest Smart Grid project, San Diego Smart Grid project, construction of California Smart Grid and miniature Smart Grid project in coastal city.

(2) The Smart Grid in China

According to characteristics that Chinese geographical distribution of energy and imbalance of load demand, in May 2009 the State Grid Corporation of China announced a plan to build a unified, strong and smart grid for the first time. In addition, the Ministry of Science and Technology deployed "Smart Grid Research and Development of Key Technologies (one-stage)" major projects in the field of advanced energy technologies of the "863" plan, focusing on key technologies to overcome and form a standard system, building demonstration projects and carrying out its application.

The first batch of State Grid Corporation smart grid pilot project is Shanghai World Expo smart grid comprehensive demonstration project. It is in accordance with the core content of smart grid and displays smart grid from there aspects, green energy, strong smart grid and rational use of electricity. Sino-Singapore Tianjin Eco-city comprehensive smart grid demonstration project is the second batch of State Grid Corporation smart grid pilot projects. Its purpose is to promote breakthroughs and application of key technologies of all aspects of strong smart grid in urban construction, to achieve the harmonious development of grid and the natural environment.

Besides, in 2009 China had built UHV 1000 kV Southeastern Shanxi - Nanyang - Jingmen demonstration project, ± 800 kV HVDC Xiangjiaba - Shanghai demonstration project, and planned to construct "three vertical three horizontal" ultra-high voltage grid during the "12th Five-year". In March 2011, State Grid Corporation claimed that China's strong smart grid would be into the all-round construction stage and would build 67 smart substations, seven-fold electric vehicle charging facilities, 11 smart grid demonstration projects and 88 smart grid standards. China will basically complete the smart grid in 2020.

Analysis and Comparison on Smart Grid in U.S., E.U. and China

There are different features in several aspects because of different comprehension of smart grid and different situation of power system in U.S., E.U., Japan and China.The focus of the development of smart grid in U.S. is to update the basic infrastructure of power grid and establish the intelligent distribution network based on informatization. Meanwhile, it emphasized developments in the basic services fields such as information technology, customer service, policies and regulations, labor support and fund guarantee. The construction of a "Unified National Smart Grid" proposed by United States is a combination of scattered smart grids in order to form a national network system aiming at building an intelligent, stable, efficient and reliable power grid.The focuses of European smart grid development are connecting renewable energy into the power grid, the construction of system based on distributed energy and integration and large-scale use of renewable energy, so that it will combine the wide area power transmission network with smart grid to become a wide area intelligent network.

China's smart grid features are: ultra-high voltage power grid as the backbone, the coordinated development of power at all levels, to achieve a strong physical power; solving planning, forecasting, monitoring, analysis, operation and control problems of distributed energy and renewable energy connected to grid; solving safe and stable operation problems of large grid, and improving abilities of making scientific decision and management, to achieve intelligent dispatch; building efficient, flexible and rational distribution grid architecture; building intelligent electricity service system, to carry out two-way interactive electricity services. Compared with other countries, the unique challenge of the development of smart grid in China is to protect the special large-scale, ultra-high voltage, large capacity transmission grid clean, safe, self-healing, economic, and interactive operation.

Thinking of Strengthening Smart Grid Construction with Chinese Characteristics

Compared to the level of research in developed countries, China still has many weaknesses in smart grid construction although China has had lots of achievements recent years. Several suggestions for China to carry out Smart grid are as follows:

1) To enhance government energy assurance capabilities and plan for smart grid resiliency. A clear and supported pricing mechanism for active and reactive power components exchange must be developed. Besides, raise power investment and construction efficiency on the premise of continuously supporting the national economic growth.

2) The concept of smart grid greatly expanded, and attention should be closely paid to domestic and foreign smart grid technology research and development trends. Key equipment is still lack, such as mass storage devices, smart energy meters, unified power flow controller, etc. So that it can't meet the technical demand of a unity strong smart grid. It needs to increased research efforts.

4) To strengthen the research and development of smart grid technical standards and communication standard architecture. Currently, there are many kinds of technical standards and communication standards, and their compatibility are poor and there are a lot of proprietary protocols, making the power system of information sharing difficult, unable to meet the smart home, the smart meters and other new requirements.

Conclusion

Smart grid will be the next generation power grid tend. It has been approved by a number of international energy policy-making departments and power companies. But because of different national conditions, starting points and cognition, the development and implementation of smart grid are distinctive among all the world countries. The paper describes the background and basic concepts of the smart grid, studies on technical application and characteristics of smart grid in world's major countries and areas and gives related suggestions on the key issues of the development of smart grid in China.

References

[1] VADARI M, "Demystifying intelligent networks," Public Utilities Fortnightly, Vol. 145, No. 11, p. 61-64, 2006.

[2] BROWN R E, "Impact of Smart Grid on distribution system design," Power and Energy Society General Meeting-Conversion and Delivery of Electrical Energy in the 21st Century, 2008 IEEE, p. 1-4, 2008.

[3] HUGHES J, "IntelliGrid Architecture Concepts and IEC61850," Transmission and Distribution Conference and Exhibition, 2005/2006 IEEE PES, p. 401-404, 2006.

[4] Zhou Xiaoxin, Chen Shuyong, Lu Zongxiang. "Review and Prospect for Power System Development and Related Technologies: a Concept of Three generation Power System," Vol. 33, No. 22, p. 1-11, 2013.

[5] YU Yixin and LUAN Wenpeng, "Smart Grid and Its Implementations. Proceedings of the CSEE," Vol. 29, No. 34, p. 1-8, 2009.

Advanced Materials Research Vols. 986-987 (2014) pp 537-541

doi:10.4028/www.scientific.net/AMR.986-987.537

Smart Grid in China

Shi Wei

China Petroleum Pipeline Engineering Corporation(CPPE)

Heping Road No.146, LangFang, Hebei province, China

cppeshiwei@cnpc.com.cn

Keywords: Smart Grid, China, Execution, Prospect

Abstract: The concept of Smart Grid is created this century, with the focus of whole world. With the social development, the requirement of power security is growing fast. China, as a great power towards to industrialized country, its requirement is more intense. This paper introduces the generation of the concept ‘smart grid’, as well as the inevitable trend of future development, plans of China for smart grid construction and some achievements, finally explains the advantages of China's smart grid development and prospects of the future.

Smart Grid comes from U.S.

"Smart Grid (IntelliGrid)" was first proposed by the U.S. Electric Power Research Institute (EPRI) in 2001. They proposed further research framework of smart grid in 2003. Subsequently, the U.S. Department of Energy released the "Grid2030" to promote construction and development of the smart grid. In 2009, U.S. government announced planning to invest $ 4 billion to promote smart grid construction. In the same year, U.S. government promulgated the ‘American Clean Energy and Security Act’ (ACES), emphasizing the importance of the smart grid in increasing the power transmission efficiency. In May 18, 2009, U.S. Secretary of Commerce Luo Jiahui (Gary Faye Locke) and Secretary of Energy Zhu Diwen (Steven Chu) announced the first batch of standards for smart grid construction, marking the U.S. smart grid construction officially started[1]. U.S. Institute of Electrical and Electronics Engineers (IEEE) and National Institute of Standards and Technology (NIST) also developed standards and principles for interactive smart grid (IEEE2030) in 2009. Then many countries formulate the development plan of smart grid according to their own reality.

Smart Grid is the Future

The electric power industry is basic industry related to people's livelihood and the important guarantee for economic and social development. Electrical power grid has been the basic and important part of industrialization, information technology and social development. At the same time, power grid constantly absorbs achievements of industrialization and information technology, so that many advanced technologies have been integrated in the power grid, which greatly enhance the power system functions.

(1) Smart grid technology is the inevitable trend for the technology development. Recently, Telecommunication, Computer, Automation and other technologies in the power grid has been extensively and organic integrated with traditional power technology, the integration greatly improves the intelligence level of the power grid. The application of Sensor & Information technology in power grid provides technical supports for system analysis and decision-making, and makes grid self-recovery to be possible. Mature development of scheduling technology, automation technology and flexible transmission technology provide basic guarantees for the development and utilization of renewable energy and distributed power source. Improvement of communication network and popularization of user information collection technology, promote two-way interaction between power grid and the user. With the further development and application of new technologies and highly integrated with physical grid, smart grid came into being.

(2) Developing smart grid is the inevitable choice of social & economic development. To achieve the development, transportation, and consumption of clean energy, the power grid must improve its flexibility and compatibility. To counter the increasing of natural disasters and external interference, the power grid must rely on smart grid to continuously improve its security and defense capability

and self-recovery capabilities. To reduce operating costs and promote energy conservation and pollution reduction, power grid must be more economic and effective, and intelligent in controlling equipments to minimize power consumption. The rapid development of distributed power generation, energy storage technologies, and electric vehicles has changed the traditional mode of power supply, and prompt the power flow, information flow and business flow integration, in order to meet increasingly diverse requirements of users.

The smart grid will be the core of future power industry. It is not only structural upgrade of the modern power grid, but also profound change for the global power industry.

Plan and Execution of China

Smart grid represents the new direction of power grid transformation. At present, many countries are actively planning to promote smart grid. State Grid Corporation of China for the first time public the "smart grid development plan" and preliminary construction schedule on May 21, 2009, which marks that the Chinese smart grid construction was officially put on the agenda. We are gradually building our smart grid:

The first stage is plan and experiment phase (2009 - 2010): Focus on smart grid development planning, drafting technical standards and management practices, researching and developing key technologies and equipments, carrying out all aspects of the experimental work.

Table -1 The first group 22 core standards for smart grid recommended by State Grid Corporation[2]

No.	Title	
1	DL755—2001 Guide on security and stability for power system	
2	Terminology and Methodology of Smart Grid	Reference IEC/PAS 62559 IntelliGrid Methodology for Developing Requirements for Energy Systems
3	Q/GDW 392—2009 Technical Rule for connecting wind farm into power grid	
4	Technical Rule for connecting wind farm into power grid	
5	DL/T 837—2012 Reliability evaluation code for transmission and distribution installation	
6	overhead transmission line monitoring device standards	Including Q/GDW242～Q/GDW245
7	Q/GDW383—2009 Technical guide for smart substation	
8	DL/T860 Communication networks and systems in substations	Equal IEC61850 Substation communication networks and systems
9	Q/GDW382—2009 Technical Guide for Distribution Automation	Equal IEC61968 Application integration at electric utilities--System

		interfaces for distribution management
10	DL/T1080 Application integration at electric utilities-System interfaces for distribution management	
11	Open Geodata Interoperability Specification	Equal Open Geodata Interoperability Specification，OpenGIS
12	Q/GDW480—2010 Technical rule for distributed resources connected to power grid	
13	Intelligent power meter standards	Including Q/GDW1354～Q/GDW1365
14	Electric vehicles standards	Including GB/T 18487(Equal IEC61851), Q/GDW233～Q/GDW 238, Q/GDW Z423, Q/GDW397～Q/GDW400
15	DL/T890 Energy management system application program interface(EMS-API)	Equal IEC61970 Energy management system application program interface (EMS-API)
16	GB/T18700.5 Telecontrol equipment and systems	Equal IEC60870−5
17	GB/T22239—2008 Information security technology—Baseline for classified protection of information system	
18	IEC62351 Power System Control and Associated Communications-Data and Communication Security	
19	IEC62357 Power System Control and Associated Communications Reference Architecture for Object Models, Services and Protocols	
20	GB/T 22080~22081—2008《Information technology—Security techniques》	Equal ISO/IEC27000 Information security management system fundamentals and

		vocabulary
21	GB/T 18336—2008 Information technology - Security techniques - Evaluation criteria for IT security	Equal ISO/IEC15408 Information technology – Security techniques -- Evaluation criteria for IT security
22	GB/T 20279—2006 Information security technology Security techniques requirements of separation components of network and terminal equipment	

The second phase is the comprehensive construction phase (2011 to 2015): Accelerate construction for UHV power grid and distribution network in urban and rural, Initially Forming the smart grid operation and interactive service system, key technologies and equipments achieve breakthrough and be widely used.

On June 26, 2010, the first ±800kV / 4750A UHVDC converter valve in the world developed by China EPRI successfully passed all type tests in State Grid Corp's power electronics laboratory[3]

On July 8, 2010, ±800kV UHVDC SiChuan~ShangHai Line as a main artery of West-East electricity transmission project successfully put into operation. SiChuan~ShangHai Line has the maximum voltage (±800kV), the maximum transmission capacity (6.4GW), the maximum distance (1907kM), the most advanced technology. It bears the task of sending out clean energy from Jinsha River hydropower base[4].

The third stage is the leading and ascension phase (2016 to 2020): Basically complete the smart grid, the grid resource allocation capability, safety, efficiency, and the interaction between power grid, power source, and the users could significantly increase.

These three phases are the overall arrangements for the implementation of smart grid construction and cannot be completely separated. Technology research, equipment development, testing, standard perfecting and popularizing work will be throughout.

Our Advantage and Prospect in China

Over the years, China's power industry vigorously strengthen power grid infrastructure, while paying close attention to the international power technology development, emphasis on research and innovation and integration of various new technologies, enhance independent innovation capability quickly, good condition for the construction of smart grid has been created.

1) In power grid construction, China continue to strengthen and improve the network structure, fully mastered the core technology of UHV power transmission, UHV AC pilot project and HVDC demonstration project are stable in operation, lay the solid foundation for grid development.

2) In large power grid operation control, China has the advantages of "unified management" system and rich operation experience, technology and equipment of scheduling are international advanced; dispatching automation systems and relay protection devices which independent researched are widely used.

3) In the construction of communication and information platform, many power communication nets have been finished; it forms the communication network structure in which optical fiber, microwave, carrier and other means coexists.

4) In the aspect of test detection means, China has set up large-scale wind power, solar power and electricity technology testing center according to the needs of development of smart grid.

5) In the development of smart grid pilot practice, each link has been fully carried out, the smart grid dispatching technical support system, intelligent substation, electric information

acquisition system, electric vehicle charging infrastructure, FTTH pilot projects progress smoothly.

6) In the field of electric vehicle charging and discharging, China carried out a large number of accesses, in charging and discharging facility monitoring and billing and so on, and has completed the electric vehicle charging operation site on a part of cities.

7) In the aspect of power grid development mechanism, business scope of Chinese power enterprise covers each link from the generation, transmission, distribution to substation; there are obvious advantages in unified planning, unified standards, and fast forward.

Smart grid has become the direction of future development; the core of smart grid is a comprehensive, dynamic integration of user side resources, including relevant information of load and electricity use. Therefore, the demand side management is one of the most important parts of smart grid. Although the demand side management framework of smart grid has good development opportunity, China must learn experiences of foreign countries in the concrete implementation process and combine with the actual situation, actively carry out innovation. While smart grid promote bidirectional interactive information to bring convenience for the development of demand side management, it also brings the risk of information security; for information acquisition security (sensor), communication and data security work, we should attach great importance, in order to prevent hackers and virus attacks; China shall actively prevent investment risk when paying attention to increase supports of the construction of smart grid, demand side management, and because it is a system engineering, conspicuous gains will be achieved piecemeal.

References

[1] JingMin Ni, GuangYu He: *Assessment on the American smart grid:* Automation of Electric Power Systems Vol.34 (2010.4.25), p. 9

[2] Information on http://www.sgcc.com.cn/ztzl/newzndw/.

[3] Information on http://www.epri.sgcc.com.cn/.

[4] Information on http://www.cpnn.com.cn/.

[5] LiSha Zhou: *Low-Carbon Performance Evaluation Model for Smart Grid Considering Environmental Effects 2013*

Advanced Materials Research Vols. 986-987 (2014) pp 542-545

doi:10.4028/www.scientific.net/AMR.986-987.542

Spatial Electric Load Forecasting Based on Least Squares Support Vector

Li Yanbin[1, a], Li Yun[2,b], Cao Le[1,c] and Li Weiguo[2,d]

[1] School of Economics and Management, North China Electric Power University,Changping District, Beijing102206, China

[2] School of Electrical and Electronic Engineering,North China Electric Power University,ChangpingDistrict,Beijing 102206,China

[a]gslyb2000@sohu.com, [b]leal_ly@hotmail.com, [c]517694144@qq.com, [d]lwglixi@tom.com

Keywords: spatial load forecasting,least square support vector machine,matlab simulation

Abstract. This paper proposes a new spatial load forecasting method for distribution network based on least squares support vector machine. The method adopt data, the characteristic of which is similar with forecast sample, to training in order to obtain the regression coefficients and bias, which we need to do the forecasting.Atthe same time,compare with artificial neural network model,The least squares support vector machine transforms quadratic programming problems into linear equations, thus avoiding the insensitive loss function, greatly reducing the computational complexity and further improving the accuracy of the prediction model. Finally, the effectiveness and practicality are verified by examples.

Introduction

1980s American H. L. Willis made on the basis of spatial power distribution network load forecasting (Spatial Load Forecasting, SLF) this concept [1-2] . Spatial load forecasting not only need to load forecasting , spatial information needed to predict the load . Domestic space in line with forecasts , there are four main methods : trend method , multivariate methods , land use simulation method [3-7] . As the trend of law are many and difficult to choose a template , multivariate methods of data overload and prone to large errors , these two methods have gradually been eliminated. Currently, most of the land is to use simulation to predict method, which is divided by the cell , the law of the land in order to analyze the development of predictive models for simulation, get a load of the total amount of space , the average amount allocated to give each cell load distribution , this method has higher accuracy.

Literature [8-9] proposed the use of fuzzy logic for spatial load forecasting , however, the choice of model for the membership functions with obvious subjectivity. Literature [10-11] , fuzzy logic and rough set theory, spatial load forecasting, but this method ignores the uncertainty in the data itself . [12] proposed a method based on ant colony algorithm to predict the load space , the method of slow convergence and easy to fall into local optimum . [13] is the spatial load forecasting based on cellular automata , although the method can describe the relevant factors affecting the development of spatial load from many angles , but the relevant rules and parameters still need improvement. The characteristics of the grid for distribution , we propose a method based on least squares support vector machine room load forecasting method to construct least squares support vector machine model , and then predict the target year , and in Taiwan , for example, to verify superiority.

Spatial load forecasting basic steps

Spatial load forecasting prediction by following these steps .

(1) Prepare data load , the total load prediction

Historical data extracted from the GIS and other loads . The total load cell is carried out by combined forecasting model to predict the total . Each of the prediction model according to the information useful to combine the organic , the load prediction accuracy is greatly improved.

(2)classification and classification load forecast

Through the different needs of users of the land use classification of the load is divided into industrial , residential , commercial, administrative and educational four categories. Load has certain synthetic load density.

(3) cell division

Spatial load forecasting is the most important cell division , in order to be able to predict a good position to increase the load on the distribution network planning to provide useful information that will be tested area is divided into a plurality of cells . The concept of the cell as the smallest geographic unit for spatial load forecasting . In order to simplify the steps of spatial load forecasting and improve forecast accuracy , a reasonable division of the cell . After analysis , the predicted three layers , the total layer , the acquisition layer and the data layer of the simulation , the model can effectively control the interval of data collection work , while ensuring the accuracy and resolution of land classification.

(4) land use simulation

Simulation is a lot of land for the extraction of spatial information. The first step is a multi-partition, a city that is divided into several layers , such as industrial level , school level , transport layer , residential layer. By dividing each of the smallest unit cell computing and industrial areas, schools , residential areas, commercial areas , such as the shortest distance . According to the data , analyze each cell salable area of land available , and can be used in the future to develop the land area . The introduction of GIS spatial load forecasting , can reduce high spatial information collection effort , which is valid for spatial load forecasting is extremely important .

(5) the use of least squares support vector machine load space

① Select the kernel function.Mercer Theorem is the kernel function interpreted as the product of tectonic kernel feature space technology can be found in many papers. Select a Gaussian radial basis (RBF) function as kernel function, as shown in Equation(1) as shown in this article.

$$K(X, x_i) = exp\{-\|x - x_i\|^2/2\sigma^2\} \quad (1)$$

② data preprocessing.In order to meet network requirements for input and output , according to the model before training

$$X_i = (X_i - X_{min})/(X_{max} - X_{min}) \quad (2)$$

The batch data after linear normalization processing transformed data values between 0-1.

③ set parameters , using the training sample data , build the model. With trainlssvm () to achieve the network training , the regression coefficients and bias, thereby obtaining predictive models. Predict the trained model, and predictions by the anti- normalization restored.

④ error checking to obtain the predicted results.

Cases considered

In order to verify the least squares support vector machine algorithm proposed text on the effectiveness of long-term power load forecasting , the choice of Taiwan from 1981 to 2000, a total of 20 years of electricity load data for validation. In forecasting process to 1981-1995 annual load data as two -dimensional input vector data , training samples after the establishment of appropriate mathematical model to predict back five years or even longer in electricity load . We put Taiwan geographically divided into four parts , namely, northern, central , eastern and southern .

Uses need to set the width δ^2 kernel function parameters to establish calibration model based on radial basis function (RBF) kernel function method of least squares support vector machine .

Caution should be taken to determine the model parameters.Least squares support vector machine σ^2 has a great influence on the performance of the algorithm.Regularization parameter σ^2 is proportional to the sample data punishment,the training error and generalization ability compared with the inverse algorithm ; regularization parameter values $\omega^t\omega$ right on the relative weight of the inverse algorithm generalization ability will worse.So,we passed the test method to obtain the optimal solution.

To measure the mean difference model to predict the effect of the expression

$$E_{A.D} = \left(\frac{\frac{\Sigma |y_{pre} - \hat{y_{pre}}|}{n_{pre}}}{y_{pre}} \right) * 100\% \quad (3)$$

Corrected sample y_{pre} dependent variable $\hat{y_{pre}}$ measured values , n_{pre} number of samples for the calibration data set.

According to a good tune model parameters , get the final predictions . Select $\gamma = 1 \sim 100$, $\sigma^2 = 0.01$, according matlab calculation to get the predicted load of the load them with the actual amount of contrast, to obtain comparative diagram in Figure 1.

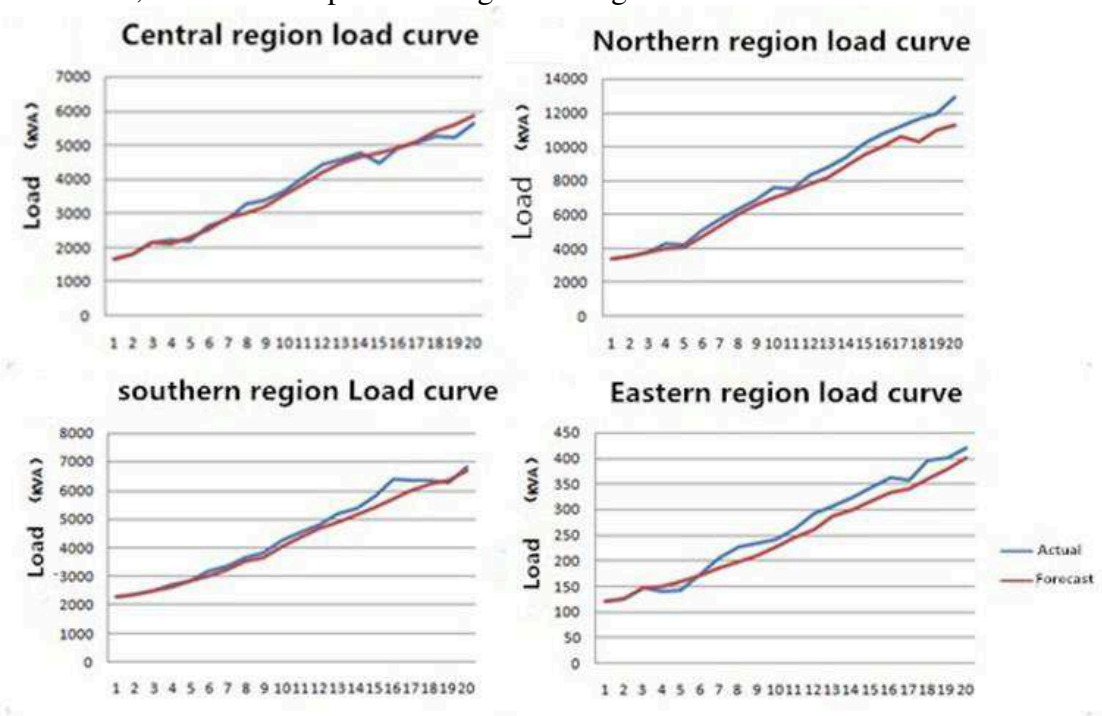

Fig.1 Taiwan's actual load compared with predicted annual load

In the above figures , the blue is the actual annual load curve , red is forecast load curve .

Charts available in the method of least squares support vector machine , the error can be controlled within a narrow range , with some accuracy.

The mean difference in various regions shown in Table 1:

Tab.1 The mean difference in Taiwan

Parameter	Northern	Central	Southern	East	Taiwan
The mean difference (%)	5.67	6.03	6.75	5.98	6.14

Conclusion

This paper focuses on the method of least squares support vector machines , and related models proposed derivation . Through practical examples and analysis , to overcome the past to predict the results of subjective poor results due to quantization , get vector machines have the advantage of least squares support , small sample needed , a small error range, and enhanced versatility , high accuracy . To strike spatial load forecasting provides a new thinking and new methods.

Acknowledge

This work is supported by the Natural Science Foundation of China (51277063), the Beijing Central Universities in Beijing to build the project funding.

References

[1] Willis H L.Spatial Electric Load Forecasting[M].New York:MarcelDekker,2002.
[2] Tianhua Wang, Mingtian Fan, Pingyang Wang,et al:Power System Technology. Vol.25 (1999),p. 42
[3] Manman Yang,Jinfeng Wang,Yanqing Li,etal:Electric Power Science and Engineering. Vol.27(2011),p.35
[4] Bai Xiao, Xiuyu Yang,Gang Mu,et al:Journal of Northeast Dianli University. Vol.33(2013),p39
[5] Guiling Yi,Yan Zhang:Electric Power Automation Equipment.Vol.24(2004),p.20
[6] Quan Zhou, Caixin Sun, Guoqing Chen,et al.GIS based distribution system spatial load forecasting and the optimal planning of substation location and capacity[C].Proceedings of the Power Con.Kunming(China):2002:885-889.
[7] Yixin Yu, Hongpeng Zhang, Chongjian Zhang,et al:Journal of Tianjin University.Vol.35(2002),p.135
[8] Moyuen Chow,Hahn Tram:IEEE Transactions on Power System.Vol.12(1997),p.1360
[9] Vladimiro Miranda,Claudio Monteiro:Power Engineering Society Winter Meeting.Vol.2(2000),p.1063
[10] Hao Xiong, Weiguo Li, Yanhao Huang:Power System Technology.Vol.31(2007),p.36
[11] Hungchih Wu,Channan Lu:IEEE Transactions on Power Apparatus and Systems.Vol.17(2002),p.516
[12] Quan Zhou,Jingyun Deng,Haijun Ren,et al:Power System Protection and Control. Vol.38(2010),p.99
[13] Lixi Yang,Jinfeng Wang,Genyong Chen,et al:Proceedings of the CSEE.Vol.27(2007),p. 15
[14] Weiwu Yan,Hongdong Zhu,Huihe Shao:Journal of System Simulation.Vol.15(2003),p. 1494
[15] Yujun Li,Xiaojun Tang,Junhua Liu:Spectroscopy and Spectral Analysis.Vol.30(2010),p. 774

Advanced Materials Research Vols. 986-987 (2014) pp 546-550

doi:10.4028/www.scientific.net/AMR.986-987.546

Study for Wind Farm Power Quality Based on Wind Turbine's Characteristic Parameters

Zhao Kuo[1,a], Zhang Yibin[1,b] and Wang Yaguang[1,c]

[1]Northeastern University, No. 3-11, Wenhua Road, Heping District, Shenyang, 110819, P.R.China

[a]zhaokuo13@126.com, [b]zhangyibinneu@163.com, [c]dbdxwyg@sina.com

Keywords: wind power generation; harmonic; voltage fluctuation and flicker; assessment method.

Abstract. The grid-connected wind farms bring power quality problems to power system due to the volatility and random of wind power generation. Analysis and calculation are carried out in this paper for the main influence factors of wind power harmonics, voltage fluctuations and flicker, and the assessment methods of the above power quality problems. For a certain wind farm, the corresponding power quality index limits can be calculated. Assessment conclusions can also be given by comparing the calculated power quality index values and the index limits.

Introduction

Recently, more and more attentions are paid to the power quality problems of grid-connected wind farms. The stochastic volatility of wind power and the use of power electronic devices may cause voltage fluctuation and flicker [1, 2], harmonic [3] and other power quality problems. According to the characteristics of wind power generation, reference [4] established a wind farm simulation platform in Matlab and analyzed the influence of voltage fluctuation and flicker. Reference [5] studied the voltage flicker issue at the point of common coupling (PCC) by reference to IEC 61400-21[6]. Reference [7] analyzed harmonic problems in wind farms, but the evaluation methods of voltage fluctuation and flicker is not given. In addition, there are some other references studied the assessment method of the grid-connected wind farm power quality [8, 9, 10].

Wind farm harmonic problem

Harmonic current analysis

Reference [11] fundamentally regulates harmonic current limits on different voltage levels. For specific wind farm, the limit value should be determined according to the actual short-circuit capacity of PCC, as it is shown in Eq. 1.

$$I_h = \frac{S_{SC}}{S_{k1}} I_{hp} \tag{1}$$

where S_{SC} is minimum short-circuit capacity of PCC, MVA, S_{k1} is benchmark short-circuit capacity, MVA, I_{hp} is the h harmonic current limit value, A, I_h is the h harmonic current limit value corresponds to S_{SC}, A.

For each wind farm connected to the same PCC, harmonic current allowable value can be calculated by Eq. 2.

$$I_{hi} = \left(S_i / S_t\right)^{\frac{1}{\alpha}} I_h \tag{2}$$

where I_{hi} is the i wind farm's h harmonic current limit value, A, S_i is the i wind farm's agreement electricity capacity, MVA, S_t is power devices capacity of PCC, MVA, α is phase superposition coefficient.

The total wind farm harmonics injected into PCC can be superposition calculate by Eq. 3, in which coefficient K_h selection reference to Table 1.

$$I_h = \sqrt{{I_{h1}}^2 + {I_{h2}}^2 + K_h I_{h1} I_{h2}} \tag{3}$$

Table 1 Value of coefficient K_h

h	3	5	7	11	13	9	>13	even
K_h	1.62	1.28	0.72	0.18	0.08		0	

After calculating the superposition harmonic current of all turbines, it's necessary to convert the superposition value into the PCC side, and then judge whether they exceed or not by comparing the calculated value with the limited value.

Harmonic voltage analysis

The *h* harmonic voltage ratio HRU_h in PCC can be calculated by Eq. 4.

$$HRU_h = \frac{\sqrt{3} U_N h I_h}{10 S_k} \tag{4}$$

where, U_N is nominal voltage of power grid, kV, S_k is PCC short-circuit capacity, MVA.

Eq. 5 calculates the total harmonic voltage distortion THD_u.

$$THD_u = \sqrt{\sum_{h=2}^{\infty} (HRU_h)^2} \times 100 \tag{5}$$

Assessment and exceed judgment of harmonic voltage can be made by HRU_h, THD_u and limit value.

Wind farm voltage fluctuation and flicker

Voltage fluctuation analysis

Relative voltage fluctuation by single turbine switching operation can be measured according to Eq.6.

$$d = 100 \cdot \varphi_u \cdot \frac{S_n}{S_k} \tag{6}$$

where, d is relative voltage fluctuation, %, φ_u is voltage fluctuation of grid connecting point, S_n is single turbine rated apparent power, MVA.

When limit start-up and shut down number of wind turbines, voltage fluctuation is calculated by Eq. 7.

$$d \approx \frac{\Delta S_i}{S_{SC}} \times 100\% \tag{7}$$

where, ΔS_i is three-phase load change value, MVA.

Voltage flicker analysis

As for wind power generation, user's load, agreement electricity capacity, and system voltage should be considered in voltage flicker limit configuration. Comparing with the standard limit [12, 13], we should first measure the total PCC voltage flicker G caused by all turbines.

$$G = \sqrt[3]{L_P^3 - T^3 L_H^3} \tag{8}$$

where, L_P is long time voltage flicker limit, L_H is long time voltage flicker limit for a higher voltage level, T is voltage flicker transfer coefficient.

Voltage flicker limit E_i is,

$$E_i = G \sqrt[3]{\frac{S_i}{S_t} \cdot \frac{1}{F}} \tag{9}$$

where, F is simultaneous factor for fluctuating load, the typical value F=0.2~0.3(But $S_i / F \le S_t$ must meet).

Voltage flicker for wind turbine is,

a. Continuous operation

When wind turbines works in continuous operation state, the total voltage flicker value they generate is calculated by Eq. 10.

$$P_{lt\Sigma} = \frac{1}{S_k}\sqrt{\sum_{i=1}^{I}\left(\varphi_C \cdot S_n\right)^2} \tag{10}$$

where, φ_C is flicker coefficient of a single unit, I is the number of wind turbines connected to the grid.

b. Switching operation

The total flicker value produced by several units switching operation is,

$$P_{lt\Sigma} = \frac{8}{S_k}\left[\sum_{i=1}^{I} k_{120,a}\left(\varphi_S \cdot S_n\right)^{3.2}\right]^{0.31} \tag{11}$$

where, φ_S is flicker step coefficient of a single unit, $k_{120,a}$ is switching time for wind turbines in 120min.

The system bus flicker value that comes from wind turbines outlet is get by wind turbine flicker multiply transfer coefficient, as it is shown in Eq. 12 and Eq. 13.

$$P_{ltA} = T_{BA} \cdot P_{ltB} \tag{12}$$

$$T_{BA} = \frac{S'_{lcA}}{S_{lcA} - S'_{lcB}} \tag{13}$$

where, T_{BA} is transfer coefficient, P_{ltA} is node A long time voltage flicker value caused by node B, P_{ltB} is node B long time voltage flicker value, S'_{lcA} is short-circuit capacity that node A transfer to node B, S_{lcA} is node A short-circuit capacity, S'_{lcB} is short-circuit capacity that node B transfer to node A.

Assessment case

To analyze the problem, this paper takes a typical 49.5MW wind farm case as an example, using 1.5MW GW82/1500 wind turbines, 1.6MVA S9-1600 box-type transformers and LGJ-400 transmission line to access to the grid. Fig. 1 shows the wind farm equivalent wiring diagram, assemble line short-circuit capacity is 900MVA, PCC minimum short-circuit capacity is 3030MVA, PCC power devices capacity account by planning capacity 1410MVA.

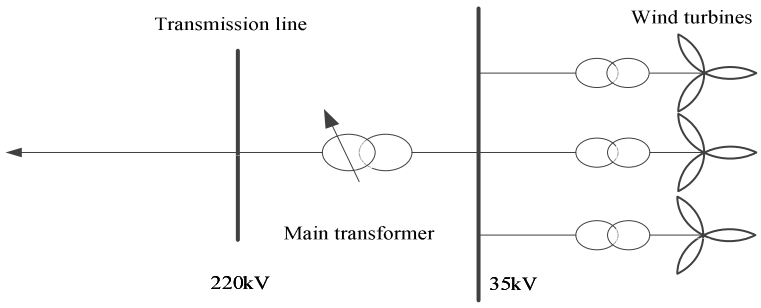

Fig.1 Equivalent wiring diagram of wind farm

According to the test data of the assess wind farm, each harmonic current histogram is shown in Fig. 2.

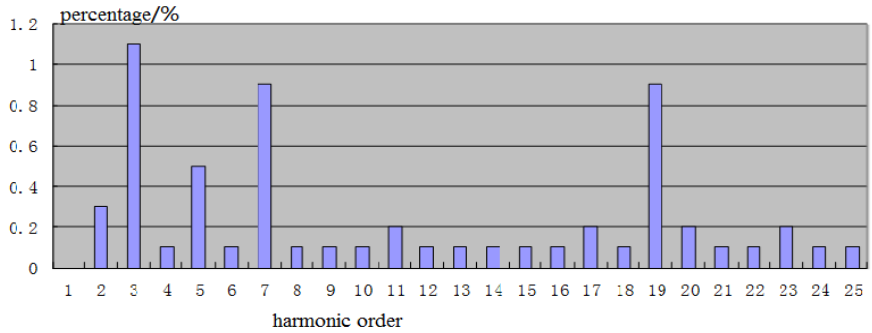

Fig. 2 Harmonic current histogram of a single wind turbine

Evaluating harmonic current according to the above method, the results is shown in Table 2.

Table 2 Assessment result for harmonic current

Harmonic order	PCC harmonic current limit /A	Harmonic current value /A	Conclusion
2	0.92	0.07	qualified
3	0.19	1.27	unqualified
4	0.46	0.03	qualified
5	0.24	0.47	unqualified
6	0.31	0.03	qualified
7	0.54	0.54	unqualified
8	0.23	0.03	qualified
9	0.24	0.03	qualified
10	0.18	0.03	qualified
11	0.27	0.06	qualified
12	0.15	0.03	qualified
13	0.26	0.03	qualified

Total injection harmonic is mainly affected by the single turbine harmonic current value, as can be seen from Fig. 2, the 3rd, 5th and 7th harmonic current of this case is larger. Among them, the 3rd harmonic current even exceeds the rated current 1%, which is one of the important factors affecting wind farm. Besides, PCC short-circuit capacity is small, while the access capacity is large, which makes user's assigned limit value smaller and more rigorous.

Table 3 shows the comparison result of total harmonic voltage distortion and PCC harmonic voltage limit.

Table 3 Assessment result for harmonic voltage

Total harmonic voltage distortion /%	PCC harmonic voltage limit /%	Percentage/%	Conclusion
0.36	2.0	18	qualified

According to the calculation result, the harmonic voltage caused by harmonic current injection is lower than the standard limit, which is qualified.

Table 4 analyses the voltage fluctuation value caused by several wind turbines. In the process of field-testing, the biggest voltage change value is about 1.35%, which matches the theoretical analysis result, and did not exceed the standard limit at all.

Table 4 Calculation data of voltage fluctuate

Number	Calculated value/%	Standard limit/%	Conclusion
1	0.0105	1.5	qualified
33	1.3434	1.5	qualified

For voltage flicker analysis, continuous operation and switching operation state are different. Take continuous operation as an example, flicker coefficient is shown in Table 5, voltage flicker comparison result is shown in Table 6.

The wind farm voltage flicker transfer to PCC is 0.27, less than PCC allowed value 0.31, voltage flicker is qualified, but close to the limit. It's advised that the wind farm should take some corresponding measures, in order to reduce operation voltage flicker.

Table 5 Value of flicker coefficient

Impedance angle	30°	50°	70°	85°
Annual average wind speed	Flicker coefficient			
6.0	2.71	2.57	2.50	2.50
7.5	2.60	2.48	2.38	2.37
8.5	2.58	2.44	2.33	2.30
10.0	2.56	2.38	2.24	2.23

Table 6 Voltage flicker assessment for PCC

PCC voltage flicker /%	Voltage flicker limit/%	Percentage/%	Conclusion
0.27	0.31	87	qualified

Summary

As to the increasing numbers of the problem of the poor power quality influenced by grid-connected wind farms, this paper studies the main influence factors of wind farm harmonic, voltage fluctuation and flicker, as well as their calculation and assessment methods. Harmonic is mainly affected by the types of wind turbines. As for the voltage fluctuation and flicker, the influence factors mainly include wind conditions, wind turbines types, control strategy, system conditions and etc. Furthermore, a wind farm case validates the feasibility of the above assessment method.

References

[1] Zhao Haixiang: Studies on Voltage Fluctuation and Flicker Caused by Integrated Wind Power [D]. Beijing: China Electric Power Research Institute, 2004.

[2] Huang Zhuangsheng: Measurement and Analysis for Harmonics Generated by Nanao Wind Power Plants [J]. Power System Technology, 2001, 25(11):80-82.

[3] Wu Yichun, Ding Ming: Simulation Study on Voltage Fluctuation and Flicker Caused by Wind Farms [J]. Power System Technology. 2009, 33(20):125-130.

[4] Wang Haiyun, Wang Weiqing, Liang Bin: Wind Farm voltage Flicker at he Point of Common Coupling [J]. Electric Power Automation Euipment, 2008, 28(12):81-83.

[5] IEC 61400-21, Measurement and Assessment of Power Quality Characteristics of Grid Connected Wind Turbines [S].

[6] Bai Xue-song, Yu Haiyang, Lu Feikong, et al: Evaluation for Power Quality of Wind Power[J]. Heilongjiang Electric Power, 2011, 33(1):46-49.

[7] He Shien, Zheng Wei, Zhi Yong, et al: Power quality issues of large-scale cluster wind power integration [J]. Power System Protection and Control, 2013, 41(2):39-44.

[8] Sainz L, Mesas J: A. Deterministic and Stochastic Study of Wind Farm Harmonic Currents[C]. IEEE Transaction on Energy Conversion, 2010, 25(4):1071-1080.

[9] Wang Shenzhe, Gao Shan, Li Haifeng, et al: Evaluation of Power Quality in Grid Planning Scheme with Wind Power Integration [J]. Transactions of China Electrotechnical Society. 2013, 28(8):56-65.

[10] GB/T 14549-1993, Harmonic Power Quality Utility Grid[S].

[11] GB/T 12326-2008, Power quality Voltage Fluctuation and Flicker[S].

[12] Q/GDW 392-2009, Technical Rule for Connecting Wind Farm to Power System[S].

Advanced Materials Research Vols. 986-987 (2014) pp 551-555

doi:10.4028/www.scientific.net/AMR.986-987.551

Study in the application of PSIM software in the teaching of curriculums related to the new energy power generation

Hongwei Li[a], Gui Chen[b]

School of electrical information, Southwest Petroleum University, Chengdu, 610500, P.R.C.

[a]lhwmail@126.com, [b]chengui@swpu.edu.cn

Keywords: Teaching, PSIM software, wind power system, Permanent magnet synchronous generator (PMSG), full power converter.

Abstract. In view of the teaching requirements of the new curriculums about new energy power generation technology in electrical engineering field, this paper has proposed and designed a rated 3kW wind power system under the environment of PSIM9.0 software. Through systematically analyzing the mathematics and theory knowledge of the small and medium sized permanent-magnet direct-drive wind power system (PDWPS for short), the wind power system model has been built and the back-to-back double-PWM control circuit has been designed. Then the whole PDWPS has been established based on PSIM. The simulation results show that, when the wind speed changes, the output power of the generator is stable and the DC voltage of the inverter is constant. The results prove that the control strategy is correct and valid. As a powerful auxiliary teaching tool, PSIM can be used to strengthen student's understanding of theoretical knowledge and improve the students' learning interest and enthusiasm. The contents in this paper provide a new method to the teaching and practice in electrical engineering courses.

Introduction

Smart grid has a very wide range of content and the integration of renewable energy is its one important feature. In recent years, a lot of ordinary colleges and universities have opened the courses such as "distributed generation", "new energy power generation and interconnection", "wind and photovoltaic power generation" and other courses about new energy power. But those curriculums need wide knowledge base, the concepts are relatively abstract, and all of them are strong theoretical and practical comprehensive courses. In order to improve the teaching effectiveness, the experiment teaching is necessary. But now, the ordinary colleges and universities are lack of corresponding experiment equipment, the teaching time is cut down and teaching content increases. All these questions result in poor teaching effectiveness. The introduction of the simulation software maybe can solve those problems well.

At present, there are many power electronics and power system simulation tools used in the commercial and educational power system [1-4]. The PSIM is a kind of simulation software packages used in the field of power electronics and motor control. PSIM has simple user interface and is easy to learn and use. And it also has fast simulation speed and clear simulation waveform. Moreover, compared with the MATLAB simulation tools, PSIM has the properties of very small setup capacity (less than 100M bytes), fast operation speed and good expansibility and transplantation (even it can run directly without setup process)[4].Especially, PSIM9.0 and later version add new energy power generation models such as solar cell and wind power generation. So, PSIM provides an excellent platform for its application in the development of new energy power generation or distributed generation virtual experiments.

Currently, the small and medium-sized independent wind power generation found strong support from the national policies. They are mainly used in remote areas, where lack of electricity but lack not of wind energy, and in parts of the self-supply power plants, such as remote mountains, border posts, lonely islands large oil fields, etc. [5] Small and medium-sized wind turbine system is an important content of "distributed generation", and the permanent-magnet direct-drive wind power generation

system (PDWPS for short) is an investigative hot spot in recent years. Through the simulation and modeling of PDWPS, this paper described the application of PSIM in the above mentioned courses teaching.

Overview of PDWPS

PDWPS, whose basic structure are shown in Fig.1, is mainly composed of four modules: wind turbine, PMSG, converter and control system. Unlike traditional asynchronous wind power generator system, PDWPS saves heavy speed-increasing gearbox, and this increases the utilization efficiency of wind power and improves the unit operation reliability. Moreover, PDWPS does not consume reactive power from the main grid, and the power converter can improve the low voltage ride-through of the system. All those provide a strong guarantee for the wind power to meet increasingly stringent interconnection requirements. PDWPS has the following main characteristics [6]: 1) smaller size and lighter weight for generator; 2) smaller electromagnetic interference and good EMC performance; 3) simple structure, good reliability, long service life; 4) high efficiency, obvious energy saving; 5) better adaptation even under the bad environment; 6) good voltage waveform and strong adaptive capacity to variation of load.

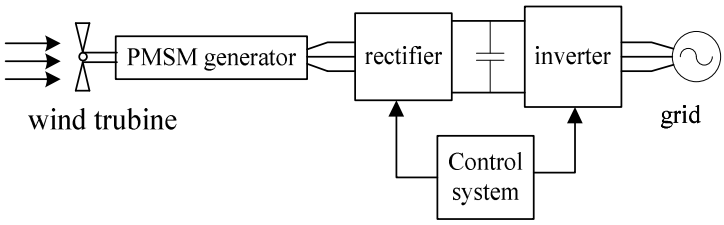

Fig.1 Diagram of basic structure for PDWPS

Mathematical model of PDWPS

3.1 power characteristics for wind turbine

As a key component of the wind power generation system, the main function of wind turbine is to intercept wind energy and convert the wind energy to the mechanical kinetic energy efficiently. So, the wind turbine not only affects the effectiveness and stability of the output of the wind power generation system, but also directly decides whether the system can run normally.

According to the hydrodynamics knowledge, the input power of the wind turbine equals to the kinetic energy produced by flow of air. The expression is,

$$E = mv^2 / 2 = \rho S v^2 / 2 \tag{1}$$

Based on Betz limit theorem [5], the theoretical maximum output power of wind turbine is,

$$P_{\max} = EC_{\max} = \rho S v^2 C_{\max} / 2 \tag{2}$$

Where, m is the intercepted air quality, S is the swept area by wind leaf, v is wind speed, ρ is air density. And $C_{\max}$ is the maximum power conversion coefficient, its theoretical value is 0.593, but the actual value is about 0.4 because it is impossible to achieve the theoretical value in the actual operation.

The output torque formula of the wind turbine is,

$$T_m = P / \omega = \rho S v^2 C_p / 2\omega \tag{3}$$

Where, P is the output active power, C_p is the power conversion coefficient, ω is the blades rotating angular velocity of wind turbine.

3.2 The model of PMSG

During the running process of PMSG, the electromagnetic relations are very complex, so it is hard to establish its accurate mathematical model. For the sake of analysis, it is usual to make the following assumptions: 1) Y type connection for the stator winding; 2) the back EMF be sine-wave and do not consider the effect of space harmonic and magnetic circuit saturation; 3) do not consider the losses of eddy current and hysteresis; 4) no dynamic response process for excitation current.

In d-q axis rotation coordinates, the mathematical relationships for PMSG voltage and electromagnetic torque are as following [6].

Voltage equations are,

$$\begin{cases} U_d = -\omega_c \psi_q + (R_s + pL_d) i_d \\ U_q = \omega_c \psi_d + (R_s + pL_q) i_q \end{cases} \tag{4}$$

Flux linkage equations are,

$$\begin{cases} \psi_d = L_d i_d + \psi_f \\ \psi_q = L_q i_q \end{cases} \tag{5}$$

Electromagnetic torque equation is,

$$T_e = 3n_p[\psi_f i_q + (L_d - L_q) i_q i_d]/2 \tag{6}$$

Where, ψ_q and ψ_d are the d-axis and q-axis flux linkages respectively, L_d and L_q are the d-axis and q-axis self-inductances for stator windings, R_s is the stator resistance, i_d and i_q are the d-axis and q-axis armature currents, ω_c is the rotor angular velocity, p is the differential operator symbol, n_p is the poles pares of PMSG, ψ_f is the flux linkage of permanent magnets and is constant.

Modeling and control strategies

Back-to-back double PWM converter consists of the generator side rectifier, DC bus and the grid side inverter. The rectifier accepts the active power from the generator then converts them to DC power, and then through the DC bus, the inverter converts the DC power to AC power and injects AC power into the grid. Due to wind speed and generator speed continuously changing, the generator output voltage and frequency change with them. In order to meet the interconnection requirements of voltage and frequency, the control method and strategy of the dual PWM converter are very critical.

4.1 Modeling and control strategy in generator side

The control objective of rectifier in generator side is to achieve the maximum power point tracking (MPPT) by adjusting the speed and torque of PMSG when the wind speed changes. Under the rotating coordinates, the equation (6) shows that the torque is only related to q-axis armature current when $L_d = L_q$, so the torque control is the current control. In short, the rectifier adopts current-speed double closed loop control. The speed and torque depend on the space vector currents. It can achieve control objectives by making i_d and i_q track the given signals i_d^* and i_q^*. The control models and diagram are shown in Fig. 2 based on PSIM.

4.2 Modeling and control strategy in grid side

The control objective of inverter in grid side is to make the DC bus voltage more stable and the grid run under unit power factor. In order to overcome the drawbacks of the single current control method in traditional small and medium-sized wind power system, this paper adopts double closed loop voltage oriented vector control method [7-8]. Voltage oriented vector control method include indirect control and direct control. Here, the direct current control method has been adopted for it uses the current closed-loop control and has better dynamic performance and good robustness [9]. In the method, the outer loop voltage signal was controlled by the given DC voltage U_{dc}^* and the actual feedback DC voltage U_{dc}, and the inner loop current signal was controlled by the currents in grid side and the output of outer loop. The control models and diagram are shown in Fig.3 based on PSIM.

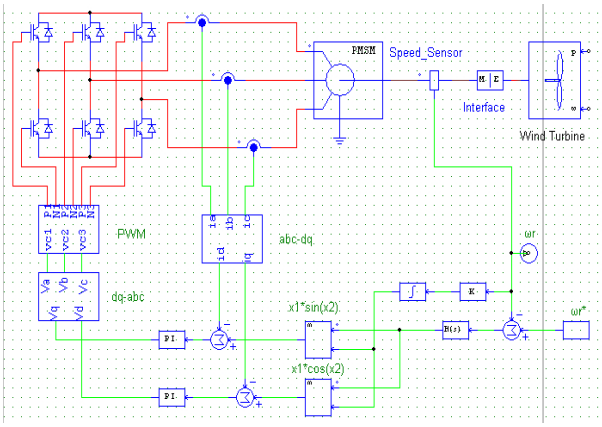

Fig.2 Control system model of PMSG side rectifier

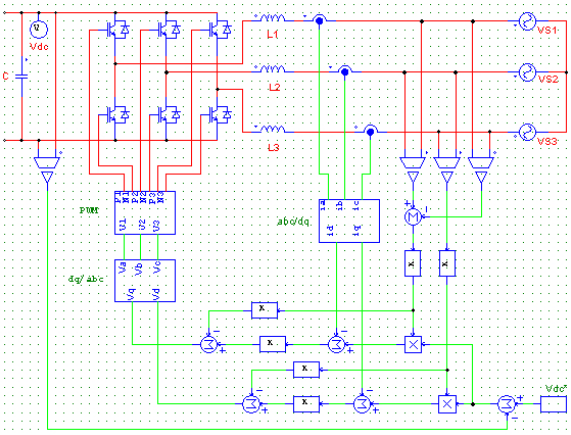

Fig.3 Control system model of Grid side inverter

Simulation and results analysis

In order to verify the feasibility of the small and medium-sized permanent-magnet wind power system, this paper, based on PSIM, design a system with the rated power of 3 kW whose main parameters are shown in table 1. To verify the stability of proposed system, the wind speed has a sudden change from the rated speed 12m/s to 9m/s (shown in Fig.4) during the simulation. After the simulation, the speed and torque of PMSG are shown in Fig. 5, the output active power of PMSG is shown in Fig. 6, the DC bus voltage is shown in Fig. 7 and the output currents of inverter is shown in Fig. 8.

It can be seen from Fig.5~8, when the wind speed has a sudden change, the system has a fast dynamic response and very small overshoot. When the system runs below the rated wind speed, the DC bus voltage is almost constant 400 V and the inverter output voltage frequency is the same as the grid voltage frequency. The simulation results show that the model was correct, the system was stable and the control strategies were feasible and valid.

Table 1 Parameters of the complete system

item	parameter	item	parameter
Air density	1.2kg/m3	Grid frequency	50Hz
Radius of the blades	2m	Dc bus voltage	400V
Rated wind speed	12m/s	Dc bus capacitance value	1.9mF
Rated power	3kW	Converter switching frequency	10kHZ
Phase voltage	180V		

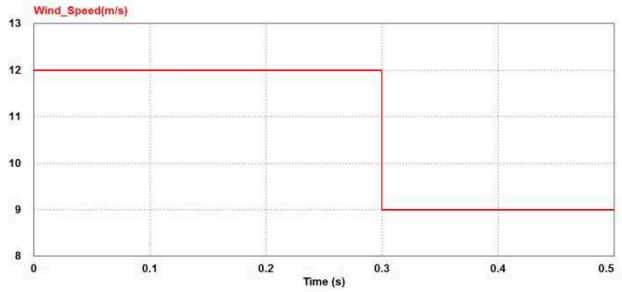

Fig.4 Step change of the wind speed

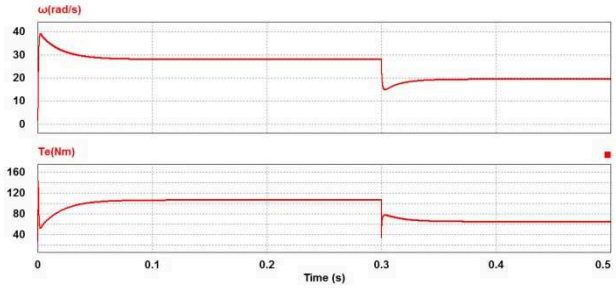

Fig.5 Speed and torque waveforms of PMSG

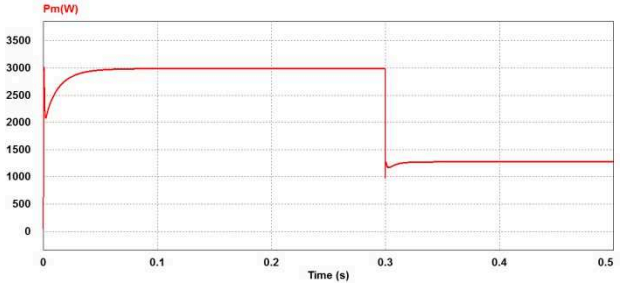

Fig.6Output active power of PMSG

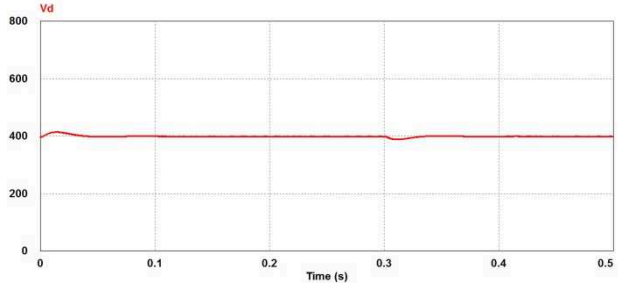

Fig.7 DC busvoltage waveform

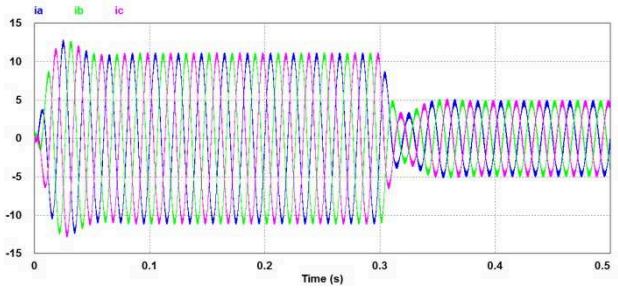

Fig.8 Output current of inverter

Conclusion

This paper discusses the modeling and simulation of the small and medium-sized permanent magnet wind power system based on PSIM9.0. The simulation results are in agreement with the theoretical calculation values. Compared with PSIM, although PSCAD and MATLAB/Simulink software is so powerful and can realize the simulation of complex system, they launch slowly and have long running time and software transplantation is relatively difficult.

In the teaching, the working principles of the system are analyzed first, and then the system are modeled based on PSIM. The parameter correction designs need to be done based on the requirement of engineering design before running the simulation system. Finally, the simulation system is used to verify whether the designs and the models are correct or not. By introducing PSIM into the classes to develop corresponding virtual experiments, it can solve the problem of insufficient experimental time, provide students with a good platform for integration of theory with practice, grasp the corresponding professional theoretical knowledge better and enrich the teaching content, method and means. Moreover, it also can stimulate students' interest in learning, train students comprehensive and scientific research, practice and innovation ability.

References

[1] LI Guangkai, LI Gengyin, The Summary of Power System Simulation Software[J]. Journal of Electrical &Electronic Engineering Education,, 2005,27(3):61-65.

[2] Wang Yao, Wu Yanping, Zheng Dan, Power electronics curriculum design based on PSIM simulation [J]. Experimental Technology and Management, 2013,30(12): 108-110.

[3] GUO Jin, ZHANG Youpeng Simulation research on direct-driven wind turbine with permanent magnet synchronous generator grid-connected power system [J]. Chinese Journal of Power Sources,2013,37(4): 617-620.

[4] Tu Qingrui, Xu Zheng, Zhang Jing, Modeling and simulation on connection of direct-drive wind turbine based on PSCAD/EMTDC [J]. Acta Energiae Solaris Sinica, 2010, 31(4):523-530.

[5] Li Defu, Small and medium-sized wind power industry development report in 2012, Wind Energy [J].2013, (5): 44-50.

[6] OliveiraDS, ReisMM, Silva CEA, et al. A Three-Phase High Frequency Semi-Controlled Rectifier For PMWECS [J]. IEEE Trans. Power Electronics, 2009, 25(3): 677-685.

[7] Agarwal V, Aggarwal RK, Patidar P, etal. A Novel Scheme for Rapid Tracking of Maximum Power Point in Wind Energy Generation Systems [J]. IEEE Trans. Energy Conversion, 2010, 25(1): 228-236.

[8] Chinchilla M, Arnaltes S, Burgos JC. Control of Permanent-Magnet Generators Applied to Variable-Speed Wind-Energy Systems Connected to the Grid [J]. IEEE Trans. Energy Conversion, 2006, 21(1): 130-135.

[9] YaoJun, LiaoYong, LiHui, et al. Unity power factor control of a direct-driven permanent magnet synchronous wind-power generator[J]. Electric Machines and Control, 2010,14 (6): 13-20.

Advanced Materials Research Vols. 986-987 (2014) pp 556-559

doi:10.4028/www.scientific.net/AMR.986-987.556

Study on Cooperative Games in Electric Vehicle Charging Market on account of Shapley Distribution Model

Shuang Yang[1, a] ,Min Yang[2, b]

[1]Economic Management Institute, Beihang University, 100191, China

[2]Economic Management Institute, Beihang University, 100191, China

[a]email: yangshuang9008@126.com, [b]email: yangmin7901@163.com

Keywords: Electric vehicle, Charging market, Supply chain, Cooperative games, Shapley distribution model.

Abstract. This thesis applies the thought of cooperative game and studies on the best mode of cooperation and benefit distribution in the charging market in supply chain. Firstly by researching the relationship between the unit cost and the number of charging pile construction, the thesis concludes that grid, gas station and car park three party will participate at the same time. Then, with the data of Beijing charging market, it makes specific accounting of five unions of profit model, and finds out the best program in which the three-party union could be established. Finally, it uses classic Shapley method, getting the distribution models of enterprise union.

Introduction.

As the best choice for the low-carbon economy, electric vehicles contain huge market potential. The construction of charging facilities is the vital basis of its extensive promotion. Commonly used electric vehicle charging way are slow filling and fast filling.But now, the application of electric vehicles is also in the testing and demonstration phase, and the construction of charging stations and operation mode select are still in exploration. It has become an urgently important task of research to find out the kind of cooperation and allocation mechanisms, which the parties of supply chain should establish to maximize the benefits and fair and reasonable.

Introduction to Supply Chain Cooperative Game and Shapley Value Method.

Supply Chain Cooperative Game.

Supply Chain Cooperation. Supply chain cooperation is supply, production, sales, mutual cooperation between two or more nodes on the supply chain enterprises in order to achieve the common goal, obtaining the biggest value with the minimum cost.

Mathematical Model. N={1, 2, 3,... , n}, S, any subset of the N, is called union. V (S) is the corresponding characteristic function, indicating participators of union S can get the maximum utility in mutual cooperation, namely:

$$v(s_1 \cup s_2) \geq v(s_1) + v(s_2), \quad s_1 \cap s_2 = \emptyset \qquad (1)$$

Shapley Distribution Model.

Shapley value of cooperative game theory method are widely used in the supply chain cooperation profit distribution problem. The Shapley value of game (N, v) will apportion major league benefit v (N) according to the following formula:

$$\emptyset_i(v) = \sum_{S \subseteq S_i} \frac{(n-|s|)!(|s|-1)!}{n!}(v(S) - v(S\backslash i) \qquad (2)$$

$$v(\emptyset)=0$$

Research Hypothesis.

Hypothesis 1. In a certain area, fast charging price P_k and slow charging price P_m were determined.

Hypothesis 2. In a certain area, total number of charging pile M is determined, the corresponding total charge amount Q is also determined.

Hypothesis 3. After charging market actual formation, there exist fast and slow filling charging methods at the same time, relations between the number of two kinds charging piles is established in proportion, the corresponding annual charging amount also have fixed relation.

Hypothesis 4. Grid companies provide quick charging service, while charging station provide slow filling services.

Charging cooperation models.

Analysis of market participants. According to the existing optional way of charging, there are three possible participants in the market: the grid companies A_1, gas station A_2 and a parking lot A_3.Assuming that a certain area in the specified period, the number of fast charging piles and slow charging piles is M_k and M_m respectively, corresponding charging amount is Q_k, Q_m. It is set that the number of fast and slow charging piles A_1built is m_1 and m_2, the number of A_2 is$(M_k - m_1)$, the number of A_3 is $(M_m - m_2)$. $m_1 \in [0, M_k]$, $m_2 \in [0, M_m]$.

General income of all participants is:

$$Y(S) = \sum_{i=k,m} P_i \times Q_i \qquad (3)$$

Cooperation Pattern Analysis. For all the possible coalition, there are five kinds of possibilities, Hj , j=1,2,3,4,5, as shown in table.1.

Table.1 Cooperation Pattern

	Fives Cooperation Pattern
H_1	{1}，{2}，{3}
H_2	{1，3}，{2}
H_3	{1，2}，{3}
H_4	{1}，{2，3}
H_5	{1，2，3}

Income Analysis. Benefit analysis of all kinds of cooperation mode.

Mode 1. 1,2,3 operate independent respectively, namely {1}，{2}，{3}.

$$Y(1) = P_k Q_{k1} + P_m Q_{m1} + P_{b1} Q_{k2} + P_{b2} Q_{m2}$$

$$Y(2) = P_k Q_{k2}$$

$$Y(3) = P_m Q_{m2}$$

$$C(1) = P_c(Q_{k1} + Q_{m1}) + C_{k1} + C_{m1} + C_{rm} + C_{rk} + C_{ek} + C_{em}$$

$$C(2) = P_{b1} Q_{k2} + C_{k2} + C_{r2}$$

$$C(3) = P_{b2} Q_{m2} + C_{m3} + C_{r3}$$

$$V(1) = P_k Q_{k1} + P_m Q_{m1} + P_{b1} Q_{k2} + P_{b2} Q_{m2} - (P_c(Q_{k1} + Q_{m1}) + C_{k1} + C_{m1} + C_{rm} + C_{rk} + C_{ek} + C_{em})$$

$$V(2) = P_k Q_{k2} - P_{b1} Q_{k2} + C_{k2} + C_{r2}$$

$V(3) = P_m Q_{m2} - P_{b2} Q_{m2} + C_{m3} + C_{r3}$

Mode 2. 2 operate by oneself, 1, 3 cooperate with each other, namely {1,3},{2}. In this opinion, Union may establish. It is the same with Mode 3 and Mode 4.

Mode 5. 1,2,3cooperate with each other, namely{1， 2， 3}, establishing league union.

$$Y(1,2,3) = P_k(Q_{k1} + Q_{k2}) + P_m(Q_{m1} + Q_{m2})$$
$$= P_k Q_{k1} + P_m Q_{m1} + P_k Q_{k2} + P_m Q_{m2}$$

$C(1,2,3) =$

$P_c(Q_{k1} + Q_{m1} + Q_{k2} + Q_{m2}) + C_{k1} + C_{m1} + C_{rm} + C_{rk} + C_{k2} + C_{r2} + C_{m3} + C_{r3})$

$$V(1,2,3) = (P_k Q_{k1} + P_m Q_{m1} + P_k Q_{k2} + P_m Q_{m2}) -$$
$$(P_c(Q_{k1} + Q_{m1} + Q_{k2} + Q_{m2}) + C_{k1} + C_{m1} + C_{rm} +$$
$$C_{rk} + C_{k2} + C_{r2} + C_{m3} + C_{r3})$$
$$\Delta V_{5a} = V(1,2,3) - \big(V(1,2) + V(3)\big) = \Delta C_{em} + \Delta C_{q5} > 0$$
$$\Delta V_{5b} = V(1,2,3) - \big(V(1,3) + V(2)\big) > 0$$
$$\Delta V_{5c} = V(1,2,3) - \big(V(2,3) + V(1)\big) > 0$$

Through the model test, researcher can get Mode 5 is one of the best cooperation mode.

Shapley Value Method in Profit Distribution. Shapley value of (N,v) will distribute benefit v(N) according to Eq.4:

$$\emptyset_i(v) = \sum_{S \subseteq S_i} \frac{(n-|s|)!(|s|-1)!}{n!} (v(S) - v(S \backslash i)) \quad (4)$$

In this equation, $v(\emptyset) = 0$, $w(|s|) = \frac{(n-|s|)!(|s|-1)!}{n!}$ can be taken as the weighting factor, S_i is the subset of all contains members of N collection, |s| is the number of elements in subset S.

Conclusions. This paper discuss five kinds of electric vehicle charging market operation mode, using Shapley value method to calculate the charging market profit distribution situation of the parties. Results and conclusions are as follows:

League Alliance. Power grid companies, gas stations and parking lots will be participating at the same time in the market, when the tripartite cooperation, alliance assembly will be greatly reduced, and the enthusiasm is higher. Establishing the operation mode is the most appropriate.

Necessity of Cooperation. Shapley value method is used to undertake three parties profit allocation, further verifying the necessity of the big leagues.

Additional Recommendations. When the participants actual profits is inconsistent with Shapley value distribution, government can adjust the price participants purchase electric power. If the expected income gap is still big, government should subside to solve the problem.

References

[1] Shaik.Amjad, S.Neelakrishnan, R.Rudramoorthy. Review of design considerations and technological challenges for successful development and deployment of plug-in hybrid electric vehicles[J].Renewable and Sustainable Energy Reviews,2010,14(3):1104-1110.

[2] Allen F. Hybrid vehicles and the future of personal transportation. New York: CRC Press，2008：10-13.

[3] Shen Xiaofei, in: The future development of Chinese electric cars, the McKinsey study. 2010, (Z2): 100-102.

[4] Yang Junqian, in: Thinking about electric vehicle charging mode, Electrical technology, 2010, (10): 10-11.

[5] Information on http://china.toocle.com,2010-06-25

[6] Information on http://www.bjgtj.gov.cn, 2010-01-19.

Advanced Materials Research Vols. 986-987 (2014) pp 560-563

doi:10.4028/www.scientific.net/AMR.986-987.560

Study on Effects of Solar Generation on Power Grid

Zhaozhi LONG[1, a], Fei LU[2,b]

[1] Measurement Research Institute, China Electric Power Research Institute, Wuhan, China

[2] Hubei Electric Power Research Institute, Wuhan, China

[a]longzhaozhi@epri.sgcc.com.cn,[b]lufei@qq.com

Keywords: Solar Generation; Power Grid; Power Fluctuation; Solar Utilization Factor; Solar Electricity Share

Abstract. The climate change and the shortage of energy have made the solar energy as the priority renewable energy in many countries, and solar energy is under the fast development. Since the solar energy has the intrinsic intermittence and fluctuation, its integration into the power grid will lead to the power fluctuations. The paper proposes a method of deploying the photovoltaic generation which is the main solar generation technology in China to meet the load demand in order to reduce the storage investment. The analysis shows that there is a strong correlation between daytime solar generation fluctuations and grid load fluctuations, and it is able to use solar plant instead of some peek-load regulating generator units. Therefore, solar generation technology also has great potential of integration ability even without the use of energy storage, and the purpose of solar generation is to increase the share of solar electriciy at the lowest unit cost rather than to guarantee 100% utilization factor.

Introduction

The climate change and the shortage of energy have made the solar energy as one of the promising renewable energy resources in many countries. Solar energy does not require fuel costs and can be used in any sunshine place. At present, solar generation mainly includes two technologies: photovoltaic generation and solar thermal power generation. Photovoltaic generation technology has been used worldwide popularly, and currently there are more than 200,000,000 running solar cell matrixes [1]. Solar thermal power generation is an important project for the use of solar energy by heating the fluid to drive the steam or warm air turbine, and it can be broadly divided into three categories: concentrating solar power systems, solar pond technology and solar chimney power generation [2-4]. Compared with the photovoltaic generation, solar thermal power generation has lower investment costs but has not yet implemented wide commercial applications.

Nowadays, solar energy industry is under the fast development. In China, the large-scale solar power plants which use photovoltaic technology have been built and connected to the power grid. Since the solar energy has the intrinsic intermittence and fluctuation, its integration into the power grid will lead to the power fluctuations. The traditional grid is designed for the centralized production, dispatch and distribution of electricity. When the share of solar energy is small, the traditional generation can compensate the power fluctuation of the solar generation by itself. However, with the increase in the share of solar generation, the power fluctuation may go beyond the adjusting limitation, adding difficulties to the system operation and making the integration of solar energy limited.

Thus to the grid, the crucial issue of solar energy integration is to maintain the balance between the generation and the demand. The solar power and the grid demand are all fluctuating and they add the complexity of the grid planning and operating [5, 6]. The objective of solar energy is to maintain the power balance with an acceptable cost and maximize the utilization of the solar energy. Based on the correlation between the solar irradiation and the grid load fluctuations, the paper proposes a method of deploying the photovoltaic generation which is the main solar generation technology in China to meet the load demand in order to reduce the storage investment. It is proved that the share of solar electricity can increase remarkably by reducing the solar utilization rate slightly while keeping the cost stable.

Power grid load and supply configuration

The main task of grid scheduling is scheduling generators to meet changes in the load demand. Normally, the grid load can be decomposed into two parts of fixed component (base load) and changed component (peak load). Seen from the load structure, part of the base load demand is from the continuous operation of electrical equipment, and the rest is from the intermittent load. When the intermittent loads are demanded at different times, it will smooth the overall load fluctuations. However, the overall fluctuations will increase when the intermittent loads with certain synchronicity which related to the season, the weather, the daily routine and habits. In some power grids, the daytime maximum load demand is about 40%~70% higher than the demand at night, and the average daytime demand in summer is about 30% higher than the daytime demand in winter. Since the load volatility exists in the grid, the grid requires peek-load regulating generator units else to meet the load demand in real time except the stable base generator units. Base generator units usually include nuclear power plants, coal-fired power plants and some large gas-fired power plants which have the relatively low cost of power generation and stable operation throughout the year. In contrast with the base generator unit, the peak-load regulating generator units only start in the case of meeting the load fluctuations with short and random running time in minutes or few hours. Obviously, the base units have higher utilization of equipment than the peek-load regulating units. Although the base units provide the most power required by the grid, it is often about 50% of the total installed capacity in the grid to meet load fluctuations.

For the characteristics of power grid mentioned as above and the actual situation of solar generation in China, the paper argues that solar generation has a great potential of supplying peak power to the grid. The solar plants can take the place of peek-load generator units for the reasons as follow:

1) Compared with the base generator units, the solar generation has higher Levelized Energy Costs (LECs) which are closer to those of peek-load regulating generator units;

2) Since the daytime load is always higher than the load at night, the peek-load regulating generator units most operate in the day, and the solar generation just conforms to this characteristic.

The characteristics of solar generation

With the movement of the sun in a day, the received radiation power of solar plant related directly to the solar electricity also constantly changes, as shown in Fig. 1. Different day conditions have a direct impact on the cost of solar generation. Besides, purchase of equipment, conversion efficiency and useful time must be considered to estimate the cost [7, 8]. The better day conditions, the higher conversion efficiency and the longer useful time can reduce the unit cost of solar generation.

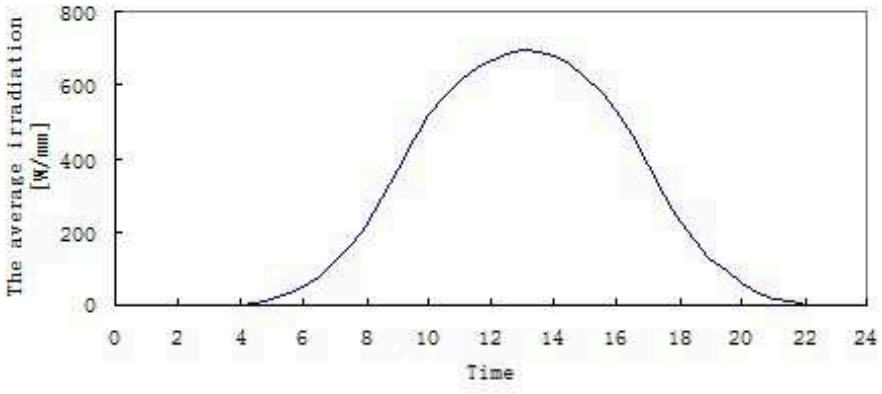

Fig.1 The diurnal irradiation curve

Analysis and discussion

In the paper, the hourly load data of a regional grid and the local annual solar radiation are used to calculate the grid acceptance of solar generation, and to analyze the relationship among utilization factor, solar electricity share and unit cost with the increase in capacity of solar generation.

Daily load curve of the grid has seasonal differences, as shown in Fig.2 [9]. According to the data curves in Fig.1 and Fig.2, it is obvious that the visible grid load fluctuations and solar generation have a significant correlation which is conductive to solar energy integration into the power grid. Basically, the increase or decrease in the load is the same as solar power generation in a day, especially from 12:00 to 14:00 which is the period of the maximum load coinciding with the maximum solar electricity. Similarly, the grid load in summer is higher than the load in winter, and the solar utilization factor is also higher than the utilization factor in winter. The consistency of curves is just to meet the needs of the peek-load regulating.

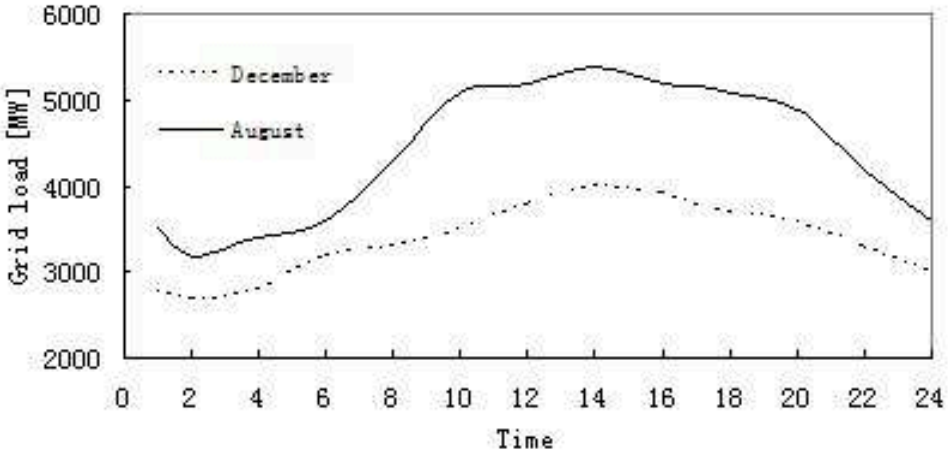

Fig.2 The average grid load curve

The paper defines the solar utilization factor is the ratio of solar power to the grid and maximum solar power, and the solar electricity share is the ratio of solar power to the grid and grid load. In theory, it can be found out directly that solar unit cost will reduce with the improvement of solar utilization factor, but the relationship between solar electricity share and utilization factor is not clear. Fig.3 shows the simulation results that the grid is able to accept all solar generation power when solar electricity share is lower than 2.5%. With the increased installed capacity of solar generation, the power grid starts to abandon the solar generation power and the unit cost of solar electricity rises.

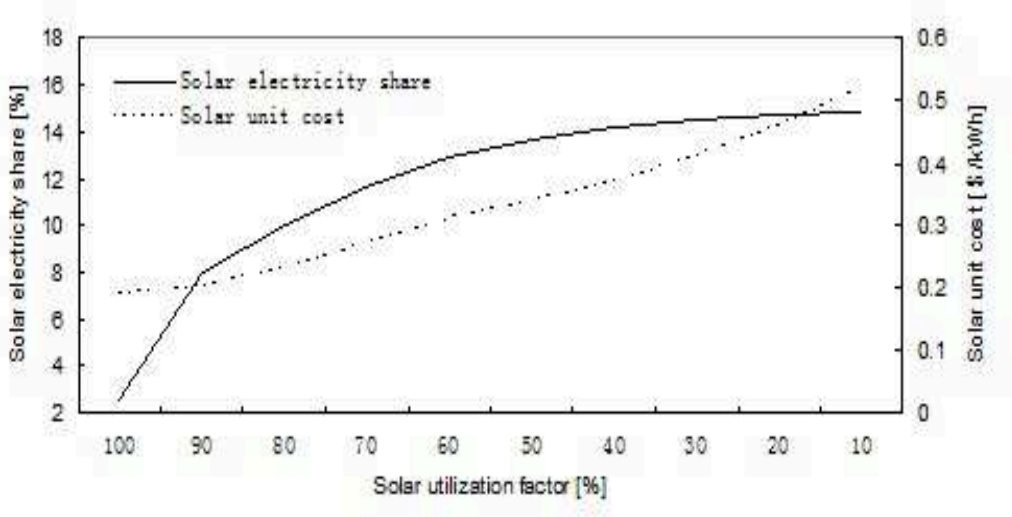

Fig.3 The relationship among utilization factor, solar electricity share and unit cost

It is worth noting that, when the utilization factor decreases from 100% to 90%, the unit cost increases from 0.19$/kW·h to 0.20$/kW·h. At this stage, the unit cost basically does not change, while the share of solar electricity is accounted for 2.5% to 8% with an increase by 220% which means better effective use of renewable energy. By increasing solar installed capacity continuously, the unit cost continues to increase, but the increase in the share of solar electricity is significantly weakened.

Conclusions

Based on the analysis in the paper, there is a strong correlation between daytime solar generation fluctuations and grid load fluctuations, and it is able to use solar plant instead of some peek-load regulating generator units. Therefore, solar generation technology also has great potential of integration ability even without the use of energy storage. Simulation results show that the utilization factor decreases from 100% to 90%, as well as the unit cost increases to 0.20$/kW·h from 0.19$/kW·h. At this stage, the unit cost basically does not change, while the share of solar electricity is accounted for 2.5% to 8% with an increase by 220%. It means the purpose of solar generation is to increase the share of solar electricity at the lowest unit cost rather than to guarantee 100% utilization factor.

References

[1] H.L. Willis, W.G. Scott, Distributed Power Generation Planning and Evaluation, Marcel Decker, Inc., New York, 2000.

[2] S.A. Kalogirou, Solar thermal collectors and applications, Prog. Energ. Combust. Sci., 30 (2004) 231-295.

[3] P.D. Lund, R.S. Keinonen, Radiation transmission measurements for solar ponds, Sol. Energ., 33 (1984) 237-240.

[4] X. Zhou, F. Wang, R.M. Ochieng, A review of solar chimney power technology. Renewable and Sustainable Energy Reviews 14 (2010) 2315-2338.

[5] T. Meyer, J. Luther, On the correlation of electricity spot market prices and photovoltaic electricity generation, Energy. Convers. Manage., 45 (2004) 2639-2644.

[6] J.I. Prieto, J.C. Martinez-Garcia, D. Garcia, Correlation between global solar irradiation and air temperature in Asturias, SPAN Sol. Energ., 83 (2009) 1076-1085.

[7] P.P. Singh, S. Singh, Realistic generation cost of solar photovoltaic electricity, Renew. Energ., 35 (2010) 563-569.

[8] I.A. Zahed, J. Hallenstain, Effect of non-technical factors on the electricity cost of the photovoltaic systems, Desalination, 209 (2007) 108-112.

[9] Zhao Zhengming, Liu Jianzheng, Meng shuo. The Integrated application system of solar energy generation[J], Power Electronics, 1 (2)7-10.

Advanced Materials Research Vols. 986-987 (2014) pp 564-571

doi:10.4028/www.scientific.net/AMR.986-987.564

Study on the Framework of Fission Product Source Term for Nuclear Power Plants

Xinhua LIU[1,a], Lan FANG[2,b], Zhaowen ZHU[1.c]

[1]Nuclear and Radiation Safety Center, Beijing, 100082, China

[2]China National Nuclear Operation Company, Haiyan, Zhejiang, 314300, China

[a]liuxhua225@sina.com, [b]fanglan.happy@163.com, [c]zhuzhw@126.com

Keywords: dose equivalent I-131; fission product; primary coolant source term; release source term;

Abstract. The problems occurring in the fission product source term calculations for M310/CPR1000, EPR and AP1000 are briefly analyzed, based on the related regulations and standards, as well as operational feedback, review experiences and recent research achievements for nuclear power plants in China. The framework of fission product source term proper to China has been first studied and proposed in perspective of the purpose of source terms. The calculation processes of fission product source term are rearranged and the requirements for deferent reactor types are specified. The proposed framework can be taken as a foundation for solution of the long-standing problems in the calculation of fission product source term and provide reference for source term calculation.

Introduction

The reactor types of nuclear power plants (NPPs) that will be constructed in China mainly include CPR1000, EPR and AP1000. The CPR1000 originated from the M310, which are GWe-level NPP introduced from French, while EPR and AP1000 are advanced Generation-Ⅲ NPPs, with the power output of 1.75GWe and 1.25GWe, respectively. The designs of these three reactor types have evolved for several decades and the safety, reliability and economy have been enhanced greatly. Although some improvements have been made in their source term calculation, problems still exist which would lead to the incoherence between the designs and realistic operation, influence the radioactive waste minimization, release optimization and environmental impact assessment, and even limit the development of the nuclear power industry.

The problems occurring in the fission product source term estimations for M310/CPR1000, EPR and AP1000 are briefly analyzed, based on the related regulations and standards, as well as operational feedback, review experiences and recent research achievements for nuclear power plants in China. The calculation framework of fission product source term proper to China has been firstly studied and proposed in perspective of the purpose of source terms. The calculation processes of fission product source term are rearranged and the requirements for deferent reactor types are specified. The proposed calculation framework can be taken as a foundation for solution of the long-standing problems in the calculation of fission product source term and provide reference for source term calculation.

The problems existing in the fission product source term calculations

Introduction of the fission product source term

The source terms for NPPs under normal operation include the radwaste management source term (RMST) and the radiation shielding design source term. The former is mainly used for environmental impact assessment while the latter is used for radiation protection management. The RMST can be divided as core inventories, primary coolant source terms and release source terms following the calculating processes, and be divided as fission products, activated corrosion products, tritium and carbon-14, according to their origins.

Radioactive materials are generated from the fission of heavy nuclides and the activation of corrosion products within the core. The information such as the total activities and concentrations of the fluid in various systems and effluent, as well as the concentration of solid waste during the normal operation should be precisely estimated for radiation protection management, radwaste management, environmental impact assessment and environmental monitoring.

The fission products in pressed water reactors (PWR) are generated within the fuel, its source term is named as core inventories. A small part of the fission products are transferred into the primary coolant during the normal operation and then transported to the other systems. The majority of these nuclides are finally solidified into the solid wastes, with a tiny amount released into the environment by the means of gaseous and liquid effluent. Therefore, the fission product source terms includes the core inventories, primary coolant source term, gaseous and liquid effluent source term, among which the core inventories are the origin, the second one is used for radwaste management and radiation protection management, and the last one aimed for effluent discharge control, environmental impact assessment and monitoring.

The primary coolant source term consists of activated corrosion products, tritium, and carbon-14 besides the fission products. The fission product source term in the primary coolant is influenced by several factors, such as the fuel defect rate, escape rate coefficient etc. It can be lowered by updating the core design and improving fuel cladding materials so as to reduce the fuel defects. Tritium is chiefly produced by the ternary fission of uranium and the neutron activation of boron, lithium and deuterium. The principal ways of carbon-14 production are neutron reaction with oxygen-17, nitrogen-14 and carbon-13. This article is focusing on the calculation framework of fission product source term.

The Problems in Fission Product Source Term for M310/CRP1000

The source terms of M310, provided by Electricite De France (EDF) in 1980s, generally reflected the operation level and design requirements at that time, which was rational as it met the regulations and standards then.

The realistic and conservative primary coolant source terms have been provided by M310, which are calculated employing PROFIP code. The calculation of realistic source term is based on 0.55GBq/t dose equivalent I-131, which is the average concentration of iodine activity at the end of the cycle of nearly 200 unit·years (except the 2^{nd} and 8^{th} cycles of Bugey unit 2) of 900MW French PWRs in 1980s. The conservative source, which assumes 0.25% fuel defects and is normalized to 37GBq/t dose equivalent I-131, is consistent with the technical specification limits.

The term dose equivalent I-131 is the concentration of I-131that alone would produce the same thyroid dose as the quantity and isotopic mixture of I-131, I-132, I-133, I-134, andI-135 actually present.

Two release source terms of M310, case A and case B, are based on different assumptions of the concentration of primary coolant radionuclide. In Case A, the dose equivalent I-131 in the primary coolant is assumed to be 0.55GBq/t during the whole cycle, while for the case B, a mixture of 0.55 GBq/t for the initial 1/4 cycle, 4.44 GBq/t for the intermediate 1/2 cycle and 37 GBq/t for the last 1/4 cycle is assumed, the average of which is 11.6GBq/t. These two sources are calculated using the REJGAS and REJLIQ code developed by EDF.

Several problems have been found in the subsequent CPR1000 design and review[1]. For example, there is no scientific basis for the calculation method of the technical specification source term, including the parameters used to describe the nuclide transportation from the fuel to the coolant and the combination used in the primary coolant source calculation. And the assumptions of the source calculation are on controversial as well. Therefore, the issues of source terms were listed as the common problems in the M310 review in 2008. Plenty of investigations on the rate and size of fuel failure, the sensitivity analysis on the defects distribution, the contribution of the uranium contamination on the cladding surface and differences of the core inventories given by ORIGEN-S and PROFIP5.1 were launched since then. The method for calculating the technical specification of primary coolant source term has been determined based on the present research achievements.

However, the basic assumptions of the primary coolant activity in the release source terms calculation for case A and case B still have not reached consensus.

In spite of the recalculation of the radwaste management source term for the newly constructed CPR1000 such as Hongyanhe NPP[2], has been done, its design ideas and calculation processes are generally the same with that of M310. Consequently it inherits the source problems from M310.

The recent feedback from NPPs shows that the fuel defects under normal operation has been dramatically reduced profiting from the improvement of the core design, fuel design and fabrication, and the dose equivalent I-131 in primary coolant is thus significantly lower than the value in 1980s. Therefore, the basic assumption of 0.55GBq/t dose equivalent I-131 in Case A seems too conservative. Thus, the fission product source would be overestimated while the corrosion product source be under-evaluated. On the other hand, the combination of three different dose equivalent I-131 values for Case B has not been justified. The recently revised national standards, GB6249-2011 and GB14587-2011, provide the discharge limits of radionuclide activities at the outlet (1000Bq/L for coastal NPPs while 100Bq/L for inland NPPs) and bring stricter requirements on the design of liquid waste systems and the calculation of release source term.

The irrational basic assumptions of the release source term affect the veracity of the estimation and corrupt the rationality of environmental impact assessment source term. It would also cause the incoherence between the designs and realistic operations, and interfere the optimization of the emission application and pertinence of the environmental impact assessment. The determination of environmental impact assessment source term is still controversial. For example, the Case A+Case B or 2Case B model are widely accepted in the environmental impact assessment during the stages of sitting, designing and first fuel loading for double units site while various combinations of case A and case B are used for multi units site. The source term used for critical nuclide, group, and exposure pathway analyses is not unified yet. All these problems are related with the irrational basic assumptions and the indistinct destination of release source terms.

The Problems in Fission Product Source Term for EPR

The EPR is designed following the European utility requirement document and based on the French N4 series and the German KONVOI plants and meets. Three sets of source terms for the primary coolant have been provided: realistic, design and technical specification source term[3], of which the last two are identical. Two suits of release source terms, expected source and the maximum source are provided for EPR.

The realistic source term for primary coolant, based on total 244 unit·years operational experience feedback of 1300MW plants and N4 series in French, is estimated to about 0.2 GBq/t dose equivalent I-131. The fuel defect of 0.25% is assumed for the technical specification source term. In the calculation, the core inventories are established with the ORIGEN-S code, and the radionuclide concentrations in the primary coolant are estimated by considering the escape rate from the fuel defects, letdown flow, purification and radioactive decay. This source term is about 23GBq/t dose equivalent I-131and is the same with the design basis and shielding design source terms.

The release source term of EPR encompasses the experience feedback from the 1300MWe units in 8 operating French NPPs during 2001-2003, with the improvements of materials, coolant chemistry, radwaste system. The expected release source term represents the average values of the experience feedback, while the maximum one takes all situations under the normal operations (including the shutdown transients) into account. The emission data from 900MW, 1300MW and the N4 NPPs in Franch during 2001-2003 are provided by EDF to support the conservativity of the design release source term.

The EPR source terms are derived from the experience feedback, and the maximum release source term was used for environmental impact assessment during the stages of sitting, designing and first fuel loading. However, the issues such as the sufficiency of the data and the rationality of the radioactive measurements, data statistics and processes etc. became the focuses of the reviews and the investigations. Therefore, the theoretical calculation of the release source term is queried by the authorities to reconfirm its conservativity, and the issues of which were listed as the

construction permit conditions in the ongoing review of Taishan NPP primary safety analysis reports.

The Problems in Fission Product Source Term for AP1000

AP1000 is a Generation-Ⅲ reactor type designed by Westinghouse Electric Company LLC. It provides two sources for the primary coolant, including the realistic source term which is 3.0 GBq/t dose equivalent I-131 approximately and the conservative, or design basis, source term which is about 37GBq/t dose equivalent I-131[4]. The latter assumes 0.25% fuel defects and employs ORIGEN-S code in the calculation.

Only one release source, called operational release source term, is provided by AP1000. It is calculated using the PWR-GALE code[5] based on the basis of realistic source term in primary coolant, thus it is not related with the technical specifications. The realistic source term for the primary coolant is determined by applying the reference plant values, which is derived from the data obtained from the experience of 26 units in 20 operating US PWRs such as H.B, Rohbinson, Arkansas, D. C. Cook etc. during 1971-1979, and the adjustment factors provided in ANSI-18.1-1984[6].

Although this source has been used for environmental impact assessment, site capacity assessment, and critical nuclide, group, and exposure pathway analyses during the stages of sitting, designing and first fuel loading, it has not been authorized by the reviewer yet because of its low conservativity for a design basis release source term. The Westinghouse compared the calculated effluent concentrations in the case of 0.25% fuel defects with it to justify that the effluent release satisfies the appendix B of 10CFR20[7], implying that it was not been regarded as a conservative source. On the other hand, this source is too stringent to be the realistic release source term. The reference data collected about four decades ago are out of date to a certain extent to effectively guide the design and operation management of nowadays NPPs, because the fuel defect rate has been significantly lowered since 1970s with the development of nuclear industry, profiting from the improvement of the levels of core design, fuel design and manufacture and operation management.

In the situation that the problems in AP1000 source terms have not been resolved and the applicability of different versions of ANSI/ANS-18.1 continues to be controversial, they were put on the list of construction permit conditions in the ongoing review of Sanmen and Haiyang NPP primary safety analysis reports.

Study on the Framework of Fission Product Source Term

As analyzed above, problems still exist in the fission product source term calculations for the three reactor types. For example, the design requirements and purpose of the release source term are not clear, and the assumptions about the primary coolant are irrational as well. Based on the national codes and standards and operational experiences from both domestic and international NPPs, this article dedicates to resolve the existing problems in source estimation, rationalize the calculation processes, normalize the calculation method for different reactor types and finally establish a calculation framework of fission product source term for Chinese NPPs, which will lay the foundation for the formulation of the standard review plan of radwaste management source term.

The Requirements of the Codes and Standards

As shown in Table-1, the main authorities referenced in the radwaste management source design and the safety analysis report reviews of Chinese NPPs, GB6249-2011 and GB14587-2011 give the discharge control values of gaseous and liquid effluent for a single unit and for the whole site, the radioactivity concentration limits of liquid effluent except H-3 and C-14 and the requirements of release management as well. However, the calculation method of design release source term is not involved. The design requirements and calculation methods are prescribed in ANSI/ANS-18.1-1984, NUREG-0017(Rev.1985) and GB13976-2008, which referenced the first two, but they are not applicable for M310/CPR1000 and EPR types. For Ap1000, although these

standards are principally appropriate, the disputes on the applicability of the two different versions of ANSI/ANS-18.1, 1984 and 1999, are not ended yet notwithstanding their principal appropriation.

In respect that the standards guiding the radwaste management source calculations are not consummate and systematic yet, the problems existed in the source terms for the three reactor types have not been resolved. The diversity of the reactor types in China, and accordingly of the calculation methods, increases the difficulty of standards setting. The standard review plan is presently in preparation and it will be helpful to resolve the problems.

Table-1 Requirements of the relative standards.

Serial Number	Title	Main requirements
GB6249-2011	Regulations for environmental radiation protection of nuclear power plant	● Provides the concentration limits of radionuclide in liquid effluents, except H-3 and C-14; ● Provides the control values of gaseous and liquid effluents discharge quantity; ● The personal equivalent dose for public caused by the radioactive materials emitted from all nuclear power reactors in the site should be less than 0.25mSv/a.
GB14587-2011	Technical requirements for discharge of radioactive liquid effluents from nuclear power plant	● Environmental impact assessment should be made according to the design discharge quantity of the reference plant at the stage of siting, and principally design value and applied value of discharge quantity at the stages of designing and first fuel loading, respectively; ● Provides the concentration limits of radionuclide in the liquid effluents, except H-3 and C-14.
GB13976-2008	Radioactive source term of PWR nuclear power plant for operational states	● Provides the requirements of release source term for normally operational NPPs; ● This standard mainly referenced ANSI/ANS-18.1-1984 and NUREG-0017(Rev.1985).
SRP11	NRC Standard review plan，Chapter11	● Radioactive effluents discharge of NPPs should meet the principle of ALARA; ● Other requirements in the standard are the same with ANSI/ANS-18.1-1984 and NUREG-0017(Rev.1985).

Operational Data of Primary Coolant Activities

As the primary coolant source terms are the basic assumption and initial condition for the release source term calculation, the collection and analysis of relative operational data, which is a very tough task, are crucial for the primary coolant source term optimization. A mass of relative investigations were carried out in recent years. The collected data of dose equivalent I-131 in primary coolant from some French, American and Chinese NPPs is listed in Table-2.

It is obviously shown that the fuel defects were continuously reducing due to the improvement of the core design, fuel design and fabrication, which caused the dose equivalent I-131 a trend of decline. The average value of French and Chinese NPPs in recent twenty years is less than 0.1GBq/t, and the maximum of French NPPs is 4.44 GBq/t.

Table 2 Collected data of dose equivalent I-131 in primary coolant

State	Dose equivalent I-131 [GBq/t]	Time	Notes
China	0.06	2000s	The average value of 23 cycles of Daya Bay Nuclear Power Base (including the cycles with fuel defects)[8]
France	0.07	1990s-2000s	The average value of 44 unit·years data from the French N4 series (including the cycles with fuel defects)
	0.10	1990s	The average value of 200 unit·years data from 1300MW NPPs in French (including the cycles with fuel defects)
	0.55	1980s	The average value of 200 unit·years data from French NPPs (including the cycles with fuel defects)
	4.44	1980s	The maximum value of the data from 900MW NPPs in French (the cycle with fuel defects)
USA	0.36	1980s-1990s	The average value of the data from American NPPs (including the cycles with fuel defects)
	3.0	1970s	The average value of the data from American NPPs (including the cycles with fuel defects)
China	0.55	/	The realistic source term of the primary coolant for M310/CPR1000
France	0.2	/	The realistic source term of the primary coolant for EPR
USA	3.0	/	The realistic source term of the primary coolant for AP1000

To estimate the expectation and the maximum of risk caused to the public, the basic assumptions of realistic source terms should be realistic, while that of conservative source terms moderately conservative. Taking M310/CRP1000 as an example, 0.1GBq/t dose equivalent I-131 in the primary coolant will be a rational assumption for the realistic release source term, while the present used assumption, 0.55GBq/t, is a bit conservative and affects the radiation shielding optimization and the radwaste minimization. According to the technical specification, the reactor should be shutdown in two months if the average dose equivalent I-131 is more than 2.2GBq/t, and it should be shutdown in 6hours if the transient value exceeds 37GBq/t. Therefore, the basic assumption of 5GBq/t is more rational than the present used 11.6GBq/t, which is over-conservative.

The fuel defects mainly depend on the fuel design and the cladding materials, whereas have little relations with the reactor type. Since the cladding materials of all the three types are Zr-Nb alloy and the improvements on the fuel design are similar, the basic assumption of the primary coolant source term for M310/CPR1000 are valuable reference for EPR and AP1000.

Framework of Fission Product Source Term

The framework of fission product source term calculation, encompassing a considerable amount of investigation achievements, is demonstrated in Figure1. It is oriented to the purposes of release source term estimation, and combines the experience feedback with theoretical calculation.

The design of the radiation shielding and radwaste management should meet the requirements of normal operation (including the anticipated operational occurrences), and the radwaste minimization and radiation shielding optimization are closely related with the practical operations. Therefore, the source terms are divided into two sets: design basis and realistic.

It is clarified in the framework that the limits of the technical specification (such as 37GBq/t dose equivalent for M310/CPR1000) make the boundary between the normal operations and

accidents, the radiation shielding and the radwaste management under normal operation are considered within the range under the limits, and the parameters describing the rate and the size of fuel defects are used as a part of the basic assumptions of the calculation. The clarification of the basic assumptions of design basis source term will definitely benefit the normalization of the design of radiation shielding and radwaste management.

The design requirements and purposes of the release source term for the three reactor types are specified in the framework. Three sets of release source terms, including design basis, operational and realistic, are required so as to accurately evaluate and monitor the public risks. These sources also contribute to assess the feasibility of the sitting and program the effluent monitoring and environmental monitoring.

The issue of the irrational assumptions in the release source term calculations has also been resolved within the framework. The dose equivalent I-131 in primary coolant of the realistic and the design basis release sources are assumed to 0.1GBq/t and 5GBq/t, respectively, and that of operational release source can be deduced on the basis of the optimization of the latter.

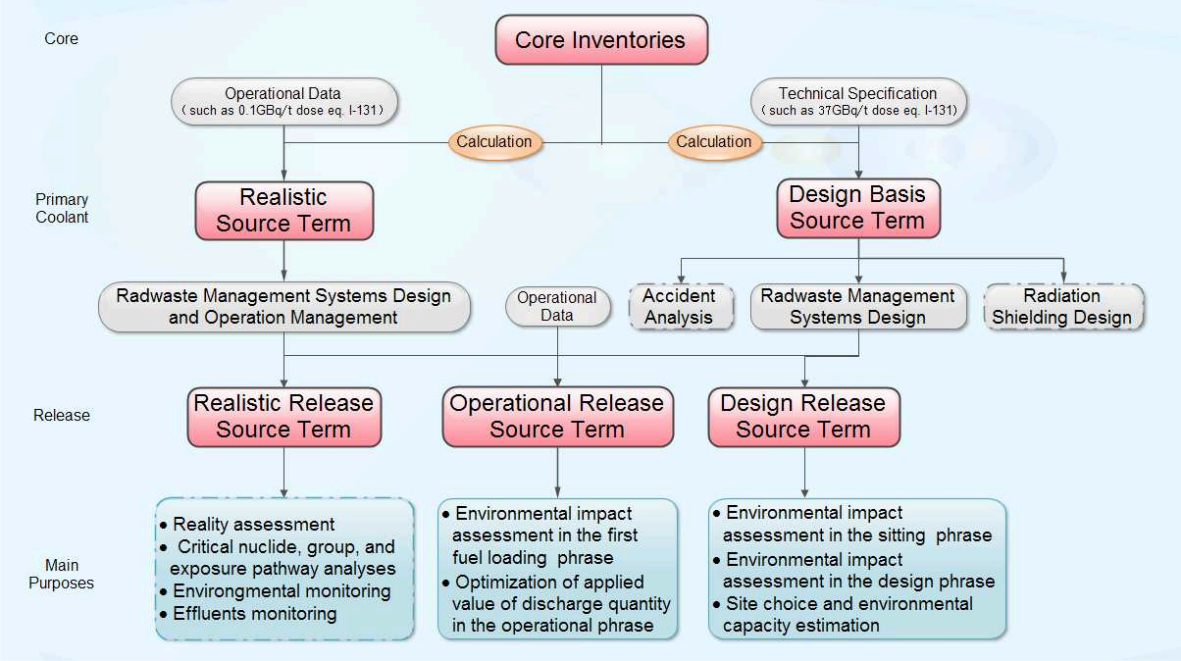

Figure1. The framework of fission product source termfor NPPs

This framework is applicable to the fission product source term calculations for CPR1000, EPR and AP1000, and can be referenced for WWER, HTGR and HWR as well. The basic ideas of the framework can not only guide the source estimation of fission products, but also be used for activated corrosion products, tritium and carbon-14.

Being a part of the complicated works of product source term calculations, this article is focusing on the construction of the framework and the formulation of the processes. Further investigations are needed on the calculation methods, basic assumptions and parameters used in the source estimation for different reactor types.

Conclusions and Suggestions

The problems in the fission product source terms for M310/CPR1000, EPR and AP1000 are analyzed,based on the codes and standards, operational feedback, review experiences and research achievements. The framework, which is applicable to the fission product source term calculation for Chinese NPPs, is established for the first time, oriented to the purposes of these sources. It provides the processes and requirements of product source term estimation, and lays the foundation for resolving the relative existing problems, and can be referenced in future calculations.

The primary coolant source terms include the design basis source and realistic source, as shown in Figure1. It is clarified in the framework that the limits of the technical specification make the boundary between the normal operations and accidents, the radiation shielding and the radwaste

management under normal operation are considered within the range under the limits, and the parameters such as the rate and the size of fuel defects are used as a part of the basic assumptions of calculation. The clarification of the basic assumptions of design basis source term will definitely benefit the normalization of the design of radiation shielding and radwaste management.

Three sets of release source terms, including design basis, operational and realistic, are required according to the framework so as to accuratelyevaluate and monitor the maximum and the realistic public risks. These sources also contribute to assess the feasibility of the sitting and program the effluent monitoring and environmental monitoring.

It is suggested thatdomestic NPPs accumulate data to support the source term estimations. Further investigations on the calculation methods and recalculations of sources for the NPPs, including newly constructed, on-building and operational ones, should be made as soon as possible to lay the foundation for the radiation shielding design, radwaste management, environmental impact assessment and environmental monitoring of NPPs under normal operation.

Acknowledgements

The writers acknowledge the valuable comments and discussions withQiliang Mei of Shanghai Nuclear Engineering Research & Design Institute, DechangCai of China Nuclear Power Technology Research Institute, Shaohua Tang of China Nuclear Power Design Co., Ltd(ShenZhen), Yawei Mao of China Nuclear Power Engineering Co., Ltd., Lan Li of Nuclear Power Institute of China, ZhihongShangguan of Suzhou Nuclear Power Research Institute, Hong Li of Tsinghua University, Xiaoqiu Chen and Hao Wu of Nuclear and Radiation Safety Center.

References

[1] Lingdong Nuclear Power Co., Ltd., Final safety analysis report of LDNPC unit 3&4, 2009.

[2] Liaoning Hongyanhe Nuclear Power Co., Ltd., Final safety analysis report of LHNPC unit 1&2, 2011.

[3] Taishan Nuclear Power Joint Venture Co., Ltd., Final safety analysis report of TNPJVC unit 1&2, 2012.

[4] Sanmen Nuclear Power Co., Ltd., Final safety analysis report of SMNPC unit 1&2, 2012.

[5] NUREG-0017 Calculation of Releases of Radioactive Materials in Gaseous and Liquid Effluents from Pressurized Water Reactors PWR-GALE Code, 1985.

[6] ANSI/ANS-18.1-1984.American National Standard Radioactive Source Term for Normal Operation of Light Water Reactors, 1984.

[7] 10CFR20 Standards for Protection against Radiation, Appendix B. Annual Limits on Intake(ALIs) and Derived Air Concentration(DACs) of Radionuclides for Occupation Exposure; Effluent Concentrations; Concentrations for Release to Sewerage, 1991.

[8] China Nuclear Power Technology Research Institute. Study on the optimization of primary coolant source terms—corrosion products and fission products, 2013.

Advanced Materials Research Vols. 986-987 (2014) pp 572-576

doi:10.4028/www.scientific.net/AMR.986-987.572

SUMMARY OF STUDY ON ERROR EVALUATION INDICES OF POWER SYSTEM SIMULATION MODEL

Zhaolei Qin[1,a], Xiaohui Ye [2,b], Lina Wu[1,c], Guanqi Liu[1,d], Xinli Song [2,e], Suna Jiang[3,f], and Tao Liu[2,g]

[1] School of Electrical & Electronic Engineering, North China Electric Power University, Baoding, 071003, China
[2] Power System Department, Electric Power Research Institute, Beijing, 100192, China
[3] School of Electrical & Electronic Engineering, North China Electric Power University, Beijing, 102206, China

[a]993787002@qq.com, [b]yexiaohui@epri.sgcc.com.cn, [c]wlnlovely@163.com, [d]liugq566@sina.com, [e]songxl@epri.sgcc.com.cn, [f]jsn2008@ncepu.edu.cn, [g]liutao@epri.sgcc.com.cn

Keywords: power system, simulation model, error evaluation, index classification

Abstract. The integrity, objectivity and science of the evaluation index system will be directly related to the accuracy of the evaluation results. However, studies on the quantitative assessment of the effectiveness of the simulation model are not still perfect, comprehensive, and links between relevant literatures are not close enough. The main thing is the lack of systematic summary of the theoretical literatures. Therefore, this paper is summarized in three aspects, the research results, indices classification and their respective advantages and disadvantages, the applicable range of indicators.

Introduction

Power system dynamic simulation plays an increasingly important role in the operation of the system, the credibility of the simulation results directly affect security and economy of system operation [1]. Improving the credibility of the dynamic simulation is only based on ensuring the effectiveness of the model and the parameters involved in the simulation [2], with the increasing complexity of modeling and simulation, the validity and reliability of the simulation model are paid more and more attention.

Currently, there are a number of domestic and foreign literatures for the quantitative assessment of the simulation model error indicators conducted in-depth study [3], and achieved certain results. In [4], it marks the arrival of an accurate simulation of the times, which is a landmark article. In [5], in order to find error sources and validate effectiveness of the model, measurement data based on WAMS (wide-area measurement system) were used to simulate the grid block. But the number of components in each sub-block is still large, how to further confirm the validity of the model is still difficult. In [6], the method of spectral analysis were used to verify simulation model validation, but spectral estimation, which need zero mean and smooth processing for sequence, changed the original information of the timing, and the problem of the algorithm‘s order was not solved. In [7], the frequency, damping, energy and other characteristics were extracted by Prony transformation method. In [8], the similarity principle, which calculated numerical similarity of measurement and simulation sequence, was exploited to quantitatively analyze simulation accuracy. In [9], a method of evaluating the model effectiveness considering the numerical similarity and the shape similarity was proposed, this method applied specification coefficient method, landmark boundary method and correlation analysis to calculate shape similarity. In [10], the types of residual analysis and Theil coefficient were introduced in detail, a dynamic simulation method based on residual analysis for the load model was proposed. In [11], a simulation evaluation method based on fuzzy analytic hierarchy process was raised, and error sources backtracking theory based on PMU measurement data block was proposed. In [12], in order to make a quantitative assessment of the confidence level for simulation system, the system identification method combining similarity was used to measure the similarity between actual model and simulation model.

As can be seen from the above literature review, studies on the accuracy of the power system simulation model are mostly in its infancy. The relevant literatures are very little, mostly confined to a detail study, or lacked a solid theoretical foundation.

Classification of Error Indices

At present, there is no systematic theory specifically for dynamic simulation model error within the power discipline [13]. But from the literature review, some experts use some error methods in dealing with the specific research topic, Integrated into two types: qualitative analysis and quantitative analysis.

The qualitative error indicators include mainly visual and graphic error method etc [14]. Qualitative indicators errors under certain circumstances, is intuitive and effective, but it is largely constrained by the subjective will of the analysts, and it is difficult to accurately assess the accuracy of the model, so there is no more introduced in detail.

Currently, researches on the quantitative error evaluation method are mainly concentrated in the numerical analysis, eigenvalue analysis, correlation-based analysis and pattern recognition analysis [15]. In this paper, take the generator model as an example, according to mechanism and application of several quantitative analyses, error indicators are classified, summarized in Table 1.

Table 1 List of several error indicators

Indices Type Name	Indices name		Objective function	Advantages and disadvantages
Numerical Indices	Residual analysis	Error sum of squares (SSE)	$\mathrm{SSE}=\sum_{i=1}^{n} w_i(y_i-\hat{y}_i)^2$	Numeric indices method: simple, easy to calculate, ignoring the parallel drift, noise and other factors, not effectively reflect the dynamic characteristics of time sequence [16]; AE and MSE: reflect the average error; SSE: absolute error accumulation, high requirements for sampling points; REE: true and reliable results, physical information-rich, strong guidance.
		Mean absolute error (MAE)	$\mathrm{MAE}=\frac{1}{n}\sum_{i=1}^{n}\lvert y_i-\hat{y}_i\rvert$	
		Mean square error (MSE)	$\mathrm{MSE}=\frac{1}{n}\sqrt{\sum_{i=1}^{n}(y_i-\hat{y}_i)^2}$	
		Mean absolute percentage error (MAPE)	$\mathrm{MAPE}=\frac{1}{n}\sum_{i=1}^{n}\left\lvert\frac{y_i-\hat{y}_i}{y_i}\right\rvert$	
		Mean square percentage error (MSPE)	$\mathrm{MSPE}=\frac{1}{n}\sqrt{\sum_{i=1}^{n}(\frac{y_i-\hat{y}_i}{y_i})^2}$	
		Average error(AE)	$\mathrm{AE}=\frac{1}{4}(\mathrm{MAE}+\mathrm{MSE}+\mathrm{MAPE}+\mathrm{MSPE})$	
	Ratio of error energy(REE)		$\mathrm{REE}=\frac{\sum_{i=1}^{n}(y_s(i)-y_m(i))^2}{\sum_{i=1}^{n}(y_m(i)-y_{stab})^2}$	
Eigenvalue Type Indices	Frequency similarity(FS)		$\varphi_t=\sum_{i=1}^{n_s}(\gamma_i\delta_i)$ Value close to 1 description error is smaller.	FS and DS can measure the dynamic variable mode [17]. Prony can give characteristic quantities of dynamic response variables in each oscillation mode, such as damping, frequency, amplitude, phase, and energy, etc. Sensitive to the noise signal, Must avoid the strong non-linear [18,19]. FSAE: Relative value form,
	Damping similarity(DS)		$\varphi_\zeta=\sum_{i=1}^{n_s}(\gamma_i\eta_i)$ Value close to 1 description error is smaller.	

	The first swing characteristic Indices	The first swing amplitude error (FSAE)	$FSAE = \frac{M_S - M_m}{M_m}$ Value close to 0 description error is smaller.	reflecting the impact of the size of the fault.
		The first swing error energy ratio (FSEE)	$FSEE = \frac{\sum_{i=1}^{n}(y_s(i) - y_m(i))^2}{\sum_{i=1}^{n}(y_m(i) - y_{stab})^2}$ The indices share similar physical meaning with REE	
Related Type Indices	Correlation coefficient shape similarity(CCSS)		$CCSS = \frac{\sum_{i=1}^{n}(x_i - \bar{x})(y_i - \bar{y})}{\sqrt{\sum_{i=1}^{n}(x_i - \bar{x})^2}\sqrt{\sum_{i=1}^{n}(y_i - \bar{y})^2}}$ Value is larger, the higher the trajectory similarity	Correlation coefficien Can effectively measure the shape similarity of two time series [20]. DGI: Principle is simple, easy to master, easy to calculate, sort clear. TIC: Easing the requirements for data sequence does not require independence and normality.
	Degree of grey incidence(DGI)		$DGI = \frac{1}{n}\sum_{k=1}^{n}\gamma(x_0(k), x_i(k))$ If greater than the given values, that satisfy the accuracy requirements	
	Theil's inequality coefficients(TIC)		$TIC = \frac{\sqrt{\sum_{i=1}^{n}(y - \hat{y})^2}}{\sqrt{\sum_{i=1}^{n} y^2} + \sqrt{\sum_{i=1}^{n} \hat{y}^2}}$ Value close to 0 description error is smaller.	
Pattern Recognition Indices (PRI)	Statistical pattern recognition method(SPRM)		---	PRI can analyze complex signals and image, dependent samples and expert scoring, complex calculation process.
	Structural pattern recognition method(SPRM)			

The alphabet notes are as follows:

n: Dynamic response variable sampling points; $y_i, \hat{y}_i$: Sampled values of the measurement and simulation dynamic response variables at the i point; w_i: Weights; $y_s(i)$: simulation Variables; $y_m(i)$: Measurement Variables; y_{stab}: Measurement value of the variable before oscillation occur; n_3: The number of signal processing decomposition; $\gamma_i = \frac{\lambda_i'}{\sum_{j=1}^{n}\lambda_j'}$: Signal Weights ($\lambda_i'$: signal energy); $\delta_i = 1 - |\frac{f_{mi}' - f_{si}'}{f_{mi}'}|$: Frequency similarity ($f_{mi}'$、$f_{si}'$ frequency of measurement and simulation); $\eta_i = \begin{cases} 1 - \left|\frac{\zeta_{mi}' - \zeta_{si}'}{\zeta_{mi}'}\right| & \zeta_{si}' > 0 \\ 0 & \zeta_{mi}'\zeta_{si}' < 0 \end{cases}$: Damping similarity ($\zeta_{mi}'$、$\zeta_{si}'$: Damping of measurement and simulation Variables);

M_S: Measurement variable value of the first swing; M_m: Simulation variable value of the first swing.

The scope of application

The each method of above has its own merits. When selecting the error calculation methods, the selected indices must reflect the characteristics of dynamic variables, and can provide enough information to find the source of error.

Curves that represent the dynamic characteristics of the system include the swing curves, power curves and voltage curves in studies on the dynamic characteristics of the power system [21]. Those curves will be taken for example to illustrate the scope of the above several error indices' application in table 2.

Table 2: The scope of the above several error indices' application

Error evaluation indices		Swing curve	Power curve	Voltage curve
Numerical Indices	Error sum of squares(SSE)	✓	✓	✓
	Mean absolute error(MAE)	✓	✓	✓
	Mean square error(MSE)	✓	✓	✓
	Mean absolute percentage error(MAPE)	✓	✓	✓
	Mean square percentage error(MSPE)	✓	✓	✓
	Average error(AE)	✓	✓	✓
	Ratio of error energy(REE)	✓	✓	✓
Eigenvalue type Indices	Frequency similarity(FS)	✓	✓	×
	Damping similarity(DS)	✓	✓	×
	The first swing amplitude error(FSAE)	✓	✓	×
	The first swing error energy ratio(FSEE)	✓	✓	×
Related type indices	Correlation coefficient shape similarity(CCSS)	✓	✓	×
	Degree of grey incidence(DGI)	✓	✓	✓
	Theil's inequality coefficients(TIC)	✓	✓	✓
Pattern Recognition indices	Statistical pattern recognition method(SPRM)	✓	✓	✓
	Structural pattern recognition method(SPRM)	✓	✓	✓

Comment：✓: Applicable; ×: Inapplicable.

As can be seen from the table, most of the error indices in these three curves can all be used. The specific method of selecting the error indices should depend on the specific circumstances and information of elements.

Conclusion and Outlook

This paper have done a more detailed collate and summarize about studies on the error evaluation indices in the field of power system, divided error evaluation indices of simulation model into four categories, provided a method reference for the study on error evaluation, and had certain guiding significance for analyzing and selecting a different indices system.

Study on model error evaluation of power system dynamic simulation still need to dig deeper dynamic characteristics, and error evaluation indices that can reflect dynamics characteristics well should be put forward dynamic performance good to guide research.

References

[1] Renmu He. Research into veracity of power system dynamic simulation[J]. Power System Technology, 2000, 24(12): 1-4(in Chinese).

[2] Cheng Zhou and Renmu He. Assessment on simulation a accuracy of power system component models[J]. Power System Technology, 2009, 33(14): 12-15(in Chinese).

[3] Huang Z Y, Kosterev M and Guttromson R. Model validation with hybrid dynamic simulation[C]. Proceedings of IEEE Power Engineering Society General Meeting 2006, Montreal, Canada, 2006.

[4] Huang Z, Guttromson R and Hauer J. Large-scale hybrid dynamic simulation employing field measurements[C]. Proceedings of the IEEE Power Engineering Society General Meeting, 2004,Denver, USA, 2004.

[5] Pereira L, Undrill J and Kosterev D. A new thermal governor modeling approach in the WECC[J]. IEEE Trans on Power Systems, 2003,18(2): 819-829.

[6] Patterson S, Kosterev D, Davies D. New thermal governor model selection and validation in the WECC[J]. IEEE Trans on Power Systems, 2004, 19(1): 517-523.

[7] Kosterev D. Hydro turbine-governor model validation in pacific northwest power systems[J]. IEEE Trans on Power Systems, 2004, 19(2): 1144-1149.

[8] Kosterev D N,Tylor C W,et al.Model validation for the august10, 1996 WSCC system outage[J]. IEEE Trans on Power Sys-tems,1999,14(3).

[9] Jin Ma, Wenjin Sheng, Renmu He. A simulation validation strategy based on wide area measurement[J]. Automation of Electric Power Systems, 2007, 31(18): 11-16(in Chinese).

[10] Bo Bo, Ma Jin. A hybrid dynamic simulation validation strategy based on time-varied impedance[J]. Automation of Electric Power Systems, 2009, 33(6): 6-10(in Chinese).

[11] Song Gao, Renmu He, Jin Ma. Error Criteriaon Power System Dynamie Simulation Validation [J]. Automation of Electric Power Systems, 2006, 30（4）：6-10.

[12] Cheng Zhou, Renmu He, Jili Wang. Dynamic Evaluation of Effectiveness of Power System Simulation Models[J]. Power System Technology, 2009, 33（14）：12-15.

[13] Han Dong, Ma Jin, He Renmu, et al. Uncertainty analysis in dynamic characteristics of load model based on probabilistic collocation method[J] . Proceedings of the CSEE , 2008 , 28(19) : 71-76(in Chinese).

[14] Wu Di, Xin Huanhai, Gan Deqiang. Evaluation on impact ofparameter uncertainty in power system dynamic simulation[J]. Automation of Electric Power Systems, 2008, 32(5)：15-19(in Chinese).

[15] Zhu Fang, Tang Yong, Zhang Dongxia, et al. Influence of excitation and governor model parameters on simulation of large-disturbance test in Northeast China power grid[J]. Power System Technology, 2007, 31(4)：69-74(in Chinese).

[16] Shikao Liu, Xingtang Liu, Wen Zhang. Fixed Quantity Evaluation to Reliability of Simulation System with Similar Degree[J]. Journal of System Simulation, 2002, 14（2）：143-145.

[17] Cheng Zhou, Renmu He. Accuracy Assessment of Power System Dynamic Simulation Based on Landmark Method[J]. Proceedings of the CSEE, 2010, 30（7）：42-47.

[18] Jin Zhang. Research on Validation of Power System Dynamic Simulation[D]. Beijing: North China Electric Power University, 2005.

[19] Hongjun Li. Researches on Power System Dynamic Simulation Error[D]. Beijing: North China Electric Power University, 2005.

[20] Jiang He. Research on Validity Evaluation and Paramter Calibration of Generator Model Based on Hybrid Dynamic Simulation[D]. Chongqing: Chongqing University, 2011.

[21] Zhaoqiang Wu. Research on Power System Dynamic Simulation Error Criteria[D]. Beijing: North China Electric Power University,2008.

Advanced Materials Research Vols. 986-987 (2014) pp 577-580

doi:10.4028/www.scientific.net/AMR.986-987.577

Sustained Overvoltage Control Considering Power System Restoration Dynamic Process

Bin Chen[1, a], Hongtao Wang[1, b], Zhongkang Wei[2], Chunyi Wang[3]

[1]Key Laboratory of Power System Intelligent Dispatch and Control of Ministry of Education, Shandong University, Jinan 250061, China; [2]State Grid Jibei Electric Power Company, Beijing 100053, China; [3]State Grid Shandong Electric Power Company, Jinan 250001, China

[a]rcuhvg@163.com, [b]whtwhm@sdu.edu.cn

Keywords: Sustained overvoltage; Power system restoration; Sensitivity and safety margin

Abstract. Changeable sensitivity and safety margin are proposed in this paper, which can avoid the voltage violation according to the operation of the current situation. A simulation test is presented to demonstrate the proposed method can decrease adjusting amounts and restoration time efficiently.

Introduction

In order to speed up the process of power system restoration (PSR), it's necessary to energy some high and extra-high voltage transmission lines during the early stages. Most of these transmission lines are unloaded or lightly loaded, which will cause sustained power frequency overvoltage because of the serious reactive power imbalance.

Reference [1] presented a simple and approximate approach for evaluating sustained and transient voltages, which can provide approximate solutions. Reference [2] presented sensitivity analysis and Efficiency Coefficients method to determine the most efficient control variables for the correction of voltage violations. Reference [3] compared PSR with normal system, applied expert system technique and nonlinear programming to provide the control scheme.

However, the methods mentioned above are static optimization without considering the whole process of PSR and global optimization. This paper takes sensitivity analysis and safety margin into consideration, adjusts the coefficient properly according to the PSR process, which can coordinate the voltage safety and the PSR time preferably.

Problem Formulation

Compared with the normal condition of power system, during the early stages of restoration, most of the control devices and loads are out of service. Adjusting these new control variables uses less time than readjusting those already in-service control variables, so these new control variables take the higher priority. It's preferable to find a solution which has less adjusting amounts of control variables and enough safety margin to cope with the subsequent operations.

Objective Function. The proposed object is to minimize the adjusting amounts of control variables and the voltage deviation, which can be formulated as follows

$$\min \ f = \sum_{i \in N} \left(V_i - 1.0\right)^2 + \sum_{j \in K} C_j \Delta u_j^{\ 2}, \tag{1}$$

where N is the number of bus; K is the number of control variables; V_i is the bus voltage; C_j is the coefficient decided by the reciprocal of sensitivity; Δu_j is the deviation of control variables.

Constraints. During PSR, the objective function is subjected to the power flow equations and the operating limits like voltage, power limits and device limits, which can be written as

$$\begin{aligned} &\mathrm{F}(u, x) = 0 \\ &\mathrm{G}(u, x) \le 0 \end{aligned}, \tag{2}$$

where x is bus voltage; u is control variable.

Sustained Overvoltage Control Strategy

Sensitivity Analysis Based on Adjoint Network Method[4]**.** The power flow equation can be expressed as

$$E_M^* Y_T V_M = S_M^*, \tag{3}$$

where E_M is a diagonal matrix with node voltage of each elements; Y_T is the nodal admittance matrix; V_M is the nodal voltage matrix ; S_M is the nodal injection power matrix.

The follow equation can be obtained from adjoint network,

$$\begin{bmatrix} K^T & (\overline{K}^*)^T \\ \overline{K}^T & (K^*)^T \end{bmatrix} \begin{bmatrix} \hat{\dot{V}} \\ \hat{\dot{V}}^* \end{bmatrix} = \begin{bmatrix} \hat{\mu} \\ \hat{\mu}^* \end{bmatrix}, \tag{4}$$

where $\hat{\mu} = \dfrac{\partial f}{\partial \dot{V}_M}$; $\hat{\dot{V}}$ is the adjoint voltage; K and $\overline{K}$ is decided by the type of node.

If defining $d = \delta S_M^* - \dot{E}_M^* \delta Y_T \dot{V}_M$, Where δS_M^* , δY_T are the first order change of S_M^* , Y_T , respectively, then the first order change of f can be expressed as

$$\delta f = [(\hat{\dot{V}})^T \quad (\hat{\dot{V}}^*)^T] \begin{bmatrix} d \\ d^* \end{bmatrix} + \delta f_P, \tag{5}$$

take the adjoint voltage into the above function can get the first order change of f and sensitivity.

The Value of Coefficient C. When sustained overvoltage occurred during PSR, adjusting the control variables according to the sensitivity can decrease the adjusting amounts efficiently. If the bus voltage is higher than safety limits, switching the control variables can lower the bus voltage level in the whole system, however it can also cause bigger deviation to the bus whose voltage is lower than safety limits, vice versa.

Suppose the voltage of bus *i* is the highest and greater than 1.0 p.u. , the voltage of bus *j* is the lowest and less than 1.0 p.u. ; the sensitivities of the voltage at bus *i* to the all control variables is S_i , where S_i={ $S_{n1,i}$, $S_{n2,i}$, … , $S_{nk,i}$ }, the sensitivities of the voltage at bus *j* to the all control variables is S_j , where S_j={ $S_{n1,j}$, $S_{n2,j}$,… , $S_{nk,j}$ }. Defining the sensitivities of all control variables to the system is S, where $S = S_i - S_j$, S={ S_{n1}, S_{n2}, … , S_{nk}}.

As mentioned above, switching unadjusted device uses less time than readjusting already switched device. If there are D control variables unadjusted under the present condition, the sensitivities of these variables is S_{new} = {S_{i1}, S_{i2}, … , S_{id} }, then it can be redefined as

$$S'_{id} = 10 * S_{max} * \frac{S_{id}}{S_{idmax}}, \tag{6}$$

where S_{max} is the max sensitivity of all control variables, S_{idmax} is the max sensitivity of unadjusted control variables.

Define C_i=1/ S'_{ni}, then C_i can have the similar function as unit adjustment cost used in optimal reactive power dispatch, which will get the minimum adjusting amounts.

During the PSR, if adjust the bus voltage according to the sensitivity of voltage alone, the bus voltage may stay near the safety limits. When restore next element, it is very likely to cause new voltage violation. So it's reasonable to adjust the control variables as less as possible, and meanwhile, leave appropriate safety margin to keep the voltage safe in the following steps.

Solving Method

PSO is adopted to solve this reactive/voltage control problem. The position of particle is corresponding to the control variables, including the voltage of generator bus, the tap position of reactive compensator and transformer, this paper only take the generator bus voltage and tap position of reactive compensator into consideration, so the x_{id} can be expressed as

$$x_{id} = [V_{G1}, ..., V_{GN_G}, Q_{C1}, ..., Q_{CN_C}]. \tag{7}$$

The position of each iteration is shown as follows

$$\begin{aligned} v_{id}^{k+1} &= \omega v_{id}^{k} + c_1 r_1 (p_{id}^{k} - x_{id}^{k}) + c_2 r_2 (p_{gd}^{k} - x_{id}^{k}) \\ x_{id}^{k+1} &= x_{id}^{k} + v_{id}^{k+1} \end{aligned}, \quad (8)$$

where ω is the weight; v_{id} is velocity of particle; c_1 and c_2 are positive constants; r_1 and r_2 are random numbers between [0,1]; p_{id} and p_{gd} are the best position of individual and particle swarm, respectively.

Simulation Study

IEEE 39-bus system is used to evaluate the proposed model, as shown in Fig1, where including ten generators, and four reactive compensators at bus 2,13,22,26, the capacity is 6*-0.2 respectively.

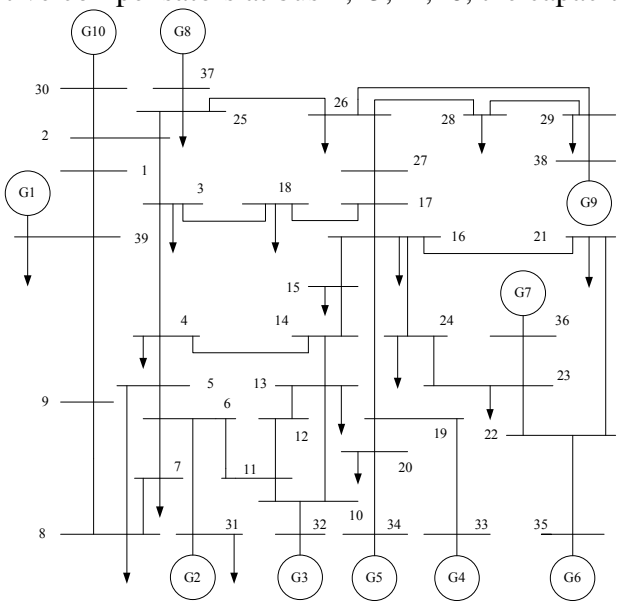

Fig.1. IEEE 39-bus New England test system

According to restoration plan in [5], the system is restored from bus30 using G10 as BSU. The steps before cranking a NBSU are shown in Table 1, the voltage limitation is [0.95, 1.05], and if the voltage adjustment of generator bus is less than 0.001 p.u., it is regarded as unchanged.

Table 1 Comparison of the result for different methods

	The method in this paper		Consider sensitivity alone	
	Voltage violation	Adjusted variable	Voltage violation	Adjusted variable
Bus 2	No	None	No	None
Bus 25	No	None	No	None
Bus 1	No	None	No	None
Bus 3	No	None	No	None
Bus 37	No	None	No	None
Bus 39	Yes	G10, C2	Yes	G10
Bus 26	No	None	Yes	G10
Bus 4	No	None	Yes	G10
Bus18	No	None	Yes	G10
Bus27	No	None	No	None
Bus5	No	None	Yes	G10,C2
Bus14	Yes	G10,C26	Yes	G10,C2
Bus17	No	None	Yes	G10
Bus6	No	None	Yes	G10

As the data shown in Table1, the method proposed in this paper has less adjusting amounts. Also the control variables adjusted firstly in the method are unadjusted or new devices, which means this method uses less time than considering sensitivity alone.

Summary

This paper presents a new method for sustained overvoltage control during PSR, in which the safety margin and changeable sensitivity according to the current situation are considered. Simulation test demonstrates that the proposed method can decrease adjusting amounts and restoration time of the PSR process efficiently.

Acknowledgments

This paper was supported by National Natural Science Foundation of China(51177092); National High-tech Research and Development Program of China(863 Program) (2011AA05A101).

References

[1] M. M. Adibi, R. W. Alexander and D. P. Milanicz. Energizing high and extra-high voltage lines during restoration. IEEE Transactions on Power Systems, vol. 14, pp. 1121-1126, Aug. 1999.
[2] Cheng G H, Xu Z. A method for sustained overvoltage control during power system restoration. Power Systems Conference and Exposition, 2004. IEEE, 2004: 473-477.
[3] Ruan Y, Yuan R, Tang X, et al. A new method for control of sustained over-voltage during the early stages of power system restoration. Power and Energy Engineering Conference, 2009. APPEEC 2009. Asia-Pacific. IEEE, 2009: 1-5.
[4] E. Z. Wang and Y. H. Zhao, Sensitivity Analysis and Load Flow of Power Networks. Beijing: China Machine Press, 1992.
[5] Sun W, Liu C C, Zhang L. Optimal generator start-up strategy for bulk power system restoration . Power Systems, IEEE Transactions on, 2011, 26(3): 1357-1366.

Advanced Materials Research Vols. 986-987 (2014) pp 581-585

doi:10.4028/www.scientific.net/AMR.986-987.581

The Application of Cluster Analysis Algorithm in The Indicators Comparison of Grid Enterprise

Xue wanlei[1],Lu kuan[1], Zhao xin[1],Liu xiaoli[2],Xu nan[1], Wei yang[2]

([1] Economic & Technology Research Institute, State Grid Shandong Electric Power Company, Shandong Jinan 250021;[2] North China Electric Power University college of economic and management,Beijing Changping 102206)

Keywords: cluster analysis algorithm; the indicators comparison of industry; power supply quality; Grid Enterprise

Abstract. This paper focuses on the application of cluster analysis algorithm in the indicators comparison of power industry. The provincial power companies are classified by the power supply quality indicator with K-means clustering algorithm to identify the standard companies and to verify the feasibility and effectiveness of the algorithm. The results show that the cluster analysis enable the power companies to accurately identify the gap between the enterprise and the benchmark of industry, so as to continuously improve the level of management and benefit.

CLC number：TM715

Introduction

With the development of power industry benchmarking activities, benchmarking enterprises continue to increase, the benchmarking index system has been improved.In order to quickly find out the potential distribution of indicators from the index data where a large number of irregular in,it is necessary to conduct a reasonable division to the standard enterprise,cluster analysis is a very effective method. Common modeling methods including K-means algorithm, fuzzy C-means algorithm and improved neural network algorithm.

This paper will select the index data of 24 provincial power companies,By K-means algorithm cluster analyzed the supply quality indicators of provincial company.and benchmarking Enterprise elected from each of the power companies in the index,through the analysis of the gap between benchmarking enterprise. identify their own deficiencies, and enhance the management level.

K-means algorithm

1.1 Data processing

Because of the complexity of the benchmarking index system and the diversity of the data,we need to process the data comparability before performing indicators cluster analysis,it mainly includes forward processing and the dimensionless processing two aspects.

（1） Forward processing

The evaluation standard of the benchmarking index the benchmarking index are not the same, some index value bigger is better,these index values are called the forward index, such as the rate of return on total assets, the tariff rate etc;Some index value smaller is better,these index values are called the reverse index, such as the line loss rate etc;Some index value need to reach a certain standard, these index values are called appropriate index,such as asset-liability ratio etc.In order to facilitate a comprehensive evaluation of the indexes.we need to do forward processing for the indexes, for the reverse index we can take it's opposite number,for appropriate index can take it's absolute value of the difference between the actual value and the standard.

（2）Dimensionless processing

Statistical unit is different between different indexes. Statistical unit in different grid enterprises of the same index may be different. Therefore, we need to do dimensionless processing for the original data of the indexes.Dimensionless method includes the following.

①Extreme value method

Through the calculation of the index which between its actual value and extreme value (Maxima or minima),we can do dimensionless processing for the indexes:

$$v_i' = \frac{v_i}{\max v_i} \quad (1)$$

②Standard deviation method

Using the standard deviation of index, we also can do dimensionless processing for the indexes,But this method is more reasonable when the original data of index in a normal distribution , and the processing method as follows:

$$v_i' = \frac{v_i - \overline{v_i}}{s} = \frac{v_i - \overline{v_i}}{\sqrt{\frac{1}{n}\sum (v_i - \overline{v_i})^2}} \quad (2)$$

In which, v_i is the actual value of a index, v_i' is the dimensionless value of this index and s is the standard deviation of it.

These two dimensionless methods assume that the actual value of index and the dimensionless value is linear relationship,however, in practice the two are not necessarily proportional change,therefore, the dimensionless processing needs concrete analysis according to the actual situation.

1.2 K- means Algorithm process

The basic idea of the K-means algorithm is firstly selected K points as the initial cluster centers, and then calculated the distance that each sample to the cluster center , the sample was attributed to the location which is nearest to the cluster center of class.Calculate of the clustering center of new class after the adjustment,If the clustering center adjacent two times without any changes,it shows that the sample have adjusted, clustering criterion function J_c convergence.After finishing the adjustment of the whole sample, modified the cluster center, go to the next iteration[1-3].The results of K-means algorithm depends on the choice of the initial cluster centers. Accurate selection of the initial centers will greatly reduce the iterative steps.Specific steps as the following:

Step1:given *n* sample dates,at the same time select *K* clustering centers C_j, $j = 1,2,...,K$

Step2:Calculate the distance $d(v_i, C_j)$ $i = 1,2,...,n;$ $j = 1,2,...,K$ of each sample data and the *K* clustering centers, if the distance satisfied $d(v_i, C_b) = \min\{d(v_i, C_j), i = 1,2,...,n\}$

if the distance satisfied $d(v_i, C_b) = \min\{d(v_i, C_j), i = 1,2,...,n\}$ the sample data should be categorized as the *b* clustering center.

Step 3:Recalculate the clustering center $C_j(i+1)$ and the clustering criterion function *Jc*

$$C_j(i+1) = \frac{1}{n_j}\sum_{i=1}^{n_j} v_i^{(j)}, j = 1,2,...,K \quad (3)$$

$$J_c(i+1) = \sum_{j=1}^{K}\sum_{b=1}^{n_j}\left\| v_b^{(j)} - C_j(i)\right\|^2 \quad (4)$$

Among them, n_j is the number of sample data in section *j* clustering , $v_i^{(j)}$as the sample data of the section *j* clustering.

Step 4:If $|J_c(i+1) - J_c(i)| < \varepsilon$,then the algorithm end,else let *i=i+1,*back to the step2 to reclassify.

1.3 The application of K- means algorithm

In the electric power enterprise benchmarking process,determining the benchmark enterprise is a very important content .Cluster analyzed the electric power enterprise benchmarking with K-means algorithm ,which can be divided into the following steps.

(1)Data processing

The good or bad of data processing will determine the efficiency, the accuracy and effectiveness of the final result of the clustering analysis.Therefore, we should do pretreatment for the original data of each index benchmarking ,using the formula (1) or (2) do the forward processing and dimensionless processing for the data, which can be directly carried out cluster analysis.

(2)Choose clustering index

Because the electric power enterprise benchmarking index system is more complex, the data which need to collect is complex,therefore, in the selection of cluster index, only need to cluster the core of index data.

(3)Using K-means algorithm for clustering analysis

K-means algorithm is a key step in clustering analysis.When using K-means algorithm, the determining of the K value will directly affect the clustering results, thus affect the evaluation of the index.Therefore, the selection of clustering center should be clearly reflected the gap between enterprises.

(4)Enterprise classification

According to the results of clustering index data we can classify the enterprise ,choose the benchmarking enterprises and determine the actual development level and the gap between benchmarking enterprises of each enterprise ,thus promote the enterprises to put the benchmarking enterprise as goal, continue to improve the ability of sustainable development and competitive ability of enterprises.

The analysis of example

Power quality has an important impact on the industrial and the safety in production, economic and living of utility users,it is not only reflected in the planning, design, construction, construction, operation and management level of electric power enterprise, is also an important indicator of the domestic and foreign various power enterprises .Therefore, this paper will use the K-means algorithm, clustering analyzed the power quality index of 24 provincial power company, established benchmarking enterprises and provided guidance and decision support for power supply quality of benchmarking management .

Assessment of China's power supply quality indicators enterprise mainly through four indicators,such as the qualified rate of city comprehensive supply voltage, the qualified rate of rural comprehensive power supply voltage, city and rural power supply reliability rate etc.Power quality related indicators of provincial power corporation in 2011 as shown in table 1.

Tab.1 Data of the power supply quality indicators of provincial power corporation in 2011

enterprise	The qualified rate of city comprehensive supply voltage %	The qualified rate of rural comprehensive supply voltage %	City power supply reliability rate %	Rural power supply reliability rate %
enterprise1	99.86	99.62	99.9813	99.9303
enterprise2	99.45	98.108	99.9309	99.762
enterprise3	97.16	97.16	99.9105	99.7653
enterprise4	99.48	98.81	99.9712	99.9401
enterprise5	99.805	98.921	99.9702	99.9066
enterprise6	96.5	96.403	99.9535	99.8085
enterprise7	99.689	99.6	99.9249	99.6262
enterprise8	99.301	94.88	99.8936	99.761
enterprise9	99.954	99.826	99.9526	99.8785
enterprise10	99.953	99.864	99.9729	99.8062
enterprise11	96.68	96.65	99.9473	99.7692
enterprise12	99.811	97.456	99.9832	99.9404
enterprise13	99.791	97.1	99.9379	99.7387
enterprise14	99.731	96.888	99.9562	99.8567
enterprise15	99.822	97.826	99.945	99.7678
enterprise16	98.24	96.567	99.943	99.7809
enterprise17	99.708	99.776	99.9403	99.6842
enterprise18	99.876	97.312	99.9182	99.7901
enterprise19	99.94	96.98	99.9286	99.7445
enterprise20	98.93	98.29	99.9287	99.8869
enterprise21	99.281	99.832	99.9209	99.6086
enterprise22	98.075	98.2638	99.8559	99.6194
enterprise23	99.656	98.35	99.9427	99.8183
enterprise24	98.98	98.56	99.8766	99.7418

Because these four indicators of power supply are positive indicators of quality, therefore it does not need to be pretreated, we can directly use K-means clustering.Can be seen from table 1.The qualified rate of city and rural comprehensive supply voltage ,city and rural power supply reliability rate all wave in three levels.In order to reflect the true difference between the various power companies,distinguish excellent, good and poor among enterprises,in this paper, K the number of clusters is determined as 3,and uses SPSS software to clustering analyze.Assuming when the clustering criterion function $J_c < \varepsilon = 0.05$, the algorithm end,the results of cluster analysis and the cluster centers are as shown in table 2 and table 3.

Tab.2 The output table of cluster analysis

enterprise	K-means algorithm		enterprise	K-means algorithm	
	Distance to the cluster center	Clustering categories		Distance to the cluster center	Clustering categories
enterprise1	0.590	1	enterprise13	0.194	2
enterprise2	1.029	1	enterprise14	0.071	2
enterprise3	0.229	3	enterprise15	0.909	2
enterprise4	0.360	1	enterprise16	1.011	3
enterprise5	0.339	1	enterprise17	0.672	1
enterprise6	1.031	3	enterprise18	0.411	2
enterprise7	0.517	1	enterprise19	0.204	2
enterprise8	2.091	2	enterprise20	1.055	1
enterprise9	0.803	1	enterprise21	0.780	1
enterprise10	0.832	1	enterprise22	1.466	3
enterprise11	0.744	3	enterprise23	0.786	1
enterprise12	0.559	2	enterprise24	0.819	1

Tab.3 The clustering center table of K-means algorithm

Clustering categories	center of clustering		
	1	2	3
Qualified rate of city comprehensive supply voltage	99.5622	99.7531	97.3310
Qualified rate of rural comprehensive supply voltage	99.1297	96.9203	97.0088
City power supply reliability rate	99.9428	99.9375	99.9220
Rural power supply reliability rate	99.7991	99.7999	99.7487

From table 2 and 3 we can see, the first class enterprises including 12 electric power enterprises, these enterprises' performance on the four indicators are good, and the indicators show a relatively balanced;the second class enterprises including 7 electric power enterprises,these enterprises' indicators of 'qualified rate of city comprehensive supply voltage' and ' rural power supply reliability rate ' is better than the first class,but the other two indicators is worse, especially 'qualified rate of rural comprehensive supply voltage' ;The third class enterprises only includes five electric power enterprises,these enterprises' performance on the 'qualified rate of rural comprehensive supply voltage'is better than the second class,but the other three indicators is worse.In summary, we can choose first class as the benchmark companies of the power supply quality benchmarking.

Considering the in the power enterprises which participate in benchmarking, first class enterprises accounted for a larger proportion, so we can choose the clustering center of the first class enterprise as a reference index value of the first type of electric power enterprise benchmarking .By comparing the gap between the first class power companies's indicators and cluster centers indicators, The power supply quality benchmarking management of the first class power company can be get more in-depth and meticulous guidance. Those enterprises which index

value is not reached the reference index value through analyzing the lagging indicator corresponding, and give some suggestions of improvement, to further strengthen the backward index management level.Those enterprises which index value reaches or exceeds the standard data, on one hand should summarize advanced experience, improve the management level of the enterprise, on the other hand, should be aimed at enterprise index more advanced, and further enhance the quality of power supply to enterprise level.

For the second and third class enterprises,they should identify the gaps with the first class enterprises, strengthen grid security management, improve the overall quality of power supply.Among them, the "Qualified rate of rural comprehensive supply voltage" is the short board of the second class enterprise , it affected the power supply quality comprehensive evaluation results of this kind enterprises .Therefore, this seven power companies should pay more attention to "rural power supply voltage integrated pass rate" indicator assessment, comparing and referring to the rural power supply management measures of the first class , dig the reason why the "Qualified rate of rural comprehensive supply voltage" behind ,then explore targeted measures and improvement programs,to achieve a balanced improvement of enterprise power quality level .

By K-means algorithm cluster analyzed the supply quality indicators of power enterprise.On the one hand, the development level of all power enterprises power quality indexes can be clear, help enterprises to put benchmark enterprises as the target to continuously improve their own deficiencies, and enhance their competitiveness;On the other hand, by clustering analysis the various indicators not only to conduct a comprehensive analysis and comparison of power enterprise quality management, and can accurately identify the root causes of the the quality of power supply gap between power enterprises.

Conclusion

In this paper, through combine the K-means algorithm with the theory and practice of electric power enterprise benchmarking , to provide decision support for electric benchmarking. Based on the basic principle of K-means algorithm, this paper studies the application of this algorithm on the power quality index in 24 provincial power company benchmarking.As can be seen from the results of cluster analysis, K-means algorithm for power enterprises peer benchmarking has a positive effect,through indicator cluster we can not only achieve a evaluation of comprehensive index, but also correctly classify the enterprise, establish business models to achieve contrast and catch up between the enterprises.

This paper is the preliminary attempt application of K-means algorithm in the electric power enterprise benchmarking.Committed to explore and verify k-means algorithm’s viability in power peer benchmarking ,there is still a lack in the establishment of analysis of electric power enterprise benchmarking.The example of this paper does not consider the impact of different power enterprise location and other objective factors, so the results lack of certain practical significance, and the k-means algorithm itself has some limitations. When the power enterprises using K-means algorithm to benchmark,the electric power enterprises need to combine their own actual situation, at the same time effectively combine with other methods such as discriminant analysis, principal component analysis etc, so as to achieve better calibration effect, provide more reliable decision support for the further development of electric power enterprises.

References

[1] Zhang jianping,Liu xiyu.Research and application of K-means algorithm based on clustering analysis[J].The research and application of computer,2007,24(05):166-168.

[2] Xu yifeng,Chen chunming,XU yunqing.An improved K2 clustering algorithm[J].Computer applications and software,2008，25(03)：275-277.

[3] Liu ludeng.The application of data mining technology in electric benchmarking[D]. Beijing:North China Electric Power University,2006:

Advanced Materials Research Vols. 986-987 (2014) pp 586-588

doi:10.4028/www.scientific.net/AMR.986-987.586

The Applications of Series Compensation Device in 10kv Voltage Level

Lijun QIN[1, a], Jiadi LI[1,b]

[1] Department of Electrical and Electronic Engineering, North China Electric Power University, Changping District, Beijing 102206, China

[b]ljd881102@163.com

Keywords: Series Compensation, Fast Switching, Voltage Quality

Abstract. This paper analyzes the voltage quality problems on transmission line of 10kv distribution network, and then introduces a series compensation device, which is based on fast switching and can effectively solve the above problem. Furthermore, this paper calculates the voltage under a actual situation, which fits the expected results.

Introduction

Currently, with the development of economic and rapid growth of electricity load, the majority of the most remote regions grid extends to areas without electricity. Due to the length of the radius of the transmission line, the quality of power supply has become increasingly prominent in the remote rural areas and low-voltage of 10kv distribution network, which is embodied in the low voltage and voltage fluctuation rate and results that the load side of the supply voltage goes far beyond the quality standards prescribed by the state and affects the production and people life. To overcome the deficiencies of existing technology described above, this paper provides a series compensated equipment based on fast switching， which can improve the terminal voltage and effectively solve the voltage quality problem so that we can make full use of energy.

The principle of series compensation device structure

This series compensation device is composed of the series capacitor, metal oxide（ZnO）, fast switching, current limiting resistors and other components. Among them, the series capacitor fits to compensate for line inductance drop and improve voltage quality. The metal oxide fits to limit the voltage across the capacitor to prevent from burning capacitor under short circuit. Fast switching fits to short-circuit capacitors and metal oxide to protect them. Limiting resistor is to prevent that the line current gets too high when switch is closed. The diagram of the device structure principle is shown below:

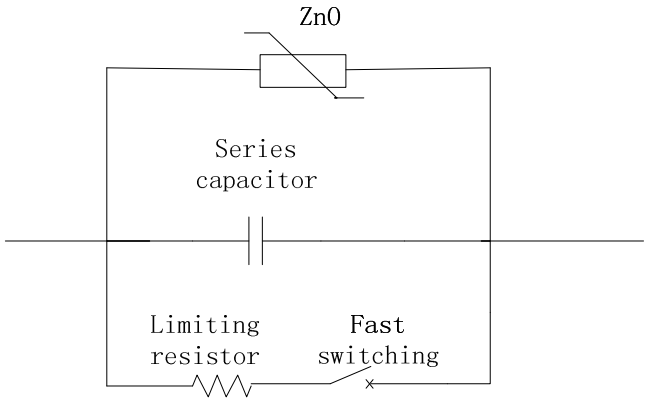

Fig.1. Series compensation device structure

When the series compensation device works properly, the capacitor is seriesed connected in line. Fast switch is open and the metal oxide is in a non-conducting state. Once the short-circuit fault occurs, the voltage across the metal oxide increases rapidly. When the voltage across the capacitor reaches the level of ZnO protection, the current through the ZnO increased rapidly. ZnO will limit the voltage added to the capacitor connected in series, and then immediately put capacitor into effect with the fault current gone.

The fast switching

The device uses a quick series of vacuum circuit breaker with fast eddy drive technology as a control executive compensation capacitor switching components. It will close in about 10ms and open less than 5ms. Combined with the rapid recognition of short circuit fault, rapid vacuum circuit breaker can be accomplished short series capacitor in about 15ms after a short-circuit fault occurs. It can significantly shorten the duration of the over-voltage so that the required energy capacity of ZnO components can be greatly reduced.

Instead of the traditional use of spark gap and 10kv circuit breakers, fast switching greatly simplifies the structure of device, improve the reliability of the device, reduce the volume and lower the cost.

Examples of simulation

Line information and operating data is shown in Table.1.

Line Information	Line length	27km	
	Taps number	33	
	Main/branch linear	LGJ-120/ LGJ-50	
Operating Data	Required data	Maximum load	Average load
	Head of the line voltage (kv)	10.49	10.51
	End of the line voltage (kv)	8.8	9.9
	Head bus current	118	83
	Head bus Power Factor	0.93	0.98

In order to improve the terminal voltage, a series capacitor is put in the middle of the line where the location voltage is 9.6kv.The capacitance values 7.15 ohms and the degree of compensation is 1.55. The compensation effect is shown in Fig.2 and Fig.3.

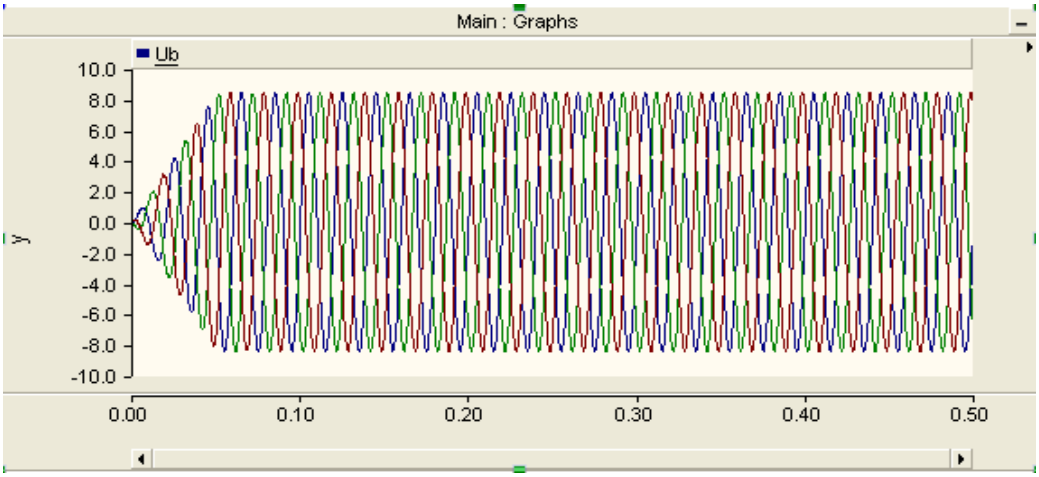

Fig.2 The end of the voltage when not compensated

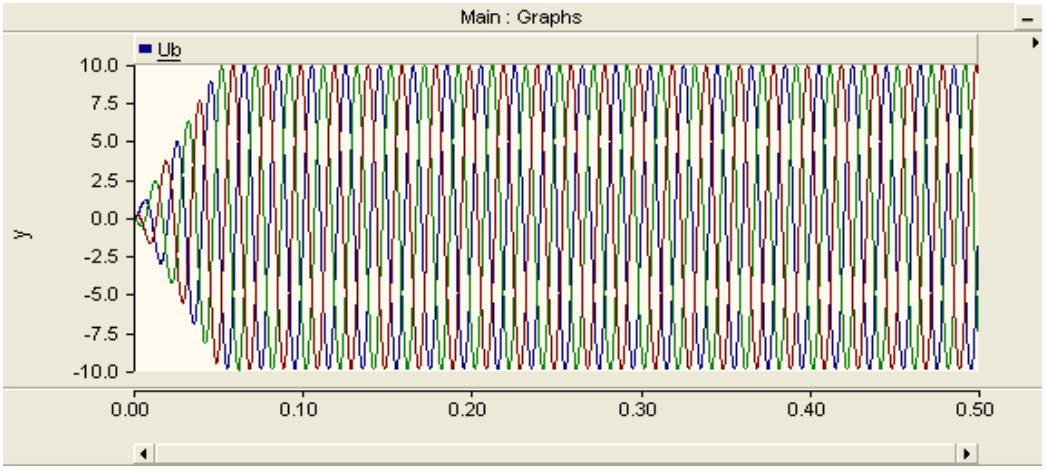

Fig.3 The end of the voltage when compensated

The compensation data under different conditions is shown in Table.2.

		Not Compensated	Compensated	Voltage Increase
End of the line voltage	Maximum load	8.8kv	9.6kv	0.8kv
	Average load	9.9kv	10.5kv	0.6kv

Visible seen from the above table, the adding series compensation not only along make the voltage meet the requirements, but also not cause excessive voltage under the average load operating conditions. The effect to improve voltage quality is apparent.

Conclusion

This paper proposed a series compensation device based on fast switching. On one hand, the fast switching can quickly short capacitance when fault is coming. On the other hand, the series compensation device makes a perfect effect on improving voltage quality.

References

[1] A new modeling and control scheme for thyristor-controlled series capacitor. Journal of Control Theory and Applications, 2009(1):P81-86.

[2] Bifurcation analysis for an SMIB power system with series capacitor compensation associated with sub synchronous resonance. Science in China(Series E:Technological Sciences), 2009(2): P.436-441.

[3] S.A.Miske. Considerations for the Application of Series Capacitors to Radial Power Distribution Circuits. IEEE Transactions on Power Delivery, 2001, 16(2).

[4] Sherif Omar Faried, Saleh Aboreshaid. Stochastic Evaluation of Voltage Sags in Series Capacitor Compensated Radial Distribution Systems. IEEE Transactions on Power Delivery, 2003, 18(3).

[5] Zhou Xiaoxin. Series compensation of power system[M]. Beijing：China Electric Power Press, 2008.

Advanced Materials Research Vols. 986-987 (2014) pp 589-592

doi:10.4028/www.scientific.net/AMR.986-987.589

The Criticality Safety Analysis of the Spent Fuel Storage Pool Area I in Small Modular Reactor

Xiangzhen HAN[a], Guoshun YOU[b]

Nuclear and Radiation Safety Center, Beijing, 100082, China

[a] email: nearly119@sina.com, [b] email:gsyou77@yahoo.com

Keywords: Criticality Safety; Spent Fuel Pool; Storage Rack

Abstract. Based on the Monte Carlo calculation method, geometric model of spent fuel storage pool Area I of small modular reactor is established, assuming infinite 6×6 type storage racks. Calculation results show that the reactivity is maximal when the water density is 1.0g/cm3. The value of k_{eff} is 0.8729 in normal storage condition. The spacing of storage racks in spent fuel pool would change in an earthquake accident condition. The values of reactivity of spent fuel pool in the assumed earthquake accident condition are also calculated. The values of k_{eff} are between 0.872 and 0.876. Both in normal condition and assumed earthquake accident condition, the values of k_{eff} are less than 0.95, to meet nuclear safety regulatory requirements.

Introduction

Maintaining sub-criticality of the fuel should be fulfilled at all times to the fuel handling and storage systems. It is 24 months fuel management program in small modular reactor. Spent fuel storage pool of small modular reactor is designed to partition layout, which is divided into storage area I and storage area II. Area I is used for the storage of new fuel assemblies before loaded into the reactor, the assemblies which are unloaded out of the core during unplanned shutdown, and the spent fuel assemblies which don't meet burn-up limit and are not allowed stored in Area II. The design of the storage racks in Area II uses burn-up credit. Area II is used for storage of spent fuel assemblies which reach a predetermined burn-up limit. Burn-up credit means taking into account the reactivity reduced of fuel irradiated in the criticality safety analysis of spent fuel storage pool. This can increase the number of storage spent fuel assemblies and the storage economy of spent fuel. In this paper, we study the criticality safety analysis of spent fuel storage pool in small modular reactor.

Calculation Code

The code used in our study is MCNP, which is a general-purpose Monte Carlo N–Particle code that can be used for neutron, photon, electron, or coupled neutron/photon/electron transport, including the capability to calculate eigenvalues for critical systems. The code treats an arbitrary three-dimensional configuration of materials in geometric cells bounded by first- and second-degree surfaces and fourth-degree elliptical tori. Pointwise cross-section data are used in MCNP. For neutrons, all reactions given in a particular cross-section evaluation (such as ENDF/B-VI) are accounted for. Thermal neutrons are described by both the free gas and S (α, β) models. Important standard features that make MCNP very versatile and easy to use include a powerful general source, criticality source, and surface source; both geometry and output tally plotters; a rich collection of variance reduction techniques; a flexible tally structure; and an extensive collection of cross-section data. MCNP code is widely used in the evaluation of criticality safety for nuclear facilities [1].

Regulations and Standards

The following are regulations and standards which are adopted and referenced in criticality safety analysis of nuclear safety review:

HAF102 "Nuclear Power Plant Design and Safety Requirements," 2004[2];

HAD102/15 "Nuclear Power Plant Fuel Handling and Storage Systems," 2007[3];

GB15146.1-2008 Nuclear criticality safety of fissile materials outside reactors - Part 1: Administrative practices for nuclear criticality safety [4];

GB15146.2-2008 Nuclear criticality safety of fissile materials outside reactors - Part 2: Basic technical practices and subcritical limits for handling, processing and operations with fissile materials [4];

GB15146.3-2008 Nuclear criticality safety of fissile materials outside reactors - Part 3: Requirements for nuclear criticality safety in the storage of fissile materials [4];

GB15146.8-2008 Nuclear criticality safety of fissile materials outside reactors - Part 8:Criticality safety criteria for the handling, storage, and transportation of LWR fuel outside reactors [4];

RCC-P "Design and Construction Rules for System Design of 900 MW PWR Nuclear Power Plants", 1991. (Amended in 1995) [5].

Critical Safety Standards

During criticality safety analysis of spent fuel storage pool Area I of small modular reactor, the enrichment of spent fuel assemblies is considered as newwith the maximal expected enrichment. It means that the enrichment of spent fuel assemblies is taken 4.2%. The design of Area I racks of spent fuel storage pool should be ensure that: At the maximal design capacity of spent fuel storage pool and the maximal acceptable new fuel enrichment of fuel asseblies, considering various uncertainties, normal and credible accident conditions, the value of keff should not be exceeded 0.95.

Geometric Model

Fuel Assemblies

Each fuel assembly contains a 17×17 rod array composed nominally of 264 fuel rods, 24 rod cluster control thimbles, and an in-core instrumentation thimble. Figure 1 shows a cross-sectional view of a 17×17 fuel assembly and the related rod cluster control guide thimble locations. The fuel rods are fabricated from cylindrical tubes made lf zirconium based alloy(s) containing uranium dioxide fuel pellets. Area I of spent fuel storage pool is used for the storage of new fuel assemblies and spent fuel assemblies which has not been reached burn-up limit. When calculating the criticality safety of spent fuel storage pool, the enrichment of fuel assemblies is assumed to 4.2% for considering conservative.

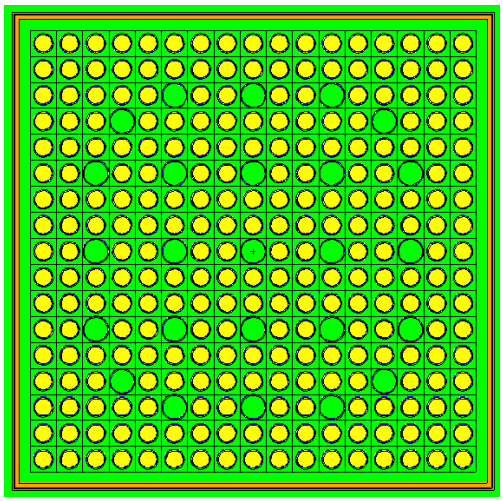

Fig.1. Fuel assembly diagram

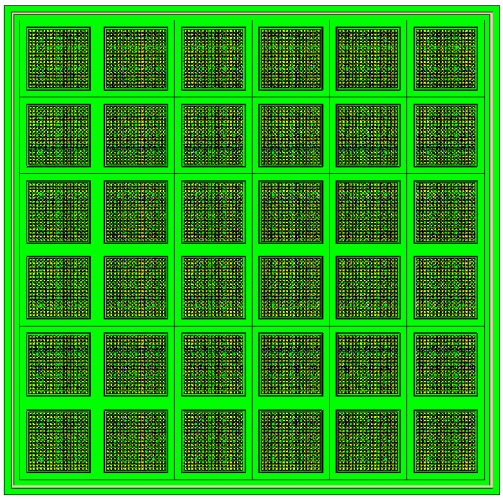

Fig.2. Storage rack model diagram

Storage Racks

New fuel is stored in a high density rack which includes integral neutron absorbing material which is cadmium to maintain the required degree of sub-criticality. The rack is designed to store fuel of the maximum design basis enrichment. Each fuel assembly is stored in stainless steel sleeve

in which cadmium panels insert. (Figure 1) The rack array center-to-center spacing of 28cm provides a minimum separation between adjacent fuel assemblies sufficient with neutron absorbing material to maintain a subcritical array.

Boundary Conditions

During criticality safety analysis of Area I of spent fuel storage pool, we analyze the relatively of 6×6 type spent fuel storage racks which are dense stored in the pool. The new fuel rack includes storage locations for 36 fuel assemblies. The rack layout and array center-to-center spacing is shown in Figure 2. There is water reflection layer of 30cm thick set on the rack. And another water reflection layer is set under the rack. For considering conservative, the boundary condition surrounded the rack of the calculation model is assumed to specular reflection. The physical meaning of the model is infinite 6×6 type storage rack arranged. The water in spent fuel storage pool is assumed to be pure, without considering the effects of neutron absorbing of boron.

Calculated Results

A calculation model of infinite storage racks arranged in space is established to calculate the reactivity in normal storage condition. This is conservative for criticality safety analysis in normal condition. In order to determine the effect of the pool reactivity on the water density caused by water temperature change, we analyze the pool k_{eff} on the influence of water temperature. The calculated results are shown in Figure 3.

It is clearly that the value of k_{eff} is lower with reduced density of water in the pool which is fulfilled with 4.2% enrichment fuel assemblies. According to Figure 3, the calculated assumed 1.0 g/cm^3 as the density of water is conserved in both conditions of normal storage and incident of criticality safety analysis.

Data in Table 1 show that the spent fuel pool k_{eff} is the maximum of 0.8729 when the density of water is assumed 1.0g/cm^3 at normal storage condition. At 95% confidence level, the values of k_{eff} are in the range from 0.87209 to 0.87372, which are all less than 0.95 and meet nuclear safety regulatory requirements.

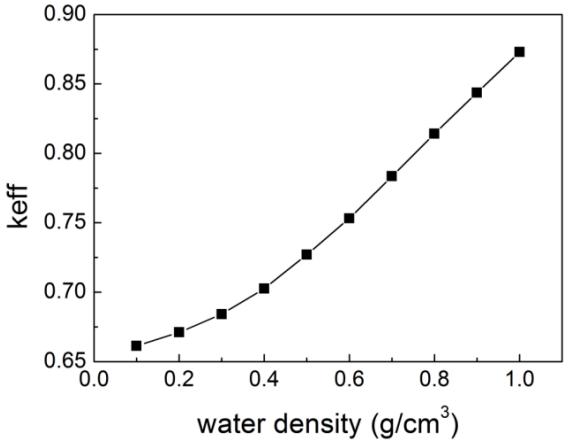

Fig.3. The function of k_{eff} with water density

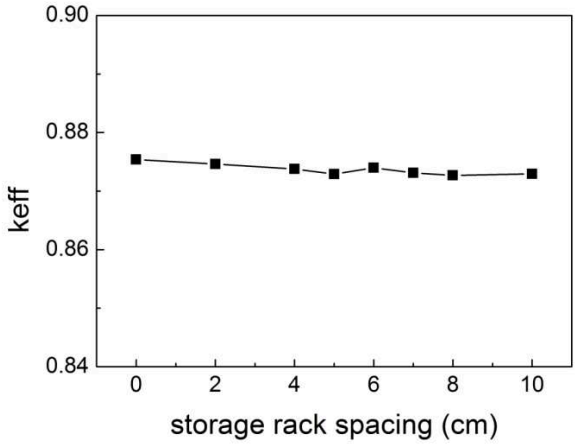

Fig.4. The function of k_{eff} with racks spacing

Accident Analysis

In this paper, we analyze the accident safety in the earthquake, and study the effect of criticality safety of spent fuel storage pool on storage racks spacing caused by the earthquake. Figure 4 shows the earthquake accident analysis results. The spacing of normal conditions between adjacent storage racks is 5cm. The calculation model simulates the effect of reactivity when rack is close to or away from each other. Figure 4 shows that the reactivity change is not obvious when the storage racks spacing change. This is due to the spacing of fuel assemblies which are in adjacent racks is maintained a certain distance when the storage racks are close to each other. So the reactivity insertion is not obvious when the spacing of storage racks change, and the value of k_{eff} is nearly the calculated value of k_{eff} of normal condition.

Conclusion

Based on the Monte Carlo calculation method, geometric model of spent fuel storage pool Area I of small modular reactor is established, assuming infinite 6×6 type storage racks. As the pool temperature will affect the moderator density, the reactivity of spent fuel pool is calculated with different water density. Calculation results show that the reactivity is maximal when the water density is 1.0g/cm^3. For considering conservative, the value of density of moderator in the pool is assumed to 1.0g/cm^3. The value of k_{eff} is 0.8729 in normal storage condition. The spacing of storage racks in spent fuel pool would change in an earthquake accident condition. The values of reactivity of spent fuel pool in the assumed earthquake accident condition are also calculated. The values of k_{eff} are between 0.872 and 0.876. Both in normal condition and assumed earthquake accident condition, the values of k_{eff} are less than 0.95, to meet nuclear safety regulatory requirements.

References

[1] Los Alamos National Laboratory, “MCNP—A General Monte Carlo N-Particle Transport Code”.

[2] HAF102 "Nuclear Power Plant Design and Safety Requirements," 2004.

[3] HAD102/15 "Nuclear Power Plant Fuel Handling and Storage Systems," 2007.

[4] GB15146-2008 Nuclear Criticality Safety of Fissile Materials Outside Reactors, 2008.

[5] RCC-P "Design and Construction Rules for System Design of 900 MW PWR Nuclear Power Plants", 1991 (amended in 1995).

Advanced Materials Research Vols. 986-987 (2014) pp 593-596

doi:10.4028/www.scientific.net/AMR.986-987.593

The Data Planning Methodology Researching on the Construction of Nuclear Plant Engineering

Xiaoling Zhu[1, a], Zhijun Wang[1, b] and Pan Chen[1, c]

[1]China General Nuclear Power Corporation

[a]zhuxiaoling@cgnpc.com.cn, [b]wangzhijun@cgnpc.com.cn, [c]chenpan@cgnpc.com.cn

Keywords: Nuclear power Plant; AEC; Data Planning（DP）; Business Model; Data Model

Abstract. Data plays more and more important roles in the AEC field, especially in Nuclear power plant constructing and engineering. In this paper, except introduce the basic DP theory and methodology, we analyzed the key points while doing the DP in nuclear power plant. Based on the analyzed results, which is an actuality of Nuclear power engineering, the paper proposed the ways to improve the data integration solution to standardize the data of project data, reduce the redundant data in the database and improve the system integration efficiency.

A. Foreword

"Development of Nuclear Power in a safe and efficient way" has been listed as a part of the "125"state planning. The development of Nuclear power now is a part of the country's energy development plan and state strategies, which has very important significance to the supply and insurance of energy usage, environment protection, structure optimization of energy chain, sustainable development strategy as well as promoting the economic and technical competitive force. But meanwhile, there are lots of challenges have been detected in nuclear power development, including the technical difficulties, large-scale construction, long-time construction period and big team collaboration, etc.

To overcome these challenges, IT technology as the backend of the business is very important as well. With the investigation and analyzation of the business process and the related data of EPCS in the whole lifecycle of nuclear plant construction, the team tried to figure out how to build up the stander of the data to improve the data quality and dig the value to serve the entire business. In our DP project, we also analyzed the data from project perspective, and focused on project planning, cost control, security, quality, experience learning. With the work above, we were trying to mitigate the islands of redundant and inconsistent data during the information system development and build up a stander to unify the way of data creating and sharing, so that the overall quality of the data can be improved to serve the business efficiently.

B. Enterprise Data Planning Overview

a) About Enterprise data planning

Data Planning is a branch of enterprise resource planning, which is focusing on the particular segment of enterprise business data model development. The so-called data planning means to follow the basic rule of database, investigate the business information and information access, and design to create a practical business oriented database model, which is used to ensure the accuracy, consistency and security of data. With the using of the data model, the information sharing will be improved, meanwhile, the core value of the enterprise business will be enhanced by leverage the value of data.

To serve the nuclear power plant building process, business process data and management information are included in data planning. And it can work as an overall blue print for the information system development during the engineering process. Understanding the business requirements and build an information data stander to close the gap during the business collaboration is one of the main purpose of data planning. With data planning implemented, the isolated data island can be mitigate, and the maturity level of system development can be improved as well. While working in the qualified information data environment, the technical and efficiency of nuclear engineering will be ultimately improved as well.

b) The Necessity of Data Planning Project

During the development of enterprises informaization, same as the other resources, like people, money, properties, etc., data resources are as important as they are, which play a more and more role to the entire company. Therefore, it should be managed like managing the other important assets. Data resources are one of the core assets of the company, and it is the core objects for data planning as well. So to establish a high-end enterprise information environment, data planning should have a global viewpoint, holistic strategy and uniform standards. The data planning project can not only serve a single department adjustment or reform, but also may related to most of the other departments. It's an enterprise-level strategic planning.

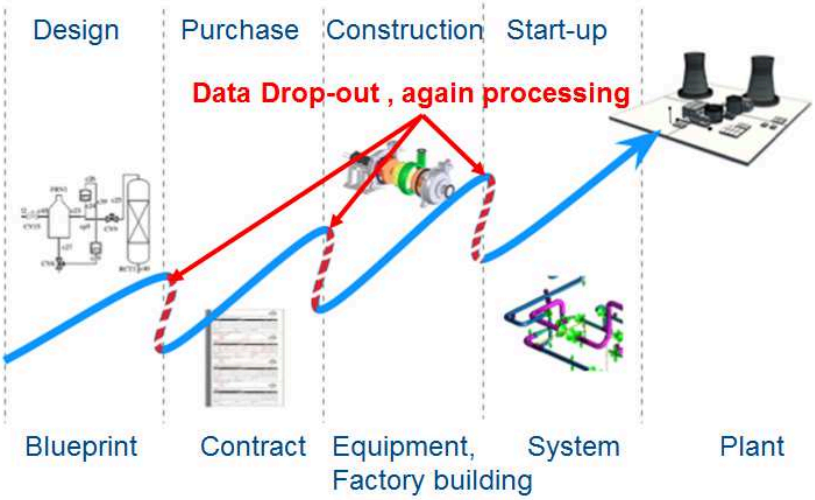

In the nuclear power engineering process, no matter the plant design, materials and equipment procurement, or the construction, installation commissioning business will generate mass of data. In order to improve the collaboration of the department and data sharing amount the complex business units, we need to ensure the quality of data flow, which not only satisfy the management's requirements, but also can serve the leadership's decision making. Without the enterprise level data planning, it's will impossible to achieve the goal.

C. The Methodology in Data Planning project

The fundamental goal of data planning is to build the business and data model to reflect the business activities. Meanwhile, with the in-depth and meticulous analysis of the business model, master data will be recognized and the relationship between the master data will be figured out as well. The master data is the core framework, and we need to setup the standard for data and data table, which can be a foundation for the database application system.

In our data planning for nuclear power engineering, while build the data model, the flexibility for the end user should be considered, so that we can encourage the business user to implement the data model during the information system development; in the other aspect, the certain rules should be applied, so that it can guide the different system development to keep the data on the same page, which can mitigate the gap and improve the data sharing efficiency amount the different system.

a) Establish the Project Team

Data planning is fundamental and core part of the enterprise resources planning. Therefore, the support and involvement of leadership are vital important for the success of the project. Meanwhile, to ensure the success of the project, the project team needs to have a clear responsibilities and rights for each team member who are involved in it. The data planning project team is directly under the lead of the senior leadership, and we also have a project manager to manager the detail action plan of the team. At the same time, some of the senior business experts and professionals were involved.

It is also worth noting that all the members involved should be have the commitment of the time. If there are too much time conflict while running the projects, we would recommend to stop until the time can be committed.

b) Business tackling and Modeling

Business and data analysis are the second step for the data planning project. The goal of the analysis is to understand the enterprise requirements deeply in a systematically way, which is also known as “business tackling”. During the business tackling, business function domain, business process and business activity are the critical part we need to take care of.

Business function domain is an abstract for the major business activities. Define the domain is the first step. After getting the domain list, project team will setup various group to take charge of the domain area. Each group will start to dig into the domain, and analyze the business function domain. We will find the domain can be made up by number of business process, and in each business process will have number of business activities. So the business model can be described by three tiers structure, which is “Business function domain – Business process – Business Activities”.

For example, during nuclear power engineering, the major business domains are usually have design, procurement (including manufacture and supervision), construction (including building and deployment) and System commission & delivery; the major management domains are usually have project plan, finance, security & quality assurance, human resource, and risk control. And the procurement domain is consisted by some procurement related processes, such as procurement planning and implementation, contract execution and implementation, equipment manufacture and supervision, and Delivery etc. In procurement planning and implementation is consisted by procurement plan, procurement request, technical specification, supplier selection, ordering, etc. Similarly, in system commission and delivery business domain, commission preparation, commission execution, system commission delivery and commission support are the main business process; and TOB, TOM, TOTO, FW, OT are the main business activity in the process of system commission delivery.

Meanwhile, while learning the business model, the interface of the domains, process and activities should be analyzed as well. For example, the procurement implementation in procurement domain and system commission preparation in system commission domain are related to the domain of project plan domain.

c) Data Analyzing and Modeling

Data analyzing and modeling are based on the business tackling and modeling. The process is to generate the data model, which including extract the data from the user view to master database, from data flow to ER diagram, from data entities to data table. According to the business process and activities, we need to extract the entities in these business, and group them to a specific group, which is called master data. We can also create the relationship of the master data, to map it back on the domain, process as well as activities. This can help us to double check the data and make it more reasonable.

The purpose of data modeling is to determine the relationship between the data and business and create a corresponding data structure to represent the business. Generally, the steps are listed as below:

Firstly, identify and define the business domain based on the user view, and then create the Conceptual Data Model.

Secondly, analyze the entity, and standardize the data structure, then build up the Logical Data Model.

Thirdly, standardize the data elements, and implement the data and coding standard in the database table, which is also called Physical Data Model.

With the help of data analyzing and modeling, we can build a more robust information recourse management structure. The model can serve as a system development guide line at the top level, and it's a foundation work for the high-end data environment.

D. Conclusion

To mitigate or clear the redundancy data in the enterprise, which has been accumulated for years of system development, is the essential goal of data planning. With the success of the project, it can help the enterprise to setup the basic data standard, reduce the isolated date island and improve the quality of the data. In a data environment with chaos, it not only a west a money during the system development, but also a bottleneck for the entire company to move the next step. Now is the time to take all the data and business to consideration, learning the experience and transform the way of thinking for our strategy of system and information development.

References

[1] James Martin - Information engineering 1989
[2] Fuxian Gao, Enterprise Data recourse planning training [Z]. 2003
[3] Industrial automation systems and integration - Integration of life-cycle data for process plants including oil and gas production facilities(ISO 15926) - Part 2: Data model
[4] Building construction - Organization of information about construction works(ISO 12006) - Part 3: Framework for object-oriented information
[5] Claudia Imhoff - Mastering Data Warehouse Design:Relational and Dimensional Techniques. 2004

Advanced Materials Research Vols. 986-987 (2014) pp 597-600

doi:10.4028/www.scientific.net/AMR.986-987.597

The energy management of Chinese tourist hotel under the background of low-carbon economy

Feilong Liu

School of Economics and Management Hunan Institute of Science and Technology, 414006,Yueyang, Hunan, China

E-mail:liufeilong12@126.com

Keywords: Low carbon economy; China; Tourist hotel; Energy management

Abstract. Tourist hotel is a “high energy consumption high emission high pollution” industry. So it is of great realistic significance of strengthening Chinese tourist hotel energy management under the background of low carbon economy. Aiming at the main problems of energy management of Chinese tourist hotel, we should begin from the following several aspects: First,To establish a scientific concept of hotel energy management and combine energy management training and assessment closely;The second is to build and improve energy management system and strengthen scientific and effective implement;The third is to establish a sound mechanism of hotel computer remote monitoring system to achieve hotel energy management information and automation.

In contemporary society, the change of energy environment and climate has become the focus of world attention, "low carbon economy" which based on low energy consumption, low emission, low pollution is becoming a global focus. The influence of low carbon economy on the development of hotel industry is very profound. Green hotel construction has made some useful attempts in the development of low-carbon economy. Under the background of low carbon economy, we can understand it is the hotel that is constructed and operated by the core value concept of low carbon economy, low carbon economy development mode and low-carbon science and technology. In fact, the hotel industry is " a high energy consumption, high emissions, high pollution" industry, coupled with the global energy demand is growing, resources shortage problem has become increasingly prominent, naturally led to rising energy prices. At the same time the hotel energy costs accounted for the proportion of expenditure for operating expenses showed a trend of rising. Therefore, in the condition of low carbon economic development, to strengthen the hotel energy management, and reduce energy consumption and operation cost of the hotel is an important research task in the China Hotel industry.[1]

The hotel energy management has an extremely important meaning

The so-called hotel energy management means that the hotel uses the modern scientific management methods and the advanced and mature technology and experience to give a comprehensive, multifunctional management to the hotel energy use. It also can say the hotel energy management is a scientific and effective management through the use of equipment and the consumption energy used by all people on the equipment using. Energy management under the background of low carbon economy is in line with the modern hotel development trend and the green hotel construction idea is come down in one continuous line. Green hotel was born in the last century 80's, the developed countries in Europe and America, and it’s proposed and initiated by a green sign organization of Germany, it is only an academic research at first. Late in twentieth Century 90 years, the White Swan ,Canadian maple leaf, German blue angel environmental labeling system organization and the nation of Israel ,American, Britain and other hotel management organization and green environmental protection agencies start to develop and publish the national or regional green hotel standards. For example in the Nordic (Sweden, Norway, Finland, Denmark) White Swan environmental labeling promulgated by the system of organization in the green hotel standards, It provides detailed energy-saving, water-saving, limited use of cleaning and chemicals

standard. Also provides the method and index of consumer goods reduction, classification of waste disposal, indoor facilities to encourage the use of environmentally friendly products and file management. The European and American countries Green Hotel growth rate is annually at a rate of 18.2%. According to the relevant data shows, the developed countries generally green hotel can reduce energy consumption by 5% to 10%, saving 10% to 20%, with great economic value. Now the developed countries have gone through the concept of "Green Hotel" into the popularization and application of substantive universal stage. So for energy management the important link of the construction of the green hotel, on the basis of the advanced management experience of European and American countries on how science works more effective, undoubtedly has become a tourist hotel industry in China need to complete a very urgent task. [2]

After joining WTO, foreign capital hotel as well as foreign hotel group gets into the China hotel market is in the accelerating speed, so the competition of the hotel industry will be more intense. If China hotel want to gain a firm foothold in the fierce market competition, it must work along both lines, not only to improve market share and operation revenue constantly, but also control costs, however the hotel energy management is an important part of the cost control of hotel. Therefore, to strengthen energy management of Tourist Hotel under the background of low carbon economy has very important practical significance.

The major problems of China Tourist Hotel energy management

So far, China tourism Star Hotel has reached about 15000, there are many times non star hotel more than the Star hotel Tourist Hotel, which is a large energy consumption ranks. From the actual operation of China Tourist Hotel, to control hotel hydropower oil and gas energy has always been a priority among priorities of its energy saving. But the internal cost control of many restaurants is often on the publicity and education and other flexible mode, the effect is not obvious. Energy management is not only the engineering work but involves all departments of the hotel. Many restaurants do not establish strict internal assessment system, which makes the hotel energy management difficult to implement. Generally speaking, the hotel energy management is mainly related to the hotel power supply system, drainage system, heating system, cooling system, central air conditioning system and so on. Energy consumption of the operation of the hotel equipment becomes an important part of the hotel product which is diverse, widely distributed, concealed installation and advanced technology. However, the equipment management of the hotel, especially the repair usually belongs to the engineering department, which resulted in the separation of duty use and maintenance. While energy consumption to produce concrete data cost also tend to stay in the financial department, resulting in consumption and pay for separation of duty. So, it will inevitably lead to many problems of energy management of tourist Hotel. To sum up, mainly in the following areas:

The tourist hotel energy management is not active

Strengthening the hotel energy management is exactly how to maximize the energy saving work in hotel in the guarantee of the normal operation of the hotel .According to "the people's Republic of China energy conservation law", energy-saving means to strengthen energy management and take technically feasible, economically rational and socially and environmentally acceptable measures to reduce the various segments of the loss and waste from energy production to consumption, and make more effectively and rational use of energy. Therefore, in the understanding of the concept, we must turn the simple "energy conservation" to "energy efficiency"; in the energy-saving ideas, we should turn the "want me to save energy "to I want energy-saving". However, in the fierce market competition, Chinese tourist Hotel industry has been in the stage of the hotel product pile up in excess of requirement. In order to gain more market share and revenue, hotel operators and managers have to take a variety of ways, such as price, to develop new products, to provide personalized service. They often focus on improving the hotel sales and market share, but the repeatability and long-term energy management is difficult to in-depth, Tourist Hotel management personnel many still remain in the "want me to energy-saving" passive stage. [3]

The tourist hotel energy management lack training and strict appraisal mechanism

In the era of green hotels, restaurants usually propagate green consumption to the guests, such as room will not changed daily disposable goods any longer. Replacement of the sheets, towels is also on the basis of the needs of customers. Many hotels placed that the card called "if you need to change the sheets, please put the cards on your pillow" in the room to cultivate the green consciousness and consumption of the spiritual. However, in actual operation, the hotel staff energy-saving awareness is weak. They often forget to turn off the lights. The daylight lamp, incandescent light is very common. Hotel staff training is a very important work, which should be involved in all aspects of the hotel management services. such as from the hotel new employees training to the fire protection knowledge training to service skills training to the reception of foreign language training etc. However, from the actual operation of the hotel, the hotel equipment often lacks the proper use and maintenance training and energy management training. From the aspects of appraisal system, hotel appraisal of department managers still focus on sales most, while the appraisal of employees, focus on attendance, service attitude and service skills, etc. Neither the hotel management nor general staff are lack of energy management system review. This situation is bound to cause the hotel's energy consumption will appear "everyone to use, no one is responsible for" phenomenon when using hotel facilities.

Tourist Hotel energy management is lack of scientific and rational technology and method

Hotel energy management involves all aspects of the hotel; the demand for both technical and hotel management level are high. From the developing trend of China's tourist hotel, the hotel industry in the future will pay more attention to the development of coordination with the balance of ecological environment and saving energy. But the actual situation is that most hotel energy management is very simple, especially lack of modern scientific management methods and advanced or mature energy management technology and experience to the comprehensive and multi-functional management of the hotel energy using. Of course, its reason is in many ways. First, from the point of environment, hotel energy conservation of China starts late, and don't have much experience. Second，due to the current status of development of the hotel, most of its engineering technology strength relatively weak restrict the implement and carry out energy saving work of the hotel. Third，modern science and technology changes every day, energy-saving new technologies, new methods constantly emerging, how to choose the most suitable technology and method for the hotel energy saving as soon as possible is also the problem.[4]

The measures and countermeasures of strengthening Chinese tourist hotel energy management

Establish scientific concept of hotel energy management, combining energy management training and examination closely

There are three conceptual change of subject that is the general hotel management, hotel staff and guests of the restaurant. To shift their concept of hotel managers' energy saving should be determined by the "energy-saving" want me to "I want to" energy saving, energy and the hotel management concept from "reduce cost" to "internal revenue", must be closely combined with the immediate interests of the hotel managers. Changing the hotel's general staff energy-saving idea, we must require the hotel full participation, also should closely combine with their vital interests, enabling them to consciously start from their own, thus eliminating daylight lamp and incandescent light, to promote the energy saving everyone good atmosphere. The idea of hotel staff transformed, improve the environmental consciousness, will also improve work quality, and, in turn, can affect the employee's family and the next generation, resulting in a huge social benefits. Changing attitudes of hotel guests, focuses on the cultivation of the green consumption spirit, from the perspective of the guests, should focus on guides them to strengthen the consciousness of energy conservation and environmental protection, and the pursuit of the civilized way of life.[5]In readjusting the tourist hotel will be the basis of scientific concept of energy management energy management training and examination of organic combine to form a complete and effective system.

To establish and improve hotel energy management system and strengthen scientific and effective implementation

In order to make the hotel energy management more scientific and institutionalized, must establish and improve a casing can, can use, energy saving regulations, clear the hotel energy management organization and management of division of labor and job responsibility, the hotel energy management departments in the work of the relationship as well as to the production and use of energy, such as saving requirements of each part. The hotel's energy management system to establish and perfect work should focus on the following several aspects:

First，the hotel management system for economic operation of the equipment. Economic operation management is mainly for energy dissipation (or capacity) equipment (system) how to improve the efficiency of management. The operation and management system, the provisions of the post responsibility system, each operation to make each device system, there is someone who's in charge of, according to the actual need to start or stop. Hotel equipment and economic operation management system including the management of economic operation of the boiler, central air conditioning system and the management of the economic operation and management and lighting electricity.

Second, the hotel use energy management system including water, electricity, oil, gas and other transport, use, energy saving index as well as the inspection and appraisal.

Third，the hotel departments of energy management system. Each department shall, according to the actual situation of unit energy consumption for the energy management system. The basis of energy management and hotel job mainly includes two aspects, namely, to establish complete system of energy measurement and energy consumption statistical work that is to emphasize on the hotel's energy consumption digital management.

To Establish and improve the hotel computer remote monitoring system in order to achieve the hotel energy management information and automation

By establishing and improving the computer remote monitoring system of the hotel, we can analysis the hotel energy usage scientifically during the operation and find and solve problems timely so as to realize the information and automation of the hotel energy management. The system should include hotels energy resource assessment, energy cost analysis, financial budget, real-time management of energy consumption, financial analysis of energy project, dynamic monitoring of energy-saving equipment, the accurately confirmation of the amount of energy-saving etc. we can realize scientific management and effective application of terminal equipment by taking advantage of the remote computer monitoring technology, scheduling energy load reasonably ,using the equipment in the long-term optimal energy state and the principle of " needs is the supply" .The hotel management personnel should make use of computer remote monitoring technology comprehensively and communicate about the problems and results of computer remote monitoring information system timely to share Information to accumulate the hotel staff energy-saving experience.

Reference

[1] JianGang Huang.Tourist hotels of China's energy management and energy saving strategy research[J].Special Zone Economy.2006 (10)228-230.

[2] Lixin Ruan .The hotel industry energy conservation and emissions reduction evaluation method research, in jiangsu province as an example[J]. Jiangsu Commercial Forum.2011 (4)26-27.

[3] Yanping Lin, Xue-qiong CHen. The influence factors of energy consumption of mountain tourist scenic spot in China hotel[J].Journal of Shenyang University of Technology(Social Science Edition).2011 (4)38-41.

[4]CaiJing.Strengthen the hotel energy management efforts to improve the economic benefits[J].Journal of Guizhou Commercial College.2005 (3)62-65.

[5] Zou Jian.Based on the energy consumption of China green star hotel to create a study[J]. Science & Technology Information. 2012 (3)69-71.

Advanced Materials Research Vols. 986-987 (2014) pp 601-605

doi:10.4028/www.scientific.net/AMR.986-987.601

The Influence of Detailed Onshore and Offshore Wind Farm Models on the System Voltage Level

Jiantao Gao[1,a], Xiaorong Zhu[1]

([1]School of Electrical & Electronic Engineering, North China Electric Power University, Baoding, China, 071003)

[a]hdgaojiantao@126.com

Keywords: PSD-BPA; Offshore Wind Power (OWP); Simulation; Detailed Model

Abstract. For the power load centers in china coast, large-scale development of new energy(such as offshore wind power and onshore wind power) is not only an effective means of control the bad weather(such as fog and haze), but also the practical requirements of coastal power shortage. In this paper, according to actual situation of China's large-scale wind power accessing to the coastal load centers centrally, also the characteristics of onshore and offshore wind farm models is considered, The voltage variation in the centralized model and detailed model is analyzed based on the platform of PSD-BPA, and the characteristic of each model is obtained. Research results have a certain reference value for China's coastal onshore and offshore wind power development.

Introduction

Currently, compared to other renewable energy resources, the industry foundation and application technology of wind power are relatively mature, so it is very suitable for commercial development of new energy power generation. As onshore quality wind resource is drained, more and more coastal countries are focusing attention on offshore wind power. Recently, the report of "2013 China's wind power installed capacity statistics" released by Chinese Wind Energy Association shows that, by the end of 2013, the totally installed capacity of offshore wind power projects is only 428.8 MW, which is far from the target of cumulative installed capacity of 5000MW by the end of "Twelfth Five-Year plan".

Modeling of wind farms has gone through two phases: in the early development of wind power, the capacity of wind farm is small, people are more concerned about the detailed model of single wind turbine, they consider that the composition of wind farm is a large number of small-capacity generators, boosting transformers and connecting lines; With the expansion of grid and wind farm scale, the way of detailed modeling appears poor convergence, long simulation time and other issues. So the centralization (equivalents) model, which studies the interaction between whole wind farm and power system, has been proposed [1]. As a large number of offshore wind farm planning, construction and operation, the proportion of offshore wind power in wind power industry will gradually expand. However considering the differences between offshore wind power and onshore wind power, for example, the unit capacity and the system characteristics [2], it is really a question whether the traditional land-based centralization model is suitable for offshore wind farms.

Based on the above analysis, and combine the research findings of offshore wind power at home and abroad, in this paper, a detailed model of offshore wind farm is built including the equipment models of wind turbine, package transformer, submarine cable and transformer, etc. So local grid voltage change and fluctuation rule is studied under different wind power output, the conclusions of this paper have reference value to depth research the characteristics of wind power model and offshore wind power.

Modeling of Wind Farm and its Influence on the Static Voltage

Onshore Wind Farm. The applied technology of onshore wind power is quite mature, each field of land wind power (such as site selection, wind resource assessment, collection system design, LVRT

capability and so on) has an associated normative guideline. Therefore, the classic model will be referenced in the detailed model of onshore wind power, specific methods will not repeat.

Offshore Wind Farm. The difference between offshore wind power and onshore wind power is embodied in the following points: 1) larger unit capacity, the wind turbine around 5MW has been the mainstream turbine at present; 2) a great influence of submarine cable on the reactive voltage, the submarine cable must be used to collect or transmit electrical energy in the field of OWP, AC cable will bring a lot of charging current. It not only limits the transmission distance and capacity, but also raise the voltage of OWF bus; 3) more choices of integration mode (HVAC, LCC-HVDC, VSC-HVDC and so on), by the requirement of transmission capacity and system stability, VSC-HVDC using in offshore wind power will be the future development trend.

For studying the static voltage level, we pay close attention on the effects of submarine cables and collector system architecture on static voltage level in offshore wind farm modeling. The structure of a detailed OWF model is shown in Figure 1 after referred the offshore wind projects (Donghai Bridge offshore wind farms, etc.) and wind farm design and integration standards.

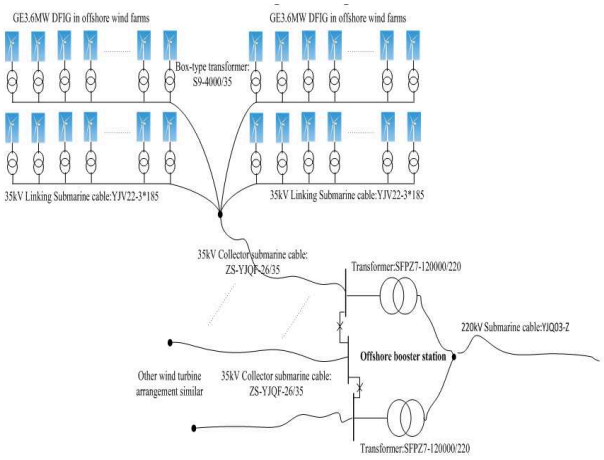

Figure 1

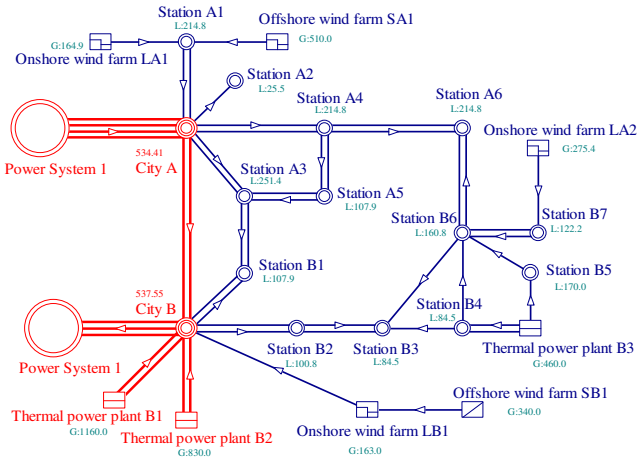

Figure 2

The Impact of Wind Farm on Static Voltage Levels. Due to the intermittent and random of wind power, large-scale wind power connecting to grid will have more and more obvious influence on grid structure design, operation scheduling scheme, reactive compensation measure and power quality[4]. For wind farms have been built, the impact of wind farm on grid voltage is mainly reflected in the WTG characteristics and reactive power compensation.

Active power output from WTG mainly depends on the wind speed; in terms of reactive power, constant speed wind turbine absorbs reactive power influenced by the active power, the fluctuation of reactive power is less for DFIG generally using constant power factor control mode. During the process of grid-connected wind turbine operation, the output of wind turbine will be influenced by tower shadow, yaw error and other factors, and the fluctuation is changed with turbulent intensity [5]. In addition, wind turbine in the process of starting, stopping and switching will produce voltage fluctuations and flicker [6].

The integration operation of wind power farm will consume some reactive power and have a negative impact on the voltage quality. This effect comes from the reactive power losses of wind turbine, collection system and boosting transformer. Existing reactive power compensation device can basically meet the system requirements of reactive power, but it has the drawback of slow adjustment and discrete adjustment. SVC can achieve quickly compensate and smooth adjustment, provide dynamic voltage support and improve the operating performance because it has introduced power electronic components into the traditional static reactive power compensation device. In addition to compensating to the wind farm, SVC can also improve the voltage quality and system stability [7].

Simulation Analysis

System Outline. In this paper, the research object is a power system of China's eastern coast. It plans to build five wind power farms (total installed capacity of 1711MW, and total output of 1454MW) in this region, including two offshore wind farms (SA1 and SB1, output respectively 510MW and 340MW). Considering the limited scale of OWP at this stage, two offshore wind farms have been accessed into the 220kV region power grid. Schematic diagram of the system is shown in Figure 2.

The Influence of Wind Farm Model on System Voltage level. In this paper, 1.5MW and 3.6MW double-fed wind turbine models produced by GE Corporation are used in onshore and offshore wind farms respectively, and the maximum output is considered as 85 percent of the installed capacity of wind farm. Also wind turbines run at constant power factor control mode (power factor of 1.0) and the wind farms consider the role of reactive power compensation device (SVC).

A coastal power system in eastern China is studied here. The voltage fluctuation is analyzed respectively in condition of centralized model, detailed model of onshore wind power and detailed model of onshore and offshore wind power. The system prerequisites of reactive power compensation, other generator status and terminal voltage remain unchanged during the change process of wind power output. In above conditions, the voltage fluctuation results are shown in Table 1 and Table 2.

Table 1 The impact of centralized model and detailed model on static voltage level under the minimum and maximum output of wind farm

Bus Station	Centralized model(kV)		Detailed model of onshore wind power(kV)		Detailed model of onshore and offshore wind power(kV)	
	Min (0%)	Max (85%)	Min (0%)	Max (85%)	Min (0%)	Max (85%)
SA1	241.8	238.4	241.9	239.2	241.7	237.9
LA1	237.7	235.2	237.9	235.9	237.6	235.3
A1	237.4	234.8	237.6	235.5	237.3	234.9
City AL	237.2	235.0	237.4	235.7	237.1	235.1
A4	236.2	233.9	236.4	234.6	236.0	234.1
A6	235.3	233.4	235.5	234.0	235.1	233.5
B6	235.5	233.8	235.7	234.3	235.4	233.9
B3	235.8	233.9	236.1	234.4	235.7	234.0
B2	236.2	233.9	236.5	234.6	235.9	234.1
City BL	236.5	234.1	236.9	234.9	236.2	234.4
LB1	240.6	236.7	241.9	237.6	239.7	237.1
SB1	241.7	239.5	243.5	240.1	242.0	239.8
B7	236.2	234.4	236.5	234.9	236.1	234.5
LA2	238.0	235.9	238.3	236.4	237.9	236.0

Table 2 The impact of wind power output change on voltage fluctuation ratio under different models

Bus Station	Rated voltage (kV)	Centralized model	Detailed model of onshore wind power	Detailed model of onshore and offshore wind power
SA1	220	1.55%	1.23%	1.73%
LA1	220	1.14%	0.91%	1.05%
A1	220	1.18%	0.95%	1.09%
City AL	220	1.00%	0.77%	0.91%
A4	220	1.05%	0.82%	0.86%
A6	220	0.86%	0.68%	0.73%
B6	220	0.77%	0.64%	0.68%
B3	220	0.86%	0.77%	0.77%
B2	220	1.05%	0.86%	0.82%
City BL	220	1.09%	0.91%	0.82%
LB1	220	1.77%	1.95%	1.18%
SB1	220	1.00%	1.55%	1.00%
B7	220	0.82%	0.73%	0.73%
LA2	220	0.95%	0.86%	0.86%
City B	500	0.56%	0.30%	0.38%
B1	220	1.09%	0.82%	0.86%
A3	220	1.05%	0.82%	0.91%
City A	500	0.40%	0.18%	0.28%
Plant B3	220	0.55%	0.41%	0.45%

According to Table 1, the distribution curve of static voltage level can be drawn under the six operation case, specifically as shown in Figure 3. According to Table 2, the distribution ratio curve of static voltage can be drawn under three models, specifically as shown in Figure 4.

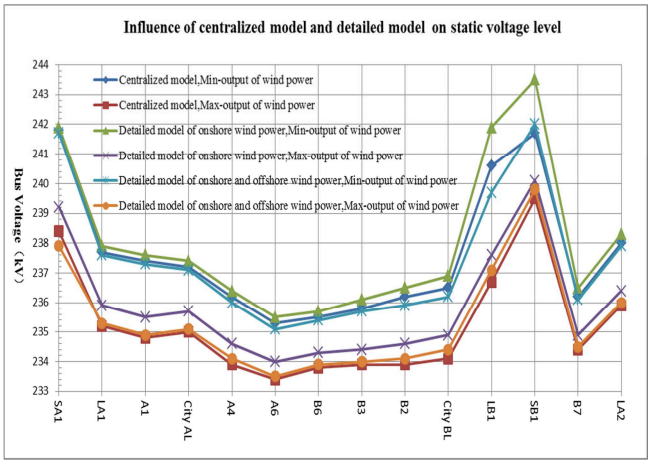

Figure 3

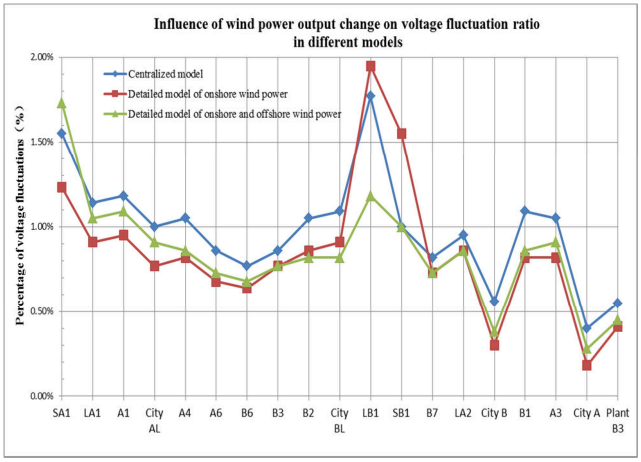

Figure 4

The following conclusions can be obtained from Table 1 and Figure 3: 1) in the models of centralized model, detailed model of onshore and detailed model of onshore and offshore, the changing trend of static voltage is consistent, so the three models are effective and realistic; 2) Stations of the highest voltage appear in bus SA1 and bus SB1, higher than the adjacent bus about 4kV and 2.4kV respectively. This fully confirms that the charging power produced by submarine cable can make the related bus voltage higher than others; 3) The bus voltage in intermediate area of the three wind farm groups is lower generally, the lowest voltage appears in station A6. So it should pay attention on station A6, for example, the reactive power compensation device should be installed in case of voltage collapse problem; 4) From the three models, the voltage level of minimum output of wind power is higher than the maximum output of wind power. The voltage level of detailed model of onshore is the highest in minimum output of wind power, and the lowest is the centralized model in maximum output of wind power. The voltage level of considering a detailed model of offshore wind power is very close to the voltage level of centralized model, but it has a gap with voltage level of detailed model of onshore wind power.

The following conclusions can be obtained from Table 2 and Figure 4: Among the simulation results, the maximum percentage of voltage fluctuation appears in centralized model, and the minimum - appears in detailed model of onshore wind power. But the rule does not be complied in the buses of SA1 and SB1, the voltage fluctuation percentage of SA1 and SB1 in detailed onshore model is higher than other models significantly, but the bus of LB1 is lower. This phenomenon is mainly caused by the charging power of OWP submarine cable.

Summary

Network architectures and integration characteristics of OWP have a large difference compared with onshore wind power. As can be seen from the simulation result, the outlet port voltage of offshore wind farms have been raised significantly, and even raised voltage of the nearby area. So necessary measures should be taken to inhibit the phenomenon, for example, it shows that compensating the charging power of the submarine cable through high voltage reactors can effectively weaken the capacitance effect of the line when the power factor is set to -0.98 [8]. In addition, it can be seen by comparing three models that the static voltage fluctuation trend is consistent, but there are some differences in voltage level and complexity of the models. Therefore, this paper suggests that the researchers can choose the right model to simplify difficulty based on research accuracy, research subject and voltage fluctuation, etc. From the research status home and abroad, the OWP development has been focusing attention on large-scale offshore wind farms. The research of China's OWP is still in the exploratory stage, in the future, the theoretical research of OWP should focus on internal wind farm and integration characteristics.

References

[1] Jiangbei Ge, Ming Zhou, Gengyin Li. Review on Large Scale Wind Farm Modeling [J]. Power System Protection and Control, Vol. 41(17), p. 146-153. (2013).
[2] Heyun Lin, Yujing Guo, Beibei Sun. Overview of offshore wind power key technologies [J]. Journal of Southeast University (Natural Science Edition), Vol. 41(04), p. 882-888. (2011).
[3] Jing Jin, Qian Ai, Lingling Xi, Xin Zhang. Internal electrical wiring systems of off-shore wind farms [J].East China Electric Power, Vol. 35(10), p. 20-23. (2007).
[4] Delong Yu, Haixiang Zhao, Na Cao: Electric Power, Vol. 39(6), p. 10-14. (2006).
[5] Suhua Lou, Zhiheng Li, Sujie Gao. Wind Farms Models and Its Impacts on Wind Farms Integration into Power System [J].Power System Technology, Vol. 31(2), p. 330-334. (2007).
[6] SUN Tao Sun, Weisheng Wang, Huizhu Dai. Voltage Fluctuation and Flicker Caused By Wind Power Generation [J]. Power System Technology, Vol. 27(12), p. 62-66. (2003).
[7] Puchun Ren, Wenhui Shi, Xiaoyan Xu: Electric Power, Vol. 40(11), p. 97-101. (2007).
[8] Guoqiang Zha, Yue Yuan, Zhixin Fu, Chunjun Sun: Power System and Clean Energy, Vol. 29(02), p. 54-60. (2013).

Advanced Materials Research Vols. 986-987 (2014) pp 606-610

doi:10.4028/www.scientific.net/AMR.986-987.606

The influence of wind power grid to power system small disturbance stability study

Wang Zhijie[1, a], Liu Sanming[1, b], Xi Pan[1,.c], Pei Zeyang[1, d], Su Xinxia[1, e], Chen Lijuan[1, f]

[1]School of Electrical Engineering, Shanghai DianJi University, Shanghai 200240, China

[a]wzjsdstu@163.com, [b]liusanmingxy@163.com, [c]467946001@qq.com, [d]yangyang0818ab@163.com, [e]suxinxia1991@126.com, [f]chenlijuancom@163.com,

Keywords: wind power integration, power system, small disturbance stability

Abstract. Setting up a practical power system containing wind farm small disturbance stability mathematical model, and the linearized equation of wind turbines and original equations of linear system, power system containing wind turbines augmented state formation matrix, turn the inverse iteration with PSASP software Rayleigh (Rayleigh quotient iterative algorithm and sparse matrix technique for large state matrix eigenvalues. In this paper, the Inner Mongolia power grid, wind power access to power system oscillation mode and the influence of the oscillation characteristics and meet the requirements of small disturbance stability of wind scale and operation control scheme. The influence of the wind farm is proposed for power system damping characteristics will not greater than the same capacity of synchronous generator's point of view.

Introduction

Small disturbance stability refers to the power system under small disturbance in sync operation ability, in math, it said in a running point near the stability of the system equations are linearized embodied.

For small disturbance stability analysis is presented in this paper the mathematical model of wind turbine for power system containing wind farm small disturbance stability calculation, combined with the actual power grid, the large capacity of wind power grid for power system oscillation mode and the influence of the damping characteristics.

Doubly-fed wind turbine mathematical model small disturbance

Doubly-fed wind turbine model writing form as follows:

$$\begin{aligned} \dot{y}_{\mathrm{g}} &= f_1(y_g, u_g) \\ \dot{y}_{\mathrm{e}} &= f_2(y_e, u_e) \\ \dot{y}_t &= f_3(y_t, u_t) \\ 0 &= g_1(y_g, u_g) \\ 0 &= g_2(y_e, u_e) \\ 0 &= g_3(y_t, u_t) \end{aligned} \tag{1}$$

Including, $\mathrm{f} = [\mathrm{f}_1^{\mathrm{T}}, \mathrm{f}_2^{\mathrm{T}}, \mathrm{f}_3^{\mathrm{T}}]^{\mathrm{T}}$ and $\mathrm{g} = [\mathrm{g}_1^{\mathrm{T}}, \mathrm{g}_2^{\mathrm{T}}, \mathrm{g}_3^{\mathrm{T}}]^{\mathrm{T}}$ are for doubly-fed wind turbine model of the dynamic equation and algebraic equation, $\mathrm{f}_1, \mathrm{g}_1$ are parts of the dynamic equation and algebraic equation for generator, $\mathrm{f}_2, \mathrm{g}_2$ for the inverter electrical control parts of the dynamic equation and algebraic equation, $\mathrm{f}_3, \mathrm{g}_3$ for the wind machine and control system parts of the dynamic equation and algebraic equation;

$\mathrm{y} = \left[y_g^T, y_e^T, y_t^T\right]^T$ and $\mathrm{u} = \left[u_g^T, u_e^T, u_t^T\right]^T$ are for the doubly-fed wind power generator sets of state variables and input variables, y_g, u_g are for generator part states variables and input variables, y_e, u_e are for the inverter electrical control parts state variables and input variables, y_t, u_t are for the wind machine and control system parts state variables and input variables.

For the stability of small disturbance linearization, available:

$$\Delta \mathrm{y} = \left[\Delta y_g^T, \Delta y_e^T, \Delta y_t^T\right]^T \tag{2}$$

The corresponding state after linearization matrix, input matrix and output matrix and feedforward matrix, respectively:

$$A_2 = \begin{bmatrix} \frac{\partial f_1}{\partial y_g} & \frac{\partial f_1}{\partial y_e} & \frac{\partial f_1}{\partial y_t} \\ \frac{\partial f_2}{\partial y_g} & \frac{\partial f_2}{\partial y_e} & \frac{\partial f_2}{\partial y_t} \\ \frac{\partial f_3}{\partial y_g} & \frac{\partial f_3}{\partial y_e} & \frac{\partial f_3}{\partial y_t} \end{bmatrix} \tag{3}$$

$$B_2 = \begin{bmatrix} \frac{\partial f_1}{\partial u_g} & \frac{\partial f_1}{\partial u_e} & \frac{\partial f_1}{\partial u_t} \\ \frac{\partial f_2}{\partial u_g} & \frac{\partial f_2}{\partial u_e} & \frac{\partial f_2}{\partial u_t} \\ \frac{\partial f_3}{\partial u_g} & \frac{\partial f_3}{\partial u_e} & \frac{\partial f_3}{\partial u_t} \end{bmatrix} \tag{4}$$

$$C_2 = \begin{bmatrix} \frac{\partial g_1}{\partial y_g} & \frac{\partial g_1}{\partial y_e} & \frac{\partial g_1}{\partial y_t} \\ \frac{\partial g_2}{\partial y_g} & \frac{\partial g_2}{\partial y_e} & \frac{\partial g_2}{\partial y_t} \\ \frac{\partial g_3}{\partial y_g} & \frac{\partial g_3}{\partial y_e} & \frac{\partial g_3}{\partial y_t} \end{bmatrix} \tag{5}$$

$$D_2 = \begin{bmatrix} \frac{\partial g_1}{\partial u_g} & \frac{\partial g_1}{\partial u_e} & \frac{\partial g_1}{\partial u_t} \\ \frac{\partial g_2}{\partial u_g} & \frac{\partial g_2}{\partial u_e} & \frac{\partial g_2}{\partial u_t} \\ \frac{\partial g_3}{\partial u_g} & \frac{\partial g_3}{\partial u_e} & \frac{\partial g_3}{\partial u_t} \end{bmatrix} \tag{6}$$

After the linearization with the system and the equation of wind turbine components and the equations of linear network, the system can be augmented state matrixA', can be obtained by solving the characteristic value of small disturbance stability of all kinds of information system. Based on integrated power system analysis program (PSASP) the small disturbance stability analysis software, realizes the wind linearized equation and original of simultaneous linear equation system, using the software of the inverse iteration to Rayleigh and sparse matrix technology (Rayleigh) quotient iteration method to calculate large state matrix eigenvalue, and implements the power grid containing wind farm small disturbance stability calculation function.

Wind power grid in Inner Mongolia power grid after small disturbance stability analysis

Calculation Conditions

Calculation used in wind turbines and control system parameters are as follows:

A single asynchronous wind turbine parameters (unit capacity standard MAO value): $P_g = 0.7\text{MW}$, $U_g = 690\text{V}$, V_r=15/ms, $V_{cr} = 4\text{m/s}$, $V_{co} = 25\text{m/s}$, r_r=0.01718p.u, x_r=0.124p.u, $x_s = 0.11\text{p.u}$, $T'_{do} = 47\text{s}$, $T_j = 6\text{s}$, $\tau_s = 1s$.

A single main parameters doubly-fed wind power generator (unit capacity standard MAO value): $P_g = 1.5\text{MW}$, $U_\text{g} = 690\text{V}$, $\text{V}_r = 11.8\text{m/s}$, $V_\text{ci} = 3\text{m/s}$, $V_{co} = 25\text{m/s}$, $X^{''} = 0.55\text{p.u}$, $\text{R} = 35.2\text{m}$, $T_\text{t} = 7.64\text{s}$, $T_g = 1.14\text{s}$, $K_{tg} = 1.246\text{p.u.torque/rad}$, $D_{tg} = 1.5\text{p.u.torque/p.u.speed}$, $\text{w}_d = 125.66\text{rad/s}$, $\theta_{max} = 27\text{deg}$, $\theta_{min} = 0deg$, $P_{max} = 1.12\text{p.u.}$, $P_{min} = 0.1\text{p.u.}$, $Q_{max} = 0.312\text{p.u.}$, $Q_{min} = -0.436\text{p.u.}$.

Through calculation, the wind power grid power grid in Inner Mongolia area oscillation mode comparison between before and after.

Wind power grid power grid in Inner Mongolia area oscillation mode comparison between before and after verified through the calculation of small disturbance stability of Inner Mongolia power grid, related to the power grid in Inner Mongolia mainly have six regional oscillation mode, respectively is: (1) cylinder unit area on the system oscillation mode; (2) Inner Mongolia, Shanxi unit of north China provides oscillation mode; (3) Inner Mongolia units of Shanxi units oscillation mode.

Table 1 to table 3, respectively, as well as the characteristics of wind power grid before and after the oscillation mode, the comparison, among them, Z, f, alpha, beta, respectively is oscillation mode corresponding characteristic value, frequency, damping ratio and the related mechanical and electrical circuits.

(1) Cylinder unit area on the system oscillation mode

Table 1 Wind power grid before and after the cylinder unit area on the system vibration model

	Z	$f(Hz)$	$\alpha(\%)$	β
nonfan	-0.2374+j6.4879	1.0325	3.6566	5.1204
asynchronous motor	-0.0024+j6.1427	0.9776	0.0396	3.0490
DFIG	0.0085+j6.1515	0.9790	-0.1395	3.0983

The corresponding modal diagram as shown in figure 1.

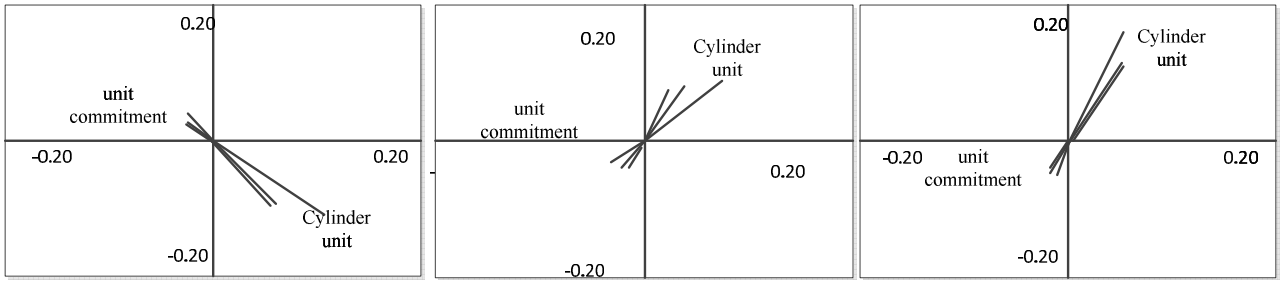

(a) no wind power (b) wind turbine with asynchronous generator (c) doubly-fed induction generators

Fig. 1 Cylinder region unit of system modal oscillation mode

(2) Inner Mongolia, Shanxi unit of north China provide oscillation mode

(3)

Table 2 Before and after the wind power grid in Inner Mongolia unit in Shanxi Province to north China provide oscillation mode

	Z	$f(Hz)$	$\alpha(\%)$	β
nonfan	-0.3977+j4.8013	0.7641	8.2554	0.8764
asynchronous motor	-0.3873+j4.7963	0.7634	8.0483	0.9138
DFIG	-0.3906+j4.8023	0.7643	8.1071	0.8867

The corresponding modal diagram is shown in figure 2.

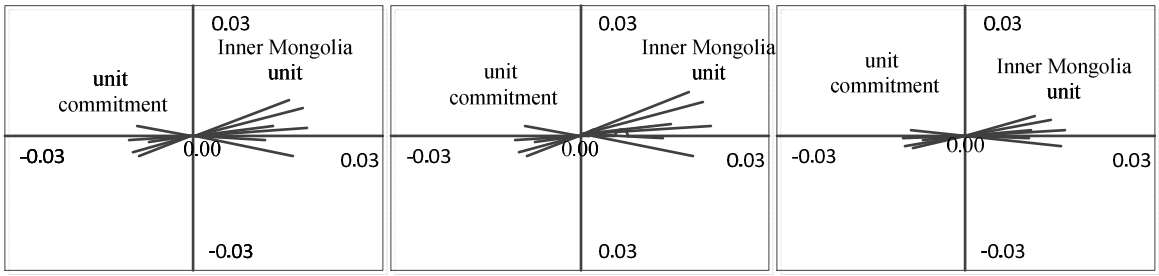

(a) no wind power (b) wind turbine with asynchronous generator (c) doubly-fed induction generators

Fig. 2 Inner Mongolia, Shanxi unit of north China provide modal oscillation mode

(4) Inner Mongolia units of Shanxi units oscillation mode

Table 3 Wind power grid in Inner Mongolia units of Shanxi units before and after the oscillation mode

	Z	$f(Hz)$	$\alpha(\%)$	β
nonfan	-0.2788+j3.7612	0.5986	7.3922	0.9512
asynchronous motor	-0.2564+j3.7927	0.6036	6.7440	1.1294
DFIG	-0.2524+j3.8087	0.6061	6.6127	1.0844

The corresponding modal diagram as shown in figure 3.

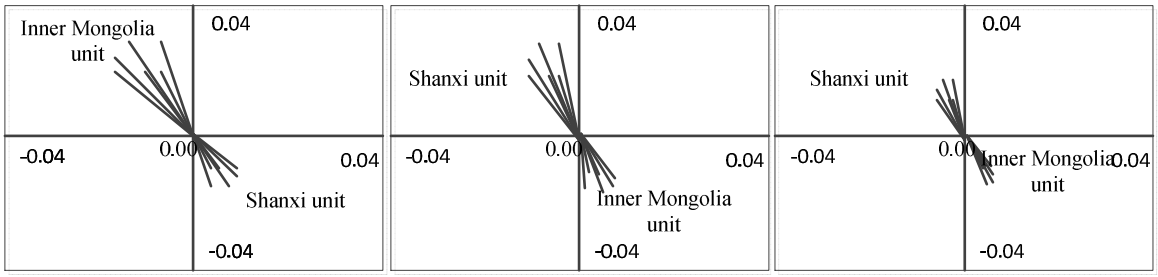

(a) no wind power (b) wind turbine with asynchronous generator (c) doubly-fed induction generators

Fig. 3 Inner Mongolia units of Shanxi units modal oscillation mode

Analysis of the above calculation results can get the following conclusion:

(1) Larger capacity of wind, both asynchronous wind power generator and doubly-fed wind power generator, related to the power grid in Inner Mongolia regional oscillation pattern has not changed, and two kinds of models of the calculation results are basically identical.

(2) Inner Mongolia, Shanxi unit of north China provides oscillation of Shanxi, Inner Mongolia unit model in wind turbines characteristics after the access to the root distribution, there was no big change, damping ratio decreased but not by much.

(3) Cylinder area through a 430km, 500kv line contact with the main system is weak, the wind generator in the region have no access, cylinder unit area the main oscillation mode damping ratio 3.65; Access to a larger capacity of wind power units (500mw), the oscillation mode damping characteristics have fallen sharply, even became negative damping, the unstable operation of the system of the actual working condition.

Conclusion

This paper sets up a small disturbance stability power system containing wind farm mathematical model. By small disturbance stability calculation of Inner Mongolia power grid, and analyses the influence of large-scale wind power system oscillation mode and the influence of the oscillation characteristics, this paper discusses the weak power grid wind that could satisfy the requirement of small disturbance stability operation scale and system operation control measures.

Fund program: Scientific research innovation project of Shanghai education committee (12ZZ197), Natural science fund project in Shanghai(12ZR1411600), Shanghai education innovation project number (14YZ157), The national natural science fund project (11201267)。

References

[1] Li Jun feng, Gao Hu and Wang Zhong-ying: China wind power development report (Environmental Science Press, China2008)

[2] Fengquan Zhou, Geza Joos and Senior Member: Voltage Stability in Weak Connection Wind Farms[J].Power Engineering Society General Meeting, IEEE: Vo12,Jun12-16,San Francisvo, USA. 2005: 1483- 1488.

[3] Morren J, de Haan S W H. Ridethrough of wind turbines with doubly-fed induction generator during a voltage Dip[J]. IEEE Trans on Energy Conversion, 2005, 20(2).

[4] Petersson A，hmdberg S，Thiringer T. A DFIG Wind Turbine Ride-through System，Influence on The Energy Production[J]. Wind Energy，2005，8(3)：251-263.

[5] Jiang Xuedong Zhao Fang. Cope with power grid voltage sag Crowbar double-fed induction wind generator control strategy [J]. Power grid technology, 2008, 32 (12) : 84-89.

Advanced Materials Research Vols. 986-987 (2014) pp 611-614

doi:10.4028/www.scientific.net/AMR.986-987.611

The numerical research on the jumping induced by the uniform and non-uniform ice-shedding of transmission lines

Yizhen Wei[1] , Pan Su[1,a]

[1]Institute of Electrical and new energy, Three Gorges University, Yichang, 443002, China

[a]email:supan417226850@163.com

Key words: Iced conductor; Uniform; Non-uniform ; Jumping off the ice

Abstract: This paper introduces several kinds of icing and ice-off simulation method: the equivalent load method, quality method, Támás model method and cell death method. With a large span cross section as an example, using finite element method, established the finite element model of single span icing wire, analyzed the non-uniform ice-off and the even ice-off,the results show that: Non-uniform ice-off dynamic tension is significantly smaller than even ice-off dynamic tension,the smallest dynamic tension is closely related to wire jump amplitude, the greater jump amplitude leads to the smaller dynamic tension，the essence of which is determined by the conductor slack.

Introduction

When weather conditions change, wind load and the external mechanical forces, then the icing lines will happen various forms of ice-off. At home and abroad, for overhead lines ice-off bouncing, the research focuses on the ice thickness, ice-off mode and wind load analysis, but the research of simulating icing and ice-off is tiny little. This article start from the simulation method of icing and ice-off, carefully clarify the mechanism and applicability of these methods, and employ the finite element method for a large span wire, numerically simulate the non-uniform and uniform ice-off.

Simulation method of the ice- off

The equivalent load method

When research on icing, the usual method is look it as the circle model which locates at the outside of the wire. The equivalent load method, in short, is dispersing icing load to some points on wire, and the method can be divided into concentrated load and uniformly distributed load.the reference [1] has been validated: Using the former method for lines icing and ice-off jumping off to simulate, found that the tension of line and the jumping height are conformity with the actual, so this method is feasible.

The quality method

When dynamic and static analysis of lines, only take the own weight of the icing into consideration, without considering the other influence. In finite element model, directly simulate the icing as the quality block of the unit node or the equivalent increasing density of the wire. At the time of simulation to ice-off, accordingly unload the equivalent mass block or reduce wire density. The method's principle is simple, the quality block commonly uses Mass21 to simulate, and program design is more concise[2].

Támás model

The quality method and the equivalent load method only take the own weight of the ice into consideration, without considering the other influences, but in fact, the icing has some mechanical properties. The icing has the other capacity, such as tensile, compression, torsion, shear. In order to consider the mechanical properties of the ice wires, Támás used beam element instead of stem cell, and used the finite element method to study the single line, analyzed this model's dynamic response of ice-off machine[3].

This method need to set up two models in finite element modeling, the first step is to simulate the wire with cable or stick, then the second step is to simulate icing with beam at the same node with stem cell.

Birth and death element method

When research on a model, sometimes need one or some unit do not exist, use the birth and death element method to study these problems will be a good choice at this time. The birth and death element method's essence is the element stiffness settings. When some unit is needed, they can exist like other units. Otherwise, can set it inexistence. The principle is that use a small formulas to decrease the stiffness matrix, and the other parameters are set to zero[4].

For the characteristics of the birth and death element method, in the simulation of overhead line ice-off, can simulate deicing with the element's birth and death. For the entity model which's ice locates on the outside of the line, the method can conveniently simulate ice-off.

The above analyzed several ice and deice method, and then the paper will give a simulation ice-off example using the first kind of simulation method.

The example analysis

Wire and the icing parameters

Set a single wire horizontal span L=1000m, wire model is LGJ-400 / 35,, two suspension points have no height difference., the wire cross area S is 435 $mm2$. Modulus of elasticity E=6.5×10 ^{10}Pa, Unit mass m=1.349kg / m , Poisson's ratio=0.3. In a weather condition, the ice thickness is 12 mm . Density is 900kg / m^3 , the wire horizontal stress σ =58.27 MPa ,the wire material damping ratio is 0.02.

Build the finite element model

With the finite element software ANSYS, selects the LINK10 to establish the finite element model with dividing line into 1000 units.

The wire shape finding

Wire self-weight shape finding

With the ANSYS, in the study of the single suspension cable, can adopt direct iterative method or the shape finding analysis. This paper use the direct iteration method to analyze the line self-weight shape finding. The basic principle: When the finite element modeling, can first built a straight line, at the meshing stage, use the LINK10 to transform it into a sufficient number of units. Restrict on the two endpoints and set the real material parameters , then set initial dependent variable into enough small, then add the acceleration of gravity and set the suspension cable tension as the convergence conditions, through a series of iterative update model, finally complete self-weight shape finding[5].

Icing wire shape finding

After wire covered by ice, the shape finding is called the second shape finding, which applying ice shape based on self-weight shape finding, this step use the load step in ANSYS. Using the equivalent load method to simulate the ice, when icing shape finding, with the form of load step, it's easy to determine the shape of wire in the end. As shown in Figure 1, shape finding is completed.

Figure1-1 The final shape of the wire after shape finding

Simulate non-uniform ice jump off of the iced wire

In fact, wire's ice-off is a complex process, uniform ice-off and uneven ice-off are all exist, and the randomness is strong. In order to simulate non-uniform ice-off, this paper take the simulation method that shown in the figure to simulate non-uniform ice-off and uniform ice-off.

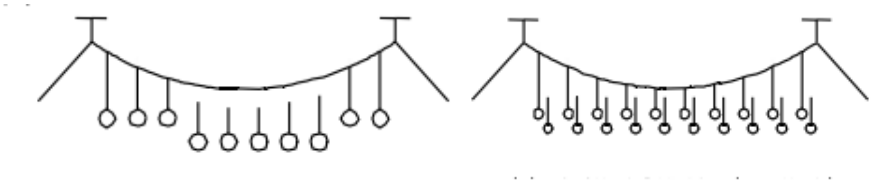

(a) Non-uniform off the ice simulation (b) Even off the ice simulation

Figure1-2 Iced wire uniform and non-uniform ice-off simulating method

For the same example to simulate the wire's uneven ice-off.(50% ice-off)

Choose the nodes of middle-span, left of middle-span and right of middle-span, to plot the S-t graph of ice-off process. The Figure 1-3 show the Y-direction S-t graph of middle-span 500 node.

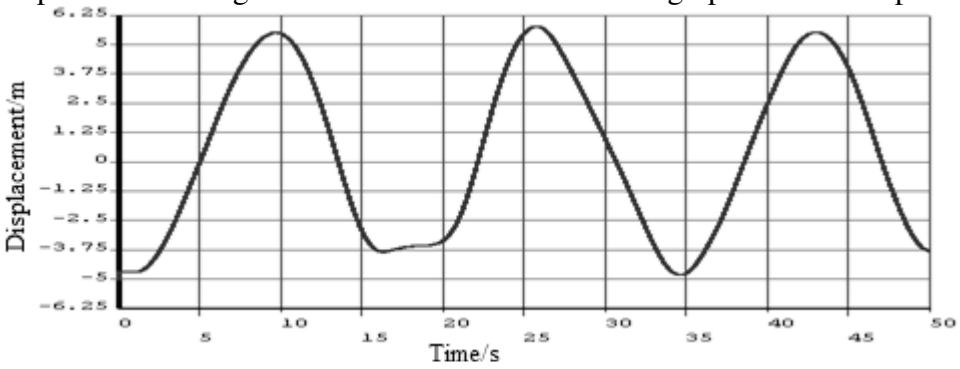

Figure1-3 Y-direction S-t graph of middle-span 500 node

Chart1-1 The maximum displacement of each node jumping

Node number	Y negative displacement	Y forward displacement
500	-5.030m	+5.765m
250	-3.770m	-1.849m
750	-3.810m	-2.054m

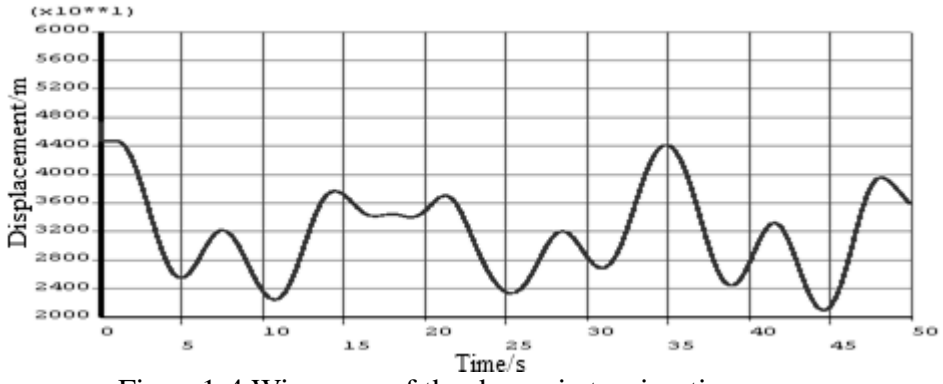

Figure1-4 Wire span of the dynamic tension time curve

The above is the rule about the wire ice-off displacement changed with time. The figure1-4 show the ice-off span dynamic tension variation.

Chart1-2 Ice-off conditions of wire tension control table

wire tension kN	100% ice-off	50% non-uniform ice-off	50% uniform ice-off
The initial tension	25.345	25.345	25.345
Iced wire tension	48.319	48.319	48.319
The maximum dynamic tension	37.815	43.738	40.378
The minimum dynamic tension	8.327	21.002	15.673

Through the wire tension comparison table, it can be seen that the tension increase obviously after the wire icing. The wires ice-off is either 100% or 50%.After ice-off, middle-span's tension is small than icing, on the three kinds of work condition, 50% non-uniform ice-off dynamic tension is maximum, 100% ice-off dynamic tension is minimum. At the same time, minimum wire dynamic tension is closely linked with jump height, and more wire jump height will lead dynamic tension to decrease, its essence is due to the wire relaxation degree.

Conclusion

To simulation of overhead line jumping, the key step is the simulation of icing and ice-off, which is less researched in the past. This paper introduces several kinds of icing and ice-off simulation method: the equivalent load method, quality method, Támás model method and cell death method. With a large span cross section as an example, using finite element method, analyzed the non-uniform ice-off and the even ice-off, the conclusion are:

When the lines ice-off jumping, middle span's amplitude is largest. The inappropriate design will lead the interphase flashover, so the line design need to be care, especially at heavy ice area, large span, and bad meteorological condition.

Either 100% or 50% ice-off jumping, middle-span's tension is small than icing line tension, on the three kinds of work condition, 50% non-uniform ice-off dynamic tension is maximum, 100% ice-off dynamic tension is minimum, at the same time, minimum wire dynamic tension is closely linked with line's jump height, and more wire jump height will lead dynamic tension to decrease, its essence is due to the wire relaxation degree.

After 100% ice-off, middle span's tension will be less then icing, which is due to line's slack, the great harm of 100% ice-off is not due to tension's increase, but wire's oscillate up and down repeatedly. In a short time, the tension's sudden change will lead the line to be damaged seriously. The suspension points need more address.

References

[1]Chen Yong, Hu Wei, Wang Liming, et al. Research jump off the ice iced conductor characteristics [J]. China CSEE, 2009,28 (7): 1-2

[2]ROSHAN FEKR M, MCCLURE G. Numerical modeling of the dynamic response of ice-shedding on electric transmission lines [J]. Atmospheric Research,1998, 46(3/4):1-11.

[3] Támás Kálmán. Dynamic behavior of iced cables subjected to mechanical shoeks[Ph.D].Qu6bee，Canada: Université du Qu6bec Chicoutimi，2007：233～243

[4] Guoqiang Wang. Practical engineering simulation technology and its practice on the ANSYS [J]. Northwestern Polytechnical University Press, 1999,8:282 ~ 283

[5] Xinmin Wang. ANSYS structural engineering numerical analysis [M] Beijing: People's Communications Press, 2007.10:468 ~ 469

Advanced Materials Research Vols. 986-987 (2014) pp 615-618

doi:10.4028/www.scientific.net/AMR.986-987.615

The Optimal Energy Storage Capacity Configuration of Photovoltaic Generation under Changing Meteorological Conditions

Bei Zhao[1, a], Mingyang Wu[2, b], Jianliang Zhong[1, b], Hai Bao[1, c]

[1]State Key Laboratory of Alternate Electrical Power System With Renewable Energy Sources (North China Electric Power University), Changping District, Beijing, 102206, China

[2] State Grid Liaoning Electric Power Company Limited Benxi Electric Power Supply Company, Benxi, Liaoning, 117000, China

[a]email: alabei@126.com, [b]email: zhongjl@ncepu.edu.cn, [c]email: hdbh@vip.sina.com

Keywords: Changing Meteorological Conditions; Photovoltaic; SC; Charge and Discharge Control; Optimal Energy Storage Capacity Configuration

Abstract. In the paper, energy storage system and charge and discharge control strategy for large-scale photovoltaic generation are designed. The optimal energy storage capacity is configurated for PV array. The energy storage system and control module for PV generation are built in MATLAB-Simulink platform. Supercapacitor (SC) is the energy storage element. Considering the insolation and temperature under the changing meteorological conditions, the output power would be fluctuant. By controlling MOSFET switches based on power signal, SC will charge when the lighting is adequate and discharge in the instance of lack of light to keep DC bus voltage in constant. Configuring the optimal energy storage capacity by simulation, the result proves that the control strategy is feasible and the configuration is optimal.

Introduction

With the rapid development of large-scale photovoltaic generation, energy storage control strategy develops fast since the storage system is the obbligato link. The energy storage system has a very important function on promoting the quality of photovoltaic generation. The solar energy is fluctuant and stochastic, thus the output power of PV array is not constant. Charging or discharging of SC balance the fluctuant output power caused by adequate and scarce sunlight. The process is implemented by controlling SC in PV generation with energy storage system.

SC is widely used as storage element in electric power system. The main contribution of paper [1] is to propose an SC control strategy for a bidirectional DC/DC converter in an micro grid ESS based on SCs. The primary objective of paper [2] is to solve above problems and improve the performance of the isolated symmetry half-bridge bidirectional DC/DC converter, novel design guidelines, novel modeling of the converter and novel control strategy are proposed by analyzing the principle of the converter and the characteristics of SC module. Paper [3] analyzed the working mode of DC/DC converter when the SC is charging, and designed the closed loop control parameters.

In this paper, a control strategy of energy storage system including PV array and SC is proposed to smooth the output power of DC bus for the grid-connected PV generation. The proposed charging and discharging control method reduces the fluctuant of output power caused by the changing meteorological conditions and configurates the optimal energy storage capacity by simulation for the PV generation system. This paper is organized as followed. In section of 'SC Energy Storage Structure of PV Generation', PV characteristics and mathematical model are analyzed, and the main parameters' formula derivations of the circuit are given. In section of 'The Optimal Energy Storage Capacity Configuration', SC charge and discharge control module based on power signal is given. The control strategy keeps the DC bus voltage in constant before the PV generation connects to grid. In section of 'Simulate Results', the SC energy storage control system of PV generation is built, which includes PV array module and charging and discharging control strategy module in MATLAB-Simulink. And the waveform of SC input and output power caused by changing meteorological conditions is showed.

SC Energy Storage Structure of PV Generation

Fig.1 shows the SC energy storage structure of PV generation. It consists of a PV array, a SC connected by a boost-buck DC/DC convertor and a boost DC/DC converter.

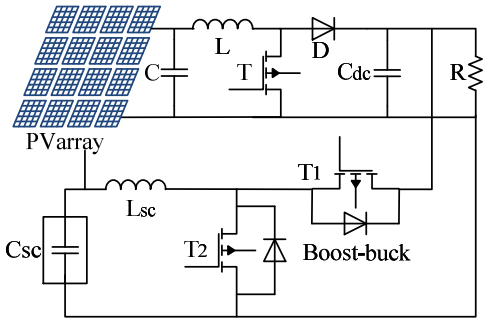

Fig.1. SC energy storage structure of PV generation

In fig.1, C is filter capacitor which makes the output power of PV array continuous. It will lead to a big amplitude ripple wave if its value is relatively small. Also, C will cause the response time to increase if its value is too big. Inductance L is chosen in the continuous mode. According to the volt-second balance theory, the integral for voltage of both ends of L is zero, which is expressed as:

$$U_{pv}DT_S + \left(U_{pv} - U_{dc}\right)\left(1 - DT_S\right) = 0 \tag{1}$$

In equation (1): U_{pv} is the output voltage of PV array; U_{dc} is the voltage of DC bus; D is the duty ratio of MOSFET, T_S is switching period, we can divide both sides of the equation, then the relationship of U_{pv}, U_{dc} and D is expressed as follows:

$$\frac{U_{dc}}{U_{pv}} = \frac{1}{1-D} \tag{2}$$

In the condition of no loss, input power equals to output power $P_{pv} = P_{dc}$, which is equivalents to $U_{pv} I_{pv} = U_{dc} I_{dc}$. The relationship between current and duty ratio is $I_{dc} / I_{pv} = 1\text{-}D$. Because the inductance current equals to PV output current, $I_{dc}/I_L = 1\text{-}D$. Considering $U_L = L*di/dt$, the ripple current of the inductance is expressed as:

$$\Delta i_L = \frac{U_{pv}DT_S}{L} \tag{3}$$

In equation (3): Δi_L can be expressed as $\Delta i_L = \eta_I / i_L$, in which η_I is ripple factor of the ripple current of the inductance. Based on equations (1) (2) (3), the calculation formula of inductance L could be expressed as equation (4). Seeking the extreme L by taking derivative with D, L is obtained the maximum with D =1/3 and the computational formula of the maximal L is expressed as:

$$L = \frac{U_{dc}{}^2\left(1-D\right)^2 DT_S}{\eta_l P_{dc}} \xrightarrow{D=\frac{1}{3}} L_{\max} = \frac{4U_{dc}^2 T_S}{27\eta_l P_{dc}} \tag{4}$$

The DC bus capacitor C_{dc}, the capacitor of DC-link, is the key link between PV array, SC energy storage system and grid-connected invertor. When choosing the capacity of C_{dc}, the circuit has to working under the condition of continuous mode. The quantity of electric charge or discharge ΔQ causes a voltage ripple of DC bus, which can be expressed as:

$$\Delta U_{dc} = \frac{\Delta Q}{C_{dc}} = \frac{I_{dc}DT_S}{C_{dc}} = \frac{P_{dc}DT_S}{U_{dc}C_{dc}} \tag{5}$$

In equation (5): ΔU_{dc} can be expressed as $\Delta U_{dc} = \eta_U U_{dc}$, in which η_U is the ripple factor of the ripple voltage. Add η_U into equation (5), the DC bus voltage C_{dc} is expressed as:

$$C_{dc} = \frac{P_{dc}DT_S}{\eta_U U_{dc}^2} \tag{6}$$

The formula of the SC inductance L_{SC} is the same as L_{max} showed in equation (5).

The Optimal Energy Storage Capacity Configuration

The control objective of energy storage is to stabilize the fluctuation caused by meteorological condition. Charge and discharge control of SC keeps the DC bus voltage in constant before the PV generation connects to grid. In the SC energy storage system, power signal is used as a switch signal to control MOSFET M_1 and M_2. Fig.2 shows the SC charge and discharge control module.

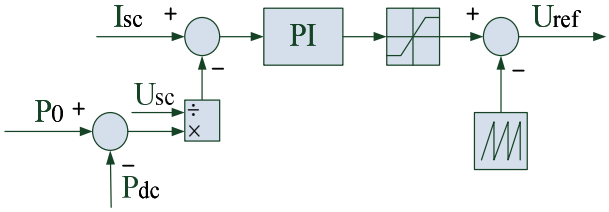

Fig.2. SC charge and discharge control module

In fig.2, P_0 is the reference power. The fluctuating power is the difference between reference power and output power, which serves as control signal to control the state of the MOSFET M_1 and M_2. When the output power is much bigger than the reference power P_0, the fluctuating power difference value is negative and M_1 is on by PWM signal of PI control of the electric current loop. On the contrary, M_2 is on. The switching table is showed as followed:

TABLE 1 Switching table of SC boost-buck circuit

$P_0 < P_{dc}$	SC charging	M_1 is on, M_2 is off
$P_0 > P_{dc}$	SC discharging	M_1 is off, M_2 is on

For large-scale PV generation, generating capacity is high so it is arduous task for SC energy storage system when weather changes. Larger capacity energy has a better storage capacity. But considering the economic efficiency, the optimal storage capacity is configurated for the requirements of large-scale PV generation.

$$C_{SC} = \frac{\Delta Q}{U_{SC}} = \frac{I \cdot t}{U_{SC}} = \frac{\Delta P_{SC} \cdot t}{U_{sc}^2} \tag{7}$$

Equation (7) is the computational formula of SC. By calculating the output power under large carving illumination and low light intensity, the ΔP could be obtained which equals to ΔP_{SC}. The capacity of SC could be calculated by equation (7).

Simulate Results

This paper builds the SC energy storage control system of PV generation, which includes PV array module and charging and discharging control strategy module in MATLAB-Simulink. The parameters of the simulation are followed: Set the initial voltage of SC to 160V, the capacity of SC to 6F, set the reference voltage U_0 to 600V. The variable illuminations are 800-600-800-1000-800 kW/m^2 in each 0.1 second showed in fig.3. The simulation time is 0.5s, and the simulation arithmetic is ode23tb. The simulation waveform of SC is showed in fig.4.

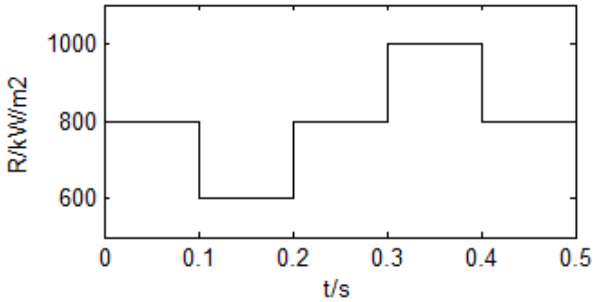

Fig.3. Variable illuminations

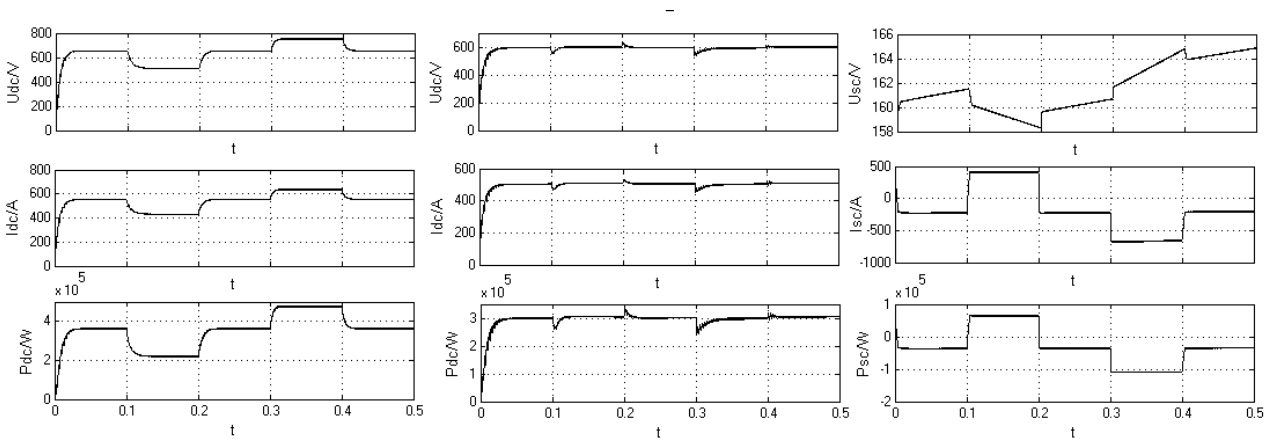

(a) U_{dc}, I_{dc}, P_{dc} without SC (b) U_{dc}, I_{dc}, P_{dc} with SC (C) U_{dc}, I_{dc}, P_{dc} of SC

Fig.4. Output voltage, current, power of DC bus and SC

In fig.4 (a), output power fluctuates as the variable illumination. The minimum output power is 220kW when illumination is 600 kW/m^2 while the maximum output power is 490kW when illumination is 1000 kW/m^2. The capacity of SC is 5.27F after calculation. In fig.4 (b), SC is used to store energy to keep the DC bus voltage in constant. Fig.4 (c) shows that when the fluctuating power is bigger than reference power, SC charged and on the contrary, SC discharged. The simulation result proves that the capacity of SC equal 6F is reasonable.

Conclusion

In this paper, the correct parameters of the PV generation system with SC are chosen. Based on the analysis of the SC boost-buck circuit, a switching table of the MOSFET is constructed to control the SC to charge and reduce the DC bus voltage or to discharge and increase the DC bus voltage. Considering both of the capacity requirement and economic efficiency, an exact capacity of SC is chosen to keep the DC bus voltage in constant. And the simulation result proves it reasonable.

Acknowledgement

This paper is supported by the National High Technology Research and Development of China (863 Program) No.2011AA05A301.

References

[1] Jiang W, Hu R, Chen W, et al. Improved performance of a DC/DC converter for supercapacitor energy storage system[C]//Energy Conversion Congress and Exposition (ECCE), 2013 IEEE. IEEE, 2013: 682-689.

[2] Inthamoussou F A, Pegueroles-Queralt J, Bianchi F D. Control of a Supercapacitor Energy Storage System for Microgrid Applications[J]. Energy Conversion, IEEE Transactions on, 2013, 28(3): 690-697.

[3] Kui-an M A, Min C. Charge mode control design for super-capacitor energy storage system[J]. Journal of Mechanical & Electrical Engineering, 2010, 7: 023.

[4] Kang Q, Xiao X, Yi H, et al. Energy management in grid connected PV systems with supercapacitor energy storage[C]//Electrical Machines and Systems (ICEMS), 2011 International Conference on. IEEE, 2011: 1-5.

[5] Seo H R, Kim G H, Kim S Y, et al. Power quality control strategy for grid-connected renewable energy sources using PV array and supercapacitor[C]//Electrical Machines and Systems (ICEMS), 2010 International Conference on. IEEE, 2010: 437-441.

Advanced Materials Research Vols. 986-987 (2014) pp 619-621

doi:10.4028/www.scientific.net/AMR.986-987.619

The Research of Variable Speed Constant Frequency Wind Power Generation Technology

Yuan FEI[a], Quan LIU[b], Yong CHEN[c]

School of Electromechanical Engineering, Beijing Information Science and Technology University, Haidian District, Beijing 100192, China

[a]125008982@qq.com, [b]bjgs2000@163.com [c]chenyong_jz@126.com

Keywords: Wind power; Unit capacity; Power regulation; Variable speed operation; Tip speed ratio; Wind energy utilization coefficient

Abstract. This paper briefly introduces the characteristics of wind power technology and its development process, Through data comparison, demonstrate the superiority of the variable speed wind turbine operation. In keeping the best tip speed ratio, the variable speed constant frequency control for the biggest wind power.

Introduction

Due to the worldwide coal, petroleum and other non-renewable energy is reduced,and coal as the main energy of the electric power industry brings the serious problems of environmental pollution,all countries in the world to focus shifted to renewable and clean energy research, development and utilization.For the use of renewable and clean energy, the most mature is wind power technology[1].

In recent years, the rapid development of wind power technology.Capacity of constantly improve, commercially available megawatt wind power unit;The variable pitch wind turbine power regulation replaced the fixed pitch adjustment, the generator of variable speed constant frequency operation replaced the traditional constant speed constant frequency operation, further improve the system efficiency;Implements the wind farm in real-time monitoring, remote controlling and computer group control, improve the stability of distribution or parallel operation and power quality.

Wind power generation technology

Wind power technology is the aerodynamics, electrical machinery, materials science, mechanical transmission, automatic control, power electronics technology and other multi-disciplinary comprehensive technology. Although wind power development has been about 100 years, but it wasn't until the 1970 s brought to the attention of the people gradually, domestic and foreign existing wind power technology has failed to fully show the advantage of wind power, wind power technology and larger development space. Large wind power generators to large capacity, good power quality, improve material utilization, reduce noise, reduce cost and improve efficiency of direction[2].

Unit capacity increase

In the early 1980 s, commercialization of the stand-alone capacity of wind turbines is given priority to with 55 kW, the middle 1980s to the early 1990s to give priority to with 100 ~ 450 kW, 90 s to 500 kW ~ 1 MW.At present, large and medium-sized units connected to the grid, has become the main form of wind energy.To reduce the cost of unit kw, save the using area of wind farm, speed up the construction of wind farms, improve the economic benefits of wind power, many wind power manufacturers committed to improve the capacity of producing capacity is greater than 1 MW commodity unit,see table 1[3-4].

Power regulation mode

Power control is one of the key technology of wind power generators.Wind generating set in more than the rated wind speed (generally for 12 ~ 16 m/s), due to the mechanical strength and

physical properties such as generators, power electronics capacity constraints, have to reduce the energy capture of wind turbines, to keep the power output near the rating, at the same time reduce the load and the whole wind turbine blade have been hit, to ensure wind turbine.Power regulation ways mainly have a fixed pitch stall adjustment, variable pitch adjustment, take the initiative to stall adjustment three ways [3].

Table 1. Megawatt wind turbine

Manufacturers/wind turbine model	Rated power/kW	Wind turbines control	Speed control	The rotor diameter/m
DeWind	1250	Variable pitch	Variable speed	70
AN BONUS	1500	Take the initiative to stall	Constant speed	80
Enron EW1.5s	2000	Variable pitch	Variable speed	70
Enron EW3.6	1800	Variable pitch	Variable speed	90
Pro&Pro MD70	1250	Variable pitch	Variable speed	70
Vestas V80	1500	Variable pitch	Variable speed	80
Nordex N80	2250	Variable pitch	Variable speed	80
Enercon E-66	1500	Variable pitch	Variable speed	90

Variable speed operation

The output power of the wind turbine mainly by three factors: the available wind power, generator power curve and generator's ability to response changes in wind speed.The fan to power from wind energy capture for:

$$P_r = \frac{1}{2} C_P(\beta, \lambda) \rho \pi R^2 V_\omega \tag{1}$$

$$\lambda = \frac{\omega R}{V_\omega} \tag{2}$$

P_r: Turbine power absorption（W）, ρ: Air density（kg/m^3）,R:The rotor radius（m）, λ: Tip speed ratio，ω: Rotor speed（rad/s）. $C_P(\beta, \lambda)$:Wind energy utilization coefficient，The maximum is Bates limit of 59.3%， C_P Curve [5] as shown in figure 1.

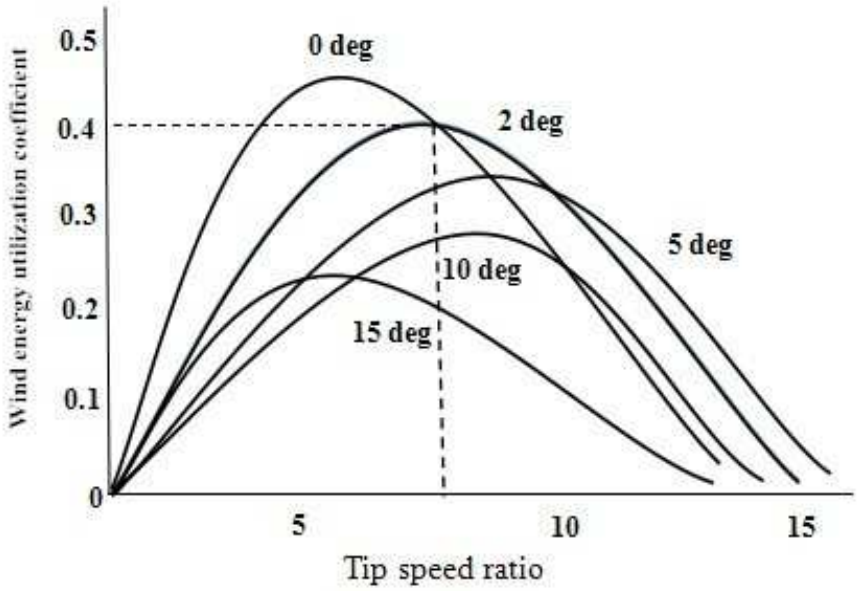

Fig.1 C_P -Curve

If they remain β constant, A curve can be used to describe the performance of it as λ.According to the figure 1,as long as you make the rotor blade tip speed ratio $\lambda = \lambda_{opt}$,can keep the unit running under $C_{p,\max}$ .Variable speed control make the wind turbines to follow the change of

wind speed change the rotation speed and maintain optimal tip speed ratio of basic constant λ_{opt} ,Relative to the constant speed operation, speed system has the following advantages:

①Have a higher efficiency, can make the pitch adjusting simplification.Variable speed operation to relax the requirement of pitch control response speed and reduce the complexity of the control system of pitch, reducing peak power demand.Low wind speed, pitch Angle is fixed, the high wind speed, adjust the pitch Angle limit maximum output power.

②Can absorb wind energy, the energy stored in the moment of inertia of rotor machinery, reduce wind fatigue damage incurred by the impact of wind generating set, reduce mechanical stress and torque ripple, extend the life of the unit.When the wind speed dropped, high-speed rotor kinetic energy is released into electricity to power grid.

③System with high efficiency.Variable speed running fan run at optimal tip speed ratio, maximum power point, improve the efficiency of wind turbine, compared to constant speed constant frequency wind power system, power generating capacity can increase more than 10% in general.

④To improve power quality.Because of the flexibility of the rotor system to reduce the torque ripple, thereby reducing the output power fluctuations.

⑤Reduce the running noise.Low wind speed, wind turbines at a low speed running state, the lower the noise.

Summary

To improve the efficiency of wind power, reduce costs, improve power quality, reduce noise, stable and reliable running, wind power technology will continue to large capacity, brushless, intelligence and control of variable speed constant frequency direction.

Acknowledgements

The research work was supported by ： the Importation and Development of High-Caliber Talents Project of Beijing Municipal Institutions，（CIT&TCD20130328） Science and technology achievements transformation and industrialization project of Beijing Education Commission in 2013.And Beijing municipal education commission research base construction projects (PXM2013_014224_000005).

References

[1] JinMei SONG,Bo WANG,HaiBo XIAO Chinese and foreign commonly used wind power technology, and the wind motor overview [J]Electrical technology2009

[2] XiaoShan ZHANG，QiangHui XIAO Wind power generation system and simulation [J]Journal of hunan university of technology2013

[3] Rolf Hoffman. A comparison of control concepts for wind turbines in terms of energy capture.[D].2002

[4] Mutschler P, Hoffman R. Comparison of wind Turbines Regarding Their Energy Generation[J]. Power Electronics Specialists Conference .IEEE.2002,1:6-11

[5] Slootweg J G,Kling W L, Polinder H. Dynamic modeling of a wind turbine with doubly fed induction generator [J], Power Engineering Society Summer Meeting,IEEE,2001,11:644-649

Advanced Materials Research Vols. 986-987 (2014) pp 622-629

doi:10.4028/www.scientific.net/AMR.986-987.622

The Research of Wasting Wind Power and Methods of Its Consumption Based on that of Fuxin

Shao Tianlong, Zhang Jian and Zhao Xunan

State Grid Liaoning Electric Power Supply Co., Ltd., Fuxin Power Supply Company, Liaoning, Fuxin 123000

stlnever@163.com

Keywords: Wind power, Difficulty of peak regulation, Wasting wind power, Consumption, Output

Abstract. As a kind of renewable clean energy, the constant access of wind power to power grids is bound to have a great impact on the power system. Based on the grid structure in Fuxin, this paper will state the difficulty of peak regulation and the matter of wasting wind power caused by the large-scale wind power integration and put forward some reasonable methods for using the wasting wind power in the heating in winter. The relevant results indicate that capacity of local consumption of wasting wind power can be improved. Under the circumstances, it can be conductive to solve the problem of wasting wind power results from the difficulty of peak regulation as well as inspire the power system planners.

Introduction

Clean energy refers to the energy that does not emit pollutants, which includes nuclear energy, hydropower, wind power, solar energy, biological energy (biogas), and tidal energy. From the Fukushima nuclear explosion we can see that compared with the wind power, nuclear energy has lower security, hydropower and solar energy have higher construction cost, the location of biological energy and tidal energy is less flexible, so the wind power has become the main force in the clean energy.

In 2012, China issued the *Five-year Development Program of Wind Power*, which clearly expounded the grand goal of future development of wind power: by 2015 the installed wind turbine capacity of wind power integration will reach 100,000,000KWH and by 2020 it will reach 200,000,000KWH. Although our wind power industry has been rapid developed in recent years, the speed of power grid construction is relatively lagging behind and the wind power consumption need to be further improved. The difficulty of peak regulation in the power system caused by the large-scale wind power integration is becoming more and more serious and the wasting wind power has also become an important factor restricting the development of wind power.

The situation of wasting wind power in China

At present, China owns the most installed wind turbines throughout the world, which accounts for 26% of all countries. However, compared with Germany, Denmark and other European countries, the percentage of wind power in China's overall energy structure is very low. As such it has a huge space for development.

In April 2013, the *Notice about Dealing Well with the Related Work of Wind Power Integration and Consumption in 2013* (hereinafter referred to as the *Notice*) showed that Northeast has become the "hardest-hit area" of wasting wind power and power rationing ,which accounted for half of that in China , that is 10 billion KWH. In 2012 the national wasting wind power is about 20 billion KWH, which is double of that in 2011. Calculate to the current state of coal consumption of generating power, 20 billion KWHs of electricity is equivalent to burning about 6,000,000 tons of coal. According to the electricity price, the direct economic loss is more than10 billion yuan.

In April 2014, the National Energy Administration issued the *Notice about Dealing Well with the Related Work of Wind Power Integration and Consumption in 2014*. *Notice* pointed out that in 2013, the using time of national wind power rose by an average of 180 hours and the wasting wind power

declined by about 5 billion KWH. The matter of wasting wind power and power rationing, however, has not been fundamentally solved, so regional wasting of wind power still restricts the development of wind power industry in China.

From the consecutive two-year notices about the work of wind power integration and consumption released by the National Energy Administration, we can see that the wasting wind power problem has been eased and the overall data is not bad, but due to the increasing load and the limit of wind power access to power grids, in China, there is still a big problem in the context of the development of wind power industry. The problem of wasting wind power not only restricted the development of wind power, but also not contributed to the overall healthy development of China's renewable energy industry due to the huge waste of investment and energy caused by the direct consequence of wasting wind power led by the difficulty of peak regulation.

Fuxin is located in west of Liaoning province in Northeast China and cogeneration is to be used for heating in winter, at the same time it will produce electricity, which has been largely enough for local electricity load of winter. Because of this most of the wind power and wind turbines must be stopped, which will inevitably cause a large amount of wasting wind power, namely northeast has particularly acute problem of wasting wind power in China. Fuxin, as the area of available wind resource, has typical problem of wasting wind power and its consumption in the process of wind power development. This paper will study the problem of wasting wind power and its consumption based on the actual data of 66 KV wind farm in Fuxin.

The situation of wasting wind power in Fuxin (2013)

Form 1 Five Wind Farms of 66 KV in Fuxin（Administrated by area)

No.	Name of Wind Farm	installed wind turbines capacity GW
1	Huadian Jinshan ZhangWu Wind Farm	24.65
2	Huadian Jinshan Kangping Wind Farm	24.65
3	Huarun Guben Wind Farm	99
4	Huaneng Gaoshanzi Wind Farm	100.5
5	Datang International Shijingao Wind Farm	49.5

The form above shows that grids have been incorporated in Fuxin area and the capacity of installed wind turbines of 66 KV is 298.3 GW in 2013.

Form 2 Statistical Form of Power Rationing in 66 KV Wind Farms of Fuxin in 2013

Statistical Form of Power Rationing in Local Wind Farms					
Name of Wind Farm	Month	Reason of Power Rationing	Times of Power Rationing	Accumulated electric quantity MWH）	Accumulated hours H）
Gaoshanzi Wind Farm	1	Difficulty of peak regulation	15	3046	80.94
	2	Difficulty of peak reguation	24	6809	218.91
	3	Difficulty of peak regulation	8	2651	56.61
	4	Difficulty of peak regulation	4	907	41.27
	5	Difficulty of peak regulation	27	4415	150.61
	6	Difficulty of peak regulation	8	367	35.36
	7	No power rationing	0	0	0
	8	No power rationing	0	0	0
	9	No power rationing	0	0	0
	10	No power	0	0	0

		rationing			
	11	Difficulty of peak regulation	9	1619.3	35.7
	12	Difficulty of peak regulation	21	2662	108
	In total		116	22476.3	727.4
Shijingao Wind Farm	1	Difficulty of peak regulation	15	1577	76.92
	2	Difficulty of peak regulation	21	2780	186.56
	3	Difficulty of peak regulation	16	1873	75.22
	4	Difficulty of peak regulation	4	663	19.41
	5	Difficulty of peak regulation	30	6505	151.90
	6	Difficulty of peak regulation	10	1275	38.39
	7	No power rationing	0	0	0
	8	No power rationing	0	0	0
	9	Difficulty of peak regulation	1	302.68	7.9
	10	No power rationing	0	0	0
	11	Difficulty of peak regulation	4	649.4	15.54
	12	Difficulty of peak regulation	20	2857.896	93.14
	In total		121	18482.98	664.98
Guben Wind Farm	1	Difficulty of peak regulation	16	4631	122.02
	2	Difficulty of peak regulation	18	11247	226.42
	3	Difficulty of peak regulation	14	6396	82.08
	4	Difficulty of peak regulation	4	1387	16.54
	5	Difficulty of peak regulation	17	6546	98.72
	6	Difficulty of peak regulation	9	2434	40.4
	7	No power rationing	0	0	0
	8	No power rationing	0	0	0
	9	Difficulty of peak regulation	1	634	5.75
	10	No power rationing	0	0	0
	11	Difficulty of peak regulation	4	371.085	8.96
	12	Difficulty of peak regulation	18	321.2426	83.4
	In total		101	33967.33	684.29
Zhangwu Wind Farm	1	Difficulty of peak regulation	5	216	30
	2	Difficulty of peak regulation	15	409	120
	3	Difficulty of peak regulation	8	210	42
	4	Difficulty of peak regulation	2	17	1
	5	Difficulty of peak regulation	13	224	23

	6	Difficulty of peak regulation	2	38	3
	7	No power rationing	0	0	0
	8	No power rationing	0	0	0
	9	Difficulty of peak regulation	1	12.6	1
	10	No power rationing	0	0	0
	11	Difficulty of peak regulation	5	17.424	18
	12	Difficulty of peak regulation	12	239.785	60
	In total		63	1383.809	298
Kangping Wind Farm	1	Difficulty of peak regulation	6	571	12.98
	2	Difficulty of peak regulation	14	126	194.74
	3	Difficulty of peak regulation	12	637	25.33
	4	Difficulty of peak regulation	1	10	1.4
	5	Difficulty of peak regulation	10	181	22.74
	6	Difficulty of peak regulation	2	14	10.57
	7	No power rationing	0	0	0
	8	No power rationing	0	0	0
	9	Difficulty of peak regulation	1	4.9	0.7
	10	No power rationing	0	0	0
	11	Difficulty of peak regulation	4	19.85	18.68
	12	Difficulty of peak regulation	14	359	22.55
	In total		64	1922.75	309.69
Totally			465	78233.16	2684.36

We can know from the above form, there are 5 online wind farms of 66KV administrated by Fuxin area in the whole year of 2013, in which the times of power rationing in Gaoshanzi Wind Farm are 116 times, the time are 727.4 hours, accumulative total of 22476.3 MWH, the times of power rationing in ShiJingao Wind Farm are 121 times throughout the year, 664.98 hours, accumulative total of 18482.98 MWH, the times of power rationing in Guben Wind Farm are 101 times throughout the year, the time are 308.25 hours, accumulative total of 33967.33 MWH, the times of power rationing in ZhangWu Wind Farm are 63 times throughout the year, the time are 122.38 hours, accumulative total of 1383.809 MWH, the times of power rationing in Kangping Wind Farm are 64 times throughout the year, the time are 309.69 hours, accumulative total of 1922.75 MWh. Due to the difficulty of peak regulation, the total times of 5 wind farms of 66 KV are 465 times, the total time are 2684 hours and the total power 78233.16 MWH.

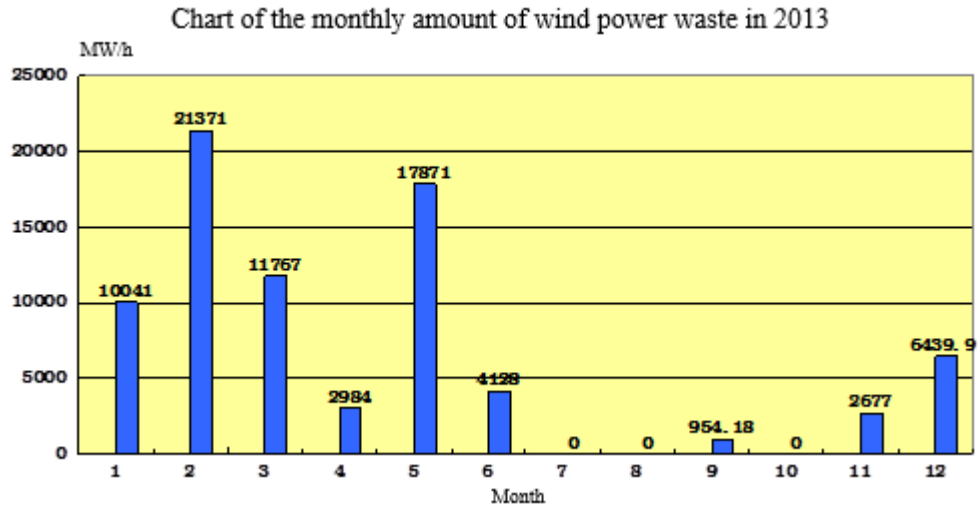

Figure 1 The monthly wasting wind power in 66KV wind farms of Fuxin in 2013

From the Figure 1 we can see that, the phenomenon of wasting wind power occurs mainly in the first five months and November to December, that is the winter heating period with off-peak load (the Fuxin's wind is heavy in May 2013, so the wasting wind power is higher).The wasting wind power is 52280 MWH in heating period, which accounted for 66.83% of the whole year's wind power; The wasting wind power of the off-peak heating period accounts for a great proportion. In winter heating period, the proportion of Fuxin coal heating increased, the crowding out the online space of wind power, therefore the difficulty of peak regulation led to the wasting wind power.

Set the Guben Wind Farm of 66 KV as an example (the curves are from the OPEN3000 system of Fuxin Power Supply Company):

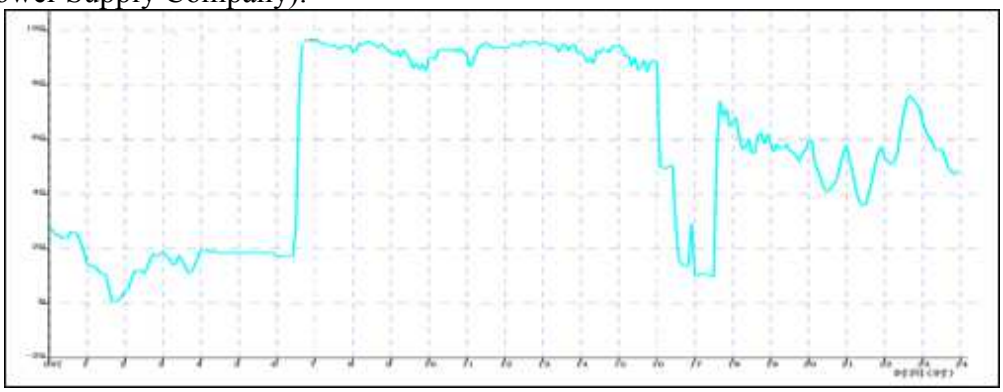

Figure 2 The curve of actual active power output on 3rd in January 2013 of 66KV wind farm

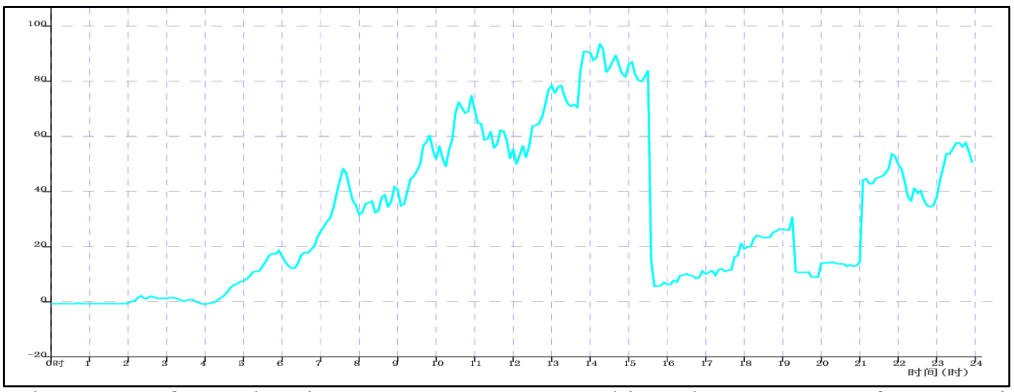

Figure3 The curve of actual active power output on 2nd in February 2013 of 66KV wind farm

In the field of power, especially of new energy, wind power is one of the fastest growing fields in the past a few years. Fuxin plans to build a super wind power demonstration base (including 220 KV wind farm), whose installed size will be over million kilowatt, so the development of the mass

concentration model is bound to make the consumption of wind power become the biggest problem. According to the present situation, the phenomenon of wasting wind power is inevitable.

Analyze the reasons of the difficulty of peak regulation

Affected by the weather, the wind power is not so stable that the wind can't completely replace thermal power, but to mutually combine and complement. Wind power development is too fast to be consumed by the local power grid. As electricity cannot be stored, and users' demand for electric power has a real-time change, the electricity is generated according to the demand. So there are much more wind power, there are less thermal power and others and vice versa. Therefore, where there are more installed wind turbines, there are more difficulties of peak regulation.

Fuxin is an area of available wind, but the wind resource and load is reverse. The fast speed of wind often occurs at night, while the load of night is low. According to the present level of wind power prediction and development of power grid, peak regulation is doubtlessly difficult and the wasting wind power is now inevitable.

The quality of wind power in winter is very good, but winter temperatures in Fuxin is very low and the heating of people's daily life need to be ensured. In order to reduce the scattered heating supply of small boilers, Fuxin supplies heating by using cogeneration, which is decided by thermal electricity. Because the heating can't be stopped, the thermal electricity, which could have to give way to wind power, cannot do that. Therefore only can the wind power stop. That is why Fuxin could have more wind power in recent years and the phenomenon of wasting of wind power increased.

Methods for improving potential of consumption

Implement of *Heating by Using the Wasting Wind Power*

Heating by Using the Wasting Wind Power is mainly to solve the difficulties of peak regulation caused by cogeneration in winter.

Concept

Heating by Using the Wasting Wind Power refers to make full use of wasting wind power, one part of which is for heating, and the other part is for storing heat that is to guarantee the supply of heating in the period without wind. Compared with the storage of electricity, storing heating is much easier. Any objects has the function of absorbing, storing and releasing heat, so as long as we find the object of storing heat, the electricity can be transformed into heat to solve the problem of supplying heating in the period without wind.

Economic problem

In terms of current technology, Heating by Using the Wasting Wind Power can be achieved completely. Its advantage lies in that the power transmission has less lose than the thermal transmission, which not only can supply heating centrally, but also can supply heating dispersedly and even to neighborhood or a single family. But the reason that so convenient way of supplying heating can't be promoted today is the price of electricity. Compared with the cost of heating transmitted by electricity, waste heat of thermal and power unit costs lower and the price is also low. Because of the electricity price, even if the families have the condition of using the heating transmitted by electricity will choose the waste heat. So the reasonable electricity price is the root cause of changing the cost gap of waste heat and electric heating.

1)The introduction of the concept of the electric price of regional wasting wind power

In November 2010, the six ministries such as the National Development and Reform Commission and the State Electricity Regulatory Commission jointly issued the "Side Measures for the Management of Power Demand ". It has put forward 16 qualitative or quantitative managerial and incentive measures for the electric power demand, in which they mentioned that they would promote and improve the system of peak price and encourage off-peak energy storage". But compared with the cost of waste heat, the cost of off-peak electricity price is still slightly higher

This paper put forward the concept of the electric price of regional wasting wind power, namely the price of some wind farm's wind power that should be stopped bought by the grid in some certain area and time. Due to the different proportion of wind power in different areas, electricity price of wasting wind power should also be slightly different. For example, the wind power in Fuxin is much richer, through analyzing the proportion of wasting wind power and adopting the method of electricity price bidding to get online for wasting wind power, they will choose the wind field whose electricity price is lower to generate electricity as a priority. So in Fuxin, electricity price of wasting wind power is lower than other regions, the scheme can be implemented more likely. Hereinafter referred to as the "the price of wasting wind power".

2)Orientation of the electricity price of wasting wind power

The waste heat cost of the residents in Fuxin is $26 /㎡, every year the heating time is from November 1 to March 31, about 150 days in total. Its average temperature in winter is from- 12 ℃ to 0 ℃. The general electric heaters, for example, an electric heater of 1000w is big enough for 10-square-meter room in winter.

Set the electric heaters occupy heating for a 10-square-meter room in continuous 8 hours as an example:

Waste heat cost of the residents: 26yuan /㎡* 10 ㎡= 260yuan

Power consumption of electric heaters in winter: 1KW * 8 hours/day *150 days = 1200 KWH

∴ Residents' reasonable electricity price of wasting wind power is less than or equals to 260yuan / 1200 KWH, is about 0.22yuan/KWH

Because of some actual reasons, such as the electric heaters can't be used in continuous full 8 hours, the space of a room can't be make full use and the area need to pay heating fee includes the shared area, the above standard price of wasting wind power: 0.22yuan/KWH is lower, so it can be appropriately increased

The environmental cost in a heating of cogeneration costs can't be ignored, and the clean energy like wind power will not impact on the environment, and it can reduce the cost of government to beautify the environment, so the government can give a wind farm proper green subsidies.

Selection of the heating places

In 2013, the wasting wind power in Fuxin during the heating period is 78233.16MWH, which can, theoretically, supply heat for 650,000-square space. In Fuxin, the actual heating area is 26,450,000 ㎡ in 2013, 2.4% of which can consume the present wasting wind power. The heating places should be chosen at the edge of waste heat radiation web with the users whose heating effect is poorer, and the selection principle should be considered as the real heating demand of users.

Operative method of electricity price

According to the price of wasting wind power, the grid company purchases the wasting wind power, and users buy the electricity from the grid company. In the ideal model, only the price of electricity used during the period of the wasting wind power can be settled accounts according to electricity price of wasting wind power, but it is difficult to be strictly divided by time, so we need to take some new marketing modes.

1)The mode of charging by two kinds of electricity price

To charge power fee by proportion and based on user's property area, for example, daily use is 0.8 KWH per square meter and the area of the house is 100 square meters, for example, the wasting wind power for about a month is: 100 * 0.8 * 30 = 2400KWH

The electricity used by a 100 - square - meter house during the winter is about 200KWH to 300KWH , in order to facilitate understanding and calculation, we take 266KWH, or the ratio of wasting wind power and the normal power is 9:1, so finally the charge standard of the user is that 90% of power is charged by 0.22yuan/KWH, and the rest 10% is charged by 0.50yuan/KWH.

2)The mode of ladder electricity price

Still set the above user as an example:

First stage: the first 266 KWH will charge according to 0.50yuan/KWH;

Second stage: 266 KWH to 3000 KWH will charge according to 0.22yuan/KWH;

Third stage: above 3000 KWHs above will charge according to 0.50yuan/KWH.

3)The mode of charging by different periods

Assume the average time of stopping the wind power is from 08:00 to 19:00 of the next day in winter:

Still set the above user as an example, During the time of using the wasting wind power, the electricity fee will be charged according to 0.22yuan/KWH, but the cap is 2400KWH, exceeding part will be charged by 0.50yuan/KWH, also in other time. In addition, in order to ensure the wasting wind power can be really consumed and avoid phenomenon of only using the wasting wind power, they should do the assessment on the users of using wasting wind power and establish a long-term relations of cooperation with a large number and stable electricity users.

The calculation method of electricity consumption

Because the output power can't be regarded as wasting wind power, which is hard to define, so adopting the following methods:

According to fit the related data of the wind power generation growth curve, wasting wind power curve and the regional increasing load curve, you can calculate the theoretical wasting wind power during the heating period of the year, issue the target generating electricity, and settle amounts of trading fee of electricity by the wasting wind power.

Based on the planed electricity generation of a wind farm, we make the coefficient of wasting wind power and generate electricity according to the agreement. In a whole year, a big part of electricity belongs to the wasting wind power, which will be charged by the price of wasting wind power.

Conclusion

As the world's most promising new energy technology, wind power has got a rapid development in China. In the wave of the wind power, China is facing a serious problem of wasting wind power caused by the introduction of large-scale wind power, so the study of the wasting wind power and its methods of consumption is very significant in the reality. This article has carried on the preliminary research, mainly including:

1) Fuxin belongs to the typical area of cogeneration, this paper analyzes, under the influence of this power supply, the reasons of wasting wind power caused by the difficulties of peak regulation.

2) Based on the marketing mode of electricity, this paper put forward the new concept of regional electricity price of wasting wind power, the system of heating by using the wasting wind power and the methods of managing the electricity price.

3) In terms of the heating by using the wasting wind power and comparing the costs of different ways of heating, this paper figures out the electricity price of wasting wind power that is suitable for Fuxin in details.

4) This paper gives us three modes of electricity price, they are charging by two kinds of electricity price, ladder electricity price and charging by different periods. And it also gives us a primary mode of figuring out he electricity.

5) From the proportion of heating by using the wasting wind power accounts for only 2% of heating in Fuxin area we can see when large-scale wind power is introduced into grid of Fuxin region, the above mode also can be used and further to develop the potential of the regional wasting wind power consumption in the area of Three-North regions relying on heating.

6) The concept of "regional electricity price of wasting wind power" not only can be used in the problems of local consumption during the heating period, and even can be extended to the mode of prices during the period without heating supply to further complement and improve the electricity price leverage led by the price during the peak period—restrain the rapid growth of the peak power consumption during peak period and improve the low electricity consumption during the off-peak period, so as to improve the efficiency of the whole society and further regulate the balance between supply and demand.

References

[1] LuoNi etc. *The Research Development of Energy Storage Technology in Power System* [J]; *The Power Grid and Clean Energy*, 2012, 2.

[2] Xu Guofeng. *The Research of Problem of Stability and Reliability of Wind Power Grid Consumption Mechanism* [D]. Zhejiang: Zhejiang University, 2012.

Advanced Materials Research Vols. 986-987 (2014) pp 630-634

doi:10.4028/www.scientific.net/AMR.986-987.630

Theoretical line loss calculation of distribution network considering wind turbine power constraint

Ke Li [a], Zhenquan Sun [b] and Meng Wang [c]

Shaanxi Regional Electric Power Group Co., Ltd, Xi'an 710061，China

[a]57454793@qq.com, [b]Zhenquansun@163.com, [c]717500985@qq.com

Keywords: distribution network, Monte Carlo simulation, forward/backward power flow

Abstract. This paper presents a theoretical line loss calculation of distribution network containing an uncertainty power of wind turbine. First, this paper establishes the theoretical line loss mathematical model considering wind turbine power constraint within the sampling period. Then this paper gets multi group wind turbine output data satisfied the power constraints through Monte Carlo simulation. By combining with the first power coefficient method and Monte Carlo simulation technique, this paper also generates multi groups load pseudo measurement test of non real time. By combining the real-time measurement of power flow calculation, a group of simulated data with minimum error between the power flow results and the real time measurement are selected. Finally based on the selected pseudo measurement, the theoretical line loss within the given time period based on periodic accumulative calculation of real-time measurement are calculated. 14 nodes example is given to verify the accuracy and practicality of the algorithm.

Introduction

Due to be influenced by the speed of wind, the wind output is random and the change is big. It cannot be simply considered as the hourly constant load to calculate the theoretical line loss. But it is rarely considered the influence of the distributed power supply in traditional theoretical line loss calculation [1-14].

Therefore, reference [15] put forward a kind of calculation method for distribution network line loss based on the theory of power flow calculation. It preferably solved the line loss change issues caused by the trend reverse flow which is induced by the distributed power in interval time. But it is assumed that the active power and reactive power of intermittent distributed power per hour is constant. Due to the distribution of intermittent power supply, such as wind turbine output affected by wind speed, this paper assumes that influenced the accuracy of line loss calculation. Reference [16] studies the influence of distribution network in different location, capacity, and operation mode after the intermittent distributed power accessed distribution network. But it does not take into account the theoretical line loss calculation problem under the condition of uncertainty of intermittent distributed power outputs.

The above methods do not consider the theoretical line loss calculation problem caused by the intermittent randomness of output capacity of distributed power supply. This paper proposes a theoretical line loss calculation model under the condition of the randomness of intermittent distributed power output.

Theoretical line loss calculation model with wind turbine

Theoretical line loss calculation model of distribution network is as follows:

$$E_T = P_{loss} \times \Delta t \tag{1}$$

Where: E_T is line loss in cycle calculation; Δt is sampling time interval in Real-time measurement data; P_{loss} is theoretical line loss in the period Δt .

Because the wind turbine power exports usually exist active and reactive power electrical degrees at every hour. The time interval of real time measurement Δt are usually less than 1 hour, so it is need to transfer wind turbine output of integral point into the wind turbine output of time interval of Δt, and wind turbine output multiplied by the sum of time is equal to the wind turbine capacity per hour, which is satisfied by the following conditions:

$$\begin{aligned} E_w^P &= \sum_{i=1}^{n} P_{w,i} \times \Delta t_i \\ E_w^Q &= \sum_{i=1}^{n} Q_{w,i} \times \Delta t_i \end{aligned} \tag{2}$$

Where: E_w^P, E_w^Q are represent the active and reactive power of wind turbine export for one hour, respectively; $P_{w,i}, Q_{w,i}$ are the pseudo measurement of wind turbine active and reactive power output for the period of Δt_i; n is the number contained Δt for one hour.

Estimation of Pseudo measurement for non-measured nodes. In the semi-automatic distribution network, here were plenty of non real-time measurement nodes; the head end power method [4] could generate pseudo measurement for non measurement nodes by the hour as the unit. The precision are low. Reference [4-7] with matching trend technology effectively enhanced the precision of pseudo measurement, but only use the measurement of the first node of the feeder. They do not make full use of the measurement of other section switches, impacted the calculation accuracy for the trend, and then reduced the theoretical line loss calculation accuracy

The Monte Carlo simulation of non measurement data. The load power of non measured load node usually obeys the normal distribution, considered the pseudo measurement of the head end power method as the average power, and also considered the electricity per hour for the active and reactive power of the wind turbine output as the average pseudo measurement, under the condition of a given variance, now gave below in the period of time Δt_i, the probability density function of active and reactive power for measurement node j is as follows:

$$\begin{cases} f_{\Delta t_i,P}(P_{\Delta t_i,j}) = \dfrac{1}{\delta_{P_{\Delta t_i,j}}\sqrt{2\pi}} \exp[-\dfrac{(P_{\Delta t_i,j} - P_{\Delta t_i,j}^{real})}{2\delta_{p_{\Delta t,j}}^2}] \\ f_{\Delta t_i,Q}(Q_{\Delta t_i,j}) = \dfrac{1}{\delta_{Q_{\Delta t_i,j}}\sqrt{2\pi}} \exp[-\dfrac{(Q_{\Delta t_i,j} - Q_{\Delta t_i,j}^{real})}{2\delta_{Q_{\Delta t_i,j}}^2}] \end{cases} \tag{3}$$

Where: $f_{\Delta t_i,P}$ and $f_{\Delta t_i,Q}$ are the probability density function obeyed the normal distribution of active and reactive power; $\delta_{P_{\Delta t_i,j}}$ and $\delta_{Q_{\Delta t_i,j}}$ are the given variances of the active power and reactive power; $P_{\Delta t_i,j}^{real}$ and $Q_{\Delta t_i,j}^{real}$ are the average active power and reactive power determined by the head end power coefficient method.

Based on the probability density function of the active and reactive load, under the condition of a given variance, if processing Monte Carlo simulation for all the non measurement load nodes of feeder and the active and reactive power output of the wind turbine, there will produce multiple sets of data. Take a set of data satisfied the constraints (2) for wind turbine, if the non real-time measurement nodes with historical electricity data have the statistical power by the hour, the Monte Carlo simulation results also need to satisfy the constraints of similar type (2).

Ensure the pseudo measurement based on the least square method. We can be forward sweep power flow to calculate each node voltage and power of branch and branch current value, if the error between these values and the measured values is smaller, that illustrates that it is more possible for estimating the pseudo measurement accuracy.

Below using the weighted least square method, we can get the mathematical model aiming at minimum error, which stands for the error between the real-time measurement and the pseudo measurement flow calculation results of measured nodes and wind turbine output.

$$\min \varepsilon_{\Delta t_i} = \sum_{i=1}^{n_V} w_{V,i} \mid V_{i,w} - V_i \mid + \sum_{ij=1}^{n_I} w_{I,ij} \mid I_{ij,w} - I_{ij} \mid + \sum_{ij=1}^{n_P} w_{p,ij} \mid P_{ij,w} - P_{ij} \mid + \sum_{ij=1}^{n_Q} w_{Q,ij} \mid Q_{ij,w} - Q_{ij} \mid \quad (4)$$

Where: $w_{V,i}, w_{I,ij}, w_{P,ij}, w_{Q,ij}$ are respectively represented measurement node voltage amplitude, branch current amplitude, the weight of branch active power and reactive power. n_V, n_I, n_P, n_Q are the number of variables of real-time measuring for the node voltage amplitude, branch current amplitude, branch active power and reactive power. $V_{i,w}, V_i$ are the power flow calculation values of node voltage amplitude for node i and the real-time measurement. $I_{ij,w}, I_{ij}$ are the power flow calculation of branch current amplitude and real-time measurement values for node i and j. $P_{ij,w}, P_{ij}$ are the branch of active power flow calculation and live measured values for node i and j. $Q_{ij,w}, Q_{ij}$ are the branch of reactive power for power flow calculation and real-time measurement values for node i and j.

By type (4), the more the real-time measurement nodes, the more accurate of the pseudo measurement's estimate results. The introduction of distributed power supply, may result in the changes of the trend direction, if there are a section switch on the branch of trend changes and real-time measurement, in this case, if only use the head end power measurement matching trend to estimate pseudo measurement, it cannot use the measurement section switch, can't consider the direction of the trend of change, and affects the accuracy of evaluation of pseudo measurement.

The whole algorithm process. Here are calculation steps of theoretical line loss based on the forward sweep trend:

1) Put in network structure parameters, power with the real-time measurement of load node in the calculation time within of each time interval Δt_i, the electricity per hour of wind turbine in computing time cycle, electricity of power load node with historical electricity and the parameters of power distribution transformer, make $i = 1$;

2) For the period of time Δt_i, construct the probability density function according to type (3) for all the measured load node and the active and reactive power of the wind turbine;

3) according to the probability density function of step 2), we can get multiple sets of the measured load node and the pseudo measurement data of the wind turbine through monte carlo simulation;

4) if the difference between more groups of pseudo measurement data from wind turbine simulation and the hourly power were greater than the given value, transfer to step 3). Otherwise, for the satisfied group of pseudo measurement data, calculate out the branch power, node voltage and load current according to the forward sweep power flow calculation;

5) according to the type 4), take a group of minimum error ε of non measurement nodes and pseudo measurement data of wind turbine as the result, calculate the losses in period of Δt_i forward sweep power flow calculation;

Examples and analysis.

As is shown in figure 1, there is a circuit of 11 nodes system[17], of which distribution transferred rated voltage is 10 kV, and average bus voltage is 10.5 kV, adds a wind turbine of which capacity is 800 kW respectively in the node of i and j, assumes that the wind turbine keeps the power factor as 0.95, the wind power characteristics and parameters can be found in the literature [18].

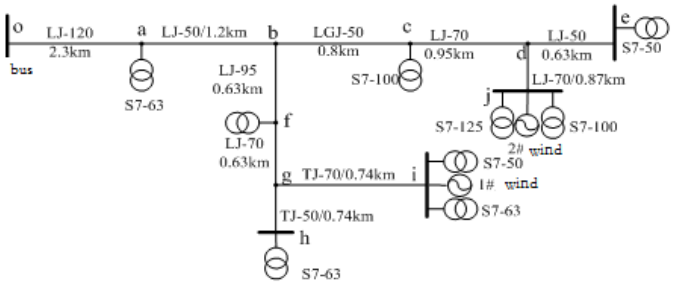

Figure 1. 11 nodes distribution network structure contains the wind turbine

Assume that the head power of branch $o-a$ and $b-c$ have real-time measurement values, wind turbine record export capacity per hour, real-time data sampling interval is 10 minutes, table 1 shows the history data for one hour one day, the wind speed change of the wind turbine is not very big, but the calculation of output power changes is very big, and has great volatility

Table 1. Historical data

Measurement amount	Time					
	00:00	00:10	00:20	00:30	00:40	00:50
1# wind turbine speed (m/s)	5.1	5.2	5.4	5.6	6	6
1# wind turbine active power (kW)	59	63	72	81	99	99
1# wind turbine reactive power (kvar)	19.5	20.8	23.8	26.7	32.7	32.7
2# wind turbine speed (m/s)	6.8	6.7	6.2	6.5	6.6	6.2
2# wind turbine active power (kW)	160	153	115	138	145	115
2# wind turbine reactive power (kvar)	52.8	50.5	38	45.5	47.9	38
Active power of branch o-a head (kW)	332.7	335.7	364.6	332.7	307.7	337.7
Reactive power of branch o-a head(kvar)	149.1	150.1	159.7	149.2	140.8	150.7
Current of branch o-a head (A)	3.645	3.677	3.98	3.646	3.38	3.697
Voltage of node o (kV)	10.5					
Active power of branch b-c head (kW)	137.2	144.2	181.8	159.1	152.2	181.9
Reactive power of branch b-c head (kW)	66.9	69.2	81.6	74.2	71.8	81.67
Current of branch b-c head (A)	1.535	1.607	2	1.764	1.69	2
Voltage of node b (kV)	10.44	10.44	10.44	10.45	10.45	10.4
1# wind turbine (kW ·h)	80					
1# wind turbine (kvar·h)	26					
2# wind turbine (kW ·h)	138					
2# wind turbine (kvar·h)	46					

Due to the changes of load power in one hour is small, assume that the pseudo measurement of every load calculating through the head end power coefficient method is maintained constant in one hour, so the case only aim at type (4) to calculate the pseudo measurement of output capacity of 1 # and 2 # wind turbine , and satisfy the wind turbine power constraints of type (2), the calculation results are shown in table 2.

Table 2. Simulated data of wind turbine

Measurement amount	Time					
	00:00	00:10	00:20	00:30	00:40	00:50
1# wind turbine analog wind speed(m/s)	5.06	5.24	5.37	5.65	6.04	5.97
1# wind turbine active power (kW)	57	65	71.5	83	102	97
1# wind turbine reactive power (kvar)	18.8	21.5	23.5	27.4	33.7	32.1
2# wind turbine simulated wind speed (m/s)	6.75	6.74	6.16	6.55	6.66	6.18
2# wind turbine active power (kW)	157	156	112	142	149	113
2# wind turbine reactive power (kvar)	51.8	51.5	37	46.9	49.2	37.3

Contrast to the Reference [4-7] using only the measurement value of the branch $o-a$, the above example also takes advantage of the measurement of the branch $b-c$ to improve the estimation accuracy of the wind turbine output power.

Table 3 shows the contrast results of the example for network loss calculation in one hour.

Table 3. The calculation result of line loss

Output result	Branch loss	Iron loss of transform	Copper loss of transform	Total losses
Reference value	1.71135	2.21666	10.6333	14.566
document[] method	1.6857	2.2221	10.6373	14.452
This paper method	1.70373	2.22208	10.6405	14.563

The table 3 shows that contrasting to literature [7], this algorithm considered the randomness of the output of the wind turbine, so it not only matched the measurement of root node branch $o-a$ in the process of power flow calculation, but also matched the measurement of branch $b-c$, and also improved the accuracy of the power flow calculation, made the calculation results more close to the real value.

Conclusions

This paper put forward to the distribution network line loss calculation method theory using of all the real time measurement and considering the uncertainty of wind turbine output, it can accurately simulate the uncertainty of wind turbine output through Monte Carlo simulation method. The example results show that, compared with the existing literature, this paper considers the theoretical line loss calculation under the condition of the uncertainty of wind turbine output, and improves the precision of theoretical line loss calculation.

References

[1] Xiutai Yang. Theoretical calculation and analysis of the power grid line loss. The front page. Water resources and electric power press. 1985,5.
[2] Weidong Han. Distribution network line loss calculation and application. Xi'an jiaotong university, master's degree thesis. Journal of xi'an jiaotong, 2001.3.
[3] Gangjun Wang, Chengmin Wang, Heng Li. Network loss calculated method for the distribution network theory based on measured data[J]. Power system technology. 2002, 26(12): 18-20.
[4] Lin Yang, Weidong Wang, Dezhi Chen. Based on the measurement of medium voltage distribution network line loss calculation[J]. Relay. 2005,33(3)：28-33.
[5] Dezhi Chen，Zhizhong Guo. Theoretical line loss calculation of the distribution network based on load obtaining and matching trend method[J]. Power system technology. 2005，29(1)：80-84．
[6] Buhan Zhang , Kewen Li, Lihua Sha. Electric energy loss calculation of distribution network based on a tree[J] . Journal of huazhong university of science.2000, 28(2): 58-59.
[7] Jianchun Wen，Xueshan Han，Li Zhang．An improved algorithm of theoretical line loss calculation for distribution network．Electric power system and its automation. 2008，20(4)：72-76．
[8] Fushuan Wen, Zhenxiang Han. Distribution network line loss calculation based on the clustering algorithm and artificial[J]. Proceeding of the CSEE. 1993, 13(3):41-50.
[9] Kaiyuan Xin, Yuhua Yang, Fu Chen. Computing distribution network line loss, a new method of the combination of GA and BP[J]. Proceedings of the CSEE. 2002, 22(2):79-82.
[10] Xiuqing Li, Lina Zhao, Qingran Meng. IGA optimization of neural network theory of distribution network line loss calculation[J]. Electric power system and its automation. 2009, 21(5):87-91.
[11] Huilan Jiang, Min An, Xiaojin Liu. Distribution network line loss calculation based on dynamic clustering algorithm radial basis function network[J]. Proceedings of the CSEE. 2005,25(10):35-39.
[12] Yuwen Peng, Kewen Liu. Theory of distribution network line loss calculation method based on the improved core vector machine (SVM)[J]. Proceedings of the CSEE. 2011,31(34):120-126.
[13] Xuncheng Huang, Wind turbinegguo He, Huan Qi. The distribution network line loss calculation model based on support vector regression[J]. Power system protection and control. 2008,36(18):51-58.
[14] Xiuqing Li, Hai Wang, Chuanwei Xu. Distribution network loss calculation based on immune genetic algorithm (ga) optimization[J]. Power system protection and control. 2009,37(11):36-39.
[15] Xianhao He. Contains the theory of distributed power distribution network line loss calculation method[M]. Changsha：Hunan university. 2009.
[16] Shenxue Dong, Yusheng Zhou, Xunwei Cao, Lei Zhu, Wei He, Wind turbine Zhang. Research on voltage line losses of distribution network with distributed generation.ICEE 2011.
[17] Xinhai Ding，Yiwind turbineg Luo, Wei Liu. Distribution network method, the improved iterative method to calculate the theoretical line loss. Power system technology. 2002,4(1)：39-42.
[18] Hong Shen. Variable speed constant frequency wind turbines parallel operation model and its application[D]. Beijing：China electric power research institute. 2003.

Advanced Materials Research Vols. 986-987 (2014) pp 635-638

doi:10.4028/www.scientific.net/AMR.986-987.635

Transient stability of wind power system with DFIG

Guo li-sa

College of Electrical Engineering,GuiZhou University,Guiyang 550003,China

email: 373196924@qq.com

Keywords: Wind power, Transient stability , DFIG

Abstract. Analyzed mathematical model of wind power which consist doubly-fed wind turbine (DFIG).Strategies for pitch angle control were developed.Used MATLAB to establish equivalent model contain infinite power system concluding DFIG ,The results showed that wind power with DFIG have good transient stability.

Introduction

Wind power is the new research field in the power system study.Wind power is gradually to the scale and industrialization. The international wind power technology research hot spot is coming from Small capacity of stand-alone wind power generation technology to the large capacity system,coming from studying the steady state behavior of the large capacity of wind farm to studying the dynamic transient behavior after the access to the grid[1].Because the DFIG using the conventional synchronous generator technology. The transient characteristics have great difference with traditional synchronous generator when fault takes place in network[2].

Wind power application has long history.Wind power development began in the 19th century.Until the nineteen-eighties century wind farms to enter the modern electric power system[3]. China have rich wind energy resources in the world.The utilization wind energy about 250 million kW[4].

Double-Fed Induction generation(DFIG) consist wound-rotor induction generator that connection to the grid and Insulated Gate Bipolar Transistor (IGBT) that installed in the rotor winding by back to back[5].Normal operation, the stator side accesses to the three phase power frequency grid, the rotor gains low frequency through current frequency converter.When the DFIG is operated in super-synchronous speeds, energy is transferred to the grid through the stator side and the rotor side.

The Models of wind turbine

Wind turbine is made up of blade,hub,gearbox and coupling.Wind energy is the third power of wind speed,shown as followers:

$$P_m = \frac{1}{2} C_p \rho S V_0^3 \tag{1}$$

In the type:P_m is wind turbine output of wind power;C_p is rotor power coefficient,the maximum C_p can not exceed 0.59[6];ρ is air density;S is the rotor swept area;V_0 is wind speed before into wind turbine.

The mathematical model of transmission

Therefore, the performance of mechanical properties,wind turbine blades and hub have a big inertia, The speed of wind turbine output mechanical power lag behind the wind conditions change.The models of transmission machine is represented by equation:

$$\frac{dT_M}{dt} = \frac{1}{\tau_w}(T_w - T_M) \tag{2}$$

In the type:$T_w$is the output torque of wind turbine; T_M is the input torque of generator;$\tau_w$is the inertia time constant of wind turbine.

The models of DFIG

The electromagnetic torque of doubly-fed induction generator is as follows:

$$T_e = \frac{P_s - sP_s}{\omega_r} = \frac{(1-s)P_s}{\omega_r} \approx \frac{3}{2}(i_{sq}\psi_{sd} - i_{sd}\psi_{sq}) \quad (3)$$

Same as the derivation of induction generator, electromagnetic power is as followers:

$$P_{em} = \frac{P_r}{s} - \frac{P_{cu2}}{s} \quad (4)$$

$$sP_{em} = P_r - P_{cu2} \quad (5)$$

$$P_{mech} = P_{em}(1-s) \quad (6)$$

The energy transfer of doubly-fed induction generator in connection with the state of the generator, when it produce electricity, $P_{mech} \rangle 0$.

The control system of DFIG:

Wind turbine generator system is a complex,multivariable,and nonlinear system.The control system of DFIG include pitch angle control model,max power point track method and converter control. The control system of DFIG plays an important role.

Doubly-fed wind power generator module is vector control in MATLAB. Only consider positive-sequence component of the stator voltage, the variable pitch blades are rigid,the wind speed is invariant.When the wind turbines in less than rated speed,Pitch Angle remains 0° .When the wind turbines in less than rated speed,use the strategies for pitch angle control to limit the maximum output active power.The control system is as follows:

$$\frac{d\beta}{dt} = \frac{1}{\tau_\beta}(\beta_r - \beta) \quad (7)$$

Energy flow between the rotor and power grid is depend on the running state of the generator.Transducer is bidirectional power flow in the variable speed constant frequency wind turbine. RSC and GSC are connected in the voltage source conversion by back to back[7].

Control strategy of the grid side converter is vector control. The current of frequency converter resolve into two current component that are mutually perpendicular.There are active current that located in the direct axis and reactive current that located in the quadrature axis. Reactive power of grid side converter is related to the reactive current that located in the quadrature axis[8]. Control objectives of the rotor-side converter is active power changes with reference value,at the same time,the power factor is constant.

Power electronic element of frequency converter is sensitive to transient disturbance. Frequency converter need to configure relay protection equipment.Breaker with fixed switching on-off time can avoid the influence of transient current and recover frequency converter quickly.It is advantageous to transient stability.

The simulation of power system with wind power

Synchronous generators stability is one of the basic conditions to ensure safe power system operation. Load distribution and interaction effect between component are not included in this study.In the power simulation system,using of DFIG instead of the whole power station[9].

In order to make the simulation comparable,Two simulation system are established, there are power system with DFIG and only synchronous generator(SG).The diagram is as followers:

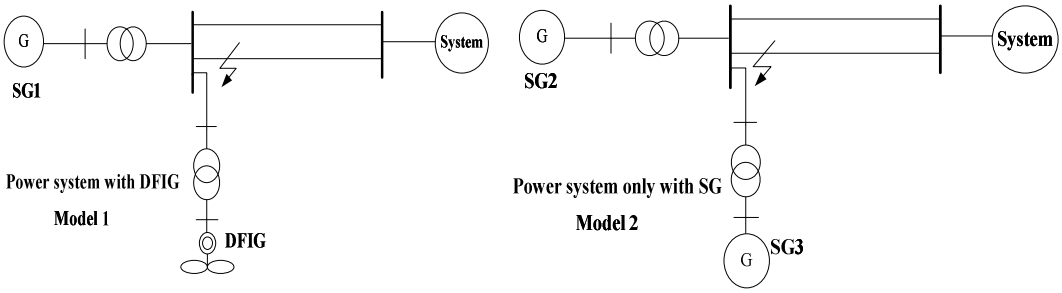

Figure 1.Simulation model diagram

Power system transient stability when three-phase short circuit occurs

Run time is 8s,step-size is 0.03ms.when t=5s,three-phase short circuit occurs in double-circuit transmission lines(as shown in figure 1).After 0.1s,the fault is removed. As shown in figure 2,the active power curve of SG in the same location is made a comparison.Curve of SG1 tend to the balance point smoothly,the recovery speed of SG2 is slower than SG1.The power wind with DFIG have a better transient stability.In Figure2,orizontal axis is time(t/s);vertical axis is power curve(P/Kw).

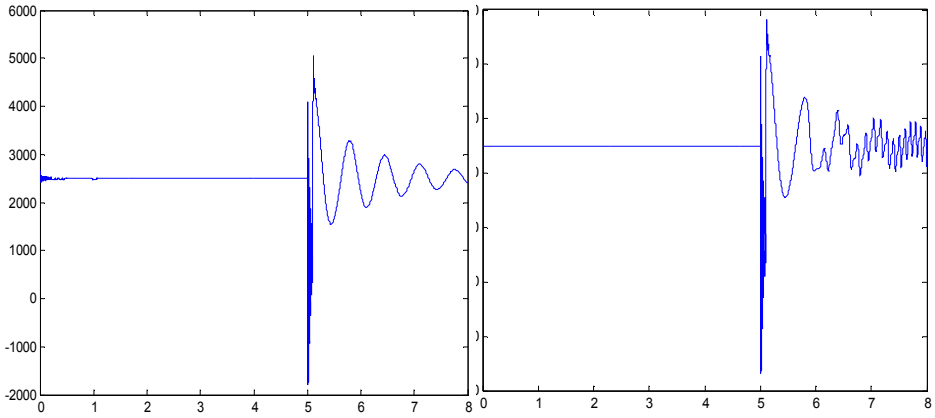

SG1 of Model1 SG2 of Model 2

Figure 2.Diagram of active power

As shown in figure 3,the power angle characteristics of SG in the same location is made a comparison.Orizontal axis is time(t/s);vertical axis is power angle.

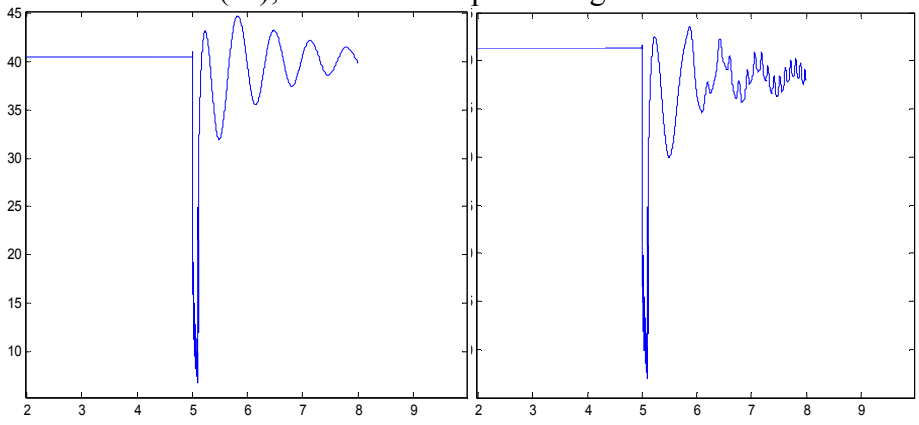

SG1 of Model1 SG2 of Model 2

Figure 3.Diagram of power angle characteristics

After cutting off the fault,power angle characteristics of SG1 is more fluctuant than SG2, The results show damping of Model 1 is smaller than SG.But curve of SG1 tend to the balance point smoothly and quickly.The power wind with DFIG have a better transient stability.

Chang the time of duration of three-phase shortcircuit.In the model 2,three-phase shortcircuit happen in 5s.If fault duration is 258ms in model 2,the system will loss the stability.If fault duration is 265ms in model 1,the system will loss the stability.The critical clearing time of system with DFIG

is longer than the system only with SG.The power wind with DFIG have a better transient stability than system only with SG.

Conclusion

Based on the control system of DFIG,the models of transmission machine and the models of DFIG,a simple power system with DFIG is studied by simulation using MATLAB. Three-phase short circuit occurs in the power system with DFIG and the system only with SG,depend on the active of power curve,angle characteristics and critical clearing time,The power wind with DFIG have a better transient stability.

References

[1]Zhao Bin,Studies of Transient Stability for Grid-Connected Wind Turbine with Induction Generator[D], Chongqing University,2008,5.

[2]Chi Yong-ning,Wang Wei-sheng1,Liu Yan-hua,Dai Hui-zhu.Impact of Large Scale Wind Farm Integration on Power System Transient Stability[J],Automation of Electric Power System,2006,30(15):10-14

[3]Ren Yong-feng,AC-excited Doubly-fed Induction Generator Wind Power Generation for Grid Connection[D],Inner Mongol University of Technology,2008,5

[4]Ye Hang-zhi,Wind turbine control technology[M],Beijing:China Machine Press,2002,5

[5]Wanf Hang-yu,Research on Model of Wind Farm and Its Applications[D],Beijing Jiaotong University,2008,5

[6]Zhou Zhi-Qiang,Research on DFIG electro-magnetic transient model,control and validation[D],Northeast Dianli University,2008,3

[7]Hou Hong-jing,Study on Operation Characteristics of Wind Farm based on DFIG[D],North China Electric Power University,2010,1

[8]Jiang yan,Research on Transient Voltage Stability of Grid-Connected wind Farms Based on VSC-HVDC[D],North China Electric Power University,2010,12.

[9]Yu Hui,Zhou Cheng, Liu Lu-ning,Study on impact of large scale wind farm integration with DFIG on power system transient stability[J],Journal of Shenyang Institute of Engineering(Natural Science),2009,5(4):305-307

Advanced Materials Research Vols. 986-987 (2014) pp 639-642

doi:10.4028/www.scientific.net/AMR.986-987.639

Transmission Network Planning scheme considering N-2 security under the market environment

Shenquan Yang [1], Xingwang Hu [2], Zhijie Zheng [1],Kuihua Wu [1], Yiqun Wang [1]

([1.]Economic&Technology Research Institute,State Grid Shandong Electric Power Company, Jinan, 250021, china;

[2.] State Grid Shandong Electric Power Company, Jinan 250002, China)

Keywords: transmission planning; electricity market; N-2

Abstract. Traditional Transmission Network Planning scheme only considers N and N-1 security , with little regard for safety of N-2 system. This paper introduces the relaxation factor establishing Transmission Network Planning model, and further considers the N-2 secure of double-circuit transmission line on the basis of relaxation on the N-1 constraints. A hierarchical genetic algorithm(HGA) Model is proposed to solve the model.The final Transmission Network Planning scheme meets the reliability requirements under uncertain environment and has the minimum overall cost.A simulation model to simulate the impact of construction of the same tower line on the investment and security of transmission network planning is builded.

0 Introduction

Large scale blackout many times at home and abroad show that with the increase in the complexity of the grid interconnection,a small perturbation of the system is likely to occur cascading failure, bringing huge economic losses to the power system and the whole society when the system is in a state of emergency after a single failure.At the same time, the existence of the power system planning maintenance also makes the power grid only meet N - 1 safety criterion not enough.Therefore, considering the N-2 security of system from planning level has important practical significance[1-2].But considering all the lines N-2 breaking not only computes intensively and for a long time, but also makes the plan too conservative, leading to excessive investment and impacting the power company benefits. [3]

1 Power Transmission System Model

Uncertain market environment factors mentioned above, can be expressed as M power injection vectors $\boldsymbol{P}=\{\xi_1,\xi_2,\xi_3...\xi_M\}$, ξ_k is the k-th power injection vector.

Transmission network planning model further considering the security when same tower double circuits are simultaneously breaking and investment savings on the basis of N-1 security constraint shows as follows.

$$\min C = \sum_{ij\in S} U_{ij} I_{ij} L_{ij} + \sum_{ij\in D} V_{ij}(B_{ij}) B_{ij} L_{ij} + \alpha Z_1 \tag{1}$$

$$Z_1 = \sum_{k\in M} C_k^s + \sum_{k\in M} C_k^d \tag{2}$$

st.

$$\left.\begin{aligned} \boldsymbol{B\theta} &= \xi_k \\ P_b &= B_b \theta_b \\ |P_b| &\le P_{b.max} \end{aligned}\right\} \tag{3}$$

$$\left.\begin{aligned} \boldsymbol{B}_b^l \boldsymbol{\theta}_b^l &= \xi_k \\ \boldsymbol{P}_b^l &= \boldsymbol{B}_b^l \theta_b^l \\ r &\le \delta \end{aligned}\right\} \tag{4}$$

$$I_{ij} = \begin{cases} 0 \\ 1 \end{cases} \quad (5)$$

$$0 \le B_{ij} \le 2 \quad (6)$$

In formula (1), C is the investment and construction costs, including the cost of building the line and load shedding costs; S, D are single loop to be chosen and double-circuit lines on the same tower set; U_{ij} is branch ij unit invetistment costs; I_{ij} is 0-1 decision variables of branch ij; B_{ij} is double-circuit on the same tower decision variables of branch ij, V_{ij} is the unit investment costs of dual-circuit branches ij to be selected, its value varies with B_{ij}; L_{ij} is line length. Z_1 is the minimum shed load of the system, including the minimum shed load of N-1 breaking and double-circuit breaking at the same time under M power injection vectors. C_k^s and C_k^d are shed loadscaused by N-1 breaking and double-circuit breaking at the same time under the k-th power injection vector, α is unit load sheddingpenaltyfee.

Formular(3) is security constraints for normal operation; Formular (4) is the relax N-1 static security constraints. ξ_k is the k-th power injection vector. $\boldsymbol{B}$ and ^{l} are Node admittance matrix, corresponding to the non-breaking way and breaking way of branch I. θ and θ^l are node voltage phase angles of the above two ways . $\boldsymbol{P}_b$ and $\boldsymbol{P}_b^l$ are the corresponding branch current, and are phase angle difference on both ends of the branch. and $\boldsymbol{B}$ are diagonal matrix consisted by each branch admittance. $\boldsymbol{P}_{b.\max}$ are heat capacity limit of the branch, δ is given relaxation factor threshold value.

1.1 Description and calculation of the relaxation factor

The uncertainty of node power injection can lead to the diversity of power grid operation mode. Power transmission system determined by the power grid planning X. There may be N – 1 overload risk under the various operation modes. In this paper, the relaxation factor is introduced to quantitatively measure the relaxation. the relaxation factor is defined as follows,

$$r = \frac{\sum_{l=1}^{N} q^l P_r^l \left\{ \left(\left| P_b^l(\xi_k) \right| > P_{b.\max} \right) / X \right\}}{\sum_{l=1}^{N} q^l} \quad (7)$$

q^l is the probability of only branch x failure breaking, P_b^l is the branch wave vector which corresponds to branch l failure breaking way. ℓ represents the probability the event E established in conditions of F.So $P_r^l\left\{\left(\left|P_b^l(\xi_k)\right| > P_{b.\max}\right)/X\right\}$ is the system overload probability after line I failure breaking. Overload probability of all N-1 failure breaking $\sum_{l=1}^{N} q^l P_r^l \left\{ \left(\left| P_b^l(\xi_k) \right| > P_{b.\max} \right) / X \right\}$,r∈[0,1]since $0 \le \sum_{l=1}^{N} q^l P_r^l \left\{ \left(\left| P_b^l(\xi_k) \right| > P_{b.\max} \right) / X \right\} \le \sum_{l=1}^{N} q^l$. value the greater the r is, the higher risk of overload the N-1 breaking will have. through the set, the transmission grid planners can set r values based on the development stage of the grid and risk appetite.

2 Simulation result

This example uses the"18 nodes system" in reference [4]. Because there is no feasible plan under N – 1 standards of static safety can increase the limit of the line transport capacity to 3000 mw. Because all line corridors of the"18 nodes system" are no more than 3, a double loop is set up as multi-circuit transmission line in this paper. For easy calculation, we assume all single-circuit line investment cost is 800000 yuan/km and the same tower double-circuit single-circuit line unit construction cost is 600000 yuan/km. When two lines appears in the designated same tower double circuit line of the planning scheme, select the double-circuit lines installed on same tower ; if only one line, select the single circuit line. The original node load values are the same as those in reference [4]. Node 11,14,16,18 are new power source nodes that may occur whose probability distribution functions follow the two-point distribution, new load node loads obey the law of normal distribution. Specific parameters of each probability distribution functions can be seen in reference [5].

This paper constructs the following simulation models. Simulation 1: single loop is applied to all lines; Simulation 2:designate some line sets $ij \in \{(4,16),(5,11),(6,14),(7,13),(9,16),(16,17)\}$ as double circuit lines installed on same tower to be chosen;Simulation3: designate all multi-circuits lines as double circuit lines on same tower. In addition, the simulation 4 and 5 simulate relaxation factor and cutting load punishment's influence on grid planning, as shown in Table1:

Table 1. Emulational modal

simulation	Relaxation factor threshold value	Wiring way	Load-shedding punishment Ten thousand yuan /MW
1	$\delta=0$	All multi-circuit lines are single-circuit line	8
2	$\delta=0$	Some multi-circuit lines are on same tower	8
3	$\delta=0$	All multi-circuit lines are on same tower	8
4	$\delta=0.1$	All multi-circuit lines are on same tower	8
5	$\delta=0.1$	All multi-circuit lines are on same tower	80

Solve the above five situations using the hierarchical genetic algorithm.The planning scheme is shown in Table 2 as the number of underlying iteration and high-level iteration are all 100.

Table 2. Planning scheme of emulational modal

scheme	Planning scheme
1	1-11, 4-7, 4-16 2）, 5-11, 6-13, 6-14 2）, 7-9, 7-13, 7-15, 8-9, 9-10 2）, 10-18, 11-12, 12-13, 14-15 2）, 16-17 2）, 17-18 2）
2	1-11, 4-7, 4-16 2）, 5-11, 6-14 2）, 7-9, 7-13 2）, 7-15, 8-9, 9-10 2）, 10-18, 11-12, 12-13, 14-15 2）, 16-17 2）, 17-18 2）
3	Same to 2
4	1-11, 4-16, 5-11, 5-12, 6-14 2）, 7-9, 7-13, 7-15, 8-9, 9-10 2）, 9-16, 10-18, 12-13, 14-15 2）, 16-17 2）, 17-18 2）
5	1-11, 4-16 2）, 5-11, 5-12, 6-13, 6-14 2）, 7-8, 7-9, 7-13, 7-15, 8-9, 9-10 2）, 9-16 2）, 10-18, 11-12, 12-13, 14-15 2）, 16-17 2）, 17-18 2）

In Table 2,the number in the bracket behind two nodes indicates an increase in the number of lines as 4-16 (2) means toextend two 4-16lines.

Table 3. Planning scheme comparison

scheme	investment cost Ten thousand yuan）	load-shedding cost Ten thousand yuan）	comprehensive cost Ten thousand yuan）
1	221120	0	221120
2	199920	4800	204720
3	182902	23680	206582
4	172120	25360	197480
5	200920	121600	322520

Scheme 2 increases 7-1 and decreases 6-13 comparing scheme 1 with 2.Double circuit lines installed on same tower are constructed to save costs by increasing 7-13 which is designated by scheme 2 as double circuit lines and save more than load-shedding costs of connecting and disconnecting at the same time. The planning schemes of plan 2 and 3 are the same. From the perspective of the investment cost, because Scheme 3 specifies that all loops are built as same-tower double-circuit lines, saving a lot of investment costs while increasing the load-shedding cost of the system, comprehensive cost increases. Line 9 and 10 in Scheme 3 are in the same tower, saving line investment costs 80 million yuan while increasing the load-shedding cost to 182.4 million yuan, therefore, line 9-10 should not be built as double-circuit lines installed on the same tower. In the actual process of planning, construction of lines installed on the same tower should be based on quantitative analysis. The scheme has minimum comprehensive cost 1 2 3 analysis often sets up double-circuit lines installed on same tower.

In scheme 3 and 4, in the same way of stringing and load-shedding punishment, the planning scheme needs to meet more operation mode, and the cost of investment increase with the decrease of the threshold value of the risk factor δ.Comparing Scheme 3 and 4,line 9-16 replaces line 4-7, line 4-16, 11-12 are decreased, and line 5-12 are increased. Line 9-16makes it easier to increase relaxation factor than Line 4-7, but reduces the shed loads in the system. Therefore, no 9-16occurresin Simulation 1, 2, 3 where the threshold value of relaxation factor is 0 while 9-16 occurs to reduce the load-shedding costs in Simulation 4 where the relaxation factor is larger.

By plan 4 and 5, with the increase of load-shedding punishment, planning scheme needs to expand more lines to eliminate overload ,which makes investment costs increase and shed load reduce, but increases load-shedding costs due to the increase in load punishment.

3 Conclusions

This paper describes the uncertainty of market environment using uncertain power injection, further considers the situation of double-circuit lines installed on same tower connecting and disconnecting at the same time under the condition of relaxation N-1 constraint, and gives the quantitative indicators of double-circuit lines, providing decision basis for planners at the beginning of the planning.

The intervention of relaxation factor constraints can make the planning scheme further consider N-2 security when the same tower lines connect and disconnect simultaneously, bringing the model solution with flexibility and hierarchy.

Solving speed and iteration efficiency are improved using hierarchical genetic algorithm for the grid planning model. Flexible setup of the feasible region makes the model solution more convenient and flexible. The example demonstrates that it is an effective method of solving complex grid planning problems.

References

[1] Haifeng, Cheng Haozhong, Zhang Yan, et al. A review of electric power network flexeible planning. Power System Technology,1999,23 (17):38-41

[2] Fan Hong , Cheng Haozhong Zhang Jietan,et al. TransmissionNetwork Planning Considering Electric PowerSystem Security. Automation of Electric Power Systems, 2007,31(11): 35-38

[3] Zhu Zhonglie,LIJianhua, Zhu Ruijing,et al.Common Tower Quadruple Circuits Fault and Transient Simulation Analysis Method. Automation of Electric Power Systems,2008,32(8): 49-54

[4] Wang Xifan. Power System Optimization and Planning. Beijing: Hydro and Power System Press, 1990. Author:Shenquan Yang（1983-）is master graduate student.His main research direction is power grid planning.

[5] Ma Chang-hui, Xue Yusheng, Wang Xiaoying,etal.Optimal Transmission Planning Based on Both Static and Dynamic Risks Part Two With Uncertain Injection Power. Power System Technology,2006,30(14):10-13

Advanced Materials Research Vols. 986-987 (2014) pp 643-647

doi:10.4028/www.scientific.net/AMR.986-987.643

Transmission Section Search for Vulnerable Line Based on Power Transfer Distribution Factor

Junjiao Wei, Jianwen Ren

North China Electric Power University, Baoding, Hebei, 071003, China

Wjj903239@163.com

Keywords: power transfer distribution factor; integrative electrical betweenness; vulnerable line; transmission section; Coefficient of difference

Abstract: For the purpose of considering characteristics of transmission line in the round, with utilization of related knowledge in complex network, Integrative Electrical Betweenness has been put forward. The proposed index, on one hand, over comes shortcoming of assuming power only transmit along the shortest path existed in previous indexes. On the other hand, ability of transferring power when other lines removal is considered. In order to further facility to grid security control, a novel method is proposed to search key transmission section of vulnerable line. The algorithm only needs simple calculation, there is no large-scale computation. The proposed algorithm has been tested on New England IEEE 39-bus system to validate its efficacy.

Introduction

Frequent blackouts, which happen in recent years, has brought new challenges to security and stability control work in power systems. The upsurge of transmission section research emerges as time requires. Through deep analysis of several typical blackouts, it's knowable that cascading failure caused by outage of individual line, plays a vital role on the occurrence of blackout. Based on this reason, in order to prevent blackouts happening again, Scholars carry on embed researches at the following two aspects：searching individual lines that cause cascading failure[1] , identify the set of lines[3,4,5].

Through analysis of previous literature, it's obvious that current research on these two aspects exist problems of caring for this and losing that. For the first aspect, the scholars put forward corresponding index to characterize vulnerability lines, in accordance with different study focus, as a result, it cannot fully reflect comprehensive transfer contribution of line. As for the latter, when finding transmission section, current researches are mostly based on the overload / heavy-load line. However, it's known that the impact of vulnerable line outage on the grid is far more serious than overload line. At the same time, previous section search methods mostly need matrix calculation or other large-scale computation, which limits its application in large scale power network.

This paper considers not only normal operating conditions, but also the status after some rest lines out of service. Then combined with PTDF, Integrative Electrical Betweenness (B_{ie}) is proposed to identify vulnerable line. The index takes both distribution network topological structure and current operation into account, creatively consider the transmission line's capability to transfer power after some fault occur. What is more, a new method is proposed to find out transmission section of specific vulnerable line，the algorithm only needs some simple calculations.

Identification of Vulnerable Line Based on Integrative Electrical Betweenness.

Betweenness(B_0). In complex network, B_0 is applied to glass concrete role of line plays in the communication process of information. With hypothesis that information of two nodes is only transmit through the shortest path, B_0 of given line l is identified as the ratio of shortest paths between node pairs (s,t) (resp. (s,t)) which through line l ($\delta_{st}(l)$) and total shortest paths between (s,t) (δ_{st}), as follows:

$$B_0(l) = \sum_{s \neq t \in V} \frac{\delta_{st}(l)}{\delta_{st}} \tag{1}$$

Integrative Electrical Betweenness. As a transmission lines, there is no doubt that it's first and foremost task is transfer power. From the definition of B_0, we know that it exist limitation to reflect the effect of transmission line by using B_0 directly. The fundamental reason is that power transmission system not only has common feature of transmission network, but also has its own 'characteristic', power transfer, not only along the shortest path, but also in all possible transmission path.

Owing to the inevitable problem of B_0, and considering transmission characteristics of power system itself, this paper puts forward Integrative Electrical Betweenness(B_{ie}) of line l to indicate its transmission contribution during electricity transmission. $B_{ie}(l)$ is defined as follows:

$$B_{ie}(l) = \sum_{s \in G, t \in L} \sqrt{R_s * R_t} * T_{st}(l) + \sum_{s \in G, t \in L} \sqrt{R_s * R_t} * A_{st}(l) * \frac{P^{\max}(l) - P^0(l)}{P^{\max}(l)} \tag{2}$$

$$T_{st}(l) = \frac{\Delta P_{ij}}{\Delta P_{st}} = \frac{X_{is} - X_{js} - X_{it} + X_{jt}}{x_{ij}} \tag{3}$$

$$A_{st}(l) = \begin{cases} 0 & , T_{st}(l) \leq 0.8 \\ \dfrac{1}{T_{st}(l)} & T_{st}(l) > 0.8 \end{cases} \tag{4}$$

Where R_s, R_t are power capacity of node s and node t respectively; Q_{st} reflects weight of different (s,t); $P^0(l)$, $P^{\max}(l)$ separately reflect current power and maximum transmission power of line l; $T_{st}(l)$ is PTDF of line l as to (s,t),it means that ,when power transaction volume between s to t has an augment of ΔP_{st} , there has a variation of ΔP_{ij} of line l connected between bus i and bus j; X_{is} is the corresponding elements of is th elements in node impedance matrix; means of X_{js}, X_{it}, X_{jt} are similar to X_{is}; x_{ij} means self-reactance of line l.

From (2), it is not difficult to find out that B_{ie} is composed of two parts:

1. $\sum_{s \in G, t \in L} Q_{st} * T_{st}(l)$, which illustrates the total transmission contribution of line l to all node pair. Its magnitude means whether an important role or not that line l plays.

2. $\sum_{s \in G, t \in L} Q_{st} * A_{st}(l) * \frac{P^{\max}(l) - P^0(l)}{P^{\max}(l)}$ reflects remain transmission capability of line l. We explain the prime reason of define $A_{st}(l)$ as (4) here: firstly without considering value of $T_{st}(l)$, the remain transmission capacity can be expressed as $\sum_{s \in G, t \in L} Q_{st} * \frac{P^{\max}(l) - P^0(l)}{T_{st}(l) * P^{\max}(l)}$.However, a potential problem will emerge, under the condition that $T_{st}(l)$ is rather small. On account of $\sum_{s \in G, t \in L} Q_{st} * \frac{P^{\max}(l) - P^0(l)}{T_{st}(l) * P^{\max}(l)}$, remain transmission capacity of line l is extraordinary large. However, the real fact is that, when $T_{st}(l)$ is small, it implies that line l is insensitive to the transmission power about (s,t), in other words, the contribution of line l on power transmission is tiny. In order to solve this issue, (4) is adopted in this paper, assumed that only when the magnitude of $T_{st}(l)$ is greater than a certain threshold value (0.8), line l use its surplus capacity to transfer power from (s,t).

B_{ie} ,proposed in this paper, not only reflects the real transmission contribution under present conditions of transmission network, but also innovatively take the ability of line l about taking shift power when a fault(such as one line outage) occurs in power system into account . With greater

value of $B_{ie}(l)$, line l has the greater degree of fragile, thus its outage is likely to affect the entire network. As a result, security analysis work should be focus on these vulnerable lines.

Transmission Section Search Based on PTDF

In order to prevent occurrence of cascading failure, and for the purpose of reducing supervision range of security and stability control, it's necessary to search transmission section of vulnerable line l, and carry online safety monitor on it.

With the common sense that parallel transmission lines are main components of transmission section. Therefore, before introduce the proposed search algorithm, this paper, firstly, analyses the relationship of parallel transmission line in the aspect of PTDF.

1. line l and line k are two parallel lines of power supply source s to load t, as shown in Fig. 1:

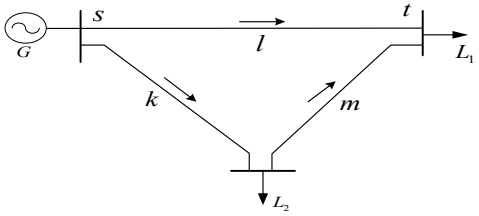

Fig.1 Schematic diagram of same source power to loads

According to the definition of PTDF, it's knowable that line l and line k take all incremental power of (s,t). Therefore, $T_{st}(l)$ of line l and $T_{st}(k)$ of line k satisfy the following equation:

$$T_{st}(l)+T_{st}(k)=1 \tag{5}$$

2. When line l, line k and line m are transmission lines for different power bus to the same load t, as shown in Fig. 2:

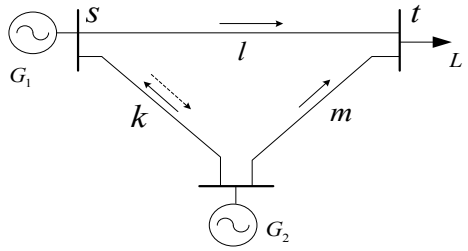

Fig.2 Schematic diagram of sources to same load

As shown in Figure 2, when transmittal power from source node s to node t increases a unit, power flow on line k will 'reverse', it forms another path to transmit power for (s,t), with line m, except path l. Then in solving process of PTDF, it need to exchange first node and end node of line k, namely $T_{st}(k)^{*}=-T_{st}(k)$ ($T_{st}(k)$ is the former PTDF of line k before exchange of node), so $T_{st}(l)$, $T_{st}(k)$ and $T_{st}(m)$ meet the following relationship:

$$T_{st}(l)+T_{st}(m)=1 \tag{6}$$

$$T_{st}(l)-T_{st}(k)=1 \tag{7}$$

$$T_{st}(k)=-T_{st}(m) \tag{8}$$

Equations (5) ~ (7) are equivalent to (9):

$$\left|T_{st}(l)\right|+\left|T_{st}(k)\right|=1 \tag{9}$$

Based on the mentioned relationship of PTDF between parallel transmission lines, a novel search method $T_{st}(k)$ is proposed. The basic principle of this algorithm is as follows:

Computing Coefficient of Difference of PTDF Between Vulnerable Line l and Line k . First of all, corresponding measures as (11) are taken when PTDF satisfy (9) and (10) ,then coefficient of difference($D(l,k)$) is quantified as (12).

$$d_{st}=\begin{cases}\left(T_{st}(l)+T_{st}(k)\right)^2, & -\varepsilon \le T_{st}(l)-T_{st}(k)\le \varepsilon \\ \left(\left|T_{st}(l)\right|+\left|T_{st}(k)\right|-1\right)^2, & -\varepsilon \le \left|T_{st}(l)\right|+\left|T_{st}(k)\right|-1\le \varepsilon \\ \left(T_{st}(l)-T_{st}(k)\right)^2, & else\end{cases} \quad (11)$$

$$D(l,k)=\sum_{s\in G,t\in L} d_{st} \quad (12)$$

Where ε is a small positive number. Thought (11) ~ (12), it shows that two line are likely to be parallel transmission lines under the conditions that $D(l,k)$ of these two lines is small.

Determine Key Transmission Section of Vulnerable Line l **.**Through calculation of $D(l,k)$, the sort $P(l)$ of $D(l,k)$ about line l and the rest lines in power system is achieved. It is knowable that lines, which have large growth of active power when line l outage, make up key transmission section of line l. Therefore, , this paper utilize relationship of size between Branch Outage Distribution Coefficient $\lambda(l,k)$ and the threshold $\lambda_{set}(l,k)$($\lambda_{set}(l,k)$ in this paper is 0.2), to ascertain whether line k belongs to key transmission section of line l When $\lambda(l,k)<\lambda_{set}(l,k)$ takes place for the first time, the search ends, then key transmission section of line l is obtained.

Example Analysis

In order to verify its validity, the proposed algorithm has been tested on IEEE39-bus system, which has 10 generators, 39 nodes, 34 lines.

Results of Identify Vulnerable Line. As a matter of fact, it's effect on the whole network, when vulnerable line l out of operation, is manifested by the total amount of changed transfer flow in entire lines to a large extent .Therefore, in this paper, identification results of vulnerable line is compared with entire change rate of active power of remaining lines under the condition that vulnerable line l out of operation (resp. C_r) and B_0, as shown in Table 1.

Tab.1 Comparison table of some line indicators sort of IEEE39 bus-system

line		B_{ie}	sort	B_0	sort	C_r	sort	load[MW]	sort
first node	end node								
16	17	39233.20	1	12	1	9.42	4	201.1	18
16	19	30049.75	2	6	5	9.53	2	451.3	3
19	20	27318.58	3	1	29	10.2	1	174.7	22
16	15	23559.18	4	3	15	9.45	3	292.6	13
17	27	22584.22	5	3	15	8.51	9	13.1	33

From Table 1, although load rate of line $l_{16\text{-}17}$ is too small to rank $18th$, however it ranks top, not only in the aspect of B_{ie}, but also in B_0. It is able to obtain ,because of $l_{16\text{-}17}$ is the only way must be passed ,when centralized supply areas transmit power to load zone, its outage will cause transmission path of generation nodes, such as 33, 34, 35 and36 get snagged without doubt. Furthermore, transmission section of load nodes such as node 3, 18 and 27 reduce to a great degree. Similarly, outage of $l_{16\text{-}19}$ and $l_{19\text{-}20}$, will directly cause the issue that power of generation node 33 and 34 cannot delivery and require of large capacity load 20 cannot be satisfied.

Analysis of Transmission Section Search Results. For the purpose of verifying effectiveness and feasibility of proposed method, transmission section of vulnerable line $l_{16\text{-}17}$ was searched, the search result is compared with outcome of Power World Simulation Software, as shown in Table 2. From Table 2, it is know that the proposed method can search out all lines whose flow change in a large degree, when line $l_{16\text{-}17}$ outage. In addition, the proposed method can effectively line, whose

power is reversed and increased ($l_{3\text{-}4}$, $l_{18\text{-}3}$, l_{17-27} , $l_{14\text{-}15}$).It can reduce leakage problem, because of power reverse. Undeniable, the proposed method has few leakage lines, investigating its fundamental reason, PTDF obtained by DC model, lake of considering load effect. But $\lambda(l,k)$ of leakage line is only 0.22, and its load is 29/34 (77.1MW), as a result, its active margin is too large to transfer increased power, without being overload, when $l_{16\text{-}17}$ is outage.

Tab.2 Search results for key transmission section of line $l_{16\text{-}17}$

	line		$D\ l,k$ of $l_{16\text{-}17}$	sort	$\lambda\ l\ k$	results of AC
	first node	end node				
search result	16	15	0.1075372	1	0.9921	increase
	14	4	0.1129526	2	0.7121	increases
	3	4	0.1238404	3	-0.8359	increase ∪ reverse
	18	3	0.5272180	4	-0.7812	increase ∪ reverse
	17	18	1.1906396	5	-0.7812	reduce ∪ reverse
	11	6	1.3303654	6	0.2740	increases
	10	11	1.3509434	7	0.2511	increases
	26	27	1.4168168	8	0.2193	increases
	17	27	1.5644251	9	-0.2178	increase ∪ reverse
	14	15	1.5739188	10	-0.9901	increase ∪ reverse
boundary line	6	5	1.6027826	11	0.1919	increases
leakage line	25	26	1.8930206	12	0.2202	increases

Summary

In this paper, on the basis of analyzing the influence factors of transmission line contribution in electric power system all-around, Integrative Electrical Betweenness B_{ie} is putted forward to identify the weak links of power grid - vulnerable line correctly and reliably. On this basis, using coefficient of difference of PTDF to obtain key transmission section, thus further reduce monitoring range of grid security and stability control on this account.

References

[1] CHEN Xiao-gang, SUN Ke, CAO Yi-jia. Structural vulnerability analysis of large power grid based on complex network theory[J]. Transactions of China Electro technical Society, 2007, 22(10): 138-144(in Chinese).

[2]CAO Yi-jia, CHEN Xiao-gang, SUN Ke. Identification of vulnerable lines in power grid based on complex network theory [J]. Electric Power Automation Equipment, 2006, 26(12): 1-5, 31(in Chinese).

[3]Zhou Decai, Zhang Baohui, Yao Feng. Fast search for transmission section based on graph theory[J]. Proceedings of the CSEE，2006， 26(12)：32-38(in Chinese).

[4]Ni Hongkun, Xu Yuqin. Fast search for the key transmission section based on dynamic programming principle [J]. Journal of North China Electric Power University，2009，36(4)：11-15(in Chinese).

[5] REN Jianwen, LI Gang, WANG Zengping, ZHEN Xufeng. New Algorithm for Searching Tie Lines Based on Deviation Path[J]. Power System Technology，2012，36(4)：121-127(in Chinese).

[6] Hua Ke,Xie, Kai,Guo, Zhizhong. Research on power flow-based transmission by use of DC and AC power transfer distribution factor, 2007，31(13)：71-74(in Chinese).

[7] Xu Lin, Wang Xiuli, Wang Xifan. Small-world feature identification based on equivalent admittance for power system[J]. Proceedings of the CSEE，2009，29(19)：20-26(in Chinese).

[8] Ju Wenyun,Li Yinhong. Identification of Critical lines and nodes in power grid on maximum flow transmission contribution degree [J]. Automation of Electric Power Systems，2012，36(9)：6-12(in Chinese).

[9] E. Bompard, R. Napoli, F. Xue. Extended topological approach for the assessment of structural vulnerability in transmission networks [J].IEEE System Journal.2012，6(3)：481-487

Advanced Materials Research Vols. 986-987 (2014) pp 648-651

doi:10.4028/www.scientific.net/AMR.986-987.648

Using Fuzzy Synthetic Evaluation Model to assess technical risk of China's alternative fuel vehicle industry

Jinfeng Lin

School of Economics & Management, Harbin Engineering University, Harbin 150001, China

linjinfeng2006@163.com

Keywords: Industry technical risk, China's alternative fuel vehicle industry, Fuzzy Synthetic Evaluation Model

Abstract. The energy, which has a close bearing on the national economy and the people's livelihood, is always a world-wide attention issues. To promote the development of alternative fuel vehicle, we have to break through many technical difficulties, at the same time, as one of strategic emerging industry, China's alternative fuel vehicle industry future development has a high degree of uncertainty, will face a lot of risks. In this paper, we set up an evaluation index system of those risks and use AHP method and Fuzzy Synthetic Evaluation Model to assess technical risk of China's alternative fuel vehicle industry.

Introduction

After nearly a century with the internal combustion engine dominating the personal transportation sector, it now appears that the alternative fuel vehicle is on the verge of experiencing rapid growth in both developed and developing vehicle markets(see table1). [1-2]

The rapid growth of vehicles has resulted in continuing growth in China's oil demand. since 2009, China's automobile production and sales has been ranked first in the world, data prediction of the NDRC Energy Research Institute shows that the number of China's automobile on the road will reach 1.5 billion by 2020, the rapid growth of automobile will result in oil consumption exceeding 2.5 billion tons, accounting for the country's total oil demand in 57%, will further aggravate the carbon emissions and environmental problems, increasing difficulty of realization of China's carbon emission reduction targets [3]. In this context, to accelerate the development of alternative fuel vehicle industry becomes the inevitable choice to break this plight.

Table 1 Some countries alternative fuel vehicle sales from 2010—2012 [4]

	2010		2011		2012	
	EV	Plug-in	EV	Plug-in	EV	Plug-in
American	37	326	10144	7671	14592	38585
Japan	2361	—	13449	—	15943	7241
China	63	417	5576	613	11375	1416
France	57	—	4012	36	8880	225
Germany	—	—	1800	241	2976	863

Alternative fuel vehicle belongs to the emerging industry, using the new technology or developing technology, technology plays the most important role in development of alternative fuel vehicle industry, but the reality is that, there are many uncertainties on alternative fuel vehicle technology, such as associated with the technical level, technology is mature or not? Whether the technology is advanced, technology is facing risk being replaced? Associated with the technical social & environment adaptability， such as technology policy is effective or not? What about the complementary technology development, etc.. So, scientific assess alternative fuel vehicle technology risk has the important significance.

Technical risk is a kind of non clear concept; the causes leading to the risk of are complex, multifaceted. Many risk factors not only the relationship between perplexing, and the risk factors and

external factors permeate each other alternately, the levels of the risk no clear extension. At the risk of between "big" or "small" exists a gradual change and transition, namely technology with fuzzy attribute of "sensory risk" [5].

In this paper, we set up an evaluation index system of those risks and use AHP method and Fuzzy Synthetic Evaluation Model to assess technical risk of China's alternative fuel vehicle industry.

Establishment of technical risk evaluation indexes set and weights determination

According to related literatures, this paper constructs the technical risk evaluation index system as shown in table 2 [6-8].

Table 2 The alternative fuel vehicle technical risk evaluation index

Target layer	Index layers	Weights	Sub index layers	Weights
Technical risk factors (U)	Technical level (U_1)	0.5000	Technology Independence (X_{11})	0.2701
			Technology Advancement (X_{12})	0.2122
			Competition and Barrier (such as patents, licensing etc.) (X_{13})	0.2412
			Technology Replacement (X_{14})	0.1334
			Technology readiness level (X_{15})	0.0900
			Technology endowment (X_{16})	0.0531
	Technical social & environment adaptability (U_2)	0.5000	Technology policy (X_{21})	0.4576
			Raw material supply ability (X_{22})	0.2203
			The Improvement and stability of technical standards (X_{23})	0.1525
			The development of complementary technologies (X_{24})	0.1695

The index weight is determined by AHP and Delphi method.

Evaluation grades determination

Evaluation grade is the criteria for evaluation, evaluation grade set is $V=(v_1,v_2,\cdots v_k)$, this paper select 5 grades, i.e. {very low, low, medium, high, very high}.

Fuzzy evaluation matrix constructions

After determining the evaluation grades, sub index layers of alternative fuel vehicle risk were evaluated respectively, use membership grades to represent sub index's membership to evaluation grade, and then get the fuzzy relation matrix(see equation 1), wherein $j=(1,2,\cdots m)$.

$$R_i=\begin{bmatrix} r_{i11} & r_{i12} & \cdots & r_{i1k} \\ r_{i21} & r_{i22} & \ddots & r_{i2k} \\ \cdots & \cdots & \cdots & \cdots \\ r_{im1} & r_{im2} & r_{im2} & r_{imk} \end{bmatrix} \quad (1)$$

Usually, on the basis of the questionnaire, r_{ijk} determined by the following equation:

$$r_{ijk}=\frac{d_{ijk}}{d} \quad (2)$$

Wherein d is the total number of experts, d_{ijk} is the number of experts made comments on k grade to the index ij .

This study invited 10 experts to give evaluation to index layers, through data processing, the two evaluation matrixes are:

$$R_1 = \begin{bmatrix} 0 & 0 & 0.20 & 0.30 & 0.50 \\ 0 & 0.20 & 0.30 & 0.30 & 0.20 \\ 0 & 0.10 & 0.30 & 0.60 & 0 \\ 0 & 0.30 & 0.50 & 0.20 & 0 \\ 0 & 0 & 0.20 & 0.70 & 0.10 \\ 0 & 0.20 & 0.30 & 0.40 & 0.10 \end{bmatrix}; \quad R_2 = \begin{bmatrix} 0 & 0.10 & 0.20 & 0.40 & 0.30 \\ 0 & 0.30 & 0.40 & 0.20 & 0.10 \\ 0 & 0.10 & 0.30 & 0.50 & 0.10 \\ 0 & 0.20 & 0.20 & 0.30 & 0.30 \end{bmatrix}$$

Evaluation vector

Use following equation calculating the evaluation vector:

$$E_i = W_i R_i = (w_{i1}, w_{i2}, \cdots, w_{im}) \begin{bmatrix} r_{i11} & r_{i12} & \cdots & r_{i1k} \\ r_{i21} & r_{i22} & \ddots & r_{i2k} \\ \cdots & \cdots & \cdots & \cdots \\ r_{im1} & r_{im2} & r_{im2} & r_{imk} \end{bmatrix} \tag{3}$$

$$E_1 = \begin{bmatrix} 0.2701 \\ 0.2122 \\ 0.2412 \\ 0.1334 \\ 0.900 \\ 0.0531 \end{bmatrix}^T \begin{bmatrix} 0 & 0 & 0.20 & 0.30 & 0.50 \\ 0 & 0.20 & 0.30 & 0.30 & 0.20 \\ 0 & 0.10 & 0.30 & 0.60 & 0 \\ 0 & 0.30 & 0.50 & 0.20 & 0 \\ 0 & 0 & 0.20 & 0.70 & 0.10 \\ 0 & 0.20 & 0.30 & 0.40 & 0.10 \end{bmatrix} = \begin{bmatrix} 0.0000 \\ 0.1172 \\ 0.2907 \\ 0.4003 \\ 0.1918 \end{bmatrix}^T$$

$$E_2 = \begin{bmatrix} 0.4576 \\ 0.2203 \\ 0.1525 \\ 0.1695 \end{bmatrix}^T \begin{bmatrix} 0 & 0.10 & 0.20 & 0.40 & 0.30 \\ 0 & 0.30 & 0.40 & 0.20 & 0.10 \\ 0 & 0.10 & 0.30 & 0.50 & 0.10 \\ 0 & 0.20 & 0.20 & 0.30 & 0.30 \end{bmatrix} = \begin{bmatrix} 0.0000 \\ 0.1610 \\ 0.2593 \\ 0.3542 \\ 0.2254 \end{bmatrix}^T$$

Evaluation vector E_1 and E_2 can present the index layers risk levels respectively.

Comprehensive evaluation of technical risk as a result of:

$$B = WR = 0.5 \begin{bmatrix} 0.0000 \\ 0.1172 \\ 0.2907 \\ 0.4003 \\ 0.1918 \end{bmatrix}^T + 0.5 \begin{bmatrix} 0.0000 \\ 0.1610 \\ 0.2593 \\ 0.3542 \\ 0.2254 \end{bmatrix}^T = \begin{bmatrix} 0.0000 \\ 0.1391 \\ 0.2750 \\ 0.3773 \\ 0.2086 \end{bmatrix}^T$$

B is showing the degree of technical risk level belonging to each grade. In order to make the evaluation result more specific, we can introduce the membership degree vector K, as shown in table3.

Table3 Evaluation grade set and corresponding intervals and median

Grade	Very low	Low	Medium,	High	Very high
Intervals	0-20	20-40	40-60	60-80	80-100
Median	10	30	50	70	90

Use medians to constitute the membership vector, i.e. $K = (10,30,50,70,90)$.Then the comprehensive evaluation results can be expressed as:

$$R = KB = (10,30,50,70,90)\begin{bmatrix} 0.0000 \\ 0.1391 \\ 0.2750 \\ 0.3773 \\ 0.2086 \end{bmatrix} = 63.1080$$

This shows that China's alternative fuel vehicle industry technical risk is at a high level.

References

[1] Stephen Brown, David Pyke, Paul Steenhof. Electric vehicles: The role and importance of standards in an emerging market. Energy Policy 38 (2010) 3797–3806.
[2] Yimin Liu , Gloria E. Helfand. The Alternative Motor Fuels Act, alternative-fuel vehicles, and greenhouse gas emissions. Transportation Research Part A 43 (2009) 755–764.
[3] Xunmin Ou, Xiliang Zhang, Shiyan Chang. Scenario analysis on alternative fuel/vehicle for China's future road transport: Life-cycle energy demand and GHG emissions.Energy Policy, Volume 38, Issue 8, August 2010, Pages 3943-3956.
[4] China automotive technology and Research Center, Nissan (China) Investment Co. Ltd., Dongfeng Motor Company Chinese. Report on the development of new energy automotive industry (2013). Beijing: Social Sciences Academic Press,.2013 (9).
[5]Zhang Donghua. Technical risk evaluation model based on fuzzy method. Science technology and management. 2005 (1) .
[6]Mou Qinyao; Zhang Suodi.Quantization of upstream semiconductor lighting technology risk. Research technology management.2010(5).
[7]Jonathan H Klein. An approach to technical risk assessment. International Journal of Project Management. Vol. 16, No. 6, pp. 345–351, 1998.
[8]Xue Zhen. Research on the risk of alternative fuel vehicle industrialization. Fudan University master's degree thesis.2009.

Advanced Materials Research Vols. 986-987 (2014) pp 652-655

doi:10.4028/www.scientific.net/AMR.986-987.652

Vulnerability Assessment Method for Distribution Network

Xiao REN[1,a]，Jun LIU[2,b]，Yafang WANG[1,c]

[1]College of Electrical Engineering, Guizhou University, Guiyang, 55003, China

[2]Electric Power Testing & Research Institute of Guizhou, Guiyang, 550002, China

[a]email: 275323875@qq.com, [b]email: 147088790@qq.com, [c]email: 840944579@qq.com

Keywords: Distribution Network; Vulnerability Assessment; Transient Energy Function; Monte-Carlo Simulation; Risk Indices; Brittleness of System;

Abstract. This article is based on the concept of vulnerability for power system, and focuses on vulnerable source of distribution network and summarizes the characteristics of vulnerability assessment methodologies and inadequate for the distribution network.And pointed out that domestic and international research for distribution network vulnerability is still in the initial stages,evaluation of existing methods are accessible only from one side distribution system's security status,the vulnerability assessment methodology of distribution network can be more fully reflected the global distribution network of security that will be researched in the future.

Introduction

In recent years,power system Blackouts occur frequently all over the world,experts from various countries come to realize that traditional security analysis has been insufficient..In the Past,power system security only contains stability and reliability,most of the safety analysis is set up on the basis of screening and storting on expect accidents,which can't reflect the change from one or more of the operating parameters in the system on impact of the trend and stability margin change.The future development direction of power system safety analysis should be run fast accurate analysis of status and trends on the basis of avoiding the occurrence of major accidents, guarantee safe operation of power system.For this reason, some literature to expand conventional power system safety, vulnerability theory is a theory developed by this one.This article summarizes the distribution network vulnerability assessment , analysis and research the different kind of theories and methods, aims to establish a distribution network vulnerability assessment method and index system for reference.

Vulnerability for Distribution Network and its Definition

The vulnerability for distribution caused by human intervention, calculation errors, communication failures, factors such as internal elements and protection systems and for the potential of large scope blackout risk.Such hidden dangers fault is only exposed when the accident occurred, which performance the ability for the power grid remain normal and stable supply of electricity to users.Distribution network vulnerability assessment includes the following 4 aspects :event recognition, risk calculation, network analysis and decision analysis.At this point, vulnerability for distribution network can be defined as extension of the safety and stability of power distribution network.

vulnerable source of distribution network

Categorize and summarize the vulnerable sources in distribution networks, can be divided into external and internal sources.

1 External Source.External sources can be summed up in two aspects.1.Force majeure such as natural disasters and weather conditions.Mainly includes:Earthquakes and typhoons, storms, high temperatures, hail, thunderstorms, flooding, forest fires, as well as plants and animals triggered failures;2.Artificial fault.Include the misuse of the system operator, controls and protection system error , vandalism,etc.

2 Internal Source.Mainly includes:1.Main components of fault in distribution networks;2. Protection and control systems failure;3.Information and communication system failures;4.Distribution system is unstable;5.Distribution network modeling and assessment is inadequate;6.Electricity market competition leads to vulnerability;7.Unable to access, integrate and use of reliable information;8.Some criminals have used high-tech data intrusion and tampering.All of the above are major vulnerable source of distribution network.

Method for Distribution Network Vulnerability Assessment

Summary

Now,Vulnerability assessment method for power system has no recognized and unified analysis standards.Vulnerability assessment for distribution network is an aspect of vulnerability assessment in power system and its assessment methods need to be improved and summarized as appropriate.At present, methods could be applied to assessment vulnerability for distribution network can broken down into the following three categories

1 Assessment methods based on brittleness of system.

2 Assessment methods based on probability theory,which include assessment methods based on risk theory and Monte-Carlo simulation.

3 Assessment methods based on transient stability analysis,which include assessment methods based on transient energy function.

Assessment methods based on brittleness of system

Brittleness analysis is an theory that attempt to explain and analysis a cascading failures in the system.[3] based on the mechanisms of cellular automata, elaborates specific modeling steps for vulnerability assessment model,defining brittleness risk function based on probabilistic risk method,quantitative analysis of probability of brittleness risk.Proposed power grid is a self-organized critical system and the brittleness inspired because of the system is self-organized criticality.

This paper study components due to failure to quit running based on self-organized criticality of power system,other elements of a system overload because of the current redistribution,caused by breaking one after another, eventually caused the system to crash.Because it does not take into account other aspects such as voltage stability and transient stability of system,which do not work for complex power system in today.

Assessment methods based on probability theory

Assessment methods based on risk theory

Risk theory study the possibility and severity of disaster.Use risk indicators to quantitatively grasp the possibility and severity of an accident , so as to more fully reflect the impact of accidents on power system.Risk is defined as the product of the probability and the consequences of the accident.Risk indicators calculated as follow

$$R(C/Y_t)=\sum P(E_i/Y_t)\times S(C/E_i) \tag{1}$$

In this formula,i:The collection of normal operating elements;Yt:The running state before failure;Ei:Uncertain accident in future moment t;P(Ei/Yt):The probability of accidents Ei in case Yt;S(C/Ei):After the accident Ei, the severity of the consequences;R(C/Yt): vulnerable indicators of system in accident Ei.Calculation of risk indicators for distribution network requires the probability and consequences of accidents caused by two important parameters.The probability of Power system accidents largely satisfies the Poisson distribution

$$P(E_i)=(1-e^{-\lambda_i})\times e^{-\sum_{j\neq i}\lambda_j} \tag{2}$$

The severity of consequences of the accident impact on power system security.Define the appropriate severity link to specific systems, specific requirements as well as the risks types.

Risk calculation of decoupling,which calculated separately each incident or each category of security issues, each component.Therefore, you can rewrite the formula(1),according to security assessments, calculate different kinds of vulnerability indicators , reflect the overall vulnerability of different power system problems.Finally, the combined vulnerability indicators can be integrated to reflect your overall system vulnerability risk index.

Theory of risk-based assessment methodology is merely a response to an aspect of the system or any part of the security problem, not reaction system-global security

Assessment methods based on Monte-Carlo simulation

Monte Carlo simulation is for solving the problems associated with a certain degree of probability model to obtain the approximate solution of the problem.[7] noted that indicators of vulnerability analysis of power system based on Monte Carlo method can be summarized as:Using random probability sampling to determine the System State,study on dynamic and static characteristics,indicators of risk through statistical analysis computing system outages.These can be divided into three parts1.State selection;2.State estimation;3.Index calculation.The advantage of this method is 1.This is a statistical testing method, easy to understand and master;2.This method can discover unexpected accidents, easier to deal with its random variation;3.Easy to handle system for operations in chronological order;4.Ideal for intensive low-reliability components, and multiple failures affect systems that cannot be ignored.Its shortage is mainly calculated time and calculated accuracy is closely related to, in order to achieve high precision reliability index, often takes a long time.

[7] serious blackout occurred in the simulation system of probability is defined as the vulnerability of the system.Its formula is

$$V = \sum \left[F(i) / N \right] \tag{3}$$

Among them, V is vulnerability of system.;I is loss of total load is greater than the threshold to take emergency control still unstable after a simulation. F (i) = 1;N is the total number of system simulation.

Computation not scale or level of complexity of the system affected, ideally suited to handle a variety of complex factors.In a certain precision and study all decrease the variance in skills is the key to improve the convergence speed of Monte-Carlo method.

Assessment methods based on transient stability analysis

Assessment methods based on transient energy function

Evaluation method based on transient stability analysis,[8] taking into account the expected probability of accidents and use potential energy boundary method for solving critical energy and fault removal of energy, composition the vulnerability indicators of system.In the literature,The absolute indicators is definite as vulnerability indicators for the contingency of i .

$$P_i^J = P_i e^{-V^i{}_{critical}} \tag{4}$$

In this formula,Pi is Probability in accident of i;Vicritical is critical energy of the contingency of i.According to the critical energy of contingency and transient energy within the time of fault clearing defined the relative indices of contingency of i.

$$P_i^X = P_i e^{V^i{}_{clear} - V^i{}_{critical}} \tag{5}$$

In the formula,V^i_{clear} is critical energy of the time of Contingency i removal .

A combination of these two indicators could get the integrated indicators of vulnerability:

$$P_S = \frac{1}{2}\left(\frac{1}{N} \left\| I_s \right\|_1 + \left\| I_s \right\|_\infty \right) \tag{6}$$

In this formula,I is integrated indicators of vulnerability within Contingency.

Set S is an acceptable benchmark thresholds and assess the system's security status.System's vulnerability mainly depends on the assessment of vulnerability index is greater than or less than the specified threshold value of S.

Conclusion

This article is based on the concept of vulnerability as well as sources of vulnerability for distribution network, Summed up vulnerability assessment method for distribution network in different literature at home and abroad.However evaluation methods mentioned in this article are available only from some aspect of power systems to assess the vulnerability index,combining multiple assessment indicators to establish comprehensive assessment indicators is research direction of distribution network vulnerability assessments need to focus.

References

[1] Weihua Chen,Quanyuan Jiang,Yijia Cao and so on.Risk-based vulnerability assessment in complex power systems [J].Power System Technology.2005:29(4):12-17

[2] Weihua Chen,Quanyuan Jiang,Yijia Cao.Voltage vulnerability assessment based on risk theory and fuzzy reasoning [J].Proceedings of the CSEE.2005:25(24):20-25

[3] Limei Yan.Brittleness Theory of System and Application to Electric Power System[D].Harbin:Harbin Engineering University.2006

[4] Jialin Bai,Tianqi Liu,Guoyun Cao and so on.A survey on vulnerability assessment method for power system [J].Power System Technology.2008:32(2):26-30

[5] Kang Lin,Keith E H.PRA for vulnerability assessment of power system infrastructure security[C].Proceedings of the 37th Annual North American,Illinois,USA,2005.

[6] Kamwa I,Béland J,Cnabb D.PMU-based vulnerability assessment using wide-area severity indices and tracking modal analysis[C].Power Systems Conference and Exposition,Atlanta,USA,2006.

[7] Le Wang.Application Study on Vulnerability Assessment in Power System Security Defense System[D].Beijing:North China Electric Power University.2005

[8] Jinling Lu,Qunxing Ji,Yongli Zhu.Power Grid Vulnerability Assessment Based on Energy Function[J].Power System Technology.2008:32(7):30-33.

[9] Zhenbo Wei,Junyong Liu,Guojun Zhu and so on.Theoretical study on the vulnerability of power system[J].Electric Power Automation Equipment.2009:29(7):38-42

[10] Tao Lin,Xingyuan Fan,Xialing Xu.Summary of power system vulnerability assessment method[j].Journal of Electric Power Science and Technology.2010:25(4):20-23

[11] Qian Li,Huaqiang Li,Zhaomeng Huang and so on.Power system vulnerability assessment based on transient energy hybrid method[J].Power System Protection and Control.2013:41(20):1-6.

Advanced Materials Research Vols. 986-987 (2014) pp 656-659

doi:10.4028/www.scientific.net/AMR.986-987.656

The central air-conditioning energy saving system

Zhengqian Feng[1,a], Chongchao Pan[2,b]

[1]Department of Shandong Provincial Key Laboratory of computer Network, Shandong Computer Science Center, Jinan, 250000, China

[2]Department of Resources and Environment Branch, China National Institute of Standardization, Beijing, 100000, China

[a]email: fengzhengqianf@126.com, [b]email:fengzhengqianf@126.com

Keywords: Central Air-Conditioning, Energy saving, Control

Abstract. At present most of the research is aimed at the end of the central air conditioning equipment, not considering the inner link between each component of the central air conditioning. In order to achieve economic operation of equipment and systems, to maximize energy saving of central air conditioning, we designed and implemented a monitoring system analysis which considered in the system more equipments linkage, multi parameter coupling, and a variety of factor. It collected energy consumption data of each device, to get the system running in typical operating conditions of the system by simulating the optimal process parameters and guide debugging critical control equipment.

Introduction

With China's rapid economic development, energy issues become increasingly prominent. Energy has become an important factor in the healthy and sustainable development of our national economy. According to incomplete statistics, China's building energy consumption has accounted for 30% of the total social energy. With the advancement of China's urbanization process, the continuous improvement of people's living standard, Experts predict if not timely solve the problems existing in the aspects of building energy consumption, this proportion will rise rapidly to about 40%. Building energy has enormous social and economic benefits. Energy consumption is one of the central air conditioning system, and heating, air conditioning, ventilation energy consumption accounts for about two-thirds of the total energy consumption. Related data show that the building of central air conditioning in operation load rate is low. Generally less than 50% of the design load running time accounts for more than 70%. So building energy-saving central air conditioning system has great potential and significance. Moreover, according to the predict calculation, if not take effective energy saving measures, China's energy consumption of building will grow by more than three times the current building energy consumption by 2020. Thus, the building energy problem is imminent. Therefore, we have developed a comprehensive analysis of the monitoring system in this situation which considered in the system more equipment linkage, multi parameter coupling, and a variety of factor. It collected energy consumption data of each device, to get the system running in typical operating conditions of the system by simulating the optimal process parameters and guide debugging critical control equipment. It implements the economical operation of equipment and systems and saves the energy consumption of central air conditioner to the maximum [1].

System Design

The system adopts the technology of the Internet of things, and realizes the date collection of monitoring and saving energy control in building central air conditioning system through the wireless and IP network. Building central air monitoring data collection includes the chiller, chilled water pump motors, cooling water pump motors, air conditioning blower motor, cooling tower fan related parameters as well as the indoor environment. Meanwhile, it is not suitable adopting the way of the cable for the part of the data collection such as indoor temperature, humidity and other

micro-meteorological environmental data. Because if deployed conventional devices, the data output in the form of cable, data lines must be deployed to the installation of the interior of each point and each device, and it is bound to cause the refrigeration circuit messy and complicated installation, therefore, we adopt wireless way. Moreover, adopting the way of wireless in the central air conditioning system has been running can avoid the transformation of the existing air conditioning and avoid wiring [2]. Figure 1 is the overall scheme of the system.

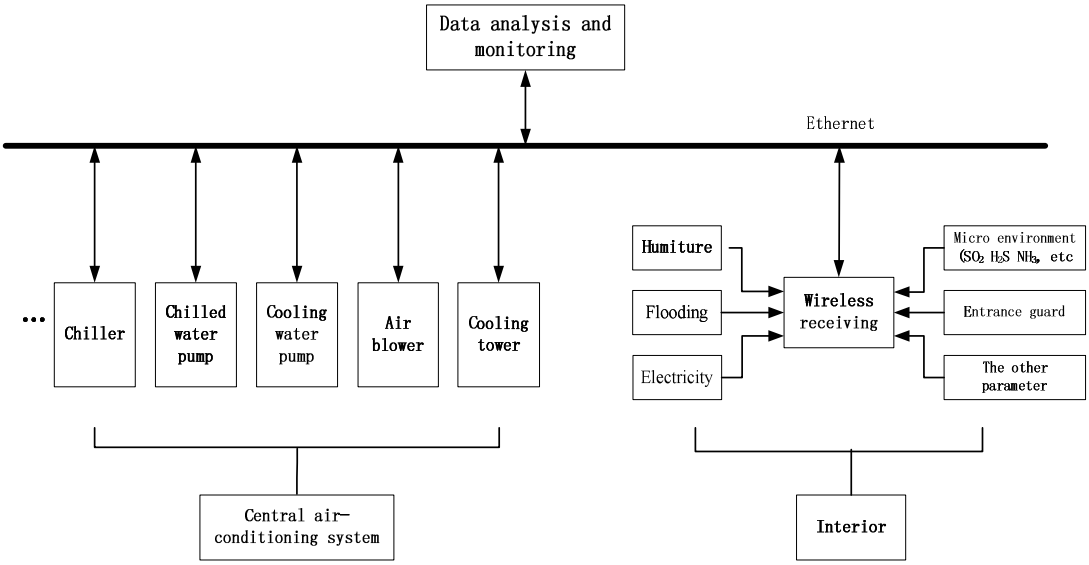

Fig.1. The overall scheme of the figure system

Central Air-conditioning System

Capacity of the central air conditioning system is selected by the maximum design load of the building, and have left margin. According to the American Air-Conditioning and Refrigeration Institute statistics, the central air conditioning equipment in 90% time runs at rated load under 70%. Due to the change of the season, day and night, and the user load, the actual air conditioning of heat load in the most time is lower than the design load. Central air conditioner can automatically adjust its operating power according to the heat load, but its circulating pump system working under a fixed maximum flow for a long time all the year which makes the system most of the time in a large flow of low temperature condition. Most of the circulating pump energy becomes pipeline transportation losses, meanwhile results in the decrease of efficiency of the host [3].

Table 1. The annual distribution imbalance of air conditioning load

Load rate	75 100	50 75	25 50	25
Percentage of the total running time	10	50	30	10

From table 1 can be seen that the distribution of the air conditioning load, within a year is not balanced. Design load accounts for about 6%～8% of the total run time, the running time of load rate is more than 75 accounts for only 10%, the running time of load rate is 50% to 75% accounts for 50%, the running time of load rate is below 50% reaches up to 40%. Therefore, for central air conditioning reasonable running, we can refer to the following:

(1) Operation and stop of the device. Analysis of overheating too cold case continues to operate and preheat pre cooling operation and as far as possible to increase the stop time.

(2) Air volume control. In the operation of the blower, the air flow control method to control the damper manually is very poor. Since the shaft power of blower and air volume are proportional to the size, so according to the heat load to control the air volume can greatly save power.

(3) Flow control. Requirements of cooling water, hot water, cold water are different with of heat load, water supply and water drainage difference in temperature. Therefore, we should control the

flow according to the above conditions. Pump power and the flow rate are proportional to the size, so the flow control can save energy significantly.

(4) The temperature and humidity control. Determining the operating state of air conditioner such as running, stop, for air conditioning should be according to the indoor temperature. Thermostatic control can prevent the waste caused by extreme cold or heat. There are a function of humidity and temperature, relative humidity decreased by 5%, equivalent to a temperature decrease 1 ℃.

The host is a major component of the air conditioning system and energy saving of host should be considered in combination with frozen water pump, cooling water pump, cooling towers, air conditioner, fan and other equipment. Therefore, we need to find the best system device configuration in co-operation between all the devices, and not just in a single device performance analysis to replace the energy-saving operation analysis of entire air conditioning system.

Inner environment

(1) Sensor

Temperature and humidity sensors used in solution are designed by Shandong Computing Science Center and which are low-power wireless sensors. Wireless communication frequency of sensors is 2.4 GHz, and which can ensure that the wireless communication distance is more than 300 meters. Temperature measuring range of sensors is -40 ℃～+125 ℃ and temperature measurement accuracy is between ± 0.3 ℃～± 2.5%. Relative humidity measurement range is 0.5% RH～100% RH and the relative humidity measurement accuracy is between ±1.8% RH ± 20%. More prominent advantages for this sensor it that electronic battery it built-in the sensor and current average is less than 7μA. Furthermore, it can work for 6 consecutive years without replacing the battery.

Other micro-environmental sensors used are all are independent designed by Shandong Computer Science Center. The current output signal of probe in detecting is very weak and need to develop special processing signal extraction circuit. Meanwhile circuit design requirements to prevent the circuit reverse connection, high voltage and high current. The signal communicates with the host through the circuit module using RS485 serial port or RF and transmits data in a wireless way.

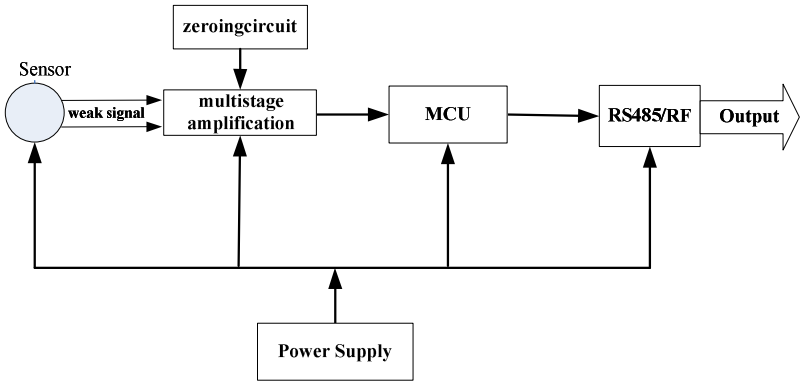

Fig.2. Circuit schematic diagram

Figure 2 is the schematic diagram of the sensor circuit. Detection circuit module receives the weak current signal which is produced by the electrochemical reaction of some parameters microenvironment. The current signal needs to make further amplification processing before A/D conversion. The signal input of the first amplifier stage must be able to pick up weak current output signal from sensor and the amplified signal is output to the amplifier. In the signal amplification process, the effective signal is amplified, noise is filtered out. Therefore, in this session we chose the small signal precision amplifiers produced by TI. The amplified signal needs to do the A/D conversion, that is converting analog signals into digital signals and after further processed, the signal output through RS485/RF. Taking into account the signal can be easily connected to an

external circuit after AD conversion, where the choice of chips are with low power consumption, small size, stability, development and simple. The transformed signal chip acquisition ultimately converted into RS485 or into the RF signal to ensure the longest transmission distance.

(2) Acquisition

Timing acquisition. Specific feature is that users can choose the type of equipment acquisition and flexible set timing acquisition time. The system can automatically collect data timed according to the user setting.

Real-time acquisition. The specific function is user generated commands to the device through the interface of data acquisition, the system responds by calling the data acquisition interface devices to obtain data. Real time data acquisition can be collected by a key, and can also select the type of device for separate collection.

Remote Control. The system processes and analyzes the data collected to get the system running in typical operating conditions of the system by simulating the optimal process parameters, and then sent the instructions in manual or automated form controlling the central air-conditioning of the building to reach the scientific operation.

At present, most of the building air conditioning system is running at part load conditions in most of the time. For the air-conditioning operation control department, they can formulate corresponding operation strategy according to the technical characteristics of building, equipment, collection and analysis of the external environment temperature inside the building and other technical parameters in all kinds of weather conditions as the basic data [4].

Conclusion

This design has reached the expected target, and achieved the desired function and which considered in the system more equipment linkage, multi parameter coupling, and a variety of factors. It collected energy consumption data of each device, to get the system running in typical operating conditions of the system by simulating the optimal process parameters and finally implemented the operation instruction of the central air conditioning. Meanwhile, this system not only can be used with the construction of the central air-conditioning energy saving, but also can be applied to the computer data center energy efficiency and other similar applications, so the potential is tremendous [5].

Acknowledgement

In this paper, the research was supported by China's National Science and Technology Support Program (Project No.2012BAK30B01).

References

[1] Yang Xiangdong, Zuo Shuaiying.Research on the energy saving method of a Central air-conditioning [J]. Construction equipment and construction materials. 2008.03(28).

[2] Guo Shangyi, Lei Xiaofeng. The monitoring and analysis of central air conditioning system energy consumption [J]. Modern Architecture Electrical, 2012.03(03).

[3] He Dehui. Discussion on the central air-conditioning energy saving and reduction of energy consumption [J]. Monograph of Science and Technology. 2013.09.

[4] Xing Junbin. The Design and Realization of Central Air-conditioning Energy Saving Control System Based on FDES [D].Shanghai: Donghua University, 2013.

[5] Shen Shiping. The Energy-saving Transformation and Energy Consumption Analysis of a Central Air-conditioning System [D].Chongqing: Chongqing University, 2011.

Advanced Materials Research Vols. 986-987 (2014) pp 660-663

doi:10.4028/www.scientific.net/AMR.986-987.660

Probe on Questions and Mode of Renewable Resource Development and Utilization on Small Islands

Yunpeng Zhao[1,a], Haibo Jiang[1,b],Zhongqing Cheng[1c]

[1]Logistics College, Naval University of Engineering, TangGu,TianJin 300450 China

[a1]zyp73115@163.com, [b1]Jianghaibo022@126.com,czq@163.com

Keywords: Small islands; Renewable Resource; NO-Energy-Storage; Direct development and utilization

Abstract: Aiming at small islands location limits and the established power grid characteristics, the paper analyses some practical problems to be dealt with when renewable resource is utilized. Combined with the characteristics of small islands, the paper puts forward the new mode without energy storage devices, and designs a renewable resource application system driven directly by photovoltaic devices, emphatically analyses the key technology of no energy storage mode. The new mode effectively resolves the battle neck problem of traditional off-net mode.

Introductions

Renewable resource Utilization on small islands is an effective way to improve the energy supply mode of the islands; but there are still many problems, such as small islands often lacking of large power grid and renewable energy application often being off-net mode. Actually the cost factors and lifespan of the indispensable energy storage battery component are their natural defects in off-net mode. Meanwhile the extremely corrosive conditions on small islands are often beyond the technical conditions of routine renewable energy use, which makes the renewable energy utilization on small islands is still at a very low level. Combined with the engineering test, the paper discusses some practical problems to solve, and gives a typical design of no-energy-storage application system being suitable for small island features system.

1 Questions analysis of renewable resource development and utilization on small islands

At present, the renewable energy technology has been used in various forms even with super large scale in china. At the same time China's photovoltaic power generation capacity and installed wind power capacity are first in the world. But there are still many problems to be solved when these mature technologies are applied on small islands.

1.1 Discuss on the utilization mode

There are two basic forms in development and utilization of renewable energy application, one is grid-connected model, another form is Off-grid model. In grid-connected model, the outside power grid are indispensable, the power generated by renewable energy is transferred to large power grid through modulation to reduce the other energy needs of electric power. In off-grid model, without external power grid the energy generated by renewable resource must be stored and converted, and then provided to the necessary loads. On many small islands diesel generators or gas turbines supply power for load, the capacity of generators and scale of grid all can not meet the large disturbance requirements of renewable resource power connected to grid. The cost and life span of energy storage batteries, the stringent requirements for loads and converting efficiency limit the application scale of off-grid model. So the renewable resource utilization on small islands is still decorative such as street lighting etc.

1.2 About environment corrosion characteristics and equipment protection problem on small islands

More harsh application environment conditions are considered when renewable resource utilization is performed. However usually when temperature is considered, the environmental temperature limit and working temperature limit are focused on. About the corrosion condition, mainly considering the oxidation corrosion of metal, which is mainly considered moisture and oxygen in the air. About equipments protection grade I level, dust and sands are emphasis. But the

characteristics of environmental corrosion on small islands are manifested in the following aspects, the main consideration of environmental temperature is the seasonal temperature difference, the temperature difference between day and night or in a short time is very small. In addition to oxidation corrosion of high humidity, salt ion corrosion and salt spray are extremely serious. About the dust protection, the main protective object on small islands is salt spray and constantly high humidity. Practical experience shows that the life span is about 1/3 if environment corrosion characteristics and equipment protection have not been considered.

2 Probe on the utilization model of renewable resource on small islands

In the case of lacking of large power grid relying on, reasonable optimization of renewable energy exploitation patterns is an effective way to improve the independent ability of small islands. Aiming at the defect of the common off-grid patterns, we proposed a zero-energy-storage renewable energy application model as follow. The system principle is shown in figure 1.

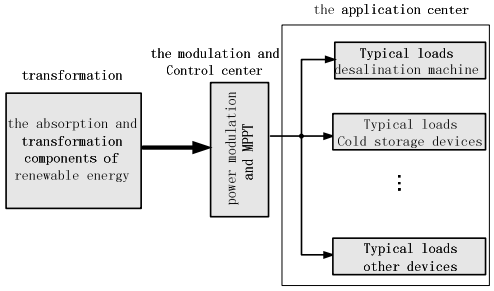

Fig.1 No-energy-storage model of renewable resource

The basic idea of the zero-energy-storage model is that energy converted by renewable resource is consumed instantaneously to the greatest degree of the conversion. The model consists of three parts. One is the absorption and transformation component of renewable energy, which coverts the most richly existing renewable resource on small islands into other forms of energy-usually electrical energy. Two is the control and modulating component. It should at least meet three requirements. First is the power modulation, which modulates the irregular electrical energy to the regular electrical energy which can meet the application center load directly; Second is the maximum power tracking, which demands the converted energy consuming at possibly high efficiency; Third is the loads regulation at application center, such as loads preferred starting right and optimal load working state, in order to make the whole system coordinated working. Three are the loads at application center, which should have enough flexibility. The flexibility here means not only that the loads can be starting or stopping according to the orders from the control components but also that the working states of the loads can be adjusted according to the power supplying from energy converting components.

3 A classical design of the zero-energy-storage model

The No-energy-storage application model is structured aiming at the problems of electrical power storage. According to the current technology level, the cost of storage 1KWH electricity is about 3000￥ or more, while the storage cost of 1 tons of water only a few yuan. On small islands, freshwater, cold and heat energy are fast consumable essential, the problems of electrical power storage will be resolved easily if using the energy converted from renewable resource directly. Based on the idea that water storage is better electricity storage, we give a classical design of solar desalination system driven directly by PV.

3.1 The whole consist of the system

Through the control of intelligent management unit, the energy from the solar photovoltaic components makes the reverse osmosis desalination machine dynamically adjusting its working state, so that the dynamic consumption instantaneously is less than or equal to the PV maximum output power, which ensure the whole system balance. The designed Peak power of the system is eight thousand warts, consisting of 48 pieces of photovoltaic components connected by 16 series connection and 3 parallel connections. All these components collected by lightning protection

confluence box supply energy to seawater desalination devices directly by intelligent management unit without energy storage devices. The minimum operating frequency and the minimum operating power is 20Hz and 600warts.The best operating frequency and power is 50Hz and 4000warts. It produces 5t fresh water daily under normal lighting circumstances. The framework of the system is as shown in figure 2.

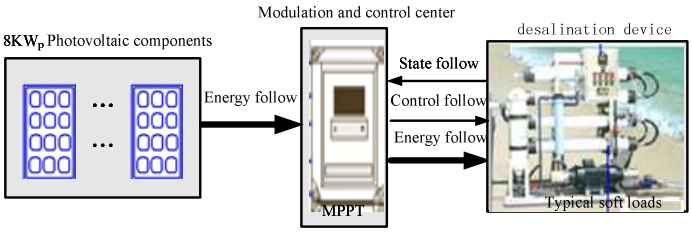

Fig.2 The frame of the photovoltaic desalination device

3.2 Analysis of the critical technology

Knowing from the typical application diagram of no-energy-storage model, the key parts of the whole system are intelligent management or conversion control units, which basic function is the energy conversion and management. Though the photovoltaic components can converts light energy into DC power which varies whit light intensity, however the electricity driving the desalination devices must three-phase alternating current. All these require intelligent management unit can not only complete the energy conversion, and according to the real-time solar illumination intensity, make desalination device stability and maximum use of the PV module converting electrical energy. Another main function is realizing the starting and stopping control automatically according to the external light. The hardware design of the system is simple relatively. Now we discuss the software programming.

The software design of the system mainly embodies the programming of power tracking unit, which mainly includes system start determining, maximum power point tracking method and the transition process of weather transients. The starting delay time is critical. Too short waiting time makes the pump starting frequently within a short time, which can not work continuously, and also shorten the life of the devices. Too long waiting time decreases the efficiency of the whole system. The starting flow of the system is shown in figure 3.

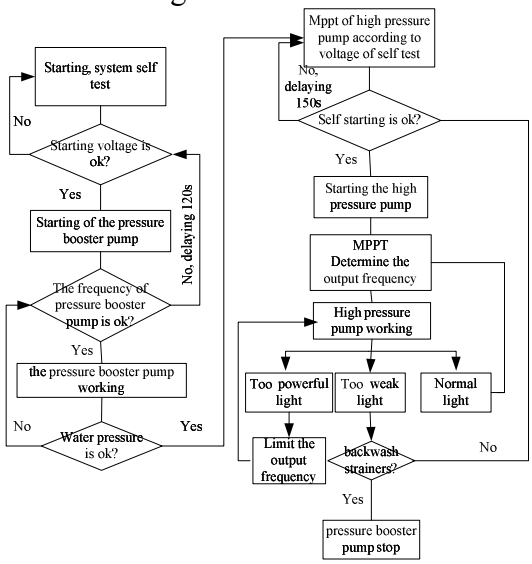

Fig.3 Flow chart of intelligent PV control unit

4 Conclusions

According to application model brought out in this paper, we established application on a small island in 2009. It has worked more five years placidly. The experiment practice of the no-energy-storage model shows that the new application model well resolved the problems of traditional model. It can improve the existing ability of the small islands greatly.

References

[1]Zhao YunPeng, Jiang HaiBo.Design and Optimizing of PV-RO Seawater Desalination Device.China Water & Wastewater,Vol.28(2012),P.77-80

[2]Wang DongLin. Issues in the application of solar photovoltaic power technology. Electrical Technology of Intelligent Buildings,Vol.5(2011),P14-17

[3] Galvea J B，Garcia-Rodriguez L，Martín-Mateos I. Seawater desalination by an innovative solar-powered membrane distillation system [J]. Desalination，2009，246（1/3）：567-576.

[4]Zhao YunPeng, Cheng Zhongqing, Li Nan.Research on System Structure of Renewable Resource Micro Power Grid Distributed Independently.Advanced Materials Research Vols. 347-353 (2012) pp 912-916

[5] Haibo Jiang, Yunpeng Zhao and Yanru Li.Problems and Solutions of Wind Energy Development and Utilization in Coral Reefs. Advanced Materials Research Vols. 347-353 (2012) pp 3529-3532

Advanced Materials Research Vols. 986-987 (2014) pp 664-668

doi:10.4028/www.scientific.net/AMR.986-987.664

Explore on High-rise Residential Appearance and Integration of Solar Flat Plate Collector Design in Panzhihua City

Qian ZHANG[1, a], Chunlin BIAN[2, b]

[1] Department of Civil Engineering and Architecture, Panzhihua University, Panzhihua, 617000, China

[2] Department of Civil Engineering and Architecture, Panzhihua University, Panzhihua, 617000, China

[a]email: 418677556@qq.com, [b]email: 342257149@qq.com

Keywords: Solar Integrated, High-rise residential, Row spacing, Flat-plate collector

Abstract. Firstly, this paper briefly introduces Panzhihua City's location, climatic conditions and hours of sunshine. Secondly, it proposes alternative solution of integrating the heat collector with high-rise residential building's facades. Thirdly, several equations on heat collector's area, row distance, and azimuth are explained and discussed.

Introduction

With the rapid growth in energy demand, resulting in increasingly serious environmental pollution, China is facing the dual pressures and challenges of unprecedented energy and the environment. Since the beginning of the 20th century, 90 years, China has increased the research and application of solar energy and building integration, but now China has nearly 2 billion m^2 building completed about 70% of the residential annually, the proportion of high-rise residential is also increasing large year by year, while 99% of these buildings are high energy consumers, urban water supply in order to meet more and more high-density high-rise buildings do not affect the appearance of building facades, solar collectors how to more effectively together and building facades [1]. The author quote Panzhihua City an example of high-rise residential solar panels and exterior design integrated exploration, hoping to promote and facilitate the application of solar collectors in high-rise buildings, faster realization of our energy reduction targets.

Panzhihua City high-rise residential buildings selection analysis

More and more modern high-rise residential buildings in the city appeared an important part of the overall image of the city (Figure 1). Due to the important influence of its huge scale and massing of city landscape, we require high-rise residential buildings not only to meet the general residence requirements. Also requires a certain aesthetic value and ornamental. Panzhihua is located in the Southwest, Northwest, Southwest belongs to the city, mainly in the following three high-rise residential style forms:

Figure1 Panzhihua City building close-up view

1. Modernism. In the form of binding function, the overall style is simple, crisp. Focus on stress points, lines, composition principles plane. Simple and elegant facade colors, no frills (Figure 2 (a)).

2. Neoclassicism. Emphasize the relevance of history in the design practices; refine the language of classical architecture and innovation, the use of a large number of modern materials, reflecting the overall atmosphere, elegant architectural style (Figure 2 (b)).

3. Art Deco. It is currently one of the more popular styles of high-rise residential buildings. It is enough of a new classicism to modernism style transition, showing the characteristics of modern elegance, emphasizing vertical lines and abstract decorative pattern (Figure 2 (c)).

（a）modernism （b）Neoclassicism （c）Art Deco

Figure 2 Vertical lines and abstract decorative pattern

Functional solar collector design parameters

A solar collector installation location

In building surface choose a suitable installation location is the key to ensuring a solar hot water system functional requirements, installation location is the most ideal building roof, followed by building facades, such as walls, balconies and other parts (due to the mounting angle of the collector limit the amount of radiation to get affected by certain impacts) should be avoided in the bottom of the building facade, surrounded by green areas or building block recess shape of the installation.

Solar collector area calculations.

① design average daily water consumption

Design Day Average water consumption: from December 1, 2010 implementation of the "civil-saving design standards" (GB50555-2010), the provisions of the average daily water consumption of residential hot water, specifically for solar water heating systems and hot water mining quota selection. The average daily water consumption rise residential Panzhihua value should be in accordance with Table 1.

Table 1 Residential average daily water consumption quota of hot water

Hot water supply and equipment	average water quota (L)	Unit
owned heating water supply and bath equipment	20 60	L / person · d
central Heating water supply and bath equipment	25 70	

②Solar system guaranteed rate

Solar fraction F is the total load in the percentage of solar water heating system consists of solar burden is an important parameter to determine the solar collector area of the key factors also affect the economic performance of the system, which is calculated as follows:

$$F = Q / L \qquad (1)$$

In the formula, Q is the system effective heat gain from the sun; L is the system total load.

③ collector area calculation

"Civil solar water heating system technical specifications" in accordance with the different types of solar water heating systems heat the solar collector area calculation is divided into two cases:

The first is a direct system collector area calculation: total collector area of direct system according to the daily water consumption and water temperature to determine the user, calculated as follows:

$$A_C = \frac{Q_W C_W (t_{end} - t_i) f \rho}{J_T \eta_{cd} (1 - \eta_L)} \qquad (2)$$

In the formula, A_c is the collector system for the direct total area, m^2; Q_W is the average daily water consumption, L; C_w is the water specific heat capacity, 4.187kJ / (kg.℃); t_{end} is the design temperature of the water storage tank,℃, usually take 60℃; t_i is the initial water temperature,℃; ρ is the density of water, 1.0kg / L; Annual average daily amount of solar radiation collector J_T is

local lighting up, kJ/m^2, Panzhihua City's average amount of radiation can press the summer months and winter months, respectively, where the surface of the collector lighting calculations; f is the solar fraction,%, based on the life of the solar irradiation system, economic system and user requirements and other factors after considering identified, should be 30% to 80%; η_{cd} is annual average thermal efficiency of the collector, the value should be based on the experience of 0.25 to 0.50; η_L is the rate of heat loss from the storage tank and piping, the value should be based on the experience of 0.20 ~ 0.30.

The second is indirect area of the collector system: the system to be considered an indirect heat exchanger factor, so compared to the direct system, to obtain the same quantity of water, which requires relatively large area, the collector the area is calculated as follows:

$$A_{IN} = A_C \left(1 + \frac{F_R U_L \cdot A_C}{U_{hx} \cdot A_{hx}} \right) \qquad (3)$$

In the formula, the total collector area of indirect systems, m^2; collector system for the direct total area, m^2; total loss coefficient for the collector, W/m^2.℃, for flat plate collectors, should take 4~6 W/m^2.℃. For vacuum tube collectors, should take1~2W/m^2.℃, the specific values should be based on actual test data collector products may be; as heat transfer coefficient, W/m^2.℃; Ripe for the change called the plot's heat, m^2.

Azimuth solar collectors

According to the solar radiation Panzhihua typical local weather parameters, the collector angle is set to 60° and 30° change in azimuth 0°~90° range of azimuth calculation under different circumstances change the size of the received solar radiation on the surface of the inclined . Known horizontal surface daily average direct sun radiation (H_{bH}) and monthly average daily diffuse radiation (H_{dH}) per month, according to Klein derivation formula R_b direct radiation factor and Liu-Jordan derivation of scattered radiation factor Rd, the horizontal solar radiation is converted to an inclined surface solar radiation (H_β):

$$H_\beta = H_{bH} R_b + H_{dH} R_d \qquad (4)$$

Collector row spacing

When the collector is installed, it is should avoid blocking the surrounding shade or collectors. The length of buildings' shadow which is a minimum level of clearance of collectors from the shade, It is the collector row spacing. Calculated according to the following formula (Figure 3):

$$D = H \cdot \cos X_S \qquad (5)$$

In the formula, D is the horizontal distance from the collector minimum spacing (m) shade or between front and rear; H is the vertical height (m) the highest point of the shade light collector surface between the lowest point; X_s is building location solstice 10:00 sun elevation angle (year-round use) (°) (in order to ensure that no less than any time in the sunshine of the winter solstice on the collector 4 hours).

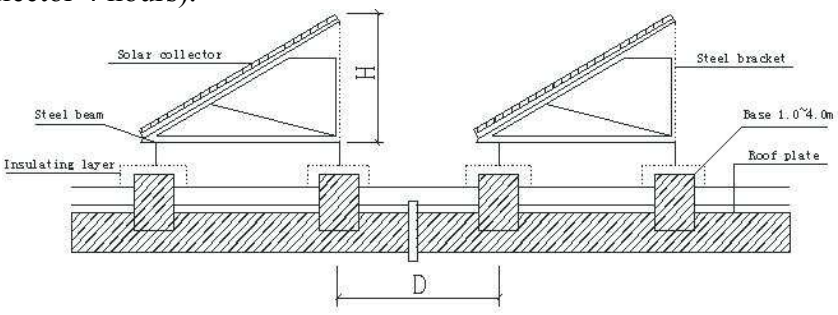

Figure 3 Schematic cross-sections of solar collectors

Solar collectors and residential facades specific binding mode

Combined with flat roofs

Installation of solar collectors on flat roofs is the most simple and feasible way for residential and collector toward no special requirements, and sufficient solar radiation. It should be noted collectors front row spacing, to avoid blocking. Through the bracket and solar collectors on the roof base with fixed, neatly arranged in a certain inclination, embedded base, good waterproofing measures pipeline through the floor, should not affect the existing roof waterproofing, insulation and drainage structures. Since the height of high-rise residential and the roof-mounted solar collectors are not in the normal field view, as long as the organized arrangement, there is no significant impact on the building exterior.

(a) Flat roof solar cell - Tube Products

(b) the cell demonstration projects - Flat-plate collector products

Figure 5 Examples of collectors installed on flat roofs

Combined with the sloping roof

The solar collectors mounted on the south to the top of the hill, and the roof slope consistent with the inclination, better reflects the collector and architecture combined effect (Figure 6). Different forms of roof material texture add richness, especially textured glass roof flat plate collector surface to form skylight effect. But if it uses high-rise residential pitched roof shape, roof area is smaller than the flat roof and pitched roof due to the various changes in the body, so that the effective available area is also smaller, generally only a few households to meet top hot water load requirements. Installation technology is more complex to avoid impact on the roofing, insulation, bois, and drainage. According to the relationship between the collector and the roof points, there is overhead, style and down slope embedded surface covered three installation methods.

Figure 6 The sloping roof-mounted solar collector heat instance

Combined with metope

In conjunction with the wall solar collectors and wall combination can reduce the length of the pipeline, but also solve the high-rise buildings due to limited roof area and cannot put collectors' problem. First, the analysis should be carried out when the sun collectors and wall combination. For Panzhihua City, but also to the south wall sunshine is good, but more balconies, bay windows, the walls are divided into smaller areas, collectors can choose between the installation location window walls, the window wall. Something, which is may be a large area of the wall installation that using union tube form.

In conjunction with balcony

Flat-plate collector plate appearance and balcony railing similar to the vacuum tube and the grid-like texture is similar to the balcony railing. The collector and balcony bar coordination, increasing the market for color, texture, form a sense of rhythm, is more suited to the combination

of high-rise residential. In consideration of the aesthetics, the solar collectors in general and balcony railings (board) parallel or install a larger inclination. The solar radiation collector would be less acceptable to some, should be considered in the design of this adverse effect (Figure 7)

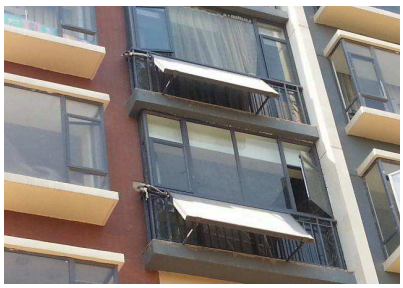

Figure 7 Examples of a district collector balcony

In conjunction with grill

Tend to be reserved for high-rise residential air conditioner outdoor unit design position and cover with a wooden or metal grille. Vacuum tubes and grille texture similar architectural design can leave the position of a collector tube installed in the vicinity of the air conditioner bit. Decorative grille and air integration does not increase the amount of facade elements (Figure 8).

In conjunction with floating panels, decorative frame

Vacuum tube solar collector combined to form an array of floating panels, frame mounting, forming a strong sense of rhythm, solar collectors play a shading effect, but also form a rich shade variations, roof trusses overhead space can become a resident of activities. (Figure 9).

Figure 8 Examples of grille with

Figure 9 Demonstration and application of a plot

Conclusion

When accelerate the process of high-rise residential solar panels with integrated design applications, there are two main issues restricting the development of solar collectors and high-rise residential appearance of the integrated design. On the one hand, the solar collectors on the market, this is poor fitting with the architectural appearance [3]. On the other hand, the importance of the architect solar hot water system has not been designed to understand the existing solar hot water system products is still lacking. Therefore, architects need to gradually increase the emphasis on subjective solar hot water system, which was used as one of the elements of architectural design[4]; addition, the development of solar collector products not only pay attention to improve product performance, but also the architectural requirements should be changed type and new product development.

References

[1] Zhangxishun. Construction technology of integration of solar energy and building. [M]. China State Construction Engineering Press,2014.04(16).

[2] Panzhihua City, Housing and Urban Planning and Construction Bureau. Panzhihua City, Housing and Urban Planning and Construction Bureau Notice on accelerating the civil applications of solar hot water systems, (2)

[3] ZhuHua,ZhangWingHao. Qinghai Tibetan areas use solar energy development path in this paper [J]. Qinghai social science，2010,(3).

[4] LinBoYu.Modern energy economics [M]. BeiJing ： Chinafinancial and economic publishing house，2007.

[5] LiuJianMing. Solar thermal power generation technology [M]. BeiJing ： Chemical Industry Press，2012.04(1).

Advanced Materials Research Vols. 986-987 (2014) pp 669-672

doi:10.4028/www.scientific.net/AMR.986-987.669

System optimization model and path analysis for sustainable development of coal industry

Xiaoxia Yu [1, a], Jianguo Gao [1, b] and Yizheng Liu [1, c]

[1]Faculty of Land Resource Engineering, Kunming University of Science and Technology, Yunnan 650093, China.

[a]274420797@qq.com, [b]335150686@qq.com, [c]237706109@qq.com

Keywords: Sustainable development, optimization model, coal industry

Abstract. China's increasing demand for energy, the energy development and utilization patterns of traditional high exploitation, high emission and low use, not only caused a serious waste of resources and environmental damage, but also is difficult to meet the needs of economic development and facing the industry crisis of survival. Entered a new period of development, the coal industry how to get out of a resource conservation and production intensive road of sustainable development becomes an important strategic task. In this paper, by constructing and using efficiency of coal resources optimal allocation model and path analysis for the sustainable development of coal industry, circular economy, as a kind of advanced development model to promote the coordinated development of resources, environment and economy, becomes the inevitable choice of the coal industry to explore a new road to industrialization.

Introduction

According to the related statistics data, expected by 2030, fossil energy including oil, natural gas and coal still occupies the mainstream energy status in the world. Especially for coal resources, the total amount of coal resources that at the present stage of China possession is among the world top, and it belong to the world's largest producer and consumer of coal resources supported by the current technical conditions[1-2]. From the perspective of one-time energy consumption structure, the coal resources consumption proportion in primary energy sources in total consumption always control the proportion of over 70%, and this trend will not change in a certain period of development. In order to ensure the sustainable development of the modern economic society, except for making full use of clean and renewable energy, it is also very important that based on the circulation economic perspective to explore the sustainable application of primary energy sources in measures. Combining with the development of coal industry, model and strategic analysis should be build for the sustainable development of the coal industry under the circular economy[3-4].

The necessity of the coal industry to develop circular economy

The coal industry to develop recycling economy is to realize the sustainable development strategy. The opening of the UN climate change conference in Copenhagen, it marks a green, low carbon economy as the theme of the new development mode is sweeping the globe. China's economy accounts for about 7% of the world economy. However, the yearly consumption of coal accounts for 40% of the world and CO2 emissions account for 18% of the global total. China is already one of the world's largest emitter of carbon. That's a tall order for China, which puts forward to 2020 carbon dioxide emissions per unit of GDP than in 2005 decreased by 40% to 45% and the primary energy consumption of non fossil energy ratio reaches 15%. China’s "Twelfth Five Year Plan" clearly pointed out the need to accelerate the construction of resource-saving and environment-friendly society, save energy, reduce greenhouse gas emissions intensity, the development of circular economy, promote low-carbon technologies, actively respond to climate change, promote economic and social development in harmony with the population resources environment, and walk the road of

sustainable development. Coal as the important basic energy in China, we must change the mode of development, control the total quantity of coal, vigorously develop circular economy, accelerate the clean production and utilization of coal, promote the coal industry to achieve "green development". That's China's strategy development direction according to optimize energy structure, fulfill commitment on carbon emission reduction and actively respond to climate change.

The development of circular economy of coal industry is the fundamental way outof environmental pollution. For a long time, the serious ecological problems brought by large-scale and high strength development of coal resources and energy production-consumption structure based coal coke thermal power. First of all, coal annually produces a lot of poisonous gases methane and coal direct combustion emissions, as well as some gangue spontaneous combustion caused serious air pollution. Second, the surface subsidence caused by underground mining area already amounted to 4.0 * 1010 m^2, resulting in a large number of farmland abandoned, village forced relocation, seriously affecting the development of mining economic and regional economy. In addition, coal mining serious damage to water resources. Ever year, the national coal mine water is discharged about 2.2 * 109 m^3, which utilization rate is less than 30%. However, the coal mining area of the underground water level falling, causing parts of human and animal drinking water spare hard, severely affected agricultural production. Also, the annual production of coal gangue is 1.5 × 108 t, which occupy land more than 1.2 x 108m^2 and increase the rate at 2 × 106 ~ 3 × 106 m^2 every year[5].

In order to change this situation, development and utilization of coal resources must be based on the core of circular economy, promoting clean coal production, circulation efficiency and energy-saving emission reduction, the exploitation and utilization of the demand for natural resources and ecological environment will reduce to the lowest degree with minimal resource consumption.

The development of circular economy is an important measure to improve the economic efficiency of coal enterprises. Coal resources as the exhaustible resources, once be exploited, the physical form will be permanently lost resources. Non-renewable characteristics determines the scarcity of coal resources; nevertheless, circular economy is a powerful weapon to solve the scarcity of resources. To the recycling of resources as the basic form of circular economy, it changes the traditional "resources-products-pollution discharge" as the process of economic form, through the progress of science and technology to fully explore the added value of coal products, coal gangue, coal bed methane generated in the traditional coal production and mine water "waste". It forms a new economic growth point that waste to treasure.

In recent years, China has been accelerating the reform of the coal market, creating a good development environment to coal industry and promoting increased economic benefits of trade[6]. However, to improve the economic benefits of the current coal are heavily dependent on coal production capacity expansion and the coal price promotion. Therefore, endogenous growth momentum is insufficient. So, the development of circular economy in coal enterprise, change from the exploitation of resources and primary processing to the resources development, deep processing, has become an important guarantee for improving the economic efficiency and market competitiveness.

System optimization model for sustainable development of coal industry

Based on the concept of sustainable development system of the coal industry and to maximize the net effect by using the value of coal resources, coal industry is the important way of sustainable development. Therefore, construction and utilization of coal resources and optimal allocation model has important realistic value.

Within a certain time T, to maximize the net benefit value to get the discount with the resources use, and to meet the constraints of sustainability, namely the final make production possibility set a collection at the beginning of all productive. Belongs to the non-renewable resources of coal resources, considering the intergenerational equilibrium using non-renewable resources, mining rate of non-renewable resources should not be greater than its development reserves growth rate, or less

than to seek alternative renewable resources replacement rate. Non-renewable resources in the net benefits for t years of exploitation are as follows:

$$E_t = P_t Y_t - c_t(Y_t,\ X_t) - W_t Y_t \tag{1}$$

Refer with: E_t. Net benefit value, P_t. Resource unit price, X_t. Resources exploitation for t years, $c_t(Y_t,\ X_t)$. Resources exploitation cost for t years, W_t. Resources exploitation quantity change unit rents and royalties.

Non-renewable resources of the optimal model for mining system as follows:

$$\max E = \int_0^T E_t e^{-\rho t} dt \tag{2}$$
$$\text{s.t } setZ_0(k_0,\ L_0,\ X_0) \subset setZ_T(k_T,\ L_T,\ X_T)$$
$$Y_t \le X_t \le Q_t$$

Refer with: ρ. Discount rate, $Z_0(k_0,\ L_0,\ X_0)$. Initial production possibility set, $Z_T(k_T,\ L_T,\ X_T)$. Final production possibility set, L. Labor capital, K. Material capital, Q .Available amount of substitution for non-renewable resources.

The optimal mining mathematical model of non-renewable resource can be used to describe the general nature of sustainable utilization of non-renewable resources[7]. The pursuit of the rational use for non-renewable resources, so that it make the net benefit maximization of resources. With the finite time instead of the maximization of the infinite time, model achieves the sustainable development of coal resources by principle of precession rolling forward or dynamic methods.

Path analysis for sustainable development of coal industry

(1)The aid of the relevant laws and regulations of the repairs, ensure the sustainable development of the coal industry under the Perspective of circular economy can always be in a good policy and legal environment to support them:

First, for the coal industry needs to be revised policies and regulations, improve the audit system to maximize of coal production and operation permit, the reasonable control of enterprise access. At the same time, related to coal enterprises involved in the process of production and operation of coal resource consumption and pollutant emissions issues should be implemented to the specific legal provisions and standards, and clearly the appropriate liability regime. On this basis also need the help of integrated applications on a variety of new technology, new materials and new technology, the progressive realization of the optimization and upgrading of the entire coal industry.

Second, the need to combine our corporate social functions related to the separation of policy and requirements for coal companies to do the separation process of social functions performed significantly advance its purpose is reasonable to reduce the production and management of coal enterprises in the process undertaken by the social and historical burden problem.

Third, the need to build the cumulative of aging converting coal industry funding system, which is part of the application should be implemented in special funds to take over the work of the development of the coal industry among, for the development of coal resources depleted mines, through the construction of infrastructure and the implementation of the fostering of fiscal transfer payment policy in application, to accelerate its economic restructuring efforts and the process of economic transformation and development.

(2)With the aid of to give full play to economic leverage, full development based on the coal industry chain of circular economy.

First, formulate preferential fiscal and tax policies. For our country, by the presence of a long and continuing influence on policy under low background of the planned economy, the vast majority of coal enterprises with limited sources of development funding, to ensure that this part of the business cycle in the process of developing sustainable economic development able to have adequate sources

of funding should be based on financial regulation and taxation as a means of control, to ensure the effectiveness of the tax treatment through price subsidies, financial discount, pre-tax loan loss allowance and a variety of ways.

Second, it should be combined with coal production and management enterprise actual situation, to be effective against the coal companies to improve and perfect the existing cost accounting system, by effectively increasing the environmental costs through cost-effective handling of the price mechanism, with coal enterprises environmental awareness effectively strengthened, to ensure sustainable development of coal enterprises with economic development and ecological environment.

Third, by the reasonable control of emissions from waste coal companies to ensure that the drainage plan and pollution indexes were able to get effective implementation to ensure that the cost of coal enterprises themselves sewage pollution has been effectively implemented.

Conclusion

As we all know, energy is the human society to stabilize the foundation of survival and development. Under the process of global economic integration and growing urbanization continues to expand the scale of the background action, communication and exchange of energy issues for many aspects of economic, political, military and cultural world between the various countries and regions attention is only to rise in. In the background of this development, the development of circular economy and promote the process of the national economic and social development can be said to be the key measures and strategy to achieve conservation of resources both in technical and economic basis of reasonable and feasible and the environment protection purposes, the key for the development of disposable resources such as coal energy is undoubtedly a class is crucial. In conclusion, the article for the sustainable development path issues related to the coal industry and made a brief analysis of the model and description, hoping to provide some help for future reference and to carry out related research and practice work.

References

[1] Linna Hu. The Mode Design and the Cultivation Mechanism of the Composition Coal Circular Economic Industrial District. *Science and Technology Management Research*, vol. 31(2011) no. 12, p. 195-198.

[2] Xueke Yang. Perfecting the accounting system to promote the development of circular economy of coal. *China Management Informationization*, vol. 14(2011) no. 24, p. 9-10.

[3] Huiren Bai. The Mode Design and the Cultivation Mechanism of the Composition Coal CircularEconomic Industrial District. *Technoeconomics & Management Research*, (2007) no. 2, p. 123-124.

[4] Lei Zhang, Hongmei Wu. Sustainable Development of Shanxi's Coal Industry. *Reformation &Strategy*, vol. 26(2010) no. 1, p. 129-131.

[5] Minggao Qian. On sustainable coal mining in China. *Reformation & Strategy*, vol. 35(2010) no. 4, p. 529-534.

[6] Bin Yan. To realize the sustainable development of China's coaleconomy strategy. *China Business Monthly*, (2011) no. 12, p. 19-20.

[7] Yuqing Wang. Development Countermeasure of Coal Economy From Perspective of Sustainable Development. *Coal Technology,* vol. 32(2013) no. 5, p. 5-6.

Advanced Materials Research Vols. 986-987 (2014) pp 673-676

doi:10.4028/www.scientific.net/AMR.986-987.673

Research on the Workshop Structures of Aluminum Potroom on High Temperature Condition

Bo Sun[1,a], Tao Ding[1,a], Yiming Li[2,b], Qianbo Zhao[1,a], Mingxiao Zhao[1,a]

[1]School of Mechanical and Power Engineering, Harbin University of Science and Technology, Harbin, 150080, China

[2]Department of Basic Teaching and Research, Harbin Finance University, Harbin, 150030, China

[a]email: sunbosting@126.com, [b]email:liyiming1682@163.com

Keywords: Aluminum potroom; Natural Ventilation; Workshop Structure; CFD

Abstract. This paper aims to eliminate the danger of high temperature in the aluminum potroom by natural ventilation. According to the history of aluminum potroom, two different workshop structures are proposed to improve the natural ventilation effect. The first structure is called the inner-partition potroom, which contains blind grilles located at certain distance from the two sides of electrolytic cell. The second structure, called the large-opening potroom, directly set up a large opening on the outer wall of aluminum potroom. Two structures are compared with the aid of CFD simulation, and the physical model is established based on the field measurement. The velocity and temperature fields are simulated under three different outdoor conditions. By the comparative analysis of temperatures on the electrolytic cell and operating area, this paper indicates the large-opening potroom has better performance on high temperature condition.

Introduction

The main equipments in the aluminum potroom includes the electrolytic cell and other auxiliary equipments, which equipments as heat source release constantly heat and pollutants into surroundings environment[1]. The superfluous heat and pollutants enter into working area will cause heat dissipation problem of electrolytic cell and severe working environment, which make a negative effect on product quality and work efficiency [2]. In China, the hot potroom usually uses natural ventilation to eliminate superfluous heat and pollutants and provide fresh air [3]. The workshop structure directly affects natural ventilation performance. The current structure that contains blind grilles located at certain distance from the two sides of electrolytic cell, shown in Figure 1, is called inner-partition potroom in this paper.

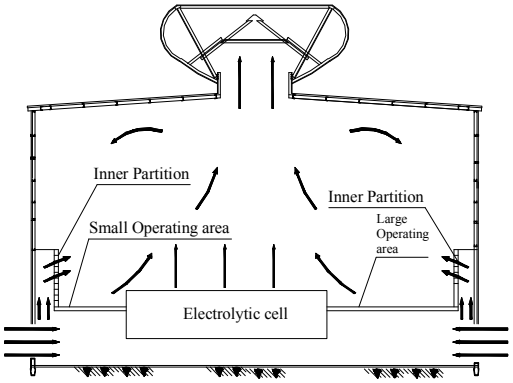

Fig.1. The inner-partition aluminum potroom

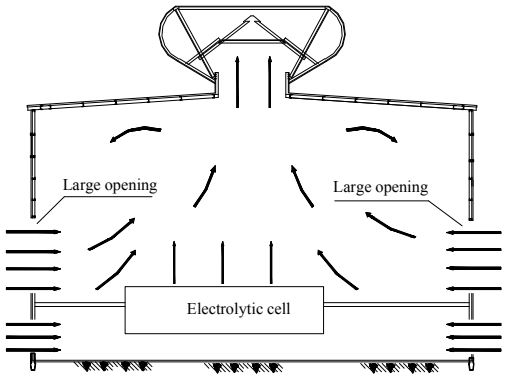

Fig.2. The large-opening aluminum potroom

When fresh air enter the potroom from the opening at the bottom of outdoor, most fresh air flows through the surfaces of electrolytic cell by the way of fixed grilles and take away superfluous heat and pollutants discharged by skylight. The rest fresh air enter workshop through the inner partition. This kind of structure can effectively reduce the surface temperature of cell and improve the product quality [4]. But, in some hot region, this structure may make high temperature operating area where workers must stay some time. So this paper proposes the large-opening potroom shown

in Figure 2, which leads more outdoor air into the operating area by enlarging the opening of second floor. In the paper, CFD method is used to analyze ventilation effects in two kinds of workshop structures.

Simulation model

Since the aluminum potroom has complicate structure and many kinds of equipment, it is necessary to simplify the physical model properly [5]. This paper constructs the physical model about 300KA electrolytic cell based on the field measurement in the aluminum factory of shanxi qingjian. The details of objects in the model are shown in Table 1, which displays all the sizes and parameters. For the large-opening potroom, the opening on outer wall is from the ground of first floor to the elevation 8 meters, which will not affect the normal operation of crane. In a practical application, the large opening on the second floor can be considered installing the electric blind or shutter on it to keep the workshop from rainwater.

Table 1. The sizes and parameters for all the objects

Object	Name	x (m)	y (m)	z (m)	Parameter
Wall	Workshop	27	18.21	6.2	
Blocks	Beam	0.25	0.6	6.2	
	Oblique bus	0.46	1.6	1.6	
	Upright bus	0.46	1.5	0.38	
	Level bus	15.78	0.534	0.38	
	Feed box	13.28	1.4	0.45	
	Tip	0	1.334	2.015	Heat:4570.14W
	Electrolyte layer	14.65	0.3	2.015	Heat:29611.46W
	Aluminum layer	14.65	0.2	2.015	Heat:15410.05W
	Carbon layer	14.65	0.45	2.015	Heat:40791.30W
	Insulating layer	14.65	0.384	2.015	Heat:2417.26W
Opening	Air inlet	4.8	0	6.2	
Partitions	shield plate	14.65	1.1	1.1	
	Small operating area	3.48	0	6.2	
	Large operating area	8.87	0	6.2	
	Rib plate	0	1.334	0.38	
Resistances	Grille of cells	14.65	0	1.41	ξ=0.5
	Inlet window	0	2.4	6.2	ξ=2.37
	Outlet window	2.7	0	6.2	ξ=1.42

In simulation, standard k-ε turbulent model and discrete ordinate radiation model are chosen to predict the velocity and temperature fields in the workshop [6] [7]. To consider the potroom locates in hot region, the outdoor air temperature selects a extreme value 50℃ as the high temperature condition. The outdoor wind speed chooses 0, 2m/s and 4m/s representing real outdoor conditions named Condition Ⅰ, Condition Ⅱ, and Condition Ⅲ, and the wind direction always keeps perpendicular with the large operating area side of potroom.

Simulation results and analysis

According to the above simulation model, the velocity and temperature fields in two workshop structures are obtained. The temperature distributions under Condition Ⅰ are shown in Figure 2. The results display the thermals appear in two structures, which cause the obvious temperature gradient in the whole workshop. By comparison, the temperatures in small and large operating area

in the large-opening potroom are lower than in the inner-partition potroom, because more fresh air flows into the workshop without the resistance of inner partition. But because of the resistance of inner partition, more fresh air enter in the first floor of inner-partition potroom and then flow through the surfaces of electrolytic cell to take more heat away by thermal. So the temperatures on the cell surfaces in the inner-partition potroom are lower than in the large-opening potroom. Meanwhile, the temperature distribution in the inner-partition potroom is more uniform in that the interference from fresh air is less. Owing to space constraints, the other temperature and velocity distributions do not discuss in this paper.

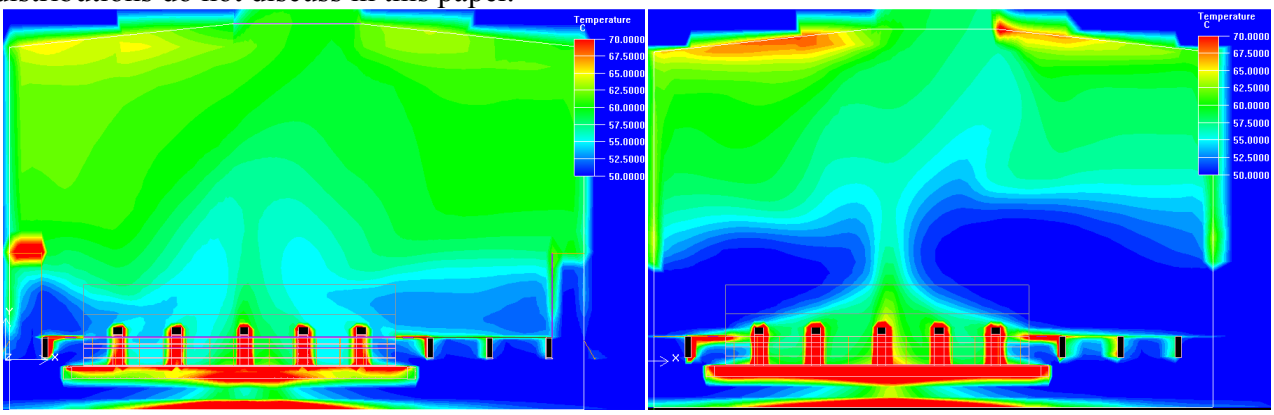

(a) The inner-partition potroom (b) The large-opening potroon

Fig.2. Temperature distribution in the potroom

The operating area worker must stay some time, includes small operating area, large operating area and the operating area between electrolytic cells. To fully describe the temperatures of operating area, the paper gives the air temperatures on the middle section between cells by selecting 17 data points about 0.5m apart from 1.8 meters above the operating area, which are shown in Figure 3. Figure 3(a) indicates that the temperatures in small and large operating area with large opening are lower than with inner partition because of more fresh air, but the temperatures in the middle part are higher since hot airflow intensely passes the middle region into the upper workshop. Figure 3(b) shows that the temperatures in the large-opening potroom are mainly lower than in the inner-partition potroom because outdoor fresh air through the passage between cells takes more heat away. At the same time, the highest temperature in the inner-partition potroom appears the region deviating leeward side due to the outdoor wind interference. Figure 3(c) has the same tendency with Figure 3(b), but only the highest-temperature region in the inner-partition potroom is closer to leeward side and the temperature decline in the large-opening potroom is greater on account of more wind speed. Comprehensively, all the air temperatures of operating area in two kinds of structures decrease with the increasing of outdoor wind speed.

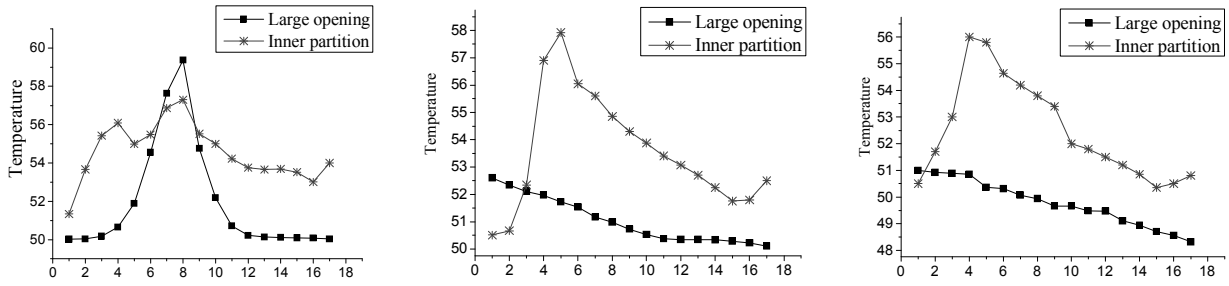

(a) Condition Ⅰ (b) Condition Ⅱ (c) Condition Ⅲ

Fig.3. Comparison of air temperatures of operating area

Table 2 displays the temperatures on the surfaces of electrolytic cell. According to the results for Condition Ⅰ, the temperatures on cell surfaces in the large-opening potroom is slightly below them in the inner-partition potroom, and the reason is that fresh air cooling the cell enter the first floor less without the resistance of inner partition. For Condition Ⅱ, the temperatures on the Aluminum, Electrolyte and Carbon layers with the large opening is higher than with the inner partition, but

those on the other objects is lower. The cause for this is that the Aluminum, Electrolyte and Carbon layers are mainly cooled by thermal from the first floor which is destroyed by outdoor wind, and the other objects can be directly cooled by the transverse airflow from the second floor wind. As outdoor wind speed increases, which results in strong transverse airflow in all floors, only the Aluminum layer has higher temperature in the large-opening potroom according to Condition Ⅲ. On the whole, the temperatures on the cell surfaces in large-opening potroom is higher when outdoor wind has small speed, but the highest temperature is also below 400℃ the limit on the electrolytic cell.

Table 2. Temperatures on the electrolytic cell surfaces Unit: ℃

Condition	Structure	Position	Layer				Equipment	
		Object	Aluminum	Electrolyte	Carbon	Insulating	Shield plate	Feed box
Ⅱ	Inner partition	Highest	344.214	317.926	366.953	286.754	366.953	125.939
		Average	292.543	247.562	238.641	118.591	142.714	85.4628
	Large opening	Highest	337.058	380.873	321.183	292.089	380.873	124.288
		Average	299.740	269.085	259.298	127.914	149.122	85.4708
	Inner partition	Highest	343.621	352.791	319.484	301.878	352.791	142.934
		Average	285.860	224.197	241.435	115.944	132.707	84.9818
	Large opening	Highest	396.040	390.791	340.279	230.027	230.027	138.738
		Average	299.278	255.460	249.800	112.653	127.658	82.5246
	Inner partition	Highest	393.784	389.588	317.237	264.464	389.588	149.180
		Average	283.486	227.943	235.811	105.784	137.925	84.6380
	Large opening	Highest	362.910	373.015	316.891	207.590	373.015	128.736
		Average	274.633	236.553	224.416	97.2570	110.531	81.3031

Conclusion

Based on the analysis of the simulation results under three conditions, the potroom with large opening on the outer wall generally has lower temperature in the operating area. Although the temperatures on the electrolytic cell surfaces are higher than them in the inner-partition potroom, the highest temperature is also below the limit 400℃. At the same time, the cooling effect for electrolytic cell will better in the large-opening potroom with the increasing of outdoor wind speed. In conclusion, the workshop structure of aluminum potroom on high temperature condition should be designed as the larger opening on the outer wall to improve natural ventilation.

References

[1] Nancy J.Holt, Nigel M.Anderson. Ventilation of Potrooms in Aluminum Production. [J]. TMS Light metals, 1999, 263~268.

[2] W.Haupin, H.Kvande. Thermodynamics of Electrochemical Reduction of Alumina. [J]. TMS Light metals. 2000, 379~384.

[3] Wan Mu and so on. Analysis of Affecting Factors on Natural Ventilation in Aluminum Electrolytic plants. [J]. Journal HV&AC, 2006 (10), 79-81.

[4] Wan Mu, Zhan Xutao, Li Xiaodong. Experiment on Coefficient of Local Resistance for Perforated Interior Walls in a New-style Aluminum Potroom. [J]. HV&AC, 2006(7), 100-102.

[5] Wang Yinfu and so on. Spot Measurement and Analysis of Natural Ventilation in Aluminum Potroom. [J]. Light metals, 2005 (8) 80-86.

[6] J.Bos, G.Bouzat. Numerical Simulation, Tools to Design and Optimize Smelting Technology. [J]. TMS Light metals.1998, 393~402.

[7] Marc Dupuis. 3D Modeling of the Ventilation Pattern in an Aluminum Smelter “Potroom” Building Using CFX-4. [J]. CIM Light Metals, 2001, 172~183.

Advanced Materials Research Vols. 986-987 (2014) pp 677-680

doi:10.4028/www.scientific.net/AMR.986-987.677

The research on seismic performance of tower under icing condition

Yuchen TIAN[1], Weijian XUE[1],Ying ZHOU[1],Lan JIANG[1, a]

[1]College of Electrical Engineering and New Energy, China Three Gorges University, Yichang, 443002, China

[a]email:jianglanctgu@163.com

Keywords: Transmission tower icing; The dynamic Characteristic: seismic performance

Abstract. Southwest area of china is the zone of the transmission lines which often happens icing disaster. It is also an earthquake-prone area, also influenced by the interaction between ice and earthquake. This article uses the finite element method (fem), establishing three-dimensional model for steel towers in southwest china, to analyze the dynamic performance of the ice condition and the analysis of seismic action. The aim is to get internal forces for steel towers under the action of earthquake and deformation law along with the change of ice thickness.

Introduction

High voltage grade of transmission lines is the lifeline engineering of the national project. China is an earthquake-prone country. The southwest of china, which located on the earthquake fault zone, its power transmission facilities should be considered more on its safe operation. Only in Yunnan province from 1993 to 2003, the losses of electric power facilities in all previous earthquakes are more than 218 million [3]. The earthquake in Wenchuan brings 185lines to rest [4].With the power grid construction is going to have large capacity, high pressure, the tower of the seismic performance should take enough attention to research and design.

In addition, the congelation or frequent climate region in southwest China easily makes the tower and conductor frozen in winter. Only in Guizhou province in 2008, 184875 towers collapsed [5].Tower, under the condition of icing, its dynamic characteristics of the great changes have been taken place [1].

This paper takes a type glass tower in southwest China as an example, with the help of finite element method, established a three-dimensional finite element analysis model for iron tower, using the equivalent density method considering ice tower, seismic response analysis of structure, discussed the influence of ice thickness on the structural seismic performance.

Engineering background

In this paper, we choose a 500kV transmission line tower which has been built in the west high altitude localities as an example to analyze. The height of the tower is 55.3 m, and the practical height is 50m. the schematic is shown in figure 1(a).

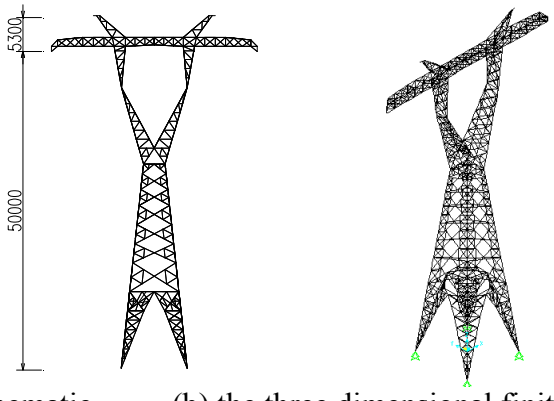

(a) Plane schematic (b) the three dimensional finite element model

Fig.1 The diagram of the transmission tower

The tower, assembled by Q235 angle steel could be separated to three parts: the first tower, the tower and the tower legs. There are three main types of materials which can constitute a tower bar: advocate material, oblique materials and auxiliary materials, respectively, the Angle steel models could be adopt by ∟160 x 12, ∟80 x 6 and ∟45 x 4. There is a bolt between rods and bars; the finite element model is shown in figure 1(b).

Calculation model

Establish the three-dimensional finite element analysis model of the tower by using SAP2000 as finite element analysis tool to. According to the connection characteristics of tower structure, advocate material, oblique materials and auxiliary materials used space beam element. The auxiliary material bar bending moment has been put in the end. In addition to both computational efficiency and computational accuracy requirements, we should divide the stab about 1 m into the unit. Steel [6], [7] ice calculation parameters are shown in table 1:

Table 1 The physical properties of the material indicators

material	E (N/m2)	υ	α(cent degree)	ρ(kg/m3)
steel	2.06×10^{11}	0.3	1.2×10^{-5}	7850
Yu Song ice	5.2×109	0.3	—	900

We do not consider the tower icing contribution to the structural stiffness [1] in the analysis .The ice is calculated by using the equivalent density method for structural dynamic characteristics. The influence of equivalent density could be calculated according to the equation(1).

$$\rho_o = \frac{A_i\rho_i + A_s\rho_s}{A_s + A_i} \tag{1}$$

ρ_o is the equivalent density，kg/m^3 ；

A_s , A_i is the area of the steel bar and ice, m^2；

ρ_s , ρ_i is the density of the steel bar and ice, kg/m^3 .

Adopting finite element analysis software SAP2000, establishing the three-dimensional truss model, using the subspace iteration method, the dynamic characteristics analysis and using the mode superposition to response spectrum method, seismic response analysis of structure.

Dynamic characteristic analysis

Dynamic characteristic analysis is the basement of the dynamic analysis. Before the seismic performance, power transmission tower's dynamic characteristic analysis should be first. Particularly, to calculate tower's dynamic characteristic, we could ignore the weight of ground wire. Its weight could be put into the load only.

Table 2 The top 3 order natural frequency of vibration Hz

frequent	ice free	5mm	10mm	15mm	20mm	25mm	30mm
X	1.2329	1.1218	1.0313	0.9559	0.8919	0.8367	0.7886
Y	1.2937	1.1776	1.0829	1.0041	0.9370	0.8792	0.8287
Torsion	1.6100	1.4591	1.3373	1.2365	1.1513	1.0782	1.0146

It can be seen from figure 2，, the structure of the first three order vibration frequency of the vibration mode include X to translation, Y to translation and torsional as a whole. With the increase of ice thickness structure, the corresponding frequencies decrease.

Spectrum analysis

Mode-superposition response spectrum method is used for tower analysis under the action of the more severe earthquake internal force and deformation. Assuming that the region seismic fortification intensity of 7 degrees, design earthquake acceleration of 0.1 g. A maximum horizontal earthquake influence coefficient is 0.08.The second field, earthquake are grouped into the second group, site characteristic period of 0.4 s. Analyze the tower structure to seismic action in X and Y to

the earthquake under the action of displacement value and the counteracting force. X to the earthquake under the action of overall structure deformation as shown in figure 2 (a), Y to the deformation of the structure under seismic loading are shown in figure 2 (b) .Displacement value trends along with the change of ice thickness as shown in figure 3.

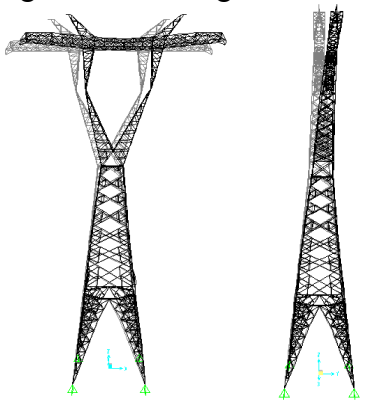

(a) (b)

Fig.2 Seismic deformation

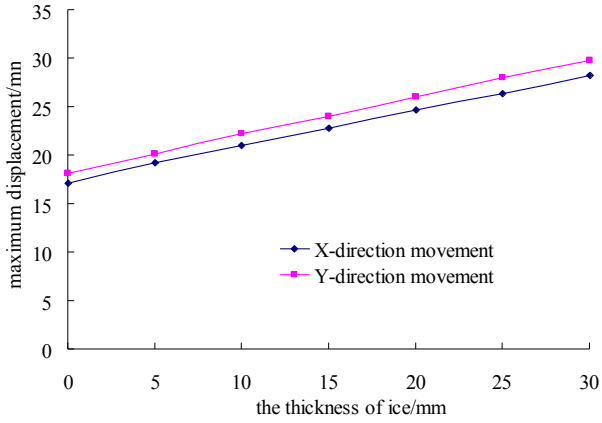

Fig.3 The value of seismic deformation

It can be seen from the figure 2, under the action of earthquake, the structure of each position displacement size associated with the height from the ground. The greater the height from the ground, the greater the displacement value is. It can be seen from the figure 3, Y to the displacement value is slightly greater than X to the displacement, Y to the stiffness is larger than X to the stiffness. With the increase of ice thickness, the maximum of tower displacement increases, and it approximately equals to linear relationship.

For tower, marked four bearing Numbers for A, B, C, D, as shown in figure 4.And statistics when ice thickness is not at the same time, each bearing in X and Y to the earthquake in all directions under the action of reactions, as shown in table 3.

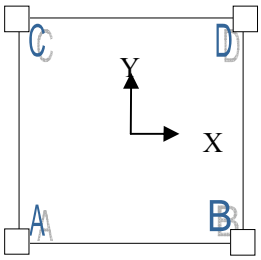

Fig.4 The support of tower

Table 3 Force of support

Bearing Serial number	The earthquake direction	direction	The thickness of the ice/mm						
			0	5	10	15	20	25	30
A	seismic action(X)	X	4.747	5.685	6.659	7.714	8.850	10.104	11.477
		Y	3.620	4.207	4.786	5.404	6.055	6.716	7.435
		Z	26.640	30.616	34.456	38.561	42.879	47.167	51.096
	seismic action(Y)	X	4.127	4.714	5.336	5.971	6.681	7.407	8.159
		Y	4.765	5.554	6.436	7.343	8.374	9.659	10.962
		Z	28.956	32.678	36.618	40.446	44.841	49.315	53.776
B	seismic action(X)	X	3.890	4.576	5.269	5.985	6.763	7.559	8.429
		Y	3.311	3.794	4.247	4.719	5.204	5.697	6.258
		Z	24.830	28.187	31.272	34.481	37.821	41.064	44.687
	seismic action(Y)	X	3.481	3.998	4.536	5.078	5.658	6.229	6.817
		Y	4.575	5.381	6.239	7.129	8.104	9.325	10.566
		Z	27.240	30.834	34.558	38.024	41.990	46.041	49.993

C	seismic action(X)	X	4.949	5.938	6.957	8.035	9.203	10.471	11.863
		Y	3.815	4.449	5.079	5.739	6.433	7.138	7.893
		Z	27.399	31.588	35.622	39.881	44.359	48.853	53.785
	seismic action(Y)	X	3.457	3.935	3.708	4.884	5.382	5.896	6.431
		Y	3.586	4.167	4.568	5.351	6.022	6.698	7.422
		Z	25.616	28.742	31.663	34.735	38.007	41.181	44.222
D	seismic action(X)	X	3.461	4.071	4.686	5.336	6.021	6.724	7.479
		Y	2.788	3.154	3.489	3.842	4.209	4.561	4.956
		Z	2.351	26.589	29.386	32.321	35.356	38.206	41.413
	seismic action(Y)	X	2.982	3.343	3.709	4.044	4.431	4.807	5.173
		Y	3.452	3.987	4.568	5.157	5.810	6.478	7.166
		Z	25.544	28.558	31.663	34.475	37.757	40.910	43.922

It can be seen from table 3, X to the earthquake, the support to the reaction force is less than X to Y reaction, as the change of ice thickness, the ratio showed a trend of expansion. X under the action of earthquake, bearing A and C that X to the reaction force is greater than B C support that X to the reaction; Y to the earthquake, the A and B bearing Y to the bearing reaction force is larger than C D that Y to reaction. The reasons for this phenomenon are limited by the response spectrum method. Overall, with the increase of ice thickness, the bearing under the action of earthquake reaction are also increasing.

Conclusion

Through the analysis, we can get the following conclusion:

1, the tower in the first three order vibration mode respectively characterized by X to translation, Y to translational and torsional. With the increase of thickness of ice, each order frequency is on the decline.

2, under the effect of more severe earthquake, the displacement in the Y to the displacement value is slightly greater than X value that is slightly greater than X Y to the stiffness of the stiffness.

3, with the increase of ice thickness, tower under seismic action of reactions are also increasing.

References

[1] Du Yue; Jiang Lan; Zhou Yuxin; Li Qiaorong; Wang Tairan; Pan Zijun. Research on Dynamic Characteristics of Large Span Transmission Tower in Icing Environment，Advanced Materials Research Vols.756-759（2013）:0155~0159

[2] Li H N，Bai H F. State-of-the-art review on studies of disaster resistance of high-voltage transmission tower line systems [J].China Civil Engineering Journal.2007, 40(2): 39-46

[3] Li H N. Transmission tower seismic analysis and design [M]. China electric power press.2009.11

[4]Zhang Z Y, Zhao B, Cao W W .Investigation and Preliminary Analysis of Damages on the Power Grid in the Wenchuan Earquake of M8.0[J].Electric Power Technologic Economics.Vol:20,No.4.Aug.2008

[5]Ruan L L, Du Z J , Su H Y, ELECTRICAL EQUIPMENT .2008 and ice storms in early the Guizhou power industry disaster impact assessment [J]. The Guizhou Meteorological, 2009 Supp 33:89-91

[6] National standards of P.R.C. Code for design of steel structures[S]. China plans to press.beijing:2003

[7]Chen Kequan, Yan Bo, Zhang Hongyan, Zhou Song. Numerical simulation of de-icing on transmission lines under shock load [J] ， CHINESE JOURNAL OF APPLIED MECHANICS.2010,27(4):761-766

[8] PRC National Standard. Code for seismic design of electrical installations(GB50260-2013) [S]. China plans to press.beijing 2013

Advanced Materials Research Vols. 986-987 (2014) pp 681-684

doi:10.4028/www.scientific.net/AMR.986-987.681

Research on the dynamic characteristics of strain tower in heavy icing area based on SAP2000

Shilong WANG[1],Qixiang LIN[2],Ying Qian[3]

[1,2]College of Electrical Engineering & New Energy of China Three Gorges University

[3]State Grid of Hubei Xianning Power Supply Company,Xianning,437000,China

email: ctgulin@sina.com

Keywords: heavy icing area; strain tower; SAP2000; Dynamic analysis;

Abstract. This paper is a further analysis of the strain tower on 1YD - JC4.After making a static analysis of 1YD - JC4 strain tower,we select the best offset point and make a dynamic analysis of it.Based on the finite element analysis software SAP2000, we set up a three-dimensional model of 1YD - JC4 strain tower of 110kv about heavy icing area,and then obtain the first six modal frequencies after making a dynamic analysis . We then draw the response spectrum curve.in the end, we select the safe and economic value of damping according to the curve.

Introduction

The ice disaster damage to the line is mainly to damage the tower , such as tower collapsing, deformation, insulator off. The ice disaster has caused enormous loss to the power grid in the year of 2008. After that,State Grid Corporation of China has promulgated new codes and specifications in which we improve the safety level of the important lines,strengthen the vertical strength of lines from external load and internal force calculation conditions , and improve safety coefficient of the tower,[1].Because of this,Yichang Electric Power Survey and Design Institute of Electric Power Co., Ltd has specially designed tower-1YD series which are used in heavy icing area.For the high-rise structures under the control of deformation.We should adapt the appropriate vibration control technology to reduce the deformation and acceleration of the structure[2]. The real tower test is usually needed to do to ensure the safety and accuracy though the really tower test is expensive.So this paper simulate and analyze 110kv 1YD - JC4 strain tower based on the finite element analysis software SAP2000,which has proved reference for the Subsequent transmission tower test simulation, tower optimization and the simulation of disaster prevention.

calculation model and analysis methods

1.1 calculation model

The 1YD series tower is specially designed by Yichang Electric Power Survey and Design Institute Co.,Ltd. according to the actual conditions of Shennongjia heavy icing area. The practical height is 30.0 m,the total height is 37.5m,the weight of the tower is 20.4 t,the horizontal span is 400m and the vertical span is 900m.We take Q345 steel for the main member of tower body and we take Q235 steel for the auxiliary member .the icing thickness is set as 30mm.We set up A three-dimensional model of the 1YD-JC4 tower in the finite element analysis software SAP2000 and all the rods piece use the space bar element. See chart 1.

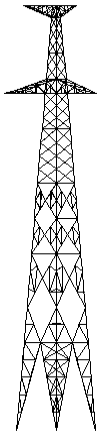

Fig.1 Dimensional model of the 1YD tower

1.2 The load on the tower

The loads of pole tower are generally divided into the vertical loads(The direction perpendiculars to the ground), the transverse horizontal loads(parallel plane along the horizontal direction)and the longitudinal horizontal loads(The vertical plane which is vertical horizontal direction).The vertical loads include the gravity loads of wire, ground wire,insulator strings and fittings,tower self weight loads and the vertical loads in installation and maintenance of which include the gravity loads of workers, tools and accessories and so on.The transverse horizontal loads include the wind pressure of wire ,ground wire ,insulator strings and fittings,the wind loads of tower and tower body and the angel force of the wire and the ground wire on the angle tower . The longitudinal horizontal loads include the unbalanced tension of wire and ground wire(the direction of unbalanced tension of no corner tower is along the line, and the unbalanced tension of corner tower perpendicular the cross arm of the tower),the tension of broken wire and broken ground wire ,the support of the normal force from the ground wire to the tower when the wire breaks and the tight line tension when installing wire[3].

The Circuit parameters :①The wire model is LGJ-240/55,and the ground wire model is JLBIA-120.②The weight of the insulator tension string of wire and ground wire are 500N, 100 N.③The spacer weights 30 N.

(1)Condition 1—The stiuation of the operation situation.The strain tower load combination consists of the minimum temperature, no wind, ice free,and not breaking load （$v=0, T=-20^0C, b=0$）. Ground gravity GB=7246 N ,wire gravity GD=10 310 N, wire pressure PD=3 140 N.

(2)Condition 2—The stiuation of the broken wire situation.Load combination for ice free, calm, off any two phases.Random phase wires broken will produce two kinds of deformation because there are upper, middle and lower three-phase conducting wires.The breakage of random phase wires,upper wire and a lower or two lower wires.The gravity of ground wire GB=7246 N ,not broken wire gravity GD=10313 N.The broken phase wire gravity GD=5422 N,and the wire gravity TD=14294 N.

(3)Condition 3—The stiuation of the broken ground wire situation.Load combination consists of ice free, calm, not broken wires , broken in any one ground wire.wire gravity GD=10310N,Ground wire gravity GB=3723 N,Ground wire tension TD=10593N.

(4)Condition 4— The stiuation of the installation I situation.Lifting the upper wire.And the load combination for a corresponding wind, ice free.（V=15 m/s, T=-10℃，b=0）.Ground wire gravity GB=7 248 N,ground wire pressure PB=900 N,Wire gravity GD=10 310 N,wire pressure PD=1 413 N.When hanging the wire,wire gravity GD=27 955 N,wire pressure PD=6 284 N.

(5)Condition 5—The stiuation of the installation II situation.Lifting the lower wire.The load combination is the same to the condition 4.Ground wire gravity GB=7 248N,ground wire pressure PB=900N,wire gravity GD=10310N,wire pressure PD=1 413N.When lifting the lower wire,the lower crossarm total gravity GD=14841 N,wire pressure PD=1413N.

We apply the calculated tower load to the 3D model operation to analysis.

1.3 analysis methods

The structural vibration instability of tower under dynamic loading is an important factor of causing tower collapse accident.Therefore, in order to avoid huge economic loss brought by tower collapse accident,it is necessary to grasp the dynamic response of tower unde the effect of the wind loads and the impact loads caused by the earthquake or other reasons and the influence of those dynamic on tower strength based on taking tower strength into consideration in the process of the design[4].

Time-history analysis is a dynamic analysis hose structure is more realistic.Linear time-history analysis is essentially based on the basic to solute dynamic differential equations (1) ,and then obtain the basic size of structural response under the action of dynamic load[5].

$$M\ddot{u}_a(t)+C\dot{u}_a(t)+Ku_a(t)=F(t) \tag{1}$$

In the formula: M—The mass matrix

C—A viscous damping matrix

K—Static structural element system stiffness matrix

$\ddot{u}_a(\mathrm{t})$, $\dot{u}_a(\mathrm{t})$, $u_a(\mathrm{t})$ are the absolute displacement, velocity and acceleration of the nodes, and they are all vector related to time.

A typical modality equation is :

$$\ddot{y}(t)_n+2\xi_n\omega_n\dot{y}(t)_n=\overline{f}(t)_n \tag{2}$$

$\overline{f}(\mathrm{t})_n$ is the modality load

According to the method of solving the differential equation of arbitrary loading solution, we can obtain the approximate solution of load in smaller time increments using the polynomial.

$$\ddot{y}(t)_n+2\xi_n\omega_n\dot{y}(t)_n+\omega_n^2y(t)=R_{i-1}+t\dot{R}_{i-1}+t^2\ddot{R}_{i-1}+\frac{t^3}{6}\dddot{R}_{i-1} \tag{3}$$

Dynamics analysis

When the structure suffers earthquake action,even if the main structural component structure remains elastic deformation,the permanent deformation of secondary structure will dissipate some energy.However ,this part of the energy is difficult to estimate in theory.In the dynamic analysis of structures, the energy dissipation is defined and implemented by damping[5].

The structural damping should be taken into consideration when doing the structure Time-history analysis. In general,Structural damping is defined by the modality damping ratio,and it is the ratio of the modality damping and critical damping.

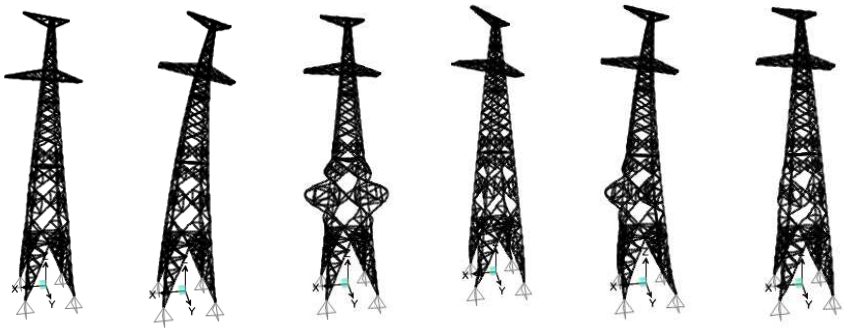

Modality1 Modality 2 Modality 3 Modality 4 Modality 5 Modality 6

Fig 2.1～6 Modality figures

Since we have done the static analysis to the model, we find that the point of 250 is the largest offset.Consequently,we choose the point 250 to do linear dynamic analysis.After running the software,The first six modality graphs(Fig 2) and frequencies can be calculated and they are shown in the following table.

Table 1 The first six frequencies of strain tower

	Modality 1	Modality 2	Modality 3	Modality 4	Modality 5	Modality 6
Frequency(f)	4.11	4.11	7.39	7.72	8.23	8.39

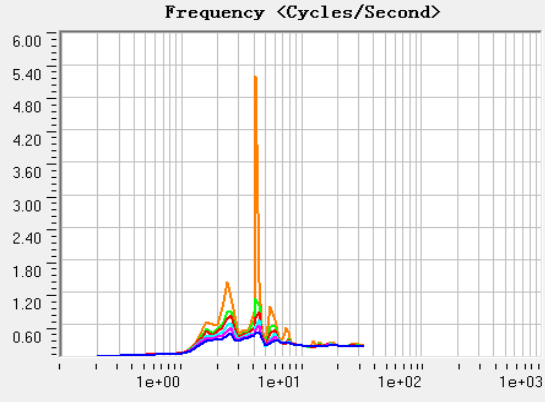

Fig 3.The response spectrum curve

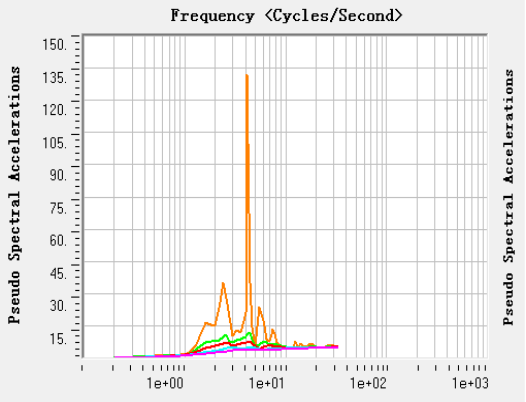

Fig 4. The response spectrum curve

In Fig. 3, the abscissa represents the frequency,and the ordinate shows pseudo acceleration.The software can generate a corresponding response spectrum curve for each value of damping. From the figure,We can see that when the damping value is assigned as 0,the acceleration is the maximum and the curve volatility is very extreme.While the damping values are 0.02, 0.03, 0.05, 0.07, 0.10,the acceleration decreased gradually, and the curve is more gentle.If the damping value is 0.2, 0.4, 0.6,The curves gradually tend to be straightas shown in Fig 4.However,at this time, the anti elastic ability of the structure is very high, and the economic investment is very large.Therefor, the most economical way is that the structure vibration in safe condition.In conclusion,taking economic and security into consideration,the modality damping ratio of steel structure is generally selected as 0.02.And the attenuation ratio which shows vibration between two adjacent maximum is 0.88[5].

Conclusion

On the basis of the static analysis,We do a further analysis of the strain tower in heavy icing area based on SAP2000 .We can obtain the response spectrum curves of damping value of 0, 0.02, 0.03, 0.05, 0.07, 0.10, 0.2, 0.4 and 0.6.In the end,we select the damping ratio of tension tower as 0.02 considering the two factors of economic and security .

References

[1] China Power Engineering Consulting Group Corporation ,Southwest Electric Power Design Institute,Central Southern Electric Power Design Institute.Design technique regulation of heavy ice overhead transmission line (DL/T5440-2009)[S].Beijing.China Electric Power Press ,2009.

[2] Construction and communication committee of shanghai,Code for Design of Tall-slender Structures（GB50135-2006）[S].Beijing .China Plan Press ,2006

[3] Xianghe Chen,Zaiguo Liu,Qi Xiao and so on .Design of tower and foundation of transmission [M].Beijing.China Electric Power Press ,2008.

[4] Qi Chen ,Analysis of bearing capacity of 220kV cat transmission tower dynamic characteristics and limit.[D],Nan Chang . Nanchang University ,2009 .

[5] Beijing Civil King Software Technology Co., Ltd.,Chinese building standard design and Research Institute . SAP2000 guide Chinese version (The second edition) [S]. Beijing.China Communications Press ,2012.

Advanced Materials Research Vols. 986-987 (2014) pp 685-688

doi:10.4028/www.scientific.net/AMR.986-987.685

Three-dimensional Wind Field Simulation on the Two Typical Roofs of the Building

Shuqin Liu[1] ,Zhongguo Bian[1] ,Yuanbo Cai[2] ,Fang Zhao[2]

[1.] Shandong University, Jinan, 250061 [2.] University of Jinan,Jinan, 250022
lshuqin@sdu.edu.cn, bzhongguo@sdu.edu.cn

Keywords: wind field; wind energy; building roofs; wind turbine installation; built environment;

Abstract: Wind energy utilization in the building environment has the advantage that it can avoid transporting effectively, especially it has important significance for residents without electricity. This paper mainly analyzed the basic situation of three-dimensional wind field around the buildings with the theoretical analysis and CFD numerical simulation method. By simulating the wind with different directions and different speeds, the characteristics of the wind field around single flat and pitched roof building are analyzed.

Introduction

With the large number of fossil energy used, the shortages of energy have become increasingly prominent; meanwhile, using fossil fuels can also cause many negative effects to the natural environment[1]. Wind energy development is one important way to solve the energy shortage and environmental pollution. But the wind field around the building is relatively complex, and because of the buildings' block, the wind velocities in different areas around the building vary greatly[2]. This paper presented the wind flow condition around the flat roof building and pitched roof building by Computational Fluid Dynamic (CFD) technique, including the wind energy on building roof. And then this paper discussed the suitable installation site of wind turbines on the building roof from the analysis results of wind velocity and turbulence intensity.

1 wind field analysis around single flat roof building

The building model is designed two-story high, which is 10m length, 8m wide and 8m height. It is used Gambit to generate meshes and simulated by Fluent. The inlet velocity was specified by constant wind velocity because the building is low. Turbulence condition is set by turbulence intensity I and hydraulic diameter L. equations are as following[3]:

$$I=0.16Re\text{^}(-1/8) \quad (1)$$

$$Re=vd\rho/\eta \quad (2)$$

$$L=4A/P \quad (3)$$

Where: Re- Reynolds number; v-average velocity; d-flow diameter; ρ-medium density; η-medium power coefficient of viscosity; A-Inflow surface area; P- Inflow surface perimeter.

In this simulation turbulent flow equation adopted *standard k-e* model. Second order wind schemes should be used for solving the algebraic equations in convective term. The fluid adopted Newtonian fluid and steady flow. Medium is air which is low-speed and incompressible. The scaled residuals should be in the range of 10^{-3} which mean the calculation reach steady state[4,5].

For the building, 9 points at the front, middle and back of the building top are selected as the reference site for installing a turbine to analyze wind energy aggregation. Meanwhile, in order to study the effect of wind speed and direction to buildings, wind velocity is designed 5m/s, and wind direction(α) is 0°and 45°as shown in Fig. 1. The computed normalized, U/Ue, measure the wind energy effect of building roof.

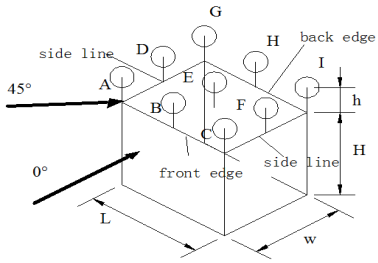

Fig.1 Flat roof building model

1.1 wind flow around flat roof building under wind direction α=0°

Fig.2 show the wind speed contour and turbulence intensity contour of building middle vertical section(x=0). From Fig.2 (a), wind velocities is generally improved on the top of the roof when wind flow through the building. But turbulence intensity is also improved around building shown in Fig.2 (b).

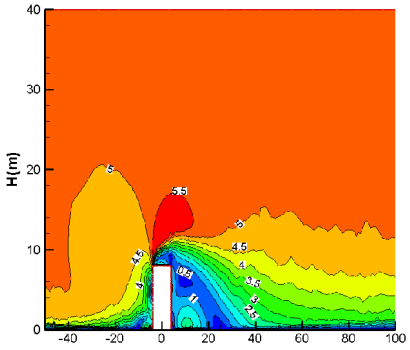

Fig.2 (a) Velocity contours at x=0

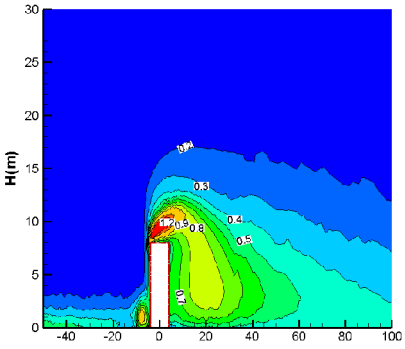

Fig.2 (b) Turbulence intensity contours at x=0

In order to make full use of space to install wind turbines, this section focused on analysis the changes of wind speed and turbulence intensity in the roof top. Fig. 3 shows the changes of wind velocity ratio and turbulence intensity at each reference point as the change of the height (h) above roof. From fig. 3(a), the wind velocity ratio of point B achieved highest when h=0.5m, and gradually stabilized at 1.18 with *h* increasing, that wind speed of 5.59m/s. Wind velocity ratio of point E reached maximum when h=3m, and stabilized at 1.2 with h increasing, that wind speed of 6m / s. And when h=4.5m, wind velocity ratio of point H achieved highest and gradually stabilized at 1.1 with *h* increasing.

Wind turbulence intensity of the wind turbine installation location is usually lower than 25%, and not more than 30%[4]. The changes of turbulence intensity can be found in Fig.3(b). Turbulence intensity of point A, point B and point C is lower than 30% when h=3m; when h=3m, turbulence intensity of point D, point E and point F is lower than 30%; and turbulence intensity of point G, point H and point I is lower than 30% as h=6m.

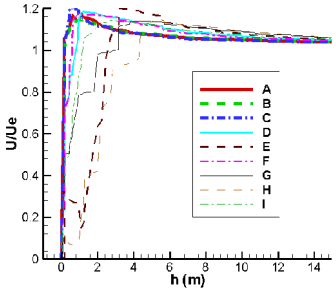

Fig.3(a) Wind velocity ratio for *α=0°*

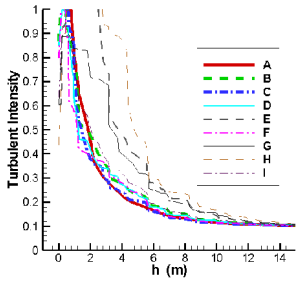

Fig.3(b) Turbulence intensity for *α=0°*

1.2 wind flow around flat roof building under wind direction α=45°

Fig.4 shows the changes of and turbulence intensity at each reference point as the change of the height (h) above roof. From Fig. 4(a), wind velocity ratio of each point is more than 1, which means that wind velocities of roof points are improved. Fig.4(b) shows the changes of turbulence

intensity with h changing. Turbulence intensity of point A and point D is lower than 20% when h=2m, other points are becoming stationary when h=4m.

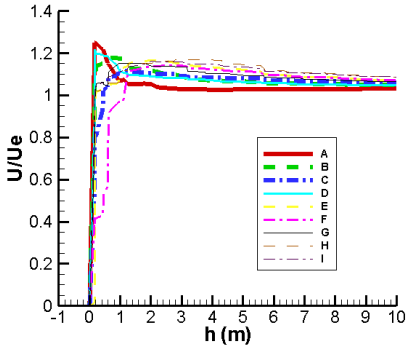

Fig. 4(a) Wind velocity ratio for α=45°

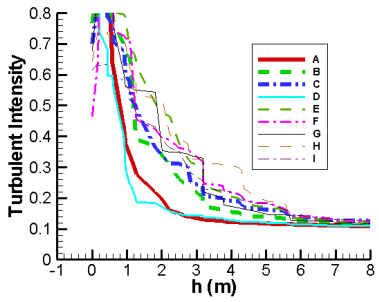

Fig. 4(b) Turbulence intensity for α=45°

It can be seen from the changes of wind velocity ratio and turbulence intensity under wind direction α=0° and α=45°: there are no obvious changes about the heights above the roof reference points, this shows that different wind directions have little influences to the heights above roof which are suitable to install wind turbines. Therefore the heights of each reference point suitable for installation of wind turbines on the rooftop not only reducing wind turbine installation height appropriately, but also satisfying the installation requirements of wind turbine. Fig. 5 shows the uniform wind turbine installation heights under different wind direction for U=5m/s.

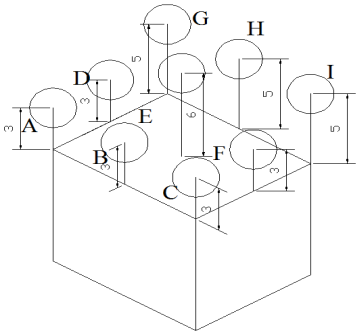

Fig. 5 Suitable installation height of each reference point

2 wind field analysis around pitched roof building

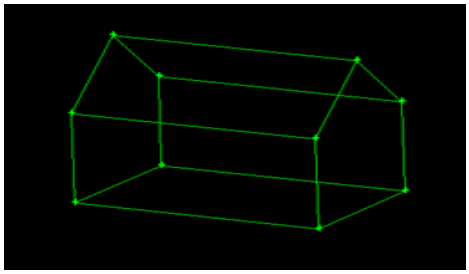

Fig. 6(a) patched roof building model

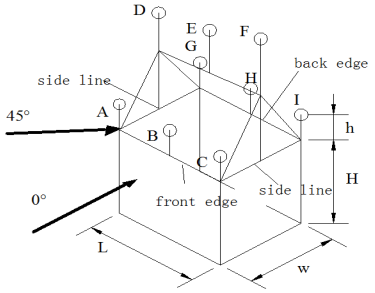

Fig.6 (b) Reference points of patched roof

Relative to the roof, pitched roof is also a very common typical roof. The sizes of pitched roof building are: L=10m, W=10m and H=12m which contain pitched height is 4m, the reference points are shown by Fig.6.

Fig.7 shows the changes of velocity and turbulence intensity at each reference point as the change of the height (H) above ground under wind direction α=0°. From Fig.7(a), the velocity of each point is over 5m/s and the highest wind velocity reached 6.5m/s because of the building. But points G,H,I of back edge appear low velocity areas because the pitched roof resisted, and then the velocity sharp increase. Fig.7(b) presents that when the wind is just connected the building, the turbulent intensity is low, which shows the turbulent intensity of points A ,B ,C can low than 20% as H=14m. But turbulent intensity become higher because the building obstructs, and the turbulent intensity of back edge can reach 20% as H =17m.

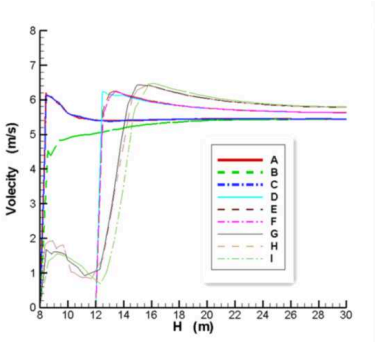

Fig.7(a) Wind velocity ratio for $\alpha=0°$

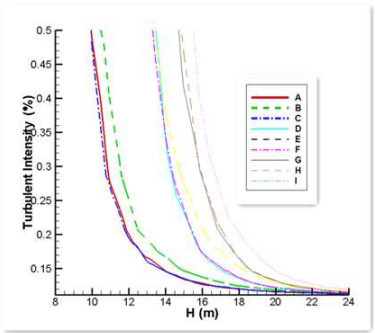

Fig.7(b) Turbulence intensity for $\alpha=0°$

3 Conclusions

CFD simulations for the cuboids buildings have been performed, and analyzed the wind energy of building rooftop at different roofs and different wind directions. Some conclusions are as follows:

1) The flat roofs of cuboids building have gather effects for wind energy, and the wind velocity above roof can increase more than 20%.

2) Under the same wind velocity, the wind turbine suitable installation heights at building front edge are lower than heights at building back edge, but the heights of building middle areas should be higher because the turbulence intensity is much large at the middle areas of building roof. Therefore, if the building is wide enough, wind turbines can be installed with height differences at the building roof, which can increase the installation quantities of wind turbine and then increase the total generating capacity.

Acknowledgement

The investigation presented in this paper was Supported by Natural Science Foundation of Shandong province(ZR2012EEM031). IEA Wind Task 27 .

Reference:

[1]Yu Zhenhong, Talk about wind energy development and use of mountain resources [J]. private science and technology, 2012,10:51

[2]Yuan Xingfei, Zhang Yu, Wind power utilization efficiency on roof of rectangular buildings [J]. civil, architectural and Environmental Engineering, 2012,24(3): 117-123

[3]Zhang Yu, Wind-energy efficiency study and structural analysis of building integrated/ mounted wind turbines

[4]Islam Abohela, Neveen Hamza, Steven Dudek. Effect of roof shape, wind direction, building height and urban configuration on the energy yield and positioning of roof mounted wind turbines [J]. Renewable Energy, 2013, 50:1106-1118.

[5]L. Ledo, P.B. Kosasih, P. Cooper. Roof mounting site analysis for micro-wind turbines [J]. Renewable Energy,2011,36:1379-1391

Advanced Materials Research Vols. 986-987 (2014) pp 689-693

doi:10.4028/www.scientific.net/AMR.986-987.689

Summary on wind speed distribution and its parameter estimation

LI Hui, ZHANG Fang

School of Automation, Beijing Information Science & Technology University, Beijing 100192, China
lhbxy21@sina.com, zhfang101@163.com

Keywords: wind farm; medium-and-long term; wind speed distribution; parameter estimation

Abstract: The main objective of this paper is to review some models of medium-and-long-term wind speed distribution in wind farms, for example Gamma distribution, Log-normal distribution, Weibull distribution, Rayleigh distribution and Burr distribution. On the base of the Weibull distribution, some kinds of parameter estimation approaches are introduced. Meanwhile, the advantages and the disadvantages of various algorithms are analyzed and compared. The prospects of this research are put forward at the end of this paper.

I. Introduction

Recently, generation power technology of renewable energies has been paid more and more attention because most countries in the world have focused on environmental protection and sustainable development. Wind energy, as a non-polluted renewable energy, has been used to generate power aiming to improve energy structure and protect ecologic environment in many countries. However, wind power has random, undulated and intermittent property, which makes output wind power fluctuate larger. In addition, the safety of power network will be influenced seriously if penetration power reaches an extreme value [1-2]. Therefore, it is necessary to study distribution characteristic of wind speed for optimizing dispatching, reducing reserved capacity, enhancing penetration limit and satisfying business needs of power market.

The probability distribution of wind speed can describe statistics character of wind power. According to the difference of time scale, there are short-term, medium-term and long-term wind speed distributions. However, the majority of researches involve medium-and-long term wind speed distributions [3]. The aim of this paper is to sum up statistical characteristics of current wind speed distributions. As an example of Weibull model, some common methods of parameter estimation are intruduced. Finally, some suggestions are presented for wind power exploitation and utilizing in China.

II. Probability distribution models of wind speed

Nowadays, there are several probability density functions (pdf) and their cumulative distribution functions (cdf) that can be used to model wind speed, such as Gamma function, Log-normal function, Weibull function, Rayleigh function and Burr function, in which two-parameter Weibull function has been generalised. Then the pdf, cdf and their characteristics are introduced as follows.

A. Gamma distribution

In development and utilization of wind energy, the earliest model was Gamma distribution, which represented the sum of exponentially distributed random variables. Gamma distribution nearly can imitate all of circumstances in Europe continent [4]. Its pdf was given by [1]:

$$f(v)=\frac{v^{k-1}}{c^{k}\Gamma(k)}\exp\left(-\frac{v}{c}\right) \tag{1}$$

where v is wind speed. k is the dimensionless shape parameter and c is the scale parameter. Γ is the gamma function. The relationship between the mean or expected value μ, variance σ^2 and parameters of the Gamma distribution are respectively shown:

$$\mu=ck \quad \text{and} \quad \sigma^2=c^2k \tag{2}$$

Its cdf was defined in [4]

$$F(v)=\frac{\Gamma_{v/c}(k)}{\Gamma(k)} \tag{3}$$

where $\Gamma_{v/c}$ is an incompletable gamma function.

B. Log-normal distribution

Excepted for Gamma distribution, the log-normal distribution often was used to describe wind speed frequency distribution. The pdf of a log-normal distribution was [5]:

$$f(v)=\frac{1}{vk\sqrt{2\pi}}\exp\left[\frac{-(\ln v-c)^2}{2k^2}\right] \quad (4)$$

The mean μ and variance σ^2 of Log-normal distribution are found to be:

$$\mu=\exp\left(c+k^2/2\right) \quad \text{and} \quad \sigma^2=\exp\left(2c+k^2\right)\left[\exp\left(k^2\right)-1\right] \quad (5)$$

Its cdf was shown in [6]:

$$F(v)=\frac{1}{\sqrt{2\pi}k}\int_0^v\frac{1}{x}\exp[-\frac{(\ln x-c)^2}{2k^2}]\mathrm{d}x=\Phi\left(\frac{\ln v-c}{k}\right) \quad (6)$$

As the Log-normal distribution could't be used well to imitate the instances of low or high wind speed, it hasn't be advocated to apply now [7].

C. Weilbull distribution

In wind studies, the Weibull pdf has been widely adopted. The general form of the Weibull distribution, which has two parameters, was given by [6]:

$$f(v)=\frac{k}{c}\left(\frac{v}{c}\right)^{k-1}\exp\left[-\left(\frac{v}{c}\right)^k\right] \quad (7)$$

where $f(v)$ is the probability function of wind speed v, k is the dimensionless shape parameter and c is the scale parameter, which has a reference value in the units of wind speed.

The mean μ and variance σ^2 of the Weibull distribution can then be calculated from

$$\mu=c\Gamma(1+1/k) \quad \text{and} \quad \sigma^2=c^2\Gamma(1+2/k)-\mu^2 \quad (8)$$

The corresponding cdf of the Weibull distribution was [8]:

$$F(V)=P(v\le V)=1-\exp\left[-\left(\frac{V}{c}\right)^k\right] \quad (9)$$

where V is known usually.

In general, k ranges from 1.5 to 3 at most conditions. c shows the average speed of wind farm. When c is equal to 1, it is named by the standard Weibull distribution. Note that the Weibull function can't model some extreme wind speed distribution [9].

D. Rayleigh distribution

The Rayleigh distribution is a special case of the Weibull distribution in which the shape parameter is taken as 2.0, and it has only one parameter namely the average wind speed, that makes it simpler to use. When wind data in one year or several years were obtained at certain site, the Rayleigh distribution can depict accurately wind speed. But the result is relatively worse when the average wind speed is less than 4.5 m/s. when the average wind speed is less than 3.6 m/s, the Rayleigh distribution can't be completely suitable to use. The Rayleigh pdf was [6]:

$$f(v)=\frac{v}{c^2}\exp\left(-\frac{v^2}{2c^2}\right) \quad (10)$$

The mean μ and variance σ^2 of the Rayleigh distribution can then be obtained from

$$\mu=c\sqrt{\frac{\pi}{2}}\approx 1.253c \quad \text{and} \quad \sigma^2=c^2(2-\pi/2)\approx 0.429c^2 \quad (11)$$

its cdf was given by [10]:

$$F(v)=1-\exp\left(-\frac{v^2}{2c^2}\right) \quad (12)$$

Generally speaking, the results of Rayleigh distribution exist to 10% errors. When there isn't better wind data, we can use them to estimate wind speed, but this function can't be used to model wind speed at any sites.

E. Burr distribution

In recent years, Burr distribution has been gradually applied to simulate wind speed. It had better effect [11-12], but it has slowly calculated speed. The pdf of Burr distribution was [11]:

$$f(v)=\frac{\alpha k\left(\frac{v}{\beta}\right)^{\alpha-1}}{\beta\left[1+\left(\frac{v}{\beta}\right)^{\alpha}\right]^{k+1}} \tag{13}$$

where α is the scale parameter, β and k *are* the shape parameters. The mean μ and variance σ^2 of the Burr distribution can then be calculated from

$$\mu=\frac{\beta\Gamma\left(1+\frac{1}{\alpha}\right)\Gamma\left(k-\frac{1}{\alpha}\right)}{\Gamma(k)} \quad \text{and} \quad \sigma^2=\frac{\Gamma\left(1+\frac{1}{\alpha}\right)\Gamma\left(k-\frac{2}{\alpha}\right)}{\Gamma(k)}-\mu^2 \tag{14}$$

The corresponding cdf of the Burr distribution was:

$$F(v)=1-\left(1+\left(\frac{v}{\beta}\right)^{\alpha}\right)^{-k} \tag{15}$$

In a word, note that select the distribution model according to the real condition of wind resource at some area. If geography climates are different, the distributed rules of wind speeds are different.

III. Parameter estimation methods

In the above-mentioned distribution models, as long as the related parameters are gained, the form of distribution can be determined. At present, there are some parameter evaluated approaches, for instance graphic method, maximum likelihood method, and moment method. Then they will be introduced separately for example of Weibull distribution.

A. Graphic method

Graphic method is derived by using cdf. Take twice the logarithm of Eq. 9.

$$\ln[-\ln[1-F(V)]]=k\ln V-k\ln c \tag{16}$$

We obtain $y=ax+b$ form respect to ln[-ln[1-$F(V)$]] and ln$V$ and also k is the slope of the straight line. Using cdf, we evaluate (lnV_i,ln[-ln[1-$F(V_i)$]]) pairs and then we solve linear least squares problem to obtain coefficients of straight line *a, b*. Hence

$$k=a \tag{17}$$

$$c=\exp(-b/a) \tag{18}$$

Implementation of this method consists of three stages such that: (i) using wind speed data, calculate cumulative frequency distribution or first evaluate frequency distribution, which requires sorting wind speed data into bins, and then using frequency distribution, obtain cumulative frequency distribution, (ii) calculate (lnV_i,ln[-ln[1-$F(V_i)$]]) pairs and (iii) solve linear least squares problem and find scale and shape parameters using Eq. 17 and Eq. 18.

B. Maximum likelihood method

Maximum likelihood method is an approach suggested by Stevens and Smulders [13], details on the development of this method can be found in [14]. Maximum likelihood method requires extensive iterative calculations. Shape and scale parameters of Weibull distribution are estimated by these two equations

$$k=\left(\frac{\sum_{i=1}^{n}v_i^k\ln(v_i)}{\sum_{i=1}^{n}v_i^k}-\frac{\sum_{i=1}^{n}\ln(v_i)}{n}\right)^{-1} \tag{19}$$

$$c=\left(\frac{1}{n}\sum_{i=1}^{n}v_i^k\right)^{\frac{1}{k}} \tag{20}$$

where v_i is the wind speed and n is the number of nonzero wind speeds.

This method is implemented in two stages such that: (i) using wind speed data, calculate summations in Eq. 19 and Eq. 20 with taking care of zero wind speeds which make logarithm indefinite and then calculate shape parameter with Eq. 20 and (ii) find scale parameter using a numerical technique in order to find the root of Eq. 19 around $k = 2$.

C. Moment method

This method is suggested by Justus et al. [15]. When the mean wind speed $\overline{V}$ and standard deviation are available, shape and scale parameters can be estimated with this method using

$$k = \left(\frac{\sigma}{\overline{V}}\right)^{-1.086} \quad 1 \le k \le 10 \tag{21}$$

$$c = \frac{\overline{v}}{\Gamma(1+1/k))} \tag{22}$$

Also mean wind speed is calculated by

$$\overline{V} = \frac{1}{n}\sum_{i=1}^{n} v_i \tag{23}$$

and standard deviation is calculated by

$$\sigma = \left[\frac{1}{n-1}\sum_{i=1}^{n}(v_i - \overline{V})^2\right]^{0.5} \tag{24}$$

This method also requires two stages such that: (i) using wind speed data, calculate summations in Eq. 23 and Eq. 24, calculate mean wind speed $\overline{V}$ and standard deviation σ and (ii) find scale parameter k and shape parameter c using Eq. 21 and Eq. 22.

The advantages or disadvantages of parameter estimated methods aforementioned are shown in Table 1. The graphic method is the method of choice because it could be performed by hand with minimal computation. But the maximum likelihood method and the moment method are the more accuracy and more appropriate computer-based method.

Tab.1 Comparison of parameter estimated methods

method	character
Graphic method	It is simple and easy to realize, but it is less accurate and less robust.
Maximum likelihood method	It has high accuracy, but complex transcendental equations must be calculated and results are sensitive to initial values.
Moment method	It is simple and has higher precision, but it cannot use the whole sample information.

IV. Conclusions and prospects

Studies showed that the two-parameter Weilbull function can well imitate medium-and-long-term wind speed, but it cannot describe accurately the situation of two peaks or even three peaks existing in the short-term wind speed distribution when sudden climates change [12]. Therefore, the author suggests that the next emphasis in study will be the feature research of short-term wind speed. For example, we can make better by applying to some combined approaches, builting multiple parameter Weibull distribution, increasing calculated speed and accuracy of parameter estimation, simplifying complicated distributed models, and so on. In general, it is very important to accurately model wind speed for pre-judging the change trend of wind, enhancing accepted capacity, and promoting massive exploitation and utilizing of wind power.

Acknowledgment

This work is supported by the Importation and Development of High-Caliber Talents Project of Beijing Municipal Institutions (CIT&TCD201304113).

References

[1] Chen Z., Blaabjerg F. Wind farm: a power source in future power systems. Renewable and Sustainable Energy Reviews,Vol.13 (2009), p.1288-1300
[2] Brano V.L., Orioli A., Ciulla G., et al. Quality of wind fitting distributions for the urban area of Palarmo, Italy. Renewable Energy, Vol.36 (2011), p.1026-1039
[3] Peng Hu, Guo Yufeng, Wang Songyan, et al. Pattern analysis on characteristics of wind speed distribution in wind farms. Power System Technology, Vol. 34 (2010), p. 206-210
[4] Kiss P., Jánosi I.M. Comprehensive empirical analysis of ERA-40 surface wind speed distribution over Europe. Energy Conversion and Management, Vol.49 (2008), p. 2142-2151
[5] Azami Z., Ahmad M.R. Fitting of statistical distributions to wind speed data in Malaysia. European Journal of Scientific Research, Vol. 26 (2009), p. 6-12
[6] Safari B., Gasore J. A statistical investigation of wind characteristics and wind energy potential based on the Weibull and Rayleigh models in Rwanda. Renewable Energy, Vol. 35 (2010), p. 2874-2880
[7] Wang Miao, Zeng Lihua. Study of wind speed frequency distribution model. Journal of Hydroelectric Engineering, Vol. 30 (2011), p. 204-209
[8] Hafzullah A.Z. Stochastic generation of hourly mean wind speed data. Renewable Energy, Vol. 29 (2004), p. 2111-2131
[9] Kececioglu D.B., Wang W.D. Parameter estimation for mixed-Weibull distribution. Proceedings of Annual Reliability and Maintainability Symposium. Forum (1998), p. 247-252
[10] Carta J.A., Ramírez P. Analysis of two-component mixture Weibull statistics for estimation of wind speed distributions. Renewable Energy, Vol. 32 (2007), p. 518-531
[11] Waal D.J., Gelder P.H., Beirlant J. Joint modeling of daily maximum wind strengths through the Multivariate Burr-Gamma distribution. Journal of Wind Engineering and Industrial Aerodynamics, Vol. 92 (2004), p.1025-1037
[12] Azami Zaharim, Siti Khadijah Najid, Ahmad Mahir Razali, et al. Analyzing Malaysian wind speed data using statistical distribution. Proceedings of the 4th IASME/WSEAS international conference on energy & environment. Forum (2009), p. 363-370
[13] M.J.M. Stevens, P.T. Smulders. The estimation of the parameters of the Weibull wind speed distribution for wind energy utilization purposes. Wind Eng, Vol.3 (1979), p. 132-145
[14] A. Genc et al. Estimation of wind power potential using Weibull distribution. Energy Sources, Part A: Recov, Utiliz Environ Eff, Vol.27 (2005), p. 809-822
[15] C.G. Justus, W.R. Hargraves, A. Mikhail, D. Graber. Methods for estimating wind speed frequency distributions. J Appl Meteorol, Vol.17 (1978), pp. 350-353

Advanced Materials Research Vols. 986-987 (2014) pp 694-697

doi:10.4028/www.scientific.net/AMR.986-987.694

Modeling and Uncertainty Estimation of Wind Power Curve Based on Recorded Field Data

Peng Lin[a], Shu-qiang Zhao[b]

State Key Laboratory of Alternate Electric Power System with Renewable Energy Sources, North China Electric Power University, Beijing, 102206, China

[a]jamiedsg@163.com, [b]shuqiang_zhao@163.com

Keywords: method of bins; measured wind power curve; uncertainty estimation; non-parametric interval estimation; confidence interval.

Abstract. Wind power curve of wind turbine has great importance in the prediction of wind power. The measured wind power curve is drawn by method of bins based on recorded field data; the uncertainty factors of the wind power curve is analyzed, and a non-parametric confidence interval estimation method is proposed based on analyzing the statistical characteristics of the data distribution. By means of the method, a probability density function model for wind power in each wind speed level is established, and the uncertainty estimation confidence interval of wind power curve is obtained on the basis of deterministic estimation. The example analysis proves the efficiency and feasibility of the method proposed in this paper.

Introduction

Wind power resources, widely distributed, is a kind of clean and cheap renewable green energy. Because the wind randomness and volatility has a negative effect on the economic operation, security and stability of power grids, the research on wind power prediction is deepening fast. Wind power curve is the key to wind power prediction. Wind power curve is influenced by many factors, and the wind power is not only related to wind speed, but also other factors such as air density , the swept area and fan mechanical conditions, so wind power curve itself exists great uncertainty. Wind power curve is one of the major curves reflecting the wind turbine output performance [1]. The existing research on wind power curve is almost deterministic analysis, which gives the corresponding point value of output under a certain wind speed, while there is a big risk [2]. In this paper, the uncertainty method proposed enriches the information of wind power curve and improves the reliability of the estimation results.

Modeling of the wind power curve

In accordance with the international electrotechnical commission (IEC) standard of IEC61400-12, wind power curve of wind turbines represents the relationship between the average wind speed and power for 10 min [3,4], and it should be obtained by the measured way, different from the standard wind power curve provided by manufacturer [5]. Because wind speed and power is not a one-to-one correspondence, so the measured data should be modeled and analyzed. Method of bins is used in this paper [6,7,8].

Wind speed is equally divided into M intervals according to the method of bins, which is called wind speed bin. For an example, take 0.5 m/s for a small bin. Then calculate the average wind speed and power of each bean respectively to receive M (V_{imean}, P_{imean}) data:

$$V_{imean} = \frac{1}{n_i}\sum_{j=1}^{n_i} V_{ij} \ . \tag{1}$$

$$P_{imean} = \frac{1}{n_i}\sum_{j=1}^{n_i} P_{ij} \ . \tag{2}$$

Finally use spline interpolation method to synthesize a smooth curve with M (V_{imean}, P_{imean}) point, namely the wind power curve by method of bins. This method involves all the measured data in the model, so the error of the wind power curve obtained is small, the smoothness is good, and the model is stable.

Uncertainty estimation

Probability density function estimation problem is to estimate the probability density function through the samples, containing parametric, semi-parametric and non-parametric estimation method [9, 10].

Non-parametric method doesn't need to give any priori assumptions of the distribution so it is more in line with the actual distribution. Compared to the parametric method, the functional form and parameters of non-parametric estimation method are unknown [11]. Its advantage is: when doing overall estimate, the form of function is freedom and doesn't rely on the distribution of the sample; it is suitable for nonlinear, inhomogeneous data and the data of which the overall distribution is unknown. For the distribution of the measured wind power curve, there is not a specific form to carry on the accurate description. Therefore, in this paper, the non-parametric estimation method is adopted to establish the probability density function of wind power curve.

Kernel function regression is one of the non-parameters estimation methods. It mainly adopts kernel density estimation. Kernel density estimation function is:

$$f(x)=\frac{1}{nh}\sum_{i=1}^{n}K\left(\frac{x-X_i}{h}\right). \tag{3}$$

Gaussian kernel function $K=\frac{1}{\sqrt{2\pi}}e^{-\frac{u^2}{2}}$ is used in this paper.

Interval estimation

Interval estimation is a method describing the uncertainty of estimator [12]. Based on the deterministic point estimation, interval estimation gets probability density function by wind power curve error measurement, and uses the theory of probability to calculate estimate interval under a given confidence level.

ξ is a random variable, and $F(\xi)$ is the probability distribution function, the non-parametric estimation technique is adopted to establish the $1-\alpha$ estimate interval $\left[G(\alpha_1),G(\alpha_2)\right]$ ($\alpha_2-\alpha_1=1-\alpha$). Take symmetric probability interval, this is to say, $\alpha_1=\alpha/2$ $\alpha_2=1-\alpha/2$. The probability confidence interval is:

$$\left[G(\alpha_1),G(\alpha_2)\right]=\left[G\left(\frac{\alpha}{2}\right),G\left(1-\frac{\alpha}{2}\right)\right]. \tag{4}$$

$G(q)$ is the inverse function of $F(\xi)$, so $\Pr\{\xi\le G(q)\}=q$ through which estimate interval boundary value can be obtained under the given confidence level.

The error of wind power curve is associated with a variety of factors such as wind speed and air density. Data analysis shows that when the wind speed is different, the power probability density distribution function varies greatly. As a result, in this paper, wind speed considered as the main influencing factors of wind power curve error, is divided into 50 levels by 0.5 m/s (under normal circumstances, wind speed at wind farms is under 25 m/s). Respectively, set up different power probability distribution.

According to the deterministic estimate of wind power curve and probability density function, estimate interval under a given confidence level can be received, so as to reflect the range of output.

Example analysis

Select the recorded field data of a wind turbine from Colorado as an example for analysis. The data contains the actual wind speed and power output from 0:00 on January 1, 2006 to 23:50 on December 31, 2006 every ten minutes.

Figure.1 depicts scattered data points and the measured wind power curve drawn by method of bins. The measured data points are evenly distributed on both sides of the wind power curve, and the curve is smooth.

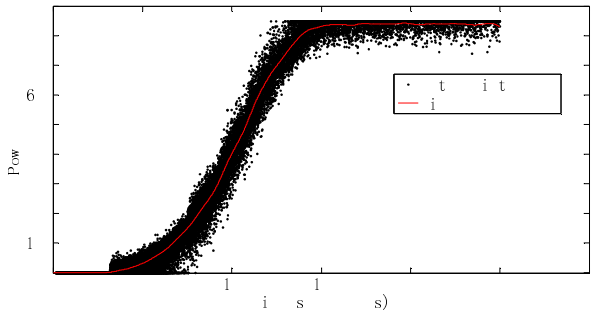

Fig.1 Measured wind power curve drawn by method of bins

Figure.2 shows wind power probability density curve of the 10th wind speed level and it is shaped like the double-peak normal distribution. Figure.3 shows wind power probability density curve of the 25th wind speed level and it is shaped like the normal distribution. The different results illustrate that power output distribution varies. That is to say, the classification method proposed in this paper is feasible and can well describe the power output distribution at different wind speed levels.

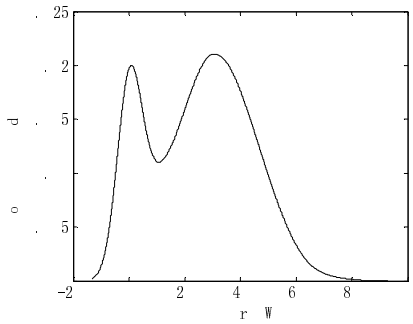

Fig.2 Wind power probability density curve of the 10th level

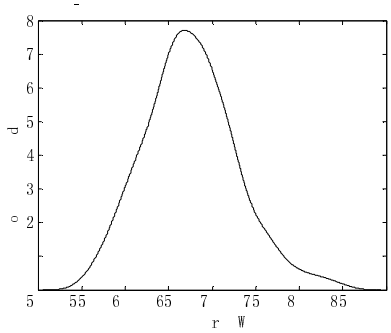

Fig.3 Wind power probability density curve of the 25th level

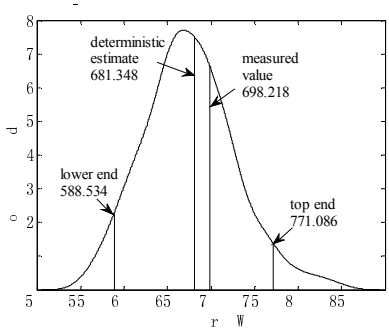

Fig.4 Wind power probability density curve of the 10th level and the 90% confidence interval

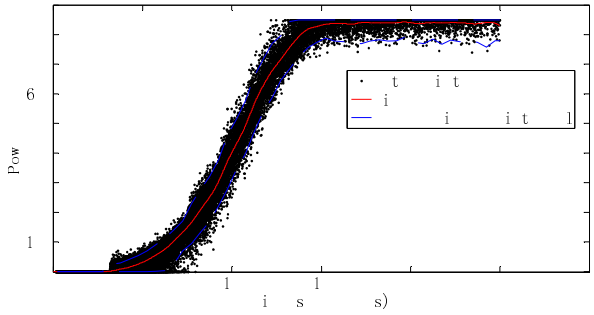

Fig.5 The 90% confidence interval of wind power curve

Figure.4 depicts the power probability density curve of the 22380th data of 09:50 on June 5, 2006 and the 90% confidence interval. Its deterministic estimate value is 681.348 kW, and the 90% confidence interval is [588.534, 771.086] kW. The measured value is 698.218 kW included in the range of the confidence interval. The result proves that the non-parametric interval estimation method is feasible and effective.

Using the same method, confidence interval of each wind speed level can be obtained. Connect the boundaries of all the confidence intervals then two envelopes can be formed up and down on the wind power curve. Figure.5 shows the result of 90% interval estimation.

Summary

Method of bins is proposed to build the measured wind power curve, which reflects the actual operation of wind turbine. Furthermore, method of non-parametric kernel density interval estimation based on the deterministic estimation is adopted to calculate the uncertainty estimation interval of output under a given confidence level. The approach improves the reliability of the estimation results. In this paper, the proposed approach extends the traditional deterministic research on wind power curve, gives the uncertainty range of wind power curve estimation and provides technical support for wind power prediction and power grid dispatch.

References

[1] Zhou Yan, Tan Yinglian, Liu Biao, et al. Overview on prediction research of wind power [J]. Electric Drive Automation, 2013, 35(1): 11-14.

[2] Fan Gaofeng, Wang Weisheng, Liu Chun, et al. Wind power prediction based on artificial neural network [J]. Proceedings of the CSEE, 2008, 28 (34):118- 123.

[3] Lang Binbin, Mu Gang, Yan Gangui, et al. Research on wind speed vs output power characteristic curve of wind power generator interconnected with power grid [J]. Power System Technology, 2008, 32(12):70~74.

[4] Wind turbine generator systems-Part 12: Wind turbine power performance testing [S]. International Electro technical Commission, 2005.

[5] Gamesa Eolica S.A.. Gamesa G52/G58-850 kW Technical Files [R]. Spain:Gamesa Eolica S.A., 2001.

[6] Li Yuan. Method research on wind turbine optimal selection based on wind resource characteristics [D]. North China Electric Power University(Beijing), 2008.

[7] Liu Hao, Liu Yibing, Xin Weidong, et al. Wind turbine power performance based on the operation data [J]. Power System and Clean Energy, 2009, 25(7):53-56.

[8] Li Mengyan, Liu Xingjie, Mi Zengqiang. Research on modeling method of wind turbine power curve [J]. Yunnan Electric Power, 2012, 40(3):1-5.

[9] KRZYZAK A, WALK H. A distribution-free theory of nonparametric regression [C]//New York, NY, USA: Springer-Verlag, 2002:70- 80.

[10] Wang Caixia, Lu Zongxiang, Qiao Ying, et al. Short-term wind power forecast based on non-parametric regression model [J]. Automation of Electric Power Systems, 2010, 34(16):78-82,91.

[11] Zhou Songlin, Mao Meiqin, Su Jianhui. Short-term forecasting of wind power and non-parametric confidence interval estimation [J]. Proceedings of the CSEE, 2011, 31(25):10-16.

[12] OLIVE D J. Prediction intervals for regression models [J]. Computational Statistics & Data Analysis, 2007, 51 (6) :3115-3122.

Advanced Materials Research Vols. 986-987 (2014) pp 698-701

doi:10.4028/www.scientific.net/AMR.986-987.698

Application of PSO in the optimization of nuclear power unit's heat regenerative system

FU Wenfeng, LI Fe[a], ZHOU Lanxin

North China Electric Power University, Key Laboratory of Condition Monitoring and Control for Power Plant Equipment, Baoding: 071003, China

[a]email: lfei_1988@163.com

Keywords: feed-water heating allocation; nuclear power secondary loop; PSO; optimal design

Abstract. Based on theoretical deduction, according to the characteristics of nuclear power unit, a universal heat economic framework for PWR nuclear power plant heat regenerative system was established. And on this basis, the cycle thermal efficiency was chosen as the optimization goal, the extraction steam pressures were chosen as optimization variables, a universal nuclear power unit regenerative system optimization model was established. A 900 MW nuclear power unit was taken for example, it's the first time that AWPSO was applied to optimize the regenerative heat system of nuclear power unit. The result shows that the convergence ability and search performance of PSO are superior to other methods and the original design scheme. A new and convenient design is provided for PWR nuclear power plant heat regenerative system in this paper.

Introduction

The regenerative feed-water heating system is the core of whole thermodynamic cycle in thermal power plants. It plays a decisive role for the thermo-economy of a steam turbine unit [1]. Therefore, many experts and scholars at home and abroad carried out a lot of research in order to get the best allocation scheme of feed-water enthalpy rise and produced important results in this field. In fact, some traditional methods have been attempting to solve the feed-water heating allocation problems, such as average allocation, enthalpy drop allocation, geometric series allocation, etc. [2-4]. The systems are all further simplified by these allocation schemes, and it leads to fall short of result and facts. Some scholars optimized by direct optimization method, such as dynamic programming, the simplex method, the nonlinear optimization method, etc. [5], but the calculation processes of these methods are very tedious and the versatility and accuracy are not high, so they're difficult to popularize. In recent years, simulated natural ecosystem mechanism is introduced to optimize the regenerative heating system by some scholars, and some certain achievements are obtained, such as genetic algorithm (GA) and simulated annealing algorithm, but these algorithms have some shortcomings such as easy to bring immature convergence, poor stability, and etc.

In this paper, adaptive weight particle swarm optimization (AWPSO) was applied to solve the feed-water heating allocation problem of nuclear power units for the first time. The calculation result demonstrates that AWPSO is superior to other methods and the original design scheme. A new and convenient design was provides for PWR nuclear power plant heat regenerative system.

Mathematical model

General regenerative system of nuclear power unit is shown in Figure 1. Different from conventional thermal power unit, the high pressure cylinder exhaust steam of nuclear power unit is separated by steam separator (after separation, the "steam" is used as reheat steam, the "water" is fed into the deaerator). And the new steam and extraction steam of the first stage of high pressure cylinder are used as reheating source, the drain is fed into one high pressure heater. On the other hand, one pipe of reheated steam is used as the steam source of feed-water pump usually in nuclear power unit, which is also different from general thermal power unit. These factors make steam circulation system very complex, increase the calculation difficulty, and the ever optimized methods

for thermal power unit are no longer suitable for nuclear power unit. It is need to establish a new optimization model, which is suitable for nuclear power unit.

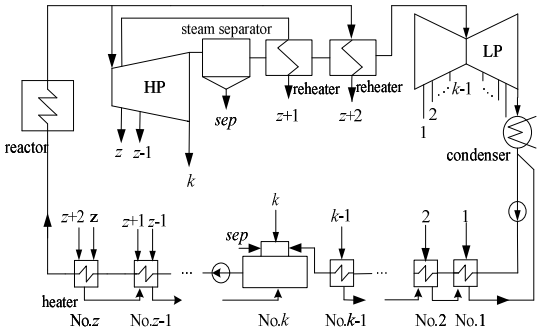

Fig.1 Thermodynamic system of nuclear power unit

Construction of steam-water distribution equation

According to the divided steam-water system, considering the energy balance and mass balance, steam-water distribution equation of unclear power unit secondary loop can be written as follow:

$$[A][\alpha_j]+[A_\tau][\alpha_\tau]+[A_f][\alpha_f]+[\Delta q]=[B][\tau] \tag{1}$$

The significance and composition rules of each element of the matrix are as follows:

1) $[A][\alpha_j]$ represents the main steam-water. $[\alpha_j]=[\alpha_1,\alpha_2\cdots\alpha_{z+2}]^{\mathrm{T}}$ are the shares of each extration steam of heaters and reheaters; $[A]$ is $z+2$ factorial square matrix, constituted as follow:

$$A=\begin{pmatrix}
q_1 & \gamma_1 & \gamma_1 & \cdots & \gamma_1 & \beta\tau_1 & \beta\tau_1 & & \cdots & & \beta\tau_1 \\
0 & q_2 & \gamma_2 & \cdots & \gamma_2 & \beta\tau_2 & \beta\tau_2 & & \cdots & & \beta\tau_2 \\
0 & 0 & \ddots & \ddots & \vdots & \vdots & & & & & \\
 & & & q_{k-1} & \gamma_{k-1} & \beta\tau_{k-1} & \beta\tau_{k-1} & & \cdots & & \beta\tau_{k-1} \\
 & & & & q_k & \gamma_k & \gamma_k & & \cdots & & \gamma_k \\
\vdots & \vdots & \ddots & & \ddots & q_{k+1} & \gamma_{k+1} & & \cdots & & \gamma_{k+1} \\
 & & & & & & \ddots & \ddots & \ddots & & \vdots \\
 & & & & & & & q_{z-1} & \gamma_{z-1} & \gamma_{z-1} & \gamma_{z-1} \\
0 & 0 & & & \cdots & & & 0 & q_z & 0 & \gamma_{z+2} \\
0 & 0 & \cdots & 0 & \beta\tau_{z+1} & \beta\tau_{z+1} & \cdots & & \beta\tau_{z+1} & q_{z+1} & \beta\tau_{z+1} \\
0 & 0 & \cdots & 0 & \beta\tau_{z+2} & \beta\tau_{z+2} & \cdots & & & \beta\tau_{z+2} & q_{z+2}
\end{pmatrix}$$

where q is the heat of steam, τ is the enthalpy rise of feed-water in each heater, γ is heat of the drain water, β is the flow coefficient in steam-water separator.

2) $[\alpha_\tau]$ represents the share of auxiliary water ; $[\alpha_f]$ represents the share of auxiliary steam; $[A_\tau]$ and $[A_f]$ are $z+2$ factorial square matrix, whose composition rule and determine method are identical to matrix $[A]$.

3) $\Delta q=[\Delta q_1,\Delta q_2,\cdots\Delta q_{z+2}]^{\mathrm{T}}$ represents the pure heat that in and out of the system. $\Delta q_i\neq 0$ means that Δq_i pure heat is let into the i^{th} heater. For ease in writing, the drain water heat of the steam separator in deaerator and the pump power of the feed- water pump are classed as this category. Thus, Δq_k contains $\alpha_{sep}\gamma_{sep}$ and τ_b.

4) $[\tau]$ represents the feed-water enthalpy rise of each heater and the reheat steam enthalpy rise in the reheaters. $[B]$ is a $z+2$ factorial diagonal matrix, constituted as follow:

$$B=diag[\underbrace{\beta(1-\alpha_p),\beta(1-\alpha_p),\cdots\beta(1-\alpha_p)}_{k-1\text{项}},\underbrace{1,1,\cdots 1}_{z+1-k\text{项}},\ \beta,\ \beta]$$

Transforming formula (1), combining the definition of q, τ and γ, α_j can be expressed by p_j as follow:

$$\alpha_j=f^j_{p\to\alpha}(p_1,p_2,\cdots p_z) \tag{2}$$

Establish the optimal model

Thus, the cycle thermal efficiency of the unit can be calculated as follow:

$$\eta_i = \frac{w}{\bar{q}} = [(1-\alpha_{z+2})(h_0 - h_k) - (\alpha_z + \alpha_{z+1})(h_z - h_k) + \alpha_{rh}(h_{rh} - h_c) - \sum_{j=k}^{z-1}\alpha_j(h_j - h_k) - \sum_{j=1}^{k-1}\alpha_j(h_j - h_c) - \Pi]/(h_0 - h_{fw}) \quad (3)$$

where α_{rh} represents the share of the reheat steam; h_c represents exhaust enthalpy; h_{fw} represents the feed-water enthalpy; Π is the power losses caused by steam leakage of the shaft gland, gateway and etc.

Combining the formula (2) and formula (3), the cycle thermal efficiency η_i can be expressed by extraction steam pressure p_j as follow:

$$\eta_i = f(p_1, p_2, \cdots, p_z) \quad (4)$$

Considering some constraints, the optimal mathematical model of nuclear power unit thermal system can be described as follows:

$$\begin{cases} \max \eta_i \\ s.t \quad G_j(\vec{x}) \geq 0, j = 1,2,\cdots z \end{cases}, \quad \text{where } G_j(\vec{x}) = \begin{cases} G_1(\vec{x}) = p_1 - p_c; G_2(\vec{x}) = p_2 - p_1; \\ \cdots; G_z(\vec{x}) = p_z - p_{z\text{-}1}; G_{z+1}(\vec{x}) = p_0 - p_z \end{cases} \quad (5)$$

The example calculation and the result analysis

A certain 900 MW pressurized water reactor nuclear power unit thermodynamic system as shown in Figure 2. The terminal temperature difference of feed-water heaters and pipe extraction pressure losses are shown in Tab.1

Tab.1Entropy extraction efficiency of all levels, pressure drop and temperature difference of heaters

items	symbols	units	H5	H4	H3	H2	H1	SEP	RH
Extraction pressure loss	Δp_j	%	5	5	5	5	5	2	2.6
outlet terminmal difference	θ_j	◦C	3	0	2.5	2.5	2.5	0	13.4
inlet terminmal difference	φ_j	◦C	8	-	5	5	-	-	-

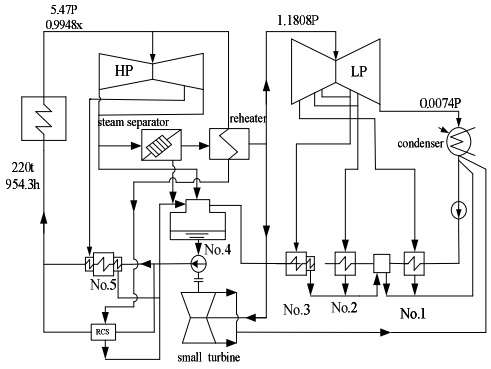

Fig. 2. The secondary loop system of a 900MW PWR nuclear power unit

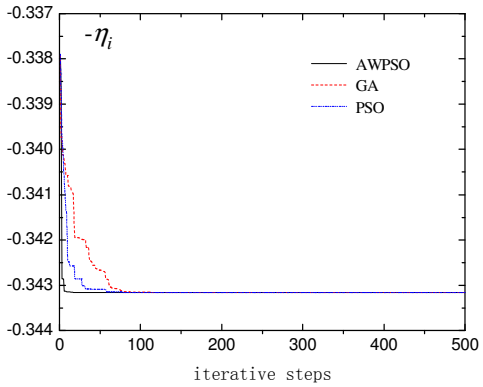

Fig.3. The evolution curves of AWPSO, PSO and GA

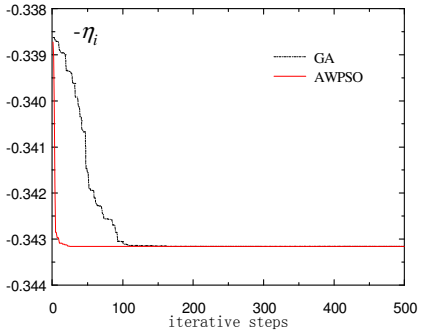

Fig.4. The evolution curves of AWPS0 and GA in population of 10

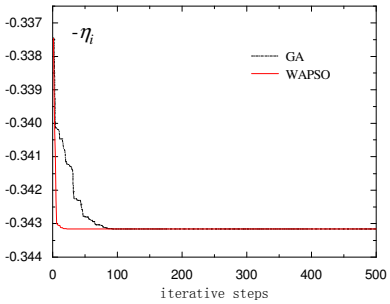

Fig.5. The evolution curves of AWPS0 and GA in population of 30

Due to PSO is usually to find the minimum value of fitness function, so when optimize the regenerative heating system, combining the formula (5), the fitness function is constructed as $F = -\eta_i$. Parameter Settings: Population size is 20; Learning factors c1=c2=2; Inertia weigh w_{max}=0.9, w_{min}=0.5; Iteration steps t=500. Compare the optimization result with the original design value, the average distribution method, GA and standard PSO, as shown in Table 2. Fig.3-Fig.5 are the evolution curves of different methods under different population sizes.

The Table 2 shows that result of AWPSO compared with the original design is relatively increased about 0.051%. If the annual utilization hours are 7000, extra generating capacity will be made by one unit each year. If the average power produce fuel consumption is 320 KW/h in the country, 1028.613 tons of standard coal will be saved by one unit, which gives considerable economic benefit.

Tab.2 The optimization results of all programs

items	Original design	Average divide	GA	standard PSO	AWPSO
p_1	0.0244	0.0393	0.0267	0.0273	0.0267
p_2	0.0898	0.1295	0.1053	0.1028	0.1056
p_3	0.3531	0.3242	0.3489	0.3417	0.3487
α_1	0.0282785	0.0429497	0.0309876	0.0316551	0.0309873
α_2	0.0381076	0.0381067	0.0410939	0.0397166	0.0410312
α_3	0.0536341	0.0375159	0.0479189	0.0477821	0.0479573
α_4	0.0854198	0.0898916	0.0860544	0.0871591	0.0861064
α_5	0.0696247	0.0696948	0.0696346	0.0696519	0.0696129
α_{rh}	0.6907854	0.6874193	0.6902595	0.6889778	0.6902452
$\alpha_{0,\ rh}$	0.0743967	0.0739969	0.0743496	0.0742412	0.0743348
η_i	0.342986	0.342905	0.343158	0.343157	0.343161

Note: α_{rh} represents the share of reheat steam; $\alpha_{0,\ rh}$ represents the share of the new steam that used to heat the reheat steam.

Conclusion

According to the characteristics of the secondary loop system of nuclear power unit, a universal heat economic framework for PWR nuclear power plant heat regenerative system was established based on theoretical deduction. The cycle thermal efficiency was chosen as the optimization goal, the extraction steam pressures were chosen as optimization variables, a universal nuclear power unit regenerative system optimization model was established. PSO was applied to optimize the thermal system of nuclear power units for the first time. The practical calculation shows that the AWPSO can achieve or approximate the optimal value, with high efficiency and good stability, and it's easy to master and apply in the practical work for the simple procedure and less operations. An effective way is provided to analyzing and solving the problem of nuclear power unit thermal system optimization.

Acknowledgement

The Fundamental Research Funds for the Central Universities(2014MS109).

References

[1] Zheng Tikuan. Thermal power plant [M]. Beijing: China Electric Power Press, 2008:138.

[2] Salisbury JK. Steam turbines and their cycles[M]. New York: Robert E. Krieger Publishing Company, 1974.

[3] Zhang Yi, Chen Zhigang, Huang Liping, Li Yong. The Approach and Analysis of Optimal Distribution of Feed-water Enthalpy rise for Steam Turbine[J]. Journal of Northeast Dianli University, 2008, 28(4): 52-56.

[4] Zhao Yi, An Minshan. Comprehensive optimization of Regenerative and reheat steam turbine thermal system parameters [J]. Proceedings of the CSEE, 1991, 11(1): 47-54.

[5] Zhang Chunfa, Zhang Suxiang, Cui Yinghong. Thermo-economy state equation of modern power system[J]. Journal of Engineering Thermophysics, 2001, 22(6): 665-667.

Advanced Materials Research Vols. 986-987 (2014) pp 702-705

doi:10.4028/www.scientific.net/AMR.986-987.702

Calculation of Capacitance and Inductance Parameters of Transformer Winding under Very Fast Transient Overvoltage

Yan Li, Yang Li, Yinjun Guan, Tianyuan Li

Research Institute of Special Electrical Machines, Shenyang University of Technology, China

Email: tlly0808@yeah.net

Keywords: Transformer, VFTO, Capacitance, Inductance, FEM

Abstract. The distributed parameters of transformer windings are indispensable in analyzing the transients particularly caused by the very fast transients which occur at the time of disconnecting switch operations in GIS. Winding insulation structure and the safe and stable operation of the transformer are determined by the accuracy of the calculation. In this paper, finite element method(FEM) is used to model and simulate the electromagnetic field calculation of winding capacitance and inductance parameters. The simulation calculation results are consistent with the experimental measurements on a transformer model, which verifies this method is feasible.

Introduction

Disconnect switch restriking causes very fast transient overvoltage (VFTO) in gas insulated substations (GIS) which can damage power equipment, especially inductance devices in the substations[1][2]. The very fast transient overvoltage has a steep wave front of time, the main oscillation frequency depends on the length of the GIS, general is 1 ~ 40 MHz. The directly invading of Very Fast Transient Overvoltage caused by the switching operation in GIS to transformer windings may severely damage their longitudinal insulation. Research in transformer windings under VFTO wave process of transformer insulation design and protection has significance meanings [3][4].

The transformer windings can be regard as a complex networks composed by capacitance, inductance, resistance and conductance, under very fast transient overvoltage. During the process of transient response of transformer windings to impulse waves, transformer winding can be seen as a lumped parameter network [5]. During the process of transient response of transformer windings to impulse waves, the initial voltage distribution along transformer winding due to a step voltage input was determined by the capacitances within the winding. The final voltage distribution along transformer winding was determined by the inductance of the winding [6][7][8]. Therefore, to obtain a more accurate result, it is necessary to improve the method of the analytical formula or to find a new method other than analytical formulation method in calculating the parameters of capacitance and inductance [9][10].

This paper presents a finite element method by using Ansoft software to calculate the parameters of capacitance and inductance of different kind of winding forms in the high-voltage transformer. In order to validate the correctness of this method, the parameters of one practical transformer is taken for analyzing, and the results are read by the self-compiling software to realize the analysis of the wave process under VFTO.

Calculation of Inductance Parameter

In the process of impact, when the impulse waves' equivalent frequency is low enough, the effect of impulse waves on the winding is completely determined by the inductance. For the infinite without iron yoke core model, simulate the magnetic field distribution, to improve the accuracy of the inductance calculation. The calculation of distributing inductance is based on the magnetic static. By applying the boundary conditions the infinite long core will be better simulated, and the distribution of magnetic field around windings will be more close to the actual situation. Consequently the accuracy of the calculation of inductance will be improved significantly.

Calculation method and procedure of Inductance is based on a three-phase double-winding without on-load tap-changer 400MVA/500kV power transformer. The finite element method calculation model is shown in Fig.1.

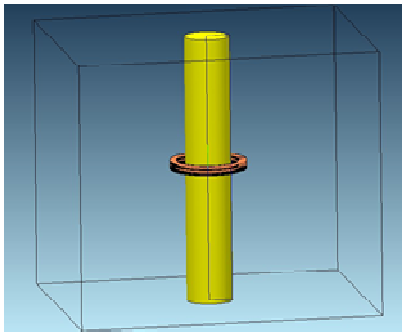

Fig.1.Inductance model of disk to disk

Inductance consists of two parts, hollow inductance component and core inductive component. Self-inductance is calculated by planar coil inductance formula, the structure as shown in Fig.2.

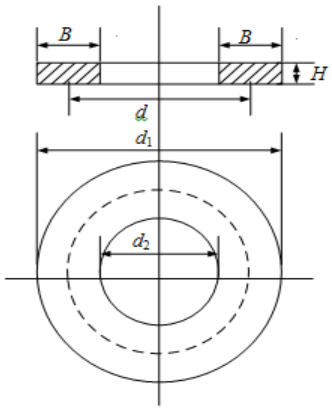

Fig.2 Structure size of plane coil

The calculation of self-inductance is given by

$$L = \frac{\mu_0}{8\pi} d \psi w^2 \quad (1)$$

Where μ_0 is the permeability of vacuum, d is the average diameter of disk, w is the number of turns per disk, Ψ is a function of associated with ρ=B/d.

Mutual inductance is obtained by the coupling coefficient method.The calculation of mutual inductance is given by

$$M_{ij}=L_i q^{|i-j|}, \quad i \neq j \quad (2)$$

Where L_i is the self-induction of the unit i, q=0.97~0.99 is coupling coefficient.

The results of mutual inductance calculated are shown in the Table 1.

Table 1. Inductance value of the first disk with the top 6 cake（μH）

Numbering	Finite element method	Analytical method
$M_{1,1}$	1052.9	1101.4
$M_{1,2}$	1022.4	1071.5
$M_{1,3}$	1003.2	1038.8
$M_{1,4}$	981.1	1015.9
$M_{1,5}$	1023.5	1073.7
$M_{1,6}$	1012.7	1053.5

It can be seen from the Table 1, the difference of the result calculated by the both methods is not significant which shows the correctness of the new method. The main reason of causing difference is that, analytical method has been simplified and not considered the entire structure.

Calculation of Capacitance Parameter

Electric field analysis is the basis for calculating the capacitance of the transformer, the finite element method of electric field analysis is most close to the actual situation of the transformer, reduce the assumptions, the calculation results can be obtained with high accuracy. The capacitance is calculated using the finite element software of electrostatic field. Through a series of electrostatic simulation, the capacitance matrix will be calculated. In every simulation process, one conductor was set to 1V voltage, other conductors was set to be grounding.

The capacitance C of conductors i and j is calculated by energy formula. The capacitance C of conductors i and j is given by

$$C = \frac{2W_{ij}}{U^2} = \int_{\Omega} D_i \cdot E_j \, \mathrm{d}\Omega \tag{3}$$

Where W_{ij} is the electrostatic energy stored in the volume between the conductors i and j, D_i is the electric flux density of conductor i, E_j is the electric field intensity of conductor j. U is the voltage difference between i and j.

Calculation method of capacitance is similar to the process of inductance. The calculation of capacitance is based on the 400MVA/500KV mentioned above, the calculation model built by a disk as a unit is shown in Fig.3. To verify the results, the analytical formula is used to calculate capacitance of the winding. The calculation of disk to disk capacitance is given by

$$C_s = \frac{\varepsilon_{de} d_a B}{4 a_d} \times 0.11 \tag{4}$$

Where ε_{de} is the permittivity of compound insulation, d_a is the average diameter of one disk, B is the radial width of one disk, a_d is the insulation wide between disks.

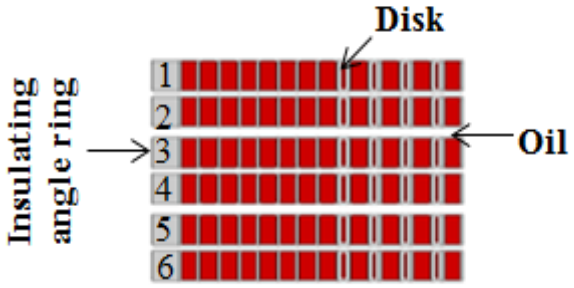

Fig.3. Disk winding model

The results of capacitance calculated are shown in the Table 2.

Table 2. The capacitance of disk to disk (F)

Numbering	Finite element method	Analytical method
$C_{s1,2}$	$3.32e^{-9}$	$3.16e^{-9}$
$C_{s2,3}$	$1.97e^{-9}$	$1.86e^{-9}$
$C_{s3,4}$	$3.28e^{-9}$	$3.16e^{-9}$
$C_{s4,5}$	$1.97e^{-9}$	$1.86e^{-9}$
$C_{s5,6}$	$3.32e^{-9}$	$3.16e^{-9}$

From the data comparison of Table 2, the results calculate by the finite element method is slightly larger than analytic method, that illustrate the validity of the finite element method. The difference mainly comes from the approximate calculation as the analytic formula cannot figure out the actual condition that electric field distribution influences the capacitance.

Conclusion

A finite element method is presented in this paper to calculate the electric and magnetic fields of transformer and then figure out the distributed capacitance and inductance parameters of windings. The calculation of disk-to-disk parameters of capacitance and inductance in a high voltage transformer compared with result of analytical method is similar. That means this method is feasible and accurate.

Acknowledgement

In this paper, the work was supported by NSFC (Project No. 51177103) and Program for LNIRT in University (Project No. LT2011002).

References

[1] RUN Quanrong, SHI wei. Suppression of VFTO by disconnector with opening and closing resistor in GIS [J].High Voltage Engineering, 2005, 31(12):6-8.

[2] JIN Lijun, ZHENG Yuanbing, PENG Ge, et al. Research on the ferrite for suppressing VFTO in GIS [J]. Transactions of China Electrotechnical Society, 2006, 21(4):7-10.

[3] Shibuya Y, Fujita S, Hosokawa N. Analysis of very fast transient overvoltage in transformer wingding [J]. IEE Proc Gistrib, 1997, 144(9):461-468.

[4] Fujita S, Hosokawa Y. Experimental investigation of high frequency voltage oscillation in transformer wingding [J]. IEEE Trans on Power Delivery, 1999, 13:1201-1206.

[5] A. A. Dahab, P. E. Burke and T. H Fawzi, "A Complete Model of a Single Layer Air-cored Reactor for Impulse Voltage Distribution", IEEE Trans. Power Delivery. Vol. 3, No. 4, pp. 1745-1753.

[6] SUN Haifeng,CHEN Honghai. MATLAB based Simulating Calculation of oltageDistributionin Transformer Windings under VFTO [J]. Hebei Electric Power Technology,2004,23(4)

[7] B. M. Dent. E. R. Hartill and J. G. Miles, "Method of Analysis of Transformer Impulse Distribution Using a Digital Computer", Proc. IEE, Vol.105, pp. 445-459.

[8] P. Waldvogel and R.Rouxel, "A New Method of Calculating the Electric Stresses in the Winding Subjected to a Surge Voltage", Brown Boveri Review, Vol. 6, pp. 206-213.

[9] J. H. McWhirter, C. D. Fahrnkopf and J. H. Steele, "Determination of Impulse Stresses within Transformer Winding by Computers", AIEE Trans., Vol.75, pp. 1027-1279.

[10] K. Okuyama, "A Numerical Analysis of Impulse Voltage Distribution in Transformer Windings", Elect. Eng. Japan, Vol.87, 1967, pp. 80-88.

CHAPTER 3:

Environmental Engineering and Resource Development in Energy Industry

Advanced Materials Research Vols. 986-987 (2014) pp 709-712

doi:10.4028/www.scientific.net/AMR.986-987.709

Duplicate Confluence Precipitation Technology Processing Desulphurization Dust Removal Actual Waste Water Experimental Study

Gao Yunxia, Dai Xuemin, Yao Li, Nan Guoying

Hebei Institute of Architecture Civil Engineering, Zhangjiakou Hebei, China 075024,

Email: wljgyx@163.com

Keywords：Settling Technique of Compound Flow; Desulphurization Precipitator; Surface Load, impact

Abstract：In order to discuss the treatment performance of wastewater from desulphurization precipitator by settling technique of compound flow, the field test rendered the effluents of integrated desulfurization precipitator as the handing objects. The results show that the critical load of the sediment separator is 4mm/s. When the surface load is less than or equal to 4 mm / s, the turbidity of effluent is less then 10 degrees and the maximum is less then 18.2 degrees. The effect of hydraulic load impact on the water treatment system is greater than that of pH and SS of inlet. The treatment efficiency of field test is equivalent that of laboratory simulation.

The main source of the pollutants of industrial coal-fired boiler desulfurization dust catcher in the wastewater is coal combustion in boiler flue gas from coal-fired industrial boilers. In China, desulfurization precipitator for supporting the use of coal-fired industrial boiler can be divided into two generations and three categories. The second generation of desulfurization precipitator has the function of simultaneous desulfurization and dust removal with high efficiency. Industrial boiler desulfurization dust catcher is the core producer of waste water, property of flue gas, working fluid (water) and precipitator itself is the three basic ways of influencing wastewater quality. The coal quality, combustion and furnace of boiler, boiler load, structure and operation management of boiler, the types and performance of dust catcher, supply mode and property of working fluid influence the wastewater quality through their own way, SS of wastewater changes during the operation. At present, the industrial boiler in China have treatment technology of wastewater recovery in desulfurization precipitator like coagulating sedimentation [1-3], alkaline medium deep filtering technology [4], microporous ceramic surface filtering technology [5] and neutralization treatment technology of alkaline industrial wastewater [6]. Precipitation technology is widely used in the field of water treatment because of its economy and effectiveness. Advection sedimentation, inclined plate sedimentation and inclined tube sedimentation is the most traditional precipitation technology. The development of new high efficiency and widely suitable precipitation technology is the most active research direction [7]. The common characteristics of Industrial boiler desulfurization precipitator wastewater quality is high SS, high Al^{3+}, high Fe^{3+}, and low pH [8].

1 Experiment Device

As it is shown Chart 1, the treatment processing system includes inflow lifting system, coagulant medication system, pH value adjustment system, mixture flocculation unit, the composite sedimentation processing unit and flocculation by swirling flocculation column, with 2 types, which are type I D×h = 153mm×2080mm = 38.2L and type II D×h = 250mm×1733mm = 85.0L. Composite flow inclined plate settler are all single composite precipitator for the downward flow and upward flow.

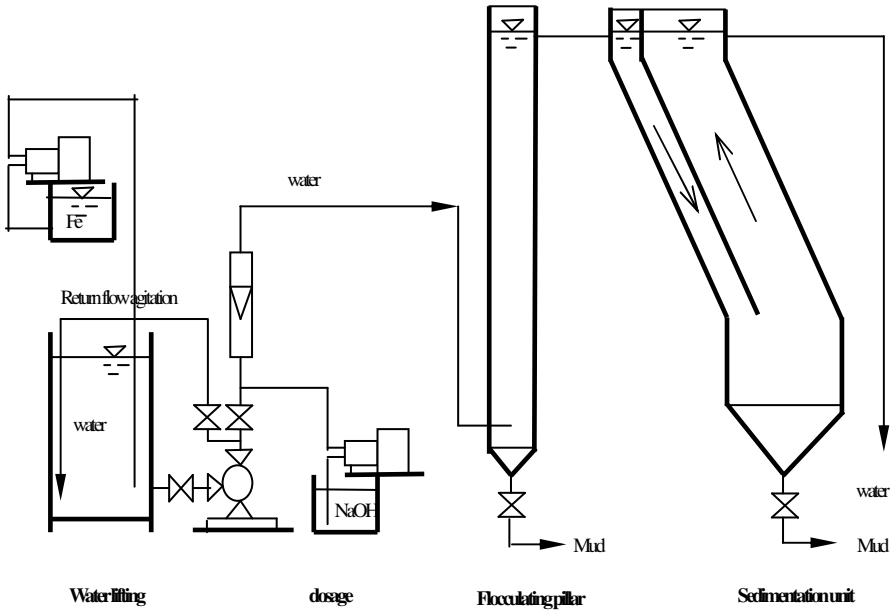

Chart 1: Process of Experiment

2 Experiment Water Sample

Experiments were carried out in an industrial boiler flue gas desulphurization and dust removal area, with waste water from integrated desulfurization precipitator, with SS 1596mg/L, 320 FTU of turbidity, total solids 2590mg/L, pH value 3.1, the average temperature 18.1 ℃. Using $FeCl_3$ and NaOH combined medication dosing method. Add $FeCl_3$ in the pump suction mouth, dosage of 10mg/L; Add NaOH in anterior pipeline of the measuring equipment, dosage of 20-40mg/L.

3 Experiment Equipment and Methods

3.1 Main Analytical Instrument and Equipment

Turbidity Measurement: By using phototurbidometry, we determined the value of extinction through type 721 Spectrophotometer made by Shanghai Second Analytical Instrument Factory. The testing sample is compounded with diatomaceous and the regression equation of standard curve as follows:

When turbidity between 3-10FTU：Y=110.57X-0.4936

When turbidity between 10-100FTU：Y=168.32X-7.1054.

pH Measurement: By the pHS-2 acidity meter made by Shanghai Second Analytical Instrument Factory, the method to measure pH is glass electrode method.

3.2 Experiment Content and Method

Steady running performance test uses the experiment method of inflow gradually to increase the load step by step. Table 1 is shown all the system performance of all experiment working condition. In the working condition 3 includes 2 different flocculation times.

The impact resistance performance experiment can change the water load, the inflow water quality (SS and pH) with the basis of certain running result to observe the impact resistance performance.

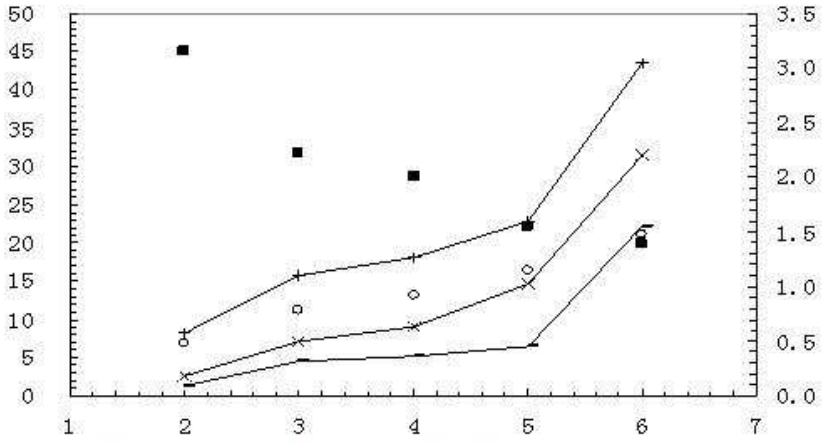

Chart 2: Effluent Turbidity-Net Surface

Table 1: Test Experiment Conditions of Working Condition

Experiment Working Condition	1	2	3-I	3-Ⅱ	4	5
Water Quality of Inflow Water						
pH Value	3.1	4.2	3.0	2.8	3.5	2.9
Turbidity Degree	325	365	330	310	310	345
Flocculation conditions						
Flocculation column No.	Ⅰ#	Ⅰ#	Ⅰ#	Ⅱ#	Ⅱ#	Ⅱ#
Flocculation time/min	7.1	4.7	3.5	7.9	6.3	5.2
Precipitation Surface Unit Load /mm/s	2	3	4	4	5	6

4 Experiment Result and Discussion

Steady Running Treatment Performance

Chart 2 displays the relationship that the effluent turbidity and removal rate are changing with surface load convert. In this table, the data of working condition 3 comes from 3-II operation status. The water quality fluctuation coefficient is the ratio of the max value of the effluent turbidity and the average value when $K_{\max}$ is running at the certain working condition. ΔC_{max} means the water quality fluctuation is poor.

Chart 2 shows that the effluent turbidity is increasing with the rise of sedimentation unit surface load. When $u_0 \leqslant 4$mm/s, the effluent turbidity is increasing slowly; When $u_0 > 4$mm/s, the effluent turbidity is increasing fast. Thus, from the experiment we find the critical value of the surface load is 4mm/s. The gradually decrease of $K_{\max}$ indicate the range of the relative volatility of effluent turbidity becomes smaller, and the rapid increasing of $\Delta C_{\max}$ indicate Absolute amplitude is on the increase. When the surface load is $u_0 \leqslant 4$mm/s, the average of effluent turbidity is <10FTU, the max value is <18.2FTU; When $u_0 \leqslant 5$mm/s, the average value of the effluent turbidity is <15FTU, the max value is $\leqslant$22.8FTU; When $u_0 \leqslant 6$mm/s, the average of effluent turbidity <32FTU and the max value is <43.5FTU.

Comparing with the traditional precipitation technique, duplicate confluence precipitation technology does not only achieve the same level of removal rate but it also has better adaptability of the inflow water quality as well as concentrating function.

5 Conclusions

1) Duplicate confluence precipitation technology processing desulphurization dust removal actual waste water has the reliable performance, with simple technology, combining the sediment and concentration together.
2) When the surface loading is $u_0 \leq 4$mm/s, the average value of effluent turbidity is <10FTU and the maximum value <18.2FTU. With the rise of surface loading, the effluent turbidity is increasing but the relative fluctuation range is lower with rise of absolute rangeability.
3) In the three elements of water load including water load, inflow SS and pH, the water load impact has the largest impact to the system treatment effect, when the water impact level reach to 1.2, the turbidity responsibility reach to 1.2.
4）Treatment processing performance of boiler desulfurization precipitator and laboratory prepared samples are basically the same, but affected raw water quality fluctuation in the field test, the effluent turbidity is more volatile.

Reference

[1] Yumin An, Ning Kang. *Industrial Boiler Dust Removal Mechanism in Wet Cyclone and Waste Water Chemical Coagulation*, Environmental Technology, 1994, 16(2) p.24-26.

[2] Xiaojun Wang, Jin Xiao. *Flocculant in the Treatment of Boiler Dedusting Ash Washing Wastewater by Modified Cationic Natural Polymer*, Guangdong Chemical, 1990, 25(3)p.33-34.

[3] Rulu Zhou, Zhongquan Guo, Jianguo Fang. *Experimental Study on Reuse Wastewater by Using Small and Medium-Sized Coal-fired Boiler Technology.* Coal Mine Environmental Protection, 2003, 12(3) p.17-19.

[4] Jingjin Liu, Zhuxin Chen, Huiying Zhang. *Application of the Boiler Slag in the Wet Dust Wastewater Removal Treatment*, Industrial Safety and Dustproof, 2001, 27(5)p.14-16.

[5] Jingjin Liu, *Application of Quartz Microporous Ceramic in the Boiler Wet Dust Removal in Wastewater*, Pollution Prevention Technique, 1996, 9(4) p.230-232.

[6] Zhiyi Ma. *In Dealing with A Case of Printing and Dyeing Wastewater*, Water Supply and Drainage, 1995, 13(11) p.24-25.

[7] Hongfeng Ding, Shigang Yang, Leifeng Han etc. *Boiler Wastewater Treatment and Reuse of Process Design*, Marine Meteorological and Hydrological Instrument, 2002, 15(2) p.52-54.

[8] Guoying Nan, Lin Li, Sun Dongtao and etc. *Industrial Coal-fired Boiler Desulphurization and Dust Removal Wastewater Quality Characteristics and Treatment Strategy*, In the Fourth Conference on Environmental Protection and Environmental Engineering, Chengdu, 2004 p.98-302.

Advanced Materials Research Vols. 986-987 (2014) pp 713-718

doi:10.4028/www.scientific.net/AMR.986-987.713

Numerical Simulation on U(Ⅵ) in Uranium Tailing Impoundment affected by acid rain

Ouyang Shuanglong[1a], Li Shuzhan[2], Zhou Shukui[1], Li Hua[1], Jiang Haihao[1], Deng Wenjing[1]

[1]Municipal Engineering, University of South China, Hengyang, 412001, China;

[2]Civil Engineering. Zhengzhou University, Zhengzhou, 450001, China

[a]ouyang1019@126.com

Keywords: uranium tailings impoundment, nuclide migration, static experiment, partitioning coefficient, numerical simulation

Abstract. As acid rain getting more and more serious, increasing attention is given to environmental effect assessment of uranium tailings under the condition of acid rain. In the paper, influence of acid rain to partitioning coefficient (Kd) of U(Ⅵ) in soil was studied, and migration of radionuclide uranium in soil was simulated by computer. The static experiment results showed that the Kd value of U(Ⅵ) in soil reaches minimum value when pH is 2.0. When 2.0＜pH＜3.5, the Kd showed a rising tendency； The Kd in soil reaches maximum value when pH is 3.5. And when 3.5＜pH＜8.0, the Kd showed a decreasing tendency. This paper has taken a large uranium tailings impoundment in South China as an example studied by VisualModflow. After setting up models of groundwater movement and radionuclide migration in the study area, migration tendency of radionuclide U(Ⅵ) was simulated and pollution of radionuclide to environment was predicted. The results of simulation show that the migration of uranium speed to be the slowest when pH = 2.0, and the figure to be the fastest when pH = 3.5. Furthermore, maximum speed is about 1.24 times of minimum speed.

Introduction

Since the early 1950s，our country has already started to uranium geology work. China is a big mining country, the capacity of tailings in China is more than one hundred million tons [1-3].Uranium slag is a product of uranium hydrometallurgical processes, which is usually stored in the uranium tailings. Uranium tailings contain depleted ore that have extracted uranium and various contaminants produced during the process of mining, also includes not recycled uranium and all decay daughters of uranium series [4-6]. It is usually open-air stacking in the tailings area. Due to the effect of leaching of the atmospheric precipitation, heavy metal in the tailings and radionuclide are easy to enter the shallow groundwater, which have serious impact on the ecological environment of the uranium tailings and its surroundings[7-8]. Therefore, the development on simulation research of radionuclide migration in uranium tailings may well make sense to analysis the groundwater pollution that uranium tailings could produce and offer some solutions to this problem.

The studies about transport dispersion law of pollutant in ground water adopted more and more frequently over these years [9]. With the development of computer simulation technology on groundwater movement and pollutant diffusion, we have got surprising evolvement in quantitative description of pollutant migration. Computer simulation study of nuclide migration refers to predicting the activity and distribution of radionuclide in geological environment of tailings area and it's surrounding in hundreds, thousands or even millions of years. To finish the work, we need analysis a large number of hydro geological data, experimental data and technical information from relevant experiment. Meanwhile, we must combine with the related discipline theory model for computer simulation and calculation [10-11].

The research subject of uranium tailings is located in southern China, with abundant precipitation, but also a large acid rain region. Acid rain has an influence on the pH of the mining area. pH mainly

bring effects on the existence form of uranium in soil and the adsorption characteristics on the surface of soil particles, it also change the soil absorbability of uranium [12]. The main parameter reflects the soil on the absorption ability of the metal is the partitioning coefficient (Kd). A small Kd means metal ions mainly dissolved in the liquid phase, when Various chemical reactions occur easily. A large Kd shows that the soil absorbability of metal ions is strong [13].

This paper proposed adopts the method of experiments combined with simulation, study the effect of pH on the partitioning coefficient of U(VI) in the soil by static experiment firstly, then use groundwater numerical simulation software Visual MODFLOW to simulate the migration of U(VI) with different partitioning coefficient. These may provide the necessary theoretical base for comprehensive control of uranium tailings. Visual MODFLOW is a three-dimensional visualization professional software which is the most popular software in the international field of assessment and forecast of groundwater [14-15].

Solute movement equation

Migration partial differential equation in three dimensions of homogeneous chemical compositions was established in this study, considering the groundwater convection, dispersion, and fluid sink/source term, equilibrium adsorption, first-order irreversible reaction

$$\theta R\frac{\partial C}{\partial t}=\frac{\partial}{\partial x_i}\left(\theta D_{ij}\frac{\partial C}{\partial x_i}\right)-\frac{\partial}{\partial x_i}(q_i C)+q_s C_s-\lambda_1\theta C-\lambda_2\rho_b\overline{C} \tag{1}$$

Retardation factor is defined as:

$$R=1+\frac{\rho_b}{\theta}\frac{\partial\overline{C}}{\partial C} \tag{2}$$

In this formula, C is the dissolving concentration (ML-3); $\overline{C}$ is adsorption concentration (MM-1), which is the function of dissolving concentration C according to the adsorption isotherm relationship; q_i is Darcy velocity (LT-1); D_{ij} is diffusion coefficient tensor (L2T-1); q_s is flow of aquifer per unit volume in source/sink(T-1); C_s is concentration in source/sink (ML-3); λ_1 is reaction rate constant of dissolved phase (T-1); λ_2 is reaction rate constant of adsorbed phase (T-1); θ is porosity (dimension is 1); ρ_b is bulk density of medium in gap (ML-3)。

Materials and methods

Collection soil in field

Soil used in this paper is undisturbed soil, which is unpolluted and able to represent the main characteristics of the research region undisturbed soil. The physical structure of the soil should not be destroyed if there is a possibility when collecting.

The influence of different pH on the adsorption test

In this experiment, ten 250mL Erlenmeyer flasks were divided into two groups, A and B, each group has five Erlenmeyer flasks. Then added 1g mining soil sample which sifted by a No. 35 sieve to group A; and added 1g soil sample around the area which sifted by a No. 35 sieve to group B. Next, added equivalent dose of U3O8 solution which CU(VI)=5mg/L into group A and B. then adjusted pH value to 2.0, 3.5, 5.0, 6.5, 8.0 using sodium hydroxide solution and nitric acid(error was plus or minus 0.05). At the same time, kept the water-soil ratio was 100: 1(mass). Shook the sample solution for 2 hours then let it stand for 24 hours, centrifuged the sample solution in the end. After centrifugation, the uranium content of supernatant was measured.

Method of analysis

This paper measured the uranium content of solution using GB6768-86-spectrophotometry.

Results analysis on static adsorption experiment

According to data measured by static adsorption experiment, the partitioning coefficient (Kd) were calculated by using the following formula: $\mathrm{Kd} = \frac{\mathrm{V}}{W}\left(\frac{C_0}{C} - 1\right)$

In this formula,

Kd ——partitioning coefficient (mL/g);

V ——volume of the soil solution (mL);

W ——mass of the soil sample (g);

C_0 ——initial concentration of heavy metal ions in the liquid phase (mg/L);

C ——initial concentration of heavy metal ions in the liquid phase after the soil adsorption (mg/L).

Curves of partitioning coefficient affected by different pH in soil were graphed after calculating (figure 1).

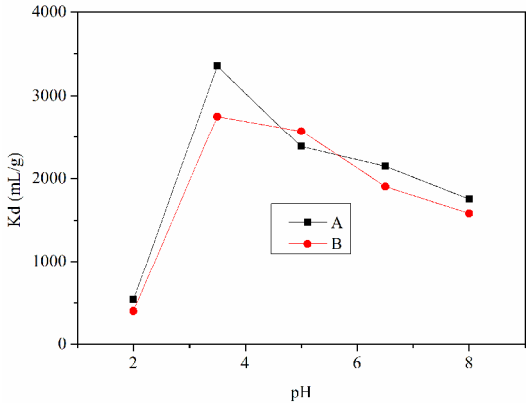

Fig. 1 The effect of pH on Kd of uranium in the soil

Transport and transform simulation of U(Ⅵ) in uranium tailing site

Boundary conditions

The east and west sides of the uranium tailing are surrounded by rivers, and the north side is a mountain range that sort of run east-west. Set the north side as water boundary, and set east, west, south sides as constant head boundary after comprehensive analysis of hydrogeology geological conditions in the study area. Moreover, set the entire ground surface in the study area as rainfall infiltration.

Set the aquifer as unconfined aquifer which is a same thickness and homogenization single layer according to the hydrogeology geological conditions in the study area. Assumed the flow state was steady flow at the same time. Set the entire tailing as an equivalent water head distribution surface, and infiltration of the tailing was simplified into uniform infiltration. The entire ground surface in tailing was supposed to equivalent concentrations surface.

Subdivision model

The area of simulating region was about 80 square kilometers. The plan of whole region was divided into 100 rows and 80 columns, and the length and width of each grid was 100 meters. In order to make the simulation results in more reliable, and the distance and direction of nuclides migration exactly, the plan of Uranium Tailing was divided into 200 rows and 160 columns. Then the accuracy of grid was doubled. The model was subdivided into two layers in vertical direction. The first layer was phreatic aquifer and the second layer was aquiclude. The elevation of simulating region was about 30 meters. Phreatic aquifer was set as 15 meters in this study.

Determine the model parameters

According to the hydrogeology geological conditions in the study area, the percolation coefficient of aquiclude in simulating region was divided into three different parts. And percolation coefficient, specific yield, porosity, etc were assigned respectively in each area.

The mock object was radioactive nuclides of uranium in this study. Concentration in simulating region except for uranium tailing was zero. Infiltration supplement of the uranium tailing was generalized into uniform infiltration, and concentration boundary was supposed to uniform. According to the maximization principle of pollution damage, set the average concentration of U(VI) before the uranium tailing operate as initial concentration in simulation.

Correct the model

In order to accurately describe the characteristics of the aquifer, each parameter such as percolation coefficient was adjusted for several times. Thus, head by simulation corresponds closely to the measurements by drilling, and the modeling result would be exact.

Percolation coefficient, dispersion coefficient, specific yield in each part was listed in table 1.

Table 1 Values of parameters involved in model

parameter	1	2	3
percolation coefficient K(m/d)	30	6.5	4.0
specific yield	0.014	0.009	0.007

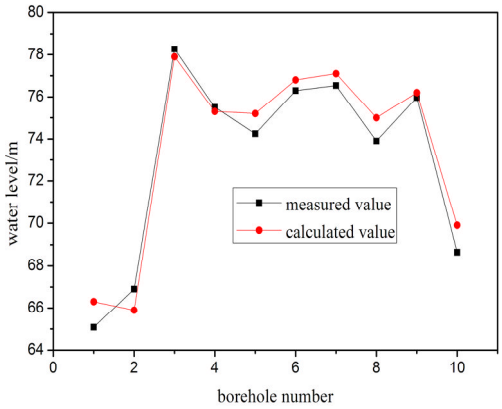

Fig.2 Water level fitting of observation boreholes

The simulated heads were compared with the drilling ones (as shown in figure 2), and a good agreement was obtained, which indicated the model founded was reasonable and reliable. Therefore, the model founded was used to simulate the migration of U(VI) in uranium tailing.

Analyses on migration simulation results

Basing upon the experimental data, three groups of partitioning coefficient (pH=2.0, 3.5, 8.0) were input the model. Following results were listed after running the model.

(1) pH=2.0, Kd_1= 398mL/g (partitioning coefficient in uranium tailing); Kd_2 = 532 mL/g (partitioning coefficient around the mining area), concentration distribution of U(VI) in groundwater after a year as shown in figure 3:

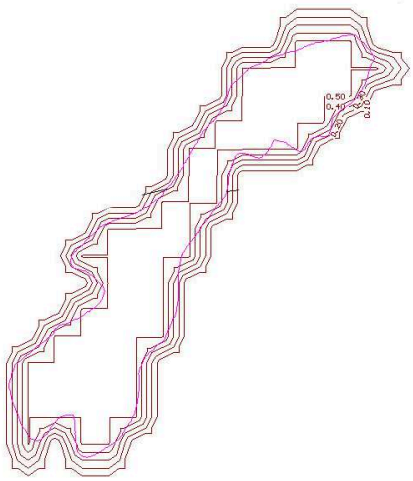

Fig.3 Contour map of the uranium mass concentration in the groundwater in 1 year (pH=2.0)

(2) pH=3.5, Kd_1= 2754mL/g (partitioning coefficient in uranium tailing); Kd_2 = 3357 mL/g (partitioning coefficient around the mining area), concentration distribution of U(VI) in groundwater after a year as shown in figure 4:

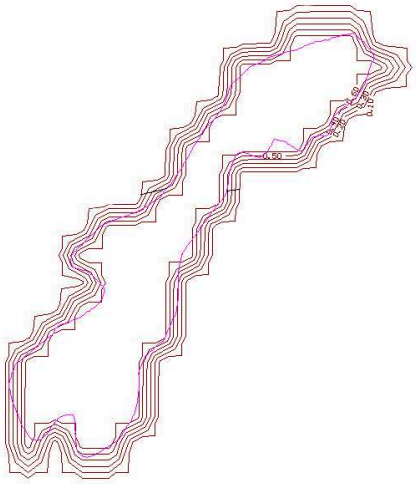

Fig.4 Contour map of the uranium mass concentration in the groundwater in 1 year (pH=3.5)

(3) pH=8.0, Kd_1= 1582mL/g (partitioning coefficient in uranium tailing); Kd_2 = 1751mL/g (partitioning coefficient around the mining area), concentration distribution of U(VI) in groundwater after a year as shown in figure 5:

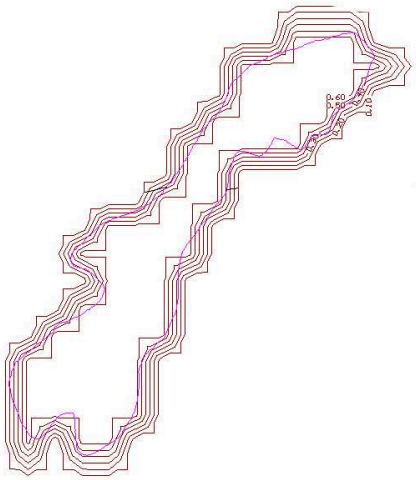

Fig.5 Contour map of the uranium mass concentration in the groundwater in 1 year (pH=8.0)

As can be seen from these three figures, the variation of pH value had definite influence on migration of U(VI) under the same conditions. The migration of uranium speed to be the slowest when pH = 2.0 and the figure to be the fastest when pH = 3.5. Furthermore, maximum speed is about 1.24 times of minimum speed. Therefore, control of the pH value in uranium tailings has certain actual significance in prevention and control of radioactive pollution.

Conclusions

1) From the results of numerical simulation, the migration of U(VI) in aquifer is relatively slow, surface water isn't polluted so far. But since long half-life of uranium, it is necessary to take long-term monitoring to it.

2) The pH value has impact on partitioning coefficient, thus affecting the migration of U(VI) in groundwater. So, control of the pH value in uranium tailings and acid rain management has much practical significance in prediction and controlling the pollution problem in uranium tailings.

Reference

[1] Under DH, Analysis of uranium supply to 2050[M].IAEA, The uranium production cycle and the environment. IAEA-S-M-362/2. Vienna:IAEA,2002.

[2] LI he-llian, CHEN jia-jun, GU zhi-jie. Study on Environmental Impact of Uranium Mill Tailings on Groundwater [J]. Techniques and Equipments for Environmental Pollution Control, 2000,1(3):82-88.

[3] LI GEN, WANG lai-gui, CHEN LEI, ect. Numerical Simulation of the Seepage Stability of A Tailing Reservoir [J]. Metal mine, 2008,(9):123-125.

[4] PAN ying-jie. Environmental Protection Technologies and Prospect for Uranium Mining and Metallurgy in China [J]. Uranium Mining and Metallurgy, 2002,21(1):43-46.

[5] LI he-llian, CHEN jia-jun. Numerical Simulation of ^{238}U in Uranium Mill Tailing Impoundment [J]. Safety and Environmental Engineering,2007,14(1):36-38.

[6] PAN ying-jie. Exploration on Final Disposal Technologies of Uranium Waste Ore and Tailings [J]. Uranium Mining and Metallurgy, 994, 13(4): 223-227

[7] ZHANG xiao-wen, ZHOU yao-hui, LI cong-kui, ect. Study on Filling Treatment of Heap Leaching Tailings of Uranium Ore [J]. Environmental Engineering, 2004,22(1):51-53.

[8] MA cong-an, LI ke-min, SHI LEI, ect. Application of Visual MODFLOW in Simulation of an Opencast Mine Underground Water [J]. Environmental Engineering, 2011,29(1):98-101.

[9] ZHONGHE WANG and MYRON B. ALLEN. Modeling Full-Tensor Anisotropy in Groundwater Flow Via an Iterative Scheme for Mixed Finite Elements [J].Transport in Porous Media,1996,25:147-165..

[10] YANG ming-tai. The status quo of radionuclide migration [J]. Nuclear Electronics & Detection Technoligy, 2006,26(1):126-128.

[11] TUO xian-guo, XU zheng-qi, MU ke-liang. Development of Radioactive Nuclide Migration Study in Different Mediums. Computing Techniques for Geophysical and Geochemical Exploration, 2006,28(1):36-40.

[12] ZHAO jin-yan, WANG jin-sheng, SUN fu-li, ect. Experimental research on the pH influence of lead and mercury absorption on the soil in the unsaturated zone [J]. Hydrogeology & Engineering Geology,2005,6:16-19.

[13] H Veeresh,S Tripathy,et al. Sorption and distribution of absorbed metals in three soils of India[J].Applied Geochemistry,2003 ,18:1723-1731.

[14] WU jian-feng, ZHU xue-yu. Discuss the Developing Trends of Groundwater Simulation Software by MODFLOW [J].Geotechnical Investigation & Surveying, 2000(2):12-15.

[15] Laura K Lautz, Donald I Siegel. Modeling surface and ground water mixing in the hypothetical zone using MODFLOW and MT3D[J]. Advances in Water Resources,2006(29):1618-1633.

Advanced Materials Research Vols. 986-987 (2014) pp 719-721

doi:10.4028/www.scientific.net/AMR.986-987.719

Petrological, geochronological and geochemical constraints on Hot Dry Rock geothermal applications

Andong WANG[1,a], Zhanxue SUN[1,b], Baoqun HU[1,c], JinHui LIU[2,d], Jianjun WAN[1,e]

[1]State Key Laboratory Breeding Base of Nuclear Resources and Environment (Ministry of Education), College of Earth Sciences, East China Institute of Technology, Nanchang 330013, China

[2]School of Water Resources and Environmental Engineering, East China Institute of Technology, Nanchang 330013, China

[a]adw008@mail.ustc.edu.cn [b]zhxsun@ecit.cn [c]bqhu@ecit.cn [d]liujh@ecit.cn [e]932106487@qq.com

Keywords: Hot Dry rock, petrology, geochronology, geochemistry, geothermal application

Abstract. In the past forty years, the investigation on Hot Dry Rock (HDR) geothermal resource has been a hot topic. A great number of investigations confirm that electricity power generated from HDR is feasible and propose that a right HDR site is composed of basement rock and its overlying cover. In the present study, we explore the petrology, geochronology and geochemistry features of the HDR basement rocks with the aim to further optimize HDR siting conditions. Combined analyses show that young S-type or crustally-derived granites with high U, Th and K contents have great potential to develop HDR geothermal resources.

Introduction

The concept of HDR, which is defined as the deep hot crystalline rock, has firstly been proposed by American scientists at early 1970s during the first oil crisis [1]. Subsequently, American and other seven countries have carried out HDR experiments at several different locations like Fenton Hill (American), Soultz-sous-Forêts (France), and so on [2] [3] [4]. Generally, a suitable HDR site should be composed of "basement" rocks (i.e., the deep crystallization rocks) and their overlying "cover" [5]. A large number of HDR experiments and numerical simulations indicate that electricity power generated from HDR is feasible and also suggest that HDR geothermal resource is a kind of renewable and local energy resources with great potential [3]. In this regard, many other countries including developed and developing ones will plan to develop HDR geothermal resources in the near future. However, in order to reduce the cost and skill risks, we should select the most possible HDR extraction sites for geothermal applications [5]. In the present contribution, we explore the possible constraints from petrology, geochronology and geochemistry data for basement rocks with the aim to further optimize HDR siting conditions.

Petrology constraints

In theory, any position on the Earth has potential for developing HDR geothermal applications because the temperature becomes higher from surface to bottom. However, due to the skill, cost and other factors, the site should be located in some special locations. Voluminous investigations exhibit that the most suitable rock types for HDR geothermal applications are S-type or crustally-derived granites including K-feldspar granites, mica- or biotite-bearing granites, monzogranites, leucogranites, syenogranites, and so on [4]. Petrologically, the main composition minerals for these granites are K-feldspar, mica (biotite or muscovite), plagioclase, quartz with minor accessory and secondary minerals like zircon and chlorite [5] [6]. Most of the major minerals belong to felsic or leucocratic minerals [6]. In contrast to the metamorphic rocks, basic rocks and A-type granites, the above-mentioned granites are predominantly sourced from remelting or differentiation of pre-existing crustal materials with minor or no involvement of mantle-derived materials [4]. Analytical results also indicate that the S-type or crustally-derived granites have relatively higher

volumetric heat production rates than those of gneisses, schists, amphibolites, quartzites, ultrabasites and basalts [5] [6]. Thus, the major rock types for HDR basement rocks are S-type or crustally-derived granites.

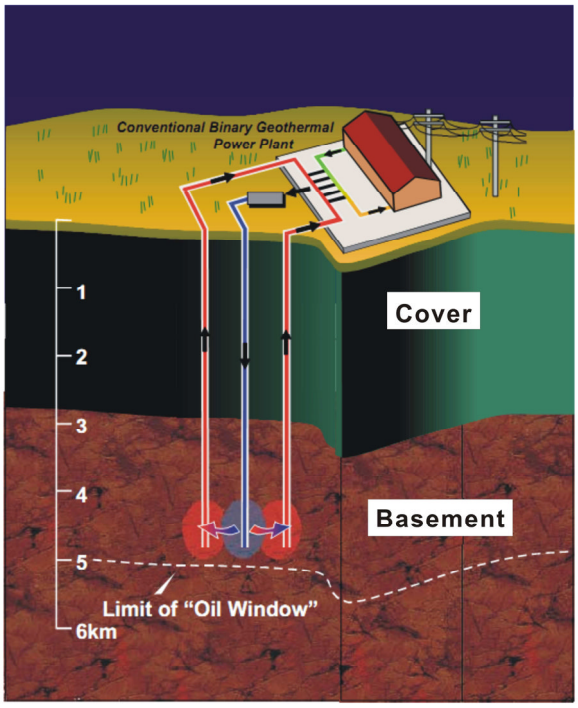

Figure 1. A carton diagram showing that a HDR site is composed of basement rocks and cover sedimentary rocks (modified from [7])

Geochronology constraints

The formation or emplacement timing of the basement rocks is also vital for developing HDR geothermal resources. Voluminous surface heat flow data show that the Precambrian continental crust or landmass like shield displays low heat flow value but relatively younger terrains exhibit high heat flow, implying that the ancient shield is cold and the HDR sites should be located in the younger terranes [8]. Elemental determination results suggest that ancient basement rocks are easily exposed and eroded, which result in the loss of mobile radioactive elements U, Th and K. Therefore, the Precambrian basement rocks generally display low volumetric heat production rate and geothermic gradient. As an example, the Sweden Fjällbacka HDR project is located in the Precambrian (about 920Ma) crystalline bedrock with low heat flow density of 35-65 mW/m^2 and temperature gradients of 10-18 °C/km [9]. Based on these conditions, we suggest that Fjällbacka HDR project is not suitable for generating electric power. In fact, the Sweden government has ended it in 1989.

Geochemistry constraints

The heat sources of HDR are predominantly stemmed from the long half-life radioactive elements U, Th and K, which are incompatible and easily concentrated in continental crust. In this regard, the mantle-derived rocks are generally depleted in U, Th and K, while crustally-remelting granites are commonly enriched in U, Th and K [4]. It is noted here that not all but a small proportion of crustally-remelting granites can be used to abstract HDR geothermal sources. Generally, the right HDR basement rocks display high K_2O/Na_2O ratios larger than 1.0 belonging to the K-rich granites, and show U, Th and K peaks in the primitive-mantle normalized trace element diagrams. The thermal ability of basement rocks can be evaluated by volumetric heat production rate. On the basis of previous data, it is proposed in the present study that the granites can be used to develop HDR geothermal resources when their volumetric heat production rates are equal to or larger than 5.0 μW/m^3 [5].

Conclusion

Coupled analyses from petrology, geochronology and geochemistry for HDR basement rocks suggest that young or Phanerozoic especially Mesozoic and Cenozoic S-type or crustally-derived granites with high U, Th and K contents have great potential to develop HDR geothermal resources. However, as is stated above, a right HDR site should be composed of basement rocks and cover sedimentary rocks or sediments. The feature of cover sedimentary rocks or sediments is another subject in the next study.

Acknowledgement

This study was financially supported by grants from geothermal survey project of China Geological Survey (No. [2011]01-17-31), Doctoral Fund from East China Institute of Technology (NO. DHBK2013101) and Opening Fund from State Key Laboratory Breeding Base of Nuclear Resources and Environment (NRE1306).

References

[1] Robinson E S, Potter R M, McInterr B B, et al. A preliminary study of the nuclear subterrene. In: M C Smith (Editor), Geothermal Energy. Los Alamos Natl Lab Rep, 1971, LA-4547: Appendix F.

[2] Tenzer H. Development of hot dry rock technology. International Workshop on Hot Dry Rock Technology, 2001, pp 1-14.

[3] Ledésert B A, Hébert R L. The Soultz-sous-Forĕts' enhanced geothermal system: a granitic basement used as a heat exchanger to produce electricity. In: Heat Exchanges—Basic Design Applications. 2012, pp 477-504.

[4] Wang A D, Sun Z X, Hu, B Q, et al. Guangdong, a potential province for developing Hot Dry Rock geothermal resource. Applied Mechanics and Materials, 2014, 492: 583-585.

[5] Rybach L, Bodmer P, Pavoni N, et al. Siting Criteria for heat extraction from hot dry rock: application to Switzerland. Pageoph, 1978, 116: 1211-1224.

[6] Zhao P. Investigation of heat production in southeast China [D]. Beijing: Chinese academy of sciences, 1993.

[7] Chopra P, Wyborn D. Australia's first hot dry rock geothermal energy extraction project in up and running in granite beneath the Cooper Basin, NE South Australia. The Ishihara Symposium: Granite and Associated Metallogenesis, Geos. Au., 2003, PP43-45.

[8] Sclater J G, Francheteau J. The implications of terrestrial heat flow observations on current tectonic and geochemical models of the crust and upper mantle of the Earth. Geophys. J. R. astr. Soc., 1970, 20: 509-542.

[9] Wallroth T, Eliasson T, Sundquist U. Hot dry rock research experiments at Fjällbacka, Swden. Geothermics, 1999, 28: 617-625.

Advanced Materials Research Vols. 986-987 (2014) pp 722-724

doi:10.4028/www.scientific.net/AMR.986-987.722

Research on reservoir characteristics in San Zhao Peripheral zone

Sun Fei[1, a], Qiuhan Qin [2,b] ,Shenghao Zhou[3,c] ,Li Peng[4,d]

[1, 2,4]Northeast Petroleum University,Daqing ,China

[3]The third production technology research institution of petroleum,ChangQing,China

[a, b] woaiwangguai@126.com, [c] 57989809@qq.com, [d] 755088447@qq.com

Keywords: FuYu oil layer; Yang DaChengZi reservoir; reservoir pore space; reservoir permeability; diagenic metamorphism of reservoir.

Abstract. Using a large number of core, logging and seismic data, on the basis of sequence stratigraphy, reservoir geology, sedimentology, such as theory, the San Zhao peripheral zone were studied. FuYu reservoir is studied and Yang DaChengZi reservoir structure of reservoir. Based on coring well cores observation and rock thin section, casting thin sections and scanning electron microscopy (sem) analysis techniques, such as the SQ3–Y1 a sedimentary period main sedimentary, main lithological types, and different oil reservoir is studied.

Regional Geology Overview

San Zhao surrounding the zone through years of exploration, the principal part of the construction of a total of exploratory well, evaluation Wells and development Wells, seismic exploration degree is higher, the basic is covered by 3 d seismic.The main purpose of the study area layer to help Yang oil layer. Fu Yang oil reservoir pore types as follows: primary intergranular pore, narrow primary intergranular pore, dissolution to expand intergranular pore and intragranular dissolved pore, mold holes and cracks.Various pore types, Fu Yang oil reservoirs are mainly composed of secondary pores.

Reservoir petrology characteristics

Reservoir petrology characteristics mainly reflect reservoir sandstone of compositional maturity and structural maturity, is to control the reservoir physical property of original sedimentary conditions and evaluation index, at the same time affect the reservoir in the late diagenesis and diagenetic evolution.

2.1 Fuyu oil layer

FuYu reservoir rock types in the delta plain sedimentary grey lithic feldspar sandstone (powder), a small amount of transition to feldspathic lithic sandstone .The feldspar content is 25%~45%;Quartz content is 12%~42%;Cuttings content is 16%~62%, the Yang DaChengZi reservoir rock debris content increased slightly, the average is about 32%. Lithic types are mainly acidic extrusive rock cuttings and metamorphic rock cuttings. Through the casting thin sections, rock thin sections and scanning electron microscopy (sem) analysis shows that the rock-good sorting, rounded way round - edge is given priority to. Cement and mixed base content and features similar to Yang DaChengZi reservoir. Overall, FuYu reservoir sandstone rock particle size, structure and composition of medium-low maturity of petrology characteristics.

2.2 Yang DaChengZi reservoir

Through core observation and microscopic microscopic analysis showed that Yang DaChengZi reservoir rock types in fluvial facies sedimentary grey lithic feldspar sandstone (fine) quality is given priority to, a small amount of transition to feldspathic lithic sandstone .The feldspar content is 27%~47%; Quartz content is 24% ~36%; Cuttings content is 22%~48%, lithic types are mainly acidic extrusive rock cuttings, followed by metamorphic rock cuttings. Rock-good sorting, rounded way round-edge is given priority to. Calcite and argillaceous cement development, content is generally greater than 10%;Impurity content of the base is less, generally less than 5%.In general, Yang DaChengZi reservoir sandstone of rock fine granularity, structure and component maturity middle-class petrology characteristics.

Reservoir diagenesis and diagenetic sequence

3.1 Diagenesis

Diagenesis is one of the main factors affecting reservoir physical properties. Ro value is between 0.5%~1.3%, and in the study area is in A rock up phase.

3.1.1 Compaction

In the study area, sandstone reservoir, shallow buried depth overall, general distribution in the range 1200 m to 2400 m depth, compaction degree is weak, grain contact relationship to a point-line contact is given priority to, residual intergranular pore is development. With the increase of buried depth, occasional line contact, concave and convex contact, plastic debris was compaction deformation and the plastic debris is compaction are false mixed base. As compaction gradually increases, characterized by primary intergranular pore, grain contact relationship closer, rock density increases.

3.1.2 Dissolution

Dissolution is mineral type and volume conversion process. Accompany the feldspar dissolution of authigenic minerals such as kaolinite and quartz are precipitated. In the study area, acidic water may come from compaction of argillaceous rock.

3.2 Diagenetic stages and diagenetic sequence

By Ro data and the microscopic analysis of characteristics of mineral, springs for A period of Three to Yao in the study area is at A rock into A subage. The main diagenetic events can be described as: The medium intensity compaction: point - line contact, a small amount of concave and convex contact; The plastic debris compaction deformation; Primary pores gradually reduce, compaction residual intergranular pore. Late calcite cementation development: rich calcium ions under CO_2 involved in the formation water in occur between pore precipitation, precipitation of calcite.

In conclusion, early diagenetic sequence can be summarized as follows: compaction-calcite cementation-feldspar dissolution-calcite replacement of silica particles-occasional lysis pressure-a small amount of quartz overgrowth and surrounding particles of illite and chlorite envelope.

3.3 The reservoir pore type and pore evolution

Based on key Wells in the study area the casting thin sections and scanning electron microscope, spring for a period of three to Yao sandstone reservoir space types of the reservoir is given priority to with residual intergranular pore and dissolution pore, microfracture rare.

Overall, the changes of pore types in the study area from top to bottom is: the primary pore is given priority to, mixed pore, secondary dissolution pore. Transformation of influencing pore types and diagenesis are: the damage of calcite cementation, compaction, clay mineral formation and transformation; Improve the role of feldspar dissolution.

3.4 Reservoir control factors analysis and evaluation

Through the study of a mere 273 Wells in the core physical property data analysis, reservoir quality differences between different reservoir is obvious.

Table 1-1 Reservoir classification evaluation standard

Reservoir classification	Porosity (%)	Permeability (mD)	Reservoir space	Exploration results	Evaluation
	>12	>0.5	Intergranular pore,intragranular pore,fracture	Found oil gas fields	good
Ⅱ	8~12	0.1~0.5	Intergranular pore,intragranular pore,fracture	Found oil and gas fields	preferably
	5~8	0.01~0.1	Intergranular pore and fracture	Oil and gas showsgood	general
Ⅳ	<5	<0.01	Intergranular pore and fracture	Trace gas show	poor

3.4.1 Fuyu oil layer

FuYu reservoir buried depth is mainly for the 1600 m to 2000 m, is under FuYang DaChengZi reservoir significantly. Porosity is mainly distributed between 5% ~ 20%, average 12.1%.Permeability is generally less than $10\times10^{-3}\mu m^2$, with a mean of $13.82\times10^{-3}\mu m^2$. Strongly the cementation of FuYu oil reservoir property significantly lower than the overlying putaohua oil layer, and Yang DaChengZi reservoir.

By studying FuYu oil layer thickness of single sand body statistical histogram can be seen, FuYu oil layer thickness of single sand bodies are mainly distributed in 1~2 m, about 41%, the second is less than 1 m single sand body, accounted for 36%, on the whole the thin sand body dominant, but these sand body vertical superimposed each other and accumulated considerable thickness.

3.4.2 Yang DaChengZi reservoir

Yang DaChengZi reservoir porosity is mainly distributed between 5% ~ 15%, the average of 10.8%.Permeability is generally less than $10\times10^{-3}\mu m^2$, with a mean of $1.8\times10^{-3}\mu m^2$.

By carbonate content and depth of diagram analysis shows that in the 1900 m and 2200 m or so, appear unusually high value with two carbonate content corresponding to the porosity and permeability of low-value belt, with dense calcite cementation. Carbonate content and porosity is very good relationship, shows that the decrease of porosity in the study area is closely related with calcite cementation.

Conclusion

(1) FuYu oil layer due to the intense calcite cementation have a poor reservoir property, and the underlying Yang DaChengZi reservoir reservoir property.

(2)The physical properties of the reservoir in the study area are mainly controlled Yu Changshi selective dissolution and compaction.

(3)The feldspar dissolution and calcite cement difficult soluble or insoluble;Kept good for weak compaction, primary pore and the late acid dissolution in water easily into the rock.

(4)Use of FuYu reservoir strata slice technology can obtain the key layer of shallow water delta sand body distribution characteristics and Yang DaChengZi reservoir river sedimentary sand body distribution characteristics.

(5)In the shallow water delta distributary channel, underwater distributary channel sand body and fluvial channel sand body distribution range is wide, vertically superimposed each other, on the transverse fault fold shall, constitute a favorable oil and gas reservoir.

References

[1] Taiju Yin, Changmin Zhang,Tang jun, etc. The plant oil storage layers of structure analysis [J].Journal of JiangHan petroleum institute,2001, 23 (4):19-22.

[2] Yinan Qiu , Ailin Jia. Reservoir geological model 10 years [J]. Journal of oil, 2007, 21 (4):101-104.

[3] Chen bo, Haitao Zhao. The research method system and ideas of the fine reservoir characterization study [J]. Journal of henan oil, 2006, 20 (1):21-24.

[4] Jianwei Feng, Junsheng Dai, GuoSheng Ji, etc. Logging data quantitative identification river reservoir structure elements [J], journal of China university of petroleum, 2007, 31 (5): 21-26.

[5] Guangqing Yao, Lianwu Li, Shangru Sun. Sandstone reservoirs constitute the research idea and method of quantitative analysis [J]. Journal of geological science and technology intelligence, 2001, 20 (1):35-38.

[6] Jiyu Liu, Jinbiao Yun, Lv Jing. Reservoir parameter quantitative prediction methods, JiLin geological, 2001, 20 (1):70-75.

[7] Shaobin Guo, Shaobo Sun, SongLiao basin sequence stratigraphy study new knowledge. Lithofacies palaeogeography, 1998, 18 (1):54-60.

Advanced Materials Research Vols. 986-987 (2014) pp 725-729

doi:10.4028/www.scientific.net/AMR.986-987.725

Study on coal's green mining technology roadmap of Jurassic coalfield in northern Shaanxi

Wei ZHANG[1,a], Jinsuo ZHANG[2,b], Jian XU[3,c]

[1,2,3] Research Centre for Energy Economy and Management ,Xi'an University of Science and Technology, 710054, China

[a]email: davidzw75@139.com, [b]email:mark56zhang@163.com, [c] email: xujian@xust.edu.cn

Keywords: Coal's green mining; Technology roadmap; Jurassic coalfield of northern Shaanxi

Abstract. Jurassic coalfield in northern Shaanxi is a typical ecologically fragile area. In recent years, with the rapid development of coal mining industry in this area, the environmental problems were caused by coal mining have become so serious that threat seriously to the sustainable development of northern Shaanxi. In this paper, the research team use multi-round expert seminar to design a coal's green mining technology roadmap(CGM-TRM) for Jurassic coalfield of northern Shaanxi, which will provide a macro guidance for related government, institutions and enterprises, and produce wide range of utility in relevant R&D activity.

Introduction

As a kind of low cost energy, coal play very important role in China's energy security and economic development, but with the continuous expansion of coal development in China, the environment destruction that caused by coal mining is highlighted, and has become serious problem that not only constrained healthy development of china's coal industry, but also seriously impact the sustainable development of coal area. So realize the green mining of coal is an important measure for scientific development of coal industry in China, also is the only route which must be passed to realize sustainable development in coal-rich regions.

There are a variety of reasons that initiate the environment destruction in the process of coal mining, among them, the technical failure (it means existing technology cannot take into account both efficient exploitation and environmental protection) is the most important one. At present, there are a lot of related research focus on the technology of coal's green mining in China, but the focus of existing research are mainly on the technology system and technology applications, for example, QIAN Ming-gao, MIAO Xie-xing, XU Jia-lin put forward the concept of coal's green mining, and analyzed the technical framework and application situation[1][2][3][4], ZhANG Guo-qiao,LI Gang analyzed the application of green mining technology coal in China[5], YU Xue-yi, HUANG Sen-lin analyzed the falling crack failure of overburden strata of shallow coal seam and its control method[6], WANG Shuang-ming, HUANG Qing-xiang, et al put forward the water protection mining technology based on the regionalization method [7], MIAO Xie-xing, ZHANG Ji-xiong, et al analyzed the waste-filling method and its application in fully-mechanized coal mining[8]. In contrast with the above research, the research on the technology foresight and R&D planning of coal's green mining is very lack in China, especially the coal's green mining technology roadmap (CGM-TRM) is still blank. Therefore, it is necessary to research and design CGM-TRM for strengthening the foreseen and planning of coal's green mining technology according with the real situation of typical mining area.

The general situation in the study area

Jurassic coalfield in northern Shaanxi, that is one of the seven major coalfield in the world, is located in the northern six counties of yulin city, namely Fugu, Shenmu, Yuyang, Hengshan, Jingbian and Dingbian, that covers an area of 27000 km^2 and buried 138.8 billion tons of proved reserves of coal resources, that accounts for about 53.5% of total amount of coal resources in

Shanxi Province. Since the turn of the century, has not yet been used 131.5 billion tons. Since the turn of the century, Jurassic coalfield of northern Shaanxi has entered into the phase of large-scale development. In 2009, China's central government set up 13 large coal base, among them, the main part of "Shaanbei" and "Shendong" base located in the Jurassic coalfield in northern Shaanxi. Up to now, the accumulative production of coal amount to 6.17 billion tons in this coalfield. In 2012, the coal output of Jurassic coalfield in northern Shaanxi amount to 300 million tons that accounting for 8.19% of the total coal production in China. This above shows that Jurassic coalfield of northern Shaanxi has become one of the most important coal base of China to support China's modernization construction, and will play an indispensable strategic role in the national energy security system.

In recent years, with a large number of coal resources was developed, the ecological environment destruction of the Jurassic coal field of northern Shaanxi is becoming more and more serious. In this coal field, Gob area is continuously expanding that cause the serious surface subsidence disaster, and destruct of the earth's surface buildings, land and other important production and living facilities. At the same time, coal mining also cause serious destruction of underground water resources, a large number of wells springs and stream dried up that lead a lot of ground vegetation to dying, and then raises the serious soil erosion and land desertification. For "Shenfu" mining area as an example, by the end of 2011, the coal mine gob area totaling 35446.57 hm^2, among them the subsidence area totaling 4410.8 hm^2, the underground water level of this area decrease from 1~2m to less than 31~50m, 4 rivers disappeared, lakes number reduced from 869 to 79. In Shenmu county, the area of soil and water loss is totaled 6700 km^2, erosion modulus is as high as 20-40 thousands t/km^2, soil and water loss amounted to nearly 100 million tons every year, land desertification is continuous expanding to the southeast at the rate of 0.5%/t. These above problems not only severely restricted the healthy development of coal industry in northern Shaanxi, but also serious threat the region's sustainable development.

Methodologies

Technology roadmap(TRM) is a kind of efficient tool for carry out technology foresight and R&D planning. It uses some simple form of graphics, tables and text to describe the step of technology innovation and logical relationship between them. It is useful to assistant the users to clear the technology development direction in specific technology areas, to identify the key technology, and to foresee the technical bottlenecks, and to choose suitable strategy for technology innovation. At present, TRM has been acknowledged as one of the basic tools of R&D management for government, institution and enterprises.

Execution flow of CGM-TRM. The research and develop of CGM-TRM of Jurassic coalfield in northern Shaanxi including four stages, it is as shown in table 1. In the first stage, the preparatory work for designing CGM-TRM was carried out by research team that including establishing expert database, formulating research plan and field investigations, etc. In the second stage, the first expert seminar was carried out to discuss the present situation and problems existing in the coal mining of the Jurassic coalfield of northern Shaanxi, and to set up the goals of CGM-TRM. In the third stage, the second expert seminar was carried out to select key technologies of CGM-TRM, and to analyze the possible bottleneck of key technologies, and then to discuss the strategies for breaking through the technology bottlenecks that including R&D project and R&D organizer, R&D schedule and R&D mode, etc. In the fourth stage, the first version of CGM-TRM was prepared by research team, and it was audited by the third expert seminar, and then according to the expert's opinions, the final CGM-TRM was formulated by the research team.

Tab 1 The Execution flow and method of designing CGM-TRM

Stage	Work Contents	Methodologies
1	Establishing expert database, formulating research plan and field investigations	Literature analysis, Questionnaire survey, Field investigation
2	Analysis of the present situation and problems, and set the targets of CGM-TRM of the Jurassic coalfield of northern Shaanxi	Expert seminar, Scenario analysis
3	Selection and analysis of key technology， and R&D strategy analysis	Questionnaire survey ,Expert seminar
4	CGM-TRM preparation, review and revision	Expert seminar

Targets setting. The target setting is the precondition for selection of key technology, thus it is the foundation for CGM-TRM designing. According to the resources occurrence and mining conditions in the study area, the research team grasps the status quo of R&D and application of related technology by literature analysis, questionnaire survey and field investigation. Based on the above works, the targets of CGM-TRM were determined by expert's opinion, that include establishing technological system of coal's green mining of Jurassic coalfield in northern Shaanxi from two aspects of feed forward prevention and environmental restoration, from 2013 to 2020 ,the subsidence damage reclamation rate reach 85%, the mine water utilization rate reach 100% and the waste rock and other solid waste utilization rate above 80%.

Key technologies analysis. Key technologies analysis, which mainly includes three contents namely key technology selection, technology bottleneck analysis and R&D project setting in this study, has been completed by the second expert seminar. According to the expert's opinion, water-preserved coal mining technology, filling mining technology and ecological restoration technology in subsidence area were selected as key technologies firstly, then the bottlenecks of every key technology were listed in detail, and then the R&D projects for breaking through the technology bottlenecks are designed respectively, the result of key technology analysis are listed in table 2.

Tab2 Key technologies analysis of coal's green mining of Jurassic coalfield in northern Shaanxi

Key technology	Technology bottlenecks	Project
Water-preserved coal mining technology	● Detailed exploration of hydrologic condition in mining area ● The influence mechanism of different mining method on water-resisting layer ● The technical specifications of water-preserved coal mining technology	◆ Detailed exploration of hydrologic condition in mining area ◆Research and design the specifications of water-preserved coal mining technology ◆ Demonstration project construction of water-preserved coal mining technology
Filling mining technology	● Low cost filling materials ● Filling equipment system that matching high-efficient coal exploitation mode	◆ Low cost filling materials ◆ High speed filling material transport system ◆ Integration hydraulic support for working face support and filling ◆ Industrial test and demonstration project construction of filling mining technology system
Ecological restoration technology in subsidence area	● Land reclamation technology in subsidence area ● Ecological reconstruction technology in subsidence area	◆ Experimental research of land reclamation and ecological reconstruction technology ◆ Comprehensive ecological restoration mode research of subsidence disasters

R&D strategies analysis. R&D strategy analysis, which also mainly includes three contents namely determining R&D organizers, designing R&D schedule and selecting R&D mode in this study, has been completed by the third expert seminar. As far as R&D organizers is concerned, there are one project should be organized by government, five projects should be organized by related university and institution, three projects should be organized by coal mine enterprises. In aspects of R&D schedule, the kind of technology R&D projects should be completed within 2-3 years, and the kind of industrial test and engineering demonstration project should be completed within 3-4 years. In the aspect of R&D mode, there are two projects should use technology introduction, three projects should use independent innovation, and four projects should use cooperative innovation. The R&D strategies are shown in the table 3.

Tab 3 R&D strategy analysis of key technology in CGM-TRM

Key technology	Project	Organizer	Schedule	Mode
Water-preserved coal mining technology	◆ Detailed exploration of hydrologic condition in mining area	☆	2-3	◈
	◆ Research and design the specifications of water-preserved coal mining technology	✦	3-4	◈
	◆ Demonstration project construction of water-preserved coal mining technology	△	3-4	⧖
Filling mining technology	◆ Low cost filling materials	✦	2-3	◈
	◆ High speed filling material transport system	✦	2-3	◇
	◆ Integration hydraulic support for working face support and filling	✦	2-3	◇
	◆ Industrial test and demonstration project construction of filling mining technology system	△	3-4	⧖
Ecological restoration technology in subsidence area	◆ Experimental research of land reclamation and ecological reconstruction technology	✦	2-2.5	⧖
	◆ Comprehensive ecological restoration mode research of subsidence disasters	△	3-4	⧖

☆ Government ✦ University and research institution △ Enterprises
◈ Independent R&D ⧖ Cooperative R&D ◇ Technology Introduction

Results

Based on two round expert seminar, research team draw up the first vision of CGM-TRM. After this, the third expert seminar was carried out to audit the first vision of CGM-TRM, according to the expert's opinion, research team modified the CGM-TRM correspondingly, then the final CGM-TRM were completed, it is shown in figure 1.

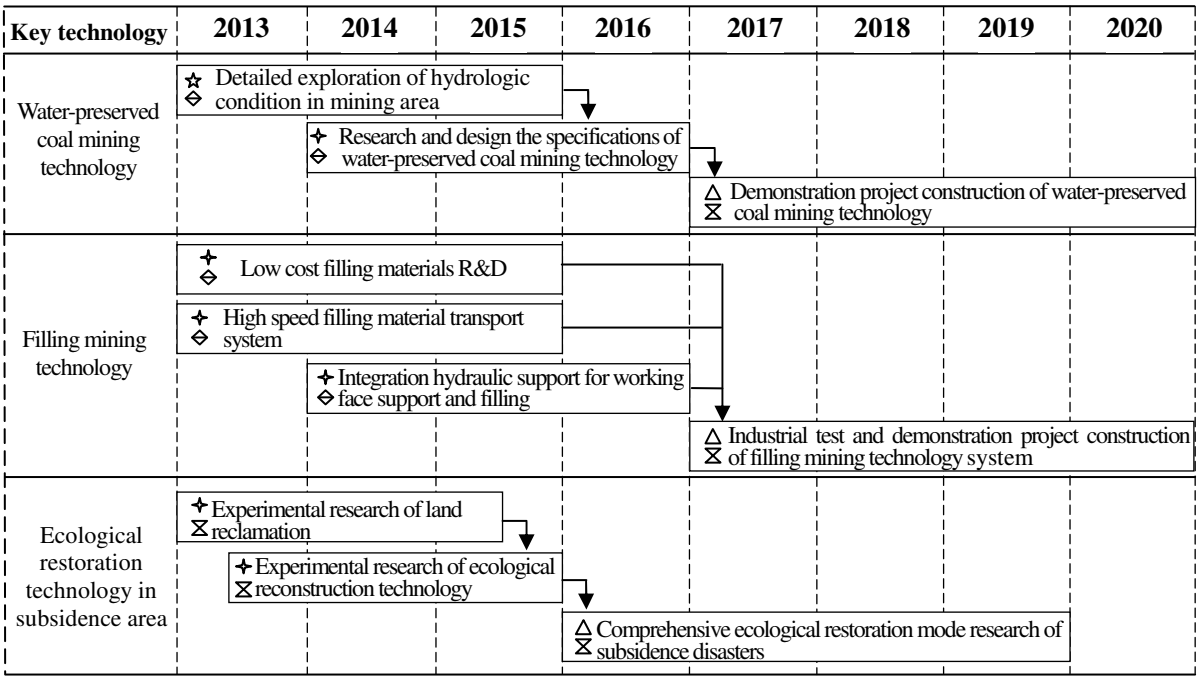

Fig 1 The CGM-TRM in Jurassic coalfield of northern Shaanxi: 2013-2010

Conclusions and Discussion

In this paper, the CGM-TRM of Jurassic coalfield in northern Shaanxi was designed by multi-round expert seminar, in which the key technologies and its R&D strategy were analyzed detailed. It will provide macro guidance for coal's green mining technology innovation, and help related governmental departments, institutions and enterprises to make clear the direction of future coal's green mining technology needs of Jurassic coalfield in northern Shaanxi, then help them to develop reasonable R&D plan accordingly for optimizing the allocation of innovation resources.

In next stage, an important work is to communicate the CGM-TRM with government departments, related institutions and enterprises, to reach a consensus in a wide range of relevant subjects. At the same time, as far as a lot of uncertain factors in the process of R&D as concerned, it is necessary to update and adjustment the CGM-TRM according with the changing conditions.

Acknowledgement

In this paper, the research was sponsored by the national soft science research program (Project No. 2013GXS4D151) and soft science research program of Shaanxi province (Project No. 2012KR2-01).

References

[1] QIAN Ming-gao, XU Jia-lin,MIAO Xie-xing. Green Technique in Coal Mining[J]. Journal of China University of Ming & Technology, 2003,32(4):343-348

[2] QIAN Ming-gao,MIAO Xie-xing,XU Jia-lin. Green mining of coal resources harmonizing with environment[J].Journal of China Coal Society,2007,32(1):1-7

[3] MIAO Xie-xing,QIAN Ming-gao. Research on Green Mining of Coal Resources in China: Current Status and Future Prospects [J].Journal of Mining & Safety Engineering, 2009,26(1):1-14

[4] XU Jia-lin,QlAN Ming-gao. Concept of green mining and its technical framework[J]. Science &Technology Review,2007,25(7):61-65

[5] ZhANG Guo-qiao,LI Gang. Green mining technology of coal and its application in China [J].China Coal, 2008,34(8):112-113

[6] YU Xue-yi, HUANG Sen-lin. Analyzing falling crack failure of overburden strata of shallow coal seam and its control method [J].Coal Geology and exploration, 2006,34(2):18-21

[7] WANG Shuang-ming, HUANG Qing-xiang, FAN Li-ming, et al. Study on overburden aquiclude and water protection mining regionalization in the ecological fragile mining area[J]. Journal of China Coal Society,2010,35(1):8-14

[8] MIAO Xie-xing, ZHANG Ji-xiong, GUO Guang-li. Study on waste-filling method and technology in fully-mechanized coal mining [J]. Journal of China Coal Society,2010,35(1):1-6

Advanced Materials Research Vols. 986-987 (2014) pp 730-733

doi:10.4028/www.scientific.net/AMR.986-987.730

Study on Dust Hazard in Coal Mine and Its Countermeasures

Shi-bin Wang[a], Ri-hui Chen*[, b] and Xiang-yun Meng[c]
Faculty of Land Resource Engineering, Kunming University of Science and Technology, Kunming 650093, China
[a]wsb18288667554@163.com, [b]chenrihui555@126.com (Corresponding author),
[c]yan761415498@163.com

Keywords: mineral dust, disaster, dust collection, prevention and control

Abstract. With the development of modern coal mining equipment, high-yield, high efficiency, high-speed mining technology was achieved, but also a sharp increase in the amount of dust generated in the mine at the same time, it damage workers health and bring insecurity to mine production. This paper has summarized the existing domestic and international prevention and control technology of dusts, elaborated mineral dust prevention and control work from the dust control, dust generation and dust diffusion three major aspects, and noted that the current technology trends.

Introduction

Mine dust is the inevitable outcome of the mine production and construction process, is the general term for all kinds of particles, but also led to one of the main mine production disasters. Mine dust bring hazardous to workers' health workers, cause pneumoconiosis, affect work efficiency; accelerate wear of mechanical equipment, reducing the life of some of the instruments; impede vision worker increases the occurrence of accidents; even some mineral dust (such as sulfide dust, coal dust)can explosive, have a serious threat to mine production safety.

Pneumoconiosis is the most serious occupational disease in our country and the majority of patients are mine workers, but people do not have enough hazard awareness on mine dust. A large amount of mine have less investment on preventing and controlling technology of dusts. Make mine dust prevention theory and application technology research is relatively weak, and less using. So far there is no complete set of prevention and control system and adequate attention.

Dust source control

Coal dusts mainly be produced in heading and wining faces, a large number of coal dusts would float in the face, hinder the normal production and harm the operator if don't take any dust control measures, so it is need to take appropriate measures to control and reduce mine dusts in heading and wining faces.

Coal seam infusion. In the coal body in advance before playing a number of drilling in coal mining, injection pressure water into the interior of coal, increasing moisture and reduce coal dust generated during mining. Practical experience has proved that water can get to a certain coal dust suppression effect, this method is also used in many coal mines abroad. Our preliminary trials to date, coal injection devices have a theoretical and rapid changes, accumulated a lot of experience.

Factors affecting coal seam water effects are follows: wetting properties of liquids, coal gas pressure and internal gas pressure on coal, cracks and pores of the degree of development and injection parameters. Injection parameters including injection pressure, velocity, flow, time and drilling depth, spacing, etc.. Different coal corresponding to different water parameters, they can be determined in accordance with successful experience of the same coal face reality. Injection equipments consist of drilling rigs, pumps, sealing, splitters, etc., the achievements have been developed in Xi'an branch of Coal Academy can be resolved into soft coal seam drilling equipment porosity problems, Chongqing branch of Coal Academy developed the coal mine linkage hydraulic drilling rig, and so on.

Chemical inhibitors. Chemical inhibitor is an aqueous solution when the additive injection coal, the purpose is to reduce the surface tension of water, reduce the polarity of the water, and enhance the dust trapping ability of the coal to improve wetting effect and strengthen the dust. Chemical inhibitors, also known as wetting agents, it can improve the effectiveness of coal seam water injection. WANG Huibing, who at the time of injection Yaoqiao conducted tests and found that after adding a wetting agent, injection speed increased, injection pressure reduced, the moist scope of coal expanded and water incremental increased, removal rate is improved and for the more obvious effects of respirable dust[1]. Development of new chemical inhibitors has made a lot of achievements in recent years.

Mining dusting

In the mining and tunneling face, coal continue to be destroyed, a large amount of dusts in the process of fragmentation, so it is need to take measures to collect dusts. Coal mining processes mainly have blasted mining, conventional mining and mechanized mining, according to the principle of the destruction of the coal dust to arrange different measures.

Water stemming blasting. Water stemming blasting is a new technology blasting that uses a special bag filled with water instead of solid stemming explosives filled in the front and rear. When blasted, water was atomized under high temperature and pressure into water vapor and fine water droplets to spread around rapidly penetrate into the coal weight, adsorbed gases and capture dust, which can reduce the harmful gases and dust concentration, but also have the flash suppressor, a cooling effect on the gas mines[2]. Notably PVC bag may generate new harmful substances in the explosion, the harmful to the human body should to be discussed and studied further.

Spraying dust technology. Water sprayed from nozzle with the help of pressure facilities, the water is atomized into fine droplets sprayed in the air, the movement of water droplets collide with dusts and moisture they to be dust-laden water droplets and sink under gravity; adhesion dust particles fall into pieces and make it difficult flying.

Air curtain dust technology. The air curtain is a transparent wall, formed by the use of strip-shaped slit blowing air jet wind, isolating contaminants to protect the health conditions of the workspace. In life there are widely used, such as the use to prevent mosquito flying into the kitchen. Air curtain was installed at the shearer to jet air to prevent the driver from the proliferation of cutting coal dust. Air curtain isolation technology is also applied in the heading face, Mainly have two forms of air nozzles and mural chimney. Air nozzle is similar to air curtain in shearer to form air wall. The air of mural chimney generated wall attachment effect, changed the axial wind into rotating wind in the section tunnel of heading face, and built air curtain to block the dust in front of the machine driver[3].

Dust diffusion controlled

Water curtain purification technology. Water pipe in the tunnel at the top or at the side, is provided with a plurality of sprays on the water pipe, the water curtain was jet by sprays to capture mine dusts. So the sprays shall be arranged so that the water curtain covered the whole cross section of tunnel. Water curtain can be arranged in the gateways of the full-mechanized caving faces and the driving working faces and other dust generating sources. Increasing the number of water curtain can improve the cleaning efficiency. According to mine conditions, water curtain spray can use the automatic mode of photoelectric and touch.

Precipitators. High efficient dust precipitator is so large that is unsuitable to be installed directly on the shearer and tunneling machine, usually installed in the return airway and into the face. At present, The dust collector in mine commonly used with SCF series fan, MAD series air purifier, KGC series dust tunneling machine and PSCF water jet fan etc[4]. They can be divided into dry dust remover, wet scrubbers and electrostatic precipitators three categories. Dry dust removal methods are gravitational settling, inertial dust, centrifugal dust removal and filtration. It needed to clean the collectors regularly, otherwise they would be blocked by dust and reduce

efficiency. Wet dust collector consumes a large amount of water, and sewage treatment, with low operation costing mine which have lots of water. Electrostatic precipitator dust removal efficiency is high, but the installation requirements are strict, need to consider the dust properties, installation conditions and economic cost. All series of precipitators can be divided into dry precipitators, wet scrubbers and electrostatic precipitators three categories. Dry dust removal methods are gravitational settling, inertial dust, centrifugal dust removal and filtration, to be timed for the dust to clean, to prevent dust collection efficiency decreases blocked. Wet scrubber water consumption and waste water to be treated, lower operating costs and more mines in the water. Electric precipitator have high efficiency, but the installation demanding is strict. Advantages and disadvantages of three types of dust, dust to be based on the nature of the site, installation conditions, considering the economic cost options.

Ventilation dusting. Ventilation dusting is using airflow to dilute and exhaust mineral dusts of air in operating site. The main factors of affecting the efficiency of ventilation dusting are the properties of wind speed, mineral dust density, particle size and so on. According to mineral dust choose the best wind, which can maximize exclude dust without causing secondary dust flying. The maximum wind speed in heading face specified in the "Coal Mine Safety Regulations" is 4m/s. Ventilation dusting systems about heading face has far-pressing-near-absorption, far-pressing and far- absorption -near- pressing can be selected according to production status and technical conditions of the mine. Ventilation dusting and dust catcher are often used together, for example, that dust catcher installed on extraction fan can greatly reduce dust exclude gas dust content in the heading face; with series ventilation underground, dust collector can guarantee the air quality of the next face in air return laneway in the coal face. In pressure and exhaust ventilation system, the layout of fan, air duct and dust catcher should be right, and arrange the air volume between pressure and exhaust ventilation system reasonable.

Individual Protection. The individual Protection is to reduce the inhalation of dust by wearing a variety of protective equipment. Although a series of measures are taken in the dust prevention and reducing of mine, there will be a small amount of fine dust whose concentration exceeds in some places suspended in a roadway, so individual protection is indispensable as the last checkpoint that prevents dust damage. Individual protection equipment mainly include dust mask, dust respirator wind, dust cover and so on, to let the workers wearing can breathe clean air and work normally.

Dust control is also a main measure to prevent the coal dust explosion, but from the governance of the coal dust explosion condition, it is necessary that measures are taken to prevent the coal dust burned, for example, exercise strict management over possible fire. To prevent and reduce the harm of coal dust explosion, measures of reducing the explosive power and the explosion range are also taken, including, regular cleaning the dust to prevent deposition of coal dust in explosion reaction, regularly spreading some inert powder in some tunnel to increase the ash of coal dust deposition, setting the flameproof shed to quickly absorb heat, eliminate fire and reduce the impact and so on after the coal dust explosion.

The trend of mine dust hazard control

Mine dust monitoring system used in mine will realize the networked, real-time online and intelligent development, in which the performance of dust concentration sensor is improving, and the instrumentation can automatically analyze the rule the generation and movement of mine dust. Monitoring can realize remote control and intelligent control, such as the spray system and flameproof shed automatically spraying according to the monitoring data. Mine dust monitoring system will share monitoring circuit and control platform with other monitoring system to realize the resource sharing. People will continue to study the water injection technology, equipment and technology of hard in-seam water infusion to promote the existing water injection process into automation development; improve the automation and standardization of spray dusting, do research in the formula of efficient environmental chemical inhibitor and its proportion technology, automatic feeding, the technology and its equipment of water quality filter technology; strengthen the research on the process of shearer and driving machine to reduce dust generated during the

production; actively introduce and digest the domestic and foreign advanced dustproof technology and apply foam dust[5], dust cylinder, ultrasound dust, magnetic dust in the production; strengthen the management of personnel and equipment, and develop comprehensive dustproof standard specification.

Conclusion

In view of the relationship between numerous dust control technology and the physicochemical properties of dust, the paper does testing and analysis of dust around the working face before making dustproof job. It is necessary to test and analyze the nature of true density, specific surface area, dispersion, surface tension, contact Angle, the optical properties, wettability and charged, etc. Then, based on the nature, the paper chooses different dustproof technique and technology.

References

[1] WANG Huibing, WANG Yuandong, and LU Ping. Research on Wetting Agent for Water Infusion of Coal Seams, Journal of China Coal Society1994,19(2)：151-160

[2] CHEN Dongchun, XU Peiming, and LI Ran. Comprehensive depress & removal of dust caused by mining activities in underground coal mine, Mining Engineering2010,8(3)：59-62

[3] CHENG Weimin, LIE Wei, NIE Wen, et al. The Prevention and Control Technology of Dusts in Heading and Winning Faces and Its Development Tendency. Journal of Shandong University of Science and Technology：Natural Science2012，,29(4)：77-82

[4] CHANG Haihu and LIU Zilong. KUANG CHEN FANG ZHI. Beijing: China Coal Industry Publishing House2007

[5] REN Wanxing, WANG Deming, GUO Qing, et al. Application of foam technology for dust control in underground coal mine. International Journal of Mining Science and Technology 24 (2014) 13–16

Advanced Materials Research Vols. 986-987 (2014) pp 734-737

doi:10.4028/www.scientific.net/AMR.986-987.734

Study on the Feasibility of SRV in Coal Reservoir

Linlin CHENG, Yuanfang CHENG, Chong CHEN, Dongfeng ZHU,

Wenbiao DENG

College of Petroleum Engineering, China University of Petroleum, Qingdao 266580, Shandong, P. R. China

[a]Email: chenglin_1015@126.com

Keywords: SRV; CBM; natural fracture; in-situ stress; brittleness index.

Abstract. In our country there is plenty of CBM (coalbed methane), but the state of CBM itself, unique output mechanism and low saturation, low permeability, low reservoir pressure and high gas content, et al. determine the low efficiency of it, so in order to improve CBM recovery, combined with the successful experience of north American shale gas reservoir by SRV(stimulated reservoir volume), the writer summarizes the implementation of SRV, deeply analyzes effectiveness and limitations of this new technology in CBM development. The results of practical research and theoretical analysis show that SRV in the coal reservoir can achieve the desired effect on the condition that there are great quantity of natural fractures, joints and bedding, weak structure surface development in the reservoir, the rock brittleness index is greater than 40 and horizontal principal stress difference is relatively smaller. Finally, simulating a well's condition by the MEYER software, the result shows that SRV is feasible in coal reservoir, which will create important guiding significance and practical value for the exploration of CBM.

Introduction

Our country is very rich in coalbed methane, but the low permeability of itself rusults in the low efficiency and poor economic, which means most wells must take measures such as fracturing stimulation to improve the reservoir flow capacity and thus achieve better economic. At present, the most common method is the conventional stimulation hydraulic fracturing technology by forming a single symmetrical wings cracks and complex "T" type joints, etc. to improve the flow properties of the reservoir. However, its effect is so insignificant that creativereform and innovation is necessary and urgent. Recently, SRVas a new technology has made remarkable achievements in the oil and gas exploration, especially in shale gas, which will creat a good inspiration for Coalbed methane exploration and development.

This paper proposes the conditions for SRV and analyses the effectiveness and limitations of SRV in coal reservoir combined the successful exploitation of the experience in North American shale gas; finally, takes a coalbed methane well for example to conduct numerical simulation software through MEYER, which confirms that SRV is feasible in coal reservoir.

Applicability of SRV

Being different from conventional fracturing, SRV refers to reconstructing reservoir during hydraulic fracturing, communicating simultaneously natural fractures through the man-made main cracks(fig.1), therefore three-dimensional fracture networks in which natural fractures and artificial fractures intersect is made to increase SRV and improve penetration channels. In other words, the core of this technology is to achieve 3D transformation and generate large-scale reticular flowing channel.

On the basis of the results of previous studies, the author puts forward the suitable conditions from natural fractures, the mechanism of reservoir rock composition and mechanical joints network structure: ①abundant natural fractures are queite necessary for SRV. When

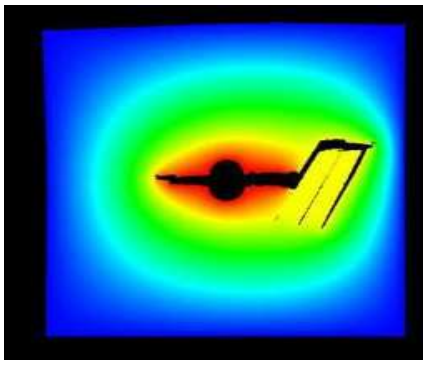

Fig.1 Seam network formation process schematic

implementing hydraulic fracturing,it can creat secondary seams as well as main cracks extending to three dimensions, which communicate natural fractures effectively.Besides, the higher the degree of development of natural fractures are, it is much easier to form complex network systems within the formation relatively. ②high content (greater than 35%) of Siliceous and high brittleness index is the material basis of SRV. In general, the higher the content of siliceous rocks are, the stronger its brittlenessis, higher consolidated Young's modulus is, the lower Poisson's ratio is, so it is far more prone to fracture failure of the reservoir. A large number of empirical data show that when the brittleness index is greater than 35, a wide crack fracture zone can be formed within reservoir; the reservoir system is easy to form a network of cracks on the condition that brittleness index is greater than 40. ③little difference betwween formation horizontal principal stresses is the basic prerequisite for SRV. It has been studied that situ-stress magnitude and orientation determines the orientation and shape of the artificial crack. As cracks always initiate and extends along the direction of maximum horizontal stress, it is easy to form a single main fracture morphology with large horizontal principal stress difference while it tends to form reticular cracks in the system.

Currently, the western has successfully develop this technology in dense shale gas, oil shale and sandstone gas and its mining efficiency has beed improved significantly, especially in the Great Basin USA 5 Fort Worth, Illinois Basin it has been close to maturity. In contrast, this technology in the domestic shale gas as well as in hypotonic, low permeability reservoirs is still at an initial stage.

Analysis on the Feasibility of SRV in coal reservoir

The characteristics of coal reservoir "three low and one high (low porosity and low permeability, low reservoir pressure and high saturation),"as well as the mode of occurrence of coalbed methane determine that fracturing process is the key of coalbed methane exploration stage.

According to the mechanism of CBM reservoir, its mining process can be summarized as Desorption-Diffusion-Seepage-Shaft output of these four stages. Among them, the flow control process is rather decisive of coalbed methane output, therefore to maximize communication between the wellbore fracture and the degree of connectivity is the most effective way to obtain high yield for single well. In addition to that, practice in field shows that low permeability in coal reservoir has dominantly limited the yield of CBM. As can be seen from the simulation results shown in Fig.2 that within the same time the larger coal reservoir permeability is, gas flows farther and corresponding the higher economic productivity is. For the reason that, in order to maximize the benefits of the exploitation of coalbed methane wells, the shortcut is to improve the flow properties of the reservoir, that is to say implementing SRV technology.

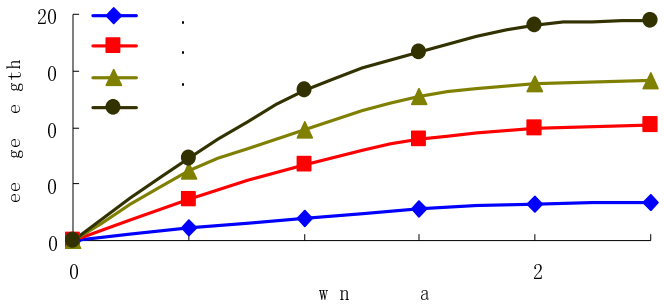

Fig.2 Different fluid flowing characteristic curves within the reservoir

Coal reservoir rock, as a feature with multiple fractures extensively develops vertical, group-based natural fractures, joints and bedding, etc, thence through SRV the produced multi-level secondary cracks cross effectively the original natural fractures, which leads to the formation of large-scale fracture network system.Apart from that, in the implementation of fracturing, coal reservoirs under high level of principal stress difference is prone to produce straight hydraulic fractures while under low stress conditions it tends to creat radial extension of the fracture network structure.

However, there are many disadvantages.At first, high content of clay minerals in the coal makes brittleness weak, whicn brings much difficulties in initiating fractures. Then, lots of cracks in reservoir makes it easier to fracturing fluid filtration, which clogs pores of the reservoir and swells the matrix. Finally, the soft texture of coal is prone to plastic deformation under external force and proppant embeds the formation of interna easily, all of which contributes to formed cracks with low conductivity capabilities.

Numerical simulation

Take a coalbed methane well in Linfen City, Shanxi Province for example to carry out numerical simulation by MEYER Software. The mechanical parameters of this well is in Table 1.

Table 1 Mechanical parameters of the target layer

Depth/m	1051.55m~1058.50m	σ_v/MPa	25.5
σ_H/MPa	18	σ_h/MPa	16
p_p/MPa	10.5	σ_t/MPa	1
E/MPa	6000	υ	0.36

Simulation results from fig.5 show that three-dimensional network of complex joints in the coal reservoir is successfully formed. Based on the results of data, SRV is up to 140m^3 which is 5 to 8 times the volume of conventional hydraulic fracture; besides, the length of fracture network extends to 3564.03m and secondary sewn as the major part of the whole network system lengthen out to 3198.88m; average high of cracks is 10.33m and the average width is 3.22mm, which has already reached effective fracture conductivity standard; moreover, the surface area arrives at 36864m^2 , SRV is about 240180m^3 and the average volume fracturing efficiency reaches up to 37.113%, which basically achieves the desired effect of fracturing.

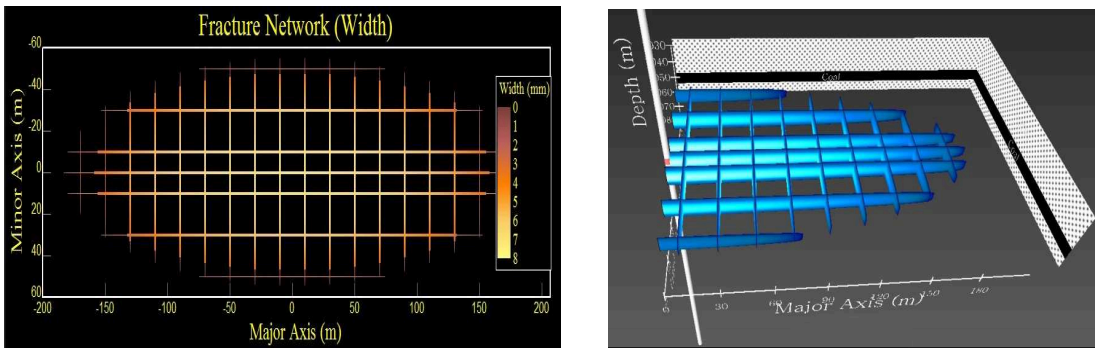

(a) **(b)**

Fig.3 Seam network plan & 3D schematic diagram

Table 2 Fracture network system parameters

	Fracture	DFN	secondary
Fracture Volume/m^3	18.395	142.567	124.169
Length/m	365.12	3564.03	3198.88
Frac Height-Avg/m	11.33	10.33	10.22
Area/m^2	4139.99	36864.27	32723.91
Avg.Hydraulic Frac Width/mm	3.7	3.22	3.16

Summary

Field practice and theoretical analysis show that the success of SRV is closely related to natural fractures' development, brittleness and horizontal stress; The higher the degree of development of natural fractures is, the greater brittleness index is, the smaller the difference between horizontal stress is, the more easily SRV forms seam network and the more significant increase the yield dose. More importantly, the numerical results indicate it is feasible to enhance CBM's production by SRV.

References

[1] Cipolla C L, Warpinski N R, Mayerhofer M J, et al. The relationship between fracture complexity, reservoir properties, and fracture treatment design[C]. SPE 115769, 2008.

[2] ZHANG Yi, XIAN Baoan, SUN Fenjin, WANG Yibing, BAO Qingying. The reasons for low yield of coal-bed methane production and technology of improvement[J]. Natural Gas Industry, 2010, 30(6): 55-59.

[3] ZHANG Yapu, YANG Zhengming, XIAN Baoan, et al. The technology of improving coal-bed methane[J]. Special Oil & Gas Reservoirs, 2006, 13(1): 95-98

[4] LI Anqi, JIANG Hai, CHEN Caihong. In China Coal-bed methane Wells' practice of hydraulic fracturing and seam crack model selection analysis[J]. Natural Gas Industry, 2004, 24(5): 91-93.

[5] Olson J E, Taleghani A D. Modeling simulation growth of multiple hydraulic fractures and their interaction with natural fracture[C]. SPE 119739, 2009.

[6] Maxwell S C, Urbancic T J, Steinsberger N, et al. Micro seismic imaging of hydraulic fracture complexity in the Barnett shale[C]. SPE 77440, 2002.

Advanced Materials Research Vols. 986-987 (2014) pp 738-741

doi:10.4028/www.scientific.net/AMR.986-987.738

Effects of thermal discharge from nuclear power plant on phytoplankton

Xinyu WEI[a], Guoliang WEI, Xiaowei XIONG[b]

Nuclear and Radiation Safety Center, Beijing, 100082, China

[a]email: weixinyu2004@163.com, [b]email: 46026@163.com

Keywords: Thermal discharge, phytoplankton, power plant, nuclear

Abstract. Elevated water temperatures are the major threats from thermal discharges of coastal power plants. The effects of thermal discharge from power plant on phytoplankton were reviewed. With increasing amount of nuclear power plants in China, The effects of thermal discharge from a nuclear power plant on phytoplankton were investigated. Several results and suggestions were proposed.

Introduction

There is great concern about the ecological impacts of coastal power plants on coastal waters. Elevated water temperatures and residual chlorine (anti-fouling agent) are major threats from thermal discharges of coastal power plants with the once-through cooling systems [1,2]. Thermal power plant (nuclear and fossil-fuelled) are the largest sources of waste heat, over 60% of the energy input as fuel is lost to the environment via cooling water [3]. As compared with fossil-fuelled power plants, a nuclear power plant with similar power rate discharges more waste heat, which may cause higher elevated temperature and more obvious impact on environment. With increasing amount of nuclear power plants in China, the effects of the thermal discharges from nuclear power plants on the abundance, productivity, and community composition of phytoplankton need to be studied.

Phytoplankton is the most important primary producer in the ocean ecosystem. It plays an important role in global carbon cycle, and is an important part of the marine food chain. It not only provides food for zooplankton, crustaceans, mollusks and larvae fish, but also indicates the change of sea water quality and global climate [4]. The following several important species of phytoplankton were concerned in the current studies: diatom, dinoflagellates, blue-green algae and chlorophyta.

The objectives of this study were (1) to summarize the effects of the thermal discharges from power plants on the abundance, productivity, and community composition of phytoplankton; (2) to determine the effects of the thermal discharges from a Chinese nuclear power plants on phytoplankton, and (3) to determine future work concerning effects of high water temperatures on phytoplankton.

Results and discussions

Effects of thermal discharge on community composition of phytoplankton

In the open waters, it was thought that the influence of thermal discharge on community composition of phytoplankton is limited, but when the surface temperature has a rise of more than 1.5 ^{o}C, water stratification may occur. This may affect the nutrient exchange in vertical direction, and finally affect phytoplankton and zooplankton [5]. For the closed or semi-closed waters, due to the restriction of water exchange, the higher elevated water temperatures may lead to the changes of phytoplankton community composition. In the Tampa bay (Florida), with a rise of 3 ^{o}C, blue-green algae become the dominant species of phytoplankton in seawater [6]. With the temperature increased from 0 to 10 ^{o}C, the species succession from the spring species (diatoms and dinoflagellates were the dominant species) to the summer species (autotrophic and heterotrophic flagellate as the dominant species) occurred in the south of the Baltic seawaters [7,8].

According to the study above, it was concluded that with increasing of water temperature, the dominant species of phytoplankton community were gradually changed into the species with stronger heat resistance.

Effects of thermal discharge on red tide

Phytoplankton play a key role in the assimilation of organic matter and excess nutrient inputs in the water column from farming, these primary producers are then grazed by groups higher in the trophic chain (e.g., ciliates, zooplankton, and shellfish). Nevertheless, eutrophic levels and the alteration of nutrient content composition (proportion) induce harmful algal blooms. Jiang[9] studied that in Xiangshan Bay (a subtropical, eutrophic, semi-enclosed bay), temperature elevation caused by thermal discharge associated with eutrophication resulted in a dominant species shifting from diatoms alone to dinoflagellates and diatoms. The stress-induced toxic dinoflagellate (Prorocentrum minimum) blooms in winter and the winter–spring transition appeared in this bay.

Sanmen nuclear power plant in China was situated on coast of Shanmen Bay which is near Xiangshan bay mentioned above. Therefore, there may be the similar phytoplankton community composition as Xiangshan bay. Thermal discharge of Sanmen nuclear power plant will result in the similar changes of phytoplankton community composition as Xiangshan bay, which should be given more attentions.

Tolerance temperature limit of phytoplankton

Breeman [10] pointed out that, in some species, ecotypic differentiation in thermal responses over the distribution range influenced the location of geographic boundaries. Breeman demonstrated the complexity of temperature control on the distribution of macroalgae. The differential tolerance of different life-stages as well as differential temperature requirements for processes such as reproduction was found. He states that while Amphi-Atlantic (Arctic) temperate species survived at sub-zero temperatures, southern boundaries are set by lethally high summer temperatures on both sides of the Atlantic; none of these species survived temperatures over 30^{o}C[11，12].

In the tropic areas, indian researchers studied the effects of thermal discharge from Madras nuclear power plant on plankton. The results showed that when the temperature is higher than 38.2 ^{o}C, the primary production of tropical phytoplankton was inhibited [13,14]. It was found that, tolerance temperature limits of phytoplankton in the tropics are generally below 40 ^{o}C.

Most sea areas in China are in temperate and subtropical zones, the main Chinese studies of the tolerance temperature limit of phytoplankton were described as follow. Liao et al. studied the effects of elevated temperature on the composition and the cell density of marine phytoplankton both in winter and summer. It was found that the number of phytoplankton species and the cell density were sharply reduced with experimental temperature more than 36 ^{o}C in summer (natural water temperature 28 ^{o}C) and with experimental temperature more than 34 ^{o}C in winter (natural water temperature of 12 ^{o}C) [15].

The experimental results of Zeng showed that the tolerance temperature limit of coscinodiscus jonesianus and coscinodiscus radiatus is 38 ^{o}C in summer, and only 34 ^{o}C in winter. the tolerance temperature limit of chaetoceros gracilis is 36 ^{o}C in summer, and only 32 ^{o}C in winter [8]. Yu studied the effects of elevated temperature on the growth of 10 kinds of typical phytoplankton species in the Chinese east sea. The results showed that The optimum temperature of the growth of these phytoplankton species were between 20 ^{o}C and 25 ^{o}C. When the temperature increased to 30 ^{o}C, these phytoplankton species showed very low growing rate or almost no growing [16].

According to the results above, it was concluded that the tolerance temperature limit of phytoplankton in China is mainly between 30 to 40 ^{o}C.

Effects of thermal discharge from a nuclear power plant

Daya Bay nuclear power plant is located in Shenzhen Dapeng peninsula of china. It is the second nuclear power plant built in mainland China.

Before the operation Daya Bay nuclear power plant, the water temperature of the west coast of Daya Bay was about 17.5 ^{o}C in winter and about 29 ^{o}C in summer. The annual average temperature was about 23.5 ^{o}C, water temperature distribution from the shallow coastal water to the deep water area had a decreasing trend. After the operation of the nuclear power plant in 1994, the isotherm of

17.5 ^{o}C in winter migrates to site of Dalajia. The influence of thermal discharge is more obvious in summer, the temperature of many sea areas is as high as 30 ^{o}C. The average annual temperature is increased to 23.88 ^{o}C, which has an increase of about 0.4 ^{o}C as compared with the value before the operation of nuclear power plant. The surface water temperature of the outfall of the nuclear power plant is high all the year, It is up to 35 ^{o}C in summer. The obvious difference between the surface and the bottom water temperature results in the formation of obvious thermocline. The elevated temperature zone of 4 ^{o}C is close to 2 km^2, and the elevated temperature zone of 1 ^{o}C in winter and summer are 27 km^2 and 12 km^2, respectively [17].

A large number of investigations and researches near Daya Bay nuclear power plant were performed [18-21]. It was found that the effects of thermal discharge on phytoplankton species mainly have the following three aspects: (1) In the ecological monitoring area of Daya Bay, the dominant phytoplankton was changed from warm water species of phytoplankton into a wide-temperature species of phytoplankton. The abundance of species is declining year by year. The diatoms are the dominant population throughout the year [18]; (2) In the past years, the proportion of diatom felled slightly, which was different from that of dinoflagellate. The proportion of diatom/dinoflagellates ratio was declining, which was more obvious in the summer [19]; the diversity index was significantly lower in the summer [19, 20]; (3) from 2005 to 2006, in the sporocysts of Alexandrium cysts researched the peak values in winter [21].

It was concluded that there is obvious impact of thermal discharge from Daya Bay nuclear power plant on the community structure of phytoplankton.

Conclusions and Suggestions

This paper studied the effects thermal discharge of power plant on phytoplankton. Several conclusions were proposed according to the available studies.

(1) With increasing of water temperature, the dominant species of phytoplankton community were gradually changed into the species with stronger heat resistance.

(2) The tolerance temperature limit of phytoplankton in China is mainly between 30 to 40 ^{o}C.

(3)There is obvious impact of thermal discharge from Daya Bay nuclear power plant on the community composition of phytoplankton.

(4) Thermal discharge of Sanmen nuclear power plant may result in the similar changes of phytoplankton community composition as Xiangshan bay, which should be given more attentions.

The following work need to be done in future: (1) to determiner interactive effects of high water temperatures and residual chlorine on phytoplankton productivities; (2) to compare of the effects of thermal discharge on phytoplankton and the effects of impingement and entrainment on phytoplankton.

Reference

[1] Yi-Li Chuang, Hsiao-Hui Yang, Hsing-Juh Lin．Effects of a thermal discharge from a nuclear power plant on phytoplankton and periphyton in subtropical coastal waters，Journal of Sea Research, 2009, (61): 197–205．

[2] W .Majewski, D.C.Miller, Predicting effects of power plant once-through cooling on aquatic systems, technical papers in hydrology,Acontributiontothe International Hydrological Programme, UNESCO.

[3] Dr AWH Turnpenny, Dr KE Liney, Review and development of temperature standards for marine and freshwater environments, JACOBS, 2011.

[4] Colin Reynolds, Ecology of Phytoplankton, Cambridge University Press, 2006.

[5] Roemmich D，McGoWan J．Climatic wanning and the decline of zooplanktonin the California current

[6] Blake NJ，Doyle LJ，Pyle T E．The macro-benthic community ofathermallyaltered areaofTampa Bay, Florida [A]．In：EschG W and McFarlane R W(Editors)．Thermal ecologyII[M]．Springfield: Viginia, Technical Information Center， Energy Research and Development Administration Symposium Series(Conf．750425)．1 976，296,--33 1．
[7] Anderson A, Haecky P, Hagstron A．Effect of temperature and light on the growth of micronano- andpico-plankton：impactonalgal succession[J]．Marine Biology,1994，120(4)：51l~520．
[8] Zeng Jiangning, Impact of thermal discharge of coastal power plant on the ecological in the subtropical area [D]. Hang zhou: Zhejiang University, 2008．
[9] Zhibing Jiang, Yibo Liao, Jingjing Liu, Lu Shou, Quanzhen Chen, Xiaojun Yan, Genhai Zhu, JiangningZeng. Effects of fish farming on phytoplankton community under the thermal stress caused by a power plant in a eutrophic, semi-enclosed bay: Induce toxic dinoflagellate (Prorocentrum minimum) blooms in cold seasons, Marine Pollution Bulletin, 2013, 76: 315-324.
[10] Breeman, A.M., 1988. Relative importance of temperature and other factors indetermining geographic boundaries of seaweeds: experimental andphenological evidence. Helgoland Marine Research 42, 199–241
[11] Andrew Wither, Roger Bamber, Steve Colclough, Keith Dyer, Mike Elliott, Peter Holmes,Henk Jenner, Colin Taylor, Andy Turnpenny, Setting new thermal standards for transitional and coastal (TraC) waters, Marine Pollution Bulletin 64 (2012) 1564–1579
[12] Breeman, A.M., 1988. Relative importance of temperature and other factors indetermining geographic boundaries of seaweeds: experimental andphenological evidence. Helgoland Marine Research 42, 199–241
[13] Ahamed, M.S. Madras Atomic Power Station: an environmental impact assessment study of the cooling system on pelagic life. Ph.D. Thesis, University of Madras, 1997.
[14] M. Rajadurai, E.H. Poornima, S.V. Narasimhan, V.N.R. Rao, V.P. Venugopalan, Phytoplankton growth under temperature stress: Laboratory studies using two diatoms from a tropical coastal power station site, Journal of Thermal Biology, 2005, (30): 299–305.
[15] Hu Deliang, Yang Huanan, Effects of heat shock on macroinvertebrates in Xiangjiang River [J], Techniques and Equipment for Environmental Pollution Control (Chinese), 2001, (2):25-27．
[16] Du Feiyan，Wang Xuehui，Li Chunhou，Jia Xiaoping．Variation characteristics of macrobenthos productivity in Daya Bay of South China Sea [J]，Chinese Journal of Applied Ecology，2008，19(4):873-880．
[17] Liu Sheng, Huang liangmin, Huang Hui, Lian Jiansheng, Long Aimin, Li Tao．Ecological response of phytoplankton to the operation of Daya Bay nuclear power station[J]．Marine Environmental Science (Chinese) 2006，25(2)：9-25．
[18] Wang Yu, Lin Mao, Lin Gengming, etc.,Yearly changes of phytoplankton in the ecological monitoring zone of Daya Bay [J]．Marine Sciences (Chinese)，2012，36(4)．
[19] Li Tao, Liu Sheng, Huang Liangmin, ect., The long-term effects of thermal discharge of Daya bay nuclear power plant on phytoplankton [C]．Chinese Society for Environmental Sciences-The academic conference proceedings (Chinese) 2010．
[20] Sun Cuici, Wang Youshao, Sun Song, etc．Analysis dynalllics of phytoplanlkton community characteristics in Daya Bay [J]．Acta Ecologica Sinica (Chinese), 2006，26(12)：3948-3958．
[21] Wang Chaohui, Cao Yu, etc. The fluxes of dinoflagellate cyst from sediment traps deployed in Dapeng-Ao area of Daya Bay from 2005 to 2006 [J]．Journal of tropical oceanography (Chinese)，2011，30(1)：113-118．

Advanced Materials Research Vols. 986-987 (2014) pp 742-746

doi:10.4028/www.scientific.net/AMR.986-987.742

Review on the supervision monitoring program for radiation environment around nuclear power plants

Yanxia Zhang[a], Jin Li*[b], Weiwei Lu*[c], and Liang He[d]

Nuclear and Radiation Safety Center of the Ministry of Environmental Protection, NO.54 HongLianNanCun, Haidian District, Beijing 100082, P. R. China

[a]zhangyanxia@chinansc.cn, *[b]lijin@chinansc.cn, *[c]luweiwei@chinansc.cn, [d]heliang@chinansc.cn

Keywords: Nuclear power plants, radiation environment, supervision monitoring, review

Abstract. The supervision monitoring program of radiation environment around nuclear power plants is an important basis for the environmental radiation monitoring work. Key elements such as source, exposure pathway and representative person are discussed in the design of the supervision monitoring program, and technical details about the review of monitoring, evaluating and quality assurance are also given in this article. For the supervision monitoring work of radiation environment around nuclear power plants, it can provide some guidance about the review of the supervision monitoring program for nuclear safety regulators, and provide some reference about the design and revision of the supervision monitoring program for nuclear safety monitoring departments.

Introduction

The radioactive pollution monitoring system has been established in China. For the nuclear and radiation facilities, there are "dual track" managements in the radiation environmental monitoring work, the government supervision management and the operating unit management. According to article 24 of the law of the People's Republic of China on Prevention and Control of Radioactive Pollution, the competent administrative department of environmental protection under the State Council should be responsible for the supervision monitoring of important nuclear facilities such as nuclear power plants.

The supervision monitoring work of nuclear power plants consists of two parts: the external radiation environment supervision monitoring and the radioactive effluent monitoring. At present, because of absence of related technical standards of the supervision monitoring, monitoring project, point and frequency are significantly different between nuclear power plants [1-2]. While taking into account the feedback of Fukushima nuclear accident experience and combing with the actual situation of existing supervisory monitoring system in China, several important questions on the review of external radiation environmental supervision monitoring program are discussed to unify and regulate the work of supervision monitoring around nuclear power plants as far as possible. It can provide some guidance about the review of the supervision monitoring program for nuclear safety regulators, and provide some reference about the design and revision of supervision monitoring program for nuclear safety monitoring departments.

Review of design information

The design information should be reviewed firstly, including the necessity and sufficiency of the description of site environment and operation situation, as well as the rationality of the source, exposure pathway and representative person [3-4].

Site environment and operation situation. The related information of the design of site environment should contain the site location information, meteorological condition, hydrologic geology, current and future land use, land resources, aquatic resources, population distribution and other important data of site environment. In addition, the status and historical trend of radiation

environment, radionuclide type, operational limits and conditions on the operating license and other important information should be given.

Source analysis. In particular, the supervision monitoring program should be designed such that radionuclides that are significant in terms of dose to the representative person are monitored. Thus, all kinds of radioactive waste gas and waste water should be analyzed, and the most critical nuclide for the exposure should be determined in the supervision monitoring program, through giving the source, release, calculation model and other parameters.

Exposure pathway. The gaseous, liquid and other exposure pathways should be given in the supervision monitoring program. Gaseous way should at least consider air immersion external exposure, surface sediment external exposure, internal radiation of inhaled air and eating vegetables, grain, milk, and meat. Liquid way should at least consider shore sediments external exposure, water immersion external exposure, waterborne external exposure, drinking water internal radiation, internal radiation of ingestion of vegetables, grain and fruit due to contaminated water, internal radiation of ingestion of aquatic organisms, internal radiation of ingestion of animal products (meat, milk) due to contaminated crops and drinking water. Meanwhile, other exposure pathways around the site those can reach or exceed 10% contribution to individual and collective dose should also be described. Through the analysis of the gaseous, liquid and other exposure pathways, the most critical pathway should be determined.

Representative person. In the operation stage of nuclear power plants, the representative person should be described, through giving living habits, diet information, resource utilization information of living place and other important information necessary to dose estimation. The information is generally associated with ages of the representative person.

Review of main content

The scope, object, point, frequency, low limit of detection and other important elements should be given a detailed review from aspects of the feasibility, rationality and regulations compliance with the law and standard.

The scope of monitoring. Supervision monitoring of radiation environment around nuclear power plants includes measurement of environmental gamma radiation level and environmental medium radiation level, and the scope of monitoring should usually satisfy: 20 km away from the nuclear power plant for the environmental gamma radiation, 10 km for the environmental medium radiation, and 30~80 km for the control point.

Monitoring objects. Monitoring objects should include terrestrial gamma radiation, gamma cumulative dose, aerosols, gases, deposition, precipitation, surface water, groundwater, drinking water, seawater, sediment, aquatic, terrestrial plants, livestock, poultry, cattle (sheep) milk, biological indicator, soil/sediment, intertidal zone and other important objects.

Sample/monitoring points. For all monitoring objects, the number, range, distance and other information about the representativeness of sample/monitoring points should be reviewed. For example, in the case of terrestrial gamma radiation, including the instantaneous monitoring and the continuous monitoring, points of the instantaneous monitoring should be:

(1) Outside the factory ground maximum concentration;

(2) In 8 cross azimuth according to the radius of 2, 5, 10, 20 km around the factory;

(3) Increased appropriately under the direction of the wind and densely populated areas [5].

Points of the continuous monitoring should be:

(1) In the range of 10 km around nuclear power plants;

(2) In 16 azimuthal uniformly;

(3) Increased appropriately under the direction of the wind and densely populated areas [6].

Points of instantaneous monitoring should take into account the continuous monitoring points, and 20%~30% overlap is generally required for the purpose of data comparison. At the same time, the supervision monitoring program should also include pre-operational monitoring of the background

levels so that the incremental contribution from the nuclear power plant can be determined. Thus, monitoring points of the terrestrial gamma radiation should be fully taken into account the consistency of survey points of pre-operation of nuclear power plants. This is particularly important with practices that discharge NORM.

Table 1 Sampling frequencies and measurement analysis projects of the supervision monitoring of radiation environment around nuclear power plants

Object	Sampling frequency	Measurement analysis project and frequency
Terrestrial gamma radiation	Quarterly	Gamma radiation dose rate, quarterly
	Continuously	Gamma radiation dose rate, continuously
Gamma cumulative dose	Quarterly	Gamma radiation dose rate, quarterly
Aerosols	Continuously	α/β , continuously
		Gamma nuclide analysis , monthly
	Accumulatively	Total α, total β, gamma nuclide analysis , monthly
Gases	Continuously	^{131}I, ^{133}I , monthly
	Monthly	^{3}H, ^{14}C, monthly
	Quarterly	noble gas quarterly
Deposition	Accumulatively	Total α, total β, ^{90}Sr, gamma nuclide analysis , quarterly
Precipitation	The precipitation period	^{3}H, ^{90}Sr, gamma nuclide analysis
Surface water	Twice a year	^{3}H, ^{90}Sr, gamma nuclide analysis, twice a year
Groundwater	Twice a year	^{3}H, ^{90}Sr, gamma nuclide analysis, twice a year
Drinking water	Quarterly	Total α, tatal β, ^{3}H, ^{90}Sr, gamma nuclide analysis, quarterly
Seawater	Twice a year	^{3}H, ^{90}Sr, gamma nuclide analysis , twice a year
Sediment	Once a year(coastal nuclear power plant), Quarterly (inland nuclear power plant)	^{3}H, ^{90}Sr, gamma nuclide analysis, same with sampling frequencies
Aquatic	Once a year	^{90}Sr, gamma nuclide analysis, twice a year
Terrestrial plants	Each month during growing season	^{3}H, ^{90}Sr, ^{14}C, gamma nuclide analysis
Livestock/poultry	Once a year	Gamma nuclide analysis, twice a year
Cattle (sheep) milk	Twice a year	^{131}I, ^{90}Sr, twice a year
Biological indicator	Once a year	Characteristic nuclide , once a year
Soil/sediment	Once a year	^{90}Sr, gamma nuclide analysis, once a year
intertidal zone	Once a year	^{90}Sr, gamma nuclide analysis, once a year

) Recommended;

) : ^{54}Mn, ^{60}Co, ^{134}Cs , ^{137}Cs, ^{144}Ce, ^{238}U, ^{232}Th, ^{226}Ra and ^{40}K are generally suggested;

3) : ^{110m}Ag is generally required.

At least, one control point should be set in all monitoring items. Control points should be under the direction of the minimum wind frequency, or up the river receiving wastewater, or in the sea unaffected by the nuclear facilities. Environments of control points and sample/monitoring points should be as consistent as possible.

Sampling frequencies and analysis of measurement projects. The frequency of monitoring and sampling should be determined by the complexity of the environment, the significance of the doses to the representative person and the properties of radionuclides. Sampling frequencies and measurement analysis projects of supervision monitoring of radiation environment around nuclear power plants are shown in table 1. According to the natural environment in different regions, monitoring items can be adjusted.

Table 2 Typical monitoring methods and low limits of detection of main monitoring projects in the supervision monitoring of radiation environment around nuclear power plants

Object	Item	Monitoring standard/method	Typical low limit of detection
Environmental radiation	Terrestrial gamma-radiation dose rate	Norm for the measurement of environmental terrestrial gamma-radiation dose rate GB/T14583-1993	10 nGy/h
Environmental media	Gamma activity concentrations of radionuclides	Gamma spectrometry method of analysing radionuclides in soil GB/T11743-1989	10 Bq/kg
		Gamma spectrometry method of analysing radionuclides in air WS/T184-1999	5×10^{-3} Bq/m^3
		Gamma spectrometry method of analysing radionuclides in biological samples GB/T16145-1995	10 Bq/kg
		Gamma spectrometry method for analysis of radionuclides in water GB/T16140-1995	1 Bq/L
	Total α, total β	Determination of gross alpha activity in water thick source method EJ/T1075-1998	5×10^{-2} Bq/L
		Determination of total β radioactivity in water Evaporation method EJ/T900-1994	5×10^{-2} Bq/L
	^{90}Sr	Analytical method for strontium-90 in soil EJ/T1035-2011	0.5 Bq/kg
		Radiochemical analysis of Sr-90 in ash of biological samples - extraction chromatography by di- (2-ethylhexyl) phosphate GB/T11222.1-1989	0.1 Bq/kg
		Radiochemical analysis of strontium-90 in water Extraction chromatography by di-(2-ethylhexyl) phosphoric acid GB/T6766-1986	10^{-2} Bq/L
	^{3}H	Analytical method of tritium in water GB/T12375-1990	0.5 Bq/L

Monitoring methods and low limits of detection. In the review of the supervision monitoring program for radiation environment around nuclear power plants, the national standards or industry standards/method should be chose, and mature methods home and abroad should be applied for the project lack of national standards and industry standards. A detailed list of standards of sampling, monitoring, analysis method and basis of the supervision monitoring program also should be given. In addition, typical low limits of detection of main monitoring projects should be given, as shown in Table 2.

Quality assurance

A complete quality assurance system should be established for the supervision monitoring work of radiation environmental around nuclear power plants, while giving detailed quality control measures.

The quality assurance system of the supervision monitoring implements a comprehensive quality management on the whole supervision monitoring process of nuclear power plants, including all activities of supervision monitoring that ensure data accurate and reliable. It mainly includes the supervision monitoring organization guarantee, equipment calibration and maintenance, supervision monitoring method validation, supervision monitoring program, supervision monitoring personnel training and exercises, supervision monitoring evaluation and quality supervision, nuclear accident supervision monitoring and sampling, laboratory analysis, monitoring data processing and result report, as shown in Figure 1.

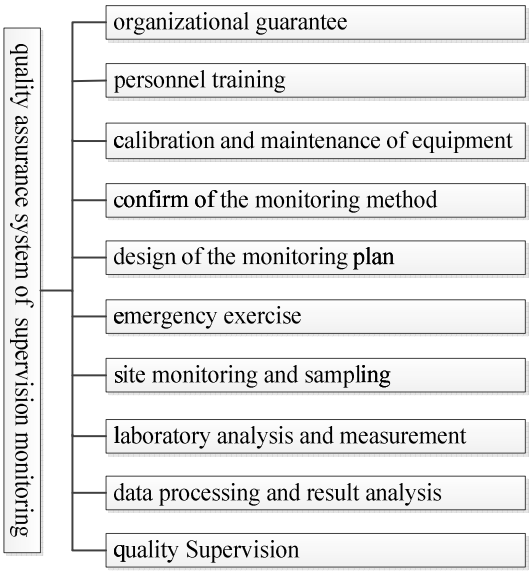

Figure1 The quality assurance system structure of the supervision monitoring in nuclear power plants

Conclusion

As an important part of supervision monitoring, through analysis of the source, exposure pathway, representative person and other key elements of the supervision monitoring program of radiation environment around nuclear power plants, technical details about the review on monitoring, evaluating and quality assurance are also given in this paper. It can provide some guidance about the review of the supervision monitoring program for nuclear safety regulators, and provide some reference about the design and revision of the supervision monitoring program for nuclear safety monitoring departments. This study will effectively promote China's nuclear power plant supervisory monitoring work around nuclear power plants and protect public health and environmental radiation safety.

References

[1] D. Hu, J. F. Song. Progress Report on China Nuclear Science & Technology Vol.2(2011), p.205-212 (In Chinese)

[2] N. M. Huang, Z. D. Chen, H. Q. Song et al. Radiation Protection Vol.24(2004), p.191-205 (In Chinese)

[3] International Atomic Energy Agency (IAEA). Environmental and Source Monitoring for Purposes of Radiation Protection. Safety Standards Series No. RS-G-1.8, Vienna(2005)

[4] International Atomic Energy Agency (IAEA). Programmes and Systems for Source and Environmental Radiation Monitoring. Safety Reports Series No.64, Vienna(2010)

[5] Ministry of Environmental Protection of the People's Republic of China. Technical Criteria for Radiation Environmental Monitoring. HJ/T61-2001(In Chinese)

[6] Department of Nuclear Safety Management of Ministry of Environmental Protection of the People's Republic of China. General Technical Requirement about Improvement Action of Nuclear Power Plants after Fukushima Nuclear Accident (Trial Implementation), 2012(In Chinese)

Advanced Materials Research Vols. 986-987 (2014) pp 747-750

doi:10.4028/www.scientific.net/AMR.986-987.747

The analysis and countermeasures for the influencing factors of power grid engineering electromagnetic environment

Youquan Zhang[1], Fei Wang[1], Shaocan Wang[1], Qing Wang[2], Xiaolei Zhang[1]

([1.] State Grid Shandong Electric Power Company, Jinan, Shandong 250001; [2.] Tai'an power supply company, State Grid Shandong Electric Power Company, Tai'an, Shandong 271000）

Keywords: Electromagnetic environment; Substation; Transmission line; The impact analysis

Abstract. In light of the increasingly prominent environmental problems and disputes of the power transmission transformation engineering, analysis many of the environmental impact of 500 kV power transmission transformation engineering, introduce the related standards of electromagnetic environmental impact, focusing on the analogy analysis and theoretical prediction for the electromagnetic environment around typical 500 kV power transmission transformation engineering , analysis the condition of the power frequency electromagnetic field and radio interference which generated by power transmission transformation engineering effects on the environment. put forward the countermeasures and technical measures to solve and alleviate the problem of environment .

1 The environmental impact factors of 500kv power transmission transformation project

The main environmental impact factors of 500kv power transmission transformation project are power frequency electric field, power frequency magnetic field, radio interference and noise generating at project runtime. And different from general construction projects, the main characteristics of electric power construction projects is the electromagnetic impact on the environment, this paper mainly refers to the impact of the power frequency electric field, power frequency magnetic field and radio interference on the environment [1].

2 The evaluation scope and standards

2.1 The evaluation scope

The evaluation scope of power frequency electric field and power frequency magnetic field in substation is the area within 500m range outside the substation fence, focus on evaluating the area within 100m range outside the fence; The site location of radio interference is the area within 2000m range outside the fence, focus on evaluating the area within 100m range outside the fence

The evaluation scope of power frequency electric field and power frequency magnetic field on transmission line is the banded region bounded by outside the transmission line edge wire 50m, and the evaluation scope of radio interference is the banded region on both sides of the transmission lines 2000m, focus on evaluating the banded region on both sides of the edge wire 100m [2].

2.2 Evaluation standard

Power frequency electric field and power frequency magnetic induction intensity execute the requirements of 4kV/m evaluation standards and 0.1mT recommended by The Technical Specifications for the Environmental Impact Assessment of Electromagnetic Radiation of 500kV EHV Transmission Transformation Project HJ/T24-1998; The radio interference value in accordance with the provisions of The Radio Interference Limits of High Voltage AC Overhead Transmission Lines GB15707-1995, in the location of the 20m distance from edge phase conductors projection, and in the condition of test frequency of 0.5 MHz and good weather, The radio interference value of the 500kv transmission line less than the limitation requirement of 55 dB (μV/m), 500kv substation with reference to the standards.

3 The environmental impact of 500kv substation

Such as the 500kv substation constructed in plain area of Shandong province ,in which substation scale is 2×1000 MVA main transformer, and 500kv, 220kv all adopt GIS power distribution unit, can adopt the Mudu 500kV substation of Suzhou city, Jiangsu province to analogy forecast.

Monitoring section select outside the walls of outlet side of the Mudu substation high voltage power distribution unit. The monitoring points of power frequency electric field and power frequency magnetic field outside the wall to 5m as the starting point. A monitoring points is arranged every 5m and monitoring to 60m outside the wall.

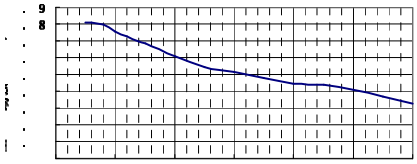

Fig1 The changing trend for the power frequency electric field intensity of Mudu 500kV substation

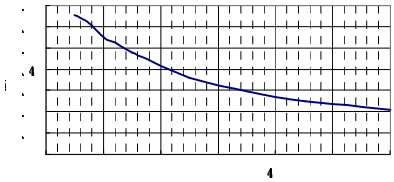

Fig2 The changing trend for the power frequency magnetic induction intensity of Mudu 500kV substation

The monitoring points of radio interference outside the wall to 1m as the starting point. A monitoring points is arranged every 2nm (n takes 0~6)and monitoring to 64m outside the wall[3].

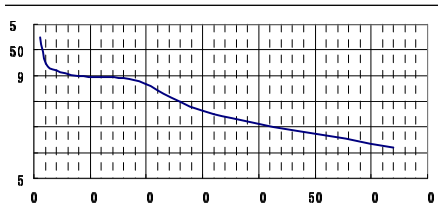

Fig3 The changing trend for the radio interference of Mudu 500kV substation

From the monitoring results of Figure 1~3 can be seen, with the increase of distance, the changes of power frequency electric field intensity and power frequency magnetic induction intensity outside the 500kV substation fence in trends were attenuated, the monitoring values outside the substation fence all can meet the evaluation standards of 4kV/m and 0.1mT. The monitoring values of radio interference outside the substation fence 20m can satisfy the limitation requirement of 55dB（μV/m）. Therefore, It generally doesn't need to take technical measures beyond design specifications outside the 500kV substation fence to satisfy the standard of environmental impact assessment.

4 The environmental impact of 500kv transmission line

Prediction calculation adopt the calculation method recommended by The Technical Specifications for the Environmental Impact Assessment of Electromagnetic Radiation of 500kV EHV Transmission&Transformation Project HT/T24-1998, in a typical design tower SZ1, for example, select the typical calculation parameters of SZ1 tower design(Figure 4) into the calculation.

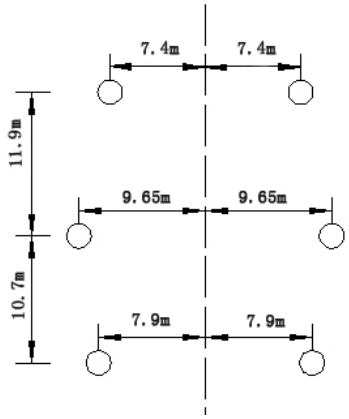

Fig 4 The parameter of SZ1 tower

The line wire is selected by 4×JL/LB20A-630/45 with wire diameter is 33.6mm and spacing split is 500mm, phase sequence alignment is considered by A-B-C and C-B-A. Consider voltage by 525kV（Go up 5% of rated voltage），and electric current by 1100A。The erection height of line is considered by wire-to-ground height with residential erection height is 14m and nonresidential erection height is 11m, calculate the power frequency electric field intensity, power frequency magnetic induction intensity and radio interference generated by its operation. The calculation results are shown in Figure 5, Figure 6, and Figure 7. In the design, power transmission transformation project often use multiple tower, and it doesn't need to calculate each tower type. Because the calculation value of power frequency electric field of the larger tower is bigger, the calculation value of radio interference of the smaller tower is larger, and the power frequency magnetic field generally doesn't become constraints, so in the theoretical calculation of the specific projects, simply select one kind of the larger and one kind of the smaller tower to calculate.

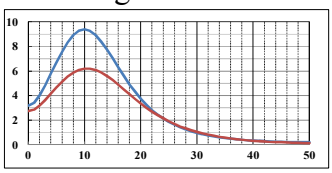

Fig5 The forecast distribution curve for the power frequency electric field intensity of 500kV tower double-circuit transmission line

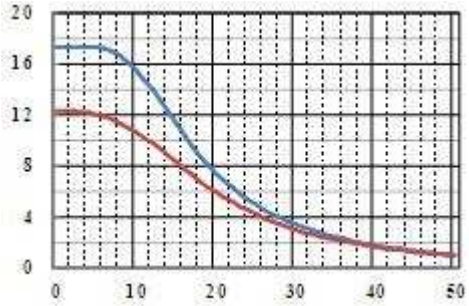

Fig6 The forecast distribution curve for the power frequency magnetic induction intensity of 500kV tower double-circuit transmission line

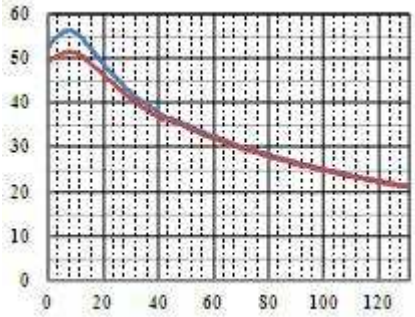

Fig7 The forecast（80%）distribution curve for the radio interference of 500kV tower double-circuit transmission line

From Figure 5 can be seen, when the line is erected in accordance with the requirements in design statutes of 14m erection height in residential area, since the demolition control requirements of 500kV transmission line project is the houses within 5m range of edge wire on both sides of the line, but the power frequency electric field intensity in the height of 1.5m from the some area ground outside 5m range outside line edge wire is more than 4kv/m, unable to meet the requirement of the evaluation standard of 4kv/m, so only according to the requirements of 500kv design procedures to execute the 500kv transmission line construction, unable to satisfy the requirements of 4kv/m environmental impact assessment standard. To 19m from the center of line (that is, 9.35m outside the edge wire), the power frequency electric field intensity in the height of 1.5m from the ground can satisfy the requirements of 4kv/m environmental impact assessment standard.

From Figure 6 and Figure 7 shows, the power frequency magnetic induction intensity of 500kv transmission transformation line is far less than 0.1mT, the radio interference at the location of 20m (that is, 29.65m from the center of line) outside line edge wire is also far less than 55dB (μV/m), the power frequency magnetic field and radio interference will not become the environmental constraints.

5 Epilogues

Through the theoretical analysis calculation and analogy monitoring for 500kv power transmission and transformation project, it generally doesn't need to take technical measures outside the design specifications to satisfy the standard of environmental impact assessment outside the 500kV substation fence. When the wires erection height of 500kv transmission line are increased to more than 17 m above residential area, after according to the circuit design rules removing the houses within 5m range of edge wire on both sides of line, the power frequency electric field, power frequency magnetic field and radio interference all can satisfy the standard of environmental impact assessment, it doesn't need to take other measures such as increasing the demolition range, and effectively reduce the civil disputes in the environmental demolition and demolition investment

References

[1] Gang Zhao, Guangjun Yang, Xiaoqin Li. The discussion on the assessment problem of electromagnetic effects and environmental impact of power transmission&transformation engineering[J]. Electric power environmental protection, 2007, 23(4):16-19.

[2] HJ/T24-1998 The Technical Specifications for the Environmental Impact Assessment of Electromagnetic Radiation of 500kV EHV Transmission&Transformation Project[S].

[3] DL/T988-2005 The Measurement Method for the Substation Power Frequency Electric Field and Magnetic Field of High Voltage AC Overhead Transmission Lines[S].

Advanced Materials Research Vols. 986-987 (2014) pp 751-754

doi:10.4028/www.scientific.net/AMR.986-987.751

Heavy Metal by Zero-valent Iron and Natural Zeolite Partitioning in Acid Mine Drainage: A Comparative Study

Changfeng Cai[a], Lin Jiang [b], Fengli Wang[c], Fuzhang Qi[d]

School of Chemical and Biological Engineering, Anhui Polytechnic University, Anhui CHINA
[a]ccf2005@ahpu.edu.cn, [b]angongchjlin@126.com, [c]mengjiang1189@163.com [d]qfzcom@sina.com

Keywords: heavy metal, zero-valent iron, natural zeolite, acid mine drainage

Abstract: In this study, two different bed materials in media filter systems were examined. Natural zeolite has the ability to take up heavy metals (Cd, Zn) from acid mine drainage (AMD) as well as zero-valent iron (ZVI). The aim of the study was to estimate the ability to remove heavy metals of Natural zeolite and compare the efficiencies of the two media. A major purpose of this report was to determine which media would have a higher permeation rate after running a period of time. It was concluded that ZVI had a higher efficiency of taking up heavy metals (>96.5%) and a faster permeation rate which had a longer operating life.

Introduction

Acid mine drainage (AMD) is a form of water pollution occurring worldwide in association with mining of coal and sulfide ore deposits [1]. AMD is always harmful with low pH (3-6) and high concentrations of heavy metals and many heavy metals are known to be toxic or carcinogenic [2]. Zero-valent iron (ZVI) has been successfully applied for the treatment of wastewater and groundwater with heavy metals, arsenic, nitrate, phenol, dyes [3]. There is an increasing trend of the use of ZVI for the removal of contaminants from wastewater and groundwater [4]. During the last few years, ZVI has been reported to demonstrate effective removal of many metallic irons, including Pb^{2+},Zn^{2+},Cu^{2+},Pb^{2+},Cr(Ⅵ)[5, 6]. Natural zeolite also has the ability to take up heavy metals [7]; either for their cation exchange or molecular sieving properties. Currently, Natural Zeolite is widely used in wastewater and soil beneficiation [7, 8].

The objective of this study was to compare the removal efficiency of Zn^{2+} and Cd^{2+} from AMD between ZVI and natural zeolite, and to investigate the changes in infiltration rate of pore media, and to select economical and effective media [9, 10].

Materials and methods

The column experiment was carried out using polyvinyl chloride resin (PVC) filter columns of 50 cm height and 16 cm internal diameter. The columns had inlet and outlet connections so that waste water could flow downwards through them. The bottom of each column was closed using PVC plate. Column 1 was packed with 15% ZVI and 85% ceramsite (2-3mm in diameter) and column 2 was packed with 30% natural zeolite (2-4mm in diameter) and 70% ceramsite (2-3mm in diameter). The wastewater was constantly supplied at the top of columns with peristaltic pumps, and the level was maintained at 10 cm depth above the media surface throughout the experiment. The flow rates in two columns are 0.05cm^3s^{-1} and hydraulic residence time is 24 hours.

Effluent was collected daily and then chemical concentration was determined. The pH was measured by electrode; heavy metals were measured with flame atomic absorption spectrometry. The hydraulic conductivity (K) indicates the ability of media to conduct wastewater through it under hydraulic gradients [1]. The hydraulic conductivity of the two columns was estimated by measuring the head loss. The head loss was measured using piezometers located 15, 25, 35 cm above the bottom. The permeability of the two columns was calculated from water head and the flux which was measured by the flow rate from the outlet using Darcy's law:

$$K=\frac{Q\cdot}{A\cdot\triangle}$$

Where Q is the flow rate(L^3T^{-1}), Δ is the head loss(L), and Δ is the distance between the two points where Δ is measured(L), and A is the cross section area of the columns(L^2). The K and the concentrations of Cd^{2+} and Zn^{2+} were measured daily. The pH values were measured every half-day.

Results and discussion

The pH value of AMD was about 5, it can be seen that pH values of the two columns reach around 9.6 rapidly after running 2-3 days, then decreased to around 9.1 and fluctuated slowly. The results may be caused by dissolution of alkaline hydrolysis, and with the advance of the experiments, pH values decreased with the slower dissolution of alkaline hydrolysis. The results are shown in Fig.1.

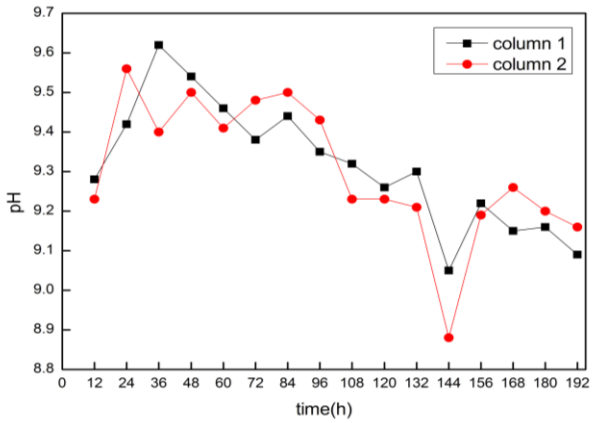

Fig.1. pH value changes during the experiment

The variations of the hydraulic conductivity during the experiment are shown in Fig.2. In the experiment, the hydraulic conductivity of column 1 decreased rapidly during the first two days, and then became smooth. At the same time the hydraulic conductivity of column 2 decreased slower than that of column 1 in the first three days. These two reductions may be due to clogging of chemical precipitation or dissolution, the mineralogical composition of the media, redox potential. The productions were adsorbed by these media which made the reductions of pore volume. The results also showed that ZVI- ceramsite mixture had a higher permeability than natural zeolite-ceramsite mixture.

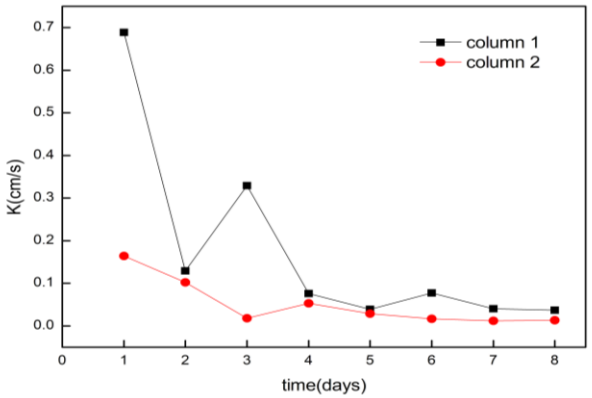

Fig.2. Permeability changes during the experiment

The removal efficiencies of Cd^{2+} and Zn^{2+} are shown in Fig.3. The results indicated that the two media can remove >94% Cd^{2+} and >99% Zn^{2+}, and ZVI had a higher removal efficiency than Natural Zeolite. It also can be seen the removal efficiencies somewhat decreased after the columns ran three to four days, but always >90%.

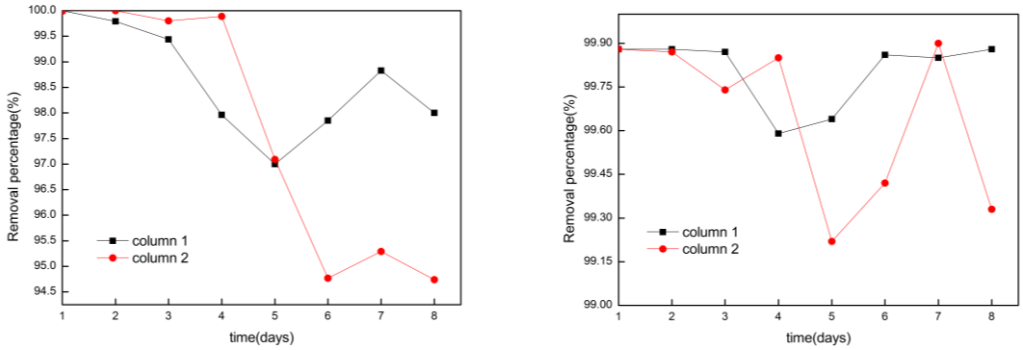

Fig.3. Removal efficiencies of Cd^{2+}, Zn^{2+}

Conclusions

The clogging of porous media is a chemical and physical phenomenon, resulting in a decrease in the capacity of permeating water and the efficiency of conducting wastewater [11]. Metals are removed as the pH increase, and the pH value is an important parameter that controls the removal of metals. Alkaline substances (ceramsite) can improve the pH of AMD, and then precipitate some heavy metals.

ZVI and natural zeolite can effectively remove heavy metals, but ZVI had a higher efficiency of removal in disposing heavy metals than natural zeolite, and a faster permeation rate [11, 12]. There is an increasing interest in the use of ZVI and artificial zeolite for the removal of contaminants from wastewater and groundwater. The two media can be combined with other media to remove many other contaminants, such as nitrate, phenol, ammonia nitrogen.

Acknowledgments

This work was supported in part by the grants from the National Natural Science Foundation of China (51274001) and the Opening Project of State Key Laboratory of Coal Recourses and Safe Mining (SKLCRSM10KFA05).Sincere gratitude is expressed to Professor Changfeng Cai for her help.

References

[1]. Cheng, H., et al., Geochemical processes controlling fate and transport of arsenic in acid mine drainage (AMD) and natural systems. Journal of hazardous materials, 2009. 165(1): p. 13-26.
[2]. Hierro, A., et al., Geochemical behavior of metals and metalloids in an estuary affected by acid mine drainage (AMD). Environmental Science and Pollution Research, 2013: p. 1-17.
[3]. Wilkin, R.T., R.W. Puls and G.W. Sewell, Long-term performance of permeable reactive barriers using zero-valent iron: Geochemical and microbiological effects. Ground Water, 2003. 41(4): p. 493-503.
[4]. Henderson, A.D. and A.H. Demond, Long-term performance of zero-valent iron permeable reactive barriers: a critical review. Environmental Engineering Science, 2007. 24(4): p. 401-423.
[5]. Fu, F., D.D. Dionysiou and H. Liu, The use of zero-valent iron for groundwater remediation and wastewater treatment: A review. Journal of hazardous materials, 2014.
[6]. Bigg, T. and S.J. Judd, Zero-valent iron for water treatment. Environmental Technology, 2000. 21(6): p. 661-670.
[7]. Zorpas, A.A., et al., Heavy metal uptake by natural zeolite and metals partitioning in sewage sludge compost. Bioresource Technology, 2000. 72(2): p. 113-119.
[8].Kesraoui Ouki, S., C.R. Cheeseman and R. Perry, Natural zeolite utilisation in pollution control: A review of applications to metals' effluents. Journal of Chemical Technology and Biotechnology, 1994. 59(2): p. 121-126.

[9]. Okubo, T. and J. Matsumoto, Effect of infiltration rate on biological clogging and water quality changes during artificial recharge. Water Resources Research, 1979. 15(6): p. 1536-1542.
[10]. Mays, D.C. and J.R. Hunt, Hydrodynamic aspects of particle clogging in porous media. Environmental science & technology, 2005. 39(2): p. 577-584.
[11]. Sani, A., et al., Impact of Water Quality Parameters on the Clogging of Vertical-Flow Constructed Wetlands Treating Urban Wastewater. Water, Air, & Soil Pollution, 2013. 224(3): p. 1-18.
[12]. Rinck-Pfeiffer, S., et al., Interrelationships between biological, chemical, and physical processes as an analog to clogging in aquifer storage and recovery (ASR) wells. Water Research, 2000. 34(7): p. 2110-2118.

Advanced Materials Research Vols. 986-987 (2014) pp 755-760

doi:10.4028/www.scientific.net/AMR.986-987.755

Factors affecting mercury oxidation by SCR catalysts

Wen Du[1,a], LibaoYin [2], Yuqun Zhuo[1,b], Qisheng Xu[2], Liang Zhang[1], Changhe Chen [2]

[1]Key Laboratory for Thermal Science and Power Engineering of Ministry of Education Thermal Engineering Department, Tsinghua University, Beijing 100084, P. R. China

[2]Electric Power Research Institute of Guangdong Power Grid Corporation, No.8 Shuijungang, Dongfengdong Road, Guangzhou 510080, China

[a]email: duw09@mails.tsinghua.edu.cn, [b]email: zhuoyq@tsinghua.edu.cn

Keywords: Mercury; SCR catalyst; Oxidation; flue gas

Abstract. The application of selective catalytic reduction (SCR) system may affect mercury speciation in coal-combustion flue gas. The factors affecting mercury oxidation efficiency by SCR catalysts have been evaluated in this research. The influencing factors investigated included hydrogen chloride (HCl), sulfur dioxide (SO_2), ammonia (NH_3) injection rate and space velocity. HCl had been found to promote mercury oxidation significantly. The Eley-Rideal mechanism was proven to be suitable to explain the reaction of Hg^0 and HCl. NH_3 injection had a strong negative effect to mercury oxidation. The deactivation of aged SCR catalysts was mainly due to loss of active sites.

Introduction

In recent years, elemental mercury emission is a major environmental issue as a consequence of its persistence, long-range mobility, bioaccumulation and neurotoxicity [1]. Coal-fired power plant is one of the largest anthropogenic sources of mercury emission, accounting for about 30% of total mercury emission in the world [2]. U.S Environmental Protection Agency finalized the Mercury and Air Toxics Standards (MATS) to limit the mercury emissions from power plants in 2012 [3]. The UN Minamata Convention on Mercury was signed worldwide in 2013 to regulate the use of mercury and reduce mercury emission [4]. There are three main forms of mercury in atmosphere, i.e. elemental (Hg^0), oxidized (Hg^{2+}) and particle-bound (Hg^P) [1]. In coal-fired power plants, most of Hg^{2+} can be removed by wet flue gas desulfurization (WFGD) systems because Hg^{2+} is soluble in water. Hg^P can be collected with fly ash by particulate material control systems [1]. It is difficult to remove Hg^0 due to its water-insoluble and highly volatility. Sorbent injection is one of the most efficient technologies in Hg^0 removal [5]. However, the application of sorbent injection has been limited due to its high cost. Efficient mercury removal technology with low cost is the main concern in mercury emission control researches.

Selective catalytic reduction (SCR) is a widely commercialized technology for NO_x emission control in power plants [6]. The SCR catalysts could oxidize Hg^0 [7]. The application of SCR exhibits co-benefit of mercury catalytic oxidation and NO_x reduction. In recent years, many power plants have installed SCR and WFGD systems. The proportion of $DeNO_x$ systems installation of power plants in China is 28% on 2012 and SCR systems accounts for 98% of $DeNO_x$ systems [8]. The proportion of SCR installation will have a sustainable growth in future due to the stringent environmental limits in China [9]. SCR systems can promote Hg^0 oxidation [1] [6] [7], while the mechanism of Hg^0 catalytic oxidation by SCR was not well confirmed.

This study investigates the effects of SCR catalysts on Hg^0 oxidation under simulated coal-fired flue gases. The effects of HCl, SO_2 and NH_3 on mercury oxidation were studied. The deactivation of SCR catalysts was also investigated.

Experimental Section

Apparatus

The experimental setup for the tests is similar to our previous research [10]. The reactor system is comprised of four parts: mercury generation, simulated flue gas mixing, fixed-bed reactor and tail gas treatment. Hg^0 was generated by a PSA Mercury Generator (Cavkit 10.534) and water vapor was generated by an IAS Hovocal Gas Generator. The fixed-bed reactor was made of a 40 mm inside diameter quartz tube. The simulated flue gas was accurately controlled by Mass Flow Controllers. All the tubes, joints and valves with Hg containing gas passing through were made of either quartz or PTFE. The concentration of NO_x was monitored by FTIR gas analyzer (Nexus 670). The concentrations of Hg^0 and Hg^{2+} were continuously monitored by an online cold vapor atomic absorption spectroscopic mercury analyzer (ThermoFisher CEMS). Hg^P absorbed by the SCR catalysts was measured by Lumex RA-915M. The total system error range was previously determined as ±10% [10].

Experimental Procedure and data processing

The SCR catalyst in the quartz tube is honeycomb structure, which is the same shape as the catalyst in SCR reactor in power plants. The height of the catalyst was about 6 mm (space velocity was 17600 /h), the wall thickness was about 1 mm, and the weight was about 1 g (±0.01 g). The inlet elemental mercury concentration was set at 20 μg/Nm^3 for all the tests and the total flow rate was controlled at 2 L/min. Normally the reaction temperature was 350°C and the gas sampling line was maintained at 140°C to avoid moisture condensation and mercury adsorption. Each test normally lasts for 5 h and three replicates were done for each test.

The total Hg^0 oxidation rate has been defined as:

$$\text{Total Oxidation Rate } \eta_{oxi} = \frac{\sum_0^t c^t_{Hg^{2+}}}{c_0 \cdot t} \times 100\% \quad (1)$$

where c_0 is the inlet Hg^0 concentration, $c^t_{Hg^{2+}}$ are the outlet Hg^{2+} concentrations at the reaction time.

The NO conversion was determined by the following equation:

$$\text{NO conversion } \eta_{NO} = \frac{(c^{in}_{NO} - c^{out}_{NO})}{c^{in}_{NO}} \times 100\% \quad (2)$$

where c^{in}_{NO} and c^{out}_{NO} are the NO concentrations in the inlet and outlet streams.

Characterization of the SCR catalysts

Both the fresh and aged SCR catalyst was obtained from the same SCR reactor in a 600 MW coal-fired power plant (Taishan, China). The catalysts are in corrugate shape. The space velocity inside SCR reactor was normally 17600 /h. The catalyst which had been operated for about 26000 h was tested as the aged SCR for comparisons.

The surface area and pore size of the catalysts were measured on an automatic nitrogen adsorption analyzer (Quanta Autosorb-1-c, USA). X-ray diffraction (XRD) analyses were conducted on a diffractometer (Bruker D8, German) using Cu Kα radiation. The elemental analysis was measured by an X-ray fluorescence spectrometer (XRF, PAN alytical Axios PW4400, Netherlands).

Results and Discussion

Catalyst Characterization

The specific surface area, pore volume and average pore diameter of the catalysts are shown in Table 1. The result indicates that the specific surface area and pore volume of the catalyst decreased after the service in power plant. The reduction may be caused by blockage by fly ash particles and sintering of TiO_2 particles.

Table 1 Physical properties of the catalysts

Sample	BET Specific Surface Area(m^2/g)	Total Pore Volume (cm^3/g)	BET Averaged Pore Size(nm)
fresh SCR catalyst	59.7	2.81E-03	11.5
aged SCR catalyst	28.4	1.67E-03	14.2

Figure 1 depicts the X-ray diffraction patterns of the catalysts. The TiO_2 crystalline phase of the catalyst was anatase. There was no obvious transition of TiO_2 crystalline phase during the service indicating no sintering of TiO_2 on the surface of the catalyst. Since other components are not observed, it can be conclude that the impurities are well dispersed on the surface of used SCR catalyst.

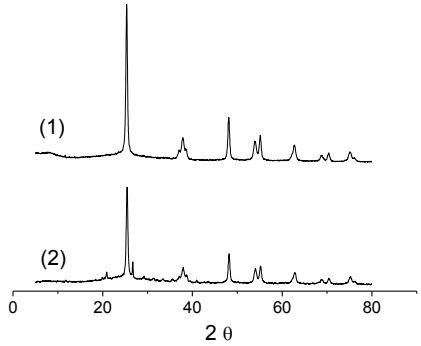

Fig. 1. X-ray diffraction patterns: (1) fresh catalyst, (2) aged catalyst

The main chemical composition of the SCR catalysts was measured by X-ray fluorescence (XRF), as shown in Table 2. The main components of the SCR catalyst are TiO_2, SiO_2, WO_3 and V_2O_5, which are widely used in commercial SCR catalysts. Compared to fresh catalyst, the content of TiO_2, WO_3 and V_2O_5 in the aged catalyst decreased and the content of K, Ca, Na, Mg, Al, S, Si, Fe increased. The mass fraction of alkali metal oxide is nearly 10% of the aged catalyst. The deactivation of aged SCR catalyst appears to be pore blocking of alkali deposition. The decrease of TiO_2 concentration was due to the deposition of fly ash constituents over the catalyst surface. The loss of active content (V, W, Ti) and fly ash deposition may cause deactivation and have negative effect to mercury oxidation.

Table 2. XRF analysis of the catalysts (w.%)

Composition	Fresh SCR	Aged SCR	Fly ash
TiO_2	67.2	55.5	1.23
SiO_2	13.7	18.2	39.6
WO_3	6.47	4.5	0.05
Al_2O_3	1.75	3.7	12.98
Fe_2O_3	0.14	1.9	9.8
CaO	2.33	3.4	9.72
P_2O_5	0.72	0.6	0.12
SO_3	0.13	2.6	17.81
V_2O_5	1.92	1.1	0.07
K_2O	0.05	0.3	1.51
MgO	0.10	0.2	0.75
Na_2O	0.05	0.3	1.53

Mercury catalytic oxidation efficiency

1) The effect of HCl

The Hg^0 oxidation activity of the SCR catalysts is greatly promoted in the presence of hydrogen chloride, and the reaction is considered to proceed as follows[11]:

$$Hg + 2HCl + 1/2\ O_2 \rightarrow HgCl_2 + H_2O \quad (3)$$

Factors that enhance surface chlorination, such as higher inlet HCl concentrations, promote Hg^0 oxidation [12]. In order to investigate the influence of HCl on the Hg^0 oxidation, tests were conducted under different HCl concentrations and the mercury speciation was shown in Figure 2. There was a trace of Hg^P on catalyst when HCl was in presence. For fresh SCR catalyst, the extent of mercury oxidation was progressively increased as the HCl concentration in the flue gas increased. The research carried out by Hocquel [13] proved that V_2O_5 could significantly promote the amount of $HgCl_2$ in the flue gas. The oxidation of mercury occurred at the active V_2O_5 sites. Mercury oxidation increased with increasing HCl content [11] [13] [14]. The Deacon process had been

suggested as the mechanism of releasing chlorine (Cl_2) via a reaction between V_2O_5 and HCl [15]. The active Cl can react with Hg^0 in the gas phase. The Eley-Rideal mechanism was suitable in explaining the reaction of Hg^0 and HCl on the catalyst, since there was no adsorbed mercury in the HCl atmosphere. However, the promotion effect on Hg^0 oxidation in the presence of high concentration HCl was limited for aged SCR, which was due to the reduced active sites on the surface of aged SCR [16]. Pore blocking of aged SCR by combined alkali and calcium sulfate deposition and growth had been proposed to explain the deactivation of SCR catalysts [17]. It had been observed that the surface was blocked and active contents were lost for the aged SCR catalyst from both SEM and XRF analyses. When all the active sites were occupied by HCl for aged SCR catalyst, the mercury oxidation efficiency would no longer increase with increasing HCl concentration.

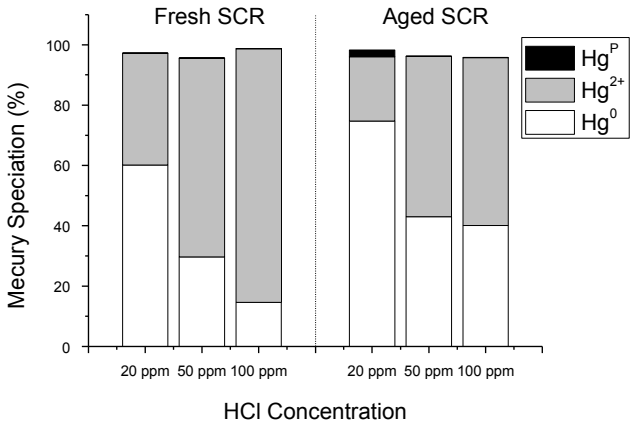

Fig. 2. The effect of HCl on mercury oxidation (6%vol. O_2,12%vol. CO_2, 5.12%vol. H_2O, 20-100 ppm HCl, 500 ppm SO_2 and 300 ppm NO balanced by N_2)

2) The effect of space velocity

The mercury oxidation rates were tested at the space velocities of 17600 /h (typical value in the boilers) and 8800 /h. The test results are illustrated in Figure 3.

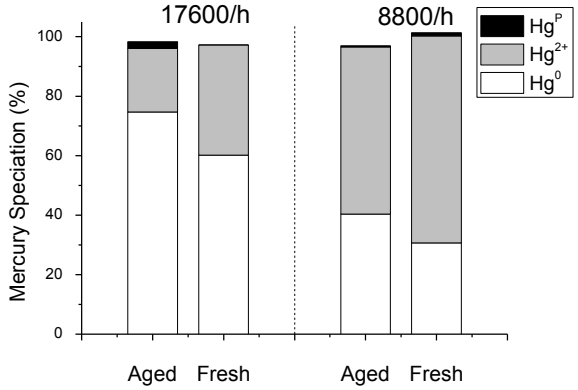

Fig.3. Mercury speciation under different space velocities(6%vol. O_2,12%vol. CO_2, 5.12%vol. H_2O, 20 ppm HCl, 500 ppm SO_2 and 300 ppm NO balanced by N_2)

As expected, Hg^0 oxidation rates increased for smaller space velocity over SCR catalysts. For the same space velocity, the extents of Hg^0 oxidation fell as the usage of the SCR catalyst. This was apparently due to the deactivation of aged SCR catalyst. When the space velocity decreases, the residence time increases. If the difference between the performances of fresh catalyst and aged catalyst is due to the disparity of the specific surface area and total pore value, the difference of Hg^0 oxidation rates between the catalysts will increase and the ratio of the Hg^0 oxidation rates will be close to the ratio of the specific areas when the space velocity decreases. However, the result is opposite. The result in Figure 3 showed that the difference of the Hg^0 oxidation rates between the catalysts decreased when the space velocity reduced to 8800 /h. This phenomenon indicates that the difference of Hg^0 oxidation rates between the catalysts is due to the decrease of active sites, which is consistent with the XRF data.

3) The effect of SO_2

Figure 4 shows the mercury speciation of fresh SCR catalyst under different SO_2 concentrations. As the SO_2 concentration in the flue gas boosted, the mercury removal process was slightly suppressed and the amount of Hg^0 increased. The result is consistent with previous research [18]. This was probably due to the adsorption active sites occupied by the high concentration SO_2. The SO_2 related chemical reactions that are of interest in coal-fired power plants include:

$$SO_2 + 1/2\ O_2 \rightarrow SO_3 \quad (4)$$

$$Hg + SO_3 + 1/2O_2 \rightarrow HgSO_4 \quad (5)$$

Further studies might be worthwhile to evaluate the active species responsible for mercury oxidation in the SO_2 simulated atmosphere.

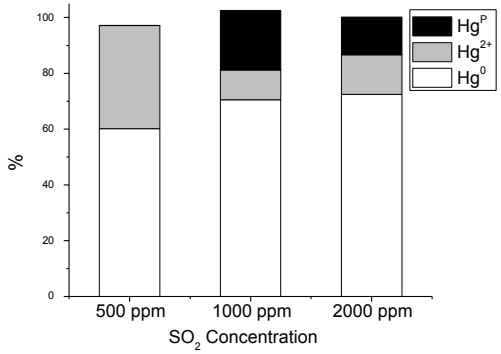

Fig.4. The effect of SO_2 on mercury speciation (6%vol. O_2,12%vol. CO_2, 5.12%vol. H_2O, 20 ppm HCl, 500-2000 ppm SO_2 and 300 ppm NO balanced by N_2)

4) The effect of NH_3 Injection

Ammonia (NH_3) has been most widely applied for NO_x reduction in the SCR process. In a SCR reactor, the reduction of NO with NH_3 proceeds according to the following reaction:

$$4NO + 4NH_3 + O_2 \rightarrow 4N_2 + 6H_2O \quad (6)$$

Figure 5 shows the Hg^0 oxidation and NO conversion over the fresh SCR catalyst as a function of NH_3/NO molar ratio. The NO conversion was almost linearly increased with NH_3/NO ratio in the presence of 50 ppm HCl, and fresh SCR catalyst exhibited good NO_x reduction catalytic activity. Hg^0 oxidation rate, on the contrary, decayed as NH_3/NO ratio rose. This interpreted that NH_3 had a strong inhibition effect on mercury oxidation. With the increase of the NH_3/NO ratios, the effect of HCl concentrations to the Hg^0 oxidation rates decreases. This indicates that the promotion effect of HCl to the Hg^0 oxidation rates was restrained when the NH_3 concentration increased. The reaction mechanism was that NH_3 competed for surface active sites against HCl, which is consistent with previous research [19]. NH_3 bound to the V_2O_5 sites on SCR catalyst as part of NO reduction process and therefore competed against Hg^0 adsorption [14]. Hg^0 contacted the chlorinated active sites from gas phase or as a weakly adsorbed species. Higher HCl concentrations promote Hg^0 oxidation.

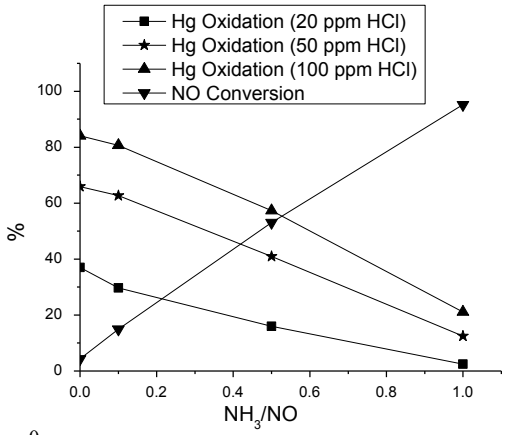

Figure 5. Dependence of Hg^0 oxidation and NO conversion on the NH_3/NO moler ratio (6%vol. O_2,12%vol. CO_2, 5.12%vol. H_2O, 20-100 ppm HCl, 500 ppm SO_2, 300 ppm NO and 0-300 ppm NH_3 balanced by N_2)

Conclusions

This study has been performed to understand the factors affecting Hg^0 oxidation rate by SCR catalyst. Tests results have indicated that SCR catalysts could oxidize elemental mercury at the temperature expected in SCR process in a variety of flue gas species. HCl was the most significant flue gas component that converted Hg^0 to Hg^{2+} under the application of SCR catalysts. NH_3 addition decreased mercury oxidation rates. Increasing the chlorine content of the flue gas could reduce the negative impact of ammonia injection. The Eley-Rideal mechanism might be appropriate to explain the reaction of Hg^0 and HCl. The deactivation of aged SCR catalysts was due to pore blocking by alkali and fly ash deposition and loss of active sites.

References

[1] Pavlish J H, Sondreal E A, Mann M D, et al. Status review of mercury control options for coal-fired power plants [J]. Fuel Process. Technol, 2003 (82) 89-165.
[2] U.S. Government Printing Office, A Study of Hazardous Air Pollutant from Electric Utility Steam Generating Units: Final Report to Congress [R]. Washington, DC, 1998.
[3] U.S. Environmental Protection Agency, Airlink Web Site at: http://www.epa.gov/ airquality/combustion/actions.html#dec12
[4] Stiftung Wissenschaft und Politik (SWP). German Institute for International and Security Affairs. The UN Minamata Convention on Mercury [S]. 2013
[5] Wilcox J, Rupp E, Ying S C, Lim D H, et al. Mercury adsorption and oxidation in coal combustion and gasification processes [J]. International Journal of Coal Geology 2012 (90) 4–20.
[6] Laudal D L, Pavlish J H, Brown T D, et al. Pilot-scale evaluation of the impact of selective catalytic reduction for NO_x on mercury speciation[C]. Proceeding of the Air and Wastc Management Association Annual Meeting, Orlando, Florida, 2001.
[7] Wang Peng-ying, Su Sheng, Xiang Jun, et al. Catalytic oxidation of Hg^0 by CuO-MnO_2-Fe_2O_3/γ-Al_2O_3 catalyst [J]. Chemical Engineering Journal, 2013 (225) 68-75.
[8] China Electricity Council. 2013. Airlink Web Site at: http://www.cec.org.cn/xinxifabu/ 2013-03-18/98950.html
[9] Chinese Research Academy of Environmental Sciences. GB 13223—2011 power plant air pollutant emission standards [S]. Beijing: Environmental Science Press of China.
[10] Du Wen, Yin Li-bao, Zhuo Yu-qun, et al. Catalytic Oxidation and Adsorption of Elemental Mercury over $CuCl_2$-Impregnated Sorbents[J]. Industrial & Engineering Chemistry Research, 2014 (53) 582-591.
[11] Lee C W, Srivastava R K, Ghorishi S B, et al. Study of Speciation of Mercury under Simulated SCR NO_x Emission Control Conditions [C]. Proceedings of the MEGA Symposium, Washington, DC, 2003.
[12] Niksa S, Fujiwara N. A Predictive Mechanism for Mercury Oxidation on Selective Catalytic Reduction Catalysts under Coal-Derived Flue Gas [J]. Journal of the Air & Waste Management Association, 2005 (55) 1866–1875.
[13] Hocquel M. The Behaviour and Fate of Mercury in Coal-Fired Power Plants with Downstream Air Pollution Control Devices [D]. Forschr.-Ber. VDI Reihe Nr. 251. Düsseldorf: VDI Verlag, Germany, 2004
[14] Senior C L. Oxidation of Mercury across Selective Catalytic Reduction Catalysts in Coal-Fired Power Plants [J]. Journal of the Air & Waste Management Association, 2006 (56) 23–31.
[15] Gutberlet H, Schlu¨ter A, Licata A. SCR Impacts on Mercury Emissions from Coal-Fired Boilers [C]. The Electric Power Research Institute SCR Workshop, Memphis, TN, 2000.
[16] Eom Y, Jeon S H, Ngo T A, et al. Heterogeneous mercury reaction on a selective catalytic reduction (SCR) catalyst [J]. Catalysis Letter, 2008 (121) 219–225.
[17] Joshua R S, Christopher J Z, Bruce C. F, et al. SCR deactivation in a full-scale cofired utility boiler [J]. Fuel 2008 (87) 1341–1347.
[18] Zhuang Y, Laumb J, Liggett R, et al. Impacts of acid gases on mercury oxidation across SCR catalyst [J]. Fuel Processing Technology, 2007 (88) 929-934.
[19] Kim M H, Ham S W, Lee J B. Oxidation of gaseous elemental mercury by hydrochloric acid over $CuCl_2$/TiO_2-based catalysts in SCR process [J]. Applied Catalysis B: Environmental, 2010 (99) 272–278.

Advanced Materials Research Vols. 986-987 (2014) pp 761-764

doi:10.4028/www.scientific.net/AMR.986-987.761

Modeling and experimental studies of SO_2 absorption in aqueous ammonia solution with Wetted-wall Column

Jian Peng[a], Dengfeng Zhang[b], Chaoqin Yang[c]; Jun Tao[d]

Faculty of Chemical Engineering, Kunming University of Science and Technology, Kunming, 650500, China

[a]Jianp2004@163.com, [b]plum0627@163.com, [c]kustycq@126.com, [d]taojun_1986@163.com

Keywords kinetics; SO_2 absorption; wetted-wall column; mass transport

Abstract. In a wetted-wall column of pilot-scale sulphur dioxide removal efficiencies were measured at 20℃ and atmospheric pressure with aqueous ammonia solutions as the scrubbing liquid for different sulphur dioxide inlet concentration in the range of 1000-3000 mg/m^3. A mathematical model with the effects of a chemical enhancement factor and sulfite concentration in the liquid phase developed to interpret laboratory experiments was adapted and the calculated values were in reasonable agreement with the experimental values. It appears that this model can provide good predictions of the absorption performances of industrial columns and be helpful to design scrubbers for SO_2 abatement with aqueous ammonia solutions.

Introduction

It is well known that sulfur dioxide exist in the flue gases of power plants and industrial boilers lead to acid rain which damages buildings, vegetation and water ground cycle [1]. SO_2 is also considered to be toxic to humans by inhalation. Throughout the world, pollutant emission standards have become increasingly strict over the past ten years [2]. The most effective wet processes use sodium or calcium hydroxides [3,4], but the liquid or solid wastes that absorption produced must be treated correctly if they are not marketable.

Ammonia-based wet flue gas desulphurization has drawn increasing attention because of its higher desulphurization efficiency, useful byproducts, and lower investment in china in recent years [5, 6]. Liu Guorong [7] investigated the effects of several key factors on the efficiency of ammonia desulphurization and established a mathematical model for ammonia desulphurization based on the two-film theory in spray towers. Jia Yong[8]studied the gas-liquid mass transfer and chemical reaction process during ammonia-based flue gas desulfurization in a packed column. Gao Xiang[9] investigated the characteristics of the gas-liquid absorption reaction between sulfur dioxide and an ammonium sulfite solution in a stirred tank reactor and indicated that the absorption of sulfur dioxide is controlled by both the gas-and liquid-films when the ammonium sulfite concentration is lower than 0.05mol/L, and mainly by the gas-film at higher concentrations.

The aim of this study was to investigate the characteristics of SO_2 absorption into aqueous ammonia solutions and the influence of operating conditions on absorption efficiency in wetted-wall column at 20±0.5℃ and atmospheric pressure.

Materils and Methods

The experimental set-up is shown schematically in Fig.1.It includes a pilot-scale column and a heat exchanger and a pump resistant to acid or alkali solutions. The tower has an inside diameter of 0.1m

and is packed with ceramic tube which has an inside diameter of 8mm and outside diameter of 10mm. The number of ceramic tube is 38 and the height of the packing is 1.2m.

The gaseous mixture is made of SO_2 supplied by a high pressure cylinder and air blown by a compressor. Sample of gas at the input and the output of the column is analyzed by UV analyzer, which gives the SO_2 contents.

Efficiency of desulphurization is defined according to measured results for gas composition.

$$\eta = \frac{c_{in} - c_{out}}{c_{in}} \tag{1}$$

The column is operated co-currently with recycle of the scrubbing liquid, aqueous ammonia solution was used.

A series of absorption tests was conducted at 20 ± 0.5℃ and atmospheric pressure. Experiments were performed with gas flow rates in the range from 15m^3/h to 85m^3/h and a liquid flow rate varying between 0.05 m^3/h and 0.15 m^3/h.

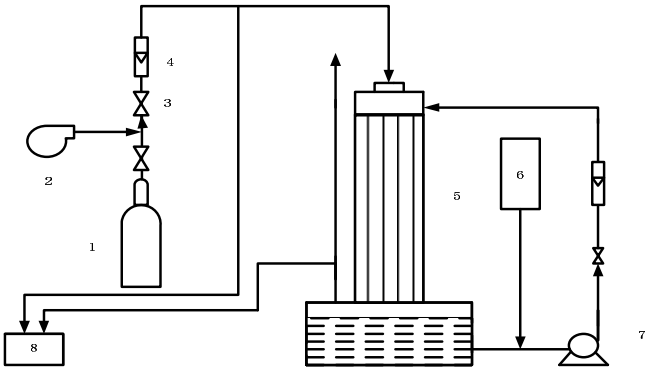

1. SO_2 cylinder 2. Compressor 3.Valve 4. rotameter 5. column 6. Ammonia liquor tank 7.Pumb 8.UV analyzer

Fig 1 Diagram of experimental system of ammonia desulphurization

Modeling of SO_2 absorption into aqueous ammonia solution

Based on the two-film theory of absorption with chemical reaction, a mathematical model was developed to simulate the SO_2 absorption into aqueous ammonia solutions. The model assumes the absorbed gas SO_2 undergoes a fast irreversible reaction with the liquid reactant $(NH_4)_2SO_3$, which is complete within the liquid film.

The following reactions will mainly occur during the absorption of SO_2 into aqueous solution with ammonia:

$$SO2+(NH4)2SO3+H2O \rightarrow 2NH4HSO3 \tag{2}$$

The model assumes that dissolved SO_2 undergoes a fast irreversible reaction which is completed in the liquid film. The absorption reaction is considered to be globally of second order with respect to the reactants according to:

$$r = k_2 c_{SO_2} c_{(NH_4)SO_3} \tag{3}$$

Based on the two-film model, the mass transfer equation of SO_2 into $(NH_4)_2SO_3$ solution is :

$$N_{SO_2} = k_G (p_{SO_2} - p_{SO_2,i}) = E k_L c_{SO_2,i} \tag{4}$$

The concentration of $(NH_4)_2SO_3$ in the bulk liquid being much greater than the SO_2 interfacial concentration $c_{SO2,i}$, the kinetics of the reaction becomes pseudo-first order and for large Hatta numbers:

$$E = \frac{Ha}{\tanh H} \approx Ha \tag{5}$$

Where H is Henry's coefficient of SO_2 for aqueous ammonia solution.

$$Ha = \sqrt{k_1 D_{SO_2}} / k_L = \sqrt{k_2 D_{SO_2} c_{(NH_4)_2SO_3}} / k_L \tag{6}$$

The following expression is finally used for the absorption rate.

$$N_{SO_2} = \frac{p_{SO_2,i}\sqrt{k_2 D_{SO_2} c_{(NH_4)_2SO_3}}}{H} \tag{7}$$

Experimental parameters and dimensions are listed in Table 1 and the physical parameters in Table 2

Table 1 Experimental parameters and dimensions

Liquid flow, Q_L	0.05-0.15m^3/h
Gas flow, Q_G, at 20℃ and 1atm	15-85m^3/h
Temperature, T	20℃
Height of column, h	1.2 m
Pressure, P	1atm

Table 2 Physical parameters at 20

Water density, ρ_L	998kg/m^3
Dry air density, ρ_G	1.205 kg/m^3
Water viscosity, μ	1 10^{-3}Pa·s
Diffusion coefficient for SO_2 in water	1.52 10^{-9} m^2/s

Results and discussion

Effect of $(NH_4)_2SO_3$ Concentration on the SO_2 absorption Rate

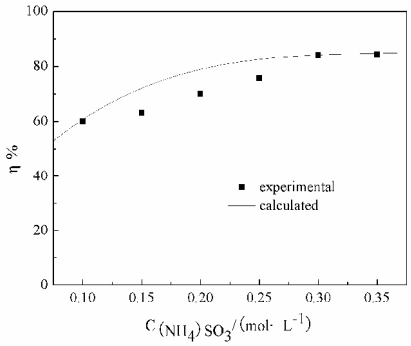

Fig 2 Relationship between absorbent concentration and desulphurization efficiency

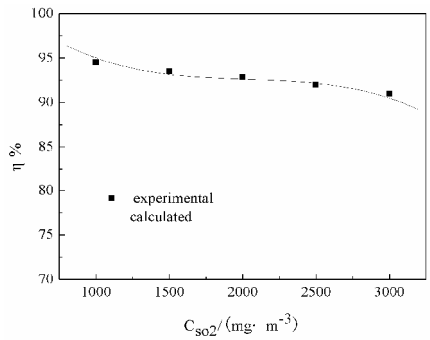

Fig 3 Effect of the SO_2 inlet concentration on desulphurizat efficiency

Fig.2 illustrates the influence of absorbent concentration and desulphurization efficiency, while the SO_2 concentration was 2500mg/m^3.The liquid flow rate was 120L/h during the runs. It appears that, for a constant acidity of the absorbent, a rise in $(NH_4)_2SO_3$ concentration involves an increasing desulphurization efficiency when $(NH_4)_2SO_3$ concentration lower than 0.3mol/L. However, the SO_2 absorption rate becomes nearly constant as the $(NH_4)_2SO_3$ concentration rises above 0.3mol/L. In the latter case, the reaction may be mainly influenced by gas-film.

Effect of Inlet Concentration on SO_2 Absorption Rate

Fig.3 shows the effect of the SO_2 inlet concentration on desulphurization efficiency. pH is 6.5 $\pm$0.1, gas flow rate is 50m^3/h and liquid flow rate is 120L/h. It reveals that desulphurization efficiency decreases with SO_2 inlet concentration increase. However, this does not imply decrease in absorption rate. In fact, the absorption rate is a simple increasing function of SO_2 inlet concentration, while the decreasing tendency of η is resulted from fast increase of SO_2 that needs to be absorbed.

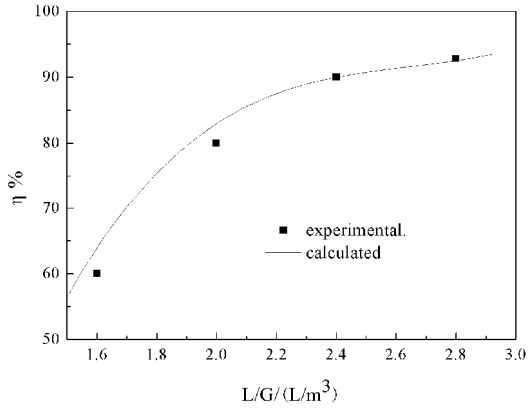

Fig 4 Effect of liquid-gas ratio on the flue gas desulphurization efficiency

Effect of Liquid-gas Ratio on the SO_2 Absorption Rate

The results of effect of liquid-gas ratio on the flue gas desulphurization efficiency are shown in fig.4.The experiments are carried at a fixed liquid flow rate, while gas flow rate is controlled according requested L/G. As can be seen from fig.7, η increases as the flow ratio increasing. When L/G is over 2.5, the change of η is smoothed. Obviously, η increases because of the increase in interface increasing. On the other hand, increase the L/G ratio leads to increased power consumption and thus operation cost.

Conclusions

On the basis of experiments with wetted-wall column it is possible to draw the following conclusions: The results demonstrate that when inlet concentration is 2500mg/m^3 the best technical parameters are 2.4 to 2.8L/m^3 for the liquid-gas ratio, 5.8 to 6.5 for the pH value of absorption. Under the best technical parameters the desulphurization rate can reach 95%. The liquid-phase and gas-phase mass transfer coefficients of the system were determined. A model with a chemical enhancement factor was developed for the prediction of the SO_2 removal efficiency. It is showed that the calculated values of the SO_2 removal efficiency are in reasonable agreement with the experimental values.

References

[1] Wang, J. S., Anthon E, J., Clean combustion of solid fuels, *Appl Energy*, 85, 73-79(2008).
[2] Versnon, J: *Int. J. Energy Res*,14: 805-812(1990).
[3] Lin, R. B., Shin, S. M., Liu, et al: *Chem Eng Sci*,58, 3659-3668(2003).
[4] Chu, H., Chien, T.W., Li, S.Y.: *Sci Total Environ*, 275, 127-135(2001).
[5] Xiao, W. D, Li, W, Fang, Y. J., et al: *Electric Power*,34(7),54-58(2001)(in Chinese).
[6] Wu, Z. B., Liu, Y., Sheng, Z. Y. et al: *Environmental Science & Technology*, 33(2), 137-137(2010) (in Chinese).
[7] Liu, G. R., Wang Z.W., Wei, Y. L. et al: *CIESC Journal,*61(6),2463-2467(2010) (in Chinese).
[8] Jia, Y., Zhong Q., Du, D. D. et al., Study on modeling of ammonia-based flue gas desulfurization process, *Journal of Power Engineering*, 29(10),960-965(2009)(in Chinese).
[9] Gao, X., Ding, H. L., Du, Z. et al: *Applied Energy* 87, 2647-2651(2010).

Advanced Materials Research Vols. 986-987 (2014) pp 765-770

doi:10.4028/www.scientific.net/AMR.986-987.765

Recent Review of Gas Hydrate Sediments Mechanics Behavior

LU Jingsheng, LI Dongliang, LIANG Deqing

Centre for Gas Hydrate Research, Guangzhou Institute of Energy Conversion, Chinese Academy of Sciences, No.2 Nengyuan Rd., Wushan, Tianhe District, Guangzhou 510640, CHINA

lujs@ms.giec.ac.cn, lidl@ms.giec.ac.cn, liangdq@ms.giec.ac.cn

Keywords: Mechanics behavior, Gas Hydrate Sediments, Review

Abstract. The purpose of this review paper is to summarize the recent research in mechanics behavior of hydrate bearing sediments (HBS). The paper will discuss recent research of the laboratories mechanics test with analysis on HBS and numerical simulation on mechanics behavior of HBS.

Introduction

As a potential energy of 21st centuries, commercial development of gas hydrate (GH) from the permafrost and oceans is put on the list of future national energy security by some countries. The main problem of GH development is geo-mechanical stabilities due to dissociation of the solid hydrates during drilling, casing and gas production. They can degrade the structural strength of the HBS which can lead to the casualties like wellbore collapse, blow-outs and even tsunamis due to large-scale geological subsidence. So it is significant to research in the mechanics behavior of HBS.[1]

China drilled out gas hydrate onshore at Qinghai-Tibet Plateau in 2009 and offshore at South China Sea in 2007 and 2013. However, due to lack of original gas hydrate cores, the laboratories' artificial HBS is widely applied while the numerical simulation on mechanics behavior applies the laboratory's data to simulate the field condition before the gas hydrate trial production. North American onshore tests at Alaska and Mackenzie Delta at beginning of this century while Japan offshore tests at Nankai Trough in 2013 were both followed this process, laboratories data-model simulation-field test.

Laboratories Mechanics Test and Theoretical Analysis on HBS

The tri-axial compressive test with theoretical analysis is the basic approach for current research of HBS mechanics behavior. American researchers had reviewed gas hydrate research in 2011, based on their mechanics review, this review will give below.[1]

Winter et al. [2] have built an instrument, named GHASTLI - Gas Hydrate and Sediment Test Laboratory Instrument, to research on the properties of ice, pure gas hydrate and HBS from Mackenzie Dealt, Alaska Mexico and India. They analyze the mechanical properties like stress-strain relationships, strength and modulus with the HBS grain properties and distribution. The strength of sediments with GH is much larger than that without GH. Furthermore, they find out the bond effect between hydrate and sediment grains in the laboratories' artificial HBS which should be considered in the prediction model because there is no cementation effect in the field HBS. Meanwhile, they researched the acoustic property for the in situ exploration, drilling, well-test and production projects.

Hyodo et al.[3, 4] discussed the relationships between GH saturation and mechanics properties. Draw the diagrams of stress-strain in the different GH saturation with temperatures, confining pressures and shear strain rates. The bonding effect was discussed on the shear strength and deformation of HBS with GH saturation and grain size of sediments.[3] With the successful trail production of marine GH by Japan in March, 2013, a series of tests for production methods, the thermal recovery method or depressurization method, were conducted to investigate the shear strength and deformation behavior of HBS. From the laboratories' test, the results indicate that:

thermal recovery method reduces the failure strength of isotropically consolidated HBS but increases the initial stiffness and volumetric strain when compare these with the pure Toyoura sand; depressurization method will not cause the collapse of HBS during depressurization and that give little effect on the ultimate deformation of HBS, while the initial deformation rate goes up with depressurization rate up. Furthermore, the larger the reduction of pore pressure is, the larger axial strain and volumetric strain are. When the axial load is higher than the strength of HBS after dissociation, both water pressure recovery and thermal recovery method will lead to failure of HBS.[4]

Masui et al.[5-9] give a conclusion that shear strength and elastic modulus increase with saturation up while shear strength decrease with porosity down at same saturation. Additionally, in the Mohr–Coulomb criteria, cohesion increases with saturation, however there is no obvious trend to the internal friction angle and poisson's ratio. They compared the HBS properties of retrieved cores from Eastern Nankai Trough with synthetic GH samples, similar strength, but different elastic modulus due to initial porosity with grain size and distribution, and different volumetric strain because of dilatancy effect by size distribution. Interestingly, they researched on the unloading-reloading tri-compression test.[8] From the Fig. 1, the total stress-stain curve of HBS unloading-reloading is similar to conventional HBS stress-strain curve. However, the tangent of the stress-strain curve diminishes throughout the unloading-reloading process. In other words, once deformed, a specimen becomes easy to deform again in the same direction. From the Fig. 2, the deformation mechanism is two parts: (1) At the beginning of axial loading, the consolidation is a dominant deformation mechanism where the slope of unloading-reloading curve influencing elastic component of deformation has increased. Then, the dilatancy is a dominant deformation mechanism because that has decreased. (2)After the peak, the dilatancy behavior is still a dominant deformation mechanism; the irreversible strain (inelastic strain) makes more contributions than the reversible strain (elastic strain) to the deformation increase of a specimen.

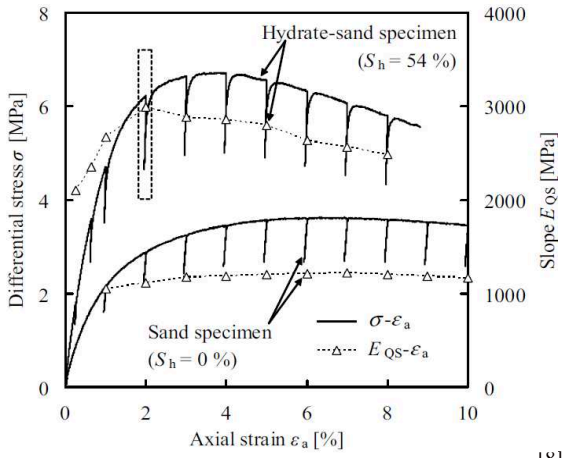

Fig.1 Differential stress-axial strain curve [8]

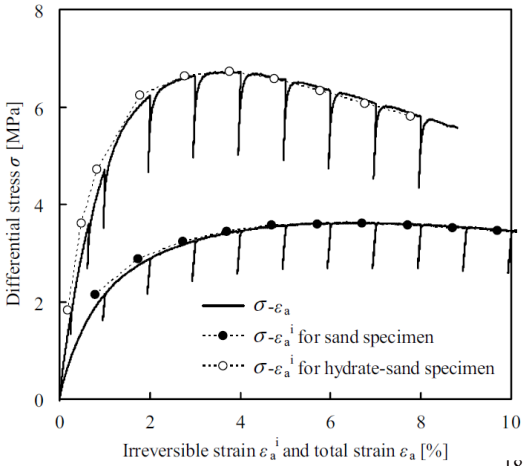

Fig. 2 Strain in unloading-reloading test [8]

The effective confining pressure σ'_3 test for the formulation of strength is given by experiment data where cohesion c and internal friction angle φ can be calculated. For the hydrate, based on the Mohr-Coulomb failure criterion, the tri-axial compressive strength $\sigma_C(S_h, \sigma'_3)$ can expand to equitation (6) [10]:

$$\sigma_C(S_h, \sigma'_3) = \frac{2\cdot\cos\varphi}{1-\sin\varphi} c(S_h = 0) + \alpha \cdot S_h^{\beta} + \frac{2\cdot\sin\varphi}{1-\sin\varphi}\sigma'_3 = \sigma_C(0,0) + \Delta\sigma_{C-sh} + \Delta\sigma_{C-cp} \quad (1)$$

(The cohesion c is a function of GH saturation S_h; the internal friction angle φ and effective normal stress σ'_3. The first, second and third terms in the right side of Eq. (1) can be explained to correspond to the apparent uniaxial compressive strength of sand specimen $\sigma_C(0,0)$, the strength increase with GH saturation $\Delta\sigma_{C-sh}$ and the strength increase with effective confining pressure $\Delta\sigma_{C-cp}$, respectively. $\Delta\sigma_{C-sh}$ can be got a equitation related to S_h from the difference of strength versus hydrate saturation chart by experiment data where α and β is coefficient and exponent for approximation of $\Delta\sigma_{C-sh}$).

The researchers from Southampton University [11-14] applied a Gas Hydrate Resonant Column (GHRC) apparatus to investigate the strength and stiffness during the hydrate formation and dissociation. In the hydrate formation, the total increase in stiffness with full hydrate formation was up to 20 times that measured when without GH was in the pore space. Furthermore, hydrate volume which affects the buckling resistance of column and effective confining stress applied to the specimen can take significant influence of stiffness during the hydrate formation.[13] For the bonding effect, the small amounts of bonding had a huge affection on the shear modulus of the sand with hydrate, and hydrate bonding had the little impact on the bulk modulus. While there was little dependence of stiffness on effective stress when above hydrate contents are enough. Hydrate-bonded sand was found to be much higher damping than the sand specimens with the same equivalent water content. A peak damping ratio was found at about 3–5% hydrate content, both in torsion and in flexure. It is suggested this should be the intrinsic damping properties of the hydrate itself.[15] In the hydrate dissociation, large decrease of specimen stiffness was detected to slight changes in hydrate saturation. Final, they give the suggestion of the nonlinear behavior will be required to more accurately model the behavior of HBS because the current model of quantifying soil strength/stiffness value for hydrate volume remaining would be overestimated.[13]

Dalian University of Technology researchers [16-19] conducted series of tri-axial compression tests on synthetic HBS cores under high confining pressures and low temperature. They take the two stages of HBS stress-strain relationship into consideration, rapid structural damage stage and complete structural damage stage, following the Duncan-Chang model. They found out the initial yield strain, initial yield strength, initial deformation modulus and ultimate deviator stress increase with the confining pressure up and temperature down while the initial yield modulus is only affected by temperature. Both cohesion and friction angle are increased with the decreased of temperature and increase of strain rate; the strength increased with decreasing porosity; the porosity has a great influence on the cohesion but not on the fraction angle. The variations of failure strength with porosity mainly were caused by the variations of cohesion.[16] Moreover, the stress-strain curves of HBS showed as a shape of hyperbola, and that deviator stress rises gradually with axial strain going upwards and eventually arrives at a constant value without significant peak value. When confining pressure over 5 MPa, the failure strength drops with confining pressure up. A new strength criterion is proposed based on the experimental results which can well reflect the failure load of HBS under high confining pressures. The Duncan–Chang model is used to describe the deformation behavior of HBS under various confining pressures, and that simulated results are well match to the experimental data.[18]

WU et al [20] established a statistical damage constitutive model of HBS. A power function is established for the damage variable which thinks about the affection of effective confining pressure based on the relationship between equivalent elastic modulus and hydrate saturation. The strength of a micro-element of HBS is described by Drucker-Prager failure criterion and the variation of the micro-element strength is assuming to follow Waybill's distribution. The statistical damage constitutive model of HBS is established.

Numerical Simulation on Mechanics Behavior of HBS

Heriot Watt University researchers [21-23] established a wellbore stability model for HBS with rock and soil mechanics software FLAC^{3D}. This model can couple the thermodynamically stability, heat transforms, porous medium flow and geo-mechanics deformation of GH.[22] Then they combined finite-element model of casing for HBS with GH simulator HWHYD with rock with soil mechanics software ABAQUS. Although this model solved the problems of fluid-solid coupling, the coupling between mechanical and thermal terms is only one-way coupling.[23]

Lawrence Berkeley National Laboratory researchers [24-27] took the numerical studies on geo-mechanical stability of HBS with hydrate simulator TOUGH2+HYDRATE (T+H) and soil mechanics software FLAC3D (F). T+H is the system hydraulic, thermal, and thermodynamic behavior in geological media containing GH. FLAC3D has built-in constitutive mechanical models suitable for soil and rocks, including various elastoplastic models for quasi-static yield and failure

analysis, and viscoplastic models for time dependent (creep) analysis, that could be used directly or modified for analysis of geo-mechanical behavior of HBS. TOUGH+HYDRATE and FLAC3D are linked through a coupled thermal/hydrological/mechanical (THM) model of the HBS (Fig. 3). In Fig. 3, the data exchanges between TOUGH+ HYDRATE and FLAC3D are illustrated with arrows going through the central THM model. The shear strength, bulk modulus, cohesion and friction angle is considered as the parameter of HBS mechanics. T+H simulator can give the results of thermodynamic parameters (such as temperature T), hydraulic parameters (such as capillary pressure Pc, intrinsic permeability k and pressure P). Then they simulated production on GH reservoir and got the stress field, strength and mechanics behavior versus time. Their simulation results indicate that gas production from oceanic deposits may affect the geo-mechanical stability of HBS. Conversely, the increased pressure caused by the weight of structures on the ocean floor increases the stability of underlying hydrates.[27, 28]

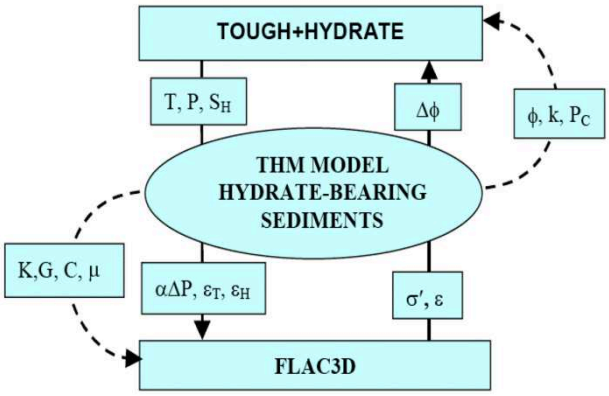

--	Direct couplings	S_H	Hydrate saturation	K	Bulk modulus	C	Cohesion
—	Indirect coupling	μ	Coefficient of friction	σ'	Effective stress	ε	Strain
T	Temperature	k	Intrinsic permeability	P	Pressure	$\emptyset$	Porosity
G	Shear modulus	P_c	Capilary pressure				

Fig. 3 Coupling of TOUGH+HYDRATE and FLAC3D for analyzing geomechnical behavior of HBS[29]

Kolditz et al.[30] developed the OpenGeoSys, a free scientific multi-platform modeling package that enables numerical simulations of individual or coupled thermo-hydro-mechanical-chemical (THMC) processes in porous and fractured media. A gas module for OpenGeoSys with coupled THMC is the subject of a study currently in progress.

Recent research of Guangzhou Institute of Energy Conversion

China's marine HBS is below 2000m water depth, much deeper than the Japan, India and North American, which the confining pressure is over 20MPa and pore pressure is about 20MPa.[1, 31] So there is not too much successful research on such high pressure in the laboratory. Recently, Guangzhou Institute of Energy Conversion built tri-axial facilities, which can apply the maximum capabilities of 250 kN for axial loading with accuracy of 0.1%/min strain-rate, 30 MPa for confining pressure and 20 MPa back pressure. The temperature inside the chamber can be controlled at the range from 243 K to 323 K with an accuracy of 0.5 K by circulating 50% ethylene alcohol solution from the refrigerator. The data of displacements, load, confining pressure, back pressure and temperature were acquired and recorded by the computer system at every 10 seconds during the test. This tri-axial facility took the advantages of laboratories mentioned above; it specially designed to simulate the high pressure condition of South China Sea.

Conclusion

In brief, it is not easy to get the mechanics data of HBS in the field, such as the permafrost and the deep marine. Thus, to get the full understanding stability of HBS for future exploitation, the laboratories test with theoretical analysis and numerical simulation have a long way to go.

Acknowledgments

This work was financially supported by the Chinese Academy of Science Program (KGZD-EW-301), NOG Program (GHZ2012006003) and National Natural Science Foundation of China (41276043).

References

[1] Moridis G, Collett T S, Pooladi-Darvish M, et al. [J]. SPE Reservoir Evaluation & Engineering. 2011, 14(1): 76-112.
[2] Winters W J, Waite W F, Mason D H, et al. Methane gas hydrate effect on sediment acoustic and strength properties[J]. 2007, 56(1-3): 127-135.
[3] Hyodo M, Yoshimoto N, Kato A, et al. Shear Strength and Deformation of Methane Hydrate Bearing Sand with Fines[J]. Proc. of the 18th ICSMGE, Paris. 2013.
[4] Hyodo M, Li Y, Yoneda J, et al. [J]. Marine and Petroleum Geology. 2014, 51(0): 52-62.
[5] Masui A, Haneda H, Ogata Y, et al. Mechanical Properties of Sandy Sediment Containing Marine Gas Hydrates In Deep Sea Offshore Japan[C]. The International Society of Offshore and Polar Engineers, 2007.
[6] Masui A, Miyazaki K, Haneda H, et al. Mechanical Properties of Natural Gas Hydrate Bearing Sediments Retrieved from Eastern Nankai Trough[C]. Houston, Texas, USA: 2008.
[7] Miyazaki K, Masui A, Sakamoto Y, et al. Investigation of Deformation Mechanism For Methane Hydrate Sediment Based Upon Mechanical Properties In Unloading And Reloading Process Under Triaxial Compression[C]. The International Society of Offshore and Polar Engineers, 2009.
[8] Miyazaki K, Masui A, Tenma N, et al. Study On Mechanical Behavior For Methane Hydrate Sediment Based On Constant Strain-Rate Test And Unloading-Reloading Test Under Triaxial Compression[J]. 2010, 20(1).
[9] Miyazaki K, Masui A, Sakamoto Y, et al. Triaxial compressive properties of artificial methane-hydrate-bearing sediment[J]. 2011, 116(B6): B6102.
[10] Miyazaki K, Masui A, Sakamoto Y, et al. Effect of Confining Pressure on Triaxial Compressive Properties of Artificial Methane Hydrate Bearing Sediments[C]. Houston, Texas, USA: 2010.
[11] Clayton C, Kingston E, Priest J, et al. Testing of pressurised cores containing gas hydrate from deep ocean sediments.[C]. 2008.
[12] Rees E V L. Methane Gas Hydrate Morphology and its Effect on the Stiffness and Damping of some Sediments[D]. University of Southampton, 2009.
[13] Priest J, Sultaniya A, Clayton C. Impact of hydrate formation and dissociation on the stiffness of a sand[C]. 2011.
[14] Sultaniya A K. Effect of dissociation on the properties of hydrate bearing sediments[D]. University of Southampton, 2011.
[15] Clayton C R I, Priest J A, Best A I. [J]. Geotechnique. 2005, 55(6): 423-434.
[16] Yu F, Song Y, Li Y, et al. Analysis of Stress-Strain Behavior And Constitutive Relation of Methane Hydrate-Bearing Sediments With Various Porosity[J]. 2011, 21(4).
[17] Li Y H, Song Y C, Liu W G, et al. Analysis of Mechanical Properties and Strength Criteria of Methane Hydrate-Bearing Sediments[J]. 2012, 22(4): 290-296.
[18] Li Y, Song Y, Liu W, et al. [J]. Journal of Petroleum Science and Engineering. 2013, 109(0): 45-50.

[19] Song Y, Zhu Y, Liu W, et al. [J]. Marine and Petroleum Geology. 2014, 51(0): 70-78.
[20] Wu E, Wei C, Wei H, et al. [J]. Rock and Soil Mechanics. 2013, 1: 8.
[21] Tan C P, Freij-Ayoub R, Clennell M B, et al. Managing Wellbore Instability Risk in Gas Hydrate-Bearing Sediments [C]. Jakarta, Indonesia: Society of Petroleum Engineers, 2005.
[22] Freij-Ayoub R, Tan C, Clennell B, et al. [J]. Journal of Petroleum Science and Engineering. 2007, 57(1–2): 209-220.
[23] Tohidi B, Salehabadi M, Jin M, et al. Finite Element Modelling of Casing in Gas Hydrate Bearing Sediments (SPE-113819)[C]. 2008.
[24] Rutqvist J, Moridis G J. Numerical Studies on the Geomechanical Stability of Hydrate-Bearing Sediments[C]. Houston, Texas: 2007.
[25] Rutqvist J, G. J. M. Development of a Numerical Simulator for Analyzing the Geomechanical Performance of Hydrate-Bearing Sediments[C]. American Rock Mechanics Association, 2008.
[26] Rutqvist J, Moridis G J, Grover T, et al. Coupled multiphase fluid flow and wellbore stability analysis associated with gas production from oceanic hydrate-bearing sediments[J]. 2012, 92–93(0): 65-81.
[27] Kim J, Moridis G, Yang D, et al. Numerical Studies on Two-Way Coupled Fluid Flow and Geomechanics in Hydrate Deposits[J]. 2012, 17(2): 485-501.
[28] Rutqvist J, Moridis G J. [J]. SPE Journal. 2009, 14(2): 267-282.
[29] Rutqvist J. Status of the TOUGH-FLAC simulator and recent applications related to coupled fluid flow and crustal deformations[J]. 2011, 37(6): 739-750.
[30] Kolditz O, Bauer S, Bilke L, et al. [J]. Environmental Earth Sciences. 2012, 67(2): 589-599.
[31] Ren H, Han L, Xu J, et al. Research on Marine Gas Hydrate Drilling Sampler of China[C]. International Society of Offshore and Polar Engineers, 2013.

Advanced Materials Research Vols. 986-987 (2014) pp 771-774

doi:10.4028/www.scientific.net/AMR.986-987.771

The Experience & Enlightenment from Low-cost Strategy of Shale Gas Development in America

Dong Xu[1, a], Lingbi Wang[2, a], Hongxiang Zhao[3, a] and Su Hu[4, b]

[1]College of Management and Economics, Tianjin University, Tianjin 300280, China;

[2] Drilling Research Institute, China National Petroleum Corporation, Beijing 100540, China;

[3]Lianda Group Corporation, Dagang Oilfield Group Company, Tianjin 300270, China;

[4] Department of Safety Technology and Engineering, China University of Petroleum (East China), Qingdao 266580, China.

[a] grammarxudong@aliyun.com, [b]globalhusu@163.com

Keywords: Shale gas, low-cost development, fiscal and taxation incenting policy, comparison.

Abstract. The experience of shale gas low-cost development in America provided production organization and management methods including horizontal well drilling, cluster well drilling, pad drilling, batch drilling, factory drilling, and reservoir volume fracturing. The policy of finance and taxation has played a positive role in promoting and encouraging shale gas development. The development of shale gas in China is different from America in sides of resource features, development process, the technical levels and the policy environment. We should learn from the technical means, management method and encouraging fiscal and financial policy of low-cost development strategy of America, study and formulate policy suitable to China's own characteristics, to promote low-cost development of shale gas.

Introduction

The progress of shale gas development technology in America has an important impact on the development of global energy [1]. It even changed several countries' economy and living standards. Oil companies are accelerating the adjustment of development strategies so as to meet the needs of unconventional resources, especially the development scale of shale gas [2]. Drilling equipment is in continuous improvement. On the other hand, the technology of well construction and drilling methods are in continuous improvement. Improvements in technology promote the emergence and development of more effective management modes. Well production management and operation management model have been an important way in the efficient development of shale gas.

Low-cost Development Method of Shale Gas

Horizontal well drilling. Vertical wells were the main drilling mode of shale gas development in America before 2002. With the great success of Devon Energy Corporation's seven horizontal wells' test of shale gas, the industry began to promote horizontal drilling. Horizontal drilling has been the main way of drilling in shale-gas drilling at present. The number of horizontal wells of shale gas increased rapidly after 2002. The number of Barnett's horizontal wells added up to 4960 from 2003 to 2007, which made up more than 50% of Barnett's horizontal wells. The number of drilled horizontal wells was 2219 and made up of 94% of Barnett's horizontal wells in 2007. The number of drilled horizontal wells was 13740 and even made up of 95% in 2009. The technology of horizontal well drilling can maximize the contact of the reservoir which can increase the recoverable reserves and single-well output. Especially the technology's breakthrough of multi-section fracture of horizontal wells improved the technology to a new level. Practice indicates that the contact area of horizontal wells is 20 times that of the vertical wells. In this case, horizontal wells can improve the recovery efficiency of oil and gas dramatically.

Cluster well drilling and pad drilling. Because shale gas is stored in low porosity and low permeability formation and the output decline is fast, so it needs to be through large-scale mining way to achieve considerable economic benefits. With the improvement of horizontal well drilling, cluster well drilling and pad drilling have been widely used in drilling operation in America. With the adoption of pad drilling, multiple horizontal wells can be drilled in the same well, which can improve the mining area of oil and gas so as to reduce the cost of single well [3]. This mode can save space, be easy for centralized operation, increase mining area and realize large-scale mining, so it has been one of the most popular ways in drilling.

Batch drilling. Batch drilling, in short, is the drilling method of using a drill in the same wellblock to complete the surface casing, intermediate casing or oil-string casing. In drilling practice, it is mainly used in surface drilling of cluster well. It will remove the drilling machine to the next well immediately and go on drilling the next one, if one well is completed. Special surface drilling machine has the characteristics of small size, flexible, convenient and cheap. Also, it is very fast in drilling surface. It only needs 36 hours to finish drilling the surface of 500 meters. It can save the time of waiting greatly, so as to improve the use ratio of drilling machine and reduce the cost of drilling.

Factory drilling. The road to success of America's high-efficient development is to reduce the cost of drilling and completion, ensure cementing and fracturing quality, so as to increase the single well production. One important way is factory operation, which is to design multiple wells. From drilling, perforation, fracturing, completion to production, the overall process is completed by central area, so as to give full play to the advantages of automated drilling machine.

The concept of factory drilling aims to solve the problems of frequent cross-operation and repetitive operation. It is formed to improve the operational efficiency and reduce operating costs. Its core is to implement the equipment and process standardization, and improve continuously in the process of drilling. Factory Drilling refers to the decoration of many similar wells and the use of plenty of standardized equipment or services in the same area. It is an effective and low cost operation mode which is in the form of production or assembly to conduct drilling and well completion. Factory drilling promotes the fast growth of the number and speed of horizontal wells in America and also plays a key role in the cost reduction of shale gas.

Reservoir volume fracturing. Factory operation can not only improve the drilling efficiency, but also improve the effect of reservoir reconstruction. The cost of single well of four shale gas reservoirs (Barnett, Haynesville, Fayetteville, Marcellus) in America, drilling expense and reservoir reconstruction make up more than 80% and each one accounts for a half. Low-cost strategy is the key to realize the effective development of shale gas. Reservoir volume fracturing could encourage the interaction in the process of hydraulic fracture to generate a more complex net to increase volume. Reservoir volume fracturing is the key technology to realize low-cost development.

Implementation methods:

(1) Simultaneous fracturing--Two sets of fracturing trucks fracture at the same time;

(2) Crossing fracturing--Two wells, one set of fracturing truck, perforation and some other operating types construct interactively and fracture by piece.

Tab 1 Production data and well cost of building in America

	Barnett	Marcellus	Haynesville	Fayetteville
Initial capacity of well $10^4m^3/d$	7	12	28	5.3
Decline rate of the first year %	70	75	81	68
Recovery ratio	0.74	0.75	0.82	0.62
Well cost of building 10^4\$	280	350	700	300

The great effect of factory operation can be shown from the following points:

(1) It raises the initial production and final recovery ratio;

(2) It reduces the operation time and moves of facility, so as to reduce the cost of construction;

(3) The average output can raise 21% to 55% compared with single fracturing.

The main features of organization form lie in drilling in bulk, truckload, storing containers, bulk operation and reducing the mud replacement.

The fiscal and taxation incenting policy to promote the low cost and efficient development of shale gas

The U.S. government in the late 1970s and early 1980s established the fiscal and taxation incenting policies, including price incentives and tax credits to develop the unconventional gas. The implementation of these policies played a key role in improving the economic benefits of shale gas and other unconventional gas, arousing the enthusiasm of producers, increasing the drilling of unconventional natural gas and promoting the technological progress and the development of shale gas industry. These policies are the successful implementation of the strategy for the development of shale gas at low cost.

Price incentives. America published '*Natural gas policy act*' in 1978 which was in view of the unconventional gas price incentives [4]. Shale gas, coal-bed methane, tight gas and other unconventional gas were classified as "high cost" of natural gas, which were allowed to increase the control price limit year by year. The act also removed the price controls of new wells of unconventional natural gas.

Tax credits. America published '*Crude oil windfall profits tax act*' in 1980 which stipulated that shale gas and tight gas were implemented tax deduction and exemption which were between 1979 and 1993 and after2003 [5]. '*Internal revenue code*' increased the tax credits of No. 29 which aimed at unconventional natural gas. It stipulated that tax credit was based on the production and the credit was 3 $/barrel, about 0.52$/ thousand cubic feet. Other unconventional fuel tax credits were adjusted according to the inflation rate year by year except for tight gas [6].

Statistical research suggests that America's price incentives and tax credits have significant positive correlation relationship with the number of unconventional gas wells. Policy incentives make unconventional gas drilling more active, the increase in the number of drilling promotes the technological progress and technological progress accelerates the drilling, reduces the cost of development of unconventional natural gas, increases the gas reserves and production. Unconventional gas production increased nearly 50% in the United States, while conventional gas production increased less than 10% between 1987 and 1992.

Comparison between the present situation of shale gas development between China and America

In the development of shale gas resources, it mainly exist the following differences in China and America at present.

Differences in the resource characteristics. China is similar to America in the development, quality and other aspects of organic shale, but enrichment region is located in the Sichuan mountains which was discovered at present, thus it is hard for the quick movement of drilling machines, which increases the difficulty and cost of development.

Differences in the development process. The shale gas development has formed eight production patterns in America, and it has been into the commercialization stage completely [7]. Unconventional natural gas production was 190 billion cubic meters in 2011 which made up 30% of gas production. While shale gas development in China is still in the stage of exploration and Chinese are carrying out the research experiments now.

Differences in the technological level. Lots of research input and technical progress were the main power to promote the development of America's unconventional gas, which formed high efficiency and low cost technology and technology integration promoted the exponential growth of shale gas production.

China's drilling well types and the ways of completion in the development of shale gas are fairly homogeneous, the technology of drilling and completion of slim hole is not matched and the technology which is suitable for shale gas' large displacement fracturing is still immature.

Differences in the policy environment. The early research input in shale gas which was dominated by government, policies support, commercial operation practices, perfect infrastructure and pipeline network provided a good environmental condition for America's shale gas industry.

Implications and suggestions

The successful implementation of the strategies for the development of low-cost shale gas was the result of market, technology, management, finance and tax and legal policy which provided the enlightenment to the development of shale gas industry in China. People in China should draw lessons from the example of America, combine China's own characteristics, study and formulate effective means and methods of the shale gas development, so as to promote the scientific development of the shale gas industry in China.

Using the experience of factory drilling for reference and promoting low cost and efficient development of shale gas. Low cost and efficient development of shale gas needs not only the continuous improvement of drilling technology, but also the improvement of production methods and the refinement of management. Factory operation is a technological progress and a kind of management innovation. It can effectively solve the problems of cooperation, time waste, cost control in the operations. The successful experience of unconventional oil and gas development in America is of great significance for promoting shale gas and other unconventional oil and gas development in China.

Emphasis on the accumulation of experience and preparing for technology. China should pay more attention to the accumulation of experience and technology, increase the technology and management of laboratories, accumulate experience rapidly, speed up the pace of learning and improvement, promote work in all areas by drawing upon the experience gained on key points, in order to move towards from experimental zone to large-scale application.

Related policies coming into being as soon as possible. To begin with, the business model which is dominated by large companies can widely attract the capital investment of shale gas development. China should insist on keeping the markets open and expanding the cooperation and introduce the foreign companies with unique technology boldly. China can also introduce key technology, equipment and management experience through acquisitions or foreign cooperation. Thirdly, the preferential amount should be increased and the subsidization criteria should be improved. Last but not least, China should speed up the policies of fiscal and taxation policies with aspiration and regulations.

References

[1] Kinnaman T C. The economic impact of shale gas extraction: A review of existing studies[J]. Ecological Economics, 2011, 70(7): 1243-1249.

[2] Li J, Dong D, Chen G, et al. Prospects and strategic position of shale gas resources in China[J]. Natural Gas Industry, 2009, 29(5): 11-16.

[3] Garza T C, Wimberg J A, Woolridge T, et al. Gyro Guidance Techniques and Telemetry Methods Prove Economical in Onshore Multiwell Pad Drilling Operations in the Piceance Basin[C]//IADC/SPE Drilling Conference and Exhibition. Society of Petroleum Engineers, 2010.

[4] MacAvoy P W. Natural Gas Policy Act of 1978, The[J]. Nat. Resources J., 1979, 19: 811.

[5] Friedmann P A, Mayer D G. Energy Tax Credits in the Energy Tax Act of 1978 and the Crude Oil Windfall Profits Tax Act of 1980[J]. Harv. J. on Legis., 1980, 17: 465.

[6] Code I R. Internal Revenue Code[J]. Income Taxes &&, 1994: 1-999.

[7] Alexander T, Baihly J, Boyer C, et al. Shale gas revolution[J]. Oilfield Review, 2011, 23(3): 40-55.

Advanced Materials Research Vols. 986-987 (2014) pp 775-778

doi:10.4028/www.scientific.net/AMR.986-987.775

Classification of surrounding rock of Bolt Supported in coal Mine Roadway

Fengshan Han[1, 2,a], Li Song[1,b]

[1]Research Center for Numerical Tests on Material Failure, Dalian University, Dalian, 116622, China

[2] State Key Laboratory of Coal Resources and Safe Ming, China University of Ming and Technology, Xuzhou, 221116, China

[a]hanfs@sohu.com, [b]438506835@qq.com

Corresponding author：hanfs@sohu.com

Keywords: Coal mine roadway, rock bolt support, surrounding rock, classification

Abstract:. Classification of Surrounding rock of roadway of Coal mine bolt supporting is the basis of bolting design, To scientifically design coal roadway bolting, classification of surrounding rock of coal roadway bolting must first be carry out. in this paper, the comprehensive application of knowledge engineering, rock mechanics, we developed the surrounding rock classification system for the bolt support of coal mine roadway engineering, the surrounding rock classification system is practical easy to use, the bolt supporting of roadway surrounding rock classification results to the coal mine roadway bolt support has important significance and practical value.

Introduction

Surrounding rock classification of roadway of Coal mine bolt supporting of roadway is the basis of bolting design, To scientifically design coal roadway bolting, classification of surrounding rock of coal roadway bolting must first be carry out. Throughout the surrounding rock classification methods at home and abroad [1-5], according to the classification of surrounding rock by considering factors and adopt different index and classification method of surrounding rock can be generally summarized as the following: (1) the single factor index classification, such as rock strong coefficient f as the classification index, although this method reflects the characteristics of the rock on the one hand, but with a single index to determine the surrounding rock which is influenced by many factors is incomplete. (2) Multiple factors combined qualitative and quantitative indexes of classification, compare with a single index classification, it has the obvious progress and caught the main influence factors of the stability of surrounding rock. (3) Multifactor composite index classification, this kind of classification method consider the effect of various factors on the stability of surrounding rock, it more fully reflect the engineering properties of surrounding rock, it is a good kind of surrounding rock classification method.

The Influence factors analysis of Coal mine roadway bolting support surrounding rock classification

Due to different roadway of coal mine corresponding to different geological conditions, the bolt support may be subjected many influence factors to its surrounding rock classification, and it is the interaction, mutual influence, it can be analyzed in the large system theory decomposition-coordination analysis, as is shown in Fig.1

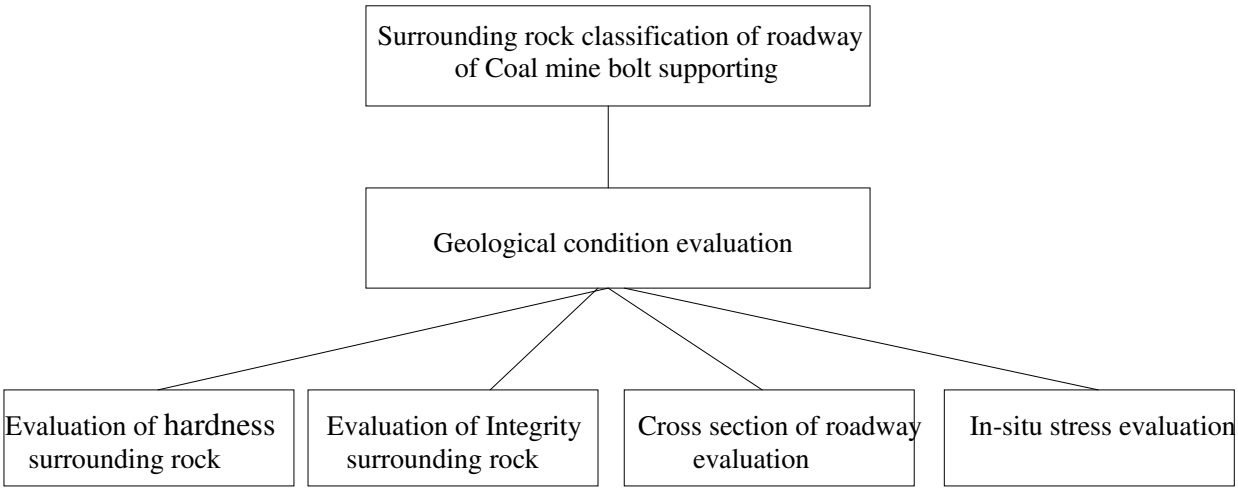

Fig.1. Factors analysis of classification of bolt support surrounding rock

Based on the experience of a large number of data and In-situ field engineering, coal mine roadway bolting surrounding rock classification should consider the following factors:

(1) Evaluation of hardness of surrounding rock

The strength of surrounding rock of roadway directly influence on the roadway stability of the roadway after excavation, the higher the strength of surrounding rock, the easier it is to support of roadway, on the other hand, supporting the more difficult. Roadway surrounding rock hardness evaluation factors is shown in Fig.2

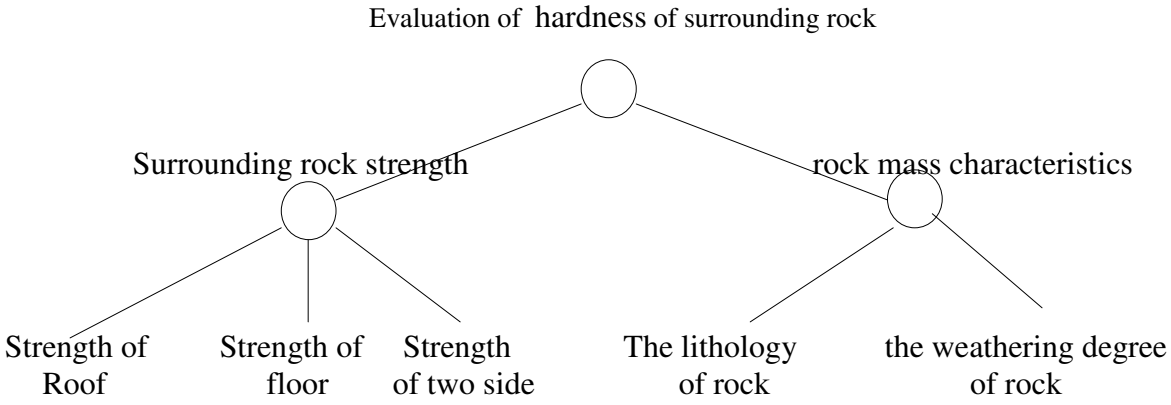

Fig.2. Evaluation factors analysis of rock hardness of roadway surrounding rock

(2) Evaluation of Integrity of surrounding rock.

Roadway surrounding rock with different geological weak surface and structural planes, such as bedding, joint and fissure, weak intercalation, the weak surface and structure surface, largely weaken the integrity of rock mass, it is weak surface and structural planes that easily lead to the unstability of the roadway, Evaluation of Integrity of surrounding rock factors analysis is shown in Fig.3

(3) Evaluation of Cross section of roadway

The cross section of roadway, the greater the balance disturbance to the surrounding rock of roadway in the greater the influence, also is not easy to support , Cross section of roadway evaluation factors analysis is shown in Fig.4

(4) In-situ stress evaluation

In-situ stress is the cause of roadway surrounding rock deformation and failure of the main force, the mining depth of roadway ground stress has a direct impact , In-situ stress evaluation factors analysis is shown in Fig.5

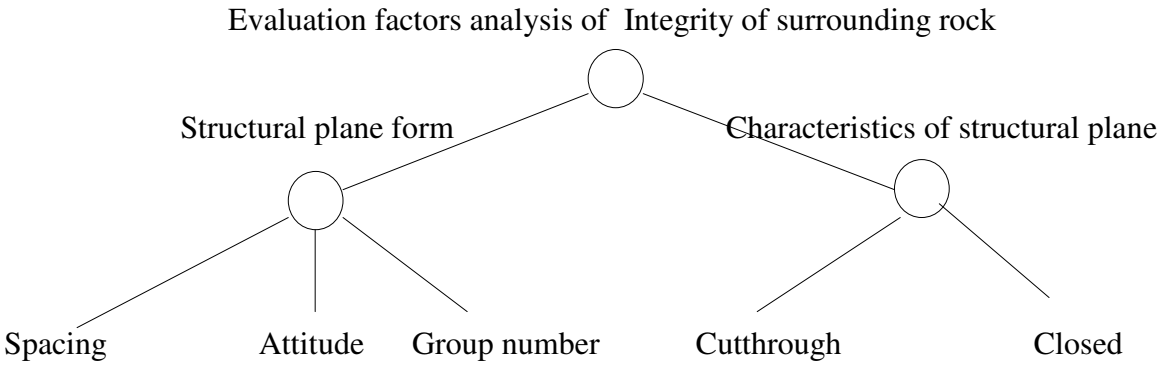

Fig.3. Evaluation factors analysis of Integrity of surrounding rock

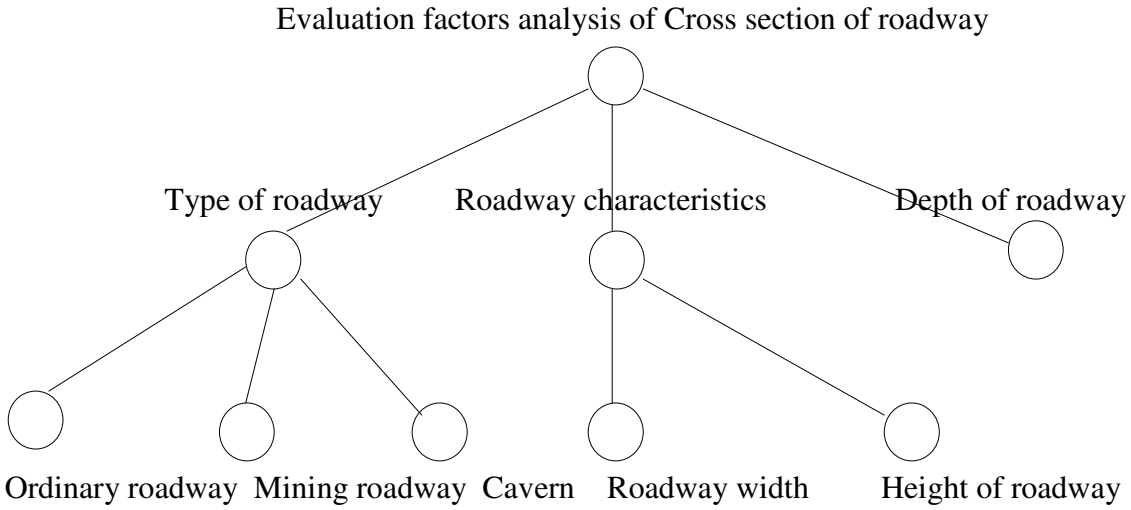

Fig.4. Evaluation factors analysis of Cross section of roadway

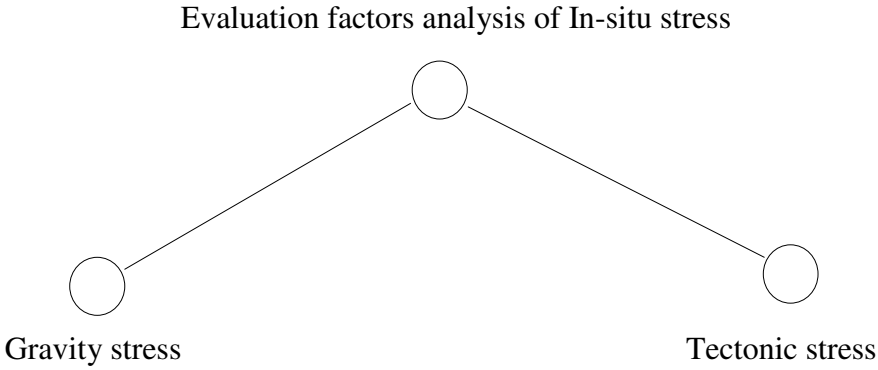

Fig.5. Evaluation factors analysis of In-situ stress

Classification of Bolt Supported Surrounding Rock in Coal Mine Roadway

Based on the experience of coal roadway bolting, Select the following coal roadway bolting surrounding rock classification indexes：（1）strength of surrounding rock of roadway σ,（2）joint influence coefficient J , (3) roadway width L, (4) mining depth H.

Classification of Bolt Supported Surrounding Rock in Coal Mine Roadway is shown in Table 1

Table 1 Classification of bolt supported of surrounding rock in coal mine roadway

Classification	Strength of surrounding rock of roadway σ / *Mpa*	Joint influence coefficient J	Roadway width L / *m*	Mining depth H / *Km*
Ⅰ	<25	<0.4	>8	>1
Ⅱ	25～40	0.4 ～ 0.6	5 ～8	0.6 ～1
Ⅲ	40～65	0.6 ～0.8	3.6～5	0.3 ～0.6
Ⅳ	>65	>0.8	<3.6	<0.3

Acknowledgements

This research is funded by the “Project of science and technical program of the Educational Department of Liaoning Province (L2012436) ” and “Open Projects of State Key Laboratory of Coal Resources and Safe Mining of China University of Ming and Technology (11KF07) ”

References

[1] He Manchao,Sun Xiaoming，China's coal mine soft rock engineering supporting design and construction guide, Science press, Beijing, 2004 (in Chines)

[2] He Manchao, zhang guofeng,, jiahe mine deep coal roadway surrounding rock stability control technology research, journal of mining and safety engineering, No.(1)(2007), p: 1-50(in Chines)

[3] Feng Xiating, Lin Yunmei, An expert system for rock mechanics and engineering， Liaoning science and technology press ，Shenyang，1993 (in Chines)

[4] Xie shengli, shuli coal mine island segment back mining roadway bolt support technology, coal science and technology, No.(1)(2008), p:15-23. (in Chines)

[5] He Manchao, Su Yonhua, Sun xiaoming, Supporting coal roadway stability analysis of the reliability of anchor rod, Chines Journal of rock mechanics and engineering, No.(12)(2002),p:15-23

Advanced Materials Research Vols. 986-987 (2014) pp 779-785

doi:10.4028/www.scientific.net/AMR.986-987.779

Shale Reservoirs Multi-fracture Fracturing Technique and Studies on Reservoirs Stresses

Guangming ZHANG[1,2,a], Jiandong LIU[1,2,b], Chunming XIONG[1,2,c], Luhe SHEN[1,2,d], Juan JIN[1,2,e]

[1]Research Institute of Petroleum Exploration & Development, PetroChina, Beijing, 100083, China

[2]Key Laboratory of Oil & Gas Production, China National Petroleum Corporation, Beijing, 100083, China

[a]email: gmzhang@petrochina.com.cn, [b]email: liujiandong@petrochina.com.cn, [c]email: xiongcm@petrochina.com.cn, [d]email: shenluhe@vip.163.com, [e]email: jinjuan022@petrochina.com.cn

Keywords: Shale; Finite Element; Stress Anisotropy; Fracturing; Fracture

Abstract. Theoretical studies have shown that the generation of the hydraulic fractures reduces or even reverses the stress anisotropy near the fractures and results in increasing the complexity of fractures. A finite element model was established in which the pore pressure elements were used to simulate the behavior of porous media and the pore pressure cohesive elements were adopted to catch the characters of hydraulic fractures. A special fracturing manner was adopted to create complicated fracture networks by reducing or even reversing the stress anisotropy between fractures. The geometries of hydraulic fractures, strains, stresses, pore pressure distributions and fluid pressures within the fractures are obtained. The results of the model are fit well with the corresponding theoretical data. The simulation results show that the stress anisotropy is reduced by the generation of the hydraulic fractures, multiple parallel transverse fractures of horizontal well even reverse the stress anisotropy in some place of the reservoir. The simulation results validate the feasibility of the theoretical studies and the expected complex network fractures could be created by adopting special fracturing manner.

Introduction

Shale is organic-rich formation and also is the source rock as well as the reservoir. The shale gas is stored in the pore space of the reservoir, and a considerable of the shale gas is adsorbed on the organic material. The shale reservoir has low or ultra-low permeability, and it is no economic productivity except the stimulation treatments are implemented. It is important to realize that economic production in these low or ultra-low permeability reservoirs can be increased by creating fracture networks.

The typical characters of shale reservoirs are：(1) The permeability is between 0.000001 mD and 0.001 mD; (2) The thickness is between 15 m and 180 m; (3) The effective porosity is 1~5%; (4) The depth is between 300 m and 3000 m; (5) The percentage composition of quartz is 40~50%; (6) The content of organic carbon is larger than 2%, and the grade of maturity is 1.4~3%; (7) The brittleness coefficient is high, and it is easy to create fracture network; (8) Shale gas in shale reservoir is mainly in free state, adsorption state and dissolved state [1].

The Conception of Fracture Network Fracturing and Multi-fracture Fracturing

For the low and ultra-low permeability shale reservoir, the major fracture and branch fractures are created simultaneously when fracture net pressure reaches the sum of horizontal differential stresses and rock tensile strength. Multiply branch fractures and the major fracture intersect and the complex fracture network is created [2]. Figure 1 is the sketch map of ideal fracture network when volume fracturing is performed. Volume fracturing is a special hydraulic fracturing in which hydraulic fractures and natural fractures propagate simultaneously and the fracture network is

created. Multi-fracture fracturing is a special volume fracturing. Volume fracturing is not only adapt to ultra-low permeability shale reservoir, but also to tight gas reservoir and coalbed methane reservoir.

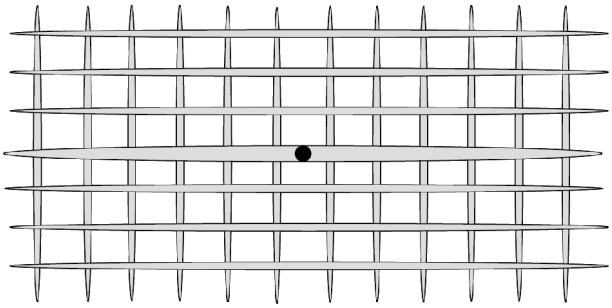

Fig.1 Sketch map of ideal fracture network

Suitable Reservoir Conditions for Fracture Network Fracturing

Stress Field of Shale Reservoir

The stress distribution in shale reservoir has a crucial effect for the generation of fracture network. For conventional reservoir, the created hydraulic fractures are perpendicular to the direction of the least principal stress. For the ultra-low permeability shale reservoir, it is need to create fracture network to maximum the conductive surface area in contact with the shale matrix. When fracture net pressure reaches the sum of horizontal differential stresses and rock tensile strength, the branch fractures initiate and propagate [2]. When the horizontal differential stresses are small, the generation of branch fractures is easy.

Modulus and Poisson's Ratio of Shale Reservoir

In the production stage, the flow conductivity of branch fractures has a considerable effect on productivity of oil gas well. The larger elastic moduli of shale reservoir results in the smaller embed distance of proppant, and the higher flow conductivity of fractures [3]. The ratio of elastic modulus to poisson's ratio represents the brittleness of rock, the larger the value, the more brittle of the rock [4]. The more brittle the shale reservoir is, the easier of creation of branch fractures and complex fracture network.

Shale Reservoir Heterogeneity

The shear fractures are easily created when shale reservoirs have many natural fractures, joints, and intercalary strata, and these discontinuity surfaces have a small angle with the horizontal maximum principal stress [5-7]. The formed shear fractures and the major fractures intersect, and the complex fracture network is generated [8].

Performance Evaluation of Shale Reservoir Fracture Network Fracturing

The Stimulated Reservoir Volume of Shale Reservoir

For the ultra-low permeability shale reservoir, it is normal to adopt the microseismic monitoring technology to estimate the stimulated reservoir volume (SRV). In the process of hydraulic fracturing, microseismic monitor technology mainly records the shear deformation which result from stress variation around fracture tip and pore pressure variation because of the leakoff of fracturing fluid. For the ultra-low permeability shale reservoir, the pore pressure variation because of the leakoff of fracturing fluid is very small, the shear deformation resulting from the pore pressure variation could be ignored, thus the signals recorded by the microseismic monitoring technology are mainly the shear deformation resulting from the stress variation around the fracture tip. The volume besieged by the boundary of all the recorded shear deformation is the stimulated reservoir volume (SRV) [9].

Fracture Spacing of Fracture Network

The stimulated reservoir volume (SRV) has no any detail about the construction of fracture network, which has considerable affect on the fracturing treatment effect. The total length of fracture network can be expressed as [9]

$$L_{ftotal} = \frac{4x_f x_n}{\Delta x_s} + 2x_f + x_n \quad (1)$$

Where: L_{ftotal} is the total length of fracture network; x_f and x_n are the half length and the width of fracture network, respectively; Δx_s is the fracture spacing of fracture network.

Form the above equation, the larger the L_{ftotal} is, the better the fracturing treatment effect, so for the same stimulated reservoir volume (SRV), the smaller the fracture spacing is, the better the fracturing treatment effect.

Petrophysical Parameters and Treatment Parameters Effect on Multi-fracture Fracturing

Properties of Fracturing Fluid

The viscosity of fracturing fluid has a considerable affect on the complexity of the fracture network. Laboratory and field experiment have verified that the complexity of fracture network near and away from the wellbore when enlarging the viscosity of fracturing fluid [3]. In the process of hydraulic fracturing, the flow distance of fracturing fluid within branch fractures can be expressed as [3, 10]

$$y = \sqrt{\frac{2k\Delta Pt}{\varphi\mu}} \quad (2)$$

Where: y is flow distance of fracturing fluid within branch fractures; k is the permeability of branch fractures; ΔP is fluid pressure gradient along the fracture; t is the opening time of fracture; φ is the porosity of fracture; μ is the viscosity of fracturing fluid.

From the above equation, the flow distance of fracturing fluid within branch fractures has a inverse ratio to the viscosity of fracturing fluid, so reducing the viscosity of fracturing fluid can increasing the complexity of fracture network.

Figure 2 is the microseismic record dots map for the same well [11]. (a) adopts the cross linked gel as the fracturing fluid, (b) employs water as fracturing fluid after (a) has been performed. The stimulated reservoir volume (SRV) in (b) is larger than (a), it can conclude that the low viscosity fracturing fluid can increase the complexity of fracture network and the stimulated reservoir volume.

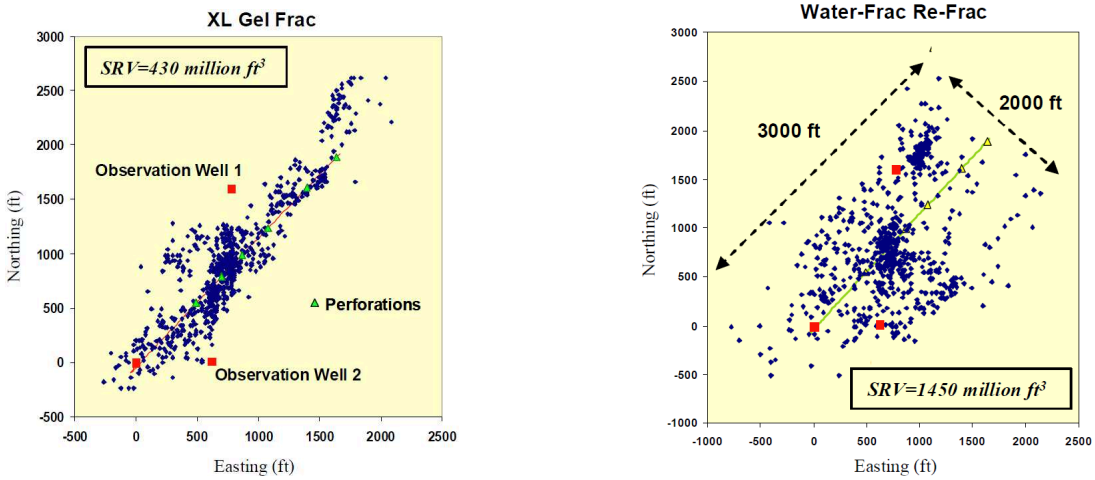

(a) Cross-linked gel fracturing (b) Water-fracturing re-fracturing

Fig.2 Microseismic event cloud structure observed by microseismic fracture mapping

Properties of Proppant

For the same proppant concentration and proppant compressive strength, smaller proppant has larger superficial area and larger contact area with fracture, so it is unbreakable [3]. Smaller proppant has larger contact area with fracturing fluid, is easily been carried into the tips of fractures, can enlarge the flow conductivity of the fracture.

Treatment Flow Rate

For the volume fracturing, because of the large stimulated reservoir volume and high net pressure to create branch fractures, it needs to adopt large injection flow rate.

Change In-situ Stress and Generate Complex Fracture Network

The Effect of Obtained Fractures on Reservoir Stress Field

The reservoir stress field has a crucial effect on the fracture network [12]. The generated fractures will change the in situ stress around the fractures, and has affect on the shape and configuration of subsequent fractures.

In 1946 Sneddon proposed the plain strain model, which gives the theoretical formulae about the changed stress resulting from the generation of fractures [13]. Figure 3 is the sketch map of the plain strain model, in which σ_h and σ_H are horizontal minimum principal stress and maximum principal stress, respectively.

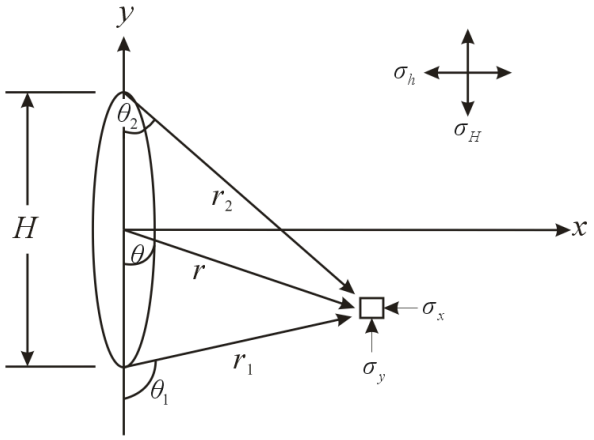

Fig.3 Sketch map of the plain strain model

The basic support is that the shale reservoir is an isotropy, homogeneous linear elastic material. Based on the plain strain model, the theoretical formulae are listed as:

$$\frac{1}{2}(\Delta\sigma_y+\Delta\sigma_x)=p_o\left\{\frac{r}{\sqrt{r_1r_2}}\cos(\theta-0.5\theta_1-0.5\theta_2)-1\right\} \tag{3}$$

$$\frac{1}{2}(\Delta\sigma_y-\Delta\sigma_x)=p_o\frac{2r\cos\theta}{H}(\frac{H}{4r_1r_2})^{3/2}\cos(\frac{3}{2}(\theta_1+\theta_2)) \tag{4}$$

$$\Delta\tau_{xy}=-p_o\frac{2r\cos\theta}{H}(\frac{H}{4r_1r_2})^{3/2}\sin(\frac{3}{2}(\theta_1+\theta_2)) \tag{5}$$

$$\Delta\sigma_z=\mu(\sigma_x+\sigma_y) \tag{6}$$

Where H is the height of fracture; p_o is the internal fluid pressure; $\Delta\sigma_x$, $\Delta\sigma_y$, and $\Delta\sigma_z$ are the induced stress in x direction, y direction and z direction, respectively; $\Delta\tau_{xy}$ is the induced shear stress in the xy plain.

The following geometry relationship could be obtained from figure 3.

$$L=\sqrt{x^2+y^2} \tag{7}$$

$$\theta=\tan^{-1}\left(-x/y\right) \tag{8}$$

$$L_1=\sqrt{x^2+(y+H/2)^2} \tag{9}$$

$$\theta_1=\tan^{-1}\left[-x/(y+H/2)\right] \tag{10}$$

$$L_2=\sqrt{x^2+(y-H/2)^2} \tag{11}$$

$$\theta_2=\tan^{-1}\left[x/(H/2-y)\right] \tag{12}$$

Basing on equations (3)~(12), Soliman obtains the relationship between the reduced stress and the distance away from the fracture [14], as depicted in figure 4. In the figure, both the vertical and the horizontal coordinates are dimensionless. The reduced stress near the fracture in the *x* direction is larger than the *y* direction, that is $\Delta\sigma_x > \Delta\sigma_y$, so the created fracture reduce of even reverse the differential stress between *x* and *y* directions, resulting in the generation of fracture network easier. In same place near the fracture where the equation $\sigma_h + \Delta\sigma_x = \sigma_H + \Delta\sigma_y$ meets, the fracture network is easiest to come into being.

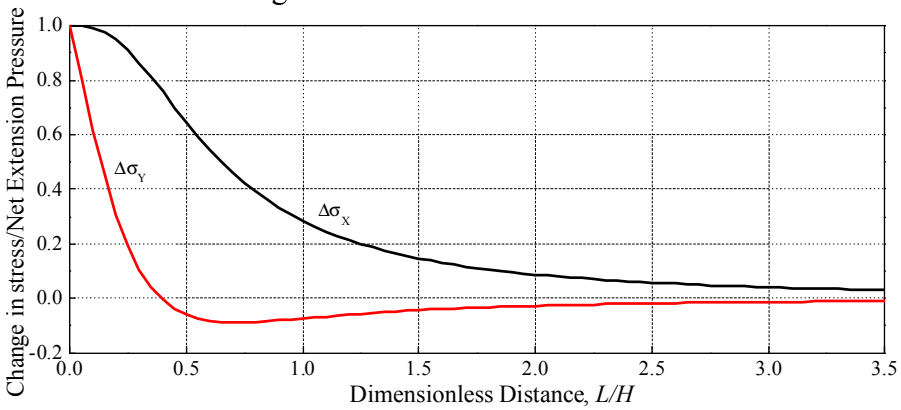

Fig.4 Reservoir stress change resulting from the presence of a plain strain fracture

Generate Fracture Network by Taking Fracturing Treatment

Shale reservoirs have a high brittleness, and are easy to create stress-relief fractures, as depicted in figure 5. Microseismic data have proved that stress-relief fractures do not intersect with the major fracture. Special fracturing treatment should be carried out to intersect stress-relief with the major fracture and to create complex fracture network.

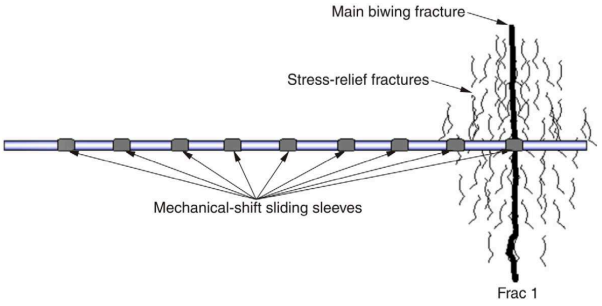

Fig.5 The generation of Fracture 1

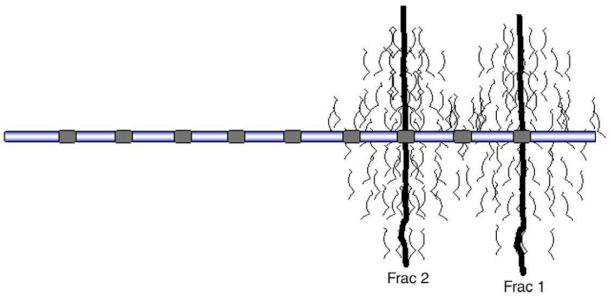

Fig.6 The generation of Fracture 2

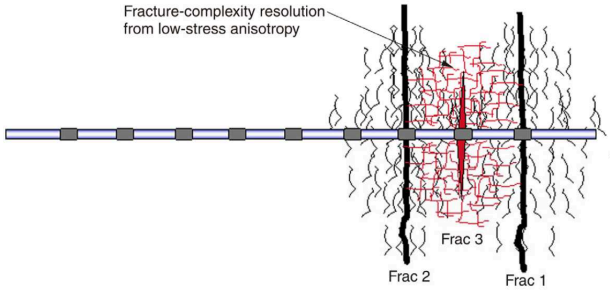

Fig.7 The generation of Fracture 3

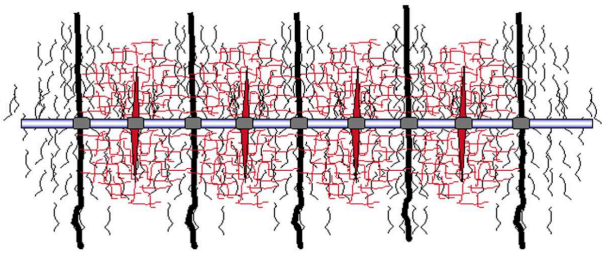

Fig.8 The final complex fracture network

The formed fracture change the stress field near the fracture, the stress anisotropy of the formation between two formed fractures is considerably reduced. Complex fracture network is easily created if hydraulic fracturing are performed in this place [15, 16]. For the horizontal well staged fracturing, it is possible to create complex fracture network by change the sequence of fractured interval. The first fracture are created at the toe of the horizontal well (Figure 5), then, moving toward the heel, a second fracture are formed (Figure 6). Then, instead of continuing toward the heel, the third fracture is generated between the two formed fractures (Figure 7). The generation of the third fracture reverses the stress field between the two formed fractures, and the

reduced stress-relief fractures intersect with the three major fractures and previous generated stress-relief fractures, and the complex fracture network are created. Following this fracturing sequence, a horizontal completion with nine fracturing intervals is illustrated in Figure 8 [17, 18].

Conclusions and Recognitions

(1) Shale reservoirs have low or ultra-low permeability. In order to get economic productivity special fracturing treatments are needed to create complex fracture network.

(2) The stimulated reservoir volume (SRV) and fracture interval of fracture network are two important parameters for evaluating the volume fracturing. Large SRV and small fracture interval could improve stimulation effect.

(3) The stress field has a crucial effect on the creation of fracture network. The fracture network is easily created when the horizontal differential stress is small. The brittleness of shale reservoirs has also important affect on the generation of fracture network.

(4) The property of fracturing fluid and proppant has considerable affect on the stimulation effect. Small viscosity of fracturing fluid can improve the complexity of fracture networks. Small particle size proppant can increase the flow conductivity of fractures.

(5) The generation of fractures can reduce the stress anisotropy around the fracture. Multiple parallel transverse fractures of horizontal well further reduce or even reverse the stress anisotropy in some place of the reservoir. Special stimulation treatment can be performed to decrease the stress anisotropy, and it is possible to create complex fracture networks by employing the special fracturing methods.

References

[1] Chen Zuo, Xue Chengjin, Jiang Tingxue, et al. The Multi-fracture fracturing technique of shale-gas wells and domestic application suggestions [J]. Natural Gas Industry, 2010, 30(10): 30-32.

[2] Lei Qun, Xu Yun, Jiang Tingxue, et al. "Fracture network" fracturing technique for improving post-fracturing performance of low and ultra-low permeability reservoirs [J]. Acta Petrolei Sinca, 2009, 30(2): 237-241.

[3] Cipolla, C.L., Warpinski, N.R., Mayerhofer, M.J., Lolon, E.P. 2008. The Relationship Between Fracture Complexity, Reservoir Properties, and Fracture Treatment Design [J]. Paper 115769 presented at the 2008 SPE Annual Technical Conference and Exhibition held in Denver, Colorado, USA, 21-24 September.

[4] George, E.K. 2010. Thirty Years of Gas Shale Fracturing: What Have We Learned [J]? Paper 133456 presented at the SPE Annual Technical Conference and Exhibition held in Florence, Italy, 19-22 September.

[5] Warpinski, N.R., and Teufel, T.W. 1987. Influence of Geologic Discontinuities on Hydraulic Fracture Propagation [J]. JPT, (39): 2.209-220. DOI: 10.2118/13224-PA.

[6] Warpinski, N.R. 1991. Hydraulic Fracturing in Tight, Fissured Media. JPT, February, 146.

[7] Warpinski, N.R., Lorenz, J.C., Branagan, P.T., Myal, R., Gall, B.L. 1993. Examination of a Cored Hydraulic Fracture in a Deep Gas Well [J]. SPE Prod & Fac. (8):3 150-158. DOI: 10.2118/22876-PA.

[8] Yao Fei, Chen Mian, Wu Xiaodong, et al. Physical simulation of hydraulic fracture propagation in naturally fractured formations [J]. Oil Drilling & Production Technology, 2008, 30(3): 83-86.

[9] Mayerhofer, M.J., Lolon, E.P., Warpinski, N.R., Cipolla, C.L., Walser, D., Rightmire, C.M. 2008. What is Stimulated Reservoir Volume (SRV) [J]? Paper 119890 presented at the 2008 SPE Shale Gas Conference held in Fort Worth, Texas, USA, 16-18 November.

[10] Warpinski, N.R., Mayerhofer, M.J., Vincent, M.C., Lolon, E.P. 2008. Stimulating Unconventional Reservoirs: Maximizing Network Growth while Optimizing Fracture Conductivity [J]. Paper 114173 presented at the 2008 SPE Unconventional Reservoirs Conference held in Keystone, Colorado, USA, 10-12 February.

[11] Cipolla, C.L., Lolon, E.P. Erdle, J.C., Tathed, V. 2009. Modeling Well Performance in Shale-Gas Reservoirs [J]. Paper 125532 presented at the 2009 SPE/EAGE Reservoir Characterization and Simulation Conference held in Abu Dhabi, UAE, 19-21 October.

[12] Rushing, J. and Sullivan, R. 2003. Evaluation of a Hybrid Water-Frac Stimulation Technology in the Bossier Tight Gas Sand Play [J]. Paper SPE 84394 presented at the Annual Technical Conference and Exhibition, Denver, Colorado, 5-8 October. DOI: 10.2118/84394-MS.

[13] Sneddon, I.N. 1946. The Distribution of Stress in the Neighborhood of a Crack in an Elastic Solid [J]. Proc., Royal Society of Lodon, Series A 187, 229-260.

[14] Soliman, M.Y., East, L., and Adams, D. 2008. Geomechanics Aspects of multiple Fracturing of Horizontal and Vertical Wells [J]. SPE Drilling and Completion. (23)3: 217-228. DOI: 10.2118/86992-PA.

[15] Soliman, M.Y., East, L., and Augustine, J. 2010. Fracturing Design Aimed at Enhancing Fracture Complexity [J]. Paper 130043 presented at the SPE EUROPEC/EAGE Annual Conference and Exhibition held in Barcelona, Spain, 14-17 June.

[16] East, L., Soliman, M.Y., and Augustine, J. 2010. Methods for Enhancing Far-field Complexity in Fracturing Operations [J]. Paper 133380 presented at the SPE Annual Technical Conference and Exhibition held in Florence, Italy, 19-22 September.

[17] Cheng, Y. 2010. Impacts of the Number of Perforation Clusters and Cluster Spacing on Production Performance of Horizontal Shale Gas Wells [J]. Paper 138843 presented at the SPE Eastern Regional Meeting held in Morgantown, West Virginia, USA, 12-14 October.

[18] Roussel, N.P., Sharma, M.M. 2010. Optimizing Fracture Spacing and Sequencing in Horizontal Well Fracturing [J]. Paper 127986 presented at the 2010 SPE International Symposium and Exhibition on Formation Damage Control held in Lafayette, Louisiana, USA, 10-12 February.

Advanced Materials Research Vols. 986-987 (2014) pp 786-789

doi:10.4028/www.scientific.net/AMR.986-987.786

The research of energy efficiency construction design with pollution control consideration

Guohaiqing

Inner Mongolia Technical College of Construction，Hohhot, Inner Mongolia，010070

Keywords: differentiations; architectural groups; landscapes; distribution model

Abstract: Focusing on the architectural proper distribution problems with low energy consumption, this paper analyzes the architectural distribution model and builds the architectural landscape target location distribution model with pollution control consideration. According to the features of the architectural landscape pollution control, the paper analyzes the architectural landscape target location distribution model with differentiations and finds the optimal distribution with less pollution for the architectural landscapes. The Oealcle spatial is used to describe the relationship model of the vegetation objects in the landscapes in order to obtain the optimal distribution model for the architectures with differentiations. The simulation experiments illustrate the proposed model can appropriate distribute the architectural landscapes with differentiations with better pollution control effects.

1 Introduction

With the rapid economic development, China's urbanization rate is gradually improving. People have more stringent requirements for the architectural landscape distribution[1]. The architectures are not only important parts for the cities, but also reflection of the changes in the landscapes. However, the pollution from the architectures is unavoidable. To seek a reasonable way to get cleaner landscape distribution model is a hot research issue for related personnel[2,3]. The architectural landscapes with less pollution have dynamic and stochastic characteristics. The traditional two-dimensional geographic analysis method[4,5] cannot handle the uncertainty characteristics caused by architectural landscape pollution. Therefore, there are big deviations of the architectural landscape distribution results with large defects.

2 The simulation analysis of the landscape distribution model with different architectures

2.1 The establishment of the landscape objective positions distribution model

Typically, the architectural landscape distribution will be affected by the surrounding complex surfaces and their own features, such as contribution ratio between input and output of the landscape type, building density, average building height and building area ratio which are dynamic architectural landscape features. Therefore, the target position data of the architectural landscape have uncertain features. According to the central limit theorem, the initial positions of the architectural landscape targets are considered to follow two-dimensional normal distribution $N(0,\sigma_0^2)$. The center of the building distribution is the initial point which follows the independent distribution of x_0 and y_0. Assuming the initial position is the origin of the coordinates and subjects to distribution of $N(0,\sigma_0^2)$. The building the joint probability density function in the polar coordinates (R,Θ) is expressed by equation (1).

$$\varphi_0(r,\theta)=f_0(r\cos\theta,r\sin\theta)\bullet\left|\partial(x,y)/(\partial(r,\theta)x)\right|=[r/(2\pi\sigma_0^2)]e^{-r^2/(2\sigma_0^2)}((r,\theta)\in D) \quad (1)$$

In the equation, $D=\{(r,\theta)|r>0,\theta\in[0,2\pi)\}$. The probability density of R and Θ can be expressed by equation (2).

$$\begin{cases} \varphi_{R_0}(r)=\int_0^{2\pi}\varphi_0(r,\theta)d\theta=(r/\sigma_0^2)]e^{-r^2/(2\sigma_0^2)}I_{(0,+\infty)} \\ \varphi_{\Theta_0}(\theta)=\int_0^{+\infty}\varphi_0(r,\theta)dr=\dfrac{1}{2\pi}I_{[0,2\pi)} \end{cases} \quad (2)$$

In the equation, I is unit function.

Equation (1) can be transformed to the format of $\varphi_0(r,\theta)=\varphi_{R_0}(r)\varphi_{\Theta_0}(\theta),(r,\theta)\in D$. In polar coordinates, R follows Rayleigh distribution, Θ following the uniform distribution on the interval of $[0,2\pi)$, and R and Θ are independent for each other.

The architectural landscape target distribution is increasingly expanding with the initial position distribution as the center and the degrees of the position distribution expand is relative to the changing modes of the architectural landscape dynamic changing features. Therefore, the architectural landscape target positions are consisted of two parts-initial distribution and distributions determined by the uncertainty of the architectural feature elements. This paper analyzes the distribution model of the architectural landscape target position with differentiations according to the architectural landscape dynamic changing features. Because of the uncertainty and dynamics of the architectural landscape features with differentiations, the distribution model of the architectural landscape with differentiations is random distribution model. The position and direction of the unknown architectural landscape target follow uniform distribution in the interval of $[0,2\pi)$. Assuming the initial position follows uniform distribution, the distribution model of random architectural landscape target can be deduced. When the source target remain stable after time t_0, the probability density function of the position of the architectural landscape is expressed by equation (3).

$$\begin{cases} \varphi(r,\theta)=[r/(2\pi\sigma^2)]e^{-r^2/(2\sigma^2)} \\ \sigma^2=\sigma_0^2+2(\bar{v}t_0)^2/\pi \end{cases} \quad (3)$$

In the equation, $\bar{v}$ denotes the mean of the objective architectural landscape distribution function which is usually considered as a reasonable landscape distribution.

2.2 The add of pollution constrains in the model

In the procedure of architecture distribution, the costs generated by the pollution control process should be considered. The architecture distribution and pollution control information have strong relativity. When the amount of architecture meets $N(t_0)<k$ in equation (1) or close to k, the constrains should be applied.

The pollution levels generated by the architecture exceed the threshold of law penalty, it should be punished. The utility of the architecture generating pollution can be expressed by equation (4).

$$u_f-(\gamma+\Delta\gamma)\ \ u_c>0 \quad (4)$$

u_f is construction cost, u_c is the extra cost due to pollution, γ is penalty proportion, $\Delta\gamma$ is penalty compensation coefficient. By analyzing equation (3), the norms the utility should meet after breaking the constrains can be expressed by

$$u_f-\Delta\gamma u_c>\gamma u_c \quad (4)$$

The pollution behavior will be completely punished and the utility norms generated by the architecture can be expressed by

$$FU=(u_f-\Delta u_f)-(\gamma+\Delta\gamma)u_c>0 \quad (5)$$

The increase of the penalty probability and reduce of the predication efficiency will prevent the trends of some polluted architecture. The norms of the architectural distribution utility after breaking the lawful constrains can be expressed by

$$u_f-\Delta u_f-\Delta\lambda u_c>\gamma u_c \quad (6)$$

The architecture enterprises who disobey the laws will pollute the environment. The equations (2) and (4) are compared and analyzed and the critical points in equation (2) and (4) are higher than those in equation (1) which illustrate the information disclosure will inhibit the process of law-abiding behaviors of some architecture enterprises.

3 Simulation experiments

In order to verify the validity of the proposed model, simulation is necessary. The simulation experiment builds models of the 3D landscape of the architectural groups with differentiations with differentiations in some regions. The region area is 150km × 120km which contains different types of vegetation, buildings and roads. The experiments analyze the representative objects, such as trees and buildings which are imported from the two-dimensional image map in the navigation shoot. The shapes of the buildings and roads are generated by the software of 3Dmax and transformed to SDO_Geometry object format. The vegetation model is generated by fractal technology and stored as SDO_Geometry format. The experimental platform is with 2.4GHz P4 processor, 512M RAM and 32M display memory. In the experiments, the plan effects with the proposed model and traditional model with two-dimension images are described in Fig. 1.

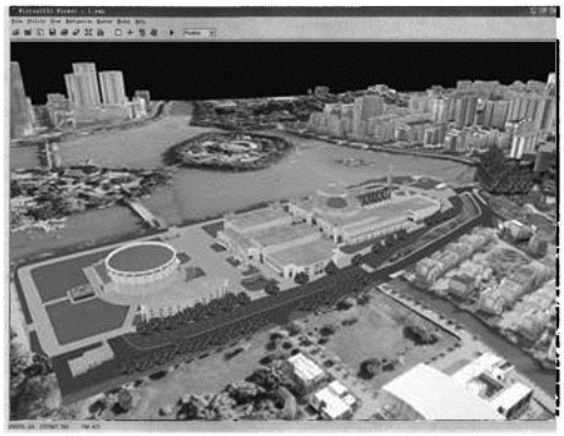

Fig.1 The architectural landscape distribution scheme with proposed model

The pollutions and energy costs caused by different layout methods are described in Table 1.

Table 1 The architectural distribution effects comparison with three algorithms

Max Energy	Mean model		Variance model		Proposed model	
	Mean costs	Mean time consuming/ms	Mean costs	Mean time consuming/ms	Mean costs	Mean time consuming/ms
200	108684.62	4.01	100558.43	1.60	99776.82	1.21
250	110694.67	3.48	101867.10	1.60	99983.74	1.22
300	108565.93	3.72	99793.46	1.61	98293.22	1.22
350	108959.22	3.82	101256.82	1.61	99939.29	1.22
400	110649.82	3.77	102124.34	1.61	99873.98	1.22
450	109466.72	3.92	100520.07	1.60	99923.87	1.21
550	108923.65	3.76	100882.76	1.61	99843.45	1.22
650	108466.23	3.46	99903.29	1.61	98329.32	1.22
750	107687.62	3.68	99035.85	1.61	98231.28	1.21
950	105827.73	3.89	102360.27	1.62	100217.62	1.22

By Fig. 1 and Table 1, the energy savings of the proposed model for the architectural landscape distribution plan are better than those in the traditional models with satisfactory results.

4 Conclusions

This paper builds the architectural landscape target location distribution model with pollution control consideration which analyzes the architectural landscape target location distribution model with differentiations and finds the optimal distribution with less pollution for the architectural landscapes. The Oealcle spatial is used to describe the relationship model of the vegetation objects in the landscapes in order to obtain the optimal distribution model for the architectures with differentiations. The simulation experiments illustrate the proposed model can appropriate distribute the architectural landscapes with differentiations with better pollution control effects.

References

[1]Ceng Bo. Often, money, Huang Ye. Urban 3 d landscape building model [J]. Chinese journal of image and graphics, 2001, 8 (6) : 590-593.

[2]. Ding Shengyan, instructions, qinfen. The research progress of landscape visualization. Journal of henan university (natural science edition) jin qiao, 35 (4) : 62 - a - 67.

[3]. Norbert Haala, Claus Brenner. Virtual city models from laster altimeter and the 2 d map data [J]. J PE&R 5, 1999, 65 (7) : 787-795.

[4]. Wait, Li Xiaoji, Chen lei, etc. A new three-dimensional JingKu modeling method [J]. Journal of system simulation technology, 2008, 4 (3) : 178-181.

[5]. Zhang Yunxia, Song Huanbin Zhong Yanjiang. Based on 3 d GIS of urban landscape modeling explore [J]. Journal of surveying and mapping and spatial geographic information, 2005, 28 (2) : 27-29.

Advanced Materials Research Vols. 986-987 (2014) pp 790-793

doi:10.4028/www.scientific.net/AMR.986-987.790

Design of heavy medium separation density control system based on PLC

Jie Zhang [1, a], Manrong Xing [2,b] and Wenjie Li [3,c]

[1] Hebei Vocational&Technical College of Building Materials, Wen Yu Road No.8,Qinhuangdao City,Hebei Province,China

[2] Hebei Vocational&Technical College of Building Materials, Wen Yu Road No.8,Qinhuangdao City,Hebei Province,China

[3] Hebei Vocational&Technical College of Building Materials, Wen Yu Road No.8,Qinhuangdao City,Hebei Province,China

[a]xue.hong.xue.bai@163.com, [b]021223@163.com, [c]shellyli@126.com

Keywords: heavy medium separation density,PID,antomatic control,PLC

Abstract. Paper in view of the dense medium coal preparation process control, carefully study the density of heavy medium coal preparation control system of the internal structure, main characteristics, control laws and the design method. Open field bus control structure is adopted in the system, Siemens S7-300 programmable controller is responsible for control, executing agencies responsible for enforcing the orders of the PLC to control the related parameters. Through the practice, this control system is powerful, easy to operate, reliable performance, has certain theoretical significance and practical application value.

Introduction

Coal preparation is to improve product quality in the production of coal industry indispensable link, is the comprehensive utilization of resources, an effective way to energy conservation and environmental protection, is also China's sustainable development strategy in the 21st century is an important part of the clean coal technology. High-tech input is the necessary way of high efficient coal, is the JianRen effect, reduce the processing cost, the effective measures to achieve maximum economic benefits. And heavy medium density automatic control system is one of the most important link, its height and stability of the link to the coal production process product quality and production rate plays a decisive role.

Dense medium coal preparation is the use of coal in a certain density of the liquid medium according to the density rise or fall, and the different density of material plant, China coal and gangue separation. Dense medium coal preparation is sorting according to density, in order to ensure product quality, must ensure that the medium density and stability. Medium density is too high, so high density material rise, affect the product quality, medium density is too low, can make the buoyancy material sinking, resulting in loss of buoyancy materials.

In traditional control methods of coal preparation plant, the relationship between the density control system of main equipment are implemented through hardware control circuit, the execution is more complex, the reliability is also poor. With the development of PLC technology, the application of PLC to the heavy medium coal preparation process parameters of detection, automatic control and production management functions such as set at an organic whole, constitute a separate subsystems. In density control system, the relationship can be implemented through software and hardware of the main equipment to complete the real-time control and regulation of heavy medium density accurately, thus to improve the product quality, increase the carbon yield, reduce the tons of coal, the purpose of the dielectric loss.

Process control

Dense medium coal preparation process is shown in fig.1. In density control system, artificial medium, the medium on the pump discharge pipe and a densitometer, tube above the barrels and electric door, when artificial add medium by pump cycle to determine the medium density, determination by densimeter, for medium density is achieved when stop adding interfaces; Sorting, barrel by dense medium through the corresponding pump will play to the sorting machine, medium medium density by another densitometer for measuring at this time. Such as medium density is greater than the separation density, through the control valve and water control system, in order to reduce the density, guarantee the stability of the density and meets the requirements; Below the separation density, such as medium density can be adjusted through the shunt volume to increase into the thin dielectric drum, through magnetic separation after a pause into the dense medium barrels, guarantee the density conform to the requirements of the separation. System operation process, high density medium plus quantitative circulating water, to supplement water and maintain stability of the density[1].

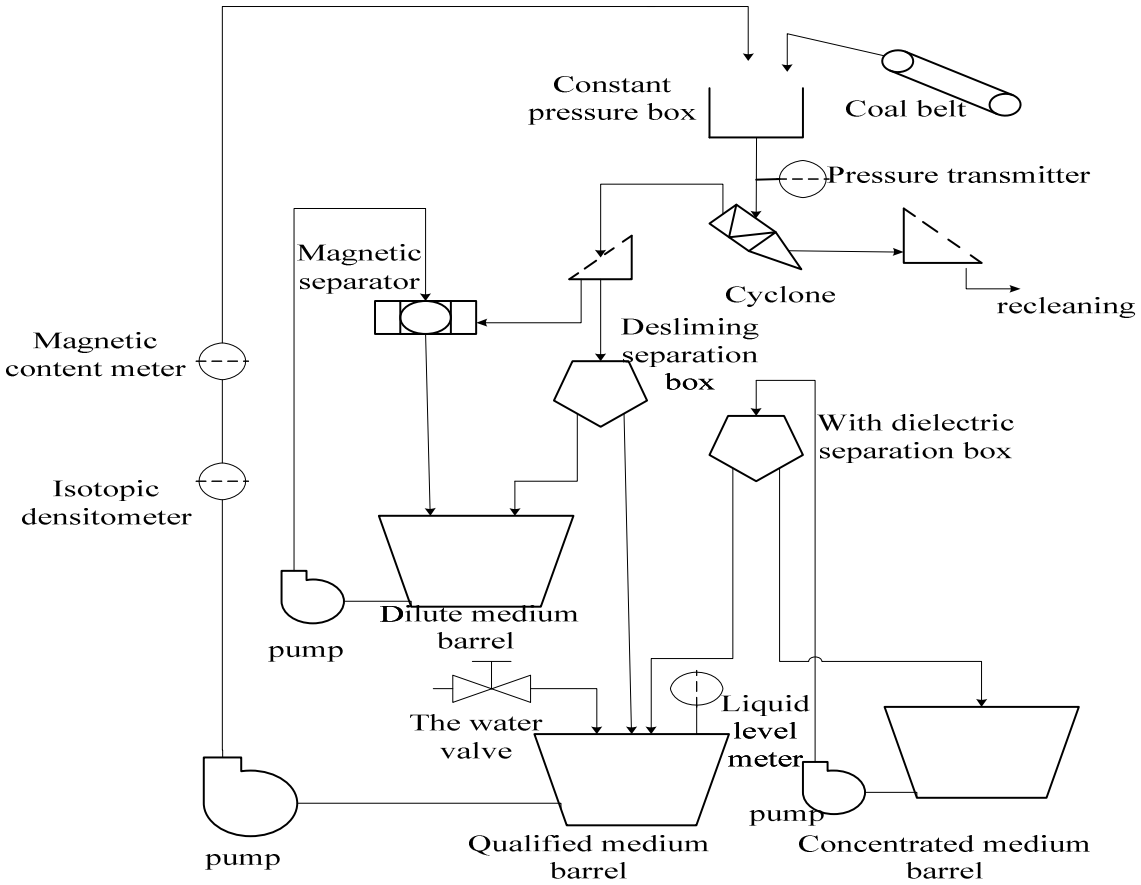

Fig.1. Diagram of dense medium coal preparation production

Density control system working principle is to use the PLC internal PID function block, analyse density gauge, level gauge, such as on-site inspection equipment of the input signal, to detect the process variables comparing with set point, through the analog output module, the output signal to drive the water regulating valve, shunt valve electric actuator, to achieve dynamic control of pressure, density, liquid level white. The PID controller parameter setting is the core content of control system design, according to the character of the charged process to determine the proportion coefficient of PID controller, the size of the integral and differential time, mainly depends on engineering experience, in the experiment of the control system[2].

Density control system set in density as the system input, feedback densitometer feedback signal as input, the PLC input to the system and feedback input count, quantification, and calculated by the algorithm, the proportional valve opening signal, through the analog output module, the output analog

signal to drive all kinds of electric actuator. Density control system principle block diagram is shown in fig.2.

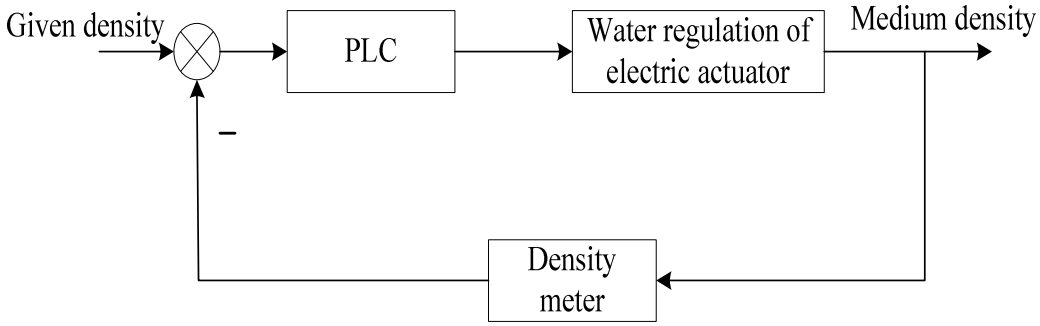

Fig.2.Block diagram of the density control system

Before the open control system, qualified medium bucket will blast first, after waiting for slurry mixing pump, circulation system implementation, the density meter in the measurement location, density signal into current signal output, transmitted to the PLC PID regulator, regulator according to the following regulation:

(1)The actual value is less than the set value, medium density is low, the dense medium cyclone separation, part of the plant into the coal system, coal into coal gangue system, reduce coal preparation efficiency. Low density, the regulator output 4 mA signal, shut off the water valve, if still can not meet the required to produce the density value density, to qualified medium barrel adding medium, in order to achieve the required density values.

(2)The actual value is greater than the set value, medium density is high, the dense medium cyclone separation, coal into the plant system, grind stone into the coal system, reduce product quality. Density is high, the regulator output 4 mA - 20 mA signal, transferred to the water regulator, add water to the qualified medium tube, gradually reduce the density, density value is equal to the set value, regulator output, add water valve is closed[3].

PLC selection

PLC has become the most important and most used in industrial automation control equipment, adopt PLC as the core and with the rotation sensor for detecting element, such as photoelectric encoder is simplified the hardware design, and improves the system reliability and stability, received the affirmation of the user. PLC selection focuses on several aspects: PLC performance, peripherals and capacity. Brand PLC has the system reliable operation, strong anti-interference ability, low failure rate, small volume, low energy consumption, abundant I / 0 interface, can be to control various devices; Through the Ethernet module can make intuitive in upper machine, equipment, stop or process display; Advanced modular structure, making it easy for users to design, combination and strong maintainability; Structure of ladder diagram, programming is easily operation.

The state in accordance with the requirements of the density control system, PLC required for various types of input/output points, such as: medium density monitoring (choose magnetic content of CE, isotopic densitometer ME); Plant ash monitoring (select ray ash gauge HE); Qualified medium level monitoring (select level gauge YE) raw coal in measuring monitoring (choose belt weigher JE); Jig water level and pressure monitoring (choose water level sensor SP1, pressure sensor SP2); Dense medium cyclone steady speed running monitoring (selection pressure transmitter PE), etc. These interfaces are analog signal, so the choice is suitable for the PLC device analog input point.

Through a comparative analysis of various aspects of PLC performance, cost-effective, and finally density control system network using S7-300 PLC and FCS field bus technology Siemens company.

S7-300 series of CPU315 2DP[4], is a stacking structure of medium-sized PLC system, instruction rich, strong function, easy to expand. PLC hardware connection diagram is shown in fig.3[5].

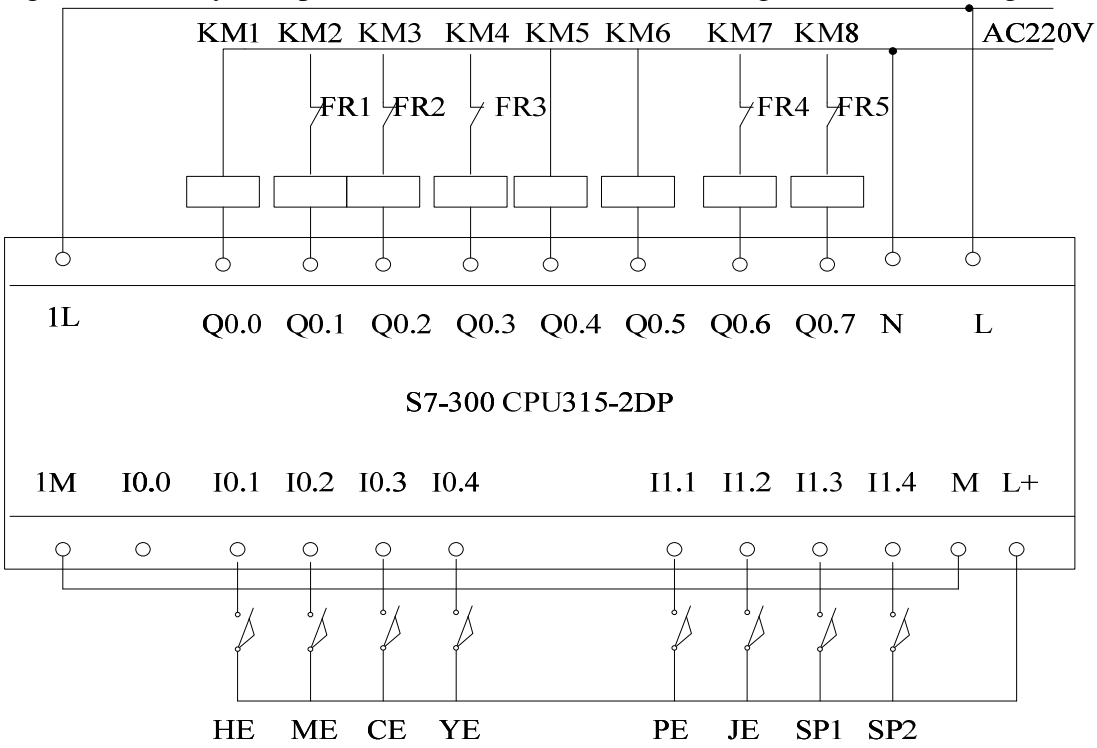

Fig.3.PLC hardware connection diagram

The system of PLC control system and communication network not only can collect and display field devices on/stop, failure state, inverter output frequency, electrical current, coal bunker coal level, liquid level, flow, medium density, such as real-time data, can also use the real-time data in systems and control, statistical main equipment operation and fault condition, asked the data sent to a more senior management, or as a reference equipment repair and related production tasks.

Conclusions

In short, dense medium density adjusting control system can complete in the process of dense medium coal preparation process of various physical parameters of display, alarm and regulating function, and a complete set of automatic detection, automatic adjustment and remote operation, process signals, etc, so as to guarantee the operation of the production process continuity, stability, reliability, and guarantee the quality of cleaned coal, increase plant yield.

References

[1] Weidong Xue ,Haining Yan. Coal preparation automation practical technology [M]. Beijing: Coal industry publishing house,(2007),p.61-68

[2] Astrom ICJ,HangCC.Persson P and Ho W K. Towards Intelligent PID Control [J].Automation.(2002),p.28

[3] Cunwei Li,Huancheng Rong and Lintu Sun. Dense medium density automatic control system research. Coal preparation technology, (2002),p.45-49

[4] SIMATIC S7-300 programmable controller system manual [K]. Beijing: (2005),p.35-48

[5] Zhuying Zhang. Dense medium suspension density meter level detection and automatic control of [J].Shanxi coking coal science and technology, 2009(10),p.37-40.

Advanced Materials Research Vols. 986-987 (2014) pp 794-797

doi:10.4028/www.scientific.net/AMR.986-987.794

Design of Hydraulic Experimental System of Oil Drilling and Production

Yongpeng Cai[a], Guangzheng Jia[b], Yongliang Ren[c], Shipeng Chen[d]

School of Mechanical Science and Engineering, Northeast Petroleum University, Daqing, Heilongjiang, 163318, China

[a]caiyongpeng516@126.com, [b]jiaguangzheng@126.com, [c]rrryyylll@126.com
[d]chenshipeng.ok@163.com

Keywords: Oil drilling and production equipments, Hydraulic experimental system, Data acquisition, Components selection

Abstract. Designed a set of hydraulic experimental system for testing some performance parameters of oil drilling and production equipments and demonstrating its functions and principles. This system provided hydraulic environment for pumping unit, ESP (Electric Submersible Pump), well control devices, drilling and workover experiments, collected and analyzed experimental data, provided an important platform for the research and development of oil drilling and production equipments and experiment teaching. The functions and principles of hydraulic system's components are introduced, and some main components are selected and designed in the system.

Introduction

There are already had some experimental apparatuses, used for testing performances and studying technology of the oil drilling and production equipments in china and abroad. In the early 1990s, Northeast Petroleum University developed a "Deep well- pumping unit test device", we can observe the working conditions of fixed valve; Jianghan Petroleum Institute designed a "Horizontal wells pump test device" in 1997, to study the horizontal wells performance [1].By summarizing the relevant researches, designed a hydraulic experimental system. Its main purpose is to simulate drilling, workover, oil production and other equipment's working principles, test the main working parameters, both for scientific experiments, and serve the teaching experiments.

The structure and functions of hydraulic experimental system

Hydraulic experimental system mainly consists of high-pressure and low-pressure hydraulic system, metering system, data acquisition and control system. The relationship of hydraulic system to the subsystems of oil drilling and production equipment is shown in Figure1.

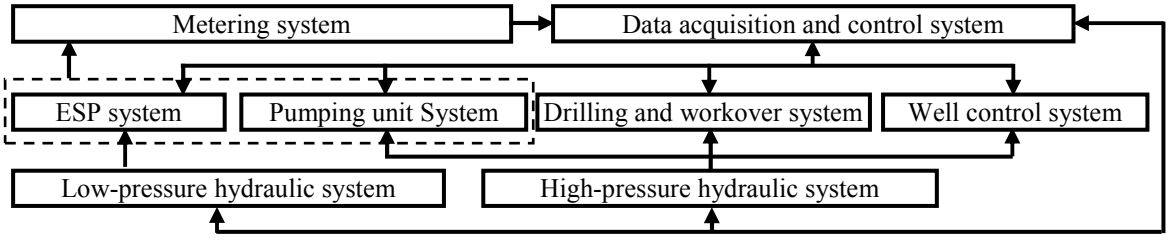

Fig.1 The relationship of hydraulic system to the subsystems of oil drilling and production equipment

Based on the process and technology requirements of pumping unit, ESP devices, well control equipments, drilling and workover equipments, the hydraulic experimental system can test the principle and performance of drilling and production equipments, in order to analyze, evaluate study and develop them efficiently.

High-pressure hydraulic system

High-pressure hydraulic system is shown in Figure 2 (a). It can provide high-pressure hydraulic experimental environment, simulate the downhole pressure, water injection pressure, circulating

pressure of workover and drilling, well control pressure, so that the experimental conditions closer to the oil field environment.

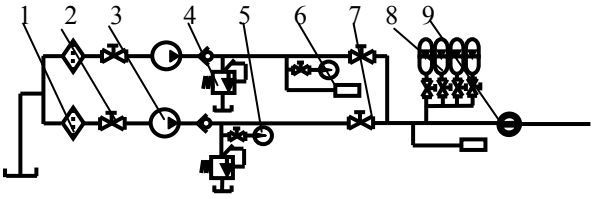

1-Filter; 2-Inlet valve; 3-High pressure plunger pump; 4-Unloading valve; 5-Pressure gauge; 6-Pressure sensor; 7-High pressure valve; 8-Accumulators; 9-Flowmeter

(a)

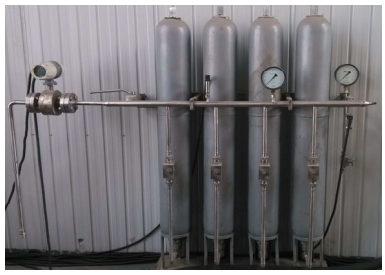

(b)

Fig.2 (a) The schematic diagram of high pressure hydraulic system. (b) The picture of high-pressure system

High-pressure hydraulic system uses both 40MPa and 15MPa high pressure plunger pumps as power source. They can work alone, or work simultaneously. The accumulators can be used as an auxiliary or emergency power source, replenish system leaks, stabilize system working pressure, absorb pulsation of the pump and hydraulic shock, etc [2]. Pressure gauges, pressure sensors and electromagnetic flow-meter main tests discharge pressure and flow-rate values of high pressure plunger pumps.

When the accumulator as the power source, can reduce the power of engine [3], the effective volume of accumulator is the largest. In this case the accumulator volume can be calculated through the equation

$$V_0 \geq \frac{V(P_1/P_0)^{\frac{1}{n}}}{1-(P_1/P_2)^{\frac{1}{n}}}. \tag{1}$$

Where V_0 is the desired effective volume of accumulator, V is the working volume of accumulator, P_0 is its charge pressure, P_1 is the lowest working pressure, P_2 is the highest working pressure, and n is the exponent. According to the experimental requirements, the relevant calculation parameters of accumulator are shown in Table 1.

Table 1 The relevant calculation parameters of accumulator

V [m3]	P_1 [MPa]	P_2 [MPa]	P_0 [MPa]	n
0.095	16	24	14	1.4

Based on the Equation (1) and relevant parameters, the volume of accumulator is $V_0 \geq 0.149 m^3$. System uses an accumulator group consists of four 40L accumulators. Manual valves installed at the outlet of accumulators, so we can choice the number of accumulators to work, as shown in Figure 2 (b).

Low-pressure hydraulic system

Low-pressure hydraulic system is shown in Figure 3. It can provide low pressure large flow water resource for ESP experiments. The resource can meet the flow-rate requirement of ESP, which will avoid cavitations, not affect ESP's performance analysis results [4].

System uses two centrifugal pumps in parallel to provide a wider range of flow-rate for experimental system. By adjusting the flow-rate regulating valve, the low-pressure hydraulic system can provide different flow-rate of water for experiments.

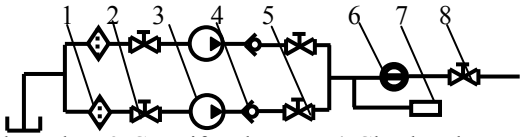

1-Filter; 2-Inlet valve; 3-Centrifugal pump; 4-Check valve; 5-Outlet valve;
6-Flowmeter; 7-Pressure sensor; 8-Flow control valve

Fig.3 The schematic diagram of low pressure hydraulic system

Metering system

Metering system connects with the discharge port of ESP and pumping unit experimental system's Christmas tree, for adjusting the pressure and flow-rate of produced fluid, and measuring the volume of it. The schematic diagram of metering system is shown in Figure 4 (a).

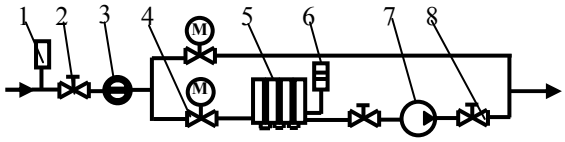

1-Pressure sensor; 2-Hand operated valve;3-Flow-meter;
4-Electric valve; 5-Gauge tanks; 6-Liquidometer;
7-Line pump; 8-Ball valve

(a)

(b)

Fig.4 (a) The schamatic diagram of metering system. (b) The picture of metering system

In the whole system, the ESP's delivery capacity is the largest [5]. The flow-rate of ESP is 150m^3/d, the volume of produced water is 0.1042m^3 per minute. If each experiment last for 6 minutes, there will have 0.6252m^3 water flow into the gauge tanks. In order to adapt to a longer time experiment, the volume of the gauge tanks designed for 1m^3.

Taking into account the wall thickness, strength, installation, transportation, floor space, and other factors, we choose four gauge tanks of 250L in series for measuring. The liquidometer mounted at the top of the gauge tanks, can measure the liquid level in the gauge tanks, as shown in Figure 4 (b).

Data acquisition and control system

Date acquisition and control system can monitor the experimental status, examine and record the experimental parameters, draw experimental curves, remotely control parts of the experiments, set and modify some system parameters. It mainly consists of IPC (Industrial Personal Computer), data acquisition card, Siemens PLC (Programmable Logic Controller) and expansion modules, display instruments, buttons, etc. System's block diagram is shown in Figure 5.

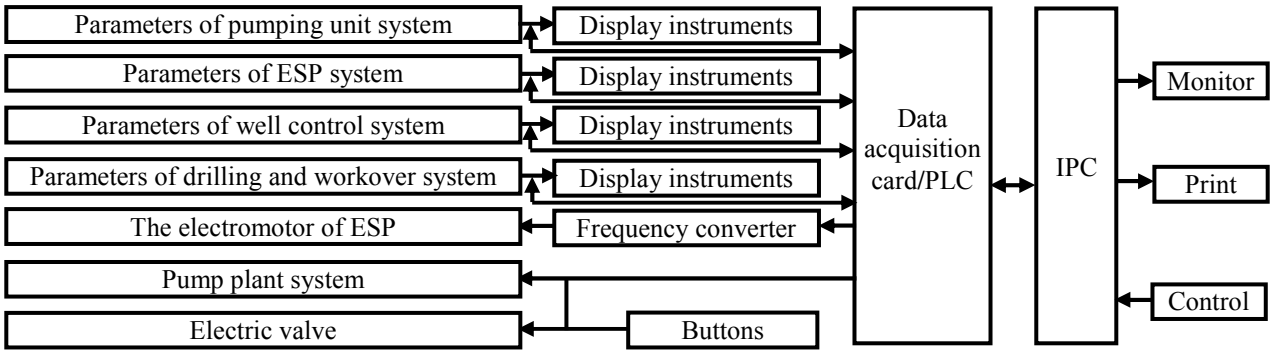

Fig.5 Block diagram of data acquisition and control system

The testing parameters of pumping unit system include the pressure of water in wellbore hole simulator, the produced water's pressure and flow-rate, and the liquid level in the gauge tanks. ESP system testing parameters, including the ESP's rotor speed and torque, the pump inlet water pressure and flow-rate, the pump outlet water pressure and flow-rate, and the fluid level in the gauge tanks. In drilling and workover system and well control system mainly tests the water pressure in the wellbore hole simulator. Pump plant system includes high-pressure plunger pump, low-pressure plunger pump, large flow-rate pump, low flow-rate pump, pipeline pump.

Experimental curves

During the experiment, some real-time curves of fluid pressure and flow-rate can be drawn by the data acquisition system, as shown in Figure 6.

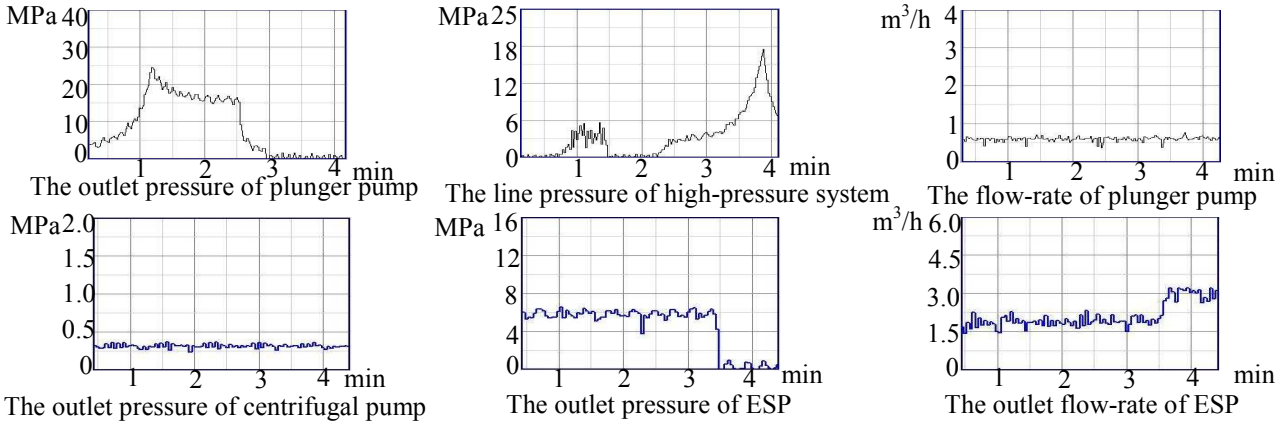

Fig.6 The experimental data curves

Conclusions

Hydraulic experimental system can provide 40MPa high pressure water resource and 50m^3/h low pressure water resource for the oil drilling-production experimental equipments. It can meet the pressure and flow-rate requirements of different tests. The data curves of pressure and flow-rate can display the performance of experimental equipments. This system can create condition for improving the standard of teaching and academic level, and cultivating innovative engineering talents with oil characteristics.

Acknowledgement

The authors would thank the project Supported by National Key Technology R&D Program (No.2012BAH28F03).

References

[1] Deshi Zhang, Ruiqing Chang, Cui WANG, Chunhong Li, Hui Zhao: Lifting Simulation Test System of Sucker Rod Pumps. The Third Mechanical Engineering Technology Forum of Ten Provinces. Heilongjiang, China, July, 2007.p418-422. In Chinese

[2] Gang ZHAO: Application of Accumulators in Hydraulic Systems. Chinese Hydraulics & Pneumatics. 2010 (01), p64-65.In Chinese

[3] Jizhi Li, Lujun Zhang, Xinyi Gu,Wei PAN: The Summary of Accumulator Type and Application. Machine Tool & Hydraulics. 2001 (06), p5-7. In Chinese

[4] Desheng Zhou, Rajesh Sachdeva: Model of electric submersible pump in gassy well. Journal of Petroleum Science and Engineering, 2010, Vol.70, No.3-4.p204-213.

[5] Ligang Liu, Houshun Jiang:Optimization Design of ESP Wells Lift. Petrochemical Industry Application. June, 2013. Vol.32, No.6. In Chinese

CHAPTER 4:

Design and Research of Components and Mechanisms of Energy Equipment and Installations

Advanced Materials Research Vols. 986-987 (2014) pp 801-804

doi:10.4028/www.scientific.net/AMR.986-987.801

A New Purification Method for Rotor Center's Orbit by Using Ensemble Empirical Mode Decomposition

Wenbin Zhang[a], Jiaxing Zhu[b],Yasong Pu[c] and Yanping Su[d]

Engineering College, Honghe University, Mengzi 661100, Yunnan, China

[a]190322507@qq.com, [b]984948084@qq.com, [c]377821053@qq.com, [d]626516683@qq.com

Keywords: Rotor center's orbit, Purification, Ensemble empirical mode decomposition, Rotating machinery

Abstract. Aiming at the purification of rotor center's orbit, a new approach was presented by using ensemble empirical mode decomposition (EEMD). Ensemble empirical mode decomposition decomposed a complicated signal into a series of intrinsic mode functions (IMFs). Then according to prior knowledge of rotating machinery, chose some interested IMFs and reconstructed the needed signal. By doing this the noises would be eliminated successfully. At last the purification of rotor center's orbit was obtained by extracting the useful signal component. Simulation and practical results show the advantage of EEMD in noise de-noising and purification of rotor center's orbit. This method also has simple algorithm and high calculating speed; it provides a new way for purification of rotor center's orbit of rotating machinery.

Introduction

Vibration monitoring is a very important content for turbine generator unit. And the rotor center's orbit can express the vibration characteristic of generator unit. Different rotor center's orbit represents different rotor condition or fault information, such as ellipse represents unbalance fault, outer eight represents misalignment and inner eight represents oil-film whirl, et al [1]. Generally speaking, the original rotor center's orbit can't be used due to the noise interference. How to eliminate noise and to obtain the refine rotor center's orbit is the main studying content for rotor center's orbit purification.

Empirical Mode Decomposition(EMD) is an adaptive signal processing method that can be applied to nonlinear and non—stationary process perfectly [2]. It may decompose any complicated signal into a set of complete, adaptive and almost orthogonal components called Intrinsic Mode Functions (IMFs). The IMFs represent the natural oscillatory mode embedded in the signal and work as the basis functions, which are determined by the signal itself, rather than predetermined kernels. EMD method is widely applied to many project fields [3-5]. However, one of the major drawbacks of the original EMD is the frequent appearance of mode mixing, which is defined as a single IMF either consisting of signals of widely disparate scales, or a signal of a similar scale residing in different IMFs, To alleviate this drawback, Ensemble Empirical Mode Decomposition (EEMD), a substantial improvement of EMD, is presented by Zhaohua Wu and N. E. Huang [6]. EEMD is a new noise-assisted data analysis method by utilizing the full advantage of the statistical characteristics of white noise to perturb the signal in its true solution neighborhood, and to remove itself after serving its purpose.

Considering the characteristic of rotating machinery, a new purification method is proposed by using EEMD. At first, the sample data is decomposed by EEMD into a series of IMFs. Then, the interested periodical sine components are extracted. In the end, the purified rotor center's orbit could be obtained from the reconstruction of useful signal component.

Conception of EEMD

The EEMD algorithm can be stated as follows [6-7]:

(1) Initialize the ensemble number M and the amplitude of the added white noise, let M=1.

(2) Execute the mth trial for the signal added white noise.

(a) Add the white noise series with the given amplitude to the investigated signal, i.e.

$$x_m(t)=x(t)+n_m(t) \quad (1)$$

Where $n_m(t)$ represents the mth added white noise, and $x_m(t)$ indicates the noise-added signal of the mth trial.

(b) Decompose the noise-added signal $x_m(t)$ into l IMFs $c_{i,m}(i=1,2,\ldots l, m=1,2,\ldots,M)$ using the EMD method. Where $c_{i,m}$ indicates the ith IMF of the mth trial; l is the number of IMFs and M means the number of the ensemble.

(c) If $m<M$, then let $m=m+1$ and repeat the step (a) and (b) again and again until $m=M$, but with different white noise each time.

(3) Compute the ensemble mean $\bar{c}_i$ of the M trials for each IMF, and we obtain

$$\bar{c}=\frac{1}{M}\sum c \quad (2)$$

(4) Report the mean $\bar{c}_i$ ($i=1,2,\ldots,l$) of each of l IMFs as the final ith IMF.

Simulation

To verify the good performance of the EEMD method in noise de-noising, the simulation signal showed as follows:

$$f(x)=\sin(2\pi x f_1/f_s)+\sin(2\pi x f_2/fs)+i(x) \quad (3)$$

In which $i(x)$ refers to the noise interferences. Fig.1 shows waveform of the original simulation signal in time domain and its spectrum.

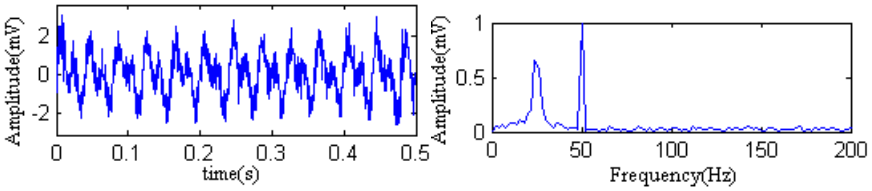

Figure 1. Original signal in time domain and frequency domain.

Take sampling frequency as f_s=2000Hz, and f_1=25Hz, f_2=50Hz. Now we use EEMD method to decompose the original signal into some IMFs. Fig.2 shows the decomposed results.

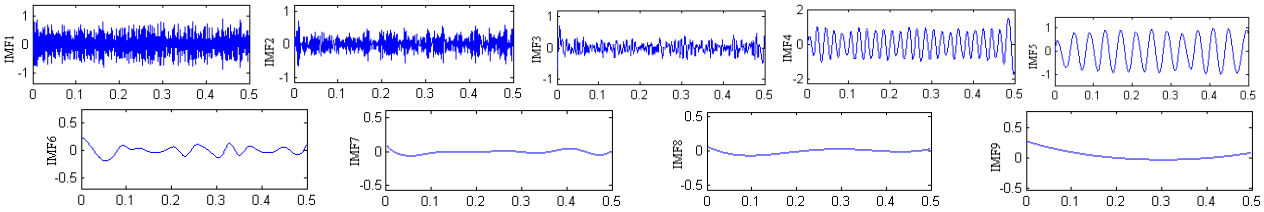

Figure 2. EEMD decomposition results of simulation signal

From Fig.2 we can see that simulation vibration signal is decomposed into a finite number of stationary intrinsic mode functions (IMFs). In Fig. 2 we can know that IMF4 and IMF5 are the periodical sine signals. Fig.3 gives the frequency spectrum of these two IMFs. We know that the periodical components of the simulation signal are extracted by EEMD respectively.

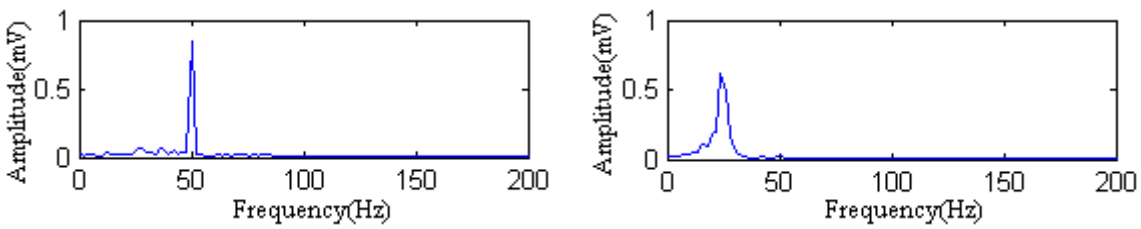

Figure 3. Frequency spectrum of IMF4 and IMF5

Purification of Practical Rotor Center's Orbit

In this section, the EEMD method is applied to purify the rotor center's orbit. The sample date comes from a practical rotor center's orbit of the turbine generator units in the power plant. The speed of the rotor is near 3000 rpm. Let the sampling frequency equal to 6400Hz. Due to the serious noise interference, the original rotor center's orbit is too disordered to get any fault information. Fig. 4 shows original two vertical vibration signals and the periodical component extracted by EEMD decomposition for them.

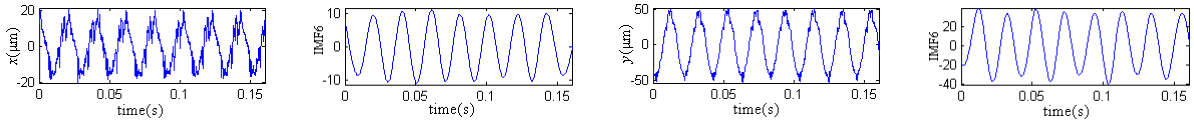

Figure 4. Two vertical signals before and after extracted by EEMD.

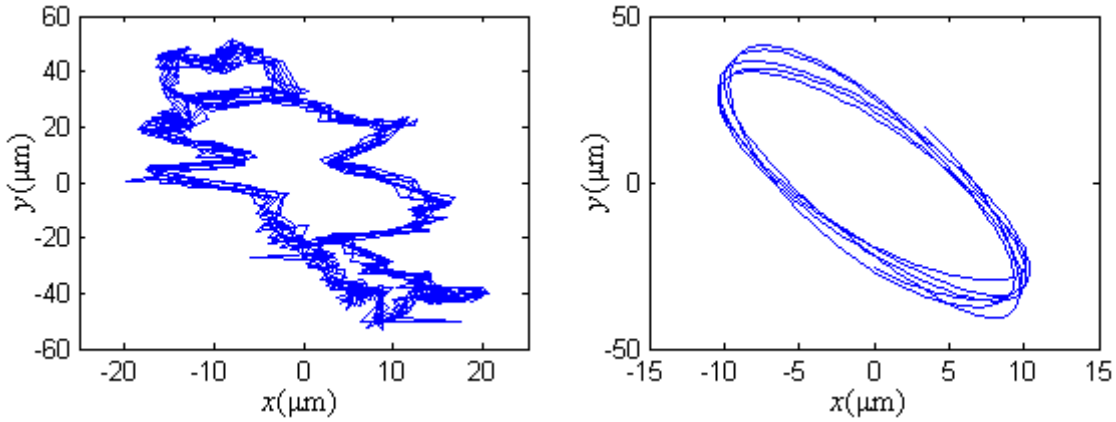

Figure 5. Original rotor center's orbit and the purified result.

Now we combine the rotor center's orbit by these two periodical components. Fig. 5 shows the purified rotor center's orbit by EEMD and the original signal. According to the common fault spectrum feature, we know that elliptical axis trace means unbalanced fault.

Conclusion

The EEMD method is proposed to purify rotor center's orbit of rotating machinery, effectively overcoming the shortcoming of the mode mixing occurring in the empirical mode decomposition method. Simulation and practical results show that this method has good advantage in rotor fault diagnosis, it will supply a new way for fault diagnosis of rotating machinery.

Acknowledgment

The study is subsidized by Yunnan application fundamental research project fund (2013FB062). All the persons involved in the research projects are thanked for their help. Thank you for your help of corresponding author Yanping Su.

References

[1] S. T. Wang and H. M. Li, "A new method for automatically identifying the axis trace moving direction of turbine-generator unit", Proceeding of the CSEE, 2003, Vol.23, pp.146-149.

[2] N. E Huang, Z. Shen, S. R. Long, M. C. Wu, H. H. Shih, Q. N. Zheng, N. C. Yen, C. C. Tung and H. H. Liu, "The empirical mode decomposition and the hilbert spectrum for nonlinear and non-stationary time series analysis", Proc. R. Soc. Lond A, Vol. 454, pp.903-995, 1998, doi: 10.1098/rspa.1998.0193.

[3] J. C. Echeverria, J. A. Crowe, M. S. Woolfon, B. R. Hayes-Gill, "Application of empirical mode decomposition to heart rate variability analysis", Medical and Biological Engineering and Computing, Vol.39, No.4, pp.471-479,2001, doi: 10.1016/j.neucom.2004.10.007.

[4] H. L. Liang, S. L. Bressler, R. Desimone and P. Fries, “Empirical mode decomposition: a method for analyzing neural data”, Neurocomputing, Vol.65, pp.801-807, 2005. .
[5] K. Y. Qi, Z. J. He and Y. Y. Zi, “Cosing window-based boundary processing method for EMD and its application in rubbing fault diagnosis”, Mechanical Systems and Signal Processing, Vol.21, No.7, pp.2750-2760, 2007, doi: 10.1016/j.ymssp.2007.04.007.
[6] Z. H. Wu and N. E.Huang. “Ensemble empirical mode decomposition: a noise-assisted data analysis method”, Advances in Adaptive Data Analysis, Vol.1, No.1, pp.1-41, 2009, doi: 10.1142/S1793536909000047.
[7] J. S. Lin and Q. Chen, “Application of the EEMD method to multiple faults diagnosis of gearbox”, 2010 2nd International Conference on CD-ROM Purchase at Partner, Mar. 2010, pp.87-90, doi:10.1109/ICACC.2010.5487143.

Advanced Materials Research Vols. 986-987 (2014) pp 805-809

doi:10.4028/www.scientific.net/AMR.986-987.805

A Numerical Study of Wet Steam Condensation over a Corrugated Plate Separator

LIU Xiao Yi,[1,3] TIAN Rui Feng,[1,2] GAO Yan Xin,[1,2] SUN Lan Xin,[1,2] YAN Chang Qi[1,2]

[1]College of Nuclear Science and Technology, Harbin Engineering University, Harbin 150001, China
[2]Key Discipline Laboratory of Nuclear Safety and Simulation Technology, Harbin 150001, China
[3]Bohai Shipbuilding Heavy Industry Co., Ltd., Huludao 125004, China

Keywords: wet steam; corrugated plate separator; numerical simulation; condensation.

Abstract. To provide steam of appropriate quality and to improve the efficiency of steam-water separation over corrugated plates, it is necessary to study the condensation behavior of wet steam moving over a corrugated plate separator. In this paper, classical nucleation theory and a droplet growth model are used to describe the process of wet steam condensation on corrugated plates. The CFX software water droplet condensation model was employed to simulate the process and to allow analysis of the characteristics of wet steam condensation. The results show that: (1) the nucleation rate increases gradually over time and exhibits a positive correlation with the temperature of the wet steam, (2) departure from the saturated state decreases gradually along the flow direction, leading to a concurrent decrease in the steam condensation rate and (3) the steam condensation rate is elevated with increases in the local pressure gradient.

Introduction

Wet steam has the ability to produce a large number of droplets which in turn may cause serious water erosion that reduces equipment strength and service life and can even threaten the operational safety parameters of the equipment. For these reasons, a steam-liquid separator must be used to dehumidify wet steam. At present, the corrugated plate separator is the most widely used means of final stage moisture separation and so understanding the process of wet steam condensation on a corrugated plate separator is an important step in evaluating the performance of such devices and in improving separation efficiency. Herein, a numerical model for wet steam flow over a three-dimensional corrugated plate separator is described.

The calculation model

A. The physical model

This work investigated numerical simulations of the condensation characteristics of wet steam flowing over a single channel corrugated plate, as pictured in Fig. 1. The corrugated plate length applied during modeling was 175 mm, with plate spacing of 15 mm and a wave number of three with a pitch of 42 mm and a flexion angle of 30°. The straight segment length before and after each wave plate was 14 mm.

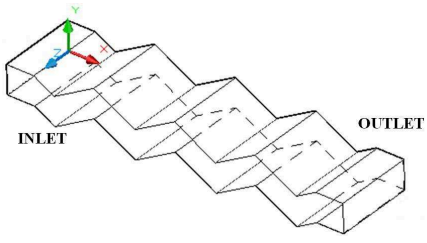

Figure1. The corrugated-plate structure

B. Condensation model

It is generally agreed that the process of spontaneous condensation can be described by a combination of classical nucleation theory and droplet growth theory.[1] To simplify calculations associated with the process of steam condensation and the modeling of droplet growth, the following was assumed[2]:

- the wet steam is homogeneous and without impurities,
- small liquid water droplets in the wet steam are spherical,
- both phases of the vapor-liquid mixture have the same velocity,
- interactions between droplets may be ignored, and

- the heat capacity of small droplets is negligible compared with the latent heat of condensation.

1) Spontaneous condensation models

In this model, the nucleation rate represents the nucleus formation rate per unit mass of mixture, denoted by J, based on the classical nucleation theory as modified by Kantrowitz and incorporating non-isothermal effects. The nucleation rate is given by[3]

$$J = q_c(2\sigma / \pi M^3)^{1/2}\ \rho_g{}^2 \exp(-4r_c^2\sigma / 3K_bT) / \rho_l(1+\Phi) \quad (1)$$

In this equation, q_c is the condensation coefficient, M is the mass of one molecule, σ is the liquid surface tension coefficient in N/m, K_b is the Boltzmann constant, Φ is a non-isothermal correction factor and r_c is the critical droplet radius which is calculated by

$$r_c = 2\sigma T_s / \rho_l h_{fg}(T_s - T) \quad (2)$$

where T_s is the saturation temperature and T denotes the droplet temperature.

2) Water droplet growth model

Based on the work of Gyarmathy,[4] Young developed a droplet growth rate expression incorporating a three layer theoretical model proposed by Langmuir.[5,6] The droplet growth rate at low pressures (0.1 to 0.3 bar) is modified to obtain better agreement between calculated and experimental values. The specific form is written as[7]

$$dr / dt = \frac{\lambda_g(T_s - T)(1 - r_c / r)}{\rho_l h_{fg} r[1/(1+2\beta K_n) + 3.78(1-\upsilon)K_n / P_{rg}]} \quad (3)$$

where λ_g is the thermal conductivity, β is the proportionality coefficient (equal to 0.75), K_n is the mean free path of the gas molecules P_{rg} is the Prandtl number and υ is an adjustable correction factor.

Determination of the computational model and mesh topology

The Reynolds number is used to calculate the flow pattern of the wet steam flow field over the wave plate. The standard k-ε model is adopted for the continuous phase, while the discrete phase is determined by means of the zero-equation model and the wall function method is used to process the region adjacent to the wall. Because of the regular geometry of the corrugated plate flow channel, a structural mesh is employed to improve the precision of calculations as well as to reduce memory occupancy, employing a total mesh number of 540,000. The resulting grid structure is shown in Figure 2.

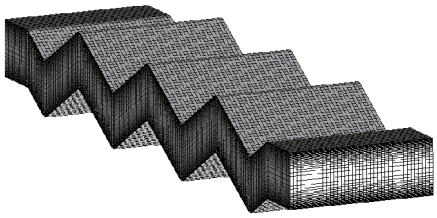

Figure2. The structure of the waveforms board

Boundary conditions and calculation methods

When modeling the condensation flow of wet steam over the corrugated plate, the Euler-Euler governing equation is employed to describe the two phase vapor-liquid characteristics. The numerical model is solved using the TVD difference method and the CFX two phase flow droplet condensation model, neglecting water droplet collisions and aggregation. The wet steam is assumed to flow as a homogeneous two-phase system at an inlet velocity of 6 m/s and 10% humidity, at a temperature of 369 K. The vapor-liquid two phase state equations were set to meet the IAPWS library conditions. The outlet relative pressure is set to 0 atm and the corrugated plate wall is assumed to be both adiabatic and non-slip. The backsplash and adsorption of droplets on the wall are not considered in the model.

Results and analysis

A. Changes in wet steam condensation characteristics over time

When modeling, the zero point of the time scale is set equal to the moment at which the flow indicated by cross section A (perpendicular to the vapor flow direction) moves past the entrance to the corrugated plate. Cross section A subsequently moves further from the entrance of the corrugated plate over time. Analysis of the area-averaged parameters of the wet steam at cross section A as the section travels to different locations is then performed, with the specific results detailed below.

Figure 3 shows that, over time, the nucleation rate gradually increases, although the rate of increase eventually slows. Based on the nucleation rate formula, an analysis of the nucleation rate variation during the process of steam condensation is performed.

In accordance with classical nucleation theory, expressions for the nucleation rate (Equation 1) and the critical radius (Equation 2) have been given. Substituting Equation 2 into 1 gives a new expression indicating that the cube of the surface tension coefficient is inversely proportional to the nucleation rate and that undercooling is proportional to the nucleation rate. Therefore reducing the value of the surface tension coefficient will produce higher nucleation rates, while a lower degree of deviation from the saturated state will lead to a lower nucleation rate. The surface tension and vapor saturation thus both have a significant effect on the nucleation rate.

The surface tension may be calculated as[8]

$$\sigma = 0.2358(1/T - T_c)^{1.256}[1 - 0.625(1 - T/T_c)] \quad (4)$$

Here T is the water temperature and T_c is the critical temperature of water (647.3 K).

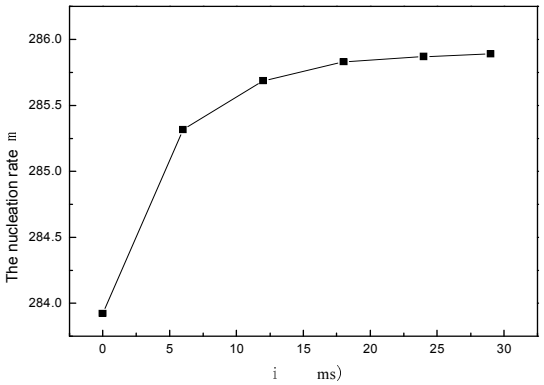

Figure3. Nucleation rate changes over time

The relationship given here between surface tension and temperature shows that higher temperatures reduce the surface tension coefficient but increase the nucleation rate. Figure 4 shows that the steam temperature increases over time and so the droplet surface tension will be reduced, leading to an increase in the nucleation rate. Because of the role of the corrugated plate as a separator of wet steam, the relative humidity of the steam also decreases and so the degree to which the steam deviates from the saturation state is lowered, which can lead to a decrease in the nucleation rate over time. The impact of such changes on the nucleation rate is small, however, relative to the effect of changes in the surface tension coefficient, and simply serves to reduce the rate of increase.

Figure 5 shows that the droplet diameter gradually increases over time until a plateau is reached, after which the diameter is relatively stable. An analysis of changes in the droplet diameter may be performed based on phase equilibrium conditions. The radius, r, of a droplet under equilibrium water vapor pressure may be incorporated into the follow expression[9]

$$P_r = P_\infty \exp(2\sigma / \rho_l R_g T_r) \quad (5)$$

In this equation, P_x is the water vapor pressure associated with water droplets of radius r, Pa is the vapor pressure at phase equilibrium and P_∞ is the water vapor saturation pressure when the droplet radius is infinity (that is, the vapor-liquid interface is infinity).

The above equation for P_x shows that P_x is larger than P_∞ and that P_x will be reduced as the droplet radius increases and thus will approach P_∞. As the vapor molecules condense into water droplets, the droplet surface area increases and the equilibrium partial pressure of the water droplets is slightly reduced. However, the water vapor pressure does not change, such that the smaller droplets will continue to grow. When the water droplets grow to a certain size the steam will attain a new thermodynamic equilibrium and no further growth will occur.

Figures 6 and 7 demonstrate that the number of drops is gradually reduced as the humidity of the steam decreases over time. The curved flow path of the wave plate occasionally changes the direction of the steam flow and thus, owing to their inertia, a portion of the water droplets deviate from the trajectory of the vapor phase as vortices are formed in the corners of the corrugated plate, leaving the droplets stranded in these locations. At each vortex site, the area over which wet steam is in contact with the wall of the corrugated plate is very large, such that the droplets inside the vortex are essentially attached to the wall and thus separated from the wet steam. As wet steam flows over the corrugated plate, therefore, the number of water droplets is gradually reduced and the humidity of the steam slowly decreases. The results also show that the wet steam traverses the first band of the corrugated plate between 6 and 12 ms from time zero and this is the time span over which the steam humidity and the number of water droplets decrease most rapidly. Thus the first band of the plate represents the most effective wet steam separator.

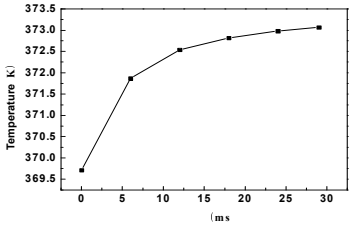

Figure4. Temperature changes over time

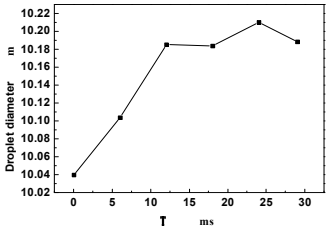

Figure5. Water droplet diameter changes over time

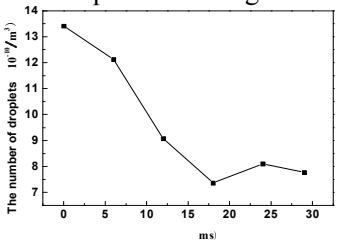

Figure6. Variations in the number of water droplets over time

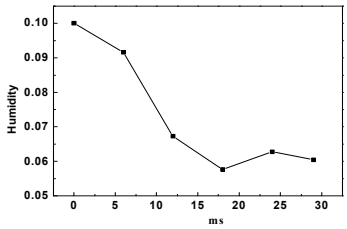

Figure7. Humidity changes over time

B. Characteristics of wet steam condensation on the waveform board at specific times

1) The effect of the saturation state of wet steam on condensation

Because of the spontaneous condensation of the wet steam and the separation effect of the wave plate, the degree of saturation of the wet steam is constantly changing, and this will have a pronounced effect on the condensation process. Cross section B, which is parallel to the direction of steam flow at Z = 20 mm is used to examine the physical parameters of the interface at any given moment and to analyze the wet steam condensation.

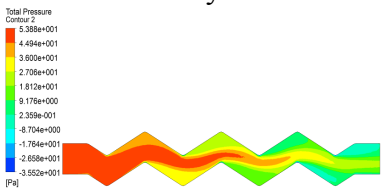

Figure8. Variations in pressure along the flow direction

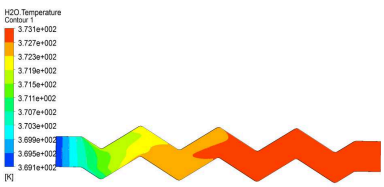

Figure9. Variations in temperature along the flow direction

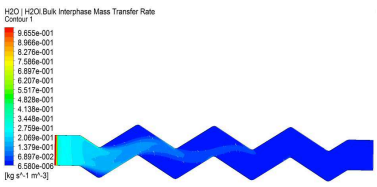

Figure10. Variations in condensation rate along the flow direction

Figures 8 and 9 demonstrate that the temperature gradually increases in the direction of the flow of the wet steam, going from the initial temperature of 369 K to a value of 373 K. The wet steam pressure also gradually decreases to a relative pressure 53.8 Pa less than the initial atmospheric pressure at the entrance. With increased extent of steam flow, the deviation of the wet steam from saturation conditions is diminished. Based on what is known of wet steam condensation, the greater the extent of deviation from saturation, the greater the degree of condensation. Thus the wet steam condensation rate decreases along the flow direction, as shown in Figure 10.

2) The effect of pressure gradient on wet steam condensation

The preceding analysis showed that the first band of the corrugated plate produces the greatest amount of steam separation. The characteristics of wet steam condensation along a cross section of the corrugated plate were analyzed using a cross section, which is perpendicular to the direction of the wet steam flow on the windward side.

Figure 11 shows the location of the most extreme pressure gradient at the cross section, and also demonstrates that this zone corresponds to the greatest quantity of droplets and the highest liquid mass fraction and condensation rate. There is, however, no obvious relationship between the distribution of the nucleation rate and the pressure gradient.

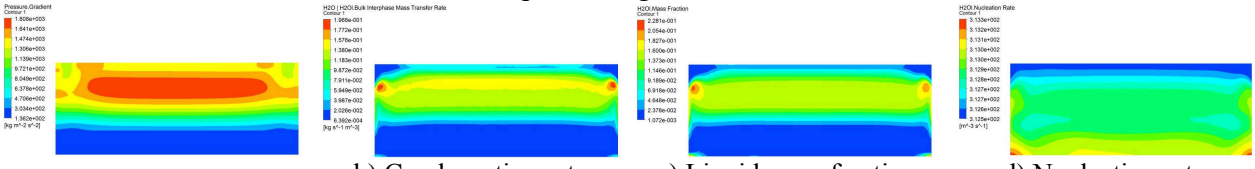

a) Pressure gradient b) Condensation rate distribution c) Liquid mass fraction distribution d) Nucleation rate distribution

Figure11. The distributions of steam parameters along the cross section

Based on the equations associated with control of the liquid phase, an analysis of the relationship between various steam parameters may be performed. The equation relating the quality setting of the speed, m_j, with the steam humidity, Y, the nucleation rate, J, and the number of drops, N, is

$$m_j = 4\pi r_c^3 \rho_l (1-Y) J / 3 + 4\pi r^2 \rho_l N \frac{dr}{dt} \quad (6)$$

The first part of this equation represents the mass that undergoes phase transition due to the nucleated condensation of water droplets, while the second part expresses the phase transition mass resulting from droplet growth. An analysis of the order of magnitude of these two parts shows that the magnitude of the first part is on the order of 10^{-9}, whereas the magnitude of the second part is on the order of 10^4. Therefore the condensation rate is primarily influenced by the quantity of water droplets. Because the pressure drop plate is small, the speed of the wet steam flow is low over the corrugated plate and this reduces the spontaneous condensation of the wet steam, hence the nucleation rate has little effect on the condensation rate. Based on an analysis of the images in Figure 11, the pressure gradient has a greater effect on the water droplet growth rate and a lesser effect on the water droplet nucleation rate. As a result, increasing the pressure gradient generates a greater amount of liquid condensation.

Conclusions

(1) The nucleation rate of wet steam passing over corrugated plates gradually increases and is positively correlated with the temperature of the steam.
(2) The degree of departure from the saturated state decreases gradually along the flow direction, leading to a concurrent decrease in the rate of steam condensation.
(3) The rate of steam condensation increases as the pressure gradient is increased.

References

[1] J.B.Young. The Spontaneous Condensation of Steam in Supersonic Nozzles. Physico Chemical Hydrodynamics, July 1982, 3(2), pp57-82.
[2] Lan Xin Sun turbine dehumidification level two-phase flow numerical study. Journal of Harbin Engineering University, 2006:17-19.
[3] Guha A, Young J.B. Time-Marching Prediction of Unsteady Condensation Phenomena due to Supercritical Heat Addition. IMech E, 199l, C423/057.
[4] South Korea together, Liu Gang, Wang Z. non-equilibrium homogeneous condensation droplets Growth Model of Wet Steam. Chinese Society of Engineering Thermophysics, conference papers, 2009, pp. 1 -10.
[5] A.J. White, S.Senoo. Numerical simulation of unsteady wet steam flows with non-equilibrium condensation in the nozzle and the steam turbine. ASME joint US-European fluid engineering summer meeting, 2006, p. 61.
[6] J.B. Young. The spontaneous condensation of steam in supersonic nozzles. Physical Chemical Hydrodynamics, 1982,3(1):57～82lows of condensing steam. J. Propul, Power, 1993, 9(4), pp 579～587.
[7] A.J. White, J.B. Young. Time-marching method for the prediction of two dimensional, unsteady flows of condensing steam. J. Propul, Power, 1993, 9(4), pp 579～587.
[8] Guangqi Liu, Malian Xiang, Jie Liu, Data Handbook of Chemistry and Chemical properties, inorganic volume. Industrial Equipment and Information Engineering, Publishing Center of Chemical Industry Press, 2002, p. 1334.
[9] Sidi Fu. The condensation in the high-speed fluid. Beijing: Science Press,1988, pp 12-26

Advanced Materials Research Vols. 986-987 (2014) pp 810-813

doi:10.4028/www.scientific.net/AMR.986-987.810

A Study on Exhaust Muffler Using Counter-phase Counteract

Ying-li Shao

Department of Statistics and Mathematics Inner Mongolia Finance and Economics College

Huhhot, P. R. China

yinglishao@163.com

Keywords: Counter-phase, Diesel engine, Muffle, Insertion loss.

Abstract. The exhaust noise, which falls into low-frequency noise, is the dominant noise source of a diesel engines and tractors. The traditional exhaust silencers, which are normally constructed by combination of expansion chamber, and perforated pipe or perforated board, are with high exhaust resistance, but poor noise reduction especially for the low-frequency band noise. For this reason, a new theory of exhaust muffler of diesel engine based on counter-phase counteracts has been proposed. The mathematical model and the corresponding experimental validation for the new exhaust muffler based on this theory were performed.

Introduction

Exhaust noise, a kind of bump, is the main noise source of diesel engines and tractors. Installing exhaust muffler is the most direct and effective method to control the exhaust noise [1]. But most of the traditional exhaust mufflers are composed of expansion chamber, and perforated pipe or perforated board [2], whose exhaust resistance is rather great and whose function of noise reduction is very poor, especially for the low frequency, which is the major part of exhaust noise [3]. Pointing at the problem in the traditional mufflers of diesel engines, the author puts forth a new theory of exhaust silencer of diesel engine based on counter-phase counteract and split-gas rushing . The dominant low-frequency noise components are controlled by counteract of two sound waves with counter-phases (180°phase difference), the other frequency-band noise is reduced by lowering the exhaust gas flow rate thus lowering exhaust noise. In addition, the author establishes a physics model of counter-phase counteract, founds a mathematics modelling on the basis of and analyses the acoustical characteristics of the above-mentioned physics model, deduces theoretical model of the transmission loss of the new muffler, and founds the relationship between its acoustic characteristics and the major parameters of framework. Thereafter, according to the new theory, taking the single-cylinder diesel engine of CG25 as the sample model machine, the author designs an exhaust muffler, and tests and verifies the new theory and the theoretical analysis.

Principle of the muffler

The principle of the new muffler is shown in Fig.1. The muffler unit is mainly composed of an outer tube and an inside tube. There are two round and opposite holes in the inside tube, and the sizes of the two holes are same, and the summation of the sectional areas of the two holes is no less than the sectional area of the entrance of the inside tube. With the help of the U-tube,the exhaust noise enters from the entrance, and counter-phase when it enters the inside tube of the muffler, along the upper passages and lower passages. In accordance with the theory of sound radiation, the author can regard the two opposite holes as the two plunger sound source, and due to the reverse oscillation, the radiation capability of the combined sound resource is reduced, so the author can reach the aim of noise reduction.

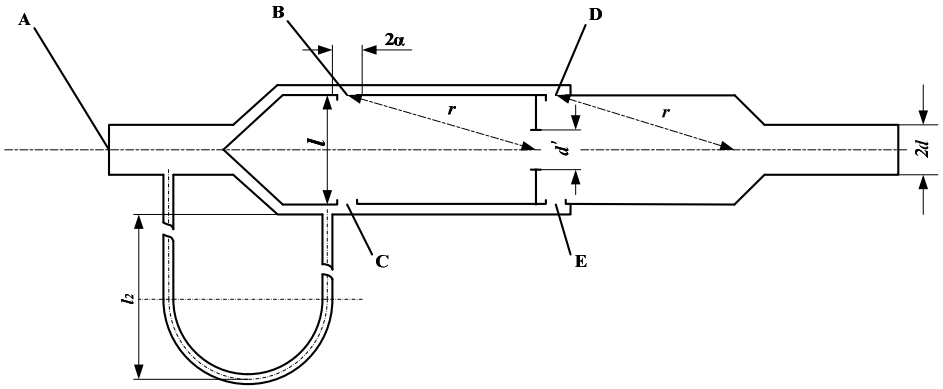

Fig. 1 Principle of the muffler using reversed-phase cancelling

Analysis to the experimental results

The theoretical formula for transmission loss of the new type muffler

$$TL=20\log\frac{2r^2}{akdl}$$

The author designs 3 series of data and name them as Muffler Type Ⅰ, Muffler Type Ⅱ and Muffler TypeⅢ, and their sizes are as the following:

Muffler Type Ⅰ: r=165mm, l=80mm;

Muffler Type Ⅱ: r=165mm, l=60mm;

Muffler TypeⅢ: r=56mm, l=80mm

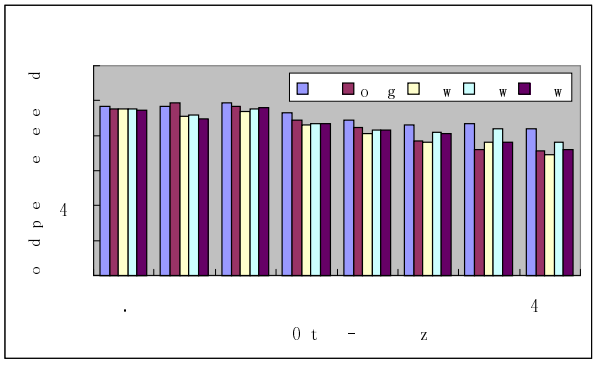

Fig. 2 The contrast on octave-band sound pressure level at 1800r/min

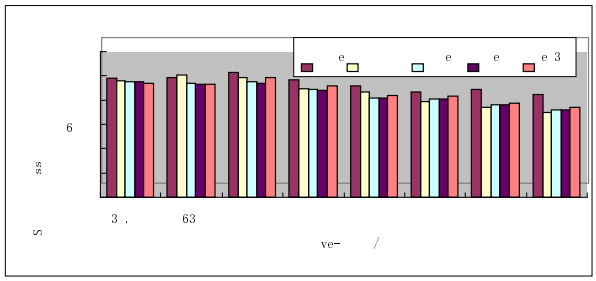

Fig. 3 The contrast on octave-band sound pressure level at 2000r/min

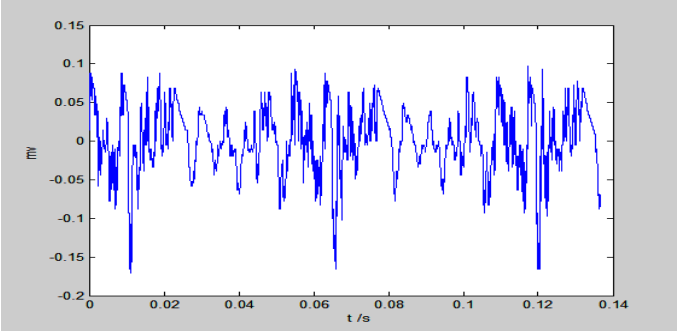

Fig. 4 The time domain signal of the new Ⅰ at 2000r/min

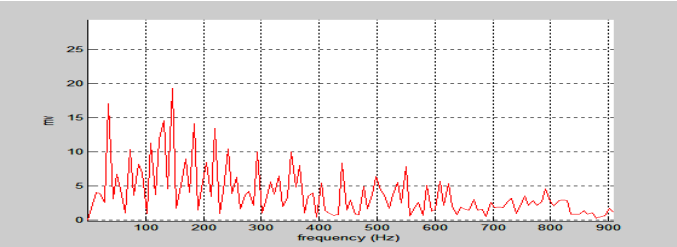

Fig. 5 The spectrum of the new Ⅰ muffler at 2200r/min

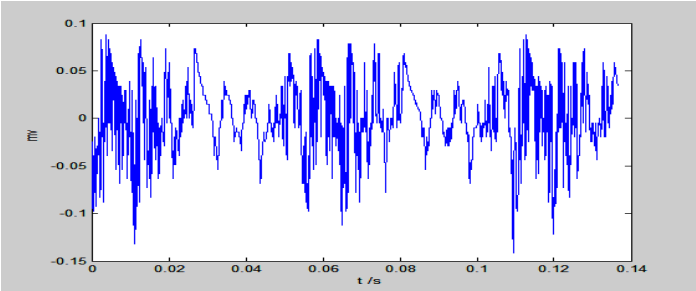

Fig. 6 The time domain signal of the new Ⅱ at 2000r/min

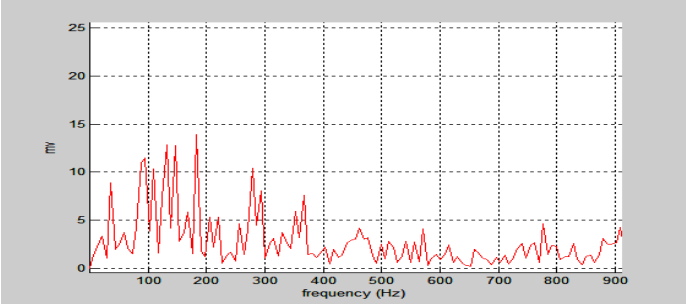

Fig. 7 The spectrum of the new Ⅱ muffler at 2200r/min

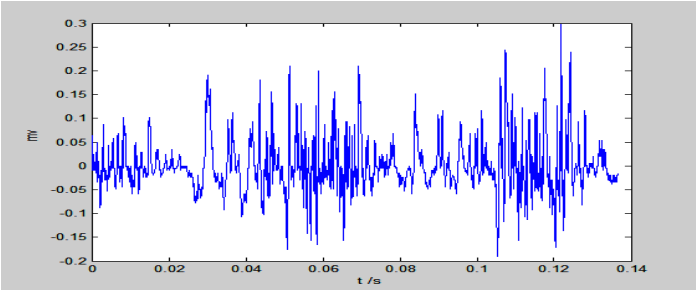

Fig. 8 The time domain signal of the newⅢat 2000r/min

The tested results show that the insertion loss of three new mufflers has all reached 7dB (A), more than 4dB (A) improved compared to original muffler. The original muffler can only reduce the high-frequency noise components, it cannot reduce, even strengthen the noise of frequency below

500 Hz, proved conventional muffler with poor capacity of lowering the low-frequency noise again. The new exhaust mufflers were obviously effective in controlling the low-frequency exhaust noise, which proved correctness of the new theory. In addition, it has been found that the new mufflers have a good effect of noise control in the whole frequency domain especially in the range of under 500 Hz. This not only proved that the new mufflers have very good performance for low-frequency noise reduction, but also proved that using split-gas rushing can lower the air flow speed thus lowering the air-regeneration noise. The counter-phase is only effective to the exhaust noise of the target frequency and its odd multiple harmonics instead of the whole frequency range, but the split-gas rushing is working to the noise in all frequency range. By comparing the results of three new mufflers, it was noticed that the new muffler type Ⅱ was the best, especially at the rated speed the effect is more pronounced, which is consistent with the theoretical model analysis, further proved the correctness of the theory.

Conclusions”

Taking the single-cylinder diesel engine CG25 as the experimental engine, the exhaust noise was measured and its spectrum was analyzed. In order to accurately extract the exhaust noise as the control target, the singular value decomposition technique was utilized for decomposition and reconstruction of the signal.

Based on this, three new mufflers with different parameters were designed and manufactured. The sound level pressure dB (A), octave-band sound pressure level as well as detailed spectrum of exhaust noise from the tested diesel engine with three new mufflers were measured and analyzed respectively at five different speeds. By comparing the results with that without muffler and with the original muffler of the engine, the new theory of muffler has been verified.

Acknowledgements

This work has been supported by Inner Mongolia Natural Science Foundation of China No. 2012MS0602.

References

[1] A.D.Sahasrabudhe,S.Anantha Ramu , M.L.Munjal.Matrix condensation and transfer matrix techniques in the 3-D analysis of expansion chamber mufflers[J].Journal of Sound and Vibration,1991,147(3),pp.371-394.

[2] Mara Cuesta,Pedro Cobo:Active Control of the Exhaust Noise Radiated by an Enclosed Generator [J]. Applied Acoustics,2000(61),pp.83-94.

[3] Y. Mishing, in: *Diffusion Processes in Advanced Technological Materials*, edtied by D. Gupta Noyes Publications/William Andrew Publising, Norwich, NY (2004), in press. T.Kar , M.L.Munjal.Generalized analysis of a muffler with any number of interacting ducts[J].JournalofSoundandVibration,2005,285(3),pp.585-596.

[4] T.W.Wu,P.Zang , C.Y.R.Cheng.Boundary element analysis of mufflers with an improved method for deriving the four-pole parameters[J].Journal of Sound and Vibration,1998,217(4),pp.767-779..

[5] R.J. Ong, J.T. Dawley and P.G. Clem: submitted to Journal of Materials Research (2003) Bilawchuk,K.R.Fyfe:Comparison and implementation of the various numerical methods used for calculating transmission loss in silencer systems.Applied Acoustic,2003,64(9),pp.903-91.

Advanced Materials Research Vols. 986-987 (2014) pp 814-818

doi:10.4028/www.scientific.net/AMR.986-987.814

An Experiment and Simulation Study on Performance Of Finned Tube Condenser

QIN Hai-jie[1,a], ZHU Wei-ying[2,b], LI Wei-zhong[1,c]

[1]Key Laboratory of Ocean Energy Utilization and Energy Conservation of MOE,School of Energy and Power Engineering, Dalian University of Technology, Dalian,116024,China;

[2]Dalian Sanyo Compressor Co., Ltd., Dalian, 116033,China

[a] hey7503@sina.com [b] zhuwy16@163.com [c] wzhongli@dlut.edu.cn

Keywords: Finned tube condenser, Test, Simulation

Abstract. In this paper, a finned tube condenser performance test platform by using hot water as heat transfer medium in the pipe was established. The air side correlations of pressure drop and heat transfer were acquired based on lots of testing datas.A segment by segment model of the finned tube condenser used in these correlations was proposed and a simulation program was developed by using Visual C++ programming tools. Experiment and simulation results show that the air side correlations of pressure drop and heat transfer are fitting well with experimental datas. The deviation between the experimental and calculated values is within ±5%.The deviation of Nu Number is within ±10% and the deviation of the pressure loss is within±15%.

Introduction

Improve the efficiency of the system in the field of refrigeration and air conditioning is an important issue. Condenser is the main component of the refrigeration and air-conditioning systems, its heat transfer performance will directly affect the entire cooling system performance. To better understand the performance characteristics of the condenser in order to improve its performance, domestic and foreign scholars have done a lot of experiments and simulation studies. 1978, McQuiston[1] presented flat fin heat exchangers general correlation in accordance with its five prototype test data . In recent years, Wang [2] summarized heat exchanger corresponding experimental correlations based on experimental data of 9 prototypes. However, the fin spacing and size of the test tube pitch are the same for these prototypes; the extended universality of correlations has not been verified. Jensen [3] established phase change heat exchanger model by using the moving boundary. Each phase moving boundary method is a distributed lumped parameter method , the refrigerant heat physical parameters in each region of the phase transformation is represented by a lumped parameter phase zone length as state variables (micro- component), making the heat exchanger zone length in the system varies with time during the simulation. Yue Ting [4] establishes a steady state simulation model of a small refrigeration unit condenser. In this simulation model , the combination of distributed parameter model and the lumped parameter model of the merits , according to the condenser refrigerant state division, district of refrigerant superheat and sub cooling zones were established distributed parameter model and experimentally validated models and the accuracy of the algorithm.

The condenser running conditions can quickly be predicted by using of the steady-state distribution parameter model to simulate finned tube condenser performance, and determine whether the parameters of the condenser meet the design requirements. Not only can avoid frequent prototype trial and experimentation, reduce costs, but also can improve design efficiency and shorten the product development cycle.

Firstly, to establish a Finned tube condenser performance test platform using hot water as heat transfer fluid, obtained heat transfer coefficient of air side and resistance characteristics parameters by experiment; then using Segment by Segment model [5], combined with the test results, to build condenser calculation model. Finally, a exchanger simulation program was compiled by using

Visual C++ programming tools. In the simulation process in the condenser is divided into three zones, namely, to solve its basic equations illustrate the impact of changes in the structural parameters of the condenser to the condenser performance.

Steady distributed parameter model

Condenser model. Condenser is using Segment-by-Segment model simulation. According to the order flow of the refrigerant tubes, each computing unit used in the calculation method for solving, calculated heat transfer process within each Segment tube inside and outside of the tube, respectively, to solve the energy conservation equation and momentum conservation equations [6]. Combined with the actual operation of the condenser, the model makes the following assumptions:

1) Air flow rate of air flowing outside the tube is regarded as one-dimensional flow patterns, regardless of its structure causes uneven distribution;
2) Using the cross-flow heat exchanger structure, but the common condenser, the refrigerant tube and the tube relative to the outer air flow to cross flow within the flow cross each calculation Segment of a distribution model;
3) Ignore tubes axial heat loss through the fins of the heat exchanger considered only in the vertical direction;
4) Assuming each Segment air flow area is one-dimensional, and air without mixing at axial direction .
5) Ignore the pressure drop at the U-tube.

The control equations within segment. Generalized thermodynamic definition of dryness in the overheated state of the super cooled state, other thermodynamic defined dryness. Segment status within the refrigerant by generalized dryness value judgments.

$$X = \frac{h - h_{bub}}{h_{dew} - h_{bub}} \tag{1}$$

For any Segment, the following equations can be established.

1) Refrigerant heat equation

Continuity equation:

$$m_r = const \tag{2}$$

Energy equation:

$$Q_r = m_r(h_{in} - h_{out}) = m_r(f(X_{in}) - f(X_{out})) = \alpha_r A_i (T_r - T_w) \tag{3}$$

Where:

Q_r —Refrigerant heat exchange capacity; m_r —Refrigerant mass; h_{in}, h_{out} —Refrigerant inlet and outlet enthalpy; α_r —Local heat transfer coefficient of refrigerant [8]; A_i —The refrigerant heat exchanger area;

T_r —Refrigerant temperature; T_w —Heat exchange tube wall temperature.

2) Air-side flow and heat transfer equations

Continuity equation:

$$m_a = const \tag{4}$$

Heat equation:

$$Q_a = m_a Cp_a \varepsilon_t (T_{a,o} - T_{a,i}) = \alpha_a A (T_w - \frac{T_{a,o} + T_{a,i}}{2}) \tag{5}$$

Where:

Q_a —Air heat exchange; Cp_a —Air specific heat capacity at constant pressure;

ε_t —Temperature efficiency; m_a —Air mass flow.

3) Tube inside and outside heat balance equation

Ignore heat loss as well as a small amount of refrigerant in the refrigeration oil influence on heat transfer from the energy conservation equation shows:

$$Q_a = Q_r \tag{6}$$

4) Calculation of the pressure loss of the refrigerant

Refrigerant pressure loss in the pipe by the static pressure loss, the pressure loss and the friction pressure loss component of acceleration, the pressure loss according to the reference [8].

5) Algorithms and processes

Figure 1 is the flow chart of the simulation process, A is a simulation flow chart for the entire condenser, B is a simulation flow chart of one segment .Said single heat exchanger simulation model based on the use of Visual C++ compiled a heat exchanger performance simulation program. In the calculation, the parameters may be parameters of the structure of the condenser and inlet and fluid parameters are set in a range of condenser simulation program according to the setting. The simulation output of the main heat load heat exchanger, the pressure loss on the air side, the air outlet temperatures.

Refrigerant properties model. In order to ensure the calculation results, the physical properties of the refrigerant used herein, is calculated using the American Institute of Standards and Technology (NIST) developed physical computing software Refprop 8.0[7], using Visual C + + for Refprop.dll encapsulation used in the simulation program to ensure that refrigerant accuracy physical properties.

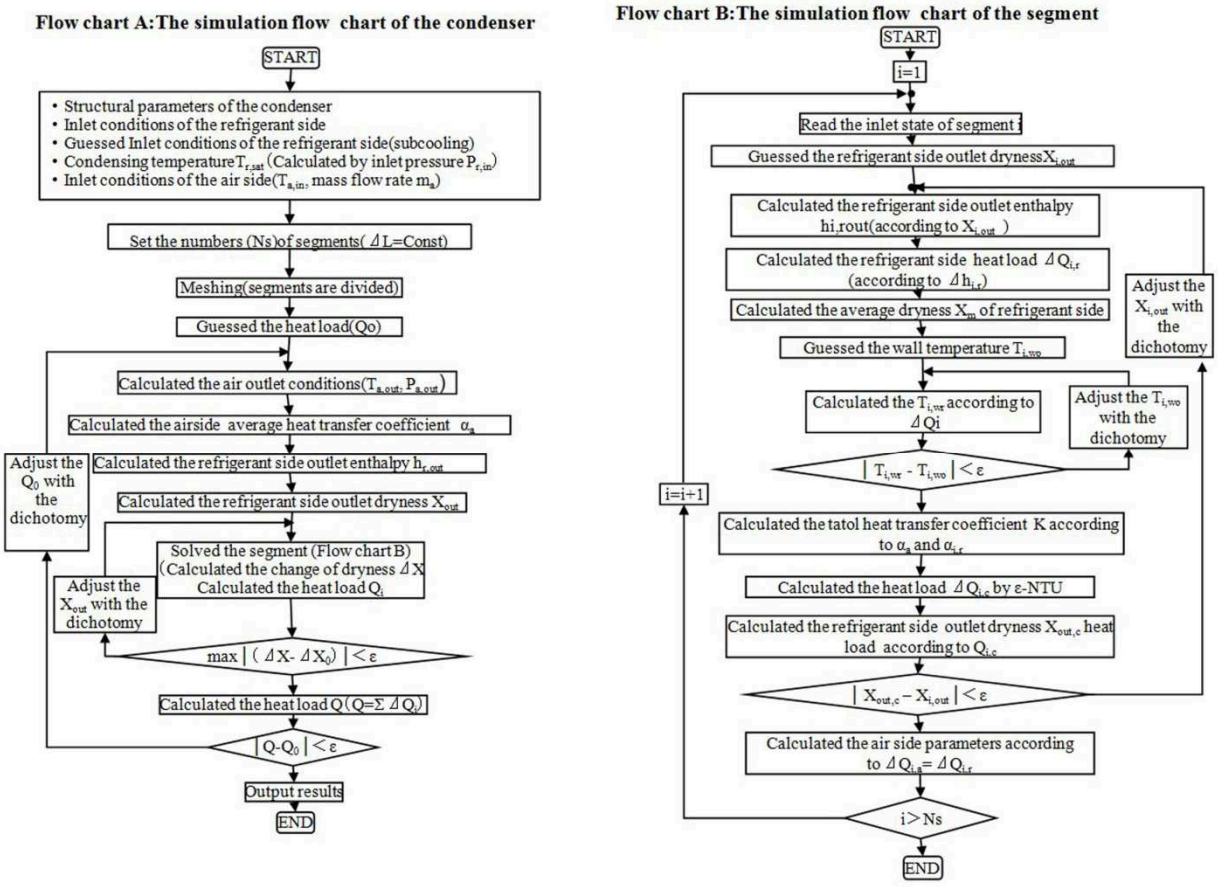

Figure 1 The Flow Chart of Simulation Calculation

Test device

Air system. Test Lab with air enthalpy-difference method for the condenser air inlet by an air handling system to control parameters; dry air side outlet of the wet bulb temperature is measured by the sampling means in the wind tunnel. The air flow through the condenser is controlled by changing the operating frequency of the induced draft fan. After the heat exchanger outlet and the nozzle are provided with static pressure measuring three points, each measuring point by the static pressure measuring hole to take four different directions, the mixture was measured by the

differential pressure transducer and the static pressure of the wind pressure nozzle before and after. The air-side heat exchanger pressure loss can calculate by the static pressure of the wind; the air temperature and humidity around the nozzle pressure and nozzle can calculate the volume of air flow through the nozzle, so you can get the air flowing through the heat exchanger and the face wind speed.

Water System. Mainly by the constant temperature water tank water system, circulating pump, a flow control device composed of a closed loop system uses a stable manner in the water flow rate and temperature were tested heat exchanger. Each in charge of road traffic through manual valve, pressure regulator and out of the water in the heat exchanger can be achieved within the water flow path for each charge is equal. Water system uses RTD sensors to measure water temperature and water temperature for each charge of the road.

Test Equipment. The RTD sensor to measure temperature, air pressure and water static pressure is measured using a differential pressure transmitter. The test datas obtained by the sensor and transmitter are transferred to the computer every 6 s.

Tests and calculations

Test results. Figure 2 shows the variation of pressure loss with tube number of columns, which can be seen, the deviation between the experimental results and the calculated results are mainly distributed within ± 15%. Figure 3 shows the variation of air side Nu number with x^*, and can be seen from the figure 3, when $x^* \le 0.3$, under the same conditions as x^*, with the increase in the number of rows, Nu number increases; while x^* relatively large , the number of columns is not significantly affected. Deviation Nu number between experimental results and the calculated results are mainly distributed within ± 10%, especially in the larger face velocity range (approximately 1.6-8m / s), the calculated and experimental values are closer fitting formula.

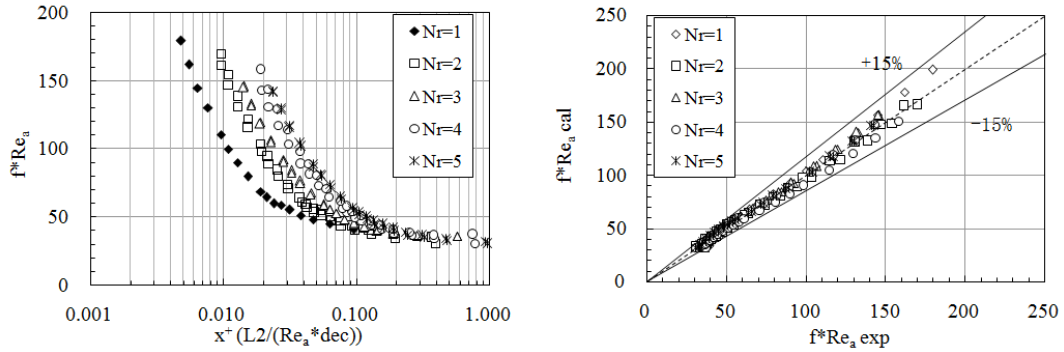

Figure 2 The relationship of the pressure loss vs. row number

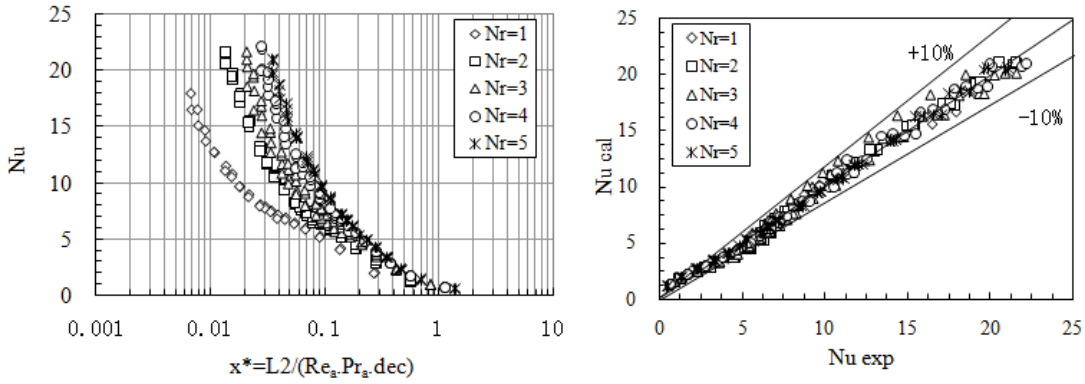

Figure 3 The relationship of the Nu number vs row number

Simulation. In order to verify the accuracy of the calculation results, a series simulation of a condenser are carried out: The air face velocity range is 1.8~2.6m/s, the step size is 0.2m/s. The data in Table 1 can be seen in the deviation between simulation results and experimental values within the allowable range (± 5%), to achieve a better description of the simulation accuracy, basically to meet the heat exchanger in the design and verification phase requirements.

Table 1 Simulation results vs test results

Heat load (kW)			Loss of air pressure(Pa)		
Experiment	Simulation	Deviation	Experiment	Simulation	Deviation
5.96	5.97	0.17%	17.22	17.78	3.40%
5.28	5.46	3.41%	25.91	24.88	-3.95%
4.85	5.02	3.51%	16.82	16.37	-2.52%
11.41	11.03	-3.33%	64.33	67.51	4.98%
4.12	4.31	4.61%	12.51	12.98	3.87%

Conclusion

In this paper, water as a medium to establish a test platform Finned tube condenser through experiments applicable to slit fin heat exchangers and pressure losses associated relational style, and apply it to the condenser of the simulation model, while preparing the condenser performance simulation program, and the condenser prototype experiment and simulation comparison. The results showed that the simulation and the experimental error can be maintained within ± 5%, a condenser designed to meet the needs. While the design cycle is shortening about 90%t, thus can greatly reducing the product development and design cycles.

References

[1] F.C. McQuiston, Heat mass and momentum transfer data for five plate-fin tube transfer surface, ASHRAE Transactions, 1978, 84(1), 266-293.

[2] Wang C C, Hsieh Y, Lin Y. Performance of plate finned tube heat exchangers under dehumidifying conditions [J]. Journal of Heat Transfer, 1997, 119(1):109-117.

[3] Jensen J M, Knudsen H J H. A new moving boundary model for transient simulations of dry-expansion evaporators[C], Proceedings of the 15th International Conference on Efficiency, Costs,Optimization,Simulation and Environmental Impact of Energy Systems. 2002.

[4] Yue Ting,Liu Chu-yun, Chen Guo-dong,Xu Lin. Study on Simulation and Experiment of Little Scale Refrigeration Device Condenser [J]. Gryogenics. 2005,(5): 46-48.

[5] P.A. Domanski, EVAP-COND, simulation models for finned tube heat exchangers, National Institute of Standards and Technology Building and Fire Research Laboratory, Gaithersburg,MD, USA, 2003.

[6] Wang H S, Rose J W, Honda H. Condensation of refrigerants in horizontal microfin tubes: comparison of correlations for frictional pressure drop [J]. International journal of refrigeration, 2003,26(4): 461-472.

[7] NIST Reference Fluid Thermodynamic and Transport Properties—REFPROP Version 8.0 User's Guide, 2007.

[8] Goto M, Inoue N, Yonemoto R. Condensation heat transfer of R410A inside internally grooved horizontal tubes[J]. International journal of refrigeration, 2003, 26(4): 410-416.

Advanced Materials Research Vols. 986-987 (2014) pp 819-822

doi:10.4028/www.scientific.net/AMR.986-987.819

Analysis of Pipe Structure Stress Affected by Double Corrosion Points

Wang Xin[1,a], Wang Jia[1,b] , Liu Xin[1,c] , Zhao Guoliang[2] ,Wang Wenjing[3], Wu Di[4,d]

[1] School of Mechanical Engineering, Dalian University of Technology, Dalian 116023, China

[2] Installation company, Offshore Oil Engineering CO., LTD Tianjin 300451, China

[3] Dalian YILIY Engineering Machinery CO., LTD, Dalian 116025, China

[4] Faculty Electronic Information and Electrical Engineering, DUT, Dalian 116023, China

[a]wangxbd21@163.com, [b]wangjia209@163.com, [c]liushi28958@163.com, [d]wudi@dlut.edu.cn

Keywords: Crane; Boom; Double corrosion points; FEA

Abstract. Currently, corrosion of offshore crane booms is serious and badly affects equipment performance and working safety. Obviously, analysis of the corrosion is necessary. In this paper, as an actual case, the boom FEM of 320t pipe-laying crane is built to analyze its double points corrosion based on analysis of single point corrosion. By analyzing stress concentration and stress distribution of different distance for double corroded points, which can be axially arranged or circularly arranged, we try to obtain some affected trends.

Introduction

Corrosion of steel structure not only causes the waste of resource, but also seriously affects the equipment performance and working safety. In practical application, structure has corrosion protection. But as time goes on, corrosion cannot be avoided due to severe working environment and poor equipment maintenance [1]. When corrosion reaches to a certain level, structure is damaged and doesn't work. So, corrosion can not to be ignored.

Offshore cranes are corroded more easily than ones on land because of marine environment. These crane booms are mostly composed of trusses. As a typical example, Fig. 1 and Fig. 2 show 320t pipe-laying crane which has worked for almost 30 years, and its serious corrosion which is found recently. The corrosion's distribution is various, such as two points corrosion distribution and multi-point corrosion distribution. These corrosions can lead stress concentration and damage structure at last.

There are many scholars to research corrosion problem. Dong Shier [2], Li Zengliang [3], Hong Laifeng [4] and other scholars used ANSYS to research the effect of point corrosion defects on oil pipeline's residual strength. Wei Huazhong [5] made a detailed description of establishing reasonable model of corrosion points. Chou Chaoui B A [6] made nonlinear FEA on point corrosion pipelines. It can be seen that existing studies have more focused on corrosion analysis of transmission pipelines. But only a few studies are about the boom corrosion of offshore cranes. We can refer to the former, but they are different. Pipeline is longer and mainly subjects to internal pressure. However, the crane boom mainly subjects to axial load and bending moment when loading. So, their research methods are similar, but different. In this paper, based on single point corrosion achievement [7], two points corrosion and its influence facts are analyzed, which are the distance between two corrosive points. The analysis example is 320t pipe-laying crane's boom, whose sizes are shown in Tab. 1.

Fig. 1 320t pipe-laying crane

Fig. 2 Points corrosion of the boom

Table 1 Size and specification of the boom

Boom length (m)	Boom cross section (mm)	Chords(angle steel) (mm)	Bracings(pipe) (mm)
75	3975x2320	203.2×203.2×25.4	Φ60.3×3.9 Φ73×5.2 Φ88.9×5.5 Φ101.6×5.8

1 FEM of corroded pipe

According to Saint-Venant's principle, in order to avoid the boundary effect, the bracing of boom is selected whose sizes are 500mm length and Φ88.9 × 5.5mm. Its FEM is built by solid95 element. According to [8], corrosion point is simply built as hemispheroid, as shown in Fig.3. The model is meshed by tetrahedron and hexahedron. For lower stress gradient area, grid size is relatively sparse, and is about 10mm. For higher stress gradient area, especially around of corrosion point, grid is subdivided, and its size is as small as 1mm. The model's node is 93334 and its element is 43184.

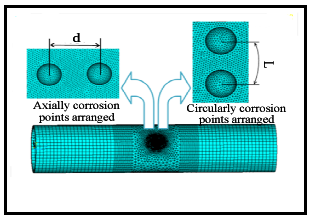

Fig. 3 Finite element model

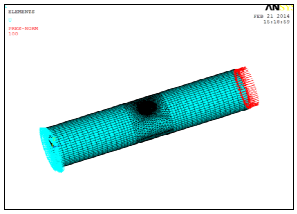

Fig. 4 Model of applying boundary conditions

It is noted that two corrosive points can be classified in axially arrange and circularly arrange, as shown in Fig. 3. The distance of two axially arranged points is defined as linear distance d between the two corrosion points center. And the distance of two circularly arranged points is defined as arc length L between the two corrosion points center. The parameters about corrosion points are shown in Tab. 2.

For crane boom, its bracings are mainly subjected to axial load. Through analyzing boom FEM, we can obtain that bracings' max. stress is about 100MPa. So, we apply a uniform compressive stress 100MPa on the side of the bracing model and apply full displacement constraints to the other side, as shown in Fig. 4.

Tab.2 Parameters of corrosion points

Parameters	Definitions
D	Diameter of corrosion points
$\alpha=d/D$	The ratio between axial distance d and diameter D
$\beta=L/D$	The ratio between arc length L and diameter D
σ_{mid}	Von mises stress on the middle between two corrosion points' center
σ_{emax}	Max. von mises stress at the edge of corrosion points(except σ_{mid})
σ_{max}	Max.{ σ_{mid} , σ_{emax}}
$K=\sigma_{max}/100$	Factor of stress concentration
α_{lim}	Ratio α when two axially arranged corrosion points cannot affect each other
β_{lim}	Ratio β when two circularly arranged corrosion points cannot affect each other

2 FEA of two axially arranged points

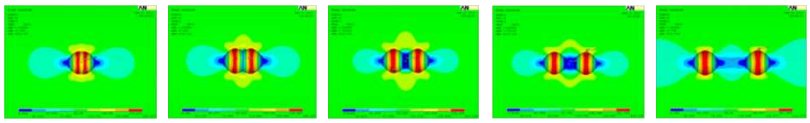

(a)α=0.2 (b)α=0.6 (c)α=1.0 (d)α=1.4 (e)α=1.8

Fig. 5 Stress distribution of different α for 45% of corrosion depth ratio

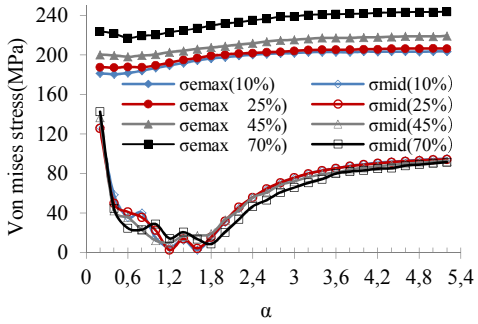

Fig. 6 Stress curves of different α

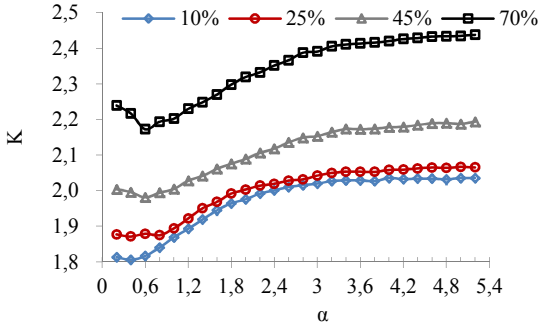

Fig. 7 K curves of different α

FEA models with different corrosion depth ratios (10%, 25%, 45%, 70%) and different d are built, in which two corrosion points are arranged axially. We can make α-σ_{mid} curves, α-σ_{emax} curves and α-K curves with different depth ratios, as shown in Fig. 5 , Fig. 6 and Fig. 7.

From these figures, different depth ratios have similar curve trend, whose max. stress occurs at the edge of the corrosion points. If α is more and more higher, σ_{emax} and σ_{mid} tend to be a stable value, and the stable values of σ_{emax} are near to their single corrosion point's max. stress. Simultaneously, the two corrosion points are unaffected, like two independent single point corrosion. Here, we can define α_{lim}. In order to uniform rule, Δ_i are calculated according to Eq. 1, and $\Delta_i < 5\%$ is as judgment rule to obtain α_{lim} [9], as shown in Tab. 3. From this table, we can show that α_{lim} is similar and between 3.0 and 3.2 with different corrosion depth ratios. So, we take α_{lim} = 3.2 as judgment if the two corrosion points are affected or not.

$$\Delta_i = \left| \frac{K_{i+1} - K_i}{\alpha_{i+1} - \alpha_i} \right| \times 100\% . \tag{1}$$

Tab.3 α_{lim} values with different corrosion depth ratios

Corrosion depth ratio	10%	25%	45%	70%
α_{lim}	3.0	3.0	3.2	3.2

3 FEA of two circularly arranged points

FEA models with different corrosion depth ratios (10%, 25%, 45%, 70%) and different L are built, two corrosion points are arranged axially. We can make β-σ_{mid} curves , β-σ_{emax} curves and β-K curves with different depth ratios, as shown in Fig. 8 , Fig. 9 and Fig. 10.

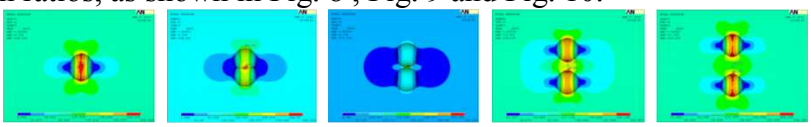

(a) β=0.2 (b) β=0.6 (c) β=1.0 (d) β=1.4 (e) β=1.8

Fig. 8 Stress distribution of different β for 45% of corrosion depth ratio

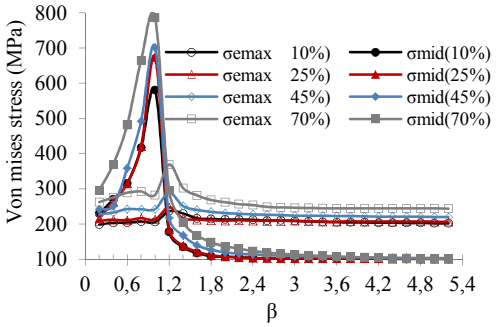

Fig. 9 Stress curves of different β

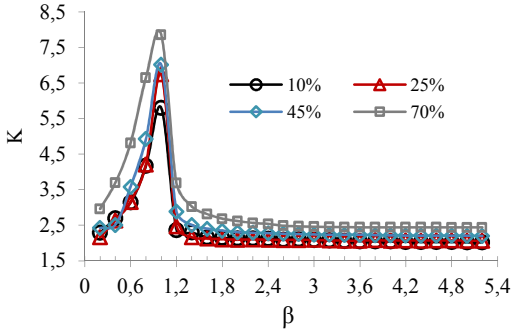

Fig. 10 K curves of different β

From these figures, different depth ratios have similar curve trend, whose cutoff point is β = 1. When β≤1, the max. stress is σ_{mid}. And when β>1, the max. stress occurs at the edge of the corrosion points. If β is more and more higher, σ_{emax} and σ_{mid} tend to be a stable value, and the stable values of

σ_{emax} are near to their single corrosion point's max. stress. Simultaneously, the two corrosion points are unaffected, like two independent single point corrosion. Here, we can define β_{lim}. Also using Eq. 1, β_{lim} of different depth ratios are shown in Tab. 4. β_{lim} is between 4.0 and 4.2. So, we take β_{lim} = 4.2 as judgment if the two corrosion points are affected or not.

Tab.4 β_{lim} values with different corrosion depth ratios

Corrosion depth ratio	10%	25%	45%	70%
β_{lim}	4.2	4.0	4.0	4.0

Conclusions

For the two-point corrosion of boom pipes, FEA model is built and analyzed and make some conclusions as follow:

(1) In the corrosion case of two axially arranged points, stress concentration is not very obvious than single point corrosion. The limitation ratio α_{lim}=3.2 can be as judgment to judge if two corrosion points affect each other or not. That is to say, when α<3.2, stress of the two corrosion points are affected. When $\alpha \geq 3.2$, the two corrosion points are unaffected, like two independent single point corrosion.

(2) In the corrosion case of two circularly arranged points, stress concentration is more obvious than single point corrosion. Also there exists limitation ratio β_{lim}=4.2 as judgment. When α<4.2, stress of the two corrosion points are affected. When $\alpha \geq 4.2$, the two corrosion points are unaffected.

(3) Stress concentration in two circularly arranged points is more serious than ones in two axially arranged points, so we should pay more attention to the formers.

Acknowledgement

This work is supported by the Fundamental Research Funds for the Central Universities (DUT14ZD221) and Dalian Science and Technology Plan Project (2013A16GX111).

References

[1] QI Minhua, in: *Antisepsis and Safeguard of Chemical Equipment*, edited by China Petroleum and Chemical Standard and Quality, Vol. 04 (2013), p. 30-31.

[2] Dong Shier, He Dongsheng and Zhang Peng, in: *The Elastic and Plastic Finite Element Analysis of Double Points Corrosive Pipe*, edited by Design and Research, Vol. 32 (2005), p. 20-23.

[3] Li Zengliang and Chen Meng, in: *Finite Element Analysis of The Residual Strength and Life for Outside Corroded Pipelines*, edited by Lubrication Engneerng, Vol. 35 (2010), p. 86-89.

[4] Hong Laifeng and Sun Tie, in: *The Effect of Double Corrosive Points on Remaining Storage of Line Pipe*, edited by Oil & Gas Storage and Transportation, Vol. 29 (2010), p. 916-918.

[5] Wei Huazhong and Zhou Xiaobing, in: *Residue Strength Analysis of Pressure Piping With Combined Corrosion Defects*, edited by Process Euipment & Piping, Vol. 44 (2007), p. 42-44.

[6] Chou Chaoui B A and Pick R J, in: *Behaviour of Longitudinally Aligned Corrosion Pits*, edited by International Journal of Pressure Vessels and Piping, Vol. 57 (1994), p. 197-200.

[7] Wang Wenjing, Geng Shou and Jia Xiaonan, in: *The Influence of Corrosion on Structure and Method of Improvement*, edited by Chinese Journal of Construction Machinery, Vol. 13 (2014).

[8] Meliani M H and Matvienko Y G, in: *Corrosion Defect Assessment on Pipes Using Limitation Analysis and Notch Fracture Mechanics*, edited by Eng. Fail. Anal, Vol. 18 (2011), p. 271.

[9] Zhang Rixiang, Gu Zichang and Jiang Meng, in: *Finite Element Analysis on Inside-pressured Pipeline with Double Corrosion Defects* , edited by Steel Construction, Vol. 25 (2010), p. 79-81.

Advanced Materials Research Vols. 986-987 (2014) pp 823-827

doi:10.4028/www.scientific.net/AMR.986-987.823

Analysis of Transient Thermal Stress of IGBT Module Based on Electrical-thermal-mechanical Coupling Model

Qingyuan Zheng[a], Minyou Chen[b], Bing Gao[c], Nan Jiang[d]

State Key Laboratory of Power Transmission Equipment & System Security and New Technology

School of Electrical Engineering, Chongqing University, Chongqing, P.R. China

[a]eaglerupt@gmail.com, [b]mchencqu@126.com, [c]gaobingcqu@gmail.com, [d]jnhappy0204@hotmail.com

Keywords: IGBT, Electrical-thermal-mechanical coupling, Thermal stress

Abstract. Reliability of IGBT power module is one of the biggest concerns regarding wind power system, which generates the non-uniform distribution of temperature and thermal stress. The effects of non-uniform distribution will cause failure of IGBT module. Therefore, analysis of thermal-mechanical stress distribution is crucially important for investigation of IGBT failure mechanism. This paper uses FEM method to establish an electrical-thermal-mechanical coupling model of IGBT power module. Firstly, thermal stress distribution of solder layer is studied under power cycling. Then, the effects of initial failure of solder layer on the characteristic of IGBT module is investigated. Experimental results indicate that the strain energy density and inelastic strain are higher which will reduce reliability and lifetime of power modules.

Introduction

Insulated Gate Bipolar Transistor (IGBT) is commonly used in wind power systems, which often surfs severe environments. Thus, reliability is of great importance for that matter[1,2]. A reliable wind power system calls for a good working condition for its wind power converter, of which IGBT is the central part. So a close study of the failure mechanism of the power module is very important to improve the reliability of converters.

In real operation, IGBT modules burden huge amount of heat which is produce by the conducting and switching state, also leading to an non-uniform temperature distribution in IGBT module, because of the multi-layer structure and the mismatching of the expansion coefficient of every layer producing thermal stress in IGBT module. At the interface of different layers, the shear stress will firstly cause crack in solder layer, and eventually accumulate into failure.

Aiming at the effects of power cycling, an electro-thermal-mechanical model is built to analyze the thermal stress characteristic, including the common used parameters for lifetime prediction. Then, the effects of center void in solder layer was discussed, impact of size of void on the junction temperature was analyzed, and effects of the corresponding of thermal stress parameters was also discussed. By analyzing the variation of thermal stress, the real operation of IGBT can help to understand the failure mechanism and improve the lifetime prediction model, overcoming the current module in which the temperature was taken into account.

IGBT Structure Module

Figure 1 shows the typical structure of a IGBT power module. Fatigue and aging of solder materials can be caused by its special multilayer structure as well as the mismatching of thermal expansion coefficient among different materials. This can lead to failure of the device as a result of rupture of chip bong wires, breakage in solder layers or an increase in temperature[3-5].

In thermal aging, the solder layer has creep effects under constant stress where the layer has relatively low melting point. When building a finite element model for IGBT power module, all the

materials are assumed to be elastic, while the elastic-plastic-creep effect of layer is explained by Anand model[6].

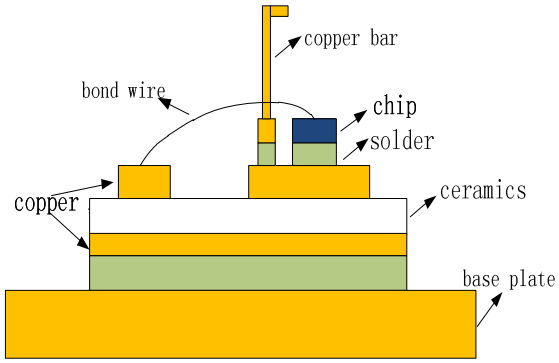

(a)Cross-section graph of the IGBT module

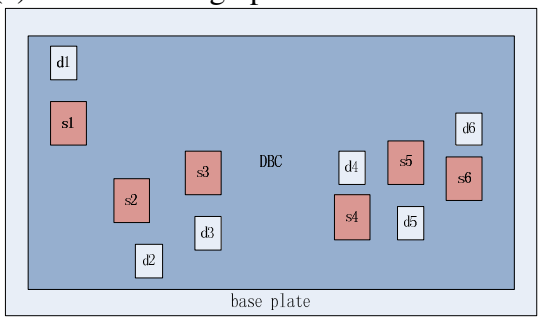

(b)Top view of the IGBT module

Fig. 1 Cross-section graph and top view of the IGBT module under study

Thermal-Mechanical Stress Analysis

Power Cycling Model. In real operation, IGBT always keeps conduction and switching state, which can generate huge amount of heat, exposing the IGBT chip to constant temperature fluctuation. Together with the mismatching of thermal expanding coefficient of the inner structure of model, the temperature fluctuation gives rise to alternating thermal stress between interfaces of different materials. This leads to cracks in solder layer, which means a reduction in heat dissipation, a concentrating of heats and even more serious failure of the layer[7,8].

In this paper, the transient thermal stress distribution of the solder layer under power cycling failure model is analyzed. Because transient temperature fluctuation in switching period is negligible to the failure of a device. Therefore, by considering the aging acceleration and changing the period of loading current, we could attain the heat source variation to the pattern shown in Fig. 3. All together 3 power cycling periods are chosen to analyze the thermal-stress variation of IGBT power module in power cycling. The Von Mises stress distribution of the last moment can be seen in Figure 4.

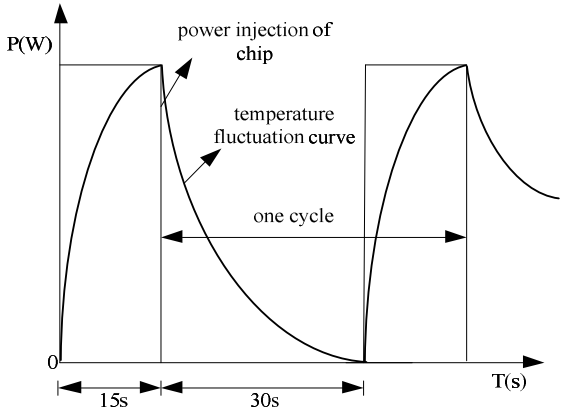

Fig. 3 Illustration of power cycling

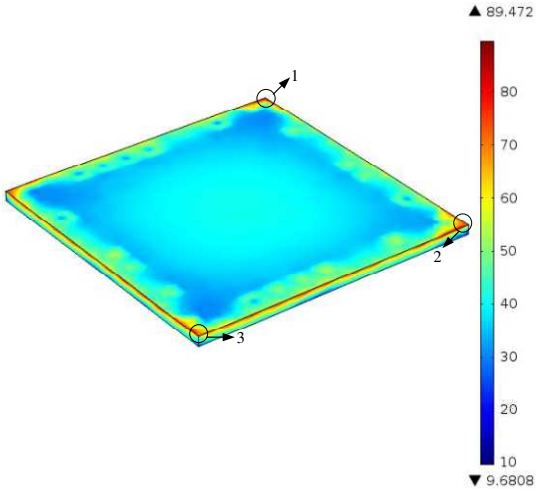

Fig. 4 Distribution of Von Mises stress for solder

It can be concluded that thermal stress mainly concentrates on the edges of the solder layer, especially on the vertexes, which agrees with former experimental findings[9]. Edges and vertexes are the most delicate parts defined as dangerous points, where cracks generally stem from here and gradually expand towards the center. In addition, more strain and strain energy appear in these areas for the reason that the thermal mismatching from CTE differences are the most serious here.

We then analyze strain energy density of solder layer in different moment. As can be seen in Figure 5, the density increases with the time in an approximately ladder-like pattern. When the circulation reaches steady state, the lifetime of a solder layer can be calculated by fluctuation amplitude and Kliman energy fatigue model.

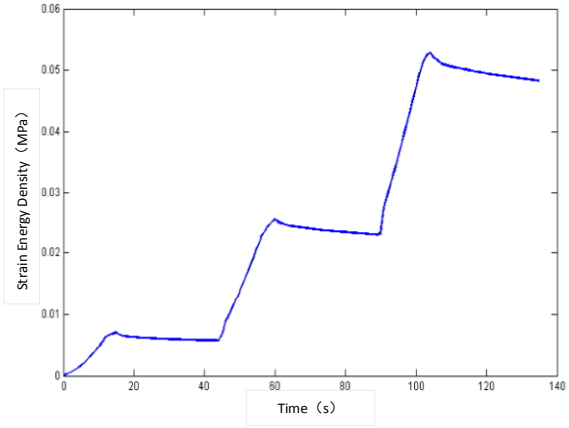

Fig. 5 Contour map of strain energy density of solder

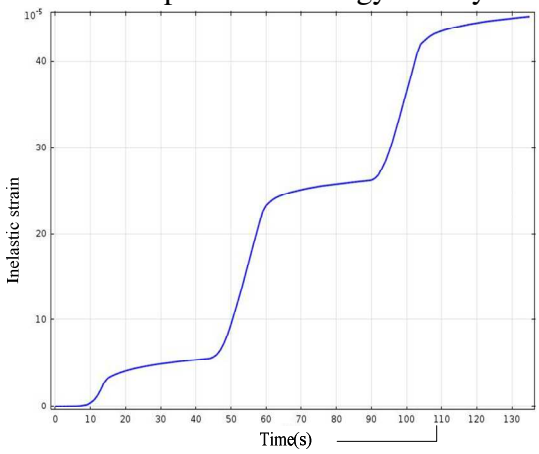

Fig. 6 Contour map of inelastic strain of solder

Fig. 6 shows the variation curve of the inelastic strain of solder layer. The inelastic strain increases with the time in a ladder-like pattern. It can also be seen that strain variation rate varies with the

heating stage. In the early stages, the rate is low because the material's elastic deformation occur. So inelastic deformation is approximately is 0 in the early stages. In this process, strain variation rates are distinct in different power cycling.

Influence of Initial Voids on the IGBT Solder Layer Failure. The solder layer of power module is vital for the properties and reliability of a device as it lies in the main course of heat and electric conduction[8]. Void can frequently be seen in solder layers as a result of technologic factors in manufacturing. Changes in temperature caused by power cycling can lead to circulating shear strain and spatial temperature gradient, causing the void to expand and the layer to crack or even stratify.

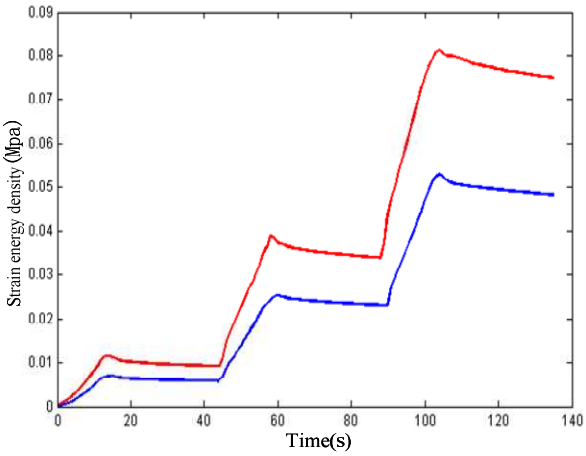

Fig. 7 Comparisons of strain energy density for danger point of solder layer

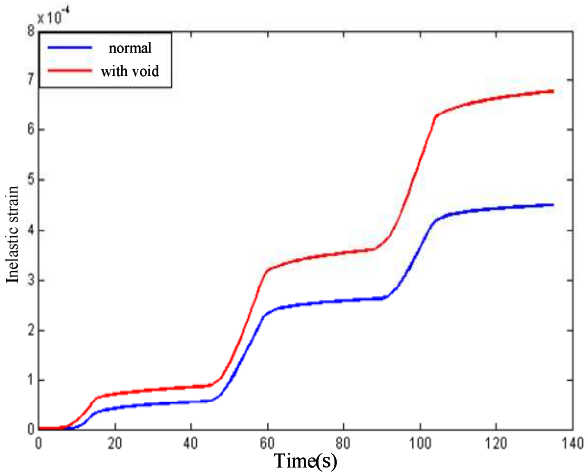

Fig. 8 Comparisons of inelastic strain for danger point of solder layer

Strain energy density and inelastic strain are two parameters to describe the lifetime of an IGBT power module. When encountering voids, the changes is shown in Fig. 7 and Fig. 8 where strain energy density increases 0.032MPa as well as inelastic strain rises $1.53e^{-4}$. Also, according to the Coffin-Mason lifetime formula and the Kliman formula, the thermal fatigue lifetime of a solder layer is in inverse relation to the strain energy density amplitude and strain amplitude. As a result, voids in solder layer leads to shorter lifetime. Layer with previous faults suffers from serious deformation when overvoltage or overcurrent. The temperature impact caused by the voltage and current may accelerate the cracking of the layer and the bonding wires lift-off, leading to the failure of the module.

Conclusions

The self-circulating heating process of the IGBT power module can bring diversity in the inner temperature and thermal stress of the module. Taking the impact of inconsistency on the aging of power module into consideration, the electro-thermal-mechanical coupling model which based on accelerate aging method is established to analyze the variation of the transient thermal stress characteristics of the IGBT power module. The result demonstrates that in such case:

1. In the power cycling, a higher frequency of dangerous point's heat exchange brings about a greater temperature gradient and greater Von Mises stress, which means more possibility in failure.

2. In the initial failure of the solder layer, the strain energy density and inelastic strain are 0.032MPa and $1.53e^{-4}$ higher. These shorten the lifetime of the solder layer which results decreasing the reliability as well as the lifetime of the module.

Acknowledgements

The authors gratefully acknowledge the support from 973 project of China (2012CB215200) and State Key Lab of Power Transmission Equipment project (2007DA10512713202).

References

[1] L. Wei, , R. J. Kerkman, R. A. Lukaszewski, H. Lu and Z. Yuan: *Industry Applications*, Vol. 47 (2011) No.3, p.1794.

[2] P. J. Tavner, G. J. W.Van Bussel, F. and Spinato: *Power Electronics, Machines and Drives* (Dublin, Ireland, April 4-6, 2006) p.127.

[3] K. Shinohara and Q. Yu: *Electronic Packaging Technology & High Density Packaging* (Beijing, China, Aug. 10-13, 2009) p.1277.

[4] T. Y. Hung, S. Y. Chiang, C. J. Huang, C. C. Lee and K. N. Chiang: *Microelectronics Reliability*, Vol. 51 (2011) No.9, p.1819.

[5] L. B. Zheng, L. Han, J. Liu and X. H. Wen: *Transactions of China Electrotechnical Society*, Vol. 26 (2011) No.7, p.242.

[6] B. A. Zahn: *In Electronic Components and Technology Conference, 2002. Proceedings. 52nd* (San Diego, USA, May 31, 2002) p.1475.

[7] T. Anzawa, Q. Yu, T. Shibutani and M. Shiratori. *In Electronics Packaging Technology Conference, 2007. EPTC 2007. 9th* (Singapore, Dec. 10-12, 2007) p.94.

[8] X. P. Xie, X. D. Bi, J. Hu and G. Y. Li. *Semiconductor Technology*, Vol. 34 (2009) No.10, p.960.

[9] Boettcher, Matthias, and F. W. Fuchs. *In Power Electronics and Applications, Proceedings of the 2011-14th European Conference on* (Birmingham, Aug. 30-Sept. 1, 2011) p.1.

Advanced Materials Research Vols. 986-987 (2014) pp 828-831

doi:10.4028/www.scientific.net/AMR.986-987.828

Analysis of Viscoelastic Fluid Flow over a Suddenly Moved Flat Plat

Xiaoyan Liu[1,a], Zhiping Li[1,a], Libing Fu[1,a], Lixiang Wang[2,a], Yongxia Pang[3,a]

[1]Beijing Key Laboratory of Unconventional Natural Gas Geology Evaluation and Development Engineering, School of Energy Resources, China University of Geosciences, Beijing, 100083, China

[2]Changzheng Engineering Co., Limited, Beijing, 101111, China

[3]Zhuangxi Oil Production Plant of Shengli Oilfield management area, ShanDong, 257237, China

[a]liuxiaoyan2183@163.com

Keywords: Viscoelastic fluid; Velocity field; Tangential tension; Laplace transform; Modeling

Abstract. The velocity field and the associated tangential tension corresponding to the flow of the viscoelastic fluid over an infinite rigid plate are determined in this paper. The characteristic of the non-Newtonian viscoelastic fluid flow is analyzed using the Stehfest method of the numerical inversion of Laplace transform. It indicates that the flow of the viscoelastic fluid is very sensitive to the material constants. Finally, some comparative diagrams concerning the velocity and tangential tension profiles are presented.

Introduction

In recent years, due to its practical applications, non-Newtonian fluid has received much attention in some areas such as oil drilling, food industry and paper industry [1,2]. The rheological properties of these fluids are determined by their so-called constitutive equations. For a Newtonian fluid, its flow is described by the Navier-Stokes equations[3]. However, these equations are not enough to describe many real fluids, especially those of high molecular weight such as polymeric liquids, food stuffs, biological fluids, etc. Recently, one of the most popular non-Newtonian fluid model is the so-called Burger fluid model [4,5].

The velocity field and the associated tangential tension corresponding to the motion of a viscoelastic fluid over a suddenly moved flat plat are determined in present paper. The well-known solutions of this problem for an Oldroyd-B fluid, Maxwell fluid, second-grade fluid and a Newtonian fluid appear as a limiting case of our solution. Finally, some comparative diagrams concerning the velocity and tangential tension profiles are presented.

Mathematical formulation

Several kinds of fluid model have been developed to describe the flow of viscoelastic fluid [6,7]. A rate type model due to Oldroyd will be considered in the following mathematical models, in which the second convected derivative of the strain tensor is included. The model contains one retardation time and two relaxation times.

Initially, the fluid is at rest and at time t=0+ the plate is impulsively brought to the constant velocity V (at y=0). The fluid occupies the space y > 0. The x-axis is taken parallel to the flow. The differential equation for the tangential tension $\tau_y(y,t)$ is of the form

$$\tau_y(y,t) + \lambda\partial_t\tau_y(y,t) = \mu(1+\lambda_r\partial_t+\beta\partial_t^2)\partial_y v(y,t) \tag{1}$$

Where λ is relaxation time, λr and β are retardation times, μ is the dynamic viscosity of the fluid.

In the absence of a pressure gradient in the x-direction, the equation for fluid motion is

$$\partial_y \tau_y(y,t) = \rho \partial_t v(y,t) \tag{2}$$

Where ρ is the constant density of the fluid.

Eliminating $\tau_y(y,t)$ between Eq.1 and 2, we attain to the governing equation

$$\partial_t v(y,t) + \lambda \partial_t^2 v(y,t) = \gamma(1 + \lambda_r \partial_t + \beta \partial_t^2)\partial_y^2 v(y,t), \quad y,t > 0 \tag{3}$$

Where $\gamma=\mu/\rho$ is the kinematic viscosity of the fluid.

The initial conditions are

$$v(y,0) = 0, y > 0 \tag{4}$$

$$\partial_t v(y,t) \to 0 \quad \text{as } t \to 0 \tag{5}$$

The boundary conditions are

$$v(0,t) = V, t > 0 \tag{6}$$

$$v(y,t), \partial_y v(y,t) \to 0 \text{ as } y \to \infty \tag{7}$$

Solution of the problem

Calculation of velocity[8,9]

Multiplying Eq.3 by exp(-st), integrating with respect to t from 0 to ∞ and taking into account the initial conditions (4), (5), we find that

$$\lambda s^2 v_s(y,s) + s v_s(y,s) = \gamma(1 + \lambda_r s + \beta s^2)\partial_y^2 v_s(y,s) \qquad y,s>0 \tag{8}$$

Where $v_s(y,s)$ is the Laplace transform of the function $v_t(y,t)$. From the boundary conditions (6) and (7) we also get the equations:

$$\begin{aligned} &v_s(0,s) = \frac{V}{s} \\ &v_s(y,s) \to 0, \ \partial_y v_s(y,s) \to 0 \quad as \ y \to \infty \end{aligned} \tag{9}$$

The solution to Eq.8 subjected to the boundary conditions (9) is

$$v_s(y,s) = \frac{V}{s}\exp\left(-\sqrt{\frac{\lambda s^2 + s}{\gamma(1 + \lambda_r s + \beta s^2)}}\, y\right) \tag{10}$$

Calculation of the tangential tension

Having in mind the fluid being at rest up to the moment t=0, the initial condition for the tangential tension is of the form

$$\tau_y(y,0) = 0 \tag{11}$$

Multiplying Eq.(1) by exp(-st), integrating with respect to t from 0 to ∞ and taking into account the initial condition(11), we find that

$$(1+\lambda s)\tau_s(y,s) = \mu(1+\lambda_r s+\beta s^2)\partial_y v(y,s) \tag{12}$$

Where $\tau_s(y,s)$ is the Laplace transform of the function $\tau_y(y,t)$.

Substituting (10) in (12), we attain to the tangential tension $\tau_s(y,s)$:

$$\tau_s(y,s) = -\frac{V\rho}{\sqrt{\frac{\lambda s^2+s}{\gamma(1+\lambda_r s+\beta s^2)}}} e^{-\sqrt{\frac{\lambda s^2+s}{\gamma(1+\lambda_r s+\beta s^2)}}y} \tag{13}$$

Limiting cases

By letting $\beta\to 0$ in Eq.10 and 13, we attain to the Laplace space solutions corresponding to an Oldroyd-B fluid. In the special case when $\beta\to 0$ and $\lambda r\to 0$, the Eq.10 and 13 can be put into the form corresponding to a Maxwell fluid. Taking the limit of equation (10) and (13) as $\beta\to 0$ and $\lambda\to 0$, we get the velocity field and the tangential tension corresponding to a second grad fluid. Finally, as$\beta\to 0$, $\lambda\to 0$ and $\lambda r\to 0$, the equation (10) and (13) yield the Laplace space solution corresponding to a Navier-Stokes fluid .

Results and Discussion

The velocity and tangential tension profiles corresponding to the viscoelastic fluid are obtained using the Stehfest method of the numerical inversion of Laplace transform. The influence of the material constants on the viscoelastic fluid flow is studied in this part.

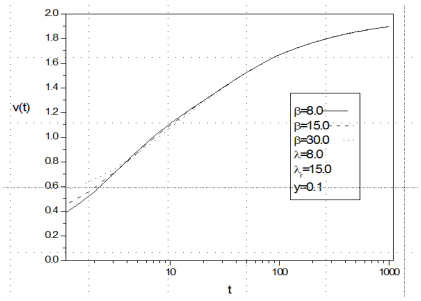

Fig.1 y=0.1, velocity profiles v (t) corresponding to a viscoelastic fluid for V=2, γ=0.0011746, λ=8.0,λr=15.0.

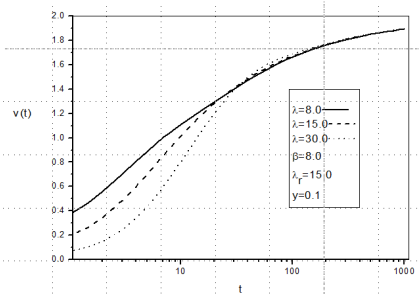

Fig. 2 y=0.1, velocity profiles v (t) corresponding to a viscoelastic fluid for V=2,γ=0.0011746, λr=15.0, β=8.0.

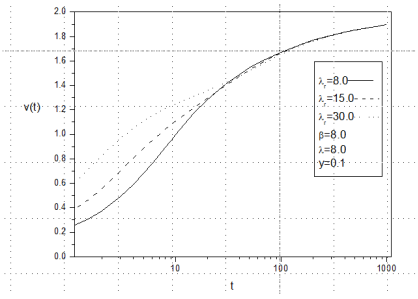

Fig.3. y=0.1, velocity profiles v (t) corresponding to a viscoelastic fluid for V=2, γ =0.0011746, β =8.0, λ =8.0.

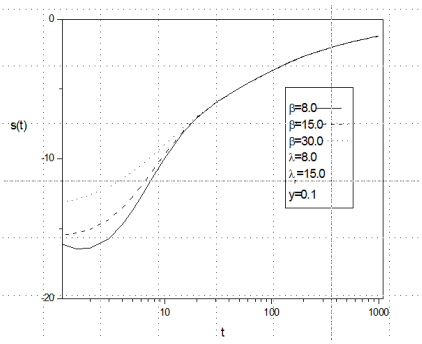

Fig.4 γ=0.1, tangential tension profiles s(t) corresponding to a viscoelastic fluid for V=2, γ=0.0011746, λ=8.0,λr=15.0.

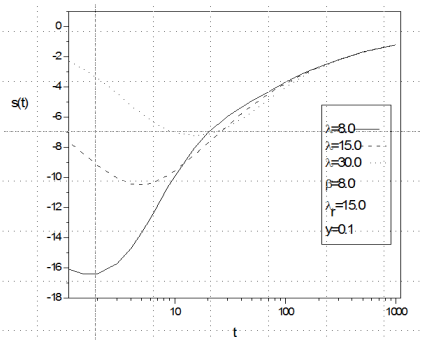

Fig.5 γ=0.1, tangential tension profiles s(t) corresponding to a viscoelastic fluid for V=2, γ=0.0011746, λr=15.0, β=8.0.

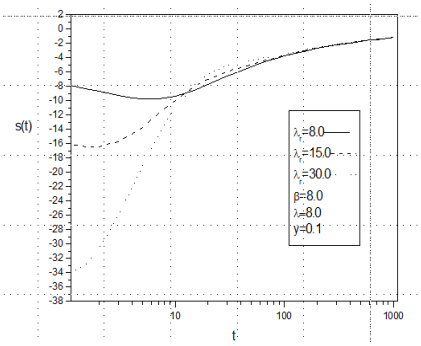

Fig.6 γ=0.1, tangential tension profiles s(t) corresponding to a viscoelastic fluid for V=2, γ=0.0011746, β=8.0, λ=8.0.

In figs. 1, 2 and 3, the variations of velocity field v(y,t) are plotted for different material constants. For different values of the retardation time β (fig. 1.) and λr (fig. 3.), the larger of its value, the velocity v(y,t) is bigger at t=0. The opposite is true for the relaxation time λ (fig. 2.). In each case the velocity is going to the initial velocity V for $t \to \infty$. Figs 4, 5 and 6 depict the effect of the relaxation time λ (fig. 5.) and the retardation time β (fig. 4.) and λr (fig. 6.) on the associated tangential tensions. In each case the tangential tension tend to zero for $t \to \infty$. The influence of the material parameters on the fluid velocity and associated tangential tensions is mainly in early stage.

Acknowledgment

This work was financially supported by the National Key Projects (2011ZX05009-006).

References

[1] T.HAYAT, S.AFZAL, A.HENDI: Exact solution of electroosmotic flow in generalized Burgers fluid. Applied Mathematics and Mechanics, Vol.32 (2011), no. 9, p.1119-1126.

[2] Wang Qing-he, Tong Deng-ke: Analysis of Burgers fluid flow in double cylinder rheometer. Chinese Journal of hydrodynamics, Vol.25 (2010),no. 2, P.183-189.

[3] C. Fetecau, Corina Fetecau: Decay of potential vortex in an Oldroyd-B fluid. Department of Mathematics, Technical University of Iasi, Iasi6600, Romania, Vol.43 (2005), P.340-351.

[4] Constantin Fetecau, Corina Fetecau: The first problem of Stokes for an Oldroyd-B fluid. International Journal of Non-Linear Mechanics, Vol.38 (2003), p.1539-1544.

[5] C. Fetecau, T. Hayat, et al: Steady-state solutions for some simple flows of generalized Burgers fluids, International Journal of Non-Linear Mechanics, Vol.41 (2006), p.880-887.

[6] R. Penton, The transient for Stoke's oscillating plane: a solution in terms of tabulated functions, J. Fluid Mech. Vol. 31(1986), p. 819-825.

[7]M. E. Erdogan. A note on an unsteady flow of a viscous fluid due to an oscillating plane wall, Int. J. Non-Linear Mech. Vol. 35 (2000), p. 1-6.

[8] Stehfest H. Algorithm368 numerical inversion of Laplace transform [J]. Communications of ACM, Vol. 13(1970) no.1, p.47-49.

[9] Stehfest H. Remark on Algorithm368 numerical inversion of Laplace transform [J]. Communications of ACM, Vol. 13(1970) no.10, p.624-625.

Advanced Materials Research Vols. 986-987 (2014) pp 832-836

doi:10.4028/www.scientific.net/AMR.986-987.832

Dynamic Characteristic Analysis of the Internal Combustion Air Compressor

Shengtong Zhang[1,a], Jizhong Zhang[1,b *], Mei Zhao[2], Lianjun Cheng [1], Ning Zhang [1]

[1]College of Mechanical and Electronic Engineering, Qingdao University, Qingdao 266071, China

[2]International Colleges, Qingdao University, Qingdao 266071, China

[a]zhangshengtong0921@163.com, [b]zjzqdu@163.com

* Corresponding Author

Keywords: I. C. engine; Compressor; Dynamic characteristic analysis; Simulation

Abstract. By applying the seamless data interface between SolidWorks and ADAMS, the model of the internal combustion compressor was imported. The internal combustion compressor virtual prototype model was established, the kinematics and dynamics analysis were completed, and the dynamic load on crankshaft was given. After we use finite element analysis software ANSYS, the modal analysis of crankshaft were accomplished, the modes of vibration and response frequency in the first five orders were obtained. The mixed body dynamics model was established, and the crankshaft force curves under the rigid body and flexible body morphology were obtained.

Introduction

The internal combustion air compressor is a simple, highly efficient and convenient new type air compressing device which can transform heat energy into air pressure energy. It uses a connecting rod to connect dynamic piston with compressive piston as a whole in order to move right and left, which realizes the action of air induction and air compress. This device reserves the advantages of crank and connecting rod mechanism in the traditional piston internal combustion engine, which can restrict piston motion and realize the timing of system. So it has the advantages of piston internal combustion engine, piston compressor and HFPE. The Internal Combustion Air Compressor can be the power source of all kinds of air power mechanisms in field operation[1-2].

Operational Principles and Features

Operational Principles of the internal combustion air compressor is as shown in Fig. 1.

In the operational process fuel mixed gases combust to push dynamic piston and do work. Compressive piston is in the middle of piston component which outputs air pressure energy. The internal combustion air compressor realizes the retrace of piston component by means of crank and connecting rod mechanism; meanwhile, crank and connecting rod mechanism drive the operation of the subsidiary system of internal combustion engine. In the operational process described above, the 1st operation room realizes transformation from fuel heat energy to mechanical energy of piston component, just as the theory of energy transformation of four-stroke internal combustion engine; the 2nd operation room realizes energy transformation from mechanical energy of piston component to air pressure energy.

However, because of the newly components like added compressive piston, guiding sliding chunk and connecting rod , the weight of the components in the internal combusting air compressor which moves left and right will increase, so will the inertia force of the system. Consequently, dynamic performance of the internal combustion air compressor will decrease. Studying dynamic characteristics of the internal combustion air compressor by means of building dynamics simulation model of crankshaft system in the internal combustion air compressor through combining finite element analysis technology and virtual prototyping technology and simulating crankshaft system through rigid-flexible coupling multi-body kinematics and dynamics becomes one of pressing issues in the designing process of the internal combustion air compressor.

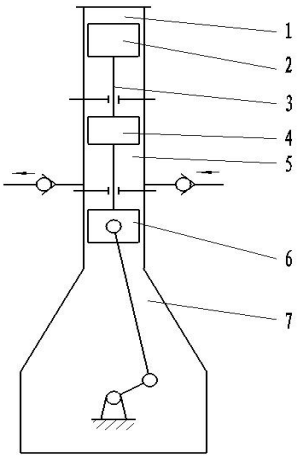

1—the 1st operation room 2—dynamic piston 3—connecting rod
4—compressive piston 5—the 2nd operation room 6—guiding sliding chunk
7—crankcase

Fig. 1 Working principle diagram

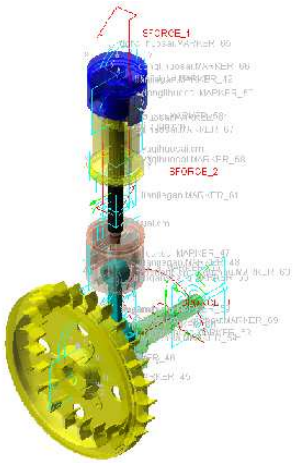

Fig. 2 Simulation model

The multi-rigid body dynamics simulation of crankshaft system

The article adopt the method of combining 3D modeling software named Solidworks and dynamics simulation software named ADAMS to build and analyze multi-rigid body dynamics simulation model of the internal combustion air compressor. Please see specific method in literature[3]. Simulation model consists of piston, connecting rod, cylinder block, compressive piston, sliding chunk, Crank and connecting rod mechanism and fly wheel. Simulation is as shown in Fig. 2.

Through the software named AVL Boost, operation pressure on the dynamic piston is obtained by simulation for the process of thermodynamics in the combustor of the internal combustion air compressor. The calculation of the force pressed on the compressive piston and the friction on the internal combustion air compressor can be seen in literature[4].

After finishing modeling and simulation under the circumstance of ADAMS/View, we can use post processor in ADAMS to obtain not only kinematics parameter curve of compressive piston component like position, velocity and acceleration but also changing force curve of both sides of connecting rod.

Fig. 3 is the stress distribution curve of the big side of the connecting rod. We can see that when the crankshaft turns around about 12 degrees, the peak value of stress will be 35000N. Afterwards, the stress of the connecting rod is relatively steady in a period, the impact force of dynamic piston on the crankshaft is relatively small.

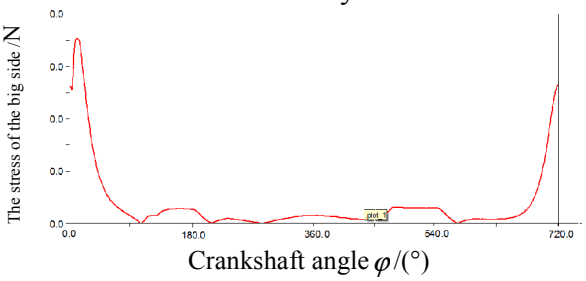

Fig. 3 The stress distribution curve of the big side of the connecting rod

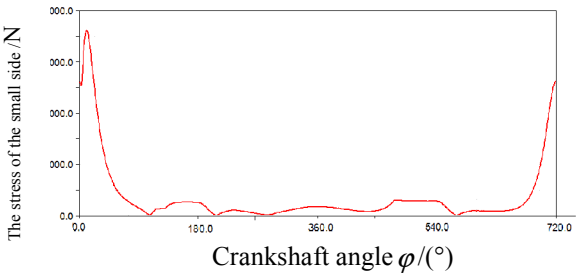

Fig. 4 The stress distribution curve of the small side of the connecting rod

Through calculating the stress between the small side of the connecting rod and the sliding block, we obtain the stress distribution curve of the small side of the connecting rod which is shown as Fig. 4. Peak value of stress is a little larger than the big side of the connecting rod, which is about 36000N. Other times the stress of the kinematics pair is relatively steady.

The stress on both sides of the connecting rod is primarily influenced by combustion pressure in different operating conditions, which is maximum when the combustion pressure is maximum.

Analysis on crankshaft mode

Firstly, we import its 3D model of parasolid into ANSYS to finish the transformation of its wireframe style. The finite element mesh generation uses tetrahedron, and mesh generation is the smart one. Crankshaft generation produces 104361 nodes and 21207 units. The finite element mode after mesh generation of the crankshaft is shown as Fig. 5:

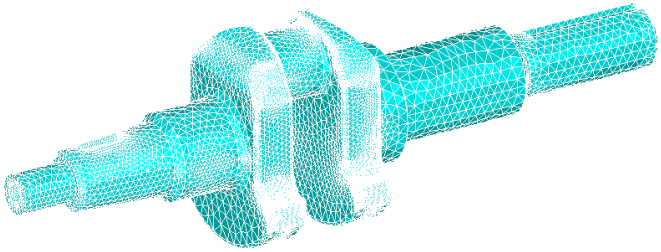

Fig. 5 Finite element model of crankshaft

The modal analysis is a technique used to define the vibration features (solid frequency and vibration modes) of designing mechanism and components. Solid frequency and vibration modes are important parameters of designing framework supporting dynamic load, which are also the key to analyze other kinematics questions.

The methods of mode analysis in ANSYS are: Subspace, Lanczos, PowerDynamics, ReducedHolder, Unsymmetic, etc[5]. We choose Lanczos in this article, in which we use eigenvector to realize iterative algorithm. The modes of vibration in the first five orders were obtained through calculation, which are as follows:

(1) The frequency of the crankshaft's first order is 1319.2HZ, and the change of the vibration mode is shown Fig. 6: its main performance is roughly along radial elastic vibration around 2 endpoints.

(2) The frequency of the crankshaft's second order is 1705.44 HZ, and the change of the vibration mode is shown Fig. 7: its main performance is slight elastic vibration along direction y around 2 endpoints.

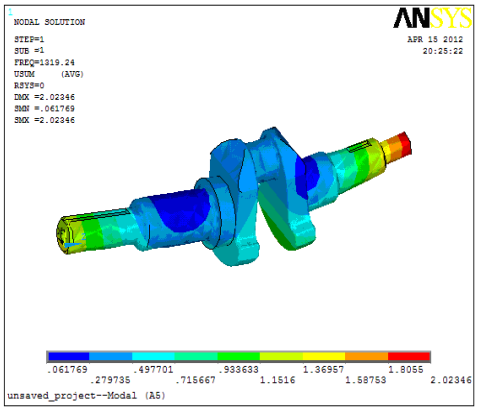

Fig. 6 The modal of the crankshaft's first order

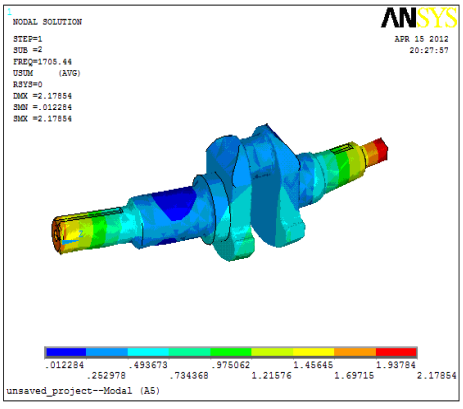

Fig. 7 The modal of the crankshaft's second order

(3) The frequency of the crankshaft's third order is 2742.04HZ, and the change of the vibration mode is shown Fig. 8: its main performance is roughly torsion around spindle direction y.

(4) The frequency of the crankshaft's fourth order is 3518.73 HZ, and the change of the vibration mode is shown Fig. 9: its main performance is that the bottom of main axle neck keeps still while wavelike vibration happens to other parts along direction y.

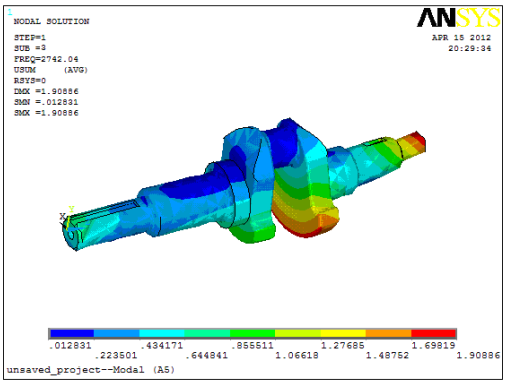

Fig. 8 The modal of the crankshaft's third order

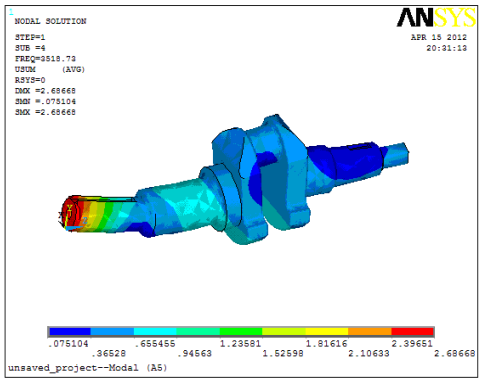

Fig. 9 The modal of the crankshaft's fourth order

(5) The frequency of the crankshaft's fifth order is 4826.53HZ, and the change of the vibration mode is shown Fig. 10: its main performance is wholely wavelike vibration along direction x.

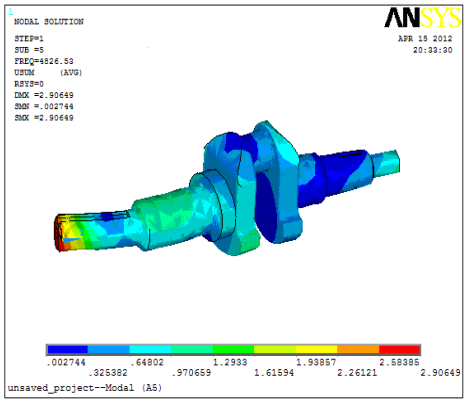

Fig. 10 The modal of the crankshaft's fifth order

Analysis on kinematics of the flexible body in the crankshaft system

After the mesh generation of modals in ANSYS, through choosing spots on the boundary, it will export CFL which can be imported into ADAMS/Flex in order to create the mixed (rigid and flexible) kinematics modals.

After the simulation, we can obtain the stress of the kinematics pair between the crankshaft flexible body and the connecting rod, and compare with the stress of the crankshaft when the rigid body is loading. The stress of the hinge in the flexible body crankshaft condition is shown as Fig. 11.

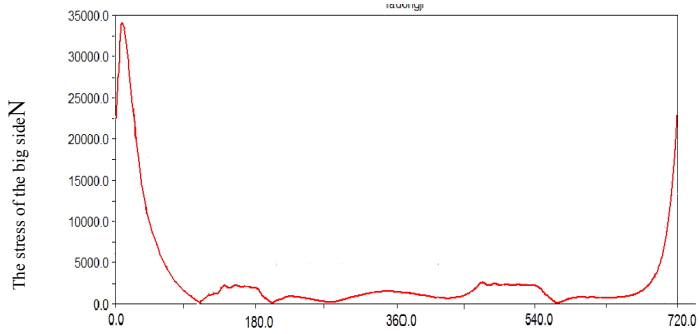

Fig. 11 The stress of the hinge in the flexible body crankshaft condition

Through comparing and analyzing it with the rigid one, we can know that when the crankshaft is loading as the flexible body, its stress curve doesn't change so much. However, the peak value declines, so it reveals that the replacement will have some influence on the kinematics features of the whole crankshaft system.

Conclusion

By applying the seamless data interface between SolidWorks and ADAMS, the model of the internal combustion compressor was imported. The internal combustion compressor virtual prototype model was established, the kinematics and dynamics analysis were completed, and the dynamic load on crankshaft was given. After we use finite element analysis software ANSYS, the modal analysis of crankshaft were accomplished, the modes of vibration and response frequency in the first five orders were obtained. After calculating and comparing the hinge stress of the rigid body and the flexible body, we know that peak values of them are 35000N and 33000N, which lays the foundation of following reliability study and optimal design.

References

[1] Zhang Tiezhu, Zhang Jizhong. Method and Device of Transforming Mechanism Energy into Fluid Pressure: China,200410075662.6[P]. 2008-01-23.

[2] Zhang Jizhong, Zhang Tiezhu, Zhang Hongxin, Dai Zuoqiang. Conception Design of The Internal Combustion Air Compressor[J]. Modern Manufacture Engineering,2005,(12):90-92

[3] Sui Bo, Zhang Jizhong, Zhang Tiezhu, Dai Zuoqiang. Dynamics Simulation of Virtual Prototype Technique Integrated Power Water Pump[J], Modern Manufacture Engineering,2009(8):19-22.

[4] Zhang Jizhong, Shang Pengfei, Zhao Hong, Zhang Yi, Dynamics Analysis of The Internal Combustion Air Compressor [J]. Chinese Mechanism Engineering,2008,19(20):2415-2418.

[5] Yang Kang, Han Tao. The Application Study of ANSYS in the Modal Analysis [J]. Journal of Jiamusi University (Natural Science Edition) ,2005,23(1):81-84

Advanced Materials Research Vols. 986-987 (2014) pp 837-840

doi:10.4028/www.scientific.net/AMR.986-987.837

Effects of Geometry Parameters on Mechanical Expanding of Large Diameter Welding Pipe

Lifeng Fan [1, a], Ying Gao[2, b] , Jiaxin Yan[1, c] , Jianbin Yun[3, d]

[1]Transportation of Institute, Inner Mongolia University, Hohhot, China

[2]College of Material Science and Engineering, Hebei University of Science and Technology, Shijiazhuang, China

[3]Product quality inspection institute of Inner Mongolia, Hohhot, Inner Mongolia China

[a]ysufanlifeng@foxmail.com, [b]gaoyingch@sina.com, [c]1577438681@qq.com, [d]119356871@qq.com

Keywords: mechanical expanding, welding pipe, finite element method, deformation characteristic

Abstract. Mechanical expanding is widely used in production of large diameter submerged-arc welding pipes. To improve welded pipe quality, it is necessary to investigated effects of geometry parameters on mechanical expanding forming process. So, effects of geometry parameters on mechanical expanding is obtained using finite element method..

Taking the expanding of X80 steel Φ1219mm×22mm×12000mm welding pipe for instance, the mechanical expanding forming process is simulated by finite element (FE) code ABAQUS. In this paper, the simulation data is validated by experiments and a comparison showed a good agreement with experiments results. The effects of geometry parameters on mechanical expanding are discussed. Thus, the result of research provides a basis to improve welded pipe quality.

Introduction

Mechanical expanding technology is widely used in large-diameter straight seam submerged arc weld (LSAW) pipes. In the forming process. Expansion is accomplished by an internal mandrel. The mandrel consists of 8, 10, or 12 segments. Segments are chosen so that their radii are near that of the inside of the pipe. The mandrel is hydraulically actuated, and in one step it typically expands a length of one half to one diameter (depending on the wall thickness). Each step maintains some overlap between the expanded and unexpanded pipe sections. Expansion improves the roundness of the pipe and brings it to its desired final size. To achieve low ovality, the pipe is typically expanded 0.8 – 1.3% from its diameter.

Affected by the previous forming process, there have been ellipse and pouting in welded pipe before expanding. To evaluate ellipse and pouting, this paper proposed two indicators: ovality T and pouting f.

$$T = \frac{D_{\max} - D_{\min}}{D_{nor}} \times 100\%$$

Where $D_{\max}$ —Maximum diameter/mm,

$D_{\min}$ —Minimum diameter/mm,

D_{nor} —Nominal diameter/mm.

Pouting f is defined as maximum radial deviation with theory of circular arc within 75mm scope of welds.

The mechanical expanding is a very complicated procedure since it is usually influenced by many factors. It is difficult to control the forming quality. Thus there have been many researches about mechanical expanding. In early stage, the research on mechanical expanding is depended on experiments[1, 2]. Although the results are an useful to guide production， they are lack of universality and difficult to promote in further. The analytical method of analysis is based upon simplifications of

process and material behavior. The analytical method of analysis generally has to be formulated with significant simplifications of forming conditions which can considerably affect the accuracy of the results [3- 5]. With the advent of computation technology, most of research is depend on finite element methods. So many scholars analyzed the effect of mechanical expanding to the pipe quality using the finite element method respectively, such as G. Palumbo[6], M. D. Herynk[7], Guo[8], Wu[9], Liu[10], and Cai[11]. But they do not consider about the effect of front process.

The aim of this paper is to show that effects of geometry parameters of welded pipe on mechanical expanding. This research is based on commercial FEA code ABAQUS. By using FEA, the shape of welded pipe is obtained. The results of research provide a basis to guide mechanical expanding production.

Finite element analysis

FEA of expanding was carried out using the commercial code Abaqus/Standard. A 2D finite element model is established for the plane strain condition. In simulation, the mandrels are defined as analytical rigid which would not need requiring elements is divided for simple geometric shapes. In analysis process of forming, one of the most important factors is the calculation of springback. So, considering both efficiency and accuracy in the deformation process, the 2mm four-node plane strain reduced integration quadrilateral element CPE4R which had high efficiency and accuracy for calculating springback is set in deformable sheet. The sheet metal is defined as elastic–plastic. Also, simple limited slid master-slave contact algorithm in which the mould was master surface, the sheet was slave surface is selected, and the penalty function model of friction coefficient 0.1 is established to judge the contacting state. The objectives of this analysis are to investigate the deformation characteristic in expanding.

Validation experiments Experiments were carried out using a hydraulic press as a platform to develop the expanding process. An experimental mould system, where the welded pipe is set around it, was placed on the horizontal table of the hydraulic press. Inclined plane and segmented design provide expanding during the movement of the internal mandrel. The material used for the investigations corresponds to Q235A. The size of the welded pipe corresponds to Φ333mm×4.75.Displacement of segments are realized by controlling displacement of internal mandrel. Several experiments were carried out and the resulting welded pipe profiles were measured. A validation of the FE model has been carried out through the comparison between ovality and expanding force calculated through FE simulation and the experimentally measured in Fig. 1-Fig. 2. In summary about the comparison between numerical and experimental results, a proper correlation could be observed. The results are demonstrated that FEA could obtain accurately the forming process.

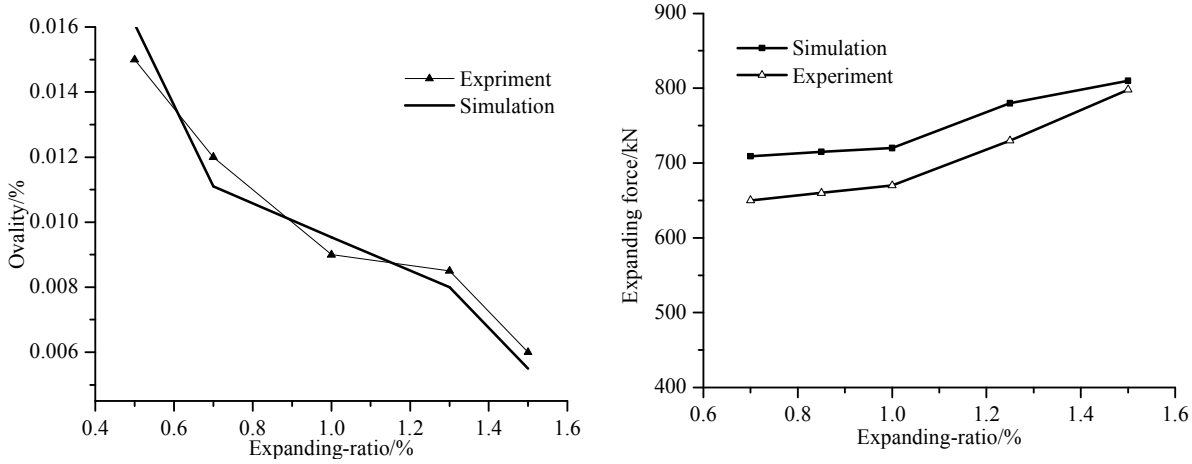

(a) Ovality (b) Expanding force

Figure 1 Comparison between simulation and production

Results and discussion

A welding pipe of Φ1219mm×22 mm×12000mm was taken as research objective. The material X80 grade pipeline steel, where is E = 245 Gpa, σ_s = 569.5 Mpa. A 2D plane model of the pipe for the expanding process was constructed from the geometry obtained from production after welding. The deformed weld pipe was obtained from the FE analysis and the effects of geometry parameters of welded pipe on mechanical expanding were investigated.

The pipe diameter and thickness of sheet for different ovality after expanding predicted from the FE analyses are shown in Figs. 3 respectively. With the changing of polar angle, the pipe diameter and thickness of sheet is cycle fluctuation change. It is indicated that the pipe diameter and thickness of sheet mainly affected with segments of mandrel. From Fig. 3a, it is observed that the larger the ovality, the greater need of expanding rate, which caused welded pipe diameter increased obviously. From Fig. 3b, it is shown that the wave shape appeared suspended parts between two segments, The thickness of sheet reduced overall, and it has the thinnest in the edge area of segments. It is demonstrated that the plastic deformation mainly occurred in suspended parts between two segments.

At the same time, small plastic deformation with small ovality (such as ovality =4%) lead to nonuniformity of thickness.

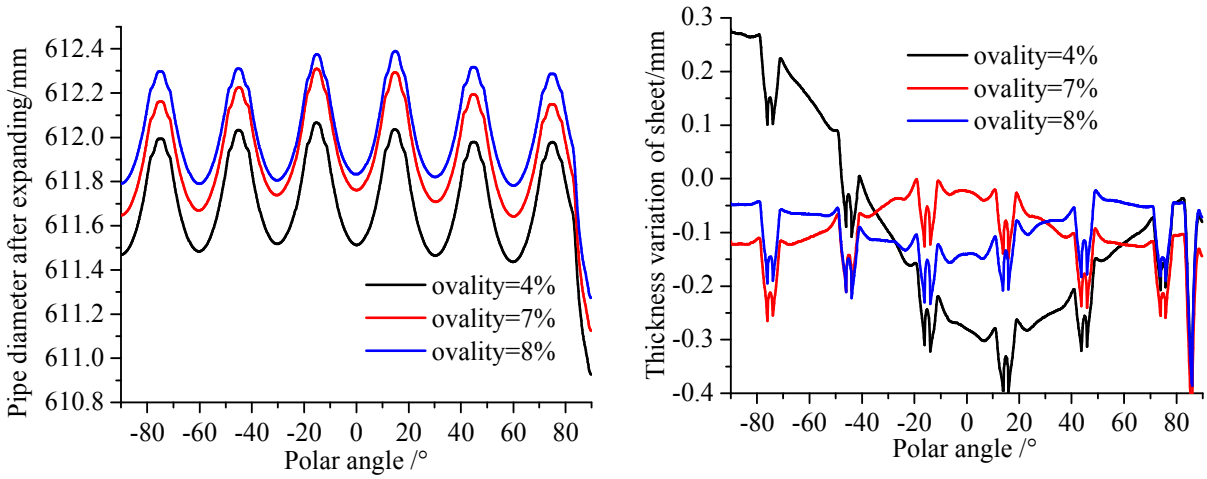

(a) Pipe diameter after expanding (b) Thickness of sheet

Figure 3 Pipe diameter and thickness of sheet for different ovality after expanding

In Fig. 3c, section geometry of welded pipe regularly changed and it is obviously observed that there is pouting in weld pipe. The results indicated that the pipe diameter increases with increase of pouting.

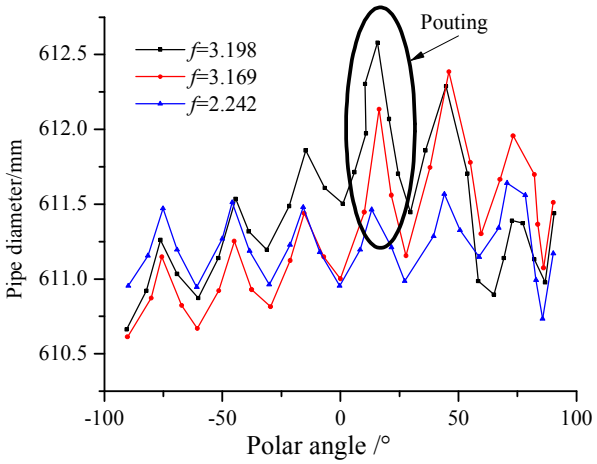

Figure 8 Pipe diameter for different pouting

In general, it can be seen that the pipe diameter and thickness of sheet regularly changed with segments of mandrel in whole pipe. Thus, the segments number of mandrel is the main factor

affecting the pipe diameter and thickness of sheet. So less segments number of mandrel is used, which can improve the residual stress distribution and quality of welded pipe.

Conclusion

The present work has been to analysis effects of geometry parameters of welded pipe on mechanical expanding for improving quality of welded pipe. In this paper, The mechanical expanding forming process is simulated using the finite element code ABAQUS. In this work, the following conclusions can be drawn:

(1)In mechanical expanding forming process, the pipe diameter, thickness of sheet and pouting mainly affected with segments of mandrel.

(2) Less segments number of mandrel will benefit to improve the residual stress distribution and quality of welded pipe.

Acknowledgement

The authors are grateful for the financial support provided by the Program of Higher-level Talents of Inner Mongolia University, China(Grant No. 135143), The Scientific Research Projects of the Inner Mongolia Provincial Education Department (Grant No. NJZY14006) , the Natural Science Foundation of Hebei Provincial Education Department, China (Grant No. Y2012035) and the Natural Science Foundation of Hebei Provincial Technology Department, China (Grant No. 12211014).

References

[1] Youliang He, Guangrun Bai, Kerang Zhou. Theory research on expanding process of welded pipe diameter[J]. *Welding Pipe and Tube*, 1997, 20(6): 9-11(In Chinese)

[2] Zhengrong Fu. Expriment research on expanding process of spiral welded pipe [J]. *Heavy Machinery*, 1995, (5): 18-22(In Chinese)

[3] Jingda Cai, Xi Cheng. Analysis and calculation on mechanical expanding force of conical die [J], *Chinese Mechanical Engineering* , 2010, 21(5): 599-602(In Chinese)

[4] Xidai Du, Haibo Du. Tension analysis of mechanical expanding with single-end machine[J]. *China Metal Forming Equipment & Manufacturing Technology*, 2010, (1): 72-74(In Chinese)

[5] Xuliang Qu. Research on expanding machine spiral of large diameter welded pipe. *Machine & Hydraulic* [J]. 2009, 37(1): 183-187

[6] G. Palumbo, L Tricarico. Effect of forming and calibration operations on the final shape of large diameter welded tubes[J]. *Journal of Materials Processing Technology*, 2005, 164~165(5): 1089-1098

[7] M. D. Herynk, S. Kyriakider, A Onoufriou, et al. Effects of the UOE/UOC pipe manufacturing processes on pipe collapse pressure[J]. *International Journal of Mechanical Sciences*, 2007, 49(5): 533-553

[8] Baofeng Guo. Simulation and experimental research on mechanical expanding process of pipeline steel pipe[D]. *Yanshan university*, 2001.

[9] Peng Wu. Simulation and experimental research on mechanical expanding process of large diameter spiral welded pipe [D]. *Yanshan university*, 2001.

[10] Qian Liu. Simulation of radial expanding to release stresses of large diameter straight weld pipe[D]. *Tianjing university*, 2006.

Advanced Materials Research Vols. 986-987 (2014) pp 841-843

doi:10.4028/www.scientific.net/AMR.986-987.841

Experimental study on emission characteristics of methanol gasoline in the GW491QE engine

Zexu WU, Yinshan WANG

School of Automotive and Transportation, Tianjin University of Technology and Education, Tianjin, China, 300222

Email:wuzexu2007@126.com

Keywords: Methanol gasoline; Experimental study; Engine emission Performance

Abstract. M10, M15, M50 methanol gasoline and 93 # gasoline engine emission performance test were researched on the engine GW491QE. Always stayed in 60 N·m torque and rotational speed increased from 1000 r/min to 3000 r/min, recorded the corresponding data, performance, emission performance curve was drawn respectively, comparison and analysis, the influencing factors of GW491QE engine emission performance were discussed, practical application on engine GW491QE suitable blending ratio of methanol gasoline was chosen. The experimental results show that: three kinds of methanol gasoline of HC emissions is lower, M15 improvement is most obvious; NOx emissions are reduced. GW491QE engine emission performance is taken into account, M15 methanol gasoline is a good proportion of the actual application.

Introduction

Methanol (CH_3OH) is a kind of similar to gasoline with the physical and chemical properties of the fuel, the molecular structure of simple, high octane number and oxygen percentage, synthesis process is simple, is regarded as one of the most promising future oil alternative fuel[1] . However, there are some problems in the methanol fuel engine in practical application, after methanol combustion such as formaldehyde, acetaldehyde produces harmful emissions[2] , and methanol cold start performance is poorer, low calorific value, burning ability is poor. And the methanol gasoline can improve the situation in some degree.

Methanol gasoline is usually marked by the content of methanol fuel mix, such as M20 mixed fuel is marking the volume fraction of 20% methanol and 80% of gasoline. Analysis of this paper mainly introduces and discusses three kinds of proportion of methanol gasoline (M10, M15 and M50) and 93 # gasoline(M0) emission performance experiment on engine GW491QE, choose to practical application in engine GW491QE suitable blending ratio of methanol gasoline.

Test fuel, equipment and methods

Test with fuel, the physical and chemical characteristics of methanol and 93 # gasoline are shown in table 1.

Table 1 Comparison of several physical and chemical properties of methanol and gasoline

Performance indicators	methanol	gasoline
Density (20 ° C) /(g·L^{-1})	810	700 ~ 800
Gasification hot /(MJ·kg^{-1})	1100	350
Theoretical air-fuel ratio	6.45	14.7
Limits on fire /(%)	6.7 ~ 36.5	1.4 ~ 7.6
Low calorific value /(MJ·kg^{-1})	19.7	42.5

This experiment with GW491QE gasoline engine, which is produced in the Great Wall internal combustion engine manufacturing co., LTD, the structure form for four-cylinder inline, four stroke, vertical, and water-cooled. Main performance parameters: 2.237 L displacement, cylinder diameter of 91 mm, compression ratio of 8.8:1, the maximum output power of 78 kW, rated power speed is 4800 $r \cdot min^{-1}$,the maximum torque of 190 N·m, minimum fuel consumption rate 270 $g \cdot (kW \cdot h)^{-1}$.

The test equipment used for the test:engine FST2E CNC system;eddy current dynamometer CW160; the engine exhaust emission analyzer AVL - 4000; the engine coolant temperature device.

Test condition requirements: the engine keep under 60 N·m torque , experiment is conducted to study the characteristics of velocity; The other engine performance parameters are no longer adjust in the test. Select five sites speed measurement to do emission test[3], accurately record test data. The four types of fuel are test three times, finally the data take 3 times of the average data, data charts are drawn.

Test results and analysis

HC emissions

On GW491QE engines M10, M15, M50 methanol gasoline and 93 # gasoline(M0) were burned ,HC emissions curve was drawn, as shown in figure 1.

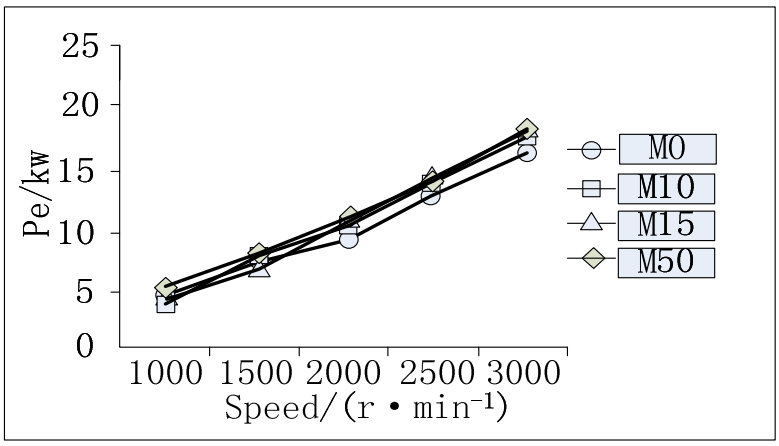

Fig.1 When 60 N • m 93 # gasoline and M10, M15, M50 HC emissions comparison

According to the shown in figure 1, 3 kinds of proportion of methanol gasoline HC emissions are less than 93 # gasoline(M0), and fell more obvious. With the increase of rotational speed, four kinds of basic same HC emissions change trend of fuel; In the three kinds of methanol gasoline, with the increase of methanol proportion, gradually reduce the HC emissions. In addition, in terms of degree of curve, while burning M15 drops fastest HC emissions curve, namely the M15 HC is most obvious.

Analysis reasons: (1) because methanol (CH_3OH) is only a carbon atom, burning with autonomous oxygen effect, which can speed up the combustion and promote complete combustion. After adding a certain proportion of methanol gasoline combustion, flame propagation speed and reduces the surface quenching effect, thus reduce the HC emissions [7]. (2) methanol can dissolve obstruction of HC emissions of carbon deposition sediments, also reduces the HC emissions.

NOx emissions

On GW491QE engines M10, M15, M50 methanol gasoline and 93 # gasoline were burned, NO*x* emissions curve was drawn, as shown in figure 2.

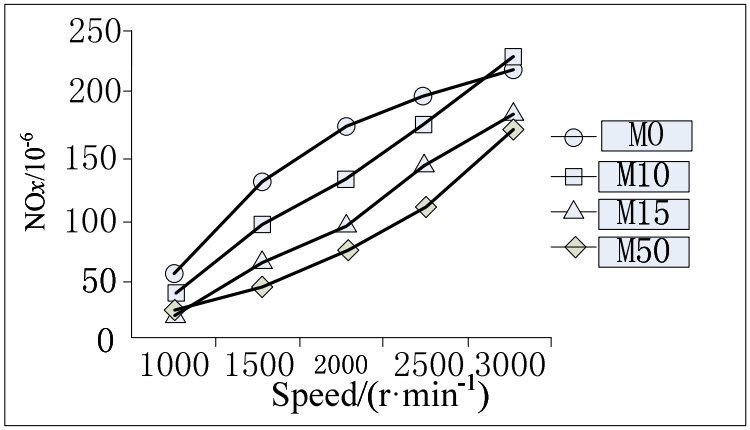

Fig. 2 The When 60 N, m 93 # gasoline and M10, M15, M50 NO*x* emissions comparison

According to figure 2, 3 kinds of methanol gasoline NO*x* emissions is less than 93 # gasoline on the whole. Analysis of reasons: NO*x* emissions increase and decrease, which depend on the temperature and concentration of oxygen in cylinder, on the one hand because of methanol as oxygen fuel and the combustion speed, promote the formation of NO*x* oxygen-rich conditions. But on the other hand, low calorific values of methanol, latent heat of vaporization is 3 times of gasoline , reduces the maximum combustion temperature and exhaust temperature, to a certain extent inhibit the formation of NO*x*, which make the methanol gasoline NO*x* emissions increase with the increase of the content of methanol.

Summary

Emissions performance was tested on the GW491QE engine , got the following conclusion:

(1) The M10, M15, M50 of HC emissions decreased obviously, and M15 improved the most obvious.

(2) Methanol gasoline NO*x* emissions were less than 93 # gasoline on the whole.

(3) GW491QE engine emission performance is taken into account, M15 methanol gasoline is a good proportion of the actual application.

References

[1] Han Xuedong, Li Zhongmo. Fuel methanol technology cooperation fair review [J]. Journal of large nitrogenous fertilizer, 2002, 25 (5): 342.

[2] Chen Weifang. Effect of M15 Methanol Gasoline on Engine Emissions [J]. Chinese Internal Combustion Engine Engineering, 2009, 30 (3): 27-29.

[3] T, HU WEI Y. Improvement of spark - ignition (SI) engine combustion and emission during cold start, fueled with methanol/gasoline blends [J]. Energy Fuels, 2007, 21 (1): 171-175.

[4] Liu Ruofei. Simulation and Test Study of Combustion and Emissions of SI Engine Fueled with Methanol Gasoline[D]. Zhejiang: Zhejiang university, 2012.

[5] Feng Xing, Wang Tie. Experimental Research of the Effects of Methanol-gasoline Fuels on EFI Engine Emissions, Internal Combustion Engines, 2010.3:45-48.

[6] Yin Hang ,Hao Chun. Emission Characteristics of Vehicles Fueled with Different Proportion Mixture of Methanol-Gasoline Fuel, Research of Environmental Sciences,2011, 24 (8): 917-924.

[7] Cao jie ,Wang Tie. Experimental Study on an EFI Engine Fueled with Low Proportional Methanol-Gasoline, Internal Combustion Engines, 2010.3:52-56.

Advanced Materials Research Vols. 986-987 (2014) pp 844-847

doi:10.4028/www.scientific.net/AMR.986-987.844

Finite Element Analysis of the Stiffness and Strength of Large Power Plant Condenser

Yang Yabin[1,a], Lai Xide[1,b], Chen Xiaoming[1,c], Zhou Xiang[1,d], Lei Mingchuan[1,e], Song Bingjie[2,f]

[1]School of Energy and Environment，Xihua University，Chengdu，China

[2]School of Management，Xihua University，Chengdu，China

[a]18781967668@163.com, [b]laixd@mail.xhu.edu.cn

Keywords: Condenser; Strength and Stiffness; Finite element analysis

Abstract: Using finite element method to simulate complex operations of the whole condenser under extreme water pressure, this paper aims at predicting the strength and stiffness of the condenser components under extreme pressure conditions. The results show that the max stress of the components is less than the allowable stress, and the max deformation is also within the permitted scope. The results will provide necessary reference for the further optimization design of condenser.

1 Introduction

The application and development of the once-through boilers and nuclear power devices in the electricity industry lead to higher requirements for condenser performance [1].To analyze the stiffness and strength of large-scale condenser by using economic and efficient methods, it is particularly important to instruct condenser optimization design and to study the mechanical operation properties of the condenser components. So far, some academics have done some important work on condenser. For example, Lanxin Zhou and Mingzhi Zhang have achieved a comprehensive assessment of condenser running performance [2]. Shuguang Gong and Guilan Xie have completed optimization design of the ultra-specification tube sheets system [3].

A typical structure of condenser from a company is applied in this paper. Considering the contact problems of condenser tube bundles with the support plates and steel beams, the contact problems of bolts and the effect of the bolt preloads on structure strength, we conduct a numerical simulation of the whole condenser under extreme water pressure. At the same time, an analysis of stiffness and strength of condenser components is made in this study and it will provide some useful theoretical reference for the optimization design of condenser.

2 Finite element analysis model of condenser

2.1 The three-dimensional model and finite element mesh of condenser

Since the number of tubes is too large, we must simplify it. Tubes are established under the rules of constant volume and equivalent elastic modulus. At the same time, the perforated area of the tube sheets is established solid boards under the rules of considering the rigid weakening coefficient [4].The whole three-dimensional condenser model is shown in Fig.1. As the condenser is a symmetrical model, half of the model is selected as the analysis object. The number of nodes is 1,720,530, and of elements are 465,461. Mesh results are shown in Fig. 2.

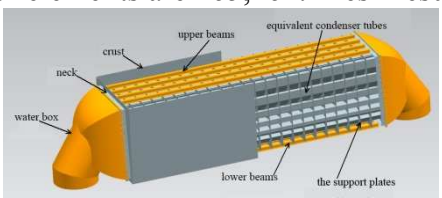

Fig.1 Model of condenser

Fig.2 Condenser grid model

2.2 Determination of the calculation conditions and boundary conditions

As for calculation condition, the max work pressure of condenser is less than 0.4MPa, so 0.4MPa is the max required hydrostatic test pressure in this study. The effects of hydrostatic pressure are also under consideration, so the pressure of unperforated area is P_1=1E-5×z+0.4, and perforated

area is P_2=(1E-5×z+0.4)×0.6575, where z-axis is the height direction of the tube sheet and the positive z-axis pointing to the bottom of the tube sheet.

In terms of loads applied, the loads include gravity, water pressure and bolt preloads. The specification of bolt in the study is 8.8 class, M27. The specific parameters are shown in Tab.1.

And for constraints imposed, the condenser is fixed by anchor bolt (M28) on the bearing through the lower beams and the constraint surfaces are shown in Fig.3.

Tab.1 Bolt preloads of M27

Bolt	M27
Preload（kN）	190.9

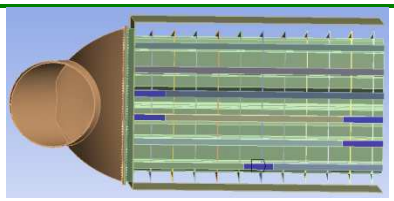

Fig 3 Constraint surfaces of condenser

The contact problems of the condenser relates to water box, tube sheets, neck, rectangular plates, the support plates, condensing tube bundles and the steel beams. Water box bolts the flange of tube sheets via plate. Since the contact area between water box, tube sheets flange and the neck is basically unchanged and contact surfaces had no relative sliding and separation either, the contact type is set bonded. The connect type of perforated area and the tubes equivalent entity is expanding and welding. With contact surfaces no relative sliding, the contact type is set bonded. Similarly, air cooling zone of the tube sheets and air-cooled equivalent entity is also set bonded.

2.3 Mechanical properties of the tube sheets materials and condensing tubes

As the tube sheet is a composite of different materials, we need to calculate its equivalent results. These equivalent results of material mechanical properties in this paper are calculated according to relevant standards HEI. The specific calculation method is in bibliography [5,6] The results are shown in Tab.2.

Table2 Equivalent Mechanical performance parameters of tube sheets and tubes

machinery performance	equivalent elastic modulus[MPa]	allowable stress S_m[MPa]
perforated area	41147.12	50.23
unperforated area	189481.43	173
equivalent condensing tubes	5080	132.7

3 Results and analysis

Stress and deformation are two main factors in finite element analysis.After calculation, the results of stress and deformation of condenser components are shown in Figure a~g, and the maximum equivalent stress and maximum deformation of components are shown in Tab. 3.

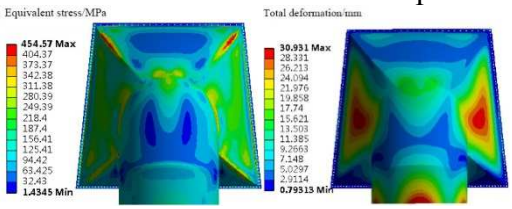

(a)Total deformation and equivalent stress of water box

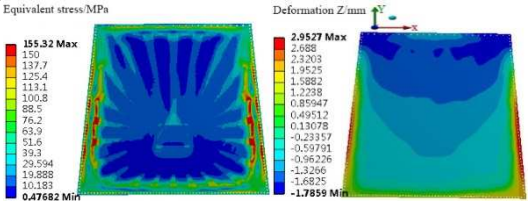

(b)Z axis deformation and equivalent stress of tube sheet

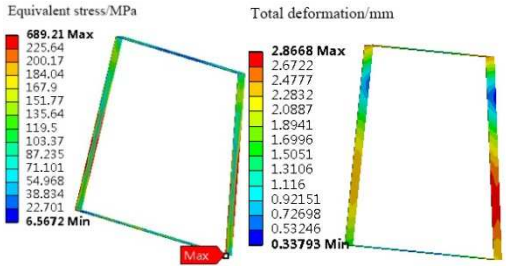

(c)Equivalent stress and total deformation of neck

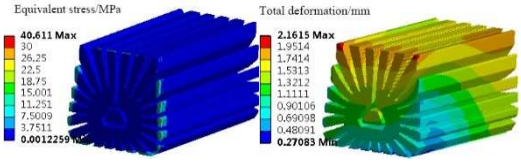

(d) Equivalent stress and total deformation of condensing tubes equivalent entity

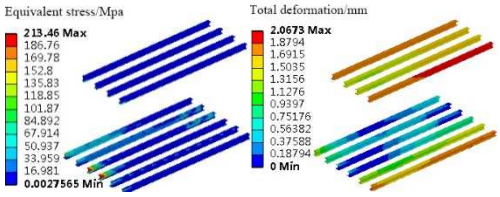

(e)Equivalent stress and total deformation of beams

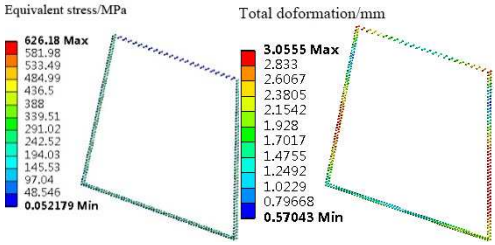

(f)Equivalent stress and total deformation of bolts

Tab.3 Results of max von-misers stress and deformation of components

condenser components	max equivalent stress[MPa]	max equivalent deformation[mm]	yield strength/ allowable stress[MPa]
water box	454.73	30.635	460
neck	225.64	2.8668	285
bolt	626.18	3.0555	735
support plate	134.45	±1.78	285
H steel beams	213.46	2.067	370
perforated area	39.3	-1.7859	50.23
unperforated area	155.81	+1.9525	173
tubes equivalent entity	40.611	2.1615	132.7

As can be seen from Tab.3, the tube sheet max stress is less than allowable stress; the max stress of components is less than yield strength, so the strength requirements are met, plastic deformation of components does not occur.

Fig. a shows that the max stress of water box appears on the seal of four surfaces consist water box, the protruding edges in the seal lead to local stress concentration. The max deformation appears at the center of both sides of water box, reaching 30.6mm.The height of water box is 4,460mm and the max percentage of elongation is 30.6/4460=0.69%, but it is too small to affect the operation of the water box. Fig. b shows that max stress in perforated area concentrated on the outer region of the tube and the unperforated area concentrated on the edge of tube sheets. The support reinforcement role of the condensing tube bundles leading to the stress in perforated area is less than unperforated area, while unperforated area had larger stress for the greater torque effect transmitted from water box. However, the strength requirements are met. Deformation of the tube sheets along the z-axis is small which meets the project requirements. Fig. c shows that above 95% stress of the neck is far less than its yield strength. The two corners of the neck bottom has local

stress concentration phenomenon, which is related to the corner curvature of the neck. The deformation of the neck is small, so it is safe for them to be judged from the function. Fig. d shows that equivalent stress of condensing tubes is generally lower, because it is not the force components. In fig. e, the beams stress is generally less than 39.7MPa; the max deformation occurs on the two upper outermost beams: it reaches 2.1mm. Fig. f shows that the stress in upper bolts is smaller with its value below 56.97MPa, But the stress in left and right side and the lower portion of the bolt is larger, and the max stress area occurs on the left and right sides of the nuts, with the value of 626.18MPa, bolt safety factor of $s_2=[\sigma_b]/\sigma=835/626.18=1.33$. As for the connection of control bolt preloads, the safety factor is within the requirements: from 1.2 to 1.5[7]. Max deformation occurs in the lower region of both sides of the bolts with the value of 3.06mm, the nut length of 180mm, and the percentage of elongation of 3.06/180=1.69%, which are too small to affect the seal.

4 Conclusions

(1)The method of finite element numerical simulation is used to calculate the equivalence stress and components deformation of the condenser, as well as the max deformation and the max equivalence stress of components. The results show that the stiffness and strength of the condenser exactly meet the requirements.

(2)The results show that at the seal of different surfaces, local stress concentration exists in the water box and the bottom corner of the neck, which leads to the stress of local points suddenly increasing greatly. Therefore, transferring the corners of tube sheets rounded design and the water box corners into circle transition leads to the curvature in the seal of surfaces changes uniformly, thereby improving the stress concentration. This idea can be applied in neck corner design.

(3)The results of stress distribution of the tube sheets, bolts and neck come to a conclusion that greater stress area occurs below the center of both sides of the tube sheets flanges, and the stress here can be reduced by appropriately increasing the effective local supports.

Acknowledgements

The research presented in this paper was supported by Natural Science Foundation of China under the Grant No.51379179，and the Foundation of Key Laboratory of Fluid and Power Machinery (Xihua University), Ministry of Education, PRC, and "XIHUA Cup" College Science and Technology Innovation Program of Xihua University (2014186). The Large Power Plant Condenserhad been implemented at Dongfang Steam Turbine Co. Ltd in China. Their supports are greatly appreciated.

References

[1]Guoshan Wang, *Thermal Performance Numerical Simulation and Application of Power Plant Condenser*(China Electric Power Press, Beijing 2009)

[2] Xinlan Zhou, Mingzhi Zhang, Xuelei Zhang: submitted to Electricity Information, 2001(1) pp.29-31.

[3] Shuguang Gong, Guilan Xie: submitted to Design and Research, 2002,31(6):49-51

[4] Xiaobao Zhang, Xide Lai: submitted to Energy Research and Management, 2010(2) pp.34-37.

[5] ASME SECTION Ⅷ Division 2 2007.Alternative Rules for Construction of Pressure Vessels. New York: ASME, 2007

[6] SECTION VIII Rulers for Construction of Pressure Vessels Division 2-Alternative Rules. China Petrochemical Press, Beijing 2004

[7] Lianggui Pu. *Mechanical Design*(Higher Education Press, 2006)

Advanced Materials Research Vols. 986-987 (2014) pp 848-851

doi:10.4028/www.scientific.net/AMR.986-987.848

Modeling and Optimization of Heat Exchanger in Automotive Exhaust Thermoelectric Generator Based on Fluid Kinematics

Xinyu Wang[1,a], Shunmin Wang[1,b], Liang Zhou[1,c] and Xichao Li[2,d]

[1] School of Automotive Engineering, Wuhan University of Technology, Wuhan 430070, China

[2] Hubei Research Institute of Products Quality Supervision and Inspection, Wuhan 430070, China

[a] best.1987@163.com, [b] wanpok@163.com, [c] ZhouLwhut@sina.com, [d] juliking0403@126.com

Keywords: modeling, optimization, fluid kinematics, fluid path-lines, fluid turbulence intensity

Abstract. The HE (heat exchanger) of automotive exhaust TEG (thermoelectric generator) plays a vital role in converting thermal energy into electrical energy, therefore achieves the goal of energy conservation and emission reduction. A new regular-octagon HE is modeled and simulated in FLUENT to obtain the velocity path-lines of fluid. Through simulation results, the velocity path-line is tracked and analyzed, in order to evaluate the fluid resistance and fluid turbulence intensity. By using control variable method, a variety of HE models with different structural parameters are modeled and simulated, to optimize the structure of HE. Eventually, it is intended to design a HE with proper fluid resistance and remarkable turbulence intensity.

Introduction

Recently, it is a hot theme to do research on automotive exhaust TEG, for the sake of the growing shortage of resources and energy crisis [1]. The HE is a one of the key component in TEG, which can efficiently converts thermal energy into electrical energy [2]. Moreover, its internal structure plays an important role in the thermal performance of HE. And a relatively optimal thermal performance can be achieved by designing different internal guiding fins and setting different structural parameters of these guiding fins, and analyzing the velocity of fluid path-line. This paper mainly focused on the fluid kinematics analysis. By analyzing the shape of the fluid path-line and the velocity magnitude, a relatively optimal HE with proper fluid resistance and remarkable turbulence intensity is obtained.

Based on this idea, a new HE, whose middle structure is regular-octagon, is designed to explore its structure to the fluid kinematical characteristics. What's more, both the front part and the extreme part of this new HE are wedge cavity structures. The three-dimensional structure is shown in Fig.1.

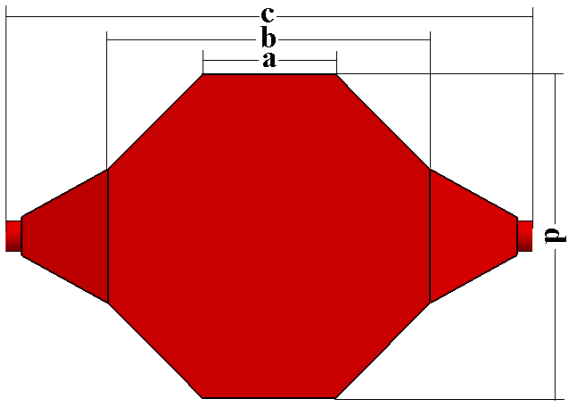

Fig.1 The three-dimensional structure of HE

As shown in Fig.1, the structural parameters are as follows: a is170mm, b is 420mm, c is 670mm, d is 420mm. In addition, both the inlet diameter and outlet diameter is 40mm, and its thickness is 4mm, and its inner cavity height is 14mm.

Modeling and Simulation of the HE

Modeling of Three-dimensional Models. At first, only half part of each HE is modeled for the sake of their axis-symmetry property on structure [3]. There are three kinds of HE models, all of their external structure is the same as the three-dimensional structure of HE shown in Fig.1. Meanwhile, inside the HE, there are a certain number of guiding fins installed on both sides of its interface. The guiding fins respectively are "fish-bone" (named model-1, shown in Fig.2 (a)), "annular" (named model-2, shown in Fig.2 (b)) and "labyrinth"(named model-3, shown in Fig.2 (c)). The thickness of the guiding fins is 4mm, and the height of those is 14mm.

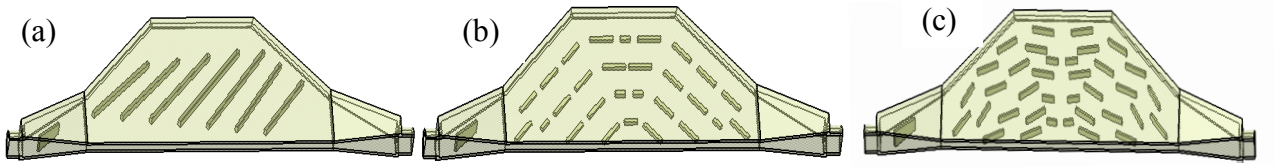

Fig.2 Three-dimensional models of HEs of model-1 (a) , model-2 (b) and model-3 (c)

Theoretical Basis of Fluid Kinematics. Basically, there are three condition equations applied in the fluid kinematics to calculate varieties of fluid kinematical problems. Which are three dimensional continuous equation, momentum equation and energy conservation equation [3, 4].

The three dimensional continuous equation is shown as below.

$$\frac{\partial u}{\partial x}+\frac{\partial v}{\partial y}+\frac{\partial w}{\partial z}=0$$

In the equation, u v w are the velocity components on x, y and z direction.

The momentum equation is shown as below.

$$\begin{cases}\rho\left(u\dfrac{\partial u}{\partial x}+v\dfrac{\partial u}{\partial y}+w\dfrac{\partial u}{\partial z}\right)=-\dfrac{\partial p}{\partial x}+\mu\left(\dfrac{\partial^2 u}{\partial x^2}+\dfrac{\partial^2 u}{\partial y^2}+\dfrac{\partial^2 u}{\partial z^2}\right)\\ \rho\left(v\dfrac{\partial v}{\partial x}+u\dfrac{\partial v}{\partial y}+w\dfrac{\partial v}{\partial z}\right)=-\dfrac{\partial p}{\partial y}+\mu\left(\dfrac{\partial^2 v}{\partial x^2}+\dfrac{\partial^2 v}{\partial y^2}+\dfrac{\partial^2 v}{\partial z^2}\right)\\ \rho\left(u\dfrac{\partial w}{\partial x}+v\dfrac{\partial w}{\partial y}+w\dfrac{\partial w}{\partial z}\right)=-\dfrac{\partial p}{\partial z}+\mu\left(\dfrac{\partial^2 w}{\partial x^2}+\dfrac{\partial^2 w}{\partial y^2}+\dfrac{\partial^2 w}{\partial z^2}\right)\end{cases}$$

In the equation, u , v , w are the velocity components on x, y and z direction, ρ is the fluid density , μ is the dynamic viscosity coefficient of the fluid.

The energy conservation equation is shown as below.

$$\rho c_p\left(u\frac{\partial T}{\partial x}+v\frac{\partial T}{\partial y}+w\frac{\partial T}{\partial z}\right)=\lambda\left(\frac{\partial^2 T}{\partial x^2}+\frac{\partial^2 T}{\partial y^2}+\frac{\partial^2 T}{\partial z^2}\right)$$

In order to make clear the condition of fluid, some fluid kinematical parameters should be given or calculated, such as Reynolds number (Re) and turbulence intensity (I).

The Reynolds number (Re) can be calculated out through the equation as below.

$$\mathrm{Re}=\frac{\rho u d}{\mu}$$

In the equation, Re is the Reynolds number, ρ is the density of fluid, u is the average speed of fluid, d is the fluid diameter, μ is the dynamic viscosity coefficient of the fluid.

The turbulence intensity (I) can be calculated out through the equation as below.

$$I=0.16\,\mathrm{Re}^{-}\cdot$$

In the equation, Re is the Reynolds number, I is the turbulence intensity.

Boundary Condition Parameters Setting. Based on bench test data, the inlet velocity is 21 m/s, the inlet temperature is 340℃, the exhaust gas density is 0.6 kg/m³, and the dynamic viscosity coefficient is 2.96×105 Pa·s. In this condition, the exhaust gas can be regarded as incompressible air [4]. What's more, the HE is made of brass. In order to get the exact and precise result, heat conduction and heat convection are considered in the FLUENT simulation.

Based on the given parameters, Re is calculated to be 14890. For Re is a low Reynolds number, according to previous study, Wilcox $-\omega$ model is best suitable for the simulation of exhaust gas. Thus the standard $-\omega$ equation is taken to calculate the fluid mechanics [3, 4]. The boundary condition is set as velocity inlet and pressure outlet [5]. The boundary condition parameters are: inlet velocity 21 m/s, inlet temperature340℃, inlet turbulence intensity 0.05,outlet gauge pressure 0 bar, outlet turbulence intensity 0.03, inlet and outlet hydraulic diameter 40mm, convection heat transfer coefficient is 21 W/(㎡·K).

Discussion

Velocity Path-lines of Exhaust Gas with Different Guiding Fins. Taking model-1, model-2 and model-3 in to the FLUENT simulation, the velocity path-lines are shown in Fig.3. Fig.3 (a) is the velocity path-lines of model-1, Fig.3 (b) is the velocity path-lines of model-2, and Fig.3(c) is the velocity path-lines of model-3.

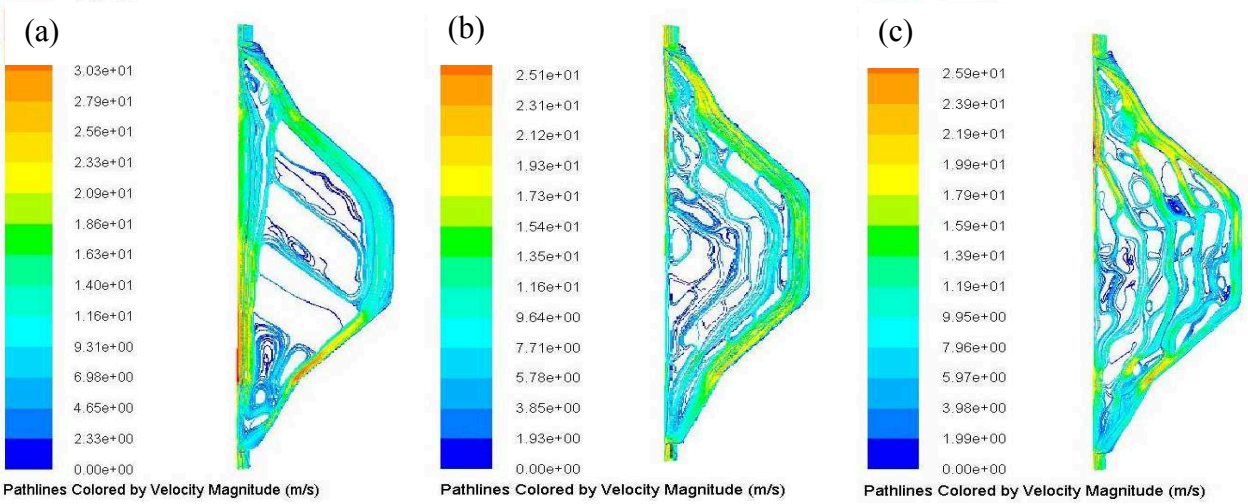

Fig.3 Velocity path-lines of exhaust gas of model-1 (a) , model-2 (b) and model-3 (c)

From the velocity path-lines simulation results, it is apparently that model-3's fluid distribution is the best among the three models. Model-1, with "fish-bone" guiding fins, contains too many zones where the fluid can't pass through directly. And its velocity ranges from 0 to 32.6m/s, the velocity difference is so huge that exhaust gas can't flow uniformly inside the HE.

Taking model-2 and model-3 into comparison, the fluid velocity difference of these two models are approximately the same, while model-3's average velocity is about 5m/s higher. Moreover, there are more turbulence flows generating inside model-3, which can enhance the heat convection.

Through the comparison, the conclusion is that, the HE with "labyrinth" guiding fins can obtain the relatively optimal fluid velocity magnitude and relatively optimal turbulence intensity of fluid.

Velocity Path-lines of Exhaust Gas with Different Thickness of "Labyrinth" Guiding Fins. Based on the previous simulation, the HE with "labyrinth" guiding fins can obtain relatively optimal fluid kinematical performance. Therefore, control variable method can be used to explore the problem, which is that how different thickness of guiding fins influences the fluid kinematical performance of exhaust gas. And then mode-4 and model-5 are modeled, in comparison with model-3. The thickness of mode-4 and model-5 respectively are 3mm and 3.5mm. Other parameters are the same with model-3. The simulation results are shown in Fig.4 (a) (velocity path-lines of model-4) and Fig.4 (b) (velocity path-lines of model-5).

Comparing model-3, model-4 and model-5, the optimal model is still model-3, whose average velocity is not too high, whose turbulence intensity is remarkable. The turbulence intensity of model-4 and model-5 is higher than model-3, however, their fluid speed is higher, most of the exhaust gas can't exchange heat energy with HE.

Velocity Path-lines of Exhaust Gas with Different Height of "Labyrinth" Guiding Fins. By using control variable method once again, model-6 and model-7 are modeled, in contrast with

model-3. The height of "labyrinth" guiding fins of model-6 and model-7 respectively are 10mm and 12mm, other parameters are the same with model-3.

Comparing model-3, model-6 and model-7, the optimal model is model-7, which owes the maximum turbulence flow and minimum velocity difference. The reason is that, model-6's fins height is too low, most of the fluid rushes through the HE without exchanging heat with HE. And the turbulence flow of model-3 is fewer than that of model-7. Therefore, the fins' height of model-7 is ideal, which promotes fluid mixes with each other [5]. Thus, the turbulence flow is remarkable.

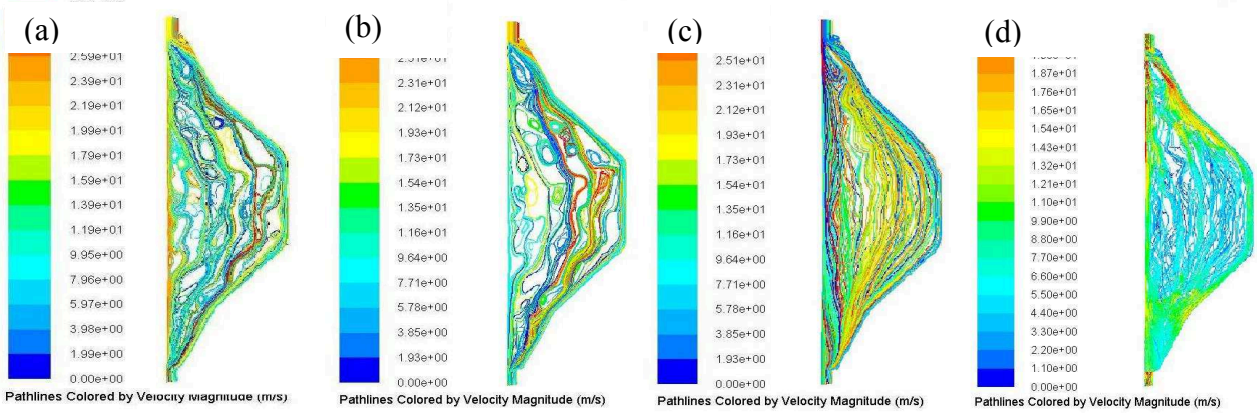

Fig.4 Velocity path-lines of exhaust gas of model-4 (a) , model-5 (b), model-6 (c) and model-7 (d)

Conclusion

This paper mainly concentrates on modeling and optimization of HE in automotive exhaust TEG, so as to obtain an optimal structure and fluid kinematical performance of HE. Therefore, the regular octagon HE is installed with "fish-bone", "annular" and "labyrinth" guiding fins one by one. Then three different models are modeled and simulated in FLUENT. By analyzing velocity magnitude, path-line and turbulence intensity, the HE with "labyrinth" guiding fins is evaluated to be the optimal one. Then the simulation models with different height and thickness of guiding fins are modeled. By using control variable method, a series of simulation results are compared one by one, thus the HE is optimized. Finally, the HE with the shape of regular octagon, with "labyrinth" guiding fins installed in the inner cavity, with the guiding fins height 12mm and thickness 4mm, is the optimal structure.

However, this study is limited to modeling and simulation in FLUENT to optimize the HE based on fluid kinematic, more research should be carried out on exploring the heat transfer mode between exhaust gas and HE. Therefore, in the future study, the research emphasis is focused on the thermal performance of HE.

References

[1] Su C Q, Ye B Q, Guo X. "Acoustic Optimization of Automotive Exhaust Heat Thermoelectric Generator [J]." Journal of Electronic Materials, 2012, 41(6): 1686-1692.

[2] LI XueFang, GUO JiangFeng, XU MingTian , CHENG Lin Min. "Entransy dissipation minimization for optimization of heat exchanger design." Chinese Science Bulletin. July 2011,Vol.56 No.20: 2174 2178

[3] SONG JiWei, XU MingTian, CHENG Lin."Theoretical analysis of a method for segmented heat exchanger design[J]." Chinese Science Bulletin.July 2011, Vol.56 No.20: 2179–2184

[4] L. Wang, B. Sunden. "Optimal design of plate heat exchangers with and without pressure drop specifications, Appl[J]." Therm. Eng. 23(2003) 295–311.

[5] Babu B V, Munawar S A. "Differential evolution strategies for optimal design of shell-and-tube heat exchanger[J]." Chem Eng Sci, 2007, 62:3720–3739

Advanced Materials Research Vols. 986-987 (2014) pp 852-857

doi:10.4028/www.scientific.net/AMR.986-987.852

Physical Parameters Consistency Based 3D Temperature Field Reconstruction for Combustion Flame

Xuguang Wang[1,2, a], Haipeng Zhang[1,b]

[1] School of Control & Computer Engineering, North China Electric Power University, Baoding 071003

[2]Hebei Engineering Research Center of Simulation & Optimized Control for Power Generation, Baoding, China, 071003

[a]wang_xuguang@163.com, [b]zhpng1980@163.cm

Keywords: Physical parameters consistency; Refractive effects; Temperature field; Refractive index field

Abstract. We present a novel solution to accurately recover 3D dynamic flame temperature field based on physical parameters consistency. First, a new optical model is proposed to establish the relationship between the flame radiation and the radiance field, this model fully considers refractive effect caused by refraction index changing; Second, high dynamic range (HDR) cameras are used to take flame images, a lookup table is employed calculate temperature from radiance; Third, an algorithm is put forward to reconstruct the flame temperature field. Experimental results on real flame accord with physical facts, which demonstrate that our solution is validate.

Introduction

Since temperature is one of the most essential physical parameters to flame, reconstructing flame temperature field becomes the hotspot, and is significantly valuable to related industries [1].

Temperature field measurements can be divided into two categories, i.e. the intrusive measurements and the non-intrusive ones. Early methods belong to the former category. They are easy to implement, but only applicable to measure single point temperature each time. Non-intrusive measurements can be further divided into two subcategories, i.e. active methods and passive ones. Typical technologies such as acoustic thermometry [2] belong to the former one. The needs of costly facilities limit its application. Passive methods rely on the radiation of the flame. The radiation from flame is captured by sensors and shown through images. Then the temperature field is reconstructed based on those flame images. Shimoda et al [3] introduced a flame temperature field measurement method, namely two-color method, which is only suitable for two dimensional cases. Wu[4] investigated the relationship between flame image brightness and flame temperature. Wang et al[5] made an intensive study of reconstruction of flame temperature field as well as concentration field. Wang and Zhao[6] made important contribution to flame image process and 3D flame temperature field reconstruction. Wang et al[7] takes flame images with high dynamic range cameras and reconstructs the radiance field on camera band for the flame, then obtains the flame temperature field through the lookup table between radiance and temperature.

There exist two drawbacks of the passive methods mentioned above. First, all the methods ignore the refraction of the flame and assume that light rays travel through the flame along straight lines. Since flame is a kind of inhomogeneous medium, it bends the light rays internally. Second, except for the work proposed by Wang et al[7], other works do not take into account the fact that the dynamic range of the flame emission is larger than that of general industrial cameras.

Our approach belongs to the passive methods. In our work, we offer three contributions over the existing state of the art. First, a new model, which takes account refraction caused by refraction index changing, is put forward. Second, lookup table between temperature and radiance is established to effectively reduce the computational complexity. Third, an algorithm that reconstructs the

temperature field based on the consistency between temperature and refractive index is proposed. Experimental results indicate that our improvements are successful.

1. Optical model

Fire is typically defined as an oxygen-fueled chemical decompositioon that releases heat to the environment, and flame is the visible luminous reaction products of fire. When the radiation from flame arrives at the sensor (CCD or CMOS), it is converted into electrical signals by a photoelectric convertor. The electrical signals are then digitized and formed images on the image processor. Before reaching the sensor, radiant energy inevitably undergoes several kinds of attenuation, including reflection, refraction and absorption.

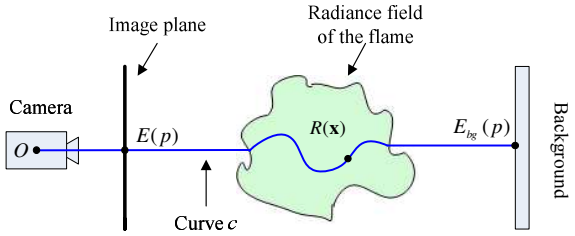

Fig.1 Optical model of flame.

The radiant energy $E(p)$, a pixel p in a flame image received, consists of two parts (as shown in Fig.1): The radiant energy emitted from flame along curve c and background's contribution $E_{bg}(p)$. Curve c is the path, which light rays travel along, before reaching pixel p. The reason why light rays travel through the flame along a curve path lies that, flame is inhomogeneous, the density of fire products varies in different areas of the flame. As a result, light rays are bent inside the flame. Thus, $E(p)$ can be expressed as

$$E(p) = \int_c \alpha(\mathbf{x})\mathbf{R}(\mathbf{x})\tau(\mathbf{x})d\mathbf{x} + E_{bg}(p) \tag{1}$$

Where $\alpha(\mathbf{x})$ is the view factor from $\mathbf{x}$, a point locating on curve c, to pixel p. $\mathbf{R}(\mathbf{x})$ is the radiance field. Here, we make an assumption on the structure of $\mathbf{R}(\mathbf{x})$, we do this by assuming that $\mathbf{R}(\mathbf{x})$ can be represented by a linear combination of base functions $R_i(\mathbf{x})$:

$$\mathbf{R}(\mathbf{x}) = \sum_i a_i R_i(\mathbf{x}) \tag{2}$$

a_i is the corresponding coefficient of $R_i(\mathbf{x})$. The choice of the base functions $R_i(\mathbf{x})$ is essential for the tractability of the model. In order to simply the calculation, we chose the box function as the base functions. $\tau(\mathbf{x})$ denotes the transmissivity of light rays travel along curve c. For simplicity, we assume that the transmissivity is only determined by path length of light rays. Particularly, if curve c is parameterized by t, t_1 is the nearest intersection to the lens between curve c and the flame bound, and $\mathbf{x}$ corresponds to t_2 on curve c, $\tau(\mathbf{x})$ can be calculated by the following formula

$$\tau(\mathbf{x}) = \exp[-\sigma\int_{t_1}^{t_2}\sqrt{1+[c'(t)]^2}\,dt] \tag{3}$$

where σ is a positive medium-dependent constant known as the extinction cross-section, and is assumed to constant throughout the flame. $E_{bg}(p)$ denotes the radiant energy contribution from background. Under certain conditions, e.g. in a completely dark room, $E_{bg}(p)$ can be neglected. If no special instructions, we let $E_{bg}(p)$ equals 0 in this paper.

With the discussion above, the radiant energy that pixel p received can be formulated as

$$E(p) = \sum_i a_i \int_c \tau(\mathbf{x})\alpha(\mathbf{x})R_i(\mathbf{x})d\mathbf{x} \tag{4}$$

Eq.(4) describes a nonlinear system of equations

$$E(\mathbf{p}) = \mathbf{Sa} \tag{5}$$

Where vector $E(\mathbf{p})=[E(p_1),\cdots,E(p_m)]^T$ represents the radiant energy that the flame image received, $\mathbf{a}=[a_1,\cdots,a_n]^T$ denotes the coefficient vector of the basic functions. The coefficient matrix $\mathbf{S}$ has the following form

$$\mathbf{S}=\begin{bmatrix} \int_{c_1}\tau(\mathbf{x})\alpha(\mathbf{x})R_1(\mathbf{x})d\mathbf{x} & \cdots & \int_{c_1}\tau(\mathbf{x})\alpha(\mathbf{x})R_n(\mathbf{x})d\mathbf{x} \\ \vdots & \vdots & \vdots \\ \int_{c_m}\tau(\mathbf{x})\alpha(\mathbf{x})R_1(\mathbf{x})d\mathbf{x} & \cdots & \int_{c_m}\tau(\mathbf{x})\alpha(\mathbf{x})R_n(\mathbf{x})d\mathbf{x} \end{bmatrix} \tag{6}$$

In the coefficient matrix $\mathbf{S}$, $c_i, i=1,\cdots,m$ is completely determined by the refractive index field $\Phi(\mathbf{x})$ of the flame.

Given the radiant energy that the flame image received as well as the refractive index field $\Phi(\mathbf{x})$, the radiance field of the flame can be solved. The radiant energy of the flame image received could be obtained by calibrating the camera response function.

According to [7], the temperature field $\mathbf{T}(\mathbf{x})$ (If no special instructions, temperature refers to Kelvin temperature) can be obtained via the lookup table after given the radiance field $\mathbf{R}(\mathbf{x})$. When no confusion happens, $\mathbf{R}(\mathbf{x})$, $R_i(\mathbf{x})$, $\Phi(\mathbf{x})$ and $\mathbf{T}(\mathbf{x})$ are denoted as $\mathbf{R}$, R_i, Φ and $\mathbf{T}$ respectively for short in the following content of this paper.

2. Temperature field reconstruction

During the flame imaging process, irradiance plays a key role. After experiencing a certain optical system, the irradiance $\hat{E}(p)$ that pixel p receives can be described as[8]

$$\hat{E}(p)=\beta\gamma\zeta^2E(p) \tag{7}$$

where β denotes the optical system's transmittance, and γ demonstrates the sensor's spectral response. The two parameters can be obtained through calibration process. ζ is the ratio of aperture radius to focal length.

The camera response function could be calculated via images taken from the same scene with different exposure times[8].

After calibrating the camera response function, we derive the linear system from Eq.(5) and Eq.(7)

$$\theta\hat{E}(\mathbf{p})=\mathbf{Sa} \tag{8}$$

with $\theta=1/(J_0\beta\lambda\zeta^2)$, $\hat{E}(\mathbf{p})=[\hat{E}(p_1),\cdots,\hat{E}(p_m)]^T$. Note that coefficient matrix $\mathbf{S}$ is completely determined by refractive index field Φ, which must be calculated before solving the linear system (8). In a least squares sense, the solution is

$$\mathbf{a}=\theta\mathbf{S}^+\hat{E}(\mathbf{p}) \tag{9}$$

Here $\mathbf{S}^+$ is the generalized inverse matrix of $\mathbf{S}$. Since coefficient vector of the base functions $\mathbf{a}$ is determined by radiance field $\mathbf{R}$, and $\mathbf{S}^+$ is determined by Φ, Eq.(9) could be rewritten as

$$\mathbf{a}(\mathbf{R})=\theta\mathbf{S}^+(\Phi)\hat{E}(\mathbf{p}) \tag{10}$$

That is to say, solving linear system (19) equals to finding a appropriate combination of radiance and refractive index field $(\hat{\mathbf{R}},\hat{\Phi})$, which satisfies Eq.(10).

Based on Wang's work [7], there is a one-to-one mapping between $\mathbf{T}$ and $\mathbf{R}$. Under the assumption that the air pressure remains unchanged during the burning process, the flame temperature T and the flame density ρ satisfy the following equation according to the ideal gas law

$$\rho=\frac{P\mu}{rT} \tag{11}$$

where μ denotes the molar mass of the flame's products, $r=8.32J/(K\cdot mol)$ is a scalar. According to Gladstone-Dale equation [9], the relationship between ρ and the flame refractive index ϕ is

$$\rho=\frac{\phi-1}{\kappa} \tag{12}$$

Here, κ represents the Gladstone-Dale constant. According to Eq.(11) and Eq.(12), we obtain the mathematical relation between T and ϕ

$$T = h(\phi) = \frac{P\mu\kappa}{r(\phi - 1)} \tag{13}$$

That is to say, there exists a one-to-one mapping $h(\cdot): \Phi \to \mathbf{T}$.

In this paper, we adopt $\Phi_0(\mathbf{x}) = \mathbf{1} \in \mathbf{R}^{m \times n}$ as the initial value of Φ. After calculating the initial coefficient matrix $\mathbf{S}_0$ according to formula (6), we obtain the coefficient vector $\mathbf{a}_0 = [a_1^0, \cdots, a_n^0]^T$ from the following OP

$$\begin{cases} \min \quad \sum_{i=1}^{m} [\mathbf{S}_i^0 \mathbf{a}_0 - \theta \hat{E}(p_i)]^2 + \eta \sum_{j=1}^{n} [\Delta A_0(\mathbf{x}_j)]^2 \\ s.t. \quad \mathbf{a}_0 \geq \mathbf{0} \end{cases} \tag{14}$$

where $\mathbf{S}_i^0$ denotes the *ith* line of $\mathbf{S}_0$. In the objective function, the first term is the data fitting term, it ensures that the solution satisfies Eq.(8-9) in a least squares sense; the second term is the smoothness term. Scalar η is used to weight the smoothness term relative to the data fitting term. $A_0(\mathbf{x}_j) = \sum_{q=1}^{n} a_q^0 R_q(\mathbf{x}_j) = a_j^0$, $\mathbf{x}_j$ denotes the center of the support region of base functions R_j. Laplace operator Δ is employed here, because if $\Delta A_0(\mathbf{x}) = 0$ holds, $A_0(\mathbf{x})$ is harmonic, and harmonic function is smooth enough. The constrain $\mathbf{a}_0 \geq \mathbf{0}$ is used to guarantee the non-negativity of the solution. Then, we can calculate the initial value of the radiance field via formula $\mathbf{R}_0 = \sum_{q=1}^{n} a_q^0 R_q$. Now, the initial value of the temperature field $\mathbf{T}_0$ can be obtained too through the lookup table between radiance and temperature.

The iteration strategy we adopt is: In step k, Φ_k denotes the refractive index field. We calculate $\mathbf{S}_k$ according to Eq.(6), and get $\mathbf{a}_k = [a_1^k, \cdots, a_n^k]^T$ via the following convex problem (CP)

$$\begin{cases} \min \quad \sum_{i=1}^{m} [\mathbf{S}_i^k \mathbf{a}_k - \theta \hat{E}(p_i)]^2 + \eta \sum_{j=1}^{n} [\Delta A_k(\mathbf{x}_j)]^2 \\ s.t. \quad \|\mathbf{a}_k - \mathbf{a}_{k-1}\| \leq \delta D_k, \quad \mathbf{a}_k \geq \mathbf{0} \end{cases} \tag{15}$$

Here, $\mathbf{S}_i^k$ denotes the *ith* line of $\mathbf{S}_k$, $A_k(\mathbf{x}_j) = \sum_{q=1}^{n} a_q^k R_q(\mathbf{x}_j) = a_j^k$. Scalar $\delta \in (0,1)$, $D_k = \|\mathbf{a}_k - \mathbf{a}_{k-1}\|$.

The smaller and smaller search radius δD_k ensures the convergence of $\{\mathbf{a}_k\}$. With $\mathbf{a}_k$, $\mathbf{R}_k$ is calculated conveniently. After obtaining $\mathbf{T}_k$ through the lookup table, Φ_{k+1} can be got too according to Eq.(14). The iteration terminates when $\|\Phi_{k+1} - \Phi_k\|$ is small enough. The terminate condition based on the fact that the temperature and the refractive index field of flame must be consistent with each other all the time. $\|\Phi_{k+1} - \Phi_k\|$ describes the consistency of the temperature and the refractive index field, i.e. the smaller $\|\Phi_{k+1} - \Phi_k\|$ is, the more consistent $\mathbf{T}$ and Φ are.

4. Results and discussion

We use two kinds of cameras to take flame images, i.e. HDR cameras and general industrial ones. HDR cameras are used to take HDR flame images for the purpose of minimizing the information loss caused by overexposure or underexposure. The other cameras are used to add views. More views of the flame will lead to more accurate visual hull. The experimental setup is shown in Fig. 2.

To guarantee the accuracy of the reconstruction results, flame images must not be polluted by ambient illumination. So our setup is placed in a totally dark room. We use the industrial 95% ethyl alcohol as the fuel, and put the fuel into an ordinary alcohol burner. We tried 8 bit, 10 bit and 12 bit flame images in our experiments, only to find trivial difference in smoothness and resolution of the reconstructing results. So the following results are all based on 8 bit flame images.

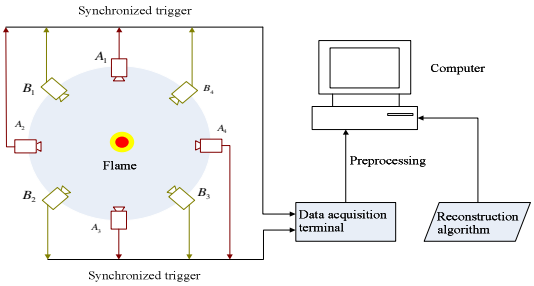

Fig.2 Schematic of the imaging system. A_1-A_4 are HDR cameras, B_1-B_4 are general industrial cameras.

Before reconstruct the flame temperature field, the support region of the base function R_i must be determined first. In our work, we calculate the flame visual hull of flame with eight viewed images, and divide the flame body inside the visual hull into voxels. The resolution of the flame body is determined by the number of effective pixels of the flame images. Here effective pixel refers to the pixel, which locating on the flame in the flame images. We take voxels of the flame body as the support region of R_i for simplicity. In this case, the number of base functions equals that of voxels.

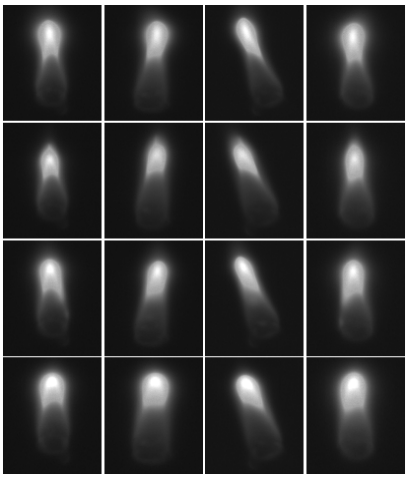

Fig.3 Multi-view HDR images of alcohol lamb flame.

Fig.3 shows the HDR flame images of the alcohol lamb. Each line shows the images taken from four different views at the same time, and each column corresponds to four images taken from the same view. Obviously, the flame can be divided into two parts, the bright head and the rest loom part. For the loom part is ambiguous, we only reconstruct temperature field and refractive index field for the bright head. Then we generate the back-projected images for the bright head. The comparison is restricted inside the bright head. The bright head can be easily detected by threshold based methods.

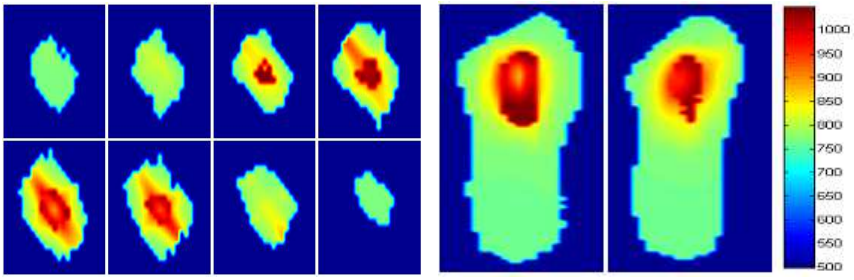

(a) (b)

Fig.4 Cross- and longitudinal-section of the flame temperature field.

Fig.4 shows the cross- and longitudinal-sections of the flame temperature field from HDR images in Line 1 of Fig.3. In this figure, the dark red represents the greatest temperature level and the dark blue represents the lowest temperature level. According to the temperature distribution, the

temperature in the central region is relatively low, rises along radial direction, and drops when it reaches the outermost layer. So the flame can be divided into three levels, i.e. flame core, inner flame and outer flame. The very center of the "brain" is the flame core, the highest temperature appears in the inner flame, and the rest region belongs to the outer flame. In the flame core, the gaseous alcohol's concentration is relative high but the oxygen's is low, which makes the alcohol unable to burn completely. In inner flame, with sufficient oxygen supplied by surrounding air, the temperature rises reasonably and reaches its maximum. In the outmost layer, flowing air cools the flame, making the temperature lower than that in inner flame. The distribution of the flame temperature field agrees well with the physical law of the real world, which confirms the validity of our solution.

4. Conclusions

In this paper we present an optical model of flame imaging, this model fully considers light deflection caused by refraction index changing. To avoid solving a complex transcendental equation, we use a lookup table to effectively reduce the computational complexity. An algorithm based on the consistency between temperature and refractive index is proposed. The algorithm starts under the assumption that light rays travel along straight line inside the flame, and terminates when temperature and refractive index field physically consistent with each other. The reconstructed temperature field of alcohol flame confirms the validity of our approach.

Acknowledgment

This work is partly supported by National Natural Science Foundation of China (No.61300066) and the Fundamental Research Funds for the Central Universities (No.2014MS141).

References

[1] B.W. Albers and A.K. Agrawal, "Schlieren Analysis of an Oscillating Gas-Jet Diffusion Flame," *Combustion and Flame*, vol.199, pp.84-94, 1999.

[2] C. Mougenot et al. "Three-dimensional spatial and temporal temperature control with MR thermometry-guided focused ultrasound (MRgHIFU)," *Magnetic Resonance in Medicine*, vol.61, no.3, pp.603-614, 2009.

[3] M. Shimoda M, A. Sugano, T. Kimura, Y. Watanabe and K. Ishiyama. "Prediction method of unburnt carbon for coal fired utility boiler using image processing technique of combustion fame," *IEEE Transactions on Energy Conversion*, vol.5, no.4, pp.640-645, 1990.

[4] Z.S. Wu. "Luminous fame image processing and its application in combustion monitoring," Ph.D. Dissertation, Tsinghua University, China, 1998.

[5] F. Wang F, Z.Y. Ma, J.H. Yan et al. "Experimental study of temperature and concentration distribution measurement based on fame image," *Journal of Power Engineering*, vol.23, no.3, pp.2404-2408, 2003.

[6] S.W. Wang, Y.J. Zhao and F.L. Wang. "Study of reconstruction 3D temperature field of fame using OST," *Journal of Engineering Thermophysics*, vol.23, no.3, pp.2404-2408, 2002.

[7] X.G. Wang, Z.H. Wu, Z. Zhou, Y.P. Wang and W. Wu. "Temperature field reconstruction of combustion flame based on high dynamic range images," *Optical Engineering*, vol.52, no.4, 043601, 2013.

[8] P.E. Debevec and J. Malik. "Recovering high dynamic range radiance maps from photographs," *SIGGRAPH*, pp.369-378, 1997.

[9] J.H. Gladstone and T.P. Dale. "Researches on the refraction, dispersion, and sensitiveness of liquids," *Philosophical Transactions of the Royal Society of London*, vol.153, pp.317-343, 1863.

Advanced Materials Research Vols. 986-987 (2014) pp 858-861

doi:10.4028/www.scientific.net/AMR.986-987.858

Reliability Assessment of the Small Sample Aero-engine Bearings

Feng Ding [1, a], Jiucheng Yin[2,b], Junqiang Dang [3c]

[1,2,3]School of Mechanical and Electronic Engineering, Xi'an Technological University,No.2 Xue Fu Middle Road, Xi'an, Shanxi Province,710021, China

[a]dfeng88@gmail.com, [b]yinjiucheng163@163.com

Keywords: aero-engine bearing; reliability; small sample; Weibull distribution

Abstract: Aiming at the test of Aero-engine bearing is expensive, small sample without failure, and bearing life obeys Weibull distribution, small sample data is introduced in order to estimate the reliability of bearing with the method of Bayesian point estimation. The weighted least squares method is utilized to estimate the shape and scale parameters of Weibull distribution in the case of no failure. The bearing cumulative failure function, failure rate and average life can be gotten. Finally, the bearing experiment data is used to verify the validity of the small sample evaluation. It is proved that the method has an important value for the replacement and maintenance of Aero-engine bearing.

0. Introduction

Aero engine main bearing is a key work part, in high temperature, high speed, variable load and in poor working conditions, which results in the rolling bearings failure problems often appears in the process of aircraft engine application. According to statistics, the main bearing failure accounts for 30% of the total engine failure. So strengthening the reliability of aero engine bearing, is great of significance to shorten the development cycle of aero engine. Compared with ordinary bearing, the reliability of aero engine bearing is relatively high. Therefore, it can not do the complete test in the experiment, but it only can do truncation test regularly with small sample and short time. So the evaluation of small sample and no failure data is put forward.

1. Evaluation Methods in Small Sample Data

1.1 No Failure Data of Small Sample Censored Time

N set of samples are randomly selected to test from the product of a group (n less than or equal to 2), doing the sample's test life about timing censored test for k times[1], truncated time is (t_i,s_i) i=1,2,…k , sample number without failure is denoted as n_i before the i^{th} truncation, then n=n_i.

All samples data without failure is expressed as: (t_i,s_i) i=1,2,...,k. Where:s_i=n_1+n_2+...+n_k, it is expressed at cut-off time t_i during the k^{th} s_i sample truncation test regularly.

1.2 The Cumulative Failure Probability Analysis of p_i Multilayer Bayesian

In the condition the cumulative failure probability of p_i is known at the t_i moment, by the binomial theorem, r_i sample failure probability of s_i samples is shown as follows:

$$L(r_i / p_i) = C_{s_i}^{r_i} p_i^{r_i} (1 - p_i)^{s_i - r_i} \tag{1}$$

Where: $C_{s_i}^{r_i}$ expresses failure combination of r_i samples in s_i samples.

According to the test results of bearing which is only failure or no-failure, conjugate distribution Beta (a, b) of binomial distribution is selected to regard as the prior distribution of the cumulative failure probability p_i[2,3].

For the Beta distribution, the probability density function of the incomplete $Beta(\theta_1,\theta_2,a,b)$ distribution in the interval (θ_1,θ_2) is shown as following:

$$f(x)=\frac{(x-\theta_1)^{a-1}(\theta_2-x)^{b-1}}{B(a,b)(\theta_2-\theta_1)^{a+b-1}},\theta_1<x<\theta_2 \tag{2}$$

Combined with the test analysis of bearing, the failure probability p_i of bearing is obviously smaller. For the convenience of calculation, usually taking a=1, b>1.

1.3 The Estimation of Cumulative Failure Probability p_1, p_2, p_i

Taking $Beta(0,1,1,b)$ distribution as the prior distribution of cumulative failure probability p_1 in the interval (0,1), the multilayer prior distribution of cumulative failure probability p_1 can be obtained under the condition of the hyper parameter b obeying uniform distribution in the interval (1,u).

$$f(p_1/u)=\frac{1}{u-1}[\frac{u(1-p_1)^{u-1}}{\ln(1-p_1)}-\frac{(1-p_1)^{u-1}}{[\ln(1-p_1)]^2}-\frac{1}{\ln(1-p_1)}+\frac{1}{[(1-p_1)]^2}] \tag{3}$$

According to the Bayesian theorem, the posterior distribution of p_1 is shown as following:

$$\pi(p_1/s_1)=[f(p_1/u)L(0/p_1)]/\int_0^1 f(p_1/u)L(0/p_1)dp_1 \tag{4}$$

Because the Bayesian point estimation is the minimum in terms of risk compared with other loss functions, so $L(\hat{p},p)=(\hat{p}-p)^2$ is usually used as loss function. $L(\hat{p},p)$ is expressed the loss derived from parameter p when it is adopted decision $\hat{p}$.

$$\hat{p}_1=\int_0^1\pi(p_1/s_1)dp_1=[(1+s_1)\ln\frac{s_1+u+1}{s_1+2}-s_1\ln\frac{s_1+u}{s_1+1}]/[u-1-s_1\ln\frac{s_1+u}{s_1+1}] \tag{5}$$

Similarly the cumulative failure probability p_2 can be launched:

$$\hat{p}_2=\int_{\hat{p}_1}^1\pi(p_2/s_2)dp_2=\hat{p}_1+(1-\hat{p}_1)[(1+s_2)\ln\frac{s_2+u+1}{s_2+2}-s_2\ln\frac{s_2+u}{s_2+1}]/[u-1-s_2\ln\frac{s_2+u}{s_2+1}] \tag{6}$$

According to the derivation about the analysis of the cumulative failure probability for p_1, p_2, using inductive method, taking parameter b as uniform distribution in the interval (1, u), incomplete $Beta(\hat{p}_i,1,1,b)$ distribution is the prior distribution of cumulative failure probability p_i in the interval $(\hat{p}_{i-1},1)$, then the cumulative failure probability analysis of multilayer is shown as below:

$$f(p_i/u,\hat{p}_{i-1})=\int_1^u\frac{(1-p_i)^{b-1}}{B(1,b)(1-\hat{p}_{i-1})^b}*\frac{1}{u-1}db \tag{7}$$

The cumulative failure probability p_i formula can be derived by the Bayesian method:

$$\hat{p}_i=\int_{\hat{p}_{i-1}}^1\pi(p_i/s_i)dp_i=\hat{p}_{i-1}+(1-\hat{p}_{i-1})[(1+s_i)\ln\frac{s_i+u+1}{s_i+2}-s_i\ln\frac{s_i+u}{s_i+1}]/[u-1-s_i\ln\frac{s_i+u}{s_i+1}] \tag{8}$$

2. Analysis of Bearing Life and Reliability of the Weibull Distribution

According to a lot of experimental proof, bearing life approximately obeys Weibull distribution. Bearing life obeyed Weibull distribution with two parameters will be discussed[4]. The function of bearing reliability is shown as follow:

$$R(t)=\mathrm{e}^{[-(t/\eta)^m]} \tag{9}$$

The estimation $\hat{p}_i$ of cumulative failure probability $\hat{p}_i$ at the moment of t_i can be gotten by the Bayesian method, using the weighted least squares method to calculate the shape and scale parameters of bearing life model in the case of no failure[5].

$$p_i=p(t_i\le t)=1-e^{-(\frac{t_i}{\eta})^m} \tag{10}$$

Using the calculation $\hat{p}_i$ instead of the cumulative failure probability p_i, the shape and scale parameters will be obtained by the weighted least squares method. Taking the weight: $w_i = n_i t_i / \sum_{i=1}^{k} n_i t_i$, ($i$=1,2,..,$k$).

Order: $$Q(m,\eta) = \sum_{i=1}^{k} w_i [1 - p_i - e^{-(t_i/\eta)^m}]^2 \tag{11}$$

Derive partial derivative of the function of $Q(m,\eta)$, then the numerical number of $\hat{m}$ and $\hat{\eta}$ will be obtained. $\hat{m} = (B - A^2)/(D - A*C)$, $\hat{\eta} = e^{[(B*C - A*D)/(B - A^2)]}$

Where: $A = \sum_{i=1}^{k} w_i \ln(\ln \frac{1}{1-\hat{p}_i})$, $B = \sum_{i=1}^{k} w_i [\ln(\ln \frac{1}{1-\hat{p}_i})]^2$ $C = \sum_{i=1}^{k} w_i \ln t_i$, $D = \sum_{i=1}^{k} w_i \ln t_i \ln(\ln \frac{1}{1-\hat{p}_i})$

So it can calculate reliability, failure rate and average life of bearing:
$R(t) = e^{-(t/\hat{\eta})^{\hat{m}}}$, $\lambda(t) = (\hat{m}/\hat{\eta})/(t/\hat{\eta})^{\hat{m}-1}$, $ET = \hat{\eta}\Gamma(1+1/m)$

3. The Reliability Case of Aero-engine Bearing without Failure Data

Aiming at some type of bearing, Randomly selected 2 sets from the whole truncated life test is done regularly for five times, no failure data obtained is shown in Table 1 no failure data.

Table 1 No failure data

Truncated sequence (i)	censored data (h)	sample number n_i / a	no failure number s_i / a
1	180	2	10
2	300	2	8
3	500	2	6
4	600	2	4
5	800	2	2

According to the conclusion of reference[6], b should not be made too large, the upper limit of b is designated as u temporarily. U is selected in the interval (2, 8). Usually u is respectively selected 2, 3, 4, 5, 6, 7, 8. According to equation (5), (6), (8), (10) and (11), getting the numerical number of $\hat{m}$, $\hat{\eta}$ and R(t), whose results are shown in table 2 the cumulative failure probability and table 3 reliability.

Table 2 The cumulative failure probability

Parameters	2	3	4	5	6	7	8
P_1	0.0443	0.0432	0.0421	0.0411	0.0401	0.0391	0.0383
P_2	0.0908	0.0876	0.0862	0.0840	0.0820	0.0799	0.0782
P_3	0.1458	0.1409	0.1378	0.1340	0.1306	0.1271	0.1242
P_4	0.2045	0.1977	0.1927	0.1871	0.1821	0.1771	0.1728
P_5	0.2800	0.2699	0.2618	0.2535	0.2460	0.2388	0.2324

It can be seen from table 3, the selection of u has some influence on shape parameters $\hat{m}$ and scale parameters $\hat{\eta}$, but has little effect on the reliability estimation. For example: When the time is 60 hours, the reliability is below 0.0001; When it is 180 hours, the reliability is below 0.001; When it is 600 hours, the reliability is below 0.01. From figure 1 and figure 2, the reliability and failure rate of different shape parameters at different time can be seen, the selection of u has little effect on the change of reliability and failure rate curve. Therefore, u=5 is right in the interval (2, 8) .

Table 3 Reliability

Parameters	2	3	4	5	6	7	8
$\hat{m}$	1.4659	1.4378	1.4119	1.3921	1.3784	1.3605	1.3449
$\hat{\eta}$	1015.4631	1078.1480	1141.0452	1202.1898	1259.4117	1320.8094	1380.7747
R(60)	0.9843	0.9844	0.9845	0.9847	0.9850	0.9852	0.9854
R(180)	0.9239	0.9265	0.9290	0.9314	0.9338	0.9358	0.9374
R(300)	0.8459	0.8531	0.8593	0.8652	0.8708	0.8754	0.8796
R(500)	0.7019	0.7180	0.7321	0.7446	0.7559	0.7659	0.7748
R(600)	0.6298	0.6501	0.6680	0.6839	0.6977	0.7105	0.7218
R(800)	0.4941	0.5218	0.5457	0.5671	0.5857	0.6032	0.6188

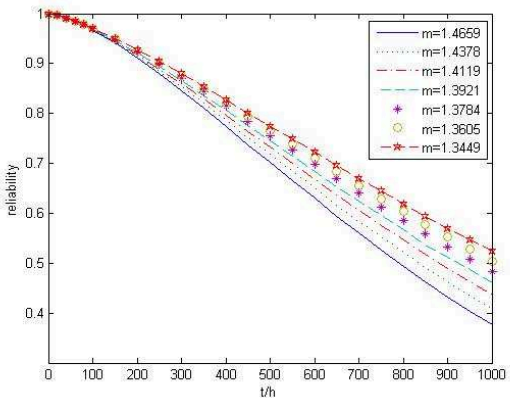

Fig. 1 Reliability curve

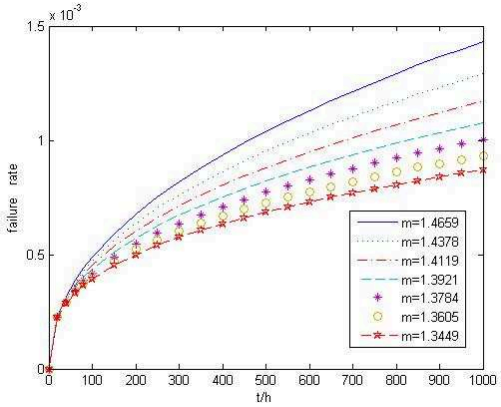

Fig. 2 Failure rate curve

When u is equal to 5, shape and scale parameters are respectively 1.3921 and 1202.1898. So the reliability, failure rate and average life can be concluded.

4. Conclusion

In this paper, conjugate distribution Beta(a,b) of binomial distribution is regarded as prior distribution of cumulative failure probability by using the Bayesian method. The model of bearing reliability evaluation can be gotten, the assessment accuracy of bearing reliability will be improved. Prior information should be continued to accumulate and collected in order to ensure reliability evaluation results more accurate.

Acknowledgment

This research was supported by the National Natural Science Foundation of China under grant 51275374.

References

[1] Tang Xuemei, Zhang Jinkui. Analysis and evaluation of small sample experiment of weapon equipment [M], National Defence Industry Press 2001.
[2] Zhao Yu. Reliability data analysis [M], Bei Jing: National Defence Industry Press 2011.
[3] Liu Tengteng Prediction and reliability analysis study of ball bearing life [D], Henan University of Science and Technology, 2009:27-29.
[4] Mao Zhizhong Application of mechanical reliability theory method [M], Bei Jing: Machinery Industry Press, 2011.
[5] Xu Xianzhao Study on the reliability evaluation method of rolling bearing [D], Chinese Metrologica Journal, 2012:15-25.
[6] Mao Shisong. Zero failure data process of bearing life test [J], Application of probability and statistics, Vol.9.No.3.p.327-330.1993.

Advanced Materials Research Vols. 986-987 (2014) pp 862-865

doi:10.4028/www.scientific.net/AMR.986-987.862

Research on Hydraulic Turbine Cavitation Based on Cordon

zhuo ma qiong da [1, a]

[1] Department of mechanical and electronic, Tibet Vocational technical college, Lhasa 850000,China

[a]basang666@yeah.net

Keywords: Hydraulic turbine, cavitation, Cordon method

Abstract. Since the first hydraulic mechanical erosion discovered in the later stage of 19th century, researchers from both abroad and home have devoted a large amount of time and energy, ranging from fluid dynamics of multiphase systems and dynamics of materials to design of impeller, processing craft and material application with multi-subject research.

Although great achievements have been acquired, some problems are still waiting to be resolved. At present, the fundamental principle of hydraulic turbine's erosion has been found out. When temperature of water is kept at a stable level and pressure of fluid's internal part decreases to a critical point, the fluid will evaporate, forming a vacant cave which will be destroyed in a short moment and cause pressure wave of hundreds of MPa to intensely vibrate hydraulic turbine and leave trails shaping like honeycomb.

However, reasons of hydraulic turbine's cavitation are extremely diverse and complicated, not only involving factors such as waterpower and mechanism, but also working conditions of hydraulic turbines, setting conditions of hydropower stations as well as working environment. Causes of hydraulic turbine cavitation in every hydropower station differ due to different factors, which undoubtedly increases the difficulty to prevent and predict cavitation.

This passage is to apply Cordon method to predict destruction volume of cavitation and compare it with the real conditions of hydropower station. In additions, both reasons and measures will also be researched in order to gain a favorable effect.

Cavitation phenomenon in hydraulic turbines

Cavitation is caused by the bursting of bubbles due to swirls, producing large pressures on the surface of the metal and ripping the surface metal. If it happens in a caustic environment, damage will be larger.

As the sites with lower pressures produce more bubbles, water in the sites with high pressures will destroy the bubbles and strike the metal in a fast speed, making the surface of the metal shaping like what is bitten by mice. Attacked by cavitation, all the notches and flaws may speed up the erosion at the surface of the metal despite of smearing the protection layer. The damage of cavitation on the materials is accumulated with each day, thus, designers are supposed to get a better understanding of cavitation and make effective measures. Figure 1 indicates the cavitation phenomenon occurring in hudraulic turbines.

Figure 1. Cavitation phenomenon in hydraulic turbines

Prediction formula of cavitation.

At present, few methods can be utilized to predict cavitation. But Cordon method is a comprehensive formula which refers to the cavitation characters of hundreds of hydraulic turbines in North America.

Weight loss W(kg) of hydraulic turbines' impellers after eight thousand hours' working can be calculated according to Formula (1).

$$W = K_1 d^2 \tag{1}$$

In the above formula, K_1 represents cavitation intensity index of hydraulic turbines, d the throat diameter（m） of wheels. Cavitation intensity index of hydraulic turbines can K_1 can be calculated referring to Formula (2):

$$K_1 = 2.178^n \tag{2}$$

$$n = 0.45v^2 b^{-0.56} + 2.3C_f - S_a - R_1 - B \tag{3}$$

n------represents the effect index of K_1;
v------average fluid speed of unit;
b------ number of wheels' impellers;
C_f------utilization index of unit loading;
S_a------drowning depth of hydraulic turbine(m);
R_1------material index of hydraulic turbine;
B------ local air pressure.

According to Formula (1), (2), (3), based on real references of power stations, the weight loss, 162.6kg for one year, can be predicted. Compared with that of 2009, the weight loss is 150kg from which we are able to draw a conclusion that the error is just 12.6kg.

Therefore, Cordon method is not only feasible, but also credible.

Causes of Cavitation

As Cordon method is able to well predict the conditions of cavitation in hydropower stations, causes of cavitation can be analyzed through decomposition of Cordon.

According to Cordon method, the main factors which influence cavitation index K_1 include average fluid speed, number of impellers, loading utilizing index, drowning depth, material index as well as local air pressure. To rule out the fixed factors like design and local air pressure, the effect factors of cavitation in the hydropower can be indicted in Chart 1:

Item	Parameter	Item	parameter
Type of wheel	HL220-LJ-380	Loading utilizing index	0.95
Fluid volume of unit(m^3/s)	112	Drowning depth of lower reach/m	-0.86
Water head/m	51	Material index of impellers	2.8
Diameter of wheel/m	3.8	Air pressure/kPa	93.8
Fluid speed/(m/s)	10.8	Weight loss of current year	162.6
Number of impellers	14	Real weight loss of current year	150

Chart 1. Prediction of weight loss for hydraulic turbine

The wheel material in this station is made from ZG45 carbon steel which is easy for forging but soft. Obviously, ZG45 carbon steel's cavitation resistance ability is worse, which is one of the most important reasons causing severe erosion in hydraulic turbine.

What's more, drowning depth of lower reach is also firmly related with cavitation. When pressure of the fluid in which hydraulic turbine works is low, cavitation will be easy to be made. The real extracting height when hydropower unit works directly influences pressure of the fluid and extracting height is largely related with the drowning height of lower reach. As investigation has indicated, the larger extracting height is, the bigger possibility of cavitation will be.

Loading utilizing index is also a vital factor affecting hydraulic turbine. It can be expressed through the ratio between full operating time of hydraulic turbine and its normal operating time of a year. As indicated in the investigation, loading utilizing index will exert negative impact on hydraulic turbine no matter it is higher or lower.

Measures dealing with cavitation.

4.1 Serious research on problems of sand discharging.

One vital step is to make feasible sand discharging plans in the hydropower station with large amounts of mud and sand to decrease the amount of sand accumulation. Hasty work without investigation of sand discharging will not only bring tremendous waste to people, but also potential catastrophes.

4.2 Basic research on hydraulic turbines' cavitation.

It is essential to found a foundation which exclusively supports the research of hydraulic turbines' cavitation and actively take part in the research of mechanism of cavitation and abrasion. The fact that old experts who research in these aspects have retired, the majority of people in middle ages have experienced career change and young people are reluctant to engage in this job should inspire more people to work hard to create an active atmosphere for the development of this research.

4.3 Making of reasonable operating plan.

Reasonable plans are supposed to be made in order to reduce extracting height. According to local hydrological conditions, based on situations of sea levels in both high and low reaches, reasonable operating plans are supposed to be made to reduce extracting height on condition that adequate amount of power is generated.

4.4 Fulfilling mending regulations.

Despite the softness of materials and bad capability of resisting erosion, wheel should not be changed directly based on economical reasons. Therefore, it is quite significant to fulfilling mending regulations. It will not only shorten mending time and prolong using lifetime, but also make more economic profits and guarantee safe operation with good use of Cordon method to predict the developing process of cavitation.

4.5 Welding of wheels.

Stainless welding bars of new type which resist cavitation and abrasion must be used in the process of further welding. To take OCr13Ni4~6Mo stainless welding bar for example, it matches the mechanical facilities whose mother material is carbon steel. Besides, it is in possession of features such as easy welding and processing as well as resistance of cavitation and crack which have been applied in a great many large-scale hydropower stations in both abroad and home.

4.6 Protection of coverage.

In order to further strengthen the resistance of cavitation, coverage protection is supposed to be implemented in hydraulic turbines. Common spraying materials include mental, alloy, pottery and plastic. Spraying craft includes surface brushing, arc spraying and electroplating. For instance, Dongchuan hydropower station applies electroplating to strengthen the ability of cavitation and achieves great effects.

Summary

China's hydropower development has a quite promising future, but a great many hydropower stations which have been established are experiencing severe cavitaion and abrasion. These damages reduce operating efficiency and intensify vibration, not only threatening the safety of hydropower stations, but also bringing troubles to the normal operation of power grid.

Although the mechanism of cavitation is simple, its causes are supposed to be analyzed from diverse respects. Measures implemented also continuously change and their effects are difficult to be predicted. Therefore, conclusion of mending experience, utilization of Cordon method, confirmation of causes of cavitation as well as good selection of resisting measures are greatly meaningful to stations' economical operation and technological transformation.

References

[1] Duan Shengxiao, Cavitation and Abrasion Damage Condition of Hydraulic Turbine and Countermeasures in China, 2001.

[2] Gui Jiazhang, Liang Xing, Hydraulic Turbine Cavitation Analysis Based on the Cordon Method, 2013.

[3] J. GA Bitter. A Study of Cavitation Phenomena[J]. Wear, 1963, (5).

[4]Finnie. On the Velocity Dependence of the Cavitation of Ductile Metals by Solid Particles at Low Angles of Incidence[J]. Wear, 1978, 48.

Advanced Materials Research Vols. 986-987 (2014) pp 866-869

doi:10.4028/www.scientific.net/AMR.986-987.866

Review of Research Development on Slurry Pipeline Drag Reduction Technology

Ping Sun[1,a],Dongdong Wang[1,b],Yuzhang Sha[1,c] and Luxi Liu[1,d]

[1]School of Shenyang, Shenyang University, Liaoning 110044, China.

[a]ssunpp@263.net,[b]1039716857@qq.com,[c]shayuzhang@163.com,[d]373752621@qq.com

Keywords: Slurry pipeline transportation, Drag reduction technology, Micro-bubble drag reduction, Vibration drag reduction.

Abstract. The resistance of slurry pipeline transportation has greatly impact on slurry transportation system. In order to improve transportation efficiency,energy utilization rate,taking the appropriate drag reduction technology has a very important significance.This paper presents drag reduction technologies for slurry transportation applications,including micro-bubble drag reduction technology and vibration drag reduction technology.

Introduction

Slurry pipeline transportation has greatly advantages such as less investment, construction period shortly, less environmental pollution and ease of management,causing various aspects of attention.It has been used widely in many fields.With increasing depletion of energy and intensification environmental pollution,energy-saving and emission reduction have to be solved.Thus the research of drag reduction technology plays an increasingly important role.There appears a variety of drag reduction methods.For instance,soluble high molecular weight polymer,fiber material, spiral flow, changing pipe geometry,heating drag reduction and adjusting the size of particles etc.With the analysis of the theoretical knowledge and experimental data to be established,the above drag reduction technologies had been made great progress, but there are some disadvantages and some of the drag reduction technology apply in reality still for a long time.This article will discuss micro-bubble drag reduction technology and vibration drag reduction technology.

The Technology of Micro-bubble Drag Reduction

The Development of Micro-bubble Drag Reduction Technology. In 1949 Locknar and Mantinelli firstly proposed the injection of gas in the pipeline.They found, however, that the injection of gas increased the pressure gradient in the pipe.In other words, the injected gas increased transport resistance [1].Nevertheless,Heywood N.I .and Rechardson J.F. et al, through experimental studies found that gas injection drag reduction in the laminar flow was best [2].Chinese scholar Xingrong Zhang et al, in1982, Conducted a three-phase flow pipeline experimental in Qingshan power plant and got some preliminary results of this trial: drag reduction rate was up to 6.2% [5].In 1996, Chinese scholar Yonggang Zheng and other scholars,in the study of circular pipe aerated flow drag reduction,considered that circular pipeline aerated drag reduction was actually achieved lower resistance by bubbles attached in the boundary layer of pipeline as same as polymer additive [8].Under the assumption of gas-liquid stratified flow situation,they studied the theory of drag reduction pipeline aeration.In the theoretical model proposed,drag reduction rate reached 30% to 50% [7].

In 2005,Aluf Orell conducted systemic research and presented complete set of its governing equations for predicting the slug unit pressure gradient [4].In 2007,Aluf Orell first attended to proposed model for evaluating the pressure gradients for stationary and moving solid beds overlaid by three-phase slug flow.His research came to the conclusion that in critical value for slurry speed ,it could achieve better effect on reducing resistance [3].

In 2008,Chinese scholars Bo Tang, Jianyi Kong and Runsheng Rao,in the three-phase flow experiment of pipeline drag reduction,investigated many factors about the drag reduction.For example, the flow rate of the slurry, adding content of the gas, the impact of gas pressure and the movement patterns of gas in transportation pipeline and other factors of the performance of slurry.Concluded when adding gas volume fraction reached to 12%, it will obtain the minimum drag coefficient [9].

Meanwhile,in recent years in the test for the different aerated device trials,which generally considered that rotating jets spray gas device has prominent advantage.Because the design of this device can obtain abundant Micro-bubbles and achieve the size less than 1mm [10].This design can still produce a negative pressure air vortex, has the ability to self-inspiratory ,avoid the drawback of blocking phenomenon.In further studies of the nozzle device,Chinese scholars Ting Xiong, Shidong Fan and Zixuan Yang drawn that diameter of the Spiral pipe in 10mm, the mixing effect is better and the pitch in 60mm, the pressure loss is minimum [11].

Micro-bubble drag reduction technology has made great progress and theoretical research.Meanwhile it has been applied slurry transportation in short distance such as cutter suction dredgers and other fields.

The Mechanism of Micro-bubble Drag Reduction. Chinese scholars Xingrong Zhang, Shaoqiang Zhang and Lvtai Zou came to conclusion of drag reduction mechanism [5]:Under certain velocity of slurry condition , when added to a appropriate amount of gas, the gas destroyed the movement mechanism and the structure of two-phase flow in slurry pipeline ,which enhance turbulence of slurry.It made numerous small bubbles in the slurry flow evenly blended among,then result in the cross-sectional velocity and concentration of the slurry more evenly distributed.The velocity gradient and concentration gradient were reduced, so that reduced the shear force of the pipe wall , and achieved the effect of drag reduction.

In 1989,Chinese scholars Baowei Song, Jingquan Huang[6],in Northwestern Polytechnical University,studied the effects of friction in the boundary layer on the flat surface of micro-bubbles. They thought the drag reduction mechanism that properties of micro-bubbles within the boundary layer viscous and elastic in itself,a portion of the fluid shear force transits into deformation energy stored, thereby reducing the energy loss.the key was to change the density of the boundary layer, and thus got drag reduction effect.

The Mechanism of Micro-bubble drag reduction is generally summed up that at conditions of high concentrations and low flow rate, to inject the right amount of gas can get a better drag reduction result. And vice verse. The joined bubbles changed the viscous and the density of boundary layer,flow structure and velocity gradient, so that the friction coefficient of pipe wall surface reduced and the direct friction of slurry pipe wall weaken.Meantime,it destroyed the flocculation reticular of slurry flow and enhanced the internal turbulence intensity ,which made the slurry concentration more well-distributed in cross-section.In additiont,the properties of viscosity and volatility of the bubbles, it can store up the energy of fluid in contact with the pipe wall as well as play a role of lubrication , such that transmission of resistance is reduced.

The Deficiency and Prospect of Micro-bubble Drag Reduction Technology. Although micro-bubble drag reduction even relatively low cost and easy to implement, but there are shortcomings that in the long distances,micro-bubbles is unstable, prone to burst, and certainly generate more large resistance and noise.At the same time the size of the bubble is not easy to control.Small bubble drag reduction effect is not obvious, and large bubbles can influence efficiency of pipeline, so the control of the bubble size and stability which is worthwhile for us to have a further discussion and study. For example,to improve the adsorption characteristics of piping material and make the bubbles to scroll along the wall and to change the physical stability of the bubble characteristics that the bubble is not easily broken.It is also that do some changes on the inner wall of the pipeline structure shape, making the bubble more evenly distributed around the perimeter of the pipe wall.As well as try to make micro-bubble drag reduction technology and other drag reduction for joint,which find out the drag reduction effect more obvious and easy to implement method of drag reduction.

The Technology of Vibration Drag Reduction

The Development of Vibration Drag Reduction. In 1960,M.O. Kramer put forward a drag reduction method of the bionic:artificial dolphins skin.The drag reduction rate could reach to 50% [14].This method can be understood that the movement of fluid contributed to the outer membrane of volatility, making the boundary layer in fluctuation , which increase the thickness of boundary layer , so as to achieve the effect of drag reduction [12].

In 1993,Chinese scholars DeSheng Gu, Guangwen Chen[12]thought that the drag reduction method was internal, passive method of drag reduction, so that it was not easy to control.Therefore,they proposed the external force as vibration source,realizing dynamic drag reduction of drag reduction method ,which was vibrating drag reduction.

In 1995,Chinese scholar Youyuan Tan[16]proceeded the experiment of vibration drag reduction in tailing.She concluded that: the concentration and the transmission speed of slurry and vibration parameters in the process of drag reduction were the main parameters, and within the low speed and high concentration (< 72.6%) could get good drag reduction effect.

In 2001,Chinese scholars Yezhi Sun, Aixiang Wu and Jianhua Li[13]in tailing test of drag reduction vibration, also confirmed the above conclusion, at the same time analyzed the reflection and transmission of stress wave and the stability of boundary layer thickness and change, and acquainted the feasibility of drag reduction vibration.

Vibration drag reduction technology is a novel drag reduction method and its basic idea which is use wall vibration to lower the concentration gradient and the velocity gradient of the boundary layer , in order to achieve the effect of drag reduction. But the usability and stability of this method needs further study.

The Mechanism of Vibration Drag Reduction Technology. Chinese scholars Desheng Gu, Guangwen Chen[12]hold the mechanism of vibration drag reduction : There were three aspects that elaborate the mechanism of vibration drag reduction technology.First boundary layer fluctuation was caused by the external force in the pipeline, contributed to the movement of the slurry particles of the boundary layer, reduced the velocity gradient and the shear stress on the boundary layer.Moreover, vibration made the boundary layer more stability, and its thickness was also increase.Finally,vibration promoted slurry particles to easily suspended, which made the slurry concentration gradient reduced. So as to achieve the effect of drag reduction.

About the mechanism of drag reduction of vibration ,There are some else points [15]:On the one hand ,drag reduction associated with the vortex state in the spanwise direction ,which is produced by the periodic stokes layer on the vibratory pipe wall.On the other hand ,boundary layer exists the phenomenon of flow to the vortex of recycling.

The Deficiency and Prospect of Vibration Drag Reduction Technology. Due to lack of theoretical consensus of the mechanism of vibration drag reduction, so it still need further in-depth studies on theory.Moreover, when transporting slurry concentration is higher, the vibration of the pipeline could produce the phenomenon of segregation of slurry,resulting in the effect of drag reduction significantly lower. In addition, the vibration source produces the optimal amplitude and frequency which is not clear.The relationship between the velocity and concentration of slurry flow and vibration parameters far from clear. These questions need further study.

Summary

In this paper, the micro-bubble drag reduction technology and the vibration drag reduction technology are simple summarized. There applied prospects is extensive and economical.But their respective theoretical studies are not very perfect, which also should be deepened.At the same time, combined with other drag reduction technology experiment also need to be researched, thus obtain good drag reduction effect.

References

[1] T. Xiong, S.D. Fan and P. Jiang: Testing System Optimization and Design for Slurry Pipeline Transportation. Research Journal of Applied Sciences,Engineering and Technology, Vol. 5 (2013) No.5,p.1646-1651.

[2] S.Z. Wang: *Granular Materials of Slurry Pipeline Transportation* (Ocean Publication,China 1998).p.67-68.(in china)

[3] Aluf Orell: The Effect of Gas Injection on The Hydraulic Transport of Slurries in Horizontal Pipes.Chemical Engineering Science,Vol.62 (2007) , p.6659 – 6676.

[4] Aluf Orell: Experimental Validation of A Simple Model for Gas-liquid Slug Flow in Horizontal Pipes. Chemical Engineering Science,Vol.60 (2005), p.1371 – 1381.

[5] X.R Zhang, S.Q. Zhang and L.T. Zou: The Primary Exploration of Three-phase Flow High Concentrations of Pipeline. Electric Power Environmental Protection,Vol. 1 (1986),p.43-44.(in china)

[6] B.W Song, J.Q. Huang: A Study on The Drag Reduction of The Plate by Mico-bubbles. Journal of Hydrodynamics, Vol. 4 (1989) No.4, p.105-114.(in china)

[7] Y.G. Zheng, D. Fang and G.F. Li: Gas-liquid Stratified Laminar Flows and Laws of Drag-reducing in Pipe. Journal of Chengdu University of Science and Technology, (1996) No.3, p.89-94.(in china)

[8] Y.G. Zheng, D. Fang and G.F. Li: A Theoretical Study of Drag Reduction by Aeration in Pipe Flow. Journal of Hydrodynamics, Vol. 11 (1996) No.2,p.162-171.(in china)

[9] B. Tang, J.Y. Kong and R.SH. Rao: The Research on Drag Reduction and Transportation by Ejecting Compressed-air to Pipeline. Machine Tool & Hydraulics, Vol. 12 (2008), p.90-92+95.(in china)

[10] B. Tang, J.Y. Kong and R.SH. Rao: Experimental Research on Air-ejecting Device for Pipeline Transportation. Machinery Design & Manufacture, (2011) No.6, p.152-154.(in china)

[11] T. Xiong, SH.D. Fan and Z.X. Yan: Numerical Simulation of Optimized Air Injector. Ship&Ocean Engineering,Vol. 5 (2011), p.94-96+100.(in china)

[12] D.SH. Gu, G.W. Chen: Analysis of The Dynamic Drag Reduction Effect Slurry Pipeline. Jiangxi Nonferrous Metals, Vol. 1 (1993), p.1-4.(in china)

[13] Y.ZH. Sun, A.X. Wu and J.H. Li: Vibration Drag-reduction of Pipeline Transport of High Density Slurry. Mining and Metallurgical Engineering, Vol. 4 (2001), p.4-6+9.(in china)

[14] M.O. Kramer: Boundary Layer Stabilization by Distributed Damping. Journal of the American Society for Naval Engineers, Vol. 72 (1960) No.1, p. 25-34.

[15] Y.K. Wang, CH.B. Jiang and L. Li: Review of Research on Drag Reduction. Hydroelectric Power, Vol. 32 (2008) No. 2, p.67-70.(in china)

[16] Y.Y. Tan: A Study on Transportation Characteristics of High-density Slurries. Mining Research & Development, Vol. 2 (1995), p.9-13.(in china)

Advanced Materials Research Vols. 986-987 (2014) pp 870-873
© (2014) Trans Tech Publications, Switzerland
doi:10.4028/www.scientific.net/AMR.986-987.870

Simulation study on effects of Ignition Time on Particle Emission for GDI Engine

Chuanfang Wei[a], Wei Dong, Xiumin Yu, Ping Sun, Ling He

State Key Laboratory of Automotive Simulation and Control, College of Automotive Engineering, Jilin University, Changchun 130025, China

[a]1049907048@qq.com

Keywords: GDI engine, AVL-Fire, simulation, ignition timing, particle

Abstract. In this paper, the AVL-Fire software was used to research the effects of ignition timing on homogeneous combustion and particle emission in a GDI engine. The result shows that the highest temperature and pressure reduce with the delay of ignition timing under the homogeneous charge mode in which gasoline is injected in the intake process. But the soot mass fraction decrease first and increase subsequently.

Introduction

In recent decades, how to improve the fuel economy and emissions of the internal combustion engine has been an important research direction in face of global energy crisis and strict emission regulations. Because the gasoline direct injection (GDI) in cylinder can effectively increase the engine power and fuel economy, so it has become a research hotspot. But particle emission of GDI is high in comparison to traditional gasoline engine, close to that of diesel engine. So it's necessary to study the particle emission of the GDI engine. This paper uses the AVL-Fire software to study how the ignition timing affects the particle emission under the homogeneous combustion mode in GDI engine [1-3].

The Establishment of Three-dimensional Model

The EA888 engine parameters show in table 1.

Table 1 EA888 engine parameters

Form	Four cylinders
Compression Ratio	9.6
Stroke(mm)	84.2
Cylinder Diameter(mm)	82.5
Nozzle Diameter(mm)	0.18

Table 2 Initial Conditions and Boundary Conditions

Boundary conditions	Inlet temperature(k)	330
	Combustion chamber crown(k)	550
	Cylinder wall temperature(k)	450
	Piston crown temperature (k)	600
Initial conditions	Intake port temperature(k)	333.15
	Intake port pressure(Pa)	100000
	Cylinder temperature(k)	951

The Establishment of Model. First, EA888 geometric model was built in Pro/E software. Then AVL-Fire software is used to treat the model. Dynamic grid was generated in the range of 0-540 degrees crank angle. The valve open time is 0°crank angle and the compression top dead center is 360°crank angle.

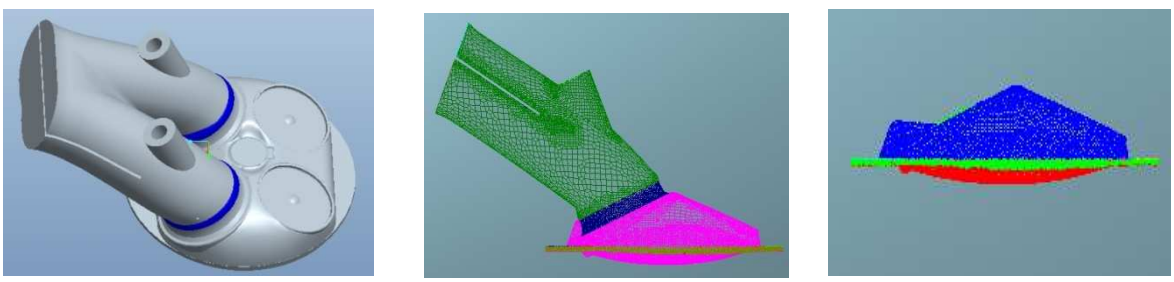

(a) Geometry model (b) 360°CA BTDC (c) 0°CA BTDC

Fig. 1 EA888 engine model

The dynamic grid is showed in Fig.1b and the model adopts hexahedral grid. In order to shorten the calculation time, the inlet and exhaust ports are removed when the inlet and outlet valves close. The largest mesh size is 2 mm and the minimum mesh size is 0.25 mm.

The Initial Conditions and Boundary Conditions. The initial conditions and boundary conditions of model show in table 2.

Model Validation

Fig.2 shows the EA888 engine bench. The engine speed is 2000r/min and the injection time is 40°CA BTDC. The fuel injection duration is 20 degrees crank angle, the fuel injection amount is 25mg and the ignition timing is 19°CA BTDC. From the Fig. 3, the model is proved correct.

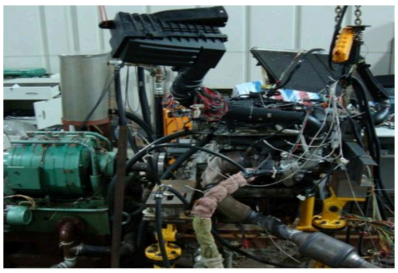

Fig.2 EA888 engine bench test

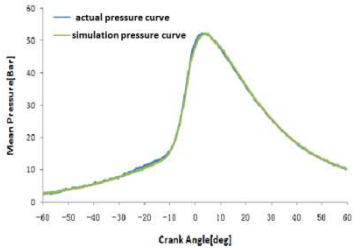

Fig.3 Model validation curve

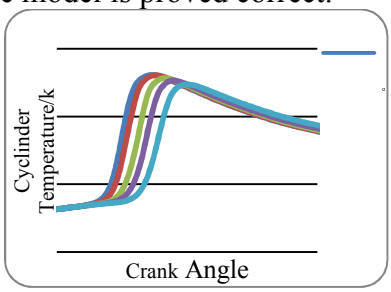

Fig. 4 Cylinder temperature curves

The Results of Numerical Simulation Analysis

This article researches how the ignition timing affects the combustion and soot emission of GDI gasoline engine under the homogeneous combustion mode. In this mode, the mixture formation time is long and relatively uniform. Thus the ignition timing has an important impact on the combustion and soot emission.

The engine speed is 2000 r/min, injection quantity is 25mg per cycle, the injection time is from 40 to 60 degrees crank angle and the ignition time is 24°CA BTDC ,21°CA BTDC,17°CA BTDC,14°CA BTDC,10°CA BTDC respectively.

Combustion Analysis. Fig.4 and Fig.5 show the temperature curve and pressure curve with different ignition timings. The highest temperature and pressure increase and the peaks are closer to the compression top dead center with the advance of ignition timing.

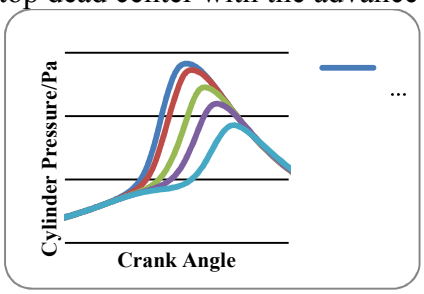

Fig.5 Cylinder pressure curves with crank angle

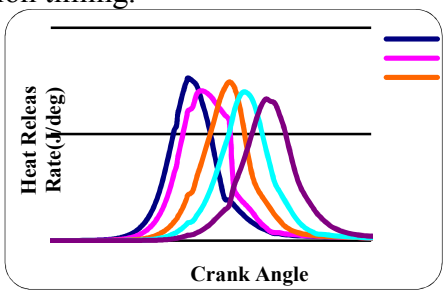

Fig.6 Heat release rate curves with crank angle

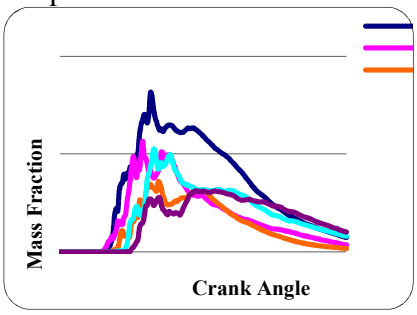

(a)Soot mass fraction curves with crank angle

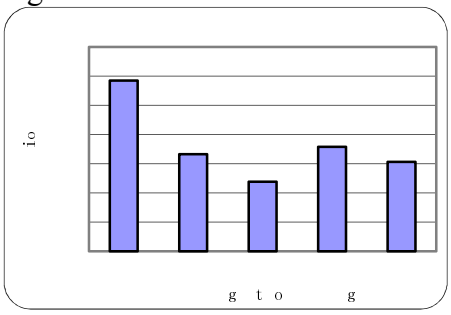

(b)Soot mass fraction with different ignition timing

Fig. 7 Soot mass fraction

Emissions analysis. From fig.6, the heat release rate shows an increasing trend, but a peak at 17°CA BTDC appears. And the soot mass fraction decrease first and increase subsequently from fig.7b. There are some reasons for this phenomenon.

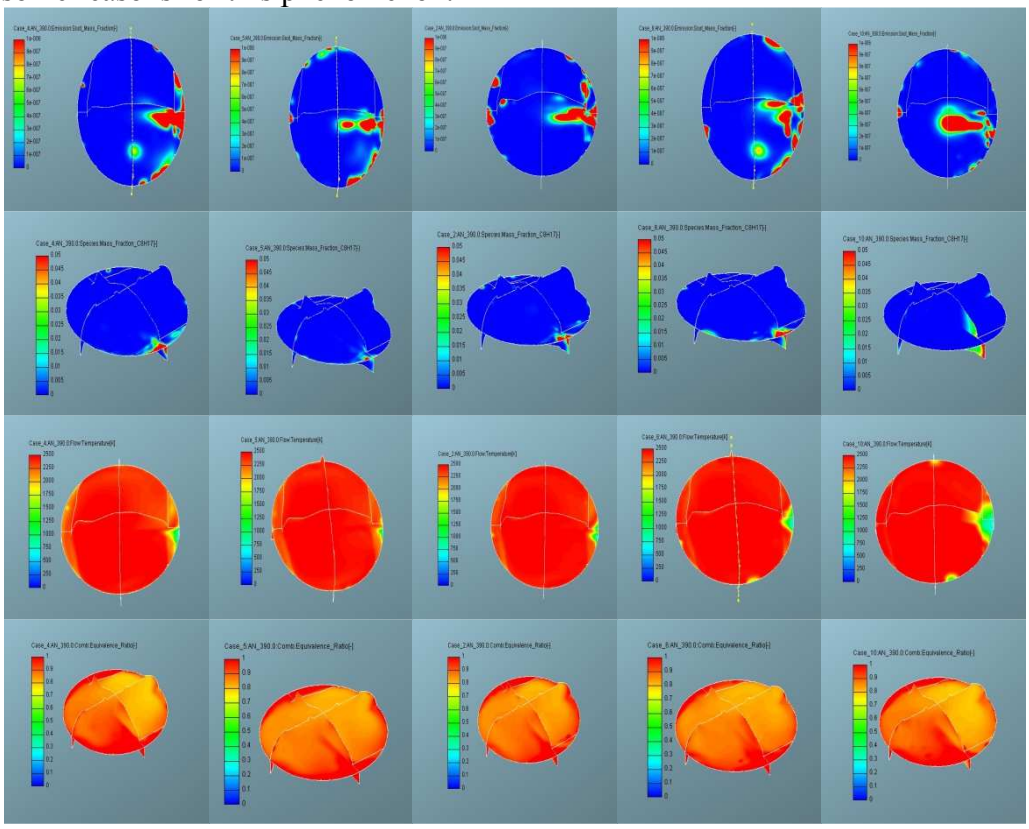

Fig. 8a SOOT, 8b HC, 8c temperature, 8d equivalent ration (20°CA ATDC)

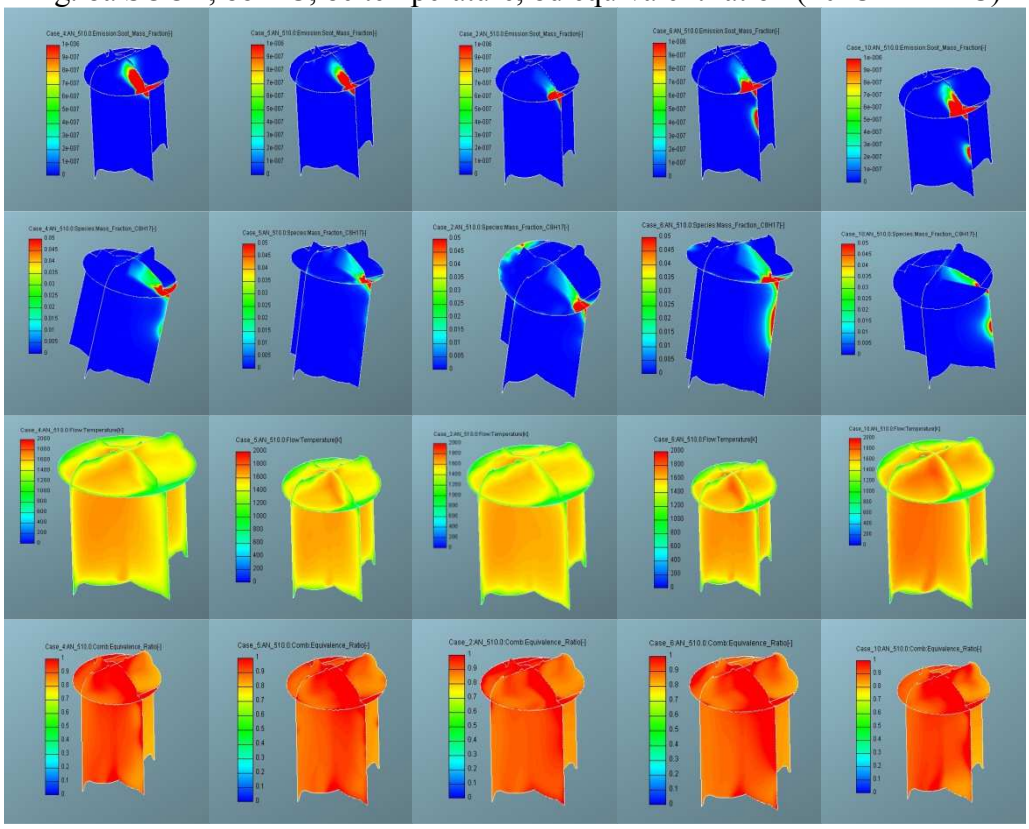

Fig. 9a SOOT, 9b HC, 9c temperature, 9d equivalent ration (150°CA ATDC)

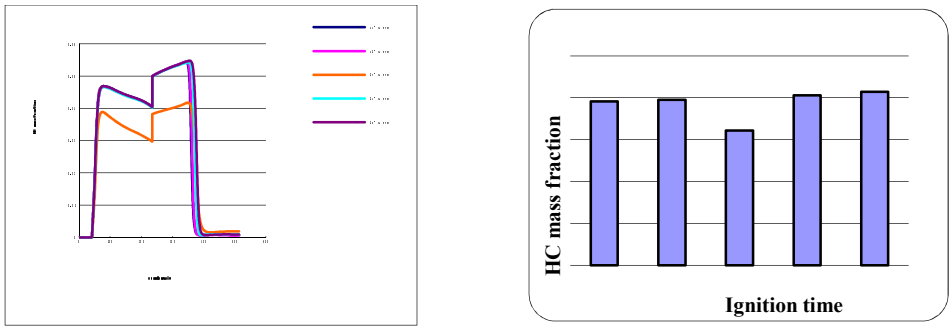

(a)HC mass fraction curves with crank angle (b)HC mass fraction with different ignition timing

Fig. 10 HC mass fraction

Soot formation condition is high temperature and oxygen, so it is necessary to analyze the cylinder temperature, equivalent ratio and HC. Because, Kleeman found that organic compounds were the main components for the gasoline engine particles [4]. Soot and HC are in the similar areas at 20°CA ATDC from fig.8a and fig.8b. From the fig.8c, the cylinder temperature is about 2500k except that a small part in cylinder is 2000 k. However, the area is the soot area when the temperature is under 2000k. (Research showed that the soot formation was between 1500k and 2400k, no matter how high the equivalence ratio was, there was almost no soot formation. And when the temperature exceeded 2400K, there was no soot[5].) And the fig.8d shows that the equivalence ratio is about 1.1 in the soot area. All of this is the best conditions for soot.

At the moment of the exhaust valve open, the combustion in cylinder is shown in fig.9. This phase is mainly for the soot oxidation. The fig.9c shows that the cylinder temperature is lower than 1800k at 150°CA ATDC. (The research showed when the temperature was below 2000k, the soot wouldn't be oxidized in the later phase[6].) So the soot will not be oxidized from 150°CA ATDC.

Conclusions

(1) Using the simulation software, the paper analyzes how the ignition timing affects the combustion. And with the delay of ignition timing, the maximum pressure and the highest temperature peak decrease.

(2) Analyze the factors how affect the particle generation, and pointed out the main soot formation area.

(3) Last, a conclusion is concluded that 17°CA BTDC is the best ignition timing in this condition.

References

[1] Schwarz C, Schunemann E, Durst B, et al. Potentials of the spray-guided BMW DI combustion system . SAE Paper 2006-01-1265, 2006.

[2] Zhao F, Lai M C, Harrington D L Automotive spark-ignited direct-injection gasoline engin . Progerss in Energy and Combustion Science, 1999, 25(5) : 437-562

[3] Mohr M, Steffen D, Forss A M. Particulate emissions of gasoline vehicles and influence of the sampling procedure . SAE Paper 2000-01-1137, 2000

[4] Kleeman M J, Schauer J J, Cass G R, et al. Size and composition distribution offine particulate matter emitted from motor vehicles. Environmental Science& Technology,2000,34(7):1132–1142

[5] Kanda T. Hakozaki, T. Uchimoto, T. Hatan, J. Kitayama, N. andSono, H. "PCCI Operation with Fuel Injection Timing Set Close to TDC", SAE Paper 2006-01-0920.

[6] Jianqin Wei Study the Formation and Oxidation of Diesel Particulate Journal of Xi'an Highway 1994-3

Advanced Materials Research Vols. 986-987 (2014) pp 874-877

doi:10.4028/www.scientific.net/AMR.986-987.874

SOC Estimation on PNGV model and Hybrid Electric Vehicle

Junling Xu[1, a], Liwei Li[1,b], Anna Jiang[1,b]

[1]Dept. of automation engineering, Qingdao University, Qingdao, 266071，China

[a]454923806@qq.com, [b] ytllw@163.com, [c] an_na_jiang@163.com

Keywords: PNGV equivalent battery mode; SOC estimation; UKF arithmetic

Abstract: Based on PNGV (the Partnership for a New Generation of Vehicles) equivalent battery model, establishing state-space equations, discrediting them and using UKF (Unsvented Kalman Filtering) arithmetic to achieve an exact SOC estimation under the non-linear condition. According to simulation experiment, UKF estimation just has an error rate of less than 6 percent, and has a quite high use value.

Introduction

Battery management system as an important part of hybrid electric vehicle mainly responsible for collecting information, estimating SOC and enabling real time communication with the vehicle control unit. This can help to extend battery life, remind the distance per charge and insurance the traffic safety. As a result, the research of battery management system has important applications.

Battery equivalent circuit model

Typical equivalent circuit models are Rint, Thevenin and PNGV. Rint does not involve the battery internal dynamic characteristics and just be used to simulate the simple circuits but not for EV. The precision of Thevinin model is higher than that of Rint，but lower than PNGV. PNGV medal is standard battery model in PNGV Battery Test Manual in 2001, and still use in Freedom CAR Battery Test Manual in 2003. It is consisted of resistance and Capacitance and be used to formulate operating characteristics of battery. This method has clear physical meaning and can easily distinguish model parameters. Considering the temperature influence to model parameters can obtain more correct PNGV model parameters, and then it raises the battery SOC estimation accuracy. Base on such advantages, this paper chooses PNGV equivalent circuit model. As shown in the fig 1.

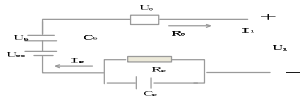

Fig.1 PNGV equivalent circuit model

In the model, U_{oc} is ideal voltage source, referring the open circuit voltage of batter; R_0 is ohmic resistance, R_p is the polarization resistance, I_p is By current of passing polarization impedance, C_p is polarization capacity, I_l is the battery load current, C_b capacitance describe the accumulative open circuit voltage changes when it loads current.

From the figure 1-1, following equations can be get:

$$U_b = U_{oc} - \frac{1}{C_b}\left[\int I_l d_t\right] - R_0 I_l - R_p I_p \tag{1}$$

state equation is shown as figure1-1:

$$\begin{cases}\begin{bmatrix}\dot{U}_b\\ \dot{U}_p\end{bmatrix}=\begin{pmatrix}0 & 0\\ 0 & -\dfrac{1}{C_pR_p}\end{pmatrix}\begin{bmatrix}U_b\\ U_p\end{bmatrix}+\begin{bmatrix}\dfrac{1}{C_b}\\ \dfrac{1}{C_p}\end{bmatrix}I_l\\ \dot{S}=-\dfrac{\eta}{Q_0}I_l\end{cases} \tag{2}$$

In this state equation, the voltage value of the capacitance of PNGV model is state variable, and the terminal voltage of battery is output variable. of which, Q_0 is battery available capacity,S is functions of SOC about current. That is:

$$S(t)=S(t_0)-\frac{1}{Q_0}\int_{t_1}^{t}\eta I_l d_t \tag{3}$$

$S(t_0)$ is initial value of SOC, η is coulomb efficiency.Following state-space equations can be obtained after the discretization of equation(1)and equation(2)

$$U_{b,\varepsilon}=F[S_\varepsilon]-\frac{1}{C_b}\left(\sum I_l\Delta t\right)_\varepsilon-I_{l,\varepsilon}R_0-I_{p,\varepsilon}R_p+V_\varepsilon \tag{4}$$

$$\begin{bmatrix}U_{b,\varepsilon+1}\\ U_{p,\varepsilon+1}\\ U_{\varepsilon+1}\end{bmatrix}=\begin{bmatrix}1 & 0 & 0\\ 0 & \exp\left(-\Delta t/\left(R_pC_p\right)\right) & 0\\ 0 & 0 & 1\end{bmatrix}\begin{bmatrix}U_{b,\varepsilon}\\ U_{p,\varepsilon}\\ S_\varepsilon\end{bmatrix}+\begin{bmatrix}\Delta t/C_p\\ R_p\left[1-\exp(-\Delta t/(R_pC_p))\right]\\ -\Delta t\eta_\varepsilon/Q_0\end{bmatrix}I_{l,\varepsilon}-\begin{bmatrix}W_{1,\varepsilon}\\ W_{2,\varepsilon}\\ W_{3,\varepsilon}\end{bmatrix} \tag{5}$$

$F[S_\varepsilon]$ is functional relation of SOC and electromotive force, W_1,W_2,W_3 is system white noise, V_ε is observation noise

In Document [3], battery model has been given an accuracy test. By simulation and experiment, using HPPC test to calculate model parameters estimates SOC error rate is less than 6 percent. According to the experiment, the PNGV model parameters gained under normal temperature is reasonable, and this model has a high accuracy. Fig 2 is HPPC current schematic diagram.

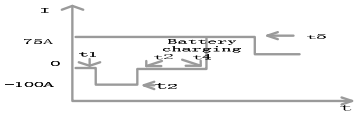

Fig 2 HPPC current schematic diagram

The UKF estimation based on PNGV

UKF filtering method dealing with noise includes extension and non-extension such two ways. In this paper, UKF filtering method of non-extension form is used, because non-extension rule can reduce the dimension of system and the number of sigma point. Filtering has a better real-time performance, so it is propitious to deal with the Gaussian Noise.

UKF filtering calculation method:

For non-linear system

$$X_k+1=f(X_k)+W_k \tag{6}$$

$$Y_k=h(X_k)+V_k \tag{7}$$

Supposing state is gaussian random vector ,statistic characteristics of process noise and measurement noise are:

$W_k \sim N(0, Q_k)$ $V_k \sim N(0, R_k)$

(1) initialization

$$\hat{X}_0 = E[X_0] \tag{8}$$

$$P_0 = E[(X_0 - \hat{X}_0)(X_0 - \hat{X}_0)^T] \tag{9}$$

(2) State estimation

(a) calculating Sigma point

$$X_{k-1}^0 = \hat{X}_{k-1} \tag{10}$$

$$X_{k-1}^1 = \hat{X}_{k-1} + (\sqrt{(n+k)P_{k-1}})_i, i = 1, 2, 3....n \tag{11}$$

$$X_{k-1}^i = \hat{X}_{k-1} + (\sqrt{(n+k)P_{k-1}})_i, i = n+1, ..., 2n \tag{12}$$

(b) time dissemination equations

$$X_{k\backslash k-1}^i = f(X_{k+1}^i) \tag{13}$$

$$X_k^1 = \sum_{i=0}^{2n} W_i^{(m)} X_{k\backslash k-1}^i \tag{14}$$

$$P_{x,k}^- = \sum_{i=0}^{2n} W_i^{(c)} [X_{k\backslash k-1}^i - \hat{X}_k^-][X_{k\backslash k-1}^i - \hat{X}_k^i]^T \tag{15}$$

$$r_{k\backslash k-1}^i = h(X_{k\backslash k-1}^i) \tag{16}$$

$$\hat{y}_k^- = \sum_{i=0}^{2n} W_i^{(m)} r_{k\backslash k-1}^i \tag{17}$$

(c) measure updating equations

$$P_{y,k} = \sum_{i=0}^{2n} W_i^{(c)} [r_{k\backslash k-1}^i - \hat{y}_k^-][r_{k\backslash k-1}^i - \hat{y}_k^-]^T + R_k \tag{18}$$

$$P_{xy,k} = \sum_{i=0}^{2n} W_i^{(c)} [X_{k\backslash k-1}^i - \hat{X}_k^-][r_{k\backslash k-1}^i - \hat{y}_k^-]^T \tag{19}$$

$$K = P_{xy,k} P_{y,k}^{-1} \tag{20}$$

$$\hat{X}_k = \hat{X}_k^- + K(Y_k - \hat{Y}_k^-) \tag{21}$$

$$P_{x,k} = P_{x,k}^- - K P_{y,k} K^T \tag{22}$$

Combine PNGV battery model equation (3), (4), (5). the UKF calculation can be used in SOC estimation of nickel-metal hydride batteries.

Experiment and the result

In order to verify The feasibility and accuracy of SOC estimation of Unsvented Kalman Filtering arithmetic based on PNGV model to the energy management system of hybrid electric vehicle, in Laboratory, by using test data and MATLAB simulation, we get SOC estimated curve as shown in the fig 3. That shows it is efficient for Unsvented Kalman Filtering arithmetic to give an online SOC estimation on nickel metal hydride battery, and can calculate SOC data rather correctly.

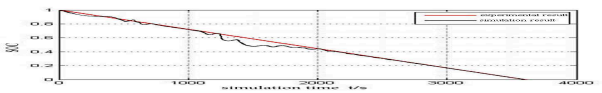

Fig.3 SOC estimation on PNGV model and UKF

Summary

This paper establishes two-dimensional state-space equations on the foundation of PNGV model, using UKF arithmetic which has two functions in non-linear filtering field to the SOC estimation of nickel metal hydride battery, and achieving good results. SOC error is within 6 percent.

However, temperature has a significant impact on characteristics of nickel metal hydride battery. PNGV model Parameter also has an evident change with temperature. So in BMS research, we must have a systematic consideration on the influence of temperature changes to battery model.

Acknowledgements

The work was supported by the Shandong province Natural Science Foundation of China (No.Y2008F23), Shandong province Science and Technology Development Plan (No. 2011GGB01123) and 863 programme (No.2012AA110407).

Reference

[1] Wang Lifang, Hu Yunfei, Liao Chenglin, “Research on SOC estimation of NIMH batteries in hybrid electric vehicles based on improved Thevenin model,” Chinese High Technology Letters, , 2008, 18(9),p.948-952.

[2] James H A, Alfred T, Barry W J. A battery state of charge indicator for electric wheelchairs [C]// IEEE Transactions on Industrial Electronics (SO278-0046).USA: IEEE, 1990, (10).

[3] Yang Yan, Taofen Tang, Electric vehicle PNGV equivalent circuit model and the estimation method of SOC for lithium batteries[J] .journal of system simulation,2012,24(12), p. 938 – 941.

[4] Battelle Energy Alliance. Battery Test Manual for Plug-In Hybrid Electric Vehicles, revision 0[M].USA: US Department of Energy National Laboratory, 2008, (3),p.22-29.

[5] Minxin Zheng. Dynamic Model for Characteristics of Li-ion Battery on electric vehicle [C]// Proceedings of ICIEA 2009.May, 2009, Xi’an, China. New York, USA: IEEE , 2009,p.2967-2870.

Advanced Materials Research Vols. 986-987 (2014) pp 878-881

doi:10.4028/www.scientific.net/AMR.986-987.878

Stress Analysis and Measures Resistance to Deformation of Coal Pipeline Above Goaf

Guo KeYi

Tangshan Research Institute of coal science and Industry Group Co., Ltd.,Hebei, Tangshan,063012, China

email: tsjxgky@163.com

Keyword: coal pipeline; mining influence; force analysis; anti-deformation measure

Abstract. Based on one company's engineering of constructing underground coal pipeline above goaf, calculation analysis the influence of residual subsidence deformation and stress distribution of the coal pipeline engineering. The mining subsidence make the underground coal pipeline bearing not only the earth pressure of upper, lower and lateral, but also the result of the subsidence deformation include of vertical and horizontal in-plane bending moment. Based on this, put forward the anti-deformation technical measures to build new coal pipeline and provide scientific basis for anti-deformation design.

Basic situation

One company is planning to build the underground coal pipeline, the project covers an area of 229.09 mu, the north-south longitudinal length is 2.4 km. The cross-section of the coal pipeline is rectangular and section size is 3.9 * 2.5 m, the pipeline is all buried and is for cast-in-situ reinforced concrete structure. The amateur is in the range of the seventh coal mining belong to the PingMei group. The coal seam extracted by the seventh mine in the area has three sets of coal, WU,JI, GENG, extractive time is between 1961 to 2009, the total mining thickness is about 12.5 m, mining depth is 70 m~ 323 m, and dip Angle of coal seam is 8 ~ 10°. In addition, some small mining such as Hualian mining, Wenji mining and Xinhua mining have exploited for a long time in the nearby, Mainly exploited residual coal of JI and fault coal pillar. The area affected by faults and the small fold associated with faults, the coal seam is discontinuous across pitch and tendency, thickness change is big, coal seam is fragmentary, geological structure is relatively complex.

Condition of the surface deformation

To study the estimated surface subsidence deformation, the domestic and foreign experts put forward many methods. At present in our country the commonly used method in calculating the surface movement deformation include of probability integral method, the negative exponential function method, the Weibull function method and typical curve method. The probability integral method has the advantages of parameters are easy to determine and strong practicability, so it is widely used in the mining area and is the most commonly used method. The estimate of ground residual subsidence deformation is according to the probability integral method calculated the ground residual subsidence deformation along the longitudinal and transverse direction of the coal pipe. The selected parameters of predicting surface movement is shown in table 1.

Table 1 The selected parameters of subsidence technology

Subsidence coefficient, q	Horizontal transfer coefficient, b	the tangent of mainly affect ,tgβ	Mining influence transmission coefficient, k	Movement distance of inflection point, s/H
0.03 0.15	0.30	2.0	0.7	0.05

After calculation, can see that the maximum ground subsidence is 355 mmalong coal pipeline, the maximum deformation of slope is 5.0 mm/m along the longitudinal direction of coal pipeline, the maximum horizontal deformation is -2.1 mm/m, the maximum deformation of slope is 3.0

mm/m in transverse direction, the maximum horizontal deformation is 1.3 mm/m, so will be affected by mining Ⅱ level[1-2].

The structure stress analysis

Can know from past numerous domestic ground construction above mine mining area and the goaf, the new building above mined-out area will cause the activation of old mined-out area, the surface movement deformation will intensify. Combined with the project, under the influence of mining additional force, pipeline structure produces excessive deformation and failure. First of all, we make force analysis of the coal pipeline in the normal condition (not affected by the condition of mining underground). The pipeline bear except the uniformly distributed earth pressure, there are some tiny deformation caused by heat bilges cold shrink might be slightly friction with the soil and these basically are negligible. Based on the analysis of its stress distribution, underground coal pipeline mainly bear bending moment (M), shear force (V) and axial force (N), the stress distribution is showed in figure 1.

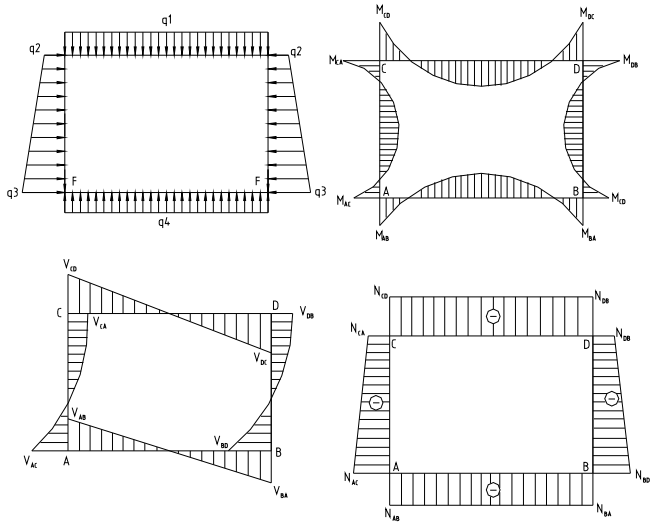

note:q- Uniformly distributed load,F-Concentrated load,M-Bending moment,V-Shear,N-Axial force

Fig.1 Coal piping stress analysis diagram regardless of the mining influence under the condition

Mining subsidence make underground building generating additional force mainly include three fields: First is the holding role generated by the relative motion of soil along the underground building surface caused by the earth's surface horizontal deformation, it will produce certain friction force and bending moment, make the structure failure or extrusion fracture; Followed by the earth's surface curvature distortion because of uneven subsidence, that will cause the underground building (structure) produce bending moment around a vertical in-plane, make underground building produce concentrated bending deformation and fracture; Again is the uneven level of mobile of the earth's along the transverse of underground building, that will make the underground building produce bending moment in the plane of the horizon and fracture damage [3-5].

Due to the project structure similar to surrounding rock of roadway, influenced by mining, surrounding rock stress becomes more complicated.In view of the coal pipeline cross-sectional area is not large, and the structure is simple, let's see a coal pipeline as linear geometric structure, For this structure, the main damaged deformation is the lateral deformation (tensile, compression).

Assume that underground coal pipe for a rigid rod, underground coal mining influence the overburden deformation pipeline soil shear, produce sliding friction, on the one hand can prevent soil movement, on the other hand make the coal pipe movement and deformation. Friction Fr is equal to the product of the positive pressure Fn and friction coefficient μ, that is

$$Fr=\mu Fn$$

Here in order to further simplify the force analysis, we do not consider the soil of different impact of friction coefficient and the effects of the whole channel in different depth of the underground coal, positive pressure Fn is the whole coal pipe load.

In general, regard he halfway point of the mining building as the center of gravity of the slip resistance, in this point the building movement with the soil completely, namely the relative displacement Vx is zero. Outside the scope, underground coal pipeline produce relative displacement between soil. These relative displacement make friction passing to the coal pipeline and generate additional strain. Add up the friction transmit to coal pipeline as elastic deformation force, its value increases gradually from center to the ends of buildings, as shown in figure 2.

The maximum friction force is: $Fr_{\max} = \frac{1}{2} Fr = \mu \bullet \frac{l}{2} q$

In the formula, q is uniformly distributed load generated by coal pipeline's weight.

Therefore, additional tension due to the friction increases along with the length L of coal pipeline on the direction of movement.

So, in constructing the coal underground pipelines affected by goaf, setting deformation joint to the entire coal pipeline to reduce length of the monomers is need.

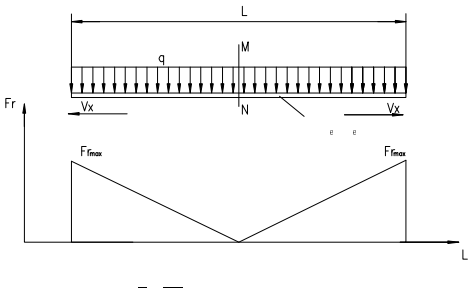

Figure 2 Coal piping stress analysis diagram consider of the mining influence under the condition

Anti-deformation protection technology

Due to underground coal pipe moves with the earth's surface (subsidence, inclination, horizontal movement), so the structural safeguard procedures applies simply to soil transformation of direct close to the mining coal pipe and additional stress transfer to coal pipeline.

The anti-deformation measures including flexible and rigid measures, Two kinds of measures can be used to prevent the destruction of the surface curvature and surface horizontal parallel effect. In general, in order to save money, the rigid of many building (structure) is not big, So when the earth's surface occur uneven movement, the building(structure) will produce deformation, And then only when the deformation exceeds a certain value, the building(structure) damage. Flexible measures allow the building(structure) to produce small deformation, in order to reduce the increased cost of rigid measures. Flexible measures generally include setting deformation joint, the excavation buffer groove, add foundation pad and sliding layer, etc.; Rigid measures generally includes as much as possible to adjust structure form and enlarging section and structure reinforcement of primary member such as foundation according to the deformation situation appropriately, etc. The new underground coal pipe is cast-in-place reinforced concrete structure, its anti-deformation technology measures including flexible measures, rigid measures and the combination of flexible measures and rigid measures, in order to make buildings can withstand different types of mining subsidence deformation without damage [6-7]. Based on past experience and calculation, the specific anti- deformation technical measures is as follows:

(1) Setting one deformation joint every 30 m, from base to top all apart, deformation joint's width is 70㎜, the body type of each monomer separated by the deformation should strive to simple.

(2) Setting sliding layer under the concrete foundation, practice: 100㎜ thick C15 concrete cushion, with cement mortar screeding, with two layers of linoleum. Compare to width of the base, 100㎜ more per side.

(3) make waterproof layer on all around and top of the outsid concrete wall' outside, make protective layer on waterproof layer and outside of the protective layer fill 200㎜ thickness of slag.

(4) increase coal pipeline' stiffness and the amount of reinforcement appropriately.

Measures of resistance to deformation is the precondition of building structural design, can refer to in the design of the new building measures of resistance to deformation and resistance to

deformation of concrete design still need to calculate according to the deformation of the concrete situation in detail.

Summary

1.The new coal pipeline engineering is a cast-in-place reinforced concrete structure and all buried, will undergo Ⅱ stage mining influence affected by the residual subsidence deformation of the seventh coal mining belong to the PingMei group.

2. The mining subsidence make the underground coal pipeline bearing not only the earth pressure of upper, lower and lateral, but also the result of the subsidence deformation include of vertical and horizontal in-plane bending moment.

3.Through comprehensive analysis of underground mining influence and stress distribution of coal pipeline, put forward the scientific and reasonable anti-deformation technical measures, providing basis for anti-deformation design.

Reference

[1] State Bureau of coal industry: Buildings, water, railway and coal pillar and coal mining regulations[M].BeiJing:China Coal Industry Publishing House,2000.

[2] Teng YongHai,Tang ZhiXin,Zheng ZhiGang. Research and application of fully mechanized top coal caving mining subsidence[M]. BeiJing:China Coal Industry Publishing House,2009.

[3] Zhou GuoQuan,Cui JiXian,Liu GuangRong,et. Coal mining under buildings[M].Beijing:China Coal Industry Publishing House,1983.

[4] Liu ZhaoPei,Zhang WenMei. Structural mechanics[M].The 1 edition. TianJin: TianJin University press, 1998.

[5] Sun XunFang,Fang XiaoShu,Guan LaiTai. Mechanics of materials [M]. the 5 edition. BeiJing: Higher Education Press, 2009

[6] Teng YongHai, Wang JinZhuang. China's study on coal mining beneath surface buildings-state-of-the-aet and developing trend[C]. Transactions of Nonferrous Metals Society of China, 2005,15,(1): 6～8.

[7] Yang WeiGuang. Ground and foundation [M]. 3 edition. Beijing: Chinese Architecture Industry Press, 1998.

Advanced Materials Research Vols. 986-987 (2014) pp 882-886

doi:10.4028/www.scientific.net/AMR.986-987.882

Stress intensity factors for high aspect ratio semi-elliptical external surface cracks in cylindrical vessels

QI Hong-yu[1,2,a], GUO Peng-chao[1,b]

[1]School of Energy and Power Engineering, Beihang University, Beijing 100191, China;

[2]Collaborative Innovation Center of Advanced Aero-Engine, Beijing 100191, China;

[a]qhy@buaa.edu.cn, [b]guopengchao2013@163.com

Keywords: Aspect ratio; External longitudinal crack; Influence coefficient; Stress-intensity factors (SIFs).

Abstract. External surface cracks can occur in cylindrical vessels due to damage and propagate in the manufacturing process and during service life. Most of research focuses on stress intensity factors for surface cracks with low aspect ratios, i.e., a/c ≤1.0. Situation may well arise where the aspect ratio of cracks is larger than one. An external longitudinal surface crack is assumed to be subjected to different types of hoop stress distributions acting perpendicular to the crack faces. The stress intensity factors (SIFs) along the crack front were determined through the three-dimensional finite element method. Then these results are used to compute approximate values of SIFs in the case of complex loadings by employing both the superposition principle and the power series expansions of the actual hoop stresses. It is found that the maximum stress intensity factor for external surface cracks with high aspect ratio occurs at different point to that with low aspect ratio.

Introduction

Cylindrical vessels are widely used as pressure vessels in infrastructure engineering, for example, in the power plant and chemical industries and in the manufacturing process and during service life, semi-elliptical surface cracks may initiate on internal or external surface. These cracks can extend quickly under applied loads which may cause catastrophic failure. Therefore,accurate stress intensity factors (SIFs) for such elastic surface cracks are necessary for reliable prediction of fatigue crack growth rates of pressure vessels.

Lots of efforts has been devoted to the calculation of SIFs for the semi-elliptical surface cracks. Despite of the accuracy, analytical solutions are complex and only applicable to some simple crack configurations and boundary conditions [1]. To avoid this limitation, numerical solutions have proved to be an effective approach.Newman and Raju[2] used 3-dimensional finite-element methods （FEM）to calculate stress intensity factors for semi-elliptical surface cracks as well as Roberto Brighenti[3]. Bueckner HF [4,5]used weight function method to obtain the SIFs. Others numerical methods also have been used, boundary element method (BEM) [6, 7], and element-free method [8].

However,much focus has been (see references above) on SIFs for semi-elliptical surface cracks with aspect ratio a/c≤1. Kou and Burdekin [9] used finite element method to calculate SIFs with high aspect ratio up to 2.0 for circumferential semi-elliptical surface cracks but not longitudinal cracks. C.Q. Li and S.T. Yang[10] obtained the SIFs of longitudinal internal cracks with the aspect ratio a/c ≥1 but not the external cracks. External surface cracks can occur in cylindrical vessels due to damage and propagate, for instance, by fatigue.

The present study is to calculate the SIFs for cylindrical vessels with high aspect ratio semielliptical longitudinal external surface cracks and subjected to internal pressure (Fig.1)

Loading Conditions

Based on the principle of superposition[2], for a cylinder with an external surface crack, the stress induced by the internal pressure P_I is equal to that caused by the hoop stress P_a produced by the

internal pressure acting on the crack surface plus the stress produced by the internal pressure acting on the intact cylinder

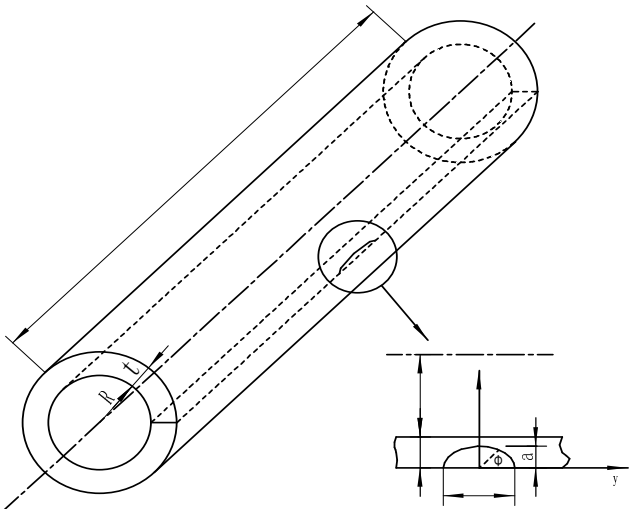

Fig.1 External longitudinal flaw in a cylinder

Such a principle can be used together with the Tylor-expand principle. The cylinder is subject to a load (p) which is applied to the surface crack with five different types of distribution, defined in a local coordinate system as shown in Fig.1 along the thickness direction (x direction). These five loading distributions are constant, linear, quadratic, cubic and quartic and can be expressed as follows:

$$p=(\frac{x}{a})^n \tag{1}$$

where n is equal to 0,1, 2,3 or 4 representing five types of load distribution. For any arbitrary load distribution at the crack face p_a, it can approximately be represented by a fourth order polynomial according to Tylor-expand principle as follows:

$$p_a=\sum_{n=0}^{4} Y_n(\frac{x}{a})^n \tag{2}$$

where $Y_n$is the coefficients that determine the form of the polynomial and will be derived in the next section. The dimensionless Mode I stress-intensity factor for the *n*th stress distribution is calculated as follows:

$$K^*_{I(n)}=\frac{K_{I(n)}}{\sigma_{ref}\sqrt{\pi a/Q}} \tag{3}$$

where $K^*_{I(n)}$ is referred to as the influence coefficient and $K_{I(n)}$ is the stress intensity factor for each given loading case p (n = 0,1, 2 ,3 or 4). σ_{ref}represents the reference stress, i.e., $\sigma_{ref}=1$.

$$Q = 1 + 1.464(\frac{a}{c})^{1.65} \text{ for } a/c\leqslant 1 \tag{4a}$$

$$Q = [1 + 1.464\left(\frac{a}{c}\right)^{1.65}](\frac{a}{c})^2 \text{ for } a/c>1 \tag{4b}$$

The given loading case p (Eq.(1)) can be replaced by an arbitrary p_a (Eq.(2)) by multiplying the term$\sum_{n=0}^{4} Y_n$. With the principle of superposition the stress intensity factor under the arbitrary load p_a, should be $\sum_{n=0}^{4} Y_n K_{I(n)}$ which can be expanded by substituting $K^*_{I(n)}$(Eq. (3)) for $K_{I(n)}$ as follows:

$$K_I=\sum_{n=0}^{4} Y_n K_{I(n)} =\sum_{n=0}^{4} Y_n K^*_{I(n)}\ \sigma_{ref}\sqrt{\pi a/Q}=$$

$$\sqrt{\frac{\pi a}{Q}}\,(Y_0K^*_{I(0)}+Y_{10}K^*_{I(1)}+Y_2K^*_{I(2)}+Y_3K^*_{I(3)}+Y_4K^*_{I(4)}) \qquad (\sigma_{ref}=1) \tag{5}$$

Application of internal pressure

Most cylinders are subjected to internal pressures.Acorrding to the above depiction, the cylinder is subjected to internal pressures P_I, then [11]

$$p_a=\frac{P_I R^2}{(R+t)^2-R^2}(\frac{(R+t)^2}{(R-x)^2}+1) \tag{6}$$

By the Tylor-expand P_I can be expanded at x=0 as follows:

$$p_a=f(x)=\sum_{n=0}^{4}\frac{x^n}{n!}f^{(n)}(0)^n$$
$$=\frac{P_I R^2}{(R+t)^2-R^2}\left(2+\frac{2}{R+t}x+\frac{3}{(R+t)^2}x^2+\frac{4}{(R+t)^3}x^3+\frac{5}{(R+t)^4}x^4\right) \quad (7)$$

Since the stress distribution is in the form of $(\frac{x}{a})^n$, (n=0, 1, 2, 3, or4), p_a can be written as

$$p_a=f(x)=\frac{P_I R^2}{(R+t)^2-R^2}\left(2+\frac{2a}{R+t}\frac{x}{a}+\frac{3a^2}{(R+t)^2}\frac{x^2}{a^2}+\frac{4a^3}{(R+t)^3}\frac{x^3}{a^3}+\frac{5a^4}{(R+t)^4}\frac{x^4}{a^4}\right) \quad (8)$$

Denoting Y_n for the coefficients in Eq. (8), then

$Y_0=\frac{2P_I R^2}{(R+t)^2-R^2}$, $Y_1=\frac{2aP_I R^2}{(R+t)a[(R+t)^2-R^2]}$, $Y_3=\frac{4a^3P_I R^2}{(R+t)^3a^3[(R+t)^2-R^2]}$, $Y_4=\frac{5a^4P_I R^2}{(R+t)^4a^4[(R+t)^2-R^2]}$

Numerical Analysis

As discussed above the key obtain the stress intensity factor is to determine the influence coefficients$K^*_{I(n)}$. Before working out the influence coefficients for, it is necessary to verify the 3D finite element method proposed above. A finite element model with a quarter of cracked cylinder is used to analyze the SIFs under each of the five elementary stresses because of the symmetry (Fig.2). In the 3D FEA, wedge finite elements are created by collapsing one side of each brick element near the crack front; the mid-side nodes of the wedge elements are shifted to quarter-point positions to model the theoretical square root singularity of the stresses and strains. The quarter cylinder was then carefully partitioned with the purpose of creating desired mesh around the crack front. The influence coefficients are determined under each stress distribution respectively based on Eq. (3). The results of the influence coefficients are presented in Table 1 together with those of Raju and Newman [2]. The difference between the two for most results is within 3.0% with the maximum difference less than 6.0%.The comparison suggests that the proposed 3D FE model and method as accurate as those of Raju and Newman [2].

With the proposed 3D FE method verified, the influence coefficients for high aspect ratio semi-elliptical surface crack (a/c=1.2 or 1.5) in a cylindrical vessel subjected to constant, linear, quadratic ,cubic or quartic stress distributions have been calculated using ANSYS software. As discussed above, there are many geometric and loading factors that affect the stress intensity factor K_I among which are: a/t, a/c, t/R. And the K_I varies along the crack front. In the 3D FEA, the influence coefficients were calculated on the crack front of the elements as determined by the angle ϕ.

As shown in Fig.3-6 ,influence coefficients distribution along the crack front in terms of the angle ϕ for various values of a/c, a/t and t/R. As can be seen the influence coefficients K^*_n at the same points on the crack front considerably vary with the different type of load distribution. For example, in Fig.3,at the surface point, $\phi=0$, the influence coefficient of constant load distribution is about 52 times that of quartic load distribution. Moreover, not only the magnitude of the influence coefficient is affected by load distributions, but also the trend along the crack front is different. As can be seen in Fig.3-6, under the constant load distribution the influence coefficients mainly decrease from the surface point($\phi=0$) to the deepest point($\phi=\pi/2$).However, under the other four load distributions the influence coefficients increase from the surface point($\phi=0$) to the deepest point($\phi=\pi/2$).

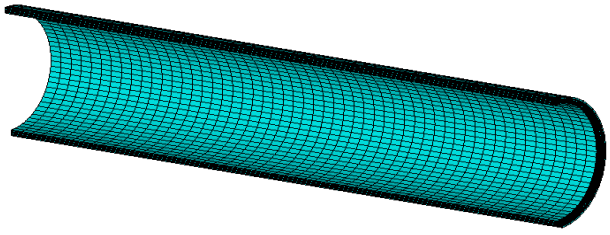

a FE model of a quarter of the cylinder

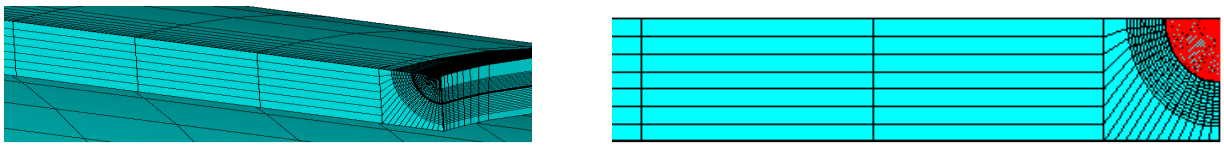

b the crack face **c** the distribution of load on crack face (in red)

Fig.2 Finite element model for the cylinder

On the other hand, the ratio of wall thickness to the radius of the cylinder vessel t/R almost have no effect on influence coefficient at present study. As can be compared Fig.5 and Fig.6 with the same condition other than t/R, when the t/R from 0.1 to 0.25,the difference between the two value of influence coefficient is within 1%. However, it is found that the higher the aspect ratio of cracks the larger the stress intensity factors at the surface point when compared Fig.3 with Fig.5.

According to the Eq. (5), the SIFs of the crack front from the surface point ($\phi=0$) to the deepest point ($\phi=\pi/2$) can be obtained with the cylinder subjected to internal pressure p_I through the 3D FE model. The K_n has been shown in Fig.7, which define the p_I equal to 1, with the different of a/c.

From above results it has been shown that, the maximum stress intensity factor can occur at the deepest point ($\phi=\pi/2$) of the crack front for cracks with low aspect ratio while it may occur at the surface point ($\phi=0$) when the crack has high aspect ratio. Therefore, aspect ratio of the crack may cause different modes of failure for the cylinder vessels. These results vindicate the need for further research on cylinders with semi-elliptical surface crack for high aspect ratio (a/c＞1) even though almost all current research focuses on low aspect ratio (a/c≤1).

Table 1 Verification of influence coefficients with Raju and Newman (1982) (a/c=1.0 and t/R=0.1)

loading		a/t=0.2			a/t=0.5		
		Eq.(3)	Raju and Newman	difference	Eq.(3)	Raju and Newman	difference
Constant (K_0^*)	π/2	1.0193	1.025	0.55	1.1279	1.118	0.88
	π/4	1.0474	1.044	0.32	1.2077	1.144	5.56
	0	1.1753	1.156	1.66	1.4726	1.453	1.3
Liner(K_1^*)	π/2	0.7143	0.718	0.51	0.7823	0.765	2.26
	π/4	0.5619	0.544	3.29	0.6056	0.570	5.26
	0	0.1950	0.202	3.46	0.2696	0.286	8.73
Quadratic (K_2^*)	π/2	0.5904	0.590	0.06	0.6418	0.619	3.6
	π/4	0.3353	0.335	0.08	0.3574	0.344	3.89
	0	0.0750	0.076	1.31	0.1112	0.1113	0.89
Cubic(K_3^*)	π/2	0.5157	0.513	0.52	0.5575	0.533	4.59
	π/4	0.2199	0.219	0.41	0.2327	0.222	4.81
	0	0.0392	0.039	0.51	0.0589	0.059	0.16

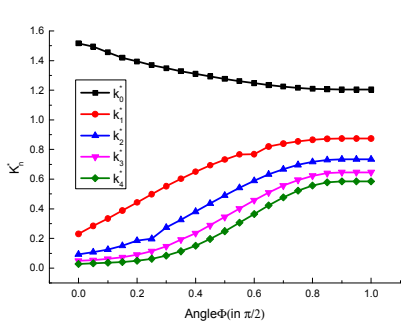

Fig.3 Influence coefficients distribution along the crack front for a/c=1.2 ,t/R=0.1 and a/t=0.2

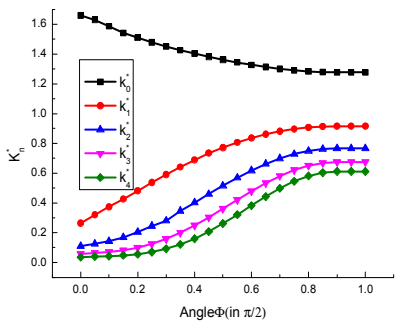

Fig.4 Influence coefficients distribution along the crack front for a/c=1.2,t/R=0.1 and a/t=0.5

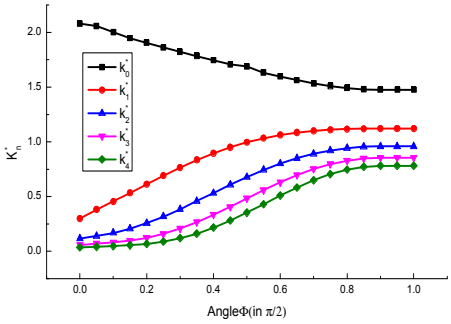

Fig.5 Influence coefficients distribution along the crack front for a/c=1.5,a/t=0.2 and t/R=0.1

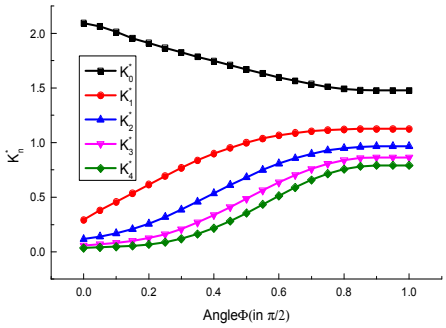

Fig.6 Influence coefficients distribution along the crack front for a/c=1.5,a/t=0.2 and t/R=0.25

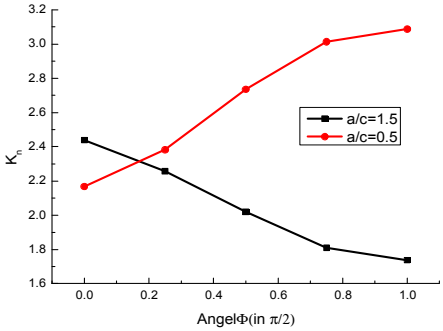

Fig.7 K_n along the crack front for a/t=0.2,t/R=0.1

Conclusions

The stress intensity factors of high aspect ratio semi-elliptical longitudinal external surface cracks in metallic cylindrical vessels have been examined through employing a three-dimensional finite element model. It has been found that the maximum stress intensity factor for external surface cracks with high aspect ratio occurs at different point to that with low aspect ratio and hence may lead to different modes of failure. It has also been found that the type of loading is the most significant factor that affects the stress intensity factor. It can be concluded that the method presented in the paper can be used to determine the stress intensity factors for cylindrical vessels with surface cracks of a large range of aspect ratios. This will enable more accurate prediction of crack growth rate and shape parameter of cylindrical vessels with various longitudinal semi-elliptical surface cracks.

Acknowledgements

This project was supported by the Beijing Municipal Science & Technology Commission (D131100003113003) and the Hi-Tech Research and Development Program (863) of China (2012AA052102) and Program of International S&T Cooperation of China (2013DFA61590).

Reference

[1] S.T. Yang, Y.L. Ni, C.Q. Li: Eng Fract Mech Vol.109 (2013), p.138
[2] Raju IS, Newman JC: J Press Vess-T Vol.104 (1982), p.293
[3] Roberto Brighenti: J Press Vess-T Vol.123 (2001), p.139
[4] Bueckner HF: ZAMM Vol.50 (1970), p.529
[5] Bueckner HF: ZAMM Vol.51 (1971), p.97
[6] Pan E. A: Int J Fract Vol.88 (1997), p.41
[7] Blandford GE, Ingraffea AR, Liggett JA: Int J Numer Methods Engng Vol.17 (1981), p.387
[8] Krysl P, Belytschko T: Int J Numer Methods Engng Vol.44 (1999), p.767
[9] Kou KP, Burdekin FM: Eng Fract Mech Vol.73 (2007), p.1693
[10] C.Q. Li, S.T. Yang: Int J Pres Ves Pip Vol.96-97(2012), p.13
[11] Timoshenko SP, Goodier JN:Theory of elasticity,(International edition,Singapore 1970).

Advanced Materials Research Vols. 986-987 (2014) pp 887-890

doi:10.4028/www.scientific.net/AMR.986-987.887

Structure dynamic response analysis of pipe string under the action of Perforating detonation wave

Xiang Sun[1,a], Zong-zhi Yang[2,b], Yun-gang Liu [3,c],
Mai-quan Zhang[4,d], Yuan-fei Zhu[5,e]

[1]China University of Petroleum, No.66, Changjiangxi Road, Huangdao District, Qingdao

[2]China University of Petroleum, No.66, Changjiangxi Road, Huangdao District, Qingdao

[3]Shengli Oilfield Well Logging Company，Beier Road, Dongying District, Dongying

[4]Shengli Oilfield Well Logging Company，Beier Road, Dongying District, Dongying

[5]Shengli Oilfield Well Logging Company，Beier Road, Dongying District, Dongying

[a]sunx839@126.com, [b]yangzongzhi621@126.com, [c]13515467972@139.com,
[d]zhmq8112@163.com, [e]zhuyuanfei@126.com

Keywords: Impact perforation; Pipe string ; Dynamic response; Finite element analysis

Abstract. Impact load of perforation will result in strong vibration of downhole string, string operated such as bending fracture accidents. Considering the clearance between string and casing, using space beam and spring element to solve the nonlinear contact problems between oil jacket, established the numerical model of string structure dynamic response analysis in horizontal well. Extracting downhole perforation pressure wave monitoring data, using the finite element software ANSYS, analyzed the dynamic response of the tubing under perforation of detonation shock wave impact, got the displacement of the tubing, acceleration time history. The results show that, without packer, the maximum Mises equivalent stress in the end of the string, the deformation and stress changes in deflecting section of the tubing string are bigger than in vertical Wells.

Introduction

Perforation completion is adopted widely in oilfield, The enormous detonation wave generated When perforating gun firing is released within the wellbore. This part of the detonation wave will push string strong shock vibration[1,2] upwards,may cause tubing string bend, fracture etc. Due to the horizontal well string thousands of meters long, it is very difficult to solve the process of string dynamics when perforating with analytical method . a lot of simplification is needed for the model, even without a lot of simplification can't get analytical solutions[3,4] . But this kind of problem can be solved by the finite element method,even without simplification, only need to establish a correct finite element model. This paper, using finite element method of transient dynamic problems, theoretical studied the perforating tubing string vibration problem in horizontal well.

The transient dynamics fundamental equations

The basic equation of transient dynamics analysis is:

$$[M]\{\ddot{u}\}+[C]\{\dot{u}\}+[K]\{u\}=\{F(t)\} \quad (1)$$

Where:

$[M]$=mass matrix

$[C]$=damping matrix

$[C]$=stiffness matrix

$\{\ddot{u}\}$=acceleration vector of the node

$\{\dot{u}\}$=velocity vector of the node

$\{u\}$=displacement vector of the node

At any given time t, these equations can be considered as a series of the static equilibrium equations ,which considering the inertial force and damping force.

String structure dynamic model

Select the entire string as the research object, the initial position of the string and borehole axis is a coincidence. String in the wellbore distorted under a variety of load combination such as gravity, buoyancy force, internal and external pressure, perforating impact etc,and multidirectional random contact with the inner wall of the casing will happen.

Because considering the initial clearance of the string and casing , the contact problem of string and casing is a random contact nonlinear mechanics problem, the calculation method has the certain difficulty and complexity. Each beam element string can list a unit balance equation, all the balance equation after coordinate transformation and assembled unit, the whole string of overall balance equation is obtained:

$$\{K\}\{u\} = \{P\} \tag{2}$$

Where:

$\{K\}$=global stiffness matrix

$\{u\}$=the overall displacement vector

$\{P\}$=the overall load vector

with the balance equation of beam element and spring element equilibrium equation are combined after assembling, string contact nonlinear problem of overall balance equation is obtained as follows:

$$\{K + K_T\}\{u\} = \{P\} \tag{3}$$

Where:

$\{K_T\}$=the whole stiffness matrix for all the spring element after conversion to assemble

A large number of numerical examples show that when perforating the longitudinal vibration load produced by the tubing string is much higher than on the tubing string lateral load. That is to say longitudinal vibration (axial) plays a main role[5,6], therefore the model only need apply the longitudinal vibration impact load in the end of the perforation .

Analysis of examples

The finite element model

For example , the string in a perforation completion horizontal well, according to the survey data, established the whole interval finite element analysis model . Among them, the column diameter is 73 mm, inner diameter is 62 mm, the material is N80 steel, the density is 7846 kg/m3, poisson's ratio is 0.3, the elastic modulus is 206 GPa, yield limit is 564 mpa and shear modulus is 79.4 GPa.

Use Beam4 and Combination14 unit established the string structure finite element model as shown in figure 1.

The boundary conditions

Imposing fixed constraints in the location of the well head, using coordinate system in the other nodes of the column, imposing the constraint of double spring element along the radial and axial direction of the column, even at the end of the spring on the column node, the other end is fixed.

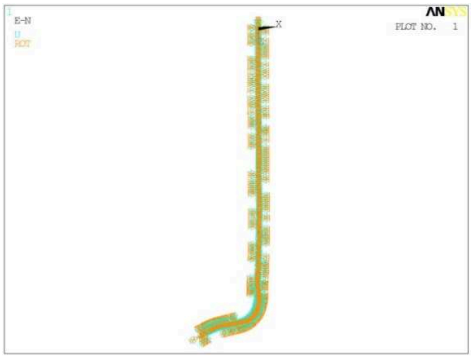

(a) whole

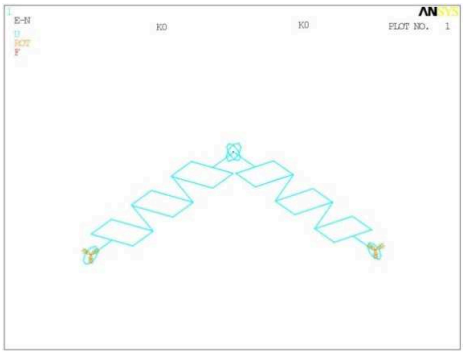

(b) a node applied two-way spring

Figure 1.String finite element model

Column loads

Through pressure monitor we gather the distribution of wellbore pressure, and extract the data as the dynamic load of the column structure.

The simplified perforation detonation wave load as shown in figure 2, the figure shows that the longitudinal impact load increases rapidly firstly , and then fail to a certain value ,lastly flunctuate around it during the process of blasting. Lengthwise perforation impact load as shown in figure 2 is imposed to the end of horizontal pipe column.

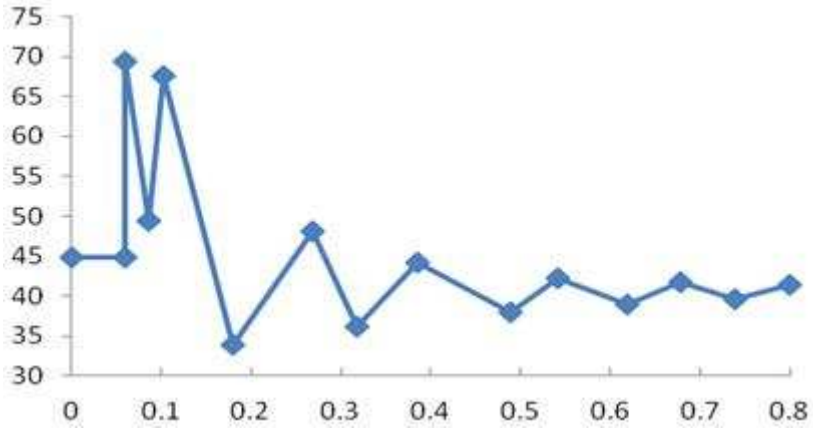

Figure 2.Perforating impact load curve

Analysis of the results

Through the numerical analysis of dynamic response of the column under the action of detonation wave by the finite element software ANASYS, we obtain the deformation and stress contours of the whole model as shown in figure 3.

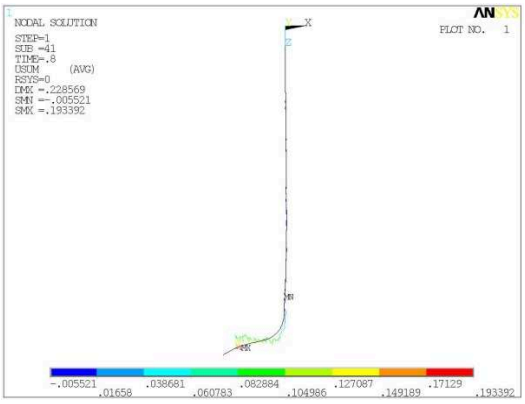

(a) Model displacement nephogram

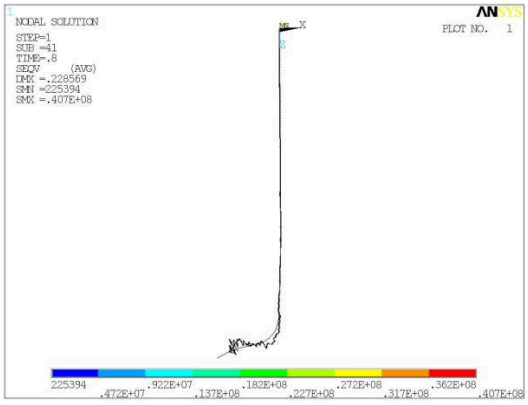

(b) Model stress nephogram

Figure 3.String structure dynamic response

By the figure, we know the maximum displacement of column node is about 0.229m, located NO.268 node, and deformation of tubing string on the deflecting section are much larger than on the vertical section. The maximum Mises stress is 40.7MP, located at the end of the column; the minimum value is 0.225MP, in the tube end of the mouth of the well.

Extract the result data of node 278, and analysis the column longitudinal vibration displacement, velocity and the time history of acceleration as shown in figure 4, 5 after perforating. As shown in the figure 2, under the action of perforation impact load, node 278 longitudinal displacement trend along with the change of time and impact load are of a similar change trend, which is rapidly increasing first, then the attenuation, the maximum value is about 0.3m. Without considering damping, the biggest vibration velocity of the column is about 2.08m/s.

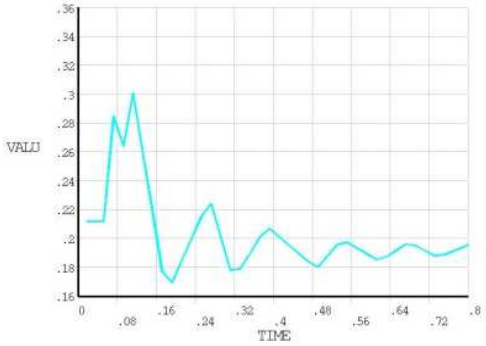

Figure 4.Displacement-Time curve

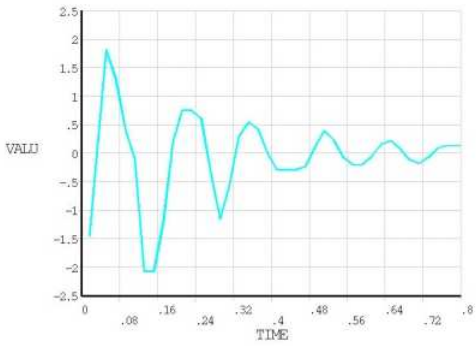

Figure 5.Speed-Time curve

Conclusions

(1)By the clearance between column and casing, the introduction of spring element model, finite element dynamic model of horizontal well tubing string, we can easily carry out the perforating dynamic analysis on the tubing column.

(2)In order to analysis the vibration mechanics problems of tubing string under the action of impact load accurately and reasonably, first we must accurately measure the relations that the perforating shock wave change along with the time, and effect on the tubing string as the transient initial dynamic load of the tubing string finite element dynamic analysis.

(3)Without arrangement of the packer, the maximum Mises equivalent stress occurred in the end of the tubing string, the stress and deformation of tubing string on the deflecting section are much larger than on the vertical section under the effect of perforating impact load.

Reference

[1] Feng Chen, Huabin Chen,Kai Tang,Guohui Ren. Influence of perforating impact load on the operating string and the countermeasures, NATUR.GAS IND.VOLUME30,ISSUE5,2010.

[2] Hongdong Yin,Shiyi Li,Jianjun Zhang. Mechanics analysis of perforating combined well testing string and protection technology of downhole instrument,Oil drilling&Production technology,Vol.25 No.3,June 2003

[3] Zhanghua Lian, Tiejun Lin, Jian Liu, Bin Le,Jufen Chen, Yuexia Xu,Tao Yang. Finite element analysis of tube string vibration on horizontal well, Oil drilling&Production technology,Vol 28 No1,Feb 2006

[4] Hongcai Zhang,Bo He. The finite element analysis - ANSYS13.0 from entry to practice, Beijing industry press,2011

[5] Xuehong Zhang,Lunyuan Chen,Jubao Liu.Finite element analysis of the contact and friction of a whole drillpipe string,ACTA PETROLEI SINICA,Vol13 No 3,1992

[6] Zhendong Yu,Yan Li. Finite Clearance Element Analysis of Perforation Tube String for Testing for Oil,Chinese Journal Of Applied Mechanics,Vol.20 No.1,Mar.2003

Advanced Materials Research Vols. 986-987 (2014) pp 891-894

doi:10.4028/www.scientific.net/AMR.986-987.891

Study on desorption temperature of adsorption bed in typical weather conditions

Hua Zhang, Xu Ji*, Ming Li, Jieqing Fan, Bin Luo, Congbin Leng

Solar Energy Research Institute, Yunnan Normal University, Kunming 650092, China

* Corresponding author: jixu@ynnu.edu.cn

Keywords: adsorption bed; typical weather conditions; desorption temperature

Abstract. In this paper, the desorption temperature of adsorption bed in typical weather condition is studied though the solar adsorption refrigeration experiment with conditions of different weather. The results showed that: the better the weather condition is, the higher the highest temperature of the adsorption bed is, so the better the effect of desorption is. No matter in cloudless sunny or partly cloudy sunny conditions, the desorption temperature of adsorption bed can reach 93.4℃, and the amount of desorption also will be larger; however, in cloudy weather conditions, desorption temperature can reach 88.5℃, and desorption quantity is relatively fewer than it in cloudless sunny days.

Introduction

The solar energy refrigeration way mainly includes the solar energy light hot refrigeration and the solar energy photoelectricity refrigeration. The photoelectricity refrigeration is mainly photovoltaic refrigerator; the light hot refrigeration mainly has adsorption type, absorption type, the jet type, dehumidification type, etc. Adsorption refrigeration has the advantages of a simple structure, low operating cost, the long lifetime and thermal coefficient of performance (COP) higher, etc. Therefore, the adsorption refrigeration technology is widely concerned by refrigeration field [1].

Adsorption refrigeration as a environment-friendly refrigeration way, many domestic and foreign scholars have done a lot of research from theory and experiment: Y. Zhong [2-3] study on the isothermal adsorption characteristics of barium chloride. He pointed out that the barium chloride - ammonia working pairs can be used for air conditioning and refrigeration. For the air conditioning performance, when the cooling temperature is 35℃ and refrigeration temperature is 15 ℃, system COP as high as 0.6. Shanghai Jiao tong University, Y.Z. Lu [4] applies thezeolite molecular sieve - water adsorption refrigeration in the locomotive air conditioning. The research indicated the zeolite molecular sieve - water working pairs has the very high cold storage capacity and 1 kg zeolite molecular sieve stores cold up to 600 kJ. D.M. Li[5] established a Thermodynamic calculation model of the adsorbent bed, which take into account the interactions in absorption bed temperature, pressure and the quality. By using the numerical calculation method give a reasonable explanation of equation in solar energy radiation intensity change, for further analysis of dynamic characteristics in adsorption bed laid a foundation. To reduce the adsorption bed thermal resistance, D.S. Zhu[6] has carried on the experimental study of adsorption bed and adsorbent (Polyaniline) particles on the surface of the contact thermal resistance. He analyzed the influence on the contact surface coated with conductive gel and pressurizing method on thermal contact resistance. The experiments show that this method can effectively reduce the contact heat resistance, and no influence on the mass transfer process in the adsorbent bed of adsorbent.

The weather conditions has important effect on the performance of adsorption bed, but there is still no mature theoretical analysis [7-8], and also lack of corresponding experimental research. Therefore, this paper mainly experimental research and analysis from the influence of weather condtions on the desorption temperature of adsorption bed, and provides a theoretical basis for the application of adsorption refrigeration technology.

Solar adsorption refrigeration principle

Solar adsorption refrigeration system is mainly composed of adsorbent bed, condenser, evaporator and valve, etc. As shown in Figure 1. The adsorption bed temperature increased after absorbed solar energy. When it reaches the temperature of refrigerant desorption, the refrigerant desorbed from the adsorbent. Refrigerant vapor desorbed by condenser into liquid, and stored in the evaporator. The temperature and pressure of adsorption bed decreases in the night. Desorption of refrigerant vapors in the daytime again by adsorbents. Thus the refrigerant in the evaporator evaporation heat generated cooling, in order for the refrigeration cycle [9].

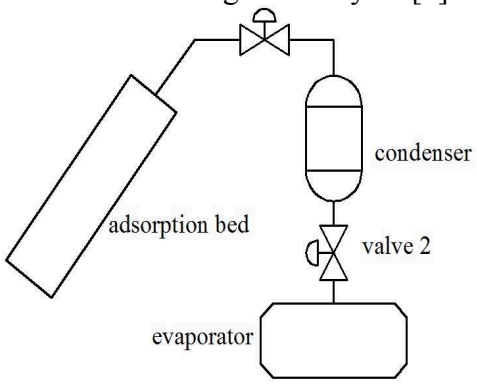

Fig. 1 Principle of adsorption refrigeration system

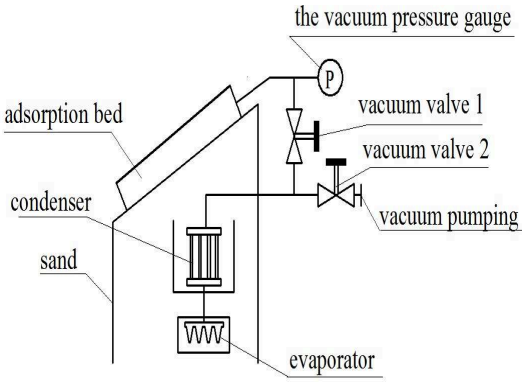

Fig. 2 Schematic diagram of adsorption refrigeration experiment

Experimental study of typical weather conditions on adsorption desorption temperature

The experiment adopts the integral fin tube as the adsorption collector bed, the effective heat collecting area of 1.5 square meters, and uses the multi tube adsorption structure of adsorbent bed and with valve control solar adsorption cooling system [10]. Refrigeration working pairs using Active carbon-methanol. Adsorption refrigeration system experiment schematic diagram is shown in Figure 2.

The effect of typical weather conditions on the temperature change of the adsorption bed

In order to accurate illustrate the effects of typical weather conditions on the desorption temperature of adsorption bed, this paper makes some research on solar adsorption refrigeration experiment under the cloudless sunny, partly clouds in the sunny, cloudy with strong solar radiation and cloudy with weak solar radiation environments, and analyses the temperature changes of adsorption bed in four typical weather conditions. The curves of temperature of adsorption bed and solar radiation under the four typical weather conditions are shown in Figure 3.

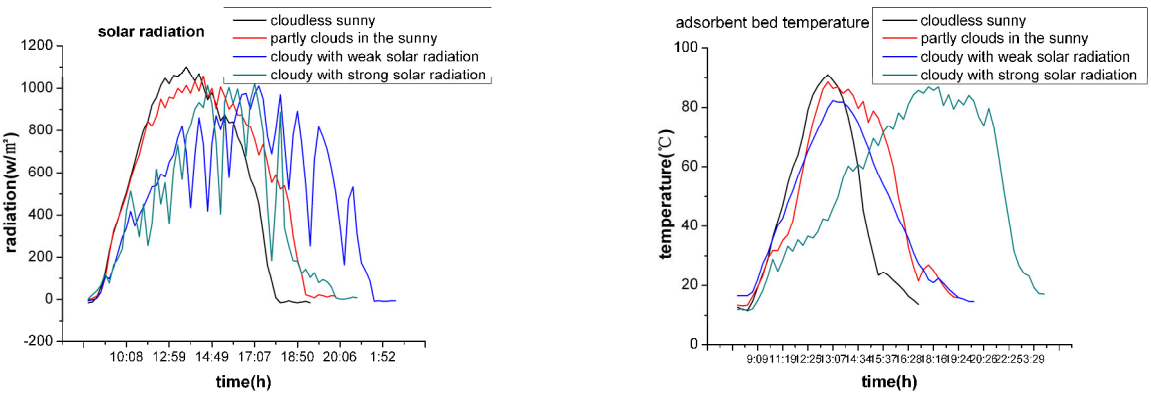

Figure.3 The curves of the temperature of adsorption bed and solar radiation

Analysis of Figure 3 indicate that the temperature of adsorbent bed mainly depends on the weather conditions. In the heating stage, the adsorption bed received solar radiation, the temperature of

adsorption bed begin to rise gently until the temperature rises to the highest point, then the temperature of adsorption bed maintains stably. In the heating stage, adsorption bed is mainly used for desorption of methanol in adsorbent. During the cooling stage, closed the valve, and the temperature of adsorption bed begins to decline until the temperature of adsorption bed tends to be stable. Then opened the valve, the pressure of adsorption bed is reduced. However, the temperature of adsorption bed will rise owing to releasing the adsorption heat that it is generated from the evaporation of methanol in evaporator. Eventually, adsorption equilibrium and adsorption bed temperature tend to be stable.

In cloudless sunny weather, the temperature of adsorption bed rises the fastest and the temperature curve is smooth. There was no significant fluctuation in temperature; in partly clouds in the sunny weather, the temperature of adsorption bed appears small fluctuations and the curves of temperature have concaves; in cloudy with strong solar radiation weather, clouds cover a long time, the temperature of adsorption bed change scope is big, and the curves of temperature has a lot of concaves; in the three kinds of weather conditions which given above, the temperature of adsorption bed in high temperature (greater than 80℃) time is greater than 3 hours, and the effect of desorption is better. In cloudy with weak solar radiation, temperature's variation of the adsorption bed is not obvious, whereas the temperature of adsorption bed maintains at above 80 ℃ less than 2 hours, and the function of desorption is poor.

The effect of typical weather conditions on the maximum desorption temperature of adsorption bed

In order to further illustrate the influence of typical weather conditions on the desorption temperature of adsorption bed, this paper studies on the highest temperature of adsorption bed. Then it compares and analysis the highest temperature of adsorption bed under the cloudless sunny day, partly clouds in the sunny and cloudy with strong solar radiation environments. Experimental data is shown in Figure 4.

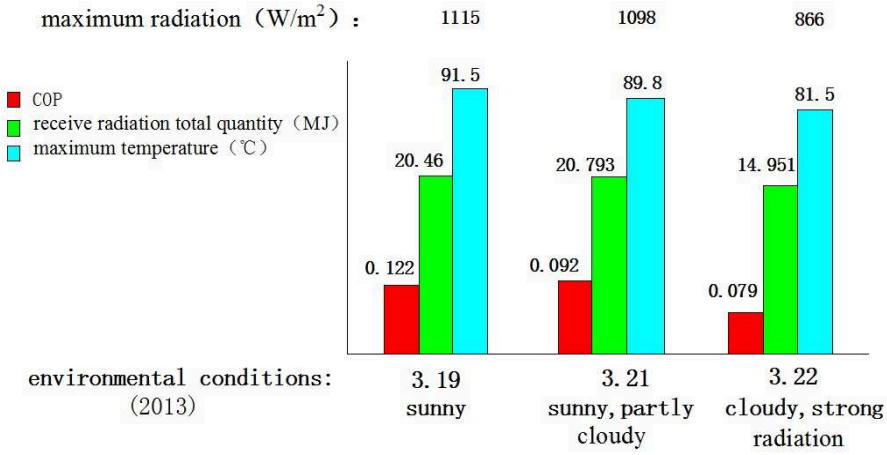

Figure.4 Typical weather conditions and the highest temperature of adsorption bed

Compared the cloudless sunny and partly clouds in the sunny weather, although the total amount of radiation received by adsorption bed in partly clouds in the sunny weather more than that in the cloudless sunny weather, however the largest amount of radiation received by adsorption bed in cloudless sunny weather is 1115 W/㎡, and it is 1098 W/㎡ in partly clouds in the sunny weather. So the highest temperature of adsorption bed in the cloudless sunny weather is 1.7℃ higher than it in partly clouds in the sunny weather. In addition, the COP is also greater than it in partly clouds in the sunny weather. The total solar radiation and the maximum amount of radiation received by adsorption bed in partly clouds in the sunny weather is greater than those in cloudy with strong radiation weather. Therefore, the maximum temperature of adsorption bed is 8.3 ℃ higher than it in cloudy with strong radiation weather. Through the above analyses, the maximum temperature of adsorption bed has very significant relation with weather conditions. The better the weather conditions are, the higher the

highest desorption temperature of adsorption bed is, and the adsorption refrigeration system has a high cooling efficiency.

Summary

In this paper, the desorption temperature of adsorption bed under typical weather conditions are studied though the solar adsorption refrigeration experiment and then drawing the following conclusions:

(1)The temperature of adsorbent bed mainly depends on the weather conditions, the better the weather conditions are , the higher the highest desorption temperature of adsorption bed is. So this state is advantageous to the adsorbent desorption and the adsorption refrigeration system has a high cooling efficiency.

(2)In cloudless weather, temperature of adsorption bed almost has no fluctuations, it maintains at high temperature for long periods of time. Hence, this state is advantageous to the adsorbent desorption; In partly clouds in the sunny, cloudy with strong solar radiation weather, the adsorbent desorption efficiency is not good; Meanwhile, in cloudy with weak solar radiation weather, the variation range of adsorption bed temperature is not obvious, and the temperature maintains at high temperature for a short time. So the adsorbent desorption condition is poor, and it has less contribution to the refrigeration system. The progress of research on new adsorbent bed

Acknowledgements

The present study was supported by National Natural Science Foundation, China (Grant No.: 51366014).

References

[1] X. Ji, M. Li, J.Q. Fan. Structure optimization and performance experiments of a solar-powered finned-tube adsorption refrigeration system. Applied Energy, 113 (2014): 1293–1300.
[2] Y. Zhong, R.E. Critoph, R.N. Thorpe. Isothermal sorption characteristics of the BaCl2-NH3 pair in a vermiculite host matrix. Applied Thermal Engineering, 27(2007): 2455-2462.
[3] Y. Zhong, R.E. Critoph, R.N. Thorpe. Dynamics of BaCl2-NH3 adsorption pair. Applied Thermal Engineering, 29(2009): 1180-1186.
[4] Y.Z. Lu, R. Z, M. Zhang. Adsorption cold storage system with zeolite water working pair used for locomotive air conditioning. Energy Conversion and Management, 44(2003): 1733-1743.
[5] D.M. Li, Y.J. Jiang. Thermodynamic calculating method of adsorption bed in the solar adsorption refrigeration system. Acta Energiae Solaris Sinica, 24(2003): 483-487.
[6] D.S. Zhu, S.W. Wang. Experimental investigation of contact resistance in adsorber of solar adsorption refrigeration. Solar Energy, 73(2002): 177-185.
[7] W.Z. An, Z.Q. Liu. Experimental study and exploration of adsorption working pair in adsorption refrigeration system. Chinese Journal of Refrigeration Technology, 41(2012): 65-69.
[8] Z.G. He. Research progress in new types of adsorber. Chemical Engineering, 39(2011): 34-38.
[9] X.C. Yang, X.X. Zhang. Research status of solar energy in absorption and adsorption refrigeration systems. Vacuum and Cryogenics, 19(2013): 130-134.
[10] J.L. Liu, X.L. Zheng. Research and development of solar solid adsorption refrigeration technology. Journal of Green Science and Technology, 9(2011): 188-191.

Advanced Materials Research Vols. 986-987 (2014) pp 895-899

doi:10.4028/www.scientific.net/AMR.986-987.895

Study on milling deformation of ruled surface blade

Maoyue L I [1, a], Haibin YU [1, b], Yunzhong FU[2, c]

[1]Mechanical and Power Engineering College, Harbin Univ. Sci. Tech., Harbin, 150080, China

[2]School of Mechatronics Engineering, Harbin Institute of Technology, Harbin, 150001, China

[a]email: lmynjfu@sina.com, [b]email: 1012959811 @qq.com, [c]email: fyz@hit.edu.cn.com

Keywords: Ruled surface blade; Deformation; Finite element simulation

Abstract. Integral impeller is the key component in aviation, aerospace and other fields, and the deformation has an important effect to the machining quality and precision of the integral impeller. Because of the complexity of the geometry and surface curvature changes for the integral impeller, and the semi suspended state during the processing, force analysis and control technology for the deformation have become the key and difficulty to realize high quality processing. In this paper, the situation about the blade machining with the finite element analysis is introduced, and the factors about the blade machining deformation is also summarized. The deformation of a single cutter location point are computed and analyzed with finite element method, and the application problems to the machining deformation with the finite element are presented.

Introduction

Impeller parts are the typical and representative parts with complex surfaces. The processing precision and quality directly determine the effectiveness of the related mechanical equipment. It is still a research spot on the tool path planning and processing technology in the field of numerical control machining for high speed and stable impeller parts. It is easy to make a deformation during blade machining, which causes the errors of parts dimension and leaf thickness non-uniformity. On the other hand, it will have a complex stress and large vibration amplitude for the blade surface during the work processing. In order to improve the efficiency of product processing, it usually works in the milling deformation limit state for the machine systems and the cutting process. Therefore, the analysis of deformation of the impeller machining process is directly related to the processing quality of impeller and its working performance in the future.

Before the work-pieces are machined, it can make a good preparation for the thin walled work-piece milling if the model is analyzed with finite element, which can know about the parameters, such as stress changes, temperature changes and yield limit. Compared to the traditional experimental methods, the finite element simulation for the surface quality analysis, tools' design, process selection and so on, can save more time. The most important is the mechanical and physical properties can be obtained from the finite element simulation results. However, it is difficult to achieve the result with the traditional experiment.

Thin blade machining situation with finite element

At present, the research direction about the finite element model can be divided into two types: only considering the work-piece deformation and considering both the work-piece and the tools deformation. Wang Zhigang [1] analyzed the milling processing deformation of Aeronautical thin-wall box parts by the finite element software, which was under the assumption that the tool was a rigid body and the feedback effect of deformation was ignored. Ratchev [2] established the surface error prediction model of the thin-walled parts round side milling using the finite element software ABAQUS. A flexible prediction model was established which included the work-piece deformation and surface error with the changes of entry angle and exit angle [3].

Kline [4] studied the milling deformation model of a rectangular thin plate. Budak [5] confirmed the instantaneous un-deformed chip thickness converged to the nominal value in the static milling

process. So only the correction value of radial cutting depth is considered, but the correction value of the instantaneous un-deformed chip thickness isn't considered during considering the deformation coupling model of the tool and work-piece deformation. The iterative algorithm would be used to analyze the coupling effects between tool and work-piece deformation and the material removal effect in the processing. Budak [6] established a tool model by using the equivalent cylindrical cantilever beam unit along the axial length. On this basis, Wan Min [7] proposed a method to discrete the structure with irregular finite element grids, which provides a general method for complex parts to discrete the grid. In addition, Zhang Zhihai [8] established a model to predict the work-piece surface error in the end milling, which considered the relationship between the milling force / torque and instantaneous un-deformed chip thickness. The deformations of the tool, work-piece and machine tools and other factors were considered in this model, but the coupling effect between the tool deformation and work-piece deformation were not considered.

At present, it is not perfect in the field of thin-walled components machining deformation by finite element analysis, but it was able to simulate the relationships among different parameters. In the model of only considering the deformation of the work-piece, it cannot reflect the characteristics of periodic fluctuation in milling processing and the distribution law of milling force along the direction of the cutting edge, and has a certain effect on the deformation prediction accuracy, because the applied milling force is the average values according to the empirical formula. In the model of considering both the deformation of the work-piece and cutter, although the deformation factors including the tool and work-piece and machine are considered, but the coupling effects of the tool and work-piece deformation are ignored, so it must have some influences on the machining simulation precision.

Deformation analysis of the blade machining

The deformation caused by the low stiffness is very important in milling thin-walled components, because it is related to the thin-walled components machining quality and precision. The elastic deformation for the thin blade will be generated due to the effects of the force. The impeller blades' deformation can not be ignored because it is in the semi suspended state during the processing, which is shown as Fig. 1. Generated parts size errors and leaf thickness non-uniformity errors will directly influence the overall performance of the impeller. However, it will be an effective method for machining the integral impeller to reduce the machining deformation by adjusting the radial depth parameters, after analysis the deformation of blade, and calculating the final deformation of thin-walled blades with the iterative algorithm.

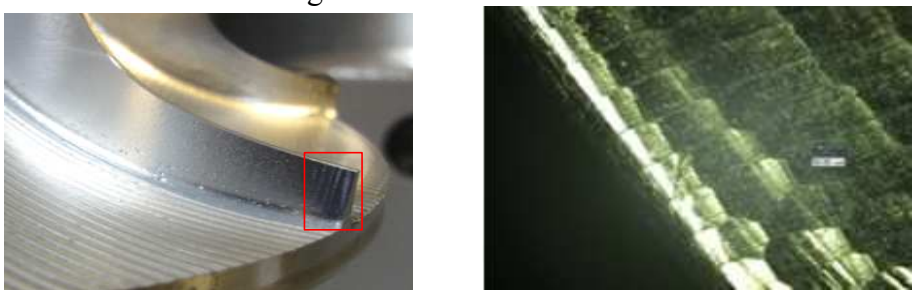

Fig. 1 High speed milling blade surface morphology

The deformation of the blade will be analyzed by ANSYS, and the studied blade machining deformation is decomposed into two directions, including the normal direction and the tangent direction. The deformation along the normal direction mainly inflects the effects on processing parameters with the work-piece deformation, while the tangential direction mainly inflects the effects on the compression tension deformation for blade. Deformation of materials in actual processing is often negligible, and blade deformation is mainly elastic deformation along the normal direction.

In the cutting process of single blade, it will have an elastic deformation generated by milling force to cause the changes of radial cutting depth. At the same time, the new milling force will generate a new deformation. It actually means the work-piece deformation has a feedback effect on

machining parameters. So it leads the radial cut depth becomes small by deformation with the milling force, and then it will make the cutting force become smaller. The smaller cutting force will generate a smaller deformation, which will make the radial cutting depth and the cutting force increase. After the cutting force increases, it will make the work-piece deformation increase. And this will result in radial cutting depth decrease, causing the milling force decrease. This repeated process will make the parameters influence each other until the convergence condition with a stable equilibrium state. It is shown as in Fig. 2. Therefore, the factors of the milling force, deformation and radial cutting depth will affect each other.

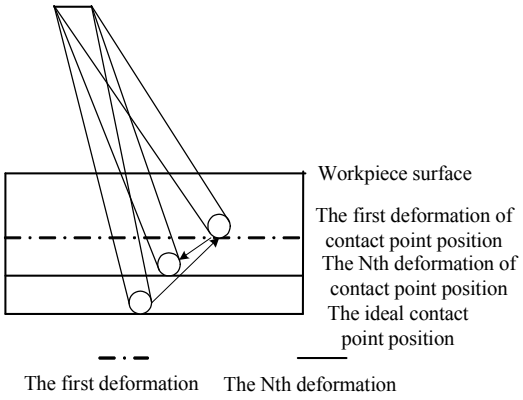

Fig. 2 Deformation iteration process

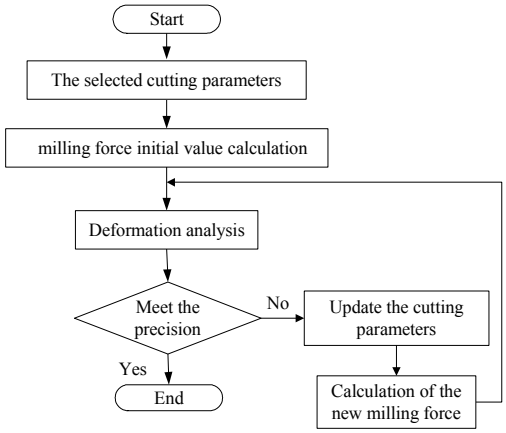

Fig. 3 Analysis flow for a single cutter location point

It is difficult to describe the relationship between the deformation and cutting force with two-dimensional graph, because the milling force and the deformation have a nonlinear relationship for the non-developable ruled surface blade. So the blade deformation can be obtained with the finite element technology, which is shown in Fig. 3. Then the new milling force can be computed with the new deformation, and iterate this process until the desired accuracy is realized.

Blade deformation calculation based on finite element analysis

The blade surface studied in this paper belongs to the undevelopable ruled surface, which has a complicated geometry. However, the ANSYS finite element software cannot realize blade's geometric modeling well. To solve this problem, the solid geometry model using 3D UG software to establish an impeller. In order to facilitate grid, blade model is a simple model (without blade root part connected with hub). Blade model with the blade root will lead to identify the interface wrong, and can't have meshes. Graphic conversion will be executed using the graphical interface between ANSYS and UG. The final model is saved as IGES format ANSYS can identify, and the 3D lead geometric model into ANSYS software is shown as in Fig. 4 a).

After the blade entity construction is completed, the grid division can be directly carried. Although the blade is thin part, it isn't suitable to grid in accordance with shell element because the blade thickness difference is very large. Therefore 3-D solid element division should be adopted. The 3-D solid element mainly has 4 nodes tetrahedron element and 20 node hexahedron unit. Tetrahedron mesh is relatively easy, but the grid is not regular, especially the distribution of nodes is irregular. Hexahedral nodes distribution is in each vertex and the midpoint of each edge, which is a hexahedron with 20 nodes. Because the node is located on the cutter location points, cutting force will not be applied to the cutter location accurately if the nodes distribution are irregular. This will be not conducive to the subsequent deformation analysis, and calculation accuracy will be bad compared with hexahedral tetrahedral. So the hexahedral element mesh will be used in the paper. Element type is selected as solid186, material is aluminum alloy T7075-651, elastic modulus EX is set to 71Gpa, Poisson's ratio PRXY is set to 0.33. The number of grid thickness needs to pay attention, and it must be in 2 or more than 2. Otherwise, the mesh cannot be generated. The result is shown as in Figure 4 b). It contains 3360 elements, 17962 nodes. It also can be seen that grid is regular, and the nodes numbers are sequential.

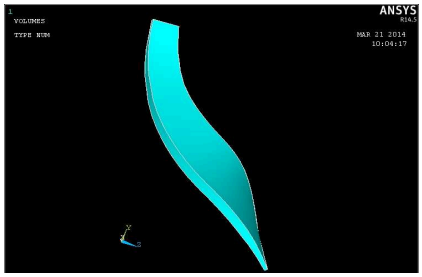

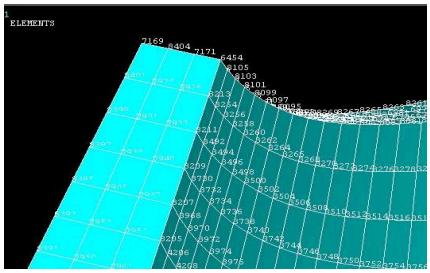

a) A blade solid model lead into ANSYS b) Grid node number

Fig. 4 A blade solid model and its mesh division

The integral impeller hub strength is greater, so the deformation is very small, and it can be neglected. So the blade root part should be constrained when adding a constraint. The blade root part can be selected using the Displacement-On Areas command, and zero can be filled in VALVE after selecting ALL DOF (full freedom constraint). It also means the displacement constraint in blade root is set as zero.

Take the numbers of 6534 single point deformation analysis for an example, the initial value of the milling force can be calculated after applying the initial milling force. Select the command of Force/Moment-On Nodes, and input node number 6534, the milling force value can be computed according to the experience formula. The results can be solved after respectively applying milling force in Fx, Fy, Fz directions. During the application process, the red milling force arrows node can be seen, then the Contour Plot-Nodal Solu command can be selected, and the deformation cloud chart can be viewed from the DOF Solution in the Nodal Solution option, which is shown as Fig. 5.

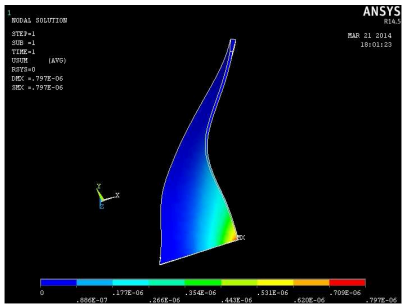

Fig. 5 Blade milling force deformation cloud chart Fig. 6 Node processing deformation

The deformation at 6534 can be observed via the command of Scalar Parameters. The total output deformation result is shown as Fig. 6.

Since the output deformations in x, y and z are not the studied result, but the total deformation is needed, and it needs to decompose the total deformation into elastic deformation along the normal direction, so as to adjust the radial cutting depth to calculate a new milling force, to calculate a new deformation until equilibrium is realized. With this process, the analysis of a single point deformation is over. Deformation calculation for the next cutter location point can go on like this.

In conclusion, the finite element analysis can be divided into three stages, including preprocessing, calculation analysis and post-processing. Preprocessing is to establish the finite element model to complete the mesh analysis. Calculation analysis can complete the computation of the force and the displacement with the relevant finite element theory. Post processing can obtain the acquired and processed results, and output it in a simple way, which is convenient for the user to quickly extract the required information.

Conclusion

The thin-walled blade deformation caused by cutting force is studied in this paper, and the calculation of single point machining deformation is analyzed by finite element method.

(1) The setting methods of blade grid and constraint conditions are shown, which is according to the geometric characteristics and the actual situation of blade machining. The finite element blade machining process analysis can be realized accurately with this method.

(2) Overall deformation size and deformation trend for individual cutter location point are calculated by finite element method, which set the foundation for deformation compensation for each cutter location point.

Acknowledgement

This research has been supported by the Natural Science Foundation of China (51205098), China Postdoctoral Science Foundation funded project (2013M531055).

References

[1] Wang Zhigang, He ning, Zhang ning , etc. Finite element analysis of deformation of machining Aerospace Thin-walled Parts [J]. Aviation Precision Manufacturing Technology, 2000, 36(6): 7-11.

[2] S. Ratchev, E. Govender, S. Nikov, etc. Force and deflection modeling in milling of low-rigidity complex parts [J]. Journal of Materials Processing Technology, 2003, 143-144:796-801.

[3] S. Ratchev, S. Liu, W. Huang, etc. Milling error prediction and compensation in machining of low-rigidity parts [J]. International Journal of Machine Tools & Manufacture, 2004,44(15): 1629-1641.

[4] W. A. Kline, R. E. Devor, I. A. Shareef. The prediction of surface accuracy in end milling [J].Journal of Engineering for Industry, 1982, 104: 272-278.

[5] J. S. Tsai, C. L. Liao. Finite-element modeling of static surface errors in the peripheral milling of thin-walled workpieces [J]. Journal of Materials Processing Technology, 1999, 94:235-246.

[6] E. Budak, Y. Altintas. Modeling and avoidance of static form errors in peripheral milling of plates [J]. International Journal of Machine Tools & Manufacture, 1995, 35(3): 459-476.

[7] Wan Min. Research on the key technology of prediction of surface static errors in peripheral milling of thin-walled workpiece machining process [D]. Xi'an: Northwestern Polytechnical University, 2005.

[8] Zhang Zhihai , Zheng li, Li zhizhong, etc. Based on milling surface geometric error model of milling force / torque model [J]. Chinese Journal of Mechanical Engineering, 2001, 37(1): 6-10.

Advanced Materials Research Vols. 986-987 (2014) pp 900-903

doi:10.4028/www.scientific.net/AMR.986-987.900

Test and Analysis on Assembly Deformation of Diesel Engine Cylinder Liner

WU Bo[1, a], WANG Zeng-quan, Liu Chang-zhen and YAO Liang-yu

[1] China North Engine Research Institute, Tian jin 300400, China

[a]wubo-cneri@163.com

Keywords: diesel engine; cylinder liner; Fourier series; finite element.

Abstract. The measurement of deformation of one diesel engine water cooling cylinder liner under free condition and assembly load case is carried out by V-INCOMETER testing system. The basic principles of radial deformation for this cylinder liner are obtained through the test data Fourier transformation. And the affect principles of cylinder liner original distort, which results from mechanical machining and heat treatment process, to the cylinder liner assembly deformation are carried out.

Introduction

The liner of water-cooled internal combustion engine embedded in block body is composed of the combustion chamber with piston set, cylinder head and cylinder head gasket. While cylinder liner also plays a guiding role for the reciprocating motion of the piston. When the diesel engine is working, the inner walls of cylinder liner contact with high temperature high pressure gas in combustion chamber directly.The outer walls contact with cooling water. Thermal stress is generated due to the temperature difference between the inner and outer walls. Combustion pressure, piston side pressure and cylinder head bolt preload, make cylinder liner to become one part in the worst working environment of the entire engine. Due to manufacture processing errors, working load and other factors, cylinder liners will appear distortion which can not be completely eliminated. The excessive cylinder liner deformation causes the piston ring and cylinder liner wall not to be fit completely. So that the piston ring sealed performance degradation will increase combustion chamber leak. At the same time that also causes poor lubrication of piston ring-cylinder liner friction pair, the piston rings excessive wear, cylinder scoring and other failures in engine operating. So the cylinder liner deformation is closely related to oil consumption, friction work, the friction pair wear and exhaust emission.

Although the total deformation of cylinder liner in working state is bigger than the assembly deformation an order of magnitude or so, it is mainly radial deformation under heat loading and combustion presure based on the assembly deformation. Thermal deformation and deformation under gas presure are mainly concentric expansion deformation and the piston ring has strong adaptability for it. The testing and simulation calculations of the cylinder liner dynamic deformation are still very difficult. The test and the calculation precision of dynamic deformation can not to be guaranteed. Therefore, to carry out the test and simulation of assembly deformation and to get the basic rules and information of cylinder liner deformation in present engine development process still have important engineering application value.

In this paper, one wet cylinder liner of a certain type of diesel engine is as the research object. Fourier transform analysis of the test results of cylinder liner deformation in free state and different preload conditions were carried out. The radial deformation rules of cylinder liner in top, middle and bottom position are obtained. The influence laws of cylinder deformation by initial deformation, which caused by mechanical processing and heat treatment, are researched systematically. The study results provided the basis support to find the main reasons of cylinder liner excessive deformation in engineering practice.

Testing of cylinder liner deformation

V-Incometer form and roughness measurement system is shown in Fig.1. It can be used to make a flexible measurement of cylinder bore deformation, wear, temperature influences and dimensioning of piston rings in engine development. The measurement system is flexible and mobile due to simple adaptation of the measuring probe to different cylinder dimensions. Using the V-Incometer system, the cylinder liner radial deformations of one 6V type diesel engine were measured under three different conditions: free state, free installation state in which the cylinder liner set into block body without installing the cylinder head, assembly state in which the cylinder head fixed by four bolts with 60kN preload. And the relative deformation of cylinder liner of assembly state is obtained by removed the free installation deformation from assembly deformation. The test device was fixed from the crankshaft end and located position to the inner cylindrical surface of the inferior cylinder. The whole cylinder liner's inner surface radial deformation can be measured with high accuracy by controlling the measuring arm rotation and axial movement. The measurement system reproducibility is less than 2μm.

Fig.1 V-Incometer：Form and Roughness Measurement System

Though the deformation value of each cylinder liner in this 6V type diesel engine is different, the basic laws of deformation are identical. So in this paper only one cylinder deformation data and analysis results are provided. The section position in which deformation data extracted are shown as Fig.2. Comparison analysis of deformation between section 1, section 2 and section 3 under various load case are performed. The section 1 is the position of the first piston ring location when the piston reaches upper stopping spot. The section 2 is the position when the piston reaches maximum velocity. And the section 3 is the position of the first piston ring location when the piston reaches lower stopping spot.

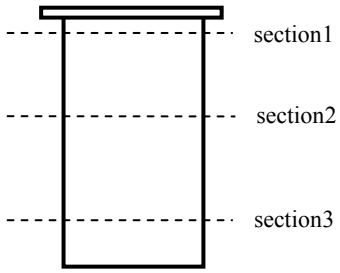

Fig.2 Sketch of deformation data extracted section position on cylinder liner

Analysis of testing results

Fig.3, Fig.5 and Fig.7 provided the testing results of radial deformation in three cylinder liner sections under various load cases. Fig.4, Fig.6 and Fig.8 gave the Fourier transformation results of above radial deformations.

Fig.3 and Fig.4 show that the cylinder liner deformations under free state in section 1, which are caused by machining and heat treatment, have obviously thrice curve characteristic. The 0 to 3 order Fourier deformation coefficient are relative bigger than others, but the deformation amplitude is small

(≤3μm). After the cylinder head bolt force preloaded, the assembly deformation and relative deformation become quadratic curve. Comparison to free state, the 2 order Fourier deformation increase obviously, which deformation amplitude reaches above 12μm. And other 0 ,3 and 4 order deformations are also increased at a certain extent. Moreover, the profiles of cylinder liner assembly and relative deformation are consistent, which shows the deformation caused by bolt preload is dominant to the final form of section 1 in cylinder liner.

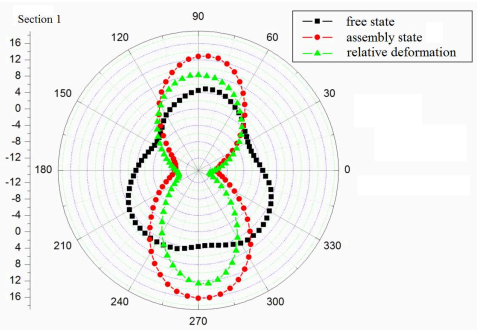

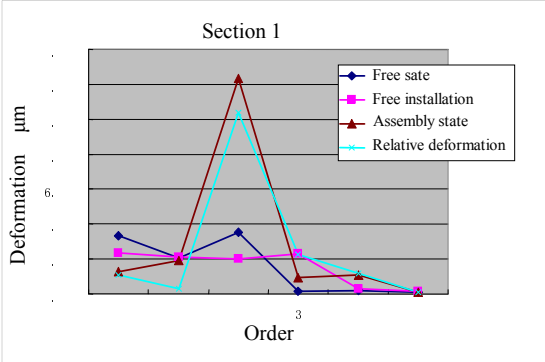

Fig.3 Radial deformation of section 1 Fig.4 Each Fourier deformation coefficients of section 1

The deformation of section 2 of cylinder liner is similar with section 1. The deformation amplitude is gradually decreased with the liner section position moving down. And comparison to the section1, the Fourier deformation coefficient of 0 order is decreased obviously as shown in Fig.5 and Fig.6.

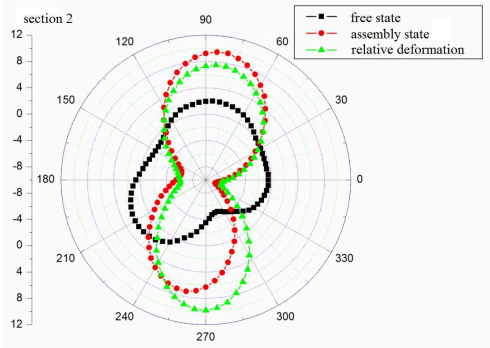

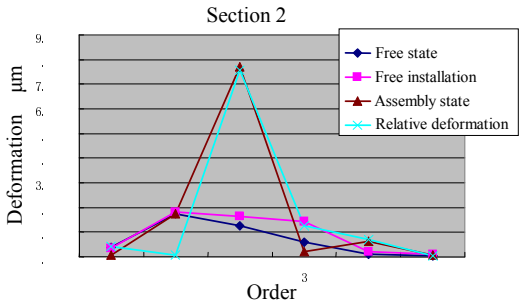

Fig.5 Radial deformation of section 2 Fig.6 Each Fourier deformation coefficients of section 2

As shown in Fig.7, the profile of section 3 is changed from thrice curve to quadratic curve under free state and free installation state, and the deformation amplitude is increased greatly. From Fourier deformation transfer results shown in Fig.8, the origin deformation which caused machining and heat treatment mainly is the secondary order deformation. The deformation amplitude is up to 10μm. Nevertheless the relative deformation in section 3 is very small, which is less than 2μm. These results show that the influence of cylinder head bolt preload on cylinder liner bottom deformation is very small. The assembly deformations of liner bottom section are mainly composed of origin deformation caused by machining and heat treatment in progress of cylinder liner production.

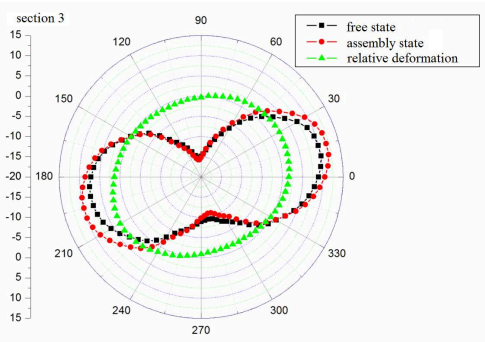

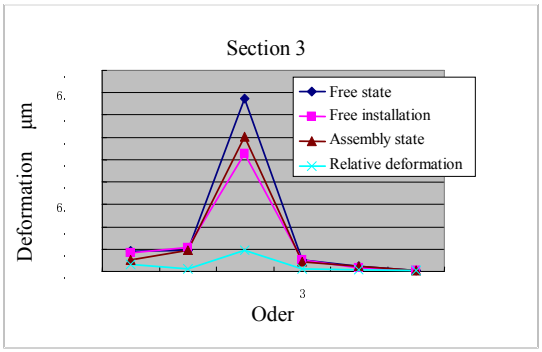

Fig.7 Radial deformation of section 3 Fig.8 Each Fourier deformation coefficients of section 3

Through synthesis analysis of the three sections deformation results and other testing results not given in this paper, the origin deformations caused from liner production are thrice curve with small

amplitude on the top liner. And with the section moved to the liner bottom, the origin radial deformations are changed to quadratic curve. Cylinder head bolt preload force has a significant effect on the deformation of upper part of cylinder liner. And bolt preload mainly affects the 2 order, 3 order and 4 order Fourier deformation coefficients, but the influence on the lower part deformation is gradually weakened.

Summary

Through a comprehensive analysis of the test results of the cylinder liner deformation, we get the following conclusions:

(1) Initial twist generated in the production process of the cylinder liner affect the final assembly deformation significantly, particularly in the lower part of the cylinder liner, the initial deformation of the cylinder liner substantially dominated the final assembly deformation.

(2) When using the finite element method to calculate deformation of the cylinder liner, it is difficult to consider the initial deformation, and therefore must be used the relative deformation of the cylinder liner to effectively correct and verify the calculate model.

(3) Deformed shape of the cylinder liners are not the same for each section. Fourier coefficients of each section of the deformation are not the same trend. The deformation profiles are closely related to particular structures form. So when the analysis and evaluation of deformation of the cylinder liner are performed, need to select a typical cross-section according to different structural forms.

References

[1] Schneider E, Blossfeld D, Lechman D, et al. effect of cylinder bore out-of-roundness on piston ring rotation and engine oil consumption.[J]. SAE paper, 930796

[2] Kakade N N, Chow J G. Finite element analysis of engine bore distributions during boring operation [J]. Transactions of the ASME Journal of Engineering for Industry, 1993, 115(4):379-384

[3] Loenne K, Ziemba R. The GOETZE Cylinder Distortion: Measurement System and the Possibilities of Reducing Cylinder Distortions.[J]. SAE Paper, 880142.

[4] F Koch, P Decker, R Guelpen, et al. Cylinder liner deformation analysis-measurements and calculations [J]. SAE Paper, 980567

[5] Wei hai-qiao, Shu ge-qun. Study on the relation between piston impinging vibration and combustion noise of internal combustion engines [J]. Transactions of CSICE, 2004,22(1): 27-32.

Advanced Materials Research Vols. 986-987 (2014) pp 904-907
© (2014) Trans Tech Publications, Switzerland
doi:10.4028/www.scientific.net/AMR.986-987.904

The method of finding the center of steam turbine shaft coupling based on multiple practice

Jing Liu[1, a], Yong-Sheng Kuang[2,b]

[1]Changsha university of science and technology, Energy and Power engineering national laboratory , Changsha, Hunan province, China.

[2]NingXiang town by the open area development road, Changsha, Hunan province，China.

[a]jimmydeloveu@163.com , [b]149760665@qq.com,

Keywords: multiple practice; center axis ; coupling; calculation method.

Abstract. It is magnificent to find the center of the coupling after many calculations, test and optimization. It presents a check based on looking methods and determine the centering of this calculation method after repeatedly overhaul of a 200mw extraction condensing steam turbine adjusting center practice. The effectiveness of its application in practice can duration, and the average time and its consumption of money could be reduced to 1/3, 1/3 and 1/5of its original, illustrates the adjustment process issues which should pay attention to,and provides technical reference for the safe operation of the same type of rotating machinery .

Introduction

It is the foundation of the normal operation of the steam turbine within the prescribed scope of steam turbine shaft coupling center in the factory. Hot bolt ,setting error, uneven sedimentation, cylinder deformation, unsteady thermal expansion etc, however, will cause the shaft center measurement deviation,combined with long-term solid particle impact will led to the steam turbine cracking and corrosion [1], the repair process is very difficult [2].By repeatedly overhaul the 200MW smoke condensate steam turbine,it could be possible to find center adjustment after the practical process for multiply times,.Then,it would be no hard to achieve the minimum quantity adjustment, the easiest design and most efficient adjustment process . Generally,according to the lack of a precise systematic, streamline processes, this process is time-consuming and waste of energy.This paper deduces the a simplified calculation method based on center adjustment, among them, clearly adjust center calculation is divided into several specific part, and clearly describe the key processes of it , and applied to other analogous process of finding center.

1 Center adjustment method of the application

1.1 Initial parameters

In this example,the diameter of coupling of two rod plane table is referred to,which is D 603.00 mm, the distance of circular table to 2 # bearing center is 327.00 mm, center distance of2# bearing is 2220.00 mm,the angle of bearing adjustment block center and the shim the centerline named a=75 °, and cosa =0.28, sina= 0.92.Coupling circumference value and openings deviation as shown in Fig. 1,

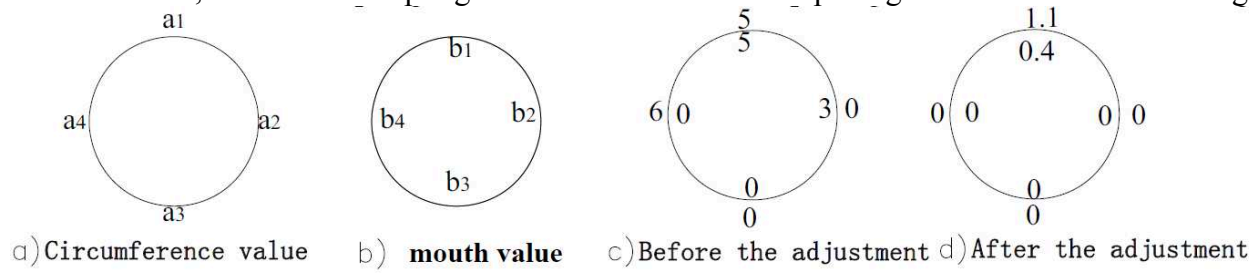

Fig. 1, Numerical coupling center before and after the adjustment

1.2 Calculation process and results

Using formula (1-6) to calculate. The specific calculation process of gasket adjustment method is shown in Tab. 1.it is necessary to increase the left side of the gasket(displacement) △ H_{2zc} = 0.0236 mm, and △ H_2 = 0.0118 mm on the right side;3 # bearing:increases gasket vertical direction t △ H_3 = 0.2022 mm, increase the left side of the gasket △ H_{3zc}= 0.2727 mm, cut right gasket △ H_{3zc} = 0.1059 mm,After adjusting the circumference the results are shown in Tab. 1.

Tab. 1, Coupling center adjustment calculation

serial number	name	symbol	Calculate formulation	Numerical unit 0.01mm	note
1	2 # bearing vertical adjustment value △ H_2 on both sides of the gasket	$\triangle H_2$	$\triangle H_{2c}=\triangle H_2\cos\alpha$	2.32	
2	2 # bearing horizontal modifier △ H_2 'on both sides of the gasket modifier	$\triangle H_2'$	$\triangle H_2'c=\triangle H_2'\sin\alpha$	1.09	
3	2 # left the gasket at the bottom of the bearing adjustment value	$\triangle H_{2zc}$	$\triangle H_{2zc}=\triangle H_2+\triangle H_2'$	2.75	Increase the gasket
3	2 # bearing right at the bottom of the gasket modifier	$\triangle H_{2yc}$	$\triangle H_{2yc}=\triangle H_2-\triangle H_2'$	1.19	Increase the gasket
5	3 # bearing vertical adjustment $\triangle H_3$ on both sides of the gasket	$\triangle H_3$	$\triangle H_{3c}=\triangle H_3\cos\alpha$	12.68	
6	3 # bearing horizontal modifier$\triangle H_3$'on both sides of the gasket modifier	$\triangle H_3'$	$\triangle H_3'_c=\triangle H_3'\sin\alpha$	22.32	
7	3 # left the gasket at the bottom of the bearing adjustment value	$\triangle H_{3zc}$	$\triangle H_{3zc}=\triangle H_3+\triangle H_3'$	26.05	Increase the gasket
8	3 # bearing right at the bottom of the gasket modifier	$\triangle H_{3yc}$	$\triangle H_{3yc}=\triangle H_3-\triangle H_3'$	-11.0262	Reduce the gasket

Calculation results are as follows: 2 # bearing: vertical increase gasket △ H_2 = 0.0519mm,

1.2 The result analyses

From 2 # and 3 # two bearing ,those in the vertical direction, the left and the right side : the adding displacement of value of the gasket can be identified by using this method, hence, this method is applicable for the same type of steam turbine shaft coupling, and, by making a systematic calculation in Tab. 1,it could accelerate corresponding calculation efficiency . The results of all the circumference of a circle and openings deviation values conform to the technical requirements for cylindrical is less than 0.02 mm, the opening is less than 0.01mm, half coupling axis eccentricity is less than 0.01 mm, other uncertain factors of differential settlement of the foundation, uneven subsidence is less than 18mm,which is superior to the standard .Not only that, due to the use of summarized recent overhaul ,the elimination amount of its openings deviation and circumference value is 2/3 and 2/3, respectively than the original average level. Applying this method could actual eliminate the error and uneven subsidence value of finding the axis of coupling than the original 1/5.The above calculation is the result of the multiple overhauls, lots of calculation statistics. With other collaborate process of adjusting coupling center, the circumference of a circle, openings deviation eccentric degree, the uneven subsidence equivalent amount can be adjusted to the corresponding result.

2 Coupling center finding method

2.1 Finding center

Finding Coupling center, is to make the rotor axis balanced into a smooth curve,which did not fold point in the middle of the rotor. The connection of rotor will have a periodic alternating on bearing force, which cause vibration and noise. The center will not affect the bearing load distribution, whether poor circular excursion or openings deviation of unbalanced load have influence on the coupling.

2.2 Finding process

(1) Establish standard adjustment: according to the former bearing shell temperature and vibration situation, considering all the factors,provide standard which affect the shaft system

adjustment and the center of the manufacturer, start solid cylinder shaft center adjustment after the establishment of standard.(2) determine the adjustment quantity: after setting major repair and overhaul of solid cylinder standard, half cylinder has to be calculated, then the reserved acceptance standard of half cylinder adjustment after overhaul has to be determined, to determine the amount of adjustment according to overhaul before half cylinder center and reserved after overhaul of half cylinder standard .(2) the adjustment steps: Main steps of measurement, calculation and adjustment of three main links of grinding bearing pad iron .

2.2 Calculation method

It has five circle center adjustment of coupling measurement by every step of the data,to record the location of the center value,namely 0 to 90 °, 180 °, 270 ° and the total average of every numerical as shown in Fig. 2(a). Considering there is circular offset and open openings deviation and its direction changes.To meet the requirements,the steam turbine rotor, generator rotor bearing center have to be adjusted, the center adjustment calculation method can be divided into the following two aspects.

2.2.1 Eliminate the circumference difference

Coupling center and 2 #, 3 # poor bearing circular adjustment quantity as shown in figure, 2 #, 3 # . It is on the left represents the center of the coupling in figure.the rail on behalf of the rotor, h on behalf of the up and down or left and right amount of translation, at the same time will be 2 #, 3 # bearing to the upper left translation h after coupling center for namely. H value calculation is as follows:

Upper and lower center panning.

$$h_{sx} = \frac{(a_{1/0.99} - a_{3/0.98})}{2}. \quad (1)$$

Left and right center panning:

$$h_{zy} = \frac{(a_{2/0.99} - a_{2/0.98})}{2}. \quad (2)$$

Type of a1, a2, a2, a3 is circumference value, h_{sx}, h_{zy} represent the displacement of vertical and horizontal direction , which have been taking comprehensive consideration of table direction and the value of a1, a2, a2, a3 and symbols.

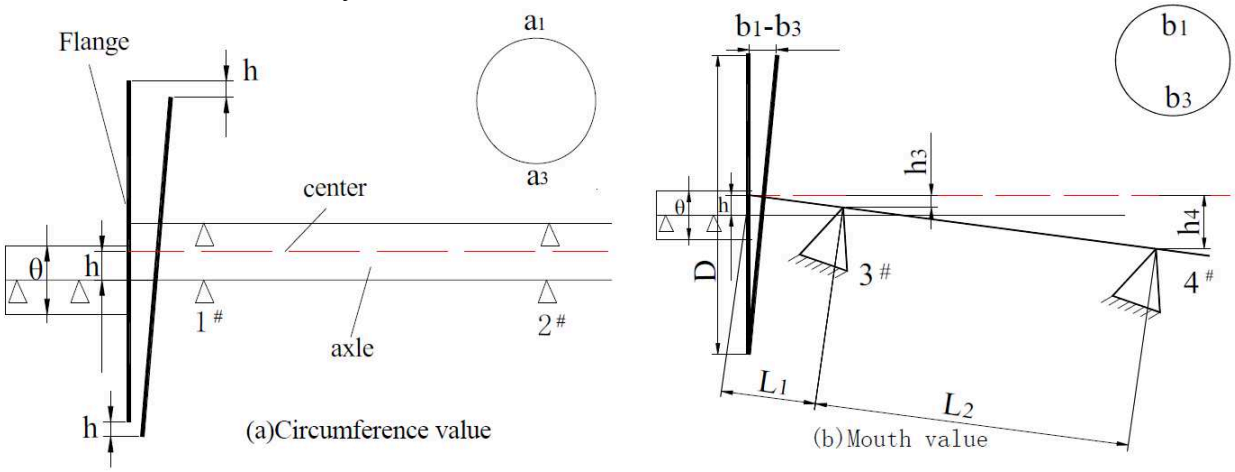

Fig. 2, Schematic of eliminate the circumferential difference(a) and illustration of the removal of coupling openings deviation(b).

2.2.2 Remove openings deviation

As shown in Fig. 2(b),coupling center and 2 #, 3 # of bearing flat openings deviation adjustment quantity is different. The bearing up of 2 # is h_2, bearing up after the of3 # is h_3,respectively. two coupling openings deviation b_1, b_2.The h_2, h_3 calculation is as follows, the calculation of eliminate the openings deviation is as follows:

$$h_2 = \frac{(b_1 - b_2) \times L_1}{D} \quad h_2' = \frac{(b_1 + b_2) \times L_1}{D} \quad . \tag{2}$$

$$h_3 = \frac{(b_1 - b_2) \times (L_1 + L_2)}{D} \quad h_3 = \frac{(b_1 + b_2) \times (L_1 + L_2)}{D} \tag{3}$$

shim adjustment numerical algebra sum of 2 #, 3 # bearing should take two parts,

$$\Delta H_2 = h + h_2 - 0.1h_2', \qquad \Delta H_3 = h + h_3 - 0.1h_3' \tag{4}$$

Type of b1, b2, b2, b3 end face, respectively, h2, h3 symbol has respectively, fixed around openings deviation instead of b1 b2 can be used to calculate the h2 respectively, b2 instead of b3 to calculate the h3;Referred to in rod coupling diameter, D - two plane table L1 - circular table to 2 # bearing center distance of measuring points and L2, 2 #, 3 # bearing center distance. Considering plane table direction, b1, b2, values and symbols and the h value, to adjust gasket to eliminate the openings deviation. Second, change the position of the upper and lower gasket at the same time, must be a corresponding change on both sides of the gasket thickness, to maintain good spherical contact.

2.2.2 Adjust volume of the gaskets.

On both sides of the gasket to adjust quantity calculation method , which takes gasket center Angle to △H_b on behalf of the vertical direction of gasket, △ Ha on behalf of the horizontal direction. When vertical direction △H_b add and subtract to lower gasket thickness and the bearing shell mobile△H_b equal on both sides of the gasket thickness at the same time, plus or minus △ $H_b$cos a;If the horizontal direction mobile △ Ha, lower gasket, on both sides of the gasket thickness respectively add (subtract) △ $H_a$sina. Each of the shim under the adjusting shim shoulds not be more than three pieces.To adjust gasket sheet steel should be adopted and phosphor copper, unfavorable use copper skin soft material such as Single chip thickness is not less than 0.02 mm, the aperture should be bigger than shim aperture of 1 ~ 2 mm; Gasket assembly, should be carefully cleaned its burring and rough edge. In the center deviation within the scope allowed the position for turbine center is higher than the generator, and lay on the above position to its openings deviation. Adjustment is within 0.1 mm gasket contact with hollow nest situation doesn't have to check. If adjustment quantity more than 0.1 mm, which should be re-examine and crapping block, after crapping again review center. Center after the adjustment to the bearing oil gear measurement, adjustment and repair, and are able to be adjusted on tile gasket to keep bearing force.

Conclusions

This method of coupling center adjustment is based on predecessors experience and practice application for many times, the adjustment process of steam turbine generator shaft system has shown in the form of chart compiled.To sum up ,it is an accurate calculation method of a calibration center. This method was applied to concrete coupling overhaul center adjustment process of turbo-generator set.It has proved in multiple practice by applying this method to adjust the unit operation, the result shows that shaft system is stable, related parameters of the bearing is superior to the requirement. The effect is good after the unit running because this method is feasible and maintenance, the time , procedure, money consuming can be reduced to 1/3 ,1/3and 1/5 of the original, In a nutshell,it can offer reference for the application of the same type unit, but for the big unit shaft system aspect application, needs further research.

References

[1]R.Macchinia,M.S.A.Bradleyb,T. Dengb. Influence of particle size, density, particle concentration on bend erosive wear in pneumatic conveyors, J. Wear.2012(202)21–29.

[2]Xuefei Guana,Jingdan Zhanga,El Mahjoub Rasselkordeb,Waheed A. Abbasib,S. Kevin Zhoua. Material damage diagnosis and characterization for turbine rotors using three-dimensional adaptive ultrasonic NDE data reconstruction techniques, J. Ultrasonics. 2013(53) 516–525.

Advanced Materials Research Vols. 986-987 (2014) pp 908-914

doi:10.4028/www.scientific.net/AMR.986-987.908

Concept of limited corrosion dew point for coal-fired boiler and experimental research

Baokui CHEN[1, a], Fengzhong SUN[2, b]

[1] School of Energy and Power Engineering, Shandong University, No.17923 Jingshi Road, Jinan 250061, China

[2] School of Energy and Power Engineering, Shandong University, No.17923 Jingshi Road, Jinan 250061, China

[a]email: chenbaokui2568@sina.com, [b]email: sfzh@sdu.edu.cn

Keywords: Low temperature corrosion; Acid dew point; Phase equilibrium; Fugacity equation

Abstract. Inadequacy was discussed of using acid dew point temperature (ADT) as safe low limitation of exhaust gas temperature on the background of waste heat deep utilization of flue gases. Concept of limited corrosion dew point (LCT) was presented based on corrosion property of ordinary carbon steel and binary phase equilibrium of H_2SO_4-H_2O system,. Calculation formula of LCT was solved by establishing fugacity equation of H2O with a fixed concentration and constant pressure. The results show that LCT lies during 68-84℃ when volume percentage of H_2O vapor varies from 6-12% which is in line with that of exhaust gas of boiler. The maximum relative error of the calculated data is 1.43% in contrast to reported data. Ordinary carbon steel in contact with flue gas with its surface temperature above LCT will not occur obvious corrosion and wet soot deposition through observation of experiment on site. It is available for exhaust gas temperature to decline below ADT but above LCT in process of deep utilization of waste heat of flue gas.

Introduction

Whenever fossil fuels containing sulfur are fired in heaters or boilers, sulfur dioxide, and to a small extent sulfur trioxide, are formed in addition to water vapor. The SO_3 combines with water vapor in the flue gas to form sulfuric acid and condenses on heat transfer surfaces, which could lead to corrosion and destruction of the surfaces. Significant efforts have been devoted for establishing methods to predict the sulfuric acid dew point (ADT) of flue gas [1-3]. A thermodynamic approach has been used for predicting ADT with very low sulfuric acid vapor concentration by Muller [4], based on partial pressure data of vapor-liquid phase equilibrium of H_2SO_4-H_2O derived by Abel [5-6]. Later experimental work using a SO3 condenser method confirmed Muller theoretical calculations expressed by Muller curve.

Muller curve is now the bases for evaluating various methods for measuring SO_3 and widely cited in lots of literatures [7-9]. About 1-50 ppm of H_2SO_4 vapor remains in the flue gas. The ADT varies from 117-147℃ by Muller Curve with 10% water vapor concentration by volume. It has been an important parameter for designers to determine the temperature of exhaust gas [10]. With more and more strict request for environment protection and energy saving in China, exhaust gas temperature of widely using heat recovery equipments has been reduced to 100℃, the wall temperature of metal tube is about 80-90℃, Which is obvious lower than ADT. The unacceptable corrosion and ash deposition did not occur without using special anticorrosive material. From the operation experience of the power plant, as long as the wall temperature of ARH is above 75℃, obvious corrosion will not occur [11]. As a result, in the background of deep utilization of waste heat of flue gases, it is inadequate to use ADT as safe low limitation of exhaust gas.

The ADT is only the starting temperature which could lead to sulfuric acid corrosion, but corrosion rate is not only connected with ACD but also the concentration and condensed amount of sulfuric acid. When surface temperature is below ADT, condensation occurs with high concentration of sulfuric acid and little condensed amount. Valid corrosion and sulfuric ash deposition will not happen for heat recovery system made from the ordinary carbon steel, such as

#20C, in contact with aqueous of high sulfuric acid concentration 60-90(Wt%). Some scholars proposed that temperature of available corrosion point should lie somewhere between acid dew point and water dew point and gave an experienced formula, but lacking theory bases [12].

According to theory of binary phase equilibrium and corrosion property of ordinary carbon steel, concept of limited corrosion point temperature was presented. The formula associated with single variable of water vapor partial pressure is solved by setting up water fugacity equation.

Concept of limited corrosion point temperature and its connection with thermodynamics acid dew point temperature

Concept of limited corrosion dew point temperature

The exhaust gas of boiler is a complicated and compound system including N_2, O_2, CO_X, NO_X, SO_2, SO_3, and so on. From thermodynamics point of view, the ADT can be solved by theory of multi-phase equilibrium. Due to the complex of theoretical study, it is necessary to reasonably simplify exhaust gas system. The following hypothesis are main points:

1) The exhaust gas is considered as ideal gas.

2) Gases apart from H_2SO_4 and H_2O are considered as inactive gases.

Based on these two points, the exhaust gas system is considered as a binary system of H_2SO_4-H_2O.

By Gibbs phase rule, the degree of freedom of the binary liquid-vapor system equals 2, i.e., the numbers of independent intensive variable are 2. Only two parameters are independent among T, P, X1 or Y1 (the mole fraction of liquid H_2SO_4 or H_2O), X2 or Y2 (the mole fraction of vapor phase H_2SO_4 or H_2O). If choosing P and Y2 as independent variables, thus the partial pressure of water vapor can be expressed: P1=P*Y2.

Limited corrosion point temperature is defined as a temperature value which the state point lies at equilibrium with 60% liquid weight concentration of H_2SO_4 under pressure 1 bar.

Reasons for LCP to be more valid than ADT as basis of valid corrosion temperature.

The reasons are based the following two points:

1) ADT is only the starting point of low temperature corrosion, it does not mean that at the ADT the valid corrosion and sulfuric deposition happen.

2) According to the corrosion property of ordinary steel carbon, weight concentration 60-90 percent sulfuric aqueous has a low corrosion rate(about 6 g/m2.h) in contact with ordinary steel carbon ,which is much less than the fastest corrosion rate(about 80 g/m2.h) at 56 percent weight concentration.

Connection with thermodynamic acid dew point

T-X fig of binary system of H_2SO_4-H_2O under pressure 1bar is showed in fig.1. The temperature of superheated vapor with state A falls to point B where the first liquid drop appears in the liquid-steam equilibrium state, this temperature is called the ACP. We assume that the concentration of liquid phase sulfuric acid is 80 percent (wt %). When the temperature continues falling to a point C where the concentration of liquid phase sulfuric acid is 60 percent (wt %), we call the temperature of the point C as LCP.

So both ADP and LCP are state points of liquid-vapor phase equilibrium. ADP lies in a state with fraction of liquid phase being zero, but LCP lies in a state with a few fraction of liquid phase, its value can be achieved by data of phase equilibrium.

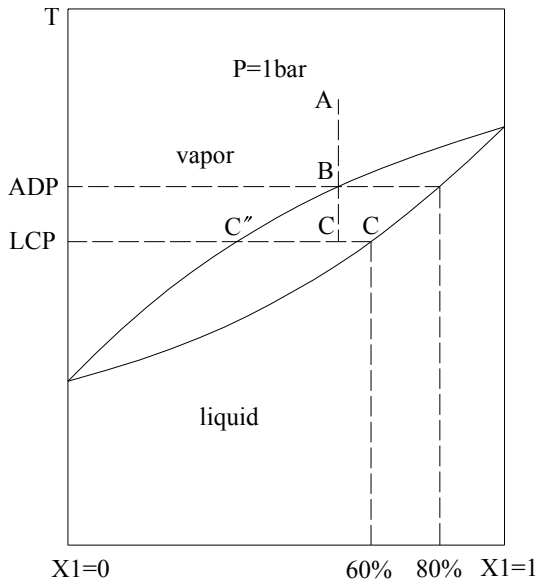

Fig.1. T-X figure of H_2SO_4-H_2O syetem

Establishment of mathematical model and derivation of LCP equation

Mathematical model establishing

The Fugacity equation as mathematical model for solving phase equilibrium of H2SO4 and H2O was first established by Abel, which was expressed by thermodynamics parameters and temperature functions through the hypothesis of ideal gases. Then displace Fugacity with partial pressure. At last, partial pressure of vapor phase of binary system was solved. Gmitro and Vermeulen used the renewed thermodynamics parameters and revised the fugacity equation [13].

Based on the hypothesis of ideal gases, the fugacity of water vapor was derived by using the latest thermodynamics parameters here. The LCP was worked out expressed by a single variable function of partial pressure of water vapor.

Derivation of LCP equation

At equilibrium, the partial mole free energy of water vapor $\Delta\bar{G}_\pi(g)$ is equal to the partial mole free energy of the liquid water $\Delta\bar{G}_\pi(l)$:

$$\bar{G}_\pi(g) = \bar{G}_\pi(l) \tag{1}$$

Suppose the vapor acts as perfect gas, we obtain:

$$G^0(g) + RT\ln p_\pi = G^0(l) + RT\ln a_\pi \tag{2}$$

$$\ln p_\pi = \frac{G^0(l) - G^0(g)}{RT} + \ln a_\pi \tag{2a}$$

$$\ln p_\pi = \frac{-\Delta G^0}{RT} + \ln a_\pi \tag{2b}$$

Equation (2b) holds at any temperature and composition. The partial pressure under consideration is given by the sum of two terms: a pure-component term $-\Delta G^0 / RT$, a function of temperature only; and an activity term $\ln a_\pi$, a function of both temperature and composition.

The derivation process can be seen from literature [13]

At last, we obtain：

$$\ln p_\pi = A\ln\frac{298}{T} + \frac{B}{T} + C + DT + ET^2$$

where

$$A=\frac{1}{R}\left[-a+\bar{c}_p(298)-298\alpha\right]$$

$$B=\frac{1}{R}\left[-\Delta H^0_{298}+298a+\frac{298^2}{2}b+\frac{298^3}{3}c+\bar{L}_{298}-298\bar{c}_p(298)+\frac{298^2}{2}\alpha\right]$$

$$C=\frac{1}{R}\left\{-\Delta S^0_{298}-a-298b-\frac{298^2}{2}c+\bar{c}_p(298)+\left[(\bar{G}_\pi(l)-G^0(l))_{298}-\bar{L}_{298}\right]\frac{1}{298}\right\}$$

$$D=\frac{1}{2R}(b-\alpha)$$

$$E=\frac{1}{6R}c$$

Strictly speaking, α is a function of temperature and composition. When the temperature is below 200℃, the influence of composition can be omitted [13].

For H_2SO4 aqueous (wt60%), the latest thermal data and the results are shown in table 1. [14]

Table1 Pure composition H_2O, H_2SO4 and H_2SO4 aqueous（wt60%） thermal data

Parameter	Unit		H2O	H2SO4
ΔH^0_{298}	kJ/mol	K	44.014	79.131
ΔS^0_{298}	J/mol	K	118.884	144.152
$\bar{L}_{298}$	J/mol	K	-4710.15	-35190.1
$\bar{c}_p(298)$	J/mol	K	68.39138	112.8343
$(\bar{G}_\pi(l)-G^0(l))_{298}$	J/mol	K	-4502.07	-29458.3
a	J/mol	K	32.838	32.908
b	J/mol	K2	2.42E-3	193.221 E-3
c	J/mol	K3	0	-10.936 E-5
α	J/mol	K2	0.0485	-0.00460
A	none		2.530	9.623
B	K		-6860.669	-15690.51
C	none		18.554	22.902
D	(K)-1		-2.77E-3	1.16E-2
E	(K)-2		0	-2.19E-6

Note: Any coefficient or subscript shown as 298 is actually computed as 298.15K (25℃); The standard state pressure is 1bar.

From above data, the partial pressure of H_2O (bar) can be solved：

$$\ln p_\pi = 2.530\ln\frac{298}{T}-\frac{6860.669}{T}+18.554-0.00277T \tag{3}$$

Contrast to thermal equilibrium data of associated literature

Flue gas moisture content of coal-fired boiler of is usually around 10%, which changes between 5% and 15%. The contrast results are shown in table 2 between thermal equilibrium data and data calculated by formula (6).

Table 2 Contrast of data

Temperature ( )	Pressure (KPa [15])	Pressure (KPa[16])	Data (KPa)	Relative error (%)
65	5.03	5	5.02	0.40
70	6.40	6.39	6.41	0.31
75	8.03	8.09	8.12	1.12
80	10.04	10.19	10.22	1.43
85	12.57	12.72	12.75	1.19
90	15.60	15.80	15.81	1.28

Note: The pressure unit is mmHg in (15), converted to KPa here; data of the third column from equation (3)

Test verification on corrosion and ash deposition on site

Test was carried out respectively in 200MW unit, 300MW unit, 600MW unit, test position is located after air pre-heater and before electric precipitation. The test material is ordinary 20# carbon steel. The aim of test is to check up corrosion and ash deposition of the surface which temperature lies between water dew point and LCP. The original data, operation parameters, and thermal data are shown in the table 3.

The process of corrosion test on site

The parameters of the test are shown in fig 2. The system is composed of constant temperature box; water tube and its accessories, including pump, flow meter, temperature measuring point, and so on; heating tube in gas duct). Due to LCP of different unit varying from 64-74℃, three constant temperature boxes with different temperature (70℃, 65℃, 40-60℃) were designed.

Table3 Original data and operation parameters

Parameter	Unit	200WM	325WM	600WM
Electrical load	WM	150-220	210-325	40-55
Flue gas temperature	℃	120-135	132-147	115-129
Flue gas velocity	m/s	8-10	7-11	7-10
$Q_{ar.net}$	KJ/kg	19000-21000	18250-19750	17500-19500
V_{daf}	%	15-19	14-18	16-22
S_{ar}	%	0.8-1.5	1.2-1.8	1.3-2.2
M_{ar}	%	6-8	6-9	6-10
Concentration by volume	%	6.0-6.6	6.3-6.9	6.8-7.6
Dew point of water		42-44	43-45	45-47
SO_2 concentration	mg/Nm3	1900-2000	2100-2300	2200-2400
SO_3 concentration	ppm	7-42	8-48	9-54
ADP		121-147	123-149	126-151
LCP		64-67	70-72	72-74

The system is divided into four sections: (1) section without water; (2) section with water temperature 70℃; (3) section with water temperature 65℃; (4) section with water temperature 40-60℃.

Heat transfer and ash deposition of the surface were recorded. The test time is about 3 months for each unit (200 MW unit, 300 MW unit, 600 MW unit)

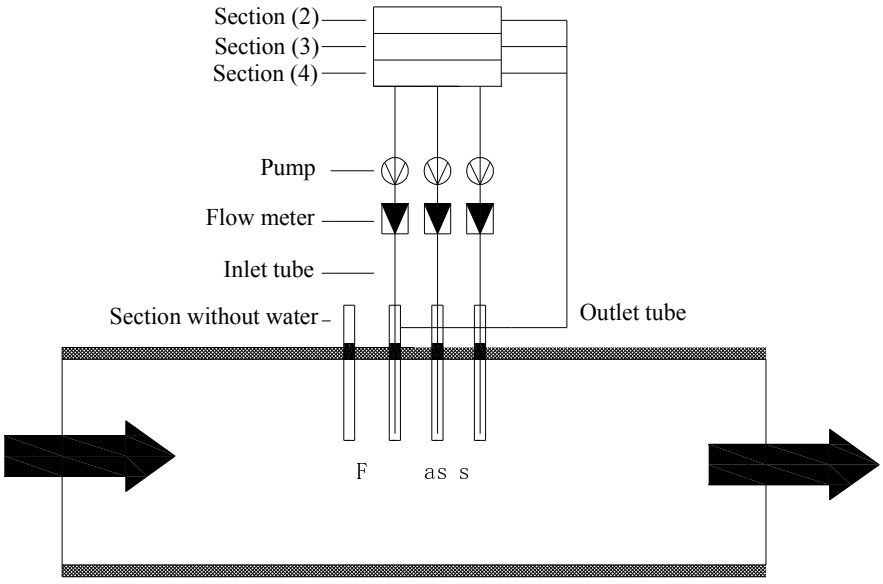

Fig. 2 Figure of the test system

Results of test

The following results are achieved by the test on site (different ash deposition on surface are shown in fig 3：

(1) No water test section: wall temperature of the steel tube is equal to that of flue gas. The upwind side is smooth and have no ash deposition, the backwind side with stable float ash, no corrosion phenomena appears.

(2) Water temperature 65℃ test section and the water temperature 70℃ test section (wall temperature is higher about 3-5℃ than the water temperature via computation), the windward side is smooth without dust, the backwind side with stable float ash, did not see the yellow sulfuric corrosion layer after the removal of the float ash layer.

(3) Test section with the water temperature 40-60℃: water temperature below 65℃, the upwind ash deposition began to accumulate, yellow sulfuric corrosion layer can be seen after the removal of the float ash layer.

(4) Water temperature below 40 ℃ is close to the water dew point, the upwind side appeared granular ash with ash layer obvious thickening and obvious corrosion.

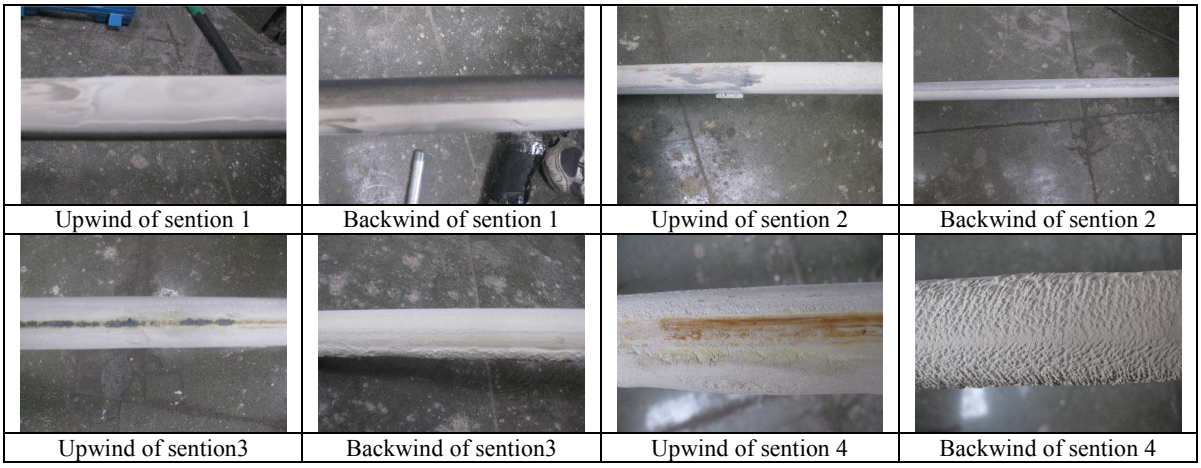

Fig. 3 Corrosion and ash depositon of different test elections

Discussion of the test

(1) Ordinary steel heat exchanger can be safe and stable operation for a long time with its wall temperature below ADP and above CLP, no valid corrosion phenomenon was observed.

(2) When the wall temperature is lower than LCP, the effective corrosion and dust deposition of windward side gradually appear, the corrosion layer thickens gradually as the temperature decreases.

(3) When the wall temperature is near the water dew point, the windward side appears a large number of granular ash, corrosion is serious.

Conclusion

The concept of limited corrosion dew point temperature was presented based on corrosion property of ordinary carbon steel and binary phase equilibrium of H2SO4-H2O. It is more valid and has a more significance in engineering practice of wasted heat utilization than ADT as the basis on low-temperature corrosion of flue gas in coal-fired boilers.

(1) The limited corrosion dew point temperature (LCT) was worked out by fugacity of H_2O, its relative error is less than 2% compared with reported data.

(2) Ordinary carbon steel in contact with flue gas with its surface temperature above LCT which is far lower than ADT will not occur obvious corrosion and wet soot deposition through observation of experiment on site.

References

[1] A.G. Okkes, Get acid point of flue gas, Hydrocarbon Process. 1987, 7, 53-55.

[2] Srivastava R K, MILLER C A. Emissions of sulfur trioxide from coal-fired power plants[C]. Power Gen International 2002: Orlando Florida 2002, 11.

[3] Lisle E S, Sensenbanch. The determination of sulfuric trioxide and acid-point in flue gases [J]. Combustion, 1965, 36(1):12-15.

[4] Muller P. A. contribution to the problem of the action of sulfuric acid in flue gases [J]. Combustion, 1965.36(1):47-49

[5] Abel E. The vapor phase above the system sulfuric acid-water [J]. Journal of Physical Chemistry, 1946,50:260-282.

[6] Abel E. On the experimental bases for the calculation of the sulfuric acid vapor pressure above the sulfuric acid-water system [J]. Journal of Physical Chemistry, 1947, 50: 908-914.

[7] Verhoff F H, Banchero J T. Predicting Dew Points of Flue Gases [J]. Chem.Eng. Prog. 1974, 70(8): 71-72.

[8] Kiang, YenHsing. Predicting dewpoints of acid gases [J]. Chemical engineering, 1981,2(9):127.

[9] Pierce R R. Estimating acid dew points in stack gases [J]. Chemical engineering, 1977,4(11):125-128.

[10] Jin Baoshenge, Tang Zhiyong, Sun Keqin, Zhong Zhaoping. Numerical Prediction of the Deposit Rate of Condensed Sulfurci Acid from the Flue Gas of Power Plant Chimney[J], Proceedings of the CSEE 2006,26(9): 40-44(in Chinese)

[11] Zhao Zhijun, Lu Fengshi, Zhang Shuji, et al. New-type steam air heater and the application of its automatic control device[J], Electric Power 2007, 40(9): 54-56(in Chinese)

[12] Zhang Jibiao, Hao Wei, Zhao Zhijun, et al. Theoretical and Practical Research on Mechanism of Low–temperature Corrosion Caused by Boiler Flue Gas[J], Journal of Chinese Society of Power Engineering, 2011, 31(10): 730-734(in Chinese)

[13] Gmitro J I. Vermeulen T. Vapor-liquid equilibrium for aqueous sulfuric acid [J]. AICHE Journal, 1964, 10: 740-746.

[14] Giauque W F., et al. The thermodynamics for aqueous sulfuric acid solutions and hydrate from 15 to 300K[J]. Journal of the American Chemical Society, 1963, 85: 287-289.

[15] Manual of Sulfuric Acid (Revised Edition)(Japanese version of the translation, 1978)[M]. Beijing: Chemical industry press 1981, 27.

[16] Design handbook of sulfuric acid process design(physical and chemical data) Design institute of Nanjing chemical industry company[M]. Nanjing: Sulfuric acid industry intelligence center of science and technology of ministry of chemical industry, 1990:11.

Advanced Materials Research Vols. 986-987 (2014) pp 915-918

doi:10.4028/www.scientific.net/AMR.986-987.915

Design and Research of offshore Drilling Platform Electric Power System

[1,a] Chen Pingliang

[1]CNPC offshore engineering co., LTD, Beijing, China, 100028

[a]chenpl.cpoe@cnpc.com.cn

Keywords: offshore Drilling Platform, Electric System, Design.

Abstract. In order to design a reasonable safe power control system and realize the automated management of offshore drilling system, this paper analyzes the electric system features and grid configuration of drilling platform; power station design and short circuit calculation; electrical power system electroplax selection. This system adopts oceanographic engineering software EDSA for construction and parameter input and conducts short-circuit calculation for modeling and simulation. The electric system design and short-circuit calculation can be examined by simulation result and real platform.

Introduction

Petroleum is the blood of economy and sufficient and stable supply of oil and gas resources is the essential conditions for economy steady development. 21 century is the is the age of energy scarcity.a lot of countries have turned their eyes on ocean and put abundant manpower and material into marine energy resource development. Self-elevating drilling platform is one of offshore drilling equipment the wildly used at present in the word, mostly operating at intertidal zone and shallow sea. In recent years, the quantity of self-elevating drilling platform is increasing. The design, construction, check and research of the offshore drilling platform of our country cry for development, especially in basic technology design. We lack of independent design and mostly rely on foreign design technology. Thus, improving the above-mentioned research work can enhance our country's offshore structure design and manufacture ability and international competitiveness, which is of great significance to the marine resource exploitation and oceanographic engineering development. offshore drilling platform is the base of marine oil gas exploitation. Electric system of the platform is a set of independent electricity generation, electricity transmission, and electricity distribution system, and real-time reliable electric monitoring system is of great significance to the offshore drilling platform.

Engineering Background

The two drilling platform is launched at China offshore oil engineering construction base dock at the west coast of Qingdao, and head for Bohai bay for mud oil. The two drilling platform is triangular-formed truss-spud-legged self-elevating drilling platform with the maximum drilling depth of 6,000 meters, which is designed and built according to the norm of American bureau of shipping and China bureau of shipping. At present, two more platforms are built at the base. The four drilling platforms will operate at the same time and same site, which is beyond example in Chinese mainland. The basic components of semi-submersible drilling platform are offshore system, drilling system and dynamic positioning system. offshore system is mainly composed by the motives providing power station, stability maintaining ballasting system, offshore control system and other systems like commination system. Drilling system is mainly composed by drilling equipment, mud system and bop system. Dynamic positioning system is mainly composed by controller, power distributor and thruster etc.

Design and Analysis of Drilling Platform Electric System

Power Grid Calculating in Power supply schema Translation: The relation between delivery and load electricity consumption of platform diesel generating set is shown in formula (1) and (2).

$$P_{G1}+P_{G2}+P_{G3}+P_{G4}+P_{G5}+P_{G6}+P_{G7}+P_{G8}=P_{\text{Network loss}}+\text{P}_{\text{Load}} \quad (1)$$

$$P_{\text{Network loss}}=5/100(P_{G1}+P_{G2}+P_{G3}+P_{G4}+P_{G5}+P_{G6}+P_{G7}+P_{G8}) \quad (2)$$

In (4.1), PG1 to PG8 separately represent the delivery of eight diesel generating sets. Load P is the electricity consumption the platform load needed. In formula (2), the loss coefficient of 5/100 is the common empirical data in current application system.

Pre-diagnostic Analysis of Power Supply Schema Translation: Power supply mode needs transmission for the drilling needs. The load, power supply and charging line of these two power supply modes differ. Thus, in the transmission, the constraint conditions and switching paths of the associated equipment require consideration. The main factors influencing power supply mode transmission mainly contains power/electricity consumption, breaker conditions and diesel generating sets conditions. In the switching process from mode two to mode one, assume that diesel generating set G6 is in breakdown maintenance and breaker P is broken. According to the task decomposition figure, detail the task to each underlying device. The loads in Mode one are thruster 1,2,3,4,5,6; main winch motor 1,2,3,4 and main top drive motor 1,2.

Partial realized program of pre-diagnostic function is shown as follows:

```
Sub a1() as bool                          // examining the feasibility of schema translation
If   Fix32.Fix.Lode.F_CV/0.95> Fix32.Fix.PL.F_CV
// Fix32.Fix.Lode.F_CV load power in model one, Fix32.Fix.PL.F_CV maximum available power of
power grid remain
       a1=false
else
a1=true
end if
end sub
Sub a2 () as bool
Dim s As Integer                          // examining how many diesel generating sets are on
      a2=false
exit sub
S=Fix32.Fix.Lode.F_CV/4896
a2=true
end sub
```

2.3. Power Supply and Power Distribution System Design of Drilling Platform Electric System

This platform selects alternator (synchronous generator). Galvanic magnet exciting coil produces structural magnetic field. Put magnet exciting coil on the rotor and put armature winding on the stator. Put two sets of power transformer in the cabin transformer room and the rated capacity is voltage: 1000kVA. The alternating–current distribution system on this platform is supplied by two parallel-operated main generators with 600v rating and 50Hz three phase insulation. The1000kVA 600/400v main transformer provides the platform with 400V power, and VFD and 2 sets of drilling motor provide with AC600V. The single line drawing of power distribution system is shown in figure 1:

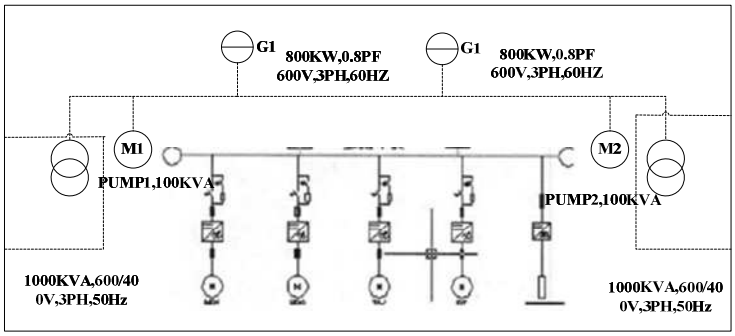

Figure 1: Single Line Drawing of power Distribution System

Variable Frequency Drive and Platform Grid Construction: We have completed the electricity distribution of drilling platform variable frequency drive system, analysis and single line drawing

design and calculating of frequency conversion system. The electricity distribution single line drawing of variable frequency drive system is shown in figure 2. In the figure, the main drilling equipment is constituted by four VFD-connected alternating current dynamos. Each dynamo contain a set of electrical machine cable and a set of controlling cable to connect air blower, air space heater, pull-rod cooling water pump, chain lubrication oil pump and safety isolating switch. The alternating current dynamo connected into the system is: one winch motor, two slush pump motors, one 600kW turntable drive motor, and one winch brake energy absorption resistance control panel.

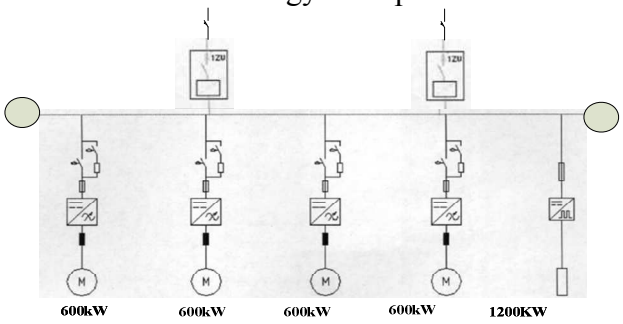

Figure2： VFD Control System

The electrical design of daily drilling drive electromechanical adopts AC variable frequency speed regulating. Full digital technical AC variable frequency speed regulating generates harmonic generation, which can be inhabited by increasing transducer pulse count.

All cables should satisfy the standard of IEEE-45, IEC33 etc. except some dedicated device adopting machine cables. Voltage class of power cable is 0.6/kV. Voltage class of instrument and controlling cable is 250V. Low-smoke, halogen-free, inflaming retarding set or fire-resistant offshore cable is with double sheath and tinned copper wire armoured, whose cable core can resist the degree of 85℃.

Electric Installation Selection of Main Distribution Board: According to power distribution system and application, this platform can be divided into 600V main distributing board, 400V switchboard. Power distribution unit structure contains switchboard protection grade, electric installation install ways, and framework and operation panel. Main switch of electric generator in offshore engineering project adopts air circuit breaker, like Terasaki AR12, Schnelder, MT, Siemens 3WL etc. the switch is selected according to formula (3) and (4) to ensure the overload protection.

$$I_{ac} = I_{acG2} + I_{acM1} \times 2 \quad (3)$$

$$i_{pc} = i_{pG2} + i_{pM1} \times 2 \quad (4)$$

Rated current should be larger than the electric generator's rated 860A current, rated 600V voltage, and rated 50Hz frequency. Rated short circuit making capacity is larger than the maximum expected peak current, namely the effective value of Iac(3.79kA). In conclusion, considering the price factors, this platform adopts Terasaki AR12 air circuit breaker (extraction type) as the main switch of the electric generator. There are many kinds of similar switches as the main switch of the load screen, like Terasaki XS, Schneider NS, Siemens 3VF, and ABB IsomaxS etc. This Platform adopts the Terasaki XS225NS moulded case circuit breaker. This platform adopts the Terasaki AR12 air circuit breaker (extraction type) as the switch of primary side of the transformer ACB6, 7, and adopts Terasaki ARZ165 air circuit breaker (extraction type) as the switch of transform vice side ACBS,9.

System Implementation

This paper adopts ESDA electrical modelling and analysis to conduct electric power design analysis. Firstly, we draw the single line drawing, and then we turn short-circuits calculation toolbar and select the different calculation standard in the standard selection menu. We adopt the IEC909 calculation basis, as shown in Figure 3.

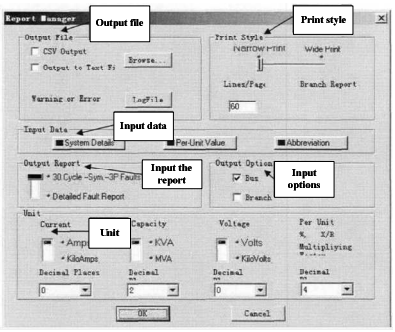

Figure3: IECgOg Standard Control Options

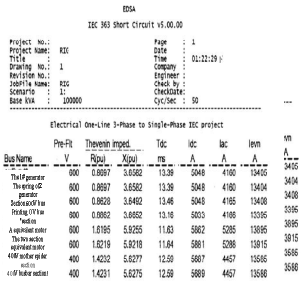

Figure4: EDSA calculation data

Short-circuit calculation adopts the computing method of IEC61363 three-phase alternating current system. Calculating software adopts EDSAZO05 (Revl), which is certificated by Sweden platform level club. Working conditions of calculation: three-phase short circuit current of two main generators in full-load operation and one main generator in full-load operation.

Summary: we can see from the EDSA calculating results that the calculating data of drilling platform power station get from EDSA is identical to the former calculation result. Hand computation lays emphasis on formula, ignoring a lot of parameters, while software relies on parameter adjustment, paying more attention to parameters. The value difference of formula computing and software computing is under 10%. Calculating result fully proves the correctness of drilling platform power station based on EDSA software and the design and short circuit calculation, which achieves the purpose of using EDSA for simulation.

Conclusion

By the drilling platform electric system design, this paper grasps the steps of platform power station design, understands comprehensively controller switching equipment like generator, switchboard etc. and gets familiar with the short-circuit current and distribution switch examination. By EDSA modelling, we compute the short-circuit current and the simulation result design is similar to the calculating result, which proves the correctness in two ways and can be the reference and of engineering significance to the development of offshore platform electric system design.

References

[1]Bi Yujia, Wu Feiwen.DP-2/P-3 Key Design Points of offshore Electric Power System [J].Shanghai Shipbuilding, 2008, (04):59-63.

[2]Wang Liang. Deepwater Semi-submersible Drilling Platform Dynamic Position Capacity Analysis [D]. Master Degree Thesis of Shanghai Jiaotong University.2010:3-45.

[3] Halim Setan, Rusli Othman. Monitoring of offshore platform subsidence using permanent GPS stations [J]. Journal of Global Positioning Systems.2006, 5(1-2):17-21.

[4]Zhang Zhiwang. Design Characteristic of the Monitoring Alarm System of Bottom Supporting Drilling Platform [J].China Offershore Platform.2006, 21(6):51-53.

[5] Zhang Hui. Electric System Design and Research of Deepwater Semi-submersible Drilling Platform [J].Electrical Technology, 2010,(4):43-45.

[6]Miao Huaming. Local Area Network Research of Monitoring and Alarm System in Drilling Platform [J].Manufacturing Automation,2005, 27:597-599.

[7] Jiu Xiansheng.8530TEU Configuration of Pressure Power System in Container Platform [J].Shanghai Shipbuilding,2008,37(5):78-82.

[8] Sun Caiqin, Guo Chen, Shi Chengjun. Model Analysis of Power Station Simulation System [J].World Shipping, 2003,26(03):38-39.

[9] Li Fuxin. The Generation and inhabitation of Harmonic Wave in offshore Petroleum Platform Electric System [J].Ocean Engineering Academic Meeting, 2007:374-377.

[10] Yu Ying. Harmonic Wave Analysis and Simulation Research of offshore Platform Electric Power System [J].Petroleum Machinery, 2006, 34(12):10-13.

Advanced Materials Research Vols. 986-987 (2014) pp 919-922

doi:10.4028/www.scientific.net/AMR.986-987.919

Experimental Research on Ice Accretion Characteristic of Energy-Saving Conductor

Hanjie Huang[1,2,a], Hua Jin[1,b], Zhixiang Huang[2,c], Xinmin Li[3,d]

[1] China Aerodynamics Research and Development Center, Mianyang, 621000, China

[2] State Key laboratory of Aerodynamics, Mianyang, 621000, China

[3] China Electric Power Research Institute, Beijing, 100075, China

[a]email: Hansjie@hotmail.com, [b]email:jh80103440@sohu.com, [c]email: xjtu331hzx@163.com, [d]email: Xinmin_li@163.com

Keywords: energy-saving conductor, ice accretion characteristic, icing test

Abstract. New type of energy-saving conductor which can obviously reduce the transmission losses was recently developed in power project. However, considering ice-coating and galloping in winter, it is necessary to investigate its ice accretion characteristic compared with conventional conductor. Research was conducted by icing wind tunnel test. Ice mass and ice shape of conductor with different diameter were examined. There is no clear advantage on the ice-coating resistance capability of energy-saving conductor with small diameter, while for conductor with larger diameter, energy-saving conductor's ice-coating resistance capability is better than conventional conductor. The test result is helpful for choosing suitable type of large diameter conductor in high and ultra-high voltage transmission project.

Introduction

In recent year, a new type of conductor for transmission lines has been developed. Small semi-circular or trapezoid grooves are spirally engraved on the newly designed conductor's surface, as shown in Fig.1a. The global surface configuration of newly developed conductor is much smoother than that of a conventional conductor, shown in Fig.1b (Eguchi [1]).

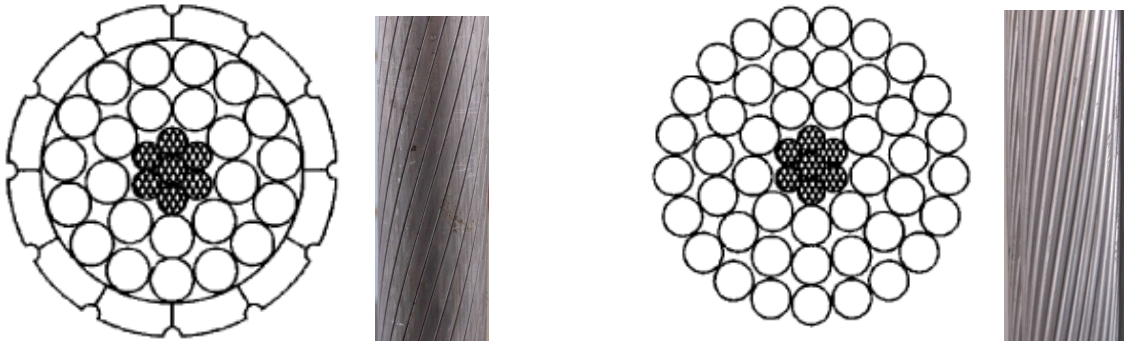

(a) Recently developed conductor (b) Conventional conductor

Fig. 1 Cross-section of two types of conductors

It has been found that because of the smoother surface and smaller ruggedness, the electric property of the new type of conductor is better than that of conventional conductor. It is called energy-saving conductor for less electric loss than conventional conductor in long distance power transmission. It seems that the new conductor is more suitable for the high and ultra-high voltage transmission projects being set up in China. However, more and more transmission lines will cross valleys, rivers and micrometeorological area in mountainous regions of west and south China, ice accretion on conductor is inevitable in winter. Under certain condition, wind can induce galloping--large amplitude, low frequency self-oscillation of ice-coated conductor (Nigol [2]). Galloping can be extremely harmful to the safe operation of power transmission system. It is necessary to investigate energy-saving conductor's ice accretion characteristic by test, comparing

with that of conventional conductor. There are certain limits of using the current available test results, which all focus on conventional conductor (Long [3] and Fu [4]). In this research, small size ice wind tunnel was used to investigate ice accretion characteristic on 4 different diameter groups of energy-saving and conventional conductor commonly used in transmission project.

Experiment Design

Icing test was conducted in 0.3 m×0.2m ice wind tunnel at Low Speed Aerodynamics Institute of China Aerodynamics Research and Development Center (CARDC). The ice wind tunnel is a close-circuit wind tunnel with two sections in tandem. The second section where test was conducted, is 0.3m×0.2m, as shown in Fig.2. The maximum wind speed in the second section is 60m/s, the lowest temperature is -30℃. In test, the temperature was dropped to the preset value by cooling system, while water spraying device was used to generate mist. MVD was 50 μm in the test, which was comparable to the size of water droplet in natural rainy and foggy weather.

The test models are sections of real conductor. There are 14 types of conductor, which divided into 4 groups with diameter about 25mm, 30mm, 34mm and 40mm respectively, as shown in Fig.3. For every group, there are one conventional conductor, which is No.4, No.5, No.10 and No.14 respectively, and other 2~3 energy-saving conductors. Models were firmly mounted horizontally in the tunnel, the test wind speed was 8m/s and 15m/s, temperature was -6℃. After 30minutes icing, the ice mass and ice shape would be recorded and analyzed.

Fig.2 Test section of ice wind tunnel

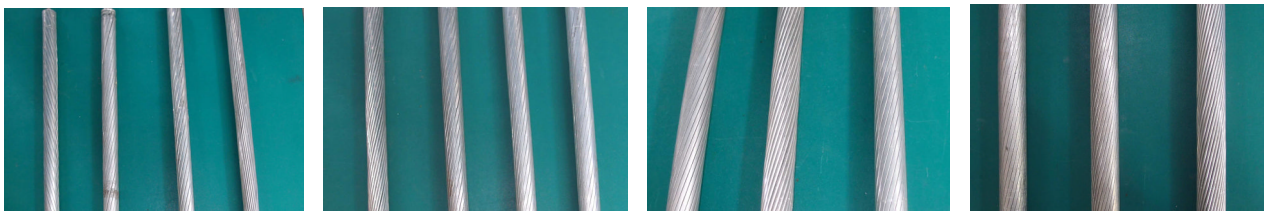

No.01～04 No.05～08 No.09～11 No.12～14

Fig.3 4 Groups of conductors

Analysis of Ice Accretion Characteristic

Kind of Ice Shape. Ice accretion phenomena on conductors are clearly, the most common ice shapes on conductor are fan-shaped, crescent and shape similar to crescent with smoother outline. Under natural condition, the most common ice shapes on conductor are crescent and fan-shaped, which is confirmed in this study, as shown in Fig4.

Influence of Wind Speed. Some conductors with detail geometric data of ice shape at different wind speed are shownd in Fig4. The change of ice mass of all conductors is shown in Tab.1. For every conductor, there is a noticeable increase of ice mass with the increase of wind speed. There is even more than 3 times larger amount of ice mass at wind speed 15m/s than that of at 8m/s. This mainly because that over-frozen droplet in mist moves with the air flow, the larger the speed is, the

more amounts of droplets will collide directly with conductor's surface and solidifying and freezing on the surfac. From literature [5], "when temperature is mild (higher than -10℃), wind speed 15m/s is more favorable for ice accretion", considering comman climate condition in power project operation, 8m/s and 15m/s reasonably reprents conductor's ice accretion characteristic at low and high wind speed respectivly. Basically, the thickness and cross-section areas of ice shape at 15m/s is also larger. For some conductors, the increase of ice mass with the speed may even cause the ice shape change from crescent or shape similar to crescent to fan-shaped, for example, conductor No.4, which means larger aerodynamic forces on conductor. This may pose safety issues to the transmission system and should be taken into great consideration in design and operation.

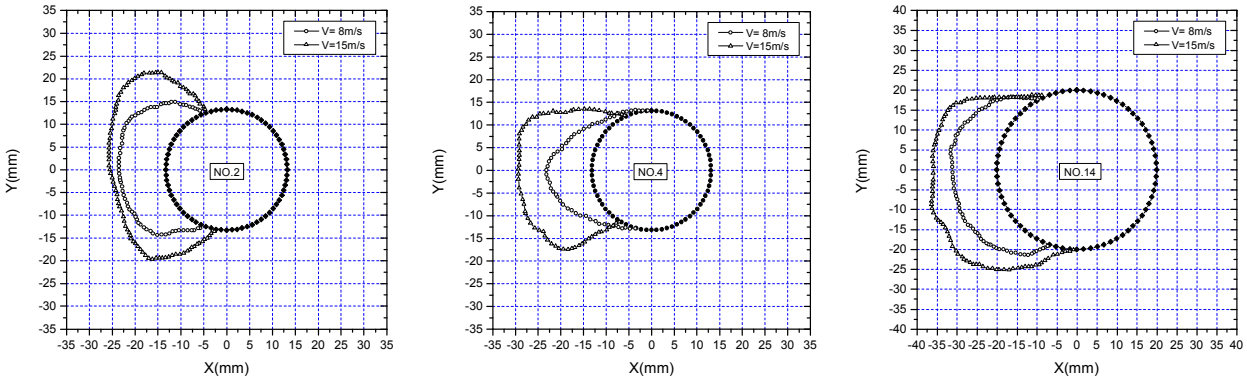

Fig.4 Geometric form of ice shapes

Table 1 Ice mass changes with types of conductors (g)

Group No.	Type No.	Ice mass V= 8m/s	Ice mass V= 15m/s	Type No.	Ice mass V= 8m/s	Ice mass V= 15m/s
1	No.1 d=25mm	93.6	152.7	No.2 d=25.2mm	98.9	193.6
	No.3 d=25.94mm	72.5	183.9	No.4 d=26.67mm	53.3	196.3
2	No.5 d=30mm	103.8	158.2	No.6 d=30.2mm	110.6	230.0
	No.7 d=30.2mm	80.2	160.8	No.8 d=30.5mm	102.7	202.6
3	No.9 d=32.4mm	129.2	229.4	No.10 d=33.75mm	64.3	98.2
	No.11 d=33.9mm	48.9	84.4	---	----	---
4	No.12 d=39.5mm	107.8	172.7	No.13 d=39.5mm	76.7	101.7
	No.14 d=39.9mm	124.8	197.0	---	---	---

Comparison of Ice-coating Resistance Capability of Two Kinds of Conductors

As shown in Tab.1, when wind speed is 8m/s, from group1 to group 4, conductor with smallest value of ice mass in each group is conventional conductor No.4, energy-saving conductor No.7, energy-saving conductor No.11, energy-saving conductor No.13 respectively. Conductor with largest value of ice mass in each group is energy-saving conductor No.2, energy-saving conductor No.6, energy-saving conductor No.9, conventional conductor No.14.

As for 15m/s, conductor with smallest value of ice mass is energy-saving conductor No.1, conventional conductor No.5, energy-saving conductor No.11, energy-saving conductor No.13. Conductor with largest value of ice mass is conventional conductor No.4, energy-saving conductor No.6, energy-saving conductor No.9, conventional conductor No.14.

It can be found that, when the diameter of conductor is less than 30.5mm, for example group 1&2, there is no clear advantage in ice-coating resistance capability for energy-saving conductor compared with conventional conductor. Sometimes, the value of ice mass of conventional conductor is the smallest. While with the increase of conductor's diameter, the advantage of energy-saving conductor becomes more and more clear. In group 3, the ice accretion characteristic of energy-saving conductor No.11 is better than conventional conductor No.10. While for the group 4 with relative larger diameter, all two types of energy-saving conductors' ice accretion characteristic are better than conventional conductor at all testing wind speed, especially No.13. This conclusion can be helpful for choosing suitable type of large diameter conductor in high and ultra-high voltage transmission project.

Ice mass and ice thickness do not increase linearly with the increase of conductor's diameter. Attention should be paid that, for the conventional conductor series, the value of ice mass of No.14 conductor with largest diameter is the largest at different testing speed, while for the energy-saving conductor series, the value of ice mass of No.9 and No.6 conductor with smaller diameter is the largest respectively. That also means that energy-saving conductor with large diameter may has the better ice accretion characteristic.

Conclusions

Ice accretion phenomena on conductors are clearly, the most common ice shapes on conductor are fan-shaped, crescent and shape similar to crescent. There is a noticeable increase of ice mass with the wind speed, 3 times larger amount of ice mass at higher speed than at lower speed was observed. The increase of ice mass with the speed may even result in the change of ice shape's type. Ice mass and ice thickness do not increase linearly with the increase of conductor's diameter. Comparing with conventional conductor, there is no clear advantage on the ice-coating resistance capability of energy-saving conductor with small diameter, while for conductor with large diameter, particular type of energy-saving conductor's ice-coating resistance capability is much better.

Acknowledgements

This work was financially supported by the National Natural Science Funds (Project No. 41272832, 50908218).

References

[1] Y. Eguchi, et al. Drag reduction mechanism and aerodynamic characteristics of a newly developed overhead electric wire. Journal of Wind Engineering and Industrial Aerodynamics, 2002, 90, 293-304.

[2] Nigol, P.g.Buchan, Conductor Galloping Part I-Den Hartog mechanism [J]. IEEE Transactions on Power Apparatus and System, 1981. 100(2), 699-707.

[3] Long X.l, et al. Study of coagulated ice on power transmission conductors. Journal of High Voltage Engineerin (in Chinese) , 1996, 36, 1096-1100.

[4] Ping Fu, et al. Two-dimensional modeling of the ice accretion process on transmission line wires and conductors. Journal of Cold Regions Science and Technology, 2006, 46, 132-146.

[5] Hanjie Huang etc. Test study on transmission line's ice accretion. 13th International Conference on Wind Engineering, 2011, Netherlands.

Advanced Materials Research Vols. 986-987 (2014) pp 923-926

doi:10.4028/www.scientific.net/AMR.986-987.923

Exploration on Automatic Welding Methods for Battery Pack of New Energy Automobiles

Jiandong Yang [1,a], Hui Yan[1, b] , Chunlin Tian [2,c,]and Jing Li [2,d]

[1]Jilin Business and Technology College ,Changchun City,China

[2]School of Mechanical and Electrical Engineering, Changchun University of Science and Technology, Changchun City, China

[a] yangjiandong@jlbtc.edu.cn, [b] yanhui7125@126.com, [c]tianchunlin@126.com, [d] lijing@126.com

Keywords: New Energy, Automobile, Battery Pack, Welding

Abstract. This article presents some research of welding methods according to battery pack working requirements of new energy automotive, for meeting the battery pack processing of new energy automotive in theory , single-sided duplex parallel resistance mass spot welding process is proposed.

Introduction

Currently, the new-energy automobile industry is listed in the seven national strategic emerging industries in China and therefore, the development of new energy automobiles is the historic opportunity of China's automobile industry. With increasingly serious environmental pollution and energy shortage, the research, development and promotion of new energy automobiles have become the core concern of governments and enterprises of all countries. Hereinto, power battery is the key technology as well as the bottleneck technology in the development of electric automobile due to its significant role in handling quality, driving safety, reliability and research and development costs of electric automobile [1]. For the secondary batteries researched and developed over the past decades such as nickel-cadmium, plumbic acid, nickel metal hydride, lithium ion and zinc air battery as well as fuel cell, they all have their own characteristics. However, considering the features required by electric automobile such as safety, high capacity, high-energy density and service life, lithium ion battery is going to become the mainstream technical trend that will be developed by all electric automobile enterprises. Apart from the performance features possessed by lithium ion battery itself, using lithium ion battery as the power supply system of electric automobile in China also possesses the following advantages: the mineral resources that manufacture lithium ion battery such as lithium, manganese, iron, vanadium, etc. are abundant; the technical level and scale of lithium ion battery in China has reached the world leading level; the production and processing of lithium ion battery have formed the integrated industry chain and the annual output of battery has reached more than 1/3 of the world's total output, which promotes the electric automobile to develop toward industrialization and large scale. Striving to develop lithium ion power battery industry will promote the development of new-energy automobile industry in China effectively.

In order to meet the requirements in terms of voltage, power and energy of the whole power supply system, lithium ion battery pack generally consists of several shunt-wound lithium-ion cell monomers and the nickel plating steel sheet and lithium ion battery core are welded through resistance spot welding technique under normal conditions during mass production. The internal resistance of battery pack will be increased if the welding strength is too low and in some severe cases, the lithium ion battery core and nickel plating steel sheet will be separated because the welding is not firm and this can lead to the failure of power supply; if the welding strength is too high, then it will cause the leakage of electrolyte and the combustion or explosion of lithium ion battery pack due to short circuit [2]. Therefore, resistance spot welding becomes a significant procedure in the production process of battery pack. Welding quality has a decisive effect on quality of lithium ion battery pack and its service life. As a result, the automatic welding machine principle in series-parallel welding of Model 18650 cylinder-shaped lithium ion battery commonly used in power supply system for new energy automobiles is discussed in this paper.

Determining the Welding Method

Fig. 1 below is the real photo of lithium ion battery pack applied in power supply system of new energy automobiles. Fig. 2 is the dimensional sketch of lithium-ion cell monomer.

Fig. 1 Real Photo of Lithium Ion Battery Pack

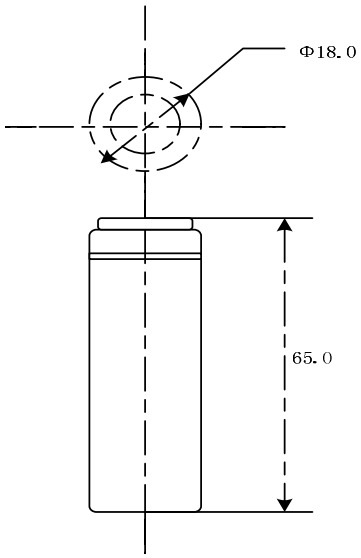

Fig.2 Dimensional Sketch of Lithium Ion Battery

The welding methods of metals can be divided into three categories according to the characteristics of technical process and they are fusion welding, pressure welding and braze welding. The welding heat sources are varied, including flame, electric arc, resistance, ultrasonic wave, friction, plasma, electron beam, laser beam, microwave, etc. Considering the welding of lithium ion battery pack is the lap welding of thin plate, pressure welding technique of resistance spot welding is adopted in this paper.

Through utilizing the resistance heat from the contact surface when the current flows through the workpiece to heat the workpiece to be welded which is pressed between electrodes to melting state and finally, the efficient and economical metal binding welding-and-forming technique is formed. This technique possesses many advantages such as concentrated heat quantity, small welding deformation, without using welding material, less auxiliary processes, low energy consumption and non-pollution, simple processing and achieving welding automation easily, etc. The operating principle is shown in Fig. 3.

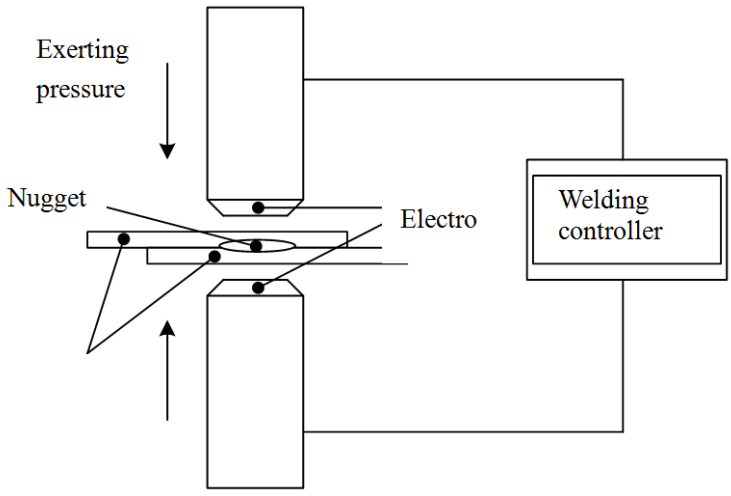

Fig. 3. Diagram for Operating Principle of Resistance Spot Welding

Determining the Electrification Method

Based on the different discharge methods of electrode to workpiece to be welded, resistance spot welding mainly can be divided into four categories: direct spot welding, indirect spot welding, series spot welding and duplex spot welding. Some common electrification methods in spot welding are presented in Fig. 4.

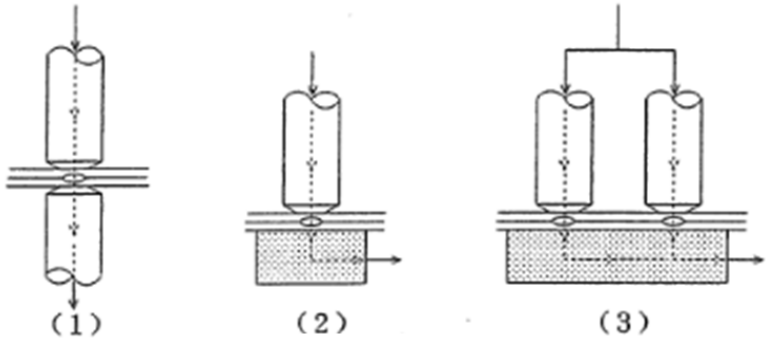

a) Direct spot welding

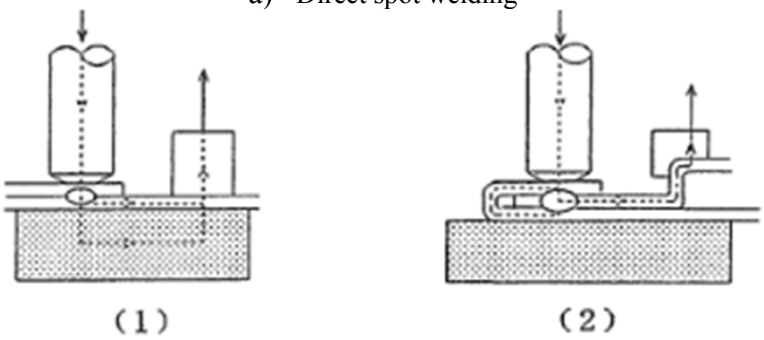

b) Indirect spot welding

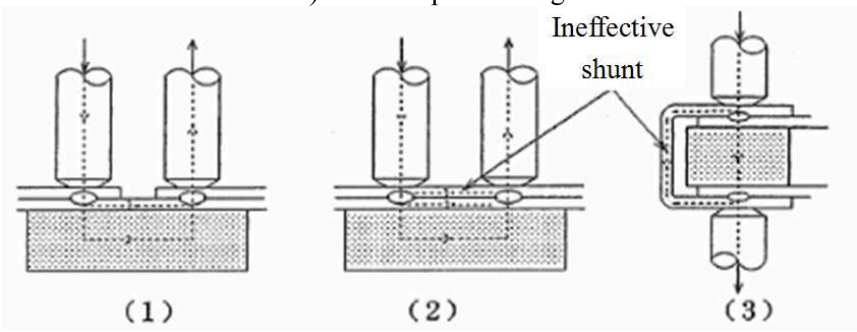

c) Series spot welding

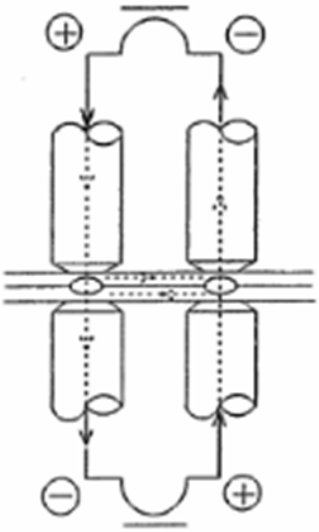

d) Duplex spot welding(Push-pull spot welding)

Fig. 4. Some Common Electrifying Methods in Spot Welding

In direct spot welding, a group of electrodes directly clamp the workpiece to be welded tightly through exerting pressure and the welding current flows through one of the electrode and the contact surface of workpiece to be welded to another electrode and forms conducting state; while indirect spot welding is the current of the contact surface of workpiece to be welded flows through one certain part of the workpiece from one electrode to another; series spot welding refers to the case in which the current flows through two contact regions in sequence and performs spot welding when there are two contact regions in one welding current circuit, however, in some cases, the current may be shunted and the electrode shall be increased in order to prevent the decrease of current efficiency and to guarantee the welding quality; duplex spot welding is using the welding transformer of both ends of the electrode and performing duplex spot welding simultaneously. Compared with series spot welding, this method can decrease shunt phenomena. Due to the structure and characteristics of lithium ion battery core, direct spot welding method is hard to achieve the welding between battery core and the connecting sheet. Therefore, the unilateral duplex parallel spot welding method shall be adopted.

Conclusion

Based on the practical situation of lithium ion battery pack used in the power supply system of new energy automobiles in this paper, the existing welding techniques and process are analyzed. It is believed that resistance mash spot welding technique is more reasonable and the single-sided duplex parallel spot welding method shall be adopted in terms of electrification methods. This paper only focuses on theoretical discussion currently and the next step is to conduct experimental investigation systematically in order to determine the proper welding method and corresponding technological parameters and achieve better welding effects.

Acknowledgment

The authors gratefully acknowledge the funding of this study by Science and Technology Development Plan of Jilin province (20130204024GX) and Talent Development Project of Jilin province (20091328) and Venture Fund Project for Personnel Studying Abroad of Jilin province (2010273).

References

[1] Huiming Gong, Michael Q. Wang, Hewu Wang. New energy vehicles in China: policies, demonstration, and progress [J]. Mitigation and Adaptation Strategies for Global Change, 2013 (18):207~228.

[2] Qingsong Wang, Ping Ping, Jinhua Sun. Catastrophe analysis of cylindrical lithium ion battery [J]. Nonlinear Dynamics, 2010(61):763~772.

[3] MeiChen,BinghuiWu,JingYang,NanfengZheng. Small Adsorbate-Assisted Shape Control of Pd and Pt Nanocrystals[J]. Adv. Mater. . 2012 (7).

[4] Min-Kyu Song,Soojin Park,Faisal M. Alamgir,Jaephil Cho,Meilin Liu. Nanostructured electrodes for lithium-ion and lithium-air batteries: the latest developments, challenges, and perspectives[J]. Materials Science & Engineering R . 2011 (11)

[5] LI Yong, SONG Jian, YANG Jie,Damage effects of heterogeneous material of new energy automotivebatteries under thermomechanical shocks[J]. Science China Press.2013(30): 3037 ~ 3044

Advanced Materials Research Vols. 986-987 (2014) pp 927-930

doi:10.4028/www.scientific.net/AMR.986-987.927

Finite Element Analysis for the Collapse Accident of A 110kV Transmission Tower

Yi Zhu，Bo Li，Hao Wang，Kun Li

Economic & Technology Research Institute, State Grid Shandong Electric Power Company, Shandong Jinan 250021;

Keywords: straight-line tower ; the strong wind ; collapse ; the finite element analysis ; line tower coupling

Abstract. Put the finite element analysis of line tower coupling modeling to the collapse of a 110 kV line straight-line tower, study the effect of strong wind on transmission tower and wire. The results show that under the action of strong wind, the material specification selected by the part of the rods on the type of tower is lower, cross section is smaller, the principal material of tower will be instable and flexional under the compression, resulting in tower collapsed.

Introduction

On April 29, 2011, the rainstorm appeared in the via area of a 110kV line, gust grade is 10, local wind grade is 11. On ten past zero, April 30, the line zero-sequence I segment and distance I segment generate protective action, so that superposition is not successful. Through inspection the cause is that the tower body of the line # 11, # 12 and # 13 tower collapsed due to storm wind.

Fig.1 A case of #12 tower failure for 110 kV transmission line

Fig.2 A case of No.13 tower failure for 110 kV transmission line

Free-standing transmission tower, which is connected by Angle steel or steel pipe, is a large space hyperstatic truss structure. Many of the running transmission tower in actual lines are designed in the 1980s or even earlier, when due to the limitations of design methods and analytic means, it is difficult to make a comprehensive & detailed analysis and evaluation for the design structure, and unable to fully consider the issues of strength, stiffness and stability of each component in the structure. With frequent extreme weather in recent years, some security issues on transmission tower putting into use in earlier times become more prominent [1].

Using general finite element analysis software ANSYS, this paper aimed at the local weather conditions to establish mechanical calculation model of transmission tower, research the structure characteristics of transmission tower in line, determine the condition of tower structure strength in such extreme operating condition, to get stress state in each rod, and find out the reasons for the collapse of transmission towers.

1 The finite element modeling for transmission tower

1.1 Transmission tower structure

11 and # 12, # 13 tower are 110kv ZGU2-21 (7727) straight-line dual-circuits tower, the type of tower is designed in the late 1970s.The nominal height of the tower is 21 m, and the total height is 31 m. The root open is 4.595 m for front, and 3.214 m for side. The design for horizontal span is 350 m, vertical span is 350 m,and the actual span is 328 m.The landing leg and the main limb on body part 1 of the tower are connected by different specifications of the Q345 angle steel, and the

others are all connected by Q235 angle steel. The structure type is shown in figure 3. The model number of wire is LGJ - 240/40, the model number of ground wire is GJ - 50.

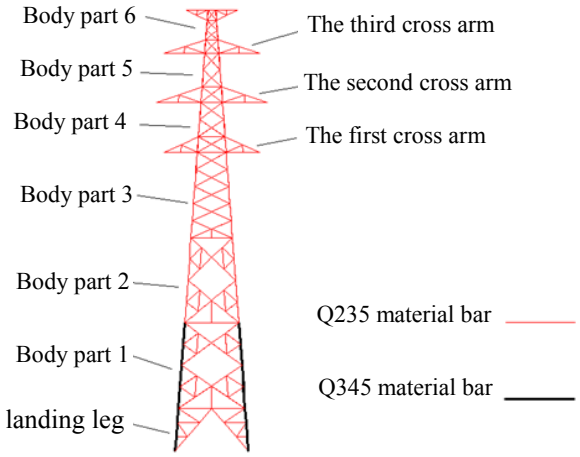

Fig.3 Subsection numbers and structures of #11-#13 straight-line towers

1.2 Finite element analysis model

Due to the interaction of the stress of wire, ground wire and transmission tower, in order to accurately simulate the stress status of tower, build a model for wire (ground wire) together with the tower, build a three-towers&four-wire finite element model. Transmission towers using beam elements Beam188 to disperse all rods, the rods are connected with each other through steel node, ignore the specific structure of the junction, only consider the quality of the connection, and regardless of the impact of the jumper wire connection and the altitude difference of the wire suspension point[2]. On the basis of the wire (ground wire)"form-finding"[3], according to the deformation and mechanical characteristics of wire (ground wire), using the rod element of LINK10 to conduct the model, when calculating the geometric nonlinear effects should be considered.

1.3 Computational load

As far as analysis for working condition, the load auctioning on transmission tower can be divided into three parts: the first part is the self-weight of transmission tower structure; the second part is the role of the wire (ground wire) to the transmission tower; the third part is the impact of wind loads. According to local meteorological conditions, use the wind of grade 11 to account in this calculation(30m/s), the wind direction with the line is 90°. Load combination considers the combined action of these three part load.

2 The assessment for structural strength of transmission tower structure

According to the specification requirements, base on the design theory of probability limit, in accordance with the requirements of The Technical Specification For 110～750kV Overhead Transmission Lines GB50545-2010[4], the transmission tower components were categorically assessed according to the nature of stress.

2.1 The strength calculation of tension components

According to the specification requirements, use the following formula to calculate the strength of tension components：

$$\sigma = \frac{N}{m \cdot A_n} \pm \frac{M}{m_M \cdot W} \le f \tag{1}$$

In this formula, N is the axial force ; An is the net sectional area of components ; m is the strength reduction factor for the axial stress components, regarding to the single limb connection angle steel components, m=0.85[5] ; mM is the stable strength reduction factor for flexural components, regarding to the single limb connection angle steel components, mM=1.0 ; M is the bending moment design value ; W is the net section resistance moment of components ; f is the strength design value of the material.

2.2 Local stability calculation of compression member

After the transmission tower structure under load, about half of the rods bear the combined action of the axial pressure and bending moment, these rods may exist the possibility of instability. Loss of overall stability of transmission tower is because of the accumulation of each rod local instability, which changes the structure into mechanism. According to the specification requirements, use the following formula to calculate the local stability of the compression member:

$$\sigma = \frac{N}{\phi \cdot m_N \cdot A} \pm \frac{M}{m_M \cdot W} \le f \qquad (2)$$

In this formula, A is gross sectional area of components ; ϕ is axial compression stability coefficient of components ; mN is the stable strength reduction factor for compressive rod, regarding to the equilateral double angle steel components, mN=1.0[5] ;W is the gross section resistance moment of components.

3 The analysis for calculation results and collapsed reasons.

3.1 The analysis for structural strength

For the same three-tower structure and the similar runtime environment, the calculation results of the three-tower are basically the same. In order o save space, this article only specifically describe the calculation of # 12 straight tower. Under the action of strong wind (wind direction is perpendicular to the line direction), the tension member of # 12 straight tower account for 48.8% of the total rods, the compression member account for 51.2%. The maximum stress and the location of bars of two kinds of material for transmission towers are shown in Table 1 and Figure 4.

Tab.1 The maximum stress and the location of bars

Rod material	The maximum tensile stress of tension member(MPa)	The maximum compressive stress of compression member(MPa)	Strength design values[6] (MPa)	The location of the maximum stress
Q345	306.6	332.2	310	The rods in leeward side of the root of landing leg
Q235	217.8	272.2	215	The rods in leeward side of the connection location of body part 1 and body part 2

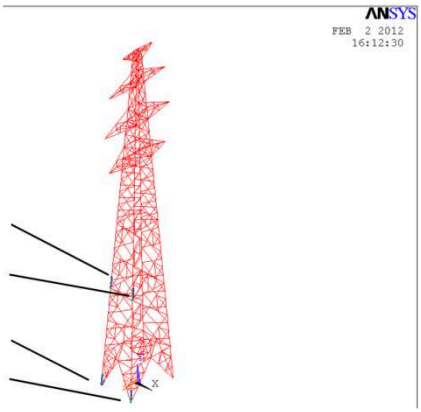

Fig.4 The location of the maximum stress of Q345 and Q235 rod members.

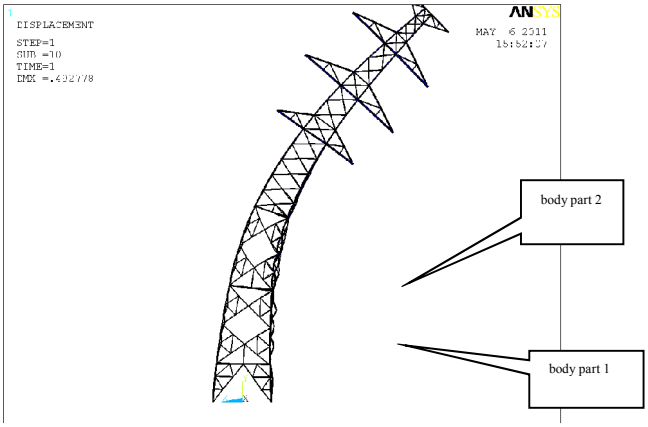

Fig.5 The deformation of tower body

3.2 The analysis for the structural deformation

Under the action of strong wind (wind direction is perpendicular to the wire), the transmission tower rods in the connection location of body part 1 and body part 2 all generate the larger deformation, as shown in Figure 5.

3.3 The analysis for collapsed reasons

Sample the principal material and auxiliary material of the collapsed #11-#13 line tower, and make the material testing analysis for the chemical composition, organizational analysis, mechanical properties, according to the test results, the tissue of the principal material and auxiliary

material are normal, element content and mechanical properties at room temperature conform to the requirements of *The Carbon Structural Steel* GB/T700-2006[11] for Q235 and Q345 structural steel.

Synthesize the calculation results of stress and displacement, and combine the design strength value of the component material, the principal material of the root of landing leg, and the rod material of the connection location etc of body part 1 and body part 2 all generated overstressing. Among them the maximum overstressing proportion of the principal material is 4%, and the maximum overstressing proportion of the rod material of the connection location of body part 1 and body part 2 is 26%. In terms of deformation, the overall structure on the location of body part 1 and body part 2 generate the maximum deformation, so under the action of strong wind (wind direction is perpendicular to the line direction), this position is the most dangerous position, which may be damaged because of the strength and the insufficient local stability, the analysis results are consistent with the the actual collapsed situation of tower, as shown in Figure 1 and Figure 2.

In view of the collapse accidents have occurred many times in the region in history (the year of 2002 and 2005), when the wind speed all exceed 30.0 m/s. So it should be appropriate to improve the design standards of wind resistance in the region, and it is suggest that the collapse of the 110kV line 7727 type tower in the region is generally surveyed. On the basis of the wind speed no less than 33m/s (wind grade is 12), again according to *The Technical Specification For 110～750kV Overhead Transmission Lines* (GB50545-2010) to check reinforcement ; In densely populated areas and tuyere areas, it is suggest that make a reinforcement processing for under 300m span transmission tower, and make a redesigned replacement for more than 300 m span transmission tower, in order to prevent the collapse accidents from happening again.

4 Conclusion

1) The reason for the collapse of the line is that under the action of the strong wind of grade 11, the connection location of tower body 1 and body 2 generate overstressing, take place larger deformation, cause the principal material of tower instability and flexion under the compression.

2) The tower type (7727) is finalized in 1977, according to The Technical Specification For 110～750kV Overhead Transmission Lines (GB50545-2010) accounting, found the body part 2 and above the main limb bar choose Q235, material specifications is lower, unable to meet the using demand of the strong wind of grade 11.

3) It is suggest that suitably improve the wind-resistant design standards in the wind prone areas in history, the old lines in such regions need a re-checking reinforcement, in order to prevent the collapse accidents from happening again.

References

[1] Changyuan Wu, Yu Zhang. The reason and emergency countermeasures for the collapse of the 220 kV lines in South mountain[J]. Electric power construction, 2009, 30(1): 47~49.

[2] Yunwei Feng. The research of ANSYS modeling and dynamic characteristics for transmission tower[J]. The steel structure, 2008, 23(1): 21~25.

[3] Jianguo Xu, Huajun Shi, Yong Guo, etc. The finite element modeling for the large span transmission tower line system[J]. Electric power construction, 2011, 32(3): 15-19.

[4] Xiaohui Liu, Bo Yan, Xuesong Lin, Wenyun Li, etc. The research of monsoon numerical simulation for500kV extra high voltage transmission lines. Engineering mechanics, 2009, 26(1): 244-249.

[5] The Ministry of Construction of the People's Republic of China. GB 50017-2003 The design specification of steel structure[S]. Beijing: China Electric Power Publishing House, 2003.

Advanced Materials Research Vols. 986-987 (2014) pp 931-935

doi:10.4028/www.scientific.net/AMR.986-987.931

Impacts of Diverting Potential Difference on Armored Cables in Substations

Li CHEN

Transmission and Distribution Line Training Department, Sichuan Electric Power Corporation, Skills Training Centre, Chengdu 611133, China

email: chitangyuan@163.com

Keywords: Grounding Grid; Ground Resistance; Diverting Potential Difference; Armored Cable; CDEGS

Abstract. To reduce the interference on communication equipments caused by transient electromagnetic field of switching operation, the shields of cables are connected to grounding grid on both sides in the substations grounding designs. However, when the substation is stroke by lightning or shorted, the huge potential difference called diverting potential difference between the cable core and the shield is generated, which can easily destroy insulation of cables, even producing electrical tree or dielectric breakdown in insulation material. Moreover, the large current flowing through the shield of cables will cause personnel accidents and equipment damages. In this paper, the electric model of cables is established using grounding grid simulation software—CEDGS. The way diverting potential difference changes influenced by grounding grids, soil and other parameters is analyzed. Measures to reduce diverting potential difference are proposed for providing a theoretical basis of construction in practice.

Introduction

Diverting potential [1] refers to the potential which is transferred from grounding device to the equipment with bonding conductors when the short-circuit current or the lightning current flows through the grounding device. To reduce the interference on communication equipments caused by transient electromagnetic field of switching operation, the shields of cables are connected to grounding grid on both sides in the substations grounding designs. However, when the substation is stroke by lightning or shorted, the huge potential difference called diverting potential difference between the cable core and the shield is generated, which can easily destroy insulation of cables, even producing electrical tree or dielectric breakdown in insulation material. Moreover, the large current flowing through the shield of cables will cause personnel accidents and equipment damages [2] [3].

In addition, the grounding grids in China are made from steel instead of copper because steel is much cheaper than copper. As a result, the problem of ground potential unbalance is more outstanding than that at abroad. Especially on the condition that substation is stroke by lightning which produce high-frequency current, along with the facts that permeability of steel is much larger —200 times than copper, so the gradient of grounding grid potential is much too big [4]. In order to solve the above problems, it is necessary to analysis impacts of diverting potential difference on armored cables in substations [5].

In this paper, the diverting potential caused short circuit in substations is discussed merely, because characteristics of lightning stroke in the substations are much more complex.

Cable model and grounding grid model

The current flowing through armor tier is composed of short-circuit current. Not only it's related to short-circuit current and the location where the current empties into earth, but also it's affected by the topology of the network. It's difficult to calculate the result by numerical analysis in practice [6] [7] [8]. With grounding grids simulation software—CEDGS, the rule of diverting potential influenced by grounding grids and soil can easily be obtained.

We assume that the grounding gird is a square, the length of one side is 100 meters. The distance of equalizing conductors is 10 meters. Grounding grid which is made from copper is buried 0.8 meters deep. The grounding conductors' radius is 10.1 millimeters, and the shape is cylindrical. Homogeneous soil resistivity is 500 $\Omega \bullet m$. There is a VV22 armored cable in substation transferring status signals from primary side to central control room. The length of the cable is 60 meters. This single core cable's nominal cross section area is 10 square millimeters. The material of the core is copper, and the material of the armor tier is steel. The inner diameter of armor tier is 4.9 millimeters, the external diameter is 5.0 millimeters. The armor tier is stretched over with PVC of 2 millimeters thickness. The cable's parameters are shown in Figure1.

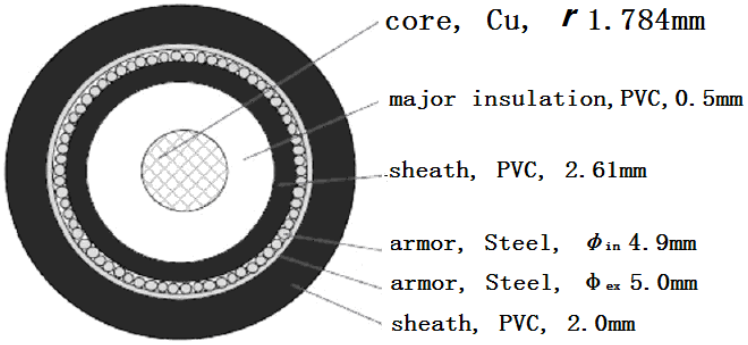

Fig.1. The armor cable—VV22

The cable is buried in 0.1 meters depth. Core conductor is connected to grounding grid through equivalent output impedance which is 300 Ω at primary side, and is connected to grounding grid through equivalent input impedance which is 1 Ω in the control room. Armored shield is connected to grounding grid at both sides by earth connecting conductors which is made from steel. The radius of earth connecting conductors is 2 millimeters. Suppose 10kA short-circuit current flows into grounding grid, the location where the current empties into earth is shown in Figure2.

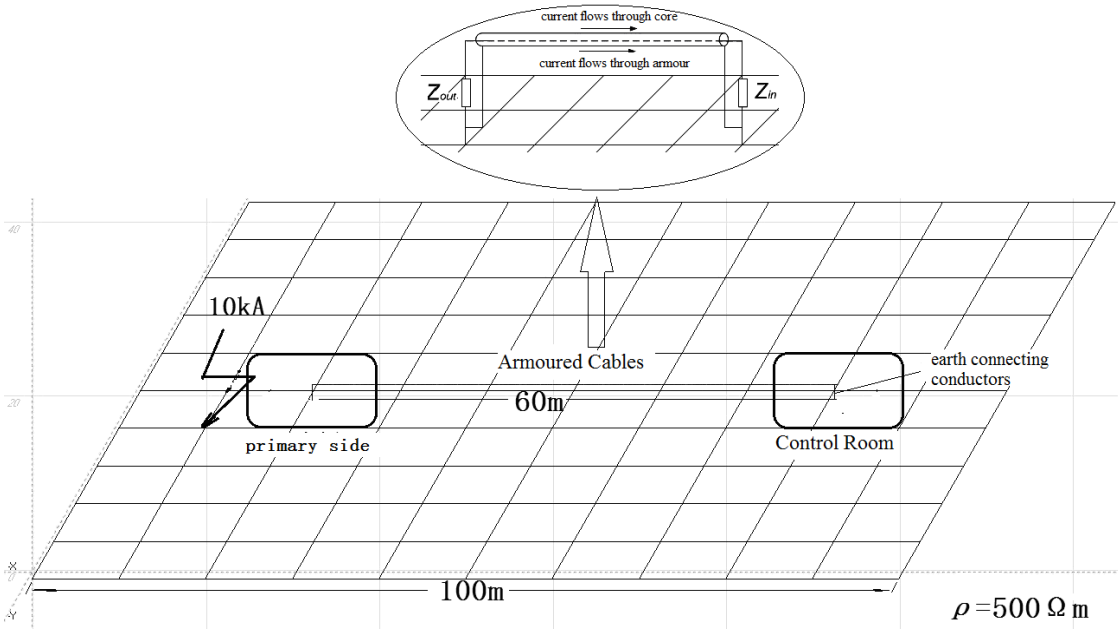

Fig.2. Simulation model of grounding grid and armored cable

Test results of homogeneous soil model

Through the simulation of CDEGS, the biggest diverting potential difference between the core and the armor can be obtained near primary side, because the gradient of grounding grids potential is much bigger in this area [9]. Diverting potential difference discussed later in this paper refers the biggest voltage between the core and the armor.

Put the calculation parameters into CDEGS, and assume respectively the radius of grounding conductor will be 0.001m, 0.002m, 0.003m, 0.005m, 0.007m, 0.009m, 0.010m, 0.012m, 0.015m, 0.020m, 0.025m and 0.030m. The change rules can be obtained shown in Figure3.

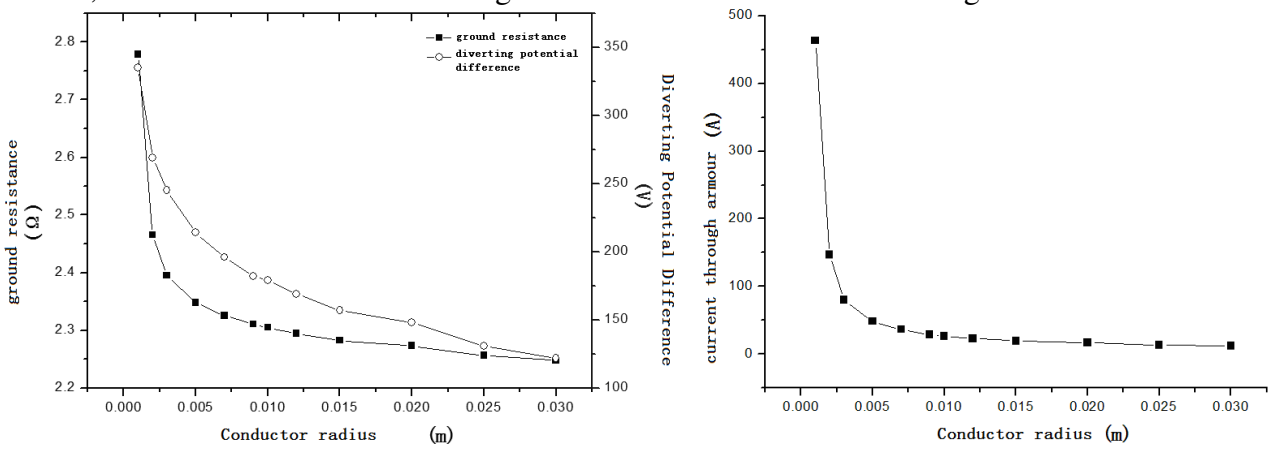

(a) The influence on diverting potential difference (b) The influence on current through armor

Fig.3. The simulation result influenced by conductor radius

Analyzing the data, we can draw a conclusion that conductor radius is smaller, ground potential is more unbalanced, which will lead to the bigger diverting potential difference. When the radius becomes bigger, the fault current is prone to flow into earth and the potential unbalanced degree of grounding grid is declining, so the diverting potential difference and current flow through armor becomes smaller.

Keep the parameters of grounding grid and armored cable unchanged, and assume respectively homogeneous soil resistivity will be $500\,\Omega \bullet m$, $1000\,\Omega \bullet m$, $1500\,\Omega \bullet m$, $2000\,\Omega \bullet m$, $2500\,\Omega \bullet m$ and $3000\,\Omega \bullet m$. The change rules can be obtained shown in Figure4.

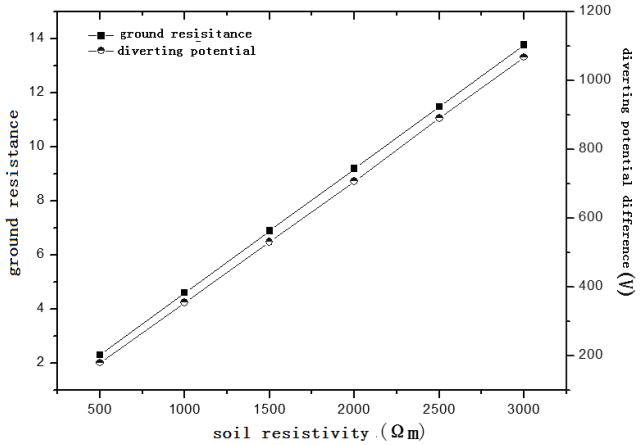

Fig.4. The simulation result influenced by soil resistivity

The result is obvious that soil resistivity is proportional to ground resistance and diverting potential difference. However, the current which flows through armor tier keeps no change.

It's been proved that in engineering design inductive effect of grounding grids can't be ignored for 500kV large substations or substations stroke by lightning because potential unbalanced degree becomes bigger. In this simulation, homogeneous soil resistivity doesn't affect potential unbalanced degree of the grounding grid due to current remaining unchanged, so the reason why diverting potential increase is that the potential of the whole grounding grid becomes larger. The soil resistivity is bigger, the more difficulty for current to disperse in the soil.

Test results of horizontal two layer soil model

Keep the parameters of grounding grid and armored cable unchanged, and assume the bottom layer soil resistivity is 500 $\Omega \bullet m$ which the thickness is infinite and the top layer thickness is 50 meters. Put $500\,\Omega \bullet m$, $1000\,\Omega \bullet m$, $1500\,\Omega \bullet m$, $2000\,\Omega \bullet m$ and $2500\,\Omega \bullet m$ into the top layer soil resistivity. The change rules can be obtained shown in Figure5.

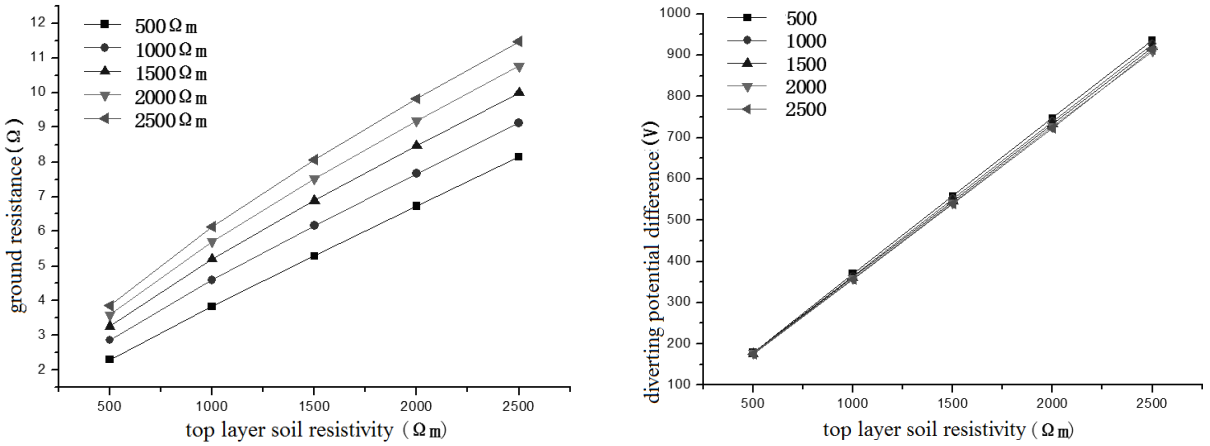

(a) The influence on ground resistance (b) The influence on diverting potential difference

Fig.5. The simulation result influenced by top layer soil resistivity

The result shows that top soil resistivity is proportional to ground resistance, diverting potential difference and current flowing through armor tier. With the increasing of soil resistivity, the ground resistance increases. As a result, diverting potential difference becomes larger due to the increasing of unbalanced degree of grounding grid.

In this simulation, the current flowing through armor tier remains unchanged. That's because the impedance of the armor loop is very large—armor tier is made from steel which have the high resistivity and the thickness of that is only 0.1mm.

Keep the parameters of grounding grid and armored cable unchanged, and assume the top layer soil resistivity is 500 $\Omega \bullet m$ and the thickness is 50 meters. Put $500\,\Omega \bullet m$, $1000\,\Omega \bullet m$, $1500\,\Omega \bullet m$, $2000\,\Omega \bullet m$ and $2500\,\Omega \bullet m$ into the bottom layer soil resistivity. The change rules can be obtained shown in Figure6.

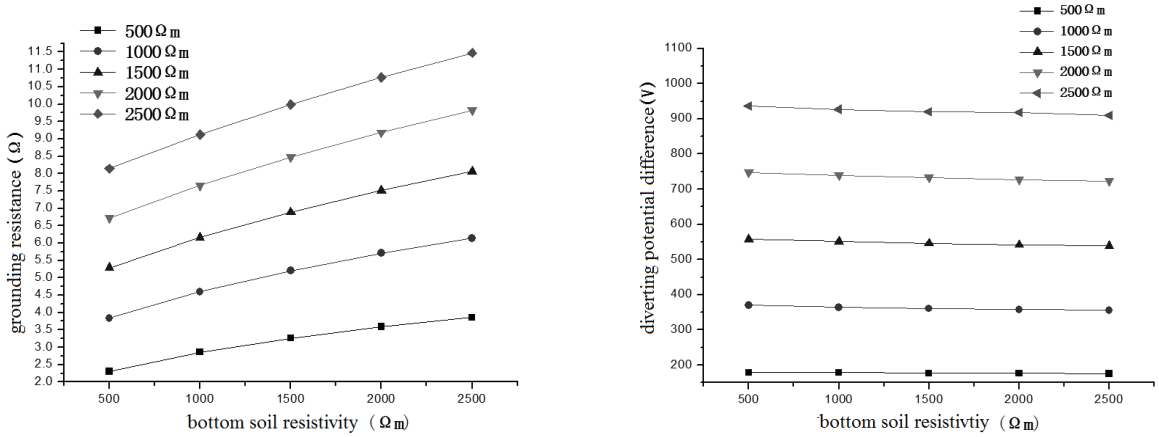

(a) The influence on ground resistance (b) The influence on diverting potential difference

Fig.6. The simulation result influenced by bottom layer soil resistivity

The results showed that with bottom soil resistivity increasing, ground resistance increases and diverting potential difference decreases slightly, current flows through armor tier stays the same.

Analyzing the data above, it's found easily that there is no direct relationship between ground resistance and diverting potential difference. Diverting potential difference is mainly affected by the top soil rather than bottom soil. It's obvious that the unbalanced degree of grounding grid is decreasing due to the increasing of the bottom soil resistivity.

Conclusion

Based on grounding grid simulation software—CEDGS, established the model of grounding gird and armored cable, select variables to simulate and calculate. Through the simulations to get the way diverting potential difference how to change influenced by grounding grid, soil and other

parameters. Measures to reduce diverting potential difference are proposed for providing a theoretical basis of substations construction.

References

[1] DL/T 620-1999 Over-voltage protection and insulation coordination for AC electrical installations [S]. Electric power industry ministry of the People's Republic of China, 1999.

[2] Qi Lei and so on. Measurement of distributed parameters and transient analysis of shielded cable [J]. Proceedings of the CSEE, 2005, 25(6):119-123.

[3] Wu Maolin and so on. Analysis of electromagnetic interference in shielded cables caused by ground potential difference in substations [J]. High Voltage Engineering, 2005, 31(3):53-55.

[4] Wang Zhongren and so on. Hydropower station grounding design [M]. China WaterPower Press, 2008.

[5] Hu Yi. The analyses of substation grounding systems and improving measures [J]. High Voltage Engineering, 1987(1):59-62.

[6] Lu Zhiwei and so on. Potential difference within grounding net for large substations [J]. electric power construction, 2004, 25(9):39-40.

[7] Li Shenglin and so on. Study of influence factors of dual-layered soil on vertical grounding rod performance [J]. Insulators And Surge Arresters, 2007, (5).

[8] Otero A F. Frequency-dependent grounding system calculation by means of a conventional nodal analysis technique [J].IEEE Transaction on Power Delivery,1999,14(3):873-878.

[9] R D Southey,F P Dawalibi,W Vukonich. Recent Advances in the Mitigation of AC Voltages Occurring in Pipelines Located Close to Electric Transmission Lines [J].IEEE Transactions on Power Delivery,1994,9(2):1090-1097.

Advanced Materials Research Vols. 986-987 (2014) pp 936-939

doi:10.4028/www.scientific.net/AMR.986-987.936

Modal Analysis of Vibration and its Program Development in Power Transformer Core

Fangxu Han, Yan Li, Xin Sun , Huan Wang

Research Institute of Special Electrical Machines, Shenyang University of Technology, China

email: hanfangxu021532@163.com

Keywords: Power transformer; Natural vibration frequency; Program development

Abstract. In this paper, based on the modal analysis combined with power transformer product structure, using the empirical formula calculation method and finite element simulation analysis software calculates the natural vibration frequency of power transformer core, respectively, while making the VB language as a tool to develop the calculation software of natural vibration frequency of power transformer, provides a strong support for product tenders, design and optimization.

Introduction

Power transformer is an elastic vibration system composed of kinds of structures. The system has a lot of natural vibration frequency. When transformer core, winding, fuel tanks and other structure mechanical vibration natural frequency is equal to or close to the core of silicon steel sheet of the magnetostrictive vibration fundamental frequency and integer times, will produce a resonance phenomenon, make the transformer noise significantly increased[1,2]. Therefore, according to the structural parameters of power transformer core calculating the natural frequency of vibration accurately is important for reducing the vibration noise, to avoid structure resonance and improve the quality of the product design.

Mode analysis of transformer core is the basis of the transformer body vibration noise, modal vibration mode and natural frequency can be obtained, analyzes the possibility of resonance structure, and then guide the transformer construction design, to avoid the resonance. In this paper, the application of ANSYS finite element software to modal analysis the core structure of a DSP-24650/132 type transformer, finds resonance modes, gives structure to avoid resonance rationalization proposals. At the same time, based on the empirical formula and Visual Basic language as a tool develop the power transformer core vibration frequency calculation software.

The natural vibration frequency of core empirical formula：

According to the empirical formula, the natural vibration frequency of core can use the type to calculate[3]：

$$\mathrm{F}_0 = 1.08K_c \frac{(Z+h)}{(H_0+h)^2} \times 10^5 \tag{1}$$

Definition function is: F_0 is natural vibration frequency of core, Hz ; $H_1 = H_0 + h$,cm; $M_1 = B_0 + z$,cm; K_c is and $(H_0+h)/(B_0+Z)$ related coefficient, and its relation as shown：

Figure 2 by the curve fitting coefficient K_c is calculated by the following formula:

$$K_c = 0.125(\frac{H_1}{M_0}) + 0.725 \quad \text{(For single phase)} \tag{2}$$

$$K_c = 0.0625(\frac{H_1}{M_0}) + 0.78125 \quad \text{(For the three phase)} \tag{3}$$

The fundamental frequency, two, three, four high frequency to 50Hz of the magnetostrictive vibration frequency is 100Hz, 200Hz, 300Hz and 400 Hz, etc, respectively. And its corresponding frequency band range usually take 75～125Hz, 175～225Hz, 275～325Hz, 375～425Hz. In order

to avoid the resonance, should make its core natural frequencies avoid the magnetostrictive vibration frequency range[4].

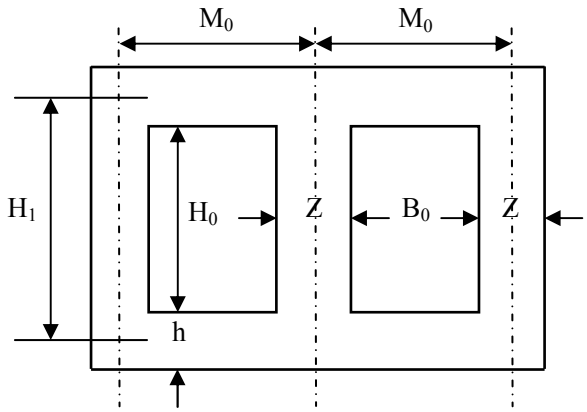

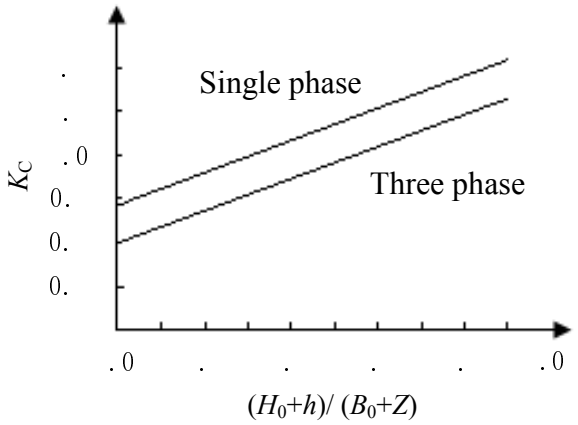

Fig.1.Natural vibration frequency variable parameters Fig.2.Relation curve of K_c and $\frac{(H_0+h)}{(B_0+Z)}$

The natural frequency of core model is about 236 which obtained by analytical formulas, the specific calculation process is as follows:

$$K_c = 0.0625(\frac{H_1}{M_0}) + 0.78125 = 0.0625 \times (\frac{212}{83.5}) + 0.78125 \approx 0.94$$

$$F_0 = 1.08K_c \frac{(Z+h)}{(H_0+h)^2} \times 10^5 = 1.08 \times 0.94 \times \frac{(70+34.5)}{(177.5+34.5)^2} \times 10^5 \approx 236$$

Core vibration modal analysis

Modal analysis is in fact to convert the vector which described in the original physical coordinate to the "modal coordinates", it can be said modal analysis is actually a form of coordinate transformation[5]. Power transformer core natural vibration frequency simulation calculation can obtain by ANSYS software, its modal analysis calculation module provides six modal extraction methods, DSP-24650/132 type transformer core, for example, the modal analysis of the specific process is as follows:

(1) Modeling and meshing: power transformer core is a complicated multi freedom degree system, its modeling necessary to simplify. Since modal calculation does not support non-linear characteristics, the calculation will be considered as a whole, ignoring the laminated structure and the joint structure between the yokes of iron. Modal analysis shall establish a three-dimensional entity model, adopt SOLID186 unit meshing core model and generate 2808 units 14660 nodes. The solid model and finite element calculation model as shown in figure 3 and 4 respectively.

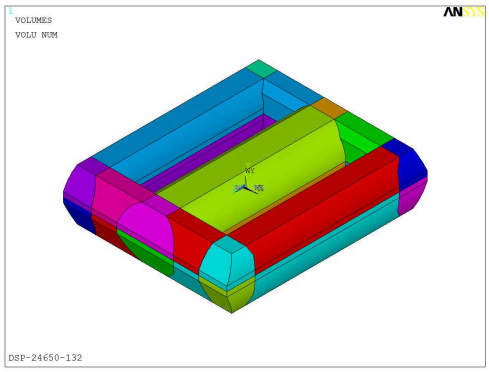

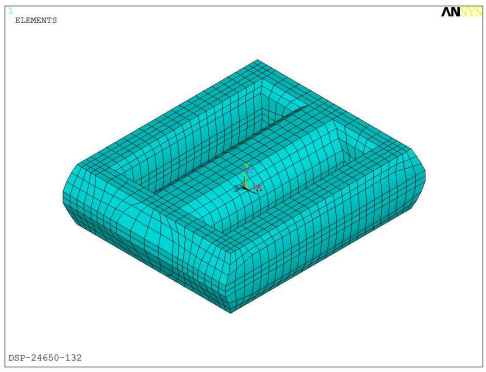

Fig.3. Core entity model Fig.4. Core modal calculation model

(2) The determination of material parameters: modal analysis to determine the material properties include: elastic modulus, poisson's ratio and density of core. The density and poisson's ratio of silicon steel sheet can be provided by the manufacturer or manual detected, because the core

is made of laminated silicon steel, the density of core should be the density of silicon steel sheet multiplied by pile coefficient, the transformer core pile coefficient is 0.95, so the density of core is 7650 * 0.95 = 7267.5. Elastic modulus accurate or not directly determine the accuracy of the results of the modal analysis, based on past papers and research results mainly has the following two kinds: $E=2.06\times10^{11}$Pa(ignoring the impact of the laminated structure); $E=1.50\times10^{11}$Pa(consider the impact of laminate structure).

（3）Boundary conditions and loading: In modal analysis, the different boundary conditions will directly affect the core structure of the modal vibration and natural frequency. According to the actual situation of the transformer installation, at present mainly adopts two kinds of boundary conditions: bottom constraint and free boundary. Bottom constraint refers to the transformer core model at the bottom of the nodes on the x y z three directions of the degrees of freedom is defined as zero.

（4）The solution and result analysis: type select Model Analysis, modal extraction method selection Subspace, solving the frequency range is defined as 0 ~ 1000Hz. Table 1 shows the power transformer core free-bound and bottom constraint in the first 10 order natural frequency. As the calculation results can be seen in table 1, analytical value and freedom condition of 1 order simulation value match, and its error was 8.7%.

Table 1 Core inherent frequency simulation calculation results

Order number	Free constraint / Hz	Bottom constraint/ Hz
1	215.39	31.831
2	265.99	97.247
3	275.00	114.22
4	277.70	290.68
5	292.44	296.92
6	369.44	311.75
7	407.63	322.05
8	453.06	379.73
9	531.23	451.25
10	539.22	456.34

Using ANSYS finite element software objects modal analysis, can know the structure of each order natural frequency and each order natural frequency of the vibration mode. The vibration mode of the core at free boundary and bottom constraint is shown in figure 5.

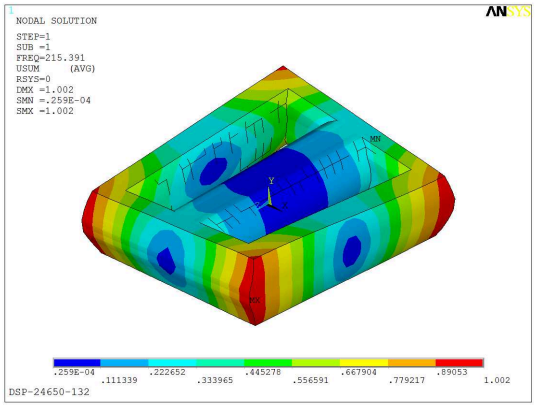

First-order (freedom constraint)

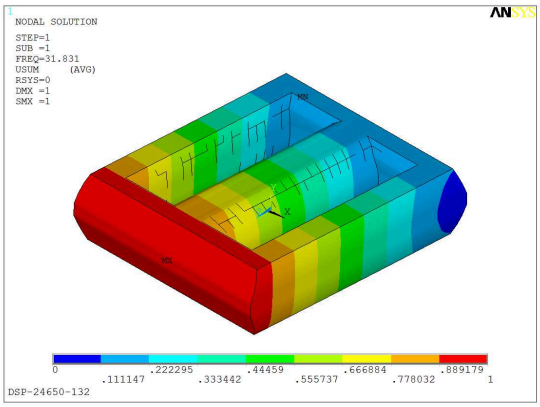

First-order (underside constraints)

Fig.5. Core modal vibration mode

Core natural vibration frequency calculation program development

Based on the above calculation method, using VB language as a tool to design software parameter input interface, based on the input parameters obtain the natural vibration frequency of core. Software parameters input interface shown in Figure 6.

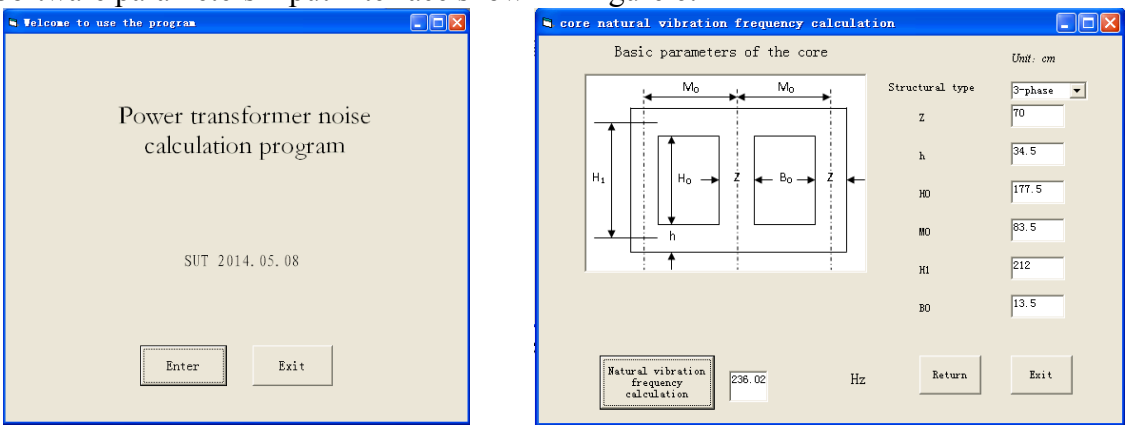

a) Login interface b) Calculate the interface

Fig.6 Core natural frequencies calculation program

Conclusion

Product design can be through the selection of reasonable core size, make its natural frequency to avoid the fundamental frequency and two, three, four high frequency band（75～125Hz, 175～225Hz, 275～325Hz, 375～425Hz）of magnetostrictive vibration, to prevent noise caused by the resonance increases effectively. Before core structure parameters selected can be calculate natural vibration frequency preliminary for the core through author design software, in order to improve the efficiency of designers. At the same time by Visual Basic language as a tool develops a power transformer core natural vibration frequency calculation procedure, for products bidding, design and optimization provides a strong support.

Acknowledgement

In this paper, the work was supported by NSFC, under Project No. 51177103 and Program for LNIRT in University (Project No. LT2011002).

Reference

[1] Yucheng Xie. Power transformer Handbook[M]. Beijing: China machine press, 2003.

[2]Xiaoan Gu. Study on the vibration and noise control techniques in large power transformers. Transformer[J], 2001, 10 (5):7-11.

[3] Xiantu Zhou. The noise of distribution transformer[J], 2006, 43(12): 1-6.

[4] Zhigang Dong. The noise of a transformer. Transformer[J], 1996, 33 (3): 30-35.

[5] Zhifang Fu. Theory and application of modal analysis[M]. Shanghai: Shanghai Jiao Tong University press, 2001.

Advanced Materials Research Vols. 986-987 (2014) pp 940-943

doi:10.4028/www.scientific.net/AMR.986-987.940

Numerical Analysis about the Effects of PV Panels on the Mechanical Properties of Frame-shear Structure

Wei Peng[1,a],Guoquan Zhu[1,b],Guoping Chen[1,c] and Shifeng Zeng[2,a]

[1]School of Civil Engineering and Architecture, Southwest University of Science and Technology, Mianyang, Sichuan, China, 621010

[a]email:weipengswust@163.com,[b]email:zhgq10000@163.com,
[c]email:guopingchen2002@163.com,[d]email:shifengzeng@163.com

Keywords: Frame-shear Wall Structure, PV Panels, Numerical Analysis, Structural Analysis

Abstract. As a kind of pollution-free and sustainable energy, solar energy has received people's favor increasingly. Integration of solar power and architecture has become one of the important ways that people use solar energy. In this paper, numerical analysis of four frame-shear wall structure models on which PV panels are installed or not installed is conducted by ANSYS. The results show that integration of solar power and architecture meets the requirements of technical specification for concrete structures of tall building. But PV panels installed on the building surface will increase story displacement and produce stress and strain redistribution, which have negative effects on structural safety. This study provides a reference for the structure design of integration of solar power and architecture.

Introduction

Now the energy crisis is getting more and more nervous. As a respond to this condition, the architect have to consider how to reduce the energy consumption of the building in the process of designing architectural style[1]. Solar energy is abundant, recyclable, clean and it brings low environmental loads[2], so that integration of solar power and architecture structure[3] is becoming more and more popular with the builder. However, the builder don't consider the adverse effects generated by the PV panels when solar energy facilities are installed on the buildings. Considering this problem, numerical analysis is made under four frame-shear wall structure models on which PV panels are installed or not installed by using the finite-element software ANSYS in the paper. The results show that installing PV panels in high-rise frame-shear wall structure meets the requirements of technical specification for concrete structures of tall building[4]. But PV panels installed on the building surface will increase story displacement and produce stress and strain redistribution which have negative effects on structural safety, so that these negative effects should be valued particularly in the structure design of integration of solar power and architecture.

Establishment of Finite Element Model

Structure Parameters. The main body of calculation models is a 12-floor frame-shear wall structure. The bottom floor is 6m in height. The top floor is 3.5m in height and other standard floors are 3m. The total height of the building is 39.5m from the land surface. The section size of frame column is 500m×500m and frame beam is 300m×200m. Thickness of transition floor slab is 100mm and thickness of shear wall is 250mm. The standard floor layouts of frame-shear wall structure are shown in Fig.1.

Polycrystalline silicon photovoltaic panels which are installed on the side of structure from the second floor to the top floor are used in solar panels. In order to simplify the calculation models, the solar panels are installed on frame column with brackets. The distance of the panels and column is 200mm[5]. The size of PV panels is 265mm×265mm×25mm and its density is 2500kg/m^3. The location schematic diagram of PV panels are shown in Fig.2.

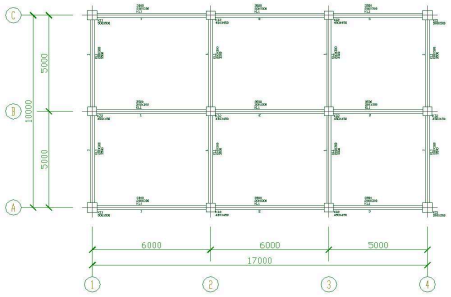

Fig.1. The standard floor layouts

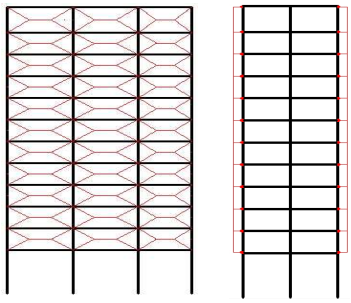

Fig.2. The location schematic diagram of PV panels

Selection of elements and modeling. The selection of material parameters and elements is based on the material texture and section shape of components, as shown in Table1.

Table1. Material parameters and elements selection[6]

Component	Material	Modulus of elasticity [N/mm^2]	Poisson ratio	Density [Kg/m^3]	element selection
Beam, Column	concrete	3.0×10^{10}	0.2	2500	Beam4
Shear wall	concrete	3.0×10^{10}	0.2	2500	Shell63
slab	concrete	3.0×10^{10}	0.2	2500	Shell63

The finite element analysis software ANSYS is used to analysis the models. The APDL command stream is used to build geometric model and Do statement is used to build model from the bottom to the top. First the key points are established according to the specific coordinates of structure, then column, beam, slab and shear wall are created by connecting the key points. The grids are meshed into the same elements. Geometric and element model is shown in Fig.3.

The unitary deformation performance and distribution of stress and strain of the structure under gravity loads and solar panel loads is analyzed in this paper.

Calculation model. Model1: under the gravity loads not being installed PV panels. Model2: PV panels being installed on the side away from the shear wall. Model3: PV panels being installed close to the side of the shear wall. Model4: PV panels being installed on both sides of the frame-shear structure.

Loading and Solving. The vertical influence of PV panels´ gravity loads is ignored when numerical simulation of the frame-shear structure is made by ANSYS. The effects on frame-shear structure from horizontal loads generated by PV panels are emphatically considered. The loading position of horizontal loads is set on beam-column joints from 2 floor to 11 floor. In the same layer, the loads on middle beam-column joints are twice times compared with the edges. Gravity loads on each node are set to the acceleration of gravity (g=9.8m/s2)[6]. Displacement and degree of freedom of all nodes on X,Y and Z directions are constrained at the bottom. Taking an example of Model4, the model loading and constraint diagram is shown in Fig.4.

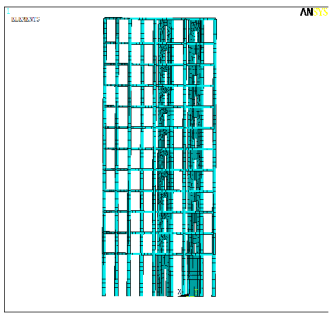

Fig.3. Geometric and element model

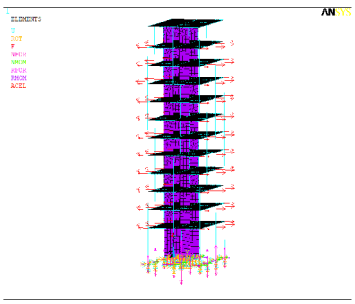

Fig.4. The model loading and constraint diagram

Results analysis

The deformation and distribution of stress and strain of four calculation models are obtained. And the maximum story drift, maximum stress and strain are also obtained.

Results analysis—Model1. The distribution diagram of displacement is shown in Fig.5(a). The distribution diagrams of stress and strain are shown in Fig.5(b) and Fig.5(c).

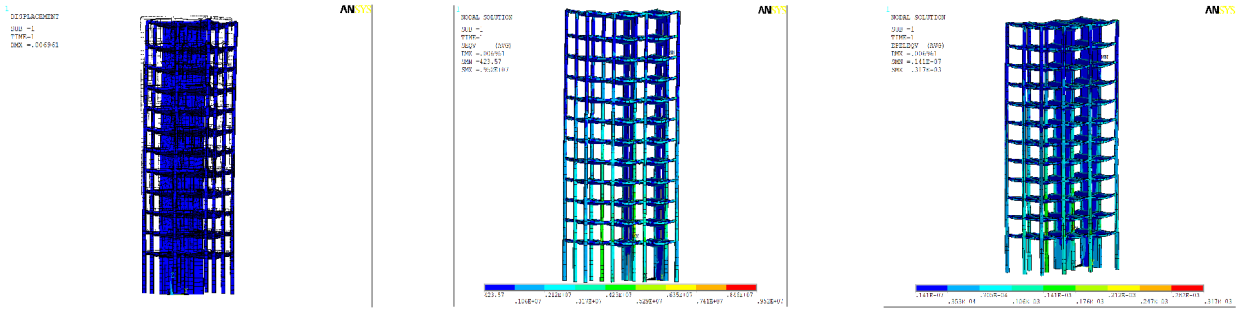

(a) (b) (c)

Fig.5: (a)The distribution diagram of displacement (b)The distribution diagrams of stress (c)The distribution diagrams of strain

According to the calculation results, when the structure bears the gravity loads, the maximum story drift of the model appears to be 6.961mm, the maximum stress is 9.52Mpa and the maximum strain is 3.17×10^{-4} . The stress and strain are mainly distributed at the bottom of column and shear wall evenly.

Results analysis—Model2. The distribution diagram of displacement is shown in Fig.6(a). The distribution diagrams of stress and strain are shown in Fig.6(b) and Fig.6(c).

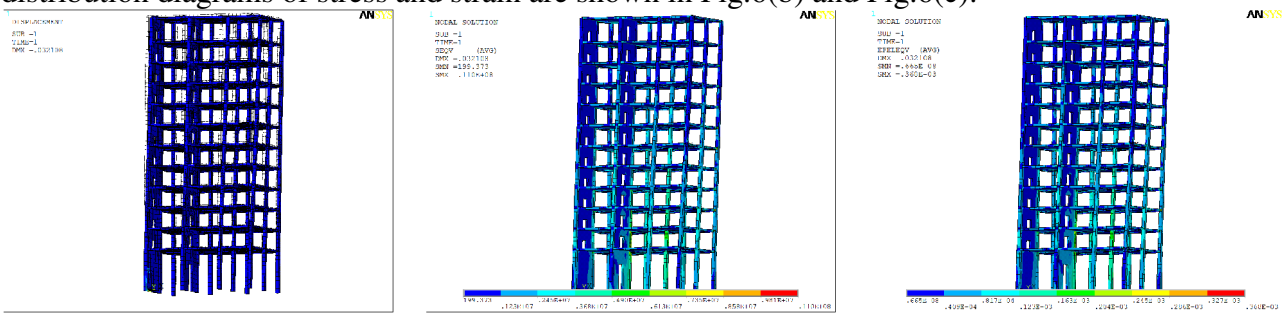

(a) (b) (c)

Fig.6:(a)The distribution diagram of displacement (b)The distribution diagrams of stress (c)The distribution diagrams of strain

According to the calculation results, when the structure bears the gravity loads and horizontal loads closing to the side of shear wall, the maximum story drift of the model appears to be 32.108mm. It produces stress and strain redistribution and produces torque. The maximum stress is 11Mpa, the maximum strain is 3.68×10^{-4}. The maximum stress and strain are close to the side of the bottom of the column and shear wall on which PV panels have been installed.

Results analysis—Model3. The calculation results of Model3 are close to the value of Model2. The maximum story drift of the model appears to be 26.365mm, the maximum stress is 9.98Mpa and the maximum strain is 3.33×10^{-4} . The stress and strain are mainly distributed at the bottom of column and shear wall. Comparing the two models, there are less effects on structure when PV panels are installed close to the shear wall.

Results analysis—Model4. Taking no account of the vertical loads of PV panels, the calculation results of Model4 are close to the value of Model1. Because horizontal loads imposed on both sides of the structure are the same. The maximum story drift of the model appears to be 6.958mm, the maximum stress is 9.55Mpa and the maximum strain is 3.18×10^{-4} .

Analysis and Comparison

According to the calculation results, the maximum layer displacement, the maximum stress and the maximum strain of frame-shear wall structure are compared, as shown in Fig.7(a), (b) and (c).

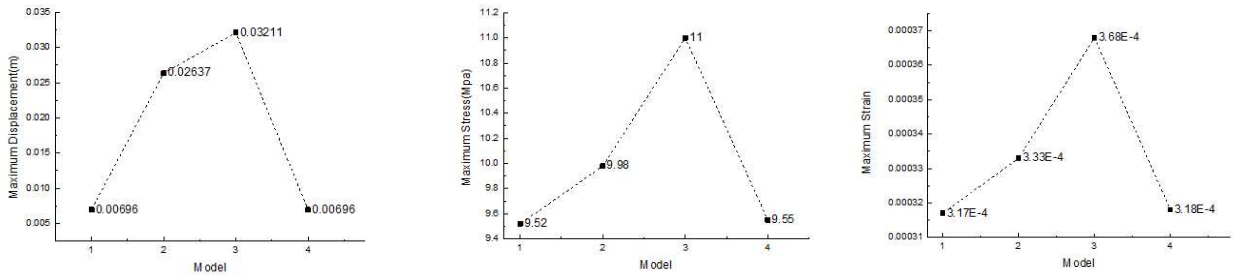

(a) (b) (c)

Fig.7:(a)The contrast of maximum layer displacement (b)The contrast of maximum stress (c)The contrast of maximum strain

After the comparison, the results show that the maximum layer displacement of Model2 is 5 times compared with Model1 when vertical loads are not considered. As well, stress and strain redistribute and increase accordingly. There are small effects among the maximum layer displacement, the maximum stress and the maximum strain of architectural structure when PV panels are installed symmetrically on both sides of the building.

Conclusions

(1)Integration of solar power and architecture meets the requirements of technical specification for concrete structures of tall building. But PV panels installed on the building surface will increase story displacement and produce stress and strain redistribution. Horizontal loads should be valued seriously in the process of design.

(2)Solar panels should be installed in the symmetrical position to reduce the maximum structural displacement and ensure the safety of building structure.

(3)As for integration of solar power and high-rise architecture, more attention should be paid to the influence of PV panels for buildings.

References

[1] LiYun Tang.Solar power in the application of green building[D].South China University of Technology Guangzhou,2012.1-8.(in Chinese)

[2] YaoWang.The application and Research of Solar Energy Technology on the Building[D].Xi'an University of Science and Technology,2007.3-5.(in Chinese)

[3] Zhaozhao Qie.The Study of Integration Design on Solar Building[D].Hebei University of Technology.2007.

[4] JGJ203-2010,Technical specification for concrete structures of tall building.China architecture & building press,Beijing,2010.(in Chinese)

[5] JGJ203-2010,Civil technical specifications of solar photovoltaic systems.China architecture & building press.Beijing,2010.(in Chinese)

[6] Meiling Li.Study on Shear reallocation of High-rise Frame-shear Wall Structure under Earthquake based on Elastoplastic method[D].2012.19-23.(in Chinese)

Advanced Materials Research Vols. 986-987 (2014) pp 944-947

doi:10.4028/www.scientific.net/AMR.986-987.944

Numerical Calculation of Short Circuit Electromagnetic Force In Isolated Phase Bus

Tusongjiang Kari[1, a], Xiwang Abuduwayiti[1, b] and Ming Ma[2, c]

[1]School of electrical engineering, Xin Jiang University, Xinjiang 830046, China;

[2]Electric power research institution of Guangdong Grid Corporation, Guangdong 510080, China;

[a]minyun229@163.com, [b]xiwang_x@163.com, [c]sdmaming@126.com

Keywords: 2D finite element, isolated phase buses, short circuit electromagnetic force

Abstract. Short circuit electromagnetic forces are one of the most important factors in design and operation of buses. 2D infinite element models are set up with ANSOFT for isolated phase buses, simulating with transient method and calculating short circuit electromagnetic force taking eddy effect and proximity effect into account. The result reveals that the maximum electromagnetic force under short circuit condition is a periodic function of current phase angle.

Introduction

There phase isolated phase buses (IPBs) have been widely used in power plants to delivery power from generators to transforms, due to magnetic field density between phases and eddy current loss are reduced significantly[1]. Electromagnetic force impose on buses under short circuit condition will cause large deformation or even permanent damages, which effect safety of power delivery, therefore it is important to calculate accurately in design and operation of IPBs.

As development of simulation technique, finite element methods on multi-physics are applied in electromagnetic design. Finite element methods are used to calculate eddy current, power loss of IPB [2-3]. It also is used to compute transient electromagnetic force on other type of buses [4-5]. Finite element methods based on ANSYS are used to calculate electromagnetic force [6]. However, more efforts is still needed to investigate characteristic of short circuit electromagnetic force. In this paper, 2D finite element model taking buses size, skin effect and proximity effect into account is established. Magnetic field distribution and force imposed on conductor and shell are calculated with ANSOFT parametric method and the results provide advices and reference for design and optimization of IPBs.

IPB modeling

Physical model. IPB consists of three tubular conductors fixed in three cylindrical shaped shells. The conductor is supported by insulators made of epoxy material. The conductors and shells are made of aluminum material and welding the joints. The shells are connected together at each end by bonding plates and are grounded at one end. The cross section of IPB is shown in Fig. 1

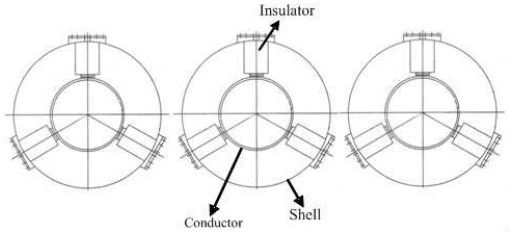

Fig 1 Cross section of IPBs

Mathematical model. The numerical calculation was processed under the ANSOFT software. In order to simplify the calculation, we proposed several hypotheses below in mathematical modeling :

A. Longitudinal dimension of bus is significantly greater then the cross section.
B. characteristics of materials are constant
C. displacements currents are neglected.

Based on the physical model and hypotheses above, the electromagnetic field control equation can be expressed as [7]:

$$\nabla\times(\upsilon\nabla\times A)=J$$

There is only Z component of current density and magnetic vector potential, that means

$$A_x=A_y=0,\quad J_x=J_y=0$$

So the control equation is expressed as

$$\frac{\partial}{\partial x}(\upsilon\frac{\partial A_z}{\partial x})+\frac{\partial}{\partial y}(\upsilon\frac{\partial A_z}{\partial y})=-J_{sz}+\sigma\frac{\partial A_z}{\partial t}$$

In the equations above, A_z is the Z component of magnetic vector potential, J_{sz} is the source current density, J_{cz} is the eddy current density of conducting region, σ is conductivity. The Coulomb gauge $\nabla\cdot A=0$ is employed to ensure the uniqueness of vector potential.

The largest electromagnetic force occurs during short circuit condition and the transient three phase short circuit currents in phase conductors are function of time as follows:

$$i_A=\sqrt{2}I_0\left[e^{-\frac{t}{T_a}}\cos a-\cos(\omega t+a)\right]$$

$$i_B=\sqrt{2}I_0\left[e^{-\frac{t}{T_a}}\cos\left(a-\frac{2\pi}{3}\right)-\cos\left(\omega t+a-\frac{2\pi}{3}\right)\right]$$

$$i_C=\sqrt{2}I_0\left[e^{-\frac{t}{T_a}}\cos\left(a+\frac{2\pi}{3}\right)-\cos\left(\omega t+a+\frac{2\pi}{3}\right)\right]$$

Where I_0, T_a, ω, A_z and a are effective short circuit current, decay constant of direct current component, angular frequency and phase angle. Value of I_0, T_a, ω and a used in simulation is 160kA, 45ms,314.15 and 30^o respectively.

Determination of physical property parameter. The model for simulation and analysis is built as Fig 2 shown. The number of elements and nodes in finite element model are 14460 and 29157.

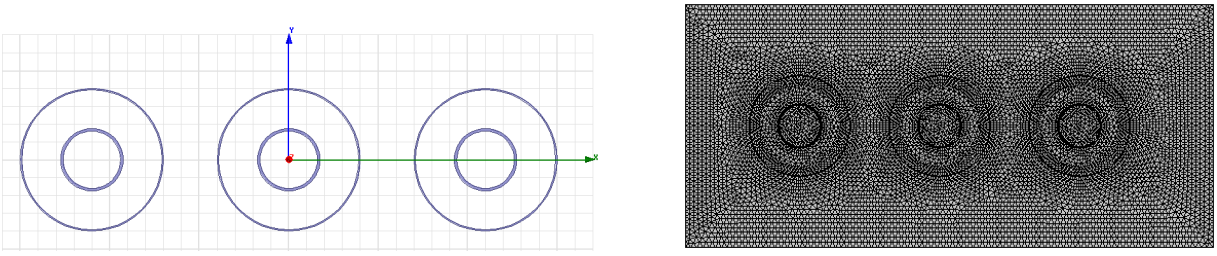

(a) Model of IPB (b) finite element mesh

Fig 2 Analyzed models

The geometry data and physical property parameter are shown as table 1

Table.1 Geometry data and physical property

parameter / type	Material	Inner radius (mm)	Outer radius(mm)	Permeability	Resistivity($\Omega\cdot m$)
Conductor	Aluminum	320	350	1	2.6e-8
Shell	Aluminum	784	800	1	2.6e-8

Setting of rest conditions.

A. The boundary condition is $A_z=0$ on the border of air region;

B. Applied current on conductors taking eddy current into account;

C. Set simulation time $T=0.4s$ and time step $\Delta T=0.001s$

Analysis of simulation results. Parametric method of ANSOFT is use to compute electromagnetic force. The distribution of magnetic field shown as Fig 3 shown:

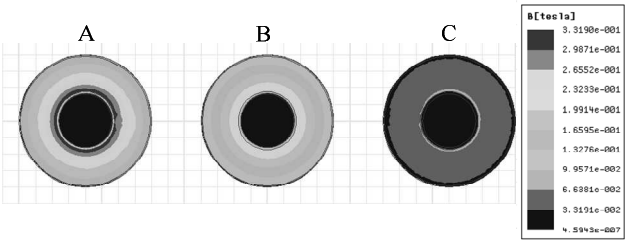

Fig 3 Distribution of magnetic field at t=0.005s

Electromagnetic force imposed on conductor and shell varies as short circuit changes. It is known form Fig 4 and Fig 5 that short circuit electromagnetic force has a large x-direction component and the y-direction component is so small that it can be neglected.

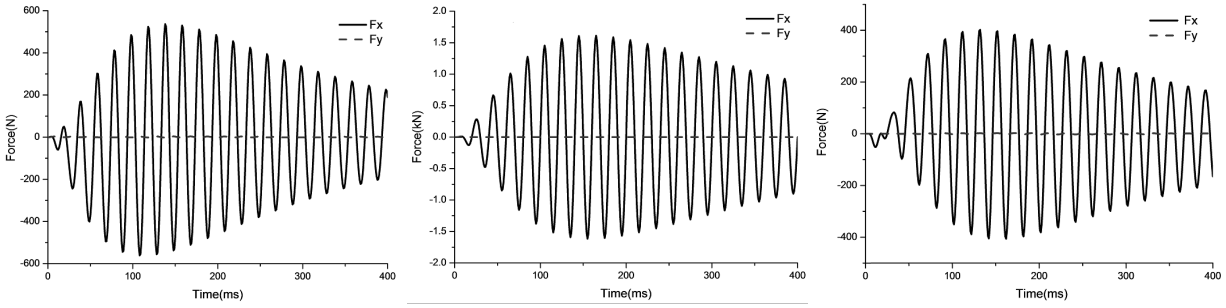

(a) Phase A (b) Phase B (c) Phase C

Fig 4 Force on the conductors ($a = 30^0$)

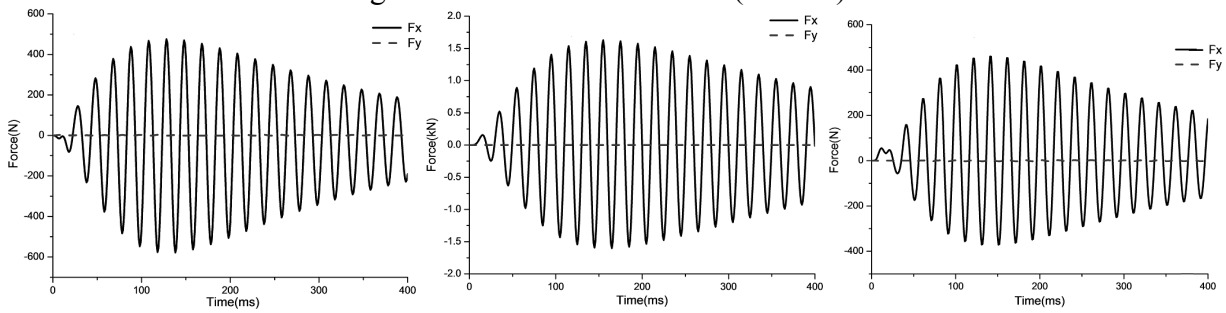

(a) A Phase (b) B Phase (c) C Phase

Fig 5 Force on the shells ($a = 30^0$)

Electromagnetic force on phase B is larger than other phase and the force is about 1616N per meter of IPB. The comparison of x-direction component of force at different phase angle is shown as Fig6.

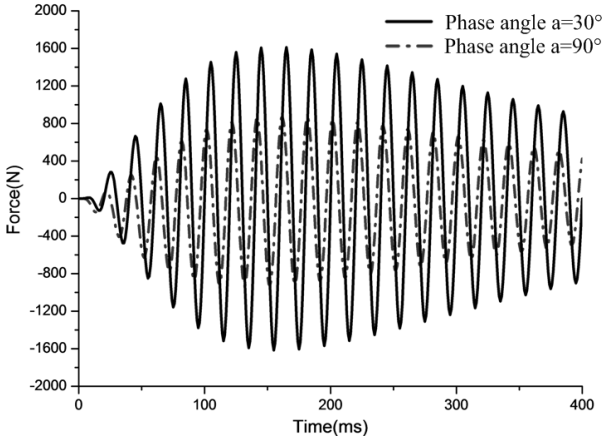

Fig6 Force on conductor B versus phase angles

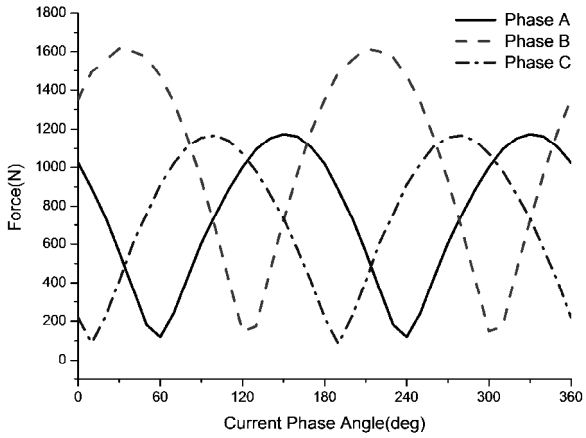

Fig7 Force on conductors versus phase angles

Regarding current phase angle as an unknown parameter, peak value of electromagnetic force is calculating by sweeping current phase angle from 0^o to 360^o with ANSOFT.

By analyzing Fig 7 we found that the peak values of short circuit electromagnetic force is a periodic function of current phase angle and the cycle is 180^o. The maximum electromagnetic force occurs when current phase angle $a = 30^o$ and minimum force as $a = 120^o$. Besides, the maximum

force of phase A and phase C almost identical, which is about 72% of phase B's peak value; what's more, the minimum force of phase A and phase C is approximately 10% of maximum force of phase B.

Conclusion

This paper built 2D finite element model of the isolated phase buses and compute magnetic field and transient electromagnetic force with ANSOFT fast and accurately. The results reveal that the middle phase conductor experience largest force, maximum short circuit electromagnetic force is a periodic function of current phase angle and the cycle is 180^o. In addition, horizontal component of force is much greater than vertical component. The result could be applied to design and optimize IPBs.

Acknowledgement

The authors would like to acknowledge the funding of the National Natural Science Foundation of China (Grant No. 51367016)

References

[1] J.P.A. Bastos, N. Sadowski, Electromagnetic modeling by finite element method, Marcel Dekker, Inc., 2003.
[2] S. K. Choi, Analysis on the magnetic properties of an isolated phase bus system, in Proc. 5th Int. Conf. Electrical Machines and Systems, 2001, p. 1166-1169.
[3] S. L. Ho, Y. Li, Edward W. C. Lo, J. Y. Xu, Analyses of three-dimensional eddy current field and thermal problems in an isolated phase bus, IEEE Trans. Magn, vol. 39, May 2003, pp. 1515-1518.
[4] D. G. Triantafyllidis, P. S. Dokopoulos, and D. P. Labridis, Parametric short-circuit force analysis of three-phase busbars-A fully automated finite element approach, IEEE Trans. Power Delivery, vol. 18, Apr. 2003, pp. 531-537.
[5] M.R. Shah, G. Bedrosian, J. Joseph, Steady-State Loss and Short-Circuit Force Analysis of a Three-Phase Bus Using a Coupled Finite Element Circuit Approach, IEEE Transactions on Energy Conversion, Vol. 14, No. 4, December 1999.
[6] A.H. Isfahani, S. Vaez-Zadeh, Accurate Determination of Electromagnetic Circuit Forces in Isolated Phase Buses under Short Conditions, in Tampa. Power Engineering Society General
[7] Bhag Singh Guru, Huseyin R. Hiziroglu, Electromagnetic Field Theory Fundamentals, Cambridge University Press, 2009

Advanced Materials Research Vols. 986-987 (2014) pp 948-951

doi:10.4028/www.scientific.net/AMR.986-987.948

Power Transformer core column section optimization model and design

Qu Zihang, Tang Bo, Chen bin, Li Yu, Peng Youxian

China Three Gorges University Yichang, China

email: tangboemail@sina.com, 420720119@qq.com

Keywords: Power Transformer; Core Column; Nonlinear Regression; Integer Programming; Optimized Design

Abstract. The progression of power transformer core is usually determined by the core diameter and the width and thickness of the silicon-steel sheet is determined by the graphing method. Therefore, coil section can't be fully utilized. To analyze the manufacturing characteristics of power transformer core columns from the performance and material savings and the nonlinear integer regression programming model is established. Taking the circumscribed circle diameter is 800mm, progression equal to 17 as an example. The optimized design of column section is solved by using the MATLAB. The results show that the optimized design can increase the cross-section fill factor by 3.8% and the diameter of the core columns larger, the optimization results better.

Introduction

The rectangular sizes at various levels of power transformer core column section is the key factor of the ultimate performance and costing, is very important to optimization and design. However, in the traditional transformer design, every diameter progression of core column is reference to the production experience. Subjectively, in consideration of achieve to certain number of stages in order to meet certain geometric cross-sectional area without exact or scientific solving process. After determining the core column diameter, the various core cross-sectional geometric dimensioning uniquely determined according to a unified national standard core design manual [1]. This will lead to progression of the core columns increasing unnecessarily, increasing the cost of power transformers and reducing the performance of the transformer. Therefore, a reasonable choice of progression power transformer core column section to determine the geometry dimensioning of all levels is a crux to improve the performance and reduce the transformer costs. With the development of computer applications and mathematics software, according to these practical problems to establish optimization model abstractly and simplified by mathematical method. Then using the computer technology to solve the problem and providing a solution.

At present the traditional methods in engineering is graphing method, but the course is very inconvenient and the deviations is large from the optimal solution. Thus, by building the nonlinear regression integer programming model about stepped rectangular cross-section dimensions at all levels and using the MATLAB to carry out standardization solving and obtain the optimization results about various types of core column section according to this optimization model [2, 3]. The main focus of this paper is optimization model establishing, the computer solving and data analysis.

Traditional methods to determine the silicon steel progression

Core section design is an important part of the column power transformer design. Power transformer core columns usually within a circular coil, in order to make full use of the space within the circular coil, the core column section is designed as a multi-stage axial symmetry and down the ladder. By properly selecting the size of each rectangle ladder in the design to strive to make the core cross-sectional geometry has a largest column. When the diameter circular of coil constant, the more core pillar progression, cross-sectional area larger, and the better the performance of the transformer, but the specifications of silicon steel be going to complicated if the progression too much, manufacturing hours increasing. So must be considered utilization factor and workmanship of core column synthetically. In the conventional transformer design, if the core diameter is

determined, the size which is the core section of the stack at all levels will be uniquely determined according to the design manual. The experience correspondence between the core column diameter and progression as shown in Table 1, which is usually on the basis of the scope of the core column diameter to determine the core columns progression.

Table 1 Selection of core column section progression

Core column diameter mm	progression
80-195	5-7
200-265	8-10
270-390	11
400-740	12-14
760-800	15-17
1000	19
1200	22

Choosing the ratio of the actual geometry cross-sectional and the area of the circumscribed circle to measure the fill factor of power transformer core column section [4], the specific formula is:

$$\eta=\frac{S_{Core}}{S_{circle}}\times 100\%=\frac{S}{\pi r^2}\times 100\% \tag{1}$$

The effective area of the core columns

The effective area of the core columns refers to the sum of all levels of silicon steel geometric cross-sectional area (excluding oil channel). Because of assuming the lamination factor is 1, the effective cross-sectional area of the core columns can be considered approximately equal to its sum of multi-level cross-sectional area of the geometry [5, 6]. Due to the axial symmetry of cross-section in a circle up and down, left and right, the theoretical calculation of the effective cross-sectional area of the core columns:

$$S=\sum_{i=1}^{n}2x_i y_i \tag{2}$$

Where the x_i is the level i width ($i=1,2,3\cdots n$), the y_i is the level i thickness ($i=1,2,3\cdots n$), S is the effective cross-sectional area of the core columns (Unit: mm^2).

$$y_i=\sqrt{r^2-x_i^2}-\sum_{k=1}^{i-1}y_k \quad (i=1,2,3\ldots,n) \tag{3}$$

In order to simplify the equation (2) into a single objective function, can be determined the relationship between x_i and y_i according to geometric relation of the each size from figure 1. In the figure 1, $x_1=OA$, $x_2=DC$, $y_1=AB$, $y_2=BC$, $OD=y_1+y_2$, $OC=OB=r$ (the r is the radius of the circle). From the Pythagorean Theorem could be obtained the $x_1^2+y_1^2=r^2$ from the $Rt\Delta OAB$, that is $y_1=\sqrt{r^2-x_1^2}$, $y_2=\sqrt{r^2-x_2^2}-y_1$. Thus obtained the relationship between x_i and y_i.

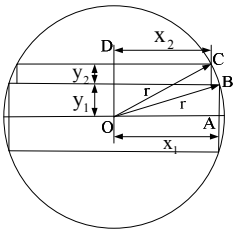

Fig.1 Schematic cross section of the core columns

The slice width mantissa dimensions at all levels is 0 or 5 generally at cross-section optimization, according to the width of each class film can be calculated from the corresponding stack thickness. Because of the actual thickness of the stack must be an integer multiple of the thickness of the silicon steel sheet, the given limiting value of the outer diameter by core can be controlled necessarily[7,8]. Width at all levels must be a multiple of w:

$$\left[\frac{x_i}{w}\right] = \frac{x_i}{w} \tag{4}$$

The level 1 must be greater than the thickness of 26mm, that is:

$$y_1 \geq 26 \tag{5}$$

The level n width greater than 20mm:

$$x_n \geq 20 \tag{6}$$

Width increasing with levels increasing:

$$x_1 \geq x_2 \geq x_3 \geq \cdots \geq x_n \tag{7}$$

The total thickness and maximum width of the silicon steel could not be greater than the diameter of the core columns circumscribed circle:

$$x_1 < d, \sum_{i=1}^{n} y_t < d \tag{8}$$

Solving and analysis of the effective area of the core columns

A. Specific examples

Take the $d = 800\text{mm}$ as an example, the core columns cross-sectional area optimization method uses the MATLAB to solve nonlinear integer programming. Using the constr function to solve the optimal solution for each unknown from the nonlinear programming objective function, but the results is decimal which need programming to adjust. Making the mantissa is 0 if the range between (0, 2.4) and (7.5, 0) and making the mantissa is 5 if the range between (2.5, 7.4) when number 5 as a multiple; Making the mantissa rounding when number 10 as a multiple. Then get the solution about the width, thickness, effective area and the filling factor of the iron core shown in Figures 2.

Figure 2 shows the corresponding levels of silicon thickness and width. When the mantissa number is 5 and 0, there is no big difference at all levels of the corresponding silicon steel sheet width and thickness. Take the level eight silicon steel as an example, the slice width is 600mm and the slice height is 43mm when the mantissa is 5; The slice width is 600mm and the slice height is 49mm when the mantissa is 0.

The fill factor of the core columns is lower according to the traditional design methods of core pillar, is 93.48%. After the above optimization, while the mantissa is 5, the fill factor is 97.24%; while the mantissa is 0, the fill factor is 97.25%. It can be seen, the fill factor of the optimized core columns were higher than the traditional core column fill factor.

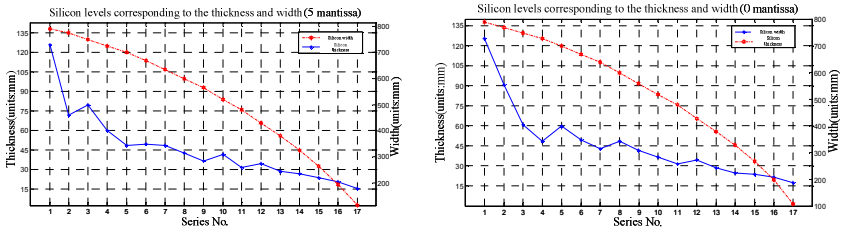

(a) 5 mantissa (b) 0 mantissa

Fig.2 Silicon levels corresponding to the thickness and width

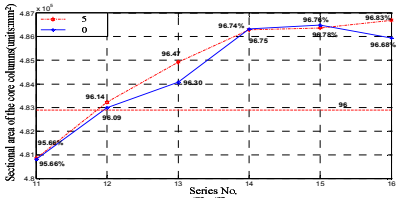

Fig.3 The effective area and fill factor of the core columns when the progression is 11-16

B. The impact of progression on the optimization results

Currently the core column design which is uniformly used by 17 level, the fill factor is lower, only 93.48%. Enhancing the fill factor to reduce the manufacturing costs of core columns and improve the performance of power transformers [9]. Figure 3 shows the effective area and fill factor of the core columns progression between 11 and 16.

Contrasted the effective area and the fill factor of the core by progression between 11 and 17 from the conclusions, the effective cross-sectional area and the fill factor of the core columns increasing with silicon steel progression increasing, when $n=17$, the effective cross-sectional area of the core columns is 488850 mm2 and the maximum value of fill factor is 97.25%. This is means the number of stages of the core columns increasing appropriately could improving the effective area and fill factor effectively.

From figure 3, if $n=12$, the fill factor of silicon is still greater than 96%. So if the choice about silicon steel is level 12, the manufacturing cost of the entire core columns will be greatly reduced.

C. The impact of diameter on the optimization results

Take the $d=800\text{mm}\ 1000\text{mm}\ 1200\text{mm}$ as an example, through the method of linear programming to calculate the indicators of different diameter core columns, and the make a compare with the traditional core columns manufacturing index. The specific results are shown in Table 2.

Table 2 Contrast between optimization results of the index and traditional manufacturing index

Core column diameter	800mm	1000mm	1200mm
circumscribed circle area	502650 mm2	785400 mm2	1131000 mm2
progression	17	19	22
Original cross-sectional area	469860 mm^2	736320 mm^2	1065440 mm^2
Now cross-sectional area	488850 mm^2	765740 mm^2	1104155 mm^2
Original fill factor	93.48%	93.75%	94.2%
Now fill factor	97.25	97.5%	97.63%

Data can be seen from Table 2, the larger of core column diameter, the greater of the circumscribed circle area, the more stages, the effective area of core column and the larger the fill factor, the better optimization results.

Conclusion

1) By nonlinear programming method for power transformer core column section to optimize the design, and in an examples which is the diameter is 800mm and the progression is 17, the cross-sectional area fill factor improved by 3.8%;

2) In the same diameter of circumscribed circle, the effective area and fill factor of the core columns will increase with the core pillar progression increases. When the design is level 12, the relative original fill factor also increased 2.5%. And for the entire transformer to reduce 10 laminated layers will greatly improve production efficiency and reduce costs;

3) The larger the diameter of the core columns, the more progression of core columns, the effective area and fill factor of the core columns greater, the optimization results better.

References

[1] Lu Changbo, Zhu Yinghao, Zhang Huailing. To calculate the power transformers [M].Haerbin: Heilongjiang Science & Technology Press, 1986: 37-39

[2] Wang Juan, Yang Yi. Power transformer core column section optimization design [J]. Transformer, 2011, 42(09): 26-27

[3] Si Shuhong, Yao Xiping, Pei Wansheng. Oil Ducts Optimization Design on the Iron Beam Sectional of the Electricity Transformer [J] Journal of Anhui Electrical Engineering Professional Technique College, 2010, 15(03):1-5

[4] Qiu Qingquan, Li Qingfu. Research on Optimization Design for Cross Section of Transformer Core Based on Improved Genetic Algorithm [J]. Transformer, 2004, 41(09):70-72

[5] Wu Fuzhuan, Li Yuling. The Optimum Design of Core Section of Transformer [J]. Journal of Zhongyuan University of Technology, 2000, 11(04):70-72

[6] Li Xiangsheng, Chen Qiaofu. Theory calculation and optimization design of transformer [M]. Wuhan: Huazhong University Press, 1990: 200-205

Advanced Materials Research Vols. 986-987 (2014) pp 952-955

doi:10.4028/www.scientific.net/AMR.986-987.952

Research on the energy recovery of the excavator slewing system based on hybrid technology

Wang Dongyun [1, a], Zhang Yu [1,b]

[1] College of engineering, Zhejiang Normal University, Jinhua, Zhejiang Province, 321005, China

[a]zsdwdy@zjnu.edu.cn, [b]zjnuzy@zjnu.cn,

Keywords: Hybrid excavator, energy recovery, slewing mechanism, electric motor

Abstract. In the traditional excavator, the slewing braking energy cannot be recovered and eventually became heat. As the hybrid technology was introduced into the hydraulic excavator, it makes energy recovery possible. In this article, a new energy recovery method based on hybrid, using an electric motor instead of a hydraulic motor to drive the swing mechanism. When braking, the electric motor will enter the generator mode and the energy will be recovered and stored in super-capacitors. This method has been proved to have high energy recovery efficiency.

Introduction

The energy saving effect of hybrid hydraulic excavator has been widely recognized, and its energy-saving features focused on two main areas: 1) by improving the working conditions of the engine and down-sizing engine rated power, to achieve energy; 2) to further improve energy efficiency through energy recovery effect. Currently, researchers are mainly focused on two aspects. The fist one is to recycle the potential energy of the boom when it is dropping, the second is to recover the kinetic energy of the slewing system when it is braking. Some researchers take the measure of single motor driven single joint programs in order to achieve flexible control and energy recovery. There are also researchers those choose a hydraulic accumulator scheme to recover the kinetic energy of the rotating mechanism. Both programs would increase the system cost a lot, and they may not be used on traditional powered excavators. But it is not the case for hybrid powered exactors. Because they are already equipped with electric motor, the energy storage unit and electric controller, it is relatively a low-cost solution to drive the slewing mechanism by a electric motor / generator and recover the kinetic energy when it is braking.

Analysis on the power loss of slewing mechanism

The standard digging cycle time of a 7-Ton excavator is about 10 ~ 15senconds, and the two rotary motion of time contains about half of the total time. The rotary motion also contains a single start acceleration, constant speed (longer turnaround time), the braking of the three stages. During braking, the rotational speed of the motor abruptly changes, much heat is generated, causing a great loss of energy. According to the most commonly used devices and working conditions to estimate the rotational inertia of the platform, according to the following empirical formula using backhoe working device when estimating [4] [5]:

Rotate with full-load $$J = 128G^{\frac{5}{3}}\left(kg \cdot m^2\right) \quad (1)$$

Rotate with no load $$J_0 = 72G^{\frac{5}{3}}\left(kg \cdot m^2\right) \quad (2)$$

Where G is the mass of the excavator。

If G=7 Ton, then we can get $J = 3278.7\,kg \cdot m^2$, $J_0 = 1844.3\,kg \cdot m^2$ 。

And so ,in a digging cycle, the braking energy can be calculated as follow,

$$W = \frac{1}{2} \cdot J \cdot w^2 = \frac{1}{2} \cdot J \cdot \left(\frac{2\pi \cdot n}{60} \right)^2 + \frac{1}{2} \cdot J_0 \cdot \left(\frac{2\pi \cdot n_0}{60} \right)^2 \qquad (3)$$

Where n is the start rotate speed with full load, and here it is set to 14RPM； similarly, n_0 is the start rotate speed with no load, and here it is also set to 14RPM.

Then we get the total braking energy W=5.5KJ.

The electric motor drive strategy

In the traditional hydraulic excavator, it may cost too much to reuse the braking energy by electric method for many electric components such as battery, capacitor, electric motor and generator must be used. But in the hybrid hydraulic excavator, due to its system has a kind of electrical components, the cost can be achieved without spending too much energy recovery electric type, so the use of electric hybrid hydraulic excavator-style energy recovery is quite feasible, with the energy storage element is the direction of recovery energy recovery hybrid hydraulic excavator development [3].

As shown in fig.1, when the rotational speed of the motor torque when both positive or both negative, the motor for the generator; conversely, was the motor. When the rotation motor is initiated, the super capacitor begins to discharge with the super capacitor or SOC reaches a certain stage of the handle operator to stop the rotation shake super capacitor stops discharging, due to the inertia continues rotating platform driven rotary motor rotational power, and the to the super capacitor energy storage.

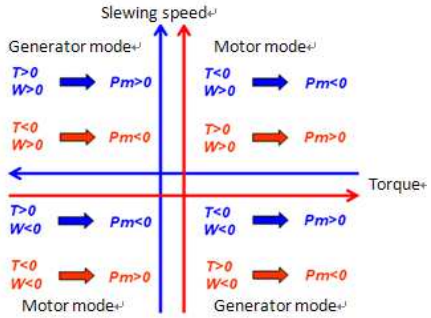

Fig.1 The work type of the electric motor

The simulation model of the slewing mechanism

The electric generator using AmeSim model motor controller model and a capacitor model, such as integrated model consisting of inertia rotary folder rotating brake simulation model is shown below, where the rotary motor parameters for the selected model TYB325-42-80's permanent magnet synchronous motor, which is rated at 5.22kw, bus rated voltage of 380V, rated speed 2400RPM, rated current o:10A, rated torque: 20.69Nm.

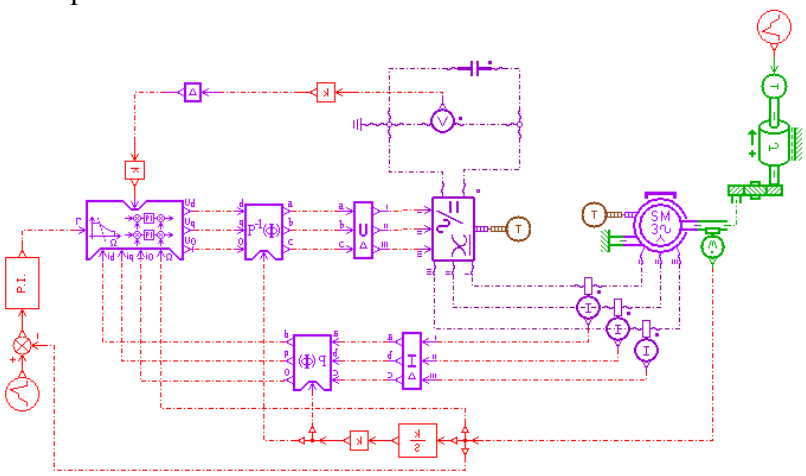

Fig.2 The Simulation based model of the slewing mechanism driven by electric motor

Simulation Result

Fig.3 and fig.4 shown the target motor speed and load torque which are the simulation inputs. In 0s ~ 0.1s stage, the motor starts to rotate, the sharp increase torque by 0Nm into-25Nm; in 0.1s ~ 1s phase motors do accelerated motion, in addition to a portion of the output torque of the motor to resist friction, wind, etc. drag torque generated, the majority of the torque is used to drive the motor to make accelerated motion, and the motor output torque of about-19Nm; in 1s ~ 2.5s phase motors do uniform motion. Then all the motor output torque to resist friction and wind resistance torque generated by the motor output torque at this time about-4.9Nm; in 2.5s ~ 3.5s phase brake motors turning into a generator, this when the output torque of the motor is not mainly rely on inertia rotary motor driven rotary platform, and the motor torque is 8.5Nm. The parameters of the electric motor are shown in fig.5- fig.7.

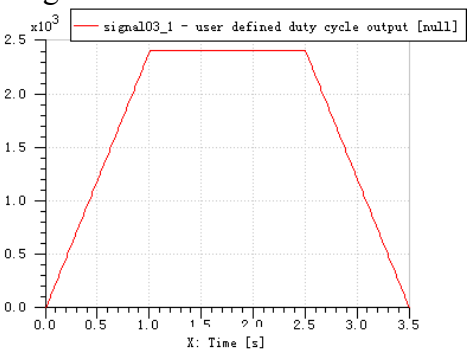

Fig.3 The target speed

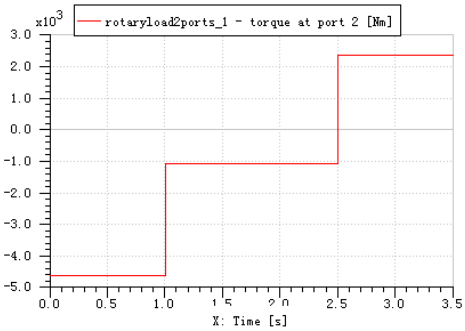

Fig.4 The load torque

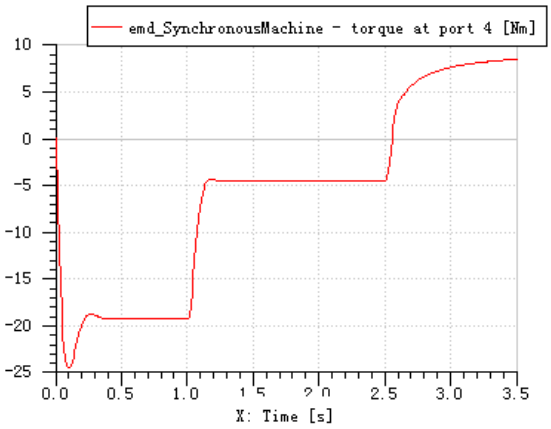

Fig.5 The output torque of the electric motor

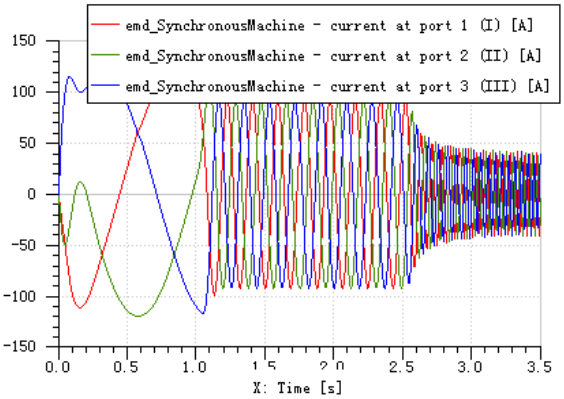

Fig.6 The current of the electric motor

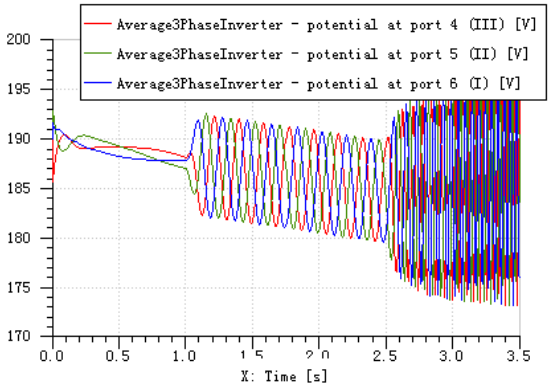

Fig.7 The voltage of DC line of the electric motor

Super-capacitor current variation shown in fig.8. From the figure difficult to find current changes corresponding to the state of the motor sport can be divided into three parts. The first part of the motor acceleration to do, then the super capacitor current sharply increases to about 1.5A, and the

fluctuation about 1.5A; motor as a second portion of uniform rotary motion, when the current is reduced to the super capacitor 1.2A; s Third part of the motor deceleration done, this time due to the motor torque is positive, the motor power, the current becomes negative, the capacitor begins to charge.

Super-capacitor voltage curve shown in fig.9. 2.5s to change the voltage dividing line is divided into two parts: the first part of the motor for the electric motor, the voltage falling capacitance falling; the latter half of the motor as a generator, the voltage starts to rise, the capacitance increases.

the SOC of the super-capacitor is：

$$SOC = \frac{0.5CV_c^2}{0.5CV_{cR}^2} = 95.42\%$$

The energy storage of the super capacitor is

$$Q = \frac{1}{2}CU^2$$

After calculation, the recovery energy for one slewing cycle is 2153J。

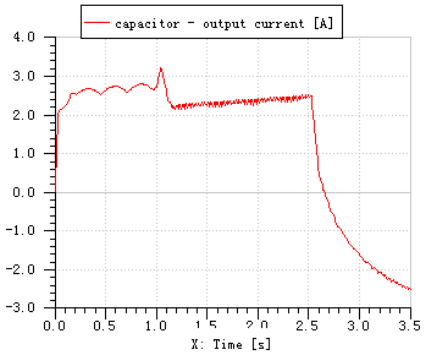

Fig.8 The current curve of the super-capacitor

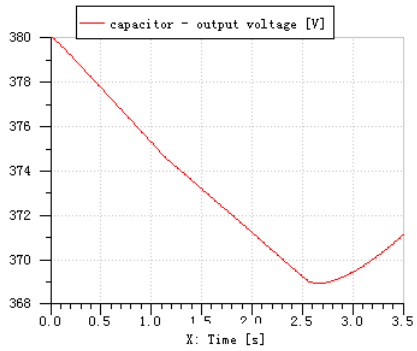

Fig.9 The voltage curve of the super-capacitor

Conclusion

Based on motor-driven rotary super-capacitor energy storage and energy recovery solutions, with high energy recovery efficiency, and does not affect the overall handling, the hybrid excavator equipped with a great value.

Acknowledgements

The financial support of national natural science foundation (Granted NO. 51205368) and the natural science foundation of Zhejiang Province (Grant No.LQ12E05003) are gratefully acknowledged.

Reference

[1]D.Y.Wang, S.X.Pan, G.Chen, el.al, “Performance analysis of hydraulic excavator powertrain hybridization”， Automation in construction, vol.18(3), May 2009, pp. 249-257.

[2]C.Guan, X.Xu, X.Lin, Recovering system of swing braking energy in hydraulic excavator[J], Journal of Zhejiang University(Engineering Science) , 2012 46(1) , 142-149.

[3]Matsubara M,Hybrid system for construction machine,Japan：JP2001173024[P]，2001-02-06.

[4]K.Chen, J.Zhang, P.Y.Wang,The modeling and analysis of slewing mechanism of hybrid hydraulic excavator[J], Construction Machinery, Vol.6,2011,pp:81-86.

[5]X. Lin, S. X. Pan and D.Y. Wang, “Dynamic simulation and optimal control strategy for a parallel hybrid hydraulic excavator”, Journal of Zhejiang University Science A, Vol.9, 2008 pp.624-632,.

[6]

Advanced Materials Research Vols. 986-987 (2014) pp 956-962

doi:10.4028/www.scientific.net/AMR.986-987.956

Research on the Hydrodynamic Performance of a Wave Energy Converter

ZHENG Xiongbo[1, a], YANG Yunong[2,b]

[1]College of Science, Harbin Engineering University, Harbin 150001, China

[2]College of Power and Energy Engineering, Harbin Engineering University, Harbin 150001, China

[a]zhengxiongbo@hrbeu.edu.cn, [b]yangyunonghrbeu@163.com

Keywords: wave energy, hydrodynamic performance,numerical calculation

Abstract. Under the pressure of fossil energy shortage, rational exploitation of ocean wave energy is propitious to establish an environmentally friendly society. This paper presents the results of a practical research done in a test tank, on the hydrodynamic performance of a wave energy converter with swing arms and floaters designed purposely. Fixed on a trailer, the converter was composed of two floaters, two swing arms, mechanical transmission devices and generators. The method of this research was to measure the floater's acceleration and the output voltages of the generator under the movement of waves, analysis the influence of wave height and period on floaters' movement, then compute the wave energy conversion efficiency. At last, the research findings show that the converter performed well with heaving motion performance and high energy conversion efficiency.

Introduction

As the economy and the population are growing rapidly, the traditional fossil energy resources are consumed increasingly. Under the pressure of the energy shortage, countries attach great importance to rational exploitations of traditional energy and researches on new energy. As a sort of clean marine renewable energy, wave energy has been recognized as an available choice. It has a impressive prospects with its abundant reserves and wide distribution. Hence, researches on ocean wave energy development became active in recent years[1-4].

Wave power generation is the main form for wave energy developing and utilizing. Since the first wave energy device came out in 1955, hundreds of different converter forms have been found all over the world. Generally, they consisted of three parts: wave energy capturing system, mechanical conversion system and generation system[5,6]. Among them, wave energy capturing system is used to capture wave energy. So far there has been pendulum, canard, mussels, oscillating water column type, float type and other forms. Mechanical conversion system is used to convert the captured wave energy to a particular form of mechanical energy (such as air or water pressure energy).Generation system plays the role of using turbine or mechanical transmission device to transmit mechanical energy to generator, and then, generator converts the mechanical to electric energy[7-9]. Some devices only contain wave energy capturing system and generation system while eliminating mechanical conversion system, such as direct-driven generator. Currently, researches of wave energy conversion device mainly focus on conversion efficiencies, reliability and cost issues of the three main systems. Researchers, at home and abroad, have done a lot of theoretical and experimental researches on that, and pay close attention to the oscillating water-column type and the oscillating floater type nowadays. Moreover, the oscillating floater type has been a hot research point gradually, due to its simple structure and high conversion efficiency[10].

A wave energy converter with swing arms and floaters was designed in this paper. This device capture wave energy by floaters, then convey it to generator with the help of swing arms and the mechanical transmission device. We set up model experiments under different wave height and period on floaters' movement, by measuring the vertical acceleration of floaters and average output power of the device, to research floaters' moving rules and the device's energy conversion performance, and then, to provide reference for further research on wave energy converter.

1. Test Scheme

1.1 Principle of the Wave Energy Device

The converter was composed of two floaters, two swing arms, a mechanical transmission device and generators. Among them, floaters floated on the water, and each of them fixed with one end of the swing arms. The other end of the swing arms was connected with the projecting shaft to the mechanical transmission device which was installed in a container structure. The overall structure of the model and the internal structure of the container are shown as the figure 1 respectively. Under the effect of waves, the floaters moved upward and downward, pushed the swing arms reciprocating. Then, the oscillating traverse motions of the swing arms drove the transmission device work. In addition, the transmission device contained a reversing mechanism and a speed-increasing box. The reversing mechanism converted the oscillating traverse motions of the swing arms to one-way rotation motion of the shaft, connected to the speed-increasing box through the shaft coupling to increase the rotation speed. The speed-increasing box drove the rotating generator rotate, which can convert mechanical energy into electric energy. Each floater corresponded to each generator.

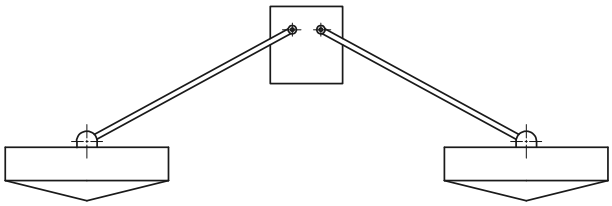

Fig.1 The overall structure of the model

1.2 Equipment and Instruments

This experiment was conducted in Harbin Engineering University's towing tank, which is 108m long, 7m wide, and 3.5m depth. The experimental equipment and instruments mainly consisted of a rocker-flap wave maker, wave shore, a trailer, Donghua DH5920 dynamic signal test and analysis system, the acceleration sensor, and the resistance box. The wave maker can produce regular wave with cycle ranges from 0.4 to 4 seconds while maximum wave height can reach at 0.4 meters, it can simulate ITTC spectrum under single and double parameters, JONSWAP spectrum, P-M spectrum, wave spectrum of the actual sampling and so on. Also, the wave maker can produce irregular wave whose significant height can reach at 0.32 meters; The signal testing and analyzing system had 16 working channels, it can sample the frequency ranging from 10 to 100kHz, with system error less than 0.5% and instability less than 0.05%.It was used to collect acceleration, force and the voltage and the current of the generator.

1.3 Method of Experiment

The purpose of this experiment was to measure the floater's acceleration and the output power of generator under the action of waves, grasp the effect laws of floater motion performance and energy conversion performance in the factors like wave height, period, damping and so on, and finally provided the experimental basis for the study of the wave energy device. The model was fixed in the trailer by a framework and the float was floating on water. The trailer was parked in towing tank and 48m far away from the wave maker (shown in figure 2). Stuck on the center of the two floaters, the acceleration sensor was connected to the dynamic signal measurement and analysis system through cable. The output terminal of the generator was connected to rheostat, which was in parallel with the dynamic signal measurement and analysis system to measure the voltage of the rheostat and finally to obtain the output power of the generator.

Fig.2 Picture of experiment

The main parameters of the experimental model are shown in Table 1. The signal sampling frequency of the dynamic signal test and analysis system was 50Hz. The wave was regular, and wave height and period are as follows:

(1) wave height: 0.125m, 0.15m, 0.175m;

⑵ period: 1.2s, 1.4s, 1.6s, 1.8s, 2.0s, 2.2s, 2.4s, 2.6s;

Table 1 Major Parameters of the model

Number	Items	Parameter	Unit
1	Diameter of floaters	750	mm
2	Shape of floaters	cone	
3	Height of floaters	265	mm
4	Length of swing arms	900	mm
5	draft	89	mm
6	Weight of swing arms	17	kg
7	Angle between swing arms and horizontal in equilibrium	24	º
8	Power rating of generator	50	W

2. Data Processing and Result Analysis

2.1 Experiment of the Floaters'Movement Performance

The floaters were arranged perpendicularly to the direction of wave, which was regular produced by the wave maker. After finishing the collection of the acceleration of the floaters under the function of the waves with the help of the acceleration transducer, we declined noise and integrated the experimental data by matlab, then we got the speed and displacement of the floaters and analyzed the movement discipline of the floaters according to the result. In addition, the changes of the waves in real time were measured by the wave height recorder. In figure 3, it was a curve of the regular wave, whose wave height was 0.15cm and period was 1.4s.

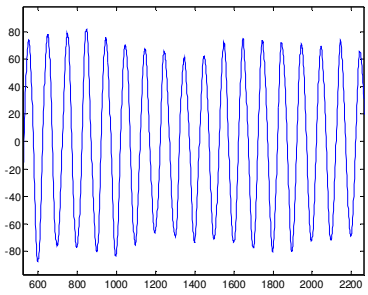

Fig.3 Wave curve

Next, the vertical accelerations of the two floaters under the same experimental condition were compared. Figure 4 was the vertical acceleration curve of the two floaters when the height of the incident wave was 0.15m and the period was 2.0s. The abscissa of the figure was the sampling number, and the ordinate was the displacement of floaters.

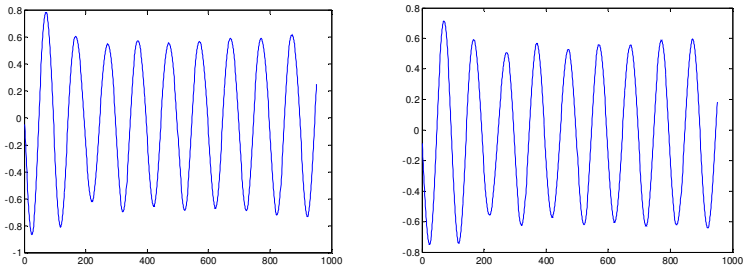

Fig.4 Acceleration curve of two floaters

Ignored the factors such as the irregularity of wave itself and measuring errors, it can be seen from the figure 4 that the motion curve of the floaters is sine curve and the vibration period of the floaters is 2.0s, just same as the wave period under the function of the regular wave. On the other hand, it can be seen from figure 4 that the vertical accelerations of the two floaters are nearly same and the average error of them is 1.2%. The error mainly were caused by mechanical transmission device and measuring instruments. Thus, the movements of the two floaters were the same under the same experimental condition. Hence, we only analyzed the energy output of one floater's movement in following discussion.

In order to analyze the connection of the vertical displacement amplitude and incident wave period of the floaters, the wave height was fixed on 0.15m. When the wave period is 1.2s, 1.4s, 1.6s, 1.8s, 2.0s, 2.2s, 2.4s, 2.6s respectively, we measure the vertical displacement of the floaters, and calculate the vertical displacement of the floaters and the ratio of its average during the calculate time and the wave height. Figure 5 was the change curve of the trend that the ratio of the average displacement amplitude and the wave height（z/h）varied in different period. The abscissa was the wave period and the ordinate was the ratio of the average displacement amplitude and the wave height.

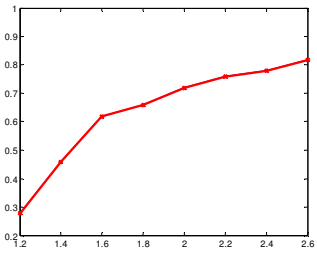

Fig.5 The change curve of the growth rate of displacement amplitude

It can be seen from the experimental result above that under the function of the regular wave which period ranged between 1.2s to 2.6s and the ratio of the displacement amplitude and the wave height between 0.2s to 0.8s, the displacement amplitude of the floaters decrease with the increasing of the wave period.

Now, comparing the relationship of the movement displacement amplitude of the floaters and the wave when wave periods were the same and wave heights were different. Preset the wave period at 1.8s and the wave height at 0,125m, 0.15m, 0.175m. In the measurement cycle, the change curve of the floater's mean displacement amplitude just as figure 6, of which, the abscissa was the wave height and the ordinate was the displacement amplitude of the floaters.

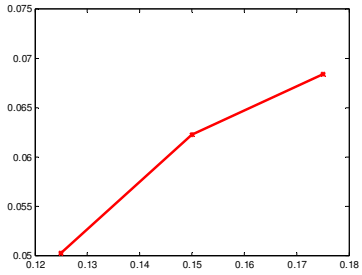

Fig.6 The change curve of the floater's mean displacement amplitude

When the wave period was 1.8s, the wave length λ was nearly 5.1m, the wave height was 0.175λ, and this curve can be seen as linear wave. It showed that the displacement amplitude of the floaters increased with the increasing of wave height. However, the connection was the non-linear damping of the mechanical actuating mechanism, not linear increment.

2.2 Energy Conversion Efficient of the Converter

For counting the energy conversion efficiency of the device, it need to count the power of the incident wave in the width of the floaters and the output power of the device separately. Meanwhile, the conversion efficiency was measured by ratio of the device's output power and the power of the incident wave in the width of the floaters.

The efficiency of the incident wave in the unit size can be counted by the eq. 1:

$$P_{\mathrm{w}} = \frac{\rho g^2}{32\pi} H^2 T \tag{1}$$

The output power of the device can be counted by the eq. 2:

$$P_{\mathrm{out}} = \frac{1}{T}\int_0^T \frac{U^2(t)}{R}\,dt \tag{2}$$

In the two formulas above, ρ is the density of the water, H is the height of the wave, T is the period of the wave, R is the external resistor of the generator, $U(t)$ is the functions that vary with the voltage across this resistor gathered by the dynamic signal analysis system, $U(t)$ is discrete function, the number of the data is N, the spacing interval is, so the eq. 2 should be counted as the following formula[11,12] in the actual calculation process[11,1 Δt 2].

$$P_{\mathrm{out}} = \frac{1}{N\times\Delta t}\sum_{k=0}^{N-1}\frac{U^2(k)}{R}\Delta t \tag{3}$$

Supposing that the diameter of the floater is D, the conversion efficient can be counted by the eq. 4.

$$\eta = \frac{P_{\mathrm{out}}}{P_{\mathrm{w}}\times D}\times 100\% \tag{4}$$

This experiment takes the voltage across this resistor gathered by the dynamic signal analysis system, and when the resistance was 100 Ω, the spacing interval was 0.02s. Then we have the result counted the energy conversion efficient under different condition according to eq. 1 to eq. 4, as table 2.

Table 2 Corresponding relation of the efficiency with wave height and period

Period(s)	Efficiency（%） of Wave height: 0.125m	Efficiency（%） of Wave height: 0.15m	Efficiency（%） of Wave height: 0.175m
1.2	12.3	16.2	18.1
1.4	18.7	23.5	25.7
1.6	22.4	27.5	30.8
1.8	28.6	31.6	33.8
2.0	21.9	25.7	29.1
2.2	12.3	16.1	20.4
2.4	7.8	10.2	13.1
2.6	5.6	6.4	8.6

From the table 2, it can be seen that, under the condition of the wave height is 0.125m, 0.15m, 0.175m, and the period ranged from 1.2s to 1.8s, the output power of the device increases with the increasing of wave period. When the wave period is 1.8s, the output power increases to the top, and then decreases with the increasing of the period. While under the same period, the higher the wave is, the higher efficiency of the device's energy conversion performances; The higher the wave is, the larger the amplitude of the floater is. And the efficiency of the mechanical transmission device and generators are the highest in that time. The experiment showed that under the condition above, the maximum efficiency of the device can reach to 33.8%.

3.Conclusion

This paper designed a wave energy converter with swing arms and floaters, and took experiment of electricity generation in test towing tank. The experiment mainly study on the hydrodynamic performance of the converter, and analyze the influence of regular wave height and period on the efficient of floaters' movement and energy conversion. The experiment results show that in the effect of regular wave, when the two floaters arranged perpendicularly to the direction of incoming wave, the movement of them are synchronous. The displacement amplitude of the floaters' vertical movement increases by degrees with the augment of the wave's period, and increasing of the wave's height, but the speed of the increment decreased; Under the same condition of the wave height, the energy conversion efficiency of the device firstly increases and then decreases with the increasing of wave period. In this converter, when the wave period is 1.8s, the efficiency is the highest. On the other hand, when the wave periods are the same, the higher the wave is, the higher the efficiency of the converter is. Synthesize the result of the experiment above, the wave energy converter possessed superior energy conversion performance.

Acknowledgment

This work was supported by the National Ocean Renewable Energy Special Funds(TJME2011BL03) and the Fundamental Research Funds for the Central University.

References

[1] Cruz J. Ocean wave energy: Current status and future prepectives[M]. Berlin: Springer-Verlag Berlin Heidelberg, 2008.
[2] British Petroleum. Statistical Review of World Energy[Z].2010
[3] Wang Chuankun, Lu Wei. Analysis method of ocean energy resource and storage estimation[R]. Beijing: Ocean Publisher, 2009.

[4] You Yage. Ocean energy progress of China[J]. China Science and Technology Achievements, 2007,16(3):18-20.
[5] Ren Jiali, Zhong Yingjie, Zhang Xuemei, et al. State of arts and prospects in the power generation from oceanic wave[J]. Journal of Zhejiang University of Technology,2006,2(1):69-73.
[6] Clement A, McCullen, Falcao A, et al. Wave energy in Europe: current status and perspectives[J]. Renewable and Sustainable Energy Reviews,2002,6(5):405-431.
[7] Smith H C M, Pearce C, Millar D L. Further analysis of change in nearshore wave climate due to an offshore wave farm: An enhanced case study for the Wave Hub site[J]. Renewable energy, 2012,40(1):51-64.
[8] Henderson R. Design , simulation, and testing of a novel hydraulic power take-off system for the Pelamis wave energy converter[J]. Renewable Energy, 2006, 31(2):271-283.
[9] Pecher A, Kofoed J P, Espedal J. et al. Results of an experimental study of the langlee wave energy converter[C]. Proceedings of the 20th International Offshore and Polar Engineering Conference, Beijing, China, June 20-25,2010.
[10] Gou Yanfen, Ye Jiawei, Li Feng, Wang Dongjiao. Investigation on the wave power device[J]. Acta Energiae Solaris Sinica,2008,29(4):498-501
[11] Su Y L, You Y G, Zheng Y H. Investigation on the oscillating buoy wave power device[J]. China Ocean Engineering, 2002,16(1):142-145.
[12] M.E. Mccormick. Ocean wave energy conversion[M]. Beijing: Ocean Publisher,1985.

Advanced Materials Research Vols. 986-987 (2014) pp 963-966

doi:10.4028/www.scientific.net/AMR.986-987.963

Research on the noise comprehensive management of HVDC converter station

Ye Chun-yan[1]

[1]State Grid Electric Power Research Institute, Sichuan Electric Power Company, Chengdu, 610072,China

[a]email: 173139168@qq.com

Keywords: HVDC converter station; converter transformers; spectral characteristics; noise source control; comprehensive management

Abstract. HVDC converter station noise problem is getting attention by the relevant departments. The noise of converter stations is mainly generates by the converter transformers, smoothing reactor, AC and DC filter and valve outer cooling fan equipment, on this basis, the converter station noise control must be integrated into a variety of factors. In this paper, the noise source control, noise propagation route control and protection noise receptor were studied and explored.

Introduction

Compared with AC Transmission,HVDC has many advantages ,such as large transmission capacity,small active power loss of line,reliable operation and quick speed adjustment .In the HVDC system,Converter station is the site ,which is in order to complete the DC and AC power conversion,and to achieve power system for stability and power quality.But it brings the optimal allocation of power resources ,at the same time, will also have the effect of noise on the surrounding environment,and caused widespread concern in the community.This paper analyse the converter station equipment noise and study the noise reduction measures.

The analysis of main noise sources in converter station

The main noise sources in converter station include converter transformers, smoothing reactor, AC and DC filter, valve outer cooling fan equipment and so on .Among them, converter transformers,smoothing reactor, AC and DC filter noise was generated by the electromagnetic noise,and valve outer cooling fan equipment noise was generated by the mechanical noise and aerodynamic noise.

1)The noise of converter transformers

The converter transformer is the noise source,which is of the maximum sound level ,and the noise source is divided into three parts:① electromagnetic noise: under the action of an alternating magnetic field, the core leads small changes of the transformer silicon steel sheet .called magnetostriction [1],resulting in vibration noise②The noise of the transformer and magnetic materials ,which is caused by the electromagnetic force between the coil and the coil wire[2].③The noise ,which is caused by the converter transformer cooling system fan.

Figure 1 is a converter transformer noise spectrum (Figure A-weighted noise amplitude with measurements), hereinafter,and its frequency is to 100Hz fundamental frequency and its harmonics based.As can be seen from Figure 1, the frequency of converter transformer noise distribution is very wide,and is In the low-frequency-based.The peak value is appeared in the low band center frequency of 100,200,400 HZ,and it becomes flat in the mid and high frequency flatten. the mean noise level in front of the converter transformer is 85-100 dB (A).

2)The noise of smoothing reactor

The size of the smoothing reactor noise is related to the Structure, operating power and factory model.The Smoothing reactor core is devided into oil and dry air core ,and its noise is mainly caused by that the coil vibration of the DC current and harmonic currents interaction[3].Oil core

smoothing reactor noise generation principle, sound level intensity, frequency range was similar to converter transformer.The coil of the dry smoothing reactor is made up of the one or more epoxy impregnation and sealing coil layers,and the material is the insulated aluminum.The main reason of the noise caused by the air core smoothing reactors is the coil vibration and the currents of the coil magnetic field interaction.

As can be seen from Figure 2, the frequency of smoothing reactor noise distribution is very wide,The peak value is appeared in the low band center frequency of 100,400 HZ,and the frequency components is rich in the medium and high frequency and becomes flat .At rated power,the total noise level of the oil smoothing reactor is 85~90 dB[4],the total noise level of the dry smoothing reactor is 70 dB.

3)The noise of the AC filter group

The AC filter group is made up of the filter reactor and filter capacitor,。The filter reactor often use the dry hollow reactor.The reactor coil noise is generated by the alternating electromagnetic field, causing the cyclical magnetostrictive effect ,and there is significant peak in the low frequency.The noise,producted by the bottom and top of the capacitor element,is the highest,which is the main noise source[5].and the sound level is lower than the noise producted by the converter transformer and smothing reactor.

As can be seen from Figure 3, the frequency of smoothing reactor noise distribution is very wide,The peak value is appeared in the low band center frequency of 50， 100 HZ,and it becomes flat in the medium and high frequency,the total noise level of the AC filter group reactor is 60.6~66.6 dBdB[6] .

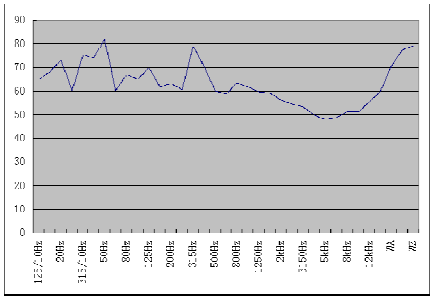

Figure 1 Converter transformer noise spectrum

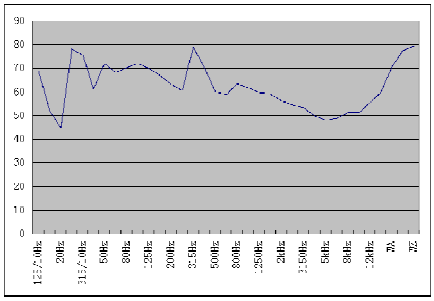

Figure 2 Smoothing reactor noise spectrum

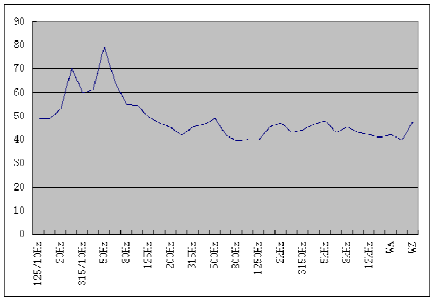

Figure 3 AC filter group noise spectrum

4)The noise of valve outer cooling fan equipment

The converter valve external cooling devices cooled units and the valve cooling tower can produce large noise.The spectral characteristics of the valve cooling tower fan noise is a typical fan noise spectrum,and the frequency of smoothing reactor noise distribution is very wide,low, medium and high band frequency components is rich and average, and have no significant peak.

The study of the noise comprehensive treatment in converter station

Noise control channels in converter station , including the following three ways: ①control the noise source; ② cut noise transmission routes; ③protection of noise receptors. Below with the actual situation of the converter station equipment were described.

1)control the noise source

Converter transformer : ①Reduce core flux density. Tests showed that each lower flux density 0.1T, the core can reduce noise 2 ~ 3dB (A) ;②Due to the size and rate of silicon steel magnetostrictive material related,magnetostrictive rate can be a small high permeability material,Such as high permeability silicon steel core noise at the same flux density reduced 2 ~ 4dB (A),however, this method costs higher.3)use low-noise fan;

Smoothing reactors :①For dry-type smoothing reactors, vibration limit the coil, adjust the structure size, spacing and mechanical support rods away from the critical frequency resonance frequency,the use of large amplitude conductor increases and other measures to reduce inertia can be reduced 5-10dB noise;②respectively, using the top and bottom of the package installation mode noise shield, the shield noise reduction of up to 15-20dB .

2)Noise control transmission route

If the above method does not significantly reduce noise,or to further reduce the high cost of equipment required for the noise,noise may be considered off main route of transmission noise reduction measures, such as insulation, silencers, acoustic and vibration isolation.

Converter station design optimization

①converter transformer valve hall and arranged face to face should be adopted;②try to control the floor, hall and converter transformer valve disposed in the central region of station site;③ AC filter and converter transformer should be arranged separately, while reducing the AC filter height,And bounded away from the station.By using noise analysis software SOUNDPLAN converter station area on the simulated noise,Figures 4 and 5, respectively, when using a face-arranged to change shape and noise distribution flow stations.

As can be seen from Figure 4 and Figure 5, when compared with a zigzag arrangement according to the valve hall and converter transformers are arranged face to face can be improved by the converter station outside noise environments.

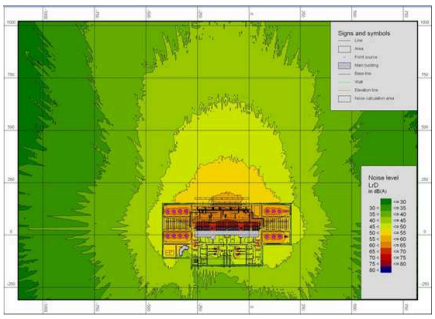

Figure 4 Valve hall an in-line converter station noise distribution

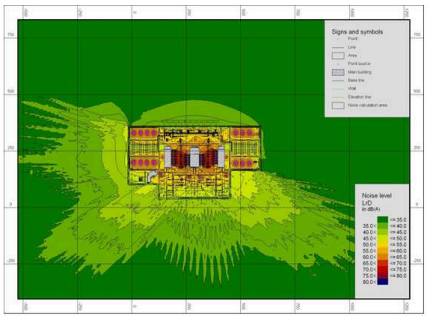

Figure 5 Valve hall-face arrangement converter station noise distribution

Set the sound barrier

①sound barrier materials are brick, steel, various types of composite structure, the insertion loss of the sound barrier (ie noise reduction) depends on the acoustic sound barrier transmission, diffraction and reflection case , the general can get 5 ~ 15dB of noise reduction②fan muffler: generally available 15 ~ 30dB (A) noise reduction.③isolation device: you can reduce the noise 1 ~ 5dB (A). Such as converter transformers and other equipment in the installation of the bottom structure damping device to reduce low frequency noise.④Acoustic enclosures: its sound effect is better than the sound barrier, the general noise reduction can reach 15 ~ 25dB (A).

Noise control effect analysis

A converter station on the main noise source noise reduction program are as follows:

Scenario 1: change sides transformer plus converter transformer sides of a firewall, surrounded by walls and ventilation plant noise reduction device settings sound barriers, sound-absorbing material posted firewall (composite absorber), and extend the length of the firewall.

Scenario 2: converter station capacitors using towers structure, thereby reducing the height of the sound source, and reduces noise transmission range.

Scenario 3: Converter Transformer BOX-IN packages noise, the converter station to minimize the noise level has been standing boundary noise level is less than 50dB.

Contrast these noise reduction program, using noise analysis using software SOUNDPLAN converter station area on noise simulation, which makes the program 1 a converter station to minimize the noise level has been, so stop the noise control community at 50 dB (A) or less, residential noise levels are controlled in the acoustic environment quality standard class II standards[7].

Conclusion

Converter transformers, smoothing reactors, AC filter group, the valve is the main source of noise outside Cooler converter station within the noise types include electromagnetic noise, mechanical noise and aerodynamic noise. Noise reduction measures should be taken to co-ordinate the planning, follow environmental standards, technical feasibility, economic rationality principle of governance.Equipment noise spectral characteristics in converter stations with a wide band characteristics, which mainly low-frequency noise, high frequency component is weak.converter station noise control should be a reasonable choice of converter station sites, followed as much as possible to reduce the number and intensity of noise sources, then consider a reasonable choice and optimization of the design, and finally consider the necessary sound insulation, noise reduction, etc. noise control measures.

References

[1] Martha Emirates Noise and Vibration Control Engineering Manual [M] Beijing: Mechanical Industry Press, 2002.

[2] Lan T S,Chiu M C.Optimal noise control on plant using simulated annealing[J].Transactions of the Canadian Society for Mechanical Engineering,2008，32 (3-4):423-437.

[3] High-yuan, Zhaoqing SOCIETY OF Guiguang DC Converter Station Noise Control Engineering Design [R] Beijing: Beijing Green Year Acoustic Engineering Co., Ltd., 2006.

[4] Yang Yiming, Zhang Xu Wen. HVDC converter station equipment noise reduction measures [J]. High Voltage Engineering, 2006,32 (9) :149-152.

[5] Southern Power Grid Technology Research Center of Yunnan - Guangdong ± 800kV HVDC project audible noise study report [R] Guangzhou: China Southern Power Grid Technology Research Center, 2006.

[6] GB12348-1990, Standard of noise at boundary of industrial enterprises.

[7] Henan Electric Power Research Institute. Lingbao Converter Station audible noise test report [R]. Zhengzhou, 2005.

Advanced Materials Research Vols. 986-987 (2014) pp 967-970

doi:10.4028/www.scientific.net/AMR.986-987.967

Study on 110kV Composite Material Transmission Poles and Towers

Yan QIN[1], Yanhai WANG[1, a,*], Long HAI[1], Yufeng LI[1], Yao FENG[1]

[1] College of Electrical Engineering & New Energy, China Three Gorges University, Yichang 443002, China

[a]email:45245356@qq.com

Keywords: FRP; Transmission line; cross section form; wire grounding scheme; pole

Abstract. Traditional transmission line poles and towers have many problems, such as higher corrosion, heavy weight, poor durability and maintenance cost is high. Use of fiber reinforced polymer composites (FRP), based on the theory of poles and towers design, 110 kV FRP pole structure size parameters are calculated, designed the 110 kV FRP pole structure, cross section form and wire grounding scheme. Design results show that compared with traditional pole, 110 kV FRP pole has the characteristics of compact structure, small occupied line corridors.

Introduction

At present, the use of traditional transmission line towers are mainly steel tube tower, angle steel tower and concrete pole, they are exposed to the atmosphere all year round, prone to corrosion in the external factors. In addition, there is the heavy weight, poor durability, maintenance cost is high, prone to various security risks [1-2]. Fiber reinforced polymer composites (FRP) has a light weight, high strength, corrosion resistance and good insulation performance characteristics. FRP used for transmission line poles and towers, steel can be saved and easy to solve the transmission line wind deviation and the pollution flashover accident, reduce the width of line corridors, reduce the maintenance costs of transportation and operation[3-6]. In this paper, according to the characteristics of FRP to planning and design of 110 kV transmission line FRP pole, and to explore the section form and wire grounding scheme.

The characteristics of FRP

Light weight. The density of FRP is about a quarter of the steel, one tenth of the concrete. FRP transmission poles with light weight characteristics can greatly reduce transport costs, especially in traffic difficult mountain.

Good insulation properties. FRP has high insulation resistance, under the condition of wet and dirty, still has a certain insulation properties. FRP transmission poles can reduce lightning accident; reduce the gap between the conductor and the poles, reduce the width of line corridors occupied, saving scarce land resources; without insulator string, decrease the shaft height.

High strength, corrosion resisting. The strength of FRP is close to the yield value of Q235 which commonly used in transmission line towers. FRP transmission poles to corrosive medium such as acid, alkali, salt and organic solvents, corrosion resistance can be excellent, it is particularly suitable for concrete and steel with special anti-corrosion requirements of environments such as coastal areas, industrial zones and acid rain-prone areas and so on.

110kV pole design condition

Conductor selection of LGJ-300/25, earth wire selection of LGJ-95/55, span 250m. Design of meteorological conditions such as shown in Tab.1.

Calculation parameters

Calculate of conductor and ground wire Kilo Newton per cubic miter load. According to the conductor and ground wire specifications and other design conditions, calculation of conductor and ground wire Kilo Newton per cubic miter load, the results are shown in Tab. 2.

Tab. 1 Meteorological conditions

Meteorological conditions	Temperature ( )	Wind speed(m/s)	Thickness of ice (mm)
Maximum temperature	+40	0	0
Minimum temperature	-20	0	0
Maximum wind speed	-5	30	0
Icing situation	-5	10	10
Mean temperature	5	0	0
Installation situation	-15	10	0

Tab.2 Conductor and ground wire Kilo Newton per cubic miter load value (10^{-3}MPa/m)

Kilo Newton per cubic miter load	conductor	ground wire
Kilo Newton per cubic miter weight (γ_1)	31.13	45.42
Kilo Newton per cubic miter ice (γ_2)	28.08	47.18
Kilo Newton per cubic miter total vertical load (γ_3)	59.21	92.60
Kilo Newton per cubic miter wind without ice (γ_4)	33.08	53.01
Kilo Newton per cubic miter ice and wind (γ_5)	9.85	17.67
Kilo Newton per cubic miter total load without ice (γ_6)	45.42	69.80
Kilo Newton per cubic miter total load with ice and wind (γ_7)	60.03	94.27

Calculate of conductor and ground wire maximum sag. With an average annual temperature is the first state, the maximum temperature for the second state. According to the equation of state of hanging point of overhead lines:

$$\sigma_{02}-\frac{E\gamma_2^2l^2}{24\sigma_{02}^2}=\sigma_{01}-\frac{E\gamma_1^2l^2}{24\sigma_{01}^2}-\alpha E(t_2-t_1) \tag{1}$$

$$f_C=\frac{\gamma_1 l^2}{8\sigma_{02}} \tag{2}$$

By the formula 2, calculate of conductor and ground wire maximum sag. The maximum sag of conductor is 5.55m; the maximum sag of ground wire is 3.31m.

Determine of practical height. Tower cross-arm bottom edge line onto the floor of the vertical distance of the ground is called practical height; it is important to the tower safety and economy. The practical height of FRP poles calculates by formula 3.

$$H=f_{\max}+h_x+\Delta h \tag{3}$$

Where, $f_{\max}$ is maximum conductor sag, m; h_x is conductor from the ground and the across safety distance, m; h is construction margin, m. The calculated practical height is 12.5m.

Conductor arrangement

Horizontal distance between conductors. Under normal operating voltage of weather conditions, because of the action of wind load, swaying in the conductor, the middle of the span conductor swing amplitude is the largest. When the wire rolling is not synchronous, span central conductors will close to breakdown air gap between conductors, occurrence of flashover. When the span follows 1000m, the horizontal distance calculates by formula 4[7].

$$D=\frac{U}{110}+0.65\sqrt{f_{\max}} \tag{4}$$

Where, D is conductor horizontal distance; U is system nominal voltage; $f_{\max}$ is maximum conductor sag. According to the results and control the results of other studies, 110kV FRP pole horizontal distance is 3.6m.

Vertical distance between conductors. When two-phase conductors are arranged vertically, the main factors that determine the vertical line spacing is: Conductors' uneven ice or ice shedding lead the conductors jump sharply. In order to ensure the conductors galloping without collision, two

phase conductors must ensure a safe distance. The vertical distance of 110kV FRP pole between the phase conductors is not less than 3.5m [7].

Horizontal migration between conductors. Ice-shedding will make the conductors to produce vertical jump, if the upper and lower conductors of the adjacent no design level offset, it is easier to produce collision, so that occurrence of power system fault.

110kV transmission line, adjacent the upper and lower conductors' horizontal migration is not less than 0.5m [7].

Determine the pole structure size and cross section form

Because of FRP has good insulation performance, so the conductors fixed on the cross arm directly, eliminating the insulator string, also don't need to check wind deviation. According to the design parameters are calculated; take the upward-form pole as the prototype, the FRP pole structure size design as shown in Figure 1. Pole section is circular, diameter 350mm, wall thickness 10mm, adding triangular ribs, as shown in Figure 2.

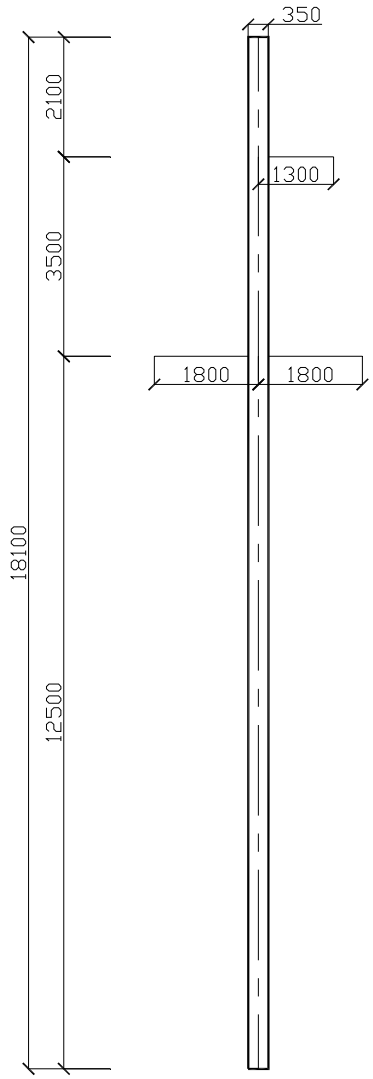

Fig.1. 110kV FRP pole structure size

Fig.2. 110kV FRP pole cross section form

Ground wire grounding scheme

Installation of ground wire in the FRP pole at the top, a ground down lead is arranged in the inner pole, set a short gap in the central of the ground down lead, so that under normal operating conditions can not be broken down, when lightning current flows, gap breakdown occurs, the ground down lead short circuit, and the lightning current smoothly discharged into the ground.

Conclusion

According to FRP itself good insulation and related specifications, designs and gives a 110 kV FRP pole structure size. Structure and size of the FRP pole is significantly less than the traditional pole with the same voltage level, more compact and smaller occupy line corridor.

References

[1] QIAN Xi-hui, LIANG Hao, WU Jian-gang. Corroded Component Durability Evaluation for Service Tower of Transmission Line [J] .East China Electric Power, 2013, 41（8）:1695-1698.

[2] LIU Hanli. Research and Application of Composite Transmission Poles and Towers [J] .Fiber Composites, 2011,（1）:38-40.

[3] LIU Huan-huan1, LIU Ming-hui, YU Xin. The Discussion of Designing Fiber Reinforce Plastic Transmission Tower[J]. Fiber Reinforced Plastics/Composites, 2013,（6）:48-52.

[4] YU Jibo, WU Xiong. Development and Application of GRP Poles for Power Transmission[J]. Fiber Glass, 2013,(6):40-47.

[5]Debbie Fox. Market for FRP Grows in the Power Industry[J]. Reinforced Plastics, 2008, 52(9):40-43.

[6] Awad M M, Heggi N, Tshoun F. The Future of Towers Made of Organic Compound Materials [A]. 12th International Middle-east Power System Conference. Aswan: 2008 Mepcon, 2008.

[7] Code for design of 110kV～750kV overhead transmission line（GB50545-2010）.Beijing:China planning press,2010.

Advanced Materials Research Vols. 986-987 (2014) pp 971-974

doi:10.4028/www.scientific.net/AMR.986-987.971

The design and calculation of 500 kv transmission line RPC double pole based on the ANSYS

Longshi WANG[1,a], Xu LI[2,b], Xiaobing SONG [2]

[1]College of Electrical Engineering and Renewable Energy, China Three Gorges University,Yichang,443000,China

[2]College of Electrical Engineering and Renewable Energy, China Three Gorges University,Yichang,443000,China

[3]College of Electrical Engineering and Renewable Energy, China Three Gorges University,Yichang,443000,China

[a]email:2578096252@qq.com, [b]email:lixuyichang@163.com

Keywords: RPC pole, design and calculate,finite element analysis

Abstract. Reactive Powder Concrete（RPC） material has good performances such as great strength, good durability and good stability,Therefore it has higher application value.In this paper, We design and calculate theoretically for the transmission lines of RPC door type double pole , and use the finite element analysis software ANSYS analysis the RPC double pole. Then we compare the results of numerical calculation we have get with the theoretical calculation results .It turned out that the RPC pole in the 500 kv transmission line designed application is feasible.

Introduction

RPC (Reactive Powder Concrete) materials is the combination of DSP and fiber reinforced materials of high technology concrete materials, with high strength, high toughness, high durability and the characteristics of high density［2-4］.The material in those aspects such as raw material composition and preparation technology are great differences with high performance concrete, and the durability and compactness of its internal structure got improved significantly. At present, the main research work of RPC is focused on the material mechanical properties and micro aspects of the production process, The structure of applied research is less, much more less in the application of transmission line pole research［4］.

The theoretical design and calculation of 500kv transmission line RPC pole

1.1 The design parameters and load calculation of tower head

The conductor we take is LGJ - 400/35 and the ground wire is JLB4-150. The RPC pole designed according to the typical weather zone II,the horizontal span is 400 m,the vertical span is 580 m, the pole with φ 500 diameter and the wall thickness of 100mm.The RPC pole composed of six rods which section of 6m long, and each Paragraph with welded connections.Tension control stress is 700 M Pa.Suspension insulator string consists of 28 pieces XWP2-160 insulator,the String length （λd） is 4340mm.The total mass of wire insulator strings and its fittings for 218.49kg.Wire fittings length λb is 645 mm,The total mass of wire insulators and its fittings for 7.03 kg. The lightning line maximum and minimum support force are T_D=9.97kN and T_D=9.97kN .Preliminary selection of pole geometry size are:Overall length (L) is 36m,outside diameter (R) is 500 mm, inner diameter (r) is 400 mm.According to the design requirements, insulation coordination and lightning protection and so on.

Reinforcement in accordance with the constitution requirement to use of partially prestressed stell. The prestressed reinforcement with 16 high strength steels which the diameter is 12. The non-prestressed reinforcement with 12 ordinary steels which its diameter is 14［6］.

The rod head design load values calculated by the design conditions as shown in Fig 1:

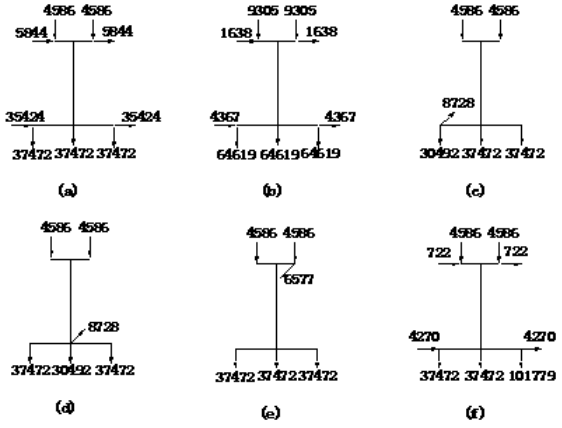

(a)Operation of Ⅰ, (b) Operation of Ⅱ, (c)Off the left wire,
(d)Off the middle wire,（e）The ground uneven tension, (f)The installation situation
Fig 1.The rod head design value of load (N)

1.2 The internal force calculation

The maximum wind conditions, the wire-off side circumstances and ground of the unbalanced tension situation cause internal forces greater ,and we calculate the bending moment separately caused by operation Ⅰ (maximum wind), the wire-off side and the ground wire unbalanced tension , bending moment diagram as follows:

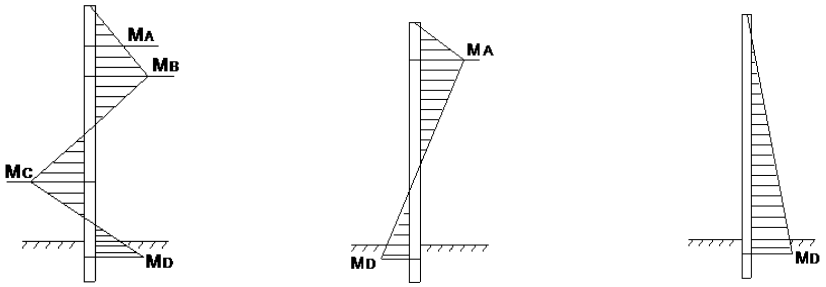

(a)The gale case (b)Broken edge wire (c)Ground wire unbalanced tension
Fig 2. Bending moment diagram of electric pole

The calculation results as follows: The wind: M_A=78.8kN·m, M_B=415.5kN·m, M_C=426.4kN·m, M_D=426.4kN·m ; Broken edge wire:M_A=74.8kN·m, M_D=13.7kN·m ; Ground unbalanced caused tension:M_D =175.2kN·m. From the results,we can see that everywhere of Poles'strength are controlled by the normal wind conditions.

1.3 The bending bearing capacity calculation

According to the literature 1, a new formula of calculation of bending bearing capacity, crack resistance and deflection on the basis of the original design specification. In this paper, We calculate those situations by referring to the calculation formula［1-3］.

The bearing capacity of bending is:

$$M_p = f_{cm}A(r_1+r_2)\frac{\sin\pi\alpha}{2\pi} + f_p' A_p r_p \frac{\sin\pi\alpha}{\pi} + (f_p - \sigma_{po})A_p r_p \frac{\sin\pi\alpha_1}{\pi} + f_{cy}(r_1+r_2)\frac{\sin\pi\alpha}{\pi} + f_y A_s r_s \frac{\sin\pi\alpha + \sin\pi a}{\pi}$$
$$= 460.5kN\cdot m > 426.4kN\cdot m$$

During the calculation,M_P is the bending moment design value,A is the member area, A_P is the All interface area of the prestressed reinforcement,r_1 and r_2 are the radius of circular cross section inside and outside respectively, r_p is longitudinal prestressed reinforced circle radius,$\alpha_1$is the ratio of longitudinal reinforcement sectional area and pull all longitudinal section area of steel,f_{cm} is the

design value of concrete flexural compressive,f_p and f'_p are the prestressed tensile and compressive strength design values,$\delta_{p0}$is the effective prestress of prestressed reinforcement.The bearing capacity of bending meets the design requirements.

1.4 Crack width checking

Stage allows the cracks in prestressed steel fiber reinforced concrete poles checking cross-section (normal section) cracking when subjected to bending moment is:

$$M_{cr} = \gamma f_{tk} W_d \left(1 + \beta_c \alpha_{pL} \lambda_f\right) + \sigma_{pc} W_d = 175kN \cdot m$$

During the calculation, r is the plastic influence coefficient of concrete in tension zone, f_{tk} is the matrix of concrete tensile strength standard values,W_d is the conversion section elastic resistance moment,and ,α_{PL} is the coefficient of steel fiber on the tensile strength of reactive powder concrete(When reactive powder concrete strength grade during CF35~CF45,α_{PL}=0.55;and when Steel fiber reinforced concrete strength grade is CF50~CF60,α_{PL}=0.63).

Considering the reinforcement effect of steel fiber, under the combination of short-term effects of loading,and in the using phase , the pole steel fiber prestressed concrete crack bending cross-section (normal section) is allowed the maximum crack width:

$$\delta_{f\max} = (200 + S)\frac{M_s - M_{fcr}}{A_s E_s r_s} \upsilon\left(1 - \beta_c \beta_{cw}\right) = 0.0197mm \angle 0.05mm$$

During the calculation,M_s is the moment of reactive powder concrete pole by the combination of short-term effects of load calculation of bending section (section) .S is the spiral rib spacing,V is the coefficient of associated with longitudinal reinforced surface characteristics(Ribbed bar is 0.7,high strength spiral rib steel wire is 0.6), β_{CW} is the coefficient of steel fiber reactive powder concrete effect on pole crack width(When reactive powder concrete strength grade during CF35~CF60, β_{CW}=0.5)

According to the regulation, circular crack width should less than or equal to 0.05 mm, so the crack width meets the specification requirements［5］.

1.5 The deflection calculation

The stiffness of RPC(Reactive Powder Concrete) pole after appears cracks :

$$B_s = \left[0.65 + \frac{2}{3}\left(\frac{M_{cr}}{M_s} - 0.7\right)\right] E_c I_c \left(1 + \beta_G\right) = 2.1 \times 10^{14} N \cdot mm^2$$

During the calculation,β_G is the influence coefficient of steel fiber bending stiffness of reactive powder concrete pole of the short-term(When reactive powder concrete strength grade during CF35~CF60,β_G=0.35),E_C is the elastic modulus of concrete and I_C is the moment of inertia of conversion section.Calculation method of load combination of long term effect is same to the front.

The top of the pole displacement:

$$y = \frac{K \Sigma P H^3}{3 B_s} = 172.4mm$$

$$\Sigma P = 15.2 \times 36.5 + 642 \times 2 + 126 \times 2 = 2090.8N$$

The pole under the action of horizontal force, and structural material elastically deform ,which make the peak produce the deflection as follows:

$$\omega = \frac{y}{L} = \frac{172.4}{36.5 \times 10^3} = \frac{4.71}{1000} < \frac{5}{1000}$$

Therefore the pole deflection meets specification requirements［5］.

The 500kV transmission line RPC electric poles of finite element calculation

Establishing RPC double pole finite element model , setting up the unit type, and using solid 45 unit concrete, steel and cross arm use BEAM3 element[6], then define material properties, division of grid, load and solve.After loading the finite element model and the calculation results are as follows:

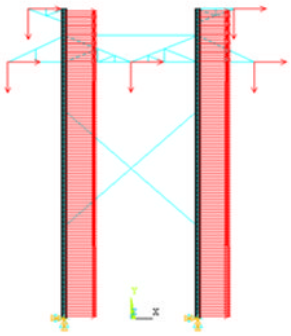

Fig3 After loading the Finite element model

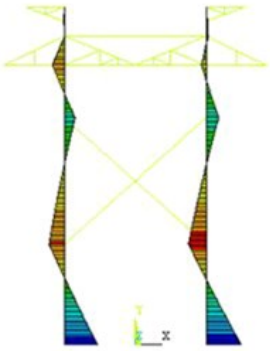

Fig4 Under the combination of long-term effects of deformation figure

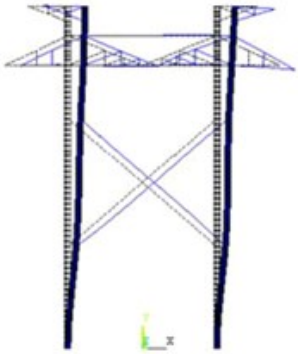

Fig 5 The bending moment diagram of structure

The maximum deflection of ANSYS simulation structure is 193.75 mm, the theoretical calculation value is 172.4 mm,and the error is 12.4%, within a reasonable range.The maximum bending moment value of ANSYS simulation structure is $4.19\times10^{8}N\cdot mm$, the theoretical calculation value is $4.26\times10^{8}N\cdot mm$,and the error is 1.6%, within a reasonable range.From the results of the analysis ,we can conclude that RPC concrete pole has higher bearing capacity, better crack resistance and anti deformation ability.

Conclusion

In this paper, We design and calculate for the pole by an example.And we use the finite element analysis software ANSYS to analyze the RPC pole, and then extract its deformation figure and deflection under the combination of long-term effects.From the analyze results,we can conclude that RPC concrete pole has broad prospective market which can be applied to the 500 kv transmission line.

References

[1] WANG Dehong，JU Yanzhong，KANG Mengxin. Study on Design of Prestessed Reactive Powder Concrete Pole [J]. GuangDong Electric Power ,2013

[2] JU Yan-zhong，WANG De-hong，ZHANG Chao. Advance of Research and Application on Reactive Powder Concrete [J]. Journal of Northeast Dianli University 2011

[3] JU Yanzhong, SHAN Ming, L I Xu, M ENG Xian an. Design of h igh2endurance reactive powder concrete poles for transmission lines [J]. Northeast Electric Power, 2008.

[4] WANG Ju，PENG Xing-min .The application research on reactive powder concrete [J] Technological Development Of Enterprise .2008

[5] FANG Qiang .The design of high-strength annular partial prestressed concrete pole [J]. Electric Power Construction.1999

[6] JU Yanzhong. Study on practical design method of 500kV double rod transmission Line [D]. JI Lin : Northeast Dianli University, 2009

Advanced Materials Research Vols. 986-987 (2014) pp 975-979

doi:10.4028/www.scientific.net/AMR.986-987.975

The Study on the SIT Technology of Subsea ILM

Zhao Xiaolei[1,a], Wu Zhixing[1,b], Chu Leping[1,c], Guo Xingwei[1,d], Chen Jinyu[1,e]

[1] China Offshore Oil Engineering Corporation, Ltd Tianjin, 300452

[a]Email: zhaoxiaol@mail.cooec.com.cn, [b]Email: wuzx@mail.cooec.com.cn,
[c]Email: chulp@mail.cooec.com.cn, [d]Email: guoxw@mail.cooec.com.cn,
[e]Email: chenjy@mail.cooec.com.cn.

Keywords: subsea production facilities; ILM; SIT; pipe line end termination; deep water;

Abstract. With the development of offshore oil and gas field enters into deep water constantly, subsea production system has become the main development mode in deep water development. Subsea Inline manifold (ILM) is common facilities in subsea production system and is used to gather oil and gas from the side subsea wells. Two subsea ILMs has been adopted in Panyu 35-1/35-2 Gas field with water depth range from 194 to 338 m in South China Sea. System integration test (SIT) is very important for the subsea production facilities. This paper states the flow chart, master equipment, purpose and precautions for each test of ILM SIT, which collects great technology for the development of subsea production system.

Introduction

With the gradual dying out of the land and shallow water petroleum energy, the oil and gas from the offshore deep water is increasing constantly. Depending on the good reliability, economy and outstanding achievements, the subsea production system has become the important model for the deep water oil field development. The water depth explored by this mode has reached 3000m[1].

Panyu 35-1/35-2 Gas field lies in South China Sea. The subsea charismas trees, PLETs(pipeline end termination), ILMs, jumpers and SUTUs(subsea umbilical termination unit)and other subsea facilities have been adopted in this subsea production system. The oil, gas and water from PY34-1/35-2/35-1 will be processed at PY34-1 central processing platform (CEP) and then transported to Liwan 3-1 natural gas central processing platform[2]. After separation, metering and pressurization, the oil and gas are transported to CNOOC Deepwater Gas Plant onshore terminal for further processing. The field layout is shown in Fig 1.

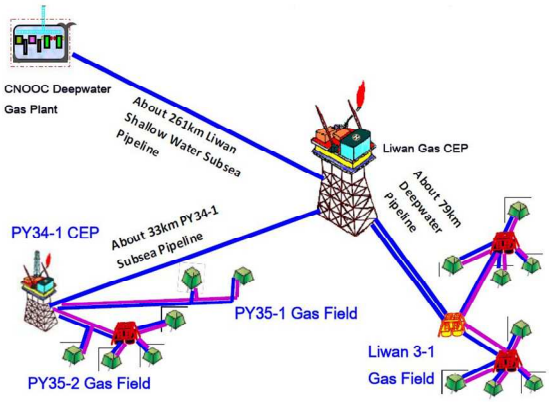

Fig.1. The schematic gas field layout of PY35-1/2

Subsea ILM is one kind of subsea manifolds which is integrated with subsea valves, hubs, bullseyes, etc. It is adopted when there are oil wells near the side of the subsea pipeline and the manifold is required to be laid together with the pipeline[3]. After the fabrication of subsea facilities, the ILM will be laid together with pipeline through the tensioner of the pipe-laying vessel. Then, jumper will be installed to connect the ILM with charismas trees under water. All the interfaces during installation and future production operations should be tested during SIT to validate the fabrication compliance with requested functionality of ILM[8]. Since there are many

interfaces, further many operations have to be carried out by remotely operated vehicle (ROV), the unknown risk is very high. If any issue happened during installation or production, the whole gas field may be affected. Therefore, the SIT is a very important test for subsea facilities.

This paper states in detail the flowchart, key equipment, purpose and precautions for each test included in SIT for subsea ILMs in PY35-1/2 project. The laying of ILMs has been completed successfully.

ILM composition

The ILM structure is designed into two parts.

1) Upper structure

The upper structure is a rigid frame which supports the valves, CAMERON vertical type connectors, jumpers and pipeline. The upper structure can be lifted using 4 padeyes and it slides on a rail system to allow to cater for thermal expansion of flow line and transfers load to mudmat.

2) Mudmat with protection frame

The mudmat is made up of single mat with skirts to increase the bearing capacity. Guiding rails sit over the mudmat to guide the upper structure during pipeline expansion and prevent lateral movement of upper structure in transverse direction [4].

6 in ILM composition is shown in Fig 2.

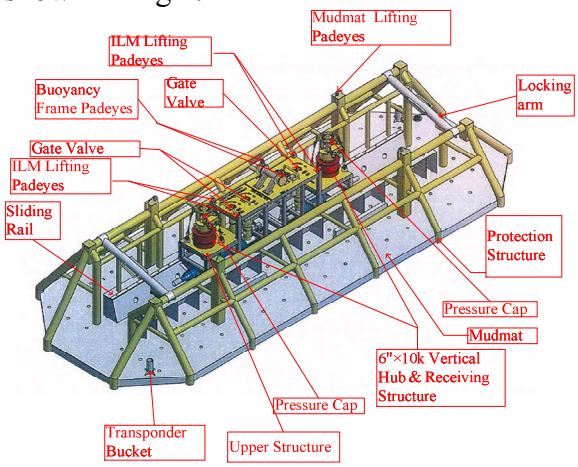

Fig.2. ILM components

Flow chart

There are 8 tests in the SIT for ILM. The test flow chart after optimization is shown in Fig.3.

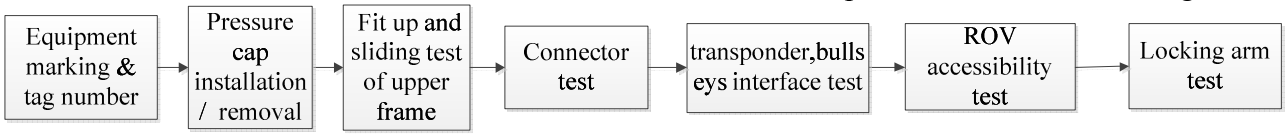

Fig.3. SIT flow chart

Master equipment list

The key equipment used in SIT for ILM is shown is table 1.

Table 1 SIT master equipment list

Equipment Required for Test	Qty.	remarks
Bullseye	4	Max inclined degeree:5
Camera	1	10m pixel
Cranes	3	One 35t, two 100t
Certified shackles	12	
Fork Lifts	2	8t
Block chains	2	10t

Cameron Vertical Connector(CVC) Hub Cleaing Tool	1	Provided by equipment supplier
CVC Seal Replacement tool	1	Provided by equipment supplier
CVC Test Gasket 6” x 10 k`	1	Provided by equipment supplier
Pressure cap 6” x 10 k	1	Provided by equipment supplier
Debris Cap – 6”	1	Provided by equipment supplier
CVC Running Tool	1	Provided by equipment supplier
On Shore Rigging Assembly	1	
Dummy/real ROV	1	
Torque Wrench	1	Max 2000N M
Total Station	1	
Piping borescope	1 set	Wire length longer than 25m,waterproof

SIT

Initial status

Before carrying out any activity, the following points have to be completed [5]:

1) Before SIT carried out, the unit FAT for each component of ILM should be completed. The sequence of SIT can be changed to meet the offshore schedule if required.

2) Equipment to conduct the tests has been received on the yard and is fit for purpose, including calibration, certification, etc.

3) Specific work that has to be completed ahead of each task has been identified.

4) Specific task plan (for each major activity) has been prepared and approved.

5) Toolbox talk has been conducted with all personnel involved in the operation. Roles and responsibilities are clearly identified

6) Permits to work are in place

Lifting plans

All non-routine lifting operations shall have a lift plan supported by an analysis of the hazards and risks.

Equipment marking & tag number

1) The objective is to verify equipment marking & tag number as per related data sheets (DDS), specifications and drawings.

2) Precautions:

a) if there is inconformity between DDS and nameplates, the information should be fed back to client.

b) The number of subsea valves for opening and closing is different from the DDS, the actual turns should be followed.

Pressure cap installation/removal

1) The purpose of this test is to trial fit the Pressure caps and to verify its integrity with ILM CVC hubs. The pressure cap installation test is shown in Fig.4.

Fig.4. Pressure cap installation test

2) Precautions:
   a) Seal verification will be performed during this test if client required.
   b) The lifting force to remove the pressure should not exceed 4 ton.
   c) Levelness of the pressure should be monitored during installation and removal.

Fit up and sliding test of upper structure

1) The purpose of this test is to verify the fit-up of the ILM upper structure with the protection frame and simulate the pipeline expansion during the field production.

2) Precautions:

Two forklift should be prepared, one for ILM sliding, the other one for emergency hold back. The sliding test scheme is shown in Fig.5.

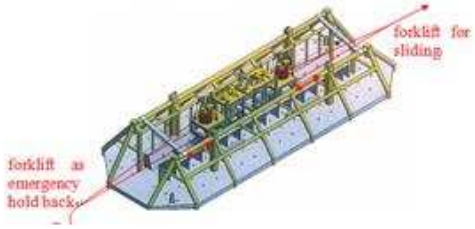

Fig.5. ILM upper structure sliding test

Connector test

1) The purpose of this test is to verify:

a) Interface between CVC hub and CVC connector

b) Interface between CVC RT and CVC connectors[6].

The on-site connector test is shown in Fig.6.

Fig.6. Connector test

Fig.7. Bullseye fit-up test

2) Precautions:

a) The Cameron operation manual for operating RT to connect the connector to the hub should be followed strictly.

b) The cleanliness of water-based hydraulic oil to operation Running Tool(RT) to connect the connector to hub should be tested. The cleanliness should be no higher than NAS 1638 class8.

c) The pressure of HPU used for driving the RT should no less than 5000psi, and the volume should be bigger than 50L.

Survey Equipment fit-up.

1) The objective of this test is to perform the fit up test for all surveying aids to be used offshore during installation. This fit-up include bullseye and transponder with the ILM[7].

2) Precautions: There is requirement for the installed direction of the bullseye. The longitudinal axis of the bullseye should be parallel to the main longitudinal axis of ILM. The installed bullseye is shown in Fig.7.

ROV accessibility test

1) The purpose of this test is to verify the ROV interface with ILM components for subsea operation[8]. The yard ROV access test is shown in Fig.8.

Fig.8. ROV access test

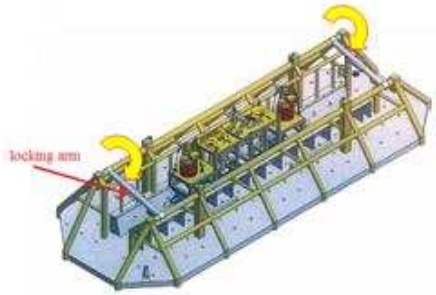

Fig.9. Locking arm swivel test

2) Precautions:

a) All the access of ROV during offshore installation and future field production should be checked.

b) The operation related to ROV should be careful in case causing the damage of ROV.

Locking arm test

1) The purpose of this test is to check the swiveling function of locking arm of ILM. The test scheme is shown in Fig.9.

2) Precautions: lubricating oil should be used in the swiveling trunnions and locking latches of ILM.

Conclusion

This paper in detail states the flow chart, master equipment, purpose and precautions for each test included in ILM SIT first time depending on PY35-1/2 subsea project. It provides technical references for other subsea facilities such as central manifold, pipeline end manifold, pipe line end termination, subsea jumper, enhancing the SIT technology further. It is very good for the development of vast unexploited deep water oil field, causing great social and economic benefit.

Acknowledgement

The financial support of China National Important Science and Technology Foundation 2011ZX05027-004 " The technology and equipment for fabrication, testing technology of deep water production facilities " is appreciated.

References

[1] Wang Wei, Sun Liping, Bai Yong. Investigation on Subsea Production System[J]. CHINA OFFSHORE PLATFORM，2009 ，24（6）：41-45；

[2] Yu Fangfang, Duan Menglan, Guohong. Design of Deep Water Manifold And Structure Design Study on Subsea Manifold for LW3-1 Gas Field[J] . Oil Field Equipment，2012，41（1），24~29.

[3] ISO13628-1, General requirements and recommendations[S]. TC67/SC4, 2010

[4] Tanyue, Shiyun, Liuming. Structure Analysis of PLET And Mudmat [J]. offshore oil，2011(9)：93-96.

[5] Liang Ji, Yao Baoheng, Qu Youjie. China measure and test[J].China Measure&Test，2012,01, 38~39.

[6] Zhang Xianzhen,Sun Wei, Deng Jisong. The analysis for subsea production system and its commissioning [J]. Shipbuilding Of China，2009- 2010：146-151；

[7] ISO13628-15, Subsea manifold and structure General requirements and recommendations[S]. TC67/SC4, 2010.

[8] ISO13628-8, Remotely Operated Vehicle on Subsea Production System[S]. TC67/SC4, 2008.

Advanced Materials Research Vols. 986-987 (2014) pp 980-984

doi:10.4028/www.scientific.net/AMR.986-987.980

Thermal Analysis of Gas Insulated Bus based on Multiple Species Transport Technique

Yang Zhang[1],Cuiling Shao[2] , Shuangshuang Tian[3]

School of Electrical Engineering, Wuhan University, Wuhan, China

zhangyangsai@163.com,sclingwhu@163.com

Keywords: GIB, temperature distribution, multiple species

Abstract: The temperature field distribution is a most important part we pay close attention to when gas insulated bus is designed. In this paper, finite element method is employed to calculate the temperature rise of gas insulated bus based on fluid governing equation and heat conduction equation. The problem of convection heat transfer between fluid and solid is solved by multiple species transport technique which provides convenience for the calculation of convection heat transfer coefficient. The solution region includes SF_6 gas, ambient air, conduct and tank whose electrical and thermal properties are dependent of temperature. Analysis result illustrates that the thermal field distribution is symmetrical, the lowest temperature is at the bottom of the tank, while the highest temperature is on the top of the conductor.

1. Introduction

The study of gas insulated bus began in 1960s, which has the advantages of large transmission capacity, low power loss, small electromagnetic interference, low maintenance cost and long service life etc [1]. With the continuous expansion of city size and power demand, the power supply should have higher reliability. In addition, environmental factors are becoming more and more serious for the construction of power facilities. Therefore, GIB becomes one of the ideal choices to transfer power which will be possible to replace the overhead transmission line[2].

The calculation of temperature rise of GIB will couple electromagnetic field and thermal field analysis. The common calculation methods include finite element method and analytical method. The conductor and tank temperature is solved by analytical method through establishing heat balance of iterative loss equation, convection heat transfer equation and the heat radiation equation. The treatment of convection and radiation heat transfer of air and insulating gas is different in finite element methods which have been reported [3]. The convective and radiation heat transfer is equivalent to the heat conduction in GIB. However, heat transfer coefficient is often difficult to compute because of the unknown surface temperature and there is deviation of calculated results with the actual temperature distribution [4].The convective heat transfer coefficient, which is calculated by dimensionless parameters, is regarded as constant [5]. Although this method can simplify the calculation, the result is inconsistent with the actual situation.

Due to the different installation environment, the temperature of running GIB will be certainly affected by ambient temperature and operating current. Research shows that all the parameters of the fluid are the function of temperature and the convective heat transfer coefficient is not same in different surface orientation of fluid-solid heat transfer surface. Because of sophisticated temperature factors in GIB, it is difficult to study these problems only by experiments. The numerical calculation method has the advantages of low cost which can simulate any complex environment. On the basis of the analysis mentioned above, considering the nonlinear characteristics of the temperature of gas physical parameters, this paper has established GIB finite element model to calculate the temperature rise with multiple species transport technique. The technique, which avoids applying constant convective heat transfer coefficient to tank surface, reduces the computational error. Through analyzing the related factors, the paper provides a theoretical basis for the design of GIB size and temperature monitoring.

2. Steady-state mathematical model of the electromagnetic field

The simulation based on a 500KV 4600A GIB for the original model. Its structure is shown in Fig.1. As the temperature field calculation of the heat source, electromagnetic field analysis must compute GIB conductor and tank Power loss accurately. In order to facilitate the simulation, simplifying assumptions make the following four points:

1) Due to the symmetrical structure of GIB and its axial length is much larger than the outer diameter of the tank, in order to reduce the amount of computation, two-dimensional finite element analysis is used to solve the electromagnetic fields of GIB.

2) The relative permeability of conductor and tank is constant.

3) The resistivity of the conductor and tank are a function of temperature.

4) The impact of bus contact structure on temperature distribution is ignored.

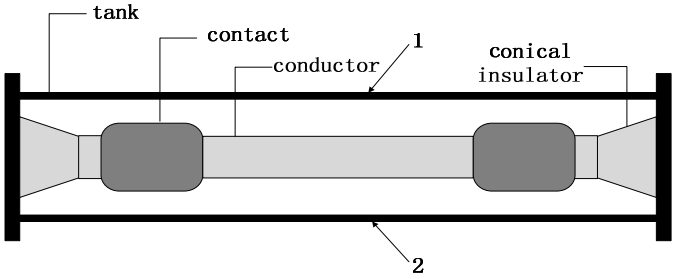

Fig. 1 Structure of the GIB and the locations of measurement points

Therefore, under the above assumptions, GIB cross section including the outside air is selected to solution region because the tank permeability is close to air. The solution region is shown in Fig.2.

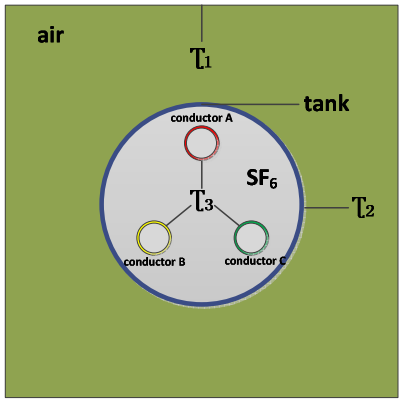

Fig. 2 Solution region of the model

Combining the specific model parameters and finite element analysis of the electromagnetic field, the 2-D current diffusion problem in a time-harmonic regime can be stated as follows :

$$\begin{cases} \Omega : \dfrac{1}{\mu}\left(\dfrac{\partial^2 A}{\partial x^2}+\dfrac{\partial^2 A}{\partial y^2}\right)=-J_z \\ \Gamma_1 : A_z = 0 \end{cases} \tag{1}$$

Where Ω is the solution region, Γ1 is the Dirichlet boundary condition, μ is the magnetic permeability, A_z is the z component of the magnetic vector potential, J_z is the total current density. Considering the change of resistivity with temperature, GIB power losses per unit length of the conductor and tank can be written as:

$$Q=\sum_{i=1}^{n} q_i^e=\sum_{i=1}^{n}\frac{J_i^e J_i^{e^*}}{\sigma(T)S_i^e} \tag{2}$$

$$\sigma(T)=\sigma_{20}/[1+0.004(T-20)] \tag{3}$$

Where n is the number of elements, q_i^e is the power losses of typical finite element, J_i^e and σ_{20} are the total current density and the electric conductivity of the element in 20℃ , respectively. S_i^e is the area of element, T is the temperature of tank.

The material and size parameters of GIB are shown in table.1.

Tab. 1 Dimensions and parameters of the GIB

parameter	conductor	tank
material	A6063-T5	A5005-0
internal diameter[mm]	140	480
external diameter[mm]	160	490

3. Mathematical model of thermal field

A. Heat transfer mechanism and the basic assumptions

The solution region of thermal field which is same with electromagnetic field is shown in Fig.2.The heat of conductor and tank is dissipated through ambient air. Conductors, insulators and tank composed of a closed cavity, which is filled with SF_6 gas. The power losses of the conductor warm the surrounding, which causes insulating gas to expand. Therefore, the heat from conductor gets into the insulating gas primarily through the natural convection heat transfer. Similar with conductor, there is a same heat exchanger manner between the tank and ambient air. The difference is that the former is a limited space within the convective and radiation heat transfer, the latter belongs to the large space of convection and radiation heat transfer.

The calculation of GIB thermal field is based on the following assumptions:

1) *GIB is in a room, thus ignoring the temperature effects caused by wind speed and solar radiation.*

2) The radiation heat transfer of SF6 gas is not considered.

3) The density, viscosity and thermal conductivity of SF_6 gas and air are related to temperature but gas specific heat are considered constant.

B. The natural convection heat transfer

In order to avoid calculating the convective heat transfer coefficient of the tank surface, ambient air is introduced to analyze the convection heat transfer of GIB. It is worth noting that there are two fluids which have different physical parameters after the introduction of ambient air. The equation is stated as:

$$\alpha_{\text{bulk}}=Y_{SF_6}\alpha_{SF_6}+Y_{air}\alpha_{air} \tag{4}$$

Where α is density, thermal conductivity or viscosity of air or SF_6, Y is mass fraction of air or SF_6 , α_{bulk} is the physical parameters of two fluid combination.

The gas density, thermal conductivity and viscosity are the function of temperature and it can be written as:

$$\rho_{\text{bulk}}(T)=\rho_0 PC_1/(TC_2) \tag{5}$$

$$\lambda_{\text{bulk}}(T)=\lambda_0(T/C_1)^{1.5}(C_1+C_2)/(T+C_2) \tag{6}$$

$$\mu_{\text{bulk}}(T)=\mu_0(T/C_1)^{1.5}(C_1+C_2)/(T+C_2) \tag{7}$$

Where ρ_0, λ_0 , μ_0 is density, thermal conductivity or viscosity of SF_6 or air respectively in environment temperature, P is gas pressure, C_1 and C_2 is constant associated with the gas physical parameters.

4. Analysis of simulation results

A. Multi-field coupling calculation method

As the resistivity of conductor and tank is relevant to temperature, therefore the power losses of them, which are used as input conditions of thermal field analysis model, can be iteratively calculated according to the initial temperature. There is a comparison of calculated and the initial value of conductor temperature to decide whether to update the initial temperature, which finally helps calculate the correct temperature distribution of GIB.

B. Analysis of simulation results

The power losses of GIB conductor and tank for different load currents are shown in Tab.2

Tab. 2 Power losses of the conductor and tank for different load currents

Current A	Conductor losses $W \cdot m^{-1}$	Tank losses $W \cdot m^{-1}$
2400	43.31	24.15
3500	73.99	41.03
4600	141.22	80.99

The load current is 4600A, environment temperature is 21.5 ℃, emission rate of tank surface is 0.9. the thermal field distribution is shown in Figure 3. By the GIB fluid thermal field simulation results that the internal temperature distribution of GIB general rule is: The thermal field of solution region is symmetrically distributed. The maximum temperature of the solution region locates at the top of conductor, whereas the temperature of ambient air is lowest. The section temperature of conductor which is approximately equal rises 40K.The differences of temperature in insulating gas are significant. The temperature of gas in bottom is lower than the top. Compared with the conductor, the temperature gradient of tank is more obvious because of the larger diameter. The maximum and minimum temperature of the tank locates at the top and button of tank respectively. The gas flowing characteristics is the main cause of the temperature distribution above.

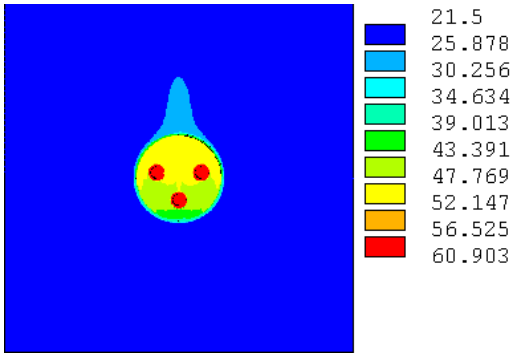

Fig. 3 Temperature profile of the GIB

The results comparison is shown in Tab.3. The measuring points are shown in Fig1.The result shows that the simulation results are consistent with the experimental results.

Tab. 3 Comparison between the calculated and tested results of temperature field

Current (A)	Test point 1		Test point 2		T_0 (°C)
	calculated value (°C)	experimental value (°C)	calculated value (°C)	experimental value (°C)	
2400	32.97	34.0	31.7	31.0	26.0
3500	34.21	35.0	32.05	31.7	22.0
4600	36.37	37.0	32.65	32.0	21.5

5. Conclusion

1) Compared with conventional finite element method, the multiple species transport technique has higher accuracy to calculate coupled fluid and thermal fields. It avoids applying the convective heat transfer boundary conditions.

2) The temperature rise of conductor is not obvious compared with the tank.

3) Convective heat transfer coefficient is not constant. So when calculating the temperature rise of GIB, the nonlinear thermophysical parameters of SF6 on the tank must be considered to reduce the computational error.

References

[1] Benato R, Carlini E M, Mario C D, et al. Gas-Insulated Transmission Lines in railway galleries[J]. IEEE Transactions on Power Delivery,2005,20(2): 704-709.

[2] Volcker O, Koch H. Insulation co-ordination for Gas-Insulated Transmission Lines(GIL)[J]. IEEE Transactions on Power Delivery,2001,16(1): 122-130.

[3] Benato R,Dughiero F,Forzan M,et al. Proximity effect and magnetic field calculation in GIL and in isolated phase bus ducts[J]. IEEE Transactions on Magnetics,2002,38(2): 781-784.

[4] Benato R,Dughiero F. Solution of coupled electromagnetic and thermal problems in gas-insulated transmission lines[J]. IEEE Transactions on Magnetics,2003,39(3): 1741-1744.

[5] Kim S W,Kim H H,Hahn S C,et al. Coupled finite-element-analytic technique for prediction of temperature rise in power apparatus[J]. IEEE Transactions on Magnetics,2002,38(2): 921-924.

[6] Eteiba M B,Aziz M M A,Shazly J H. Heat conduction problems in SF6 gas cooled-insulated power transformers solved by the finite element method[J]. IEEE Transactions on Power Delivery,2008,23(3): 1457-1463.

Advanced Materials Research Vols. 986-987 (2014) pp 985-989

doi:10.4028/www.scientific.net/AMR.986-987.985

Verifying Calculation of Reactor Pressure Vessel Fast Neutron Fluence

Qiaofeng LIU[a], Jingru HAN[b], Haiying CHEN[c], Chunming ZHANG[e*]

Nuclear and Radiation Safety Center of MEP, Beijing 100082, China

[a]email: liuqiaofeng01@163.com, [b]email: hanjingru@163.com,
[c]email: chy1025@126.com, [d]email: zcm1106@sohu.com
*The Corresponding Author

Keywords: Fast Neutron Fluence; Monte Carlo Method; verifying Calculation

Abstract. The reactor pressure vessel is an unchangeable component of the light water reactor. To some extent, the life of the pressure vessel depends on the fast neutron fluence. In addition, the fast neutron fluence is an important parameter for radiation protection. So, the fast neutron fluence is one of the main parameters which should be verifying calculated by the reviewers. The verifying calculation of the fast neutron fluence of one reactor pressure vessel is presented in this paper, and the standard deviation between the verifying and designing calculations is lower than 10%. The reasons for the deviation are discussed.

Introduction

The reactor pressure vessel is an unchangeable component of the light water reactor. The life of the nuclear power plants depends on the service life of the pressure vessel, which is under the influence of the fast neutron fluence. At present, the designed life of the reactors under operation in China is 40 years, and many of them are planning to extent to 60 years such as Qinshan nuclear power plant. The pressure vessel fast neutron fluence is an important factor to estimate whether it is actionable. And, the fast neutron fluence is one of the important parameters of radiation protection, and also included in the area of review in Standard Review Plan for the Review of Safety Analysis Reports for Nuclear Power Plants LWR Edition (SRP) [1]. Thus, the reactor pressure vessel fast neutron fluence should be verifying calculated by the nuclear safety reviewers to determine the accuracy and reasonableness of the designing values [2][3].

The reactor pressure vessel fast neutron fluence can be calculated by the discrete ordinate (SN) method and Monte Carlo (MC) method [4][5][6]. Both methods are approved by Nuclear Regulatory Commission of USA, and widely used in designing and reviewing [7]. The SN method is based on deterministic theory with high calculation efficiency. And it could obtain the distribution of the pressure vessel fast neutron in a single calculation. In contrast, the MC method is based on the probability theory with lower efficiency. But the parameters of geometry can be described in detail with MC method, which is the disadvantage of the SN method. Besides, in recent years, both of the methods have been improved very much with the development of the computer technology. The description of geometry with SN method is more and more accurate, and the efficiency of the MC has a substantial increased.

In this paper, pressure vessel fast neutron fluence of a reactor is verifying calculated. The results of the verifying and the designing calculations are compared, and there are some reasons for the relative deviation between them. The pressure vessel fast neutron fluence of the sample reactor is designed by the SN method and verifying calculated by the MC method [8][9][10].

The theory of the verifying calculation of reactor pressure vessel fast neutron fluence

The neutrons with energy above 0.1MeV or 1MeV are called fast neutrons. In the light water reactor, the life of the pressure vessel is depends on the radiation effect of the fast neutrons fluence with energy above 0.1MeV (E>0.1MeV). And the fast neutron fluence with energy above 1MeV (E>1MeV) plays an important role in the materials embrittlement and damage under the radiation. Both kinds of the neutrons are simulated in the verifying calculation. And in this paper, the calculations are at the inner surface of the reactor pressure vessel.

There are a few simplified handlings in the process of modeling depending on some experience. There is a brief introduction at follows. Some sensitivity analysis had been done to confirm the reliability of the handlings, which is not a major task in this paper. Only the conclusions of the sensitivity analysis are described.

First, in the modeling, the materials like water, void and some metal supports are mixed into the fuel rods as a whole. What's more, as the influences of the outer fuel assemblies are more important to the pressure vessel fast neutron fluence than the inner ones, the fuel rods which contained in the outer fuel assemblies are modeled pin-by-pin, but the inner ones are mixed in further. The sensitivity analysis shows that if fuel rods of the inner fuel assemblies are also modeled pin-by-pin, the calculation results could converge slowly but with a few influences to the results of the fast neutron fluence.

Second, to obtain the maximum value of the fast neutron fluence at the inner surface of the reactor pressure vessel, the distribution of the fast neutrons in the circumferential direction is calculated in the first step, and there would be a maximum value in an azimuth angle. Then, the distribution in the axial direction is calculated at this azimuth angle. The maximum value obtained by the second step is considered to be the maximum value at the inner surface of the pressure vessel as an approximate. The sensitivity analysis shows that the calculation results of the maximum value at the other azimuth angle are lower than this value, only a few are higher with very small deviation.

Third, because of the symmetry of the reactor core, 1/4 of the core model is enough, and the results could be corrected to the real at last or in the process of the calculation.

In addition, to make sure the accuracy of the results, the statistical variances are controlled to be lower than 0.03 in the calculation with the Monte Carlo method. The energy of the neutron is cut at 1E-11MeV in the calculation, and it hardly affects the fast neutron fluence. The ENDF/B library is chosen as the cross section library in the calculation.

The method and discussion of the verifying calculation

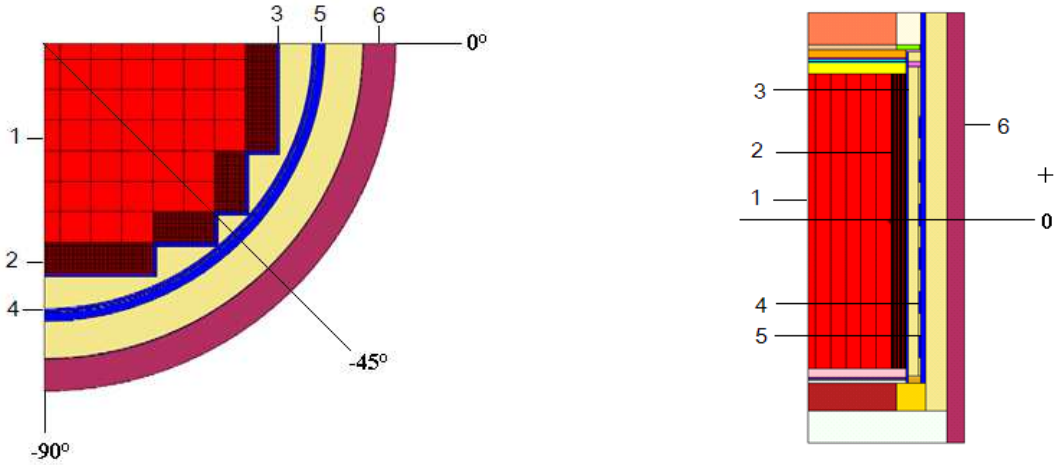

(a) The model in radial cross section (b) The model in axial cross section

1-inner fuel assemble; 2-outer fuel assemble; 3-core baffle; 4-core shroud; 5-core barrel; 6-reactor pressure vessel.

Fig.1. The geometry model of the verifying calculation

All the parameters of the reactor are provided by the designers. The geometry model is built with the MC method. The models for verifying calculation is shown in Figure 1(a) and (b), the model is shown in radial and axial cross section respectively. As it is shown in Figure 1, the origin in the radial is on the horizontal line, and the origin in the axial is on the mid-plane of the reactor core. In the geometry model, there are fuel assembles and their upper and lower support structures, the reactor internals, pressure vessel, and water between them. The reactor internals are out of the reactor core, and they are core baffle, core shrouds and core barrel from the inside out. There are 6 reactor shrouds surrounding the core baffle. Different colors in the figure stand for different

materials. In this sample, the core baffle, core shrouds, and the core barrel is made of stainless steel. The reactor pressure vessel is made of carbon steel.

The distribution of the fast neutron fluence in the circumferential direction with steps of 2° is calculated at first. As it is shown in figure 2(a), the fast neutron fluence of either E>0.1MeV or E>1MeV is low at 0° and -90°, and the maximum value is 2.45E+10n·cm^{-2}s^{-1} in the azimuth angle of -46° to -44° and 1.12E+10 n·cm^{-2}s^{-1} in the azimuth angle of -44° to -42° respectively. The obtained azimuth angles are mostly agreed with a few deviations.

Then, the distribution in the axial direction is calculated in the azimuth angle of -46° to -44°, and a step of 5cm is used in this calculation. As it is shown in figure 2(b), the maximum value of the fast neutron fluence is 3.83E+10n·cm^{-2}s^{-1} at -89.98cm to -99.98cm in the axial direction (E>0.1MeV) and 1.75E+10n·cm^{-2}s^{-1} at -9.98cm to -19.98cm in the axial direction (E>1MeV) respectively, which are the maximum values at the inner surface of the pressure vessel as an approximate.

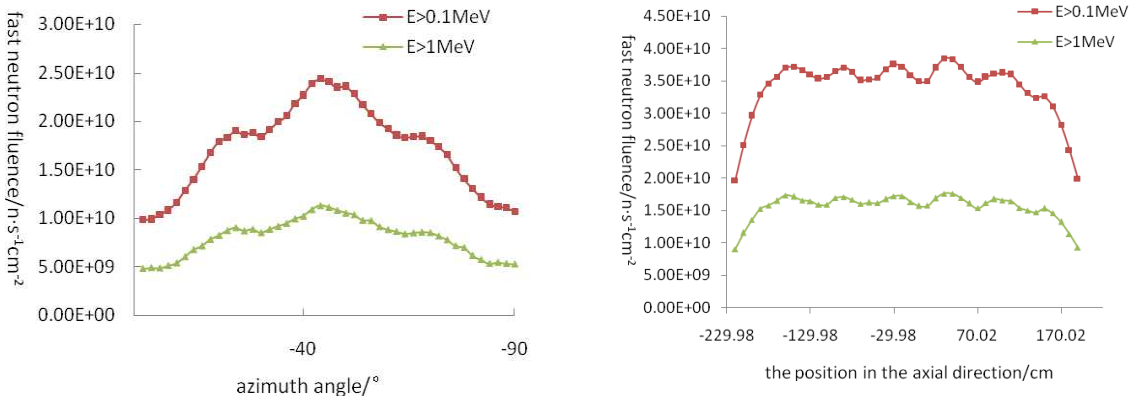

(a) The distribution of the fast neutron fluence in the circumferential direction
(b) The distribution of the fast neutron fluence in the axial direction
Fig.2. Distribution of the fast neutron fluence

The verifying results of the maximum value at the inner surface of the pressure vessel are compared with the designing ones, and the comparison is shown in table 1. The standard deviation is within 10%. Relatively speaking, the former ones are higher, and they are more conservative than the latter. The results of both kinds of methods are up to the required standards of the SRP. (The provision in the SRP: The peak vessel wall fluence for the design life of the plant is less than 1E+20 neutrons per square centimeter (n/cm^2) for neutrons of energy greater than 1MeV.)

Tab.1. Comparison between the verifying and designing calculation of the maximum value at the inner surface of the reactor pressure vessel

Energy	Verifying Calculation (MC Method)	Designing Calculation (SN Method)	Standard Deviation
E>0.1MeV(n·cm^{-2}s^{-1})	3.83E+10	3.54E+10	-8.2%
E>1MeV (n·cm^{-2}s^{-1})	1.75E+10	1.66E+10	-5.4%

There are some reasons for the relative deviation between the verifying and designing calculation.

First, different methods are used in the verifying and the designing calculation. Either method could be used to the calculation of the fast neutron fluence. When using the same method, only systemic errors for different users would be shown. Otherwise, it may bring in some deviations depending on different methods. In this verifying calculation, a three-dimensional model is built by the Monte Carlo method, while a two-dimensional model is used in the discrete ordinate method. The latter is less detailed than the former.

Second, the methods in the simplification of the geometry are different. In the designing calculation, some reactor internals, such as core shrouds, are omitted. Hence the average value of the pressure vessel fast neutron fluence would be higher than the actual value. It could leads to a

more conservative result. However, the geometry is described more resemble real in the verifying calculation. This kind of simplification can generally be accepted by the calculation of the fast neutron fluence, because the more conservative result would lead to the less damage to the reactor pressure vessel.

Third, the methods for handling the results are different. The results of verifying calculation with the Monte Carlo method are ensured their accuracy by controlling the statistical variances, although there are some uncertainties because of the cross section of the neutrons, the geometry simplifies, and so on. Because the history of each single particle could be simulated with this method, and a statistical result could be obtained at last. However, after the calculation with the discrete ordinate method, the results should be multiplied by two factors. One is the uncertainty factor of the method and the other is the distribution factor in axial direction. The two factors are elected from experiments. In this condition, the accuracy or rationality of the factors should be evaluated.

In addition, some other different conditions are set in the designing and the verifying calculations respectively. It would bring in some influences to the results. For example, the units of the counting are surfaces and grids respectively in the verifying calculation with the Monte Carlo method and the designing calculation with the discrete ordinate method. Different sizes of the surfaces or the grids may lead to different results. In general, the smaller of the sizes, the more accurate of the results, and usually at the expense of the calculation speed.

Conclusion

The Monte Carlo method is applied to the verifying calculation of the reactor pressure vessel fast neutron fluence, which is different of the discrete ordinate method in the designing. The standard deviation between the results of the verifying and the designing calculations is within 10%. Although the verifying calculation results are more conservative than the designing calculation results, both methods are allowed to calculate the fast neutron fluence of reactor pressure vessel, and the calculation results could meet the specified requirements of SRP. The deviation between the results of the two calculation methods may result from the different calculation methods, the simplicity of the geometry, the handling of the calculation results, the conditions setting in the designing, and so on. These considerations which could lead to the deviation should be taken seriously in the verifying calculation of the reactor pressure vessel fast neutron fluence to make sure the scientific of the verifying calculation. If it is necessary, some of the accuracy or rationality of the treatment should be evaluated both in the verifying and the designing calculation.

Acknowledgement

In this paper, the research was sponsored by the National Science and Technology Major Project (Project No. 2011ZX06002-010 and No. 2013ZX06002-001).

References

[1] U.S. Nuclear Regulatory Commission. NUREG-0800 Standard Review Plan for the Review of Safety Analysis Reports for Nuclear Power Plants LWR Edition [R]. March 2007.

[2] National Nuclear Safety Administration of China, HAF001 Civilian nuclear facilities safety and management regulations of People's Republic of China[S], October 1987.

[3] National Nuclear Safety Administration of China, HAF102 Nuclear Power Plant Design Safety requirements[S]. July 1991.

[4] John Charles Wagner. Monte Carlo Transport Calculations and Analysis for Reactor Pressure Vessel Neutron Fluence[D]. The Pennsylvania State University, December 1994.

[5] U.S. Nuclear Regulatory Commission. NUREG/CR-6115 H. B. Robinson-2 Pressure Vessel Benchmark[R]. July 1996.

[6] U.S. Nuclear Regulatory Commission. NUREG/CR-6115 PWR and BWR Pressure Vessel Fluence Calculation Benchmark Problems and Solutions[R]. September 2001.

[7] U.S. Nuclear Regulatory Commission. Regulatory Guide 1.190 Calculational and Dosimetry Methods for Determining Pressure Vessel Neutron Fluence[R]. March 2001.

[8] Deng Li. The Parallel Design of Monte Carlo Code and Measures of Enhance Speedup[J]. Chinese Journal of Computational Physics, 2001, 18(2): 177-180.

[9] Xu Qi. Research on GPU-based Acceleration Method for Monte Carlo Neutron Geometry Treatment[J]. Atomic Energy Science and Technology, 2013, 47: 689-695.

[10] Zhou Diyu. An Improved Parallel Sn Sweeping Algorithm for Solving Transport Equations[J]. Computer Engineering & Science, 2008, 30(4): 62-65.

Advanced Materials Research Vols. 986-987 (2014) pp 990-993

doi:10.4028/www.scientific.net/AMR.986-987.990

Application of Biomass Burning Stove in the Greenhouse Environment

Shuang Cui[1,a], Zhiping Xue[1], Qingyu LIU[1,b*], Yingyu Zhu[2], Baoquan Zhao[1]

[1] College of Engineering, Shengyang Agricultural University, Shenyang 110866,China

[2] Organic Food Corporation of Liaoning Livelihood, Shenyang 110023,China

[a]email: cshuangzhao@163.com, [b*]Corresponding Author: Qingyu Liu(1967-), professor of Shenyang Agricultural University, engaging in development and research of renewable energy sources. E-mail:qyliu@126.com

Keywords: Biomass; Burner; Greenhouse environment; Research application

Abstract. According to the demands of greenhouse environmental conditions, this paper examines a solid fuel burning stove applied to compression molding of biomass in order to solve the issues which temperature is too low in greenhouses in winter north of China and carbon dioxide concentration is too low caused by insufficient ventilation number. The burning stove designed with big furnace, no grate and recalculated secondary air. Fuel utilization was improved in the largest degree in this design. Feed amount, feed rate and time are controlled by the PLC system which is adopted to make fuel fully burning, low pollution emissions and more automation. The temperature field and gas flow field changes is simulated by the FLUENT. The temperature of various sections and the formation of nitrogen oxides is reduced by the special design when burning. Experiment shows that sulfur dioxide concentration is about 0.41mg/m^3, nitrogen dioxide is about 0.498mg/m^3 which have no effect in growth and development of crops. This paper provides theoretic guidance for improving greenhouse conditions.

Introduction

Biomass solid fuel [1] belongs to renewable energy, it's a kind of clean energy, high-density, low pollution, low cost, easy to transport, easy to store, etc. Biomass solid fuel burner is efficient combustion equipment, stable combustion, heat output uniform [2]. Greenhouse heat mainly from solar radiation, temperature is too low in the winter north of China, low temperature is not conducive to the growth of greenhouse crops; Insufficient ventilation number result in insufficient ventilation restricted concentrations of carbon dioxide, reducing the photosynthetic rate of greenhouse crops; Additions burner equipment can be used, while heat by burning fuel to produce carbon dioxide, greenhouse environmental conditions is improved. Biomass burning stove applied in greenhouse environment conditions can change the traditional way of carbon dioxide warming and supplying viewed from energy conservation and environmental meet the need of environmental conditions of growth and development of plants required ,contribute to the growth of crops, increase production, achieve zero pollution, maintain the ecological greenhouse in the circulatory system.

Demands of Greenhouse Environmental Conditions

Arch greenhouses are selected in this experiment, it has three sides wall and a rear wall, lighting structure is provided on the front wall, the total area of approximately 1152m^2, four townhouses, single buildings heat required about 6500W by theoretical calculations.[3]the greenhouse crops` most suitable temperature is 20~25℃, the carbon dioxide concentration of 0.11% to 0.13%. Within a certain range of concentrations, plants for sulfur dioxide, nitrogen oxides have some resistance, and some have evolved ability to absorb in a considerable degree. Research shows that plants will be damaged when the concentration of sulfur dioxide in the air reach to 0.05~10mg/L, nitrogen dioxide concentration of 2~3mg/L [5] [6].

Structural Design of Biomass Burning Stove

No grate design, batch combustion method; Feed amount, speed and time were controlled by the feeder; Combustion furnace automation degree is improved by PLC control system; Low moisture solid biomass compression molding fuel is selected, the amount of combustion air is controlled by the induced fan, fuel is complete burning, lowest the pollution emissions, meet the environmental requirements of greenhouse crops.

The specific structure of new design compression molding of biomass solid fuel burning stove [7] [8] as shown below:

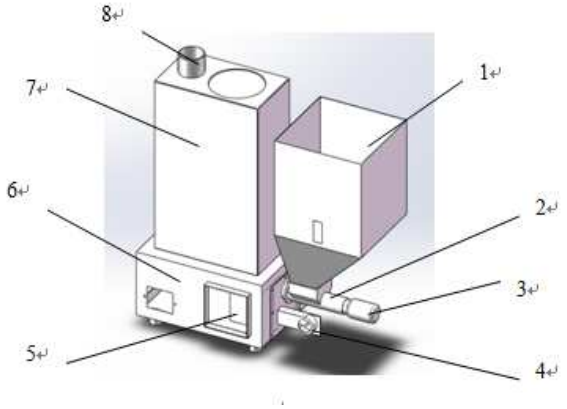

1.Feed tank 2.Screw feeder 3.Motor 4.Blower 5.Combustion chamber 6.Ash chamber 7.Cooling zone 8. Exhaust port

Fig.1.Combustion furnace structure

Calculating the fuel consumption according to the formula [8]:

$$B = \frac{Q}{Q_{net,ar} \cdot \eta} \quad (1)$$

In the type: B_j is fuel consumption (kg/h); Q is heat required (kJ/h); $Q_{net,ar}$ is base low calorific value (kJ/kg); η is thermal efficiency (%).

Burning stove efficiency takes 45.5% when theoretical calculation, the fuel is corn stalk solid modeling pellet, its low calorific value is 15.75 MJ/kg, calories is about 6500 W, fuel consumption (fuel consumption rate) of biomass compression modeling solid fuel burning stove is calculated of 3.27 kg/h according to the energy balance [9].To provide enough heat and carbon dioxide for the whole greenhouse, burning stove need work continuously for 4 hours, the packing density of particle is 100 kg/m^3, so need combustion chamber volume is 0.141 m^3. Designed burning stove is mainly composed of the cooling area, ash chamber and the combustion chamber three parts, the overall volume is greater than the minimum required volume.

Screw feeder is controlled by PLC control system. Overall design of the combustor is an inverted trapezoid structure, volume is 0.0135m^3. Air distribution system is composed of induced fan, primary wind plat and secondary wind ring. Primary wind plat is composed of 135 holes that diameter is 5mm, the area is about 0.106m^2, air through the hole in the bottom space of the chamber into combustor. Secondary wind ring is composed of 20 holes that diameter is 5mm, air from the ash chamber wall through the top of wind ring into combustor. Corn stalk compression modeling solid fuel completely burn need air volume is 4.36 m^3/ kg by theoretical calculation.

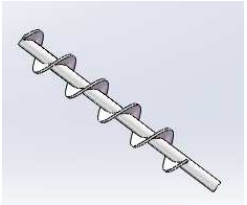

Fig.2 Screw feeder

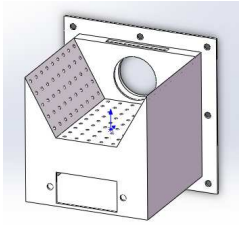

Fig.3 Combustor

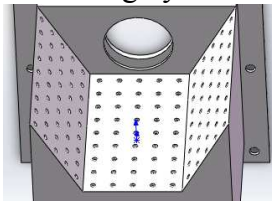

Fig.4 Primary wind plat

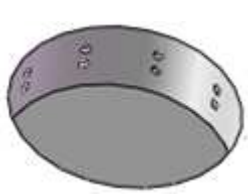

Fig.5 Secondary wind ring

Simulation Analysis and Temperature Measurement of Burning Stove

Two-dimensional compression molding of biomass solid fuel burning stove is simulated according to FLUENT software-Eddy dissipation (ED) model [9]. The simulation conditions are as follows: room temperature is 21℃, standard atmospheric pressure, the specific flow of 0.3, continue wind, the wind speed is 170.68 m^3/h, mainly set up factor is the wind, burning main composition is methane, feed speed is 3 kg/h, the ignition temperature is 343K, continuous burning,[10]. Speed scalar figure and the static temperature figure are analysis treatment results as follows . Maximum speed can be find on the primary wind plat, secondary wind ring and smoke outlet, velocity scalar presents a top-to-down trend; Static temperature figure shows that the highest temperature at the exit of fuel combustion, the cooling zone has uniform temperature decreasing changes.

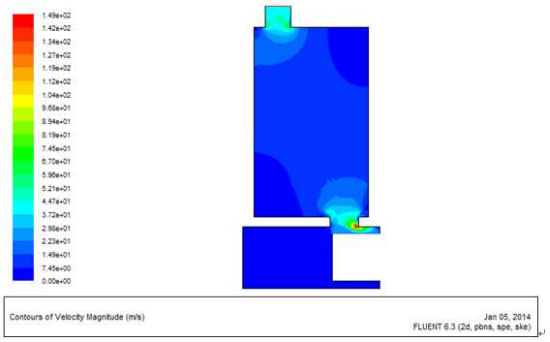

Fig.6. Velocity scalar

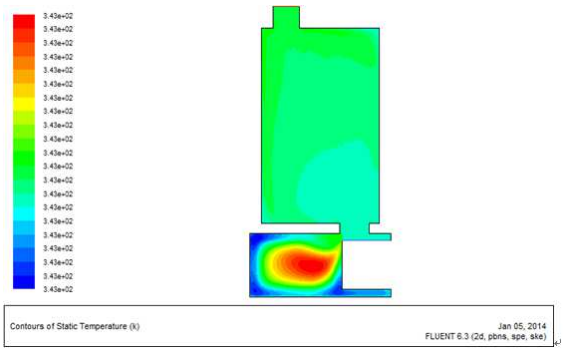

Fig.7. Static temperature

This paper finds that the wall temperature have a obviously influences on the inside temperature field during gas phase flow field simulation in burning stove This is the result of gas movement heat transfer [11] [12]. If burning stove has lower temperature, nitrogen content will be less. The changing of each part of the burning stove in the test as follows:

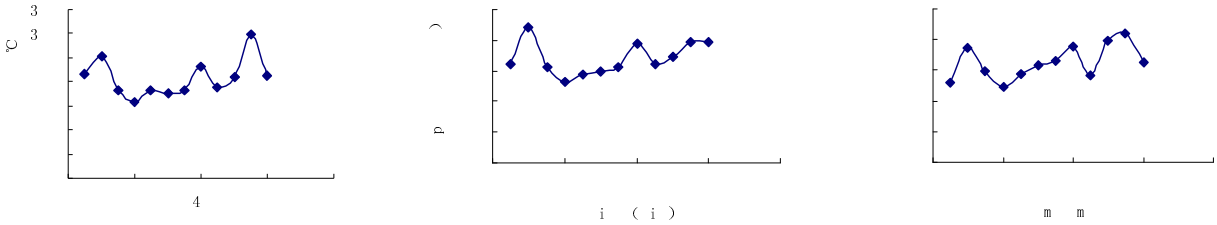

(a) Vent pipe wall (b) Radiation zone wall center (c) Combustion chamber wall

Fig.8 Various parts of the temperature change

The biomass compression molding solid fuel are ignited, temperatures continue to rise, due to the intermittent feed, feeding the second time before fuel fully burned, the flame by pressure, smoke temperature is reduced, when fuel burning temperature rise again, until to the end of the test. The design features of this burning stove is proved that reduce inside temperature and bring down the formation of nitrogen oxides pollution

Emissions Measurement of Sulfur Dioxide and Nitrogen Dioxide

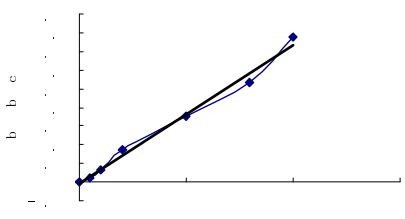

Fig.9 SO_2standard curve regression equation

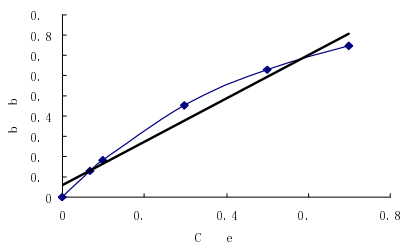

Fig.10.NO_2^-standard curve regression equation

Experimental sulfur dioxide and nitrite standard curve regression equations were Y=0.037X-0.0022, Y=1.0684X+0.0588. Ambient air was drawn through the air sampler, in the samples of the test, sulfur dioxide and reagent blank absorbance was 0.176 and 0.042; nitrite and reagent blank absorbance were 0.517 and 0.132. The contents of each pollutions which existed in the state of gases is calculated by the method of chemical analysis, sulfur dioxide and nitrogen dioxide concentrations were approximately 0.41mg/m^3 and 0.498mg/m^3,the measurement results u limited range of crops pollutant concentrations, does not affect the normal growth of greenhouse crops.

Conclusion

The result shows that with the big furnace design can dispersion heat and lower the temperature in the stove and reduce the formation of nitrogen oxides. No grate design, batch combustion method and the way which feed amount, feed rate and time controlled by the PLC control system are adopted to make fuel fully burning, lowest the pollution emissions and more automation. The air into combustor is controlled by induced fan. Primary wind plat and secondary wind ring are designed to meet the needs of primary wind and to ensure unburned volatile gases and smoke fully burn in the furnace with the secondary wind at the same time. The results provide theoretical guidance for improving greenhouse conditions and provide a certain degree of scientific basis for the application and popularization of biomass burning stove in greenhouses.

References

[1] Shengyong Liu, Yingfong Zhao, Bailiang Zhang. Combustion theory of him briquette fuel, Energy Research and Utilization[J],2002.
[2] Fei Xu, Shulin Hou, Lixin Zhao,Yishui Tian, Haibo Meng. Biomass pellet fuel combustion technology Development Status and Trends [J]. Journal of Safety and Environment, 2011.
[3] Libo Wang , Zhongjing Tian , Shuncai Cheng. Development of vegetable greenhouse heating equipment and intelligent control systems. Cheng Shi Jianshe Li Lun Yan Jiu [J], 2013.
[4] Food and Agriculture Organization of Unition Nations. Rural Energy in the Asia-Pouific Region Combustion and Gasification of Biomass[J]. 2002.
[5] Feng Zhang.Study on the Design of Tobacco Seedling Greenhouse and Ancillary Machinery Equipment. [D]. Henan Agricultural University,2012.5.
[6] Jipeng Zhang. Plant Physiology [M]. Higher Education Press,2006..
[7] Xinhua Li. Optimal design of biomass pellet fuel burner [D] Beijing Technology University,2011.6.
[8] Xiao Li. Experimental study typical gasification of biomass pellet fuel burning [D]. Shandong Jianzhu University,2012.5.
[9] Taichun Xiu. Development and experimental study of biomass briquette stoves [D]. Harbin Technology University,2009.7.
[10] Qiaoyue Wang. The research progress on monitoring technology and equipments of biomass briquette combustion. Renewable Energy Resources[J],2012. 30(8):88-94.
[11] Wenyi Dai. Experimental study on kinetic characteristics of biomass pellet fuel combustion and combustion [D]. Jilin University,2008.5.

Advanced Materials Research Vols. 986-987 (2014) pp 994-997

doi:10.4028/www.scientific.net/AMR.986-987.994

Research on Destruction and Preventive Measures of Geological Disasters Damage on Transmission Lines in the Seismically Active Belt

Yu Fan[1, a], Xing wang[2, b], Guoguang Zhu[3, c], Xiuqing Li[4, d]

[1] Skills Training Center Of State Grid Sichuan Electric Power Company, Chengdu, 610072, China

[2] Skills Training Center Of State Grid Sichuan Electric Power Company, Chengdu, 610072, China

[3]State Grid Power Company in Chengdu, Chengdu, 610042, China

[4]State Grid Power Company in Xianning, Xianning, 437100, China,

[a]email: scdyfanyu@163.com, [b]email: 20601112@qq.com, [c]email: 413545607@qq.com, [d]email:85322261@qq.com

Keywords: Seismically Active Belt; Transmission Lines; Geological Hazards; Measures

Abstract. In the seismically active belt, frequent landslides, debris flow, avalanches, rock and soil creep and uneven ground subsidence and other geological disasters regularly cause risk to transmission lines, and even risk the safe operation of the power network. The main reasons of geological disasters occur are: fragile geological environment, heavy rain, the foundation defect, the destruction of vegetation, artificial spoil, unauthorized mining etc. Transmission line route optimization design, suitable use of the new technology in construction and technical innovations are effective measures to prevent geological disasters.

Introduction

The main inland seismically active belt topography is plateau and mountainous. Geological disasters in these areas has the characteristics of various kinds, caused disaster soon, frequency occurrence, wide influence, heavy damage, long term influence etc. These regional geological disasters regularly cause damage to the tower base, foundation collapse, tower deformation, tower break down, etc., which seriously risk transmission lines even the safe operation of electricity networks. This paper intends to classified analyze geological disasters occurrence of transmission lines in the seismically active belt, and combined with preventive measures of common geological disasters to exploration and research on destruction and preventive measures for geological damage on transmission lines from transmission lines management and operation and the use of new technology, etc.

Destruction and Cause Reason Analyze of Geological Disaster on Transmission Lines in the Seismically Active Belt

In the seismically active belt, transmission lines generally impact by frequent landslides, debris flow, avalanches, rock and soil creep and uneven ground subsidence and other geological disasters.

Landslide is quantities, large-scale, serious destruction, complex characteristics, but has a certain regularity natural geological disasters in the mountain deformation. It is the major representation of geological disasters in the seismically active belt which contains 90% of the total number of geological disasters risk transmission lines or more. The main destruction representation on transmission lines are the resurrection of the ancient landslide, landslides occurred within the shallow layer of loosely packed and occur along the contact surface of the cover layer and bedrock landslides and other forms of damage.

Figure 1 Impact on transmission lines by the resurrection of ancient landslides

Resurrection of ancient landslides means transmission line tower is located on the ancient landslide has occurred in the past, the latter due to the impact of natural or man-made factors, resulting in partial or whole resurrection landslide deformation, causing the tower displacement, deformation damage or even collapse. It shown in Figure 1, the resurrection of ancient landslides caused by tower shift, severe deformation, and the maximum displacement over 4m, surface cracking, tower severely deformed, and other elements to pull off.

Overburden and bedrock landslide along the contact surface also means loose deposits occur along the base layer of the top surface of the slide occurred, such relatively large landslide thickness, generally thicker than 6 meters, which has a heavy risk on the tower foundation. For example, in China the Longmen Shan fault zone, by impact of the "5.12" earthquake and "4.20 Lushan" earthquake, such landslide occurrence have increased significantly on size, distribution and frequency, resulting in a large number of transmission line towers main member bent, tower foundation subsidence settling even tower collapse and other major safety incidents. As shown in Figure 2, by the “5.12" earthquake and aftershocks impact to induce such landslides, causing serious destruction to 500kV line tower.

Figure 2 Impact of landslide for 500kV transmission line

According to years of analysis on seismically active belt geological disasters condition, fragile geological environment is an essential factor in the development of geological disasters. The hydro power transmission lines typically locate in geological fault zones. Normally, the zones along the

complex terrain conditions (deep valleys, steep terrain), slippery ground (clay stone, marl) development, covering a wide layer of loosely distributed, huge thickness, fracture structure development , much active fracture have stronger seismic activity. The rains are the major factors that induce geological disasters like: landslides, mudslides, etc. According to statistics, in recent years, China's major seismically active belts had an average annual rainfall of 900 to 1800 mm, which also increases the possibility of local geological disasters. For seasons, summer has the maximum rainfall, basically from the beginning of May to the end of October, accounting for 80% of the total annual rainfall. Regularly, concentrated rainfall, long duration is the incentive of geological disaster-prone. According to years of real transmission lines operation and management condition in the seismically active belt, the main human-cause geological disasters more regularity occurring are: the destruction of vegetation, artificial spoil, unauthorized mining etc.

Preventive Measures of Geological Disasters Damage on Transmission Lines in the Seismically Active Belt

Choose route of transmission lines and towers location reasonably.

In the design stage of transmission lines, geological disaster-prone areas with seismic activity area characteristics should be considered. The design choices of the transmission line's geological conditions need to be full analyzed, especially on geological disasters and demonstration to avoid the range of geological disaster-prone, principally focused on disaster region. The tower located in the zones with ditches, scarp edge and slope side condition, slope stability and growth should be estimate analyzed to ensure that within a long-term trend the tower location can against collapse or landslide risks. Large instability ancient landslide should be identification timely during the survey design. The tower in this area will be arranged with the department's position shift. It cannot only pursue the route toward convenient transmission lines, while ignoring the huge losses future geological disasters.

Foundation improvements

Improvement of foundation type and construction process can be used in transmission lines construction on mountain, which excavation is too large to form a high-cut slope and generate a lot of spoil, resulting in manmade geological disasters. In the case of the tower steep slopes, it can excavation inclined inserted straight excavating the foundation for the improvement of excavating the foundation with helical column. It also can change the traditional fort-like ridge, slope protection, excavation practice small platform way, into high above the ground oblique column excavating the foundation and tower leg length combined method to improve, shown in Figure 3.

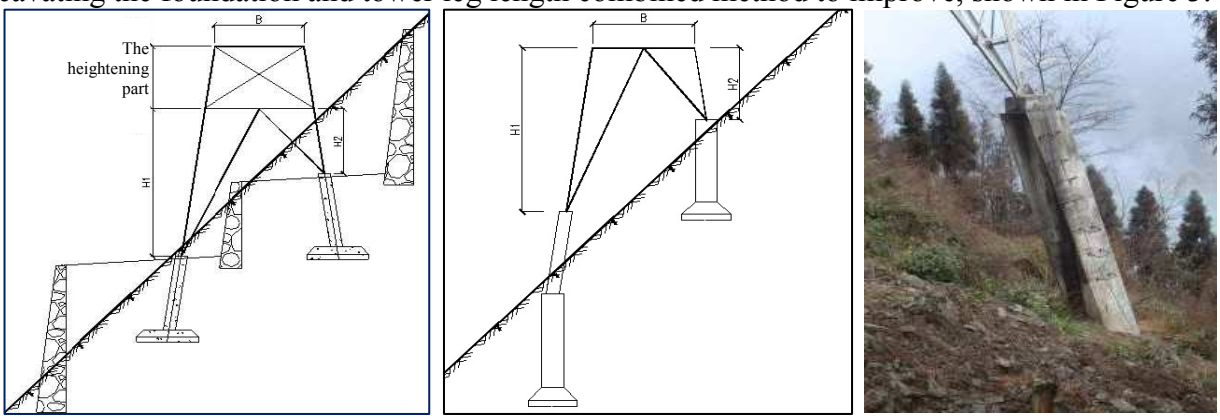

(a)Traditional (b) Improvement (c) Real photo

Figure 3 Tower foundation improvements on steep slope

When the tower located on a narrow ridge, change the traditional group and fort-like ridge practice, into not lower the foundation and straight column excavating the foundation, combine using integrated foundation with the four basic composition of the coupling beam, which can make it a frame structure to improve the stability of the foundation. If the tower is located in the scarp edge, improve traditional fort-like ridge, slope protection and excavation small platform measures, into

use full-length leg combine and high and low foundation with oblique beams, which besides improve the ability of foundation anti-overturning. These improvements not only lower the height of the tower to reduce project costs, but also as much as possible to maintain the original topography and vegetation. The amount of construction waste soil and surface wound is small, which greatly benefit landslides, collapses and other geological to prevent disasters.

Lines transitive

For such large-scale revival of ancient landslides, deep landslides and other location with huge geological risk, take general measures such as the construction of revetment effect, fort-like ridge, and anchor piles obvious lower effect, which would cause too much reconstruction. Recent seismic activity experience with regional geological disaster prevention work has proved that only way to complete solve the problem is using reconstruction, diversions and high cross-avoidance to transformation landslide and other measures to improve the technology.

Slope reinforcement and rocks anti-flying

For shallow landslides, the contact surface bedrock landslides, landslides and other geological disasters, it can use pile, anchor piles, anchor grouting etc. to reinforced slope. Anti-slide pile can use Φ600 reinforced concrete piles with 8m interval setting. Dump piles deep to bedrock surface. The main strip use four Φ40, Φ24 of four of Class II threaded steel reinforcement with a pile rib cage hoop stirrups, concrete grade 250, by way of construction of bored pile construction, concrete pouring underwater perfusion, which has good treatment effect. Prevention of geological disasters such as landslides can use SNS flexible slope protection nets. According to the terrain, it can choose passive or active protection network protection network to use.

Long-term prevention

Emphasis on fort-like ridge, slope, and drainage ditches inspections and timely repair the defects. Plant vegetation in poor geological conditions enhances the ability to resist soil erosion. In the transmission line construction, the selection of model aircraft wire-laying, avoiding the pay-channel tree felling, but also to protect the environment, minimizing the human factors of geological disasters desirable approach.

Conclusion

In recent years , the actual experience of geological disasters prevention and treatment showed that preventive measures on the foundation of the traditional emphasis during the design of geological survey work, and more to analyze the possibility of geological disasters to prevent; use of a new foundation, avoid large foundation excavation; discovered problem should be handled, select the appropriate, targeted pre-control measures can minimize the risks of geological disasters on transmission lines, and effectively ensuring the long-term safe and reliable operation of the transmission line.

References

[1] Zhang Yanfu, Wu Lihua, Miao Shengkun Ertan - Zigong transmission Line Segment Liangshan State Geological damage Analysis and Countermeasures [J] energy technology economy, 2010 (1), P31 ~ 35,50

[2] Tang Guilin. Guangyuan - Mountain geological disaster damage and countermeasures on high-voltage transmission line tower [J]. Journal of Engineering Geology, 2000 (Suppl.), P291 ~ 292,295

[3] Ding, Weilen Wu, Qin Jianhua, Chen Yuliang, Yang Quanzhong thinking. Southwest Geological Disaster Investigation. Sedimentary Geology and Tethyan Geology, 2006 (3), P77 ~ 80

[4] Zeng Mengchuan, Tan Shiwei. Impact of the Earthquake Effects on the Stability of the Mountains Transmission Line Tower Of [J]. Chinese new technologies and products, 2011 (09), P100 ~ 101

[5] Cao Meigen,Zhu Quanjun,MO Zenglu,Yang Jingbo,Zhou Fulin.Current Research Status of HVTransmission Line Earthquake Prevention and Disaster Relief and Earthquake Countermeasures[J].Electric Power Construction,2011(5),P123~ 27

Advanced Materials Research Vols. 986-987 (2014) pp 998-1003

doi:10.4028/www.scientific.net/AMR.986-987.998

The analysis of the effect of fouling on the performance of the fill layer

Luping Bai[a], Li Zhang[b] and Xiaofeng Lu[c]

College of Energy and Mechanical Engineering, Shanghai University Of Electric Power
Yangpu, Shanghai, 200090, China

[a]15121020690@163.com, [b]zhangli@163.com ,[c]21465777@qq.com

Keywords: fouling; performance; the fill layer; analysis

Abstract: Based on that the film filling was simplified to the flat plate model, the heat and mass transfer of the filling zone with fouling in cooling tower were analyzed. The effect of fouling on the performance of filler was analyzed according to the dirt growth model. The work done in this paper can simply forecast changes in cooling tower performance caused by the filler fouling. It will lay a theoretical foundation for accurately calculating the performance coefficient of filler. And it is helpful to solving the problem of no the ripe empirical formula of filler performance with fouling for engineering applications.

Introduction

Cooling tower is the final equipment of low-temperature heat releasing in turbine cold junction system, within the cooling tower, the filler zone is an important zone. The temperature drop in the filler zone usually occupies about 60-70% of the total drop. So the performance of the filler zone directly affects the temperature of the outlet water. Among the many affecting factors, such as filling method, filling height, filling depth ect, the cleanliness of the filler should not be underestimated. The dirt is inevitably flocked in gap of the filling during the operating time of cooling tower. Once the filling of the cooling tower is not clean, the heat and mass transfer performance of the filling would change.

Currently, the empirical formula of heat and mass transfer coefficients given by the references are for the clean filler layer to make analysis of thermal and resistance performance. However the empirical formula with fouling has not been reported. This is mainly because the complex shapes of the filling which is more complex with fouling. But, just as previously described, the accumulation of dirt is bound to happen. It is imperative to study how fouling affects the filler's heat and mass transfer performance. Because of the limitations of the experimental conditions, it is quite difficult to get the heat and mass transfer performance from the experiments. So, one simplified approach was tried to get the heat and mass transfer performance of the filler layer with fouling in this paper. The work would be help for researching the performance changing of the cooling tower.

Heat and mass transfer model of flat plate filler

The flat plate model. There are several types of filling for cooling tower: drip, film and bit thin film.[1] Usually the film filling could provide more contact surface between water and air. It is widly used because of its high cooling efficiency. Fig1 is the schematic diagram of the film filling commonly used in engineering. According to the different surface shape, the film filling is divided into several cases. There are composite wave, S wave, sine wave, two-way wave and so on. In order to analyze heat and mass transfer mechanism of the film filler, the model B, C in Fig.1 can be simplified as the model of A, namely the flat plate model.

Although the fouling on the flat plate filler layer would change the mass and heat transfer coefficient, the filler layer with fouling still can be considered to be flat plate if the fouling is simplified to distribute on the plate evenly. The only change is that the spacing between the flat plate becomes smaller.

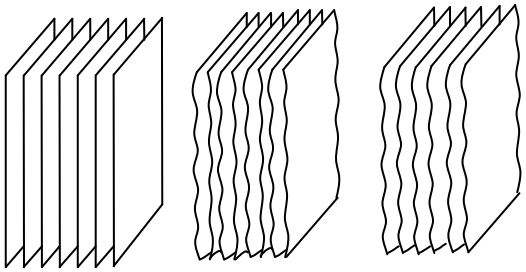

Fig.1 Schematic diagram of film filling

Heat transfer model of steam-water in the flat plate. Compared to the width and the height of the plate, the filler layer spacing is much smaller. The spacing could be usually neglected. And the change scope of the air velocity and temperature in filling zone is also small. In addition, the wind velocity of the filler and the water spray strength can be controlled in a certain range. Taking these factors, we can assume the following: firstly, the air flow is two-dimensional; secondly, the shear carrying when air sweeps over the water film can be ignored. According to physical conservation conditions,the heat transfer process of filler layer can be represented by those differential equations:

1) The mass conservation equation

$$\nabla \cdot (\rho \vec{v}) = 0 \tag{1}$$

In the formula: $\vec{v}$ is the air velocity vector; ρ is the air density, kg/m^3.

2) The momentum equation

$$\nabla \cdot (\rho \vec{v}\vec{v}) = -\nabla p + \mu \nabla \cdot \left(\nabla \cdot \vec{v} - \frac{2}{3} \nabla \cdot \vec{v} I \right) + \rho \vec{g} + S_F \tag{2}$$

In the formula: p is the air partial pressure; μ is the laminar and turbulent viscosity coefficient, kg/(m·s); I is unit tensor $\vec{g}$ is the gravity acceleration vector; $\vec{S}_F$ is the force between air and cooling water film.

3) The energy conservation equation

$$\nabla \cdot \left(\rho \vec{v} \int_{t_{ref}}^{t} c_a dt \right) = \nabla \cdot \left[\lambda \nabla t - \sum_j h_j J_j \right] + S_e \tag{3}$$

In the formula: t_{ref} is the reference temperature of enthalpy calculation, 0℃; h_i is the corresponding enthalpy of component i, J/(kg·K) , the formula is $h_i = \int_{t_{ref}}^{t} c_a dt$; λ is the thermal conductivity coefficient, W/(m·K); $\sum_j h_j J_j$ is sensible enthalpy transfer caused by component diffusion; S_e is the energy source term, W.

4) The component conservation equation

$$\nabla \cdot (\rho \vec{v} Y_V) = \nabla \cdot [\rho D_c \nabla Y_V] + S_m \tag{4}$$

D_c is the diffusion coefficient of water vapor in humid air , m^2/s; S_m is the source term, namely the cooling water evaporation quantity of per unit volume and per unit time, kg/(m^3·s).

Mass transfer model of steam-water in the flat plate. The heat transfer process is always accompanied with mass transfer in the filling layer. Water film mass transfer process of flat plate can be drawing as Fig.2 [2]. In the picture, the shadow part is flat; and the curve represents the water-air interface namely the falling surface of water film. b is the imaginary plane, infinitely closed to the actual interface. In order to simplify the calculation, when all components are water the water component is assumed to be 1. Generally, the mass percentage of water vapor in the air is usually quite small, and in this case the highest value is on the b plane. Although the temperature is high to 50 ℃ and the total pressure is 1atm, the corresponding value of the water mass percentage is only 0.077. The driving potential of vapor leaving the water-air interface is the difference of the water vapor mass percentage. Since the water vapor mass percentage of surface b and the infinity

are both small, the difference is much smaller than which between water film and b(approximately 1). So the diffusion of water vapor mainly occurs on the imaginary plane b.

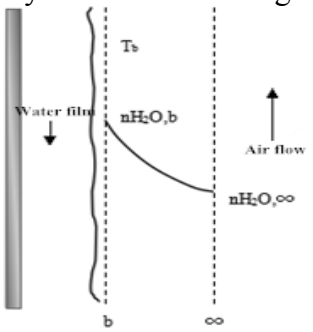

Fig.2 Schematic diagram of falling water film evaporation in air

Because the heat and mass transfer diffusion have same form in physics laws, there is a close analogy relationship between them.Based on the heat transfer diffusion model,the mass transfer diffusion could be dealt with using the analogy method. In order to make the analogy coefficient be more consistent with the model of mass transfer, the water film is idealized as follows:

1) The property of water film is constant and the surface is adiabatic.
2) The flow rate reduction caused by water evaporation is ignored；
3) The thickness of water film is uniform, no fluctuation；
4) There is no sliding on the surface;
5) The velocity of flow in water film is uniform;
6) There is no temperature gradient on the water film cross-section；
7) The thermal conduction through the flow direction is neglected；

With these assumptions, the differential equations and the boundary conditions of the mass transfer boundary layer is completely similar to the heat transfer boundary layer. So the mass transfer can be analyzed using the mathematical model of heat transfer.

Calculation of relevant parameters in the filler layer. As we all know, the flow, and the heat transfer and the mass transfer in the filling layer are associated with many parameters. Through the above analysis, these parameters (i.e. the average drag coefficient, heat transfer number Nu, mass transfer number Sh) can be calculated referencing the knowledge of flow between the two plates[3]. When the cooling tower runs, the wind speed is generally 1~3m/s. And the gap of the filler is usually between 20~30mm. Under the above conditions, the corresponding Re is greater than the critical value of laminar flow(2300). Therefore the air flow in the filler is turbulent. Calculating formulas of the related parameters are as follows：

1) The average drag coefficient

$$C_{fm}=\frac{\frac{1}{l}\int_0^l \tau_w dx}{\frac{1}{2}\rho u_\infty^2}=0.0792\ \mathrm{Re}^{-\frac{1}{4}} \qquad (10^4<\mathrm{Re}<1.2\times10^5) \tag{5}$$

In the formula: l is the plate length, m； μ_∞ is the mainstream velocity of the air , kg/(m^2·s).

2) Heat transfer number Nu

$$Nu_m=\frac{\alpha_m l}{\lambda}=0.023\ \mathrm{Re}^{\frac{4}{5}}\ \mathrm{Pr}^{\frac{2}{5}} \qquad (10^4<\mathrm{Re}<1.2\times10^5) \tag{6}$$

In the formula: α_m is the convective heat transfer coefficient of plate, W/(m^2·K)； λ is thermal conductivity of wet air molecules, W/(m·K).

3) Mass transfer number Sh

$$Sh_m=\frac{\beta_m l}{\rho D_c}=0.023\ \mathrm{Re}^{\frac{4}{5}}\ Sc^{\frac{4}{5}} \qquad (10^4<\mathrm{Re}<1.2\times10^5) \tag{7}$$

In the formula: β_m is the convective mass transfer coefficient of flat plate, kg/(m^2·s)； D_c is the water vapor diffusion coefficient, kg/m^2.

4) The volumetric mass transfer coefficient

$$\beta_{xv} = 1439(g/1000)^{0.54}(q/1000)^{0.47} \tag{8}$$

In the formula: g is mass air flow, t/(m^2·h)； q is water-spraying density, t/(m^2·h)；

5) Resistance characteristics of the filler:

$$\Delta p = \gamma_a A v^M \tag{9}$$

In the formula: ΔP is filler resistance, N/m； γ_a is air bulk density, N/m^3； v is the airflow velocity through filler, m/s；

$$A = -9.2354\times10^{-4}q^2 + 4.3290\times10^{-2}q + 0.760 \tag{10}$$

$$M = 2.1783\times10^{-4}q^2 - 9.3581\times10^{-3}q + 1.982 \tag{11}$$

The fouling growth model of filler layer.

Steam-water heat and mass transfer model of flat plate given in the last section is suitable for completely clean filler layer. Once the filler layer is fouled, the heat and mass transfer performance is affected. Since the fouling is accumulated gradually, different degree of fouling has different influences on the filler layer. Therefore, the calculation of mass and heat transfer performance of the filler layer with fouling must be matched with the growth model.

Fouling of cooling tower filler is divided into two parts. One part is the external material deposition. The other part is microbial growth (biofouling) on the surface of filler which occurs mainly in the plastic thin wall surface when water flows through. With the passage of time, the dirt accumulates and results in the decreases of filler layer spacing gradually. This will affect the water cooling, ultimately result in declining efficiency of cooling tower.

The increases of dirt thickness lead to the increases of the filling weight. Generally speaking, the dirt changes with time can be divided into linear, exponential, drop rate and asymptotic growth model. Because of different filling ways, the changes are not the same. In this paper, the asymptotic fouling growth model was selected.

For the asymptotic fouling model, Kern and Seaton[4] assumes that the dirt sedimentation velocity is constant, and the dirt denudation rate is proportional to the quality:

$$\frac{dm}{d\theta} = \dot{m}_d - \dot{m}_r = \dot{m}_d - bm \tag{12}$$

In the formular, b is denudation proportionality constant, 1/s. Integrating (12) :

$$m = m_f\left[1-\exp(-\theta/\theta_c)\right] \tag{13}$$

In the formula, $m_f = m_d/b$, it is the asymptotic deposition quality, kg/m^2； $\theta c=1/b$, it is time constant. It can be interpreted as the mean residence time for a component of fouling deposited on the surface. It can also be interpreted as the time required for the dirt growing to the asymptotic value by constant linear rate[5] (assuming $\dot{m}_r$ = O), as shown in fig.3.

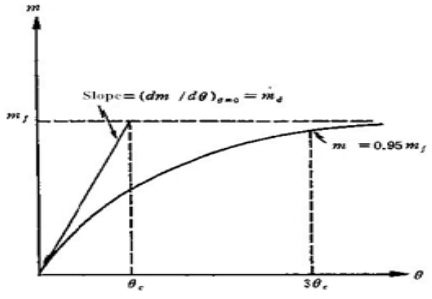

Fig.3 The meaning of θ_c

Calculation of the filling performance with fouling.

The calculation was done under the condition of taking filler (TJ-10) as an example and supposing that the dirt was evenly on the plate. According to the experimental analysis of Michel[6], dirt

growth was in accordance with the asymptotic model. The corresponding time constant is 40, and the asymptotic quality m_f is 8.5. According to the Eq.13, dirt quality can be calculated under different time. Conversely, since the uniform fouling on the flat surface leads the decreases of the spacing between the flats, the diaphragm spacing can reflect the fouling thickness. This can be used to calculate the dirt quality and the required time. Because of the complex components, the density is difficult to be determined. Therefore, in this paper, the selected dirt was simple dirt (calcium, magnesium carbonate). The density is 2.6×10^3 kg/m^3. The distance change reflects the growth of fouling, then the performance changes of the filler was analyzed.

Table 1. Filler fouling calculation data

Distance b/m	Equivalent diameter d/m	the coverage rate of dirt %	time/days	Re	C_{fm}	Nu_m	Sh_m	ΔP/Pa	ΔP reducti-on/%	β_{xv} /kg·m^{-3}·s^{-1}	B_{xv} reducti-on/%
0.030	0.060	—	0	12337.079	0.00751	39.075	37.540	114.844	—	0.039	—
0.029	0.058	3.33	6.64	11925.843	0.00757	36.800	34.886	115.518	-0.59	0.036	7.2
0.028	0.056	6.67	14.60	11514.607	0.00764	35.782	33.921	116.199	-1.18	0.035	9.8
0.027	0.054	10	24.56	11103.371	0.00771	34.756	32.948	116.884	-1.78	0.034	12.5
0.026	0.052	13.33	37.86	10692.135	0.00778	33.722	31.968	117.573	-2.38	0.033	15.2
0.025	0.050	16.67	57.88	10280.899	0.00786	32.680	30.981	-0.693	-2.98	0.032	17.9
0.024	0.048	20	99.87	9869.663	—	—	—	—	—	—	—

The filling width and filling height are both supposed to be 1m, and film distance is 30mm. Because the wind speed in filling is 3m/s, so the corresponding Re>10^4. The water spraying density is 15m^3/(m^2·h), and the air density is 1.22kg/m. The viscous coefficient is 1.78×10^{-5}kg/ (m·s), and water vapor diffusion coefficient Dc is 2.2×10^{-5}m^2/s. According to the Eq.8~9, volumetric mass transfer coefficient β_{XV} was 0.039kg/(m^3·s), and ΔP was 114.844Pa. According to Eq.5~11, relevant data could be calculated as shown in table 1.

The changes of ΔP and β_{XV} in table 1 was plotted in Fig.4. It was clear to see: with the fouling increasing, the filler layer's resistance was increased, and the volumetric mass transfer coefficient was decreased , and the heat and mass transfer performance was reduced. The trend of dirt analysis on the simplified flat plate was consistent with the experiment result. This proved the correctness of the simplified analysis and laid a theoretical foundation to accurately calculate the performance coefficient of filling dirt.

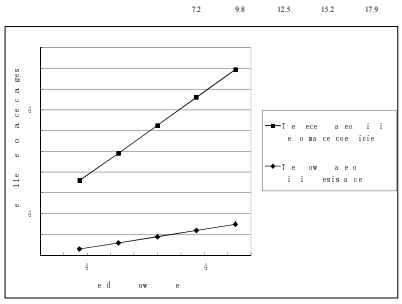

Fig.4 The relationship between filler performance and dirt growth

Conclusions

In this paper, firstly complex film filler was simplified to flat plate model, then the heat and mass transfer model of plat plate was discussed. Secondly, the asymptotic fouling growth model was explained in brief and this model was used to calculate the filling performance under different fouling. At last, compared with the experimental results, it proved that this model could simply forecast the filler performance changes due to fouling growth in cooling tower.

Acknowledgments

This paper was supported by Shanghai Engineering Research Center of Energy-Saving in Heat Exchange Systems (11DZ2210500 and 12DZ2280300).

References

[1] Zhenguo Zhao. The cooling tower[M]. China Water Power Press, 1997.
[2] Jianmin Liu. Heat and mass transfer principle and its application in power science and technology[M]. China Power Press, 2005.
[3] Qiangsheng Yang, Baorong Pu. Advanced Heat Transfer[M].Shanghai Jiao Tong University press, 2004.
[4] Kern D Q, Seaton R E.Surface Fouling: How to limit.Br Chem Eng, 1999, 55(6) :71-73.
[5] Shanrang Yang, Zhiming Xu, Lingfang Sun. Fouling and Countermeasures for heat transfer equipment[M]. Beijing: Science Press, 2004.
[6] Michel, M. , Noble, R.and Gary, R.M.Research of fouling.lm .ll.Presented at Cooling Tower Institute Annual Meeting, New Orleans, Louisiana, 17-19 February 1993, Paper TP93-06.

Advanced Materials Research Vols. 986-987 (2014) pp 1004-1010

doi:10.4028/www.scientific.net/AMR.986-987.1004

Optimization of Remaining Useful Life for Paralleled Battery Packs on Expansion Mode

Huang Shengjun[1, a], Zhangyan[1, b], Zhang Tao[1, 2, c] and Guo Bo[1, d]

[1] College of Information System and Management, National University of Defense Technology, Changsha, Hunan, P. R. China, 410073

[2] State Key Laboratory of High Performance Computing, National University of Defense Technology, Changsha, Hunan, P. R. China, 410073

[a]huangshengjun89@gmail.com, [b]zy331214534@126.com, [c]zhangtao@nudt.edu.cn, [d]boguo@nudt.edu.cn

Keywords: Paralleled Battery Pack, Expansion Mode, Remaining Useful Life, Genetic Algorithm.

Abstract. Remaining useful life (RUL) is of great importance to energy supply systems, such as battery pack. In this paper, an optimization model of RUL for the paralleled battery pack on expansion mode is proposed based on the basic concept of RUL and the capacity fading model. genetic algorithm (GA) is adopted to solve the problem. Case study shows that the battery pack's RUL can be extended by using the optimization model and GA.

Introduction

The capacity of each battery cell is relatively small due to the restrictions on manufacture and security, resulting in a big gap between cell and load, which is usually eliminated by constructing battery pack in the connection of series and parallel. If the last step is the parallel connection, the pack could be looked as paralleled battery pack, and each paralleled circuitry could be regard as a module. The Paralleled battery pack has many advantages, e.g., the system capacity could be expanded easily by paralleling a new module.

The life of paralleled battery pack is expressed by RUL regularity, which has been researched by a group of scholars with several papers published: in order to estimate the power battery's RUL, an electrochemical impedance spectra (EIS) method for calendar ageing quantification of batteries is presented in [1], with the effects of State of Charge (SOC) and temperature (T) taken into account; the commonly used RUL prediction methods are reviewed in [2]; and reference [3] compares various RUL prediction algorithms, etc.

All the works mentioned above have made some significant progress on RUL prediction and estimation; however the optimization of RUL is ignored. In order to fulfill the optimization, a great deal of meaningful thoughts have been put forward: reference [4] improves the utilization rate and RUL of battery by using micro-controller which is driven by detected battery operation data to perform equilibrium; the life of battery pack is extended in [5] with the help of good battery operation management; the battery equalization management is discussed in detail in [6], etc. Generally, the consistency control and balance management mainly concentrate on the self-adjustment of circuit, for example using resistance to share current in order to protect the weak battery, lacking some quantitative description.

The objective of this work is to enhance the quantitative analysis in RUL extending for paralleled battery pack by the refined discharge current control of each module, which is performed with the help of the newly designed RUL optimization model and GA.

Case study shows that the battery pack's RUL could be extended by using the optimization model and GA, and some conclusions on the efficiency of optimization is given as well.

RUL and Expansion Mode

Remaining Useful Life. The service life of battery is usually expressed by the State of Health (SOH), which is defined as the ratio between current capacity detected by instrument and original capacity given by the manufacture company [7].

The SOH value of brand new battery usually equals 100%, and will decline as the cycles increase. When the SOH value is reduced to 80%, the IEEE standard 1188-1996 claims that the battery should be replaced [8]. The time before the service life ending is called RUL, which can be expressed as RUL_i, where i (i =*1*~*N*) indicates the #*i* battery and N is the scale of paralleled battery pack.

The paralleled battery pack can be regard as series system from the view point of reliability, because the pack acts as an independent power supply system. Thus the RUL of paralleled battery pack denoted as RUL_P can be achieved by Eq. 1:

$$RUL_P = \min_{i=1\sim N}\{RUL_i\}. \tag{1}$$

Expansion Mode. Due to less estimation of load demand growth rate, power supply system may need to enlarge its capacity during operation, which is called expansion mode. At the expansion point, the group of N used units which is expressed as B_N, and the another group of M fresh units is expressed as B_M.

As B_N has been used before expansion, so its RUL value is smaller than that of B_M, but the pack's RUL is limited to the minimum module according to Eq. 1, thus the expansion does nothing positive to the pack's RUL. Besides, when B_N meets its end point of life, there may be some utilizable cycles on B_M. In order to improve the pack's RUL as well as reduce the cycle waste of B_M, effective strategy should be proposed.

RUL optimization model

The RUL model of single cells. The calculation of RUL for cell i (RUL_i) is needed when optimizing the pack's RUL, which relays largely on an accurate SOH degradation model. The SOH degradation model can be transferred from capacity fading model to some extent, which has been proposed by previous research [9-11].

The literature [11] establishes an empirical model which could be used to evaluate the cycle life of battery by means of data fitting and regression based on the test data:

$$\begin{aligned} &C_r(T,I,n_c) = A(T,I)\times n_c^{B(T,I)} \\ &A(T,I) = 2674.698e^{0.734/T} - 0.155/I - 2679.913 \\ &B(T,I) = 785.460e^{-0.844/T} + 0.122I - 782.972 \end{aligned} \tag{2}$$

Eq. 2 describes the capacity fading model, where T is the environmental temperature (the absolute temperature *K*); I is the discharge current (the current rate *C*); n_c is cycled times; $C_r(T,I,n_c)$ is the capacity when the battery has been cycled n_c times with the discharge current I in the ambient temperature T.

According to the definition of SOH, the SOH degradation model can be derived from Eq. 2:

$$S(T,I,n_c) = 1 - \frac{C_r(T,I,n_c)}{100} = 1 - 0.01A(T,I)\times n_c^{B(T,I)}. \tag{3}$$

Eq. 3 describes the SOH degradation model, where $S(T,I,n_c)$ is the SOH when the battery has been cycled n_c times with the discharge current I in the ambient temperature T. Then the inverse function of n_c for Eq. 3 is available:

$$n_c(T,I,S) = \left(100(1-S)/A(T,I)\right)^{1/B(T,I)}. \tag{4}$$

Where $n_c(T,I,S)$ is the cycled times when the battery has been cycled until the SOH decreased to S with the discharge current I in the ambient temperature T, that is, the battery's "age". Therefore, $n_c(T,I,0.8)$ is the total life of the battery, so the battery's RUL can be expressed as:

$$RUL(T,I,S) = n_c(T,I,0.8) - n_c(T,I,S) \quad (5)$$

Where $RUL(T,I,S)$ is the RUL of battery with its SOH value equals S if discharging with the current of I at ambient temperature T.

The optimization model of paralleled battery pack's RUL. The RUL of paralleled battery pack (shown as Eq. 6) could be generated by the Eq. 5 and Eq. 2:

$$RUL_P(\vec{T},\vec{I},\vec{S}) = \min_{i=1\sim M+N}\{RUL(T_i,I_i,S_i)\} \quad \vec{T}=[T_1,T_2,\cdots,T_{M+N}] \quad \vec{I}=[I_1,I_2,\cdots,I_{M+N}] \quad \vec{S}=[S_1,S_2,\cdots,S_{M+N}]. \quad (6)$$

Therefore, the optimization model of paralleled battery pack's RUL can be expressed as:

$$\begin{aligned} &Object: \ max\{RUL_P(\vec{T},\vec{I},\vec{S})\} \\ &S.\ t. \ I_1+I_2+\cdots+I_{M+N}=I_{load} \\ &\quad 0\le I_i\le I_{max}, i=1\sim M+N \end{aligned} \quad (7)$$

Where $\vec{I}$ is decision variable, $\vec{T},\vec{S},I_{load},I_{max}$ are state and constraints parameters, the first constraint indicates that the output current of paralleled battery pack should meet the load current demand, the second constraint represents the limited discharge current zone of each module.

Genetic Algorithm

GA is a heuristic algorithm first proposed by John Holland in 1960s, describing a solution as an individual consisted of a string of code. In this paper, the classical genetic algorithm is adopted to solve the optimization model (Eq. 7) with several key steps newly designed.

Encoding. There are several encoding modes: binary encoding, real encoding, orderly string encoding and structured encoding, which make big difference in the performance and population diversity of genetic algorithm. In this paper, the real coding is adopted as follows:

Set the population of generation t $(t=0,1,2,\cdots)$ as $X_t=\left(x_t^1\ x_t^2\ \ldots\ x_t^n\right)^T$, where n is the number of individuals in a population; x_t^i $(i=1,2,\cdots,n)$ is the individual i, made up of m ($m=M+N$) real numbers, which can be expressed as a $1\times m$ vector $x_t^i=\left(x_t^{i(1)}\ x_t^{i(2)}\ \ldots\ x_t^{i(m)}\right)$. So the population can be expressed as a matrix:

$$X_t=\begin{bmatrix} x_t^{1(1)} & x_t^{1(2)} & \cdots & x_t^{1(m)} \\ x_t^{2(1)} & x_t^{2(2)} & \cdots & x_t^{2(m)} \\ \vdots & \vdots & \ddots & \vdots \\ x_t^{n(1)} & x_t^{n(2)} & \cdots & x_t^{n(m)} \end{bmatrix}. \quad (8)$$

Initialization. The initialization is that generating a series of random feasible solution satisfied the constraints. The following steps are implemented in this paper:

① Generate m random numbers $r_i(1\le i\le m)$, and normalize these numbers into m new numbers;

$$R_i=r_i/\sum_{j=1}^m r_j \quad (1\le i\le m). \quad (9)$$

② Get each current value $I_i(1\le i\le m)$ according to Eq. 10;

$$I_i=R_i\times I_{load} \quad (1\le i\le m) \quad (10)$$

③ Check out whether each current value $I_i(1\le i\le m)$ meets the constraints $0\le I_i\le I_{max}$ or not. If satisfied, then go to step ⑤, otherwise, go to step ④;

④ Distribute the exceeded part $I_{max}-I_i$ into $\lfloor n/2\rfloor$ batteries with smaller discharge current on average, then go to step ⑤;

⑤ Repeat the above steps n times, constituting a $n\times m$ matrix.

Selection. The purpose of selection is reserving outstanding individuals with larger fitness value to the next generation and eliminating some bad ones. This paper adopts "roulette gambling + β% elitist reserving" strategy, where β is a parameter values $[0 \sim 50]$, which is carried out as follows:

① Get the fitness value $F_i (i = 1,2,\cdots,n)$ of each individual in population X_t according to fitness function;

② Get the probability that individual i is selected according to Eq. 11;

$$P_i = F_i \Big/ \sum_{i=1}^{n} F_i \quad (i = 1,2,\cdots,n) \tag{11}$$

③ Generate the roulette wheel. Get the cumulative probability of individual i according to Eq. 12, and additionally set $CP_0 = 0$;

$$CP_i = \sum_{j=1}^{i} P_j \quad (i = 1,2,\cdots,n) \tag{12}$$

④ Roulette wheel selection. Generate a random number $r \in (0,1]$, if r locates in the interval $(CP_{i-1}, CP_i]$ $(i = 1,2,\cdots,n)$, and then select the individual i to reserve to the next generation. Repeat the roulette wheel selection n times, select n individuals to constitute population X_{t+1}.

⑤ Elitist reserving. Sort the individuals of population X_t according to the fitness value decrease, then use the β% individuals to replace the other β% individuals which were random selected from population X_{t+1}, the result is population X_{t+1}.

Crossover. Crossover refers to swapping genes of two individuals, thereby generating two new individual, which is performed in three steps:

① Choose the individual and make pairs. The probability for each individual being selected is p_c. The selected M individuals were paired in a random way, if M is odd, then an individual would be deleted or added.

② Perform crossover operation on paired individuals. There are two kinds of crossovers: discrete crossover and arithmetic crossover, this paper uses the latter one, which was described below:

x_t^i and x_t^j $(i, j = 1,2,\cdots,n)$ are two individuals in population t, the new individuals would be generated according to the crossover operation shown by Eq. 13:

$$x_{t+1}^i = \alpha x_t^j + (1-\alpha) x_t^j \qquad x_{t+1}^j = \alpha x_t^j + (1-\alpha) x_t^i \tag{13}$$

Where α is the parameter for the crossover operation valued in the interval $[0,1]$.

③ Check the new individuals whether meet the constraints or not. Firstly, if $\sum_{k=1}^{m} x_{t+1}^{i(k)} > I_{load}$ or $\sum_{k=1}^{m} x_{t+1}^{i(k)} < I_{load}$, then distribute the margin $\sum_{k=1}^{m} x_{t+1}^{i(k)} - I_{load}$ or $\sum_{k=1}^{m} x_{t+1}^{i(k)} < I_{load}$ to m modules averagely. Secondly, check the individuals again with the step ③ described in chapter 3.2.

Mutation. Mutation refers to randomly change the value of certain genes of individual by a relatively small probability p_m, with the purpose of improving the local search ability of genetic algorithm.

The mutation operation is divided into two steps, firstly individual was selected at the probability of p_m. Then the selected individuals are put into the process of mutation. There are several mutations, including uniform mutation, non-uniform mutation, normal mutation and adaptive mutation, etc. The normal mutation is adopt by this paper and described below:

If $x_t^i = (x_t^{i(1)}\ x_t^{i(2)} \ldots x_t^{i(k)} \ldots x_t^{i(m)})$ is the selected individual in population X_t, and the gene k is the mutation point, then the newly individual after mutation is $\widehat{x_t^i} = (x_t^{i(1)}\ x_t^{i(2)} \ldots \widehat{x_t^{i(k)}} \ldots x_t^{i(m)})$, where $\widehat{x_t^{i(k)}}$ is determined by Eq. 14:

$$\widehat{x_t^{i(k)}} = Normal(x_t^{i(k)}, \sigma^2) \tag{14}$$

Where $Normal(x_t^{i(k)},\sigma^2)$ is a normal distribution random number generator with the mean of $x_t^{i(k)}$ and the standard deviation of σ.

In addition, the new individual $\hat{x}_t^i$ is also need to do constraints check as step ③ shown in chapter 3.4.

The values of mutation operator p_m cannot be too large, if $p_m > 0.5$, then the genetic algorithm will degenerate into a random search.

Termination condition. The termination condition of the algorithm proposed by this paper is that the global optimal solution kept the same for N_{sd} continuously evolutionary generations.

Case study and discussion

In order to verify the validity of RUL optimization model and the effectiveness of genetic algorithm, the following case was presented and discussed.

The paralleled Li-ion battery pack's initial parallel scale is $N=7$, expansion scale is $M=3$, the SOH of pack at the expansion point is $S_P=0.88$, and all the batteries' capacity fading follows the law described by Eq. 2.

The load current requirement is 8.0 C, the maximum discharge rate is 2.0 C, the SOH value of fresh battery is 100%, the ambient temperature is room temperature and keeps constant, and the difference between each model's SOH can be ignored. To sum up, the parameter value of optimization model (Eq. 7) as shown in Table 1.

TABLE 1. THE VALUE OF OPTIMIZATION MODEL PARAMETER

Parameter	t_0	S_P	N	M	I_{load}	I_{max}
Value	318 [K]	0.88	7	3	8.00 [C]	2.00 [C]

TABLE 2. THE VALUE OF GENETIC ALGORITHM PARAMETER

Parameter	n	m	β	p_c	α	p_m	σ	N_{sd}
Value	200	10	10	0.95	0.8	0.10	0.02	400

According to Table 1, both $\vec{T}$ and $\vec{S}$ are 1×10 vectors, equal $[t_0\ t_0\ t_0\ t_0\ t_0\ t_0\ t_0\ t_0\ t_0\ t_0]$ and $[S_P\ S_P\ S_P\ S_P\ S_P\ S_P\ S_P\ 1.00\ 1.00\ 1.00]$ respectively.

For the given optimization model, the parameter of newly designed genetic algorithm is shown in Table 2.

The result of optimization model solved by GA defined in Table 2 is showed in Fig 1.

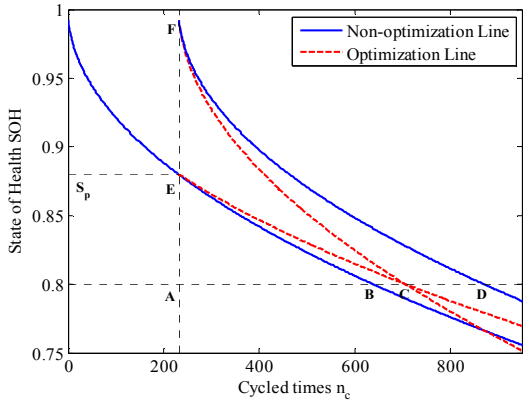

Fig. 1. The optimization Result ($S_P=0.88$)

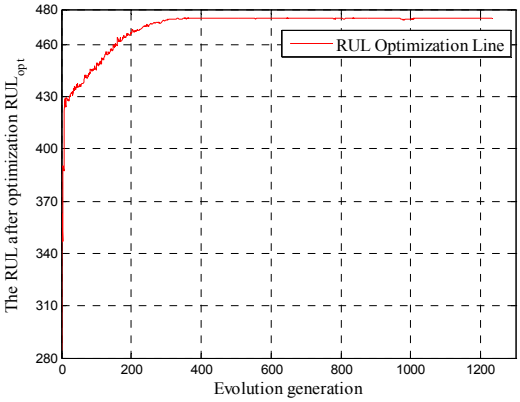

Fig. 2 The process of optimization for GA

As Fig. 1 shows, the load current is 5.6 C with each module shared 0.8 C at the beginning, and this value keeps constant before it increases to 8.0 C when the pack's SOH decreases to $S_P=0.88$ (point A). Faced with large load demand, the expansion decision is made, and the expansion scale is 3. The real line starts from point E and point F is the SOH fading line if the pack discharges in non-optimization mode, point B and point D represents the end of life point for the expanded and initial battery respectively; the dotted line starts from point E and point F is the SOH fading line if the pack discharges in optimization mode, point C indicates the end of life point for both expanded and initial battery. The discharge plan for every module in non-optimization mode is $[800\ 800\ 800\ 800\ 800\ 800\ 800\ 800\ 800\ 800]\times 10^{-3}$ C, the pack's RUL is the length of line AB, that is $RUL_{ini}=408$;

the discharge plan for every module in optimization mode is $[737\ 737\ 737\ 737\ 737\ 737\ 737\ 948\ 948\ 948]\times10^{-3}$ C, and the pack's RUL is the length of line AC, which is $RUL_{opt}=475$ (the process of optimization for GA is shown in Fig. 2); thus the increasing rate of RUL is $\Delta RUL=(475-408)/408\times100\%=16.67\%$.

In order to further discuss the optimization model, three main parameters in Table 1 S_P, M and I_{load} are adjusted, and the results are as follows:

① Set S_P vary at the step of 0.01 in $(1\ \ 0.8)$ with the others in Table 1 kept as constant, and each kind of circumstance is solved by GA with the result showed in Table 3. As Table 3 shows, the lower S_P, the higher ΔRUL, which indicates that the optimization is easily achieved for the pack with poor performance, and the main reason is that the poor pack's initial RUL is relatively small, so the growth could impact ΔRUL easily.

② Set M vary at the step of 1 in $[1\ \ 5]$ with the others in I kept as constant, the results is shown in Fig. 3. As Fig. 3 shows, the growth amount increases as M increases, indicating that increasing the expansion scale has a promoting effect on extending RUL.

③ Set I_{load} vary at the step of 1 in $[6\ \ 10]$ with the others in table I kept constant, the results is shown in Fig. 4. As Fig. 4 shows, the growth rate ΔRUL kept almost the same as I_{load} increases, indicating that ΔRUL has little relation on I_{load}.

TABLE 3. THE EFFECT OF S_P ON THE OPTIMIZATION RESULTS

S_P	RUL_{ini}	RUL_{opt}	ΔRUL	I_{low} / C	I_{high} / C
0.99	638	639	0.16%	0.800	0.801
0.98	633	635	0.32%	0.799	0.803
0.97	625	629	0.64%	0.797	0.808
0.96	614	621	1.14%	0.794	0.813
0.95	599	611	2.00%	0.791	0.821
0.94	581	599	3.10%	0.787	0.831
0.93	560	584	4.29%	0.782	0.843
0.92	536	567	5.78%	0.776	0.857
0.91	509	548	7.66%	0.768	0.874
0.90	478	526	10.04%	0.759	0.895
0.89	445	502	12.81%	0.749	0.919
0.88	408	475	16.42%	0.737	0.948
0.87	368	446	21.20%	0.722	0.983
0.86	325	414	27.38%	0.703	1.026
0.85	278	378	35.97%	0.680	1.079
0.84	229	339	48.03%	0.651	1.147
0.83	176	295	67.61%	0.612	1.239
0.82	121	245	102.48%	0.555	1.371
0.81	62	186	200.00%	0.461	1.591

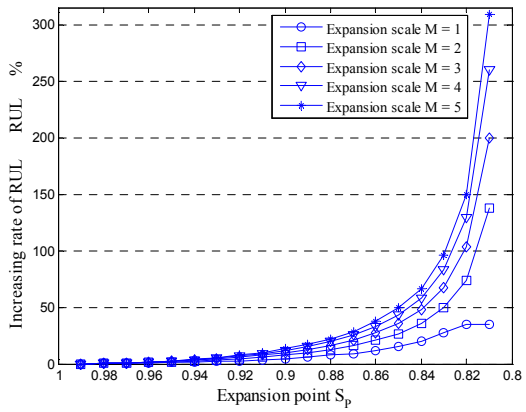

Fig. 3 The effect of expansion scale M on the optimization results

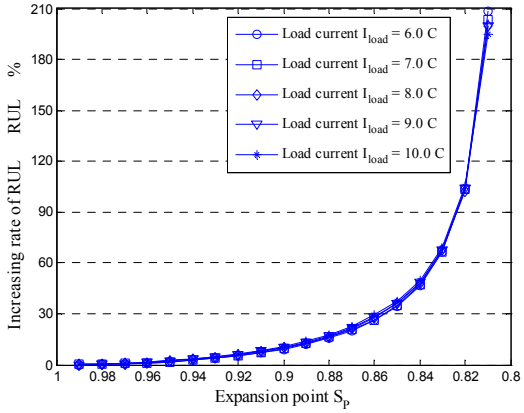

Fig. 4 The effect of load current on the optimization results

④ Parameter t_0 determines the degradation trend of SOH in Eq. 3, leaving some impact on the sensitivity of model, as literature [11] has analyzed the characteristic of parameter T in Eq. 2, this paper leaves this part out. Parameter N and I_{max} have similar effect on optimization results with parameter M and I_{load}, so this part is also omitted.

Conclusion

This paper analyzes the paralleled Li-ion battery pack's RUL under the conditions of expansion, the pack's RUL optimization model has been established based on the capacity fading model proposed in literature [11], for solving the model, the traditional genetic algorithm is improved by some special design, and finally the RUL optimization model and algorithm are analyzed and discussed in a case.

The case study proved that the pack's RUL can be extended and optimized by current distribution, and three rules are gained:

① The RUL growth amount and rate is larger if the expansion time is later (the pack's SOH value is low at the expansion point);

② The larger expansion of scale is, the higher RUL growth amount and rate are;

③ The load current is smaller, the RUL growth amount is larger, but the growth rate of RUL remains constant.

References

[1] A. Eddahech, O. Briat, E. Woirgard, and J. M. Vinassa, "Remaining useful life prediction of lithium batteries in calendar ageing for automotive applications", Microelectronics Reliability, vol. 52, no. 9, pp. 2438-2442, Sep. 2012.

[2] S. E. Samadani, R. A. Fraser, and M. Fowler, "A review study of methods for lithium-ion battery health monitoring and remaining life estimation in hybrid electric vehicles", SAE 2012 World Congress and Exhibition, pp. 41-56.

[3] B. Saha, K. Goebel, and J. Christophersen, "Comparison of prognostic algorithms for estimating remaining useful life of batteries", Transactions of the Institute of Measurement and Control, vol. 31, no. 3, pp. 293-308, Jun. 2009.

[4] C. H. Lin, H. Y. Chao , C. M. Wang, and M. H. Hung, "Battery management system with dual-balancing mechanism for LiFePO4 battery module", TENCON 2011 - 2011 IEEE Region 10 Conference, pp. 863-867.

[5] A. Keeli and R. K. Sharma, "Optimal use of second life battery for peak load management and improving the life of the battery", Electric Vehicle Conference (IEVC), 2012 IEEE International. pp. 1-6.

[6] J. Cao, N. Schofield and A. Emadi, "Battery balancing methods: A comprehensive review", Vehicle Power and Propulsion Conference 2008, pp. 1-6.

[7] T. Kim, W. Qiao and L. Qu, "Online SOC and SOH estimation for multicell lithium-ion batteries based on an adaptive hybrid battery model and sliding-mode observer", Energy Conversion Congress and Exposition (ECCE), 2013 IEEE, pp. 292-298.

[8] IEEE Recommended Practice for Maintenance, Testing, and Replacement of Valve-Regulated Lead-Acic (VRLA) Batteries for Stationary Applications, IEEE Standard 1188-1996.

[9] S. Shankar, D. Matthew, S. Abhinav and G. Kai, "Analytical algorithms to quantify the uncertainty in remaining useful life prediction", 2013 IEEE Aerospace Conference, pp. 1-11.

[10] F. Wang, B. Fan, S. Q. Liu, G. G. Qian, X. Huang and S. Han, "Attenuation test and duplication of power battery's cycle life", Journal of Automotive Safety and Energy, vol. 3, no. 1, pp. 71-76, Mar. 2012.

[11] H. L. Li and J. R. Su , "Cycle-life prediction model studies of lithium-ion batteries", Chinese Journal of Power Sources, vol. 32, no. 4, pp. 242-246, Apr. 2008.

[12] J. J. Grefenstette, "Optimization of Control Parameters for Genetic Algorithms", Systems, Man and Cybernetics, IEEE Transactions on, vol. 16, no. 1, pp. 122-128, Jan. 1986.

Advanced Materials Research Vols. 986-987 (2014) pp 1011-1014

doi:10.4028/www.scientific.net/AMR.986-987.1011

Deformation Characteristic Analysis on Crimping of Large Diameter Welding Pipe

Lifeng Fan [1, a], Ying Gao[2, b] , Jianbin Yun[3, c], Jiaxin Yan[1, d]

[1]Transportation of Institute, Inner Mongolia University, Hohhot, China

[2]College of Material Science and Engineering, Hebei University of Science and Technology, Shijiazhuang, China

[3]Product quality inspection institute of Inner Mongolia, Hohhot, Inner Mongolia China

[a]ysufanlifeng@foxmail.com, [b]gaoyingch@sina.com, [c]119356871@qq.com, [d]1577438681@qq.com

Keywords: crimping, welding pipe, finite element method, deformation Characteristic

Abstract. Crimping is widely used in production of large diameter submerged-arc welding pipes. In order to improve crimping forming quality, it is necessary to analysis deformation characteristic of crimping forming process. So, crimping is analyzed using finite element method.
Taking the crimping of X80 steel Φ1219mm×22mm×12000mm welding pipe for instance, the crimping forming process is simulated by finite element (FE) code ABAQUS. In this paper, the simulation data is validated by product and a comparison showed a good agreement with product results. The stress/strain from simulation is discussed. Thus, the results of research provides a basis to improve crimping quality.

Introduction

Crimping forming technology is widely used in large-diameter straight seam submerged arc weld (LSAW) pipes. In the forming process, both edges of sheet are bended into a certain curvature by crimping die. And the edges of sheet are made close to or reach the nominal curvature of pipe. The geometry and dimensional accuracy of final products are obtained. The peach beak and the cracking in expanding are prevented effectively by the crimping.

In the present investigation, several papers have been published dealing with these parameters and their effect on crimping quality. In early stage, the research on crimping is depended on experience in production[1, 2]. Although the results are an useful to guide production，they are lack of universality and difficult to promote in further. The analytical method of analysis is based upon simplifications of process and material behavior. There are following relevant literatures on the crimping: design parameters[3], bending moment/forming force[4], springback[5] and stress/strain[6]. With the advent of computation technology, simulation of crimping can be analyzed using finite element methods. So many scholars analyzed the effect of crimping to the pipe quality using the finite element method respectively, such as PALUMBO G [6], Liu [7], HERYNK M D[8] , TONG[9], GAO, [10] and REN[11]. Finite element analysis (FEA) is an efficient tool for researching crimping forming process. But the most significant disadvantage in the design of crimping parameters are time consuming.

The aim of this paper is to provides a basis to improve crimping quality. This research is based on the forming analysis performed by the commercial FEA code ABAQUS. By using FEA, the distribution of stress/strain before and after forming are obtained.

Finite element analysis

FEA of crimping was carried out using the commercial code Abaqus/Standard. A 2D finite element model is established for the plane strain condition. In simulation, the holders are defined as analytical rigid which would not need requiring elements is divided for simple geometric shapes. The

discrete rigid body and 2.5mm R2D2 element are defined in punch and die without considering the deformation. In analysis process of forming, one of the most important factors is the calculation of springback. So, considering both efficiency and accuracy in the deformation process, the 2mm four-node plane strain reduced integration quadrilateral element CPE4R which had high efficiency and accuracy for calculating springback is set in deformable sheet. The sheet metal is defined as elastic–plastic. Also, simple limited slid master-slave contact algorithm in which the mould was master surface, the sheet was slave surface is selected, and the penalty function model of friction coefficient 0.1 is established to judge the contacting state.

A welding pipe of X80 level Φ1219mm×22 mm×12000mm was taken as research objective. The Fig. 1 show the curve of true stress and strain X80 grade pipeline steel real, including E = 245 GPa, σ s = 569.5 MPa. In Fig. 5, finite element analysis is compared with the profile of sheet in top surface after crimping measured with a portable three-coordinate measuring system. The results are demonstrated that FEA could predict accurately the crimping profile. The crimping parameters in simulation are shown in table 1.

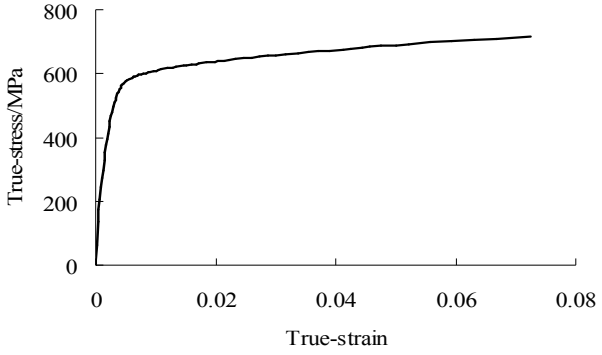

Figure 1 X80 uniaxial tension

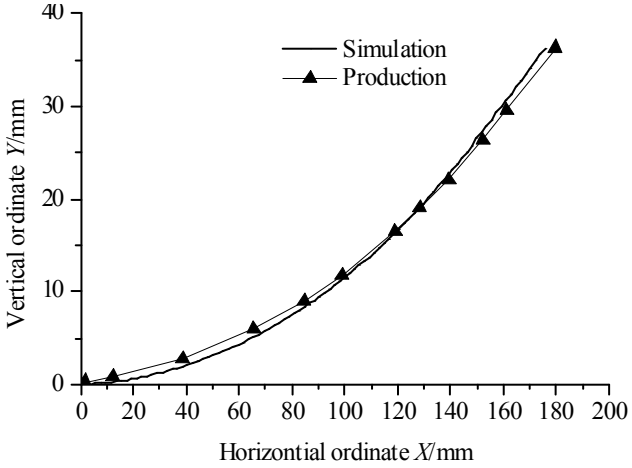

Figure 2 Comparison between simulation and production

Table 1 Parameters of the crimping simulation

Parameters	Description	Value
R_p /mm	Base radius of punch	303.20
β_p /°	Terminal angle of the punch	88
ρ_p/mm	Radius of curvature of the punch termination	465.7
R_d/mm	Base radius of die	303.20
β_d /°	Terminal angle of die	88
ρ_d/mm	Radius of curvature of the die termination	465.7
h/mm	Die displacement	42.1
B/mm	Length of crimping	190
D/mm	Horizontal distance between punch and die	80

Results and discussion

Distribution of stress Fig. 3 shows that the Mises stress is symmetrically along the sheet layer and the maximum Mises stress distributes at the top and bottom of sheet surface. The Mises stress in the tangential direction is increased with decreasing the radius of curvature gradually. Fig. 4 for geometry and residual stress distribution after unloading, from which it is known that the cloud is no stress no deformation near the edge of sheet.

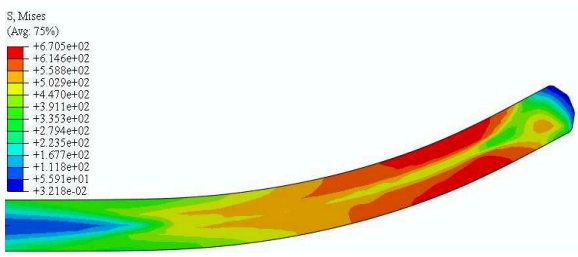

Figure 3 Mises stress of crimping in load

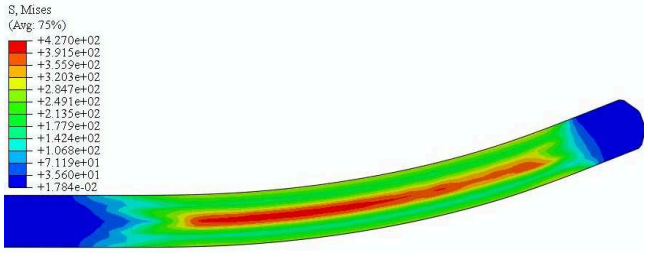

Figure 4 Mises stress of crimping after springback

Analysis of stress and strain The stress and strain value form simulation are researched in Fig. 5- Fig. 7. In Fig. 5, the Mises stress vary with horizontial ordinate which ranges from 0 mm to 190 mm. And the maximum Mises stress value $\sigma = 650MPa$ in upper surface and lower surface are at x = 130mm. From the trend of curve, it is indicated that the stress value increases with increased curvature. In Fig. 6, The curve of residual stress from surface showed that the value changes more gently and the residual stress fluctuation is less. The results indicated that after forming the stress is rearranged and the even distribution of residual stress is the main element to assure the crimping quality. In Fig. 7, The curve of plastic strain from surface can be divided into three parts: small deformation, main deformation and difficult-to-deformation. When x $45mm$, small curvature caused elastic deformation is larger than plastic deformation in small deformation part, so the plastic strain is little. When $45mm$ x $130mm$, most of the sheet material is yield and increasing of small curvature caused plastic deformation is larger than elastic deformation, so the plastic strain is maximum in main deformation part. When $x \geq 130mm$, decreases of Forming torque Increased the difficulty to occurr plastic deformation, so the plastic strain is decreases obviously.

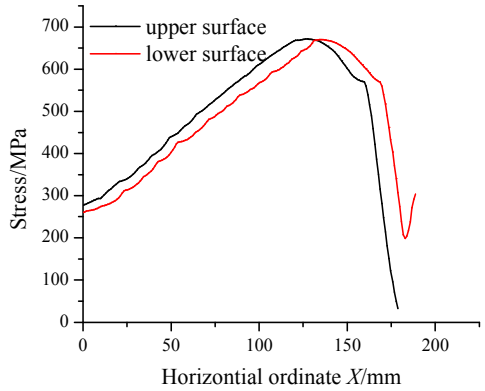

Figure 5 Curve of stress in horizontial ordinate

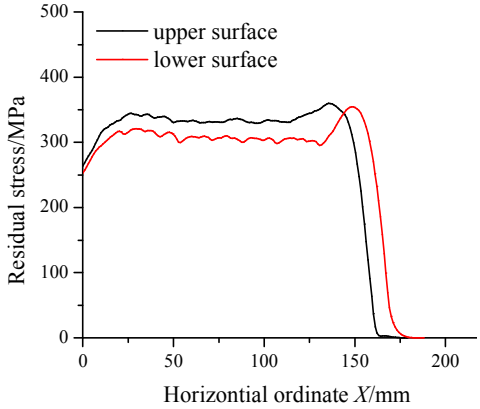

Figure 6 Curve of residual stress in horizontial ordinate

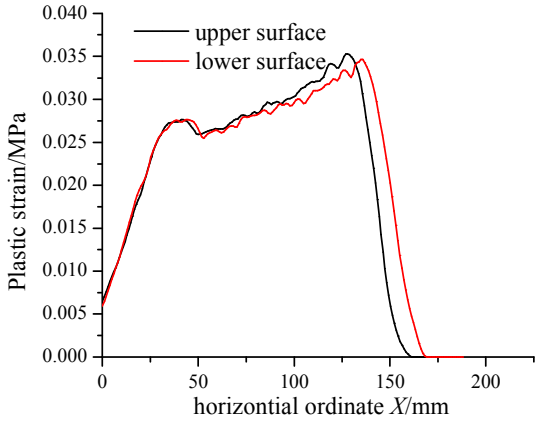

Figure 7 Curve of plastic strain in horizontial ordinate

It also can be seen that there is straight flange in the edge of sheet because of no stress and no deformation. In production, larger straight flange directly reduce the quality of welded pipe. So, it indicated that crimping forming process still needed to be improved.

Conclusion

In this paper, the following conclusions can be drawn:

(1) Crimping forming process is simulated by finite element (FE) code ABAQUS, and the simulation data is validated by product and a comparison showed a good agreement with product results.

(2) The distribution of stress and strain are investigated. Thus, the present work has been to study deformation characteristic of crimping forming for improving forming quality.

Acknowledgement

The authors are grateful for the financial support provided by the Program of Higher-level Talents of Inner Mongolia University, China(Grant No. 135143), The Scientific Research Projects of the Inner Mongolia Provincial Education Department (Grant No. NJZY14006) , the Natural Science Foundation of Hebei Provincial Education Department, China (Grant No. Y2012035) and the Natural Science Foundation of Hebei Provincial Technology Department, China (Grant No. 12211014).

References

[1] Hong Li. Prebending process of longitudinal submerged arc welding production line [J]. *Welding Pipe and Tube*, 2006, 29(1): 55-57(In Chinese)

[2] Zhimin Xie, Jinming Xia. Prebending process parameter design of longitudinal submerged arc welding pipe [J]. *Welding Pipe and Tube*, 2007, 30(3): 52-54(In Chinese)

[3] Shiyan Zhao. Study on quality control strategy and simulation system development of UOE pipe forming[D], Yanshan university 2010(In Chinese)

[4] Qiang Yang. Springback analytic and process parameters optimization of plate edge preflex for the forming of large diameter longitudinal seam welded pipe[D], Yanshan university 2012(In Chinese)

[5] Lifeng Fan, Ying Gao, Qiang Li, Hongshen Xu, Quality Control on Crimping of Large Diameter Welding Pipe. Chinese Jounal of Mechanical Engineering [J]. 2012, 25(6): 1264-1273

[6] G. Palumbo, L Tricarico. Effect of forming and calibration operations on the final shape of large diameter welded tubes. *Journal of Materials Processing Technology*, 2005, 164~165(5): 1089-1098

[7] Jinglei Liu, Kcjian Huang, Feng Ruan. Effects of the parameters of prebending on O-forming of pipe in UOE process [J]. *Journal of Plasticity Engineering*, 2005, 12(3): 72-75(In Chinese)

[8] M. D. Herynk, S. Kyriakider, A Onoufriou, et al. Effects of the UOE/UOC pipe manufacturing processes on pipe collapse pressure. *International Journal of Mechanical Sciences*, 2007, 49(5): 533-553

[9] Xiaogang Tong. *Study on groove shape and the open angle of end tab of UOE pipe* [D], 2008(In Chinese)

[10] Ying Gao, Qiang Li, Lifeng Fan. Finite element analysis of JCO forming process for longitudinal seam submerged arc welded pipes[J]. *Journal of Modelling, Identification and Control*, 2010, 11(3/4): 2

[11] Qiang Ren, Dayong LI, Tianxia Zhou, et al. The simulation of UOE pipe forming by three-dimensional finite element method[J]. *Journal of Netshape Forming Engineering*, 2011, 3(6): 80-84(In Chinese)

Advanced Materials Research Vols. 986-987 (2014) pp 1015-1018

doi:10.4028/www.scientific.net/AMR.986-987.1015

Research on the Lithium Battery Pack Cooling by Thermal Simulation

Yining Chen[1, a], Ceyuan Li[2, b]

[1] Power Management of Liaoning Provincial Government, Shenyang 110035, China;

[2]State Key Laboratory of Automotive Simulation and Control, Jilin University, Changchun 130022, China.

[a]cyn5853@163.com, [b]1002856086@qq.com

Keywords: Lithium-ion Battery Pack Thermal Characteristic, Thermo Physical Parameters, Temperature Field Simulation, Experimental Verification.

Abstract. Batteries are used the energy storage of the pure electric vehicle. When the battery pack work in the high temperature environment for a long-term, permanent damage that high temperature does to the battery cannot be restored, the battery life will be drastically reduced. When the batteries temperature reaches a relatively high value, the battery pack will caught fire. This paper firstly analyzed the characteristic of the Lithium-ion Battery by batteries experiment. On the basis of the thermal experiment ,this paper do a lot of research of the cooling method by ANSYS and verified the accuracy of the model of the thermal model.

Introduction

In recent years, because the energy crisis and environmental pollution are worsening, all countries put a lot of energy and money to accelerate the commercialization process of pure electric vehicles. As the only source of power for electric vehicle, the battery performance directly affects the use performance of electric vehicles. Because environmental temperature has a significant influence on the performance of the batteries, battery pack thermal management technology, which regards the control of the battery internal temperature range and uniformity as the goal, becomes an important research topic.

The ambient temperature is the main factor which affects the performance of lithium batteries. When the temperature is relatively high, a large current discharge causes the battery pack temperature rises too fast. Although the high temperature will cause the speed of battery pack chemical reaction become faster, but also will cause great harm to the battery pack. High temperatures cause the battery generate irreversible internal substance, which makes the battery life reduced.

Experimental study on the thermal characteristics of the battery

Noboru Sato analyzes the causes of lithium battery generating heat, summed up the heat source of lithium battery[1]. the specific heat production is calculated as shown in Formula1.

$$Q_t = Q_r + Q_p + Q_s + Q_j \tag{1}$$

Among them, Q_t is the total heat production of lithium battery, Q_r is the chemical reaction heat lithium ion and electron transfer generate in the reaction, Q_p is the heat generated from the difference between cutoff voltage and the balance voltage, which is called polarization reaction heat, Q_s is called the vice reaction heat generated by the electrolyte electrolysis in lithium battery charging and discharging process or the discharge side reaction which is called a sub-reaction, Q_j is the Joule heat generated by the internal resistance of lithium battery.

Beinad etc. see lithium battery as a uniform internal heat production[1], Base on the lithium battery internal resistance and reaction principle of entropy increase, Beinad proposed a theoretical formula to calculate the rate of heat generation of lithium battery, as specified shown in Equation2.

$$\Phi = -IT\frac{dE}{dT} + I(E-V) \tag{2}$$

$-IT\frac{dE}{dT}$ is lithium battery reversible reaction heat, I(E-V) represents the ohmic resistance or irreversible thermal reaction, I is lithium battery charge and discharge current, E is the open circuit voltage of the lithium battery, T is the inside temperature of the lithium battery, V is the voltage.

Research on the thermal Simulation of lithium batteries pack

This paper does some research on the Lithium battery temperature field by a three-dimensional thermal model. Assuming that each part of the material inside the battery properties are consistent, thermal conductivity, etc. is approximately constant in the process of charging and discharging , we can obtain lithium battery heat model[3][4]:

$$\rho C_p \frac{\partial T}{\partial t} = k_x \frac{\partial^2 T}{\partial x^2} + k_y \frac{\partial^2 T}{\partial y^2} + k_z \frac{\partial^2 T}{\partial z^2} + q \tag{3}$$

ρ represents an average density of lithium batteries ,T represents the temperature of the lithium battery, C_p is the lithium battery specific heat capacity, t represents time, respectively, K_x,K_y,K_z represents the thermal conductivity inside lithium battery.

This paper designs the battery pack cooling system, using CFD simulation software to study the effects of battery pack cooling structure on the battery pack temperature field. Firstly,this paper establish the batteries model, Natural cooling model is showed in the Fig.1.

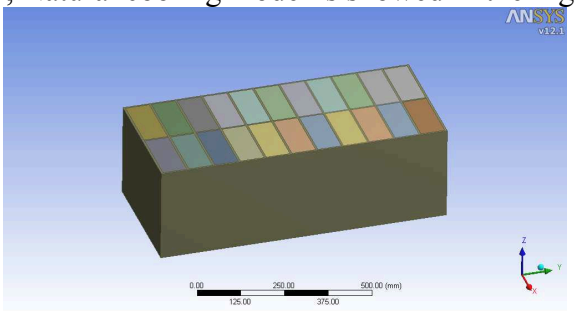

Fig.1 Natural cooling model

In the natural convection simulation , air movement of the lithium battery surface and flow field wall are selected as natural convection ,heat transfer coefficient is set as 4w/m^2.K ,air and lithium battery pack contacts are set as fluid and structure interaction. Figure2 is lithium battery use 120A discharge one hour natural cooling results. Figure3 is a lithium battery serial cooling temperature field simulation, the simulation discharge current is set as 120A, the convective heat transfer coefficient is 10w/m2.k, air is from the left into the battery pack.

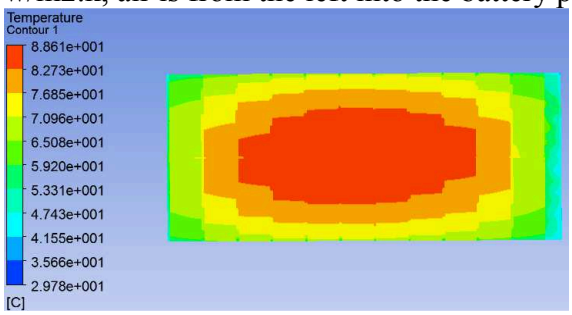

Fig.2 Natural cooling simulation result

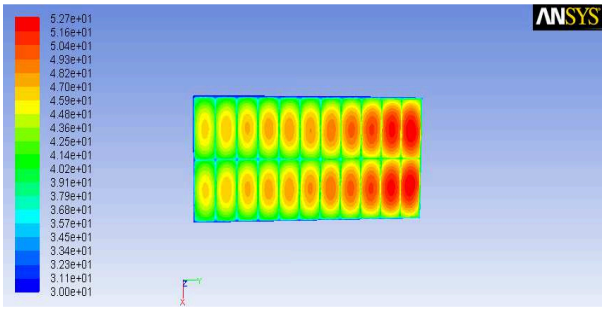

Fig.3 String-type cooling simulation result

From the results in Figure 2, when lithium battery pack use 120A discharge one hour and outside temperature is 30℃, the batteries maximum temperature reaches 88℃, which will cause serious damage to the batteries. Figure 3 is the result of battery pack serial cooling. From this result, it can be seen that the maximum temperature of the battery pack is reduced to 57℃, but the temperature uniformity of the battery pack become worse.Therefore, the battery pack must be designed thermal structure.

In order to solve the heat problem, this paper designs the following cooling structure, gray part is the battery box, blue part represents the battery pack ,the structure is shown in Fig.4.Fig.5 is Battery pack and air field simulation model.

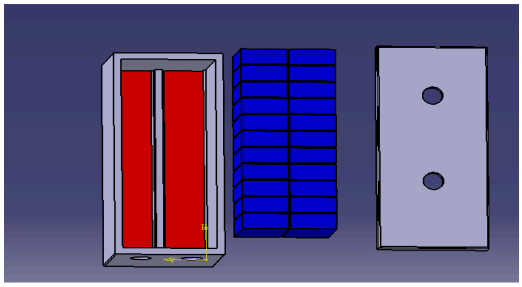

Fig.4 Arrangement relationship between batteries and battery box

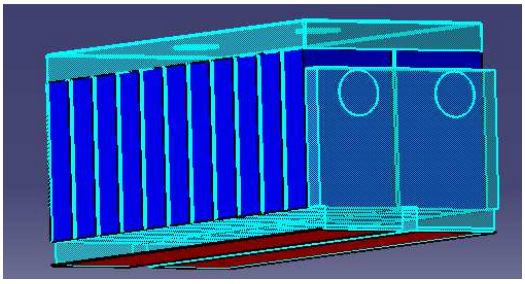

Fig.5 Battery pack and air field simulation model

This paper study temperature field of the design of the thermal structure by the CFD simulation, the simulation results show that although this structure can effectively reduce the temperature of the battery pack, but can cause the temperature dead zone of battery pack. Figure 6 is the temperature contours of the lithium battery center plane, the simulation conditions were set: time is 20min; current is 120A;the wind speed is 8m/s.

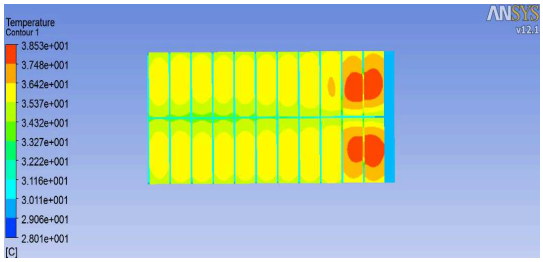

Fig.6 Battery pack and air field simulation model

In order to remove the dead zone temperature caused by heat dissipation structure, This article improves the cooling structure by installing the windshield at the bottom of battery box, Improvements are shown in the following two figure.

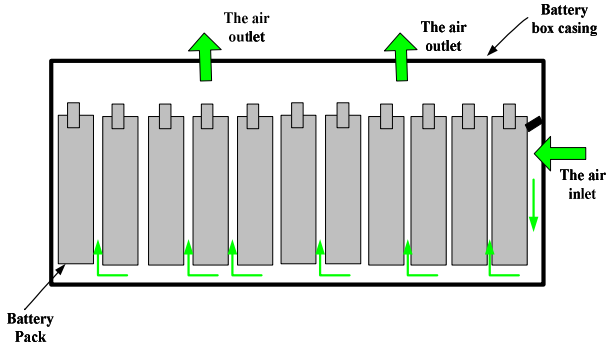

Fig.7 Air flow field before improvement

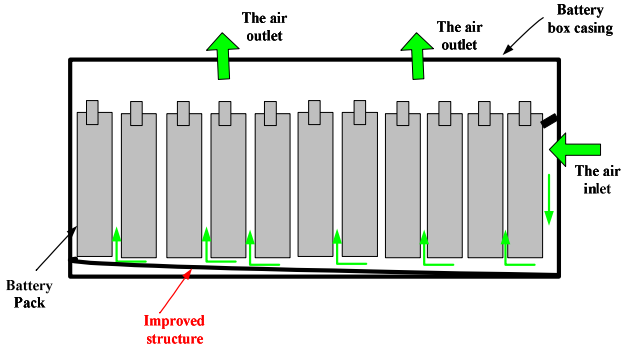

Fig.8 Air flow field after improvement

Improved structure significantly improves the battery pack cooling temperature uniformity, Fig.9 is the temperature contours of the lithium battery center plane, the simulation conditions were set: time is 20min; current is 120A;the wind speed is 8m/s.

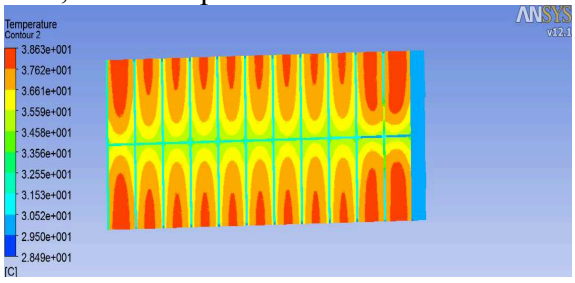

Fig.9 Battery pack and air field simulation model

Thermal model experimental verification

Figure 11 is the comparison chart of monitoring points temperature obtained by experiment and ANSYS simulation results of lithium battery pack, simulation and experiment conditions are set Consistent : discharge current is120A, time is half an hour, cooling wind speed is 5m/s. Figure 10 is the layout of the cooling test temperature sensor.

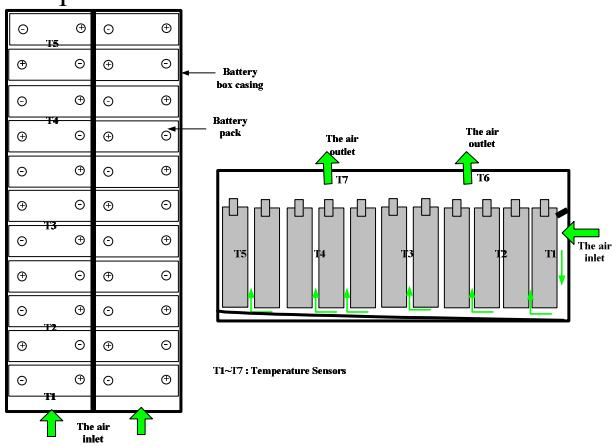

Fig.10 Cooling test temperature sensor layout

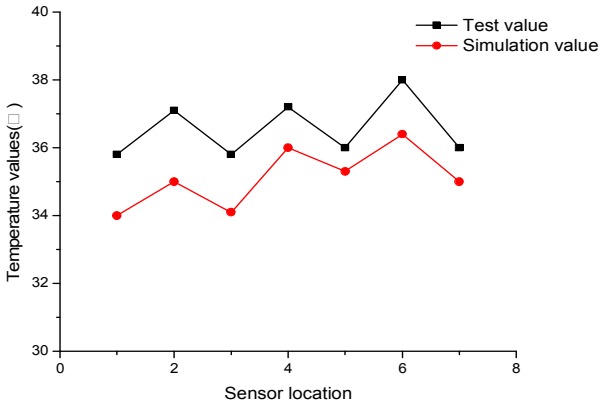

Fig.11 Cooling test temperature sensor layout

Summary

This paper do some theoretical analysis on the battery pack's internal heat production and designs a cooling structure of the battery pack, and improves and optimizes the structure, finally validates the accuracy of the cooling simulation system through experimental study.

References

[1] Noboru Saco.Thermal behavior analysis of lithium-ion batteries for electric And hybrid vehicles[J].Journal of Power Sources,2001,99:70-77.

[2] Kim Yeow, Ho Teng, Marina Thelliez, Eugene Tan.Thermal Analysis of a Li-ion Battery System with Indirect Liquid Cooling Using Finite Element Analysis Approach[J].SAE Int.J.Engines,2010,3(2): 65-78.

[3] Michael R. Giuliano, Suresh G. Advani, Ajay K. Prasad∗. Thermal analysis and management of lithium–titanate batteries[J]. Journal of power sources, 2011,196: 6517-6524.

[4] Hongguang Sun∗, XiaohuiWang, Brian Tossan, Regan Dixon. Three-dimensional thermal modeling of a lithium-ion battery pack[J].Journal of power sources,2012,206: 349-356.

Advanced Materials Research Vols. 986-987 (2014) pp 1019-1022

doi:10.4028/www.scientific.net/AMR.986-987.1019

A research on superheater mechanism model of intelligent optimization based on spot data

Changliang Liu[1, a], Meng Ni[2, b]

[1]State Key Laboratory Of Alternate Electrical Power System With Renewable Energy Sources (NCEPU)

[2]School of Control and Computer Engineering, North China Electric Power University, Baoding 071003, China

[a]email:changliang_liu@163.com, [b]email:15100209669@163.com

Keywords: Nonlinear; Mechanical Analysis; Superheater; Particle swarm optimization

Abstract. In order to solve the problems of strong coupling and nonlinear parameters of superheater model, in this paper, we aimed at a 600MW subcritical drum boiler high temperature superheater as the object of study .On the basis of mechanism analysis and its dynamic characteristics I built a dynamic model of high superheater contains 9 typical working conditions .I optimized the model parameters by using field data. A continuous nonlinear model is obtained by curve fitting. The simulation results show that superheater model built by this method can better simulate the field characteristic. This model provides a reference design of automatic control system of main steam temperature .This paper aims to provide the basis for the application of advanced control algorithms in the field. Furthermore, this model can provide higher accuracy for on-site training to improve training effect.

Introduction

Summarize the existing in Superheater model as followed, Yongsheng Fan, Zhigao Xu proposed a Transfer function of the 600MW concurrent boiler to simulate the dynamic characteristics of different working conditions in 1997[1]. According to this theory provides a new idea for nonlinear models .As different working conditions of transfer function is calculated by manual work, not through the optimization parameter identification .Therefore this model may lack of precision .Pu Han in 1994 proposed an experimental method to obtain the object of Dynamic characteristics .Including the step response method with correlation analysis and identification methods [2]. Literature [3] discusses the application of genetic algorithm in thermal process identification .But did not resolve the problem of nonlinear thermal model. Literature [4] presented an automatic optimization algorithm framework parameter thermodynamic system model based on genetic algorithm and neural network .Providing a simple and practical method for the thermal power plant simulator mathematical modeling and parameter optimization .Document [5] by the research of data mining rough set reduct, using the quantum Particle swarm optimization, parametering the main steam temperature transfer function, finally get accurate results.

Superheater Mechanism Model

In order to make the model simplified making the following assumptions in this paper:

- All of the parallel tube is equivalent to a heated tube.
- The metal tube has the same temperature. Neglect the axial changes in metal temperature.
- As a medium in the pipe flow along the length direction.

These assumptions can make the model simplified maximum based on the right to reflect the main physical phenomena .The mass conservation equation (1), energy conservation equation (2), the unit length of metal heat balance equation (3) and the unit length of metal pipe medium heat equation (4) which can be used to develop the boiler.

$$\frac{\partial D}{\partial y}-(\frac{F}{v^2})(\frac{\partial v}{\partial \tau})=0 \tag{1}$$

$$Q_2=\frac{\partial(\mathrm{DH})}{\partial y}+F\frac{\partial(\rho u)}{\partial \tau} \tag{2}$$

$$Q_1-Q_2=m_j c_j\frac{\partial T_j}{\partial \tau} \tag{3}$$

$$Q_2=\alpha_2\pi d_2(T_j-T)=\alpha_2 a_2(T_j-T) \tag{4}$$

The above formula, Q_1 representative absorption of heat pipe wall; Q_2 is released to the steam heat pipe wall; a_2 is the unit length of pipe inner surface area; d_2 as the inner diameter of the pipe; T_j and T is a metal and medium temperature; α_2 is exothermic coefficient; m_j is metal mass per unit length of pipe; c_j is the metal specific heat; D is the medium flow; v as a medium specific heat capacity; F is the cross-sectional area; y as the tube length.

We can be obtained by using single phase relative variables represent the dynamic equations of heat pipe by equation (1) (2) (3) (4) linear .In order to get the expression of η enthalpy, we can use the time τ for variables on Laplasse change with the equations been linearized .Then we can get the equation (5).

$$\eta_2(s)=\frac{1}{1+T_m s}e^{-\frac{a^*}{2}\frac{shB}{B}}q_1(s)-\left\{\frac{c^*}{b^*}\left[1-e^{-\frac{a^*}{2}\left(chB+\frac{a^*}{2B}shB\right)}\right]-\frac{FP_0}{Q_0}e^{-\frac{a^*}{2}\frac{shB}{B}s}\right\}$$

$$+p(s)e^{-\frac{a^*}{2}\left(chB-\frac{a^*}{2B}shB\right)}\eta_1(s)+\frac{1+(1-n)T_m s}{1+T_m s}e^{-\frac{a^*}{2}\frac{shB}{B}}d_1(s) \tag{5}$$

Obviously equation (5) has a transcendental function in the form of the transfer function and very complex .It also needs to simplify. It can be assumed that the medium heat capacity v remain unchanged .And take an entire section of the inlet and outlet of the arithmetic mean value .So $T_a=0$ $b^*=0$ and (5) can be simplified as follows.

$$\eta_2(s)=e^{-\tau_0 s-\frac{\alpha_d T_m s}{1+T_m s}}\eta_1(s)-\frac{1+(1-n)T_m s}{T_a s(1+T_b s)}\left(1-e^{-\tau_0 s-\frac{\alpha_d T_m s}{1+T_m s}}\right)d_1(s)$$

$$+\frac{1}{T_a s(1+T_b s)}\left(1-e^{-\tau_0 s-\frac{\alpha_d T_m s}{1+T_m s}}\right)q_1(s) \tag{6}$$

By formula (6) can get the relationship between $\eta_1(s)$ and $\eta_2(s)$ for (7).

$$\frac{\eta_2(s)}{\eta_1(s)}=e^{-\tau_0 s-\frac{\alpha_d T_m s}{1+T_m s}} \tag{7}$$

From the formula can be pushed to the transfer function (8) of the superheater outlet temperature and water flow.

$$\frac{T(s)}{D_{sp}(s)}=-Ke^{-\tau_0 s-\frac{\alpha_d T_m s}{1+T_m s}} \tag{8}$$

$$K=(I_1-I_{sp})/(D\cdot C_{p2}) \tag{9}$$

The above formula, I_1 and I_{sp} as the water steam enthalpy and the enthalpy of water; C_{p2} is the link of export of specific heat at constant pressure.

Identification of Superheater Transfer Function in Different Working Points

The research object of this paper is the high temperature superheater of a 600MW subcritical boiler. Therefore we choosing 50%, 57%, 65%, 73%, 80%, 83%, 92%, 97% and 100% working condition data for research .Formula (8) can be approximated by higher-order inertia link (10).

$$G(s)=\frac{K}{(1+Ts)^n} \tag{10}$$

The transfer function of the use of particle swarm algorithm (10) identification in the MATLAB environment .We finding out the temperature transfer function of water disturbance with nine typical load point .As shown in TABLE I

TABLE I. THE DYNAMIC CHARACTERISTICS OF WATER JET DISTURBANCE IN TYPICAL WORKING CONDITION

Load	main steam flow (t/s)	Pilot area （℃/kg/s）	Inert area （℃/℃）
50%	830	$-2.2564/(1+700s)^2$	$1.1498/(1+399s)^4$
57%	961	$-1.8478/(1+626s)^2$	$1.2299/(1+368.6759s)^4$
65%	1106	$-1.3199/(1+511.5374s)^2$	$1.0756/(1+316.905s)^4$
73%	1270	$-1.1251/(1+543.9224s)^2$	$0.9272/(1+300s)^4$
80%	1370	$-0.7358/(1+557s)^2$	$0.799/(1+327.4529s)^4$
83%	1440	$-0.6893/(1+531.7262s)^2$	$1.2952/(1+300s)^4$
92%	1608	$-0.6537/(1+520.48s)^2$	$1.7966/(1+210.8951s)^4$
97%	1713	$-0.5378/(1+513.0724s)^2$	$1.4252/(1+157.3597s)^4$
100%	1800	$-0.5362/(1+406.1298s)^2$	$1.8153/(1+115.772s)^4$

A Nonlinear Model of Superherater

From the TABLE I we can see that the relationship between leading region gain and the main steam flow should be through 9 points. Function as shown in Figure 1 and the Function relation:

$f_1(x)=0.0662x^3-2.3442x^2+7.5809x-6.986$

Empathy can be obtained with the pilot area time constant of the main steam flow .Shown in Figure 2 and the Function relation: $f_2(x)=-162.52x^3+652.45x^2-864.62x+432.15$

Similarly we can get the relation curve of the inert region gain and the main steam flow .Shown in Figure 3 and the Function relation: $f_3(x)=-0.8296x^3+5.2721x^2-8.7861x+5.3826$

Similarly we can get the relation curve of the inert zone time constant and the main steam flow .Shown in Figure 4 and the Function: $f_4(x)=-703.1488x^3+252.93x^2-314.46x+116.91$

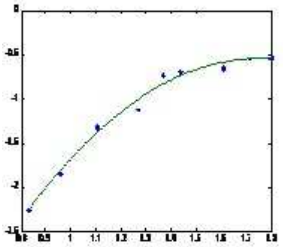

Figure 1
Pilot area gain

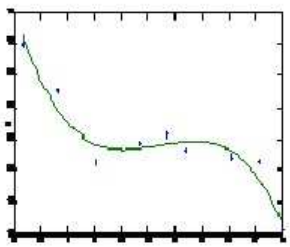

Figure 2
Pilot area time

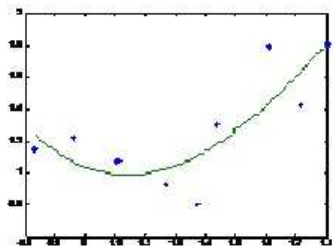

Figure 3
Inert area gain

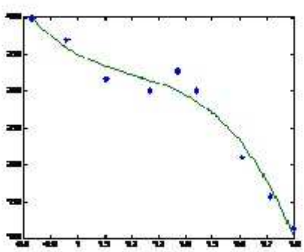

Figure 4
Inert area time

Figure 5 is a block diagram of a nonlinear model and the Fnc1 to Fnc4 corresponding $f_1(x)$ to $f_2(x)$. Getting a wider range of model because the model according to the current main steam flow to calculate the transfer function of the corresponding .The operation results in any condition of the model, as shown in Figure 6 .We can see tracking characteristic of this model is great .Because the system is not only in operation for several operating points, with the help of a new model can describe any working condition.

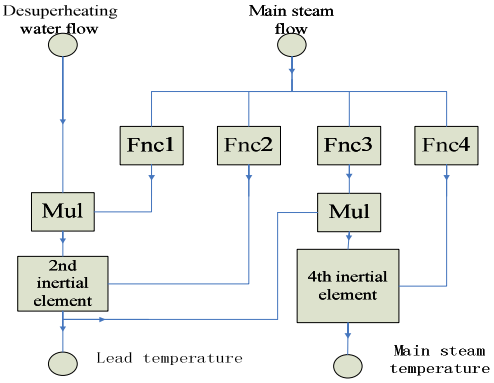

Figure 5
Model diagram

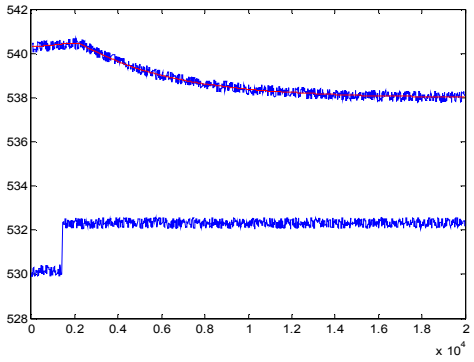

Figure 6
Simulation result

Conclusion

In this paper, with a power plant boiler superheater temperature controlled object for research background, I explored a method of modeling which can describe a class of nonlinear systems .The dynamic characteristics of the superheater temperature controlled object that can be described by a unified mathematical model .This model avoided some technical problems when using piecewise linear modeling with a plurality of transfer functions.

Acknowledgement

This paper is supported by State Key Laboratory of Alternate Electrical Power System with Renewable Energy, the Fundamental Research Funds for the Central Universities (13MS102), National Natural Science Foundation of China(61203107), National Key Technology Support Program (2012BAA12B06).

References

[1] Yongsheng Fan, Zhigao Xu, Laijiu Chen. Research on adaptive fuzzy control system of boiler superheated steam temperature based on dynamic mechanism analysis. Chinese. Proceedings of the CSEE, 1997,01:23-28

[2] Pu Han, Jizhen Liu, Ze Dong.Research and application of thermal process modeling methods [J].Journal of north China institute of electric power, 1994, 11:87-92..

[3] Jin Ma, Bingshu Wang, Liping Li, Ning Cui. Research on parameter optimization method of superheater mechanism model genetic algorithm [J]. Journal of system simulation, 2008, 09: 2433-2436

[4] Changliang Liu, Xining Yu,Wanye Yao,Jizhen Liu. Thermal power plant process model identification based on genetic algorithms[J]. Chinese Society for Electrical Engineering, 2003,03:170-174.

[5] Pu Han, Shitong Yuan, Jinying Zhang. Research on Modeling of ultra supercritical boiler main steam temperature control system[J]. Computer simulation, 2013,12:115-120.

Advanced Materials Research Vols. 986-987 (2014) pp 1023-1025

doi:10.4028/www.scientific.net/AMR.986-987.1023

Analyze for Design Philosophy on the Route and Process for Gas Pipeline in the Middle-Asia District

Wei He[a], Guoxing Wang[b], Changhua Ji[c], Yunfeng Gong[d]

146 He Ping Road, Lang Fang City, He Bei Province, China

[a] hew202309@126.com, [b]cppewangguoxing@gmail.com, [c]23048356@qq.com, [d]75335677@qq.com

Keywords: middle-asia district, pipeline layout, process scheme, wall thickness selection, SNIP, ASME, design feature, difference, analyze

Abstract. According the experience of gas pipeline project in the Middle-Asia district, the writer analyzes and concludes the design feature for the pipeline route and the process scheme for the gas pipeline project in the Middle-Asia district. For the requirement of code SNIP, ASME and Chinese specification, the writer analyzes the difference and design feature on the design requirement and draws the conclusion. The pipe grade, design parameter, wall thickness selection and the process design for station are detailed described in the article, which can expand the design thought and provide the reference for the similar project.

Introduction

As the project increasing in the Middle-Asia district, the design philosophy and the code are difference with European and America districts. The SNIP code system of Russian is adopted in these districts which are difference with the code system of ASME code. So, the feature and difference are obvious in the design of route and process of gas pipeline.

Design feature and Analyze

Pipeline grade and design factor

On the choosing of pipeline grade and the design factor of pipe wall thickness, it is decided by the purpose and scope of the position and line pipe laying location in the SNIP code. In the ASME code, the location class is a geographic area along the pipeline classified according to the number and proximity of buildings intended for human occupancy and other characteristics that are considered when prescribing design factors for construction, operation pressures and methods of testing pipelines and mains located in the area and applying certain operating and maintenance requirements. For the details of SNIP code are as follows:

Table 1 Pipeline grade distribution

Pipeline grade	Factor on Strength, stability and working conditions of pipeline	Scope（for example）
B	0.60	Compressor stations, gas pressure reducing station, underground gas stations, gas stations, gas metering station；
I	0.75	Waters wear across segments, railway and road wear crossing segments, the swamp crossing segment; pigging transceiver station and 100m long pipe connected thereto; gas pipeline hub is turned on, compressor station inlet outlet pipeline
II	0.75	Pipeline block valve station and the length of 250m from the valve center to both side, crossing with the underground pipe and cable
III	0.90	Diameter of pipe is more than 1200mm, northern climate construction area, grade V road
IV	0.90	Diameter of pipe is less than 1200mm

Calculation of wall thickness

On the pipe wall thickness calculation scheme, calculated formulas between SNIP norms and ASME code system are not the same. the author calculate the wall thickness using the design parameters for the same conditions, according to a different formula to calculate and compare different diameters, can analyze the basic trends: for grade B pipe, wall thickness calculated according to SNIP norms is in the middle of result between factor of 0.4 and 0.5 by the ASME B31.8 Code; for grade I pipe sections, wall thickness calculated according to SNIP norms is in the middle of result between factor of 0.5 and 0.6 by the ASME B31.8 Code. For the details, please see the following table:

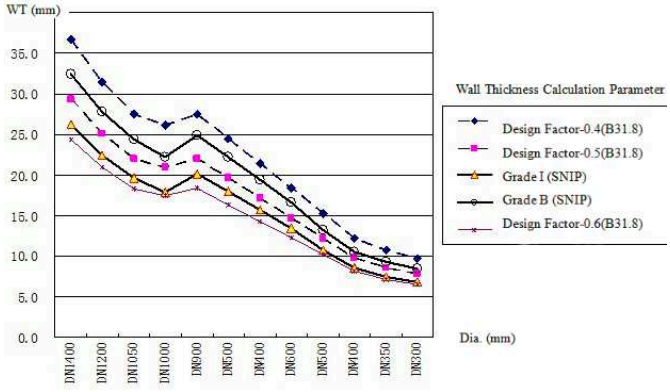

Fig.1 Calculate the wall thickness comparison chart

Block valve station

For the ordinary pipeline block valve station design, which must have an emergency shutdown automatic device or remote control function according to the SNIP standards, emergency shutdown devices should drop rate decreased by 10% to 15% within 1 to 3 minutes, the distance for the adjacent block valve stations shall be not more than 30Km. But, according to ASME standards there is no explicitly requested block valve station need to have emergency shut-off function drop rate, the distance of adjacent block valve stations is designed in accordance with the regional class, as follows: in the class I region, the distance shall be not more than 32Km, in the class II region, the distance shall be not more than 24Km, in the class III region, the distance shall be not more than 16Km, in the class IV region, the distance shall be not more than 8Km.

For the Compressor Station downstream protection valve station design, the block valve station shall be installed in the 750m of upstream and downstream of the gas pipeline to protect the compressor station and shall be remote controlled by compressor station; But, according to ASME standards there is no explicitly requested block valve station to install, only the minimum distance is not more than 8Km.

Venting pipe

In SNIP code, the distance between the venting pipe and the block vale is clearly defined: if the diameter is less than 1000mm, the distance is not less than 15m, if the diameter is more than 1000mm, the distance is not less than 50m, and the distance from other buildings or structures shall be not less than 300m. the ascertain of vent pipe diameter should meet the finish venting empty of adjacent trunk line section in the 1.5 ~ 2h, the height of venting pipe from the ground is not less than 3m. Due to security requirements from a large set of vent shorter and lower height, the torch is generally not adopted. In the ASME code, the height of venting pipe shall be not less than 10m above the natural ground.

Pig trap station

According to SNIP code, pig trap stations are separate with the compressor stations and the distance is not less than 200m.the condensate collector shall be set and the filter separating device shall be set in the compressor station. The condensate collector can use the same wall thickness pipe in the class I section, the features including venting with liquid loading, vacuum purge, clean up the bottom of the tube, sampling and level display.

According to the ASME code, pig trap station and compressor station can be set in the same yard, the cyclone separation and filtration equipment shall be set in the pig trap station.

Gas metering device

According to SNIP code, the gas flow metering station shall be set on the bypass pipe of gas pipeline. for accurate measurement requirements, Transmission Pipeline Set double valve to protect the measurement accuracy. When pigging, open Trunk line valve, but do not close the metering station and export valve. Since the pigging device does not set, some gas can not be measured during the pigging, the main solution for the calculation of time through ball and pass the ball stage based on the average output rate can be calculated pass the ball during the bypass flow. But in the ASME code, The bypass line does not allow to set and the pig trap devices must be set.

Gas purifying device

For the SNIP standards, specifications require the use of dust on the gas purification level, after three to five compressor stations for individual compressor stations, usually filter - gas separator for secondary purification. The above requirements are different setup with ASME which requires the cyclone filter and filter separator set in each compressor stations.

Lube stock

For SNIP standards, the cleaning oil tank (not less than $50m^3$) and waste oil tank (not less than $25m^3$) shall be set in the lubrication stock on compressor station, and a fuel pressure unit to supply clean oil to the fuel pump and libraries waste tank pumping waste oil pump. lubricants plant set in a separate compartment near the fuel pressure unit. ASME specification does not require oil workshop set.

Safe distance of compressor station

For SNIP standards, compressor stations and gas transmission lines need to follow the safety distance requirements for the design. for the 1000mm diameter pipeline, the pressure of the gas station and trunk spacing is not less than 225m, shift quarters and trunk spacing is not less than 300m, shift dormitory and compressor stations is not less than 700m, each compressor stations shall have a tarmac.

Summary

Listed in this article are just some of the main features and differences in line and process design encountered in practice. With the development of the CIS, the current Middle Asia countries revise their specifications in accordance with their characteristics. because its specifications system is very complex, these should be integrated in the design process analysis problems encountered and should not be applied mechanically.

References

[1] SNIP 2.05.06-85 Trunk pipeline design specifications

[2] SNIP-85 Trunk pipeline process design specification

[3] ASME B31.8-2007 Gas Transmission and distribution Piping System

[4] KMK2.3.06-97 Code for Design of Trunk pipeline Engineering

[5] KMK 3.06.08-97 Trunk Pipeline Construction and Acceptance Specification

Advanced Materials Research Vols. 986-987 (2014) pp 1026-1028

doi:10.4028/www.scientific.net/AMR.986-987.1026

Research and simulation of energy-saving hierarchical design model for differentiate architecture

Guo haiqing

Inner Mongolia Technical College of Construction，Hohhot, Inner Mongolia，010070）

Keywords: building energy-saving; energy consumption; evaluation indicator system

Abstract: Energy-saving hierarchical design model is established for differentiate architecture. From current status of China's construction, exploration research is established on energy-saving hierarchical design model of differentiate architecture to evaluate indicator system of energy-saving building. Availability of evaluation information in index system is low, so it is difficult to play the role of evaluation of building energy-efficiency. EHTV difference method is used to calculate and evaluate energy-saving design of hierarchical building, including: heat transfer indicator of building envelope targets, air conditioning and heating consumption, basis of EHTV indicators.

1 Introduction

In the background of the depletion of non-renewable energy, building energy economy accounts is about 30% (20% to 25% in our country) of the total energy consumption, which gains concern of all walks of life [1,2]. Many countries have made clear legal provisions in energy consumption and developed a variety of assessment methods and technical standards [3]. China in the early 1980s began to promulgate the relevant national and industry standards, due to the lack of necessary evaluation system of building energy consumption and effective measures to regulate building energy efficiency standards, standards in the implementation meet lots of difficulties [4]. There are terms of mature practice in developed countries on promoting building energy efficiency, such as the implementation of DSM (demand-side energy management), National Housing Energy Rating system, building energy audits, etc., but smooth implementation of these measures are based on scientific building energy assessment [5]. This article points out the necessity of establishing energy evaluation system in line with China's national conditions, and then construct hierarchical model of differentiate architecture energy for our country's current situation.

2 energy hierarchical design model for differentiate building

2.1 single building model

Ground floor heating in the building envelope gains increasing proportion. Ground floor heating is a two-dimensional or three-dimensional dynamic heat transfer process, with computational complexity and heavy calculating workload.

The basic principles of heat transfer calculation method for ground floor heating: Ignoring thermal properties changes with temperature of ground floor area, according to different influencing factors, heating of ground floor is divided into three heat transfer process: ① heat transfer process of outdoor under the influence of the earth's surface temperature; ②heat transfer process of indoor ground floor③ heat transfer of difference of temperature between adjoining room.

2.2 establish energy hierarchical design model of differentiate building

Heat transfer Q0 of building envelope structure including three parts as walls, windows and roof, can be expressed as:

$$Q_0=Q_w+Q_f+Q_r \tag{1}$$

where: Q_w : heat transfer of exterior wall,W.

$$Q_w=\sum(F_W\times K_W\times\rho_W\times\Delta_{TEQW}) \tag{2}$$

Q_f : Heat transfer of windows, W. window heat transfer includes two parts: heat from solar radiation and heat from temperature difference.

$$Q_f=\sum(F_f\times K_f\times\Delta_t)+\sum(F_f\times SC\times ESC_K\times SF) \tag{3}$$

Q_r :heat transfer of inner wall,W.

$$Q_r = \sum (F_r \times K_r \times \rho_r \times \Delta_{tEQr}) \quad (4)$$

In equation(2), (3), (4): F_w: area of exterior wall, m^2; F_f: outside area of window, m^2; Fr: roof area, m^2; Δt: difference between indoor and outdoor temperature , ℃, For air conditioning energy consumption calculation: difference between average outdoor temperature of calculated local air conditioning and designed indoor temperature (26 ℃); For the heating energy consumption calculation: difference between average outdoor temperature of calculated local heating and designed indoor temperature (18 ℃);

When carrying out energy consumption calculation of building air conditioning and heating, it needs to calculate partially heat transfer estimate of air conditioning Qoc and heating estimate

Q_{oh}: $Q_{oc} = Q_{wc} + Q_{fc} + Q_{rc}$, $Q_{oh} = Q_{wh} + Q_{fh} + Q_{rh}$ 。

Heat transfer index EHTV of building envelope structure is average of units area converted from sum energy of building envelope structure.

Corresponding heat index of air-conditioning $EHTV_c = Q_{oc}/F_0 (W/m^2)$; indicators of heat transfer $EHTV_h = Q_{oc}/F_0 (W/m^2)$ 。

wherein: F_0 : construction area, m^2 .

From above analysis, to obtain heat transfer index EHTV of building envelope, in addition to the parameters of building design, the key is to get parameters such as equivalent temperature difference between the walls and roof, shading coefficients, and radiation heat of standard window solar.

3 Simulation experiments and results

Select computing five cities such as Harbin, Guang Zhou and Wei Fang etal., as examples, some only need heating, some only need conditioning, some need both. Numerical example is a form of residential buildings, three floors, whose height is 2.5m, construction area is about 1500m2. Comparing results by calculating the effective heat transfer coefficient using traditional methods and EHTV methods are shown in Table 1.

Table1 Comparison to different examples

	Haerbin	Guangzhou	Weifang air conditioning	Weifang heating	Shanghai air conditioning	Shang Hai heating	Beiing air conditioning	Beijing heating
EHTV	-14.97	19.05	21.71	-4.30	17.85	-9.30	13.07	-10.44
Energy consumption per year	224.32	42.98	31.96	36.43	18.07	72.21	12.80	85.29
DOE	249.34	48.63	34.08	45.00	19.67	83.44	14.11	95.13
Relative errors	1.13	-0.88	6.01	-9.76	3.52	-3.43	1.89	0.69

EHTV envelope method is a simplified method of calculation of heat transfer and energy consumption structure. When EHTV method evaluates using the equivalent temperature difference parameters, simplifies calculations of transfer envelope. Meanwhile, calculating annual energy consumption for heating in air conditioning, an exponential equation is also employed, substituting consumption parameters and shape correction factor. Moreover, EHTV indicators include the effects of shape factor.

4 Conclusions

Based EHTV algorithm energy-saving hierarchical design model of differentiated building is in simulation and research. Taking Harbin, Guangzhou, Weifang and other five cities as residential samples, a specific test is carried out to obtain heating and air conditioning of the environment indicators and comparative analysis from samples of residential energy. The results show that: energy-saving building layered design is significantly better than residential energy-saving design.

Establishment of energy hierarchical design system, for the purpose of energy conservation lays a good foundation to help the healthy and sustainable development of urban construction.

Reference

[1] Aydin H, Melhem R, Mosse D, Power-aware scheduling for periodic real-time tasks. IEEE Transactions on Computers 2004; 53(5): 584-600.

[2] Pappala V S, Erlich I. A New Approach for Solving the Unit Commitment Problem by Adaptive Particle Swarm Optimization [A]. Power and Energy Society General Meeting Conversion and Delivery of Electrical Energy in the 21st Century, 2008 IEEE [C]. 2008: 1~6.

[3] S.Hemamalini, sishaj P Simon. Emission Constrained Economic Dispatch with Value-point Effect using Particle Swarm Optimization [J]. TENCON 2008 - 2008 IEEE Region 10 Conference,2009,Vol.27(3):1-6.

[4] Chen Y S, Chen D R. An efficient DVS algorithm for fixed-priority real-time applications. International Symposium on Parallel and Distributed Processing with Applications. 2010; 29-37.

[5] T．Nishioka,K．Ohtak．Hashimoto，H．Onoj ima，Measurement and Evaluation of TheIndoor Thermal Environment In A large Domed Stadium[J]，Energy and Buildings．2000 3

CHAPTER 5:

Electrical Machines, Mechatronics, Automation and Control

Advanced Materials Research Vols. 986-987 (2014) pp 1031-1034

doi:10.4028/www.scientific.net/AMR.986-987.1031

A New Type of Brushless DC Motor Control Strategy

Zhang xiaolei[1], Wu kuihua[2], Wang jian[3], Sun wei[1], Wu kuizhong[4], Du peng[1]

[1] State Grid Shandong Electric Power Company, Jinan 250001, China;
[2] Economic & Technology Research Institute, State Grid Shandong Electric Power Company, Shandong Jinan 250021;
[3] State Grid Shandong Electric Power Research Institute, Shandong Jinan 250001
[4]State Grid Electric Power Company in Jilin Province, Jilin Changchun 130000)

Keywords: the brushless dc motor, the control strategy, the torque ripple

Abstract. Because torque ripple disturbance can be created when the brushless dc motor is communicating, In this paper, from two aspects of energy feedback and the torque ripple, H/L - PWM - ON control strategy is analyzed .And a simulation system is set up. Through the trials, it shows that H/L - PWM - ON strategy can efficiently complete the energy feedback, has small torque ripple, and fully proves the feasibility and practicability of this control strategy.

Introduction

The commonly used PWM - ON and ON - PWM, H - PWM - L – PWM [1, 2] is included in the PWM strategy of Brushless DC Motor. The existing main problem is that commutation has torque ripple when the BLDCM is running, When the ripple is solved, it is beneficial to extern the scope of motor application . In this paper, H/L - PWM modulation control strategy is presented . The paper analyses the energy flow and the commutation torque ripple when machine is stop . The following conclusion is obtained: H/L - PWM - ON strategy can quickly achieve energy feedback. It has small torque ripple. And it is Suitable for the control of the brushless dc motor.

Strategic analysis

Brushless dc motor control system is shown in figure 1. The whole circuit is supplied by the dc power . and the Three-phase half bridge inverter is a power -supply source of the brushless dc motor. The model of the motor and the number of Switch tube and diode has been shown in the figure.

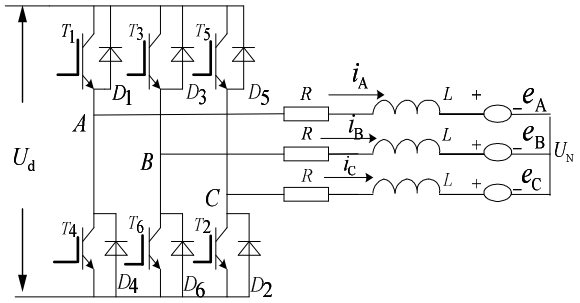

Figure 1 System circuit

This article focuses on another modulation H / L-PWM-ON mode. This modulation scheme is proposed, based on the Complementary switch tube up and down. However another one with a lower arm is reached . Its timing is shown in Figure 7.

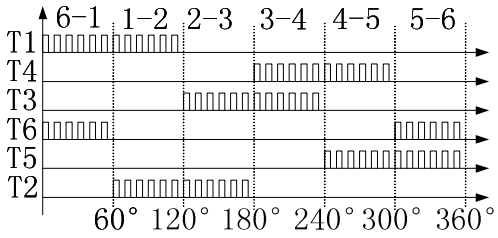

Figure 2 H_PWM-L_PWM type

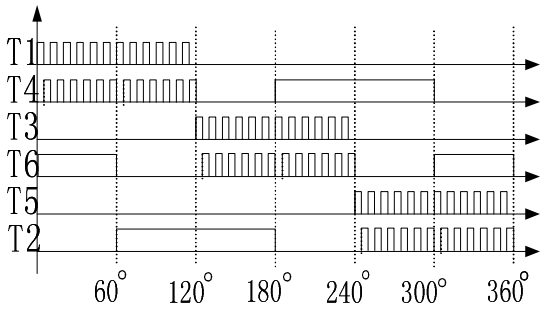

Figure 3 H/L-PWM-ON type

According to the figure 7, it is obtained that any one of the six states has three state switch work in this modulation method . This is different from the first five kands. The advantage is that when the motor is running , it is in favor of the feedback energy so that the motor stopped and reversed more quickly. Because when the motor is running, from the single-phase ,it is the current double quadrant circuit.

Such as in a moment that T4 and T1 is modulating while T6 is reached , the motot is running on a duty ratio. The circuit is as simplified as Figure 8 . In the figure , UA0 is the sum of the middle voltage U_N and the counter electromotive force

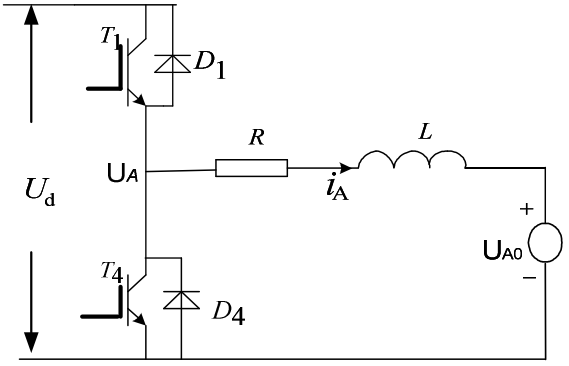

Figure 4 Current double quadrant circuits

From the positive point of current, power, T1, D4 and load are Buck circuit; When the reverse electricity is flowing, the switch T4 and D1 make up the Boost boost circuit. When the duty ratio of the motor decreases, the voltage UA will be less than UA0. When the motor is required to stop running, the same results will happen .Then the Current will reduce or even reverse. At the moment, the circuit is Boost circuit. The energy is provided from the motor to the power –supply. it can achieve the positive braking to achieve the purpose of energy-saving and fast shutdown .

In contrast, the first four modulation, because of two different phase of the switch tube, slow down or stop the process, form the Internal free-wheeling only by the corresponding lower arm freewheeling diode. But they have no corresponding the boost boost circuit for energy feedback channel so that energy efficiency is not high and the braking performance motor is poor. Because it is double polarity modulation, the feedback channel of the fifth kand of way is completed by the corresponding diodes to stream. Motor load and power always have energy exchange . But the switching loss is about two times that of other methods, which impacts its range of applications.

The torque ripple analysis

Literature [6] carefully analyzes the influence of modulation of the torque ripple. Next, it will take a look at the comparison of the effects of H / L-PWM-ON mode for torque ripple.

First Electromagnetic torque size is analyzed when the motor is running smoothly. That is to say the phase is not changed . It is supposed to be electromagnetic torque(unit N·m) which is generated by the brushless motor. Then Three-phase electromagnetic torque sum can be expressed as the follow :

$$T_e = (e_A i_A + e_B i_B + e_C i_C) / \omega$$

In this formula, ω represent the rotor mechanical angular velocity .

Since the magnetic potential of the brushless DC motor is trapezoidal wave, only the largest counter electromotive force value is conducting when the motor is running at any time . it means that when only two phases is opening up ,(If at this time A phase T1T4 is complementary to be opened, B phase T6 will be always reached) the following will be obtained :

$$\begin{cases} e_A = E \\ e_B = -E \end{cases} \qquad \begin{cases} i_A = -i_B = I_A \\ i_A + i_B + i_C = 0 \end{cases}$$

Then The total electromagnetic torque will be $T_e = 2EI_A / \omega$.

In this formula, I_A is the average a phase current in the stable operation.

Since the phrase commutation is divided into the bridge arm in phase and the lower bridge arm phase , therefore it needs to compare the current ripple up and down, respectively, when the arm commutation. First the current ripple is compared when the lower bridge arm phase is communicating.

first torque changes are analyzed during the phase commutation in the H/L - PWM - ON modulation mode. As shown in figure 1, With A phase modulation as an example, the up and down at this point, the switch from T1T4T6 switch to T1T4T2, namely the current bridge arm is from under the phase B to C arm phase under the bridge.

At present , it is existed. $\begin{cases} e_A = E \\ e_B = e_C = -E \end{cases}$

Because of the Continuity of the electric current, In an instant commutation, T6 tubes will be shutdown .But i_B will not instantly become 0 which lead to make diode conducting . so the following equation is shown:

$$\begin{cases} U_A = DU_d = Ri_A + L\dfrac{di_A}{dt} + e_A + U_N \\ U_B = U_d = Ri_B + L\dfrac{di_B}{dt} + e_B + U_N \\ U_C = 0 = Ri_C + L\dfrac{di_C}{dt} + e_C + U_N \end{cases} \tag{1}$$

The three equation is added , and the following equation is get :

$$(1+D)U_d = e_A + e_B + e_C + 3U_N = -E + 3U_N$$

Then the result can be obtained :

$$U_N = \frac{(1+D)U_d + E}{3} \tag{2}$$

Put the (2) into the (1) ,and it can be get :

$$U_A = DU_d = Ri_A + L\frac{di_A}{dt} + e_A + \frac{(1+D)U_d + E}{3}$$

resistance voltage change is ignored , then :

$$\Delta i_{A1} = \frac{(2D-1)U_d - 4E}{3L}\Delta t \tag{3}$$

Through the above analysis and comparison, the torque ripple of H/L - PWM - ON control strategy is small, and it is conducive to the smooth running of the motor. it's worth noting that this strategy has disadvantage which is that it exists risks in the direct connection ,when the guidance of the up and down tubes is conducting . And when the up and down tubes of only two different phases in the first five kinds types is conducting, direct connection won't be absolutely appeared.

Experimental result

Through the above analysis, theoretically , this way of modulation is feasible. Brushless dc motor parameters used in the experiment are as follows: Rated power is 550 W, Voltage ranges from 220 V to 240 V . Pole-pairs are 2. Rated current is 3.5 A . torque is 1.7 N · m . Rated speed is 3000 r/m .

In the experiment, 3KHZ switching frequency is used . Under the condition of duty ratio of 0.5, When the motor is under the low speed or under the light load, the waveform of A phase current and line voltage is shown in the figure 9.

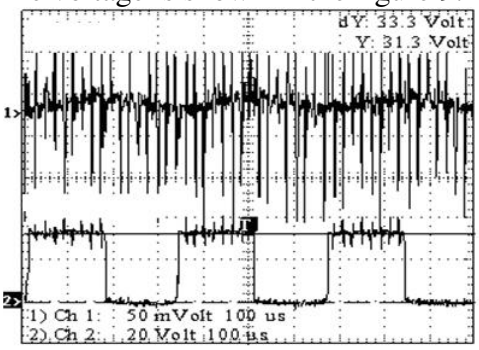

Figure 9 I_A and U_{AB}

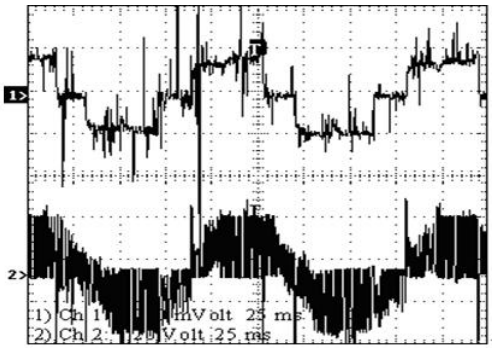

Figure 10 I_A and U_{AC}

As can be seen from the figure 9 , when T_1, T_4 are modulate up and down ,and T_6 is conducting , when the line voltage UAB is positive , A phase current is on the rise; Line voltage UAB is appositive; a phase current is on the decline.

To be sure: A complete cycle (that is, the six state), is that A phase current is negative.The waveform of A phase current and line voltage UAC when motor has load is shown in figure 10.

Conclusion

Through the theoretical analysis and experimental results, compared with other kinds of control strategy, the electromagnetic torque ripple caused by the H/L - PWM - ON this way of modulation is small. And it is conducive to the smooth running of the motor. It can realize two-way flow of energy and achieve the quick stop of the motor and energy saving.

References

[1] WEI Kun.Torque Ripple Suppression Technique in Permanent Magnetic Brushless DC Motors[D].Hangzhou :Zhejiang University,2005. (in Chinese)

[2] Sun jianzhong, Bai fengxian , Special motor and its control [M]. China Waterpower Press,2005.

[3]Sun hanfang, Intel 16-bit single chip microcomputer [M].Beijing: Beijing university of aeronautics and astronautics press, 1995.

[4] QI Ringling hui,CHEN Ming. Analysis and attenuation on commutation torque ripples of brushless DC motor[J]. Electric Machine and Control,2006,10[3]:287-295. (in Chinese)

[5]Lin weixun. Modern power electronic circuits[M].Hangzhou :Zhejiang University,Version 1, 2002.

[6] ZHANG Xiangjun,CHEN Boshi. The different influences of four PWM modes on commutation torque ripples in brushless DC motor control system[J]. Electric Machine and Control, 2003, 7[2]:87-91. (In Chinese)

Advanced Materials Research Vols. 986-987 (2014) pp 1035-1038
© (2014) Trans Tech Publications, Switzerland
doi:10.4028/www.scientific.net/AMR.986-987.1035

Active Control Model of Island Multiple Generators System

Guobin[1, a], Luoji[2,b]

[1]Heping Road No. 146, Langfang City, Hebei Province, China

[2]Heping Road No. 146, Langfang City, Hebei Province, China

[a] cppeguobin@cnpc.com.cn, [b]luoji@cppe.com.cn

Keywords: Island mode, brushless generator, isochronous load sharing, electronic governor, digital data communication

Abstract. This paper focuses on *selecting control of parallel generator* that ensures safety and efficiency operation in oil & gas offshore pipeline application. For island grid system, the advanced microcontroller based digital isochronous method of active load sharing is introduced. The programmable logic controller system is adapted to automatic load sharing.

Introduction:

One or more diesel generators without a connection to an electrical grid are operating in "island" mode.

Generator systems in island are rapidly increasing, particular on site in oil & gas offshore pipeline application.

The more than one generator provides the advantages of high flexibility, reliability and redundancy, thus an island generator plant will have at least two generators.

The automatic generator control is rapidly increasing to match the load demands. The intelligent controller has the following objectives:

To hold system constant frequency;

To maintain the correct interchange of power between generators

To ensure each generator unit at the most economic value;

Active load sharing of automatic generator control shall be digital isochronous sharing, which actively calculated the percentage of real load on generator sets.

Generator system. In general, the alternators installed in oil & gas offshore application shall be brushless, salient pole rotor self regulating type as Fig. 1 shows

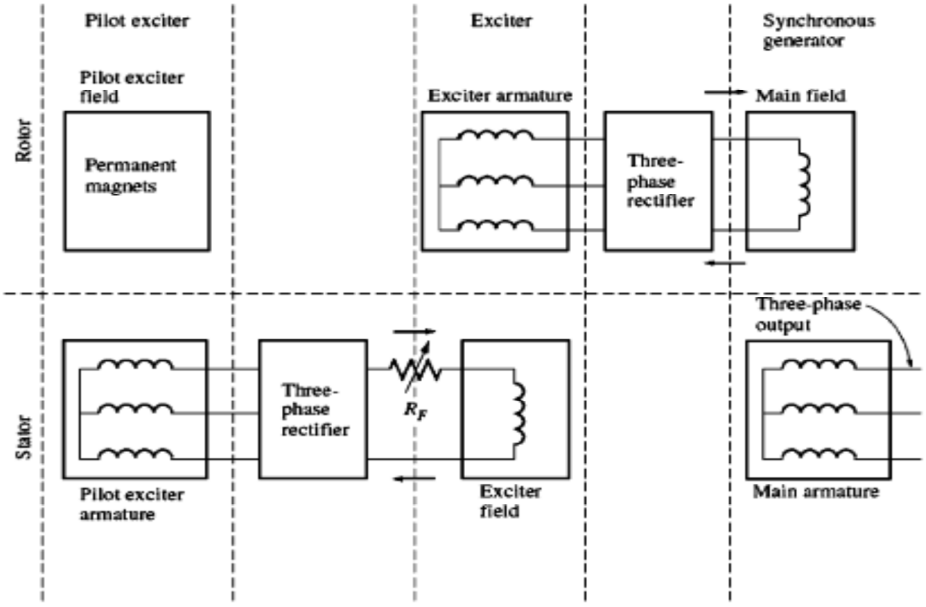

Fig. 1 Configuration of generator:

A typical configuration of parallel operating multi-generators system in oil & gas pipeline application is illustrate in Fig. 2

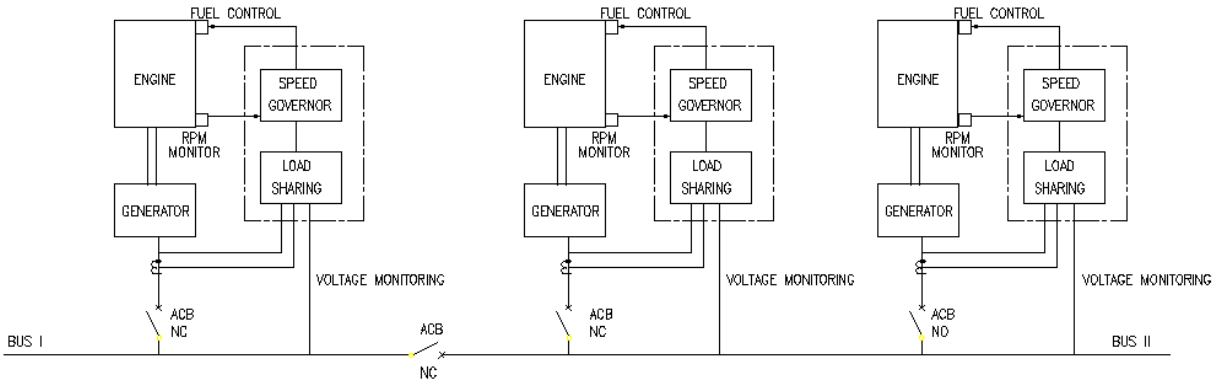

Fig. 2 Parallel operating multi-generators system

In general, electric power is generated by three diesel generators sets to supply power to loads, with operation in N+1 philosophy (2 sets running and 1 set standby), where N is the minimum number of generators required to meet the load demand. The bus bar is divided into two sections via bus couple which was in the normally closed.

Generator load sharing. Essentially, parallel running is achieve in two stages include synchronizing and load sharing. Once the Auto- synchronizing between generators to the main bus is complete, the power will be shared depending upon the generator characteristics.

There are two methods for active load sharing of the power system [1]:

1 Isochronous load sharing (constant frequency);

2 Droop load sharing(varying frequency);

The loads in offshore pipeline application mainly are continuous duty and require high quality of power supply. Frequency variation will have effects on the induction process motor. Thus, the constant frequency is required in island mode.

Generator in isochronous sharing mode can maintain the requested speed very precisely. But the generators running in parallel, it is impossible to keep load sharing stable between generators in isochronous mode [2]. Unless, communication may be employed to be increase the stability of this mode. That means digital isochronous load sharing.

The digital isochronous load sharing system shall be produced to achieve stabilize the island multiple generators operation.

Structure of load sharing. In comparison traditional generator controllers which have some different modules resulting in a lot hardwires, but intelligent generator controller can achieve the function including governor control, synchronizing and load sharing.

The digital data communication via CAN bus between generators exchanges power information (real power).

A typical schematic diagram for data communication for isochronous load sharing between generators is illustrate in Fig. 3

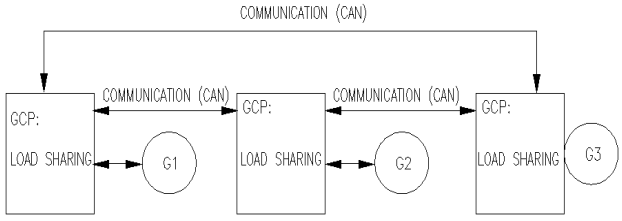

Fig. 3 Control unit communications between generators

For digital isochronous load sharing system, the key of active load sharing of island operation is mainly relaying on the generator governor and controller.

Governor. In general, governor specifically performs the speed and active power control of the engine. That is the governor applied to an engine-generator set controls engine speed to assure the driven AC generator provides the proper frequency of the AC power output. Fig 4 shows the block diagram of speed governor.

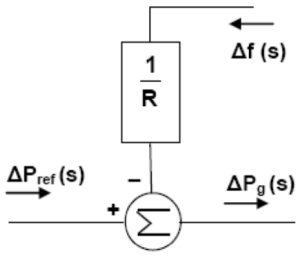

Fig. 4 Block Diagram of Speed Governor

Engine generator with electronic governor is necessary to required for digital isochronous load sharing. The electronic speed control senses actual engine speed and provides a feedback signal to the actuator, which, in turn, positions the engine throttle or fuel control to maintain a very accurate engine speed.

In general, there are two operating modes used for speed governing engine is droop and isochronous. However, the isochronous governor is used in automatic active load sharing.

Isochronous governing causes the steady state speed error to become zero, thereby producing a constant speed at the shaft and a constant frequency for the power system. Isochronous governing is also a form of 'integral control'. This method is best suited to a power system that is supplied by one generator. In multiple generators in parallel, the generators will "fight" each other in order that system is non-stable in load sharing. However, the intelligent controller is introduced to control isochronous governor in active load sharing via communication line.

Controller. The key successful of digital active load sharing is relaying on controller. Intelligent controller is automatic load sharing control functions between generators. Active load sharing is achieved by increasing/decrease fuel to engine via controller software while maintaining a fixed speed.

Fig. 5 shows the active power control block of generator, where inputs are local measurement of frequency and power output and load output, and the set points are provided by the central controller. The output is fuel demand.

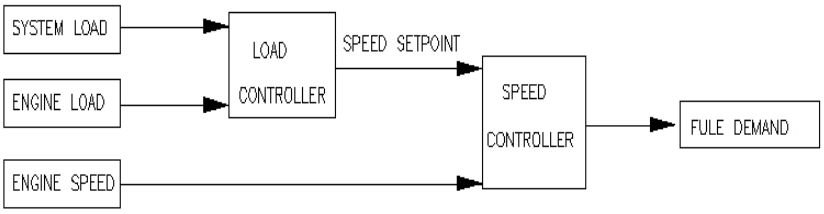

Fig. 5 Control block of generator

Controller has active control system that actively calculate the percentage of real load on a specific generator set, compare those values to the percentage of real load on the system, and then provides control to the fuel and excitation system of the generator to drive the percentage of load on the generator to the same value as the percentage of load on the system.

Communication data between generators is important to achieve isochronous active load sharing. The analogue and digital line is used. But digital line is superior to the analogue line since more data can be communicated to perform complex and accurate load sharing function. Moreover, data line can be more suitable for long distance in comparison with analogue line.

Summary. Microcontroller based on digital isochronous has been automatically achieved for the load sharing. The controller is simple and reliable. In comparison to traditional, it decrease different module and can be give easy and liable operation about load sharing.

References

[1] Governing Fundamentals, Woodward Governor Company, Product Manual 26260

[2] Power Generator handbook

[3] Robert Worfgang, Fundamental Principles of Generator for information Technology, Schneider electric

[4] S. David Alley, Generator Basic Applied to Field Problems

Advanced Materials Research Vols. 986-987 (2014) pp 1039-1042

doi:10.4028/www.scientific.net/AMR.986-987.1039

Adaptive Control of Chaotic Motion in Fractional Order Wind Generators

Tengfei LEI[1, a],Jing MENG[1,b], Heng CHEN[1,c],Linzheng REN[1,d] ,Xu WANG[1, e]

[1] Graduate Department ,Xijing University, Xi'an

[a]leitengfeicanhe@126.com, [b]1532674448@qq.com, [c]chenhenrys@qq.com,
[d]274222649@qq.com,[e]1156539139@qq.com

Keywords: fractional order; permanent magnet synchronous generator; chaos control;circuit

Abstract. In this paper, the directly driven wind turbine with permanent magnet synchronous generator (D-PMSG) is investigated, the mathematical model of which is built up. Also, the chaotic behaviors or limit cycle phenomena is demonstrated under certain working conditions or the parameters of the model having a certain range of values. A novel adaptive controller is designed based on the quasi-Lyapunov stability theory for fractional-order systems. Also, electronic circuits are designed to realize the controllers using Multisim. The simulation results demonstrate the effectiveness and realizable ness of the proposed methods, besides, the research results will be provided as theoretical references for the study of improving control performance.

Introduction

At present,the energy and the environment are the pressing problem facing mankind[1][2].As the wind power is a kind of green energy,it is the widely recognized in general. The chaos is a new subject that started in the twentieth century.Under certain conditions,the brushless DC motor can generate chaotic phenomena in the literature[3].Brushless doubly-fed wind power generator is controlled in documents[4].The sliding mode variable structure control method is taken in the the D-PMSM chaotic system in documents[5], but the requirement for the sliding mode variable structure's accuracy of the mathematical model is not so high.Therefore,there may be some errors on the establishment of mathematical model. The paper of documents[6] proposes a adaptive control way of the chaos system in permanent magnet synchronous motor.The permanent magnet synchronous generator system above is not considered to establish the mathematical model of damping.But, the wind turbine system's study about damping is not much.

According to the characteristics of the permanent magnet synchronous generator,the system model is reestablished in damp conditions. Meanwhile, this paper presents a fractional order to describe D-PMSG.In this paper, an adaptive synchronization control method is designed by using the fractional Lyapunov stability theory[8][9] ,and the control strategy is tested through the circuit simulation.

The system model of D - PMSG

The basic structure of D-PMSG is as shown in fig1,which consists of a wind turbine,converter and other components.The wind turbine converts the wind energy into the mechanical energy and the generator converts the mechanical energy into the electrical energy.In addition,the converter moves the electrical energy into the grid.

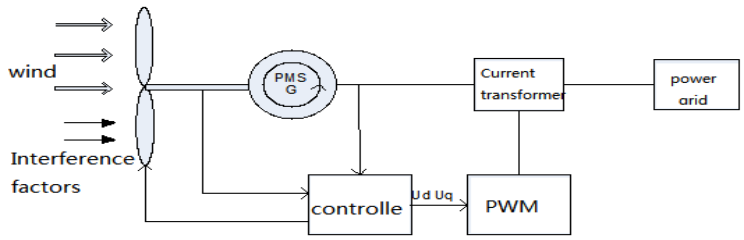

Fig.1 The basic mechanism of D- PMSG

Assuming generator has the uniform air gap and the inductance of D and Q axes are same, Considering the influence factors on the system, the system of certain properties and damping, friction and other physical quantities with fractional characteristics, it can be used for fractional differential description, rewrite rewritten dynamic mathematical model:

$$\begin{cases} D^{q_1}x_1 = -x_1 + x_2x_3 + \hat{u}_d \\ D^{q_2}x_2 = -x_2 - x_1x_3 + \sigma x_3 + \hat{u}_q \\ D^{q_3}x_3 = \gamma(x_2 - x_3) - \hat{T}_w \end{cases} \quad (1)$$

When $\hat{u}_d = 0$, $\hat{u}_q = 0, \hat{T}_w = 0$, this process can be viewed as the transient period after the wind turbine permanent magnet synchronous generator runs over. Its parameters are taken as follows: σ = 25, γ = 5.46. The formula (1) has the chaos characteristics.

Chaotic synchronization controller

According to the literature in the [6] to the motor synchronous control of chaos, we can construct the response system.

$$\begin{cases} D^{q_1}y_1 = -y_1 + y_2y_3 + k_1e_1 \\ D^{q_2}y_2 = -y_2 - y_1y_3 + \sigma y_3 + k_2e_2 \\ D^{q_3}y_3 = \gamma(y_2 - y_3) + k_3e_3 \end{cases} \quad (2)$$

Among them,it meets $e_i = y_i - x_i (i = 1,2,3)$ .Using the(1)-(2),we can obtain

$$\begin{cases} D^{q_1}e_1 = -e_1 + y_2e_3 + x_3e_2 + k_1e_1 \\ D^{q_2}e_2 = -e_2 - e_1y_3 - x_1e_3 + \sigma e_3 + k_2e_2 \\ D^{q_3}e_3 = \gamma(e_2 - e_3) + k_3e_3 \end{cases} \quad (3)$$

Therefore,we can get

$$D^q e = (B + F(x, y) + K)e \quad (4)$$

According to equation(2) ,we construct the H function

$$H = e_k^T PD^q + e_k e^T PD^q e \quad (5)$$

Expanding the formula(5),we can obtain

$$H = e^T D^q e + e_k^T ED^q e_k \quad (6)$$

From the formula(6),it can be derived the format of the text chart.

$$\max\{\tilde{k}_i\} \le -[\max\{eig(\frac{A^T + A}{2})\} + \max\{eig(\frac{F(x,y)^T + F(x,y)}{2})\}] \quad (7)$$

According to the formula(7),the value of $\tilde{k}_i$ can be obtained, which proves that the system(1) is stable .

Circuit simulation

When the system is in chaos,the minimum value of q is 0.95. According to the previous analysis,can find the value of $\widetilde{k}_i$,and write the corresponding response of the system(2).The drive system and response system are similar,so we only draw the circuit principle diagram of the system(2) .The system (2) is implemented by linear resistance, capacitance, operational amplifier LM741 and analog multiplier AD633.

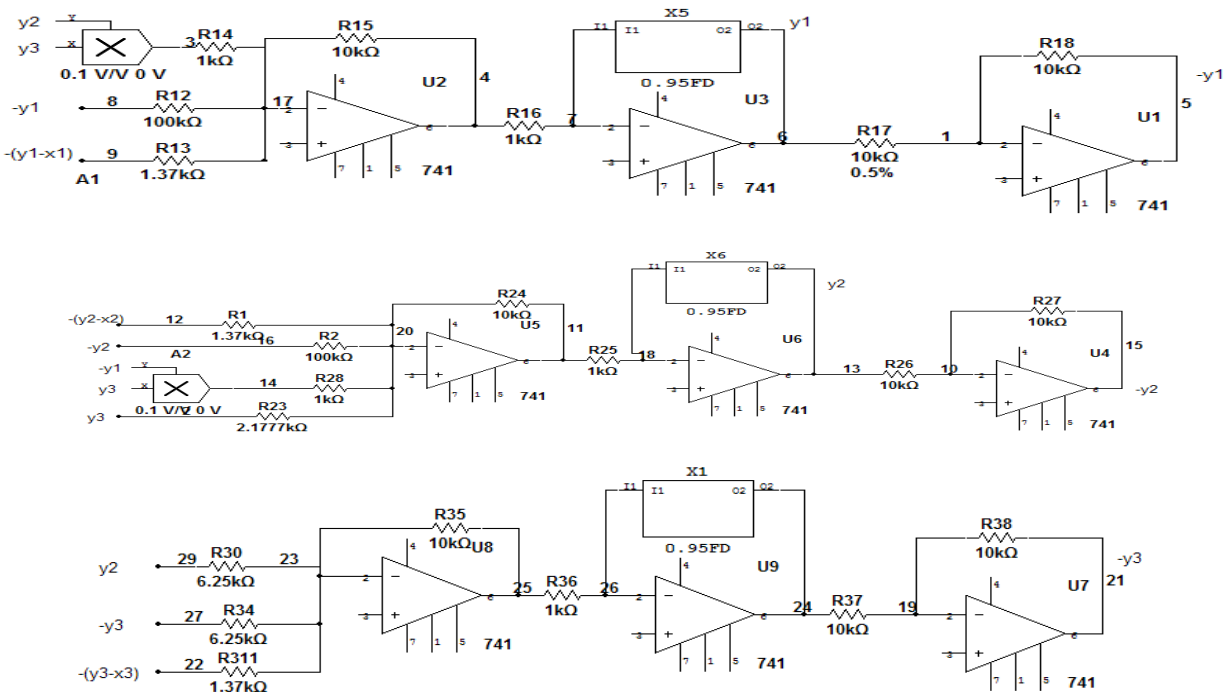

Fig. 2 The circuit principle diagram of the system(2)

Using Mutisim10 to simulate the circuit,we can get the attractor Fig.3 of the system and draw the synchronous wave form as shown in Fig.4.

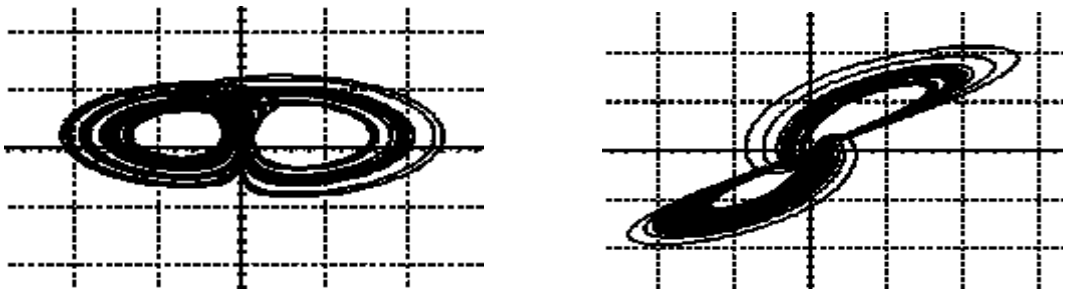

Fig. 3 Chaotic attractor of the system(1)

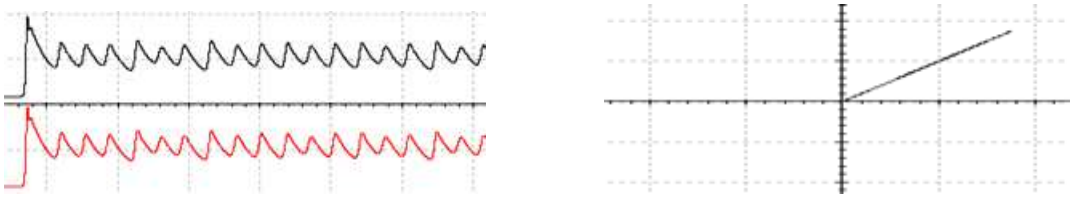

a $t-x_1, y_1$ (5V/div 5V/div) b x_1-y_1 (5V/div 5V/div)

Fig.4 Synchronous simulation results

Conclusion

In the light of the damping effect of the permanent magnet synchronous generator in the chaotic system,this paper presents a fractional order to describe the permanent magnet synchronous generator.An adaptive synchronization method is proposed.At the same time,astrict mathematical theory of this control method is proved to be given.The circuit is designed and tested by using modular design method.Furthermore,in the experiment,we receive prospective results that the experimental results is fully consistent with theoretical analysis circuit.Ultimately,the correctness and validity of the method are confirmed.

References

[1] AN XueLi, JIANG Dongxiang. Chaotic characteristics identification and trend prediction of running state for wind turbine [J]. Electric Power Automation Equipment, Mar. 2010, Vol. 30 No.3, pp. 15 - 24.

[2] ZHANG Bo, LI Zhong, MAO Zongyun. The chaotic model and Hopf bifurcation of a type of permanent-magnet synchronous motor [J]. Proceedings of the CSEE, Sep.2001, Vol21 No.9: 13-17.

[3] Yang Zhihong Yao Qiong hui. Brushless DC motor system nonlinear research. Journal of dynamics and control, Mar.2006, Vol.4 No.1: 59-62.

[4] Cai Chaohao. H ∞ Control for brushless doubly-fed wind generator [J]. Journal of electrical and control applications, 2011, 20 (3) : 45-50.

[5] Yang Guoliang, Li Huiguang. Sliding mode variable structure control of chaos in direct-driven permanent magnet synchronous wind turbine [J]. ACTA Physca SIICA. Nov.2009, Vol.58 No. 11 : 7552-7557 .

[6] ZHANG Xinghua, DING Shougang. Adaptive chaotic synchronization of permanent magnet synchronous motor with non smooth air-gap[J]. Control theory & applications. Jun.2009.Vol.26 No.6 : 661-664 .

[7] CHEN Wen,ZHANF Hongguang,Li Xicheng.mechanics and engineering problem of fractional derivative model [M] Beijing: Science Press,.2010.

[8] Matignon D 1996 IMACS.IEEE SMC Proceedings Confercelille,france,July 9-12,1996 P963.[9] WAJDI M A, AHMAD M H. On nonlinear control design for autonomous chaotic systems of integer and fractional order[J]. Chaos, Solitons and Fractals, 2003, 18: 693-701.

Advanced Materials Research Vols. 986-987 (2014) pp 1043-1047

doi:10.4028/www.scientific.net/AMR.986-987.1043

An Energy-Saving Scheme of Motor Drive Systems Based on Ultracapacitors

Quntao AN[1, a], Li SUN[2, b], Minghang Duan[3, c], Ruibo Liu[4, d]

[1]Department of Electrical Engineering, Harbin Institute of Technology, Harbin, 15001, China

[2]Department of Electrical Engineering, Harbin Institute of Technology, Harbin, 15001, China

[3]Department of Electrical Engineering, Harbin Institute of Technology, Harbin, 15001, China

[4]Department of Electrical Engineering, Harbin Institute of Technology, Harbin, 15001, China

[a]email: anquntao@163.com, [b]email: motor611@sina.com, [c]email: 991502632@qq.com,

[d]email: 840701511@qq.com

Keywords: Motor Drive System; Energy-Saving Scheme; Ultracapacitor; DC-DC Converter

Abstract. In order to prevent DC link voltage pump during braking, a paralleled release circuit composed of chopper and resistor is often employed. As a result of energy waste on the resistor, the efficiency of the motor drive system is low in the case of frequent braking. To improve the efficiency, an energy-saving scheme of motor drive systems based on ultracapacitors is proposed in this paper. An energy storage system (ESS) paralleled with the DC link of the motor drive is adopted in the scheme, which is composed of a bidirectional DC-DC converter and ultracapacitors. The ESS can realize recycling of the braking energy. Compared with PWM rectifier, this scheme can avoid various technical requirements for grid-connected inverters.

Introduction

The modern drive system has been applied in fields of industry and electric vehicles since they can improve the performance and efficiency of motors substantially. To brake the motor, resistors or the winding are often used to consume regenerative energy during braking, which results in low efficiency of the motor drive system [1] [2]. To improve the overall efficiency and performance of the motor drive system, an four-quadrant drive in which the diode rectifier is replaced by PWM rectifier is adopted, as shown in Fig.1(b) [3]-[6]. As the four-quadrant drive, since the related standards for grid-connected inverters should be complied with, the design requirement and complexity are increased.

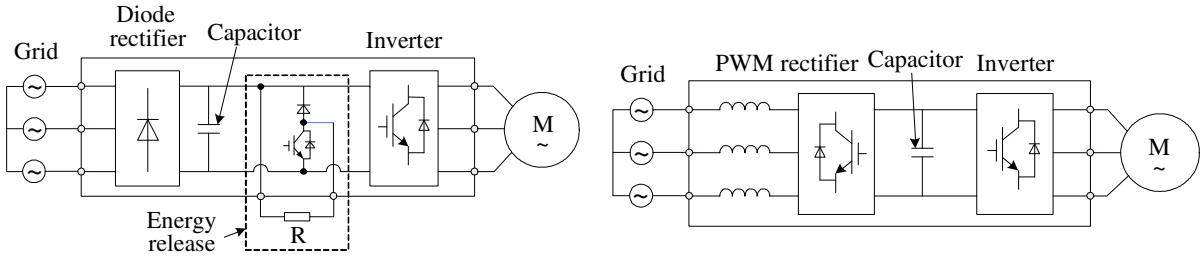

(a) Diode rectifier-inverter topology with brake resistor (b) PWM rectifier-inverter topology

Fig.1. Typical topologies of motor drive systems

To simplify the design, an energy-saving scheme based on ESS paralleled with DC link is proposed in this paper. This scheme can be used to reform traditional motor drive systems with diode rectifiers, since it can recycle regenerative energy and improve the efficiency of motor drive systems.

Proposal of the energy-saving control scheme

The proposed energy-saving scheme for motor drive systems is shown in Fig.2. In the scheme, the energy storage and management unit paralleled with the DC link is used to recycle the braking energy. The unit is consists of a bidirectional multiple DC-DC converter and ultracapacitor group. The high level end of the converter is connected to DC link and the low level end is the ultracapacitor group.

The operation principle of the energy-saving scheme can be described as follows. When the motor brakes, the regenerative energy is fed to capacitors on DC link, and then pumps DC link voltage. The controller of energy storage units measures the DC link voltage, and when the voltage reaches a preset value U_{ch}, the DC-DC converter runs in Buck. At this moment, the energy storage unit is equivalent to a virtual load for the motor drive. By hysteretic chopping control of DC link voltage, the feedback energy from the motor can be absorbed. When the motor runs, the DC link voltage declines to U_{disch} and the DC-DC converter operates in Boost. And DC link voltage closed-loop is carried with U_{disch} as the reference. Since U_{disch} is larger than the diode-rectified voltage value, the energy required by the motor is offered by the energy storage unit prior to the rectifier. When the voltage of ultracapacitors is less than the preset value, the DC-DC converter will stop and the DC link is supported by the diode rectifier again.

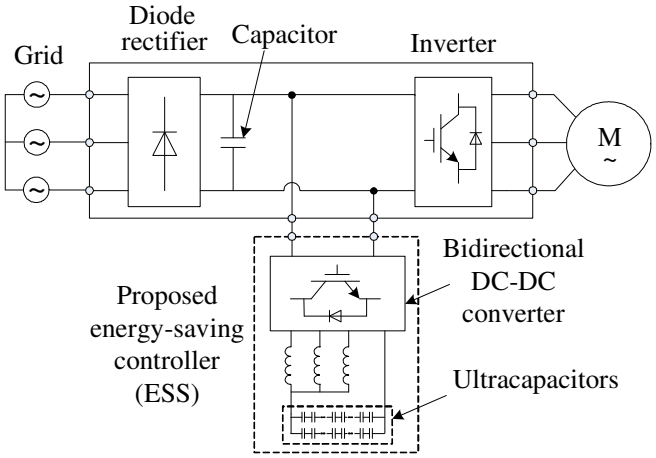

Fig.2. The proposed energy-saving scheme of motor drive systems

Design and control strategy of the energy-saving scheme

The function of the energy storage unit is to store regenerative energy of the motor, and to supply the motor with the energy again when the motor needs. Energy recycling is achieved and the overall efficiency of the system is improved. To realize the above-mentioned function, the DC-DC converter together with its control strategy and the ultracapacitor group are required to design, as shown in Fig.3. Triple structure is employed in the bidirectional DC-DC converter, in which the low level end is connected to ultracapacitors and the high level end with the DC link.

The relationship between DC voltage U_{dc} and effective value U_{ac} of the AC supply is:

$$U_{dc} \approx 1.4U_{ac} \tag{1}$$

For a system powered by three-phase 380V voltage, U_{dc} is around 530V. Taking the grid voltage fluctuation into account, the rated voltage on the high level end of the DC-DC converter is designed as 650V and 480V for the low level end.

As shown in Fig.2, the control system of the bidirectional triple DC-DC converter includes a charging controller (Buck) and a discharging controller (Boost). Both of them employ double closed-loop structure with current loop and voltage one. Regulators in both voltage loop and current loop use PI controller. Output of the voltage loop is regarded as the current reference, and output of the current loop is used for PWM modulation. In order to reduce current ripples of inductors, the carrier phase-shifted PWM is adopted.

Operation state of the controller is decided by the switch logic, as shown in Fig.3. The DC link voltage can be controlled like Fig.4 under the motor brake and electromotion. When the DC link voltage increases when the motor brakes, a hysteretic comparator is carried out between the threshold value U_{dcch} (650V) and the measured voltage U_{dc} to chopper for charging. Considering the current limitation in the closed-loop control of Buck as I_{lmax}, and duty of the chopper as D, the

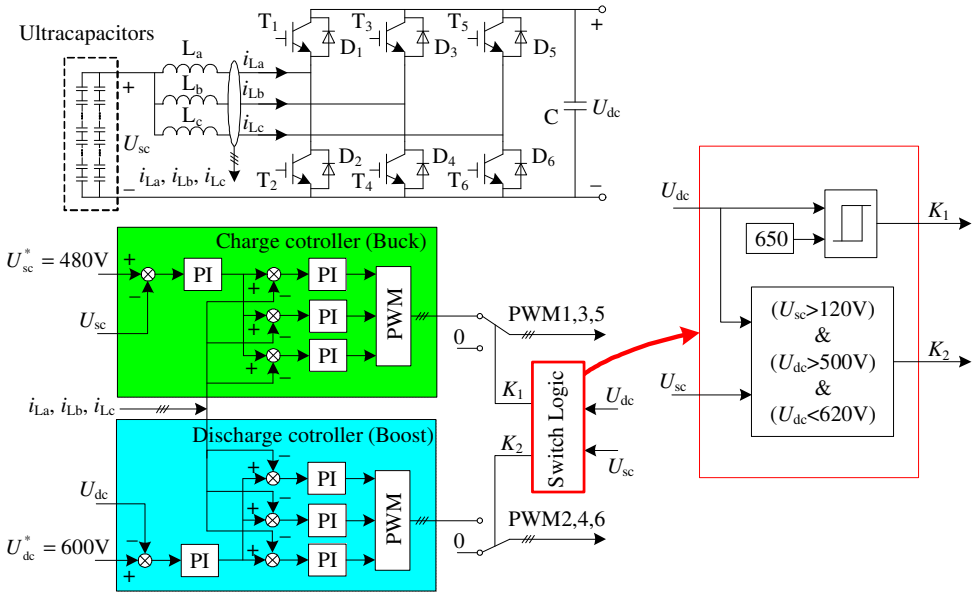

Fig.3. Topology and control strategy of the energy storage unit

DC-DC converter can be equivalent to a resistor R_{eq} for the DC link:

$$R_{eq} = \frac{U_{dc}}{3DI_{Lmax}} \tag{2}$$

And, the regenerative energy is stored into the ultracapacitor group by chopper with the hysteresis comparation between U_{dc} and U_{dcch}.

When the motor transit from brake to electromotion, the DC link voltage will decline to $U_{dcdisch}$ (620V). Then Boost control starts work, and the DC link voltage is controlled as the reference U_{dc}^{*}. Here, the energy in ultracapacitors is offered to the motor. With declining of the voltage on the ultracapacitor group, the DC-DC converter will stop when the ultracapacitor voltage declines to U_{scmin}. And then, the motor is powered by the AC supply. These threshold voltage values in the scheme meet the following relationship:

$$U_{dcrec} < U_{dc}^{*} < U_{dcdisch} < U_{dcch} \tag{3}$$

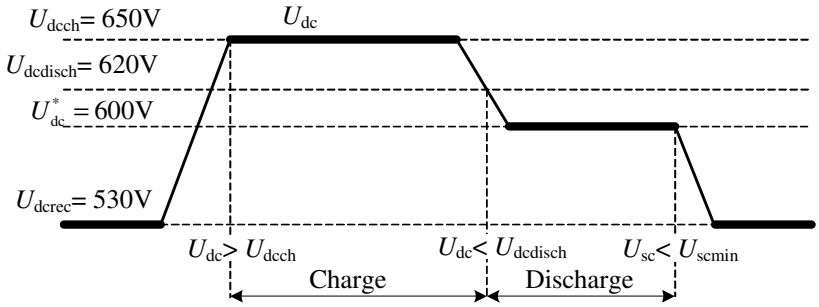

Fig.4. DC link voltage waveform during charge and discharge

Simulation results

The simulation model of the proposed energy-saving control scheme is set up by Matlab. Vector controlled three-phase permanent magnet synchronous motor is considered, the motor parameters include: rated rotate speed 2000rpm, rated current 24.5A, rated torque 27Nm, torque coefficient

1.1Nm/A and rotational inertia 89.5×10^{-4}Kgm^2. The AC supply voltage is 380V, switching frequency is 4kHz and the load is 27Nm. The initial voltage of ultracapacitor group is 100V with limited value U_{scmin} 120V. The simulation results are shown in Fig.5. The initial speed of the motor is zero, and change to –2000rpm at 0.1s and 2000rpm at 0.4s, respectively. The speed, torque and current waveforms are shown in Fig.4(a)(b). Before 0.1s, the speed is zero, motor does not need energy and the ESS does not work, which is shown in Fig.4(e)(f). At 0.1s, the speed is –2000rpm, and the motor works as a generator. At this moment, the regenerative energy is used to charge ultracapacitors through the bidirectional DC-DC converter as a Buck, shown in Fig.4(c)(d). The charge controller keeps the DC link voltage stable at 650V, as shown in Fig.4(g). At 0.4s, the speed is changed to 2000rpm, the energy that the motor needs is offered by the ESS. Meanwhile, the DC link voltage is stable at 600V. The voltage on ultracapacitors declines until to 120V, the ESS will stop and then the motor fed by the AC supply. Totally, the simulation results demonstrate that the proposed energy-saving scheme can realize recycling of regenerative energy of the motor and improve efficiency of the motor drive system.

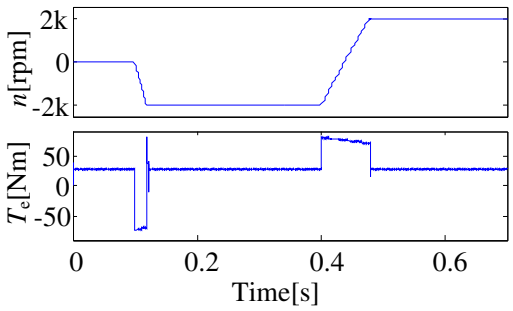

(a) Motor speed and torque

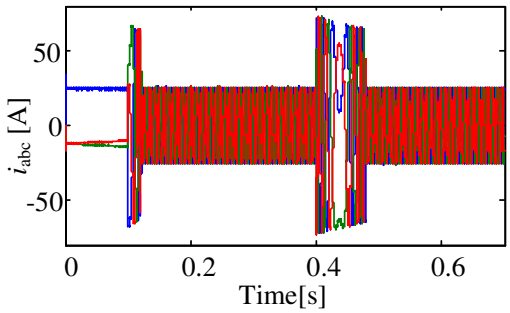

(b) Three phase currents of the motor

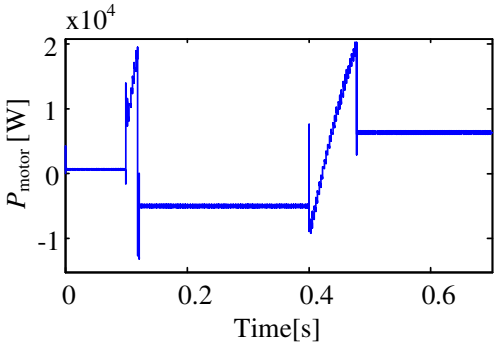

(c) Input power of the motor

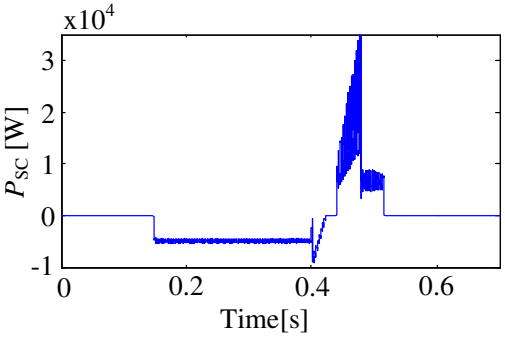

(d) Output power of the ESS

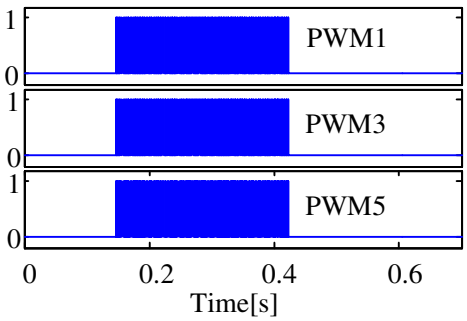

(e) PWM signals of the upper switches

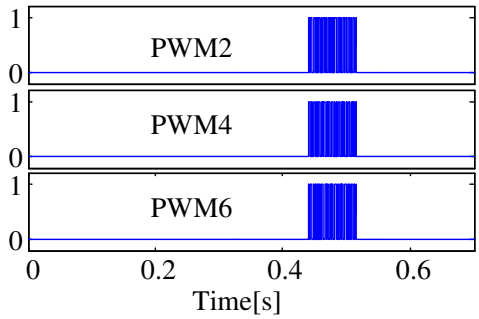

(f) PWM signals of the lower switches

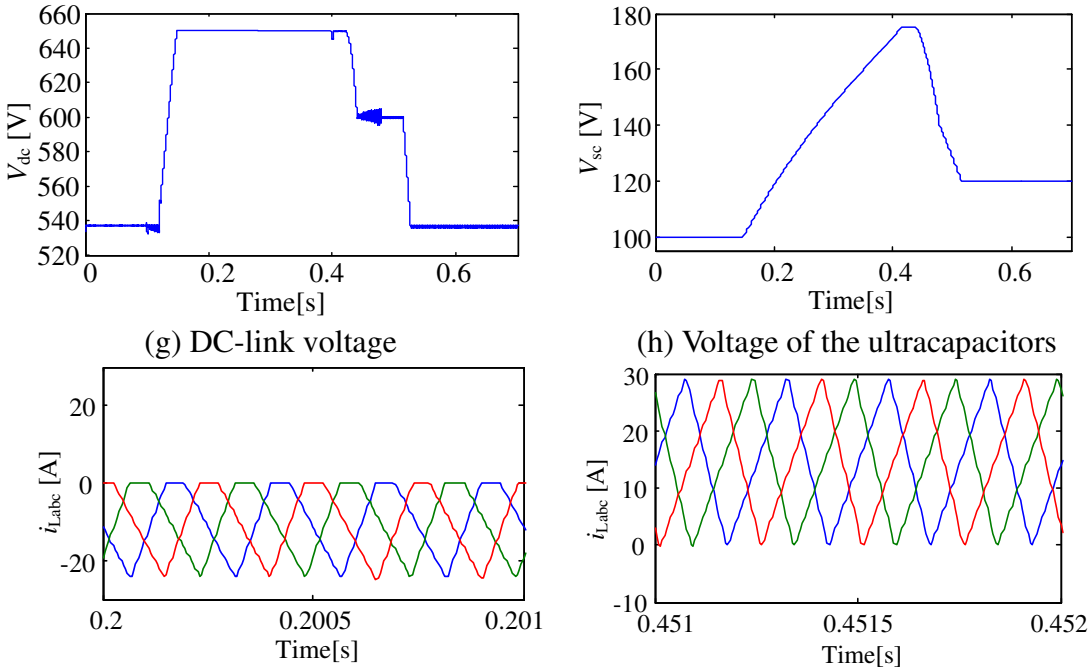

(g) DC-link voltage (h) Voltage of the ultracapacitors

(i) Inductor currents under Buck mode (j) Inductor currents under Boost mode

Fig.5. The simulation results

Conclusion

An energy-saving control scheme for motor drive systems is proposed in this paper, which is in parallel with the DC link as the energy storage system composed of a bidirectional DC-DC converter and ultracapacitor group. When the motor brakes, the regenerative energy is absorbed, and when the motor runs as electromotion, the stored energy is offered to motor again. The proposed scheme can recycle the braking energy and improve efficiency of the motor drive system, which is validated by the simulation results.

Acknowledgement

In this paper, the research was sponsored by the National Nature Science Foundation of China (Project No. 51207029), China Postdoctoral Science Foundation (Project No. 2012M510089), Heilongjiang Postdoctoral Fund (Project No. LBH-Z11145) and the Fundamental Research Funds for the Central Universities (Project No. HIT.NSRIF.2015012).

References

[1] A.V. Ravi Teja, Chandan Chakraborty, Suman Maiti, Yoichi Hori. A new model reference adaptive controller for four quadrant vector controlled induction motor drives[J]. IEEE Transactions on Industrial Electronics, 2012:59(10):3757-3767.

[2] Mahesh M. Swamy, Tsuneo Kume, Yoshiaki Yukihira, Shuichi Fujii, Mitsujiro Sawamura. A novel stopping method for induction motors operating from variable frequency drives[J]. IEEE Transactions on Power Electronics, 2004:19(4):1100-1107.

[3] Liming Liu, Hui Li, Seon-Hwan Hwang, Jang-Mok Kim. An energy-efficient motor drive with autonomous power regenerative control system based on cascaded multilevel inverters and segmented energy storage[J]. IEEE Transactions on Industry Applications, 2013:49(1):178-188.

[4] Feng Wang, Jianguo Jiang. A novel operation mode of synchronous motor used as generator in pump station using four-quadrant variable frequency technology[C]. International Conference on Computer, Mechatronics, Control and Electronic Engineering, Wuhan, 2010:136-138.

[5] Yan Cheng, Wei Zhang. SVPWM-based predictive current controller for four-quadrant induction motor drive system[C]. ICEMS, Beijing, 2011.

[6] Yuhua Wang, Jianlin Miao, Yuanfang Wei. The research of traction motor energy-saving regenerative braking control technology[C]. International Conference on Intelligent Computation Technology and Automation, Changcha, 2010:930-933.

Advanced Materials Research Vols. 986-987 (2014) pp 1048-1053

doi:10.4028/www.scientific.net/AMR.986-987.1048

Analysis and Suppression of Common-Mode Voltage in Open-End Winding Induction Motor Drive System Fed by Dual Inverter

Quntao AN[1,3, a], Guanglin Wang[2, b], Minghang Duan[3, c], Li SUN[4, d]

[1]School of Mechatronics Engineering, Harbin Institute of Technology, Harbin, 15001, China

[2]School of Mechatronics Engineering, Harbin Institute of Technology, Harbin, 15001, China

[3]Department of Electrical Engineering, Harbin Institute of Technology, Harbin, 15001, China

[4]Department of Electrical Engineering, Harbin Institute of Technology, Harbin, 15001, China

[a]email: anquntao@163.com, [b]email: glwang@hit.edu.cn, [c]email: 991502632@qq.com, [d]email: motor611@sina.com

Keywords: Induction Motor; Open-End Winding; Dual Inverter; SVPWM Strategy; Common-Mode Voltage

Abstract. Dual inverter fed open-end winding induction motor (OEW-IM) is a new solution for multilevel drive. Comparing with traditional multilevel converters, the dual inverter is being interested in for its more flexible current control, the absence of fluctuating neutral point, and fault-tolerant capability. This paper analyzes the potential common-mode voltage (CMV) in the open-end winding induction motor system, and proposes a new space vector PWM (SVPWM) strategy to reduce the CMV. The proposed method is validated by simulations and experiments.

Introduction

With the development of multilevel converters, a dual inverter fed open-end winding induction motor drive is proposed [1] [2]. The dual two-level inverter can produce space voltage vector locations identical to that of a three-level inverter, and avoids the undesirable fluctuating voltage on the series DC capacitors. Recently, several power converter configurations derived from the dual inverter are presented [3]-[5]. A common DC link or isolated DC sources can be adopted in the dual inverters. In the common DC-link dual inverter, the zero-sequence current is detrimental to the system performance [6]-[8]. As to the dual inverter with isolated DC sources, the zero-sequence current can be eliminated but the common-mode voltage may produce axis current and shorten longevity of the motor. In order to eliminate the CMV in the dual inverter fed by isolated DC sources, the SVPWM strategy employing these switching combinations that do not contribute to the CMV is introduced [9]. Nevertheless, the maximum amplitude of reference voltage vector by these combinations is equal to DC link voltage V_{dc}, and the maximum DC link voltage utilization can not be obtained. To increase the DC voltage utilization, a new SVPWM strategy is proposed in this paper. The proposed strategy can eliminate the CMV completely when the magnitude of reference voltage is less than V_{dc} and the CMV can be restrained when the reference is larger than V_{dc}. The realization algorithms are introduced, and the method is validated by the simulation and experimental results.

Dual Inverter Fed Open-End Winding Motor System

The open-end winding induction motor drive system fed by dual inverters is shown in Fig.1. In this configuration, neutral connection of the motor is separated and fed by the dual two-level inverter from the both ends of the winding.

In Fig.1, the dual inverter is composed of two inverters, INV1 and INV2. The voltage vectors of the two inverters can be defined as follows:

$$\begin{cases} \boldsymbol{V}_{s1} = 2(v_{a1o} + v_{b1o}e^{j2\pi/3} + v_{c1o}e^{j4\pi/3})/3 \\ \boldsymbol{V}_{s2} = 2(v_{a2o'} + v_{b2o'}e^{j2\pi/3} + v_{c2o'}e^{j4\pi/3})/3 \end{cases} \tag{1}$$

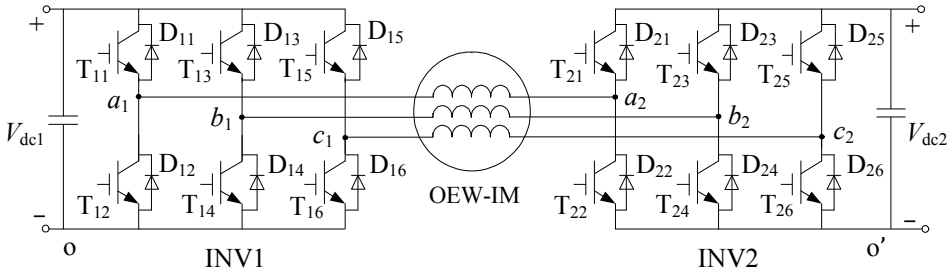

Fig.1. Open-end winding induction motor fed by dual inverter with isolated DC sources

In a two-level inverter, there are six switches on three legs. Eight combinations of these switches can produce eight voltage vectors including two zero vectors. Accordingly, space distribution of the voltage vectors by a single inverter is shown in Fig.2(a) for INV1 and Fig.2(b) for INV2, respectively.

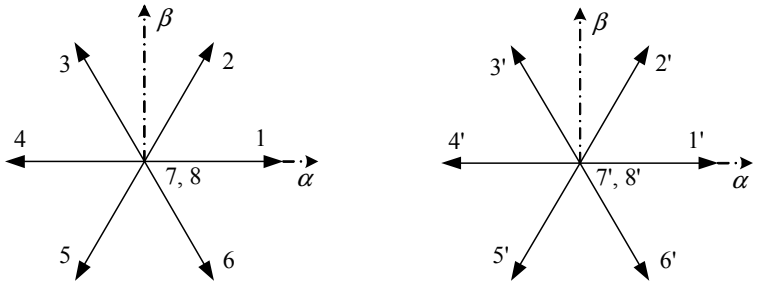

(a) INV1 (b) INV2

Fig.2. Space voltage vectors produced by INV1 and INV2

Thus, three phase voltages of the induction motor in Fig.1 are described by:

$$\begin{cases} v_{a1a2} = v_{a1o} - v_{a2o'} + v_{oo'} \\ v_{b1b2} = v_{b1o} - v_{b2o'} + v_{oo'} \\ v_{c1c2} = v_{c1o} - v_{c2o'} + v_{oo'} \end{cases} \tag{2}$$

Then, the space voltage vectors produced by the dual inverter can be solved by:

$$\boldsymbol{V}_s = 2(v_{a1a2} + v_{b1b2}e^{j2\pi/3} + v_{c1c2}e^{j4\pi/3})/3 = \boldsymbol{V}_{s1} - \boldsymbol{V}_{s2} \tag{3}$$

In other words, the output voltage vectors of the dual inverter can be combined by those from two inverters. There are 64 states totally, corresponding to 64 switching combinations, which can produce 18 non-zero space vector locations and a zero one. The distribution of these vectors in αβ reference frame is shown in Fig.3. The 19 vectors form 3 hexagons, the small hexagon ABCDEF, the middle one HJLNQS and the large one GIKMPQ respectively. According to the modulation principle of SVPWM, voltage vectors of the three hexagons can be used to synthesize the expected reference vector. Different from the two-level SVPWM, some vectors in the dual inverter may bring the CMV in the open-end induction motor drive.

SVPWM and Analysis of Common-Mode Voltage

For the system described in Fig.1, the sum of three phase currents is zero. As a result of the symmetrical back electromotive forces in the motor, the sum of three phase winding voltages is also zero, that is $u_{a1a2}+ u_{b1b2}+ u_{c1c2}=0$. Based on (2), the CMV can be obtained by:

$$u_{oo'} = -\frac{1}{3}(u_{a1o} + u_{b1o} + u_{c1o} - u_{a2o'} - u_{b2o'} - u_{c2o'}) \tag{4}$$

For a three-phase open-end winding motor, the 64 switching combinations are substituted into (4), respectively, and then their CMVs are shown in Table 1.

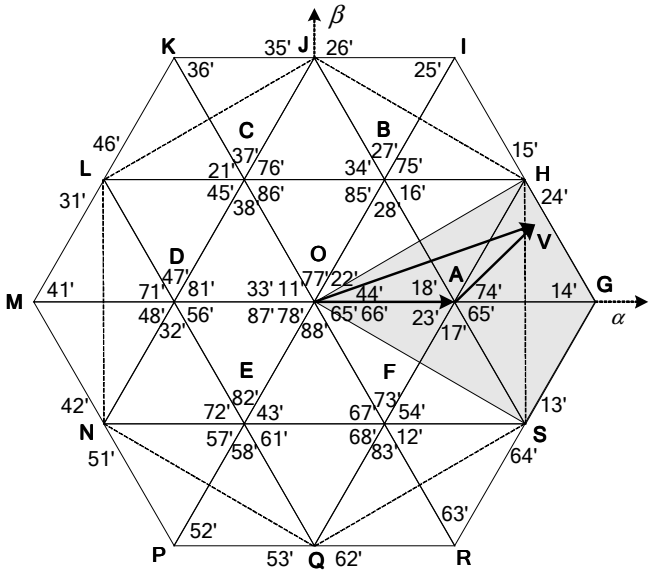

Fig.3. Distribution of space voltage vectors

Table 1 CMVs under various switching states

CMV	$-V_{dc}$	$-2V_{dc}/3$	$-V_{dc}/3$	0	$V_{dc}/3$	$2V_{dc}/3$	V_{dc}
Space voltage vectors	78’	74’, 76’, 72’, 58’, 38’, 18’	75’, 73’, 54’, 34’, 14’, 71’, 56’, 36’, 52’, 32’, 48’, 16’, 12’, 68’, 28’	88’, 77’, 66’, 55’, 44’, 33’, 22’, 11’, 53’, 35’, 15’, 51’, 13’, 31’, 46’, 64’, 24’, 42’, 26’, 62’	57’, 37,’ 45’, 43’, 41’, 17’, 65’, 63’, 25’, 23’, 84’, 61’, 21’, 86’, 82’	47’, 67’, 27’, 85’, 83’, 81’	87’

From Table 1, the CMVs produced by these voltage vectors on the middle hexagon HJLNQS are zero. Therefore, the CMVs will not be produced by employing these voltage vectors in SVPWM strategy. The traditional two-level SVPWM algorithm can be used to accomplish the modulation of the middle hexagon, but the sectors in the middle hexagon rotate 30 degree clockwise corresponding to that in the small one.

The modulation index m is defined to denote DC link voltage utilization as:

$$m = \left|\boldsymbol{V}_{\text{ref}}\right| / V_{\text{dc}} \tag{5}$$

Where, $\boldsymbol{V}_{\text{ref}}$ is the reference voltage vector. From Fig.3, the maximum linear modulation index of the dual inverter is $m_{\max}$=1.15. According to the modulation principle of SVPWM, the maximum amplitude of the synthesized reference voltage vector is V_{dc} by the middle hexagon, which is the radius of inscribed circle of the middle hexagon. Under this condition, the modulation index is one, and does not reach the maximum one obviously. Thus, when the amplitude of the reference vector is larger than V_{dc}, namely m>1, voltage vectors on the large hexagon are required to synthesize. The region of the large hexagon can be divided into 6 small hexagons, OBHGSF, OCJIHA, ODLKJB, OENMLC, OFQPND and OASRQE, which center on A, B, C, D, E and F, respectively. As shown in Fig.3, when the reference vector **OV** locates inside the shadow of the hexagon OBHGSF, it can be divided into two parts, namely **OV**=**OA**+**AV.** Moreover, **OA** can be obtained by vector 1 from INV1 (shown in Fig.2(a)), and the fixed switching state remains during one switching period. Meanwhile, **AV** can be obtained by modulating in the hexagon OBHGSF. In other words, **OV** can be achieved by making INV1 locate on vector 1 and modulating INV2. Then, **AV**=**OV**–**OA**, and the relationship for αβ components of vector **AV** and **OV** is:

$$v_{\text{AV}\alpha} = v_{\alpha} - \frac{2}{3}V_{\text{dc}};\ \ v_{\text{AV}\beta} = v_{\beta} \tag{6}$$

Similarly, when **OV** locates inside the hexagon OCJIHA, there is **OV**=**OB**+**BV**. **OB** is obtained by the vector 2 from INV2, and **BV** by modulation of INV1 in the hexagon OCJIHA. Successively, **OV** can be achieved by separating **OV** in to two parts, as **OV**=**OX**+**XV, (X**=**A**, **B**, **C**, **D**, **E**, **F)**. Here, **OX** is produced by one inverter and **XV** by the other one. To simplify the algorithm, the unified

pulse width modulation [10] is adopted to synthesize **XV** in these small hexagons. First, convert the reference vector into three phase reference frame by the inverse Clarke transformation:

$$\begin{bmatrix} v_{\mathrm{XVa}} \\ v_{\mathrm{XVb}} \\ v_{\mathrm{XVc}} \end{bmatrix} = \frac{2}{3}\begin{bmatrix} 1 & 0 \\ -1/2 & \sqrt{3}/2 \\ -1/2 & -\sqrt{3}/2 \end{bmatrix}\begin{bmatrix} v_{\mathrm{XV}\alpha} \\ v_{\mathrm{XV}\beta} \end{bmatrix} \tag{7}$$

The corresponding active times are defined as, respectively:

$$T_{\mathrm{a}} = Tv_{\mathrm{XVa}}/V_{\mathrm{dc}};\ \ T_b = Tv_{\mathrm{XVb}}/V_{\mathrm{dc}};\ \ T_{\mathrm{c}} = Tv_{\mathrm{XVc}}/V_{\mathrm{dc}} \tag{8}$$

Where, T is the switching period. The effective time T_{eff}, zero vector time T_0, and offset time T_{offset} are defined as, respectively:

$$T_{\mathrm{eff}} = T_{\max} - T_{\min};\ \ T_0 = T - T_{\mathrm{eff}};\ \ T_{\mathrm{offset}} = T_0/2 - T_{\min} \tag{9}$$

Where, $T_{\max}$ and $T_{\min}$ represent the maximum and minimum value of T_{a}, T_{b}, T_{c}, respectively. Then, conducting times of top switches in the inverter are:

$$T_{\mathrm{ga}} = T_{\mathrm{a}} + T_{\mathrm{offset}};\ \ T_{\mathrm{gb}} = T_{\mathrm{b}} + T_{\mathrm{offset}};\ \ T_{\mathrm{gc}} = T_{\mathrm{c}} + T_{\mathrm{offset}} \tag{10}$$

According to the modulation method above, the voltage vector with maximum amplitude of $2\sqrt{3}V_{\mathrm{dc}}/3$ can be achieved. However, the CMV may be produced during modulating with the large hexagon vectors. For example, when the reference vector **OV** locates inside the triangle AHG, vector 17', 14', 15', and 18' are used and the CMVs contributed by each vectors are $V_{\mathrm{dc}}/3$, $-V_{\mathrm{dc}}/3$, 0, and $-2V_{\mathrm{dc}}/3$, respectively. And their active times are $T_0/2$, T_1, T_2, and $T_0/2$. Then, the CMV during one PWM period is:

$$v_{\mathrm{oo'}} = \frac{V_{\mathrm{dc}}}{3}\times\frac{T_0}{2} + (-\frac{V_{\mathrm{dc}}}{3})\times T_1 + (-\frac{2V_{\mathrm{dc}}}{3})\times\frac{T_0}{2} = -\frac{V_{\mathrm{dc}}}{6}(T_0 + 2T_1) \neq 0 \tag{11}$$

Where, T_1, T_2 and T_0 are the active times of **AG**, **AH** and point **A**. From (11), the CMV is not zero when the modulation strategy above is adopted.

New SVPWM Strategy Suppressing Zero-Sequence Voltage

Here, how to restrain the CMV will be discussed. If one defines active time distribution factor x （0<x<1）for zero vectors, and supposes the active time of vector 17' is xT0 and that of 18' is (1-x)T0 , then the CMVs can be expressed as:

$$v_{\mathrm{oo'}} = \frac{V_{\mathrm{dc}}}{3}\times\frac{xT_0}{2} + (-\frac{V_{\mathrm{dc}}}{3})\times T_1 + (-\frac{2V_{\mathrm{dc}}}{3})\times\frac{(1-x)T_0}{2} \tag{12}$$

To restrain the CMV furthest, one can let $v_{\mathrm{oo'}}$=0 and obtain:

$$x = \frac{2}{3} + \frac{T_1}{3T_0} \tag{13}$$

By redistributing the active time for zero voltage vectors, one can obtain (14) based on (8).

$$T_{\mathrm{offset}} = \frac{1}{3}(T_0 - T_2) - T_{\min} \tag{14}$$

When vector AV locates in the shadow in Fig.3, T1=Tmid–Tmin. And based on Tmax+Tmid+Tmin=0, one can get the offset time according to (9) as:

$$T_{\mathrm{offset}} = \frac{T_0 + T_{\mathrm{eff}}}{3} = T/3 \tag{15}$$

Substituting the results into (10), the conducting times of top switches in INV2 can be achieved. The same process can be used for the situations that vector OV locates in other regions. Further analysis shows that the same result Toffset =T/3 can be obtained wherever OV locates. Thus, the modulation strategy restraining the CMV can be simplified according to the conclusion.

Based on (13), when T1=T0, x=1, and the limitation for eliminating the CMV is reached, and meanwhile |OV|=$2\sqrt{3}V_{\mathrm{dc}}/3$. When the amplitude of the reference vector OV is larger than $2\sqrt{3}V_{\mathrm{dc}}/3$, the proposed modulation strategy can not eliminate the CMV completely but retrain it to the greatest degree fortunately.

Simulation and Experimental Results

The model of a vector controlled open-end winding induction drive fed by the dual inverter is established by Matlab/Simulink. The induction motor's parameters are as follows: rated voltage 380V, rated current 6.8A, rated frequency 50Hz, stator resistance 2.375Ω, stator inductance 189.2mH, mutual inductance 181.4mH, rotor resistance 1.741Ω, rotor inductance 188.9mH, rotary inertia 0.0109 Kgm² and polepairs 2. The simulation results are shown in Fig.4. Phase-a voltage is shown in Fig.4(a), three phase currents are shown in Fig.4(b), and motor speed and torque are shown in Fig.4(c). Fig.4(d)(e) and (f) show the CMV waveforms by modulating with the middle hexagon, the large hexagon and the proposed SVPWM, respectively. From the simulation results, the CMV is almost zero when the middle hexagon is used for modulation. However there is obvious CMV when the large hexagon is adopted. When the modulation index is larger that one (m>1), the CMV can be restrained effectively by the proposed method. The experiment results for the modulation with the large hexagon and the proposed method are shown in Fig.5, respectively. The experiment results are consistent with the simulation ones, which validate the proposed SVPWM strategy.

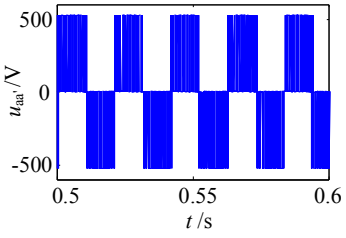

(a) Phase a voltage

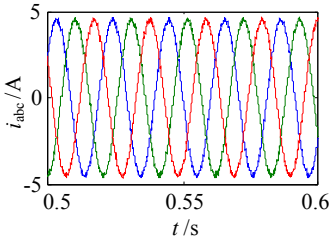

(b) Three phase currents

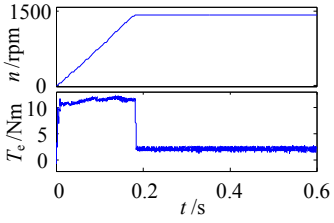

(c) Speed and torque

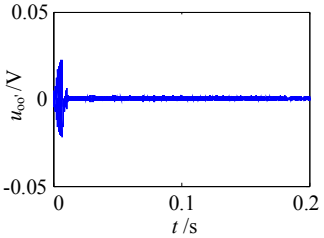

(d) CMV under mid-hexagon SVPWM

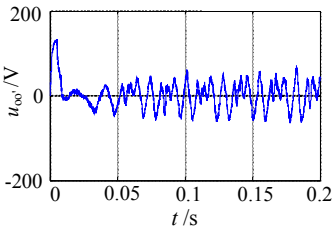

(e) CMV under large-hexagon SVPWM

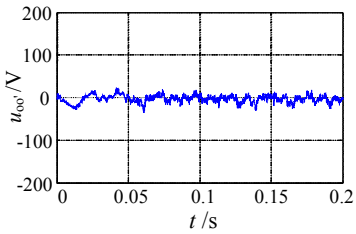

(f) CMV under the proposed SVPWM

Fig.4. The simulation results

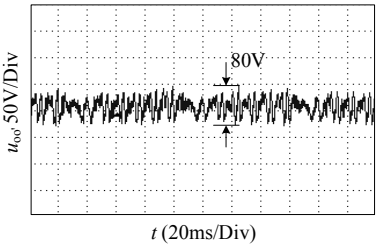

(e) CMV under large-hexagon SVPWM

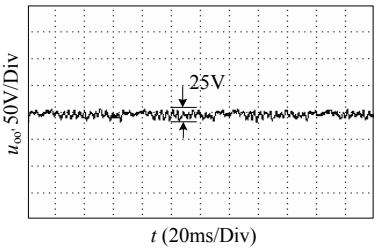

(f) CMV under the proposed SVPWM

Fig.5. The experimental results

Conclusion

The same voltage vector locations can be obtained in the open-end winding induction motor system fed by dual inverters as those in three-level inverters. Comparing with two-level inverters, the configuration can improve the DC link voltage utilization significantly. The CMV problem in dual inverters fed by isolated DC sources is discussed in this paper, and a now SVPWM modulation strategy for restraining the CMV is proposed. The proposed strategy can eliminate the CMV completely when the modulation index m<1 and restrain the CMV effectively when m>1. The simulation results as well as experimental ones validate the presented method.

Acknowledgement

In this paper, the research was sponsored by the National Nature Science Foundation of China (Project No. 51207029), China Postdoctoral Science Foundation (Project No. 2012M510089), Heilongjiang Postdoctoral Fund (Project No. LBH-Z11145) and the Fundamental Research Funds for the Central Universities (Project No. HIT.NSRIF.2015012).

References

[1] J. Rodriguez, J.S. Lai, F.Z. Peng. Multilevel inverters: a survey of topologies, controls, and applications[J]. IEEE Trans. Ind. Electron., 2002:49(4):724-738.
[2] K.R. Sekhar, S. Srinivas. Discontinuous decoupled PWMs for reduced current ripple in a dual two-level inverter fed open-end winding induction motor drive[J]. IEEE Trans. Power Electron., 2013:28(5):2493-2502.
[3] M. Jones, I.N.W. Satiawan, N. Bodo, E. Levi. A dual five-phase space-vector modulation algorithm based on the decomposition method[J]. IEEE Trans. Ind. Appl., 2012:48(6):2110-2120.
[4] R.S. Kanchan, P.N. Tekwani, K. Gopakumar. Three-level inverter scheme with common mode voltage elimination and DC link capacitor voltage balancing for an open-end winding induction motor drive[J]. IEEE Trans. Power Electron., 2006:21(6):1676-1683.
[5] G. Mondal, K. Sivakumar, R. Ramchand, K. Gopakumar. A dual seven-level inverter supply for an open-end winding induction motor drive[J]. IEEE Trans. Ind. Electron., 2009:56(5):1665-1673.
[6] V.T. Somasekhar, K. Gopakumar, A. Pittet, V.T. Ranganathan. PWM inverter switching strategy for a dual two-level inverter fed open-end winding induction motor drive with a switched neutral[J]. IEE Proc.-Electr. Power Appl., 2002:149(2):154-160.
[7] S. Srinivas, V.T. Somasekhar. Space-vector-based PWM switching strategies for a three-level dual-inverter-fed open-end winding induction motor drive and their comparative evaluation[J]. IET Electr. Power Appl., 2008:2(1):19-31.
[8] V.T. Somasekhar, S. Srinivas, B.P. Reddy, C.N. Reddy, K. Sivakumar. Pulse width-modulated switching strategy for the dynamic balancing of zero-sequence current for a dual-inverter fed open-end winding induction motor drive[J]. IET Electr. Power Appl., 2007:1(4):591-600.
[9] M.R. Baiju, K.K. Mohapatra. A dual two-level inverter scheme with common mode voltage elimination for an induction motor drive[J]. IEEE Trans. Power Electron., 2004:19(3):794-805.
[10] D.W. Chung, J.S. Kim, S.K. Sul. Unified voltage modulation technique for real-time three-phase power conversion[J]. IEEE Trans. Ind. Appl., 1998:34 (2):374-380.

Advanced Materials Research Vols. 986-987 (2014) pp 1054-1057

doi:10.4028/www.scientific.net/AMR.986-987.1054

Brake pedal feel verification of the energy recovery system

CAI Jian-wei[1, a],CHU Liang[1, b], FU Zi-cheng[1, c], LIU En-fen[2,d]

[1] Jilin University, Changchun, Jilin Province 130022, P.R. China

[2] Jilin Dongguang Aowei Automobile Brake System Co., Ltd., Changchun, China

[a]jianweicai@163.com,[b]chuliang@jlu.edu.cn, [c] fzc-010@163.com,[d] jabflef@126.com

Keywords: Braking Strategy; brake pedal simulator; pedal feel; vehicle test.

Abstract. Brake pedal feel is intuitive feelings for the driver and affected vehicle safety performance. Due to the participation of the motor, brake force distribution and the original pedal feel of the driver would be changed. Based on the traditional hydraulic unit of ESC, Jilin University developed a braking energy recovery system of uniaxial decoupled. A series of fixed partition coefficient control strategy was developed, coordinated control of electrical regenerative braking and hydraulic braking was carried out. Vehicle test was carried out for coordinated braking strategy, parallel strategy and traditional control strategy. Vehicle test results show that the brake pedal travel simulator and the coordinated braking strategy can improve the energy recovery, and ensure that the brake pedal feel is consistent with the traditional vehicle.

Introduction

Regenerative braking system converted the kinetic energy into other forms of energy and reused when vehicle was deceleration or braking [1]. Due to the participation of the motor, brake force distribution and the original pedal feel of the driver would be changed and vehicle safety, economy and comfort were affected. In order to improve the braking energy recovery rate and ensure the brake pedal feel, foreign car manufacturers developed many mature brake energy recovery systems[2-5], Such as the ECB system of Toyota , the EDIBS system of Nissan developed with Hitachi, the ESP-hev and HAS-hev system of BOSCH, regenerative braking system based ESC of Continental. Domestic was in infancy, some companies and universities proposed some new configuration system, and applied for a patent, but no actual product appearance. To solve the above problems and avoid the patents, Jilin University proposed a solution, that the hydraulic brake system and motor regenerative is decoupled for one axis, the pedal travel simulator was designed and developed independent [6].

System Architecture

Vehicle Introduction. In this paper, the target vehicle was a hybrid vehicle of domestic [7]. The vehicle technical parameters was shown in Table 1

Table 1 The main technical parameters

Parameter	Value
Vehicle mass	1524kg
Wheelbase	2675mm
Rolling radius	307mm
Motor rated power	20kw
Maximum motor power	40kw
Motor rated torque	130Nm
Maximum motor torque	260Nm
Battery voltage	288V
Battery capacity	6Ah
Main reduction ratio	4.313

Hardware Introduction. Jilin University brake system hardware solution was as shown in Figure 1. Normal state, the valve 1 is normally open, valve 2 is normally closed. When the vehicle was braking, valve 1 and valve 2 was energized, the valve 1 was used to cut off the hydraulic brake circuit between front axle and master cylinder. Valve 2 was used to control the work state of the simulator and simulate the pedal feel of the front axle. When the braking torque of the motor is insufficient or braking torque of demand increases, It need to be compensated by hydraulic brake, Active increase pressure was achieved by hydraulic pump of the ESC hydraulic unit and the check valve. When the pedal travel simulator fails, vehicle restored the traditional braking to ensure the safety of vehicle.

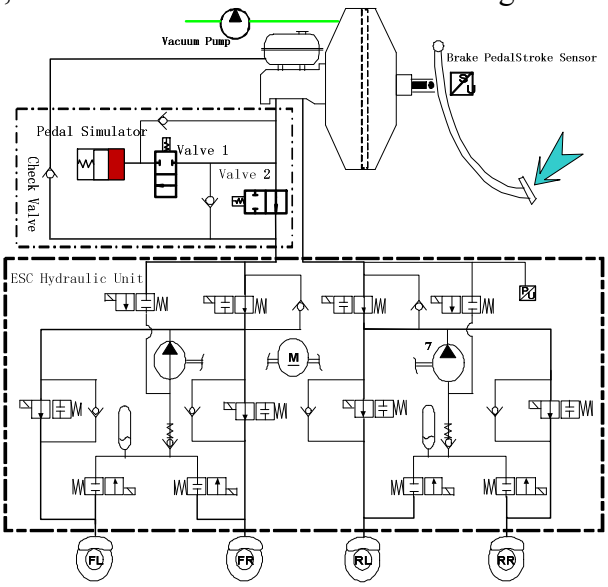

Fig 1 Hardware solutions of hydraulic braking system

Control Strategies.

In this paper, there are three control strategies: a fixed percentage of brake force distribution control strategy, parallel regenerative braking control strategies and the traditional control strategy were divided into two cases, the motor braking torque was 80Nm for parallel regenerative braking control strategy. That these four control strategies were strategy A, strategy B, and strategy C.

Strategy A: a fixed percentage of brake force distribution control strategy [8] is used as brake torque distribution for the front and rear axles based on traditional distribution vehicles , that the front axle during braking remains a traditional car brake force distribution coefficient β unchanged. As shown in Figure 2.

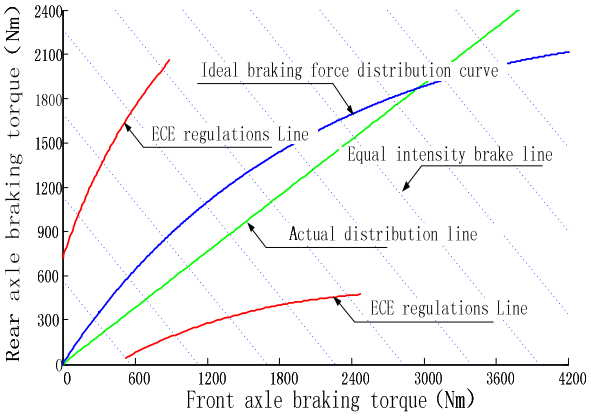

Fig2 Braking torque distribution method

Demand braking torque of front axle is described as:

$$T\_Req\_FA = \beta * T\_require \quad (1)$$

Demand braking torque of front axle is described as:

$$T\_Req\_RA = (1-\beta) * T\_require \quad (2)$$

Demand braking torque of front axle is described as:

$$T\_require = 2 * P\_RR * (C_f + C_r) \quad (3)$$

Here, T_Req_FA-demand braking torque of front axle; T_Req_RA-demand braking torque of front axle; T_require-demand braking torque of driver. P_RR-wheel cylinder pressure of right reart; C_f-brake effectiveness factor of front wheel; C_r-brake effectiveness factor of rear wheel.

Front axle braking torque could be consisted by motor torque and hydraulic braking torque. The demand braking force of front axle was the goal, to maximize the regenerative braking force of the motor, the shortfall was complemented by the hydraulic braking force of front axle. When the vehicle speed is below the minimum speed, reducing the braking force of the motor gradually and increasing front axle hydraulic braking force to ensure that the total braking force unchanged.

So the demand braking torque of motor and the demand hydraulic braking torque of the front axle were calculated as:

$$T\_Mot\_Req = \min(T\_Mot\_Max, T\_Req\_FA) \quad (4)$$

$$T\_Hyd\_FA\_Req = T\_Req\_FA - T\_Mot\_Act \quad (5)$$

Here, T_Mot_Req -demand braking torque of motor; T_Mot_max -maximum braking torque of motor; T_Hyd_FA_Req -demand hydraulic braking torque of front axle; T_Mot_Act -actual braking torque of motor.

Strategy B: Cancel simulator control, set the demand motor braking torque is 80Nm.

Strategy C: Cancel simulator control, set the demand motor braking torque is 0Nm.

Vehicle Test

Real vehicle test verification was carried out on high adhesion road, under speed 60km / h to verify the four control strategies proposed above, the brake pedal is divided into fast and slow speeds. Test results are shown in Figs.

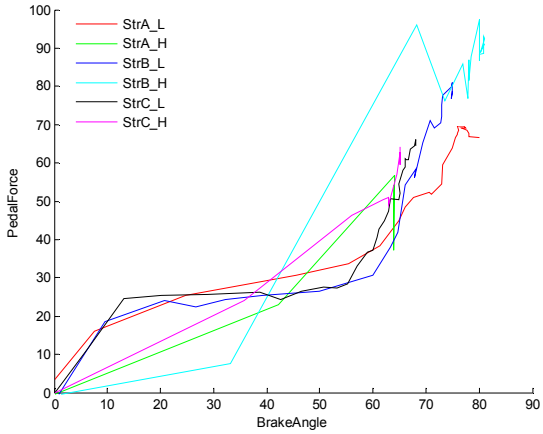

Fig3 brake pedal angle and force

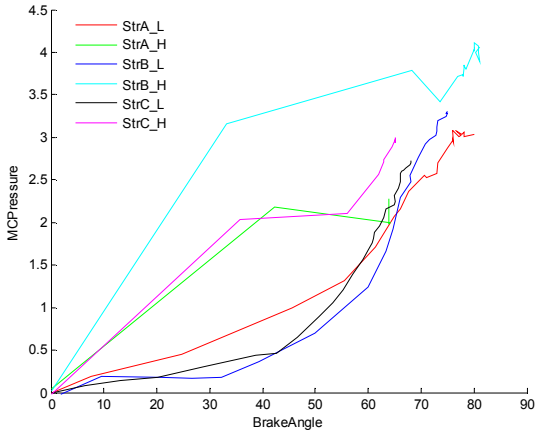

Fig4 Brake pedal angle and vehicle deceleration

StrA_L is the condition of strategy A and pedal speed is low; StrA_H is the condition of strategy A and pedal speed is high; StrB_L is the condition of strategy B and pedal speed is low; StrB_H is the condition of strategy B and pedal speed is high; StrC_L is the condition of strategy C and pedal speed is low; StrC_H is the condition of strategy C and pedal speed is high.

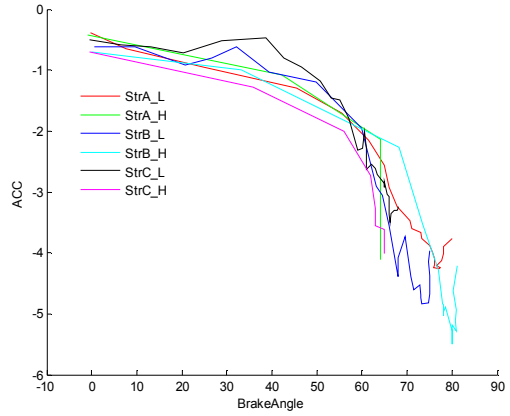

Fig5 Brake pedal angle and master pressure

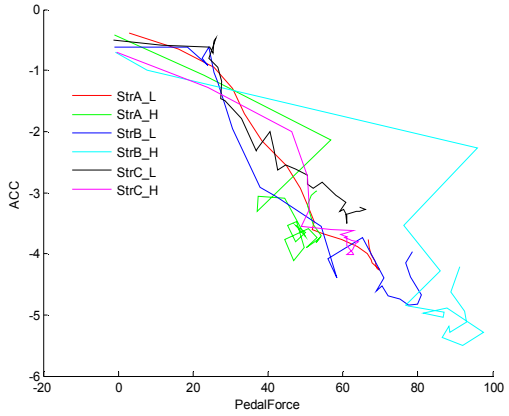

Fig6 Brake pedal force and vehicle deceleration

Pedal feel of coordinated control algorithm is basically same with the original car pedal feel , Parallel braking control strategy, due to entry and exit of the motor braking torque pedal feel changes, especially exit stage, the driver braking feeling becomes 'soft' and impacts vehicle safety.

Results

Parallel braking strategy, in order to ensure safety, motor braking torque values cannot be too large, and therefore energy recovery is finite, the driver braking feel becomes 'soft' when motor torque exits and impact vehicle safety performance. Coordinated braking strategy can use torque motor fully and ensure the pedal feel to consistency with the original vehicle.

Acknowledge

Supported by Graduate Innovation Fund of Jilin University

Reference

[1] Cai J W, Chu L, Fu Z C, et al. Regenerative Braking System for a Pure Electric Bus[C]. Applied Mechanics and Materials, 2014, 543: 1405-1408.

[2] Nakamura E, Soga M, Sakai A, et al. Development of electronically controlled brake system for hybrid vehicle[J]. SAE paper, 2002: 01-0300.

[3] Oshima T, Fujiki N, Nakao S, et al. Development of an Electrically Driven Intelligent Brake System[J]. SAE International Journal of Passenger Cars-Mechanical Systems, 2011, 4(1): 399-405.

[4] Sunao Hano ,Motomu Hakiai. New Challenges for Brake and Modulation Systemsin Hybrid Electric Vehicles (HEVs) and Electric Vehicles (EVs) [J].SAE paper, 2011: 39-7210.

[5]von Albrichsfeld C, Karner J, von Albrichsfeld-Continental C, et al. Brake system for hybrid and electric vehicles[J]. SAE Technical Paper, 2009: 01-1217

[6] Wang Cong, Liu Hongwei, Yao Liang, et al. Design of Brake Pedal Stroke Simulator for Hybrid Electric Car[C]. Advanced Materials Research, 2013, Vols. 694-697, pp73-76

[7] Cai J W, Chu L, Fu Z C, et al. Study on Regenerative Braking Control Algorithm[C]. Advanced Materials Research, 2014, 898: 873-877.

[8] Chu L, Yao L, Chen J, et al. Integrative braking control system for electric vehicles[C]//Vehicle Power and Propulsion Conference (VPPC), 2011 IEEE. IEEE, 2011: 1-5.

Advanced Materials Research Vols. 986-987 (2014) pp 1058-1062

doi:10.4028/www.scientific.net/AMR.986-987.1058

Design and test of the control system for the fast disruption mitigation valve on J-TEXT

Shenyang Wang[1, 2, a], Zhongyong Chen[1, 2, b] and Yihui Luo[1, 2, c]

[1]State Key Laboratory of Advanced Electromagnetic Engineering and Technology, 430074, Wuhan, China

[2]College of Electrical and Electronic Engineering, Huazhong University of Science and Technology, 430074, Wuhan, China

[a]yyqf23@163.com, [b]chenzy1003@163.com, [c]yhluoceee@163.com

Keywords: Fast disruption mitigation valve, Control system

Abstract. Disruptions are highly undesired events during tokamak plasma discharge, and now massive gas injection (MGI) is the most promising technique mitigating all negative consequences of a disruption. A fast disruption mitigation valve has been designed and tested for J-TEXT tokamak based on eddy-current repulsion mechanism. In order to get the key operating parameters of the valve such as voltage and gas pressure in real time and to realize remote automatic control, a control system on LabVIEW software platform based on hardwires of sensors, relays, Advantech industrial computer and NI-6221 data acquisition card has also been designed. The experimental test results show that the control system works well.

Introduction

Tokamak is the most advanced device of artificial fusion machines. The tokamak operation on several mega-ampere（MA） and thus contains an abundant source of energy. But during tokamak plasma discharge, because of plasma MHD instability, an unfavorable current distribution can lead to the creation of internal plasma modes and to enhanced losses of energy and particles or, in the worst case, to an abrupt termination of the plasma current. This process is called disruption [1].

Disruptions are highly undesired events. In current large size tokamaks, they can cause significant machine damage. Major disruption during tokamak operation can cause a severe damage on tokamak, especially in the next step large devices such as ITER. During disruptions, the plasma energy would loss within 1 ms and result in a large force load on vessel components. The runaway electrons (REs) with hundreds mega-electron-volt (MeV) energy also generate due to the high electrical field. The REs could impact and damage the plasma facing components [1, 2].

In order to mitigate the negative effects of a disruption, MGI is selected because of its important advantages: the gas flows very fast and can fill the whole vessel immediately which leaving no space for the development of runaway electrons. As the warning time prior to the disruption given by MHD modes or other signatures can only amount to 100 ms or even shorter, the most important for mitigation is a very fast reaction of massive gas injection device.

A fast disruption mitigation valve has been developed on J-TEXT successfully. This paper introduces a detailed design and test of the control system for the fast disruption mitigation valve which could open 0.5 ms after a TTL trigger signal, the control system can get key operating parameters of the valve such as voltage and gas pressure in real time and realize remote automatic control. The basic construction of the valve system will be presented firstly, and then a detailed design of the valve control system based on LabVIEW will be shown, test results and summary are given at last.

Construction of the valve system

Figure 1 shows a sketch and an assembled image of the valve:

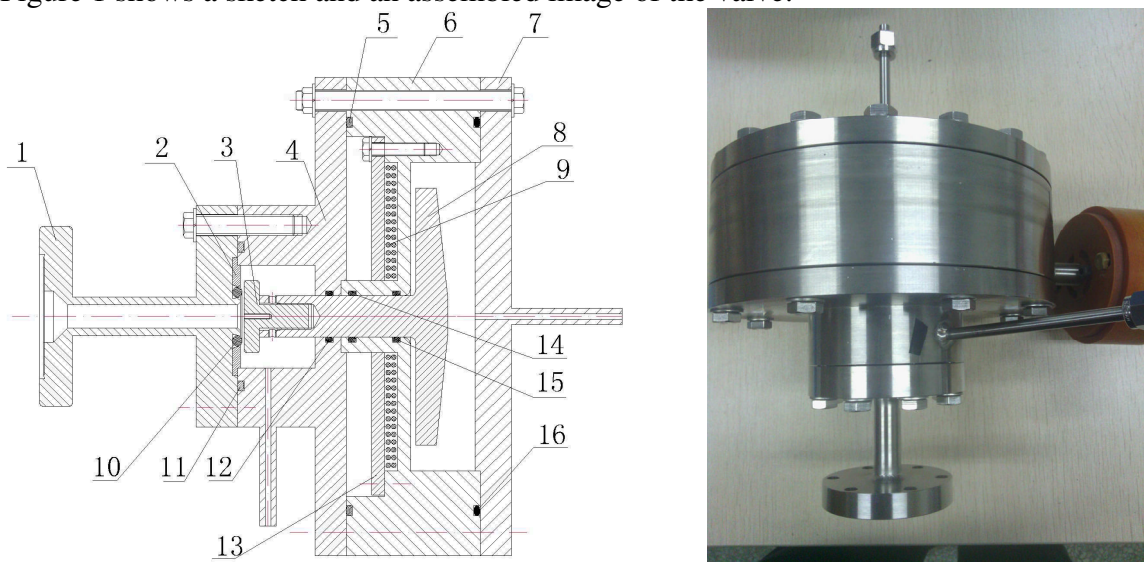

(a) (b)

FIG. 1, (a) Structure of the valve: (1) CF 35 flange; (2) washer; (3) removable piston; (4) work chamber; (5), (10), (11), (12), (14), (15), (16) o-rings; (6) back chamber; (7) cover; (8) mushroom piston; (9) coil; (13) platen, (b) image of the fast valve.

Figure 1 (a) shows structure of the valve. All the components contacted with vacuum vessel are made of stainless steel, except for the aluminum piston. To begin with its principle, the work and back chamber are filled with helium or argon, there's a strong force pressed on the mushroom piston and the o-ring (10) because of the difference of the actual areas on which the pressures are acting, when the capacitor (C=0.5 mF) is discharged through the coil an eddy current excited by a time-varying magnetic field will generate an electromagnetic force which opens the valve [2, 3]. The work chamber volume is about 30ml. The gas pressure can be selected between 1 and 50 bar but should be high enough in order to guarantee a fast gas flow into the discharge vacuum. The assembled image of the valve is shown in Fig.1. (b)

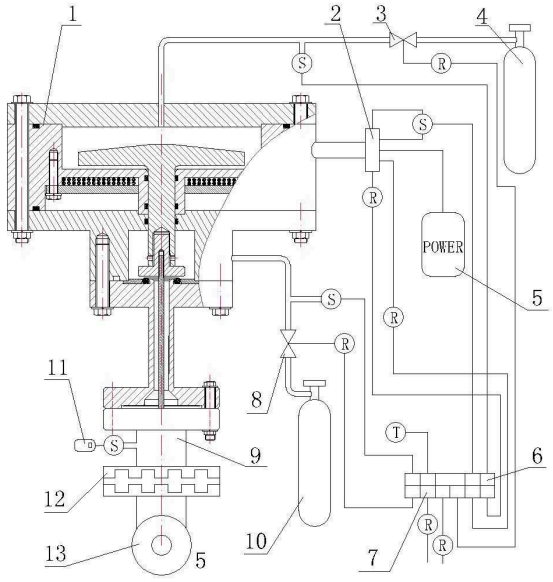

FIG. 2, Test bench (1) the valve; (2) capacitor; (3),(8) safety valves; (4),(10) gas bottles; (5) high voltage power supply of the capacitor; (6) signal input of the integrated controller; (7) signal output of the integrated controller; (9) vacuum chamber; (11) vacuum gauge; (12) flapper valve; (13) vacuum pump; S represents the sensors, T represents the trigger and R represents solid state relay.

For checking the valve and control system performance, a basic test and calibration bench system has been assembled in laboratory shown in Fig. 2 [2]. The valve system contains the disruption mitigation valve (1) assembled with a vacuum chamber (9), pressure sensors represented as S, trigger signal represented as T and solid state relays represented as R in the figure, a vacuum pump (13), a high voltage supply (5), and gas bottles (4), (10). The vacuum pump is located to pump out the injection chamber after each test. An integrated controller which contains signal input (6) and output (7) has been used.

First the safety valve (3) is opened which provides a force on the mushroom piston leading the fast valve (1) separated from the vacuum chamber (11). After that, the capacitance voltage, pressures in work chamber are changed to the desired value. The values of the capacitance voltage and pressures in both two chambers can be detected by the sensors and changed by switching the relays. At last, when the valve control system detects the trigger, it will output an open signal and the energy storage in the capacitor will be released through the coil and thus the fast valve will be opened.

Design and test of the valve control system

The main function of the control system is when a trigger signal of an intended disruption is detected, it outputs a high level TTL signal which will open the valve and thus a certain amount of gas is injected into the tokamak vacuum. The amount needed of gas injected vary on different plasma operation parameters. And during research, the mitigation effects of different capacitor voltage and different amount of the gas injected are very important. All the valve operation parameters need to be adjusted manually or automatically. In order to facilitate the experiment, two channels of A and B for charging the capacitor have been used as shown in Fig. 3(b). Channel A is used for automatic charge and B for manual. Another important consideration is keeping functions of aeration and charging the capacitor of the fast valve closed when detected the trigger signal for one second. And the fast valve opens a certain time that can be adjusted after getting the trigger signal for requirements of physical experiment.

Due to the complexity of the valve work environment (strong electromagnetic radiation), the output values of sensors have a small fluctuation which can cause repeated action of the relay. For the gas pressure and capacitance voltage is very high, the control system could have a noise tolerance ΔN, when the gas pressure or voltage exceed these settings, the control system will output a low TTL level and only when it decreases to ΔN smaller than the settings will the control system output a high TTL level (so called threshold protection).

Main functions of the control system are listed below [4]:

a) Analog signal acquisition of the coil voltage and gas pressures of both work and back chamber
b) Digital signal acquisition of the trigger
c) Automatic aeration
d) Automatic and manual charging
e) Save specific data for further checking
f) Threshold protection

As shown in Fig. 2, the whole hardware bench is based on sensors, relays, Advantech industrial computer and NI-6221 data acquisition card. According to the requirements mentioned above, LabVIEW is chosen as the most suitable software development bench because of its great capabilities in the field of test, measurement and control. LabVIEW is a graphical programming language and it has a straightforward development interface which can reduce the development time of prototype design significantly and make it easier for future maintenance [4, 5].

To make the system performance better and solve contradiction between rapid trigger signal acquisition and relatively slow analog data indication, multithreading design is selected. A text file is created and the acquainted data will be saved into it when getting the trigger and data storage only lasts for one second.

The basic program flow diagrams are given below in Fig.3. [6]

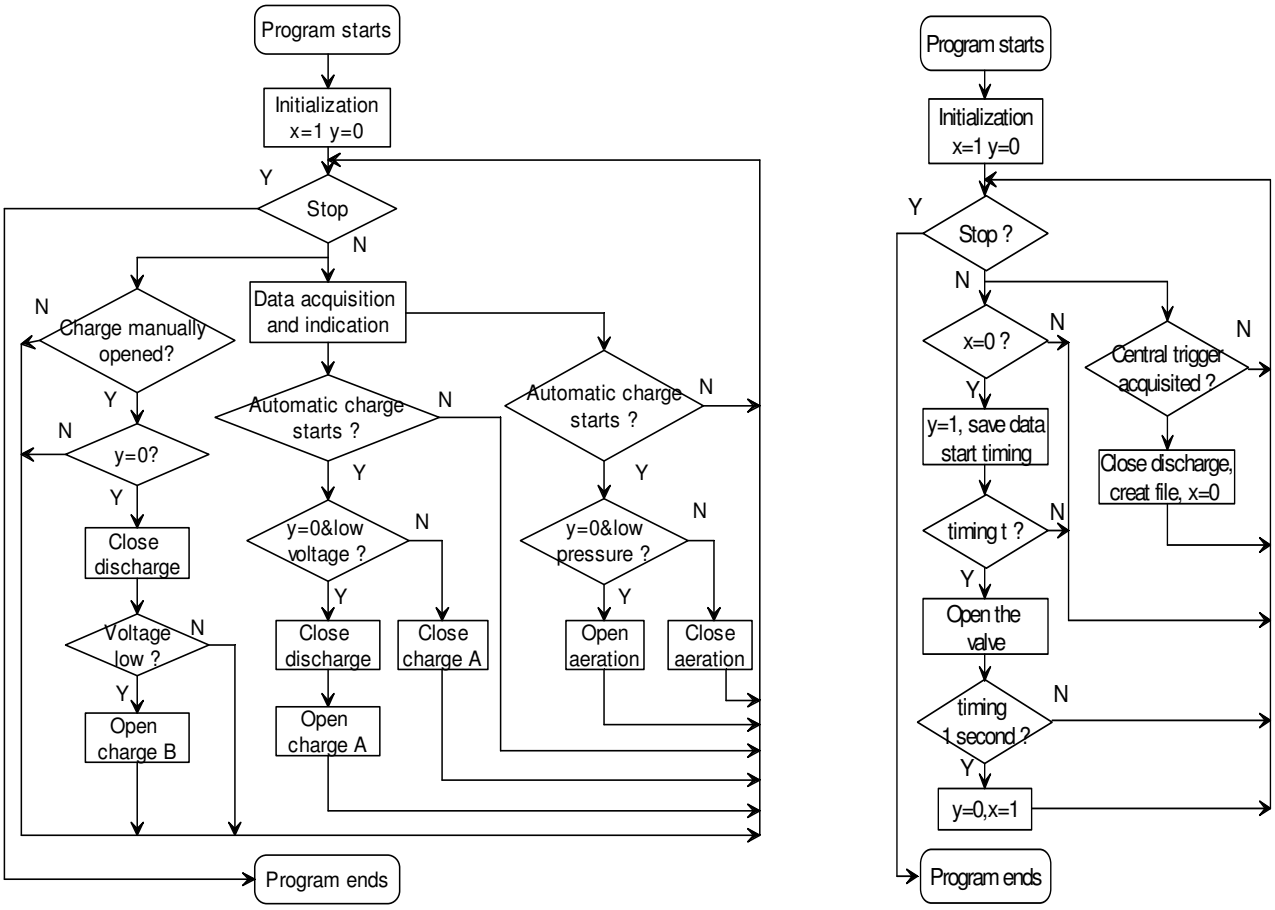

(a) (b)

FIG. 3, (a) Control thread of the valve; (b) Trigger detection, timing and data storage thread

The interface of the control system is shown in Fig. 4.

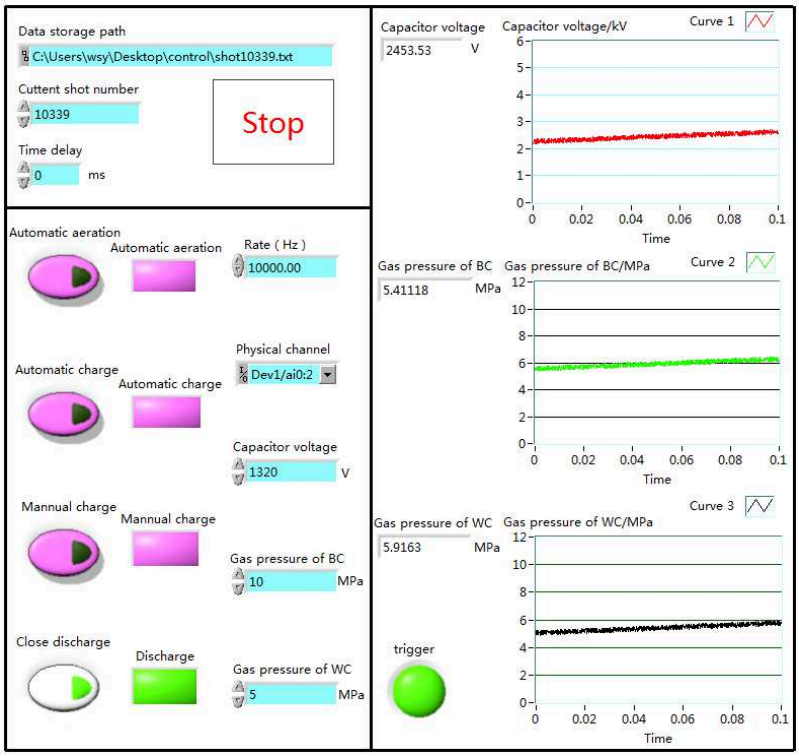

FIG. 4, Operation interface of the control system

As shown in Fig.4, the part of data acquisition and indication is on the right. And the parameters settings and control area are on the left. The software threshold protection is an important function of the control system and its realization is shown in Fig. 5. It is used as a subroutine in the system.

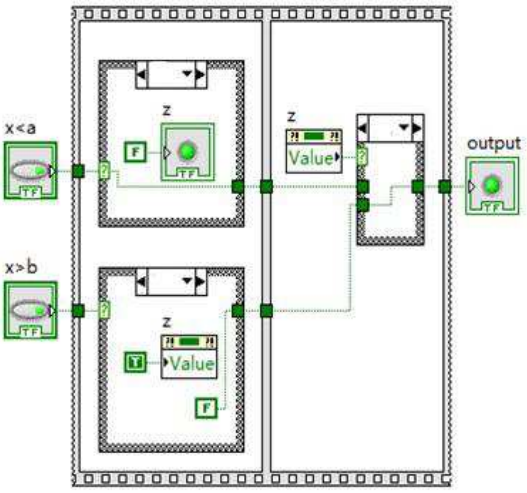

FIG. 5, Realization of the threshold protection

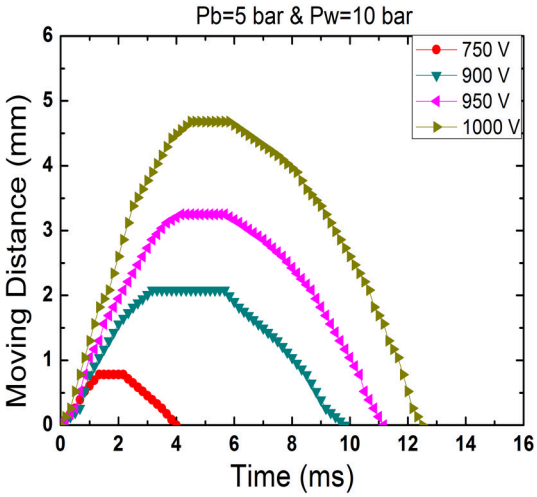

FIG. 6, Opening characteristics of the valve

Fig. 6 shows a typical waveform of the opening characteristics of the valve by a fast camera under different capacitor voltages ranging from 750V to 1000V (Pb represents gas pressure in back chamber and Pw in work chamber, both gases are argon). One can see the valve starts to open about 0.3ms after the trigger signal. After about 3ms, it is nearly completely open and 10ms later is closed again due to the high gas pressure in the back chamber when the capacitor voltage is 900V.

Summary

In this paper, a fast valve test bench and its real-time control system have been introduced. The control system can quickly get and adjust various parameters of the valve， which is very convenient for relevant physical experiments. To meet some special experimental requirements, the control system also has some particular functions such as accurate delayed trigger of the capacitor and locking functions of aeration and charge when the valve is open. The control system has a friendly interface and stable operation. During tests, it works well and will be used in the next round physical experiments on J-TEXT tokamak.

References

[1] ITER Physics Basis, Nuclear. Fusion 39, 2137 (1999)
[2] A. Savtchkov, K.H. Finken, and G. Mank. Development of a fast valve for mitigating disruptions in tokamaks. Review of Scientific Instruments, 73, 3490(2002)
[3] S.A. Bozhenkov, K.H. Finken, M. Lehnen, and R.C. Wolf. Main characteristics of the fast disruption mitigation valve. Review of Scientific Instruments, 78, 033503(2007)
[4] National Instruments Corporation. LabVIEW Basic I: Development Course Manual. 2008.
[5] Liu Rui, et al. Design of tokamak synchronous data acquisition system based on PXI Express. Atomic Energy Science and Technology, 48,170(2014.1) (In Chinese)
[6] Young Ok Kim, et al. Control and operation of the gas injection systems for KSTAR tokamak. Fusion Engineering and Design, 88, 1132(2013)

Advanced Materials Research Vols. 986-987 (2014) pp 1063-1066

doi:10.4028/www.scientific.net/AMR.986-987.1063

Design of controller of permanent magnet brushless Dc motor for electric vehicle

Haining Jiao[1,a], Xiping Liu[2,b] and Jie Yang[3,c]

[1]Jiangxi University of Science and Technology, Ganzhou Jiangxi 341000,China

[2]Jiangxi University of Science and Technology, Ganzhou Jiangxi 341000,China

[3]Jiangxi University of Science and Technology, Ganzhou Jiangxi 341000,China

[a]email:jiaohaining@yeah.net,[b]email:759247639@qq.com,[c]email:15405993@qq.com

Keywords: electric vehicle; brushless dc motor; STM32; PID controller

Abstract. In view of the defects of the electric car driver motor technology, considering actual needs of the car running, relaxing the electrical power density and the limitation of the moment of inertia etc, focusing on the reliability, speed range and high efficient operation area of the motor, based on the analysis of permanent magnet brushless dc motor operation principle, this paper designed a low cost, high intelligent electric car permanent magnet brushless dc motor controller. Through the analysis, simulation, experiment and comparison, the results show that the control system has good dynamic response and steady state properties.

Introduction

With the advantages of high efficiency, high torque, easy to control, easy to cooling, maintenance costs low, long life, safe and reliable, low noise, magnetic brushless dc motor are widely used as a drive motor for electric vehicles. There are many factors restricting the development of electric vehicles, while motor controller is one of the important reasons. In general, permanent magnet brushless dc motor can be broken down into ontology, electronic commutation device and the rotor position sensor and so on three parts. The principle block diagram is shown in fig.1. in this diagram, the dc power provides power; the rotor position sensors detect the rotor position information and send signals to the electronic commutation circuit processing, then get the next position electronic switch signal conduction.

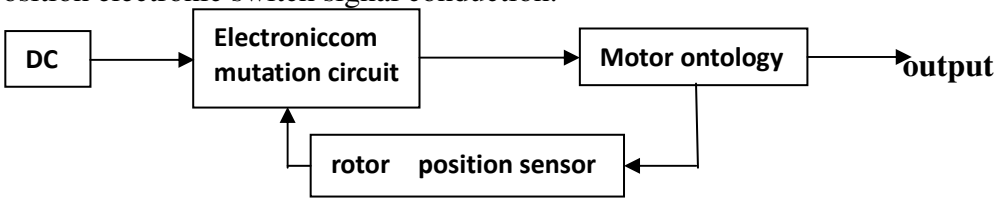

Fig.1 Brushless dc motor working principle diagram

Applied to motor control system of micro controller must be short interrupt time delay, namely good real-time response, and must have the superior control performance. Based on the above requirements, this design employ the STM32 series microcontrollers STM32F103, which is the core of the drive system. STM32F103 uses the 32-bit ARM Coaex-M3 kernel and it has the advantages of operation speed, high performance, low power consumption, high code density, etc. The kernel is specifically designed to meet the high performance, low power consumption, competitive price in the integration of embedded in the field of requirements. The traditional PID control algorithm is simple and has good robustness and reliability, so it is often used to control motor control system of position loop, current loop and speed loop.

Permanent Magnet Brushless Dc Motor Control System

The electric car driving system

In general, the electric car motor drive system include motor, sensor, control circuit and peripheral circuit, etc, as shown in Fig.2. The dc power which is provided by storage battery is

converting by IGBT power circuit for brushless dc motor, the system uses pulse width modulation to adjust the motor speed, and the current detecting circuit detects that the current signal and the torque for a given value for PID arithmetic to control the generation of PWM wave. By controlling the width of the pulse width of PWM waves to realize speed regulation; When the system is greater than the current over-current protection setting, the system produces the interruption, and interrupt handling subroutine into fault protection, blockading PWM wave output until the fault elimination.

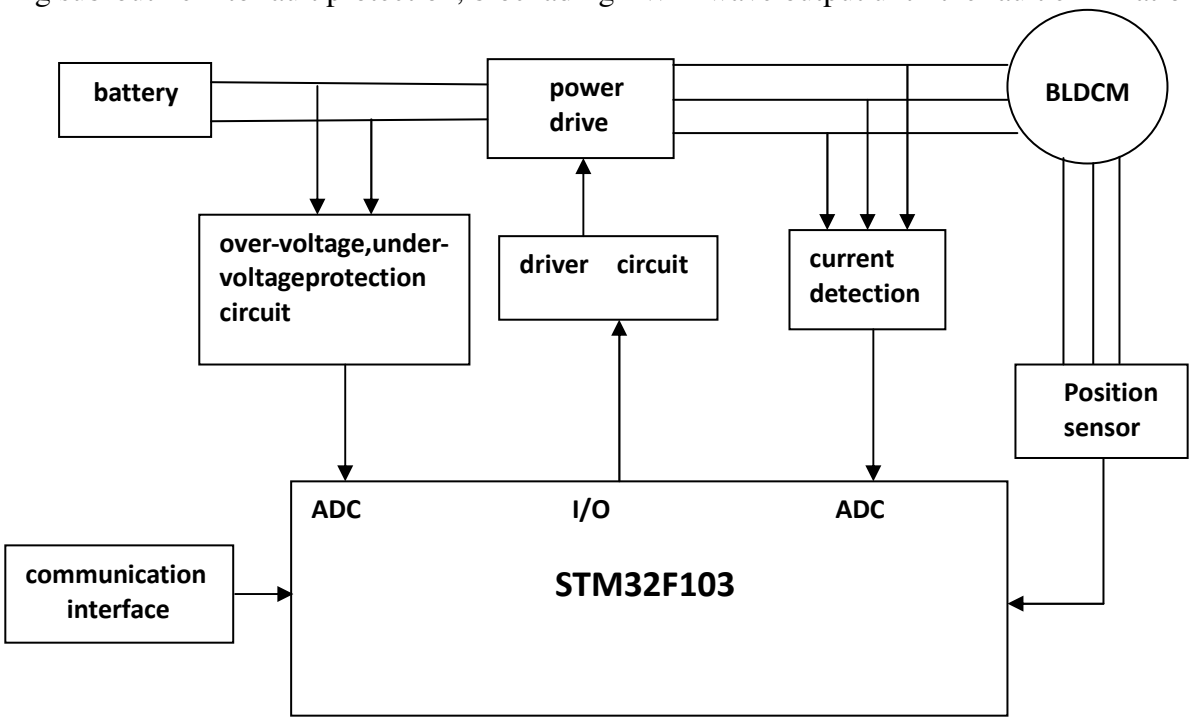

Fig.2 The hardware of control system block diagram

The Design of Controller Hardware Circuit

Controller hardware circuit is mainly composed of two parts: one is the peripheral control circuit, including the auxiliary power circuit, MOSF ET drive circuit and protection circuit and the contactor of driving circuit; Another piece is the core control circuit, the main STM32 micro-processor as the core, including two kinds of protection circuit, detection circuit, signal modulation circuit, CAN bus communication circuit, watchdog circuit and isolation of auxiliary power supply circuit.

①The Design Of The Hall Sensor Interface Circuit

The power supply for Hall sensor driver is usually 5v, so as to prevent the power against, it add a diode ,the hall sensor is open circuit output, have to be connected to a resistance, and add a low pass for hall sensor RC filter to prevent the strong magnetic fields in the brushless motors and brushless motor controller PWM carrier frequency interference.

②The Design Of The Protection Circuit

Over-current protection is the key content of the controller design, this scheme adopts the combination of hard and soft can effectively protect the security of the controller and motor load, and can play out the overload capacity of the load to reflect the intelligent control of the system. Over-current protection circuit must first solve the problems of the power circuit current sampling, this scheme adopts the hall transformer for high current sampling, can detect alternating current and direct current, even the transient peaks, which can realize power circuit and control circuit of electrical isolation; At the same time,it has good linearity, precision, fast dynamic response and superior electrical properties. In order to prevent the motor overload, controllers, temperature and battery aging damage, this scheme also designs the overvoltage protection circuit, temperature protection, low voltage protection circuit.

③The Design Of The Detection Circuit

Detection circuit system is divided into system self-check and running status detection, system self-check detect power detection module, motor, accelerator, brake state, battery voltage before the

operation the boot system, to ensure control system reliable. Running state detection detect the loop current, temperature and motor speed controller in the normal work process of the controller , through a serial port communication to transfer system parameters to the front of the instrument panel to make driving personnel's judgment convenient.

Control Strategy And Software Design

The system realizes current closed-loop PID control strategy by software, control algorithm for incremental PID is increment control algorithm. As a high intelligent degree of the controller, software is an important part of the controller. Fig.3 is the initialization program flow diagram and Fig.4 is the main program diagram.

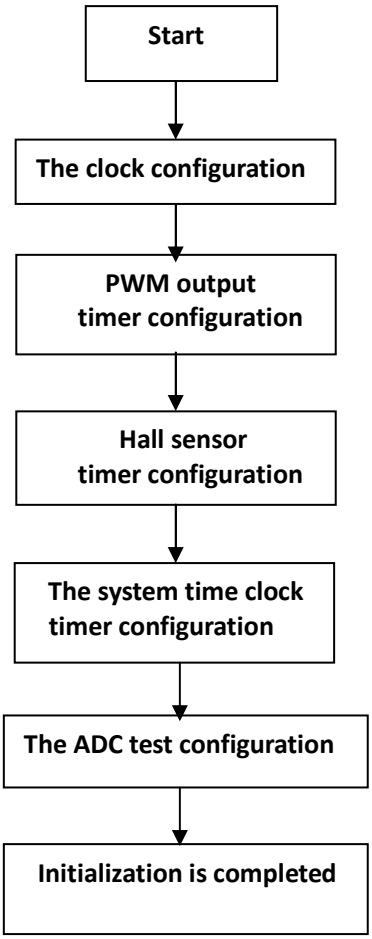

Fig.3 System initialization module block diagram

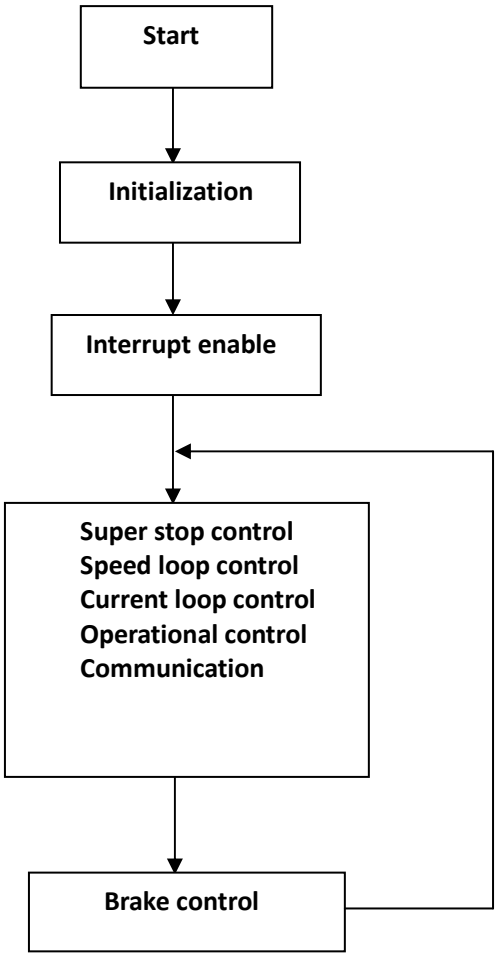

Fig.4 System main program module block diagram

The software is the embodiment of the intelligent controller software design including the generation of PWM function module, the signal detection module design, the software design overload protection, temperature protection, low voltage protection software design, communication module, software design and self-inspection process design and programmable power speed curve design. The controller for a variety of signal detection and communication processing happens in the interrupt. And in a reasonable amount of time the automatic updates occur. When the controller receives the external command it can respond immediately, so that the main loop or other modules can be read immediately when it needs to use a test of its corresponding variables, without need to wait, And read the latest data, make the main loop can focus on data processing and all kinds of exception handling. After systems reset every time, they first perform initialization program, then open another interruption, finally execute the main program.When systems have an interrupt request, they implement the interrupt service subroutine. Initialization programs include the definition of setting all kinds of system clock, interrupt vectors, initializes the I/O port initialization, the control

register setting and each function module. After the initialization is finished, the motor is started by the main programs to detect the rotor position information, and then to control the current loop speed loop, etc.

Experiment Results

The rated power in the experiment is 500w brushless direct current motor, under the condition of laboratory. The dc power supply a voltage of 72 v and the experimental results are observed by the oscilloscope. In the experiment, the motor can be safe and reliable to operation, and control effect is better, so the motor's overall experimental results are good.

Conclusions

The control design regard safety, reliability and stability as a goal, the designed controller has a more perfect protection function, self diagnosis and fault response function, and has good scalability, easy hardware upgrade ability. The controller hardware circuit is simple, low cost, easy to operation and maintenance.

Acknowledgment

2013 Education Department project of Jiangxi Province: Fundamental Research of PMSM for Electric Vehicle Based on Variable Magnetic Reluctance Field Adjustment.

References

[1] G.Liu,z.Q.Wang,J.C.Fang.Permanent magnet brushless dc motor control technology and application[M].Beijing;Mechanical Industry Press,2010:5-10.

[2] Vincent Onde.STM32 micro-control processing advanced motor control method[J].Chinese integrated circuit,2011,20(4):83.

[3] w.hu,H.X.He.Electric cars with permanent magnet brushless direct current motor automatic control[J].Journal of university of Guang dong industry,2004,21(1):13-16.

[4] Z.P.Chu.The electric motor with brushless direct current motor controller based on STM32{D].Cheng Dou:XiHua university,2011.

[5] B.Liu.Permanent magnet brushless direct current motor control system research[J],Coal mine electrical and mechanical,2010(2):17-19.

[6] J.K.Liu.Advanced PID control MATLAB simulation[M].The third edition.Beijing:Electronic industry Press,2011:25-27.

[7] Y.C.LI.Brushless direct current controller is applied in bicycle research[D].GuangZhou:Journal of university of Guang dong industry,2009.

Advanced Materials Research Vols. 986-987 (2014) pp 1067-1070

doi:10.4028/www.scientific.net/AMR.986-987.1067

Design of Permanent Magnet Synchronous Motor Servo System

Hao He[a] , Jiaoyu Liu[b] , Xianxi Pan[c] and Limin Kan[d]

School of Automation, Wuhan University of Technology, Wuhan, 430070, China

[a]hhczfy@163.com,[b]liujiaoyu_2006@163.com,
[c]706816214@qq.com, [d]1028520132@qq.com

Keywords: Permanent Magnet Synchronous Motor; Servo System; Vector Control

Abstract. The objective of this work is to improve the control performance by redesigning the permanent magnet synchronous motor servo system .The vector control thought is used to control the permanent magnet synchronous motor. So it is easy to realize the torque current characteristic of linear. The design of the permanent magnet synchronous motor servo system is first proposed. The hardware and software designs are realized in this paper, and it is subsequently verified experimentally. Experimental results show that the DSP controller for the permanent magnet synchronous motor servo system has extensive applicability, high reliability and high performance price ratio.

Introduction

In this paper, permanent magnet synchronous motor servo system is a researched object. And the AC permanent magnet motor is a servo drive control object. The position, speed and torque of the permanent magnet synchronous motor are controlled by the servo drive controller. In addition, the high precision, large range and constant torque speed regulation are implemented in this servo system.

The vector control technology and control strategy of permanent magnet synchronous motor are proposed in [1] by authors. Vector control is based on the direction of the magnetic field vector as axes. The size and direction of the motor current vector is represented by the instantaneous value. At the same time, the control torque problem is solved by the coordinate transformation. The size and direction of the motor current vector is represented by the instantaneous value. So the problem of the torque control is solved by coordinate transformation.

The basic idea of vector control of permanent magnet synchronous motor is as follows: The DC motor torque control law is simulated when the permanent magnet synchronous motor is controlled. And the stator current of permanent magnet synchronous motor is decomposed in the rotating coordinate axes. Then the excitation current of flux and the torque of the torque current are gotten. The amplitude and phase of the stator current are controlled. Then the excitation current and torque current are changed. Because of the excitation current and torque current is orthogonal relationship, the excitation current and torque current are controlled separately. So the Torque is controlled effectively.

Hardware Design of Permanent Magnet Synchronous Motor Servo System

The design of the DSP controller for the servo system of permanent magnet synchronous motor is proposed in this paper. The hardware design of the DSP controller for the permanent magnet synchronous motor servo system as depicted in Fig. 1 was developed in the laboratory and used to start the motor.

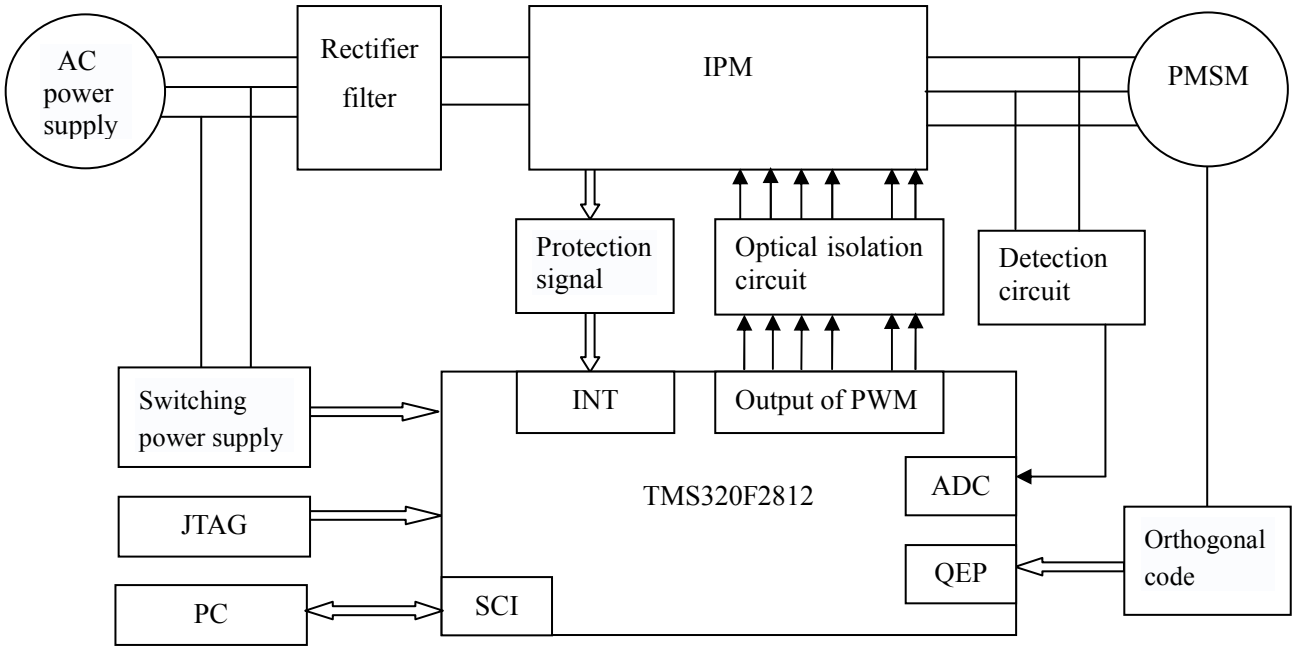

Fig.1 The hardware block diagram of the DSP controller for the PWSM servo system

The system has better dynamic and static performance in this design. The system can be realized functions, such as the change of the internal parameters, interface, communication with controller, debugging and monitoring.

This hardware mainly consists of the control circuit and the power circuit. The control circuit consists of the DSP minimum system, external input and output circuit, current and voltage detection circuit, motor speed and position detection circuit, the communication circuit and protection circuit. The power circuit consists of rectifier circuit, filter circuit and inverter circuit.

Process of the design can be divided into three important parts as follows:

Rectifier and filter circuit: The alternating current is transformed into direct the current by the rectifier circuit. The rectifier circuit is composed of the three-phase uncontrolled rectifier diode. After current is rectified by the three-phase uncontrolled rectifier bridge, the output voltage has the harmonics. In order to reduce the fluctuation of DC bus voltage, the filter circuit is designed. The rectifier and filter circuit is shown in Fig. 2.

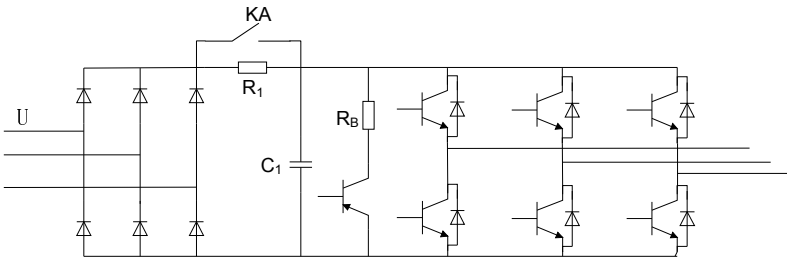

Fig.2 The rectifier and filter circuit

Optical isolation circuit: The DSP signal can't drive IGBT directly, so the optical isolation circuit is designed.

The control unit of DSP: The TMS320LF2812 DSP microprocessor DSP controller for the permanent magnet synchronous motor to achieve higher control accuracy under the conditions of external interference.

Software Design of Permanent Magnet Synchronous Motor Servo System

The modularized programming is used to design the software of DSP controller for the permanent magnet synchronous motor servo system. The procedure includes main program, timer interrupt service program, serial port interrupt program, the unusual interrupt program and so on. The software flow chart of the main procedure is shown in Fig. 3.

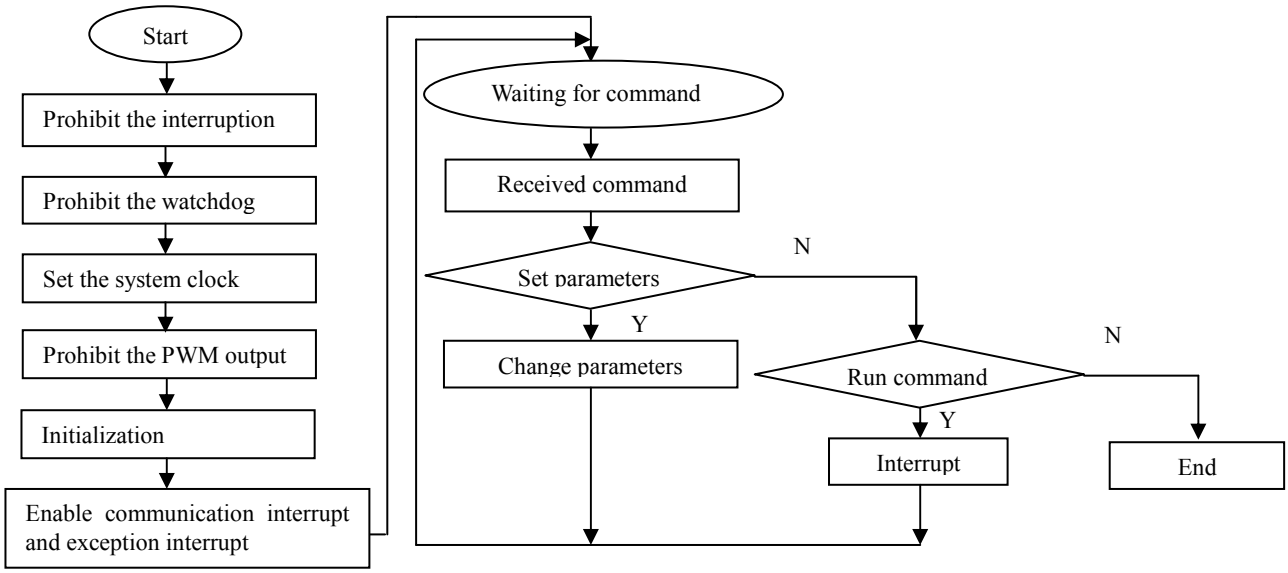

Fig.3 The software flow chart of the main procedure

The software flow chart of the main procedure is described as follows:
1) When the system start, the interruption and the watchdog are prohibited. Then the system clock is set, and then the PWM output is prohibited.
2) After the PWM output is prohibited, the system is initialization.
3) According to the different operation instructions, the system is operated by the different ways.
4) When the operation instruction is “waiting for command”, the process of the command is received. The run procedure is run as Fig. 3.
The main procedure can be divided into four steps as follows: the system clock, interrupt initialization, the register allocation on AD conversion and the initialization time management module and IO port.

Conclusion

This work has focused on the design and implementation of permanent magnet synchronous motor servo system based on DSP. The control performance of the permanent magnet synchronous motor servo system is improved. Towards this goal, the DSP controller for the permanent magnet synchronous motor servo system is first designed in the laboratory. The characteristics of this controller are described below.
1) The powerful data processing capability and high operating speed DSP is employed in this paper. The proposed DSP controller has extensive applicability, high reliability and high performance price ratio. The speed and precision of data processing, the integration and the real-time performance have all been obviously improved.
2) It is easy to realize the torque current characteristic of linear.
Overall, the successful implementation with a low cost micro controller illustrates the feasibility of the new approach in this paper.

References

[1] Pan Xianxi, Research and implementation of the permanent magnet synchronous motor servo system [D].Wuhan: Wuhan University of Technology, 2013(In Chinese)
[2] Liu Kaipei, Lu Penggang, Luo Huan, Fuzzy frequency conversion driving system basedon DSP and IPM[J]. IEEE Conference on Power System Technology, 2002
[3] K.Chikh, A.Saad, M.Khafallah, D.Yousfi, PMSM vector control performance improvement by using pulse with modulation and anti-windup PI controller [J]. IEEE Conference on Multimedia Computing and Systems (ICMCS), 2011
[4] Xu Dan, Huanqiang Luo, Wang Feng, Xiaomei Yin, Nianxing Fang, Research on the sliding-mode variable structure control based on the vector control of PMSM[J]. IEEE Conference on Electrical and Control Engineering, 2011
[5] Zhao Kaiqi. The study of improved PI method for PMSM vector control system based On SVPWM[J]. IEEE Conference on Industry Applications Society Annual Meeting , 2011

Advanced Materials Research Vols. 986-987 (2014) pp 1071-1076

doi:10.4028/www.scientific.net/AMR.986-987.1071

Design of Shearer Electrical Control System Based on STM32

Zhongchu Wang[1,a], Jiaqi Liu[1,b]

[1]School of Electronic and Information Engineering, University of Science and Technology Liaoning, Anshan, Liaoning, China, 114051

[a]wangzhongchu01@126.com,[b]gh54007@163.com

Keywords: Shearer, STM32, CAN bus, Electrical control system

Abstract. This paper introduces a new type of electric traction shearer control device based on the STM32. This kind of device is constituted by three different function modules and some peripheral modules. The different modules are interconnected through RS-485 and CAN bus. According to this paper,we make a detailed description about the structure and hardware of the shearer electrical control system, and expound the characteristics of RS-485 and CAN network communication. This electric control system can highly improve the stability and safety of the shearer.

Introduction

China is a big country in coal production and consumption. The total output of national raw coal reached 3.33 billion tons while the consumption was about 3.62 billion tons in 2012[1]. And annual coal imports amounted to 289 million tons. Shearer is an important equipment of domestic coal mining in our country. Due to its special working environment and complex internal structure, its stability and efficiency are directly affecting the output of coal and the safety of the coal miners. Therefore, it has an important significance for the sustainable development of Chinese economy and the energy security to improve the automation level of coal winning equipment, to make the existing coal mine production more productive, efficient and safe, and reduce the dependency of external coal.

This paper introduces an electrical traction shearer control device based on embedded technology which uses the STM32F107 processor as the core, using the distributed technology to make different functional modules respectively complete data acquisition and processing, receives and sends control command, achieves a real-time display of various parameters of the system, and finally through the output relay signals control frequency converter to control each motor complete coal mining actions.

The Composition of Shearer Control System

The designing scheme of this control system is shown in Fig.1, consisting of the main control module, DAQ module, traction control module and some peripheral devices. The CPU in three function modules uses STM32F107VCT microprocessor produced by ARM's Cortex as core. The processor is based on the Cortex-M3 core, high-performance micro-controller chip, clocked at 72MHZ, its interior contains 256KB of Flash and 64KB of SRAM, the built-in resource-rich, including: SPI, I2C, UART, CAN, etc.[2], supporting JTAG online debug mode, compatible on the pin and software in the same series of different models[3]. System peripherals include RF Wireless Remote Module (intrinsically safety), LCB/RCB (intrinsically safety), gas breaker, leakage protector, LCD, etc.

Considering the implementation , maturity and economy of the practical engineering , the communication network among various modules is established by CAN bus and RS-485. The RS-485 interface consists of a balancing driver and differential receiver, which has good noise immunity and high transmission rate[4]. Its main mission is the transmission of data between modules;The CAN bus has the advantages of high information transmission stability and good real-time performance, and it has been successfully used in the automotive and other industrial fields[5]. Because the STM32F107 has two built-in integration CAN bus controller, only one more external receiver can realize the function and reduce the volume and complexity of hardware circuit. In this control system, the task of CAN bus is to receive and send the commands from the LCB/RCB and RF Wireless Remote Module.

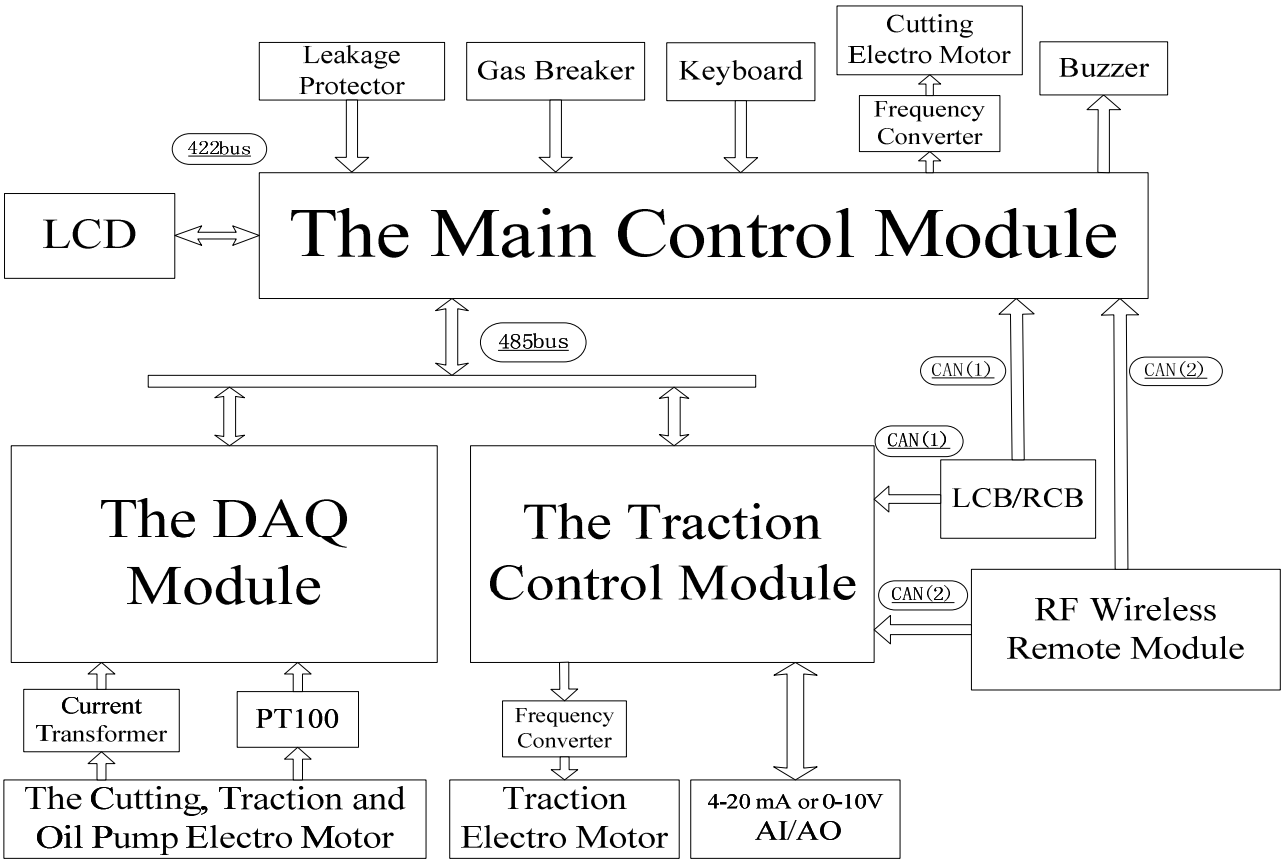

Fig.1.The structure of the control system of shearer

The LCD uses, in the GP series, 5.7 inch touch screen of PRO-FACE. This kind of LCD is widely used in industrial field with high resolution and its power is supplied by 24V DC. With the setting function, parameters can be manually set by the touch screen such as the pulling speed, alert limit of the motor temperature and current. And the screen can storage a lot of warning and fault information in order to rapidly locate the fault location and shorten the maintenance time.

The Hardware Design of Control System

The Main Control Module. As the core of the whole control system, the main control module is responsible for receiving data and commands from the DAQ module, the LCB/RCB and RF Wireless Remote Module. After calculating, processing and packaging, the data will be sent to the traction control module and LCD to complete the corresponding action and information display. In addition, the main control module also directly control the main start, stop, arm up, down, and some other high priority functions whose actions are made by the relay or solenoid valve. The hardware structure of the main control module is as shown in Fig.2.

The hardware circuit mainly consists of the CPU, reset circuit, clock circuit, storage circuit, I/O, etc. The I/O signal channels are all made of optical coupling isolation to prevent the external disturbance. It uses ULN2003 with high current gain and load ability as output driver chip. And the main control module itself still has a gas concentration in 200-1000 Hz frequency input signal interface and an Ethernet interface which can be used to upload information of shearer to the PC over telephone wire.

The DAQ Module. The DAQ module can be regarded as sensory organs of the whole control system, responsible for collecting the real-time temperature and current data of the cutting motor, traction motor and oil pump motor in the system, and sending the signals to the master control module through RS-485 bus after the analog signal acquired is converted into digital signals. The temperature sensor adopts PT100 platinum thermal resistance that is stable performance and easy to use in -50℃ to 200 ℃ temperature range and the current transformer is adopted to test the current[6]. The system uses

high-performances AD converter to complete the conversion of analog signal to digital signal and realize inverse time over current protection of all electrical circuits. All the digital signals converted are sent to the CPU through the photoelectric isolation, ensuring the integrity of the data and the stability in the process of data transmission.

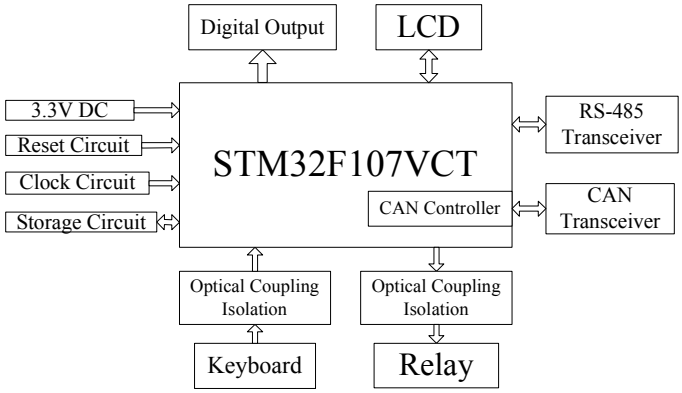

Fig.2. The hardware structure of the main control module

The Traction Control Module. The control of the traction motor is accomplished by controlling frequency converter through the output relay signals, including the control of the traction motor traction right and left, speed up and slow down, pine and brake operations. In addition to the reset circuit, clock circuit, communication circuit, traction control module also contains 2 road AO feedback contact, 2 road (0-10 V) AI, which can be directly connected to frequency controlling the acceleration and deceleration of traction motor [7]. Moreover designed CAN bus communication circuit in the traction control module can directly receive the commands from the LCB/RCB and RF Wireless Remote Module under the condition of damage in the main control module, making the system complete a simple control action in the case of downgrade. It controls the normal traction direction of coal winning machine.

Hardware Design of Power Supply Part. Control system as a whole uses 24V DC power supply, using DC-DC power modules. The module standard input voltage is 24V, and output voltage is 5V. It has the functions of short circuit protection, self-resumption, output shutdown and large isolation voltage .etc. Using tiny SIP encapsulation, it can allow more space for other devices and wiring in the limited space of each module.

In order to minimize the interference between each other and ensure the stability of the system, the communication circuit, temperature collection circuit and AD conversion circuit adopt independent power supply module power supply respectively on the hardware design of a power supply.In addition, the system keeps a special power supply module with low dropout linear regulators, which changes 5 DCV to 3.3DCV, for powering the CPU and other chips.

Hardware Design of the Communication Network. The CAN bus is mainly responsible for the reception and dispatch of the control commands in this system. Inside the STM32F107VCT processor, there are two CAN bus channels, each of them has its own transmitter TX and receiver RX, which respectively located on chip GPIO pins PD0 and PD1, PB5, and PB6 [8]. When using two CAN bus channels, it will be directly connected to the CAN bus repeater, and then hooked up to CAN bus, which can greatly simplify the complexity of hardware circuit.

ISO1050, as the transceiver of CAN bus, is conformed to the technical manual of ISO11898-2 standard, which used with isolated power supply, ISO1050 can prevent noise of the data bus or other circuit current into the local ground to interfere and damage sensitive circuits. It has some merits such as high transmission rate, strong anti-interference ability, high reliability, and provides check grade emission ability and difference within the capacity for the CAN controller of STM32F107VCT. In hardware design, CAN bus network at both ends are equipped with 120 Ω terminal resistance to prevent the signal reflection. PSM712 is the ESD. The CAN bus interface hardware construction is as shown in Fig.3.

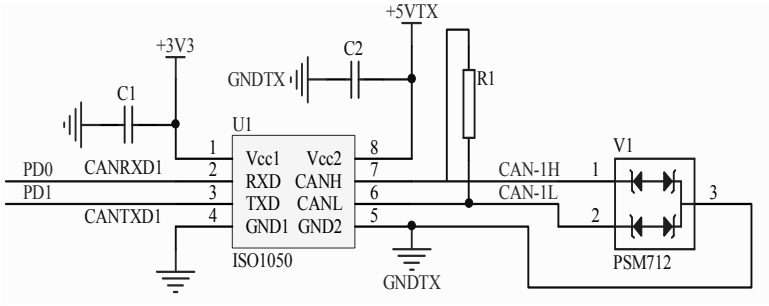

Fig.3. CAN bus interface hardware construction

RS-485 bus is mainly responsible for the communication of the main control module with the DAQ and the traction control module. Each module in the control system has a SP3485. The chip is +3.3V low power half duplex transceiver, fully meeting the required RS-485 electrical specifications of the serial protocol, and data transfer of the data transmisson rates up to 10Mbps (load), which, on the same serial bus, allows connection of up to 32 transceivers. The RS-485 interface hardware construction is as shown in Fig.4.

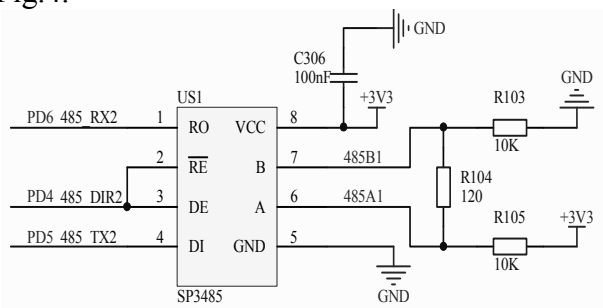

Fig.4. Hardware interface of RS-485

Software Design of the System

The software debugging work is completed based on RealView MDK development tool in the environment of Keil uVision.The software integrates with editor, compiler, emulator and debugger. The RealView MDK, a software development tool designed for all kinds of embedded processors by ARM, contains numerous case template and firmware instance. The system supports JLINK online simulation, and simplifies the program debugging process. It also can reduce the development difficulty, shorten the development cycle and can make developers more convenient in the process of debugging. Using JLINK emulator supports JTAG debug interface for online debugging [9].

Specific workflow in control system is as follow: After the system boots, initializes and then completes self-test, the DAQ module firstly tests temperature acquisition node and the integrity of and current collection node, and then enters the stage of data collection after receiving the feedback information and confirming the correct; After transforming digital signals of the electricity and the temperature signals acquired to analog signals, which packages in the data buffer, waiting for the inquiries from the main control module and eventually the data passes to it through RS - 485 bus network; The display sends the internal stored parameters to the main control module through RS-422 bus; The RF Wireless Remote Module and the LCB/RCB can send commands to the main control module through their respective CAN bus; The main control module transmits real-time parameters and control commands received of Shearer to the screen and traction control module to complete the corresponding action. Software flow chart of the control system is shown in Fig.5.

Control system adopts the design of distributed structure. The control module can effectively deal with the relevant data from other nodes, so as to determine the current working condition of coal winning machine. The control system preferentially detects the links such as the gas density and whether there is electric leakage in the shearer after the system boots, which fully guarantees shearer in a safe working environment all the time.

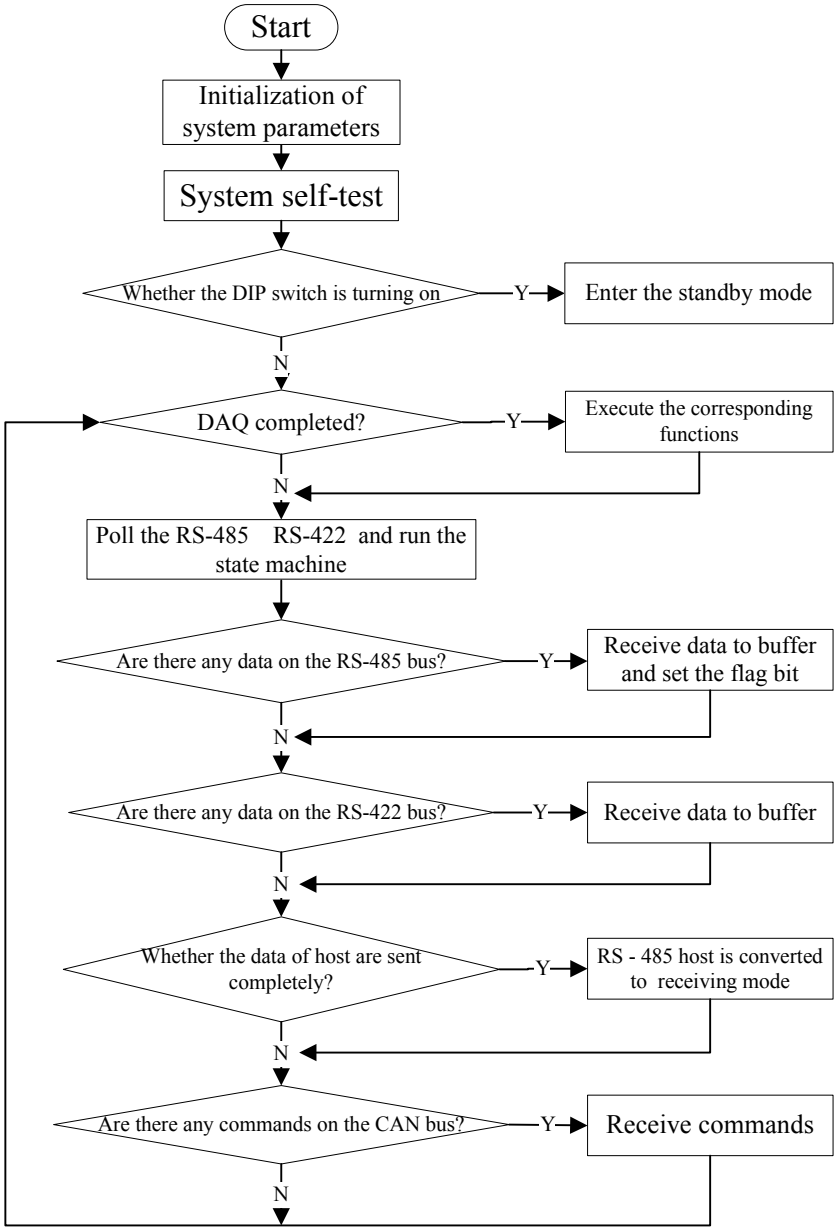

Fig.5. The system flow chart

Fault Tolerance Design of the System

Because coal mining machine need long time to adapt to the wicked underground work under harsh conditions, the safety, reliability and easy maintainability are higher required, so it is a certain fault tolerance. In this way, even if part of the shearer control system break down, it is still safe to do some basic operations. When the overall shearer breaks down, it can quickly find the cause of the problem, locate the fault module and restore system running in a short period of time. When compiling, the software program designs the multiple standby modes to maintain the basic operating functions of the system. For example, the CAN bus module setting in the traction control module can be activated by turning on the toggle switch to complete initialization when the main control module communication is damaged or completely interrupted. The traction control module through the CAN bus directly receive the commands from the LCB/RCB and the RF Wireless Remote Module, controlling the direction of coal winning machine around traction to protect the safety of underground workers. When lower communication network malfunction in the system breaks down, the shearer control system can control transducer through AO reserved 2 way switch and analog quantity to achieve control of the frequency converter operation. A large amount of redundancy is designed to improve

the reliability of coal winning machine as a whole, to reduce the probability of breaking down in control system.

Conclusions

STM32F107VCT as the core, shearer electrical control system is designed based on CAN bus and RS-485 bus, with high reliability, strong anti-jamming capability of the CAN bus interface which can realize the communication between the remote control and the main control system. Each module in the control system adopts RS - 485 bus to constitute the internal communication network, whose advantages are fast data transfer rate and strong ability to resist noise. It can monitor the real time working status of shearer by LCD and PC. Under the strong magnetic interference, through repeated tests,the system is working properly and the communication network is working steadily.It overcomes some weaknesses of traditional PLC control system such as the bad anti-jamming ability and shortcomings in real-time performance,etc. At the same time, the design of modular hardware structure has great advantage in the aspect of maintenance.

References

[1] The Gazette of Land and Resources in 2012. Beijing: Ministry of Land and Resources of the People's Republic of China (2012), in Chinese.

[2] Jun Liu. *Examples of STM32*.edtied by Beihang University Publishers, Beijing (2011),in Chinese.

[3] Jiwei Chen, Junwei Xiang and Yao Zhang: submitted to Journal of Development & Innovation of Machinery & Electrical Products (2013), in Chinese.

[4] Lihua Meng: Research on RS-485 communication manager based on STM32.Master thesis: Hebei University of Technology (2012), in Chinese.

[5] Robert Bosch GmbH, CAN Specification, Version2.0, 1991.

[6] Linna Zhang, Wufa Liu: *The Sensing Detection Technology and Application*, edtied by China Metrology Publishing House, Beijing (1999), in Chinese.

[7] Jinbo Qiu, Zhenjian Liu: submitted to Coal Science and Technology (2008), in Chinese.

[8] Hongpo Hu, Shujian Liang, Zhenhua Zheng, Tiejun Wang, Hua Yang: submitted to Microcontrollers & Embedded Systems (2012) , in Chinese.

[9] Hexin Zhang, Xiaohui Wang, Xiaodong Huang: submitted to Control and Instruments in Chemical Industry (2012), in Chinese.

Advanced Materials Research Vols. 986-987 (2014) pp 1077-1080

doi:10.4028/www.scientific.net/AMR.986-987.1077

Design of the Stepper Motor Control System Based on FPGA

Xuehui HAN[1, a], Lihong LEI[1,b], Yongbin YANG[1]

[1]School of Electronics and Information , Changchun University of Science and Technology, Changchun,130022,China

[a]email: hxhrp@163.com;[b]email: llhrp@aliyun.com

Keywords: FPGA (Field Programmable Gata Array); stepper motor; LabView

Abstract. A stepper motor control system is designed based on the stepper motor controller and EP2C5Q208C8. The control system of the host human-computer interaction interface is designed by LabView; through RS232 to communicate with the PC. According to the characteristic of the stepper motor control system , Verilog HDL language program and the software of Quartus Ⅱ are used to simulate each function modules. The analysis of simulation results and experiment show that using the method of FPGA+LabView can simplify the complexity of the system design and possess a very high stability on the running status. The motor running status can be easily observed in the PC interface.

Introduction

This paper proposes that adopting LabView to set up the host human-computer interaction interface and using FPGA as the master chip to control stepper motor through the stepper motor controller and sending data to human-computer interaction interface to display the motor running status. The design makes full use of the advantages of FPGA: it can quickly process the data; all of the control logic is high reliable and is completed by hardware. So the electrical interference with the control system has been reduced and the operation mode which is used to set up the motor running status is simplified by the interactive interface.

The Overall Program Design of the System

As is shown in Fig.1, a block diagram of a stepper motor control system mainly consists of a PC interface, a Field Programmable Gata Array (FPGA), a stepper motor controller and a motor. FPGA receive data via RS232 from PC and process the data. On the one hand, the corresponding control command and data are transmitted to the stepper motor controller in order to control the stepper motor. On the other hand, the processed data sent to the host computer through the RS232 for allowing the host computer interface to clearly see the stepper motor running.

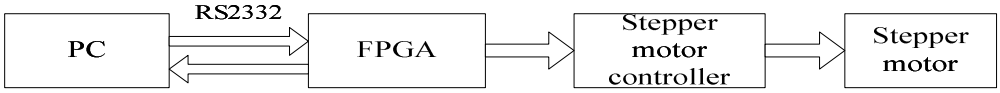

Figure1.Stepper motor control system block diagram

Hardware Design

EP2C5Q208C8, which is produced by Altera, is used as a master chip, and L298N is used in this system by stepper motor controller. L298N is a high-voltage, high current motor driver chip produced by SGS. It can be controlled by standard TTL logic level signal. FPGA can output LVTTL level. As the output range of the LVTTL level is a subset of the TTL-level input voltage range, the output port of FPGA can be connected directly with the pin of stepper motor controller. System connection diagram is shown in Fig.2.

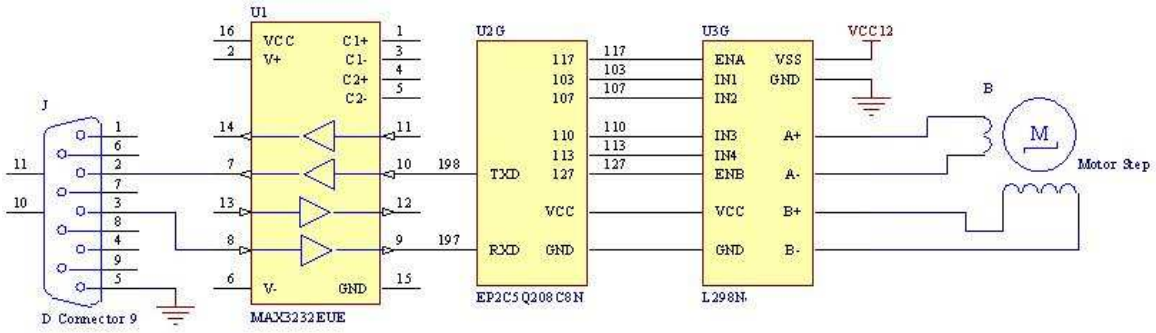

Figure2. System connection diagram

A. EP2C5Q208C8

EP2C5Q208C8 input / output power voltage is 3.3V and it has 288 logical blocks, 142 input / output lines, 208 pins and a PQFP package. It is composed of input / output unit, basic programmable logic unit, Global Clock Network & Phase-Locked Loops, embedded memory, multitrack interconnect, and embedded multipliers[2].

B. The stepper motor and stepper motor controller

Stepper motor is an open-loop control element that can transmit the electrical pulse signal to the angular or linear displacement. The motor speed and stopped position only depend on the frequency and number of pulses of the pulse signal, regardless of load changes in the case of non-overloaded, i.e. a pulse signal is sent to the motor, and the motor is rotated by one step angle[4]. Stepper motor do not have cumulative error, only periodic errors, this feature is widely used in the areas of controlling of the stepper motor speed and position control in areas.

L298N controller is selected to be stepper motor driver. Its instantaneous peak current can be up to 3A, and continuous operating current is 2A. TLP521optocoupler is used in L298N controller for optical isolation to prevent the spikes impact on FPGA generated when the controller is started and stopped.

The two-phase four-wire stepper motor is used in this system. Considering the influence of torque, smooth, noise, and other aspects, we adopt the eight-shot way of working. According to the characteristics of stepper motor control system, the system uses modular design principle; a top-down design, functional separation design and level design are all used according to the modern EDA project[5].

Software Design

The design of the program is based on Quartus Ⅱ software platform and written by the language of Verilog HDL.. The program contains three major modules: rx_module, tx_motor and data_conversion. FPGA uses EP2C5Q208C8, and the external clock is 20MHz.

A. The rx_module module

The rx_module module consists of rx_fifo_module module, rx_top_control module and rx module. Rx module also contains detect module, rx_bps module and rx_control module. Its main role is to receive the data via the serial port from PC and send the data into the FIFO buffer.

When detect module detects a start bit, it outputs a high level signal to the rx_control modules. The rx_control module controls rx_bps module to generate timing, reads the useful data received by rx_control module according to the signal output by rx_bps module and outputs the data. The rx_top_control module receives the data and sends them into the rx_fifo_module in order to cache data, wherein FIFO depth is set to 16.

B. The data_conversion module

The main role of data_conversion module is to take out the data which are located in FIFO data buffer and send them to rx_module module so that the data can be processed by the follow-up module.

C. The tx_motor module

The tx_module module consists of tx_fifo_module module, tx_top_control module, data_motor module and tx module. Data_motor module also contains data_control module and motor module. The main roles of tx_motor module, on the one hand, is to send data to PC through tx so as to display the motor's running status; on the other hand, is to transfer control module commands and data to the stepper motor driver through data_motor output to control the motor.

The data_control module is used to set the operation mode of the stepper motor based on the received serial data, including the direction of rotation, the initial velocity, acceleration and deceleration, operation mode and the number of steps. The motor module is used to set the stepper motor's running configuration, perform command according to the data_control module.

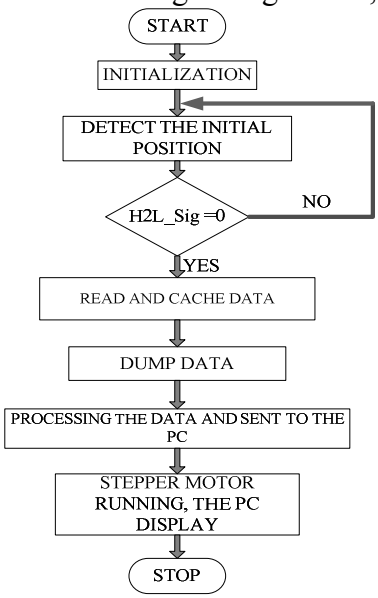

Figure 3. Software design flow chart

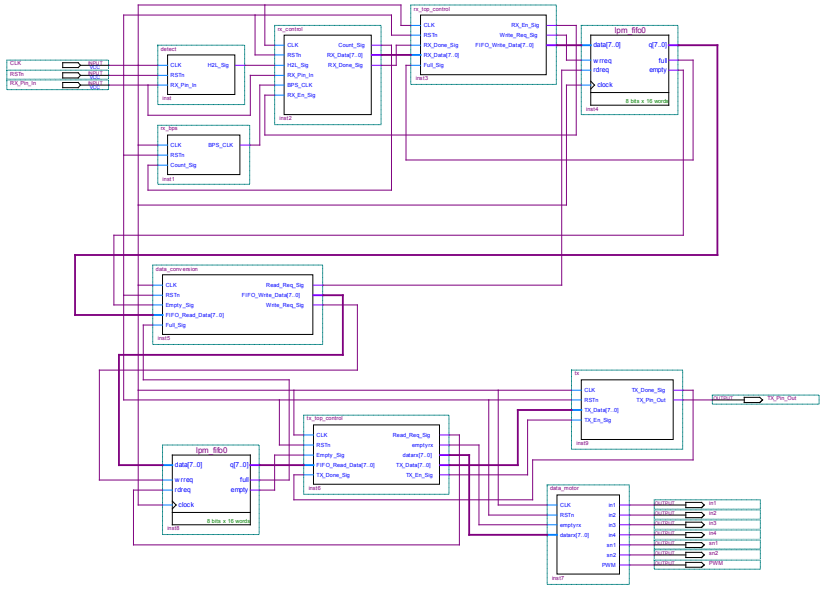

Figure 4. Module connection diagram

D.The Software Design Flow Chart and Connection Diagram

1) Software Design Flow Chart

The software design flow chart is shown in Fig.3. Firstly, system is initialized and each module signal is reset; detect module will detect the initial position. When detect module is pulled low level, the rx_module module will read the data and cache the data; after dumping the data through the data_conversion module, the tx_module module will process the data, control the stepper motor, and send the data back to the PC for display.

2) Module connection diagram

The Module connection diagram is shown in Figure 4.

E. The upper monitor

Host-computer keeps in touch with console-computer via serial communication. Using the LabVIEW platform to develop serial communication is relatively simple because the LabVIEW function template provides several serial communication subroutines. The left side of the front panel is used to initialize the serial port settings of the computer; the right side of the front panel is used to set the motor running and displaying. There are two modes of operation: continuous operation mode can be set to the motor rotation direction, speed, etc.; step by-step operation mode can also set the number of steps. After configuring the serial port parameters, we need to click the button of 'setting the parameters' to set the parameters for final confirmation. When motor state is set up, if we click the Run button, the motor will start to run. The motor running status will be shown according to the information which is sent back from the console-computer.

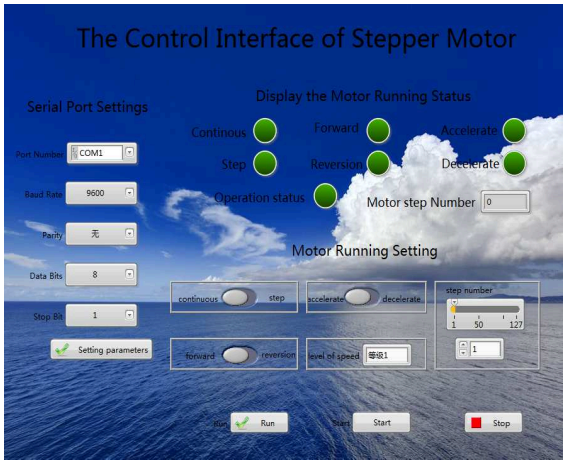

Figure 5. The front panel

Conclusion

After repeated experiments, using the method of FPGA+L298N can simplify the design's complexity and ensure the stability of the system; the motor running control and display are set by host-computer designed by LabVIEW with the advantage of simple interface, simple control and being easily observed to the motor running. LabVIEW+FPGA+L298N are used in stepper motor control system. The stepper motor now can run continuously with given number of steps, controlled speed and direction.

Reference

[1]Cyclone Ⅱ Handbook [Z].Altera Coporation, 2008

[2]Xu Yang, Huang Zhiyu, Li yan, Chen Zhuo, The design and engineering application of Verilog HDL based FPGA [M], Beijing: POSTS&TELECOM PRESS, 2009. 5

[3] Cyclone Ⅱ Device Handbook [Z], Altera Coporation,2008

[4] Wang Yanping. Stepper motor control system design [J]. Modern electronic technology, 2010, 329(18): 205-210

[5] Gao Yanyan, Wu Yunsong, Wu Xuejie, Huang Hongguo. MCU and FPGA based multi-channel stepper motor control system design [J]. High Power Converter Technology, 2012, (5): 43-46

Advanced Materials Research Vols. 986-987 (2014) pp 1081-1085

doi:10.4028/www.scientific.net/AMR.986-987.1081

Design of the Voltage-controlled Bandpass Filter Based on Current Feedback Op Amp

Sheng-qian Ma[1, a], Yan-ping Ji[1, b], Xing-ping Ran[1, c], Wei-zhao Zhang[1, d], Yang Yang[1, e]

[1]College of Physics and Electronic Engineering, Northwest Normal University, Lanzhou 730070, China

[a]email: s.q.ma@163.com, [b]email:416894253@qq.com, [c]email:574721414@qq.com, [d]email:410358095@qq.com, [e]email:yangyangking@qq.com,

Keywords: Current feedback operational amplifier; bi-quad loop filter circuit; analog multiplier; voltage-controlled band-pass filter.

Abstract. This paper puts forward structure and realization method of the voltage-controlled band-pass filter based on the current feedback operational amplifier (CFA) which uses bi-quad loop filter circuit model to design the new filter circuit. Input voltage signal is input to voltage-controlled band-pass filter circuit composed by an analog multiplier AD835 and a current feedback operational amplifier AD8001 which are the core. Using the voltage signal to adjust the center frequency of the filter, the filter has wide frequency band and good high-frequency performance. This paper describes the design principles, infers the design formulas and designs the circuit of the voltage-controlled first-order and second-order band-pass filter.Through the simulation, the filter can realize the scope of the center frequency from 200KHz to 10MHz.

Introduction

In the field of signal processing, data collection and communication systems, the filter has a wide range of applications, including the voltage-controlled filter with a simple circuit structure, convenient adjustment, high accuracy, and solving the wide variations of the pending signal frequency, which plays an important role in the field of signal processing[1][2][3] .The voltage-controlled filter can achieve automatic adjustment of the filter frequency[4].The voltage-controlled filter is mainly composed by an analog multipliers and an operational amplifiers. Using the current feedback operational amplifier to design the voltage-controlled filter is common method. Compared with the voltage feedback operational amplifier[5],the current feedback operational amplifier has the high-inverting input impedance, the low-inverting input impedance, distortion, so it can achieve the high frequency filter . The basic design methods of the voltage-controlled band-pass filter based on the voltage and the current feedback operational amplifier are similar[6]. These methods include the component replacement method[7], the cascade method[8], RLC-CRD transformation method[9], and trapezoidal network simulation method[10]. The design uses a current feedback operational amplifier AD8001.While the analog multiplier uses a voltage-output four-quadrant multiplier AD835. The voltage-controlled band-pass filter based on the voltage feedback operational amplifier uses the current feedback operational amplifier to replace the voltage feedback operational amplifier [11][12], and then the adjoint network to replace the original network, by which we gain the current feedback filter. Compared the voltage-controlled filter designed in this thesis with other voltage-controlled filters, its center frequency is high, waveform is smooth, distortion is small and other features.

The design and principle of the voltage controlled band-pass filter

2.1 The design and principle of the voltage-controlled first-order band-pass filter

The voltage-controlled first-order band-pass filter based on the current feedback operational amplifier mainly uses the four-quadrant multiplier voltage output, the current feedback operational

amplifier and a few resistors and capacitors. The band-pass filter is formed by the simple high-pass and low-pass filter in series, whose sequence is bound, it must connect the high-pass filter with the low-pass filter in series and meet the condition of $f_{LP}>f_{HP}$, And when taking $f_{LP}<f_{HP}$, all the signals will be filtered out. To form a 20dB attenuation band-pass filter, it should make a first-order high-pass filter and a first-order low-pass filter connected in series; to form a 40dB attenuation band-pass filter, it should make a second-order high-pass filter and a second-order low-pass filter connected in series, and so on. Therefore, to form a voltage-controlled first-order band-pass filter, which just need to make a voltage-controlled first-order high-pass filter and a voltage-controlled first-order low-pass filter connected in series.

The voltage-controlled first-order band-pass filter circuit uses the above method to design is shown in Figure1.In the circuit, U_5, U_6, the resistors R_{10}~R_{14} and the capacitor C_2 form the voltage-controlled first-order low-pass filter. While U_1~U_4,the resistors R_1~R_9 and the capacitor C_1 form the voltage-controlled first-order high-pass filter. To connect a voltage-controlled first-order high-pass and low-pass in series forms a voltage-controlled first-order band-pass filter. The upper cut-off frequency of the voltage-controlled first-order band-pass filter is the cut-off frequency f_{HP} of the high-pass filter. The lower frequency is the cutoff frequency f_{LP} of the low-pass filter. Its bandwidth is BW=f_{LP}-f_{HP}, and the center frequency is $f_0=\sqrt{f_{LP}f_{HP}}$. By adjusting the cut-off frequency of the voltage-controlled high-pass and low-pass filter to adjust the bandwidth, thereby the center frequency of the voltage-controlled band-pass filter is adjusted. And because the cutoff frequency of the voltage-controlled high-pass and low-pass filter is adjusted by the control voltage V_f ,so the upper and lower frequency of the voltage-controlled band-pass filter is also adjusted by the control voltage V_f.

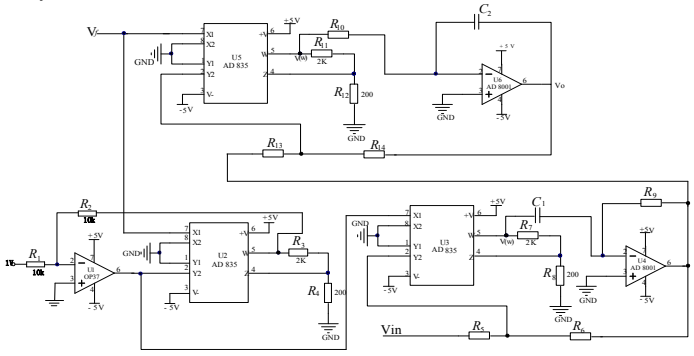

Figure 1 The voltage-controlled first-order band-pass filter

According to Kirchhoff's law and Figure1,the transfer function of the voltage-controlled first-order low-pass filter transfer function is:

$$H_{LP}(s)=-(R_{14}/R_{13})/\{s[(R_{13}+R_{14})/R_{13}]\times(R_{10}C_2/V_f)+1\} \quad (1.1)$$

Formula（1.1），it can deduced the cut-off frequency of the filter is :

$$f_{LP}=\omega_{LP}/2\pi=V_fR_{13}/[2\pi(R_{13}+R_{14})R_{10}C_2] \quad (1.2)$$

When takingR_{13}=R_{14},formula (1.2) becomes to be :

$$f_{LP}=V_f/(4\pi R_{10}C_2) \quad (1.3)$$

Similarly, the transfer function of the voltage-controlled first-order high-pass filter is:

$$H_{HP}(s)=-(sR_6/R_5)/\{s+[V_f(R_6+R_5)]/(R_5R_9C_1)\} \quad (1.4)$$

formula（1.4）,it can deduced the cutoff frequency of the filter is :

$$f_{HP}=\omega_{HP}/2\pi=V_f(R_6+R_5)/(2\pi R_5R_9C_1) \quad (1.5)$$

When taking R_5=R_6, formula (1.5) becomes to be:

$$f_{HP}=V_f/(\pi R_9C_1) \quad (1.6)$$

So the central frequency of the voltage-controlled first-order filter is:

$$f_0=\sqrt{f_{LP}f_{HP}}=\sqrt{V_f^2/(4\pi^2R_9R_{10}C_1C_2)}=V_f\sqrt{1/(R_9R_{10}C_1C_2)}/2\pi \quad (1.7)$$

In the experiment ,when taking R_5=R_6=1k,R_9=1.416k,C_1=60pF,then it can deduced f_{HP}=3.75*10^6 V_f, when taking R_{13}=R_{14}=500Ω,R_{10}=88.5Ω,C_2=30pF,then f_{LP}=3.0*10^7 V_f. When V_f taking 0.3v, 0.4v, 0.6v, 0.8v, 1.0v,the simulation results using ORCAD is shown in Figure 2.

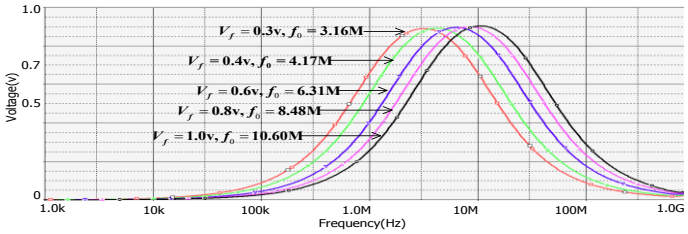

Figure 2 The amplitude-frequency characteristics simulation curve of the voltage-controlled first-order band-pass filter

After testing, when the control voltage V_f taking 0.3v,0.4v,0.6v,0.8v,1.0v,the measured and calculated values of the center frequency f_0 is shown in below Table 1.

Table 1 Comparison of the measured and theoretical values of the center frequency of the first-order band-pass filter

V_f / v	theoretical value	0.3	0.4	0.6	0.8	1.0
f_0 / *M*Hz	measured value	3.16	4.17	6.31	8.48	10.60
	Calculated	3.18	4.24	6.36	8.51	10.72
δ_f （Relative error）(%)		0.63	1.65	0.79	0.35	1.12

2.2 The design of the voltage-controlled second-order band-pass filter

The circuit of the voltage-controlled second-order band-pass filter based on the current feedback operational amplifier is shown in Figure 3. In the figure 3, U_5, R_{10}, R_9, R_8 and C_2 form a summing integrator damper, U_3, R_5, R_7 form an inverting input of the operational amplifier closed-loop, and U_4,R_6 and C_1 form an inverting integrator. The role of $U_1$is to achieve the square of the signal, which makes a linear relationship between the cut-off frequency and the input frequency. While U_2 is to realize multiplied signal to control the voltage. In the circuit, V_f is the control voltage.

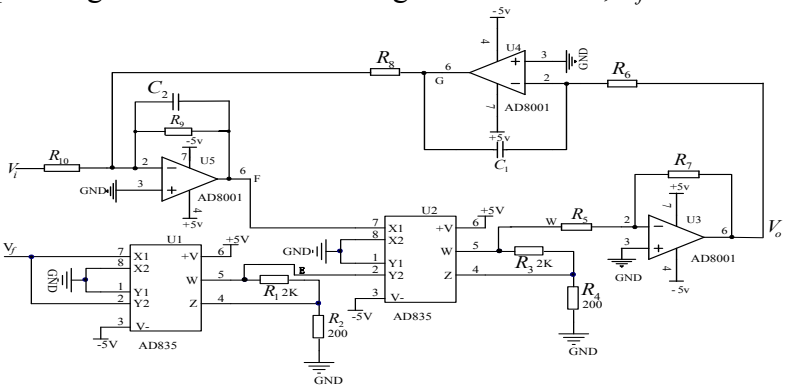

Figure 3 The voltage-controlled second-order band-pass filter

According to Kirchhoff's law：

$$V_E = 0.4V_f^2 \quad (2.1)$$

$$0.4V_E V_F = V_W \quad (2.2)$$

$$V_W / R_5 = V_Q / R_7 \quad (2.3)$$

$$V_Q / R_6 = V_G C_1 S \quad (2.4)$$

$$V_i / R_{10} = (V_F / R_9) + (V_F C_2 S) + (V_G / R_8) \quad (2.5)$$

$$V_D = 0.4V_f^2 V_O \quad (2.6)$$

$$V_Q / R_{11} = -V_D / R_{12} = -0.4V_f^2 V_O / R_{12} \quad (2.7)$$

According to the formula(2.1~2.7),it deduce the transfer function of the filter is:

$$H(s) = [R_7 s / (C_2 R_{10} R_5)] / [s^2 + s / (C_2 R_9) + V_f^2 R_7 / (C_1 C_2 R_5 R_6 R_8)] \quad (2.8)$$

formula(2.8),it can deduce the center angular frequency is

$$\omega_{BP} = V_f \sqrt{R_7} / \sqrt{C_1 C_2 R_5 R_6 R_8} \quad (2.9)$$

The gain factor is $K = R_9 R_7 / (R_{10} R_5)$ (2.10)

The quality factor is $Q_{BP} = V_f R_9 \sqrt{C_2 R_7} / \sqrt{C_1 R_5 R_6 R_8}$ (2.11)

So ,the central frequency is $f_0 = V_f \sqrt{R_7} / (2\pi \sqrt{C_1 C_2 R_5 R_6 R_8})$ (2.12)

From formula(2.10)and (2.11),it can see the quality factor Q_{BP} of filter is controlled by voltage V_f, but the gain K is not controlled by voltage V_f, When taking $C_1=C_2=C$,$R_6=R_8=R$,$R_5=R_7$,it can deduce

$$f_0 = V_f / (2\pi RC) \quad (2.13)$$

Considering the maximum input voltage of the AD835 is 1.0V, when the control voltage V_f taking 0.4v, 0.5v, 0.7v,0.9v,1.0v,the simulate results using ORCAD to is shown in Figure 4

.

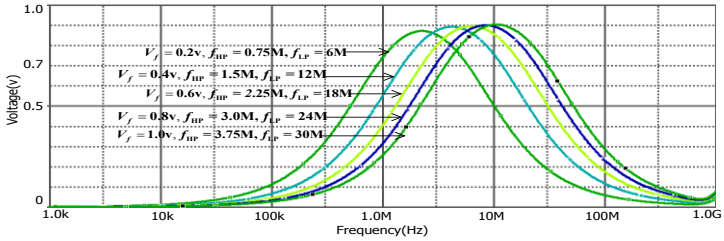

Figure 4 The amplitude-frequency characteristics simulation curve of the voltage-controlled second-order filter

After testing , when the control voltage V_f taking 0.4v,0.5v,0.7v,0.9v,1.0v,the measured and calculated values of the central frequency f_0 is shown in below Table 2.

Table2 Comparison of the measured and theoretical values of the center frequency of the second-order band-pass filter

V_f / v	heoretical value	0.4	0.5	0.7	0.9	1.0
f_0 / KHz	measured value	316.2	501.2	631.0	794.3	1000
	Calculated	318.6	502.3	632.5	795.9	1001
δ_f （Relative error）(%)		0.75	0.22	0.24	0.20	0.10

Conclusion

This paper provides a new design method and circuit of the voltage-controlled band-pass filter based on the current feedback operational amplifiers .The design uses the model of the double second-order loop filter, by making the analog multiplier and the current feedback operational amplifier to lead into the model of the double second-order loop filter to design the new filter circuit. Input voltage signal is input the voltage-controlled band-pass filter circuit constituted by an analog multiplier AD835 and a current feedback operational amplifier AD8001,through which to adjust the the center frequency of the filter to design a filter with frequency bandwidth, high-frequency filters, good performance, simple circuit structure, real-time, low cost, easy to adjust. Besides, the scope of its center frequency is 200KHz-10MHz.If adding the frequency voltage conversion circuit and other circuits to the filter circuit, it can achieve the adaptive voltage controlled band-pass filter. Therefore, the voltage-controlled band-pass filter designed in the thesis based on the current feedback operational amplifier (CFA) has good practical value and broad application prospects.

Acknowledgement

In this paper, the research was sponsored by the Natural Science Foundation of China(61162017),Department of Education-fund projects in Gan su(1101-03) and Northwest Normal University NWNU-LKQN-13-16.

Reference

[1]S.Q.Ma,X.P.Ran,M.H.Fan,et,al.The design adaptive low-pass filter[J],Piezoelectrics & Acoustooptics, 2013，35(2):245-249.

[2]X.P.Li,J.Xu,J.Li,et,al.The principle and implementation method of the voltage-controlled filter,[J],Modern Manufacturing Engineering ,2006,10:114-115.

[3]C.P.Guo,W.Q.Ni.Analysis of stability of the voltage controlled voltage source filter[J],Journal of Luoyang Normal University,2013,32(5):32-34.

[4]J.G.Jiang,Y.N.Wang.Realization of Gm-C Filter with Accurate Tunable Frequency[J], Electronics & Information Technology, 2006, 28(7): 1335-1339.

[5]Fleischer P E, Tow J. Design formulas for biquad active filters using three operational amplifiers[J]. Proceedings of the IEEE, 1973, 61(5): 662-663.

[6]Tangsrirat W.Single- input three-output electronically tunable universal current-mode filter using current follower transconductance amplifiers[J]. AEU-International Journal of Electronics and Communications, 2011, 65(10): 783-787.

[7]A.Li. New active simulated inductance and its application[J]. Hainan University: Natural Science, 2010, 28(004): 327-331.

[8]L.Zhao,W.Liu. Broadband LC bandpass filter design cascade method[J]. Radio Engineering, 2010, 40(8): 42-45.

[9]H.K.Shen. Active simulation bandpass network design[J]. Wired communication technology, 1990 (2): 7-9.

[10]Y.L.Wang,P.Q.Yang. Log-domain filter design LC ladder network simulation based computing[J]. Xiangtan Normal University: Natural Science, 2004, 25(4): 33-35.

[11]Y.A.Li.A simple method of calculating the CFA voltage negative feedback amplifier[J]Electronic Engineer,2004，30(7):31-33.

[12] Jiraseree-amornkun A, Surakampontorn W. Efficient implementation of tunable ladder filters using multi-output current controlled conveyors[J]. AEU-International Journal of Electronics and Communications, 2008, 62(1): 11-23.

Advanced Materials Research Vols. 986-987 (2014) pp 1086-1089

doi:10.4028/www.scientific.net/AMR.986-987.1086

Drive Circuit Design of H-bridge Permanent-magnet DC Moment Motor Based on HIP4081 Chip

Bing Zhao

Yantai Engineering Technology College

zb6933517@163.com

Keywords: HIP4081, H-bridge, PWM, Permanent-magnet DC moment motor

Abstract. In order to achieve reliable drive for Permanent-magnet DC moment motor and high-precision control, we use special chips designed HIP4081 H-bridge PWM motor drive circuit bipolar reversible, with DSP as the controller completed a two-way rotation and permanent magnet DC motor speed control . Experiments show that the circuit is safe, reliable, environmental adaptability, good thermal conductivity, high efficiency, applicable to Permanent-magnet DC moment motor powered a variety of control systems.

Introduction

Permanent-magnet DC moment motor is a low speed, high torque motor, which can be long-term work in the stall, you can directly drive the low-load, with optical encoder or encoder can be composed of high-precision servo system, due to its regulation characteristics and mechanical characteristics, speed and torque ripple small advantages have been widely used[1].

Permanent-magnet DC moment motor is currently widely used PWM drive mode, this drive mode can achieve a wide range of speed and position control, as compared with the conventional driving method has a great advantage. Although PWM technology has made great achievements, but DC PWM control technology and associated power drive technology will continue to develop. Since the market is relatively small permanent magnet DC torque motor supporting power drive components, so for a certain type of permanent magnet DC torque motor developed a driver card. HIP4081 driver chip using the chip as NMOSFET power tube, using a digital signal processor (DSP) to generate the PWM pulse width modulated wave, the drive mode can not only drive Permanent-magnet DC moment motor[2], you can also drive other medium-power DC motors.

H-bridge PWM driving principle

PWM drive motor armature voltage polarity by way of reversible and irreversible drive into two categories, irreversible PWM motor driving one or two-quadrant operation, poor speed performance. In order to ensure permanent magnet DC torque in four quadrant operation with good speed performance, using a reversible PWM drive, reversible PWM drive can be divided into two kinds of unipolar and bipolar. Reversible PWM different main circuit structure is divided into H-type and T-type, in which the H-type widely used in the actual system[3], which is composed of four power switching elements and four-wheeling diode bridge circuit composed.

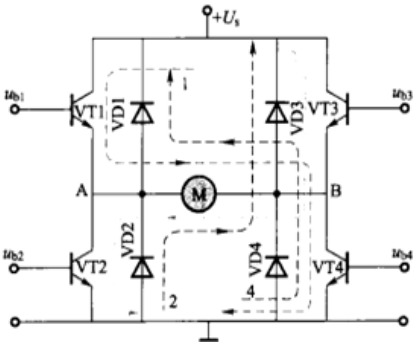

Figure1 H-bridge driver circuit bipolar PWM basic principle reversible

Four power switches driving voltage is divided into two groups, the driving voltage of opposite polarity. The driving voltage $u_{b1} = u_{b4}$ and VT1 VT4 driving power switch turned on and off simultaneously. The driving voltage $u_{b2} = u_{b3}$, and the driving power on member VT2 and V3 are simultaneously turned off. In a driving cycle, when $0 \le t \le t_{on}$, the driving voltage is positive u_{b1} and u_{b4}, and the power switch VT1 VT4 saturated conduction; the driving voltage u_{b2} and u_{b3} is negative, the power switching device off VT2 and VT3. Then the forward voltage is applied to both ends of the motor armature, the armature voltage $u_a = U_s$, and the armature voltage is greater than the inductor voltage $u_a > E_a$, forward current flows through the circuit 1. In time $t_{on} \le t \le T$, the driving voltages u_{b1} and u_{b4} is negative, and the power switching device VT1 VT4 full off; driving voltage u_{b2} and u_{b3} is positive, VT2 and VT3, but not the power switch is turned on immediately, releasing stored energy in the motor armature under the action of the motor armature current along the circuit 2 via the diode VD2, VD3 freewheeling current direction remains positive, the diode VD2, VD3 drop on the power switching device VT2, VT3 withstand back pressure, when the armature voltage $u_a = -U_s$.

Introduction HIP4081 driver chip

In the small motor applications, due to the integrated power amplifier power amplifier circuit performance parameters than ordinary electronic components higher and better overall performance, smaller volume amplifier circuit, system failure may be lower, and enhance the reliability of the system. But conventional driver IC operating current is not large, so the chip design with HIP4081 H-bridge motor drive circuit[4]. HIP4081 chip pin as shown in Figure 2.

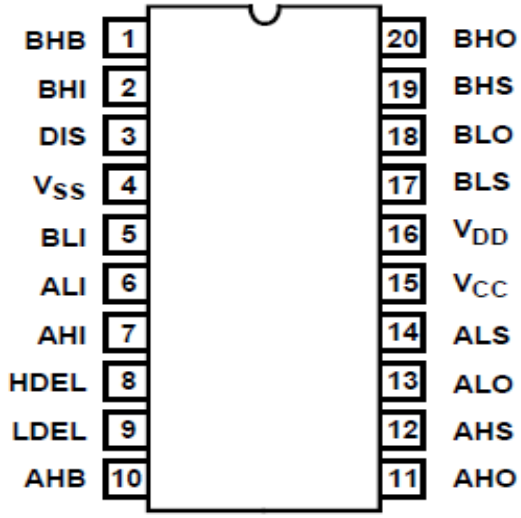

Figure 2 HIP4081 chip pin

HIP4081 chip is intersil company launched a high-frequency full-bridge driver chips, widely used in the control H bridge. This chip has a separate low and high input channels, each drive four N-channel MOS transistor; peak output current of 2.5 A; internal charge pump and chips with dead time set; suspended supply using bootstrap circuit, its high-end working voltage up to 80 V, the logic supply voltage range 6 ~ 15 V, high operating frequency up to 1 MHz; has to control all inputs ban ends, can easily form a protective circuit with external components.

Power switching component selection

With the development of electronic technology, power electronics has experienced rapid technological change. Development of IGBT, MOSFET and including intelligent components, including the power module technology has made tremendous progress[5]. This selection of enhanced NMOSFET IRF3205 HEXFET as power conversion devices, with very low on-resistance internal dynamic dv/dt rating, enhanced with a combination of high-speed switching reliability.

Drive circuit design of permanent magnet DC moment motor

PWM driver circuit shown in Figure 3:

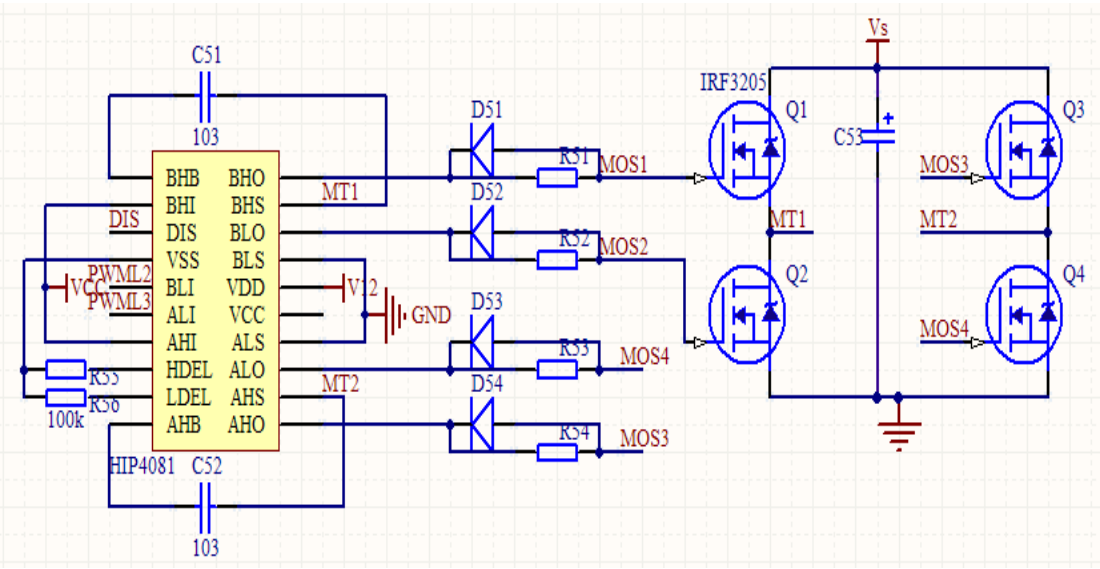

Figure 3 Permanent magnet DC torque motor drive circuit PWM

State of motion and motor work follows a logical sequence in Table 1 below[6][7]:

Table 1 Logical relationship

ALI	AHI	BLI	BHI	DIS	ALO	AHO	BLO	BHO	H-bridge state	Function
×	×	×	×	1	0	0	0	0	M1~M4 Close	Stop
1	1	0	1	0	1	0	0	1	M1,M4 Conduction	Forward
0	1	1	1	0	0	1	1	0	M2,M3 Conduction	Reversion
0	1	0	1	0	0	1	0	1	M1,M3 Conduction	Brake
1	1	1	1	0	1	0	1	0	M2,M4 Conduction	Brake

PWM input is TTL compatible PWM signal, dutycycle between 0% ~ 100%; Vs for the H-bridge power supply, MOS tube to obtain the output current from the power supply terminal. 4-quadrant mode, changing the direction controlled by dutycycle compatible with TTL level PWM signal to get. In addition, to ensure the ipsilateral H bridge two simultaneous conduction MOS tube is not very important. For Q1 and Q2 or Q3 and Q4 in the conduction time there is a delay, the dead time in the circuit. In order to increase the power density and thermal capacity of the circuit, by the thick film printing process ALN substrate and burning metal welding.

Conclusion

The practical application shows: H-bridge PWM reversible bipolar driver circuit designed in this paper is not only safe and reliable way to achieve a two-way rotation and speed permanent magnet DC torque motor, improve the reliability of the drive circuits and systems, and small product size, thermal performance well, high efficiency, safe working in harsh environments, can be applied by a permanent magnet DC torque motor as the drag of the original variety of control systems.

References

[1] Intersil. Application Note AN9325[Z].2003.

[2] Intersil. HIP4081 Data Sheet[Z].1996

[3] DIAO Xiao-ling. Hybrid Integrated Technology H Bridge Motor Driver Based on the HIP4081 [J]. Modern Electronics Technique, 2009(4): 8-10.

[4] QIAN W, GUO X, JIANG Y, et al. Design of the DC-DC Converter Control with Phase-Shift Full-Bridge Based on HIP4081[J]. Measurement & Control Technology, 2011(12):13.

[5] ZHOU Shao-lei, PENG Xian, ZHANG Yu-tong, et al.Design of A PWM Drived Card for DC Torque Motor [J]. Journal of Naval Aeronautical and Astronautical University.2008,23(1):.83-85.

[6] Kazmierkowski M P, Dzieniakowski M A. Review of Current ControlRegulation Techniques for 3-phase PWM Inverters[J]. IEEE IECON conf. 1994: 567～575.

[7] Kiyoshi Ohishi, Tomoniri Mashimo. Digital Robust Speed Servo Systemwith Complete Avoidance of Output Saturation Effect[C], Power Conversion Conference，1997, (1): 501～506.

Advanced Materials Research Vols. 986-987 (2014) pp 1090-1093

doi:10.4028/www.scientific.net/AMR.986-987.1090

Modeling and Simulation of UAV Electric Servo System

Zheng Xing

Wuhan Mechanical Technology College, Wuhan 430075

zhengxcn@foxmail.com

Keywords: Electric Servo System; MATLAB; Dynamic Simulation

Abstract. With the dynamic simulation tool of MATLAB named SIMULINK, modeling and simulation are made for a certain type of UAV electric servo system. Through detailed performance analysis of simulation results, the simulation experiment is confirmed to be accuracy.

Introduction

Electric servo System is an important and indispensable part of the aerospace vehicle flight control system. it is a force application device of the controller. Electric servo system generates force and torque, manipulate control surface and boost guide mechanism in order to achieve flight attitude and trajectory control [1-2]. Therefore, the performance of servo system directly affects the performance and flight safety of the flight control system.

In this paper, the dynamic simulation tool of MATLAB named SIMULINK is used to construct simulation model of the electric servo control system [3]. From the simulation of a commonly used electric servo system example, the detailed analysis of the system performance is made and the accuracy of the results is verified.

System components and principles

Energy of the Electric servo is electric. Because of its simple structure, easy maintenance, reliable, it is widely used in UAV flight control system. A certain type UAV electric servo system is a position servo feedback system. It is mainly made up of servo amplifier, DC servo motor, reducer, position feedback potentiometer and output rack etc, as shown in Figure 1.

When the difference of the input signal u_i and the feedback potentiometer feedback signal u_f is not zero, servo amplifier amplifies the error signal e_i to make the DC servo motor rotation and the reducer makes the output rack move to the required direction. At the same time, the brush of the feedback potentiometer synchronously motion with the rack. When the rack is moved to the position where the difference between the control signal and the feedback signal is zero, the error signal e_i disappears, DC servo motor and the rack stop. The displacement and the direction of the rack are in direct ratio with the size and polarity of the control signals [4].

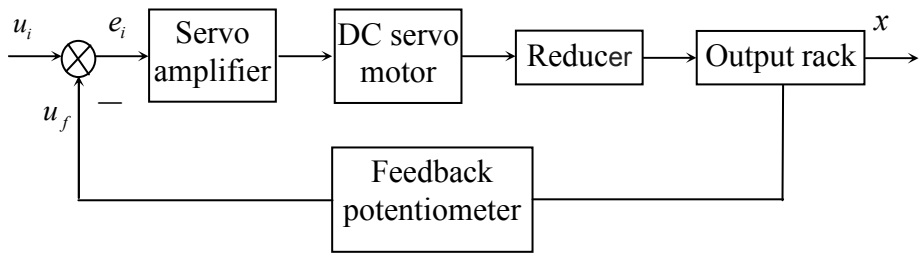

Fig.1 Block diagram of the electric servo system

The mathematical model of the system

Before the simulation, the mathematical model of the various parts of the system is established.

Servo amplifier. The error signal equation is shown as Eq. 1.

$$e_i = u_i - u_f \tag{1}$$

The Amplifier circuit equation is shown as Eq. 2.

$$u_o = Ke_i \tag{2}$$

Among them, u_i the input signal, u_f the feedback signal, e_i is an error signal, K is a magnification, u_o the amplifier output signal.

DC servo motor. The armature circuit voltage balance equation is shown as Eq. 3.

$$u_o = L_a \frac{di}{dt} + i(r_a + r_b) + E_a \tag{3}$$

The armature back EMF equation is shown as Eq. 4.

$$E_a = C_e \frac{d\theta}{dt} \tag{4}$$

The torque balance equation of the motor shaft is shown as Eq. 5.

$$J\frac{d^2\theta}{dt^2} + f\frac{d\theta}{dt} = M - M_l \tag{5}$$

The electromagnetic torque equation is shown as Eq. 6.

$$M = C_T i \tag{6}$$

Among them, L_a is the inductance of the armature winding, r_a is the resistance of the armature winding, r_b is The equivalent resistance of the servo amplifier, i is the current in the armature winding, E_a is the The back EMF, C_e is the back EMF coefficients, θ is the angular displacement of the motor shaft, J is the motor and load inertia referred to the motor shaft, f is the motor and load viscous friction coefficient referred to the motor shaft, M is the torque generated by the motor, M_l is the load torque.

Reducer. The reducer equations are shown as Eq.7 and Eq.8.

$$x = \frac{1}{n}s \tag{7}$$

$$s = r\theta \tag{8}$$

Among them, x is the output displacement of the rack, n is the reduction ratio, s is the linear displacement of the motor shaft, *and* r is the motor shaft radius.

Feedback. Potentiometer The feedback potentiometer equation is shown as Eq.9.

$$u_f = K_f x \tag{9}$$

Among them, K_f is the Feedback coefficient.

Based on the above equations, after simplification, we can establish the structure of the electric servo system, as shown in Figure 2.

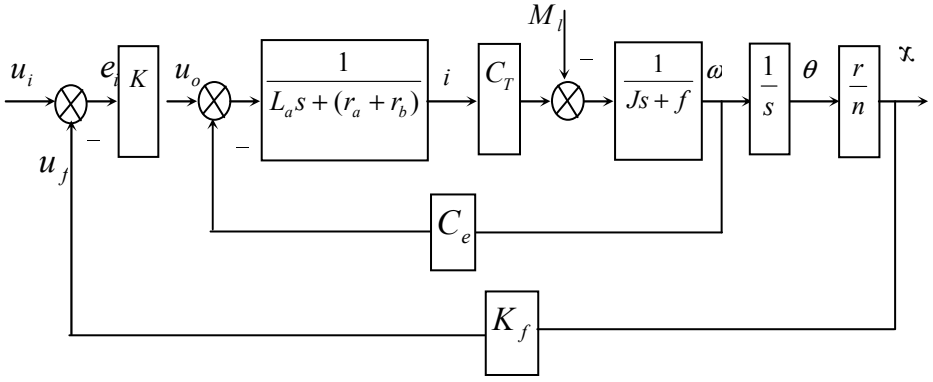

Fig.2 Structure of the electric servo system

Simulation Analyses

MATLAB/SIMULINK provides the basic function module, which is stored in the Module library of the SIMULINK. Run SIMULINK in MATLAB [5], create a Model file. Based on the system structure, don't consider the effect of load torque M_i, after substituting the corresponding parameters, a simulation example as figure3 is built.

Run the command [a,b,c,d]=linmod(fz.mdl) and step(a,b,c,d) in MATLAB, a system step response curve can be obtained, as figure 4. The figure shows that the system is stable. The rise time is 0.053s, the overshoot is 23%, and oscillation frequency is 2.5 times, regulation time is 0.35s, magnification is 5mm/1v. (The actual rise time of the system is 0.046s, the overshoot is 20%, oscillation frequency is 2.5 times, regulation time is 0.3s, magnification is 10±0.5mm/2v). Then, run bode(a,b,c,d), The amplitude frequency characteristics of system can be obtained, as figure5. The system bandwidth is about 8.7 Hz (The actual bandwidth is 10Hz). The above analysis shows that the simulation results close to the actual system, also proves the correctness of the system model.

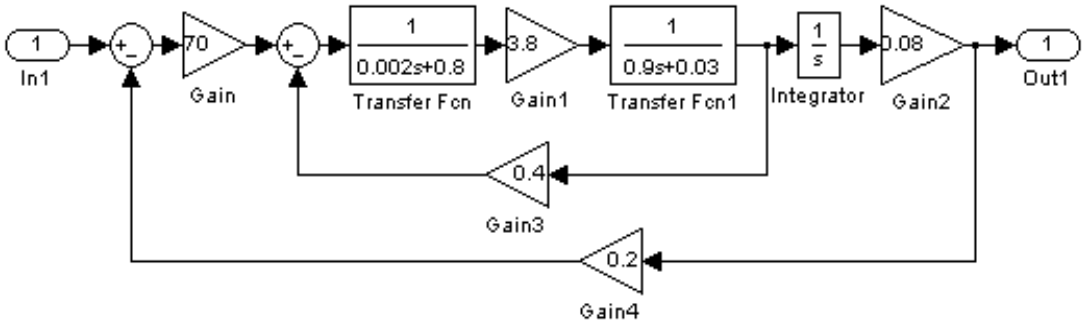

Fig.3 A System simulation example

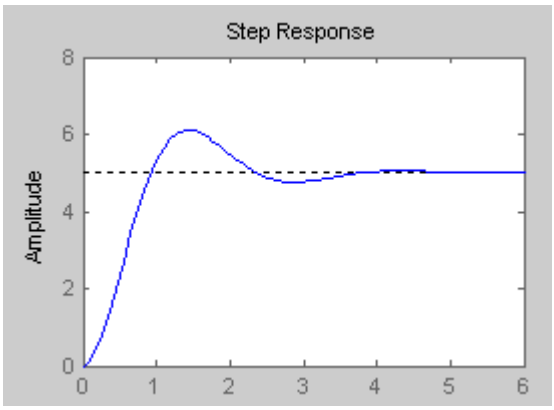

Fig.4 Step response characteristic simulation results

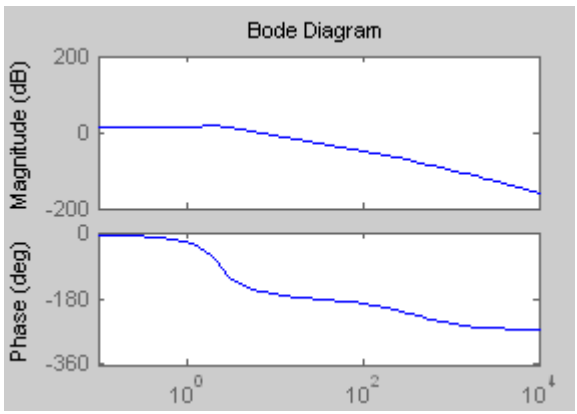

Fig.5 Amplitude-frequency characteristic simulation results

Conclusion

The established mathematical model reflect the actual situation of the system very well, the simulation result is close to the actual system. Using SIMULINK to simulate the electric servo control system, we can modify the parameters, and intuitively obtain simulation results. This method is Convenient and practical. According to the simulation model to analyze the static and dynamic performance of the electric servo system has important practical value of the electric servo system design, research and performance testing

References

[1] Li Linglong, Huo Liangqing, Zhang Qifeng, Sun bin, Design and Simulation Analysis of Servo Amplifier, Process Automation Instrumentation 2012, 33(12).

[2] Yin Dayi, Huang Yuting, Liu Yunfang, Simulation of double-motor speed tracking servo system based MATLAB/Simulink, JOURNAL OF CHINESE INERTIAL TECHNOLOGY, 2011, 19(2).

[3] Sun Jun, Liu Wei, Tian Long, Zhu Wei, Tang Hailun, Servo Feed Drive System Simulation Model and Analysis Based on SIMULINK, Modular Machine Tool & Automatic Manufacturing Technique, 2013, (3).

[4] Jing Qin, Applications of MATLAB/SIMULINK in System Simulation, Journal of Xi‘an University of Arts & Science:Natural Science Edition, 2012, 15(1)

[5] Wang Guixia, Modeling and Simulation of Random Control System Based on MATLAB/Simulink, Ship Engineering, 2012, 34(3)

Advanced Materials Research Vols. 986-987 (2014) pp 1094-1097

doi:10.4028/www.scientific.net/AMR.986-987.1094

Optimization Study of CVT Speed ratio to Plug-in Hybrid Electric Vehicle

Min Zhou [1,a], Yanfang Zhang [1,b]

[1]Chongqing College of Electronic Engineering, Chongqing 401331 ,China,;

[a] 303325025@qq.com, [b] 45923563@qq.com

Keywords: CVT; plug-in hybrid electric vehicle; target speed ratio; energy economy

Abstract: Taking CVT plug-in hybrid electric vehicle as the study subject, the objective function of the energy economy is created. In view of engine, motor efficiency and CVT efficiency coupled relationship; proposed reverse optimization algorithm to solve function. The target speed ratio of optimal energy economy is obtained in different SOC (State Of Charge), velocity, acceleration and slope. On the Matlab/Simulink platform, the system simulation model is built and simulated. The results shows that the target speed ration optimized control law in the case of no additional hardware cost , energy economy save about respectively 3.6% ,4.6%,6.7% in driving cycles of the NEDC,UDDS,HWFET before optimization.

Introduction

Traditional best economy control strategy of continuously variable transmission (CVT) only make the engine work in high efficient area . If plug-in hybrid electric vehicle(PHEV) adopts CVT as the transmission，its energy consumption is not only related to the engine efficiency, but also affected by CVT efficiency, motor efficiency and battery efficiency.

In this paper, the objective function of the energy consumption is set up, which is calculated by reverse calculation method. Then the best target speed ratio of CVT MAP is get under different state of charge (SOC), velocity, acceleration and grade. The PHEV model is built based on Matlab/Simulink, and the control laws of before and after optimization has carried on the simulation analysis.

Systen Configuration

The baseline vehicle studied in this paper is a parallel car with single-shaft and torque coupling as shown in Fig.1. The powertrain is composed of engine, motor, one-way clutch (C1), friction clutch (C2), CVT, differential,batteries and other parts. The role of the one-way clutch is to ensure that the speed of the one-way clutch is to ensure that the speed of the drive system is not lower than the engine speed. The friction clutch is used to start the engine and transfer engine torque.

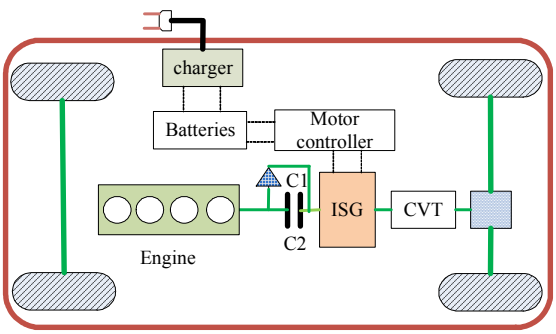

Fig.1. Drivetrain configuration of a parallel PHEV

CVT Speed Ratio Control Strategy

Influence factors.PHEV is different from ordinary sense of the hybrid electric vehicle. Part of its energy from the fuel, the other part is from the power grid. In order to unify the two energy measurement, defined in this article, the energy consumption economy function is the sum of two kinds of energy consumption of the cost.

The consumption of electricity cost can be expressed in equation (1).

$$Q_{electric} = \frac{a_{electric}\int_0^t P_m dt}{3600\eta_m\eta_{bat\_discharge}} \tag{1}$$

where $Q_{electric}$ is the consumption of electricity cost; $a_{electirc}$ is the price of power grid; P_m is the power of motor; η_m and $\eta_{bat-discharge}$ are the efficiency of motor and batteries.

The consumption of fuel cost can be expressed in equation (2).

$$Q_{fuel} = \frac{a_{fuel}\cdot g\int_0^t b_e P_e / 3600dt}{1000\gamma} \tag{2}$$

where Q_{fuel} is the consumption of fuel cost; a_{fuel} is the price of gasoline; g is the acceleration of gravity; P_e is the power of engine; b_e is the fuel consumption rate; γ is the heavy of fuel oil.

$$b_e = \frac{3.6\times10^6}{\eta_e Hu} \tag{3}$$

where η_e is the efficiency of engine; Hu is the low calorific value of gasoline.

Then the equation (3) is taken into equation (2). $$Q_{fuel} = \frac{a_{fuel}\cdot g\int_0^t P_e dt}{\gamma Hu\eta_e} \tag{4}$$

When the demand of vehicle power is P_v, the efficiency of CVT is η_{cvt}, the vehicle power from the actual need is indicated in equation（5）and（6）.

$$P_m + P_e = \frac{P_v}{\eta_{cvt}} \tag{5}$$

$$P_v = (mg\cos(\alpha)\cdot f_r + \frac{C_D A\cdot v_r^2}{21.15} + \ldots \cdots mg\sin(\alpha) + \delta ma)\cdot\frac{v}{3600\eta_{cvt}} \tag{6}$$

where m is the weight of vehicle; f_r is the rolling resistance coefficient; C_D is the drag coefficient; A is the frontal area; δ is the correction coefficient of rotating mass; v_r is the relative velocity; v is the velocity; α is the grade.

The energy consumption economy can be expressed as indicated in equation (7).

$$Q = \frac{a_{electric}\int_0^t P_m dt}{3600\eta_m\eta_{cvt}\cdot\eta_{bat\_discharge}} + \frac{a_{fuel}\cdot g\int_0^t P_e dt}{\gamma Hu\eta_e\eta_{cvt}} \tag{7}$$

By the equation (7) can be concluded that energy consumption economy is mainly affected by the efficiency of the engine, motor, batteries and CVT.

The definition of the optimization problem. According to the equation (7) can be seen that the optimization of energy consumption economy about PHEV, it comes down to the following optimization problem that seeks the best target speed ratio and the speed and torque of engine and motor under the given SOC, velocity and acceleration.

In this way, the system optimization objective function can be expressed as indicated in $\max Q$ (8).

The Analysis of Simulation Result

Based on the vehicle simulate model, a simulation for the optimization of CVT target speed ratio and the traditional economy embed the control target speed ratio are performed.

The figure 2 is the efficiency profile of motor and CVT in combined NEDC drive cycle. It can be seen that under most of the working point, the CVT efficiency and motor efficiency of after speed ratio optimization is more than before optimization.

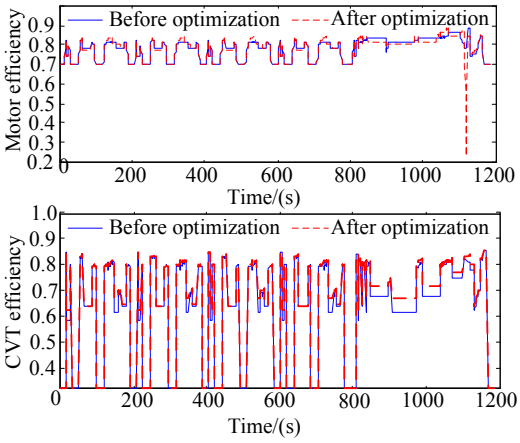

Fig.2. Simulation result in combined NEDC drive cycle

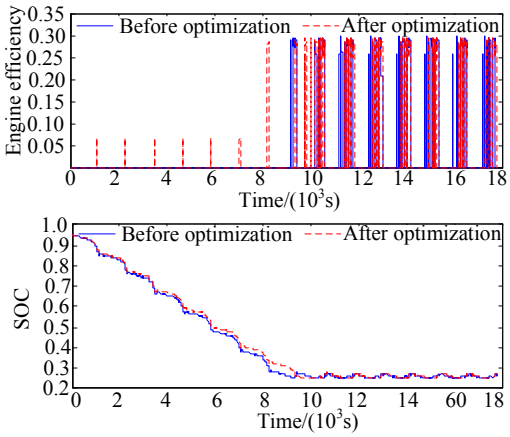

Fig.3.Simulation result in combined 15 NEDC drive cycles

The figure 3 shows the engine efficiency profile and battery SOC profile in combined 15 NEDC driving cycle. It can be seen that the engine participate in the work time is slightly different before and after speed ratio optimization; the most operations points have higher efficiency after optimization. This is because CVT better adjusts the engine working points.

Table.1.Simulation result in combined three drive cycles

Drive cycle	Q /Yuan			
	times	Before	After	Save
NEDC	1	0.88	0.86	2.27%
	10	19.57	18.57	5.11%
	15	42.73	41.2	3.58%
UDDS	1	0.88	0.85	3.41%
	10	18.48	17.34	6.17%
	15	41.64	39.87	4.25%
HWFET	1	1.54	1.47	4.55%
	5	12.47	11.02	11.63%
	10	50.14	48.15	3.97%

From the changing curve of the battery SOC, it can be seen that running time in CD mode is slightly greater than before optimization. This is because the optimized CVT speed ratio can improve the powertrain efficiency of the system. The simulation results of several drive cycles

shows in Table.1. It can be seen that the optimized target speed ratio can make the energy consumption economy save about 3.6 percent, 4.6 percent, 6.7 percent under NEDC, UDDS, HWFET, respectively.

Conclusion

In this paper, three contributions are proposed:

1) For plug-in hybrid cars can recharge the characteristics of the cost of objective function is established.

2) In view of the efficiency of CVT has coupling relationship between the efficiency of engine and motor, the reverse calculation of optimization method is designed to solve best CVT speed ratio under different SOC, velocity, acceleration and slope grade.

3) The simulation results shows that the energy consumption economy can save about 3.6 percent, 4.6 percent, 6.7 percent in NEDC, UDDS, HWFET, respectively, under the condition of without increasing hardware cost.

References

[1]Aoyama T, Takahara H, Kuwabara S, et al. Development of new generation continuously variable transmission[J]. SAE technical paper 2014-01-1728.

[2]Wang Yuan-zhi. Speed ratio control study on CVT with electrical pulley actuation system[J].Advanced Materials Research, 2010,39(342), 342-346.

[3]Lee H, Kim H. Improvement in fuel economy for a parallel hybrid electric vehicle by continuously variable transmission ratio control [J]. Journal of Automobile Engineering, 2005,219(1):43-51.

[4]Montazeri M, Asadi M. Genetic-fuzzy shifting strategy for continuously variable transmission in parallel HEV[C]//. IEEE. International Symposium on Mechatronics and its Applications : Jordan, IEEE, 2008: 1-6.

[5]Huang Wei, Zhou Yun-shan, Xue Dian-lun, et al. A study on driveline control strategy of the fou-wheel drive hybrid electric vehicle based on CVT [J]. Automotive Engineering. 2008, 6(30):501-505.

[6]Hu Ming-hui. Study on energy management strategy for mild hybrid electrical vehicle with CVT[D],Chongqing:Chongqing University,2007.

Advanced Materials Research Vols. 986-987 (2014) pp 1098-1102

doi:10.4028/www.scientific.net/AMR.986-987.1098

Photovoltaic Grid-connected Micro-inverter Based on Self-tuning Fuzzy-PI Controller

Liu Chang-liang[1,a],Zhang Hui-chao[2,b]

[1]State Key Laboratory Of Alternate Electrical Power System With Renewable Energy Sources(NCEPU),Beijing,102206,China

[2]North China Electric power university,Baoding,071000,China

[a]changliang_liu@163.com, [b]zhanghuichao0915@126.com

Keywords: PV Grid; Micro-inverter; Self-tuning PID Control; Fuzzy Control;

Abstract. This paper introduces a kind of grid-connected micro-inverter system. Photovoltaic micro-inverter system is a highly nonlinear and time-varying system. Compared to traditional linear control strategy, Fuzzy Controller has better robustness and stability in the changing or non-linear application. Matlab simulation model for current tracking PV Grid-connected Micro-inverter was completed based on the Fuzzy self-tuning PI controller and the control strategy was tested on the micro-inverter prototype. The resu1ts show that this control strategy can effectively reduce the tracking error of the net current, and improve the system's dynamic response.

Introduction

The micro inverter device can realize the maximum power tracking in panel level and support hot-plugging. The PV power generation system possesses the advantages of high power density, high conversion efficiency, high reliability, and flexible system scalability. Hence, the grid-connected micro-inverter system will be the trend of photovoltaic power generation[1-4].Photovoltaic power generation system is a multi-variable, time-varying system. In the absence of the precise mathematical model traditional linear control strategies is difficult to achieve the perfect performance[5].

In order to overcome the conventional PID controller's deficiencies and improve system performance，a certain intelligence Fuzzy reasoning will be applied to the PID parameter self-tuning in this paper. The parameters K_p,K_i of the PI controller can be tuned according to the operating status of the system. Therefore, the system can get a better dynamic and static performance.

Model and Characterization

2.1 Topology Structure of Micro-inverter

In this paper the photovoltaic micro-inverter power generation system is mainly composed of PV module, micro-inverter and Grid, as shown in Fig.1 a. The micro-inverter mainly includes three parts, the DC/DC converter using flyback topology and the DC/AC converter using MOSFET full-bridge, and the filter circuit using Electro-Magnetic Interference (EMI).Functionally, the DC/DC part can achieve boost transformation, maximum power point tracking (MPPT), and it converts the DC output of the solar panels to a half-wave sinusoidal current. The output half-wave sinusoidal current is converted to be full-wave sinusoidal current by the DC/AC part, and then the current is fed to the EMI filter before the grid.

2.2 Model of Photovoltaic Grid-connected Micro-inverter

Flyback converter is the core part of the micro inverter, and its equivalent non-isolated circuit is a Buck-Boost converter. In order to facilitate analysis, the grid voltage V_{grid} is equivalent to half sine wave, and the system equivalent circuit is shown in Fig.1 b.

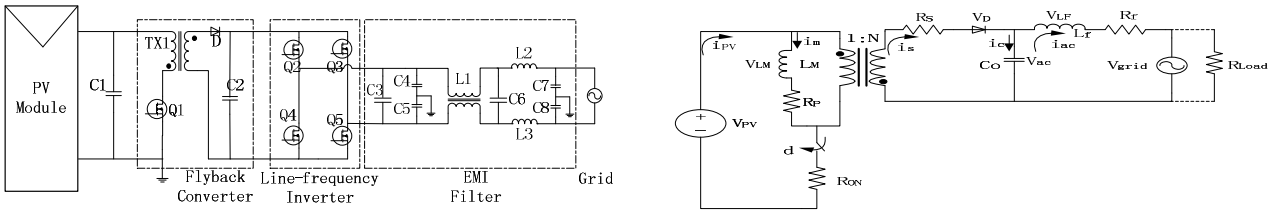

a Topology Structure b Equivalent circuit of micro-inverter

Fig.1 Topology Structure and Equivalent circuit of Photovoltaic Grid-connected Micro-inverter

Flyback converter has the following three states that need to be analyzed corresponding to three energy storage elements: flyback inductor current I_m, flyback output capacitor voltage V_{ac}, System output current I_{ac}. The averaged Kirchhoff's Voltage Law and Current Law (KVL and KCL) equations of the converter over one switching cycle are shown in Eqs.1-6.

$$V_{LM}=L_M\frac{d(i_m)}{d(t)}=d\cdot V_{pv}-d\cdot i_m(R_{ON}+R_P)-d'(\frac{V_{ac}+i_m\cdot R_s}{N}) \tag{1}$$

$$i_s=\frac{i_m}{N}\cdot d' \tag{2}$$

$$V_{LF}=L_f\cdot\frac{d(i_{ac})}{d(t)}=V_{ac}-i_{ac}\cdot R_f-V_{grid} \tag{3}$$

$$i_c=C_o\cdot\frac{d(V_{ac})}{d(t)}=i_s-i_{ac} \tag{4}$$

$$V_{grid}=R_{load}\cdot i_{ac} \tag{5}$$

$$i_{pv}=d\cdot i_m \tag{6}$$

Where d is the duty cycle of modulation signal, d' is the off-time (1-d), N is the turns ratio of flyback transformer. Assume X, U and Y represent the system static working point, $\tilde{x},\tilde{u}$ and $\tilde{y}$ are the perturbations over the operating point, then there are

$$x=X+\tilde{x}=[I_m\ \ I_{ac}\ V_{ac}]+[\tilde{i}_m\ \tilde{i}_{ac}\ \tilde{v}_{ac}] \tag{7}$$

$$u=U+\tilde{u}=[D\ V_{grid}\ V_{pv}]+[\tilde{d}\ \tilde{v}_{grid}\ \tilde{v}_{pv}] \tag{8}$$

$$y=Y+\tilde{y}=[I_{ac}]+[\tilde{i}_{ac}] \tag{9}$$

Substituting Eqs.7-9 into Eqs.1-6, the small signal linearized model is obtained, as shown in Eq.10 and Eq.11.

$$\begin{bmatrix}\dot{\tilde{i}}_m\\ \dot{\tilde{i}}_{ac}\\ \dot{\tilde{V}}_{ac}\end{bmatrix}=\begin{bmatrix}-\frac{R}{L_m} & 0 & -\frac{D'}{L_m\cdot N}\\ 0 & -\frac{R_f}{L_f} & \frac{1}{L_f}\\ \frac{D'}{N\cdot C_o} & -\frac{1}{C_o} & 0\end{bmatrix}\begin{bmatrix}\tilde{i}_m\\ \tilde{i}_{ac}\\ \tilde{V}_{ac}\end{bmatrix}+\begin{bmatrix}\frac{k}{L_m}\\ 0\\ -\frac{I_m}{N\cdot C_o}\end{bmatrix}[\tilde{d}]+\begin{bmatrix}\frac{D}{L_m}\\ 0\\ 0\end{bmatrix}[\tilde{V}_{pv}]+\begin{bmatrix}0\\ -\frac{1}{L_f}\\ 0\end{bmatrix}[\tilde{V}_{grid}] \tag{10}$$

$$\tilde{i}_{ac}=\begin{bmatrix}0 & 1 & 0\end{bmatrix}\begin{bmatrix}\tilde{i}_m\\ \tilde{i}_{ac}\\ \tilde{V}_{ac}\end{bmatrix} \tag{11}$$

where

$$D'=1-D$$

$$k=V_{pv}-I_m(R_{ON}+R_P)+\frac{V_{ac}+I_m\cdot R_s}{N}$$

$$R=D(R_{ON}+R_P)+\frac{D'R_s}{N}$$

In order to obtain the relationship between the micro-inverter output AC current (i_{ac}) and modulation input (d), the disturbance of other variables are not considered. Therefore, the transfer function is obtained between output AC current and modulation input, as shown in Eq.12.

$$G(s)=\frac{\frac{kD'-I_mR}{L_mN^2L_fC_o}-\frac{I_m}{L_mC_oN^2}s}{s^3+(\frac{R}{L_m}+\frac{R_f}{L_f})s^2+(\frac{RR_f}{L_mL_f}+\frac{1}{L_fC_o}+\frac{D^2}{N^2L_mC_o})s+(\frac{R}{L_mL_fC_o}+\frac{R_fD^2}{N^2L_mC_o})} \tag{12}$$

Self-tuning Fuzzy-PI Control Strategy

By Eq.12 shows that the transfer function of micro-inverter output current (i_{ac}) and PWM duty cycle (d) varies as the inductor(L_m) current (i_m). Self-tuning Fuzzy-PI control strategy is applied. The parameters (K_p, K_i)of the PI controller can be tuned according to the operating status of the system. Therefore, the system can get a better dynamic and static performance.

3.1 Fuzzy controller design

For fuzzy reasoning, take the grid-connected current deviation E and its rate of change E_c as input variables, the proportion coefficient increment ΔK_p, integral coefficient increment ΔK_i as output variables. Fuzzy subsets of the all the four variables are defined as {NB, NM, NS, O, PS, PM, PB}.

Triangular membership function is chosen in this paper. The membership functions of the current deviation E, the current deviation rate E_c, the proportional coefficient ΔK_p and the integral coefficient ΔK_i are shown in Fig.2.

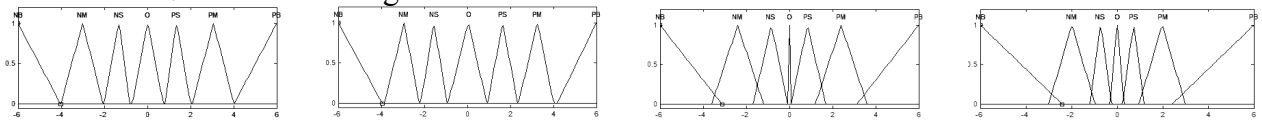

Fig.2 Membership Functions of the Input and Output variables

According to the knowledge of control theory and human control experience summary, in the design of adjustment rules to PI controller parameters, fuzzy rule tables are established , as shown in Table 1 and Table 2.

Table 1 Fuzzy rules of ΔK_p

ΔK_p		E_c						
		NB	NM	NS	O	PS	PM	PB
E	PB	O	PM	PM	PB	PB	PB	PB
	PM	O	PS	PS	PM	PM	PM	PB
	PS	PS	O	O	PS	PS	PM	PM
	O	PS	PS	O	O	O	PS	PS
	NS	PM	PM	PS	PS	O	O	PS
	NM	PB	PM	PM	PM	PS	PS	O
	NB	PB	PB	PB	PB	PM	PM	O

Table 2 Fuzzy rules of ΔK_i.

ΔK_i		E_c						
		NB	NM	NS	O	PS	PM	PB
E	PB	PS	PS	PS	PM	PS	PS	O
	PM	PM	PM	PM	PM	PM	PS	PS
	PS	PB	PM	PM	PB	PB	PM	PM
	O	PB	PB	PB	PB	PB	PB	PB
	NS	PM	PM	PB	PB	PM	PM	PB
	NM	PS	PS	PM	PM	PM	PM	PM
	NB	O	PS	PS	PS	PS	PS	PS

3.2 Structure of Self-tuning Fuzzy-PI

The idea of self-tuning Fuzzy-PI controller is to accommodate both the advantages of the traditional PI control and Fuzzy control. The system of the PV micro-inverter not only has a strong adaptability of Fuzzy controller, but also has a high precision of PI controller.The current deviation E and its rate of change E_c are selected as the two input variables of the two-dimensional fuzzy controller. Then, Fuzzy rules are built to make a reasonable and logical inference. The PID parameters are modified according to the Fuzzy control rules. $K_p=K'_p+\triangle K_p$, $K_i=K'_i+\triangle K_i$. The structure of self-tuning Fuzzy-PI Controller is shown in Fig.3.

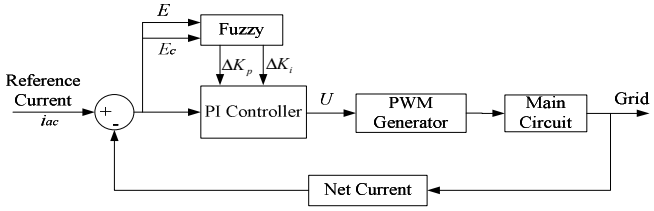

Fig.3 Structure of the Self-tuning Fuzzy-PI Controller

Simulation and Experiment

4.1 Simulation of micro-inverter system

Simulation model of the system is established using the Matlab SimElectronics component library. The Initial value of the fuzzy PI controller parameters are K_p= 0.01, K_i=500. Simulation structure of the micro-inverter system is shown in Fig.4

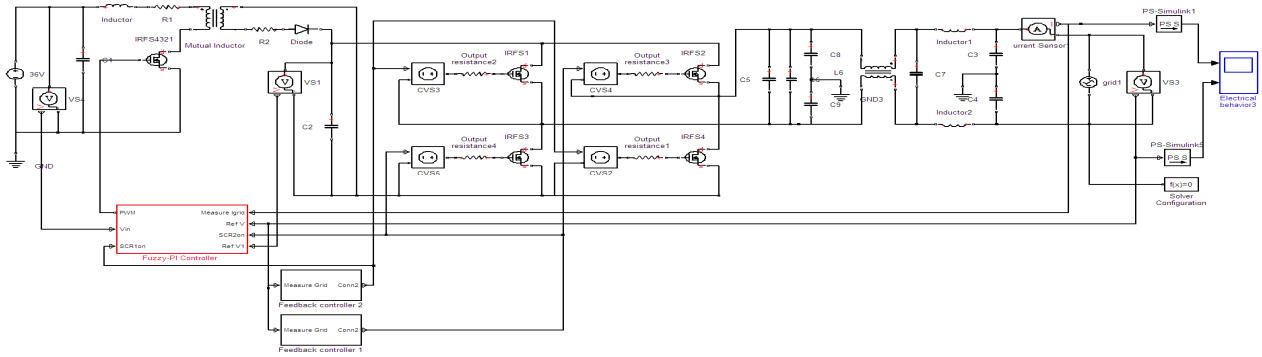

Fig 4 Simulation of micro-inverter system

Control method of fixed parameter PI controller and control method of Fuzzy-PI controller are performed respectively. Grid-connected current waveforms of the two methods are shown in Fig.5 and Fig.6. Obviously, compared with the grid-connected current obtained by fixed parameter PI controller, the grid-connected current obtained by Fuzzy-PI controller has higher sine degree and less harmonic content.

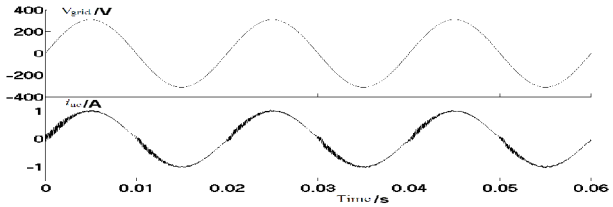

Fig.5 Simulation of fixed parameter PI controller

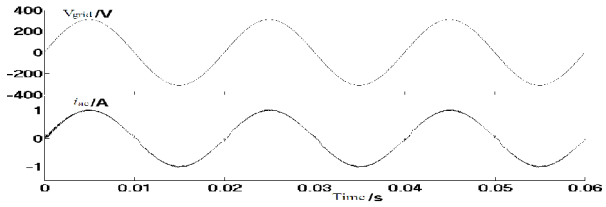

Fig.6 Simulation of Fuzzy-PI controller

4.2 Experiment of micro-inverter system

In order to verify the effectiveness of the system control method further, a 160w micro inverter prototype is completed, which is in accordance with the simulation of the system. DsPIC33 microcomputer is adopted as the main control chip, the turns ratio of the flyback transformer is 1:12, original side switch tubeQ1 is IRF3710, and switch frequency is 57 KHZ, vice side diode is C2D05120E, switch tubes Q2-Q5 of full bridge inverter part are IPB60R190C6, C1=12000 uF,C2=0.1 uF, C3=0.47uF, and L1=600 uH. The results of the experiment are shown in Fig.7 and Fig.8.

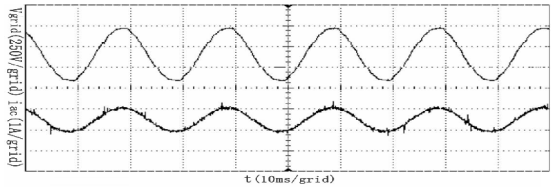

Fig.7 Experiment of fixed parameter PI controller

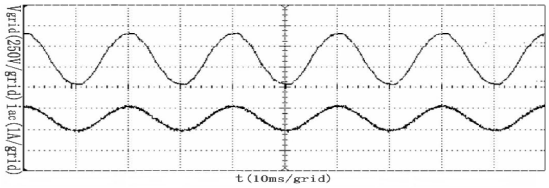

Fig.8 Experiment of Fuzzy-PI controller

Conclusion

In this paper, small signal analysis model of micro-inverter is established. As a high nonlinear and time-varying system, it is difficult to achieve good control effect using traditional PI controller. Self-tuning Fuzzy-PI control strategy is put forward for photovoltaic grid-connected micro-inverter. Simulation and experiment results show that the control strategy has the virtues of good robustness, and could reduce the harmonic content of grid-connected current. Therefore, the system gets a better dynamic and static performance.

Acknowledgements

This paper is supported by State Key Laboratory of Alternate Electrical Power System with Renewable Energy，the Fundamental Research Funds for the Central Universities (13MS102), National Natural Science Foundation of China(61203107).

References

[1] Wenxiang Gao, Mingyu Wang, Lijian Wang, et al. “Review of research on photovoltaic micro-inverter”, Power System Protection and Control, 2012,21,p.147-155.
[2] Haibing HU, Xiaobo HUANG, Wanbao WANG, et al. “A PV Micro-inverter Based on Three-port Flyback With Power Decoupling Function”, Proceedings of the CSEE, 2013,12,p.47-54,185.
[3] Haibing Hu, Harb S, Kutkut N, et al. “Power decoupling techniques for micro-inverters in PV systems-a review”, 2010 IEEE Conference on Energy Conversion Congress, 2010,p.3235- 3240.
[4] Meshram S, Agnihotri G, Gupta S. “The steady state analysis of Z-Source Inverter based Solar Power Generation System”, 2012 IEEE 5th India International Conference on Power Electronics, 2012,pp.1-6.
[5] Hai Wang, Tianyou Hu, Yang Liu,Xuesong Zhang. “Analysis and Design of PV Inverter Based on Fuzzy Control Strategy”, Power Electronics,2013,47,p.50-52

Advanced Materials Research Vols. 986-987 (2014) pp 1103-1107

doi:10.4028/www.scientific.net/AMR.986-987.1103

Research of a Robust Control for Electro Hydraulic Servo System

Xiaogang Tang[1,a], Chao Zhang[2, b]

[1]Jiangsu electric power equipment co., LTD，Changzhou, Jiangsu 213000, China

[2] Jiangsu Institute of Urban and Rural Construction, Changzhou, Jiangsu 213000, China

[a]1186532017@qq.com, [b]zhangchaohyit@163.com

Keywords: electro hydraulic, servo system, robust control, PID, accurate tacking.

Abstract. In recent years, electro hydraulic servo systems are more and more widely used in the aerospace, manufacturing industry and the agricultural machinery. As a result, higher requirements are put forward for the performance and application environment, including better tracking precision and respond speed. Aiming at the shortcomings of conventional PID controller, such as the large overshoot, long transfer time and poor robustness performance, a robust control scheme with dual-loop structure is proposed in this paper. Simulation results show that better performances are acquired in the novel approach in contrast with the PID control scheme and the structure of the proposed scheme is simple and easy to implement.

Introduction

Electro hydraulic servo control is an emerging science and technology, which was firstly presented in the 1950s and developed gradually to form a discipline. Especially in the late 1970s and early 1980s, great improvement and popularity of computer control technology laid the foundation of the combination of electronics and hydraulic technology, making a breakthrough in the capacity of the hydraulic servo control system used in complex systems. Electro hydraulic control system combines the advantages of both electric and hydraumatic. The tracking precision is relatively high and the whole system is fast and easy to tune. Moreover the control output power can be very large, resulting in a wide implement. It was firstly applied in military field, and latterly applied in varieties of industry areas such as mechanical manufacturing, mining, environment and electric power engineering and other automatic control of mobile devices [1-3].

In practical engineering, the most widely used control scheme is the proportional, integral and differential approach which is referred as PID control. Based on the system errors, the PID controller calculates the command by employing the proportional, integral and differential method. Owing to its simple structure, great stability and reliability, PID control scheme has remained a leading position in the industry control technologies. However, due to the nonlinear load torques and the uncertainties caused by the electro hydraulic servo system and the environment, PID parameters are inefficiently tuned which make it difficult to meet the control requirements [1]. As a result, a novel robust approach which can be applied to electro hydraulic servo system based on PID technology is studied in this paper.

Disturbance observer (DOB) [4] which is confirmed to be simple and practical ,is the most effective approach to solve the aforementioned problems. The main idea of DOB is to measure the errors between the outputs of the nominal and actual systems, and the estimated disturbance is adopted to eliminate interference. DOB holds capacity of anti-interferences and improve the system robustness against uncertainties including parameter perturbations and the disturbance of load torque [5-7]. Hence, DOB is introduced in the design of the robust controller for electro hydraulic servo system in this paper.

Problem Description

Electro hydraulic servo target is a hydraulic device composed of servo controller, power amplifier, hydraulic control component and actuators. The control component can be chosen as hydraulic valve or servo variable displacement pump and the actuators can be hydraulic cylinder or hydraulic motor.

Within a certain range, the amplifier output current i_v and the control voltage signal u are in proportion

$$i_v = K_u u \tag{1}$$

Where K_u represents the static amplification coefficient.

The linear flow equation of the control component is shown as

$$Q_f = K_Q i_v - K_C p_f \tag{2}$$

Where Q_f describes the load flow, K_Q describes the amplification coefficient and K_C represents the flow-pressure factor coefficient, after all p_f represents load pressure difference.

The continuity flow equation of the hydraulic cylinder is presented as

$$Q_f = A_t R \frac{\mathrm{d}\theta}{\mathrm{d}t} + \frac{V_t}{4E_y}\frac{\mathrm{d}p_f}{\mathrm{d}t} + C_{s1} p_f \tag{3}$$

Where A_t describes the piston area of the hydraulic cylinder, R describes the arm length, θ denotes the rotation angle correspond to the displacement of the piston, V_t is the total volume and E_y represents equivalent volume elasticity coefficient while C_{s1} indicates the total leakage coefficient.

The load torque balance equation is described as below

$$A_t R p_f = I\frac{\mathrm{d}^2\theta}{\mathrm{d}t^2} + B_t\frac{\mathrm{d}\theta}{\mathrm{d}t} + K_t\theta + M_L \tag{4}$$

Where I denotes the total moment of inertia of the piston and load, B_t represents viscous damping coefficients, K_t describes the stiffness of the loading spring and M_L describes the load moment.

Taking Laplace transform, if there is no elastic load and the value of B_t is small, the open loop function of the electro hydraulic system is described as

$$G_P(s) = \frac{\theta(s)}{u(s)} = \frac{K_a}{s\left(\frac{s^2}{\omega_h^2} + 2\frac{\xi_h}{\omega_h}s + 1\right)} \tag{5}$$

Here $\omega_h = 2A_t R\sqrt{\frac{E_y}{IV_t}}$ represents natural frequency of the hydraulic pressure, $\xi_h = \frac{K_{ce}}{A_t R}\sqrt{\frac{E_y I}{V_t}}$ denotes the damping factor and $K_a = \frac{K_Q K_u}{A_t R}$ describes the open loop amplification coefficient.

The load torque of the electro hydraulic servo targets consist of moment of inertia M_J, moment of coulomb friction M_f, damping moment M_v, and position moment M_θ.The expressions of them are

$$\begin{cases} M_J = J\dfrac{\mathrm{d}^2\theta}{\mathrm{d}t^2} \\ M_f = M_{f0}\mathrm{sgn}\left(\dfrac{\mathrm{d}\theta}{\mathrm{d}t}\right) \\ M_v = K_v\dfrac{\mathrm{d}\theta}{\mathrm{d}t} \\ M_\theta = K_\theta\theta \end{cases} \tag{6}$$

So far, the modeling process of the electro hydraulic servo system has been completed.

Robust Control Design and Analyze

DOB based inner loop control. The basic idea of DOB is to observe the difference between the output of actual system and nominal model [4], which is caused by the external torque disturbance and the parameter perturbations, and take it into consideration in the design of control input. In other words, equivalent interference is observed and compensated in the control command. The construction of the DOB is illustrated in Fig.1:

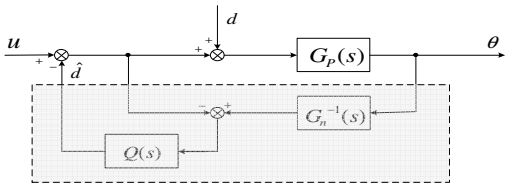

Fig.1 The construction of DOB

In Fig.1, $G_P(s)$ denotes the actual target, $G_n(s)$ is the nominal model, $Q(s)$ describes the low filter, d and $\hat{d}$ represent the equivalent interfering moment and its estimation respectively.

Consider u and d as control input and the system output is shown as

$$\theta = G_{U\theta}(s)u + G_{D\theta}(s)d \tag{7}$$

Where

$$G_{U\theta}(s) = \frac{G_P(s)G_n(s)}{G_n(s)+[G_P(s)-G_n(s)]Q(s)} \tag{8}$$

$$G_{D\theta}(s) = \frac{G_P(s)G_n(s)[1-Q(s)]}{G_n(s)+[G_P(s)-G_n(s)]Q(s)} \tag{9}$$

The frequency band of the filter $Q(s)$ is f_0, which indicates that in the low frequency, when $f \le f_0$, $Q(s) \approx 1$ .As a result, $G_{U\theta}(s) \approx G_n(s)$, $G_{D\theta}(s) \approx 0$. The results show that DOB leads the actual system be equal to the nominal model approximately, and hold strong suppression ability against various disturbance as well as parameter perturbations. Comprise between the robustness and the interference rejection capability is made by choosing appropriate $G_n(s)$ and $Q(s)$.

$G_n(s)$ is considered as unconstructed uncertainty and the simplified nominal model is established as

$$G_n(s) = \frac{K_{an}}{s\left(\dfrac{s^2}{\omega_{hn}^2} + 2\dfrac{\xi_{hn}}{\omega_{hn}}s + 1\right)} \tag{10}$$

Where K_{an} , ω_{hn} and ξ_{hn} are nominal parameters.

$Q(s)$ is a very important step in the DOB design, firstly to make $Q(s)G_n^{-1}(s)$ regular, the relative order of $Q(s)$ must be larger than that of $G_n^{-1}(s)$. For the nominal model $G_n(s)$, we can choose

$$Q(s)=\frac{4\tau s+1}{\tau^4 s^4+4\tau^3 s^3+6\tau^2 s^2+4\tau s+1} \tag{11}$$

The bandwidth design of $Q(s)$ is a comprise between the robustness and the interference rejection capability, which is decided by choosing appropriate τ.

Outer loop control based on PID. In order to achieve good tracing performance of the angular position, a PID controller using angular tracking errors based on DOB is designed in this section. The construction of the controller is shown in Fig.2

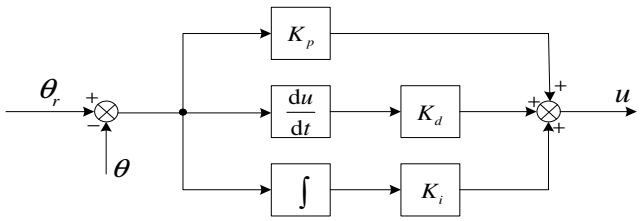

Fig.2 The construction of the PID controller of outer loop system

In Fig.2, θ_r describes the desired output of the electro hydraulic servo system, hence the output u is chosen as part of the input of the DOB.

Simulations

The parameters of the actual object are shown as $K_a=18.5$, $\omega_h=92.0$ rad/s, $\xi_h=0.32$.While the model parameters are $K_{an}=17.5$, $\omega_{hn}=94.0$ rad/s, $\xi_{hn}=0.30$.

We can conclude that model errors exist between the nominal and actual model, and the load torque coefficients are illustrated as

$J=0.00012\,\mathrm{N\cdot s^2/rad^2}$, $M_{f0}=0.55\,\mathrm{N}$, $K_v=0.0025\,\mathrm{N\cdot s/rad}$, $K_\theta=0.025\,\mathrm{N/rad}$

Considering the practice engineering, the control input of the servo controller is limited to ±10V.

The parameters of the control scheme are illustrated as

$\tau=0.0012$ s/rad, $K_p=6.0$, $K_i=0.0$, $K_d=0.25$.

While the conventional PID scheme is shown $K_p=1.2$, $K_i=2.5$, $K_d=0.065$.

The step signal is set as 10deg and the response curves under the control schemes above are shown in Fig.3.Conclusion can be made from Fig.3 that, in contrast with conventional PID control scheme, the setting time of the robust control approach in this paper is much smaller, in other words, the tracking velocity is increased and no obvious overshot emerges.

Then the desired angle signal is set as a 1Hz sine wave with amplitude of 1deg. The tracking error curves in both control approaches are shown as in Fig.4.From Fig.4, we can see that the tracking errors in the robust control method proposed in this paper are smaller than that of the traditional PID control. So far, the rationality and validity of the control scheme in this paper is demonstrated.

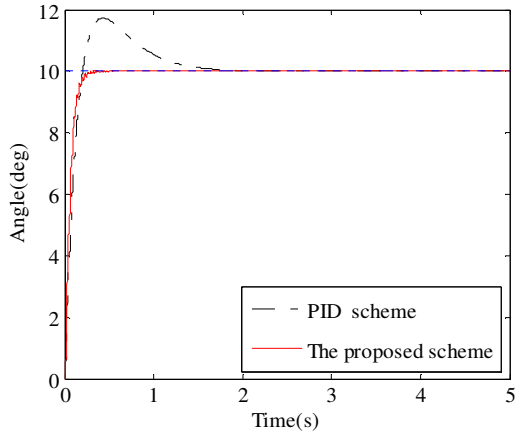

Fig.3 Curves of angle tracking under two control schemes.

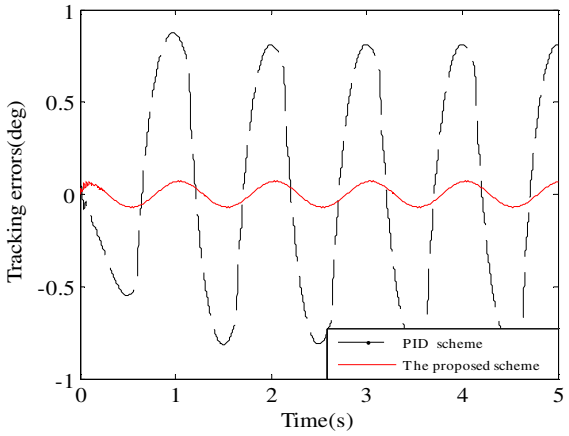

Fig.4 Curves of angle tracking error under two control schemes

Conclusion

In this paper, a novel robust control scheme using a dual-loop structure is proposed for the electro hydraulic servo systems with multi load torques. Simulations show that in contrast with conventional PID control approach, the electro hydraulic system achieves better performances under the robust control scheme with higher response speed and angular tracing precision, as well as smaller overshoot. As a result, the rationality and validity of the novel control scheme is demonstrated.

References

[1] B. Y. Wang, Y. L. Dong, and K. D. Zhao. Compound control for hydraulic flight motion simulator[J]. *Chinese Journal of Aeronautics*, 2010, 23(2): 240–245.

[2] T. A. Minav, J. J. Pyrhonen, and L. I. E. Laurila. Permanent magnet synchronous machine aizing: Effect on the energy efficiency of an electro-hydraulic forklift[J]. *IEEE Transactions on Industrial Electronics*, 2012, 59(6): 2466–2474.

[3] X. H. Li, F. Xu, J. H. Zhang, and S. N. Wang. A multilayer feed forward small-world neural network controller and its application on electrohydraulic actuation system. *Journal of Applied Mathematics*, 2013, 2013, Article ID 872790, 8 pages.

[4] H S Lee, M Tomizuka. Robust Motion Controller Design for High-Accuary Positioning Systems [J]. IEEE Transactions on Industrial Electronics, 1996, 43(1): 48-55.

[5] Q W Jia. Disturbance Rejection through Disturbance Observer with Adaptive Frequency Estimation [J]. IEEE Transactions on Magnetics, 2009, 45(6): 2675-2678.

[6] B K Kim, W K Chung, and K Ohba. Design and Performance Tuning of Sliding-mode Controller for High-speed and High-accuracy Positioning Systems in Disturbance Observer Framework [J]. IEEE Transactions on Industrial Electronics, 2009, 56(10): 3798-3809.

[7] C Du, H Li, C K Thum, et al. Simple Disturbance Observer for Disturbance Compensation [J]. IET Control Theory and Applications, 2010, 4(9): 1748-1755.

Advanced Materials Research Vols. 986-987 (2014) pp 1108-1111

doi:10.4028/www.scientific.net/AMR.986-987.1108

Research of Chain-SVG PWM Modulation Strategy

Lin Liu[a], Zhongchu Wang[b] and Chunbo Gu[c]

University of Science and Technology LiaoNing, Anshan 114051, China

[a]liulin_204@126.com, [b] Wangzhongchu01@126.com, [c]361047793@qq.com

Keywords: SVG, PWM control, multilevel

Abstract. With the rapid development of control theory and microprocessor, many new rectifier control strategy has been born. In current power system, the rapid development of full-control devices, the high application of converter makes the electricity demand is higher and higher. At the same time the increase of power grid users, also bring more harmonic wave pollution, noise and other problems. Therefore, in the field of researching on inverter control has attracted more attention of more people. In order to meet the capacity of switching devices and reduce the switching frequency, often adopts multilevel topology structure [1]. This page based on the cascaded multilevel based on SVG topology structure, analysis of PWM control method and put forward a simple and feasible PWM control method and improve the utilization rate of DC side.

Introduction

According to the working principle of three-phase voltage source PWM rectifier [2-3], figure 1 is the basic unit topology of H bridge, it outputs three levels of +E,−E,0 under the different breakover combination of switching devices.

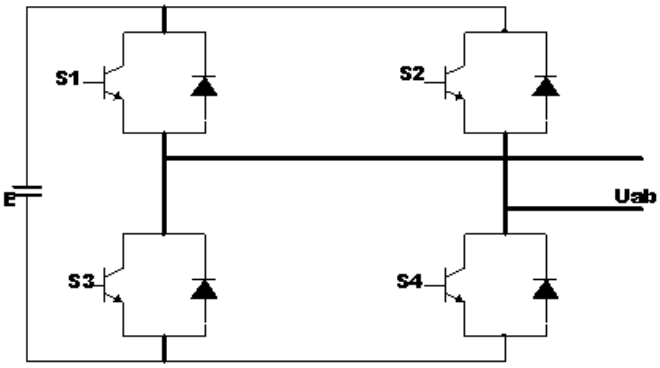

Fig. 1 The basic H-bridge topology

In order to avoid causing short because of the switching tube breakover in a common H bridge, so the IGBT of S1 and S3 do not on at the same time, and their pulse drive signals of T1 and T3 is complementary relationship [4]. In the same way, the S2 and S4 also don't on at the same time. When the IGBT of S_1 and S_4 on at the same time, H bridge output level = E, and when the IGBT of S_2 and S_3 on at the same time, H bridge output level = -E. Carrier wave use triangle wave or use sawtooth wave[5], in this paper to illustrate the optimization effect of the modulation wave, so the carrier still adopts triangle wave.

Putting the basic H bridges unit together constitute the cascaded multilevel SVG, n kind of cascaded structure of multiple units in series as a valve group, three valve form a complete set of three-phase inverter, the cascaded structure is easy to output the multilevel, figure 2 shows the main circuit structure of three-phase H bridge on multilevel SVG , the level number is 2n+1.

The Improved Control Algorithm of Cascaded Multilevel Converter

For cascaded multilevel converter PWM control, with the increase of number of level, its control strategy is also more and more complex, the triangular carrier phase shift PWM control method is only suitable for cascaded multilevel inverter, as long as the carrier ratio is high enough, it contains no

low harmonic and only contain higher harmonic which is related to carrier frequency in the PWM. To inject the zero sequence component to sine wave[6-7], the zero sequence component is a weighted average of the maximum and minimum values in three-phase transient sine wave, assume formula of a three-phase voltage are:

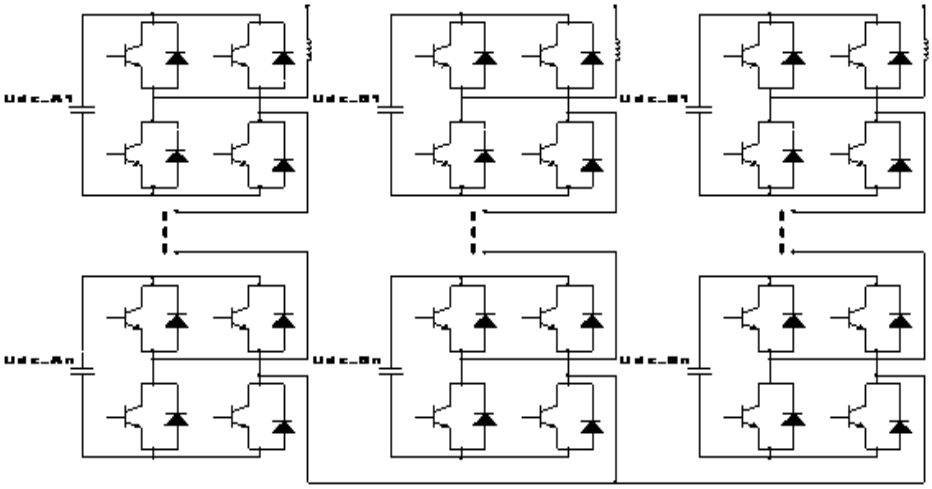

Fig. 2 Cascaded multilevel SVG topology

$$\begin{cases} U_{\alpha 1} = \mathrm{Ur}\sin(\omega t) \\ U_{\beta 1} = \mathrm{Ur}\sin(\omega t + 120°) \\ \mathrm{U}_{\gamma 1} = \mathrm{Ur}\sin(\omega t + 240°) \end{cases} \tag{1}$$

According to the above definition, the zero sequence component:

$$\mathrm{U}_0 = -\frac{\mathrm{MAX}(\mathrm{U}_{\alpha 1},\ \mathrm{U}_{\beta 1},\ \mathrm{U}_{\gamma 1}) + \mathrm{MIN}(\mathrm{U}_{\alpha 1},\ \mathrm{U}_{\beta 1},\ \mathrm{U}_{\gamma 1})}{2} \tag{2}$$

$$\begin{cases} \mathrm{U_a} = \mathrm{U}_{\alpha 1} + \mathrm{U}_0 \\ \mathrm{U_b} = \mathrm{U}_{\beta 1} + \mathrm{U}_0 \\ \mathrm{U_c} = \mathrm{U}_{\gamma 1} + \mathrm{U}_0 \end{cases} \tag{3}$$

Taking an example of seven power unit of cascaded multilevel converter, the carrier adopts triangle wave, the modulation waveform adopts the injected zero sequence component, the triangle wave sampling the sine wave and getting the step wave, the intersection point of the triangle wave and step wave controls the switching devices of conduction and shut off, so output the SPWM, the pulse width which is determined by the intersection point of the triangle wave and step wave when the triangle wave only in its vertex positions (or low) sampling sine wave, the method is only applicable to three-phase system, because of the injected zero sequence component cannot cancel each other in a single phase system, which contains three harmonics in output waveform, and this situation is not exist in the three-phase system.

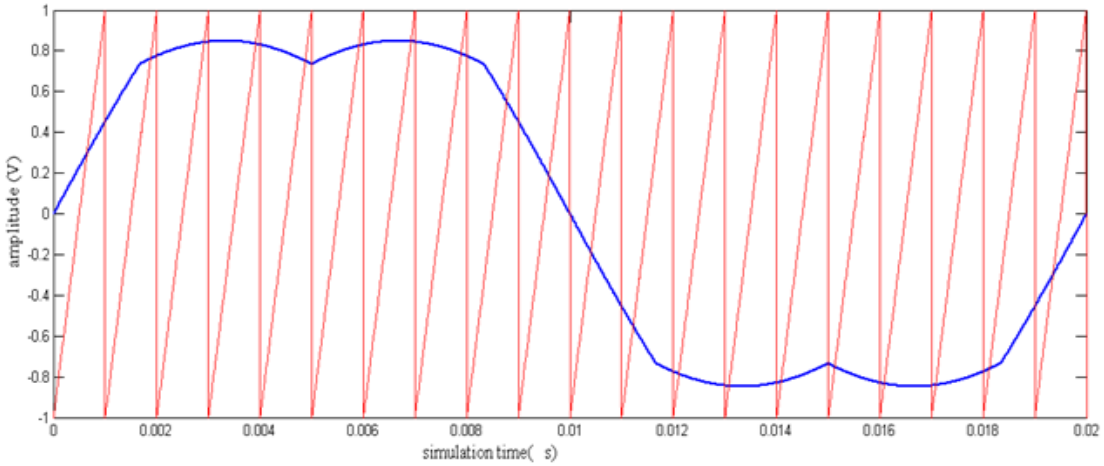

Fig. 3 The comparison of modulated wave with carrier wave

Simulated Analysis

According to the analysis above, built simulation model in the MATLAB, figure 5 is the overall structural model, figure 4 is the module of modulation wave formation after injecting zero sequence component, getting the transient value of maximum and the minimum of three phase by MAX and MIN module, and through the gain module to count its weighted average to get zero sequence component, and add the zero sequence component to sine signal to get the required waveform, out1 is the modulation waveform after injecting zero sequence component.

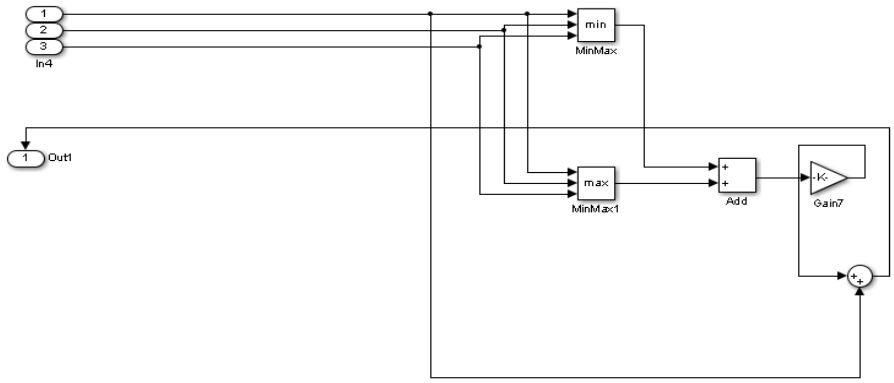

Fig.4 The module of modulated wave

Sine wave modulation frequency is 50Hz, phase difference is 120°, the triangular wave frequency is 1KHz, modulation ratio M = 0.9[8-9], the power supply of power unit is DC 700V, load is in series of resistance of 60Ω and inductance of 20mh. The picture below is the whole simulation graphics.

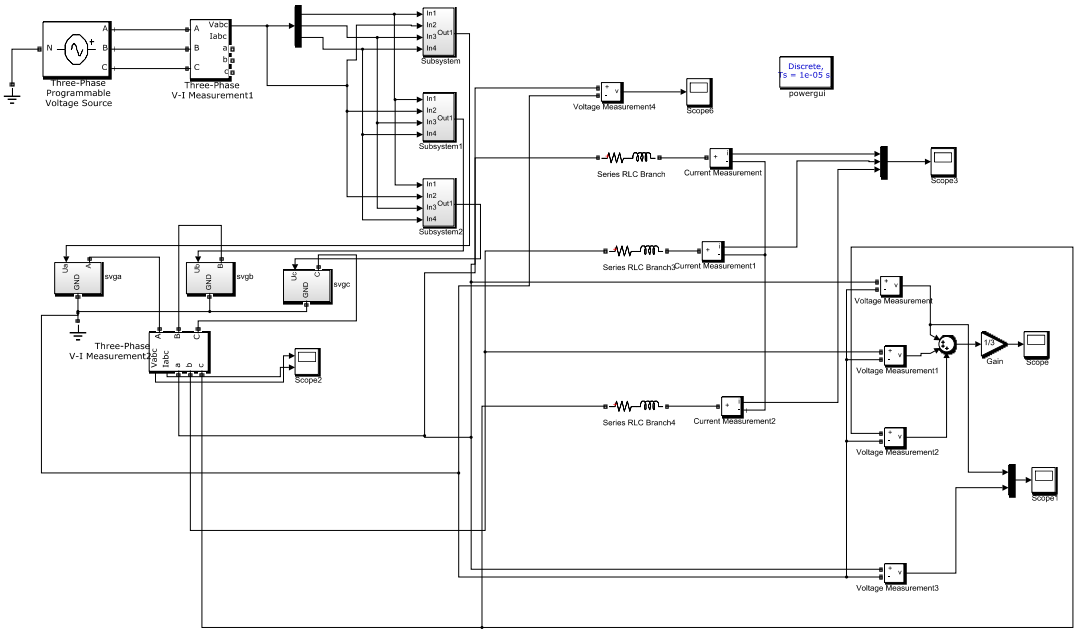

Fig. 5 Entirety simulation figure

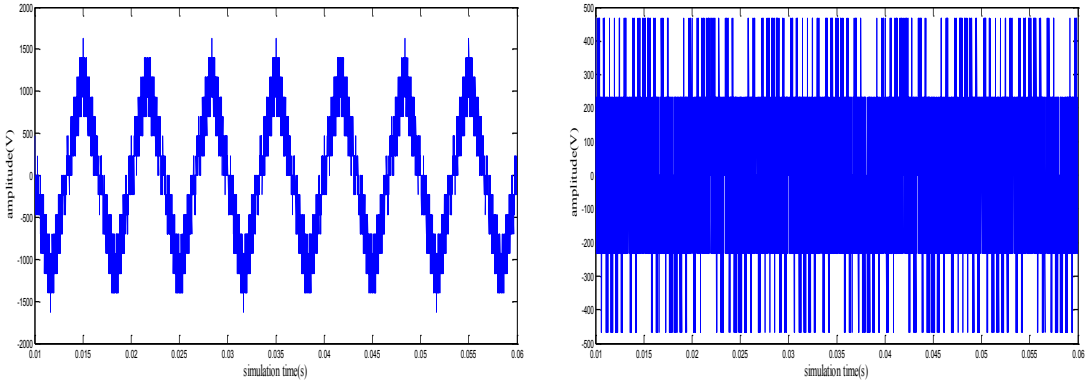

Fig. 6 The line voltage of system compare with unimproved

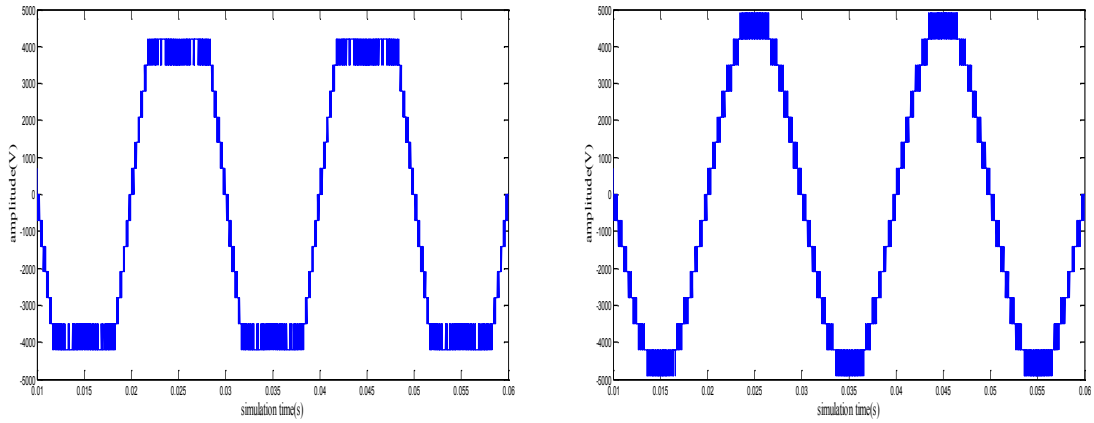

Fig. 7 The phase voltage of A-phase compare with unimproved

Conclusion

Figure 7 is A phase voltage after simulating. The system's line voltage as shown in figure 6, because of the influence of injecting zero sequence component, A phase voltage had a high time harmonic component, because of the harmonics in three-phase system offset each other, phase voltage fluctuation is serious, line voltage have a good harmonic characteristic.

From PWM control method of mechanism analysis, this paper deduced the improvement ideas of the PWM control method, an improved method of modulation wave modulation wave greatly reduces the complexity of calculation on for the high pressure of multilevel inverter control provides a simple and feasible method of PWM control, and in the MATLAB simulation to prove the validity of the theory and feasibility.

References

[1] Xing Zhang, Chongwei Zhang: PWM rectifier and control. Beijing: Mechanical Industry Press. (2012), p. 5-11.

[2] Min Xu: Research and Implementation on the SVG based on PWM Rectifier. Taiyuan: Taiyuan University of Technology. (2013)

[3] Wei Chen, Yongyan Deng, Shiying Gong: DC Voltage Balancing Strategy of SVG Based on Cascaded H-Bridge Converter. Computer & Digital Engineering, 41(10): 1625-1627. (2013)

[4] Shuqin Yu: The nonlinear control method and PWM strategy of Cascaded STATCOM: Beijing Jiaotong University. (2012)

[5] Huibo Lou, Chengxiong Mao, Jiming Lu: Carrier Phase Shifted Pulse Width Modulation Technique Based on Sawtooth Wave. High Voltage Engineering, 38(004): 993-998.(2012)

[6] Ang Liu: The Research on Control Strategy of Carrier Phase Shifted Algorithm for Cells Cascaded High-Voltage Inverter. (2009)

[7] Tao Li, Xiaofeng Zhang, Qiao Zhang: Target-optimum-oriented PWM Algorithm Based on SPWM and SVPWM. Proceedings of the CSEE, (2012)

[8] Biyang Yuan, Xiangzhong Wang: Cascaded voltage inverter power unit carrier phase SPWM improved algorithm. Electronics World, 1. 31-33.(2013)

[9] Caijuan Wang: Research of STATCOM Based on Multilevel Cascaded Technology. Taiyuan University of Science and Technology, (2013)

Advanced Materials Research Vols. 986-987 (2014) pp 1112-1116

doi:10.4028/www.scientific.net/AMR.986-987.1112

Research of direct torque control of asynchronous motor

Chunbo Gu[a, *], Zhongchu Wang, Lin Liu

University of Science and Technology Liaoning, Anshan 114000, China

[a]361047793@qq.com

Keywords: Asynchronous motor; direct torque control; Simulink

Abstract. Direct torque control (DTC) as a new type of motor control strategy, make the control system has good dynamic regulation performance. In this paper, we use the theory of direct torque control to research the speed regulation system of asynchronous motor direct torque control principle and its main component. Use Matlab/Simulink library to build the simulation model of induction motor DTC complete simulation and results show that the direct torque control run time has good control effect in asynchronous motor.

Introduction

Due to the torque control obtained the very good solve, ac motor won a wide application in industry [1]. Direct torque control is a kind of typical control theory after induction motor vector control theory. Direct torque control system is different from the vector torque control system, it static coordinates calculation and control stator flux linkage and torque of the motor directly with space vector concept by detecting the stator voltage and current and then to obtain high dynamic performance of the torque. Direct torque control has the advantage of fast dynamic response, simple control and small parameters dependence [2].

Dynamic mathematical model of asynchronous motor

The mathematical model of three -phase asynchronous motor is a high-order nonlinear and strong coupling multivariable system, in order to facilitate analysis the mathematical model of asynchronous motor, we have to idealize the motor model and make some assumptions, these assumptions are:

1.Uniform air gap, motor radial magnetic circuit isotropic, then, self-inductance of rotor winding don't changes over rotor position;

2.The rotor three-phase winding of the stator and rotor is symmetrical, the conductor space make sine distribution along the air gap effectively;

3.Ignore the harmonic magnetic field;

4.The rotor measurement are all converted to the stator side, so that the stator and rotor winding have the same number of turns;

5.Ignore the effect of magnetic saturation and the iron loss[3].

Based on the analysis of the direct torque control, we generally use the mathematical analysis method of space vector. Asynchronous motor is usually described in orthogonal stator coordinate system (α-β coordinate system), as shown in figure1 is the equivalent circuit diagram of space vector of asynchronous motor.

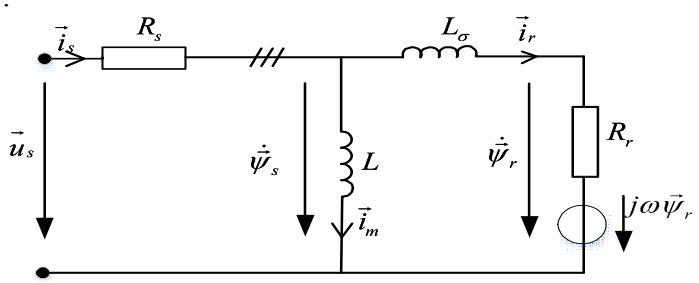

Fig.1 Space vector of asynchronous motor equivalent figure

Where $\vec{u_s}$ is the stator voltage space vector ; $\vec{i_s}$ is the stator current space vector; $\vec{\varphi_s}$ is the stator flux linkage space vector; $\vec{i_r}$ is the rotor current space vector; $\vec{\varphi_r}$: is the rotor flux space vector; ω is the electrical angular velocity.

And rules, we will be rotating space vector projection is called the alpha component on the shaft in the alpha and call the beta component in the beta axis in the orthogonal projection. By above knowable, asynchronous motor in stator coordinate system represented by the following formula:

$$u_s = R_s i_s + \dot{\varphi}_\mu \tag{1-1}$$

$$0 = R_r i_r - \dot{\varphi}_r + j\omega\varphi_r \tag{1-2}$$

It can be deduced stator and the rotor flux and electromagnetic torque equation by Eq. 1-2:

$$\vec{\varphi}_r = \vec{\varphi}_s - L_\sigma \vec{i}_r \tag{1-3}$$

$$\vec{\varphi}_s = \int (\vec{U}_s - R_s \vec{i}_s) dt \tag{1-4}$$

$$\vec{\varphi}_r + (\frac{1}{T_\sigma} - j\omega_r)\vec{\varphi}_r = \frac{1}{T_\sigma}\vec{\varphi}_s \tag{1-5}$$

$$T_e = \frac{3}{2} n_p (\varphi_{s\alpha} i_{s\beta} - \varphi_{s\beta} i_{s\alpha}) = \frac{1}{L_\sigma}\frac{3}{2}|\vec{\varphi}_s||\vec{\varphi}_r|\sin\theta \tag{1-6}$$

The formula for the rotor angular velocity, ω_r is the rotor angular velocity, θ is flux angle, $T_\sigma = L_\sigma / R_r$ is time constant of motor rotor. n actual operation of the asynchronous motor, it is necessary to keep the amplitude of the stator flux linkage as the rating, so as to make full use of the motor ferromagnetic materials; And the rotor flux linkage amplitude generally determined by the load. Because when the stator flux changing, the rotor flux vector basically remains unchanged, so as long as the change of the stator flux linkage vector space position, you can change the flux Angle theta and to change the electromagnetic torque of the motor. The rotor flux can be according to the type(1-3)by changing the rotor current. The stator flux linkage can be changed according to the type(1-4)to the integral of the stator voltage .Steady-state torque calculation can be finished according to the type(1-6)based on rotor flux and the flux Angle theta calculation.

Induction motor direct torque control theory

In recent years, the ac technique develops rapidly and gains a lot of creative achievements. Among them, Depenbrock who is a German professor put forward direct torque control(DTC)system in 1985.Direct torque is different from the vector control technology, it has its own features: simple structure, good performance, direct control means and so on. It rejected the idea of decoupling vector control and let the rotor flux orientation change of the stator flux orientation[5].In the operation of the motor, we just need to know the resistance of the motor parameters, so the direct torque control for motor parameters are lower than the dependence of vector control[6].

We analysis and control direct torque system which is based on voltage space vector. It convert the motor of sone physical quantity to vector by introducing the park transformation[7] and then using stator flux to analysis mathematical model of asynchronous motor in αβ0 coordinates. Then calculate the electromagnetic torque equation and the expression of the stator flux linkage according to u-n model [8]. After getting the electromagnetic torque and stator flux linkage, we make it and the value which has been given for hysteresis comparison. PWM inverter signal is obtained by look-up table and direct control of inverter switch state, so as to control the torque of the motor in real-time. The schematic diagram is shown in figure 2.

As we can see from the figure 2, A direct torque control system is made up collectively of motor, inverter, voltage, torque observer, flux observer, current two-thirds of converter, torque hysteresis comparator, flux hysteresis comparator, sector selection, speed regulator, switch selector and so on, it can be divided into three parts:

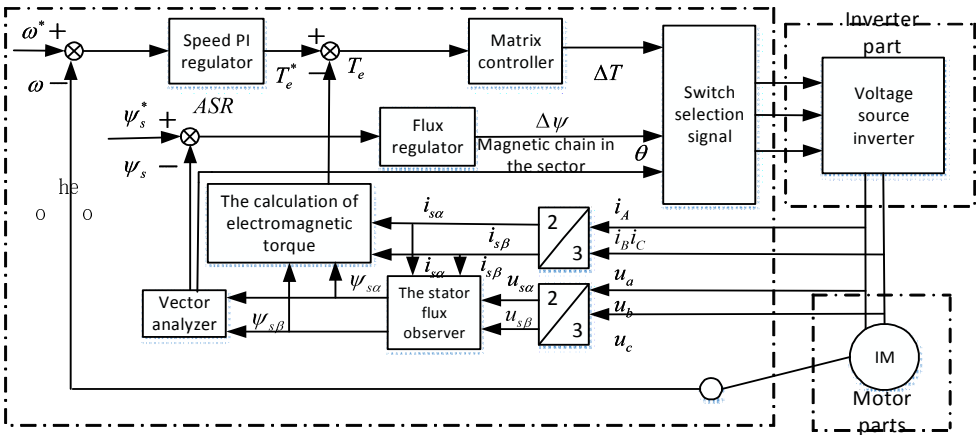

Fig.2 The basic component of direct torque control block diagram

The control part: voltage, torque observer, flux observer, current two-thirds of converter, torque hysteresis comparator, flux hysteresis comparator, sector selection, speed regulator, switch selector. This part mainly adjust torque, flux of interval judgment, stator flux linkage, it select the unit output of the inverter switching state through switch signal. Motor part: motor. Inverter part: inverter.

Among them, the flux observer and torque observer which are by sampling values of voltage and current through two-thirds change according to the asynchronous motor mathematical model to calculate the stator flux linkage and torque of the stator; Voltage state of the unit of flux position detecting should not only depend on the choice of flux linkage and torque control signal, but also on the stator flux linkage section, this unit is based on the stator flux linkage of alpha and beta component to determine the position of the stator flux linkage; Speed regulator control the speed by using of a given speed and feedback speed difference and then output a given value of torque through regulator; Flux regulator is to facilitate the control the change of the stator flux near the set value and then output flux control signal; The function of torque controller is that export torque control signal in a given output torque by using hysteresis control, thereby control the torque of the motor directly; The unit of switch state selector output appropriate switch state to control the inverter drive motor and stable operation according to the torque, stator flux linkage position and the stator flux linkage.

Direct torque control system simulation model

In this paper, the simulation based on Matlab 7.9,it is built in simulink which invokes the visualization module and combinate S function, its structure is simple,clear outline and control idea. System simulation is shown in figure 3:

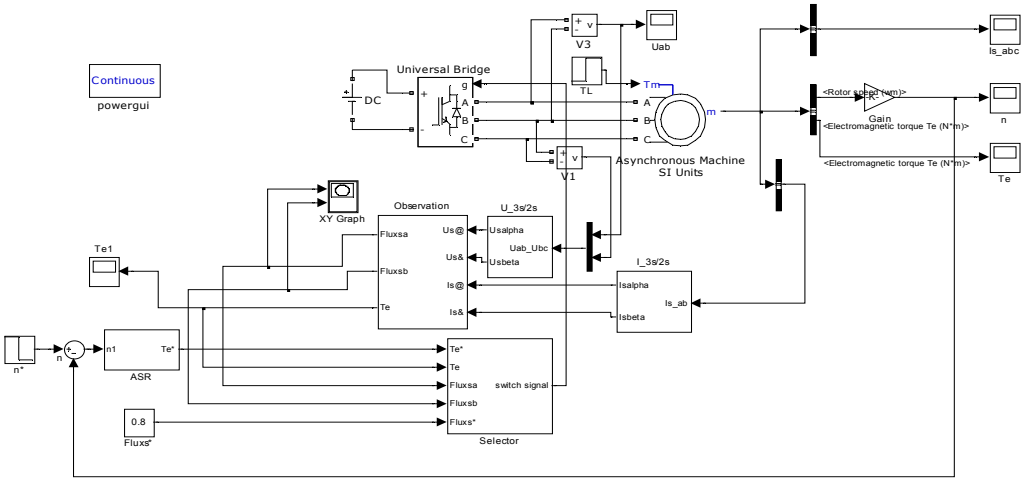

Fig.3 Induction motor direct torque control system simulation diagram

In figure 3, it use the three-phase asynchronous motor module which is provided by the Simulink Simpower systems. Its parameter selection are as follows: three-phase inter switch device IGBT power, the parallel feedback diode, IGBT buffer resistance R_s =100 $K\Omega$,buffer capacity C_s =inf. we

use asynchronous motor parameters in simulation experiments as: power rating P_N =15 KW , rated voltage U_N =400V,rated frequency f =50HZ,moment of inertia J =0.102 $kg \cdot m^2$, logarithmic n_p =2, stator resistance R_s =0.2147 Ω , stator inductance L_s =0.000991H,rotor resistance R_r =0.2205 Ω , rotor inductance L_r =0.000991H, stator mutual inductance L_m =0.06419H.System of other parameters: magnetic chain set in_flux =0.8Wb,voltage of dc side U_{dc} =490V,load torque T_L =60 $N \cdot m$, proportion coefficient of the PI controller K_p =50 and integral coefficient K_i =10,system sampling time T_s =1s,the given value of speed n_e in step 0.5s from 1420 $r/\min$ to 1200 $r/\min$,motor control method has always been a round flux control[10].All sorts of motor startup and steady-state waveform as shown in figure 4 to 7:

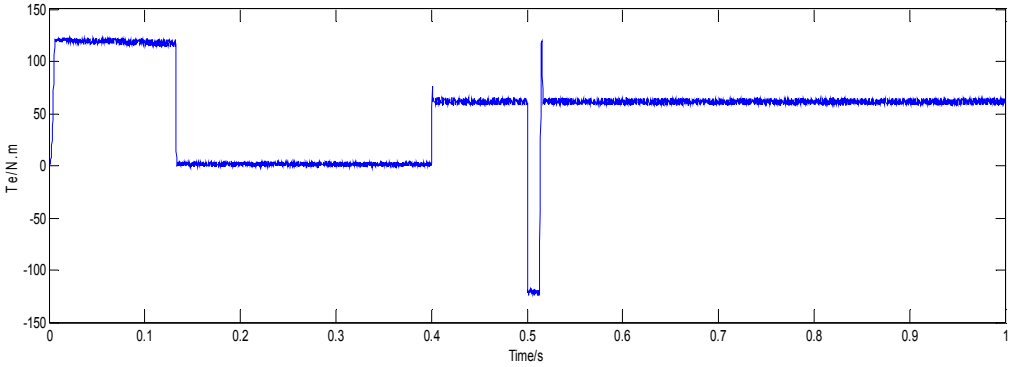

Fig.4 Electromagnetic torque waveform

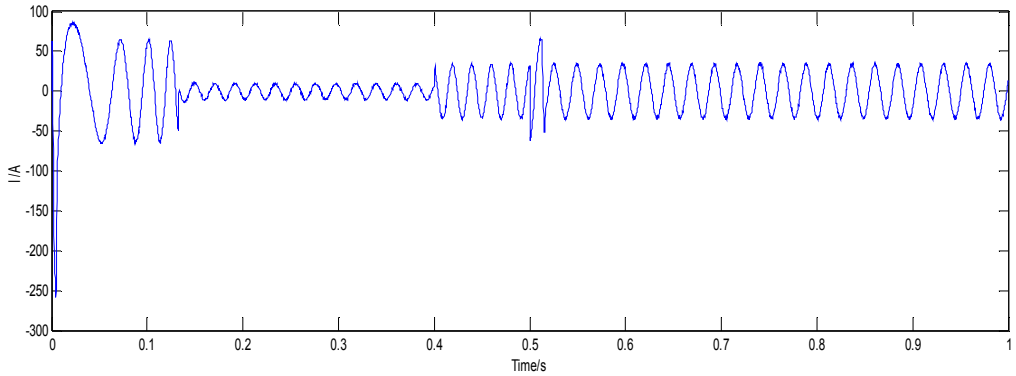

Fig.5 Motor stator current

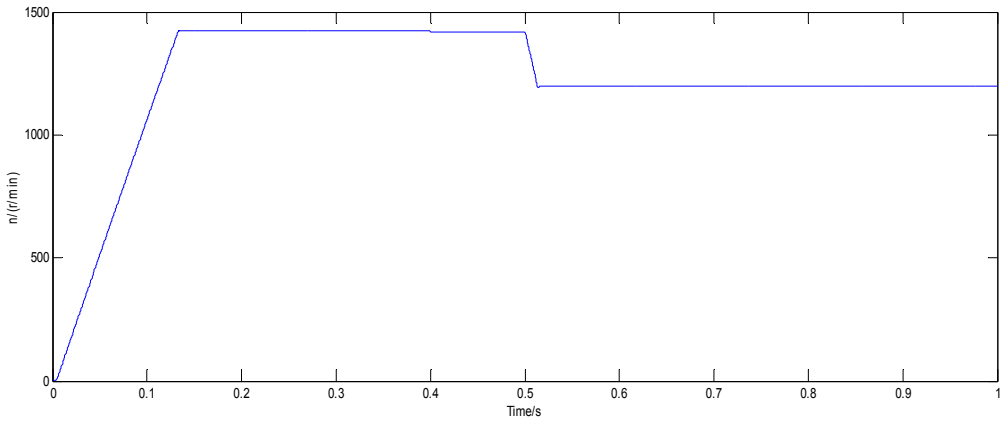

Fig.6 Motor speed waveform

Figure 4 and 5 respectively are motor electromagnetic torque waveforms and stator current waveform diagram. Figure 6 shows the waveform of motor speed, the simulation speed for a given value is 0.5s speed from 1420 $r/\min$ to 1200 $r/\min$, it can be see that speed feedback is good to follow a given that the system can meet the requirements of the speed control. Figure 7 shows the stator begin from the center, counterclockwise and amplitude increases gradually, achieve stable circle finally, it simulate the motor start-up process very well and its effect is very good. The reason is

that tolerance width of flux hysteresis regulator and the torque hysteresis regulator is smaller. If the tolerance of flux linkage and torque is large, the overall of flux is also circular but fluctuation of the circular will increase [11].

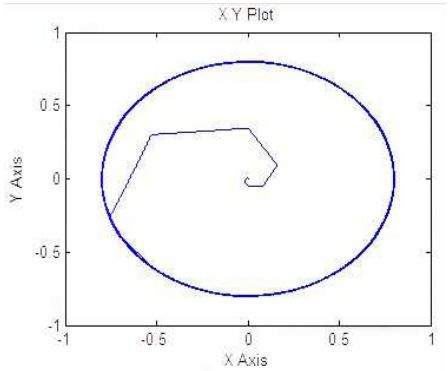

Fig.7 Stator flux linkage waveform

Conclusion

Direct torque control analysis the asynchronous motor of the mathematical model, control motor flux linkage and torque under stator coordinate system directly to make the system structure become simple and to implement more easy. It solved largely that control computation complex, features affected easily by motor parameters change and the actual performance is difficult to achieve the results of theoretical analysis and some major problems in the control of the vector.

Reference:

[1] Hu yu-wen,Huang wen-xin,Zhang lan-hong,Li lei and so on.Asynchronous motor(electric,power generation)direct torque control system. Beijing:mechanical industry press,2012:1-7.
[2] Guo zheng-ping,Ai hong.Asynchronous motor direct torque control simulation.Beijing:Beijing university of information science and technology,2012,27(3):1-1.
[3] Zhou yang-zhong,Hu yu-wen.Ac motor direct torque control.Beijing:mechanical industry press,2009:33-34.
[4] Yao dan,Wang bao-zhong.Asynchronous motor direct torque control.Jiangsu,jiangsu university of science and technology,2012,3:7-10.
[5] Li yue,Xie da-qin.Three-phase ac motor direct torque control research.Journal of baoji college of arts and science(natural science edition),2013,2:45-48.
[6] Yang le,Cheng ming-sheng.Asynchronous motor direct torque control method research.Inverter world,2012,6:83-87.
[7] Bai huang-dong,Chen jia-cheng,Wu su-lian.Based on park transformation of three-phase alternating current phase sequence judgment research.Electric technology,2013,7:43-46.
[8] Luo jian-xin,Fan sheng-wen.The study of the ac asynchronous motor direct torque control.The northern industrial university,2012,5:23-25.
[9] Nie xiang-ju,Miao xing-lei,Li ping.Asynchronous motor DTC of Matlab simulation.Journal of heilongjiang institute of engineering,2012,6,26(2):50-55.
[10] Li xin-yu,Ma ming-zhi,Liao yan-pei.Induction motor direct torque control system.Electric power science and engineering,2013,7,29(7):27-32.
[11] He zhi,Wang dan.Based on the design and implementation of direct torque control inverter.Dalian maritime university,2013,6:33-34.

Advanced Materials Research Vols. 986-987 (2014) pp 1117-1120

doi:10.4028/www.scientific.net/AMR.986-987.1117

Research on CNC AC Servo System design and parameters' tuning and optimization

Xianlong Han[1,a], Yaojuan Zhang[2,b]

[1] Engineering Training Center, Beihua University, Jilin, China

[2] College of Mechanical Engineering , Beihua University, Jilin, China

[a]bhhxl@126.com, [b]zhangyaojuan0714@163.coml

Keywords: servo system; CNC; GISE; PID parameter tuning

Abstract. In this paper, the tricyclic control block diagram for CNC AC servo system of three phase permanent magnet synchronous motor was established. And three loop PID controller tuning was analyzed. At the same time, this paper proposed the tuning tricyclic PID parameters adopting GISE. Then take the CNC milling machine for example, simulation tuning was conducted in MATLAB using GISE. The results show that the servo system is no overshoot, fast response and good stability. So GISE is more suitable for parameter's optimization and tuning of permanent magnet synchronous motors' AC position servo system.

Introduction

With the development of power electronics technology, computer technology, control technology and sensor technology, the AC motor and DC motor control performance can become parable with good dynamic performance, so the AC drive system is widely used in CNC machine tools position servo system. Currently, the NC machine AC servo systems generally use tricyclic (current loop, velocity loop and position loop) PID regulator control technology, the traditional PID parameter tuning method has low efficiency, large errors shortcomings. In order to further improve the performance of CNC servo system; there is need for further research CNC servo system PID parameter tuning and optimization problems.

CNC AC servo system PID controller tuning tricyclic

CNC machine tools in AC Servo System uses a lot of three-phase permanent magnet synchronous servomotor(PMSM),three-phase permanent magnet synchronous servomotor with three-phase AC power supply, and its mathematical model with multi-variable, strong coupling and nonlinear characteristics, control them more complex, currently the most commonly used method is the use of vector transform method for linear motor decoupling control, getting mathematical model similar to the DC motor, the dynamic structure shown in Figure 1.

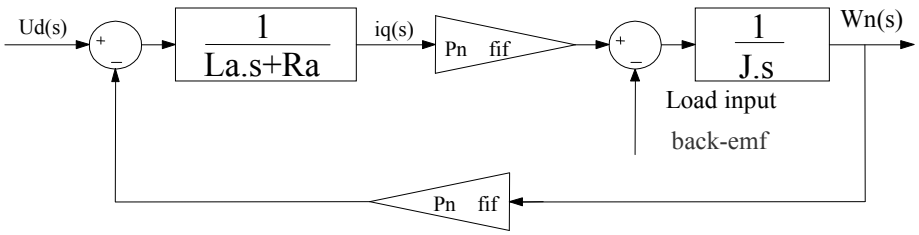

Fig.1 The block diagram of the PMSM

A. Design of the current loop tuning

In the tricyclic structure of permanent magnet synchronous servo system, high current loop is the fundamental of high performance servo system; its dynamic response is directly related to the implementation of vector control strategy or not, directly affecting the dynamic performance of the whole system. Decoupling the permanent magnet synchronous motor based on the model together with the above components, you can create permanent magnet synchronous motor current loop control block diagram shown in Figure 2.

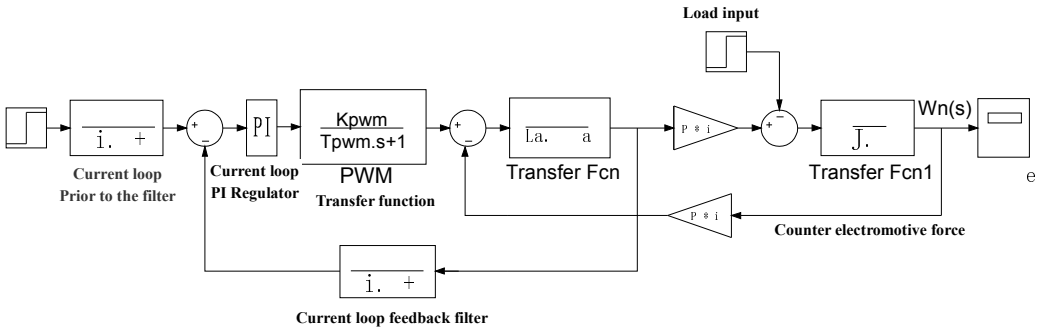

Fig.2 The block diagram of current loop

As the motor SPWM electrical time constant greater than the time constant, to offset the large inertia of the system delay, and improve the response speed of the current loop, taking the time constant equal to the motor controller electrical time constant, that is to take: adjust the current loop open after loop transfer function is:

$$G_1(s)=\frac{K_I K_{P1} K_{PWM}/R_d}{\tau_I s(T_\Sigma s+1)} \tag{1}$$

At this point, the current loop is adjusted second-order system, in accordance with order "best" system design to take:

$$\frac{K_I K_{p1} K_{PWM}}{R_a \tau_I} T_\Sigma = 0.5$$

Therefore $K_I = \frac{R_a \tau_I}{2K_{p1}K_{PWM}T_\Sigma}$, thus the current loop tuning regulator design is completed.

B. The design speed loop tuning

AC servo system speed control is an extremely important aspect. The servo control performance of its overall system performance is an important component of the speed servo control should have a high accuracy, fast response characteristics. When the design of the current loop similar to that in the speed loop in the feedback path and the low-pass filter link (filter time constant of0.01s), and after the given signal with the corresponding part of the balance filter. Speed loop control system block diagram shown in Figure 3.

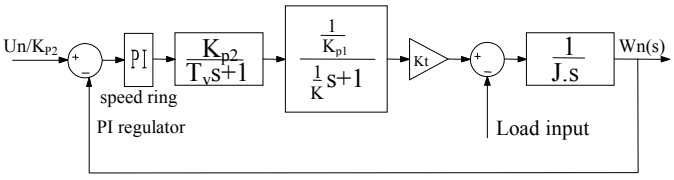

Fig.3 The simplified block diagram of speed loop

The role of the speed loop is usually resistant to load disturbances, inhibition rate fluctuations, the project will usually speed loop tuning into a type II system, so the speed loop regulator should also be designed as PI controller, the transfer function is:

$$G_{Pn}(s)=K_v\frac{\tau_v s+1}{\tau_v s} \tag{2}$$

At this point, the speed loop open-loop transfer unction is:

$$G_P(s)=K_v\frac{\tau_v s+1}{\tau_v s}\frac{K_{p2}K_t}{JK_{p1}s(T_v s+1)(\frac{1}{K}s+1)}=K_N\frac{\tau_v s+1}{s^2(T_{\Sigma v}s+1)} \tag{3}$$

Among: $K_N=\frac{K_v K_{p2} K_t}{K_{p1} J\tau_v}$, $T_{\Sigma v}=T_v+\frac{1}{K}$, Adopt $M_{r\min}$ criteria for selecting parameters, can be obtained:

$$K_N=\frac{h+1}{2h^2T_{\Sigma v}^2} \quad \tau_v=hT_{\Sigma v} \quad h=5 \tag{4}$$

Associated vertical (3) and (4) can be solved and, thus speed loop controller design tuning is completed.

C. Position loop tuning design

The main objective of the position loop is to quickly track the command value changes, the main performance indicator is the steady-state position tracking error and position loop gain. When the system processes the input after the end of the transient response, the servo system at steady operation the actual position error between the target value and the command is defined as the steady-state position tracking errors. Simplify the system structure shown in Figure 4.

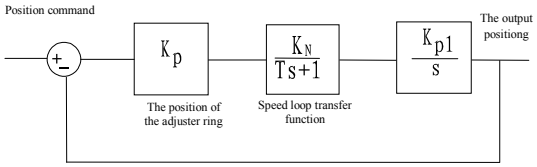

Fig.4 The simplified block diagram of position loop

CNC machine tools in the application, the general ramp input command signal to determine the location of the system tracking error, the unit ramp function input, position loop tracking error is:

$$\varepsilon = \frac{1}{K_{pp}} \tag{5}$$

Where is the position loop gain for the speed loop proportional coefficient for the speed loop gain for optical encoder detects amplification factor.

CNC milling machine servo system tricyclic setting calculation

Select Normal After transformation of NC milling machine Z-feed motor as the research object, the model for1FK6102, motor parameters are as follows:

$n_r = 3000rpm$, $I_r = 11.6A$, $M_r = 16.5Nm$, $J = 0.01215kgm^2$, $R_a = 0.15\Omega$, $T_s = 0.0022s$, $T_L = 0.0113s$, $K_{p1} = 1$, $T_v = 0.01s$, $K_E = 100V/1000rpm = 0.96V/(rad/s)$, $K_t = 1.51N \cdot m/A$, $K_{p2} = 1$, $K_{PWM} = 7.78V/A$, $T_{PWM} = 167us$, $T_i = 100us$.

The manual calculation of system parameters into the model test results of the tuning, analysis in time domain and frequency domain, the results after the setting shown in Table 1.

Table1 The quality of the corrected system

Performance	Current loop	Speed loop	Position loop
Regulation time s）	0.0025	0.2	0.4
Overshoot	2%	27%	0
Amplitude-frequency margin db）	19.5	26.8	10.6
Phase frequency margin deg）	65.6	42.2	74.2
Angular frequency amplitude-frequency shear rad/s）	1620	40.8	19.4
Phase frequency shear angular frequency rad/s）	7740	580	51.8

From the results, the position loop, velocity loop, current loop design results basically meet the needs of engineering controls. As for the speed loop overshoot, in practical applications, since the input is not a unit step, the actual overshoot to be much smaller.

AC servo system parameter optimization

As mentioned earlier, traditional AC Position Servo System parameter tuning regulator was designed to simplify all aspects of the transfer function into the corresponding typical link of frequency characteristics and root locus method regulator tuning parameters, which makes tuning parameters more complicated, and to some extent dependent on the engineer's experience, there is a certain degree of error, the system does not work in the best condition. In order to make the system optimal or sub-optimal mode of operation, experts and scholars put forward the optimal PID parameter tuning method, the optimal PID parameters self-tuning is the key performance index function selection and optimization algorithm, its direct impact to system optimization results. Common objective function includes ITAE, IST2E, GISE guidelines, criteria GIST example to do this in order to explore further.

Self-tuning PID parameter optimization criterion of GISE index function can be expressed as:

$$Q=\int_0^{\infty}\left[e(t)^2+\rho\dot{e}(t)^2\right]dt$$

Take GISE guide lines different? Valuesto optimize the system to optimize the results in Table2.

Table 2 Effect of initial value on optimum results

Initial [kp kv tsv]	optimization results [kp kv tsv]		
	?=0.001	?=0.01	?=0.05
[30 4 2]	[68.668 8.0495 0.207]	[46.666 11.491 0.544]	[16.523 9.257 2.132]
[50 50 10]	[72.119 13.729 12.469]	[46.958 10.443 16.50]	[16.429 8.761 13.426]
[20 1 0.1]	[71.681 13.703 1.130]	[45.563 11.929 0.351]	[16.304 10.751 0.3531]
[20 1 0.01]	[71.903 13.773 0.588]	[42.625 11.429 0.049]	[16.159 9.476 0.790]

The results of the optimization objective function to the system model for the generation of the unit step response system and bode diagram shown in Figure 5 and Table 3.

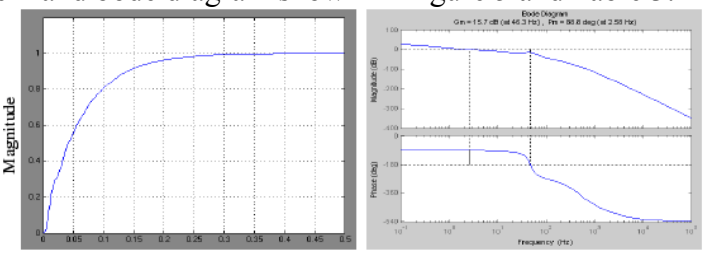

Fig.5 Optimized results of GISE rule

Table3 Effect of optimization rules on optimum results

Regulation time s）	Overshoot %）	Amplitude-frequency margin db）	Phase frequency margin deg）
0.35	0	15.7	88.8

GISE criteria optimization is the key to a reasonable selection parameter ρ, the smaller the parameter ρ take the optimized parameter valuesgreater choice in this case?=0.05, the optimized system regulation time of0.4s,no overshoot, and the transition process without oscillation.

To sum up, the generalized integral square error(GISE)as the optimization criterion, the optimized system has no overshoot, short response time(0.4s),the transition relatively stable, steady-state error characteristics of small, more suitable and permanent magnet synchronous motors AC position Servo System parameter Tuning.

Conclusion

In the traditional CNC position servo system tuning adjustment, the model simplification is bound to bring error for tuning results of PID parameters, and manual calculation is tedious and inefficient. While using MATLAB optimizing the system parameters can improve the efficiency and accuracy of the system parameter adjustment and the dynamic performance after tuning the system. The selection of optimal objective function has a great influence to the performance of the system after tuning; this research shows that it is more suitable to take GISE as the optimization criterion for permanent magnet synchronous motor.

References

[1] X.J.Zhu, J.Q.Wang, Q.Chen. Research on Dynamic Grinding Force in Ultrasonic Honing Chatter［J］. Key Engineering Materials,2011,487: 433-437

[2] Li Xu, Bin Yao. Adaptive Robust Control of Mechanical Systems with Nonlinear Dynamic Friction Compensation. American Control Conf. Chicago. 2000: 2595~2599.

[3] H.S.Chang, S.E.Baek, J.H.Park, andY.K.Byun. Modeling of Pivot Friction Using Relay Function and Estimation of Its Frictional Parameters. Proc. of the American Control Conf, San Diego, USA. 1999: 3784~3789.

[4] Li Yi.Two Degree of Freedom Control for Disk Drive Servo Systems.[Ph.D. Dissertation]. University of California at Berkeley . 2000.

[5] Hexu Sun,Lianbing Li,Xiaojun,Guiying Song. A study on predictive control for multi-modes of synchronous motor in servo system. Power Conversion conference. 2002(3):1285-1289

Advanced Materials Research Vols. 986-987 (2014) pp 1121-1124

doi:10.4028/www.scientific.net/AMR.986-987.1121

Research on Controller of Micro-hydro Power System

Nan XIE[1,a], Dezhi QI[2,b], Weimin CHEN[2,c], Wei WANG[2,d]

[1]Dept. of Computer and Information Engineering of Zhejiang Conservancy and Hydropower College, Hangzhou, 310018,China

[2]College of Mechanical and Electrical Engineering, China Jiliang University, Hangzhou, 310018, China

[a]email:nkxiexie@163.com, [b]email: qdz_001@126.com,
[c]email:c9419@sina.com, [d]email:wangwei@cjlu.edu.cn

Keywords: Micro-hydro Power;Self-excited Asynchronous Generator;Double Loop Control;Circuit Topology.

Abstract. On the existing independent operation of micro-hydro systems, a kind of circuit topology of micro hydro power based on self-excited asynchronous generator are studied. Using power electronic devices to meet power standard and reduce circuit losses. The double loop to control of inner current loop and outer voltage loop is studied, realizes the fast control of system and injected into the grid in the form of current, it's safety and high efficiency. Last,using experimental platform to verify the feasibility of the system.

Introduction

With increasing shortages for energy , people have a more deeply research on renewable energy power generation technology such as wind power , photovoltaic , micro- hydro,and distributed generation and grid technology has been known to the public. China is rich in micro- hydro resources , micro-hydro [1]have the advantages which power transmission line is simple , low cost, low maintenance costs , environmental pollution-free.etc, as one of important micro power is increasingly people's attention . From the cost analysis, if micro- hydro uses the traditional control of small and medium hydro electric power, it will have a high cost,therefore, micro-hydro use the asynchronous generator which does not control, the output power is constant. When users load changes , micro- hydro systems need to maintain a constant power outp ut for the power balance [2][3] , users load will absorb excess power through certain controls to ensure that the terminal voltage is constant. At present, micro- hydro power is used in remote mountainous areas in China , with the popularity of the grid, the grid in remote mountainous areas have been covered , but they are basically on the tip of the grid ,and have poor power quality , high electricity costs. On the basis of new energy technology on the network [4][5][6] , this paper proposes a new micro- hydro power topology and control strategy that based on the self-excited induction generator which is not control, it can be achieved a complementary between micro-hydro and electric power ,and reduce electricity cost of users.

Micro-hydro Systems Topology

When turbine drives in asynchronous generators, through the excitation and electromagnetic induction, the stator current and stator voltage are generated in the side of generator stator. The hydropower potential difference in the input side and the output load is fixed, the turbine speed is constant, the induction generator to maintain constant voltage and frequency values, so that the generator output voltage and frequency is constant, namely ,power generation devices have a constant power output.

The topology structure of micro-hydro power system as shown in Fig.1, the user load is directly connected to the asynchronous generator, the generator supply power to the local user load.The difference between the generator output power and load demand power will be backed to the grid by control circuit, thus ensuring the stability of the system. In order to avoid increasing the

harmonic to generator by the control loop, the control circuit is divided into two parts, before part adopts controllable rectifier, after part uses grid inverter, and then access LC filter circuit. The advantage of this design is the only difference power through electronic circuits, which reduces the capacity requirements of power electronic devices and equipment costs.

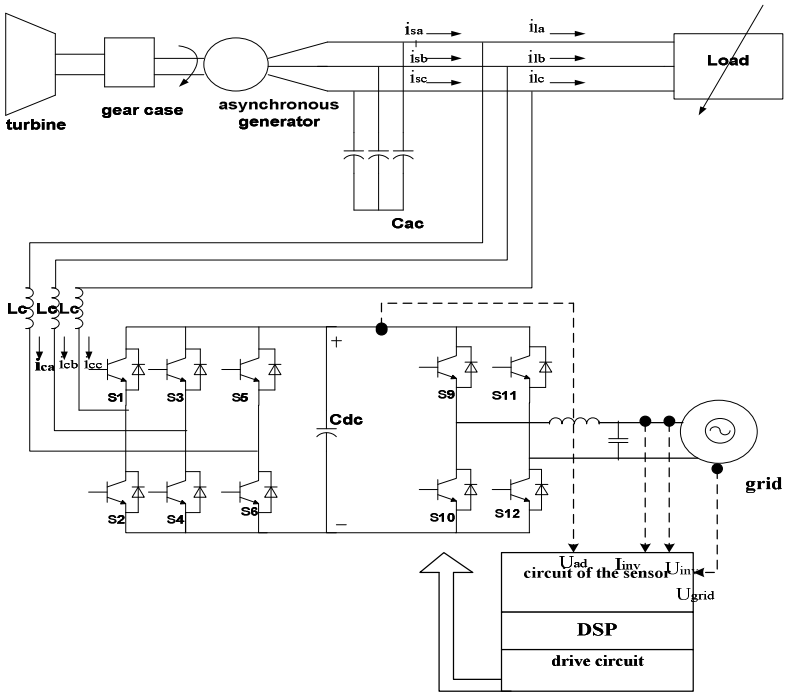

Fig.1. The grid-connected circuit topology of micro-hydro power system

The Grid-connected Control Strategy of Micro-hydro Systems

Analysis of the previous section, the no-controlled mirco-hydro output power is stability, once the users load changes, the generator voltage will also changes. In order to maintain the generator output voltage is stability, corresponding control strategy is used to calculate the difference power which depends on the load side voltage changes, then the difference power is injected into the grid in the current form, thus ensuring clients voltage is stability. In this paper, double-loop control strategy is used. Figure 2 is a block diagram of double-loop control. Current loop control and voltage loop control can be analyzed separately. In the inner current loop, including the current PI controller transfer function, the transfer function of the inverter, the filter transfer function. Its grid-connected process: given the reference current i*L, compared with the inverter side of the inductor current iL, the difference is accommodated by PI current controller, and then get modulated signal Ur through the inverter part, which will be corrected by the grid voltage, the sinusoidal current will be outputted with same frequency and phase of the grid after filtered links, system achieves grid-connected.

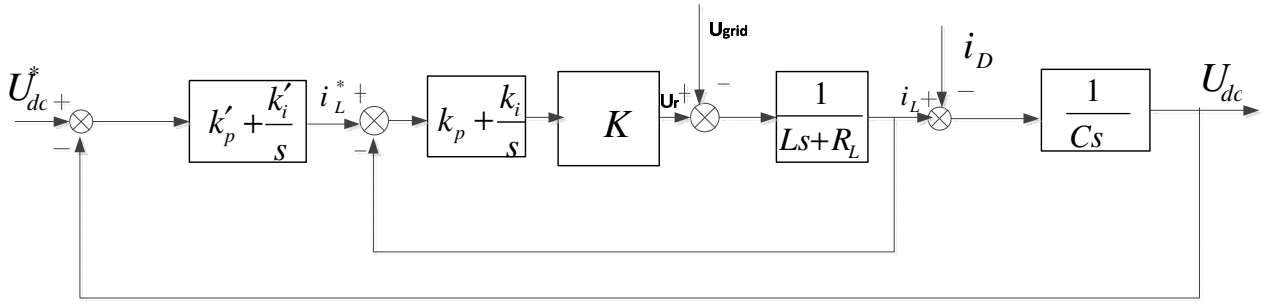

Fig.2. The block diagram of double closed loop

The inner current loop transfer function is:

$$G(s)=\frac{\frac{Kk_p}{L}s+\frac{Kk_i}{L}}{s^2+\frac{R_L+Kk_p}{L}s+\frac{Kk_i}{L}} \tag{1}$$

In Fig.2, the voltage loop control is analysised, which ignores the voltage sampling delay link, it consists of outer voltage transfer function of the PI controller, the current inner loop transfer function, the transfer function of the DC bus side. U*dc is reference voltage of DC bus, iD is the DC current perturbation, Udcis the actual DC link voltage. Its operation process is: compared the actual DC voltage with the reference voltage, the voltage difference is processed by the PI controller, it will generate reference value inner current, adjusted through the current inner loop, the actual current of the output inverter side is disturbed by disturbance current and decoupling control,so that the DC bus voltage is stability.

The outer voltage loop transfer function:

$$G(s)=\frac{\frac{k_p'K'}{C}+\frac{k_i'K'}{C}}{s^2+\frac{k_p'K'}{C}s+\frac{k_i'K'}{C}} \tag{2}$$

Experiment Results

In this paper, the experimental platform is builded to verify the feasibility of systems. In the experiment, using frequency converter control 2.2kW three-phase asynchronous motors that simulates micro-hydro turbine, 1.5kW three-phase squirrel cage induction motor is choosed as self-excited generator, the output side of generator connects to the variable resistive load.

Figure3(a) is the waveform of generator output voltage and output current with the load side changes, the curve 1 is output voltage of the generator, the curve 2 is load current in the user side. Figure3 (b) is the waveform of generator output current and inverter output current when the load side changes, the curve 2 is load current in the user side, the curve 3 is the output current of the inverter side. Before the point of m, when the generator is opened, as the local load power is 0W, load current in generator side is 0A, the maximum output voltage is 220V, the output maximum current of the inverter is 2.3A. When the load power increases 400W at the point of m, the load current is 1.2A, the output current of the inverter side that grid current is automatically reduced, the voltage is essentially unchanged. It illustrates that the system which uses a self-excited induction generator-controlled has a good operating performance and feasible.

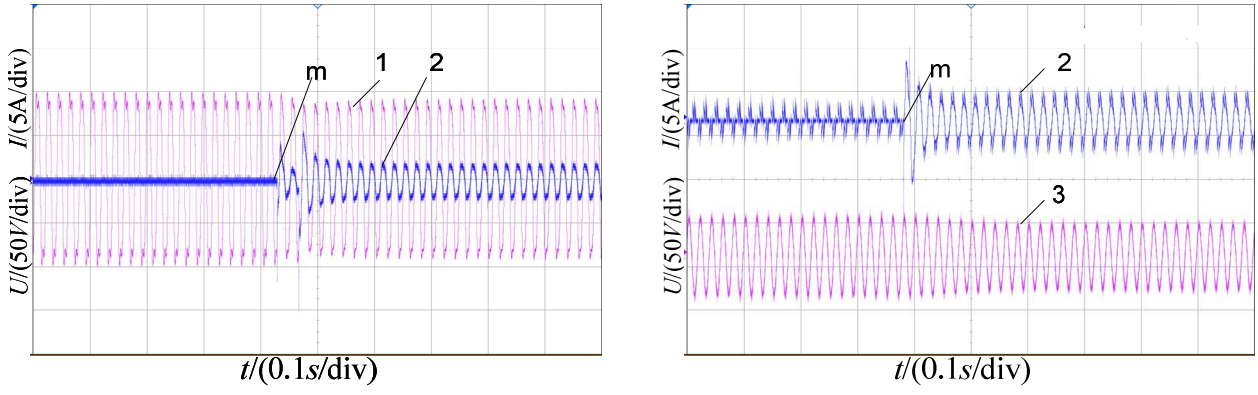

(a) (b)

Fig.3 The waveform of output voltage in generator side and current of load and output current in inverter side with the load power changes

Fig.4 is the waveform of output current in the inverter side and the grid voltage, the curve 4 is the output current in inverter side, curve 5 is the grid voltage. From the Fig.4 ,as the phase and frequency of the inverter output current and grid voltage, the grid current has a good tracking variation with the grid voltage, and the output current is stable, the power factor is close to 1.

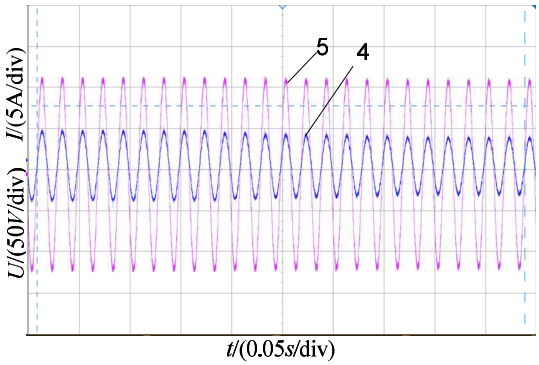

Fig.4. The waveform of output current in inverter side and grid voltage with the load power changes

Conclusion

This paper presents a novel micro-hydro system circuit topology and the corresponding control strategy. Experimental results show that when the load changes, the output voltage of the generator-side remains substantially constant, the generator-side load current increases, the output current of the inverter side decreases, that is in line with the theoretical analysis. The output current of the inverter can maintain the same frequency and phase with the grid voltage , power factor closes to 1, the system is reliable.

References

[1] YUAN Lin-juan, ZHANG Xin, HE Xiang-li, The Progress and Developing Trend of Rural Micro-hydropower Stations, China Rural Water and Hydropower, 2011(7), 147-152.

[2] Youssef, K.H.Wahba, M.A.Yousef, Hasan A. A New Method for Voltage and Frequency Control of Stand-Alone Self-Excited Induction Generator Using PWM Converter with Variable DC link Voltage,American Control Conference, 2008 Digital Object Identifier,2008,2486 – 2491

[3] Ramirez, J.M. Torres, M.E.An Electronic Load Controller for Self-Excited Induction Generators, Power Engineering Society General Meeting,2007,1-8.

[4] LIU Yang-hua,WU Zheng-qiu,TU You-qing, A Survey on Distributed Generation and Its Networking Technology,Power System Technology, 2008,32(15), 70-76.

[5] YIN Guiliang,ZHANG Shengming, Modeling and Simulation of Micro-Hydropower Unit System,Power System Technology,2012,36(2),147-152.

[6] WU Zhen-xing, ZOU Xu-dong, HUANG Qing-jun, Research on Grid Connection Converter of Three-phase Power Electronic Load,Proceedings of the CSEE,2012, 30(24),2622-2628.

Advanced Materials Research Vols. 986-987 (2014) pp 1125-1128

doi:10.4028/www.scientific.net/AMR.986-987.1125

Research on Design Methods and Experiments of the Electro-hydraulic Power Steering Pump

Yong Chen[1,a], Jingjing Xia[2, b]

[1,2]School of Traffic Engineering,Huaiyin Institute of Technology,Jiangsu,Huaian,223003,China

[a]56348008@qq.com, [b]xjj741025@163.com

Keywords: electro-hydraulic power steering; steering pump; design method; experiment research

Abstract. In order to improve the performance of vehicle steering system and reduce the system energy consumption, the structure and operation principle of an electro-hydraulic power steering(EHPS) system with a electro-hydraulic steering pump are described, on this basis, with the function requirement of steering system, and by using vehicle design and fluid drive theory, the design method of this electro-hydraulic steering pump and its matching with the vehicle are presented. Through building electro-hydraulic steering pump test platform to test its performance parameters, the results prove the correctness and effectiveness of this kind of design method, provide the basis for subsequent development of the electronic control system.

Introduction

EHPS system is developed on the basis of the hydraulic power steering(HPS) system, the use of electric motor to drive the steering pump. EHPS system has three advantages relative to the HPS system: (1)steering light; 2 good fuel economy; (3) steering road feeling good[1-3].

Based on the vehicle design and fluid drive theory, this paper puts forward the design method of this electro-hydraulic steering pump and its matching with the vehicle. Through building electro-hydraulic steering pump test platform to test its performance parameters, it provides the basis for subsequent development of the electronic control system.

Composition and Working Principle of EHPS System

EHPS system is mainly composed of electric steering pump, electric control unit (ECU), steering wheel angle sensor, vehicle speed sensor, power steering gear, cylinder, etc, shown in Fig.1.

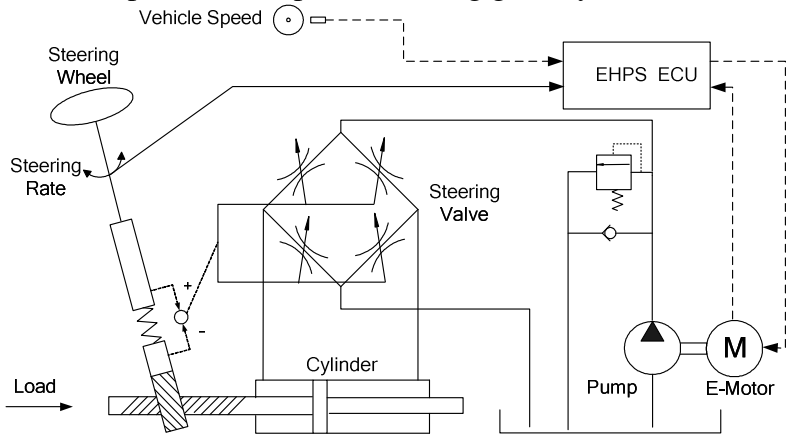

Fig.1 EHPS Working Principle

In the process of vehicle steering, according to the speed of vehicle, the steering wheel angular velocity sensor signal, the EHPS system controller output a pulse width modulation(PWM) duty ratio signal to control the speed of the motor, so as to control the steering pump output flow rate change, and to control the pressure into the power cylinder oil, to control the steering force.

Design of Steering Pump Working Parameters

In the parking steering, a steering wheel steering resistance torque T_1 can be used to estimate as follows[4,5].

$$T_1 = \frac{\mu}{3}\sqrt{\frac{G^3}{P_w}} \tag{1}$$

Where: T_1 is a steering wheel steering resistance torque at the time of the parking steering, N•m; G is acting on a tire normal load, N; μ is sliding friction coefficient between the tire and the road surface; P_w is tire pressure, Pa.

The front axle steering resistance torque T_2 of the parking steering is $2T_1$.

In the parking steering, power steering gear output torque T_3 is described as follows.

$$T_3 = P \cdot A \cdot L \cdot (\cos\theta_1 + \cos\theta_2)/\eta \tag{2}$$

Where: P is power cylinder maximum pressure, MPa; A is power cylinder piston effective area, mm^2; L is knuckle arm length, mm; θ_1,θ_2 are respectively inside and outside the maximum steering angle of the front wheels, °; η is mechanical efficiency of the transmission mechanism of the steering.

Generally approximate that T_2 and T_3 are equal, Eq.3 can be calculated by the system maximum working pressure P.

$$P = \frac{T_3 \cdot \eta}{A \cdot L \cdot (\cos\theta_1 + \cos\theta_2)} \tag{3}$$

According to the maximum pressure of the hydraulic cylinder P and loss of the system pressure $\Sigma\Delta P$ to determine the maximum working pressure P_{max} of pump.

$$P_{max} = P + \sum \Delta P \tag{4}$$

Where: P_{max} is maximum working pressure of pump, MPa; $\Sigma\Delta P$ is loss of system pressure, MPa.

Steering desired flow Q_0 is generally determined by power piston effective area A, rack & pinion steering gain G_R and steering wheel maximum rotational speed n. It can be approximated by the volume change of the power cylinder as a function of time with the leakage flow Q_2 within the steering gear.

$$Q_0 = G_R \cdot n \cdot A \times 60 \times 10^{-6} \tag{5}$$

Where: Q_0 is steering desired flow, L/min; G_R is rack & pinion steering gain, mm/r; n is steering wheel maximum rotational speed, r/min.

The actual need for the pump maximum flow Q_1 (L / min) is:

$$Q_1 = (1.5 \sim 2)Q_0 + Q_2 \tag{6}$$

Where: Q_1 is actual need for the pump maximum flow, L/min; Q_2 is leakage flow within the steering gear, L/min.

By calculating the above parameters, hydraulic power required by the system can be estimated by the Eq.7.

$$W = Q_1 \cdot P_{max}/\eta_p \tag{7}$$

Where: W is hydraulic power required by system, W; η_p is total efficiency of steering pump.

Then pump structure, the size of the pump cavity is optimized design, make it accord with common displacement values in the series. According to the calculated pressure and flow to design the steering pump.

Design of Motor Parameter

Motor is one of the important parts of EHPS system, the power of the motor is slightly bigger than steering pump power.

The output torque of the motor T_i (N, m) as follows.

$$T_i = \frac{P_{\max} \cdot q}{2\pi \cdot \eta_m} \tag{8}$$

Where: η_m is mechanical transmission efficiency between the pump and motor.

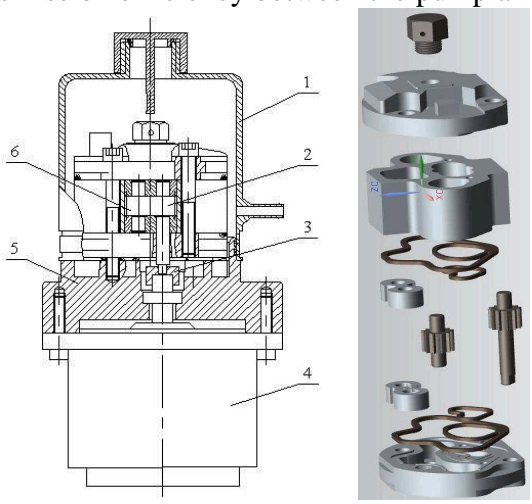

Fig.2 Electric Steering Pump Structure
1-oil tank 2-active gear members 3-coupling 4-motor
5-pump and motor coupling body 6-driven gear

Experiment Research of Electric Steering Pump

Experiment principle is shown in fig.3. In the experiment, through the throttle valve 5 to adjust the size of the steering pump 2 export work pressure, adjust the speed of motor 1 to control the steering pump output flow, motor speed by rotating speed sensor 5 acquisition, acquisition the actual output flow of steering pump under different working pressure through the pressure and flow sensor group 4.

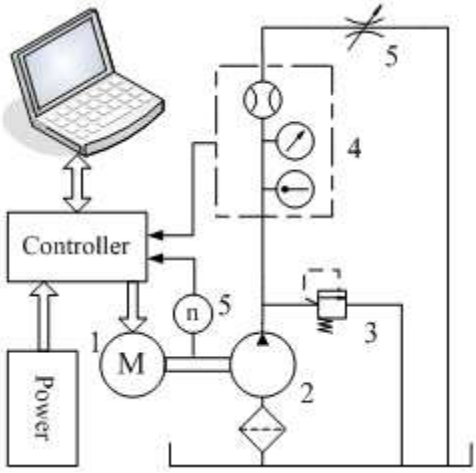

Fig.3 Principle Diagram of Electric Steering Pump Test

Flow-Pressure Characteristics of Steering Pump. Under different speed and different working pressure of steering pump output flow is measured, the output flow and pressure characteristic curve is obtained, as shown in Fig 4. Steering pump flow rate decreases with the increase of test pressure, with the increase of test speed increases.

Volumetric efficiency of Steering Pump. Under different rotation speed and in different working pressure, the volumetric efficiency of the pump features along with the change of pressure is measured.

$$\eta_v = \frac{Q}{Q_0} \tag{9}$$

Where: Q_0 is the theory flow of the pump under different rotational speed, L/min; Q is the actual flow of the pump under different pressure, L/min.

As shown in Fig.5, the volumetric efficiency of the pump decreases with the increase of test pressure, with the increase of test speed increases.

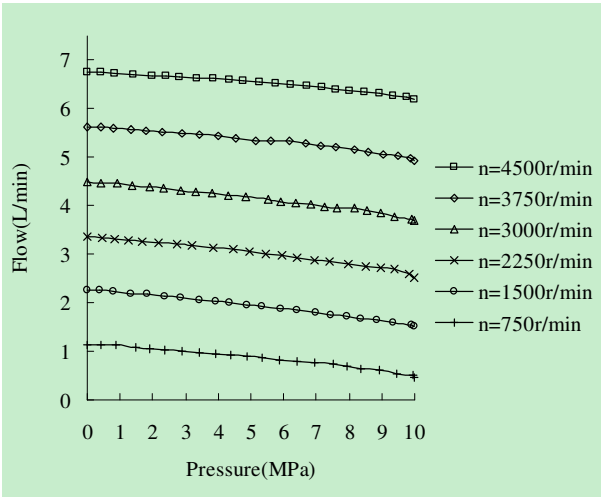

Fig.4 Flow and Pressure Characteristic Curve of Electric Steering Pump

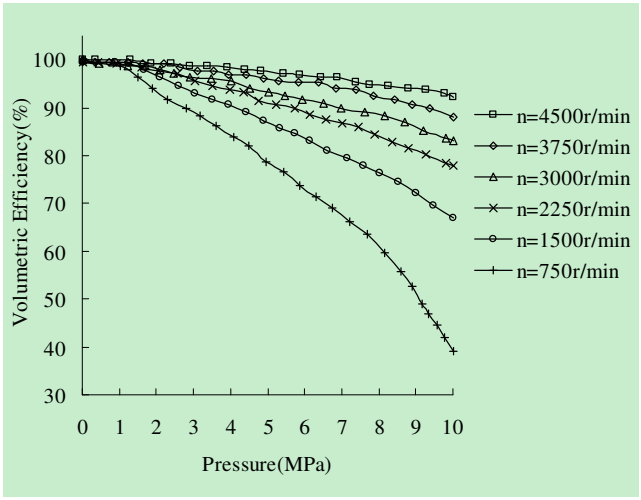

Fig.5 Volumetric Efficiency of the Steering Pump

As shown in Fig.5, with the pressure rising, the volumetric efficiency of the pump was significantly decreased trend when the rotating speed of 750 r/min, the volumetric efficiency is low; When speed up to 1500 r/min, volumetric efficiency is obvious rise, but it is still not ideal. Speed of 2250 r/min, 3000 r/min and 3750 r/min and 4500 r/min of volumetric efficiency curve were similar, the volumetric efficiency is over 80%, it is ideal.

Summary

EHPS system is new concept of vehicle steering system. At present, domestic is lack of mature design theory and method of EHPS system. In this paper, the key parts of electric hydraulic pump of EHPS system was designed, the design method is verified for the correctness and validity through experiment, and provides a theoretical basis for the research and development of the electric hydraulic pump.

References

[1] Badawy A, Fehlings D, Alexander W, et al. Development of a new concept of electrically powered hydraulic steering. SAE Paper No. 2004-01-2070, 2004.

[2] Chen Yong, Xia Jingjing, Chang Lü. Energy consumption of EHPS system based on hardware-in-loop simulation test[J]. Transactions of the CSAE, 2010,26(8):117-112.(in Chinese).

[3] Peter E, Pfefer D, Niqel J, et al. Energy consumption of electro-hydraulic steering systems, SAE Paper No.2005-01-1262,2005.

[4] Guoqing Geng, Lidong Miao, Qiang Li. Design Method Discussion of the Electro-hydraulic Power Steering System [J]. Journal of Agricultural Mechanization Research, 2006, (6): 207-210 (in Chinese).

[5] Xiaofeng Wang. Automotive Chassis Design[M]. Beijing:Tsinghua university press, 2010 (in Chinese).

Advanced Materials Research Vols. 986-987 (2014) pp 1129-1133

doi:10.4028/www.scientific.net/AMR.986-987.1129

Research on Electric Power Control Technique for Stable Operation of DC Micro-grid

Xiao XU[1, a], Xiaochun Ma[1], Zhenning Zi[2], Baoqiang Ben[2], Hua Li[2], Siming Wei[3]

[1]Department of Electrical Engineering,Beijing Jiaotong University,Beijing,100044,China

[2]China EPRI Science & Technology CO.LTD.,State Grid Smart Grid Research Institute,102200,China

[3]Department of Electrical Engineering,North China Electric Power University,102206,China

[a]email: xuxiaoxiao39@126.com

Keywords: Distributed Generation; DC Micro-grid; Energy Saving; Voltage Stability;

Abstract. Distributed generation(DG) into DC micro-grid can save a lot of converter equipments compared with AC micro-grid,.So,with the popularity of DG,DC micro-grid technology also has get great development.However,the key technology of DC micro-grid is not yet mature.This paper is based on shanghai DC micro-grid demonstration project of Sate Grid Smart Grid Research Institute.Firstly,we analysis the advantages and disadvantages of AC,DC and AC/DC hybrid micro-grid.Then, after comparison and analysis of DC micro-grid topology,we put forward system scheme and corresponding control strategy.The simulation results show that, the proposed control strategy is feasible,simple,real-time and effective.This design scheme is applicable for radiant topology and would provide guidance to the development direction of DC micro-grid project later.

Introduction

Nowadays,traditional fossil fuel resources,not only generate global environmental pollution and climate change,but also has reduced gradually.This has threated the world development and human survival.At the same time, the traditional electric system intensifies the energy crisis because of its disadvantages of complex structure and big loss [1].In the threat of resources and environment, development of new energy has become an important developing direction all over the world.Thus,distributed generation(DG) can solve the problems of large electric system by saving power lines and loss of converter devices.This is a huge advantage in Environmental friendly society today.

Micro-grid is posed to make full use of large-scale DG.It scales between electric systems and DG,which not only couples electric systems and DG,but also can run independently.It can provide electricity of high power quality and security safety to loads.Articles [2-4] introduces systematically the concept of micro-grid and micro-grid research status of the United States,Europe,Japan,etc.This paper is based on shanghai DC micro-grid demonstration project.After DC micro-grid current situation study,we design system topology structure,operation modes,stability control strategy and key equipments for the project.Last,we verify The accuracy of the topology and control strategy to provide theoretical support for demonstration project.

Key Technology of DC Micro-grid

Nowadays, micro-grid structure mainly includes AC type,DC type and AC/DC hybrid type at home and abroad [5].Among them,AC type is main realization form.Distributed electric resource（DER)and energy storage devices connect to AC bus through converters.For example,solar cells, fuel cells and other DC power need inverters.But for wind power generation,gas turbine and other AC power,they need both rectifiers and inverters.To meet the requirements of power supply reliability,electric system must connect a large number of converters.This not only adds the cost of the electric system,but also increases the system complexity and failure rate.

In DC micro-grid,DER and energy storage devices connect to DC bus with less converters.For example,personal computers,workstation servers and other sensitive digital electricity equipments can connect to bus with just DC chopper.By selecting suitable DC bus voltage,DC power can connect to bus directly and AC power just need to a simple rectifier.The most obvious advantage is the introduction of large capacity battery and super capacitor as a backup.On one hand, they can be used as the power battery for electric cars.On the other hand ,they also can improve the reliability of micro system.Now,DC micro-grid technology is still in initial stage.It is only researched in some universities and used in some special application,such as aerospace and ships.There's no commercial DC micro-grid engineering examples.The shanghai DC micro-grid is the first large demonstration project in China.

In AC/DC hybrid micro-grid,AC bus provide power for AC loads and DC bus for DC loads.Compared with AC micro-grid,it can reduce converter devices and make less cost.Compared with DC micro-grid,it can simplify frequency conversion process,but it has more problems such as complex control links,difficult power supply and apparent power quality problems.Considering its transitional nature,it may become an important direction of DC micro-grid application.

Transmission power,transmission radius,line loss and load voltage are the most important factors of setting DC micro-grid voltage level.In addition,matched degreed with AC power system and practical engineering investment is in considering,too.Now,DC micro-grid voltage level has not reached consensus all over the world.But most experts tend to750V,380V,220V,110Vand 48V level [6].Considering DC micro-grid needs at home,this system sets up three voltage grades.750V bus mainly connect DER and energy storage, and maintain the whole system stability.380V high voltage directly provide DC power for lighting,air conditioning system, large electrical appliances and other DC loads.In addition,48V low voltage level is setted for small DC loads.

Shanghai DC Micro-grid Example

The structure of DC micro-grid can be divided into the ring,mesh and radiant type.For ring topology,there are two current path between any two stations [7].It would improve reliability,security and quality of power supply.But,the fault diagnosis and protection control are relatively difficult.Meanwhile,the ring type need large equipment investment.Moreover ,mesh type consists of two or more rings,which needs more complex control strategy.This type is still in the stage of theoretical research, no relevant pilot and applications.

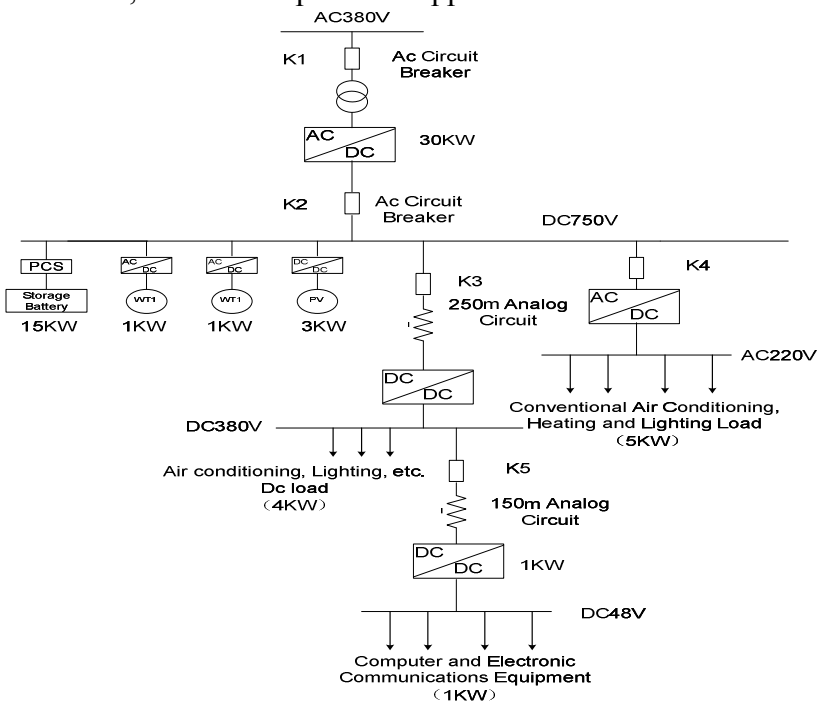

Fig.1 System Structure of Shanghai DC Micro-grid

Shanghai DC micro-grid project adopts radiant topology.Radiant topology has great advantages,such as easy flow control,simple fault protection,low line investment,etc.It's the most practical value structure currently.As shown in figure 1,the micro-grid power is 30KW,including three DC micro-grids.Electric system connect to 750V bus through isolation transformer.750V bus power flow is large ,including photovoltaic cells,wind power,energy storage devices and AC loads, etc.Small wind turbines are located in the periphery of project area,because it covers a lager area.So that,750V bus also is setted in periphery.750V bucks to 380V to,then 380V bucks to 48V.The power flow is smaller in this two DC buses,which are located in center of project area.

Meanwhile, two simulation circuit devices are setted in system to strengthen scientific research function.One simulates 250m low line between 750V and 380V.The other simulates 150m between 750V and 380V.They both can adjust continuous line length and install faults in any position.

The Control Strategy

This system adopts multi-layer control mode, dividing into total distribution network control, DC layer control and micro-grid element control.

As shown in figure 2,total distribution network control is at the top of system.On one hand, it monitors the information trend between electrical power system and micro-grid real-time.According to system energy state,it would choose point of common coupling(PCC)to control working condition of 30KW AC/DC module.At this time, micro-grid become grid connection state.When there is a grid fault in electric system,micro-grid transforms working condition from grid connection to isolated island operation.DER and energy storage equipments could safeguard important loads demand.On the other hand,the top control can adjust micro-grid operation mode according to collecting information of voltage, current and power.

DC layer control is the core of the whole control system.Its task is receiving the top command signal and controlling each part of micro-grid.When system is running normally,system takes master-slave control.Electric system act as main power supply and 30KW AC/DC module acts as main control.Meanwhile,other DER operate in PQ control mode.When a system fault occurs,control system first maks judgment on the fault rapidly,then it isolates fault zone.Thus,it can ensure normal area power supply and limit fault current in a certain extent.For example,when a short trouble occurs,DC layer control first determine fault location.If fault occurs in 220V,380V and 48V net,it would lock relevant pulses to isolate fault nets from 750V net to prevent fault expanding.If fault occurs in 750V net,it isolate 750V net from 220V and 380V net.At the same time,it blockade IGBT trigger pulse of wind turbines and photovoltaic cells to ensure DER not be affected.

Micro-grid element control is the underlying control.It mainly controls start-stop of DER,loads and energy storage devices to maintain voltage and frequency stable and provide relevant protection.With environment changing,it must monitor work condition of DER real-time.Photovoltaic battery capacity is affected by light and wind generator is affected by weather,temperature and monsoon significantly.Their generation is random and rolling.So,it need calculate power of each grid node to adjust output power,through controlling input numbers of photovoltaic battery and the proportion of wind turbine blade tip.Through load forecast and reasonable monitoring of DER,it can plan battery groups' number reasonable to optimize load demands.It is called peak clipping and valley filling.The underlying control manages photovoltaic battery,wind generator and energy storage battery.Because they act different roles in system,they adopt different control strategies.The key is that,their voltage and current instructions from controller is different.DER is in voltage and current double closed loop control at low voltage side,and energy storage battery is in voltage and current double closed loop control at high voltage side.Energy storage battery absorbs DER short-term fluctuations and maintains DC bus voltage.The control principle as shown in figure 3,voltage outer loop is to stabilize DC bus voltage,and current inner loop is to stabilize energy storage battery current.U^*_{dc} is given bus voltage,U_{dc} is measured bus voltage,I^*_{dc} is given energy storage battery current,I_{dc} is measured energy storage battery current.The difference between U^*_{dc} and U_{dc} passes PI regulator to get the required output current instantaneous value of energy storage battery I^*_{dc}.Then,the difference between I_{dc} and I^*_{dc} passes PI to get the

switch tube.With controlling IGBT, battery can achieve constant output current.However,For DER,U^*_{dc} and I^*_{dc} are given by their own value.

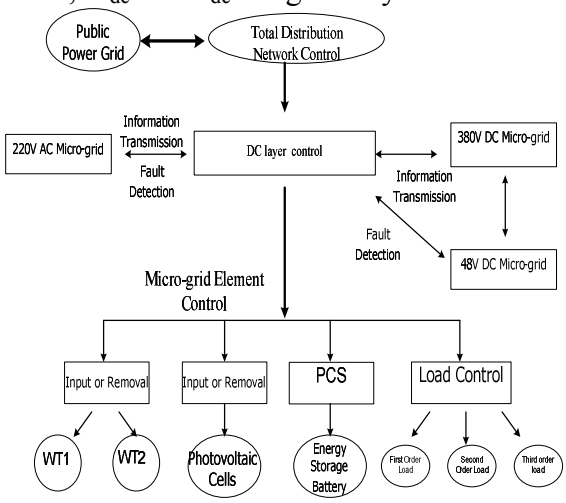

Fig.2 Multi-layer Control Mode of DC Micro-grid

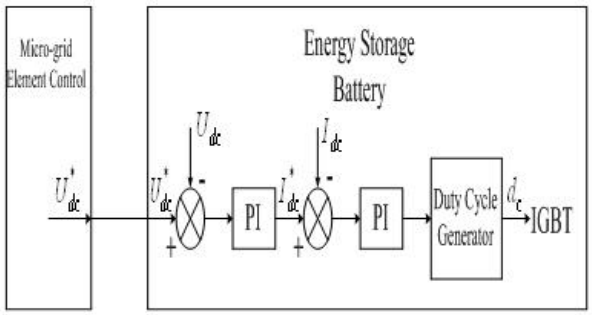

Fig.3 Battery Control Principle Diagram

Simulation Analysis

According to the figure 1, we set up corresponding PSCAD simulation model.By simulating grid connection and isolated island condition,we can further study characteristics of DC micro-grid and verify feasibility of control strategy.

When system is running normally,system takes master-slave control.30KW AC/DC module acts as main control unit.Meanwhile,other DER operate in PQ control mode.Traditional power quality problems won't happen on DC bus,so the key of DC power supply is maintaining bus voltage stable.

The simulation shows in figure 4,bus voltage fluctuate slightly at the start.Then,voltage remain stable with fluctuation less than 0.1%.

Micro system is susceptible to disturbance because of limited capacity.Distribution network nodes are so numerous that short circuit faults occur occasionally.As shown in figure 5 and figure 6,when t=1s,we simulate short circuit fault for 0.2s between 380V micro-grid and 250m power line.At that time,380V micro-grid is cut off rapidly and DC bus voltage drops to zero.when t=1.2s, voltage returns to normal working condition.Throughout the process,750V micro-grid,which is effected little, still can run normally.After a brief fluctuations less than 2.0%,DC voltage quickly return to rating.

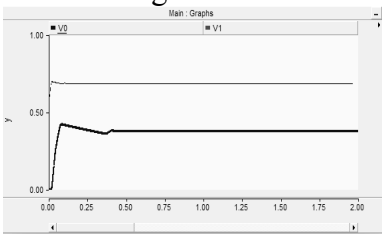

Fig.4 Normal Operation Voltage

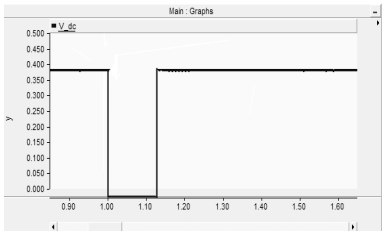

Fig.5 380V Bus Voltage

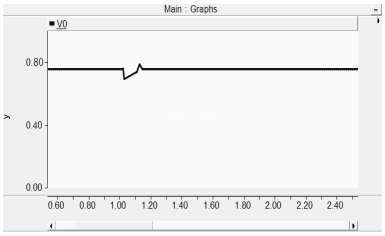

Fig.6 750V Bus Voltage

Micro-grid transforms work modes between grid connection and isolated island by PCC control.When system run in isolated island,energy storage battery converts to V/F control mode to maintain the whole system voltage stable.As shown in figure 7,we simulate inputting and removing loads to cause transient disturbance.when t=0.5s,asynchronous motor connects to micro-grid.At the same time, the bus voltage appear larger fluctuation and recover in a short time.

The size of the battery capacity is the most important factor to maintain isolated island operation.Small capacity is difficult to maintain voltage stable and large capacity would cause resources waste.The battery power output is shown in figure 8,battery increases the power output to meet the loads demand.From theoretical calculation and simulation,15KW capacity is a good choice for this system,which can provide enough power for isolated island.When DER and battery energy

can not meet loads need,bus voltage is lower than the preset threshold.The system needs to control the load shedding to ensure the continuity of important loads power supply.

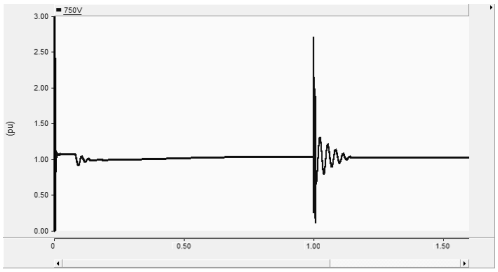

Fig.750V Bus Voltage Changes

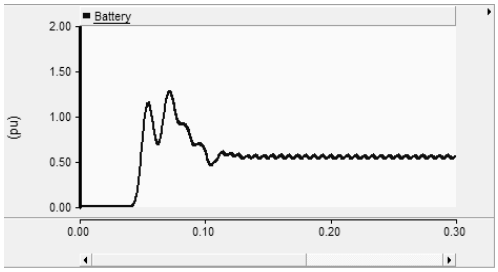

Fig.8 Battery Power Changes

Conclusion

DC micro-grid is better compatible with future renewable power supply,distributed energy storage and bidirectional current demand electric vehicle charging stations.Traditional power quality problems,such as frequency, reactive power and harmonic problems,would not happen on DC bus.DC system only prevent DC voltage from flickering or dropping,that it can get good power quality.In this paper ,we design a radiant system structure and calculate technical parameters of the relevant equipments for shanghai DC micro-grid demonstration project.On the basis,we put forward multi-layer control strategy,whose main task is to maintain DC bus voltage stable.The simulation results show that,the established strategy can ensure DC micro-grid operate normally in grid connection and isolated island condition.This paper results would provide theoretical guidance for the demonstration project.

Acknowledgement

In this paper, the research was sponsored by Reactive Power Optimization in Dc Area(Project No. 5455DD140006-C).

References

[1] Jiang Dao-zhuo,Zhen Huan.Research Status and Prospect of DC Power Distribution Network[J].Automation of Electric Power Systems.2012,36(8):98-104.

[2] Wang Chang-gui,Cui Rong-qiang,Zhou huang.New energy technologies[M].China Electric Power Press.2010.150—178.

[3] Zhu Yong-qiang,Yin Zhong-dong,TianJun.Microgrids Based on DC Energy Pool[C].IEEE Energy2030,Atlanta,17-18 November,2008.

[4] Ding Ming,Zhang,Ying-yuan,Mao Mei-qin.Key tech-nologies for microgrids being researched[J]. Power System Technology,2009,33(11):5-12.

[5] H.Kakigano,M.Nomura,T.Ise.Loss Evaluation of DC Distribution for Residential Houses Compared with AC System[J],June21—24,2010.

[6] Zou San-hong,Pei Wei,Qi Zhi-ping.Universal inter-face unit of distributed power and microgrid inter connection[J]. Automation of Electric Power Systems,2010,34(3):91-95.

[7] Yang Wenjie,Zeng De-rong.Simulation Research on Photovoltaic Generation Switching in the Microgrid Operation Control.Electric Switchgear,2011（No.1）.

Advanced Materials Research Vols. 986-987 (2014) pp 1134-1137

doi:10.4028/www.scientific.net/AMR.986-987.1134

Sensorless Control of High Speed Permanent Magnet Synchronous Motor Based on Modified Sliding-mode Observer

Xiaodong Wang[1, a], Gang Liu[2, b]

[1 2]School of Instrumentation Science and Opto-electronics Engineering, Beihang University, Beijing 100191, China;

[a]sosa1988@126.com, [b]lgang@buaa.edu.cn,

Keywords: permanent magnet synchronous motor; vector control; sliding mode observer; Sigmoid function.

Abstract. In sensorless vector control of permanent magnet synchronous motor, it is necessary to achieve an accurate estimate of the motor speed and position of the rotor. Traditional sliding mode observer algorithm has the inherent chattering problem which reduces accuracy. The Sigmoid function was used to replace the sign function in the traditional sliding mode observer as the switching control function to cancel the filter and phase compensation links. A new sliding mode observer was designed and its stability was proved. High-speed permanent magnet synchronous motor simulation and experimental results show: the new modified sliding mode observer based on Sigmoid function can eliminate the severe buffeting of the traditional sliding mode observer, achieve the accurate estimation of the rotor speed and position for high-speed permanent magnet synchronous motor to complete a wide range of speed control; the correctness and feasibility of the sensorless control strategy based on this method is verified.

Introduction

PMSM(Permanent Magnet Synchronous Motor) has advantages of high power density, fast dynamic response and small torque ripple[1]. Combined with magnetic bearings the rated speed of high speed PMSM can reach tens of thousands or even hundreds of thousands of revolutions per minute. It can be widely used in molecular pumps, compressors, centrifuges and other high-speed drive applications. For vector control of PMSM, the accurate rotor position signals is the prerequisite. In conventional PMSM vector control system, to obtain the rotor position information we need optical encoder position sensor, etc., which not only increases the cost and complexity of the system, but also reduces the reliability of the system. Thus, in recent years the control methods without position sensors of PMSM has been a hot research field.

At present, the common position sensorless control method for PMSM is mainly divided into two categories [2]: one is the motor saliency-based methods, such as high-frequency signal injection method, these methods at zero speed and low-speed work better, but they are not suitable for high-speed applications, and is only applicable for saliency effects interior permanent magnet synchronous motor; other is based on the back-EMF or flux estimation method to estimate the rotor position, for example, the estimation method based on electromagnetic relations [3,4], the model reference adaptive method [5], extended Kalman filter method [6], sliding mode observer method [7] and so on. Estimation method based on the electromagnetic relations are mostly working in the open-loop state, so it's vulnerable to motor parameter variation; model reference adaptive method is simple, but it's also very sensitive to parameter variations; extended Kalman filter method is too large, it is difficult for high-speed situations; sliding mode observer method is simple and easy to implementation, and it has good robustness.

In order to achieve the sensorless control of PMSM, this paper selected a new switch function, Sigmoid function , to take place of the traditional switch function. At the same time, low-pass filter and phase compensation are removed. The system was simplified and the estimation accuracy was improved. Finally, experimental verification showed the correctness and effectiveness of this method.

1 Mathematical Model of the Permanent Magnet Synchronous Motor

The rotor structure of PMSM can be divided into the surface-mount and the buried. This article focused on surface mount PMSM. For the establishment of mathematical model of PMSM ,without affecting the performance of the premise, we made the following assumptions [4]:

(1) Ignore the magnetic core saturation;

(2) Exclude the impact of hysteresis and eddy current losses;

(3) Wind EMF waveform is a sine wave.

In the two-phase stationary coordinate system, the mathematical model of PMSM can be expressed as:

$$\frac{di_\alpha}{dt} = -\frac{R}{L}i_\alpha + \frac{1}{L}V_\alpha - \frac{1}{L}e_\alpha \tag{1}$$

$$\frac{di_\beta}{dt} = -\frac{R}{L}i_\beta + \frac{1}{L}V_\beta - \frac{1}{L}e_\beta \tag{2}$$

Back-EMF equation can be expressed as:

$$e_\alpha = -k_e\omega_r \sin\theta_r \tag{3}$$

$$e_\beta = k_e\omega_r \cos\theta_r \tag{4}$$

2 Modified Sliding Mode Observer

According to the mathematical model of PMSM, the sliding mode current observer equation can be constructed:

$$\frac{d\hat{i}_\alpha}{dt} = -\frac{R}{L}\hat{i}_\alpha + \frac{1}{L}V_\alpha - \frac{1}{L}u_\alpha \tag{5}$$

$$\frac{d\hat{i}_\beta}{dt} = -\frac{R}{L}\hat{i}_\beta + \frac{1}{L}V_\beta - \frac{1}{L}u_\beta \tag{6}$$

$$u_\alpha = k_{sw}sign(\hat{i}_\alpha - i_\alpha) \tag{7}$$

$$u_\beta = k_{sw}sign(\hat{i}_\beta - i_\beta) \tag{8}$$

By equation (1), (2), (5), (6) a current observer error equation is obtained:

$$\frac{d\left(\hat{i}_\alpha - i_\alpha\right)}{dt} = -\frac{R}{L}\left(\hat{i}_\alpha - i_\alpha\right) + \frac{1}{L}\left(e_\alpha - u_\alpha\right) \tag{9}$$

$$\frac{d\left(\hat{i}_\beta - i_\beta\right)}{dt} = -\frac{R}{L}\left(\hat{i}_\beta - i_\beta\right) + \frac{1}{L}\left(e_\beta - u_\beta\right) \tag{10}$$

The current difference between the estimated value and the actual current is selected as a sliding switch plane:

$$s = s(x) = \hat{i}_s - i_s \tag{11}$$

When the system is in the sliding surface movement, s = 0.The back-EMF $e_s = u_s = k_{sw}sign(\hat{i}_s - i_s)$. As can be seen, sliding switch function expression contains the information of back-EMF of the motor. Because it contains a high-frequency switching signal ,and the results must be filtered.By low-pass filter to obtain the back-EMF takes the phase delay. Therefore, the conventional sliding mode observer needs to be compensated.

The final expression for the angular position of the rotor:

$$\hat{\theta} = -\arctan(\frac{\hat{e}_\alpha}{\hat{e}_\beta}) + \Delta\theta \tag{12}$$

In conventional sliding mode observer, the introduction of a low-pass filter brought significant phase delay and it would affect the position estimation accuracy. In addition, due to the non-ideal characteristics of the switching function, we must adopt a certain angle compensation. In such a high precision high speed system, the output of the low pass filter, it is difficult to meet the requirements. It is necessary for observer to be improved. In order to obtain better observation results, this paper introduces Sigmoid function as a sliding switch function, designed a new type of sliding mode observer.

The current difference between the estimated value and the actual current is selected as a sliding switch plane. The current observer equation is established:

$$\frac{d\hat{i}_\alpha}{dt} = -\frac{R}{L}\hat{i}_\alpha + \frac{1}{L}V_\alpha - \frac{1}{L}k_{sw}H(\hat{i}_\alpha - i_\alpha) \tag{13}$$

$$\frac{d\hat{i}_\beta}{dt} = -\frac{R}{L}\hat{i}_\beta + \frac{1}{L}V_\beta - \frac{1}{L}k_{sw}H(\hat{i}_\beta - i_\beta) \tag{14}$$

The traditional sliding mode observer uses symbolic function as a switch control function, its inherent discontinuity switching characteristics result in serious chattering. To reduce this chattering, we used a new switch control function, that is Sigmoid function.

$$H(x) = \frac{2}{1+e^{-k\cdot x}} - 1 \tag{15}$$

When the system reaches the sliding surface and moves in the sliding surface, the back-EMF is expressed as:

$$\hat{e}_\alpha = k_{sw}\cdot H(\hat{i}_\alpha - i_\alpha) \tag{16}$$

$$\hat{e}_\beta = k_{sw}\cdot H(\hat{i}_\beta - i_\beta) \tag{17}$$

Combined with the back-EMF equation (3), (4), the rotor angular position and speed equation is established:

$$\hat{\theta} = -\arctan\left(\frac{\hat{e}_\alpha}{\hat{e}_\beta}\right) \tag{18}$$

$$\hat{\omega} = \frac{\sqrt{\hat{e}_\alpha{}^2 + \hat{e}_\beta{}^2}}{\psi_f} \tag{19}$$

In order to prove the stability of the new sliding mode observer, Lyapunov function can be constructed:

$$V = \frac{1}{2}S^T S \tag{20}$$

The stability condition of the new sliding mode observer is:

$$\dot{V} = S^T\dot{S} \le 0 \tag{21}$$

When the sliding gain k value is large enough, we can guarantee the existence of sliding motion and ensure that the system is asymptotically stable.

$$k \ge \max(|e_\alpha|, |e_\beta|) \tag{22}$$

3 Experimental Verification

In order to verify the feasibility of the proposed method, 4kW high-speed PMSM was used to build a motor control system experimental platform. The TMS320F28335DSP was used as the core of control system and power amplifier module is Mitsubishi PM25RLA120 IPM, the switch frequency is 10KHz. The rotor position signals of two kind of sliding mode observers were put into oscilloscope by external DA chip.

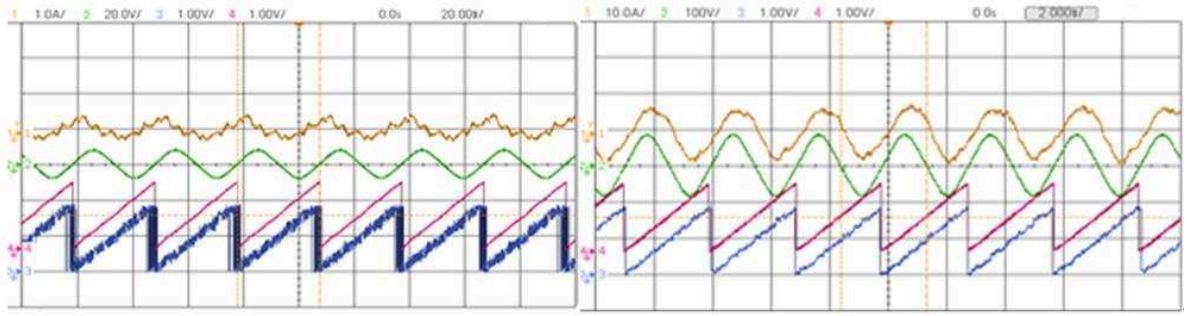

Fig. 1 Comparison of the rotor position at 2000r/min(L) and 20000r/min(R)

The third signal from top down is rotor position signal which is provided by improved sliding mode observer, and the fourth signal from top down is the rotor position signal which is provided by traditional sliding mode observer . As can be seen from the figure, the rotor position signal estimated by the traditional sliding mode observer contained severe chattering , but the method used herein significantly reduced chattering.

4 Summary

Based on the analysis of traditional sliding mode observer structure and characteristics, Sigmoid function was used to replace the traditional symbol function or saturation function as a switch control function. Phase compensation and filter link were cancelled. A new sliding mode observer was designed. Experimental results showed that: the new sliding mode observer can output more accurate estimation of the rotor position and speed to achieve position sensorless control of PMSM. The stable operation of experimental motor at high speed range (0-20000r/min), verified the correctness and feasibility of the proposed method.

References

[1] Bon-Ho Bae，Seung-Ki Sul，Jeong-Hyeck Kwon，et al．Implementation of Sensorless Vector Control for Super-High-Speed PMSM of Turbo-Compressor [J]. IEEE Transactions on Industry Applications，2003，39(3)：811-818．

[2] Silverio Bolognani，Roberto Oboe，Mauro Zigliotto．Sensorless Full-Digital PMSM Drive With EKF Estimation of Speed and Rotor Position [J]. IEEE Transactions on Industrial Electronics ，1999，46(1)：184-191．

[3] Bianchi N, Bolognani S, Jang, J.H., et al. Comparison of PM Motor Structures and Sensorless Control Techniques for Zero-Speed Rotor Position Detection[J]. IEEE Transcations on Power Electronics, 2007, V22(6):2466-2475.

[4] Ozturk S.B., Toliyat H.A. Direct Torque and Indirect Flux Control of PMSM[J]. IEEE/ASME Transcations on Mechatronics, 2011, V16:351-360.

[5] Zhaowei Qiao，Tingna Shi，Yindong Wang，et al．New Sliding-Mode Observer for Position Sensorless Control of Permanent-Magnet Synchronous Motor [J]．IEEE Transactions on Industrial Electronics，2013，60(2)：710-719．

[6] Bozo Terzic, Martin Jadric. Design and Implementation of the Extended Kalman Filter for the Speed and Rotor Position Estimation of Brushless DC Motor[J]. IEEE Transactions on Industrial Electronics, 2001, 48(6):1065~1073.

[7] Fakham H, Djemai M, Blazevic P. Sliding modes observer for position and speed estimations in brushless DC motor(BLDC motor) [J]. IEEE ICIT, Tunisia, 2004, 10(12):121-126.

Advanced Materials Research Vols. 986-987 (2014) pp 1138-1141

doi:10.4028/www.scientific.net/AMR.986-987.1138

Simulation of Permanent Magnet Linear Synchronous Motor's Self-organizing rule and self-regulared parameter fuzzy control

Lijuan Zhang[a], DanYu Luo [b] ,Junliang Cui[c] and Li He[d]

Zhengzhou electric power college, Henan Zhengzhou 450004, China;

[a]zhanglijuan0406@163.com, [b] sunny.ldy@163.com, [c]cjunliang@sina.com,[d]heli1985_85@163.com

Keywords: permanent magnet linear synchronous motor, Self-organizing rule and self-regulared parameter fuzzy control, speed controller, Simulation

Abstract. In view of the permanent magnet linear synchronous motor vector control system, this paper proposes a model reference adaptive speed controller gain fuzzy self-tuning neurons. The simulation results show that when a sudden load disturbance or parameter mutation, the gain of model reference adaptive fuzzy self-tuning neuron speed control has quick response, strong robustness, good dynamic and static characteristic, etc.

Introduction

In the coal Direct drive permanent magnet linear synchronous motor, because it saved the middle of the transmission link, eliminating the effects of mechanical transmission chain; and its high-performance permanent magnets with high intensity electromagnetic thrust, low loss, small electrical time constant, fast response time, etc. [1]. Compared with the traditional rotary motor, although eliminates some of the adverse effects brought by the mechanical transmission, but it increases the difficulty to control. For perturbation and uncertainties such as the impact of disturbance on the system, in this paper, the design speed loop gain of the model reference adaptive fuzzy self-tuning neuron speed controller to ensure the robustness of the system.

Permanent magnet linear synchronous motor mathematical model

Establishment of permanent magnet linear synchronous motor mathematical model is a computer simulation of the premise. In the derivation process, make the following assumptions [2]:
Ignore the core saturation;

Excluding the eddy current and hysteresis effects; On the active cell without damping windings, permanent magnets are no damping effect; Counter-electromotive force is sinusoidal.

Under the condition of field oriented vector control, PMLSM mathematical model can be described as follows [2]:

Mechanical equations of motion : $F_e = M \cdot dv/dt + Bv + F_f = K_f \cdot i_q$, $K_f = \pi \cdot \psi_f / \tau_n$

In the formula, M is the mass of the motor mover, B is a viscous friction coefficient, F_f representative of the load resistance, F_e representative of the electromagnetic thrust, τ_n representative of the permanent magnet flux effectively, v is the linear velocity of the mover, and $v = 2\tau_n f = v_s$.

In the formula, f is the frequency of the inverter output power, v_s is the motor synchronous speed, K_f is the thrust coefficient.

d-q-axis voltage and current equation. $\begin{cases} u_d = -\pi v \psi_q / \tau_n + d(\psi_f + \psi_d)/dt \\ u_q = -r_q i_q + \pi v \psi_f / \tau_n + d\psi_q / dt \end{cases}$.

In the formula: $\psi_d = L_d i_d$; $\psi_q = L_q i_q$ .In the formula, u_d, u_q denote d-axis mover, the q-axis voltage; i_d, i_q denote d-axis mover, the q-axis armature current; ψ_d, ψ_q denote move d axis, the q axis armature

current d and q axis magnetic chain; r_d, r_q denote d-axis mover, the q-axis resistance; L_d, L_q denote d-axis mover, the q-axis inductance.

According to the equivalent mathematical model of these kinds have PMLSM shown in Figure 1.

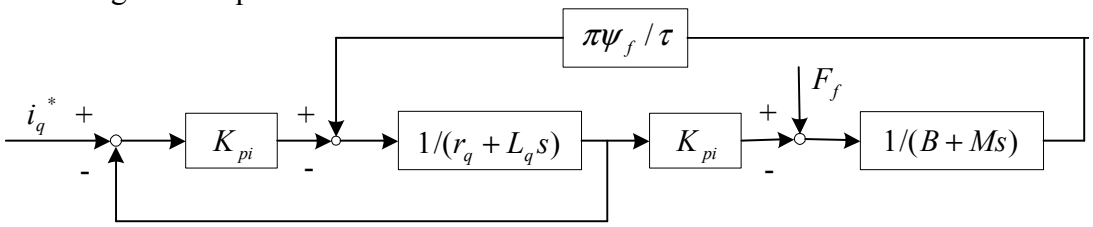

Figure 1 Vector control ($i_d = 0$) when the mathematical model of PMLSM

Model reference adaptive gain fuzzy self-tuning adaptive speed controller design

Model reference adaptive neuron adaptive control and speed control is to model neuron adaptive control with the combination of control technology, can enhance the performance of the servo system. It combines a model reference adaptive control with dual characteristics of neural control.

Reference model assumes that the selected mathematical model, the mathematical model can provide a proper reference for the desired output, the desired system response speed. Through continuous tracking the reference model output, timely correction neurons teacher value of the speed controller, which makes neural neurons speed controller supervision learning part with correct and timely signals, which ensures the weights learning convergence in the right direction. Thus, the output neuron controller is adjusted to force the output speed of the system follows the reference model output [3].

Neuron model reference adaptive speed controller shown in Figure 2.

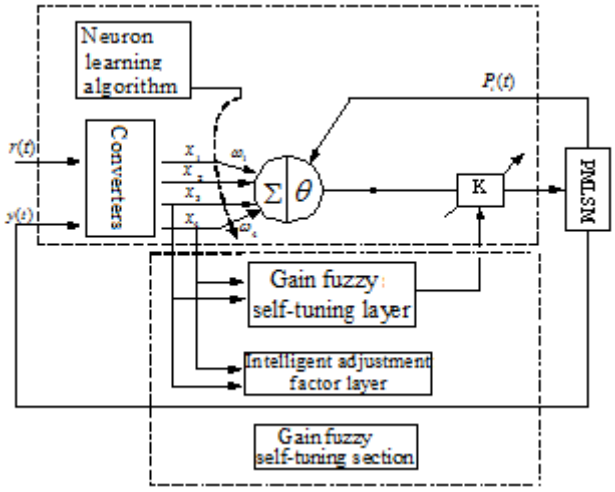

Figure 2 Adaptive neuron controller fuzzy self-tuning of gain

The choice of reference model. Reference model selection system of one-order inertial system, its transfer function is [4]: $G(s) = y(s)/u(s) = 1/(T_1 + 1)$

In the formula, u is a step input reference model, but also neurons speed controller speed command signal; y is the reference model output, $y(t) = (1 - e^{-t/T_1})u(t)$; T_1 represents the time constant, as required, by selecting the value of T_1, to obtain the desired exponential rate curve.

Neuron controller to calculate the value of the speed of teachers. To translate into time domain differential equation formula: $dy/dt = -my + mu$ .In the formula, $m = 1/T_1$. Dynamic error e is defined as the difference between output and the time lag compensator output of the reference model.

Rated motor parameters to take the case, the mechanical equations of motion have PMLSM speed differential equations can be obtained: $dv_t/dt = K_f \widetilde{I}_q^* / M_n - B_n v_t / M_n - F_n / M_n$ .In the formula, M_n, B_n respectively mover mass nominal value and the nominal value of the viscous friction coefficient, F_n is the nominal resistance value of the load, $\widetilde{I}_q^*$ load resistance is not considered representative of the disturbance, the mover mass change, viscous friction coefficient change the value of the reference section neurons teacher case calculation. Therefore, the dynamic error e is the derivative:

$$de/dt = dv_t/dt - dy/dt = K_f \widetilde{I}_q^* / M_n - (mM_n - B_n)v_t / M_n - F_n / M_n - me - mu$$

Take *L*yapunov function $V = e^2/2$, then $dV/dt = ede/dt$. Select $de/dt = -ge$ (Constant $g > 0$), then $dV/dt = -ge^2 < 0$, so that the system meets the asymptotically stable. Substituted into $de/dt = -ge$, to be launched:

$$\widetilde{I}_q^* = (m-g)/M_n e/K_f - (mM_n - B_n)v_t / K_f + F_n / K_f + mM_n u / K_f$$

$$= (m-g)M_n e/(\pi\psi_f/\tau_n) - (mM_n - B_n)v_t/(\pi\psi_f/\tau_n) + F_n/(\pi\psi_f/\tau_n) + mM_n u/(\pi\psi_f/\tau_n)$$

Formula calculated $\widetilde{I}_q^*$ is only part of the neuron controller teachers' value calculation, which includes compensation for the permanent magnet flux perturbation harmonic disturbances and time delay, is not added to the system parameters (i.e.: load resistance changes mover mass changes, changes in viscous friction coefficient) compensation for disturbance.

Also, consider the load resistance changes, the situation mover mass changes, changes in the viscous friction coefficient, and teachers value neurons compensate. Here the end effect of PMLSM's influence on the thrust can be equivalent load disturbance resistance, so as part of the load disturbance resistance to compensate [3].

Teachers value through online correction neuron controller values, and constantly to neurons on-line training speed controller, the controller of the actual output is equal to the desired current instructions.

Simulation results analysis

(1) When the load is 10kg, tuning PID parameters, the parameters fixed gain adaptive neuron controller is: K = 0.05; d = 120; initial weights were taken 10. Gain fuzzy self-tuning parameters adaptive neuron controller is: K=0.05; d = 120; initial weights were taken 10. $K_{Min} = 0.05, K_{Max} = 1.0$. The actual belt load 20kg, the response curve shown in Figure 3.

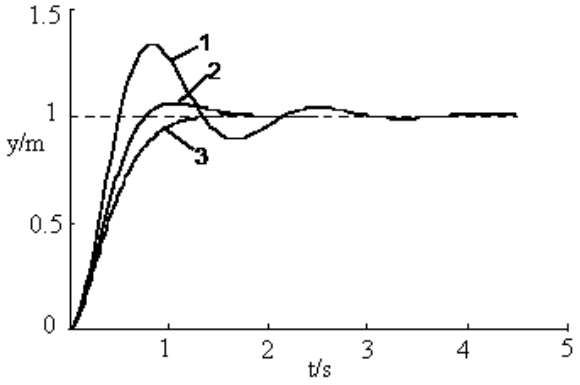

Figure 3 Effect of change in the three parameters

Curve 1 is the PID control; Curve 2 is a fixed gain of adaptive neuron controller; curve 3 to gain self-tuning adaptive fuzzy neuron controller.

Clearly, because of the PID parameter is sensitive to changes in the object, when the operating state changes PMLSM drive system, the control action is almost lost. Fixed gain adaptive neuron

controller, while having some control, but not very effective. Two gain self-tuning adaptive fuzzy neuron controllers for this case has a good control effect.

(2) Setting PID when load for 10 kg, fixed gain adaptive neuron controller does not use deviation nonlinear transformation; gain self-tuning adaptive fuzzy neuron controller uses a nonlinear transformation deviation, both still on the same parameters. 5kg perturbation added in 3.5s, shown in Figure 4.

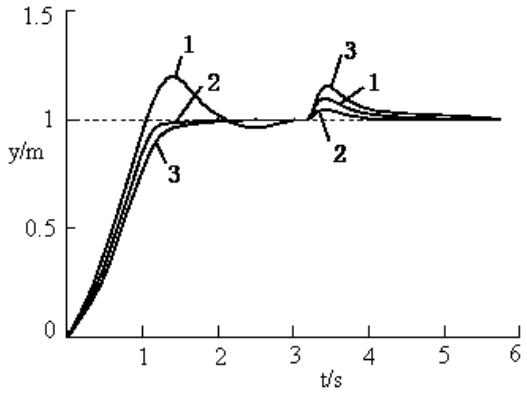

Figure 4 External disturbance control performance comparison of three

Curve 1 is the PID control; Curve 2 is a fixed gain of adaptive neuron controller; curve 3 to gain self-tuning adaptive fuzzy neuron controller.

Visible deviation neuron controller did not use non-linear transformation of the system when there is disturbance relatively large super pick, adjust the recovery time is longer, so the use of non-linear transformation deviation significantly strengthened the immunity of the controller.

From comparing these two cases, the gain of fuzzy self-tuning layer neuron controller makes adding significantly faster dynamic response, overshoot suppression capability significantly strengthened.

Conclusions

On the basis of adaptive neuron controllers joined the gain on fuzzy self-tuning layer, thereby improving the response speed controller inhibited overshoot, while exhibiting a strong and robust line model changes PMLSM servo system to adapt sex.

References

[1] Q.D.Guo, C.Y,Wang, M.W.Zhou:Tingyu Sun linear precision AC servo system control technology[M], Beijing: Mechanical Industry Press, 2000.1

[2] L.Gang, L.C.Jiao: Multi-mode adaptive fuzzy controller and its application in police Servo System[M], Control Theory and Applications ,2004

[3] Y. Shi et. MATLAB language essence and dynamic simulation tools SINMULINK[M], Northwestern Polytechnical University Press, 1999.4

[4] Y.Y .Ye: Principles and Applications of Linear Motor [M], Beijing: Mechanical Industry Press, 2000.

Advanced Materials Research Vols. 986-987 (2014) pp 1142-1145

doi:10.4028/www.scientific.net/AMR.986-987.1142

SSP Podded Propulsion Motor Control Based on SR-CDKF

YAO Wenlong[1, 2]

[1]College of Marine Engineering,Dalian Maritime University,Dalian, China

[2]Department of Marine Engineering,Qingdao Ocean Shipping Mariners College,Qingdao,China

yaowl@coscoqmc.com.cn

Keywords: ship electric proplusion, SSP Podded Propulsion, Propulsion Motor, CDKF,SR-CDKF

Abstract. In this paper,the rotor speed and the position of the SSP propulsion motor are estimated for building sensorless vector control system with speed and current double closed loops based on square root center difference Kalman filter(SR-CDKF) algorithm. This method makes use of the QR decomposition linear algebra techniques and so on, and it updates the matrix square-root of the state covariance by the Cholesky factor updating. This method can not only get the more steady results but also improve the estimation accuracy of the SSP podded propulsion system. Simulation result shows that the improved CDKF algorithm is not only more accurate but also has higher rate of convergence compared with CDKF speed controller.

Introduction

Podded propulsion is the new type of ship electrical propulsion system which has developed in recent years. It is mainly made up of stents, pod and propeller parts, the propulsion motor was placed in a 360^0 rotary podding, the propeller was directly driven on both ends of the propulsion motor, thus the many complex mechanism (such as clutch, gearbox, intermediate shaft, thrust, etc.) were simplified and it was replaced by the electric control system that has the higher reliability than mechanical system. The redundancy has been greatly improved, which can realize the quick start, quick reversals, stepless speed regulation, low speed stability and excellent control performance [1].

Square Root center difference Kalman filter (SR-CDKF) is a novel filtering method of the nonlinear systems, and it is different with the central Difference Kalman filtering (CDKF), it doesn't need to calculate the square root of the covariance matrix of state during the every time update[2]. In view of the nonlinear problem of Podded propulsion system, the CDKF covariance square array is used instead of covariance matrix iterative arithmetic in this paper, it can avoid the filter divergence effectively, and the convergence speed and stability of the filtering algorithm were improved, it can meet the mobility characteristics of Podded propulsion system.

Square Root center difference Kalman filter algorithm

The central difference was adopted to instead of the first and second order derivative of Taylor series expansion.

$$f'(\overline{x}) \approx \frac{f(\overline{x}+h\delta x)-f(\overline{x}-h\delta x)}{2h} \tag{1}$$

$$f''(\overline{x}) \approx \frac{f(\overline{x}+h\delta x)+f(\overline{x}-h\delta x)-2f(\overline{x})}{2h^2} \tag{2}$$

For state vector, Sigma points and weights according to the type (2) structure:

The number of CDKF Sigma point is 2n+1 for n state vector, and the Sigma points and weights were structured according to the type (2)

$$\chi_0 = \overline{x}\,,\ \chi_i = \overline{x} + \left(h\sqrt{P_{xx}}\right)_i, i = 1,\cdots,n$$

$$\chi_i = \overline{x} - \left(h\sqrt{P_{xx}}\right)_i, i = n+1,\cdots,2n \tag{3}$$

$$W_0 = h^2 - n/h^2 , W_i = 1/\left(2h^2\right), i = 1,\cdots,2n$$

The square-root form of the CDKF makes use of three powerful linear algebra techniques, QR decomposition, Cholesky factor updating and efficient least squares, which

QR decomposition.

The QR decomposition or factorization of a matrix $A \in \mathbb{R}^{L\times N}$ is given by, $A^T = QR$, where $Q \in \mathbb{R}^{N\times N}$ is orthogonal, $R \in \mathbb{R}^{N\times L}$ is upper triangular and N ≥ L. The upper triangular part of R , $\tilde{R}$, is the transpose of the Cholesky factor of $P = AA^T$, i.e., $\tilde{R} = S^T$,such that $\tilde{R}^T\tilde{R} = AA^T$ .We use the shorthand notation qr{•} donate a QR decomposition of a matrix where only «± is returned[3].

Cholesky factor updating.

If S is the original Cholesky factor of $P = AA^T$, then the Cholesky factor of the $P \pm \sqrt{vuu}$ is denoted as $S = cholupdate\{S, u, \pm v\}$. This algorithm (available in Matlab as cholupdate) is only $O(L^2)$ per update.

Efficient least squares.

The solution to the equation $(AA^T)x = A^Tb$ Þ also corresponds to the solution of the over determined least squares problem $Ax = b$.

The detail algorithm is obtained as follows:

Initialize with:

$$\hat{x}_0 = E[x_0] , \ S_0 = chol\left\{E[(x_0 - \hat{x}_0)(x_0 - \hat{x}_0)^T]\right\} \tag{4}$$

Where: $\hat{x}_0$ is initial value of the fixed state estimation, S_0 is the value which is initialized by calculating the matrix square-root of the state covariance via a Cholesky factorization.

$$S^-_k = \text{chol}(P_{k-1}) \tag{5}$$

For $k \geq 1$, $2n+1$ Sigma points were adopted[7]:

$$\chi_{k-1} = \left[\hat{x}_{k-1} \quad \hat{x}_{k-1} + \eta S^-_k \quad \hat{x}_{k-1} - \eta S^-_k\right] \tag{6}$$

Time update equations:

$$\chi_{k|k-1} = F[\chi_{k-1}, u_{k-1}], \ \hat{x}_k^- = \sum_{i=0}^{2L} W_i^{(m)} \chi_{i,k|k-1} \tag{7}$$

$$S_k^- = \text{qr}\left\{\left[\sqrt{W_1^{(c)}}(\chi_{1:2L,k|k-1} - \hat{x}_k^-) \quad \sqrt{Q^v}\right]\right\}, S_k^- = \text{cholupdate}\left\{S_k^-, \chi_{0,k} - \hat{x}_k^-, W_0^{(c)}\right\} \tag{8}$$

$$Z_{k|k-1} = H[\chi_{k|k-1}], \hat{z}_k^- = \sum_{i=0}^{2L} W_i^{(m)} Z_{i,k|k-1} \tag{9}$$

Measurement updates equations:

$$S_{\tilde{z}_k} = \text{qr}\left\{\left[\sqrt{W_1^{(c)}}\left[Z_{1:2L,k} - \hat{z}_k\right] \quad \sqrt{R_k^n}\right]\right\}, \ S_{\tilde{z}_k} = \text{cholupdate}\left\{S_{\tilde{z}_k}, Z_{0,k} - \hat{z}_k, W_0^{(c)}\right\} \tag{10}$$

$$P_{x_k z_k} = \sum_{i=0}^{2L} W_i^{(c)}[\chi_{i,k|k-1} - \hat{x}_k^-][Z_{i,k|k-1} - \hat{z}_k^-]^T , \kappa_k = \left(P_{x_k z_k} / S^T_{\tilde{z}_k}\right) / S_{\tilde{z}_k} \tag{11}$$

$$\hat{x}_k = \hat{x}_k^- + \kappa_k(z_k - \hat{z}_k^-), \ U = \kappa_k S_{\tilde{z}_k} , S_k = \text{cholupdate}\left\{S^-_k, U, -1\right\} \tag{12}$$

Model Analysis of Ship Electrical Propulsion Motor Control System

Electromagnetic torque of the SSP propulsion is

$$T_e = \frac{3p}{2}\frac{\psi_r^2}{R_r}\omega_s^* \tag{13}$$

Where Te is electromagnetic torque, P is the number of magnetic poles, Rr is the rotor resistance, ψr is the rotor flux valid values[4].

The friction torque of SSP propulsion system Tf is

$$T_{\mathrm{f}}=\mathrm{sign}(\omega)T_{\mathrm{s}}+k_{\omega}\omega \tag{14}$$

Where $\omega=2\pi n/60$, n is propeller speed, Ts is the static friction torque, n is the linear friction coefficient.

The motion equation of the SSP propulsion system is

$$\frac{d\omega}{dt}=\frac{1}{J}(T_{\mathrm{e}}-F\omega-T_{\mathrm{L}}),\ \frac{d\theta}{dt}=\omega \tag{15}$$

Where J is SSP moment of inertia, Tm is the load torque[5].

The dynamic model of SSP propulsion system is

$$T_{\mathrm{p}}=K_{\mathrm{T}}(J)\cdot\rho D^5 n|n| \tag{16}$$

$$F_{\mathrm{e}}=K_{\mathrm{F}}(J)\cdot\rho D^4 n|n|\cdot(1-\tau) \tag{17}$$

$$P_P=2\pi nT_{\mathrm{p}}=K_{\mathrm{T}}(J)\cdot 2\pi\rho D^5 n^3 \tag{18}$$

Where $T_{\mathrm{e}}(i_{\mathrm{a}},i_{\mathrm{b}},i_{\mathrm{c}},\theta)=P\dfrac{\partial \mathbf{W}_{\mathrm{m}}(\psi,\theta)}{\partial\theta}$, i_{a} is thrust deduction coefficient, i_{b} is wake fraction, the value can be obtained by ship's manual, Tp is propeller torque, Fe is propeller effective thrust, ρ is density of water,D is propeller diameter.During stable sailing in the sea, the ratio of propeller is a constant value, it shows that propeller will work on the speed ratio of the characteristic curve[6].

Simulation and Results

The simulation parameter of propulsion motor was based on "Taiankou", as follows: power rating= 4700kW, rated voltage=660V,rated speed=155 r/min, rated torque=1185KN·m, rotor permanent magnet flux linkage= 4.55Wb,stator resistance=1.632m,number of motor pole=8, inductance of d axis=0.25 mH,inductance of q axis=0.47 mH.

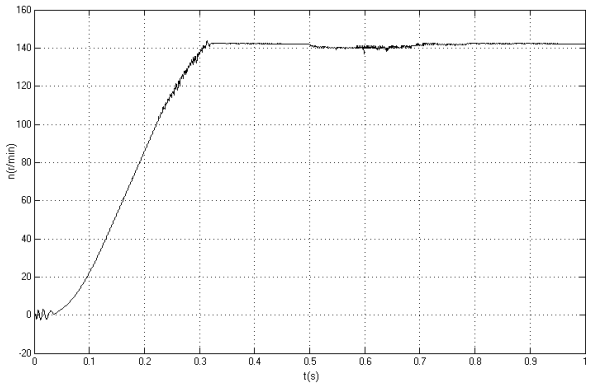

Fig.1 Speed curve based on CDKF

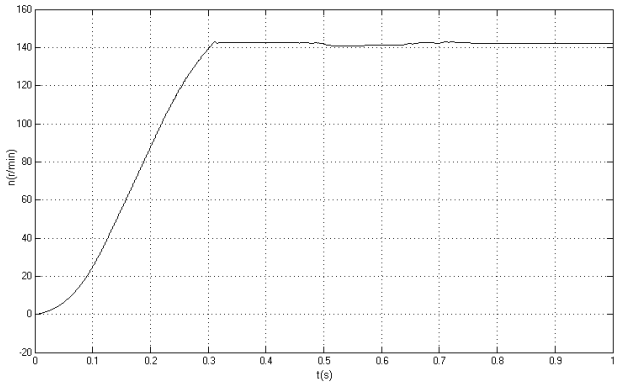

Fig.2 Speed curve based on SR-CDKF

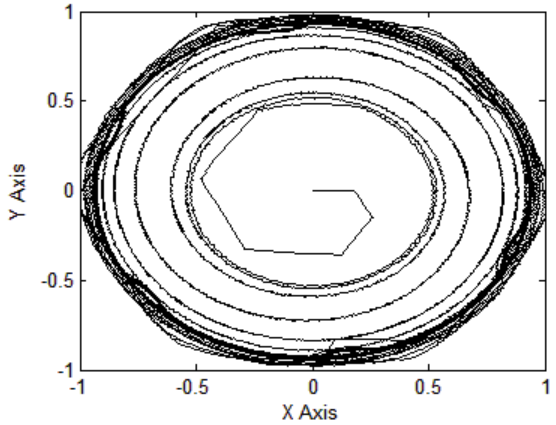

Fig.3 Stator flux based on CDKF

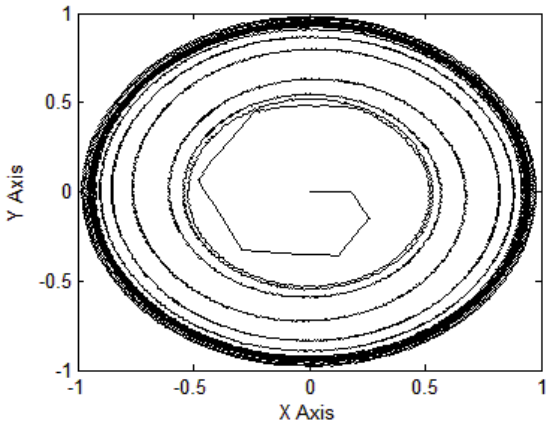

Fig.4 Stator flux based on SR-CDKF

When ship sailing in navigation at 142r/min, sea condition suddenly changes (such as the rough waves,etc.),so that the torque of the propeller load will change, the simulation analysis was carried out on this working condition. The simulation time is 1s, the initial speed is 142 r/min, at the beginning of the simulation, the motor load torque is 1100KN·m, at the time of 0.5 s propeller load torque changes to 400KN·m.The simulation results about the control method of SSP propulsion motor based on vector control with CDKF and SR-CDKF composite algorithm are shown as Fig.1-Fig.4.

The simulation results show that: When sea condition changes, under the two control modes, speed up smoothly, and the speed changes slightly after the the torque of the propeller load changes but back then. The system reaches the given speed after 0.31 s and propeller load changes in 0.5 s, the controller, torque and current have a corresponding response by the SR-CDKF. The speed oscillation of propulsion system based on SR-CDKF composite control was less than 6r/min,but the speed oscillation based on CDKF reached 15r/min, and the propulsion system based on SR-CDKF composite control can be achieved the setting speed in a short period of time, it has the faster response speed character.

Conclusions

In this paper the SR-CDKF control algorithm was introduced into the sensorless vector control of ship propulsion motor control system due to the CDKF algorithm is the optimal estimation method and the model of the propulsion motor in the process of actual operation can't be identical with the actual system, adopting PI speed controller system unavoidably affected by parameters change, but the SR-CDKF has better numerical properties and guarantees positive semi-definiteness of the underlying state covariance, it is not sensitive to external disturbance and parameter variation, it has very strong robustness. The simulation results show that the SR-CDKF propulsion motor control system can provide higher precision than the CDKF propulsion motor control system. It has the better ability to resist load disturbance, it has faster response speed, smaller dynamic overshoot and ripple, it can satisfy the maneuvering requirements under rough sea.

Acknowledgment

This work is supported by National Natural Science Foundation (NNSF) of China under Grant 61104187 and 51179102,the Shandong Province Higher Educational Science and Technology Program under Grant J13LN72,COSCO Science and Technology Development Project 2012-1-H-004.

References

[1] LI Bingqiang, LIN Hui. Direct Control of Current Vector for Surface-mounted Permanent Magnet Synchronous Motor[J]. Proceedings of the CSEE,2011,31:288-294

[2] Norgaard M, Poulsen N, Ravn O. New developments in state estimation for nonlinear systems[J] . Automatica, 2000, 36 (11): 1627 - 1638.

[3] S. J. Julier, J. K. Uhlmann. Unscented filtering and nonlinear estimation. Proc of the IEEE Aerospace and Electronic Systems, 2004,92(3):401-422.

[4] Wenlong Yao, Yuan Liu . Design of Vector Control based on MFAC for SSP Podded Propulsion, Proc. of the Int. Conf. on Robotics and Biomimetics (ROBIO 2013), 2013(12):2418-2423

[5] Ji Feng,Fu Lijun,Ye Zhihao. Study on Vector Control for Vessel Electric Propulsion[J]. Journal of wuhan university of science and technology,2011,35(2): 361-364

[6] Ma Cheng.The technology of Podded propulsion [M].Shanghai: Shanghai Jiaotong University Press,2007,5.

Advanced Materials Research Vols. 986-987 (2014) pp 1146-1150

doi:10.4028/www.scientific.net/AMR.986-987.1146

Stator Resistance Identification and Simulation Analysis Based on Fuzzy Logic

Qing TIAN[1, a], Junling ZHU[*,2,b]

[1] School of Computer Science, Zhao Qing University, Guang Dong 526061,China

[2] School of Computer Science, Zhao Qing University, Guang Dong 526061,China

[a]email: zdtina@qq.com, [b]email:zhuzhu000011@163.com

*Corresponding Author

Keywords: Stator Resistance; Fuzzy Logic; Vector Control; MRAS

Abstract: To improve the speed sensorless speed control system's performance, this paper analyzes the rotor flux and speed estimation principle based on MRAS. On this basis, a new online identification method of induction motor stator resistance based on fuzzy logic is proposed. This method takes rotor flux and stator current vector as input and the stator resistance changes as the output. In the simulation environment, we compare the speed waveforms after the increase of stator resistance identification and conduct simulation to the identification effect when doubling the original value of stator resistance suddenly. The experiments show that the method has simple structure, high reliability, low computational complexity and obvious ability to identify the stator resistance changes, and besides, it can significantly improve the speed control system performance.

Introduction

If the vector control technology is widely used in the high-performance induction motor speed control system, the speed estimation accuracy and system robustness have high sensitivity to the motor parameters. Observation of the rotor flux is an important issue for vector control, and the observation precision of rotor flux directly affects the performance of vector control system. No matter what method is taken to estimate the rotor flux, it will inevitably be affected by the motor parameters. For example, when computing the rotor flux based on the voltage model, the stator resistance changes will make the flux observations inaccurate, and the control effect of vector control system will be reduced, because the stator resistance changes with the changes of current frequency, temperature and other factors and is also affected by the skin effect and flux saturation effects. In order to improve the performance of speed sensorless vector control system, online identification or compensation for the stator resistance has become a hot topic [1-4]. Many scholars have studied the identification methods of stator resistance: calculating the stator resistance by using the measured motor parameters and motor steady-state model; building the stator resistance signals based on the adaptive algorithm; and online stator resistance identification based on neural network technology [5-6]. This paper puts forward a speed sensorless vector control strategy based on fuzzy logic. It takes the rotor flux and the stator current vector as the fuzzy controller input, and the variation of stator resistance as the output. Simulation results verify the feasibility and effectiveness of this control strategy.

Rotor Flux and Speed Estimation Principle

According to the design method of MRAS, this paper selects the rotor flux voltage model as the reference model, and takes the rotor flux current model as the adjustable model, because the voltage model only uses the two signals of stator voltage and stator current without using the speed signal, and it is less affected by changes in motor parameters. Current model has a speed signal, so the rotor speed can be estimated by using the positive real dynamic system and Popov hyperstability theory to design the appropriate adaptive law. The block diagram of MRAS speed estimation based on rotor flux is as shown in Figure 1.

To realize the rotor flux speed sensorless field-oriented vector control of the induction motor, this paper needs the accurate phase position and amplitude of rotor flux ψ_r, but it is difficult to directly detect the rotor flux ψ_r in the engineering technology application, and the rotor flux vector shall be indirectly estimated by using the state observer.

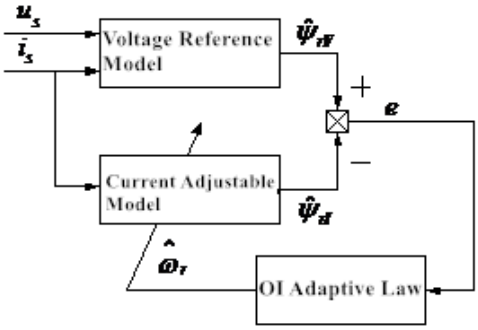

Figure 1 Block Diagram of MRAS Speed Estimation based on Rotor Flux

Equation (1) and Equation (2) are based on the stator voltage and stator current, whereas Equation (3) and Equation (4) are based on the stator current and motor speed. Equation (5) is based on MRAS speed estimation expression.

$$\psi_{r\alpha V} = \frac{L_r}{L_m}\int \left[u_{s\alpha} - (R_s + \sigma L_s P) i_{s\alpha} \right] dt \quad (1)$$

$$\psi_{r\beta V} = \frac{L_r}{L_m}\int \left[u_{s\beta} - (R_s + \sigma L_s P) i_{s\beta} \right] dt \quad (2)$$

$$\psi_{r\alpha I} = \frac{1}{1 + T_r p}\left[L_m i_{s\alpha} - T_r \psi_{r\beta} \omega_r \right] \quad (3)$$

$$\psi_{r\beta I} = \frac{1}{1 + T_r p}\left[L_m i_{s\beta} - T_r \psi_{r\alpha} \omega_r \right] \quad (4)$$

$$\hat{\omega}_r = (K_p + \frac{K_i}{s})(\hat{\psi}_{r\alpha I}\hat{\psi}_{r\beta V} - \hat{\psi}_{r\beta I}\hat{\psi}_{r\alpha V}) \quad (5)$$

Where R_s and R_r respectively represent the stator resistance and rotor resistance, L_r, L_s, L_m respectively represent the rotor inductance, stator inductance and mutual inductance, $T_r = L_r / R_r$ represents the rotor time constant, $\sigma = 1 - L_m^2 / L_s L_r$ represents the leakage inductance coefficient.

The method estimates the speed by firstly estimating the rotor flux. However, the temperature, current frequency and other factors make the stator resistance R_s change and deviate from the nominal value during operation of the motor, so the stator resistance is different from the true resistance under the actual motor operating conditions. From the above speed estimation method, in equations (1) and (2), R_s changes result in the speed estimation error. In MRAS model, the reference model is related to R_s, so that error exists when the adjustable model approaches the reference model, and finally there is a greater error between the speed estimation and the real speed. At the same time, when the system operates at low speeds, the stator resistance has obvious voltage drop effects, the measurement error submerges the counter electromotive force, and brings greater systematic errors and poor system low-speed performance, which may cause serious system instability[7].

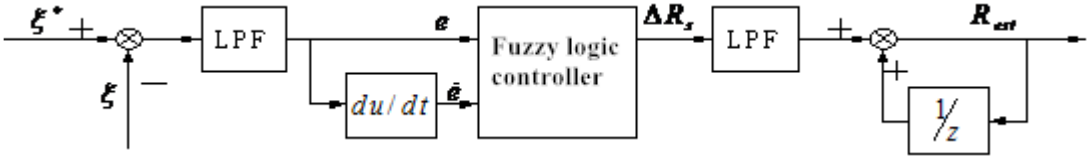

Figure 2 Block Diagram of Stator Resistance Identification based on Fuzzy Logic

Stator Resistance Identification Based on Fuzzy Logic

The block diagram of the proposed stator resistance online identification based on fuzzy logic is as shown in Figure 2. ξ^* and ξ are calculated by flux observer based on the rotor flux obtained from equations (1)-(4) and the stator current obtained from equations (6)-(7), and $i_{\alpha s}$ and $i_{\beta s}$ can be obtained by CLARKE transformation.

$$\xi^* = i_{\alpha s}\psi_{\alpha rV} + i_{\beta s}\psi_{\beta rV} \tag{6}$$

$$\xi = i_{\alpha s}\psi_{\alpha rI} + i_{\beta s}\psi_{\beta rI} \tag{7}$$

Where, $\psi_{\alpha rV}$ is the rotor flux voltage model's component on the α axis, $\psi_{\beta rV}$ is the rotor flux voltage model's component on the β axis, $\psi_{\alpha rI}$ is the rotor flux current model's component on the α axis, $\psi_{\beta rI}$ is the rotor flux current model's component on the β axis, the deviation signal e of ξ^* and ξ removes the high frequency harmonics in the signal through a low-pass filter, and then feeds the deviation signal and its differential components to the fuzzy logic controller, and the controller's output variable is the variation of stator resistance identification ΔR_s. Similarly, the variation of stator resistance identification ΔR_s obtains a smoother variation of the stator resistance through a low-pass filter.

In the design of the rule base, quantify the fuzzy controller's input signal deviation signal e and $\dot{e}$ as well as the output ΔR_s into seven fuzzy subsets, namely negative big (NB), negative medium (NM), negative small (NS), zero (ZE), positive small (PS), positive medium (PM) and positive big (PB). Where, the domain range of ΔR_s and e is [-3, 3], and the domain of $\dot{e}$ is between [-60,60]. Select the triangular membership function. Control rules are designed as:

If e is A_i and $\dot{e}$ is B_i, then ΔR_s is C_i。

Fuzzy control rule table is shown in Table 1. Fuzzy inference uses the direct product method. The weighting factor of i-th fuzzy rule is:

$$\alpha_i = \mu_{ei}(e)\cdot\mu_{\dot{e}i}(\dot{e}) \tag{8}$$

$$\mu_{\Delta R_n Rule_i}(\Delta R_s) = \sup[\alpha_i \mu_{\Delta R_n'}(\Delta R_s)] \tag{9}$$

Where, $\mu_{\Delta R_n Rule_i}(\Delta R_s)$ represents the membership of controller output ΔR_s in the i-th fuzzy rule. $\mu_{\Delta R_n'}(\Delta R_s)$ represents the membership function of fuzzy sets $\Delta R_n'$ on the controller output ΔR_s domain. The membership are shown in Figure 3, Figure 4 and Figure 5.

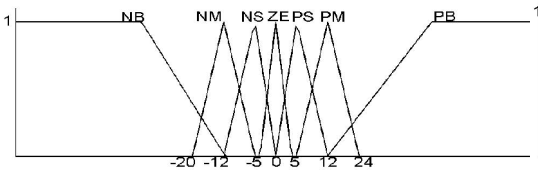

Figure 3 e Membership Function Graph

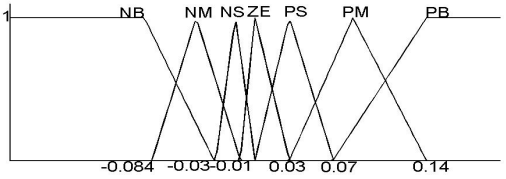

Figure 4 $\dot{e}$ Membership Function Graph

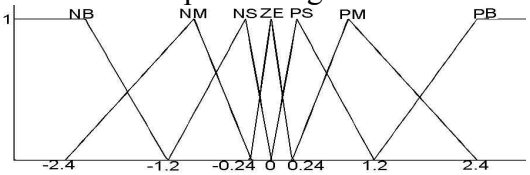

Figure 5 ΔR_s Membership Function Graph

The membership function $\mu_{\Delta R_n}$ of controller output ΔR_s is:

$$\mu_{\Delta R_n} = \max_{j=1}^{49} \mu\Delta R_n Rule_j(\Delta R_s) \tag{12}$$

Finally, this paper adopts the centroid method to solve ambiguity for the resulted fuzzy sets, and obtains the exact value. The value of output ΔR_s on the discrete domain can be obtained.

$$\Delta R_s = \frac{\sum_{j=1}^{49} \mu_{\Delta R_n}\left(\Delta R_{sj} \bullet C\left(\Delta R_{sj}\right)\right)}{\sum_{j=1}^{49} \mu_{\Delta R_n}\left(\Delta R_{sj}\right)} \tag{13}$$

Simulation Results and Analysis

This paper uses Matlab/Simulink tool to simulate the speed sensorless vector control system, the simulation selects the three-phase squirrel-cage induction motor, and its parameters are: rated power of 1.1kw, rated voltage of 380V, rated frequency of 50Hz, stator resistance $R_s = 0.93\,\Omega$, rotor resistance $R_r = 0.71\,\Omega$, stator leakage inductance $L_{\sigma r} = L_r - L_m = 0.0035$H, mutual induction $L_m = 0.082$H and friction coefficient $F = 0.006\text{N}\cdot\text{m}\cdot\text{s}$. Rotor leakage inductance $L_{\sigma s} = L_s - L_m = 0.0035$H, and the inertia coefficient is $J = 0.19\text{Kg}\cdot\text{m}^2$. In the simulation process, the system given speed is 50rad/s. Given that the motor stator resistance mutates into 2 times of the original value when it is at 2s, namely, mutating from 0.933Ω to 1.866Ω. Simulation experiments have made comparative analysis for the waveforms of stator resistance identification and no stator resistance identification. Figure 6 and Figure 7 respectively show the speed waveform of no stator resistance identification and torque simulation curve waveform of no stator resistance identification.

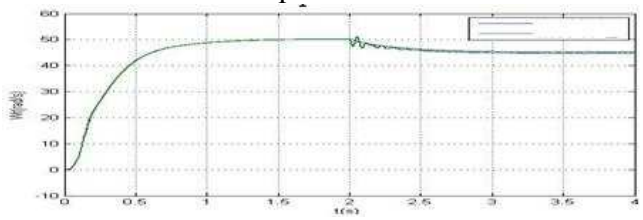

Figure 6 Speed Waveform of No Stator Resistance Identification with a given speed of 50rad/s, and stator resistance increases by 100% at 2s

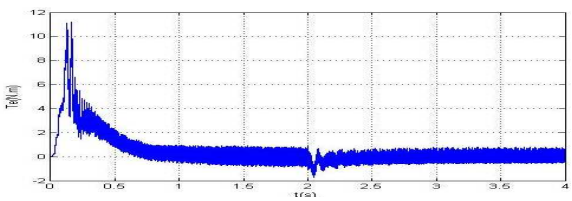

Figure 7 Torque Waveform of No Stator Resistance Identification, given the speed is 50rad/s, and stator resistance increases by 100% at 2s

Figure 6 and Figure 7 are respectively the speed and torque simulation curve waveforms of stator resistance identification. As seen in Figure 6, the speed estimation and the actual speed have significantly deviated from the given value and oscillation is generated, indicating that the changes of stator resistance have a great impact on the speed accuracy and result in a serious decline of the system performance. As seen in Figure 8, the damped oscillation occurs when the speed is at 2s, yet does not deviate from the given value, so the system is stable. As seen in Figure 7, the electromagnetic torque has a greater disturbance when the motor starts, and larger oscillation and pulsation are generated when the motor stator resistance changes. As seen in Figure 7, the oscillation and torque pulsation are relatively smaller for the torque with stator resistance identification.

According to the simulation results, under the condition of severe stator resistance mutations, the speed and torque waveforms presented in this paper are obviously better than the waveforms without stator resistance identification. Besides, the speed does not deviate from the given value, and it has good stability. Also, the torque has better smoothness and a good identification of the stator resistance dynamic changes.

Conclusions

In the speed sensorless vector control system based on MRAS method, this paper proposes a new stator resistance online identification solution based on fuzzy logic, which takes the rotor flux and the stator current vector as the input as well as the stator resistance changes as the output. Then, this paper makes a simple analysis of rotor flux and speed estimation principle, adopts new method to handle the effects of stator resistance changes, and establishes a stator resistance identification method based on fuzzy logic.

Simulation results show that the stator resistance changes have a greater influence on the speed estimation, and the proposed stator resistance identification strategy can achieve real-time estimation of the actual stator resistance. The method has simple structure, high reliability and low computational complexity. The application of stator resistance identification system can significantly improve the speed control system performance.

Acknowledgment

National Natural Science Foundation of China（NO.61379041）；Guangdong Zhaoqing Science and technology innovation project（NO：2012G26）Guangdong Zhaoqing University Natural Science （NO：201212）Support Fund。

References

[1] Riccardo Marino, Sergei Peresada, and Patrizio Tomei. On-Line Stator and Rotor Resistance Estimation for Induction Motors[J]. IEEE Transactions on Control Systems Technology. 2000,8(3):570-579

[2] Veran Vasic, Slobodan N. Vukosavic, Emil Levi. A Stator Resistance Estimation Scheme for Speed Sensorless Rotor Flux Oriented Induction Motor Drives[J]. IEEE Transactions on Energy Conversion, 2003,18,(4):476-481

[3] Kojabadi, H.M., Chang, L., Doraiswami. R. A novel adaptive observer for very fast estimation of stator resistance in sensorless induction motor drives[J]. Power Electronics Specialist Conference. 2003. 3:1455-1459

[4] Li Zicheng, Cheng Shanmei. Research on Stator Resistance Identification Strategies in Speed Sensorless Induction Motor Control [J]. Journal of System Simulation. 2009,21(8):2355-2357,2376

[5] Baburaj Karanayil, Muhammed Fazlur Rahman and Colin Grantham. Stator and rotor resistance observers for induction motor drive using Fuzzy Logic and Artificial Neural Networks[J]. IEEE ,2003:124-131

[6] Yanping Xu, Yanru Zhong, Jie Li . Fuzzy Stator Resistance Estimator for a Direct Torque Controlled Interior Permanent Magnet Synchronous Motor[J]. IEEE Transactions on Energy Conversion, 2003:438-441

Advanced Materials Research Vols. 986-987 (2014) pp 1151-1154

doi:10.4028/www.scientific.net/AMR.986-987.1151

Study on optimal-power Ratio Optimization of Automatic Transmission

Fengping Cao

Automotive Department, Shandong Jiaotong University, Jinan, Shandong, China

cao2138@163.com

Keywords: Compound Automotive Transmission, Optimal Power, Ratio Optimization, SimulationX Software.

Abstract. Regards the compound auto transmission as the object of research, an optimal-power ratio optimization algorithm that takes into account the efficiency of CVT was presented in the paper. Firstly, the numerical models of drivetrain were established, which included the engine output torque model and the efficiency model of CVT. Then, the driving power was chosen as the dynamic target, and the optimized objective function was built. According to the requirement of shift gear, the ratio of shuttle transmission components was determined. Based on the Simulation X, the simulation car model with the compound auto transmission was design to confirm the validity and effectiveness of the proposed method.

Introduction

In recent years, cars production and ownership are increased rapidly, which brought a lot of harm to the society, such as air pollution and energy consumption. In order to improve the performance of vehicles, several measures were adopted in the world [1, 2, 3]. Among them, the matching and optimized designing of the power transmission system is largely determines the automotive dynamics and fuel economy, and is considered as an important measure to improve the automobile general performance. Regards the compound auto transmission as the research object, an optimal-power ratio optimization algorithm is presented in the paper.

Organization of the Text

The Structure and Workings of Compound Auto Transmission

The transmission composed of a metal belt CVT unit and a shuttle transmission component, and can realize continuously variable transmission and a variable transmission according to the automotive operation mode. It not only can play the advantage of gear transmission efficiency, but also overcome the shortages of low efficiency of metal belt type continuously variable transmission in high-speed and high-power [4].

Establishment the Mathematics Model of Drivetrain

The Engine Output Torque Model. Engine output torque is the function of throttle opening and engine speed, that is $T_e = f(\alpha, n_e)$. Through the engine bench test, and using interpolating fitting methods can get the steady numerical model of engine output torque, which is shown as Fig. 1.

Because of the impact of mixture concentration, the engine is usually worked under non steady state. Modified the engine output torque under steady conditions using formula (1), and take this as the engine output torque under non steady state [5].

$$T_{ed} = T_e - K \cdot W_e \tag{1}$$

Where, T_{ed} is the engine output torque under non steady state, T_e is the engine output torque under steady conditions, W_e is the angle acceleration of the Crankshaft, and k is the falling coefficient of engine torque.

The Efficiency Model of CVT. For the metal belt CVT unit, power loss is inevitable during energy transferring. In order to optimize the drivetrain, it is need to build the efficiency model of CVT. Research indicates that the efficiency model of metal belt CVT is the function of its ratio and engine torque [6]. The relational data are gained through experiment, and the efficiency model of CVT built is shown as Fig. 2.

The Model of Optimal Power Ratio Optimization for the CVT

The driving power is not just the engine power, but also the efficiency of CVT. It is need to consider the efficiency of CVT for automotive dynamics when optimizing the ratio of CVT.

For a car with the compound auto transmission, if the ratio of shuttle transmission component is determined, in order to ensure best automotive dynamics, there requires the car obtain the maximum driving power at any throttle opening and car speed. The driving power of the car can be calculated by formula (2) regardless of the main reducer efficiency.

$$P_d = P_e \eta_{cvt} \tag{2}$$

Where, P_d is the driving power, P_e is the engine power, and η_{cvt} is the efficiency of CVT.

Simulation and Analysis

According to the structure and workings of compound auto transmission, the mathematics model of drivetrain, and simplified the driving resistance to air resistance and rolling resistance, the

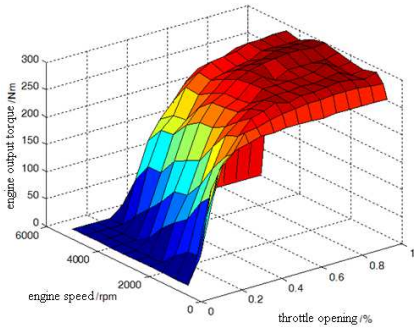

Fig. 1 The numerical model of engine output torque

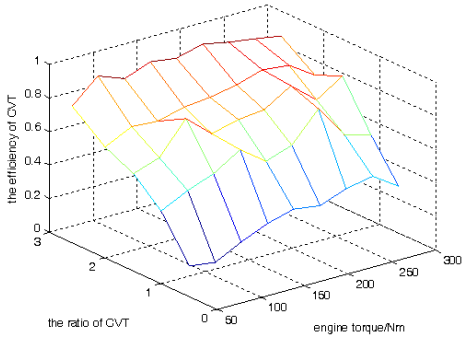

Fig. 2 The CVT efficiency numerical model

simulation model is established based on SimulationX software as Fig. 3. The ratio of shuttle transmission components is determined as 1.5, and the range of CVT ratio is set as [0.5, 2.6], and according to the transmission's radius, the original ratio of CVT is shown as Fig. 4.

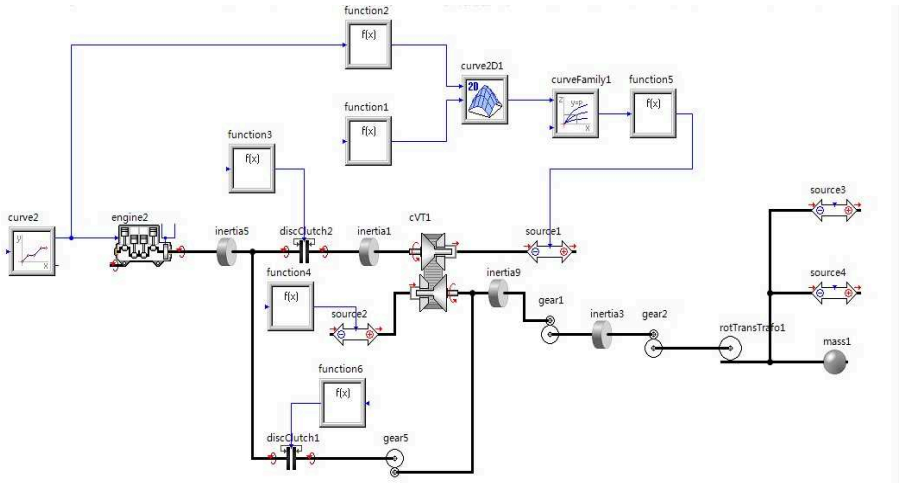

Fig. 3 Simulation model with compound auto transmission based on SimulationX

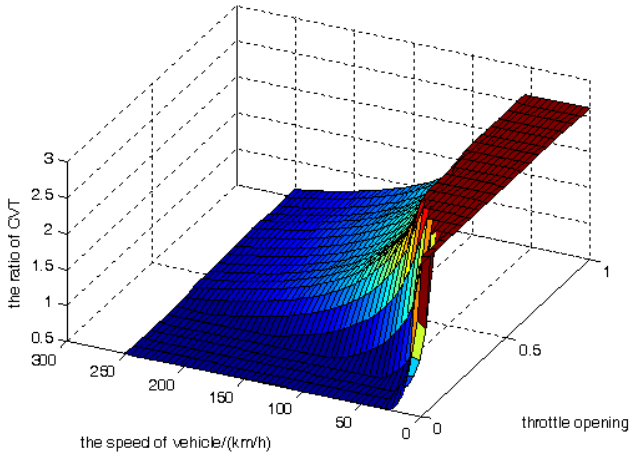

Fig. 4 The original ratio of CVT

Set the simulation time as 50s, and the simulation results of automotive speed is shown as Fig. 5.

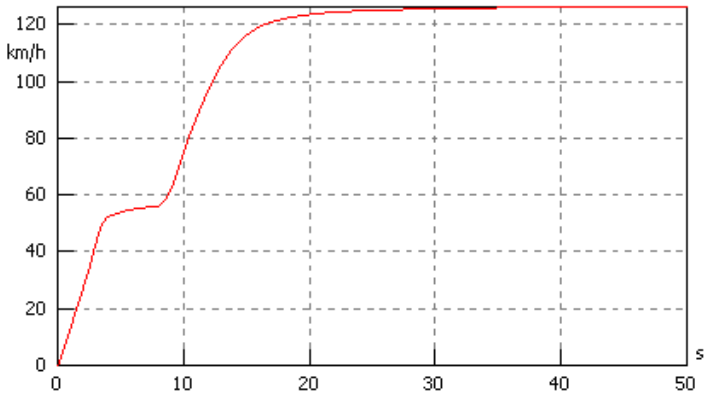

Fig. 5 The automotive speed

Using the above simulation model and the ratio optimization model, optimize the ratio of CVT. Fig. 6 is the ratio optimization result for the CVT.

For the transmission, set the ratio of CVT as the optimization results, and in this case, the automotive speed is shown as Fig.7.

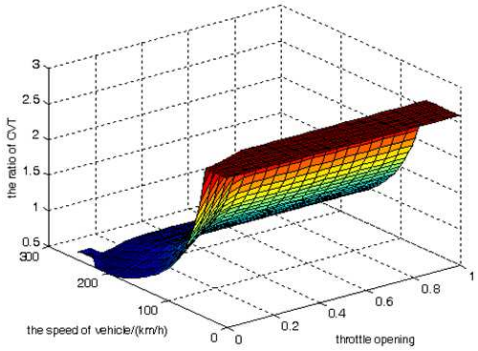

Fig. 6 The CVT ratio optimization results

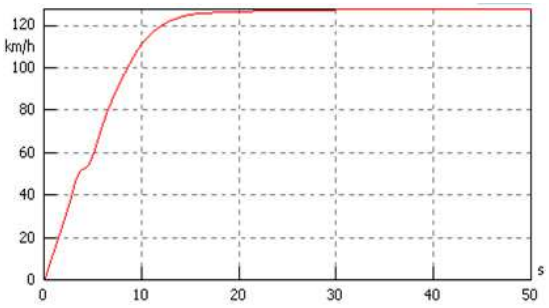

Fig. 7 The automotive speed after optimization

From Fig. 5 and Fig. 7, we can see that the 0-100km/h acceleration time before and after optimization is 12.31s and 8.58s, the acceleration time reduced 30.3%. This shows that the car's dynamic characteristic improved significantly.

Conclusions

In the paper, an optimal-power ratio optimization algorithm that takes into account the efficiency of CVT is presented.

The numerical models of drivetrain, which included the engine output torque model and the efficiency model of CVT, are established.

The optimized objective function is built, which considered the efficiency of CVT. Using the simulation car model based on the SimulationX software, the validity and effectiveness of the optimization method is confirmed.

Acknowledgements

This work is sponsored by Shandong science and technology develop project (2012G0020504), thanks to Shandong Science and Technology Department, as well as the references authors.

References

[1] Plotkin. Steven E, Greene. David, in: Energy Policy, Vol.12(14), (1997), p. 179-188.

[2] Zhangsong Zhan, Zhengjun Yang, Xingchun Liu, in: design, compute and research, Vol.3, (2007), p. 17-20. (In Chinese).

[3] Weidong Luo, Wangbiao Qiu, in: modern machine, Vol.2, (2008), p. 32-34. (In Chinese).

[4] Jinxiang Feng, Huijun Wang, China, Patent. ZL10115088.1. (2007). (In Chinese).

[5]Weisheng Chen, in: Study on the Ratio Control for CVT, Hu Nan University, (2008). (In Chinese).

[6] Xuedong Lin: Automobile Power Matching Technology. (2010).(In Chinese).

Advanced Materials Research Vols. 986-987 (2014) pp 1155-1158

doi:10.4028/www.scientific.net/AMR.986-987.1155

VSC-HVDC Control Strategy Research and Simulation Analysis

Yang Hu[1, a], Huiqi Li[1, b]

[1]School of Electrical and Electronic Engineering, North China Electric Power University, Baoding, Hebei, 071000, China,

[a]huyang_ncepu@163.com, [b]460378470@qq.com

Keywords: VSC-HVDC; Control Strategy; SIMULINK.

Abstract. With the development of high-power full-controlled power electronic devices based HVDC voltage source converter (VSC) and pulse width modulation (PWM) technology (VSC-H VDC) technology has become a reality. Currently VSC - HVDC technology in foreign countries in the theoretical study of the transition phase to the experimental system, while the domestic is just beginning, many of the basic theory and applications related to basic issues to be studied. In this paper, based on existing research, analyzes power VSC-HVDC system control strategy proposed *dq0* coordinates using a steady state model, and based on the model , designing the control program. Finally, to build a system using SIMULINK simulation model for a steady-state simulation analysis.

Introduction

As the power electronics technology developing, the use of full-controlled devices based on voltage source converter (Voltage Source Converter, VSC) in HVDC has become possible. In 1990, McGill University, Boon-Teek Ooi put forward HVDC concept with PWM control VSC, the so-called HVDC (HVDC light) [1,2]. In 1999, Gotland ,ABB put into operation in the world's first commercialization of VSC-HVDC system [3], the rated operating capacity of the system is 50MW, both ends of the VSC rated capacity of 65MW, transmission voltage is ± 80kv, transmission distance is 70km, it is the southern tip of the South Island Gothic with a wind farm 70km outside the city of Visby to link up with the existing AC lines run in parallel. In the ABB company IGBT switching devices developed for the VSC-HVDC, while Japan has also developed a switching element GTO for the VSC-HVDC interconnection and back to back, at present, CIGRE 14th meeting of the group has set up a working group for the VSC-HVDC [4,5].

In this paper, based on existing research, analyzes VSC-HVDC system rectifier and inverter power control strategy, using a steady state model proposed dq0 coordinate, and design control strategy. Finally, to build a system using SIMULINK simulation model for a steady-state analysis.

Research control strategy for steady state

For steady state, assuming symmetrical three-phase system is running, there is no zero-sequence component, the first derivative of the state variable to 0, we obtain:

$$\begin{cases} 0 = u_{cd} - Ri_d - u_{sd} + \omega L i_q \\ 0 = u_{cq} - Ri_q - u_{sq} - \omega L i_d \end{cases} \quad (1)$$

Decoupling control for the search, where the initial phase angle of voltage is 0° on AC side . Thus $u_{sd} = |u_s|$, $u_{sq} = 0$ and let ωL is the fundamental reactance , Then the formula (1) can be simplified as:

$$\begin{cases} u_{cd} = Ri_d + u_{sd} - X_T i_q \\ u_{cq} = Ri_q + X_T i_d \end{cases} \quad (2)$$

Variables research is needed into the AC system reactive power Q_s And DC side injection of active power P_c. Loss simulated by a resistor. We can get:

$$P_c = \frac{3}{2}(u_{cd}i_d + u_{cq}i_q) = \frac{3}{2}\left[u_{sd}i_d + R(i_d^2 + i_q^2)\right] \quad (3)$$

$$Q_s = \frac{3}{2}(u_{sq}i_d - u_{sd}i_q) = -\frac{3}{2}u_{sd}i_q \quad (4)$$

Formula (3) and formula (4) have a relatively clear physical meaning. Assuming AC system is strong enough, u_{sd} is a constant value, the reactive power on the AC side is obviously only the *q*-axis current proportional. The active side of the inverter consists of two parts, the first part representatives of the desired power converter, the inverter and the representative part of the reactor loss.

Therefore, the alternating current component can be decomposed into two separate i_d and i_q. Although in the formula (3) i_q is also the vatiable quantity of P_c, but the actual control process can be calculated based on the reactive value of i_q, therefore the active side of the inverter P_c can be considered only with i_d been related. So the model is active and reactive decoupled. Further, considering the normal operation active power transmission loss is much less than the value, so P_c and i_d ,Their approximate linear relationship is also very conducive to controller design.

By controlling i_d and i_q ,can reach the active and reactive power control purposes. Generally, however, the real power is the VSC-HVDC direct current or DC voltage by the control of either the AC side may be required to control the reactive power control of the AC voltage may also be required. The following can be a PI controller are designed, respectively, for controlling i_d and i_q.

A. **Active Power Controller.** A controller for controlling the active i_d in modeling, we use the DC power controller. To improve system response speed, steady-state inverse model provided by i_d reference value.

DC power controller shown in Figure 1.

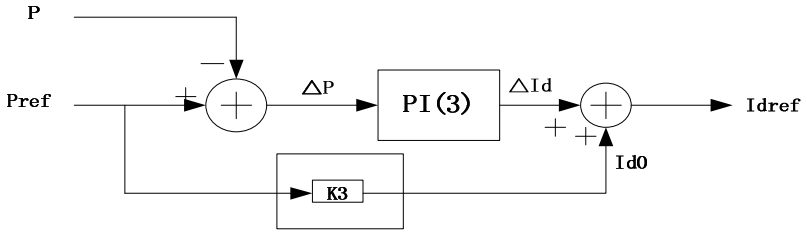

Fig. 1 DC power controller structure

B. Reactive Power Controller. A controller for controlling the reactive power i_q AC reactive power controller shown in Figure 2.

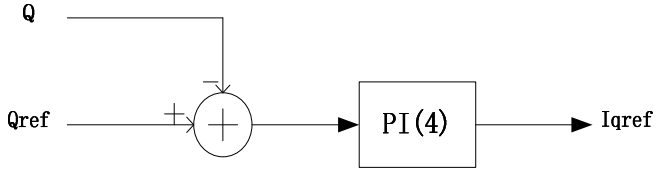

Fig. 2 AC reactive power controller structure

C. modulation wave synthesis. By the amount of control i_d and i_q VSC modulated wave can be synthesized. Synthesis of the inverter modulation wave structure shown in Figure 3. *R* is the

equivalent loss resistance of the analog; U_{cd} , U_{cq} after Park inversing become i modulated signal form, PLL links for locking phase.

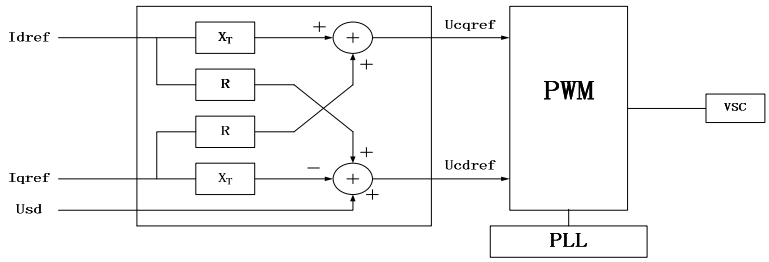

Fig. 3 Inverter modulation wave synthesis structure

MATLAB simulation-based analysis of VSC-HVDC

Using fixed-step discrete algorithms, Ts_Power = 7.407e-6; Ts_Control = 74.07e-6. To analysis steady-state and step response. Figure 4 is a system main circuit simulation model. First, in the model of three-phase programmable so that no short circuit between the power supply voltage failure without fluctuation, "Station2" and "AC System2", research VSC control system performance under normal conditions [6].

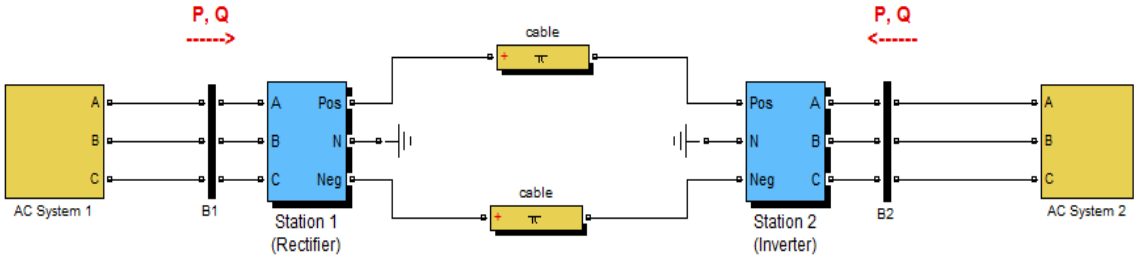

Fig. 4 System main circuit simulation model

Run the program to obtain simulation results shown in Figure 5 to Figure 6, namely "Station1" and "Station2" DC voltage, active power and reactive power.

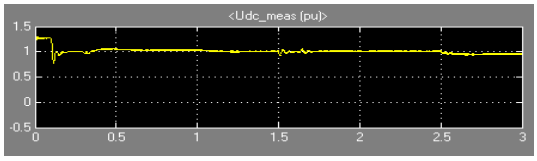

Fig. 5 (a) Station1 DC voltage waveform

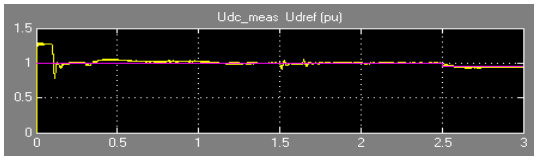

Fig. 6 (a) Station2 DC voltage waveform

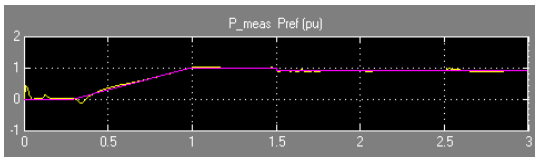

Fig. 5 (b) Station1 active waveform

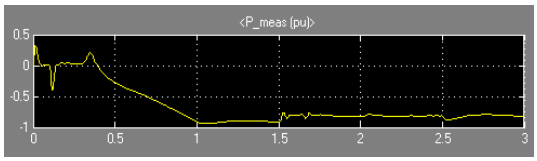

Fig. 6 (b) Station2 active waveform

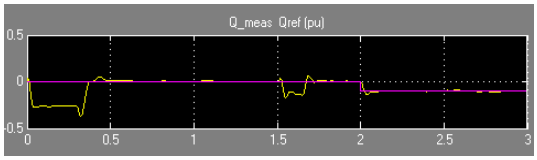

Fig. 5 (c) Station1 reactive power waveform

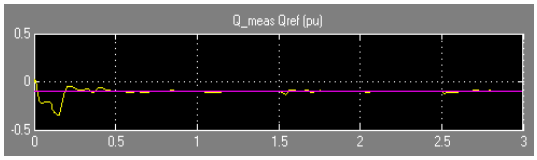

Fig. 6 (c) Station2 reactive power waveform

Seen from the waveform, in converter station 1and station 2 ,control system working with 1.3s time to reach steady state. After the steady state, the DC voltage is 1.0 p.u (200kV), steady-state power of 1.0 p.u (200MW). Reactive power rectifier side is 0, the inverter side reactive power is -0.1 p.u (20Mvar).

When 1.5s, the converter station power command a mutation, the actual active power can change quickly follow instructions to achieve stable within 0.3s, while active two converter stations also change accordingly. When 2.0s, after commutation reactive power command station a mutation, seen from Figure 5 (c) the actual reactive power corresponding change rapidly, and on the DC voltage and active power is small, a control system Good decoupling performance. When 2.5s, the DC voltage command converter station 2 mutation, a DC voltage converter station will follow changes in the short-term fluctuations in active settings quickly restored, fundamental reactive power is not affected . Active and reactive power reference value and the DC voltage changes, the system needs to re-enter the steady 0.3s time. Active and reactive power control is theoretically independent, but the visible waveform analysis, or a certain degree of interaction between the two.

Conclusion

In this paper, VSC-HVDC system control strategies were studied by using a steady state model based on dq0 coordinates. Using the SIMULINK to build the model. Simulation and analysis includ steady state of active and reactive power, voltage control. Studying the various operating conditions of the VSC-HVDC system, the model reflects the good operating performance.

References

[1] X.Wang, Boon-Teeh: PESC '90 Record volume I :325-332.

[2] Boon-Teeh Ooi, X.Wang: IEEE Transaction on Power Electronics, 1990, 5 (2) : 229-235.

[3] U.Axelsson, A.Holm, C.Liljegren, K.Eriksson, L.Weimers. CIRED Conference, May1999, Niee.Franee.

[4] A.S.Cook, M.Wyckmans, L.Weimers, K.Eriksson. Network Interconneetion using HVDC Light.Distribution 2000 Conferenee, Brisbane. Australia, November 1999.

[5] S.Hirokazu, N.Tatsuhitoetal: IEEE Trans. On Power Delivery,1997:12 (4) :1589-1597.

[6] MathWorks. SimPowerSystems. User Guide.2012

Advanced Materials Research Vols. 986-987 (2014) pp 1159-1162

doi:10.4028/www.scientific.net/AMR.986-987.1159

A parametric study of microfluidic power generator based on reverse electrowetting in a microchannel geometry

Wencheng Han[1], Diansheng Wang [1, a], Liping Xiang[1], Yudou Wang[1], Zhaoqin Huang[2], Aifen Li[2, b]

[1]Key Labratory of New Energy Physics & Materials Science in Universities of Shandong, College of Science, China University of Petroleum, Qingdao 266580, China.

[2]College of Petroleum Engineering, China University of Petroleum, Qingdao 266580, China.

[a]dshw@upc.edu.cn, [b]aifenli@upc.edu.cn

Keywords: microfluidic power generator, reverse electrowetting, mechanical-to-electrical energy conversion mechanism, influencing parameter, power output.

Abstract. The micro power generators that depend on converting the ambient energy into usable electrical energy for portable electronic devices have attracted much attention in recent years. A novel microfluidic power generator which is based on reverse electrowetting in a microchannel geometry was presented by Tom Krupenkin and J. Ashley Taylor. This generator overcomes the defects such as low output and low resource utilization of traditional energy converters. Understanding the parameters influencing output of this generator is a key to enhance the power output of it. This paper discussed the effects of factors on generator output by numerical simulation. The results show that promising performance of REWOD-based power generator can be achieved by choosing a thinner dielectric film with high dielectric constant and high break strength, and increasing the droplet oscillation frequency.

Introduction

With the rapid development of portable electronic devices, electrical batteries characteristics such as short lifespan, limited capacity, poor portability, etc. have become the critical bottleneck of its applications. Alternative power sources which overcame these limitations are thus highly desirable. More recently years efforts have been focused on ways to convert environmental energy into electrical power. Actually there exist many ways to convert ambient energy into usable electrical energy [1-4]. The general opinion from the literatures is that mechanical energy in the form of motion is particularly the most versatile and ubiquitous ambient energy source available for portable applications[5-8], but currently its use is substantially limited by low power output of energy converters. To solve this problem, Tom Krupenkin and J. Ashley Taylor developed a completely new mechanical-to-electrical energy conversion method which is based on reverse electrowetting-on-dielectric (REWOD), the approach and apparatus are introduced in the patent [9]. Fig. 1 show the schematics of microfluidic power generator based on reverse electrowetting in a microchannel geometry. The main parts of this generator are a plurality of electrodes and a fluidic body which comprise spatially separated conductive droplets and dielectric droplets. Electrodes are covered by dielectric film and the hydrophobic film, the hydrophobic film provides low-hysteresis surface for droplets motion. Fluidic body is configured to reversibly move as a whole with respect to plurality of electrodes under the influence of a mechanical force. Each cycle of alternations of the amount of electrical charge accumulated by the electrodes, whereby generating electrical current flow between electrodes.

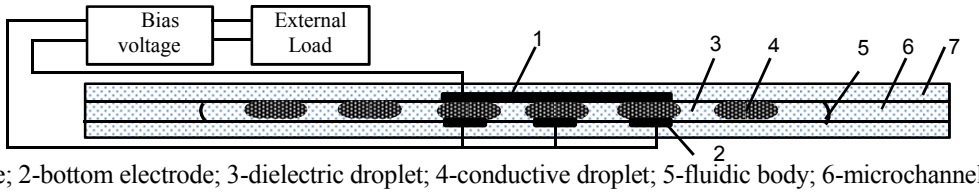

1-top electrode; 2-bottom electrode; 3-dielectric droplet; 4-conductive droplet; 5-fluidic body; 6-microchannel; 7-substrate.

Fig. 1 Schematics of REWOD generator of microchannel geometry [9]

The microfluidic power generation based on REWOD is a novel method of mechanical-to-electrical energy conversion, which had not been previously described in the

literatures besides the mentioned in Tom Krupenkin and J. Ashley Taylor's article[10], the research about influencing parameters of the reverse electrowetting process is lacking. In this paper, we discussed the influences of dielectric film material and thickness, and droplet oscillation frequency on the REWOD-based microfluidic power generator output by numerical simulation.

Simulation

In this section, according to the mechanism of microfluidic power generator based on the reverse electrowetting which described in the patent [9], we provide a numerical simulation of finite element method to discuss the influences of factors on the generator output.

The entire apparatus of the REWOD-based power generator in a microchannel geometry is consisting of some REWOD units with the same structure, and one of the units is schematically shown in Fig. 2. In the simplest approximation, we neglect the intricacy of the wetting-dewetting process associated with the motion of liquid droplets during the REWOD process and treat each droplet simply as a variable capacitor [10] shown in Fig. 2. The value of bias voltage V_{app} is switched from zero to V_0 during the whole process is shown in Fig. 3, where T is the cycle time period of the droplet oscillation.

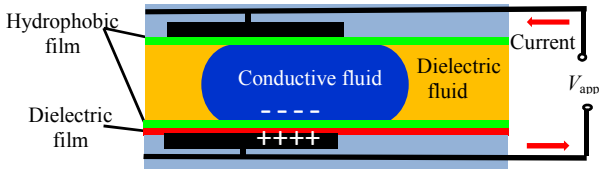

Fig. 2 Schematics of REWOD unit mechanisms

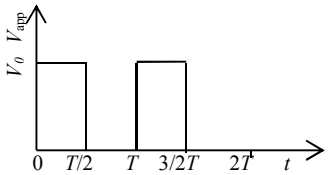

Fig. 3 Value of the V_{app} switched with time

The simplified calculation model of the REWOD unit is shown in Fig. 4, The entire simplified model size is 2.5mm×150μm, bottom electrode size is 1mm×20μm, conductive droplet length is 1mm, the gap between top and bottom electrode is 100μm. The value of parameters for the simulation are shown in Table1.

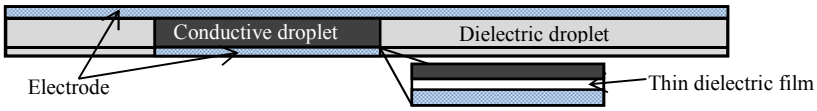

Fig. 4. The simplified calculation model of the REWOD unit

Table 1. The value of parameters for the simulation

Item	Material	Dielectric Constant	Breakdown strength
Dielectric film	Si_3N_4	9.7	1000[V/μm]
	ParyleneC	3.0	200[V/μm]
	SiO_2	4.2	100-1000[V/μm]
Dielectric fluid	Transform oil	2.36	18-20[V/μm]
Conductive fluid	Hg	Approaching infinity	–
Electrode	Cu	Approaching infinity	–

The domain of conductive droplet, dielectric droplet and the dielectric film comply with Eq. (1), where V is the electric potential, ε_d is the dielectric constant of the medium.

$$\nabla\cdot(\varepsilon_0\varepsilon_d(-\nabla V))=0 \tag{1}$$

The boundary conditions on the surface of the top and bottom electrode respectively are V=0 and V=V_{app}.The boundary conditions about the interface between the liquid-solid and liquid-liquid are as follows Eq.(2), where ρ_s is the surface charge density, $\boldsymbol{E}$ is the electric field, $\boldsymbol{D}$ is the electric displacement vector, $\boldsymbol{n}$ is the (outward) unit normal vector.

$$\boldsymbol{n}\cdot(\boldsymbol{D}_1-\boldsymbol{D}_2)=\rho_s \quad \boldsymbol{n}\times(\boldsymbol{E}_1-\boldsymbol{E}_2)=0 \tag{2}$$

The charge on the electrode plate and the net energy generated are calculated following Eq. (3), where the S is the surface of the electrode, the Q_0 is the total charge.

$$\int \rho_s \mathrm{d}S = Q_0 \quad W_t = 0.5Q_0V \tag{3}$$

The Eq. (3) showed that the energy of REWOD process generated in one cycle is equal in amount to the capacitor stored actually. Assuming that the conductive droplet moved periodically in the x direction as follows x=0.5[mm](1-cos2πft), where the f is the droplet oscillation frequency, t is time. Charge and net electrical energy generated under different conditions by the microfluidic power generator based on REWOD in a microchannel geometry are calculated in two cycles.

Dielectric Film Material. As shown in Fig. 5, for three different dielectric films with the 10μm thickness, charge are decreasing from the maximum to zero while the energy generated is increasing from zero to the maximum as the movement of the conductive droplet in a cycle. What's more, dielectric films with different dielectric constant have important influence on the net energy generated. The charge and net energy are both most for dielectric film Si_3N_4, on the contrast, which are both less for dielectric film paryleneC. This can be interpreted as the dielectric constant of Si_3N_4 and paryleneC is the largest and smallest respectively in the three kinds of films. It is concluded from the above results that the higher dielectric constant is, the more charge and net energy are.

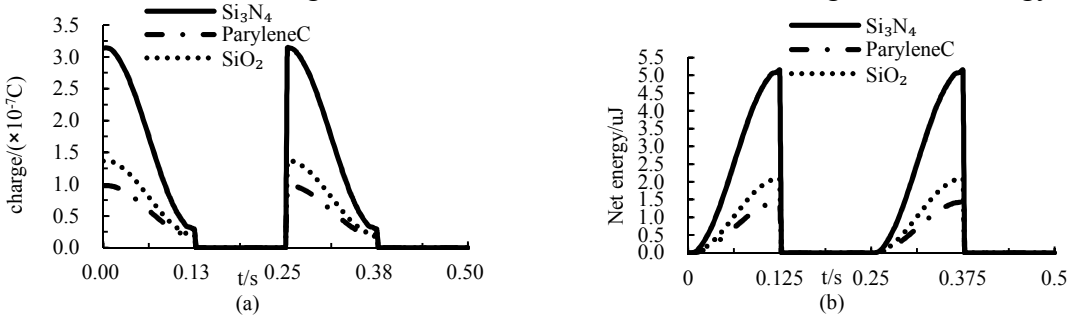

Fig. 5 The (a) variation of charge and (b) net energy generated for three different dielectric films with thickness of 10μm, bias voltage applied is 36V, and droplet oscillation frequency is 4Hz.

Dielectric Film Thickness. The plot of charge and net energy generated in two cycles for three different thickness of Si_3N_4 film was given in Fig. 6. The general trend of charge and generated net energy curves are quite similar in all three cases. Charge decreased from maximum to zero and net energy generated increased from zero to maximum along with the motion of the droplets. However, from the results one can see that the net energy of almost 10μJ is obtained for the 5μm thickness Si_3N_4 film, but only 3μJ energy generated for the 15μm case. Thus it can be seen that decreasing the thickness of the dielectric film lead to increase the energy generated effectively. But meanwhile, it brings the challenges to electric breakdown resistance of dielectric material and the technology of thin film fabrication.

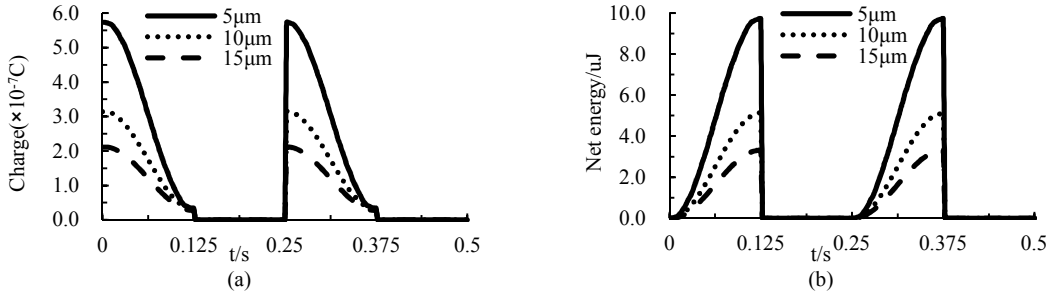

Fig. 6 The (a) variation of charge and (b) net energy generated for different thickness of Si_3N_4 film. Bias voltage applied is 36V, and droplet oscillation frequency is 4Hz.

Droplet Oscillation Frequency. Droplet oscillation frequency is another important parameter to the output of generator based on REWOD. We calculated variations of the charge and net energy for three different droplet oscillation frequencies as shown in Fig. 7. The maximum amount of charge and net energy are equivalent for three cases in per period, but the higher oscillation frequency, the shorter cycle of wetting-dewetting, net energy generated almost 52μJ in a second for oscillation frequency of 10Hz, while for low frequency of 1Hz, only 5.2μJ generated. It is obvious that more electrical charge flowed back to circuit and more energy generated per unit time for the case of higher oscillation frequency. Apparently, higher oscillation frequency can increase power output remarkably, and that the generated net energy linearly increases with droplet oscillation frequency.

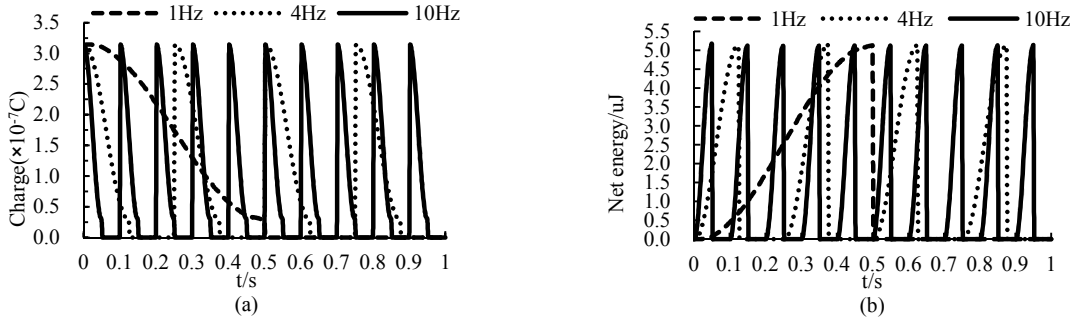

Fig. 7 The (a) variation of charge and (b) net energy generated for different droplet oscillation frequency. Dielectric film is Si_3N_4 with 10μm thickness, bias voltage applied is 36V.

Summary

In this paper, we discussed the influences of parameters on the output of the microfluidic power generator based on REWOD in a microchannel geometry by simulating this process. The results show that: (1) more net energy can be generated by using dielectric layer with high dielectric constant and high break strength such as Si_3N_4; (2) the thin film show far better performance than the thick film; (3)The generated net energy increases linearly with droplet oscillation frequency, and the net energy generated under 10Hz frequency is ten times more than the case of 1Hz within the same time.

From the above, one can conclude that the promising performance of microfluidic power generator based on REWOD in a microchannel geometry can be achieved by choosing a thinner dielectric film with high dielectric constant and high break strength, and increasing the droplet oscillation frequency.

Acknowledgement

The authors wish to acknowledge the support of this work by Fundamental Research Funds for the Central Universities (13CX05017A, 14CX02026A) and CNPC Innovation Foundation (2012D-5006-0207).

References

[1] Roy Want, I. Keith Farkas, and Chandra Narayanaswami: IEEE Journal of Pervasive Computing. Vol. 4(2005), p. 14-17.

[2] R.J.M. Vullers, R. van Schaijk, I. Doms, C. Van Hoof, and R. Mertens: Solid-State Electronics. Vol. 53(2009), p. 684-693.

[3] Adnan Harb: Renewable Energy. Vol. 36(2011), p. 2641-2654.

[4] Liang Liu, Rui Zhang, and Kee-Chaing Chua: IEEE TRANSACTIONS ON WIRELESS COMMUNICATIONS. Vol 12(2013), p. 288-300.

[5] F. Moll, A. Rubio, in: Proc. Mixed Design Integr. Circuits Syst. Conf., Gdynia, Poland, Jun. (2000).

[6] S. Roundy, P. K. Wright, and J. M. Rabaey: Comput. Commun. Vol. 26(2003), p. 1131-1144.

[7] T. Starner, J. A. Paradiso, in: Low-Power Electronics Design, C. Piquet, Ed. Boca Raton, FL: CRC Press (2004).

[8] T. Starner: IBM Syst. J. Vol. 35(1996), p. 618-629.

[9] T. Krupenkin, USA. Patent 17,898,096. (2011).

[10] T. Krupenkin, J. A. Taylor: Nat. Commun. 2:448. doi: 10.1038 / ncomms1454 (2011).

Advanced Materials Research Vols. 986-987 (2014) pp 1163-1168

doi:10.4028/www.scientific.net/AMR.986-987.1163

A smart PV cooler based on solar thermoelectric generator with phase change material

Qi ZHANG[1, a], Amen AGBOSSOU[2, b]

[1]Chongqing Institute of Green and Intelligent Technology, Chinese Academy of Sciences, Chongqing, China, 400714

[2]Université de Savoie, LOCIE - CNRS UMR 5271, Campus Scientifique - Savoie Technolac, 73376 Le Bourget du Lac Cedex, France

[a]email: zhangqi@cigit.ac.cn, [b]email: amen.agbossou@univ-savoie.fr

Keywords: Smart system; Thermoelectric generator; Solar energy; Energy harvest

Abstract. This paper presents a typical application for a newly developed thermoelectric energy harvesting system. The proposed solar thermoelectric generator (TEG) operates with phase change material (PCM) day and night. An energy management system was connected with the TEG to increase the output voltage while the harvested power was used to drive a wireless transmitter. The wireless receiver controlled the switch of a water tap which functions as a smart cooler of a photovoltaic cell. This study demonstrates a way of using micro-energy to improve macro-energy production smartly.

Introduction

Solar micro energy harvesting has become an attractive topic in researches for a long time [1]. The most popular technology includes thermoelectric effect [2] with space variation of temperature and pyroelectric effect [3][4] with time variation of temperature. A newly developed solar thermoelectric generator uses phase change material to accompany the working process of the TEG [5-6], improving the temperature stability on its cold face during the day and extending the work time of the TEG into the night. The newly proposed TEG had been proved with a maximum power generation 17μW outside, which is insufficient with a majority of wireless application. The focus of this study is to realize a typical wireless application with this TEG, taking advantage of a group of the micro generator and impedance matching.

Constitution of the Experimental System

It is well known that the weakness of photovoltaic power is that the power generation decreases when the panels become hot. This decrease is often greatest when solar radiation is high. So our experiment uses the developed TEG group as a (self-powered) smart system in order to improve photovoltaic power generation. The proposed smart system aims to refresh the photovoltaic panel through water evaporation. The constitution of the smart system is shown in Fig.1(a) which mainly includes: (1) a TEG work unit (2) a smart controller which was powered by the TEG, it monitors the temperature in two PVs and sends out a wireless signal to activate the cooler. (3) two identical photovoltaic panels: one serves as a reference while the other is fitted with a cooling system on its shaded side where it is not irradiated by the sun. (4) a water tap which was controlled by a wireless switch. Solar radiation is measured with a cmp3 pyranometer from Kipp & Zonen company. All data were recorded with a data acquisition system (NI USB-6259 BNC).

The TEG in work unit is made of 12 pieces of TEC-12708 module which were connected in series electrically. The equivalent seebeck coefficient of each module is 30mV/°c and its internal resistance is 2.5Ω. The TEG was connected to the PCM with two heat exchangers (63730 AAVID THERMALLOY). A paraffin wax from Dupont company is used as the PCM; its melting point is 21.7°C. Between 18°C and 22°C, the heat storage capacity is 40mJ/m3. Solar radiation is the heat source and the PCM is the heat sink during the day. At night, heat from the PCM is dissipated into

the environment by convection. The TEG has two separately treated work statuses: during the day, a glass cover is used to increase the absorption of solar radiation while at night; the glass is taken off to enhance convection.

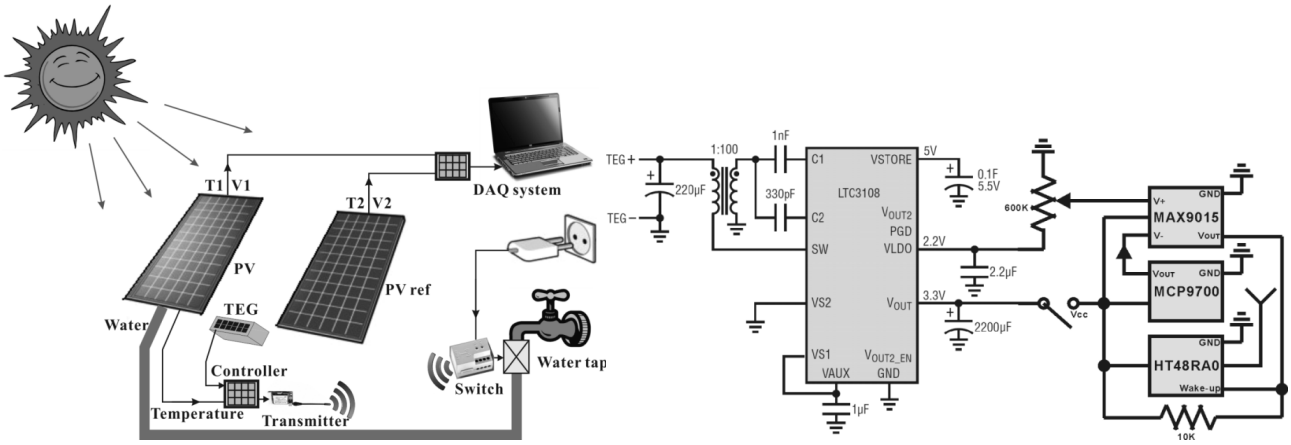

(a) The entire system (b) The controller

Fig.1. Constitution of the experimental system

A diagram of the smart controller is shown in Fig.1(b). It contains transformer, DC-DC converter, temperature sensor, comparator, micro-controller and wireless transmitter. The maximum output voltage of the TEG is 1V according to a previous test outside. It is not sufficient to power common commercial electronic devices directly. A DC-DC converter is a solution to this problem. The ultra-low voltage step-up converter (LTC3108 from Linear Technology Corporation) was adopted, allowing the system to operate with such a low TEG output voltage. A coupled inductor (LPR6235-752SML from Coilcraft INC.) with a ratio of 1:100 is used as the transformer. The main output of the converter is set to 3.3V and a 2200μF capacitor is used to temporarily store the energy. It is able to drive the temperature sensor, comparator, micro-controller and wireless transmitter at the same time. The output for the battery in the converter is connected to a 0.1F capacitor, storing energy from the TEG when the primary capacitor is fully charged. A low-power linear active thermistor (MCP9700 from Microchip Technology INC.) is used to sense the temperature on the PV panel. It is placed on the back of the panel and it transfers the temperature, giving analog output. In order to limit our test to the demonstration of the efficient use of harvested micro-energy without developing a specific wireless transmitter and electric switch receiver, we chose a commercial wireless doorbell (D403 from Friedland company) with an integrated transmitting micro-controller (ht48ra0-2 from Holtek Semiconductor INC.) working at 433MHz. The wireless switch is activated automatically when the doorbell rang. The micro-controller was put on standby most of the time when no command was sent to the transmitter. It is “woken up” by grounded triggering from the voltage comparator (MAX9015A from Maxim Integrated Products, INC.) and the doorbell rings. The inverting input of the comparator is connected to the output of the temperature sensor while the non-inverting input receives a given reference temperature from the potentiometer driven by the low drop-out linear regulator in the step-up converter.

The principle of the panel cooling system is based on drying combined with solar radiation. The first layer of a water-pipe system (such as waterSmart drip line) was glued to the back of the PV panel. The drip line is associated with a tap timer in order to create an automatic drip system designed to work at low pressure without a pump. A layer of superabsorbent cloth was glued to this first layer of the water-pipe system. A second layer of drip line was added and it was covered with another layer of superabsorbent cloth. So there were then two layers of drip line and superabsorbent cloth. When the water drip line was open, the superabsorbent cloth was impregnated. Once the water supply was cut off, the PV panel was refreshed through the drying of the superabsorbent cloth.

The energy from the PV panel made the water in the cloth evaporate into the surroundings and thus refreshed the PV panel. To clearly show the possible effect of such a smart system and to guarantee the correct status of all the power consumers after the converter, we present in this paper the results for when the switch is turned on manually for ten minutes every hour.

Experimental results

The tests were performed over several autumn days in Aix-Les-Bains (France). We present the results of two consecutive days with very similar solar radiation and the same ambient thermal loads. Fig.2 shows the sunshine and ambient temperature measured on these two days. Solar radiation ranged from 0 to 900W/m^2. The relatively low ambient temperature varied between 10 and 26°C at midday and fell by around 10°C at night. The two days were windless and the convection effect was considered as natural convection. The maximum daily temperature could not be very high in our test conditions. However, these conditions are still interesting for us because if the performance of the PV is improved during the autumn, the improvement should be even more significant in the summer.

The performed test considered two PV panels: one equipped with the cooling system and the other one left in its normal working state. On the first day, the two panels worked without any special management. For the second day, the cooling system was activated at the back of one panel. The analysis of the results aims to (i) present the micro-energy harvest by TEG work unit in a real situation and (ii) demonstrate the improvement provided by the cooling system controlled by the self-powered wireless system powered by harvested micro-energy.

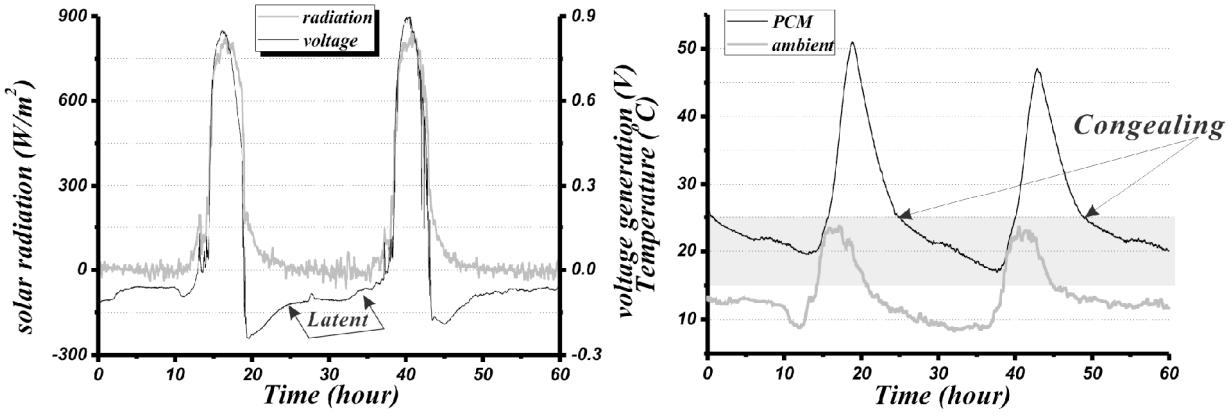

a) Recorded radiation and TEG voltage (b) Temperature in the PCM and environment

Fig.2. Experimental results of the TEG

Fig.2 shows also the recorded voltage generation on an external resistor of 40Ω with the TEG and temperature variation inside the PCM over 60 hours. Analysis of this figure lead to five comments: (i) the energy harvested was 465J over 60hours - an average power of 2.15mW. The daily maximum power reached 20mW (a power density of 2.7mW/cm^3 or 1W/m^2). Energy harvested at night by the TEG formed 10% of the total energy. This real situation test was carried out in autumn. Logically, the performance would be better in summer and not so good in winter. (ii) the voltage generated in daytime reached 0.9V for a solar radiation intensity of 900W/m^2. Although less voltage was generated at night than during the day, the absolute value was generally greater than 0.02V (more than 90% of the time). It can be regulated with the step-up converter and utilized in a some application at night. (iii) the phase change process occurred during our test. The decrease in ambient temperature was gradual from hour 21 to 27, but there was a definite change in the PCM

temperature variation at hour 25. This change of slope recurs at hour 49 at the same temperature, 25°C. As this fits with the manufacturer's stated melting point, we believe that this is the congealing point of the PCM. When the PCM releases the latent heat, the generated voltage becomes stable, as indicated in Fig.2(a). However, the latent heat in the developed prototype generator is still insufficient. Its sensible heat is utilized during the experiment. It can be expected that with more PCM or more latent heat capacity, the performance would be better. (iv) the temperature curve (Fig.2(b)) clearly shows the inertial effects of PCM in generating a temperature gradient in the TEG. There is indeed a shift in the peak ambient temperature and the peak internal temperature of the PCM. The shift of temperature, between ambient and PCM internal temperature, is favorable for maintaining a temperature gradient in the TEG. It can be noted that, in the absence of solar radiation, the temperature inside the PCM remains high. This confirms the idea of heat storage in the PCM for the generation of micro-energy at night. (v) the voltage generated by the TEG was very sensitive to solar radiation during the day. The night performance depends mainly on convection and ambient temperature. Variations in voltage generation can be used for sensing radiation during the day; this confirms the possible use of the TEG device to carry out smart control strategies in some processes.

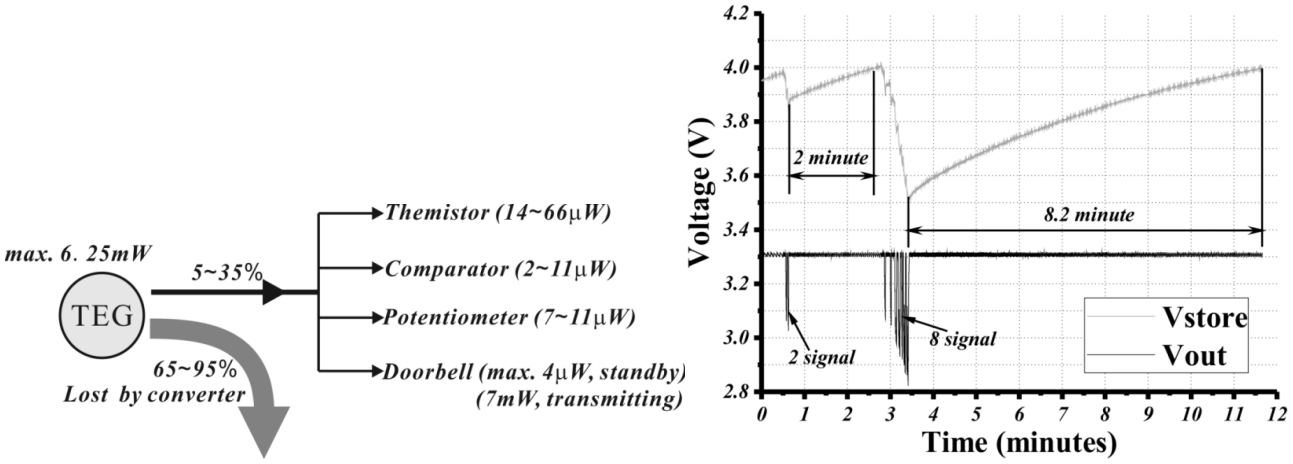

(a) Energy balance in the controller (b) Transmitting process of temperature sensor

Fig.3. Experimental results of the controller

The characteristics of the self-powered controller depend on the power capability of the TEG, the DC-DC energy conversion efficiency and the power consumption of the electronic devices. A diagram of the energy balance in the system can be seen in Fig.3(a). The TEG system can provide a maximum power of 20mW. When the TEG is connected to the step-up converter, the output DC signal is first changed into a switched AC signal and then amplified by the transformer. The amount of energy lost in this process depends on both the transformer ratio and the input voltage to the converter. The maximum energy conversion efficiency reaches 35% in our case. Intended as the study of a typical case, one TEG module was constantly irradiated with the maximum recorded value in the environment and it generated 150 mV in an open circuit status. It was used to drive the sensing system and the performance is shown in Fig.3(b). The voltage variation in the two capacitors (V_{out} is connected to 2200μF and V_{store} to 0.1F) was recorded. When the TEG was connected to the converter, the generated voltage fell to 100mV. The calculated input power to the converter was 1.67mW. With V_{out} fully charged and V_{store} charged to 4V, two groups of doorbell commands were sent out by manual activation of the temperature sensor. The recorded pattern of voltage variation shows that V_{out} was used to drive the electronic consumers directly while V_{store} sensed the change of V_{out} and quickly recharged it. The drop in V_{store} was in relation to the power consumption of the doorbell and the increase corresponded to the major part of energy harvested from the TEG. The measured harvested power after the converter was between 0.39 and 0.47mW. The calculated energy conversion efficiency was 23-28%; this is in line with the characteristics

provided by the manufacturer. In short, the step-up converter is a good solution for a self-powered controller when the generated power from the TEG is not enough to drive the electronic devices directly. With one module of the TEG and without matched impedance, the system can send out at least one signal every two minutes. It is expected that this kind of system could work as an independent sensor node within a well-designed control strategy.

Fig.4 shows the results of the water cooling application of harvested micro-energy related to macro-energy. The two PV panels work without any special treatment during the first day. The cooling system is activated on the second day. Fig.4 (a) and (b) present the voltage generation from the PV panels and the temperature variation on their rear side. The results of the two PV panels are also compared with dimensionless values. Fig.4 (c) and (d) present the ratio of measured data. These graphs clearly show that: (i) the two PV panels have almost the same behavior on the first day, without cooling. The variation in their temperature ratios is less than 15% while that of their voltage generation is less than 3%. The temperature of the PV panels with the cooling system is a little higher when the water is not supplied because the cloth on the rear side reduces convection. (ii) when the cooling system is active at hour 39.7, as shown in Fig.4(d), significant improvements in voltage generation are achieved. The variation of their temperature ratios is more than 50%, while that of their voltage generation is 10%. It is thus seen that temperature monitoring by our self-powered wireless sensor can improve the output of PV panels by controlling a water-cooling system automatically.

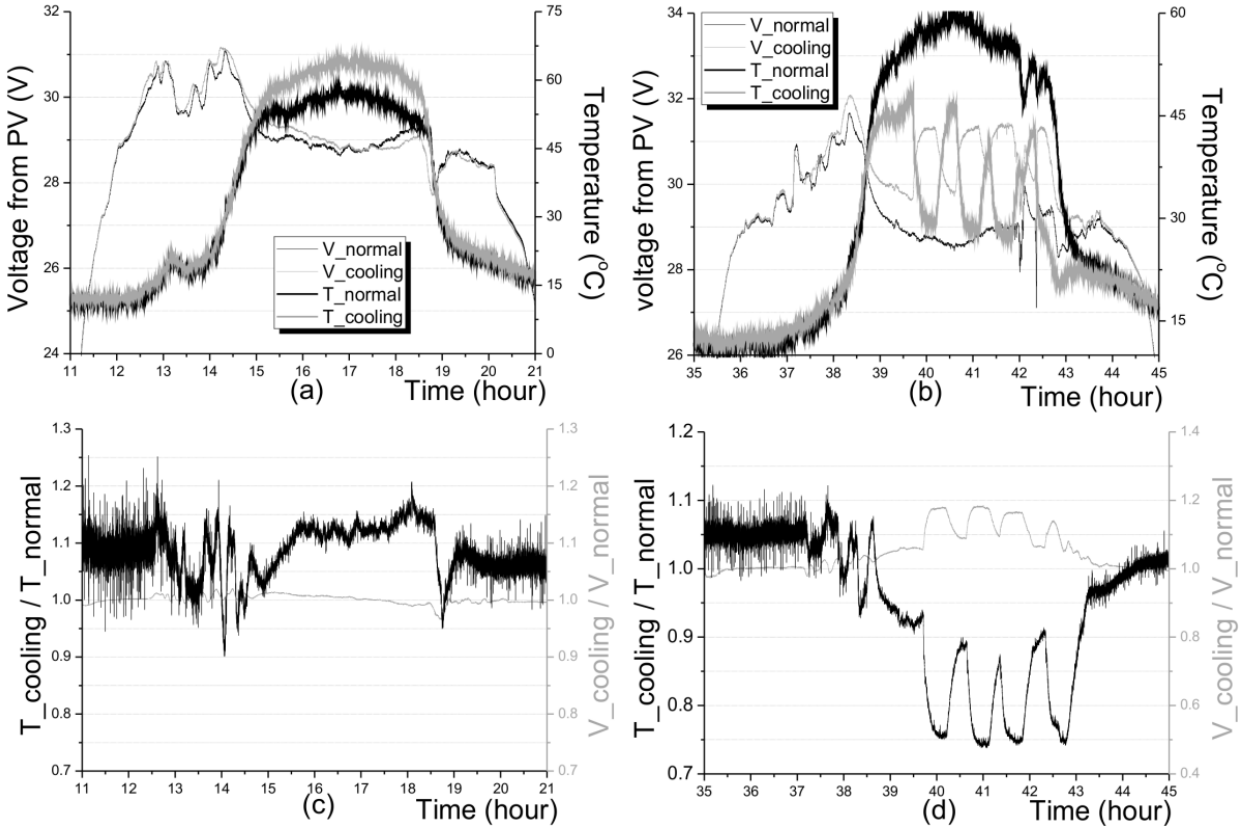

Fig. 4. Experimental results of the PVs with and without cooling: (a) and (c) are performance during the first day; (b) and (d) are performance during the second day.

Conclusion

In this study, a smart cooling system for PV panel is developed. The framework of independent wireless temperature sensor nodes was used to improve the performance of a PV panel. The feasibility of the proposed wireless application was proved step by step. The solar thermal micro-generator based on a thermoelectric device and phase change material was first tested for its

output voltage and power in outside conditions. The generated power was 2.15mw on a typical sunny autumn day, sufficient to drive both a temperature sensor and a wireless transmitter intermittently. Since the generated voltage was not sufficient to drive the electronic consumers directly, a step-up converter was adopted in the proposed power management circuit. The converter also solves the problem of the storage of electric energy, as the output of the TEG changes continually. With our prototype self-powered temperature sensing system, it can respond to the target temperature every two minutes when the input solar radiation is around 900W/m^2. The results of the autonomous temperature monitoring show that with a simple cooling system and with the harvested micro-energy, one can increase the performance of a PV panel (10% of voltage increase with ambient thermal loading in autumn).

Acknowledgement

This work was supported by Region Rhone-Alpes (France) through the project “Pivoter”, the National Natural Science Foundation of China (51205435) and the Key Scientific & Technological Projects of Chongqing (cstc2012ggC70001).

References

[1] Z. Abdin, M.A. Alim, R. Saidur, M.R. Islam, W. Rashmi, S. Mekhilef, A. Wadi, Solar energy harvesting with the application of nanotechnology, Renew.& Sust. Energ. Rev., 26 (2013) 837-852

[2] Q. Zhang, A. Agbossou, Z.H. Feng, A. Grillet, Phase change material and the thermoelectric effect for solar energy harvesting and storage, Proceedings of the ASME/JSME 2011 8th Thermal Engineering Joint Conference, March 13-17, 2011, Honolulu, Hawaii, USA (2011)

[3] S. Harihara Krishnan, D. Ezhilarasi, G. Uma, and M. Umapathy, Pyroelectric-Based Solar and Wind Energy Harvesting System, IEEE T. Sust. Energ., 5 (2014) 73-81

[4] Q. Zhang, A. Agbossou, Z.H. Feng, M. Cosnier, Solar micro-energy harvesting with pyroelectric effect and wind, Sens. Actuators A: Phys. 168 (2011) 335-342.

[5] A. Agbossou, Q. Zhang, G. Sebald, D. Guyomar, Solar micro-energy harvesting based on thermoelectric and latent heat effects. Part I: Theoretical analysis, Sens. Actuators A: Phys. 163 (2010) 277-283.

[6] Q. Zhang, A. Agbossou, Z.H. Feng, Mathieu Cosnier, Solar micro-energy harvesting based on thermoelectric and latent heat effects. Part II: Experimental analysis, Sens. Actuators A: Phys. 163 (2010) 284-290.

Advanced Materials Research Vols. 986-987 (2014) pp 1169-1172

doi:10.4028/www.scientific.net/AMR.986-987.1169

Adaptive Notch Filter Based Active Damping Control for Grid-connected Inverter

Ping WANG[1, a], Mengmeng CAI[2, b]

[1] Electrical Engineering and Automation Department Smart Grid Key Laboratory of Education Ministry, Tianjin University, Tianjin, 300072, China

[2] Electrical Engineering and Automation Department Smart Grid Key Laboratory of Education Ministry, Tianjin University, Tianjin, 300072, China

[a]email: pingw@tju.edu.cn, [b]email:cmm1990@hotmail.com

Keywords: Weak Grid; Adaptive Notch Filter; Active Damping Control

Abstract. The LCL filter is widely applied as interface between grid-connected inverter and grid due to the preferable high frequency attenuation characteristic. Under the condition of weak grid, impedance value of grid model cannot be ignored, the existence of grid impedance results in different LCL resonant frequencies, which will arise challenges of traditional active damping control. Based on the analysis of band pass filter using active damping control strategy, an adaptive active damping control is proposed in this paper by introducing the application of active notch filter, which can adjust the position of negative resonance point adaptively so as to manage sudden grid changes. Theoretical analysis and simulation results presented on the platform of grid-connected PV inverter system indicate the effectiveness and adaptability of this active damping strategy.

Introduction

Since more and more power electronic equipments have accessed to power grid, a plenty of non-linear loads have been introduced. Additionally, long-distance transmission lines could bring a possibility of superabundant line impedance, which will harm the grid due to underlying harmonic pollution and line voltage distortion. Gird in this condition called weak-grid, according to its weak connection with power secondary equipments. Simulation model of weak-grid does no longer consist of 220V AC stabilized-voltage power but annexed with a serial RL branch instead [1].

Weak-grid can impact on the inverter, which is the interface between distributed power generator and grid, conversely. References [2] indicates that variable line impedance can challenge the inverter stability, current control strategy, parameter design of LCL filter as well as the adaptability of active damping control and so on.

This paper aims at the resonance point offset problem arisen by grid impedance variation. Applying the adaptive notch filter as a breakthrough, the paper proposes a new active damping method which can adjust the position of negative resonance point adaptively so as to manage sudden grid changes.

Adaptive Notch Filter Based Active Damping Control Strategy

Since band-reject filter can realize a complementary function of band-pass filter, which means band-pass filter can be replaced by band-reject filter to achieve the same active damping control efficiency showed in references [3]. Besides, adaptive notch filter is derived to have the equivalent transfer function of band-reject filter expressed as Eq.(1) [4].

$$\frac{\varepsilon(\mathrm{s})}{x(\mathrm{s})}=\frac{s^2+\omega_o^{\,2}}{s^2+\dfrac{\mu A^2}{\tau}s+\omega_o^{\,2}} \tag{1}$$

Without adding excess sensor, inserting the adaptive notch filter in front of the generator element of modulating wave, a new adaptive notch filter based active damping control strategy is proposed whose overall framework is demonstrated in Fig.1.

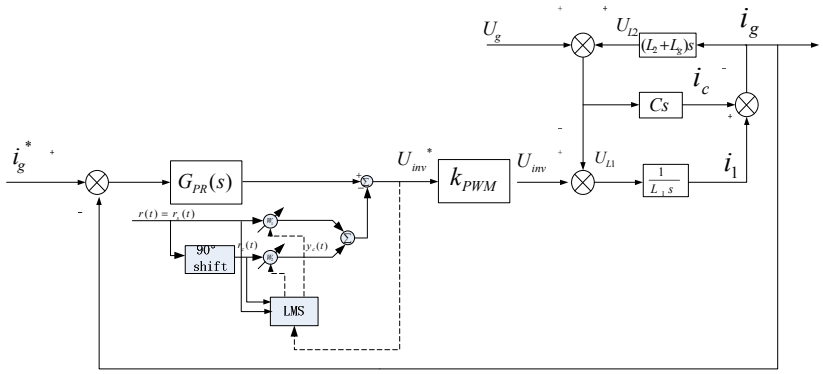

Fig.1.Framework of Adaptive notch filter based active damping control strategy

Where signal U_{inv} stands for the finally modulation wave, which comes out through a calculation of PR current regulator, is being sent into PWM generator module. A unity-negative feedback circuit is applied here by taking sampling of the grid-side current signal I_g, forming the whole control framework.

Accordingly, system open loop transfer function can be obtained as below:

$$G_o(s)=\mathrm{G}_{PR}(s)\frac{k_{pwm}G_{ANF}(s)}{L_1(L_2+L_g)Cs^3+(L_1+L_2+L_g)s} \tag{2}$$

$$G_{ANF}(\mathrm{s})=\frac{\varepsilon(\mathrm{s})}{x(\mathrm{s})}=\frac{s^2+\omega_o^{\,2}}{s^2+\frac{\mu A^2}{\tau}s+\omega_o^{\,2}}$$

Where represents the transfer function of adaptive notch filter. When resonance frequency is reached, system pole - zero cancellations happen. As a result, resonance peak of old system is effectively controlled.

Eq.(2) could be written in the simplified form as follows:

$$G_o(s)=G_{PR}(s)\frac{k_{pwm}}{L_1(L_2+L_g)Cs(s^2+\frac{\mu A^2}{\tau}s+\omega_o^{\,2})} \tag{3}$$

System comparison open loop bode plot is drawn as Fig.2 for further analysis, according to Eq.(2) and Eq.(3).

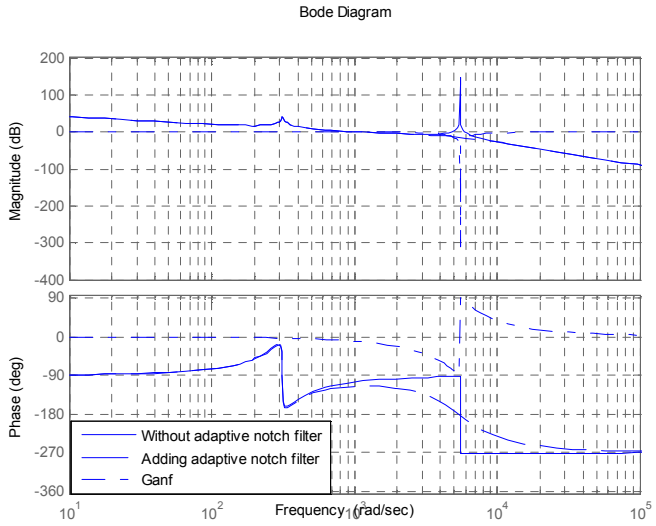

$(L_1=1.2\mathrm{mH}, L_2=0.5\mathrm{mH}, C=83\mu\mathrm{F}, L_g=0.1\mathrm{mH})$

Fig.2. System Bode Plot

Comparing three curves in the figure, an obvious positive resonance peak could be found in straight line represented system, which demonstrates a potential instable factor included in the original system. At the same frequency point, band-reject filter link represented chain dotted line system shows a negative resonance peak, which can overlay with the preceding positive resonance

peak. Therefore there is no resonance peak existing in the new method introduced system, consequently unstable factor has been eliminated.

Additionally, Bode plot of high-frequency band and low-frequency band are completely unaffected by the introduction of band-reject filter, which means this active damping control strategy has no negative influence on the high-frequency attenuation efficiency of LCL filter and it also preserves the favorable tracing performance of PR controller. From the phase perspective, original system has a 180° phase mutation problem generated by conjugate poles, which is introduced by LCL filter, has been resolved to some extent.

Test results

Fig.3 and Fig.4 respectively represents the grid-connected current FFT diagrams for system before and after introducing the adaptive notch filter based active damping method. Comparing these two pictures, we can easily find a significant decrease of harmonic contents happened in Fig.4 at the resonance frequency (873Hz) and near frequency band compared to Fig.3. Meanwhile, table.2 lists the detail percent content of specific frequency point, which also reflects a remarkable harmonic attenuation characteristic around resonance frequency by this new method. Accordingly the effectiveness of this active damping method has been testified.

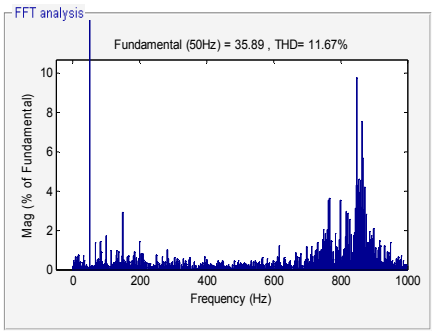

Fig.3 Grid-connected current I_g FFT (Without adopting active damping control)

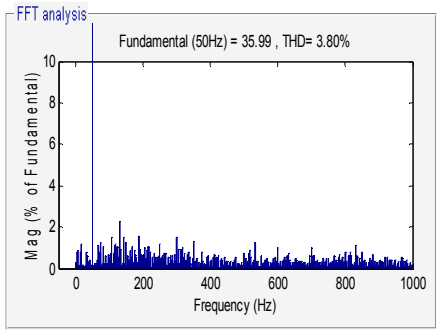

Fig.4 Grid-connected current I_g FFT (Adopting active damping control)

Table.1 Harmonic contents comparison

Frequency/Hz	contents/%(Fig.3)	Frequency/Hz	contents/%(Fig.4)
860	4.56	860	0.20
865	7.53	865	0.20
870	3.08	870	0.45
875	1.11	875	0.07
880	0.14	880	0.12
885	1.33	885	0.23
890	1.49	890	0.18

After varying the value of L_g from 0.1mH to 0.5m, the new resonance frequency changes to 748Hz. Still using resonance frequency harmonic suppression results to measure the efficiency of two control strategies shown in Fig.5 and Fig.6. In Fig.5[5], the frequency percent content around new resonance frequency shows a slightly decrease, which prove that there has no adaptability for the traditional control method under a weak-grid condition. Also Table.2 demonstrates the detail harmonic content of each frequency point.

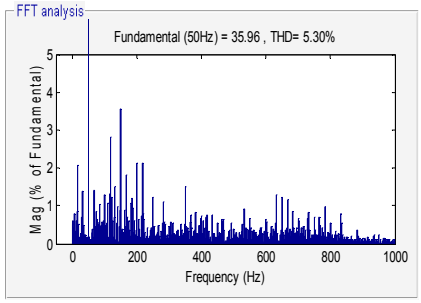

Fig.5 Traditional active damping control result

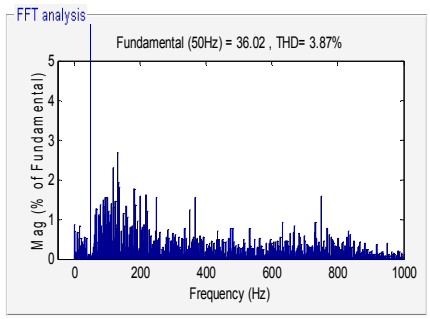

Fig.6 Adaptive active damping control result

In this group of comparison, the harmonic contents of new resonant frequency and adjacent frequency in Fig.6 is smaller than what in Fig.5, which proves that adaptive notch filter based active damping control has a better attenuation performance compared to traditional band-reject filter based active damping control.

Table.2 Harmonic contents comparison

Frequency/Hz	Content/%(Fig.5	Frequency/Hz	Content/%(Fig.6)
735	0.91	735	0.31
740	0.19	740	0.05
745	0.52	745	0.34
750	0.70	750	0.05
755	0.14	755	0.01
760	0.44	760	0.23
765	0.19	765	0.12

Although the downward trend in this comparison experiment is not as significant as the former one, when system resonance frequency shifts slightly, the new resonance frequency still can be attenuated by traditional active damping control to some extent for the reason that original system bandwidth is wide enough. However, according to the data shown in Table.2, some difference control result between the traditional active damping control and new control method still can be found by observing above data. Therefore, the adaptability of proposed method in this paper is verified also.

Conclusion

This new active damping control method needs to be implemented on a premise of accurate measurement of power grid impedance value. Although extra power grid impedance on-line measurement technology is costly, however control structure proposed in this paper is quite simple and can be easily implement, besides will not bring other harmonics. What's most important, it can bring a remarkable improvement of adaptability for adaptive damping control under weak-grid situation. Above all, adaptive notch filter based active damping control proposed in this paper has a certain application prospect and development space.

Acknowledgement

In this paper, the research was sponsored by the Research Fund for the Doctoral Program of Higher Education (Project No. 20120032110070).

References

[1] LU Li, LIU Fang, ZHANG Xing, et al. Study of controlling a single-phase photovoltaic Grid-connected Inverter operating in a weak grid [J]. Power Electronics, 2012: 46(5):36-38.

[2] Liserre, M., Teodorescu, R., Blaabjerg, F.. Stability of photovoltaic and wind turbine grid-connected inverters for a large set of grid impedance values [J]. IEEE Transactions on Power Electronics, 2006: 21(1):263-272.

[3] HUI Junying, CAI Ping, MA Xiao-min. Applied study of active notch filter[J]. Acta Acustica,1991: 16(1):19-24.

[4] CHANG Jianhua, QUAN Shuhai. Algorithm, Principle and Computer Simulation of the Adaptive Filter Wave Trap [J]. Journal of Wuhan automotive polytechnic university, 1998: 20(3):46-49.

[5] XU Jinming, XIE Shaojun, XIAO Huafeng. Research on Control Mechanism of Active Damping for LCL Filters [J]. Proceedings of the CSEE, 2012:32(9):27-33.

Advanced Materials Research Vols. 986-987 (2014) pp 1173-1177

doi:10.4028/www.scientific.net/AMR.986-987.1173

Advanced Metering Infrastructure and its Back Software Architecture for Future Power System

Xiangyu Kong[1, a], Bo ZENG[2], Kai WANG[2], Yi Zeng[1, b], Qun Yang[1]

[1] Key Laboratory of Smart Grid (Tianjin University), Ministry of Education, Tianjin, 300072, China

[2] Electric Power Research Institute of Guangxi Power Grid Corporation, Nanning, China

[a]email: kongxy06@163.com, [b]email: zengyiroom@163.com,

Keywords: Advanced Metering Infrastructure, Meter Data Management System, Network Management System, Demand Response

Abstract. Governments have become increasingly concerned about the development of the smart grid, and a series of smart grid demonstration projects have been started. Multi-levels common and integrated infrastructure architecture for smart grid demonstration project was proposed in the paper. The implementation and operation of its back office systems were presented, which include the design, development and deployment of network management system, meter data management system, load control systems, community level and home energy management system, and web portal. The integration between different parts and their managements were also were proposed.

Introduction

Advanced Metering Infrastructure (AMI) is recognized to be the first step for power system to move towards smart grid, which will not only support automated meter readings, customer home appliance connections, but also future distribution automation, substation automation and possibly mobile workforce management and other advanced applications [2]. Areas of AMI that cover the scope of a smart grid include the following [3-6]: (1) the end-use systems and related distributed-energy resources (e.g., building and factory loads, distributed generation, storage, electric vehicles); (2) management of the generation and delivery infrastructure at the various levels of system coordination (e.g., transmission and distribution control centers, regional reliability coordination centers, national emergency response centers); (3) the information networks themselves (e.g., remote measurement and control communications networks, inter and intra enterprise communications, public Internet), and (4) the financial and regulatory environment that fuels investment and motivates decision makers to procure, implement, and maintain all aspects of the system (e.g., stock and bond markets, government incentives, regulated or non-regulated rate-of-return on investment).

Fig.1 shows the technological development of smart grid from the conventional grid. In conventional electric grids we have only one direction of communication from the grid to the consumer. In smart grids we have two way communications between the utility and the consumers. With the help of the bi-directional communication the generation of electricity can be made dynamic. In smart grids with distributed resources a design of grid which is smart with bi-directional communication is implemented and it will most importantly include more number of renewable and eco-friendly sources of power gene ration [7].

The purpose of this paper is to present a description of advanced metering infrastructure for smart grid demonstration project of China, which is

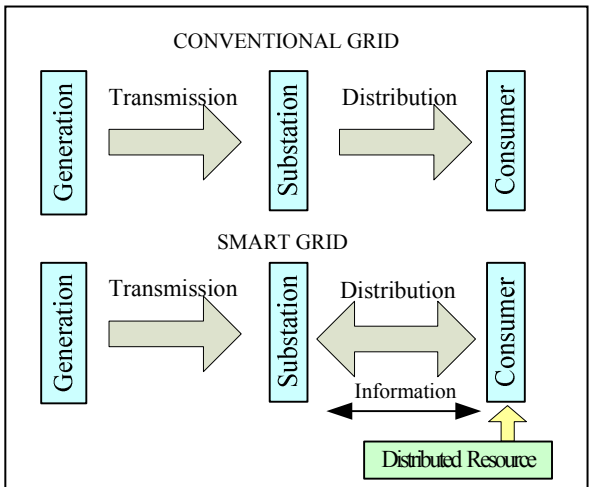

Fig. 1 Technological development of Smart Grid

aimed at improving customer understanding and efficiency of their electricity usage, making distributed power "plug and play accesses", reducing operations and maintenance costs, and so on. The project AMI and its back office architecture were promoted, which may provide a source of inspiration for the demonstration and application of other smart grid projects

Smart Grid Infrastructure Architecture

The smart grid is proposed use digital technology to improve reliability, security, and efficiency (both economic and energy) of the electric system from large generation, through the delivery systems to electricity consumers and a growing number of distributed-generation and storage resources [8]. Integrated smart gird infrastructure architecture is illustrated in Fig. 2, which contains three network levels, WAN, LAN and HAN. The communication network also serves as the control link or information link between the operational command center to different end devices for control or customer services display and alarm. These end devices can be control switches for capacitor banks or load control devices. Hence the communication system, by implication, is basically a two-way communication system and practically serves as a neural network of the system.

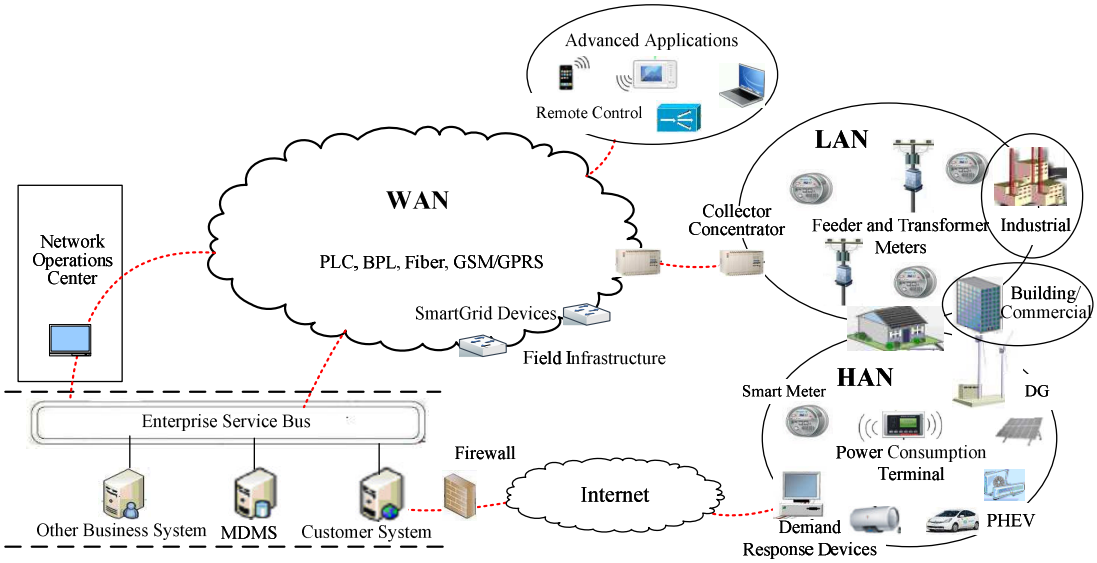

Fig. 2 Multi-level common and integrated smart gird infrastructure architecture

AMI is not a single technology, but rather an integration of many technologies that provides an intelligent connection between consumers and system operators. AMI gives consumers the information they need to make intelligent decisions, the ability to execute those decisions and a variety of choices leading to substantial benefits they do not currently enjoy. In addition, system operators are able to greatly improve consumer service by refining utility operating and asset management processes based on AMI data.

Through the integration of multiple technologies (such as smart metering, home area networks, integrated communications, data management applications, and standardized software interfaces) with existing utility operations and asset management processes, AMI provides an essential link between the grid, consumers and their loads, and generation and storage resources. Such a link is a fundamental requirement of a Modern Grid.

Back Software Architecture for Future Power System

Back Software of the AMI is responsible for managing all of the activities associated with identifying and designing the appropriate business process requirements for the information technology needs and then designing, developing, procuring and implementing the resulting automation (hardware and software) that will be required to establish two-way system communications between meter at the customer's premise and power company's back office

systems. Critical elements of these systems include the design, development and deployment of the Network Management System, Meter Data Management System (MDMS), load control systems, Community level and home Energy Management system (EMS), web portal development for energy information and program support, along with integration between these systems and other legacy systems, such as outage management.

In the back software architecture, Network Management System is the gateway, with which, all commands sent to and all data received from the smart meters and field infrastructure. The system includes three subcomponents: the head-end component to communicate with the meters; the network management console to optimize and manage the individual meters and network field infrastructure and how they work together; and the cryptographic services component to secure the data and communications of the entire network. A network operations center should be setup to oversee the operations of the AMI telecommunications network.

MDMS is the repository of the meter and event data from smart meters and variety sensors. The important system provides all of the validation, editing and estimating necessary to support customer usage calculation. As the system of record for meter data, other systems that require meter data will retrieve such data from the MDMS. Aside from meter reading and billing support functions, the MDMS also receives and routes all messages from the meter population to the appropriate systems. This includes alarms for meter failures, power outage, demand response messages, service switch operation and messages from associated HAN devices.

Load Control Systems are the management and control system to manage the smart thermostat and other new dispatchable load resources. For customers that sign up for demand response programs allowing power company to control their devices, remotely during demand response events, the Load Control Systems are responsible for dispatching the commands through the network to the devices that will ultimately respond. The information about the customer, their participation in demand response programs and the configuration of their meters and devices must be received from the MDMS and Network Management System.

With bi-directional flows of energy and coordination through communication mechanisms, a smart grid should help balance supply and demand and enhance reliability by modifying the manner in which customers use and purchase electricity. These modifications can be the result of consumer choices that motivate shifting patterns of behavior and consumption. These choices involve community level EMS and home EMS.

Distributed energy resources management is an important part of this EMS: The ability to connect distributed generation, storage, and renewable resources is becoming more standardized and cost effective. Several other concepts associated with a smart grid are in a nascent phase of deployment these include the integration of micro-grids, electric vehicles, and demand response initiatives, including grid-sensitive appliances [9]. Another important function is the capability to interface with meters for plug-in hybrids through the HAN communication interface which might allow for design of special plug-in hybrid programs. MDMS would need to be aware of the program the customer is participating in and the customer's vehicle information. This would require some additional enhancements to the MDMS and surrounding interfaces.

Web Portal will provide each customer the opportunity to view their own usage data, collected by smart meters, through the internet via the internet website. In order to accomplish this task, the MDMS system will process and send the customer's data to a web portal for access to their meter data. The system may require some analytical preparation of the data so the customer can use it as well as integration with web portal so the data may be displayed. The connection is secure so that customers only may view their own personalized data. Further development that support personalization and simplification of choice related to programs and services available, such as more robust functionality including sophisticated analytics that would relate the usage data to the customer's program and bill, is developing.

The Way to Integration of Different Parts

The relationship between the smart gird back office systems is depicted in Fig.3. The lines in between the systems represent integrations that transfer data and information between the systems that allow each system to operate and enable the proposed business processes.

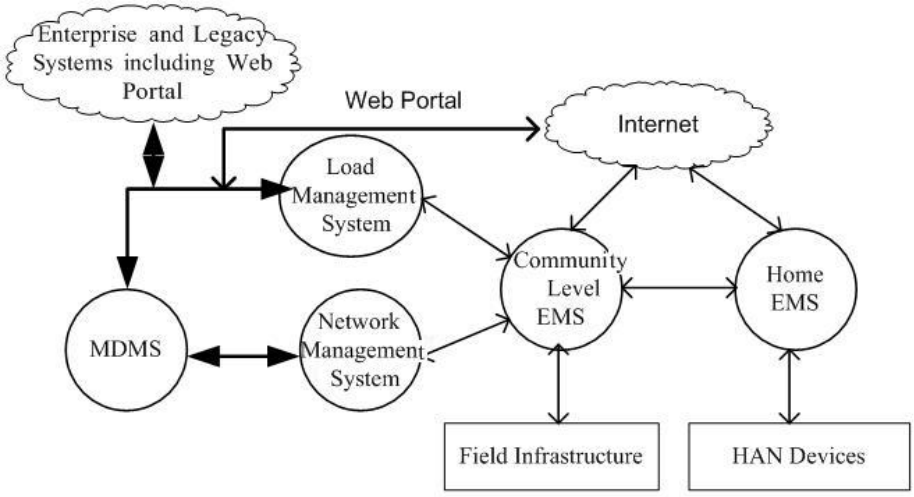

Fig. 3 Back software architecture for demand response

The integration of different parts to architecture of smart grid are shown as follow way.

A. Integrating Network Management System and MDMS

The MDMS integrates with Network Management System to facilitate two way communications between the meter at each customer's premise with MDMS, load control systems and Community level and home EMS. The first step is to identify business processes that are changed or enabled through the implementation of power company. These business processes are designed and then analyzed to identify the data and commands necessary to enable the new or changed business process. Individual interfaces are designed and developed to enable the flow of data between these two systems. The volume of the data and frequency with which each interface must run determines the software and hardware design and sizing necessary to support the integration.

B. Integrating MDMS with Load Control Systems

The Load Control systems are designed to support enabled demand response programs across distribution control area. As such, the MDMS must be aware of those customers who are on demand response rates, which demand response program each customer is enrolled in, and when a demand response event has occurred. This will allow the MDMS to calculate the customer's usage and monitor their response to the event accordingly. In turn, the billing system, through the integration described above will receive the information necessary to accurately bill the customer according to the terms of the appropriate demand response program.

C. Integrating MDMS with Community level and home EMS

Community-level and home EMS require integration with the MDMS should include time-of-use rates with a critical peak price overlay (subject to regulatory approval) and related information services in conjunction with advanced metering to encourage consumers to reduce peak demands or shift consumption from on-to off-peak periods and then to measure and validate the demand response. The capability to perform contract meter reading (gas/water meter reads) is possible.

D. Integrating MDMS with Web Portal

The MDMS integrates with web portal to provide interval usage data for each customer via the Internet. In order to accomplish this task, the MDMS system will process and send the customer's data to a web portal to provide customer to access their meter data, and it expenses include labor necessary to maintain software and hardware for integration and within the MDMS and Web Portal to provide customers access to their meter data on-line.

To ensure successful development and implementation of back office systems, structured project management oversight and governance will be utilized. Processes and tools will be put in place to manage scope, schedule, budget, and resources consistent with the Project Management Institute's Project Management Body of Knowledge. Appropriate governance will also be put in place to manage issues identification, escalation, and resolution.

Conclusion

There are various uncertainties and risks that may affect the integration and enhancements of the integrated infrastructure architecture. Risks including vendor and the integration and enhancements of the power company legacy systems should be analyzed. With the implementation of the project, Nanning, the capital city of Guangxi Province and the demonstration city of this project, is installing two-way communication AMI system, customer systems and programs to provide consumers with information, choices, and technologies to better manage their electricity costs while reducing distribution system peak demand and correlated pollution and cost impacts.

Acknowledgement

In this paper, the research was sponsored by the National High Technology Research and Development Program 863 of China (2011AA05A115).

References

[1] United States Department of Energy Office of Electric Transmission and Distribution. Grid 2030: a national version for electricity's second 100 years[R] [EB/OL]. http://www.oe.energy.gov/Documents_and_ Media/ Elec_Vision_2-9-4.pdf.

[2] Wenpeng Luan，Sharp D，Lancashire S. Smart grid communication network capacity planning for power utilities [C]. IEEE/PES Transmission & Distribution Conference & Exposition (T&D), 2010, (4) 1-5.

[3] Rosemead, California. EDISON SMARTCONNECT development funding and cost recovery Volume 2: Deployment Plan[R], 2007.

[4] Zhang Luhua, Yi Zhonglin,Wang Sitong. Effects of Advanced Metering Infrastructure (AMI) on relations of Power Supply and Application in smart grid [C]. China International Conference on Electricity Distribution (CICED), 13-16 Sept. 2010, Beijing, China: 1-5.

[5] Gungor V C, Sahin D, Kocak T. Smart Grid Technologies: Communication Technologies and Standards [J]. IEEE Transactions on Industrial Informatics. 2011, 7(4):529-539.

[6] Thimmapuram P R, Kim Jinho. Consumers' price elasticity of demand modeling with economic effects on electricity markets using an agent-based model [J]. IEEE Transactions on Smart Grid, 2013, 4(1): 390-397.

[7] Sellvam, K Srinivas, G S Ayyappan, et al. Advanced Meterring Infrastructure for Smart Grid Applications [C. International Conference of Recent Trends In Information Technology (ICRTIT), 19-21 April 2012, Chennai, Tamil Nadu: 145-150.

[8] Rahimi F, Ipakchi A. Demand Response as a Market Resource under the Smart Grid Paradigm[J]. IEEE Transactions on Smart Grid, 2010, 1(1): 82-88.

[9] Beidou F B, Morsi W G, Diduch C P, et al. Smart Grid: Challenges, Research Directions and Possible Solutions[C]. 2010, 2nd IEEE International Symposium on Power Electronics for Distributed Generation Systems (PEDG), 670-673.

Advanced Materials Research Vols. 986-987 (2014) pp 1178-1182

doi:10.4028/www.scientific.net/AMR.986-987.1178

An Earthquake Emergency Alarm System for Power Plants based on Programmable Automation Controller

Jihua FU[1, a], Zhitao LI[1, b], Qiao TAN[1], Jianjun WANG[1]

[1]Key Laboratory of Crustal Dynamics, Institute of Crustal Dynamics, China Earthquake Administration, Beijing, 100085, China

[a]email: fujh@email.eq-icd.cn, [b]email: zhitao.lee@163.com

Keywords: Power Plants; Earthquake; Emergency Alarm System; Programmable Automation Controller

Abstract. To avoid or relief the fatal damage of an earthquake, a seismic automatic alarm system was put forward to meet the needs of power plant. Both a digital accelerometer AKE392B and a programmable automation controller SC200AD-1 were introduced to compose the earthquake emergency alarm system. The AKE392B converts the acceleration of ground motion into a series of digital signal, and this digital signal is transferred to the SC200AD-1 by the field bus EIA485. The PAC in the system is applied to collect the ground motion data, remove the non-seismic interrupts, access an earthquake's intensity, carry out emergency auto-handling actions by ON/OFF values, and generate emergency alarm to its parent system, power plant management system. Through theory and experiment analysis, the earthquake emergency alarm system could be easily built to measure the ground motion acceleration in accuracy, and generate the seismic emergency alarm rapidly.

Introduction

Power plant, one of the most important parts of lifeline engineering systems, maintains the functions of our modern society. Many kinds of natural disasters especially earthquake can do the greatest threats to power plants and power supply systems. These threats are not only reflected in the severe damages of the power supply system itself in an earthquake, but also in a series of serious secondary disasters, such as triggering fire and hazardous substances leaking [1] [2]. Power plant is supposed to be strong enough to survive from the attacks by an earthquake. But only by strengthening of the buildings and components is a non-commercial and time-consuming plan [3]. An earthquake early warning system could probably provide the critical alarms and information needed to protect power plants against an earthquake. Unfortunately, research on earthquake early warning system was not good enough to solve the problem completely: one reason is that there is about a 30 kilometers' blind zone on the meizoseismal area of an earthquake and another reason lies in that the false rate is still too high to impact the routines of a power plant [4]. Although earthquake early warning system does not work at present, the ground motion measurement can assessed the earthquake damage rapidly. Therefore, an earthquake emergency alarm system based on the onsite ground motion measurement might provide an easy, effective and reliable way of disaster reduction. A seismic emergency auto-handling system was put forward to protect the water supply system [5]. Considering the complexity of the power plant management system, a programmable automation controller (PAC) based earthquake emergency alarm system was proposed, which was regarded as a subsystem of the power plant management system. Comparing with the programmable logic controller (PLC), PAC is much powerful in data processing beside its openness and flexibility.

The Earthquake Emergency Alarm System's Development

As shown in Fig. 1, the earthquake emergency alarm system was composed by some distributed seismic accelerometers, a PAC, and several actuators, for example ON/OFF values. The earthquake emergency alarm system was connected by the field bus EIA-485, and performed as a subsystem of the power plant management system.

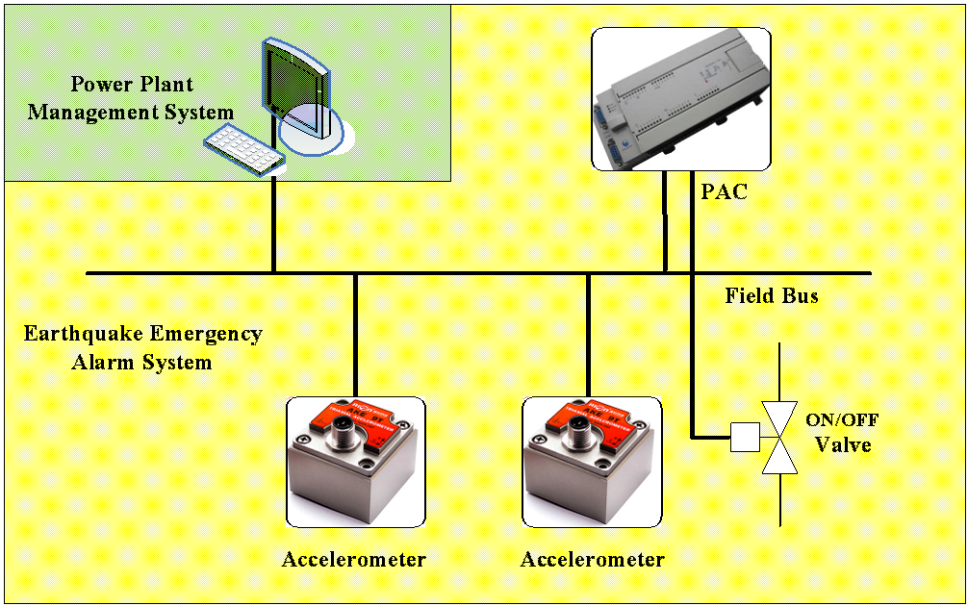

Fig.1. The block diagram of the earthquake emergency alarm system

Several three-axis accelerometers, AKE392B, were mounted around a power plant distributed to measure the acceleration of the ground motion. AKE392B's scale factor in the full range of long-term stability and the deviation are typically less than 0.1%. This specification makes AKE392B a reliable solution for the seismic acceleration measurement. In addition, due to its digital output and different address codes, several AKE392Bs were used to form a multi-point measurement system, which helped the earthquake emergency alarm system to cover a broad range and to reduce false operation.

The specifications of the AKE392B were listed below:

- Measuring Range: ±2g (X, Y, and Z axis);
- Frequency Band width: 1-80Hz;
- Nonlinearity: ±1% F. S.;
- Resolution/threshold (@1Hz): < 1mg;
- Interface: EIA-485;
- Power Supply：9-36V DC.

A PAC, SC200AD-1 was introduced to the earthquake emergency alarm system. The SC200AD-1 acted as a captain of the alarm system: collecting ground motion data from accelerometers, removing the non-seismic interrupts, accessing an earthquake's intensity, carrying out emergency auto-handling actions by ON/OFF values, and generating emergency alarm to its parent system, power plant management system. SC200AD-1, one of PAC, combined the good features of a personal computer (PC) and a PLC, which made it openness, reliability, and high-performance computing.

Software's Design

Due to the flexible interface of AKE392B and the openness of SC200AD-1, the software of the earthquake emergency alarm system was easily built. The AKE392B's acceleration data frame was shown by Fig. 2.

Identifier (1byte)	Data Length (1byte)	Address code (1byte)	Command word (1byte)	Date domain	Check sum (1byte)
0x68	0x0D	0x00	0x84	0x00 0x02 0x10 0x10 0x08 0x50 0x00 0x05 0x04	0x32

Fig.2. The acceleration data frame of AKE392B

The data domain given by hexadecimal in the example above was the acceleration values measured by AKE392B, where the acceleration on X axis was 0.210 g, the acceleration on Y axis was -0.850 g, and the acceleration on Y axis was 0.504 g.

SC200AD-1 supports the NI's Labview to develop its software. Based on the data frame given by Fig. 2, the acceleration data's collection program was built, which was shown by Fig. 3.

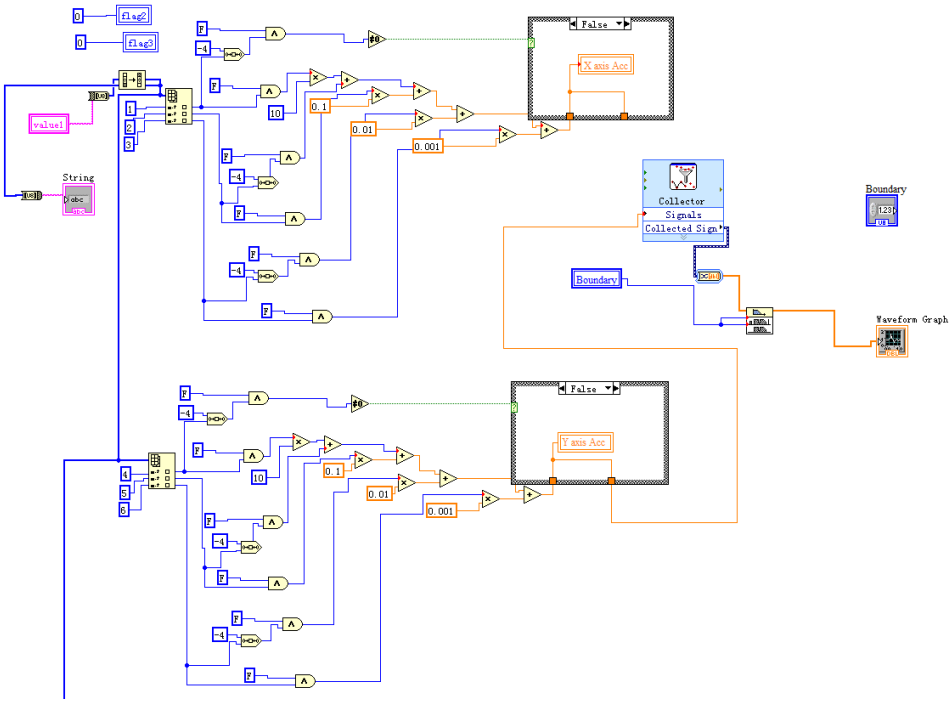

Fig.3. The program of acceleration data's collection

Using the program above, the back ground noise of the ground motion and a small ground motion event were recorded, which were shown by Fig. 4 (a) and (b) respectively.

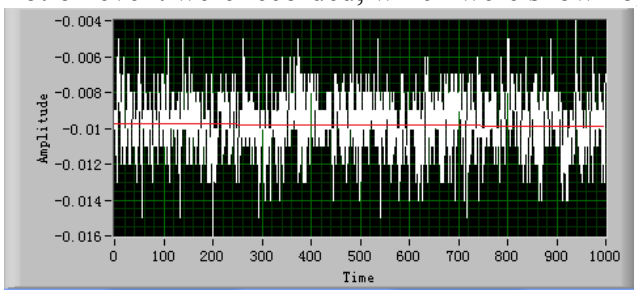

(a) The back ground noise

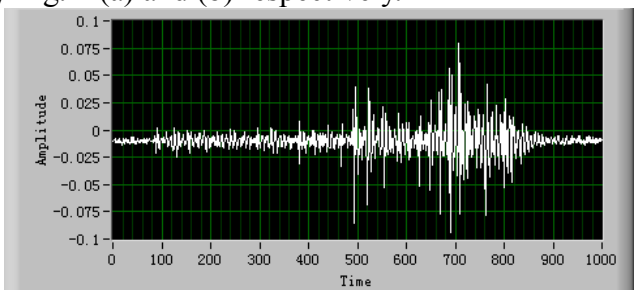

(b) The small ground motion event

Fig.4. The acceleration data collected

There are two non-seismic interrupts: the baseline drift and the impulse noise. These interrupts not only would cut down the accuracy of the earthquake intensity's assessment, but also might cause some serious false operations for the earthquake emergency alarm system. Therefore these two noises should be removed as much as possible. And two kinds of digital filters were used to do the signal pretreatments.

One filter was a high pass filter, which was used to revise the baseline drift in long period. It could be described by the recursion Eq. (1) [6].

$$a_j = \frac{1+q}{2} \cdot (a_j^* - a_{j-1}^*) + q \cdot a_{j-1} \tag{1}$$

where $a_j^* (j = 1, 2, \cdots$ was the acceleration sequence before filtering, and $a_j (j = 1, 2, \cdots$ was the acceleration sequence after filtering. And q was a filter parameter. The q's value determined the cutoff frequency of the high pass filter, and it was close to 1 but less than 1. Here the q's value was set to 0.99. By applying the high pass filter the baseline was shown by the red line on Fig. 3 (a).

After high pass filter, another filter, median filter, was employed to remove the impulse noise. Median filtering is a popular method of noise removal, because its non-linear technique could effectively suppress impulse noise while preserving edge information. Specifically, the main idea of the median filter was to run through the signal entry by entry, replacing each entry with the median of neighboring entries:

$$y(i) = meadian\{x(j), j \in (i-m, i+m)\} \quad (2)$$

where $(i-m, i+m)$ represents a neighborhood centered around location i in the acceleration sequence. m was the maximum of the distance between i and j. Here m was set to 2.

By applying the median filter above the back ground noise of the ground motion and a small ground motion event were both presented by Fig. 5 (a) and (b). And it was clearly shown by comparing Fig. 5 (a) with Fig. 4 (a) that the back ground noise was compressed effectively.

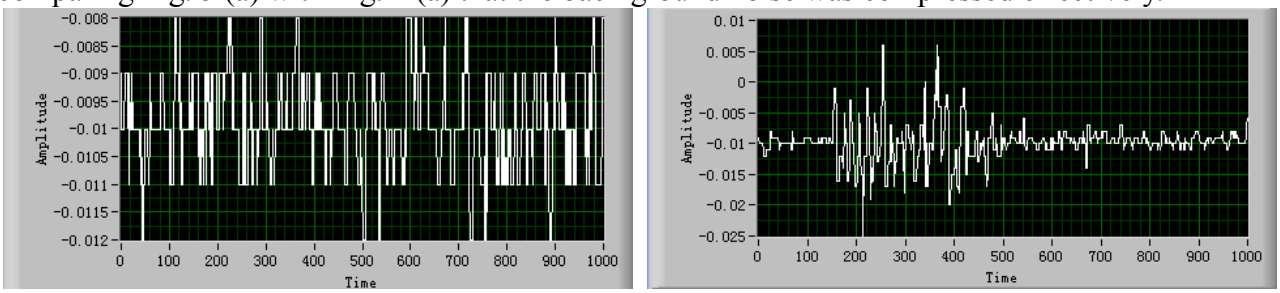

(a) The back ground noise (b) The small ground motion event

Fig.5. The acceleration data filtered

Before carrying out emergency auto-handling actions or generating emergency alarm, the earthquake emergency alarm system should access the earthquake's intensity at first. Recent research showed that the misjudging rate was the smallest using spectral intensity to assess seismic intensity or the damages of the lifeline engineering system [7]. Taking this into account, the spectral intensity was employed in the alarm system, and it was obtained by:

$$SI = \int_{0.1}^{2.5} S_v(\xi, T)dt \quad (3)$$

where ξ was the damp of the single degree of freedom (SDOF), T was the period, and S_v was the SDOF's velocity response. To get the peak spectral intensity in time, some immediate processing methods in the time domain were used [8].

Experiment Analysis

The seismic accelerometers were the front end of the earthquake emergency alarm system. Their performances would affect the whole system's abilities. AKE392B's performances were tested by attached on a closed-loop control vibration system WS-Z30. The WS-Z30 exported a serial of acceleration signals with the same amplitude (0.25g). The outputs of AKE392B and the standard sensor were both recorded at different frequency points (1, 2, 5, 10, 20, 40, 60, and 80Hz). The test results were shown by Tab. 1.

Tab.1. The test results of AKE392B's performance

Frequency (Hz)	1	2	5	10	20	40	60	80
Sensitivity (V/g)	0.857	0.857	0.856	0.855	0.857	0.855	0.848	0.852
Deviation (%)	0.23	0.23	0.12	0.00	0.23	0.00	-0.82	-0.35

The test results indicated the sensor AKE392B could measure ground motion with sufficient accuracy, and their maximum of sensitivity deviations on frequency response were -0.82% and less than 1%.

Conclusion

Through the preliminary theory and experiment analysis, the earthquake emergency alarm system possessed the following features:

- The earthquake emergency alarm system could be easily built and act as a subsystem of power plant's management system;
- The PAC, SC200AD-1, made the earthquake emergency alarm system a full use of the advantages of PC and PLC;

- High pass filter and median filter were both effective to remove the non-seismic interrupts, which could improve the accuracy of the earthquake intensity's assessment and avoid some false operations unwanted;
- The accelerometer AKE392B in the earthquake emergency alarm system could measure the ground motion acceleration with adequate accuracy in real-time.

Acknowledgement

This paper is supported by the research grant from Institute of Crustal Dynamics, China Earthquake Administration (No. ZDJ2012-16, No. ZDJ2013-27) and the National Nature Science Foundation of China (No. 50908215).

References

[1] O'Rourke, T., Bonneau, A. lifeline performance under extreme loading during earthquakes [J]. Earthquake Geotechnical Engineering, 2007 (6) 407-432.

[2] Li, H., Liu, C. Trends and prospects for research on disaster mitigation in lifeline engineering system [J]. Journal of Dalian University of Technology, 2005 45 (6) 156-161 (in Chinese)

[3] Martin WIELAND, Lothar GRIESSER, Christoph KUENDIG. Seismic early warning system for a nuclear power plant [C]. 12WCEE, 2000 (1781) 1-8.

[4] Allen, R., Kanamori, H., The potential for earthquake early warning in Southern California [J]. Science, 2003 (300) 786-789.

[5] Fu Jihua, Li Zhitao, Tan Qiao, et al. A seismic emergency auto-handling application system for the lifeline engineering system [C]. Disaster Advances, 2012 5(4) 833-837.

[6] Kanamori, H., Maechling, P., Hauksson, E. Continuous monitoring of strong motion parameters [J]. Bull. Seism. Soc. Am., 1999 89(1) 311-316.

[7] Wang, Y., Zhou, Z., Lan, R. A proposed method for instrumental intensity determination in west China using modified spectrum intensity [J]. Journal of Basic Science and Engineering, 2010 18(S) 119-128. (in Chinese)

[8] Rosenberger, A., Beverley, K., Rogers, G. The new strong motion seismic network in Southwest British Columbia, CANADA [C]. 13th World Conference on Earthquake Engineering Vancouver, B. C., Canada. 2004.

Advanced Materials Research Vols. 986-987 (2014) pp 1183-1186

doi:10.4028/www.scientific.net/AMR.986-987.1183

Analysis of Braking Energy Recovery in EV with EHB

Liang Zhou [1, a], Mengyang Zhao[1, b] , Xinyu Wang[1, c] and and Xichao Li [2,d]

[1] School of Automotive Engineering, Wuhan University of Technology, Wuhan 430070, China

[2] Hubei Research Institute of Products Quality Supervision and Inspection, Wuhan 430070, China

[a] ZhouLwhut@sina.com, [b] zmy469120891 @163.com,
[c] best.1987@163.com, [d] juliking0403@126.com

Keywords: Braking recovery, EHB, Coupling relationship, Energy flow

Abstract. The battery ability of recovering electricity plays a significant role in improving the regenerative braking performance. In this paper, a control for recovery of braking energy in Electric Vehicles (EVs) with electro hydraulic brake (EHB) is proposed, which makes the recovery transfer to the electric hydraulic pump of EHB directly, rather than being stored statically in the battery. An energy flow strategy was designed for the maximum braking energy recovery based on this control. The simulation results show higher energy recovery rate in comparison to the general recycling control.

Introduction

The amount of energy dissipated during vehicle braking is significant. The most advantageous development is to find a method to extend the mileage of EVs by recycling part of braking energy. However, the battery ability of recovering electricity is a decisive role to the process of the energy recovery. [1]

During the process of braking energy recovery in general EVs, the electric energy, transformed from kinetic energy, stores in the battery and releases when EVs starts. But the battery ability of recovering electricity hiders EVs maximize braking energy recovery. In EVs with EHB, the recovery transfers to the electric pump of EHB directly, which is utilized dynamically in the process of vehicle braking, so the battery is no longer the main energy storage unit. [2]

Control model

The actuator of EHB is a high-pressure accumulator, which power is supplied by a electric hydraulic pump. As the pressure of the accumulator will reduce during brake, the recovery can transfers to the electric pump of EHB directly to pump oil to maintain enough pressure. Excess electricity transfers to the battery if the generator is performing a power higher than the required power of EHB electric pump, otherwise, the battery to supplement electricity. That is to say, the recovery is utilized dynamically in the process of vehicle braking in the EV with EHB.

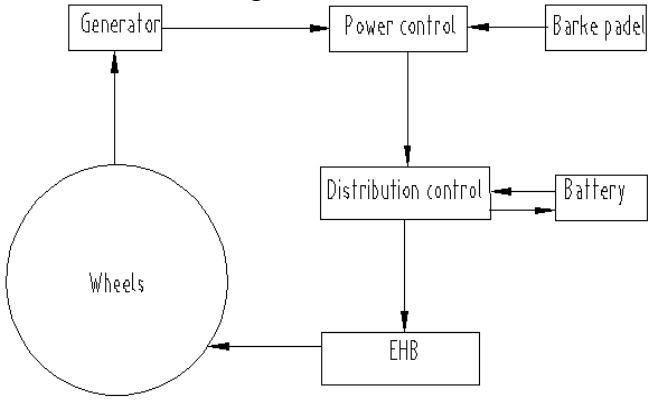

Fig 1. Model structure

Coupling between force and power

Brake Force Distribution. At the view of energy recovery, motor should supply brake force as much as possible by working as a generator during braking. As the motor is only connected to the front axle in this model, it means the actual brake force distribution curve more closing to horizontal axis in the braking force distribution diagram, more energy can be regenerated. But in order to avoid side slipping and keep the steering ability, this curve should be above the regulations limit curve declared by the ECR13. [3] The requirements are taken to design a control for brake force distribution to maximize braking energy recovery based on maintaining braking performance during braking, which does not need to take the battery ability of recovering electricity the into account.

Strategy for Braking Energy Recovery. Brake intensity, speed and the State of Charge (SOC) of battery are the key factors to the strategy for braking energy recovery, which are taken as the strategy inputs. The brake intensity can be reflected by the brake pedal position, while the actual speed can be traced by the current generated by the generator.

If the vehicle is in a state of emergency braking, regeneration doesn't work in the emergency braking in this strategy for the security.

If the EV speed is lower than a minimum vehicle speed, the charging efficiency of battery is very low to be charged. The regenerative brake force is no longer in existence at this state.

To supply sufficient brake torque and prevent overcharging, the regenerative braking should be prohibited to charge the battery when the SOC reaches the limit.

Linked with the motor characteristics between torque and speed, ultimate regenerative brake force can be calculated in various vehicle speed.

The brake force between front and rear wheels are distributed by the braking control module according to the maximal principal mentioned above. The front wheels brake force is divided into motor brake force and the front EHB brake force. All of the brake force act on EV power system to get the actual deceleration. The cooperation algorithm can be described as Fig 2.The regenerative force showed in Fig 3.

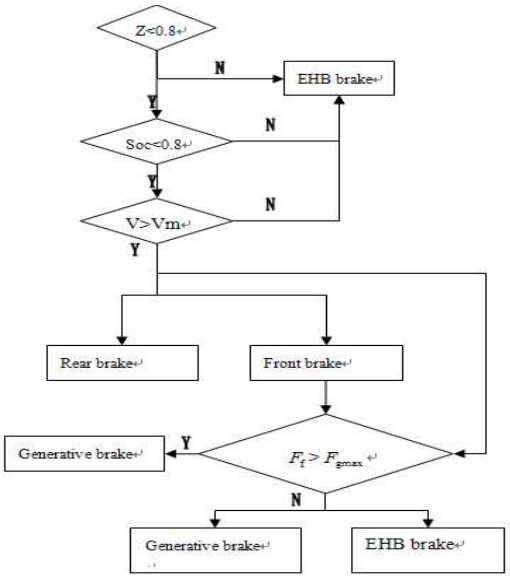

Fig 2. Brake force distribution algorithm

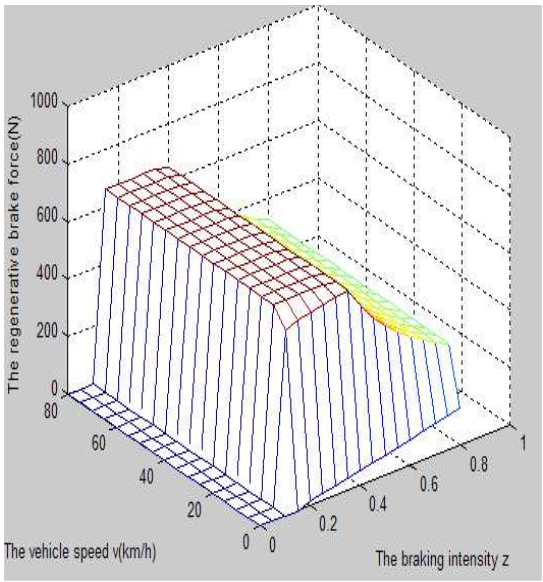

Fig 3. The regenerative brake force

The Strategy of Energy Flow. The motor is taken as a generator during brake, the output power changes with the speed, The expression between them can be got by fitting the load characteristic of the motor: I = f (n).

In the process of braking, the recovery is affected by SOC of the battery, which reflects the change of the battery capacity.

EHB with a electric hydraulic pump starts to pump after giving it the certain energy. The relationship between output flow and rotate speed is presented in Eq.1.

$$q_b = V_b \cdot S_m \frac{E}{E - (a \cdot P_{bin} + (1-\alpha) \cdot P_{bout})} \tag{1}$$

Above, V_b is the pump displacement, P_{bin}, P_{bout} are the Inlet and outlet pressure of the pump. The rotate speed of the pump can be got from the load characteristic of the pump.

The brake fluid is stored in the accumulator to establish a high pressure. The brake force of the EHB can be adjusted by using the valves to control the flow to brake cylinder. When the brake fluid drives brake pads to touch the brake disc, a relationship between the positive pressure and the relative displacement is determined, that can be obtained by Eq.2.

$$\mathrm{m}_c \frac{d^2 x_c}{dt^2} = -p_{cy1} A_p + C_{ec} \frac{dx_c}{dt} + k_{ec} x_c \tag{2}$$

Above, m_c, C_{ec}, k_{ec} are mass, damping, spring stiffness of the brake caliper. When the EHB is supplied by power, the brake force of it can be calculated by Eq.1, Eq.2.

The energy flow strategy was designed to utilize the recovery dynamically described as following Fig. 4.

The Results of the Simulation

The consumption or recovery of the battery can be calculated by the change of its voltage and current, showed in Eq.3. The energy consumption value is calculated if the current value is greater than 0. Otherwise, energy recovery value is calculated when the current value is less than 0.

$$E_0 = \int_0^{\mathrm{t}} (\mathrm{E_k} - I(\mathrm{t})R) I(t)\mathrm{dt}. \tag{3}$$

Where E_{k} is the initial voltage of battery, R is the internal resistance of battery.

EHB utilizes the regenerative current generated by generator dynamically, which power can be presented in Eq.4.

$$E_{\mathrm{m}} = \int_0^{\mathrm{t}} F_{\mathrm{m}} \mathrm{v(t)}\ \mathrm{dt} \tag{4}$$

Where F_m is the brake force of EHB.

The entire consumption of energy without the process of recovery is calculated in Eq.5.

$$E = P_{\mathrm{w}} \mathrm{tv}(F_w + F_{rr} + mzg). \tag{5}$$

Where F_{w} is air resistance, F_{rr} is rolling resistance.

The energy recovery rate, that is the ratio of regenerative energy and entire consumption of energy, is used to evaluate the design:

$$\eta = \frac{E_0 + E_{\mathrm{m}}}{E} \times 100\%. \tag{6}$$

When initial braking speed is 60km / h, the braking intensity of 0.3， was simulated. The initial SOC was selected as 0.8. Simulation results are showed in Fig. 5.

Simulation results show the SOC changes smaller than the general EVs. It means that EV with EMB has a higher energy recovery rate to the general EVs, which rate is about 30%. Another is that general EV cannot recover energy during the SOC is higher than 0.8, while EV with EHB can make the recovery transfer to the EHB.

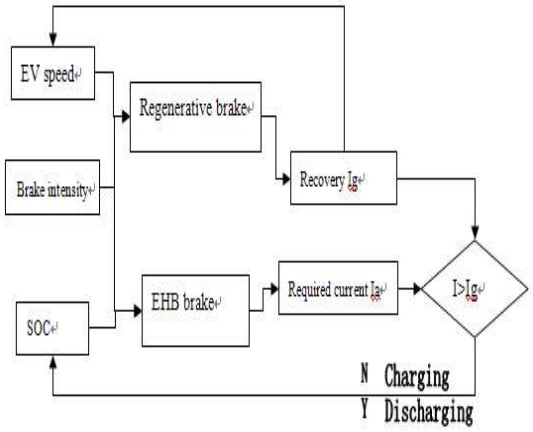

Fig 4 Energy flow strategy

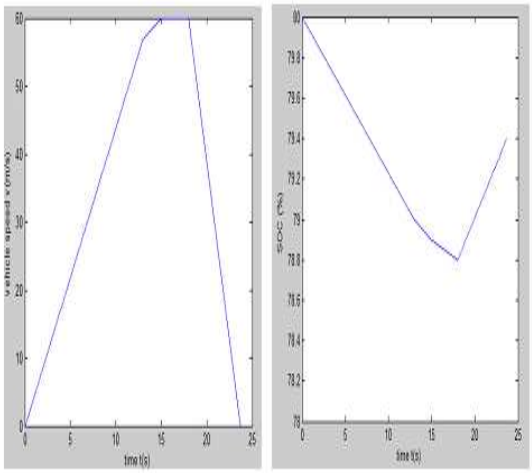

Fig 5. Simulation results

Conclusion

In this paper, a strategy to utilize the generative brake force dynamically during brake is proposed for the EV with EHB. The coupling relationship between distribution of brake force and the energy flow is pointed out. The front-drive EV with EHB has been built in the MATLAB/Simulink to simulate its energy recovery rate. The simulation results demonstrate that EHB braking and regenerative braking can work cooperatively to capture more energy than general HEV storing the recovery statically. These analytical procedures forecast that energy recovery utilized timely can provide some guidelines in terms of a method to extend the mileage of EVs.

References

[1] Line C，Manzie C．Electromechancial Brake Modeling and Control．IEEE Transactions on Control System Technology，2008，16(3)：446-457.

[2] Ahn J K，Jung K H.et a1．Analysis of a Regenerative Braking System Using Electro-Mechanical Brake．International Journal of Automotive Technology，2009(12): 229—234．

[3] Ruan, J. and Walker, P., "An Optimal Regenerative Braking Energy Recovery System in Electric Vehicles," SAE Technical Paper (2014).

[4] Jihong Zhang, “Research of Electric Vehicle Regenerative Braking Control Based on EHB System ,” JiLin University, JiLin, China 2008, Master's thesis 2008:01

[5] Templin, P., “A Diesel Engine Model, including Compression Brake for, Powertrain Control,” SAE Technical Paper 2002-01-3125, 2002, doi:10.4271/2002-01-3125.

Advanced Materials Research Vols. 986-987 (2014) pp 1187-1190

doi:10.4028/www.scientific.net/AMR.986-987.1187

Analysis on Primary Frequency Regulation function tests for Thermal Power Units

Lijie Kang[1, a], Weiping Liang[2, b]

[1]Department of Automation North China Electric Power University, Baoding 071003, China

[a]tanhuahenmei@163.com, [b]lwp-123a@vip.sina.com

Keywords: thermal power unit, primary frequency regulation, analysis

Abstract. With the increase of the load capacity and the development of the automation degree, the power dispatching center has a higher requirement for the primary frequency regulation function of the unit aircrew. After a certain period of time when the unit has been put into operation, the primary frequency regulation function must have the conditions to be put into operation, so that the unit can be involved in grid frequency at any time when the conditions are satisfied and the power supply quality can be fully guaranteed [1]. The regulation performance of primary frequency regulation plays a vital role in maintaining the stability of the unit aircrew and the power grid, so it is very necessary to conduct the frequency tests for the thermal power units [2]. In this paper, we describe the disturbance tests and recovery tests under different load points and different network frequencies. Through the analysis, we can draw the conclusion that the primary frequency regulation function of unit 1 can fully meet the requirement of the frequency regulation of the power grid.

Introduction

Primary frequency regulation is also known as the primary regulation for the frequency of the power grid [3]. The primary frequency regulation function refers to that when the grid frequency beyond the normal limits, the speed control system of each unit which is to participate in the grid's primary frequency regulation will automatically increase or decrease the unit power according to the changes of the grid frequency, so as to achieve a new balance and limit the grid frequency within a certain range. Primary frequency regulation is related to the structure and working principle of the speed governor and the working characteristics of the speed control system [4]. The principle of primary frequency regulation of thermal power unit is that the imbalance between the generator's input and output power results in the frequency instability of the electric power system, the mathematical formula is shown as follow:

$$\mathrm{Pm} - \mathrm{Pe} = 2\mathrm{Hs}\Delta\omega \tag{1}$$

In the formula: Pm refers to mechanical power, which is related to the generator's prime mover and governor's characteristics; Pe is the electromagnetic power, which not only is related to the generator's electromagnetic characteristics, but also depends on the load characteristics of the electric power system; Hs refers to the generator's inertia constant; $\Delta\omega$ is the speed deviation of the generator [4]. Figure 1 is the schematic diagram of primary frequency regulation of thermal power unit, which is made up by the coordinated control system (CCS), governor, steam turbine and boiler. In the mode of turbine following boiler, we regulate the opening of the turbine tones according to the changes of the main steam pressure. In this mode, the load variation rate is so slow that the unit does not have the primary frequency modulation function. Thus, we establish the model based on the coordinated control system in the mode of boiler following turbine[4].

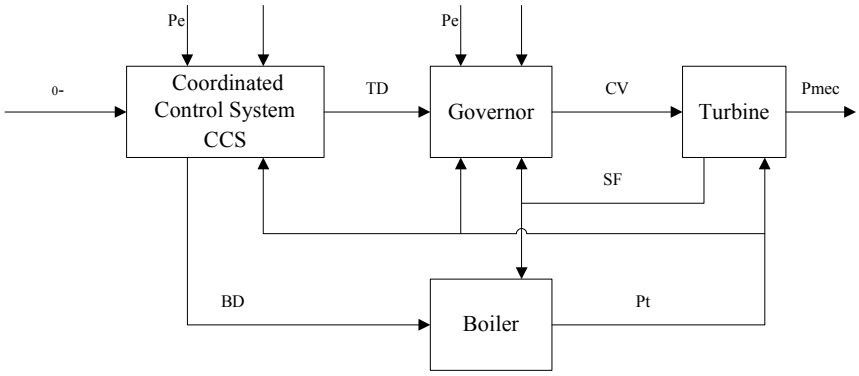

Figure 1 Schematic diagram of primary frequency regulation of thermal power unit

Major Technical Indicators of Primary Frequency Regulation

The main technical indexes of primary frequency regulation contain speed droop, dead band, power compensation, slow rate, lag time of response, stability time.

Speed droop is defined as that the unit aircrew adopt the grid connected mode in the way of differential speed regulation. When the synchronizer is in a position, this regulation system keeps the speed in the vicinity of the ratings. Meanwhile, each power (P) corresponds to a speed (N). The variation of speed following power is shown in Figure 2.

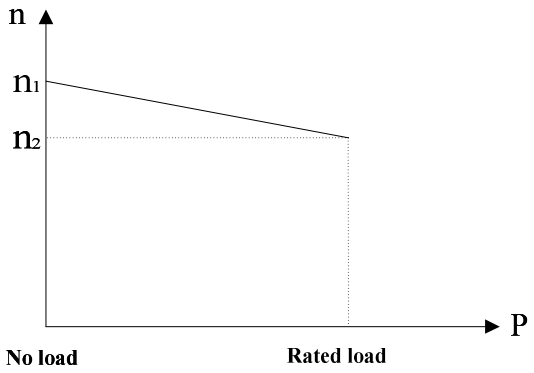

Figure 2 The variation of speed following power

Under the condition that the given value of the control system is unchanged, the ratio of the rotation speed variation rate (Δn) and the rated speed (n_0) which is corresponding to the unit power from zero to the rated speed is usually expressed in percentage [4].

$$\delta = \frac{\Delta n}{n_0} * 100\% \tag{2}$$

For the unit that undertakes basic load, the speed droop is generally a bit more, in the hope that the changes of the grid frequency have a small impact on its power, so that the unit can run a long time under the economic condition. As to the unit that bears the peak load, the speed droop is smaller, in the hope that it will undertake more varying load after the grid frequency changes.

Dead band refers to the insensitive area in the vicinity of the rated speed. The setting of the dead band is mainly to prevent the turbine tones' unnecessary frequent movement when the grid frequency fluctuates in a small scope, which is not conducive to the safe operation of the equipment. Otherwise, in order to maintain the stability, the actual frequency regulation capacity and the safety of the unit, we also need to limit the frequency regulation load, in case that the unit is in overload condition when the primary frequency regulation acts [4].

Power compensation is calculated by the speed droop (δ) and the grid frequency deviation which can be converted to the speed difference (Δn) [5]. The formula is as follow:

$$\Delta p = -\frac{\frac{\Delta n}{n_0} * 100\%}{\delta} * P_N \tag{3}$$

In the formula, n_0 is the rated speed and P_N refers to rated power.

For example, the unit which the speed droop is 5%, when the speed difference (Δn) is -6 and the grid frequency deviation (Δf) is -0.10Hz, Δp is calculated as follow:

$$\Delta p = -\left(\frac{\frac{-6}{3000}*100\%}{5\%} * P_N\right) = 0.04 * P_N = 4\%P_N \quad (4)$$

Slow rate is that due to the friction and clearance of the governor, the transmission amplification mechanism and the steam distribution mechanism component, there is a retardation phenomenon between the input and the output. This phenomenon acts on the control system so that in a certain range of the speed difference (Δn), the power remains unchanged [5]. The computational formula of slow rate (ε) is as follow:

$$\varepsilon = (\Delta n/n_0) * 100\% \quad (5)$$

In the formula, n_0 refers to the rated speed.

Lag time of response refers to the time needed from the change of the grid frequency meets the primary frequency regulation required value to the unit's load begins to change, which should be less than 3 seconds [5].

Stability time is the time the unit's load needed to reach stability in the process of primary frequency regulation after the grid frequency is stable, which should be less than 1 minute. The load instruction changes factors should be excluded, when the coordinate control system (CCS) or the automatic generation control system (AGC) is running [5].

The Implement of Primary Frequency Regulation

The primary frequency regulation function is an important means to maintain the frequency stability of the grid. The unit 1 of one power plant uses the C145/N200-130/535/535 turbine generator which is designed and manufactured by Harbin Steam Turbine Plant. We modify the turbine generator as C150/N220-12.75/535/535. The boiler is the natural circulation boiler which is produced by Beijing Babcock Willcocks and the type is B&W-670/13.7-M. After adjusting, the approval max load is 215MW. The DCS system of the unit is composited by the Beijing Hitachi HIACS5000 system, while the steam turbine electro-hydraulic control system is the Xinhua control system. When the unit load is in the range of 95MW-215MW, the primary frequency regulation should be put into use automatically. The primary frequency regulation speed change is set to 4% to meet the requirement of the grid frequency regulation.

Function Tests of Primary Frequency Regulation

Subjects and Requirements

1) Turbine generator and DEH, CCS

2) Speed variation rate is set to 4% and the speed drop of DEH-side is directly added to the turbine control valve instructions through the speed varying law setting function. We design frequency correction circuit at the CCS-side, while the corrective commands are not limited by the speed. The dead band is set to ±2r/min (±0.033Hz). For the thermal power unit which the rated load is 215MW, we limit the magnitude to 20MW. There is no load limit that is set by the operating personnel. According to the thermal power plant's safety evaluation requirements, the primary frequency regulation function and the major technical indicators after the maintenance of the unit meet the needs of the grid frequency regulation and the requirement of the national grid company's "The Guidelines of primary frequency regulation tests of Thermal power generating units".

Tests and Analysis

We conducted several primary frequency regulation tests on unit 1 on June 9, 2013, which were 0.067Hz, 0.1Hz and 0.2Hz step frequency modulation at three load points (140MW, 160MW and 190MW). Here we mainly analyze the disturbance test and the recovery test which were conducted when the load was 140MW and the high grid frequency was 0.1Hz. Other experiments' results are shown in Table 4.1.

1) The disturbance test

The grid frequency was 50Hz and the speed was 3000r/min, while the real load was 140.07MW and the actual speed stage pressure was 5.93MPa at 15:11:45 under the mode that turbine follows boiler. 3 seconds later, the grid frequency and the speed deviation were manually set to 50.1Hz and -6r/min. At that time, the calculation result of the regulation system was that the frequency difference load is -9.06MW (the rate of speed fluctuation is less than 4%) and the real load is 134.46MW. The unit actually reduced the load by 5.41MW within 3 seconds, which meets the requirement of the primary frequency regulation rules that the lag time of load response should be less than 3 seconds. 15 seconds later, the real load was 127.92MW and the speed stage pressure was 5.14MPa. The unit's load raised 12.15MW within 15 seconds since the grid frequency began to change, which meets the requirement that the load adjustment should reach 90% of the maximum theoretical load adjustment within 15 seconds.

2) The recovery test

The grid frequency was 50.1Hz and the speed was 3006r/min, while the real load was 131.71MW and the actual speed stage pressure was 5.51MPa at 15:15:04 under the mode that turbine follows boiler. 3 seconds later, the grid frequency and the speed deviation were manually set to 50Hz and 0r/min. At that time, the calculation result of the regulation system was that the frequency difference load is 0MW (the rate of speed fluctuation is less than 4%) and the real load is 136.87MW. The unit actually reduced the load by 5.16MW within 3 seconds, which meets the requirement of the primary frequency regulation rules that the lag time of load response should be less than 3 seconds. 15 seconds later, the real load was 144.38MW and the speed stage pressure was 6.24MPa. The unit's load raised 13.67MW within 15 seconds since the grid frequency began to change, which meets the requirement that the load adjustment should reach 90% of the maximum theoretical load adjustment within 15 seconds.

Conclusions

Through the tests, we can draw the conclusion that the lag time of response is less than 3 seconds, the stability time is less than 1 minute and the load adjustment reaches 90% of the maximum theoretical load adjustment within 15 seconds. It can proof that the primary frequency regulation function can fully meet the requirement of the rules and the frequency regulation indicators are better than the requirement of the national grid company's "The Guidelines of primary frequency regulation tests of Thermal power generating units".

References

[1] Yong Lu, Yu Gong: Modern Electric Power Vol.28 (2011), p.69-74, (In Chinese).

[2] Weijian Huang, Xi Zhang, Shihe Chen,etc...: Electric Power Vol.44 (2011), p.73-77, (In Chinese).

[3] Wenhua Duan: Science and Technology of West China Vol.13 (2014), p. 39–41, (In Chinese).

[4] Tierui Wang, JiLin Electric Power Vol.41 (2013), p.38-40, (In Chinese).

[5] Baishan Mei,Delan Zhang,Rong Chen: Electric Power Science and Engineering Vol.29 (2013), p.54-58, (In Chinese).

[6] Yiming Zhang, Chenglian Luo, Yuanjing Meng, etc...: Electric Power Vol.35 (2002), p.35-38, (In Chinese).

Advanced Materials Research Vols. 986-987 (2014) pp 1191-1195

doi:10.4028/www.scientific.net/AMR.986-987.1191

Application of Special Optical Fiber Sensing Technology in New Generation of Smart Substation

Ruirui Yang[1, a], Huiyuan Yang[1, b] and Weichi Ou[1,c]

[1] School of Automation, Wuhan University of technology, Wuhan, China, 430070

[a]ctyrr@163.com, [b]13006372909@163.com, [c]780448508@qq.com

Keywords: new generation of smart substation; special optical fiber; sensing technology; online monitoring

Abstract. The new generation of smart substation puts forward higher requirements to sensing technology. Based on the needs of these requirements, four kinds of special optical fiber sensing technology in power systems were researched: all-optical current transformer, distributed temperature sensing technology, fiber grating vibration sensing technology and fiber Bragg grating sensing technology. These kinds of optical fiber sensing technology for the new generation of smart substation to enhance its performance were analyzed. Finally, based on the fiber Bragg grating sensing technology, the online oil and winding temperature monitoring system was constructed for the new generation of smart substation.

Introduction

The smart grid is a breakthrough in the 21st century. It is also a trend of development in the field of power systems. As an important foundation for the smart grid, smart substation is the source of operational data collection and command execution units. The development of smart grid smart substation raises higher requirements for smart substation: constructing professional maintenance mode, the device status visualization technology and online monitoring techniques; developing new materials, equipments and communication technology that satisfies the greater capacity for information exchanging and processing functions [1].

Optimizing smart substation secondary system while ensuring its operational reliability is an important way to improve the economic benefits and achieve long-term development of smart substation. The new generation of smart substation proposed four main aspects of optimization for its secondary system: the automation system network; the allocation and integration of secondary equipment functions to achieve data monitoring with panoramic views; the function of smart assistance systems; the configuration of monitoring system and propose the device online monitoring optimization program [2].

Sensing system bears the inspection tasks of related parameters in smart substation. The use of online monitoring technology to monitor the operational status of smart substation is the key to guarantee its security, reliability, efficiency.

The new generation of smart substation proposes higher demands for its sensing technology in many aspects such as monitoring accuracy, fault tolerance, area covered, remote control monitoring, self-organizing, multi-hop path. However, in some high-pressure environments needed to be measured that requires better insulating properties such as online monitoring of smart switch, real-time measuring of high-voltage transformer winding temperature, current and other parameters, electrical sensing technology using in traditional smart substation is not applicable.

Special optical fiber sensing have features of electrical insulation, high temperature resistance, low energy consumption, no spark, no short circuit fault, anti-electromagnetic interference, small size and high sensitivity. Special optical fiber sensing can achieve goals of precise acquainting, accurate passing and significantly reduces the occupied area. The special optical fiber sensing technology has immeasurable prospects in the new generation of smart substation.

Special optical fiber sensing technology

Special optical fiber sensing technology has many advantages: small energy loss, stable chemical properties, small cross-section, strong anti-noise capability, anti-electromagnetic interference, no spark, no short circuit fault, high temperature resistance and so on. It is applicable in the field of electric power system to achieve the function of devices online monitoring and ensuring its operation safety and reliability.

There are four kinds of special optical fiber sensing technology being researched now.

Fiber Optical Current Transformer. Currently, the new developing fiber optical current transformer (FOCT) uses special fibers as the current sensing material. The sensing fiber ring is twined around measured current carrying wires. Based on the polarization properties of optical fibers, it measures current indirectly by measuring Faraday rotation angles in optical fibers. Each component in FOCT system is connected via fibers that welding together. It has a simple insulated structure, large dynamic range, reliable connection, no explosion, no danger of secondary circuit open, long-term stability, good consistency, mature technology and no discrete components in it. FOCT fiber sensing ring also has a light weight, small size and low cost.

The installation of FOCT is flexibility. It is suitable for traditional types of independent strut, transformer bushing or hanging. Because of its strong interference capability, it is ideally suited for gas-insulated switchgear (GIS) and other high-voltage equipment in complex electromagnetic environment without having to install the remote module. FOCT fiber ring has no heating phenomenon, thus the measurement accuracy will not be affected by increscent current. It has no saturation and anti-electromagnetic interference, thus can also be used for DC measurements.

However FOCT still has defects, affected by external magnetic and electric fields, the all-fiber current sensor inside will produce Faraday effect and optical Kerr effect, causing circular birefringence and linear birefringence. At this time, the polarization state is not only affected by the strain and temperature, but also by changes in the polarization plane of the incident light, which makes it impossible to distinguish the cause of changes in polarization state between changes in magnetic field and external disturbance.

For this problem, the influence of linear birefringence effects can be reduced or compensated mainly from the following aspects [3]: First, finding glass materials of low photoelastic coefficient to produce fiber and reducing photoelastic effect in the fiber to reduce the linear birefringence. The birefringence of ZF6 in flint glass is small, and it is little affected by temperature, makes it an ideal new material for sensing fiber in FOCT. Second, using fiber with double cladding structures can reduce the linear birefringence. Choose silicon material which has the most stable Young's modulus over a wide temperature range to be the first cladding layer. Because of its fragile mechanical properties, choose acrylate material to be the second cladding layer. Optical fiber of this structure has a good stability. Third, use new fiber processing technique to suppress birefringence: spun fiber has a good stability to environmental changes; twisted fiber can significantly reduce the linear birefringence inside; annealing to eliminate the birefringence caused by the bending of light. Last, by improving the measurement methods, like using Sagnac interferometer to achieve all-fiber current sensor program, reducing the impact of birefringence on the measurement [4].

Distributed temperature sensing. Distributed Temperature Sensing technology is suitable for the real-time measurement of space temperature distribution. Its optical fiber is the transmission medium as well as the sensing medium. Distributed Temperature Sensing technology can accomplish the task of distributed measurement of temperature field distribution along the fiber uninterrupted. It has many advantages that conventional sensors cannot match, such as anti-electromagnetic interference, high spatial resolution, flameproof, small size, long span, and little effect on the measured temperature field etc. Currently, distributed optical fiber temperature sensor mainly based on Raman scattering effect and optical time domain reflectometer (OTDR) technology to achieve continuous distributed measurement. Time domain and frequency domain optical system based on Brillouin is also a current hotspot.

Distributed Temperature Sensing technology is mainly used for inlet and outlet temperature monitoring of high-voltage cables in the new generation of smart substation. It can not only extend

the life of power cables but also improve the power transmission capacity. It can also be used for the fault warning of power system cables and power system sensing cables.

The distributed optical fiber temperature sensor detects the Raman scattered light which contains temperature information is very weak, or even submerged in noise. The noise elimination level of the anti-Stokes and Stokes backscatter is directly related to the accuracy of temperature measurement in the entire system. To improve the strength of long-distance optical transmission signal, fluorine-doped optical fiber can be used. The main task of fluorine is to reduce the refractive index of the silica. Because its Rayleigh scattering is small and the loss is also close to the theoretical minimum value, fluorine-doped optical is mainly applied for optical signal transmission over long distances.

Optical fiber interferometric vibration sensing. Optical fiber interferometric vibration sensing technology uses vibration sensing fiber as the sensing unit. When it is affected by the external disturbance, the vibration it caused changes some characteristic of the light transmitting part (wavelength, phase, attenuation, polarization, propagation time, and mode field distribution). By monitoring the optical signal, vibration interference information can be got. Using special sensing device in optical fiber monitoring changes of light characteristics, the detection of events and states (including: temperature, strain, destruction, damage, shock, sound waves, vibration load and displacement) can be achieved. This sensing technology has a high precision and a wide frequency range. It will never cause the grid resonance and has a strong immunity to electromagnetic interference outside.

Optical fiber interferometric vibration sensor can be laid along walls, fences or under the gravel, soil and turf. It can also be installed on masonry or concrete wall, the fiber perimeter monitoring system (FPMS) mounted around can monitor the system and alarm when foreign invasions are detected. At the same time, it applies to the online monitoring of iced transmission line galloping under certain wind velocity to prevent serious incidents and ensure the reliability and safety of auxiliary systems and infrastructures in the new generation of smart substation.

Optical fiber interferometric vibration sensing technology mainly uses ordinary communication optical fiber cable as transmission cable, 2-48 core fiber cable mostly, based on system requirements.

Fiber Bragg Grating Sensing. Fiber Bragg Grating (FBG) sensing technology is based on the photosensitivity of fibers. The interaction of germanium ions in the core and external incident photon causes permanent changes in the refractive index. However, the perturbations of periodic refractive index only affect a narrow section of the spectrum. When the broadband light wave transmitting inside, the incident light will be reflected on the corresponding frequency, and the remaining transmitted light waves are largely unaffected.

FBG sensing technology can directly measure the temperature and strain two basic physical quantities. It has many advantages such as anti-interference ability, simple sensing probe structure, small size, good repeatability of measurement results, etc. FBG sensing technology can be applied to current detecting, GIS system temperature measuring, pressure testing and other auxiliary facilities monitoring.

But for now, problems still exist in FBG sensing technology. That the response sensitivity of bare FBG is low is the critical one of these problems. In order to improve the sensitivity of the fiber Bragg grating, material's thermal expansion coefficients and thermo-optic coefficients can be appropriately increased. Pressure and Temperature are two main factors in improving its sensitivity: First, since the refractive index of light caused by temperature has the most significant impact on coupling wavelength, the temperature sensitivity of fiber grating can be improved by selecting the appropriate core or cladding doped materials and there density. Adding germanium and boron to optical fiber materials can increase the photosensitivity and decrease its numerical aperture. Polymer material with larger coefficient of thermal expansion like polyester fiber can also be applied to achieve embedding encapsulation. Second, in terms of the pressure factor, choose special polymer material with relatively small elastic modulus and low thermal expansion coefficient (like Polytetrafluoroethene) to achieve embedding encapsulation. Using a special cavity structure for Grating encapsulation may also increase the pressure-sensitive characteristics [5].

Transformer parameters monitoring

Transformer online monitoring is based on a variety of electrical and mechanical characteristics of the transformer to achieve the monitoring purpose of the transformer through the methods of partial discharge analysis, oil dissolved gas analysis, oil and winding temperature analysis, and transformer vibration online analysis [6]. This part mainly describes the online monitoring system of transformer oil and winding temperature based on FBG sensing technology and its installation.

Transformer burning occurs frequently due to the high oil temperature. One important reason is that the transformer overloads, its oil temperature exceeds the preset temperature. Meanwhile, oil and winding temperature directly affects the operation of the transformer cooling system. Therefore, transformer oil and winding temperature online monitoring system is of great importance to the safety and reliability of the new generation of smart substation.

Temperature of the transformer top is oil-immersed transformer's detecting temperature. In order to be easy for installation and maintenance, sensors are usually mounted on top of the transformer enclosure. The highest temperature of transformer windings situated in its upper part where is hard to measure, thus the surface temperature of the windings is often used as an alternative. Conventional temperature sensors are larger and susceptible to electromagnetic interference [7].

The temperature online monitoring system of transformer oil is based on FBG sensing technology. The system mainly consists of the temperature host, probes and connecting cables. The structure of transformer oil temperature online monitoring system is shown in Fig 1.

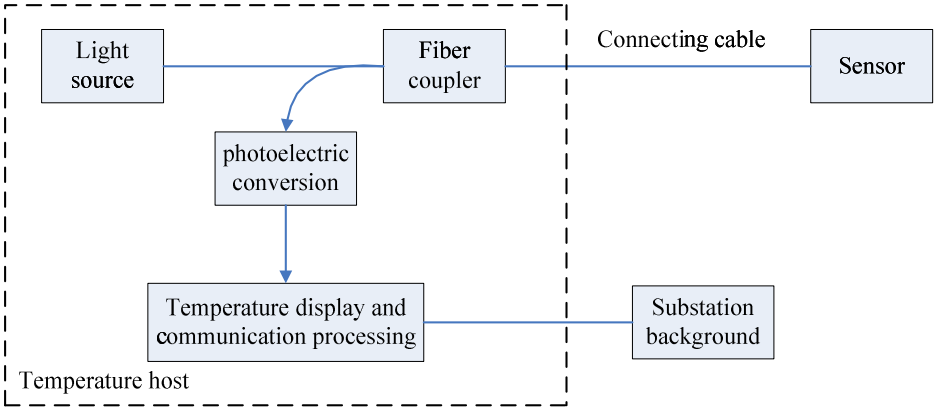

Fig.1 Structure of transformer oil temperature online monitoring system

FBG sensor is sensitive to temperature changes and of small size. After special designed， it can be embedded to the oil temperature detecting hole or pasted in a small plane on the upper surface of the windings to achieve real-time measurement. FBG sensing technology has strong anti-interference characteristics. It is very suitable for high pressure, high magnetic field environments. The probe of FBG sensor can work across a long distance without being affected. Thus, FBG sensing technology is ideal for temperature online monitoring of transformer oil and windings.

In addition, special optical fiber technologies can also achieve transformer current, partial discharge, gas dissolved in oil, transformers vibration and other aspects of online monitoring: through measuring optical radiation caused by partial discharge, FBG sensing technology can make various researches like partial discharge detection, location and analysis possible to conduct; Optical fiber interferometric vibration sensing technology can achieve the propose of online monitoring of gas dissolved in oil and transformer vibration by detecting the strain of transformer oil, transformer windings and core; the online monitoring of transformer current can be realized by FOCT sensing technology.

Conclusion

Special optical fiber sensing technology can achieve the goal of constructing transformer online monitoring system for the new generation of smart substation, effectively ensure its operating

security and reliable as well as improve its economic benefits. Therefore making it possible for the new generation of smart substation to meet the higher demands put forward by the smart grid. Based on traditional fiber sensing technology, special optical fiber sensing technologies improve and refine the materials, structure, etc. The application of special optical fiber sensing technology has broad prospects in the new generation of smart substation.

Acknowledgment

This work was financially supported by the National Nature Science Foundation (51177114) and Wuhan Applied Basic Research Projects in 2014.

References

[1] Xuankun Song, Jiang Shen, Jingru Li, Zhihong Xiao, Zhenyu Li, Guohui Zhou and Baoying Huang: Electric Power Construction, p.11-15, Jun (2013), in Chinese.

[2] Yousong Zeng: Public Communication of Science and Technology, p. 57+56 Volume:23 (2013), in Chinese.

[3] Shiqing Xu, Shixun Dai, Junjie Zhang, Guonian Wang, Lili Hu, Zhonghong Jiang: Laser and Optoelectronics Progress, p. 41-45, Jan (2004), in Chinese.

[4] Jintao Xu, Yingli Wang, Jia Wang, Jianhua Feng, Yongming Yu, Wei Zheng: China Electrical Equipment Industry, p. 53-57, Jan (2011) in Chinese.

[5] Dequan Feng: Northwestern University, (2007) in Chinese.

[6] Zhongbao Liu, Yongqing Wang: China Electric Power Education, p. 213-214, Volume:36 (2013), in Chinese.

[7] Fanchao Zeng, Yubing Wei, Guoan Kuang: Electric Engineering, p. 12-13, Jun (2009), in Chinese.

Advanced Materials Research Vols. 986-987 (2014) pp 1196-1200

doi:10.4028/www.scientific.net/AMR.986-987.1196

Development of Engine Exhaust Active Noise Control System

Jie Wang[1, a*], Zhien Liu[1,b], Jiawei Zeng[1,c], Chao Wang[1,d]

[1] Wuhan University of Technology, Wuhan 430070, China;

[a]wjie@whut.edu.cn, [b]Lzen@whut.edu.cn, [c]840497918@qq.com, [d]281284730@qq.com

Keywords: Engine exhaust noise reduction, Active noise elimination, Acoustic interference

Abstract: In order to enhance the capacity of elimination of engine exhaust low frequency noise, a set of engine exhaust active noise control system was developed. The system was developed by using MC9S12XS128 MCU, and it is based on the theory of sound wave interference. The system can realize the voice signal acquisition, reverse phase processing and output, and can eliminate engine exhaust low frequency noise. Experimental results showed that the system has good silencing effects on the engine exhaust noise under the steady state.

Introduction

In recent years, with the vigorous development of Chinese automobile industry, car ownership in China is increasing year by year. At present, Chinese annual growth in the amount of cars is more than 20 million or more. The increasing of vehicles has brought the adverse effect for the environment, including the main part of the urban noise pollution casued by vehicles. Engine exhaust noise, which accounts for a significant proportion of the whole machine noise, is the largest noise source. The traditional method for controlling engine exhaust noise is installing a muffle. But traditional muffler may cause an increase in engine exhaust back pressure, increase the overall weight of the vehicle and have other defects. Active muffler system has been increasingly favored by the major car manufacturers because of its small size, light weight and can effectively reduce engine exhaust back pressure, etc. U.S. Bose active noise control system has been developed from research and development to advance market applications. Many other foreign examples can also prove the feasibility of its technology. China also has begun a series of research and has achieved some results in the field of active noise control. In the future, with more wide application of the active noise elimination technology, the costs will be lower. Active noise elimination technology has a broad prospect in China as a new kind of automotive noise control technology.

This article describes the development process of an engine exhaust active noise control system. The system was developed based on MC9S12XS128 single chip. The development of the system verified the feasibility of active noise elimination, put forward the idea of active noise elimination, found some problems need to be solved and pointed out the direction of the deep development of engine exhaust active noise control system.

Brief introduction to the Active Noise Control system

Active Noise Control is based on destructively interfere between two sound waves or the principle of sound radiation suppression. Acoustic radiation, which has the equal pressure and the opposite phase with the primary source, is generated by the secondary source. The two waves offset each other, so as to achieve the aim of reducing noise [1]. The basic theory of active noise control is the young's interference theory of sound wave. When the two same frequency and opposite phase columns of sound waves met in space, interference phenomenon will be produced. Its principle is shown in Figure1.

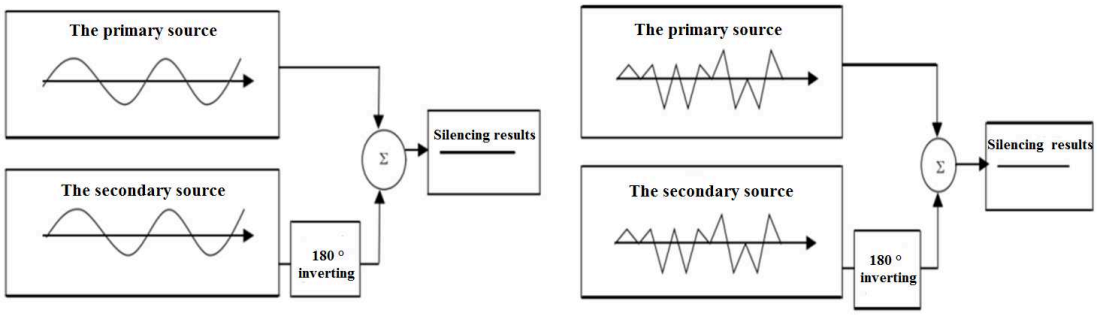

Fig.1. The principle diagram of the young's interference of sound waves

This paper describes an active noise control system for the engine tailpipe exhaust noise, so the system was designed with the particular sound field of the pipe as the research object. System structure diagram as shown in Figure2. The system picks up noise signal through the microphone installed on the upstream of the exhaust pipe. After inverse processing, then noise signal will be feed to the secondary sound source (speaker) installed on the downstream of the exhaust pipe. By adjusting the output of secondary sound source to make it have the equal amplitude and opposite phase with the original noise signal, the purpose of eliminating noise can be achieved[3].

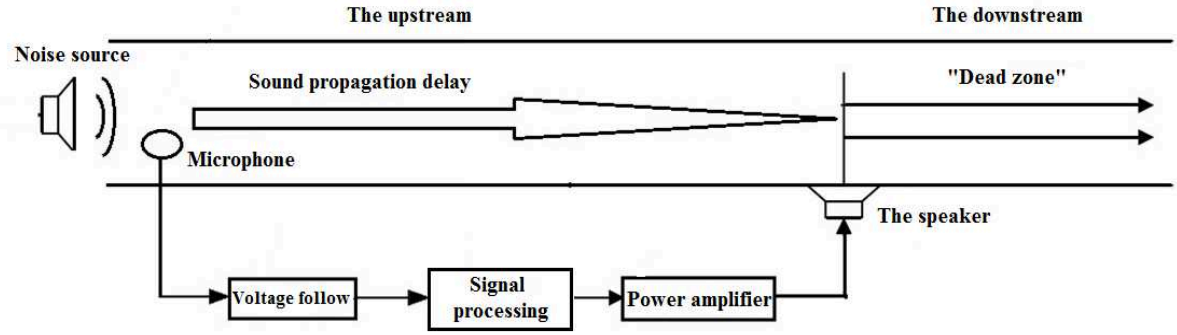

Fig. 2. System structure diagram

sound interference can be easily achieved by using audio processing software. Audio signals collected by audio processing software will be reverse phase processing. Then making the left and right sound channel output are equal in amplitude and opposite on the phase, noise elimination can be realized.Common audio processing software is Cool Edit Pro. Cool Edit Pro is a powerful multi-track recording and processing software developed by the U.S. Adobe Systems. It can handle multiple files at the same time, easy to cut and paste in several files, merging and overlapping sound operation[4].

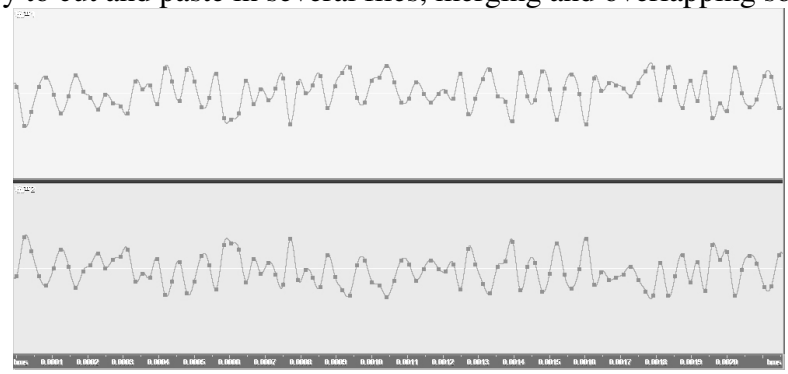

Fig.3. Diagram of noise signal waveform before and after reverse phase

This paper uses the Cool Edit Pro to Generate a random noise signal, Then we can generate a signal with opposite phase and the same frequency with the original signal. Waveform diagram before and after being Inverted is shown in Figure3. Finally, the two waveform overlap. Experimental results show that when the two waveform overlap, one can be seen as a noise source, another can be seen as the secondary sound sources in active noise control system, two sound source will produce interference phenomenon. Since the waveform is completely inverted, when excluding the impact of error factors, the noise signal is completely eliminated. The successful elimination of noise signals

showed that destructively interfering of sound waves can be used as the principle means of eliminating noise.

Active noise control system design

The controller of the active noise control system described in this article is realized by MC9S12XS128 MCU. Microcontroller is used to process signals coming from the sound sensor, adjust the control system to keep it always in the best control effect mode. System is designed in blocks, which includes three parts: single chip processing module, microphone module, speaker module. Two blocks combine with connectors, which can facilitate the future extension improvement, testing, and replacement. Hardwares included in the System are shown in Figure4, and the several modules will be introduced in the following.

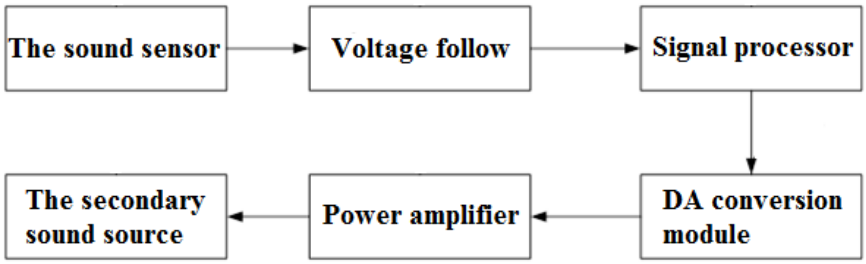

Fig.4. Hardwares included in the System

Microphone module includes sound sensor and a voltage follower circuit module. Sound sensors is used to detect the intensity of the sound on the noise source, the output can use 3.3 V and 5 V reference voltage signal which is available for the AD converter acquisition[5]; The voltage follower circuit module is connected with the sound sensor, which is used for increasing the input impedance, so that the voltage is more closer to the true value of AD module.

Signal processing module include a processor and a DA converter module. Signal processor uses MCS12XS128 MCU to process voltage signal. the AD module is used to complete the switch from the voltage signal to the digital signal. Single chip microcomputer completed the inverse processing of digital signal. Digital signal after inverse processing output to the DA conversion module. DA conversion module is connected to the signal processor, is used to switch the processed digital signals into analog voltage signal, and output to power amplifier. DA conversion module adopts TLC5615, TLC5615 is a D/A converter with serial interface, whose output is voltage type, and output voltage is double the maximum voltage reference. In this system, TLC5615 uses SPI serial transmission for single chip microcomputer CPU interface. The maximum transmission rate is 1.21 Mhz. DA conversion time is 12.5us. The conversion accuracy of TLC5615 is 10 bit, and the converted output is voltage. The maximum output voltage is VDD-0.4 V. The logic voltage input is 5 V (+ 5%). If using 5 V logic level, the maximum input voltage is 4.6 V.

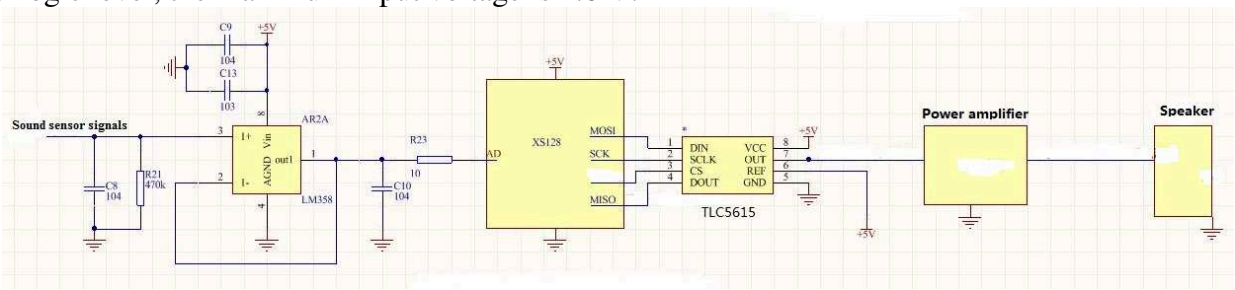

Fig.5. Schematic circuit diagram of system

Speaker module contains power amplifier and speakers. Connection with the DA conversion module, power amplifier is used to amplify the signal to meet the needs of the speaker. Power amplifier use TEA2025 amplifier integration module, which can directly amplify the output signal of the DA module. Secondary sound source module adopts full frequency electrodynamic loudspeaker to

meet the needs of the low frequency sound wave. Schematic circuit diagram of system is shown in Figure5.

Active noise control system function debugging

Combination of a signal generator and oscilloscope was used to debug the inverse function of the system.

Functional verification of inverting was completed by using dual channel oscilloscope. A certain frequency signal from a signal generator was collected. Signals after dealing with the inverse system and without inverse processing are showed at the same by using dual channel oscilloscope. During the experimental process, different frequency square wave, sawtooth wave and sine wave were generated by using signal generator, the 20 hz square wave and sine wave diagram are respectively shown in Figure6.

Experimental results of inverse function showed that for low frequency sound signal, the system has good capability of reverse phase, but with the increasing of frequency, the system will show a certain of ductility. The higher the frequency, the more obvious time delay phenomenon. By changing different signal source, we can get the same conclusion that for low frequency sound signal, the system has good inverse function; for high frequency signal, the delay phenomenon is serious, the system doesn‘t have a good ability of reverse phase. Reason analysis showed that when the frequency of the sound source signal is too high, the speed of signal transmission and DA converting can not meet the requirements, whcan lead to a voice signal processing is not timely, resulting in signal delay.

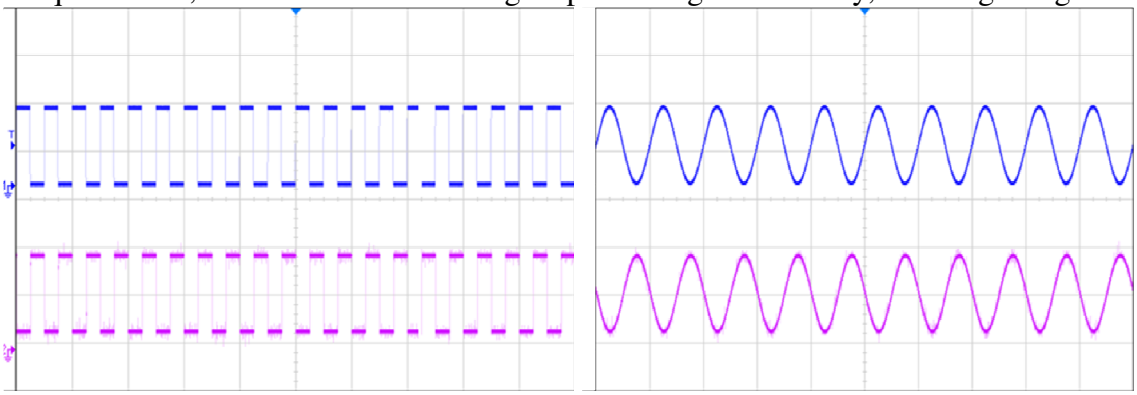

Fig.6. Diagram of the 20Hz square wave and sine wave

According to the actual measured engine exhaust noise, further inverse function of this system was debugged. The inverse function was debugged mainly for engine low frequency noise on the steady state. Figure 7 is the engine exhaust noise on a steady speed of 2500rpm (Abscissa is time, ordinate is samples values). Figure 8 is the noise spectrum of the engine exhaust noise after the Fourier transform based on external audio processing method(Abscissa is frequency, ordinate is sound pressure level).

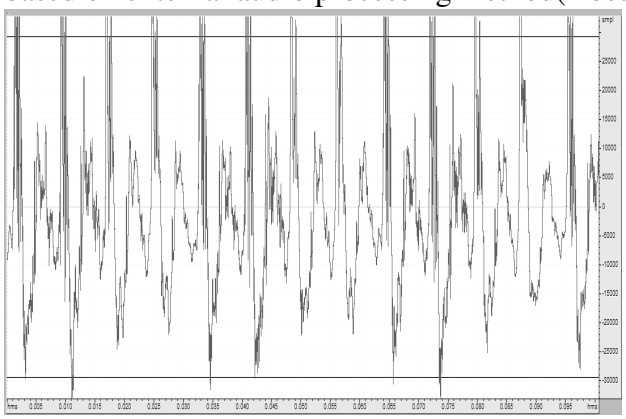

Fig. 7 Exhaust noise on speed of 2500rpm

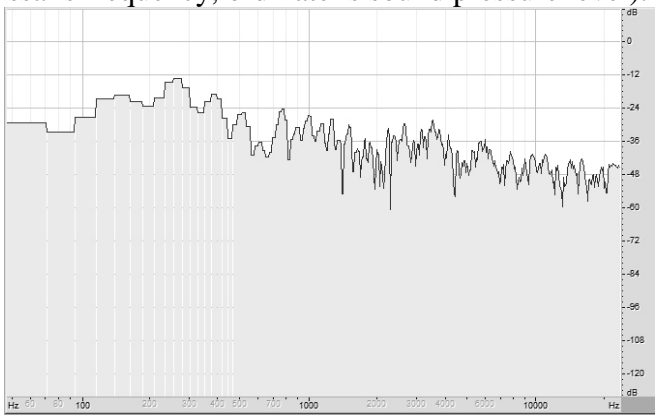

Fig.8 Spectrum obtained by Fourier transformation

According to the analysis of the noise spectrum diagram shown in figure 8, on low frequency range of engine exhaust noise, the sound pressure level on nearly 140Hz and 257Hz and 375Hz frequency

are in the peak position. By using audio processing software, we generated sine wave with the corresponding frequency and sound pressure level, and stacking output it for the system to acquire. System will output the voice signal which has been inverted. And the voice signal will eliminate the original engine exhaust noise by interference cancellation. By collecting and processing the sound signal, the spectrum diagram of processed signal can be obtained and shown in Figure9. From the figure we can see that the sound pressure decreased about 10dB in the low frequency range, particularly on the above location of the three frequencies, which means this system has good silencing effect on the elimination of engine exhaust low- frequency noise.

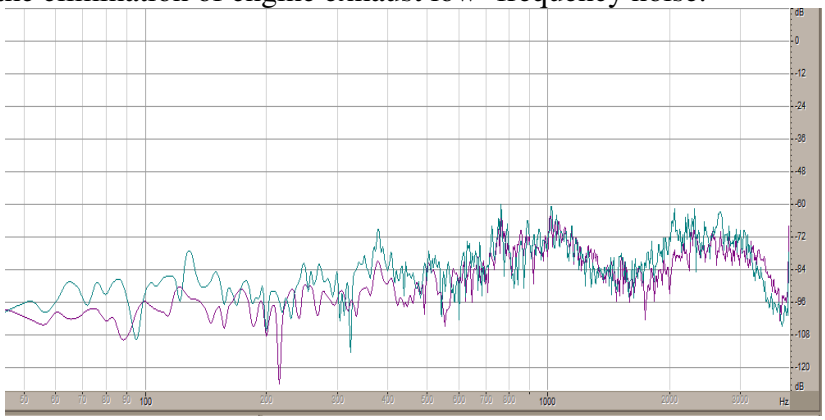

Fig. 9 Spectrum diagram of sound signal before and after interference cancellation

Conclusions

a. By using the audio processing software, the principle of active noise elimination was simulated. The Verification results showed that acoustic interference principle can achieve good silencing effect. The system has the advantages especially on the low frequency steady noise processing. Active noise elimination principle can be used as a silencer technical means to eliminate engine exhaust noise to more in-depth study.

b. Paper designed and developed a kind of engine exhaust active noise control system. The noise signal was processed and inverted by using MC9S12XS128 micro-computer. The system successfully realized processing of 140Hz, 257Hz and 375Hz exhaust noise, which were measured by the engine bench test. The actual exhaust noise in the above frequencies droped by about 10dB. The effectiveness of the system was proved.

c. System designed in this paper has a better handling capacity for stationary noise. But for transient noise, the effect is not good due to factors such as signal delay. So improvement will be continued in subsequent research.

References

[1] Zhaoxiang Deng, Haijun Zhao, Jie Yang, Fusheng Pan; The semi-active muffler performance exhaust muffler research based on CFD[J]. Internal Combustion Engine Engineering, 2009,v.30; No.13605:83-87.

[2] Yang Zhao, Heji Yu; Review of Active Noise Control Technology [J]. Noise and Vibration Control, 1997,04:6-9.

[3] Xiaoli Zhang, Haipeng Hou; Active Noise Control System in pipeline[J]. Light Industry Machinery, 2010,v.28, No.10402:103-106.

[4] Nelson, P.A. and Elliott, S.J., “Active Control of Sound”, Academic Press, London, 1992.

[5] Hansen, C.P.: Understanding Active Noise Control. Spon Press, New York (2001).

Advanced Materials Research Vols. 986-987 (2014) pp 1201-1204

doi:10.4028/www.scientific.net/AMR.986-987.1201

Coordinated Control of Variable-speed Constant-frequency Wind Farms in Weak Grids

Chao Li [1, a], Hongtao Wang[1, b], Zhongkang Wei[2], Chunyi Wang[3]

[1]Key Laboratory of Power System Intelligent Dispatch and Control of Ministry of Education, Shandong University, Jinan 250061, China; [2]State Grid Jibei Electric Power Company, Beijing 100053, China; [3]State Grid Shandong Electric Power Company, Jinan 250001, China

[a] lichao2008@mail.sdu.edu.cn, [b] whtwhm@sdu.edu.cn

Keywords: weak grids, frequency control; voltage control; coordinated control

Abstract: Variable-speed constant-frequency (VSCF) wind farms are gradually becoming a significant proportion of generation in weak grids with constantly increasing penetration rate, and it should certainly take responsibility of the grid frequency and voltage stability. Based on the P-Q performance curve of doubly fed induction generator (DFIG), by introducing static synchronous compensator (STATCOM), this paper presents a coordinated control strategy of active power and reactive power to deal with fault and load disturbance in weak grids. Simulation results show that the proposed coordinated control strategy can effectively improve the frequency and voltage stability of the grids.

Introduction

In recent years, wind power has developed rapidly, which occupies the increasing proportion of weak grids. When fault and load fluctuation occur in weak grids, the wind farm should undertake part of the frequcency and voltage modulation tasks[1, 2]. Cooperating with STATCOM, VSCF wind turbine has the voltage adjustment ability [3] and frequency regulation ability [4, 5].

In the present paper, a coordinated control strategy based on the active power deload control and voltage compensation is proposed such that, when weak grids frequency excursion or fault occurs, wind farms change active power output and reactive power output together with STATCOM. The effectiveness of this control approach was tested in weak grids, where wind generation plays an important role.

Power Regulation Capability Analysis of DFIG Wind Turbines

To develop frequency regulation ability of DFIG, this paper proposed a coordinated control method based on pitch angle control and overspeed control. In this control approach, wind generators operate according to a deload optimum power extraction curve compared to the maximum power point tracking (MPPT), such that the active power provided by each wind turbine increases or decreases during system frequency changes, as depicted in Figure 1(a).

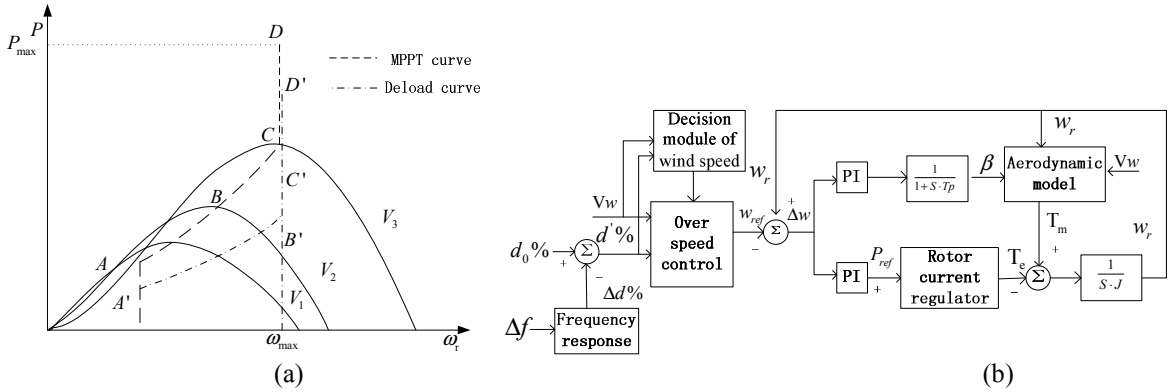

(a) (b)

Fig. 1. Frequency characteristics of DFIG. (a) Power-speed performance curves. (b) Frequency controller

The principle of this control approch is that overspeed control is used in preference to pitch angle control to obtain a faster response speed, and pitch angle control starts when the overspeed control can not meet the demand of frequency regulation. Depending on the wind speed, control strategy is divided into three modes: low wind condition, medium wind condition, and high wind condition. Assuming reserve power of DFIG can be expressed as:

$$\Delta P_R = d\% \cdot P_{\mathrm{MPPT}} \tag{1}$$

Where, $d\%$ is deload coefficient, P_{MPPT} is value of MPPT. $d\%$ can be changed according to different circumstances needed to support. This paper proposes an improved active power control for DFIG at all regions of wind speed. The frequency regulation controller is designed as Figure 1 (b).

The input are rotor speed w_r, wind speed V_W, frequency f and the initial level of deload coefficient $d_0\%$. The output are pitch angle β and active power reference value P_w. Wind speed mode is selected first according to each input, and wind generators operate according to a deload optimum power extraction curve such that the DFIG is able to provide a proportional frequency response. When the system frequency drops, the controller will reduce the rotor speed or increase the pitch angle to increase the active output, vice versa.

Considering reactive power output of the converter, P-Q performance curve of DFIG and reactive control block are shown in Figure 2.

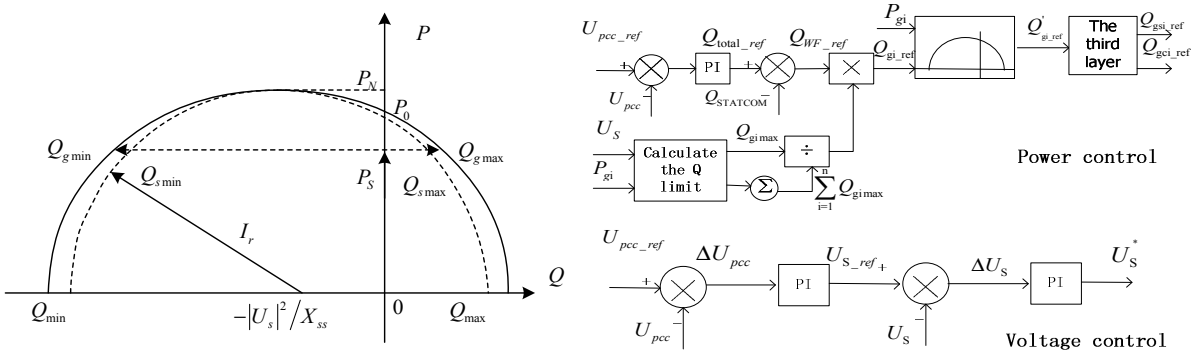

(a) (b)

Fig. 2. Reactive power characteristics of DFIG. (a) P-Q performance curve. (b) Reactive power control

As shown in Figure 2(a), when active output is under the given conditions, the reactive power has different operation mode; the adjusting range of reactive power is different when active power output under different conditions. As the change of wind speed, the active power output varies accordingly within $[0, P_N]$, while the reactive power output range is also changing. When the active power output is within $[P_0, P_N]$, the closer active power output to P_N, the more reactive power needed. Control block diagram of reactive power is shown in Figure 2(b), including power control and voltage control. Power control is applicable for the condition of crowbar inaction, and voltage control is applicable for the condition of crowbar action. In the power control mode, reactive power is allocated through three levels. The first is between wind farm and STATCOM; the second is between different wind turbines; the third is between rotor side converter and grid side converter.

Central Control System in Weak Grids

In order to maintain the stability of the grid voltage, a certain reactive power value is needed to inject to the weak grids. As shown in Figure 2, reactive power output is strong volatility for stochastic volatility of the active power and grid fault. This paper studies the effect of injecting optimum reacitve power using STATCOM on voltage of weak grids connected DFIG. Also, DFIG operates on deload mode to ensure that DFIG has sufficient active capacity and provides active power support for weak grids. The block diagram with proposed central control is shown in Figure 3.

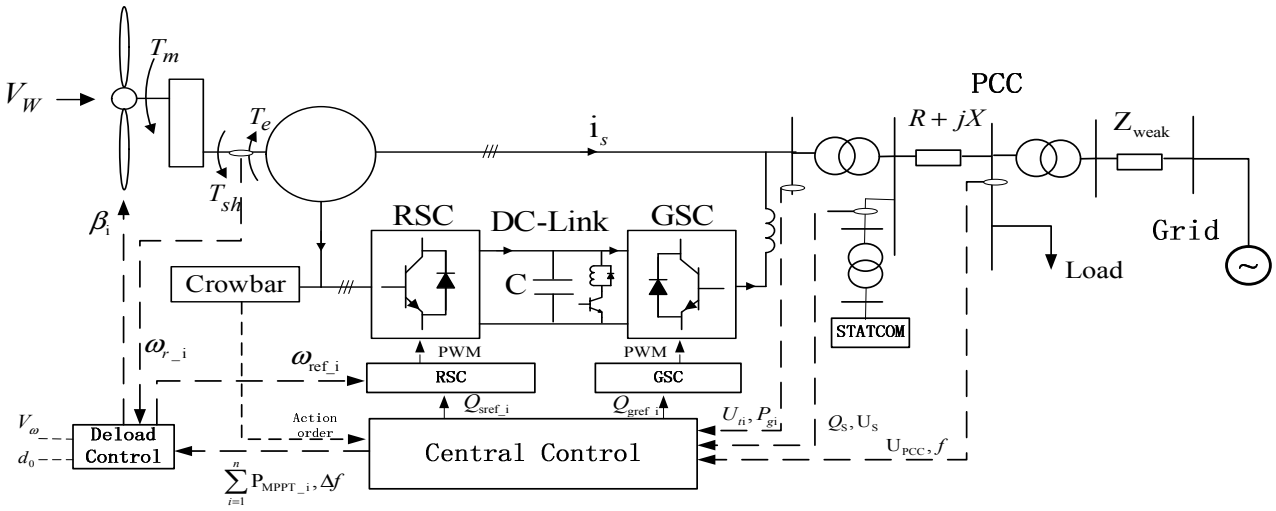

Fig. 3. Simplified block diagram with central control system

In the control diagram of Figure 3, the central control system achieves the active and reactive power balance objectives through real-time coordinated control among the wind farm, the compensation unit and grid system. The central control system contains three operational mode: power control , voltage control and frequency control. The control process is shown in Figure 4.

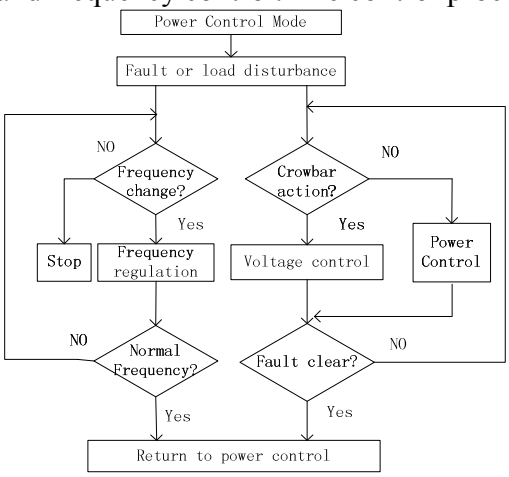

Fig. 4. Central control system flow chart

Test System and Simulation Results

The test system within PSCAD/EMTDC used for this study is shown in Figure 3. Two different cases studied on this test system are: (1) 3-phase, high impendance fault to ground, (2) sudden increase in load in the weak system.

Case 1 Three phase to ground fault

In this case, the 3-phase fault at t=0.5s is studied at PCC. The voltage drop are 20% and 50%, respectively. As shown in Figure 5(a)(c), after providing reactive power compensation by using the central control, the voltage drop during the fault has improved, and recovered to original value quickly after the clearance of fault. Figure 5(b)(d) are reactive power allocation between wind farm and STATCOM of different needs.

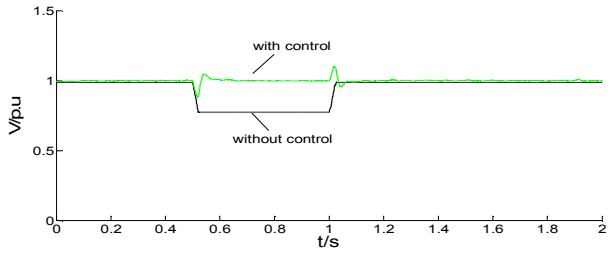

(a)

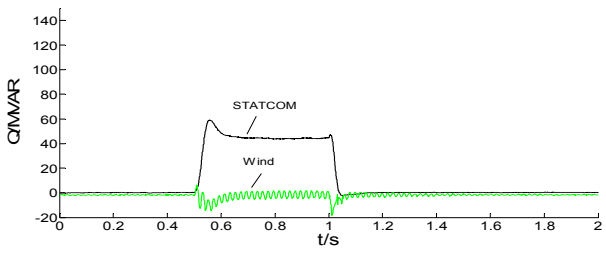

(b)

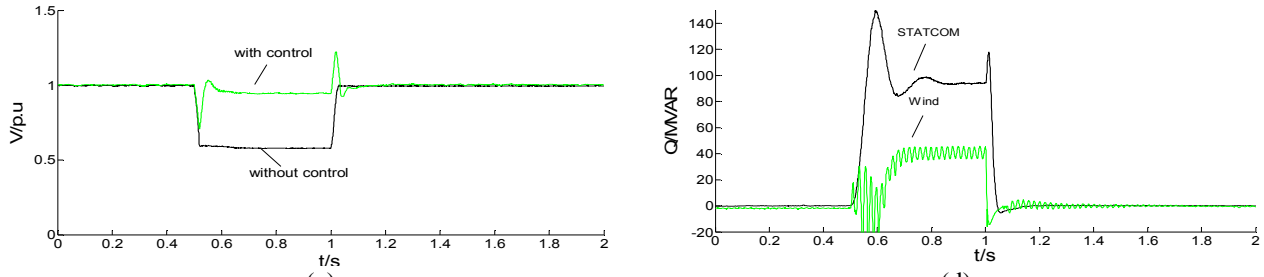

(c) (d)

Fig. 5. Simulation results of testing on voltage response. (a) 20% voltage drop. (b) 20% reactive power compensation. (c) 50% voltage drop. (d) 50% reactive power compensation.

Case 2: Sudden increase in load

In this case, sudden increase in load at t=1s is studied at PCC. The frequency improvement and active power output response to frequency are shown in Figure 6.

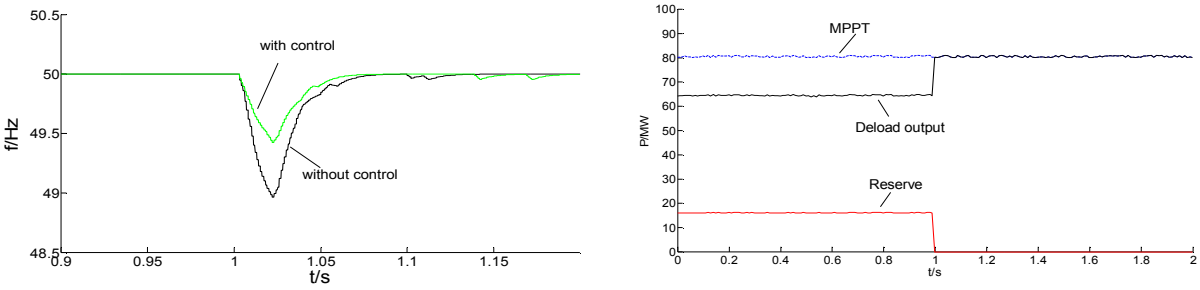

(a) (b)

Fig. 6. Simulation results of frequency response. (a) Traces of frequency. (b) Wind farm's frequency response

Summary

This paper presents an active-reactive power coordinated control strategy based on the P-Q performance curve of DFIG. Center control system is established to improve the frequency and voltage stability in weak grids. The Robustness of the control system is the focus of future research.

Acknowledgment

This paper was supported by National Natural Science Foundation of China(51177092); National High-tech Research and Development Program of China(863 Program) (2011AA05A101).

References

[1] Kanellos, F.D. and N.D. Hatziargyriou, The effect of variable-speed wind turbines on the operation of weak distribution networks. IEEE Transactions on Energy Conversion, 2002. 17(4): p. 543-548.

[2] Eduard Muljadi, C.P.B., Brian Parsons, Abraham Ellis, Effect of variable speed wind turbine generator on stability of a weak grid. IEEE Trans on Energy Conversion, 2007. 22(1): p. 29-36.

[3] Ferdous, M.J., Y. Arafat, and M.A. Azam, Flicker level mitigation of weak grid connected wind turbine with DFIG by injecting optimum reactive power using STATCOM, in 2013 International Conference on Informatics, Electronics & Vision (ICIEV). 2013: Dhaka. p. 1-5.

[4] Yuan, X., J. Chai, and Y. Li, Control of variable pitch, variable speed wind turbine in weak grid systems. 2010 IEEE Energy Conversion Congress and Exposition (ECCE), 2010. p. 3778-3785.

[5] G., d.A.R. and P.J. A., Participation of Doubly Fed Induction Wind Generators in System Frequency Regulation. IEEE Transactions on Power Systems, 2007. 22(3): p. 944-950.

Advanced Materials Research Vols. 986-987 (2014) pp 1205-1209

doi:10.4028/www.scientific.net/AMR.986-987.1205

Decoupling control strategy for Conergy three-level three phase grid converter

Shimin Shan[1, a], Weichi Ou[1, b] and Ya Feng[1]

[1] School of Automation, Wuhan University of technology, Wuhan, China, 430070

[a]jerry299288@whut.edu.cn, [b]7844508@qq.com

Keywords: grid converter; three-level NPC; decoupling control; closed-loop control; power factor;

Abstract. Conergy three-level NPC topology is often used in grid connected inverter due to its high efficiency, fewer switching devices and better EMI performance. Traditional half-bridge topology can be transformed to Conergy NPC topology by adding bi-direction switches. This paper proposed a novel control strategy for Conergy three-level NPC three phase grid converter with real and reactive power closed-loop controller in the synchronous d-q rotating frame. The power control loop is based on the feed forward decoupling of d-axis and q-axis components of the output current, thus the active and reactive power can be controlled separately. Additionally a proportional-integral controller is added to enhance the robustness of the power controller. Simulation results verify the effectiveness of the proposed strategy.

Introduction

Grid converters for applications such as wind power system and photovoltaic have gained more and more attention in recent years, demanding for outstanding efficiency and relatively low cost [1]. Neutral point clamped (NPC) multi-level topology has a lower voltage rising rate, lower switching losses and higher inverter efficiency compared to the traditional two-level full-bridge circuit. As a variant of classical NPC three-level topology, Conergy NPC three-level topology is suitable for grid converters due to its high efficiency, fewer switching devices and better EMI performance [2].

Grid converters should comply with strict power quality requirements before they are allowed to be connected to the power grid. Apart from those requirements, power factor is frequently mentioned. Usually the power factor for photovoltaic inverters should be interpreted as a requirement to operate at a unit power factor [3]. In wind power generation, Grid Codes require the grid converter to behave like conventional synchronous generator and the reactive power demand can be calculated by its set point, power factor controller or voltage controller. In smart grid concept, flexible AC transmission devices such as STATCOM and UPFC are required to injected specific reactive power into the power system for local compensation or to support the AC voltage.

In this paper, a novel control strategy for Conergy NPC three-level three phase grid converter is proposed. The topology and its modulation method are first introduced. Then the mathematical model of the proposed grid converter in synchronous d-q rotating frame is studied and analyzed. Forward decoupling current control is employed to realize the separate control of real and reactive current. Then the closed-loop controller for active and reactive power is implemented, with PI controllers regulating the reference current in synchronous d-q rotating frame. Finally some simulation results are presented and conclusion made.

Topology and modulation method

A transformation from classical 2-level full bridge topology to the Conergy NPC 3-level is achieved by adding “clamping circuit”, which differs from the diode clamp three-level NPC topology. Alternate choices for the “clamping circuit” include two IGBTs connected in inverse parallel, or a single reverse blocking IGBT [4] [5].

The topology is shown in Fig. 1 (a), in addition to the buses “P” and “N” connected to the positive and negative of DC source respectively, the neutral point bus “M” is also essential. The ‘midpoint’ or ‘neutral point’ is obtained by adding capacitors of exactly the same capacity between bus P and M

and between bus N and M. Compared to the diode-clamping NPC, there is no need for additional diodes meanwhile the IGBT body diodes are used as current path. The new topology would require six additional isolated gate drives for the clamping switches.

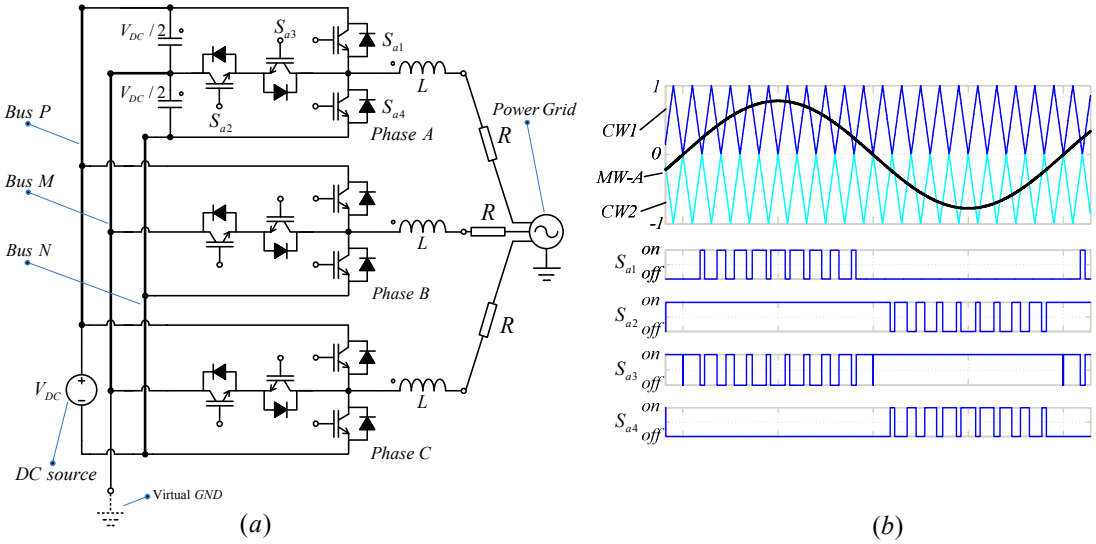

Fig. 1 (a) Schematic of the three-level Conergy NPC three-phase Grid Converter; (b) Bipolar SPWM modulation for phase A of the grid converter

In general three-phase SPWM modulation method three sinusoidal modulation signals with a phase shift of 120 degrees to each other are used to produce balanced three phase AC voltages. New pulse generation method for the proposed converter requires some modifications. Take phase A as an example, the only difference for the other two phases is the phase shift angle [6].

Apart from positive and negative states, the new method should also generate zero states for the converter. Like the bipolar SPWM modulation method, carrier are bipolar isosceles triangle waves, modulated wave is in phase with the output sine wave. The modulation method is shown in Fig .1(b). The corresponding switch states for generating positive and negative voltage is show in Table 1.

Table 1 Switch states

Voltage	Sa1	Sa2	Sa3	Sa4
Positive	on	on	off	off
0	off	on	on	off
Negative	off	off	on	on

Positive polarity carrier *cw1* and negative polarity carrier *cw2* were compared with the modulation wave *mw-A*. In the positive half cycle of the modulation sine wave, *Sa2* remains conductive and Sa4 remain off short, compare *mw-A* with *cw1* to generate two complementary drive signals for *Sa1* and *Sa3*; During the negative half cycle of the sine wave, it is similar to the positive situation.

Mathematic model

Assume the converter is connected to ideal three phase power grid through a low pass L-R filter shown in Fig. 1(a). The general mathematical model in the three phase system is first established and transformed into a d-q frame which is rotating at the angular speed omega. The mathematic model of the Grid converter in the d-q frame can be expressed Eq. 1 [7].

In equation Eq. 1 *ed* and *eq* represent components of the grid voltage. *Vd* and *Vq* are components of the equivalent output voltage of the converter. The coupling terms in the equation will affect the dynamic characteristics of the grid converter. In order to control real power and reactive power separately, some decoupling method is necessary.

$$\begin{cases} e_d = L\dfrac{di_d}{dt} + Ri_d - \omega L i_q + v_d \\ e_q = \omega L i_d + L\dfrac{di_q}{dt} + Ri_q + v_q \end{cases} \tag{1}$$

Decoupled d-q current control

Grid converter's power control is based on the instantaneous power theory and the control strategy is implemented in the d-q frame [8]. This method makes it very convenient to control real and reactive current directly, which are in proportion to the real and reactive power. The current regulator also employs the proportional-integral control method and the expression is the controller is Eq. 2.

$$\begin{cases} v_q = -(k_{iP} + \dfrac{k_{iI}}{s})(i_{q,ref} - i_q) - \omega L i_d + e_q \\ v_d = -(-k_{iP} + \dfrac{k_{iI}}{s})(i_{d,ref} - i_d) + \omega L i_q + e_d \end{cases} \tag{2}$$

kiP and *kiI* are parameters in current loop proportional integral controller. *Idref* and *iqref* are current command in d-q frame. Substituted the current controller Eq. 2 into the mathematic model Eq. 1, expression of id in Eq. 3 does not contain the variable *iq*, the decoupling is realized.

$$\begin{cases} \dfrac{di_d}{dt} = -\left[R - (k_{iP} + \dfrac{k_{iI}}{s})\dfrac{1}{L} \right] i_d - \dfrac{1}{L}(k_{iP} + \dfrac{k_{iI}}{s}) i_{d,ref} \\ \dfrac{di_q}{dt} = -\left[R - (k_{iP} + \dfrac{k_{iI}}{s})\dfrac{1}{L} \right] i_q - \dfrac{1}{L}(k_{iP} + \dfrac{k_{iI}}{s}) i_{q,ref} \end{cases} \tag{3}$$

The above results indicate that after the feed forward decoupling process, the cross effect between the d and q axis components of the output current will be eliminated. Therefore real and reactive current can be controlled separately shown in Fig. 2(a).

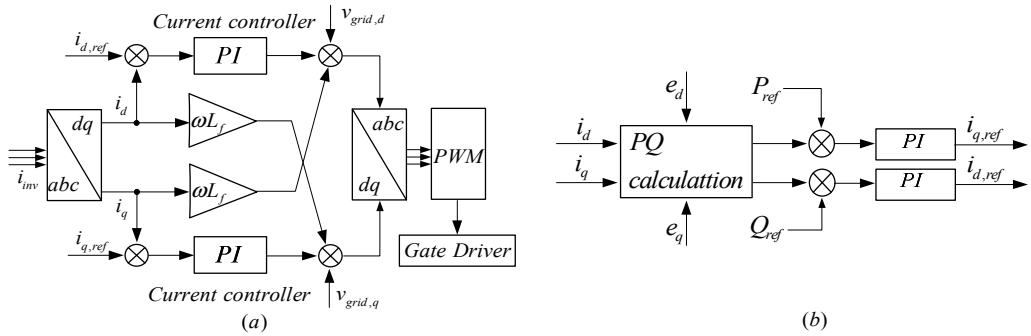

Fig. 2 (a) Decoupled current control in d-q frame; (b) Real and reactive power closed-loop control

The expression of d axis and q axis component are similar to each other and they share the same system parameters. Same controller can be applied to both d axis and q axis components, whether in the double closed-loop situation or just a single current closed-loop situation.

Power Control

In instantaneous power theory, the active and reactive power of a balanced three-phase system in the synchronous d-q frame is calculated by Eq. 4.

$$\begin{bmatrix} P \\ Q \end{bmatrix} = \begin{bmatrix} e_d & e_q \\ -e_q & e_d \end{bmatrix} \begin{bmatrix} i_d \\ i_q \end{bmatrix} \tag{4}$$

Feed-back method can be introduced to enhance this strategy. The reference real power *Pref* and reactive power *Qref* are interpreted to the reference current in d-q frame as the output of PI controller. The proposed power closed-loop controller is show in Fig. 2(b). The proportional integral power controller has the advantage to stabilize the output power when grid voltage fluctuates. Accuracy of output real and reactive power is also increased.

Simulation Results

A 5KVA simulation model for Conergy NPC 3-level 3-phase grid converter has been constructed to verify the proposed control strategy. The real and reactive power regulation command is given in the form of per unit (also known as p.u.). Base voltage is 380V and base power is 5KVA. DC bus voltage is 800V and switching frequency is 10 kHz with 2-microseconds dead time inserted. The L-R filter parameters are 4.8mH and 0.5 ohm.

Case 1: Unit power factor operation. First set the reactive power at zero and maintain unit power factor operation. Fig. 3 shows the phase voltage before L-R filter have three values: 800V, -800V and zero. The output current is sinusoidal and in phase with the grid voltage.

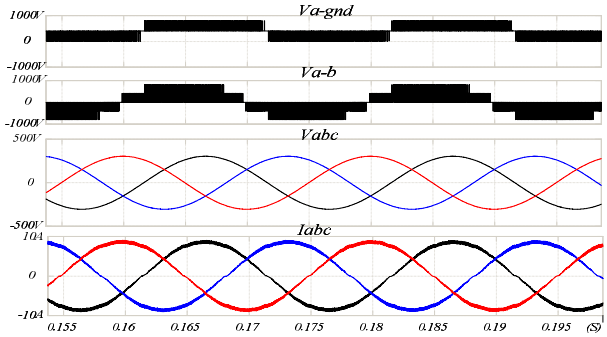

Fig. 3 Unit power factor operation

Case 2: Power command changes. Change the output real and reactive power command at 0.22s. The active power command jumps from 0.5 per unit to 0.8 per unit and the reactive power command jumps from 0 to 0.62 per unit. Power factor changes from unit to 0.627. Grid voltage, inverter current and real and reactive power is shown in Fig. 4(a) and Fig. 4(b).

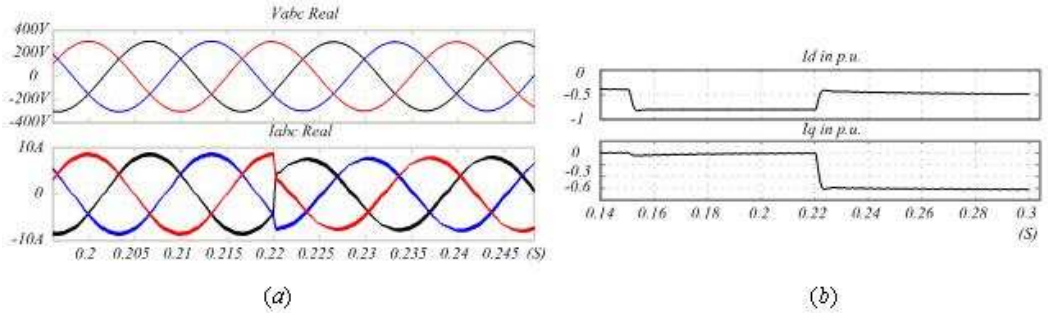

Fig. 4: (a) Grid voltage and current; (b) Real and reactive power.

Case 3: Grid voltage fluctuation. The grid voltage drops to 0.9 p.u. at 0.35s and jump back to 1.0 p.u. at 0.4s, grid voltage and inverter current is shown in Fig. 5(a). The output real power and reactive power are shown in Fig. 5(b). When grid voltage fluctuates, the output current will be adjusted to maintain the output power at its set point.

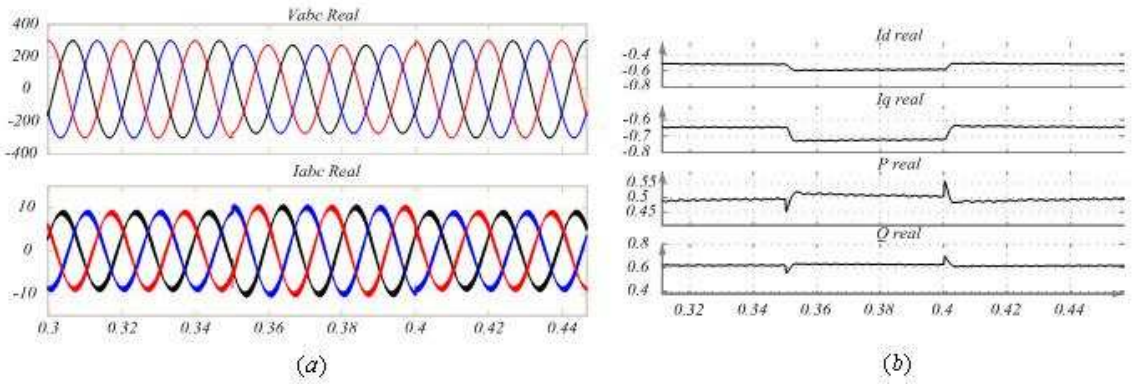

Fig. 5: (a) Grid voltage and current; (b) Real and reactive power injected into the power grid.

Conclusion

A SPWM modulation strategy for three-level Conergy NPC three-phase Grid converter with real and reactive power control based on the synchronous d-q frame is proposed. The feed forward decoupling current control loop can control the real and reactive current separately. Thus the power factor can be controlled to reach its set point. With a proportional-integral power controller, the grid converter can generate specified amount of real and reactive power. During the grid voltage fluctuation, the output power maintain constant. The proposed control strategy can enhance the robustness of the grid converter.

Acknowledgment

This work was financially supported by the National Nature Science Foundation (51177114) and Wuhan Applied Basic Research Projects in 2014.

References

[1] Li Zhang, Kai Sun, Yu Fang, in Energy Conversion Congress and Exposition (ECCE), 2013 IEEE, Sept. 2013, pp. 1623-1627.
[2] Mario Schweizer, Johann W. Kolar, IEEE Trans. Power Electron., vol. 28, no. 2, pp. 899-907, Feb. 2013.
[3] Dung H Pham, Gregory Hunter, Li Li and Jianguo Zhu, Australasian Universities Power Engineering Conference, AUPEC 2013, Sept. 2013, pp. 1-5.
[4] Xuehua Wang, Xinbo Ruan, Shangwei Liu, and Chi K. Tse, Power Electronics, IEEE Trans. Power Electron., vol. 25, issue. 12, pp. 3119-3127, Sept. 2010.
[5] Lin Ma, Kai Sun, Xinmin Jin, Electrical Machines and Systems (ICEMS) 2011, Aug. 2011, pp. 1-5.
[6] Tang Lei, Zeng Chengbi, Miao Hong, Xu Wei, Yang Yan, Power System Protection and Control, vol. 41, no. 14, pp. 13-17, Jul. 2013, in Chinese.
[7] Shuitao Yang, Fan Zhang, Jinyun Liu, Zhaoming Qian, Transaction of China electrotechnical society, vol. 21, no. 7, pp. 31-35, Jul. 2006, in Chinese.
[8] Yong Wang, Ning Gao, Yuehua Luo, Xu Cai, Proceedings of the Chinese Society for Electrical Engineering, vol. 31, no. 21, pp. 70-73, Jul. 2011, in Chinese.

Advanced Materials Research Vols. 986-987 (2014) pp 1210-1213

doi:10.4028/www.scientific.net/AMR.986-987.1210

Development and application of power transformer Oil Purifier in Line

Wang Enlu, Wang Qinghao, Zhao Chuanzong, Zhang Wenguang, Huang Yanhai, Liu Chuanbo, Liu Xiao, Zhang Xiaoshu, Tong Rui, Zhang Hua

Fushun Power Supply Company, Liaoning Electric Power Company Limited, State Grid, China,

wts55@126.com

Keywords: Transformer; Purify in line; Breakdown Voltage; Purifier; Transformer oil

Abstract. Power transformer oil purifier described in this article is equipment that filters charged transformer oil in running transformers. Transformer oil can be filtered on line to improve performance of the transformer oil. This article analyzes the necessity of the purification and filtration on processing power transformer oil, describes the overall design ideas of oil purifier in line. Through examples, power transformer oil purifier in line is further discussed the steps and precautions in the application. By comparing the power outage transformer oil purifier and oil purifier in line, the superiority and science of oil purifier in line are clarified.

Introduction

Power transformer is the core of energy conversion and transmission, also the most important and critical equipment in grid. Currently, oil-immersed transformers have been used most widely. Transformer oil is a fractionated product of petroleum. It combined with Paraffin, Naphthenic hydrocarbon, Aromatic unsaturated hydrocarbons .ect. Commonly known as the Fang Peng oil, Light yellow transparent liquid, relative density is 0.895, Freezing point less than -45 ℃[1-3].

Mainly there are effects like insulation, thermal and protective mainly on transformer oil in transformers. With the running time increased, transformer oil will be gradually deteriorated and generate a series of harmful substances. Not only degrade the insulation of transformer oil, but also affect the cooling effect because of clogging the cooling oil circuit that drive transformer heat, the safe operation of transformer is posed a threat [4,5].

In operation, degradation of transformer oil is a process which resulting in degraded performance of liquid dielectric or physical and chemical properties gradually deteriorated due to the free discharge of the electric field, magnetic field, electric arc or corona. In order to ensure the indicators of transformer oil reaches operating procedures required, the purification is needed. The role of purifier is filter, distill the deterioration transformer oil and a series of operations, remove impurities in transformer oil (water is mainly), making the index reach close to new oil standards. Then purifier is put into use in transformers again. The purpose is to achieve energy saving[6].

Significance of purify in line

As users' increasingly demanding on voltage quality and reliable continuous power supply, development and application of power transformer oil purifier online become very important. Purifier online is to purify transformer oil in running transformers, this device is using to effectively remove free carbon, water, metal particles and its oxides in the oil under normal operating conditions, dielectric strength and service life of transformer oil is ensured, safety and reliability of running transformer is effectively improved, thereby maintenance outage is reduced, maintenance cycle is extended.

According to the "Decision on accelerating the development of strategic emerging industries" made by the State Council. "Guiding Catalogue of strategic emerging industries focused on products and services," drafting of such as the National Development and Reform Commission and the Ministry of Science, the Ministry of Finance and other relevant departments, outfits of waste oil regeneration is included in renewable resources projects. This shows filtering equipment, and other similar devices will get more attention and be more widely used.

Performance and indicators

The main structure of oil purifier in line is consisted of inlet pipe, inlet valve, prefilter, heater, thermometer, automatic valve, vacuum cylinder, nozzle, buoys, suction tubes, vacuum gauge, condensers, water Chu, vacuum pumps, oil drain pump, pressure gauge, fine filter, pump, reservoir tanks, flowlines, check valves, etc. As shown in Figure 1.

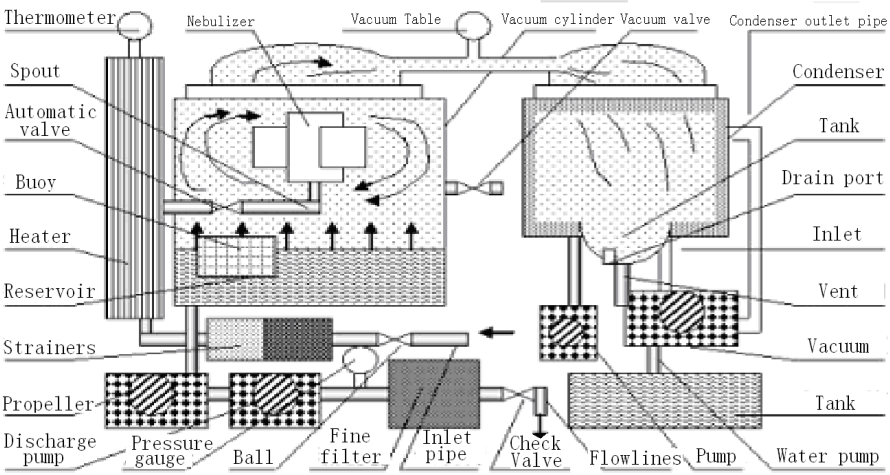

Figure 1 Technology Schematic of Oil Purifier in Line

Electrical control is another important part of the Oil Purifier in Line. The main electrical control automatically tracked by the programmable controller and inverter composed. The frequency of inverter motor kept within a certain range by electrical control, ensure that the device starts to accelerate the impact does not appear instantly. So that the whole flow stabilizes, no flow charged phenomena arises by shock, acetylene, ions flow. As shown in Figure 2.

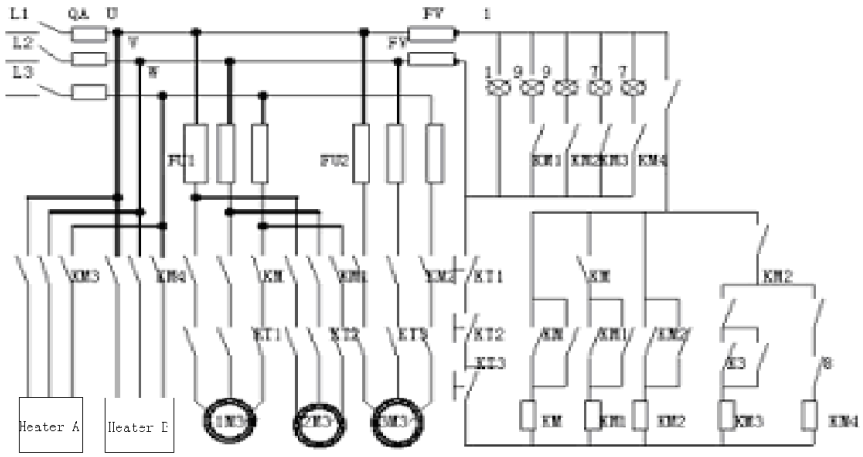

Figure 2 Electrical control of Oil Purifier in Line

Operation procedure

Two oil tank and outside-circulation line are provided, which can realize the two system trading off and subsection optimizing of change and purify oil. With filling value and outlet value are autocontrolled, synchronization effect of circulation oil flow is achieved best.Then the security of oil purifier in line is ensured. Using about one year, operating steps of oil purifier in line is tidied:

(1)Oil purifier in line should be placed on flat space (which can move, adjust direction and height), so that degassing efficiency of oil purifier in line is expressed fully.

(2)Oil purifier in line should be placed near oil level indicator, so that the accommodation of oil level can be watched.

(3) Oil purifier in line has a return value, in order to control the oil flow in operation. To avoid part of oil flow rate make too large, static friction and other disturbing factors are produced.

(4) The oil valve or reliable check valve should be installed on outlet of oil purifier in line, in order to avoid oil in storage tanks siphon back or running oil phenomenon after a temporary shutdown (such as rain), thus affecting the normal oil level in the conservator.

(5) The insertion tube of oil tanks must be inserted into the oil above 30mm.

(6) Gas in the oil escape more thorough when using oil purifier in line. Oil has a stronger intake performance, oil in the oil tank has a certain intake process and after that will produce negative pressure.

(7) The gas relay should be put into signal position before running, in order to avoid purifying gas make malfunction.

(8)Qualified oil ,about 5%～6% of all transformer oil, is prepared.

(9) Oil drain valve port at transformer bottom should be matched with the purifier tube, if not a flowline should be removed to re-weld.

(10) Regenerator in oil purifier in line must be filled with qualified oil

(11) Open the transformer oil pillow cover; the flowlines of the purifier are put into the pillow of the oil level.

(12) Inlet pipe of oil purifier in line is put into the prepared qualified oil.

(13) The oil drain valve under the transformer is opened.1%～2% of oil in the transformer is discharged.

(14) While performing step 13, oil purifier in line should be vacuumized (Not less than-0.09Mpa), and oil is synchronize supplemented into transformer oil pillow.

(15) While “Waste oil” is drained 1%～2% of all using the oil drain valve under the transformer, inlet pipe of the purifier is connected to the drain valve.

(16) At this point the purifier can work normally.

Precautions in using oil purifier on line

(1) Purifying in line must be taken in sunny day.

(2) Into and out oil of a maximum of 60L/min, with the decrease of transformer oil capacity is reduced.

(3) When purifying in line, the authenticity of oil level must be ensured and transformer oil is ensured enough.

(4) When transformer oil regenerating online, regenerating must after purifying, regenerator must be filled with qualified oil.

(5) Connections of the into-out oil tube must be carried out under the command of professionals.

(6) Before purifying in line, the purifier must be checked carefully. Oil purified performance is ensured (heating, vacuum function, filter systems) before work.

Application results of oil purifier in line

There is a S9—500/10 transformer in Li Shih Fushun Economic Development Zone, Northern Heating Co., Ltd. Because of the special requirements of electricity, the user’s power supply can not be interrupted. Otherwise it will damage the boiler and other equipment. As often running at full capacity, the phenomenon of aging comes to the transformer insulating oil. From the observation of oil pillow standard, transformer oil become black. The electrical in the plant worry about there is hidden in transformer. So they contact testing department of Power Administration test the oil sample. In accordance with national standards, breakdown voltage of transformer oil should be greater than 45kV. The test results of the transformer oil is only 19.5kV which does not meet the national standard, and also water content of 89mg/kg.According to user needs, 7th December, 2013 to 8th December,2013, “oil purifier in line” is used to the transformer purifying for 15 hours. After purifying, the results of testing the transformer oil shows that breakdown voltage reach 46kV and

water content of 41mg/kg that complying with national standards. Test results of transformer oil are shown in Table 1.Reliable protection for safe and stable operation of transformer is provided by using oil purifier in line. Potential pitfalls are solved and problems are not caused for power users.

Table 1 Test results of transformer oil

Project	Flow L/min	Moisture mg/kg	Breakdown Voltage kV
Before	---	89	19.5
After	50	41	46

Conclusion

Currently, State Grid Power Company of Fushun use oil purifier in line on transformers for 10kV and below, and obtain successful experience. The effect is also satisfactory. For 66kV and above voltage level of transformer has no courage to adopt oil purifier in line. The main consideration is when purifying in line transformer oil is pressured into the transformer by purifier. The oil may contain a lot of bubbles. These bubbles will produce free at a higher voltage. Perhaps insulation of transformer oil will be declined. In severe cases, even lead to internal discharge.

With the development of electronics, sensors, and control and other technology, carried out oil purifying on 66kV and above voltage level transformer is not only feasible, but also is the future research directions and goals.

Reference

[1] Baoding Tianwei Electric Co., Ltd. Transformer Test Technology [M].Machinery Industry Press,2000

[2] "Transformers" magazine editorial department. Power transformer design and calculation methods [M]. Liaoning Science and Technology Press, 1988

[3] Zhang Zhibao. Transformer Principles and Applications [M]. Chemical Industry Press, 2007

[4] Fang Daqian. Quick-speed manual count transformer [M]. China Water Power Press,2004

[5] Yin Kening. Transformer Design Principles [M]. China Electric Power Press,2003

[6] Ping Shaoxun ,Zhou Yufang. And analysis of operation of power system neutral grounding. China Electric Power Press,2010

Advanced Materials Research Vols. 986-987 (2014) pp 1214-1217

doi:10.4028/www.scientific.net/AMR.986-987.1214

Distributed Reactive Power-Voltage Control Method of Micro-grid

Yuwei Li

School of Electrical & Electronic Engineering,

North China Electric Power University, Beijing 102206, China

Email: 1162062263@qq.com

Keywords: Micro-grid; Distributed generation; Droop control; Distributed control.

Abstract. For micro-grid with multiple distributed power supply, a micro-grid distributed reactive power-voltage control method is proposed in this paper. By introducing active power disturbance, the load reactive power can be distributed in accordance with the distributed generation power rate, which leads to accurate distribution. At the same time, in order to ensure system voltage output stability in the rate, based on consistency and input/output linearization theory, under the distributed power multi-agent network topology, the distributed nonlinear co-droop controller is designed to make up for voltage fluctuation caused by active power disturbance. The simulation results verified the correctness and feasibility of the proposed control method.

Introduction

Micro-grid is a kind of medium or low voltage distribution power system, which assembled by a variety of forms of distributed power supplies, energy storage devices, loads, the control units and protections. In recent years, many scholars have carried out related researches on above issues: When the resistive and inductive components of micro-grid line impedance can not be ignored, paper [1-2] proposed a decoupling coordinate transformation method which based on virtual power, virtual frequency and voltage, to solve the problem of power control coupling. However, these methods can not completely eliminate the reactive power allocation errors while improving the stability of the micro-grid system, also, they need more accurate line parameters. In [3], it adopts virtual output impedance to overcome power coupling, inhibit the affection of impedance differences on the accuracy of power allocation. However, the introduction of virtue impedance makes the system voltage quality lower, and increased instability in the system at the same time. In [4-5], a method is put forward to compensate for the line impedance characteristics and distribution errors caused by local loads by introducing virtual inductance, but the droop coefficient of this method is difficult to get.

Under the distributed power multi-agent network topology, based on consistency and input/output linearization theory, the distributed nonlinear co-droop controlling is used to keep the micro-grid voltage stable. Power controller based on distributed control design is improved, which makes it can not only ensure the reasonable distribution of the load reactive power, but improve the quality of the system output voltage at the same time. In this paper, a power control method is proposed, it introduced active power disturbance to compensate for reactive power distribution error. The proposed method can not be affected by micro-grid line impedance characteristics, the influence of local loads and the influence of the topology structure, in another word, it can not only ensure the accuracy of load reactive power allocation but also maintain the stability of the system voltage.

Distributed Voltage-reactive Power Control Method

For each distributed power supply with its multi-agent, the general form of the distributed control is:

$$\boldsymbol{u}_i = \alpha_i(s_{i0}\boldsymbol{y}_0, s_{i1}\boldsymbol{y}_1, s_{i2}\boldsymbol{y}_2, \ldots, s_{in}\boldsymbol{y}_n) \quad i = 1,2,\ldots,n \tag{1}$$

where $\boldsymbol{y}_0$ represents the output of distributed control. $\boldsymbol{y}_i, i=1,2,\cdots,n$ represents the output of distributed power number i. The multi-agent network topology matrix is showed as following:

$$\boldsymbol{S}=\begin{bmatrix} s_{10}(t) & s_{11} & & \cdots & s_{1n}(t) \\ s_{20}(t) & s_{21}(t) & s_{22} & \cdots & s_{2n}(t) \\ \vdots & \vdots & & \ddots & \\ s_{n0}(t) & s_{n1}(t) & s_{n2}(t) & \cdots & s_{nn} \end{bmatrix} \in \mathbb{R}^{n\times(n+1)} \tag{2}$$

where $s_{ii}(t)=1$.when the distributed power number i can get the information of distributed power number j: $s_{ij}(t)=1$, otherwise: $s_{ij}(t)=0$. When the distributed power number i can get the information of leading agent: $s_{i0}(t)=1$, otherwise: $s_{i0}(t)=0$.

For reactive power-voltage droop control, derivative should be introduced for linearization. As following, in the distributed power multi-agent network topology, based on input/output linearization and consistency theory, the distributed nonlinear co-droop controlling is used to keep the micro-grid voltage stable.

For the nonlinear system:

$$\begin{cases} \dot{\boldsymbol{x}}_i = \boldsymbol{f}(\boldsymbol{x}_i)+g(\boldsymbol{x}_i)u_i \\ y_i = h(\boldsymbol{x}_i)+D_i u_i \end{cases} \tag{4}$$

where $\boldsymbol{x}_i$ is state variable; u_i is control input;$u_i=E_{oi}$; $\boldsymbol{\zeta}_i$ is disturbance input; y_i is the output of the system; $y_i=v_{odi}$; h_i is output function; $\boldsymbol{A}_i$, $\boldsymbol{B}_{1i}$, $\boldsymbol{B}_{2i}$, D_i are corresponding matrix; vector field $\boldsymbol{f}(\boldsymbol{x}_i)=\boldsymbol{A}_i\boldsymbol{x}_i+\boldsymbol{B}_{1i}\boldsymbol{\zeta}_i$, $g(\boldsymbol{x}_i)u_i=B_{2i}u_i$, $D_i=0$.

Due to the control input $u_i=E_{oi}$, the output of the system $y_i=v_{odi}$ is nonlinear, and it meets the equation $v_{odi}^2=E_{oi}^2-v_{oqi}^2$, by solving two differential, we can get:

$$\ddot{y}_i = L_f^2 h(\boldsymbol{x}_i)+L_g L_f h(\boldsymbol{x}_i)u_i \tag{5}$$

$$u_{vi}=\frac{-L_f^2 h(\boldsymbol{x}_i)+v_i}{L_g L_f h(\boldsymbol{x}_i)} \tag{6}$$

In that case, a system which has been accurate linearized can be got, it has new coordinate system: $\boldsymbol{z}_i=[z_{1i},z_{2i}]^{\mathrm{T}}=[v_{odi},\dot{v}_{odi}]^{\mathrm{T}}$. The linear relationship can be described as $z_{1i}=y_i$, $\dot{z}_{1i}=z_{2i}$, $\dot{z}_{2i}=v_i$; $\boldsymbol{A}$, $\boldsymbol{B}$ are the coefficient matrices of the newly established linear equation.

Assuming the distributed control law to be:

$$v_i=-\boldsymbol{\alpha}_{vi}[D_{i0}\boldsymbol{z}_{oref}+\sum_{j=1}^{n}D_{ij}\boldsymbol{z}_j-\boldsymbol{z}_i]=-\boldsymbol{\alpha}_{vi}\boldsymbol{e}_{vi} \tag{7}$$

where $\boldsymbol{\alpha}_{vi}$ represents the voltage feedback matrix, $\boldsymbol{e}_{vi}$ represents voltage error, $\boldsymbol{z}_{oref}=[v_{oref},0]^{\mathrm{T}}$.

According to the theory of optimal control for linear systems, optimal control volume meets the following conditions:

$$\begin{cases} v_i=-\boldsymbol{\alpha}_{vi}[D_{i0}\boldsymbol{z}_{oref}+\sum_{j=1}^{n}D_{ij}\boldsymbol{z}_j-\boldsymbol{z}_i] \\ \boldsymbol{\alpha}_{vi}=\boldsymbol{B}^{\mathrm{T}}\boldsymbol{P} \\ \boldsymbol{P}\boldsymbol{A}+\boldsymbol{A}^{\mathrm{T}}\boldsymbol{P}-\boldsymbol{P}\boldsymbol{B}\boldsymbol{B}^{\mathrm{T}}\boldsymbol{P}+\boldsymbol{Q}=\boldsymbol{0} \end{cases} \tag{9}$$

Improved Power Controller

Firstly, the distributed collaborative droop control make the load power an initial allocation, when a compensate signal is sent by the distributed control system, using sampling/retainer to preserver the active distribution state at this time, so a preparation for the next step can be made. Secondly, introducing the active disturbance to realize the accurate distribution of load power in improved power controller, also reactive power distribution error caused by the distributed collaborative droop control can be compensated by introducing active disturbance. The expression of the proposed improved power controller can be got as following:

$$\begin{cases} w_i = w_{oi} - (m_{Pi} \cdot P_i + K_{\mathrm{I}} \cdot n_{Qi} \cdot G \cdot Q_i) \\ E_i = E_{0i} - n_{Qi} \cdot Q_i + K_{\mathrm{C}} \cdot G \cdot \int_t Q_i \mathrm{d}t \\ E_{oi} = \dfrac{-L_f^2 h(\boldsymbol{x}_i) + \{-\boldsymbol{\alpha}_{vi}[D_{i0}\boldsymbol{z}_{oref} + \sum_{j=1}^{n} D_{ij}\boldsymbol{z}_j - \boldsymbol{z}_i]\}}{L_g L_f h(\boldsymbol{x}_i)} \end{cases} \tag{12}$$

In the equations above: G represents the soft gain compensation of the synchronization signal; K_{I}, K_{C} respectively represent the active disturbance gain and the integral control gain. All distributed generations choose the same K_{C}.

Due to the introduction of active disturbance, the voltage quality will be affected in the process of power control; the proposed distributed collaborative droop control can make the precise distribution of voltage quality in power load and improve the voltage quality at the same time through dynamic adjustment.

Simulation Analysis

In order to test and verify the correctness of the presented control method, the 380V/50Hz independent micro-grid system which is in island operation is used to make simulation experiment; the system is showed in Fig.1. In this micro-grid system, there is 5 DG and 6 loads, the line parameters are mostly with resistance, are Z_i=3.46+j1.52Ω. Load parameters of this system are: $P_{L_1} = P_{L_2} = 20k\mathrm{W}$, $Q_{L_1} = Q_{L_2} = 9.75k\mathrm{Var}$, $P_{L_3} = P_{L_4} = 6.67k\mathrm{W}$, $Q_{L_3} = Q_{L4} = 3.75k\mathrm{Var}$, $P_{L_5} = P_{L_6} = 20k\mathrm{W}$, $Q_{L_5} = Q_{L_6}$ $7.5k\mathrm{Var}$, the output impedance of each distributed generation is: Z_{g1}=0.1+j0.2Ω, Z_{g2}=0.4+j0.4Ω, Z_{g3}=0.5+j0.5Ω, Z_{g4}=0.7+j0.8Ω and Z_{g5}=1+j0.8Ω.

The droop control module is made up of power control, voltage control and current control. In the distributed collaborative control, let $\boldsymbol{Q} = diag\{6000,10\}$, voltage feedback matrix can be got by equation (9): $\boldsymbol{\alpha}_v = [77.4597 \quad 12.8421]$.

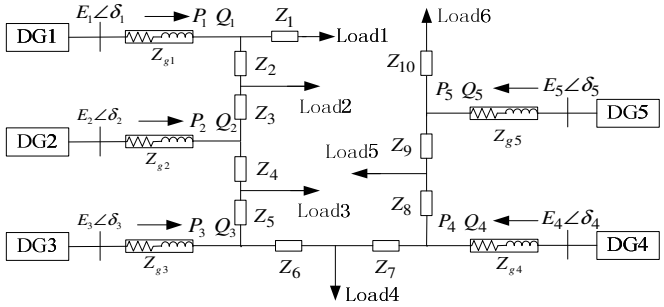

Fig. 1 Structure of simulated micro-grid system

In order to make the distributed power allocate according to the proportion of the load capacity S_i^*, the droop coefficient should be inversely proportional to its capacity, where $Q_{i\text{-}j}$ represents the power sharing ratio $Q_i : Q_j$.

According to Fig.2(a-b), DG3, which has the smallest droop coefficient, takes the least reactive power, this kind of reactive power allocation is unfavorable to the stable operation of the micro-grid. After the introduction of active disturbance power controller, the distributed power can share the reactive load according to its own capacity, The ratio among the output power of the distributed power $Q_{1\text{-}5}$, $Q_{2(3)\text{-}5}$ and $Q_{4\text{-}5}$ are tending to the required power sharing ratio 3, 2.5 and 1.5.

In order to verify the effectiveness of the proposed improved control method, each distributed power droop coefficient was reduced to 1/10 of the original, and the simulation result is shown in figure 2(c) of the dotted line. The overshoot and oscillations of the dynamic response are also improved comparing to the distributed collaborative droop control.

In order to get a further verification of the distributed collaborative droop control method, as it shown in Fig.3 (a-b), comparing to the traditional droop control, the distributed collaborative control can make the output of DG voltage stable in the rating or make the deviation very small. Therefore, the improved load power allocation method which based on the distributed collaborative

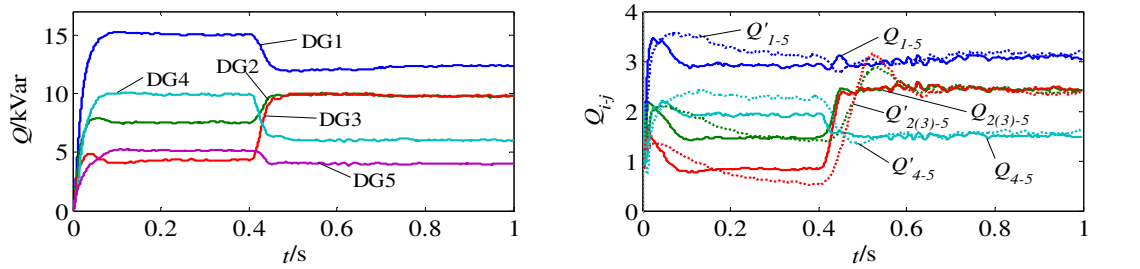

(a) DG reactive power distribution (b) DG reactive power ratio change among

Fig. 2 Simulation results of power sharing

droop control can ensure an accurate allocation of reactive power; also, it can make the control system with a control function of making the voltage constant.

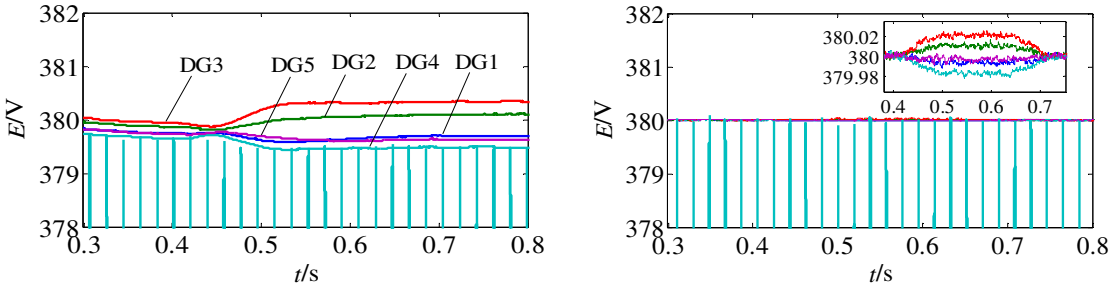

(a) (b)

Fig. 3 DG voltage curves under different control modes (a) with traditional droop control method (b) with distributed collaborative droop control method

Conclusion

In the independent micro-grid, to solve the problem of reactive power allocation among the distributed power supplies and the voltage quality problem, in this paper, a islanded micro-grid distributed reactive power-voltage control method has been put forward, the method is based on the analysis of factors that influencing the power allocation. In the distributed generation with multi-agent, based on the theory of consistency and input/output linearization, the nonlinear distributed collaborative droop controller was designed. Furthermore, on the above basis, we introduced active power disturbance to compensate the distribute error of the load reactive power. In that cases, the reactive power can be distributed precisely, at the same time, the stability of the system voltage can be guaranteed and the system can get good dynamic and steady-state characteristics.

References

[1] De Brabandere K, Bolsens B, Van-den-Keybus J, et al. A voltage and frequency droop control method for parallel inverters[J]. IEEE Trans on Power Electronics, 2007, 22(4): p. 1107-1115.

[2] Li Y, Li Y W. Power management of inverter interfaced autonomous microgrid based on virtual frequency-voltage frame[J]. IEEE Transactions on Smart Grid, 2011, 2(1): p. 30-40.

[3] Guerrero J M, Garciade V L, Matas J, et al. Output impedance design of parallel-connected UPS inverters with wireless load-sharing control[J]. IEEE Transactions on Industrial Electronics, 2005, 52(4): p. 1126-1135.

[4] Li Y W, Kao C N. An accurate power control strategy for power-electronics-interfaced distributed generation units operating in a low-voltage multibus microgrid[J]. IEEE Transactions on Power Electronics, 2009, 24(12): p. 2977-2988.

[5] Li Y, Li Y W. Power management of inverter interfaced autonomous microgrid based on virtual frequency-voltage frame[J]. IEEE Transactions on Smart Grid, 2011, 2(1): p. 30-40.

Advanced Materials Research Vols. 986-987 (2014) pp 1218-1221

doi:10.4028/www.scientific.net/AMR.986-987.1218

Marine fuel boiler system design platform

Hou Ying-ying

Zaozhuang Vocational College of Science & Technology, TengZhou , 277500

Keywords: Signal interface, analog, digital, PLC Design

Abstract. This design platform consists of a computer control, signal interface and PLC or IPC and other components. Signal interface consists of analog and digital input and output board composition, these boards are equipped with signal conditioning and terminal board, the input and output to meet industry standards, can be directly connected with the actual computer control system, this article will focus on the signal interface.

Introduction

There are a lot of marine fuel boilers and analog switches, when the boiler system simulation, it involves a lot of input and output analog switch status and size[1]. The design of the boiler simulation system made of industrial objects connected via simulation platform and actual PLC controller via analog input and digital input boards USB2832 card PCI2310 read control signal PLC controllers into the boiler simulation system , and calculate the corresponding action in the model, and then the switch state model and calculate the analog output board USB2833 and PCI2310 information to the PLC via analog controller as input PLC, constitutes hardware-in -the-loop (HIL) simulation systems. This HIL simulation platform can be used for a variety of test and validate the control system development process, but also as curriculum design, graduate design and other aspects of the control algorithm or the controlled object validation tools in teaching.

Platform structure

This design platform consists of a computer, signal interface and PLC or IPC and other controller. Signal interface consists of analog and digital input and output board composition, these boards are equipped with signal conditioning and terminal board, the input and output to meet the industry standard, you can connect directly with the actual computer control system, will be the focus of this chapter describes the signal interface[2]. To achieve the controlled object model and the controller signal via signal interface, can be composed of HIL simulation system.

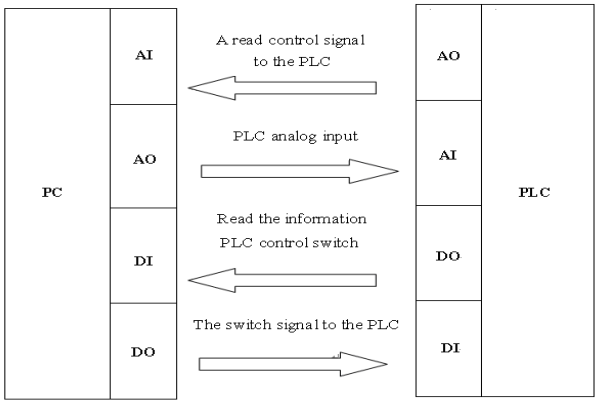

Figure1 Computer and PLC connection diagram

Figure 1, for example in marine fuel boiler, analog and digital simulation model output signal is the output signal is regarded as the boiler pressure and temperature sensors as the input signal from the controller; analog simulation model inputs and switches semaphore signals seen as a controller for the water supply valve and fuel valve.

Signal Interface

Analog input data acquisition card. USB2832 is a USB bus-based data acquisition card, the computer is directly connected to the USB interface can be achieved. Can be used in the laboratory and product testing in areas such as data acquisition, waveform analysis and processing systems. USB2832 card with AD, DA, DI, DO, and CNT timer /counter functions, where it's used in the AD analog input function, the AD has the following characteristics[3]:

1) Converter Type: AD7321
2) Input Range: ±10V, ±5V, ±2.5V, 0~10V
3) Conversion Accuracy: 13 (Bit)
4) Sampling rate: Maximum switching frequency 500KHz chip
5) Physical Channels: 32 channels, 16 channels
6) Analog input: Single-ended and double-ended analog input
7) Sampling channels: The end of the channel - the first channel +1
8) Channel switching mode: The first end of the channel in order to switch
9) Acquisition mode: Continuous acquisition
10) Clock: Board internal clock
11) Non-linear error: ±1LSB
12) System Accuracy: 0.1%
13) Operating temperature range: 0℃~+50℃

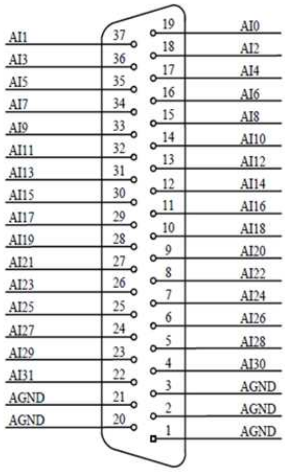

Figure2 37-pin D-type connector pin definitions Figure

Figure 2, the signal connector pin definitions: AI0 ~ AI31 as analog input pin, when a single-ended input, to 32 analog channels; When is a double-ended input, the first 16 to the positive input terminal after 16 corresponding to the negative input terminal is a terminal. AGND analog signal common ground that the analog signal input and output regarded it as a reference. Is a single-ended input channel one signal when multiple signals, they use the same ground. When the number of channels required more environmental disturbance is relatively small and can be used single-ended mode. Figure 3 is a single-ended wiring methods[4].

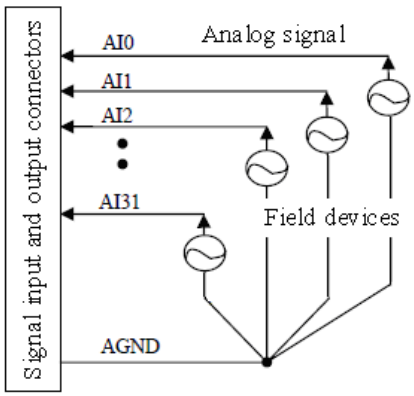

Figure3 AD single-ended input connection diagram

Analog output data acquisition card. USB2833 data acquisition card with AD, DA, DI, DO, CNT timer / counter functions used here its DA analog output function, the DA features are as follows:

1) Converter Type: AD5724
2) Output Range: 0~5V, 0~10V, 0~10.8V, ±5V, ±10V, ±10.8V
3) Conversion Accuracy: 12Bit
4) Number of channels:4
5) Setup time: 10 ms
6) Non-linear error: ±1LSB
7) Operating Temperature: 0℃~+50℃

The design of the large ones due to be greater than the analog output of 4, used a two USB2833. In order to distinguish between two USB2833, their physical ID number will be set to 0 and 1 respectively.

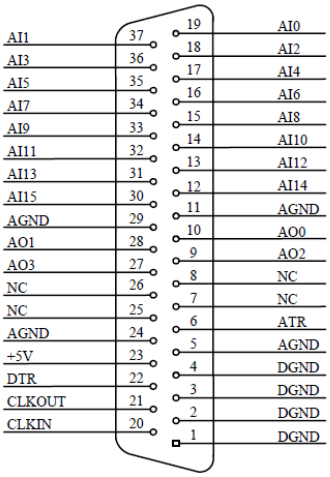

Figure4 37-pin D-type socket pins

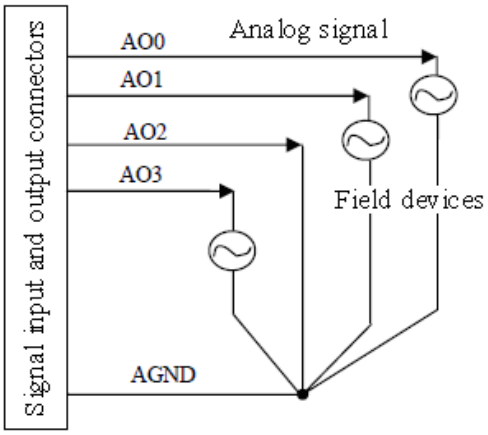

Figure5 Signal connection method DA analog output

Pin defined in Figure 4, USB2833 is: AO0 ~ AO3 analog signal output pins. AGND analog signal, the input and output analog signals it as a reference. In this design does not use the rest of the pins will not repeat them. Figure 5 is a terminal connection methods.

Connected to circuit design and PLC

In order to match the PLC connection circuit in the switch input circuit and output circuits were added to the ULN2803, namely eight NPN Darlington[5]. ULN2803 internal circuit diagram is shown in Figure 11.

Figure 6 with the first switch output DO0 example, on the basis of the actual circuit of Figure 9 plus the external power supply and pull-up resistors, ULN2803 also added the external power supply and pull-up resistors. When the output bDOSts [0] is high, the transistor is turned on, the voltage at the collector within PCI2310 low, Darlington is not conducting, DO0 is high. When the output bDOSts [0] is low, transistor PCI2310 within the non-conducting, the collector voltage is high. Darlington conduction, DO0 at a low level.

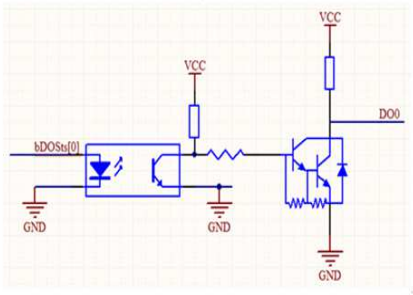

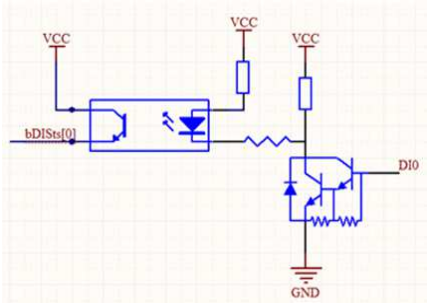

Figure6 Witch output adjustment circuit Figure7 Witch input adjustment circuit

Figure 7 with the first switch input DI0 road for example, DI0 is high Darlington conduction, the output low emitting diode conduction, and thus the transistor conduction PCI2310 inside, bDISts [0] is high. DI0 is low Darlington is not conducting, the output of the high level cannot make light-emitting diode conduction in the transistor PCI2310 have not turned on, bDISts [0] is low.

Conclusion

Industrial object simulation platform in the joint action of the hardware and software of the computer simulation model and PLC control systems to connect and communicate. Complete hardware conditions, the correct tool for the entire design is to achieve security features, and software conditions are a function of the hardware design can be achieved. In connection with the PLC controller also take into account matching of both voltage and current, load capacity issues. Constitute a virtual simulation system with the actual PLC controller connected hardware loop simulation system. When the accuracy of the computer simulation model to reach a certain requirement, this system can be developed or validation controller.

References

[1] Nei xiu-jun.Water control character analysis and design for marine boiler[J]. Journal of wuhan uniwersity of technology .2009(7):149-152

[2] Gan Hui-bing,Zhang Jun-dong. Design and realization of simulation system ofmarine boiler based on PLC[J]. Journal of Dalian Maritime University.2006(2):5-7

[3] HU Xian-fu, CHEN Ban-Zhang,XU zhi-de,et al.Proceedings of Asian simulation conference[C], 2002:491-495.

[4] S rensen K,Condra T. Modeling and Simulating Fire Tube Boiler Performance [C]. Proceedings of SIMS 2003-44th Conference on Simulation and Modeling. Sweden: Malardalen University, 2003:9-12.

[5] M E Flynn, M J O'Malley. A Drum Boiler Model for Long Term Power System Dynamic Simulation [J]. IEEE Transactions on Power Systems (S0885-8950), 1999, 14(1): 209-217.55

Advanced Materials Research Vols. 986-987 (2014) pp 1222-1225

doi:10.4028/www.scientific.net/AMR.986-987.1222

Energy Saving Matching of Power Equipment for four-footed Robot Dog

Wang Jun[1,a], Hu chuan[1,b], Zhang You-tong[2,c]

[1]Department of Mechanical Engineering, Academy of Armored Forces Engineering, China

[2]School of Mechanical Engineering, Beijing Institute of Technology, Beijing 100081,China

[a]joe4126@163.com, [b] chuanhu@126.com, [c]youtongzhang@163.com

Keywords: energy matching, power equipment, robot

Abstract. To increase the flexibility performance of robot dog, dynamic performance matching of power equipment in four-footed robot dog is made. Demand for power and configure in robot dog power equipment is briefly analyzed, improved backward power match between gasoline and pump is presented, power and flow rate match between gasoline and pump is calculated, control strategy based on pump pressure feedback is applied into gasoline engine control in order to save energy. With experimental bench test, experimental results showed that energy saving matching of power equipment can meet the requirement of fast dynamic meditation for robot dog .

Introduction

Combined with many techonolgies of articulation mechanism, hydraulic pressure transmission, electronic control and intelligent control[1], robot dog used four–footed constructure motion style so that it can do work in the harsh condition, robot dog plays an important role in emergency-saving and disaster-saving and explosion-proof. In order to make rapid reaction to the change of road surface and weight, good mobility is needed for bearing burdern four-footed robot dog, power equipment with high power density and flexible control is needed, since there are some advantages of small volume, large torque and easy control for variable bump system, and small volume, easy starting for gasoline engine[2], small gasoline engine and variable bump are selected to form power equipment. When it worked, regular change load of variable bump made gasoline engine to operate in range of high fuel consumption, engine power is not reached optimal value, power match between gasoline engine and variable pump directly affected dynamic character and stabilization, there are many literatures and technology matertials published in professional periodicals, most for hydraulic prssure grab, such as, [3] presented nomal work range in max power and lower fuel consumption area when power match between gasoline engine and variable pump is made for full hydraulic prssure grab, in order to prevent large rotation speed undulation, rotation speed of gasoline engine is controlled to optimal speed range by means of digital PID using limit load. [4] used rotation speed sensoring control strategy to adjust pump input power to match output power in gasoline engine. in order to keep operation speed of gasoline engine in range of saving energy.[5] used step-motor to reform mechical throttle valve to preform electronic control, and control step motor by microprocess 68376, so that opening angle of electricity throttle valve is effectively controlled, all these literatures are focus on stable condition. According to requirement of high speed reaction to transient operation of robot dog, based on electronic controlled reforming for foreign single cylinder, improved backward match method based on bump pressure feedback is presented, calculation process of work flow rate for variable pump and savign energy match of gasoline engine is given, final match test is made to verify match validity.

1 Power Equipment

Four-footed bearing-burden robot dog is made up of power equipment, articulation structure, hydraulic pressure system, electric control system, sensoring system and top controller, as shown in figure 1.

According to overall sketch requirement, overall index for power equipment is large power, light weight, high reliability, high ratio of performance and price, its technical parameter is : power 20kW, weight 20kg , hydraulic pressure 20MPa, foreign gasoline engine with two strokes and

single cylinder is selected as power resource, electronic controlled threttle valve and electric control system are added to this gasoline engine,it performs precision control and profile mediation, power equipment arrangement is shown in figure 2, the technical parameter of gasoline engine is power 20kW, Max rotational speed 18000 r/minm, Max torque 100N m and hydraulic bump is power 14kW, Max rotational speed 4000 r/minm, Max torque 80N m. Gasoline engine provided power to robot dog, rotation of variable pump is driven by crankshaft of gasoline engine, load is input torque of variable pump, according to change of road surface and weight, flow rate is continued to mediate and to keep hydraulic pressure system in stable condition, electronic control system automatically regulated throttle valve angle to meet real power demand according to system pressure.

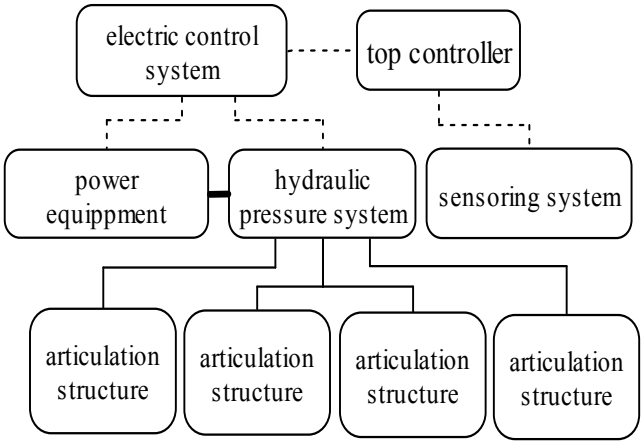

Fig.1 Basic constructure of robot dog

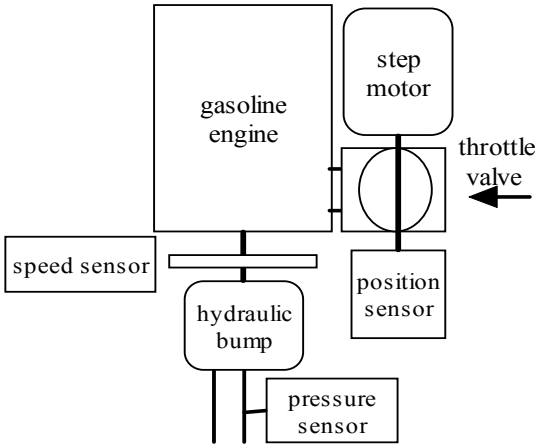

Fig.2 Arrangement of power equipment

2 Match Method

The goal of saving energy match in dynamic equipment is that rotation speed and output torque of gaoline engine can adapt to external load and continue to change, and it makes real work point of gasoline engine to optimal saving energy point: high power and lower fuel consumption. while it fullfils basic match among gasoline, variable pump and external load. Three are two kind of traditional match method: forward match and backward match, backward match method is improved to increase dynamic equipment, its principle is shown in figure 3.

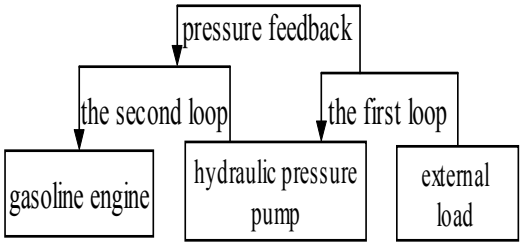

Fig.3 Match principle of backward match method

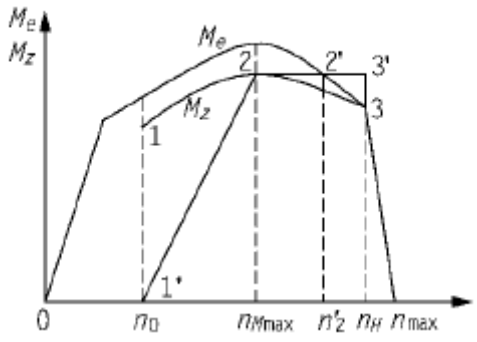

—effective engine torque z —pump load torque

Fig.4 Max engine torque character and pump target load

The first loop fullfils match between pump and external load, self–adaption control is used to adjust output flow to meet the demand of robot dog. The second loop makes match btween gasoline engine and pump, closed-loop control for throttle valve is made to gasoline engine, the third loop is a connection between first loop and second loop, hydraulic pressure is used as feedback to gasoline engine to sensor the work condition of robot dog. Since road surface makes walking posture change, in order to keep balance condition of robot dog walking, it needed to fast response change of external load to gasoline engine control, output pressure of variable pump conresponds to external load, pressure change speed is higher than rotation speed in indicating change of external load, hydraulic pressure connects the two loop, hydraulic pressure is used to predict to relative torque of gasoline engine, closed-loop control for throttle valve is made to gasoline engine

according to prediction torque, it makes gasoline engine output torque to reach target and assure pump to absorb all output power of gasoline engine

3 Match Calculation

3.1 Gasoline engine

Different performance is corresponding to different operation profile of gasoline engine. When external resistance torque is equal to near 75 precent of max torque of gasoline eneine, gasoline engine will operate in optimal saving energy point and keep high ecnomy index.When external resistance torque is near max torque of gasoline eneine, gasoline engine will operate in max power point and keep high dynamic index.

When output torque of gasoline engine $M_e \in [75\%M_{e\max}, M_{e\max}]$ resistance torque M_i is given,angle acceleration speed a, rotation speed n is shown as follow.

Angle acceleration speed a: $a = \dfrac{M_e - M_1}{j_e}$ rotation speed n_e $n_e = \dfrac{\omega_0 + \alpha t}{2\pi}$ (1)

Where, M_1 is external resistance torque, Me is output torque, J_e is running inertia.

3.2 hydraulic pressure pump

Gasoline engine connects with hydraulic pressure pump by transmission case, absorbing power N_p of hydraulic pressure pump is equal to output power N_e of gasoline engine in optimal operation point.

$$N_p = p_p q_p n_p = N_e \tag{2}$$

To keep pump to work in high efficiency point and gasoline engine in good dynamic and fuel consumption, max power of engine target load is selected as control target for hydraulic transmission, pressure difference Δp is used as sensor value, output flow rate of optimal profile in pump is followed.

$$q_p = \frac{6000 N_{e\max} \eta_{pt}}{\Delta p \cdot n} \tag{3}$$

Where, Δp is pressure difference, n is rotational speed of pump, q_p is output flow rate, $N_{e\max}$ is rating power of gasoline engine.

Relation of Max torque character in gasoline engine and target load in pump is shown in figure 4. When 90 percent of max power of gasoline engine is selected as pump power,corresponding ideal load curve MZ 1-2-3, combined real condition, ‘- - ’ line is real target curve, out put flow of pump is followed.

When $n_0 \le n \le n_{M\max}$ $q_p = \dfrac{6000 \times 0.9 N_{e\max}(n - n_0)}{n_{M\max} - n_0} \times \dfrac{\eta_{pt}}{\Delta p \cdot n}$

When $n \ge n_{M\max}$ $q = q_{p\max}$

Where, $N_{M\max}$ and $n_{M\max}$ is power and rotation speed in max torque profile respectively, n_0 is starting speed of pump, $N_{e\max}$ is rated power, $n_{\min}$ is idle speed of gasoline engine.

4 Experimental verification

4.1 Matching performance

According to operation requirement of robot dog, idle speed of gasoline engine is set to 2300r/min, stable operation speed is 12000r/min, max rotation speed is 16000r/min, torque of engine and pressure of pump is measured dynamically, when engine operated in stable speed range, parameters of pump and engine are shown in figure 5. From figure 5, pump pressure change is located in 11000-12000r/min range, this rotation speed is work range of max torque in engine, it showed that load change of pump is suited to optimal operation range of gasoline.

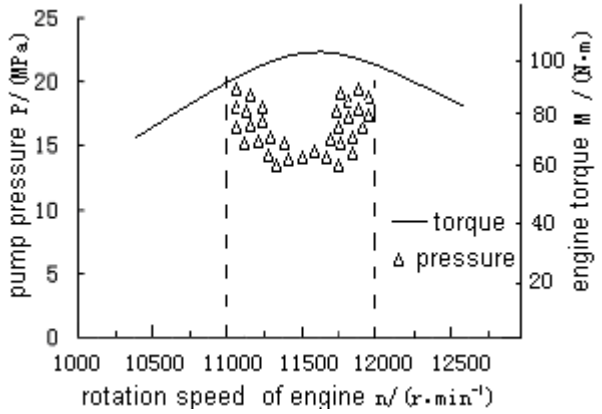

Fig.5 Parameter change of gasoline and variable pump

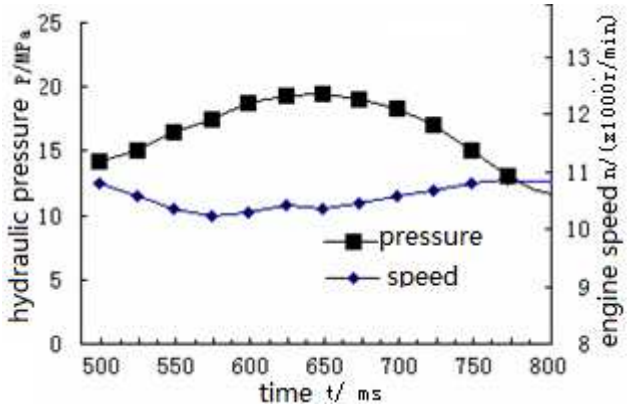

Fig.6 Rotation speed change of gasoline

4.2 Control Effect

Power equipment load is varied with walk gesture and bearing-burden condition of robot dog, in order to keep hydraulic system pressure to a fixed range, rotational speed of gasoline engine is required to control in real time by ECU and change in a given range. When hydraulic system pressure is fixed to 15-20MPa and gasoline engine rotation speed target is 10500r/min, real speed control effect under varying load is shown in figure 6. Seen from fig.6, when hydraulic system pressure is changed, real speed varied under the setting speed target, varied amplitude is about ±100r/min, and there is no oscillation speed to appear.

5 Conclusions

Acccordingto operation requirement of power equipment in robot dog, improving backward match method is presented, match calculation process of saving energy between pump and engine is provided, fast prediciton torqure by sensoring pump pressure is found for gasoline engine, saving engine in transient condition of power equipment is effectively resolved. Experimental result showed that gasoline engine can operate in high efficiency range and fast reaction meditation is achieved.

Reference

[1] Siegwart R. *Guide Theroy of Self–motion Robot*. Press of Xian Jiaotong university(2006)
[2] Yao hui xin. *Hydraulic Pressure Transmission and Control of Walking Mechanism*.Press of people transportation(2002)
[3] SU Xiuping, LI Wei,WANG Yuqiao. Machine Tool &Hydraulic, Vol.37(12)(2009),p.104-107
[4] PENG Tianhao, YANG Hua yong, FU Xin.Engineering Machine. Vol. 32(08)(2001),p:37-40
[5] Wang Dongyun, Guan Cheng.Transactions of the Chinese Society for Agricultural Machinery, 2009,40(4), p.91-96.(in Chinese)
[6] CHEN Qian gen, FEI Wang long, JIANG ping. Civil Machine. Vol. 12 (2007) ,p.64-69

Advanced Materials Research Vols. 986-987 (2014) pp 1226-1230

doi:10.4028/www.scientific.net/AMR.986-987.1226

Power Tracking Control Strategy Based on Feedback Frequency of Large-scale Grid-connected PV Generation

Ling Wang[1, a], Bei Zhao[2, b], Jianliang Zhong[2, a], Sarmad Malik[2, c], Hai Bao[2, d]

[1] State Grid Liaoning Electric Power Company Limited Benxi Electric Power Supply Company, Benxi, Liaoning, 117000, China

[2] State Key Laboratory of Alternate Electrical Power System With Renewable Energy Sources (North China Electric Power University), Changping District, Beijing, 102206, China

[a]email: email: zhongjl@ncepu.edu.cn, [b]email: alabei@126.com,

[c]email: sarmadmalik90@gmail.com, [d]hdbh@vip.sina.com

Keywords: Photovoltaic; Frequency Regulation; Power Tracking Control Strategy; Droop Control

Abstract. PV (Photovoltaic) generation output with MPPT (Maximum power point tracking) is unadjustable. In this paper, PV generation is expected to regulate grid frequency. Thus a power tracking control strategy based on feedback frequency instead of MPPT is put forward. The feedback frequency is transferred to controlling unit of DC-DC inverter. The DC bus voltage is adjusted by controlling the duty cycle of DC-DC invertor. A grid-connected PV system with a power tracking control strategy based on feedback frequency and a DC-AC inverter control module are built in MATLAB-Simulink platform. Experiment result indicates that PV generation could regulate grid frequency by the control strategy based on feedback frequency.

Introduction

Maximum power point tracking (MPPT) is widely used in Photovoltaic (PV) to make the output efficient since MPPT could achieve the max PV outputs. Nowadays with the development of large-scaled PV generation, PV generation is expected to regulate grid frequency. PV generation output with MPPT is unadjustable so that PV generation cannot participate in frequency regulation. A new control strategy is needed to take place of MPPT, which can make DC bus voltage adjustable to regulate grid frequency.

Analyzing the PV characteristic curve is the first thing to research the PV generation. In paper [1], a simulation model of PV module based on Simulink is built in accordance with PV module's physical and mathematical model. The $I \sim V$ curve of PV is determined by this physical and mathematical model. There are a lot of methods of MPPT used in PV generation, and paper [2] introduces a tracking method named P&O (Perturbation and Observation), which is the most widely applied in MPPT control for PV generation. A DC-AC inverter is the key link of the grid-connected PV generation. Paper [3] studied the deadbeat control strategy for the grid-connected current in three-phase voltage-type PV grid-connected inverter. In paper [4], the hierarchical control is applied to ac micro grids, solving the tradeoff of the droop method by implementing a secondary control loop and capable of operating in grid-connected and islanded modes.

In this paper, a power tracking control strategy based on feedback frequency is put forward. DC bus voltage is adjusted by controlling the duty cycle of DC-DC invertor. Then PV could regulate grid frequency when the frequency is fluctuating. This paper is organized as followed. In section of 'Power Tracking Control Strategy based on Feedback Frequency', PV characteristics and mathematical model are analyzed, and a new control strategy is put forward. In section of 'Control Structure of DC-AC Inverter', droop control and double loop control strategy are used in large-scale grid-connected photovoltaic inverter, which assume unbalance power of inverter. In section of 'Simulate Results', a grid-connected PV system with power tracking control strategy based on feedback frequency and a DC-AC inverter control module are built in MATLAB-Simulink platform and the waveform of DC bus voltage and active power is obtained.

Power Tracking Control Strategy based on Feedback Frequency

The solar cell equivalent model is made up of ideal current source I_s, antiparallel freewheeling diode D, series resistance R_s, and parallel resistance R_{sh}. The value of I_s is equal to the short-circuit current, which reflects the insolation and temperature of the solar cell. The I~V characteristic equation of the solar cell is shown as equation (1):

$$I = I_s - I_0 \left\{ \exp\left[\frac{q(V + R_s I)}{AKT} \right] - 1 \right\} - \frac{(V + R_s I)}{R_{sh}} \tag{1}$$

In equation (1): I is operating current of solar cell; I_s is short-circuit current; I_0 is reverse saturation current; q is charge constant; V is output voltage; A is diode P-N junction coefficient; K is Boltzmann constant; T is absolute temperature. The I~V curve will be got by equation (1). But the five coefficients including I_s, I_0, R_s, R_{sh}, A, which are related to the temperature of solar cell and insolation, and they are difficult to confirm. This model is not convenient for engineering application. Solar cells used in engineering application require several important parameters, such as I_{sc}, V_{oc}, I_m, V_m, P_m. The PV array character is equivalent to an engineering simplifying model by ignore $(V+R_sI)/R_{sh}$, and considering I=0 $I = 0$, V=V_{oc} at the condition of open circuit, while V=V_m, I=I_m at the condition of short circuit. The engineering simplified mode is showed as:

$$I = I_{sc}\left\{1 - C_1\left[\exp V/(C_2 V_{oc}) - 1\right]\right\} \tag{2}$$

$$C_1 = (1 - I_m/I_{sc})\exp\left[-V_m/(C_2 V_{oc})\right] \tag{3}$$

$$C_2 = (V_m/V_{oc} - 1)\left[\ln(1 - I_m/I_{sc})\right]^{-1} \tag{4}$$

In equations (2), (3) and (4), C_1 and C_2 can be determined by I_{sc}, V_{oc}, I_m, V_m. The I~V curve is determined by equation (2). The P~V curve is a single peak curve determined by I*V~V .

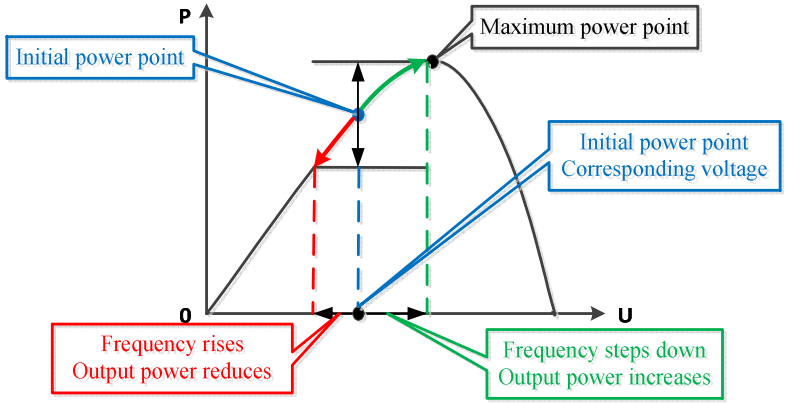

Fig.1. Power tracking control strategy on P~V curve

Fig.1 shows the theory of power tracking control strategy. In order to make the PV generation participate in regulating frequency, the output power of the DC-DC inverter control unit will not export at the maximum power point with MPPT. So the PV generation sacrifices some power. And the output voltage of DC-DC inverter is a little bit smaller than the maximum power point voltage. When the grid frequency is fluctuating, the voltage has an allowance to increase or decrease to change the duty cycle of DC-DC inverter. So the corresponding output active power is changed to regulate frequency.

TABLE 1 Adjustment of output voltage and active power based on grid frequency

		Power point on P~V curve	DC bus voltage	DC bus power
grid frequency	rise	move left	decrease	decrease
	decrease	move right	increase	increase

The power tracking control strategy is based on feedback frequency. Set the initial output power point a little bit lower than the maximum power point, in other words, the corresponding voltage is

on the left side of the maximum power point voltage. When the system frequency rises, the tracking point moves left and the output active power reduces. On the contrary, when the frequency reduces, the output active power increases. The adjustment of output voltage and active power based on grid frequency is showed in Table 1. This tracking strategy makes the PV generation output power adjustable, so the PV generation could participate in regulating frequency.

Control Structure of DC-AC Inverter

By analyzing the output characteristic of inverter, the output power is expressed as:

$$S = P + jQ = \dot{E}\dot{I}^* = \dot{E}\left(\frac{\dot{U} - \dot{E}}{\dot{Z}}\right)^* \tag{5}$$

In equation (5): E is the bus voltage of the grid side; U is the output voltage of the inverter. Suppose the angle of the grid is 0, and the power angle isφ. Z is the impedance between inverter and the grid and θ is the impedance angle with $Z\angle\theta = R + jX$. X is much bigger than R when Z is inductive by ignoring the resistance R . So Z would be considered as X, thus $\theta \approx 90°, \sin\theta \approx 1, \cos\theta \approx 0$, and then the active power and reactive power can be expressed as:

$$\begin{cases} P = \left(\dfrac{EU}{Z}\cos\phi - \dfrac{E^2}{Z}\right)\cos\theta + \dfrac{EU}{Z}\sin\phi\sin\theta \\ Q = \left(\dfrac{EU}{Z}\cos\phi - \dfrac{E^2}{Z}\right)\sin\theta - \dfrac{EU}{Z}\sin\phi\cos\theta \end{cases} \Rightarrow \begin{cases} P = \dfrac{EU}{Z}\sin\phi \\ Q = \dfrac{E}{Z}\left(U\cos\phi - E\right) \end{cases} \tag{6}$$

According equation (6), it could be obtained that P is determined byφ and Q is determined by U-E when the power angleφ is so small that it could be ignored. In this condition, P and Q could be controlled independently. Classical droop control strategy $P \sim \omega$ and $Q \sim U$ are used as the control theory of the inverter. The droop characteristic equations are expressed as:

$$\begin{cases} \omega = \omega - m_p P \\ U = U_0 - n_q Q \end{cases} \tag{7}$$

In equation (7): ω_0 and U_0 are the frequency and voltage at non-load; ω and U are the frequency and voltage in reality; m_p and n_q are the droop gain of frequency and voltage. On the basis of traditional inverter strategy, the closed-loop dynamic behavior of inverter output voltage and current control loop have to be considered. Fig.2 shows the control structure of the inverter.

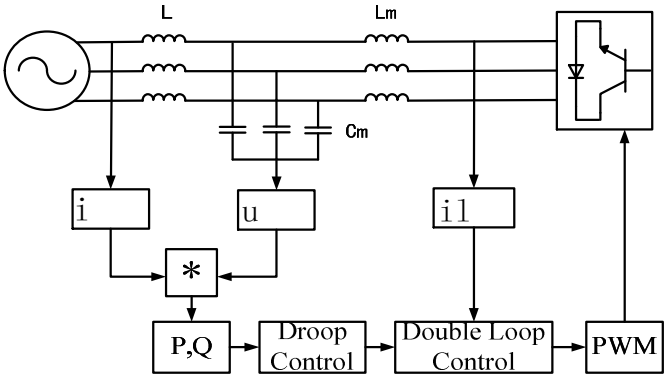

Fig.2. Control structure of the DC-AC inverter

The control structure in fig.2 includes three parts: the first part is used to calculate P and Q. The current and voltage on the AC side are transformed into the ones in dq coordinates by introducing Park's Transformation, and then P and Q could be calculated. The second part is droop control, which calculates the output voltage and frequency by PQ droop characteristic showed in equation (7). The third part is double loop control, which could reduce the high frequency interference and keep frequency stable. The double loop control structure is showed in fig.3.

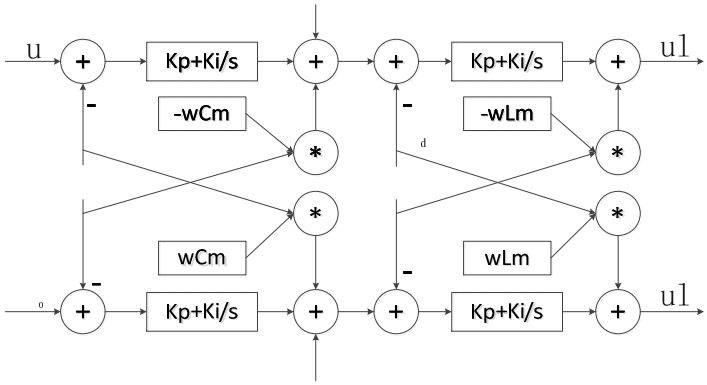

Fig.3. Double loop control structure of the inverter

Simulate Results

The grid-connected PV module is built in MATLAB-Simulink. The system simulation is showed in fig.4. Set a frequency fluctuation of the system and feed it back to DC-DC inverter control unit. According to the control of duty cycle, the DC bus output voltage and active power is adjustable. The system frequency keeps stable with PQ droop control and double loop control strategy.

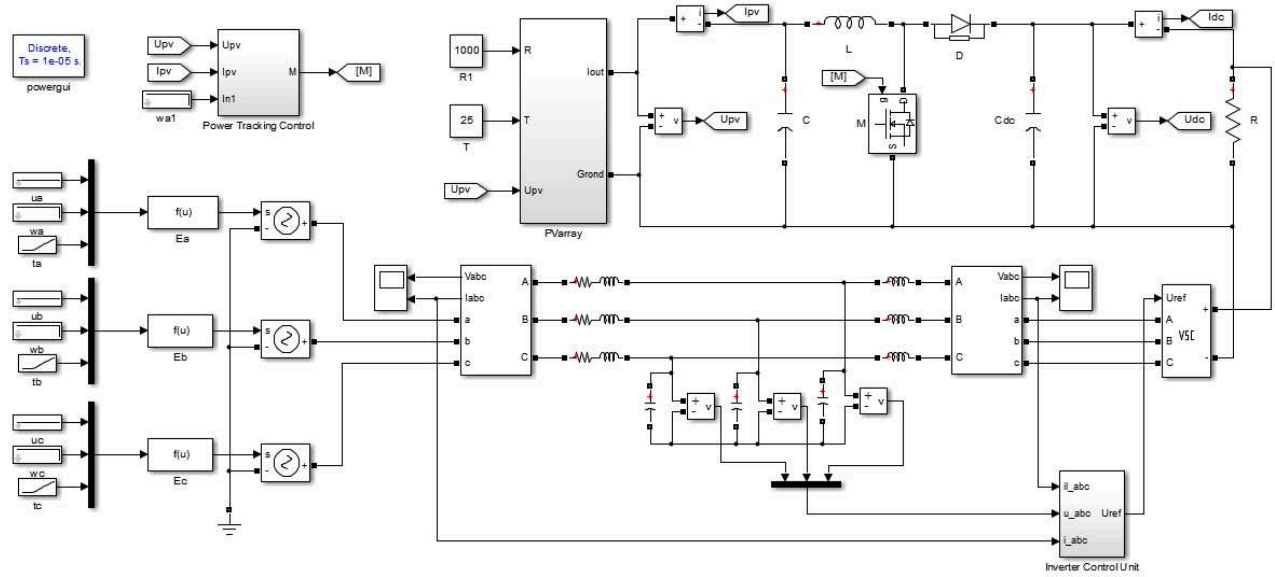

Fig.4. PV system simulation

There is a frequency fluctuation at 0.05s and the grid frequency reduces 1Hz from 50Hz to 49Hz. The tracking point on *P*~*V* curve moves to the right and the output active power increases. The duty cycle of DC-DC inverter changes to adjust the DC bus voltage. PV output power increases to regulate grid frequency. The simulation of PV output voltage and power is showed in fig.5.

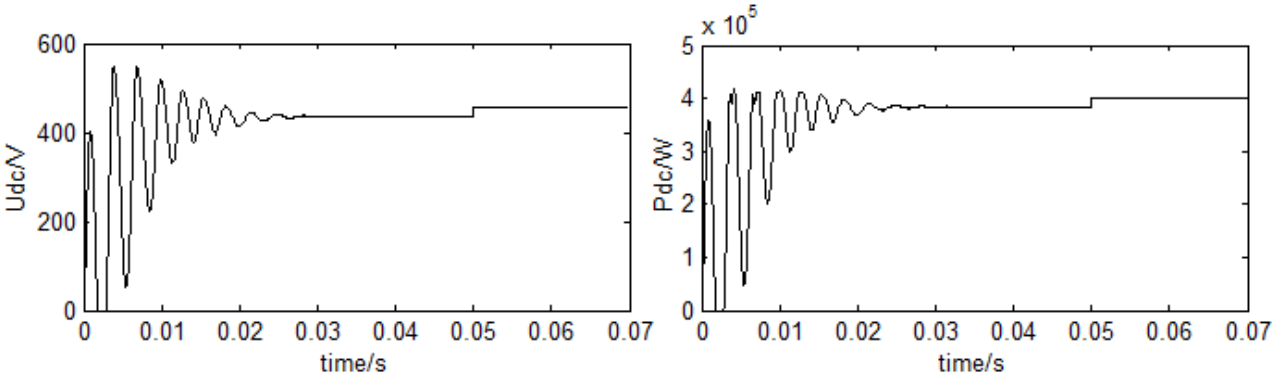

Fig.5. DC bus output voltage and power wave of the PV system simulation

When the system frequency steps down, the tracking point moves to the right then the voltage increases from 437V to 457V, and the output active power increases from 384kW to 402kW. The PV generation output adjusts quickly to adapt to the frequency and stabilize the fluctuation to keep the system frequency stable. By PQ droop control, it has a batter effect on frequency stability.

Conclusion

Based on power tracking control strategy and the control of duty cycle, the DC bus output voltage and active power are adjustable. Thus PV generation could participate in regulating frequency when the grid frequency is fluctuating. The system frequency keeps stable with PQ droop control. Double loop control could reduce the high frequency interference and keep frequency stable. The control strategy is feasible and it makes a contribution to regulate grid frequency and keep frequency constant.

Acknowledgement

This paper is supported by the National High Technology Research and Development of China (863 Program) No.2011AA05A301.

References

[1] Ding K, Bian X G, Liu H H. Matlab-Simulink Based Modeling to Study the Influence of Nonuniform Insolation Photovoltaic Array[C]//Power and Energy Engineering Conference (APPEEC), 2011 Asia-Pacific. IEEE, 2011: 1-4.

[2] Femia N, Petrone G, Spagnuolo G, et al. Optimizing duty-cycle perturbation of P&O MPPT technique[C]//Power Electronics Specialists Conference, 2004. PESC 04. 2004 IEEE 35th Annual. IEEE, 2004, 3: 1939-1944.

[3] Han G, Xia Y, Min W. Study on the three-phase PV grid-connected inverter based on deadbeat control[C]//Power Engineering and Automation Conference (PEAM), 2012 IEEE. IEEE, 2012: 1-4.

[4] Guerrero J M, Vasquez J C, Matas J, et al. Hierarchical control of droop-controlled AC and DC microgrids—a general approach toward standardization[J]. Industrial Electronics, IEEE Transactions on, 2011, 58(1): 158-172.

[5] YAO W, CHEN M, MOU S, et al. Paralleling Control Technique of Microgrid Inverters Based on Improved Droop Method [J][J]. Automation of Electric Power Systems, 2009, 6: 021.

[6] Lei X, Da X, Yanchi Z. Three-level inverter based on direct power control connecting offshore wind farm[C]//Sustainable Power Generation and Supply, 2009. SUPERGEN'09. International Conference on. IEEE, 2009: 1-6.

[7] Sato A, Noguchi T. Voltage-source PWM rectifier–inverter based on direct power control and its operation characteristics [J]. Power Electronics, IEEE Transactions on, 2011, 26(5): 1559-1567.

[8] Dannehl J, Fuchs F W, Hansen S, et al. Investigation of active damping approaches for PI-based current control of grid-connected PWM converters with LCL filters[C]//Energy Conversion Congress and Exposition, 2009. ECCE 2009. IEEE. IEEE, 2009: 2998-3005.

[9] Guo W, Lin F, Zheng T. Nonlinear PI control for three-phase PWM AC-DC converter[C]//Industrial Electronics Society, 2005. IECON 2005. 31st Annual Conference of IEEE. IEEE, 2005: 5 pp.

[10] Pogaku N, Prodanovic M, Green T C. Modeling, analysis and testing of autonomous operation of an inverter-based microgrid[J]. Power Electronics, IEEE Transactions on, 2007, 22(2): 613-625.

Advanced Materials Research Vols. 986-987 (2014) pp 1231-1235

doi:10.4028/www.scientific.net/AMR.986-987.1231

Research and development of the wind power monitoring system for North China Power Grid

Li Lixing

Department of electric power engineering, North China Electric Power University, Baoding, China

Email: lilixing123123@gmail.com

Keywords: North China Power Grid, wind power, monitoring system, output characteristics

Abstract. Facing to the current environment, energy pressure and wind power development at home and abroad, combined with the actual situation of North China Power Grid, this paper analyzes the wind development in North China firstly, and then based on C# language and the Oracle database develops based on B/S mode of wind power monitoring informing system. This system includes monitoring module, wind data mining module, data management module, real-time alarm module, and the user management module, which realized the wind power in North China Grid remote monitoring and statistical analysis of the data, to ensure data consistency.

Introduction

North China Power Grid Company made response to the new national energy policy actively, active docking for planning of power grid construction and new energy development. There are abundant wind resources in north China, such as Inner Mongolia region, zhangjiakou in BTT (Beijing-Tianjin-Tangshan) region and Chengde bashang region. At the end of 2008, the BTT power grid scheduling directly under wind power installed capacity of 797 MW (megawatt), reached 1378 MW by the end of 2009, and the total installed capacity of wind has been researched 3.3 million kilowatts in the end of 2010 [1-3]. Now, Tens of millions of MW level wind power base in hebei province is planning, predicts a total installed capacity of wind electricity will be 7.5 million kilowatts in 2015 for north region of hebei. Wind power plant is developed from the situation that small-scale access to the low-voltage power grid to the other, which based on large-scale and accessed to high voltage level. With the establish of millions of wind power and wind power base level, wind power will develop at an unprecedented speed.

With the rapid development of wind power technology, the scale of wind power expanded as well. There is different from the small-scale wind power, the influence made by the large one have been expanded from a simple voltage fluctuation problem to the power adjustment control, quality of electric energy and power system stability [4]. The intensive production of Large-scale grid wind farms will make the power grid peak shaving contradictions become more prominent. Output of the wind turbine is determined by the crew size characteristics and wind speed, and the characteristics of wind speed are change uncertainty. Considering the worst case, that in the load peak situation the wind generator output is zero and in the low load the output of wind become largest [5]. In this situation, the wind power not only can not participate in peak shaving, but also increasing the difficulty of the load peak shaving and increase the requirements for the thermal power unit [6, 7].

Based on the former introduction, real-time monitoring of wind power system operation condition and reasonable scheduling wind power resource is very important. The wind monitoring system could monitoring the operation condition real time of wind farms in the scheduling area, analyze the historical accumulation of wind data and provide a Data platform for further research, such as wind software development, wind power forecast and so on.

Summary of the monitoring system

The wind monitoring system is a monitoring and control system for wind power system based on the date of scheduling system and the energy management system. Its main purpose is to realize the real-time monitoring of grid wind farm operation, DM (data mining) according to the accumulation

of basic data and understand the operation of the wind characteristics. Then provide a powerful basis for wind guiding and as a subsequent management of data platform. This system processing and analysis the collected data at the same time and realize the global monitoring and macro management. The final purpose of this system is wind power prediction function and scheduling based on the prediction.

This system is developed by three layer architecture of B/S mode. The communication principle is as follows [8]:

(1) The client browser makes a request to the server for accessing the database and the requirement in the form of HTTP.

(2) The Web server accepts the client request, transfers the request to SQL syntax, and sends it to the database server.

(3) The database server receives the request and verifies its legitimacy, then carries on data processing and return the results back to the Web server.

(4) The Web server transfers the results in the form of HTML, forwarded to the client browser and displays the results in a form of friendly Web page.

The structural model is shown in figures 1.

Fig.1 Structural model

Data sources

The data of wind power monitoring system for North China Power Grid mainly comes from the scheduling monitoring system and the energy management system [9]. They are all based on the scheduling platform of North China Power Grid Dispatching Center (NCPGD).

According to the data of different nature, wind power monitoring system data sources are different. The data mainly come from the provincial scheduling, local scheduling and the direct dispatching. Some data consist of the real-time data and historical data of monitoring system, some data consist of artificial data and statistics date of management system, and other data consist of wind power plant and scheduling center. Whatever the kinds of the data, they are all transferred by the follow ways:

(1) Using the terminal way from the site or region and the province reported data.

(2) PI (Plant Information System) database data.

(3) OMS (Open Mobile System) data.

Systematic designs

The overall structure of data mining and analying system is shown in Fig 2, and the Fig 3 shows the way of data transmission.

The system extract the data of real-time wind power by PI data interface module and the electricity data from Oracle database by OMS module. Then deposit the real-time wind power and electricity data to the Oracle database of the data mining and analysis system of North China Power Grid., and proide the synchronous storage by interpolation processing. The delayed data system needed typed in manually and realize the important function, such as wind power real-time monitoring, wind power data query, data mining analysis and WebGIS function. This function can be realized through the IE browesr for the LAN users.

The system decomposed the information processing into five parts: basic information, real-time data, alarm data, historical data and report data. Every informations are mainly processed by database.

This syetem is mainly composed by six modules: monitoring function module, data mining function module, data management module, real-time alarm module, user's system management module and help module of the system.

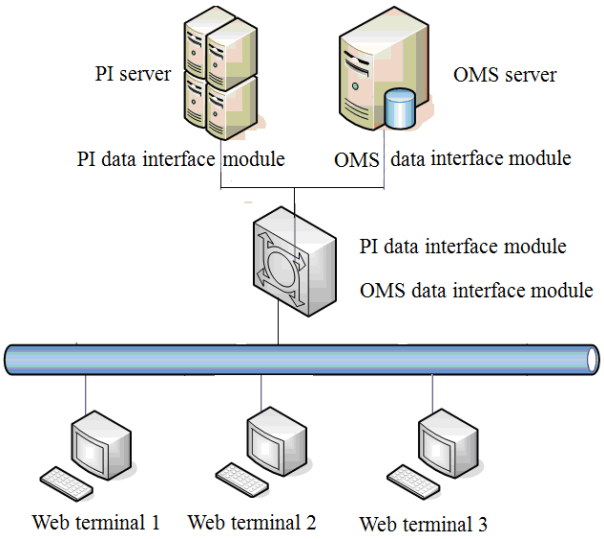

Fig.2 Overall structure of system

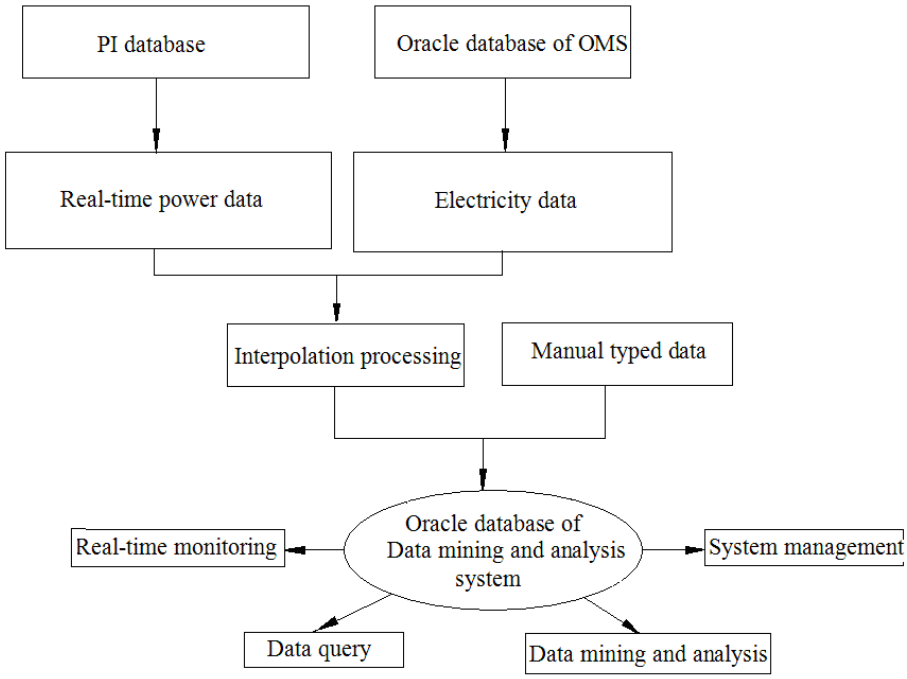

Fig.3 Data flowchart

Analysis of system function

Data mining and auxiliary decision-making function is based on the collection of real-time and historical data. This function can not only analyze all sorts of equipment running status, format related statements and analyze results according to the statement, but also evaluate the current situation of equipment operation. The evaluation is easy to adjust equipment maintenance and product selection, so as to decide whether to continue to promote a device, rather than simply reflects the current problems. The content of analysis includes the daily wind power, the difference between peak and valley, short-term fluctuations, wind power utilization hours etc.

Output sequence features of wind power

Wind power generation is the main rely on wind energy and the biggest characteristic of wind energy is uncertainty and instability. For this reason, the wind power generation also has the instability and volatility. But on the other hand, the wind power has some regularity with a day a quarter or a year. It is important to analyze the output sequence features for mastering the regular pattern of wind power output change, increasing the accuracy of the scheduling staff and improving the system security and economy.

1) Circannual output features of wind power

This system drew the monthly average output during January 2010 to January 2011 through the real-time data of wind power. The data in figures is the average values of the data in one day, which is typical day every month. The figures show in Fig 4.

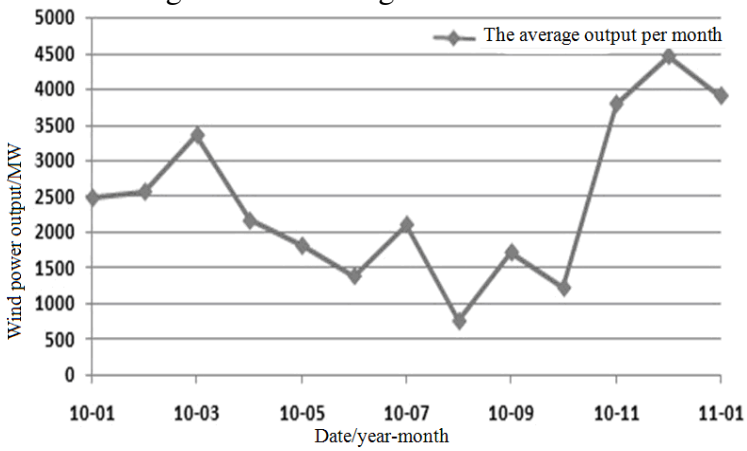

Fig.4 Monthly average wind power output

Wind power output has certain seasonal characteristics of North China Power Grid: wind power output significantly larger in spring and winter, but slightly low in summer and autumn. The maximum average output in winter is about twice the summer and fall wind power output.

2) Daily output features of wind power

Because of the obvious seasonal characteristics, this paper averaged wind power output data which exist in every season in the same time and drew the typical daily output curve of different seasons, as shown in Fig.5.

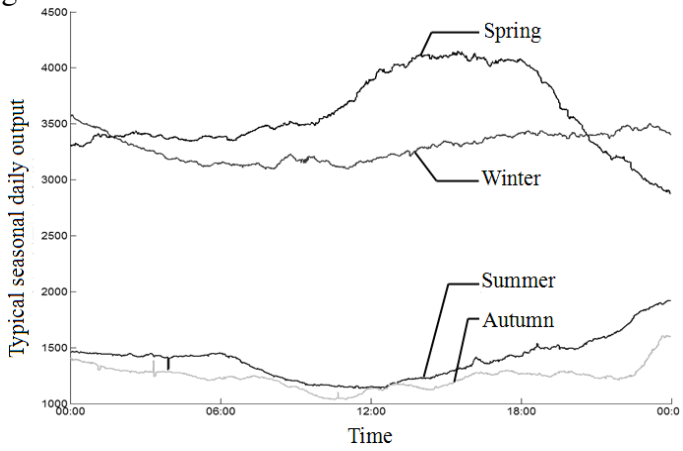

Fig.5 Typical daily curves of seasonal wind power output

Quantity of electricity

This system could display the quantity of electricity of wind power plant, such as Provinces North China Power Grid, BTT Power Grid and each straight scheduling wind farm. Taking an example of BTT Power Grid, figure 6 shows the quantity of wind electricity in 1-5 month.

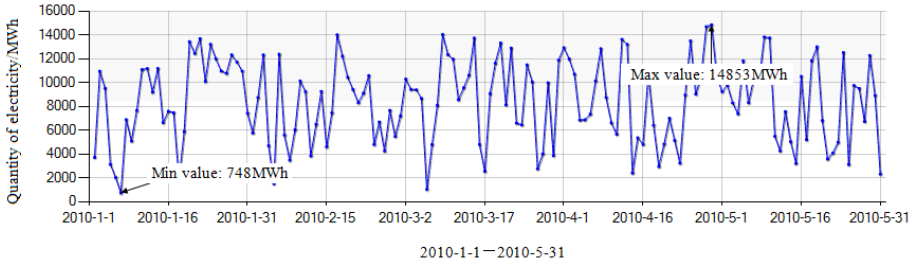

Fig.6 The quantity of wind electricity

Wind power utilization hours

Wind power utilization hours equal to using hours at full power, reflect the generated energy of wind power plant in the statistical cycle. It could visually check the wind power situation. Taking an

example of BTT Power Grid, figure 7 shows the wind power utilization hours and converted value for all the year round.

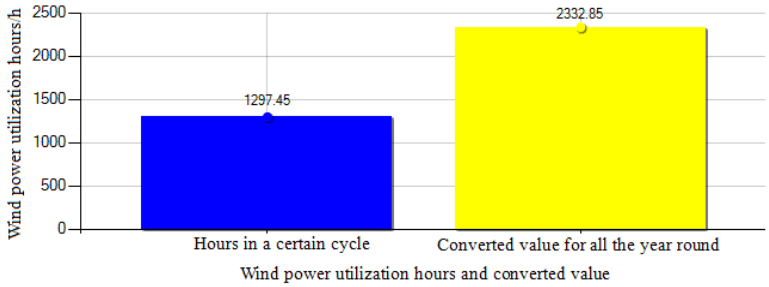

Fig.7 Wind power utilization hours

Alarm module

The wind power alarm module is necessary to monitor the wind plant. It related to normal operation of the wind farm monitoring, safety of the wind farm and even safety of the power grid. In this system, alarm module contrapose the problem of a certain wind farm, as Fan repair or closing down. If there are some problems of a wind farm, this system will display the source and flashing alarm lamp. It will eliminate when the farm become normal.

Conclusions

The wind power monitoring system real-time monitoring the North China Power Grid and the wind farm based on the real-time data. This system analyze the related statistics and data mining at the same time and provide powerful basis for guiding wind power operation.

The system is not perfect, the monitoring system should predict the wind power and wind power scheduling based on monitoring data the in the future. This monitoring system makes the analysis of the effect of wind farm on line possible, and lay a foundation for large wind power grid safe and stable operation and reasonable allocate resources.

References

[1]. Wei ZHongkang. Prospect of Wind power in North China Power Grid. North China Electric Power. 2006 34(03):52-54

[2]. Li Fuqiang, Wang Bin and Xu Shaoliang. Analysis on Peak Load Regulation Performance of Beijing-Tianjin-Tangshan Power Grid with Wind Farms Connected. Power System Technology. 2009,33(18):128-132

[3]. Li Feng, Lu Yicuan. Influence of large-scale wind energy converters on transmission systems. Electric Power, 2006,39(11):80-84

[4]. Yih-Huei Wan.Wind power plant behaviors: analyses of long-term wind power data. U.S:U.S. department of energy office and renewable energy, 2004.

[5]. Zhang Ning, Zhou Tianrui and Duan Changgeng etc. Impact of Large-Scale Wind Farm Connecting With Power Grid on Peak Load Regulation. Demand Power System Technology, 2010,34(1):152-158

[6]. Gao Debin, Li Qun. Analysis and Research of Operational Characteristics of Wind Power Generation in Northeast Power Grid. Electric Power Technology, 2010,19 (2):33-37

[7]. Chen Zhen, Ni Weidou and Li Zheng. Preliminary Study on Wind Power Characteristics. ACTA Energiae Solaris Sinica ,2011,32(2):210-215

[8]. Hou Youhua, Fang Dazhong. Analysis on Active Power Fluctuation Characteristics of Large-Scale Grid-Connected Wind Farm and Generation Scheduling Simulation Under Different Capacity Power Injected From Wind Farms Into Power Grid. Power System Technology,2010,34(5):60-66

[9]. Xiao Chuangying, Wang Ningbo. Power Characteristics of Jiuquan Wind Power Base. Automation of electric Power System ,2010,34 (17):64-67

Advanced Materials Research Vols. 986-987 (2014) pp 1236-1239

doi:10.4028/www.scientific.net/AMR.986-987.1236

Research and simulation on the energy-saving control model of large-scale intelligent electromechanical device

ZHANG Yun-long

BaoTou Light Industry Vocational college，Mongolia,Baotou,014035

Keywords: electromechanical device; energy-saving design; non-essential energy

Abstract: In energy-saving control process of large-scale-scale intelligent electromechanical device, it is need to consume non-essential energy. To reduce energy consumption, energy-saving design method is proposed based on adaptive linear genetic algorithms. According to theory of adaptive particle swarm optimization, optimal particle is searched in the global domain, which provides basis for energy-saving control of large-scale-scale intelligent electromechanical device. According to adaptive linear genetic theory, energy-saving control model of large-scale intelligent electromechanical device is built to complete energy-saving control. Experimental results show that algorithm can effectively reduce energy consumption and obtain satisfactory results.

1 Introduction

With worldwide energy shortage, China's energy is continually in emergency [1]. To relieve energy crisis of production and life, energy conservation measures need to be spread to different areas [2]. Therefore, energy-saving control design for large-scale intelligent electrical and mechanical devices becomes a hot issue in the field of energy research by the attention of many experts [3]. At this stage, major methods for control design of large-scale-scale intelligent electromechanical device includes energy-saving control methods based on dynamic adjustment algorithm, multi-core embedded algorithms and dynamic balance algorithms [4]. Among them, the most commonly control method is based on dynamic adjustment algorithm. Due to constantly expanding application of energy-saving control methods for large-scale intelligent electromechanical device, there is a broad space for development, as is the main subject of research in energy field [5].

2 Relevant principles of energy-saving control method for large-scale intelligent electromechanical device

2.1 Energy saving control parameters calculating

According to theory of adaptive particle swarm optimization, global optimal particle is searched to calculate energy-saving control parameters, which provides technical support of energy-saving control for large-scale intelligent electromechanical device. Specific steps are as follows:

Step1：Generate random particle populations and speed according to a given search space.

Step2：Calculate value of objective function according to objective function and all generated particles.

Step3：Calculate the global optimum.

Step4：Vary weight and learning factors according to evolutionary generation,.

Step5：Modify position and velocity of particles according to updating formula of speed and position.

Step6：Calculate objective function value by updating particles.

Step7：Determine whether objective function value is less than global optimum.

Step8：Unchange global optimum value if objective function value is large-scale; replace objective function value if global optimum is large-scale.

Step9：Determine whether to meet maximum evolutionary generation, if not go to Step 4; if is go to Step 10.

Step10：Output global optimum value and obtain global optimum variable values.

As optimizing energy-saving control system of electromechanical device, test functions employed are: in Sphere Model $f_1=\sum_{i=1}^{N}x_i^2$ function， in Schwefel's Problem 2.22 $f_2=\sum_{i=1}^{N}|x_i|+\prod_{i=1}^{N}|x_i|$ function, in Schwefel's Problem 1.2 $f_3=\sum_{i=1}^{N}(\sum_{j=1}^{i}x_i)^2$ function， in Schwefel's Problem $f_4=\max\{|x_i|\}$ function, in Schwefel's Problem 2.22 $f_2=\sum_{i=1}^{N}|x_i|+\prod_{i=1}^{N}|x_i|$ function。

For above 5 test functions, search space is the range [-100,100]. In order to simplify search process, search variable dimension is 5. To use the ability of close search, a lot of random particles are generated in search space, and then position and velocity of a particle are updated based on current best position and global best position. In the iterative process of continuous adjustment factor inertia weight and learning, all particles are gradually approaching optimal value of global energy-saving control.

2.2 energy-saving control model establishment of large-scale intelligent electromechanical

Employing adaptive linear genetic algorithm, adaptive parameter can be effectively adjusted for energy-saving control of large-scale electromechanical device, so as to reduce energy consumption. Details are described below:

Spatial location of electromechanical components and spatial position of the element as a chromosome can be expressed by following sets:

$$Y=\left[(U_1,IM_1),(U_2,IM_2)\ldots(U_k,IM_k)\ldots(U_N,IM_N)\right] \tag{1}$$

Where， U_k can be used to describe position of $k(k=1,2,\cdots,N)$ th electromechanical components, U_k can be used to describe encoding of electromechanical components,， N is the length of the chromosome.

In control process of large-scale intelligent electromechanical device energy-saving, there are many types of constraints, which can be expressed by following penalty function:

$$H_{\min}=S+\chi\times(|x_U|+|U-U_{set}|+|V-V_{set}|+load1+load2)$$
$$H_{\max}=\frac{1}{H_{\min}} \tag{2}$$

where：

$$load1=\begin{cases}\gamma & (x_k\geq x_k)\\ 0 & (w_j<\mathrm{w}_{\lim,j})\end{cases}$$
$$load2=\begin{cases}\gamma & (\frac{dc}{dv}\geq v)\\ 0 & (\frac{dc}{dv}<v)\end{cases}$$

In the above formula, c , γ and η are all corresponding penalty coefficient.

Using the following formula population conversion can be cross, in order to gain diversity of chromosome populations in control process of large-scale intelligent electromechanical device energy-saving:

$$V_{1k}^{'}=w\cdot Z_{1k}+(1-w)\cdot Z_{2k}$$
$$Z_{2k}^{'}=w\cdot Z_{2k}+(1-w)\cdot Z_{1k} \tag{3}$$

Where， $w\in(0,1)$ 。 Z_{1k} and $Z_{2k}^{'}$ are samples of chromosomes population。

3 Analysis of experimental results

In order to verify effectiveness of proposed method, an experiment is done in Visual C + +6.0 as experimental environment. Set element number of large-scale intelligent as m , necessary energy consumption as f , unnecessary energy consumption as g . Energy efficiency of energy-saving control for large-scale electromechanical device can be calculated by the following formula:

$$\omega = \frac{\sqrt{m-f}}{g^2-\varphi^2-1} \tag{4}$$

According to energy efficiency of energy saving control for these large-scale intelligent electromechanical device, effects of energy-saving control is accurately measured by different methods.

Experiments are performed by traditional energy-saving control algorithm, as obtained results are described by the following figure:

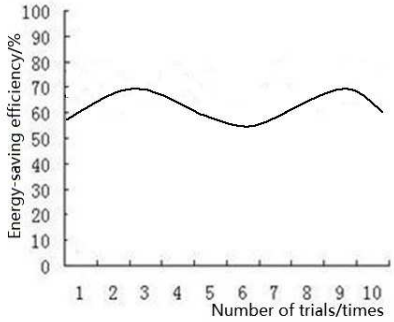

Figure1 Energy-saving control results of traditional algorithm

Experiments are performed energy-saving control algorithm in this paper to obtain results as described by the following figure:

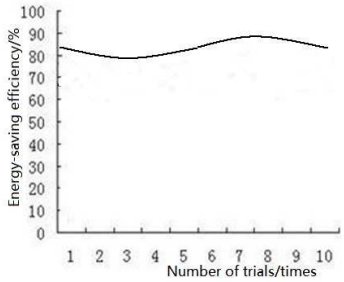

Figure2 Results of energy-saving control algorithm in this paper

Based on the above two figures, it is presented that this algorithm is employed to energy-saving control of intelligent electromechanical device; energy-saving effect is much higher than conventional algorithms.

For energy-saving control of large-scale intelligent electromechanical device by different methods, results are classified and analyzed. Table 1 can be obtained as follows:

Table1 Datasheets of energy-saving control

Algorithms	Times	Energy-saving efficiency
Traditional algorithm	10	27%
Proposed algorithm	10	46%

According to Table 1, proposed algorithm is employed for energy-saving control of intelligent electromechanical device and reduces energy effectively.

4 Conclusions

A method for energy-saving design based on adaptive linear genetic algorithm is presented in this paper. According to theory of adaptive particle swarm, optimal particle is searched in global range so as to provide the basis for energy-saving control of large-scale intelligent electromechanical device. According to adaptive linear genetic theory, energy-saving control model of large-scale intelligent electromechanical device is established and energy-saving control is completed. Experimental results show that proposed algorithm can effectively reduce the energy consumption which obtains satisfactory results.

5 References

[1] Marija Trčka,Jan L.M.Hensen. Overview of HVAC system simulation[J]. Automation in Construction,2010,19,93-99
[2] Jong-Seob, W. Fuzzy Torque Distribution Control Design for a Parallel Hybrid Electric Vehicle. Expert Systems[J],2002,19(1):4-10.
[3] Jejurikar R, Gup ta R. Energy Aware Task Scheduling with TaskSynchr onizati on for Embedded Real2 Time Systems[J] Computer2Aided Design of I ntegrated Circuits and Systems, IEEE Transac2 tions on, June 2006: 1024 - 1037.
[4] Wang Xiaoying, Zhao Hai, Chen Yingge, et al. Dual Power Aware Task Scheduling in Sensor Network[J]. Acta electronica snica, 2006,34(5):798-783
[5] R Jejurikar, R Gupta. Energy Aware Task Scheduling with TaskSynchr onizati on for Embedded Real2 Time Systems[J] Computer2Aided Design of I ntegrated Circuits and Systems, IEEE Transac2 tions on, June 2006:1024-1037

Advanced Materials Research Vols. 986-987 (2014) pp 1240-1244

doi:10.4028/www.scientific.net/AMR.986-987.1240

Research of Effect of Battery Participating in Demand Response

Rong Zhang[1, a], Bing Qi[1,b]

[1] School of Electrical and Electronic Engineering, North China Electric Power University, Beijing 102206, China

[a]zhangrong3992@163.com, [b]qbing@ncepu.edu.cn

Keywords: demand response, battery, model, ordered charging, free charging.

Abstract. Batteries have been widely used in the residential electric systems. This paper firstly analyzes the characteristics and feasibility of using the battery to participate in Demand Response (DR) programs. Secondly, the load characteristics in the two different kinds of battery systems are studied, including the power battery of electric bicycles and the battery which are used as the standby power for communication systems and computer systems. Thirdly, this paper studies the DR implementation method of reducing peak and filling valley and related impact on power grid load.

Introduction

Nowadays, the number of battery power users is growing rapidly. Battery can be used for electric bicycles (EBs), tricycles (ETs), vehicles, and also can be used for information systems such as communication systems, computer systems, automatic control systems and so on [1]. According to incomplete statistics, the number of EBs and personal notebook computers in china has reached hundreds of millions and the quantity of wireless base stations, communication rooms and data centers have reached millions. The proportion of these battery loads in residential electricity load keeps sustained growing and the load characteristics of battery have attracted the attention of Power Supply Companies and relevant departments of government. But so far the research emphases in this field still focus on the impact of electric vehicle [2] battery and energy storage battery [3] on the grid. Few articles study the relationship between DR [4-5] and battery of EBs, communication and computer systems in depth, or put forward the specific methods and effects of the battery systems participating in DR.

Based on the research of the battery's using features and charging characteristics, we know that most of equipment and systems include battery can participate in DR by changing the charge and discharge schedule. This paper presents a new approach to control the battery's charging and discharging time. We can change the behavior of the battery through DR time controller based on DR signals, to charge as much as possible at the off-peak time in order to reduce grid load and difference between peak and valley.

Strategies of battery participating in DR

Power users who want to participate in DR need the equipment include DR ability. Battery can be used as a load when charging and can be used as a power source when discharging [6]. According to related tariffs or incentives, power users change the charging and discharging behavior of battery products spontaneously, to make them discharging during the peak hours, offering energy to the load instead of the grid, and charging during the valley hours. Battery control flow is shown in Fig. 1.

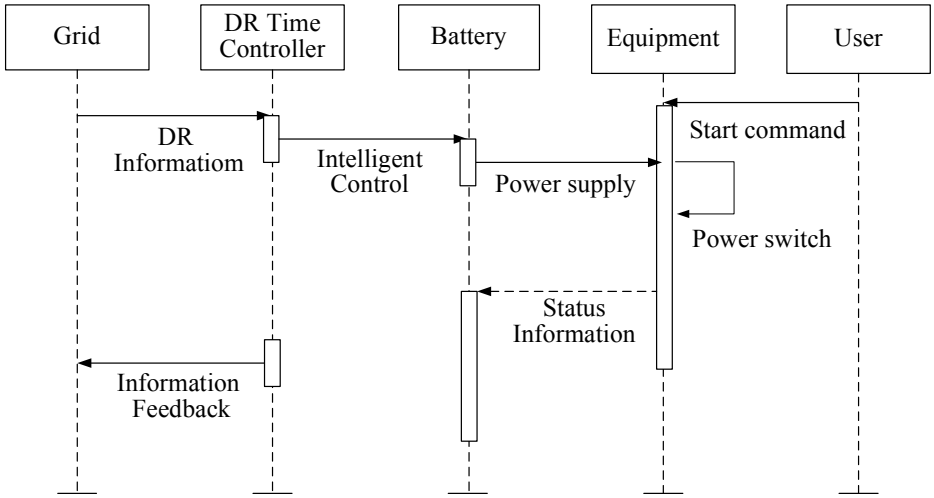

Fig. 1. Battery control flow on DR

According to their using features, the battery can be divided into two different kinds of model. One is the power battery of EBs (include ETs) whose load characteristics can be affected by the habits of the users, and the charging behavior is of randomness and intermittent which is in a disordered state of charging. The other one is the batteries which are used as the standby power of communication and computer systems. When the system is supplied by mains power, the battery has been charged fully in a floating state, and almost have no impact on the grid. In this paper, two charging models are established for these two battery systems [7], investigating the characteristics of the load of battery system and, how load affect to the grid when a certain scale of battery participate in DR.

Battery charging characteristic analysis

When battery connected to the grid, its power demand is determined by charging voltage and current. Battery charge mode can be divided into common charge and fast charge. Common charge current is 0.1C ~ 0.3C and fast charge current is 1C. Battery charging voltage is about 1.2 times of the rated voltage (U). When charging by the way of limited voltage and constant current, the battery charging power can be obtained by the charging current and charging voltage as (1).

$$P_c = U_c I_c \tag{1}$$

In the formula above, P_c represents charging power, U_c denotes charging voltage, $U_c = U \times 120\%$, I_c stands for charging current.

Battery charging time can be obtained through charging power and state-of-charge (SOC). SOC can be determined by subtracting the depth of discharge (DOD) from total capacity (C). We can get the charging time as follow (2)

$$t_c = (C - SOC) / I_c \tag{2}$$

Battery charging time can also be obtained through electricity used by battery load. If P_l represents load power, t_l represents load working time, then charging time can be estimated as follow (3).

$$t_c = P_l \times t_l / P_c \tag{3}$$

For different battery equipment, the charging time connected to the grid will be subject to certain restrictions. Different uses of batteries have different design standards which shown in Table 1.

Table 1. Standards for Different Uses of Batteries

Use of Battery	Capacity(C)	Voltage(U)	Discharge time
Electric Bicycle	10 20Ah	48V	2 4h
Electric tricycle	60 120Ah	48V	2 4h
Laptop	2 8Ah	12V	2 8h
Wireless base	500 1000Ah	48V	2 8h
Communications	2000 6000Ah	48V	2 8h

EB battery charging modeling. For EBs, we refer to the data of people's travel habits from the National Household Travel Survey (NHTS 2001) [8]. Potential interconnection hours were derived from the likely residential customer home arrival times. If it is assumed that the start time of charging is equal to end time of the last trip, the start time of charging can be considered approximately as a normal distribution model N (μ, σ2). The values of μ and σ as well as the average charging time of EBs can be estimated under certain precondition. It is generally used to take into account that EBs are charged after work, taking μ is 19 and σ is 4.

The charging load curves that a large number of EBs connected to the grid in a day can be obtained by the start time of charging, charging length, charging power and other data of every EB. Assumptions are as follows: battery capacity of EB is 20Ah and ET is 100Ah, all EBs and ETs rated charging current is 0.1C and the average depth of discharge is 50%. When the battery is fully charged, we can find the average charging time equal 5 hours, the charging power of EB is 115.2W and ET is 576W. Based on the data above, the charging load curves of 24 hours in a day can be calculated using the Monte Carlo simulation method.

Communications system load charging modeling. Standby power is to provide safe, stable and reliable power protection for reliable operation of the system. For communication base stations and communications rooms, refer to their battery capacity configuration, the equipment power of some kind of communication base station and communication room is assumed to be 2kW and 40kW and the power change is negligible. Setting N_b is the number of communication base stations, N_r is the number of communications rooms, then the system loads on the grid can be obtained as follow (4)

$$P_s = 2N_b + 40N_r \tag{4}$$

Battery resource characteristics analysis

Simulation scenario is set in Zhuji City, Zhejiang Province, China, taking the load curve of one day in the summer of 2013 for example. The number of people is about 1.2 million in Zhuji City. Assuming that ET ownership is 50,000, the number of communication base stations is 1000 and the number of communications rooms is 100. Each family has four people and one EB, EB ownership is calculated to be 300,000. When batteries do not participate in DR, the main parameters of the system, including the equipment power, charging power, charging time, discharging time, are analyzed and the daily power probability distribution of the system can be derived which shown in Fig. 2.

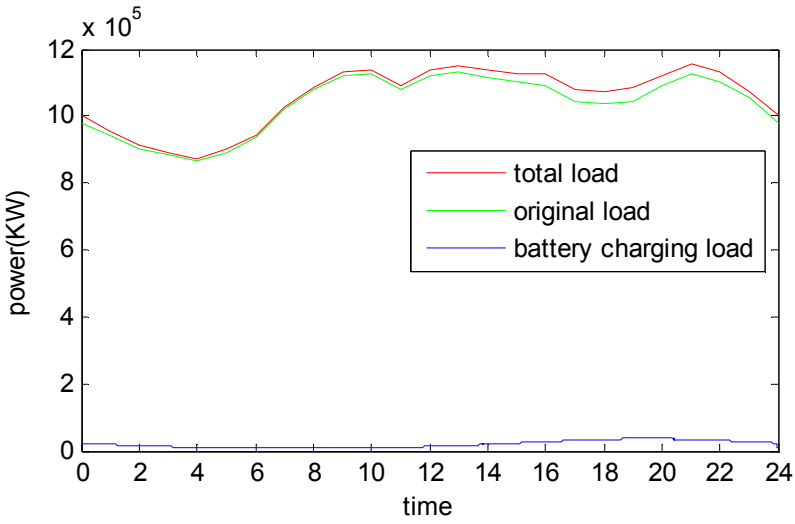

Fig. 2. Summer day load curve not participating in DR

When batteries participate in DR, a typical simulation scenario is set as follow. On the base of load curve on the grid, 24 hours was divided into three sessions in a day: Peak Hours (8:00-16:00 and 19:00-22:00）, common hours (6:00-8:00, 16:00-19:00 and 22:00-24:00) and valley hours (0:00-6:00). Price strategy of power supply companies implementing the measure is TOU. Battery obtain pricing information through DR time controller participating in DR. When participating in DR, EBs and ETs are controlled to charge as much as possible at the valley hours. 90% of the EBs (include ETs) need to participate in DR, 10% of them remain free charging. For communication base stations and communications rooms, battery DOD need to be controlled to ensure the safe operation of the system. When the system can be supplied by batteries for 10 hours, batteries are discharged 20% at the peak hours by DR time controller, i.e., two hours, and charged fully at valley hours. According to the power grid load curve, the system is supplied at 10:00-11:00 and 12:00-13:00 by batteries and then batteries are charged by the gird at 3:00-5:00.

According to the simulation of battery participating in DR, daily battery charging power probability distribution can be calculated. The change of grid load curve shown in Fig. 3.

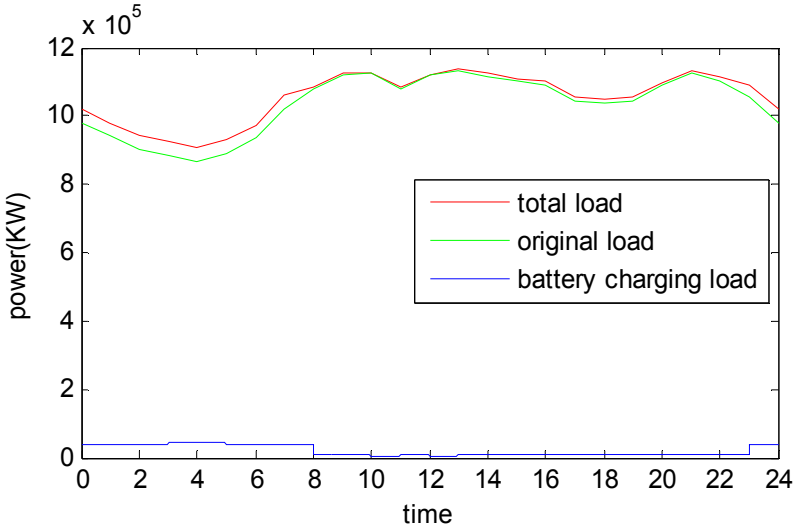

Fig. 3. Summer day load curve participating in DR

Particular targets of load characteristics shown in Table 2.

Table 2. Particular targets of grid load characteristics considering battery charging load

Mode	maximum power kW	minimum power kW	valley-to-peak kW	valley-to-peak rate
original load	1130740	865500	265240	23.4%
Free charge	1155400	874010	281390	24.4%
Ordered charge	1137892	919510	218382	19.2%

According to the simulation results, after changing battery from free charging mode to ordered charging mode, day peak value decrease by approximately 1.5%, day valley value increase 5.2%, valley-to-peak value decrease 63008kW, valley-to-peak rate decreased from 24.4% to 19.2%.

Conclusion

In this paper, we have studied two charging models which are established for the two battery systems to forecast the battery load. The simulation results have demonstrate that optimizing and controlling charging and discharging time of the battery, the operating characteristics and operational efficiency of the grid will be improved significantly, which shows the battery to participate in DR is effective.

References

[1] Mikko Rasanen, Heikki Summala. Attention and Expectation Problems in Bicycle-car Collisions ：an In-depth Study［J］. Accident Analysis and Prevention, 1998, 30(5)：571-639.

[2] Casey Quinn, Daniel Zimmerle, Thomas H. Bradley. The effect of communication architecture on the availability, reliability, and economics of plug-in hybrid electric vehicle-to-grid ancillary services[J]. Journal of Power Sources, 2010, 195(5)：1500-1509.

[3] Zhaohong B, Gengfeng L, Xifan W. Review on reliability evaluation of new distribution system with micro-grid[J]. Electric Power Automation Equipment, 2011, 31(1): 1-6.

[4] Abreu K. PG&E ’ s Perspective on Demand Response under the Smart Grid Paradigm[C]//Proceedings of IEEE Power Systems. Conference and Exhibition (PSCE’09). Seattle, WA, USA：IEEE, 2009：1-32.

[5] Su C L, Kirschen D. Quantifying the effect of demand response on electricity markets[J]. IEEE Transactions on Power Systems, 2009, 24(3)：1199-1207.

[6] Hu Weihao, Chen Zhe, Birgitte B J. Optimal operation strategy of battery energy storage system to real-time electricity price in Denmark[C]//IEEE Power and Energy Society General Meeting. Minneapolis, Minnesota：IEEE, 2010：25-29.

[7] Staats P T, Grady W M, Arapostathis A. A statistical method for predicting the net harmonic currents generated by a concentration of electric vehicle battery chargers[J]. IEEE Transs on Power Delivery,1997, 12(3)：1258-1266.

[8] Taylor M J, Alexander A. Evaluation of the impact of plug-in electric vehicle loading on distribution system operations[C]//IEEE Power & Energy Society General Meeting, Calgary, Canada, 2009：1-6.

Advanced Materials Research Vols. 986-987 (2014) pp 1245-1249

doi:10.4028/www.scientific.net/AMR.986-987.1245

Research on Condition Monitoring of Protection System Based on Substation Area Protection

Shiyong WANG[1, a], Tingting SHI[2, b]

[1]Beijing Electric Power Corporation of SGCC, Beijing, 100031, China

[2]Feidong Electric Power Corporation of SGCC, Hefei, 230000, China

[a]email: wsy00158@sina.com, [b]email: shitingting365 @163.com

Keywords: Intelligent Substation; Substation-area Protection; Condition Monitoring; GOOSE

Abstract. Protection equipment in intelligent substation includes Merging Unit, protection equipment and Intelligent Terminal. At present, the status of the intelligent electronic device in intelligent substation protection system is still lack of effective monitoring means. According to the characteristics that substation area protection can obtain current information of all circuits in substation through GOOSE network, a protection system conditioning monitoring relay named PSCMR is designed in this paper. Based on the principle of current differential, PSCMR can accurately identify the abnormal condition or malfunction of Merging Unit or Electronic Current Transformer and realize condition monitoring of intelligent electronic device in protection system.

Introduction

In intelligent substation, protection system contains Merging Unit, protective equipment and Intelligent Terminal [1]. At present, the intelligent electronic devices in protection system are lack of effective monitoring measures. Failure of protective equipment cannot be found in time which cannot trip for the faults in power system. And it may results in disastrous consequences [2].

In the new generation of intelligent substation, hierarchical protection system is adopted [3]. As shown in figure 1, the protection system includes local protection, Substation-area Protection and Wide-area Protection. Local protection is traditional protection, such as line protection, bus bar protection, and so on. Substation-area Protection collects voltage and current data of all circuit in substation and provide the function of backup protection, the under frequency load shedding, and so on[4-6]. Wide-area Protection installed in pivotal substation can realize backup protection, network topology analysis, power flow analysis, and so on [7-11].

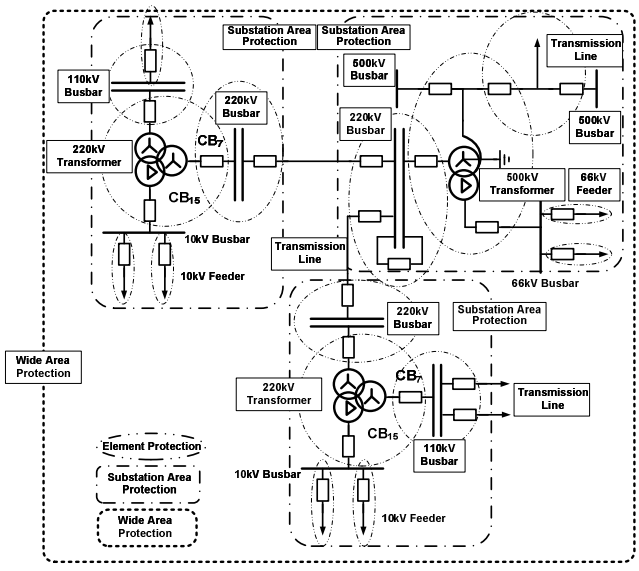

Fig.1 Function scope of hierarchical protection system

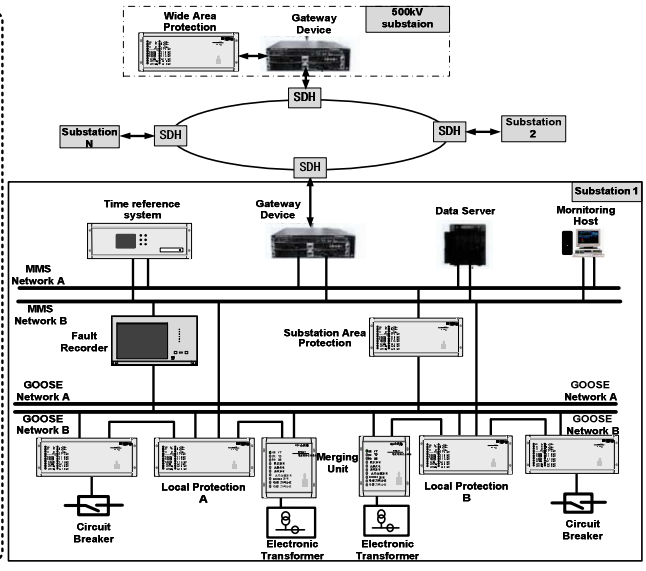

Fig.2 Framework of hierarchical protection system

As shown in figure 2，Substation-area protection can collect the data of current and voltage of every circuit in whole substation through GOOSE network. A Protection System State Supervision Relay (PSCMR) which utilizes the currents of all circuit in whole substation is designed in this paper. Through comparing the difference of substation-area protection and local protection, PSCMR can identify those faulty intelligent electronic devices and send alarm message in time. It can avoid the malfunction or refusing trip of protection system, and provide the safety of power system.

Basic Principle of PSCMR

Kirchhoff's current law based current differential protection has advantage of natural phase selection，operates very fast and is immune to power swing and widely used in power system [12].

Current differential protection based Protection System Condition Monitoring Relay has been developed in this paper. As shown in Figure 3, a typical 220kV substation is studied. 16 current differential circuits labeled as D1 ~ D16 are constructed in whole substation. As shown in Table 1, D1~D2 are current different circuits for transformers, D3~D8 are current different circuits for bus bar. D9~D16 are current different circuits for four 220kV transmission lines and four 110kV transmission lines.

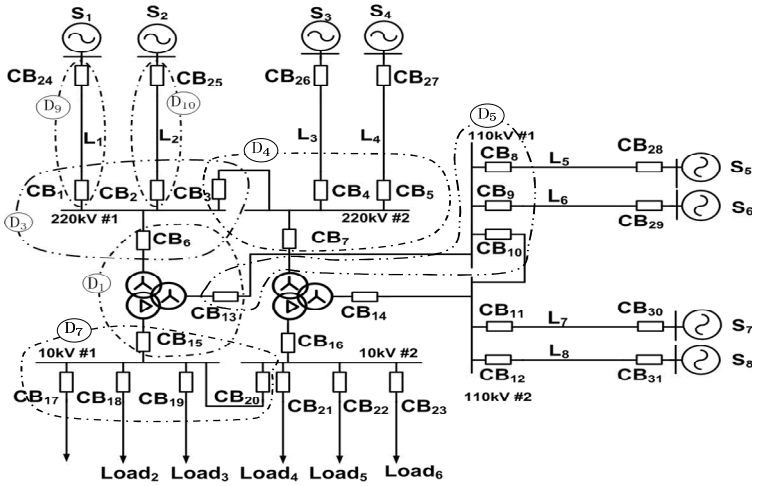

Fig.3 Electric diagram of a typical 220kV substation

PSCMR calculates the differential current for every current differential circuit in real time. Different current of D1~D16 will be zero during normal operation of protection system. As shown in figure 3, in the presence of abnormal condition of Electronic Transformer or Merge Unit will cause differential currents in at least two differential circuit circuits. By analyzing the differential current circuit, PSCMR can recognize the faulty Merging Unit or Electronic Transformer.

Tab.1 The scope of differential circuits in substation

Differential Circuit	Protected Device	Scope of Circuit Breaker	Differential Circuit	Protected Device	Scope of Circuit Breaker
D_1	Transformer T1	CB_6,CB_{13},CB_{15}	D9	Line L1	CB_1,CB_{24}
D_2	Transformer T2	CB_7,CB_{14},CB_{16}	D10	Line L2	CB_2,CB_{25}
D_3	220kV#1Busbar	CB_1,CB_2,CB_3,CB_6	D11	Line L3	CB_4,CB_{26}
D_4	220kV#2 Busbar	CB_3,CB_4,CB_5,CB_7	D12	Line L4	CB_5,CB_{27}
D_5	110kV#1 Busbar	CB_8,CB_9,CB_{10},CB_{13}	D13	Line L5	CB_8,CB_{28}
D_6	110kV#2 Busbar	CB_{10},CB_{11},CB_{12},CB_{14}	D14	Line L6	CB_9,CB_{29}
D7	10kV#1 Busbar	CB_{15},CB_{17},CB_{18},CB_{19},CB_{20}	D15	Line L7	CB_{11},CB_{30}
D8	10kV#2 Busbar	CB_{16}, CB_{20},CB_{21},CB_{22},CB_{23}	D16	Line L8	CB_{12},CB_{31}

For example, Merging Unit of CB1 has fault, differential currents will appear in D3 and D9. When PSCMR recognizing differential currents in D3，it can utilize traversal algorithm shown in figure 4 to locate the faulty intelligent electronic device.

Since differential current circuit D3 includes CB1, CB2, CB3 and CB6, PSCMR can detect whether D1 is normal firstly. If there is no differential current in D_1, PSCMR will continue to

traverse D4, So in turn, until differential current is found in D9. Thus it can determine whether Merging Unit or Electronic Transformer abnormality or failure happened in CB1.

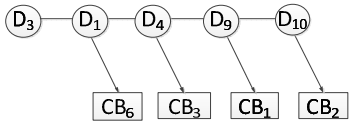

Fig.4 Differential Circuit Traversal Algorithm

Tab.2 Malfunction Identification of Differential Circuit

Circuit Breaker	Differential Circuit for Abnormal Identification	Circuit Breaker	Differential Circuit for Abnormal Identification
CB_1	D_3,D_9	CB_9	D_5,D_{14}
CB_2	D_3,D_{10}	CB_{10}	D_5,D_6
CB_3	D_3,D_4	CB_{11}	D_6,D_{15}
CB_4	D_4,D_{11}	CB_{12}	D_6,D_{16}
CB_5	D_4,D_{12}	CB_{13}	D_5,D_1
CB_6	D_3,D_1	CB_{14}	D_6,D_2
CB_7	D_4,D_2	CB_{15}	D_1,D_7
CB_8	D_5,D_{13}	CB_{16}	D_2,D_8

Algorithm of PSCMR

Phase segregated current differential protection principle is adopted in PSCMR, and its ratio-restrained characteristic[13] is shown in figure 5 and expressed in equation (1).

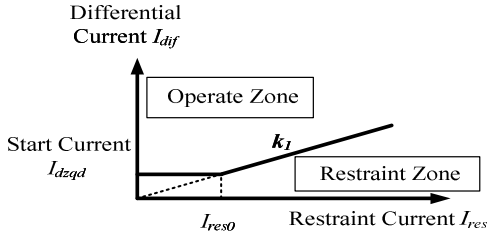

Fig.5 Ratio-restrained characteristic of differential principle

$$\begin{cases} I_{dif} > I_{dzqd} & (I_{res} < I_{res0}) \\ I_{dif} > k_1 I_{res} & (I_{res0} \le I_{res}) \end{cases} \tag{1}$$

The main function of PSCMR is monitoring whether there are faults in Merging Unit or Electronic Transformer during normal operation of power system. According to 10% Error Curve of Current Transformers, error of Current Transformer is no more than 10%. Ratio coefficient k_1 in this paper is set 0.1.

Phase A for example, differential current is the sum of vector current in each branch; resistant current is the sum of scalar current in each branch. Assumed positive direction of current is from Bus to Line.

$$I_{dif\,A} = \left| \alpha_1 \cdot \dot{I}'_{1A} + \alpha_2 \cdot \dot{I}'_{2A} + \cdots + \alpha_n \cdot \dot{I}'_{nA} \right| \tag{2}$$

$$I_{res\,A} = \alpha_1 \cdot \left| \dot{I}'_{1A} \right| + \alpha_2 \cdot \left| \dot{I}'_{2A} \right| + \cdots + \alpha_n \cdot \left| \dot{I}'_{nA} \right| \tag{3}$$

α_1, $\cdots$, α_n are factors to balance the different ratio of Current Transformer in each side of transformer.

Software Diagram of PSCMR

Shown in figure 6, PSCMR calculate differential current in D_1~D_{16} in order, and determine whether differential protection of D_1~D_{16} should act. If differential protection of D_1 act，PSCMR run into traverse subroutine of D1. First, PSCMR detect whether differential protection of D_3 acts. If

differential protection of D_3 act, it can be determined that intellectual electronic device in protection system of CB_6 have occurred abnormal situation. Otherwise，PSMCR will continue to detect differential current of D_5. If differential protection of D_5 act, it can be determined that intellectual electronic device in protection system of CB_{13} have occurred abnormal situation. Otherwise, PSMCR will continue to detect differential current of D_7. If differential protection of D_7 act, it can be determined that intellectual electronic device in protection system of CB_{15} have occurred abnormal situation, and traverse subroutine of differential circuit D_1 end，algorithm of PSCMR returns to main program, and continues to detect differential current of D_2 ~ D_{16} in sequence until the program ends.

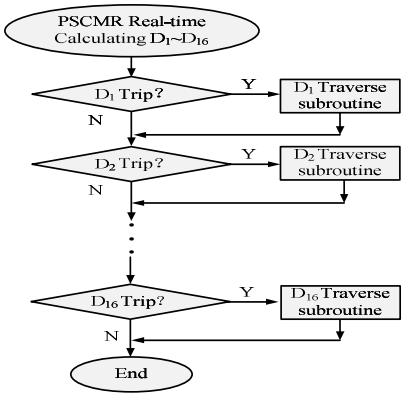

Fig.6 Main program of PSCMR software algorithm

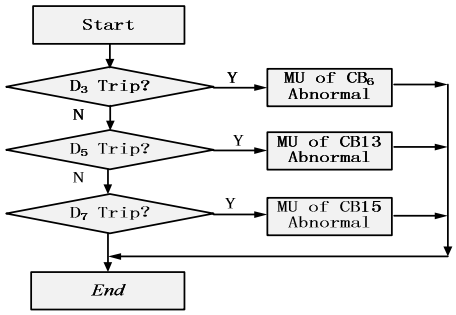

Fig.7 Traverse subroutine of differential circuit D_1

Simulation and Evaluation

A typical 220kV substation simulation model shown in Figure 3 has been established in the Alternative Transient Program (ATP), and algorithm of PSCMR is programmed in MATLAB. Data get from ATP is used to test the algorithm of PSCMR.

Normal operation conditions, abnormal operation of Merging Unit all have been simulated to test the algorithm of PSCMR in this paper. Some simulation results to abnormal operation of Merging Unit in CB1are shown in Figure 8.

It can be seen that D3 and D9 have acted. PSCMR can locate the abnormal situation in protection system of CB1 accurately and send alarm signal.

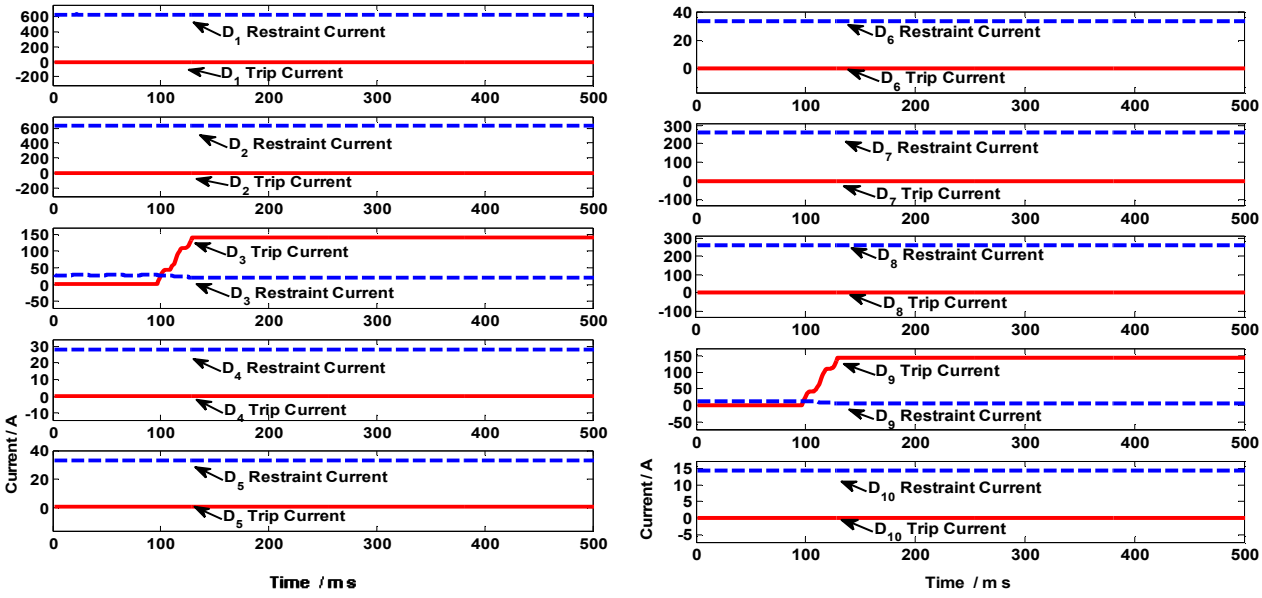

Fig.8 Currents in differential circuit caused by abnormal Merging Unit of CB1

Simulation results of ATP indicate that PSCMR can monitor the operating situation of protection system in whole substation, and can identify abnormal Merging Unit or Electronic Transformer accurately.

Patrol Function of PSCMR

PSCMR can communicate with all local protection devices and Intelligent Terminals in whole substation. It can call all local protection devices and Intelligent Terminals periodically. If any local protection device or Intelligent Terminals have no response, alarm signal will be sent by PSCMR.

Conclusion

Online condition monitoring of intelligent electronic devices in intelligent substation is very important to improve the reliability of protection system. According to the characteristics that Substation-area protection can obtain current information of all circuits in substation through GOOSE network, current differential protection based Protection System Conditioning Monitoring Relay named PSCMR is designed in this paper. PSCMR can identify the abnormal device through the action results of each differential current circuit and patrol local protection device and intelligent terminals through GOOSE network. Alarm signals will be sent out by PSCMR in the presence of abnormal conditions of intelligent electronic device. PSCMR is a valuable try of online condition monitoring of protection system, it also enrich the function of Substation-area protection.

References

[1] Bin Wang, Xinzhou Dong, Fei Xu, et al. Analysis of data sharing for protection and control system in smart distribution substation[J], Proceedings of the CSEE,2011,31:1-6.
[2] Baohui Zhang. Problems on protection relay and urgency control system in interconnected power network of China and studies needed [J], Electric Power Automation Equipment,2004,24(07): 1-6.
[3] Xuankun Song, Yinchao Li, Jun Li, et al. Hierarchical protection and control system for new generation smart substation. Electric Power Construction，2013,34(7):24-29.
[4] Xianggen Yin, Shang Wang, Zhe Zhang. Zone-division and tripping strategy for limited wide area protection adapting to smart grid [J],Proceedings of the CSEE),2010,30(7):1-7.
[5] Baohui Zhang, Liangcai Zhou. Centralized substation backup protection [J], Electric Power Automation Equipment, 2009,29(6): 1-5.
[6] Xinzhou Dong, Lei Ding. Research on design of digital integrated protection and control system [J],Power System Protection and Control,2009,37(01):1-5.
[7] Wei Cong, Zhencun Pan, Jianguo Zhao. A wide area relaying protection algorithm based on longitudinal comparison principle[J],Proceedings of the CSEE,2006,26(21):8-14.
[8] Tianqi Xu, Xianggen Yin, Dahai You, et al. Analysis on functionality and feasible structure of wide area protection system [J], Power System Protection and Control,2009,37(03):93-97.
[9] Yusheng Xue, Xing Lei, Feng Xue, et al. Review on wide area protection of electric power systems[J],High Voltage Engineering,2012,38(03): 513-520.
[10] Fei Zeng, Shihong Miao, Xiangning Lin. A wide area backup protection algorithm for power grid based on sequence component[J],Automation of Electric Power Systems, 2010,34(23): 57-63.
[11] Xiaoling Cai, Liwei Wang, Chan Lin, et al. Principle and realization of substation-area protection based on smart substation[J], Proceedings of the CSU-EPSA,2012,24(6):128-133.
[12] Yaozhong Ge. The new principles and techniques of protection and fault location. Xi'an Jiaotong University Press，2007.
[13] Yiqing Liu. Study on principle and implementation technology of substation-area backup protection in intelligent substation [D]. College of electrical engineering, Shandong University，2012.

Advanced Materials Research Vols. 986-987 (2014) pp 1250-1253

doi:10.4028/www.scientific.net/AMR.986-987.1250

Research on Distributed Power Quality Monitoring System of Oilfield

Mengtao Huang[1, a] ,HaoWang[2,b]

[1]College of Electrical and Control Engineering ,Xi'an University of Sience and Technology,Xi'An 710054, China

[2]College of Electrical and Control Engineering ,Xi'an University of Sience and Technology,Xi'An 710054, China

[a]email:275489567@qq.com, [b]email:656228336@qq.com

Keywords: LabVIEW,power quality,ATT7022C,oilfield

Abstract: For the specific requirements of power quality in the process of oil exploration,this paper designs a distributed intelligent monitoring systems,including oilfield power quality monitoring center and single oil well monitoring terminal.Among them,Single well terminal hardware is composed of high precision meter chip ATT7022C and ARM9 processor, it can complete the accurate measurement of the electrical parameters.The monitoring center is designed with LabVIEW as the carrier of the power quality comprehensive platform.Using ethernet for data transmission between the terminal and monitoring center. The results show that the system is comprehensive, it can effectively detect multiple power quality parameters and harmonic variation of the grid side,and also can provide technical support for oilfield power quality monitorng automation.

0 Preface

Petroleum is an important energy in China. There are two main problems in the current oil exploitation:1.With the rectifier, inverter and switching power supply technology, new energy-saving equipment put into use in the field of oil exploitation, inevitably resulting in a frequency deviation, as well as three-phase unbalanced and harmonic problems. 2.Oilfield is composed of a plurality of single well set.In the case of a wider range monitoring, only using a single monitor of power quality monitoring system is not flexible enough, and it is difficult to analyze the overall situation.Therefore,it is necessary to establish a monitoring and control system of distributed, networked, intelligent.

1 Overall system design

Oilfield power quality monitoring system is composed of the power quality monitoring center and some monitoring terminals.Monitoring center is located at each substation, is responsible for the management and maintenance of the monitoring terminal data transmission.And the role of the monitoring terminal is to report each real-time electricity parameters of oil pumping well.Its structure is shown in figure 1.

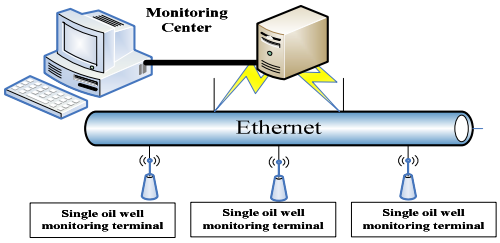

Fig.1 The overall structure of the system

2 structure and function of the single well monitoring terminal

The design of the single well monitoring terminal with high precision in the three-phase electric meter IC ATT7022C can achieve its own recuperated for electrical signal filtering, the voltage, current, frequency, reactive power detection accuracy reached 0.5%,meeting the standards at the national level of the instrument.The measurement of electrical parameters meter chip and ARM9 processor send the data to the PC machine by the Ethernet .Through the calculation of basic electrical parameters，It implements the voltage deviation, three-phase imbalance degree deviation, current steady-state power and reactive power index analysis.In this paper, windowed interpolation FFT algorithm combined with wavelet transform Mallat, thus completing the positioning harmonic measurement and transient perturbation signal.LabVIEW has powerful functions and data programming ability, can complete the programming and the realization of interface index.In figure 2, you can see its structure diagram.

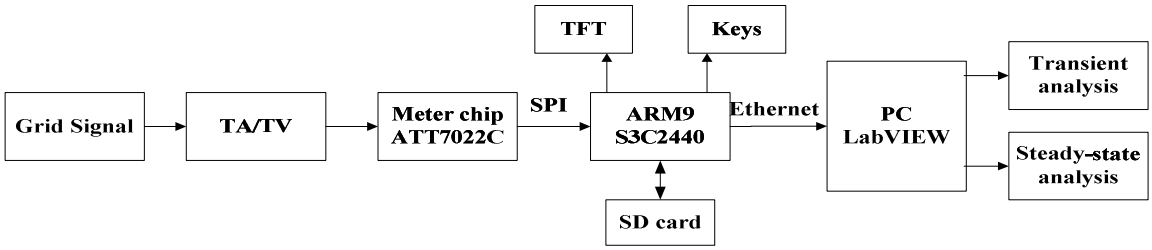

Fig.2 The overall structure of the system

Figure 2, the voltage or current transformer is in proportion to the transformation of the equipment.Its main function is to convert the high voltage and large current power grid into a standard low voltage scaling transformation (380/5V) or standard small current (10A/5mA).In order to achieve real-time transmission of data, use the check more accurate TCP protocol, using multifunctional monolithic network interface chip W5300, which integrates an10/100M Ethernet controller ， its speed can reach 80Mbps.In LabVIEW, with support for serial interface,GPIB, VXI, PXI and Ethernet standard bus data acquisition equipment VISA interface software library which could realize the communication between the upper and lower computer[2].

3 Harmonic and transient power quality parameters

3.1 Harmonic Analysis

From the IEC standards and national standard definition, harmonic frequency spectral component is defined as an integer multiple of.When the power grid is in steady state ,FFT algorithm is the most common method in Harmonic Analysis[3].Any function can be used in the form of a Fourier series launched：

$$f(t) = A_0 + \sum_{1}^{\infty} [A_n \cos(nwt + \varphi_n)] \quad (1)$$

Wherein, T represents periodic, A_n represents the corresponding amplitude, φ_n represents the initial phase angle.

Real FFT analysis of frequency spectrum leakage effect.In order to reduce leakage, need to add window fuction.Frequency-domain response function sidelobe amplitude and width of the main lobe will cause a certain process is not complete, so it should look at the performance of the frequency domain window function closest to the impact function, that is, the side lobe is small and narrow main lobe window function.In this paper, using the Hanning window.

This paper processes the signal through LabVIEW signal processing for conversion under the menu controls FFT.vi,it can be able to get HRU and THD.As shown in Figure4.

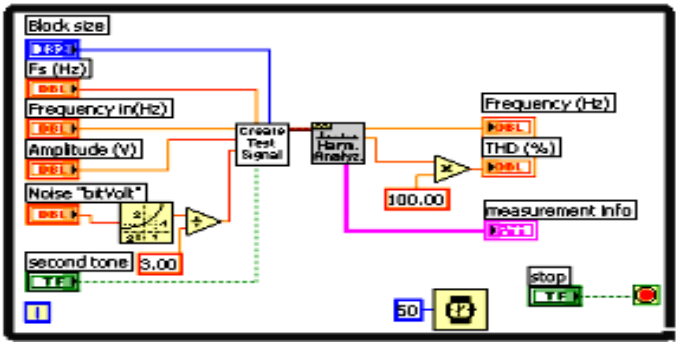

Fig. 4 Harmonic analysis program

3.2 Wavelet localization of transient disturbance parameters

Due to the high-power oil pumping unit works with a high-frequency DC-DC power conversion technology and three-phase rectifier technology, the distribution network will lead to a certain line voltage and current disturbances. However, once the state is bound to contain a mutation abnormal signal (voltage sags, swells) or high-frequency resonant interference, Fourier transform look powerless.Using an improved algorithm based on wavelet decomposition and reconstruction,it can deal with signal of high frequency and low frequency part respectively.For the high frequency component contains noise and singular information,wavelet transform is used to determine the signal mutation point time and amplitude and high frequency resonance happened[4].

Wavelet transform is a special kind of waveform with finite length, its average value is 0. Wavelet sequence defined as:

$$\Psi_{a,b}(t)=\frac{1}{\sqrt{|a|}}\Psi(\frac{t-b}{a}) \qquad a,b\in R \tag{2}$$

In the formula, a represents the frequency factor, b indicates the time shift factor.

Mallat algorithm is a fast algorithm of wavelet transform,its steps are as follows：

(1)The selection of wavelet base.This paper selects db4 wavelet,compared to other dbn wavelet, it has the most short time window, better time resolution.

(2)To determine the decomposition level.As far as possible to ensure that the fundamental frequency of the lowest subband is located in the center of the fundamental frequency component, thereby reducing the interference of the other sub bands.The formula is:

$$N=(\log_2 f_s / f)-2 \tag{3}$$

（3）Wavelet denoising[5]. Treatment of each layer of wavelet coefficients in the larger and smaller than a certain threshold model coefficients, and then the wavelet coefficients are processed and then inverse transform, reconstruction of the signal over noise, so as to achieve the purpose of denoising.

4.The experimental analysis

High-power pumping unit has voltage sag effect when it is working, and the characteristic of high frequency disturbance is obvious.We mainly use sag duration and temporary decline in value to describe voltage sags.The mathematical model of its expression is:

$$f(t)=\begin{cases}\sin(wt+\varphi_1) & t<t_1,t>t_2\\ a\sin(wt+\varphi_2) & t_1\le t\le t_2\end{cases} \quad (0.1<a<0.9) \tag{4}$$

The programmable AC power（The Chroma 61703Programmable AC Power Source） to produce a common transient power quality disturbance signals.The effective value of the fundamental signal set 220V, frequency of 50Hz,Harmonic signals were 3 harmonic 3%, 5 harmonic 2%, 7 and 9 harmonics 1%.To use this system for voltage sag real-time signal analysis, db4 wavelet is uesd as the wavelet basis in the process of experiments.The sampling frequency is 12.8kHz, the sampling length is 10 cycles.The analysis results as shown below.

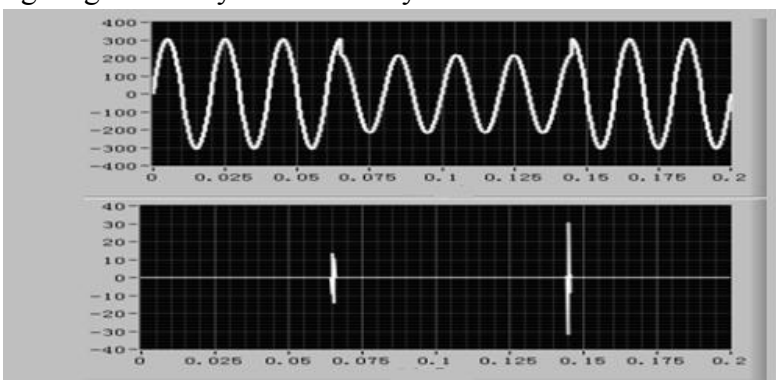

Fig.6 Detection of voltage sags by running mallat

The results can be obtained: Test duration 0.0802s, the magnitude of change was 29.8291%. The actual duration of 0.08s, the amplitude variation rate is 30%. The results show that the transient analysis module of the system has higher accuracy and amplitude in the time domain.

5 Conclusion

In this paper, the authors design a distributed power quality monitoring system of oilfield,the following conclusions can be obtained:

1) This design has realized the monitoring terminal hardware design, software design, to achieve the expected goals,and solving the oilfield network integrated wiring difficult problems caused by the dispersed.

2) Power quality monitoring platform constituted by the embedded hardware and LabVIEW,it can effectively analyze each phase harmonic distortion rate, every harmonic containing rate , transient parameter of time domain and amplitude. It also possess a good monitoring effect on the steady state phase voltage deviation, frequency deviation, three-phase unbalance degree.Its error precision instruments to meet Class A standards, which is expected to be used in practice.

References

[1] Lu Yanxia, Zhang Xiumin,Pu Xiaowen. Harmonic study of electric vehicle chargers[J]. Proceedings of the CSU-EPSA, 2006, 18(3): 51-54.

[2] SHAHID E.KHALID.Advanced Topics in LabWindows/CVI[M]. National Instruments，2001

[3] SHEN Bin,Hu Yangcheng. Application of LabVIEW in Power Quality Monitoring System [J]. Industrial control computer,2010,23(9):29-30.

[4] Chu Jun, MA Jianwei. Detection of power quality disturbed signals based on wavelet transform[J].Power System Protection and Control, 2009, 37(5): 34-36.

[5] Huang Mei, Huang Shaofang. A harmonic engineering calculation method for electric vehicle charging station[J].Power System Technology, 200832（20）：20-23.

Advanced Materials Research Vols. 986-987 (2014) pp 1254-1257

doi:10.4028/www.scientific.net/AMR.986-987.1254

Research on Intelligent Auxiliary Decision-making System for Regional Power Grid Faults

Lijun QIN[1, a], Xiaoteng WU[1,b]

[1] Department of electrical and Electronic Engineering, North China Electric Power University, Changping District, Beijing 102206, China

[b]wuxiaoteng_vic@126.com

Keywords: power grid failure, auxiliary decision-making, failure diagnosis

Abstract. a secure and stable operation of power grid will provide critical assurance for sustainable development of society and economy. Through power grid dispatching auxiliary decision-making system, key information could be obtained from various information sources of the control center such as energy management system, security and stability control system and safety production information system. In case that accident occurs, this intelligent auxiliary decision-making system will provide full assistance to dispatcher with dealing with accidents by starting failure diagnosis function and producing project for coping with accidents. Accelerate transformation of accident handling style from empirical style to analytical and intelligent handling style to improve technical level of sensing of power grid operation status, risks assessment, failure diagnosis and dispatching.

Introduction

When accident occur to power grid, the dispatcher should analyze accident, find out the focus problem, eliminate off-limits of the system and provide referenced scheme for recovering power-supplying in the area where accident occur with assistance of accident auxiliary decision-making system. General flow chart for regional power grid accident auxiliary decision-making system is as shown in Fig.1.

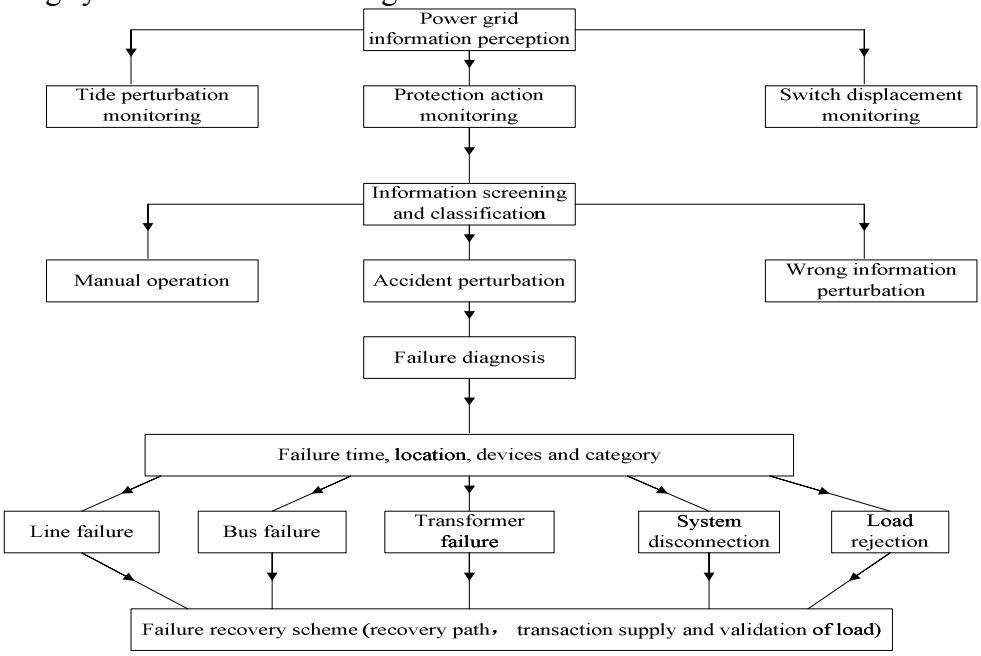

Fig.1.General process for making decision

Production of Sequential Network Topology

Replication and reproduction of the model of the whole network in scale of 1:1 provide reliable data base for power grid failure diagnosis technology which is based on network topology analysis.

The key process for carrying out analysis and recovery of system accident is to maximally restore loads in the power-losing area within the shortest time and transfer loads of over-loaded equipment and then put out reasonable plan for coping with accident.

It could be observed from this that restoration of controlling is a constraint optimized dispatching process with multiple targets which should be carried out by stages. It is of the objective to restore the maximal loads with the shortest time. Constraint conditions to be fulfilled for accident recovery control are to make sure that loads of all devices are within limit values and all node voltages are fulfilling requirements. Due to particularity of elements for electric system of discrete type in system construction, topology analysis algorithm is critical for the device search process.

Shading Network Topology Analysis

Shading method applied in network topology analysis for this system is based on accident handling auxiliary decision-making system which is basing on shading network topology analysis. Comparing with the conventional topology analysis algorithm applying stack for searching, shading network topology analysis algorithm is free from low efficiency with process rolled back during searching and it is of high speed, high efficiency and with simply designed program.

Progress for Sequential Network Topology Analysis

During normal operation, turn on a switch displacement monitoring and when a switch is shifted (regardless of manual operation or protection action), network topology module will initiate whole network topology once and topology information will be stored in a CASE when topology is completed. By one time, the system can store 30 CASE with each CASE has timing mark, activating signal and flag value. Connectivity, load, voltage and current information will also be stored together with storage of CASE. In case that failure occurs to the system, when switch is shifted, the former and the latter CASE are implying data variations before and after failures occur. Fault area and load loss could be figured out by comparing the two CASEs.

During normal operation, in case that no displacement of switch occurs, renovate all remote measurements with certain interval to update to the new CASE. By this operation, to make sure that the connectivity and operation status stored are consistent. Topology monitoring process is as shown in Fig.2.

Finally, after the power restoration program is generated, mark running load rate, load limit value of each line and transformer after expert system finishes strategic analysis to provide power constraint for further restoration scheme.

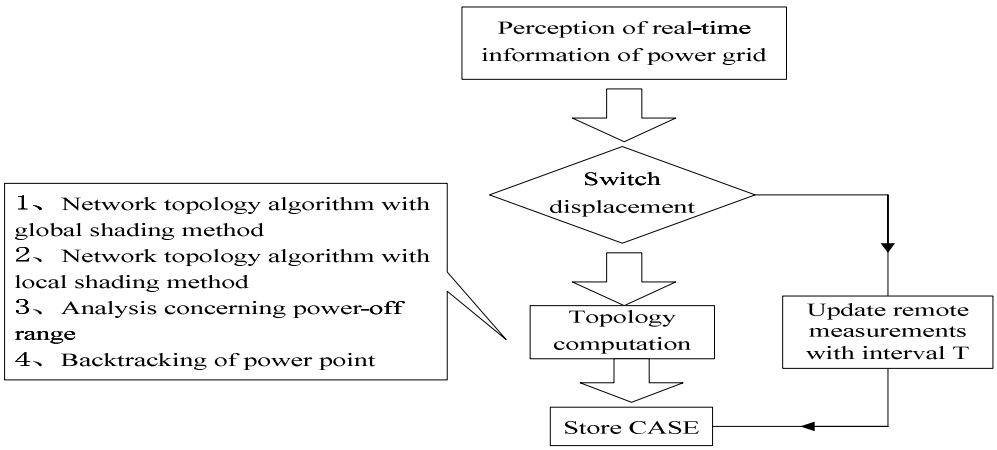

Fig.2.Sequential network topology analysis process

Power Grid Failure Diagnosis

The four most significant characteristics，also be called as the four failure elements appear after various faults occur to electric system are:

(1)Various protection action configured for components for relating electric system with simultaneous protection and being put out;

(2) Tripping of switch for connecting components of electric system;

(3) Resultant failure signal given by transformer with fault components.

(4) Electrical running parameters of components, such as current, power rate are changed,

Through the above four elements, summarize various faults and corresponding statistic features to failures of components and fulfill intelligent diagnosis of failures. An alarm could be defined by figuring out the four elements for alarming, the definition is as follows:

① Protection of general export

② A protection action

③ Displacement of a switch

④ Corresponding zero of remote measuring

①+②+③+④=fully defined failure occurred；

②+③+④=fully defined failure occurred, but general accident is not received;

①+③+④=failure occurred while failure type cannot be defined;

①+②+④=failure possibly occur, but deflection of remote communication is not received, verification should be carried out.

①+②+③=failure possibly occur, but zero of remote measuring is not received. Reclosing is possible fulfilled and record of reclosing action is required; it is possible that zero of remote measuring is not received; verification should be carried out through other methods.

Fulfill power grid failure diagnosis to figure out power-off area of power grid which could be taken as the starting condition for failure diagnosis. With support from relaying protection failure information and displacement signal of remote communication of automatic dispatching system, real-time network topology analysis will be carried out. Fault area should be defined first. Simple failures, such as the fault area with only one fault component could be directly defined as the fault component. For complicated failure (switch, protection action failure, wrong action), reliability of failure of each component in power-off area could be computerized by the system and failures will be sorted from high reliability to low reliability and then the dispatcher will determine the fault device eventually according to the inspection report results. Failure diagnosis process is as follows:

Decision-making for Recovery of Power Grid Accident

Accident recovery decision-making system of power grid will report the power-off area, station, load loosing value, area to be restored with power, off-limit of fault devices and other information after failures occur. For the area to be restored with power, power restoration path should be searched first and alternative schemes should be provided. Filter alternative schemes according to constraint conditions configured by customer and get the final optimal route recovery scheme complying with the objective function. For off-limited devices, method to eliminate off-limits should be provided basing on principle concerning sensitivity. Meanwhile, carry out risk assessment for fault power grid and figure out weak point of fault power grid and provide corresponding correcting and controlling strategy.

Conclusion

With rapid development of national economy, the power grid is continuously expanded and the electric power industry plays an increasingly important role in people's lives and work. How to eliminate failures promptly, restore power supplying within power-off areas, or to minimize the power-off area and short power-off time to minimize losses caused by power failure with presumption of a safe and stable power grid is of important and practical significance to

development of the whole electronic industry, regional power grid accident auxiliary decision-making system can solve these problems.

References

[1] Xin Shan; Ze-mei Dai; Yi-jun Yu; Zhe Zhang; Yong Zhang; Jing Zhang, "Design and realization of large grid online decision-making support system for accident treatment," Developments in Power Systems Protection, 2012. DPSP 2012. 11th International Conference on , vol., no., pp.1,5, 23-26 April 2012

[2] Xilin Zhang; Jiyong Li; Chenghong Jiang; Bing Liu; Aizhou Yang, "Aided decision-making system of accident operation and command for local power grid in Changchun," Automation and Logistics (ICAL), 2011 IEEE International Conference on , vol., no., pp.442,445, 15-16 Aug. 2011

[3] Sheng Si-qing，Ma Zhi-gang，et al. Distribution network fault restoration based on improved adaptive genetic algorithm[C]. //Second International Conference on Intelligent Computation Technology and Automation.2009：318-321.

[4] Zhang Yongjun，Ren Zhen，Li Bangfeng．Survey on optimal reactive power dispatch of power systems[J]．Power System Technology，2005，29(2)：50-56．

[5] Jia DongLi; Song Xiaohui, "Study on technology system of self-healing control in smart distribution grid," Advanced Power System Automation and Protection (APAP), 2011 International Conference on , vol.1, no., pp.26,30, 16-20 Oct. 2011

Advanced Materials Research Vols. 986-987 (2014) pp 1258-1262

doi:10.4028/www.scientific.net/AMR.986-987.1258

Research on multicast flooding suppression in smart substation

WANG Xiangqun[1, a], HUANG ZaiChao[1, b], LI Chunlong[1, c], HUANG Zhi[1, d], WANG XiaoBo[2, e]

[1]China Electric Power Research Institute,Nanjing 210003

[2]Jiangsu Electric Power Company Research Institute,Nanjing 210024

[a,b,c,d] email:{wangxiangqun,huangzaichao,lichunlong,huangz}@epri.sgcc.com.cn
[e]email:wangxb1987@qq.com

Keywords: intelligent substation, multicast, flooding, VLAN, GMRP

Abstract. The existence of a large number of multicast flooding data in the process level of smart substation,causes serious influence on the real-time performance and reliability of network.Through the exchange principle of Ethernet,the forwarding process of second-layer multicast in network is introduced. Combined with the application in intelligent substation and some experimental data, through in-depth analysis of the 802.1Q VLAN isolating broadcast domain,setting static multicast to change the static MAC address table ,and GMRP to change the multicast information on Ethernet switch through the interactive protocol data, the multicast flooding suppression method is illustrated. And based on the practical engineering situation, the three kinds of methods are compared from the characteristics of debugging operation and maintenance convenience and reliability of intelligent equipment,then the technology route recommendation is given.

Introduction

The intelligent substation adopt the concept of hierarchical information of automation system in substation proposed by IEC61850 ,and it is divided into three levels:the station level, bay level, process level.The process level consists mainly of two types of packets GOOSE and SV.The GOOSE packets transmitted information includes latching signal, position signal , status signal and control signal , and it has high requirement to the real-time and reliability .Sampling packet transmission information from process level to bay level,and this kind of message has high requirement to real-time.Currently SV and GOOSE messages are second-layer multicast packets in process level network.The general processing of this type of packet in industrial Ethernet switch is that ,if the port mapping corresponding to the multicast destination address is not existent in the MAC address table,the packet will forward to all the ports except the input port in the same VLAN.As the SV flow of MU is very large ,the IED in the SV network will receive a lot of irrelevant message,then the network bandwidth will be wasted,and the IED will receive serious impact ,especially in mixed network of SV and GOOSE,GOOSE message will be blocked in the absence of preferential measures,the performance of real-time can not be ensured,also the reliability and safety will be jeopardized[1-6].

The article firstly introduce the principle of multicast communication,then describe several technology of multicast flooding suppression,and the proposal is given combined with project practice.

The principle of multicast communication

The principle of switch

In smart substation,especially the process level,the IED communicate via Ethernet,and the Ethernet switch can learn the MAC address of the equipment connected to the port.The process of learning is that switch listens all the incoming packets,and examines the source MAC address,then forms a mapping of MAC address to the corresponding port,and the mappings are stored in the MAC address table in the switch.When a frame arrives at the switch,the switch determine how

to transmit the frame by the lookup of the MAC address table.If the destination address exists in the MAC address table,the frame will be forwarded to the corresponding port,otherwise the frame will be forwarded to all the ports except the source port.

The principle of multicast

Multicast technology, is a technique that allows one or more hosts to transmit a single packet to multiple hosts. The difference between multicast MAC address and unicast MAC address (physical MAC address) is that, in the six bytes of the multicast MAC address,the lowest bit of the highest byte is 1, while the bit of unicast MAC address is 0, as shown in Figure 1. GOOSE message and SV message are both multicast message.The second-layer multicast has a mapping to a group of Ethernet port in the MAC address table,when such a message arrives at Ethernet switch,the switch will analytic the destination address of the message and query the MAC address in MAC address table of the switch .If the address appears in the table , check the corresponding multicast members of the address,and the message will forward to all the member ports,else the message will forward to all the ports in the same VLAN.

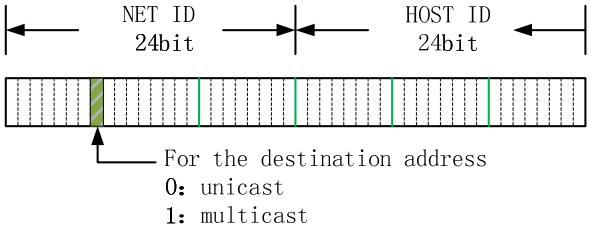

Figure 1 The MAC address of unicast and multicast

The suppression of VLAN

The concept of VLAN

VLAN is an end-to-end logical network constructed by network management software,and it can step across different segment and network.A VLAN forms a logical subnet, which is a logical broadcast domain,and it can cover multiple network devices in different geographic locations, allowingInternet users to join a logical subnet.In brief,VLAN can divide a physical network into several logical network, then it can control the broadcast domain, improve network security, simplify network management,also, it makes the construction and expansion of network more convenient.

The isolation of unknown multicast flooding by VLAN

When a multicast packet arrives at a port of the switch, the switch port will check whether the message has 802.1Q tag,if not ,the switch will insert a tag into the frame according to the default VLAN ID of this port . If the message contains the 802.1Q tag, the switch determines whether to allow the message to the port according to the VLAN the port belonging to. After the multicast packet entering the switch,it will forward to corresponding destination port by querying the multicast MAC address table.If there is no the multicast in the MAC table ,the packet will forward to all the other ports in the same VLAN. The division of VLAN has greatly reduced the scope of flooding, therefore the network system is more stable and reliable.

In order to limit the scope of multicast flooding and improve the utilization rate of network resources,some IED and multicast source will be configed into a same VLAN.In general,the substation will be divided into different logic zone according to the voltage level,such as 220kv system region, 110kv system region, 35kv system region.VLAN is set according to different bay in different voltage levels,and a VLAN is set in one bay,such as 110 kV line bay,110kv section bay, 110 kV PT control bay[7,8].

Assuming in a switch of SV network, each merging unit sends out the multicast traffic for 6Mbps,we can contrast the flooding flow between before and after VLAN config according to different amount of MU,and the experimental data:

Table 1: The comparison of SV flooding between before and after setting VLAN

The count of MU	1	2	4	6	8	10
SV flooding before VLAN setting (Mbps)	6	12	24	36	48	60
SV flooding after VLAN setting (Mbps)	0	0	0	0	0	0

If there are ten MUs connected to a Ethernet switch ,these ten MUs will send out data of 60Mbps without VLAN setting, and most of these flow is useless to the other IED connected to the same switch and will cause the tremendous impact on the IEDs.If each MU is in the independent VLAN,the SV packet will not flood to other VLAN,and the network reliability will greatly enhanced.

Suppression of static multicast

Static multicast refers to the static multicast group with manual configuration,and the multicast address will not disappear automatically when the ageing time is overtime.To add or delete multicast address entries in MAC address table staticly can realize the management of multicast group member.When a multicast packet arrives,the switch will query the multicast address table,then the packet will forward to corresponding destination ports.

In order to solve the problem of multicast flooding in intelligent substation,especially the serious impact on the IED caused by SV packet in process level,static multicast group can be created in switch according to the destination address of the packet.When the SV or GOOSE packet arrive at the switch,the the switch will query the multicast address table,then the packet will forward to corresponding destination ports,instead of forwarding all the other ports.

According to the design of network and the business needs,it can be determined that which ports will be connected to the switch by the IEDs,and the communication service among the IEDs can be confirmed.According to the destination of each multicast service on the IED,the destination IED can be confirmed ,then the switch ports will also be confirmed,after that,the mapping of the multicast to the switch ports.The static multicast group can be created through the management software of Ethernet switch,then the mapping entry will be added in the MAC address table. Then,all the other multicast group could be created,and the multicast address can be found in the MAC address table.And all the multicast packet will forward to de designated ports,and will not flood to all the ports.All the Ethernet swith in the process level will be set the same config for the multicast group.If the multicast packet will be sent out across the switch,the cascaded ports would be added to the multicast group.By creating static multicast in all the cascaded Ethernet switches,the whole process layer network can be made no multicast flooding.

The suppression of dynamic multicast

Dynamic multicast is changeable relative the static multicast,and the entry of the multicast address in the MAC address table will change when the switch receives the protocol message,so,the multicast packet may be sent out to different ports although it has the same destination address. GMRP is defined in IEEE 802.1P,and it is used to maintain the multicast registration information in the Ethernet switch.GMRP can filter the second-layer multicast,so it is suitable for SV and GOOSE message in smart substation.

The destination address of GMRP is a specific multicast MAC(01-80-C2-00-00-20),and switch or host can distinguish GMRP message from other message.When a terminal device want to join a multicast group,it will send join-in information.After receiving the message,the switch will join the port connected to the device in the multicast group,also ,the swith will broadcast the GMRP join-in information in the VLAN the port belonging to, then the multicast source in the VLAN can know the presence of new multicast members.When the multicast source send a multicast packet,the switch will query the MAC address table,then forward the packet to the corresponding ports,so as to

realize the forwarding of second-layer multicast in the VLAN.The process can be described in schematic as shown below.Also, the Ethernet switch will periodically send a GMRP querying message(LeaveAll),if the device want to stay in the multicast group,it should respond to the querying by sending join-in message,otherwise,it can send a leaving message or do not respond to the querying.If the switch can not receive a responding message or receive a leaving message ,it will delelte the corresponding port of the multicast group in the MAC address table.A device can join multiple multicast groups,and this can meet the need of that a protection may require data from more than one MU.GMRP can effectively control the multicast flooding,and it is especially suitable for information transmission of MSV9-2 and GOOSE based on the pubish/subscribe mechanism in smart substation[9-11].

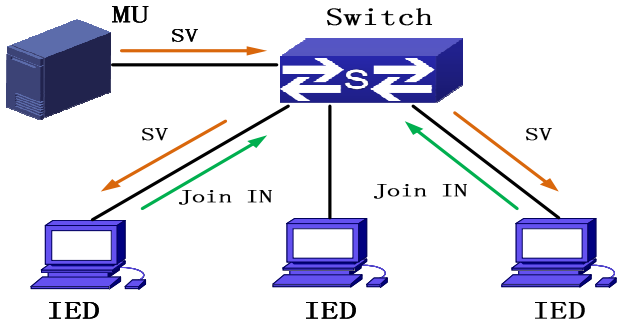

Figure 2 The description of joining in the multicast group

Conclusion

At present,VLAN technology is the most widely used isolation technology of multicast message,and the VLAN can be configured in Ethernet switch by the connection between switch ports and IED,also by the interaction relationship among the IEDs,and it does not need to do much operation at IEDs.But the function configuration of the Ethernet switch is complicated,and this will increase the difficulty of debugging and maintenance.But once configured,the correspondence between the IEDs and the Ethernet switch ports is not free to change,otherwise,the IEDs can not communicate normally.Static multicast is suitable for the situation of that the multicast group only has a small number of members,when there is a lager number of members or frequent changes,this method of static multicast is not suitable.Ethernet switch only need to open the function when the GMRP is used,also,do not need to define a specific port,so the work of configuration is greatly simplified.But,the IED should support the GMRP protocol,and this will improve the requirements of function and reliability of the IEDs.But considering the simplicity of the switch configuration and the convenience of substation expansion,the GMRP technology will become the mainstream packet filtering in process layer of intelligent substation in future.At the same time ,static multicast technology can be used as the supplement of GMRP when the IED can not support GMRP.

References

[1] IEC61850， Communication networks and systems in substations[S]. 2003.

[2] XU Cheng-bin，SUN Yi. min. A communication solution of process layer GOOSE in digitized substation[J]. Automation of Electric Power Systems，2007，3 1(1 9)：91-94.

[3] CAO Jinping，LI Wei，QIN Yingli，HUANG Xin. Research on digital substation proless level communication technology[J]. Power System Protection and Control，2008，36(12)：60-63.

[4] CAO Jinming，FANG Xinyan，WU Rong. Reliable substation communication based on IEC61850[J]. Electric Power Automation Equipment, 2008,28(9):89-93

[5] TONG Xiaoyang,L I Yingchuan, CHEN Deming, ZHA NG Li , XU Kelai. Refined Management Study of the Digital Substation Secondary System Based on IEC61850[J]. Automation of Electric Power Systems, 2009,33(22):44-48

[6] CAO Haiou, YAN Guoping, XU Ning, LI Cheng. GOOSE networking scheme for mgital substation[J]. Electric Power Automation Equipment,2011,31(4):143-146

[7] NIU Zhan-ping. Application of VLAN technology in the intelligent substation network[J]. Power System Protection and Control，2009,37(23):75-78.

[8] DING Teng-bo , LIN Ya-nan , ZHAO Meng. Research of the virtual local area network in smart substation[J]. Power System Protection and Control, 2012,40(1):115-119

[9] DING Daiyong，WANG Liping，WANG Xiaoru. Research on Application of Multicast in Low Voltage Substation Communication[J]. Power System Technology, 2011,31(4):143-146.

[10] YIN Haichun．Implementation of IGMP snooping protocol on the switch layer[D]．Chengdu Chim University of ElectronicScience and Technology,2004．

[11] LI Jing,DUAN Bin,ZHOU Jianglong,LIU Lili.Design of a Publish/Subscribe Communication Model Based on GMRP for Substation Communication[J].Power System Technology, 2008, 32(16):16-21

Advanced Materials Research Vols. 986-987 (2014) pp 1263-1267

doi:10.4028/www.scientific.net/AMR.986-987.1263

Review of AGC and Primary Frequency Regulation

SUN Peng[1, a], TANG Xiaojun[2, b], WANG Haohuai[3, c],
ZHONG Wuzhi[2], WANG Jian[3] and LUO Hongmei[2]

[1] North China Electric Power University, Beijing, China
[2] China Electric Power Research Institute, China
[3] China Southern Power Grid, China
[a]sunflower198961643@163.com, [b]tangxj@epri.sgcc.com.cn, [c]wanghh@csg.cn

Keywords: Frequency Characteristics, AGC Control Strategy; Primary Frequency Regulation; AGC

Abstract. This paper introduces the current research status of primary frequency regulation and AGC control strategy. Firstly, some important parameters about primary frequency regulation are introduced. Secondly, describes the development on the theory of AGC. Thirdly, the basic concept of CPS and ACE were briefly described, and then the difference between CPS and former A1/A2 standard were compared. Finally, outlook on the coordination between AGC control strategies and primary frequency regulation.

Introduction

With the expansion of the power grid interconnection and the power market, the application of technological innovation to conventional automatic generation control (AGC) will become a hot spot. Mainly in the following areas：Research on interconnected power grid of AGC control strategy and methods； The operating with AGC and primary frequency regulation under special mode. This literature describes the factors of primary frequency regulation, development status and trends of AGC basic control strategy and outlook the operating strategy between AGC and primary frequency regulation in a special power shortage situation.

1 Analysis on Primary Frequency Regulation Parameter of Power Grid

Primary Frequency Regulation(PFR)[1] means automatic control unit of generators conditioning control system will increase or decrease active power so that the grid frequency can quickly return to the rating range when the grid frequency deviation. Literature [3] studied the following characteristics of PFR: (1) Function of PFR is shared in an interconnected power system so that bigger system is more likely to get stronger ability of PFR. (2) The response time of PFR is very short, generally not more than 15s after frequency changes. (3) Working time can be more than 15min. (4) PFR requests generators in system to retain enough reserve capacity. Below describes the parameters of PFR.

1.1 Regulation dead zone

The function of regulating dead zone contributes to stable operation, when the grid frequency is basically stable near the rating value and is not going beyond the regulation dead zone, units don't have to take regulation against the tiny fluctuation of frequency, reduce the changes of valve position and improve the stability of generator operation. On the other hand, when frequency deviation is beyond regulation dead zone, frequency regulation will be taken to meet the need of primary frequency of power system. The regulation dead zone of generators involved in primary frequency regulation domestic is generally restricted to ± 0.033 Hz. Literature [2] pointed out that in practical applications, the artificial failure zone of domestic speed control system can only be set to achieve two decimal places, the dead zone of primary frequency regulation in most power plant is

set to $\pm$0.04 Hz. Generator units of the hydroelectric power plant built in the mountains away from load center whose frequency are volatile, dead zone can properly be extended.

1.2 Regulation coefficient

Regulation coefficient δ reflects the relationship between generator output power and frequency that is the static characteristic of power - frequency; it can be approximated to a straight line, as shown in figure 1.

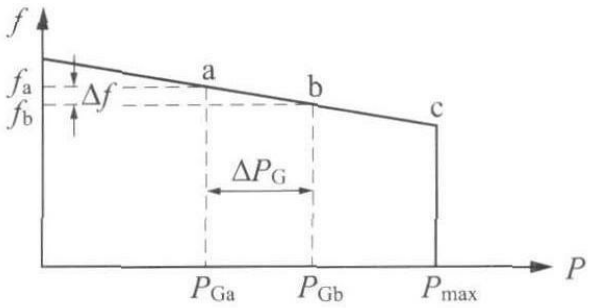

Figure1 Static characteristic of power - frequency

Regulation coefficient is defined as:

$$\delta = -\frac{f_a - f_b}{P_{Ga} - P_{Gb}} = -\frac{\Delta f}{\Delta P_G}$$

Which:

Δf —— changes of power grid frequency from f_a to f_b;

ΔP_G ——changes of generator output from P_{Ga} to P_{Gb}.

In addition, from the concept of speed regulation system, a parameter, speed unequal rate, used in larger range is put forward. Speed unequal rate and relative regulation coefficient in essence is the same, and the difference is that speed unequal rate is a parameter of the regulation system, but regulation coefficient is raised from the angle of power grid frequency regulation. Regulation coefficient is of a great influence on maintaining the stability of system frequency.

Studies in reference [2] show that regulation coefficient values in a system should be different. When system load changes, generators with smaller regulation coefficient values should undertake the load changes first, and then do the generators with larger regulation coefficient. Basing on this principle, δ of hydropower generators that take the task of peaking and frequency modulation will lager than that plants excluding the peaking and frequency modulation tasks.

1.3 Delay rate

The above static characteristic curve of regulating system is completely theoretical. It is based on the corresponding of speed and load of the unit. Once the speed of the unit has a deviation, the speed control system will immediately act, and the unit power is immediately changed. However, with the influence of factors such as friction and clearance, when the speed of the unit changes, the static characteristic curve is no longer a curve, but turns into a pair of parallel curves. It is usually referred to the delay phenomenon of the regulation system. The delay rate parameter of the unit is proposed in literature [3].

Formula is defined as follows

$$\varepsilon = \frac{\Delta n}{n_0} \times 100\% \quad ;$$

Which:

Δn ——Speed difference of the characteristic line between the speed ascent and descent;

n ——Unit rated speed.

Delay rate of turbine operation is very unfavorable, because the slow rate is higher, indicating the interval time from the turbine speed changes to the regulating valve starts operation is larger, which causing the turbine cannot be adjust the external load changes. Especially when load rejection, regulation valve closed behind caused by delay rate, make speed increases too much, causing a critical security control action. In addition, due to the presence of delay rate, in the parallel operation, the unit load swing cause the swing of the speed when stand-alone operation, that the supply frequency fluctuations. Therefore, it required delay rate the smaller the better.

1.4 Response time

Primary frequency regulation response time is the time from when the grid frequency changes by the action time of primary frequency regulation to the unit load began to change, which should be less than 3 seconds.

1.5 Setting time

Primary frequency regulation settling time is the time when unit load reach a stable line after the grid frequency stabilized, which should be less than 1 minute. It should be excluded from the load instruction changes when unit coordinated control system or automatic generation control (AGC) is running.

Literature [4] gives the related tracking unit primary frequency regulation parameters settings of China Southern Power Grid：

Table1 PFR parameter settings of China Southern Power Grid

Regulation coefficient	4%~ 5% Thermal power
	3%~ 4% Hydro
Regulation dead zone	± 0.033Hz Thermal power
	± 0.05Hz Hydro
Response time	≤ 3*s*
Setting time	< 60*s*
Delay rate	< 0.07% ~ 0.1%
Magnitude of the load	≥ ±6% ~ ±10%

2 Development on the Theory of AGC

As early as the 1950s, based on the principle of the transfer function in classical control theory, Kirchmayer proposed a mathematical model of interconnected system LFC to study the PI control method, which is widely used in AGC PI control link nowadays.

With the development of computer technology, AGC system technology has developed from the early analog systems into a digital system now. That is, from the simple, strong robustness and decentralized system control to complex, highly nonlinear and continuous variation of the power system. In 1970, Elgerd and Fosha first applied modern control theory to the interconnected system of LFC problem, but because of the centralized control, the LFC met the problem of "curse of

dimensionality" in the information delivery. Literature [5] reviewed the characteristics of the traditional AGC systems and the features of the proposed system based on modern control theory. The application of modern control theory proposed method may improve the effect of the traditional methods based on modern control theory. On the basis of a large number of practical engineering applications, Literature [6] improved AGC control cycle, control strategy, database models, unit control mode and the Area Control Error smooth handling in conventional AGC algorithm, introducing dynamic filters to remove some dead-ACE effects of high frequency noise, reducing unnecessary control commands.

According to AGC control characteristics, the model system can be described using the no-model control method, intelligent AGC is an important research direction with the development of intelligent control. Literature [7] did a pioneering work in the application of fuzzy control theory of complex multi-area interconnected power system of LFC and improved fuzzy control rules with correction factors. However, due to the normal two-dimensional fuzzy controller only set error and error change as input variables and lack of integral action, combined with the fuzzy controller specific quantization process, the conventional fuzzy control system cannot eliminate the steady state error, which limiting the accuracy requirements for steady higher process control applications. Literature [8] used a PID controller design experts for large-area interconnected load frequency control. Rules of experts are made up of two parts. One part comes from the standard analysis and practical experience of the CPS, the other part is based on the PID dynamic characteristics of the controller and the actual situation of load frequency control.

3 Research Status on AGC Strategy

Automatic generation control (AGC) regional interconnection has become the most important subject of power grid in the modern design and operation. The goal of AGC is by adjusting the power output of AGC generators with fluctuating load requirements to maintain the grid frequency constant and tie-line power close to the planning. To assess the effect of AGC control, the North American electric reliability council (NERC) has put forward several control performance assessment criterion successively. Have A1/A2 standards then CPS standards [9] in 1996 in order.

According to the character analysis of interconnected power grid in China composed by grid dispatching center and provincial dispatching center, literature [10] proposed grid/provincial dispatching center AGC hierarchical control and coordination technology based on tie-line and frequency bias control. It also put forward AGC control methods based on CPS standard. Because provincial dispatching centers adopt TBC control, it can keep balance between generators power and load in each province. The main use of AGC in grid dispatching center is monitoring. Whether if the AGC taking part in regulation and the size of regulation depend on specific conditions. CPS standard is based on the ACE value in A1/A2 standard. ACE control area is divided into 4 parts: dead zone, normal area, sub-emergency zone, emergency zone, each control zone with processing on the change of CPS index.

Literature [11] illustrated AGC control strategy under CPS and proposed the concept of CPS regulation power component. Then the concept is combined with proportional component and integral component, and constituted the region's total power regulation. More, the total regulating power of the region can be amended to further enhance the CPS indicators according to the size and direction of the area control error and frequency deviation. Finally, the paper proposed a method of dividing the AGC control area according to the total regulating power of the region rather than ACE. These control strategies helps improve the quality of grid frequency, and reflects the mutual support function between interconnected AGC control areas in emergency situations.

Literature [12] analyses the difference between CPS and A1/A2 standard, the AGC control strategy based on the CPS should be considered the relationship between ACE and the system frequency synthetically. We put forward a kind of ideal AGC control strategy based on the CPS standard, that is when the frequency deviation is big, the control objectives of the AGC is to make the ACE and the frequency deviation opposite , when the frequency deviation reduce, AGC control strategy make the ACE to minimum. Using the methods of "AGC control strategy based on frequency change", “combined primary frequency regulation with AGC coordination “and " AGC unit cluster control mode", improved the level of the AGC operation and CPS assessment effectively.

4 Summary

The interconnection and marketization of regional power grid are two important reforming directions of state grid, it is meaningful to research parameter of primary frequency regulation and set reasonable parameter values. The control of AGC based on CPS standard will be a hot spot in future. Nowadays AGC control strategies are unformed, and AGC control strategies in coordination with multiple types of generators will be carried out. And the coordination between AGC control strategies and primary frequency regulation under power shortage conditions should be more deeply researched.

References

[1] Erlich I, Rensch K, Shewarega F. Impact of large wind power generation on frequency stability[C] Power Engineering Society General Meeting, 2006. IEEE. IEEE, 2006: 8 pp.

[2] SHU Rong, ZHOU Binqiang. Discussion on Primary Frequency Regulation Parameters Optimization of Hydroelectric Generators[J]. Yunnan Electric Power, 2009, 37(4): 35-36.

[3] LIU Quanshe, Research on Vertiginous Rate and Stagnant Rate of Turbine's Variable System[J]. Turbine Technology, 2001, 43(4): 244-245.

[4] WEN Xue, ZHANG Kun. Research on the Primary Frequency Regulation of China Southern Power Grid[J]. Southern Power System Technology, 2008, 2(3): 70-72.

[5] Jaleeli N, VanSlyck L S, Ewart D N, et, al. Understanding automatic generation control[J]. Power Systems, IEEE Transactions on, 1992, 7(3): 1106-1122.

[6] GAO Zonghe, Some Algorithmic Improvements on Agc Software[J].Automa -tion of Electric Power Systems , 2001, 25(22): 49-51.

[7] GAO Feng, QIN Yihong. Optimum Design of Fuzzy Load-Frequency Controllers for Interconnected Power Systems[J]. Proceedings of The Chinese Society for Electrical Engineering, 1995, 15(6): 384-390.

[8] Hao Fei, Liu Jizhen, Tan Wen. Design and Application of Expert Controller on the Load Frequency Control[J]. Modern Electric Power, 2006, 23(1): 61-65.

[9] YU Tao, CHEN Liang, CAI Guanglin. CPS Statistic Information Self-learning Methodology Based Adaptive Automatic Generation Control[J]. Proceedings of The Chinese Society for Electrical Engineering, 2008, 28(10): 82-87.

[10] GAO Zonghe, Teng Xianliang, Tu Liqun. Hierarchical Agc Mode and Cps Control Strategy for Interconnected Power Systems[J]. Automation of Electric Power Systems , 2004, 28(1): 78-81.

[11] GAO Zonghe, TENG Xianliang, ZHANG Xiaobai. Automatic Generation Control Strategy Under Control Performance Standard for Interconnected Power Grids[J] . Automation of Electric Power Systems , 2006, 29(19): 40-44.

[12] TANG Yuezhong, ZHANG Wangjun, ZHANG Jian, CHEN Ming. Research on Control Performance Based Control Strategy for Automatic Generation Control [J]. Power System Technology, 2004, 28(21): 75-79.

Advanced Materials Research Vols. 986-987 (2014) pp 1268-1272

doi:10.4028/www.scientific.net/AMR.986-987.1268

Simulation on Superconducting Magnetic Energy Storage in a grid-connected photovoltaic system

Yang Xie[1,2,a], Ming Zhang[1,2,b], Guozhong Jiang[1,2], Peng Geng[1,2], Kexun Yu[1,2]

[1]State Key laboratory of Advanced Electromagnetic Engineering and Technology, 430074, Wuhan China

[2] School of Electrical and Electronic Engineering, Huazhong University of science and Technology, 430074, Wuhan, China

[a]email: xy00792@qq.com [b]email: zhangming@mail.hust.edu.cn

Keywords: Photovoltaic, Superconducting Magnetic Energy Storage, Photovoltaic Generation;

Abstract. Photovoltaic (PV) generation is widely used to solve energy shortage and environment problem. Since the output current of the solar cell will change with the sunlight irradiation, the power of the solar cells are not stable, so there is a need of a storage equipment connected to the PV system. With the characteristics of high efficient energy storage and quick response of the power exchange, the superconducting magnetic energy storage (SMES) can be used to meet the balance between the grid and the PV. A SMES and PV subsystem are connected together with the DC bus, which have less power electronics elements and can control power quality efficiently than linked with the AC bus. This hybrid system is composed of a DC/AC converter on the grid side, a DC/DC converter with the PV arrays, and a DC chopper with the superconducting magnet. A detailed model of the hybrid system is built with MATLAB/SIMULINK. Simulation results with and without SMES connected to the grid-connected photovoltaic system are presented, compared, and analyzed. The results of simulation demonstrate that the SMES system can maintain the DC bus as a constant value which can contribute to the stability and reliability of the grid-connected PV system.

Introduction

Solar resource is an effective way to be the main alternative energy source to replace traditional ones in the future. The photovoltaic (PV) cell is an all-electrical device, which produces electrical power when exposed to sunlight and connected to a suitable load. Without any moving parts inside the PV module, the tear-and-wear is very low.

Since the output current of the solar cell will change with the sunlight irradiation, the power of the solar cells are not stable. As a result, PV cells' output cannot always meet demand power, the power mismatch should be compensated with the power from the main grid. On the other hand, they sometimes generate more power than load need, excessive power flows to the grid. It is not good to have a big influence on the grid, there is a need of energy storage equipment to make power from the grid stable. Superconducting magnetic energy storage (SMES) have lots of advantages such as high power density, long periodic life, a high speed, can be used to meet the balance between the grid and the PV.

Among the earlier work in the literature, there are some studies about SMES, such as stabilization of the power system [1][2] and the transient stability [3][4]. And it is proved that SMES is effective as an energy storage device. Also in terms of practical use of renewable energy, the PV and SMES combined system is focused on recently. In the combined system, energy storage device is essential because PV needs power management in the particular area. Many of the former study linked the SMES on the AC side of the grid. However, linked with DC bus will have less power electronics elements and can control power quality efficiently than linked with the AC bus. Study of applying SMES to the PV[5] linked with DC bus is introduced. In this manuscript, the authors focus on the power characteristic of SMES, no detailed model of the PV cells or the SMES. And the power of the system is up to only 5KW.What's more, the irradiation of the sunlight impact on the power has not been fully considered.

In this paper, each part of the hybrid system is introduced and the control strategy is clarified in section II and III. In section IV, with and without SMES are simulated on the grid-connected photovoltaic system to investigate their impacts on the dynamic performance and power flow of the PV generation system.

System Model

The main circuit of the combined system is shown in Fig. 1. The system is composed of PV cell array, PV side DC/DC converter, DC chopper, superconducting magnet and the grid side converter. In a grid-connected PV system, the energy storages equipment must have the characteristic of high energy storage efficiency and quick power response, and the energy storage capacity is also enough. So the superconducting magnet is selected as the energy storage equipment of the PV system. It is linked with the PV system with the DC bus. The DC chopper is set to manage the energy pass through the superconducting magnet by charging and discharging of the current of the superconducting magnet. With the coordinate control of converter, the power transfer between the superconducting magnet and the PV units or the power grid can be controlled effectively.

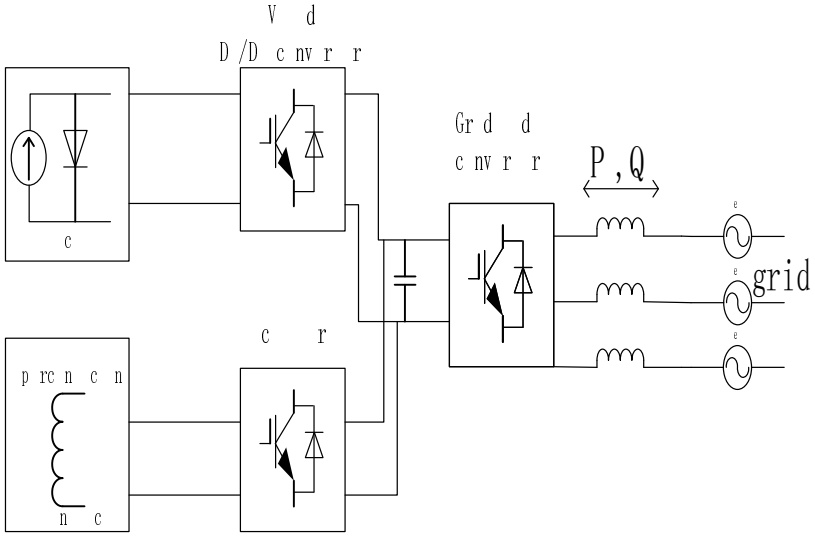

Fig. 1. The main circuit of PV with SMES.

The structure of SMES circuit is as shown in Fig 2.

It contains two main part, one is the voltage source converter (VSC), and the DC chopper. The VSC is used to control the active power P and the reactive power Q respectively, the function of the DC chopper is to control the magnitude and polarity of the current flowing through the superconducting coil (SC); the energy is stored in the SC in magnetic field.

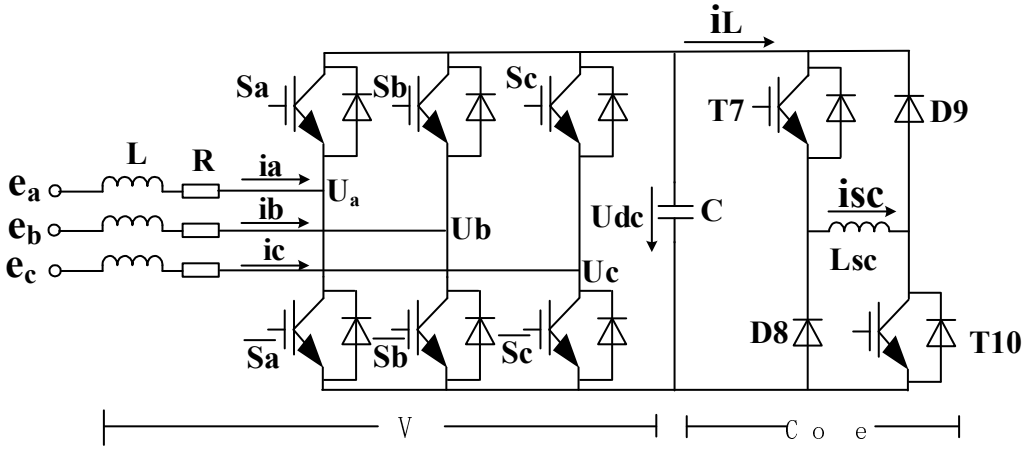

Fig. 2. The main circuit of SMES

A typical PV module is made up around 36 or 72 cells connected in series, encapsulated in a structure made of, e.g., aluminum and Tedlar®. A simplified electrical model of the PV cell is depicted in Fig. 3.

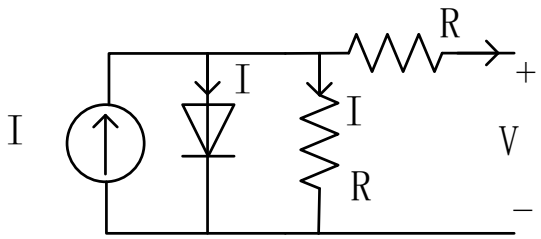

Fig. 3. The main circuit of PV.

System Control

The system level control can be divided into two conditions. In normal operation state of the grid, the PV can realize the operation of maximizing the energy capture based on Maximum PowerPoint Tracker (MPPT). In the condition of less insolation, the control objective is to make the SMES to supply the capability of the PV. This control level gives out the power demand for the SMES, which is represented in the Fig. 4.

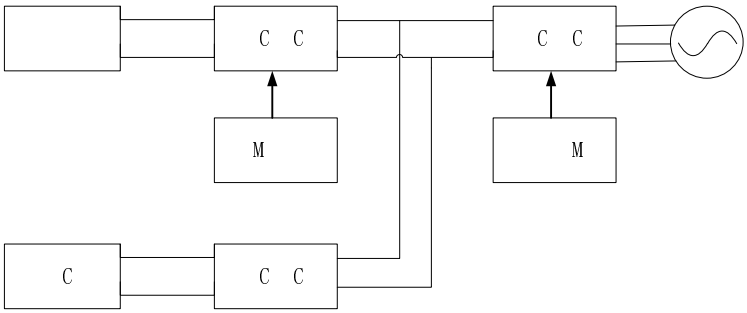

Fig.4 System control

The control of the SMES can be divided into two parts, that one is the active power current control, and the other is the reactive power. It is shown in Fig 5.

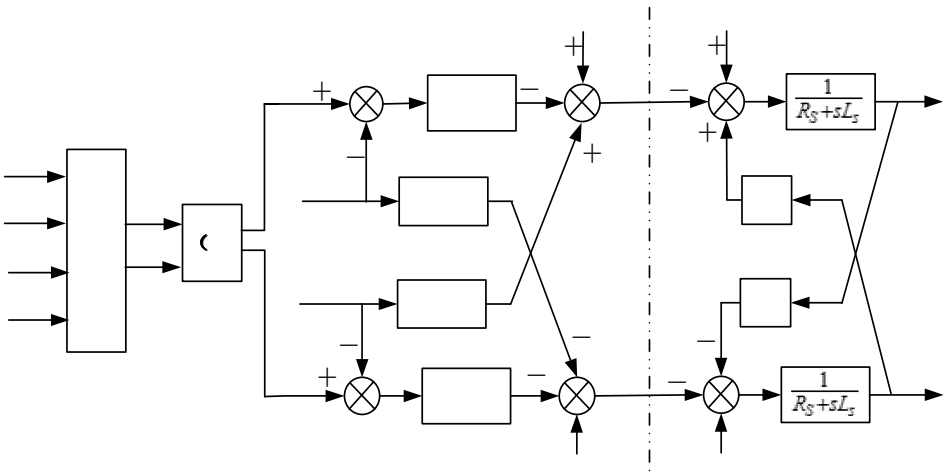

Fig.5 The control block diagram of VSC

The Perturb and observe (P&O) method operates periodically incrementing or decrementing the output terminal voltage of the PV and comparing the power obtained in the current cycle with the power of the previous cycle. If the voltage varies and the power increases, the control system changes the operating point in that direction, otherwise change the operating point opposite direction. Once the direction for the change of current is known, the current is varied at a constant rate. This rate is a parameter that should be adjusted to allow the balance between faster responses with less fluctuation in steady state.

Simulation

To evaluate the system performance, the model of the combined system is established using MATLAB /SIMULINK. The model contains a PV cell array, three power converters and associated controllers, a DC-link capacitor, a superconducting magnet, and an equivalent power grid.

According to the parameters of the SunPower SPR-305-WHT, the parameter of PV cell arrays are designed in Table I. For the grid-connected converter of the hybrid system, the capacity design should consider the power requirement for different control objective within the 50% rating power of the PV system. Considering the current carrying level of the high temperature superconducting tapes, the rating current of the magnet is selected as 160A.

TABLE I Design Parameters

Item		Parameters
PV	Rating power	45kVA
	Rating voltage	64.2V
	Rsh	0.038Ohm
Grid-side Converter	Rating power	100kVA
	Switching frequency	5kHz
	Filter inductor L	1mH
DC chopper	Rating power	100kVA
	Switching frequency	10kHz
	DC link capacitor	10000uF
	DC rating voltage	630V

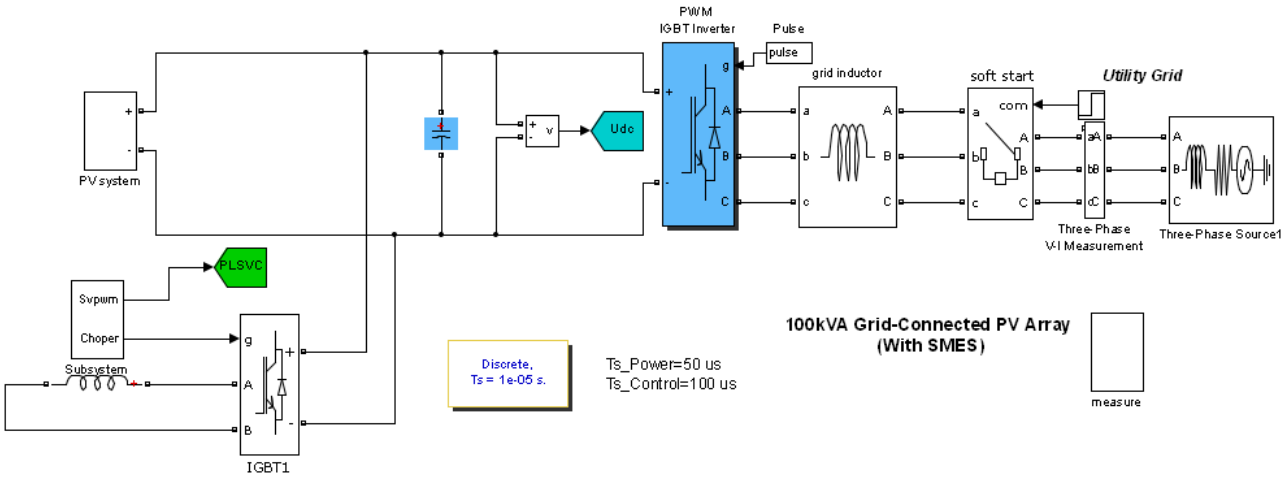

Fig.6 The simulation circuit with SMES

The simulation was set as shown in Fig.6. And then the result was given in Fig 7 and 8.

Fig. 7(a) shows the DC bus voltage dropped down from 630V to 580V without SMES. Fig. 7(b) shows the grid side current was influenced and cannot meet the stand to connect to the grid. Fig. 7(c) shows the grid side power the set power of the VSC the PV output power and the irradiation all in per-unit value. And the grid absorbs power from the PV as the line is below zero. As shown in Fig. 7(c) the PV output power can catch up with the irradiation using the MPPT. But the grid side power cannot meet the demand power. Fig. 8(a) shows the results with SMES, in which the DC bus voltage can keep as nearly a constant 630V. Fig. 8(b) shows the grid side voltage and the current is in high power factor. Fig. 8(c) shows that power of the PV can also track the maxim point and have no oscillation. The grid absorbs the exactly power as the demand. It can be seen that the SMES can smooth the power fluctuation of the PV effectively.

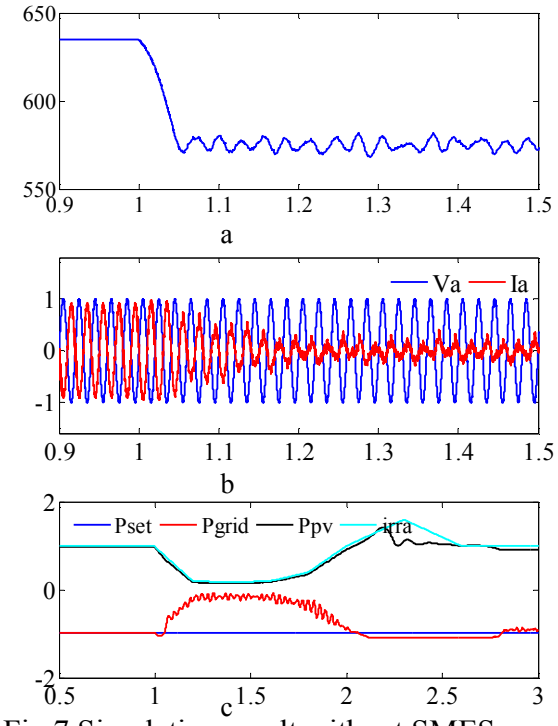

Fig.7 Simulation result without SMES

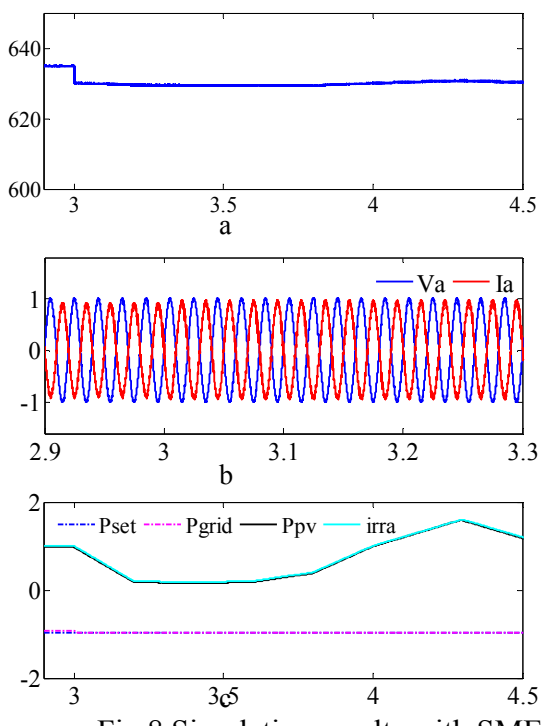

Fig.8 Simulation results with SMES

Conclusion

This paper presents a SMES based hybrid system for PV used in photovoltaic power generation. The SMES is designed to improve the stability and reliability of the grid-connected photovoltaic system. To evaluate the dynamic response of the hybrid system, simulation tests are carried out using MATLAB/SIMULINK. The results of simulation demonstrate that the SMES system can contribute to the stability and reliability of the grid-connected PV system.

References

[1] Yunus, AMShiddiq, Mohammad AS Masoum, and Ahmed Abu-Siada. "Application of SMES to enhance the dynamic performance of DFIG during voltage sag and swell." Applied Superconductivity, IEEE Transactions on 22.4 (2012): 5702009-5702009.

[2] Tam, Kwa-Sur, Prem Kumar, and Mark Foreman. "Enhancing the utilization of photovoltaic power generation by superconductive magnetic energy storage." Energy Conversion, IEEE Transactions on 4.3 (1989): 314-321.

[3] Abu-Siada, A., and Syed Islam. "Application of SMES unit in improving the performance of an AC/DC power system." Sustainable Energy, IEEE Transactions on 2.2 (2011): 109-121.

[4] Ali, Mohd, Toshiaki Murata, and Junji Tamura. "A fuzzy logic-controlled superconducting magnetic energy storage for transient stability augmentation." Control Systems Technology, IEEE Transactions on 15.1 (2007): 144-150.

[5] Zhang, Hui, Xin Wang, Jing Ren, Bo Deng, Hai Dou, and Yongjun Gao. "Research on superconducting magnetic energy storage in the photovoltaic distributed generation." In Power Electronics and Motion Control Conference, 2009. IPEMC'09. IEEE 6th International, pp. 2198-2202. IEEE, 2009.

Advanced Materials Research Vols. 986-987 (2014) pp 1273-1276

doi:10.4028/www.scientific.net/AMR.986-987.1273

Study of Five-level inverter SHEPWM Control Technology Based on Walsh Function

Li Song

Department of Electrical Engineering School, East China jiaotong University

Nanchang , 330013 Jiangxi Province, China

email: jxlisong1@163.com

Keywords: Five-level inverter; Walsh function; Multi-band ;selected harmonic elimination

Abstract. SHEPWM technique applicable to multi-level voltage inverter via Walsh function can be solved by linear equations instead of nonlinear transcendental equations. This method don't need a large number of initial values, it's suitable for online calculation because of its advantages such as high speed calculation and high-accuracy. For the traditional SHEPWM technique based on Walsh function has modulation index restricted problem. This paper proposes a multilevel SHEPWM technique, which Combined Walsh function with multi-band modulation technique. Through the analysis of multi-level multi-band SHEPWM voltage waveform based on Fourier series transform, summarized the multi-level multi-band SHEPWM nonlinear equations when modulation index changed from 0 to 1, and solved the problem with on-line control calculating and modulation index expanding by Walsh function transform. Take five-level inverter as an example, according to the values obtained and considering some equations have several solutions under certain modulation index, using the MATLAB/SIMULINK software do simulation research. The result confirmed that the multi-level multi-band SHEPWM technique based on Walsh function transform is correct and practical.

Introduction

H type bridge cascade inverter is a kind of multilevel topology that has a good application prospect [1]. The pulse width modulation control method for multilevel inverter includes sine pulse width modulation technology [2], space vector pulse width modulation technology [3] and the selected harmonics elimination pulse width modulation technology [4]. Among these technologies the SHEPWM technology's low switching frequency and high quality output features has receive more attentions on inverter's control research. The traditional SHEPWM technology need to be solved for nonlinear equations, and can not realize online calculation, real-time control for switch angles [5]. For multilevel inverter can not calculate the nonlinear equations if take the traditional SHE control method when the modulation ratio is very low. This is also a main problem that limits the method for practical application.

The literature [6] put forward a SHEPWM technology based on Walsh function, analyzed the transformation relation between the Walsh domain and Fourier domain, convert the nonlinear transcendental equations based on Fourier domain to piecewise linear equations based on Walsh domain. The literature [7-10] improved the calculation steps of conversion process, proposed the recursive solution method between harmonic elimination switch angle and each amplitude fundamental voltage subsection. Walsh function transformation technology has low requirements for initial value of switching angles; a set of initial values can calculate each fundamental voltage amplitude piecewise. The literature [11] conclude that when the multilevel inverter under low modulation ratio control, piecewise linear system of equations can not solved based on Walsh function. On the basis of the above research results, this paper proposes a multi-band modulation scheme [12] that can broaden the multilevel inverter's modulation ratio and applied to Walsh function's transformation. The method analyzed the SHEPWM voltage waveform for multilevel inverter based on different waveband modulation mode, conclude unified SHEPWM solving model for multilevel inverter multi-band modulation when modulation ratio changes from high to low.

Through Walsh function transform the SHEPWM nonlinear equations based on unified solving model to piecewise linear system of equations.

Multi-band multilevel inverter SHEPWM harmonic elimination model

Figure 1(a) is a half-wave symmetric two-level staircase waveform; by Fourier transform can get the formula (1)

$$u(\omega t) = \frac{a_0}{2} + \sum_{n=1}^{\infty} (a_n \cos(n\omega t) + b_n \sin(n\omega t)) \quad n = 0,1,2,3... \tag{1}$$

Analyze the above formula can change as following general form

$$u(\omega t) = \begin{cases} b_n = 0, n \text{ is even} \\ b_n = \dfrac{4E}{n\pi} \sum_{k=1}^{N} p_k \cos(n\theta_k), n \text{ is odd} \end{cases} \tag{2}$$

In the formula, Mark b_n as the harmonic coefficient matrix, p_k at the rising edge of θ_k record +1, at the falling edge record -1.

Figure 1(b) is five-level trapezoidal modulation half cycle waveform, according to the formula (2) establish the harmonic elimination system of linear equations, eliminate 5 times harmonics, adopt the numerical algorithm to solve. When the modulation ratio is below 0.373, the equations have no solution. Aim at the above situation, this paper proposes a multi-band modulation scheme that can broaden the modulation ratio, take turns to broaden the modulation ratio by figure 1(a) and 1(b).

(a) Five-level A waveband model staircase waveform

b) Five-level B waveband model staircase waveform

Figure 1.Multi-band SHEPWM waveform for multi-level inverter

Observe the above staircase waveform, it is not hard to see that the waveform transformation rules between the different bands is take turns to downward folded the top waveform according to the dotted line. The applicable range modulation ratio for model A and B respectively is [0.373 1] and [0 0.373]. It can be see that adopt the multi-band modulation method can broaden the modulation ratio to [0 1]. When the modulation ratio is in different range can take the correspond waveband to establish the SHEPWM nonlinear equations, so you can get the different modulation ratio's correct switch angle.

The transformation of Walsh function and the establish of harmonic elimination model

The Walsh can be represented as Wal(n,t).n usually represent as the number of passing zero within time T under a certain order for Walsh function, t is the normalized time interval within time T.

Normalized the 1/4 periodic waveform figure 1(a) as figure 2 show, T (0-1) divided into 2^m equal parts, and mark c as the normalized value, the interval number for rising edge is N. Similar to Fourier expression, the above waveform by Walsh transform can get a group of Walsh function gather, as shown below

$$f(t) = a_0 Wal(0,t) + \sum_{i=1}^{N-1} a_i Wal(i,t) \tag{3}$$

$$\begin{cases} a_0 = \dfrac{2}{T}\int_0^T f(t)Wal(0,t)dt \\ a_i = \dfrac{1}{T}\int_0^T f(t)Wal(i,t)dt \end{cases} \quad \text{i} = 1,2,3... \tag{4}$$

Formula (3) simplified as follows on the basis of symmetry

$$f(t)=\sum_{i=1}^{N/2}W_{4i-3}Wal(4i-3,t) \tag{5}$$

Mark $W_{4i-3}=F^{\omega}(4i-3)$ as the Walsh coefficient of waveform f (t) that the Walsh function correspond, combined with figure 2

$$F^{\omega}(4i-3)=\frac{1}{2^{m-2}}\sum_{n=N+1}^{2^m/4}Wal(4i-3,n)+(\frac{N}{2^{m-2}}-4c)\cdot Wal(4i-3,N)\quad \text{i}=1,2,3\ldots \tag{6}$$

The simulation result

According to the data of above table draw the harmonic elimination switch angle trajectory as figure 3 show, the figure shows that modulation ratio in the range of 0 to 1 each band can get the correct switch angles. At each bands' transform place near minizone has multiple sets of switch Angle trajectory, These seemingly redundant switch angles can increase the select flexibility and control performance of switch angles when actual control.

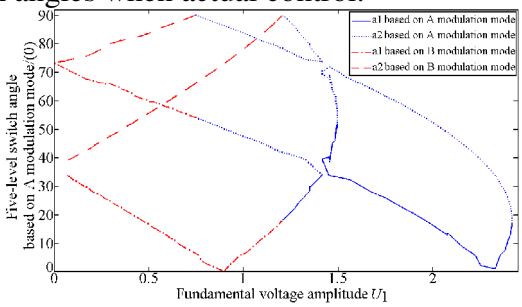

Figure 3. Switch angle trajectory for each waveband

In order to validate the above theoretical analysis and the solve results, This paper use Matlab/Simulink simulation software to set up the simulation model and conduct researches for five-level inverter multi-band SHEPWM control technology based on Walsh transform. The simulation parameters: Independent dc voltage source voltage 50V; A and B band take U1 for 2.0 and 1.2 respectively when the switch angles are solved. Figure 4 and 5 give the five-level inverter output voltage waveform and spectrum distribution that the three kinds of the switch angles correspond.

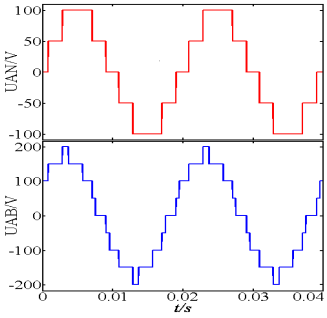

(a) Phase voltage and line voltage simulation waveform

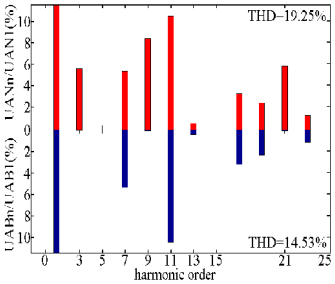

b) Phase voltage and line voltage spectrum distribution

Figure 4. A mode the simulation waveform

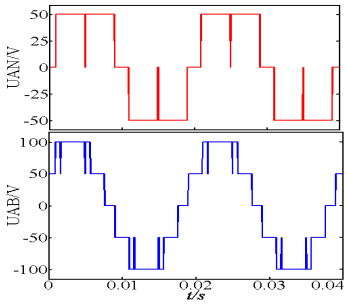

(a) Phase voltage and line voltage simulation waveform

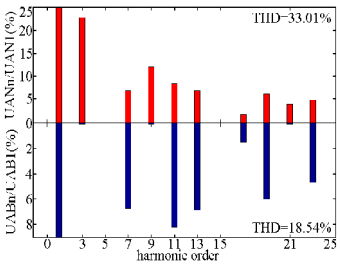

(b) Phase voltage and line voltage spectrum distribution

Figure 5. B mode the simulation waveform

Conclusion

This paper on the basis of analysis the multi-band multi-level inverter SHEPWM control method based on Walsh function transform, get the following conclusion:

The paper proposed the multi-band multi-level inverter SHEPWM control method based on Walsh function transform is able to expand the modulation ratio from 0 to 1 and transform the traditional SHEPWM nonlinear equations to piecewise linear system of equations to solve, Make the multi-level inverter can calculate the SHEPWM switch angles online, and able to eliminate harmonic by real-time.

The simulation results verify that 5 times harmonic of each band modulation mode is eliminated, Proved the paper that proposed linear multi-band solving method based on Walsh function is correct and practical.

References

[1] Hammond P W. A new approach to enhance power quality for medium voltage AC drives[J]. IEEE Trans on Industry Applications, 1997, 33(1): 202-208.

[2] Wu Hongyang, He Xiangning. Research on PWM control of a cascade multilevel converter[J]. Proceeding of the CSEE, 2001, 21(8): 42-46(in Chinese).

[3] Hu Yinghong, Wang Jianze, Shen Ke, et al. One-dimensional space vector modulation for single-phase cascaded multilevel inverter[J]. Power system technology, 2012, 39(6): 120-125(in Chinese).

[4] Fei Wanmin, L Zhengyu, Yao wenxi. Research of selected harmonic elimination PWM technique applicable to multi-level voltage inverters[J]. Proceeding of the CSEE, 2004, 24(1): 102-106(in Chinese).

[5] Fei Wanmin, Ruan xinbo, Zhang Yanli, et al. Research on the initial values of SHEPWM method for multi-level voltage inverters. [J] Proceeding of the CESS, 2007, 27(13): 87-92(in Chinese).

[6] Asumadu J A, Hoft R G. Microprocessor-based sinusoidal waveform synthesis using Walsh and related orthogonal functions[J]. IEEE Trans on Power Electronics, 1989, 4(2): 234-241.

[7] Swift F, Kamberis A. A new Walsh domain technique of harmonic elimination and voltage control in pulse-width modulated inverters[J]. IEEE Trans on Power Electronics, 1993, 8(2): 170-185.

[8] Liang T J, Hoft R G. Walsh function method of harmonic elimination[C]//IEEE APEC'93.CA: San Diego, 1993: 847-853.

[9] Tsorng-Juu L, O'Connell R M, Hoft R G. Inverter harmonic reduction using Walsh function harmonic elimination method[J]. IEEE Trans on Power Electronics, 1997, 12(6): 971-982.

[10] Zhao Yanlei, He Biao, Tong Jianzhong. Application of Selective Harmonic Elimination PWM Technique Based on Walsh Transform in DVR[J]. Power system technology, 2006, 30(10): 45-49(in Chinese).

[11] Zheng Chunfang, Zhang Bo, Qiu Dongyuan. Selective Harmonic Elimination Technique Based on Walsh Transform for Multilevel Inverters[J]. Trans of China Electronics Society, 2006, 21(7): 121-126(in Chinese).

[12] Guan E Y, Song P G, Ye M Y, et al. Selective harmonic elimination techniques for multilevel cascaded H-bridge inverters[C]//IEEE PEDS'05.Malaysia: Kuala Lumpur, 2005: 1441-1446.

Advanced Materials Research Vols. 986-987 (2014) pp 1277-1281

doi:10.4028/www.scientific.net/AMR.986-987.1277

Study of Low Voltage Ride Through in Photovoltaic Grid-Tied Inverter Based on Unsymmetrical Grid Voltage Fall

LIAO Tian-fa[1,2,a], Chun-yang[2], SI Wen[1], DONG Chang-wen[1], XUE Jia-xiang[1]

[1]School of Mechanical and Automotive Engineering, South China University of Technology, Guangzhou 510640, China

[2]Department of electronic engineering, Huizhou University, Huizhou 516007, China;

[a]liaotianfa@163.com

Keywords: grid-tied inverter, unsymmetrical fall, P-R controller, LVPT

Abstract. In this paper, 10KW three-phase three-level photovoltaic grid-tied inverter is applied as hardware platform. Considering the insufficiency of PV arrays power output and low overall efficiency due to grid voltage falls asymmetrically, P-R current controller is used to provide unsymmetrical positive and negative sequence current to the grid so that low voltage ride through (LVPT) in photovoltaic inverter can be achieved. Through the implement of experiments, it is well proved that the requirement of LVPT when the grid voltage falls asymmetrically can be met by applying the solution proposed in this paper.

Introduction

In recent years, as the increasing of photovoltaic power penetration, especially more and more large-scale photovoltaic power stations are gradually connected to the grid, the photovoltaic inverter disconnection will arise when there is a short time grid failure occurring (such as short-circuit, component failure, launch of heavy load, etc.). Since there is a period of time before the gird recovers to normal condition, the losses of power will cause the disconnection of near inverters. Then, because of the disconnection of distributed power generation systems, energy will be accumulated at DC side to bring forth overvoltage of bus capacitor and over-current or distortion of grid-connected current. Thus, power quality will be seriously impacted. Consequently, PV grid-tied inverter is required to have the capability for LVPT.

Considering the factors that grid voltage fall unsymmetrically will result in insufficiency of PV arrays power output and low overall efficiency, comparison between decoupled dual synchronous current controller and Proportion-Resonant current controller is made. Finally Proportion-Resonant current controller is selected to achieve LVPT when the grid voltage falls unsymmetrically[1,2].

Hardware platform of low voltage ride through(LVRT)

The platform of LVRT is 10KW three-phase three-level photovoltaic grid-connected inverter, a simplified figure of the hardware topology is shown as Figure 1.

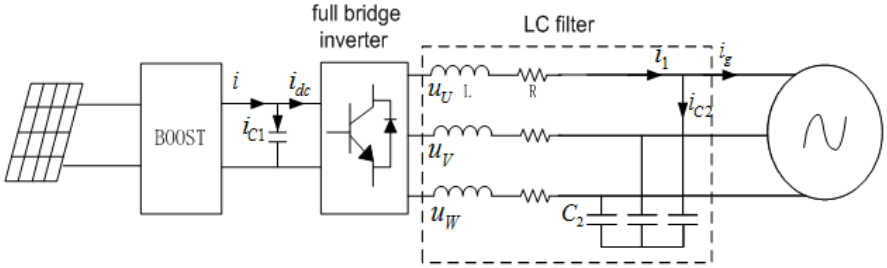

Figure1 Simplified topology of LVRT

Double Boost converter is used in the first stage in order to reduce the Boost current flowing through each channel, current pressure, switching losses and line losses of the switches of Boost circuit. Three-phase full-bridge inverter based on clamping diodes is applied as the second stage circuit to realize inverter transformation. The inverter current flows through LC filter to the grid.

Double Boost circuit is connected to two PV arrays and independent MPPT control is implemented to accommodate the power difference between two photovoltaic arrays due to hot spot effect or other elements. Film capacitance is used to connect the first stage and the second stage. On the one hand, stable bus voltage can be achieved, on the other hand, DC power of DC side and AC power of AC side can be decoupled. Usually, filters are applied to filter output current of inverter for the purpose of reducing switch losses and EMI. Considering the elements of control easiness, dynamic response, filter effects, switching loss, cost and size, LC filter is designed in the circuit. LEM sensor is applied to sample current and voltage, and then signals are transferred to control chips DSP2808 and CPLD. Multiple computation and control of the circuit are conducted in the control chip. ARM3S811 is selected as the core chip of monitoring system and standard Modbus Protocol is applied as the communication protocol. All of the inverter status are shown in the LCD256160.

Design of current controller

For single-phase systems, when grid voltage falls, the amplitude m and phase θ of voltage will change，it is easy to achieve LVPT if the PV grid-connected inverter adjusts the amplitude and phase of inverter current. Currently, current controller of three-phase system usually adopts PI controller in rotating coordinate system. When three-phase voltage falls symmetrically, traditional PI controller provides symmetrical current to the grid to achieve LVPT. However, when three-phase voltage falls asymmetrically, traditional PI controller only considers positive sequence component of inverter current, neglects the negative sequence component of inverter current, so traditional PI controller is not suitable for unsymmetrical voltage fall of three-phase system. To solve the situation mentioned above, there are two kind of current controllers can provide unsymmetrical current to the grid to achieve LVPT[3,4]

Decoupled dual synchronous current controller

Decoupled dual synchronous current controller controls positive current and negative current respectively through rotating of $\pm\omega$.

Because of PV grid-connected inverter is connected to the grid by three-phase three-wire, there is no residual current or residual voltage. When the grid has unsymmetrical malfunctions, the inverter current is shown in following formula 1

$$i = I^{+}\begin{bmatrix}\cos(\omega t+\phi^{+})\\ \cos(\omega t+\phi^{+}-\frac{2\pi}{3})\\ \cos(\omega t+\phi^{+}+\frac{2\pi}{3})\end{bmatrix}+I^{-}\begin{bmatrix}\cos(\omega t+\phi^{+})\\ \cos(\omega t+\phi^{+}+\frac{2\pi}{3})\\ \cos(\omega t+\phi^{+}-\frac{2\pi}{3})\end{bmatrix} \quad (1)$$

Current i transfer to positive current of dq axis by Park coordinate:

$$i_d^{+} = I^{+}\cos\phi^{+} + I^{-}\cos\phi^{-}\cos(2\omega t) + I^{-}\sin\phi^{-}\sin(2\omega t) \quad (2)$$

$$i_q^{+} = I^{+}\sin\phi^{+} - I^{-}\cos\phi^{-}\sin(2\omega t) + I^{-}\sin\phi^{-}\cos(2\omega t) \quad (3)$$

negative current of dq axis：

$$i_d^{-} = I^{-}\cos\phi^{-} + I^{+}\cos\phi^{+}\cos(2\omega t) - I^{+}\sin\phi^{+}\sin(2\omega t) \quad (4)$$

$$i_q^{-} = I^{-}\sin\phi^{-} + I^{+}\cos\phi^{+}\sin(2\omega t) + I^{+}\sin\phi^{+}\cos(2\omega t) \quad (5)$$

i_d^{+}, i_q^{+}, i_d^{-}, i_q^{-} are all constitute of DC component and double -frequency(2ω)alternating vibrate component，positive component i_d^{+}, i_q^{+} and negative component i_d^{-}, i_q^{-} have coupling, so it is necessary to filter alternating vibrating component, decoupling positive component and negative component.

On the base of decoupled dual synchronous current controller, a decoupling circuit and low-pass filter are applied to eliminate the need for complex designs of damping ratio and decouple the coupling of positive component and negative component. However, there are disadvantages of this method, PI controller needs tracking on DC reference values without static error. In fact, PI

controller is a time-varying function, it will generate static error while tracking DC parameters. Feed-forward net is adopted based on this problem, which means that the feed-forward negative current reference value can offset the double-frequency vibrate of positive component, the feed-forward positive current reference value offset the double-frequency vibrate of negative component. So the coupling of DC component and AC component can be relieved. The control block diagram is shown in Figure 2.

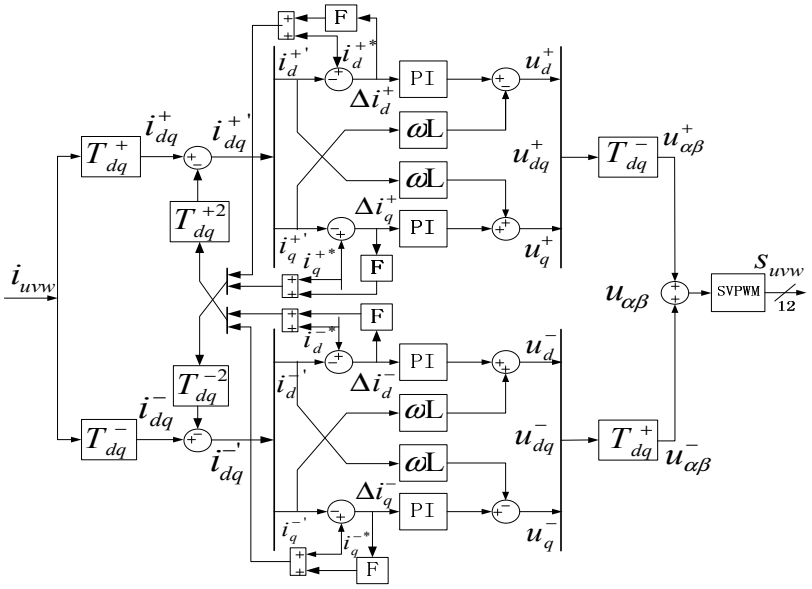

Figure2 Decoupled dual synchronous current controller based on feed-forward and low-pass filter

T_{dq}^{+}, T_{dq}^{-} are Park transform matrix, sampling current transfer to positive component and negative component of d axis and q axis, $T_{dq}^{+} = \left(T_{dq}^{-}\right)^{T} = \begin{pmatrix} \cos\theta & \sin\theta \\ -\sin\theta & \cos\theta \end{pmatrix}$, θ is grid phase.

Proportion-Resonant current controller

Decoupled dual synchronous current controller can provide unsymmetrical positive and negative current to the grid without static error only when DC reference values are perfectly tracked by PI controller, but it is hard to achieve in practical application. Introduction of feed-forward can compensate the double-frequency vibration, but decoupled dual synchronous current controller needs two current loops that complex algorithm and huge calculation is required. In contrast, P-R current controller works in static frame, all calculation are based on grid frequency f and only one current loop is needed to control positive and negative current. Output without static error can be achieved.[5] For the factors mentioned above, a P-R current controller is used in this paper to provide unsymmetrical positive and negative current to the grid so that the inverter can achieve LVPT when grid voltage falls asymmetrically.

The P-R current controller used in this paper consists of proportional part and second order undamped vibration part, in the transfer function, $G_{PR}(s) = K_p + \frac{K_i s}{s^2 + \omega^2}$, K_p is scaling factor, K_i is gain coefficient. The control block diagram of P-R current controller is shown as Figure 3.

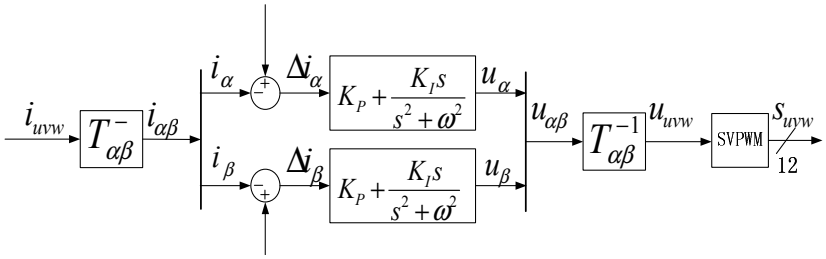

Figure3 P-R current controller based on static abc Coordinate system

$$u_\alpha = G_{PR} \cdot \Delta i_\alpha, u_\beta = G_{PR} \cdot \Delta i_\beta \quad (6)$$

From Figure 3, u_α, u_β do not interfere with each other, P-R current controller can achieve static error-free output, and Δi_α, Δi_β ripple wave are reduced, this is what PI current controller can not achieve[6,7].

Analysis of experimental results

When grid voltage falls asymmetrically, LVPT in photovoltaic inverter can be achieved by tracking positive component of the gird falling voltage fundamental wave and providing unsymmetrical positive and negative current to the grid. The result of the experiments is shown in Figure 4 and 5.

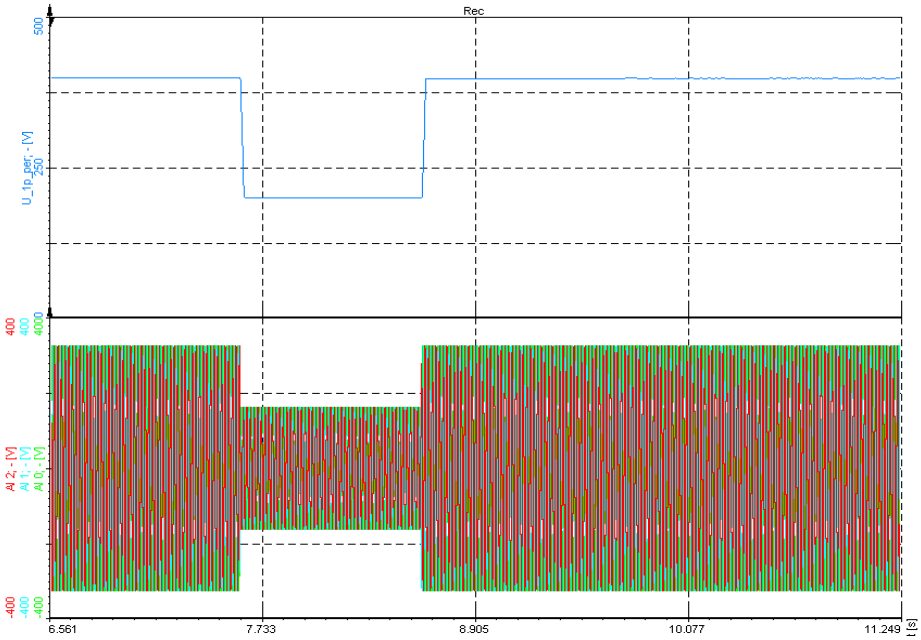

Figure 4 Three-phase voltage unsymmetrical falls and positive component track

The lower part of Figure4 indicates U and V voltage fall simultaneously. The unsymmetrical drop depth of voltage is less than 50%, downtime is about 8600-7400=1200ms, which meets the needs of LVPT: voltage unsymmetrical drop depth is between 20% and 90%, crossing time is less than 3 seconds. The upper part indicates that positive component of falling voltage fundamental wave keeps good consistency with the actual voltage drop.

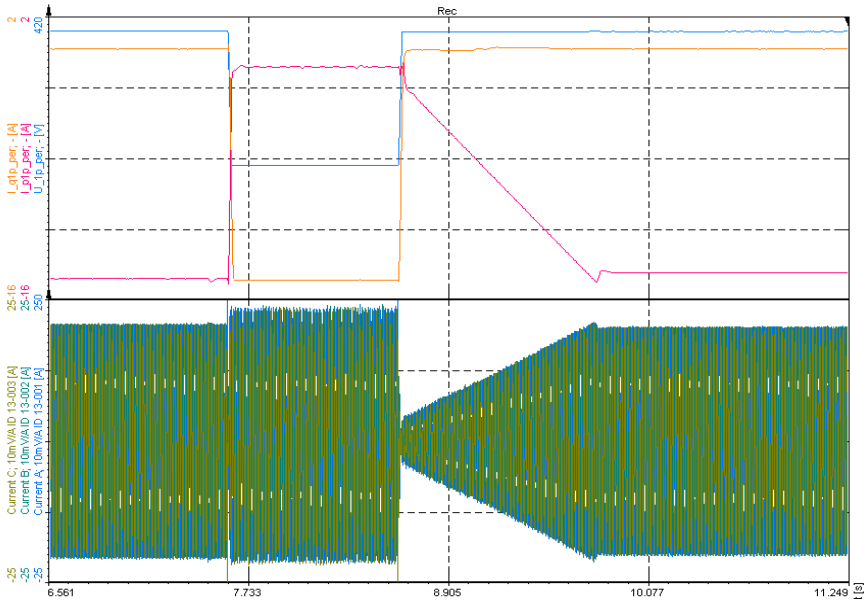

Figure 5 Unsymmetrical positive and negative current inject to the grid simultaneously to achieve LVPT

As Figure 5 shows, when the fault occurs at 7400ms, positive component of voltage fundamental wave is rapidly captured by the control loop. Thus, inverter can rapidly increase negative current input to the grid and decrease positive current input to the grid. When fault occurs, the inverter output current suddenly increases. At 8600ms，positive component of voltage fundamental wave recovers to normal level, inverter increases positive current, decreases negative current, grid current is gradually increased to the pre-fault level until 9400ms and downtime is 9400-7400=2000ms, less than 3s, which also meets the requirement of LVPT.

Conclusion

In this paper, the hardware platforms of LVPT is briefly introduced. Besides, comparison between decoupled dual synchronous current controller and P-R current controller is made and come to the solution of applying P-R current controller to provide unsymmetrical positive and negative current to the grid to achieve LVPT. Through experiments, the results shows that the proposed solution can rapidly recover to normal working status by achieving output without static error, reducing grid-tied vibration frequency and also meeting the requirements of achieving LVPT when grid voltage falls asymmetrically.

References

[1] P. Rodriguez, A. V. Timbus, R. Teodorescu, M. Liserre, and F. Blaabjerg,“Flexible active power control of distributed power generation systems during grid faults,” IEEE Trans. Ind. Electron., vol. 54, no. 5, pp. 2583–2592, Oct. 2007.

[2] Low and high voltage ride-through of DFIG wind turbines using hybrid current controlled converters[J].Electric Power Systems Research,2011,81:1456-1465

[3] Remus Teodorescu, Marco Liserre, Pedro Rodriguez. Power Converters for Photovolatic and Wind Power Systems[M]. Advanced Technology of Electrical Engineering,2011

[4] HU Peng,ZHANG Qian,LIU Yang,SHENG ChunChen,CHENG XiaoFang,CHEN ZeShao. Optical analysis of a hybrid solar concentrating Photovoltaic /Thermal (CPV/T) system with beam splitting technique[J]. Science China(Technological Sciences),2013,06:1387-1394.

[5] Proportional integral plus multi-frequency resonant current controller for grid-connected voltage source converter under imbalanced and distorted supply voltage conditions[J]. Journal of Zhejiang University(ScienceA:An International Applied Physics & Engineering Journal),2009,10:1532-1540.

[6] SONG ZhanFeng,XIA ChangLiang,LIU Tao,DONG Nan. A modified predictive control strategy of three-phase grid-connected converters with optimized action time sequence[J]. Science China(Technological Sciences),2013,04:1017-1028.

[7] Mary Kaye,Chris Diduch,Idris Gadoura. Grid Harmonic and Control Delay Compensation for Three-phase Grid-connected VSIs in Small Wind Turbine Systems[J]. Power Electronics, 2011,08:24-31.

Advanced Materials Research Vols. 986-987 (2014) pp 1282-1285

doi:10.4028/www.scientific.net/AMR.986-987.1282

Study on control strategy of the grid-side converter on doubly-fed induction generator system

Feng Yuan [a], Zhili Tan [b]

Faculty of Mechanical & Electronic Information, China University of Geosciences, Wuhan 430074, China

[a]yuanfeng0505@163.com, [b]Tanzhili@cug.edu.com

Keywords: Double-fed induction generator, grid-side convertor, SVPWM, vector control.

Abstract. Double-fed induction generator has the characteristic that voltage signal output maintain stable with the stable rotate speed, which leads to the wide utility of double-fed induction generator in the area of distributed power generation. In this paper, the basic structure and control method of double-fed induction generator were introduced and emphasis was put on the control technique of grid-side convertor of double-fed interaction power generation system. Simplified model of grid-side convertor was given in the double-fed interaction power generation system. On this basis, the performance was analyzed and control scheme of grid-side convertor was designed. Through Matlab/Simulink, simulation of stable output of DC side voltage was realized.

Introduction

With the unceasing exploit of fossil fuel, the ecological environment problem becomes increasingly fierce. Reproducible and clean alternative energy sources are badly needed. Doubly-fed asynchronous motor can get rid of the restriction of rotate speed. With doubly-fed asynchronous motor, distributed power generation system can improve the energy transfer efficiency remarkably, which has been increasingly used in new energy power generation systems such as solar energy, wind energy, biomass energy and geothermal energy etc.

For grid side converter, many kinds of control strategy were proposed in recent years. With the control strategy of space vector pulse width modulation (SVPWM) and the grid voltage vector orientation, voltage closed loop keeps the stability of DC bus voltage. Through the two current close loop of d, q axis, active power and reactive power decoupling control is realized, and arbitrary adjustable of power factor is realized. Based on the mathematical model of the grid side converter, to its principle and steady-state characteristics is analyzed. According to the dynamic model of the synchronous rotating coordinate system, with the design method of the double closed loop system, double closed loops control system is designed, include voltage closed loop and current closed loop. The simulation of Matlab/Simulink verified the feasibility and validity of the scheme.

Basic structure and principle of double-fed induction generator

In this system, the stator of double-fed induction generator is connected to the power grid directly, the rotor proceeds AC excitation, to change the phase position, frequency and amplitude of field current. Of the field current. When the power input changes, generator rotate speed changes to control the frequency of field current, which can realize variable speed constant frequency power generation. Principle of double-fed induction generator is showed in fig.1.

From grid convertor to rotor side convertor, capacitance and rotor side convertor can be seen as load, grid convertor is a one-third phase voltage type PWM rectifier. Simplified model of three-phase voltage type PWM rectifier is in fig.2. According to the kirchhoff voltage and current law,

$$L_s \frac{di_{gk}}{dt} + R_s i_{gk} = u_{gk} - (v_{kN} + v_{No}) \qquad (k = a,b,c) \tag{1}$$

From fig.2, $v_{kn} = v_{dc} S_k$.

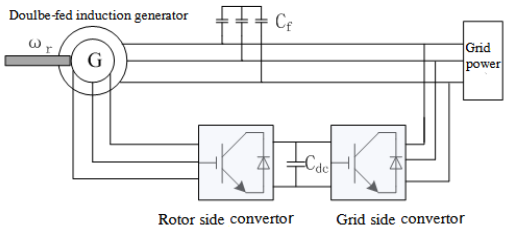

Fig.1 Structure diagram of independent double-fed power generation system

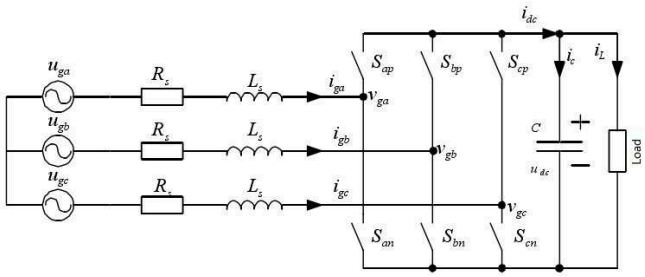

Fig.2 Simplified model of three-phase voltage type PWM rectifier

For three phase system of equilibrium state,

$$i_{ga} + i_{gb} + i_{gc} = 0 \,,\; u_{ga} + u_{gb} + u_{gc} = 0$$

We get,

$$v_{No} = -\frac{v_{dc}}{3} \sum_{k=a,b,c} S_k \tag{2}$$

Making $v_{kN} + v_{No} = v_{gk}$

From (1), (2) and capacitance current equation of direct current side, we get the mathematic model of grid side convertor of three phase in rest frame. With park transformational matrix, we get the mathematic model of grid side convertor in dq synchronous rotating reference frame.

$$\begin{cases} L_s \dfrac{di_{gd}}{dt} = -R_s i_{gd} + \omega L_s i_{gq} - v_{gd} + u_{gd} \\ L_s \dfrac{di_{gq}}{dt} = -R_s i_{gq} + \omega L_s i_{gd} - v_{gq} + u_{gq} \\ C \dfrac{du_{dc}}{dt} = S_d i_{gd} + S_q i_{gq} - i_L \end{cases} \tag{3}$$

Where, u_{gd} , u_{gq} are components of network voltage of d, q axle; i_{gd} , i_{gq} are components of current input of d,q axle; v_{gd} , v_{gq} are components of rectifier bridge voltage of d, q axle; S_d , S_q are components of switch function of d, q axle. ω is frequency of exchange network.

Control method of grid side convertor

The vector control is used in exchange network voltage control of grid side convertor. The principle is that equation above showed the mathematic model of three phase PWM rectifier in d, q synchronous rotating reference frame. If the orientation of d axle is the orientation of network voltage comprehensive vector $\vec{u}_g$, then

$$\begin{cases} u_{gd} = |\vec{u}_g| = \sqrt{\dfrac{3}{2}} U_{gm} \\ u_{gq} = 0 \end{cases} \tag{4}$$

Where, U_{gm} is phase voltage peak.

Transform (3) and get the first two equations,

$$\begin{cases} v_{gd} = -R_s i_{gd} - L_s \dfrac{di_{gd}}{dt} + \omega L_s i_{gq} + u_{gd} \\ v_{gq} = -R_s i_{gq} - L_s \dfrac{di_{gq}}{dt} - \omega L_s i_{gd} \end{cases} \tag{5}$$

The influence of electricity cross coupling items $\omega L_s i_{gd}$, $\omega L_s i_{gq}$ and network voltage u_{gd} existed. A control method is needed to relieve current coupling between d and q axis and remove network voltage disturbance. Feed forward decoupling control strategy can achieve this goal.
Transform (5) as follows:

$$\begin{bmatrix} v_{gd} \\ v_{gq} \end{bmatrix} = \begin{bmatrix} -v'_{gd} \\ -v'_{gq} \end{bmatrix} + \begin{bmatrix} \Delta v_{gd} \\ \Delta v_{gq} \end{bmatrix} + \begin{bmatrix} u_{gd} \\ 0 \end{bmatrix} \tag{6}$$

Where, v'_{gd}, v'_{gq} are first-order differential of voltage component related to i_{gd}, i_{gq}; $\Delta v_{gd}, \Delta v_{gq}$ are voltage compensation coupling term of d and q axis.

Meanwhile, 1-7 alternating current side disturbance voltage u_{gd} was used to proceed feed foreword compensation. Then, feed forward control of d and q axis is realized.

Active power and inactive power of d and q axis were as follows:

$$\begin{cases} P = u_{gd} i_{gd} + u_{gq} i_{gq} \\ Q = u_{gd} i_{gq} + u_{gq} i_{gd} \end{cases} \tag{7}$$

Where, when p>0, it means the convertor is in rectification, absorbing active power from the network; when p<0, it means the convertor is in contravariant, absorbing active power from the network.

The rectifier uses double closed loop control. The main function of outer loop, Dc voltage control loop, is Trace output voltage outer loop current instruction to realize fast current control. The specific control block diagram is in fig.3.

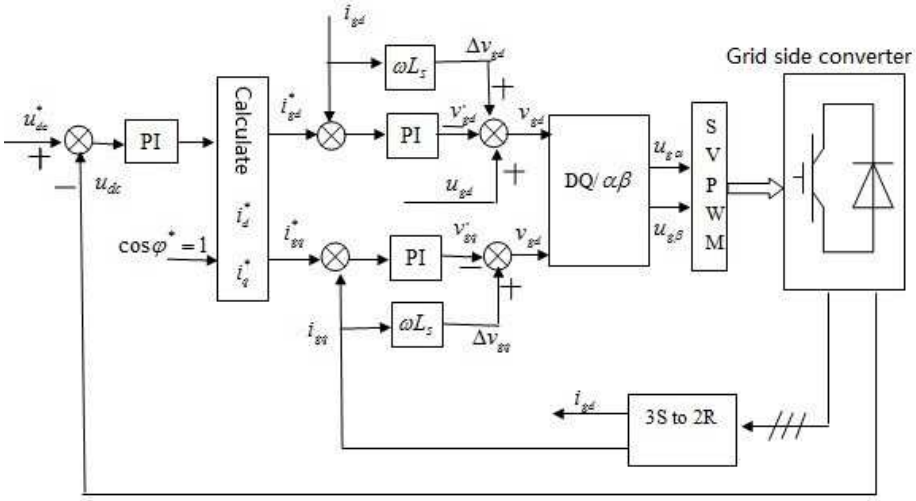

Fig.3 Diagram of grid side convertor control

In direct current link, present voltage u^*_{gd} and feedback voltage u_{gd} were compared and the error would be output through PI regulator. Power factor was set as unity power factor. i^*_{gd}, i^*_{gq} were compared with feedback current i_{gd}, i_{gq}, and the result v'_{gd}, v'_{gq} would be outputted through PI regulator. Then, v'_{gd}, v'_{gq} would be calculated with their own compensation items $\Delta v_{gd}, \Delta v_{gq}$ and power grid voltage disturbance feed-forward compensation term u_{gd}. AC side converter reference voltage v_{gd}, v_{gq} would be get. After transformation of coordinates of reference voltage, component values $v_{g\alpha}, v_{g\beta}$ of coordinate system were get. And after SVPWM modulation, driving signal appeared.

Simulation and analysis

According to the mathematic model and control diagram, Matlab was used to build the system model. network voltage 220V, frequency 50Hz, DC side stabilivolt capacitance 3300μf, AC side filter

inductance 5mH, DC side reference voltage 300V, system simulation would be normalized. SVPWM pulse modulation mode was used to strike the on/off of IGBT.

Simulated tests of unity power factor rectification and unity power factor contravariant were undertaken to test its performance in steady state. Two different conditions were simulated.

Rectification operation simulation of unity power factor.

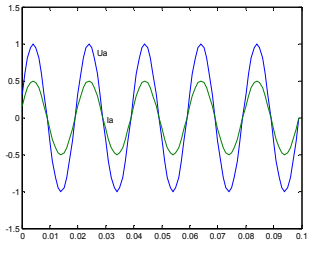

Fig.4 Phase voltage vs. phase current in rectification

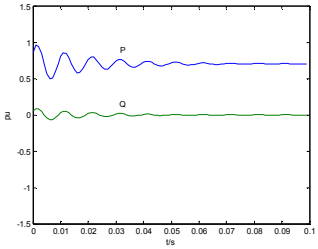

Fig.5 Active power vs. inactive power in rectification

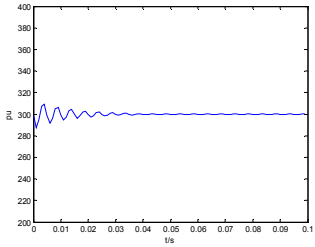

Fig.6 DC side tracking voltage waveform in rectification

In the unity power factor rectification (fig.4-6), fundamental wave of phase current is sinusoidal, keeping in phase with phase voltage. The power flows into rectifier from the network entirely. In this time, active power of the system is greater than 0, and inactive power is 0, power factor is 1, and DC side voltage is stable at a given reference voltage through regulating.

Contravariant operation simulation of unity power factor.

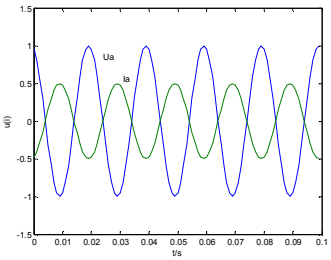

Fig.7 Waveform of phase voltage and phase current in contravariant

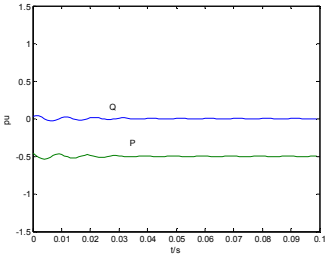

Fig.8 Active power and inactive power in contravariant

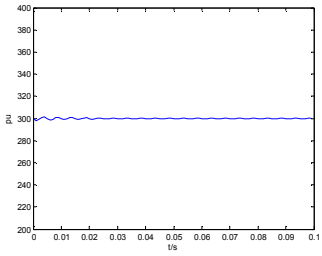

Fig.9 DC side tracking voltage waveform in contravariant

In the contravariant of unity power factor (fig.7-9), fundamental wave of phase current is sinusoidal, keeping in opposite phase with phase voltage. The power flows into the network from DC side entirely. In this time, active power of the system is less than 0, and inactive power is 0. There is no current between the network and rectifier. Power factor is 1, and DC side voltage is stable at a given reference voltage through regulating.

Conclusion

The mathematic model of grid-side convertor of double-fed interaction power generation system is established. On this basis, voltage and current double closed-loop control system was adopted. According to SVMWP, simulation and experimental study were preceded to this system. Research results showed that grid-side convertor can get sine-input current with adjustable power factor, and can maintain DC bus voltage stable, which meet the design requirement of double-fed interaction power generation system.

References

[1] R.Pena, J.C.Clare, G.M.Asher: IEEE Proceedings, 1996, 143(3),231-241.
[2] Ruben Pena, Roberto Cardenas: .IEEE, 2002, 3297-3302.
[3] H.Y. Ye: *Control technology of wind turbines* (Machinery Industry Press, China 2002).
[4] Y.K. Huo, Q.H. Liu: High Technology Letter, 2003(supp), p. 35-40.
[5] Y.Y. Ren: Daqing Petroleum Institute 2001, 25(2), 87-89.
[6] H. Li, S.C. Yang, Y. Liao: Proceedings of the CSEE, 2003, 23(8), p. 159-162.
[7] C.L. Gu, Z.C. Wei, X.S. Tao, et al: Proceedings of the CSEE, 1996, 16(2), p. 119-124.

Advanced Materials Research Vols. 986-987 (2014) pp 1286-1290

doi:10.4028/www.scientific.net/AMR.986-987.1286

STUDY ON IMPROVING POWER SYSTEM DAMPING BY USING DPFC

Jin Li[1, a] YaMin Pi [1, b] HuiYuan Yang [1, c]
[1]School of Automation, Wuhan University of technology, Wuhan, China, 430070
[a]happylimy@163.com,[b]ya23902@163.com, [c]13006372909@163.com

Keywords: Distributed Power Flow Controller; suppress oscillation; PSCAD/EMTDC; improve system stability

Abstract. In this paper, the series converters of Distributed Power Flow Controller are the main object of study. Its mechanism of suppressing power system oscillations is studied by theoretical analysis and formula derivation, which relies on a single-machine infinite-bus power system, installed the series converters. Then based on the mechanism, adopting the classic PI control and the damping controller, designed the transient stability control loop for the series converters. Finally, simulations performed by PSCAD/EMTDC, the results show that DPFC device can effectively suppress oscillation and improve system stability.

Introduction

With the characteristics of large units, ultra-high voltage, long distance and heavy load, the modern power system has become a typically strong nonlinear, high-dimension and dynamic system, along with its rapid development. As a result, it's more and more possible to cause oscillation in the power system. The essential reason of generating oscillation in power system is the absence of damping. Presently, additional controls are commonly used to provide extra damping to suppress it and control measures are generally focused on the generation and transmission parts. In the generation part, the traditional method used to increase the damping of a power system is by adding a Power System Stabilizer (PSS) in the excitation and governing system of the generator, while in the transmission part, the flexible and fast power electronic devices are mainly used on the line to provide additional control.

More current research is in the transmission part by using FACTS devices. A Phillips-Heffron model is established in literature [1-2] to analyze the mechanism of damping low frequency oscillation in power system by Thyristor Controlled Series Capacitor (TCSC), Static Var Compensator (SVC) and other FACTS devices. While, Lyapunov method is introduced in literature [3] for analyzing the damping mechanism of the Unified Power Flow Controller (UPFC). Distributed Power Flow Controller (DPFC) is the latest FACTS devices with the combined functions of series compensation and shunt compensation, however, the domestic research on it is relatively less. A single-machine infinite-bus system established with the dynamic model of the series converters of DPFC is adopted in this paper to study the mechanism of damping oscillation. Then based on the mechanism, adopting the classic PI control and the damping controller, designed the transient stability control loop for the series converters. Finally, simulations performed by PSCAD/EMTDC, the results show that DPFC device can effectively suppress oscillation and improve system stability.

The Principle of DPFC

DPFC consists of several low-power series converters and one shunt large-power converter without common dc link. The shunt converter is similar to a STATCOM; primarily used to maintain stability of the bus voltage and provide the third harmonic power the series converters are required. While the series converters employs the DSSC concept. It uses multiple low-power single-phase voltage inverters instead of a centralized large-capacity three-phase inverter in UPFC. Each converter within DPFC is independently controlled. The configuration of the DPFC is shown in shown in Fig.1.

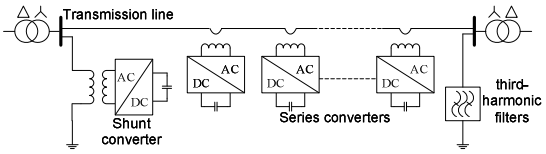

Fig.1.DPFC configuration

In order to study the function of DPFC inhibiting oscillation, a simplified equivalent model is adopted in this paper: The DPFC is accessed to a single infinite system and the shunt converter is equivalent to a third harmonic current source (derivation ignored, the simulation uses).

The Mechanism of Damping Oscillation

The output voltage is in series with the circuit via a single-phase inverter [4]. Based on the pulse width modulation (PWM), the dynamic model of the series converter can be expressed in Eq.1:

$$\begin{cases} \dot{V}_{ss} = m\dfrac{V_{dc}}{\sqrt{2}}(\sin\delta_{ss} + j\cos\delta_{ss}) \\ \dfrac{dV_{dc}}{dt} = \dfrac{3m}{2C}(I_d \sin\delta_{ss} + I_q \cos\delta_{ss}) \end{cases} \tag{1}$$

Where: m, δss are amplitude modulation ratio and phase angle of the series injected voltage; Vdc is the voltage of the series converters in DC side, Iq and Id are q-axis and d-axis current component of the series converter in AC side.

After series converter of DPFC access to system, the generator voltage equation is shown in Eq.2.

$$\begin{cases} E_q^{'} = V_{bq} + V_{ssq} + I_d x_{d\Sigma}^{'} \\ 0 = V_{bd} + V_{ssd} - I_q x_{q\Sigma}^{'} \end{cases} \tag{2}$$

Where: Xd=XL1+XL2+XT+Xss+Xd′, XqΣ=XL1 +XL2+XT+Xss+Xq, Xd is d-axis transient reactance, Xq is q-axis reactance, Vssq and Vssd are the q-axis and d-axis component of the injected voltage of series converters, Vbq and Vbd are q-axis and d-axis components of infinite bus voltage. Associated (1) and (2) yields Eq.3 for the line current. Substituted Eq.3 to nonlinear dynamic equations [5] of single-machine infinite system and linearize it at a stable operating point can obtained Eq.4.

$$\begin{cases} I_q = \dfrac{1}{x_{q\Sigma}}\left[\dfrac{mV_{dc}\sin\delta_{ss}}{\sqrt{2}} + V_{bd}\right] \\ I_d = \dfrac{1}{x_{d\Sigma}^{'}}\left[E_q^{'} - V_{bq} - \dfrac{mV_{dc}\cos\delta_{ss}}{\sqrt{2}}\right] \end{cases} \tag{3}$$

Eq.4 is the Phillips-Heffron model of single-machine infinite system installed series converters of DPFC. Phillips-Heffron model has been used in analyzing the feasibility of utilizing FACTS devices in damping oscillation and designing the corresponding controller [5-7], whose torque to the system is shown in Eq.5. Where: [Δm, Δδss]T is input signal of series converters; Kp=[Kpm, Kpδ]T, Kq=[Kqm, Kqδ]T and Ku=[Kum, Kuδ]T are definite value based on stable operating point; [Cm(jωs), Cδ(jωs)]T is the damping controller transfer function. Eq.5 shows that the torque DPFC can be provided to the system contains synchronizing torque and damping torque. Its size and negative are determined by the phase of ΔT in the plane composed of Δδ and Δω. As long as control the damping torque within a certain range can suppress system oscillation well.

$$\begin{bmatrix} \Delta\dot{\delta} \\ \Delta\dot{\omega} \\ \Delta\dot{E}'_q \\ \Delta\dot{E}_f \end{bmatrix} = \begin{bmatrix} 0 & 1 & 0 & 0 \\ \frac{-\omega_0 K_1}{M} & \frac{-D}{M} & \frac{-\omega_0 K_2}{M} & 0 \\ \frac{-K_4}{T'_{d0}} & 0 & \frac{-K_3}{T'_{d0}} & \frac{1}{T'_{d0}} \\ \frac{-K_E K_5}{T_E} & 0 & \frac{-K_E K_6}{T_E} & \frac{-1}{T_E} \end{bmatrix} \begin{bmatrix} \Delta\delta \\ \Delta\omega \\ \Delta E'_q \\ \Delta E_f \end{bmatrix} + \begin{bmatrix} 0 & 0 \\ \frac{-K_{pm}}{M} & \frac{-K_{q\delta}}{M} \\ \frac{-K_{qm}}{T'_{d0}} & \frac{-K_{q\delta}}{T'_{d0}} \\ \frac{-K_E K_{um}}{T_E} & \frac{-K_E K_{u\delta}}{T_E} \end{bmatrix} \begin{bmatrix} \Delta m \\ \Delta\delta_{ss} \end{bmatrix} \tag{4}$$

$$\Delta T = \left[K_{\mathrm{p}} - \frac{K_E K_2 K_q + K_2(1 + j\omega_s T_E) K_u}{(K_3 + j\omega_s T'_{d0})(1 + j\omega_s T_E) + K_6 K_E} \right] \begin{bmatrix} C_m(j\omega_s) \\ C_\delta(j\omega_s) \end{bmatrix} \begin{bmatrix} \Delta m \\ \Delta\delta_{ss} \end{bmatrix} \tag{5}$$

The Control Strategy of DPFC

Since the integrals of all the cross product of terms with different frequencies are zero and the active powers at different frequencies are independent from each other, a converter without a power source can generate active power at one frequency and absorb this power from other frequencies [8]. Based on this conclusion, the 3rd harmonic is selected to replace DC link for active power exchange in DPFC, due to the unique features of 3rd harmonic frequency components in a three-phase system. Control for shunt converter contains Three-phase voltage at the fundamental frequency and single-phase 3rd harmonic currents. Control block diagram is shown in Fig.2.

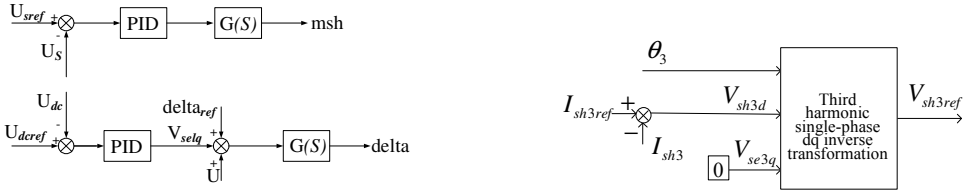

Fig.2.Control block for shunt converter

Series converters are absorbed 3rd harmonic active power and generate the fundamental frequency voltage. By injecting the voltage change the transmission characteristics of the grid. The control scheme of series converters uses the PI control and dq decoupling control. The entire control block diagram is shown in Fig.3.

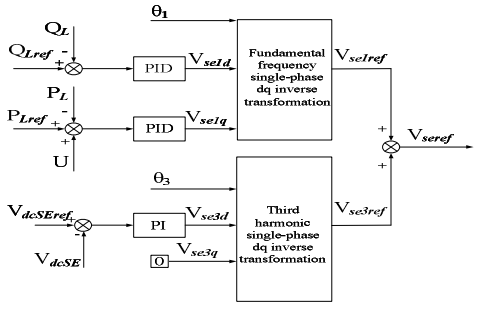

Fig.3.Control scheme of the series converter

Damping controller is used to improve the damping capacity of power system. Output parameter of damping controller is to modify the reference signal of the power flow controller. DPFC controllable parameters include voltage amplitude, phase angle of shunt converters and voltage amplitude, phase angle of series converter. All these can be used to modify the damping torque. Modulating the voltage phase angle of shunt converters or the voltage amplitude of series converters is best. In this paper, the block diagram of damping controller is shown in Fig.4.

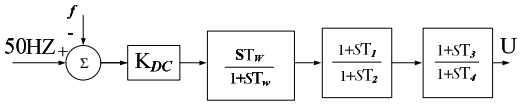

Fig.4.Block diagram of damping controller

Simulations

Simulation system of single phase diagram used in this article is shown in Fig.5, DPFC device connected to a double circuit in the network. In this graph, the valid value of line voltage of G1 is 230V, the initial phase angle is 35°, the output power is 0.65KW, and the power factor is 0.8.G2 is infinite power, the valid value is 230V, and initial phase angle is 0°. The equivalent impedance of two transmission lines L1, L2 is 1.69+j22.70. The turn ratio of transform T1, T3 is 0.23KV/0.8KV, the capacity is 15KVA, and leakage reactance is 13%, Y-△connection. The turn ratio of transform T2, T4 is 0.8KV/0.23KV; others are the same as T1, T3. Specific generator parameters are: Ta=0.125sec,Xp=0.113pu,Xd=0.56pu,Xd'=0.132pu,Tdo'=1.3323sec,Xd"=0.113pu,Tdo"=0.045sec, Xq=0.4pu,Xq"=0.135pu,Tqo"=0.034pu,W0=100π; Initial operating conditions are: Vt0=0.913pu, degv0=0.5393rad.

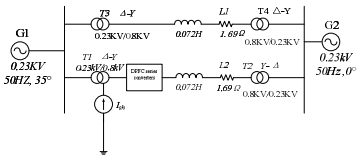

Fig.5.Simulation system wiring diagram

Simulation when mechanical torque mutation in 20s (shown in Fig.6.(a)), load power mutation in 20s (shown in Fig.6.(b)), three-phase fault in 25s (shown in Fig.6.(c)).

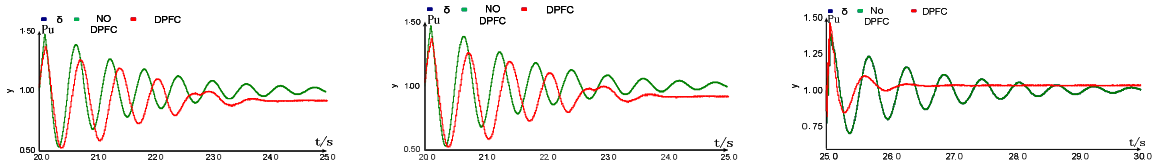

(a) (b) (c)

Fig.6.Damping simulation

To further validate the damping ability of the DPFC for inter-area oscillation, build a two-area four-machine system, installing DPFC in the two regional tie-lines. Set three-phase fault in the tie-lines in 20s, the simulation results shown in Fig.7.

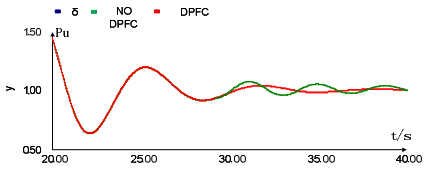

Fig.7.Damping Simulation of two-area four-machine system

As can be seen from the simulation results, the power angle of the generator can suddenly change, lose stability or even cause oscillation when mechanical torque mutation, load power mutation and three-phase fault occur. When DPFC is not connected to the system, depending on the damping ability of the system, the time to re-stabilize the system to reach a new power balance is much longer than the system access DPFC.

Conclusions

The paper derived its mechanism of damping oscillation after introduced the structure of DPFC, and then described the control strategy for the shunt converter and series converters. Adopting the classic PI control and the damping controller, designed the transient stability control loop for the series converters. Through simulation, the results show that when the system oscillation occurs, DPFC able to quickly damping oscillation of local system, allowing the system to reach a new

Acknowledge

This work was financially supported by the National Nature Science Foundation (51177114) and Wuhan Applied Basic Research Projects in 2014.

References

[1] Xiaofang Yang, et al. Proceedings of the CSEE, in Chinese, Vol.23, No.1, pp 19-23, Jan.2003.

[2] Jiangfeng ZOU, et al. High Voltage Engineering, in Chinese, Vol.31, No.7, pp 45-47, July.2005.

[3] Guizhi XU, et al. Power System Technology, in Chinese, Vol.28, No.15, pp 45-48, Aug.2004.

[4] Yang Zhao, Xiangning Xiao. Automation of Electric Power Systems, in Chinese, Vol.31, No.17, pp 40-44, Sept.2007.

[5] WANG H F, SWIFT F J. IEEE Trans on power Delivery, Vol.12, No.2, pp 941-946, 1997.

[6] WANG H F, SWIFT F J, MA L. IEEE Trans on Power Delivery, Vol.13, No.4, pp 1355-1362, 1998.

[7] WANG H F. Proceedings of the 5th IEEE African Conference in Africa, Sep 28-Oct 1, 1999, Cape Town, South Africa. Piscataway, NJ, USA: IEEE, 1999, pp 495-500.

[8] Aihong TANG, et al. Power System Protection and Control, in Chinese, Vol.39, No.16, pp 89-94, Aug.2011.

Advanced Materials Research Vols. 986-987 (2014) pp 1291-1295

doi:10.4028/www.scientific.net/AMR.986-987.1291

The Applications of New energy at high altitudes in intelligent greenhouses

Ji Changwei[1, a],Li Min[2,b]

[1]College of electrical and Information Engineering,Southwest University for Nationalities, Chengdu 610041, Sichuan,P.R.China
[2]College of electrical and Information Engineering,Southwest University for Nationalities, Chengdu 610041, Sichuan,P.R.China
[a]E-mail: 1510794471@qq.com, [b]E-mail:1340519118@qq.com

Keywords: New energy, High altitude area, Solar energy, Wind energy, Biomass energy, Intelligent Greenhouse

Abstract: In the high altitude, solar energy, biomass energy and wind energy are widely available and renewable energy sources. It will improve the region's living levels at high altitude and the ecological environment when developed efficiently and in low cost. Making full use of renewable natural resources is of great value and significance to sustain the development of high-altitude areas of the economy. This paper is a kind of research and study, which based on new energy and aims at making full use of solar energy, wind energy, biomass energy complementary relationship and physical changes between planting and breeding to improve the renewable energy industry, integrated, modular for the high altitude area residents gathered .

Introduction

The advanced biological modeling technology and the automatic control program will be used in the Intelligent greenhouse[1]. The comprehensive development of planting and breeding technology in intelligent greenhouse is a new try. Microcomputer will apperceive the environmental indicators by water level sensors, temperature sensors, humidity sensors, carbon dioxide concentration sensors, oxygen concentration sensors, light intensity sensors and other sensors. Microcomputer collects , analyses and process data, to control relative drip irrigation pipe system, wind power, solar power equipment, storage equipment, ventilation equipment, planting areas, breeding areas, the biogas production facilities to do the implementation of real-time monitoring. Microcomputer adjusts the concentration of different materials in the area and farming area, then simulates the most appropriate relative optimal environment. Finally, the greenhouse changes the growth environment of the plants and animals by former progresses in order to avoid the production losses due to human' factors.

Intelligent greenhouse structure

(1) General structure

Gradually, along with the decrease of traditional fossil energy, new energy came into the stage of history. It is a bold attempt to make the solar energy, wind energy, biomass energy and other new energy apply to intelligent greenhouse[2]. The new type of intelligent greenhouse is established to change the structure of the traditional intelligent greenhouse and makes full use of the material advantages of planting and breeding, and improves the production efficiently.

New intelligent greenhouse is divided into nine parts such as the tent body, breeding areas, planting areas, wind power, solar power, biogas digester, reservoir, living area, control area (following pictures in Fig. 1 and Fig. 2). Modules are independent and cooperative with each other forms the basis of the new intelligent greenhouse structure. And it is necessary for the normal running of the greenhouses to provide the protection.

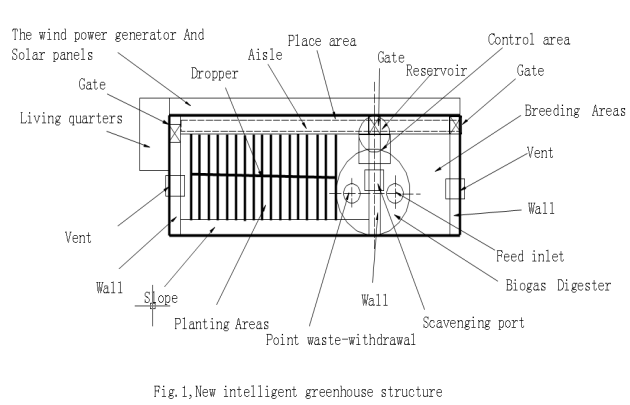

Fig. 1

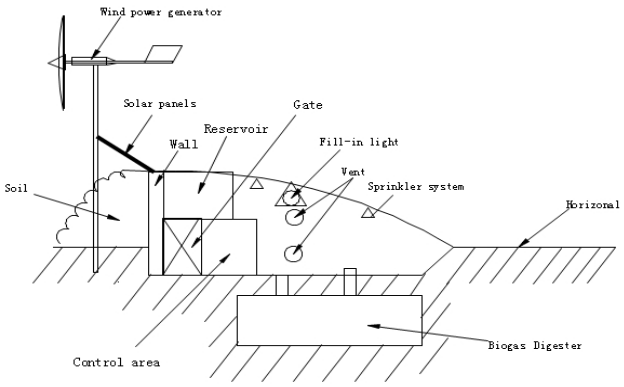

Fig. 2

(2)Tent body

The whole structure of greenhouses is covered by PE or PVC films, of which the thickness is 0.1 mm, the color is colorless and transparent. Distance between the bottom and horizontal is 1.0-1.5 m inside the greenhouse. The soil which is digged inside the greenhouse will be put on the rear of the casing body in order to form slope type for heat insulation. There is a wall between the planting areas and breeding areas to isolate them with controlled areas, biogas digester and reservoir around. On the wall , there are ventilation, adjustable gas content between the belt and farming districts.

(3)Planting areas

Planting areas is one of the main structures of the Tent body. The front of planting areas is a slope which is helpful to collect the sunlight and increase the area of shade plants. Above tent body, is the corresponding arrangement with methane and the fill light lamp. It is mainly used for plants to provide necessary light conditions during the night or cloudy day, to make plants better to do the photosynthesis to generate organic matter and release oxygen. Experiments show that use of plant growth lamp and the calefacient lamp for animals and plants can make warming lamp 15cm ground temperature inside the greenhouse increased averagely by 1.33℃, 667 m^2 cucumber yield increased by 17.4% on average, 667 m^2 production increased by 8195.4 yuan. Under the low temperature according to the weather, the average temperature increased by 1.13℃, the cucumber yield increased by 19.32%; delicious, can obviously resist the influence of low temperature according to the weather[3].Dropper pipelines which is scattered throughout ,can save the water resources,can provide the necessary water for plant growth, and achieve the goal of science with water.

(4)Breeding areas

The breeding areas is in order to carry on animal husbandry and aquaculture besides planting areas. Its demand is not so high like the planting areas. Animals will be centralized management in here. Above the tent body, there are the fill lights that will provide illumination and temperature under the right conditions for animals that needs to grow.It will help animals to avoid high altitude coldness. There is an entrance of biogas digester .The animals waste is put into biogas digester, providing the necessary raw materials for the methane production. The CO2 from the animals will become the main source in planting areas.

(5)Planting and Breeding areas

The areas is scattered with the temperature sensor, humidity sensor, the concentration sensor of carbon dioxide, the concentration sensor of oxygen, light sensor. The sensors collect the planting and breeding areas of changing parameters.

(6)Biogas Digester

It is in the middle of planting areas and breeding areas under the earth. It facilitates the original materials which produced by breeding areas for the biogas digester . Besides it provides fertilizer to Planting areas. Biogas digester generated biogas to delivery to residential areas, at the same time as a part of the planting areas sources of energy and raw materials.

(7)Reservoir

It is the main source of water demanded in the whole system. Reservoir has water level detection sensor. It provides water through the water supply pump. Water will be assigned by the control system to breeding areas as animal drinking water,as well as sealing water digester, and the area of drip irrigation system water, and source of domestic water for residential area, etc.

(8)Solar power area

Solar power area is located in the rear of the greenhouses, beneath the wind turbines, and horizontal ground into 45° .The 45° is the best accept of the solar illumination. Solar panels produced a steady stream of energy by photo-production volt phenomenon-electricity[4].

(9)Wind power area

Behind the tent body is vertical wind power device, this place is conducive to gather the maximum wind power, and avoid the influence for tent body and solar panels, light collection. When the wind comes, wind turbines will generate a steady stream of alternating current.

(10)Control area

It is the core of the whole system and it locates at the isolated wall. It is conducive to a better collect information in order to achieve better control modules. Wind power, solar energy that generated electricity will be stored here by the control system for unified management and distribution. Control system accepts all massages from each sensor. These messages through a conductor journey will be sent to the controlled area, through the modulus conversion device convert analog to digital quantity, passed to the microcomputer. The microcomputer receives the data, transform, storage, processing, reasonable judgment, deployment of resources of the whole system, establishes the whole system log, and allows all parameters of Planting and Breeding areas to meet the optimal parameters of plant and animal need.

New energy structure

When the morning's first ray of sunlight on the solar panels of new intelligent greenhouse, solar device would start preparation. With the height increase of the sun, light intensity gradually strengthened, and tens of thousands of photons will play to the panels. Enough energy photons can be in p-type silicon and n-type silicon electronic excitation from covalent bond, so that produce electronic-hole pair, produced more strikes with electronic-hole, and the Photovoltaic phenomenon is happened.This current is affected by light, it is unstable, and instantaneity. It needs us to add the charge controller between solar panels and batteries .

Compared with solar energy, wind energy is not stable. Wind power generation device is in standby state, waiting for the arrival of suitable wind. When the powerful currents of wind turbine impeller rotates, alternating current (AC) is produced. This kind of an alternating current is not stable, the amplitude and frequency of the voltage is as the size of the wind of change, is cannot be used directly. This requires DC/AC transform to produce a stable DC, which is stored in the battery.

At high altitude there is ideal lighting conditions, and wind conditions are satisfactory. Here we use the solar wind with complementary power generation that can completely meet the needs of the whole system.Solar energy, as energy of generating electricity, is not only just here ,but also the tent area heat and an important source of animal and plant grow light source[5].

High altitude air is thin and less oxygen, and farming proportion is very important in people's life.This needs the combination with the planting and breeding. We found that the biogas digester is the best device to connect the planting and breeding by data at home and abroad. The waste of breeding animals gets into the entrance of the biogas digester, after the biogas fermentation, it becomes a part of the organic matter decomposition inorganic substances, with the main combustible gas produced. These gases can be used to the life of people, burning the gas to the area to provide heat, light in the long dark night. Produced biogas fertilizer can be further used in the area of increasing crop production cost reduction.The area of organic compounds can be used to sell, at the same time also can be supplied to breeding areas, and the oxygen is indispensable to plants and animals living conditions. Thus formed an interconnected network. We know that the entire

network normal operation requires a powerful control system to adjust and various auxiliary power facilities help, like wind and solar power into the network makes the whole network interconnected interdependence[6].

Intelligent control system

According to the relative different kinds of animals and plants in different periods of temperature and humidity, concentration of carbon oxide, oxygen concentration, light intensity, temperature different needs, such as system of sensor collected data by using PID algorithm to control[7], in order to make intelligent greenhouse environment to achieve the best environment for plant and animal growth. Now we will show the main structure of control system in intelligent greenhouse in Fig. 3.

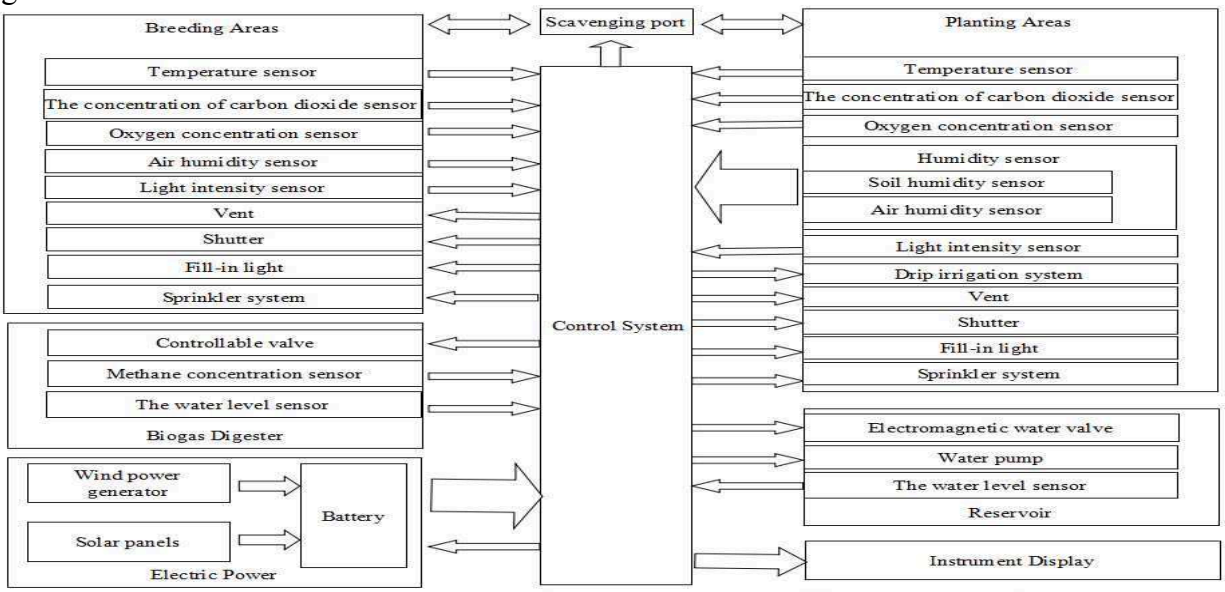

Fig. 3, the main structure of control system in intelligent greenhouse.

Main control system management is an important guarantee normal operation of the system. All process are through the control system of unified management function module.

Power system is made up of solar panels and wind turbines, as well as the battery together. Complementary wind and solar power provides a powerful source of energy to the whole system. the operation of the electric equipment provides the foundation for the entire system security. Every moment of electricity is different, but rechargeable batteries need to be better,so it still need our control system, for the power equipment of electric power monitoring and control. Make our system more stable work.

In the greenhouse,humidity in the air, temperature,light, concentration of oxygen concentration data constantly intertwined, and converged into the control system.The AD after AD collection, changes the analog quantity into digital quantity.Main control system receives and processes the data,and uses them to build a model and log to generates growth.At the same time control is gonging on.By drip irrigation control system to control the humidity of the soil, through spray system to change the planting areas and breeding areas air humidity, by controlling the air vents to change the temperature of the planting areas and breeding areas,the Control system got its aim.To change the temperature,CO_2 concentrations,and light intensity of planting areas is by Biogas lamp. Through the liquid level detection meter to change the water within the reservoir and the biogas digester, so as to better regulate the amount of water. All data will be displayed on the screen that really could easy to understand the operation of system.

Summary

This system is based on new energy which makes full use of not only complementary relationship of solar energy,wind energy and biomass energy but also adequate illumination time,

and sufficient wind in high altitude areas.It is for the normal operation of the whole system provides energy basis. Material is flowing from planting areas to breeding areas and the breeding area gains some different materials from planting areas at the same time.This process is an exchange. The intelligent greenhouse has a strong intelligent control system,so that it can reasonably adjust the needs in the process of the growth of animals and plants. It will provide a new exploration road for high altitude area to increase the economic development.

References

[1]Zhong Yafei, the CO_2 greenhouse based on single-chip microcomputer measurement and control system design [D] : Qingdao in shandong province,University of science and technology, 2011:13.
[2]Li Jingjing, Zhuang Xing. China's new energy and renewable energy policies and future development trend analysis [J]. China energy Source, 2001.
[3]Zhu Junqi,Huang Ying,Application of warming light on Cucumber in Sunlight Greenhouse in Qishan County,Vegetables,2013(10).
[4]G.M.Masters Renewable and Efficient Electric Power Systems [M].John Wiley＆Sons.Inc.,2004.
[5]LI Jin-bin,CHEN Jun,Research on the Optimization of Comprehensive Benefits of Wind_solar Habrid Renewable Generation System,Electric Automation,2013 Section 35 Volume 5.
[6]Gao Haitao, Performence of Integrated System with wind Energy and Solar Energy and Biogas,the performance of master degree theses of master of Lanzhou university of technology,June,2012.
[7]Shao Zhengfen,Research of the Automatic Control System Based on Pic16F877 in Vegetable Shed,Journal of Agricultural Mechanization Research,2007(8).

Advanced Materials Research Vols. 986-987 (2014) pp 1296-1299

doi:10.4028/www.scientific.net/AMR.986-987.1296

The Control of Low Voltage Ride Through Based on STATCOM and Crowbar Circuit

Chen Lijuan[1, a], Wang Zhijie[1, b], Su Xinxia[1, c]

[1]School of Electrical Engineering, Shanghai DianJi University, Shanghai 201306, China

[a]chenlijuancom@163.com, [b]wzjsdstu@163.com, [c]suxinxia1991@126.com

Keywords: DFIG, STATCOM, Crowbar, low voltage ride through

Abstract. When the grid voltage dips, in order to keep DFIG connected to grid and accelerate the recovery of grid voltage, reactive power compensation STATCOM is adapted to provide reactive power for grid, and crowbar circuit is installed to protect the converter of DIFG. Transient stability of power system is improved and the low voltage ride through is realized.

Introduction

In china, majority of wind farms are located in remote areas and the grid which wind power connected to is far away from the load center. This grid is relatively weak, prone to fluctuate, Even more serious is that the grid voltage greatly drop may exist, and eventually lead to wind turbines splitting, so it's a serious threat to the safe operation of power grid.

In order to protect safety of wind turbine, if the wind turbine still uses the passive split protection[1] when voltage drops, the difficulty of recovery of the whole grid will increase, the severity of the failure may be aggravated, eventually lead to all other units split from the grid. So we must take effective measures of LVRT[2] to keep the stability of grid.

This paper established the mathematic model of STATCOM, and analyzed the working principle of crowbar circuit, then established the overall implementation to realize the low voltage ride through of DFIG.

The mathematical model of STATCOM

Synchronous compensator STATCOM[3] is one of the important members of FACTS controller. It plays an important role in maintaining node voltage, suppressing the voltage flicker, preventing system oscillation, improving the system transient stability.

The device principle block of STATCOM is shown in figure1:

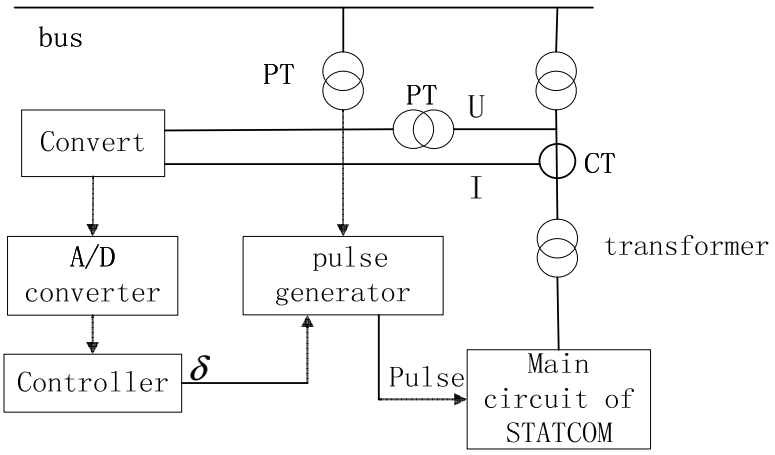

Fig. 1 The device principle block of STATCOM

In fig 1.1, PT is the voltage transformer and CT is current transformer, I_{abc} is three-phase current of system, U_{abc} is three-phase voltage of system, δ is the Angle between the output voltage of STATCOM and the system voltage.

The mathematical model of STATCOM is shown in type (1) :

$$\frac{d}{dt}\begin{bmatrix} i \\ i \\ V \end{bmatrix} = \begin{bmatrix} -\frac{R}{L} & \omega & \frac{m}{L}\cos\delta \\ -\omega & -\frac{R}{L} & \frac{m}{L}\sin\delta \\ -\frac{3m}{2C}\cos\delta & -\frac{3m}{2C}\sin\delta & 0 \end{bmatrix}\begin{bmatrix} i \\ i \\ V \end{bmatrix} - \frac{1}{L}\begin{bmatrix} u \\ 0 \\ 0 \end{bmatrix} \quad (1)$$

In the type (1), ω is the rotational angular frequency in d-q coordinate system; the same as the angular frequency of the three-phase voltage; L and R are the Connection inductance and the Equivalent resistance of STATCOM; C is the capacitor value of DC side of STATCOM; m is inverter modulation ratio of inverter; U_s is the instantaneous effective value of System voltage; V_{dc} is the DC capacitor voltage.

Block diagram of STATCOM controller structure as shown in figure 2.

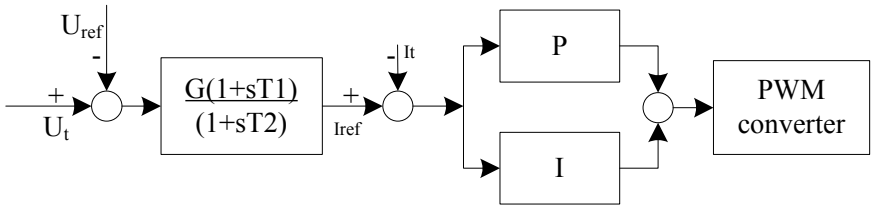

Fig. 2 The control block diagram of STATCOM

In this figure, U_t is bus voltage; U_{ref} is the expectations of bus voltage. Input the gap between the bus voltage and the expectation to the current regulator; obtain the desired current signal I_{ref}. Then compared I_{ref} with the actual output current of STATCOM, and input the resulting gap to PI regulator, obtain the phase difference δ between the output voltage of the AC side and the voltage of the Access system. Then by the PWM frequency converter, obtain the ON signal of switching devices in the main circuit of STATCOM.

Crowbar circuit

The voltage drop will cause large impulse current in the stator winding, because of the electromagnetic coupling relationship between the rotor and the stator of generator, voltage drop can also cause the overcurrent in the rotor side[4, 5], Damage the rotor side converter, and Over voltage may damage the generator rotor winding. In order to protect the rotor side converter, Crowbar circuit is installed in the rotor side, provides a bypass for the large current of rotor side.

The operation diagram of DFIG with crowbar as shown in Figure 3:

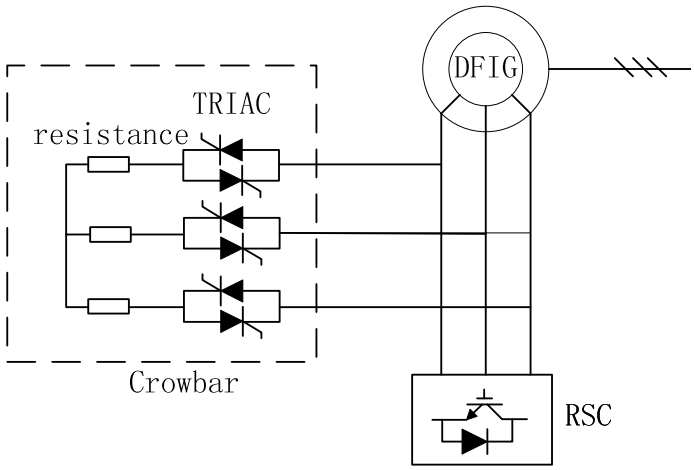

Fig. 3 The operation diagram of DFIG with crowbar

When the grid voltage dips, the rotor side converter stop working and the crowbar circuit start to work, then fault transient current will decline rapidly, and after a period of time (60ms-120ms), the pulse of bidirectional thyristor was locked. And the current gradually was gradually declined to below the thyristor holding current, at last the converter went back to work and the grid voltage recovered.

The overall implementation scheme

The overall implementation of LVRT with STATCOM and crowbar circuit as shown in figure 4:

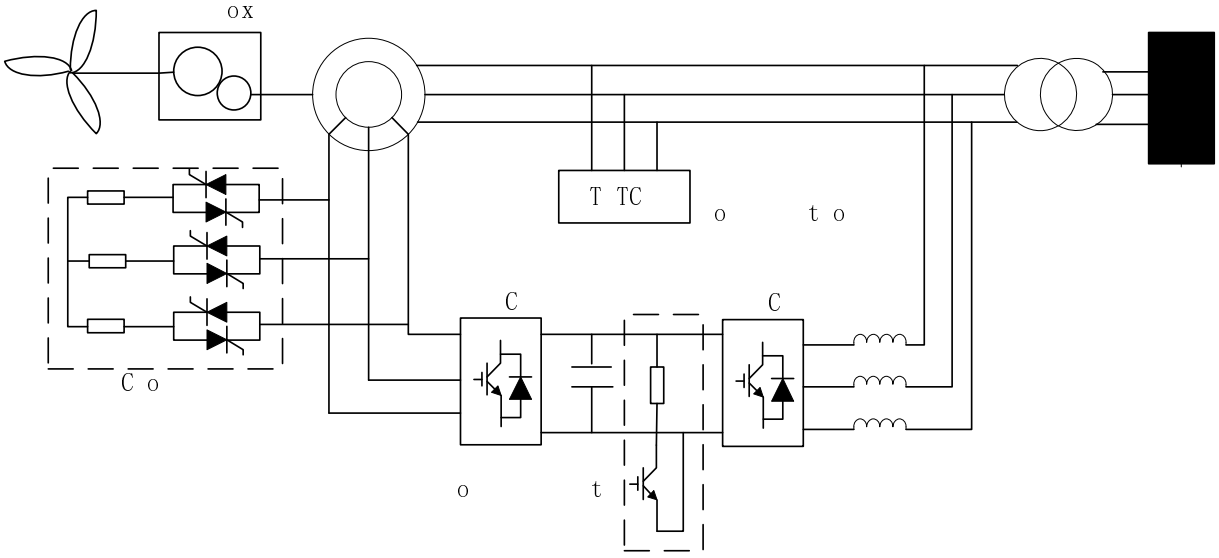

Fig. 4 The overall implementation scheme of LVRT with STATCOM and crowbar circuit

When the grid voltage dips, on the one hand, wind turbine uses the crowbar circuit to protect the equipment of wind power, and the rotor side converter can stay connected with the rotor at same time; on the other hand STATCOM is installed to compensate he reactive power for grid and Promote the recovery of grid voltage. And because STATCOM and crowbar circuit are installed, the wind turbine have the ability of Low voltage ride through. After the failure was eliminated, the crowbar circuit would exit, the power system returned to normal operation.

Conclusion

The implementation scheme of LVRT could compensate reactive power and promote the recovery of grid voltage when the grid voltage dips, and protect the converter at same time, provide a solution for integration of wind power to overcome the problem of LVRT.

Acknowledgement

This paper is funded by the Shanghai municipal education commission key projects of scientific research innovation (12 zz197), Shanghai natural science fund (12 zr1411600), and national natural science foundation of China (11201267) projects.

References

[1] Xiang Dawei, Li Ran．Control of a doubly fed induction generator ina wind turbine during grid fault ride-through[C]. Proceedings of IEEEPower Engineering Society General Meeting, Montreal, Canada, 2006.

[2] Morren J, de Haan S W H. Ridethrough of wind turbines with doubly-fed induction generator during a voltage Dip[J]. IEEE Trans on Energy Conversion, 2005, 20(2).

[3] Zhou Wei, The var compensator research of wind-power plant based on SVC and STATCOM[D], Master's thesis of Xinjiang University, 2008

[4] D. Xiang, L. Ran, P. J. Tavner, S. Yang. Control of a Doubly fed Induction Generator in a Windurbine During Grid Fault Ride-through [J]. IEEE transactions on energy conversion, 2006,21(3):652-662.

[5] QIN Yuan-wei，LIU Shuang. Doubly -fed induction generatorlow voltage ride through based on crowbar circuit [J]. Power Electronics, 2011, 45(8):51-53.

Advanced Materials Research Vols. 986-987 (2014) pp 1300-1304

doi:10.4028/www.scientific.net/AMR.986-987.1300

The Optimized Configuration Simulation of the Wind Turbine Control System Based on E-WT

Chunyan Dai[1, a], Jianhua Yuan[2, b,*] and Fanghu Zhang[3, c]

[1] Electrical Engineering & Renewable Energy School China Three Gorges University Yichang, China

[2] Electrical Engineering & Renewable Energy School China Three Gorges University Yichang, China

[3] Guandi Hydroelectric Power Station Yalong River Hydropower Development Company, Ltd. Chengdu , China

[a]1210445424@qq.com [b]sd.yjh@mail.sdu.edu.cn [c]554766314@qq.com

[*] corresponding author

Keywords: S7-1200; E-Wind Turbine; HMI; Optimum Selection

Abstract. This paper proposed, with the constant speed and variable pitch wind turbine as the research object, and E-Wind Turbine software as simulation platform, S7-1200 PLC as the master controller, the system control module were optimized for selection and configuration，thereby improving system performance and reducing design costs. Finally, in the STEP7 Basic V11 the modules which had been a good selection and configuration were connected, then to complete the configuration of communication, to verify the feasibility of communication and the effectiveness of the system optimize configuration when the wind turbine implemented the simulation in the E-WT platform.

Introduction

Wind power is the main form of wind energy[1,2]. Master the operating characteristics of wind turbines, as well as by improving its control performance to improve operation efficiency is a hot point work of the science and technology personnel. The conditions of actual wind field are random and uncontrolled, and the wind turbine is large scale, complex, high risk and high cost, these factors brought inconvenience to researchers. Simulation equipment just can overcome these deficiencies, compared it to the actual wind farms, we can find its low cost, low risk operation, flexible operation, and it can according to set conditions to run. So we can learn to wind turbine operation characteristics and study the control performance by simulation equipment.

E-WT can embed PLC program be compatible control, so it can be directly used for the actual wind turbine control system, and has occupied a certain application markets; At the same time, it has a specific fan simulation interface, 3D dynamic effect is good, and that has the certain scene simulation effect, so this paper takes E-WT as the simulation platform. There are a lot of research focused on the two aspects which are the object characteristic analysis and the design of control strategy of the wind turbine. The references [3] on the aerodynamic characteristics, variable pitch and yaw characteristics of the wind turbine were carried out detailed analysis and research. The references [4] and [5] are studied the yaw control strategy and variable pitch control strategy respectively, which are the major parts of the air blower control system. In contrast, the research of the control modules selection is relatively scarce, in the references [6], it analyzed the choice of PLC and system configuration, but it is not to do the specific research for one control object.

In this paper, it will with the constant speed and variable pitch wind turbine as the research object, and E-Wind Turbine software as simulation platform，the selection and connection of the control module as the key research, to make up for the inadequacy of the wind turbine system simulation in this study. It is worth noting that large capacity and low cost are the optimization targets of the wind turbine control system configuration.

Wind turbine control structure

Wind turbine control structure includes main circuit, control circuit and sensor and interface circuit, the connection of different parts is shown in Fig.1.

The Fig.1 shows main controller through communicate with power acquisition module to get power data, these data include electrical signals which were converted by wind speed, rotational speed, liquid level analog signal, connected to power grid's electrical signals, the site of the digital signal, and Mutual transfer electrical signals between PC and control module, etc. In addition the controller module output control signals, which is used to control wind turbine yaw system, hydraulic system, etc. For wind turbine's physical structure, it passes through the transmission system which is composed by the rotor, shaft, gear box, high speed growth axis, mechanical brake and the generator, accomplish the transformation of energy ,when achieve interconnection conditions it will be made into electricity grid.

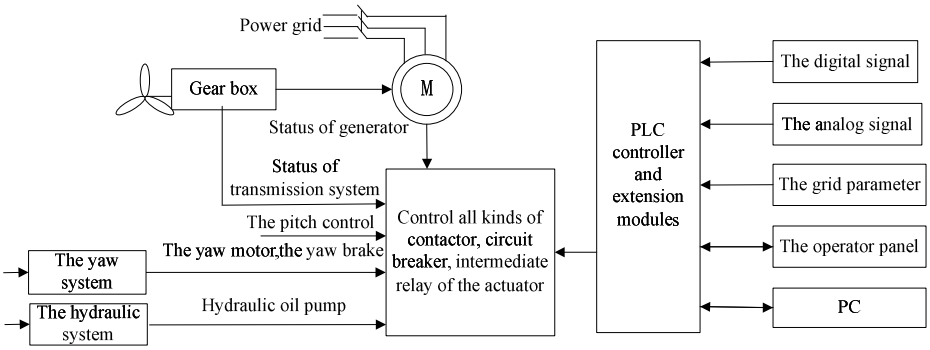

Fig.1. The control structure and the principle diagram

Wind turbine control module selection

According to the control requirements of the wind turbine operation, in order to realize the basic function to select the appropriate controller, communication equipment and power supply module, etc.

The selection of PLC. S7-1200 compared with S7-200 stronger control function, then has lower prices than S7-200, S7-300 and S7-400, and can achieve the same control effect, combined with S7-1200 controller is used flexible and powerful, can control all kinds of equipment in order to satisfy the demands of automation, and its compact design, flexible configuration and has a powerful set of instructions, so this article chooses its as the embedded controller of E - Wind Turbine platform.

The selection of I/O modules. Variable pitch and constant speed wind turbine control system with a total of 54 I/O points, including 28 digital I/O points and 26 analog I/O points. S7-1200 PLC has four kinds of CPU models, this paper selected models for CPU 1214C. CPU 1214C has 14 digital input points and 10 digital output, moreover the CPU nested a signal board, on the signal board has four digital quantity input point, it can be used as extend the digital input, and it is meet the system demand for digital I/O points.

In this case, we just need to expand analog I/O module. Wind turbine has many analog input points which is total of 22, and only has 4 analog output points. For there is a feature that the number of analog input points is far more than the number of output points, then in order to make the expansion modules can be fully utilized ,it expanded 2 SM 1231 and 2 SM 1234. SM1231 is an analog input module with 8 analog inputs on each module; SM1234 is an analog input and output module with 4 inputs and 2o outputs on each module, able to meet the system requirements for analog input and output points.

According to the above principles for the selection of I/O modules, namely on the basis of meet the requirements of input and output channels, then the maximum extent, improve the utilization rate of the module, and effectively reduce the design cost, it helps the system to achieve the optimal configuration.

The selection of communication network elements. On the basis of SIMATIC S7-1200 controller, matching using KTP600 Basic color PN, it can realize the power monitoring and the control of wind turbine real-time , and its basic protection grade is high, reaches IP65, can adapt to bad environment.

Communication module is using CSM 1277, it is a industrial Ethernet switch which is applied to the compact structure of SIMATIC S7-1200 and modular design, compared with the use of external network components, it reduced the assembly costs and installation space.

R4233A is a kind of intelligent three-phase electric parameters of the integrated data acquisition module, it can be widely used for power monitoring system in various industrial control and measurement system, and can replace transmitter or input module of measurement, which related to the current, voltage, power, etc, to reduce the system cost, convenient wiring, improve the reliability of the system.

The data is exchanged between PLC and E-WT using ProfiBus DP communication agreement. S7-1200 PLC configuration of the main communication module for CM1243-5, the ProfiBus DP slave station communication module is used PM125.

Finally, it also need to configure the power supply module which is STIOP to meet the requirement of the CPU and the extension module power supply, to ensure the normal operation of the whole system.

Based on E - WT of wind turbine control modules connection

The system hardware configuration. Based on the selection of the wind turbine control modules, get the system main hardware configuration as shown in Table 1. Other required universal devices, such as ProfiBus DP, ROFIBUS S7 bus, data acquisition card, all kinds of connecting line, etc, can follow the general principles and requirements.

Table 1. The hardware system's configuration list

	Module Type	Number(piece)	instruction
CPU	CPU 1214C DC/DC/DC	1	The controller
Frame	SIMATIC IC S7-1200	1	The fixed component of extension module
Power module	SITOP	1	——
Analog input module	SM 1231 AI 8x13 bit	2	Analog input channel
Analog input and output module	SM 1234 AI 4x13 bit AQ 2x14 bit	2	Analog input and output channels
Profibus master station	CM 1243-5	1	——
Communication module	CSM 1277	1	Communication with the operator panel
The operator interface	KTP600 Basic color PN	1	The operator panel
Signal board	DI 4*24VDC	1	Extended digital input
The power acquisition module	R4233A	1	Electric parameter acquisition
Si Bo PM125	PM125	1	Connecting the CPU with the power acquisition module

Communication configuration. STEP7 Basic V11 is used to the connection between the PLC modules, as shown in Fig.2 [7].

As shown in the Fig. 2, when the controller download the corresponding program, the CPU 1214C is responsible for the execution of the program; the two SM 1231 and the two SM 1234 on the left side are the transmission port of analog signal; CM1243-5 DP on the right side is used to implement a data exchange between PLC and E-WT. Connect the controller with other modules, forming the

communication network as shown in Fig.3. As a result of the S7-1200 with the integrated PROFINET interface, it can be a direct communication with these devices which are the programming device, HMI communication equipment and other SIMATIC controllers, and the connection between the equipment is simple. That is to say, only need a switchboard which is CSM1277 can achieve the connection. Communication configuration and the actual hardware connection is absolutely match, and after a correct communication configuration, it need a prefect fit between software and hardware, so that it can realize the information transmission between the simulation equipment and the controller, and can complete the simulation of wind turbine operation.

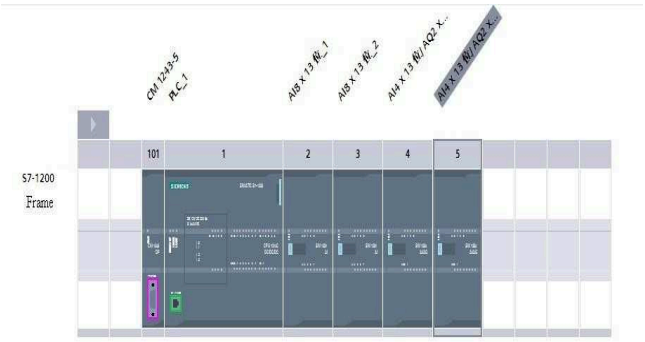

Fig.2. The connection between CPU and extension modules

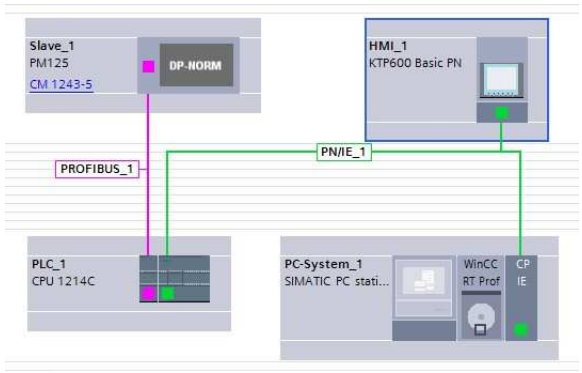

Fig.3. Communication configuration

Conclusions

In this paper, based on E-WT simulation equipment, it studied the optimal allocation of wind turbine control system, in order to make the control system to realize high performance and low cost the double optimization goals. Draw the following conclusions：

(1) The PLC S7-1200 has compact design, flexible configuration and has a powerful set of instructions, with it as the controller, can control all kinds of equipment in order to satisfy the demands of automation, and its price is low.

(2) In view the feature of the number of input and output points of control object，it used signal board as the digital quantity extension module, analog extended module choice two 1231 and two SM 1234 SM, as far as possible to reduce the number of extension module, so as to reduce the design cost.

(3) KTP600 Basic color PN with high degree of protection, so that it can improve the system performance; using CSM 1277, can reduce the difficulty of the connection between the modules in the control system, and reduce the design cost; electrical parameter acquisition module selected R4233A, using its intelligent, integrated features to reduce system cost and improve system reliability.

(4) In this paper, the optimization configuration of the control system is feasible, it plays an important role to realize simulation of wind turbine's operation .

Acknowledgment

This work was supported by the Innovation Foundation of Guozhiheng & CTGU Power Technology Co. Ltd., the Natural Science Foundation of Hubei Province (2012FFB03703), the Foundation for Young Scientists of Hubei Department of Education (Q20131301), the Development Foundation of Yichang City (A13-302a-09).

References

[1] Zhiying Zhang, in chinese: Wind Energy and Wind Power Generation Technology, the second edition, Beijing, Chemical Industry Press, (2010).
[2] Zhenyu Zhao and Yuan Zhen, in chinese: Principle and Application of Wind Turbines, China water conservancy and hydropower press, (2011).
[3] Xingjia Yao, in chinese: Principle and Application of Wind Turbines, Beijing, Mechanical industry press, (2009).
[4] Jiaying Zhang and Wenlan Wang, in chinese: The yaw Control System of Wind Turbine, Ordnance Industry Automation, Vol. 28, Section 11, (2009.11).
[5] Jiawen Wang and Huajun Gong, in chinese: The Design and Simulation of Large Wind Turbines' Variable Pitch Control System, New energy power generation control technology, Vol. 33, Section 5, (2011).
[6] Guixiang Zhang and Zhijun Zhang, in chinese: PLC Selection and System Configuration, Micro computer information, Vol. 21, Section 7-1, (2005).
[7] Renxiang Wang, in chinese : S7-1200 PLC Programming Methods and Engineering Application, Beijing, China electric power press, (2011).

Advanced Materials Research Vols. 986-987 (2014) pp 1305-1309

doi:10.4028/www.scientific.net/AMR.986-987.1305

The research of Low voltage control at Li Tang Trunk line in Li Jia Transformer substation

Liu Bo, Liu Chenyang, Cheng Pengfei, Liu Chuanbo, Wang Enlu, Zhu Bo, Xie Xinnan, Guan Ling, Bi Chuanbing, Wang Qinghao, Lin Bin

Fushun Power Supply Company, Liaoning Electric Power Company Limited, State Grid, China, wts55@126.com

Keywords: Low Voltage; MSE Power; Reactive secondary exact moment; Power Quality.

Abstract. In this paper, the rural power low-voltage of Li-Tang mains Trunk line raised the issue of secondary boost more than two groups reactive power compensation solutions, focusing on both the load power load variance method to calculate the location and placement of the regulator boost ratio, using precise moment method and reactive secondary terminal voltage rises method calculates the load side of intelligent reactive compensation on the trunk and installation location and capacity, to achieve the optimum design load tap rural power lines and intelligent var compensator configuration. The program changed in Fushun Li-Tang Trunk line in Li-Jia Transformer substation significantly after the implementation of effective, so that the end of the 31km-long line of power quality standards. Economic operation efficiency is improved.

Introduction

Li-Tang Trunk line in Li-Jia Transformer substation is a dispersed in rural area, long lines, largely load 10kV rural power grid. There is a peak period at the end of the line voltage is too low, The problem of power factor decreasing, line losing seriously which not only affect the power index, but also causing great economic losses of power supply. The effective solution to the problem of low voltage power line is important and urgen[1

The main parameters of Li-Tang Trunk line at table 1 lines which runes status and power flow calculation and analysis show that only rely on the circuit non reactive power compensation and adjustment of main transformer is not fundamentally governance Li Tang line low voltage problem. Effective way is in the middle long trunk with load ratio voltage regulator to increase at the end of the line voltage, at the same time, matching the appropriate non power compensator to compensate for the shortage of reactive power. When using intelligent load ratio voltage regulator and non power compensator combined treatment line in low voltage, according to the line structure, flow calculation, the mathematical model of equivalent rational calculation, determine the pressure regulator resettlement sites, pressure ratio, as well as to determine the capacity and with power compensator[2,3].

Table1 The parameter of Li-Tang Trunk line

length kM	The number of the transformer	The total capacity of the transformer kVA	The maximum power load kW	The maximum non reactive power load kvar
31	100	5068	2480	714

A voltage load coefficient of variance method to determine the load voltage regulating device configuration

(1) Long lines with voltage regulating transformer need to select appropriate locations, ratio and capacity, when the line is in the maximum load, The line has the best load voltage qualified rate. In order to reflect the accurate selection of voltage deviation, voltage mean variance and mean as the evaluation parameters.

The mean value of voltage:

$$U_M = \frac{\sum_{i\in\ell} U_i}{N} \tag{1}$$

Which U_i is the first load voltage, ℓ is the circuit transformer of line, N is the transformer number.

The mean variance:

$$\Delta U_s^2 = \frac{1}{N}\sum_{i\in\ell}(U_i - U_M)^2 \tag{2}$$

(2) Formula （2）describes the deviation of voltage in the mean near U_M . Because power load point does not influence the rated voltage, voltage deviation is not the same: impact load is large, so the voltage deviation should contain the load factor:

$$J = \frac{1}{N}\sum_{i\in\ell}\frac{S_i}{S_{avg}}(U_i - U_M)^2 \tag{3}$$

S_i is the node of I transformer in power, $S_{avg} = \frac{\sum_{i\in\ell} S_i}{N}$ is the node of I transformer in power, if we ignore the line loss, NS_{avg} is practical approximate to the line input end in power S_{IN} .

In the model of the first as an example, assume that line in the j rod is arranged on load voltage regulator, voltage regulator of the line is divided into 2 sections, calculation of variance were calculated Respectively also, A_j is the transformer before J , after J is the B_j transformer.

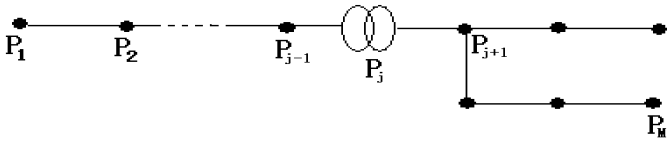

Fig.1 The distribution network line model

The boundary condition of the model:

A. Line load from the historical maximum load, the transformer's load capacity according to the distribution share.

B. Transformer active power P_i , inactive power Q_i corresponding model is equivalent to the resistance and inductance

$$\begin{cases} R_i = \dfrac{U_i^2}{P_i} \\ X_i = \dfrac{U_i^2}{Q_i} \end{cases} \tag{4}$$

U_i is the load voltage node i; R_i , X_i respectively, resistance, reactance of the node i of load, remained unchanged in the current iteration. Fig. 1 voltage variance can be expressed as:

$$\begin{cases} J_A(j) = \sum_{i\in A_j}\dfrac{S_i}{S_{IN1}}(U_i - U_{AM})^2 \\ J_B(j) = \sum_{i\in B_j}\dfrac{S_i}{S_{IN2}}(U_i - U_{BM})^2 \\ J(j) = J_A(j) + J_B(j) \end{cases} \tag{5}$$

In (5) formula, S_{IN1} is the transformer total apparent power of The A_j collection, S_{IN2} is the transformer total apparent power of The B_j collection, U_{AM} , U_{BM} by calculating.

$$\begin{cases} U_{AM} = \dfrac{\sum U_i}{N_A} \\ U_{BM} = \dfrac{\sum U_i}{N_B} \end{cases} \quad (6)$$

Which N_A is the number of A_j transformer set; N_B is the number of B_j transformer set.

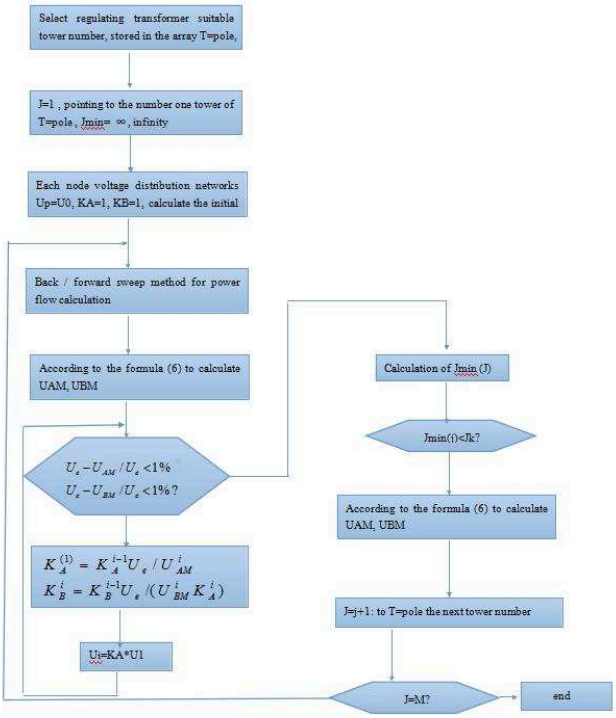

Figure 2 Load regulator position and ratio calculation flow chart

The entrance end of line voltage coefficient $k_A = \dfrac{U_1}{U_e}$, U_1 is the line entrance voltage, U_e is the rated voltage. The on load tap changer ratio is $k_B = \dfrac{U_{jout}}{U_{jin}}$, U_{jin} is the regulator input voltage, U_{jout} voltage regulator outlet voltage. U_{AM} is the regulator outlet voltage. Obviously, $U_{AM} \propto k_A$, $U_{BM} \propto k_A k_B$, in power flow calculation can be adjusted correction, correction of $U_i (i \in A)$ with k_A. Modification of U_{jout} $U_i (i \in B)$ with k_A, k_B, Calculation of the target is to make (6) in $U_{AM} = U_e$, $U_{BM} = U_e$, found for all $j \in l$ minimum $J(j)$ corresponding to k_A, k_B and J, then the regulator's capacity is determined according to the current and voltage of J.

The two tree data link back / forward sweep method based on [2], the beginning of the distribution network voltage and rated voltage, terminal load according to the transformer capacity allocation table 1 of the maximum load, the calculation flow chart shown in Figure 2, $k_A^{(i-1)}$ $k_A^{(i)}$ is the respectively I-1, I iteration of k_A , $k_B^{(i-1)}$ $k_B^{(i)}$ $U_{AM}^{(i)}$ $U_{BM}^{(i)}$ similarly explain. The calculated value of Jmin delay line distribution as shown in figure 3.

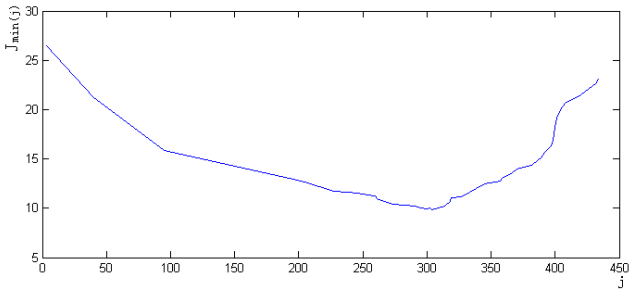

Figure 3 Dstribution of Li Tang trunks Jmin

Wattless power compensation of location and capacity

Considering Li Tang trunk line has the characteristics of too long line, wide distribution and too many transformer, in this study, the line selection on the terminal voltage boosting is a set of large nodes, the compensation In order to selection of low voltage load transformer, according to the calculation of compensation node position relative to the upper trunk load point of wattless power two times accurate moment sort. Select the value of load torque, in the low-pressure side of the local compensation.

Calculation formula of the non reactive power two precise matrix is $T_j^2 = R_{dj}(\frac{Q_{bj}^2}{U_j^2} - \sum_{s\in j}\frac{Q_{bs}^2}{U_s^2})$.Rdj means the total of j node to the source node or upstream compensation point encountered branch resistance and Qbj means the wattless power branch inflow from J node,Qbs into the node s (s is directly adjacent to the node j of wattless power). The second moment T_j^2 reflect J node has no influence on the power load on the line. Through the power flow calculation, the arrangement to each load point T_j^2, choose the maximum node as the compensation point.

In the trunk, due to long lines, the nonreactive power load is big, so we need to select more than one node important dispersion compensation. Considering the compensation capacity downstream compensation point will affect the compensation capacity current compensation node, therefore in the calculation, we should select the increasing the maximum trunk terminal voltage of a group from the same number of nodes in the selection of compensation. The amount of compensation point, depends on the non reactive power optimization on the line: the degree of compensation point is the more line reactive power, the less equipment investment, To Li Tang line as an example, its trunk nonreactive power distribution and compensation as shown in figure 4.

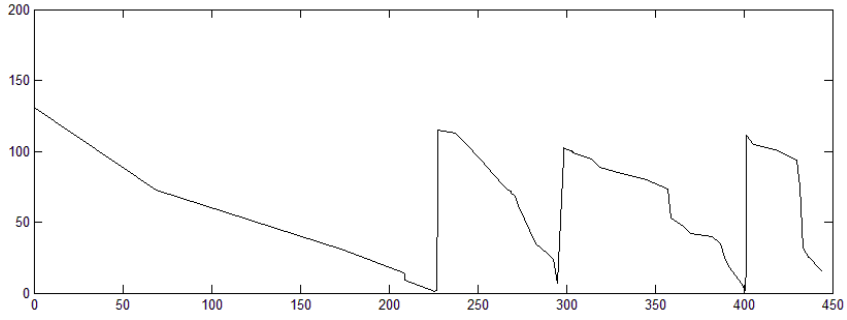

Figure 4 Trunk Li Tang trunk wattless power compensation

Calculate the Li Tang trunk line installation location of load voltage regulating transformer and nonreactive power compensator capacity, the installation location using the above method. Li Tang trunk load voltage regulating transformer capacity is 2000kVA, the location of the installation of the 300# rod, step-up ratio $k_B = 1.20$ 10kV reactive power compensator are respectively installed on the 227# rod (double verb complement 50+65kvar), 300# rod (single verb complement 100kvar), 401# rod (double verb complement 50+65kvar). The limitation of length, capacity and location related 0.4kV reactive power compensator no particular.

Governance effect

Li Tang trunk government before the 2012 January peak period of one end of the transmission line voltage is 10.3kV, the end of the lowest voltage up to 9.0kV. In 2014 January after the line control electricity peak period of one end of the transmission line voltage is 10.3kV, the terminal voltage is 9.7kV. From the operating data before and after Li Tang line low voltage government, has fundamentally solved the problem of low voltage, effectively ensure the terminal power quality standards.

Computer monitoring network based on GPRS

Intelligent load voltage regulating transformer, intelligent circuit reactive power compensator, intelligent distribution transformer voltage, current nonreactive compensator are real-time sampling at the nodes and grid operation data, operation data and equipment through GPRS network to upload sample itself.

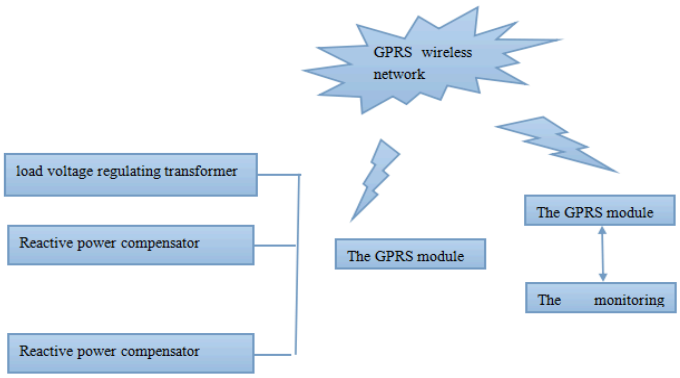

Fig. 5 The supervisory system based on GPRS

GPRS communication intelligent voltage and reactive power compensation system can timely measurement of access point voltage, current, reactive power and other data based on condition monitoring equipment, operation, and can according to the operating personnel, select the control line of non reactive compensator switching combination and the pressure regulation level, the system structure as shown in Figure 5.

The computer timing sampling measurement data of each device save for the historical data, convenient query running status line operation data and equipment. Through analysis of the historical data, summarizes the characteristics of grid voltage and reactive power without changes, through remote setting function of equipment to adjust and improve of equipment automatic operation mode.

Conclusion

In this study, in order to solve Li Tang trunk rural network line low voltage as the starting point, we use the mean of variance method using load of power on load tap changer configuration, the capacity and the site two times without power moment method to determine the load end reactive power compensator and trunk reactive power compensator, received a significant effect in Li Tang trunk line, ensure the qualification rate of the power index. Intelligent voltage and compensating device is realized by GPRS communication mode of automatic control network optimization of computer, the efficient operation of rural economic main Li Tang trunk line.

Reference

[1] Zhao Hong. The voltage quality of 10KV distribution network analysis. Rural electrician, 2003
[2] Zhang Zhi-bao. Transformer principles and applications. Chemical Industry Press, 2007
[3] Fang Da-qian. Transformer quick checking and calculating Handbook. China water power Press, 2004
[4] Yin Ke-ning. Transformer design principle. China electric power press, 2003

Advanced Materials Research Vols. 986-987 (2014) pp 1310-1314

doi:10.4028/www.scientific.net/AMR.986-987.1310

The Simulation research of SVG control algorithm based on Unbalanced Power System

Sunwei HUANG [1], SHI Jin[2]

[1.]Tianjin Key Laboratory for Control Theory & Applications in Complicated System (Tianjin University of Technology), Tianjin 300384, China

[2.]Architectural Design and Research Institute of Tianjin University Tianjin 300073, China

email: hsunwei@163.com

Keywords: static var compensator ; control algorithm ; MATLAB simulation

Abstract. For three-wire three-phase system load imbalance in the system when the current imbalance of power grid, The SVG control strategy which was applied in the unbalanced system was proposed by the paper, and carried on the research and analysis by MATLAB simulation function. The simulation results proved that the control strategy could achieve compensation control requirements， at the same time can effectively restrain the negative sequence current.

Introduction

In the case of active power remains the same，reactive power would be to lower the power factor,thus need to increase the capacity of power generation equipment and transmission equipment. So it will lead to increase investment, power loss, operating cost, the transmission line drop, at the same time, electric power equipment can not get full application and it is not conducive to electric power transmission and reasonable application. With the rapid development of power electronic technology,SVG has become the development trend of intelligent reactive power compensation; it also is hot spot of the world of reactive power compensation device research[1].

The research of SVG control strategy

Symmetry in the three-phase power network load balancing, only considering fundamental component,the common current inner loop decoupling control strategy is used which is based on dq transform[2][3]. But when the system load unbalanced, the AC current composed of positive sequence current and negative sequence current. Therefore we need to separately achieve the positive sequence current dq orthogonal coordinate transformation and negative sequence dq[4] [5]. In other words, the phase of d-axis is same as the grid voltage vector, which signifies the axis of active-component; while q-axis represents reactive-component axis. Taking rotation frequency ω_0 as positive sequence transformation, regarded rotation frequency $-\omega_0$ as negative sequence transformation. Through transformation we got Positive sequence dq coordinate transformation:

$$\begin{bmatrix} i_d^p \\ i_q^p \end{bmatrix} = C_{abc-dq}^p \cdot i_{sp} + C_{abc-dq}^p \cdot i_{sn} = \sqrt{\frac{2}{3}} I_{sm}^p \begin{bmatrix} \sin\phi_p \\ \cos\phi_p \end{bmatrix} + \sqrt{\frac{2}{3}} I_{smn} \begin{bmatrix} \sin(2\omega t + \phi_n) \\ \cos(2\omega t + \phi_n) \end{bmatrix} \quad (1)$$

Negative sequence dq coordinate transformation:

$$\begin{bmatrix} i_d^n \\ i_q^n \end{bmatrix} = C_{abc-dq}^n \cdot i_{sp} + C_{abc-dq}^n \cdot i_{sn} = \sqrt{\frac{2}{3}} I_{sm}^n \begin{bmatrix} -\sin(2\omega t - \phi_n) \\ \cos(2\omega t - \phi_n) \end{bmatrix} + \sqrt{\frac{2}{3}} I_{smp} \begin{bmatrix} \sin\phi_p \\ \cos\phi_p \end{bmatrix} \quad (2)$$

Through coordinate transformation， i_{dp} is positive sequence fundamental current active component and i_{qp} is reactive component, i_{dn} is negative sequence fundamental current active component and i_{qp} is reactive component, Then the positive sequence reactive current and negative sequence current control can achieve the anticipated goal. From the formula (1) it can be seen that through the positive sequence dq coordinate transformation, we get the positive sequence component. From the formula (2) it can be seen that through the negative sequence dq coordinate

transformation, we get the negative sequence component. the positive sequence and negative sequence double sequence synchronization control strategy was designed.. The article bases on dq coordinate transformation of positive sequence current inner loop decoupling control, the negative sequence transformation also uses the same control strategy.

The positive sequence current decoupling control algorithm for the inner ring could be represented as:

$$\begin{cases} u_d^{p*} = u_{sd}^p + (k_{iP}^p + \dfrac{k_{iI}^p}{s})(i_{dref}^P - i_d^p) + \omega L i_d^p \\ u_q^{p*} = u_{sq}^p + (k_{iP}^p + \dfrac{k_{iI}^p}{s})(i_{qref}^P - i_q^p) - \omega L i_q^p \end{cases} \quad (3)$$

The negative sequence current decoupling control algorithm for the inner ring could be represented as:

$$\begin{cases} u_d^{n*} = u_{sd}^n + (k_{iP}^n + \dfrac{k_{iI}^n}{s})(i_{dref}^n - i_d^n) - \omega L i_d^n \\ u_q^{n*} = u_{sq}^n + (k_{iP}^n + \dfrac{k_{iI}^n}{s})(i_{qref}^n - i_q^n) + \omega L i_q^n \end{cases} \quad (4)$$

It concluded that the structural schematic diagram of control strategy can be shown as Fig.1.

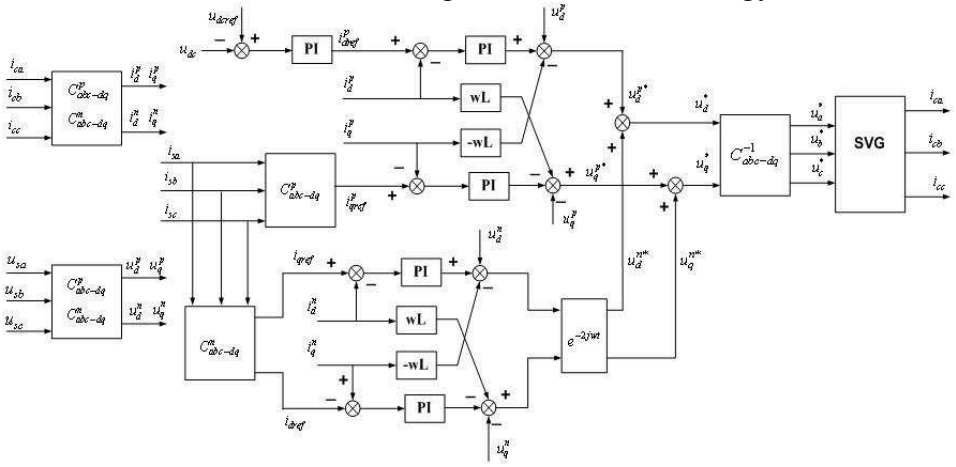

Fig.1 The diagram of based on dq coordinate transformation of positive and negative double sequence synchronization control strategy

Positive sequence adopts voltage outside loop and current inner loop decoupling control structure, The i_d^p and i_q^p are the instantaneous active and reactive power current value when SVG inverter side feedback current signal go through the positive sequence dq coordinate transformation; The i_d^n and i_q^n are instantaneous active and reactive power current value after negative sequence dq coordinate transformation; The u_d^p, u_q^p and u_d^n, u_q^n are voltage signal of the positive sequence and negative sequence active and reactive components after coordinate transformation; The subtraction between DC side voltage instantaneous value u_{dc} and reference value u_{dcref} after PI regulator operation is positive sequence active current reference value i_{dref}^p; Load side current go through positive sequence dq coordinate transformation becomes positive sequence reactive current reference value i_{qref}^p;Voltage ring ensure the SVG converter dc side voltage stability, current loop realize the decoupling control to complete the positive sequence of the reactive current in real time to follow. Through this control strategy, the systems achieve positive sequence reactive current compensation.

Negative sequence uses negative sequence current inner loop decoupling control, load side current becomes negative sequence active current reference i_{dref}^n and reactive current reference

i_{qref}^{n} through negative sequence dq coordinate transformation. Through the current inner loop decoupling control, the system realize the full compensation of negative sequence current, thus inhibiting the effects of negative sequence current to power grids due to unbalanced load of.

u_d^{p*} and u_q^{p*} are the positive sequence voltage control instruction signal through positive sequence control; u_d^{n*} and u_q^{n*} are the negative sequence voltage control instruction signal through negative sequence control. Negative sequence voltage instruction signal convert to positive sequence dq coordinate system, so that we get the input voltage instruction signal of SPWM module:

$$\begin{cases} u_d^* = u_d^{p*} + e^{-2j\omega t} u_d^{n*} \\ u_q^* = u_q^{p*} + e^{-2j\omega t} u_q^{n*} \end{cases} \quad (5)$$

The system applies the positive sequence and negative sequence synchronization independent control strategy. The detection methods of positive sequence current and negative sequence current applies the positive sequence and negative sequence synchronization test which bases on dq coordinate transformation by above-mentioned. After processing, the corresponding variables become direct component. The system uses PI controller to realize astatic control of positive sequence and negative sequence reactive current.

The simulation research of SVG control strategy

According to above analysis, with the aid of MATLAB simulation function the SVG system is set up and shown in Fig.2. The parameters of SVG system simulation are as follows: the voltage valid values Us is 690 V, the SVG connection inductance L is 1.5 mH, the device equivalent resistance R is 0.5 Ω, the inverter dc side capacitor C is 4700uF*5, the inverter dc side voltage value U_{dcref} is set to 1200 V. The system adopts SPWM pulse drive technology and the positive sequence and negative sequence synchronization control strategy which can be applied to the unbalanced system based on dq coordinate transformation.

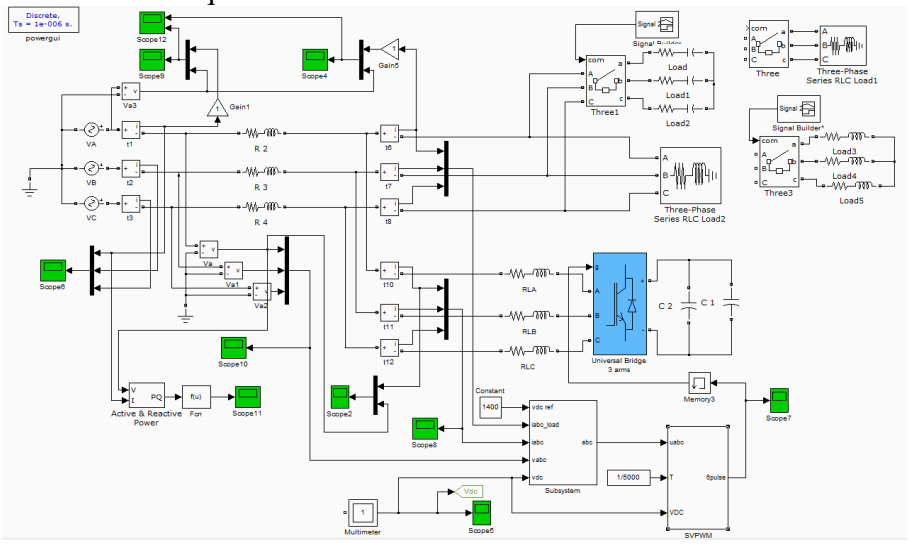

Fig2. The whole simulation model of SVG system

(1) simulation experiment with unbalanced RL load

The system simulation process is 0.6 s and it starts with power of 60 kw resistive load. When system run at 0.2 s, three-phase unbalanced load is suddenly applied: A phase load of active power is 10 kw, reactive power is 50 kvar. B phase load and C phase load is the same. Then A phase load suddenly change: active power becomes 10 kw, reactive power becomes 300 kvar. In the end, the load is removed at 0.4 s. The simulation waveform is shown in Fig. 3.

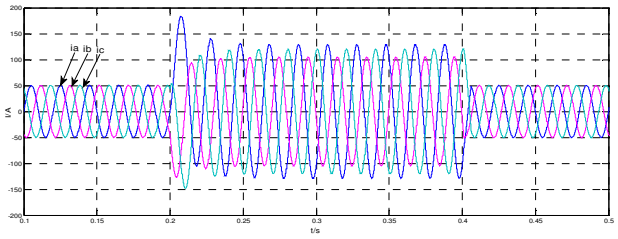

Fig.a Three phase current waveform of SVG without compensation

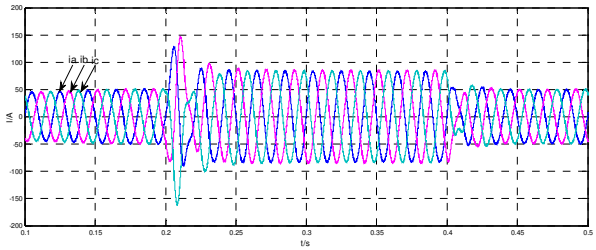

Fig.b Three phase current waveform with double sequence synchronization control strategy compensation

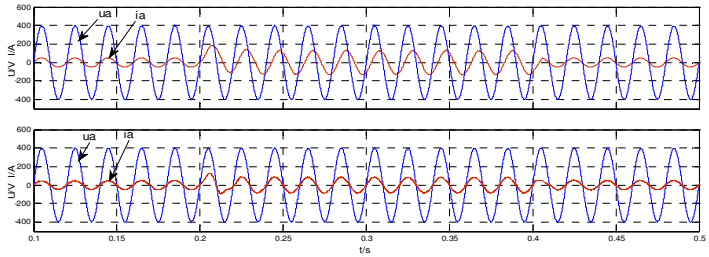

Fig.c A phase current waveform with double sequence synchronization control strategy compensation

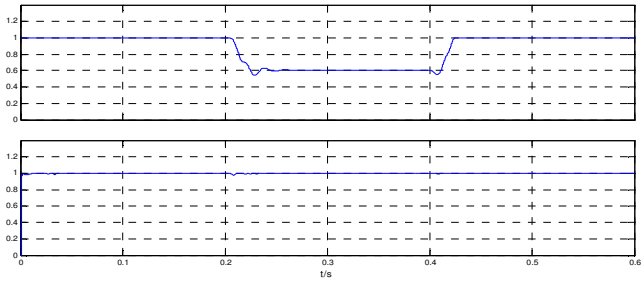

Fig.d A phase power factor before and after compensation

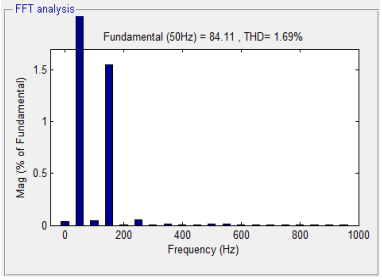

Fig.e current harmonic content with SVG compensation

Fig.3 Simulation waveform with three-phase unbalanced RL load

Through the simulation results in Fig. 3, it can be seen that when the load is unbalanced, three phase current of system is in a state of imbalance. The negative sequence current will form in three phase system. Each user of the common connection point cause that point of negative sequence voltage imbalance is not more than 2%, short time should not exceed 4%. According to the no zero sequence current unbalanced degree calculation formula:

$$\varepsilon = \sqrt{\frac{1-\sqrt{3-6L}}{1+\sqrt{3-6L}}} \times 100\% \qquad (6)$$

where $L = (i_a^4 + i_b^4 + i_c^4) / (i_a^2 + i_b^2 + i_c^2)^2$.

After load of system changing,. The unbalanced degree of three phase current without compensation is 15% in Fig.a. As shown in Fig.b, after applying single sequence of dq decoupling control strategy to compensate the inner ring, the unbalanced degree of three phase current is still 13%. When taking double sequence synchronization control strategy, three phase current wave is shown in Fig.c. By the simulation result, the unbalanced degree which is 0.05% reaches the national standard requirements. The wave of A phase power factor is shown in Fig.d. Power factor is 0.6% before compensation, after the compensation, it becomes unit power factor, system response time is less than 40 ms. The THD of AC current harmonic content is 1.69% as shown in Fig.e. The current inner loop decoupling control strategy based on positive sequence dq coordinate transformation can't realize negative sequence of reactive current compensation separately. The positive and negative sequence synchronization control strategy can realize the compensation of inductive reactive power and negative sequence current. Taking this control strategy has a good compensation effect.

(2) simulation experiment with unbalanced RC load

The system simulation process is 0.6 s and it starts with power of 60 kW resistive load. When system run at 0.2 s, three-phase capacitive unbalanced load is suddenly applied: A phase load of active power is 10 kW, reactive power is 50 kVar. B phase load and C phase load is the same. Then

A phase load suddenly change: active power adds 10 kW, reactive power becomes 300 kVar. In the end, the load is removed at 0.4 s. The simulation waveform is shown in Fig. 4.

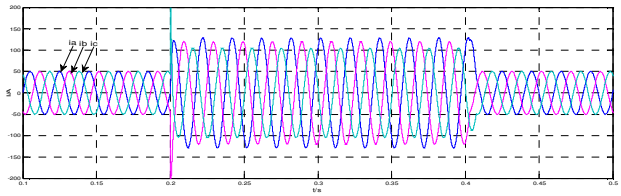

Fig.a Three phase current without compensation

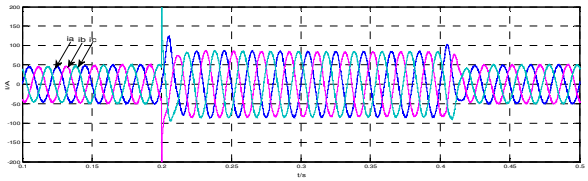

Fig.b Three phase current with compensation

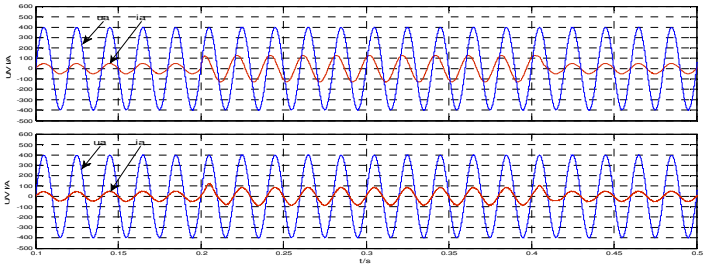

Fig.c A phase current waveform with double sequence synchronization control strategy compensation

Fig.4 Simulation waveform with three-phase unbalanced RC load

The simulation results can be seen through Fig 4. After load of system changing, three phase current includes reactive current of positive sequence current and negative sequence current. The unbalanced degree of three phase current without compensation is 15% in Fig.a. After compensation, the unbalanced degree becomes 0.045%.It achieves the national standard requirements. in the Fig.c, compare to A phase voltage, the current advances when given a sudden loading, but they are in the same phase after compensation; The power factor is 0.6 before compensation, after the compensation, it becomes unit power factor. The system response time is less than 40 ms. The THD of AC current harmonic content is 1.14%.The overshoot amount of DC side voltage is 0.32%.The control strategy of research can achieve the effect that the strategy compensates the capacitive reactive power and negative sequence current at the same time. Meanwhile, the strategy has a good compensation effect.

Conclusion

Through analysis and research, the positive sequence and negative sequence control strategy based on dq coordinate sequence synchronization has he function of the SVG reactive power compensation, at the same time it improves the ability which can inhibit negative sequence current caused by unbalanced load. In addition, system realizes compensation function of negative sequence current in simulation process. Meanwhile, the effect of reactive current signal, dynamic compensation and harmonic achieve the design requirements. And the system has good dynamic characteristics, provided a certain reference for the further application of SVG.

References

[1] Wang Zhao-an, Yang Jun, Liu Jin-jun. Harmonic suppression and reactive power compensation[M].(Beijing: China Machine Press, 1998).

[2] Liang Zhe, Chen Jing, Ou-Yang Ming-San. Research on the Operation Characteristics and Control Method of Load SVG[J]. Low voltage electrical apparatus, 2008，19(1)：37-39.

[3] Li Fu-liang, Zhou You-qing, Wu Tao. Design of advanced static var generator based on the instantaneous reactive-power theory[J]. Power System Protection and Control, 2010，38 (1)：75-78.

[4] Blazic, B. Papic, I. Improved D-StatCom control for operation with unbalanced currents and voltages[J] .IEEE Transactions on Power Delivery, 2006, 21(1): 225-233.

[5] Zhuo Fang, Chen Bo, Rao Yun-tang, Wang Zhao-an. Application of Improved TTA in SVG with Three-phase Four-wire Power System[J].Automation of Electric Power System,2007，31(13)：72-76

Advanced Materials Research Vols. 986-987 (2014) pp 1315-1318

doi:10.4028/www.scientific.net/AMR.986-987.1315

Development of the Sphere-Toroidal Continuously Variable Transmission

Shunmin Wang[1, a], Zhuo Li[1, b], Xinyu Wang[1, c] and Xichao Li[2, d]

[1]School of Automotive Engineering, Wuhan University of Technology, Wuhan 430070, China;

[2] Hubei Research Institute of Products Quality Supervision and Inspection, Wuhan 430070, China

[a]wanpok@163.com, [b]lubenn@163.com,[c]best.1987@163.com, [d]juliking0403@126.com

Keywords: STCVT, kinematics, dynamic analysis, torque-transfer

Abstract. This paper describes a new genre of Toroidal-CVT system, called the Sphere-Toroidal Continuously Variable Transmission (STCVT), which is derived from the half-toroidal traction drive (TCVT) and introduces its structure and working principle. The torque transfers from the input shaft to the cross-axle universal shaft coupling connected with the driven shaft. By discussing the difference between the torque-transfer, the paper will show the possibility of the application in the vehicle. To conclude, the system has the potential to implement infinite extension for the CVT theoretically.

Introduction

In response to global demands for environment conservation, the automobile industry is placing greater focus on the development of fuel-efficient technologies to reduce the Carbon dioxide emission [1]. Now as people are paying growing attention to driving comfort and stability, automatic transmission has been widely applied [2]. However, automatic transmission itself combines sophisticated structure with high cost, meanwhile, its maintenance cost is expensive, and all of these shortcomings hinder its development. While Continuously Variable Transmission (CVT),which has been identified as a strategic technology for improving fuel economy, as well as power performance and ride comfort of vehicles, enjoys a linear transmission ratio [3].

For decades now the half-Toroidal Continuously Variable Transmission (TCVT),which mainly consists of an input disc that is connected to the vehicle's engine, an output disc that is connected to the transmission output shaft, and the power rollers that are located between the discs has been widely studied [4,5]. But it still has many defections which restrict its development. This paper introduces a new design for the power transmission, which called Sphere-toroidal Continuously Variable Transmission (STCVT). The theoretical study has shown that STCVT has the ability to implement the change of transmission ratio continuously.

Structure and working Principle

Physical model. The half-toroidal CVT has a input toroidal disc and output toroidal disc (see Fig.1). The power is transmitted from the input disc to the output disc via a set of identical rollers regularly fitted around the discs common rotation axis. The transmission ratio change is achieved through the inclination of the roller rotation axis. The transmission ratio change is achieved through the inclination of the roller rotation axis. Inclining the pivoting roller support changes the two rollers to disc contact point positions relative to the toroidal discs common rotation axis. To force the roller to roll on the disc surfaces without slippage, all the elements are pre-loaded by introducing an axial thrust on the discs so as to push one toward the other along their common rotation axis. The housing reaction forces then press the rollers on to the disc surfaces.

The STCVT is similar to the TCVT, but remove the output disc and change the construction of the input disc (see Fig.2).

The output shaft connected with the sphere is fixed on the slider, which can move along with the slider to change the position of the sphere. Power is ultimately output through cross-axle universal

shaft coupling connected with the driven shaft. A sphere moves in the slots, accordingly, the power transmitted through the friction of the sphere and tank wall. By changing the position of the sphere, the transmission ratio changes as well.

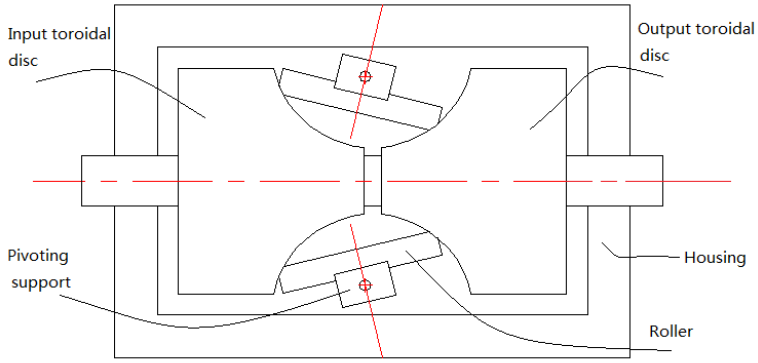

Fig.1 The construction of TCVT

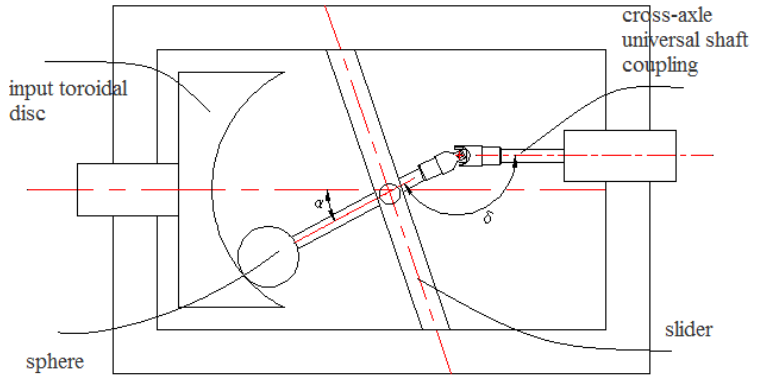

Fig.2 The construction of STCVT

Transmission ratio. As shown in Figure 3, the sphere and the input disc linear velocities at the point of tangency are equal, i.e. $v_1 = v_2$. We assume that the drive shaft angular velocity is ω_1, and active sphere driven shaft is ω_1, then we can get the following equations:

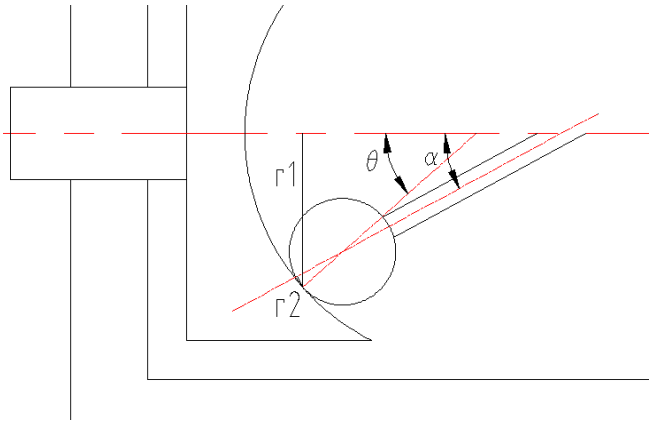

Fig.3 The transmission ratio

$$v = \omega \times r (r = R \sin \theta)$$

$$v = \omega \times r (r = r \times \sin(\theta - \alpha))$$

Among them, θ: The inclined angle between the line connecting the center of the groove and the point of tangency and horizontal direction. The two hemispheres must do remain contact α The

incline angle between the line connecting the center of the sphere and the point of tangency and horizontal direction.

So the transmission ratio can be calculated:

$$i = \frac{\omega}{\omega} = \frac{r \times \sin(\theta - \alpha)}{R \times \sin\theta}$$

The cross shaft driving mechanism motion analysis

Since the axis of the driven shaft is removable, we use the cross-axle universal shaft coupling to accomplish power take-off. As shown in the reference [6], when the axis angle of the active and driven shaft of the single cross-axle universal shaft coupling (σ is not 0), we have the equation as follows:

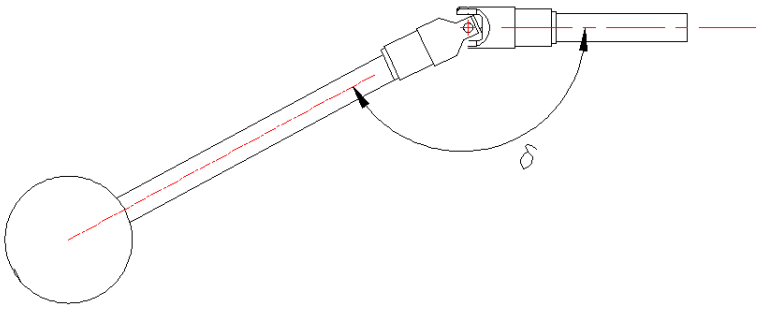

Fig.4 Diagram of the cross-axle universal shaft coupling

$$\frac{\tan\varphi}{\tan\varphi} = \cos\sigma$$

Here, φ_1, φ_2 is the rotation angle of the active and driven shaft.

We take the derivation versus time of this equation, and then get:

$$\omega = \frac{\cos\sigma}{1 - \sin\sigma\cos\varphi}\omega$$

Here, ω_1, ω_2 is the angular velocity of the active and driven shaft.

Because φ_1 remains to be 0 all the while, so

$$\omega = \frac{\omega}{\cos\sigma} = \frac{\omega}{\cos\sigma}\frac{R \times \sin\theta}{r \times \sin(\theta - \alpha)}$$

The general transmission ratio i is:

$$i = i \times i = \frac{\cos\sigma \times r \times \sin(\theta - \alpha)}{R \times \sin\theta}$$

Simulation

We choose the dynamics simulation software ADAMS to test and verify the performance of TCVT and STCVT. First of all, we build the mechanical modes in the ADAMS/VIEW and impose joint revolute constraint respectively on driving part and phantom element, and then apply contact constraint between them. Set the friction force as coulomb, and add drive motion to active part. Set the simulation time for 5s, step size for 0.05s. The result is shown in Fig.5 and Fig.6.

The result shows that the TCVT conveys larger torque. Because TCVT transfer torque through a circular arc surface, while STCVT through a point contact. The torque-transfer capability of TCVT is almost twice of that of the STCVT. The two figures show that transmission characteristic is smooth in the simulation.

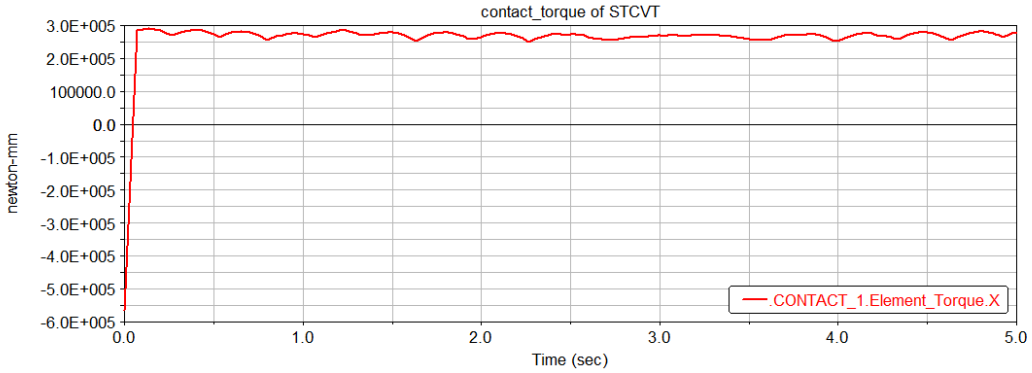

Fig.5 Contact-torque of STCVT

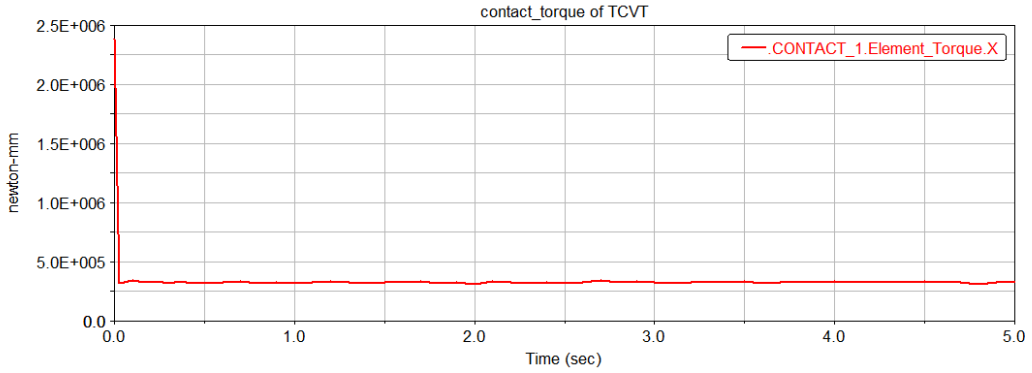

Fig.6 Contact-torque TCVT

Conclusion

Through above analysis, this paper reaches the conclusion that: The STCVT system could realize continuously change of the transmission ratio. And it has a poorer performance than the TCVT in torque transmission. But STCVT has a simple structure, and can be convenient operated, which makes it easily to cooperate with other transmission device. All in all, STCVT is an extension of the half-Toroidal CVT, and provides a profitable reference for the optimization and development of TCVT in the future.

References

[1] Heera Lee. CVT Ratio Control for Improvement of Fuel Economy by Considering Powertrain Response Lag [C]. KSME International Journal, Vol. 17 No. 11, pp. 1725~1731, 2003.

[2] Juergen Greiner. Automatic Transmission Systems Beyond 2020 - Challenges and Competition[C]. SAE 2013 World Congress & Exhibition,2013.

[3] Kenji Shimizu, Hironobu Waki. Development of a New-Generation CVT with Medium Torque Capacity for Front-Drive Cars[C]. transmission and driveline 2006,(sp-2001).

[4] VOLKER W. Drivability and control aspects of the vehicles with continuously variable transmission [D].Bath: university of bath, 2001.

[5] Robert D.Fuchs. Full Toroidal IVT Variator Dynamics[C]. Transmission and Driveline Systems Symposium 2002(sp-1655).

[6] Jin Ping, Nie Hong. Kinematics and dynamics simulation of cross-axle universal shaft coupling based on CATIA and ADAMS software[J].Modern Manufacturing Engineering,2011.2(in Chinese).

Advanced Materials Research Vols. 986-987 (2014) pp 1319-1322

doi:10.4028/www.scientific.net/AMR.986-987.1319

Design of Control System for Oil and Gas Field Pipe Production Line

Hao Ye[1, a], Yan Hou [1,b], Hong Yu Wang[1,c] and Wen Long Cai[1,d]

[1]North China Institute of Aerospace Engineering, Lang Fang He Bei, China, 065000

[a]baobaoye@hotmail.com, [b]houyan0311@163.com, [c]7666287@163.com, [d]13833633564@126.com

Keywords: Pipe Production Line, S7-300, Handshake Mode, Virtual Sensor, WinCC

Abstract. Steel pipe for pipeline have to go through multiple procedure in the whole process, and steel pipe transportation problem exists between the various processes. According to the specific requirements of the workshop environment and control tasks, a new communication mode that use S7-300PLC as the control core, connect 8 DP substation, involve 1077 output and input dot was adopted in the whole system. In the automatic mode, requirements of the complex technological process were realized; shake hands work mode was adopted between the production; using the proximity switch completed the material length measurement; in the location of inconvenience sensor installation, adopted virtual sensor in positioning. The HMI software in PC was WinCC V7.0, and communicated with PLC by Ethernet.

Introduction

Advantages of pipeline in relation to other transportation for oil and gas include large amount of transportation and low cost. The control system for pipe production line is developed based on the requirement of oil and gas project.

The automatic conveyor system utilizes the modular structure with centralized management and discrete control. The infrastructure consists of computer (or HMI), console with local/remote mode selector by which operation can be performed at either control room or field. In manual mode the motors and/or valves are operated through push buttons on the console or local panel, while in automatic mode the control is modulated based on the process parameters in the system.

The system controller is Siemens S7-300 series 315-2DP CPU module. DP (decentralized peripherals) interface which consist of Profibus-DP port for the production line interfaces with eight ET200 modules.CP343-1 lean module is connected to PC through Ethernet TCP/IP for Supervisory control and data acquisition and human machine interface(HMI) is configured for future process monitoring. The total physical input/output count is 1077. The HMI software is Siemens WinCC V7.0.

Process Flow Requirement

The whole system is divided into thirteen sections and convey rollers which include A,B,C,D (interior longitudinal seam welding), E (Cited arc plate cutting), F1 (Required corrected circular steel storage), F2 (Corrected steel pipe storage), G (longitudinal seam inspection), H1 (Storage), H2(Storage), J (waste district), N (steel group girth weld) and O (inspection).Each section is part of process flow while steel pipes produced in each stage is transferred to the next by convey roller. Sections A~E are located in one factory and others are at another location. The trolleys are used to transport the steel pipes between two factories. The steel pipe length is around 1200mm~3000mm and outer diameter is in the range of 400~900mm. The control requirements for section A,B,C is stated in below sections.

Stage A - Cited Arc Plate Welded Storage. This section has 3 steps A11,A12, A13. The design requirement as: After rolling and spot welding is complete, the pipes are lifted and transported to the required position by crane. There are sensors installed in the area. In manual mode, the pipes are moved by trolleys to the required position. In automatic mode, the A11, A12 and A13 will response to the command sent from next stage B11 and consequently instruct the trolleys to load the steel pipes onto the convey rollers which will transport the pipes to the section B11.

Stage B - Exterior longitudinal seam Welding. Section B has four positions.B11 is set for pre-welding; B12, B13 and B14 is for welding. All four positions can be operated manually and automatically. In automatic mode, steel pipes are shifted from A onto the current convey roller once the LOAD button is pressed. The pipes then are transported by trolleys and are welding on the operation station.

Stage C - Emergency Buffer. Upon the status of B12, B12, B14 of sent out pipes and status of D of no incoming pipes, the trolleys will transport the pipes to the emergency buffer after system checks the enough space in the area. Once received the load demand, the trolleys will enter storage buffer, load the pipes onto the conveyor. Then system will start conveyor which transport the pipes to section D.

Hardware structure and configuration

Hardware Configuration specifies the required modules, network architecture, assigns the module parameters and addresses, etc. The graphic configuration is illustrated in Fig.1.

Siemens S7-300 controller (CPU315-2DP) has two built-in DP ports which are connected to sub-stations. The baud rate is adjusted based on the application. Lower speed would be benefit for reducing the interference. At rate of 187.5K the maximum communication distance is limited to 1000 meters. If the actual distance between the control cabinets is greater than 1000 meters, the repeater is required

Discrete inputs on the center control cabinet is used to start while discrete outputs to indicate the status of sub-stations. Each sub-station is equipped with RUN, MAINTENANCE push buttons as well as corresponding indicators.

Software implementation

Here an example is given to demonstrate section A to B11 and B11 to B12. The same consideration would be applied to the pipe transports among others.

Pipe transportation between A and B11. When A is in manual mode, the pipes can be loaded on the roller by operating the trolley through FORWARD, BACKWARD, UP and DOWN push buttons on the local console, then pipes are removed from storage racks and transferred to specified location by operating the motors to rotate roller through CLOCKWISE and COUNTERCLOCKWISE buttons. Storage racks, trolley and rollers are shown in Fig 2. The storage racks have V shapes. The sensors are installed to detect pipes inventory and the trolley backward position. When the trolley is running right under the roller, the sensor detects forward position. After the pipes are transported to the front of B11, the trolley in section B11 is run by operator to remove them from roller to the welding station.

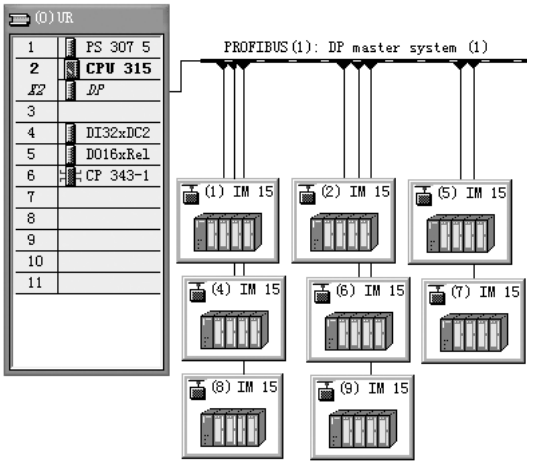

Fig. 1. Hardware configuration

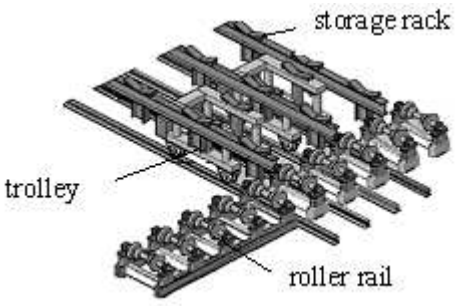

Fig. 2. Storage rack, trolley and roller rail schematic

In the automation mode the control requirements is shown in Fig3. B11 loading command is valid and there are steel pipes available in section A, the system will instruct the trolley in B11 to load the

pipes onto the conveyor and send the run command to roller so the pipes are transported to B11 forward position and are unloaded at the welding station. The B11 will go to idol mode if no pipes are available on the A storage racks after the LOAD push button at B11 is pressed.

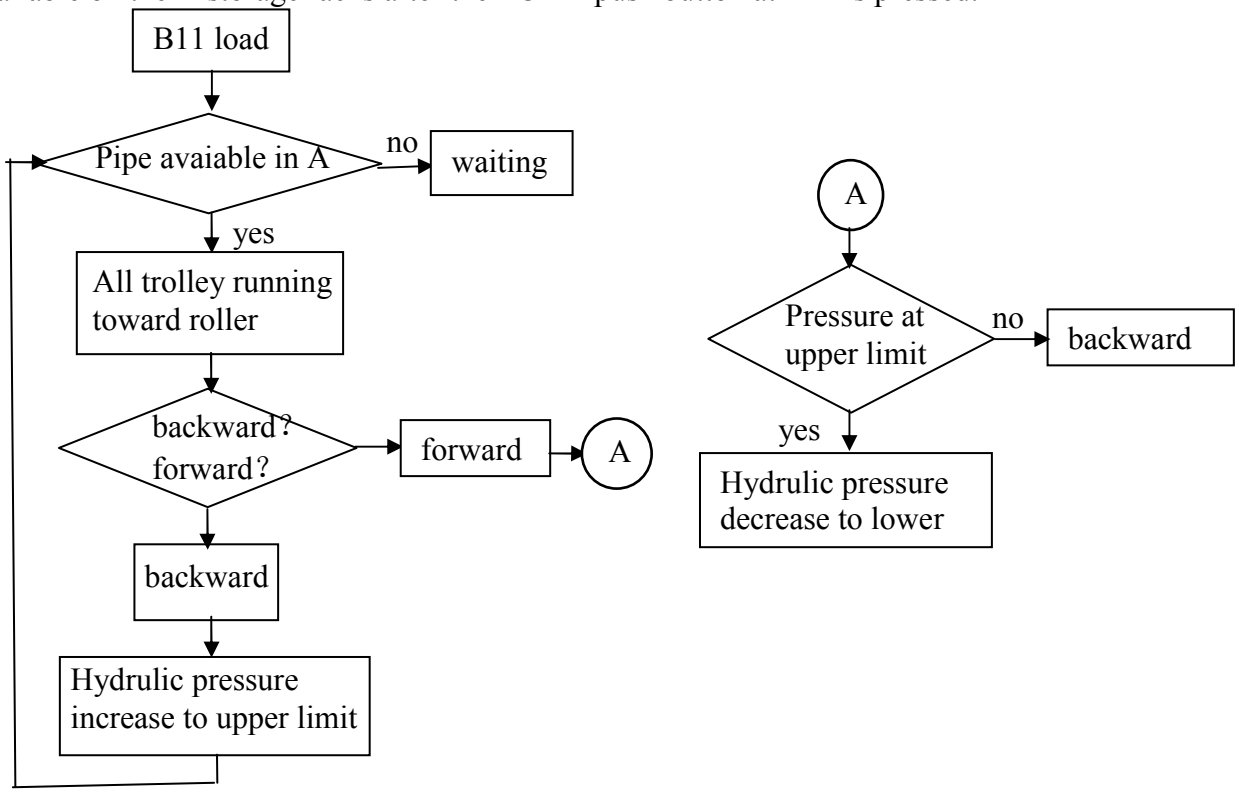

Fig. 3. Trolley of a11 control flow diagram

In the manual mode the trolley could be stopped at any position on rail. Switched to the automatic mode when trolley is at run status, the system needs to know the actual position, run direction (forward or backward) and hydraulic pressure level (upper/lower limit) before sends trolley instruction for next move. There are no upper/lower position limit sensors installed for the trolley hydraulic pressure system. The functions are achieved by timer plus SET/RESET instructions to simulate the upper/lower position. The control ladder diagram is shown in Fig.4.

Steel pipe transfer between section B11 and B12.B11 is for pre-welding and B12 is for welding. Control panel with LOAD and SENT buttons are installed in both areas. When B11 is set to auto and the LOAD button is pressed, the pipes in A should be transferred to the area automatically. After pre-welding is complete, the pipes are sent to B12, B13 or B14.If B11 is preceding the current procedure which indicates the inventory, the B11 is set to idol mode. Override by pressing the LOAD button, trolley in B11 will start movement and transfer the pipes onto the roller which transports the pipes in front of B12.consequently the trolley in B12 takes the pipes to the welding station. Simultaneously a shake hand signal is sent to confirm the SEND command from B11 and RECEIVE status of B12.If the signal is fail, both B11 and B12 will stay in idol modes. The welded pipes are transported to C storage area upon the RECEIVE command from B12.

Pipe length measurement. This section illustrates the importance of length measurement for pipe between sections A and B11. Fig.5 shows the control ladder diagram.

After the pipes are unloaded from roller and moved in front of B11, the length of pipes must be known so that they can be lifted and transported to welding station by trolley in the area. The length will be measured in B11 as well. The two values are compared and an error is calculated in the system. The error within 0.5 would ensure firm lift and transportation. A proximity switch is installed on the rail between *A* and *B11* for this purpose. When pipes are approaching the switch it starts counting, from which the length is able to be calculated. A proximity switch is required in front of B11 as well. The ladder logic for implementing length measurement is shown in figure 5: M0.0 is defined as a 100ms pulse and M1.0 is valid status set by shake hand signal between *A* and B11.

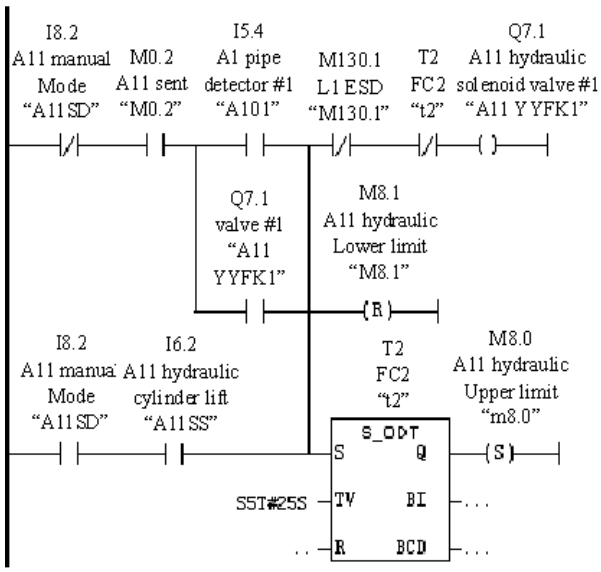

Fig. 4. Codes for simulating sensor

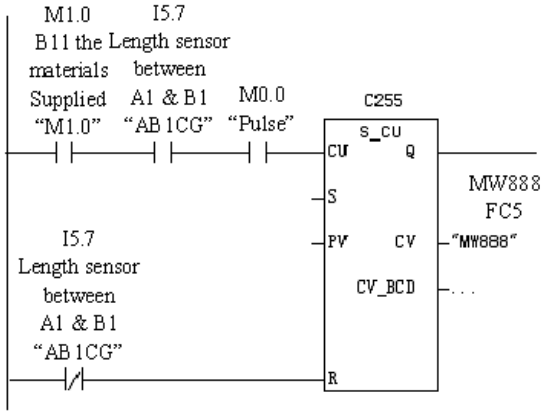

Fig. 5. Implementation of pipe length measurement

Length calculation for Pipe in B11, programmed with STL language

```
L    "mw888"
ITD
DTR
L    4.500000e-001
*R
RND
T    MW    22
```

Pipe transportation between two plants. The pipes backward transportation between two plants is performed by the backward trolleys installed on the rail. The trolley power is supplied by either rail or backup battery and controlled by S7-200 controller. The control signals are sent from S7-300 discrete output module and relay to S7-200 through the rail. The flow diagram as: the backward trolley will start if it received the SEND command from E and confirmed the RECEIVE mode from F; otherwise the E will enter into WAITING mode.

Summary

After one year's installation and commissioning, the functionalities of control system are met the client's requirement. The system realizes the discrete control and centralized management. The plant-wide real time human machine interface is designed clearly, friendly and operated easily. The system design includes process flow tracking, alarms, History data storage, display and inquiry. The implementation of project improves the operation procedure which was performed by the crane. The efficiency and safety are also made better.

References

[1] Dong Liyong: Journal of Shandong Institute of Light Industry. Sci. Vol. 25 (2011), p. 68-70
[2] SIMATIC: *SITRANS P,DS ⅡPax Reference Manual*(SIEMENS, Beijing 2003).
[3] SIMATIC: *SIPART PS2 Electropneumatic Positioner for Liner and Rotary Actuators* (SIEMENS, Beijing 2003).
[4] SIMATIC: *Micromaster440 universal frequency converty manual* (SIEMENS, Beijing 2003).
[5] SIMATIC: *SIMATIC DP/PA coupler Operating Instructions* (SIEMENS, Beijing 2006).
[6] Liao Changchu: Large and medium PLC application tutorial (Machine, Beijing 2003).

Advanced Materials Research Vols. 986-987 (2014) pp 1323-1327

doi:10.4028/www.scientific.net/AMR.986-987.1323

A Power Control Technology Adapting to Temperature Change

Hongling Zhang[1,a], Yan Wang[2,b], Yan Yang*[3,c]

[1]451 People's Liberation Army Hospital, Xi'an, 710010, China

[2]Department of Electronic Information, Northwestern polytechnical university, Xi'an, 710072, China

[3]Department of Electronic Information, Northwestern polytechnical university, Xi'an, 710072, China

[c]email: yangyan7003@nwpu.edu.cn

Keywords: power control, fault protection, temperature sensor of P-N Junction transistors, LED power supply

Abstract. Power control technology of LED is proposed, which can be adaptive to the change of temperature while online. The input power of LED will be adjusted according to the current value and its change rate of LED radiator. Reducing input power can balance the decreasing of the capacity of heat dissipation caused by the rise of ambient temperature in order to keep radiator temperature in a safe range. This avoids the vicious circle of the temperature excursion of P-N Junction caused by the rise of the temperature of LED light source characteristic of negative temperature. This, in turn, avoids damage to LED at high temperature.

Introduction

LED lamps, especially LED street lamps work under the condition of a wide temperature differential. In winter the temperature may reach to below -20℃ and in summer goes to more than 60℃. The wide temperature differential troubles the thermal design. If we design at maxium ambient temperature may raise the cost and weight of LED, which hinders its application. Otherwise, the problem of maintaining reliability performance under high temperature condition is hard to resolve.

At present, the solutions are as follows:

Overheated power-off protection method.

The implementation of this method is: install a temperature sensor in the LED lamp radiator. As the temperature exceeds maximum value, the LED drive through the hardware circuit connected with temperature sensor is shut off and the power supply is cut off in order to avoid the light emitting diode burnt down at high temperature.

Adaptive control method.

This is the improvement of the former method, which fuses modern control theory and single chip technology. The implementation of this method is as follows a temperature sensor is installed in the LED lamp radiator. Its output is linked with the single chip's (or DSP's) A/D port. Thus the analog quantity of temperature of the radiator will enter from A/D port into single chip microcomputer to realise digital monitoring of temperature. When the exceeding temperature of the radiator is detected by the single chip microcomputer, it will control the input power of the LED lights through the PWM output port to lower calorific value and get LED lamp radiator temperature back to normal.

A self-adaptive adjusting hardware control circuit is designed in this research. On the basis of the current value and its change rate of LED radiator, the input power of LED will be adjusted while online. Reducing input power can balance the decreasing of the capacity of heat dissipation caused by the rise of ambient temperature to keep radiator temperature in a safe range. This avoids the damage of LED device. And this particularly suits the condition of wide temperature differential.

The control principle of the temperature-change-adapted power

Circuit principle

The control principle of temperature-change-adapted power shown in figure 1. As is shown in the diagram, when ambient temperature rises, V_{FT} decreases because of the negative temperature characteristic of P-N Junction's temperature sensor D_1. However, with the regulation of R_1, the decreasing rate of V_1 is limited in $\Delta V_1/\Delta T \approx \delta$. And V_1 is used to control the input power of LED lamps, which means that the volume of heat dissipation of LED chips decreases following δ. On the other hand, with the rise of ambient temperature, the capacity of heat dissipation of radiator decreases. The decreasing rate is $\Delta P_D/\Delta T \approx \eta$. Because the selection of circuit components is decided on the condition of ensuring $\delta = \eta$, The capacity of heat dissipation equals to the decreasing rate of input power. In a word, the temperature of radiator will be balanced in a regulation scope no matter how the ambient changes, and this has promoted the reliability of LED working in high temperature.

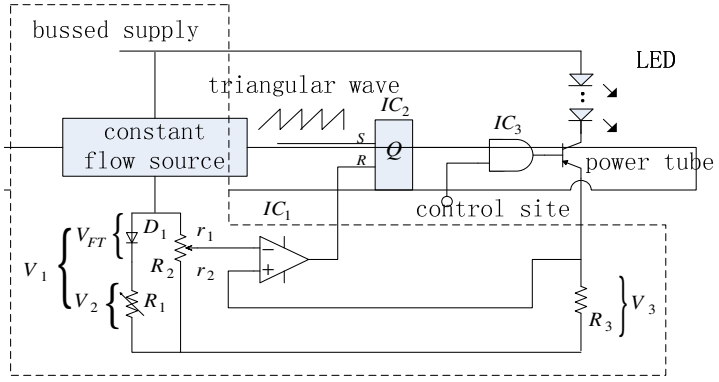

Figure. 1. The circuit principle of the LED lights temperature online adaptive adjustment

Theoretical foundation

When LED light source is working, due to the thermal resistor, the temperature of P-N Junction is[1] ,

$$T_J = T_A + R_\theta P_D \quad (1)$$

In the equation, T_J is the temperature of P-N Junction (approximately equals to the temperature of radiator), T_A is the ambient temperature, R_θ is the thermal resisitance from P-N Junction to the environment, P_D is heat dissipation. In LED, the 3%~5% of input electric power is transfered to luminous energy for output, and the rest dissipate in the device as the modality of heat, thus the heat dissipation also equals to forward voltage drop multiplied by input current, which may not cause great deviation to the experimental study[2].

The performance parameters of the effects of elevated ambient temperature are mainly reflected in two aspects. One is the monotonically decreasing of forward voltage drop V_{FT} between the two ends of LED, they can be approximated as:

$$V_{FT} = V_{F0} + K(T - T_0) \quad (2)$$

In the equation, V_{FT} is the voltage between the two ends of temperature sensor D_1 when ambient temperature is T, V_{F0} is the voltage between two ends of D_1 when ambient temperature is T_0, K is the coefficient that voltage changes with temperature, which is a negative value. For instance, the LED whose luminescent material is InGaN and substrate material is SiC, its K is: -2.66(mV/℃)[3].

And secondly, the capacity of heat dissipation of LED lamps decreases. Based on equation(1) we conclude that:

$$P_D = (T_J - T_A)/R_\theta \quad (3)$$

Obviously, as T_J, R_θ are given, when T_A rises, the power of heat dissipation P_D decreases.

It is concluded from formula(2)and (3) that: the rise of ambient temperature reduces not only the capacity of heat dissipation but also the voltage of P-N Junctions. Both of them worsen the thermal

environment of LED lamps. The measure we take in this paper is proposed to meet this need. With the change of ambient temperature, this measure adjusts the power of dissipation of P-N Junction of LED, and maintain the radiator temperature in an allowable range constantly. This avoids the vicious circle of the temperature excursion of P-N Junction caused by the rise of the temperature of LED light source, which possesses negative temperature characteristic, influenced by the rise of ambient temperature.

Technical solution

As is shown in figure 1, the method to control LED input power V_1 is as follows. In figure 1, R_1 is the gradient adjust resistor, which is used to change V_1's slope of the curve that decreases with the rise of temperature. R_2 is divider resistor(could be replaced by two constant resistors, the divider value depends on R_3 , which is the maximum of V_3 the voltage drop of R_3, R_3 is the constant current control resistor.

Selection of components and calculation of parameters[4].

①The calculation of R_1

The calculation of R_1 is the core of this paper, and it plays the role of changing V_1's slope of the curve that decreases with the rise of temperature. First of all, calculate the changing rate δ that change with the temperature:

$$V_1 = V_2 + V_{FT} = I_0 R1 + V_F T_0 + K(T - T_0) \quad (4)$$

We can deduce from formula that: $$\Delta V_1 / \Delta T \approx KT / (V_2 + V_F T_0) = \delta \quad (5)$$

In addition, with the change of ambient temperature, the dissipation rate η of radiator is regarded as: $$\Delta P_D / \Delta T = \Delta T / R_\theta = \eta \quad (6)$$

If we need to maintain radiator temperature when ambient temperature rises, we must meet: $\delta = \eta$, result in: $KT/(V_2 + V_F T_0) = \Delta T / R_\theta$, namely: $V_2 = I_0 R_1 = V_F T_0 + K R_\theta$

Thus: $$R_1 = (V_F T_0 + K R_\theta) / I_0 \quad (7)$$

In formula (7), V_F, T_0, K, R_θ, I_0 are known as quantity values.

②The calculation of R_2

Assume that: $R_2 = r_1 + r_2$, as is demanded by this patent, the selection of r_1 and r_2 must meet following requirements.

A. The requirement of bleeder

The selection of r_1, r_2 must meet: $V_1 r_1/(r_1+r_2)=I_1 R_3$, which plays the role of protecting temperature and maintaining current constant.

B. The requirement of shunt

As I_0 is constant flow source output, R_2 must be big enough to avoid it impact the precision of shunt of D_1 - R_1 branch, and the shunt of constant flow source should be as small as possible(approximately $0.02I_0$).

③The calculation of R_3

The requirements of resistors of this patent are as follows: dissipation power of R_3 should reach the minimum value, and the detected value V_3 / $I_1 R_3$ must meet the needs of voltage comparator, which includes the capacity of anti-interference and precision requirement, and in general the value ranges from decades to hundreds of million.(confirmed by the value of load current).

④the choice of the temperature sensor D_1

The temperature sensor D of the P-N Junction can be LED diode, same model to the lamps, to ensure consistency of parameters in wide temperature range. When the K value of selected LED diode cannot meet the needs when P_D decreasing. Other normal low power diode(such as 1N4148,etc) whose absolute value of K is larger also is available, but because of the impact of equivalent resistant of P-N Junction, the precision is a bit worse when other model diode in ultra-temperature is selected(T_j above 100 degrees).

The control method

As is shown in figure 1, when ambient temperature rises, V_{FT} decreases because of the negative temperature characteristic of D_1 . However, with the adjustment of R_1, the decreasing rate is limited in $\Delta V_1/\Delta T \approx \delta$. As V_1 is used to control power, we can concluded from formula 1 that the volume of heat dissipation decreases with δ . Meanwhile as temperature rises, the capacity of heat dissipation decreases in the rate of $\Delta P_D/\Delta T = \Delta T/R_\theta = \eta$. On account that the selection condition is $\delta = \eta$, the capacity of heat dissipation of radiator equals to the decreasing of input power. Thus, the temperature of radiator could be balanced in defined limits and improve the reliability of LED lamps working under high temperature, because of the ensurement that $\delta = \eta$ no matter how ambient temperature changes [6].

Examples of application

The implementation of A Power Control Technology Adapting to Temperature Change is shown in figure 2. In that, D_2(1N4148) is junction temperature sensor of P-N Junction that detects ambient temperature. R_9 is gradient adjusting resistor and R_6 is divider resistor. The calculation of these three resistors is shown in chapter Technical solution.

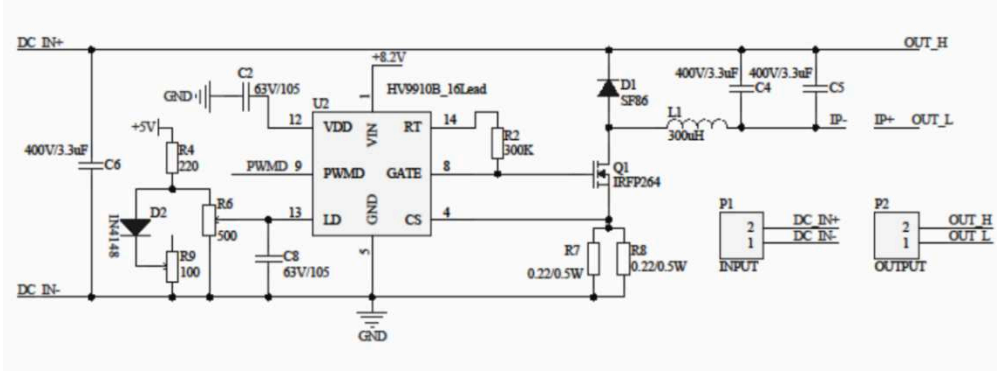

Figure .2. The Power control principle diagram of The adaptive temperature change

In figure 2, the output of Q_1 drive chip is controlled not only by the voltage drop of current-limiting resistor R_6 but also by the output voltage of R_6. In normal temperature, the voltage drop of current-limiting resistor R_7 and R_8 are lower than the output voltage of R_6 at the stage of self-adjustment, so the output power is controlled only by current-limiting resistor. Hence the output power is rated[7]. As soon as temperature rises, the output voltage of R_6 will decrease gradually due to the negative temperature characteristic of P-N Junction. When this voltage decreases to a value lower than the voltage of current limiting resistor R_7 and R_8, the drive chip of Q_1 is transfered to be controlled by self-adaptive temperature. The output power of Q_1 will be lower than the rated value. The more temperature exceeds, the lower voltage of R_6 is, the lower output power is. It makes up the decreasing of the capacity of heat dissipation of power devices caused by temperature deterioration. Since the gradient adjusts regulation resistor R_9, the power devices such as the power Q_1's capacity of heat dissipation still maintain in a safe range, the reliability of power supply working in high temperature condition.

At present, this technology has been applied to the network distributed centralized power supply system, and remarkable results have been achieved.

Conclusion

When LED lamps and lanterns are installed on road, and square where working environment temperature changes greatly, the temperature difference is often more than 80 ℃.Large temperature difference not only buys trouble to the cooling design, also brings troubles for power device selection. Tolerance selection of power devices is too big, which will further increase the cost,

leading to negative promotion of the LED light source. In this paper, the power control technology adapting to temperature changes can be used to compensate the reduction of heat dissipation and ensure the reliability of the power supply in extreme temperature environment. Moreover, the implementation cost is low, and the technology is easy to apply. In addition, due to the reduced power control within the scope of the permit, it will not impact LED light source obviously.

References

[1] Bota S A.Rosales M，Rossollo J L，et a1．Smart temperature sensor for thermal testing of cell-based Its[DB／OL]．http：／／ieeex．plore．ieee．org／Xplore／dynhome．jsp，2005,9,20．

[2] Yang ting, Jing zhanrong.etc. The design of WLED emergency lighting control circuit. Power electronic technology. (1), 13 January 2010

[3] Zhang xun, Jin dongming, Liu litian. The review of Semiconductor temperature sensor research progress.Sensor and micro system，Vol. 25, 3 June 2006

[4] Hou jing, Jing zhanrong.etc. The design of the white LED driver circuit. Power Supply Technologles and Application. Vol. 1 o, 11 November 2007

[5] Gu W．Small signal modeling for current modecontrolled Cuk and SEPI Cconverters[C]． IEEE Applied Power Electronics Conf,APEC 2005,2005,

2(2)：906—910．

[6] Liu fang, Zhang hao. The bifurcation behavior of voltage type SEPIC converter and low frequency oscillation phenomenon analysis. Transactions of China Electrotechnical Society. Vol. 23, 6 June 2008

[7] Yao shuai, Yu guiying. A drive circuit design of the car LED headlamps. China Light & Lighting. 9, 2009

Advanced Materials Research Vols. 986-987 (2014) pp 1328-1331

doi:10.4028/www.scientific.net/AMR.986-987.1328

Magnetic Field Analysis for the Dual-stator Toroidal Motor with Hybrid Excitation

Xin LIU, Ling NIE, Shouyong ZHOU

Tianjin Key Laboratory of Modern Electromechanical Equipment Technology,

Tianjin Polytechnic University, Tianjin, 300387, China

email: liuxin@tjpu.edu.cn

Keywords: Dual-stator; Toroidal Motor; Hybrid Excitation; Magnetic Field

Abstract. A dual-stator toroidal motor with hybrid excitation was proposed and its structure and operating principal were introduced. The spiral currents of worm armature coils were resolved into two orthogonal components. The FEM analytic models for current components were built. Distributions of static magnetic field were simulated. Air gap flux density curves were obtained. The simulation results justify the rationality of the electromagnetic parameters of the motor. The research results are useful for analyzing electromagnetic characteristics of the motor, and offer meaningful instruction for further research and practical application of the novel motor.

Introduction

Toroidal drive can transmit large torque in a small size and is suitable for fields such as aviation and space flight, etc[1-4]. As more and more electromagnetic and control techniques are utilized in engineering field, the new-type composite motors become advancing edge of electromechanical science. Thus the dual-stator toroidal motor with hybrid excitation has more expansive application prospect. The motor is a new concept spatial motor in which mechanical elements and magnetic ones are integrated[5,6]. It can be substituted for a servo system to simplify the structure of the existing electromechanical systems. Besides the fields that require compactness, the toroidal motor can be used in fields such as robots and aviation, etc, that require accurate control.

The dual-stator toroidal motor with hybrid excitation shown in Fig.1 consists of four basic elements: (1) the central worm inner stator; (2) radially positioned planets; (3) permanent magnetic outer stator; and (4) rotor which forms the output shaft upon which the planets are mounted. In the motor, the inner stator is fixed and armature coils are mounted in helical grooves of its surface. The outer stator has several helical beams made of magnetic steel or permanent magnets. The N and S polar helical permanent magnets are mounted alternately on the outer stator. And the planets have permanent magnetic teeth. In the same manner as the stator, the N and S polar permanent magnets are embedded alternately in a planet. The planets adopt permanent magnetic structure for excitation. The excitation method does not need exciting current, no armature wire with simple structure and high reliability, it can make the motor have smaller size and weight than the electromagnetic method[7,8]. Besides, the toroidal motor with the special rotor structure can realize direct drive that can improve efficiency significantly.

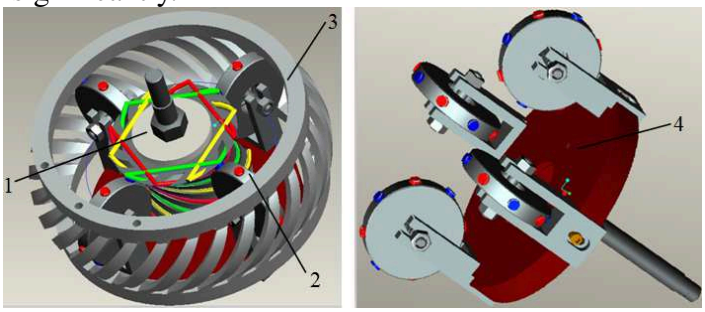

(a) Two stators of the motor (b) the rotor parts

Fig.1. The solid model of the toroidal motor

Operating Principal

Using techniques of motor driven and permanent magnet motor for reference, the authors develop the dual-stator toroidal motor. If a specific relation between planet pitch, number of pole-pairs and helical angle of the worm inner stator and tooth number of the outer stator is realized, N pole of the planets will correspond to S pole of the stators all along. The electromagnetic attractive forces between N and S pole of the different elements are driving forces. When the alternating voltage source is connected to the coils of the worm, a toroidal circular electromagnetic field is formed. It drives the planets to rotate about their own axes. The winding mode of the armature worm is related to planet teeth number. The worm is one excitation stator of the motor. The other outer stator is used to attract magnetic planets along a spiral trajectory as its helical steel beams. So the magnetic forces between the teeth of the planet and stators cause the rotor to rotate about its own axis. Thus, output power with a large torque at low speed is generated.

Toroidal motor can not only convert electrical energy into mechanical energy as general motors, but also can achieve deceleration function with a certain transmission ratio. The toroidal motor includes special mechanical structure and electromagnetic system. The coupled field between stators and rotor of the motor should be investigated further. However, the study for the magnetic field of the toroidal motor is quite difficult because the worm coils have toroidal shape and outer stator has helical beams. In this study, the current among worm coils is resolved into two orthogonal components. Circumferential and toroidal magnetic fields are simulated. The air gap flux density distributions of the motor are analyzed. The results are useful for further characteristic analysis for the new motor.

Electromagnetic Model

The magnetic field of the toroidal motor is an important subject that should be developed. Understanding the field distribution of the new motor is very important for analyzing its electromagnetic characteristics.

A worm in mesh with the planets is shown in Fig.2. The currents of armature coils run in the toroidal direction. For simplifying analysis, the current among some one phase coil can be resolved into two orthogonal components. Fig.2 shows the current and its two components at position in mesh. Let β denote the lead angle of the coil, i is the current intensity at the position for one phase coil, i_1 and i_2 are tangent and axial components of the current i respectively. From Fig.2, it is known

$$\begin{cases} i_1 = i\cos\beta \\ i_2 = i\sin\beta \end{cases} \tag{1}$$

$$\tan\beta = 2p/Z_2\left(a/R - \cos\alpha\right) \tag{2}$$

Where p is the pole pair number of the worm coils, Z_2 is the tooth number of the planet, a is the center distance between the planet and the worm, R is the circle radius of the planet, α is position angle in mesh.

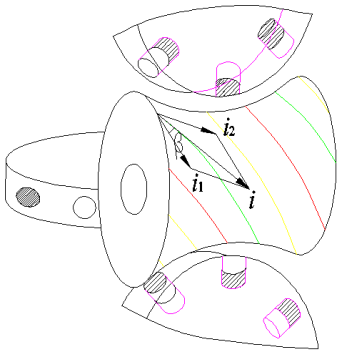

Fig.2. Current components among coil of inner stator

Based on the special structure and excitation mode of the toroidal motor, the FEM models are build by using the professional electromagnet simulation tool developed in a Ansoft environment. Fig.3(a) shows the 1/2 model of toroidal magnetic field caused by current i_1, teeth of outer stator in mesh and one planet. The view is the cross section of the worm and the planet perpendicular to current i_1. In the same manner, the view of Fig.3(b) is the cross section of the worm perpendicular to its axis through the position in mesh. It shows the model of circumferential magnetic field caused by current i_2, outer stator and all planets mounted.

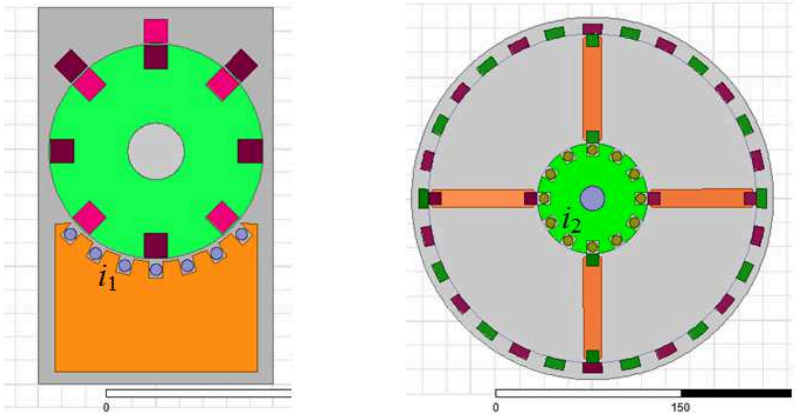

(a) (b)

Fig.3. Analytic model of current components

The distribution of material properties for different part of the model is required. For the dual-stator toroidal motor, the winding material is set to Copper, DW540-50 for the worm inner stator, the permanent-magnet material is set to NdFe30, Vacuum is the background. The boundary conditions are defined and the excitation sources are loaded.

Simulation Results and Discussion

According to the principle of finite element method, the mesh of the models for toroidal motor can be obtained by adaptive subdivision. Among the subdivisions, the part of air gap has the densest ones. Static magnetic field denotes the working state at a certain time point. The parameters of magnetic field for the motor can be obtained to prove the correction of magnetic circuit design from the static field. Setting proper excitation parameters for solver provided by simulation software, Fig.4 shows the simulation results of circumferential and toroidal magnetic fields.

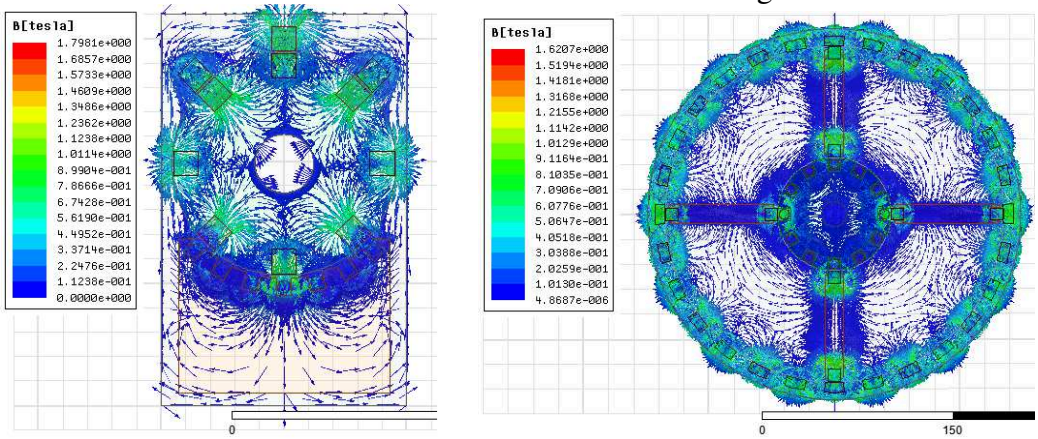

Fig.4. The simulation results

In Fig.4, different colors denote different magnetic density. From the colors distribution, it is known that there is no magnetic over-saturation phenomenon, so the magnetic parameters of the motor are reasonable. Specify a circular path in the motor air gap, the air gap flux density distributions of the specified path are given as shown in Fig.5, which calculated by field calculator of the software.

From the air gap flux density curves in Fig.5, it is known that the flux density is larger at he counterpart of planet teeth and magnetic poles of stators. Left figure shows the air gap flux density about 0.6T caused by current $i_1$along air gap circle, square waves at the outer stator side, distorted waves at the inner stator side caused by armature slot. Among the waves, the distortion is larger at throat position of the worm. Right figure shows the air gap flux density about 0.5T caused by current $i_2$at the outer circle of worm. The electromagnetic mesh between worm inner stator and planets is the main cause for the flux density distribution, and armature slot has also influence on flux density.

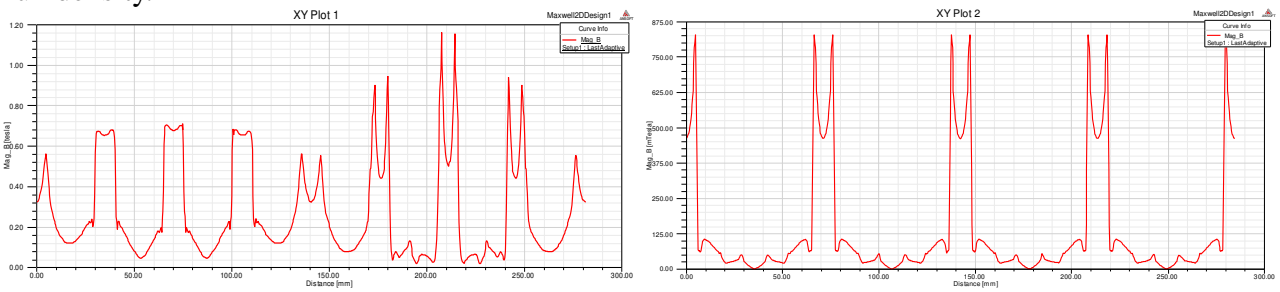

Fig.5. Air gap flux density distribution

Conclusion

Based on the special mechanical structure and excitation mode of the toroidal motor, its operating principal was introduced. The output is realized by magnetic force of planets from toroidal inner stator and outer stator. The currents of armature coils run in the toroidal direction, which was resolved into two orthogonal components. The FEM analytic models of current components were built in a Ansoft environment. Distributions of static magnetic field were simulated without magnetic over-saturation phenomenon. Air gap flux density curves were obtained with slot effect. These results are useful for design and optimum of the new motor.

Acknowledgement

This project is supported by the National Natural Science Foundation of China.(No.51207107).

References

[1] M.R.Kuehnle, H.Peeken, H.Troeder. The Toroidal drive[J]. Mechanical Engineering. 1981,32(2): 32-39.

[2] Kuehnle,M.R. Toroidal transmission and method and apparatus for making and assembling same[P]. United States Patent, 1999, 5863273.

[3] Lizhong Xu, Zhen Huang. Contact Stresses for Toroidal drive[J]. Journal of Mechanical Design. Transactions of the ASME 2003,125(3): 165-168.

[4] Lizhong. Xu, Efficiency for Toroidal drive[C], Proceedings of the 11th World Congress in Mechanism and Machine Science. China: Tianjin, 2004:737-740.

[5] Xin Liu, Lizhong Xu. Mounting and Mesh for Electromechanical Integrated Toroidal Drive[C]. The International Conference on Mechatronic and Embedded Systems and Applications. China: Beijing, 2008:142-146.

[6] Liu Xin, Xu LiZhong. Optimal servo design for the dual-stator toroidal motor[C]. Applied Mechanics and Materials. 2013, 427-429:61-64.

[7] D.M. Tsamakis, M.G. Ioannides. Torque transfer through plastic bonded Nd2Fe14B magnetic gear system[J]. Journal of Alloys and Compounds.1996, 241 (1-2):175-179.

[8] MO Huichen. Parameter Analysis on Permanent-Magnet AC Servomotors[J]. micro machine. 2005, 38(3): 3-6.

Advanced Materials Research Vols. 986-987 (2014) pp 1332-1336

doi:10.4028/www.scientific.net/AMR.986-987.1332

The Constant Voltage Composite Control Method of the SVC with Unbalanced Load Compensation

Yunshan Zhang, Yujie Pei, Jianguo Xu, Yaoding Gu, Jun Dong, Shuhan Wang

Fushun Power Supply Company, Liaoning Electric Power Company Limited, State Grid, Fushun, 113008, China

Rongxin Power Electronic Co.,Ltd, Anshan,114051,China

15842399663@163.com

Keywords: TCR, SVC, DSP, Unbalanced, Load Compensation

Abstract. in practical application of SVC, unbalanced load system exists on many sites, and the voltage at system access point is required to meet the demand of power grid operation. This paper describes a SVC constant voltage control method for an unbalanced load system. the control algorithm controls the voltage at evaluation point to reach the preset range while compensating reactive power of unbalanced load system. the control method could compensate an unbalanced load system into a balanced system, at the same time, the voltage at access point could meet the demand of power grid operation. This control method is particularly applicable to reactive control requirements of steel mills, wind power, solar power grid systems. This algorithm has been applied in Lishizhai 66kV SVC Project in Fushun, inhibits three-phase unbalance of the grid, has achieved good compensation effect.

Introduction

SVC plays many roles in power system, on the system side, SVC could increase steady state transmission capacity, prevent voltage unstability, increase transient stability of the system, enhance system damping, mitigate subsynchronous resonance, improve characteristic of direct current transmission system; on the user side, SVC could increase power factor, suppress voltage fluctuation and flicker, compensate three-phase unbalance[1-3].

For the compensation methods available now, SVC could only compensate load reactive power or system voltage at the access point, could not realize joint control of the reactive power and voltage[4, 5].

Principle of the control algorithm

With load unbalance algorithm, this control method calculates reactive power of the phase loads, compensates reactive power of the corresponding phases via SVC; at the same time, it adopts voltage closed loop algorithm, tracks the voltage at evaluation point in real time, when the value exceeds the present range, it utilizes integral method to increase or reduce the inductance value into the grid gradually, so that the voltage at evaluation point falls to the set range. This control algorithm should acquire the following parameters: voltage at the evaluation point, current and voltage of incoming line on the load side, current and other analog quantities in TCR ring. the control principle is shown in Fig.1.

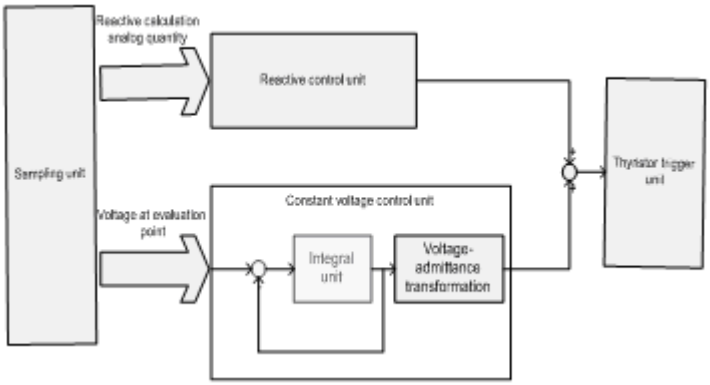

Fig. 1 System Block Diagram

(1) Reactive compensation for unbalanced load

Sampling unit acquires three-phase voltage value at SVC evaluation point, three-phase incoming line current value, and current value in three-phase TCR ring in real time. Then through Fourier transform, values of the real part and imaginary part of the acquired analog quantity are obtained. As shown in the Formula (1).

$$\mathrm{Re}[A(k)]=\sum_{n=0}^{N-1}[a(n)\cos(Qnk)+b(n)\sin(Qnk)] \quad \mathrm{Im}[A(k)]=\sum_{n=0}^{N-1}[b(n)\cos(Qnk)-a(n)\sin(Qnk)] \tag{1}$$

According to the Steinmetz split phase compensation theory, as shown in the Formula (2).

$$\begin{aligned} B_r^{ab} &= \frac{1}{3\sqrt{3}V^2}*\frac{1}{T}\int_T (v_{bc}*i_{a(l)}+v_{ca}*i_{b(l)}-v_{ab}*i_{c(l)})dt \\ B_r^{bc} &= \frac{1}{3\sqrt{3}V^2}*\frac{1}{T}\int_T (v_{ab}*i_{c(l)}+v_{ca}*i_{b(l)}-v_{bc}*i_{a(l)})dt \\ B_r^{ca} &= \frac{1}{3\sqrt{3}V^2}*\frac{1}{T}\int_T (v_{ab}*i_{c(l)}+v_{bc}*i_{a(l)}-v_{ca}*i_{b(l)})dt \end{aligned} \tag{2}$$

Three-phase reactive value on the load side may be calculated. At the same time, TCR trigger angle may be obtain according to the Formula (3).

$$Br=\frac{2\pi-2a+\sin 2a}{\pi wL} \tag{3}$$

By controlling TCR trigger angle, reactive power of unbalanced load may be compensated to the required value. As shown in Fig. 2.

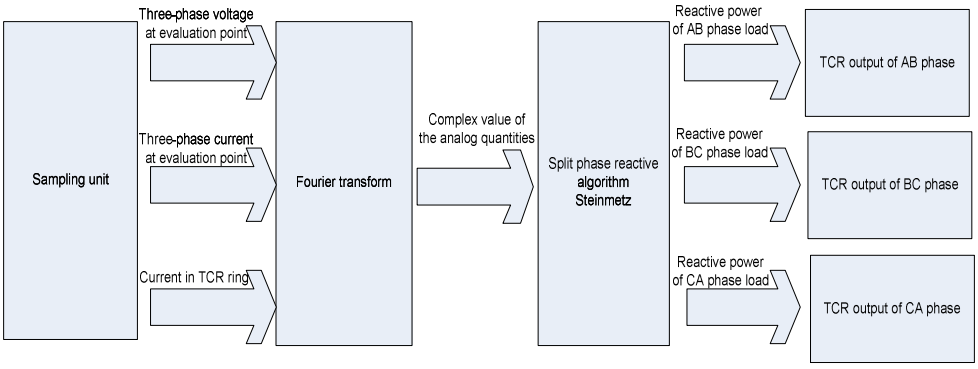

Fig. 2 Schematic Diagram of Reactive Compensation for Unbalanced Load

(2) Stabilized system voltage

Sampling unit acquires three-phase voltage value at SVC evaluation point in real time, gets full wave effective value of three-phase voltage through Fourier transform. Control algorithm adopts integral controller, compares the sampled voltage with the set section voltage.

If voltage exceeds the set upper limit value, TCR output may be increased gradually to superpose the deviation value to the unbalanced reactive output, to pull the voltage back to the set section.

If voltage is lower than the set lower limit value, TCR output may be decreased gradually, this deviation value may be subtracted from the unbalanced reactive output, so voltage at the evaluation point rises. As shown in Fig. 3.

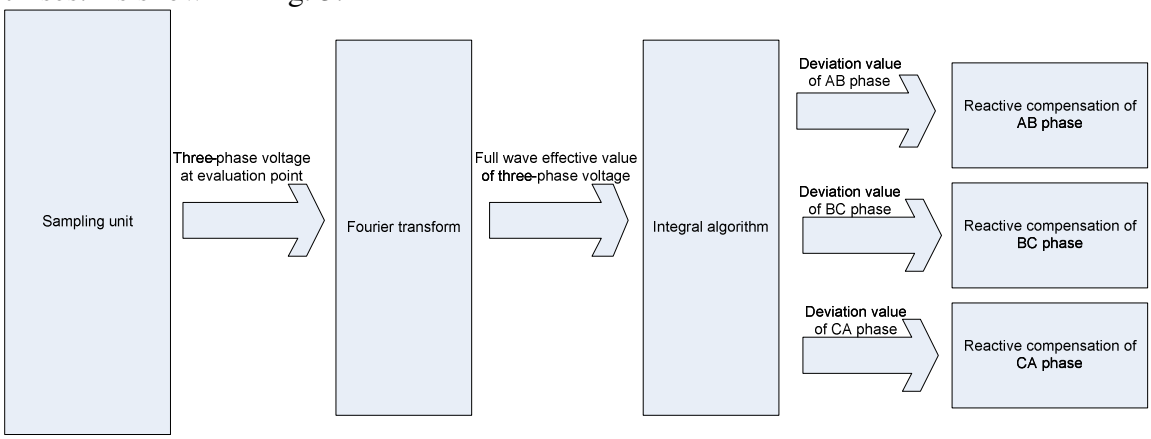

Fig. 3 Schematic Diagram of Stabilized Voltage

(3) Joint control method of reactive power and voltage for unbalanced load

In order to realize joint control of reactive power and voltage, processing result of reactive power and voltage should be combined through certain algorithm. This paper provides a weighted arithmetic method.

Weighted iterative operation is performed for the reactive power calculated according to Steinmetz reactive theory and the reactive deviation generated by voltage closed loop.

$$\begin{aligned} Br^{ab} &= Ks * Br_s^{ab} + \sum_{K=1}^{n} Ku * U^{ab}(k) \\ Br^{bc} &= Ks * Br_s^{bc} + \sum_{K=1}^{n} Ku * U^{bc}(k) \\ Br^{ca} &= Ks * Br_s^{ca} + \sum_{K=1}^{n} Ku * U^{ca}(k) \end{aligned} \tag{4}$$

Where Ks is the weighted value of Steinmetz reactive split phase calculation; Ku is the weighted value of voltage closed loop; Where, $U^x(k)$ is the deviation value obtained from voltage closed loop, given in the following formula:

$$U^x(k) = Kp * \begin{Bmatrix} [e^x(k) - e^x(k-1)] + Ki * e^x(k) \\ + Kd * [e^x(k)] + e^x(k-1) + e^x(k-2) \end{Bmatrix} \tag{5}$$

Where, K_p--- scaling factor of voltage closed loop; K_i is the integral coefficient of voltage closed loop; K_d is the differential coefficient of voltage closed loop.

After weighting, final output admittance value Br per phase is used for thyristor trigger.

Control strategy RTDS simulation

(1) A brief introduction to RTDS

RTDS is a product of computer parallel processing technology and digital simulation technology, a special computer equipment for full digital simulation of electromagnetic transient process of the power system. Its simulation principle and algorithm of electromagnetic transient process are the same as electromagnetic transient program EMTDC, the real time EMTDC. Simulation step size is 50-100μs, frequency response is accurate to 3000Hz. the biggest advantage of RTDS is the connection with actual device controller via I/O structure for mixed analog-digital simulation, if analog amplifier is added, RTDS may be connected with actual electric equipment for relevant studies.

RTDS has all features of digital simulation, for example, high precision, fast response time, convenient parameter modification, simple modeling, simulated accident will not lead to equipment damage. In addition, RTDS also has the following functions:

1) Simulation of large scale power system;
2) HVDC simulation;
3) test of relay protection device;
4) Functions of general AC transient network analyzer (TNA);
5) Expansion of analog simulator;
6) Accident analysis of scientific research and dispatch departments;

With RTDS, real time simulation analysis may be conducted for dynamic characteristic of AC/DC system, DC control protection characteristics, device test, SVC, thyristor controlled series capacitor and other FACTS equipments.

(2) RTDS simulation model building

Build SVC system for impact load in RTDS, SVC has 3 filter branches. TCR runs "Joint control algorithm of reactive power and voltage for unbalanced load". Constant voltage target is bus voltage and reactive power on 400 kV side.

Bus voltage and reactive response of the system should be verified in the test after TCR is put into operation.

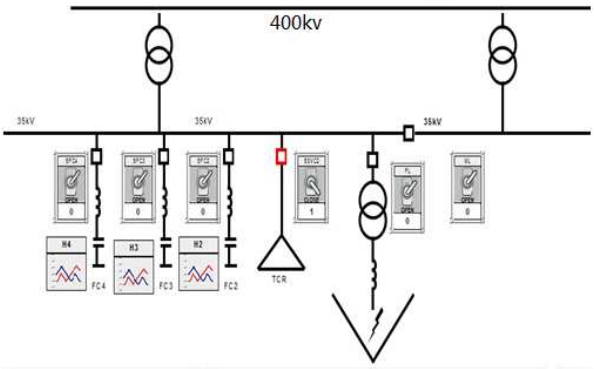

Fig. 4, RTDS Simulation Experiment Model

(3) Conclusion of RTDS simulation

Firstly input a group of fixed filters to verify reactive response of the control strategy. Reactive response of the system is shown in Fig.5.

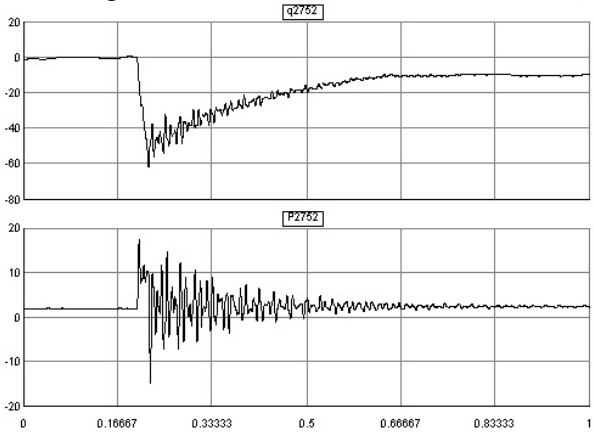

Fig. 5 The Reactive Change Curve after Input of A Group of Filters

Application of the control strategy in 66KV SVC Project

Lishizhai 220kV Primary Substation under Fushun Power Supply Company is in a complex supply network, the network contains important petrochemical, smelting loads and civil loads, maximum reactive load of this substation is 100MVar, and maximum reactive shortage is up to 60MVar. the cooperative 66kV SVC project of Fushun Power Supply Company and Rongxin Power Electronic Co., Ltd. The SVC System Wiring Diagram is shown in Fig. 6.

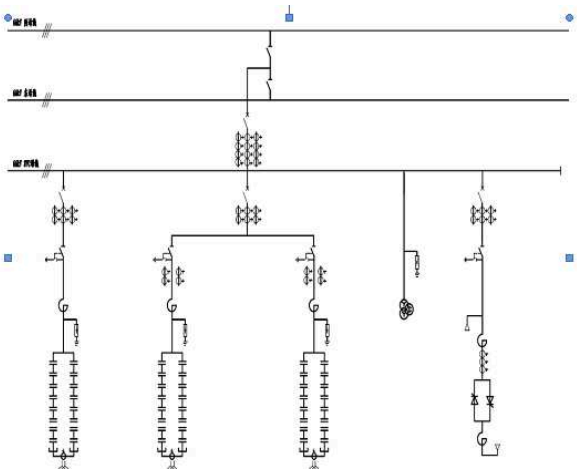

Fig. 6 Fushun Lishizhai SVC System Wiring Diagram

After this project was put into operation, good compensation effect has been achieved using "The constant voltage composite control algorithm of the SVC with unbalanced load compensation", three-phase voltage and reactive power of the phases have been compensated to a balanced state. 66kV bus voltage operation curve of the project is shown in Fig. 7.

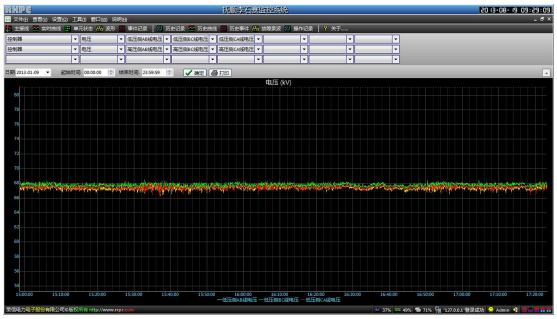

Fig. 7 Fushun Lishizhai 66kV SVC Operation Screenshot

References

[1] Jiang Qirong, Xie Xiaorong, Chen Jianye. Shunt Compensation of Power System -- Structure, Principle, Control and Application [M]. Beijing: China Machine Press, 2004. 8.

[2] Wang Zhaoan, Yang Jun, Liu Jinjun. Harmonic suppression and reactive power compensation [M]. Beijing: China Machine Press, 2004. 2.

[3] Dusan raonic,Ljubisa Stankovic,Dusan petranovic,"Adaptive Control System for Hubrid SVC,"control Applications,1995,proceedings of the 4th IEEE Conference on 28-29 Step .1995 Page(s):378-382.

[4] Bernard Widrow ,Eugene Walach.Translated by Liu Shutang and Han Chongzhao,"Adaptive Inverse Control,"Xi an:Xi an Jiao tong University Press,2000.5

[5] Qu Yong-yin,Zhou Zhen-xiong,"The Adaptive Inverse Control Strategy Research of Servo for Permanent-Magnet Synchronous AC motor,"2008 Chinese Control and Decision Conference, 2-4July2008,Page(s):3152-3155

Advanced Materials Research Vols. 986-987 (2014) pp 1337-1341

doi:10.4028/www.scientific.net/AMR.986-987.1337

The effect of dead zone mode on electric vehicle PWM speed control system

Liang Rong[1], Shanjie Jia[1], Kuihua Wu[1], ChunMei Fu[2], Qingmao Fu[3]

[1]Economic & Technology Research Institute, State Grid Shandong Electric Power Company Shandong Jinan 250021

[2]State Grid Jinan Power Supply Company,Shandong Jinan 250000

[3]State Grid Weifang Hanting Power Supply Company,Shandong Weifang Hanting 261100

Keyword: Dead zone mode; Bipolar PWM modulation; Voltage jump; Electric vehicle speed control

A**bstract.** To realize the electric vehicle braking energy recycling and driving smooth, bipolar PWM modulation mode is often adopted. To avoid the bridge arm shoot-through, a dead zone needs to be set in the complementary upper and lower bridge arm driving signal. Using hardware circuit dead zone setting has the advantages of simple setting and high reliability, is often used in the integrated driving module, however different dead zone mode has different influence on the inverter output voltage. This paper carried analysis on motor speed nonlinear problems caused by output voltage jump around a specific duty ratio in hardware dead zone setting mode, and gives the improvement of hardware circuit. Simulation and experimental results indicate that the method can well solve the output voltage jump in the vicinity of a specific duty ratio problem.

Introduction

In pulse width modulation (PWM) mode, the bipolar PWM can smoothly realize four quadrant operation of the motor, often used in electric vehicle driving system that can operate in four quadrant. In bipolar PWM mode, the driving signal of upper and lower bridge arm are complementary, to avoid the bridge arm shoot-through while the switch tube on and the shut off time difference, a dead zone must be added between the two driving signal. Using hardware circuit way of dead area setting can real-time detect the state of the PWM signal, in both normal and the PWM signal interfered situations caused misoperation can avoid switch tube on and shut off process of overlap, so it has higher reliability. At present, most of the integrated driving module itself is integrated with dead zone setting function, which not only simplified the design of the system, but also to improve the reliability of the system, but the different ways of dead zone setting produce different effect on the inverter output voltage.

About dead zone, in the study of literature at home and abroad are mainly concentrated in the research of dead zone effect and dead zone compensation, No specific way of dead zone setting caused problems are analyzed. A kind of commonly used hardware Settings Dead zone are analyzed in this paper, and analyzed the speed nonlinear problems caused by output voltage jump in the vicinity of a specific duty ratio in view of the bipolar PWM modulation mode and put forward solving measures.

1 dead zone setting circuit

Fig.1 shows a dead zone setting circuit that commonly used in integrated driving module. This way of dead zone setting is on the same bridge arm a switch tube shut off signal occurs, superimpose a fixed time width of invalid drive signal on another switch tube driving signal.

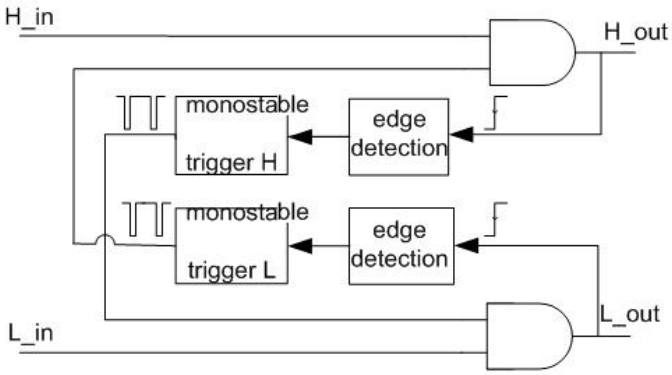

Fig.1 Schematic of dead zone setting circuit

We can see the time of the dead zone is related to the time width of the output low level of monostable trigger from Fig.1. For the time width of the monostable trigger H output low level is T_{d1}, For the time width of the monostable trigger L output low level is T_{d2},usually T_{d1} is a little bit bigger than T_{d2} in the dead zone setting circuit.

2 the effect of dead zone on output voltage

Fig.2 is the structure chart of the three-phase cascaded voltage source inverter-brushless direct current motor load. Taken phase A bridge arm for example, we analyze the effect of the above dead zone setting mode on voltage. We define Current polarity is positive that is into the motor.

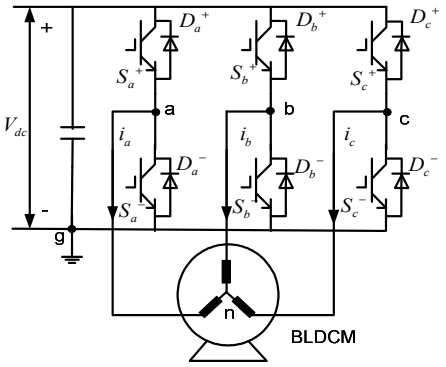

Fig.2 The structure chart of the three-phase cascaded voltage source inverter-brushless direct current motor load

Fig.3 is the waveform figure of phase A bridge arm driving signal and the output voltage, among them (Ⅰ), (Ⅱ) is the ideal switch tube drive signal, (Ⅲ), (Ⅳ) is the actual driving signal after pass the dead zone setting circuit, (Ⅴ) is the ideal output voltage of phase A, (Ⅵ) (Ⅶ) is the actual output voltage in different current polarity. The shaded part is the time of dead zone of the two switch tube of phase A bridge arm both shut off, During this time the output voltage depends on the direction of the winding current; When the winding current is positive, winding current through the diode D_a^- freewheeling, at this time the voltage of phase A is zero. When the winding current is negative, winding current through the diode D_a^+ freewheeling, at this time the voltage of phase A is V_{dc}.

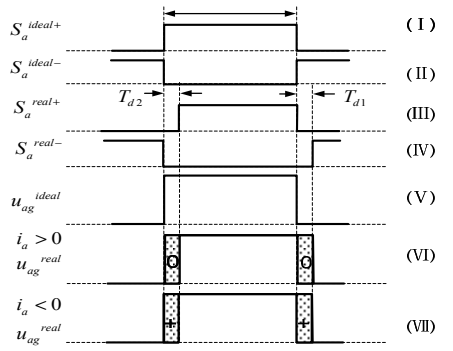

Fig.3 The waveform figure of phase A bridge arm driving signal and the output voltage

We can see from Fig.3: when the phase current is greater than zero, the actual output voltage of bridge arm is equal to the switch tube opening time width of the upper bridge arm; when the current is less than zero, equal to the switch tube cut-off time width of the lower bridge arm. In a PWM cycle, the average voltage error caused by the dead zone is:

$$\Delta u_{ag} = \begin{cases} \frac{T_{d2}}{T_s} V_{dc} & , \quad i_a > 0 \\ -\frac{T_{d1}}{T_s} V_{dc} & , \quad i_a < 0 \end{cases}$$

Where: T_s is the PWM cycle; V_{dc} is the voltage of Dc bus.

Formula (1) analyzed the effect of dead zone setting circuit on the output voltage when the two switch tubes in the same bridge arm are switching. However, as the duty ratio tend to 1, the ideal PWM signal pulse width of lower bridge arm will be more and more narrow , when the pulse width less than the dead zone width pulse loss occurs[8] and constant for the low level.

The pulse will miss and become low level, when pulse width less than dead zone width. The same, the driving signal of upper bridge arm switch tube will miss pulse, when the duty ratio is tend to 0. Fig.4 is the process of pulse missing.

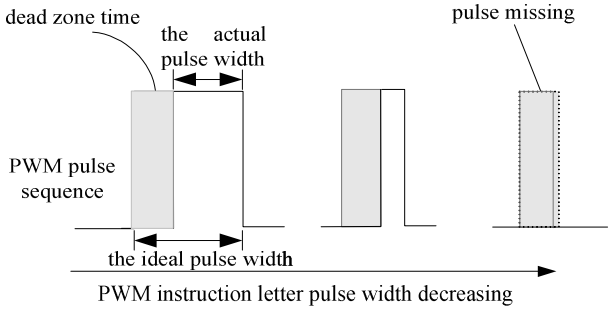

Fig.4 The process of pulse missing

The condition of pulse missing phenomenon occurs:

$$\rho < \rho_{d2} \quad \text{or} \quad \rho > 1 - \rho_{d1}$$

Where: ρ is the duty ratio of ideal driving signal; $\rho_{d1} = T_{d1}/T_s$; $\rho_{d2} = T_{d2}/T_s$.

When the pulse missed, only one of the two switch tubes of the same phase bridge arm is in a state of PWM modulation all the way, the other constant shut off, the system works in single polarity mode. At this time one way's output signal of the dead zone setting is low level all the way, thus making the other way's input signal is not affected by dead zone setting circuit. Voltage error caused by the dead zone is:

When winding current is $i_a > 0$, voltage error is:

$$\Delta u_{ag} = \begin{cases} \rho \cdot V_{dc} , \rho < \rho_{d2} \\ 0 \quad , \rho > 1 - \rho_{d1} \end{cases} \tag{3}$$

When winding current is $i_a < 0$, voltage error is:

$$\Delta u_{ag} = \begin{cases} 0 \quad , \rho < \rho_{d2} \\ (\rho - 1) \cdot V_{dc} , \rho > 1 - \rho_{d1} \end{cases} \tag{4}$$

In a PWM cycle, output voltage of phase A is:

$$u_{ag} = u_{ag}^{ideal} - \Delta u_{ag} \tag{5}$$

When the current is $i_a > 0$, output voltage of phase A is:

$$u_{ag}^{+} = \begin{cases} 0 \quad , \quad \rho < \rho_{d2} \\ (\rho - \rho_{d2}) \cdot V_{dc} , \rho_{d2} < \rho < 1 - \rho_{d1} \\ \rho \cdot V_{dc} \quad , \quad \rho > 1 - \rho_{d1} \end{cases} \tag{6}$$

We can see from formula (6) phase voltage jump when the duty ratio is near $1 - \rho_{d1}$. That's because the driving signal pulse width is T_{d2} smaller than the ideal driving signal, when the duty ratio is slightly less than $1 - \rho_{d1}$, and equals to each other, when the duty ratio slightly bigger than

$1-\rho_{d1}$,after the PWM signal pass the dead zone setting circuit. So pulse width of switch tube driving signal jump caused output voltage jump.

When current is $i_a < 0$, the output voltage of phase A is:

$$u_{ag}^{-} = \begin{cases} \rho \cdot V_{dc} & ,\rho < \rho_{d2} \\ (\rho + \rho_{d1}) \cdot V_{dc} & ,\rho_{d2} < \rho < 1-\rho_{d1} \\ V_{dc} & ,\rho > 1-\rho_{d1} \end{cases} \quad (7)$$

Obviously, output voltage jump when the duty ratio is ρ_{d2}.

3 The method of eliminating voltage jump

The dead zone setting circuit shown in Fig.1 is the use of the output signal to trigger the monostable trigger to generate the dead zone. Thus lead to the pulse width of switch tube driving signal jump when the pulse is missing.

The improved dead zone setting circuit shown in the Fig.5 below, adopted the ideal PWM signal to trigger the monostable trigger, so throughout the duty ratio interval monostable trigger H, L will be triggered, eliminated the phenomena that the pulse width switch tube driving signal jump when pulse missing in the original dead zone setting circuit.

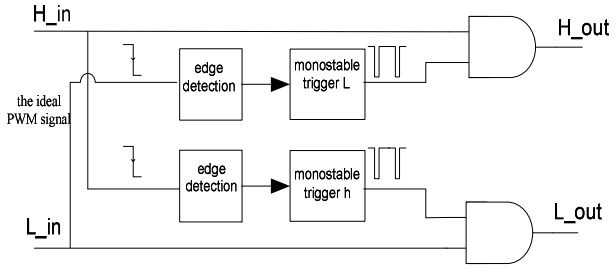

Fig.5 The improved dead zone setting circuit

4 Simulation of the improved dead zone setting circuit

Using matlab software to the dead zone setting circuit of brushless DC motor driving system establish simulation model，compare and analyze the effect of dead zone setting circuit before and after improved on system duty ratio-speed characteristics of the system. The parameters of brushless DC motor are: the resistance of stator phase is $R_s = 0.7\Omega$, the inductance of stator phase is $L = 0.5mH$, the moment of inertia is $J = 0.001kg \cdot m^2$, number of pole-pairs is $P = 2$, the width of monostable trigger H and L output low level is $T_{d1} = 5us$ and $T_{d2} = 4us$. The frequency of PWM is 20KHz.

Fig.6 is the change situation of output pulse width of dead zone setting circuit before and after the improved in the vicinity of duty ratio $\rho = 1-\rho_{d1}$. We can see that the output pulse width of the circuit jump will not occur.

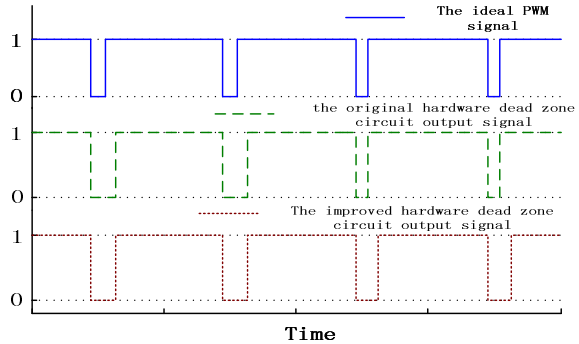

Fig.6 The switch tube PWM signal of upper bridge

Fig.7 is the simulation curve of system speed-duty ratio output characteristic, when the motor in a state of positive electric, the load torque is 0.1Nm and the dead zone setting circuit is different.

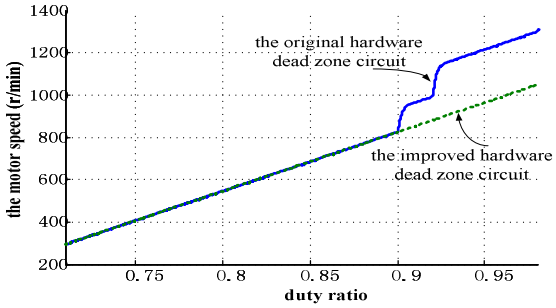

Fig.7 The duty ratio-speed curve of system before and after improved

From the simulation we can see that the original dead zone setting circuit, pulse width of switch tube driving signal will change in the vicinity of a specific duty ratio, thereby causing the jump of the average output voltage, thus affect the output characteristic of the system. And with the improved dead zone setting circuit, pulse width of switch tube driving signal will not jump, eliminated the voltage jump in the vicinity of a specific duty ratio, the motor speed smooth changed with the duty ratio.

5 conclusion

This paper analyzed the output voltage jump problem caused by a hardware dead zone setting mode, obtained the root cause of output voltage jump is the jump output pulse width in dead zone setting circuit when the pulse is missing. In speed control system of electric vehicle motor, the voltage of the motor winding jump in the vicinity of a duty ratio will cause the instability of the system operation, in order to guarantee the controllability of system in full range speed, the output voltage jump must eliminated. The dead zone setting circuit designed in this paper, using the PWM input signal to trigger the monostable trigger instead of the original dead zone using the output signal to trigger the monostable trigger circuit, the jump of the output pulse width in the dead zone setting circuit can eliminated, the problem of the voltage jump was solved.

References

[1] Yuan Qin Bing,XuYongXiang,ZoujiBing.
Electric stationary obstacle-navigation control system research[J].micromachine.2011,44(1).
[2] LI Zi Cheng,Cheng Shan Mei,Cai Kai,Qin Yi. The new PWM way of reducing torque ripples in brushless DC motor[J].Journal of huazhong university of science and technology(natural science edition), 2009, 37(11).
[3] Ben-BrahimL. The analysis and compensation of dead-time effectsin three phase PWM inverters[C]. Proceedingsof the 24th Annual Conference of the IEEE, Aachen, Germany, 1998.
[4]Seong-WhaHong,Hong-JinKim,Kang-YoonLee,JeonginCheon, Dae-HoonHan.A novel dead-time generation method of clock generator for resonant power transfer system[C], SoC Design Conference (ISOCC), Incheon, Korea, 2010.
[5] He Zhengyi, Ji Xuewu.A New Inverter Compensation Strategy Based on Adjusting Dead-Time On-Line[C]. IEEE International Symposium on Industrial Electronics, Cambridge, United Kingdom, 2008
[6] Urasaki N, Senjyu T, Uezato K, Funabashi T, An adaptive dead-time compensation strategy for voltage source inverter fed motor drives [J]. IEEE Transactions on Power Electronics, 2005, 20(5): 1150 - 1160
[7] Leggate D, Kerkman R J. Pulse-based dead-time compensator for PWM voltage inverters. Industrial Electronics[J], IEEE Transactions on, 1997, 44(2): 191 - 197
[8] Zhou B, Lau W H, Chung H. The Analysis of a Novel Dead-Time Generation and Compensation method for 2-level PWM Topology[C]. Power Electronics Specialists Conference, Jeju, Korea, 2006

CHAPTER 6:

Computation Methods and Algorithms for Modeling, Simulation and Optimization

Advanced Materials Research Vols. 986-987 (2014) pp 1345-1349

doi:10.4028/www.scientific.net/AMR.986-987.1345

A Energy Saving Routing Algorithm Based on Shortest Path Tree

Wang Run-liu[a], Yi Yun-hui[b]

School of Mathematics and Computer Science, Jiangxi Science &Technology Normal University

Nanchang, China

[a]78397475@qq.com, [b]sjxywork@163.com

Keywords: Wireless sensor network; Energy saving; Routing

Abstract. The optimal energy saving routing algorithm proposed in this paper is based on the shortest path tree. This algorithm introduces the concept of node classification and builds the weight function based on link energy consumption factor, neighbor node's residual energy factor and type weight and so on. It uses different weight factor according to different types of nodes, and finally generates the shortest path tree, all nodes send data to sink node along the shortest path tree. The simulation results show that the algorithm can prolong the network life time, balance energy consumption of each node, and reduce the average network delay**.**

Introduction

All nodes in wireless sensor network is powered by batteries, nodes have severe energy constraints [1-3]. Battery is hard to be replaced, once the node's energy is depletion, the node will be failure, it would affect the network operation, and even lead to split network and shorten the network lifetime. So every algorithm of wireless sensor network should consider saving energy, and try to prolong the lifetime of the whole network [4-5], so as to save the huge cost of deploying the wireless sensor network again.

There have many methods to prolong the lifetime of network; it must consider reducing and balancing the node's energy consumption. PEDAP_PA and PEDAP algorithm are two routing algorithm based on the minimum weight tree [6]. They defines the weight function based on link energy consumption, and build the minimum weight tree through the prim algorithm, in the end, all nodes send the data to sink node along the minimum weight tree. LET (Least Energy Tree) algorithm is proposed in reference [7], which use Dijkstra algorithm to construct the shortest path tree with minimum energy consumption from each node to the sink node, in the end, all nodes send the data to the sink node along the shortest path tree. LET algorithm is better than PEDAP and PEDAP_PA algorithm, because LET algorithm use Dijkstra algorithm to build the shortest path tree with the root of sink node. But the weight function of LET algorithm has one drawback, which ignores the residual energy of nodes. Some hub nodes are often near the sink node, if it only considers the weight function of link communication energy consumption, it is easy to cause these nodes forward too much data, and are death early for consuming energy. The Ratio_w algorithm (ratio weight routing algorithm) and Sum_w algorithm (sum weight routing algorithm) are proposed on LET algorithm, but these two kinds of algorithm don't consider the residual energy of neighbor node, the network's lifetime is also not optimal. So combining the advantages and disadvantages of above algorithm, we put forward the optimal routing algorithm based on shortest path tree (OLRA), which can prolong the lifetime of network better.

System Energy Consumption Model

In the proposed routing algorithm, it assumes that: (1) the position of all sensor nodes and sink node is fixed or slow changing, they will not affect the position and topology between nodes, and sink node has the entire network's topology information; (2) all sensor nodes have the same properties (such as initial energy, maximum sending power, the node energy consumption parameters, maximum communication radius, etc.); (3) the sending power of all sensor nodes may changes according to the communication distance; (4) each sensor node's energy is limited, but the

energy of sink node is no limited; (5) All sensor nodes in the network need to perceive and send data, so it is responsible for data collection and relay task at the same time, and send the data to the sink node by ways of direct or multiple hops.

Typical wireless sensor node's energy consumption is mainly produced by the wireless data transceiver. The energy consumption ETx of the nodes sending module is composed by the sending electronics' energy consumption and the signal amplifier circuit's electronic energy consumption. The energy consumption ERx of the receiving module only consider the electronic circuit energy consumption of receiving signal.

Among them, the energy consumption of electronic circuit is fixed as gEelec, g is the amount of sending or receiving data, Eelec is circuit electronic energy consumption of transmitting unit bits of data. Signal amplifier's electronic energy consumption is associated with node's sending power. It assumes that the nodes adjust the sending power according to communication distance, so it is related to the communication distance. The specific calculation formula is as follows:

$$E_{Tx}(g,d_{ij})=\begin{cases} gE_{elec}+g\varepsilon_{fs}d_{ij}^2, d_{ij}^2 < d_{\max} \\ 0, d_{ij} \geq d_{\max} \end{cases} \quad (1)$$

$$E_{Rx}(g)=gE_{elec} \quad (2)$$

dij is the sending distance, dmax is the maximum communication distance, εfs is electrical energy consumption which is required for amplify unit bits signal. According to formula (1) and (2), we can know that the energy consumption of transmitting gigabytes data between sensor node i and node j is computed as following formation:

$$C_{ij}(g,d_{ij})=2\times E_{elec}\times g+\varepsilon_{fs}\times g\times d_{ij}^2 \quad (3)$$

The energy consumption of transmitting gigabytes data between sensor node i and sink node is

$$C_{is}(g,d_{is})=E_{elec}\times g+\varepsilon_{fs}\times g\times d_{is}^2 \quad (4).$$

Implementation of Algorithm

In the weight function, the weight factor of different types of node's residual energy is not the same, which is described as follows: (1) standard node: if the node's residual energy value is larger than Ewarning, then it is the standard node. It is prefer to choose these nodes in the network to involve in forwarding data. The link weight value around the standard node ignores the type weight factor. (2) Warning node: if the node's residual energy is less than Ewarning, then the node is warning node. It avoid this type of node when transmit data. Now the link weight value around the warning node must consider the type weight factor, and improve the link weight value.

Assume the initial energy of node is Einital, Einital is set as following:

$$E_{warning}=E_{inital}/\delta f(x) \quad (5)$$

The specific normal number δ is to determine the value of Ewarning, x is the network parameter, f(x) is defined as following:

$$f(x)=\begin{cases} 1, x=1 \\ |(V|\bullet x)/(|V|-x). 2\leq x\leq |V| \end{cases} \quad (6)$$

|V| is the total number of nodes in the network, the initial value of x is 1, its specific calculation method is as follows: statistical the number of node whose residual energy value is lower than current Ewarning value and the proportion Yc of the warning node in the whole network. Set a threshold Ys (0< Ys <1), if Yc >Ys, then x=x+1, update the value of Ewarning. From the formula (6), we can see that f(x) is an increasing function, when x is approaching to |V|, f(x) is infinity.

So we can infer that when x is increased, Ewarning is decreased, and when Ewarning is decreased to a certain value, some warning nodes become back into the standard nodes, and continue to participate in data routing. When x is approaching to |V|, Ewarning is close to zero, the node whose value is below Ewarning is considered as the failure node which is running out of energy. The diminishing rule of Ewarning conforms to the actual situation of the sensor node energy,

in the begin, node's energy is more sufficient, The decreasing speed Ewarning is relatively fast, but when the node's energy is generally low, The decreasing amplitude of Ewarning is slower.

Considering the residual energy of node and its neighbor nodes, it introduces the node classification concept, and establishes new link weight function, OLRA algorithm is proposed. Re(i) is the node's residual energy, Re(j) is the residual energy of node j, wij is the weight value of link(i,j), Cij(g,d) is the energy consumption of transmitting gigabytes data between sensor node i and node j, dij is the distance between node i and node j. In OLRA algorithm,

$$w_{ij} = [C_{ij}(g,d)]^{\alpha}[\frac{1}{\mathrm{Re}(i)}]^{\theta \bullet \eta_j}[\frac{1}{\mathrm{Re})j)}]^{\beta \bullet \eta_i} \quad (7)$$

Among them, α is the factor of energy consumption, θ is the sending node's residual energy factor, β is the receiving node's residual energy factor, ηi is the type weighting factor of node i, and the four factors are positive constant. When α≥1, the value of α is greater, the average energy consumption of nodes is greater, the network lifetime time is smaller. When α<1, the value of α is smaller, the network lifetime is smaller, the average energy consumption of network is greater. When β is small, the weight function 7 less the effect of neighbor node's residual energy, and strengthen the effect of other parameters, so the network lifetime is increased with β.

After completed updating this round of network weights, it uses the typical shortest path tree Dijkstra algorithm to get the shortest path from source node to the destination node, and generate the optimal tree. Node generally choose the path with small energy consumption to send data, so as to avoid warning node became the hub node, and balance the node's energy consumption, prolong the network life time.

OLRA algorithm is a centralized routing algorithm, which is completed mainly on the Sink node, and the concrete implementation steps are as follows:

Step 1: Each node initializes its own information when the network starts.

Step 2: Sink node begin to collect the information. Sink node sent the information query group to all the surrounding neighbor nodes by flooding.

Step 3: After the neighbor node received the query group from the sink node, it sent its residual energy Re(i), the amount of data which is needed to be sent, coordinates information to the sink node. After sink node collected all nodes' information, it starts OLRA algorithm.

Step 4: According to the current network parameter x, it computes f(x) and Ewarning, and determines the number of standard nodes and warning nodes, judge whether the number ratio of warning node is greater than Ys. If it is greater, then x =x+1.

Step 5: It computes the network link's weight, and computes each node's data sent shortest path by Dijkstra algorithm.

Step 6: After the OLRA algorithm is completed, the sink node notify all nodes the current shortest path tree by flooding way. All the nodes find the shortest path to the sink node according to the received shortest path tree, and send data along the path.

Step 7: After the data is sent for a period of time, it jump step 2 again, the Sink node collect each node's information again, update the network link's weight.

Above steps are performed until the sensor nodes are death. The pseudo-code of OLRA algorithm is as following:

```
1   Initializes the related parameters;
2   while (E(i)>0, ∀i ∈ V )
3       Collect the related parameters of all nodes;
4       Compute f(x) and E_warning, determine link's weight;
5    U={s}, R= V-U;
6    for each v∈ V
7        if (v,s)∈ L
8            p(v)=s; Dpath(v)=w_v,s;
9        else
10           p(v)=-1; Dpath(v)=∞;
11       end
```

```
12    end
13    do while L≠Φ
14       find v0∈R, make Dpath(v0) ≡min v∈RDpath(v)} ;
15       U=U∪{v0}, R=R-{v0} ;
16       for each u∈N(v0)
17          if Dpath(v0)+wu,v0＜Dpath(u)
18                Dpath(u) = Dpath(v0) + wu,v0
19                p(u) = v0;
20          end
21         end
22       end
23    Notify each node by flooding way, and wait every node completing data transmission;
24    End
```

OLRA algorithm has three parts, which are determining the standard node and warning node, computing the link weights, and building the shortest path. Part one only need to determine all nodes, the time complexity of determining is O(|V|). Part two is two loop to compute the weight of each link, so the time complexity of computing link weight is O(|V|2). Part three is Dijkstra algorithm, so the time complexity of building shortest path is O(|V|2). OLRA algorithm's time complexity is O(|V|2), which is consistent with Dijkstra algorithm.

Simulation experiment

We choose 500×500m2 network simulation area, and randomly generate a uniform location distribution with 30, 40, 50, 60, 70, 80, 90, 100 nodes (include a sink node and other sensor nodes), the sink node's coordinates is fixed as (250, 250). In order to verify the validity of algorithm, for each wireless sensor network with fixed number of nodes, it randomly generates 10 different node positions (i.e., different network topology). Among them, the network lifetime is defined as the number of data gathering cycle (DGC) completed by sink node from the beginning of network to any one node's energy exhausted. A DGC is the time of sending data to sink node after all nodes get 1000 gigabytes of data.

Node type weighting factor η in weighting function is the around link weight value to distinguish the standard node and warning node. The around link weight of warning nodes is larger, it priority consider selecting standard node when choose path. But the value of η could not be taken too small, or it would make the influence of node's energy in weight function much larger, therefore it define the value of η of standard node is 1, the value of η of warning node is 0.25. Because there are multiple parameters in (7), the exhaustive method is adopted to get the simulation data in the process of choosing parameter. It selects 30, 40, 50, 60, 70, 80, 90, 100 wireless sensor nodes, three parameters select the value in set {0.1, 0.4, 0.7, 1, 3, 5}, all possible simulation data are get in three cycles. Analysis of simulation data shows that when study any parameter in OLRA algorithm, other two parameters can choose any value in {0.1, 0.4, 0.7, 1, 3, 5} to simulate, and the simulation results can show the law of parameter value.

Fig.1 compares the network's lifetime of each algorithm. From the figure, we can know that the network's lifetime of OLRA algorithm (number of DGC) is larger than LET, Ratio_w and Sum_w algorithm, it is optimal. For the algorithm synthetically considers the link's energy consumption, its own energy consumption and neighbor node's energy consumption, and introduces the type weight factor at the same time, avoid the nodes with smaller residual energy to participate in the data routing and death early, so OLRA can prolong the network's lifetime. Fig.2 compares each node's average energy consumption of these algorithms. From the figure, we can know that the node's average energy consumption of OLRA is smaller than that of LET, Sum_w and Ratio_w algorithm. In order to avoid the hub node's energy dead too fast, OLRA algorithm avoid choose the hub nodes on some path selection and choose the path with relative large energy consumption, so OLRA algorithm can maintain energy consumption in a low level.

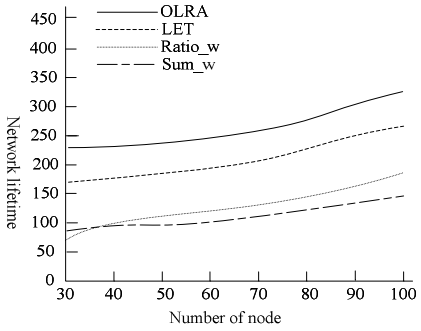

Fig.1 Network lifetime

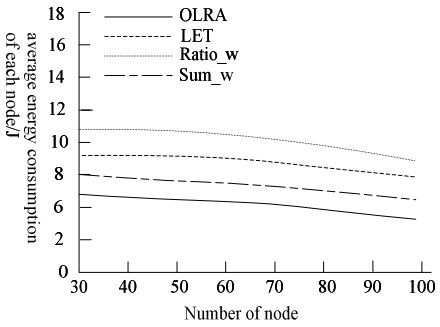

Fig.2 Average energy consumption

Conclusion

OLRA algorithm constructs the weight function based on the energy consumption factor, neighbor node's residual energy factor and type weight factor and so on, which choose different weight factor according to different types of node, and finally generates the shortest path tree by using Dijkstra algorithm. OLRA algorithm is a centralized routing algorithm of wireless sensor network. Nodes need to gather information to the sink node, and the sink node notifies other nodes the network topology after processed. Centralized routing algorithm can be applied in static network, but it is not well adapted to the wireless sensor network with dynamic topology characteristics.

Acknowledgement

In this paper, the research was sponsored by the Education Department of Jiangxi province science and technology project (GJJ14599) .

References

[1] Akyildiz I F, Su W L, Sankarasubramaniam Y, et al. A Survey on Sensor Networks [J]. IEEE Communications Magazine, 2009, 40(10), 112-116.

[2] Yick J，Mukherjee B, Ghosal D. Wireless Sensor Network Survey [J]. Computer Networks, 2010, 52(12), 2292-2330.

[3] Yi S, Heo J, Cho Y. Power-Efficient and Adaptive Clustering Hierarchy Protocol for Wireless Sensor Networks [J]. Computer Communications, 2011, (30), 2842-2852.

[4] Mhatre V, Rosenberg C. Design Guideline for Wireless Sensor Networks: Communication, Clustering and Aggregation [J]. Journal of Ad Hoc Networks, Elsevier Science, 2011, 2(1), 45-63.

[5] Chee-Yee Chong, Srikanta P. Sensor Networks: Evolution, Opportunities, and Challenges [C]. Proc. of the IEEE International Conference on Local computer Network, 2013, 9, 1247-1256.

[6] AnH O, Fahmy S, Korpeoglu I. Power Efficient Data Gathering and Aggregation in Wireless Sensor Networks [C]. SIGMD Record, 2012, 2(4), 66-71.

[7] Stanislava S, Henizelman W B. Cluster Head Election Techniques for Coverage Preservation in Wireless Sensor Networks [J]. Ad Hoc Networks, 2011, 5(7), 955-972.

Advanced Materials Research Vols. 986-987 (2014) pp 1350-1355

doi:10.4028/www.scientific.net/AMR.986-987.1350

A Low Power Way-Predicting D-cache with Partial Tag Comparison Filter

Jinxin DU[1, a], Xiangrong CAO[1, b], Xiaolin ZHANG[1, c]

[1]Department of Electronic and Information Engineering, Beijing University of Aeronautics and Astronautics (BUAA), Beijing, 100191, China

[a]email: hbdujinxin@163.com, [b]email: jackycxr@163.com, [c]email: zxl202@vip.163.com,

Keywords: Low Power D-cache; Way Prediction; Partial Tag Comparison Filter

Abstract. This paper proposes a way-predicting algorithm which is specially equipped with a Partial Tag Comparison Filter (PTCF) to reduce the energy consumption in high associative D-caches. Conventional way-predicting algorithm achieves good performance and energy efficiency on I-cache which usually can guarantee the high prediction accuracy. However, the D-cache usually cannot reach such high prediction accuracy; therefore it suffers unavoidably from severe prediction inaccuracy penalties. The introduced PTCF aims at reducing energy penalties in case of prediction-miss and thus brings improvement in energy efficiency. The experiments show that the new D-cache reduces energy consumption by about 20%~60% without any latency degradation compared to conventional way-predicting D-cache.

Introduction

On-chip cache is much smaller and faster data storage than the main memory, which transparently stores the recently accessed data blocks. Because most of computer programs have the characteristics of temporal locality (i.e. data accessed already could be needed again in the near future) and spatial locality (i.e. other data in the same accessed block may be requested soon), by fetching data in cache first other than accessing directly the main memory, computer systems can achieve high performance and high energy efficiency. Nowadays, on-chip cache has been widely used in most of microprocessors. However, while the capacity of on-chip cache keeps augmenting, energy dissipated by the cache itself increases significantly [1], which become severe restriction for further improvement in system performance. As a result, reducing the energy consumption of the cache will have great impact on the overall performance of computer systems.

In this paper we propose a way-predicting algorithm with partial tag comparison filter, which can further improve the energy efficiency on basis of conventional way-predicting algorithm for high associative D-caches.

Previous research

In traditional set-associative cache all ways are accessed in parallel and thus the cache visit could be completed in only one clock cycle. Nevertheless a lot of resource is needed to take out this process and a huge amount of energy is wasted. For example, for a 4-way set-associative cache, at most one way is potential to be the target but four ways are all visited each cache access. Avoiding the power consumption due to unnecessary accesses by modifying the cache architecture is one of the most popular principles to improve power efficiency, based on which many improved designs have been proposed, some of which are suitable for all cache types and others appropriate for dedicated cache types.

To avoid unwanted data sub-arrays access, Phased cache [2, 3] carries out tag comparisons in the first cycle and visits in the second cycle only the data sub-array with tag match. This method reduces significantly the energy consumption but at the cost of doubling the access time. In a Partial Tag Comparison cache [4], as much less time is needed to fulfill (access time is about 60%-80% of that for full tag comparisons), the partial tag comparison is completed ahead and is used to enable sense amplifiers for only matched data sub-arrays. In this way, a portion of energy consumption due to sense amplifiers can be eliminated and no latency degradation is leaded. However, as the energy

consumed by sense amplifiers is only 30% of the total energy consumed during access to a data sub-array, the amelioration in energy efficiency is limited. K. Inoue proposed the Way-Predicting cache [5] which speculatively selects a way to access in the first cycle. On prediction-hit, the cache accessing finishes in only one cycle and a great deal of energy can be saved as the accessing to all other ways is avoided; otherwise, the rest ways are accessed in parallel during the second cycle, thus both great energy and latency penalties are induced. The efficiency of Way-Predicting cache relays highly on the PHR (Predicting Hit Rate), which indicates the probability that the predicted way is just right the wanted one. There are two means to further improve the performance of Way-Predicting cache, that's to say, increasing the PHR or reducing the prediction-miss penalties. C. Tseng [6] adopted the MPLRU (Modified Pseudo Least Recently Used) replacement algorithm in Way-Predicting cache to augment the PHR and thus save energy consumption. Valid bits [7] are used in way-predicting caches with sub-block replacement policy, to pre-eliminate those hopeless sub-arrays and thus reduce average energy dissipation. M. Calogos [8] proposed a hybrid scheme combining the Way-Predicting algorithm and the Phased cache, with the objective to reduce prediction-miss penalties by switching to the Phased algorithm when the PHR is lower than expected. Other reconfigurable schemes based on prediction mechanism had also been brought up for the same purpose [9].

In this paper a Partial Tag Comparison Filter (PTCF) is introduced into the conventional Way-Predicting algorithm. This new algorithm, named as WP-PTCF (Way-Predicting with Partial Tag Comparison Filter), has proven its efficiency especially for high associative D-caches.

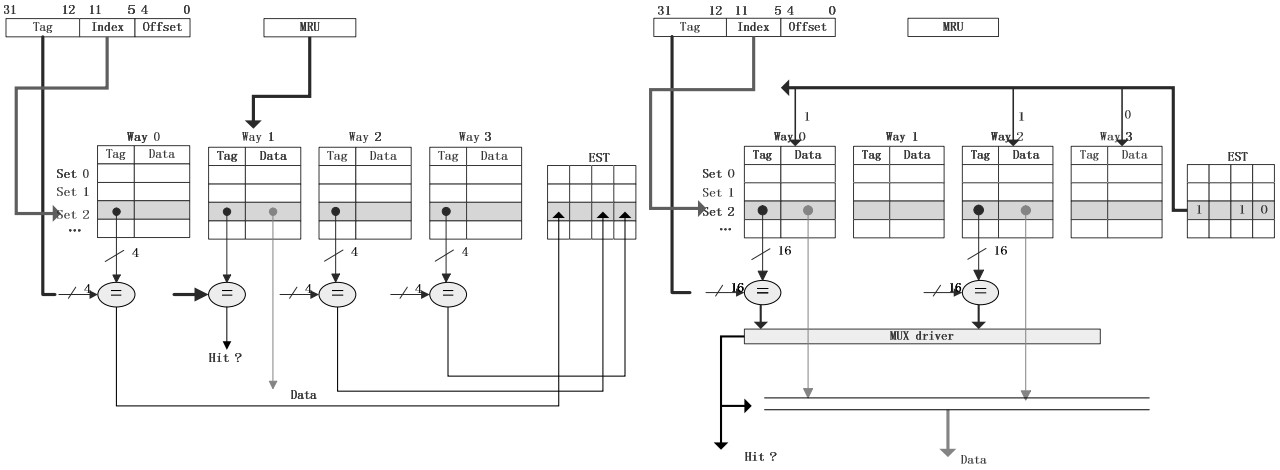

(a) First clock cycle (b) Second clock cycle

Fig.1. Architecture of WP-PTCF cache

Design of the WP-PTCF cache

In a set-associative cache each way consists of a tag sub-array and a data sub-array. While the conventional way-predicting algorithm is applied, the MRU (Most Recently Used) buffer speculatively selects a way to access in the first cycle. If prediction-hit turns out to be true then the cache accessing completes in one only cycle; in case of prediction-miss, the rest ways will be accessed in parallel in the second cycle. According to the Energy & Latency model proposed by K. Inoue [5], per-access energy consumption (E_{cache}) and latency (T_{cache}) in terms of clock cycles for a conventional N-way Way-Predicting (NWP) cache can be expressed as follows:

$$E_{NWPcache} = (E_{Tag} + E_{Data}) + (1 - PHR) * (N - 1) * (E_{Tag} + E_{Data}) \quad (1)$$

$$T_{NWPcache} = 1 + (1 - PHR) * 1 \quad (2)$$

- E_{Tag} , E_{Data} : energy consumed for accessing one tag sub-array, or one data sub-array

Obviously, the performance of a conventional Way-Predicting cache depends on the value of PHR. The higher the PHR is, the more efficient the cache turns out to be. To take two extreme cases for example, the Way-Predicting algorithm will be perfectly ideal when the PHR is approximate to 1, but will be completely awful when the PHR is approximate to 0. In fact, from the point of view of optimizing the EDP (Energy-Delay Product) which is a fundamental criterion for evaluating microprocessors, this conventional way-predicting algorithm performs even worse than a traditional set-associative cache when the PHR is lower than 48%. Generally, most of I-caches could achieve very high PHR (more than 95%), but most of D-caches could not achieve so high PHR but only about 80% in average. Therefore, for D-caches where the Way-Predicting algorithm is applied, reducing prediction-miss penalties will improve effectively the overall energy efficiency.

In this paper, we apply a Partial Tag Comparison Filter (PTCF) to the conventional Way-Predicting cache to reduce prediction-miss penalties. The architecture of a 4-way WP-PTCF cache is shown by Figure 1. In the first cycle (Figure 1(a)), not only the predicted way is accessed, but also partial tag comparisons are carried out for all rest three ways. Results of partial tag comparisons, which are 1-bit Boolean values ("1" and "0" for comparison match and mismatch respectively), will be stored in a buffer named EST (Enable Signal Table). On prediction-hit, cache access completes in the first cycle and the PTCF accounts surely for an amount of energy wasted. On prediction-miss, in the second cycle (Figure 1(b)), the EST ensures to filter out all ways with partial tag comparison mismatch and to active only the ways potential to yield a hit. By this means, a great amount of energy will be saved because the number of ways to access is largely reduced. Additionally, the tag length for comparison is shorter than original thus less energy will be needed for a tag sub-array access. In a word, at the expense of driving the PTCF, energy penalties will be largely reduced in case of prediction-miss. Just like the case in a Partial Tag Comparison cache, the PTCF is fast enough and won't cause any extra latency penalty compared to the conventional Way-Predicting cache. Generally, total energy consumption and total accessing time for an N-way WP-PTCF cache could be expressed as follows:

$$E_{NWP-PTCFcache} = (E_{Tag} + E_{Data} + (N-1) * E_{partial-Tag} + E_{EST}) + (1-PHR) * (1-PTCFR) * (N-1) * (E_{rest-Tag} + E_{Data}) \quad (3)$$

$$T_{NWP-PTCFcache} = 1 + (1-PHR) * 1 \quad (4)$$

- $E_{partial-Tag}$, energy consumed for one partial tag comparison
- E_{EST}, energy consumed for accessing the EST
- PTCFR (Partial Tag Comparison Filtered Rate), percentage of ways filtered out by partial tag comparisons in the 1st cycle
- $E_{rest-Tag}$, energy consumed for one tag comparison with reduced length in the 2nd cycle

As the EST values are of Boolean type (1 bit) which are too short in length compared to tag sub-arrays and data sub-arrays (i.e. tag size of 20 bits and data size of 256 bits for a 4-way 16KB cache with block size of 32 Bytes), the E_{EST} can be negligible in our energy model.

The energy efficiency of the WP-PTCF cache depends not only on the PHR but also on the PTCFR and the associativity (N). R. Min [4] had studied the relation between the partial tag comparison performance and the number of bits compared. Results show that using 3 or 4 bits for a partial tag comparison is the most appropriate where the PTCFR could reach more than 70% for I-caches and more than 50% for D-caches.

Power estimation based on energy consumption model

We estimate the performance of the WP-PTCF based on the energy consumption model established in the previous section. A common 4-way set-associative cache is used, of which the

number of sets is 128 and the block size is 32 Bytes, so the total capacity is 16 KB. In this example, the address size is 32 bits, the offset is of 5 bits ($=\log_2 32$), the index is of 7 bits ($=\log_2 128$), and the tag is of 20 bits (=32-5-7). Finally, the least significant 4 bits are used for partial tag comparison operations. Under the assumption that energy for accessing a tag sub-array or a data sub-array is proportional to the size, we have that:

$$E_{Tag} = \frac{20}{32*8} E_{Data}; \qquad E_{partial-Tag} = \frac{4}{32*8} E_{Data}; \qquad E_{rest-Tag} = \frac{20-4}{32*8} E_{Data} \tag{5}$$

Assuming that PHR was at 80% and the PTCFR was at 55%, the calculation shows that the WP-PTCF cache could save 18.15% energy compared to conventional Way-Predicting cache.

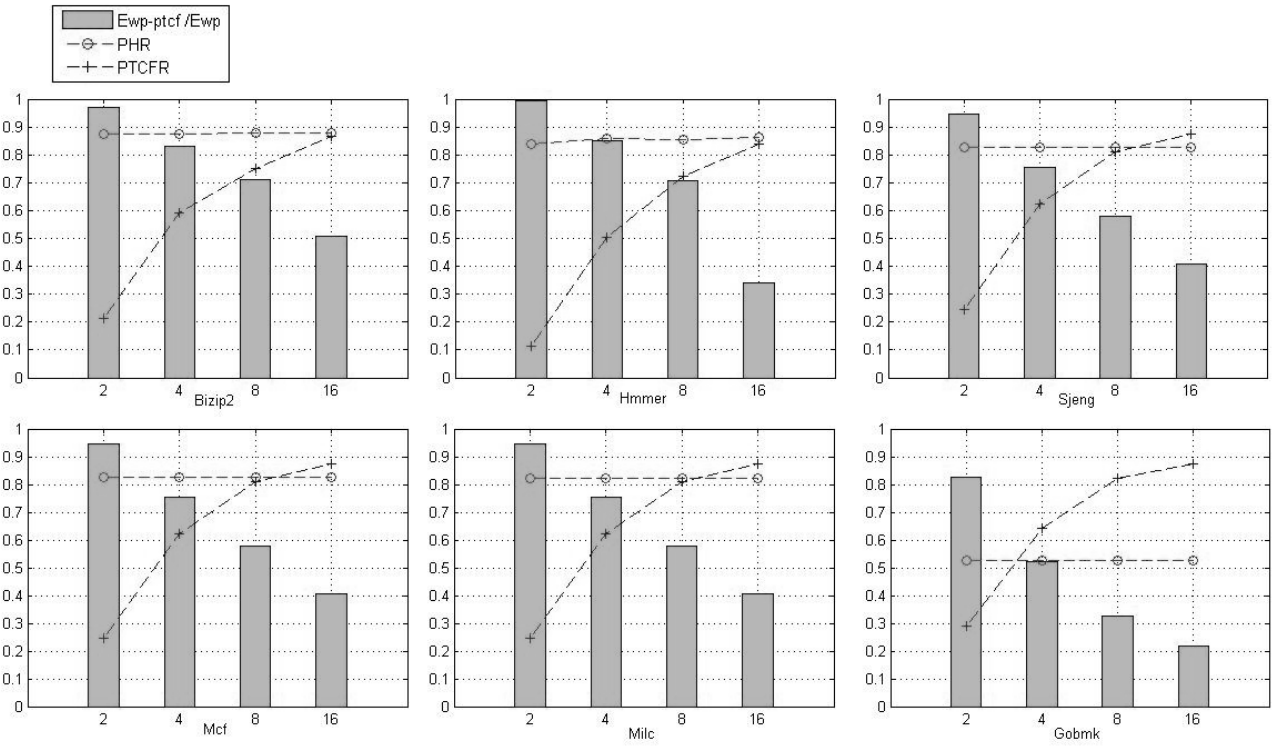

Fig.2. Results of simulations using SPEC2006 benchmarks for L1 D-cache of different associativities

Test results

We made some experiments using the Sim-Wattch simulator with several SPEC2006 benchmark programs. Sim-Wattch [10] is an architecture-level power analysis tool integrated with the Simplescalar simulator. We had modified its cache architecture so that it could simulate as conventional Way-Predicting cache or WP-PTCF cache. While program executing, Sim-Wattch calculates per-access power usage on the basis of the previously proposed power model. Simulations had been performed under four configurations for the L1 D-cache. In all configurations the block size was fixed at 32 Bytes, the number of sets was fixed at 128 and the only difference was their associativity, which was 2, 4, 8, and 16 respectively. The LRU (Least Recently Used) replacement policy was adopted in case of cache miss in all configurations. Figure 2 shows the results under the 0.10um technology.

$E_{wp-ptcf} / E_{wp}$ represents the relative energy consumed by WP-PTCF cache while the energy consumed by Way-Predicting cache is normalized. The *PHR* is calculated as the ratio of *Nb_accesses_ph* (Number of accesses with prediction-hit) divided by *Total_nb_accesses* (Total number of cache accesses). The *PTCFR* is the average way filtered rate by partial tag comparison, which is calculated as the ratio of *Nb_way_filtered* (Number of ways filtered) divided by the associcativity *N*.

Just as explained in previous section that it's meaningless to further ameliorate the Way-Predicting algorithm when the PHR is too low, the benchmark *Gobmk* (*PHR* of which is about 52%, close to the critical value 48%) will be eliminated in our analysis. For all other benchmarks, with the PHR between 80% and 90%, an energy saving of at least 15% had been achieved while the associativity is not less than four. We notice also that for the same program, as the cache set-associativity increases, the PHR maintains and meanwhile the PTCFR increases markedly, which results in significant improvement in power efficiency (i.e. average improvement of about 20%, 37% and 60% for 4-way, 8-way and 16-way respectively). On the other hand, for different programs under the same set-associativity (e.g. 4-way, 8-way, and 16-way) and with similar PTCFR, the new cache performs better where the PHR is lower.

For purpose of comparison, experiments for the L1 I-cache under the same conditions were also carried out. The results are shown by the Table 1. We conclude that our WP-PTCF cache is not suitable for I-caches, as overhead energy consumption was detected for all benchmarks and for all set associativities. The raison is that the PHR was so high (more than 99%) for I-caches that the conventional Way-Predicting algorithm is already perfectly efficient and the WP-PTCF cache could not achieve any improvement but bring unnecessary energy penalties due to the PTCF.

Table 1
Results of simulations using SPEC2006 benchmarks for L1 I-cache of different associativities

Benchmark	2-way			4-way			8-way			16-way		
	PHR	PTCFR	Ewp-ptcf/ Ewp	PHR	PTCFR	Ewp-ptcf/ Ewp	PHR	PTCFR	Ewp-ptcf/ Ewp	PHR	PTCFR	Ewp-ptcf/ Ewp
Bzip2	0.9998	0.0879	1.0233	0.9998	0.4949	1.0645	0.9998	0.7011	1.2053	0.9998	0.8174	1.3071
Hmmer	0.9985	0.0292	1.0229	0.9985	0.4907	1.0607	0.9986	0.7322	1.1933	0.9986	0.8490	1.2833
Sjeng	1.0000	0.1626	1.0233	1.0000	0.5408	1.0648	1.0000	0.7201	1.2064	1.0000	0.8065	1.3099
Mcf	1.0000	0.1921	1.0233	1.0000	0.5593	1.0648	1.0000	0.7616	1.2062	1.0000	0.8670	1.3095
Milc	0.9998	0.1604	1.0233	0.9999	0.5079	1.0646	0.9999	0.7233	1.2057	0.9999	0.8460	1.3081
Gobmk	0.9998	0.1880	1.0233	0.9998	0.5657	1.0644	0.9998	0.7625	1.2051	0.9998	0.8618	1.3066

Conclusion

In this paper a Partial Tag Comparison Filter has been introduced into the conventional Way-Predicting D-cache with the aim of reducing energy penalties in case of prediction-miss during cache access. Comparing to the conventional Way-Predicting D-cache, the new algorithm is more efficient when the PHR is relatively low (but still at a reasonable level for using the way-predicting algorithm, that's to say, between 70%~90%) and the PTCF is as high as possible. The experimental results show that this algorithm is profitable for D-caches (where the PHR is generally low, compared to I-caches) with high set-associativity (where the PTCFR is generally high). For 4-way or higher associative D-caches, an average energy saving of 20%~60% had been achieved without any latency degradation compared to conventional Way-Predicting D-caches.

References

[1] Montanaro, J., Witek, R. T., Anne, K., Black, A. J., Cooper, E. M., Dobberpuhl, D. W., ... & Thierauf, S. C. (1996). A 160-mhz, 32-b, 0.5-w CMOS RISC microprocessor. *Solid-State Circuits, IEEE Journal of*, *31*(11), 1703-1714.

[2] Hasegawa, A., Kawasaki, I., Yamada, K., Yoshioka, S., Kawasaki, S., & Biswas, P. (1995). SH3: High code density, low power. *Micro, IEEE*, *15*(6), 11-19.

[3] Megalingam, R. K., Deepu, K. B., Joseph, I. P., & Vikram, V. (2009, August). Phased set associative cache design for reduced power consumption. In *Computer Science and Information Technology, 2009. ICCSIT 2009. 2nd IEEE International Conference on* (pp. 551-556). IEEE.

[4] Min, R., Xu, Z., Hu, Y., & Jone, W. B. (2004). Partial tag comparison: A new technology for power-efficient set-associative cache designs. In *VLSI Design, 2004. Proceedings. 17th International Conference on* (pp. 183-188). IEEE.

[5] Inoue, K., Ishihara, T., & Murakami, K. (1999, August). Way-predicting set-associative cache for high performance and low energy consumption. In *Proceedings of the 1999 international symposium on Low power electronics and design* (pp. 273-275). ACM.

[6] Tseng, C. Y., & Chen, H. C. (2009, January). The design of way-prediction scheme in set-associative cache for energy efficient embedded system. In *Communications and Mobile Computing, 2009. CMC'09. WRI International Conference on* (Vol. 3, pp. 3-7). IEEE.

[7] Calagos, M., & Chu, Y. (2012). Hybrid scheme for low-power set associative caches. *Electronics letters*, *48*(14), 819-821.

[8] Chen, H. C., & Chiang, J. S. (2005, March). Low-power way-predicting cache using valid-bit pre-decision for parallel architectures. In *Advanced Information Networking and Applications, 2005. AINA 2005. 19th International Conference on* (Vol. 2, pp. 203-206). IEEE.

[9] Park, H., Yoo, S., & Lee, S. (2012). A multistep tag comparison method for a low-power L2 cache. *Computer-Aided Design of Integrated Circuits and Systems, IEEE Transactions on*, *31*(4), 559-572.

[10]Li, S., & Yao, Z. Wattch-alpha: A Power Analysis Simulator for Alpha Architecture.

Advanced Materials Research Vols. 986-987 (2014) pp 1356-1359

doi:10.4028/www.scientific.net/AMR.986-987.1356

A Model Based on BP Neural Network for Audible Noise Prediction

PENG Youxian, TANG Bo, CAO Hongying, CHEN Bin，LI Yu

China Three Gorges University Yichang, China

email:Tangboemail@sina.com, pengyouxian@163.com

Keywords: AC Transmission Lines; Prediction Model; Audible Noise; BP Neural Network; Average Absolute Error

Abstract. Audible noise prediction is a hot research area in power transmission engineering in recent years, especially come down to AC transmission lines. The conventional prediction models at present have got some problems such as big errors. In this paper, a prediction model is established based on BP network, in which the input variables are the four factors in the international common expression of power line audible noise and the noise value is the output. Take multiple measured power lines as an example, a train is made by the BP network and then the prediction model is set up in the hidden layer of the network. Using the trained model, the audible noise values are predicted. The final results show that the average absolute error in absolute terms of the values by the audible noise prediction model based on BP neural network is 1.6414 less than that predicted by the GE formula.

Introduction

The audible noise caused by transmission lines, especially by UHV power lines, has already interfered people's lives. Compared to the environmental noise at the same sound pressure level, it is much more frustrating and unbearable. In the process of designing UHVAC power lines, the influence of the audible noise is more and more significant. Reference [1] and [2] showed that audible noise is one of the main factors affecting the choice of wire structure, the costs and the determination of transmission voltage. Before the power lines design, predicting the value of audible noise is greatly helpful for designers to choosing the right type of wires.

In order to help the designers, many researchers studied out a variety of audible noise prediction models through test sections or corona cages. Reference [3] and [4] introduced these models in detail, such as the model of AEP formula by direct method and the model of GE formula by indirect method, etc. However, due to the constraint of using conditions and prediction problems such as big error, the application of these prediction models in actual line design is limited to a certain degree. Therefore, it has practical application value to carry out researches on audible noise prediction models with a strong versatility and high accuracy.

In this paper, the audible noise value is forecasted by applying the BP neural network which realizes the mathematical fitting of the complex relationship between audible noise value and its influencing factors, so as to solve the problems of the traditional prediction models in engineering applications such as the limitation in application and the low forecasting accuracy.

Determination of Audible Noise Effective Indicators

A. *Audible Noise*

Audible noise of transmission lines refers to the noise which produced when the power lines corona discharge occurs and which people can hear. It is one of the important indicators to measure the quality of transmission line electromagnetic environment.

For AC transmission lines, usually the audible noise on rainy days is 15~20 dB larger than that on sunny days. Therefore, according to international practices, in the process of the design of UHV transmission lines, commonly take L_{50} (50% of the noise value on rainy days) as the limit of audible noise. In other cases, the noise is much smaller [4]. Therefore, in this paper, the value L_{50} is considered to be the characteristic indicator of audible noise.

B. *Determination of Effective Indicators*

The international common expression of noise in prediction models is:

$$SL = f(g, N, d, D) \tag{1}$$

Seen from equation (1), the statistical noise $y = L_{50}$ from transmission lines is a function of the wire parameters $X = (g, N, d, D)$ and thus the audible noise prediction problem can be converted into a problem of finding out an optimal function $f : x \to y$ according to the given measured noise samples. Therefore, in this paper, the line parameters are considered as the audible noise effective indicators. The parameters can be trained by BP neural network and then approach to a implied nonlinear mechanism f, which can make as much accurate predictions for the unknown output noise as possible.

Audible Noise Prediction Model Based on BP Neural Network

A. *Structure of BP Neural Network*

The BP network can learn and store a lot of input and output model mapping relationships, without the description of mathematical equations of which in advance. The learning rule of BP network is to use the steepest descent method. It constantly adjusts the network weights and threshold through back-propagation till the sum of squared errors achieves the minimum. Three-layer BP neural network model topology structure includes the input layer, the hidden layer (hidden layer can be a layer or multilayer) and the output layer. Each neuron is represented by a node. The basic structure of BP network is as shown in Figure 1.

B. *Input and Output Variables in Network*

According to the features of its modeling data, audible noise prediction models can be divided into direct models and indirect models. Direct prediction models are only applicable to lines with specific structure types and specific voltage grades. While in indirect models, it mainly establishes noise prediction model for single-phase power lines.

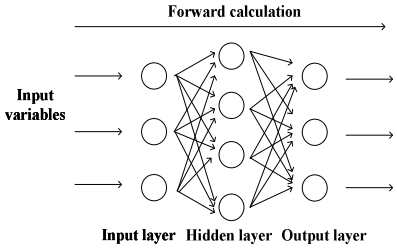

Fig.1. Structure of BP neural network

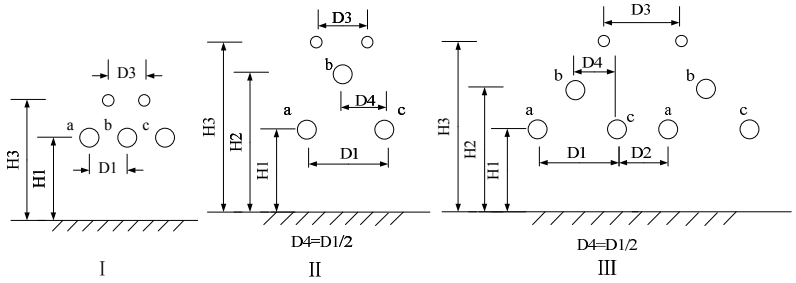

Fig.2. Structure types of transmission lines

The total noise produced by lines should be calculated further by formula (2).

$$SL_{all} = 10\lg \sum_{i=1}^{p} 10^{\frac{L_i}{10}} \tag{2}$$

Where, SL_{all} is the total noise of multiphase power lines, dB; L_i is the noise produced by each phase line(s), dB; p is the number of phases.

The indirect models are suitable for lines with different kinds of structure types and different voltage levels. Therefore, the model in this paper is established according to the theory of indirect method. The input variables in network are referred to $X = (g_{sp}, N, d, D_{sp})$. g_{sp} is the average maximum potential gradient of single-phase bundled conductors; D_{sp} is the radial distance from the single-phase conductor to point at which noise level is to be measured.

In conclusion, the input variables are single-phase line(s) parameters of the transmission lines. And correspondingly, the output variable is the audible noise value of the single-phase line(s).

Example

A. *Data Collection*

Combining the collected measured data of audible noise of multiple transmission lines [3], the audible noise samples available to indirect method are sorted out. There are 57 data samples in total which contains three structure types (as shown in Figure 2). Select 6 samples, which contain the mentioned structure types, as prediction dataset with the remaining 51 samples as training dataset. The data samples are as shown in Table 1 (Since the quantity of the samples is too much, just a small part of which is listed here) and Table 2.

Table 1. Data samples in training set

Line number	Structure Type	N	d(cm)	g(kV/cm)	D(m)	L (Single-phase) [dB(A)]	Line number	Structure Type	N	d(cm)	g(kV/cm)	D(m)	L (Single-phase) [dB(A)]
1a	I	1	6.35	15.8	27.2	56.2	10b	I	4	2.54	24.5	35.4	58.8
1b	I	1	6.35	16.8	35.6	58.1	10c	I	4	2.54	22.3	47.2	52.5
1c	I	1	6.35	15.8	44.8	53.8	11a	I	6	3.15	21.6	23.8	64.0
…	…	…	…	…	…	…	…	…	…	…	…	…	…
9b	I	4	3.52	18.4	32.7	52.1	18b	I	16	3.31	13.3	41.1	48.4
9c	I	4	3.52	17.1	45.3	46.6	18c	I	16	3.31	12.5	58.9	43.4

Table 2. Data samples in prediction set

Line Number	Structure Type	*N*	*d*(cm)	*g*(kV/cm)	*D*(m)	*L* (Single-phase) [dB(A)]
5c1	III	3	3.31	16.4	27.1	42.2
5b2	III	3	3.31	16.6	41.8	40.7
11c	I	8	3.15	18.3	41.4	55.9
12a	I	8	3.31	14.5	22.5	48.0
13b	II	7	4.07	14.6	47.0	48.1
15a	II	8	4.07	14.5	28.6	51.7

B. *Pretreatment of Data*

Since the numerical change of input and output variables is of large differences and also the dimension is different, it cannot be directly used in network training. Therefore, before the training or study, it is important to preprocess the dates. In this paper, the sample dates are normalization processed through the function 'premnmx' and then the training sample dates are totally in the range of [-1, 1].

C. *BP Neural Network Training*

In the training of the neural network, the display frequency interval is set as 50; the maximum cycling times is 100000; the target error is 10^{-4}; the initial learning rate is 0.01. Then the pretreatment dates are input into the network to have the training and after 100000 times, the training is over. The fitting curves and the residual plot are as shown in Figure 3 and Figure 4.

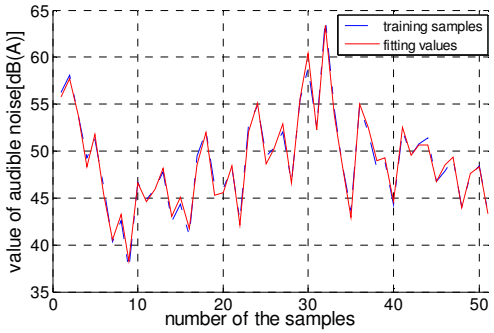

Fig.3. The fitting curves of BP network training

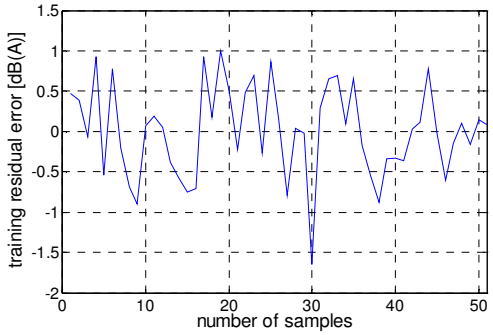

Fig.4. The residual plot of BP network training

According to Figure 3 and Figure 4, it is obviously that the fitting result is nice by applying the BP neural network. The fitting values of the training samples are very close to the actual values. And the residual errors is mostly in the range of [-1, 1], which indicates that the fitting precision of network model is relatively high.

D. *Prediction Results*

After the training, the prediction can be carried through the trained network. The line parameters of prediction samples should first be normalized by the function 'tramnmx'. Thus, the prediction results are normalized. Therefore, the results should be anti-normalized by function 'postmnmx'. The final results and errors are as shown in Table 3.

As shown in Table 3, the relative errors of the prediction model are mostly less than 2%.

Table 3. Audible noise prediction results

Line Number	Structure Type	L (Single-phase) [dB(A)]	Predictive value	Absolute Error	Relative Error (%)
5c1	Ⅲ	42.2	42.7573	-0.5283	1.1191
5b2	Ⅲ	40.7	40.9723	-0.2538	1.7407
11c	Ⅰ	55.9	57.0486	-1.1357	1.1578
12a	Ⅰ	48.0	48.1789	-0.1989	1.0321
13b	Ⅱ	48.1	47.6865	0.4169	0.9308
15a	Ⅱ	51.7	50.9937	0.7299	0.0393

Table 4. Comparison result

Line Number	Structure Type	BP Predictive value	Actual Value	GE Calculated value	Average Absolute Error	
					BP	GE
5	Ⅲ	52.0615	50.6	52.8015		
13	Ⅱ	56.5562	56.5	58.4107	-0.4147	-2.0561
14	Ⅰ	52.9265	53.2	52.8202		

E. *Comparison with GE Formula*

Select the 14th line (in class Ⅰ), the 13th line (in class Ⅱ) and the 5th line (in class Ⅲ) to carry out the BP neural network prediction. The value of the total noise can be obtained by equation (2). For comparison, calculate the noise value by GE calculation formula. The comparison result is as shown in Table 4.

Seen from the dates in Table 4, the average absolute error of BP neural network prediction model in absolute terms is 1.6414 smaller than that of GE formula.

Conclusion

1) Predicting the noise value by the model based on BP network, the maximum of absolute error in absolute terms is only 1.1357 dB, which satisfies the accuracy requirement of audible noise prediction.

2) Applying the indirect prediction method, the audible noise prediction model based on BP neural network algorithm is established. The relative errors of this prediction model are mostly less than 2%. What's more, this prediction model is applicable to the transmission lines with different kinds of structure types.

3) The audible noise value predicted by the model only refers to single-phase lines. For multiphase lines, the total noise should be calculated further by equation (2). The average absolute error of BP network prediction model in absolute terms is 1.6414 smaller than that of the GE formula. Obviously, the model based on BP neural network has a higher precision in prediction.

References

[1] Zbigniew Engel, Tadeusz Wszołek. Audible Noise of Transmission Lines Caused By the Corona Effect: Analysis, Modeling, Prediction [J]. Applied Acoustics, 1996, 47(2): 149-163

[2] Li, Q., Shuttle worth, R., Zhang G., etc. Acoustic noise evaluation for overhead line conductors [C]. Electrical Insulation Conference, 2013, pages: 119-123

[3] Yu Jinhui, Yang Yue, He Jian, etc. For AC UHV transmission line near to hear the noise prediction formula evaluation [J]. High voltage technology, 2009(3)：16-21

[4] Comber M G, Carberry R E. A comparison of methods for calculating audible noise of high voltage transmission lines [J]. IEEE Transactions on Power Apparatus and Systems, 1982, 101(10): 4090-4099

[5] Niu Lin. UHV AC transmission line electromagnetic environment parameters prediction research [D]. Shandong university, 2008

[6] Li Jingya, Cao Jie, Jiang mei. The application of BP neural network EHV transmission lines will hear noise prediction [J]. Power grid technology, 2011, 35 (2) : 173-177

Advanced Materials Research Vols. 986-987 (2014) pp 1360-1364

doi:10.4028/www.scientific.net/AMR.986-987.1360

A Review of Regional Reactive Power Optimization Techniques

Wei Wei[1], Lijie Ding[2],Yanjiao Liu[3]

[1]State Grid Electric Power Research Institute, Sichuan Electric Power Company, Chengdu,610000, China

[2]State Grid Electric Power Research Institute, Sichuan Electric Power Company, Chengdu, 610000, China

[3]Control and Computer Engineering School, North China Electric Power University, Beijing,102206,China

email: Liuyanjiao_job@163.com

Keywords: regional power grid; reactive power optimization; planning algorithm; intelligent algorithms

Abstract. With increasingly complex of the power grid structure and increasingly user requirements of power quality, Power grid voltage reactive power optimization is still the difficult points in power system operation control. This paper introduces the general optimization methods of multi-objective reactive power optimization, intelligent algorithm, the development of the hybrid method, and their respective advantages, disadvantages and improvement; It also analyzes and summarizes the simplification of search space for reactive power optimization and the key issues and research development trend of the real-time reactive voltage control system.

Introduction

Reactive power optimization is a basic problem of grid scheduling planning and operation; It has vital significance to ensure the power quality and power grid operation of the economy. Since the application of SCADA system and power grid scheduling, on-line reactive power optimization has become the basic advanced application of dispatching automation system. In power grid operation, the output adjustment of generator, transformer tap gear adjustment and through cutting of capacitor reactive power compensation equipment is the basic means for the control of reactive. Due to large number of these variables, the confounding control mode of continuous and discrete binding, it is a typical NP problem. To solve this problem, various classical methods and intelligent planning algorithm is applied to which different method of characteristics, scope of application and the solving basic conditions each are not identical, it is difficult to briefly comment on the merits.

This article points out the problem of reactive power optimization studies and the direction of their research by analyzing the basic solving principle of the common classical method and the basic solving idea of reactive power optimization problem, comparing the existing problems of different algorithms and their scope in reactive power optimization problem solving; combining Reactive Power Optimization actual needs with EMS systems development.

A review of reactive power optimization algorithm

1. Research Status of classical methods and improvements

Classic method basic principle of reactive power optimization is first determining an initial point, and then, constantly amending current solution according to the specified trajectory optimization until the satisfactory results are obtained, the calculation ends The main algorithms is planning algorithms, the algorithms use the objective function and constraint conditions of first or second order derivative as the main information of finding the optimal solution.

1.1 The classification of classical algorithm

(1) Nonlinear programming classes

Gradient method is used earlier for solving optimal power flow and voltage and reactive power optimization problem. This method uses control variables as the optimization of the negative gradient direction, Newton's method to calculate the trend to follow changes in the state variables, the penalty function to handler Inequality boundaries. Although there is strict mathematical reasoning, the actual application convergence is slow. We can't even find the optimal solution.It will appear the phenomenon of "sawtooth" near the most advantages. Later second derivative method has developed, such as Newton method and a series of non-linear programming method. Generally, the nonlinear programming method's calculation speed is slow and in a poor coordination between control variables.

(2) Linear programming classes

Usually, the objective function of control variables the partial derivative is used to establish the linear programming model. Advantages: reliable convergence. Difficulties: adjustment of linearization step; How to reduce the error caused by linearization of the model.

Reference [1] proposes a linear programming linear step dynamic adjustment strategy in reactive power optimization problem. The strategy solves the step size selection of linear reactive power optimization to some extent.

(3) Interior point method

The interior point method involves nonlinear programming and linear programming. Difficulties in the point method: there is no general rule to select the initial dual variables and Fix the obstacles parameters which is based on the original dual interior point algorithm; it requires strict control of the intermediate step so that the iteration variable is within the feasible region when Newton iterative solution method is selected; the processing of discrete variable, the processing of inequality constraints and the solution of the higher-order correction equation and so on.

1.2 The key issues of classical algorithm

(1) The processing of inequality constraints

One of the difficulties in reactive power optimization classical algorithm is the processing of inequality constraints. Commonly-used method is to construct a slack variable and a penalty function and so on. Reference [2] choose a collection filter penalty function instead of the traditional approach to process a large number of inequality constraints in the objective function, it effectively avoid the impact of the algorithm convergence and convergence rate caused by the penalty factor. Thus solving the problem of oscillation in an iterative process which led to the convergence of the algorithm is difficult. But it also increases the complexity of the algorithm.

(2) The processing of discrete variable

It often directly cut result for a simple rounding in the optimization of planning algorithms, and may misses the optimal solution. Another method is using a discrete integer branch and bound method to find the optimal solution. However, the computational efficiency is not high, when the variable dimension increases, a significant increasing will occurs in computation time. Later a continuous algorithm is introduced in the heuristic rules or penalty function and complementary constraint method. In summary, although there is strictly theoretical supporting of the algorithm, it is also easy to produce dimension disasters. And the complex real-time control of mathematical model can't meet the requirements.

Intelligent algorithm and its research status

In recent years, intelligent algorithm has been widely used in the global reactive power of regional power grid voltage real-time optimization. They do not need to form a specified optimal trajectory by using mathematical models of all kinds of information. They are applicability, and easy to deal with discrete variables. Evolutionary algorithms such as simulated annealing algorithm, genetic algorithms, particle swarm optimization, differential evolution algorithm; Tabu search algorithm and the combination of these algorithms and so on.

2.1 Evolutionary Algorithms

(1) Genetic Algorithms

The principle of this algorithm is to produce a set of initial solutions under various constraints limited by the objective function into the fitness function to evaluate their quality, eliminate low fitness, have a chance to adapt to its high degree of genetic characteristics to the next generation, retain talented individuals, and appropriate variation.

(2) Particle Swarm Optimization(PSO)

It is a little later for the use of particle swarm optimization to the reactive power optimization. This algorithm is relatively simple, fewer parameters and easier to achieve, but it is easy to fall into local optimum. Dynamic inertia weight that is used by the improved PSO algorithm of reference [3] is based on the particle fitness variance and the current search for the best position change of the particle. Reference [4] provides a parallel adaptive particle swarm optimization algorithm. Firstly, the initial populations are randomly divided into N sub-group and then optimize separately in each subgroup to the proposed method, so that it can enable the parallel computing algorithms.

(3) Evolutionary Algorithms

Differential evolution algorithm is based on the theory of swarm intelligence optimization algorithm. The algorithm produces a swarm intelligence guidance to optimize search by cooperation and competition within groups of individuals. The use of based-on a simple differential mutation and one competitive survival strategies, reduce the complexity of the genetic manipulation. The algorithm is essentially a kind of greedy genetic algorithm based on real number encoding that confirms the optimal thought.

Hybrid algorithm

Researchers have proposed a hybrid optimization algorithm for various algorithms existing problem. A hybrid strategy that is used earlier is an solution that discrete variables and continuous variables use intelligent algorithm and programming algorithm respectively and alternately. Another strategy is to use a wide range of intelligent optimization algorithm, and then use planning algorithm for local optimization.

Reference [5] combine the adaptive immune algorithm and forecast - correction interior point method, use the AIA for a wide range of global optimization to find the best candidate for the advantages, use it as an initial feasible point within the point method, and then search in the neighborhood of certainty initial feasible point through the prediction - correction interior point method for local, to improve the accuracy and speed of understanding.

The difficulty and key problem of reactive power optimization research

1. multi-objective processing method

Reactive power optimization are considering all kinds of operation indicators, such as safety margin index, voltage quality indicators, running economy index, etc. reactive power optimization objective function which is composed of these indicators tend to have different dimensional, and there is no direct analytical relationship between each other, how to balance is very difficult.

(1) the multi-objective model transformation

Multiple objective function translates into a single target by using a model transformation method. the original problem is simplified into single a objective optimization problem.

Reference [6] draws the contour corresponding to the various methods by summarizing the features of all kinds of reactive power optimization of multi-objective model transformation, on the basis of using the target space. From the geometric point of view, it discusses the model transformation method to determine optimal direction, and refers to approximate the pareto optimal solution set, studies the various kinds of model transformation method for the optimum solution of geometric meaning.

(2) Multi-objective evolutionary algorithm

The design of reference [7] contains two stage of multi-objective optimization and auxiliary decision-making method to solve the model. In the optimization stage, this paper proposes an adaptive multi-objective differential evolution algorithm, it chooses the improved not bad not bad in genetic algorithm, and crowded distance sorting; In decision-making stage, the first is to use the fuzzy c-means clustering algorithm for Pareto optimal set, and then evaluate the relative efficiency of decision schemes that is used in every kind of super efficiency data envelopment analysis method t, then help operators to extract the effective compromise solution.

Improve the efficiency of optimization algorithm

2.1 Decomposition coordination calculation

(1) partitioning method

The grid partition is based on the sensitivity, the electric distance. Reference [8] use the partition of power system according to the voltage - reactive sensitivity, makes the regional node voltage reactive power coupling the weakest. First find out the voltage - reactive sensitivity between nodes under the normal operation, search threshold partition algorithm for node partition system, use node splitting method to decompose system into several smaller network.

(2) the equivalent method after the partition

It includes NORTON equivalence, ward equivalent method and the technology of REI equivalence. Reference [9] reduced the REI equivalence partitions of external network, and compared to the centralized optimization method and the reactive power optimization based on Ward equivalent area parallel algorithms.

(3) coordinate calculation after the partition between different districts

To solve the augmented Lagrangian function in inseparable problem in reactive power optimization decomposition-coordination model, reference [10] proposed a near-the-center of all steps decomposition algorithm based on the center adjacent algorithm. The algorithm put forward a kind of applicable to special equality constraint optimization problem, which can realize calculate all the points. Numerical example results show that the proposed algorithm can realize optimizing reactive decomposition coordination calculation, and the computational efficiency is much higher than the decomposition-coordination algorithm based on auxiliary problem principle.

2.2 Simplify the search space

In the large area power grid with many nodes, the reactive power optimization model is complex, with increasing control variables, if considers the entire network of reactive power compensation point and transformer as variables of optimization algorithm, the search space increases rapidly, often cannot finish in limited time to fully search the solution space, which is difficult to meet the requirements of real-time online.

In reference [11], when particle swarm optimization algorithm is used to solve the transient stability of multi-objective optimal power flow, if encountered in the initialization invalid solution, the repeat variation for efficient solution is running until the particles, also to a certain extent, improve the efficiency of algorithm.

Conclusion

This article analyzes the common classic methods, the basic principle of solving its in reactive power optimization problem solving thinking, compares to different algorithms and their application scope in reactive power optimization problem solving problems; Pointed out that the current power grid dispatching operation of reactive power optimization calculation efficiency is not high. Besides, common algorithm search step length and the search direction with the combination of the reactive power optimization is still inadequate, these problems restrict the effect of optimization calculation.

Reactive power optimization problem is a typical NP problem, with the further development of computer hardware and intelligent algorithm, it is based on the distributed computing technology

and intelligent algorithm combined with reactive power optimization problem further, reactive power optimization of online computation efficiency will be further improved.

References

[1] qishan-fufeng-meixian ZongWei Qin Lijun. Power system reactive power optimization in linear programming problem of linear step dynamic adjustment strategy [J]. Power grid technology, 2006, 30 (18) : 40-44.

[2] Yang Shuo Zhou Jing Yang, li qiang, etc. Based on filter collection points in reactive power optimization research [J]. Power system protection and control, 2011, 19.

[3] Badar A Q H, S, B Junghare a. s. Reactive power control using dynamic Particle Swarm Optimization for real power loss minimization [J]. International Journal of Electrical power & Energy Systems, 2012, 41 (1) : 133-136.

[4] Liu Shicheng Zhang Jianhua, Liu Zongqi. Parallel adaptive particle swarm algorithm application in power system reactive power optimization [J]. Power grid technology. 2012, 4 (1) : 108-112.

[5] bypassed his Li Honglu, 8 XinYu. Based on adaptive immune algorithm and forecast - correction interior-point method of reactive power optimization [J]. Journal of tianjin university, 2008, 41 (2) : 168-174.

[6] Li Zhihuan Li Yingong, reactive power optimization of multi-objective model conversion method of contour analysis [J]. Journal of electrotechnics, 2012, 27 (6) : 153-160

[7] Qiu Wei Zhang Jianhua, Liu Nian. Considering environmental factors and voltage stability of multi-objective optimal power flow [J]. Journal of electrotechnics, 2012, 27 (2) : 190-197.

[8] Chen Canxu Liu Mingbo. Reactive power optimization decomposition coordination calculation node partition method [J]. Power system protection and control. 2010 (017) : 1-6.

[9] Liu Zhiwen Liu Mingbo. Reactive power optimization based on REI equivalence region parallel computing [J]. Power grid technology, 2012, 36 (3).

[10] li zhi, Yang Honggeng. One for decomposition coordination all points near the center of reactive power optimization algorithm [J]. Proceedings of the csee, 2013, 33 (001) : 77-83.

[11] Ye Chengjin Huang Minxiang. Considering the transient stability of multi-objective optimal power flow [J]. Proceedings of the csee, 2013, 33 (10) : 137-145..

Advanced Materials Research Vols. 986-987 (2014) pp 1365-1369

doi:10.4028/www.scientific.net/AMR.986-987.1365

Applications of Cloud model migration particle swarm optimization and Gaussian penalty function in Reactive power optimization

Qing Ma[1], Zhijun Long[1], Changhong Deng[1],Miao Li[1], Jiabin You[1] and Yong Xiao[2]

School of Electrical Engineering, Wuhan University, P.R. China

E-mail: 747942466@qq.com

Keywords: cloud model; migration operation; particle swarm optimization; Gaussian penalty function; reactive power optimization

Abstract. In order to cope with the defects of traditional particle swarm optimization (PSO) algorithm, such as its prematurity and deficiency in global optimization, a cloud model migration particle swarm optimization (CMMPSO) algorithm is proposed. Firstly, the X-condition generator based on Cloud model is introduced to adjust the inertia weights of particles; then migration action is implemented to lead the flight of global optimal particle. In allusion to the mixed integer programming problem of reactive power optimization, discrete variables are treated as continuous variables in early iterations, and a discretization operation based on Gaussian penalty function is conducted in later stages. Taking the minimum network loss and minimum voltage offset as objective functions, simulations of IEEE 30-bus system is performed to verify the feasibility and effectiveness of the proposed algorithm.

Introduction

Reactive power optimization is known as a nonlinear mixed-integer programming problem[1]. Methods for solving this problem mainly include two categories: one is mathematical optimization algorithm, but using mathematical methods often encounter some constraints like high-demanding initial value and slow convergence speed. The other is modern artificial intelligent algorithm, such as genetic algorithm, immune algorithm and particle swarm optimization(PSO). Compared with other intelligent algorithms, PSO is easier to implement and faster in convergence. But PSO has some defects, like its prematurity and deficiency in global optimization.

In recent years, a lot of scholars have done much work to improve PSO, common methods of improvement contains many kinds: one is to improve the inertia weight parameters[2]. However, many methods in this kind can't fundamentally solve the problem that particles evolve in a single direction which may not be optimal. Another is random mutation[3], this kind of random operation may cause a lot of waste in calculation, for example, it may lead the particles to fly over the feasible region.

The efficient handling of discrete variables in the OPF has been recognized as a challenging problem and has received significant attention. The simplest approach for handling discrete variables is based on the round-off strategy[4]. However, the round-off approach acts with no clear direction since it doesn’t considert the discretization effect on the objective or the constraints. Literature[5] indicates that the sensitivity-based approach combined with the merit function clearly outperforms the other approaches while the process is cumbersome.

In allusion to the above problems, this paper brings the Cloud Theory integrated with randomness and stable tendency and migration operation into PSO. Firstly, the X-condition generator based on Cloud Theory is introduced to adjust the inertia weights of particles; then migration action is implemented to lead the flight of global optimal particle. When handling discrete variables, all variables are first treated as continuous. Then, a discretization operation based on Gaussian penalty function is conducted after finding out the optimal solution.

Multi-objective model of reactive power optimization

According to grid safety and economy, the least network loss and best voltage level are chosen as the objectives of reactive power optimization, the model can be expressed as:

$$\min F = \gamma_1 P_{Loss} + \gamma_2 \Delta V_{ad} + \lambda \Delta V + \lambda \Delta Q \tag{1}$$

where $P_{loss} = \sum_{k=1}^{N_L} G_k(i,j)[U_i^2 + U_j^2 - 2U_i U_j \cos\theta_{ij}]$, $\Delta V_{ad} = \frac{\sum_{i=1}^{N} |V_i - V_i^*|}{N}$.

In Eq.1, the first item to the right of equal sign is system loss index, the second item is voltage level index , the last two parts are penalty functions .

Cloud model migration particle swarm optimization (CMMPSO)

Combination of Cloud model and PSO

X - Condition cloud generator adopted in this paper makes the corresponding membership $u(x)$ on the premise of knowing the three parameters of normal cloud (E_x, E_n, H_e) and the specific x, then generates the cloud-drop $(x, u(x))$ .Combined with PSO, aiming at controlling inertial weight parameter dynamically ,the process of algorithm generating cloud-drop is as follows:

1)Determine the parameters (E_x, E_n, H_e) of normal cloud model in each iteration:

$$E_x = f_g,\ E_n = (f_g - f_w)/K_1,\ E_n = (f_g - f_w)/K_1 \tag{2}$$

In Eq.2, f_g, f_w represent the best and the worst fitness value in the current swarm population respectively, K_1, K_2 are the parameters controlling entropy and excess entropy respectively.

2)Generate the memberships of particles :

$$u(f_i) = \mathrm{e}^{-(f_i - f_g)^2/(2*E_{ni}^{'})} \tag{3}$$

where $E_n^{'} = normrnd(E_n, H_e, 1, 1)$, f_i is the fitness value of the corresponding particle i.

3)Generate the cloud-drop $(f_i, u(f_i))$ of the corresponding particle i, and use the membership $u(f_i)$ to control the inertial parameters of each particle adaptively:

$$w_i = w_{\max} - w_{\min} * u(f_i) \tag{4}$$

Through the inertia weight adjustment strategy, particles with poor fitness can get larger inertia weight and the speed of getting rid of infeasible solution space velocity is accelerated, particles with optimal fitness can obtain the smaller inertia weight which is conducive to find the optimal solution in adjacent field.

Migration operation

In order to cope with the defects of inertia weights adjustment strategy caused by aggregation of particles, this paper puts forward the migration operation based on the introduction of normal cloud model. Its core idea is forcing the current global optimal particle to learn from other particles which are obtained randomly to get better optimization direction. The specific steps are as follows:

1) Get the current location and fitness of each particle.

2) On dimension j ,select t particles which are not global optimal from the particle swarm and migrate the value of dimension j to the global optimal particle respectively.

3) Calculate the new fitness value of the global optimal particle after migration operation and update its position information according to Eq.6:

$$p_g = \begin{cases} p_g', f_g' < f_g \\ p_g, f_g' \geq f_g \end{cases} \tag{5}$$

In Eq.5, f_g, p_g represent the best fitness value and location of global optimal particle in the current swarm population respectively.

Discretization operation based on modified Gaussian penalty function

The mathematical expression of Gaussian penalty function and reactive power optimization objective function after introducing the penalty function are shown as Eq.7 and Eq.8:

$$\varphi(x_n) = \lambda \exp[-\sum_{i=1}^{n} \frac{(x_i - b_i)^2}{c_i}] \tag{6}$$

$$F(x) = f(x) + \varphi(x) \tag{7}$$

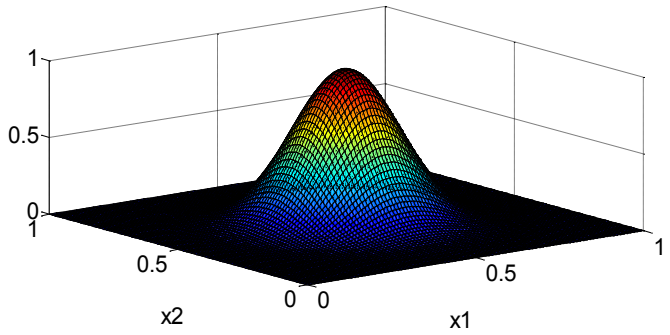

Fig.1 Distribution of Gaussian penalty function

Fig.1 shows Gaussian penalty function distribution with two discrete variables , it can be concluded that the penalty function value will decrease rapidly when the distance between center (0.5,0.5) and the vector of discrete variable increases. Therefore, when the penalty factor λ is chosen properly and the vector of discrete variable is close to the center, the objective function $F(x)$ will be significantly larger than $f(x)$ because of Gaussian penalty function $\varphi(x)$. So it has good effect to apply Gaussian penalty function to the discretization in reactive power optimization.

Based on the strategy of bringing in Gaussian penalty function proposed by literature [6], a further improved strategy aiming at PSO is put forward:

1) At the beginning of iteration, put the discrete variables into continuous variables completely before optimizing.

2) After finding out the global optimal solution, get the different integer ranges $[x_{\min}, x_{\max}]$ in which all the discrete variables lie. Then change the upper limit (lower limit) of the discrete variable i into $x_{\max}$ ($x_{\min}$).

3) Bring Gaussian penalty function into objective function as Eq.8, then start discretization.

Verification of CMMPSO and improved discretization operation

Tests are conducted respectively by standard PSO,MPSO, CAPSO and CMMPSO based on IEEE 30. Fig.2 compares the optimal capability of different methods. Fig.3 shows the nodes' voltage distribution after optimization using different methods. It can be concluded that the global optimization capability of CMMPSO is much better than any other methods. global optimal solution can be gotten with fewer iterations, and the nodes' voltage distribution is more reasonable than others. Statistics of indexes' changes are shown in Table 1. The results also shows that the improvement of energy loss and voltage deviation using CMMPSO is the best.

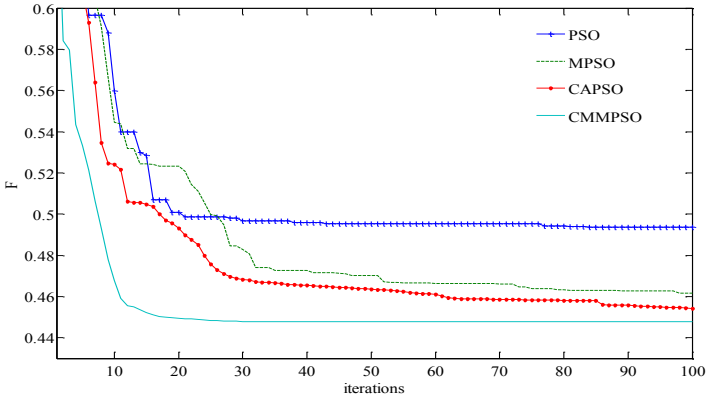

Fig.2 Comparison of different algorithms in optimal performance based on IEEE30

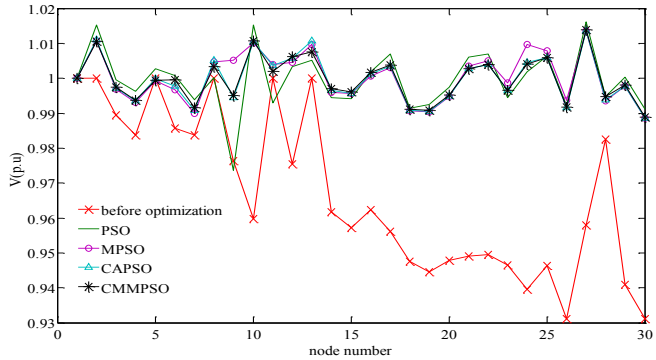

Fig.3 Comparison of different algorithms in node voltage changes

Tab.1 Index statistics of different algorithms

	$\cos\varphi$	P_{loss}	ΔV_{ad}
PSO	0.9880	0.1164	0.0021
MPSO	0.9904	0.1171	0.0013
CAPSO	0.9932	0.1167	0.0013
CMMPSO	0.9955	0.1161	0.0012

Tab.2 Results of different discretization methods

Discrete variables	global optimum	method 1	method 2	method 3	method 4
1	0.88	2	0	1	1
2	2.40	2	5	4	2
3	0.74	1	1	1	1
4	1.54	2	1	1	1
5	0.48	6	1	1	1
6	2.29	2	2	4	2
7	1.17	0	1	2	1
8	0.22	-1	3	2	0
F(x)	0.447	0.494	0.467	0.481	0.451

As is shown in Tab.2, the discretization tests are conducted respectively by Rounding-off method (method 1) , Probability adjustment method based on Heuristic rules(method 2),method of proposed by literature[6](method 3) and the method in this paper(method 4). The last line of Tab.2 shows the objective function values of different methods. The other lines shows discretization results of different discrete variables. It can be seen that both the objective function value and discretization result using method 4 in this paper are closest to global optimum which can be gotten by continuity method.

Conclusions

Integrated with Cloud theory and migration operation, CMMPSO proposed in this paper not only maintains the diversity of the particle swarm but also enhances the learning ability of the particles from the surrounding environment. It solves the problem effectively that PSO easily falls into local optimum while improving the convergence speed and accuracy of the algorithm. According to the simulation result, it is verified that this algorithm can be well applied into reactive power optimization. The system loss is reduced effectively and the system voltage is ensured to be at a good level.

Improved Gaussian penalty function strategy aiming PSO proposed in this paper introduces penalty function after the global optimization of the particle swarm. The strategy guarantees the continuity of optimization and ensures that discretization operation is operated around the global optimization. According to the simulation result, it is verified that this strategy can be well applied into handling discrete variables in reactive power optimization.

Acknowledgements

This work was supported by the National Science-technology Support Plan Projects (2013BAA02B00).

References

[1] Dai Chaohua, Chen Weirong, Zhu Yunfang, et al. Seeker optimization algorithm for optimal reactive power dispatch[J]. IEEE Transactions on Power Systems, 2009, 24(3): 1218-1231.

[2] Mengqi Hu, Teresa Wu, Jeffery D. An adaptive particle swarm optimization with multiple adaptive methods. IEEE Transactions on Evolutionary Computation, 2013, 17(5): 705-720.

[3] T. Niknam, M.R. Narimani, J. Aghaei, R. Azizipanah. Improved particle swarm optimisation for multi-objective optimal power flow considering the cost, loss, emission and voltage stability index. Generation, Transmission & Distribution, IET,.2012, 6(6):515-527.

[4] AlRashidi, M.R, Dalhousie Univ. Halifax, El-Hawary. M.E. Hybrid particle swarm optimization approach for solving the discrete OPF problem considering the valve loading effects. IEEE Transactions on Power System. 2007, 22(4): 2030-2038.

[5] Capitanescu. F, Wehenkel. L. Sensitivity-based approaches for handling discrete variables in optimal power flow computations. IEEE Transactions on Power System. 2010, 25(4):1780-1789.

[6] Li Zhigang, Wu Wenchdan, Zhang Boming, et al. A large-scale reactive power optimization method based on Gaussian penalty function with discrete control variables[J]. Proceedings of the CSEE, 2013, 33(4): 68-74.

Advanced Materials Research Vols. 986-987 (2014) pp 1370-1374

doi:10.4028/www.scientific.net/AMR.986-987.1370

Clustering Algorithm of Wireless Sensor Network Based on Energy Optimized

Yi Yun-hui[a], Wang Run-liu[b]

School of Mathematics and Computer Science,
Jiangxi Science &Technology Normal University Nanchang, China

[a]sjxywork@163.com, [b]78397475@qq.com

Keywords: Clustering; LEACH; Multi-hops; Network lifetime.

Abstract. Clustering algorithm can effectively solve the imbalance of energy consumption of different nodes. Based on the analysis of traditional LEACH protocol, we propose an improved sensor network clustering routing protocol, which reduced the cost of control information in formation process of clusters by adopting a new kind of competition parameters of cluster head, so as to solve the problem of energy heterogeneous of network node. The simulation results show that the protocol can effectively save the energy consumption of the nodes, and prolong the network life time.

Introduction

The wireless sensor network has many similarities with existing wireless self-organizing network, but there also exists big difference [1, 2]. The energy of node in wireless sensor network is provided by the built-in battery, so the lifetime of the whole sensor network is limited by the battery capacity. In order to prolong the lifetime of the whole network and improve the utilization of network, the better way is to find a better algorithm to save the network node's energy consumption. Clustering is an important network layered technology to solve these problems [3].

LEACH protocol is a kind of clustering routing algorithm which is specially used for wireless sensor network [4]. In LEACH algorithm, the nodes are self-organized to form clusters, cluster heads is randomly generated, and this random way can not guarantee the reasonable distribution of cluster head nodes. LEACH-C (LEACH-centralized) and LEACH-F (LEACH-fixed) [5] is centralized generating cluster head algorithm, the base station is responsible for selecting cluster head. LEACH-C selects the cluster head according to global information; each node sends its geographical location and the current energy to the base station. Base station calculates the average energy according to the report of all nodes, the node whose energy is lower than the average energy can't be candidate as cluster heads. LEACH-F also made a few changes based on LEACH. Cluster formation is the same as LEACH-C, at the same time, base station build a cluster head list for each cluster, which indicate the order of cluster node acting as cluster head in turns. But the LEACH-F is not suitable for the real network applications, because it can't dynamic process joining, failure and mobile of node. At the same time, it also increases the signal interference between clusters. PEGASIS (Power-Efficient Gathering in Sensor Information Systems) protocol uses the idea from the clustering algorithm [6]. According to the geographical location of the node, it uses the greedy algorithm to form all nodes as a chain with shortest distance between the adjacent nodes. Each node can send data with the minimum power, and it can randomly select a cluster head and communicate with base station in each round, so as to reduce the amount of data traffic. But PEGASIS algorithm needs to know each node's location, and the time delay of information transmission is large. TEEN (threshold sensitive energy efficient sensor network) protocol is a cluster-based routing protocol [7], it was also developed from LEACH. The implementation mechanism of TEEN is very similar to LEACH, but the former is response type, while the latter belongs to the active sensor network.

This paper analyses the characteristics and insufficiency of existing clustering routing protocol, and proposes an improved energy optimization clustering routing protocol (IEOCP). In addition to use new competition parameter of cluster head, it constructs the multiple hops routing among clusters on the cluster head set at the same time, and reduce the number of cluster head that communicate with base station directly through multiple hops transmission way, so as to reduce the energy cost in advance.

Design Principle of Algorithm

At present, the research of improving LEACH algorithm focuses on two aspects, one is to improve the cluster head selection algorithm; the other is to use multiple hops communication between clusters to transmit data to sink node. According to above design requirements, this paper improves the cluster head selection algorithm and data transmission way of LEACH algorithm respectively, we design a new wireless sensor network routing algorithm based on unequal clustering. Its basic idea is to consider the residual energy of node and its neighbor nodes in the process of cluster head competition, improve the protection of node with low energy; It schedules the active node in the clusters after clustered, and let parts of node enter the sleeping state, so the node's energy is saved and the redundancy of data information is also reduced. The communication between cluster heads and converge point adopts multiple hops routing method.

Network is composed by N sensor nodes which are randomly deployed, and we make following assumptions: (1) Sensor network is high-density static network, the base station is deployed out of the square observation area, sensor nodes and base station are no longer mobile after deployed, and the base station is unique. (2) Node has function of data fusion, each sensor node has a unique identifier (ID); (3) Node can adjust its sending power according to the distance of receiver, so as to save energy consumption; (4) Link is symmetric. If sender's transmission power is known, nodes can calculate the approximate distance to sender according to the strength of received signal. IEOCP algorithm uses the same wireless communication model as LEACH algorithm. Nodes send every bit of data to the position whose distance is d, the energy consumption is composed by the energy consumption of sending circuit and the power amplifier, so we get $E_{Tx}(l,d)$ as following:

$$E_{Tx}(l,d)=\begin{cases} lE_{elec}+l\varepsilon_{fs}d, d<d_0 \\ lE_{elec}+l\varepsilon_{mp}d^4, d\geq d_0 \end{cases} \quad (1)$$

E_{elec} is the energy consumption of emission circuit. If the transmission distance is less than threshold d_0, power amplifier loss uses the free space model; when the transmission distance is greater than or equal to threshold d_0, it uses multipath attenuation model. ε, ε_{mp} are the energy required by power amplifier in these two models respectively. The energy consumption of node receiving 1 bit of data is $E_{Rx}(l)=lE_{elec}$.

Algorithm Implementation

IEOCP algorithm is a distributed competition algorithm, each sensor node participate in the competition, make the distribution of cluster heads more uniform reasonable. In IEOCP algorithm, each node needs to keep a neighbor table, and record neighbor node's related information, which includes node ID, residual energy and distance, etc.

IEOCP uses the ratio of node's residual energy and neighbor node's average residual energy as the important parameter of the cluster head node selection. When the algorithm begin, base station firstly sends radio signal to the entire network by using a given power, node calculates the distance d to the base station according to the received signal, and get its competition radius R_i by the distance, the calculation is as follows:

$$R_i=[c\frac{E_{residual}}{\overline{E}}+(1-c)\bullet\frac{d}{d_{\max}-d_{\min}}]R_c \quad (2)$$

$0 \le c \le 1$, c is to control range of value, which is a constant coefficient. It is used to adjust the size of node's energy and node's distance. In the experiments, we can choose c=0 and c=0.5. Through simulation comparison, we can find the relationship between the number of cluster heads and R_c when c is different. $E_{residual}$ is the residual energy when node runs in the m round, $\overline{E}$ is the average energy of node in the cluster when node runs in the m round. d_{max} and d_{min} are the maximum distance and minimum distance from node to base station. R_c is the maximum competition radius of node.

Each node treats the area within the competition radius area as its competitive area, and treats all other nodes within the competition area as its neighbor nodes. Node firstly broadcast messages with radius R_i, this algorithm makes the size of cluster head coverage area limit in the area with radius R_i, so the nodes within the cluster head node's communication radius R_i can become the members of the cluster class, and has realized the uniform distribution of clustering. It updates the neighbor table according to sending message from neighbor node, it finally get the competition time t_c of cluster head, $t_c = uTE_{residual} / \overline{E}$ (3), u is a random real number that is distributed in [0.9, l], which select the appropriate constant value in the experiment. It is used to adjust the ratio of node's residual energy and the average energy within the cluster node, and control the size of competition time. T is the duration competition time of cluster head, E is the average residual energy of neighbor node, $E_{residual}$ is the residual energy of node.

After the competition of cluster head, if node has multiple neighbor node to become cluster head, then it join the nearest cluster to reduce communication interference, the node that has not joined the cluster sends messages to the neighbor nodes with largest residual energy, and became the multi-hop member of other cluster through the neighbor node. After the network has entered into the stage of stable operation, the member nodes within the cluster continuous to collect monitoring data, and send them the sink node after send to the cluster nodes. After a period of time, the whole network came into next round of working cycle, and select cluster head node again.

The algorithm improves the communication way between cluster head and sink node in advance. The cluster head uses weight to choose the next-hop route. In data transmission phase, it uses multiple hops transmission, and generates a tree which is made by cluster head nodes, the cluster head node is sink. How to choose appropriate next-hop route from neighbor cluster head set is the key to the routing policy between clusters. This paper chooses the free space model of communication, and assumes that link's energy consumption has a linear relation with the distance square d^2.

Assume cluster head i has data required to be transferred, if the relay cluster head j help to transmit data, then the cost of link's energy consumption to sink is $d_{to\sin k}(j)^2$, d_{itoj}^2 , only when $d_{to\sin k}(j)^2 + d_{itoj}^2 < d_{to\sin k}(i)^2$ is meet, the relay transmission can save energy consumption. In order to comprehensively consider the residual energy of nodes and the cost of energy consumption of link is lowest, in the choice of cluster head as the next-hop route, we introduce following definition:

$$W_j = \frac{E(j)}{E\_(r-1)} + \frac{d_{to\sin k}(i)^2}{d_{to\sin k}(j)^2 + d_{itoj}{}^2} \tag{4}$$

$d_{tosink(i)}$, $d_{tosink(j)}$ are the distance which is from cluster head i, j to sink, d_{itoj} is the distance which is from the cluster head i to cluster head j, $E(r\text{-}1)$ is the average energy of previous round, $E(j)$ is the node's residual energy. Cluster head i adds its neighbor cluster heads j to the cluster head set, and calculates the weight W_j of this neighbor cluster head, then chooses the next hop from the neighbor cluster heads whose weight value $W_j > 2$. It chooses the next hop of cluster head and records them into the routing table according to the size order of weight. The cluster head with greater weight is priority selected as the next hop routing, if the weights are equal, it chooses next hop route according to the size of node ID. The next-hop routing table is built after the cluster head of each round is formed. For node's storage capacity is limited, the next-hop routing table has just three route item, which are saved in the routing table respectively according to the size order of weight W. For example, as shown in Fig.1, the routing table of cluster head node 3 in a round is shown as table 2, the cluster head 3 would select cluster head 6 as the relay cluster head of next hop.

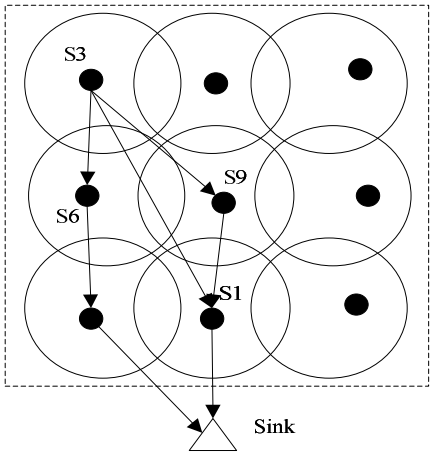

Fig. 1 Routing choosing path

Table I Route table

ID	Cluster head node ID of next hop	Weight *W*
1	6	4.5
2	9	3.6
3	1	3.4

In the practical process, some cluster heads may be as the relay of multiple cluster head, so that the energy consumption of cluster head is larger, and is easy to die quickly. The relay cluster head introduces into a reasonable energy changing threshold ΔE. For each relay node needs to send their own data and is allowed to forward the data of its two neighbor cluster head nodes, so the experiment set ΔE as $\Delta E = 3(l\varepsilon_{fs} d_{ito\sin k}^2)$ .The energy changing threshold ΔE of cluster head nodes is set according to node transmit ability, which is related with the communication energy consumption cost between nodes and sink. When the energy of relay node is larger than ΔE, it broadcast an energy message to neighbor cluster head and notify each neighbor cluster node is no longer as relaying data to forward data. Neighbor cluster heads would delete this routing item from this routing table, and select next routing item from the routing table as the next-hop routing. After the routing is finished, the cluster nodes generate a tree whose root is sink node, data is sent along the direction of sink.

Simulation Experiment

The simulation experiment randomly deployed 100 sensor nodes within 100m×100m rectangular area, Sink node is located at (50,150), the communication distance of all nodes is 20*m*. We assume that the initial energy of node is 2*J*, and generating rate of raw data is 1kb/s. When each node sends or receives data, the energy consumption of sending circuit is E_{elec}= 50*nJ*/bit, the energy consumption of power amplifier is E_{fs}=100*pJ*/bit•d^{-2}, the energy consumption of cluster head's data fusion is E_{df}= 50*pJ*/bit, the magnification times of signal amplification is ε_{mp}=0.0013pJ/bit/m^4, signal transmission distance is d_0=87m, the sampling period is 10s.

Fig.2 compares the network average residual energy of two algorithms. Compared with LEACH algorithm, IEOCP chooses new cluster head competition parameters, and the distribution of cluster head is uniform, the load in the cluster is balanced, so the balance of energy consumption of each node is improved. Fig.3 compares the number of residual nodes of two routing algorithms in each round of cycle. The figure shows that IEOCP algorithm is superiority to reduce the energy consumption. When the first node fails, LEACH algorithm has been running for 76 cycles, and IEOCP algorithm has been running for 132 cycles, the network lifetime of IEOCP algorithm improves 73.6% than that of LEACH algorithm, and from the slope of curve, the load balancing of IEOCP is obviously improved.

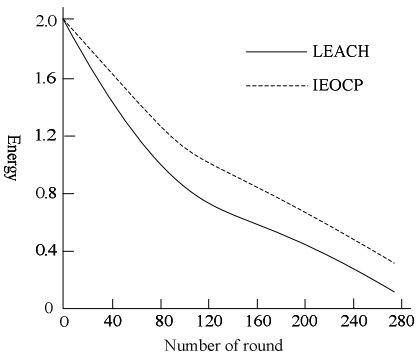

Fig. 2 Comparison of average residual energy

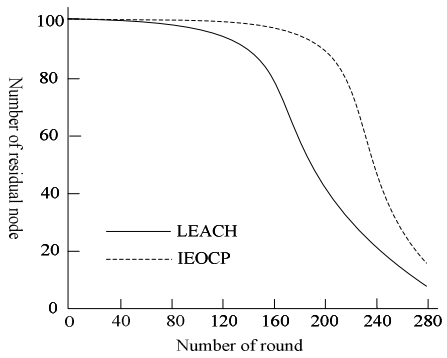

Fig. 3 Comparison of number of live node

Summary

This paper proposes a clustering algorithm based on energy optimization, which comprehensive consider the cluster head election between node and its neighbor nodes, protect nodes with low residual energy and avoid them become as cluster head early and failure, so as to prolong the network lifetime. We also improve the communication between cluster heads and sink, and put forward the dynamic multiple hops routing algorithm between cluster, which uses the weight to choose the next hop routing, and can dynamic refresh the next-hop routing table according to the relay node's residual energy, try to avoid the relay nodes dead early because of too much data forwarding.

Acknowledgements

The Project Supported by Natural Science Foundation of Jiangxi , China (20122BAB201004).

References

[1] Mhatre V, Rosenberg C. Design Guideline for Wireless Sensor Networks: Communication, Clustering and aggregation, Journal of Ad-Hoc Networks Journal, Vol.11, 2010, p.45-63.
[2] Stanislava S, Henizelman W B. Cluster Head Election Techniques for Coverage Preservation in Wireless Sensor Networks, Ad Hoc Networks, Vol.5, 2009, p.955-972.
[3] Shih E, Woo M. Physical Layer Driven Protocol and Algorithm Design for Energy-Efficient Wireless Sensor Networks, Proc. of the Seventh Annual IEEE International Conference on Mobile Computing and Networking, Vol.8(2), 2008, p.272-286.
[4] Hua C, Yum TP. Optical Routing and Data Aggregation for Maximizing Lifetime of Wireless Senor Networks, IEEE Transaction on Networking, Vol.16(4), 2012, p.892-903.
[5] Heinzelman W R, Chandrakasan A, Balakrishnan H. An Application-Specific Protocol Architecture for Wireless Micro-Sensor Networks, IEEE Transaction on Wireless Communications, Vol.1(14), 2013, p.660-670.
[6] Lindsey S, Raghavendra C, Sivalingam K M. Data Gathering Algorithms in Sensor Networks Using Energy Metrics, IEEE Transaction on Parallel and Distributed Systems, Vol.13(9), 2010, p.924-935.

Advanced Materials Research Vols. 986-987 (2014) pp 1375-1378

doi:10.4028/www.scientific.net/AMR.986-987.1375

Parameter Identification of Load Models Using the CQDPSO Algorithm

Zhenshu Wang [1, a], Shaorun Bian [1,b], Dahai Zhang [1,c],
Xiaodi Wang [2, d], Xiaoyu Liu [1, e] and Kai Yu [1,f]

[1]School of Electrical Engineering, Shandong University; Jinan250061, China.

[2]Faculty of Business Administration, The Chinese University of Hong Kong; Shatin, Hong Kong.

[a]zhenshuwang@sdu.edu.cn, [b]708898978@qq.com, [c]dhzhang@sdu.edu.cn,
[d]olivia920@hotmail.com, [e]1027725068@qq.com, [f]768469748@qq.com

Keywords: CQDPSO; PFR; Parameter identification; Load modeling; Power system modeling

Abstract. Load modeling has become a critical problem that is urgent to be solved in power system modeling. In this paper, CQDPSO algorithm, a hybrid optimization algorithm that combines quantum delta-potential-well-based particle swarm optimization (QDPSO) algorithm and chaotic optimization algorithm (COA), is proposed to identify parameters of the selected load model. Numerical results illustrate that the proposed method can improve the accuracy and reduce the computation complexity for load model parameter identifications.

Introduction

The precision of power system digital simulation is closely related to models of generators, transmission networks and loads. Load model is still at a stage of exploration while transmission network model and generator model are quite mature [1, 2]. Therefore, it is of great importance to build an accurate load model. The measurement-based load modeling method includes the following two procedures: selecting a load model structure and then performing parameter estimation using an appropriate identification technique based on field measurements.

The parameter identification methods of load model can be divided into two classes: liner methods and nonlinear methods. The nonlinear methods are mostly based on optimization, that is, to find a group of parameters to minimum the objective function. In [3], a simplified linear BP network is put forward for parameter identification of load models. A hybrid learning algorithm combines genetic algorithm (GA) and the nonlinear Levenberg-Marquardt (L-M) algorithm is proposed in [4] to identify parameters of the aggregate load model. In [5], particle swarm optimization (PSO) algorithm is applied for parameter identification. Though the PSO algorithm is easy and simple, its global search ability is constrained [6]. The QDPSO algorithm can be guaranteed to be global convergence [7] and has been successfully applied in areas such as system identification [8] and multi-objective design optimization [9]. The COA is simple and can search for optima using chaotic variables directly according to its own regularity [10]. In this paper, the CQDPSO algorithm, a hybrid algorithm that takes advantages of the global search ability of the QDPSO algorithm and the local search ability of COA, is used to identify parameters of load models.

CQDPSO Algorithm

Chaotic Optimization Algorithm. The procedures of COA based on Logistic chaotic sequence are as below.

1) Set $k = 0$, the chaotic variable s_j^k can be constructed using the optimum variable x_j^k, $j = 1, 2 \cdots, n$;

$$s_j^k = \frac{x_j^k - x_{\min, j}}{x_{\max, j} - x_{\min, j}}, \quad j = 1, 2 \cdots n . \tag{1}$$

where $x_{\max,j}$, $x_{\min,j}$ denotes the maximum and minimum values of the *j*-th dimension.

2) Calculate the next iteration of chaotic variable s_j^{k+1} ;

$$s_j^{k+1} = 4s_j^k(1-s_j^k), j = 1,2,\cdots,n. \tag{2}$$

3) Transfer the chaotic variable s_j^{k+1} to optimum variable x_j^{k+1} ;

$$x_j^{k+1} = x_{\min,j} + s_j^{k+1}(x_{\max,j} - x_{\min,j}). \tag{3}$$

4) Evaluate the new optima. If the new optima is more reasonable or the iteration number reached the predefined value, stop; otherwise, set $k = k+1$ and switch to 2).

QDPSO Algorithm. The QDPSO algorithm is described as below. Assume that there are *m* particles in a *D* dimension space. $X_i = (X_{i1}, X_{i2},\cdots, X_{iD})$ is the position of particle $i(0 < i < m)$. $pBest_i = (pBest_{i1}, pBest_{i2},\cdots, pBest_{iD})$ is the best personal position of particle i . $gBest = (gBest_1, gBest_2,\cdots, gBest_D)$ is the global best position of all the particles. Then the position of particle i can be updated using Eq. 4.

$$\begin{aligned} &p = [rand1() * pBest_{id} + rand2() * gBest_d] / [rand1() + rand2()] \\ &l = z * \left| X_{id}(t) - p \right|, 0 < z < \ln\sqrt{2} \\ &X_{id}(t+1) = \begin{cases} p - l * \ln[1/rand3()], rand3() > 0.5 \\ p + l * \ln[1/rand3()], rand3() \le 0.5 \end{cases} \end{aligned} \tag{4}$$

where $rand1()$, $rand2()$, $rand3()$ are random numbers that belong to (0,1).

CQDPSO Algorithm. The CQDPSO algorithm is a combination of the two algorithms and takes advantages of them. The procedures of the CQDPSO algorithm are listed as below.

1) Set the maximum number of iterations and population of particles; Initialize the positions of all the particles randomly; Initialize the personal best fitness value of every particle *pBest* and the global best fitness value of the initial population *gBest* .

2) Calculate the current fitness value of every particle and replace *pBest* with the current fitness value if the current fitness value is better.

3) Compare all the *pBest* values and determine the *gBest* value of current population.

4) Update positions of all the particles according to Eq. 4 and save the best particles.

5) Perform COA on the best particles and update the *pBest* values and *gBest* value.

6) If the precision requirement or maximum number of iterations is satisfied, output the results; otherwise, return to 2) and continue.

Load Model Structure

Generally, the load is represented by some combination of static and dynamic models. In this paper, exponential + difference equation based load model [11] is applied. The active power part can be expressed as Eq. 5.

$$\begin{aligned} P(k) &= a_p P_{stasic} + b_p P_{dynamic} \\ &= P_0 \left\{ a_p \left(\frac{V(k)}{V_0} \right)^{n_p} + b_p \left[1 + \left(\begin{array}{c} b_{p1}\Delta P(k-1) + b_{p2}\Delta P(k-2) + \\ c_{p0}\Delta V(k) + c_{p1}\Delta V(k-1) + c_{p2}\Delta V(k-2) \\ d_{p0}\Delta V^2(k) + d_{p1}\Delta V^2(k-1) + d_{p2}\Delta V^2(k-2) \end{array} \right) \right] \right\} \end{aligned} \tag{5}$$

where a_p , b_p are percentages of static loads and dynamic loads respectively, $a_p + b_p = 1$; n_p is the exponent of the static active power model; b_{p1}, b_{p2}, c_{p0}, c_{p1}, c_{p2}, d_{p0}, d_{p1}, d_{p2} are parameters of the dynamic active power model. There are 10 individual parameters: $\theta_P = \left[a_p, n_p, b_{p1}, b_{P2}, c_{p0}, c_{p1}, c_{p2}, d_{p0}, d_{p1}, d_{p2} \right]$.

Then the objective function for parameter identification of the dynamic active power model can be defined as below:

$$\min J\left(\theta_P\right) = \min \sum_{k=1}^{n} \varepsilon_k^2 \left(\theta_P\right) = \min \sum_{k=1}^{n} \left(P_{mk} - P_{sk}\right)^2 \tag{6}$$

where n is the number of data; P_{mk} and P_{sk} are measured active power and simulated active power respectively.

The reactive power part of the exponential + difference equation based load model and the objective function can be expressed similarly.

Case Study

The data is obtained from dynamic simulation experiment. The wiring diagram of the experiment is shown in Fig. 1. The loads are composed of six lamps (6*200W) and two induction motors (1.1kW, 2.2kW). A three phase short circuit fault occurred at the end of line L2, which lasts about 0.15 second. Power fault recorder (PFR) is installed at the high voltage side of the step-down transformer to capture fault data. Set the population to be 60 and the iteration number to be 100, calculate the parameters of the load model using the CQDPSO algorithm. The calculated parameters are listed in Table 1 and the fitting results are depicted in Fig. 2.

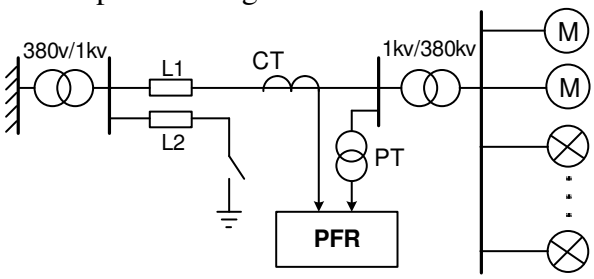

Fig. 1. Wiring diagram of the experiment

Table 1. Parameters of the load model in case study

Parameters of active power model		Parameters of reactive power model	
a_p	0.2925	a_q	0.0486
n_p	2.4350	n_q	3.9788
b_{p1}	1.7580	b_{q1}	0.6982
b_{p2}	-0.2901	b_{q2}	0.2715
c_{p0}	-0.3295	c_{q0}	-0.6584
c_{p1}	-1.5928	c_{q1}	0.3851
c_{p2}	1.1558	c_{q2}	-0.5486
d_{p0}	-1.8144	d_{q0}	-8.0042
d_{p1}	-2.9265	d_{q1}	0.4182
d_{p2}	4.6826	d_{q2}	5.5120

It can be seen from Fig. 2 that the simulated data can fit the measured data successfully with small error. As can be seen from the setting of dynamic simulation experiment, the static load (six lamps) is 1.2 kW and the dynamic load (two induction motors) is 3.3 kW. Thus, the composition of static load is about 27% and the reactive power is consumed mostly by the dynamic load. In Table 1, the calculated composition of static load is 29.25% and the reactive power consumed by the static load is

only 4.86%. The result is consistent with the theoretical value. Moreover, the exponent of the static active power model is 2.4350 and is consistent with the fact that the static load in the dynamic simulation experiment is constant impedance. It can be concluded that the parameters identification result is reasonable and precise.

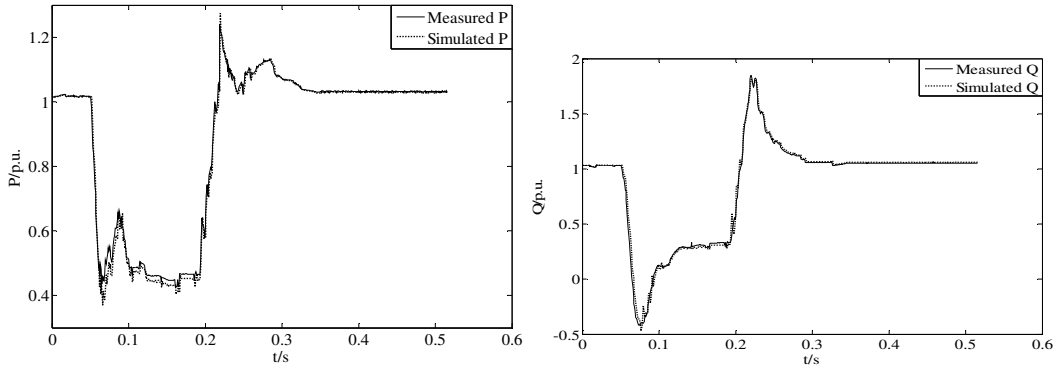

(a) Active power response (b) Reactive power response

Fig. 2. Parameter identification results of case study

Summary

In this paper, the CQDPSO algorithm is proposed for parameter identification of load models. The validity and practicality of the proposed method have been proved using data obtained from a dynamic simulation experiment. The appliance of the CQDPSO algorithm can improve the accuracy and reduce the computation complexity for load model parameter identification.

Acknowledgement

This work is supported by the National Natural Science Foundation of China (51377099), and is also supported by Shandong Provincial Natural Science Foundation of China (ZR2011EEM017).

References

[1] J. Ma, D. Han, R.M. He, Z.Y. Dong, and D. Hill: IEEE Trans. Power Syst. Vol. 23(2008), p. 76
[2] Z.S. Wang, L.C. Li, and L. Niu: Trans. China Electrotech. Soc. Vol. 24(2009), p. 127
[3] Q. Ai, C. Chen, S.D. Shen, D.Z. Gu, and Y.G. Zhou: Proc. Chin. Soc. Electrical Eng. Vol. 25(2005), p. 21
[4] H. Bai, P. Zhang and V. Ajjarapu: IEEE Trans. Power Syst. Vol. 24(2009), p. 1145
[5] Y. Cheng, P. Ju, and F. Wu: Automat. Electr. Power Syst. Vol. 27(2003), p. 25
[6] D. B. F. Van: An analysis of particle swarm optimizers (Ph.D., University of Pretoria, South Africa 2002)
[7] J. Sun, B. Feng, and W. Xu: Proceedings of the 2004 Congress on Evolutionary Computation (Portland, United states, June 19-23, 2004). Vol. 1, p.325
[8] P. Kou, J. Zhou, C. Wang, H. Xiao, H. Zhang, and C. Li: Eng. Appl. Artif. Intel. Vol. 24(2011), p. 1227
[9] S. Omkar, R. Khandelwal, T. Ananth, N.G. Narayana, and S. Gopalakrishnan: Expert Syst. Appl. Vol. 36(2009), p. 11312
[10] B. Li and W. Jiang: Control Theory & Appl. Vol. 14(1997), p. 613
[11] A. Maitra, A. Gaikwad, P. Zhang, M. Ingram, D. Mercado and W. Woitt: IEEE/PES Power Systems Conference and Exposition (Atlanta, United states, October 29- November 1, 2006). Vol. 1, p.1978

Advanced Materials Research Vols. 986-987 (2014) pp 1379-1382

doi:10.4028/www.scientific.net/AMR.986-987.1379

Research of Combined Optimum Grey Model to Mid and Long Term Electric Load Forecasting

Xiangshuo He[1, a], Li Yang[2,b] Xiaona Yu[3,c]

[1]Department of Economic Management, North China Electric Power University ,Baoding, China

[2]Human Resource Management .China University Of Geosciences, Beijing, China

[3]Environmental Design, China University Of Geosciences Great Wall college, Baoding, China

[a]hexiangshuo@126.com, [b]bdhdhe@126.com, [c]yuxiaona@126.com

Keywords: Load forecasting; Grey modeling; Partial error; Equa-l dimension and new-information; Combination optimum model

Abstract. It is well known that mid and long term electric load forecasting has many uncertain factors that influence the forecasting precision greatly, so every forecasting method has its limitation. Considering limitations of basic grey model and conventional improved models, a new practical method called combined optimum grey model for mid and long term load forecasting is introduced. The combined model is composed of partial error optimum grey model (GM) as well as equa-l dimension and new-information grey model. The forecasting algorithm can estimate model parameters, meet the requirements of dynamic power load and overcome random disturbances. Example analysis shows that the forecasting error is below 3 percent. Compared with conventional theoretical methods, the proposed scheme has the characters of simple computation, high forecasting precision and good applicability.

Introduction

Electric power system load forecasting is to achieve security, basic economic operation. Accurate load forecasting beneficial to improve power system stability and economy of which the pace of development area for the power grid, power construction scale and layout of the power industry, energy resource balancing, power swap places remaining grid of funds and human resources needs balance between regions provide a reliable basis.

Compared with short-term power load forecasting over the short, medium and long term power load forecasting, due to the historical data given less time interval long holidays or large fluctuations in the national economy as well as a wide range of seasonal factors influencing changes in load, so power load distribution can not directly identify good distribution, so the work is difficult, load forecasting model using traditional load forecasting theory can not meet the accuracy requirements established.

Medium and Long Term Power Load Forecasting Model

Is the essence of power load forecasting using the existing historical load data and related information, in a certain way to identify changes in the law of power load in order to predict future changes in electrical loaded.

Grey theory is based on the amount of random quantity as gray variation within a certain range, and the law is not obvious raw data generated by the accumulation to become law with a certain number of columns generated model equations constructed and bleaching process. Given the gray forecast unique modeling theory, this paper introduces the theory and its modeling approach in the study of long-term power load forecasting problems, thereby simplifying the problem at the same time ensure the prediction accuracy.

(1) Establish GM. GM (1,1) model is the most common form of gray model, consists of a single variable that contains only the first-order differential equation model constituted as a power load forecasting kind of effective models.

Located in an area of long-term power load history as a group had no significant change with time of the original series $x^{(0)}$,

$$x^{(0)} = [x^{(0)}(1), x^{(0)}(2), ..., x^{(0)}(n)] \quad (1)$$

Generating a first-order accumulated generating sequence with 1-AGO:

$$x^{(1)} = [x^{(1)}(1), x^{(1)}(2), ..., x^{(1)}(n)] \quad (2)$$

Take *k, i* are intermediate variables satisfies the above two:

$$x^{(1)}(k) = \sum_{i-1}^{k} x^{(0)}(i) \quad (3)$$

Since the sequence $x^{(1)}(k)$ has an exponential growth law, and the solution is just a first-order differential equations exponential growth in the form of solutions, so you can consider $x^{(1)}$ sequences satisfy the following first-order differential equation model:

$$\frac{dx^{(1)}}{dt} + ax^{(1)} = u \quad (4)$$

Wherein, a, u is a parameter. Vocabulary $A\hat{} = [a\hat{}, u\hat{}]^T$, and $a\hat{}, u\hat{}$ are *a and u* predicted value, the parameter $A\hat{}$ is determined by the least square method:

$$\hat{A} = (B^T B)^{-1} B^T Y_n = [\hat{a}, \hat{u}] \quad (5)$$

Where, *B and Yn* is a known quantity, $A\hat{}$ parameters to be determined, and *B and Yn* obtained by the following two equations:

$$B = \begin{bmatrix} -\frac{1}{2}[x^{(1)}(1) + x^{(1)}(2)] & 1 \\ -\frac{1}{2}[x^{(1)}(1) + x^{(1)}(3)] & 1 \\ \vdots & \vdots \\ -\frac{1}{2}[x^{(1)}(n-1) + x^{(1)}(n)] & 1 \end{bmatrix} \quad (6)$$

$$Y_n = \begin{bmatrix} x^{(0)}(2) \\ x^{(0)}(3) \\ \vdots \\ x^{(0)}(n) \end{bmatrix} \quad (7)$$

To the obtained $a\hat{}, u\hat{}$, Back substituting equation (4), with

$$\frac{dx^{(1)}}{dt} + \hat{a}x^{(1)} = \hat{u} \quad (8)$$

Available again after discrete GM (1,1) model to generate a gray sequence

$$\hat{x}^{(1)}(k+1) = [x^{(0)}(1) - \frac{\hat{u}}{\hat{a}}]e^{-\hat{a}k} + \frac{\hat{u}}{\hat{a}}, k = 0, 1, 2... \quad (9)$$

(2) New Information replacement projections

Improved optimization for GM (1,1) model, although as long-term forecasts, but the real practical significance and high accuracy predictive value is only the most recent one or two data, and other data only further reaction trend said the plan values or value (long-term planning of the forecast), so the model will predict new information obtained in each column of data into the same time, they remove one of the most stale data, namely

$$x^{(0)} = \left[x^{(0)}(1), x^{(0)}(2), ..., x^{(0)}(n-1), x^{(0)}(n), x^{(0)}(n+1) \right] \quad (10)$$

This metabolic data processing dimension and new information technologies is the approach the prediction accuracy is significantly improved.

Portfolio Optimization Model

Combination forecasting method is based on the maximum information utilization, which combines a variety of information on a single model, the optimal combination, in most cases, improvement can be achieved through a combination of forecasting prediction purposes.

There are two types of combination forecasting concepts : First, several forecasting methods to predict the results obtained, select the appropriate weights for a weighted average prediction method ; Second is the prediction methods were compared in several, select the goodness of fit the best or the smallest standard deviation prediction model as the best model for prediction.

This paper proposes a new portfolio optimization forecasting model, its basic idea is to improve the original sequence given gray prediction residuals, corrected for residual prediction model sequences were obtained before treatment and other reformers to improve the residual interest gray forecasting model which combines the advantages of improved prediction residuals gray prediction model and so on Innovation Gray predicted with a higher accuracy than a single prediction model their application as follows :

1) Accumulating the raw data processing ;

2) For processing data accumulated column GM (1,1) model to predict ;

3) Reduction of the prediction process ;

4) Experience poor after verification, such as the accuracy requirements are not satisfied, then take the local residual build residual data sequence ;

5) Residual data columns then create GM (1,1) model ;

6) Amended the original gray model with residual gray model ;

7) Re predictive analysis.

Advantage of the volatility of the load fitting gray combination proposed load forecasting method to optimize the existing gray prediction residuals, but also has high accuracy, such as interest law reformers and simple computation of the advantages and avoid the disadvantages of a single method.

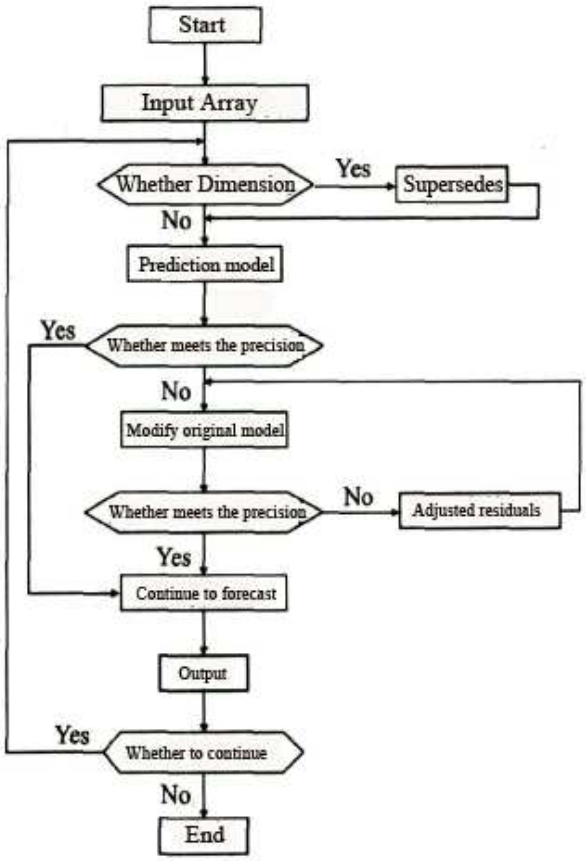

Fig.1 Main flowchart of combined optimum grey model for mid and long term forecasting

Main Program Flow Chart

Combined model presented in this paper combines both gray forecasting model based on improved Restoration interest residuals improved gray forecasting model (GM) and other by-laws based features. Compiled using C + + language to predict the main program, the main program flow chart as Figure 1.

Conclusions

Based on the study of power system problems and long-term load forecasting based on the introduction of gray system theory, a kind of high prediction accuracy of the improved model based on residual gray and gray and other reformers bearing replacement model combining both combinatorial optimization Gray predictive models. examples show that this kind of long-term power load forecasting problems related to many factors, residual gray model with improved load capacity fitting volatility, and interest and other reformers replacement gray model without increasing the amount calculated under the premise improve forecast accuracy. combines the advantages of the combination of these two models forecasting model, so that the portfolio optimization model has a simple, reliable and predictive accuracy.

References

[1] GAO Qiang,WANG Sheng-hui,XU Jian-yuan. Study of mid-term electric load forecasting based on ANN [J].Journal of Shenyang University of Technology, 2004,26(1):41-43.

[2] BAI Cun-you,FENG Xu,ZHANG Sheng-tang,et al.The application research on the gray equa-l dimension and new-info model in the prediction of irrigation water consumption [J]. Journal of Northwest Sc-i Tech Univ of Agri and For:Nat Sci Ed,2004,32(9):115-118.

[3] DENG Ju-long.Gray forecasting and decision-making [M]. Wuhan: Huazhong University of Science and Technology Press,1990.

[4] FENG Gu-i hong,YANG Xiang,ZHANG Bing-yi. The application of combined optimum grey model in med-I um and long term load forecasting [A].Proceedings of China International Conference of Electricity Distribution[C].Beijing China:2006:340-345.

[5] Guo Wenjun, Ramon Gilsanz. Nonlinear static analysis procedure) Progressive collapse evaluation [R]. Design Engineers of GilsanzMurray Steficek, LLP., 2003:1-11.

[6] Kandil M S,Debeiky S M,Hasanien N E. Overview and comparison of long-term forecasting techniques for a fast developing utility [J].Electric Power Systems Research,2001,58(1):11-17

Advanced Materials Research Vols. 986-987 (2014) pp 1383-1386

doi:10.4028/www.scientific.net/AMR.986-987.1383

Research on Energy-saving Algorithms with Migration Energy Consumption in Heterogeneous Cloud Environment

Zhenxing Yang[1, a], He Guo[1, b] ,Yulong Yu[1, c] and Yuxin Wang[2, d]

[1]School of Software, Dalian University of Technology, Dalian 116620, China;

[2]School of Computer Science and Technology, Dalian University of Technology, Dalian 116023, China.

[a]yzxlr@foxmail.com, [b]guohe@dlut.edu.cn, [c]yuylong@acm.org, [d]wyx@dlut.edu.cn

Keywords: heterogeneous cloud, data center, migration energy consumption, energy-saving, virtual machine migration.

Abstract. Cloud computing is a new emerging paradigm which delivers an infrastructure, platform and software as services in a pay-as-you-go model. However, with the development of cloud computing, the large-scale data centers consume huge amounts of electrical energy resulting in high operational costs and environment problem. Nevertheless, existing energy-saving algorithms based on live migration don't consider the migration energy consumption, and most of which are designed for homogeneous cloud environment. In this paper, we take the first step to model energy consumption in heterogeneous cloud environment with migration energy consumption. Based on this energy model, we design energy-saving Best fit decreasing (ESBFD) algorithm and energy-saving first fit decreasing (ESFFD) algorithm. We further provide results of several experiments using traces from PlanetLab in CloudSim. The experiments show that the proposed algorithms can effectively reduce the energy consumption of data center in the heterogeneous cloud environment compared to existing algorithms like NEA, DVFS, ST (Single Threshold) and DT (Double Threshold).

Introduction

Cloud computing is a new business computing model with resource pool. It is the development of distributed computing, parallel computing, utility computing and grid computing[1].To serve the growing computing services demand of consumers, many computing service providers including Amazon, Google, Microsoft, IBM and Salesforce are deploying large-scale data centers in different locations around the world. However, such data centers consume enormous amounts of electrical energy, accompanied by high operational costs and carbon dioxide emissions. Since data centers in cloud computing are widely leveraging virtualization technology, dynamic consolidation of virtual machines using live migration and switch idle servers to sleep mode or shutdown the idle servers allow cloud providers to optimize resource utilization and reduce energy consumption[2]. Existing energy-saving algorithms based on live migration does not consider migration energy consumption, and most of which are only applied to homogeneous cloud environment. Nevertheless, as the different procurement time, different tenure of use and different brands of cloud servers, making the cloud data centers tend to be heterogeneous. In this paper, we focus on energy-saving management in the heterogeneous cloud environment. The main contributions are:

(a) Model energy consumption in heterogeneous cloud environment, which contains basic energy consumption and migration energy consumption;

(b) Design overloaded and under-loaded cloud server detection policy based on median absolute deviation;

(c) Design the heterogeneous minimization of migrations policy, which is used to select the best virtual machine to be migrated;

(d) Design two algorithms to save energy consumption: energy-saving first fit decreasing (ESFFD) algorithm and energy-saving first fit decreasing (ESBFD) algorithm.

Modeling Energy Consumption

We assume there are *m* heterogeneous cloud servers and *n* virtual machines (VM), which can be expressed as $H=\{H_1,H_2,...H_m\}$ and $V=\{v_1,v_2,...v_n\}$ respectively. Because of the characteristic of heterogeneity, we chose the V2P (Virtual to Physical) live migration technology, which means the VM can be only migrated to the identically configured servers[3].

Basic Energy Consumption. Energy consumption by cloud servers in data centers are determined by the cloud infrastructure, including the CPU, memory, storage and network facilities. Among these facilities, the CPU consume main part of energy. In this paper, we focus on the CPU energy consumption. Fan et al.[4] have found that the server energy consumption grows linearly with the growth of CPU utilization, which can be expressed as in (1).

$$P(u)=P_{idle}+(P_{\max}-P_{idle})\times u \tag{1}$$

where P_{idle} is the energy consumption by an idle server, P_{max} is the energy consumption when the server is fully utilized, *u* is the current CPU utilization and $P(u)$ is the estimated energy consumption. Researchers[5,6] have further found that an idle server consumes about 70% of P_{max}, which can be expressed as in (2).

$$P_{idle}=\delta\times P_{max} \tag{2}$$

where δ is the fraction of energy consumed by the idle server. Thus, equation (1) can be rewritten as:

$$P(u)=\delta\times P_{max}+(1-\delta)\times P_{max}\times u \tag{3}$$

Due to the variety of workload in heterogeneous cloud environment, the CPU utilization changes over time. So the CPU utilization is a function of time. The CPU utilization of a server H_i can be expressed as $u_i(t)$. Thus, during a time period $[t_0,t_1]$, the basic energy consumption by a server H_i can be represented as in (4).

$$E_{basic}=\int_{t_0}^{t_1}P(u_i(t))dt \tag{4}$$

Migration Energy Consumption. When a server is verified to be overloaded, we define this situation as SLA (Service Level Agreement) violation. A single VM can be migrated out of the overload server to decrease the CPU utilization. We assume the VM v_j running in the server H_i is selected to migrate to the server H_k, the migration starts at time t_s and ends at time t_e. Therefore, the migration energy consumption occurs by the VM v_j is expressed in (5).

$$E_{mig}=\int_{t_s}^{t_e}P(\alpha\cdot u_i(t))dt+\int_{t_s}^{t_e}P(\beta\cdot u_k(t))dt \tag{5}$$

where α and β is the fraction of the CPU utilization allocated to the VM v_j in the server H_i and the server H_k respectively. Thus, the total energy of a server in the heterogeneous cloud environment can be measured by the sum of the basic energy consumption and the migration energy consumption, as shown in (6).

$$E_{total}=E_{basic}+E_{mig} \tag{6}$$

Energy-saving Algorithms Design

The energy-saving algorithms can be split into three steps: (a) detect the overloaded or under-loaded servers; (b) select the best VMs should be migrated out of the overloaded or under-loaded servers; (c) deploy the migrated VMs from overloaded or under-loaded servers.

Overloaded and Under-loaded Server Detection Policy. To determine a server is overloaded or under-loaded is usually by setting upper and lower utilization thresholds for servers. Due to the CPU utilization is changing over time, fixed values of utilization thresholds are not suitable for the dynamic workload. We use the Median Absolute Deviation (MAD), which is a robust statistics, to determine the utilization thresholds dynamically. For an ascending series, $U_1,U_2,...,U_n$, which represent the historical CPU utilization of a server, the MAD is calculated as (7).

$$MAD=median_i\left(\left|U_i-median_j(U_j)\right|\right) \tag{7}$$

We define the upper utilization threshold(T_u) and lower utilization threshold(T_l) as shown in (8).

$$\begin{cases} T_u = 1 - s \times MAD, T_l = s \times MAD, if\ (s \times MAD < 0.5) \\ T_u = 0.9, T_l = 1 - s \times MAD, if\ (s \times MAD \geq 0.5) \end{cases} \quad (8)$$

where *s* is a parameter that defines how aggressively the system consolidates VMs, the lower *s*, the less the energy consumption.

VM Selection Policy. Due to the migration energy consumption, reducing the number of migration times can reduce the total energy consumption. We design the Heterogeneous Minimization of Migrations(HMM) policy, which is to migrate the minimum number of VMs from the overloaded server to reduce the CPU utilization. If the server's CPU utilization is below the lower threshold, all the VMs running in the server will be migrated out. The HMM policy sorts the list of VMs in the decreasing order of the CPU utilization and records the hostType of the servers. Then, it repeatedly looks through the list of VMs and finds the best VM to migrate from the server. The best VM should have the utilization higher than the difference between the server's overall utilization and the upper utilization threshold. If the VM is migrated out from the overloaded server, the difference between the upper threshold and the new utilization is the minimum. The policy stops when the new utilization of the server is below the upper utilization threshold.

VM Deployment Algorithms. The problem of VM deployment can be seen as a bin packing problem with variable bin sizes and prices[7]. We propose two algorithms for VM deployment: Energy-saving First Fit Decreasing (ESFFD) algorithm and Energy-saving Best Fit Decreasing (ESBFD) algorithm. We sort all the VMs to be migrated in decreasing order by their CPU utilization. ESBFD algorithm allocates each VM to the server which provides the least increase of power consumption due to this allocation. ESFFD algorithm allocates each VM to the first server that has enough resource for this allocation. The pseudo-codes of the algorithms are presented in Algorithm 1 and Algorithm 2. The complexity of both algorithms is $n \cdot m$, where *n* is the number of VMs to be deployed and *m* is the number of servers.

Algorithm 1: Energy-saving Best Fit Decreasing (ESBFD)

```
1  Input:hostList, migrationVmList with hostType
2  Output:allocation of migrated VMs
3  migrationVmList.sortDecreasingCpuUtilization()
4  foreach vm in migrationVmList do
5    minEnergy ← MAX
6    allocatedHost ← NULL
7    foreach host in hostList do
8      if host.hostType== vm.hostType and host
     has enough resource for vm then
9        energy ← estimateEnergy(host,vm)
10       if energy < minEnergy then
11         allocatedHost ← host
12         minEnergy ← energy
13   if allocatedHost ≠ NULL then
14     allocate vm to allocatedHost
15 return allocation
```

Fig. 1 ESBFD algorithm

Algorithm 2: Energy-saving First Fit Decreasing (ESFFD)

```
1  Input:hostList, migrationVmList with hostType
2  Output:allocation of migrated VMs
3  migrationVmList.sortDecreasingCpuUtilization()
4  foreach vm in migrationVmList do
5    minEnergy ← MAX
6    allocatedHost ← NULL
7    foreach host in hostList do
8      if host.hostType== vm.hostType and host
       has enough resource for vm then
9        break
10   if allocatedHost ≠ NULL then
11     allocate vm to allocatedHost
12 return allocation
```

Fig. 2 ESFFD algorithm

Experimental Evaluation

This paper implements the proposed ESFFD algorithm and ESBFD algorithm in CloudSim[8]. The data center has two kinds of servers, half of which are HP ProLiant ML110 G4 servers, and the other half consists of HP ProLiant ML110 G5 servers. We simulate the commonly used 4 types of Amazon EC2 VM instances[9] using the PlanetLab[10] workload. We compared our algorithms with NEA (No Energy Aware) algorithm, DVFS algorithm, ST(Single Threshold) algorithm and DT(Double

Threshold) algorithm. The experimental results are shown as Fig. 3. We can see that compared to the other algorithms, EAFFD and EABFD can effectively reduce the energy consumption of the data center in the heterogeneous cloud environment. That's because the proposed algorithms make more cloud servers switch to the sleep mode.

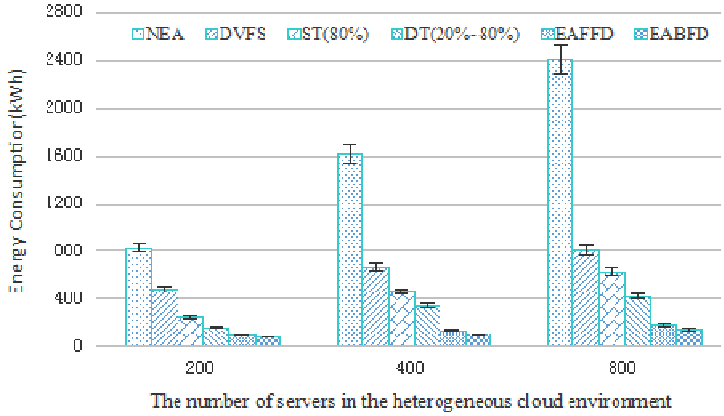

Fig. 3 The energy consumption of different algorithms under different number of servers

Conclusion

This paper investigates the energy-saving problem with migration energy consumption in the heterogeneous cloud environment. We first design the overloaded server and under-loaded server detection policy through MAD, and then design the heterogeneous minimization of migrations policy to select VMs to be migrated. Finally, we design two VM deployment algorithms: EAFFD and EABFD. Experimental results demonstrate the validity of the proposed algorithms. The future work is to consider the energy management of other devices, such as memory and network device.

Acknowledgment

This work was financially supported by the National Natural Science Foundation of China (No.11372067).

References

[1] P. Mell , T. Grance, The NIST definition of cloud computing ,NIST, 2011, 800(145).
[2] M. Armbrust, A. Fox, R. Griffith, et al. ,A view of cloud computing, Communications of the ACM, 2010, 53(4), pp. 50-58.
[3] J. H. Chiang, L. Maohua, T.Chiueh, Physical machine state migration, IEEE 17th. International Conference on Parallel and Distributed Systems (ICPADS), 2011, pp. 25-32.
[4] X. Fan, W. D. Weber, L. A. Barroso. Power provisioning for a warehouse-sized computer, ACM SIGARCH Computer Architecture News, 2007, 35(2), pp. 13-23.
[5] D. Kusic, J. O. Kephart, J. E. Hanson, et al. Power and performance management of virtualized computing environments via look ahead control, Cluster Computing, 2009, 12(1), pp. 1-15.
[6] A. Beloglazov, J. Abawajy, R. Buyya. Energy-aware resource allocation heuristics for efficient management of data centers for cloud computing, Future Generation Computer Systems, 28(5), pp. 755-768.
[7] C. F. Tiago, A. S. N. Marco, N. C. Rodrigo, et al. Server consolidation with migration control for virtualized data centers, Future Generation Computer System, 2011, 27(8), pp. 1027-1034.
[8] N. C. Rodrigo, R. Rajiv, A. Beloglazov, et al. CloudSim: A toolkit for modeling and simulation of cloud computing environments and evaluation of resource provisioning algorithms, Software: Practice and Experience (SPE), 2011, 41(1), pp. 23-50.
[9] Information on http://aws.amazon.com/cn/ec2/instance-types/.
[10] Information on https://www.planet-lab.org/.

Advanced Materials Research Vols. 986-987 (2014) pp 1387-1390

doi:10.4028/www.scientific.net/AMR.986-987.1387

Research on Market Model for China Forest Carbon-Sink in Coal Mines

Chuanghong SHANG [1, 2; a]

[1] School of Humanities &Social Sciences, North China Institute of Science & Technology, Beijing, 101601, China

[2] National Institute of International Strategy, CASS, Beijing, 100007, China

[a] email: gsshchh@163.com

Keywords: Forest Carbon-Sink in Coal Mining; Market Systems; Market Mechanisms

Abstract. In post- Kyoto Protocol times, forest carbon-sink has become one of the key path choices to realize clean development for China. Currently, China's carbon market system has not come into being. So it is necessary to take government-leading model to establish three market systems. They are property relations of coal forest, binding planning for GDP carbon emission intensity and credit trading system of forest carbon-sink. Based on market systems, certified emission reductions (CERs) and voluntary emission reductions (VERs) in mining industry can be developed.

Introduction

For a long time, coal accounts for 70 percent in China's primary energy production and consumption. In 2012, its primary energy output went to 3.32 billion tons of standard coal, in which raw coal goes up 3.3 percent in contrast with 73.2 percent in 2000[1]. Obviously, ecologic protection has been a hot issue for China's economic and social development. China's government has clearly presented the objective of which its energy consumption per GDP and carbon emission intensity will respectively go down 16 and 17 percent in 12th Five-Year Plan [2].

Through a general survey of ecologic environmental protection in coal mines domestic and overseas, it can be found out that developed countries had started the job in 1920s, big progress had been made in 1960s and enjoy much advantage to developing ones in environment assessment, technologies, equipments, policies, systems, management etc.

In 1992, Kyoto Protocol took effect. Currently the project has been carried out comprehensively focusing on forestation, reforestation in India, Brazil and China etc. [3]. China's government has attached much importance to the CDM project. In recent 10 years, 70 billions US $ has been invested to develop forestry. China's forest coverage rate has achieved 21.6 percent by the end of 2013. So forest carbon-sink has been a key path choice for China in post-Kyoto Protocol times.

Relation between forest carbon-sink and ecological environmental protection in coal mining

Forest carbon-sink plays two kinds of role. One is to preserve water and soil, prevent wind and fix sand, lessen atmospheric contamination, absorb carbon dioxide and dust, release oxygen. The other is it can form financial products and derivatives by integrating forest carbon-sink and CDM, which can gain revenue through carbon trading market[4].

At present, China is world-widely one of key countries in gas emission. In post Kyoto Protocol times, GDP carbon intensity ought to be incorporated as an obligatory target into medium and long term Plan for National Economic and Social Development. At the same time, in order to lead substantial economy, equity transaction mechanism of carbon emission also ought to be established because carbon trading is a transformation of carbon emission rights quota by financial operation.

Problems in forest carbon-sink and ecological environmental protection in coal mining

Though outstanding contribution has been made by China's mining enterprises, its low standing in global carbon trading chain leads to no corresponding speaking right. As far as year of 2008 is

concerned, 48 percent of global total CERs (Certified Emissions Reductions) trading volume is made by China. Under current CDM system, major certification authorities come from Europe. In the end, China's products prices of CERs have suffered from unfair treatment by developed countries. CERs products have been bought in and developed financial derivatives with higher market prices by developed countries.

Emission reduction is highly connected with initiative of global financial carbon market. So importance must be attached to the market. Beijing Environmental Exchange and other agencies have been set up in China after 2008, but they are not decision-makers of trading regulations in international market. In 2009, Panda Standard was released by Beijing Environmental Exchange, which marked China's beginning to take initiative of pricing right in international market. [5]

Market logic of forest carbon-sink

Coal enterprises can take part in projects trading and obtain needed capital for ecologic protection. More importantly, it can help enterprises sustainably develop forest carbon-sink.

Forest carbon-sink market consists of government agencies, internal forest carbon-sink in coal industry, domestic and international one. Firstly, obligatory targets for GDP carbon emission as quota ought to be set by government. Secondly, internal market ought to be set up as a comprehensive inter-department agency and prices of carbon trading ought to be decided by the market. Market operation can be supervised by industry association on behalf of government. Thus, effective forest carbon-sink market can be built up through participants and operational mechanism. Thirdly, domestic forest carbon-sink market can be established by the Panda Standard. Fourthly, internationalized domestic forest carbon-sink market can be set up by CDM mechanism.

Market system for forest carbon-sink

Currently government-dominant model ought to be adopted because China's market system of forest carbon-sink does not come into being. To set up final market-dominant model, such market system constraints ought to be taken shape by obligatory policies as forest property right system, obligatory target plan for GDP carbon intensity and credit trading system for forest carbon-sink.

Forest property right system in coal industry

Forest carbon-sink in coal mines is characterized as non-excludability, non-competitiveness, inseparability, commonweal and externalities. So, whether forest property right can be defined clearly is the first step to set up forest carbon-sink trading. Secondly, ownership, right of management and right to use forest land ought to be reasonably divided in forest carbon-sink project. Finally, to promote product movement of forest carbon-sink and preserve or increase their value, free transference of right to use forest land ought to be permitted and encouraged [6].

Obligatory target plan for GDP carbon intensity

According to international requirements for gas emission, obligatory target plan for GDP carbon intensity ought to be determined by government through which environmental standards will be enhanced for manufacturers. In this way, total carbon emission is speeded down. At last, balance between carbon emission and absorption can be realized. Generally emission targets are divided by state environmental department and association to manufactures whose historic emission level, predictable emission and industrial emission standards are weighted taken into consideration. Meanwhile, penalty incentives are used to punish manufacturer exceeding standards. In accordance with principle of "tragedy of the commons", under this way of obligatory target plan and non-boundary management is realized. Furthermore, carbon emission with public characteristic is turned to privatized commodity, which makes public decision-making of emission privatized. As a result, by "invisible hand" of market [7], manufacturers can make their decision for emission.

Credit trading system for forest carbon-sink

To facilitate value maximization of forest carbon-sink products, credit trading system ought to be built up to enhance efficiency of resource allocation. Under the system, on the basis of cost of carbon emission, manufacturers freely make their decision for emission and, buy in or out product

mix of emission, which implements emission reduction by them. Meanwhile, for manufacturers with emission reserve, similar futures trading system for emission ought to be established [8].

Market mechanism for forest carbon-sink

Specific market mechanism can be designed as CERs (Certified Emission Reduction) and VERs (Voluntary Emission Reduction) in coal industry.

Market mechanism of CERs (Certified Emission Reduction) in coal industry

Currently, due to administrative and legal constraints, obligatory carbon trading mechanism in coal industry ought to be dominated by government in which coal enterprises are forced to participate in carbon trading. Carbon emission volume for coal enterprises is determined by government. If the volume of enterprises exceeds limit, it ought to be bought in from carbon-sink market or be reduced through emission reduction. Or the enterprises will be punished according to GDP carbon emission limit. Meanwhile, if the enterprises emission volume is less than permitted volume, rest ought to be sold in market to gain profit. As shown in following figure 1.

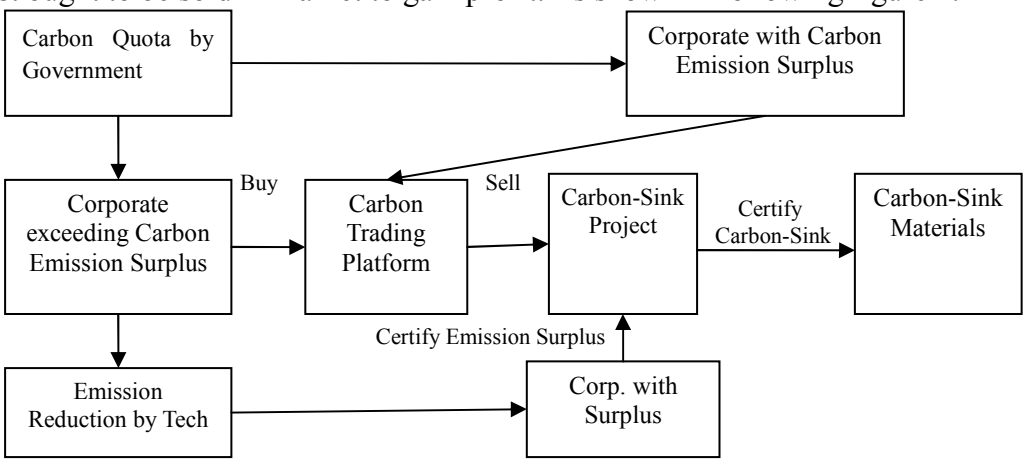

Fig.1. Market Mechanism of CERs (Certified Emission Reduction)

Market mechanism of VERs (Voluntary Emission Reduction) in coal industry

Compared with CERs, VERs is designed to make coal enterprises voluntarily transact carbon emission from profit or non-profit objectives. Profit objectives mean investment in carbon-sink products and finance. Non-profit ones are as Corporate Social Responsibility, brand building and social benefit etc. Under this mechanism, enterprises participating in carbon transaction determine their emission limit or buy in forest carbon-sink in carbon market voluntarily. As far as specific carbon trading platform is concerned, it can be set up by coal association. As shown in figure 2.

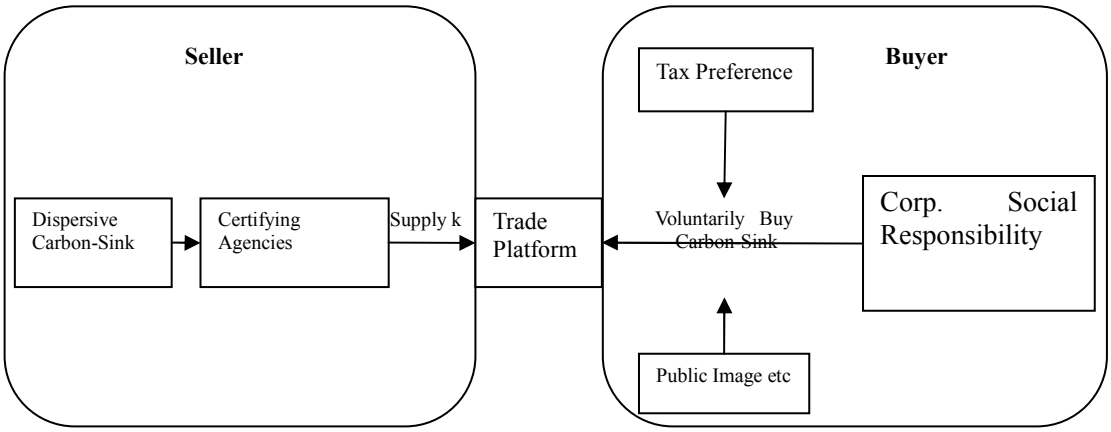

Fig.2. Market Mechanism of VERs (Voluntary Emission Reduction)

Conclusions

Currently, one of key path choices is for China to develop forest carbon-sink. GDP carbon intensity ought to be incorporated, as an obligatory target, into medium and long term Plan for National Economic and Social Development. In order to build up final real market-dominant model, such market system ought to be taken shape by obligatory government policies as forest property right system in coal industry, obligatory target plan for GDP carbon intensity and credit trading system for forest carbon-sink. Specific market mechanism can be designed as CERs (Certified Emission Reduction) and VERs (Voluntary Emission Reduction) in coal industry.

Acknowledgement

In this paper, the research was sponsored by the Basic Research Expenses for Central Subordinate Colleges and Universities (Project No. RW2013B10).

References

[1] Ministry of Land and Resources, PRC. China's Report of Mineral Resources (2013) [M]. Beijing, Geological Publishing House, 2013(10).

[2] The Twelfth Five-Year Plan for National Economic and Social Development of the People's Republic of China.[M]. Beijing, People's Publishing House, 2011.

[3] Kyoto Protocol [M]. Intergovernmental Panel on Climate Change, 1997

[4] Pei Q，Jiang M，Zhang M H. A Study of Legal Attributes of Carbon Emission Rights in Carbon Trading [J]. Ecological Economy，2009(1).

[5] Panda Standard.[M]. Beijing, Beijing Environmental Exchange, 2009.

[6] Shuxia Li, Zhiguo Zhou. Operating Mechanism of Forest Carbon Sequestration Market.[J]. Journal of Beijing Forestry University(Social Sciences), 2010(2)：88-93.

[7] Hardin, G. Tragedy of the Commons [J]. Science, 1968, 162 (3859)：1243–1248.

[8] Yan Xiao, Xiaoxue Li. Path Selection for Forest Carbon Market Cultivation in China.[J]. World Forestry Research, 2012（1）：55-59.

Advanced Materials Research Vols. 986-987 (2014) pp 1391-1395

doi:10.4028/www.scientific.net/AMR.986-987.1391

The Key Parameter Modeling of SiC MOSFET

Yonglong Peng[1,a], Rongrong Li[1,b], Yabin Li[1,c]

[1]School of Electrical and Electronic Engineering, North China Electric Power University, Baoding, 071003, China

[a]email :pylncepu@163.com ,[b]email: 859943204@.qq.com ,[c]email :418925835@qq.com

Keywords: SiC MOSFET; PSpice modeling; simulation; static and dynamic analysis.

Abstract. This thesis mainly analysed the internal relations between parameters of SiC MOSFET and its dynamic and static characteristics respectively. And furthermore, a new method for modeling of SiC MOSFET based on PSpice was proposed in this paper. By introducing voltage's controlling for voltage source E, we can compensate and correct the difference between PSpice default value of gate threshold voltage and actual value. At the same time, we can adopt two different junction capacitance models to describe the changes of junction capacitance which were brought about by the difference of the terminal voltage. In the meanwhile, there are newly increased source-drain resistance of MOSFET and gate resistance with the temperature change of variable temperature sub models. New models are able to fully and accurately reflect SiC MOSFET's static and dynamic characteristics. Moreover, it provides an important foundation for switch process analysis of SC MOSFET, loss calculation and main circuit design. The fact that the experimental testing result is highly coincident with the simulation results verifies the correctness and accuracy of the models.

Introduction

The development of the power electronics sector is always closely linked with the progress of semiconductor device. Currently, silicon power semiconductor device occupies an absolutely dominant position in the power electronics sector. However, with the development of productive forces, switching devices with the current technological level have been unable to meet the industry demands for high frequency and high power.

Once the material of SiC (silicon carbride) was born, its superior electrical properties have aroused wide public concern. SiC MOSFET is the typical application of this material. Compared with other materials' MOSFET, SiC MOSFET's on-resistance is smaller, switching loss is lower and high temperature stability is better. But because of its high price, it has not been widely used yet. But with its costs falling down, SiC MOSFET will definitely be used in more and broader areas, by virtue of its unique qualities, such as low on-resistance, high switching speed and easy drive characteristics. Therefore, it is especially important to make a circuit analysis of its static characteristics, dynamic characteristics, power loss and so on with computers before the engineering application. The accuracy of circuit analysis mainly depends on the validity and accuracy of the device model.

It is extremely urgent to make an accurate modeling for SiC MOSFET which has been regarded as the inevitable trend of semiconductor device's development in the future.

In this thesis, the modeling object mainly aims at middle and low pressure SiC MOSFET, (for example ROHM company's SiC MOSFET named SCH2080ke) to build SiC MOSFET key parametric models which are based on PSpice simulation software. First of all, we need to analyze in detail the relationship between the key parameter of SiC MOSFET and the influence factors such as voltage, temperature and so on, and then find out the fitting coefficient. Secondly, construct model in the PSpice simulation software and simulate the model to make an initial verification about the feasibility of the modeling ideas. Finally, carry out an experimental measurement for the static characteristics of SiC MOSFET, dynamic characteristics of the experimental platform and all other peculiarities to verify the correctness and accuracy of the model.

Theory and Design

Table 1 is about the PSpice model based on SiC MOSFET (SCH2080ke 1200V) coming from ROHM Company. In the table, M and D_{body} is rom build-in model and this model can simulate the basic characteristic of SiC MOSFET. However, this model can not operate very well, if you want to accurately stimulate SiC MOSFET's movement situation in the actual circuits. We must make a supplement and correction for the original model in order to obtain a more accurate simulation result before the engineering application. The key parameters which have significant impact on SiC MOSFET's static characteristics and dynamic characteristics will be modeled again.

Tab.1 Key parameter list

Key parameters	The affected objects
Threshold voltage U_T	Affect device's quiescent current And the static power consuming
On state resistance R_{ON}	Affect device's on-state voltage drop and maximum power output
Grid resistance R_G	Affect device's switching time, switching loss and a variety of other parameters
Leakage source capacitance C_{DS}	Affect device's switching characteristic
Grid source capacitance C_{GS}	Affect device's switching characteristic
Gate leakage capacitance C_G	Affect device's switching characteristic

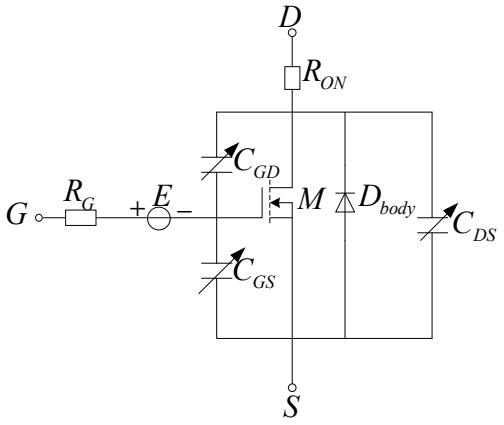

Fig. 1 New model of SiC MOSFET

Static characteristics parametric modeling

Threshold voltage U_T : it refers to the minimum gate voltage needed for channel conduction caused by strong inversion in channel areas. The size of U_T is related to the space charge quantity of unit area within the depletion region. It varies with the junction temperature and it has a negative temperature coefficient. Under the test condition where the temperature is 125℃ and the threshold voltage is 2.8V，-25℃, SCH2080ke is 4.2V. But in the simulation software PSpice, the default is that the linear change rate is -1mV/℃, obviously the fitting error is very large. According to the graph which showed the relation between SCH2080ke threshold voltage and junctional temperature, we can find that the fitting relationship is the second order nonlinear relationship. In order to make the relationship between the threshold voltage in the new model and the temperature more accurate, it is necessary to bring in a voltage-controlled voltage source to correct and compensate the difference between PSpice system defaults and actual value.

$$E = V_{T0}[1 + M_{C1}(v - V_{T0}) + M_{C2}(v - V_{T0})^2] \quad (1)$$

In this formula, M_{C1} is a voltage coefficient; M_{C2} is secondary voltage coefficient; v is the system output threshold voltage; is threshold voltage when the temperature is 25℃.

Drain-source state resistance R_{ON}: R_{ON} has a great impact on both the on-state voltage drop and maximum power output. Therefore it is an important parameter which can reflect the static characteristics of MOS pipe. becomes bigger with temperature rising and this positive temperature coefficient benefits MOS pipe's participation in multi-tube parallel application in the large power equipment. In order to make an accurate simulation to current-sharing condition and the switch state condition of SiC MOSFET in multi-tube parallel circuit, we must make a precise modeling of . We can adopt model PSpice software when model R_{ON} .The relationship as follows:

$$R_{ON} = R_0[1 + T_{C1}(T - T_0) + T_{C2}(T - T_0)^2] \quad (2)$$

Among this formula, R_0 is SiC MOSFET's on-state resistance when the temperature is 25℃; T_{C1} is linear temperature coefficient; T_{C2} is secondary temperature coefficient; T is operating temperature; and T_0 is 25℃.

Gate resistance R_G : As the grid capacitance is controlled by the grid resistance, therefore the change of R_G also influences the dynamic property of MOSFET, such as switch time, switching loss and all other parameters. As a result, it goes against the model's static and dynamic characteristic simulation to set R_G to the fixed parameter. By analyzing its characteristics, we can know that grid resistance changes with the change of temperature, so it was set up as the variable temperature resistance module which varies with temperature. The relationship as follows:

$$R_G = R_{G0}[1 + T_{C3}(T - T_0) + T_{C4}(T - T_0)^2] \quad (3)$$

In this formula, R_{G0} is grid resistance value when the temperature is 25℃; T_{C3} is linear temperature coefficient; T_{C4} is secondary voltage coefficient; is operating temperature; T_0 is 25℃.

Dynamic characteristics parametric modeling

The switching process of SiC MOSFET is mainly influenced by the dynamic characteristic parameters whose uppermost parameter is interelectrode capacitance. In addition, MOS pipe's interelectrode capacitance is not a fixed parameter, but one which forms a functional relationship along with drain-source voltage U_{DS}, gate-to-source voltage U_{GS} and temperature. Therefore, in the modeling of dynamic characteristic parameters, the emphasis is to model the capacitances.

Gate leakage capacity C_{GD}: As under the state of open and shutdown, the voltage direction imposed on will change, therefore two cases will be presented: the capacitance of C_{GD} will suddenly increase once it opens, while the capacitance of C_{GD} will decrease when it shut off. This phenomenon influences the size of input impedance, switching speed, therefore we should model it accurately.

In the sub circuit model of reference [1], when $U_{GD}<0$, we can use the characteristics of diode storge charge to describe the change of capacitance. But, it is very difficult to describe nonlinear variation of C_{GD} depending on two diodes in series to configure their junction capacitance and breakdown voltage. Even if it can be realized, its accuracy is relatively lower. When $U_{GD}>0$, we can directly switch to C_{GDMAX} without any transient process.

To avoid the limitations mentioned above, this thesis decides to adopt C_{break} module of PSpice software and describes C_{GD}'s changing process under different pressures through the functional relationship.

In Fig.2, S_1 and S_2 only functions as switch S_1 and S_2, therefore, we adopted the voltage of PSpice to control switch S_{break} module. Compared with MOSFET module of sub circuit model in reference [1], its controlling is easier, achieving instant switching is more likely to realize no matter whether the pipe is reliable and at the same time we need not to concern about the problem of triggering and shutoff. By adopting C_{break} module of PSpice software, C_1 and C_2 respectively represent variation trend when $U_{GD}<0$ and $U_{GD}>0$. Fitting function relations with voltage U_{GD} are the second order nonlinear equation.

$$C_{GD} = \begin{cases} C(1 + V_{C1}v + V_{C2}v^2) & U_{GD} \le 0 \\ C(1 + V_{C3}v + V_{C4}v^2) & U_{GD} > 0 \end{cases} \quad (4)$$

Among the variables, C is the capacity factor; V_{C1} is a fitting coefficient for C_1; V_{C2} is quadratic fitting coefficient for C_1 ; V_{C3} is a fitting coefficient for C_2 ; V_{C4} is quadratic fitting coefficient for C_2 ; v is voltage between two ends of.

Grid source capacitance C_{GS} : C_{GS} is composed of two parts: the first part is the capacitance formed by metallic oxide coming from the space between the gate and the source and it has nothing to do with operating voltage. The other part is the capacitance coming from the space between the gate and the source and it varies with different working conditions. Grid source capacitance C_{GS} mainly controlled by voltage polarities imposed on both ends of the capacitor. Bearing positive-negative pressure, the difference of the capacitive variation trend is relatively big. Thus, in reference [1] modeling, it is unreasonable to set up different fixed values only depending on the difference of the positive and negative voltage. In view of the similar variation characteristics of , we'd better adopt the model structure of C_{GD} when we model C_{GS}. The purpose is to make an

accurate simulation to the variation trend of the size of C_{GS} when voltage direction varies on both ends of .

Leakage source capacitance C_{DS} : It is made up of PN junction within the pipe. But during the process of pipe switching, the voltage direction on both ends of C_{DS} will not change, so the changing curve of C_{DS} is only influenced by size of the voltage. Thus, we need to adopt PSpice module of PSpice when we model leakage source capacitance and the relationship between voltage and it is showed as follows:

$$C_{DS} = C(1 + V_{C5}v + V_{C6}v^2) \quad (5)$$

Among the variables, C is capacity factor; v is voltage value on both ends of C_{DS}; V_{C5} is linear voltage coefficient; V_{C6} is secondary voltage coefficient.

SiC MOSFET static characteristic experiment

From the perspective of accurate measurement and observation, we mainly observe output characteristic curve and transfer characteristic curve of SiC MOSFET through static characteristic experiment. Fig.3 is a SiC MOSFET's static characteristic experiment circuit diagram; Fig.4 is a simulation and experiment comparison curve chart which describes SiC MOSFET's output characteristics; Fig.5 a simulation and experiment comparison curve chart which describes SiC MOSFET's transfer characteristics.

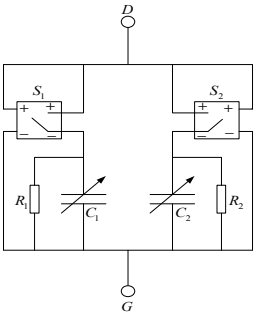

Fig. 2 Sub circuit model

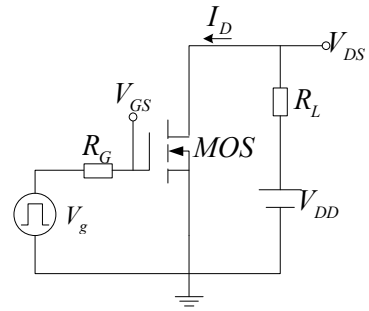

Fig. 3 Static characteristics test circuit

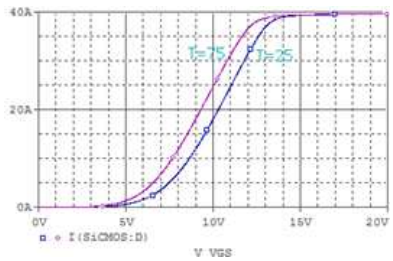

Fig. 4 (a) Transfer characteristic of the simulation waveform

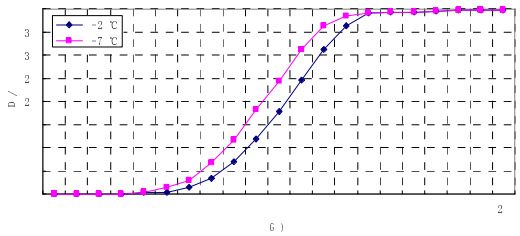

Fig. 4(b) Transfer characteristics of the experimental waveforms

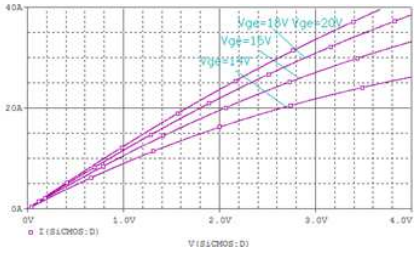

Fig. 5 (a) The output characteristics of the simulation waveforms

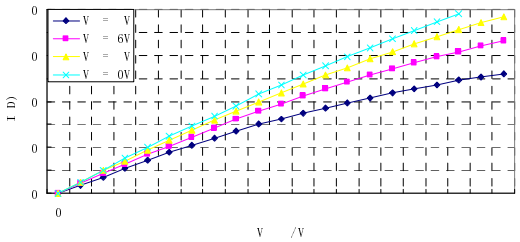

Fig. 5 (b) The output characteristics of the experimental waveforms

Compare the simulation waveform and the measured waveform in Fig.4, we can conclude that both the variation trend of the curve and data on each point are highly consistent between the two waveforms. Compare the simulation waveform and the measured waveform in Fig.5, we can get the conclusion that the test result can basically describe SiC MOSFET's output characteristics and errors are under control. The compared results demonstrate that the model we build is able to accurately describe the static characteristics of SCH2080ke by correcting some key parametric models, such as threshold voltage U_T , on-resistance R_{ON} , E and so on.

SiC MOSFET dynamic characteristic experiment

The dynamic characteristics mainly influence the switching process of SiC MOSFET. Currently, the accurate and effective way of testing the dynamic characteristics of switching devices is double-impulse test method, by which we can clearly observe switching process of the pipe. Therefore, in dynamic experiment we adopt double-impulse test method and its circuit digram is shown in Fig.6.

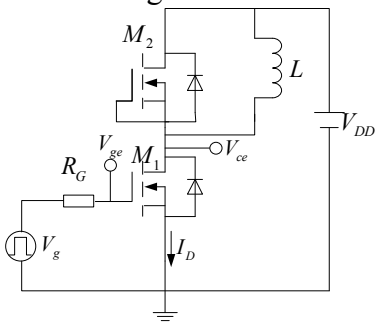

Fig.6 Dynamic characteristics test circuit

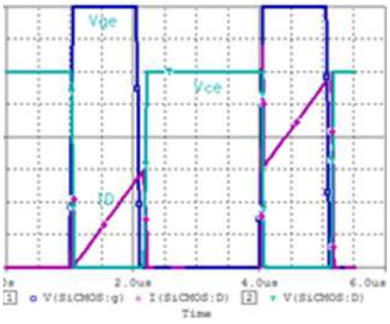

Fig.7(a) Dynamic simulation waveforms

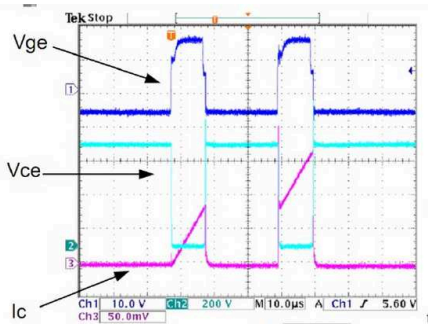

Fig.7 (b) Dynamic experimental waveforms

By comparing Fig.7(a) and Fig.7(b) we can know that the model we build in this thesis can clearly reflect voltage current waveform under the condition of open and shut-off.

Conclusion

Based on Spice procedure of SiC MOSFET offered by ROHM Company, first of all we construct a model which can describe its basic characteristics in model editor by adopting PSpice software. In order to obtain an accurate and valued computer simulation result before the engineering application, we make a specific analysis to key parameters which have great impact on dynamic and static characteristics of SiC MOSFET. In addition, we compensate and correct the original parameter model and furthermore put forward SiC MOSFET key parameter model based on PSpice simulation software.

On the premise of finishing model PSpice simulation, we do experiments on static characteristics and dynamic characteristics of No. SCH2080ke SiC MOSFET coming from ROHM Company. And we also make a comparative analysis of the degree of consistency between the simulation waveform and the experimental waveform so as to verify the correctness and accuracy of the model we built. The compared result is satisfactory and it can provide a basis for making computer circuit analysis before the engineering application.

References

[1] Kai Sun, Juejing Lu, Hongfei Wu, Yan Xing, Lipei Huang. Model of SiC MOSFET With Temperature Dependent Parameters[J]. Procreedings of the CREE, 2013, 33(3): 37-43(china)

[2] Xichuan Wang, Common Principles and Typical Applications of Electronic Devices[M]. Beijing: Mechanieal Industrial Publishing House,2012:150-154

[3] Huazhong Yang, Rong Luo, Hui Wang. Computer-aided Analysis and Design Methods of Electronic Circuits[M]. Beijing: Tsinghua University Press, 2008:57-121

[4] Hongyu Su. PSpice Circuit Design Editor[M]. Beijing: Defense Industry Press, 2004：35-55

[5] Xinchun Shi, Yi Wang, Liling Sun. Power Electronics Technology[M]. Beijing: China Electric Power Press, 2013:25-28

[6] Wang J, Zhao T, Li J, et al. Characterization, modeling and application of 10kV SiC MOSFET[J]. IEEE Trans.on Electron Devices, 2008, 55(8): 1798-1805

Advanced Materials Research Vols. 986-987 (2014) pp 1396-1400

doi:10.4028/www.scientific.net/AMR.986-987.1396

The Selection of Online Power Flow Calculation's Known Quantities

Ling WANG[1, a], Hai BAO[2, b], Yulong CHEN[2, c]

[1]State Grid Liaoning Electric Power Company Limited Benxi Electric Power Supply Company, Benxi, 117000, China

[2] North China Electric Power University, Beijing, 102206, China

[a]email:cyl_icepee@126.com, [b]email:hdbh@vip.sina.com, [c]email:chenyulong_2012@163.com

Keywords: Online Power Flow Calculation; Known Quantity; Reactive Power Flow; Accuracy

Abstract. The difference between schedule power flow and online power flow is that the former has no corresponding physical power flow, while the latter is the reappearance of existing physical power flow. Owing to the different premise, the selection of power flow calculation's known quantities can be different. A schedule power flow schedules physical power flow for power system, so the selection of known quantities has strict requirements, such as active power and reactive power regulation capability. Since the physical power flow exists, the selection of online power flow calculation's known quantities can be more flexible. For example, we can choose load bus as slack bus or replace PQ bus with PV bus. The example demonstrated that we could locate the stealing electricity buses by choosing load bus as slack bus. Considering that voltage amplitude measurement accuracy is higher than reactive power measurement accuracy, we can replace PQ bus with PV bus and make the power flow calculation results more consistent with the physical power flow. Finally, the examples show that online power flow calculation's known quantities can be selected flexibly according to the actual situation rather than strictly following the classical power flow calculation requirements.

Introduction

Power flow calculation is the significant and basic work of power system analysis and operation. According to the sequence of power flow calculation and physical power flow, it can be categorized as schedule power flow and online power flow. Schedule power flow acquires the physical system's feasible running status by calculation, and the physical system is not running under the calculated condition at the moment. That is, schedule power flow appears before physical power flow. The objective of online power flow is numerical value representation of physical power flow, and the physical system is running under this condition at the moment. That is, online power flow appears after physical power flow. Generally speaking, both kinds of power flow calculation can select the same known quantities, such as PV bus, PQ bus and slack bus, and the same power flow calculation program. However, in some cases, the selection of online power flow calculation's known quantities can be more flexible than schedule power flow calculation. The reason is that the physical system's power flow is real, and there is no need to consider the restriction of selecting slack bus and PV bus. Examples of locating the stealing electricity buses and conversion between voltage and reactive power show that the selection of online power flow calculation's known quantities can be more flexible than classical selection method. And the flexible disposal brings good effects.

Selecting Principles of Schedule Power Flow Calculation's Known Quantities [1]

The fundamental equations of power flow calculation are

$$\frac{P_i - jQ_i}{\dot{V}_i^*} = \sum_{j=1}^{n} Y_{ij}\dot{V}_j \quad , (i = 1, 2, \cdots, n) \tag{1}$$

$$\dot{V}_i = \sum_{j=1}^{n} Z_{ij} \frac{P_j - jQ_j}{\dot{V}_j^*} \quad , (i = 1, 2, \cdots, n) \tag{2}$$

where n is the bus number of the system.

Each equation set contains n nonlinear complex number equations, and they are the fundamental equations of power flow calculation. Different processing modes of these two equation sets form different calculation programs. The fundamental equations contain n complex number equations, and that is equivalent to $2n$ real number equations. Only $2n$ operational parameters could be worked out, while the other $2n$ operational parameters should be given as original data.

Generally, two operational parameters are given for every bus when calculating power flow, while the other two are taken as unknown quantities. According to the known quantities, the buses of power system are divided into three categories. For PQ bus, active power and reactive power of the bus are given, and voltage phasor is an unknown quantity. Generally, each substation bus is a PQ bus. If the power plant's active and reactive power outputs are given, it is also taken as a PQ bus. For PV bus, active power and voltage amplitude of the bus are given, while reactive power and voltage angle are unknown. Such kind of buses usually needs reactive power source to maintain the given voltage. Therefore, these buses are those who can regulate voltage of the system. Usually, power plant with reactive power reserve is taken as a PV bus. And if the substation has reactive power reserve, it can also be taken as a PV bus. There is usually one slack bus for power flow calculation. For this bus, voltage amplitude is given, and voltage phasor's direction is seen as the reference axis, which means voltage angle of the bus is zero. Generally, frequency modulation power plant is a reasonable choice for slack bus.

By observing from the selecting principles of schedule power flow calculation's known quantities, we can see that power flow calculation is to plan a working point for the physical system. Therefore, when we select known quantities, PV bus must have the capability of adjusting the reactive power, and slack bus must have the capability of adjusting the active power.

Source of Online Power Flow Calculation's Known Quantities

Online power flow calculation's known quantities come from the actual measured data, so the accuracy of the measurement system determines the matching degree between calculation results and the physical state. For the sinusoidal steady state system with single frequency, the existing measurement system acquires accurate measured data. While for the sinusoidal steady state system with harmonic, the existing measurement system produces significant errors on reactive power measurement.

(1)Reactive power definition of non-sinusoidal circuit

Budeanu proposed the classical power definition and it was written to the ANSI/IEEESdt 1459-2000 standard [2]. However, Shenherd and Zakihani thought that there was no scientific basis for the definition of Budeanu, and distortion power was just digital quantity without any physical meaning [3]. Emanuel thought that apparent power included two parts in the physical sense, that is, active power and compensation power [4]. Czanecki proposed current and power orthogonal decomposition with clear physical meaning [5]. Fryze pointed out that reactive power can be calculated by the apparent power and active power directly [6]. C.H.Page extended Fryze's definition from a certain periodic steady signal to all periodic signal waveforms in a period [7]. In 1983, Akagi proposed the instantaneous power theory and it gradually developed into a power theory appropriate for three-phase equilibrium steady-state voltage and current signal under the circumstance non-sinusoidal [8].

(2)Reactive power measurement technology

When the system suffers from severe interference or system failure, the zero-crossing point fluctuates strongly and the phase difference between voltage and current cannot be measured accurately [9]. That results in greater reactive power measurement error of formula method. When we use phase shifting method to measure signals with 10% third harmonic voltage and 20% third harmonic current, the reactive power measurement error is 4% [9][10]. When we use FFT method to measure frequency in the 49.5 Hz to 50.5 Hz range and if the signal contains ninth harmonic or inter-harmonic, amplitude measurement error can reach 10% and phase measurement error is even larger than 20% [12]. When we use Hilbert transform to measure reactive power, the maximum measurement error reaches 7% if the frequency fluctuates [13][14].

In conclusion, the principle of reactive power flow measurement exist great divergence yet, and different definition even conflicts with each other. For the non-sinusoidal steady state system, measurement error of reactive power flow is about 5% to 10%.

Selecting Principles of Online Power Flow Calculation's Known Quantities

In the premise that the measurement accuracy meets requirement, the selection of online and schedule power flow calculation's known quantities can be the same. If the measurement accuracy cannot meet requirement, we can choose operational parameters with higher measurement accuracy to replace the lower ones. For example, we can replace bus voltage amplitude with corresponding reactive power, namely converting PQ bus to PV bus. Since physical power flow already exists, the physical meaning of PV bus, PQ bus and slack bus is far less significant than schedule power flow. The restriction of known quantities' selection can be relatively broadened, and we can choose load bus as slack bus when needed.

Analysis of Examples

(1)Case 1

When there is electricity stealing at the load bus, we can locate the electricity stealing bus by power flow calculation.

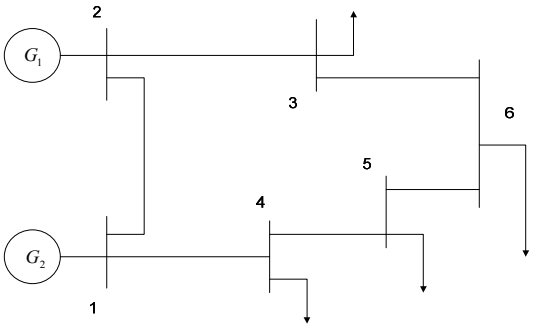

Fig.1. Schematic diagram of 6-node network

Table 1 Branch parameters

O.B	I.B	Resistance	Reactance	Susceptance
1	2	0.010	0.085	0.008
1	4	0.015	0.100	0.010
2	3	0.011	0.182	0.006
3	6	0.009	0.056	0.004
4	5	0.020	0.240	0.012
5	6	0.010	0.235	0.009

Set bus 2 as PV bus, bus 1 as slack bus and others as PQ buses. Results of power flow calculation are listed in Table 2 and Table 3. Set the results as the criteria, and the following power flow calculation uses them as references. Reference value of power is 100 MW. All the numerical values have been converted to per unit value.

Table 2 Bus data

Bus	Voltage		Generator		Load	
	Amp	Ang(^{o})	P	Q	P	Q
1	1.050	0.000	0.4066	0.3650		
2	1.040	0.198	0.4500	0.1043		
3	0.997	-3.890			0.3000	0.1600
4	1.021	-2.133			0.3000	0.1600
5	1.001	-3.832			0.1000	0.0500
6	0.993	-4.250			0.1500	0.0800

Table 3 Branch data

B.	O.B	I.B	Out-P	In-Q	Loss	
					P	Q
1	1	2	-0.0295	0.1227	0.00015	0.0013
2	1	4	0.4361	0.2423	0.00342	0.0228
3	2	3	0.4203	0.2344	0.00237	0.0392
4	3	6	0.1180	0.0414	0.00014	0.0009
5	4	5	0.1326	0.0702	0.00045	0.0054
6	5	6	0.0322	0.0271	0.00002	0.0005

When there is electricity stealing at the bus 6, the measured power is only part of the actual power. If we take half of the actual power and calculate as the standard power flow calculation, the results are listed as Table 4 and Table 5.Table 4 and Table 5 differ significantly with Table 2 and Table 3, which illustrates that those two calculation results correspond to two different power flow interfaces, and we cannot find out the electricity stealing bus.

In response to the act of electricity stealing, we adjust the known quantities of power flow calculation. Bus 1and bus 2 are set as PV buses, and the voltage amplitude is set as the value in Table 2. Bus 6 is set as slack bus, and the voltage amplitude is set as 0.933 corresponding to Table 2,

and the voltage angle is set as zero, which indicates electricity stealing has no influence on measurement accuracy of voltage. Bus 3, bus 4 and bus 5 are set as PQ buses, and the active power and reactive power is set as the value in Table 2.

Compared with Table 2, except for the voltage angle bar, all the other data of Table 6 are equal. Since bus 6 is set as slack bus, and its voltage angle is set as zero, each voltage angle of Table 6 differs by 4.250 degree from Table 2. That is a sort of translation and has no actual impacts. Compared with Table 3, all the data of Table 6 are equal. This illustrates that power flow of Table 6 and Table 7 is consistent with the standard power flow of Table 2 and Table 3. By selecting slack bus, we can locate electricity stealing at bus 6.

Table 4 Bus data when load of bus 6 is halved

Bus	Voltage		Generator		Load	
	Amp	Ang(^{o})	P	Q	P	Q
1	1.050	0.000	0.4066	0.3650		
2	1.040	0.418	0.4500	0.1043		
3	1.003	-3.178			0.3000	0.1600
4	1.023	-1.995			0.3000	0.1600
5	1.006	-3.335			0.1000	0.0500
6	1.002	-3.394			0.0750	0.0400

Table 5 Branch data when load of bus 6 is halved

B.	O.B	I.B	Out-P	In-Q	Loss	
					P	Q
1	1	2	-0.0781	0.1287	0.00022	0.00018
2	1	4	0.4085	0.2253	0.0300	0.0200
3	2	3	0.3716	0.1960	0.0181	0.0299
4	3	6	0.0698	0.0123	0.00005	0.0003
5	4	5	0.1055	0.0561	0.00029	0.0034
6	5	6	0.0522	0.0150	0.0000	0.0001

Table 6 Bus data when bus 6 set as slack bus

Bus	Voltage		Generator		Load	
	Amp	Ang(^{o})	P	Q	P	Q
1	1.050	4.251	0.4066	0.3650		
2	1.040	4.449	0.4500	0.1044		
3	0.996	0.360			0.3000	0.1600
4	1.021	2.118			0.3000	0.1600
5	1.001	0.418			0.1000	0.0500
6	0.993	0.000			0.1500	0.0800

Table 7 Branch data when bus 6 set as slack bus

B.	O.B	I.B	Out-P	In-Q	Loss	
					P	Q
1	1	2	-0.0295	0.1227	0.00015	0.0013
2	1	4	0.4361	0.2424	0.00342	0.0228
3	2	3	0.4204	0.2345	0.00237	0.0392
4	3	6	0.1180	0.0415	0.00014	0.0009
5	4	5	0.1326	0.0703	0.00045	0.0054
6	5	6	0.0322	0.0271	0.00002	0.0005

(2)Case 2

When there are measurement errors, the parameters' error degree is different, so the measurement accuracy of different electrical parameters can be ranked as follows. Voltage and current's error degree is about 1‰-2‰. Active power's error degree is about 5‰. Reactive power's error degree is above 5%. For a physical power flow interface, different selections of known quantities generate different power flow calculation results. When we replace reactive power with voltage amplitude, the classical selection method of known quantities becomes PV bus and slack bus, and the calculation's result of the latter is closer to physical power flow [15].

Conclusion

The classical selection method of power flow calculation aims at schedule power flow and there is no corresponding physical power flow. Therefore, PV bus must have the capability of adjusting the reactive power, and slack bus must have enough capability of adjusting the active power. And this provides necessary support for the expected physical power flow. The premise of online power flow calculation is that the physical power flow already exists. And the objective of power flow is numerical value representation of physical power flow. The selection of online power flow calculation's known quantities can be more flexible and it does not necessarily follow the classical selection method. This can give full play to the role of power flow calculation.

References

[1] Xi'an Jiaotong University, Tsinghua University, Zhejiang University, Hunan University, Power system calculation [M]. Water Conservancy and Electric Power Press, August 1978.

[2] Budeunu, C. Reactive and fictions power [J]. Publication NZ of the Rumanian National Institute. Bucarest, 1927.

[3] Shepherd, W., and ZAKIKHANI, P. Suggested definition of reactive power for non-sinusoidal system [J]. Proc. IEE., 1972, 119:1361-1362.

[4] Emanuel, A.E. Suggested definition of reactive power in non-sinusoidal systems and reactive power definitions and power factor improvement in nonlinear system [J]. Peoc. IEE, 1974, 121(7):705-706.

[5] Czarnecki, L.S. Considerations on the reactive power in non-sinusoidal situations [J].IEEE Trans., 1985, 1M-34:399-404.

[6] Fryze, S. Active, reactive and apparent power in circuit with non-sinusoidal waveform of current and voltage [J]. Przeglad Electrotechniczny, 1931, (7):1993-203, and, (8):225-234.

[7] Page C H. Reactive power in non-sinusoidal situation [J].IEEE Transactions and Measurement，1980，29 (4):420-423.

[8] Akagi H，Kanazawa Y，Nabae A .Generalized theory of the instantaneous reactive power in three-Phase circuits[C]. International Conference on Power Electronics，Tokyo，1983.

[9] Mei Xue, Wu Weilin. Reactive power measurement [J]. Chinese Journal of Scientific Instrument，2003，24(4)：43-45+49.

[10] Etienne Moulin．Measuring reactive power in energy meters[J]．Metering international，2002，3(1)：51-54.

[11] Liu Yuhuai,Ye Yi,Liu Jingao. The error of three phase reactive power measurement methods[J].Electrical Measurement & Instrumentation, 2003，40(453)：28-31.

[12] Qian Hao, Zhao Rongxiang. Inter-harmonics analysis based on interpolation FFT algorithm[J] .Proceedings of the CSEE, 2005， 25(21)：90-94.

[13] Wang Bolin,Liu Hua. Reactive power measurement with quasi-synchronous Hilbert arithmetic [J] .Electrical Measurement & Instrumentation, 2003，40(12)：13-15.

[14] Liu Qiankun, Li Hongwei. A novel method of reactive power measurement based on interpolation FFT algorithm refactoring Hilbert transformation [J]. Power System Protection and Control, 2009，37(15)：19-22.

[15] Bao Hai,Huang Xin,Wang Ling,Liu Gang. A new method for online steady-state power flow calculation in electric power system. 4th International Conference on Manufacturing Science and Technology, ICMST 2013: 1090-1093.

Advanced Materials Research Vols. 986-987 (2014) pp 1401-1404

doi:10.4028/www.scientific.net/AMR.986-987.1401

Wire suspension system based on fault tree analysis running condition assessment

Bing HAO [1, a] , Li ZHI [(Corresponding author) 2, b]

[1,2]The Three Gorges University,Institute of Electrical and New Energy, YiChang, 443002, China

[a]email: 605775154@qq.com, [b]email: 124857747@qq.com

Keywords: Transmission Line; Running State; The Fault Tree; Assessment

Abstract.Overhead transmission lines is an important part in the power system and the lifeblood of the transmission system.Important element of the transmission line conductor suspension system namely conductor and insulator, hardware.This paper, by using the fault tree analysis method, establishes the mathematical model of the transmission line conductor suspension system running condition assessment, reliably evaluates the running status of system, find out the weak links and the problems of the various parts, for the evaluation and maintenance of overhead transmission line provide theoretical support.

Introduction

Overhead transmission line includes tower, insulator, hardware, base, grounding device, power lines and so on, has a wide distribution area, many testing parameters, complicated operation environment characteristics. These factors cause many inconvenience to the operation, maintenance and diagnosis of the transmission line [1]. Therefore, we need to establish a set of method for overhead transmission lines to evaluate reliability and analyze, so we can according to the operation condition of the parts to decide whether to repair or inspect, which has important significance to the safety and reliability of the power grid.Fault tree analysis (FTA) is in the process of system operation, through to analyze the various factors that may result in system failure (including climate, environment, human factors, etc.), and establish the running state of the fault tree. The fault tree determines the system failure causes and probability of occurrence of the various possible combinations, and take appropriate corrective measures in order to improve the reliability of the system level.

Basic Idea of Reliability Condition Assessment

Make the running condition assessment to insulator, hardware, wire of the conductor suspension system respectively .The three main parts of running state can be thought of as independent of each other.By establishing the reliability of the suspension system overhead transmission line, and adopt the fault tree analysis method, using the principle of minimum cut set analysis of the transmission line fault tree, through the evaluation and analysis of the fault tree to find out the factors affecting the reliability of the transmission line suspension system, and find out the failure rate.

Accordingly, wire suspension system running condition assessment in general can be divided into three time, between each level events were independent of each other.In this paper, the most basic of sub event specific as follows[9]:

1）Insulator (X), a total of six basic events: X1 —the insulator surface; X2— the specific creepage distancethan from meets the pollution level of creepage distance numerical requirements; X3—porcelain insulator zero rate and the explosive rate; X4—the situation of the composite insulator damage, cracking, aging; X5—the situation of the lock pin; X6—steel leg bending and looseness.

2）Hardware (Y), a total of five basic events: Y1—hardware corrosion situation; Y2—abrasion of hardware; Y3—pin shortage; Y4—hardware looseness; Y5—hardware strength.

3）Conductor (Z), a total of seven basic child events: Z1—overhead transmission lines broken strands number; Z2—the galvanized steel strand rust; Z3—sag deviation of lead to ground; Z4—sag

deviation of each wire; Z5—sag deviation of each phase conductor; Z6—wire connector; Z7—wire strength test value.

Fault Tree of Wire Suspension System Running State

From the evaluation standard of wire suspension system, we can find out the factors affecting the reliability of overhead conductor suspension system is divided into into three broad categories.Of which the influence factors of insulator is a total of eight;The influence of hardware is a total of five;The influence factors of conductor is a total of 10. According to the logic of the relationship between these factors and through computer aided calculation of minimum cut sets and use the delete method will simplify the above factors become mutually disjoint minimal cut set.Finally the result is that insulator has six factors of minimum cut sets;The hardware has five factors of minimum cut sets;Wire has seven factors of minimum cut sets. All the eighteen basic factors constitute the incompatible minimum cut sets of wire suspension system fault tree, which become the bottom events.The three types of influence factors are become intermediate events, the reliability of whole conductor suspension system is called the top event.

According to these incompatible logical relationship between the minimum cut sets, this paper builds the fault tree model of overhead conductors suspension system as shown.

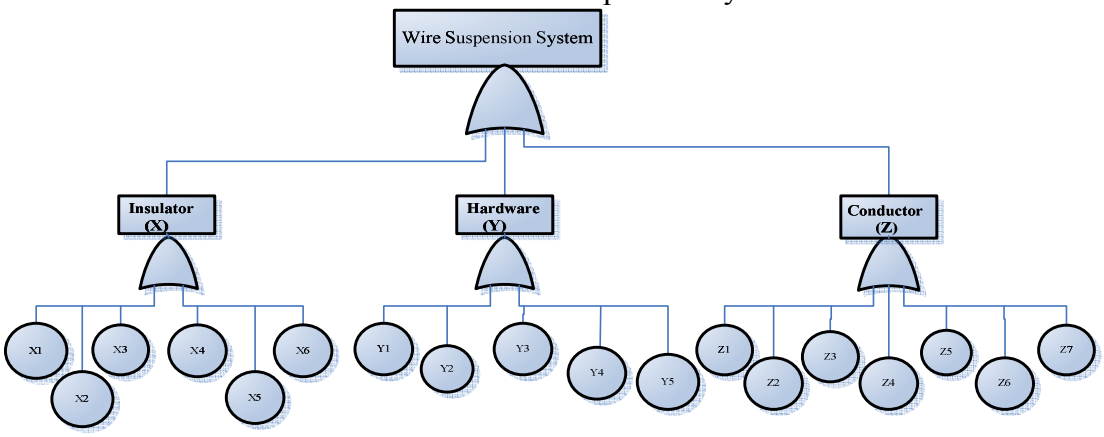

The Example Analysis

A practical transmission line, the voltage level of 220 kV, total length of 33.41 km.The insulator in the line wire suspension system is a total of 5287, including 5159 porcelain insulators and 128 composite insulators , 4830 hardwares, 318 roots wire.

By the least cut set obtain probability of top event.FTA method is used to assess the fault tree is to find out all possible failure modes which cause the top event , namely all the minimum cut sets of fault tree. A fault tree often have several minimum cut sets, or at least a minimum cut sets (corresponding to the combination of a basic failure event) happen, and the top event is bound to happen.Minimum cut sets of system failure probability approximation method is as follows: has the minimum cut sets of system one, then the system failure probability expression is:

$$Q_s = \{C_1 \bigcup C_2 \bigcup C_3 \ldots \bigcup C_i\} - \sum_{i<j=2}^{l} P(C_i \bigcap C_j) + \ldots (-1)^{l-1} P\{C_i \bigcap C_j \ldots \bigcap C_l\}$$

Using a method to make the minimum cut set by the intersection of state into mutually disjoint or using approximate calculation to reduce the amount of calculation when evaluating.

The secondary events running state probability calculation formula is:

$$N = \bigcup_{i=1}^{n} \left(\frac{N_B}{N_N} + \frac{N_A}{N_N} \bullet 0.5 \right) \qquad P(N) = N \bullet R_{Ni} \qquad (N = X, Y, Z)$$

in formula：

P(N):The unreliable probability of each secondary events；N:Each basic event unreliable matrix；N_A:State of each basic event note number；N_B:Number of each basic event bad state；N_N:The total number of each basic event overall equipment components； R_{Ni}:The right of each basic event of the coefficient matrix；N:The number of basic events；

The operation state of overhead transmission line probability calculation formula is:

$$P_S = P(X) \bullet R_X + P(Y) \bullet R_Y + P(Z) \bullet R_Z$$

in formula：

P_S:The bad state probability of operation of overhead transmission lines P(x):The unreliable probability of insulator running state ;P(Y):The unreliable probability of hardware running state;P(Z):The unreliable probability of conductor running state;

R_i:The weight coefficient of each secondary events (i=X,Y,Z)As shown in table1

Table1 Intermediate events weight value

weight	R_X	R_Y	R_Z
Value(%）	13	13	27

The above formula can be used to calculate the conductor of the various components of the suspension system is not reliable probability:

The probability of unreliable: P(X)=0.028938 P(Y)=0.00201 P(Z)=0.000111

Unreliable probability of the whole wire suspension system is：

$$P_S = P(N).R_N = 0.010156$$

The whole wires running state of suspension system are as follows:

$$A=1-P=1-0.010156=0.989844$$

Through the above data analysis can know, the transmission line of wire suspension system are in good running condition;At the same time through the adverse state probability of insulator, hardware, wire insulator is the weak link of the transmission line can be drawn from what that require timely maintenance.Compared with the actual situation, this insulator defects in wire suspension system is more, in accordance with this article model assessment results.

Conclusion

The method of fault tree analysis is a good way to analyze the running state of wire suspension system for transmission lines, which can calculate system components reliability probability and system vulnerabilities are obtained. Provides a convenient and quick reliability evaluation model for economic overhaul, maintenance overhead transmission line.

References

[1]Allan.R.N,Billinton.R,et al. Bibliography on the Application of Probability Methods in Power System Reliability Evaluation(1987-1991).IEEE. Transactions on power Systems,1994,9(l):41- 45.

[2] Qiusheng Yang, Reliability analysis and discussion of overhead transmission lines [J]. Journal of shanxi electric power, 2004,12（6）:50-53.

[3] Tao Wang, Fuchun Han. Based on the FTA method of distribution transformer running state evaluation [J]. Journal of electric power, 2009, 24 (1) : 31-34.

[4] Wei Wang,Haiying Cui, Wenhu Huang,Diagnosis method based on fault tree of minimum cut sets research [J]. Journal of data collection and processing, 1999, 14 (1) : 26-29.

[5] Fuchun Han, Yaxin Liu, Leiliang Jia, etc., The old overhead transmission lines running state evaluation standard research. [J]. Shanxi electric power. 2005,（6）：10-13.

[6] Lee, Burton Hoyt. Failure modes and effects analysis with Bayesian belief networks:Bridging the design2diagnosismodel2ing gap [D]. Stanford University, 2002: 124.

[7]jG.J.Cliteur,J.M.Wetzer,Distribution Components Condition Assessment of Power Transmission and CIRED2001,18-21June 2001,Conference PublicationNn.482.

[8] J.A.Lapworth, P.N.Jarman, I.R.Funnell, Condition Assessment Techniques For Large Power Transformers `The Reliability of Transmission and DistributionEquipment,29-31 March 1995，Conference Publication No.406.

Advanced Materials Research Vols. 986-987 (2014) pp 1405-1409

doi:10.4028/www.scientific.net/AMR.986-987.1405

Parameters Optimization of LQR for Magnet Power Supply of Accelerator

Xin ZHANG[1, a], Min LIU[2, b]

[1]School of Automation & Electrical Engineering, Lanzhou Jiaotong University, Lanzhou, 730070, China

[2]Mechatronic Engineering Department, Lanzhou Vocational Technical College, Lanzhou, 730070, China

[a]email: hdzhangx@gmail.com, [b]email:526218088@qq.com

Keywords: particle swarm optimization; LQR; parameter optimization; heavy ion accelerator; magnet power supply

Abstract. Accelerator has been widely applied to high energy, low energy physics, Medical environmental and military fields, etc. The magnet power supply is one of the most important parts of the accelerator. At the beginning, the state-space model of the magnet power supply has been established by modern control theories. Then, the PSO algorithm has been used for the weight matrices optimization of LQR controller in order to ensure that the magnet power supply can provide a magnetic field quickly which the accelerator required. The experimental results indicate that the method that proposed in the paper can meet the requirements of fast output response of the system and each control index of the LQR controller is obviously superior to that by the traditional method.

Introduction

The accelerator can make use of the electric field to drive the charged particles for high energy that can be broadly divided into cyclotron and linear accelerators, which mainly related to the content of magnet, power supply, vacuum and high – frequency control, etc. The section of the magnet power supply plays an important role in this project. The main function of the magnet power supply [1] is to provide magnetic field to the accelerator, in order to make the magnetic field increasing and decreasing synchronize with the movement of the ions, the PWM power has the advantages of simple structure[2], low manufacture cost and easy to be controlled, and can avoid the great impact on power grid and harmonic pollution[3-5]. Therefore, the research on the PWM power supply has very practical significance for the accelerator power supply.

LQR is an optimal control method with the quadratic performance indexes and these indexes have specify physical concepts generally[6], which has been successfully applied to many fields of industry control. At the same time, LQR has simple math disposal process and can achieve closed loop optimal control with the linear state feedback or output feedback. One of the key problems on the design of the controller is how to chose the weighed matrices Q and R, which will have a directly effect on the final control results. At present the commonly used weight matrix optimization algorithm are genetic algorithm, Variable Universe Fuzzy Control algorithm, particle swarm optimization.

Particle Swarm Optimization (PSO) is a evolutionary computation technique that has been successfully used for many years in different domain. In this paper, the weight matrices are optimized based on PSO for the magnet power supply and the simulation gives a nice result.

Model of the magnet power supply

The magnet power supplies of Heavy ion accelerator are mainly single phase power supply, so what this dissertation mainly specializes in is the Single-phase PWM inverter model. The model[3] of the magnet power supply is established based on the HERFL-CSR that shows in figure 1.

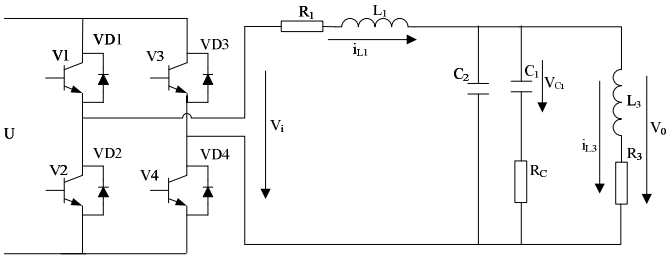

Fig.1. Accelerator magnet power supply model

When the VD1 and VD4 conduct, $V_1 = \mathrm{U}$; when the VD2 and VD3 conduct, $V_1 = -\mathrm{U}$. i_{L3} is the load current (exciting current), V_0 is output load voltage, C_1 , C_2 and L_1 are smoothing capacitors and filter inductor, R_C and R_1 are corresponding to the resistance of the smoothing capacitors and filter inductor. R_3 and L_3 are the load of magnet winding. Therefore, the mathematical model can be obtained as follow:

$$V_1 - V_0 = R_1 i_{l1} + L_1 \frac{d_{l1}}{dt} \tag{1}$$

$$i_{l1} = C \frac{dV_0}{dt} + i_{l3} + C_2 \frac{dV_{C1}}{dt} \tag{2}$$

$$V_0 = i_3 R_3 + L_3 \frac{di_3}{dt} \tag{3}$$

$$V_0 = V_{C1} + R_2 C_1 \frac{dV_{C1}}{dt} \tag{4}$$

The state space equation of the proposed model is described as (5) and (6).

Where the choosen values of each component parameter is as follows: $L_1 = 0.3\mathrm{mH}$, $L_1 = 0.3\mathrm{mH}$, $L_3 = 91.4\mathrm{mH}$, $L_3 = 91.4\mathrm{mH}$, $C_1 = 10\mu\mathrm{F}$, $C_1 = 10\mu\mathrm{F}$, $\mathrm{R}_2 = 1\Omega$.

$$\begin{bmatrix} \dot{i}_{l1} \\ \dot{i}_{l3} \\ \dot{V}_{C2} \\ \dot{V}_0 \end{bmatrix} = \begin{bmatrix} -\frac{R_1}{L_1} & 0 & 0 & -\frac{1}{L_1} \\ 0 & -\frac{R_3}{L_3} & 0 & \frac{1}{L_3} \\ 0 & 0 & -\frac{1}{R_2 C_2} & \frac{1}{R_2 C_2} \\ C_1 & -\frac{1}{C_1} & \frac{1}{R_2 C_2} & \frac{1}{R_2 C_2} \end{bmatrix} \begin{bmatrix} i_{l1} \\ i_{l3} \\ V_{C2} \\ V_0 \end{bmatrix} + \begin{bmatrix} \frac{1}{L_1} \\ 0 \\ 0 \\ 0 \end{bmatrix} V_1 \tag{5}$$

$$Y = \begin{bmatrix} 0 & 1 & 0 & 0 \end{bmatrix} \begin{bmatrix} i_{l1} \\ i_{l3} \\ V_{C2} \\ V_0 \end{bmatrix} + \begin{bmatrix} 0 \end{bmatrix} V_1 \tag{6}$$

LQR controller

Given the liner systems presented as $\dot{X} = AX + BU$, $Y = CX + DU$, the optimization of feedback control rules of LQR controller can be determinated as $U^* = -KU$, which minimizes performance index described as (7).

$$J = \int_0^\infty \left[x^T(t) Q x(t) + u^T(t) R u(t) \right] dt \tag{7}$$

Where $K = R^{-1}B^T P$, P is a definite positive symmetric matrix that can satisfy the equation Riccati $PA + A^T P - PBR^{-1}B^T P + Q = 0$. One practical method is to set Q and R to be diagonal matrix ($Q = diag(Q(1,1), Q(2,2), Q(3,3), Q(4,4))$, $R = r$) such that only 5 elements need to be decided[7,8]. The value of the elements in Q and R is related to its contribution to the cost function J.

The values of K depend on the choosing of matrices Q and R, the traditional method is realized by trial and error, the proposed method has adopted the optimization algorithm PSO in the paper. Once the feedback factor $K = [k_1 \quad k_2 \quad k_3 \quad k_4]$ is determinated, the state-space equation of this closed loop control system is obtained as (8):

$$\begin{cases} \dot{X} = A'X + B'U \\ Y = C'X + D'U \end{cases} \tag{8}$$

where $A' = A - B * K$, $B' = B * k_1$, $C' = C$, $D' = D$.

Design of PSO-LQR controller

Particle Swarm Optimization(PSO) is a evolutionary computation technique presented by Kennedy and Eberhart in1995[9,10]. In PSO algorithm[11,12], each particle in swarm represents a solution to D dimension, which is defined with its position and velocity, the mathematical description of the basic particle swarm optimization is as follows. Supposed the scale of swam is N, the position of particle i and the velocity of particle can be described as (9):

$$\begin{cases} x_i = (x_{i1}, x_{i2}, \cdots, x_{iD}) \\ v_i = (v_{i1}, v_{i2}, \cdots, v_{iD}) \end{cases} \tag{9}$$

Then ,the velocity of the particle $i(i = 1, 2, \cdots, N)$ in the $d(d = 1, 2, \cdots, D)$ -dimensional space can be adjusted according to (10) as:

$$v_{id} = v_{id} + c_1 rand_1()(p_{id} - x_{id}) + c_2 rand_2()(p_{gd} - x_{id}) \tag{10}$$

$$\begin{cases} v_{id} = v_{\max}, & if \quad v_{id} > v_{\max} \\ v_{id} = -v_{\max}, & if \quad v_{id} < -v_{\max} \end{cases}$$

Finally, the particle can adjust its position according to (11) is:

$$x_{id} = x_{id} + v_{id} \tag{11}$$

where N is the number of particles in the group, d is the dimension, v_{id} is the velocity of particle i, c_1 and c_2 is the acceleration constant, $rand_1()$ and $rand_2()$ is the random number between 0 and 1, x_{id} is the current position of particle i, p_{id} is the best previous position of the ith particle, p_{gd} is the best particle among all the particles in the population.

The structure diagram of LQR control system based on PSO is shown in figure 2.

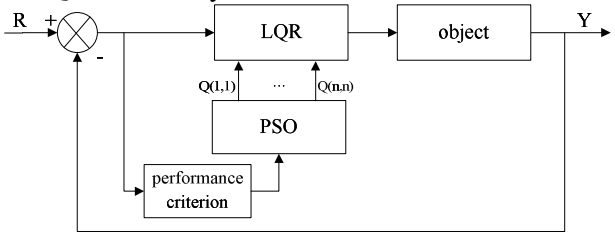

Fig.2. Structure diagram of LQR control system based on PSO

According to the operating state of the system, the module of PSO can optimize the weight matrices of the LQR controller to meet the performance requirements, and the output of this module will provide the optimized weight matrices of LQR controller.

And now, the performance criteria that also is the fitness function of the PSO in this design is defined as (12):

$$J = (1-\exp(-1))\times(M_p + M_{p1}) + \exp(-1)\times(t_s - t_r) \quad (12)$$

Where t_r is the rise time of the output current, t_s is the settling time of the output current, M_p is the overshot of the output current, and M_{p1} is the overshot of the output voltage.

With the above analysis, the specific implementation steps of the parameter optimization of PID controller based on PSO can be divided as follow:

step1: to generate initial population;

step2: to determine the fitness value of each particle using the performance criteria;

step3: to evaluate the fitness value of each particle, and update the global optimum position value;

step4: to update the velocity and position of the particles;

step5: if the maximum iteration number comes to the end or the performance criteria is satisfactory, the system gets the optimal solution. Otherwise, it returns to step 2.

Simulation and Results

As previously mentioned, the particle dimension is set to 4, the population size is set to 20, the other parameters are chosen as follows: ω(Inertia weight factor)=0.6; the acceleration constant c_1 =2 and c_2 =2; the velocity maximum of particle $v_{\max}$ =1, the velocity minimum of particle $v_{\min}$ =-1; the maximal iteration number Iteration =50, and the initial value of the particles are randomly generated within a certain space. The design takes the step signal as input signal to achieve the step response of the control system. The optimized value of the weight matrix is $Q = diag(100,1,1,1.5506)$. The curve of the optimal fitness value, which has been achieved by the proposed method, is shown in figure 3.

Another example of the trial and error for LQR controller is given to illustrate the proposed design is effective. The results of the three methods are shown in figure 4. From the simulation results, it can be conclude that the output response time and the steady time of the system, of which the LQR controller has been optimized by PSO, are much shorter with better effects.

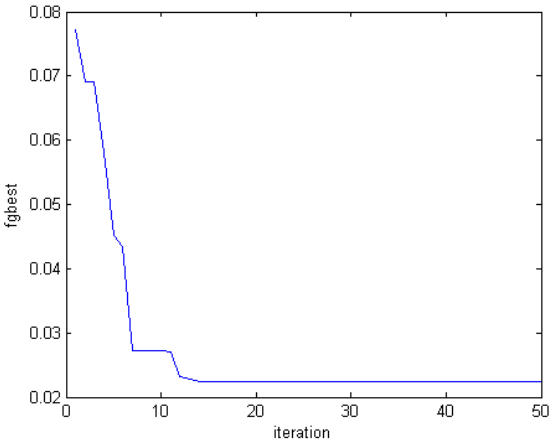

Fig.3. Curve of the global optimal fitness value

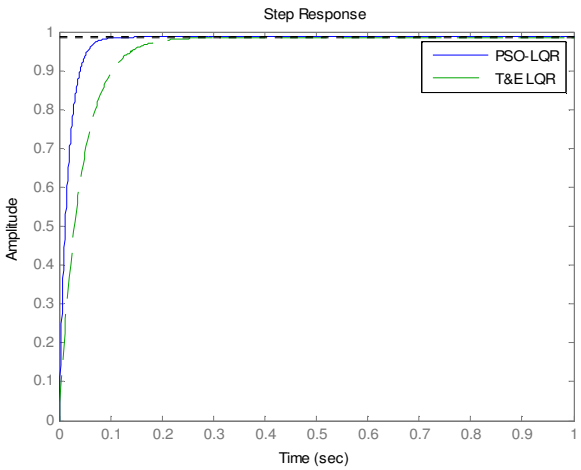

Fig.4. Step response curve of output

Conclusion

Particle Swarm algorithm is a robust, simple and very efficient optimization algorithm. In this paper, the optimization of the weighed matrix of the LQR controller has been done by PSO, which has avoided choosing the matrice Q and R artificially when the optimal LQR controller of the magnet power supply for the accelerator has been devised. The research and results show that the parameter optimization of the LQR controller with PSO has an satisfactory control effect, which is

feasible, universal and practical. The method overcomes the shortcomings of the weighted matrices selected difficultly. The result indicates that the output current can stably run according to the requirements of the accelerator.

Acknowledgement

The authors would like to thank for Project Supported by National Natural Science Foundation of China (Grant No. 61162016, 60962004) and the Lanzhou Jiaotong University Youth Foundation (No. 2011041, 2013041)

References

[1] Qi Xin,Xu Zhongxiong.magnet power supply system for rapid cycle synchrotron of Chinese spallation neutron source.atomic energy science and technology. Vol.40, No.3, pp.363-366, 2006.
[2] Zhao Tao,Wang Xiangqi,Zhang Haiyan,Wang Lin,Li Weimin.A DC stabilized current supply based on double closed-loop control technique with PS-FB converter.vol.37, No.1, pp.104-108, 2007.
[3] Qian Xiangping.Research and design of synchrotron's magnet power supply regulator on accelerator.Lanzhou:Lanzhou University.2011.
[4] Gao Daqing,Wu Rong,Zhou Zhongzu,Chen Youxin.Research and design of HIRFL-CSR pulsed switching power supply. Vol.37, No.2, pp.15-17, 2003,.
[5] QIAN Xiang-ping,QIAO Wei-ming,ZHOU Zhong-zu,Jing lan,CHEN Xi-meng.Research on genetic algorithm in accelerator power.2010 International Conference on Electrical and Control Engineering. pp.4747-4750, 2010,.
[6] P.O.M. Scokaert and J. B. Rawlings, "Constrained linear quadratic regulation," IEEE Trans. Automatic Control, vol.43, no.8, pp.1163-1169, 1998.
[7] Frank H.F.Leung,Peter K.S.Tam,C.K.Li.An Improved LQR-based Controller for Switching Dc-dc Converters. IEEE Transactions on Industrial Electronics, vol.40, no.5, pp.521-528, October 1993.
[8] Cevat Gökçek,Pierre T.Kabamba,Semyon M.Meerkov.An LQR/LQG Theory for Systems With Saturating Actuators. IEEE Transactions on Automatic control, vol. 46, no. 10, pp. 1529-1542, October 2001.
[9] J.Kennedy, R. Eberhart. Particle swarm optimization.Proceedings of the IEEE International Conference on Neural Networks. Piscataway, New Jersey. no.4, pp.1942-1948, 1995.
[10] Eberhart R C, Shi Y. Particle Swarm Optimization: Developments, Applications and Resources. Proc. Congress on Evolutionary Computation 2001. Piscataway,NJ:IEEE Press, pp.81-86, 2001.
[11] Shi Y, Eberhart R C. "A modified particle swarm optimizer". In: Proceedings of the IEEE International Conference on Evolutionary Computation, Piscataway, NJ, IEEE Press, pp.69~73, 1998.
[12] Shi Y, Eberhart R C. "Fuzzy adaptive particle swarm optimization". In: Proceedings of the IEEE Congress on Evolutionary Computation, Seoul, Korea, pp.101~ 106, 2001.

Advanced Materials Research Vols. 986-987 (2014) pp 1410-1413

doi:10.4028/www.scientific.net/AMR.986-987.1410

Prediction Model for Dissolved Gas in Transformer Oil Based on Non-parametric Regression

Chen Jin-qiang[1, a]

[1] School of Electric Engineering, Southwest Jiaotong University, Chengdu 610031, China

[a]chenjq1977@163.com

Keywords: Non-parametric regression; Prediction; Transformer; Dissolved gas in oil

Abstract. The non-parametric regression prediction model for dissolved gases in power transformer and its application are studied. As the intervals between two analytic experiments of transformer dissolved gas are unfixed，the data sequence sampled with unequal intervals is converted into the data sequences with equal intervals，which is smoothed to form a new sequence. And then use the historical samples data to establish non-parametric regression model for prediction. Compared with the grey model, the non-parametric regression model has better prediction accuracy. The case verifies the correctness and feasibility of the method.

Introduction

Based on the dissolved gases in transformer oil to predict transformer failure, which is important for the transformer state maintenance. Currently Forecast methods for Dissolved Gas in Transformer Oil mainly include the BP neural network, gray theory and linear regression prediction algorithm etc [1-3].

With the popularity of power transformer on-line monitoring system, the quantity of the gas data in the transformer oil is growing, and the data include random fluctuation, measurement error and information of oil deterioration. Non-parametric estimation method is a model fit for the Uncertainty, non-linear dynamic systems, which efficiently overcomes the random intervention factors. Non-parametric estimation is a effective model for all distribution. Currently the method has been successfully applied to econometric, electricity load forecasting and other fields [4-6]. This paper studied the prediction model of the dissolved gases in transformer oil based on the non-parametric regression, and gave an example for method validity.

The Basic Model of Non-parametric Regression

The cutting-edge of statistics field is semi-parametric and non-parametric method. Non-parametric estimation methods need not prediction equations. It can predict data by using the input-output relationship of historical samples.

In general, for t = 1, 2, ... , n, assuming that non-parametric regression model's (NAR (p)) structural formula equation is:

$$Y_t = m(X_t) + \varepsilon_t \qquad (1)$$

Where X_t is the explanatory variables; $X_t \in R^{n\times p}$; Y_t is the response variable; $Y_t \in R$; ε_t are random variables which are mutually independent and obey the same normal distribution. ε_t is the random noise error ; $\{\varepsilon_t\}$ is the sequence of random error, ε_t and $X_s\,(s \le t)$ are independent of each other. X_t is composed of several lags Y_t, namely $X_t = (Y_{t-1}, Y_{t-2}, \cdots\cdots, Y_{t-p})$; p is a positive integer representing the number of lagged variables.

Y_t is represented by a function-expression of X_t and it can be seen as a condition expectation after giving $X = x$. Here $m(\cdot)$ is called regression function. There is an approximate function of $y \approx m(x)$, so it is particularly important for the estimation of $m(\cdot)$. Just like inductive and

deductive, the kernel estimation method is used to the prediction model. The "inductive" is to get a function from given data and the "deductive" is to calculate the points value from the function.

The $m(\cdot)$ can be estimated by the N-W kernel estimation, which is a nonparametric regression method proposed by Nadaraya and Watson in 1964. The function expression is as follows:

$$W_{nt}(x)=\frac{K_h(x-X_t)}{\sum_{t=1}^{n}K_h(x-X_t)}=\frac{K_h\left(\frac{x-X_t}{h}\right)}{\sum_{t=1}^{n}K_h\left(\frac{x-X_t}{h}\right)} \tag{2}$$

Here $K_h(u)=K\left(\frac{u}{h}\right)h^{-1}, K(\cdot)$ is called the kernel function or the probability density function. Here h is the window width, X_t represents a specific value of the sample data (n). The approximation regression function $\hat{m}(x)$ can be obtained as follows:

$$\hat{m}(x)=\sum_{t=1}^{n}W_{nt}(x)Y_t=\frac{\sum_{t=1}^{n}K\left(\frac{x-X_t}{h}\right)Y_t}{\sum_{t=1}^{n}K\left(\frac{x-X_t}{h}\right)} \tag{3}$$

Prediction Process of Non-parametric Regression Model

First, use a known X_t and the corresponding time series $\{Y_t\}$ to construct the corresponding NAR (p) model, then select an estimation method, appropriately estimate the regression function $m(\cdot)$. Finally putting $X_{t'}$ into $m(\cdot)$ and equation (1), $Y_{t'}$ is calculated accordingly. The value $Y_{t'}$ is the approximate value of the sample in the future moment. The following is the process of prediction the value $Y_{t'}$ in the future moment $X_{t'}$:

1) According to a known stationary time series $\{Y_t\}$, establishing the appropriate structural equation NAR (p) model: $Y_t=m(X_t)+\varepsilon_t$.

2) Estimating the regression function $m(\cdot)$ by using non-parametric methods (eg: kernel function method, local polynomial method, k-nearest neighbor method). Though non-parametric methods and expression function are different, the essence is similar. They all can be seen as a function of a probability weighted for Y, and can achieve the similar imitative effect.

3) Calculating the parameters in the $m(\cdot)$ and to determine the order p and window width h.

4) Putting $X_{t'}$ to $m(\cdot)$, then calculating non-parametric regression prediction of $Y_{t'}$.

Nonparametric Regression Prediction of Dissolved Gas in Transformer Oil

Data Preprocessing

In this paper, the 220kV transformer of Lishui Electric Power in Zhejiang is as a example. From March 2004 to April 2006 the data of hydrogen concentration in transformer oil can be obtained [3]. First the data is processed smooothly by equal interval of time, and then the processed data is disposed for each month.

The sample data is divided into two parts: the model estimating sample and forecasting evaluation sample. The former 22 samples of data are all used for the model's non-parametric estimation; the last 4 samples are used for the evaluation of the predictive power of the model . Figure 1(a) is scatter plots of raw data, using the difference method for smoothing the raw data to obtain a processed difference data shown in Figure 1(b).

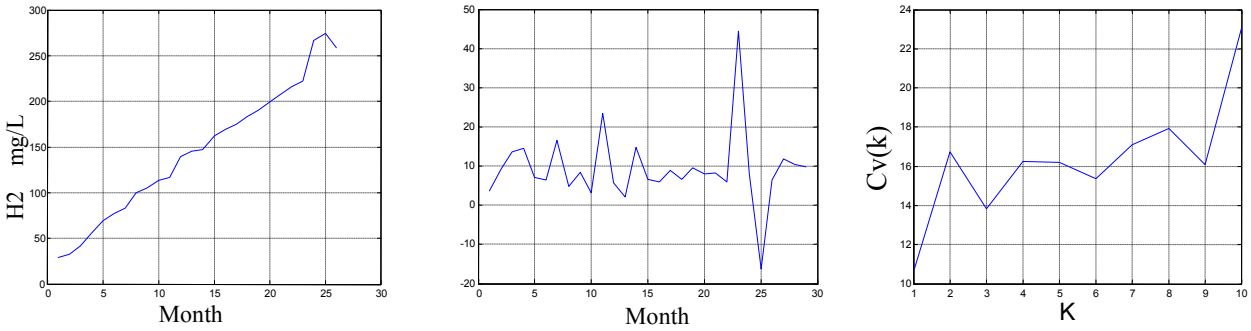

(a) Data of Original Hydrogen (b) Raw Data- First Differential (c) Orders K in Model

Fig.1. The experimental process

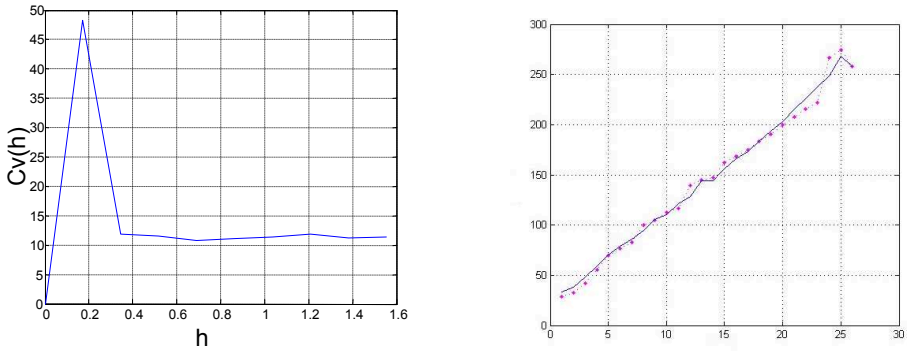

(a) Window Width h (b) Data of Fitting Curve

Fig.2. The experimental result

Establishment of NAR Model

Use Cross-validation method to determine the order p. The computed result of corresponding cv (k) value in Matlab is shown in Figure 1(c). It is known that, when k = 1, the value of cv (k) is the minimum. That means when the order of p in the best model is 1, then the non-parametric autoregressive model is as follows:

$$\nabla Y_t = m(\nabla Y_{t-1}) + \varepsilon_t \quad (4)$$

Then, select the best value of the window width by using Leave-one-out -Cross-validation and calculate the corresponding cv (h) values in Matlab. When the curve is stable, cv(h) has the smallest value 0.6913 In figure 2(a).

With the model construction, two important values of the parameters (p and h) are identified. In this case, the NAR (p) model is established and formula (1) can predict the value of the next data.

Prediction and Assessment

Normally cycle prediction method is used. This method is to use sample data $Y_1, Y_2, \cdots\cdots, Y_n$, and to predict the next value of Y_{n+1} according to structural equation in the non-parametric regression model. The result value is recorded as $\hat{Y}_{n+1}$, and then to add the value to the sample, thus a new sample is produced. The sample will contain n +1 data （$Y_1, Y_2, \cdots\cdots, Y_n, \hat{Y}_{n+1}$）, According to the new n +1 sample data , it can predict value $\hat{Y}_{n+2}$ from Y_{n+2}, and then add $\hat{Y}_{n+2}$ to the sample, forming data n +2（$Y_1, Y_2, \cdots\cdots, Y_n, \hat{Y}_{n+1}, \hat{Y}_{n+2}$）. Finally the value of $\hat{Y}_{n+k}$ is gotten from Y_{n+k} by this method. This method takes advantage of the information of the sample and predicts value in each step, so the result is more accurate. The contrast between fitting curves and original sequence curves is shown in Figure 2(b).

As the main purpose of gas content prediction in transformer oil is to forecast faults and determine maintenance plans, so short-term prediction can meet the requirements. The paper takes a four-step prediction. Grey Prediction GM (1,1) model is a mature method to the dissolved gas forecast in transformer oil. The paper also uses the gray forecasting model to predict gas content

and contrast the results are shown in Table 1. After a comparison of prediction results between gray forecasting model and non-parametric regression NAR (p) model, we see that the prediction of NAR (p) model is better, reflecting this model has strong predictive capability and high feasibility.

Table. 1 Contrast of Two Prediction Methods

time	H2(mg/L)	NAR (p) /error(%)	GM(1,1) /error(%)
2006.1	221.9	237.4/6.98	255.5/15.1
2006.2	266.3	248.3/6.76	272.8/2.44
2006.3	274.3	268.1/2.26	291.4/6.23
2006.4	276.4	258.1/6.62	311.3/12.62

Conclusion

As the situations of dissolved gases in transformer oil situation are complex and diverse, for examples load, weather and so on. The gas concentration Prediction model is difficult to fully consider various factors. Non-parametric method does not make any assumptions for the relationship between variables and analyze its data directly by modeling, thus avoiding the model deviation from parameter estimation method. In this paper, the non-parametric regression model NAR (p) for content prediction of dissolved gas in transformer oil is simple, effective, and easy to implement. The method contributes to the forecast of the state of the transformer, and provides reference to the maintenance.

References

[1] Wang You-yuan，Liao Rui-jin，Sun Cai-xin，et al．An improved grey prediction model for dissolved gas in transformer oil[J]．High Voltage Engineering，2003，29(4)：24-26(in Chinese)．

[2] SHA Li-cheng, SONG Jun. Predicting method for dissolved gas in transformer oil based on modified particle swarm optimization[J]. Journal of North China Electric Power University: Natural Science Edition,2011, 38(1): 35-38.

[3] LI Jun- qing, et al .Forecast of Mass Concentration of Dissolved Gas in Transformer Oil Based on Combinative Forecasting Model. Guangdong Electric Power, 2011(09): p. 19-23.

[4] Wang Peng，Xu Tao．An prediction model for dissolved gas in transformer oil based on statistical learning theory[J]．High Voltage Engineering，2003，29(11)：13-14(in Chinese)．

[5] ZHAO Yuan , ZHANG Xia-fei, XIE Kai-gui, Application of Nonparametric Auto- regression to Short-term Load Forecasting. High Voltage Engineering, 2011(02): p. 429-435.

[6] ZHOU Song-lin, MAO Mei-qin, SU Jian-hui. Short-term Forecasting of Wind Power and Non-parametric Confidence Interval Estimation. Proceedings of the CSEE, 2011(25): p. 10-16.

Advanced Materials Research Vols. 986-987 (2014) pp 1414-1417

doi:10.4028/www.scientific.net/AMR.986-987.1414

Transient analysis of Induction Machines Using Time-stepping Finite Element Method Coupled with the Circuit Equations

Jie LI, Yu-jiao ZHANG[a], Meng-yun SUN, Wei-nan QIN, Xin WU

College of Electrical Engineering & New Energy, China Three Gorges University, Yichang, 443000,China

email:jiao_zyj@163.com

Keywords：Time-stepping Finite element method; Field circuit coupling; Non-sinusoidal Supply; Transient analysis

Abstract. A field-circuit coupled finite element method has been applied on one induction machines for the transient analysis in case of inverter power supply and sinusoidal voltage supply in this paper. The focus is to build the time-stepping finite element method with external circuit coupled to the electromagnetic field equations and achieve voltage supply. The problem of the motion of rotor is solved through moving boundary by interpolation in the moving coordinate system. The induction machine starting transient simulation has been completed using Finite element equations indirect coupled with mechanical equation. The influence of the electromagnetic field and performance has been analyzed compared with sinusoidal condition. This method can be used for dynamic analysis of any power supply taking into account the magnetic nonlinearity of the core material. The established machine overall structure model is closer to the actual. Compared to the traditional analysis method, we can reduce the dependency of experience design. It can also be used for analysis and optimization of the new machine

Introduction

Induction machines have found wide application in industrial and agricultural production as a kind of typical alternating current machine such as the coal mining machine, which plays a vital role in the mechanization and modernization of coal mine production. In the daily operation of coal mining machine, transient process happen frequently for various reasons like poor working conditions, the starting and resection in normal operation conditions, the sudden change of load, the action of automation system and short circuit fault during accident condition [1][2]. Though the process is transient, some serious accidents such as the breakdown of power supply and important equipments are probably caused if there were lack of improving prevention measures, bringing about large economic loss. Due to the rapid development of the whole coal industry, more and more requirements are put forward for the coal mining machine which gives rise to the increasing complexity of their own structure. To study the growing accidents clearly, it is necessary to master the methods in steady-state analysis and transient analysis of motor for its core status in the coal mining machine.

The development and application of power electric device are followed by the high automation of motor. As in the alternative current motor with frequency conversion power supply, for instance. Some properties of the power change after AC-DC-AC [3]. The wave form becomes non-sinusoidal and the frequency and amplitude can be controlled flexibly. Under this circumstance, the traditional state variable method based on integrated circuit parameter is obviously improper [4]. Finite Element method is often used in the analysis of static motor like voltage transformer [5][6]. But through the study on induction machine by international scholars, it is widely acknowledged now that the Stepping Finite Element Method is an effective method for analysis on transient performance of motor, which can take many factors like the slot effect, skin effect, influence of harmonic currents and so on into account.

In this paper a description on Lagrangian grid system is used to solve the Eddy current field computation of movement velocity on motor. On the basis of this method the non-correspondence

of air gap grid is managed through moving boundary by interpolation in the moving coordinate system [7]. The voltage power supply is realized by means of the coupling of outer electric circuit equation and electromagnetic field equation. Dynamic matrix of finite element coefficient can be avoided through the coupling of electromagnetic circuit and mechanic equation, simplifying the calculation and increasing efficiency.

Moving Eddy Current Field

For the moving eddy current field $\boldsymbol{A}$ containing moving conductor, the governing equation that ϕ-$\boldsymbol{A}$ demonstrates is as follows:

$$\nabla\times\left(\upsilon\nabla\times\boldsymbol{A}\right)-\nabla\left(\upsilon\nabla\cdot\boldsymbol{A}\right)+\sigma\nabla\phi+\sigma\frac{\partial\boldsymbol{A}}{\partial t}-\sigma v\times\nabla\times\boldsymbol{A}=\boldsymbol{J}_s \tag{1}$$

Where υ is magnetic reluctivity, σ is conductivity, v is the velocity of conductor, Js is the source current density. And electromagnetic potential is introduced by B=$\nabla\times\boldsymbol{A}$ in which Coulomb's law $\nabla\cdot\boldsymbol{A}=0$ is included.

Field-circuit coupling equation

The description on Lagrangian grid is used here to eliminate the influence of speed item on finite element equation [8]. The motor governing equations are as follows:

1) Stator winding non eddy current zone

$$\nabla\times\left(\upsilon\nabla\times\boldsymbol{A}\right)=\boldsymbol{J}_s \tag{2}$$

2) Rotor bar eddy current zone

$$\nabla\times\left(\upsilon\nabla\times\boldsymbol{A}\right)=-\sigma\nabla\boldsymbol{\Phi}-\sigma\frac{\partial\boldsymbol{A}}{\partial t} \tag{3}$$

3) Non conductive zone between iron core and air gap

$$\nabla\times\left(\upsilon\nabla\times\boldsymbol{A}\right)=0 \tag{4}$$

The boundary condition for parallelism of the exterior magnetic field line of stator iron core is $\boldsymbol{A}$=0.

Coupled processing for mechanical movement

Indirect coupling method is used here, and Maxwell stress method is used after every time step to solve the electromagnetic torque Tem:

$$T_{em}=L_{ef}\oint_J\left(\frac{1}{\mu_0}B_n r\times\boldsymbol{B}-\frac{1}{2\mu_0}B^2\boldsymbol{r}\times\boldsymbol{n}\right)dl \tag{5}$$

In the computing process the discreet rotor movement equations using implicit Euler method are shown as (6)(7), time step is fixed △t and rotor is assumed to take a constant acceleration movement every time step.

$$\Omega^{(\mathrm{n})}=\Omega^{(\mathrm{n}-1)}+\frac{T_{em}{}^{(\mathrm{n})}-T_L}{J_m}\Delta t \tag{6}$$

$$\theta^{(\mathrm{n})}=\Omega^{(\mathrm{n})}\Delta t+\frac{1}{2}\frac{T_{em}{}^{(\mathrm{n})}-T_L}{J_m}\Delta t^2 \tag{7}$$

Where $\boldsymbol{\Omega}$ is angular velocity, T_L is load torque, J_m is rotary inertia of rotor.

Non sinusoidal power supply model

The field circuit coupled model, which can help to achieve power supply for stator winding using inverter [9].

The governing method of inverter is bipolar synchronous debugging, the signal carrier is triangle [10], frequency fc=1800Hz, and the modulation wave is sine shaped whose frequency fr=50Hz. The carrier wave ratio N=f0/fr=30 and modulation coefficient H=0.8.

The Amplitude-frequency characteristic can be obtained after Fourier analysis on uab. The fundamental frequency is 50Hz and the amplitude is 537.5V. Besides, only harmonics resulted from the modulation on carrier wave by signal wave exist for the signal is sine wave. High harmonic related to carrier wave frequency is relatively more which consists mainly of harmonics whose angular frequency is centralized near ωc and 2ωc.

Calculation example and result analysis

In this paper the SPWM power supply for induction machine and the simulation for it from starting to no-load under the circumstance of sinusoidal power supply.

The stator winding is double layer lapped with triangle connection. The junction of the end of rotors and stators is realized through coupling units and intermediate field coupled to the resistance and inductance circuit units. The whole model has 42846 units which are made up of 42313 field units and 533 circuit units.

Under non-sinusoidal power supply the voltage wave whose fundamental is with amplitude up to 537.5V and frequency of 50Hz.

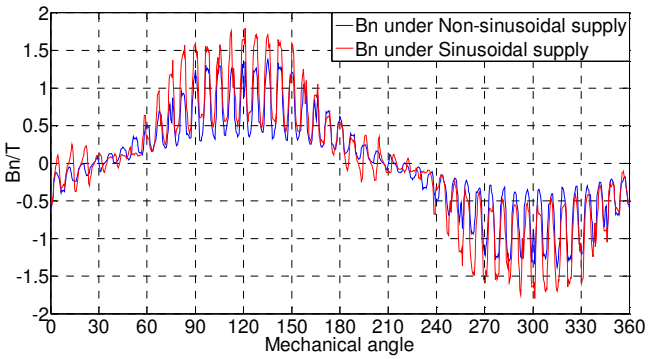

Fig.1. Air-gap flux density curve

Table 1 Harmonic distribution table of Air gap radical flux density

sinusoidal power supply		SPWM power supply	
Harmonic order	Flux density amplitude/T	Harmonic order	Flux density amplitude /T
1	1.017623549	1	0.796628395
3	0.155346293	3	0.060806632
5	0.099504387	5	0.031384919
7	0.040424641	41	0.032688609
39	0.033321184	47	0.253975605
41	0.080939932	49	0.230172262
43	0.035214767	81	0.029112554
47	0.323034675	121	0.024309191
49	0.249208135	143	0.035147652
51	0.039311799	145	0.036967425

The air-gap is an important part for electromechanical energy conversion, and the magnetic pressure drop in air-gap account for the majority of magnetic circuit. Fig1 shows the radical air gap flux density when t=2.2s. Table1 is obtained after Fourier analysis is set on the radical air gap flux density, which shows the fundamental content and harmonic content of air gap radical flux density.

It is obvious that at the time of 2.2s the amplitude of first harmonic of air gap flux density under SPWM power supply is smaller than that under sinusoidal power supply. Therefore, the air gap utilization ratio is high and the energy loss is small under sinusoidal power supply. Under the two circumstances the amplitude of 47th and 49th harmonics are all large. High-order harmonic content is high under non-sinusoidal power supply. The high high-order harmonic content may bring about more iron core loss, temperature rise, vibration noise and even the breakdown of motor, so it is necessary to take effective measures to avoid it.

Conclusion

In this paper a field-circuit coupled finite element method has been applied on induction machine for the transient analysis. Based on the transient analysis, a reasonable result that is consistent with actual instance coupled with analysis on the influence that inverter power source harmonics have on

motors are obtained. There is an advantage of high calculation precision and high convenience using moving coordination system in managing motive eddy current problem. Field-circuit coupled method takes the effect that stator end and rotor end have on the electromagnetic field of motor into account so as to realize the various power load and increase the calculation efficiency. The indirect coupling method with field-circuit coupling finite element method coupled to mechanical motion equation is relatively simple and easier to realize, however, the iteration time is relatively long. Considering these factors comprehensively, the method can be applied on the dynamic analysis on motors of various working conditions under various power supply mode. Because the material nonlinearity and motor structure resemble the normal working motor, so the model can offer certain theoretical basis for the design, research and development.

Jie Li is currently with the Department of electrical engineering for the bachelor degree. His research interests are in the multi-physical field coupling simulation.

Yujiao Zhang received the Ph.D. degree in electrical engineering from the Wuhan University, Wuhan, China, in 2012. Since 2012, she has been with China Three George University, Yichang, China, where she is currently an Associate Professor and head of the Department of Power Distribution. Her research areas are in the multi-physical field coupling analysis and design of electrical equipments and electromagnetic device. She is the host of national nature science fund item.

Reference

[1] Hui Wang, Hao Liu. Short-circuit Fault Analysis on Three-phase induction motor[J]. COAL MINE MACHINERY, 2010, 31(11): 255-257.

[2] Shenglong Guo. Transient Dynamics Response Analysis of Ranging Arm on Cutting part of Coal Shearer[J]. COAL MINE MACHINERY, 2013,34(01): 103-104.

[3] Dongyi Zhou, Wenhua Yuan, Chuping Shi,etc. Application Research on Frequency Conversion and Speed Regulating Energy saving in Ming Ventilator.[J]. COAL MINE MACHINERY,2009, 30(6); 164-165.

[4] Qiao Mingzhong, Liang Jinghui, Zhang Xiaofeng, etc. “Field-circuit Coupled Time-stepping Finite Element Analysis for Multi-phase Induction Motors.” Proceedings of the CSEE, vo1.30, no.24, pp.75-80, 2010.(in Chinese)

[5] Dou Chen. Analysis on the structure strength and vibration mode of transformer[J]. Electrotechnical Application, 2011, 30(4):82-87.

[6] Qing Zhao, Long Shao, Jingze Yu, Yi Zhang. Study on variation speed magnetic coupler[J]. Electrotechnical Application,2013,32(4): 82-87.

[7] Yan Dengjun, Liu Ruifang, Hu Minqiang, Han Jingdong. “A New Method to Deal With the Motion Problem in Electromagnetic Field Finite Element Analysis,” Proceedings of the CSEE, vo1.23, no.8, pp.163-167, 2003.(in Chinese)

[8] J.Faiz, B.M.Ebrahimi, M.B.B.Sharifian. “Time Stepping Finite Element Analysis of Broken Bars Fault in a Three-Phase Squirrel-Cage Induction Motor.” Progress in Electromagnetics Research, pp.53-70, 2007.

[9] Mi-Jung Kim, Byong-Kuk Kim, Ji-Woo Moon, etc. “Analysis of Inverter-Fed Squirrel-Cage Induction Motor During Eccentric Rotor Motion Using FEM.” IEEE Transactions on Magnetics, vol.44, no.6, pp.1538-1541, 2008.

[10] J.F.Bangura, N.A.Demerdash, “Simulation of Inverter-Fed Induction Motor Drives with Pulse-Width Modulation by a Time-Stepping Coupled Finite Element-Flux Linkage-Based State Space Model.” IEEE Transactions on Energy Conversion, vol.14, no.3, pp.518-525, 1999.

Advanced Materials Research Vols. 986-987 (2014) pp 1418-1421

doi:10.4028/www.scientific.net/AMR.986-987.1418

A meshless method for solving the mathematical model associated the leakage problem in gas pipeline

Li Junshan[1, a]

[1]Infrastucture management center, Xinglongtai oil production plant, Liaohe oil field, Panjin, China

[a] Lijunshan7000@163.com

Keywords: leakage problem. gas pipeline. meshless method.

Abstract. In this paper, we propose a meshless method for solving the mathematical model concerning the leakage problem when the pressure is tested in the gas pipeline. The method of radial basis function(RBF) can be used for solving partial differential equation by writing the solution in the form of linear combination of radius basis functions, that is, when integrating the definite conditions, one can find the combination coefficients and then the numerical solution. The leak problem is a kind of inverse problem that is focused by many engineers or mathematical researchers. The strength of the leak can find easily by the additional conditions and the numerical solutions.

Introduction

In the processing of pipeline pressure test, leakage may be happened. To determine the leak points exactly and timely is very important for repairing the pipeline. Based on the transport theory in the long pipeline and the engineering character during the pressure test, the leakage problem can be described as follows[1].

$$\begin{cases} \dfrac{\partial p_1}{\partial t} = a^2 \dfrac{\partial^2 p_1}{\partial x^2} \quad 0 < x < l, t > 0 & (1) \\ \dfrac{\partial p_2}{\partial t} = a^2 \dfrac{\partial^2 p_2}{\partial x^2} \quad l < x < L, t > 0 & (2) \\ p_i(x,0) = p_0(x)\ 0 \le x \le L, i = 1,2 & (3) \\ \dfrac{\partial p_1}{\partial x}\Big|_{x=0} = 0, \dfrac{\partial p_2}{\partial x}\Big|_{x=L} = 0, \quad t \ge 0 & (4) \\ p_1(l,t) = p_2(l,t) + \varepsilon & (5) \\ \left(\dfrac{\partial p_2}{\partial x} - \dfrac{\partial p_1}{\partial x}\right)\Big|_{x=l} = f(t), \quad t \ge 0 & (6) \end{cases}$$

Where $p_i(x,t)\ (i = 1,2)$ denote the pressure at the left/right endpoint of the pipeline respectively. a^2 is the linearized coefficient and t denotes the time variable and x is the spacial variable. p_H means the initial pressure and $\varepsilon > 0$ means the pressure difference caused by the leakage at the leakage locatio. To guarantee the well-posed of identifying the leakage location l and the leakage strength $f(t)$, we propose the realistical and convenient additional conditions as

$$p_1(0,t) = \mathrm{g}_1(t), \tag{7}$$

$$p_2(\mathrm{L},t) = g_2(t). \tag{8}$$

Where $g_i(t)\ (i = 1,2)$ denote the presure which mesured at the two endpoints respectively. The equations from (1)-(8) posed a mathematical model to identify the leakage location l and the leakage strength $f(t)$.

1.Solving the partial differential equation by radius basic function interpolation

It is well known that the usual numerical methods for solving the partial differential equations(PDEs) include the finite element method(FEM), the finite difference method(FDM) and

the finite volume method(FVM), etc. These methods are all dependent on the mesh of the domain that PDEs defined. However, the mesh is usually difficult and has effects on the efficience and the accuracy of these methods.

Since it is independent of the mesh, meshless methods have been developed dramatically in the past thirty years. In meshless methods, the interpolation is based on the scattering data and it can not be affected by the mesh.

1.1 Radius basis interpolation

Given nodes set $\{x_1,\cdots,x_N\}\in I\subset\mathbb{R}^d$, here d is the space dimensionality, we can define radius basis function on it as [2]

$$h_j(x):=h\left(\left\|x-x_j\right\|_2\right)\in\mathbb{R},\quad j=1,\cdots,N.$$

For data $y_1,\cdots,y_N\in\mathbb{R}$, radius basis function interpolation can be wrote as

$$\sum_{j=1}^{N}\alpha_j h_j(x_i)=y_i,\quad i=1,\cdots,N,$$

here α_j $(j=1,\cdots,N)$ are coefficients needed to determined.

After introducing the notations

$$H=\begin{bmatrix}h_1(x_1) & \cdots & h_N(x_1)\\ \vdots & \vdots & \vdots\\ h_1(x_N) & \cdots & h_N(x_N)\end{bmatrix}\in\mathbb{R}^{N\times N},\ \alpha=\begin{bmatrix}\alpha_1\\ \vdots\\ \alpha_N\end{bmatrix}\in\mathbb{R}^{N},\ y=\begin{bmatrix}y_1\\ \vdots\\ y_N\end{bmatrix}\in\mathbb{R}^{N},$$

we can find the linear system for the unknowns α as follows.

$$H\alpha=y \tag{9}$$

There are many radius basis functions, some frequently-used are listed below.

i. Multiquadric (MQ) function,

$$h_j(x)=(c_j^2+\left\|x-x_j\right\|^2)^{\frac{s}{2}},\ j=1,2,\cdots,N.\ s>0,\ s\neq 2N;$$

ii. Gaussian function,

$$h_j(x)=\exp[-(\left\|x-x_j\right\|/c_j)^2];$$

iii. Inverse multiquadrics function(IMQ),

$$h_j(x)=(c_j^2+\left\|x-x_j\right\|^2)^{-s},\ s>0.$$

The c_j above is called shape parameters and how to determined them are still open. As for the radius basis interpolation, one can easily find the derivative of the interpolation functions since the basis are usually infinitely differentiable.

1.2. **Kansa's method**

In [3,4], Kansa employed the radius basis function to solve the PDEs and it is named as Kansa's method.

Now, we make a brief introduction of Kansa's method. Denoting L and B are differential operator and boundary operator respectively and the problems are given as

$$\begin{cases}Lu(x)=q(x)\ when & x\in\Omega\in\mathbb{R}^d\\ Bu(x)=g(x)\ when\ x\in\partial\Omega\in\mathbb{R}^{d-1}\end{cases}. \tag{10}$$

In Kansa's method, the unknown function $u(x)$ is supposed to be in the form of

$$u(x)=\sum_{i=1}^{N}\alpha_i h\left(\left\|x-x_i\right\|_2\right) . \tag{11}$$

Moreover, we denote $\{x_1,x_2,\ldots x_I\}$ and $\{x_{I+1},x_{I+2},\ldots x_N\}$ are the inner nodal points and boundary nodal points respectively. The problem (10) can be discreted into the linear system as

$$\begin{pmatrix} H_L \\ H_B \end{pmatrix}\alpha=\begin{pmatrix} q \\ g \end{pmatrix}.$$

Here

$$H_L=\begin{pmatrix} Lh_{11} & \cdots & Lh_{1N} \\ \vdots & \ddots & \vdots \\ Lh_{I1} & \cdots & Lh_{IN} \end{pmatrix}\in\mathbb{R}^{I\times N},\ H_B=\begin{pmatrix} Bh_{I+1,1} & \cdots & Bh_{I+1,N} \\ \vdots & \ddots & \vdots \\ Bh_{N1} & \cdots & Bh_{NN} \end{pmatrix}\in\mathbb{R}^{(N-I)\times N},$$

$Lh_{ji}=Lh\left(\left\|x_i-x_j\right\|_2\right)$ and $Bh_{ji}=Bh\left(\left\|x_i-x_j\right\|_2\right)$. $q=\begin{pmatrix} q(x_1) \\ \vdots \\ q(x_I) \end{pmatrix}\in\mathbb{R}^I$, $g=\begin{pmatrix} q(x_{I+1}) \\ \vdots \\ q(x_N) \end{pmatrix}\in\mathbb{R}^{N-I}$.

2. Kansa's method for solving the leakage problem

Now we employ the Kansa's method to solve the leakage problem, i.e., Eq.1-Eq. 8.

Denote the time step as $\delta t=\frac{T}{n_t}$, here n_t means the numbers of time steps and T is the length of the time interval. For all $t\in[t^i,t^{i+1}]$ $(t^i=i\delta t,i=0,1,\cdots,n_t\delta t)$, we approximate $p(x,t)$ and $\frac{\partial p(x,t)}{\partial t}$ as

$$p(x,t)\simeq\theta p(x,t^{i+1})+(1-\theta)p(x,t^i),$$

$$\frac{\partial p(x,t)}{\partial t}\simeq\frac{p(x,t^{i+1})-p(x,t^i)}{\delta t},$$

here the parameter $\theta\in[0,1]$.

Denoting ${\alpha_j}^k$ the $k-th$ time step coefficients and $\kappa=a^2\delta t$, we discrete the PDEs in the form of $\frac{\partial p(x,t)}{\partial t}=a^2\frac{\partial^2 p(x,t)}{\partial x^2}$ as

$$\sum_{j=1}^{N}{\alpha_j}^{i+1}{g_j}^{i+1}(x)-\sum_{j=1}^{N}{\alpha_j}^{i}{g_j}^{i}(x)=\kappa\theta\sum_{j=1}^{N}{\alpha_j}^{i+1}\frac{c_i^2}{\left(c_i^2+\left|x-x_i\right|^2\right)^{\frac{3}{2}}}+\kappa(1-\theta)\sum_{j=1}^{N}{\alpha_j}^{i}\frac{c_i^2}{\left(c_i^2+\left|x-x_i\right|^2\right)^{\frac{3}{2}}}. \tag{12}$$

Algorithm

Step 1. Based on the initial condition Eq. 3, boundary condtion Eq. 4 and the interpolation formula Eq. 12, one can find the coefficients $\alpha_j^0\ (j=1,2,\cdots,N)$;

Step 2. During the time interval $t \in [t^i, t^{i+1}]\,(i = 0,1,\cdots,n_t)$ and input $N_1 - 1$ and $N_2 - 1$ equidistan points into the interval $[0,l]$ and $[l,L]$, then based on Eq.7, Eq.8 and Eq.12, we can obtain the leakage location

l and coeficients $\alpha_j^i\,(j = 1,2,\cdots,N+1)$;

Step 3. By employing Eq. 6, one can comput the leakage strength $f(t)$.

3. Tikhonov regularization for solving the linear system

In general, the matrix H in Eq. 9 is always ill-conditioned in Kansa's method especially when Gauss function or IMQ function being used. Here we employ the Tikhonov regularization to solve the system Eq. 9.

The Tikhonov regularized solution for Eq. is defined as[5,6]

$\alpha_\lambda = \arg\min\{\|H\alpha\text{-}y\|_2^2 + \lambda\|y\|_2^2\}$,

here λ is regularization paramter and ususally determined by $L-$ curve method. More details can be fond in[5] and a Matlab package for implementing the Tikhonov regularization is included in [6].

4. Numerical results

A numerical example is given to testify the efficency. We take $a^2 = 1$ and $L = \pi$, then the analytical solution $p(x,t) = e^{-t}\cos x$. The interval $[0,\pi]$ is divided into 100 subintervals and denote h as the step. The shape parameters c_j and ε are taking $c_j = \sqrt{h}$ and $\varepsilon = h$ respectively. When taking the leakage location $l = \frac{\pi}{3}$, $l = \frac{\pi}{2}$ and $l = \frac{2}{3}\pi$ respectively, we get the numerical results $\tilde{l} = 1.022$, $\tilde{l} = 1.610$ and $\tilde{l} = 2.085$.

Summary

In meshless methods, the solution to partial differential equation can be wrote in the linear combination of basis function explicitly. So it is fit for solving the inverse problems when the additional conditions are given. The numerical results for the leakage problem testify this point in the paper.

Acknowledgements

This work was financially supported by the Youth Fund of Department of Education of Jiangxi Province (No. GJJ13486), the Doctoral Foundation of Nanchang Hangkong University (No.EA201107261). The author would like to thank vice Prof. Yuan Daming(Nanchang Hangkong University) for his helpful discussions.

References

[1] Daming. Yuan: *The well-posed study on the location and the strength of a leakage problem* (in Chinese) (Master thesis , Southwest Petroleum University, Chengdu 2005).

[2] X. Zhang , K. Z. Song and M.W. Liu: Comput. Mech. Vol. 26 (2000), p. 333

[3] E.J. Kansa: Comput. Math. Appls. Vol. 19 (1990), p. 127

[4] E.J. Kansa: Comput. Math. Appls. Vol. 19 (1990), p. 147

[5] P.C. Hansen: SIAM Review Vol. 34(4)(1992), p. 561

[6] Information on http://www2.imm.dtu.dk/ pch/Regutools

Advanced Materials Research Vols. 986-987 (2014) pp 1422-1425

doi:10.4028/www.scientific.net/AMR.986-987.1422

FIR sine interpolation algorithm based on pipeline and parallel technology

Xiuli DU[1,2,a] , Huancheng JIANG[2,b] , Bo CHEN[1,2,c]

[1]University Key Laboratory of Communication and Signal Processing, Dalian University, Dalian 116622, China

[2]College of Information Engineering, Dalian University, Dalian, 116622, China

[a]email: dxlxts@126.com, [b]email: jhcxg@sina.cn, [c]email: chenbo@dlu.edu.cn

Keywords: FIR, Sine Interpolation, Pipeline Technology, Parallel Technology, FPGA

Abstract. According to the problem that the existing data interpolation algorithm has low efficiency when handling high-speed data, this paper proposes a FPGA-based FIR sine interpolation algorithm based on pipeline and parallel technology. The algorithm not only reduces the critical path so that improve the system working clock effectively, but also increases the speed of data processing to improve the speed of interpolation process significantly. Finally, according to the experiment based on FPGA, the result shows that the proposed algorithm improves the speed of data interpolation process, and reduces the system power consumption effectively. It can realize the real-time interpolation process of high-speed or hyper-speed data stream.

Introduction

Data interpolation technique is widely used in high-speed data processing field like radar imaging system, digital test equipment, and data acquisition and processing system. With the rapid development of digital signal processing technology, conventional interpolation methods can not meet the modern digital signal processing requirement of high-speed and real-time processing, and how to achieve high-speed and real-time interpolation of high-speed data stream has become an important factor in the development of high-speed digital signal processing. So the research on high-speed signal interpolation is not only important to theoretical research, but also beneficial to the application of data interpolation techniques in the field of high-speed data process.

The common algorithms of data interpolation are mainly two types: one is based on the interpolated curve, such as linear interpolation, polynomial interpolation and parabolic interpolation; the other is the sine interpolation. Linear interpolation which is easily implemented in hardware is widely used in the field of data interpolation[1], but due to the limitations of itself, it can only be used where the sampling rate is relatively high; the Lagrange polynomial interpolation[2] and parabolic interpolation[3] still have a good data recovery characteristic at a low sampling rate, but Compared to the linear interpolation, owing to the high computational complexity and complex hardware implementation, they are often used in the data interpolation of low-rate data stream; sine interpolation is widely used as it has features like good data recovery characteristic under low sampling rate , strict linear phase and easy to implement[4]; polyphase structure of FIR sine interpolation is an improvement of sine interpolation[5][6], the application of polyphase structure can improve the data processing speed , but for high-speed data stream interpolation, it still has difficult to meet the demand of high-speed and real-time processing.

This paper proposes a FIR sine interpolation algorithm based on pipeline and parallel Technology, compared to the polyphase structure of FIR sine interpolation, this algorithm can shorten the critical path, improve the interpolation processing method, so that increasing the data interpolation processing speed substantially, lowering the power consumption, it is suitable for the real-time interpolation process of high-speed data stream.

Polyphase structure of FIR sine interpolation

Through an L interpolation which insert L-1 zeros into the original data, then through a low-pass filter whose response is $h(n)$, the sampling rate of original signal $x(n)$ whose sampling rate is f_s is increased to Lf_s. The signal after insertion of zero is $x_e(n)$, the signal after sine interpolation is $y_L(n)$.

The use of polyphase structure in signal interpolation can remove unnecessary calculations, improve operation time greatly. Function (1) is the polyphase structure of sine interpolation.

$$y_L(n)=\sum_{m=-\infty}^{+\infty} h\left(mL+((n))_L\right)x\left(\left\lfloor \tfrac{n}{L}\right\rfloor -m\right)=\sum_{m=-\infty}^{+\infty} g_n(m)\,x\left(\left\lfloor \tfrac{n}{L}\right\rfloor -m\right) \tag{1}$$

For finite-length sequence, we have $N \quad L$, then $Q=N/L$, we can get the polyphase structure of FIR sine interpolation with L interpolation is as follows

$$y_L(n)=\sum_{m=0}^{Q-1} g_n(m)\,x\left(\left\lfloor \tfrac{n}{L}\right\rfloor -m\right) \tag{2}$$

FIR sine interpolation algorithm based on pipeline and parallel Technology

1. FIR sine interpolation algorithm based on pipeline

Merlino'pipeline is a kind of technology which can execute multiple instructions in a single clock cycle[6], the use of pipeline can greatly shorten the critical path, so that can improve the clock speed and the operation speed or reduce power consumption at the same clock rate. The pipeline reduces the critical path by introducing the pipeline latches along the data path. After introduction of M-stage pipeline latches, the calculation speed improves M times approximately.

For polyphase structure of FIR sine interpolation, the propagation delay of its FPGA implementation is closely related to MOS field effect transistor and stray capacity electric charge of its critical path [7], the formula for its propagation delay T_{seq} is:

$$T_{seq}=C_{charge}V_0/(k(V_0-V_t)^2) \tag{4}$$

In the formula, C_{charge} stands for charging and discharging of the capacitor in a single clock cycle, V_0 stands for supply voltage, V_t stands for threshold voltage. k stands for a constant of process parameters. The formula for its power consumption is

$$P_{seq}=C_{total}V_0^2 f \tag{5}$$

In the formula, $f=1/T_{seq}$, T_{seq} is clock cycle of polyphase structure of FIR sine interpolation.

For FIR sine interpolation algorithm based on M-stage pipeline, the critical path length is approximately reduced to $1/M$ of polyphase structure of FIR sine interpolation, the charging and discharging capacitor in one clock cycle is decreased to C_{charge}/M, but the total capacitor does not change. If the clock frequency f remains unchanged, it only need to charge and discharge C_{charge}/M during the same time of the original C_{charge}. This means that the supply voltage can be reduced to βV_0. the propagation delay of FIR sine interpolation algorithm based on M-stage pipeline is

$$T_{pip}=(C_{charge}/M)\beta V_0/(k(\beta V_0-V_t)^2) \tag{6}$$

The power consumption is

$$P_{pip}=C_{charge}\beta^2 V_0^2 f=\beta^2 P_{seq} \tag{7}$$

Therefore, power consumption is reduced to β^2 times of polyphase structure of FIR sine interpolation. At the same clock frequency, we know $T_{seq}=T_{pip}$, from (5), (7) we can calculate the value of consumption coefficient β ($0<\beta<1$).

2. FIR sine interpolation algorithm based on parallel Technology

Parallel technology is involved with architecture, algorithm mapping and programming technology; it has been a research focus [8] in the field of modern digital signal processing. In parallel processing, multiple input data can be computed in parallel at one clock cycle. Thus, the real processing speed corresponds to the number of parallel channels.

Like pipeline, the parallel technology's method of reducing power consumption is also by reducing the supply voltage, when using An N-channel parallel structure, the power consumption can be reduced to β^2 times of polyphase structure of FIR sine interpolation:

$$P_{par} = (NC_{charge})(\beta V_0)^2 f / N = \beta^2 C_{charge} V_0^2 f = \beta^2 P_{seq} \quad (8)$$

At the same clock rate, β can be obtained from the following equation:

$$LT_{seq} = C_{charge}\beta V_0 / (k(\beta V_0 - V_t)^2) = C_{charge} V_0 / (k(V_0 - V_t)^2) \quad (9)$$

3. FIR sine interpolation algorithm based on pipeline and parallel Technology

Both of Pipeline and parallel technology can be used to improve the data processing speed and lower power consumption. The speed of data process of applying these two technologies is the product of just using pipeline or parallel technology alone;

As for power consumption, the pipeline decreases the charging and discharging capacitor in one clock cycle and the parallel technology increase the clock cycle of charging and discharging capacitor, so as to achieve the purpose of reducing the supply voltage. The propagation delay T_{pd} is:

$$NT_{pd} = \frac{C_{charge}}{M}\beta V_0 / (k(\beta V_0 - V_t)^2) = NC_{charge} V_0 / (k(V_0 - V_t)^2) \quad (10)$$

The consumption coefficient β can be calculated from the equation (10).

In the FIR sine interpolation algorithm based on N-stage pipeline and M-channel parallel structure, we set N=M=3, V_e = 5 V, V_t = 0.6V, then the data processing speed approximately increased to 9 times, according to equation (10) we calculate the value of β is 0.27, which means the power consumption is reduced to 7.5% of the original. The FIR sine interpolation algorithm based on N-stage pipeline and M-channel parallel structure is shown in Figure 1.

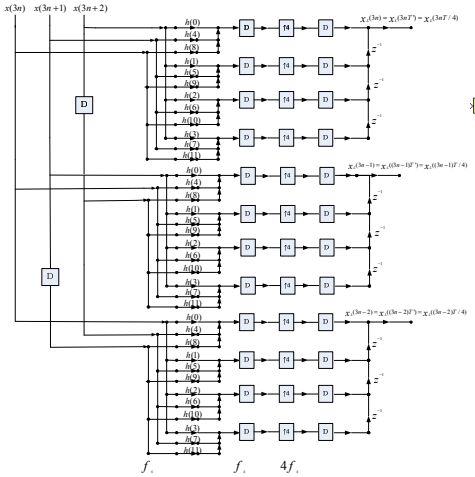

Figure 1 FIR sine interpolation algorithm based on 3-stage pipeline and 3-channel parallel structure

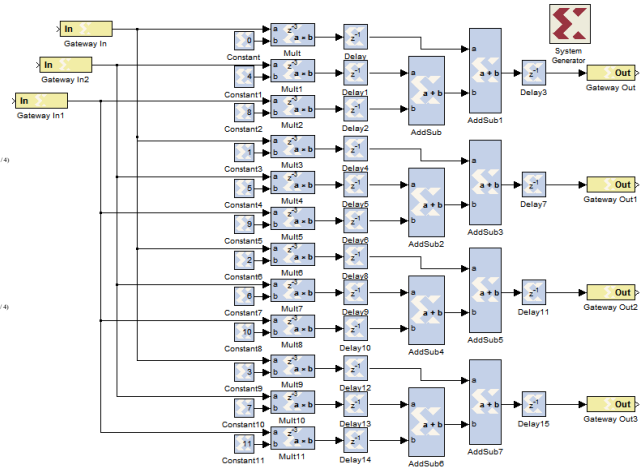

Figure 2 FIR sine interpolation based on 3-stage pipeline and 3-channel parallel structure

FPGA implementation and verification

We use the Virtex5 FPGA of Xilinx as development platform, by using the System Generator; we design and implement the FIR sine interpolation algorithm based on 3-stage pipeline and 3-channel parallel structure which is shown in Figure 2.

We get the comparison of hardware resources, critical path and power consumption between FIR sine interpolation structure based on 3-stage pipeline and 3-channel parallel structure(PPFIRSI) and Polyphase structure of FIR sine interpolation (PSFIRSI)in Table 1.

As table 1 show, with 3-stage pipeline and 3-channel parallel structure on FIR sine interpolation structure, although it uses more hardware resources, it can reduce critical path significantly, which make the clock frequency of data interpolation system increase to（$5T_M$+$2T_A$）/（T_M+$2T_A$）times of original. It significantly improves interpolation rate, while reducing system power consumption.

Table 1 The comparison of hardware resources, critical path and power consumption

interpolation structure	multiplier	adder	delay units	Critical path	power consumption
PSFIRSI	12	11	11	$5T_M + 2T_A$	P_{seq}
PPFIRSI	36	33	35	$T_M + 2T_A$	$7.5\% P_{seq}$

As Figure 3 and Figure 4 shows, when we translate the polyphase structure of FIR sine interpolation into a 3-channel MIMO parallel system, the efficiency of data processing has greatly enhanced, at the same input clock frequency, the data interpolation rate of FIR sine interpolation based 3-channel parallel structure is 3 times of the polyphase structure of FIR sine interpolation.

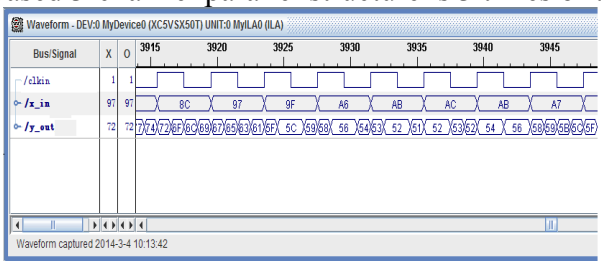

Figure 3 Polyphase structure of FIR sine interpolation

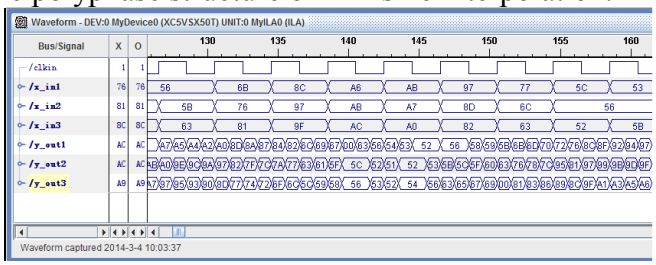

Figure 4 3-stage pipeline and 3-channel parallel system

With all analyses, applying 3-stage pipeline and 3-channel parallel structure to polyphase structure of FIR sine interpolation increase data interpolation rate to $3(5T_M+2T_A)/(T_M+2T_A)$ times of original, the power consumption is also reduced to 7.5% of the original. Thus the FIR sine interpolation algorithm based on 3-stage pipeline and 3-channel parallel structure greatly improves the speed of data processing, effectively reduces the system power consumption, which can be used in real-time interpolation of high-speed data stream.

Conclusion

In this paper, after discussing interpolation algorithm of high-speed data streams, pipeline and parallel Technology, we present a FIR sine interpolation algorithm based on pipeline and parallel Technology, which creatively uses the pipeline and parallel Technology to improve the data interpolation rate of polyphase structure of FIR sine interpolation, then we implement a FIR sine interpolation algorithm based on 3-stage pipeline and 3-channel parallel structure using FPGA. The result shows that the FIR sine interpolation algorithm based on pipeline and parallel Technology can greatly increases data processing speed and effectively reduces system power consumption though it needs more hard resources, it can be applied to real-time interpolation of high-speed data stream.

References

[1]Zhang Fangling,Jiang Defu,Gao Yang,Xue Dongwei. An Efficient Algorithm and Its FPGA Implemenation of Data Retention Interpolation. Modern Radar, 2013,35(10):62-66.

[2]Merlino P,Abramo A. A Fully Pipelined Architecture for The LOCO-I Compression Algrithm [J]. IEEE Trans on Very Large Scale Integration(VLSI) Systems, 2009, 17(7) : 967-971.

[3]Li Yaobin,Zeng Xiangbin,Shen Chengwu. Fitting algorithm of sine wave based on interpolation of parabola. Computer Engineering and Design,2009,30(11): 2793-2796.

[4]Polpo A,Pereira CAB. Reliability Nonparametric Bayesian Estimation in Parallel System[J] . IEEE Trans on Reliability,2009, 58(2) : 364-373.

[5]Wang Fang,Wang Kun qi,Shi Chun yan,Wang peng. Study and Realization of Hardware Precision Interpolation Based on CPLD Motion Control System.ICMTMA,2010,471:526-531

[6]Huang Xiaoyan,Feng Xi-an,Gao Tiande. Passive Sonar Signal Simulation of Multi- channels Based on FPGA Parallel Technology. Computer Measurement & Control, 2011,19(4):935-940.

[7]Zhou Dapeng,He Guangpu,Chen Liming. Design of FIR Digital Filter Based on Improved DA and Pipeline. Coal Technology, 2012, 31(3):33-35.

[8]Gang Tan,Yutian Feng,Hui Shen. A Combined Interpolation Method for Waveform Reconstruction in Beacon Transmitter Detector. CCWMC,2011, 8:270-274.

Advanced Materials Research Vols. 986-987 (2014) pp 1426-1430

doi:10.4028/www.scientific.net/AMR.986-987.1426

Research of Pipeline Leak Eigenvector Extracting Based On Wavelet Packet

Xiaoyun Liu[1], Xiangfen Zhang[2,*], Yan Ma[3], Yanqin Yang[4]

[1-4]Shanghai normal university, shanghai, 200234, China

[1]creatorliu@126.com,[2] xiangfen@shnu.edu.cn

Keywords: pipeline leakage; acoustic emission; wavelet packet; feature vector;

Abstract. As an important part of pipeline safety, pipeline leak detection is usually done by extracting feature vectors of leakage signal. Many researchers used wavelet packet algorithm to extract feature vector, but because of mixing effects of wavelet packet, the acquired feature vector may be not accurate. To solve this problem, the authors propose an improved wavelet packet algorithm to extract the feature vector. The improved algorithm is different from the traditional algorithm in decomposition and reconstruction and the feature vector is constituted by three time-frequency domain parameters. A lot of experiments have been performed to extract feature vector based on the proposed algorithm, with the results showing that the proposed algorithm can overcome the mixing effects and accurately extract the feature vector.

Introduction

Pipeline plays a very important role in petroleum, chemical, natural gas, urban construction and other industries. Pipeline leak can not only have a bad effect in the normal transportation, but also cause the pollution to the environment[1].

Wavelet packet algorithms are usually adopted to extract feature vectors. The authors in literature[2] decompose the acoustic emission signal of pipeline leakage with wavelet packet and reconstruct the single sub-band signal, with the energy of each frequency band as the feature vectors, which are then input to the BP neural network classifier to complete pipeline leakage diagnosis. The literature[2] use the traditional wavelet packet to reconstruct single sub-band signal, and then extract the feature vector from the reconstructed signal. However, because of the non-ideal characteristics of the traditional wavelet filter, the spectrum expansion and compression brought by the up-sample and down-sample, the single sub-band reconstructed signal might contain unwanted frequency components, and the acquired feature vector may be not accurate.

To overcome the shortcomings of the traditional wavelet packet algorithm, this article put forwards a new wavelet packet algorithm. The study select three time-frequency domain parameters to form the feature vector to detect the leakage condition. The authors performed amounts of experiments based on real pipeline leakage data, and the proposed method is used to extract the leakage feature vector.

The Improved Algorithm and Feature Parameters

The Improved Algorithm

Wavelet packet decomposition and reconstruction are implemented by convolving the signal with the filter. In the traditional wavelet packet reconstruction algorithm, the wavelet filter is non-ideal, the up-sample and down-sample will lead to the spectrum expansion and compression, which will makes the reconstructive sub-band signal contain unwanted frequency components, all of these will make the feature vector extracted from the single sub-band reconstructed signal inaccurate. This study uses FFT and IFFT transformation to process the high and low frequency coefficients, so the single sub-band reconstructed signal will not contain the unwanted frequency components[3].

This study proposes a new wavelet packet algorithm to extract the feature vectors. The proposed new algorithm can be illustrated as in Fig. 1. In Fig. 1, h0 is the decomposition low-pass filter, g0 is

the decomposition high-pass filter, h1 is reconstruction low-pass filter, g1 is reconstruction high-pass filter, $\downarrow 2$, $\uparrow 2$ are respectively the down-sample and up-sample.

Fig. 1 also describes the three main steps of the new algorithm, the abbreviations RCST is stand for reconstruction.

Step1. Eliminating the unwanted frequency component of each frequent band.

The signal convolves with h0 (low-pass filter) and g0 (high-pass filter) respectively, with the results of two filtered signals. The authors use the HF-cut-IF and LF-cut-IF operators to process the signals respectively before down-sampling. The conduct of operator HF-cut-IF, LF-cut-IF is as follows: firstly, the authors make a FFT transform to the two convolving resultant signals. Secondly, the authors set the amplitude of the high frequency (HF) or low frequency (LF) components to be zero (HF-cut, LF-cut) according to the decomposition filter (high pass and low pass filter). Finally, an IFFT transform is performed on the components-discarded data, with the results to be down-sampled to get the low and high frequency coefficients of next layer. The HF-cut-IF and LF-cut-IF operators process on each layer of the signal, which can be expressed as Eq. 1 and Eq. 2.

$$\begin{cases} X(k)=\sum_{n=0}^{N_j-1} x(n)W^{kn}, 0\le k\le \dfrac{N_j}{4} \text{ or } \dfrac{3N_j}{4}\le k\le N_j \\ X(k)=0, \quad \text{others} \\ x(n)=\sum_{k=0}^{N_j-1} X(k)W^{-kn}, n=0,1,L,N_j-1 \end{cases} . \tag{1}$$

$$\begin{cases} X(k)=\sum_{n=0}^{N_j-1} x(n)W^{kn}, \dfrac{N_j}{4}\le k\le \dfrac{3N_j}{4}. \\ X(k)=0, \quad \text{others}. \\ x(n)=\sum_{k=0}^{N_j-1} X(k)W^{-kn}, n=0,1,\cdots,N_j-1. \end{cases} . \tag{2}$$

In Eq. 1 and Eq. 2, $x(n)$ is the wavelet packet coefficient in 2^j scale, N_j is the length of the data in 2^j scale, $W=e^{\frac{-j2\pi}{N_j}}, k=0,1,\cdots,N_j-1; n=0,1,\cdots,N_j-1$.

Step2. Reconstruction of single sub-band signal.

The down-sampled signal is firstly up-sampled and then convolved with h1 or g1, with the results to be processed by the operator HF-cut-IF or LF-cut-IF. Finally, the authors can get the single sub-band reconstructed signal.

Step3. Extracting the feature vector of the single sub-band reconstructed signal got from the step 2.

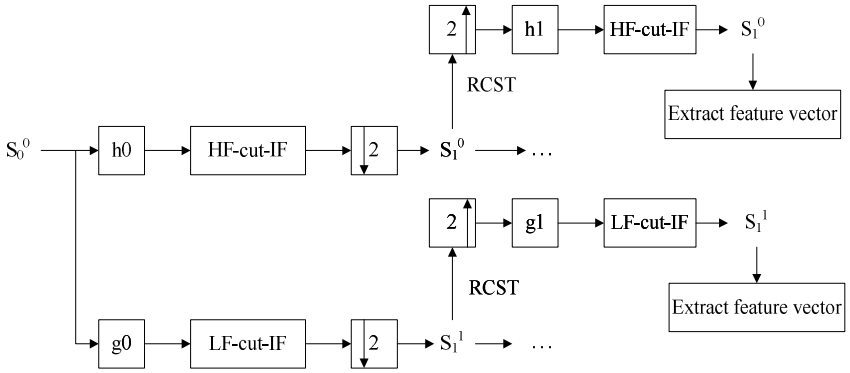

Fig. 1. The process of improved wavelet packet algorithm

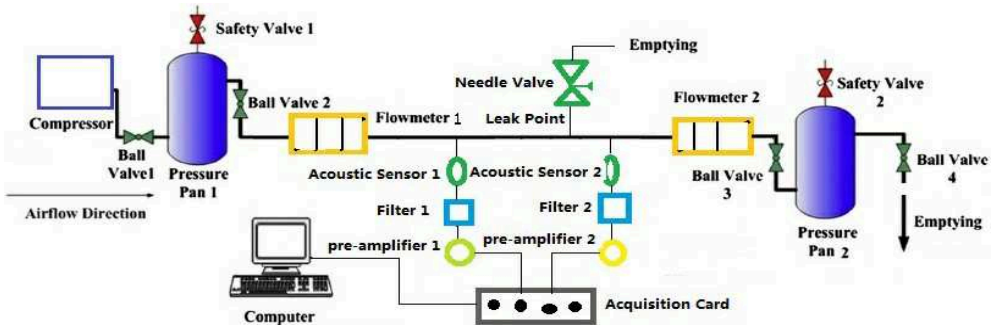

Fig. 2. Acoustic emission detection schematic diagram

Feature Parameters

The pipeline leakage signal is extremely different from the normal signal in a certain frequency band[4], the researcher can extract the feature vector from the single sub-band reconstructed signal to detect the leakage state. The time-domain parameters can be peak value, arrival time[5], time-domain energy(ET)[6], the mean(A), variance(V), skewness and kurtosis. The frequency-domain parameters can be frequency-domain energy (EF), peak value (PF).

ET is the energy of the single sub-band reconstructed signal in time-domain and can be calculated by:

$$ET = \int |S_j^i(t)|^2 dt = \sum_{k=1}^{N} |S_{j,k}^i|^2 . \quad (3)$$

Where, $S_{j,k}^i$ is the kth coefficient of the node i reconstructed signal in the jth layer. N is the length of the single sub-band reconstructed signal.

The expression of kurtosis is:

$$k_3 = \sqrt{\frac{1}{6N}} \sum_{i=0}^{N} \left[\frac{S_{j,k}^i - A}{\sqrt{V}} \right]^3 . \quad (4)$$

Where, N is the length of the single sub-band reconstructed signal.

Experiment and Result Analysis

This study did amounts of experiments to extract the feature vector from the measured acoustic emission signal. The schematic diagram of the experiment is shown in Fig. 2.

Reconstruction of the Single Sub-band Signal

The authors analyzed the measured data from sensor, with the spectra of the measured signal in normal and leakage condition shown in Fig. 3. As can be seen from Fig.3, the difference between the spectrum of normal and leakage signal is mainly concentrated in the vicinity of 64kHz. As shown in Fig.4(a), the single sub-band signal reconstructed by the traditional wavelet packet algorithm contains many redundant frequency components. The improved wavelet packet algorithm as shown in Fig.4(b), however, can accurately reconstruct the single sub-band signal which does not contain redundant frequency components.

The Extraction of Feature Vector and Result Analysis

The authors find that, for the single sub-band reconstructed signals, there are big differences in ET, PF and kurtosis coefficient (k3) between normal and leakage condition and we chose these three parameters to form the feature vector. As shown in the Fig.3, the difference is mainly concentrated in the vicinity of 64kHz in normal and leakage condition, and the frequency range of single sub-band reconstructed signal on node 7 is 62.5 ~ 75kHz, so the difference between normal and leakage signal is contained in the reconstructed signal of node 7, meanwhile, the authors can find that there is no difference in the reconstructed signal of node 3(25~37.5kHz) and node 6(50~62.5kHz) between normal and leakage signal.

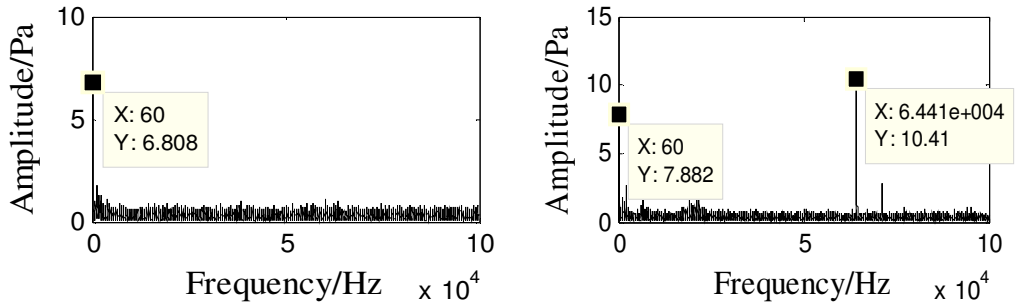

(a) Sensor 2 without leakage (b) Sensor 2 leakage

Fig. 3. Sensor measured signal spectrum

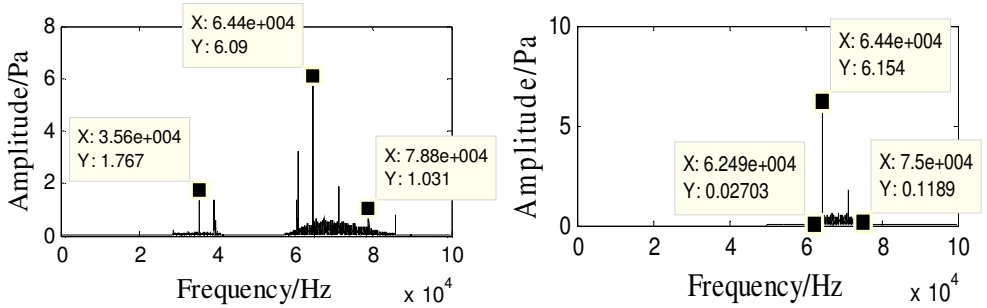

(a)Sensor 2 traditional algorithm (b)Sensor 2 improved algorithm

Fig. 4. Spectrum of reconstruction signal

Fig. 5(a), (b) and (c) are ET, k3 and PF respectively of the single sub-band reconstructed signal in node 3, 6 and 7 in normal and leakage condition, with symbol '—' and '---' represents the parameter extracted by the traditional algorithm in normal condition and leakage condition respectively, the symbol '+' and '*' represents the parameter extracted by the improved algorithm in normal condition and leakage condition respectively. According to the previous analysis, the authors can find that the characteristics parameter of the single sub-band reconstructed signal on node 3 and 6 does not change in normal and leakage condition. However, the characteristics parameters of the reconstructed signal on node 3 and 6 extracted by the traditional algorithm have big difference under normal and leakage conditions. The unreasonable phenomenon is caused by the mixing effects of the traditional algorithm in reconstructing single sub-band signal. On the contrary, the characteristics parameters extracted by our new algorithm in the two nodes do not change under the two conditions. According to the analysis, the authors can find that the improved algorithm can overcome the mixing phenomenon in reconstruction signal and exactly extract the feature vector. All of this improves the accuracy of leak detection and provide a reliable basis for pipeline leakage detection.

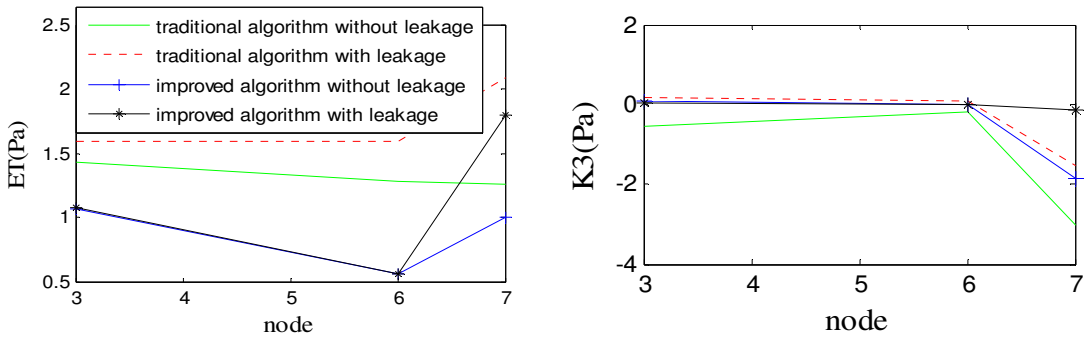

(a) the time-domain energy (b) kurtosis

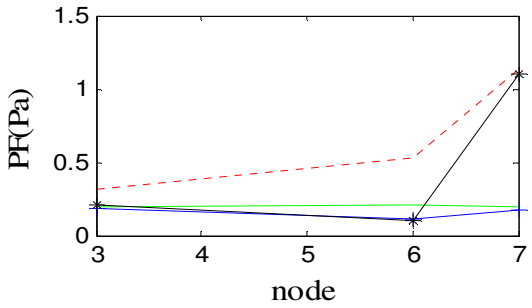

(c) frequency-domain peak

Fig. 5. Feature parameters

Conclusion

The mixing phenomenon will occur when researcher use the traditional algorithm to reconstruct the single sub-band signal, which will make the extracted feature vector not the accurate one. In this study, the authors proposed an improved wavelet packet algorithm to reconstruct single sub-band signal and extract the feature vector to overcome the disadvantage of traditional wavelet packet algorithm. The proposed algorithm use FFT and IFFT to process the convolved signal. The authors performed amounts of experiments to extract feature vector based on the proposed algorithm and the results were compared with that of the traditional algorithm. The experimental results show that the improved algorithm can overcome the mixing effects brought by the up-sample and down-sample process in the traditional wavelet packet decomposition and reconstruction and accurately extract the feature vector. The study provides good foundation for leak detection and positioning.

Acknowledgment

The project is supported by the Shanghai Science and Technology Committee (Grant No. 11510502400).

References

[1]Q.Q. Xu, L.B. Zhang, W, Liang, in: Acoustic detection technology for gas pipeline leakage, Process Safety and Environmental Protection, vol.91, no.4 (2013).

[2]J. Guan, in: Research on the System of Pipeline Leak Location Based on BP Network, M.S. thesis, Beijing Jiaotong University, Beijing, ON Beijing (2009).

[3]H.Q. Wang, Z.H. Song, P. Li, in: Improved wavelet packet frequency division algorithm and its application in fault detection, Journal of Zhejiang University (Engineering Science), vol.35, no.3 (2001).

[4]M. Ahadi, M.S. Bakhtiar, in: Leak detection in water-filled plastic pipes through the application of tuned wavelet transforms to Acoustic Emission signals, Applied Acoustics, vol.71, no.7 (2010).

[5]A. Sophian, G.Y. Tian, D. Taylor, J. Rudlin, in: A feature extraction technique based on principal component analysis for pulsed Eddy current NDT, NDT and E International, vol.36,no.1 (2003).

[6]Z.G. Qu, H. Feng, Z.M. Zeng, J.C. Zhuge, S.J. Jin, in: A SVM-based pipeline leakage detection and pre-warning system, Measurement, vol.43, no.4 (2010).

Advanced Materials Research Vols. 986-987 (2014) pp 1431-1434

doi:10.4028/www.scientific.net/AMR.986-987.1431

New research on Identification and classification of grid power quality disturbances

Ningxia Yang*[a] , Maofa Gong[b],Xiaofei Wang[c],Huiting Ge[d],Yuqing Lin[e], Bingqian Liu[f] and Feng Qiu[g]

School of Shandong University of Science and Technology,Qingdao 266590,China
*[a]yangningxia521@126.com, [b]13505324625@163.com , [c]klwz2008@126.com, [d]1020261735@qq.com, [e]838917140@qq.com, [f]lbqsjj@126.com, [g]qf35b@sina.com

Keywords: power quality,complex wavele ttransform, PSO, neuralnetwork

Abstract. To improve accuracy and speed of recognising and classifying grid power quality disturbances, this paper presents a new method which combines complex wavelet transform and particle swarm optimization(PSO) neural network to identify and classify the disturbance . This method extract both amplitude-frequency and phase-frequency information of the interference signal to make up for the lack of traditional wavelet transform which only extract the amplitude-frequency information. And on this basis, using particle swarm optimization, we seek the optimal solution of neural network weights and thresholds for the identification and classification of power quality. The MATLAB simulation result has verified the accuracy and rapidity of this method compared with the traditional method .

0 Introduction

The rapid development of the industrial control field make the serious influence on the power grid and the quality of power supply. Electric power enterprises to power quality disturbance accurate recognition and classification is the guarantee the premise of the safe and economic operation and the quality of power supply[1-2] .

At present, most studies of power quality just use the characteristics of multi-resolution analysis of wavelet transform. Different positions have different time-frequency screen resolution by amplitude feature to locate the power quality disturbance and the determination of disturbance duration, etc. But characteristics of phase frequency is not only various and phase is also very important in the disturbance signal[3-4]. In addition,most were set according to the experience, weights and threshold selection when determining the weights and threshold of neural network parameters.However, it will affect the accuracy of identification and classification of power quality disturbance[5-6].

To solve above problems, this paper will after wavelet neural network with particle swarm optimization (PSO) with the combination of the identification and classification of power quality disturbance. The analysis of jamming signal in power grid feature vectors extracted provides new ideas and new technology by complex wavelet transform to extract the signal amplitude frequency and phase information. The BP neural network combined optimization algorithm which has the global search ability of particle swarm (PSO) with the neural network weights and threshold to seek the optimal solution. The MATLAB simulation experiment show that this method has recognition speed, high accuracy and good robustness and generalization compared with the traditional method.

1 Complex wavelet analysis

1.1 Complex wavelet transform

Power grid in the common dynamic disturbance signals include voltage surge signals, voltage sag, voltage temporarily interrupt signal and transient oscillation and transient pulse signals of five. Input voltage signal after wavelet transform and extract the disturbance signal then uses the Mallat fast wavelet algorithm of db3 orthogonal tight after wavelet for five scale disturbance signals after wavelet decomposition, disturbance signals in various frequency bands get the structure information of complex wavelet coefficients.

Assume f (t) for containing the disturbance signal of the input voltage signal,then the input voltage signal f (t) for continuous wavelet transform and inverse transformation to get:

$$w_f(a,b) = \int_{-\infty}^{+\infty} f(t) \cdot \frac{1}{\sqrt{a}} \overline{\Psi(\frac{t-b}{a})} dt \quad (1)$$

$$f(t) = \frac{1}{C_\Psi}[\frac{1}{a}\int_{-\infty}^{+\infty}[W_f(a,b)\Psi(\frac{t-b}{a})db]da] \quad (2)$$

Among them, $a,b \in R, a \neq 0$, $\Psi(t)$ is continuous wavelet, $\overline{\Psi(t)}$ is complex conjugate of $\Psi(t)$, a is scaling factor, b is the translation factor.

1.2 Disturbance signals to extract feature vector

For five scale disturbance signals after wavelet decomposition, the selection of each decomposition level energy disturbance duration, mean, standard deviation and the structure of the compound disturbance signal feature vector T information. The specific practices of disturbance feature vector extraction steps are as follows:

Select the scale of the energy disturbance duration, mean, standard deviation and information composition and structure of the compound disturbance signal feature vector, expressed as:

$$T = (K_w, K_{av}, K_\delta, K_t, K_{WT}) \quad (3)$$

Type, K_W for the scale of the energy, Kav for each scale, K_δ as the standard deviation of each scale disturbance duration , Kt for each scale, K_{WT} for various scales in structure of complex information.

2 Application of PSO and BP neural network algorithm

Particle swarm optimization algorithm (PSO), a flock of birds to prey on the evolutionary algorithm. The optimal solution of the optimization space abstracted as a particle known as the "particles". Each particle has the fitness of a determined by the objective function. Each particle in a certain speed in optimization space flight decide the direction and distance of particle movement according to their own dynamic adjustment and companion's experience. The position of each particle know their current and still find the best position, this is their own experience. Each particle in groups all other known particles also found so far are the best position, a companion to the experience. According to their own experience and experience, the particle can be set for the particles with the best fitness value and continue to search in the solution space through repeated iteration update.Finally find the global best position, then it is the optimal solution. In this algorithm, the speed of the particle vi and their locations xi expression formula is:

$$v_i = v_{i-1}w + C_1 Rand\ ()(\ pBest\ [i] - x_{i-1}) + C_2 rand\ ()(\ gBest\ [i] - x_{i-1}) \quad (4)$$

$$x_i = x_{i-1} + v_i \quad (5)$$

Type, i is the number of iterative update, w as the inertia weight, xi is the iteration update particle space position, v_i is the particle iteration speed, the Rand () and rand()is a constant between interval [0, 1], C_1 and C_2 respectively is learning factor and constant.

3 Experimental analysis

The method can seek the best parameter weights and threshold through MATLAB.The sampling frequency of 1.6 kHz, disturbance signal fundamental wave frequency is 50 Hz, r (t) as white noise, signal to noise ratio of 20 db.

Through the simulation results, determine the c = 8.2645, g = 13.5708. The sample matrix randomly divided two groups, one group as the training sample, the other group as the test sample to test five kinds of common dynamic disturbance signal. The classification of the PSO - BP optimization result is shown in figure 2 and table 2.

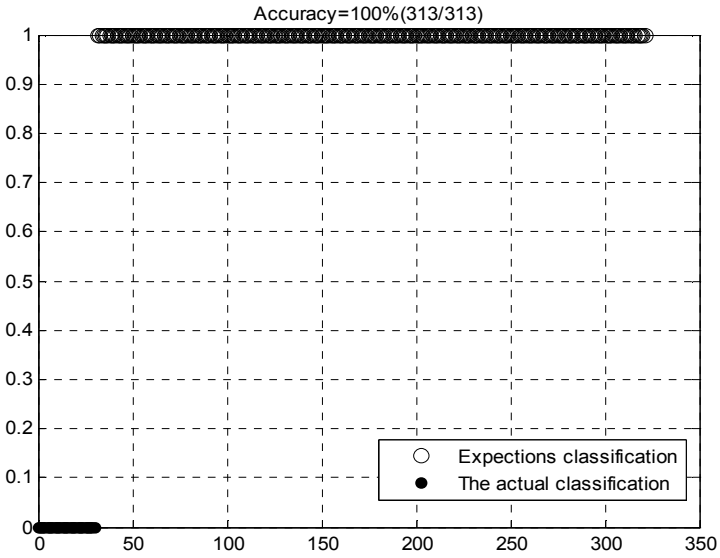

Fig.2 Classification result （Temporary transient pulse）

Tab.2 Classification result （Temporary transient pulse）

Jamming signal	Temporary transient pulse	Voltage surge	Voltage sag	Transient oscillation	Voltage interrupt
Training accuracy	100%	100%	100%	100%	100%
Test accuracy	100%	96%	99%	96%	100%

The table 2 and table 2 shows that PSO - BP for five kinds of common dynamic power quality disturbances classification accuracy as high as 100% prove that this method is effective.

4. Conclusion

This paper puts forward a kind of based on complex wavelet combined with PSO and BP network of new method for identification and classification of power quality disturbance. By complex wavelet analysis to extract the disturbance signal amplitude and phase information as the feature vector and then find the optimized by PSO algorithm neural network weights and threshold of the optimal solution, PSO - neural network based on power grid in the five kinds of common dynamic power quality disturbance recognition and classification. MATLAB simulation shows that this method can accurately and fast implementation of power quality disturbance recognition and classification.

Acknowledgements

Funded Projects: The national natural fund (61071087); Shandong province natural science foundation of China (ZR2012EEM021)

Reference

[1] LV Guang-qiang, ZHAO Jian-feng, CHENG Ming, et al. Dynamic quanlity of power supply and its solution for distribution system[J]. High Voltage Engineering, 2007,33(1):53-56.
[2]LIU Ying-ying, LI Guo-dong, GU Qiang, et al. The comprehensive evaluation of power quality based on the RBF neural network. Electrotechnical Application, 2007, 26 (1):45-48.
[3] Santoso S,Powers E J,Grady W M. Power quality disturbance data compression using wavelet transform methods[J].IEEE Trans on Power Delivery,1997,12(3):1250-1255.
[4]LIU Ying-ying,LI Guo-dong, GU Qiang, et al. The comprehensive evaluation of power quality based on the RBF neural network. Electrotechnical Application, 2007, 26 (1):45-48.
[5]SONG Xue-lei. Analysis Method of Power Quality Disturbances Based on Wavelet Transform and Support Vector Machine[D]. Harbin industrial university PhD thesis,2007.
[6] LI Lian-jie, Yao Jian-gang, Long Li-bo, et al.Application of combination weighing method in fuzzy synthetic evaluation of power quality. Automation of Electric Power Systems, 2007,31(4): 56-60.

CHAPTER 7:

Measurement and Instrumentation, Monitoring, Testing, Detection and Identification Technologies

Advanced Materials Research Vols. 986-987 (2014) pp 1437-1442

doi:10.4028/www.scientific.net/AMR.986-987.1437

A New Fault Location Method for 10 KV Distribution Lines With Branches

Yan Feng [1, a], Li Shuangshuang [2, b]

[1,2]Department of Electrical and Electronic Engineering, North China Electric Power University, Baoding, 071003, china

[a] email: yanfyyy @163.com, [b] email: lishuangshuangglm@126.com

Keywords: 10 KV distribution networks; single phase grounding fault; C-type of traveling wave; SVM; wavelet

Abstract：By using the advantages of C-type of traveling wave fault location method in distance measuring and the pattern recognition function of support vector machines(SVM)，a new fault location method is presented．The first step of the method is determining the fault distance by C-type of traveling wave location method; the second one is locating the fault section by SVM. It also adopts the wavelet to reduce the noise of fault signal，and the accuracy can be more precise when the parameters of SVM are optimized．The simulation results of ATP and MATLAB show that the method can determine the single phase grounding fault point in 10kv distribution networks with branches accurately．

Introduction

The grounding arc can be self-extinguishing when the single phase grounding fault occurs in the small current grounding system. As the fault current flows through the capacitance to earth ,its value is too small to be measured, besides the fault signal characteristics is difficult to be captured by the influence of noise. This system is widely adopted in power distribution networks of 6~35kv in China. When the single-phase ground fault occurs, the voltage to ground of non-fault-phase voltage rises to the line voltage, and the voltage remains symmetrical and the fault current is small, the system can operate about 1~2h after the fault. Although the reliability of power supply is improving, the risk of equipment insulation damage is increased at the same time. How to find the fault point rapidly is of great significance.

The10kv distribution networks in china have lots of branches, overall length and large capacitance to earth. The system can restore normal power supply generally for transient grounding faults. However, it is need to take the network offline when the permanent faults occur. In this paper, a method based on C type of traveling wave and support vector machine (SVM) is presented. The C type of traveling wave can determine the distance between the measure end and the fault point. As there are lots of branches in the 10kv distribution network, SVM is used to choose the fault section. When the distance and section are confirmed, the fault point can be found accurately.

C-type of Traveling Wave Method

Nowadays, the traveling waves consist of A, B, C, D and E five types generally[1,2]. The A and B types use the fault signal as the traveling wave. They need to detect the time when the traveling wave arrives at the measuring terminal on-line. The difference is A type of traveling wave is single-terminal location method, but B-type is two-terminal. The D and E types respectively use the signal generated by the reclosing and opening operation of breaker to determine the fault distance. C-type of traveling wave is a high voltage pulse signal injected by manual, it would not disturbed by the transition resistance, failure mode and the neutral grounding mode of power

systems, thus this method can get relatively accurate results [1,3]. Because this method is offline, it can be used several times to measure the distance. Fig.1 shows the theory of C-type traveling wave method.

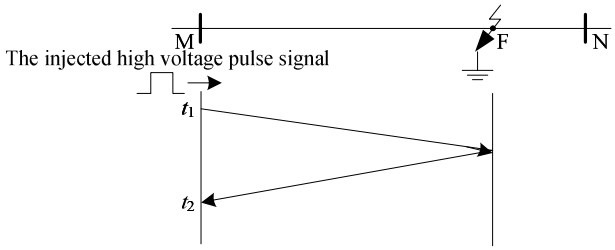

Fig.1 C-type traveling wave method

At the M end, a pulse signal is injected into the line at t_1 (commonly t_1=0), when the traveling wave arrives at the fault point F, it will reflect to the detection terminal at time t_2. The wave velocity is similar to the speed of light, $v=3\times10^8$m/s. Supposing the distance between the M and F is X_L, the calculation formula is

$$X_L = \frac{v\times(t_2 - t_1)}{2} = \frac{v\times t_2}{2} \tag{1}$$

Support Vector Machine

Support vector machine (SVM) [4, 5] is based on the theory of VC dimension and structure minimum risk theory of statistical learning. It is gonging to get the best generalization by finding the best trade-off between the model complexities of limited samples' information and learning ability. As the figure 2 shows, the main idea of SVM is to build an optimal hyperplane which can maximize the distance between the nearest separate planes of the two kinds of samples.

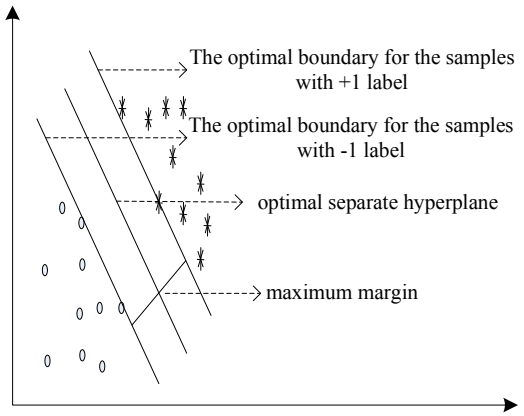

Fig.2 The optimal separating hyperplane

A .The Algorithm of SVM for Linearly Separable Samples

For linearly separable samples, supposing the input vector X is training samples X=(x_1，x_2，…，x_n), Y is the expected output vector .Setting + 1 and -1 labels respectively represent the two different kinds of samples, then Y = (y_1, y_2...y_n) has-1 and + 1 two values.

The equation of optimal hyperplane is:

$$\boldsymbol{w}\cdot x + b = 0 \tag{2}$$

$\boldsymbol{w}$ is the Weight vector and b is the bias term. The only two parameters used to control the separating function. Only there is margin between the two classification planes exist, can SVM separate the samples accurately. The constraint condition is:

$$\begin{cases} \boldsymbol{w}x_i + b \geq 1 \quad for \ y_i = -1 \\ \boldsymbol{w}x_i + b \leq -1 \quad for \ y_i = +1 \end{cases} \Rightarrow y_i(\boldsymbol{w}x_i + b) - 1 \geq 0 \tag{3}$$

The maximum margin is:

$$\frac{2}{\|\boldsymbol{w}\|} = \min_{\{x_i | y_i = +1\}} \frac{\boldsymbol{w} \cdot x_i + b}{\|\boldsymbol{w}\|} - \max_{\{x_i | y_i = -1\}} \frac{\boldsymbol{w} \cdot x_i + b}{\|\boldsymbol{w}\|} \tag{4}$$

After inducting the Lagrange function and obtaining the minimum value, we can get the result as shown below.

$$\begin{cases} L(\alpha) = \sum_{i=1}^{l} \alpha_i - \frac{1}{2} \sum_{i=1}^{l} \alpha_i \alpha_j y_i y_j (x_i \cdot x_j) \\ \sum_{i=1}^{l} \alpha_i y_i = 0 \quad \alpha_i \geq 0 \quad i = 1, \ 2, \ 3, \cdots, n \end{cases} \tag{5}$$

For most of samples α_i is 0. If the equation (3) can be set up, α_i is not 0, the corresponding samples are exactly on the optimal boundary as shown in fig.2. After the above problems are solved, the best classification function is

$$f(x) = \operatorname{sgn}\left\{ \sum_{i=1}^{l} y_i \alpha_i^* (x \cdot x_i) + b^* \right\} \tag{6}$$

B. The Algorithm of SVM for Linearly Non- separable Samples

For linearly non-separable samples, the input vector should be mapped to the high dimensional space by nonlinear transformation, and then we can utilize the algorithm of SVM for linearly separable samples to separate the samples.

$$f(x) = \operatorname{sgn}\left\{ \sum_{i=1}^{l} y_i \alpha_i^* \mathrm{K}(x \cdot x_i) + b^* \right\} \tag{7}$$

K is an inner product computation of feature space. It obeys Mercer's condition, namely kernel function. There are several kernel functions that may be used in the definition of the new classification space as presented in [6]. In addition, there are two important parameters of SVM model affect the accuracy of classification, they are kernel function parameter g and punishment parameter c, the change of g will affect mapping relationship and c decides the generalization ability of SVM

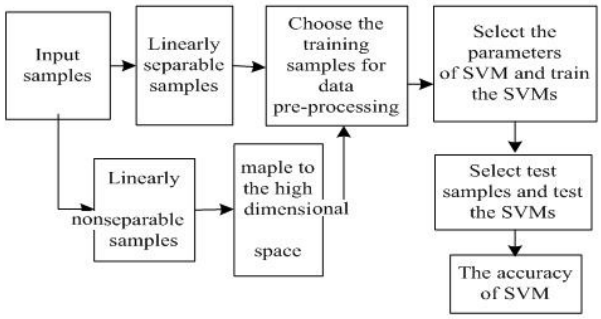

Fig.3 The flow diagram of SVM

C-type of Traveling Wave-SVM Fault Location Method

As the 10KV distribution networks have lots of branches, the strong classifying ability of SVM can determine the fault section quickly. To incorporate the advantages of C type traveling wave and SVM together, the comprehensive method can achieve fast and accurate fault location.

Figure 4 shows part of a plant's distribution circuit diagram of a substation .In order to validate the accuracy of this new method, a fault model was built by using a combination of Alternative Transient Program (ATP) software as shown in fig.5.

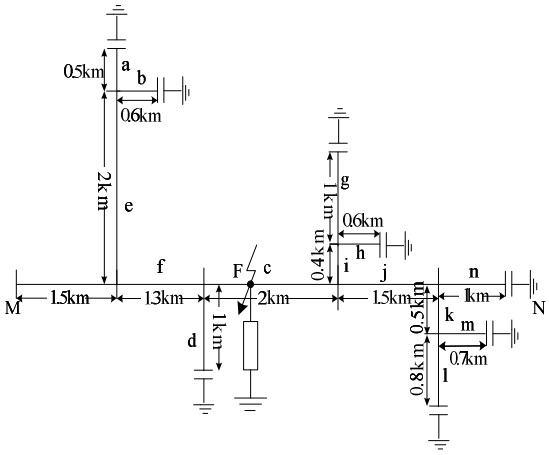

Fig.4 Schematic diagram of simplified circuit

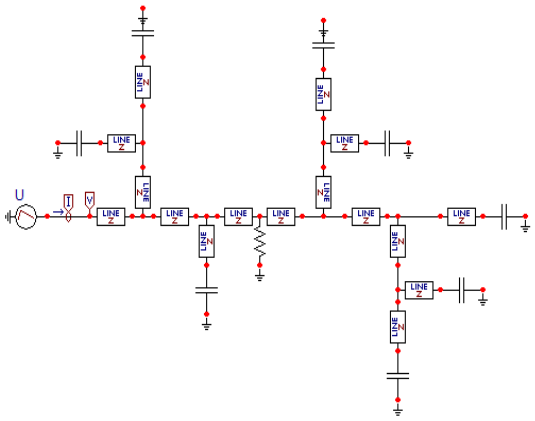

Fig.5 The simulation model of ATP

A .C-type of traveling wave distance measurement

Supposing the single-phase ground fault occurs at F point in the c section, and the ground resistance is 1000Ω. The distance between the head of the line M and F point is 3.75 km. After the fault, a high voltage pulse signal whose amplitude is 10*kv* and width is 2*us* was injected into the network, and only the entrance capacitance of transformer has an effect on traveling waves under such high frequency. The entrance capacitance of each phase winding is 423*pf* [7]. The simulation lines use the single-phase line with distribution parameters; the section of line between two points is simulated by a π type equivalent circuit. Setting the impedance of the wave is 480Ω.

The signal was injected at t_1(t_1=0), the reflected wave gets the measuring terminal M point at t_2.Before the fault point ,the waveforms from normal condition and failure condition are the same, however behind the point, the waveforms are different ,so the first non-zero point of the waveform difference can reflect the fault point distance. In order to approximate to the real fact, the waveform difference was added the white gaussian noise whose signal-to-noise ratio is 10, the noise infected waveform is shown in fig. 5. After using the Wavelet to denoise the waveform [8], we can find the break time of the waveform, from Fig.6, the break time is t_2=25.04*us*. Then the fault distance can be

obtained by formula (1). Compared with the actual distance the result differs from the reality only 6m.

$$X_L = \frac{2.504\times10^{-5}\times3\times10^{8}}{2} m = 3.756\ km$$

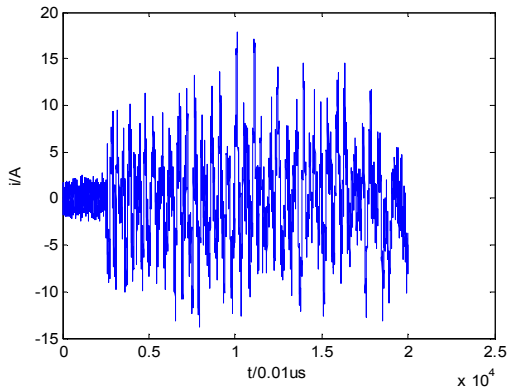

Fig.5 The difference of the two waveforms with noise

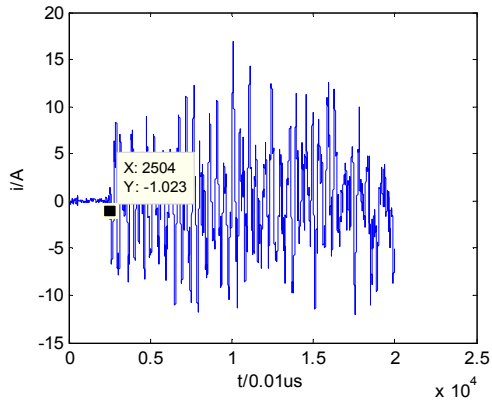

Fig.6 The denoise waveform

B .SVM Fault Section Detection

After the distance is determined , there are a , b, c and d four sections have the points whose distance to the M point is 3.75*km*.

LIBSVM [9] is a software package for SVM pattern recognition. It provides several default parameters and can classify the samples simply and fast. First, choose the training and testing samples. The total data includes 36 groups of fault waveforms. They are obtained by simulating the faults in a, b, c, and d sections with ATP-EMTP simulation software. Among them, 1-8groups of data , 9-16 groups of data, 17-24 groups of data and 25-32 groups of data came from 8 different fault points of a, b, c, and ,d respectively, they are training samples. The last 4 groups of data are testing samples; they came from the fault points whose distance to M is 3.75*km* of a, b, c, and d sections. Set the fault labels of a, b, c and d sections as 1,2,3,4. Second, choose the parameters of SVM. Researches show that Cross Validation (CV) method can find the best parameters for SVM to achieve high classification accuracy, the paper adopted it .Finally, test the classification accuracy of SVM.

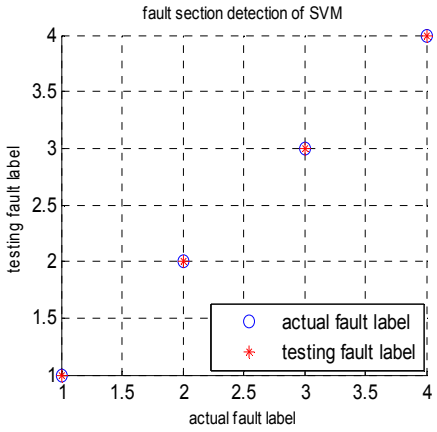

Fig.7 The result of SVM for classification

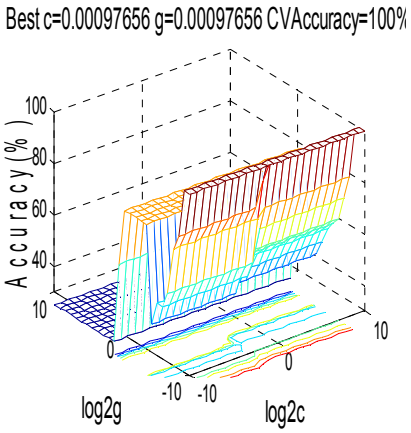

Fig.8 The optimized parameters of SVM by CV method

From Fig.7 and Fig.8, SVM can determine the fault section accurately and the best c and g are both 0.00097656. It shows that C-type of traveling wave method with SVM fault location is feasible.

Conclusion

The paper proposes a new method that combines C-type of traveling wave location and SVM method to find the fault point for distribution networks with branches. The C-type of traveling wave can determine the fault distance accurately; the optimized SVM can judge the section without error. The results show that the composite location method can accurately find the fault point of an off-line 10kV distribution line after a single phase grounding fault.

References

[1] Yan Feng, Yang Qixun, Qi Zheng, et al: Study on Fault Location Scheme for Distribution Network Based on Traveling Wave Theory [J].Proceedings of the CSEE Vol. 24(2004), p.37-43.

[2] Bo Z Q: Accurate Fault Location Technique for Distribution System Using Fault-generated High-frequency Transient Voltage Signals [J]. Generation, Transmission and Distribution, IEE Proceedings Vol.146 (1999), p. 73-79.

[3] Qi Jian: Study on Single Terminal Traveling-wave Fault Location of Transmission Line [J]. Power System Technology Vol.29 (2005), p. 65-70.

[4] Xu Zhenhua: Detection of Low-voltage Arc Fault Based on Support Vector Machine [J]. Proceedings of the CSU-EPSA Vol. 24(2012), p.128-131.

[5] J Mora-Florez, J Bedoya-Ceballos, Perez-Hernandez: Selection of Currents Patterns Using SVMs for Locating Faults in Radial Power Systems [J]. IEEE, Transmission and Distribution Conference and Exposition, Latin America (2008), p.1-7.

[6] N. Cristianini, Shawe-Taylor: An Introduction to Support Vector Machines [M].Cambridge University Press (2000).

[7] Yan Feng, Liu Wenxuan, Dong Wei, et al: A New Composite Method of Fault Location for 10KV Distribution Lines [J]. Proceedings of the CSU-EPSA Vol.24 (2012), p.117-122.

[8] KE Hui, GU Jie: Wavelet Threshold De-noising of Power System Signals [J].Proceedings of the CSU-EPSA Vol.22 (2010), p. 103-108.

[9] Information on http: //www.ilovematlab.cn/thread-35262-1-1.html.

Advanced Materials Research Vols. 986-987 (2014) pp 1443-1448

doi:10.4028/www.scientific.net/AMR.986-987.1443

A Quick Detection Approach of Magnetic Iron Grade for Magnetite

Henan Wang[1,2], Lijie Wang[1,2,a], Hebing Wang[1,2], Guanhua Men[1,2], Ye Liu[1,2], Hongyan Liu[1,2]

[1]College of measure-control technology and communication engineering, Harbin university of science and technology, China

[2]The higher educational key laboratory on measuring & control technology and instrumentations of Heilongjiang province, China

[a]wlj@hrbust.edu.cn

Keywords: magnetite, magnetic iron, grade, quick detection, winding.

Abstract. In order to achieve aims of rapid real-time monitoring iron grade during sales process or mineral processing for the iron ores, a quick detection approach to magnetic iron grade of magnetite based on electromagnetic induction is explored in the paper. Information acquisition head is focused on an iron grade sensor, and the iron grade sensor is made up of coil-windings with magnetite core. Information acquisition circuits are given adapting mode of the transformer bridge type rectifier, and construction of the head is designed and machined. Testing mechanism is analyzed from the angle of magnetic field analysis, and the magnetic field model is also built up. Furthermore, magnetic iron grade of some testing samples are measured by the detection device above. It is showed that when the grade range of the magnetic iron of magnetite is varied from 20% to 65.3%, deviation is lower than 1.0%. By research above, it is shown that the detection method of iron grade based on electromagnetic induction is feasible, and it is also significant for improving the total testing level of mineral processing fields.

Introduction

For the past few years, easy dressing iron ores are gradually decreasing in the iron ore resources. In more and more countries, mining target has begun to be focused on mineral processing, development and utilization of the low grade ores. Accordingly separation and purification of fine grained refractory ore are becoming an urgent issue in field of the mineral processing industry. There are problems of low grade, complex ore components, and fine particle size distribution, for ore resources of poor ores and ancillary minerals, which cause some difficulties to mineral separations. Therefore, from the technical perspective, advanced processing technology, equipment, and automatic on-line testing technology are all demanded urgently for promoting effective development and utilization to poor ore resources. On the other hand, from the point of the economic benefits, dressing plants have to expand the scale of production, enhance the ore processing power, save energy and reduce consumption, and reduce the mineral processing cost, for the poor iron ore production, better economic benefit just would be had. So while constantly adjusting mineral processing process, Timely developing and researching automatic real-time detecting system used for beneficiation testing fields to realize iron grade monitoring during sales processing, beneficiation processing, or tailings recycling processing [1] [2], it is a valid approach to enhance mineral separation testing level, improve the production capacity, and create good economic benefit in the field of mineral processing at present. Therefore, in the followings, an electromagnetic induction method is put forward and explored to quick detect magnetic iron grade of magnetite.

Physical Analysis for Magnetite and Detecting Approach Research

Nowadays, magnetite is the main exploited ore types within the boundary of China at present, its recoverable deposits is accounted for 50% of recoverable deposits nationwide[3]. The main

composition of magnetite is Fe_3O_4, it can be written as $FeO \cdot Fe_2O_3$. There are two kinds of valences of magnetite, that are +2 and +3, valence of one iron atomic is +2, the other two atomics are +3. In most substance, electrons move in different direction and out of order, and the magnetic effect cancel out each other, thus most substance does not show magnetism normally. Ferromagnetic material differs from general substances; internal electronic spin of the ferromagnetism may be aligned spontaneously in a small range to form a spontaneous magnetization that is called magnetic domain. As the ferromagnetism is added electricity and magnetized, its inner magnetic domain is arranged to a nicety and in the same direction, the magnetic will be enhanced to form the magnet. Grade is about 20~30% of natural magnetite. Although grade is low, the magnetite is easy to be chosen because of its natural strong magnetic. Usually iron concentrate grade after mineral processing is higher than 60%, so as a strong ferromagnetic material, the magnetite could be set in the inductive windings to be regarded as the core. Magnetic iron grade of the magnetite will be detected making use of electromagnetic induction method by AC signal exciting.

Block diagram of the detecting method for magnetic iron grade of the magnetite is shown in Fig.1. Information acquisition is completed mainly by an iron grade sensor, and the iron grade sensor is made up of coil-windings with magnetite core. Under excitation of the exciting signal, if iron grade is differing, magnetic permeability and flux would differ accordingly, output voltages of iron grade sensor would vary correspondingly; electromagnetic measurement would accomplish by the following testing circuits.

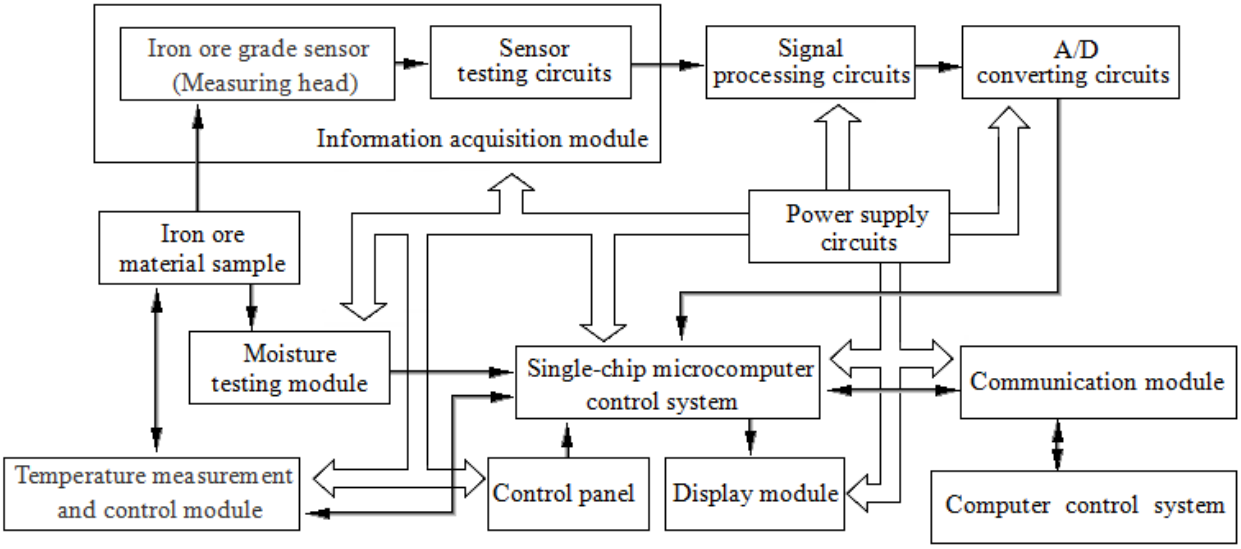

Fig.1 Block diagram of the detecting method for magnetic iron grade of the magnetite

In the Fig.1, information acquisition module is composed of iron ore grade sensor and sensor testing circuits, the iron ore grade sensor is also called measuring head in the followings. Output voltage signal of the sensor testing circuits is then transferred into signal processing circuits, nextly converted by A/D converter, lastly inputted to sing-chip microcomputer control system. Testing result of sample grade is indicated directly by display module. At the same time, the measured data can be also transferred into computer control system by means of communication module. Because iron ore oxidation degree is affected by temperature of the sample, temperature measurement and control module based on temperature sensor DS18B20 is designed to measure temperature of the tested sample and to make temperature compensation. Moisture testing module based humidity sensor AM2305 is designed to detect iron ore moisture, the moisture of iron ore not only impact grade testing, but also affect sales price. The grade and the moisture are two important factors impacting sales price of the iron ore.

Information Acquisition Module Research

Schematic diagram of the information acquisition module is given in Fig.2. The information acquisition module includes the measuring head and its testing circuits.

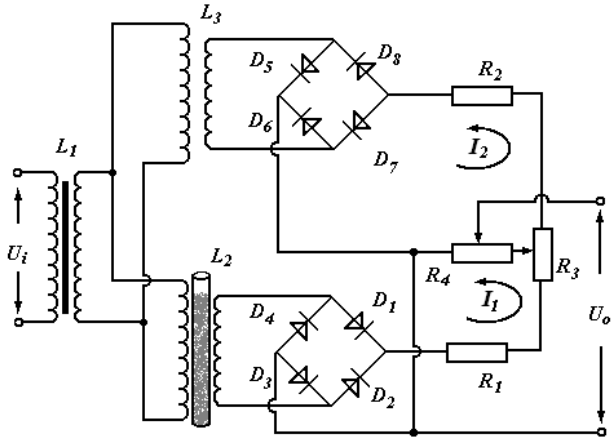

Fig.2 Schematic diagram of the information acquisition module

In Fig.2, input terminal U_i is connected the 220V output of 1KVA AC stabilified-voltage power. Aim of using the AC stabilified-voltage power is to eliminate the influence of voltage fluctuation of power grid. Output voltage of transformer L_1 is connected to the input terminals of hollow transformer L_2 and L_3, so induced voltage are generated on both ends of the secondary coil of L_2 and L_3.Magnetic resistance of the hollow transformer is very large, induced voltage is small, so two groups of bridge rectifier circuits are designed. After the bridge rectifier, two equal currents in the opposite direction I_1 and I_2 are obtained. Adjusting potentiometer R_3, so as to

$$I_1 = I_2 \tag{1}$$

At the moment, potential difference generated in resistance R_4

$$U_o = 0 \tag{2}$$

When needing to detect magnetic iron grade for magnetite, the being measured magnetite sample is set in air cavity of the inductive windings L_2 to be regarded as the transformer core. Due to the magnetite sample as the core of windings, magnetic flux become bigger, so electric current I_1 after the bridge rectifier will also increase, thus

$$I_1 > I_2 \tag{3}$$

Therefore, the potential difference U_o on resistance R_4 is no longer zero. As testing, the iron grade is higher, U_o is greater. According to the value of U_o, magnetic iron grade for magnetite thus is detected.

Setting parameters of the air-core transformer L2 and L3 are the same. When external disturbance is interfered on the transformer windings at the same time, the output of the testing circuits U_o still is zero because impact of L_2 and L_3 is cancelled out each other, the impact of L_2 and L_3 is equal in value and opposite in direction. If the detected magnetite sample is set in cavity of L_2 such as real-time testing in the process of sales, perhaps if the detected material sample on a conveyor belt is traveling through the cavity of L_2 such as on-line monitoring in the processing process, the core magnetic flux and magnetic permeability would be increased, thus U_o would be also increased, according to Faraday's law of electromagnetic induction [4], its valid value is

$$E = 4.44 f N \phi \tag{4}$$

In Eq. 4, f is frequency of alternating magnetic flux, N is number of turns of the secondary coil L2 and L3, ϕ is the maximum number of alternating magnetic flux.

Measuring Head Design

The measuring head mainly refers to two-winding transformer L_2 and L_3, structure and parameters of L_3 are the same with L_2, but there is no core within the inductance winding L_3. As the collection device of the information of grade, iron grade sensor consisting of L_2 and L_3 will realize ideally the dual electromagnetic induction testing, it is shown in Fig.3 of the structural design drawing of the measuring head L_2.

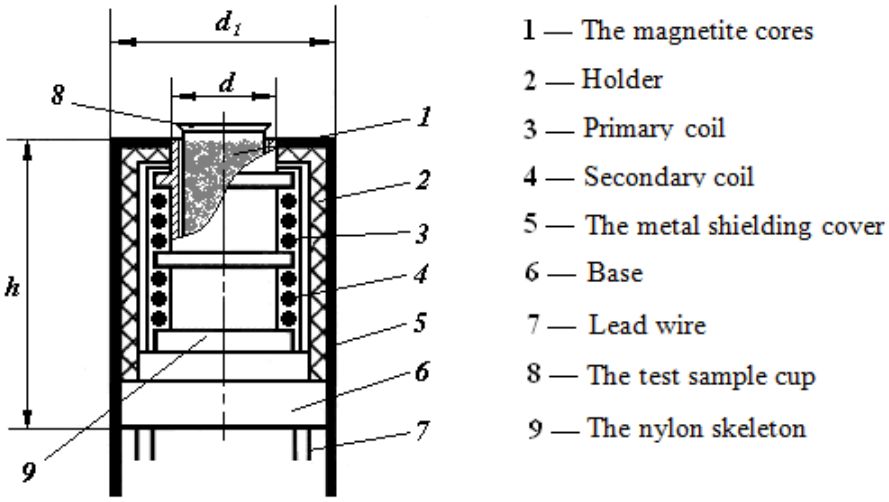

Fig.3 Structural design drawing of the measuring head

In Fig.3, frame of the measuring head is built by base 6, the nylon skeleton 9, and holder 2. Cylindrical double winding transformer L_2 constitutes the heart of iron ore grade sensor. Primary coil 3 and secondary coil 4 of the transformer are coaxial, and are respectively twisted on cylindrical nylon skeleton 9. Four wires lead out the taps of the primary coil and the secondary coil. The wires respectively connect sensor and power, sensor and testing circuits. The skeleton is processed into hollow shape to place magnetite iron core. When the power is switched on, ferromagnetic material can generate a magnetic field within limits of certain space. Making use of the electromagnetic induction, the iron grade sensor completes grade information collecting.

Enameled wire is wound into the form of solenoid to form the primary coil and the secondary coil. A very small section of enameled wire as the coil wire can reduce eddy current loss of harmonic in the wire. There is no internal joint of the coil, lead wire joint is welded to aluminum wiring wall. The coil are encapsulated and coated with silicone paint after coil winding. The skeleton and the windings are fixed on the holder, total measuring head is set in external iron metal shield to make Magnetic shield. Design above could validly enhance anti vibration mechanical strength of the measuring head, and ensure outdoor operation reliability.

Magnetic Field Analysis

As the core of information acquisition, testing mechanism of the iron ore grade sensor essentially belongs to the transformer inductance coil electromagnetic induction. Applying with alternating current for cylindrical inductance coil, alternating electromagnetic field will be formed in its surrounding space. Sketch map of the distribution of magnetic field in vertical eccentric line at the XOY plane for circular coil radius is ρ and load flow is I is given in Fig.4.

In Fig.4, magnetic field generated by electric current unit $d\alpha$ whose radius is ρ at space point $P(l,0,h)$ is dH. Line segments b is in the XOY plane, and is parallel to the radius of $d\alpha$. Length of line between intersection of b and circle tangent to the electric current unit and $P(l,0,h)$ is a. According to Maxwell's equations, the followings can be deduced.

$$dH = \frac{I\rho d\alpha}{4\pi r^2} \sin\theta$$

$$\sin\theta = \frac{a}{r} = \frac{\sqrt{h^2+b^2}}{r}$$

$$r^2 = h^2 + c^2 = h^2 + l^2 + \rho^2 - 2\rho l\cos\alpha$$

$$b^2 = (\rho - l\cos\alpha)^2 = \rho^2 + l^2\cos^2\alpha - 2\rho l\cos\alpha$$

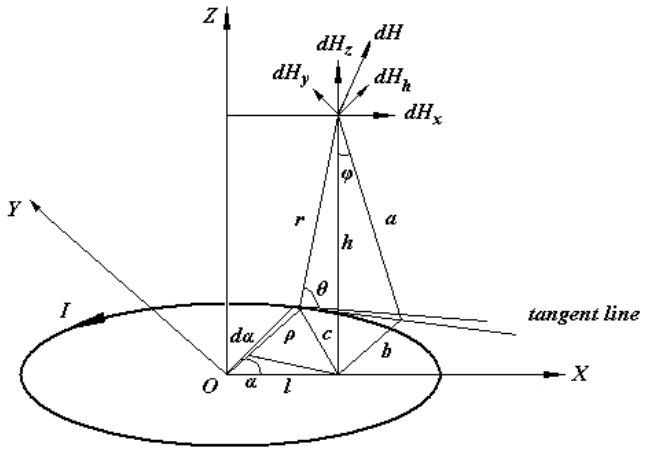

Fig. 4 The distribution of magnetic field in vertical eccentric line of circular coil

As a result,

$$dH = \frac{I\rho d\alpha}{4\pi r^2}\frac{a}{r} = \frac{I}{4\pi}\frac{\rho d\alpha\sqrt{h^2+\rho^2+l^2\cos^2\alpha-2\rho l\cos\alpha}}{\sqrt{(h^2+\rho^2+l^2-2\rho l\cos\alpha)^3}} \tag{5}$$

Component of dH is respectively dH_x, dH_y, and dH_z. dH_h is synthetic quantity of dH_x and dH_y in horizontal direction, dH is synthetic quantity of dH_h and dH_z in vertical direction.

Because of $dH \perp a$ and $dH_h \perp h$, so

$$dH_z = dH\sin\varphi = dH\frac{b}{a} = \frac{I}{4\pi}\frac{\rho(\rho - l\cos\alpha)d\alpha}{\sqrt{(h^2+\rho^2+l^2-2\rho l\cos\alpha)^3}} \tag{6}$$

$$dH_h = dH\cos\varphi = dH\frac{h}{a} = \frac{I}{4\pi}\frac{\rho h d\alpha}{\sqrt{(h^2+\rho^2+l^2-2\rho l\cos\alpha)^3}} \tag{7}$$

$$dH_x = dH_h\cos\alpha = dH\cos\varphi\cos\alpha = dH\frac{h}{a}\cos\alpha = \frac{I}{4\pi}\frac{\rho h\cos\alpha d\alpha}{\sqrt{(h^2+\rho^2+l^2-2\rho l\cos\alpha)^3}} \tag{8}$$

$$dH_y = dH_h\sin\alpha = dH\cos\varphi\sin\alpha = dH\frac{h}{a}\sin\alpha = \frac{I}{4\pi}\frac{\rho h\sin\alpha d\alpha}{\sqrt{(h^2+\rho^2+l^2-2\rho l\cos\alpha)^3}} \tag{9}$$

If respectively making integration for formula above, magnetic field intensity of arbitrary spatial point P of circular current-carrying coil would be obtained[5][6][7][8].

According to Eq. 7, if number of turns of the finite length inductor winding with cylindrical magnetite iron core is N, cross-sectional area perpendicular to the axial direction is S, relative magnetic permeability of magnetite is μ_r, and air relative permeability is taken 1, so radial micro component of magnetic induction intensity of arbitrary spatial point P *is* the following.

$$dBr = \mu_r N dH_h = \frac{\mu_r NI}{4\pi}\frac{\rho h d\alpha}{\sqrt{(h^2+\rho^2+l^2-2\rho l\cos\alpha)^3}} \tag{10}$$

Making integration to Eq.10, corresponding radial component of magnetic induction intensity is the following.

$$B_r = \frac{\mu_r NI}{4\pi}\int_0^{2\pi}\frac{\rho h d\alpha}{\sqrt{(h^2+\rho^2+l^2-2\rho l\cos\alpha)^3}} \tag{11}$$

According to Eq.11, alternating magnetic flux ϕ can be calculated.

$$\phi = B_r S = B_r \pi \rho^2 \quad (12)$$

Simultaneous Eq.4 and Eq.12, electromotive force output value can be gained, thus the iron grade value can be detected.

Experiment Results and Conclusions

Experiment samples adopt artificial mixed ore samples compounded of magnetite concentrate powder and silica sand. Concentrate powder is naturally dried. Size of the concentrate powder is that material proportion is higher than 70% under the 200 mesh sieve. TFe is 65.30% measuring by the national standard chemical analysis method, and size of the silica sand is that material proportion is higher than 100% under the 50 mesh sieve. Usually during mineral processing process, TFe at the stage of classifier overflow is about 20~40% , TFe at the stage of ore discharge of the dewatering tank is about 40~60%, and TFe of magnetic concentrate is higher than 55%. Thus, designing scope of prepared samples is from 20.00% to 65.30%, number of the measuring samples is 20.

As testing, the measuring sample is put into the test sample cup. Experiment testing is made after several times vibrating. Precision of electronic balance make samples is 0.1mg. Voltage value corresponding with iron grade is tested. Linear regression analysis method is applied to modeling between voltage and grade, measuring deviation of magnetic iron grade of the mixed magnetite samples is lower than±1.0%.

Experimental study above confirms the feasibility of the magnetic iron grade measuring method based electromagnetic induction sensor technology. Thesis research work has laid a good foundation for achieving of the apparatus of iron grade detection for iron ore. No matter from the technique prospect or from the aspects of theoretical methods, so much as application prospect, it has highly research value an

d development opportunity of the approach. As a long time topic, it has important practical significance in mineral processing.

Acknowledgements

This work was financially supported by the following projects. Scientific Research Fund of Heilongjiang Provincial Education Department of China (12531142). Natural Science Foundation of Heilongjiang Province of China (F201223). 2013 Training Programs of Innovation and Entrepreneurship for Undergraduates of Harbin University of Science and Technology of China.

References

[1] Y.Q. Pang, G. He. Acta Geologica Sichuan, vol.29(2009), p.313

[2] Y.H. Tang, L.C. Qiu. Process Automation Instrumentation, vol.32(2011), p.53 In Chinese

[3] Z.J. Wei. China Mining Magazine, vol.19(2010), p.10

[4] Information on http://www.cnki.net

[5] X.J. Kuang. Journal of Luoyang University, vol.19(2004), p.22

[6] Q. Wang. Journal of Taiyuan Normal University (Natural Science Edition), vol.5(2006), p.83

[7] L.Q. Chen. Journal of Loudi Teachers College, No.4(2000), p.77

[8] Leono S., Karankevich A., Muravlev O.. The 7th Korea-Russia International Symposium on Proeeding KORUS, vol.2(2003), p.268

Advanced Materials Research Vols. 986-987 (2014) pp 1449-1452

doi:10.4028/www.scientific.net/AMR.986-987.1449

A Rotor Speed Sensor of Cycloid Rotor Flowmeter

Shuo Liu[1, a], Fan Ding[1, b] and Chuan Ding[1,c]

[1]Zhejiang University, Hangzhou 310000, China;

[a]liushuo@sina.com, [b]fding@zju.edu.cn, [c]dc1986@zju.edu.cn

Keywords: Rotor speed sensor; Positive displacement flowmeter; Magnetic field simulation

Abstract. Positive displacement flowmeters (PDFs) are highly accurate flowmeters that are relatively insensitive to the upstream velocity distribution and fluid viscosity. Rotor speed sensors are the key components of a PDF. This paper presents the structure of a non-contact rotor speed sensor which can be used in cycloid rotor flowmeter and other PDFs. The sensor outputs a square wave which contains the speed information of the rotors. The key parameters of the rotor speed sensor are analyzed in this paper and a prototype was fabricated to confirm the rotor speed sensor work well.

Introduction

Positive displacement meters (PDFs) are one kind of flowmeters with the highest accuracy. Due to the advantages such as high accuracy, good stability, insensitivity to upstream velocity distribution and fluid viscosity, PDF plays an irreplaceable role in the application of flow rate measuring. For example, despite the new meters that are being developed nowadays, in custody transfer operations PDFs are still the most used and accurate ones[1,2]. PDF requires fluid to mechanically displace components in the meter. The flow-rate can be measured by measuring the rotation speed of the rotors. So a PDF mainly contains rotors, rotate speed sensors and secondary instrument which are used to dispose the signal and show the results.

Traditional PDF uses mechanical transmission tachometer to display the accumulate flow. This kind PDF can work without the need for electricity. But because the leak problems existed in dynamic sealing of rotating shaft, it isn't suitable for high pressure measuring. With the development of electronic technology, digital secondary instruments have replaced the mechanical secondary instruments to occupy a dominant position. Eddy current sensors and Hall sensors are used in these PDFs to measure the rotation of the rotors by non-contact measurement [3-5]. The appearance of non-contact measurement thoroughly solves the leakage problems existed in dynamic sealing of rotating shaft. And that helps PDFs to bear high pressure. Werner Ing Grad Weber proposed a volume flow meter like a gearwheel motor having a pair of round gearwheels which are mounted in a housing on stationary shafts such that they can rotate freely via ball bearings [6]. Peter Suter improved the sensor structure by increasing a magnetically conductive plate and a magnetically non-conductive sleeve to the existing structure to overcome the disadvantages in manufacture [7]. The secondary instrument presented by VSE company could improve the resolution of the flowmeter by subdividing the two channel signals [8]. Cycloid rotor flowmeter is one kind of flowmeter, which has the advantages of concise structure, low pressure loss, high accuracy and smoothly running.This paper presents the structure of a cycloid rotor flowmeter and a structure of the rotor speed sensor which can be used in cycloid rotor flowmeters.

Structure of cycloid-rotor flowmeter

The proposed flowmeter is composed of a top cover, a bottom cover, a shell, a pair of internal cycloid rotors, a central axis, sensors, and bolts. The structure of it is shown in Fig.1. The top cover, bottom cover, and shell comprised a sealed container that contains the external and internal rotors. When fluid pass the flowmeter, the rotors rotate and divide the fluid into small packets. Fig.2 presented a complete working cycle of the PDF. The internal rotor turn one third of a rotation from Fig.2(a) to Fig.2(d). During this time, one unit volume of fluid flows through the flowmeter.

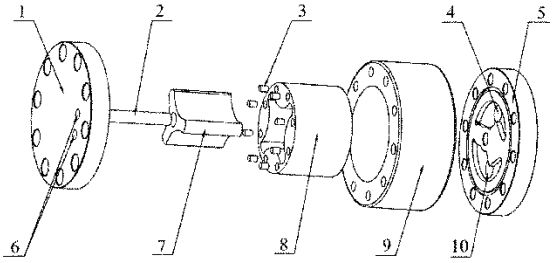

1. Top Cover, 2. Central axis, 3. Permanent magnets, 4. Inlet,5. Bottom cover,
6. Hall sensors, 7. Internal rotor, 8. External rotor, 9. Shell, 10. Outlet,

Fig.1. Structure of the high-pressure, bi-directional cycloid rotor flowmeter.

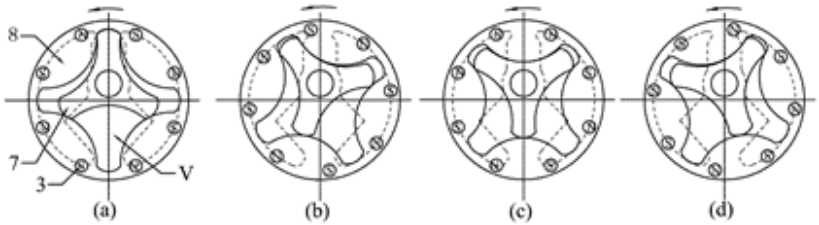

3. Permanent magnets, 7. Internal rotor, 8. External rotor, V. Unit volume

Fig.2 Rotating Process of the rotors.

Rotor speed sensor description

Rotor speed sensors design and modeling. Rotor speed sensors contain permanent magnets, Hall sensors and other components. Fig.3 (a) presented the relative position of the rotor speed sensors in the PDF, and Fig.3(b) is magnification of the magnets and Hall sensors. There are several pairs of permanent magnets in the external rotor(4 pairs in Fig.2), and two Hall sensors built in the top cover. The neighbouring permanent magnets have opposite polarities, and all the permanent magnets and Hall sensors are located at the same radius relative to rotary center. So the magnetic field around the Hall sensor is changed when permanent magnets with different polarities pass under the sensor. The Hall sensor has a square wave output with the same frequency as the alternating magnetic field.

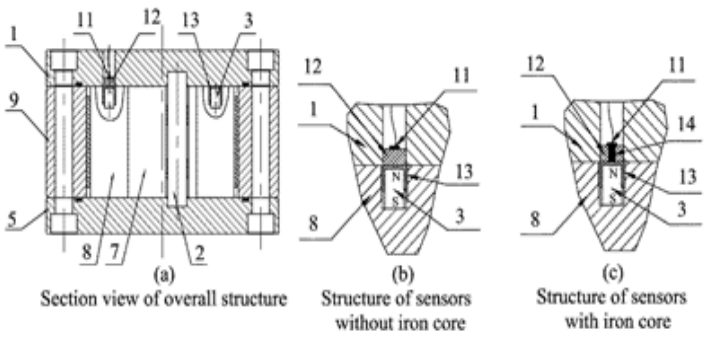

1. Top Cover, 2. Central axis, 3. Permanent magnets, 5. Bottom cover,
7. Internal rotor, 8. External rotor, 9. Shell, 11. Hall sensors,
12. Copper spacer, 13. Copper sleeve, 14. Iron core

Fig. 3 Structure of the sensors.

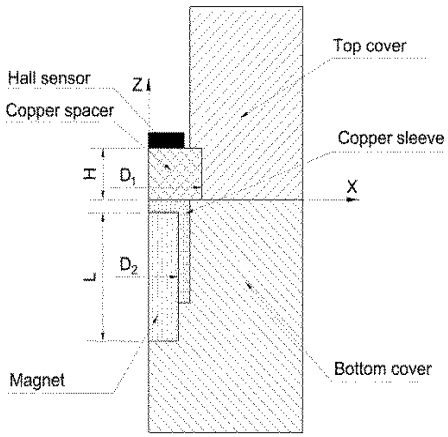

Fig.4 Simulation model of the sensor.

A simulation model of the sensors structure is built as Fig.4 to analysis the magnetic characteristic at the position of the Hall sensor. Fig.5 compared the finite element simulations for the magnetic field distributions of spacer with three different materials and structures.

In consideration of the wearability and mechanical strength of the cycloid PDF, the top cover and the rotors are made from magnetic high-strength alloy steels. And in order to fix the permanent magnets, copper sleeves are outside the permanent magnets. Because of magnetic short-circuits, if the spacer under the Hall sensors is the same material as the top cover, the magnetic field of the permanent magnets can't pass through the top cover and reach the position of the Hall sensors as shown in Fig.5(a). So the spacers must be made from magnetic isolation material (Fig.5(b)). If an external magnetic conductive core was put into the center of the magnetic isolation spacer as the structure shown in Fig.3(c), the magnetic induction intensity at the Hall sensors will be increased obviously as the result in Fig.5(c).

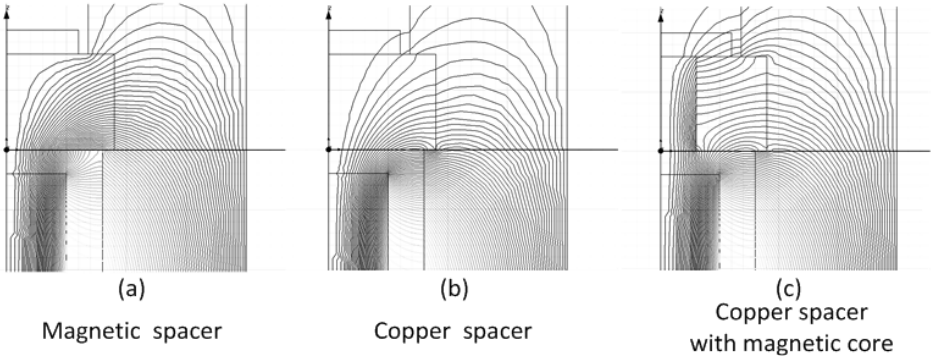

Fig.5 Distribution of the magnetic field lines

Simulation of key parameters. According to the parameters of the Hall sensors used in this research, the magnetic induction intensity around the Hall sensors must be much stronger than 5mT to ensure the Hall sensors can be triggered reliably. And improving magnetic induction intensity can assist the improvement of signal-noise ratio. So the key to design the rotor speed sensor is how to improve the strength of the magnetic induction intensity on the premise that the PDF can bear a high pressure of 31.5Mpa. Influence factors of the magnetic induction intensity include radius and thickness of the magnetic isolation spacers, radius and thickness of the permanent magnets, thicknesses of the magnetic isolation sleeves. Fig.6 presents that the magnetic induction intensity gets greater with the increase of the magnetic isolation spacer radius and the decrease of the magnetic isolation spacer thickness. Fig.7 pointed that the magnetic induction intensity is irrelevant to the length of the magnet but is positively related to the increase of the magnet radius.

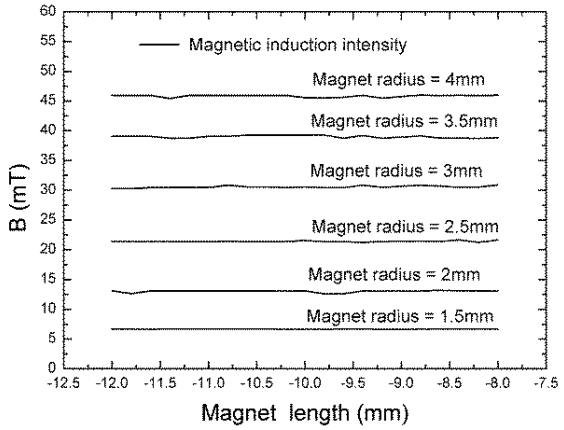

Fig.6 Variation of magnetic induction intensity with the Magnet length and radius

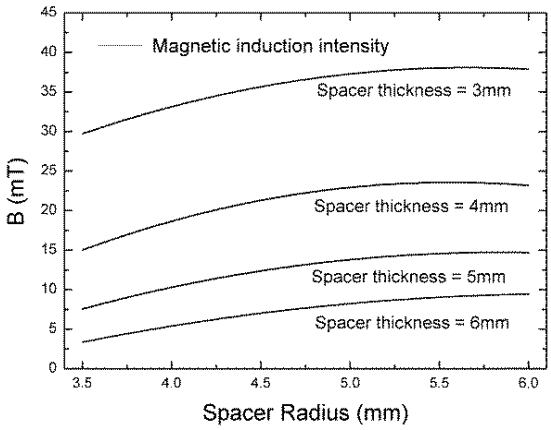

Fig.7 Variation of magnetic induction intensity with the Spacer radius and thickness

Arrangement of the Hall sensors and experiment results. There are two Hall sensors arranged in the top cover at a certain angle so that they can output two square waves with different phases. The fluid direction can be judged from the different phases.

A cycloid rotor flowmeter with the rotor speed sensors mentioned in this paper was fabricated for use in the experiments. A high accuracy standard oval gear flowmeters with the accuracy of

±0.1% is used to calibrate the cycloid rotor flowmeter. There is no bypass between the two flowmeters, so the volume of fluid through the standard flowmeter and the cycloid rotor flowmeter is same. When doing the experiment, the readings of the cycloid rotor flowmeter is the same with the standard oval flowmeter, which presents that the rotor sensors work well. The two square wave outputs shown in Fig.8 are collected by oscilloscope from the two Hall sensors while they are working at a pressure of 31.5Mpa and a flow-rate of 10.3L/min. When fluid flows forward through the PDF, the output from channel 1 advances approximately $\frac{\pi}{4}$ radians over channel 2，as shown in Fig.8(a). Conversely, the output from channel 1 lags behind channel 2 when the oil flows backwards. The clear and complete signals show that the sensors installed in the cycloid rotor flowmeter work well.

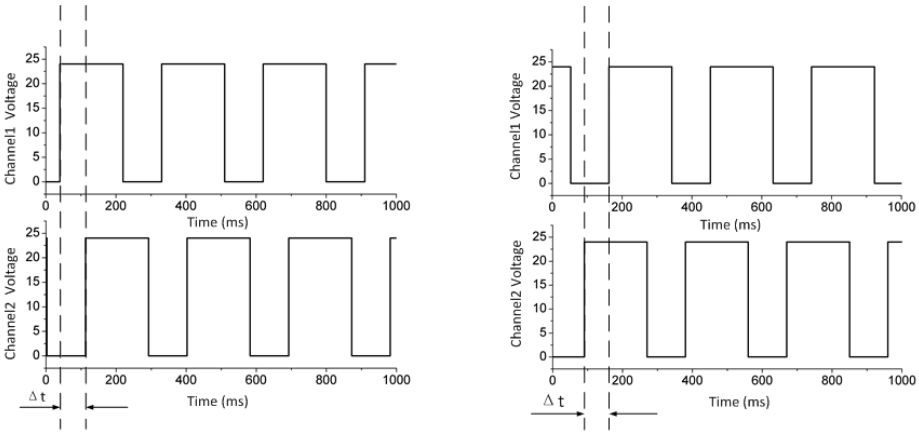

Fig.8. Square wave output by the Hall sensors

Results and Conclusions

In this work, we have discussed a kind of rotor speed sensor which can be used in the cycloid rotor flowmeters and other kind of PD meters. It contains several pairs of permanent magnets, two Hall sensors and some copper spacers and sleeves. The two Hall sensors can output a square wave respectively, which contains the speed information of the rotors, and the fluid flow direction can be judged from the phase of the two square waves. In order to analyze the influences of the structure parameters, a simulation model of the sensors structure was established and finite element analysis has been done. The results present that magnetic induction intensity gets greater with the increase of the magnetic isolation spacer radius and the decrease of the magnetic isolation spacer thickness, and the magnetic induction intensity is irrelevant to the length of the magnet but is positively related to the increase of the magnet radius. At last, a prototype was fabricated, and experiments were performed to confirm the rotor speed sensor and the cycloid rotor flowmeter can work well.

References

[1]. Su, Y.X., G.W. Liang and J. Sheng, Measurement and Test of Flow. 2007, Beijing, China: China Measure.
[2]. Li, B., F. Ding and Y. Li, Research on New-type High Pressure Bi-Directional Elliptical Gear Flowmeter. CHINESE JOURNAL OF SENSORS AND ACTUATORS, 2007. 20(1): p. 220-223.
[3]. Johannes, A.S., Volume Sensor for liquids using toothed meter wheels. US5559288, 1996.
[4]. Luker, G.J., Positive displacement flow meter. US2013/0025365 A1, 2013.
[5]. HENDRIX, A.R., POSITIVE DISPLACEMENT FLOWMETERS - HIGH-PERFORMANCE WITH A LITTLE CARE. INSTRUMENTATION TECHNOLOGY, 1982. 29(12): p. 47-49.
[6]. Charles, D.F.J. and D.F.S. Charles, Double helical flowmeter. 1995.
[7]. Hill, S.L., Positive displacement piston flow meter with damping assembly. US5562002, 1996.
[8]. Choi, T.H., et al., Design of Rotor for Internal Gear Pump Using Cycloid and Circular-Arc Curves. JOURNAL OF MECHANICAL DESIGN, 2012. 134(0110051).

Advanced Materials Research Vols. 986-987 (2014) pp 1453-1456

doi:10.4028/www.scientific.net/AMR.986-987.1453

An on-line monitoring method of interharmonics based on ANF and interpolated FFT

Jianxun WANG [a], Haihua DENG [b]

Wuhan Second Ship Design and Research Institute, Wuhan, 430064, China

[a]email: wangcoven7@163.com, [b]email:frogdeng@sina.com

Keywords: Interharmonics; ANF; Interpolated FFT; On-line monitoring; LabVIEW

Abstract. To detect interharmonics whose amplitudes are often small, a detection method based on ANF and interpolated FFT is proposed. In the method, the parallel structure of the ANF (adaptive notch filter) is firstly used to detect the fundamental and harmonic components, in which the fundamental frequency signal with high amplitude is detected with the main ANF and then the measured base frequency is output to sub-parallel ANF structure so as to extract the harmonic components. Then a separated interpolated fast Fourier transformation (FFT) analysis of interharmonic components will be effectively completed without the influence of the fundamental and harmonic components. A detection platform based on the proposed method is implemented in LabVIEW. The results of simulation and experiments show the effectiveness of the method.

Introduction

At the situation of smart grid, more and more power electronic devices, fluctuation power sourced and load are used in power system, and interharmonics pollution becomes increasingly serious [1][2]. To get actual interharmonic parameter, much research has been carried out on interharmonics detection algorithm.The existed method include time domain method and frequency domain method. The time domain detection method using EPLL [3] and ANF [4], which is based on the priori knowledge of signal frequencies, is not often used to detection interharmonics. The frequency domain algorithms including interpolated FFT methods [5][6] and parametric spectral estimation methods [7][8][9][10] are more commonly used methods. For interpolated FFT methods, when the sampling time is short, the frequency spectrum of the interharmonics with small amplitude is easily overwhelmed by fundamental and harmonics, which is the main disadvantage of interpolated FFT methods. Parametric spectral estimation methods include AR model method, prony method and eigenvalue decomposition method and so on. These methods are very sensitive to noise, and its corresponding solution of the model parameters will increase the burden of computation.

Considering the interharmonics are often small, the interharmonics' detetion will be easily influenced by fundamental and harmonics when the sampling time is small. Therefore, a detection method based on ANF and interpolated FFT is proposed in this paper so as to meet the demand of on-line monitoring detection.

The Principle of ANF

A modified version of the ANF has been recently proposed in [4].The dynamic behavior of ANF is characterized by the following set of differential equations:

$$\begin{aligned} &\ddot{x}(t)+\theta^2(t)x(t)=2\varsigma\theta e(t) \\ &\dot{\theta}(t)=-\gamma x\theta e(t) \\ &e(t)=y(t)-\dot{x} \end{aligned} \tag{1}$$

Where $y(t)$ is the input signal, θ is the estimated frequency, ς and γ are the parameters which determine the accuracy and convergence speed of the ANF. For a single-frequency sinusoid signal $y(t)=A\sin(\omega t+\varphi)$, the ANF has a steady solution of:

$$o = \begin{pmatrix} \overline{x} \\ \dot{\overline{x}} \\ \overline{\theta} \end{pmatrix} = \begin{pmatrix} -A/\omega \cos(\omega t + \varphi) \\ A\sin(\omega t + \varphi) \\ \omega \end{pmatrix} \tag{2}$$

A and ω are amplitude and angular frequency of the sinusoidal signal respectively, φ is the initial phase.

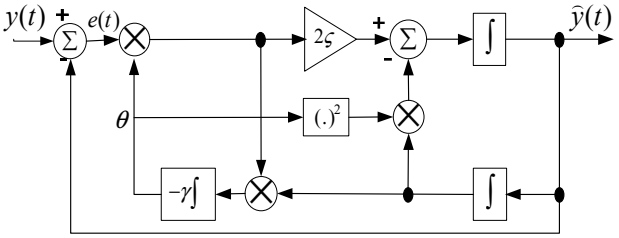

Fig.1. Block diagram of ANF structure

Block diagram of ANF structure is shown in Fig.1, the structure can exact the sinusoidal component whose frequency is closest to the input frequency, and can adaptively adjust according to the change of the amplitude, phase and frequency.

Harmonics and Interharmonics Detection Based on ANF and Interpolated FFT

This paper has proposed an improved parallel structure to detection harmonics and interharmonics which is shown in Fig.2.

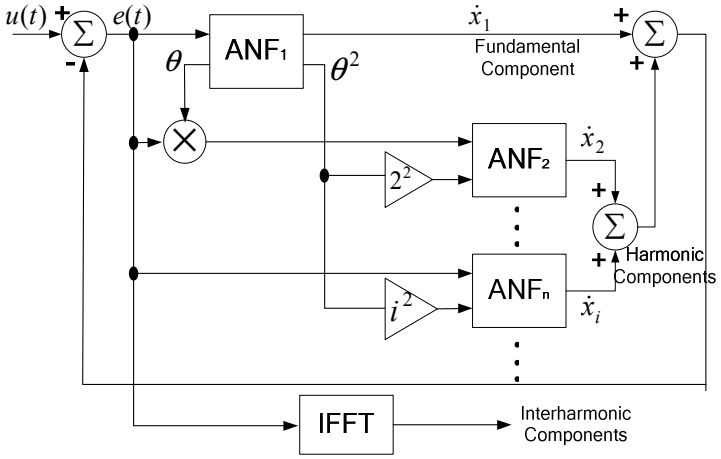

Fig.2. Improved parallel ANF structure for the measurement of harmonics and interharmonics

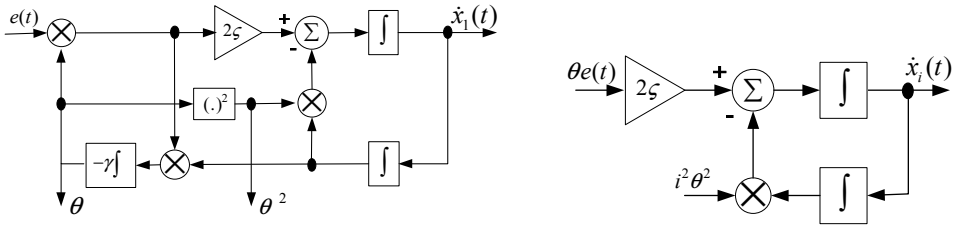

(a) ANF_1 (b) ANF_i

Fig.3. Block diagram of ANF_1 and ANF_i

In the structure, ANF1 is used to exact fundamental frequency component, and the measured fundamental frequency is output to ANF 2 ~ n; the ANF 2~n is used to exact harmonic components; the error signal is calculated by interpolated FFT to get interharmonic components. Because the frequency input of ANF 2 ~ n is limited to confirmed harmonics frequencies, the output of ANF 2~n will only contain harmonics of single harmonic frequency, then the amplitude and phase of the signal with known frequency can be calculated by Least Squares (LS) method. With the separation

of fundamental and harmonics, interhamonics' parameters can be obtained with an individual analysis of interpolated FFT.

Based on the proposed method, we establish a detection platform with LabVIEW. The implement method of ANF 1 and ANF 2~n in LabVIEW is shown in Fig.4 and Fig.5, and interpolated FFT is realized with Mathscript node.

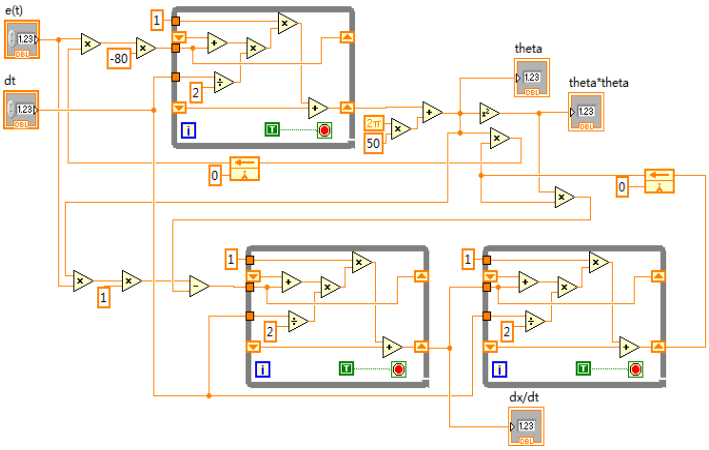

Fig.4. Implementation of ANF 1 in LabVIEW

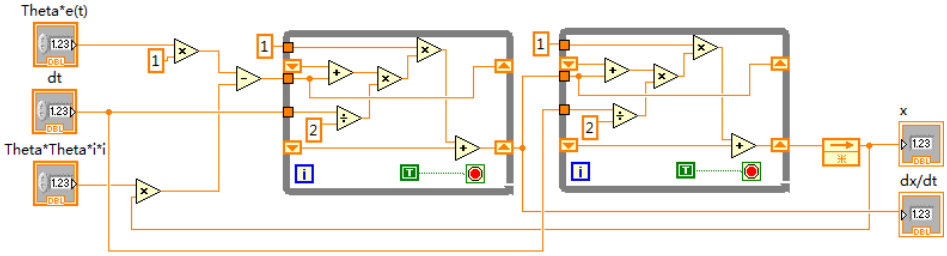

Fig.5. Implementation of ANF i in LabVIEW

Test Results

Set the simulation signal with fundamental, harmonics and interharmonics:

$$v(t)=5\sin(f\times 2\pi t+15)+1.5\sin(3f\times 2\pi t+27)+\sin(5f\times 2\pi t+32)+0.8\sin(7f\times 2\pi t+60)$$
$$+0.005\sin(35\times 2\pi t+10)+0.005\sin(45\times 2\pi t+19)+0.005\sin(310\times 2\pi t+51)+0.005\sin(486\times 2\pi t+22)$$

The fundamental frequency f=50Hz, sampling frequency is 10000Hz, sampling time is 0.2s. The interharmonics' frequencies are 30Hz, 45Hz, 310Hz and 486Hz. The test results of the proposed method are shown as follows.

Tab.1.Test results of harmonics and interharmonics

Simulation signals		Test results		Simulation signals		Test results	
f(Hz)	amp (V)	f(Hz) (error)	amp (V) (error)	f(Hz)	amp (V)	f(Hz) (error)	amp (V) (error)
50	5	50.000 (0)	5.000 (0)	30	0.005	30.000 (0)	0.00499 (0.00001)
150	1.5	150.000 (0)	1.500 (0)	45	0.005	45.067 (0)	0.00494 (0.00006)
250	1	250.000 (0)	1.000 (0)	310	0.005	310.000 (0)	0.00502 (0.00002)
350	0.8	350.000 (0)	0.800 (0)	486	0.005	486.000 (0)	0.00501 (0.00001)

Consider the case of the fundamental frequency shift, assuming $f=49.85Hz$, the test results are shown in Tab.2. From the results we can see the detection parameters of fundamental, harmonics and interhamonics are all accurate, and the results are not influenced in the situation of fundamental

frequency offset. What's more, even the interharmonics with the frequency near the fundamental and harmonics can be also accurately detected.

Tab.2. Test results of harmonics and interharmonics

Simulation signals		Test results		Simulation signals		Test results	
f(Hz)	amp (V)	f(Hz) (error)	amp (V) (error)	f(Hz)	amp (V)	f(Hz) (error)	amp (V) (error)
49.85	5	49.850 (0)	5.000 (0)	30	0.005	30.000 (0)	0.00498 (0.00002)
149.55	1.5	149.550 (0)	1.500 (0)	45	0.005	45.026 (0.026)	0.00495 (0.00005)
249.25	1	249.250 (0)	1.000 (0)	310	0.005	310.003 (0.003)	0.00502 (0.00002)
348.95	0.8	348.950 (0)	0.800 (0)	486	0.005	486.000 (0)	0.00501 (0.00001)

Conclusion

The proposed method has taken consideration of the characteristics of power signal. The fundamental and harmonic components with frequencies confirmed are firstly detected by parallel ANF, and then the interharmonics can be individually analyzed with interpolated FFT, so that fundamental, harmonics and interharmonic parameters can all be accurately detected.

References

[1] Testa A, Akram M F, Burch R, et al. Interharmonics: Theory and modeling[J]. IEEE Transactions on Power Delivery, 2007, 22(4):2335-2348.

[2] Francesco D, Roberto L, Adolfo S, et al. On the interharmonic components generated by adjustable speed drives[J].IEEE Transactions on Power Delivery, 2005, 20(4):2535-2543.

[3] Karimi Ghartemani M, RezaIravani M. Measurement of harmonics/interharmonics of time-varying frequencies[J].IEEE Trans on Power Delivery, 2005, 20(1):23-31.

[4] Mojiri M,Karimi-Gharteman M, Bakhshai A. Processing of harmonics and interharmonics using an adaptive notch filter[J]. IEEE Trans on Power Delivery, 2010, 25(2):534-542.

[5] Qian Hao, Zhao Rongxiang, Chen Tong. Interharmonics analysis based on interpolating windowed FFT algorithm[J].IEEE Trans on Power Delivery, 2007, 22(2):1064-1069.

[6] Chang G W, Chen C I, Liu Y J, et al. Measuring power system harmonics and Interharmonics by an improved fast Fourier transform-based algorithm[J].IET Generation, Transmission& Distribution, 2008, 2(2):192–201.

[7] MA Bing-wei, LIU Hui-jin, ZHOU Li, et al. An improved algorithm of interharmonic spectral estimation based on AR model[J]. Proceedings of the CSEE, 2005, 25(15):79-83.

[8] Ding Yifeng, Cheng Haozhong, Lü Ganyun, et al. Spectrum estimation of farmonics and interharmonics based on prony algorithm[J].Transactions of China Electrotechnical Society, 2005, 20(10):94-97.

[9] Guo Cheng, Li Qunzhan, He Jianmin, et al. Segmentation prony algorithm on harmonics and inter-harmonics detection of power networks[J].Power System Technology, 2010, 34(3):21-25.

[10] WANG Zhi-qun, ZHU Shou-zhen, ZHOU Shuang-xi. Inter-harmonics estimation by pisarenko harmonic decomposition method[J]. Power System Technology, 2004, 28(15):72-77.

Advanced Materials Research Vols. 986-987 (2014) pp 1457-1460

doi:10.4028/www.scientific.net/AMR.986-987.1457

Application of Vortex Generator in Ultrasonic Heat Meter Measurement

Shuo SHI [1,2, a], Jian-ting SUN [1,b], Lan-lan GUO [1,3,c], Guang-sheng DU [1d*]

[1] School of Energy and Power Engineering, Shandong University, Jinan 250061, Shandong, China

[2] Key Laboratory of Renewable Energy Utilization Technology in Building of National Education Ministry, Shandong Jianzhu University, Shandong, China

[3] College of Mechanical and Electronic Engineering, Shandong University of Science and Technology, Qingdao 266590, Shandong, China

[a]shishuo@sdjzu.edu.cn, [b] 596943233@qq.com, [c]278728206@qq.com, [d]du@sdu.edu.cn

Keywords: Vortex generator, Ultrasonic, Heat meter, impurities

Abstract. Fluids in the heat-supply pipelines have a small amount of impurities**.** Impurities can easily settle down on the ultrasonic heat meters' reflecting faces. It caused measurement inaccuracy. Vortex generator is placed in ultrasonic heat meter in this paper, which can generate vortex in the reflect fields. Vortex toke away impurities on the bottom of heat meter. Reflecting surface keeps clean. A v-shaped ultrasonic heat meter is taken for example. Numerical study of the flow field near the Reflecting surface vortex generator is carried out. Results show certain strength of vortex is caused in the reflective surface, while other palaces influenced little.

Introduction

Aiming at energy conservation and emissions reduction, more ultrasonic heat meters are used in China. But low accuracy becomes the main problem of heat metering. The main factor is the bad water quality in China heat pipes.

Measurement was carried out on the fluid with particles. At first, the readings are accurate. After several hours, the reading became disorder. After another half hour, the measurement result returned to normal again. We disassembled the ultrasonic heat meter when the readings are disorder. It is found that some impurities deposited on the reflection surface. The impurities influenced ultrasonic reflection of the surface, so the readings are not accurate。After the impurities are washed out by the vortex later, the reflection surface was restored clean, so the readings became accurate again. If vortexes can be generated in front of the reflecting surface, they can take away impurities. The accuracy of measurement can be ensured.

A profile of vortex generator

Vortex generator was put forward for the first time since 1947 by Bmynes and Tayler of united aircraft corporation USA. It mostly used to delay the separation of boundary layer, prevent the plane some deviation caused by flow separation phenomenon [1] [2]. Currently it is widely used in the field of heat transfer, descaling, etc. Winglet-type vortex generator arrays put in a compact plain-fin-and-tube heat exchanger is experimentally evaluated by Joardar A and Jacobi A.M. The result shows that it can enhance the performance of fin-tube heat exchangers markedly compared to a single-row vortex generator [3]. J.M. Wu and W.Q. Tao numerically studied a rectangular channel with winglets longitudinal vortex generator punched out from the lower wall of the channe; the results indicated that the essence of heat transfer enhancement by longitudinal vortex follows the field synergy principle [4]. Biswas G, Torii K, Fujii D placed behind a winglet type vortex generator in a fully developed laminar channel flow. The experient show the vortex generator with the optimal angle of made a big progress for heart transfer in plate-fin cross flow heat exchangers[5].

XU Zhi-Ming, WANG Yu-Peng, etc, carried experiment on vortex generator in different distance and different attack angles. They found the wing-type vortex generators can restraining

fouling of $CaCO_3$. [5] ZHANG Zhong-Bin, LI Xing-Chan, GAO Ying-Lun, ZHANG Yu-Feng studied on the $CaCO_3$ fouling characteristics of straight row of floating-point type vortex generator by weighing method. They increase angle of attack of the wing vortex generator at the specific temperature and velocity, the result showed that surface unit area fouling decreased. [6]

Because of good penetrability and strong directionality, Time ultrasonic heart meter measurement was carried out. When the ultrasonic wave travels in a fluid, it can detect and carry the information of the fluid. In the process of the spread of ultrasonic, ultrasonic walk downstream need less time than walk upstream. Time difference from downstream and upstream is related to flow velocity. transmitting transducer and receive transducer are equipped on the pipe. The travel path of ultrasonic signal is shown on fig.1， The bottom of the pipe is took as a reflective surface. ultrasound transmitting path is shown in Fig 1.

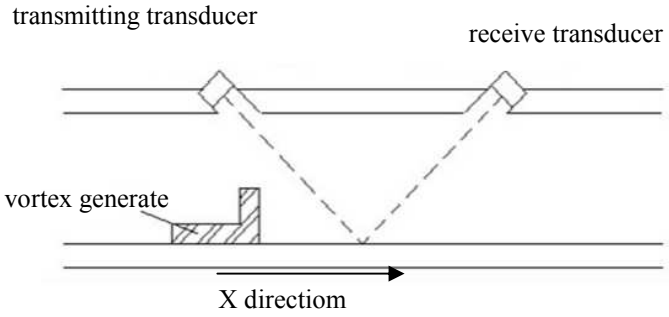

Fig.1 Ultrasonic heat meter adding vortex generator

downstream transmission time：
$$t_1 = \frac{2D/\sin\theta}{c + v\cos\theta} \quad (1)$$

upstream transmission time：
$$t_2 = \frac{2D/\sin\theta}{c - v\cos\theta} \quad (2)$$

Time difference：
$$\Delta t = t_2 - t_1 = \frac{2D/\sin\theta}{c - v\cos\theta} - \frac{2D/\sin\theta}{c + v\cos\theta} = \frac{4Dv\cot\theta}{c^2 - v^2\cos^2\theta} \approx \frac{4Dv}{c^2}\cot\theta \quad (v \ll c) \quad (3)$$

The velocity in the pipe v is proportional to the time difference, If Ultrasonic wave incident Angle θ and pipe size are fixed, We can come up with the value for the velocity of measured fluid. D is Nominal diameter, c is Ultrasonic vave propagation velocity in static fluid.

Simulation study of heat meter body with vortex generator

Different angle vortex generator was put infront of reflective surface. Numerical simulation was carried out on the fluid of heat metre body. Fig2 shows all type of generator can cause votex in reflective region. 60° vortex generator can generate stronger votex near the reflective bottom and carry impurities away. Because of the strong washing ability, 60° vortex generator selected to use.

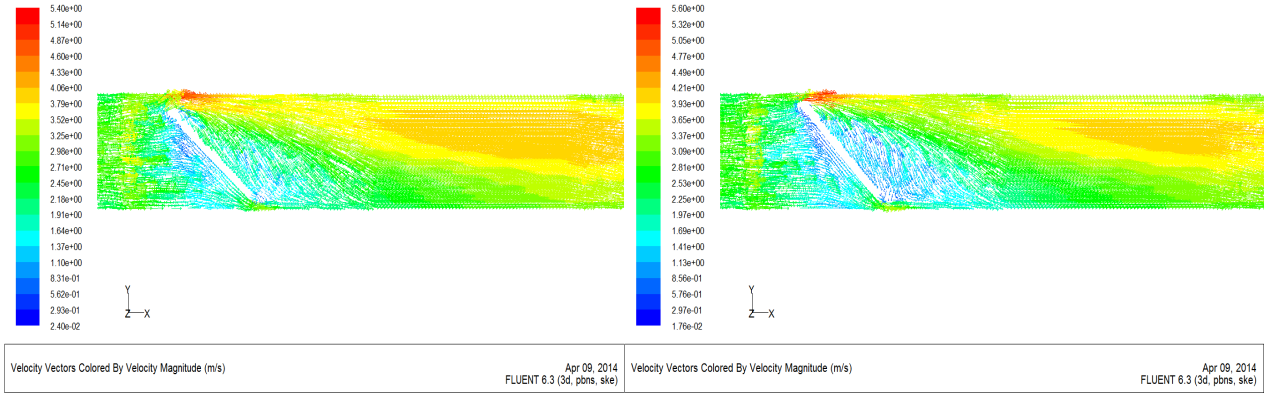

40 º 45 º

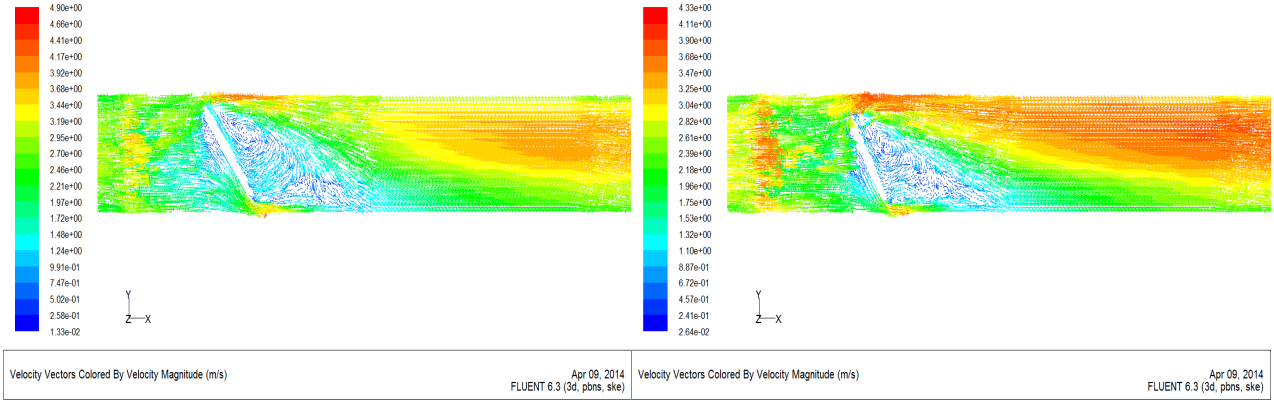

55 º 60 º

Fig.2 Velocity vectors of different angle vortex generator

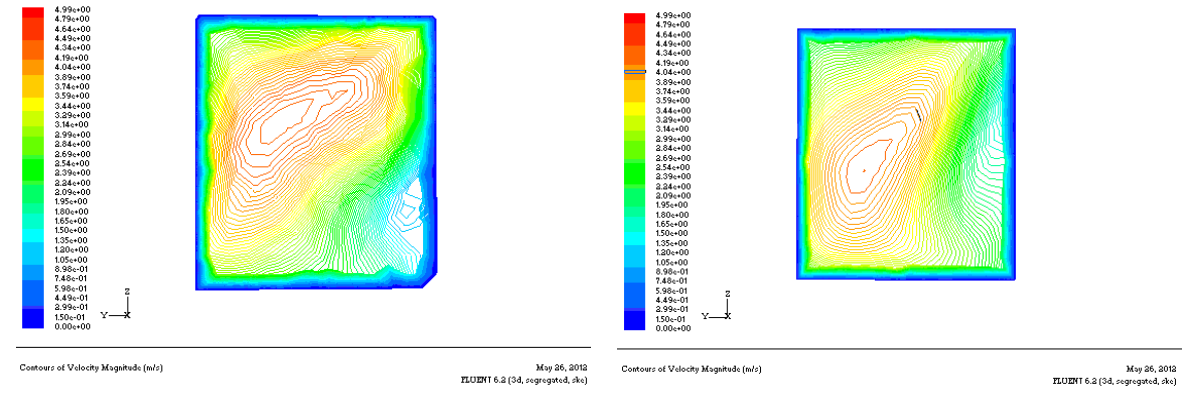

X=45 x=65

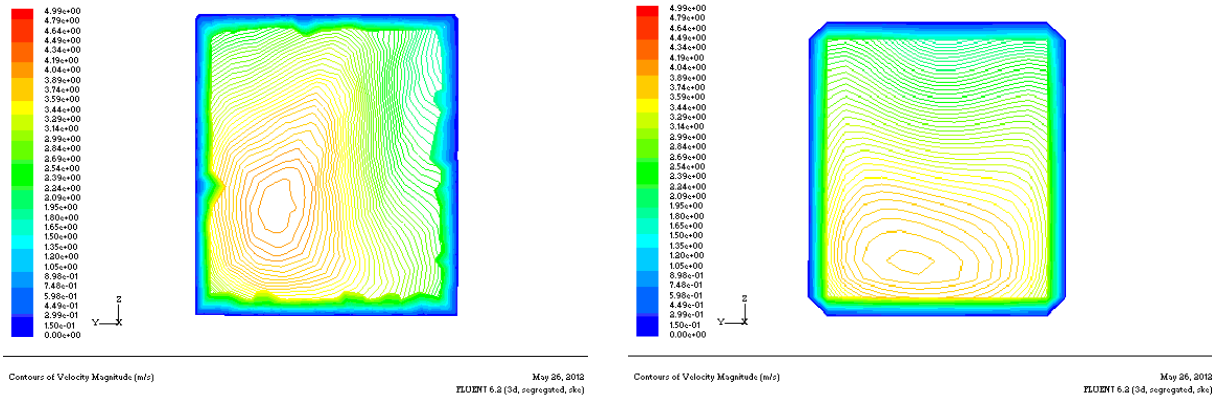

X=85 x=150

Fig3 Contour of velocity with different z coordinates

In Fig 3, x=45 in front of reflective region, it has a big change in flow field. x=65 and x=85 are in the reflective region, calculation results showed the vortex near the bottom of heat meter body. Down the reflective surface velocity magnitude turns bigger, to the bottom it becomes 0. X=150 is far from reflective region, flow field become steady. So properly placed generator can washing the reflective surface but influence other region little.

Conclusions

Sediment of the impurities in fluid is the main reason of measurement inaccuracy. Using the proper triangle vortex generator can cause strong vortex near the reflective surface, while area far away from it is influenced little. It is an effective solution to the sediment problem of reflective surface. Vortex forming mechanism and vortex operational process of vortex generator are the reason of flow controlling. Mastering the flow characteristic of two phase fluid in complex cavity and sediment law is the key problem of aplication of votex generator in ultrasonic heart meters. More attention must be paid on these problems by theoretical analysis experimental study.Useing vortex generator successfully will Improve performance of the heat meter body and raise the measure precision of measurement of inpurity fluid.

References

[1]Johnston J P, Nishi M. Vortex generator jets-means for flow separation control [J]. AIAA journal, 1990, 28(6): 989-994.

[2]Bons J P, Sondergaard R, Rivir R B. Turbine separation control using pulsed vortex generator jets [J]. Journal of Turbomachinery, 2001, 123(2): 198-206.

[3] Joardar A, Jacobi A M. Heat transfer enhancement by winglet-type vortex generator arrays in compact plain-fin-and-tube heat exchangers [J]. International journal of refrigeration, 2008, 31(1): 87-97.

[4]B Wu J M, Tao W Q. Numerical study on laminar convection heat transfer in a rectangular channel with longitudinal vortex generator. Part A: Verification of field synergy principle [J]. International Journal of Heat and Mass Transfer, 2008, 51(5): 1179-1191.

[5]Biswas G, Torii K, Fujii D, et al. Numerical and experimental determination of flow structure and heat transfer effects of longitudinal vortices in a channel flow [J]. International Journal of Heat and Mass Transfer, 1996, 39(16): 3441-3451.

[6] XU Zhi-Ming, WANG Yu-Peng, LIU Zuo-Dong, ZHANG Yi-Long. Experiment and Investigation on the Characteristic of Restraining Fouling of Wing -Type vortex Generators [J]. Journal of engineering thermophysics, 2012, 33(11): 1936-1939.In Chinese

[7] ZHANG Zhong-Bin, LI Xing-Chan, GAO Ying-Lun，ZHANG Yu-Feng. Experimental study of influence of the vortex generator on CaCO3 fouling characteristic[J]， Journal of Northeast Dianli,2010,30(4):7-10.In Chinese

Advanced Materials Research Vols. 986-987 (2014) pp 1461-1465

doi:10.4028/www.scientific.net/AMR.986-987.1461

Application of Wavelet Analysis to Eddy Current Testing for the Surface Fatigue Crack of Bolt Holes

Xiao-Li LI [1,a] , Jin-Li SUN [1,b]

[1] Naval Aeronautical Engineering Institute Qingdao branch campus, Qingdao 266041, P.R. of China

[a]qdlixl@163.com, [b] hjsjL@163.com

Keywords: nondestructive testing, eddy testing, wavelet analysis, denoise

Abstract. Eddy current testing is one of the five major routine nondestructive testing methods and it is convenient, fast and suitable for online detecting of the surface fatigue crack of bolt holes. However, the signals of eddy current testing are so weak that it is difficult to identify the signals. So more effective signal processing method must be adopted to deal with the weak signals. This paper used the wavelet analysis to process signals of the eddy current testing for the surface flaw of bolt holes. It can inhibit the noise and reinforce signal and make qualitative testing possible for quality evaluation of the surface fatigue crack of bolt holes.

Introduction

Eddy current testing (ET) is an effective method for detecting conductive material surface and near surface defect. At present, the eddy current detection in pressure vessel of nuclear power station, heat exchange tube, aircraft structure and other key equipment defect detection has been widely used[1]. However, due to the non defect signal influence of environment noise, lift-off effect and changes in the structure and equipment, the eddy current testing signal defect is often interference. In order to enhance the reliability of detection and characterization of defects and effectiveness, the applications of wavelet analysis in eddy current testing for bolt holes fatigue crack detection in this paper, detection to fatigue cracks on the surface of the bolt holes so as to evaluate the quality of bolt hole.

Experiment

2.1 Flaw Sample Facture in Plate Joint Stud Bolt Hole

In a certain type of aircraft dynamic components life study [2] found around the web first joint bolt is a typical fatigue risk point. In this experiment, the web joints were used as specimen. According to the national military standard GJB2908 – 97 NDT eddy current testing method for the quality control norms, the cracks were made in the surrounding of the bolt holes. Figure 1 is the picture of defect specimen.

On the basis of the coil impedance increment relation (equation1) [3,4,5], the crack for the same depth, phase of impedance increment is a constant, not change with the crack length.

$$\Delta Z = -\frac{1}{I^2}\int_{S_0} E_x^0(y,z)p(y,z)dydz = -\frac{1}{I^2}\int_{(l,m)} E_{l,m}^0 p_{l,m} S_{l,m} \quad (1)$$

Along with the increase of the crack depth, the amplitude of impedance increment is increase and the phase angle becomes small. When the crack depth is greater than the depth of penetration, the amplitude of impedance increment decreases. When the crack depth is greater than 3 times the depth of penetration, the amplitude of impedance increment almost keeps a constant. Therefore, the effective depth of eddy current is about 1 ~ 2 times of the depth of penetration and within the effective range of detection, using the phase discrimination defect depth to better [6].

Research shows that bolt hole crack in the web cracking length is more than 1mm, for almost all the penetrating crack. [2] Therefore, when considering the crack depth detection is meaningless,

should be concerned about is the crack length. In this study, 10 penetrating crack sample been made by wire cutting and the crack width was 0.1 mm, length were {1, 2, 3, 4, 5, 6, 7, 8, 9, 10} mm.

2.2 Acquisition Equipment

1. sensor: Standard impedance placement eddy current sensor with the coil diameter 2.5mm, the number of turns of 36 turn, the excitation frequency of 200 KHz and the center of the coil with a diameter of 2mm core.

2. Oscilloscope: Type TDS2014 with color display, bandwidth of 100 MHz, channel number of 4 and time base range of 5 ns/div to 50sec/div.

3. Card type: Type PCI-DAS4020 with four channel high speed analog channel, AD converter, trigger or gated channel, system timing controller, DA converter, 24 bit digital input and output port, dual port static 32K×24 RAM and PCI bus controller.

4. Computer: The memory of 1G and the hard disk capacity of 160 GB.

Results and analysis

3.1 Flaw Signal

Analog flaw signal of joint bolt hole of the web was presented in figure2. The output voltage of eddy current sensor increased with the length of the crack L, when $L \le 3$, a sunken appeared on the peak value of the signal, which was caused by the fact that the length crack was less than diameter of the sensor coil. And when $L \ge 8$, the voltage amplitude of the signal basically no longer increased and tended to be saturated.

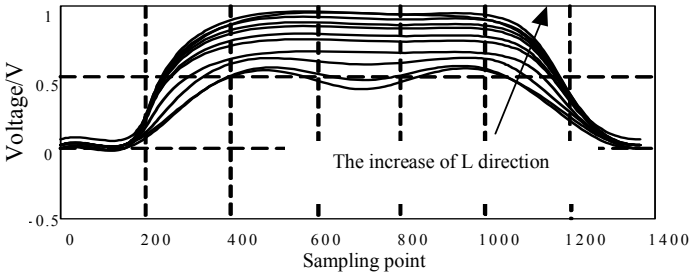

Fig. 2 Analog flaw signal of joint bolt hole of the web

The value of voltage change of the sensor which is output by the detecting system and transformed by AD acquisition card then input into the PC needs the process of signal denoising. We selected the actually detected signals of No.5 analog flaw at the detecting joint bolt hole as our object, as shown in Figure3. And adopt wavelet analysis method to eliminate the noise. On the basis of the Signal Noise Ratio (SNR) and Root Mean Square Error (RMSE) of the acquired signals and estimation signal after denoising, the performance of the denoising method is compared and the better is selected.

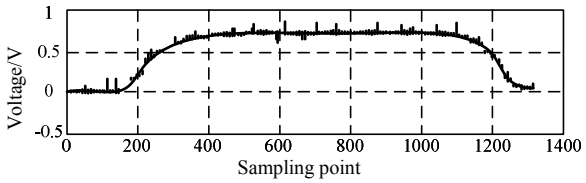

Fig. 3 Voltage change plot of eddy current testing probe on the flaw in stud bolt hole

3.2 Detection Signal Noise Reduction Based On Wavelet Analysis Method

1. Forced denoising method

Deal the original acquired signal shown in figure3 with multi-scale decomposition (the wavelet function applied is db4, and decomposed into five levels), the detailed section and approximate

section are showed in figure4, from which we can learn that the amplitude of the details part decreases as the scale increases; and the approximate part become more and more smooth with the increase of decomposition scale, which implies a rough approach of denoising, that is to replace the original signal with A5 and regard it as the signal after denoising. The feature of this processing method is that the high frequency part（details part）is removed completely, that is to say, all the coefficient of the details part is set to 0. This method is called Forced Denoising Method.

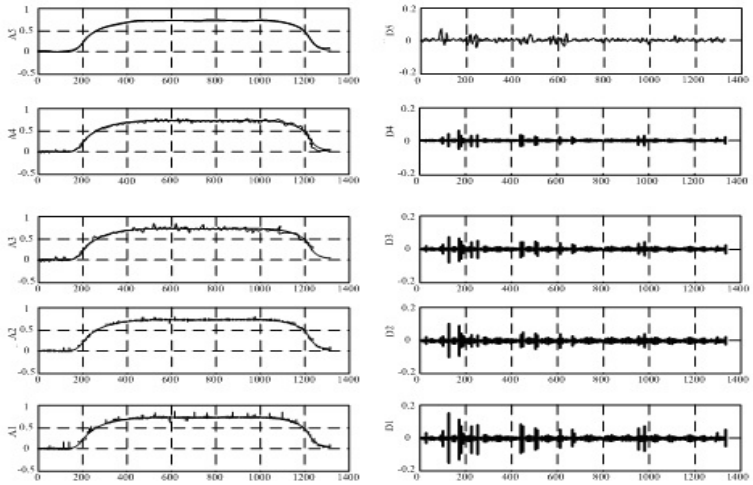

Fig.4 Multi-scale Wavelet Analysis on Eddy Current Testing Signal with Noise

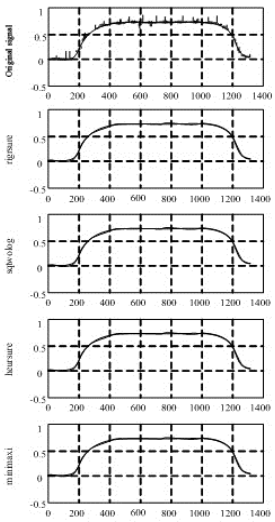

Fig.5 Effect Figure of Wavelet Transform Signal Denoise with Different Threshold Choic

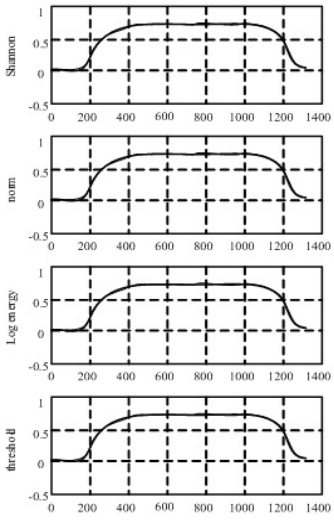

Fig. 6 Effect Contrast Figure of Denoise by WPA

2. Soft Threshold Denoising Techniques

The detecting signal as displayed in figure3, which is processed with multi-scale DWT(wavelet function is db4 and the number of levels is 5) for first, when coefficient is changed, coefficient of each level is quantized with different threshold, then IDW is implemented on the signal. The signal after denoising is presented in figure5, in which, four different principles for threshold selection are adopted, comparing the effect of the four principles with each other, the Sqtwolog mothed is the best at noise elimination. Because when modification of the wavelet coefficient is carried out, the threshold selected by this principle wipes off the high frequency characteristics of the signal completely. While the SURE and minimaxi principles are relatively conservative (only set part of coefficient to 0), thus the performance of them is poorer. However, the two kinds of methods will be useful when a little part of the high frequency of the signal s is within the scope of noise, in this circumstance, weak signal can be extracted.

3.3 Detection Signal Denoising Techniques Based On Wavelet Packet Analysis Method

For flaw detection signal as shown in figure3, wavelet Packet analysis techniques can be implemented to process denoising. Four various entropy criterions are applied, i.e. Shannon entropy, NoEn, energy entropy and soft threshold entropy, comparison between original signal and signal after denoising is presented in figure6.

3.4 Denoising Performance Comparison

Set the size of Signal Noise Ratio (SNR) and Root Mean Square Error (RMSE) as the measurement for evaluating the effect of denoising. In the context that the original signal $S = x(n)$ is the standard signal, then the Signal Noise Ratio (SNR) equation of the evaluation signal $SR = \bar{x}(n)$ on which denoising is processed with wavelet analysis is defined as:

$$SNR = 10\log\left[\frac{\sum_n x^2(n)}{\sum_n [x(n)-\bar{x}(n)]^2}\right] \tag{2}$$

And the Root Mean Square Error (RMSE) between original signal and signal after denoising is defined as:

$$RMSE = \sqrt{\frac{1}{n}\sum_n [x(n)-\bar{x}(n)]^2} \tag{3}$$

The bigger the SNR , the smaller the RMSE between original signal and evaluation signal after denoising, then the signal after denoising will be closer to the original, and the denoising effect will be better. Comparison on the SNR and RMSE between the detection signal and signal after denoising is listed in table 1.

Table 1 Denoise Effect Contrast of Testing Signal by Wavelet Analysis

	Wavelet multi-resolution decomposition and reconstruction					WPA			
	Forced denoising	rigrsure	sqtwolog	heursure	minimaxi	Shannon	norm	energy	thre
SNR	21.389	26.779	23.272	25.559	24.587	27.017	25.528	25.794	25.387
RMSE	0.0224	0.0117	0.0179	0.0135	0.0152	0.0116	0.0129	0.0126	0.0245

In table1, “Forced denoising method” refers to that the approximate part of the fifth level of the original signal is adopted directly to reconstruct signal (while the other coefficients are set to 0) after its multi-scale decomposition with wavelet, from which SNR and RMSE of the signal after denoising is obtained. “Rigrsure”, “Sqtwolog”, “Heursure”, “Minimaxi” represent four different principles for threshold selection, when WPA method is applied to signal denoising, all the criterions for threshold selection are SURE selection criterion, all of which adopt Soft Threshold quantization method, and result of denoising within the four entropy principles is shown in the table.

As we can see from table1, the value of the SNR of signal after denoising is bigger, and the value of the RMSE is smaller, which suggests that process of the denoising for detection signal obtains better result. According to the result of comparison, during the wavelet multi-scale decomposition and reconstruction method for denoising, “Rigrsure” threshold selection method performs the best, and the second is “Heursure” threshold selection method， the worst is “Forced denoising method”, Shannon entrop selection criterion embodies the best effect in denoising using wavelet packet. And denoising effect of wavelet packet is totally better than that of wavelet multi-scale decomposition and reconstruction method.

3.5 Removal of low frequency interruption caused by lift off variation in eddy current detection

The frequency of interruption caused by lift off effect is much lower than that of flaw signal. Or in other words, the scale of lift off interruption is much bigger than that of flaw signal, and it is easy to be segregated. Wavelet transformation and reconstruction is carried out firstly to remove white noise, then wavelet decomposition is implemented on the obtained signal for second time to set the wavelet coefficients which are out of certain range to 0, then reconstruct to get the flaw signal.

Conclusion

This article mainly studied wavelet denoising techniques for bolt hole crack eddy current detecting signal. Such wavelet denoising techniques as forced denoising method, soft threshold denoising method and different entropy criterion are adopted to eliminate noise in the test signal, and we set Signal Noise Ratio (SNR) and Root Mean Square Error(RMSE) as the standard for the performance of denoising, then we compared the results and select the better.

The result suggests that: (1) In multi-scale decomposition and reconstruction method, "Forced denoising method" is essentially a multi-channel bandpass filter, which mainly applies to such circumstance as deterministic noise under which the frequency band of useful signal is separated from that of noise; when the signal to noise overlaps seriously (white noise), the denoising effect of this approach is poor. (2) During the four different threshold selection criterions, SURE criterion is conservative, but during the denoising process towards this detection signal, Signal Noise Ratio (SNR) is bigger while Root Mean Square Error(RMSE) is smaller. (3) Wavelet Packet Analysis(WPA) method can process denoising at a finer frequency band, and it is more targeted, so it's more effective in signal denoising. (4) In oder to remove the influence of lift off effect during eddy current detection, "Forced denoising method" can be adopted, set the wavelet coefficient of certain scale to 0 when implementing multi-scale decomposition on signals, then carry out reconstruction, thus such interruption signals with big scale as those caused by lift off effect can be removed.

References

[1] Yu san, Chen Zhenmao, MiyaK. Siznig of stress corrosion cracknig on austenitic satinless piping in a nuclear power plant from eddy current NDT signals. Nondestructive Testing and Evaluation, 2005: 20(2): 103~114.

[2] The straight type 8 machine main rotor Ye Yanshou Report. Chinese Aviation Industry Sixth O two research institute, 2001.

[3] Sun Xiaoyun. Research and development of intelligent signal processing in eddy current nondestructive testing system. Doctoral Dissertation of Xi'an Jiao Tong University, Xi'an Jiao Tong University press, 2000.

[4] Chen Dezhi. The research on numerical simulation and signal processing in eddy current nondestructive detection, PhD thesis, Xi'an, Xi'an Jiao Tong University, 1998.

[5] Bowler J. R. Eddy current interaction with an ideal crack I the forward problem. J Appl. Phys., 1994:75(12): 8128~8137.

[6] Ren Jilin. Development of eddy current testing in China. Nondestructive Testing, 1994:16(10): 280~285.

Advanced Materials Research Vols. 986-987 (2014) pp 1466-1470

doi:10.4028/www.scientific.net/AMR.986-987.1466

Bundle Conductors Corona Current Harmonic Wave Measurement

Shaohua You[1, a], Li Chen[1, b], Jie Huang[1, c], Yunpeng Liu[2, d], and Fangcheng Lü[2,e]

[1] State Grid DC Engineering Construction Company, Beijing 100052, China

[2] North China Electric Power University, Baoding 071003, Hebei Province, China

[a]regalaxy@163.com

Keywords: Corona current, conductor, FFT, harmonic wave, Hanning window

Abstract: In order to research high level harmonic wave of six bundle conductors corona current, a measurement system was developed, and a series of wave data was obtained. Corona current is one of important corona characteristic research contents. The corona current measurement system can be used to measure the wide frequency band corona current. Six-bundle conductors was tested, and corona current was obtained. And the current signal collected in this way is safe and reliable. To research the six-bundle conductors' corona current characteristic, conductor corona current harmonic wave was analyzed, by advanced Hanning windowed interpolation FFT algorithm was adopted. Corona current harmonic characteristics before and after corona onset were compared. Research results show that, after corona onset, corona current odd harmonic increases in evidence, and even-order harmonic increase less relatively. Triple-frequency harmonics and quintuple harmonics increase obviously very much.

Introduction

Corona current is one of important corona characteristic research contents. When the surface electric field strength exceeds the breakdown field strength, the ionization occurs in the vicinity of the conductor. Accompanied with the ionization of the air, noise, light and radio interference will also take place, and the energy consumed by those kinds of effects is called corona loss. Corona current is a very important parameter that reflects the corona effect and corona onset characteristics, the accurate measure of all the frequency components of the corona current is of great importance. The effect caused by corona discharge, will effluence the economic operation of the transmission lines, corona loss etc.

Nowadays, the traditional way is to gain the current from the cage wall, and the high efficient oscilloscope is used to measure the corona current signal. But corona discharge occurs when the voltage is applied to the conductor, large quantities of charged particles, especially the electrons, are limited to the surrounding of the conductor. Collection of the signal from the conductor can better reflect the wide frequency band component of the current [1-5]. Based on wireless network technology, virtual instrumental technology, and application of the high sampling rate data acquisition card, the measurement system in this paper can realize the accurate measure of the corona current.

Harmonic analysis is to measure conductor current, and then to change analog signals to digital signals, so to analyze harmonic wave. As a result of network frequency fluctuation of network frequency, full period sampling condition is difficult to be satisfied. So "fence effect" and spectral leakage occur, and these make major phase error [6].

Windowed interpolated FFT algorithm

In order to decrease measuring error which was caused by network frequency fluctuation, windowed FFT calculation method was adopted to decrease error caused by spectra leak and fence effect. Traditional method is to average sampling first, and then to solve FFT error caused by

non-synchronous problem, namely that preferable particularity window algorithm was adopted to advance FFT transfer positional precision. Adding window is to truncate signal two terminal waveform mutation smoothly, and to drive down side lobe height in frequency domain as much as possible. Usually long range leak could be solved by adopting fine window function or measurement time increase, whereas short range leak must be solved by adopting interpolation FFT algorithm [7,8].

In allusion to harmonic analysis question, advanced windowed interpolation FFT algorithm is adopted. And assuming that spectra of discrete signal x(n) is X(k),so after Hanning windowed FFT transform, the spectra $X_1(k)$ is

$$X_1(k) = \{X(k) - [X(k-1) + X(k-a)]/2\}/2$$

After adjustment, amplitude value formulae is,

$$A_i = 2\pi d_0(1-d_0^2)\left|X_1(k_0)\right| / \sin(\pi d_0)$$

Phase angle formulae is,

$$\phi_i = phase[X_1(k_0)] - \pi d_0 + \pi/2$$

Test method and arrangement

System sketch is shown in Fig.1: in the corona current sampling section, the high-power precise no-inductance resistor is applied as the current sensor, which can assure that the resistor itself could not been destroyed by the transient voltage and current. The resistor is connected in series with the bundle conductors in the corona cage. What is more, because the resistor is almost of no inductance, when the current passes through the conductor, the voltage produced at the two ends of the resistor has the same phase as the current, which can assure that there is no distortion of the wave form and reflect the wide frequency band information of the corona current. The current signal is collected by the data acquisition card PXI-9820 installed in the upper computer 4. The whole upper computer is placed in the Faraday cage which is made-to-order.

In the voltage sampling section, the high precise capacitor voltage divider 12 is used to extract the voltage signal, and the data acquisition card is used to collect the voltage signal. The synchronous collect of the voltage and current is realized through the use of GPS synchronous clock. The trigger time can be set to 1second, 1 minute or 1 hour. The trigger time is set to 1 minute in this test, which means the trigger signal will be sent out each whole minute, after receiving the TTL trigger signal, the upper computer and lower computer collect the signal synchronously.

The current signal is transmitted via the wireless network composed of 300M/s wireless network card 7, 10 and the wireless router, which can separate the high voltage side and the low voltage side, so there is no electric connection between them.

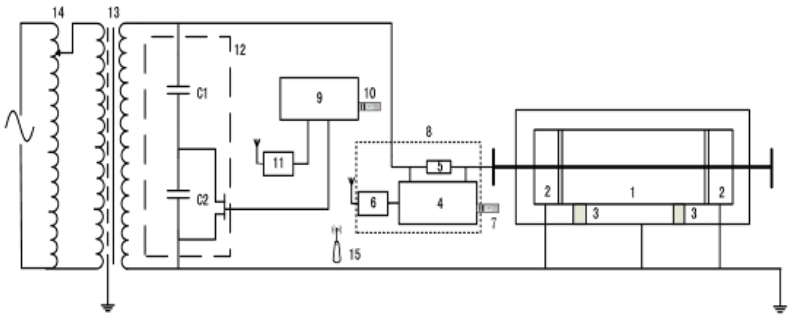

1-corona cage measurement section；2-shielding section；3-insulation support；4-upper computer; 5-resistor sampling unit； 6-upper GPS clock；7-upper wireless net card；8-Faraday cage；9-the lower computer；10-lower computer net card；11-ower GPS clock；12-TRF-800model standard capacitor divider；13- test transformer；14-voltage regulator

Fig.1 Sketch of the system structure

The whole test arrangement is shown as following figures. Fig.2 is the upper computer GPS sampling unit, which includes the GPS synchronous clock, precise no-inductance resistor, wireless net card and data acquisition card.

The upper computer is encapsulated in the metal box and place in the grading ring of the UHV corona cage together with the battery, which could make the upper be in an equal potential environment and prevent the corona discharge on the upper computer.

The lower computer is placed in the control room, and the function of the upper computer besides collecting the voltage signal is to control the corona current measure with the wireless net.

Fig.2 GPS sampling unit

Harmonic analysis

The Broad band and high sampling rate are able to decrease "fence effect". And up to eleven sub-harmonic, harmonic wave of corona current was analyzed before and after corona onset. Each sub-harmonic ingredient contents are obtained.

The corona current waves, as bundle conductors before corona onset, corona onset, in corona, and in the corona, and corona on the whole conductor, are shown as figure 3.

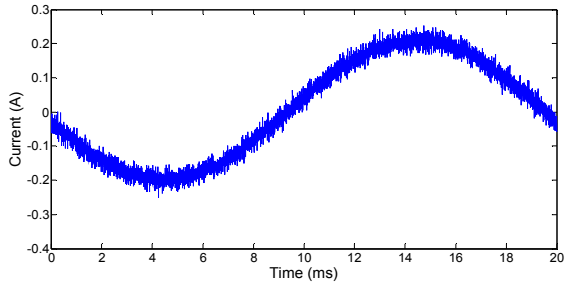

(a) Before corona onset

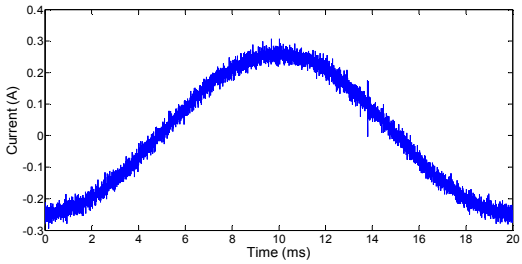

(b) Corona onset

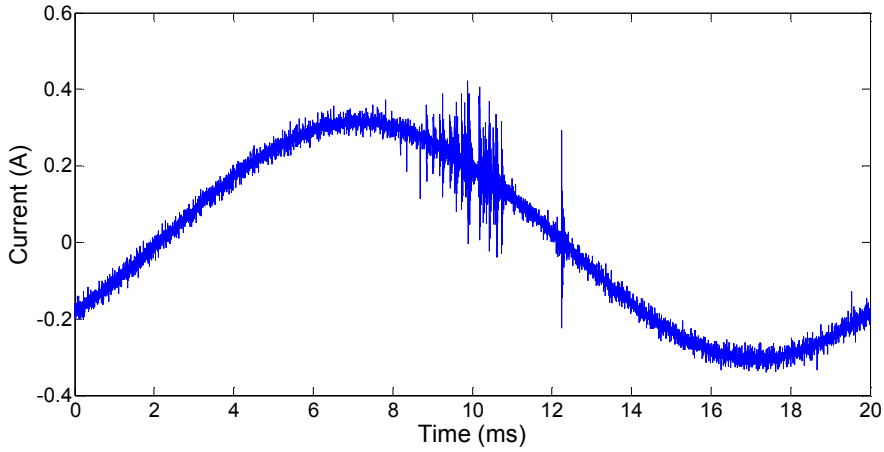

(c) Corona on the whole conductor

Fig.3 Current wave

And the harmonic analysis results, before corona onset, corona onset, in corona, and in the corona, and corona on the whole conductor are shown as figure 4.

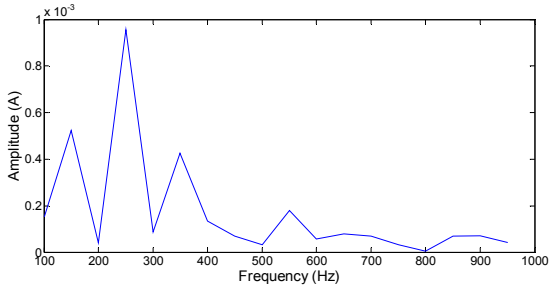

(a) Before corona onset

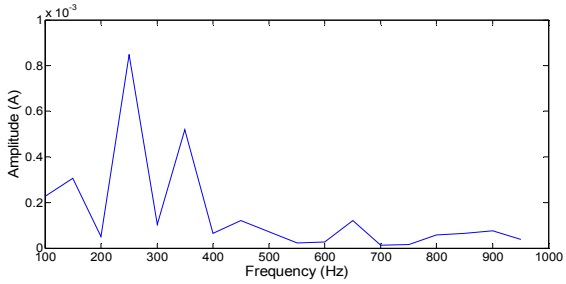

(b) Corona onset

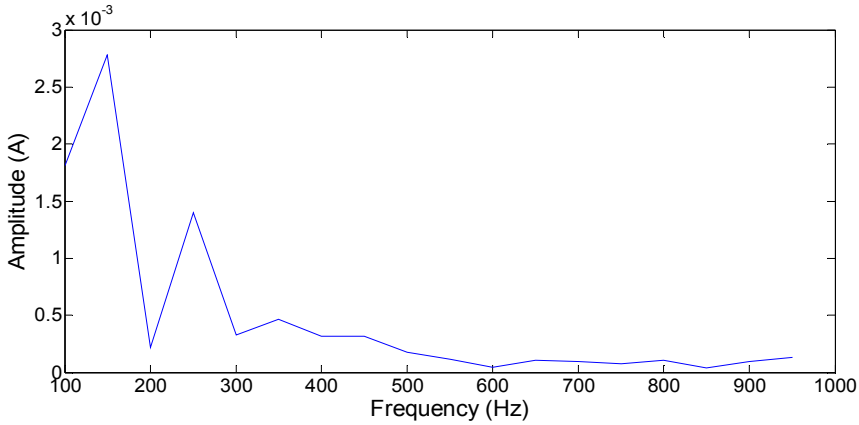

(c) Corona on the whole conductor

Fig.4 Current harmonic wave analysis

Conclusion

As wireless networks technology virtual instrument technology, and high speed synchronization data acquisition card was adopted to design a sort of synchronous clock broad band corona current measuring system. Bundle conductors corona current was measured, as before corona onset, corona onset, in corona, in the corona, and corona on the whole conductor. Hanning window was adopted. And after corona onset, corona current odd harmonic increases in evidence, and even-order harmonic increase less relatively. Triple-frequency harmonics and quintuple harmonics increase obviously very much, and conductor corona current harmonic analysis can be used to research conductor corona characteristic.

References

[1] Clade J J, Gary C H: Predetermination of corona losses under rain: experimental interpreting and checking of a method to calculate corona losses. IEEE Trans on PAS, vol. 89 (1970) no. 5, p. 853-860.

[2] P Sarma Maruvada: Corona performance of high voltage transmission lines. London, UK: Research Studies Press Ltd (2000), p. 91-108.

[3] LI Shunyuan: The application of optical fiber to measure the high voltage transmission line corona loss. Power system technology, vol. 3(1987) no. 1, p. 1-9.

[4] MAO Yingke, GUAN Zhicheng, WANG Liming, et al.: Development of a Leakage Current Monitoring System for Pollution Test Lab. High voltage apparatus, vol. 39(2003) no. 2, p. 94-96.

[5] M. Khalifa, M. Abdel-Salam: Improved method for calculating DC corona losses, IEEE Transactions on Power Apparatus and Systems, vol. 93(1974), no. 2, p. 720-726.

[6] WANG Nan, LU Fangcheng, LIANG Ying: Application of harmonics analysis approach based on modified ideal sampling frequency in on-line measuring tanδ. Electrical Measurement and Instrumentation, vol. 40(2003), no. 7, p. 12-15.
[7] WANG Nan, LU Fangcheng: Application of Wavelet Transform to Extract the Trend of tan δ On-line Monitoring. High Voltage Engineering, vol. 29(2003), no.4, p. 31-33.
[8] YANG Xiao-dong, TANG Chao, LIAO Rui-jin: Improved Harmonic Analysis Methods for Measuring Dielectric Loss of Capacitive Equipment. High Voltage Apparatus, vol. 43(2007), no. 6, n. 460-462.

Advanced Materials Research Vols. 986-987 (2014) pp 1471-1476

doi:10.4028/www.scientific.net/AMR.986-987.1471

Characteristic Analysis and Measurement of Dielectric Loss in Non-linear Insulating Materials

Rong XIA

High Voltage Research Institute, China Electric Power Research Institute, Wuhan, 430074,China

email: xiarong@epri.sgcc.com.cn

Keywords: Non-linear Insulating Material; Dielectric Loss; Characterization; Measurement

Abstract. Non-linear insulating material is widely used in the insulations of XLPE cable terminations and stator windings insulation of electric machines, and has obvious capability to improve the distribution of electric field. Actually, the dielectric loss factor of non-linear insulating materials is not equal to the *tan δ* describing linear insulating materials, and depends on applied voltage and their structures. This paper firstly discusses the difference between ac loss characteristic of non-linear dielectrics and linear dielectrics and presents a kind model of non-linear composite material. Based on the model, specific characterization and measurement methods and their numeric simulation analysis are given. Finally, a measuring system for non-linear insulating materials based on digital measuring technology is presented.

Introduction

A lossy insulating material can be represented as a parallel connection of capacitance *C* and loss resistance *R*. When an AC voltage is applied to the linear insulating material, most of the current flowing in the insulation is capacitive current leading the voltage at a phase of 90 degrees as shown in Figure 1. However a small amount of current has the same phase as the voltage. The latter (same phase) current is called loss current as it relates to power losses in the insulation. The dielectric loss angle is the angle between the current I_C and the current *I* and its tangential value (*tan δ*) is extremely important as property for showing loss in the linear insulating materials.

Non-linear insulating materials are those materials, for which the electric conductivity and/or dielectric constant as a non-linear function of electric field and possibly temperature [1]. Thus, the ac loss characteristic of non-linear dielectrics is more complicated than linear dielectrics. So far as non-linear dielectric, which only has a non-linear electrical conduction, is concerned, the resultant current waveform distorts even though the applied voltage is a sinusoidal waveform with a single frequency. The distorted waveform is mainly caused by harmonics generated in the loss current. Evaluating the harmonics generated by non-linear conductivity yields information on dielectric loss under sinusoidal and non-sinusoidal voltage that is not comprehensive when adopting *tan δ* measuring methods.

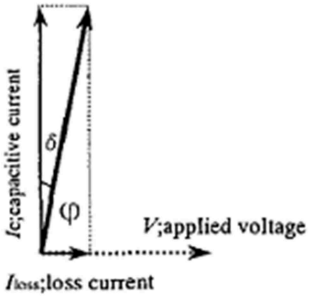

Fig.1. Vector diagram of the dielectric loss angle

Tan δ and its measuring methods for linear dielectrics can incompletely be applied for loss characteristic measurement of non-linear dielectrics. For the conventional bridge method, the bridge can only balance at a fixed frequency which is the same as the testing voltage; for phases comparison method, only the phase difference between two sine waves can be measured; for the harmonic analysis method, only the fundamental components of voltage and current are extracted by performing the discrete Fourier transform (DFT) on the digital form of the analog signals [2].

In this paper, we presented that adopting dielectric loss factor, which is defined as Pr/Pc, i.e., the ratio of the active power to the reactive power dissipated in non-linear dielectric when applying an AC voltage, instead of tan δ to describe the dielectric loss characteristic is more suitable in a general way. To discuss loss characteristic in non-linear insulating materials under AC voltage, such as an inorganic semiconductor particle filled polymer composite, a new measuring method was developed to measure active power and reactive power with high accuracy under sinusoidal and even non-sinusoidal voltage [3-4]. Based on a non-linear conductivity model of the inorganic semiconductor particle filled polymer composite sheet sample, tan δ measurement including harmonic analysis method and phase comparison method and power measurement method for dielectric loss factor were compared. In addition, recent digital measuring apparatus is getting powerful and cheap. By using this powerful digital measuring apparatus and by combining computer control and analysis technique, a measuring system was developed.

MODELING THE NON-LINEAR COMPOSITE

For convenience of modeling, some assumptions are made as follows: firstly, an inorganic semiconductor particle filled polymer composite only has a field- dependent conductivity; secondly, its dielectric constant is independent of electric field; thirdly, the composite is placed in a uniform field condition in order to eliminate the effect of the distorted electric filed. Consequently, the non-linear composite sheet sample is considered as an equivalent circuit model with a linear capacity (CL) and a non-linear resistance (RNL) connected in parallel as depicted in Figure 2.

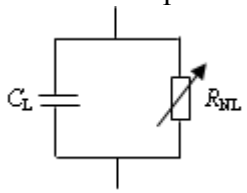

Fig.2. Equivalent circuit model of non-linear composite

If the field-dependent equivalent conductivity of RNL in the composite material is represented as

$$\sigma(E) = \sigma_0 + \alpha E + \beta E^2 + \ldots \quad (1)$$

And if the sinusoidal electric field is represented as

$$E(t) = E_0 e^{jwt} \quad (2)$$

Then the loss current density would be

$$J(E, t) = \sigma(E,t) \times E(t) = \left[\sigma_0 + \alpha E(t) + \beta E(t)^2 + \ldots\right] E \times (t)$$

$$= \sigma_0 E(t)\, e^{jwt} + \alpha\, E(t)^2 e^{j2wt} + \beta E(t)^3 e^{j3wt} + \ldots \quad (3)$$

It is evident that the field-dependent conductivity properties cause the formation and unusual changes in harmonics. And then harmonics yields the distortion of the loss current waveform.

If the area S and thickness d of the sample is known, then the current flowing in the RNL under AC applied voltage can be obtained. In practice, this current called apparent loss current can be measured by canceling the capacitive current from the resultant current flowing in the sample. As a consequence of known data it has been possible, by a curve fitting program, to derive an approximate mathematical function which describes the V-I characteristic of the apparent loss current shown as follows:

$$i_{R_{NL}}(t) = Au(t) + Bu^3(t) \quad (4)$$

Where : A: linear filed-dependent parameter given by 1.132×10^{-9}; B: non-linear filed parameter given by 4.245×10^{-15}; $i_{R_{NL}}(t)$: apparent loss current in ampere; $u(t)$: the applied voltage in volt;

The equivalent capacitance of the linear C_L is given as 200pF and the V-I character of the linear capacity follows the conventional relationship:

$$i_c(t) = C\frac{du(t)}{dt} \tag{5}$$

So the resultant current :

$$i(t) = i_{R_{NL}}(t) + i_c(t) \tag{6}$$

CONSIDERATIONS ON CHARACTERIZATION PRINCIPLES

In order to investigate the deference between the loss factor and the tangential value of the loss angle for non-linear composite material, though both quantities indicate energy dissipation, there is necessary to consider specific characterization and measurement methods.

(1) Phases Comparison:

The essential of dielectric loss angle measurement is to measure the phase difference between fundamental components of the voltage and the resultant current digitally by converting the signals to rectangular waveforms while preserving zero crossings. Subtraction of one pulse from the other gives an indication of the phase difference which is measured by counting the number of clock pulses contained in the difference pulse. The phase deference is φ, the complement of the loss angle, and then tan δ can be achieved by the following expression:

$$tan\delta = tan(\frac{\pi}{2} - \varphi) \tag{7}$$

(2) Harmonic Analysis

According to Figure 1, harmonic analysis based on DFT includes sampling the loss current and the capacitive current of the sample, transforming the analog signal into digital signal and calculating *tan δ* by performing digital frequency analysis to extract the fundamental components of both currents. According to the digital spectrum analysis theory, accurate analysis can be conducted if the sampling length is the integral multiple of the signal cycle [5]. The fundamental amplitude ratio of loss current to capacitive current is denoted by *tan δ* [6].

$$tan\,\delta = \frac{I_{loss}}{I_C} \tag{8}$$

(3) Power Measurement

The definitions of active power *P,* reactive power *Q*, and apparent power *S* for a single phase circuit in sinusoidal conditions have been accepted by the Power Engineering Society for more than a century without reservations [7]. As to the non-linear composite material sample, an accurate method is required for the measurement of the power components in the presence of distortion of voltage and current waveforms. The major question is how these power components are property defined in non-sinusoidal periodic situations. There is no divarication for the definition of active power which is the average value of the instantaneous power in one period. For reactive power, according to reference [8-9], the time domain definition of generalized reactive power is adopted.

Based on the established model of non-linear composite sample, the dielectric loss factor can be measured by the following procedures.

1) If the applied voltage *u(t)* is a sinusoidal signal and the resultant current *i(t)* is a non-sinusoidal periodic signal with peak multitude U_1 and fundamental frequency ω_0, they can be expressed as follows

$$u(t) = U_1 sin(\omega_o t + \phi_{u1}) \tag{9}$$

and

$$i(t) = \sum_{k=1}^{n} I_k \sin(k\omega_o t + \phi_{ik}) \tag{10}$$

Thus, the active power in continuous time domain form is

$$P = \frac{1}{T}\int_o^T u(t) \times i(t) dt \tag{11}$$

and the sampled and digitized P is calculated as

$$P = \frac{1}{N}\sum_{j=1}^{N} u(j) i(j) \tag{12}$$

According to the orthogonal law of triangular functions family, the active power also can be given by the following expression

$$P = \frac{1}{N}\sum_{j=1}^{N} u(t) i(t) = \frac{1}{N}\sum_{j=1}^{N} u(t)\left[i_{R_{NL}}(t) + i_c(t) \right]$$

$$= \frac{1}{N}\sum_{j=1}^{N} u(t) i_{R_{NL}}(t) = \frac{1}{N}\sum_{j=1}^{N} u(t) i_{loss}(t) = U_{1rms} I_{1rms} \tag{13}$$

Where : $U_{1rms} = U_1/\sqrt{2}$, $i_{loss}(t)$: fundamental loss current; I_{1rms} : RMS value of the fundamental loss current $I_1/\sqrt{2}$;

According to the definition of the generalized reactive power in time domain [5]:

$$Q = \sqrt{S^2 - P^2} = \sqrt{U_{1rms}^2 I_{rms}^2 - P^2} \tag{14}$$

Where : S: apparent power, I_{rms} : $\frac{1}{T}\int_o^T i(t)^2 dt$ in continuous form and $\frac{1}{N}\sum_{j=1}^{N} i(j)^2$ in discrete form.

Consequently, the dielectric loss factor can be determined as follows:

$$dlf = \frac{P}{Q} \tag{15}$$

2) If $u(t)$ and $i(t)$ are non-sinusoidal periodic signals with fundamental frequency ω_0, they can be generally given in closed form equations as follows:

$$u(t) = \sum_{k=1}^{m} U_k \sin(k\omega_o t + \phi_{uk}) \tag{16}$$

and

$$i(t) = \sum_{k=1}^{n} I_k \sin(k\omega_o t + \phi_{ik}) \tag{17}$$

Then the active power can be expressed in discrete form by the following expression:

$$P = \frac{1}{N}\sum_{j=1}^{N} u(j) i(j) = \frac{1}{N}\sum_{j=1}^{N} u(t) i_{R_{NL}}(t) \tag{18}$$

and the generalized reactive power is as follows

$$Q = \sqrt{S^2 - P^2} \tag{19}$$

The dielectric loss factor dlf can be determined by P/Q.

NUMERICAL SIMULATION ANALYSIS

If the voltage applied to the non-linear composite sample is given by:

$$u(t) = \sqrt{2} U_{m1} \sin(\omega_o t + \phi_{u1}) \tag{20}$$

and the resultant current can be obtained by (4)-(6):

$$i(t) = i_{R_{NL}}(t) + i_c(t) = Au(t) + Bu(t)^3 + C\frac{du(t)}{dt} \tag{21}$$

Considering f_o is fixed at 50Hz, the voltage and current signals are uniformly sampled up to 10,000 points in one period for phase comparison method and power measuring method. Whereas, the voltage and current waveforms are sampled at sampling frequency of 12.8 kHz for 4 periods in order to gain 1024 total sampling points. The initial values of U_{m1}, ϕ_{u1}, A, B and C are given as 1000V, 0 degree, 1.132×10^{-9}, 4.245×10^{-15} and 200pF respectively. The voltage and the apparent loss current waveforms are shown as Fig.3.

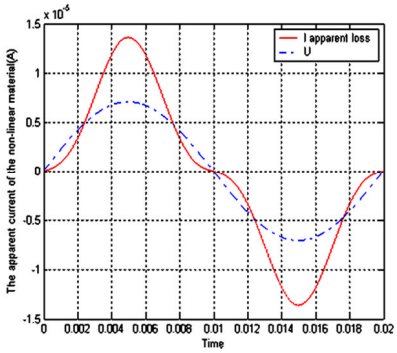

Fig.3. Sinusoidal voltage and the apparent loss current

Then each of parameters U_{m1} and B changes separately while the other parameters are fixed to known values, the numerical simulation results of the above three measuring principles are shown as Fig.4 and Fig.5.

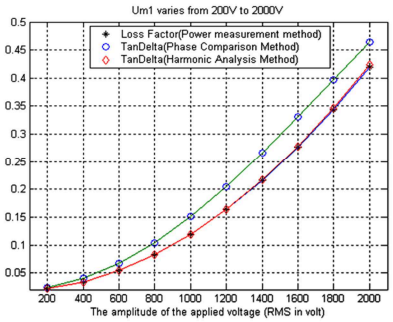

(a) When U_{m1} changes

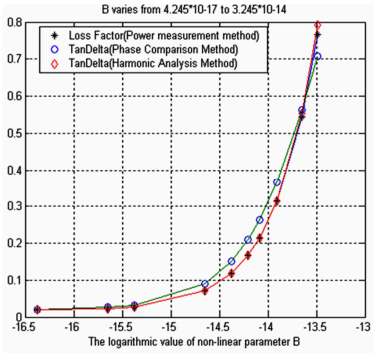

(b) When B changes

Fig.4. Curves of loss factor & *tan δ*

MEASUREMENT SYSTEM DETAILS

The outline of the dielectric loss factor measuring circuit is shown in Figure 1. Measuring was performed using a high voltage amplifier (TREK Model 20C) fed by a function generator (INSTEK Model GFG-813) which supplied up to 20 kV ac peak, at 50Hz, to a sample housed in a sample test case which has an inbuilt three terminal electrode system[10]. The amplifier also has the facility to monitor output of the applied field. The total harmonic distortion in the applied voltage is under 1%. The same ac voltage is applied to both the non-linear sheet sample and a no-loss standard capacitor connected to the ground through detecting and adjustable resistors, respectively. The voltages across those resistors are connected to a differential amplifier. The outputs of amplifier and differential amplifier are connected to a 4-CH 16-Bit 500 kS/s Simultaneous-Sampling Multi-Function DAQ card (ADVANTECH Model DAQ-2005) which is embedded in a IPC and interfaced with the IPC running a virtual instrument software package. This arrangement allows the real-time display of the voltage and current signals combined with the ability to save the waveforms as numerical data in XLS files.

By observing the output current from the differential amplifier, the variable resistor is adjusted to bring the output current in phase with the applied voltage.

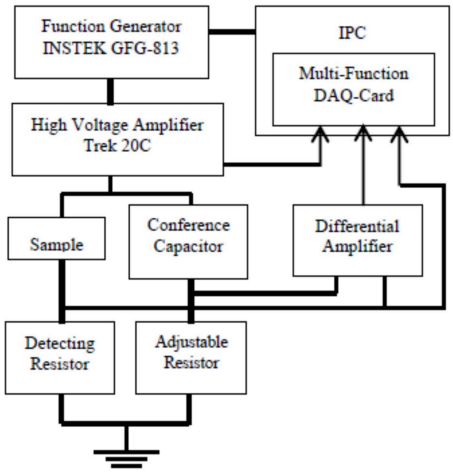

Fig.5. The structure of measuring system

Thus, the ac loss current is obtained. In this system, phase shifting does not occur at frequencies below 10 kHz. To obtain the amplitude and phase of higher harmonic waves of ac loss current, it is analyzed with the Fourier transformation method utilizing saved data files.

Conclusion

This paper discusses the dielectric loss for non-linear insulating materials, gives *dlf* as the characterization parameter and its numeric simulation analysis and presents a measuring system for non-linear insulating materials based on digital measuring technology.

References

[1] D.W. Auckland, Wenbin Su and B. R. Varlow. Non-linear fillers in electrical insulation. Proc. IEE, 1997,144: 127-133

[2] Zhengkao Zhang and M.R.Raghuveer. Some Aspects of a Digital Method for the Measurement of Loss Factor of High Voltage Insulation. Proceedings of the CEIDP, 1997,1: 279-282

[3] B.R. Varlow and K. Li. Non-linear AC properties of filled resins. IEE E Proc-Sci Meas Technol, 2003,150(2): 75-82

[4] K. S. Kelkar, N. E. Islam, C. M. Fessler, et al. Investigation of Optically Initiated Avalanche Silicon Carbide High Power Switches. Conference Record of the 2006 Twenty-Seventh International, 2006: 252 – 255

[5] Zhan Fusheng, Geng Zhongxing, Ge Yaozhong. High precision FFT algorithm for harmonic analysis in power system. Proceedings of the CSEE, 1999,19(3): 63-66

[6] T.Tsujimoto, M.Nakade, Y.Yagi, K.Adachi, et al. Development of no-site diagnostic method for XLPE cable by harmonics in AC Loss Current. Proceedings of the CPADM, 2003, 1: 73-76

[7] E.B.Makram, R.B.Haines and A.A.Girgis. Effect of Harmonic Distortion in Reactive Power Measurement. IEEE Trans. On Industry Applications, 1992,28(4): 782-787

[8] Zhang Rong, Li Zhonghua, GuoWen min, et al. Simulation of Response Characteristics of Non-linear Insulating Dielectrics in Coaxial Electrodes Under the Step Voltage. High Voltage Engineering, 2008,34: 1363-1367

[9] Wenmin Guo, Rong Zhang, Xiang Lu, et al. Simulation of Transient Response Characteristics in Coaxial Electrodes with Non-linear Insulating Dielectrics. Proceedings of the 9th International Conference on Properties and Applications of Dielectric Materials, 2009: 1145-1149

[10] Rong Xia, Hengying Xu and Zhonghua Li. Dielectric Parameters of Nonlinear Insulating Materials and Their Measurements. Properties and application of Dielectric Materials, 2006: 743-746

Advanced Materials Research Vols. 986-987 (2014) pp 1477-1480

doi:10.4028/www.scientific.net/AMR.986-987.1477

Design of a real-time detector for solution conductivity based on conductivity electrode

Jianian LI[1, a], Yan MA[1,a], Rui FENG[1,a], Huina NI[2, b]

[1] Faculty of Modern Agricultural Engineering, Kunming University of Science and Technology, Kunming, 650500, China

[2] College of Engineering, South China Agricultural University, Guangzhou 510642, China

[a]email: ljn825@163.com, [b]email: xiaohuaer89@163.com

Keywords: Solution; Conductivity; conductivity electrode; real-time detecting

Abstract. In order to realize real-time detecting for solution conductivity, an on-line detector powered with 9V battery was developed. The detector consists of conductivity electrode, excitation signal generating circuit, RMS detecting circuit, MSP430F2132 microcontroller, DS18B20 temperature sensor, HT1621 displayer and SPI interface. The solution conductivity was measured according to the principle that the electrode's output resistance varying with conductive ions concentration of the solution, the measured results could be displayed on HT1621 and be sent to other controllers through SPI interface. An optimum excitation signal that a square wave signal (the amplitude was ±3.5V, and the frequency was 1.8 kHz) had been determined by experiments, to minimize polarization effect of the conductivity electrode. Verification test had been performed for the detector, the tested results showed that maximum relative error of the detector was 2.94%, could meet the requirement of practical application.

Introduction

It has important significance that real-timely detecting and evaluating solution conductivity in many fields, such as food processing, production of purified water and distilled water, biopharming and so on. The measurement of solution conductivity was usually realized by measuring the resistance of the solution indirectly, through a resistance voltage divider circuit which consists of conductivity electrode and fixed resistance[1][2][3]. AC signals had been used as the measuring signals of conductivity electrode generally, to overcome the polarization effect of electrode caused by DC measuring signals[4][5][6][7]. Although the signal type and frequency of AC measuring signals both were different with ion concentration of the solution. So it was very important to choose reasonable signal type and frequency for different ion concentration solutions, which in turn to improve the measuring accuracy of solution conductivity. At the same time, it was an important segment that the detected results could be sent to main controller real-timely, for on-line analyzing and automatic controlling solution conductivity.

In this paper an on-line detector for solution conductivity was developed by using a conductivity electrode, a MSP430F2132 microcontroller and the corresponding circuits, the measured results of solution conductivity not only could be displayed directly, but be sent to other controllers through SPI interface.

Overall scheme design

The principle block diagram of the detector was shown in Fig.1. The detector was powered by a 9V battery which was converted to different operating voltages for supplying each circuit unit of the detector. Conductivity electrode was put into solution to detect conductivity, with a given driving signal from excitation signal generating circuit, and the output resistance of the electrode is changing with the solution conductivity. The electrode was connecting with a divider resistor in series, which formed a resistance voltage divider circuit, and then could convert the changing of solution conductivity into the form of voltage. The corresponding voltage of the conductivity was measured by the RMS (root mean square) detecting circuit, and then was sent to MSP430F2132

microcontroller for digitization processing through A/D converter interface. The results processed could be displayed on HT1621 directly and be sent to upper controller through SPI interface. DS18B20 temperature sensor was employed to feedback solution temperature, to reduce the influence of temperature for measuring accuracy of the electrode.

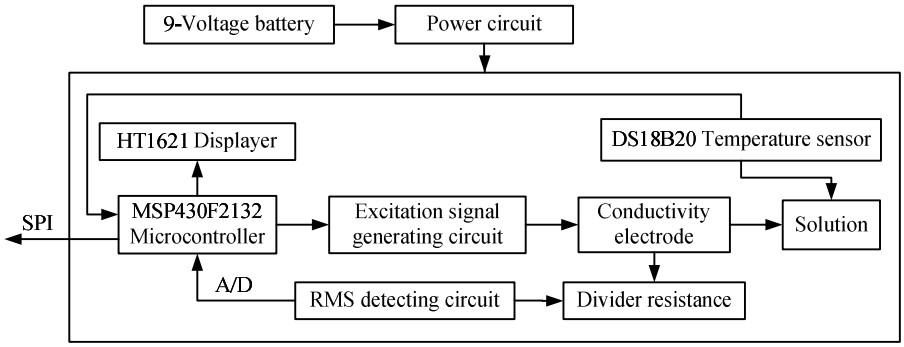

Fig.1 Principle block diagram of detector

Choice of conductivity electrode and its excitation signal source

A conductivity electrode whose range is 0.01~20 mS/cm was chosen to detecting solution conductivity, the measuring accuracy of the electrode is 0.01 mS/cm, and the electrode constant k=10 cm-1.

Polarization effect and capacity effect of the electrode are the main factors influencing the measurement of solution conductivity. The excitation signal on the electrode is closely related with polarization effect and capacity effect of the electrode, so it is necessary to determine the type, frequency and amplitude of the excitation signal by experiments.

In order to determine the excitation signal, the electrode was put into a series of different conductivity solutions to carry out conductivity detecting experiments respectively, using the output signals of SPF05 function generator as the excitation source. For each kind of conductivity of the solution under test, adjusted the SPF05 output sine wave and square wave with the step amplitude of 1V respectively, within the peak-peak range of 0~10V, and slow adjusted the frequency of each amplitude of sine wave or square wave within 0~10kHz. At the same time, a Tektronix TDS2041 oscilloscope was employed to monitor frequency, waveform, peak-peak voltage and RMS voltage of the divider resistance (2.2kΩ) of the electrode. The capacitance effect is significant when it was showed that waveform distortion or waveform overall migration or waveform asymmetry or wave frequency was different with the excitation source. When the peak-peak voltage or RMS voltage of the wave signal on the divider resistance was instability, it was showed that the polarization effect was significant. Experiments results showed that using a square wave whose amplitude is ±3.5 V and frequency is 1.8kHz as the driving signal for the electrode had optimum measuring effect, and it had optimum stability for reflecting solution conductivity by measuring the RMS voltage over the divider resistor.

Excitation signal generating circuit

Excitation signal generating circuit of the conductivity electrode was shown in Fig.2, it mainly concluded operational amplifier AD8039, metal oxide semiconductor Q4 and peripheral RC components. Its input was connected with an I/O port of MSP430F2132, a square wave signal whose frequency is 1.8 kHz was generated by the PWM controller which is internal integration of MSP430F2132 on the I/O port. With the square wave as the input signal, the excitation signal generating circuit could regulate its amplitude to ±3.5 V.

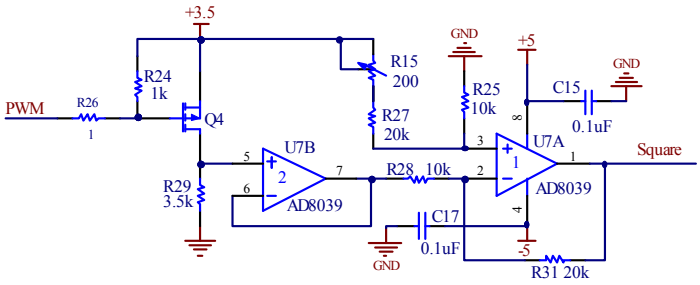

Fig.2 Schematic circuit diagram of excitation signal generating circuit

RMS detecting circuit

RMS detecting circuit of wave signal over the divider resistor was shown in Fig.3. It was comprised of RMS-DC convertor AD637, operational amplifier AD8039 and peripheral RC components. AD8039 that being connected as a voltage follower was put to the input of AD637, to improve the input impedance of AD637. AD637 was used to transform the input wave signal into equivalent DC voltage. The DC voltage was divided by R30 and R32, and then was sent to ADC interface of MSP430F2132 for detecting. The solution conductivity could be figured out according to the relationship which was obtained by experiments between voltage and conductivity.

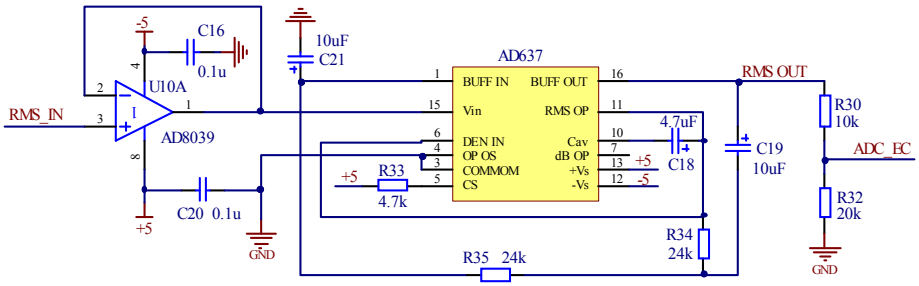

Fig.3 Schematic circuit diagram of RMS detecting circuit

Test results

In order to test and verify measurement accuracy of the detector designed, a series of solutions with different conductivity were prepared within 0~20 mS/cm, and then the detector was put into the solutions to measure conductivity. At the same time, a standard conductivity meter was employed to measure the solution conductivity, and then compared the measured results of the standard conductivity meter with that of the detector designed. The measured error of the detector was shown in fig.4, negative error indicates that detecting values are less than actual values. It was known form fig.4, the maximum relative error of the detector was 2.94%, the measurement error became stable (within 1%~1.5%) when the solution conductivity was higher than 10mS/cm. The conductivity detector designed could meet actual application requirements.

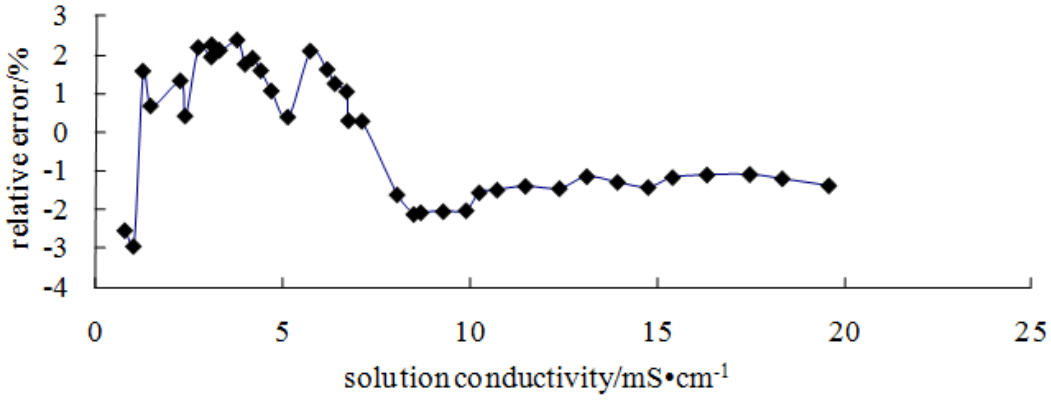

Fig.4 Measurement error of the detector

Conclusion

A conductivity detector powered with 9V battery had been developed based on conductivity electrode, to realize on-line detecting of solution conductivity. The excitation signal of the electrode was a square wave of ±3.5 V, 1.8 kHz, which was determined by experiments, could minimize polarization effect of the electrode. Test results showed that the maximum relative error was less than 3%, it could meet actual application requirements.

Acknowledgement

In this paper, the research was sponsored by the Provincial Talent Cultivation Foundation of Kunming University of Science and Technology (Project No. KKSY201323003) and Undergraduate Innovative Training Program of Kunming University of Science and Technology (Project No. 201310674245).

References

[1] Li Jianian, Hong Tiansheng, Feng Ruijue, et al. Design and experiment of automatic mixing apparatus for liquid fertilizer based on fuzzy control[J]. Transactions of the Chinese Society of Agricultural Engineering, 2013, 29(16): 22-30.

[2] Liu Zhenming,Qi Chuanhui,Wang Yunlong, et al. Based on P89C51 automatic monitor control system for on-line nutrient consistency[J]. Journal of Agricultural Mechanization Research, 2010(10): 83-86.

[3] Jia Kejin, Zhang Xiaowei, Lin Bo, et al. The intelligent on-line conductivity analyzer based on MSC1210 single chip computer[J]. Process Automation Instrumentation, 2007, 28(5): 43-46, 50.

[4] Chen Gehua, Teng Yujuan, Wang Xiaohui. A new way to measure conductance[J]. Journal of Northeast China Institute of Electric Power Engineering, 2005, 25(6): 76-78, 91.

[5] Chen Xiaoping, Chen Hongxian. Double frequency method to measure water conductivity[J]. Chinese Journal of Scientific Instrument, 2006, 27(5): 520-522.

[6] Li Lin, Chen Wenxiang. Electrical conductivity measurement using frequency self-adaptation current source to surmount the influence of capacitance[J]. Chinese Journal of Scientific Instrument, 2007, 28(12): 2256-2259.

[7] Sudduth K A, Kitchen N R, Bollero G A. Comparison of electromagnetic induction and direct sensing of electrical conductivity[J]. Agronomy Journal, 2003, 95(3): 472-482.

Advanced Materials Research Vols. 986-987 (2014) pp 1481-1485

doi:10.4028/www.scientific.net/AMR.986-987.1481

Design of high-gain amplifier for Soft X-ray imaging diagnostic system on J-TEXT tokamak

Zhengyu Xiao[1,2,a], Xiaoqing Zhang[1,2,b], Yonghua Ding[1,2,c], Jianchao Li[1,2,d]

[1]State Key laboratory of Advanced Electromagnetic Engineering and Technology, 430074, Wuhan, China

[2]School of Electrical and Electronic Engineering, Huazhong University of Science and Technology, Wuhan 430074, China

[a]zyxiao@hust.edu.cn, [b]xqzhang_1012@126.com, [c]yhding@mail.hust.edu.cn, [d]lijianchao07@126.com

Keywords: the photodiode amplifier; Soft X-ray imaging diagnostic system; J-TEXT

Abstract. Amplifier is a key component of the Soft X-ray imaging diagnostic system and the system is one of the most important diagnostic systems on J-TEXT tokamak. Signal generated by the photodiode is current and it's too small. A high-gain amplifier enable us to observe the soft x-ray radiation signal in J-TEXT tokamak accurately. So an amplifier based on transimpedance circuit was proposed. Through theoretical calculations and simulations, the designed amplifier can achieve the set goals that are the V/I gain of 10^6 and the bandwidth of 20KHz. In order to ensure the quality of the signal, interface and shell of the amplifier are designed specially. Finally designed amplifier works properly in the experiment and it can meet the needs of the experiment.

Introduction

Tokamak is a ring container and it uses magnetic confinement to achieve magnetic confinement fusion. J-TEXT (The joint texas experimental Tokamak) is a medium-sized tokamak and it was re-established at Huazhong University of Science and Technology. At first, it was developed by the University of Texas at Austin. Soft X-ray (SXR) imaging is a very important diagnostic technique for tokamaks [1]. The SXR imaging diagnostic system is as follows in Fig.1. Output amplitude of the photodiode detector is small so a photodiode of large sensing face and a resistor of high resistance are needed. However, this combination will decrease the bias, bandwidth, stability and noise performance of the system [2]. Therefore designing and choosing the relevant parameters carefully are the key point for photodiode amplifier. In order to observe the signal exactly we need an amplifier which has a gain of 10^6V/A and a bandwidth of 20KHz. Besides we need to avoid possible electromagnetic interference from space when tokamak is running. Finally we must also consider to prevent loop current caused by improper grounding [3].

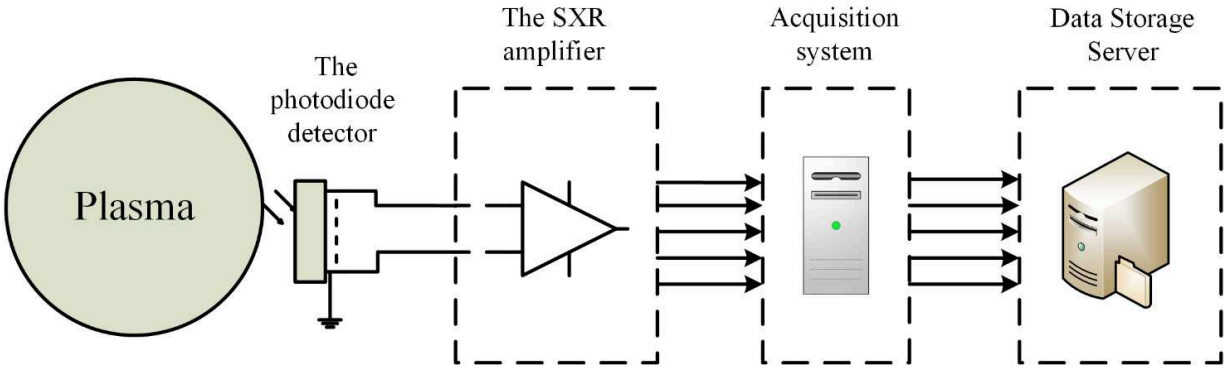

Fig.1 The SXR imaging diagnostic system

The design of amplifier on J-TEXT SXR system

As follows in Fig.2, there are three circuits which can be used with photodiode. For the circuit 1, the output voltage is in direct proportion to the input voltage. At the same time, the input voltage

is decided by $V_{in} = V_t \ln r_\phi \phi_\varepsilon / I_D$ where r_ϕ, V_t, I_D is a constant decided by photodiode and ϕ_ε is the energy flux of incident light. As a result the output voltage becomes non-linear related to the energy flux of incident light. The voltage on the photodiode just strengthens the nonlinearity. A large DC bias voltage appears because of the input bias current flowing through the junction resistance. These will increase the complexity to analyze the phenomenon. As for the circuit 2, the junction capacitance will shunt the signal current in high frequencies so as to a bandwidth limitation comes into being. By contrast, output voltage in the circuit 3 is determined by the current of photodiode. The current $i_p = r_\phi \phi_e$ and the output voltage become a linear relationship with luminous flux. Besides the voltage on the photodiode is maintained at zero so as to avoid some bad effects such as nonlinearity, DC bias voltage and bandwidth limitation [2].

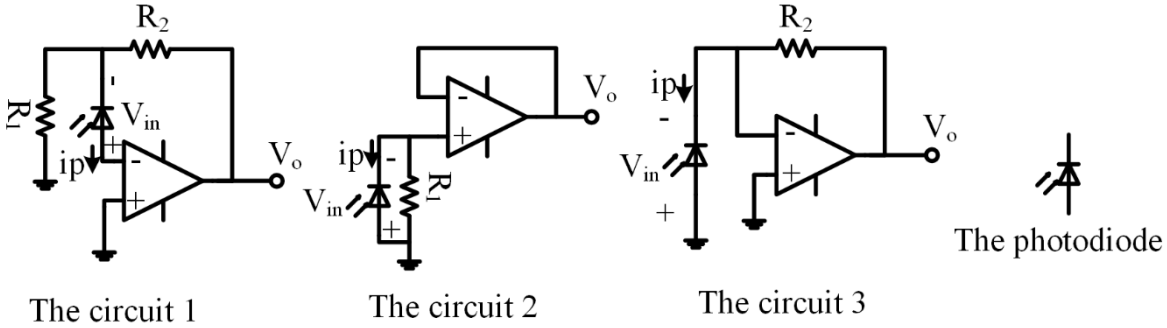

Fig.2 Three circuit can be used with photodiod

The basic equivalent circuit of the system is shown in Fig.3 (the power supply part of the circuit is omitted) and the correlative parameters are as follows in Table 1. We select AD8510 produced by ADI which has advantages in terms of input bias current, noise performance, CMRR and PSRR [4].

AD8510 can be approximated by a single-pole model. Its open loop transfer function can be expressed approximately as $A_{oL} = \omega_c / s$ where $\omega_c = 2\pi f_c$ and f_c is the unity gain crossover frequency and the f_c of AD8510 is 8 MHz. Value of R_D is so big that we can ignore it and just think it an open circuit when we analyze the circuit. So characteristics of related parameters are given in Fig.4. The figure shows that the difference on slope between the AD8510 open-loop transfer function curve and compensated noise gain curve is just 20dB/dec when they intersect with each other. This indicates a phase shift of 90° and ensures the stability of the system. The bandwidth of the circuit is f_i' shown in Fig.4 and it's about 21.81KHz [5].

Comparison of two noise gain curves reveals the decrease of noise gain peak apparently because of the compensation capacitor. The frequency range of the noise gain is nearly the same. This will allow us to reduce noise to below background noise.

The junction capacitance of the photodiode detector is variable in fact and it will have an effect on the circuit performance such as bandwidth [6]. Fig.5 provides gain versus frequency with changing C_D. Simulation result shows that the gain can stay the same before 100KHz even if the junction changes substantially. So the bandwidth is almost unaffected.

At the same time, we use aluminum frame to package the circuit in order to acquire a signal of better quality in our lab for aluminum has a high electrical conductivity. For aluminum has smaller skin depth under the same operating frequency [7].

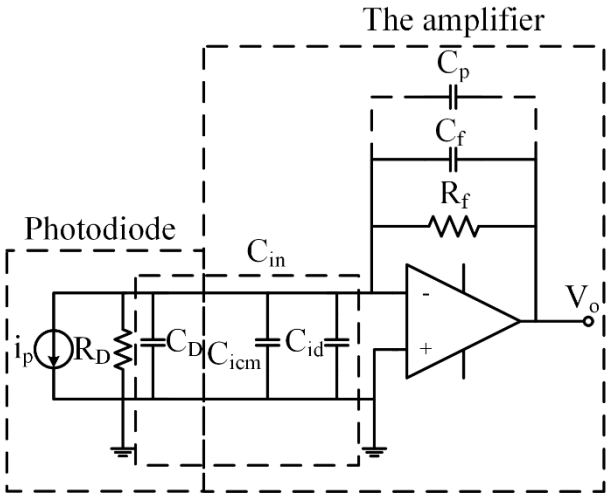

Fig.3 Basic equivalent circuit of system (C_p is parasitic capacitance across R_f)

Table 1 Correlative parameters in Fig. 3 [4]

Symbol	Values	Units
R_D	100	[MΩ]
R_f	1	[MΩ]
C_D	40(max)	[pF]
C_{icm}	11.5	[pF]
C_{id}	12.5	[pF]
C_f	6.8	[pF]
C_p	0.5	[pF]

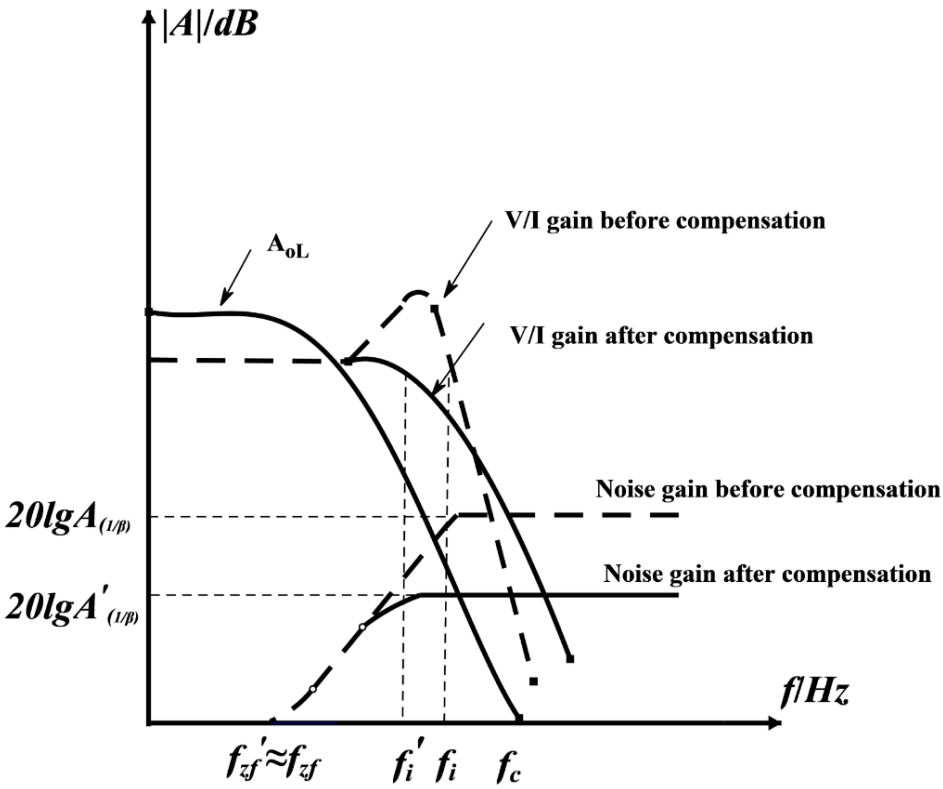

Fig.4 Open-loop gain of AD8510 and comparison of closed-loop characteristics before and after compensation

Basic working performance testing

To test the basic working performance of the amplifier it was input some specific waveforms. The equivalent test circuit is in Fig.6. The signal source is Suing TFG3150L DDS function generator. The oscilloscope is TEK MSO4034B.

The amplifier was tested with sinusoidal signal at 1Hz and22KHz. The results are presented in Fig.7 and Fig.8. Input the sinusoidal signal with 1Vp-p into the amplifier and measure the output by changing its frequency. According to the data recorded we can plot the V/I gain versus frequency as Fig.10. As we can see, the amplifier has an about -3 dB bandwidth of 22KHz and it can transmit the signal within the bandwidth well. At the same time, V/I gain is about 10^6.

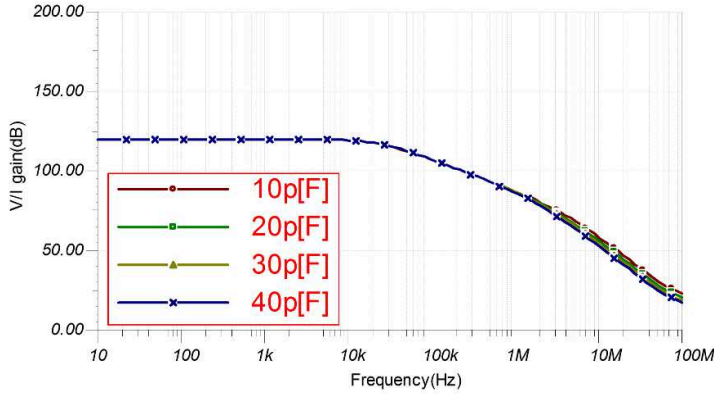

Fig.5 Gain versus frequency with changing C_D.

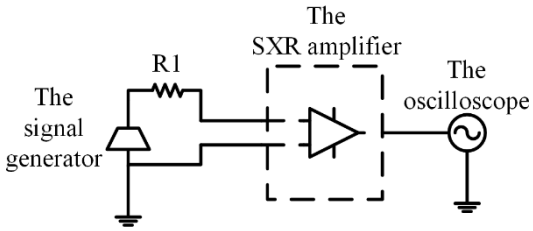

Fig.6 The equivalent test circuit(R_1=100K)

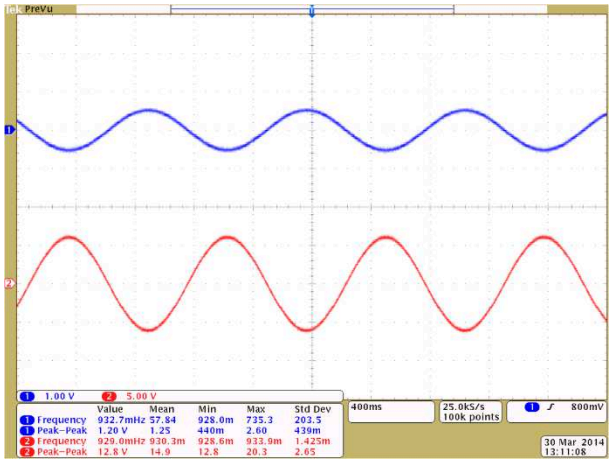

Fig.7 Upper curve: input signal (1V/div, 1Hz)
Lower curve: output signal (5V/div, 1Hz)

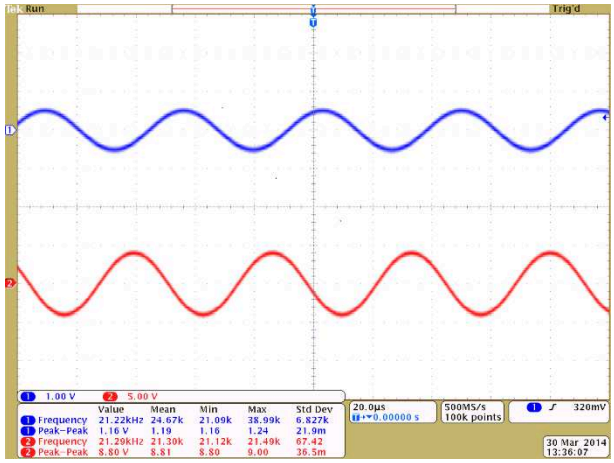

Fig.8 Upper curve: input signal (1V/div, 22KHz)
Lower curve: output signal (5V/div, 22KHz)

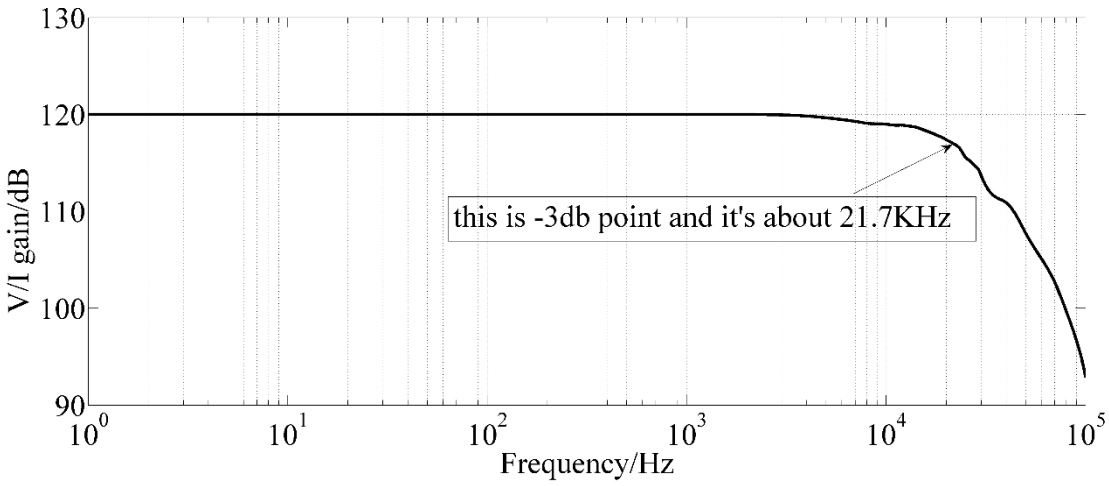

Fig.9 Amplitude-frequency response curve according to the actual measured data

Test on J-TEXT tokamak

The output signal of a typical shot when J-TEXT is running is displayed in Fig.10. As showed in Fig.10, the sawtooth activities are obvious on the J-TEXT. The phenomenon illustrates that the amplifier can run properly on the SXR diagnostic system of J-TEXT [1]. On the other hand impulse interference is strong. Burrs on the signal affect the quality of the signal seriously and so far the specific sources of these interference are unclear for high-current, high-voltage and pulse discharge are produced when tokamak is running. The next target is optimizing the signal quality.

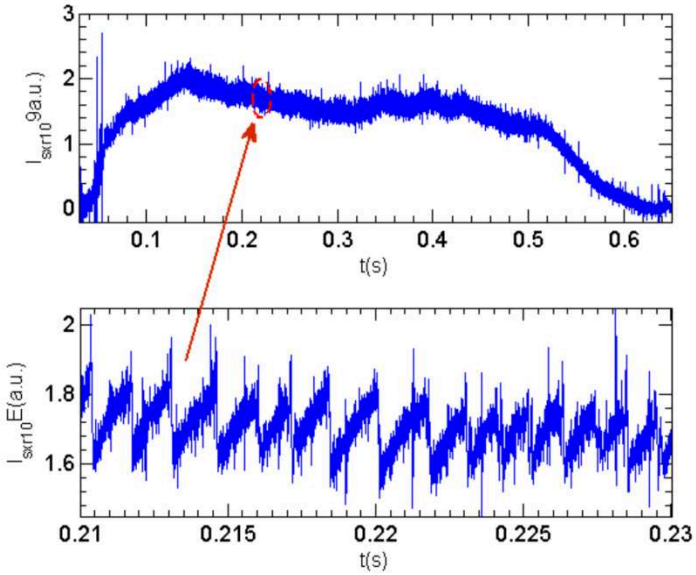

Fig.10 Test result when J-TEXT tokamak is running(shot: 1035621)

Summary

A simple transimpedance op amp circuit topology is very suitable for our amplifier after discussing. The amplifier can guarantee the gain and bandwidth needed by matching parameters. The theoretical results and the simulation results are consistent with our objectives. The amplifier can parse out the signal generated by the soft x-ray clearly and the amplifier is able to work a long time stability. Experimental results show that the amplifier meets the requirements of SXR diagnostic system for J-TEXT tokamak.

Acknowledgements

The authors thank the students of RMP Group for guidance and help. Special thanks to Bo Rao, Bin Yi, Hai Jin for their suggestions on related content.

References

[1] Y. H. Ding, et al. "Soft X-ray imaging diagnostic system on the J-TEXT tokamak." Nuclear Instruments and Methods in Physics Research Section A: Accelerators, Spectrometers, Detectors and Associated Equipment 606.3 (2009): 743-748.
[2] Graeme, Jerald G. Photodiode amplifiers: op amp solutions. McGraw Hill, 1996.
[3] M. yang, et al. "Design of weak photocurrent signal amplifier." Nuclear Electronics & Detection Technology 31.7 (2011): 734-738.
[4] The Data Sheets of AD8510 on http://www.analog.com/static/imported-files/data_sheets/AD8510__8512_8513.pdf.
[5] Mancini, Ron, and Bruce Carter. Op Amps for everyone. Newnes/Elsevier, 2009.
[6] Weckler, Gene P. "Operation of pn junction photodetectors in a photon flux integrating mode." Solid-State Circuits, IEEE Journal of 2.3 (1967): 65-73.
[7] Y. Y. Gu, et al. " Research progress of electromagnetic shielding materials." Materials Review 19.2 (2005): 53-56.

Advanced Materials Research Vols. 986-987 (2014) pp 1486-1490

doi:10.4028/www.scientific.net/AMR.986-987.1486

Design of Online Monitoring and Evaluation System for Master Station Running Status

Fang YU[1, a], Weijin ZHUANG[1, b], Jin LIU[1, c], Pan XU[1, d], Haifeng HUANG[1, e]

[1]China Electric Power Research Institute, Nanjing, 210061, China

[a]email:sosn_yf621@163.com, [b]email: zhuangweijin@epri.sgcc.com.cn,

[c]email: liujin@epri.sgcc.com.cn, [d]email: xupan@epri.sgcc.com.cn,

[e]email: huanghaifeng@epri.sgcc.com.cn

Keywords: Index System; Online Monitoring; Evaluation

Abstract. The increase of data access capacity and data types of the power grid leads to a more complex and varied grid running environment. Hence, in order to guarantee the running security of the master station, an online monitoring and evaluation system based on index system for master station is proposed in this paper. It can construct a dynamic evaluation model and complete automated collection, analysis, scoring and evaluation of indexes by using specific index calculation methods. Moreover, this system can provide comprehensive interface display for evaluation results and achieve online alarming for the abnormal situations of the master station. This system offers a new and effective way to guarantee the safe and reliable running of the master station.

Introduction

With the rapid development of the power grid, the safe running of the master station is facing great challenges, which directly affects the whole power grid's security, stability and quality operation[1][2][3]. Actually, due to the master station itself, it may also appear a variety of abnormal situations, such as: hardware failure, network interruption, software malfunctions and so on. If any of them cannot be detected and solved timely, it may take serious impact on the entire power grid. The analysis of blackouts accident happened in United States and India also shows that the fault of master station is a key factor causing power outages and incidents expansion[4][5]. Therefore, it is necessary to monitor and evaluate the functionality, performance, stability and reliability of the master station when the system is running, and it is helpful to find hidden dangers in advance and improve the safe running level of the power grid.

Due to the complexity of the master station, the existing monitoring tools have great limitations. Some only monitors and alarms for SCADA or FES communication status[6][7][8], which lacks of detecting critical data transition and data refresh status; some focuses on monitoring a signer function of the master station, which lacks of comprehensive monitoring of the whole master station including the application conditions, software conditions, hardware devices. Meanwhile, the existing monitoring tools do not have the function of data tracking, evaluation and analysis, which is not conducive to detect operation problems timely. So there is an urgently need to upgrade and improve the capabilities of online monitoring and evaluation and the risk prevention level of the master station.

In response to these problems, this paper proposes an open and universal online monitoring and evaluation system for power grid master station which can meet requirements in security and protection of power grid' s secondary systems. This system constructs a dynamic evaluation model based on the index system, achieves online monitoring and evaluation for the master station's indexes, which include application status, services, hardware resources, communication quality between the main station and the sub-station, data quality and so on.

System Architecture

Software architecture

This system uses a distributed multi-layer architecture and modular design, which can flexibly and easily be expanded without affecting the realization of system's the overall function. As Fig.1 shows , software architecture of this system is divided into three levels from top to bottom.

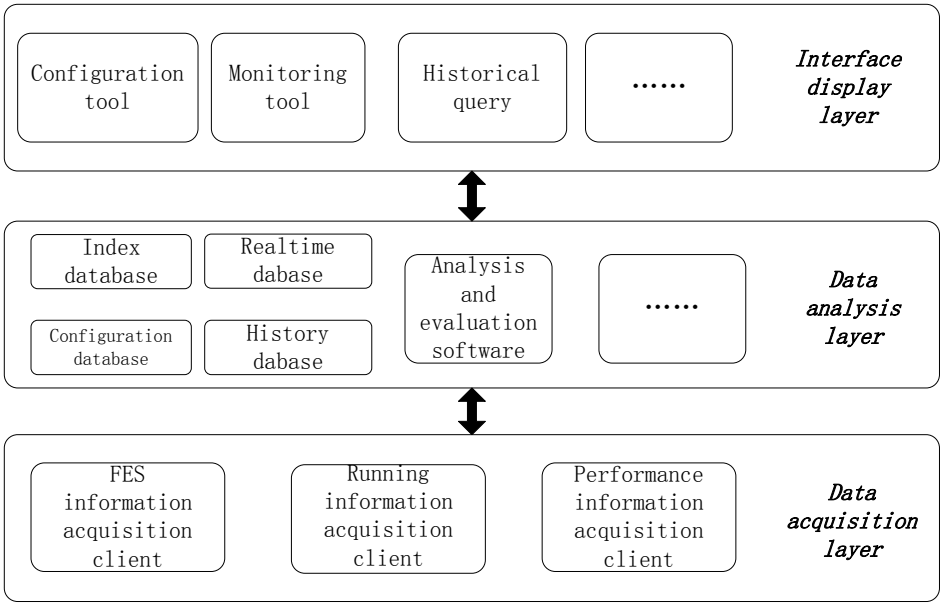

Fig.1. Software architecture diagram

- Interface display layer: an interface for interacting users with the system, achieve indexes personal configuration, real-time status monitoring, artificial detection and historical query;
- Data analysis layers: gather, process, storage and sample the data from index files, analyze and evaluate data according to the index database and configuration database;
- Data acquisition layer: accomplish data acquisition and generate index files by FES information acquisition client, running information acquisition client and performance information acquisition client.

Hardware architecture

This system only needs to increase an online monitoring server based on the original hardware architecture. FES information acquisition client is only deployed on FES servers of the master station, running information acquisition client and performance information acquisition client are deployed on database servers or application servers, analysis and evaluation software is deployed on online monitoring server, furthermore, the graphical display interface can be deployed on any machine of the master station.

Index system

Index system construction

As the master station is a multi-target, multi-dimensional and complex system, the online monitoring and evaluation index system for it is also a multi-level system. Referring to the basic theory of AHP (analytic hierarchy process, AHP)[9][10][11][12], the general design of the index system is constituted by three levels, the top layer is the total target layer, which describes the ultimate goal of this on-line monitoring evaluation system pursued; the middle layer is the guideline layer, which determines the overall framework of the index system and the bottom is the data layer, which represents the specific acquisition data. According to role the master station played and requirements of the master station, the guideline layer mentioned above is constituted by the four index groups, namely the front-end communication index group, system resources index group, applications running status index group and consistency index group from the technology point of view, as shown in Figure 2 .

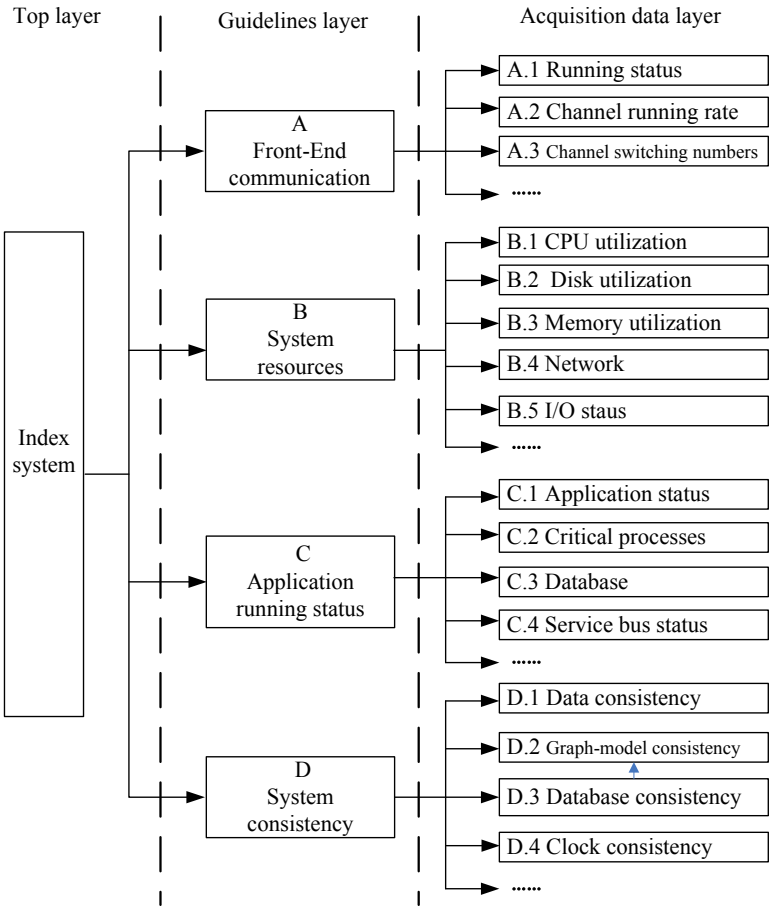

Fig.2. Index system of the master station

• Front-end communication

It is necessary to monitor the front-end communication information because the communication stability and reliability between the of the master station and sub- stations is the most important factor to guarantee the stable running of the master station. Front-end communication index group consists of conventional channel status index, channel run rate, network traffic, communication bit error rate, in addition to further, it also includes data refresh rate, channel control times and so on. The monitoring coverage of this system is more wider to characterize the running status of the front-end communication comprehensively.

• System resources

System resource index group consists of core indexes selected from the CPU, memory, disk, network, system statistics information, including system resource utilization, I / O status, file handles, network card status and so on.

• Application running status

Application running status index group consists of core indexes selected from four aspects of system application status, critical processes, service status, database, including application status, application failure times, network broken numbers, the key process status, the maximum connections numbers of database, service status (message bus, services bus, real-time database service, commercial database service and so on).

• System consistency

System consistency index group mainly evaluates the consistency of system multi-source data, consistency between graph and model, consistency between real-time database and commercial database, consistency of system time clock.

Evaluation method

After constructing the index system, the indexes are evaluated in accordance with the flowchart in Figure 3[13]. Based on the online monitoring database, which is made up of real-time data file acquired from acquisition client and historical data files, some core indexes are selected as veto

indexes firstly. It represents that the system can get a comprehensive score under the premise of all veto indexes are satisfied. If any of these veto indexes is not satisfied , the system is under a serious faulty situation, an alarming message should be sent immediately. Then every index is scored following the scoring rules, finally the comprehensive score of the system is calculated by calculating scores from every index layer. According to final score of the system, the severity of the master station running status is analyzed and the corresponding solutions are then given.

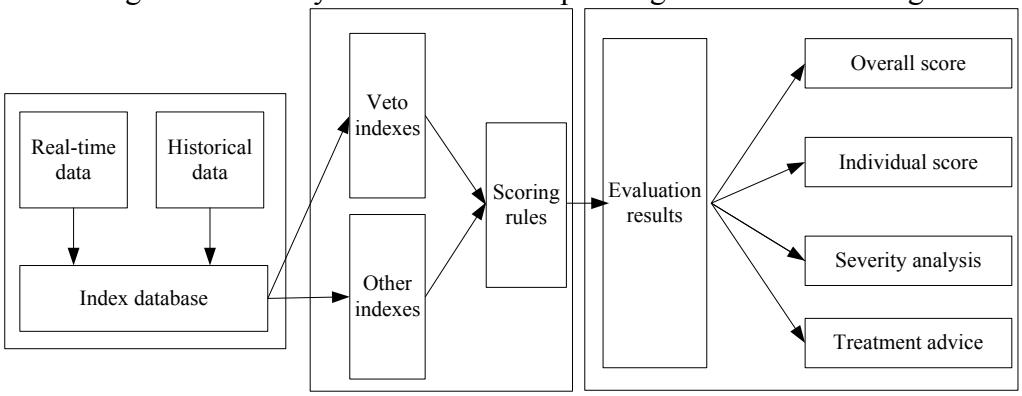

Fig.3. Flowchart of index evaluation method

In the scoring process for every index, index weight and scoring rule are introduced firstly. Index weight is introduced to distinguish the importance of one index relative to other indexes between the same index layer, which is generally represent by normalized value. Precise definition of the index weight can accurately describe the relative relationship between each index in the system and reflect the real situation of the system. Establishment of scoring rules for the underlying indexes can convert the actual value of one index into corresponding evaluated score, which is the key link to evaluate whether or what extent the master system meets the reliability requirement.

Comprehensive score is calculated according to the following formula[11]:

$$S = \sum_{j=1}^{n} S_j W_j \tag{1}$$

In the formula S_j represents the underlying index score, W_j represents the corresponding index weight , final score S is calculated by a weighted sum of scores of each layer.

System functions

Index acquisition function

Index acquisition function achieves indexes acquisition, index file generation and index file synchronization by front-end information acquisition client, system resources acquisition client and running information acquisition client.

According to the architecture of index system, acquired indexes can be divided into four types, that is front-end communication information, applications running information, system resources information and system consistency information, it also can be divided into single server information and multi-server information from the view of function implementations. Single server information refers to indexes that can be acquired by reading real-time database, reading log files or programming on one server, such as hardware resource information, channel running status, critical processes, most acquired indexes are belonged to single server information. Multi-server information refers to indexes that must be acquired by several servers working together, such as the transmission time of system change data, which requires cooperation between SCADA server and FES server. A data sending program is deployed on FES server to record the exact data sending time and the sending value, another data receiving program is deployed on SCADA server to record the exact data receiving time and exact time when real- time database updates, thus the transmission time of change data from the FES to SCADA is obtained .

Data analysis and evaluation function

Data analysis and evaluation function is used to gather and store data files transmitted from the acquisition client, analyze and evaluate the change trends of the system according to the quantitative index standards. It achieves publishing unified evaluation results and interacting with the interface display layer finally, its specific functions are as follows :

- Data summarization: receive index information files from acquisition client.
- Data storage: parse and store data into real-time database , meanwhile store historical files.
- Data evaluation: analyze and evaluate according to the index system and evaluation methods, send alarming messages and generate unified result file.

Interface display function

Interface display function is used to provide a configuration interface to users for modifying the property and the alarm thresholds of indexes. monitor the comprehensive score and specific index data of the system through online monitoring main interface. It is also used to search real-time alarm information and provide historical data query entry for conveniently batch querying or modifying.

Conclusion

The online monitoring and evaluation system for master station running status proposed in this paper can make the operation and maintenance work of the system from passive to active, detect the running security risk of the system timely, it also can enhance the reliability, security and robustness of the system, and provide decision-making basis for improving, upgrading and optimizing the master station. Finally this monitoring and evaluation system has high reliability and wide range of applications as it is independent from the master station and has no effect on the master station running status.

References

[1] Han Zhenxiang ,Cao Yijia. Power system security and its prevention [J]. Power System Technology, 2004,28(9)1-6.

[2] Ma Taotao, Guo Chuangxin, Cao Yijia, et al. Current status and development trend of intelligent dispatching automation system of power system[J]. Automation of Electric Power Systems. 2010,34(9)7-9.

[3] Xie Dawei, Yang Xiaozhong. Implementation of networking telecontrol technique in dispatching automation system[J]. Power System Technology,2004,28(8) 34-37(in Chinese).

[4] Hu Xuehao. Rethinking and enlightenment of large scope blackout in interconnected north America power grid[J]. Power System Technology, 2003,27(9)2-6.

[5] He Dayu. Rethinking over '8.14' US-Canada blackout after one year[J]. Power System Technology, 2004,28(21) 1-5(in Chinese).

[6] Wang Minkun, Tian lifeng, Gou xiaoyi. Comprehensive monitoring system for dispatching automation of sichuan power grid[J]. Power System Technology, 2006,30(21)89-93. operation of automation equipments [J]. Automation of Electric Power Systems, 2001,25(2) 66-67.

[8] YangNing ,Ma YU. The establishment of automation comprehensive supervising system for northeast power system operation control[J]. Northeast Power System, 2005,1:49-52.

[9] Wang Zhidong，Li Hui ,Li Jun ,et al. Assessment index system for smart grids[J]. Power System Technology ,2009,33(17) 14-18.

[10] Zhang Guohua, Zhang Jianhua , Peng Qian, et al. Index system and methods for power grid security assessment[J]. Power System Technology, 2009,8(33) 30-34.

[11] Li Xiaohui, Xu Jing, Li Da, et al. Index system of reliability evaluation for distribution network based on analytic hierarchy process[J]. Proceedings of the CSU-EPSA. 2009,21(3)69-74.

[12] Zhang Jian, Pu Tianjiao, Wang Wei, et al. A comprehensive assessment index system for smart grid demonstration projects[J]. Power System Technology, 2011,35(6)5-9.

[13] Yao Gang, Liu Sufei, Ma Jindong, et al. Development of evaluation index systems and methods for distribution networks[J].East China Electric Power,2009,37(12)2038-2040.

Advanced Materials Research Vols. 986-987 (2014) pp 1491-1496

doi:10.4028/www.scientific.net/AMR.986-987.1491

Fault diagnosis of bearing based on KPCA and KNN method

Wang Qiang[1, a], Liu Yong-bao[1, b], He Xing[1, c], Liu Shu-yong[1, d], Liu Jian-hua [1,e]

[1] College of Power Engineering, Naval University of Engineering, Wuhan, 430030, China

email: [a]wangqiang13000306@163.com, [b]yongbaoliu@aliyun.com, [c]hexing_mail@163.com, [d]soaringbird2008@sina.com, [e]ljh363418@sina.cn

Keywords: Bearing; Fault Diagnosis; KPCA; KNN

Abstract. Selection of secondary variables is an effective way to reduce redundant information and to improve efficiency in nonlinear system modeling. The combination of Kernel Principal Component Analysis(KPCA) and K-Nearest Neighbor(KNN) is applied to fault diagnosis of bearing. In this approach, the integral operator kernel functions is used to realize the nonlinear map from the raw feature space of vibration signals to high dimensional feature space, and structure T^2 and SPE statistics in the feature space to extract the feature vector from the fault signal with the principal component analytic method. Assessment method using the feature vector of the Kernel Principal Component Analysis, and then enter the sensitive features to K-Nearest Neighbor classification. The experimental results indicated that this method has good accuracy.

Introduction

Bearing is one of the most important component of gas turbine. And it is also a easily damaged part, especially the faults such as wear, cracking, agglutination and so on[1]. Because of long-term running or improper assembly, wear of mechanical component is a common fault in rotating machinery such as steam engine, aircraft engine, and compressor. Therefore, identification of wear is an important task for maintaining industrial facilities in the fields of mechanical and aerospace engineering.

Gu Jun et al adopt the Kernel Principal Component Analysis (KPCA) and Support Vector Machine (SVM) method to implement intrusion detection, which can not only solve the linear correlation of the input but also compress the data. This method can achieve higher detection rate and better generalization，and decrease the time of performance[2]. Liu Ailun et al apply the same method to continuous stirred tank reactor (CSTR) model by integrating the characteristics of them to avoid complex computation and improve the real time property of the fault diagnosis model[3]. TIAN Zhongda et al use the kernel principal component analysis(KPCA)and the least squares support vector machine(LSSVM) algorithm to predict the random time-delay which can eliminate the noise and interference and reduce the amount of computation[4]. A novel method based on kernel principal components analysis(KPCA) and false nearest neighbor method(FNN)is proposed on select the most suitable secondary process variables used as nonlinear modeling inputs by LI Taifu, which can be employed to overcome difficulties encountered with the existing muiticollinearity between the factors[5], and the results show that the method is effective and suitable for variable selection. Selection of secondary variables is an effective way to reduce redundant information and to improve efficiency in nonlinear system modeling. The combination of Kernel Principal Component Analysis(KPCA) and K-Nearest Neighbor(KNN) is applied to fault diagnosis of bearing.

Design of Combining KPCA and KNN

KPCA is one approach of generalizing linear Principal Component Analysis (PCA) into nonlinear case using the kernel method. Principal Component Analysis (PCA) is a very effective and popular unsupervised data-driven multivariate statistical method for feature extraction, dimensionality reduction and process monitoring. It is in its nature linear transformation which

degrades its performance for handling non-linear systems. To cope with this problem, several non-linear extensions of PCA have been developed, which allows extracting both linear and non-linear correlations among process variables.

KPCA was proposed to generalize PCA to nonlinear cases by nonlinearly mapping input samples to a higher or even infinite dimensional feature space F and performing PCA there. Specifically, let training samples $x_1,\cdots,x_N \in R^D$ be mapped to $\Phi(x_1),\cdots,\Phi(x_N)\in F$ by some nonlinear mapping $\Phi: R^D \to F$. PCA is then performed to find the principal components of mapped samples $\Phi(x_1),\cdots,\Phi(x_N)$. By formulating PCA in a way that only involves the mapped samples via dot products, we do not need to know the mapping Φ explicitly, as the dot products can be evaluated by a positive semidefinite kernel function $k(a,b)=\{\Phi(a),\Phi(b)\}$.

Assuming $\Phi(x_1),\cdots,\Phi(x_N)$ have been mean-centered, PCA is performed by finding the eigenvalues $\lambda \succ 0$, and eigenvectors $v\in F\setminus\{0\}$ satisfying $Cv=\lambda v$, where C is the empirical covariance matrix

$$C=\frac{1}{N}\sum_{i=1}^{N}\Phi(x_i)\Phi(x_i)^T \tag{1}$$

Substituting (1) into the eigenvector equation, we can see that all solutions **v** lie in the span $(\Phi(x_1),\cdots,\Phi(x_N))$ and can be expanded as

$$v=\sum_{i=1}^{N}a_i\Phi(x_i) \tag{2}$$

The problem is then reduced to finding the coefficients a_i, which can be formulated as the following eigenvalue problem by substituting (1) and (2) into the eigenvector equation.

$$K\alpha=N\lambda\alpha \tag{3}$$

where **K** is the N × N kernel matrix of training samples $K_{ij}=(\Phi(x_1),\Phi(x_j)=k(x_i,x_j)$ and $a=\left[a_1^l,\cdots,a_1^N\right]^T$ Letting λ_l be the l th largest eigenvalue of K and $a_l=\left[a_1^l,\cdots,a_1^N\right]$ be the corresponding rescaled eigenvector such that $\langle v_l,v_l\rangle=1$,(this is translated into $\lambda_l\langle v_l,v_l\rangle=1$,an input sample **x** can be mapped onto the *l* th dimension of KPCA space with coordinate value

$$\langle v_l,\Phi(x)\rangle=\sum_{i=1}^{N}a_i^l k(x_i,x) \tag{4}$$

Finally, to release the assumption that $\Phi(x_1),\cdots,\Phi(x_N)$ have been mean-centered in F, the kernel matrix K and the kernel evaluation $k(a,b)$ should be replaced by their centered versions

$$\tilde{K}=\left(I-\frac{1}{N}1_{N\times N}\right)K\left(I-\frac{1}{N}1_{N\times N}\right) \tag{5}$$

where I is the identity matrix and $1_{N\times N}\in R^{N\times N}$ with all entries set to 1, and

$$\tilde{K}(a,b)=k(a,b)-\frac{1}{N}\left(\sum_{i=1}^{N}k(x_i,a)+\sum_{i=1}^{N}k(x_i,b)\right)+\frac{1}{N^2}\sum_{i=1}^{N}\sum_{j=1}^{N}k(x_i,x_j) \tag{6}$$

In summary, three steps are needed to compute the nonlinear principal components of an input sample x: (i) compute and center the kernel matrix of training samples K, (ii) compute its nonzero eigenvectors and rescale them such that $\lambda_l\langle a_l,a_l\rangle=1$, (iii) extract d principal components of **x** by applying (3) on d dominant eigenvectors.

After the data samples are given, KPCA, performing a nonlinear data transformation into some high dimensional feature space, increases the probability of the linear separability of the patterns within the feature space. The K-Nearest Neighbor algorithm is defined not merely by the distance

between a point and its class center, but also by two different points of the sample, which is depicted as the affinity between them. Texts Categorization are classified automatically according to the K-nearest contents.

The detailed steps of the combining algorithm are illustrated.

The idea of KPCA is to firstly map the original input vectors x_t into a high-dimensional feature space $\phi(x_t)$ and then to calculate the linear PCA in $\phi(x_t)$. The linear PCA in $\phi(x_t)$ corresponds to a nonlinear PCA in x_t. By mapping xt into $\phi(x_t)$ whose dimension is assumed to be larger than the number of training samples l, KPCA solves the eigenvalue problem (7).

$$\lambda_i u_i = \tilde{C} u_i, i = 1,\ldots,l \tag{7}$$

Where $\tilde{C} = \frac{1}{l}\sum_{t=1}^{l} \phi(x_t)^T$ is the sample covariance matrix of $\phi(x_t)$. λ_i is one of the non-zero eigenvalues of $\phi(x_t)$. λ_i is one of the non-zero eigenvalues of $\tilde{C}$. u_i is the corresponding eigenvector. Eq. (1) can be transformed to the eigenvalue problem (8) -(10).

$$\tilde{\lambda}_i \alpha_i = K\alpha_i, i = 1,\ldots,l \tag{8}$$

where K is the $l \times l$ kernel matrix. The value of each element of K is equal to the inner product of two vectors x_i and x_j in the high-dimensional feature space $\phi(x_i)$ and $\phi(x_j)$. That is, $K(x_i, x_j) = \phi(x_i) \bullet \phi(x_j)$. As the calculations of the dot product $\phi(x_i) \bullet \phi(x_j)$ are all replaced with the kernel function $K(x_i, x_j)$, the mapping of $\phi(x_t)$ from x_t is implicit. The elegance of using K is that one can deal with $\phi(x_t)$ of arbitrary dimensionality without having to compute $\phi(x_t)$ explicitly. Any function satisfying can be used as K. λ_i is one of the eigenvalues of K, satisfying $\tilde{\lambda}_i = l\lambda_i$. α_i is the corresponding eigenvector of K, satisfying $u_i = \sum_{j=1}^{l} \alpha_i(j)\phi(x_j)$ ($\alpha_i(j), j = 1,\ldots,l$ are the components of α_i). Furthermore, for assuring the eigenvectors of $\phi(x_t)$ is of unit length $u_i \bullet u_i = 1$, each α_i must be normalized using the corresponding eigenvalue by $\tilde{\alpha}_i = \frac{\alpha_i}{\sqrt{\tilde{\lambda}_i}}$.

And then, based on the estimated α_i, the principal components for x_t is calculated by

$$s_t(i) = u_i^T \phi(x_t) = \sum_{j=1}^{l} \tilde{\alpha}_i(j) K(x_j, x_t), i = 1,\ldots,l \tag{9}$$

In addition, for making the sample input vectors in (X$\phi(x_t)$ centered I$\sum_{t=1}^{l} \phi(x_t) = 0$, in equation (9), the kernel matrix on the training set K and on the testing set K_t are, respectively, modified by

$$\tilde{K} = \left(I - \frac{1}{l}1_l 1_l^T\right) K \left(I - \frac{1}{l}1_l 1_l^T\right) \tag{10}$$

$$\tilde{K}_t = \left(K_t - \frac{1}{l}K 1_t 1_l^T\right)\left(I - \frac{1}{l}1_l 1_l^T\right) \tag{11}$$

where I is l-dimensional identity matrix. l_t is the number of testing data points. 1_l and 1_{l_t} represent the vectors whose elements are all ones, with length l and l_t, respectively. K_t represents the $l_t \times l$ kernel matrix for the testing data points.

From Eq. (9), it can be found that KPCA can extract more number of principal components than PCA as the maximal number of principal components in KPCA is l, instead of m. Same as PCA,

the dimension of s_t can also be reduced in KPCA if only considering the first several eigenvectors. By using the kernel method to implement nonlinear PCA, the other properties of PCA as described in (7)-(9) are all retained in KPCA except these characteristics are considered in $\phi(x_t)$. And then the K-nearest contents:

Firstly character words of training documents are extracted from KPCA, and the vector space model is constructed.

Secondly, determine the new text vector after the arrival of the new text, according to the key new text participle.

Thirdly, focus on the training selected text in the new text which is most similar to K text, and the calculation formula is:

$$Sim(d_i, d_j) = \frac{\sum_{k=1}^{M} W_{ik} \times W_{jk}}{\sqrt{(\sum_{k=1}^{M} W_{ik}^2)\left(\sum_{k=1}^{M} W_{jk}^2\right)}} \tag{12}$$

In the field of the new text of K, in turn, calculate the weight of each type, computation formula is as follows:

$$p\left(\overline{x}, C_j\right) = \sum_{\overline{d_i} \in KNN} Sim(\overline{x}, \overline{d_i}) y(\overline{d_i}, C_j) \tag{13}$$

Based on KPCA and KNN fault detection techniques

In order to verify the effectiveness of the method, the bearing fault device was designed in this paper. The experimental setup mainly included a motor, a torque transducer and a dynamometer. The motor shaft was supported by bearings with the type of 6205-2RS JEM SKF[6]. The bearing inner race, outer race and rolling element were artificially seeded a single point fault by electro-discharge machining respectively. For an inner race localized fault, a rolling element localized fault and an outer race localized fault, the accelerometers were used to sample vibration signals at 12kHz and installed at 12 o'clock, 3 o'clock and 6 o'clock positions at the drive end respectively. The specification of bearing data is listed in Table.1.

Table.1 The specification of bearing data

Bearing fault type	Speed (r/min)	Bearing failure size (cm)		Code
		Diameter	Depth	
Normal state	1795	-----	-----	1
Inner ring fault Level 1	1795	0.018	0.028	2
Out race fault	1795	0.018	0.028	3
Rolling element failure	1795	0.018	0.028	4
Inner ring fault Level 2	1795	0.036	0.028	5
Inner ring fault Level 3	1795	0.054	0.028	6

Four kinds of bearing status signals, the normal state, the inner ring and outer fault fault, rolling element failure data, the current signal of the bearing vibration signal data diagnosis.

Choose speed as N = 1797 r/min four different state bearing vibration signals such as above as the original data. In order to improve the resolution of classifier accuracy, test the performance of the network, this paper will not use the measured signal directly, but to these kinds of fault data signal processing, network as the input data.The state of each bearing a whirl number as a set of sample, each state take 30 group, write a small program calculation each group signal 13 attributes, take these feature attribute data as a network of sample data, the former and group as the training sample, after 10 group as test samples, these attributes calculation expression is as follows:

mean absolute difference, greatest peak, root mean square value, rad amplitude, variance, peak-to-peak value, skewness, kurtosis, peak factor, waveform index, impulse factor, clearance factor, kurtosis value.

Integration of these feature attribute data, a total of 120 sets of data were four categories, as fault diagnosis of input data. This section the use of training and testing data for 120 * and matrix. Each running status before each take twenty and data matrix as the training sample, a normal condition as a category, class label mark categories for digital 1; Twenty inner ring fault samples as a category, class label mark categories for digital 2; Twenty rolling element fault samples as a category, class label mark categories for digital 3; Twenty outside fault samples as a category, class label mark categories for number 4. Inner ring fault Level 2,numer 5, Inner ring fault Level 3,number 6. A total of 80*80 group of 13 data matrix, as a network of training sample. Take the rest of the four types of 10 * and data matrix as for classification of the test sample.

Test results

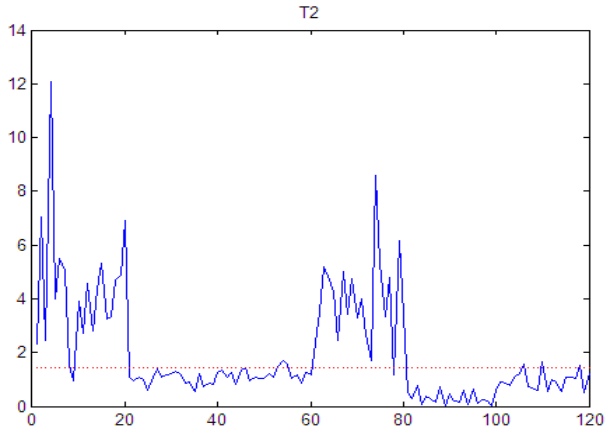

Fig.1 T^2 statistics in the feature space

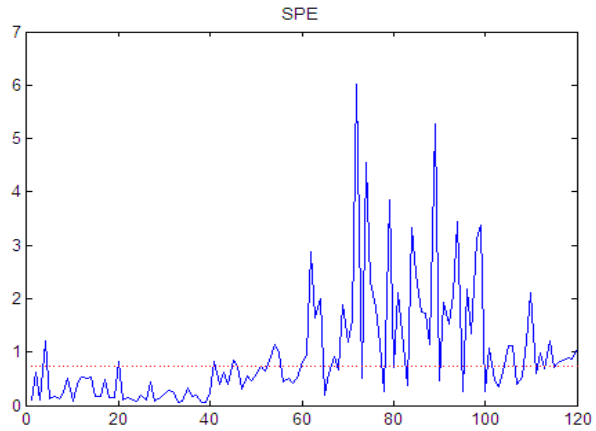

Fig.2 SPE statistics in the feature space

In this approach, the integral operator kernel functions is used to realize the nonlinear map from the raw feature space of vibration signals to high dimensional feature space, and structure T^2 and SPE statistics in the feature space to extract the feature vector from the fault signal with the principal component analytic method. And the figure is shown in Fig.1 and Fig.2. Raw data As indicated in Figure12 bearing the four fault signal data, inner ring fault level two data signal and inner ring fault level three data signals, bearing the lap data for a sample of (512), the above equation 12-24 , 13 characteristic parameters, feature extraction, training sample were 120 groups, training and test samples taken 60 group, diagnose, diagnosis above flowchart design result is shown in Fig.3.

The diagnostic accuracy rate is 96.67%, a full description of the kernel principal component analysis and k-nearest neighbor method in the validity of the fault diagnosis.

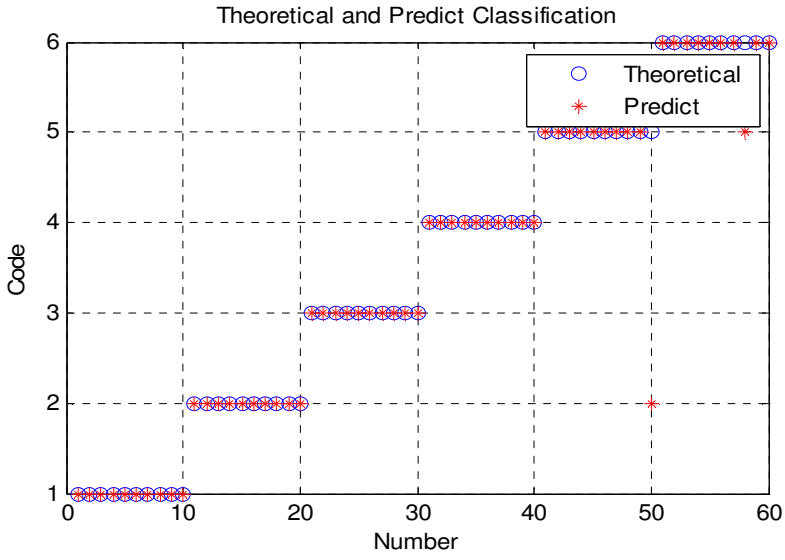

Fig.3 The diagnosis results of combining KPCA and KNN

Conclusion

In this approach, the integral operator kernel functions is used to realize the nonlinear map from the raw feature space of vibration signals to high dimensional feature space, and structure T^2 and SPE statistics in the feature space to extract the feature vector from the fault signal with the principal component analytic method. Assessment method using the feature vector of the Kernel Principal Component Analysis, and then enter the sensitive features to K-Nearest Neighbor classification. The experimental results indicated that this method has good accuracy.

Acknowledgement

Thanks for the support of National Natural Science Foundation of China (No.51179197), and State Key Laboratory of Ocean Engineering (Shanghai Jiao Tong University)(No.1009).

References

[1] He Qian, Yi-bing Liu, Peng Lv, Kernel Principal Components Analysis for Early Identification of Gear Tooth crack[C] Proceedings of the 6th World Congress on Intelligent Control and Automation, June, 2006, Dalian, China.

[2] Gu Jun. Research on Intrusion Detection System Based on KPCA and SVM.[J]Journal of Computer Simulation, 2010, 27(7): 105-107.

[3] Liu Ailun.Fault diagnosis of complex chemical process based on KPCA-SVC[J]Chinese Journal of Scientific Instrument, 2007, 28(5): 870-875.

[4] TIAN Zhong—da，GAO Xian—wen. Networked control system time。delay prediction method based on KPCA and LSSVM[J] Systems Engineering and Electronics, 2013, 35(6): 1281-1286.

[5] LI Taifu, YI JUN. Variable Selection for Nonlinear Modeling Based on False Nearest Neighbours in KPCA Subspace [J]JOURNAL OF MECHANICAL ENGINEERING, 2012, 48(10): 192-199

[6] CWRU, Bearing Data Center: http://csegroups.case.edu/bearingdatacenter/home. (Last visit, March. 21, 2012)

Advanced Materials Research Vols. 986-987 (2014) pp 1497-1501

doi:10.4028/www.scientific.net/AMR.986-987.1497

Fault Diagnosis of Communication Equipment Based on Rough Set Theory

Hai-yan ZHAO[1,a] Lin-hao HUANG[1,b] Zheng-xi XIE[1,c] Gu-sheng WEN[1,d]

[1]Wuhan Mechanical Technology College, Wuhan , 430075 , China

[a]email: haiyanzhao1979@foxmail.com, [b]email: Luckhuang137@163.com,

[c]email: xiezx2000@163.com, [d]email: wgswgs451@tom.com

KeyWords: rough set theory; fault diagnosis; decision rules

Abstract. According to the communication equipment fault characteristics of complexity, hierarchy, relevance, delay and uncertainty, the method of extracting diagnosis rules based on rough set is presented in order to obtain diagnostic decision rules with good adaptability and maximum matching capabilities. This method can process a large amount of fault data and it can reduce both attribute and attribute value.4 evaluations are selected to evaluate the effectiveness and reasonableness of decision rules, and finally core value table of decision rules which has a certain ability to adapt. Example shows that this method can remove noise in fault diagnosis sample, reduce the computation and improve the efficiency of diagnosis effectively.

Introduction

In the field of knowledge-based intelligent fault diagnosis, the purpose of diagnosis rule extraction is to find fault diagnosis reasoning guiding rules from a large number of fault sample data[1].

In 1982, Polish scholars Z.Pawlak proposed Rough Set theory to research incomplete data, inaccurate knowledge representation, learning, and the method of induction[2]. Its characteristics are the basis of the measured data does not require any additional information or prior knowledge, it can effectively extract useful information and streamline information processing[3]. Thus, relative to other methods dealing with uncertain knowledge, Rough Set theory is more practical.

Communication equipment is electronic equipment, its fault has the characteristics of complex, hierarchical, relevance, delay and uncertainty, and it is significantly different with mechanical equipment failures. In order to have a good adaptation decision rules for fault diagnosis ability and maximum matching ability, combining with the fault characteristics of communication equipment, the method of rules extraction for fault diagnosis based on Rough Set theory is proposed in this paper. Firstly, this method preprocess original data and the decision table is formed, then attribute reduction and value reduction to delete redundant attributes by Rough Set theory, and finally extract the fault diagnosis decision-making rules.

1 Establishing fault diagnosis decision table based on Rough Set theory

(1) Attribute definition

In Rough Set theory, in order to better handle data, the data and knowledge we obtained must be formulated. Because the basic components of knowledge expression system is a collection of study, knowledge about the object is described by their basic properties and the object attribute values, so the data table can also be expressed as a knowledge system with the formula S:

$S=<U, C, D, V, f>$

Where U is the study universe, that is a collection of research subjects, $C \cup D=R$ is a set of attributes, subset C and D are respectively called condition attribute set and result attribute set, $V= \cup v_r$, $r \in R$ is the collection of property values, v_r represents the value range of one attribute $r \in R$, f defines an information function, namely $f: U \times R \rightarrow V$, which specifies the property value of each object x of U. Therefore, a knowledge system S expressed in the form of a table can sometimes called decision table.

In fault diagnosis rules of communications equipment, the priori conditions are generally the measured technical parameters, and the technical parameters correspond to the condition attribute C in decision table. Most of the posterior conditional rules said the cause of the fault or parts, corresponding to the decision attribute D. Condition attributes C and decision attributes D should satisfy $C \cap D = \Phi$, and $C \cup D = R$, R is the set of all attributes in decision table.

(2) Discrete normalization processing of property value

In intelligent information processing, description of things' properties may be qualitative description or quantitative data. In Rough Set theory, this description are treated as a database, we extract useful information, infer decision rules, and ultimately applied it to the system. Because the decision is based on the finite-dimensional discrete data tables, therefore, the data should be normalization processed. If the qualitative and quantitative description of the attribute values are continuous, the data processing is called discrete normalization.

Discrete normalization method should satisfy the following two points:

① After discrete normalizing, kind of attribute values as little as possible;

② After discrete normalizing, minimize the loss of information.

2 Diagnostic rule extraction method based on Rough Set

(1) Attribute Reduction

For a description of a system, the more the system parameters used, the more profound the system is understand. However, if you use too many system parameters as data identification information, it will take up a lot of storage space and processing time. The large number of system parameters certainly contains many relevant factors, which is repeated and waste, so the problem of how to delete and simplify redundant information exists.

For communication devices, the purpose of reduction to the technical parameters of decision-fault type is to remove redundant parameters. Firstly, decision table condition attributes are reduction, namely the elimination of a column in the decision table. There are various ways to reduction decision table, here we use the method of distinguish matrix to reduction, re-organization decision table based on the condition attribute after reduction, and the duplicated rows in the decision table should be deleted.

After attribute reduction, decision tables can be viewed as a set of decision rules, and each decision rule corresponds to a fault instance, this decision rule can be further generalized value reduction.

(2) Reduction in property values

For the decision table, the attribute value reduction is the reduction of the decision-making rules. Using the decision logic, namely the elimination of unnecessary conditions for each decision rule decision algorithm, not the overall reduction properties, but for every decision rules, removing redundant attributes express the value of the rules, in order to further make the smallest decision algorithm of the rules thus obtained as the maximum of generalized rules are usually referred to as the rule.

(3) Evaluation of diagnostic rules

In general, after the attribute reduction and attribute value reduction, according to the resulting diagnosis rules extracted, the diagnosis can be stored in the knowledge base is used as a diagnostic knowledge. However, because there is a lot of noise in the sample data, some diagnostic rules may only data derived from a small sample, if the sample data is incomplete, the corresponding diagnostic rules will not be reliable. Therefore, in practical applications, we must first evaluate the knowledge of the rules, and then decide whether to retain, thereby enhancing the rule of knowledge acquired anti-jamming capability.

Let $R=\{r_1, r_2, \ldots, r_k\}$ be the set of decision rules obtained after the reduction, each r_i has identified a sequence $c_1(r_i), c_2(r_i), \ldots, c_n(r_i), d_1(r_i), d_2(r_i), \ldots, d_m(r_i)$, where $C' = \{c_1(r_i), c_2(r_i), \ldots, c_n(r_i)\}$ is a subset of the fault symptom attribute set C, $D=\{d_1(r_i), d_2(r_i), \ldots, d_m(r_i)\}$ is the decision attribute collection. This sequence is known by the decision rules r_i induction is defined as: $c_1(r_i), c_2(r_i), \ldots, c_n(r_i) \rightarrow d_1(r_i), d_2(r_i), \ldots, d_m(r_i)$.

①Several concepts

In order to evaluate the diagnostic decision rules, several related concepts are introduced.

Ⅰ. Support

Support is defined as:

$sup(r_i)=stre(r_i)/card(U)$ （1）

Where U is the object of the discussion on the field, $stre(r_i)$ is the number of rules to support the decision-making table r_i, the object property values and the number of instances of decision tables and rule matching, so $sup(r_i)$ defines the strength of the decision rules r_i.

Ⅱ.Consistent degree

Coincidence decision rules r_i certainty factor is also known, which is defined as:

$cer(r_i)=card(C'(r_i)\cap D(r_i))/card(C'(r_i))$ （2）

Where $card(C'(r_i))\neq 0$, $card(C'(r_i)\cap D(r_i))$ is the number of instances, which satisfy the condition part $C'(r_i)$ and the decision part $D(r_i)$ of rule r_i , $card(C'(r_i))$ is the number of instances which satisfy the condition part of the rule r_i. Therefore, in the fault diagnosis decision table, consistent degree reflects the credibility of ri.

Ⅲ.Coverage

Since the consistent degree can only evaluate the probability of getting the correct conclusion, and the decision rule can not be expressed in the same degree of coverage of the decision, i.e., the number of decision making rules are the same obtained based on examples. Therefore, introducing the concept of coverage, which is defined as follows:

$cov(r_i)=card(C'(r_i)\cap D(r_i))/card(D(r_i))$ （3）

Where $card(D(r_i))\neq 0$， $card(C'(r_i)\cap D(r_i))$ are the same as defined above, $card(D(r_i))$ is the number of instances $D(r_i)$ which satisfy the rule r_i. Thus, in the entire fault diagnosis decision-making table, coverage expressed support instance r_i proportion that reflects the degree of coverage of r_i.

Ⅳ.Dependence

To study how to export results attribute set D from the properties conditions set C' , we must study the degree D rely on C'. In order to measure the dependence of knowledge, dependency is defined as follows:

$k=r_{C'}(D)=card(POS_{C'}(D))/card(U)$ （4）

How to investigate whether the decision-making table of knowledge system is coordinating? The method is to calculate the condition attributes and decision attribute dependence k. If k is less than 1, which means that the decision-making results inconsistent, if k equals to 1, it means that the results fully coordinated decision-making.

②Rule evaluation

Consistent rules reflect the possibility of the rule establishment based on the establishment of the rule antecedent parts. When the coincidence degree is less than 1, indicating that the rule is satisfied in the front member, a plurality of possible conclusion, and this reflect the inconsistencies of rules.

Coverage is the proportion of data objects which satisfied the antecedent and the consequent. If the coverage is too small, the rule is not representative of data, thereby exhibiting a certain degree of randomness, randomness is too large, the ability to predict the classification of the new data object will be greatly reduced.

So we hope to get the rules with both high degree of accuracy and high degree of coverage, that is to say, two uncertainties of inconsistency and randomness are eliminated to some extent.

According to the characteristics of the actual test data and diagnostic rules knowledge base, this paper proposes a method of diagnostic rule evaluation, specific steps are as follows:

Ⅰ. First check whether the rule has a certain degree of support γ, desirable $\gamma > 1\%$;

Ⅱ. Check whether there is sufficient support for the rule of consistent class degree α, desirable $\alpha > 60\%$;

Ⅲ. Check whether there is sufficient coverage β, desirable β> 10%;

Ⅳ. If the knowledge meet the above three diagnostic rules, deposited it into the diagnosis rules knowledge base;

Ⅴ. Calculation condition attributes and decision attribute dependence k is 1 to examine the decision-making table is coordinated diagnostic rules.

Screening based support makes preliminary selected fault data set has a representative; screening coincidence makes the diagnosis based on the rule has a certain consistency; screening coverage eliminates the diagnosis based on the rule of randomness; calculation depends overall coordination of the study is the decision-making table.

3 Communications equipment fault diagnosis based on Rough Set theory

Communication devices are electronic devices, whose failure has complexity, level, relevance and uncertainty. According to electronic equipment failure signs and failure characteristics, this paper proposes a method to extract diagnostic rules based on Rough Set.

According to the data recorded in the repair process of communication device, we construct the following information system $S=(U, A\cup d)$, a_i represents a different type of communication device fault state, and $i=1, 2, \ldots, 8$; $A=\{a_1, a_2, \ldots, a_8\}$ said condition attributes, here take the measured parameters when the communication equipment is failure, namely: +5V voltage a_1, +27V voltage a_2, transmitter +24V voltage a_3, the frequency of loss of lock indication a_4, mismatch instructions a_5, transmitter power a_6, noise ratio a_7 and maximum volume a_8. d is the decision attribute, there are seven possible decision values: 1-+5V power supply failure, 2-+27V power supply failure, 3-+24V power failure, 4-frequency loss of lock, 5-receiver failure, 6-transmitter failure and 7-antenna failure.

$A=\{a_1, a_2, \ldots, a_8\}$ is the selected condition attribute, when the device is correct, the respective normal phenomena or indicators are shown in Table 1.

Tab.1 Phenomenon or Indicators When Condition Attribute is Normal

	a_1	a_2	a_3	a_4	a_5	a_6	a_7	a_8
Phenomenon or Indicators When Condition Attribute is Normal	Red Zone	Red Zone	Red Zone	Lights off	Lights off	Middle: 3W~8W High: 20W~45W	⩾23.5dB	⩾7V

When extracting failure feature using Rough Set Theory, detected data should be normalized first, eligible denoted by the number 1, does not meet the conditions referred to as the number 0. After normalization, the data was identity to facilitate subsequent processing.

38 groups of failure data was recorded, due to limited space, they are not listed here all, after normalization and attribute reduction, we obtained the decision table as shown in Table 2.

Tab.2 Decision table after pretreatment

N	*a*	*a*	*a*	*a*	*a*	*a*	*a*	*a*	*d*
1	0	1	1	0	1	1	0	0	1
2	1	0	1	0	1	1	0	0	2
3	1	1	0	1	0	0	1	1	3
4	1	1	1	0	1	1	0	0	4
5	1	1	1	1	0	1	0	0	5
6	1	1	1	1	1	0	1	1	6
7	1	1	1	1	0	1	1	1	7

Further simplification of planning decisions, the core values of decision rules is obtained as shown in Table 3.

Tab.3 Core values statement of decision rules

N	*a*	*a*	*a*	*a*	*a*	*a*	*a*	*a*	*d*
1	0	-	-	-	-	-	-	-	1
2	1	0	-	-	-	-	-	-	2
3	1	1	0	-	-	-	-	-	3
4	1	1	1	-	1	-	-	0	4
5	1	1	1	-	0	-	-	0	5
6	1	1	1	-	-	0	-	1	6
7	1	1	1	-	-	1	-	1	7

With several concepts mentioned above to evaluate core values statement of decision rules in Table 3, each decision rule r_i's support, consistent coverage of both degree and listed in Table 4. Finally, after calculation, the dependence k of condition attributes and decision attributes is also 1, core values statement that the decision rule is coordination. Indicators above meet the method of rule evaluation, therefore, it can be used as a diagnostic knowledge base for troubleshooting diagnostic rules.

Tab.4 Table and Evaluation Rules

No.	Ruleset	Support	Consistent degree	Coverage
r_1	$a_1(0)\rightarrow d(1)$	0.50	0.75	0.75
r_2	$a_1(1)a_2(0)\rightarrow d(2)$	0.33	0.67	0.50
r_3	$a_1(1)a_2(1)a_3(0)\rightarrow d(3)$	0.60	0.75	0.75
r_4	$a_1(1)a_2(1)a_3(1)a_5(1)a_8(0)\rightarrow d(4)$	0.57	1	0.80
r_5	$a_1(1)a_2(1)a_3(1)a_5(0)a_8(0)\rightarrow d(5)$	0.50	1	0.60
r_6	$a_1(1)a_2(1)a_3(1)a_6(0)a_8(1)\rightarrow d(6)$	0.60	1	0.75
r_7	$a_1(1)a_2(1)a_3(1)a_6(1)a_8(1)\rightarrow d(7)$	0.67	1	0.67

4 Conclusions

Based on the characteristics of the communication equipment failure, a diagnostic extraction method was proposed based on Rough Set Theory. This method does not require any additional information and a priori knowledge, first of all, a lot of the original fault data processing, decision rules to get the core value table, then four evaluation of decision rules to evaluate the validity and reasonableness elect fault diagnosis decision rule has some ability to adapt. Troubleshooting different from other extraction methods, this method can effectively remove noise troubleshooting sample. Stored in the knowledge base of the final diagnosis diagnostic rules can reduce the amount of computation fault diagnosis, greatly improving the efficiency of fault diagnosis.

References

[1] Xiao Xiaofeng, Electronic Equipment Diagnostics Rough Set Theory to Extract Rules [J], Fire and Command Control, 2007.12.

[2] Zeng Huangl, Intelligent Computing [M], Chongqing: Chongqing University Press, 2004.

[3] Zhang Dengfeng, Rroubleshooting Knowledge Extraction Method Based on Probability Rough Set Theory [J], Journal of Scientific Instrument, 2004.10.

[4] An Liping, Knowledge-based Expert System to Get Rough Sets, Update, and Reasoning [J], Computer Engineering and Design, 2004.01.

[5] SU Xin, Xu Xi-bin. Software Radio Theory and Technology [M]. Beijing: People's Posts and Telecommunications Press, 2010.

Advanced Materials Research Vols. 986-987 (2014) pp 1502-1505

doi:10.4028/www.scientific.net/AMR.986-987.1502

Fault Location Based on Bayesian Classifier

Lijun QIN[1, a], Jingjin CAO[2, b]

[1]Institute of Electrical and Electronic Engineering, North China Electric Power University, Beijing,102206,China

[2]Institute of Electrical and Electronic Engineering, North China Electric Power University, Beijing,102206,China

[a]email: qin3388@sina.com, [b]email: caojingjin0123@163.com

Keywords: Bayesian Classifier; Fault Location; Power System

Abstract. When a node of power system have a failure, we can deal with it by the multi-time electrical comprehensive phasor data of each node before and after the failure, introduces Bayesian Classifier to handle with the node failure case so as to distinguish and locate fault. Experiments show that Bayesian classifier is an effective method in fault location.

Introduction

Traditional classification methods often does not involve the overall distribution characteristics[1], its shortcomings are obvious: First, the traditional classification methods has nothing to do with the overall size of opportunity; Secondly, classification methods does not consider the loss caused by mistake, in some cases, the unreasonable results may occur. And Bayesian classifier is to solve the above two problems and developed on them.

In Bayesian statistics, it is always assumed that objects have a certain understanding of research, and describe the knowledge with the prior probability distribution; Then, modify priori knowledge based on extraction of sample and get a posteriori probability distribution, but the realize of a variety of statistical inference is based on the posterior distribution[2]. We can get the Bayesian classifier analysis by using the ideas of the Bayesian statistical classifier analysis.

Bayesian Classifier

Assume that there are two l universes Ω_1, Ω_2, and the corresponding probability density respectively are $f_1(x), f_2(x)$, the prior probability of two universes Ω_1, Ω_2 respectively are:

$$p_1 = P(\Omega_1), \quad p_2 = P(\Omega_2) \tag{1}$$

According to the basic requirement of the Bayesian classifier statistics[3], $p_1 + p_2 = 1$.

For some l dimensions index observation $x = (x_1, x_2, \cdots, x_l)^T$ in l European space R^l, classifying a sample by using classified rule is essentially a division of space R^l by a classified method ,we call them B_1, B_2, and they satisfy the following conditions:

$$B_1 \bigcup B_2 = R^l, \quad B_1 \bigcap B_2 = \varnothing \tag{2}$$

In Bayesian classifier analysis, a division of $R = (R_1, R_2)$ is actually the same with a criterion. Furthermore, based on the criterion R, if the samples from Ω_1 but mistaken for Ω_2, the probability is:

$$P(2 \mid 1, R) = \int_{B_2} f_1(x)\mathrm{d}x \tag{3}$$

If the samples from Ω_2 but mistaken for Ω_1, the probability is:

$$P(1 \mid 2, R) = \int_{B_1} f_2(x)\mathrm{d}x \tag{4}$$

We define the loss because of the mistake of classifying the sample in Ω_j which come from Ω_i as $L(j|i)$ in the form of notation, obviously:

$$L(1|1)=L(2|2)=\cdots=L(i|i)=L(j|j)=0 \tag{5}$$

Bayesian classifier is to look for $R=(B_1,B_2)$ to reach the smallest average misjudgment loss.

For a new sample x,we can get the posterior probability of Ω_1,Ω_2 respectively based on Bayesian posteriori criterion：

$$\begin{cases} P(\Omega_1|x)=\dfrac{p_1f_1(x)}{p_1f_1(x)+p_2f_2(x)} \\ P(\Omega_2|x)=\dfrac{p_2f_2(x)}{p_1f_1(x)+p_2f_2(x)} \end{cases} \tag{6}$$

Meanwhile，the two universes' Bayesian Classifier criterions in the case of misjudgment damage equivalent are as follows：

$$\begin{cases} x\in\Omega_1,\ if\ P(\Omega_1|x)\geq P(\Omega_2|x) \\ x\in\Omega_2,\ if\ P(\Omega_1|x)<P(\Omega_2|x) \end{cases} \tag{7}$$

Then the optimal partition R can realize misjudgment minimum：

$$p^*=p_1P(2|1,R)+p_2P(1|2,R) \tag{8}$$

If $L(2|1)\neq L(1|2)$, the average loss of Ω_1 and Ω_2 caused by misjudgment are respectively:

$$\begin{aligned} &\overline{L}(1,R)=L(2|1)P(2|1,R) \\ &\overline{L}(2,R)=L(1|2)P(1|2,R) \end{aligned} \tag{9}$$

Combined with the prior probability p_1,p_2, the comprehensive average loss caused by misjudgment can be expressed as:

$$\begin{aligned} \overline{L}&=p_1\overline{L}(1,R)+p_2\overline{L}(2,R) \\ &=L(2|1)p_1P(2|1,R)+L(1|2)p_2P(1|2,R) \end{aligned} \tag{10}$$

So, in order to achieve the minimum of comprehensive average loss $\overline{L}$ for misjudgment, optimal classifications at this time are:

$$\begin{cases} B_1=\{x:\ L(2|1)P(\Omega_1|x)\geq L(1|2)P(\Omega_2|x)\} \\ B_2=\{x:\ L(2|1)P(\Omega_1|x)<L(1|2)P(\Omega_2|x)\} \end{cases} \tag{11}$$

Particularally, when $p_1=p_2$ and $L(2|1)=L(1|2)$,

$$\begin{cases} B_1=\{x:\ f_1(x)\geq f_2(x)\} \\ B_2=\{x:\ f_1(x)<f_2(x)\} \end{cases} \tag{12}$$

It Correspond to the likelihood ratio criterion using implement classifier classification.

In terms of normal population，assume two universes Ω_1,Ω_2 have the same covariance matrix Σ, then the corresponding probability density is as follows:

$$f_j(x)=\frac{1}{(2\pi)^{\frac{p}{2}}|\Sigma|^{\frac{1}{2}}}\exp\{-\frac{1}{2}(x-\mu_j)^T\Sigma^{-1}(x-\mu_j)\},\ j=1,2 \tag{13}$$

In order to achieve the minimum of comprehensive average loss $\overline{L}$ for misjudgment, by the Bayesian posterior probability criterion, we can get[4]:

$$\begin{aligned} B_1&=\{x:-\frac{1}{2}(x-\mu_2)^T\Sigma^{-1}(x-\mu_2)+\ln p_2\leq-\frac{1}{2}(x-\mu_1)^T\Sigma^{-1}(x-\mu_1)+\ln p_1\} \\ B_2&=\{x:-\frac{1}{2}(x-\mu_2)^T\Sigma^{-1}(x-\mu_2)+\ln p_2>-\frac{1}{2}(x-\mu_1)^T\Sigma^{-1}(x-\mu_1)+\ln p_1\} \end{aligned} \tag{14}$$

Thereupon,

$$\begin{cases} F_1(x) = a_1^T x + b_1,\ a_1 = \sum^{-1} \mu_1, b_1 = -\dfrac{1}{2}\mu_1^T \sum^{-1} \mu_1 + \ln p_1 \\ F_2(x) = a_2^T x + b_2,\ a_2 = \sum^{-1} \mu_2, b_2 = -\dfrac{1}{2}\mu_2^T \sum^{-1} \mu_2 + \ln p_2 \end{cases} \tag{15}$$

That is,

$$\begin{aligned} B_1 &= \{x : F_1(x) \geq F_2(x)\} \\ B_2 &= \{x : F_1(x) < F_2(x)\} \end{aligned} \tag{16}$$

Finally, under the condition of satisfying the population variance homogeneous, Bayesian classifier criterions of two normal populations are as follows:

$$\begin{cases} x \in \Omega_1,\ if\ F_1(x) \geq F_2(x) \\ x \in \Omega_2,\ if\ F_1(x) < F_2(x) \end{cases} \tag{17}$$

In Bayesian classifier analysis of actual problems, the mean and variance of overall are often unknown, we usually use the mean and variance of sample estimates, the general forms are as follows:

$$\begin{cases} \hat{F}_1(x) = \hat{a}_1^T x + \hat{b}_1, & \hat{a}_1 = S^{-1}\overline{x^{(1)}}, \hat{b}_1 = -\dfrac{1}{2}(\overline{x^{(1)}})^T S^{-1}\overline{x^{(1)}} + \ln p_1 \\ \hat{F}_2(x) = \hat{a}_2^T x + \hat{b}_2, & \hat{a}_2 = S^{-1}\overline{x^{(2)}}, \hat{b}_2 = -\dfrac{1}{2}(\overline{x^{(2)}})^T S^{-1}\overline{x^{(2)}} + \ln p_2 \end{cases} \tag{18}$$

Then optimal criterion based on the Bayesian theorem under the sample estimate parameters is:

$$\begin{cases} x \in \Omega_1,\ if\ \hat{P}(\Omega_1 | x) \geq \hat{P}(\Omega_2 | x) \\ x \in \Omega_2,\ if\ \hat{P}(\Omega_1 | x) < \hat{P}(\Omega_2 | x) \end{cases} \tag{19}$$

The basic principle of Bayesian classifier is to treat several groups as subspace distribution in space of the research object, and each object of study is an observation point in the space. Under the condition of considering the premise of the prior probability, classification function can be built based on Bayesian classifier analysis principle, according to some rules, and then further calculating various research object into a subspace or certain other probability[5]. So when an object has a maximum probability of subspace or categories, we can determine the sample's the type of subspace or categories. Fault location component should first divide electrical components into fault component class and non-fault class under two types of a priori information, using PMU's voltage or current information of the entire network, using classification analysis of each node based on Bayesian principles build classification function analysis, finally determine the node that belongs to the fault class.

Test results

We make research on the 3 phase symmetry short circuit fault in node Bus19 of the IEEE 30 system. The linear classifier function coefficient can be calculated by Bayesian classifier analysis theory, then we can further established linear classifier model of fault nodes and non fault nodes as follows:

$$\begin{cases} F_1(x) = -279.476 + 598.987x_1 - 109.659x_2 \\ F_2(x) = -239.783 + 532.501x_1 - 80.021x_2 \end{cases} \tag{20}$$

Furthermore, for each node，we can calculate the posterior probability and posterior probability corresponding belonging to fault class and non fault class through the classification function. On the basis of the comparison of two classes of posteriori probability, we can classify the corresponding node points into the probability value of the largest group, the corresponding classification results are as shown in Table 1.

Table 1 The corresponding posterior probability and categories of IEEE30 node system under the situation of three-phase short-circuit fault for all nodes

Node	The Actual Fault Type	Posterior Probability		Fault Category
		Fault	Non-fault	
Bus-1	N	0	1.0000	N
Bus-2	N	0.00013	0.9989	N
Bus-3	N	0.1546	0.8454	N
Bus-4	N	0.00001	1.0000	N
Bus-5,6,7,8,9, 10,11,12,13	N	0	1.0000	N
Bus-14	N	0.00001	0.99999	N
Bus-15	N	0.0001	0.99992	N
Bus-16	N	0.00087	0.99913	N
Bus-17	N	0.90076	0.09924	N
Bus-18	N	0	0.99952	N
Bus-19	F	1.0000	0	F
Bus-20	N	0.90076	0.09924	F
Bus-21	N	0.00003	1.0000	N
Bus-22,23	N	0	1.0000	N
Bus-24	N	0.00042	0.9996	N
Bus-25	N	0.00006	0.9999	N
Bus-26	N	0.0015	0.9985	N
Bus-27	N	0.05881	0.9412	N
Bus-28	N	0.00001	1.0000	N
Bus-29,30	N	0	1.0000	N

System simulation experiment shows that the node fault location scheme based on Bayesian Classifier analysis theory is effective and feasible, and because the consideration of priori knowledge and a posteriori probability of the research object at the same time, node fault location results are more reliable.

Conclusion

Fault location component should first divide electrical components into fault component class and non-fault class under two types of a priori information, using PMU's voltage or current information of the entire network, using classification analysis of each node based on Bayesian principles build classification function analysis, finally determine the node that belongs to the fault class by the analysis of probability of various nodes belonging to the fault component class and the non-fault class. Experiments show that Bayesian Classifier is an effective method in fault location.

References

[1] Cheng Jie. Learning Bayesian networks from data: an information- theory based approach[J]. Artificial Intelligence, 2002, 137(1, 2):43~90.

[2] Nir Friedman. Bayesian network classifiers[J]. Machine Learning, 1997, 29:131~163.

[3] Mao Guojun. Principle and algorithm of data mining [M]. Beijing: Tsinghua University Press, 2011.

[4] Zhang Jinfang. Power network topology identification and fault location method research quickly [D].Beijing: North China Electric Power University, 2012.

[5] David Heckerman. Learning Bayesian networks: the combination of knowledge and statistical data[J]. Machine Learning, 1995, 20:197~243.

Advanced Materials Research Vols. 986-987 (2014) pp 1506-1509

doi:10.4028/www.scientific.net/AMR.986-987.1506

Flow Measurement of Primary Air Containing Pulverized Coal with Simple Venturi Tube

Xingsen YANG[1, a], Jing YIN[2]

[1]Shandong Electric Power Research Institute, Jinan, 250002, China

[2]State Grid Technology College, Jinan, 250002, China

[a]email: yxs2002@vip.sina.com

Keywords: Primary Air; Measure; Venturi

Abstract. The flow measurement of primary air is very important for thermal power plants to maintain the safe state of operation. For direct firing pulverizing system, the measuring is essentially affected by pulverized coal particles. Abrasion and occlusion would bring great trouble to the measurement. Many measuring methods are invalid under that circumstance. Lots of efforts have been made to find appropriate ways to measure the flow of primary air containing pulverized coal. Venturi tube had been successfully used to measure the flow of air. If a venturi tube is used to measure the flow velocity of primary air, the differential pressure goes higher with the increase of the concentration of pulverized coal in the primary air. The neglect of the affection of pulverized coal on the measuring would result in remarkable deviation. With the aids of coal flow rate, a method of using venturi tube to measure the velocity of primary air containing pulverized coal was established. The affection of pulverized coal on flow measuring of primary air cannot be ignored.

Introduction

Primary air may contain pulverized coal. The flow measurement of primary air is very important for thermal power plants to maintain the safe state of operation. Online measuring systems were adopted in many power plants. It is relatively easier to measure the flow of clean air. For power plants with silo system, the velocity of primary air can be measured before it's mixed with pulverized coal. Thus the velocity measuring is carried out under the state of clean air. But for direct firing pulverizing system, the flow measuring is essentially affected by pulverized coal particles. The measuring position free of pulverized coal doesn't exist in such systems. Abrasion and occlusion would bring great trouble to the measurement. Many measuring methods are invalid under such circumstance.

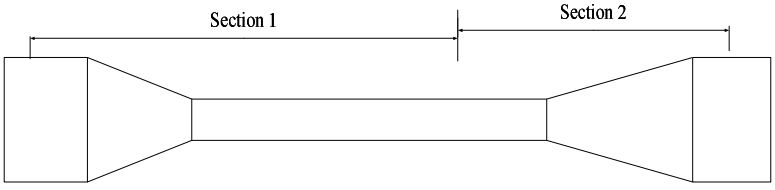

Fig.1 Sketch of Long Throat Venturi Tube

Many efforts have been made to find appropriate ways to measure the flow of primary air containing pulverized coal. As venturi tube had been successfully used to measure the flow of air, lots of attempts to use venture tube to measure gas-solid flow were made. Long throat venture tube [1][2][3][4][5] was studied and tested as an device to measure the concentration of pulverized coal in the primary air. But the venture tube that had been experimented, shown in Fig.1, was much longer than ordinary simple venturi tube. The flow resistance produced by such venturi tube would be bigger than usual. And the arrangement of such venturi tube would be difficult on site. Simple venturi tube, shown in Fig.2, which is used to measure the velocity of air was supposed to measure the flow of primary air containing pulverized coal and installed in certain power plant. Since the differential pressure goes higher with the increase of the concentration of pulverized coal in the

primary air, the measuring method should be alerted from the pattern of clean air measuring to fit the existence of pulverized coal. The deviation brought by the neglect of pulverized coal should be evaluated.

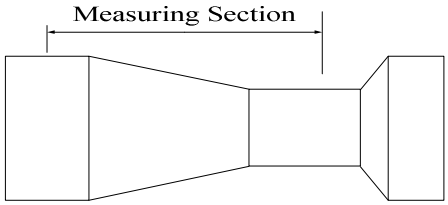

Fig.2 Simple Venturi Tube

Velocity Measuring Method

When clean air flows through a venturi tube, the differential pressure produced by the tube can be determined as:

$$\Delta P_a = k\frac{\rho V^2}{2} \quad (1)$$

In the type(1): ΔP_a stands for the differential pressure produced by the venturi tube with clean air; k stands for the coefficient for differential pressure; ρ stands for the density of air; V stands for the velocity of air flow.

When primary air containing pulverized coal flows through the same venturi tube with the same velocity *V*, the differential pressure can be determined as[1][5][6]:

$$\frac{\Delta P_m}{\Delta P_a} = 1 + f\mu \quad (2)$$

In the type(2): ΔP_m stands for the differential pressure produced by primary air containing pulverized coal; μ stands for the concentration of pulverized coal in the primary air, i.e. the mass of pulverized coal in 1kg of air; *f* stands for the coefficient of the venturi tube.

For direct firing pulverizing system, μ can be calculated as:

$$\mu = \frac{m_p}{\rho AV} \quad (3)$$

In the type(3): m_p stands for mass flow rate of pulverized coal; *A* stands for section area of the pipe.

From the above analysis, we can get:

$$\Delta P_m = k\tfrac{1}{2}\rho V^2(1 + \frac{fm_p}{\rho AV}) \quad (4)$$

Then the velocity can be got as:

$$V = \frac{\sqrt{f^2 m_p^2 + 8\frac{A^2}{k}\rho\Delta P_m} - fm_p}{2A\rho} \quad (5)$$

Type(5) can be used to measure the velocity of primary air containing pulverized coal. When the mass flow rate of pulverized equals zero, type(5) can be simplified as:

$$V = \sqrt{2\frac{\Delta P_m}{\rho k}} \quad (6)$$

Type(6) is just another form of type(1).

Measuring Deviation Analysis

In some power plants, venturi tube was installed to measure the velocity of primary air. But the calculation method that was used lost sight of the affection of pulverized coal, i.e. type(6) was used to calculate the velocity of primary air containing pulverized coal. The deviation brought by the method should be evaluated. Tab.1 shows the results of different methods.

Table 1 Results of Different Methods

Differential Pressure Pa	Result of Type(6) m/s	Result of Type(5) m/s
50	9.17	13.27
100	14.40	18.77
150	18.50	22.98
200	21.99	26.54
250	25.07	29.67
300	27.87	32.51
350	30.44	35.11
400	32.85	37.53

The parameters of the calculations in Tab.1 are given below:

k=0.56; f=0.8; A=0.1256m^2; ρ=1.014kg/m^3; m_p=1.6kg/s.

From Tab.1, we can see that the velocity deviation when the mass flow rate of pulverized coal equals 1.6 kg/s. The numerical number of deviation increases with the increase of differential pressure. But the relative deviation decrease with the increase of differential pressure. The relative deviation is within 14% to 44% in Tab.1. The deviation is intolerable. The affection of pulverized coal on the velocity measurement should be taken into account.

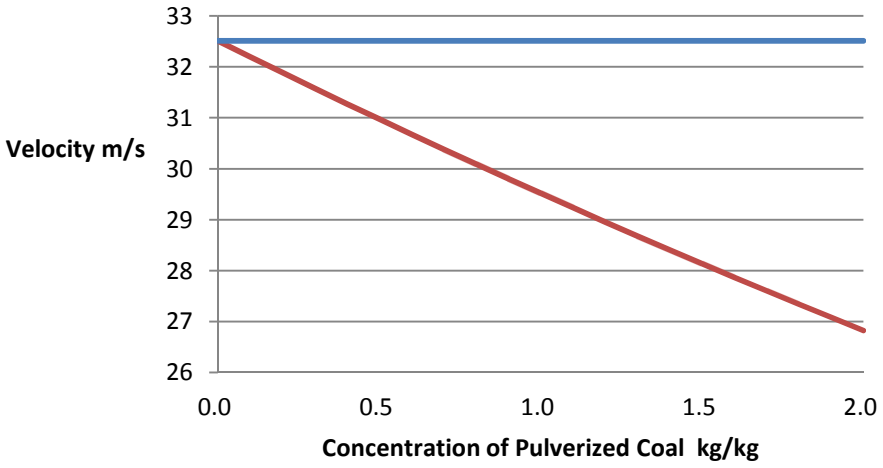

Fig.3 Velocity Variation with the Increase of Pulverized-Coal Concentration

Fig.3 and Fig.4 show the velocity variation got from type(5) and type(6) when the differential pressure equal 300Pa and 400Pa respectively. In that case, type(6) always gives the fixed value shown as the horizontal line in Fig.3 and Fig.4. The deviation between two methods is clearly shown in Fig.3 and Fig.4.

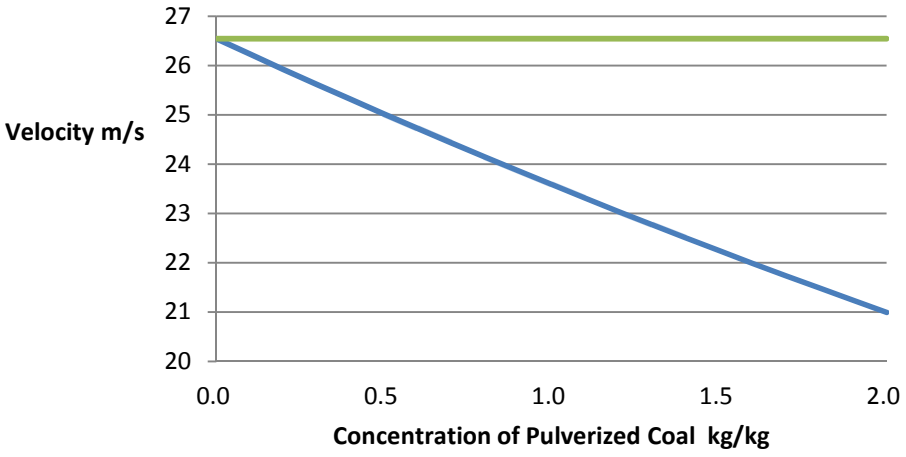

Fig.4 Velocity Variation with the Increase of Pulverized-Coal Concentration

Conclusion

If a venturi tube is used to measure the flow velocity of primary air, the differential pressure goes higher with the increase of the concentration of pulverized coal in the primary air. The neglect of the affection of pulverized coal on the measuring resulted in remarkable deviation. The affection of pulverized coal on flow measuring cannot be ignored. The measuring method of using simple venturi tube to measure the velocity of primary air should be alerted from the pattern of clean air measuring to fit the existence of pulverized coal. The method of using simple venturi tube to measure the velocity of primary air containing pulverized coal established by the paper gives the solution of the exact flow velocity. The application of the method would help to improve the accuracy of the flow measurement of primary air.

References

[1] Wang Wenqi, Yang Xingsen. Gas-Particles Measurement Using an Extended-Throat Venturimeter. Proceedings of the international Symposium on Measuring Techniques for Multiphase Flow, 1995.

[2] Xie Fei, Ding Yanjun, Wu Zhansong. Experimental Investigation of Pipeline Pulverized Coal Flow Measurements Using a Venturi Tube, J Tsinghua Univ (Sci & Tech), 2007,Vol.47.

[3] Xie Fei, Wu Zhansong. Numerical Simulation and Experimental Study of Gas-solid Two-phase Flow in Venturi Tubes. Joural of Power Engineering, April, 2007.

[4] Wu Zhansong, Xie Fei. Optimization of Venturi Tube Design for Pipeline Pulverized Coal Flow Measurements. J Tsinghua (Sci & Tech), 2007,Vol.47.

[5] Wang Wenqi, Hou Ming, Yu Rongxian. Measurement of Gas-Solid Flow Rate with an Extended-Throat Venturi Tube. J Southeast Univ, 1989.

[6] Farbar L. The Venturi as a meter for gas-solid Mixtures. Trans ASME, 1953.

Advanced Materials Research Vols. 986-987 (2014) pp 1510-1513

doi:10.4028/www.scientific.net/AMR.986-987.1510

Harmonic Detection in Power Signals Based on Fast Modified S-Transform

Guanqi LIU[1,a] , Lina WU[2,b], Zhaolei QIN[3,c]

[1,2,3] North China Electric Power University

Baoding China

[a]email: liu956888@163.com, [b]email: wlnlovely@163.com, [c]email: 993787002@qq.com,

Keywords: fast modified S-transform; harmonic detection; frequency; dynamic measurement

Abstract. In this paper, a new approach for harmonic detection in power signals based on fast modified S-transform (FMST) is proposed, which combines the advantages of the incomplete S-transform and the modified S-transform. Initially, the Fast Fourier Transform was performed and dynamic measurement values were obtained from the envelope of power spectrum, then the valid harmonic frequency points were detected by selecting the dynamic measurement values which were larger than the set thresholds. Further, the FMST was specifically performed on these major frequency points and a complex matrix was generated. The row vectors of the matrix reflected the phase and the time location information of harmonic disturbances, while the column vectors reflected the amplitude-frequency characteristics. And the feature vectors extracted from the complex matrix were used to detect the harmonic amplitude, phase and transient information. Simulation results validate the high accuracy, strong noise immunity and rapidity of the proposed approach.

Introduction

In recent years, with the rapid development of modern industry and power electronics technology, a large number of power electronic equipment are added into the power grid, which result in increased magnitude of harmonics and inter-harmonics. And these harmonic pollution will have a negative impact on power equipment, power quality and communication lines. Rapid and accurate harmonic detection is of great significance to the harmonic management.

The S-transform uses an analysis window whose width decreases with frequency for providing a frequency-dependent resolution. The S-transform has advantages in that it can extract large amounts of time-frequency characteristics and retain the absolute phase of each frequency [1]. These excellent performances contribute to its application for detection and analysis of harmonic disturbances in power signals. As the window function of S-transform is fixed, the time-frequency resolution changing trend remains unchanged, which limits its detection accuracy and positioning capability, and the detection results are sensitive to noise.

To circumvent this problem, another variant of the original S-transform known as modified S-transform (MST) is used in this paper. Since the harmonic detection is mainly for estimating the corresponding frequencies of harmonics, combing the idea of incomplete S-transform [2], this paper proposed a fast modified S-transform (FMST) for harmonic detection in power signals.

Fast Modified S-transform for harmonic detection

Modified S-transform. S-transform can be viewed as a frequency dependent short time Fourier transform or a phase corrected wavelet transform. The S-transform of a signal $h(t)$ is defined as

$$S(\tau, f) = \int_{-\infty}^{\infty} h(t)\omega(\tau - t, f)e^{-i2\pi ft}dt \tag{1}$$

where

$$\omega(t)=\frac{1}{\sigma\sqrt{2\pi}}e^{-\frac{t^2}{2\sigma^2}} \tag{2}$$

where f is the frequency, t is the time, the parameter τ is the center position of Gaussian window, and σ is the scale factor.

Reference [3] proposed and demonstrated that the modified S-transform can better highlight the valid signal than the original S-transform. Therefore, it is more suitable for analyzing noisy signals. MST is defined as

$$S_M(\tau,f)=\int_{-\infty}^{\infty}h(t)\left\{\frac{\sqrt{f/g}}{\sqrt{2\pi}}e^{\frac{-|f/g|(t-\tau)^2}{2}}\right\}e^{-i2\pi ft}dt \tag{3}$$

Equation (3) shows that, the difference between MST and the original S-transform is that the width of Gaussian window is inversely proportional to the square root of frequency, and it introduces parameter g to regulate the time-frequency resolution.

Fast Modified S-transform. In the process of the detection and analysis of power quality disturbances by S-transform, the main frequency vectors of the signal in the time-frequency matrix are usually used during the feature quantity extraction. Therefore, the literature [2] proposed a rapid algorithm of S-transform which is called incomplete S-transform. And it verified that the incomplete S-transform can detect the main frequency points of harmonic signals accurately, and it can also greatly reduce the computational burden under the precondition to ensure detection accuracy. The calculation process in MST and S-transform is similar, so a new harmonic detection algorithm based on fast modified S-transform is proposed in this paper.

The Fast Fourier Transform (FFT) was performed and dynamic measurement was utilized to describe the envelope of power spectrum, and the valid harmonic frequency points were obtained by selecting the dynamic measurement values which were larger than the set thresholds [4]. Further, the FMST was specifically performed for these major frequency points and a complex matrix was generated. Finally, these feature vectors extracted from the complex matrix were used to detect the harmonic amplitude, phase and transient information [5]. The row vector in the matrix which reflects the harmonic frequency is denoted as mode component $\mathrm{A_f}(\tau,f_k)$, and it gives an expression on the phase and the time location information of harmonic disturbances. While the column vector gives an expression on the amplitude-frequency characteristics of the moment [6].

The mode component $\mathrm{A_f}(\tau,f_k)$ of the harmonic frequency can be expressed as

$$\mathrm{A_f}(\tau,f_k)=\mathrm{A}(\tau,f_k)\,\mathrm{e}^{\mathrm{j}\Phi(\tau,f_k)} \tag{4}$$

where the amplitude corresponding to the harmonic frequency can be written as

$$\mathrm{A}(\tau,f_k)=\sqrt{\mathrm{R}\left\{\mathrm{A_f}(\tau,f_k)\right\}^2+\mathrm{I}\left\{\mathrm{A_f}(\tau,f_k)\right\}^2} \tag{5}$$

The phase can be written as

$$\Phi(\tau,f_k)=\arctan\left(\frac{\mathrm{I}\left\{\mathrm{A_f}(\tau,f_k)\right\}}{\mathrm{R}\left\{\mathrm{A_f}(\tau,f_k)\right\}}\right) \tag{6}$$

Performance comparisons

To highlight the excellent performance of the harmonics detection algorithm based on FMST proposed in this paper, the original S-transform is compared with FMST in the aspect of anti-noise performance and real-time performance.

In terms of anti-noise performance, the harmonic signal model is defined as

$$h = 0.2sin(2\pi \times 20t) + sin(2\pi \times 50t\ ) + 0.3sin(2\pi \times 150t) + 0.2sin(2\pi \times 250t) \\ +0.1sin(2\pi \times 325t) + 0.05sin(2\pi \times 375t) \tag{7}$$

This signal which has added Gaussian white noise with a SNR of 25 dB is detected by using the original S-transform, and the result is shown in Figure 1. Due to the influence of noise, the harmonics aliasing is serious, and can't separate from each other. It is clearly that the original S-transform can't detect the harmonics accurately in noisy environments.

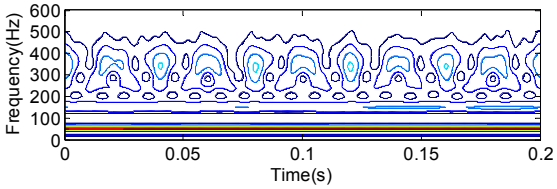

Fig.1 Detection result of S-transform

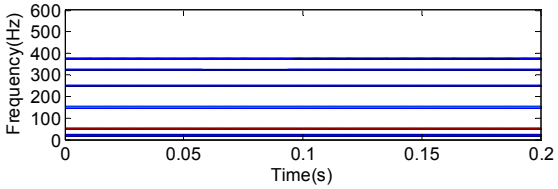

Fig.2 Detection result of FMST

The result obtained from the fast modified S-transform is shown in Figure 2. The harmonics can be seen clearly, and a further detection on the harmonic amplitude and phase can be performed on this basis. The strong anti-noise performance of the proposed method is evident from the comparison.

In terms of the real-time performance, as the algorithm proposed in this paper only performs FMST on the L major frequency points which are corresponding to the harmonics, the resulting matrix only contains L vectors, and it is far less than N/2 vectors from original S-transform.

Simulation results

The stationary and non-stationary signals containing multiple harmonics and inter-harmonics are detected by FMST through two following simulation tests, and both of them contain Gaussian white noise with a SNR of 28dB.

Stationary harmonic detection. The steady-state harmonic signal model is defined as

$$h = 0.2sin\left(2\pi \times 20t + \pi/6\right) + sin\left(2\pi \times 50t\right) + 0.2sin\left(2\pi \times 150t + \pi/3\right) \\ +0.15sin\left(2\pi \times 225t + \pi/2\right) + 0.1sin\left(2\pi \times 300t + \pi/3\right) + 0.05sin\left(2\pi \times 375t + \pi/4\right) \tag{8}$$

The chosen sample rate is 3200Hz, and the number of total sample points is 640. The original signal waveform is shown in Figure 3(a). Figure 3(b) demonstrates the fragmentary view of the dynamic measurement. The valid harmonic frequency points are accurately extracted by selecting the dynamic measurement values which were larger than the set thresholds. The FMST analysis of the signal results in a matrix with time localized frequency values. And the FMST spectrum of the major frequency points is shown in Figure 3(c). From this figure, it is clear to see that the position of peaks in the frequency axis resemble the exact frequency content with a very small estimation error. Besides, the phase of these frequency points can be obtained by Equation (6).

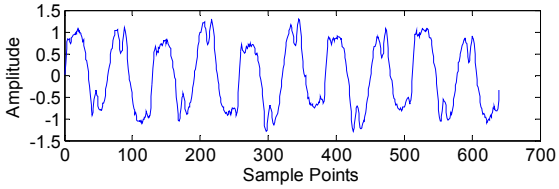

(a) Stationary harmonic signal

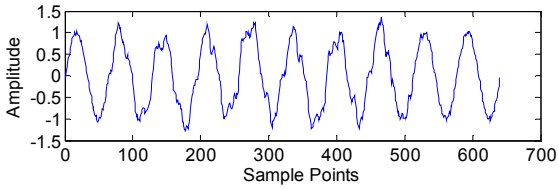

(a) Non-stationary harmonic signal

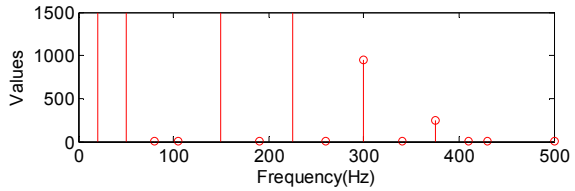

(b) Dynamic measurement values

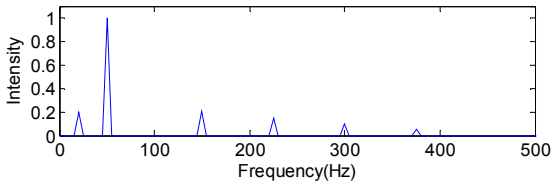

(c) Amplitude-frequency curve

Fig.3 Detection of stationary harmonic

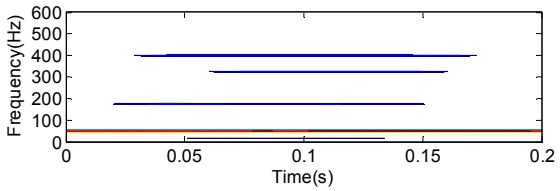

(b) Time-frequency contour plot

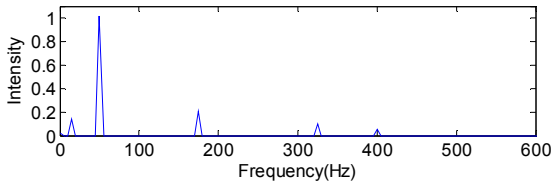

(c) Frequency envelope curve

Fig.4 Detection of non-stationary harmonic

Non-stationary harmonic detection. Another signal with time varying harmonic content is defined as

$$h = 0.15sin\left(2\pi\times15t\right)+sin\left(2\pi\times50t\right)+0.2sin\left(2\pi\times175t\right) \\ +0.1sin\left(2\pi\times325t\right)+0.05sin\left(2\pi\times400t\right) \tag{9}$$

In this non-stationary harmonic signal, the fundamental frequency 50Hz presents in the entire sample time, 15Hz harmonic in 0.05~0.135s, 175Hz harmonic in 0.02~0.15s, 325Hz harmonic in 0.06~0.16s, and 400Hz harmonic in 0.03~0.17s s. Figure 4(a) shows the generated signal..

Figure 4(b) shows the time-frequency contour plot obtained by FMST. It clearly demonstrates the harmonics and inter-harmonics contained in the signal. Meanwhile, the starting and ending time of the harmonics can be found out intuitively in this figure. The frequency envelope curve of the signal is presented in Figure 4(c). The accurate detection of the frequency amplitude is evident from the figure.

Conclusion

In this paper, a harmonic detection approach based on fast modified S-transform is proposed combing with the ideas of incomplete S-transform and modified S-transform. It can better highlight the valid signal for its good time-frequency resolution. And the computation time is greatly reduced compared with the original S-transform. The simulation results demonstrate that the approach proposed in this paper can accurately detect the harmonic frequency, amplitude and phase information in power signals. Additionally, its accurate harmonics estimation, noise immunity and transient positioning capability make it an attractive candidate for harmonic detection in practical application.

References

[1] Stockwell R G, Mansinha L, Lowe R P. IEEE trans. on signal processing, 1996, 17:998~1001.
[2] Jiliang Yi, Jianchun Peng, Huisheng Tan. High Voltage Engineering, 2009, 35(10):2562-2567.
[3] Pinnegar C R, Mansiha L. Fluctuation and Noise Letters, 2003, 3(3):357-364.
[4] Yingmei Liu, Xiaomin Bai, et al. Proceedings of the CSEE, 2003, 23(10):57-62.
[5] Li Li, Jiliang Yi, Jianlin Zhu. Transactions of China Electrotechnical Society, 2011, 6(6):187-193.
[6] Zhiyou Cheng, Dong Liang, Sui Wei, Lingdong Li. Electrical Measurement and Instrumentation, 2007, 44(3):5-8.

Advanced Materials Research Vols. 986-987 (2014) pp 1514-1517

doi:10.4028/www.scientific.net/AMR.986-987.1514

IEC61850-based Digital Watt-hour Meter Tester with Traceability

Chu HUANG[1, a], Yi TANG[1, 2, b], Bo JIANG[1], Xianshun CHEN[1], Bing AI[1]

[1]State Grid Sichuan Electric Power Corporation Metering Center, Chengdu, 610047, China

[2]College of Electrical and Electronic Engineering and, Huazhong Univ. of Science and Technology, Wuhan, 430074, China

[a]email: huangchu2341@163.com, [b]email: tangyi04@163.com

Keywords: IEC61850; Digital Watt-hour Meter; Tester; Traceability

Abstract. The IEC61850-based digital watt-hour meter is different with conventional meters. The testing method and equipment for conventional meter is no longer applicable for digital meters. A newly designed tester for digital watt-hour meter is presented. The hardware structure and working principle are described. The test has traceability to the conventional standard meter. The tracing test result shows that the tester has accuracy grade of 0.05%.

Introduction

With the development of smart grid construction, more and more smart substations have been built. In smart substations, digital metering systems based on IEC61850 [1] are employed as the substitution of conventional metering systems. New challenges arise in the practice digital metering system, one of which is the testing and traceability issue of IEC61850-based digital watt-hour meter.

Fig.1 is a typical diagram of digital metering system in substation. EVT (electronic voltage transfer) and ECT (electronic current transfer) can output secondary voltage and current sampled values. MU (merging unit) merges 3-phase voltage and current values, and then transmit them to digital watt-hour meter via IEC61850-9-1/2 communication protocol. The digital watt-hour performs the metering and measurement computation, and reports the results to substation control unit. The input of digital watt-hour meters based on IEC61850 is digital sampled values, while, the input of conventional meter is analog voltage and current. This is the essential difference between the two types of watt-hour meter. As a result, the mature valuation transfer and traceability system and testing equipment for conventional watt-hour meters is no longer applicable for digital meters.

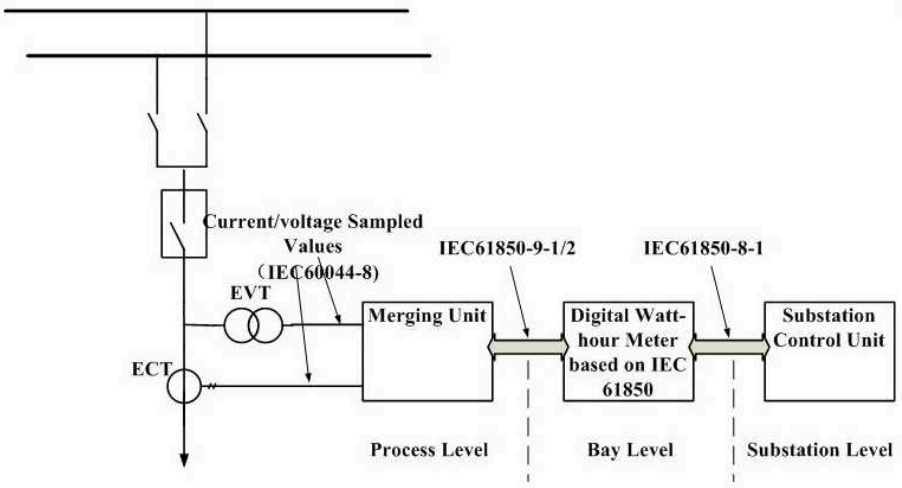

Fig. 1 Typical diagram of digital metering system

To make the testing of digital watt-hour meter feasible, a new tester is needed. And the traceability is also an important and necessary consideration in the new testing solution. Several testing solutions have been reported [2][3][4][5]. In this paper, a newly designed and novel tester for IEC61850-based digital watt-hour meter is presented, which is different with the existing testers

and traceable to conventional standard watt-hour meter. The design scheme, traceability solution and testing result of the tester will be described in the following.

Overview of the Tester for Digital Watt-hour Meter

Fig.2 is the overall diagram of the newly designed tester. The tester consists of a PC and dedicated box. The PC is responsible for MMI (man-machine interface), control and configuration of the box, sampling data transfer and internal testing data generation. The tester box is responsible for A/D conversion, power computation, IEC61850-9 handling, pulse handling and error calculation. The tester can work in 3 different modes. The detailed working principles and features will be presented in each mode respectively.

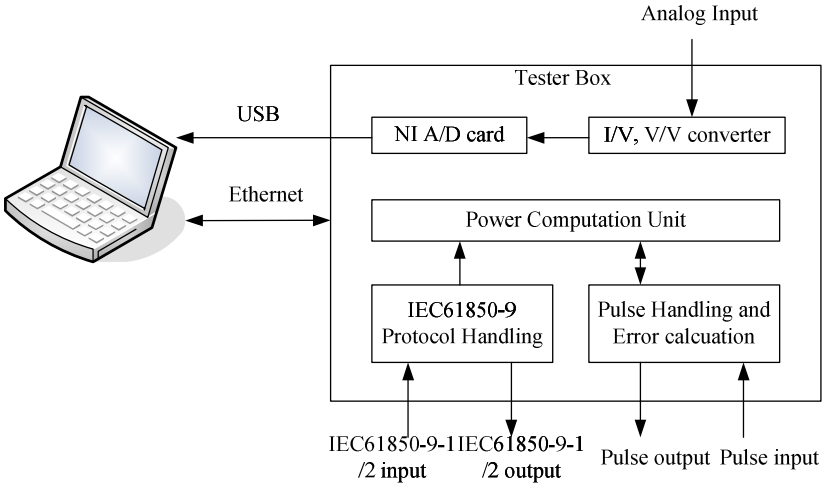

Fig.2 Overview diagram of the tester

Compared to previous testing solutions [2][3][4][5], there are several highlights in hardware design of the new tester. Firstly, high-accuracy current-to-voltage and voltage-to-voltage convertors are employed to transfer the secondary currents and voltages to small voltages, which can be sampled by A/D card. The accuracy grade of the convertor is as high as 0.01%. Secondly, a commercial A/D sampling card, USB6281, a product of NI Company, is used to implement A/D conversion. It has an 18-bit resolution and is easy to be embedded to the system, since an existing driver software is provided and the data-stream can be achieved by the USB of a PC. Thirdly, a FPGA is used to generate and receive power pulse, which has a high timing resolution and accuracy.

Working principle of the Tester

1) Virtual load testing mode

Fig.3 shows the principle of virtual load testing mode. All the out-of-use units and interfaces are omitted in the figure. In this mode, the 3-phase digital secondary currents and voltages are generated by the internal power source, which is implemented by software in PC. The digital currents and voltages are transmitted to the box via Ethernet connection. The box packs the data according to IEC61850-9 protocol and then output them to the tested digital meter via optical fiber. The tested meter will give the power values, including active power and reactive power, to the tester box in the form of pulse. Meanwhile, the computation unit will figure out the power result with the same current and voltage data. At last, the box will compare the two power values and give the error result to PC.

In this mode, the secondary currents and voltages are generated artificially according to the testing specification. In other words, the load to tested meter is not real. Thus, this mode is called *virtual load testing*. Since PC is capable and very flexible to generate the testing currents and voltages data, the internal digital power source is placed in PC. This is also a cost-saving way because no dedicated hardware is needed to implement this function.

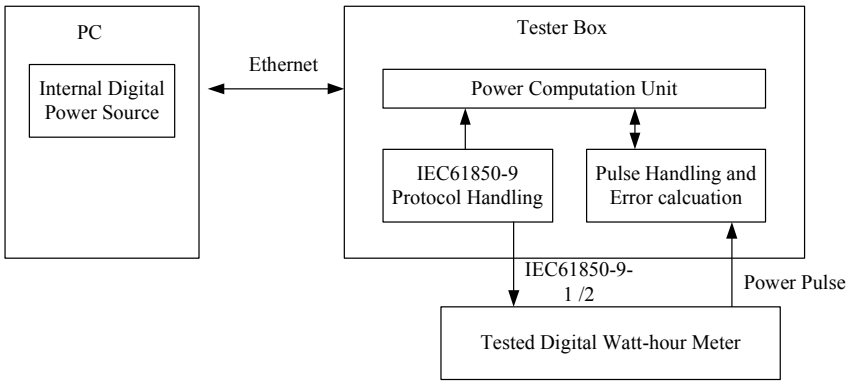

Fig.3 Virtual load testing mode

2) Actual load testing mode

Fig.4 shows the principle of actual testing mode. This mode is similar to virtual load testing mode. The difference is that this mode employs an external digital power source instead of internal source. This mode can be used in field testing scenario by using a MU as the external digital power source. In this way, the secondary currents and voltages are actual signals from the substation. So, this mode is called *actual load testing mode*.

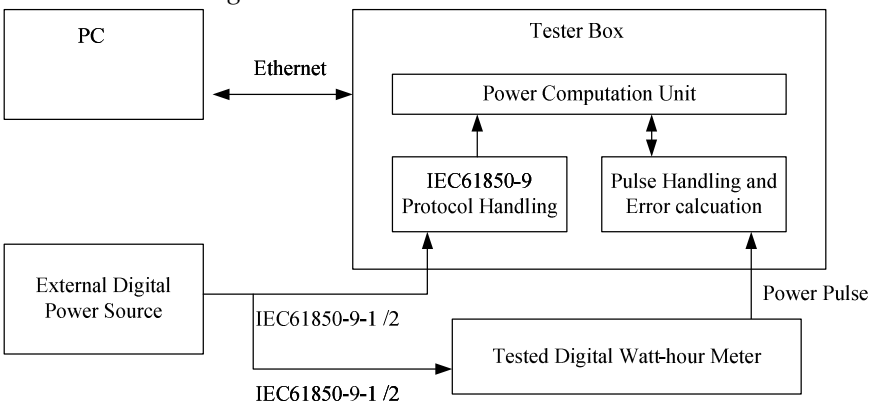

Fig.4 Actual load testing mode

3) Tracing testing mode

Fig.5 shows the principle of tracing testing mode. This mode makes the tester traceable to conventional standard meter. An external analog power source is used to generate analog 3-phase currents and voltages, which are simultaneously injected to tester box and conventional standard meter. The I/V, V/V converter will convert the currents and voltages to small voltages, which the A/D card is capable to sample. The sampled values are transmitted to PC via USB connection and then transmitted back to tester box. The box calculates power and gives active and reactive pulses. Meanwhile, the conventional standard meter will give the power pulse according to the same voltages and currents. An external error calculator will compare the pulses and give the error result.

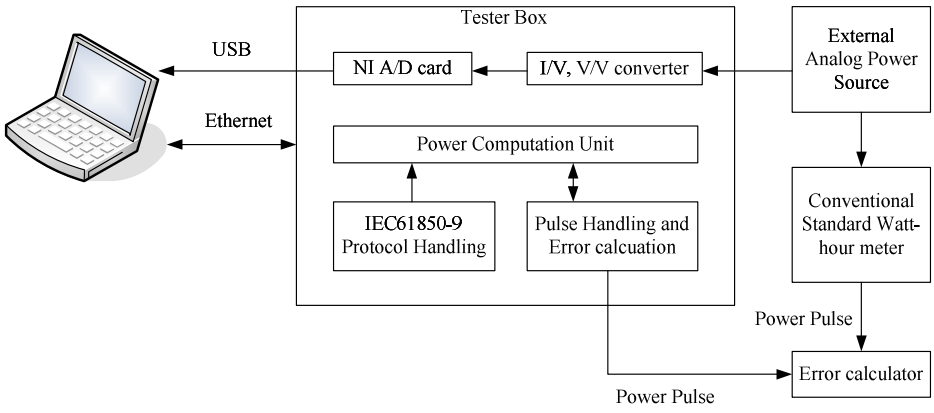

Fig.5 Tracing testing mode

Via this setup, the tester, which has an internal digital meter, is compared to conventional standard watt-hour meter with higher precision level. In other words, the tester is traceable to conventional standard meter. In this setup, the metering error is caused by not only internal digital meter, but also the A/D conversion process. However, since the A/D conversion itself has a high accuracy, the testing result still can be used to rate accuracy grade of the internal digital meter.

Test results

A tracing test is performed as fig.5. The model of conventional standard watt-hour meter is RD-33. The test result is as table 1. The basic voltage ,U_b, is set to 57.7V， and the basic current, I_b, is set to 5A. Part of the test result is shown as Table 1. The result shows that the tester can be rated to the accuracy grade of 0.05%, which makes the tester feasible to test the most-widely-used installed digital meters with the accuracy grade of 0.2% or 0.5%.

Table 1 Part result of tracing test

Current	Power factor	Standard meter RD-33（W）	Tested meter （W）	Error（%）
I_b	1	864.772	864.760	-0.00139
I_b	0.5L	432.432	432.514	0.01896
I_b	0.8C	691.576	691.513	-0.00911
$0.2I_b$	1	172.946	172.947	0.00058
$0.2I_b$	0.5L	86.548	86.569	0.02426
$0.1I_b$	1	86.62	86.613	-0.00808
$0.1I_b$	0.5L	43.275	43.275	0
$0.05I_b$	1	43.235	43.232	-0.00694

Conclusion

A newly designed IEC61850-based digital power meter tester is presented. It can work in three different modes, which are applicable with different scenarios. It is traceable to conventional standard meter. The tracing test result shows that the tester can be rated to the accuracy grade of 0.05%. And thus, the tester is valid to test digital meters with the accuracy of 0.2% and 0.5%, which are most widely used accuracy grades for installed digital meters.

References

[1] IEC61850-1. Communication Networks and Systems in Substations – Part 1: Introduction and Overview[S].

[2] Ruimin Chen, Xin Li, Zhengmin Kong. Meter calibration technology for digital watt-hour meters based on value traceability [J]. Electrical Measurement & Instrumentation, 2012, 49(562): 38-41. (In Chinese)

[3] Shui Liu, Yangjie Huang, Bin Li. The study of calibration technology for digital power metering [J]. Electrical Measurement & Instrumentation. 2011, 48(544): 66-71. (In Chinese)

[4] Yinglin Chen, Dexiang Huang. Digital Watt-hour metering system and verification equipment [J]. Electric Power Automation Equipment, 2009, 29(4): 114-117.(In Chinese)

[5] HUANG Hongtao, WANG Lei , ZHANG Jiangtao, PAN Xianlin, LU Zuliang. Traceability of Digital Electricity Meters. Proceedings of Conference on Precision Electromagnetic Measurements (CPEM 2012), Pages: 234 - 235. Washington D.C., USA, July 1 - 6, 2012.

Advanced Materials Research Vols. 986-987 (2014) pp 1518-1522

doi:10.4028/www.scientific.net/AMR.986-987.1518

Improvement and Application of Fan Fault Diagnosis of Power Plant Based on Fuzzy Rules

Liu Chang-liang[1, a], Yao Xin-tong[2,b]

[1] State Key Laboratory Of Alternate Electrical Power System With Renewable Energy Sources(NCEPU),Beijing,102206,China

[2] North China Electric power university,Baoding,071000,China

[a] changliang_liu@163.com, [b]yaoxintong1989@126.com

Key words: fan; fault diagnosis; fuzzy matrix; case-based reasoning

Abstract. In view of the nonlinear, fuzzy relationship between fan fault reason and fault symptom, put forward a kind of threshold diagnosis strategy combined with fuzzy rules and case reasoning. Using a fan fault vector through fuzzy fault diagnosis model to compare with a given threshold, then generate the initial fault solution set, and finally using case-based reasoning thinking, accurate fault location. Then we verify the method's effectiveness through a fault analysis of fan rotor vibration. The results show that the combination with fuzzy rules and case reasoning can effectively solve the problem of multi factors of failure reasons.

Introduction

Due to the highly nonlinear relationship between fault symptom and fault type, it is difficult to fault diagnosis by using mathematical model of linear relationship.[1]In recent years the fuzzy recognition method is used for the application for its fuzzy expression and good capability of nonlinear mapping.[2]

Literature[3] use mine fan rotor's fault examples to verify the method of fuzzy diagnosis. The diagnostic process set 5 fault symptoms,and diagnosis by the principle of maximum degree of membership,but only choose membership fault degree maximum is not conducive to distinguish multiple simultaneous fault conditions. Literature[4] use fuzzy fault diagnosis technology in Hunan Leiyang power plant fan fault diagnosis, under 9 fault conditions, combine the maximum membership degree and threshold principle to get a multiple fault diagnosis results, and put similar spectral structure of fault into a pattern , diagnose the fault in the model class level, to solve the false recognition problem between classes, but the process is cumbersome , and difficult to judge.

To solve the problem above, this paper combine the existing research with Case-Based Reasoning technology, to make a comprehensive analysis of the fault reason, and also reduce the occurrence of false recognition, which are illustrated by examples.

Fault diagnosis method design

2.1 Fault diagnosis model

For a vibration fault diagnosis of fan, see the vibration parts as a "sign", and the causes of these symptoms as fault. Select appropriate membership functions and use a corresponding membership to describe the tendency of changes in these parameters.

Fault symptoms: $x_1, x_2, \cdots, x_m$; The possible reasons for failure: $y_1, y_2, \cdots, y_n$. Fault symptom fuzzy vector: $X = [\mu_{x1}, \mu_{x2}, \cdots, \mu_{xm}]^T$ .Among them, is the membership of this object with the symptoms x_j. $\mu_{xj} = 0$ means the symptoms x_j do not appear, μ_{xj} more closer to 1, means the symptom is more serious. The fault reasons of fuzzy vector: $Y = [\mu_{y1}, \mu_{y2}, \cdots, \mu_{yn}]^T$, μ_{yi} $(i = 1, 2, \cdots, n)$ is the object's membership degree with this fault. The fuzzy relation between two domain is represented by the degree of membership, x_j corresponding to the faults membership is $r_{ij} = \mu_{yi}(x_j)$. It consists

a fuzzy relation matrix between domains U and V: $R=\begin{pmatrix} r_{11} & \cdots & r_{1m} \\ \vdots & \ddots & \vdots \\ r_{n1} & \cdots & r_{nm} \end{pmatrix}$.Each element in the matrix indicates the close degree between fault and symptom. Given the fuzzy relationship matrix R and fuzzy vector X, you can get fuzzy vector Y through the fuzzy relation equations $Y = R \circ X$.

2.2 The generation of diagnostic results

2.2.1 Diagnosis algorithm

(1)The principle of maximum degree of membership

Let n fuzzy subset of $U=\{x_1,x_2,\cdots,x_n\}$:A1,A2,…,An, as $x_0 \in U$ the memberships belonging to the n fuzzy subset are respectively $\mu_{A_1}(x_0),\mu_{A_2}(x_0),\cdots,\mu_{A_n}(x_0)$, if $i \in \{1,2,\cdots,n\}$, let $\mu_{A_i}(x_0)=\max\{\mu_{A_1}(x_0),\mu_{A_2}(x_0),\cdots,\mu_{A_n}(x_0)\}$,then x_0 belongs to the model that A_i represents.

(2)Threshold principle

First set the threshold level $\lambda \in [0,1]$, the value of λ is usually determined by expert scoring and experience. $\mu_{A_i}(x_0)=\max\{\mu_{A_1}(x_0),\mu_{A_2}(x_0),\cdots,\mu_{A_n}(x_0)\}$, if $\mu_{A_i}(x_0)>\lambda$, means that fault object has a threshold value that corresponds to the cause of the problem. If $\mu_{A_i}(x_0)<\lambda$, we can not identify whether there is a fault. If the membership degrees of fault are all greater than the given value, you should consider the possibility of the existence of several reasons for failure.

2.2.2 Extraction the final results based on CBR method

Through the process of diagnosis, the diagnosis results are often multiple failure modes, the form is divided into 3 types.

Mode1:fault a, b occurs only one, all the fault in the system were caused by a single fault.

Mode2:fault a, b simultaneously but unrelated. That means effects of a, b on the system are independent of each other.

Mode3:fault a, b occur simultaneously and their impact on the system have overlap, for some symptom index a,b contains in common, there may be a condition of the interactions between them.

As shown in Figure 1：

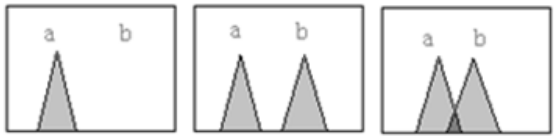

Mode 1 Mode 2 Mode 3

Fig 1 Form of multiple failure modes

Grey area in the figure respectively show the fault symptom fault set that a, b correspond , three modes correspond to three different situations. Take the mode 3 of multi-mode failure case as a whole case, then types of multiple faults at the system are mode 1 or mode 2, and mode 1 is a special case of mode 2. we can see that the maximum membership degree case is a fault occurs in the system, according to the characteristics of mode2 types, the fault symptom among the collections have no intersection, if that happened to a fault in the system, and in this case there are signs of intersection of the case will not be the fault of the system. [5] Based on this idea, the multi fault solutions can be generated from the candidate fault system.

Fuzzy diagnosis example of fan fault

3.1Build the fault set and symptom set

Take Y1 - the rotor imbalance, Y2 - rotor misalignment, Y3 - shaft coupling damage, Y4 - oil whirl, Y5 - oil film vibration, Y6-surge, Y7 - axial rubbing, Y8 - crack shaft, Y9-bearing loose this 9 faults as fault set V={y_i | i=1,2,…}.

Frequency domain analysis is an important method for vibration analysis, the characteristic frequency: fractional harmonic, 1/2 frequency, 2 times harmonic and 3 times harmonic, high order harmonics etc.. plays a main role to judge the fault. Membership function is the ratio of the amplitude of each frequency band of the total amplitude characteristic, that is: $\mu(x_i) = x_i / \sum_{j=1}^{n} x_j$ .Among them, x_i and x_j are respectively the spectral maximum in section i and section j of the characteristic bands , n is feature band number. The frequency is divided into 8 fault feature frequency as shown in table 1.

Table 1 Amplitude frequency corresponding table

Amplitude	x_1	x_2	x_3	x_4	x_5	x_6	x_7	x_8
Frequency	(0.01-0.39)f	(0.4-0.49)f	0.5f	(0.51-0.99)f	1f	2f	(3-5)f	>5f

"f" in the table is the rotor frequency. Take these characteristic spectrum as the set for fault sign diagnosis. $U = \{x_j \mid j = 1, 2, \cdots\}$

Fault diagnosis flow chart in Figure 2：

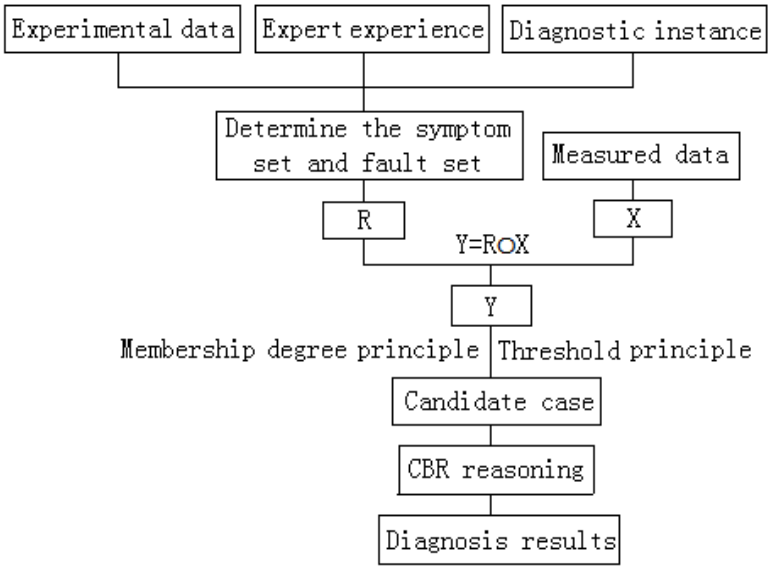

Fig 2 Fault diagnosis flow chart

3.2 Build a fuzzy relation matrix

According to the expert experience and historical data on repairing fun's fuzzy quantization , get their fault membership in different characteristics band, according to the vibration characteristics to further refinement, set the membership value which cause vibration of fan larger, and the independent factors smaller. Initially build the fuzzy relation matrix of fan vibration fault, as shown in table 2.

Table 2 The fuzzy relation matrix R

Number	Fault Category	x_1 (0.01-0.39)f	x_2 (0.4-0.49)f	x_3 0.5f	x_4 (0.51-0.99)f	x_5 1f	x_6 2f	x_7 (3-5)f	x_8 >5f
1	rotor imbalance					0.9	0.05	0.05	
2	rotor misalignment					0.3	0.6	0.1	
3	shaft coupling damage	0.1	0.2	0.1		0.2	0.3	0.1	
4	oil whirl	0.1	0.8		0.1				
5	oil film vibration		1						
6	surge	0.7				0.3			
7	axial rubbing	0.1	0.1		0.1	0.2	0.1	0.2	0.2
8	crack shaft					0.4	0.2	0.2	0.2
9	bearing loose			0.2		0.6	0.1	0.1	

As can be seen, a kind of frequency components corresponds to different kinds of fault, but the same frequency components' effect on different faults are not same .

3.3 Select sign sample and calculate the membership degree

According to the vibration spectrum diagram of vibration monitoring, select the most intense vibration value as sample, when the vibration amplitude of characteristic frequency is larger in a certain moment. as shown in table 3

Table 3 The initial data of sample set (unit：mm)

Amplitude	x_1	x_2	x_3	x_4	x_5	x_6	x_7	x_8
Frequency	0.076	0.0605	0.042	0.091	2.1893	2.6339	0.187	0.131

for $\mu(x_i) = x_i / \sum_{j=1}^{n} x_j$ we have $\mu(x_i) = [0.014 \ \ 0.011 \ \ 0.008 \ \ 0.017 \ \ 0.405 \ \ 0.487 \ \ 0.035 \ \ 0.024]^T$

Based on multi-factor comprehensive evaluation formula $Y = R \circ X$ for the fuzzy synthesis operation, calculate the fault membership: $\mu_y = [0.390 \ \ 0.417 \ \ 0.235 \ \ 0.012 \ \ 0.011 \ \ 0.131 \ \ 0.146 \ \ 0.271 \ \ 0.296]^T$

According to expert scoring and experience, this example's threshold vector is:

A={0.25，0.25，0.25，0.2，0.2，0.2，0.2，0.25，0.2}

So in the reasons of the rotor vibration, rotor imbalance, rotor misalignment, rotor crack and supporting parts loosening are most likely to occur.

3.4 Diagnostic results

1) Choose the candidate case with the biggest membership degree as a fault in the system.

2) Remove the signs of the case contains from the fault symptoms set and form a new set.

3) Exclude the case which has a mixed part with symptoms from the candidate case, forming a collection of reduced candidate.

4) Repeat the above steps, until the fault symptoms set becomes a null set. So, each time we have the biggest-membership-degreed case, then they form the solution set of the current fault.

The maximum membership degree case is "rotor misalignment", the corresponded fault symptoms set is{1f,2f},remove the signs " rotor misalignment" contained from the fault symptoms set，change the fault symptoms set as { 0.01~0.39f,0.4f~0.49f,0.5f,0.51f~0.99f,>5f}. Eliminate the candidate which has symptoms intersection with the case of Y2, Thus, Y1, Y8 and Y9 are eliminated from fault solution set, the final diagnosis is "rotor misalignment", the diagnosis result is same with the examples of vibration fault reasons. Results show that, applying fuzzy diagnosis and case based reasoning in fun vibration fault diagnosis can quickly locate the fault.

Conclusions

In this paper, by means of the fuzzy mathematics theory and the concept of degree of membership, propose a fan fault diagnosis method of the fuzzy evaluation and case reasoning integrated application. Examples show that, compared with the classification spectrum method of fault diagnosis , this method is more accurate and more intuitive, which can quickly locate the results of fault reason in many alternative, have feasibility.

Acknowledgements

This paper is supported by State Key Laboratory of Alternate Electrical Power System with Renewable Energy, the Fundamental Research Funds for the Central Universities (13MS102), National Natural Science Foundation of China(61203107)

References

[1]Yang Zhi-Ling,Wang Bin,Dong Xing-Hui, et al, Expert System of Fault Diagnosis for Gear Box in Wind Turbine. Systems Engineering Procedia,2012,4

[2]Liu Yong-kuo,Peng Min-jun,Xie Chun-li, et al,Research and design of distributed fault diagnosis system in nuclear power plant. Progress in Nuclear Energy,(2013)p.68

[3] Yu Zhi-fu, Yu Hui-rong, Wang De-fang, et al.Fault Diagnostic Expert System of Mine Ventilator Based on Fuzzy Mathematics. Coal Mine Machinery. 2013,34(1) p.271-273(In Chinese)

[4] Liu Qing-long,Researeh on The Monitor and Diagnosis System for The Air Blower of Therma1 Power Plant[D].Wuhan University, 2005,5(In Chinese)

[5]ZhiyuanWang,Marek-Sadowska,etal. Analysis and methodology for multiple-fault diagnosis. IEEE Transactions on Computer-Aided Design of Integrated Circuits and Systems, (2006) p.558-575

Advanced Materials Research Vols. 986-987 (2014) pp 1523-1526

doi:10.4028/www.scientific.net/AMR.986-987.1523

Measurement on Gas Number Density Distribution by Tunable Diode Laser Absorption Spectroscopy

ZHENG Hui-jie[1], QUAN Wei*[1]

[1.] Science and Technology on Inertial Laboratory, Fundamental Science on Novel Instrument & Navigation System Technology Laboratory, Beihang University, Beijing 100191, China

cubszhj@126.com, quanwei@buaa.edu.cn

Keywords: Atomic absorption spectrometry; gas number density distribution; Discretization method;

Abstract. An experimental technique was designed to measure the gas number density distribution of alkali vapor by tunable diode laser absorption spectroscopy. The measurement method was developed by scanning multiple gas absorption lines and fitting the experiment data with Lorentz profile to obtain the density. A discretization strategy of the equation for absorption lines is also present here as well as a constrained liner least-square fitting method. A simulation model was set up to reconstruct the two-dimensional distribution of number density and the feasibility of the reconstruction was verified. In the end, this work demonstrates the calculation error of the acquired number density and the distribution. The results indicated that the error would be no more than 5% if the measurement error is less than 9%.

Introduction

The gas atomic density distribution, an important factor to laser performance, could be measured by tunable diode laser absorption spectroscopy. Over the past few decades the development of the theory of atomic spectral line profiles and experimental measurement of the collision broadening have been studied thoroughly and numerous reviews are available[1-4]. It has been experiencing a boom driven by the technological developments to measure the gas density and proportion of trace elements [5-7], such as monitoring the methane concentration in the atmosphere with tunable diode laser absorption spectroscopy and determining the contents of SO_2 via flame-atomic absorption spectrometry. The researches above utilize the attention on- or near-resonant light propagating through the vapor cell to acquire the parameter. The number density of gas in a cell with alkali metals can be achieved with the similar method and calculated from the alkali-metal line widths and peaks utilizing the relevant broadening coefficients or collisional cross sections. The density gradient would be obtained by scanning multiple alkali metal absorption lines and fitting the experiment data with Lorentz profile discretized.

Measurement method of gas number density distribution based on absorption

2.1 The measurement principle

The alkali vapor would absorb the on- or near-resonant light as it propagates through the cell. According to the lambert-beer law [8-10], the reduction in laser intensity is

$$I_o(x) = I(0)\exp(-n\sigma(v)x) \tag{1}$$

Where $I(0)$ represents the incident light, $\sigma(v)$ the absorption cross section at frequency of v, x the position in the cell. The photon absorption cross-section depends on three chief effects: the natural lifetime broadening, Doppler broadening, and collision broadening, which are proportional to the number density of perturbing atoms. Collisions with buffer gas atoms due to electromagnetic interactions results in a broadening of the optical resonance line. When the quantity of buffer gas is more than 1 amg, the line shape has the form of Lorentzian curve[11],

$$\sigma(\mathrm{v}) = \pi r_e cf \frac{\Gamma_{\mathrm{L}} / 2\pi}{\left(\nu - \nu_0\right)^2 + \left(\Gamma_{\mathrm{L}} / 2\right)^2} \tag{2}$$

Where Γ_{L} is full width at half maximum indicating the pressure broadening of buffer gas, r_e is the classical electron radius, $c = 3\times10^8$m/s is the speed of light, and f is the oscillator strength.

The gas number density of alkali vapor is given

$$num\_den = \frac{\Gamma_{\mathrm{xL}}}{\Gamma_0} / \left(\frac{T_0}{T}\right)^n \tag{3}$$

2.2 The discretization strategy

On the basis of Eq. (1), the reduction is sensitive to the gas number density of alkali vapor. When the laser light passes through nonuniformities, multiple absorption lines can be probed to determine an approximate number density distribution along the path. The nonuniform path is modeled as being composed of m nearly uniform property path segments, each with a number density n_i absorption cross section σ_i and path length L_i. We can generalize Eq. (1) as following by denoting the product of the last two quantities as $(\sigma L)_i$,

$$\begin{bmatrix} F_1(\mathrm{n}_1) & F_1(\mathrm{n}_2) & \cdots & F_1(\mathrm{n}_n) \\ F_2(\mathrm{n}_1) & F_2(\mathrm{n}_2) & \cdots & F_2(\mathrm{n}_n) \\ \vdots & \vdots & \vdots & \vdots \\ F_m(\mathrm{n}_1) & F_m(\mathrm{n}_2) & \cdots & F_m(\mathrm{n}_n) \end{bmatrix} \begin{bmatrix} (\sigma L)_1 \\ (\sigma L)_2 \\ \vdots \\ (\sigma L)_m \end{bmatrix} = \begin{bmatrix} OD_1 \\ OD_2 \\ \vdots \\ OD_m \end{bmatrix} \tag{4}$$

Or

$$Fn = OD \tag{5}$$

Where m is the number of absorption lines probed in the measurement. Provided the densities are postulated, then the matrix F is given and the result x could be obtained. It is usually best to use a nonnegative least-squares algorithm to process Eq. (5) for each element must be positive. The result indicates the length of the number density distribution n_i. To optimize the error, a few restraints should be imposed, for example, the sum of the length L_i must be the length of the cell. The condition number of F governed the error in the solution n, which also depends on the number of absorption lines m.

Simulation

3.1 The calculated error of acquired number density

To clarify the influence of the calculated error, measurement error and the constraint, it is better to make a simulation. In the simulation, a cell with Rb vapor and He buffer gas was taken as the object. The simulation was based on two different wavelengths- 794.98 nm, the D1 line, and 780.108 nm, the D2 line under the condition of alkali atomic density 2×10^{13} cm^{-3}. The model was set up with two gas number densities, 2 amg and 3 amg, and both the total length was 10 mm. We calculated the number density distribution by dividing into eight intervals which were 1 amg, 2 amg, 3 amg and 4 amg, assuming that the concentration and the pressure of the buffer gas was uniform.

We assess the resulting error due to the measurement error by adding different random jitter to the simulation, as following shows.

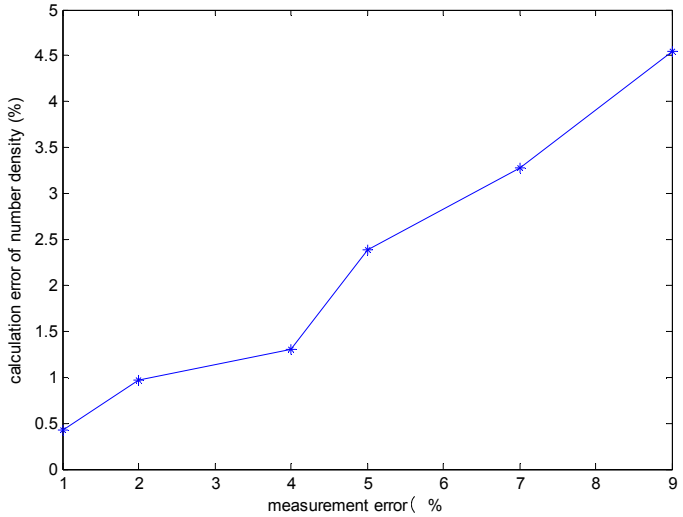

Fig. 1 Effect of measurement error on calculation result of density bins

From the figure, we conclude that the calculation error of the acquired number density would be about 5% when there is a 9% measurement error. It is essential to impose proper restraints to the actual experiment.

Summary

It is accessible to achieve the gas number density distribution by scanning multiple absorption lines with tunable diode laser. The pathlength of the density distribution can be obtained by estimating the density range, dividing into different intervals and calculating with restrained least square method. The accuracy would increase if proper constraints were added. The results will contribute to understanding of the density distribution in the cell.

References

[1] Kielkopf J F. On the precise evaluation of the complete semiclassical spectral line shape for pressure-broadened atomic spectral lines[J]. Journal of Physics B: Atomic and Molecular Physics, 1976, 9(9): 1601.

[2] Allard N, Kielkopf J. The effect of neutral nonresonant collisions on atomic spectral lines[J]. Reviews of modern physics, 1982, 54(4): 1103.

[3] Szudy J, Baylis W E. Profiles of line wings and rainbow satellites associated with optical and radiative collisions[J]. Physics reports, 1996, 266(3): 127-227.

[4] Kluttz K A, Averett T D, Wolin B A. Pressure broadening and frequency shift of the D1 and D2 lines of Rb and K in the presence of 3 He and N 2[J]. Physical Review A, 2013, 87(3): 032516.

[5] Forouhar S, Briggs R M, Frez C, et al. High-power laterally coupled distributed-feedback GaSb-based diode lasers at 2 μm wavelength[J]. Applied Physics Letters, 2012, 100(3): 031107.

[6] Cui X, Lengignon C, Tao W, et al. Photonic sensing of the atmosphere by absorption spectroscopy[J]. Journal of Quantitative Spectroscopy and Radiative Transfer, 2012, 113(11): 1300-1316.

[7] Wang J, Maiorov M, Jeffries J B, et al. A potential remote sensor of CO in vehicle exhausts using 2.3 μm diode lasers[J]. Measurement Science and Technology, 2000, 11(11): 1576.

[8] Jian W, Wei H, Haitao G. Gas temperature measurement with tunable diode laser absorption spectroscopy[J]. Acta Optica Sinica, 2007, 27(9): 1639.

[9] Liu X, Zhou X, Jeffries J B, et al. Experimental study of H< sub> 2</sub> O spectroscopic parameters in the near-IR (6940–7440cm< sup>− 1</sup>) for gas sensing applications at elevated temperature[J]. Journal of Quantitative Spectroscopy and Radiative Transfer, 2007, 103(3): 565-577.

[10] Nikkari J J, Di Iorio J M, Thomson M J. < i> In Situ</i> Combustion Measurements of CO, H< sub> 2</sub> O, and Temperature with a 1.58-μm Diode Laser and Two-Tone Frequency Modulation[J]. Applied optics, 2002, 41(3): 446-452.

[11] Seltzer S J. Developments in Alkali-metal Atomic Magnetometry[D]. Princeton: Princeton University, 2008.

Advanced Materials Research Vols. 986-987 (2014) pp 1527-1530

doi:10.4028/www.scientific.net/AMR.986-987.1527

Method of Measurement and Computing for Natural Gas Energy

Bingxiang ZHONG

College of Electrical and Information Engineering, Chongqing University of Science and Technology

email: zbxcq@126.com

Keywords: natural gas; energy computing; uncertainty; Volume calorific value; measuring system

Abstract. Energy measurement and computing can directly reflect the value of natural gas. In our country the volume flow measurement and computing will be gradually replaced by energy measurement. In this paper the principle of energy metering of natural gas is introduced and the system of energy metering of natural gas is constructed. Based on GB/T 11062, computing method of gas energy is discussed, in which quality data of natural gas, temperature, flow, pressure parameters are measured by energy metering system and the calorific value of natural gas, relative density and Wobbe index are and computed. Also the uncertainty of and computing method for natural gas energy is analyzed in which uncertainty is within 0.1%. The results show that the uncertainty of the calorific value measurement system attained accuracy requirements of GB/T 18603-2001.

Introduction

Gas metering in China has been dominated by volume measurement, namely m^3 as the unit[1]. Due to the differences of composition in natural gas, the same volume of gas generates different energy. It is generally known that natural gas contains more hydrocarbons which can burn, the unit of natural gas calorific value is higher, the value of natural gas is higher; otherwise, the calorific value is lower, the value is also lower. Therefore the volume measurement cannot fully reflect the market trading principles according to quality of natural gas, and cannot utilize scientifically and rationally natural gas resources limited. It is unfair to both sides of supply and demand. Energy metering reflects directly the value of natural gas, so most countries adopted method of energy measurement[2]. GB/T22723-2008 national standard of natural gas energy measurement [3] marks the transition gradually by volume flow measurement to energy measurement in our country, which provides the technical basis for China's natural gas measurement method with the international practice. It has the positive significance in the regulation of natural gas energy measuring and computing method.

Principle of Energy Metering of Natural Gas

According to GB/T22723-2008 national standard of natural gas energy measurement, the general principle of the measurement of natural gas is that the energy in a certain amount of gas is the product of the gas volume and the corresponding heat, that is

$$E = V_0 \cdot H_{S0} = \frac{P_m T_0}{P_0 T_M} \cdot \frac{1}{k} \cdot V_m \cdot H_{S0} \quad (1)$$

In formula, E—the energy of natural gas for a period of time; V_0 —volume flow of natural gas in standard state; H_{S0} —high position calorific value of natural gas in standard state; P_0,T_0—pressure and temperature in standard state; Pm,Tm—pressure and temperature in working conditions; k—factor of state equation of natural gas; V_m—volume flow of natural gas in working conditions.

Composition of Natural Gas Energy Metering System

The composition of natural gas energy metering system is shown in Figure 1. By gas chromatograph and matching instruments and equipment, each parameter sampling, component analyzing are completed automatically, then the natural gas compression factor, relative density , calorific value and other physical parameters are calculated. Finally, such parameters are transmitted to the host system database and energy is computed with such parameters.

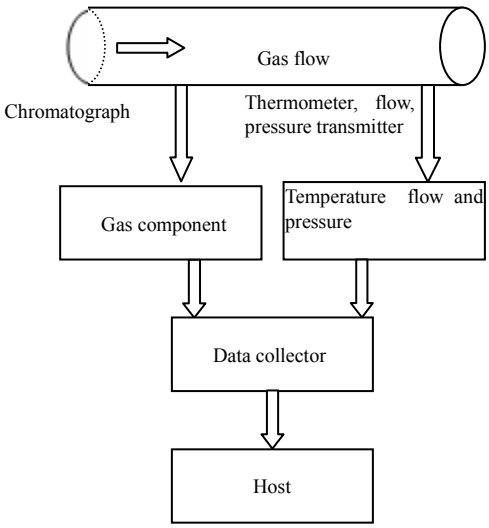

Figure 1. Composition of natural gas energy metering system

Natural Gas Energy Measurement Algorithm

Determination of calorific value is crucial segment in the energy metering of natural gas. It has direct and indirect measurement method for determining calorific value [2]. Equipment for direct measurement method are more complex than that for indirect method. In this paper the indirect measurement method will be mainly discussed. According to GB/T 11062 "calculation of calorific value, density, relative density and Wobbe index of natural gas in standard state"[4], natural gas composition are analyzed by chromatographic, then energy can be computed.

A. Calculation of the natural gas volume calorific value

Molar concentration of gas mixture components are measured by a gas chromatograph, the volume calorific value of natural gas can be calculated according to the following steps.

The first step is to calculate the molar calorific value $\bar{H}(t_1)$ of gas mixture at the combustion temperature t_1

$$\bar{H}(t_1)=\sum_{j=1}^{n} x_j \times \bar{H}_j(t_1) \quad . \tag{2}$$

In formula, x_j —mole fraction of component j; $\bar{H}_j(t_1)$ — molar calorific value of component j at temperature t_1.

The second step is to calculate the volume calorific value of gas mixture at the combustion temperature t_1， measurement temperature t2 and pressure p_2.

$$\tilde{H}\left[t_1, V\left(t_2, p_2\right)\right]=\bar{H}(t_1)\times\frac{p_2}{RT_2 \cdot Z_{mix}(t_2, p_2)} \quad . \tag{3}$$

In formula, R—molar gas constant, R = 8.314 510J / mol·K; T_2 — thermodynamic temperature, T_2= t_2 +273.15 K; $Z_{mix}(t_2, p_2)$ —compression factor of gas mixture at the measurement reference condition t_2 and p_2.

The compression factor Zmix of the gas mixture could be calculated by following formula:

$$Z_{mix}=1-\left[\sum_{j=1}^{n} x_j \sqrt{b_j}\right]^2 \quad . \tag{4}$$

In formula, x_j —mole fraction of component j; $\sqrt{b_j}$ —summation factor, $\sqrt{b_j}=\sqrt{1-Z_j}$; Z_j —the compression factor of component j.

B. Computing of the relative density of natural gas

Relative density of a gas mixture by the following formula:

$$d(t,p)=\sum_{j=1}^{n}x_j\frac{M_j}{M_{air}}\times\frac{p\cdot Z_{air}(t,p)}{RT\cdot Z_{mix}(t,p)} \quad (5)$$

In formula, x_j —mole fraction of component j; M_j —molar mass of component j; M_{air} —molar mass of standard dry air; R —molar gas constant, R = 8.314 510J / mol·K; T —thermodynamic temperature, T=t+273.15; $Z_{mix}(t,p)$ —compression factor of gas mixture at t and p; $Z_{air}(t,p)$ —compression factor of standard dry air at t and p.

C. Computing of Wobbe index of natural gas

The Wobbe index (Wobb) is a parameter representing properties of the natural gas. Supposing that calorific value and relative density of two kinds of gas are different, but if their Wobbe index are equal, they will have the same heat load at the same combustion pressure and same combustion equipment. As long as Wobbe index of one kind of gas is same as another kind of gas, the gas has the interchangeability of another gas. The definition is following:

$$\mathrm{W}\left[t_1,V\left(t_2,p_2\right)\right]=\tilde{H}\left[t_1,V\left(t_2,p_2\right)\right]/\sqrt{\mathrm{d}\left(t_2,p_2\right)} \quad (6)$$

In formula, W—Wobbe index, or heat load index; $\tilde{H}$ —calorific value of the combustible gas, kJ/m^3; d—relative density of gas.

In all countries the general prescript is that the change rate of Wobbe index allowed is not greater than ± (5 ~ 10)% when two kinds of gas exchange. Thus, Wobbe index determined by the gas calorific value and relative density has very important significance for the gas management department and users.

Uncertainty of Energy Metering of Natural Gas

Uncertainty of natural gas energy measurement mainly comes from the uncertainty of calorific value and the uncertainty of volume flow. After calculation, the uncertainty of the measuring instruments and the aspects of data processing are obtained at first, then the uncertainty of high calorific value and volume flow are synthesized. At last the uncertainty of energy measurement of natural gas are computed.

A. Uncertainty of high calorific value of natural gas

1) Uncertainty of gas component measurement

The expanded uncertainty caused by gas component measurement and varying with time was estimated to be 0.5%. Assuming it obeys normal distribution, and k=2. So the standard uncertainty is u_z =0.25%.

2) Uncertainty caused by the temperature transducer

Error allowed of temperature transmitter in system is ± 0.5 ℃. Assuming the temperature is 25 ℃, if it is distributed, $k=\sqrt{3}$, the standard uncertainty of temperature measurement is $u_T=\frac{0.5}{298.15\sqrt{3}}=0.097\%$.

3) Uncertainty caused by the pressure transducer

Accuracy of pressure transmitter adopted in the system is 0.05%. If it is distributed, $k=\sqrt{3}$, so the uncertainty of pressure measurement is $u_P=\frac{0.05\%}{\sqrt{3}}=0.029\%$.

4) Uncertainty of computing formula model

Assuming the expanded uncertainty caused by calculation model is 0.2%, If it is distributed, $k=2$, so the standard uncertainty is um=0.1%.

Synthetic uncertainty of natural gas high calorific value is

$$u(H)=\sqrt{u_Z{}^2+u_T{}^2+u_P{}^2+u_m{}^2}=0.29\%$$

B. Uncertainty of volume flow of natural gas

1) Uncertainty of measurement of ultrasonic flow meter

Error of ultrasonic flow meter allowed is 0.5%, If it is distributed, $k=\sqrt{3}$, so the standard uncertainty is $u_v=\frac{0.5\%}{\sqrt{3}}=0.29\%$.

2) Uncertainty of temperature transmitter

The standard uncertainty of temperature measurement is 0.097%.

3) Uncertainty of pressure transmitter

The standard uncertainty of pressure measurement is 0.029%.

4) Uncertainty of the model of calculation

The expanded uncertainty of models of calculation is 0.2%, If it is distributed, $k=2$, so the standard uncertainty is um=0.1%.

Synthetic uncertainty of volume flow of natural gas is $u(Q)=\sqrt{u_V{}^2+u_T{}^2+u_P{}^2+u_m{}^2}=0.32\%$.

C. The total uncertainty of Energy measurement results

The total uncertainty of Energy measurement results is $u(E)=\sqrt{u(Q)^2+u(H)^2}=0.43\%$. Assuming k=2, expanded uncertainty of the energy measurement result is $u(ef)=2u(E)=2\times0.43\%=0.86\%$.

D. Experiment

3 different gas sources are chosen on some natural gas long distance pipelines, energy of natural gas are measured. The data of calorific value and so on at 3 measurement sites were obtained by on-line gas chromatograph, flow meter and other measurement equipment, and calculated by GB/T 11062-1998. The uncertainty of high calorific value at 3 measurement sites all reached to the accuracy requirement of the calorific value measurement system of natural gas in GB/T 18603-2001[5], the uncertainty is within 0.1%.

Conclusion

In this paper the basic principle of energy metering system of natural gas was analyzed, and the system of energy metering of natural gas has established. By measuring the gas volume flow, component data, pressure, temperature and other parameters, the energy of natural gas and Wobbe index have been calculated. The uncertainty of the natural gas energy measurement results shows that the uncertainty of calorific value of natural gas is within 0.1% and meets the accuracy requirements of GB/T 18603-2001 on the calorific value of natural gas measurement system.

References

[1] Yang Hong, Dong shier, Peng Xuefeng, Chen Huang. Current Situation and Development Trend of Energy Measurement of Natural Gas in Our Country [J]. Silicon Valley, 2012,3: 44-46.

[2] Wang Chi, Li Chunhui. Measurement system of natural gas energy and method [J]. Measurement Transaction, 2008, 5 (11): 404-407.

[3] Technical supervision bureau of the people's Republic of China. GB / T22723 - 2008 Determination of Natural Gas Energy [S], 2008.

[4] Technical supervision bureau of the people's Republic of China. GB/T 11062, Computing Method of Natural Gas Calorific Value, Density, Relative Density and Wobbe Index[S], 1998.

[5] Technical supervision bureau of the people's Republic of China. GB/T 18603-2001. Technique requirements of natural gas metering system [S], 2001.

Advanced Materials Research Vols. 986-987 (2014) pp 1531-1535

doi:10.4028/www.scientific.net/AMR.986-987.1531

On a Method of Getting Test Data for Boundary Scan Interconnection Test in Multiple Scan Chains

Xianhua Yin, Cuifeng Xu

School of Electronic Engineer and Automation, Guilin University of Electronic Technology,

Guilin, 541004, China

yxh4417@guet.edu.cn, xcf4100@guet.edu.cn

Keywords: boundary scan, interconnect test, TPDF, multiple scan chains.

Abstract. The goal of this paper is to present a new innovative method of getting test data for boundary scan interconnection test in multiple scan chains, so to decrease the test time and increase the efficiency and reliability. Firstly, a new model of configuring and optimizing multiple scan chains is formed based on the researches on greedy strategy for configuring multiple scan chains for internal test and the sorting algorithm of single scan chain for Cluster test. Then, a method of establishing test project description file (TPDF) is presented in order to get the test data quickly and effectively. During the testing of two different boundary-scan circuit boards, all faults can be detected. Experiment results show that the expected objective is achieved.

Introduction

Boundary scan is an integrated method for testing interconnection on printed circuit boards (PCB) that is implemented at the integrated circuit (IC) level [1]. Boundary scan has become the technology of choice for building reliable high technology electronic products with a high degree of testability.

Using multiple scan chains, test time can be greatly reduced. And test reliability can be greatly increased. Therefore, multiple scan chains have been used extensively in test areas [2]. It is very important to study the application of multiple scan chains in interconnect test, because interconnect test is the main part of boundary scan test.

In order to generate test vectors for UUT, the data that user needs to provide is too much in some existing boundary-scan test tools. It is unavoidable to make some mistakes in the process of inputting these data during the execution of the tool. It would result in false test for UUT, and have to make other test for UUT. Thus, the testing time consumption is too large, and is low in efficiency and reliability. Some boundary-scan test tools not only need user to provide too much data during the execution of the tool, but also need user to develop test program complying with their syntax rules, which is too perplexing to be learned by user.

Getting the test data required for test generation of unit under test (UUT) is the prerequisite of automatic test pattern generation (ATPG) [2].Methods of getting test data required for test generation and fault diagnosis are studied in the paper. In order to getting the data quickly and effectively, a new innovative method of establishing TPDF(Test Project Description File) is presented.

Configuring multiple scan chains

Supposes there are K scan chains in some circuit under test. CTi is the smallest clock cycles to shift test data into or out from scan chains i. $CTIi$ is the smallest clock cycles to shift test vector into scan chains i. $CTOi$ is the smallest clock cycles to shift test responses out from scan chains i.

To reduce test time, shift out test responses at the same time of shifting the next test vector into scan chain. Therefore:

$$CTi = \max\{CTIi\ ,\ CTOi\}\ (1 \le i \le k) \tag{1}$$

Supposes the smallest clock cycles to shift test data into or out from all scan chains is CT . All scan chains is parallel, so:

$CT = \max\{CTi\}\ (1 \le i \le k)$ (2)

It is showed in expression (2) that CT will be reduced when CTi is reduced and tends to average. It is the theoretical basis for optimizing multiple scan chains.

Based on the greedy strategy, Yoon-Hwa.Choi[3] proposes a suboptimal heuristic algorithm for configuring multiple scan chains, so that internal test time is reduced to minimum. According to the algorithm, boundary scan devices are in turn configured into each scan chains based on the sequence of test length from big to small, so that the length of each scan chain tends to equality. According to expression (2), CT is reduced. Greedy strategy is a suboptimal algorithm, but the optimal solution can be obtained in many applications.

However, interconnect test is different from internal test. For some circuit under test, using some given test generation algorithm, the test generation is determined and the test length of all boundary scan devices is equal[2]. Therefore, this paper proposes a solution to configure multiple scan chains of interconnect test according to the sequence of boundary scan cells (BSC) count of boundary scan devices from big to small based on the greedy strategy. First, the boundary scan device of BSC count maximum is configured into a scan chain. CTI and CTO of the scan chain are calculated. CT of the scan chain are too calculated by CTI and CTO . Then, the boundary scan device of BSC count sub-maximum is configured into another scan chain and calculate CTI , CTO and CT of the scan chain, and so on. One boundary scan device is configured into scan chain i if and only if CTi is smaller than CTj with $1 \le j \le k$ and $j \ne i$. The configuration of multiple scan chains is completed when all boundary scan devices are in turn configured into every scan chain.

Optimizing multiple scan chains

Interconnect test needs to distinguish driver from receiver, and it is the same as that of Cluster test. So, this paper proposes a solution to optimize each of multiple scan chains of interconnect test based on the sorting algorithm of single scan chain proposed by Yoon-Hwa.Choi[4], so that CTi is reduced and CT tends to minimum. According to the sorting algorithm of single scan chain, boundary scan devices of every scan chain are sorted when all Receivers are in rear of all drivers or driver/receiver, or all drivers is in front of all receivers or driver/receiver[5]. After optimizing multiple scan chains, $CTIi$ and $CTOi$ is the minimum, so that CTi is the minimum according to expression (1).

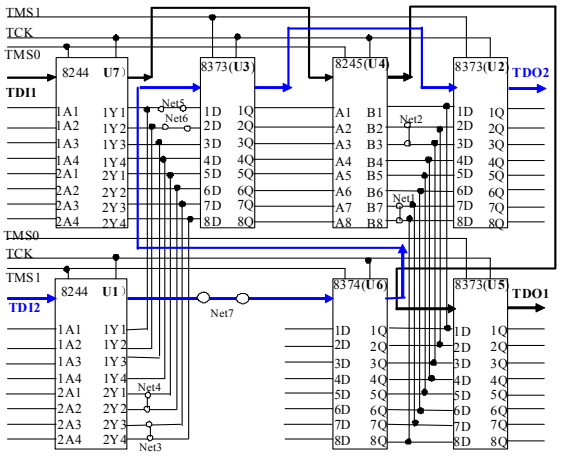

Fig.1. Demo circuit schematic diagram

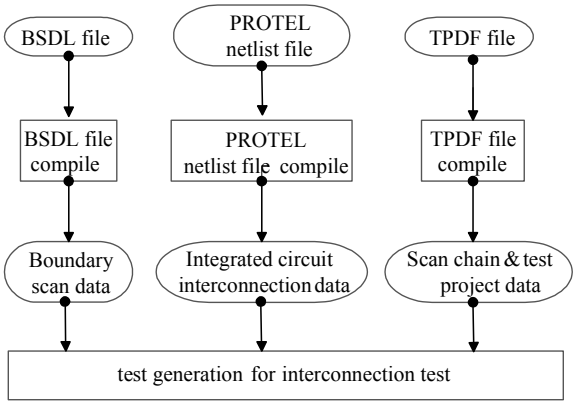

Fig.2. The flow of getting test data

The purpose of this example is to verify the result of configuration and optimization of multiple scan chains of interconnect test. Demo circuit consists of switch, jumper and seven boundary-scan chips. Switch is used for simulating open circuit fault, short circuit fault, stuck-at-0 fault, stuck-at-1 fault, bridging fault and scan chain fault. Jumper is used for setting scan chains structures of single scan chain, double scan chains and three scan chains. It is shown in Fig.1.

According to BSC number of boundary scan devices from big to small, the sequence is U4(36,D&R), U1(18,D), U2(18,R), U3(18,D&R), U5(18,R), U6(18,D), U7(18,D). Ui($1 \le i \le 7$) represents boundary scan device of Demo circuit. The digital in the bracket represents the BSC number of boundary scan device. The letter in the bracket represents the boundary scan device is a driver (D) or a receiver (R) or a driver/receiver (D&R).

For Demo circuit, results of configuring and optimizing multiple scan chains for demo circuit is shown in Table 1.The digital is the BSC number of scan chain in Table 1. The arrow indicates the sequence of boundary scan devices in scan chain From TDI to TDO. After double scan chains is configured, CT=72. After double scan chains is optimized, CT=54. Obviously, the solution proposed by this paper can works efficiently on configuring and optimizing multiple scan chains of interconnect test, the test time is reduced greatly.

Table 1. Results of configuring and optimizing multiple scan chains for Demo circuit

Scan chain		CT_i	CT
Single	U1->U6->U7->U4->U3->U2->U5	108	108
Double	Chain 1 U7->U4->U5	54	54
	Chain 2 U1->U6->U3->U2	54	
Three	Chain 1 U4	36	36
	Chain 2 U1->U7->U5	36	
	Chain 3 U6->U3->U2	36	

Establishing TPDF for multiple scan chains

In order to getting the data quickly and effectively, a new innovative method of establishing TPDF is presented. TPDF structure is shown as follows.

```
BEGIN_TPDF
<scan chain quantity description >::=
scan_chain_quantity:<integer>;
<scan chain parameter description>::=
{
    scan_chain_number:<integer>;
    scan_chain_element:<component number list>;
    TAP_name:<component number>;
    TAP_pin_map:(<TAP pin maps>);
}
<test project quantity description >::=
test_project_quantity:<integer>;
<test project parameter description>::=
[
    test_project_number:< integer>;
    scan_chain_number: < integer>;
    test_type: < integer>;
    test_chip_number: <component number list>;
    test_generation_algorithm: < integer>;
    test_generation_file_name: <file name>;
    test_no_fault_file_name: <file name>;
    test_response_file_name: <file name>;
    test_report_file_name: <file name>;
]
END_TPDF
```

BEGIN_TPDF and END_TPDF are the beginning and ending keywords of TPDF. All parameter of a scan chain is in { }. All parameter of a test project is in [ ]. For N scan chains and M test projects, there are N { } and M [ ]. The part behind "::=", is the expression of former description. ":"is a separator between the keyword and the parameter value. ";"is the ending mark of every parameter description and "&" is the connector of a parameter description between line and line. "--"is begin of a notes.

TPDF is simple in syntax rules, fixed in structure, clear in content. Therefore, it is easy for user to learn the method of establishing TPDF. In TPDF, keywords show the place that the interrelated test data should been filled in. According to test patterns for UUT, user establishes the TPDF beforehand, not during the execution of the BST tool. Once the TPDF is established successfully, the test data required for test generation and fault diagnosis can be gotten by compiling the TPDF, just only one file, not many files, for example, scan chain description (SCD) file, test generation file, non-fault test response file and test response file in some existing boundary-scan test tools. At the same time, the data that user has to provide during the execution of the tool is decreased greatly. The method of establishing TPDF increases transparence, maintainability and reliability, decreases complexity, and enhances test efficiency. TPDF is one of the most important tools for getting test data required for test generation and fault detection.

For Demo circuit as is shown in Fig.1, the TPDF is shown as follows.

```
BEGIN_TPDF
scan_chain_quantity:2;
{
    scan_chain_number:1;
    scan_chain_element: u7,u4,u5;
    TAP_name: pt1;
    TAP_pin_map: (TDI1:4,TDO1:2,TCK:3,TMS1:1,TRST:5);
}
{
    ……
}
test_project_quantity:2;
[
    test_project_number:1;
    scan_chain_number:1;
    test_type: 0；  --0: interconnection test;
    test_chip_number: u7,u4,u5;
    test_generation_algorithm: 0；--0: ant colony algorithm;
    test_generation_file_name: tgf1.txt;
    test_no_fault_file_name: tnff1.txt;
    test_response_file_name: trf1.txt;
    test_report_file_name: trpf1.txt;
]
[
  ……
]
END_TPDF
```

Flow of getting test data

By compiling TPDF file, these test data is gotten, which are scan chain parameters, test generation algorithm, test type (for example, interconnection test, cluster test), UUT, test generation file, non-fault test response file, test response file, and test report file.

Boundary scan description language (BSDL) file includes boundary-scan cells characteristics, IC pins characteristics, and connections of boundary-scan cells and IC pins, scan chain length, boundary-scan chips ID code, boundary-scan test instruction, instruction length, boundary-scan controller signal, and so on. As an important file required for boundary-scan test generation, BSDL file is provided by the manufacturer of boundary-scan components. The data noted above is gotten when BSDL file is compiled successfully.

PROTEL netlist file maps the interconnection of integrated circuit. It is generated automatically in the process of designing PCBs using EDA software of PROTEL. By electronic design interchange format (EDIF), user can transform CADENCE netlist file and ORCAD netlist file into PROTEL netlist file. Compiling PROTEL netlist file, these data relating to interconnections on PCB can be gotten. The flow of getting test data is shown in Fig.2.

Conclusion

For boundary scan interconnection test，the CT of multiple scan chains is smaller than that of single scan chains，and is more smaller after optimized. TPDF is simple in syntax rules, fixed in structure, clear in content. Therefore, it is easy for user to learn the method of establishing TPDF and use in getting test data. During the testing of two different boundary-scan demo circuit boards, the boundary-scan test software can run steadily and can detect all faults successfully. The results of experiment showed that establishing TPDF is a feasible and effective method to get test data for boundary scan interconnection test in multiple scan chains.

References

[1] Borroz, T, Using general purpose digital hardware to perform boundary scan tests. AUTOTESTCON, 2011 IEEE, pp. 328-332 ,2011.

[2] Pomeranz, I., Reddy, S.M., On Interconnecting Circuits with Multiple Scan Chains for Improved Test Data Compression. Proceedings of 17th International Conference on VLSI Design，pp.741 – 744, 2004.

[3] Yoon-Hwa Choi, Chul Kim, Jung, E, Configuring Multiple Boundary Scan Chain for Board Testing. 1995 IEEE International Symposium on Circuits and Systems,vol.3, pp.2128-2131,1995.

[4] Choi, Y.-H. , Jung, T, Configuration of a boundary scan chain for optimal testing of clusters of non-boundary scan chain devices. 1992 IEEE/ACM International Conference on Computer-Aided Design, Santa Clara, CA, USA, pp.13-16,1992.

[5] Xin-Xin Wang, Li-Ping Liang, Xing-Jun Wang, A New Solution to Implement Multi-Full-Scan-Chain Test with JTAG. 8th International Conference on Solid-State and Integrated Circuit Technology, Shanghai pp.2155-2157,2006.

[6] Berthelot, D.; Chaudhuri, S.; Savoj, H, An efficient linear time algorithm for scan chain optimization and repartitioning. Proceedings of International Test Conference, pp.781-787, 2002.

[7] Insoo Kim, Hyoung Bok Min, Operation about multiple scan chains based on system-on-chip. 2008 International SoC Design Conference, Busan, Vol.2, pp.191-194, 2008.

[8] Stamenkovic, Z., Giles, M., Russi, F, Combining internal scan chains and boundary scan register: A case study. EUROCON '09. IEEE, St.-Petersburg, pp.2064-2069, 2009.

Advanced Materials Research Vols. 986-987 (2014) pp 1536-1540

doi:10.4028/www.scientific.net/AMR.986-987.1536

On-orbit Fault Location Analysis and Solution Strategy of GEO Satellite Solar Array

Jiaoyan Zhang[1, a], Gangweng Han[1, a], Weibo Zhu[1, a], Jingyong Liu[1, a] and Na Kang[2, a]

[1]Beijing Aerospace Control Center, Beijing 100094, China

[2]Equipment College, Beijing 102249, China

[a]zhangjiaoyanhello@163.com

Keywords: GEO satellite; solar array; on-orbit fault location; solution strategy.

Abstract. Solar array is the important part of the satellite's Electrical Power Supply, the failure of the solar array may lead to the loss of some or all of the satellite's functions, so fault location in time and solution strategy of solar array is particularly important. The thesis studied the on-orbit failure of GEO satellite's solar array, analyzed the fault location according to the related telemetry, and researched the solution of all kind of the faults. The thesis contributes to the satellite control center to locate faults in time and the satellite manufacture to improve the design of the solar array, it is helpful to improve the reliability and safety of the satellite's on-orbit running.

Introduction

In recent years, in many problems plagued satellite's normal running, the failure rate of electrical power system is undoubtedly higher [1]. And once the electrical power system malfunctioned, the satellite will lose its part or all of functions. The satellite's energy mainly comes from the solar array, so after the satellite entering a preset orbit, first of all the solar array need to be able to work normally, it includes the opening and the fixation of the solar array and the normal work of Solar Array Drive Assembly (SADA). The solar array should always orient to the sun, and transfer energy to each system. At the same time, in the throughout lifetime of the solar array, the efficiency of the solar array should not t be significantly decreased. But during each process in this series of work, the failure of the solar array all occurred in recent years, and then it affected the satellite's normal operation. The studies of various aspects of fault have certain effect to the timely fault handing and the excellent design.

Fault types of solar array

The fault type of solar array is varied, and its common fault types are mainly in the following aspects.

Deployment failure of solar array. Up to the separation from the launcher, all the power is provided by the pre-charged batteries. After the separation, both batteries and folded solar array participate to the bus power. When entering the transfer orbit, the external panel is deployed, and then the power is provided by solar array. The deployment failures include that the solar array does not perform the resealed command and then gets stuck or cannot achieve completely deploying state [2].

Solar array section failure and open-circuit failure of section interconnection piece. The solar array section failure include open-circuit and short-circuit. Open circuit is that the temperature shock, space debris or micro meteorite impacts lead to the section rupture. Short circuit is the breakdown of the section caused by electrical static discharge.

The open-circuit failure of section interconnection piece is that the temperature and the shock lead to the upper and lower electrode welding, or alternating high and low temperature causes aging failure and fracture.

Sun-oriented failure of solar array. At the end of transfer phase, solar array wings rotation is initiated. Solar array positioning is made in open loop by SADA to keep the cells faces perpendicular to the sun direction, which leads to one revolution per day. Sun-oriented failure is that the SADA gets stuck, and the SADA can't control the normal direction of solar array real-time pointing toward the sun automatically.

SADA power slip ring failure. SADA is the only way of power transmission from the solar array to the power control unit. The power produced by the solar array has to transfer to the satellite body by SADA power slip ring failure. SADA power slip ring failure is the short circuit of the power slip ring or the poor contact between the brush and the ring.

Attenuation failure of solar array. The mutations of the electromagnetic environment in the space may lead to radiation damage, and then the glass cover turns black and dark, resulting in the attenuation of the photoelectric conversion efficiency of solar array.

On-orbit fault location

Deployment failure of solar array.

Judgment telemetry. Deployment failure of solar array can judge by the solar array expansion indicator telemetry and output current telemetry.

The case. In 2006, the deployment of a satellite's solar array malfunctioned, the second deployment of solar array didn't finish. After sending the deployment command, the solar array expansion indicator telemetry didn't change, and the solar array output current didn't decrease yet.

Solar array section failure and open-circuit failure of section interconnection piece.

Judgment telemetry. Solar array section failure and open-circuit failure of section interconnection piece can judge by the solar array output current telemetry. At the same time, the number of malfunctioned section also can judge by the loss power and the total power. But it is not easy to judge whether solar array section failure or open-circuit failure of section interconnection piece.

The case. In the lifetime of a satellite, there were four abnormal phenomena of the north solar array output current. In 2001 and 2002, the current all decreased sharply, and in 2009 and 2011, the current all increased sharply. After judgment by telemetry, the north solar array all lost the power of one section in 2001 and 2002 by solar array section failure or open-circuit failure of section interconnection piece.

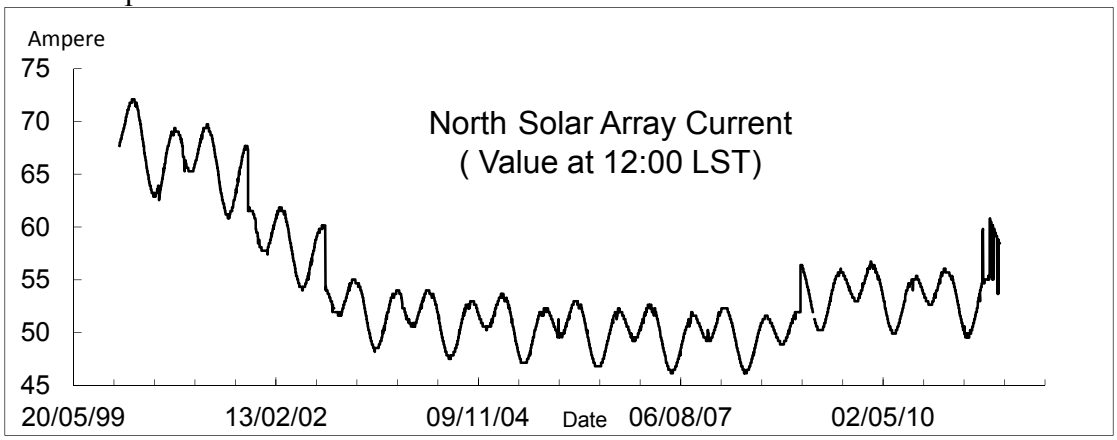

Fig. 1

Sun-oriented failure of solar array.

Judgment telemetry. Sun-oriented failure of solar array can judge by the solar array position telemetry and solar array output current.

The case. In 2011, at the end of the lifetime of a satellite, the north SADA appeared unusual, some sticking points of the SADA occurred. When the North SADA rotated to these sticking points, it would get stuck, and then the solar array can't point the sun in real time.

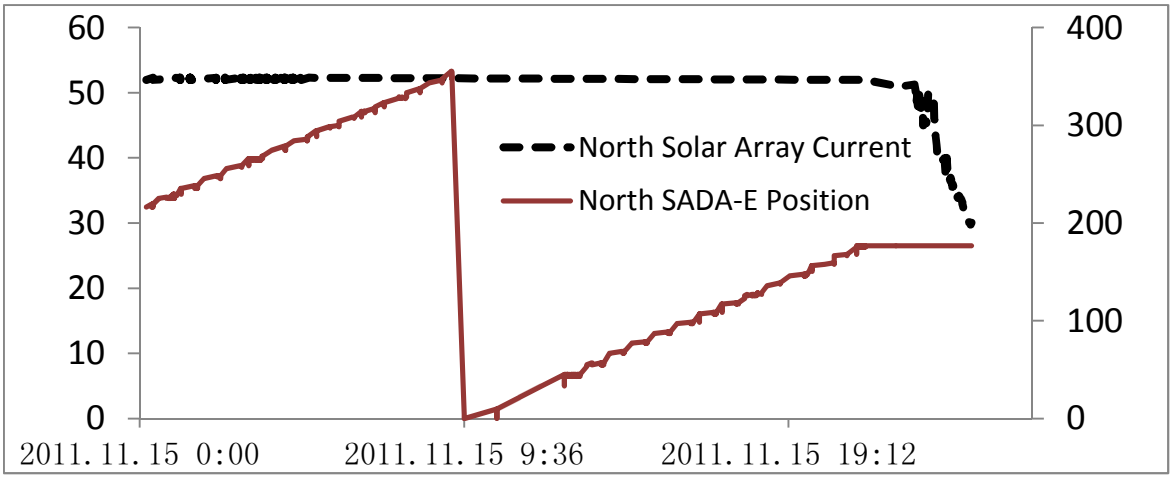

Fig. 2

SADA power slip ring failure.

Judgment telemetry. SADA power slip ring failure can judge by the SADA temperature telemetry, solar array output current telemetry and solar array position telemetry.

The case. In 2012, the north solar array current of a satellite decreased sharply, at the same time the SADA temperature increased sharply, and the solar array position appeared burr. So we can judge that, in the process of solar array's rotation, the SADA friction torque increased, and then the rotation was abnormal, and the increased torque resulted in the increase of the SADA temperature. And then the higher temperature caused the short circuit of the SADA power slip ring, so the solar array current decreased sharply.

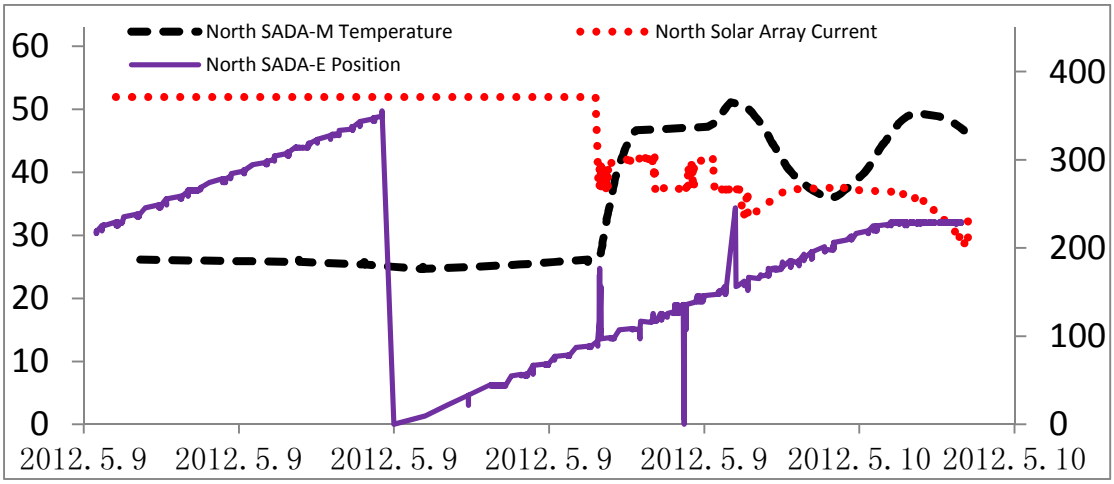

Fig. 3

Attenuation failure of solar array.

Judgment telemetry. Attenuation failure of solar array can judge by the solar array current telemetry.

The case. In 2000, because of the strong radiation of Bastille event, the surface of a satellite's solar array was eroded, and then resulting in the decrease of the output power. The decrease of solar array output current coincided with the strong radiation, so we judge that it is the strong radiation resulting in the attenuation of the solar array.

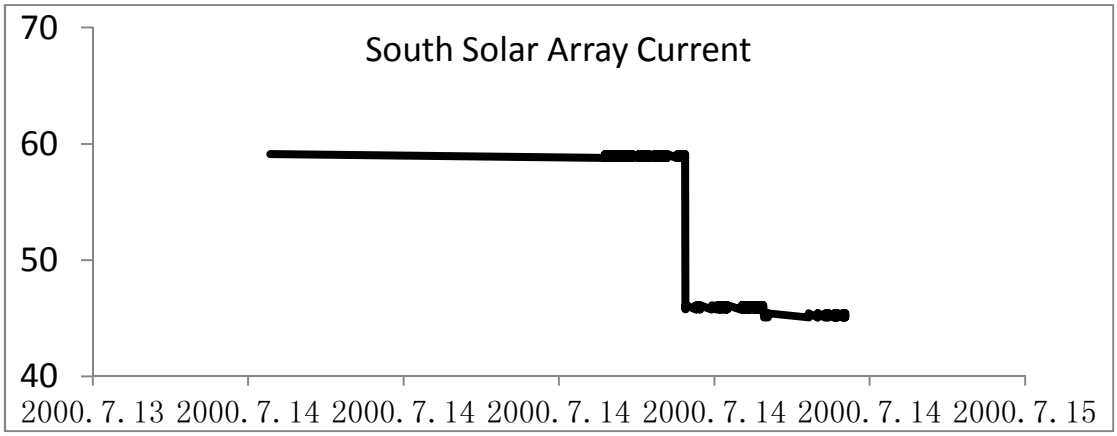

Fig. 4

Ⅳ. Solution strategy

Deployment failure of solar array.

Coping strategies for satellite control center. As a satellite control center should check the relative telemetry when the solar array is deployed. If the telemetries don't change, it can decide the following work in time according to the failure.

Better design for satellite manufacture. As satellite manufactures need to improve the reliability of the release mechanism, and the solar array could be deployed at a time instead of two times to improve the success rate. At the same time, the connection accuracy of solar array structure and the hinge also should be improved.

Solar array section failure and open-circuit failure of section interconnection piece.

Coping strategies for satellite control center. As a satellite control center should monitor the telemetry carefully in the eclipse season. The historical data suggests that this kind of malfunction usually happened in the eclipse season, therefore the satellite control center should monitor the relative telemetry carefully in the eclipse season, notice the malfunction in time and handle it, for example, reducing the power dissipation of the satellite according to the power loss of the solar array to make sure the security running of the satellite.

Better design for satellite manufacture. As satellite manufactures should take the influence of ESD and thermo elastic deformation into consideration and strengthen the stability of satellite's solar array. Electrostatic sensitive device should be designed for electrostatic discharge protection. And the manufactures should strengthen the function of thermal protection for the problem of thermo elastic deformation. At the same time, the manufactures should consider sufficient redundancy for the solar array.

Sun-oriented failure of solar array.

Coping strategies for satellite control center. As the satellite control center should monitor carefully, and notice the malfunctions in time to prevent the occurrence of serious accidents. Secondly, if the solar array gets stuck, we can try to rotate across the sticking point, for example, we can rotate the solar array backward, and then we rotate forward a bigger angle. The practice indicated that, after several attempts the solar array may rotate across the point and continue to rotate automatically. At last, if problem continue after repeated attempts, we can use both solar array and the batteries to provide the power in the high peak, and in the low peak, we can accelerate to charge the battery to supplement the battery [3].

Better design for satellite manufacture. As the satellite manufacturers should ensure that the motor and the satellite heat absorption and good thermal conductivity. At the same time, the lubricant should be added to reduce friction moment [4].

SADA power slip ring failure.

Coping strategies for satellite control center. The previous failure indicates that, the decline of output power caused by short circuit is irreversible, and there may be further diffusion. So as the satellite control center, for avoiding entire solar array failure caused by short circuit diffusion, we

should set the malfunctioned solar array rotate with back to the sun from facing the sun. And the satellite loss should be decreased to make sure the normal work of the satellite platform and the transponders.

Better design for satellite manufacture. As the satellite manufactures should consider sufficient redundancy, a conductive ring at least has two side brushes. At the same time, it should improve the thermal design of slip ring to guarantee heat radiation of the slip ring wire [5].

Attenuation failure of solar array.

Coping strategies for satellite control center. As the satellite control center, if the important space environment events are forecasted, we should monitor the relative telemetry carefully, notice the malfunction in time and handle it, for example, reducing the power dissipation of the satellite according to the power loss of the solar array to make sure the security running of the satellite.

Better design for satellite manufacture. As the satellite manufactures should consider sufficient redundancy for the solar array to ensure the adequate power of the satellite.

Ⅴ. Conclusions

Based on the relevant historical data accumulated for a long time, the thesis classified the failures of GEO satellite solar array according to its different fault components, analyzed the fault location of every kinds of failures, and researched the solution strategy of every kinds of failure The thesis has important significance to improve the reliability and security of satellite's solar array.

References

[1] Tan Chunlin, HU Taibin, WANG Dapeng, LIU Yongjian JIANG Dongsheng and SHI jun, in: *Analysis on Foreign Spacecraft In-orbit Failures*, Spacecraft Engineering Vol. 20 (2011), p. 130

[2] Baokun Zhang, in: *The Fault of satellite's solar array deploying and driving device*, Space International (1984), p. 14

[3] JIANG Dongsheng，ZHANG Pei Liu Peng and WU Lequn, in: *On-orbit Failure Analysis and Solution Strategy of Satellite Power System*, Spacecraft Engineering Vol. 22 (2013), p. 72

[4] Shaoyan Wang, in: *The Failure Analysis of Satellite Solar Array Driving Device*, Control Engineering Vol. 1 (1993), p. 55

[5] WANG Xiao，Li Chao, in: *Reliability Design and Test of One Spaceborne Slip Ring*, Electro-M echanical Engineering Vol. 25 (2009), p. 28

Advanced Materials Research Vols. 986-987 (2014) pp 1541-1544

doi:10.4028/www.scientific.net/AMR.986-987.1541

Power System Fault Diagnosis Based on Artificial Fish -Swarm Algorithm

Tianyi QU[1, a]

[1]School of Management XuZhou institute of Technology , Xuzhou, Jiangsu, 221008, China

[a]email: jdbh2001@163.com

Keywords: Fault diagnosis; Power system; Programming model; Artificial fish

Abstract. The primary method of power system fault diagnosis is that the fault section estimation is demonstrated a 0-1 programming model according to the acting theory of protective relays. This paper proposed a kind improved artificial fish -swarm algorithm: binary artificial fish -swarm algorithm(BAFA) for this kind of problem. Forward speed of optimal direction between swarm-behavior and follow-behavior is analyzed and a comparative analysis is made with genetic algorithm(GA) on this basis. Results indicate that follow-behavior is superior to swarm-behavior on forward speed of optimal direction and BAFA is superior to GA on the comprehensive performance. Meanwhile, it is shown that BAFA has the fast convergence speed and better optimization ability.

Introduction

The modern power grid with more and more scale,capcacity and coverage plays a critical role in national economy and people's life, so the fault outage will bring incalculable consequences. Timely and effective measures need to be taken to solve the fault[1][2][3]. Grid fault diagnosis is that using the fault information of protection and circuit breaker to identify the fault components of which recognition is the key problem and the protection and circuit breaker of misoperation. At present, there are many fault diagnosis methods at home and abroad. Early methods such as logical processing method, expert system, rough sets and Petri network have been widely applied in the fault diagnosis. Among them, expert system is difficult to obtain a complete knowledge base. Meanwhile it has no learning ability and poor fault tolerance. The intelligent bionic algorithm which has good generality and strong capacity in processing complex problem has a great development. Due to the nature of its numerical characteristics, the intelligent bionic algorithm is suitable to solve complicated engineering problems. Therefore, the intelligent bionic algorithm applying to power system fault diagnosis is of great significance. The algorithm features have low requirement for the initial value, insensitivity to parameter selection, strong robustness and the ability of fast-track changes, etc. Many domestic scholars have proposed improved algorithms, such as the AFA of cooperative coevolution[4][5], heuristic AFA and AFA based on mutation operatior.

This paper proposes binary artificial fish-swarm algorithm (BAFA) for solving 0-1 programming problem in power grid fault diagnosis [6], which is put forward as a new solution to solve power grid fault diagnosis.

Binary Artificial Fish-Swarm Algorithm

On the basis of existing artificial fish-swarm algorithm based on non-linear 0-1 programming model, the binary artificial fish algorithm at which each artificial fish is restricted to 0 or 1 is proposed. In a D-dimensional search space, there is a swarm formed by N artificial fish. And vector $X_i = (x_{i1}, x_{i2}, \cdots, x_{iD})$ represents the state of artificial fish i , where $i = 1, 2, \cdots N$ and $x_{ij}\ (j = 1, 2, \cdots D) \in \{0, 1\}$. The food concentration of artificial fish current location (adaptive value of object function) is represented by $Y = f(X)$ (Y is $E(S)$ in this paper), and the sate of each artificial fish is a variable to be optimized, which means each artificial fish is a potential solution. The distance between arbitrary two artificial fish

$$d_{ij} = \left\| X_j - X_i \right\| = \sum_{n=1}^{D} \left| x_{jn} - x_{in} \right| \quad (1)$$

When every artificial is to move, it need observe the movement of other fish within *visual* and food concentration to determine its own move direction every time. Where *visual* ($visual \in N \cap 1 \le visual \le D$) is the perception scope of artificial fish. *step* ($step \in N \cap 0 \le step \le visual$) is the length of the largest step of artificial fish every move. δ, crowded degree factor, represents the crowed degree around some location, which is used to avoid too crowed with nearby partners. *try_number* expresses the maximum trying times during artificial fish foraging process. At BAFA, a group of artificial fish (random solution) is initialized and then using artificial fish search for the optimal solution by iteration. It updates itself by foraging behavior, swarm behavior, follow behavior and so on in each iteration so as to realize optimization. Artificial fish algorithm is described as follows:

Here X_i is the current state of artificial fish i, and Y_i is food concentration. Selecting X_j, Y_j randomly accord (2) in the perception scope ($d_{ij} \le visual$) results in precondition.

$$x_{jk} = \begin{cases} \neg x_{ik} & n(n \le visual) \\ x_{ik} & \text{other} \end{cases} \quad (2)$$

If $Y_j < Y_i$, a step forward will be taken in this direction based on (3). Otherwise, a new random state X_j is to be selected according to (2) .This process is to be repeated until meeting the ideal condition or reaching the maximum trying times.

$$x_{ik/next} = \begin{cases} x_{jk} & m(m \le step) \\ x_{ik} & \text{other} \end{cases} \quad (3)$$

when the number of trying times meets the maximum, a random step will be made within the scope of the perception according to (4), so as to get a new state.

$$x_{ik/next} = \begin{cases} \neg x_{ik} & l(l \le step) \\ x_{ik} & \text{other} \end{cases} \quad (4)$$

X_i is denoted the current state of artificial state i; Y_i is the food concentration; N_f is the number of artificial fish within the scope of its perception. These artificial fish constitute set S_i, where

$$S_i = \left\{ X_i \middle| \left\| X_j - X_i \right\| \le visual, j = 1,2,\cdots i-1, i+1, \cdots, N \right\} \quad (5)$$

If $S_i \ne \varnothing$, the perception scope of artificial fish X_i ($N_f \ge 1$) exists other partners. The centre of set is

$$X_{centre} = \frac{\sum_{j=1}^{N_f} X_j}{N_f} \quad (6)$$

Here every artificial fish is expressed in binary system, (6) can also be expressed as under：

$$X_{centre} = \frac{\sum_{j=1}^{N_f} X_j}{N_f} \; x_{centre-k} = \begin{cases} 1 & \rho > 0.5 \\ rand()\%2 & \rho = 0.5 \\ 0 & \rho < 0.5 \end{cases} \quad (7)$$

Where $\rho = \frac{\sum_{j=1}^{N_f} X_{jk}}{N_f}$ and $rand()$ is a random integer. When calculating the central food concentration Y_{centre}, if (8) is satisfied, the state of central location is good and not crowed, and then

artificial fish moves a step towards the central location using (9). If (8) can not be satisfied, foraging behavior will be executed.

$$Y_{centre} < Y_i, N_f \cdot Y_{centre} < \delta \cdot Y_i, \delta > 1 \quad (8)$$

$$x_{ik/next} = \begin{cases} x_{centre-k} & n(n \le step) \\ x_{ik} & other \end{cases} \quad (9)$$

X_i is denoted the current state of artificial state i and Y_i is the food concentration. According to its own state, artificial fish find out the partner $X_{\min}$ whose food concentration is $Y_{\min}$ within its perception scope. If $Y_{\min} \ge Y_i$ is satisfied, foraging behavior is to be executed; if not, some artificial fish whose number is N_f will be searched within the perception scope of $X_{\min}$. If (10) are satisfied, the location of $X_{\min}$ is superior and not crowed , then the artificial fish move a step forward this direction according to (11), otherwise, foraging behavior will be executed.

$$Y_{\min} < Y_i, N_f \cdot Y_{\min} < \delta \cdot Y_i, \delta > 1 \quad (10)$$

$$x_{ik/next} = \begin{cases} x_{\min-k} & n(n \le step) \\ x_{ik} & other \end{cases} \quad (11)$$

According to the nature of problem need to be solved, the current environment of artificial fish is evaluated and then appropriate one from above behaviors is selected. Firstly, this paper attempts all behaviors to find out the one executed towards the fastest speed in the optimal derection. Secondly, the behavior that has less perfect state after execution is to be applied actually. Finally, if there is no behavior that can make the next state better than that of the current state, behavior is to be taken randomly.

Bulletin board is used to record the current optimal artificial fish state that has been researched, as well as the corresponding food concentration. After every move, every artificial fish compares the food concentration of its current state with the last record in bulletin board. If the value is more superior , the last record will be replaced by it, that keeps bulletin board maintaining optimal state of each artificial fish and the corresponding food concentration. At the end of the algorithm, the value of bulletin board is the optimal solution of the system.

Case analysis

In order to verify optimization performance of BAFA applied to power system, this paper executes a complex fault experiment in the sample power networks shown in figure 1.The test system consists of 28 elements, 40 circuit breakers and 84 protection.

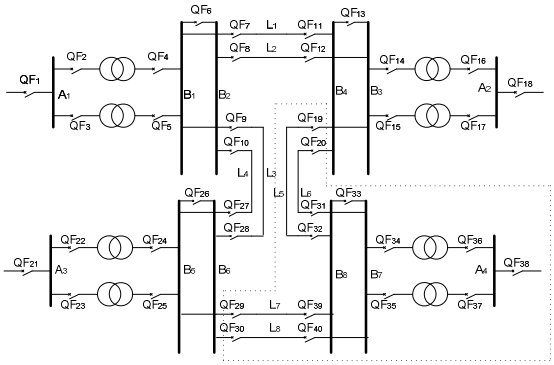

Fig.1 A sample power networks

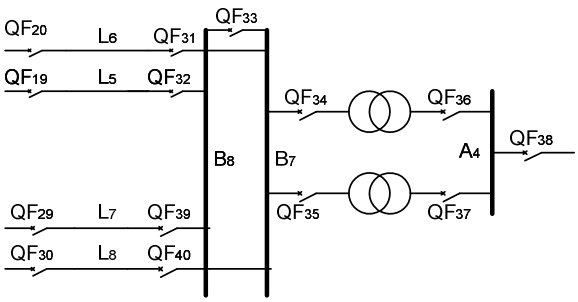

Fig.2 fault section

Suppose there is a fault in power networks (fault section is encircled by dotted line in figure 1), alarm signals are as follows: protection actions of T_{7m}, T_{8p}, B_{7m}, B_{8m}, L_{5Sm}, L_{5Rp}, L_{6Ss}, L_{7Sp}, L_{7Rm}, L_{8Ss} and circuit breaker trips of QF_{19}, QF_{20}, QF_{29}, QF_{30}, QF_{32}, QF_{33}, QF_{34}, QF_{35}, QF_{36}, QF_{37} QF_{39}.

First of all, according to the fault section concluded from the passive network formed by tripping circuit breakers, the elements that need fault diagnosis are $L_5, L_6, L_7, L_8, B_7, B_8, T_7$ and T_8. The states of these elements are represented respectively by vector $S=[s_1, s_2, \cdots, s_8]$. Then, the objective function is determined by the actual state vector of circuit breaker C, the actual state vector of protection R, the expected state vector of protection $R^*(S)$ and the expected state vector of circuit breaker $C^*(S,R)$. The objective function is

$$\begin{aligned}\min E(S) = \min\{&3(1-s_1)+4(1-s_3)+(1-s_5)+2(1-s_6)+2(1-s_7)2(1-s_8)+2(1-s_2)(1-s_5)\\&-\max(s_5,s_7)-\max(s_5,s_8)+s_1+4s_2+s_5+s_8\}\end{aligned} \quad (12)$$

Formula(12) is the food concentration of BAFA, and the experiment is operated under C language programming environment in the PC running Windows XP in this paper . The program run result shows that the optimal solution is $S=[1,0,1,0,1,1,1,1]$, $E(S)=4$,and the diagnosis is that line L_5, line L_7, bus B_7 ,bus B_8, transformer T_7 and transformer T_8 are faulted.

Conclusion

In order to ensure the accuracy and real-time performance of the power grid fault diagnosis, this paper proposes an improved AFA(the binary artificial fish algorithm)according to the characteristic of 0-1 programming optimization model for power grid fault diagnosis .The improved algorithm is to be applied in solving optimization model. Analysis shows that follow-behavior of BAFA is superior to swarm-behavior on forward speed of optimal direction. Compared with genetic algorithm under the basis of above analysis, BAFA is superior to genetic algorithm on convergence speed and optimization result. Moreover, the advantages of BAFA, such as easy programming, fast running speed, optimization strong capability of optimization are beneficial to ensure the accuracy and real-time performance of power grid fault diagnosis. However, due to the nature of 0-1 programming, whether lager step size within scope of sense is able to result in premature convergence needs further research.

References

[1] T. Sakquchi et al. Prospects of expert systems in power system operation[J]. Electrical Power & Energy Systems，1988，10(2).

[2] Cho H J，Park J K. An expert system for fault section diagnosis of power systems using fuzzy relations[J]. IEEE Trans on Power Systems, 1977, 12(1)：342-348.

[3] Li Ran，Li Jinghua，Su Lijun. Application of rough set to build electric power grid fault diagnosis model based on decision tree[J]. Relay, 2005, 33(18)：1-5.

[4] Wang Jialin，Xia Li，Wu Zhengguo，Yang Xuanfang. State of arts of fault diagnosis of power system[J]. Power System Protection and Control, 2010, 38(18)：210~214.

[5] Zang Tianlei，He Zhengyou，Li Chaowen，Qian Qingquan. Fault section estimation in transmission network based on binary swarm intelligence algorithm[J]. Power System Protection and Control, 2010, 38(14)：16~22.

[6] Zhu Zhihui，Sun Yunlian. Application of quantum immune algorithm in power system fault diagnosis[J]. Power System Protection and Control, 2010, 38(18)：22~25.

Advanced Materials Research Vols. 986-987 (2014) pp 1545-1548

doi:10.4028/www.scientific.net/AMR.986-987.1545

Research about the Testing Methods of Varistor Tester

Fuquan Wang[1, a],Jin Huang[1],Kang Gao[1,b],Zhuang Ouyang[1],Chaosheng Liang[1]

[1]Guangdong Zhaoqing Supervision & Inspection Institute of Quality and Metrology, China

[a]ddw33@163.com ,[b]gaokang2010@yeah.net

Keywords: Varistor; varistor voltage; voltage ratio

Abstract. We had described and discussed the testing methods of varistor tester about DC reference current, varistor voltage, leakage current, voltage ratio, and provided the corresponding test data,which has proved that the methods are feasible.

Introduction

Varistor Tester (referred to as "tester"), is mainly used to measure the varistor voltage, leakage current, voltage ratio or nonlinear index DC parameters[1][2]. Typically measurement value of DC reference current is 0.1mA or 1mA,MPE≤±2%; the measurement range of varistor voltage is (0～2000)V，MPE≤±2%;the measurement range of leakage current is (0～2000)μA,MPE≤±2%; the measurement range of voltage ratio is (1.020～1.300),MPE≤±0.005.

In this paper, an example of HG2516 [3] was used to introduce the testing methods. Because of DC reference current, varistor voltage, leakage current, voltage ratio parameters are all less than or equal ± 0.5 for the maximum permissible error of HG2516 tester,the calibration equipment selected are as follows: D.C. Resistance Box, type: zx84, resistance range: 100Ω ~ 100MΩ, MPE: ± (0.05% ~ 0.1%); digital multimeter, Model: 2002, range: (0～2) A, accuracy: DCI: ± (0.05% of reading + 0.002% of full scale).

DC reference current testing method

In the presented work, tested schematic, using D.C resistance box and digital multimeter had been developed (see Fig.1)[4].First of all,we determined the DC reference current value and the varistor voltage range, and then started measuring.According to the test point,we changed the resistance of D.C. resistance box ,as while as, recorded the displayed current value of digital multimeter. Indication error of DC reference current is represented by the relative error, the tested data is shown in Table 1.

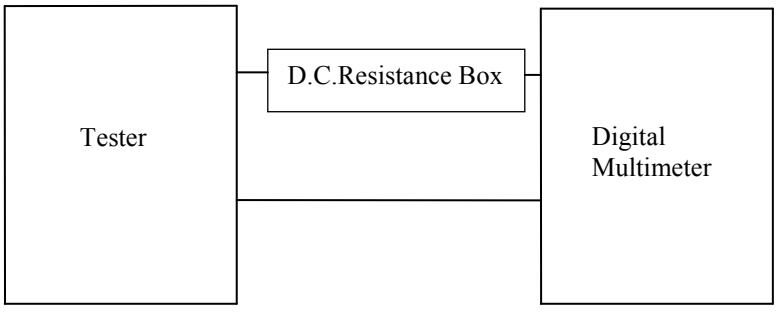

Fig.1 Wiring diagram

For measuring the DC reference current ,requiring digital Multimeter and D.C resistance is due to the tester characteristics.Resistance box tester is designed to measure the range of constant current source for the adaptation.

Table 1 Test data of dc reference current

The nominal value（mA）	Varistor voltage range	Varistor voltage test points（V）	Current measured values（mA）	Error（%）
1	1400	140	1.00131	-0.13
		420	1.00128	-0.13
		700	1.00121	-0.12
		980	1.00124	-0.12
		1400	1.00122	-0.12
The nominal value（mA）	Varistor voltage range	Varistor voltage test points（V）	Current measured values（μA）	Error（%）
0.1	1400	140	100.0576	-0.06
		420	100.0562	-0.06
		700	100.0550	-0.06
		980	100.0548	-0.05
		1400	100.0513	-0.05

Varistor voltage testing method

We need to build a connection diagram,using D.C resistance box and digital multimeter(see Fig.1)[5]. At first,we determined the value of reference current and the varistor voltage range, and then started measuring. According to the test point,we changed the resistance of D.C. resistance box, at the same time, recorded the displayed current value of the digital multimeter I_0， the resistance value of the resistor box R_0 ,and the displayed value of varistor voltage U_N .after that,we had calculated the actual value of the varistor voltage $U_{N0}=I_0 \bullet R_0$. Indication error of varistor voltage is represented by the relative error, the tested data is shown in Table 2.

The testing method of varistor voltage is actually the measurement of current, if we want to adopt the measurement method of voltage, we need to use HVDC digital voltmeter of 0.1 level, and can not adopt the voltage profile of ordinary digital multimeter, or the HVDC digital voltmeter of 0.5 level, the value of constant current source is small, so we need a high-voltage DC digital voltmeter, the reason is that it has a high input impedance.

Table 2 Varistor voltage test data

DC reference current range（mA）	Varistor voltage range	Varistor voltage displayed value（V）	Actual measured value			Error（%）
			R_0	I_0	U_{N0}（V）	
1	1400	139.9	140 kΩ	1.00131 mA	140.18	-0.20
		420.5	420 kΩ	1.00128 mA	420.54	-0.00
		701.1	700 kΩ	1.00121 mA	700.85	+0.04
		981.4	980 kΩ	1.00124 mA	981.22	+0.02
		1397.7	1.4 MΩ	1.00122 mA	1401.71	-0.29
0.1	1400	139.8	1.4 MΩ	100.0576 μA	140.08	-0.20
		420.2	4.2 MΩ	100.0562 μA	420.24	-0.00
		700.6	7.0 MΩ	100.0550 μA	700.38	+0.03
		980.7	9.8 MΩ	100.0548 μA	980.54	+0.02
		1396.6	14.0 MΩ	100.0513 μA	1400.72	-0.29

Leakage current testing method

Connection diagram was shown in Fig.1. Above all ,we still determined the value of reference current and the varistor voltage range, In addition,seted up the leakage current testing voltage and then started measuring. According to the tested point, we changed the resistance of D.C. resistance box, at the same time, recorded the measured values of the current data of digital multimeter I_{L0} ,and the displayed value of leakage current tester I_L .Indication error of leakage curren is represented by the relative error, the tested data is shown in Table 3.

When measuring the leakage current, we have two ways to input the leakage current testing voltage , one way is a percentage,the other way is a direct setting.Typically varistor leakage current is generally no more than 20μA, but when you measure the leakage current ,you need to cover the test range.

Table 3 Leakage current test data

Displayed value（μA）	Actual measured value（μA）	Error（%）
197.4	198.1	-0.35
597.0	598.8	-0.30
996.0	997.2	-0.12
1395.7	1395.7	0.00
1992.7	1995.4	-0.14

Voltage ratio testing method

The tested schematic, using D.C resistance box,digital multimeter and varistor had been developed (see Fig.2). We determined the value of reference current and the varistor voltage range, after that,according to the tested point,we changed the resistance of D.C. resistance box,besides,the displayed varistor voltage value U_N and $U_{N0.1}$ showed by the digital multimeter were recorded.We had calculated the ratio of the actual value of the voltage $k_0 = U_N / U_{N0.1}$ .the displayed voltage ratio value k or α (If the α is displayed, it need to be converted into a voltage ratio k) was recorded. Indication error of voltage ratio is represented by the relative error, the tested data is shown in Table 4.

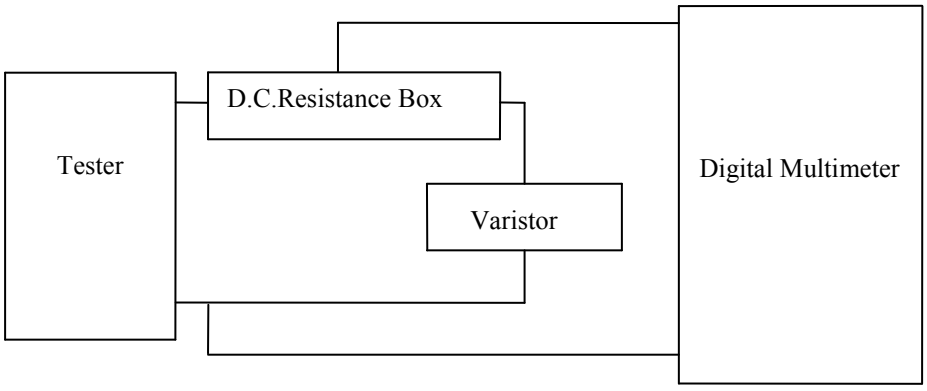

Fig.2 Voltage ratio or nonlinear index test schematic

When we measure the voltage ratio or nonlinear index , the varistor is essential , which is determined by the nonlinear characteristics of the varistor. At present, nonlinear index varistors are not low generally, therefore, when we want to measure a tester with a low α value (α<10),we need a linear resistor box to reduce the non-linear of varistor.

Table 4 Voltage ratio test data

Displayed value of voltage ratio k	Actual measured value			Error（%）
	U_N（v）	$U_{N0.1}$（v）	k_0	
1.076	504.78	469.92	1.074	0.002
1.150	544.37	472.47	1.152	0.002
1.296	619.00	476.53	1.299	0.003

Summary

In this paper, a type of varistor tester, HG2516,was choosen for discussing the methods of measuring the DC reference current, varistor voltage, leakage current, voltage ratio, and the tested data also had proved the correctness of the testing methods, which can be used in the other types of varistor testers.

References

[1]Junfeng Zhang, Bo Xia.Temporary Overvoltage Characteristic of Zinc Oxide Varisto[J]. The World of Powe r Supply,2012,(01):58-64.

[2]A.Sedky,E.El-Suheel .Structural and electronic characteristics of pure and doped ZnO varistor[J]. Chin.Phys.B,2012, 21(11).

[3]Information on http://www.cz-hgdz.com/ymdzcsy/7.html.

[4]Ying Dou, Shupeng Zhang,Weiqun Yu. Varistor tester calibration method [J]. China Metrology, 2011,(11):94-96.

[5]Junsheng Wu. Analysis and implementation of the varistor tester calibration[J]. Metrology & Measurement Technique,2005.32(7):19-20.

Advanced Materials Research Vols. 986-987 (2014) pp 1549-1553

doi:10.4028/www.scientific.net/AMR.986-987.1549

Research of Fault Monitoring And Early Warning Technology of Optical Cable

Zhang Gang[1, a], Liu Chuan[1,b], Ren Jie[1,c], Zhang Zenghua[1,d] , Chen Wei[1,e]

[1] China Electric Power Research Institute, Nanjing, 210003, China

[a]zhanggang@epri.sgcc.com.cn, [b]liuchuan@epri.sgcc.com.cn, [c]zhangzenghua@epri.sgcc.com.cn, [d]renjie3@epri.sgcc.com.cn, [e]chenwei2@epri.sgcc.com.cn

Keywords: Optical Cable NMS; Intelligent fault Analysis; Predictable Operation & Maintenance; GIS Interface.

Abstract. Electric power optic cables, as infrastructure facilities of the power communication system, are commonly affiliated to primary towers and poles of power transmission lines. And their safe and stable operation is one of important factors to guarantee the reliable power supply. At present, there are many kinds of professional application systems for equipment management in the field of Power System, so the level of their automation and intelligence is relatively high. But Management and Monitoring of outdoor lines are still staying the same as traditional methods, becoming a vulnerable part in smart grid. This paper introduces a network management system of electric power optic cables based on GIS and referred to the design method of Transmission Network Management System (TNMS). Its aims and several main developing technologies are also discussed. This system will play an important role in improving maintenance management and operational reliability for the power communication network.

Introduction

Optical cable has great frequency band resource and excellent transport performance. Since the 90s of last century, with the development of power industry and the increasing demand on the bandwidth of communication network, optical communication is more and more widely used in power system. As the infrastructure of optical fiber communication, the safe and reliable operation of optical cable has become one of the most important factors for the safe operation of power grid. Recently, with the development of on-line monitoring technology, more and more optical fiber cable lines are used on online monitoring system, and as a result, play an important role on improving the maintenance management level, discovering and solving the problem of fault line and improving the safe operation level. System construction mainly carried out around the static cable resource management and cable monitoring. The system which is built up by each company has differences among function, realization and data format. For the lack of the unified function, data, process, interface specification and the difficulty of data sharing, island of information is easily formed, as a result, it is difficult to realize the transverse and longitudinal resource sharing and result in the waste of resources and influence of work efficiency. Thus, it is necessary to design model of network management system according to communication equipment, unified design, unified standard and unified specification of optical fiber cable professional network management system. Moreover, the construction of strong network of the power system, especially for optical communication professional intelligent management work has a very important practical significance.

Aim and Content of The Development

The vast majority of power cable is attached to the first rod line and is service for the power system. The optical cable of electric power pipe is laid in the row tube invalid hole. The OPGW optical cable is erected on the ground in overhead transmission line. The ADSS optical cable is arranged in a line tower. General overhead cable is usually laid in 35KV wire rod. The optical cable in factory station is in substation cable trench and cable layer. At present, GIS is a visualization of information technology with relatively high practical, technical and economic performance. GIS uses the design idea of object-oriented. It supports the geographic information data and multiple layer control. It has a perfect performance especially on the representation and geographic information about data interface

by using vector graphics mode. Electric power transmission and distribution of GIS platform is the solution of integration system according to the demand of power intensive and large-scale power network operation and management. Professional GIS graphics and commercial database are the carriers of GIS. It is the grid data platform of the realization of graphics and data integration. For the characteristics of the power cable, the integration of GIS platform and the construction of a cable network management system seems to be very practical and feasible.

With the goal of strengthening the communication management, the core of standardized and practical, the way of the information and optical communication technology and the visible platform of GIS, power cable professional network management system improves the electric power communication optical cable network maintenance and management ability, realizes the professional application system by the fiber resource management, fault intelligent monitoring and early warning, and the business management as the support of the computer, network and standardization, enhances the ability of data analysis and standardizes data model and interface standard in order to provide technical support for the communication management of electric power system by organizing, integrating, optimizing and monitoring power cable resources. The main construction contents include the following aspects:

- Realize comprehensive management of optical cable network physical and logical resources by establishing a multi-user graphical management system to ensure the data, model, interface and interface consistency, completeness and reliability. Construct GIS cable layer to realize the visual optical fiber network resource management by using the power of GIS platform and data.
- Realize network function among GIS system, equipment management system and similar systems by designing and standardizing the system of horizontal and vertical interface.
- Realize implementation of intelligent fault alarm source judgment and complete cable fault location and fault alarm function by using optical fiber monitoring technology and through the interconnection network system and optical transmission equipment.
- Realize cable bearer service management as well as the cable fault analysis function of business impact through the method of interconnection and transmission equipment management or manual input.
- The system has two modes of online and simulation. Operation training, cable fault simulation, network optimization simulation and other functions can be realized under the mode of simulation.

System Design

Architecture Design

The system adopts three layers of system structure based on middle application server. Three layer system structure reasonably separate data storage, processing and result display. It can compute a part of data processing and application of work from the database server to application server to handle the pressure which can reduce the database server, as a result, database services can concentrate on data storage management and graphical data display and processing can make full use of graphics processing function of GIS platform which is advanced an powerful. From the system point of view, the load distribution is more uniform and the data and graphics processing ability of the whole system is improved. System structure is shown in Figure 1.

System Software Design

Cable networks do not rely on a cable manufacturer. So the network management system of optical cable could guarantee that all networks are equally supported effectively and it is particularly important to electric power communication network which has obviously diversified characteristics. The network management system of optical cable could ensure that the software design in accordance with the principle of unified design, unified standards, unified specification and be pragmatic. The whole system is divided into four parts of advanced functions, basic functions, database and data interaction interface. Advanced functions complete the standard of content and work of electric power

communication optical cable network management by optical cable network fault warning, intelligent analysis and etc. in order to enhance the communication professional management fine degree and intelligent level Basic functions complete the functions of system platform, resource management, real-time monitoring and system support to realize computerized data processing in the management of cable network. Data interaction mainly completes the relevant communication management system and monitoring station data exchange. It has the functions of data extraction, storage, forwarding and analytic. Database can make a realization of data storage and intelligent expert tactics of resources, monitoring and geographic information. The software system has cross-platform portability and it can run on different platforms. In accordance with the file of State Grid, Company Management System Construction Work, with the experience of integrated network management system, we design a set of system platform with the characteristics of high practical, high modular and degree. The function of the platform is shown in Figure 2. Each functional group is composed of a series of functional modules. The relationship between modules organizes by loose coupling and it can be flexibly deployed in different hardware environment in order to adapt to the actual needs2 of users, to achieve different management objectives.

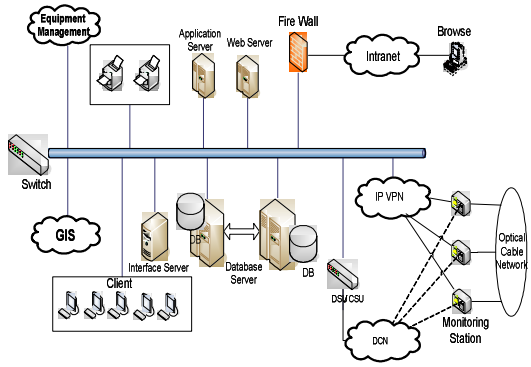

Fig 1 System Structure

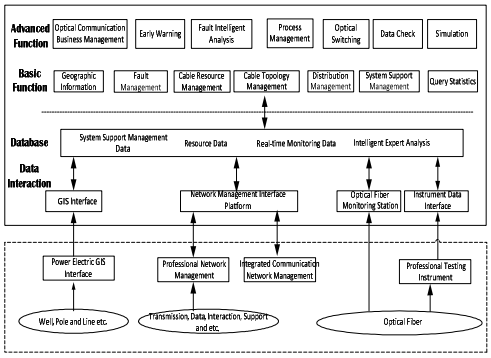

Fig 2 System Software Architecture

Interface Design

n GIS Interface

Cable network management system uses GIS as a platform of the system application interface. It can realize visible management of cable resources and to develop accurate cable, pipe, bar line, machine building and other resources on the map. By using welding and other functions to generate optical cable routing network and special network topology, it centralizes management and monitoring of optical fiber cyber source and plans network structure reasonably. By “landmarks” and vector electronic map, GIS platform accurately shows the cable routing information and improves the accuracy of fault location. In accordance with the interface specification, system designs unified GIS platform interface which is a set of universal programming interface unrelated to specific GIS. System interacts real-time data through interface and shields the heterogeneity of GIS platform in order to realize the integration of different format GIS.

n TNMS Interface.

Interconnection is realized mainly through the standard and open northbound interface between cable management system and transmission device management system, cable management system and comprehensive network management system and cable management system itself. The technology of northbound interface includes Q3, CORBA, SOAP, TL1, SNMP and etc. Among them, technology of CORBA becomes the main solution of the realization of network management northbound interface with the advantages of object-oriented, cross-platform, language independent and do not rely on network protocol. The TMF814 standard gives the definition of IDL interface set and the interface to achieve. Thus, this standard is more and more applied.

Fault intelligent Analysis.

System support the acquisition and transmission of alarm management information analysis function to realize the real-time intelligent system. System uses the real-time signal of transmission network management and monitoring system collects all these signal with analysis, filtration and concentration to transfer the useful alarm signal into interface protocol in order to realize the alarm triggering test and accurate fault location. According to the current communication network of the

cable section of business analysis, communication network influence index, influence scope, business interruption probability and other parameters can be known, as a result, realize the "n-1"and "n-2" function of cable network. According to the circuit use weight, rate of weight and other data, it quantifies the severity of blocking influence on service. The formula is as following.

$$I = \left(\sum_{i=1}^{m} \lambda_i * V_i \Big/ \sum_{i=1}^{n} \lambda_i * V_i \right) * 100\,\%$$

I is influence index, λ is circuit use weight, V is weight of weight, m is the number of all affected business influenced by fault section, n is the number of business of all network. The process of fault intelligent analysis is shown in Figure 3.

According to optical fiber monitoring equipment acquisition data, optical fiber fault judgment uses the wavelet transform algorithm to analyze fiber event judgment of events, then compares these events and the standard curve of event points, judge whether standard value and the difference beyond the event threshold range and generates a corresponding report.

As shown in Figure 4, this system uses landmarks to judge the actual position of fault point. Landmarks with name, geographical distance, optical distance, longitude, latitude and other attributes to identify optical fiber cable, well, mark stone and building geographic information. Combined event analysis technology, when the cable fault occurs, the system will automatically give the relative distance of fault location and mark the position of fault point on GIS map. The fault location method is as following.

- According to the optical distance of OTDR/COTDR test, compared with the optical cable line, landmarks of fault point can be fixed. Cable section is arranged between the two subject status to the broken fiber failure, at the same time, GIS diagram of the cable section shows red.
- Determine the geographic distance optical cable lines before and after punctuation along the fault distance, form a visual description of fault information cable. The formula is as following. "L=(length-distance1-fbobbin1)*(fgeodistance2-fgeodistance1)/(distance2-distance1-fbobbin 1-fbobbin2)", "Length" is the optical distance of fault point. "distance1, fbobbin1, distance2, fbobbin2" are optical distance and disc before and after the remaining length of landmarks respectively. "fgeodistance1, fgeodistance2" are geographic distance before and after the remaining length of landmarks respectively.
- Determine the longitude and latitude of the fault point and display the fault point location on the electronic map. According to the former formula, determine the break point of fault point and optical cable lines derived from the geographic distance. Calculate the latitude and longitude of the fault point in the segment. The formula is as following.
  msgLongitude=x2+(x1-x2)*mDis/Dist(x1,y1,x2,y2);
  msgLatitude=y2+(y1-y2)*mDis/Dist(x1,y1,x2,y2);

"x1, y1, x2, y2" are the latitude and longitude coordinates of the break point before and after respectively. "mDis" is the geographic distance between fault point and point M.

Optical Cable Network Warning

The system can do early warning analysis for cable join event, optical cable segment and different levels of cable an cable network. The flow of early warning is shown in Figure 5 Through the cable performance data periodically, system uses the least square method to acquire linear fitting for a specific period of time and to analyze point mutations. If exceeding the warning threshold, system gives the early warning information, as a result, realize the predictive maintenance of electric power communication optical cable network and improve the ability of emergency respond.

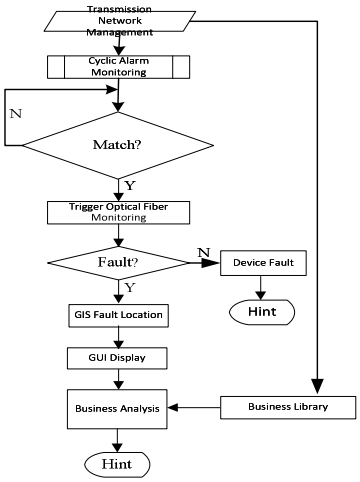

Fig 3 Flow chart of fault analysis

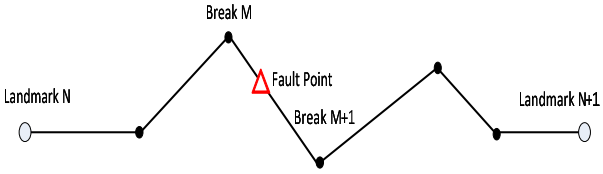

Fig 4 The diagram of Optical Cable Fault

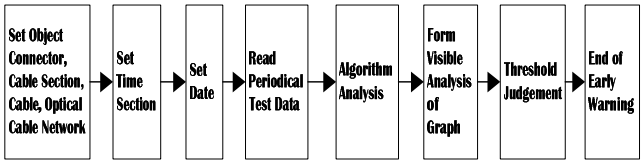

Fig 5 Flow Chart of Warning

Conclusion

As the first put forward research and development, cable professional network management is mainly used for optical cable network of electric power communication system. Meanwhile, it can also be used for telecommunications, Unicom, Netcom and mobile telecom operators, as well as all the use of optical fiber as transmission line business. It can provide network performance monitoring, the cable network maintenance, resource management and other services. With the Smart Grid construction, the demand of line monitoring and intelligent management will be increasingly high. Therefore, the cable network management system has become a new bright spot of power communication market and obtained the unprecedented development.

Acknowledgements

This work was sponsored by the Science and Technology Project Funds 2013(SGCC).

References

[1] Li Xiangrong, Hao Hanyong, Fan Tao, Tang Ruezhong. Construct Digital Power Grid and Enterprise Informatization.[J]. Power System Automation, 2007, 31(17):1-5.

[2]Cai Bin, Xu Wei, Jiang Ling, Application of A New Type of Electric Power Communication Optical Cable Inspection System.[J]. Communication of Power System. 2008, 29(6):5-7.

[3]Tang Yuezhong, Wei Xiaojing. Study on the Strategy of Implementing Informatization Engineering State Grid SG186.[J]. Electric Power Informatization, 2007, 5(10):18-22.

[4]S. L Tsao, and W.M. Cheng, Realization of an on-line fiber-optic bending loss measurement system. Instrumentation and Measurement, IEEE Transactions on 53(2004):72-79.

[5]Zhang Gang, Design of Optic Cable Monitoring System for Electric Power FTTH.[J].Modern Electronics Technique.2011,34(4):147-149.

Advanced Materials Research Vols. 986-987 (2014) pp 1554-1557

doi:10.4028/www.scientific.net/AMR.986-987.1554

Research of Process Procedures in Lighting Impulse Measurement Software

Liu Shaobo[1,a], Li Wenting[1,a], Zheng Yan[2,b], Long Zhaozhi[1,a], Zhang Shuhan[1,a]

[1] China Electric Power Research Institute, Wuhan 430074

[2] Wuhan Ordnance N.C.O Academy, Wuhan, 430075

[a] wohaio@126.com, [b] zy397037172@163.com

Keywords: lightning full-wave with oscillation, ordered sample mean clustering, TDG2.0.6

Abstract. According to the new processing requirements of lightning full-wave with oscillation in IEC60060-1 Ed.3.0, a impulse measurement calculation program based on Labview has been designed. The method of starting point determination and curve fitting has been introduced. Ordered sample mean clustering thinking was used to find the chopping point of lighting impulse tail-chopping waveform. Waveforms in TDG（test data generator）2.0.6 in IEC61083-2Ed2.0 were used to check the accuracy of the calculation program. The uncertainty of test results has also been estimated. Test results show that this calculation program meets the requirements in IEC61083-2. When the calculation program was used with oscilloscope or data capture card,the accuracy of impulse measurement system can be ensured. It is of significant importance in impulse measurement research.

Introduction

The measurement of impulse voltage is an important part in high voltage measurement and nowadays the impulse voltage measurement can meet the requirements of use. But when the process method of lighting impulse voltage wave has been changed in IEC60060-1:2010 ED.3.0 [1], the calculation program should also be changed.

Program of impulse voltage measurement system

The schematic diagram of the impulse voltage measurement is shown in Fig1: The impulse voltage generated by impulse generator is measured by impulse voltage divider, then the voltage signal is transferred to the oscilloscope or data acquisition card by the measurement coaxial cable of the divider. The waveform measured by the oscilloscope transferred to the calculation program in the computer. Then all the parameters of the impulse voltage waveform can be output .

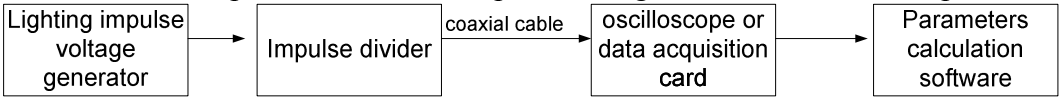

Fig.1 Schematic diagram of the impulse voltage measurement system

Most impulse voltage calculation software is programmed according to the requirements in IEC60060-1 Ed 2.0. Then all kinds of test waveforms in test data generator are used to judge the calculation accuracy of the software.The dispute of the lighting impulse voltage process methods in IEC60060-1Ed2.0 is that the definition of average curve of the waveform is too fuzzy. It is difficult to process in the actual measurement. The 0.5MHz used as the boundary frequency is not in line with the actual situation.

So in IEC60060-1Ed3.0, experimental voltage factor $k(f)$ (f is the oscillation frequency) is proposed in the process of lighting impulse voltage waveform parameters. $k(f)$ is used to filter the oscillation part of the lighting impulse waveform. Proposing of $k(f)$ is based on a lot of research results about the influence of oscillation frequency to the insulation breakdown[2-3]. The research results show that the influence of frequency to the insulation breakdown voltage is changed gradually. The propose of $k(f)$ can reflect the influence correct and it is important to the measurement of impulse voltage.

Process of lighting impulse waveform with oscillation

In IEC60060-1Ed3.0,the equation of the lighting impulse voltage to be determined Ut is :

$$Ut=Ub+k(f)(Ue-Ub) \quad (1)$$

of which: Ut: the voltage value to be determined

Ub: Peak value of reference fit curve

Ue: Peak value of initial recorded fit curve

$k(f)$: experimental voltage factor

In IEC60060-1Ed3.0, only basic process procedures are presented. There are still some difficulty in measurement Program implementation, as determination of the starting point, Fitting curve and filter structure. Discuss about these difficulties is as follows.

Determination of starting point in flat wave part For the lighting impulse voltage data recorded by the measurement instrument,firstly starting point of the waveform should be determined,then the reference level can be calculated and so on. The waveform measured by the impulse divider are often nearly flat curve but full of wrinkles,so it's difficult to determine the start point of the waveform. In paper [4], methods to determine the starting point is detailed introduced, The main idea is to cut out the flat part points and make some correlation calculation and judgment to determine the starting point.

But this method is not suitable when the rising part of the recorded waveform is oscillates seriously,the calculation program will get stuck in infinite loop. For this shortness of this method,in this paper,another method was presented:For the waveform data recorded by the data acquisition device,first find out the peak value point P of the waveform,then find the points A in the waveform before P,if $|U_A-Uo|\leqslant a|U_P-U_A|$,（a is between 0.001~0.005）,and A is the cut-off point of the flat part or called starting point of the waveform.

It is easy to realize this method in Labview and there is no limit to the rising part of the measured waveform. When the interference is existed this method is also applicable. By testing and verifying,software used this method calculates fast and can satisfy the required accuracy.

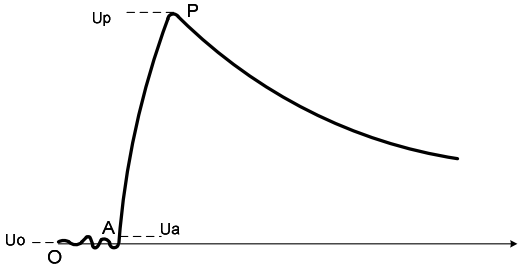

Fig.2 Determination of starting point of waveform

After determination the starting point of rising part of waveform, the average value of N points after the starting point should be calculated and determine the reference level. Then the offset compensation curve can also be determined.

Reference curve fitting of lighting impulse waveform. According to the process requirements of lighting impulse voltage waveforms in IEC60060-1,cut off the points from the point whose amplitude is 0.2 Ue（Ue e is the largest value of the recorded offset compensation curve） to the point in the tail wave whose value is 0.4 Ue. These points were used to construct the datum curve of the lighting impulse voltage waveform. The function model of datum curve in IEC60060-1Ed3.0 is:

$$U_d(t = U[e^{-(t-t_d)/\tau_1} - e^{-(t-t_d)/\tau_2}] \quad (2)$$

In this function model,four parameters need to be determined: U, τ1 , τ2 and td . This measurement software used the fit curve model in Labview to fit the datum curve.

In this calculation program,if appropriate initial values of the parameters were set,then the calculation can be convergence quickly.

When the curve fitting is finished,then the reference level curve Um(t) can be determined. The residual curve is obtained by $R(t)=U_0(t)-U_m(t)$.

Experimental voltage factor *k(f)* In IEC60060-1Ed3.0, experimental voltage factor *k(f)* was put forward to acquire the experimental voltage value. The factor is based on the frequency of the oscillation in the lighting impulse waveform. Figure 3 is the approximate curve of k(f) according to much reaserch results by relevant scholars. The equation of the curve is $k(f)=1/(1+2.2f^2)$, the broken line in Fig3 is the definition of *k(f)* in IEC60060-1Ed2.0.

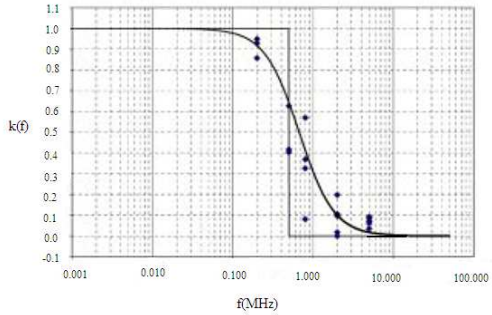

Fig.3 Curve chart of *k*(f)

In the calculation program for lighting impulse voltage, to realize the function of *k*(*f*), a digital filter based on *k*(*f*) was needed to be constructed.

In I IEC60060-1Ed3.0 annex C ,the equation of the filter to be constructed is as follows:

$$y(i)=b_0x(i)+b_1x(i-1)+a_1y(i-1) \quad (3)$$

$$b_0=b_1=x/(1+x) \quad (4)$$

$$a_1=(1-x)/(1+x) \quad (5)$$

$$x=tan[\pi Ts/\sqrt{a}] \quad (6)$$

Among them,$a=2.2\times10^{-12}$,Ts is the sampling interval of the recorded data,x(i) is the input voltage data to the filter； y(i) is the output voltage data of recorded waveform.

According to the equations (3)-(6), an IIR filter was constructed in LabView. The attenuation multiple is half the actual attenuation required. So in the process procedure, the residual curve data should pass the filter twice, flirt time , forward direction, then reverse direction.

To verify the accuracy of the lighting impulse calculation program,TDG2.06 in IEC61083-2Ed2.0:42/271/CD[5] was used to test the program. TDG is impulse waveform test data generator,LIA1-LIA12 in TDG were used. The test results of this calculation program were in table 1. The reference value of the waveforms in TDG and the deviation of measured result to the reference value is as shown in table 2. The measurement uncertainty of the program is analyzed according to annex B in IEC61083-2Ed2.0 .

From table 2, we know that when this calculation program was used to test the waveforms in TDG, the maximum absolute value of the measurement error of the test results is 6.00483×10^{-4}, so the measurement uncertainty component introduced by error of measurement is :

$$u_{B1}=6.00483\times10^{-4}/\sqrt{3}=0.035\%,$$

The maximum expanded uncertainty introduced by the reference value of the TDG waveforms is 0.016%, so this uncertainty component is $u_{B2}=0.016\%/2=0.008\%$

The composition of uB1 and uB2 is:

$$u_B=\sqrt{u_{B1}^2+u_{B2}^2}=\sqrt{0.035\%^2+0.008\%^2}=0.036\%$$

So when this calculation software used in the impulse voltage measurement system, the uncertainty compoment introduced by the software is 0.036%

Table 1. Test results of waveforms in TDG2.0.6

waveform	Ut kV		T1 us		T2 us		%	
	reference value	measured value	reference value	measured value	reference value	measured value	reference value	measured value
LI-A1	1049.6	1049.588	0.84	0.837	60.16	60.156	0	0
LI-A2	1037.64	1037.609	1.693	1.687	47.48	47.479	5.13	5.146
LI-A3	1000.22	999.963	1.117	1.108	48.15	48.16	4.57	4.589
LI-A4	856.01	855.729	0.842	0.846	47.8	47.826	7.88	7.908
LI-A5	71.973	71.972	1.711	1.692	47.7	47.687	7.74	7.776
LI-A6	100.17	100.17	1.761	1.737	41.58	41.554	17.73	17.765
LI-A7	104.348	104.349	2.12	2.087	38.36	38.331	20.14	20.199
LI-A8	96.012	96.011	1.503	1.487	44.92	44.909	14.75	14.783
LI-A9	55.927	55.924	1.215	1.208	55.74	55.732	4.02	4.047
LI-A10	81.929	81.906	0.924	0.929	42.66	42.679	12	12.05
LI-A11	86.597	86.545	0.578	0.587	56.37	56.421	4.06	4.088
LI-A12	85.584	85.555	0.587	0.596	57.36	57.394	2.27	2.286

Conclusion

A new impulse voltage measurement software according to IEC60060-1Ed3.0 was programmed. The process procedures of lighting impulse voltage and lighting impulse chopping voltage were introduced. Lighting impulse waveforms in TDG2.0.6 were used to test this software and the uncertainty of the calculation results of the software was also analyzed. The test results show that the accuracy of the software can fully satisfied the requirements in IEC60060-2[6] and IEC61083-2.

When this software was used with oscilloscope or data acquire card,it can ensure the accuracy of the impulse voltage measurement system. It is of great importance to the research of the impulse voltage measurement.

References

[1] International Standard IEC60060-1. High-Voltage Test Techniques. Part 1:General definitions and test requirements [S] . 3 rd ed . ,Geneva, Switzer-land , 2010.

[2] HALISTORM,J,BERLIJN S,GAMLIN M,et al. Applicability of Different Implementations of K -factor Filtering Schemes for the Revision of IEC 60060-1 and-2.[C].Beijing ISH,2005.

[3] LI Yi,JURIS RUNGIS. Analysis of Lightning Impulse Voltage with Overshoot[C].Beijing ISH,2005.

[4] Guo Hong, Wu Peng, Guo Zhi-feng etc, Parameter Extraction of Lighting Impulse with Overshoot or Oscillation. High Voltage Apartment[J] 2010,46 (1): 76-79.

[5] IEC61083-2Ed2.0:42/271/CD.Instruments and Software Used for Measurement in High-voltage Impulse Tests[S].

[6] International Standard IEC60060-2. High-Voltage Test Techniques. Part 2: Measuring systems [S].3 rd ed . ,Geneva, Switzer-land , 2010.

Advanced Materials Research Vols. 986-987 (2014) pp 1558-1564

doi:10.4028/www.scientific.net/AMR.986-987.1558

Research on High Bandwidth Rogowski Coil for Measuring Lightning Traveling Wave Current on Double Circuit Transmission Line

Chengju Yang[1,a] Chengwei Zhang[1,b] Gengbin Zhang[1,c] Peiling Chen[2,d] and Shijun Xie[2,e]

[1]Guangzhou Power Supply Burean of China Southern Grid, Guangzhou 510600, China

[2]Wuhan SunShine Power Science and Technology co., LTD , Wuhan 430074 , China

[A]ycj_1_2@163.com, [b]zcw_3_7@163.com, [c]zgb_z_1@163.com, [d]peilinchen@hust.edu.cn, [e]251651897@qq.com

Keywords: Rogowski coil; Traveling wave; Double circuit transmission Line; High Bandwidth

Abstract. Double circuit transmission line is an important part of the power grid, which is vulnerable to lightning and may endanger the security and stability of the power grid. In order to design a sensor which can monitor the lightning traveling wave current on double circuit transmission line, simulations of lightning on the double circuit transmission line were conducted. The simulation result shows that besides high frequency components, the traveling wave contains a lot of low frequency components. Based on the equivalent model and the frequency response of the self-integrated Rogowski coil, it turns out that the widely used self-integrated Rogowski coil is not suitable for this application as the problem of low frequency distortion. In this paper, through theoretical analysis and simulations in Matlab, an improved Rogowski coil with analog integrator is proposed which can correct the low frequency distortion of the self-integrated Rogowski coil. All the simulations, experiments and operating data installed to a double circuit transmission line in China verify the validity of the high bandwidth Rogowski coil.

Introduction

With the development of economic, the power transmission capacity is gradually growing, however the land resources for contracting transmission lines has become increasingly scarce. To solve the dilemma, double circuit transmission line on the same tower is widely used. Compared to single circuit transmission line, the tower of double circuit transmission line is higher, which causes stronger lightning attracting ability. Lightning trips frequently happened on double circuit transmission lines, which seriously endanger the safety operation of double circuit transmission lines [1,2]. In order to find the failure point timely and reduce the losses of lightning trips, accurate fault location technique is very important. Location technology based on traveling wave is widely used as it is not affected by transition resistance, asymmetry factor of line structure, terrain changes of line corridor and errors of voltage or current transformers, etc [3-5]. In this fault location method, detecting the traveling wave current is the basis. So a suitable current sensor for traveling wave current detecting on the double circuit transmission line is in urgent need to be developed.

Frequency-domain characteristics of the lightning traveling wave current

In order to design a proper traveling wave current sensor, the characteristic of the traveling wave current on the double circuit transmission line should be researched first.

Depending on the practical conditon, the model of lightning on double circuit transmission line was built in ATP-EMTP. Fig.1(a) is the waveform of the traveling wave current , Fig.1(b) is the the corresponding density distribution and cumulative probability distribution.

From the simulation result in Fig.1, it's clear that the traveling wave current on double circuit transmission line contains wide frequency component. Simulations of other parameters were done as well. According to all the of simulations, the frequecy characteristic of lightning on double circuit

transmission line is obtained. The design specifications of the frequency bandwidth of the current sensor is clear then. The low cutoff frequency of the sensor should be below 100Hz and the high cutoff frequency should be above 7MHz.

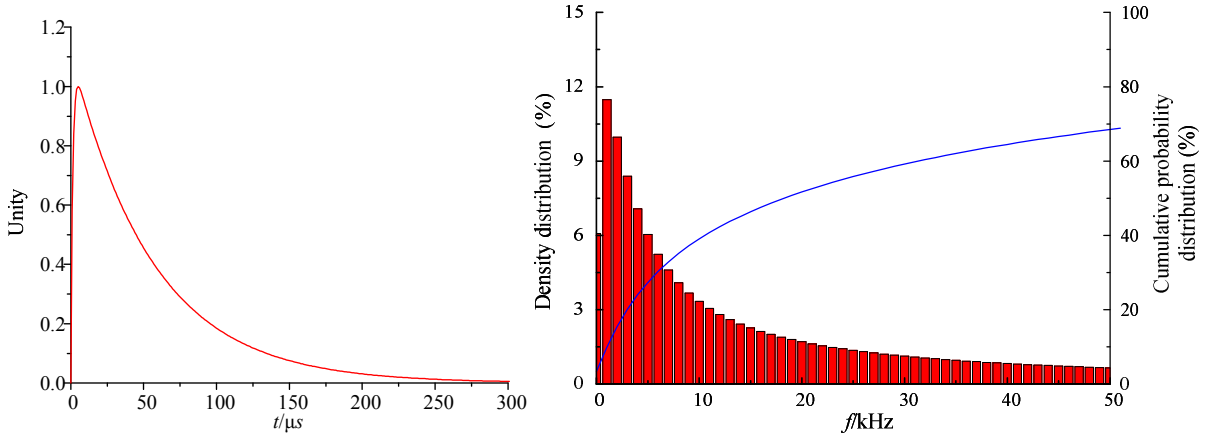

(a) (b)

Fig.1 Simulation result of the traveling wave current on double circuit transmission line

Frequency response of Rogowshi coil

The structure of Rogowski coil is shown in Fig.2. Wire is wounded on the secondary side of a skeleton of non-magnetic material. According to the theory of electromagnetic induction, when the measured current through the Rogowski coil changes, the magnetic field induces an electromotive force in the secondary side [6,7]. The equivalent circuit model is shown in Fig.3 [8-10]. $i_1(t)$ is the measured current, M is the mutual inductance between the Rogowski coil and the current-carrying conductor. L_0, R_0, C_0 and r are Rogowski coil's self-inductance, internal resistance, distributed capacitance and terminal sampling resistor respectively.

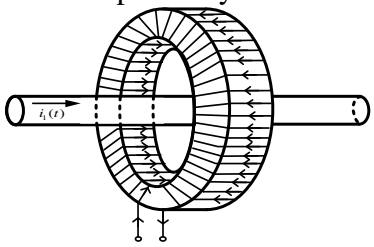

Fig.2 Structure diagram of Rogowski coil

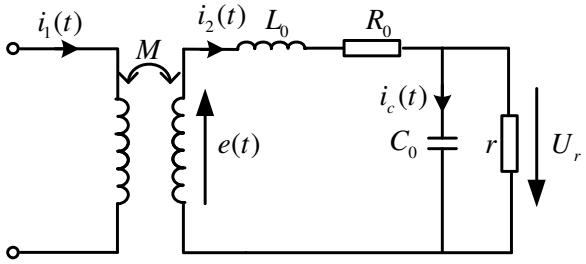

Fig.3 Equivalent circuit of self-integrator Rogowski coil

From the equivalent circuit in Fig.3 , the equations can be expressed as

$$\left.\begin{aligned} e(t) &= -M\frac{di_1(t)}{dt} \\ i_2(t) &= C_0\frac{du_r(t)}{dt} + \frac{u_r(t)}{r} \\ e(t) &= L_0\frac{di_2(t)}{dt} + (R_0 + r)i_2(t) \end{aligned}\right\} \tag{1}$$

Ignoring the influence of the distributed capacitance, the equation can be expressed as

$$e(t) = -M\frac{di_1(t)}{dt} = L_0\frac{di_2(t)}{dt} + (R_0 + r)i_2(t) \tag{2}$$

As the resistance R_0+r is small comparing to ωL_0 when the change rate of the measured current is high. Eq.2 can be simplified as

$$e(t) = -M\frac{di_1(t)}{dt} = L_0\frac{di_2(t)}{dt} \tag{3}$$

Thus, the relationship between the voltage on the sampling resistor and the measured current is

$$u_s = i_2(t)r = -\frac{Mr}{L_0}i_1(t) \tag{4}$$

Eq.4 can be valid only if R_0+r is considerable small comparing to ωL_0 and the change rate of the measured current is high.

Considering the distributed capacitance, from the equivalent circuit, the frequency response of the Rogowski coil can be obtained

$$H(s) = \frac{U_r(s)}{I_1(s)} = \frac{Ms}{L_0C_0s^2 + (\frac{L_0}{R_0} + R_0C)s + \frac{R_0 + r}{R_0}} \tag{5}$$

From Eq.5, the high cutoff frequency and the low cutoff frequency can be obtained in Eq.6 and Eq.7, respectively

$$f_H \approx \frac{1}{2\pi rC_0} \tag{6}$$

$$f_L \approx \frac{R_0 + r}{2\pi L_0} \tag{7}$$

As the change rate of the traveling wave current on the double circuit transmission line is slow and has a lot of low frequency component, the low cutoff frequency of self-integrated Rogowski coil may not cover the low-frequency component of the measured current [11,12]. Thus, the self-integrated Rogowski coil has a problem of low-frequency distortion when applying to measure the traveling wave current on the double circuit transmission line.

Analog integral compensation technology

In order to measure the traveling wave current propagating along the transmission line accurately, a compensation method is proposed in this section.

In Eq.2, the voltage on the R_0+r was ignored before, which leads to the low-frequency distortion. If we can conduct integral compensation on the differential volume on the resistor R_0+r, then the result will be accurate. Conduct integral in both sides of Eq.2, and can be expressed as

$$i_1(t) = -\frac{L_0}{M}[i_2(t) + \frac{(R_0 + r)}{L_0}\int_0^t i_2(t)] \tag{8}$$

Models were built in Simulink of MATLAB to compare the impulse response of the self-integrated Rogowski coil with and without compensation. The simulation result is in Fig.4. It shows that after compensation the current can be measured precisely.

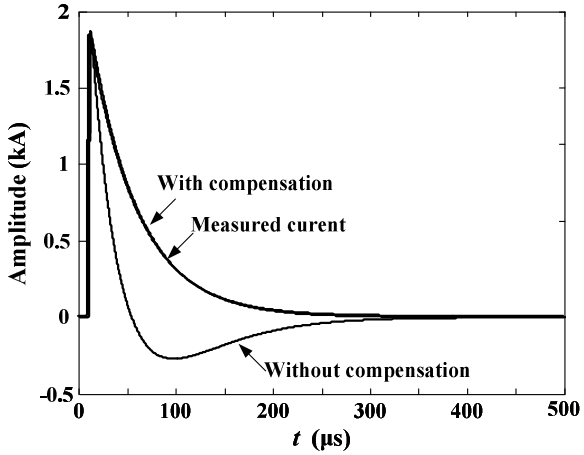

Fig.4 MATLAB simulation diagram of self-integrator Rogowski coil low-frequency distortion compensation

Analog integrator has the advantages of low cost, fast dynamic response and large range of input signal. The implementation method of analog circuit of low-frequency compensation is shown in Fig.5. Since the integrating capacitor has memory effect in the ideal integrating circuit, so in the practical application, we should place a large resistor across the integrating capacitor to form a discharge circuit. Besides, as the traveling wave current is superimposed over the power frequency current, a notch Filter is required as shown in Fig.5.

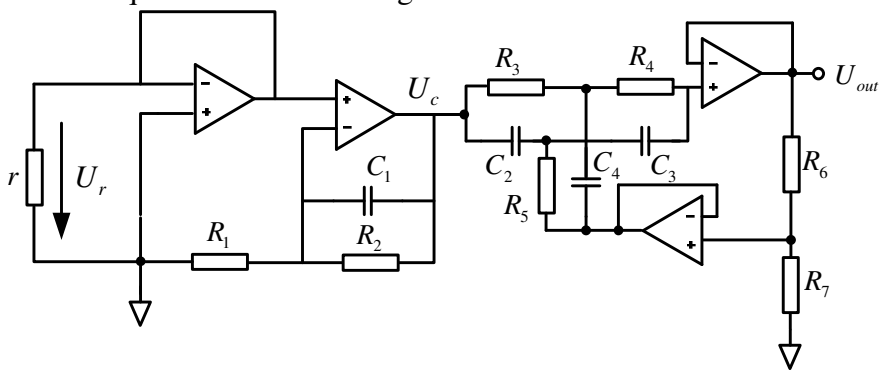

Fig.5 Low frequency distortion compensation circuit of Rogowski coil

According to the circuit in Fig.5, the relationship between the output voltage U_c and the input voltage U_r can be expressed as

$$-U_c = U_r + \frac{1}{R_1 C_1}\int U_r dt \tag{9}$$

Multiply r in both sides of Eq.8 and rearrange it, the following equation can be obtained

$$-\frac{Mr}{L_0} i_1(t) = U_r + \frac{R_0 + r}{L_0}\int U_r dt \tag{10}$$

Comparing Eq.9 and Eq.10, the following equation must be satisfied to ensure the compensation effective

$$\frac{1}{R_1 C_1} = \frac{R_0 + r}{L_0} \tag{11}$$

Use the compensation method in this paper, the output signal U_{out} and the measured current $i_1(t)$ will be a linear relationship if not considering the non-ideal characteristic of the operational amplifier and the distributed capacitance of the Rogowski coil.

To further verify the effectiveness of the proposed improved Rogowski coil with integral compensation. Relevant experiments are done in laboratory and prototype is installed on a Double Circuit Transmission Line in China. The structure parameters and electrical parameters of the Rogowski coil in the experiment are shown in Table 1. The parameters of the analog integral circuit are in Table 2.

Table 1 Structure parameters and electrical parameters of Rogowski coil

D_{in} [m]	D_{out} [m]	*Height* [m]	*Turns*	L_0 [mH]	M [μH]	R_0 [Ω]	r [Ω]	C_0 [pF]
0.7	0.9	0.5	400	0.45	1.12	11.5	1	2.1

Table 2 Parameters of the analog integral circuit

R_1 [Ω]	R_2 [kΩ]	C_1 [μF]	C_2 [nF]	C_3 [nF]	C_4 [nF]	R_3 [kΩ]	R_4 [kΩ]	R_5 [kΩ]
360	10	0.1	33	33	66	96	96	48

The experiment and online results are shown in Fig.6 and Fig.7 respectively.

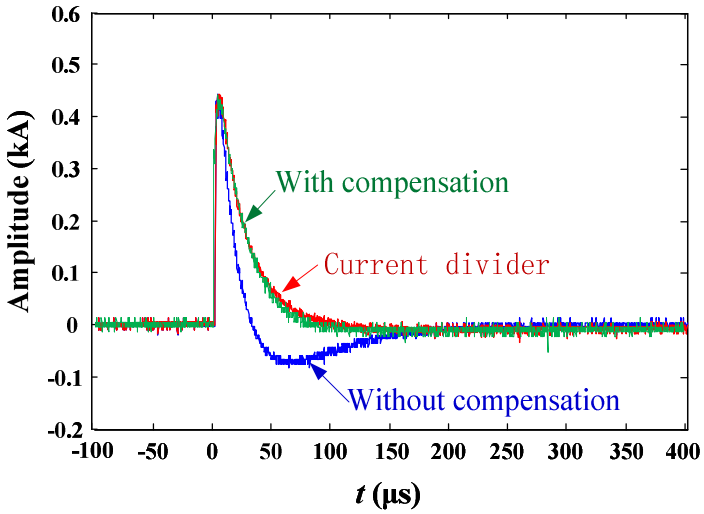

Fig.6 Waveform comparison between with and without analog integral compensation and current diverter

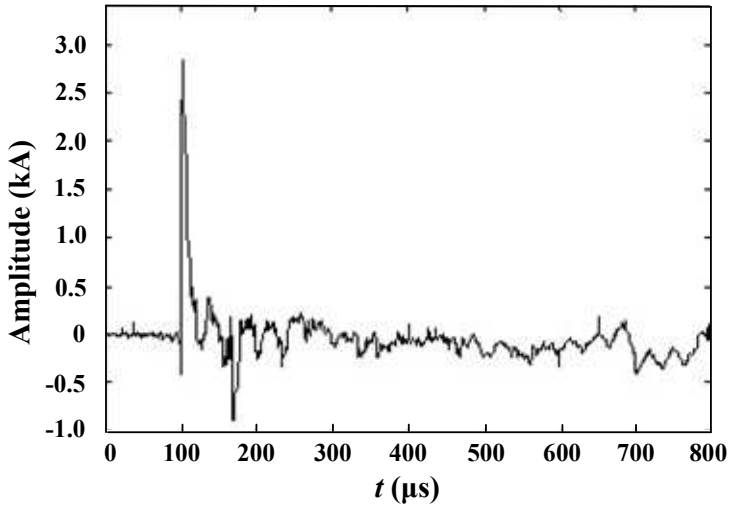

Fig.7 Lightning fault traveling current waveform measured on Double Circuit Transmission Line

In Fig.6, it's obvious that the output of the self-integrated Rogowski coil has a serious distortion problem. In comparison, using the improved Rogowski coil with integral compensation, the output waveform coincides with the waveform of the current diverter.

Fig.7 is the lightning fault traveling current waveform collected on a double circuit transmission line. Between 0.1ms to 0.2ms, there are two wave fronts of lightning wave at the point of failure and the reflected wave from the transformer substation. There is no significant low frequency distortion in the waveform.

The experiment result and the online measured waveform from a Double Circuit Transmission Line both prove the effectiveness of the improved Rogowski coil with integral compensation proposed in this paper. No significant low frequency distortion is found in the measured waveform.

Summary

Aiming at developing a traveling wave current sensor for the double circuit transmission line, the characteristic of the traveling wave current on the double circuit transmission line is researched first. It turns out that traveling wave current on the double circuit transmission line contains a lot of low frequency components. Thus the traditional self-integrated Rogowski coil with low frequency distortion can not be used. Based on the mechanism of low-frequency distortion of self-integrated Rogowski coil and by MATLAB simulation, an improved Rogowski coil with analog integral compensation is developed. Simulations, experiment results and the online monitoring data from a Double Circuit Transmission Line all prove the effectiveness of the improved Rogowski coil with integral compensation proposed in this paper.

References

[1] Gu Ding-xie, Dai Ming, Li Zhi-jun, Li Zhen-qiang. Analysis of failure trip rate of 1000kV double circuits on the same tower.[J].High Voltage Engineering, 2009, 35(3): 441-445.

[2] Hara T, Yamamoto O. Modelling of a transmission tower for lightning-surge analysis[J]. IEE Proceedings Generation, Transmission and Distribution. 1996, 143(3): 283-289.

[3] Ma Chao-ran. Prospect and development of transmission line fault location using travelling wave[J].Relay, 2007, 35(24): 1115.

[4] Schoene J, Uman M A, Rakov V A, et al. Direct lightning strikes to test power distribution lines-partiv experiment and overall results[J].IEEE Trans Power Del，2007，22(4):2236-2244.

[5] Lin Jian-hua, Yu Gang-hua. Analysis on Transmission line lightning fault traveling wave accurate measurement principle[J].Technology Wind, 2012, 202(8):39

[6] Dubickas V, Edin H. High-frequency model of the Rogowski coil with a small number of turns [J]. IEEE Trans. on Instrumentation and Measuremen，2007，56(6): 2284-2288.

[7] Zhou Bi-hua Zhu Kai-e Li Yan-xin. Output waveform oscillation of large Rogowski coil used for lightning current measurement[J]. Chinese Journal of Radio Science, 2010,25(6):1085-1089.

[8] Chen Qing, Li Hong-bin, Zhang Ming-ming, et al. Analysis and design of rogowski coils with main and assistant printed circuit boards[J]. Automation of Electric Power Systems, 2004, 28(16):79-82

[9] Li Wei, Yin Xiang-gen, Zhang Zhe, et al. New Voltage to frequency Conversion Method for Electronic Current Transformer[J]. Automation of Electric Power Systems, 2008, 32(8):88-92

[10] Shen Zhu, Qian Zheng, Luo Cheng. Development of an electronic current transformer [J] . Automation of Electric Power Systems , 2002 , 26 (18) : 41 -44 .

[11] Li Wei-bo, Mao Chen-xiong, LI Qi-yan, et.al. The Simulation Research of Rogowski Coils for Measuring f ast pulsed Heavy Current[J].High Voltage Engineering, 2002, 28(8):11-14.

[12] Wang Yu-tian, Wan Bao-juan, Sun Hai-yan, et al. Technology in Designing Integrator of Electronic Current Tran-sducer[J].Power Electronics, 2009, 43(2):76-78.

Advanced Materials Research Vols. 986-987 (2014) pp 1565-1568

doi:10.4028/www.scientific.net/AMR.986-987.1565

Research on testing parameter detection equipment of the aeroengine based on PC104

Xiao-lian Jiang[1, a], Xiu-ling Wei[2,b], Xue-yan Lv[3c]

[1] Air Force Aviation University, Changchun, China,130022

[a]xl_jiang2006@sina.com, [b]wei411036@163.com, [c]lvxueyan1974@sina.com

Keywords: Aviation engines, Trial, PC104, Controller

Abstract. Technical parameters that affect the performance of the engine include: rotor speed of the engine under high and low pressure, oil pressure, fuel pressure and exhaust temperature, etc.This article describes the features, function, structure and working principles of the testing parameter detection equipment based on the aeroengine of PC104,and we design detection circuit for the main test items.

Introduction

Aeroengine is the core components of the aircraft,aircraft power source. The maintenance quality of aeroengine directly affects the use of aircraft and even the flight safety of aircraft, therefor, in order to ensure flight safety, regular engine test must be done to check the performance of the engine.There are pointer instruments displaying testing parameters in the aircraft cabin,which is inconvenient to watch, low accuracy and large operator error, besides, crew reflect that when testing the engine , they have to record a large number of parameters,especially for the failure test, which need data analysis for the test, and making the test time long, data recording, analysis and processing inconvenient. These shortcomings can not meet the requirements of modern high-tech warfare and the maintenance of the external field. The test instrument, based on PC104 bus technology, can real-time check, display, store and print the main technical parameters engine in process of testing, allowing the crew to accurately analyze, judge and rule out engine failure and improve engine reliability, while also greatly reducing maintenance time, saving manpower, material and making the maintenance of the engine more scientific, more targeted[1-3].

Features and Functions

The parameter-testing detection equipment aeroengine is the device that draws ground testing equipment from abroad, which uses PC104 bus industry computer and EL-screen display, making the detection system with small size, light weight, easy to move, simple operation, high degree of automation, reliability, and display a wealth of information, good man-machine interface and other features to fully detect cockpit display engine performance parameters, and the accuracy of the meter pointer above the cockpit.

Equipment features include: (1)real-time detection, showing high and low pressure rotor engine speed, engine vibration speed, oil pressure, oil temperature, the primary and secondary fuel oil duct pressure and exhaust temperature; (2)render real-time test curve; (3)save the test parameter data; (4)after testing, you can view the data in the process of commissioning and commissioning curve of each parameter; (5)keep data communicating with the computer and testing instrument, and transfer data to a computer for each parameter during testing, so that the crew can see the parameters during the test data in a computer for analysis and troubleshooting.

Structure and working principle

The design ideas of parameter-testing detection equipment is using existing aircraft sensors to achieve, in the premise that aircraft instrument works and ensure that the engine work safe and reliable. Testing equipment does not affect the normal operation and maintenance personnel, which should be detected by the engine ground test program. The apparatus includes various sensors, a controller, a data acquisition card, a detection circuit, keyboard, power supply and other display components. Detection principle is shown in Fig. 1.

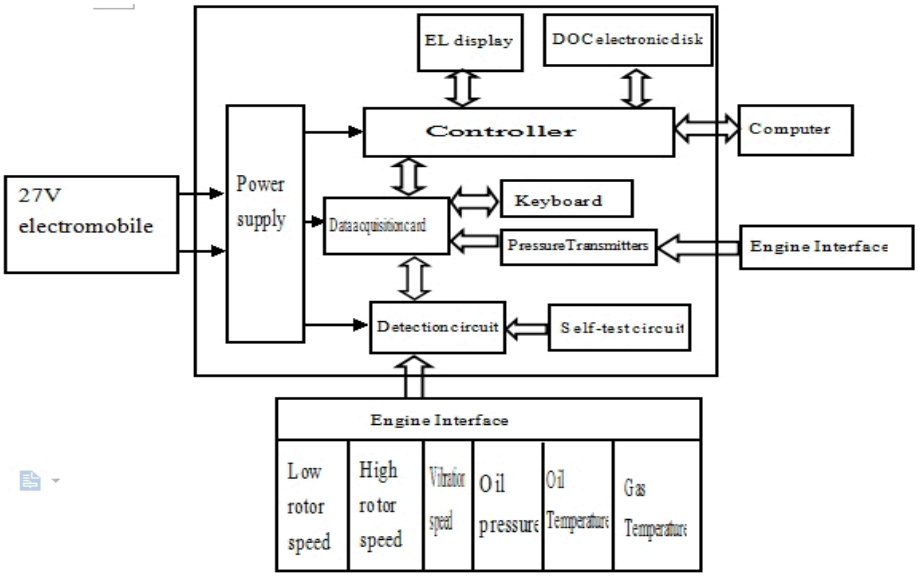

Fig.1. The working principle of test parameters detective system for aeronautical engine

When engine is testing. the analog of high and low pressure rotor speed, vibration speed, oil pressure, oil temperature and exhaust temperature output from the connector plug at aircraft, then converted into a DC voltage signal by detection circuit. Main and auxiliary pressure transmitter of oil dust is connected with main and auxiliary measuring joints on the lap of fuel oil, pressure transmitter feels the change of pressure, then outputs and the primary and secondary fuel oil channel DC voltage signal proportional to the pressure. The DC voltage signal is converted to the digital controller by the data acquisition card and is sent to controller, and controller calculate the value of parameters by program. The controller detects the data stored in the data memory for program control and displays all test data and test parameters curve on the EL display.

The controller is the core part, the main function of which is to read the data with the corresponding parameters from the data acquisition card based on the user program, and the actual value of each parameter is calculated and stored on the data storage; EL flat panel displays show human-computer interaction interface, test data for each parameter, test curves, etc. It uses an embedded industrial computer PC104 bus. EL display prompt characters HCI and the detected data, and test each parameter curve and so on. DOC electronic disk is used to store data for each parameter that is detected during the test, and to the memory controller operating system files, program files and other control equipment. DOC electronic disk capacity is 128M. Keyboard uses a simple switch keyboard, and keyboard signals are sent through the data acquisition card to the industrial computer PC104 bus. Keyboard on the front panel is used for human-computer interaction, inputting commands and data to the controller. It has six buttons, using a simple switch keyboard, Keyboard signals go through data acquisition card into the controller ang the interface is simple, easy to apply. DC power supply is used to convert the airport for 27V systems internal circuitry needed +5 V, ± 12V, +24 V DC, using two DC-DC converter to convert the 27V DC bus PC104 industrial computer and other use electrical components are required +12 V,-12V, +24 V and +5 V DC power supply. It converts the high accuracy and the can work stably in a environment -40 ℃ ~ 55 ℃.

Detection circuit design

The function of detection circuit is converting the signal that reflects the size of the parameter current, voltage, frequency, to a DC voltage signal from 0V to 5 V that data acquisition card can pick up.

4.1 Design of the rotational speed detecting circuit

Engine speed detection principle is shown in Fig.2. Isolation voltage sensor isolate the output signal of speed sensor, and outputs a voltage proportional to the speed sensor output signal frequency-5V ~ +5 V voltage signal, then the filter circuits filter the output signal to filter out high frequency interference signals, then by shaping circuit the signal is converted to a standard 5V output square wave signal and maintain product rate unchanged. The frequency of 5V square wave signal is measured by the microcontroller and the engine speed is obtained through the calculation, and the digital output is proportional to the rotational speed D / A converter, then it outputs a digital that is proportional to the speed to D / A converter. D / A converter converts the digital proportional to the speed to 0 ~ 5V DC voltage proportional to the speed and then it is fed to a data acquisition card, and converted into a digital quantity by A / D-converted in data acquisition card, and then fed into the controller. After calculation in the controller, we can get the actual value of the speed[4].

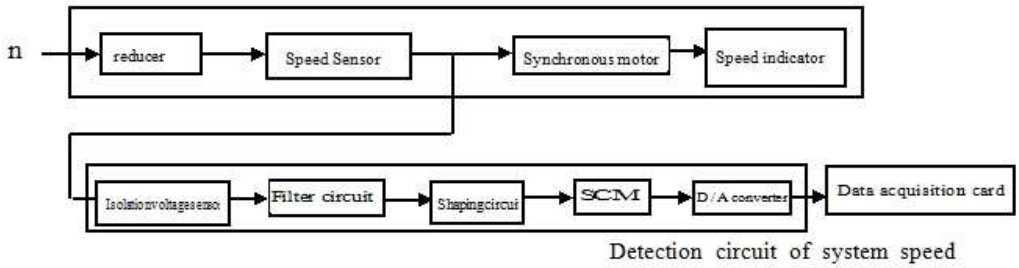

Fig.2 The principle diagram of engine speed detection

4.2 Oil pressure sensing circuit design

The left side of dashed box in Fig.3 is an oil pressure sensor, the right side oil pressure gauge, and they form the plane of the original oil pressure detection devices. Oil pressure determines the displacement of the movable armature in the pressure sensor. Displacement of the movable armature determines inductance of two coil. The inductance change of two coil changes the oil pressure gauge changing flow ratio of two current frame, and two frames of the current ratio i1/i2 and oil pressure is one to one. Oil pressure gauge is a current ratio table, and its pointer deflection angle corresponds to the current ratio i1/i2, certain oil pressure corresponding to a certain oil pressure indication[5].

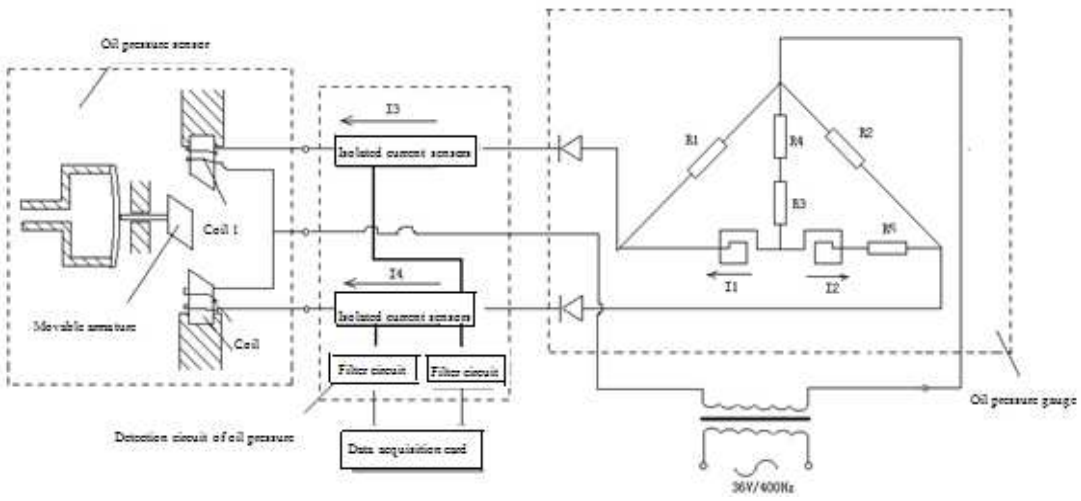

Fig.3 The principle diagram of the oil pressure detection

If the oil pressure is determined by detecting a current ratio of two frame sizes, it will destroy the original oil pressure gauge on the plane, which apparently is not allowed. We found that the oil pressure sensor and oil pressure gauge current ratio I1/I2 two connections with the oil pressure gauge flow ratio of two wireframe current ratio i1/i2 correspondence through theoretical analysis, so we can determine the size of the slide. by measuring the current oil pressure sensor and oil pressure gauge connections than two I1/I2 pressure.

In the middle of the imaginary box in Fig.3 is oil pressure detection circuit. Isolated current sensor converts current signal of oil pressure gauge and oil pressure sensor to a DC voltage signal, and then the DC voltage signal is converted into a voltage signal that can be recognized by the controller of 0 ~ 5V by scaling circuit, and send it to the data acquisition card, by which it is converted to digital by D / A conversion and sent to controller. The controller can get the actual value of the oil pressure by calculating.

The relationship between pulsating DC currents I1, I2 and the corresponding output voltage of isolated current sensor is: $u_1 = 0.1 \times l_1$, $u_2 = 0.1 \times l_2$. I1, I2 is in the range of 0 ~ 50mA, and output voltage of isolated current sensor is in the range of 0 ~ 5V. Relationship between I1/I2 and the oil pressure is shown in Table 1.

Table 1 The relationship between the oil pressure and I1/I2

Oil pressure Kg/cm^2	I_1/I_2	Oil pressure Kg/cm^2	I_1/I_2
0	0.8479	4.5	1.024
0.5	0.873	5	1.040
1	0.895	5.5	1.058
1.5	0.912	6	1.074
2	0.931	6.5	1.099
2.5	0.951	7	1.124
3	0.967	7.5	1.147
3.5	0.985	8	1.192
4	1.002		

Conclusions

Aeroengine parameter-testing detection equipment is an important equipment for the maintenance of engine, which has been used now. From the feedback of view, the system has a small size, light weight, a high degree of automation, and it is easy to operate and easy to use for outfield. Application of the system avoids the repeated disassembly of parts in the process of troubleshooting and repeated test, which can not only save time, manpower and material resources, but～ also reduce wear of engine, improve the useful time of engine. It greatly improves the efficiency of maintenance work, saves maintenance costs and will bring great economic benefits for consumers.

References

[1] Chen heng, Research on portable comprehensive detective system of aeronautical engine, Aviation Maintaineace and Engineering, 2009,37～39.

[2] Xie ping, Comprehensive detector of aeronautical engine based on PC-104, Embedded computer application, Vol.23(2007), 85～86.

[3] Li yongming. Electrical circuit of detective instruments (Northwestern Polytechnical University press, Xi-an 1992).

[4] Zhu gang, A taken aeroengine synthetic test instrument, Mechatronics, Vol.5(2003), 73～75.

[5] Cai zhongchun, Design of locationdetection circuit for aviation engine, Electronic science and technology, Vol.6(2010), 25～26.

Advanced Materials Research Vols. 986-987 (2014) pp 1569-1573

doi:10.4028/www.scientific.net/AMR.986-987.1569

Research on the Intelligent Monitoring System of Indoor Electrical Safety Based on the Internet of Things

Chen JIANG[1], Lei ZHOU[2,C], Xiaoju LIU[3], Xiaoliang XU[4]

[1]Institute for Electronic Information, Hangzhou Dianzi University, Zhejiang, 310000, China

[2,C]Institute for Electronic Information, Hangzhou Dianzi University, Zhejiang, 310000, China

[1]email: yt_jiang_chen@126.com, [2,C]email: zhoulei@hdu.edu.cn

Keywords: The Internet of things; Wireless network; Recognition; Arc detection

Abstract. This paper presents a set of schemes of centralized indoor electrical safety intelligent monitoring systems which are more intelligent, real-time and reliable based on the internet technology of things. Integrated use of wireless sensor networks, embedded microprocessor technology is realized. Hall sensor is used to collect the real-time current on the power grid. As well, This system utilizes the method of the subspace pattern recognition to identify electrical appliances and eliminate some safety risks of the domestic distribution network through the fault arc detection.

Introduction

In recent years, the leading cause of fires occurred in our country is electrical fires. Vicious load monitoring system of traditional electrical violations makes determinations by monitoring the changes of the power grid peak current. Nowadays, low-power energy-saving design is commonly made used of the intelligent electrical appliances, and large-scale accessing the low-power violation apparatus will cause the smaller mutations of the current and voltage signal waveform in a variety of appliance[1]. Thus, the method of electrical violation detection is proposed based on the analysis algorithm of the load power characteristic parameters which can accurately identify large-power electrical violation. Arc is a phenomenon of discharge, but also a kind of plasma which is generated by free gas[2]. Arc possesses a significant feature, and it has a strong randomness, short duration and high generated temperatures. When the breakdown point appears in the line, arc will occur frequently. When arc occurs frequently, a lot of heat will be released. If ignited things are around, it will ignite them resulting in a fire or explosion[3]. The arc which is caused by the loose contacts, insulation aging, breakdown, grounding fault is regarded as a fault arc[2]. The most successful one which utilizes the arc voltage detection is the arc fault circuit interrupter *(AFCI)*. In 2004, AFCI appeared in the U.S. market for power plug of household air condition [2].

The overall structure and design principle

Monitoring system is divided into four parts: data collection terminal nodes, routing nodes, servers and monitoring terminal. The current real-time collection through the sensor is realized by the current collection terminal nodes. Self-bring alarming device, relays and terminal nodes are based on the stm32 microcontroller embedded systems with the functions of some preprocessing and self-treatment. Routing node is the core of the local node groups in the whole monitoring system,which is responsible for forwarding the signals and the maintenance of the network path[4],and is responsible for transmitting front-end data into internet; The server is divided into four parts: the intelligent data analysis servers, data storage servers, security and disaster recovery server and WEB server. Monitoring terminal mainly regards the browser on the PC as a client.

The terminal node treats stm32 as master chip, so that it has a processing capacity of embedded systems. Terminal node implements a few risk discriminant algorithm, so it has the ability of independent judgment and processing; Fourier series algorithm and third-order Burg algorithm were transplanted to the terminal nodes, reducing the pressure of Wifi and data processing servers, so real-time performance of the system is further enhanced. As long as managers are in the

environments of the Internet and a browser,they can browse the analysis data provided by the Web server and make the centralized monitoring and management for the indoor electricity consumption. Fig.1. describes the system components.

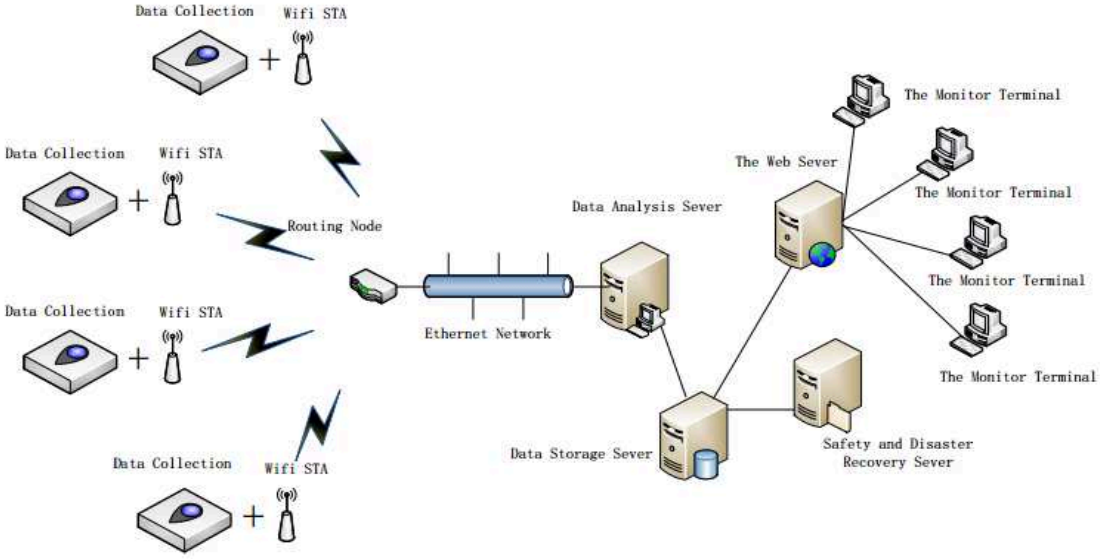

Fig.1.System structure diagram

The analysis of fault arc by Burg algorithm optimal window

The current and voltage waveforms of fault arc generally have following characteristics[5]: 1) voltage and current waveform contains high frequency noise; 2) along the arc there are voltage drops; 3) appear “Current zero-zone” ; 4) arc current rise rate is generally higher than normal currents; 5) voltage waveform is similar to rectangular; 6) arc is a flash which is usually dispersed in sporadic waves among normal current. In the previous study, linear load works normally and has no “Current zero-zone”. It appears “Current zero-zone” when there is a fault arc. Compared with the normal work, current rises relatively fast after the “Current zero-zone” and generates a little burr. So, “Current zero-zone”, a steep changes after “Current zero-zone” and burr can determine whether the fault arc occurs. But many non-linear loads under normal and arc state have a“Current zero-zone”, which has a great impact on our judgment, so we need to exclude these "normal arcs".

In this paper, the optimal window Burg algorithm is applied to calculate the eigenvalues of the fault arc. Compared with the Burg algorithm, this method is not sensitive to the initial phase, with a low degree of frequency offset and spectral splitting, and the spectrum estimation performance is better. Compared with the other eigenvalue algorithm, the computational complexity is low.

The harmonic signal among the power systems is:

$$y(n)=\sum_{i=1}^{M} A_i \sin\left(\frac{2\pi f_i n}{f_s}+\varphi_i\right)+\eta(n) \quad (1)$$

Where, M is the number of the harmonics and inter-harmonics which are contained in the signal; A_i, f_i, φ_i are the *i-th* amplitude, frequency and initial phase of the harmonics respectively; f_s is the sampling frequency; $\eta(n)$ is the white noise sequence. Then Eq.*(1)* can be converted to:

$$y(n)=-\sum_{i=1}^{m} a_m(i)y(n-i)+f_m(n) where, f_m(n)=\eta(n)+\sum_{i=1}^{m} a_m(i)\eta(n-i), m=2M \quad (2)$$

By Eq.(2) shows that harmonic signal $y(n)$ of the power system can be seen as the AR model. The most commonly used method in AR model is Burg algorithm, which utilizes Levinson recursion formulas to strike lower to higher-order AR model parameters. And the Levinson recursion formula is:

$$a_m(i)=a_{m-1}(i)+a_m(m)a_{m-1}(m-1) \quad \text{where} \quad i=1,2,\ldots,m-1. \quad (3)$$

From the Eq.(3), when the solution of *m-1*-order is known, m-order solution is desired to obtain, but only $a_m(m)$ is unknown. So the key question is how to obtain reflection coefficient $a_m(m)$. Burg algorithm uses front, backward prediction errors of minimum average power to directly solve the $a_m(m)$. Firstly, the front, backward prediction errors can be defined as:

$$f_m(n) = y(n+m) + \sum_{i=1}^{m} a_m(i) y(n+m-i) \quad (4); \quad b_m(n) = y(n) + \sum_{i=1}^{m} a_m(i) y(n+i) \qquad (5)$$

Put the Eq.(3) into Eq.(4) and Eq.(5), the order of front and backward prediction errors can be written as:

$$f_m(n) = f_{m-1}(n+1) + a_m(m) b_{m-1}(n) \quad (6); \quad b_m(n) = b_{m-1}(n) + a_m(m) f_{m-1}(n+1) \qquad (7)$$

Average power of m-order prediction error after windowing is:

$$e_m = \frac{1}{2} \sum_{n=1}^{N-m} w_m(n) \left[\left| f_m(n) \right|^2 + \left| b_m(n) \right|^2 \right] \qquad (8)$$

Where $w_m(n)$ is the m-order window function. If chose a appropriate $w_m(n)$, the deviation degree of the peak of the spectrum significantly reduces. Put Eq.(6) Eq.(7) into Eq.(8), making the $\partial e_m / \partial a_m(m) = 0$, Eq.(9) can be obtained:

$$a_m(m) = \frac{-2 \sum_{n=1}^{N-m} w_m(n) f_{m-1}(n+1) b_{m-1}(n)}{\sum_{n=1}^{N-m} w_m(n) \left[\left| f_{m-1}(n+1) \right|^2 + \left| b_{m-1}(n) \right|^2 \right]} \qquad (9)$$

We can see $|a_m(m)| < 1$, therefore, a stable AR model can be obtained by windowing Burg algorithm. Using Eq.(3), m-order solution of AR model can be obtained. Here use Eq.(9) to calculate third-order optimal window Burg AR model parameters $a_3(1)$, $a_3(2)$, $a_3(3)$. First, the parameter of normal current waveform is calculated by this method, and a feature library $A_R = f(a_{r1}, a_{r2}, a_{r3})$ is established as a reference vector. As a result, identification of the system function is converted to the identification of the parameter vector A_T. The squared Euclidean distance is obtained by Eq.(10).

$$d^2(A_R, A_T) = \sum_{i=3}^{3} (a_{ri} - a_{ti})^2 \qquad (10)$$

Through the squared Euclidean distance calculation and analysis of normal current and fault arc current about some appliances, the threshold of d^2 can be determined. It is difficult to determine due to the randomness of fault arc and lots of interference factors. In order to better achieve fault arc detection, Arc detection method of this system will adopt multi-information fusion technology which can firstly realize the current eigenvalue fusion to calculate the coefficients of AR model. Then the decision will be made combined with the mean and peak data of the statistics method.

Subspace pattern appliance recognition

Electrical appliance recognition makes use of a method of subspace pattern recognition. In this method, a linear subspace represents a model class, and the feature vectors of the linear subspace can reflect the nature of a particular category. It can calculate the space projection length of the samples in each sub-category, then according to its length, it will be included in the appropriate category. In this system, The subspace of load pattern recognition is composed of the Fourier series coefficients of current signal. Thus, by calculating dispersion degree, classification will be achieved. Since the obtained signal $x(n)$ after collection is a discrete signal, it is necessary to use the discrete Fourier transform :

$$x(n) = \sum_{n=<N>} a_k e^{jk(\frac{2\pi}{N})n} \qquad (11)$$

The coefficients of Fourier series are obtained by Eq.(12):

$$a_k = \frac{1}{N}\sum_{n=<N>} x(n)e^{-jk(\frac{2\pi}{N})n} \quad (12)$$

Since the first *15* harmonics has been taken as the characteristic value. Take a series of vector groups which are similar to $F_i=\{|a_1|,|a_2|,|a_3|,\ldots|a_{15}|\}$, and then normalize $G_i=F_i/|F_i|$. The subspace which describes the load type can be made up of the obtained results:

$$\Psi = \begin{Bmatrix} a_{11} & a_{12} & \cdots \\ a_{21} & a_{22} & \cdots \\ & & \ddots \end{Bmatrix} = \begin{Bmatrix} G_1 \\ G_2 \\ \vdots \end{Bmatrix} \quad (14)$$

For the real-time collected data, classification space vector H is obtained by calculation, and then disparity is calculated as follows:

$$m_i = |H - G_i| \times 100\% \quad (15)$$

$(1-m_i)$ is defined to represent the similarity of the two current waveforms. The computational methods of subspace pattern recognition is utilized to establish the feature library for some common electrical appliances. Then real-time current is sampled through the data acquisition system and the similarity can be calculated using the data of the sampled values and feature library.

The sampled current value and the sample of the following appliances's ten cycles of electrical have been compared and analyzed, the results are as follows:

1) Soldering iron of the pure load(the sample is the *30W* iron)

Table 1 The similarity between *25W* soldering iron and the sample

soldering iron(25w)	Period1	Period2	Period3	Period4	Period5	Period6	Period7	Period8
similarity	88.7%	89.0%	88.7%	92.1%	90.6%	89.6%	88.7%	88.8%

Table 2 The similarity between *30W* soldering iron and the sample

soldering iron(30w)	Period1	Period2	Period3	Period4	Period5	Period6	Period7	Period8
similarity	95.6%	96.7%	95.8%	97.6%	97.7%	96.9%	97.0%	97.1%

Seen from Table 1 and 2, the similarity between the measured soldering iron and iron sample expresses higher than *88%*, no matter they are the *20W* specification or *30W* specification. Small fluctuations in each cycle are due to the interferences of high frequency noise, white noise and so on which exist in the currents.

2) Computer of switching power supply(Desktop PC are as sample)

Table 3 Similarity between Notebook PC and the sample

Desktop computer1	Period1	Period2	Period3	Period4	Period5	Period6	Period7	Period8
similarity	76.8%	77.9%	78.3%	77.5%	80.1%	79.6%	77.6%	78.5%

Table 4 Similarity between Desktop PC and the sample

Desktop computer2	Period1	Period2	Period3	Period4	Period5	Period6	Period7	Period8
similarity	86.9%	88.3%	89.2%	85.4%	86.3%	85.4%	86.2%	87.5%

The similarity of the switching power supply load is lower than the Linear load .

3) Similarity of some electrical appliances

Table 6 Similarity between electrical appliances

To be identified Sample	Soldering iron	Hair dryer	Desktop PC	Notebook PC	Incandescent lamp	Electric Kettles
Soldering iron	97.1%	45.7%	25.8%	30.4%	86.9%	84.1%
Hair dryer	50.1%	85.6%	71.6%	64.3%	41.2%	45.7%
Desktop PC	29.9%	66.2%	85.3%	77.2%	30.4%	26.7%
Notebook PC	33.6%	65.4%	79.1%	88.9%	37.3%	35.4%
Incandescent lamp	82.1%	44.7%	33.7%	35.7%	93.8%	86.5%
Electric Kettles	82.3%	43.4%	30.1%	32.3%	83.5%	90.4%

Table 6 shows that the same type of electrical appliances has a higher similarity, such as linear load soldering iron, electric kettles and incandescent lamps have similarities more than *80%*. The similarities between desktop computers and laptops are at least *77%*; but the different kinds of loads

possess the lower similarity which is less than generally *40%*. Therefore, we can easily determine the type scope which the electrical appliance belongs to according to the the similarity and determine the type of electrical appliance by matching algorithm.

Conclusion and Outlook

This paper has designed the fault arc detection method based on AR model current parameters. The method calculates the parameter by third-order optimal window Burg algorithm and is combined with the the mean of current signals, peak and other statistical characteristics to generate the multi-source information. It has effectively improved the accuracy of the the fault arc detection. Subspace pattern recognition methods and characteristic parameter extraction can be used to effectively find and identify violation electrical appliance. In the terminal nodes, the algorithm is transplanted to improve the systems' reliability and real-time. Due to the electrical load types of student apartments are increasing, the analysis of more complex load types will be the emphasis of future research.

Acknowledgement

In this paper, the research was sponsored by Key scientific and technological innovation team project of Zhejiang Province "The key technology of intelligent identification and application" (Project No. 2010R50010).

References

[1] XIE Xiao-li, WANG Li-tian. Detection Method Research and Simulation of Campus Illegal Low Power Consumption Malignant Electrical Appliances[J]. Computer Simulation, 2013-3(3).

[2] YANG Yi, DONG Aihua, FU Yongli. Overview of Low Voltage Fault Arc Detection[J]. LOW VOLTAGE APPARATUS, 2009(5).

[3] Li Dongwei, Song Zhengxiang, Wang Jianhua. A method for residential series arc fault detection and identification[C]. Proceedings of the 55th IEEE Holm Conference on Electrical Contacts, 2009:8-14.

[4] LIU Xiang-ju, LIU Li-na. Research on monitoring system of indoor environment based on Internet of things[J]. Transducer and Microsystem Technologies, 2013,32(3).

[5] LU Qiwei, WANG Cong, CHENG Hong. Arc-Fault Circuit Interrupter and identification of the fault arc[J]. Electrotechnical Application, 2009, (24): 28.

Advanced Materials Research Vols. 986-987 (2014) pp 1574-1578

doi:10.4028/www.scientific.net/AMR.986-987.1574

Research on the measurement of household appliance impedance characteristic

Wang Yi[1, 2, a], Tang Han[1, b], Chen wenli[2], Hou Xingzhe[2], Sun Hongliang[2], Luo Kaibo[2],

[1]Chong Qing University of Posts and Telecommunications, Chong Qing, China

[2]Chong Qing Electric Power Research Institute, Chong Qing, China

[3]Postdoctoral Workstation of the Chong Qing Electric Power Corporation, Chong Qing, China

[a]wangyi81@cqupt.edu.cn [b]neo-chang@163.com

Keywords: PLC, power network, household appliance, impedance characteristic

Abstract. Impedance of power line channel is the most important factor for power line communication. All kinds of household appliances randomly connect or disconnect from the network, which give rise to impedance variation on power line channel. The mismatch of impedance would reduce the performance of the signal transmission. The power network is mixed with lines and loads. In order to investigate the main factors that affect power network impedance, this paper proposed a method to measure the impedance of active household appliances. Some household appliances are measured with this method, and the result shows that this method can measure the impedance effictively, which helps the study on the impedance charicteristics.

Introduction

Power line communication (PLC) is based on the power distribute infrastructure to provide data transmission. As the transmission medium, there is a huge advantage within the power distribute infrastructure for the most extensive coverage and the strong network architecture. Without additional investment, it provides convenience network access for the smart grid, meter reading system as well as the In-House LAN to solve the 'last mile' access problem. Recently, high speed PLC arouses many people's interest for the advantage above. However, the power network also suffers a great deal of interference for the sack of its open architecture. The random switch of different loads and the different ways the loads powered led to unpredictable channel characteristics. The noise and the impedance mismatch caused by the loads make the channel environment of the power network severe. For this reason, the study of the power line network is extremely important for the study of PLC [1-3].

It is obvious that the study of impedance characteristics is very helpful in improving the performance of PLC. In the paper [4], the impedance characteristics of the residential power network is measured, the band covers 5 kHz to 20 kHz. In the paper [5], input impedance characteristics of the power network in the industrial zone is measured, the band covers 100Hz to 10MHz. In order to study the feasibility of PLC based small LAN, Japanese scholars measured and analyzed the low-voltage power network impedance characteristics, which covers 20 kHz - 30MHz band [6].

Although mass measurement have been done for the power network impedance characteristics, but the impedance characteristics of household appliances in the low-voltage power network haven't been considered separately. The power network impedance characteristics are measured through calculation of the reflection coefficient and scattering parameters by a network analyzer [7]. At this point, the power network impedance characteristics include the loads and the power lines, due to the random access of the loads the power network impedance is still unpredictability. Therefore, in order to measure and analyze each factor of the power network impedance, the impedance characteristics of the loads in the power network must be studied separately.

To solve this problem, this paper proposes a method to measure the active individual household appliance, which excludes the impact of the power lines. A vector network analyzer and an artificial

main network are used in this method. With this method, the impedance characteristics of some common household appliances are measured and analyzed within 100 kHz to 10MHz band.

Measurement Method

The vector network analyzer (VNA) consists of two basic parts: source and receiver. The source signal flow through the T-biasing device, and then the bi-directional coupler to the signal transmission port. During the process, the source signal is coupled by the reference receiver to record the original signal level at the signal transmission port . The source signal flow to the connected device under test (DUT), due to impedance mismatch of the DUT, a part of source signal is reflected back to the signal transmission port. This part of signal is coupled by the receiver, and then signal level can be calculated. After all the reflection characteristic can be calculated and the impedance of the DUT can be calculated as well.

In the traditional impedance measurement, the reflection coefficient of the network is measured by the VNA. According to the relationship between the reflection coefficient and the single-port input impedance, the impedance of the DUT is calculated. The reflection coefficient r measured by the VGN is determined as follow:

$$r = \frac{Z_L - Z_0}{Z_L + Z_0} \tag{1}$$

Where ZL is the impedance of the DUT, Z0 is the impedance of the VNA input port. Since r and Z0 are known, the formula (1) can be rewritten as follow:

$$Z_L = \frac{1+r}{1-r} \times Z_0 \tag{2}$$

Measurement on the impedance of the DUT with this method is accurate when the measured impedance is close to the impedance of the VNA input port (usually 50Ω or 75Ω). The more difference between the impedance of the DUT and that of the VNA input port, the less accurate the measured impedance is. A small error in the measured reflection coefficient may cause a large deviation between the measured impedance and the true impedance. For this reason, this method should be improved.

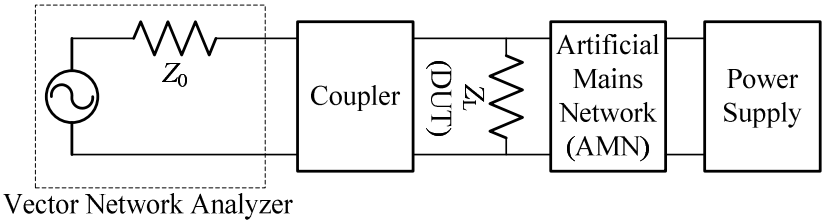

Fig.1. Improved measurement

In the traditional impedance measurement, the DUT is passive device, but in the power network the active mode is also need to be considered, so that the measurement should be conducted where the household appliances are active. Meanwhile, the interference of the external power supply must be eliminated. However, there is no appropriate solution for the impedance measurement of the active household appliances. Therefore, with some improvements on the traditional impedance measurement, a new impedance measurement method is proposed which eliminate the interference of the power network and support the measurement on the active household appliance. In the figure 1, a coupler is joined between the network analyzer and the DUT; an artificial mains network (AMN) is used to power the DUT and separate the power network. Specific measurement procedure is as follows:

- Connect the input port of VNA and the power port of AMN with a coupler and some auxiliary cables. At this point, the impedance of the AMN is measured.
- Based on the first step, access the DUT between the VNA and AMN (with a patch board). At this point, the parallel impedance of DUT and AMN can be measured.

However, the impedances are mismatch between the VNA and the DUT, which brings great trouble on the accuracy of the impedance measurement. The impedances of two ends of the coupler are frequency dependent, the input impedance changes with frequency, so that the impact of frequency should be considered in the measuring. The impedance of VNA (usually 50Ω) denote as Z0. And the measured reflection coefficient is r2, there is:

$$Z_2 = \frac{1+r_2}{1-r_2} \times Z_0 \tag{3}$$

Z_2 is the measured input impedance of the coupler and the DUT. Rewrite the r_2 with r_1: *(s* is the scattering parameters of the coupler)

$$r_2 = \frac{r_1 - s_{11}}{s_{12} \cdot s_{21} + s_{22} \cdot (r_1 - s_{12})} \tag{4}$$

Simultaneous (3) (4) (5), the impedance of the DUT can be calculated.

$$Z_L = \frac{[(1+r_1) \cdot Z_0 - (1-r_1) \cdot Z_2] \cdot Z_0}{(1-r_2) \cdot (Z_0 + Z_2) - (1+r_2) \cdot Z_2} \tag{5}$$

Measurement Arrangement

Major equipment: Rohde & Schwarz (R&S) ZNB model vector network analyzer, Agilent 33220A arbitrary waveform generator, coupler, RF cable, artificial mains network and some other auxiliary equipment.

In order to eliminate the external environment interference on the measurement results, the measurement is conducted in the shielded room in Chongqing Electric Power Research Institute.

In order to accurately measure the impedance of the DUT, the VNA needs to be calibrated before the measurement. Measurement by VNA makes use of the error model equation and the known standard calibration devices, that is to say, using the standard calibration devices the error of distributed parameter of the port under calibrated is measured and eliminate. In this measurement, the calibration is conducted by a short circuit, and a known standard resistor is used to testify the calibration correction. The result shows that this method of calibration is acceptable.

In order to get an accurate result, the measurement frequency is divided into high and low frequency bands. Low frequency band covers 100 kHz – 1 MHz, and high frequency band covers 1 MHz – 10 MHz, and the final result is combined to understand the active household appliance impedance characteristics.

Some common household appliances are chosen for this measurement, including television, washing machine, air conditioner, microwave oven, vacuum cleaner, laptop and desktop computer, fan, hair dryer, desk lamp, dryer, kettle, mobile phone chargers and so on.

Measurement Result

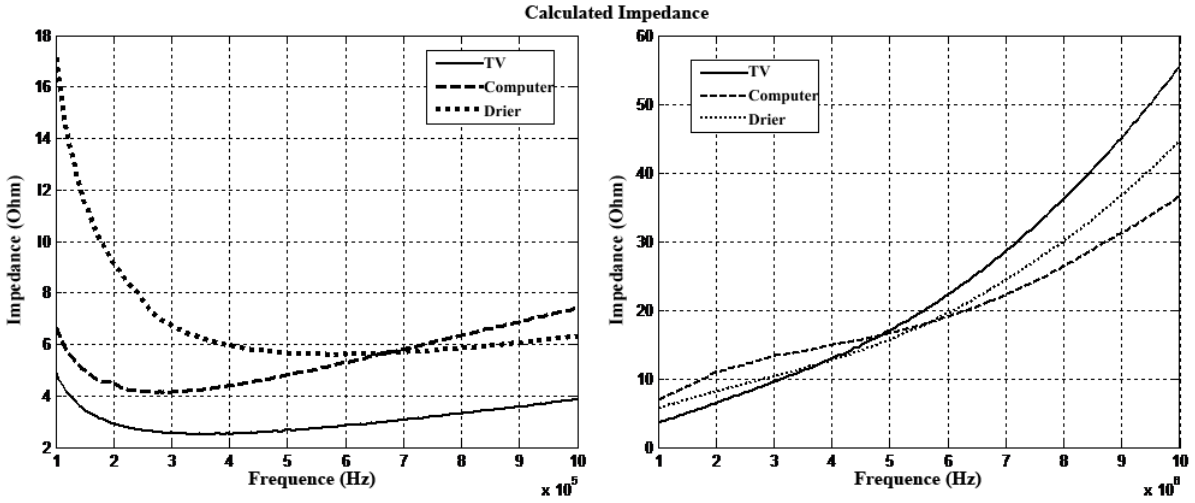

Fig.2. Measurement of TV, computer, hair dryer

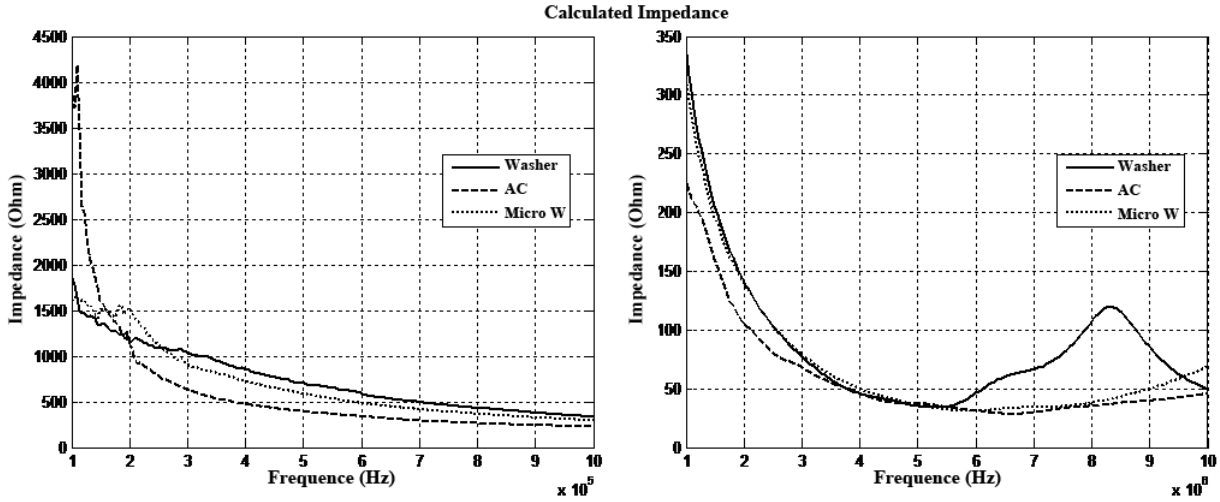

Fig.3. Measurement of washing machine, air conditioner, microwave

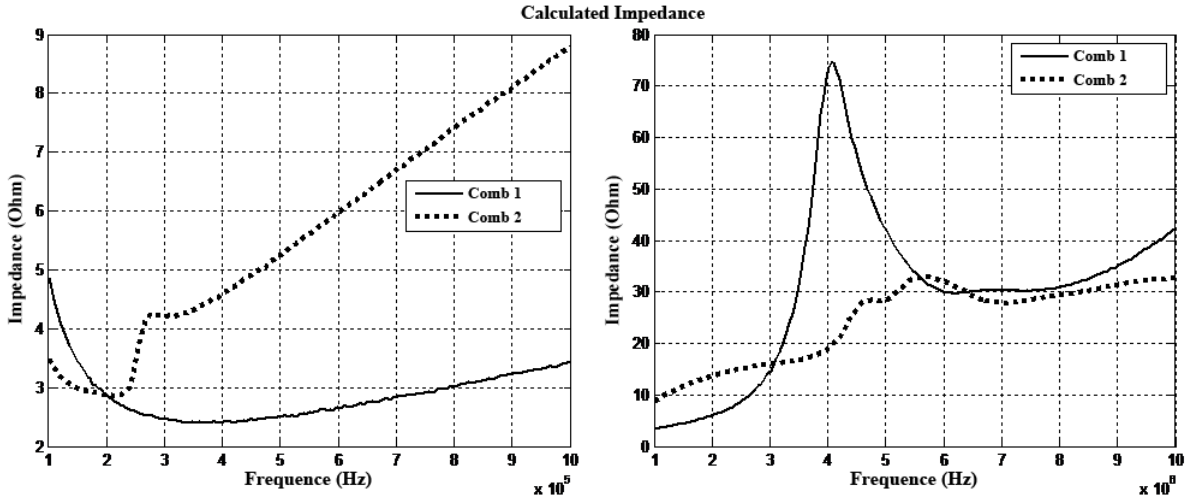

Fig.4. Measurement of combination

It can be seen in the figure 2, in the low frequency band, the impedance of hair dryer reduces the most, and through calculation all these DUTs are capacitive loads in this frequency band. In the high frequency band, with the increasing frequency the impedances increase, and all these DUTs are still capacitive loads.

In the figure 3, in the low frequency band, with the increasing frequency the impedances decrease. And through calculation, all these DUTs are capacitive loads in this frequency band. In the high frequency band, the impedances show the same characteristics as the low frequency band.

In order to inverstigate the influence of the multi household applicances, some combination are measured. Combination 1 includes television and microwave, and an additional laptop computer is added in combination 2. In the figure 4, the result shows that the total impedance is also the combination of each impedance of DUT. With more DUT involved, the impedance become more complex.

Summary

The result shows that most of the measured household appliances are capacitive load, which have a certain relationship with the internal power circuit. Therefore, the study on the household appliance impedance characteristics of the appliances should consider not only the type of the appliance, but also the characteristics of internal power circuit.

The proposed measurement method can effectively measure the impedance. With this method, the household appliance can be measured one and another to create a statistical model of the household appliance impedance characteristic. So that matching of impedance can be improved, and finally benefit the performance of PLC.

Acknowledgment

This work is supported by China Electric Power Research Institute, Chong Qing University of Posts and Telecommunications, NSFC 61201206, cstc2012jjA40045, China Postdoctoral Science Foundation funded project, Chong Qing Postdoctoral financial support Rc201314, Xm201322.

References

[1] Philipps H. Performance measurements of powerline channels at high frequencies[C]. Proceedings of the 1998 International Symposium on Power Line Communication and Its Applications. Tokyo, Japan , 1998

[2] LOPES PAC, PINTO JMM. Modeling and optimization of the access impedance of power line channels[C]. ISPLC, June 2010:142-147

[3] HAKKI C, ENGIN K. Measurements of impedance and attenuation at CENELEC bands for power line communications systems[J]. Sensors 2008 (8): 8027-8036.

[4] Vines R M, Trussell H J. Impedance of the residential power distribution circuit[J]. IEEE Trans . ElectromagnCompat, 1985, EMC-27(1): 6-12.

[5] Martzloff F D, Gauper H A. Surge and high-frequency propagation inindustrial power-lines[J]. IEEE Trans. Industr. Appl, 1986, IA-22: 634-640.

[6] Tanaka M． High frequency noise power spectrum，impedance and transmission loss of power-line in Japan on intrabuilding power-line communications[J] ． IEEE Trans.ConsumerElectr.1988，CE-34(2)：321-326．

[7] TIAN H T, YUAN R M. Measurement on narrow band power line communication channel impedance of distribution network[C]. CECNet, 2011(5) : 454-457.

Advanced Materials Research Vols. 986-987 (2014) pp 1579-1582

doi:10.4028/www.scientific.net/AMR.986-987.1579

Research on the optimization model of fault detection for large-scale electronic circuit

FENG Bao-zhen

He bei chemicai medicine of Career Technical College, Hebei 050026, China

Keywords: fault information; data collection; data excluded;

Abstract: In current large-scale electronic circuit devices, failure data calibration capacity is not strong and it is difficult to be precise classification and intelligent judgment. It lacks of the necessary mechanisms to eliminate the error message, bringing troubles to fault detection. In order to avoid the above defect, this paper presents a fault detection method for large-scale electronic circuit based on fuzzy clustering algorithm. Firstly, the use of means clustering method, the fault information is made initial classification. Then, using the second fuzzy clustering method make fault information filtering in different categories, in order to achieve the fault data confirmation. Experimental results show that the proposed algorithm can effectively improve the accuracy of fault detection of large-scale electronic circuit.

1 Introduction

With the rapid development of computer information processing technology, the ability to handle fault data of large-scale electronic circuit is growing [1]. The technique can be applied to the field of fault detection of large-scale electronic circuit and collect the fault data of different properties in the designated space, thus providing a basis for the post-operation of failure data information [2]. Fault detection of large electronic circuit has become the core content of the electronic information in the field of research, and received wide attention of scholars [3-4]. Currently, in this paper, it proposes a fault detection method of large-scale electronic circuit based on fuzzy clustering algorithm. The use of means clustering method, the fault information is made initial classification. Then, using the second fuzzy clustering method make fault information filtering in different categories, in order to achieve the fault data confirmation. Experimental results show that the proposed algorithm can effectively improve the accuracy of fault detection of large-scale electronic circuit.

2 The fault detection method for large-scale electronic circuit

2.1 Initial classification of failure information

Setting the data set formed by the collected failure data is $Y=\{Y_1,Y_2,\cdots,Y_p\}$. Each failure information packet contains l different data features, which can use $Y_l=\{y_{l1},y_{l2},\cdots,y_{lp}\}^T$ to describe. Using initial clustering method can divide the collected fault data to d different types. The data set formed by these center of categories is $W=\{w_1,w_2,\cdots,w_d\}$. For each collected fault data, there is a membership function V in the center of the cluster. The membership of the j-th signal in the k-th category is v_{jk}, it is possible to obtain the following equation:

$$\begin{cases} v_{jk}\in[0,1] \\ \forall_j=1,2,\cdots,p \\ \sum_{j=1}^{d} v_{jk}=1 \end{cases} \tag{1}$$

To use the following formula describe the objective function of initial clustering of failure data:

$$K(V,W)=\sum_{j=1}^{n}\sum_{k=1}^{d} v_{jk}^{n} e_{jk}^{2} \tag{2}$$

Thereinto, n is the weight coefficient of failure data, e_{jk} is the Euclidean distance between failure data to the center of clusting. It can be calculated using the following formula:

$$e_{jk} = \left\| y_j - w_k \right\| \tag{3}$$

Wherein, $j = 1, 2, \cdots, p$, $j = 1, 2, \cdots, d$ 。The value of w_{jk} can be calculated by using the below formula:

$$v_{jk} = \left\{ \left(\sum_{l=1}^{d} \left(\frac{\left\| w_j - w_k \right\|}{\left\| y_j - w_l \right\|} \right)^{\frac{2}{n-1}} \right)^{-1} , \left\|_j - w_l \right\| = 0 \right. \tag{4}$$

In some special cases, the following equation can be obtained:

$$v_{jk} = \begin{cases} 1 & \left\| y_j - w_l \right\| = 0 (j = l) \\ 0 & \left\| y_j - w_l \right\| = 0 (j \neq l) \end{cases} \tag{5}$$

Using the following formula can update and deal with the initial cluster centers:

$$w_k = \frac{\sum_{j=1}^{n} v_{jk}^n y_j}{\sum_{j=1}^{n} v_{jk}^n}, j = 1, 2, \cdots, d \tag{6}$$

The iterative steps of initial clustering of failure data are as follows:

(1) Select the initial cluster centers W_0 of fault data, calculate the value of v_{jk}, and set the maximum of iterative processing number.

(2) Calculate the number of cluster centers d and index n .in the of the initial classification process of failure data.

(3) Calculate the membership of different categories data in fault data.

(4) Update the membership.

(5) Repeat the above steps until the number reaches a maximum value of an iterative process.

2.2 Fault detection

When the electrical line failure, it needs to determine the location of the fault lines. Thus, it is necessary for the electrical lines to calculate the current size, and needs to determine the voltage between the neutral point of power and the neutral point of the load. In the low-voltage electrical lines, there are three-phase voltage(U_{L1}, U_{L2}, U_{L3})connecting with the neutral point MQ. At the load end, the three load impedance Z_1, Z_2 and Z_3 are connected as star class. The two neutral points MQ and ML are connected through impedance Z_{QL}. The voltage drop of this impedance is U_{QL}. The calculation formula of U_{QL} is as follows:

$$U_{QL} = \frac{\frac{U_{L1}}{Z_1} + \frac{U_{L2}}{Z_2} + \frac{U_{L3}}{Z_3}}{\frac{1}{Z_1} + \frac{1}{Z_2} + \frac{1}{Z_3} + \frac{1}{Z_{QL}}} \tag{7}$$

General configuration of the three-phase filter is the connection of three capacitor X and neutral point and through the connection of capacitor Y and the ground or the shell of the filter. For a balanced capacitance grid, leakage current can be ignored. On the other hand, when an imbalance between the phases reaches the highest, the highest leakage current of electrical network is reached. The reasons of imbalance include the tolerance of capacitor values, and the voltage imbalance of supply network. Thus, the key factors of leakage current is the generated voltage U_{QL} causing the

imbalance of capacitor C_{X1}, C_{X2} and C_{X3}. For most filters, the rated value is the same. The leakage current $I_{leak\max}$ generated by voltage drop U_{QL} in capacitor C_Y can be identified as following formula:

$$I_{leak\max} = U_{QL} \cdot j\omega \cdot C_{Yn} \tag{8}$$

Thereinto, $\omega = 2 \cdot \pi \cdot f$, The tolerance of rated value of capacitor in the passive filter is ± 20%. The highest pressure drop of C_Y occurs in which the two capacitors X have the smallest tolerances and a capacitor has a maximum tolerance. Moreover, assuming tolerance value of C_Y is the maximum. Substituting these assumptions, the leakage current is:

$$| I_{leak\max} | = \omega \cdot C_{Y,\max} \frac{U_{\max} C_{X,\max} - U_{\min} C_{X,\min}}{C_{X,\max} + 2C_{X,\min} + C_{Y,\max}} \tag{9}$$

3 Analysis of experimental results

In order to verify the effectiveness of the proposed fault diagnosis method, it needs an experiment. In the course of the experiment, the fault detection system model of large-scale electronic circuit can be divided into the underlying data layer, an intermediate processing layer, and client layer. The underlying data layer is responsible for data collection, intermediate processing layer is responsible for data pre-processing, and the top layer is the part of the user interaction with the system.

Figure 1 is the results of a fault detection model for large electronic circuit:

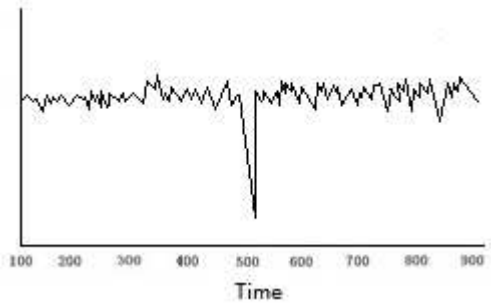

Figure 1 Test results of diagnostic model

According to Figure 1, in the user interface layer, it can be clearly found fault occurred at a certain point in time decay in large-scale electronic circuit. By improving the method can accurately locate the fault, to prove the method has high positioning accuracy and practicality.

Using traditional algorithms and the proposed algorithm for large-scale electronic circuit fault diagnosis, the diagnostic accuracy can be presented by the following diagram:

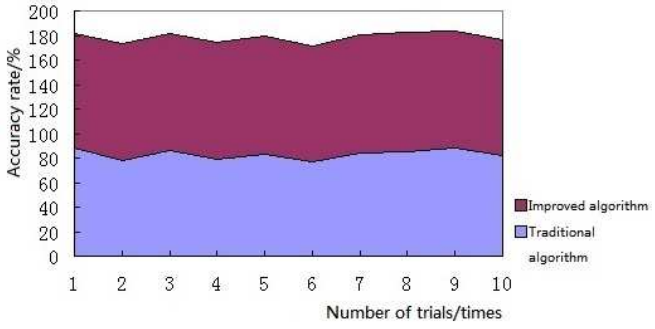

Figure 2 The diagnoses accuracy rate of different algorithms

4 Conclusions

This paper presents a fault detection method for large-scale electronic circuit based on fuzzy clustering algorithm. Firstly, the use of means clustering method, the fault information is made initial classification. Then, using the second fuzzy clustering method make fault information filtering in different categories, in order to achieve the fault data confirmation. Experimental results show that the proposed algorithm can effectively improve the accuracy of fault detection of large-scale electronic circuit.

References

[1] Cui Jianguo, Li Yibo, Li Zhonghai. Pattern recognition of complex signal based on wavelet packet and support vector machine [J]. Data acquisition and processing, 2008, 23 (2) :163-167.

[2] Guo Shuangbing. Study [J] characteristics extraction method of modulation signal based on Wavelet and Fractal Theory. Signal Processing, 2005,21 (3) :316-318.

[3] Wang Xiaoyong, Xiao Siyou, Zhang Wenxiang. Research on the fuzzy clustering algorithm of intelligent mining for Internet text [J]. Computer Simulation, 2009 (7) :216-219.

[4] Li Junfeng, Zhu Fengfeng FCM improved algorithm based on sample density [J] Science and Technology and Engineering, 2007,7 (4): 636-638.

Advanced Materials Research Vols. 986-987 (2014) pp 1583-1586

doi:10.4028/www.scientific.net/AMR.986-987.1583

Research on the Winding Deformation Testing System for Transformers Based on the FRA

ZHANG Zhongyuan[1, a], WANG Yanbo[1, b], ZHANG Linkang[1, c]

[1]School of Electrical and Electronic Engineering, North China Electric Power University, Hebei, Baoding 071003, China

[a]hvzzy_01@163.com

Keywords: Transformer, Winding deformation, Frequency-response analysis (FRA), Testing system, Module.

Abstract. Short circuit currents or forces during transport can cause mechanical displacements of transformer windings. The transfer function method is presented as a tool to detect these displacements. In order to discover the hidden trouble of the transformer, in this paper, an on-line monitoring system based on FRA method is developed, the hardware performs the main functions: signal injection, filtering, amplifying, signal conditioning, and storing the result in computer. The software includes four modules: user login, data acquisition, data analysis, data query. Finally, the monitoring system is validated by a corresponding experimental study.

Introduction

Power transformers are in service under different environmental, electrical, and mechanical conditions and may be subject to enormous hazards during the course of operation. They are commonly considered to be the heart of the transmission and distribution sectors of electric power systems; monitoring their condition and diagnosing faults are important parts of the maintenance function [1]. The large short-circuit currents result in loosen or deformation of the transformer winding with the consequence of weak mechanical strength and degraded insulation between turns. So, it is necessary to detect and diagnosis the winding deformation timely and correctly to prolong the service life of power transformer and ensure the secure and reliable operation of electric grid.

The conventional transformer winding deformation test methods include low voltage impulse test method, short-circuit impedance test method and frequency-response analysis test method [2,3]. Frequency response analysis (FRA) is a powerful diagnostic technique widely used to identify internal faults within power transformers. Transformer components such as windings, core, and insulation can be represented by equivalent circuits comprising resistors, capacitors, and self or mutual inductances whose values will be altered by a mechanical fault within the transformer [4]. Thus the frequency response of the relevant equivalent circuit winding will change. Fig.1 shows a schematic diagram of the on-line FRA method.

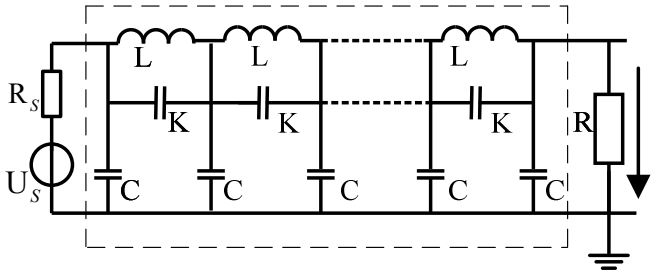

Fig.1. Schematic diagram of the FRA method

Apparatus of the FRA Testing System

The practical implementation of the FRA online monitoring system was designed for robustness and a need to fail in a safe manner. The main hardware apparatus used in this system are as follows: the pulse signal generator, protection circuit, current sensor, data acquisition card, industrial personal

computer. Configuration for the on-line monitoring apparatus is illustrated in Fig.2. A high frequency impulse signal generator is used to inject impulse signals through a noninvasive capacitor sensor (NICS) into the transformer, and the response current signal is measured on the neutral line of the transformer.

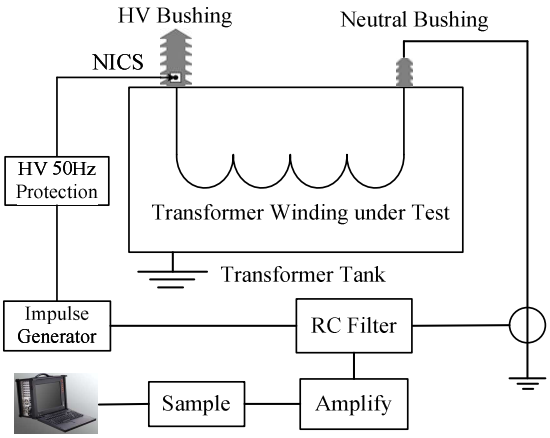

Fig.2. Schematic view of the measuring system

The NICS is installed on the surface of the transformer bushing, through this NICS, a signal can be injected into the transformer without requiring a direct connection to the main feeder [5]. It is a thin layer of conductor made of copper strap which is installed on the porcelain surface of the bushing near the ground potential, but isolated from the ground [6,7]. The basic operation principle of the NICS is the capacitive coupling mechanism between this sensor and the bushing layers.

Albeit, to avoid the effect of the 50Hz voltage on the measuring system, the signal was required to pass beyond a special protection circuit into the sensor and thereafter the winding. The protection circuit must be designed in a manner to provide a high impedance path for the 50Hz component of the network high voltage at terminals of the transformer to limit the voltage on the sensor, and hence, protect the measuring system by absorbing the system transients in the event of a failure [8]. A combination of a spark gap as the first line of defense, a small enough impedance formed by a big capacitor and a paralleled RL unit used in series with the sensor was found to be proper for this task. Fig.3 presents the designed protection circuit. Considering the transfer function of the protection circuit illustrated in Fig.4, it can be concluded that the protection system operates as a high-pass filter and can protect the measuring system against high voltage 50Hz. It should be remarked that since the protection circuit itself contributes to the response of the winding, obviously it will affect the winding transfer function in the low-frequency range. However, the major limitation of the online method comes from the noise and environmental effects at lower frequencies.

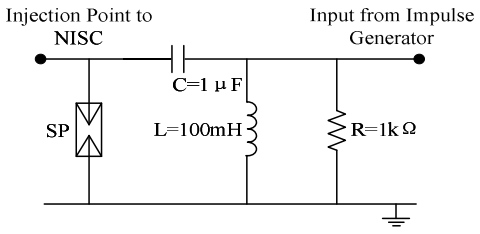

Fig.3. Designed protection circuit

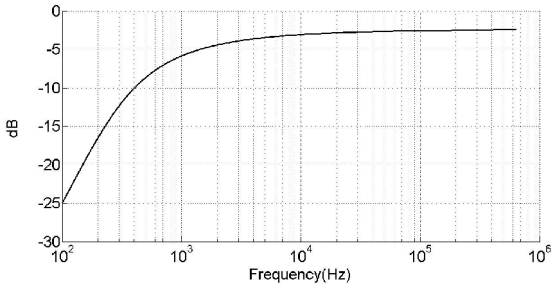

Fig.4. Corresponding transfer function of the circuit

System Software

The system software of test system is composed of user login, data acquisition, data analysis and historical data query. The data acquisition modules and data analysis modules are detailed as follows.

Data Acquisition. Data acquisition is the process of sampling signals that measure real world physical conditions and converting the resulting samples into digital numeric values that can be manipulated by a computer. Data acquisition systems typically convert analog waveforms into digital values for processing. The components of data acquisition systems include: sensors that convert physical parameters to electrical signals; signal conditioning circuitry to convert sensor signals into a form that can be converted to digital values; analog-to-digital converters, which convert conditioned sensor signals to digital values.

Data acquisition applications are controlled by software programs developed using various general purpose programming languages, and the LabVIEW is used in this system. A 4-channel 12-bit A/D converter with a simultaneous-sampling rate of 20 MHz ADLINK PCI-9812 data acquisition card is used in the system. The front panel of data acquisition module is schematically shown in Fig. 5.

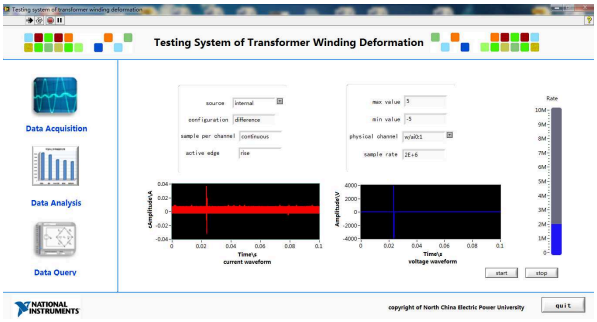

Fig.5. Front panel of data acquisition module

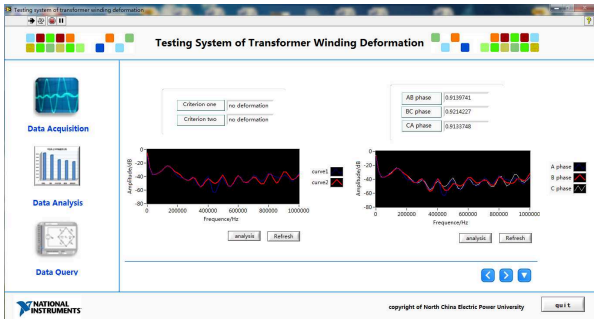

Fig.6. Front panel of data analysis module

Data stream is transmitted from the converters to the digital signal pre-processing units. For elimination the noises is performed continuously Fast Fourier Transformation on the signals. The amplitudes and phase related to signals are calculated and stored to reduce the dispersed quantities of the two high accurate measured voltage signals. The quantities of the amplitudes and phase are continuously refreshed real time in the database on the computer. User can see the variations of the waveform from the windows based on the program platform.

Data Analysis. Analysis of data is a process of inspecting, cleaning, transforming, and modeling data with the goal of discovering useful information, suggesting conclusions, and supporting decision making. The measurements were digitized and processed in a industrial personal computer using a LabVIEW program to compute and visualize the frequency-dependent characteristic of the transformer under test in real-time. The captured time-domain data are converted into the frequency domain using a DFT. It is then displayed in a graphical user interface (GUI). The GUI also allows the user to set various other system parameters. The front panel of data analysis module is schematically shown in Fig. 6.

Experiment study

The system was evaluated on a 35kV/400V, 315kVA oil-immersed distribution transformer. To better prove the newly developed online monitoring system is feasible and sensitive, the test system and a Agilent 4395A network analyzer are used to measure frequency-response curve of the same test transformer. The measured results are presented in Fig. 7.

Meanwhile, to help determine the feasibility of testing system further, a series of tests were carried out in the laboratory on the transformer, Fig.8 shows the comparison of the frequency response curve of three-phase windings of a transformer. As can be seen from the graph, the three curves are consistent with each other well.

The measurement results indicated that the online monitoring system is a practical system to realize online monitoring of transformation for the transformers.

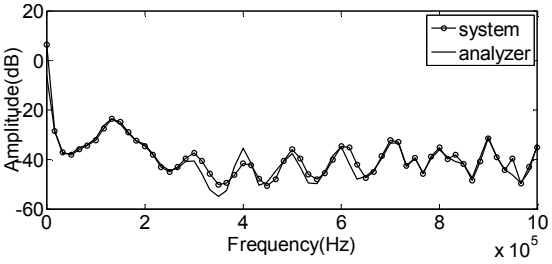

Fig.7. Curve obtained by monitoring system and spectrum analyzer

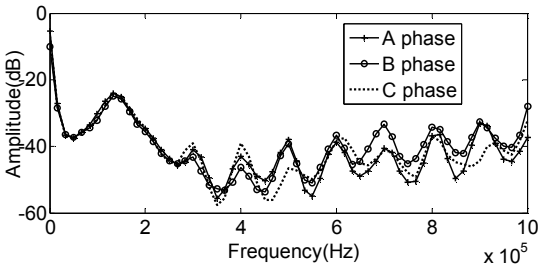

Fig.8. Frequency response curve of three-phase windings of a transformer

Summary

This contribution illustrates how to realize on-line monitoring for a transformer in service using the FRA method to detect winding deformation. The paper briefly introduces the importance of transformers and basic concept of the windings deformation, and then it expounds the development process of the software and hardware of this system. The system structure and main apparatus are discussed in hardware, the software describes the components and functions, practical experiments proved that the system can be effectively used to the online monitoring of the windings deformation.

References

[1] Ebrahim Rahimpour, Jochen Christian. "Transfer Function Method to Diagnose Axial Displacement and Radial Deformation of Transformer Windings" *IEEE Trans. Power Delivery*, Vol. 18, No. 2, pp. 493-505, 2003.

[2] M Wang, Vandermaar. A. J. "Transformer Winding movement Monitoring in service-Key Factors FRA Measurements," IEEE *Electrical Insulation Magazine*, vol. 5, no, 25, pp. 5-12, 2004.

[3] Christian J, Feser K. "Procedures for detecting winding displacements in power transformers by the transfer function method," *IEEE Trans. Power Delivery*, Vol. 19, No. 1, pp. 214-220, 2006.

[4] D. M. Sofian，Z. D. Wang. "Frequency Response Analysis in Diagnosing Transformer Winding," *IEEE* Trans. *Power Delivery*，vol. 16, no. 4, pp. 138-142, 2008.

[5] Hormatollah. "Frequency Response Analysis Low Frequency Characteristics and Fault Diagnosis on Power Transformers," *Potsdam*，vol. 10, pp. 1-4, 2010.

[6] Nagy Y. Abed, Osama A. Mohammed, "Physics-based high-frequency transformer modeling by finite elements," *IEEE Trans. Magnetics*, Vol. 46, No. 8, pp. 327-338, 2010.

[7] Marjon Popov, Lou van der Sluis, etc, "Computation of Very Fast Transient Overvoltages in Transformer windings", *IEEE Trans. Power Delivery*, vol.18, pp. 1268-1274, 2003.

[8] B. Gustavsen, "Wide band modeling of power transformers," *IEEE Trans. Power Delivery*, vol. 19, pp. 414-*422*, Jan. 2004.

Advanced Materials Research Vols. 986-987 (2014) pp 1587-1590

doi:10.4028/www.scientific.net/AMR.986-987.1587

Simulation on fault detection optimization model of large intelligent electronic inverter

HUANG Chun-ping

Department of Electronic Information Engineering, Zhongshan Polytechnic, Zhongshan Guangdong , 528404 , China

Keywords: electronic inverter; particle swarm; fault detection

Abstract: When a fault of power system occurs in grid-connected point, a serious impact is added to electronic inverter in photovoltaic micro-network internal including current, voltage and phase, the appropriate control strategies for completing fault detection of large-scale intelligent electronic inverter, is one of the currently hotspot difficulties. An engine fault diagnosis method based on PSO-SVM is proposed. Particle swarm method is used to search engine fault signals in designated space, so as to obtain optimal particle and provide the basis for an engine fault diagnosis. Support vector machine (SVM) method is applied to classify engine failure signal to complete the engine fault diagnosis. Experimental results show that the proposed algorithm for the engine fault diagnosis, can greatly improve the accuracy of diagnosis, so as to meet the needs of actual production, life, and achieve satisfactory results.

1 Introduction

Electronic inverter a new electricity production path with solar power application in the distributed photovoltaic power generation, which can improve energy utilization efficiency, and has broad prospects for development, the use of grid-connected photovoltaic power generation has become the primary application of solar energy [1]. When the large intelligent electronic inverter of micro-grid or power distribution network out of order, the traditional protection devices is likely to fail, thus, rapid recovery of large-scale intelligent electronic inverter in the fault state or restricting the fault in minimum range is particularly meaningful, many domestic and foreign scholars have done research in this field[2-4].

2 Fault detection model of large intelligent electronic inverter

A collection composed fault signal of a large intelligent electronic inverter can be represented by $\{(z_k, a_k)\}$, the engine fault signals are classified according to the following formula:

$$y \cdot z + d = 0 \tag{1}$$

Wherein $z_k \in T^q$, $a_k \in \{-1,1\}$, n is the number of all the major components of the large intelligent electronic inverter, T^q can be used to describe an electronic inverter failure space with the dimension q. The entire electronic inverter failure signal is divided into two basic categories, namely failure and non-failure class, the plane which the distance of different electronic inverter failure signal reaches maximum at can be obtained by calculation, resulting in optimal classification plane, the optimal classification plant of the electronic inverter failure has a strong generalization ability and adaptability[5].

The optimal classification plane of distance Δ from $x \cdot y + c$ and electronic inverter failure signals is as follows:

$$y \cdot z + d$$

Wherein, $\|y\| = 1$. If $y \cdot z + d \geq \Delta$, it can obtain that $a = 1$. If $y \cdot z + d \leq -\Delta$, $a = -1$.

The component z of electronic inverter failure signal in the area of radius T, the optimal classification plane should satisfy the following condition:

$$j \leq \min\left[\left[\frac{T^2}{\Delta^2}\right], n\right] + 1 \tag{2}$$

The results were normalized to make $\Delta = 1$, y and d are extending according to the actual situation. The optimal classification plane needs to meet the following conditions:

If $a = 1$, $y \cdot z + d = 1$; if $a = -1$, $y \cdot z + d = -1$

Nonlinear transformation for the above formula can transform electronic inverter failure signal classification problem into a nonlinear programming problem, its contents can be expressed by the following equation:

$$\min_{y,d} \frac{1}{2}\|y\|^2$$

$$s.t. a_k(y \cdot z_k + d) \geq 1, k = 1, 2, \cdots, n \tag{3}$$

According to the theory of SVM, the optimal solution of non-linear programming problem can be obtained, which is calculated as follows:

$$N = \frac{1}{2}\| y \|^2 + \sum_{k=1}^{n} \chi_k [1 - a_k(y \cdot z_k + d)] \tag{4}$$

Among it, the constraint condition of $a_k(y \cdot z_k + d) \geq 1$ is $\chi_k \geq 0$, the following results can be obtained:

$$\frac{\partial}{\partial y} N = y - \sum_{k=1}^{n} \chi_k a_k z_k = 0 \Rightarrow y = \sum_{k=1}^{n} \chi_k a_k z_k$$

$$\frac{\partial}{\partial d} N = \sum_{k=1}^{n} \chi_k a_k = 0 \tag{5}$$

According to wolf duality theory, these results can be brought into linear programming formulation to gain the wolf dual problem of optimal planar related to electronic inverter failure signal classification as follows:

$$z(\delta) = \sum_{l=1}^{p} \delta_l - \frac{1}{2} \sum_{l,m=1}^{p} \delta_l \delta_m b_l b_m a_l \cdot a_m$$

$$s.t. \sum_{k=1}^{n} \chi_k a_k = 0,$$

$$\delta_l \geq 0, l = 1, 2, \cdots, p \tag{6}$$

To solve the above problems, calculating the optimal classification plane of electronic inverter failure signal is needed. The optimal solution can be described by χ^*, thus, the values of the optimal solution tends to zero basically, while the remaining non-zero value is corresponding to the support vector machines of electronic inverter fault signal, the nonlinearity collection of electronic inverter failure signal is as follows:

$$y^* = \sum_{k=1}^{n} \chi_k^* a_j z_k \tag{7}$$

An electronic inverter failure signal support vector z_k is selected randomly, according to the support vector, d^* can be calculated using the following formula:

$$d^* = a_k - y^* \cdot z_k \tag{8}$$

Eventually, you can get electronic inverter failure signal classification function as follows:

$$h(z) = \text{sgn}(y^* \cdot z + d^*) = \text{sgn}(\sum_{k=1}^{n} \chi_k^* a_k z_k \cdot z + d^*) \tag{9}$$

Wherein, $\text{sgn}(\cdot)$ is the sign function, the formula is as follows:

$$\text{sgn}(v) = \begin{cases} 0 & v < 0 \\ 1 & v \geq 0 \end{cases} \tag{10}$$

According to the method described above, the particle swarm method is utilized for searching all electronic inverter failure signals within a specified space, thereby obtaining the optimal particle and providing the basis for electronic inverter fault diagnosis. SVM method is employed to classify electronic inverter failure signal, thus completing the electronic inverter fault diagnosis.

3 Simulation analysis

In the Matlab / Simulink simulation environment, simulation is conducted for common faults occurred in the running of large-scale intelligent electronic inverter, and large-scale intelligent electronic inverter is used for simulation of single-phase ground fault, two-phase ground fault, the single-phase reclosing circuit breakers at grid-connected point, and three-phase reclosing circuit breaker fault.

1) Single-phase ground fault simulation

When the single-phase ground fault occurs at grid-connected of photovoltaic power generation system and the power distribution network, the voltage and current of load changes, A phase grounds at 2.5s, the A phase ground failure is solved at 3s.

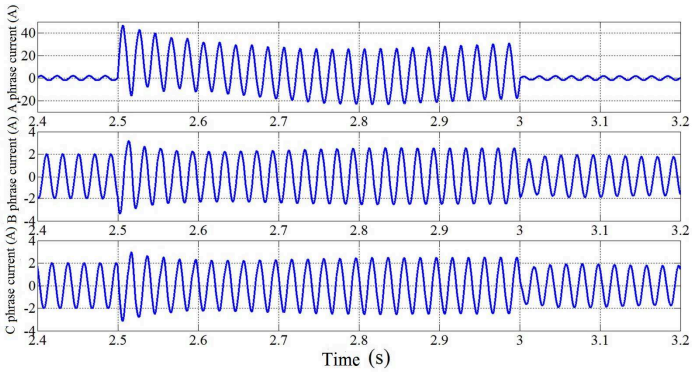

Figure 1 Three-phrase ground current waveform

Figure 1 shows the waveforms of three-phase current obtained from the load when single-phase ground fault occurs. Before the A phase connected to ground, through lock-tracking of SPLL, the phase of three-phase current waveform produced by PV inverter output is a good track to the grid phase; through PQ control, the acquired three-phase power quality meets the requirements. When the A-phase connected to ground, the current of phase A increases rapidly, the biggest peak is about 20 times the normal peak, and phase distortion occurs, the current of B phase and C phase also has increased, and the power quality is relatively poor; after troubleshooting, through SPLL phase-locked loop and PQ control, three-phase currents can quickly recover to the current waveform before A-phase ground within two cycles, the total harmonic content THD is 4.58%.

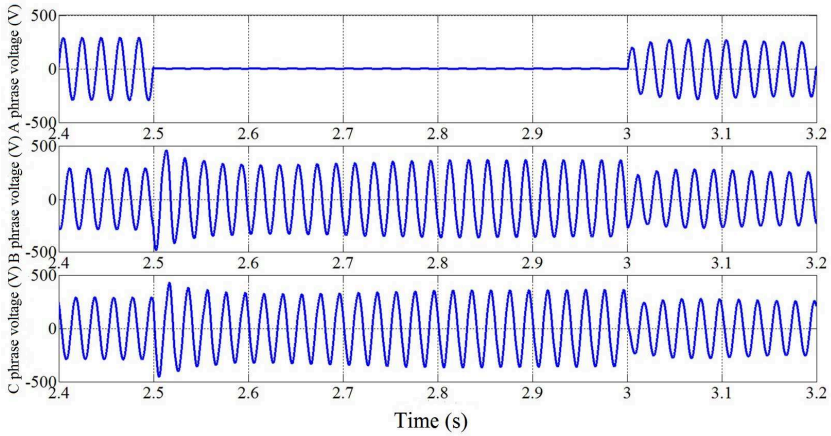

Figure 2 Three-phase ground voltage waveform

Figure 2 shows the three-phase voltage waveforms obtained from the load when large intelligent electronic inverter has single-phase ground fault, before A phase connected to ground, via phase-locked tracking by SPLL, the phase of three-phase voltage waveform outputs from

inverter is very good for tracking to the phase of grid; through PQ control, the amplitude of three-phase voltage obtained is very close to the grid voltage amplitude. When the A-phase grounds, the phase A voltage is zero, resulting in the increased voltage amplitude of B phase and C phase; After troubleshooting, through SPLL phase-locked loop and PQ control, three-phase voltage can recover to the voltage waveform before A-phase grounds within two cycles.

4 Conclusions

An engine fault diagnosis method based on PSO-SVM is proposed. Particle swarm method is used to search engine fault signals in designated space, so as to obtain optimal particle and provide the basis for an engine fault diagnosis. Support vector machine (SVM) method is applied to classify engine failure signal to complete the engine fault diagnosis. Experimental results show that the proposed algorithm for the engine fault diagnosis, can greatly improve the accuracy of diagnosis, so as to meet the needs of actual production, life, and achieve satisfactory results.

Acknowledgement

Zhongshan city, guangdong province science and technology project (project number: 20114 A243)

References

[1] Ma Shangxing, Dai Yongjun, He Jinwei. Study on grid-connected control technology of PV inverter [J]. Chinese journal of power sources, 2011, 35(6): 688-690.

[2] Zou Jianzhang, Chen Qiaofu, Zhang Changzheng. Investigation of PV Inverter Performance Test Platform [J]. Electrical measurement & instrumentation, 2010, 47(8): 20-23.

[3] Mohamed A. Eltawil, Zhengming Zhao. Grid-connected photovoltaic power systems: Technical and potential problems—A review[J]. Renewable and Sustainable Energy Reviews. 2010, 14: 112-129.

[4] Bart Meersman, Bert Renders, Lieven Degroote, et al. Three-phase inverter-connected DG units and voltage unbalance[J]. Electric Power Systems Research. 2011,81: 899-906.

[5] Cui Hong, Xia Chengjun, Luo Zongjie, et al. The impact of distributed generation synchronization on power distribution network [J]. Electrical application, 2009, 28(24): 54-58.

Advanced Materials Research Vols. 986-987 (2014) pp 1591-1595

doi:10.4028/www.scientific.net/AMR.986-987.1591

Study on a New Test and Diagnosis Method for Complex Integrated Circuit

Xiufang Wang[1, a], Jinye Peng[1], Bin Chen[2]

[1]School of Electronics and Information, Northwestern Polytechnical University, Xi'an, China

[2]College of Information System and Management, National University of Defense Technology, Changsha, China

[a]cch1725@163.com

Keywords: test signals, microprocessor, complex integrated circuit unit, test and diagnosis model.

Abstract. Due to the problem that test signals is difficult to describe and analyze in the microprocessor (CPU) and digital signal processor (DSP) circuit, this paper come up with a matrix base method to describe program signal and instruction signal, thus in theory solve the above problem. In the proposed method, simple hardware circuits can be used to produce different test signal needed in the test and diagnose of CPU circuit.

Introduction

With the development of microelectronics technique and computer technology, circuit unit in the electronic apparatus more and more adopts very large scale integrated circuits such as microprocessor (CPU) and digital signal processor (DSP). This kind of unit is called the complex integrated circuit unit with CPU. In this unit, since signals in the circuit are generated by software running of CPU, and software change very much, signals are very complex and seem unable to be described. It also brought great difficulty in test and diagnosis of circuit because of lacking the description method [1,2,3]. To overcome this difficulty, this paper puts forward a new description method that can describe signals generated by any kind of CPU software. Based on this method, simple hardware circuits can be used to produce different test signals needed in the test and diagnosis of CPU circuits.

Matrix Based Description Method of Program and Instruction

It can be known from the relationship of CPU timing signals in [4,5] that the most basic time unit of CPU operation is clock cycle T, machine cycles M is formed by multiple clock cycle T. Any instruction is composed of several machine cycle M, the whole time of carrying on an instruction is called instruction cycle time I, set of the instruction forms the program P. Such timing relationship of CPU is not merely suitable for simple structure CPU like MCS-51, 8086, ARM320, but also suitable for complex structure CPU like 80386, Pentium. In order to simplify discussion, the following takes Z-80 microprocessor as an example. Z80 has 9 machine cycles, including fetch instruction cycle, memory read cycle, memory write cycle, I/O import cycle, I/O export cycle, bus ask/respond cycle, interrupt request/response cycle, each instruction can have 1 to 6 machine cycle, Z80 altogether has 158 instructions. These 158 instructions may compose any program.

In order to use hardware to simulate operation of program, program must be described in a simple way. From the above discussion of Z80CPU time sequence, it can be know that program is changeable, and number of instruction is 158, only type of machine cycle is 9. So description question of program and instruction can be only discussed by machine cycle. In Fig.1, Instruction "LD (HL), A" contains two machine cycle, the first machine cycle is fetch instruction cycle, the second is the memory write cycle. If half clock cycle is regarded as the time unit, the voltage value of different signal line in the same time is regarded as the matrix's row, and the voltage value of different time in the same signal line is regarded as the matrix's column. Supposes A and D respectively be the vector of address bus and data bus, namely $A=[a_0,\ldots,a_{15}]^T$, $D=[d_0,\ldots,d_{15}]^T$, x is

the random voltage value, then fetch instruction cycle M_1 in Fig. 1 can be expressed by the following matrix.

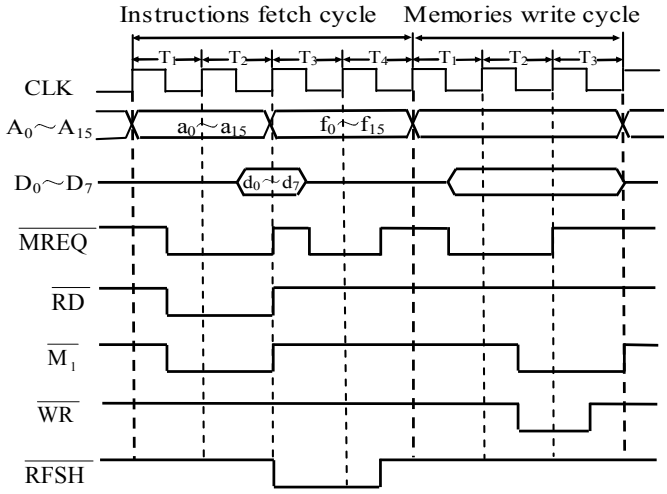

Fig. 1 Z80CPU instruction time sequence chart

M_1 matrix's 1-16th rows represent address bus information of machine cycle. M_1 matrix's 17-24th rows represent data bus information of machine cycle. M_1 matrix's 25-29th rows represent control bus information of machine cycle. Among them data of address bus include two, one is address data of the actual instruction (a_0,…,a_{15}), and another is refreshment address (f_0,…,f_{15}). In order to find out the law of instruction machine cycle expressed by this matrix, the following expression formula composed of four parts can be obtained with the resolution of matrix M_1.

$$\mathbf{M_1}=\begin{bmatrix} a_0 & a_0 & a_0 & a_0 & f_1 & f_1 & f_1 & f_1 \\ \cdots & \cdots & \cdots & \cdots & \cdots & \cdots & \cdots & \cdots \\ a_{15} & a_{15} & a_{15} & a_{15} & f_{15} & f_{15} & f_{15} & f_{15} \\ x & x & x & d_0 & d_0 & x & x & x \\ \cdots & \cdots & \cdots & \cdots & \cdots & \cdots & \cdots & \cdots \\ x & x & x & d_7 & d_7 & x & x & x \\ 1 & 0 & 0 & 0 & 1 & 0 & 0 & 1 \\ 1 & 0 & 0 & 0 & 1 & 1 & 1 & 1 \\ 0 & 0 & 0 & 0 & 1 & 1 & 1 & 1 \\ 1 & 1 & 1 & 1 & 1 & 1 & 1 & 1 \\ 1 & 1 & 1 & 1 & 0 & 0 & 0 & 0 \end{bmatrix} = \begin{bmatrix} 0 & 0 & 0 & 0 & 0 & 0 & 0 & 0 \\ \cdots & \cdots & \cdots & \cdots & \cdots & \cdots & \cdots & \cdots \\ 0 & 0 & 0 & 0 & 0 & 0 & 0 & 0 \\ 0 & 0 & 0 & 0 & 0 & 0 & 0 & 0 \\ \cdots & \cdots & \cdots & \cdots & \cdots & \cdots & \cdots & \cdots \\ 0 & 0 & 0 & 0 & 0 & 0 & 0 & 0 \\ 1 & 0 & 0 & 0 & 1 & 0 & 0 & 1 \\ 1 & 0 & 0 & 0 & 1 & 1 & 1 & 1 \\ 0 & 0 & 0 & 0 & 1 & 1 & 1 & 1 \\ 1 & 1 & 1 & 1 & 1 & 1 & 1 & 1 \\ 1 & 1 & 1 & 1 & 0 & 0 & 0 & 0 \end{bmatrix} + \begin{bmatrix} a_0 \\ \vdots \\ a_{15} \\ 0 \\ \vdots \\ 0 \\ 0 \\ 0 \\ 0 \\ 0 \\ 0 \end{bmatrix} \bullet \begin{bmatrix} 1 \\ 1 \\ 1 \\ 1 \\ 0 \\ 0 \\ 0 \\ 0 \end{bmatrix}^T + \begin{bmatrix} f_0 \\ \vdots \\ f_{15} \\ 0 \\ \vdots \\ 0 \\ 0 \\ 0 \\ 0 \\ 0 \\ 0 \end{bmatrix} \bullet \begin{bmatrix} 0 \\ 0 \\ 0 \\ 0 \\ 1 \\ 1 \\ 1 \\ 1 \end{bmatrix}^T + \begin{bmatrix} x \\ \vdots \\ x \\ d_0 \\ \vdots \\ d_7 \\ x \\ x \\ x \\ x \\ x \end{bmatrix} \bullet \begin{bmatrix} 0 \\ 0 \\ 0 \\ 1 \\ 1 \\ 0 \\ 0 \\ 0 \end{bmatrix}^T$$

$$= \begin{bmatrix} \mathbf{0}_{24\times8} \\ \mathbf{M_C} \end{bmatrix} + \begin{bmatrix} \mathbf{A} \\ 0_{13\times1} \end{bmatrix} \bullet \begin{bmatrix} 1 \\ 1 \\ 1 \\ 1 \\ 0 \\ 0 \\ 0 \\ 0 \end{bmatrix}^T + \begin{bmatrix} \mathbf{F} \\ 0_{13\times1} \end{bmatrix} \bullet \begin{bmatrix} 0 \\ 0 \\ 0 \\ 0 \\ 1 \\ 1 \\ 1 \\ 1 \end{bmatrix}^T + \begin{bmatrix} \mathbf{X}_{16\times1} \\ \mathbf{D} \\ \mathbf{X}_{5\times1} \end{bmatrix} \bullet \begin{bmatrix} 0 \\ 0 \\ 0 \\ 1 \\ 1 \\ 0 \\ 0 \\ 0 \end{bmatrix}^T = \begin{bmatrix} \mathbf{0}_{24\times8} \\ \mathbf{E_{11}} \end{bmatrix} + \begin{bmatrix} \mathbf{A} \\ 0_{13\times1} \end{bmatrix} \bullet \mathbf{E_{12}} + \begin{bmatrix} \mathbf{X}_{16\times1} \\ \mathbf{D} \\ \mathbf{X}_{5\times1} \end{bmatrix} \bullet \mathbf{E_{13}} + \begin{bmatrix} \mathbf{F} \\ 0_{13\times1} \end{bmatrix} \bullet \mathbf{E_{14}} \qquad (1)$$

Where, $\mathbf{E_{11}}=\mathbf{M_C}=\begin{bmatrix} 1 & 0 & 0 & 0 & 1 & 0 & 0 & 1 \\ 1 & 0 & 0 & 0 & 1 & 1 & 1 & 1 \\ 0 & 0 & 0 & 0 & 1 & 1 & 1 & 1 \\ 1 & 1 & 1 & 1 & 1 & 1 & 1 & 1 \\ 1 & 1 & 1 & 1 & 0 & 0 & 0 & 0 \end{bmatrix}$, $\mathbf{E_{12}}=[1\ \ 1\ \ 1\ \ 1\ \ 0\ \ 0\ \ 0\ \ 0]$, $\mathbf{E_{13}}=[0\ \ 0\ \ 0\ \ 1\ \ 1\ \ 0\ \ 0\ \ 0]$,

$\mathbf{E_{14}}=[0\ \ 0\ \ 0\ \ 0\ \ 1\ \ 1\ \ 1\ \ 1]$.

It should be noted that equation (1) considers address refreshment of dynamic RAM, Where matrix F is address value needed to refresh, $F=[f_0,\ldots,f_{15}]^T$. X is an arbitrary value 0 or 1. If does not consider address refreshment of dynamic RAM, then

$$\mathbf{M_1}=\begin{bmatrix}\mathbf{0}_{24\times8}\\ \mathbf{E_{11}}\end{bmatrix}+\begin{bmatrix}\mathbf{A}\\ 0_{13\times1}\end{bmatrix}\bullet\mathbf{E_{12}}+\begin{bmatrix}\mathbf{X}_{16\times1}\\ \mathbf{D}\\ \mathbf{X}_{5\times1}\end{bmatrix}\bullet\mathbf{E_{13}} \tag{2}$$

Similarly, memory write cycle in Fig. 1 can be indicated by the following formula.

$$\mathbf{M_2}=\begin{bmatrix}\mathbf{0}_{24\times6}\\ \mathbf{E_{21}}\end{bmatrix}+\begin{bmatrix}\mathbf{A}\\ 0_{13\times1}\end{bmatrix}\bullet\mathbf{E_{22}}+\begin{bmatrix}\mathbf{X}_{16\times1}\\ \mathbf{D}\\ \mathbf{X}_{5\times1}\end{bmatrix}\bullet\mathbf{E_{23}} \tag{3}$$

Where, $\mathbf{E_{21}}=\begin{bmatrix}1&0&0&0&1&1\\1&1&1&1&1&1\\0&0&0&1&1&1\\1&1&1&0&0&1\\1&1&1&1&1&1\end{bmatrix}$, $\mathbf{E_{22}}=[1\ \ 1\ \ 1\ \ 1\ \ 1\ \ 1]$, $\mathbf{E_{23}}=[0\ \ 1\ \ 1\ \ 1\ \ 1\ \ 1]$.

It can be discovered from equation (1) and equation (2) that M_1 is a 29×8 dimensional matrix and M_2 is a 29×6 dimensional matrix. In description matrix of two different machine cycle, matrix's row is the same and matrix's column might not be the same. For the same machine cycle, matrix E_{ij} is a constant matrix, Where E_{i1} determines the sequence format of control bus, E_{i2} determines the sequence format of the address bus, and E_{i3} determines the sequence format of data bus. Even if the machine cycle is the same, the number value on address line and data line are different. Therefore, the whole time sequence of CPU is decided by number value on the address bus and data bus, namely matrix M_i is decided by matrix A and D. On the other hand, for different machine cycle, the matrix E_{ij} is different, and time sequence of CPU is different too. Obviously any time sequence of machine cycle M_i can be expressed in the following matrix.

$$\mathbf{M_i}=\begin{bmatrix}\mathbf{0}_{24\times8}\\ \mathbf{E_{i1}}\end{bmatrix}+\begin{bmatrix}\mathbf{A}\\ \mathbf{0}_{13\times1}\end{bmatrix}\bullet\mathbf{E_{i2}}+\begin{bmatrix}\mathbf{X}_{16\times1}\\ \mathbf{D}\\ \mathbf{X}_{5\times1}\end{bmatrix}\bullet\mathbf{E_{i3}} \tag{4}$$

Or

$$\mathbf{M_i'}=\begin{bmatrix}\mathbf{0}_{24\times8}\\ \mathbf{E_{i1}}\end{bmatrix}+\begin{bmatrix}\mathbf{A}\\ \mathbf{0}_{13\times1}\end{bmatrix}\bullet\mathbf{E_{i2}}+\begin{bmatrix}\mathbf{X}_{16\times1}\\ \mathbf{D}\\ \mathbf{X}_{5\times1}\end{bmatrix}\bullet\mathbf{E_{i3}}+\begin{bmatrix}\mathbf{F}\\ \mathbf{0}_{13\times1}\end{bmatrix}\bullet\mathbf{E_{i4}} \tag{5}$$

In equation (5), M_i' is matrix of time sequence that considers the refreshment situation of dynamic RAM address. Both column of matrix M_i and M_i' are determined by the type of machine cycle. In order to facilitate further research, the following definitions are put forward.

Definition 1: Correspond to the computer instruction or program, the Boer algebra matrix which is composed by the signal in address bus, the data bus and the control bus is called computer instruction or program matrix, where the row element of this matrix is status value of bus signal in different moment, the column elements is state value of each bus signal in a certain moment. The computer program matrix is indicated with P, where the instruction matrix is indicated with I_n.

Definition 2: In matrix space V composed by the computer program matrix, instruction matrix and sub matrix, if a group of matrix $\{E_1,E_2,\ldots,E_n\}$ in space V satisfies the condition 1, and at least satisfy condition 2 or Condition 3, then $\{E_1,E_2,\ldots,E_n\}$ is called program matrix base of space V.

Condition 1: E_i can't be represented by other matrix in the matrix group $\{E_1, E_2,\ldots,E_n\}$.

Condition 2: Any program matrix and instruction matrix in the space V can be obtained by calculation between $\{E_1, E_2, \ldots, En\}$ and a unique determined matrix group $\{B_1,B_2,\ldots,B_n\}$, calculation satisfies the following form generally.

$$\mathbf{G}=\mathbf{B}_1\bullet\begin{bmatrix}\mathbf{0}\\ \mathbf{E}_1\end{bmatrix}+\begin{bmatrix}\mathbf{B}_2\\ \mathbf{0}\end{bmatrix}\bullet\mathbf{E}_2+\begin{bmatrix}\mathbf{X}\\ \mathbf{B}_3\\ \mathbf{X}\end{bmatrix}\bullet\mathbf{E}_3 \tag{6}$$

Or

$$\mathbf{G}=\mathbf{B}_1\bullet\begin{bmatrix}\mathbf{0}\\ \mathbf{E}_1\end{bmatrix}+\begin{bmatrix}\mathbf{B}_2\\ \mathbf{0}\end{bmatrix}\bullet\mathbf{E}_2+\begin{bmatrix}\mathbf{X}\\ \mathbf{B}_3\\ \mathbf{X}\end{bmatrix}\bullet\mathbf{E}_3+\begin{bmatrix}\mathbf{B}_4\\ \mathbf{0}\end{bmatrix}\bullet\mathbf{E}_4 \tag{7}$$

Condition 3: any program matrix and instruction matrix in space V can be constructed by $\{E_1,E_2,\ldots,E_n\}$ and G, construction here refers to the process that$\{E_1,E_2,\ldots,E_n\}$ and G are taken as sub matrix to form new matrix.

It is well known that function value in function space can be unlimited, but the base of function space is limited. Take three-dimensional function space as an example, its base number is 3, but function value is infinite.

Both definition 1 and 2 illustrate the significance that changeable program matrix and instruction matrix can be transformed form matrix base. Time sequence chart in Fig 1 represents instruction "LD (HL), A", and its matrix base can be expressed as the following.

$$\mathbf{I}=[\mathbf{M}_1(\mathbf{A}_1,\mathbf{D}_1)\quad\mathbf{M}_2(\mathbf{A}_2,\mathbf{D}_2)] \tag{8}$$

Suppose the content of register HL in Fig.1 is 2000H and the content of register A is 55H, instruction "LD (HL), A" is Stored in the memory at address 1000H, then

$$\mathbf{A}_1=[0\ \ 0\ \ 0\ \ 1\ \ 0\ \ 0\ \ 0\ \ 0\ \ 0\ \ 0\ \ 0\ \ 0\ \ 0\ \ 0\ \ 0\ \ 0]^T,$$

$$\mathbf{A}_2=[0\ \ 0\ \ 1\ \ 0\ \ 0\ \ 0\ \ 0\ \ 0\ \ 0\ \ 0\ \ 0\ \ 0\ \ 0\ \ 0\ \ 0\ \ 0]^T,\quad \mathbf{D}_2=[0\ \ 1\ \ 0\ \ 1\ \ 0\ \ 1\ \ 0\ \ 1]^T.$$

D_1 is the operation code of instruction "LD (HL), A". It can be known from Z80 instruction code table that D_1 is 77H, Therefore,

$$\mathbf{D}_1=[0\ \ 1\ \ 1\ \ 1\ \ 0\ \ 1\ \ 1\ \ 1]^T$$

It can be inferred from equation (8) that time sequence matrix of any instruction with n machine cycle can be expressed as follow.

$$\mathbf{I}_i=[\mathbf{M}_1(\mathbf{A}_{i1},\mathbf{D}_{i1})\quad\mathbf{M}_2(\mathbf{A}_{i2},\mathbf{D}_{i2})\quad\cdots\quad\mathbf{M}_m(\mathbf{A}_{im},\mathbf{D}_{im})] \tag{9}$$

It is obvious that a section of program written in assembly language can be expressed with matrix. The general matrix of program P is expressed as follow.

$$\mathbf{P}=[\mathbf{I}_1\quad\mathbf{I}_2\quad\cdots\quad\mathbf{I}_n] \tag{10}$$

Table 1 Examples of specific block

Instruction number	Instruction	Program mnemonic symbol	Program code	Comments
		ORG 1000H		Program start address
I_9	1000H	LD A, (2000H)	3A 00 20	Order point
I_{10}	1003H	AND 3FH	E6 3F	
I_{11}	1005H	OR B	F6 80	
I_{12}	1007H	RRC A	0F	
I_{13}	1008H	LD H A	67	
I_{14}	1009H	LD (3000H) ,HL	22 00 30	Observation point

It can be inferred from equation (9) and equation (10) that a section of program can be expressed with matrix. A section of program in Table 1 is taken as an example to obtain the matrix form of sequence signal generated by the program. Program mnemonic symbol is translated into program code according to code chart firstly. Table 1 provides concrete code of this program and precise address of instruction. Suppose fetch instruction cycle is M_1, read machine cycle is M_2 and write machine cycle is M_3, then time sequence matrix of this program can be expressed as follow.

$$\mathbf{P}_3=[\mathbf{I}_9\quad\mathbf{I}_{10}\quad\mathbf{I}_{11}\quad\mathbf{I}_{12}\quad\mathbf{I}_{13}\quad\mathbf{I}_{14}]=\begin{bmatrix}\mathbf{M}_1(1000,3A)&\mathbf{M}_2(1001,00)&\mathbf{M}_2(1002,20)&\mathbf{M}_1(1003,E6)\\ \mathbf{M}_2(1004,3F)&\mathbf{M}_2(1005,F6)&\mathbf{M}_1(1006,80)&\mathbf{M}_1(1007,0F)\\ \mathbf{M}_1(1008,67)&\mathbf{M}_1(1009,22)&\mathbf{M}_3(3000,d_L)&\mathbf{M}_3(3000,d_H)\end{bmatrix} \tag{11}$$

All data in equation (11) are in hexadecimal, d_H and d_L are data value in register H, L respectively. It is easy to calculate P_3 for 29-84 matrixes. It is obvious that matrix's row of time sequence of a program counts extraordinarily more. If does not take any treatment, store value of number directly will need large memory space for computer Simulator, which is not economic.

It can be found from equation (11) that P_3 is composed by three basic matrixes M_1, M_2, M_3. M_1 is obtained from the matrix calculation of E_{11}, E_{12}, E_{13}, E_{14}, address A, and data D. M_2 is got from the matrix operation of E_{21}, E_{22}, E_{23}, address A, and data D. M_3 is computed from the matrix operation of E_{31}, E_{32}, E_{33}, address A, and data D. Therefore, E_{11}, E_{12}, E_{13}, E_{14}, E_{21}, E_{22}, E_{23}, E_{31}, E_{32}, E_{33} make up the matrix base of this program.

Although the program of Table 1 is simple, matrix base will not change regardless of simple or complex program. Using this principle, most changeable time sequence can be obtained through calculation of time sequence corresponding to matrix base of program. This is the theoretical foundation of producing different time sequence of computer programs by universal bus simulator.

Realization of test and diagnosis

It can be inferred from above discussion that any data matrix corresponding to machine cycle of CPU will be expressed by calculation between few matrix base, address and data. That is to say that any data matrix corresponding to program can be expressed by matrix base of the program. Description of this process is described in Fig. 2(a). Since program can be expressed in matrix base and matrix is easy to deal with by using software, then software or hardware can be used to simulate time sequence. The key question is how to produce a time sequence matrix base by some hardware. We define this time sequence as time sequence base. Like matrix base, time sequence base of CPU is very limited in quantity, the collection of all time sequence base form time sequence sets of CPU.

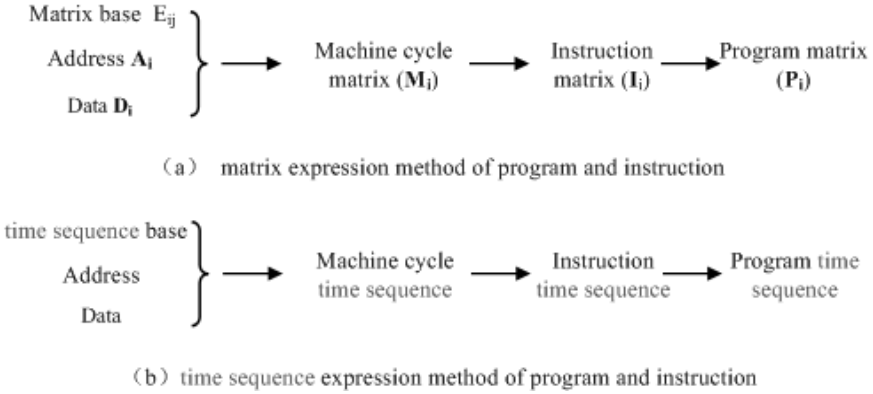

Fig. 2 Idea of emulator in simulating program and instruction

Time sequence of machine cycle can be formed by combining time sequence base with address and data, Different time sequence of machines cycle can form time sequence of instruction. Various time sequence of instruction forms the time sequence of program needed in circuit and test. Universal bus simulator can be designed according to this principle, the key to universal bus simulator is to simulate time sequence by fast logic circuit, and then add the needed time sequence signal produced by appropriate circuit to control the circuit-under-test. Test and diagnosis of complicated integrated circuit unit with CPU is realized finally. Test of different CPU circuit unit can be realized by loading different time sequence base to the same universal bus simulator.

References

[1] T. E. Funnell, Functional Test Techniques for Microprocessor-based Circuits. Electronics Test, pp.67-76, 2004.
[2] J. Masciola, G. Roberts, Testing Microprocessor Boards and Systems: a New Approach. Digest of papers, pp.46-45, 1983.
[3] G. F. Sprott. An Adaptable Emulation Support Environment for Microprocessor Systems. Digest of Papers, pp.483-488, 1983.
[4] X. X. Gao, Basis of Computer Hardware Technology. Beijing: Tsinghua University Press, 2008.
[5] X. C. Xu, Q. L. Zeng, Micro-Computer Interface Technology. Beijing: Electronic Industry Press, pp.19-32, 2003.

Advanced Materials Research Vols. 986-987 (2014) pp 1596-1599

doi:10.4028/www.scientific.net/AMR.986-987.1596

Synchronization Optimization Simulation of Optical Fiber Network Fault Features and Model Parameters

Yong Huang[1], Hengjun Liu[2],Zengliang Liu[3]

[1]School of Automation, University of Science and Technology Beijing, Beijing 100083, China

[2]94021 Unit, Ji'Nan, 250002, China

[3]Beijing University of National Defense, Beijing 410073, China

Keywords: feature optimization; genetic algorithm; K nearest neighbor algorithm; optical fiber network fault detection

Abstract. The traditional optical fiber network fault detection method has not considered the relationship between the fault characteristics and KNN parameters, it is optimized separately, and the accuracy of optical fiber network fault diagnosis is low. The synchronous optimization fault detection model of fault characteristics detection model parameters is proposed. The candidate feature subsets and K adjacent parameters are used to construct the optical fiber network fault detection model. The improved genetic algorithm is used to solve the mathematical model, and the better accurate rate of fault diagnosis for optical fiber network is obtained. The simulation is taken for testing the performance of model, compared to the traditional model, the new model has better accurate detection rate, and the detection accuracy is improved greatly, the efficiency of optical fiber network fault detection is improved, it has great application value in practice.

Introduction

With the development of optical fiber network, the fault of optical fiber network is occurred frequently, and the fault diagnosis of optical fiber network is very difficult, because the network optical fiber network fault signal is difficult to be detected, the optical fiber network optical fiber network fault signal is a typical nonlinear and non-stationary signal, the fault feature is hard to be extracted, the fault diagnosis and recognition methods are developed in lag, so the effective fault detection method should be researched, and the relative detection research has obtained more and more attention from scholar, the relation between fault feature and fault classification is not very clear, the original features are detected as far as possible to recognize the fault of optical fiber network, the traditional fault detector has high complexity with long training time, the extracted features have a large number of irrelevant and redundant features, these redundant features will have an adverse impact on the result of fault detection, therefore, some scholars have proposed some optimization algorithms such as exhaustive method, simulated annealing algorithm, genetic algorithm and particle swarm algorithm, etc[1]. In this paper, the optimization fault diagnosis detector is established based on the KNN, and the KNN detection performance is closely related to the value nearest neighbors K. Traditionally, the experience method is used to determine the K value[2], the so that the K value optimization has blindness, which easily lead to K value is not reasonable. The optical fiber network fault detection performance is bad. In order to solve the problem as above, some scholars proposed some method as: particle swarm optimization algorithm, genetic algorithm etc., the K value of KNN is optimized. The classification performance of KNN is improved. In the optical fiber network failure detection modeling, the traditional methods do not consider the link of KNN parameters, they are processed separately, and it is difficult to obtain the global optimal feature[3~5].

In order to improve the detection accuracy of optical fiber network fault, considering the features and parameters of KNN, the defects of traditional method is overcome, we propose an improved genetic algorithm (GA) optimization method of optical fiber network fault detection model, the parameter optimization model of GA-KNN is constructed, and the model is validated the effectiveness, the feasibility is proved by the simulation experiment.

Mathematical model of optical fiber network fault detection

A. Fault feature extraction problem of optical fiber network

According to a given set of fault feature optical network, assumed that F={f1,f2,…,fn}, a binary vector description is used to optimize the feature, the feature optimization formula is shown as S={s1,s2,…,sn}, }, Si ∈ {0,1}, i=1,2,... n, where, n is fault number of optical fiber network, set that 1 and 0 respectively shows that if the characteristic is selected or not, optical fiber network fault feature optimization is researched to improve the accuracy rate. So the accuracy rate (G) of optical fiber network fault detection is shown as the feature optimization number, the optical fiber network fault feature optimization problem can be described as: $\max_S G(S)$. The constraint conditions are:

$$S=\{s_1,s_2,\cdots,s_n\} \quad s_i\in\{0,1\} \quad i=1,2,\cdots,n \tag{1}$$

Analysis with formula (1) and (2), we can get that the optical fiber network fault featur e optimization is a typical multi parameter optimization problem, and the feature subset of original features is optimized from a set of dimension N.

B. KNNM parameter optimization problem

K nearest neighbor algorithm (KNN) is a very effective non parameter classifier, for an unknown sample x, we need to find out the unknown samples which is closest to the k neighbor, set that k1,k2,…,kc is the number of samples of unknown samples x, di (x) is the discriminant function of wi classification, di(x))=ki, i=1,2,3,…,c, the discriminant rule is expressed as follows: If: $d_m(x)=\max\{d_i(x)\},i=1,2,3,\cdots,c$, then x ∈ wm.

The confidence degree of K nearest neighbor classifier is defined as:

$$T=d_m(x)/k(m+1)T \tag{2}$$

In the formula, K is the number of nearest points of samples, dm(x) is number of near est neighbors category with K nearest discrimination, T*=(m-1)/m is the confidence threshol d of system, if T≥T*, K nearest neighbor classification is accurate.The constraint condition is:

$$M=\{k\} \quad K>0 \tag{3}$$

According to the optical fiber network fault detection feature optimization problem, the optimization problem of KNN parameter K takes the genetic algorithm for solution, the indi vidual shows the KNN parameter K. Detection accuracy of optical fiber network fault is th e fitness function.

Improved genetic algorithm to optimize characteristic and parameter design of KNN

A. chromosome coding

The binary coding mode is used to research the optimal combinatorial optimization of optical fiber network fault detection, and each individual is composed of 2 parts, the first part shows the optical fiber network characteristic, the second part represents the KNN value of K, KNN parameter can be transformed by formula:

$$p=\min_p+\frac{\max_p-\min_p}{2^l-1}\times d \tag{4}$$

In the formula, p shows the K parameter after transformation, l shows the K digital string length, and maxp and minp are the maximum value and the minimum value, d is the binary value. Xi is a subset of features, the corresponding fitness function *f(Xi)* is calculated as follows:

B. Design of fitness function

For the genetic algorithm, the fitness function guides the direction of its evolution, therefore, the fitness function is very important. It should meet two objectives: the dimension of the feature subset is as little as possible; to improve the accurate rate of optical fiber network fault detection.

$$f(X_i)=\frac{exp(A_{X_i}-\eta\cdot A)}{\gamma.(\sum_{j=1}^{n}x_j)/n} \tag{5}$$

Where, n is the total number of feature, and A_{X_i} is the training accuracy of X_i, A contains all the features of the training accuracy, the two parameters η and γ are used to adjust the fault detection accuracy threshold, the contribution weight degree of fitness function is reduced to improve the detection accuracy. From equation (9), it shows that when the number of features in a feature subset is less, the optical fiber network fault detection accuracy is higher, the feature subset is optimal. The genetic algorithm fitness function value is bigger.

C. Optimization operation and crossover operation

Optimization operation is the evaluation of individual quality based on the fitness value, the best individual is optimized, and the inferior individual is eliminated, which ensure the continuous evolution. The cross operation is the main way to generate new individuals, mainly has the single point crossover, multi-point crossover, uniform crossover. The procedures are shown as: firstly, the single intersection point is optimized, the 0, 1 two integers are produced, and the random number is 0, the probability of cross is the front part of it. If it is 1, the single point crossover is taken.

Simulation and result analysis

In order to test the validity of optical fiber network fault detection of GA-KNN model, the simulation is taken, the hardware environment is: CPU 3.0 G, 1 G memory, and Matlab 2007 toolbox and so on. Population size of genetic algorithm is 20, and the optimization probability is 0.6, the crossover probability P_c=0.75, and P_m=0.15, the hardware environment is: CPU 3.0G, 1G memory, hard disk space available for 80G; software environment: Windows XP operating system, Matlab 2007. Population genetic algorithm for optimization of 20, 0.6 probability, crossover probability Pc=0.75, variable cross probability Pm=0.15, Max evolution generation is 500. Experimental object for optical fiber network fault signal, and it contains 4 kinds of fault states. Each state 100 samples, the total sample number is 400. According to 4:1 proportion, they are divided into training set and test set. With different models, the experiments are taken for comparing the performance of the algorithms, the accurate rare of fault detection for different algorithms is shown in Figure 1.

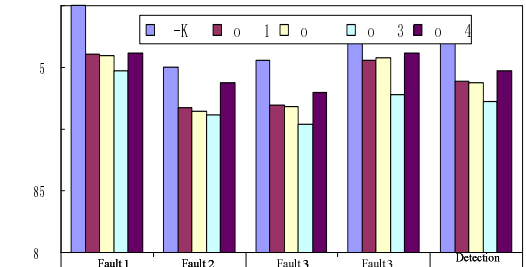

	Fault 1	Fault 2	Fault 3	Fault 3	Detection accuracy
-KNN		. 7	5. 55	7. 5	7.
	6.	. 7	.	5. 55	. 8 7 5
	5. 7	.	. 78	5. 7	. 7 7 5
	. 7	.	.	. 8	. 57 5
	6.	. 7	.	6. 5	. 7 5 5

Figure 1. Fault detection result of different algorithms

In the Figure 1, we can conclude that the result of GA-KNN detection is best, and the average detection accuracy increases by 2.25%, which indicates that the characteristics and parameters of K of Model3 are optimized. The detection calculation cost is reduced, and the fault detection speed is improved, it shows that the new method has better performance in optical fiber network fault detection.

Conclusions

In this paper, the optimization of optical fiber network fault detection method is researched, the synchronous optimization fault detection model of fault characteristics detection model parameters is proposed. The candidate feature subsets and K adjacent parameters are used to construct the optical fiber network fault detection model. The improved genetic algorithm is used to solve the fault detection problem. Results show that the new method can detect the optical fiber network fault accurately, the average detection accuracy increases by 2.25%. It has good application value in the fault detection area.

References

[1] Han Xiaodong. Fault Positioning Technology for Power Grid Based on Wavelet Neural Network[J]. Bulletin of Science and Technology. 2013; 29(6): 59-61.

[2] QIU Shi-hui. Analog Circuit Fault Diagnosis Based on Artificial Neural Network[J]. Sci ence Technology and Engineering. 2012; 12(30): 8042-8046.

[3] SVILEN D and HARALD H. Information Rate of OFDM-Based Optical Wireless Com munication Systems With Nonlinear Distortion[J]. Journal of Lightwave Technology, 201 2, 31(6): 918-929.

[4] FEMANDO N, HONG Y, and VITERBO E. Flip-OFDM for Unipolar Communication Systems[J]. IEEE Transactions on Communications, 2012, 60(12): 3726-3733.

[5] HUANG Chao，NAN Jian – guo. Simulation Analysis of Communication Optimization Algorithm of FC Fibre Channel[J]. Computer Simulation, 2013, 30(8): 194-197.

Advanced Materials Research Vols. 986-987 (2014) pp 1600-1605

doi:10.4028/www.scientific.net/AMR.986-987.1600

The Analysis of Device Model in CMOS Integrated Temperature Sensor

Qi XIONG[1, a], Shaohua ZHOU[1, b*], and Jiangping ZENG[2, c]

[1]Hunan Engineering and Technology College, Changsha, Hunan, China

[2]University of Hunan, Changsha, Hunan, China

[a]email:, [b]email:zshsa@126.com, [c]email: zengjp@hnu.edu.cn

*Corresponding author

Keywords: Intergated, Temperature sensor, Sub-threshold model, Piezoelectric effect, Resistance.

Abstract. According to the requirement of the CMOS integrated temperature sensor on the device, we analyzed the sub-threshold model of MOS device and the bipolar device under MOS technology. We found the latter is more suitable for a components of CMOS integrated temperature sensor devices. Therefore, we analyzed the influence of the substrate PNP tube's piezoelectric effect on temperature sensor and compared different types of resistance that lays a theoretical basis for the design of CMOS integrated temperature sensor.

Introduction

Nowadays, in the design of the integrated temperature sensor under standard CMOS technology, the MOS field effect transistor(MOSFET) based on sub-threshold model and substract PNP tube with fully compatible CMOS technology are widely used as a temperature sensing element. Unless the resistance is also one of the essential components in the temperature sensor, its feature has direct connection with the performance of the temperature sensor.

The Sub-threhold Model Of MOS Device

In the practical application of MOS tube, when the gate source voltage VGS tends to be approximate to the threshold voltage VTH, ID-VGS characteristic curve alters from the square law relationship to the exponantial relationship. the area when VGS is greater than the threshold voltage is called the strong inversion region. While, the area when VGS is lower than the threshold voltage is called the sub-threshold or weak inversion region(actually, the shift of those two areas is not so obvious).

Assume that the channel length is long enough, VBS= 0 and VDS>4V. Then, the drain current of the MOSEFT based on sub-threshold can be represented by equation (1) and (2) [1][2] .

$$I_D = s_\mu V_T^2 \sqrt{\frac{q\varepsilon_{si}N_{CH}}{2\phi_s}} exp\left[\frac{\phi_s - 2\phi_B}{V_T}\right] \approx s_\mu V_T^2 \sqrt{\frac{q\varepsilon_{si}N_{CH}}{4\phi_B}} exp\left[\frac{\phi_s - 2\phi_B}{V_T}\right] \quad (1)$$

Here, $\phi_S = 2\phi_B$.

$$I_D = s_\mu V_T^2 \sqrt{\frac{q\varepsilon_{si}N_{CH}}{4\phi_B}} exp\left[\frac{V_{GS} - V_{TH} - V_{OFF}}{nV_T}\right] \quad (2)$$

In the BSIM3v3 model, VOFF is a fixed constant. Compare equation (1) and (2), as we see, when the two drain current ID is equal to each other:

$$\frac{V_{GS} - V_{TH} - V_{OFF}}{n} = \phi_s - 2\phi_B \quad (3)$$

Surface barrier ϕ_S and the relationship between Fermi potential barrier ϕ_B and temperature can be obtained by the literature [1]:

$$\phi_s(T)=\phi_s(T_0)\frac{T}{T_0}-\frac{3kT}{q}\ln\left(\frac{T}{T_0}\right)+\frac{E_g(T)}{q}-\frac{E_g(T)}{q}\frac{T}{T_0} \quad (4)$$

$$\phi_B(T)=\phi_B(T_0)\frac{T}{T_0}-\frac{3kT}{2q}\ln\left(\frac{T}{T_0}\right)+\frac{E_g(T)}{2q}-\frac{E_g(T)}{2q}\frac{T}{T_0} \quad (5)$$

With equation (4) and (5), make $\phi_S - 2\phi_B$ as temperature function:

$$\phi_s(T)-2\phi_B(T)=\left(\phi_s(T_0)-2\phi_B(T_0)\right)\frac{T}{T_0} \quad (6)$$

Therefore, for a given drain current, according to the equation (3):

$$V_{GS}(T)=V_{TH}(T)+V_{OFF}+\frac{n(T)}{n(T_0)}\times \left(V_{GS}(T_0)-V_{TH}(T_0)-V_{OFF}\right)\frac{T}{T_0} \quad (7)$$

Suppose that the change of n（T） caused by temperature is minimal: n（T）= n（T0）. And the threshold voltage for the model is $V_{TH}(T)=V_{TH}(T_0)+K_T\,(T/T_0-1)$, and KT < 0:

$$V_{GS}(T)\approx V_{GS}(T_0)+K_G\left(\frac{T}{T_0}-1\right) \quad (8)$$

Here, $K_G=K_T+V_{GS}(T_0)-V_{TH}(T_0)-V_{OFF}$ (9)

The K_T, V_{OFF} and V_{GS}-V_{TH}, K_G for the typical values is negative, when the drain current I_D remains the same, V_{GS} will reduce along with the rise of temperature.

Although the power consumption of MOS tube based on sub-threshold is very low, the study on sub-threshold based MOS tube model is not perfect at present, the instability of the sub-threshold condition and its fluctuation with technology limit its application. Therefore, what is now widely used as the thermal components of integrated temperature sensor is the substrate PNP bipolar transistor which we will discuss below.

The Bipolar Transistor(BJT) And The CMOS Technology

Silicon bipolar transistor B- E junction barrier V BE is a quantity related to temperature, and has good stability. This feature can be used in the integrated temperature sensor and band gap voltage reference source. Owing to its low cost, long-term stability, high sensitivity and predictability to temperature, good compatibility with CMOS technology and low power consumption, the bipolar transistor is considered as the most attractive devices of a temperature sensor[3].

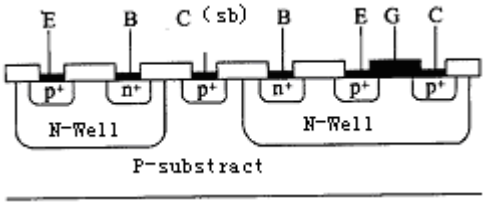

Longitudinal PNP Transversial PNP

Figure 1 The structure section of bipolar PNP transistor based on CMOS technology

There are two ways to achieve a PNP bipolar transistor in the CMOS technology, respectively known as longitudinal PNP transistor and transversial PNP transistor, as shown in Figure 1. Longitudinal PNP transistor is also called substrate PNP transistor with the P + region in the n trap (the same as the PFETs leakage source area) as emitter, N trap itself as the base area, P-type substrate as a collector area, and inevitably connects to the most negative power supply (usually grounding).

The VEB Signal of Substrate PNP Tube

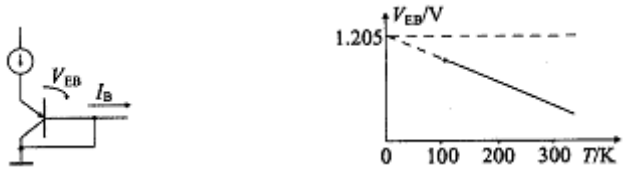

Voltage characteristic Teperature characteristic

Figure 2 Base emitter junction voltage characteristic and temperature characteristic of transistor

For substrate PNP transistor, when the relation between the collector current and the E- B junction voltage is at the forward bias situation, as shown in figure 2 (a), it can be illustrated by equation (10) [4] :

$$I_C = I_s exp(V_{EB}/V_T) \tag{10}$$

Therein, V_T= kT / q. I_S is the transistor-emitted reverse saturation current that is proportional to the $\mu kTn_i^{\ 2}$, with μ the minority carrier mobility and n_i the intrinsic carrier concentration of silicon.

Like diode, forward voltage V_{EB} can be measured by temperature signal which is expressed as:

$$V_{EB}=\frac{kT}{q} ln\left(\frac{I_C}{I_S}\right) \tag{11}$$

In PNP transistors, I_S of value is the amount which strongly depends on temperature and is expressed as:

$$I_S= \bar{\mu}_{pb} \cdot n_i^2 \frac{kTA_e}{\omega_b N_{Db}} \tag{12}$$

In the equation(12), T is the absolute temperature, unit for K. AC is the emitter area. ω_b is the base area width. NDb is the doping concentration of the base region. $\bar{\mu}_{Pb}$ is the average minority carrier mobility of the base region.

$\bar{\mu}_{Pb}$ and n_i are The quantity of related to the temperature, can be approximated as:

$$n_i = C_{TEn_i} T^{3/2} \cdot exp\left(-\frac{V_g}{2V_T}\right) \tag{13}$$

$$\bar{\mu}_{pb} = C_{TE\mu} \cdot T^{-m} \tag{14}$$

Among them, V_g is the silicon band gap voltage (equal to 1.12V at home temperature), m is effective migration rate index (for hole m = 2.2, for electronic m = 2.42), and $C_{TE\,ni}$ and $C_{TE\mu}$ are constants uncorrelated to temperature.

To obtain a general expression, we usually use the temperature of the collector current I_C related equations. It is a more simpler equation than the former ones:

$$I_C=I_{C0}\left(\frac{T}{T_0}\right)^{\alpha} \tag{15}$$

In the equation(15), α is the temperature index, I_{C0} is the current of collector at temperature zero:

$$V_{EB}=V_g - V_T \cdot ln\left(\frac{C_{TE}A_e T_0^{\gamma}}{I_{C0}\omega_b N_{Db}}\right) - (\gamma-\alpha) \cdot V_T \cdot ln\left(\frac{T}{T_0}\right) \tag{16}$$

γ = 4 - m， V_T= k T/q . At the temperature T_0, E-B junction barrier change from V_{EB} to V_{EB0} .

$$V_{EB0}=V_{g0}-\frac{kT_0}{q} \cdot ln\left(\frac{C_{TE}A_e T_0^{\gamma}}{I_{C0}\omega_b N_{Db}}\right) \tag{17}$$

V_{g0} is the band gap barrier when temperature of silicon is at T0. Equation (16) is the connection between the junction voltage drop of transistor E-B and temperature. In the formula, $(\gamma-\alpha)V_T \ln\left[\frac{T}{T_0}\right]$ does not have a significant impact on temperature. And, VT= kT / q is proportional to the temperature. Thus, VEB increase linearly with the decrease of the temperature on the whole. When the linear extrapolation reaches absolute zero, VEB achieves the silicon band gap voltage value which equals to 1.205 V, as shown in figure 2 (b).

The Voltage Proportional To The Absolute Temperature

When two collector current IC1, IC2 respectively pass through the bipolar transistor, the difference among all the junction voltage drops from different types of current and collectors can be yielded by formula (11):

$$\Delta V_{EB} = V_{EB1} - V_{EB2} = \frac{kT}{q} ln\left(\frac{I_{C1}}{I_{C2}}\right) \tag{18}$$

When the two current ratios are constant, the difference will be the quantity proportional to absolute temperature. But in practice, there are several non-ideal factors affecting the substrate bipolar PNP transistor PTAT voltage's characteristic. These factors are: the parasitic series resistance and current gain change, big injection and the Early effect.

The Influence Of The Piezoelectric Effect Of Substrate PNP Transistor On Temperature Sensor

Due to the thermal load and mechanical load caused by chip packaging will cause deformation, and junction voltage drop VEB from substrate bipolar transistor E-B can just perfectly be influencde[5]. Moreover, the piezoelectric junction effect will directly affect the accuracy of the temperature sensor. According to the theory of pressure variable resistance, take a [1 0 0] cut silicon-made substrate bipolar transistor for example, the minority carrier mobility μ produced by the changes of mechanical stress can be expressed by equation(19) :

$$\frac{\Delta\mu}{\mu} = -\pi_{12}\sigma \tag{19}$$

Therein, π_{12} is the pressure resistance coefficient, σ is the total pressure. When the minority carrier flows along the direction perpendicular to the wafer surface, the migration rate has nothing to do with the direction of the mechanical pressure. Assuming the pressure variable coefficient of minority carrier stays the same compared to the majority carrier. π_{12} , compared to holes and electrons, are respectively equal to - Pa 1.1 x 10-11-1 and 53.4 x 10-11 Pa – 11.

In figure 3 (a) and (b) shows the tendency of the current change and temperature error under the influence of substrate PNP transistor and NPN transistor. Iit is observable that PNP substrate bipolar transistor has better characteristics than NPN one, and also bears little impact of voltage change. Fabiano Fruett has demonstrated through experiments that the PTAT voltage achieved by PNP substract transistor is merely affected by this effect. So substrate PNP bipolar transistor is very suitable to be used as a component of the temperature sensor.

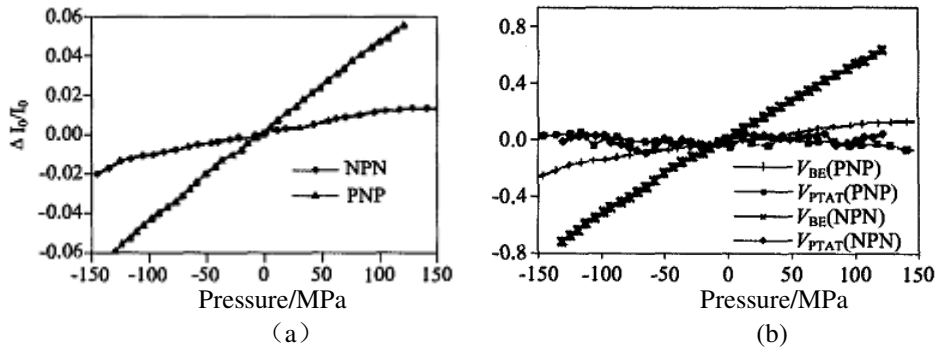

(a)The current change under pressure of PNP and NPN substract transistor
(b)Temperature error of V_{BE} and $V_{PT\ AT}$ under pressure
Figure 3 Substrate PNP and NPN transistor under pressure

Resistance And The CMOS Technology

Substrate PNP bipolar transistor of diode-connected form has emitter, collector and base parasitic series resistance. The voltage drop at the base and the emitter parasitic series resistance adds to the intrinsic E - B on pressure drop which can lead to an offset PTATA voltage. In the temperature sensor, the offset voltage will be reflected on the temperature disorder. When the base series resistance values equals to100n, it will generate temperature offset of 0.64℃. The bigger the series resistance is, the greater the disorder will be. To reduce the error brought by the series resistance, three following aspects can be adopted:

1. Change the transistor geometry size to minimize series resistance (Such as, use multi-index structure or parallel transistor structure);
2. Reduce the bias current, but it will increase the sensitivity of the noise and interference;
3. By using three phase current technology or similar technology to compensate the series resistance.

In the measurement of large temperature range, the effect that resistance changes with the temperature can no longer be ignored. Under the CSMC 0.6 μm CMOS technology, there are six kinds of resistance to choose from:

(1) n we l 1 resistance;
(2) n^+ ion implantation resistance;
(3) P^+ ion implantation resistance;
(4) Poly 1 resistance;
(5) Poly 2 resistance;
(6) h r (Poly2) resistance.

Table 1 shows some coefficient of the six resistances.

Table 1 CSMC 0.6μm CMOS process six resistance parameters

1	2	3	4	5	6	7	8
type	Rsh/Ω • □-1	dl/ μ m	dw/ μ m	VC1	VC2	tC1	tC2
nwell	849.06	-0.248	1.399	8.84 e-3	9.82e-4	5.24 e-3	9.56 e-6
n+	79.10	-0.246	-0.366	1.05 e-3	1.34 e-3	1.73 e-3	-6.17 e-7
p+	121.71	-0.925	-0.400	-2.35 e-3	7.22 e-4	9.40 e-4	1.40 e-6
poly1	27.53	0.167	0.212	2.32 e-4	1.37 e-3	7.75 e-4	-3.42 e-7
poly2	27.75	0.279	0.419	1.19 e-3	2.56 e-3	7.08 e-4	-2.53 e-7
hr (5K)	4545.68	1.144	0.055	-2.66 e-3	11.81 e-3	-4.68 e-3	1.58 e-5
hr (1K)	995.792	1.443	0.162	-4.36 e-3	-2.73 e-3	-3.04 e-3	1.15 e-5

The equation to calculate the resistance is:

$$R=Rsh\frac{l-dl}{w-dw}(1+V_{c1}|dv|+V_{c2}dv^2)(1+t_{c1}(t-tnom)+t_{c2}(t-tnom)^2) \quad (20)$$

In the equation (20), Rsh is square resistance; L the length; W the width; Vc1 and Vc2 the voltage coefficient; tc1, tc2 the temperature coefficient; T the temperature and t nom means in the room temperature of 25 ℃. In order to reduce the effect that resistance varies with change of temperature and voltage on the sensor, we choose the polyresistor poly 2 with smaller temperature coefficient. Due to its small square resistance, the negative effect is it will occupy a larger chip area, but the fact it doubles the circuit performance makes up for the defect of occuping larger area.

Acknowledgment

In this paper, the research was sponsored by the Hunan Department of Education Scientific Research Project(13C199,13C198) and Hunan Scientific and Technological Project(2011FJ4172).

References

[1]Phillip E Allen,Douglas R.Holberg.CMOS Analog Circuit Design 2nd edition[M], Beijing, Publishing House of Electronics Industry,2007.

[2] G.Giustolisi，G.Palumbo,M.Criscione eta1. A Low-Voltage Low-Power Voltage Reference Based on Subthreshold MOSFETs[J].IEEE Journal of Solid State Circuits,2003,3 8(1) :151 – 154.

[3] R.A.Bianchi,F. Vinci Dos Santos , J.M.Karam et a1. CMOS - Compatible Smart Temperature Sensors[J]. Microelectronics Journal, 1998,(29):627- 636.

[4] Chen Guican, cheng jun, Zhang Ruizhi. Analog CMOS integrated circuit design [M]. Xi 'an: xi 'an jiaotong university press, 2002.

[5]Fabiano Fruett,Guijie Wang,Gerard, C.M.Meijer.The Piezojunction effect in NPN and PNP vertical transistors and Its Influence on Silicon Temperature Sensors [J] .Sensor and Actuators,2000, 85:70-74.

Advanced Materials Research Vols. 986-987 (2014) pp 1606-1610

doi:10.4028/www.scientific.net/AMR.986-987.1606

The design and analysis of substation equipment temperature wireless monitoring system

Wei Na

Sichuan Electric Vocational and Technical College, Chengdu, China, 610019

weinapanliang@163.com

Keywords: Power equipment; Temperature; ZigBee; Temperature sensor

Abstract. The power equipment temperature monitoring within substation is one of the indicators to raise the capacity of power equipment management. From the perspective of wireless monitoring, this paper analyzed the main principles of wireless temperature monitoring of current power equipment. And with technology, according to several defects, this paper put forward a way of data forwarding, management plan by combining wireless protocol ZigBee and cable transmission, analyzed temperature monitoring system from configuration of temperature sensor, wireless temperature node and center nodes, and software design process, and finally analyzed some of the key technologies implemented by temperature monitoring system, which has a certain guiding significance.

Introduction

Substation is the hub of power supply variable distribution. Substation electrical equipments'safe, stable and reliable operation is the foundation of continuous power supply. Among the many influence factors of power equipment, temperature is one of the most important factors that influences substation. According to related statistics, the faults such as power supply suspension, electric power equipment damage, and reduced power equipment service life are caused by unreasonable temperature rise. For example, in 2013, due to the temperature of one transformer in Hefei was too high, spontaneous combustion happened to transformer and related lines which caused economic losses and power outage around the factory. In electric power equipments'stable operation, the main effect of the high temperature of power equipment is to make aging skin of electric power equipment insulation paper, which shortens the time of power equipment service on the one hand, increases the cost of power supply, on the other hand brings security hidden dangers to sustainable supply, and increases the difficulty of power equipment management. Along with the increase in electricity demands, substation plays the growing role. In order to improve safe, stable and reliable substation, it is necessary to monitor power equipment.

At present, the measurements of electric power equipment temperature are optical fiber temperature measurement, and infrared measuring temperature [1], which have a certain accuracy of measurement, but the cost is higher, and they are not conducive to substation equipment, multi-point temperature measurement requirements, and have certain limitations. Therefore, this paper uses a combination means of short-range wireless communication and wired communication, makes use of the advantages of simple, low cost, good quality transmission network by using ZigBee protocol to perform online real-time monitoring of substation transformers, all kinds of key contacts, cable connectors, switch cabinet temperature, which is easy to master the temperature parameters of power equipment and improves the reliability of substation.

Wireless Monitoring Principle of Power Equipment Temperature

Wireless network used to monitor power equipment has made a series of research results. In literature [1-3], temperature node data in transformer, contact, cable connectors, switch cabinet, inside the box are collected by using wireless temperature sensors. Via wireless transmission, unified summary may realize temperature monitoring of power equipment.

Reasonably place temperature sensors within the substation transformer, all kinds of key contact, cable connectors, and switch cabinet. Within the scope of wireless LAN, wireless temperature sensor nodes and center nodes collect temperature data in network, transformer, and relevant contact and transmit them to central nodes. By center node's transmission of temperature data received is by cable transmission (RS-485 bus), and then transmit to substation computer through bus transformation to monitor the temperature.

Wireless Monitoring Solution of Power Equipment Temperature

In Figure 1, reliable temperature monitoring of power equipment can be achieved through wireless sensor nodes and 485 bus transmissions, however, it also has some shortcomings:

(1) Temperature signal only guarantees the monitoring use in substation computer. The data communication with no realization of substation and transformer substation, substation and dispatching management center, has small promotion and application value in unmanned transformer substation, and box-type substation;

(2) Set more RS-485 and the points of contact center node with large redundancy, and put forward higher requirements for bus transmission due to electromagnetic interference.

Therefore, on this basis, design a data communication plan with low redundancy, high anti-interference ability, which can realize data communication between substation and dispatching management center..

Similar with the principle of Figure 1, the wireless monitoring of the scheme power equipment temperature configurates corresponding temperature sensor for temperature rise substation monitoring, and then put the collected temperature data summary to an intermediate nodes (network coordinator), connect to the node by using 485 bus of terminal (network coordinator) , transform data collected directly to home station computer, at the same time, through repeater, make use of electric power special communication network to transfer temperature data scheduling management center computer, realize data remote management, which has a certain reference value in box change, and unattended substation applications.

This scheme can reduce the redundancy of network, realizes data communication between substation and dispatching management center. Through repeater, the coordinate monitor of transformer substation and dispatching management center multiple computers is realized. According to temperature data of online monitoring, timely evaluate the operation of power equipment, reduce the ratio of power outage caused by temperature rise, and raise the level of management and decision-making.

Hardware Design Analysis

The design of hardware part includes temperature sensor nodes, center node (network coordinator) and network design. According to the characteristics of measured object, flexibly use different means of measuring temperature.

A. The placement of temperature sensor nodes

Temperature measuring installation of different power equipment needs has bigger difference, such as oil changes can use Figure 3 way of measuring temperature. The temperature inside the switch cabinet can be got through temperature measurement module DS18B20 in wireless MCU. Therefore, combining temperature sensor nodes places, categorize main hot parts of the equipment within substation, which is mainly divided into transformer, all kinds of connectors, contact and switchgear [4]. Sensor placement and selection analysis can be made as the following:

(1) Oil-immersed transformer temperature measuring sensor selection

Temperature measuring of oil-immersed transformer temperature depends on advanced placement of oil, winding and iron core temperature sensors. Temperature data collection makes use of fiber grating sensors placed in advance, collects oil temperature, winding and iron core, and is sent by

wireless sensor nodes to implementation of transformer oil temperature, winding and iron core temperature monitoring.

(2) Key connection joints and contact temperature sensor options

Equipment joints and contact numbers within the substation are numerous. With incomplete statistics, the joint, the contact number in a medium-sized substation for temperature measurement can reach more than 500. Large amount of temperature measurement nodes need sensors with small volume, high precision, and easy installation. A company's ZC800 series temperature sensors are adopted here because of its small volume, convenient power supply, high measurement precision, which satisfies the requirements of key connection joints and contact temperature measurement.

(3) Switch cabinet temperature measuring sensor selection

Switch cabinet temperature measurement is relatively simple, and the temperature sensor can use temperature measurement module in wireless MCU. For example, DS18B20 temperature sensor is of small size, and can adapt to different shapes of encapsulation with strong suitability.

B. Temperature sensor node hardware structure

Although there are differences in temperature sensor selection, placement, the basic parts of temperature sensor node hardware are unchanged. The temperature data collected are transmitted by temperature sensor after signal disposal such as operational amplifier, filter, A/D conversion to microprocessor, and configure data communication through wireless communication module to center node.

Signal conditioning modules include operational amplifier and filter. On the one hand, amplify the weak signal of sensor transformation, on the other hand filter interference; Microprocessor temperature data's storage, editing, and drive temperature data the wireless communication module collected real-time; Power module supplies power for microprocessors; wireless communication module adopts Zigbee communication protocol, such as in Table 1. Comparing with other kinds of communication, take considerations from transmission rate, distance and cost, Zigbee agreement in substation power equipment' wireless temperature measuring completely meets application requirements.

Table 1 Different communication ways comparison

	WiFi	3G	GPRS	Bluetooth	ZigBee
transmission rate	11Mb/s	473kb/s	171.2kb/s	1Mb/s	20~250kb/s
Transmission distance	above100m	-	-	About 10m	10~100m
cost	low	higher	High	lower	low

C. Center node and data forwarding

Center node is responsible for the data acquisition of temperature measurement nodes, whose basic structure is similar to Figure 4. The input of the microprocessor is wireless receiving module, which directly connects to repeater via 485 buses and will forward temperature data collected to site monitoring computer. Besides, private electricity network still can be used to send the temperature data collected to remote monitoring center.

Software Design Analysis

Substation monitoring temperature acquisition system software part includes greenhouse environment parameter control node program, network coordinator node (center) and PC (monitoring) computer program three parts. Network coordinator and node control program are the cores to realize substation electrical equipment temperature measurement.

Software design first is to initialize network coordinator node (center), set up a network available for substation electrical equipment temperature measurement node to join in. When need to collect data, monitor computer issues monitoring instructions. Network coordinator nodes (center) begin to

receive the corresponding ZigBee node's temperature data. And corresponding temperature measurement node receives network coordinator node (center) instruction, awakens sensing device, collects power equipment's corresponding node temperature, and forwards from center nodes for monitoring evaluation.

Various temperature measurement node and center node are initialized. Network is set up in center node. Form a network with temperature measurement node join which can send and receive data information. Monitoring computer issues instructions which require power equipment monitoring. According to the requirement, center node acquires field temperature node data, and forward it unify.

Key Technologies to Implement Wireless Monitoring Temperature

Relative to cable monitoring, the advantages of power equipment wireless control are to meet the requirements of modern power grid monitoring and management. But in wireless monitoring, it is not easy to find a really suitable way for electric power parameter monitoring. For temperature monitoring of power equipment, the keys are:

(1) The reliability of the system

The reliability of temperature monitoring system is the basis of power equipment temperature measuring practical value evaluation, which includes many angles such as the reliability of planning and design, the anti-interference ability of hardware circuit and data transmission, reliability of software design. For hardware circuit and anti-interference of data transmission, strictly follow the standards for electricity data transmission. Improve the reliability of the system from transmission line, temperature sensors, and joint angles to make the temperature data more reliable and credible. It can make accurate estimates by using these data for power equipment;

(2) Timely and effective means of monitoring maintenance

Temperature monitoring of power equipment take measures to control temperature parameters change in addition to temperature parameters monitoring. According to equipment temperature change rule, establish a set of power equipment operation management measures, including controllable temperature control and uncontrollable temperature control.

For controllable temperature control, mainly adopt its cooling measures, lower damages caused by equipment temperature rise, such as transformer forced air cooling, air conditioning temperature control installed in switch cabinet, etc. Also, realize controllable temperature intelligent adjustment, such as switchgear ideal temperature limit is M. When the temperature is higher than M, at the same time monitoring center gets data M, switchgear driver in microprocessor according to the excessive temperature turns on air conditioning control, makes temperature inside the switch cabinet lower than M, to guarantee the safe operation of power equipment.

For uncontrollable temperature control, mainly bus terminal point, insulation aging, etc., purpose equipment should be timely and effectively maintained, which requires that wireless temperature measurement node has a certain position, namely a node temperature anomalies. Managers can quickly learn the node position from monitoring computer, and eliminate hidden safety danger in time.

In general, power equipment wireless temperature monitoring also needs constant perfection, which can be more advantageous to realize the management of power equipment.

Conclusion

Remote monitoring of power equipment realized by using wireless technology is one of the main development directions of electric power measurement. This paper, on the basis of the original wireless monitoring, only considers that temperature signal is used in substation computer monitoring, and fails to realize data communication between substation and transformer substation, substation and dispatching management center, and set up more contact points between RS-485 and center node. The redundancy is bigger. Electromagnetic interference puts forward higher request on

bus transmission, and on this basis, this paper proposes a data communication and management plan to reduce network redundancy with reliable transmission and easy to implement:

(1) Based on Zigbee wireless communication and wired transmission, collect temperature measurement data by a central node, and by a RS-485 bus realize acquisition temperature data forwarding, and reduce the redundancy of network cabling;

(2) Through a HUB, forward the collected temperature data directly to monitor computer. Temperature information collected from a substation can also be forwarded through electric power private networks (VPNS), to easily realize unmanned substation management;

(3) Refer to previous wireless monitoring means, analyze hardware and software parts to make the temperature monitor system has higher reliability in terms of composition and software flow design.

References

[1] Zhou Ruishuang, Wang Chunxin, Wang Huanjuan, etc. Substation equipment on-line monitoring system based on temperature sensor and ZigBee technology [J]. Electric Power Science and Engineering, 2012, 28 (7) : 24-29.

[2] Zhang Qiaofen, Liu Yancheng, Zhang Qinjin, etc. The substation equipment temperature monitoring system design based on wireless sensor network [J]. Journal of Low Voltage Apparatus, 2011, (19) : 39-42.

[3] Chen Guoqing. Danli transformer wireless temperature monitoring system study [J]. Journal of Safety Science and Technology of China, 2012, 8 (1) : 160-163.

[4] Zou Hao. Substation equipment on-line temperature measuring system based on the Internet of things technology [D]. Jinan: Shandong University, 2011:17.

[5] Zheng Meisong. Transformer temperature detection system based on ARM [D]. Jinan: Shandong University, 2012:11.

Advanced Materials Research Vols. 986-987 (2014) pp 1611-1615

doi:10.4028/www.scientific.net/AMR.986-987.1611

The Irremovable Properties Proof of Decaying DC Component for Dynamic Phasor Measurement

Hai BAO[1, a], Jinsi HAN[1, b], Shude ZHANG[2, b], Yulong CHEN[1, c]

[1]North China Electric Power University, Beijing, 102206, China

[2]State Grid Liaoning Electric Power Company Limited Benxi Electric Power Supply Company, Benxi, 117000, China

[a]email:hdbh@vip.sina.com, [b]email:cyl_icepee@126.com, [c]email:chenyulong_2012@163.com

Keywords: Dynamic Grid; Frequency Characteristic; Phasor Measurement; Proof; WAMS

Abstract. Dynamic voltage can be described by two parts in time domain, sinusoidal steady state component and dynamic state component. The latter reflects the effect of the system's characteristic root, and is also called decaying DC component. Decaying exponential signal has continuous spectrum, and this characteristic has a bad effect on the accuracy of phase angle's measurement, therefore the idea of filtering the decaying exponential signal was proposed. To verify the possibility of this proposal, this paper analyzes the frequency formation of dynamic voltage signal mathematically, and points out that at the frequency of the sinusoidal component, measured voltage signal's time domain description is the superposition of two sinusoidal signals with the same frequency, different phase angles and different amplitudes. This is the reason for the deviation between the measured voltage angle and the theoretical phase angle. The deviation angle not only shows the combined action of steady component and dynamic component, but also illustrates that the decaying exponential signal cannot be filtered out.

Introduction

Power system wide area monitoring system (WAMS) provides information technology platform for power system dynamic monitoring, analysis, control [1-7]. Phasor measurement technology as the foundation of WAMS system, the measuring accuracy is of great concern [8-10]. In view of the internal elements of phasor measurement system, people analyze the causes of errors [8] [9]. In view of the actual operating environment, people verify the accuracy [10], as far as possible to improve the measurement accuracy. In engineering practice, generally use the zero-crossing comparison and the discrete Fourier transform method to extract the phase angle values [11] [12]. Since zero-comparison method had poor accuracy, when high-precision measurement, the discrete Fourier transform method is used to obtain the phase angle. Application premise of these phase angle measurement methods is that the system under test is in steady operation state. During the actual operation of power system, as the load changes, the electrical operation and fault etc., electric power systems often run into a dynamic process. The steady-state premise of phase angle measurement is destroyed, the test signal from a single-frequency sine becomes a composite frequency signals consisting of a sine function with exponential decay function. In order to obtain accurate voltage phasor, reference [13] proposed a method of filtering decaying DC component.

Is this method feasible? To answer this question, must carry on the detailed analysis of frequency to voltage parameter under dynamic conditions, to clarify the temporal frequency characteristics of each component and its role. In order to ensure the rigor of the argument, use mathematical proof methods. Considering that exponential decay function is the non-periodic function, continuous Fourier transform method is selected to solve the spectrum, avoiding the power spectral leakage caused by the discrete Fourier transform. Because of the dynamic component (i.e. exponential decay signal) having a continuous spectrum, especially the continuous phase spectrum, it results a deviation angle between voltage phase angle where the frequency of the steady sinusoidal (i.e. the measured phase angle) and steady-state component phase angle (i.e. the theoretical phase angle). The reason for the deviation angle arisen is, exponential decay of the signal at the specified

frequency, available sinusoidal signal description, when voltage signal is into two different phase angles of the same frequency sinusoidal signal. The existence of the deviation angle, not only embodies the combined effect of the steady-state component and a dynamic component, also proved exponential decay signal components cannot be filtered out of the role.

Frequency Characteristics of Voltage Parameters under Dynamic Conditions

Small perturbation analysis methods are commonly used to study stability system for the small perturbations of power grid operation behavior, is a linear method. For the response of linear systems, the form of the characteristic roots can be used.

$$y(t) = C_o r(t) + C_1 e^{\lambda_1 t} + C_2 e^{\lambda_2 t} + \cdots + C_n e^{\lambda_{1n} t} \tag{1}$$

Where, $y(t)$ is system response, $t \geq 0$; $\lambda_k, k \in [1, n]$ are system characteristics roots, n is the number of system characteristics roots; $C_i, i \in [0, n]$ are residues; $r(t)$ is system input; $C_o r(t)$ is steady-state component; Exponential decay of algebra and is dynamic component.

In order to simplify the process of mathematical derivation, simplifying the similar part, then (1) can be simplified as (2).

$$y(t) = C_o r(t) + C_1 e^{\lambda_1 t} \tag{2}$$

Where, $r(t) = \cos \omega_0 t$, ω_0 is system angular frequency.

Fourier transform on (2)

$$F(w) = \int_{-\infty}^{+\infty} y(t) e^{-jwt} dt = \int_{-\infty}^{+\infty} y(t) e^{-jwt} dt = \int_{-\infty}^{+\infty} [C_0 r(t) + C_1 e^{\lambda_1 t}] e^{-jwt} dt \tag{3}$$

From (3) it can be seen, Voltage signal spectrum in dynamic process is the signal spectrum sum of the sinusoidal signal and the exponential decay signal. The time-domain of the part of sinusoidal steady state signal is described as

$$C_o r(t) = A \cos(\omega_o t + \theta) \tag{4}$$

The result for the Fourier transform is

$$F_1(\omega) = F[A \cos(\omega_o t + \theta)] = \int_{-\infty}^{+\infty} A \cos(\omega_o t + \theta) \cdot e^{-j\omega t} dt$$

$$= A\pi[\delta(\omega - \omega_0) + \delta(\omega + \omega_0)] \cdot e^{j\frac{\theta}{\omega_0}\omega} \tag{5}$$

The amplitude spectrum corresponding to the formula (5)

$$|F_1(\omega)| = A\pi[\delta(\omega - \omega_0) + \delta(\omega + \omega_0)] \tag{6}$$

Illustrated that only when $\omega = \omega_0$ and $\omega = -\omega_0$, there is spectral intensity $A\pi$ values, the rest frequency intensity is zero.

Phase spectrum is

$$\arg F_1(\omega) = \frac{\theta}{\omega_0} \omega \tag{7}$$

When $\omega = \omega_0$, $\arg F_1(\omega_0) = \theta$; when $\omega = -\omega_0$, $\arg F_1(-\omega_0) = -\theta$.

With the real characteristics roots of exponential decay signal for Fourier transform

$$F_2(\omega) = F(Be^{\lambda t}) = \int_{-\infty}^{+\infty} Be^{\lambda t} e^{-j\omega t} dt = \frac{B}{\lambda + j\omega} \tag{8}$$

The amplitude spectrum corresponding to the formula (6)

$$|F_2(\omega)| = \frac{B}{\sqrt{\lambda^2 + \omega^2}} \tag{9}$$

(9) shows that, no matter what the value of the selected frequency, there are no strength of zero spectral values, namely the continuous and non-zero amplitude spectrum.

Phase spectrum is

$$\arg F_2(\omega) = -\arctan\frac{\omega}{\lambda} \tag{10}$$

(10) illustrates the continuous phase spectrum.

Since the Fourier transform result of the system response is the sum of (5) and (8), therefore

$$F(\omega) = A\pi[\delta(\omega-\omega_0)+\delta(\omega+\omega_0)]\cdot e^{j\frac{\theta}{\omega_0}\omega} + \frac{B}{\sqrt{\lambda^2+\omega^2}}\cdot e^{-\arctan\frac{\omega}{\lambda}} \tag{11}$$

(11) shows that, the system responses have continuous magnitude spectrum and phase spectrum, and spectral values at $\omega=\omega_0$ and $\omega=-\omega_0$ are combined by spectrum value of sine signal and the exponential decay signal.

The Proof of Unfiltered out of Decaying DC Component

Reference [13] points out, because the system response of exponential decay signal will influence the measurement accuracy of voltage phase angle, the signal should be filtered, to ensure the accuracy of voltage phase angle measurement. Exponential decay signals can really be filter out? In order to ensure the preciseness of the problem, use mathematical derivation methods, to discuss the possibility of decaying DC signal which is filtered.

Power system dynamic process can be divided into electromagnetic transient and electromechanical transient process, mainly refers to difference of the corresponding characteristic roots values between the two dynamic processes. Characteristic roots corresponding to electromagnetic transient far away from the imaginary axis, electromechanical transient process from the corresponding eigenvalues near the imaginary axis. In the running process of the system, we do not know when and what happened in the transient process, thus unified with λ to describe the characteristics root in dynamic processes.

Take $\omega=\omega_0$ substituted into (11), therefore

$$F(\omega_0) = A\pi[\delta(\omega-\omega_0)]\cdot e^{j\theta} + \frac{B}{\sqrt{\lambda^2+\omega_0^2}}\cdot e^{j\alpha(\omega_0)} \tag{12}$$

Where $\alpha(\omega) = -\arctan\frac{\omega}{\lambda}$.

(12) can be written as

$$F(\omega_0) = A\pi[\delta(\omega-\omega_0)]\cdot e^{j\theta} + \frac{B}{\pi\sqrt{\lambda^2+\omega_0^2}}\cdot \pi[\delta(\omega-\omega_0]e^{j\alpha(\omega_0)} \tag{13}$$

Take $\omega=-\omega_0$ substituted into (10), there

$$F(-\omega_0) = A\pi[\delta(\omega+\omega_0)]\cdot e^{-j\theta} + \frac{B}{\sqrt{\lambda^2+\omega_0^2}}\cdot e^{j\alpha(-\omega_0)} \tag{14}$$

(14) can be written as

$$F(-\omega_0) = A\pi[\delta(\omega+\omega_0)]\cdot e^{-j\theta} + \frac{B}{\pi\sqrt{\lambda^2+\omega_0^2}}\cdot \pi[\delta(\omega+\omega_0)]\cdot e^{j\alpha(-\omega_0)} \tag{15}$$

Constructed function:

$$G(\omega_0) = \frac{B}{\pi\sqrt{\lambda^2+\omega_0^2}}\pi[\delta(\omega-\omega_0)+\delta(\omega+\omega_0)]\cdot e^{j\alpha(\omega_0)} \tag{16}$$

Time domain function:

$$g(t) = F^{-1}[G(\omega_0)] = \frac{B}{\pi\sqrt{\lambda^2+\omega_0^2}}\cos(\omega_0 t+\alpha(\omega_0)) \tag{17}$$

(17) is the sinusoidal domain description of exponential decay signal in the frequency of ω_0. At the same time, this also is the filtered section of the reference [13]. The filtered signal and retention signal (as shown in the formula (4)) for the same frequency sinusoidal signal, so this proposition is not true.

The time-domain sinusoidal of measured voltage signal at the frequency of ω_0 is described as

$$f(t) = A\cos(\omega_0 t + \theta) + M\cos(\omega_0 t + \alpha(\omega_0)) = K\cos(\omega_0 t + \phi) \quad (18)$$

Where, $M = \dfrac{B}{\pi\sqrt{\lambda^2 + \omega_0^2}}$

$$K = \sqrt{[A\cos\theta + M\cos(\alpha(\omega_0))]^2 + [A\sin\theta + M\sin(\alpha(\omega_0))]^2}$$

$$\phi = \arctan\frac{A\sin\theta + M\sin(\alpha(\omega_0))}{A\cos\theta + M\cos(\alpha(\omega_0))}$$

(18) is given the sinusoidal description of measured voltage signal at the frequency of ω_0 in dynamic processes. The phase angle φ at this time differs from the steady-state component phase angle θ, and the deviation angle reflects the effect of exponential decay signal.

For the nonlinear system that input is periodic signal, the steady-state component of the response will contain harmonic components. If the variable of (16) was changed to a harmonic frequency, inevitably from (17) obtain a sinusoidal signal with same frequency, and the signal is still provided by the exponential decay signal. In other words, harmonic phase obtained at this time also contain ingredients of exponential decay signal.

Conclusions

Grid in the dynamic operation process, voltage parameter contains two parts of sinusoidal steady state component and decaying DC component, composing principles of the phase angle, become the basis of phase angle measurement. Through mathematical proof, draws the following conclusions:

1) The exponential decay signal has continuous spectrum, at any frequency, the decaying DC signal can be described by sinusoidal signal;

2) When the specified frequency is equal to the steady-state sinusoidal signal frequency, the time domain description of measured voltage signal is the sum of two same frequency sinusoidal signals with different angle, different amplitude. At this time, there is a deviation between measured and theoretical phase angle;

3) The existence of deviation angle not only illustrated the interaction of the steady-state component and dynamic component, also proved the role of exponential decay signal component cannot be filtered out.

References

[1] Phadke, J. Thorp. Synchronized phasor measurements and their applications [M]. NY.USA: Springer. 2008.

[2] He Zhiqin, Zhang Zhe, Yin Xianggen, Wang Hua. A novel wide area backup protection algorithm based on fault voltage comparison [J]. TRANSACTIONS OF CHINA ELECTROTECHNICAL SOCIETY, 2012 27 (7) 274-283.

[3] DUAN Jun-dong, GUO Zhi-zhong. On-line assessment of voltage stability of power system based on wide-area measurement system [J]. Relay, 2006 34 (15) 24-28.

[4] Gu Wei, Wan Qiulan. Linearized voltage stability index for wide-area voltage monitoring and control [J]. TRANSACTIONS OF CHINA ELECTROTECHNICAL SOCIETY, 2010 25 (6) 110-115.

[5] Li Zhenxing, Yin Xianggen, Zhang Zhe, He Zhiqing. A study of wide-area protection algorithm based on integrated impedance comparison [J]. TRANSACTIONS OF CHINA ELECTROTE--CHNICAL SOCIETY, 2012 27 (8) 179-186.

[6] Gan Lei, Kang Hewen, He Min. The dynamic monitoring of voltage stability based on wide-area measurement system [J]. Power System Protection and Control, 2010 38 (21) 152-161.

[7] Hou Wang-bin, Liu Tian-qi, Li Xing-yuan. Under-frequency load shedding based on comprehensive weight and wide area measurement system [J]. Power System Protection and Control, 2011 39 (21) 70-75.

[8] Yang Guiyu, Jiang Daozhuo, Qiu Jiaju. Synchronous measurement precision of phasor measurement unit [J]. Automation of Electric Power Systems, 2003 27 (14) 57-61.

[9] Jiang Daozhuo, Ma Jin, Zhang Xinjie. The application of phase locked loop in the data acquisition and control apparatus of power system [J]. Relay, 2000 28 (8) 43-45.

[10] Wang Mao-hai, Bao Jie, Qi Xia, Xu Zheng-shan, Guo Zi-ming. Online assessment of phasor measurement unit's performance based on sample data [J]. Power System Protection and Control, 2009 37 (10) 48-52.

[11] IEEE working group reports. Synchronized Sampling and Phasor measurements for relaying and control [R]. IEEE Trans. On PWRD.1994 9 (1) 442-449.

[12] Burnett Jr R O, Butts M M, Cease T W, et al. Synchronized Phasor Measurement of a power system event [J]. IEEE Trans. On PWRD 1994 9 (3) 1643-1649.

[13] Mai Ruikun, He Wen, He Zhengyou, Bo Zhiqian, Qian Qingquan. Dynamic phasor estimator with removing decaying DC component [J]. Proceedings of the CSEE, 2010, 30(31):123-128.

Advanced Materials Research Vols. 986-987 (2014) pp 1616-1618

doi:10.4028/www.scientific.net/AMR.986-987.1616

The research and simulation of intelligent electric leakage detection model for mining machinery

YU Mingyi

Chongqing college of electronic engineering, chongqing, 401331, China

Keywords: colliery; electric leakage; faults detection

Abstract: For today's coal mining enterprises, the mining production environment is very harsh and sometimes there are electric leakages in the automatic production equipment which cause a great impact on the stability of coal production. This paper proposes an electric leakage fault intelligent detection model. The intelligent method can fix the electric leakage faults on time which is an important prerequisite to ensure mine production stable and secure. The experimental results show that the model can effectively detect hardware failures and leakage.

1 Introduction

The application of advanced computer technology in the production in the mines can not only increase the amount of coal mining, but also save a lot of manpower, material and financial resources for the coal mining enterprises to prompt the development of coal mining enterprises[1-2]. In the process of mechanization of coal production, the electric leakage failure seriously affects the coal production stability and security which results in some economic benefits loss in coal mining enterprises. This issue causes widespread concerns in the community and it has become an important topic in the academic and industrial areas. This paper discusses the electric leakage faults in the mining machinery in accordance with the author's years of work experience. In this paper, the method for fixing the electric leakage is proposed and some rules and troubleshooting principles for excluding the leakage failures are analyzed which will provide some help for the future efforts in excluding leakage failures in mining machinery.

2 The electric leakage intelligent detection method for mining machinery

When there is some electric leakage in the circuits of mechanical equipment, the leakage position should be determined. The leakage current should be calculated first. The voltage between the source neutral point MQ and load neutral point ML should be obtained. In the low-voltage electrical lines, the three-phase voltages (U_{L1}, U_{L2}, U_{L3})are connect with the neutral point MQ. At the load ends, three load resistances Z_1, Z_2 and Z_3 are connected in the form of star. The two neutral points MQ and ML are connected by resistance Z_{QL}. The voltage between the two points is U_{QL} and the calculation is expressed by

$$U_{QL} = \frac{\frac{U_{L1}}{Z_1} + \frac{U_{L2}}{Z_2} + \frac{U_{L3}}{Z_3}}{\frac{1}{Z_1} + \frac{1}{Z_2} + \frac{1}{Z_3} + \frac{1}{Z_{QL}}} \tag{1}$$

The general configuration of the three-phrase filter is three X capacitors connecting with the neutral point and the ground via Y capacitor. For the balance capacitor power grid, the leakage current can be omitted. In another aspect, when the maximum unbalance is achieved among phrases, the leakage current will also achieve the maximum value. The reasons for the unbalance can be the tolerances of the capacitors or the voltage unbalance in the power grids. Therefore the key factors determining the leakage current are capacitors of C_{X1}, C_{X2}, C_{X3} and accordingly generated voltage U_{QL}. For most of filters, the ratings are the same. The leakage current $I_{leak\max}$ caused by voltage U_{QL} at capacitor C_Y is expressed by

$$I_{leak\max} = U_{QL} \cdot j\omega \cdot C_{Yn} \tag{2}$$

In the equation $\omega = 2 \cdot \pi \cdot f$ and tolerances of the passive filter capacitor is ±20%. C_Y is maximum when there is a minimum tolerance and a maximum tolerance between the two X capacitors. Additionally, given the tolerance of C_Y is maximum and these assumptions are put into equation (1) and (2), the leakage current is expressed by

$$| I_{leak\max} | = \omega \cdot C_{Y,\max} \frac{U_{\max} C_{X,\max} - U_{\min} C_{X,\min}}{C_{X,\max} + 2C_{X,\min} + C_{Y,\max}} \tag{3}$$

The digital signal after A/D conversion is returned as A_d.

$$A_d = \frac{I_d \times R_d}{U_{ref}} \times 1024 \tag{4}$$

in which I_d is the trigger current after amplified, R_d is the resistance at load end which is $100\,\Omega$, U_{ref} is the reference voltage for A/D conversion which is 1～5V, 1024 is the maximum resolution for the 10-bit A/D converter.

3 The software anti-interference design and experimental analysis

The coal mines electric leakage faults detection devices normally operate outdoors with lots of interference signals and electromagnetic interferences which will cause distortion of the analog input signals, control signal chaos, out of control, device crashes, and disorder of the signals on address or data buses[3-4]. Therefore, the anti-interference design of the test equipment will affect the reliability of the equipment. In addition to strengthen the anti-interference in hardware, the software also should have anti-interference design. If the device is running out of control or into an infinite loop, the equipment service program will automatically start from 0000H. For the reset circuit connecting with the RESET end of the microcontroller, a capacitor and resistor to ground will form power-on reset circuit which makes the program start from 000H once it is powered on. The power-on reset circuit and manual reset circuit can provide the reset signal which is more than 10mA. The interior of the reset chip MAX813L has a watchdog timer and voltage monitor. When the programs are into the infinite loop or the source voltages suddenly change, the system crashes and data read and write errors or malfunction will be prevented in order to ensure the normal operation of the systems.

The experiments are used to verify the validity of the proposed system in the coal pipeline leakage application. The data for the experiment is the power consumption data in the pipeline from different projects in some colliery. The experiment applies the proposed system and the traditional system respectively to detect the leakage signals in the pipelines and the results are described in Fig. 1. In the Fig. 1, the data collected from the proposed system has a high degree of matching with the actual data while the data obtained by the conventional system has a larger difference which illustrates the proposed method is feasible for the electric leakage detection in the coal pipelines.

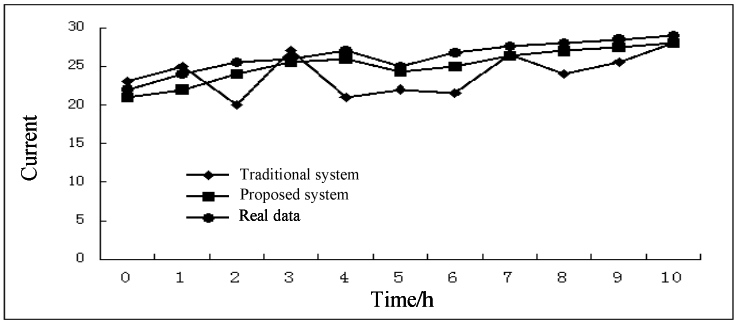

Fig. 1 The detection performance comparison among different systems and the real results

In order to testify the performance of the propose system, the energy savings by the proposed system and the traditional systems are collected from 10 mine pipeline projects which are described in Table 1. From table 1, the energy savings by the proposed system is higher than those by traditional systems and the operational efficiency and accuracy are also better than those in traditional systems which illustrate the proposed system can maximize the energy savings and ensure the power stations security with important application value.

Table 1 The real measured data

	Traditional system			Proposed system		
No.	Energy savings/J	Detection time /h	Detection accuracy/ %	Energy savings/J	Detection time/h	Detection accuracy/ %
1	245	22	80	288	13	89
2	194	20	82	290	11	90
3	255	19	81	269	10	92
4	198	18	83.5	289	12	90
5	263	21	85	308	13	91
6	232	17	79	295	14	89
7	146	18	80.5	283	12	93
8	178	20	84	305	11	95
9	193	22	83	313	10	94
10	212	19	81	295	12	96

4 Conclusions

In summary, with the continuous progress of science and technology, the computer technology is widely applied in China's, especially in coal production. The mechanized equipment is widely used to promote the application of computer technology which also brings new opportunities for the future development of the computer technology. The researches on the methods fixing electric leakage failure are not only beneficial for the future innovation and development of computer technology, but also effectively improve the extraction of coal, increase the economic benefits for mining enterprises and build foundations for the future development of the market economy in China.

References

[1] Zhang Zhipeng. Introduction to computer hardware and software maintenance and troubleshooting [J]. Journal of shihezi science and technology, 2007, 13 (5) : 176-179.

[2] Liu Xujin. Li jianping. Du Changlong fuzzy neural network fault diagnosis expert system of shearer simulation [J]. Journal of coal mine machinery, 2011, 12 (4) : 89-92.

[3] Dong Hui. Yang Jinmin Zhang Dafang. Based on the fault classification optimization of Byzantine fault tolerance service [J]. Microcomputer information, 2007,01 (25) : 132-135.

[4] Wu Bingsheng. Cai Chao. Jiang Jinjun. Study of mechanical fault diagnosis based on virtual instrument [J]. Journal of coal mine machinery, 2009 (02) : 108-111.

Advanced Materials Research Vols. 986-987 (2014) pp 1619-1623

doi:10.4028/www.scientific.net/AMR.986-987.1619

The Research on the Factory Accept Test Technology of subsea PLET

Zhao Xiaolei[1,a], Chu Leping[1,b], Guo Xingwei[1.c], Yu Guohe[1,d], Chen Jinyu[1,e]

[1] China Offshore Oil Engineering Corporation, Ltd Tianjin, 300452

[a] Email: zhaoxiaol@mail.cooec.com.cn, [b]Email: chulp@mail.cooec.com.cn,
[c] Email: guoxw@mail.cooec.com.cn, [d] Email: yugh@mail.cooec.com.cn,
[e] Email: chenjy@mail.cooec.com.cn.

Keywords: subsea production system; PLET; FAT; hydro test; deep water;

Abstract. With the development of offshore oil and gas field enters into deep water constantly, subsea production system has become the main development mode in deep water development. Pipeline End Termination (PLET) is common facilities in subsea production system and is used to provide subsea tieback interface. An embedded type PLET has been adopted in Panyu 35-1/35-2 Gas field with the water depth of 194 to 338 m. Factory Accept Test (FAT) is very important for the subsea production facilities, and the references is very limited due to technical security. This paper in detail states the flow chart, master equipment, purpose and precautions for each test of FAT for PLET, which collects great technology for the development of subsea production system.

Introduction

With the gradual dying out of the land and shallow water petroleum energy, the oil and gas from the offshore deep water is increasing constantly. Depending on the good reliability, economy and outstanding achievements, the subsea production system has become the important model for the deep water oil field development. The water depth explored by this mode has reached 3000m[1].

Panyu 35-1/35-2 Gas field lies in South China Sea. The subsea charismas trees(XT), PLETs, Inline Manifolds(ILM), jumpers, Central Manifolds (CM), Pipeline End Manifolds(PLEM) and Subsea Umbilical Termination Units (SUTU) have been adopted in this subsea production system. The field layout is shown in Fig 1. The oil, gas and water from PY34-1/35-2/35-1 will be processed at PY34-1 central processing platform (CEP) and then transported to Liwan 3-1 natural gas central processing platform[2].

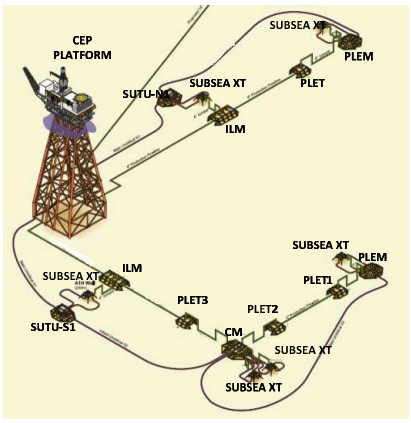

Fig.1. The schematic gas field layout of PY35-1/2

Subsea PLET is used to provide subsea tieback interface which is integrated with subsea valves, hubs, bullseyes, etc. After installation of subsea CM, PELM, the PLET will be laid together with pipeline through the tensioner of the pipe-laying vessel. Then, jumper will be installed to connect the PLET with other subsea facilities under water.[3] The FAT is to validate the fabrication compliance with the required functionality. Since there are many interfaces, further many operations have to be carried out by remotely operated vehicle (ROV), the unknown risk is very high. If any issue happened during installation or production, the whole gas field may be affected. Therefore, the FAT is a very important test for subsea facilities.

This paper in detail states the flowchart, key equipment, purpose and precautions for each test included in FAT for subsea PLETs in PY35-1/2 project. The laying of PLETs has been completed successfully.

PLET composition

The PLET structure is designed into two parts[4].

1) Upper structure

The upper structure is a rigid frame which supports the valves, CAMERON vertical type connectors (CVC), jumpers and pipeline sections with its elbow. The upper structure can be lifted using 3 padeyes and it slides on a rail system to cater for thermal expansion of flowline and transfers load to mudmat.

2) Mudmat with protection frame

The mudmat is made up of single mat with skirts to increase the bearing capacity. Guide rails sit over the mudmat to guide the upper structure during pipeline expansion and prevent lateral movement of upper structure in transverse direction.

PLET composition is shown in Fig 2.

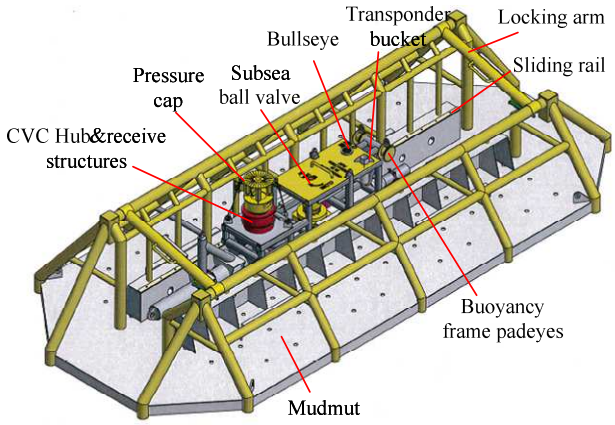

Fig.2. PLET components

Flow chart

There are 8 tests in the FAT of PLET. The test flow chart after optimization is shown in Fig.3.

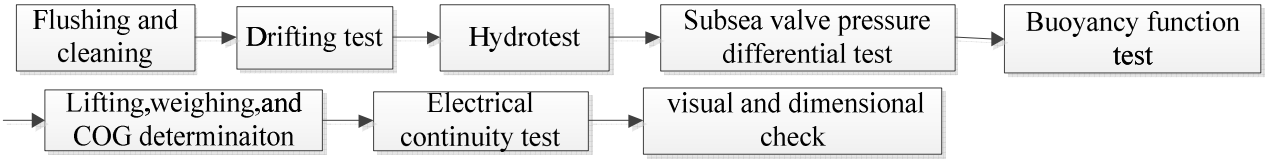

Fig.3. FAT flow chart

Master equipment list

The master test equipment used in FAT for one 6in PLET is shown is table 1.

Table 1 FAT master equipment list

Equipment Required for Test	Qty.	remarks
Drift mandrel	1	Ø 130mm x Thk 6 mm, made by alunimnum
loadcell	1	100t, accuracy 5‰
Camera	1	10m pixel
Forged pressure cap	1	6” x 7K , Used on the PLET pipeline end
Cranes	3	One 35t, two 100t
Certified shackles	8	CCS certified
Torque tool	1	3000NM, For the fastening of bolts on test clamp
6” x 10K test clamp with bolts and nuts	1	Provided by equipment supplier
6” x 10K test Gaskets	1	Provided by equipment supplier

Pressure cap 6" x 10 k	1	Provided by equipment supplier
Total Station	1	
Piping borescope	1 set	Wire length longer than 25m,waterproof
micro Ohm meter	1	accuracy0.01Ohm
adhesive force instrument	1	>5MPa

FAT

Initial status

Before carrying out any activity, the following points have to be completed [5]:

1) The assembly of PLET should be completed. Equipment to conduct the tests has been received on the yard and is fit for purpose, including calibration, certification, etc.

2) All non-routine lifting operations shall have a lift plan supported by an analysis of the hazards and risks.

Cleaning and Flushing

1) The objective is to remove all foreign material and debris such as scale, dirt, dust and slag and clean all internal piping of PLET.

2) Precautions:

a) The flushing duration should be long enough to ensure there is no foreign material left in the piping.

b) The piping should be dried by compressed air and the hub face should be protected after this test.

Drifting Test

1) The purpose of this test is to verify that the liquid piping is piggable. The test is performed using Drift Mandrel, which consist of two parallel circular metal disks (0.95 x Minimum pipe diameter and 6 mm thick).

2) Precautions:

a) The thickness of the drift mandrel should be increased to prevent to be stuck at the groove between the piping and subsea ball valve.

b) Distance between the two circular plates should be bigger than 2 times pipe nominal internal diameter.

Hydrotest

1) The purpose of this test is to verify the integrity of completed PLET piping. The test will be performed at Test pressure = 1.25 x Design Pressure for hold period of 2 hours, using inhibited water. The hydrotest plan is shown in Fig.4 [6].

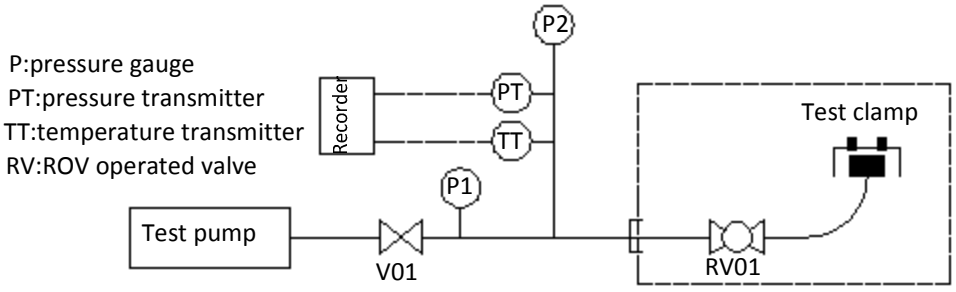

Fig.4. PLET hydrotest plan

2) Precautions:

a) The dedicated AUTOCLAVE fittings are needed for the tubing connection to the test clamp.

b) The torque for the fastening of bolts on the test clamp should be followed strictly.

c) The variation of pressure caused by the change of temperature should be taken into consideration. The formula for variation of pressure caused by 1° is:

$$\Delta P = (\beta - 3\alpha)! D3(2.5-2\nu)/(2E3T) + k$$

Variable description	
β	Expansion coefficient of test-medium (26.08 x 10^{-5}/℃)
α	Coefficient of the steel liner expansion (1.16 x 10^{-5}/℃)
ν	Poisson's ratio (0.3)
E	Young's modules of the steel (2.1 x 10^{6} kg/cm^2)
K	Compression ratio of test – medium volume (4.75 x 10^{-5}cm^{2}kg)
D	Diameter of test pipe (cm)
T	Wall thickness of the test pipe (cm)
$\swarrow\Delta P\searrow$	Change value of pressure caused by 1℃ temperature changing (kg/cm^2 x℃)

Differential pressure Test

1) The purpose of this test is to verify the interface between the valve overrides and torque tooling, to verify the torque and number of turns required to operate the valves, and to verify the seal function of valve under the design pressure.

2) Precautions:

a) If the datasheet of the valve is different from actual torque and number of turns required to operate the valve, the actual number should be followed.

b) The precautions in the hydrotest should also be followed.

Buoyancy function test

The test is to verify Swivel padeyes could swivel along the trunnion axis and installation of connection bolts.

Lifting, Weighing, center of gravity (COG) determination

1) The test is to verify handling of the PLET during lifting and to verify the overall weight.

2) Precautions: the shackles used for offshore campaign should be used to test its fit up with the padeyes of PLET.

Electrical continuity test

1) The purpose of this test is to verify the electrical continuity between all components (to be cathodically protected) in PLET.

2) Precautions: all the non-welded connection including the bolt connection, mechanical connection, and riveted connection should be tested.

Visual and dimensional Check

1) The purpose of this test is to ensure the marking of the PLET is correct , and to ensure that the overall dimension of PLET assembly and local critical dimensions (related to installation) are in line with the drawings[7].

2) Precautions:

a) The adhesive force of corrosion should be no less than 5Mpa[7].

b) The overall dimension of PLET upper sturcture should be test to ensure it could pass through the tensioner of pipe-lay vessel. The as-built structure is shown in Fig.5.

Fig.5. As-built PLET

Conclusion

This paper in detail states the flow chart, master equipment, purpose and precautions for each test included in FAT of PLET depending on PY35-1/2 subsea project. It provides technical references for other subsea facilities such as CM, PLEM, ILM, jumper, enhancing the FAT technology further. It is very good for the development of vast unexploited deep water oil field, causing great social and economic benefit.

Acknowledgement

The financial support of China National Important Science and Technology Foundation 2011ZX05027-004 " The technology and equipment for fabrication, testing of deep water production facilities " is appreciated.

References

[1] Wang Wei, Sun Liping, Bai Yong. Investigation on Subsea Production System[J]. CHINA OFFSHORE PLATFORM，2009，24（6）：41-45；

[2] Yu Fangfang, Duan Menglan, Guohong. Design of Deep Water Manifold And Structure Design Study on Subsea Manifold for LW3-1 Gas Field[J] . Oil Field Equipment，2012，41（1），24~29.

[3] ISO13628-1, General requirements and recommendations[S]. TC67/SC4, 2010

[4] Tanyue, Shiyun, Liuming. Structure Analysis of PLET And Mudmat [J]. offshore oil，2011（9): 93-96.

[5] Liang Ji, Yao Baoheng, Qu Youjie. China measure and test[J].China Measure&Test，2012,01, 38~39.

[6] Zhang Xianzhen,Sun Wei, Deng Jisong. The analysis for subsea production system and its commissioning [J]. Shipbuilding Of China，2009- 2010：146-151；

[7] ISO13628-15, Subsea manifold and structure General requirements and recommendations[S]. TC67/SC4, 2010.

Advanced Materials Research Vols. 986-987 (2014) pp 1624-1628

doi:10.4028/www.scientific.net/AMR.986-987.1624

The research on the integrational measurement device of grounding resistance

Li Bo, Pang Yanjun, Li Jianfeng, Li Ying, Ge Changxin, ShanYi, Wang Qinghao, Hai Tianshu, Li Zhi, Li Yiran

Fushun Power Supply Company, Liaoning Electric Power Company Limited, State Grid, China,

wts55@126.com

Keywords: grounding resistance, lead wire retracted and released, pluggable connection

Abstract. Measuring grounding resistance is the only basis to judge the grounding of electrical equipment is good or not. Aim at the trouble on retracting and releasing of the current lead wire and voltage lead wire;the insecure connection Lead wire and grounding resistance tramegger, grounding crooked chisel and so on； The hectic trouble such as placing or picking the grounding resistance testing equipment, we developed the integrational measurement device of grounding resistance. It mainly introduces the structure and design principle of the device, and provides the related technical essentials. Combined with the actual application,and demonstrates its convenience and flexibility by the force of contrast; Through the case analysis, fully demonstrates the device is feasible, creative and rationality.

Introduction

Grounding is the very important link to guarantee the personal safety, electrical equipment and over-voltage protection device working well. In electrical system, it can be divided into the following three categories in accordance with its purpose: (1) the working grounding: according to the need of the normal operation mode of electrical system， it will be one point grounding. Such as the transformer neutral point grounding; (2) the protective grounding: make sure the personal safety through connecting uncharged metal parts of electric equipment in normal circumstances to the earth. Such as the cover grounding of transformer and high-voltage electrical; (3)the anti-rader grounding: over-voltage protection device is grounded at one end for guiding the powerful lightning current safety, the overvoltage protection device at one end of the ground .Such as the lightning rod (wire) and lightning arrester grounding[1-5].

Table 1 The allowable values of electrical equipment grounding resistance

order	distribution transformer		The allowable values of grounding resistance
1	distributing line tower without lightning conductor		30
2	distributing line tower with lightning conductor		10 ~ 30 According to the soil resistivity
3	distribution transformer	100kVA and above	4
		Below 100kVA	10
4	valve type lightning arrester		10
5	Independent arrester		10
6	Independent microwave station		5
7	Independent fuel, explosive gas tank		10
8	The first tower of service entrance		30
9	Temporary grounding device of live-working		5~10

Grounding resistance value objectively reflect the grounding situation, large grounding resistance is harmful for the personal and electrical equipment , but blindly reducing the grounding resistance may not be reasonable because of the relationship between the price and quantity. So the commissioning and preventive test procedures made the detailed rules on the ground resistance. Measuring grounding resistance is the only basis to judge the grounding of electrical equipment is good or not. So grounding resistance must be measured in the commissioning and preventive test to test. In power grid, the working grounding, protective grounding and the anti-rader grounding is

different, so the grounding resistance value has strict standard. Table 1 is grounding resistance allowable value of common electrical equipment.

At present, grounding resistance measurement of small grounding grid usually uses the ZC-8 grounding resistance tramegger. grounding resistance tramegger has advantages of small volume, light weight and high accuracy, but current, but it still has proper corrupt practice ,such as retracting and releasing of the current lead wire and voltage lead wire ;the insecure connection lead wire and grounding resistance tramegger, grounding crooked chisel and so on. we developed the integrational measurement device of grounding resistance to solve these problems , and grounding resistance measurement will be more convenient, quick, reasonable by using it.

The principle measurement of grounding resistance

Grounding resistance Measurement is a very important item to guarantee the personal safety, electrical equipment and over-voltage protection device working well. The assignment of grounding resistance measurement is quite frequently for several hundred tests a year because of the squatter settlement rebuilding, The new substation and the pre-test on small grounding substation in recent years. This requires rapid, accurate and efficient when testing the grounding resistance. Figure 1 is the principle diagram of grounding resistance measurement.

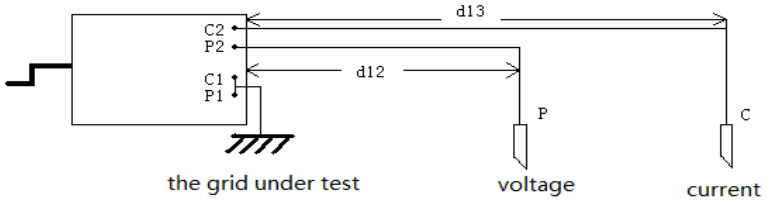

Figure 1 The principle diagram of grounding resistance measurement.

In this figure， d12 is the length between the grounding resistance and the voltage lead wire, (d12≈2.5 D）; D13 is the length between the grounding resistance and current lead wire (d13≈4 D）; D is the longest diagonal of the grounding resistance.

The disadvantage of original grounding resistance measurement.

(1) Retracting and releasing of the current lead wire and voltage lead wire

1）When retract and release lead wires ,the independent lead wires without putting spool will make current lead wire and voltage lead wire easy to disorder.

Figure 2 The original distributed measuring equipment

2）The interlaced current lead wire and voltage lead wire will cause measurement error when using the same putting spool , the vectorial angle method is not easy to be used in grounding resistance measurement ,and it also restricted by regional conditions.

3) Current lead wire and voltage lead wire adopt their own independent putting spool respectively; the increase of test items is bound to waste of resources as shown in figure 2.

(2) Transportation is not convenient

In order to standardize team construct, the instrument cabinet is furnished with grounding resistance tramegger, current lead wire, voltage lead wire, grounding grid lead wire wire , grounding crooked chisel, hammer and so on ,and all items are in accordance with the instrument, meter, tools, lead wire and so on.

The equipment must get out from different cabinet in each grounding resistance test, and need to be get back in accordance with the cabinet label after test.

(3) The connection of lead wire, grounding resistance tramegger with grounding crooked chisel

1) current lead wire, voltage lead wire and the lead wire connected to grounding grid need to be linked and removed temporarily in every test. This step not only waste time,but also easily make current lead wire and voltage lead wire wiring error,and impact the accuracy of measurement results.

2) current lead wire, voltage lead wire and grounding resistance tramegger are not easy to tighten,it may cause error measurement.As shown in figure 3.

Figure 3 The connection of original grounding with lead wire

3) current lead wire, voltage lead wire and grounding resistance tramegger use metal holder connection. Despite the connection being well,the lead wires often hung in grass, wood, stone, brick and other obstacles when retracting which brings inconvenience to the work.As shown in figure 4.

Figure 4 The retracting lead wire caught in the stick

Figure 5 Pluggable connection

The solution

According to experience for many years and the actual situation, we research the integrated measuring device of grounding resistance. It seats the items in a test box reasonably,such as grounding resistance tramegger, current lead wire, voltage lead wire, two spools, the connecting lead wire of grounding grid, grounding crooked chisel, hammer, auxiliary lead wire and so on.

1) The connection of grounding resistance tramegger to current lead wire, voltage lead wire is secure without disassembly. pluggable connection is adpoted to connected Current lead wire, voltage lead wire with grounding crooked chisel and the connection of lead wires with grounding gird is steel trap. As shown in figure 5.

2) Current lead wire and voltage lead wire wind around the two independent spools respectively, the spools move cleanly,coefficient of rolling friction $\mu \leqslant 0.15$,it is suitable for retracting and releasing the wire and more time-saving effort.Current lead wire, voltage lead wire and grounding resistance tramegger use the same spool crank. As shown in figure 6.

Figure 6 The putting spool in measuring device

Figure 7 The integrated measuring device

The integrated measuring device of grounding resistance not only put the material, equipment, etc together in a box, but aslo formed a complete system of grounding resistance test finally after a series of design, engineering processing.

Device parameters

Test cases: it adopts the stainless steel material; 0.4M long; 0.2M wide; 0.18M high; The total weight is 8kg. As shown in figure 7.

The choice of equipment material

①grounding resistance tramegger: ZC--8 ;
② Voltage lead wire:ϕ=1.5 mm2 ; 25m long;
③Current lead wire : ϕ=1.5 mm2 ; 45m long;
④Two putting spools: the coefficient of rolling friction;μ≤0.15;
⑤the connecting lead wire of grounding grid: ϕ=1.5 mm2; 2.5m long;
⑥ two connecting lead wires of grounding grid: stainless steel material, each weighing 0.5kg;
⑦ Hammer: 0.5kg;
⑧ auxiliary lead wire: ϕ=1.5 mm2;20m long;
⑨ Special crank: stainless steel material, 0.1kg weigh;
⑩ Two passive lead wires:ϕ=1.5 mm2, 15m long , using in the vectorial angle method and the bigger ground.

Technical indicator

(1)range:0～100Ω.
(2)Accuracy:≤1.5% .
(3)Working temperature:-10℃～40℃ .
(4)Earthquake intensity: The device has no damage after free-falling from 0.5m high
(5)Holding time: Its temperature changes is + 4 ℃ for 3 minutes in open box testing..

The application situation

The integrated measuring device of grounding resistance is adopted to measure the grounding resistance of the electrical equipment.Then we choose the method of contrastive to clarify that the device is convenient and quick; The details are shown in Table 2.

Table 2 The contrast between distributed equipment and integrated device

	Time of distributed equipment wasting minute	Time of integrated devicewasting minute	Time Saving in one place	Time Saving in 400 places minute
Preparatory stage	3	1	2	800
Wiring and releasing	5	2	3	1200
measure	1	1	0	0

Removing and winding	6	3	3	1200
Work end	3	1	2	800
total	18	8	10	4000

It can be seen from table 2 clearly, using the distributed equipment to test grounding resistance takes 18 minutes, but using integration device only takes 8 minutes, for saving 10 minutes.If calculated at 400 places a year, the saving total is 4000 minutes.

Field test results show that the integrated measuring device of grounding resistance meets the requirements of accurate data.The arrangement of voltage lead wire and current lead wire is not limited by geographical condition, so using straight-line method or triangle method is feasible. Measurement of soil resistivity does not need to prepare lead wire deliberately; the spare wire of device is enough. In short, this device gets the desired effect of convenience and efficiency, and fully proved that the device has the scientific nature, viewpoints and rationality.

Conclusion

The integrated measuring device of grounding resistance has accomplished more than 400 small grounding resistance test for the past year, its work performance is convenient, quick and flexible and conforms to the requirements of the test, the following is the four advantages mainly in application effect :

①The integrated measuring device of grounding resistance is very convenient to get and put because of instruments and equipment all being concentrated in one

②The effect of the integrated measuring device of grounding resistance is good in the actual production application，and this device gets the desired effect of accuracy and efficiency, it should be said that the device not only has the simple design, principle and structure, but also has the novel idea and pragmatic.

③This device meets the design and actual requirements in technical indicator and function , it has the advantage of light weight, easy to carry, convenient wiring, small floor area, easy care and will give safety production a security

④ The integrated measuring device of grounding resistance has uniqueness in terms of use. The device plays a positive role in grounding resistance test, it makes the grounding resistance test more clear, more simple and save the time of measuring grounding resistance.

References

[1] Xu Ying, Xu Shi Heng. AC Power System Overvoltage Protection and Insulation, China Electric Power Press, Beijing, 2006

[2] Qiu Zhixian. High Voltage Composite Insulators and Its Application, China Electric Power Press, Beijing, 2006

[3] Tan Qiong, Li jingLu, Li Zhiqiang. Mountainous Grid Lightning Protection Technology, China Water Power Press, Beijing, 2011

[4] Gao Jun. Grid to Prevent Pollution Flashover Technical Q&A, China Electric Power Press, Beijing, 2009

[5] Yin Kening, Principle of Transformer Design, China Power Press, Beijing, 2010

Advanced Materials Research Vols. 986-987 (2014) pp 1629-1633

doi:10.4028/www.scientific.net/AMR.986-987.1629

Videogrammetric Techniques for Wind Tunnel Testing and Applications

Zhang Zhengyu[1,2], Huang Xuhui[1], Yin Jiang[1], Lai Hanxuan[2]

[1.] State Key Laboratory of Aerodynamics, high speed Aerodynamics institute, China Aerodynamics Research and Development Center (CARDC) ,Mianyang 621000, People's Republic of China

[2.] Information Engineering College, Southwest University of Science and Technology, Mianyang 621010, People's Republic of China

Keywords: videogrammetry; model deformation; attitude; aero-optics; wind tunnel test

Abstract. Videogrammetric measurement is a research focus for the organizations of wind tunnel test because of its no special requirements on the test model, its key techniques for the vibration environment of the high speed wind tunnel are introduced by this paper, such as the solution of exterior parameters with big-angle large overlap, the algorithm of image processing for extracting marked point, the method of camera calibration and wave-front distortion field measurement. The great requirements and application prospects of videogrammetry in wind tunnel fine testing have been demonstrated by several practice experiments, including to measure test model's angle of attack, dynamic deformations and wave-front distortion field in high speed wind tunnels whose test section size is 2 meters.

Introduction

The attitude and deformation of test model under the aerodynamic loads [1-2][4-9] are measured by videogrammetry[1-11] which uses CCD images and photogrammetric techniques. On the other hand, a wavefront distortion field can be get by measuring the deviation displacement field induced by the beams from center of camera to the mark points crossing the flow field[3,11], which quantifies the aero-optic effects of the flow with disturbances and provides a tool to observe flow structures.

The fine design of modern aircraft demands the more and more precise data of wind tunnel test, therefore, the corrections on elastic angle and elastic deformation of the test models must be taken into consideration[1-2], which require to measure the attitude and deformation of test model rather than the attitude and position of supporter used to fix the test model [4-9]. In addition, for all kinds of optical systems onboard high-speed aircraft[3], it is necessary to measure and correct aero-optics effects, such as detection systems of photoelectric imaging and the optical communication system etc, which need urgently to quantify wavefront distortion in large wind tunnel with high spatial resolution to generate the correction method.

Therefore, the videogrammetric techniques for wind tunnel testing are presented; the several practice experiments in the Asia's largest transonic and supersonic wind tunnels are also introduced.

Measurement Principle

Collinear equations describe the principle of the videogrammetry[1-2], their expression is

$$\begin{cases} x+f\dfrac{a_1(X-X_s)+b_1(Y-Y_s)+c_1(Z-Z_s)}{a_3(X-X_S)+b_3(Y-Y_s)+c_3(Z-Z_s)}+x_u=x_0 \\ y+f\dfrac{a_2(X-X_s)+b_2(Y-Y_s)+c_2(Z-Z_s)}{a_3(X-X_S)+b_3(Y-Y_s)+c_3(Z-Z_s)}+y_u=y_0 \end{cases} \quad (1)$$

where(a_1, a_2, a_3, b_1, b_2, b_3, c_1, c_2, c_3) are the nine elements of rotation matrix R determined by the attitude (φ, ω, κ) of camera; (x0 , y0) are the center coordinates of camera image plane; and f is the camera focal length; x_u and y_u are the distortion parameters; (Xs, Ys, Zs) are coordinates of camera center in 3D coordinate system; (x, y) and (X,Y,Z) are the coordinates of a measuring points in 2D image and 3D coordinate system respectively. When the camera parameters as well as the 2D image coordinates of the points are known, their 3D coordinates can be computed by the equations(1).

Coplanar equations [10] describe the homologous points on the images taken by the different view angles are coplanar. Given two pictures I_A and I_B, the homologous point set is P, where $\forall p_i \in P$, $p_i = (p_i^A, p_i^B)$; $S_A u_1 v_1 w_1$ and $S_B u_2 v_2 w_2$ are 3D image coordinate systems of I_A and I_B respectively; 3D image coordinates of p_i^A and p_i^B in $S_A u_1 v_1 w_1$ and $S_B u_2 v_2 w_2$ are (u_1, v_1, w_1) and (u_2, v_2, w_2) respectively; S_1 and S_2 are origins of coordinate of $S_1 u_1 v_1 w_1$ and $S_2 u_2 v_2 w_2$ respectively. The coordinates of S_2 in $S_1 u_1 v_1 w_1$ is (b_x, b_y, b_z), then coplanar equations of p_i^A and p_i^B are

$$F(p_i) = \begin{vmatrix} b_x & b_y & b_z \\ x_1^A + x_u & y_1^A + y_u & -f \\ u_2 & v_2 & w_2 \end{vmatrix} = 0 \tag{2}$$

where

$$\begin{bmatrix} u_2 \\ v_2 \\ w_2 \end{bmatrix} = R_2 \times \begin{bmatrix} x_2^B + x_u \\ y_2^B + y_u \\ -f \end{bmatrix} \tag{3}$$

(x_1^A, y_1^A)in equation(2) and (x_2^B, y_2^B) in equation(3) are 2D image coordinates of p_i^A and p_i^B respectively; R_2 is the rotation matrix from $S_2 u_2 v_2 w_2$ to $S_A u_1 v_1 w_1$.

Key techniques

Camera calibration based on coplanar equations. Due to the limits of the space and observation windows' positions for wind tunnel test section, the CCD images taken by big rotation angles and large overlap of multi-cameras are inevitably for videogrammetric measurement in wind tunnel tests, especially for high speed wind tunnels, their vibrations as well as aerodynamic noises are larger in the testing, high-precision exterior parameters and interior parameters is needed [2-9]. The exterior parameters can be easily obtained by linear and small-angle model for the traditional (aviation) photogrammetry(it is nearly vertical photography). But for big rotation angles and large overlap of multi-cameras, the nonlinear characteristics of collinear equation must be taken into consideration to obtain the precision exterior parameters, which are basis to accurately get the 3D coordinates. The distortion models include radial distortion, eccentric aberration and thin prism distortion [10,12], shown as follow

$$\begin{cases} x_u = \delta x_r + \delta x_d + \delta x_p \\ y_u = \delta y_r + \delta y_d + \delta y_p \end{cases} \tag{4}$$

where

$$\begin{cases} \delta x_r = x[k_1(x^2 + y^2) + k_2(x^2 + y^2)^2] \\ \delta y_r = y[k_1(x^2 + y^2) + k_2(x^2 + y^2)^2] \end{cases} \tag{5}$$

$$\begin{cases} \delta x_d = p_1 x(3x^2 + y^2) + 2p_2 xy \\ \delta y_d = 2p_1 xy + p_2 x(x^2 + 3y^2) \end{cases} \tag{6}$$

$$\begin{cases} \delta x_p = s_1(x^2 + y^2) \\ \delta y_p = s_2(x^2 + y^2) \end{cases} \tag{7}$$

Because b_x describes the scale of the relative orientation, as long as the total number m of P more than 13, the five relative orientation elements $(b_y, b_z, \varphi, \omega, \kappa)$, the six distortion parameters$(k_1, k_2, p_1, p_2, s_1, s_2)$ and (x_0, y_0) can be calculated by equation(2). The generalized inverse method of least square solution is used to solve equation (2). Let a vector $X = (b_y, b_z, \varphi, \omega, \kappa, k_1, k_2, p_1, p_2, s_1, s_2, x_0, y_0)$, then the Jacobi matrix of equation (2) is shown as follow

$$f(X)=\begin{bmatrix} \frac{\partial F(p_0)}{\partial b_y} & \frac{\partial F(p_0)}{\partial b_z} & \cdots & \frac{\partial F(p_0)}{\partial y_0} \\ \frac{\partial F(p_1)}{\partial b_y} & \frac{\partial F(p_1)}{\partial b_z} & \cdots & \frac{\partial F(p_1)}{\partial y_0} \\ \cdots & \cdots & \cdots & \cdots \\ \frac{\partial F(p_m)}{\partial b_y} & \frac{\partial F(p_m)}{\partial b_z} & \cdots & \frac{\partial F(p_m)}{\partial y_0} \end{bmatrix} \tag{8}$$

The iteration of equation (2) are

$$\begin{cases} X^{(k+1)}=X^{(k)}-\alpha_k Z^{(k)} \\ A^{(k)}Z^{(k)}=(F(p_0)^{(k)},F(p_1)^{(k)},\cdots,F(p_{m-1})^{(k)})^T \end{cases} \tag{9}$$

where $A^{(k)}$ is the Jacobin matrix of the $X^{(k)}$, α_k is value which makes

$$\sum_{i=0}^{m-1}(F(p_i)^{(k)})^2 \tag{10}$$

get minimum value, the rational extremum method[10]is used to compute α_k.

Image process of mark points. The artificial coded points are pasted on surface of the test model, to produce high contrast image of mark points. The coded points use the concentric ring to encoding and the circle point located in the center to determine their location. Therefore, from the differences of concentric ring around the center point, the homologous coded points can be automatically identified[1-2].The Canny edge detector is used to generate contours of coded points and the other points. The median filtering method is employed to leach the noise in images, and the positioning precision (range from 0.01 to 0.03 pixels) can be obtained using gray center of gravity method, least square fitting method or center-weighted gray et al.

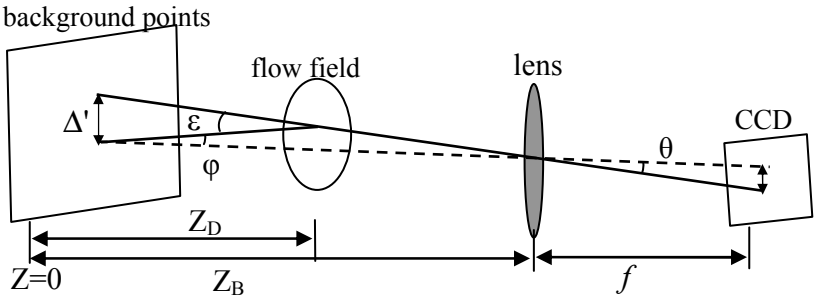

Fig.1 Principle of measurement

Aero-optics wavefront measurement. Following the principle of aero-optics wavefront distortion and ray trace, the refraction of a beam is caused by the disturbance flow. The deviation angle

$$\varepsilon=\int_s \nabla n ds \tag{11}$$

where n is the index-of-refraction, optical path length (OPL)

$$\phi=\int_s n ds \tag{12}$$

As shown in the fig.1, ε is small in aero-optics application, $ds \approx dz$ is reasonable, thus optical path difference (OPD) can be calculated by

$$\hat{\phi}=\phi-\bar{\phi}=2\Delta Z_D \varepsilon \tag{13}$$

where $\bar{\phi}$ is the OPL of the beam crossing the flow field without disturbances, ΔZ_D is the half of length of flow disturbances in Z direction. In the fig.1, because of $\Delta Z_D << Z_D$, according to projective geometry, we can get

$$\varepsilon = \arctan\left(\frac{Z_B \tan(\theta)}{Z_D - (Z_B - Z_D)\tan^2(\theta)}\right) \quad (14)$$

where

$$\tan(\theta) = \frac{\Delta'}{Z_B} = \frac{\Delta}{f} \quad (15)$$

Δ' and Δ are the displacement in world coordinate and image coordinate system respectively, Z_B is distance from lens to background points, f is focal length.

Experimental Study

Repeat measurement tests on angle of attack. The experimental facility is 2m supersonic wind tunnel of CARDC. Two cameras with 4,000,000 pixels, two computers to acquire images and two 35mm fixed focus lens are used to set up a videogrammetric system. Table 1 shows the measured results at the given supporters' angles, the largest standard deviation of the average measured angles of attack is 0.0027°; the differences of elastic angle measured by videogrammetry compared with that computed by balance are in the last column, where the biggest is -0.0256° and the smallest is -0.0119°. The differences are caused by the measuring basis, because the videogrammetric basis and the elastic angle calibration of balance are used the digital clinometers whose precision is 0.01°, thus the higher precision clinometers can be employed to decrease the differences.

Table 1 Measured results of angles of attack in 5 repeated tests

Angle of supporter (degree)	5 repeated test to measure angles of attack with videogrammetry					Average Value (degree)	Standard deviation of average value (degree)	Differences of elastic angle (degree)
	1	2	3	4	5			
-8	-8.2752	-8.2868	-8.2823	-8.2883	-8.2820	-8.2829	0.0023	-0.0256
-6	-6.1996	-6.2017	-6.1995	-6.2051	-6.1995	-6.2011	0.0011	-0.0270
-4	-4.1167	-4.1191	-4.1156	-4.1213	-4.1189	-4.1183	0.001	-0.0220
-2	-2.0385	-2.0375	-2.0323	-2.0402	-2.0351	-2.0367	0.0014	-0.0175
0	0.0493	0.0507	0.0555	0.0471	0.0524	0.0510	0.00143	-0.0149
2	2.1500	2.1514	2.1568	2.1462	2.1496	2.1508	0.0017	-0.0130
4	4.2642	4.2584	4.2626	4.2526	4.2590	4.2594	0.0022	-0.0161
6	6.4004	6.3942	6.4008	6.3896	6.3964	6.3963	0.00221	-0.0128
8	8.5452	8.5481	8.5591	8.5410	8.5559	8.5499	0.0027	-0.0119

tunnel of CARDC. Fig2 shows the positions of the mark points. The measured results of the 4 repeated tests are shown in table2, the standard uncertainty of the deformation at point 1 is 5.232±0.082mm, which indicates the precision of this videogrammetric system is good.

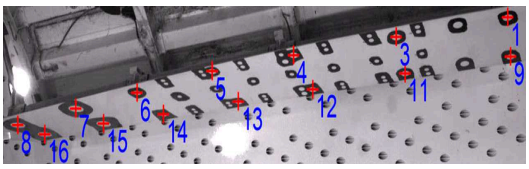

Fig 2 Mark points on the full size embedded door

Table 2 Dynamic deformation data of the first point

	1	2	3	4
Sample frequency(Hz)	80	80	80	80
Number of samples	600	1200	360	320
Average (mm)	5.120	5.246	5.348	5.215
Dynamic uncertainty(mm)	0.084	0.079	0.075	0.060

Aero-optics effects measurement. The facility is 2m supersonic wind tunnel of CARDC. Fig 3 shows the measured OPD fields described by Zernike polynomial at Ma=3.0. Fig 4 is a deflection displacement vector field generated by the airflow of an electric drier.

Conclusion

The repeated tests have demonstrated the precision of the videogrammetry is high, that is, the standard deviation of the average angle measured by videogrammetry is≤0.0027°; the standard uncertainty of the videogrammetric deformation data is 5.232±0.082mm. On the other hand, videogrammetry provides a new way to research and measure aero-optic effects, which is simple and need not expensive coherent source. Therefore, the applications of videogrammetry are great in the wind tunnel fine testing.

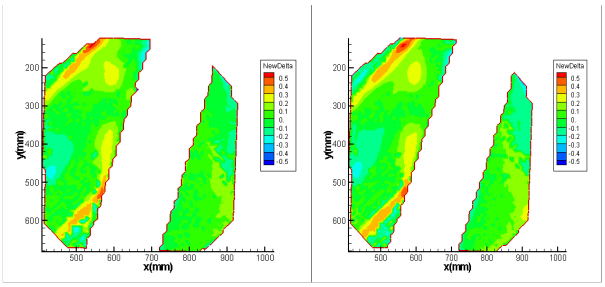

Angle of attack =16.88 Angle of attack=18.24
Fig 3 OPD described by Zernike polynomial

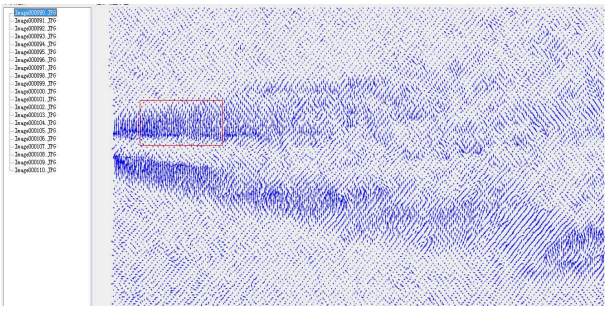

Fig4 A displacement field induced by an electric drier

References

[1] DANNY A B. Videogrammetric model deformation measurement technique for wind tunnel applications[R], AIAA Paper 2007-1163.

[2] LIU T, BURNER A W, PAPPA R. Photogrammetric techniques for aerospace applications[R], AIAA Press 2008.

[3] Zhao Tao, Zhang Zhengyu. Measurement and Reconstruction for Large Aero-Optics Wavefront Distortion Field [J]. ACTA OPTICA SINICA， 2013(33)10:10120031-10120037

[4] Zheng Yu Zhang, Shui Liang Wang. Videogrammetric measurement for model displacement in wind tunnel test [J]. Applied Mechanics and Materials, 2011, (130-134):103-107

[5] Thomas W. Jones, Charles B. Lunsford. Design and Development of a Real-Time Model Attitude Measurement System for Hypersonic Facilities. 43rd AIAA Aerospace Sciences Meeting and Exhibit 10-13 January 2005, Reno, Nevada, AIAA 2005-1411

[6] SUN Yan，Zhang Zhengyu. Vision Measurement Technology Research for Model Angle of Attack in Wind Tunnel Tests. Acta Aeronautica et Astronautica Sinica，2013, (34):1-7

[7] Luo C，Zhang Z Y. Exterior orientation for videogrammetric model deformation measurement. Journal of Experiments in Fluid Mechanics, 2010, 24(6): 88-91.

[8] Zhang Z Y, Luo C. Experimental investigation on exterior orientation in vibration environment. Journal of Experiments in Fluid Mechanics, 2011, 25(3):56-59.

[9] Zhang Z Y. Precision investigation on model displacement videogrammetric measurement in 2.4m transonic wind tunnel. Journal of Experiments in Fluid Mechanics, 2011(25):56-60

[10] Zhang zhengyu. Nonlinear Distortion Correction of CameraBased on Coplanar Condition Equations[J]. Acta Optica Sinica, Vol. 32(2012): 0115002-1- 0115002-6

[11] ZHANG Zhengyu,Huang Xuhui,Yin Jiang. Measurement and Visualization of Large Aero-optics Wavefront Distortion Field in Wind Tunnel Testing，Applied Mechanics and Materials Vo1. 389 (2013) pp 1053-1057

[12] Ahmed M, Farag A. Nonmetric calibration of camera lens distortion: Differential methods and robust estimation [J]. IEEE Transactions on Image Processing, 2005, 14 (8):1215～1230.

Advanced Materials Research Vols. 986-987 (2014) pp 1634-1637

doi:10.4028/www.scientific.net/AMR.986-987.1634

Windowed DFT Method for Frequency Measurement Involving Amplitude Modulation

Hui Xue[a], Huilan LI, Jiangbo Wang[b], Hongwei TANG,

College of Information and Electrical Engineering, China Agricultural University, Beijing, 100083, China

[a]email: xue_huicn@aliyun.com, [b]email: h00518@163.com

Keywords: Frequency Measurement; Amplitude Modulation; Discrete Fourier Transforms

Abstract. A windowed DFT method is proposed for power system frequency measurement involving amplitude modulation. First, an error analysis of conventional DFT based method considering amplitude modulation is given. Second, a noval a window DFT function is proposed method to eliminate these errors is given based on the relation among three consecutive DFT values. Due to its high precision and low required processing effort, the proposed algorithm is a good candidate for online frequency measurement.

1. Introduction

Frequency is a fundamental parameter in power system analysis, operation and control. Fast and accurate frequency measurement is an essential requisite to the control and protection of power system[1]. Among various techniques developed for frequency measurement[2-7], DFT based methods[2,3] is widely used due to its high precision and easy implementation. The basic idea of DFT based method is to calculate the phasor using DFT. Though the DFT calculated phasor is not accurate, it is found that the phase angle change in this phasor is a function of steady-state frequency deviation, therefore, the actual frequency can be estimated by the inaccurate phasors obtained using DFT[2,3]. However, when there are fluctuant bulky loads connected to the busbars, the voltage and current signal is likely to be fluctuated and the waveforms of the electrical signal are amplitude modulated. The conventional DFT based method is sensitive to these amplitude modulations and shows larges errors in these situations.

In this paper, the errors of conventional DFT based method considering amplitude modulation are studied, and an improved method to eliminate these errors is proposed based on the relation between three consecutive values of DFT.

2. The proposed method

Assume that the power system is operating close to nominal frequency, a fluctuant bulky load is connected to the busbars and voltage/current fluctuations appear, the corresponding voltage and current signals may be assumed to be amplitude modulated with a frequency ω_m as:

$$x(t) = [1 + a_m \cos(\omega_m t)]\cos(\omega t) \tag{1}$$

Where $\omega=2\pi f$, $\omega_m=2\pi f_m$, f and f_m are the fundamental and modulating frequency respectively, $a_m$is the modulating magnitude. Note (1) is equivalent to a superposition of six exponential components as:

$$x(t) = a(t) + b(t) + c(t) + d(t) + e(t) + g(t) \tag{2}$$

Where $a(t)=e^{j\omega t/2}$, $b(t)=e^{j-\omega t/2}$, $c(t) = a_m e^{j-(\omega+\omega_m)t}/2$, $d(t) = a_m e^{j-(\omega-\omega_m)t}/2$, $e(t) = a_m e^{j-(\omega+\omega_m)t}/2$, $g(t) = a_m e^{j-(\omega+\omega_m)t}/2$.

For a pure exponential signal as $s(t) = a_1 e^{j(2\pi f_1 t+\phi_1)}$, the DFT of it can be expressed as

$$S(n) = \sum_{k=0}^{N-1} s(k) W_N^{kn} = \frac{a_1 \sin(l\pi)}{N \sin(l\pi/N)} e^{j(\phi_1 - l\pi + l\pi/N)} \tag{3}$$

where n=0,1,2,…N-1, N is the size of the data window for DFT calculation, $W_N = e^{-j\frac{2\pi}{N}}$, ω_s is the sample frequency, $k_1=\omega_1 N/\omega_s$ is the spectrum line corresponding to the signal frequency, $l=n-k_1$ is the distance between n and k1 in the DFT spectrum. Due to the linearity of DFT, the DFT of $x(t)$ is a superposition of DFT of the six exponential components. Thus, the phasor of $x(t)$ can be expressed as:

$$X(1) = A(1) + B(1) + C(1) + D(1) + E(1) + F(1) \tag{4}$$

Where A(1), B(1), C(1), D(1), E(1) and F(1) can all be obtained using (3). In (4), if only A(1) or A(1)+B(1) exist in X(1), which means if the sampled signal is a pure exponential or sinusoid, the phase angle change of X(1) can be used to provide accurate frequency deviation measurement[2,3]. Notice C(1) and D(1) are two vectors that have similar magnitude and their phase angle difference with A(1) have the similar values, while one is positive and another is negative. Thus, the combination of C(1) and D(1) only affects the magnitude of X(1), while hardly affects the phase angle of X(1) and the phase angle change of X(1)=A(1)+B(1)+C(1)+D(1) can be used to provide accurate frequency deviation measurement. Therefore, the frequency measurement error mainly comes from E(1) and F(1) in (4). A method to reduce E(1) and F(1) in (4) is given in the following.

Notice the frequency is operating close to nominal frequency, therefore the values of A(0/2)(A(0) or A(2)) and B(0/2) are usually much smaller than the corresponding values of C(0/2), D(0/2), E(0/2), F(0/2) according to (3). Therefore, X(0) and X(2) can be expressed as：

$$\begin{aligned} X(0) &\approx C(0) + D(0) + E(0) + F(0) \\ X(2) &\approx C(2) + D(2) + E(2) + F(2) \end{aligned} \tag{5}$$

It can be deducted from (3), that

$$\begin{aligned} &K_1[C(0) + C(2)] \approx C(1), \quad K_2[D(0) + D(2)] \approx D(1) \\ &K_3[E(0) + E(2)] \approx E(1), \quad K_4[F(0) + F(2)] \approx F(1) \end{aligned} \tag{6}$$

And K_4 can be approximated as K_0, and

$$K_0 = CSC(2\pi / N) / [CSC(\pi / N) + CSC(3\pi / N)] \tag{7}$$

Equation (7) shows that K_0 is a constant whose value is determined by N, for example, for N=64, K_0=0.3752. And the following equation can be obtained from (5-7).

$$\begin{aligned} X(1) - K_0[X(0) + X(2)] \approx\ & A(1) + B(1) + (1 - K_0 / K_1)C(1) \\ & + (1 - K_0 / K_1)D(1) + (1 - K_0 / K_3)E(1) + (1 - K_0 / K_4)F(1) \end{aligned} \tag{8}$$

A Comparison between (4) and (8) shows that values of E(1) and F(1) have been greatly reduced in (8), Therefore, the effect of E(1) and F(1) in X(1) can be reduced by subtracting $K_0[X(0)+X(2)]$ from X(1), and the accurate frequency deviation measurement can be obtained by using the phase angle change of $X(1)$-$K_0[X(0)+X(2)]$ instead of X(1) as

$$df = \frac{1}{2\pi} \frac{d\phi\{X(1) - K_0[X(0) + X(2)]\}}{dt} \tag{9}$$

3. Numerical experiments

We will give some numerical experiments to compare the proposed method and conventional DFT based method[2] considering amplitude modulation. The sample frequency is set as 3200Hz, and the nominal frequency is set as 50Hz, the number of sample points for DFT calculation is N=64, and K_0=0.3752.

3.1 Interpolation function

The model of the test signal is as follows:

$$x(t) = (1 + a_m \cos(\omega_m t + \phi_m))\cos(\omega t + \phi) + a_3 \cos(3\omega t) + 0.1\cos(5\omega t)$$

Where $\omega=2\pi f$, f is the fundamental frequency. $\omega_m=2\pi f_m$, f_m and a_m are the modulating frequency and magnitude. The values of the parameters are given in Table1. We will perform six experiments. In each experiment, one parameter is varied and the other parameters are fixed as shown in Table 1.

In case 1, the value of is varied from 49.5Hz to 50.5Hz to study the effect of frequency variation of fundamental component. In case 2, the value of φ is varied from 0 to 2π to study the effect of phase angle variation of fundamental component. In case 3, the value of a_m is varied from 0 to 1 to study the effect of magnitude variation of modulating components. In case 4, the value of f_m is varied from 0Hz to 25Hz to study the effect of the frequency variation of modulating component. In case 5, the value of φ_m is varied from 0 to $2\pi$to study the effect of phase angle variation of modulating component. In case 6, the value of a_3 is varied from 0 to 1 to study the effect the magnitude variation of harmonic component. The frequency measurement errors(FE) are given in Fig. 1. Fig.1 shows that for all the six cases, the measurement precision of the proposed method are much higher than the conventional DFT based method.

Table 1: The values of parameters

Parameters	$f^{\perp}$ /Hz	ϕ/Radian	$a_m{}^{\perp}$ /pu	$f_m{}^{\perp}$ /Hz	ϕ_m/radian	$a_3{}^{\perp}$ /pu
Values	5 0 . 2	0	0.2	10	0	0.1

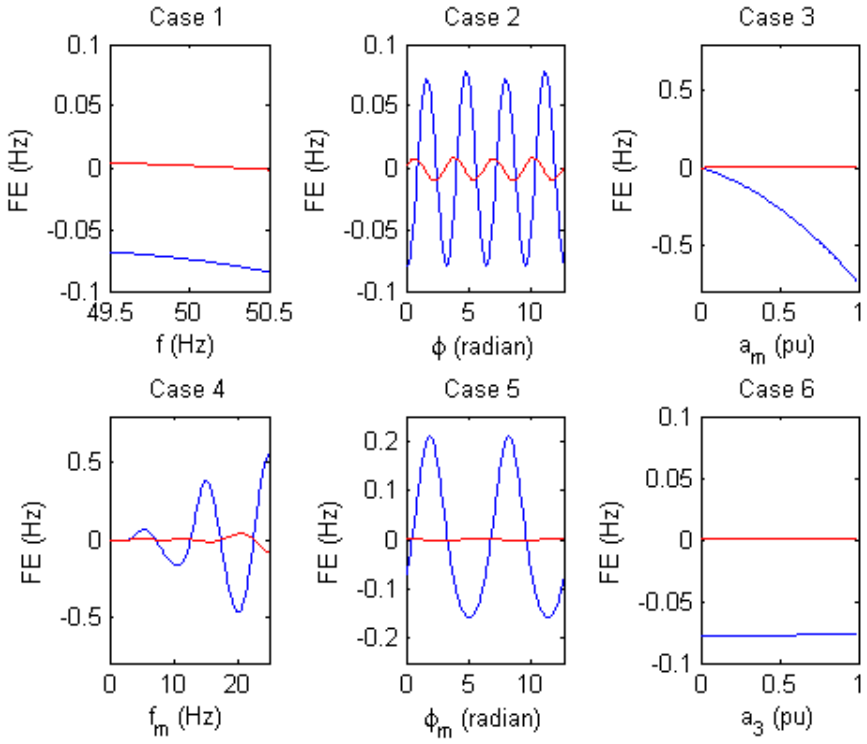

Fig.1. Frequency measurement errors (Blues are for conventional DFT, reds are for the proposed method)

3.2 The effect of noise and multi modulating components

50dB white noise is added to the signal to study the effect of noise, and the frequency measurement errors(FE) are given in Fig.2. Fig.2 shows that the proposed method performs stable and accurate in noisy environment.

Our theoretical deductions and experiments also show that the proposed method performs well under multi modulating components environment, which is not list here due to the limit of paper length.

4. Conclusion

A DFT based methods for power system frequency measurement considering amplitude modulation are proposed in this paper. Due to its high precision and low required processing effort, the algorithm is a good candidate for online frequency estimation.

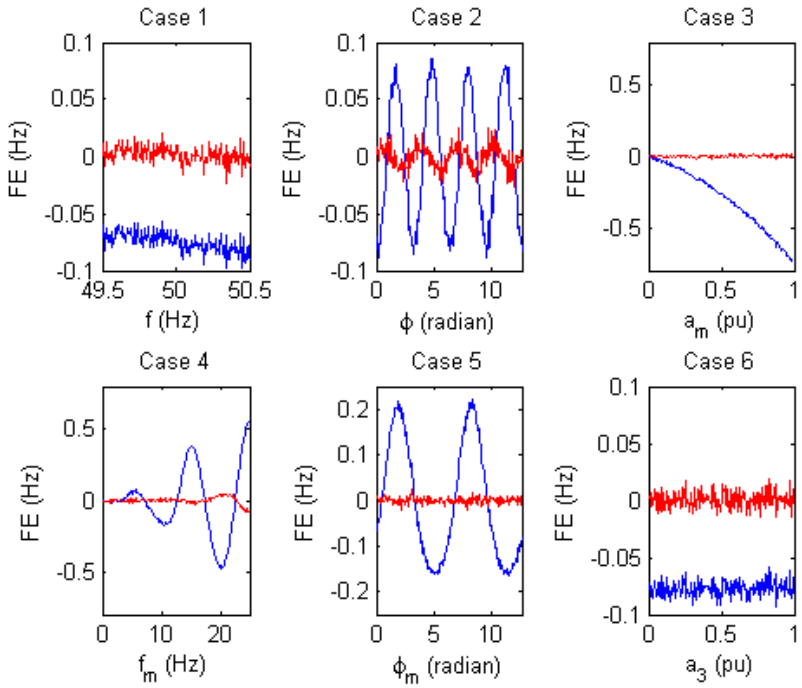

Fig.2. Frequency measurement errors (Blues are for conventional DFT, reds are for the proposed method)

Acknowledgement

This work is supported in part by the National Natural Science Foundation of China under Grant 51207160 and in part by the Program for New Century Excellent Talents under Grant NCET-13-0565.

References

[1] A. G. Phadke, J. S. Thorp, "Synchronized phasor estimations and their applications", New York: Springer, 2008.

[2] A. G. Phadke, J. S. Thorp, M. G. Adamiak, "A new estimation technique for tracking voltage phasors, local system frequency, and rate of change of frequency", IEEE Transaction on Power Apparatus and System, vol. 102, no.5, pp. 1025-1038, 1983.

[3] A. G. Phadke, B. Kasztenny, "Synchronized phasor and frequency estimation under transient conditions", IEEE Transaction on Power Delivery, vol. 24, no. 1, pp. 89 – 95, 2009.

[4] P. Zhang, H. Xue, R. G. Yang, "Shifting window average method for accurate frequency estimation in power systems," IEEE transaction on Power Delivery, vol. 26, no. 4, pp. 2887-2889, 2011.

[5] M. M. Begovic, P. M. Djuric, S. Dunlap, A. G. Phadke, "Frequency tracking in power networks in the presence of harmonics," IEEE Transaction on Power Delivery, vol. 8, no. 2, pp. 480-486, 1993.

[6] H. Karimi, M. G. Karimi, M. R. Iravani, "Estimation of frequency and its rate of change for applications in power system", IEEE Transaction on Power Delivery, vol. 19, no. 2, pp. 472-480, 2004.

[7] M. G. Karimi, H. Karimi, A. R. Bakhshai, "A filtering technique for three phase power system", IEEE Transaction on Instrumentation and Estimation, vol. 58, no. 2, pp. 389-396, 2009.

Advanced Materials Research Vols. 986-987 (2014) pp 1638-1642

doi:10.4028/www.scientific.net/AMR.986-987.1638

Analysis of Active Power Loss for Reactive Power Compensation Devices

Yingying CHENG, Feng ZHOU[a], Ji XIAO[b]

State Grid Chongqing Electric Power CO. Electric Power Research Institute, Chongqing, 401123, China

[a]email: zfocus@foxmail.com, [b]email: xiaoji114@163.com

Keywords: Reactive Power Compensation; Reactor; Capacitor; Active Power Loss

Abstract. Analyzing the active power loss of reactive power compensation device under normal reactive power output status and its influence factors and metering the active power loss of the reactor in the 500kV substation and the capacitor in the 220kV substation, concluding that the active power meter had the influencing factors of forward and reverse active and putting forward the assessment requirements for the running reactive power compensation device by analyzing the site calibration data of metering device.

Introduction

At present, the use of reactive power compensation device for reactive power compensation is the main means on stabilizing transmission line voltage and reducing line loss, while it's the common methods of reactive power compensation that the reactive power compensation device is installed in the bus side [1] [2]. The active power loss is an important economic and technical index for the power equipment and electric power enterprises. The reactive energy meter is provided at the bus side to measure the active power loss of reactive power compensation device and its secondary circuit. In the paper, the components and the influence factors of the active power loss is analyzed, and the economy of its running state is assessed reasonably, it has important reference significance for the state test and evaluation and the fault alarm and processing of reactive power compensation device.

The analysis and influencing factors of the active power loss

There are many different types of reactive power compensation devices currently, mainly including synchronous condenser, static reactive power compensation device SVC, static synchronous compensator STATCOM, the parallel capacitors, etc [3-5]. SVC mainly includes the thyristor controlled reactor (TCR) and thyristor switched capacitor (TSC), STATCOM is a kind of device, which uses such as IGBT, GTO or SIT and so on full - controlled and high-speed power electronic device as a switch device to control the current. And the parallel capacitor is currently the most main methods of reactive power compensation with the characteristics of low price, high efficiency and low operation cost, which make it be widely used in the reactive power compensation [6-10]. In this paper, the active power losses and its influencing factors of the reactive power compensation device under normal reactive power status were analyzed.

(1) The active power loss of the capacitor [11]

The theory active power loss of the capacitor includes the dielectric and the plate loss of the capacitor, and the loss of reactor active power and the wiring loss of the capacitor bank.

The capacitor may be assumed as the equivalent circuit model of the capacitor C and the resistor R who are connected in parallel, there are $R = tg\delta \cdot X_c$, in which R is the equivalent series resistance of the capacitor, X_c is capacitance of the capacitor for each phase, $tg\delta$ is the dielectric loss tangent. Therefore, the active power loss of the capacitor is:

$$P_c = I^2 R \tag{1}$$

In the type (1), I is the total current of the capacitor circuit.

(2) The active power loss of the reactor

The reactor active power loss includes the loss of the reactor coil resistance, the iron core eddy current loss, the hysteresis loss and the eddy current loss of the air gap.

The reactor can be assumed as the equivalent circuit model of the resistance R and the reactance X_l who are in series, in which X_l is the reactance of the reactor, whose value is determined by the reactor manufacturing process, R is a total impedance equivalent loss of reactor, Therefore, the active power loss of capacitor is:

$$P_l = I^2 R \tag{2}$$

In the type (2), I is the total current of the reactor circuit.

(3) The meter error and the loss of the secondary circuit

The electric energy meter of the transformer substation reactive power compensation device involved in this paper all adopt 0.5S active energy meter, and the reactor active power loss energy meter's CT ratio in 500kV transformer substation is 300/5, PT variable ratio is 35kV/0.1kV,the magnification of the metering consolidated is 21,000. In fact, the error of the electric energy meter is very small, and the loss value of the connecting wires and the secondary circuit of reactive power compensation device is not large, but it is not to be ignored for the similarly small the active power loss value of the reactive power compensation device, and it must be taken into account regarded as the part of the entire assessing and evaluating system.

(4) The effect of transformer integrated error to the measurement

Theoretically capacitive or inductive current will only cause reactive power measurement and won't produce active power, but due to the reactor is the inductive element and its power factor is very small, in this case, the influence on the measurement results is large because of using the angle difference of the voltage and the current transformer to measure. CT, PT and its secondary circuit have impact on the electric energy meter current and voltage phase, which makes the actual measurement of the secondary side of the power meter, is inconsistent with the primary side of the power and will generate errors.

The measurement of active energy meter is:

$$\begin{aligned} P = {} & U_a I_a \cos[90^\circ + (\delta_{Ia} - \delta_{ra} \pm \delta_{Ua})] + U_b I_b \cos[90^\circ + (\delta_{Ib} - \delta_{rb} \pm \delta_{Ub})] \\ & + U_c I_c \cos[90^\circ + (\delta_{Ic} - \delta_{rc} \pm \delta_{Uc})] \end{aligned} \tag{3}$$

In the type (3), in the ideal case of three-phase symmetrical, when $\delta_I - \delta_r \pm \delta_U > 0^\circ$, P is negative, the reverse of active energy metering. When $\delta_I - \delta_r \pm \delta_U < 0^\circ$, P is positive, the active energy metering is the positive. When $\delta_I - \delta_r \pm \delta_U = 0^\circ$, active power is not measured. Under normal circumstances, it is impossible to produce active power when measure the active on the reactive power compensation device, however, the integrated error of the transformer makes the electric energy meter may be able to measure the forward active and reverse active power.

In this case, in addition to reducing the PT secondary circuit load, but also a higher level of accuracy transformer should be configured to reduce the synthesis phase difference and to reduce the impact on the electric energy meter.

The analysis of field test data of active power loss

(1) The field calibration of metering device

To collect the information of the reactive power compensation device in the substation, including the voltage and current, active power loss, power factor, we tested the metering device and recorded real-time voltage and current, power factor, electric energy meter errors and other data of the reactive power compensation device under the running state. As shown in Fig.1 is the field calibration of active energy meter for the reactor in the 500kV substation.

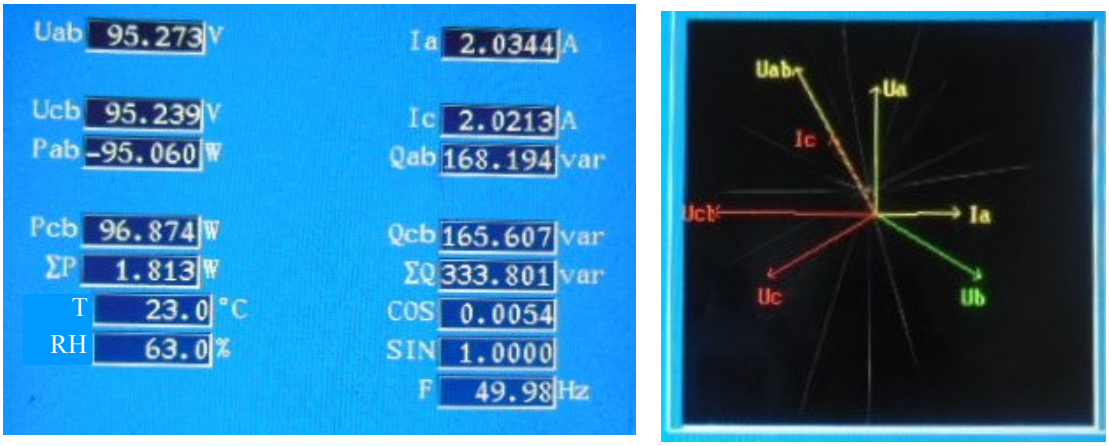

Fig.1. The field calibration of active energy meter for the reactor in 500kV substation

(2) The data analysis of the active power loss

For the convenience of analyzing the active power loss and the power factor of the reactive power compensation device, we statistics the information of the metering device for the reactor and capacitor in the substation. The configuration of metering device for reactor in 500kV substation is given in Tab.1. According to the wiring and voltage grade, the capacitors in the substation are installed in 10kV bus side, and the accuracy level of active metering electric energy meter of the capacitor is 0.5S class.

Tab.1. The configuration of metering device for reactor in 500kV substation

No.	Accuracy of meter	Wiring	Measurement of voltage	CT ratio	PT ratio	Measurement magnification
A	0.5S	Three-phase three wire	35kV	300/5	35kV/0.1kV	21000
B	0.5S	Three-phase three wire	35kV	300/5	35kV/0.1kV	21000
C	0.5S	Three-phase three wire	35kV	300/5	35kV/0.1kV	21000
D	0.5S	Three-phase three wire	35kV	300/5	35kV/0.1kV	21000

It gives the measured data of reactor metering device in the 500kV substation in Tab.2, including the check degree of electric energy meter, the voltage and current, the power factor and the electric energy meter errors.

Tab.2. The measured data of metering device for reactor in 500kV substation

No.	Electric energy meter ended degrees						The field test data					
	Forward KA	Forward KR	Backward KA	Backward KR	P	Q	Ia	Ic	Uab	Ucb	Cosφ	Error (%)
A	81.00	26358.49	0.06	57.23	1.88	523.44	3.179	3.175	95.18	95.05	0.0036	0.008
B	87.63	25077.73	0.05	38.48	1.91	522.19	3.174	3.176	94.98	94.90	0.0037	0.035
C	89.48	24714.46	0	0	1.81	530.15	3.205	3.203	95.58	95.51	0.0034	0.035
D	39.79	21270.16	0	0.002	0.80	-490.95	2.988	2.983	95.02	94.97	0.0016	0.117

According to the field test data in Tab.2, we mainly analyzed the power factor of reactive power compensation device and the error of electric energy meter, as shown in Fig.2, we provided the real-time power factor of reactor and the error of electric energy meter which in the 500kV substation.

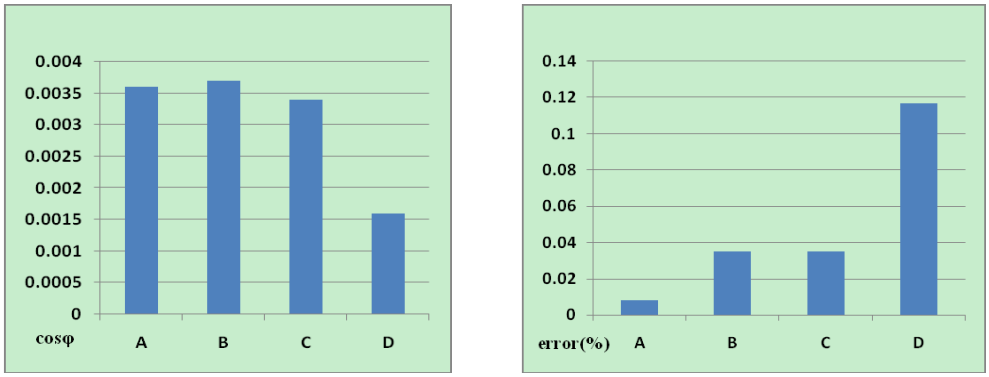

(a) The power factor of reactor (b) The error of electric energy meter

Fig.2. Power factor and energy meter error of reactor in 500kV substation

Can be seen from Fig.2, the maximum power factor value of the reactor in 500kV substation is 0.0037, and the most active loss generated from loss of reactor itself and the bias metering under the comprehensive error of transformer. The maximum error of the three-phase electric energy meter is 0.117%, it completely meet the requirement that the error of the 0.5S class electric energy meter is less than 0.5%.

The configuration of metering device for capacitor in 220kV substation is given in Tab.3. According to the wiring and voltage grade, the capacitors in the transformer substation are installed in 10kV bus side, and the accuracy level of active metering electric energy meter of the capacitor is 0.5S class.

Tab.3. The configuration of metering device for capacitor in 220kV substation

No.	Accuracy of meter	Wiring	Measurement of voltage	CT ratio	PT ratio	Measurement magnification
A	0.5S	Three-phase three wire	10kV	300/5	10kV/0.1kV	6000
B	0.5S	Three-phase four wire	10kV	600/5	10kV/0.1kV	12000
C	0.5S	Three-phase four wire	10kV	300/5	10kV/0.1kV	6000
D	0.5S	Three-phase three wire	10kV	300/5	10kV/0.1kV	6000

The measured data of the capacitor metering devices which in the 220kV substation were given in Tab.4, including the check degree of electric energy meter, the real-time power, the voltage and current during field testing, the power factor and the electric energy meter errors.

Tab.4. The measured data of metering device for capacitor in 220kV substation

No.	Electric energy meter ended degrees						The field test data							
	Forward KA	Forward KR	Backward KA	Backward KR	P	Q	Ia	Ib	Ic	Uao(ab)	Ubo	Uco(cb)	Cosφ	Error (%)
A	0	0	28.96	5507.74	-0.34	85.21	0.484	-	0.484	101.65	-	101.37	0.004	0.335
B	0	0	12.18	1501.90	-1.29	254.02	1.417	1.425	1.406	62.84	60.84	59.02	0.0051	0.06
C	0	1.3	11.23	4277.08	-0.36	100.20	0.564	0.570	0.562	61.08	59.85	56.50	0.0036	0.249
D	8.43	1257.29	0.08	252.85	0.11	-153.81	0.873	-	0.872	101.90	-	101.59	0.0007	0.135

According to the field test data in Tab.4, we mainly analyzed the power factor of reactive power compensation device and the error of the electric energy meter, as shown in Fig.3, the real-time power factor of the capacitor and the error of the electric energy meter which in the 220kV substation were given.

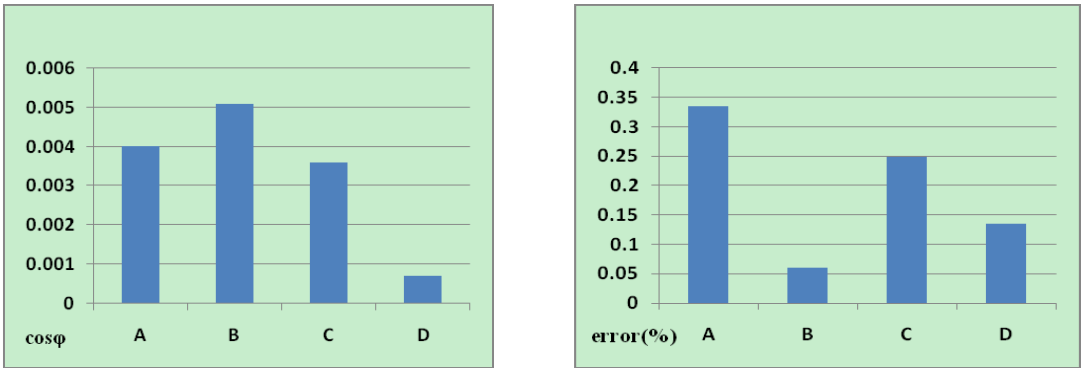

(a) The power factor of capacitor (b) The error of electric energy meter

Fig.3. Power factor and energy meter error of capacitor in 220kV substation

Can be seen from Fig.2, the real-time power factor of reactor in 200kV substation is up to 0.0051, the rest is 0.004 or less, and the most active loss generated from loss of reactor itself and the bias metering under the comprehensive error of transformer. The maximum error of the three-phase electric energy meter is 0.335%, it completely meet the requirement that the error of the 0.5S class electric energy meter is less than 0.5%.

Conclusion

In this paper, according to the field calibration of metering device for reactors and capacitors in substation, and the reactors and active power data measured in the substation was analyzed. The results showed that in the case of relatively large measurement magnification the electric energy meter error and the secondary circuit losses cannot be ignored. Electric energy meter can measure the positive and negative active power under the comprehensive error of transformer. The power loss of the reactive power compensation device measured in this paper performed well. At present, there is no uniform requirement for power factor of the reactive power compensation device, and I suggest making standards as soon as possible to assess its operational status.

References

[1] YAO Liang-zhu. Discussion on optimizing reactive compensation to decrease line loss [J]. Automation of Electric Power Systems, 2002, 22(12): 71-73.

[2] GUO Rui, LIU Guo-hai. Study on STATCOM model and its control strategy [J]. Electric Power Automation Equipment ,2006, 26(1): 21-24.

[3] SONG Shan, CHEN Jian-ye. Theory and prototype verification of thyristor based STATCOM [J]. Automation of Electric Power Systems, 2006, 30(18): 49-54.

[4] FENG Yu-cheng, CHEN Chen. Comparison and analysis between static synchronous compensator and traditionary static var compensator [J] .Power of East China, 2005, 33(9): 16-19.

[5] ZHOU Jian-feng, GU Ya-qin, WEI Shou-qi, et al. Comprehensive comparative analysis of SVC and STATCOM [J]. Electric Power Automation Equipment, 2007, 27(12): 57-61.

[6] YU Meng-ze, CHEN Bai-chao, TIAN Cui-hua, et al. High voltage static var reactive power compensator using shunt magnetically controllable reactor [J]. High Voltage Engineering, 2009, 35(7): 1770-1773.

[7] LI Shan-ying, SHI Qing-xin. Study on reactive power compensation for the integration and operation of large-scale wind farms [J]. Electric Power, 2010, 43(9): 71-74.

[8] VARMA R K, AUDDY S, SEMSEDINI Y. Mitigation of sub-synchronous resonance in a series-compensated wind farm using FACTS controllers [J]. IEEE Transactions on Power Delivery, 2008, 23(3): 1645-1655.

[9] XU Hong-bing. Analysis on economic operation of shunt capacitor for reactive power compensation [J]. Power Capacitor & Reactive Power Compensation, 2006, (12): 12-14.

[10] SHI Huan, HUANG Xiao-sheng, ZENG Wen-jun, et al. Dynamic reactive power compensation device based on magnetically controlled reactor [J]. Electric Power, 2011, 44(1):32-36.

[11] KONG Bin, WEI Ya, LIU Xian-lin. Electric energy dissipation analysis of parallel condenser based on harmonic wave [J]. Journal of Zhengzhou University (Engineering Science), 2003, 24(3) 98-100.

Advanced Materials Research Vols. 986-987 (2014) pp 1643-1646

doi:10.4028/www.scientific.net/AMR.986-987.1643

Evaluation of On-line DGA Limit Values and Calculation of Detecting Intervals for On-line Monitoring Equipment for Transformers

Yangliu LI[1, a], Zhiyong CHEN[2, b]

[1] School of Mechanical Engineering, Dalian University, Dalian, 116622,China

[2]Dalian Hi-Think Computer Technology, Corp., Dalian, 116085, China

[a]email: lylmaria@163.com, [b]email: lynxboy@sina.com

Keywords: DGA; Limit Values; On-line Detection; Detecting Intervals

Abstract. Methods presented in this paper evaluate the on-line DGA results and provide specific on-line DGA limit values. For on-line equipment monitoring transformer condition, a method to calculate specific detecting intervals according to the evaluation of on-line DGA results is proposed. An example to calculate detecting intervals is demonstrated using the field test data acquired by on-line equipment for transformer condition-monitoring service.

Introduction

For many years, dissolved gas analysis (DGA) has been widely accepted to forecast incipient faults in oil-filled transformers. As each fault produces equivalent gases (H_2, CH_4, C_2H_2, C_2H_4, C_2H_6, CO, CO_2) that dissolved in insulation oil, some faults can be diagnosed by quantification the gases before certain electrical and thermal phenomena leading to a serious failure in the grid [1]. Nowadays, the quantification of fault gases is usually done in the laboratories, which is a well-known diagnostic technique used to quantify the ratios of the fault gases. Nevertheless, there are many disadvantages of off-line DGA in the laboratories which lead to the inaccuracy in the DGA results, so considerable interest in installing on-line DGA systems which can extract dissolved gas and analyze the rations of gases in the field increased.

Nowadays, on-line monitoring devices have been installed on many transformers in China [2]. However, there is no coherent standard for on-line DGA results [3]. The accuracy of on-line DGA results needs to be evaluated, and also corresponding methods need to be taken. Although there is always some degree of inaccuracy in laboratory dissolved gas measurements, especially at low gas concentrations; the measurements evaluation can be convincing reference to evaluate the on-line measurements, which can also improve transformer condition assessment and diagnosis by DGA.

Evaluation of On-line DGA Value

It should be noted not only quality of laboratory dissolved gas measurements but also on-line dissolved gas measurements influence the assessment of transformer condition. In case the on-line monitoring equipment reported false positives, non-periodical laboratory dissolved gas testing will increase, which lead to unnecessary maintenance and repair costs. Furthermore, the type of incipient fault may be misdiagnosed if the quality of DGA results is poor, especially when the concentrations of gases are in a low range. For example, the discharging fault may be misdiagnosed as heating problem. If the detection for the increases of fault gases deviates from the real filed situation, the seriousness of the fault may be misestimated. Therefore the quality of on-line DGA measurements needs to be evaluated [4][5].

IEC 60567 defined that Repeatability, reproducibility, and accuracy are quality parameters of laboratory DGA measurements [6]. Compare with laboratory DGA measurements, repeatability and accuracy, two quality parameters are defined to describe the quality of the results. Repeatability or precision is related to the differences when multiple samples of the same oil are analyzed by the same on-line equipment over a short period of time (usually less than one day). Accuracy is related to the differences that are observed between the values measured by the on-line equipment and the

nominal values contained in a gas-in-oil sample prepared according to standard procedures [7]. In china, individual network has their own technical laboratory, so the observation can be done between the values measured by analysis in the lab and the on-line equipment. It should be known that a variety of extraction and detection methods of fault gases utilized by different on-line equipment. It is confirmed that both excellent results and poor results were obtained with all of the extraction techniques used, so that the main determinant for the quality of results appears to be gas detection performance and not the extraction technique. Meanwhile, good quality results for fault gases can be acquired by those means, including semiconductor gas sensors, Fourier Transform Infra-Red, Photoacoustic Spectroscopy. In the long term, on-line equipment provide more effective data, the stander of on-line equipment accuracy should be higher or at least reach the quality of laboratory measurements. According to the results of survey by CIGRE[8][9], using the stander of laboratory dissolved gas measurements as a reference, requirement of accuracy and repeatability of on-line DGA results are given in Table 1.

Table 1 Requirement of accuracy and repeatability of on-line DGA results

	Medium gas concentration	Low gas concentration
Accuracy	±15%	±30%
Repeatability	±7%	±27%

The ranges of typical values (gas concentrations and rates of gas increase) observed by CIGRE [10] and the IEC [11], which represent usually normal condition of transformers. In the whole network, the concentration of gases may increase slowly for each oil-filled electrical transformer, so regular gas increase may be observed. Typical values and rates of gas increase for on-line detection, which is set as C_{Ti} is shown in Table 2. They mean, for example, that hydrogen concentrations in 90% of the transformers surveyed were below 150μL/L or 50μL/L depending on the network considered.

Table 2 Typical values and rates of gas increase for on-line detection

C_{Ti}	H_2	CH_4	C_2H_4	C_2H_6	C_2H_2	CO	CO_2
Gas Concentration Values (μL/L)	50-150	30-130	60-280	20-90	0-10	400-600	3800-14000
Rates of Gas Increase (μL/L/year)	35-132	10-120	32-146	5-90	0-2	260-1060	1700-10000

In GB/T 7252-2001, only the concentrations of fault gases which may indicate the incipient fault are motioned, which can be defined as caution concentration values [4]. When the on-line DGA results reach those concentrations (C_{Ci}), utilities need to pay extra attention to the specific transformer. Nevertheless, in some old equipment, weak chemical bonds may break in the first years of operation and then stabilize. In that case no further measures need to be taken, but the changes of the concentrations need to be followed up. If the concentrations of fault gases still increase, another concentration limit value, pre-failure concentration value C_{Pi} is defined. Pre-failure concentration values were found by CIGRE [8] to be surprisingly similar on different networks, suggesting that failure occurs when a critical amount of insulation is destroyed. CIGRE pre-failure values can therefore be used as an evaluation for on-line detection of the levels of gas formation observed just before failure. They are indicated in Table 3 for gas concentrations (inμL/L) and for rates of gas increase (in μL/L /day) [9].

Table 3 Average pre-failure gas concentration values for on-line detection

C_{Pi}	H_2	CH_4	C_2H_4	C_2H_6	C_2H_2	CO	CO_2
Gas Concentration Values (μL/L)	725	400	800	900	450	2100	/
Rates of Gas Increase (μL/L/day)	3	5	5	11	0.5	/	/

Calculation of detecting intervals

In IEEE Standard 4, gas concentrations requiring monthly, weekly and daily sampling intervals have been called levels 2, 3, 4 [10]. Typical sampling intervals are those used for regular maintenance of the transformers (e.g., every year for transmission transformers and every 6 months for nuclear transformers in the US, or your own intervals) [11]. Under the circumstance that on-line devices are equipped, the detecting intervals instead of sampling intervals should be calculated.

Set the shortest detecting interval is t_{min}, and the responding time of on-line equipment is t_{rep}. Obviously, once the concentrations reach the pre-failure value, the detecting interval time, there is $t_P = t_{min} = t_{rep}$ If the concentration of one of fault gases reaches the value of Cc, there is probability of fault in the transformer, the detecting interval should be shorten. For the purpose of calculations in this paper, the sampling interval corresponding to pre-failure values has been chosen as one hour. Set p_F the probability of having a failure-related event in service, b_F and k_F coefficient of the probability, which can be calculated by equation 1.

$$\ln c_o = b_F \ln C_P + \ln(k_F p_F) \tag{1}$$

Set t_T as interval time when the concentration is in the typical value range, and set t_P as interval time when the concentration reaches the pre-failure value.

$$\frac{c_o}{C_P} = \left(\frac{t_P}{t_o}\right)^{k_F p_F} \tag{2}$$

Through on-line detection, define t_o as detecting interval time. According to equation 2, values in Tables 4 have been calculated for detecting intervals.

Table 4. Examples of Intervals and Gas concentrations Calculated

(μL/L)	H_2	CH_4	C_2H_4	C_2H_6	C_2H_2	CO	CO_2	t_O
C_T	50	15	10	5	0.5	200	1500	
	100	30	60	20	2	400	3000	$2160t_{min}$
C_C	150	60	70	40	10	500	4000	$113t_{min}$
	170	120	140	130	12	1100	12000	$78t_{min}$
	220	150	190	180	25	1200	15000	$36t_{min}$
	380	240	380	400	100	1600	27000	$7t_{min}$
C_P	725	400	800	900	450	2100	50000	t_{min}

Conclusion

On-line DGA results provide large quantity data which will be propitious to the assessment of transformers condition and diagnosis of transformers. The qualities of on-line DGA results need to be restricted. Repeatability and accuracy, two quality parameters are defined to describe the quality of the results. Also the requirement for accuracy and repeatability of on-line DGA results are presented. As only limit values of DGA for transformers are mentioned in the on-line standard for oil-filled transformers applied in state grid. Typical value (C_{Ti}), caution value (C_{Ci}) and pre-failure value (C_{Pi}) are defined to indicate probability of failure. The detecting interval should be shortened once the on-line DGA results reach the caution value. Method presented in this paper allows individual networks or transformer users to calculate detecting intervals as a function of gas concentrations in service. An example to calculate detecting intervals is demonstrated, showing the method can be complementarity to maintenance of transformers.

References

[1] Michel Duval, James Dukarm. Improving the Reliability of Transformer Gas-in-Oil Diagnosis [J]. Electrical Insulation Magazine, 2005, 21(4):21-23.

[2] Yangliu Li, Xuezeng Zhao. Estimation of the Equilibrium Concentration of H2 and CO in Transformer Oil from Membranes [J]. IEEE Electrical Insulation Magazine, 2011, 27(2):30-33.

[3] Yangliu Li, Xuezeng Zhao, Chunzhi Guo, et al. Gas Concentration Prediction Algorithm Based on Membrane Extraction for Transformer On-line Monitoring System [J]. Electric Power Automation Equipment, 2010, 30(12):36-41.

[4] GB/T 7252-2001, Guide To The Analysis And Diagnosis Of Gases Dissolved In Transformer Oil [S], 2001.

[5] Michel Duval. A Review of Faults Detectable By Gas - In - Oil Analysis in Transformers [J]. IEEE Electrical Insulation Magazine, 2002, 18(3): 8-17.

[6] IEC Publication 60599. Mineral Oil-impregnated Electrical Equipment in Service-guide to the Interpretation of Dissolved and Free Gases Analysis [S], 1999, (2).

[7] Yangliu Li, Wenda Wu. Temperature Dependence of On-line DGA Results for Transformers through Membrane Extraction [C]. Advanced Materials Research, 2013, (614-615):1163-1167.

[8] M. Duval et al. Joint Task Force D1.01/ A2.11 of CIGRE, "Recent developments in DGA interpretation," CIGRE Brochure # 296, 2006, available from publications@cigre.org. Summary in Electra, 2006, 226(6):56–60.

[9] Mineral Oil-Impregnated Electrical Equipment In Service - Guide To The Interpretation Of Dissolved And Free Gases Analysis [S], IEC Publication 60599-Amendment 1, 2007(04).

[10] Michel Duval. Calculation of DGA Limit Values and Sampling Intervals in Transformers in Service[J]. IEEE Electrical Insulation Magazine, 2008, 24(5): 7-13.

[11] M. Duval, Using Gas-In-Oil Standards to Improve Accuracy of Dissolved Gas Analysis Results and Diagnoses [J]. Electricity Today, 2002, 14(6):16-19.

Advanced Materials Research Vols. 986-987 (2014) pp 1647-1650

doi:10.4028/www.scientific.net/AMR.986-987.1647

Remote Sensing Interpretation and Early Warning System Designing of Geohazards along Transmission Lines ---A case study of the Danba - Kangding 500 kV Double Circuit Transmission Line

CAO Yongxing[1, a], CHANG Ming[2, b], TANG Chuan[2,c], LI Weile[2,d], MA Guochao[2,e]

[1]Sichuan Electric Power Company, Chengdu, 610072, China

[2]State key Laboratory of Geohazard Prevention and Geoenvironment Protection, Chengdu University of Technology, Chengdu,610059, China

[a]email: 87085306@163.com, [b]email:Changming@cdlg.edu.cn, [c]email:tangchuan@cdlg.edu.cn, [d]email:liweile21@cdlg.edu.cn,[e]email:Maguohao@cdlg.edu.cn,

Keywords: Landslide, Debris Flow, Transmission Lines, Warning System, Remote sensing

Abstract. The landslide and debris flow investigation area for Danba ~ Kangding 500 kv double-circuit transmission line route selection is within Ganzi in Tibetan autonomous prefecture, with the area of about 440 km^2. The topography, geomorphology, geologic structure, stratum lithology, natural factors, social and economic conditions have great influences on the transmission lines route selection and its construction. For comprehensive evaluation engineering rationality and construction convenience, remote sensing technology (RS) and geographic information system (GIS) technology are taken to implement geological environment survey. With field investigation, remote sensing images interpretation method is used to determine basic characteristics of the geo-hazards.

Introduction

Geohazards typically include avalanches, landslides, mudslides, etc., with characteristics such as relative complexity of their formation process, powerful destructive ability, and very huge amount of economic losses. Earthquake will lead to generate massive loose solid materials, as much as to 50-150 hundred millions m^3 [1, 2, 3, 4]. They usually accumulate at valley forming regions or talus slope at the earthquake center, as a potential source of landslide or debris flow when meets heavy rainfall. For example, after Wenchuan Earthquake, almost every rainy season, there always a large number of landslide disasters occurring in the disaster areas. Currently, abroad researchers have used a variety of monitor devices to prevent its occurring, such as mud level meter, camera and ultrasonic detectors and other devices [5]. In domestic research community, GIS technology is taken to investigate these loose materials distribution features and thus when select location of transmission lines, designers will skirt around dangerous areas [6, 7, 8, 9].

Facing great threats from such widespread distribution of landslides and debris flows, traditional survey methods failed because of its enormous cost with very long time. The most cost-effective approach is to use remote sensing to obtain overall possibility distribution of geological disasters and identify most dangerous areas [10]. GIS and remote sensing technology are introduced to help transmission lines designers to select the location of power tower in Danba-Kangding 500kV double circuits project. In this paper, relative circumstances are discussed in detail.

Characteristics of the study area

Danba - Kangding 500 kV double circuit transmission line is located in western mountains and canyons area in Sichuan province, eastern of Ganzi Tibetan Autonomous Prefecture and upstream area of Dadu River, generally same trend with Dadu River. This area is gateway to Tibet and political, economic and cultural center of Ganzi Tibetan Autonomous Prefecture. Transmission

corridor passes through this wide area, from south to north. The maximum elevation is 4440 meters, with minimum elevation 1380m and average 2910m. Maximum gradient region is 73 °, minimum slope is 5 °, average slope is 35.85 °. , relative elevation is 3060m (Figure 1).

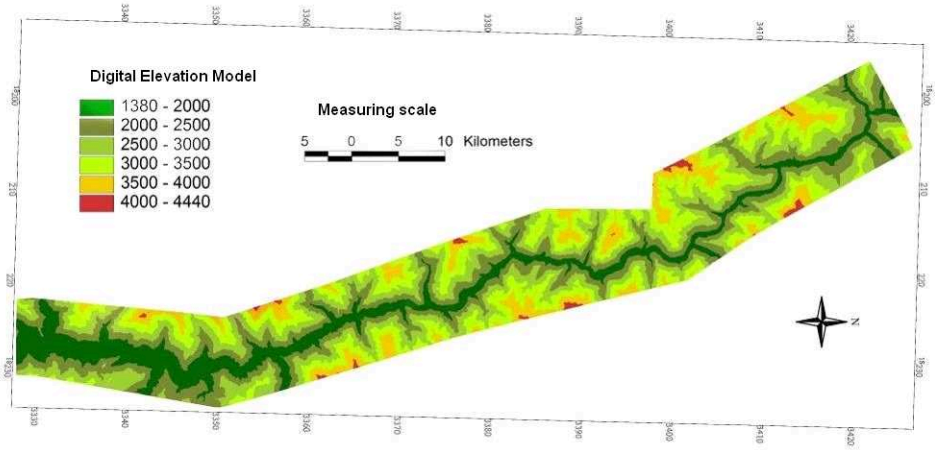

Fig.1 Elevation map of the study area

Features of remote sensing for landslide and debris flow monitoring

Data Preparation

Taking real possessive geologic situation of study area and accessibility of remote sensing data together into account, mainly phase characteristics and spatial resolution of remote sensing images are investigated. Take one scene from Landsat-7 ETM multispectral remote sensing data and three scenes from SPOT5 satellite panchromatic data. Then make fusion together. In this way, not only remaining SPOT 5 high spatial distribution rate but also obtaining ETM multispectral data rich tone and texture information, more useful information can be generated (see Figure 2 and Figure 3).

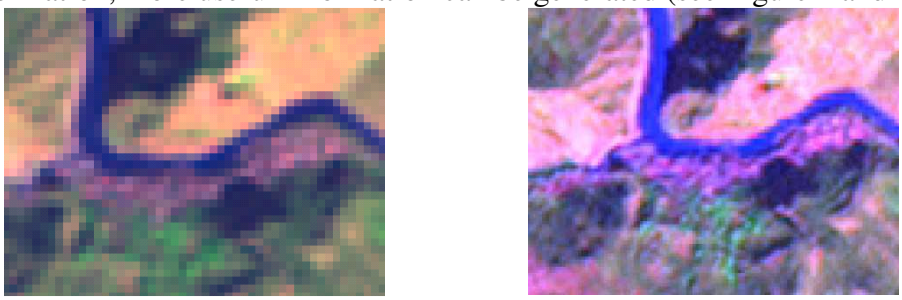

Fig.2 The before and after fusion map of ETM multi-spectral and panchromatic.(the left map show before fusion, the right after fusion)

Fig.3 The before and after fusion map of SPOT5Images and panchromatic of ETM Images(the left map show before fusion, the right after fusion)

Interpretation of landslide

Landslide always occurs with a wide range of ground movements, rock falls, deep failure of slopes and shallow debris flows. Due to difference of lithology, structure, activities, groundwater and landslide volume, landslides usually decline in different shapes. On SPOT images, landslide most typical shape is dustpan (tongue-shaped, like a V -shaped, irregular shape, etc.) flat shape, and sometimes one or two landslides can be found with complete parts such as scarp, stairs, tongue, sliding perimeter, landslide step and closed depression. The most obvious feature is chair-like

terrain landslide. On remote sensing images, these gullies show significant ribbon shade and hue difference. Based on these features, characteristics, depth of valley, and the distribution materials within ditch can be identified.

Interpretation of debris flow

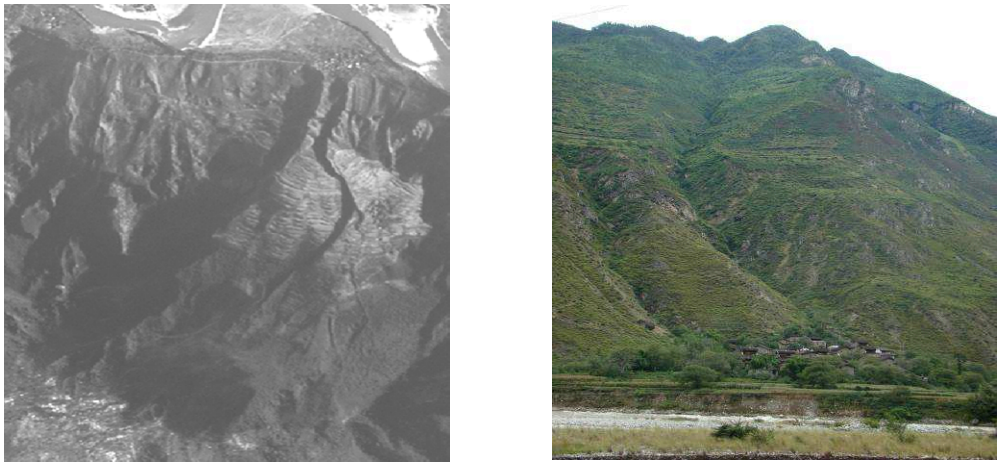

Fig.4 Panchromatic image of SPOT 5 and field photo in Bangji debris flow

Generally debris flow formation zone is with scoop-shaped, steep slope, serious rock weathering, and fully accumulated loose solid materials. On its circulation area, commonly ditch bed is straight, longitudinal slope smoother than its original formation area but steeper than its deposition area. Generally valley is relatively narrow and both-side surfaces of the hillside are stable. Accumulation area is located at valley outlet, longitudinal slope flat with obvious alluvial fan and pale shades. Just like Figure 4 shows.

Monitoring and early warning system designing

Landslide monitoring and early warning designing need to take the matter of the source, terrain features and start condition all into consideration. Instability displacement curve is often used to depict landslide trend, and critical rainfall is taken as important index to monitor the mudslides (Figure 5).

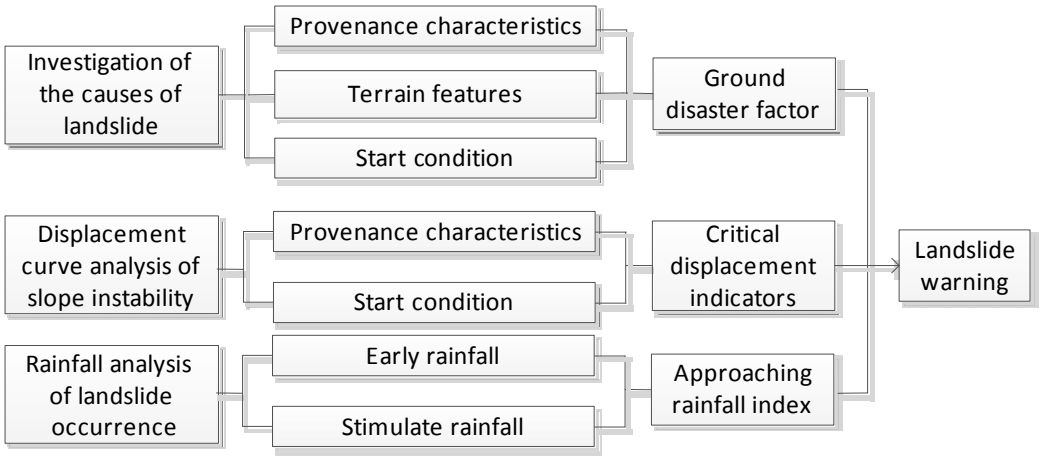

Fig.5 Monitoring and early warning technique route

Landslide monitoring and early warning

According to laws of landslide deformation generally divided into three stages, through studying roles of two factors tangent angle and acceleration [11, 12], here summarizes characteristics of slope cracks space, with taking the tangent angle and acceleration as basis for determining the landslide collapse.

General creep type landslide tangent angle can be divided into four stages: when the tangent angle is belong to 45º ~ 80º, collapse body is in its initial acceleration phase; when the tangent angle is from 80º to 85º, sliding masses is in initial acceleration phase; when the tangent angle is larger than 85º, slip sliding masses is in critical moments; generally when the tangent angle approximately equals with 89º, the body began to slide. Before landslide entering the temporary sliding stage, acceleration value is nearly 0. Once the critical stage, acceleration will increase sharply. According to these differences, the landslide monitoring and early warning can be achieved.

Debris flow monitoring and warning

Through research relationship between debris flow and average rainfall intensity & rainfall lasted time, here a formula to predict debris flow trend is established:

$$I = 72.216D^{-0.737} \quad (1)$$

where I is average rainfall intensity (mm/h); D is rainfall duration (h). This shows that when the rainfall time is longer, the corresponding average rainfall intensity would decrease and security cordon would fall. According this, a security line can be drawn to evaluate dangerous degree.

Conclusion

Danba-Kangding 500kV double circuit transmission line project is across Kangding county, where landslides and debris flows occurs frequently. For quickly identify possible points of geological disasters occurring and help transmission lines designers decide locations of power towers, this paper analyzes the characteristics of landslide and debris flow on remote sensing images. Combining with indoor remote sensing interpretation and field survey data, we can determine the basic characteristics of the geological disasters, and establish early warning and forecasting models. This greatly accelerates speed to select a proper location for power tower and can be a reference for similar work.

References

[1] Huang RQ, Li WL. A Study on the Development and Distribution Rules of Geo-hazards Triggered by “5.12”Wenchuan Earthquake [J]. Science in China (Edition E), 2009a, 52(4): 810-819.

[2] Huang RQ, Li WL. Analysis of the geo-hazards triggered by the 12 May Wenchuan Earthquake, China [J]. Bull of Engineering Geology and the Environment, 2009b, 68(2): 363–371.

[3] Huang RQ, Li WL. Research On Development And Distribution Rules Of Geohazards Induced By Wenchuan Earthquake On 12th[J]. Chinese Journal of Rock Mechanics and Engineering, 2008,27(12):2585-2592.

[4] Huang RQ, Li WL. Fault effect analysis of geo-hazard triggered by wen-chaun earthquake [J]. Journal of Engineering Geology, 2009,17(1):19- 28.

[5] Parker RN, Densmore A, Rosser NJ, Michele M, Li Y, Huang RQ, et al. Mass wasting triggered by the 2008 Wenchuan earthquake is greater than organics growth [J]. Nature Geoscience, 2011, 4 (2):449–452.

[6] Tang C, Zhu J, Li WL. Rainfall triggered debris flows after Wenchuan earthquake [J]. Bull Eng Geol Environ, 2009, 68(4):187–194.

[7] Tang C, Liang JT. Characteristics of debris flows in Beichuan epicenter of the Wenchuan earthquake triggered by rain storm on sep-tember[J]. Journal of Engineering Geology, 2008,16(6):751-758.

[8] Xie H, Zhong DL, Zhang JS. Debris Flow in Wenchuan Quake-hit Area in 2008[J]. Journal of Mountain Science, 2009,5(4):501-509.

[9] Chang M, Tang C, Fu R. Application of mike11 model in water diversion and flushing pollutants of urban river network in sihong city[J]. Water Resources and Power, 2012,30(8):103-106.

[10] Feng HF, Zhang ZM, Qian JP. Disaster characteristics and countermeasures of Huili county, Sichuan geological[J]. The Chinese Journal of Geological Hazard and Control, 2007,18(4):111-114.

[11] Xu Q, Liu HX. Large-scale shaking table test study of acceleration dynamic responses characteristics of slopes [J].Chinese Journal of Rock Mechanics and Engineering, 2010,29(12):2420-2428.

[12] Liu HX, Xu Q, Fan XM. Influence of ground motion intensity on dynamic response laws of slope accelerations [J]. Rock and Soil Mechanics, 2012,3(5):1357-1365.

Advanced Materials Research Vols. 986-987 (2014) pp 1651-1654

doi:10.4028/www.scientific.net/AMR.986-987.1651

Research of Improved On-line Power Flow Method

Hai BAO[1, a], Ling WANG[2, b], Yulong CHEN[1, c]

[1] North China Electric Power University, Beijing, 102206, China

[2]State Grid Liaoning Electric Power Company Limited Benxi Electric Power Supply Company, Benxi, 117000, China

[a]email:hdbh@vip.sina.com, [b]email:cyl_icepee@126.com, [c]email:chenyulong_2012@163.com

Keywords: Reactive Power; On-line Power Flow; Convergence

Abstract. Based on measurement accuracy of reactive power lower than the accuracy of active power and voltage magnitude, this paper proposes an improved on-line power flow method. Through simulation, compared with the conventional power flow, this method improves the accuracy of the calculation results and also has obvious advantages on the convergence rate. Finally, the article analyzes the reasons for this situation.

Introduction

Power flow calculation is the basis of reasonable, reliable and economy of power system operation and planning, but also is the basis of many non-stationary problems of power system. Since the power flow calculation problems appeared, technology is already quite mature by the descendants continue to improve [1-7]. At the same time, it has been widely used. Three types of nodes are considered in conventional power flow calculation, including *PQ* nodes, *PV* nodes and slack nodes. And the current measurement technique can ensure the measurement accuracy of active power and voltage magnitude to the thousandth. Therefore, the measurement accuracy of reactive power directly determines precision of power flow calculation results.

Measurement of Reactive Power

Before the mid 90's in last century, the measurement of active power has reached a high level in China, but the measurement level of reactive power is very low. A large number of reactive watt-hour meters were in 2 level following, which used measure structure of induction system [8]. With the rapid development of microelectronics technology and electrical measurement techniques, the measurement level of reactive power has been improved to some extent. At present, the measurement methods of reactive power mainly include the definition and indirect method.

(1) Reactive power measurement based on definition

Reactive power is defined as follows

$$Q = UI\sin\varphi \tag{1}$$

where Q is reactive power; U and I are voltage and current RMS; φ is power factor angle. Based on this definition, there are formula method, phase shifting method and integral method for measuring reactive power [9]. These methods have a higher accuracy only when the voltage and current is single frequency sine wave. Otherwise, these will bring significant errors.

With the new energy power generation and a great amount of non-linear load access power system, the traditional sine waveform has distorted and frequency has changed. It results in greater error of reactive power measurement, which based on above methods.

(2) Indirect measurement

Reactive power can also be calculated by apparent power and active power, the calculation formula is as follows

$$Q = \sqrt{S^2 - P^2} \tag{2}$$

where Q is reactive power; S is apparent power; P is active power. For 1 grade watt-hour meter that measure reactive power by this method, in order to prevent the maximum error occurrence, only when the power factor is less than 0.5774 does the accuracy of reactive power achieve to 2% [10]. However, the power factor is generally 0.85 or more in practical power system, and the measuring error of reactive power that uses this method to measure is relatively large.

Principle of Improved On-line Power Flow Method

Assume that there are n nodes in the system, where the 1~m node is PQ node, the m+1~n-1 node is PV node, the n node is slack node, and then Newton-Raphson iterative formula is as follows

$$\begin{bmatrix} \Delta P \\ \Delta Q \end{bmatrix} = J \begin{bmatrix} \Delta\theta \\ \Delta V / V \end{bmatrix} = \begin{bmatrix} H & N \\ M & L \end{bmatrix} \begin{bmatrix} \Delta\theta \\ \Delta V / V \end{bmatrix} \tag{3}$$

where J is Jacobian matrix; $\Delta\theta$ and $\Delta V/V$ are correction of node voltage phase angle and amplitude; active power changes(ΔP) and reactive power changes(ΔQ) can be calculated by formula (4) and formula (5)

$$\Delta P_i = P_i - V_i^{(0)} \sum_{j=1}^{j=m} V_j^{(0)} (G_{ij} \cos\theta_{ij} + B_{ij} \sin\theta_{ij}) - V_i^{(0)} \sum_{j=m+1}^{j=n} V_j (G_{ij} \cos\theta_{ij} + B_{ij} \sin\theta_{ij}) \tag{4}$$

$$\Delta Q_i = Q_i - V_i^{(0)} \sum_{j=1}^{j=m} V_j^{(0)} (G_{ij} \sin\theta_{ij} - B_{ij} \cos\theta_{ij}) - V_i^{(0)} \sum_{j=m+1}^{j=n} V_j (G_{ij} \sin\theta_{ij} - B_{ij} \cos\theta_{ij}) \tag{5}$$

and the element H of Jacobian matrix can be obtained by formula (6a) and formula (6b)

$$H_{ij} = V_i^{(0)} V_j^{(0)} (G_{ij} \sin\theta_{ij} - B_{ij} \cos\theta_{ij}) \tag{6a}$$

$$H_{ii} = -V_i^{(0)} \sum_{\substack{j=1 \\ j\neq i}}^{j=m} V_j^{(0)} (G_{ij} \sin\theta_{ij} - B_{ij} \cos\theta_{ij}) - V_i^{(0)} \sum_{j=m+1}^{j=n} V_j (G_{ij} \sin\theta_{ij} - B_{ij} \cos\theta_{ij}) \tag{6b}$$

The measurement error of reactive power is large from the previous analysis. That is, there is a larger difference between Q_i and actual operation, it causes the results of on-line power flow is not accurate enough. In order to obtain high accuracy results, we can use voltage amplitude, which has a higher measuring accuracy, replaces reactive power that has a lower measuring accuracy. That is to say all the load nodes as generator nodes, then calculating on-line power flow. So the formula of improved on-line power flow becomes

$$\Delta P = H \cdot \Delta\theta \tag{7}$$

where the active power changes(ΔP) can be calculated by formula (8)

$$\Delta P_i = P_i - V_i \sum_{j=1}^{j=n} V_j (G_{ij} \cos\theta_{ij} + B_{ij} \sin\theta_{ij}) \tag{8}$$

H is Jacobian matrix of improved on-line power flow, and it can be obtained by formula (9a) and formula (9b)

$$H_{ij} = V_i V_j (G_{ij} \sin\theta_{ij} - B_{ij} \cos\theta_{ij}) \tag{9a}$$

$$H_{ii} = -V_i \sum_{\substack{j=1 \\ j\neq i}}^{j=n} V_j (G_{ij} \sin\theta_{ij} - B_{ij} \cos\theta_{ij}) \tag{9b}$$

Procedure of Improved On-line Power Flow

1) Construct admittance matrix.

2) Set initial value ($\theta_i^{(0)}$)of each node voltage phase angle.

3) Initial value of voltage phase angle are used into the power equation, then calculate $\Delta P_i^{(0)}$

4) Obtaining the new Jacobian matrix elements ($H_{ij}^{(0)}$) using the initial value of voltage phase angle.

5) Solving the equation (4), and get each node correction ($\Delta\theta_i^{(0)}$).

6) Calculating new voltage value of each node, that is $\Delta\theta_i^{(k+1)}=\theta_i^{(k)}+\Delta\theta_i^{(k)}$.

7) If the absolute value of each node correction is less than the convergence accuracy, the iterative is convergent, output the result and the end of computing. Otherwise, go to step 3).

Example Analysis

This paper tested the IEEE9, 30, 57,118 standard systems. The proposed method compared with conventional power flow method, the results were shown in table 1 ($\varepsilon=10^{-5}$).

TABLE 1 Comparison of results

System nodes	Conventional method		Improved method	
	Convergence time(s)	Number of iterations	Convergence time(s)	Number of iterations
9	0.0062	4	0.0050	3
30	0.0081	4	0.0059	3
57	0.0152	3	0.0116	3
118	0.0537	5	0.0289	5

As seen from the table 1, under the same convergence precision, the convergence time of on-line power flow that is proposed in this paper is reduced, the number of iterations is also less than or equal to the conventional power flow's.

The reasons for the above phenomenon are mainly in the following two aspects:

1) The equation (3) shows that the Jacobian of conventional power flow is a matrix of order $n+m-1$; and the equation (7) shows that the Jacobian of improved on-line power flow is a matrix of order $n-1$. Thus, the Jacobian of improved method is less order m than that of conventional method. This is one of reasons why the convergence time is reduced.

2) The formula (4), (6a), (6b), (8), (9a) and (9b) shows that the ΔP and H, which are calculated based on this voltage amplitude, are closer to a real situation than that are calculated based on voltage of its own set in the conventional power flow. This is also one of the reasons why the convergence time is reduced and the number of iterations is less than or equal to the conventional power flow.

Conclusion

Based on reactive power measurement error is large, improved on-line power flow method is presented in this paper. Proven by MATLAB programming, this method has good feasibility. The method has an obvious advantage on the convergence rate compare with the conventional power flow method.

References

[1] Ward B, Hale H W. Digital computer solution of power-flow problems [J]. IEEE Trans. on Power Apparatus and Systems, 1956 75 (6) 398-404.

[2] Van J E. Iteration methods for digital load flow studies [J]. IEEE Trans. on Power Apparatus and Systems, 1959 78 (3) 583-586.

[3] Van J E, Griffin J H. Elimination methods for load-flow studies [J]. IEEE Trans. on Power Apparatus and Systems, 1961 80 (3) 299-302.

[4] Ronald M, Guffin. A computer for solving linear simultaneous equations using the residue number System [J]. IRE Trans. on Electronic Computers, 1962 11 (2) 164-173.

[5] Brown H E, Carter G K, Happ H H, Person C E. Power flow solution by impedance matrix interative method [J]. IEEE Trans. on Power Apparatus and Systems, 1963 82 (65) 1-10.

[6] Tinney W F, Hart C E. Power flow solution by Newton's method [J]. IEEE Trans. on Power Apparatus and Systems, 1967 86 (11) 1449-1460.

[7] Stott B, Alsac O. Fast decoupled load flow [J]. IEEE Trans. on Power Apparatus and Systems, 1974 93 (3) 859-869.

[8] Ma Liren, Fu Shiji, Peng Zhonghua.New techniques for reactive energy measurement [J]. Electrical Measurement & Instrumentation, 2002 39 (434) 23-26.

[9] Qin Haifeng, Zhou Hao. Summary on reactive power in power system [J]. Electrical Measurement & Instrumentation, 2007 44 (493) 5-9.

[10] Liu Yuhuai, Ye Yi, Liu Jingao. The error of three phase reactive power measurement methods [J]. Electrical Measurement & Instrumentation, 2003 40 (453) 28-31.

Advanced Materials Research Vols. 986-987 (2014) pp 1655-1660

doi:10.4028/www.scientific.net/AMR.986-987.1655

Study on A New Type of Electric Larceny Using Half-wave Rectifying Method

Ji XIAO[a], Fuping ZHAO, Yingying CHENG, Feng ZHOU[b], Rongmei LIU

State Grid Chongqing Electric Power CO. Electric Power Research Institute, Chongqing, 401123, China

[a]email: xiaoji114@163.com, [b]email: zfocus@foxmail.com

Keywords: Transformers; Secondary Circuit; Half-wave Rectification; Electric Larceny

Abstract. A new electricity larceny case is proposed in this paper, which using half-wave rectifying method. According to the fact that users consumption varies greatly, analyzing the phenomena discovered and stealing principle. Then simulating the method of electricity larceny in the laboratory, and dissecting the error of the half-wave rectifier stealing mode under different current and power factor. Finally, proposing preventive measures and proposals targeted.

Introduction

At present, with the rapid development of new technology, the means of electric larceny to develop in the direction of high technology and high concealment too, it brings difficulties to the work of anti electricity larceny. I recently found a behavior of electric larceny which use a half-wave rectifier (current transformer secondary circuit in series with the diode), through the measurement and analysis of the measuring metrologists. According to the measurement laws and regulations, this kind of behavior has been halted and processed. Outlaws electricity stealing behavior has not only caused huge economic losses to the country, but also seriously damaged the legitimate rights and interests of power supply enterprise and disrupted the normal order of power supply and posed a serious threat to the safe use of electricity. It brings to enormous bane to the society [1-7]. This paper provides an in-depth analysis of this case and put forward specific measures and suggestions to prevent electricity larceny.

Phenomena

When the copy nuclear income person analyzed the consumption, he found that the electricity consumption of a customer plummeted in the month, and fall range estimated at more than 80%. The customer's watt-hour meter and mutual inductor installed in 10kV metering cabinets, the watt-hour meter adopted three-phase and three wire connection mode. the measuring metrologists came to the scene to check the measuring device and discovered that indicating instrument displayed measurement device measuring circuit current was approximately 2.5A, but in the clamp multimeter and calibrator measured loop current was about 1.2A, and a manufacturer Q LCD multifunction power meter displayed the current was approximately 0.4A. Metrology personnel used the watt-hour meter on-site verification for the watt-hour meter error examination, it displayed error is about 84%. Then reused the waveforms and harmonic examination of the calibrator respectively to check the measuring circuit and the measuring loop wave, we found that there was missing of measure loop current waveform (as shown in Fig.1), measuring loop current and voltage waveforms were normal (as shown in Fig.2).

Can be seen from Fig.1, the secondary circuit of three-phase voltage waveform of A, B and C are normal. The secondary circuit of A and C phase current waveforms are missing half, and the current waveform happen up; Field measurement circuit waveform shows in Fig.2, A, B, C three-phase voltage and current waveforms are normal. Field staff exchanged the multi-function Watt-hour meter of Q-manufacturer for the mechanical energy meter of P-manufacturer, then they used the field calibrator for error checking again, it showed the error is about -0.8%. Through the above phenomenon, there was an apreliminary inspection that the client steals electricity. With a half wave

rectifier diode which was strung into the current in the secondary circuit. We checked the secondary circuit after power outage and found that the actual situation match with the speculation [8-10].

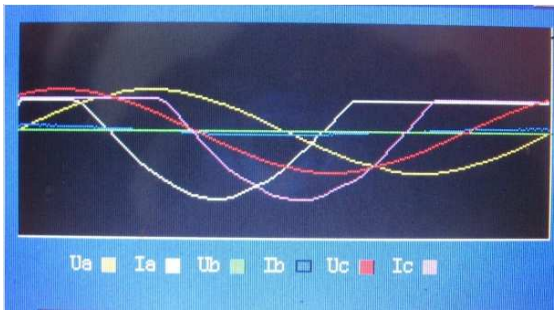

Fig.1. Field metering circuit waveforms

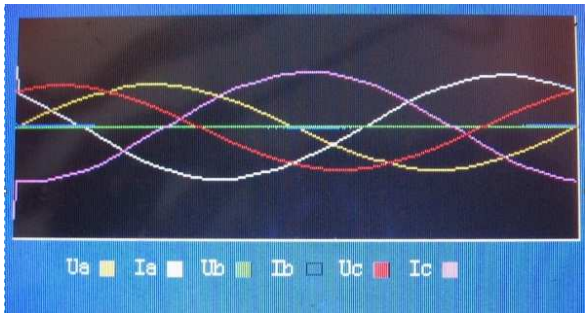

Fig.2. Field measurement circuit waveforms

The principle of electric larceny

The principle scene electric larceny

Electric energy metering system schematic diagram of power user is shown in Fig.3. The low voltage and current signals are introduced into the three-phase three wire active electric energy meter by secondary circuit, which was converted from the system power supply voltage through the voltage transformer PT and the current transformer CT. Measurement technician found that the electricity consumption of the customer plummeted in the month. Through the measurement and analysis, and checking the secondary circuit after power outage, it was confirmed that the client stole electricity through the diodes D1 and D2 which were strung into the current in the secondary circuit, as shown in dotted lines in Fig.3.

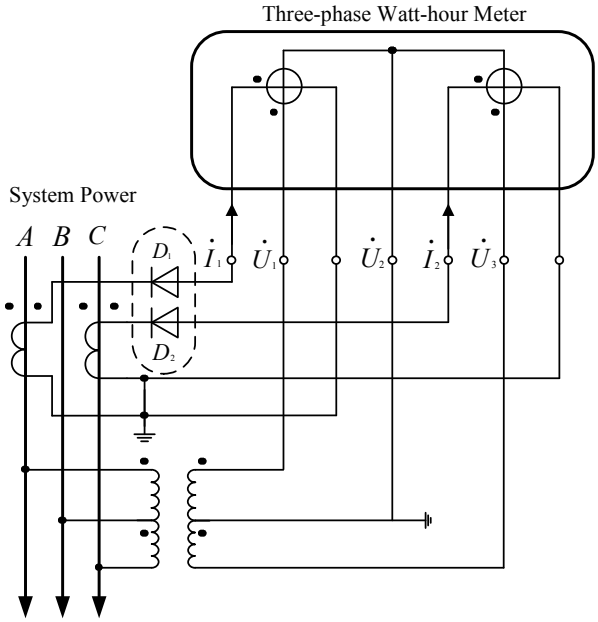

Fig.3 The schematic diagram of the power user electric energy metering system

Mathematical model analysis

Set AC current function is $E(t)=E\sin\omega t$, the Fourier series expression after a half-wave rectifier is:

$$E(t)=\frac{E}{\pi}+\frac{E}{2}\sin\omega t+\frac{2E}{\pi}\sum_{k=1}^{\infty}\frac{1}{1-4k^2}\cos 2k\omega t \tag{1}$$

From equation (1) can be seen, if we do not consider the impact of the temperature coefficient of resistance and the forward voltage drop of the diode, the frequency of current valid value is 0.5 times without the diode in the current in the secondary circuit when the current secondary circuit use half-wave rectifying method. Because the three-phase secondary circuit voltage of the metering

device are normal, both A and C phase of the current secondary circuit are strung into diodes. So, in theory, it shall be the 50% of actual electricity consumption after watt-hour meter's recording halving. But as a result of the multi-function watt-hour meter sampling element cannot correct sampling and secondary voltage drop and other factors, actually the watt-hour meter less power does not accord with 50%. Here, the author will simulate the site conditions in the laboratory experiment, design and verification of various electric energy meter error performance at different values of current and power factor.

Laboratory analysis

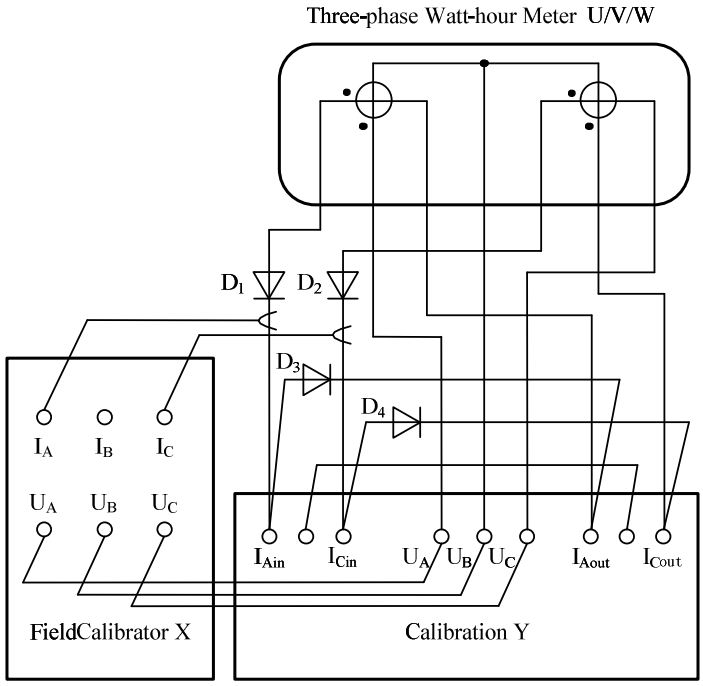

Fig.4 The experimental schematic diagram of the half- wave rectifier electric larceny

In order to analyze the measurement error accurately, we simulated the situation of electric energy measurement on site in the laboratory based on the way of the electricity consumers on-site [11-15]. The experiment principle diagram as shown in Fig.4, and the experimental analysis as follows:

(1) The experimental equipment and devices

A U manufacturer's three-phase three-line multifunction Watt-hour meter; a V manufacturer's three-phase three-wire multifunction Watt-hour meter; a W manufacturer's three-phase four-wire mechanical electric energy meter; an electric energy meter site calibrator X; a Three-phase electrical energy meter calibration Y; a multimeter Z and four diodes. The electric energy meter errors were qualified by testing indoor and experimental devices worked properly and the errors were qualified.

(2) The mode of wiring

Voltage: U, V W, X, Y of the three-phase voltages is respectively connected in parallel.

Current: B phase of the three-phase electrical energy meter calibration Y and the three-phase four-wire mechanical electric energy meter W are connected in series (without U, V), A, C-phase current of the three-phase electrical energy meter calibration Y and the electric energy meter U, V, W are respectively connected in series. And there have two diodes D1 and D2 which are strung into A, C-phase current in the secondary circuit, and the directions of the diode conduction are same. In order to prevent reverse cut-off state open when the current loop of the electric energy meter calibration therefore, there two diodes D3 and D4 are strung respectively between the current into the terminal and the current export terminal (without meter) of the A, C-phase current of the three-phase electrical energy meter calibration Y, and D4, D3's conduction direction opposite to the D1 and D2's. Electric energy meter field calibrator X, A, C-phase current pliers clamp meter into

the current loop to monitor A, C-phase current waveform, and the B-phase pliers of the field calibrator X is connected to the B-phase current loop of the electric energy meter W when using field calibrator X to inspect the error of the mechanical energy meter W.

(3) Calibration parameter setup: three-phase three-wire method (the B-phase current of the calibration Y will come up in this way

(4) Experimental data: as shown in Tab.1.

Tab.1. Laboratory and field data

Laboratory / field	Watt-hour meter		The parameters of calibration Y			Displayed value of field calibrator X		Displayed value of multimeter Z	Displayed value of Watt-hour meter	Displayed value of error (%)		The total power shown in field calibrator X / calibration Y *100(%)
			Output current(A)	Cosφ	The total power(W)	Current(A)	The total power(W)	Current(A)	Current(A)	Calibration Y	Field calibrator X	
Laboratory	Diode access A, C phase	U	2.5	1.0	433.00	1.406	216.780	1.297	0.74	-82.65	/	50.06
		V							0.305	-94.69	/	/
		W					286.009		/	-35.36	0.795	/
		U	2.5	0.5L	216.50	1.356	109.346	1.289	0.75	-75.27	/	50.51
		V							0.308	-83.43	/	/
		W					/		/	-33.02	0.969	/
		U	1.0	1.0	173.20	0.547	86.753	0.497	0.48	-63.41	/	50.09
		V							0.315	-84.21	/	/
		U	1.0	0.5L	86.60	0.545	43.933	0.498	0.46	-34.50	/	50.73
		V							0.315	-61.61	/	/
		U	1.5	1.0	259.80	0.865	130.453	0.757	0.59	-72.64	/	50.21
		U	0.75	1.0	129.90	0.410	65.128	/	0.38	-57.2	/	50.14
		U	0.3	1.0	51.96	0.164	26.048	/	0.16	-35.22	/	50.13
Field		Q	2.5	/	/	1.2	/	1.2	0.4	/	-84	/
		P	2.5	/	/	1.2	/	1.2	/	/	-0.8	/

It can be seen from Tab.1 when the half wave rectification occurs in the current loop:

(a) The meter less power or error (displayed value of error of calibration Y) may be different with a multi-function Watt-hour meter under load current and power factor in different cases.

(b) Calibration error is different from the error of electric energy meter site calibrator measured. Only the calibration error can reflect the undercount power accurately, the error of site calibrator can't serve as the basis for refundable power consumption.

(c) The power which is not measured by multifunctional electric energy meter is not always more than half of the total power, and there may be less than half of the total power.

(d) The power which is not measured or error of the meter may be different between different multi-function watt-hour meters.

(e) The error of mechanical energy meter is within the scope of qualified in case of the power which is not measured by mechanical energy meter is more than half of the total power (As the experiment mechanical energy meter access to the B-phase full-wave current in the experiment, the error displayed by calibration Y be around -33% in accordance with the wiring of three-phase four-wire).

All kinds of multi-function watt-hour meter in different current or power factor condition in Tab.1, errors of calibrations are different is because of these meter does not sampled correctly. Diode in the cut-off state, for causing the current transformer secondary open the influence on the error of the transformer do not discuss in this paper.

Conclusion and recommendation

At present, the method of half-wave rectification for electricity larceny increasingly, which is mainly aimed at the transformer connected meters. Using the current mainstream on-site checking instrument products for watt-hour meter on-site inspection, the error of electronic watt-hour meter will seriously negative, and the error does not give a true reflection of power which is not measured. For the mechanical energy meter, when the customer exist the electricity larceny behavior with a half-wave rectifier, the error of the field calibrator tested displays normal.

As a safeguard against electricity larceny by a half-wave rectifier, we specially put forward the following recommendations:

(1) We must check the current and voltage waveforms when the measurement personnel carry out the electric energy meter site inspection work, which can use the on-site checking instrument measurement functions to check. If necessary, we should be compared the current and the voltage value of the watt-hour meter with other energy meters and measuring devices.

(2) When the waveform anomalies is found in the site inspection and required further verification, the sampling locations of site calibrator's current and voltage should be selected at the measurement loop or other possibility which can reflect the secondary current and voltage values properly to validate, and the workers must compare the error results and suggest the power supply bureau to equip with hand-held electricity tester which has harmonic detection function to improve the technology.

(3) We should take effective measures immediately in accordance with the clues of electricity larceny to investigate if we found waveform deletion on-site inspection, and promptly informed of the situation to the relevant departments.

(4) The anti-stealing electric power is action of all staff, the field measurement and supervisory personnel should be good at discovering and analyzing the abnormal situation, and should also be familiar with the customer situation, strengthening power consumption analysis, finding electric larceny suspicious behavior.

(5) The related personnel should be familiar with the various functions of multifunction meter, especially the load curve. Load curve data recorded typically contains a certain time interval of current, voltage, value of power, the bottom of the equivalent (with time scale) and the recording of the history time can be kept several months. We have to enhance the analysis of load curve if there any abnormal condition happened, which is very helpful for judging when the abnormal occurs and taking actions in time.

References

[1] GUO Li-cai, PENG Zhi-wei, FAN Qiang. A survey of electric energy metering and countermeasures to electric power stealing [J]. High Voltage Apparatus, 2010, 46(5):86-88.

[2] ZHAN Qiao-song. The principle and application of the tamper preventing for the electronic single-phase electrical energy meter [J]. Electrical Measurement & Instrumentation, 2006, 43(7):18-19.

[3] SHAO Qiang, LI Dan, LIU Xiao-xiang. The research and application of single-phase prevent electricity from theft watt-hour meter's principle [J]. Electrical Measurement & Instrumentation, 2009, 46(7):59-62.

[4] NA Dong-sheng. Investigate, collect evidence and crack down electricity stealing activities according to law [J]. Power Demand Side Management, 2006, 8(5):54-55.

[5] HU Lin, YAN Yun-chang, HUANG Jing, et a1. Research on new real-time systemic anti-electricity filching system [J]. Power Demand Side Management, 2006, 8(2):47-48.

[6] Liu Yang-li, Teng Zhao-sheng, Zhou Liang-zhang, et a1. Anti-steal new technology research based on single-phase watt-hour meter [J]. Computer Measurement & Control, 2008, 16(12):1996-1998.

[7] HAN Gu-jing, YIN Xiao-gong, QIN Liang, et a1. A novel technique of preventing electricity-stealing in current method for electric power measuring equipment [J]. Electrical Measurement & Instrumentation, 2007, 44(10):29-32.

[8] QIN Jun, PAN Xiao-jun. On rebuild of energy metering [J]. Electrical Measurement & Instrumentation, 2007, 44(1):18-20.

[9] LI Tao, DU Xiao-ping, LIU Huan-guang. Realization of electricity stealing prevention in distribution transformer monitoring system [J]. Electric Power Automation Equipment, 2007, 27(11): 95-97.

[10] BU Zheng-liang, YIN Xiang-gen, TU Guang-yu. Development of HV watt-hour meter [J]. Electric Power Automation Equipment, 2006, 30(19): 89-93.

[11] ZHAO Bing, Lii Ying-jie, ZHOU He-ping. Design of a new anti- stealing electricity device [J]. Power System Protection and Control, 2009, 37(23):116-119.

[12] ZHOU Wei, ZHU Rui-De, WANG Jin-quan. GSM -based monitoring and control system against electricity stealing [J]. Electric Power Automation Equipment, 2004, 24(2):64-66.

[13] ZHANG Yi-hui, MA Yan-feng, HAN Ping-jun, et a1. Theft proof device for power load management terminal [J]. Electric Power Automation Equipment, 2009, 29(11):132-135.

[14] QIN Chun-bin, LIANG Gang. Design of a shunt-current electric larceny detecting monitoring in electric power metering system [J]. Journal of Henan University (Natural Science), 2009, 39(4):416-419.

[15] QIN Chun-bin, ZHAO Jian-jun, ZHANG Lei, et a1. Analyzing and modeling for shunt current electric larceny of electric power metering system [J]. Electrical Measurement & Instrumentation, 2009, 46(2):39-42.

Advanced Materials Research Vols. 986-987 (2014) pp 1661-1665

doi:10.4028/www.scientific.net/AMR.986-987.1661

Study on Linearity of Impulse Voltage Divider

Zhaozhi LONG [1, a], Fei LU[2,b], Wenting LI[1,c]

[1] Measurement Research Institute, China Electric Power Research Institute, Wuhan, China

[2] Hubei Electric Power Research Institute, Wuhan, China

[a]longzhaozhi@epri.sgcc.com.cn, [b]lufei@qq.com, [c]liwenting@epri.sgcc.com.cn

Keywords: Linearity; Impulse Voltage Divider; Impulse Voltage generator; Deviation; Charging Voltage

Abstract. The uncertainty contribution related to linearity shall be considered in the calculation of measurement uncertainty when using the impulse voltage measuring system. Under the condition that the national standard is not yet established at present, the paper proposed an experimental method to measure the linearity of 600kV damped capacitive impulse divider(HCR600). The paper used low voltage resistance divider R200S to measure the linearity of generator, and obtained the linearity curve. With the increase of charging voltage, the linearity of divider can be obtained by measuring the charging voltage of impulse voltage generator precisely and its ratio of indicating value of the sample divider HCR600 after corrected. The result shows that the linearity of HCR600 decreases from +0.4% to -0.8%; the maximum difference between positive polarity and negative polarity is 0.14% and the linearity of negative polarity is superior to that of positive polarity. Besides, the paper used a 500kV resistance divider(SMR 7.7/ref500) calibrated by PTB to compare with HCR600, and obtained the linearity curve. By comparison, two curves show a good agreement, the maximum difference between them is 0.15% at the same voltage. The result shows that the method proposed in the paper can be used to measure the linearity of divider accurately. It also can be used as experimental verification in the process of the national standard establishing and to calibrate the ultrahigh voltage impulse voltage measuring equipments when equipments satisfy some requirements.

Introduction

With the continuous development of UHV transmission technology, rated voltage level of transmission line is rising. In order to meet the withstand voltage test requirements of the equipment such as transformers, transformer, capacitor, the rated voltage of impulse voltage generator and measuring system is also greatly increased. Electric power research institute has established 3600 kV impulse voltage measuring system, UHV AC test base and DC test base even have established 7200 kV impulse voltage test measuring system [1-3]. The accuracy of the results of withstand voltage test can directly influences the safety of power equipment. Traceability is an effective method to guarantee the accuracy of the measuring value, through uninterrupted chains with prescribed uncertainty, make the parameters of voltage and time traceable to the national standard or international standard [4-5]. So manufacturers pay more attention to quantity traceability of measurement equipment and calibrate the equipment at regular intervals.

United States, Australia, Germany, Japan have improved impulse voltage measuring system and established standard measuring system voltage with expand uncertainty of 0.5% [6-10]. At present impulse voltage standard measuring system is not established and impulse voltage quantity traceability still stay on the theoretical analysis stage in China.

Linearity is the one of the most important characteristics of impulse voltage divider. The uncertainty contribution related to linearity shall be considered in the calculation of measurement uncertainty when using the impulse voltage measuring system. The paper try to obtain the linearity of the 600kV damped capacitive impulse divider(HCR600) in the test by measuring the charging voltage of impulse voltage generator.

Method Analysis

The scale factor of the measuring system is not a constant value over the whole voltage range due to the nonlinearity of the measuring system. In IEC60060-2 [5], the linearity test is described as "To compare the scale factors at five points equally spaced voltages between the operating ranges". There are four methods to measure the linearity of impulse voltage divider.

(1) The preferred method is comparison measurement by comparison with a higher class reference measuring system, however, such a system does not exist for comparison with a national-standard-class system.

(2) Comparison with the output of an electric-field measuring instrument. The measuring system can be checked against an electric-field responding measuring system which is so located in such a way that it measures a field proportional to the voltage being measured. The electric-field measuring system shall provide a response suitable for the type of voltage being measured. The method is only can be used in the case of no corona, even the accuracy of electric-field measuring instrument is very low, about 1%.

(3) For a voltage divider consisting of several high-voltage units, the linearity test can be performed respectively. The method requires that the divider is not significantly affected by corona and other influences at the upper limit of the assigned measurement range.

(4) Comparison with a standard sphere gap. The complete linearity test shall be made within sufficiently short time that atmospheric conditions do not change and hence corrections need not be used. For higher voltage levels, larger sphere gap is needed. It is impossible to find so big sphere gap.

(5) Comparison with input voltage of a linear high voltage generator. There is an alternative linearity test which utilizes the charging voltage of an impulse voltage generator (IG). The linearity of divider obtained by this method contain linearity of IG. If the linearity of an IG is known by any measures, we can obtain the linearity of the impulse divider. In this paper, the linearity of 600kV damped capacitive impulse divider(HCR600) is obtained by this method.

Experiment

The linearity of an IG. A reference DC divider combined with a digital voltmeter(HP 34401A), which is traceable to the national-standard DC voltage, was connected to the charging point of the IG. A 200 kV impulse voltage divider R200S with ignored nonlinearity was connected to the fourth stage of the IG. The charging voltage plots were 15kV, 23kV, 33kV, 42kV, 53kV in sequence. The nonlinearity of IG was obtained by calculating the ratio of output peak voltage and charging DC voltage at different plot. Fig. 1 shows the deviations of the output impulse voltage of the IG from linearity, dependent on the charging voltage. Each plot shows the mean value and the standard deviation for 20 measurements.

The linearity of HCR600. Then keeping the same connection scheme but using all 12 stages of IG, the linearity of HCR600 was measured. The charging voltage plots were 15kV, 23kV, 33kV, 42kV, 53kV in sequence. The linearity of whole system(HCR600 and IG) was obtained by calculating the ratio of output peak voltage of HCR600 and charging DC voltage at different plot. Fig. 2 shows the measurement results. The linearity of HCR600 was obtained by taking account of the of IG, shown in Fig. 3. In the final result of Fig. 3, the same tendency is seen in the both polarities, which seems reasonable. The maximum deviation is -0.8 %.

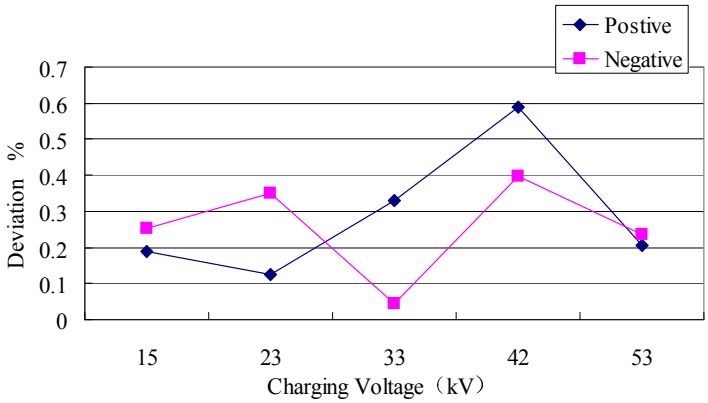

Fig.1 Linearity test results of impulse generator(IG)

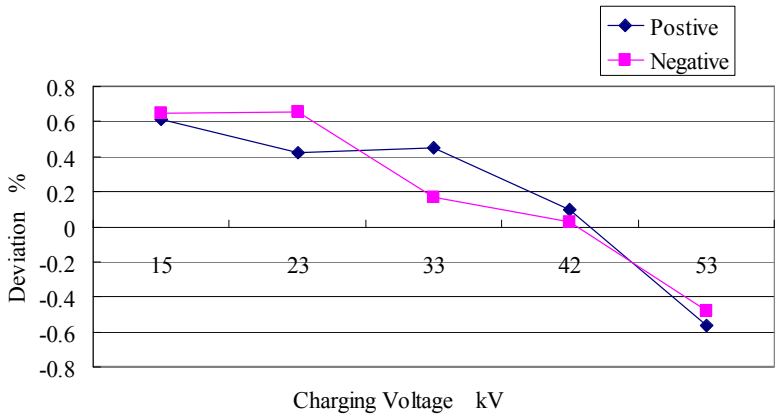

Fig.2 Linearity test results of the whole system(HCR600 and IG)

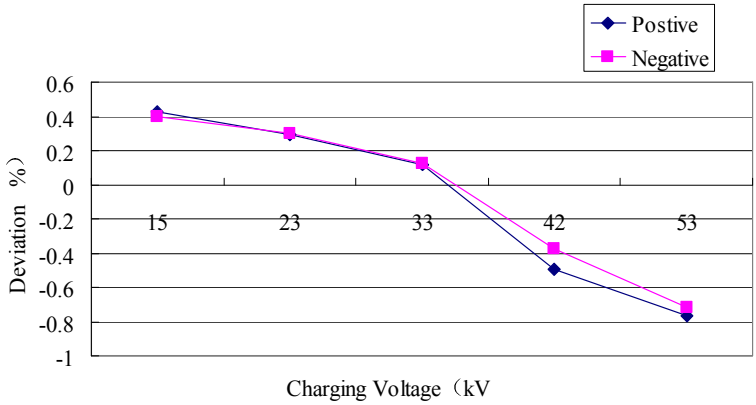

Fig.3 Linearity test results of the HCR600

Measurement Verification

To confirm the effectiveness of the above technique, a linearity test was carried out on HCR600 by using the 500kV impulse divider， This divider(SMR 7.7 ref /500) is a shielded resistive divider and its nonlinearity evaluated by PTB is 0.1 %. Comparison of two divider, the nonlinearity of HCR 600 was obtained too. Limited to the rated voltage of SMR 7.7 ref /500, the comparison voltage plots were 15kV, 23kV, 33kV, 42kV. The Fig.4 shows the linearity of HCR600 by comparing with SMR 7.7 ref /500. The Fig.4 shows a good agreement with Fig.3. The results demonstrated that the methods described in this paper is reasonable and can be used in the traceability of impulse voltage measuring system.

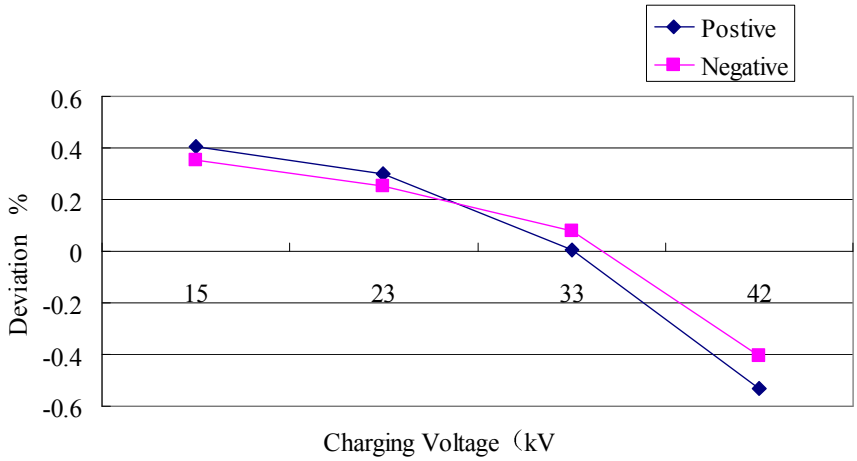

Fig.4 Linearity test results of the HCR600 comparing with SMR 7.7 ref /500

Using the above method to obtain the linearity of impulse voltage divider need to satisfy following conditions.

(1) The complete linearity test shall be made within sufficiently short time that atmospheric conditions do not change a lot.

(2) Attention should be paid to the equal charging of all stages of a voltage generator.

(3) Sufficient time should be allowed for all stages to charge before triggering the generator.

(4) The accuracy of the DC voltage divider is better than 0.5%。

(5) In the test, pay attention to the temperature rise of resistance of generator and ensure enough time interval.

Conclusions

In this paper, all the methods for measuring the linearity of impulse voltage divider are described. In addition, the paper improves the method mentioned in IEC 60060-2. First the linearity of the impulse generator(IG) is obtained by using a linear 200kV resistance diver. Then taking account of the linearity of IG, the linearity of HCR600 is obtained.

The result shows that the linearity of HCR600 decreases from +0.4% to -0.8%; the maximum difference between positive polarity and negative polarity is 0.14% and the linearity of negative polarity is superior to that of positive polarity.

In addition, the paper use the SMR 7.7 ref /500 as standard divider and obtain the linearity of HCR600. Comparing the two curves, two curves show a good agreement, the maximum difference between them is 0.15% at the same voltage. The result shows that the method proposed in the paper can be used to measure the linearity of divider accurately.

References

[1] Yang Yingjian, Tang Jian, Wu Xiong. Construction of UHV AC Test Base of SGCC[J]. High Voltage Engineering, 2007, 33(11): 6-9.

[2] Li Guangfan, Liao Weiming, Li Qingfeng. Voltage Output Performance of 7200kV/480kJ Impulse Voltage Generator[J]. Proceedings of the Chinese Society for Electrical Engineering, 2008, 28(25): 1-7.

[3] He Huiwen, Gu Dingxie, Zhou Peihong, Xiu Muhong, Dai Ming. Simulating Calculation and Analysis on Time-to-crest of Switching Impulse for Test on Chinese UHV AC Pilot Project[J]. High Voltage Engineering, 2011, 37(9): 2156-2162.

[4] IEC60060-1 High-voltage Test Techniques – Part 1: General Definitions and Test Requirements, 2010.

[5] IEC60060-2 High-voltage Test Techniques – Part 2: Measuring Systems, 2010.

[6] [3] T. Wakimoto, M. Ishii. National Standard Class Measuring System for Impulse Voltage in Japan [C]. 15th International Symposium on High Voltage Engineering, Ljubljana, Slovenia, 2007: 1-5.

[7] J. Hällström, M. Aro, Y. Zhang, B. Larzelere, et al. Progress of a worldwide Comparison of LI measuring systems - Round 1[C]. 12th International Symposium on High Voltage Engineering, Bangalore, India, 2001: 1-7.

[8] T. Harada, T. Wakimoto, S. Sato and M. Saeki. Development of national standard class reference divider for impulse voltage measurement[C]. 11th International Symposium on High Voltage Engineering, London, England 1999: 13-16.

[9] T. Harada, T. Wakamoto, M. Saeki, S. Sato. Development and performance test of the reference divider for 300kV lightning impulse voltage measurement in Japan[C]. 10th International Symposium on High Voltage Engineering, Montreal, Canada, 1997: 303-306.

[10] Pradeep M. Nirgude, K. Devender Rao, R.S.Shivakumara Aradhya. Performance tests on impulse measuring systems at ultra high voltage research laboratory[C]. 11th International Symposium on High Voltage Engineering, London, England, 1999: 1120-1123.

Advanced Materials Research Vols. 986-987 (2014) pp 1666-1668

doi:10.4028/www.scientific.net/AMR.986-987.1666

The Application of Rogowski Coil in Power System

Wang Qinghao, Zhang Yunshan, Zhang Wenguang, Li Zhi, Zhang Ning, Li Yan, Wang Zhixu, Cheng Pengfei, Lin Bin, Li Jianfeng

Fushun Power Supply Company, Liaoning Electric Power Company Limited, State Grid, China,

wts55@126.com

Keywords: Rogowski coil, current transformer, on-line monitoring

Abstract. The traditional current transformer measurement device cannot meet the requirements of the rapid development in the current power system because of the outdated structure while the Rogowski coil has significant advantages. This article introduces some applications of Rogowski coil in power system. Now the research and application of Rogowski coil current transformer has become one of the most important research directions. Rogowski coil today has been widely used in electric power system.

Introduction

In recent years, with the construction of modern high pressure, ultra-high voltage transmission network, electric power system is developing in the direction of large capacity, high voltage and large current. It puts forward higher requirements on the current measurement devices. Traditional electromagnetic current measurement device has disadvantages as big shape, narrow frequency band and low explosion-proof insulation[1-3]. The Rogowski coil current transformer has no direct contact in physical with the measured current loop but through the electromagnetic field coupling, so with a series of advantages of good electric insulation, wide current measuring range, high accuracy, no magnetic saturation, wide frequency range, good linearity, small volume, low manufacturing cost and easy to digital output etc.At present, the Rogowski coil has many applications [4,5].

The identification of detour lightning and direct lightning

Lightning breakdowns are divided into detour lightning and direct lightning. For different breakdowns, the solution is also different.

Now in power system, to identify the category of the breakdown is extremely difficult. The lightning locator, although can measures the parameters of the lightning current, it can't identify detour lightning and counterattack lightning. In this paper, we give a kind of lightning current measurement system based on transmission line tower. And on the tower in the insulator string installed the clamp type set of Rogowski coil current sensor, to measure the direction of the lightning flashover current, which is proportional to the strength of the lightning. We put another Rogowski coil current sensor at the grounded point to measure the direction. By comparing the current directions of the two sites, we can get the strike kind. In addition, the system also has the function of locating the lightning strike point. The measurement system schematic diagram is shown in Figure 1.

The measurement of U-I characteristic of the vacuum arc

As control and protection equipment, vacuum switch plays an important role in power system. The key research in vacuum switch technology is on vacuum arc characteristics, and *U-I* characteristic is one of the important characteristics of vacuum arc.

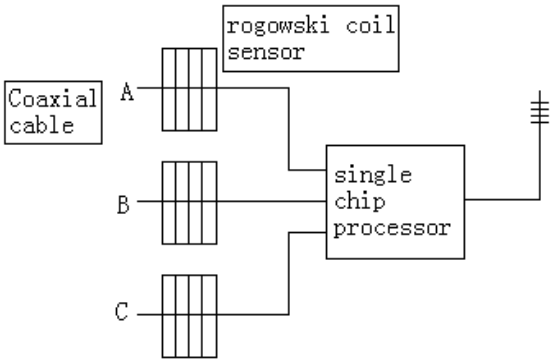

Figure1 The measurement system

Vacuum arc belongs to the strong impact current and there are many measuring methods to measure it. We use the Rogowski coil to do the trial. Rogowski coil has a special structure of air-core coil. At the same time, the Rogowski coil has low output power, simple structure and good linear excellent features. At present, it has been successfully applied to *U-I* characteristic testing. The schematic diagram is in Figure 2.

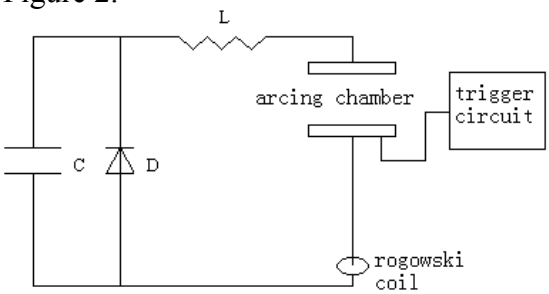

Figure 2 The schematic diagram of the system

The monitoring of grid over voltage

In 110 kV and above power grid, the transformer bushing often uses capacitive bushing. When suffering over voltage attacks, the end screen will flow the capacitive over voltage current. According to it, the over voltage monitoring can be realized.

There is the power frequency current flowing in the end screen under normal operation voltage, and abnormal current under the over voltage occasion. So, the current in the Rogowski coil is the superposition signal. According to the actual situation of power grid, we use ATP simulation respectively to show the lightning over voltage, operating over voltage and power frequency voltage. The simulation results are shown in Figure 3.

Considering the frequency range of the current in end screen with both low and high frequency, so we use a broadened frequency band Rogowski coil. Figure 3 is the Multisim simulation results of the amplitude frequency response and phase frequency response.

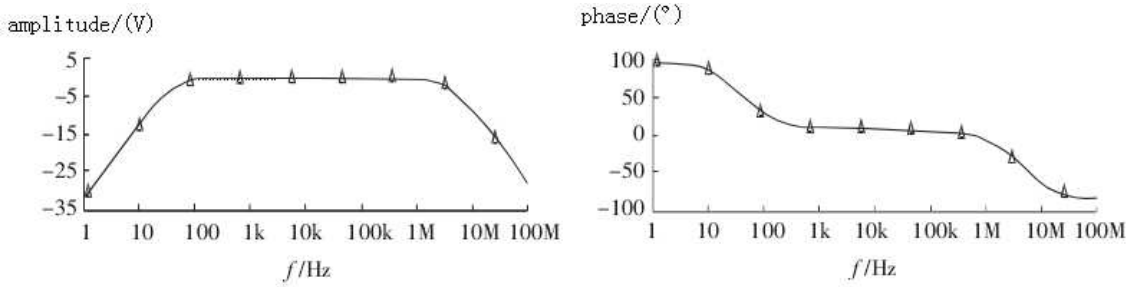

Figure 3 The amplitude frequency response and phase frequency response

The detection of cable partial discharge

The normal trial measurement of cross linked polyethylene (XLPE) cable partial discharge is mostly used the IEC60270 method. But the method is of low frequency band, vulnerable to the effects of background interference. So, at present, the focus has been shifted to the high frequency and ultra high frequency measurement to test the cable partial discharge at home and abroad, especially on gas insulated switchgear (GIS). Many experts now are trying to expand this method to the on-line monitoring technology in cable partial discharge.

Online monitoring of transmission line insulators

Transmission line insulator, as an important device of mechanically fastened and insulating effect, is widely used in electric power system. Its running state directly affects the safe and reliable operation of power system. Experimental research and site operation experience show that in adverse weather conditions, the filth of dust on the surface of the insulator will be wet. When under the effect of applied voltage, the surface conductivity and leakage current will greatly increase, results the decrease of insulator's electrical properties and even flashover. According to statistics, the insulator flashover accidents caused by pollution account for second place in power grid.

The current sensor using Rogowski coil can meet the demand for measuring the leakage current. It can accurately monitor data to facilitate staff maintenance and improve the operation reliability of the transmission line.

Conclusion

Rogowski coil is reviewed in this paper at some applications of the current transformer in power system. Due to the Rogowski coil application is very extensive, the increasing demand is becoming more and more complex. So the monitoring needs more precise measurement. The Rogowski coil is with good electric insulation and a lack of iron core saturation problems, together with current wide measuring range, high accuracy, no magnetic saturation, wide frequency range, good linearity and small volume, low manufacturing cost, easy to digital output and a series of advantages.

Proved by actual operation, it is to use a flexible form, structure, rich variety and high reliability. Therefore the using the Rogowski coil of the electric power system monitoring and protection is very reliable.

Reference

[1] Li Shiping, Liu Guiying. Modern Power Quality Detection Technology. China Power Press, 2008.

[2] Wang Hezhen. The Var Compensation of High Voltage Shunt Capacitor Technology. China Power Press, 2006.

[3] Ping Shaoxun, Zhou Yufang. Power System Neutral Grounding Mode and Operation Analysis. China Power Press, 2010.

[4] Yao Huannian, Cao Meiyue. Resonance Grounding of Power System. China Power Press, 2009.

[5] Wang Zhaoan. Harmonic Elimination and Reactive Power Compensation. Mechanical Industry Press, 2009.

Advanced Materials Research Vols. 986-987 (2014) pp 1669-1672

doi:10.4028/www.scientific.net/AMR.986-987.1669

The portable device for detecting smart meter fee control functions

Sun Zhiqiang , Zhai Feng , Liu Ying and Cen Wei

China Electric Power Research Institute, Beijing, 100192, China

sunzhiqiang@epri.sgcc.com.cn

Keywords: Smart Meter, Fee Control Functions, Portable Device

Abstract. In view of the current smart meter fee control functions heavy task, work intensity and other issues, we designed a new type of portable smart meter fee control functions test device. The device includes a parallel communication, automatic features such as card issuers, small size, light weight, easy to carry, to achieve automatic control function detects meter fees, enhanced energy meter test bench, between the host computer and the inspector who machine interaction capabilities, improve the detection efficiency of the staff, reducing the misuse rate, and enhance the flexibility of the testing work. The device is able to meet the needs of the current smart meter automatically detects work. Guarantee the accuracy and reliability of the energy meter testing.

Introduction

Smart meter fee control function is performed by local and remote two ways, and fee control function testing is a relatively new test, to be completed by the current detection device charge control function still relatively few. In the smart meter to detect the beginning, mostly borrowed inspectors have the ability to detect communications meter test bench to provide a communication channel and power, using the card reader and associated detection software testing, the detection process is a very labor participation large semi-automated process, the detection efficiency is low. After fee control function automatically detects platform appears detection efficiency has been greatly improved, but the larger units automatically detect volume, poor flexibility, high maintenance costs. Based on the above issues, we designed this portable smart meter fee control function testing device.

Application of Network Structure Portable Smart Meter Fee Control Function Testing Device

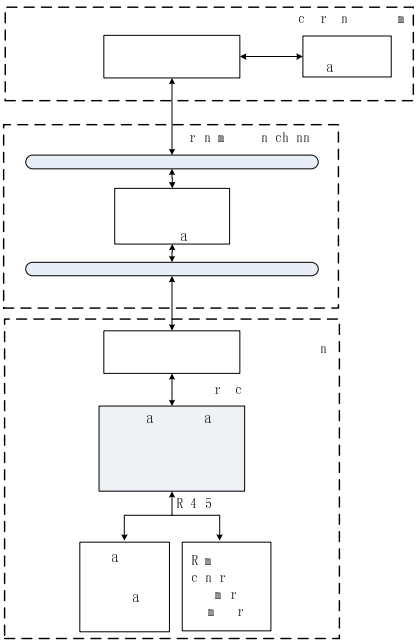

Fig.1 Smart meter fee control function testing applications network structure

Smart meter fee control function testing application system network architecture shown in Fig. 1.

The structure is mainly composed of three parts, namely, the State Grid Corporation detection key management systems, portable smart meter fee control function testing devices and smart energy meter [1,2] .

Hardware Design of Portable Smart Meter Fee Control Functions Testing Device

The detection device using the PC as the control center, a multi-port server to provide a communication channel for the detection of epitope equipped with automatic issuing emulator epitope, automatic card simulator, switching power supplies. Among them, the emulator automatically issuing smart cards issued for a variety of testing process used; automatic card detection process simulator used to complete the automatic card action; switching power supply for the emulator card issuers, card simulator, meters and other offers stable supply different voltages[3]. The overall structure is shown below in Fig. 2.

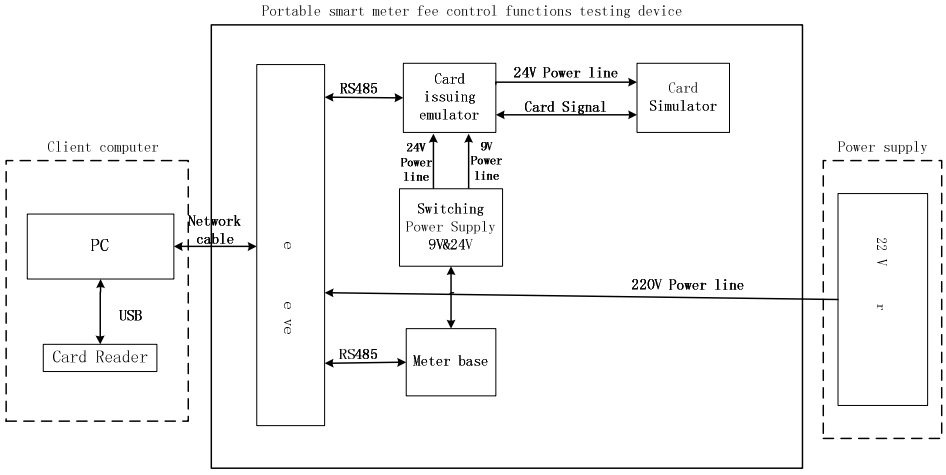

Fig. 2 Portable smart meter fee control function testing device hardware architecture

Multiport Serial Server. Card issuing emulator and the meter via RS485 serial port serial servers, each using a different port, the client computer sends commands to multiple serial server via Network cable, after many serial server the command assigned to the Card issuing emulator and the meter to ensure the instruction is correct transmission[4].

Card issuing emulator. Card issuing from the control unit emulator, IC card unit, a communication unit, a power supply unit, IC card, the output units. The main control unit is the core component of the various commands from the host computer by its resolution, and it can control other units to complete the appropriate action. The communication unit is the master unit communicates with the host computer interface. IC card unit is equipped with a card unit according to the type of smart card type used in the detection process, comprising: a user of the card unit, a key Bottoms card unit, card key recovery unit, field parameter setting unit card, master card unit parameters preset card unit and the like. They are connected with the control unit and the IC card output unit[5]. IC card output unit is a multiplexer, the output unit according to the type of card commands the master unit; power supply unit supplies power to the other main control board of each unit.

Card issuing simulator can be used to issue national grid company enterprise standard "Q / GDW 365-2009" as defined by the card. The card can be inserted into the desired slot, the card and the output channel signal. Data from the card machine with a computer and password by entering the channel input. Function depending on the configuration and number of cards, card emulator into full-configurable and dedicated configuration two categories[6]. Emulators and simulators card issuing composed kit enables smart meter inspection process issuing, card automation, greatly improving the efficiency checklist.

Card issuing emulator provides RS485 interface as an input channel to receive computer instruction, execute and return the results. Each Card issuing emulator provides a DIP switch configuration address, to facilitate the composition RS485 serial network.
Card issuing emulator provides 24V interface control card simulator.
The structure shown in Fig. 3.

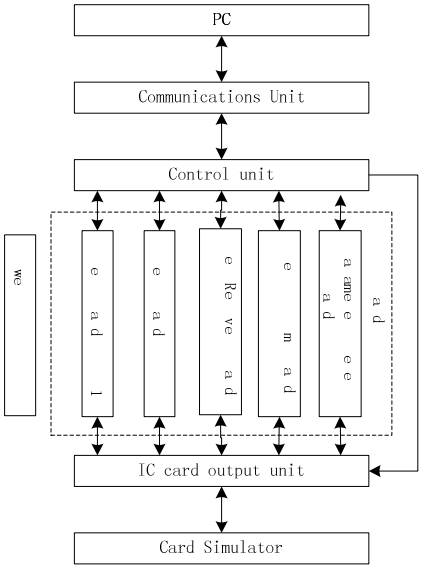

Fig. 3 Card issuing emulator structure

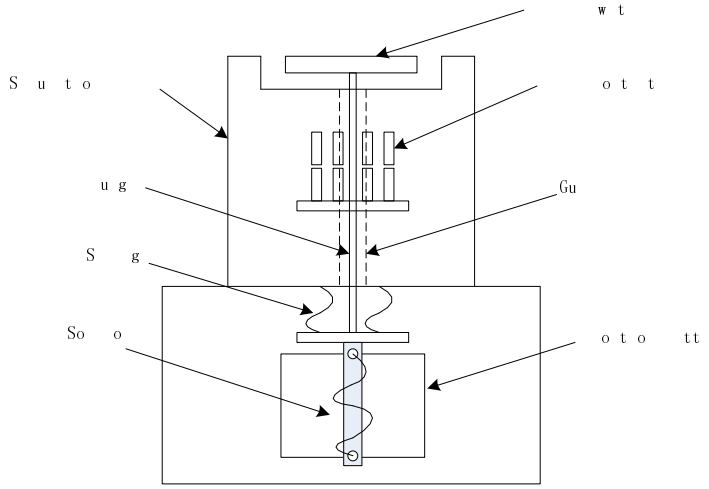

Fig. 4 Card simulator structure

Card Simulator. Card simulator can simulate the action is a device, which consists of cards and card emulation switching of two parts. Dimensions, size and arrangement of contacts and other indicators related to the simulation of the card fully meet the requirements of ISO7816. Automatic card position switch on the market to meet the majority of the deck position switch requirements. Simulator and emulator card issuing smart cards can be achieved in conjunction issuance and card automatically, greatly enhance the degree of automation of the control of local fee table detection.
The signal simulation simulator card smart card is introduced into the smart card holder table, card by card analog switch action [7,8].
Card simulator consists of a base ,control battery ,sliders ,rails , emulation cards and other components. Among them, the card emulation contacts on the card deck is used in contact with the power meter contacts, for data interaction. Control cells fixed on the base . Battery is installed in the control electromagnet core and slider connected slider top is a card switch , slider can slide in the rails so that the card deck position switch and automatic switch contact card action. In addition . Integrated single-chip controller IC card and battery control module , single-chip controller via the communication interface to communicate with the host computer , perform the card , pull the card control ; connected to the IC card module described in the previous section to issuing a signal output unit emulator . The general structure of the card shown in Fig. 4 simulator . Automatic plug the card process: insert card simulator meter IC card IC card slot the card slot of the spring clamp device . When the PC card issued instructions solenoid coil is energized , generates magnetic force. Push the core is moved forward , pushing the slider against the spring resistance of the core to move forward in the rails, the top of the slider switch card also moves forward into contact with the cartridge until the switch position of the case, the simulation of the card contact with the contact card contacts meter deck complete card action[9]. Conversely, when you need to pull the card off solenoid coil , magnetic disappear , the spring push the slider to move back . Pull the card to complete the action .

Software Design Portable Smart Meter Fee Detection Device Control Function

The software is based on. NET development environment, using Microsoft Visual Studio 2008 development tools, the use of C # programming language development, software architecture follows

a modular design, according to the hierarchical structure of the design, each level and program modules were completed some functions, as expansion and remote software upgrades function to lay the foundation.

Software for remote fee control of smart meter testing items: Test security authentication features, remote key update testing, remote control test, II parametric test, copy the data back testing, anti-attack testing, remote testing cleared. For local fee control of smart meter testing items: Test security authentication features, remote key update testing, remote control test, II parametric test, copy the data back testing, anti-attack test, a class of parametric testing, remote initialization wallet command, the user card test, remote account recharge test parameters preset card test[10,11].

Summary

New portable smart meter fee detection device control function designed in this paper have been applied in practice. After testing, the automatic detection devices to achieve a good detection system automatically Card issuing, card, parallel communication, human-computer interaction and other functions, with a high degree of automation, less repetitive operations, test cycle is short, and high detection efficiency over the a good solution to the current electricity meter detection testing department workload, weight and other problems, so that the past takes a lot of manpower and long working hours meter batch testing work has been completely changed. Make a very significant effect in practice.

References

[1] ZHANG Song, LI Yi-fei. Smart energy meter data security protection technology[J].Power Demand Side Management, 2010,12（2）:74-76

[2] CEN Wei, ZHAO Bing, FENG Zhan-cheng. Explore of the Local Cost Control Smart Mete's Anti-attack Capability Test[J]. Electrical Measurement & Instrumentation，2011,48（5）; 51-55

[3] Security techniques of information interchange authentication specification for smart electricity meters [S].2012,16-24

[4] China Electric Power Research Institute. Publicity materials of intelligent watt-hour meter information exchange security authentication[Z].2009,112-113

[5] WANG Qin-chu, YAO Yan-xia. Smart Energy Meter Information Security Technology[J]. Electrical Measurement & Instrumentation，2010,47（A08）：111-115

[6] Information Security Technology[M].Beijing: Higher Education Press, 2008:25-53

[7] YAO Li. Explore of the Prepaid Watt-hour Meter's Data Security[J].Zhe Jiang Electric Power, 2009,2:48-51

[8] CHEN Wei,ZHOU Pei-yuan.Smart card data security technology research[J].Information Safety and Information Security, 2002,3:44-47

[9] TIAN Yong-jun,ZENG Jian-ping. Secure design's strategy of card prepayment meter[J]. China Instrumentation, 2007,4:73-77

[10] FANG Yu,LI Shen-pei.An investigation on data security of IC card prepayment product systems[J]. Journal of electronics&information technology,2002,6：781-786

[11]FU Zhong-quan.The design and realization of Prepaythree-phase power meter based on CPU card[D]. Hunan:Chinese Academy of Sciences master's degree thesis, 2009：10-11，36-38

Advanced Materials Research Vols. 986-987 (2014) pp 1673-1676

doi:10.4028/www.scientific.net/AMR.986-987.1673

The application of wireless sensor networks in power engineering

Ruihui Mu

College of Computer and Information Engineering, Xinxiang University, 453003,Xinxiang,China,

muruihui@126.com

Keywords: wireless sensor networks, power engineering, power system communication

Abstract: The fast evolution of computer technology, sensor technology, MEMS and modern wireless communication technology has impelled development of wireless sensor networks. Wireless sensor networks are consist of a large number of nodes which can be capable of communicating, computing and cooperation in ad hoc model. In this paper, we study the application of wireless sensor networks in power engineering. A device for remote monitoring of electric towers is designed. This paper proposes the implementations of remote wireless centralized electricity meter reading based on wireless sensor network.

1. Introduction

A wireless sensor network (WSN) consists of spatially distributed autonomous sensors to monitor physical or environmental conditions, such as temperature, sound, pressure, etc. In computer science and telecommunications, wireless sensor networks are an active research area with numerous workshops and conferences arranged each year.

Wireless sensor networks are gaining in popularity for industrial sensing applications due to their relatively low cost and simplicity for retrofitting into existing infrastructure. They are particularly suited to power engineering applications as they do not require cabling, which will lead to shorter outages during installation and a lower capital outlay than their wired equivalent. This technology has previously been applied within the power engineering domain, in areas such as transmission system security and substation temperature monitoring, but to-date, such systems have been standalone. For wireless sensor network technology to make a valuable contribution to condition monitoring in the power domain, like any monitoring system, it must integrate with existing systems to allow monitoring engineers a unified view of equipment health.

2. Electricity tower multi-hop routing algorithm

Choose LEACH protocol to be used in sensors to collect data with a high degree of similarity of the network, ease of management. In addition, LEACH protocol to minimize network energy loss goal. More suitable for the needs of the power tower is monitoring equipment. Randomly select a cluster head node characteristics by agreement, to be shared equally between the relay communications business of wireless sensor networks. This average node energy consumption of the sensor network is devices. Equipment distant linear Communications LEACH protocol clustering algorithm must first set up a cluster. We can be seen as the hub clusters or clusters. So you want to select some electricity tower as the cluster heads node and the formation of such a cluster, to tower to tower as an example, provided that they are in mutual communication within the scope. Using LEACH algorithm, first, select a cluster head node between the four towers. Four nodes each generate a random number in the O to 1 between. Once a node is less than the set threshold r (n) random set for the cluster head node issued to around electricity tower broadcast notification has become a cluster head node. Periodically the implementation of the algorithm makes Tower 4 to Tower 7 has become possible cluster head. Each round cycle has an electricity tower cluster head node. When after a power tower cluster head node r (n) value is set to 0. The next cycle will not act as a cluster head node. So, we will be increasing the probability of remaining power tower cluster head node clusters. Last only a power tower, T (n) value becomes l, the next

round of communications will become the cluster head node. If a power tower in the intersection area of the clusters, it played a role in the data transmission to the remote.

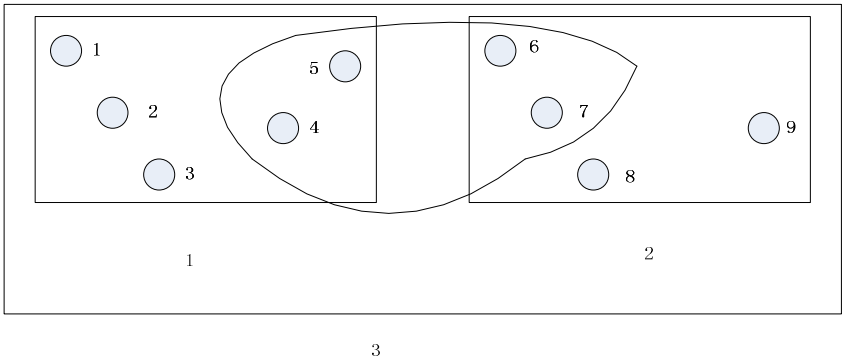

Figure 1. Schematic diagram of electric tower nodes

In Figure 1, the EACH algorithm analysis of long linear communication. Combined with the actual select the optimal number of cluster heads. Hope that each round of data communication in the cost of the total energy minimum. And the consuming energy can be more evenly distributed in the entire network. Be seen as a total of three clusters. Two general clusters and a hub for the cluster. Located in a limited area is more evenly distributed with the node 9. And it is divided into three clusters. Power tower in the communication network of the large range of power tower is far exceeding the number shown in the figure. Assume that each cluster will have a cluster head node and 2 (9/3-1) members of the node. Cluster head node in each power tower clusters in the transmission data request packet the ADV message, the receiving member node packet, data analysis, fusion. And energy consumption of the transmission data packet to the gateway is node. Set a radius r of the area distribution of the Ⅳ electricity towers. Cluster-head power tower to send data around each frame energy consumption formula for.

$$E_{Head} = n\xi_{amp} d_{farthest}^2 + 2n\frac{N}{u}E_{1hit} + n\frac{N}{u}\xi_{amp} d_{toaink}^2 + n\frac{N}{u}E^{'}$$

Where, n is the median packets sent; ξ_{amp} is the magnification of the signal amplifier; $d_{farthest}$ is the distance in a power tower within the clusters as cluster head node power tower and its farthest electricity tower: u is the number of cluster head power tower; E_{1hit} is the each sending or receiving a data circuit itself consumes energy; d_{toaink} is the power tower to the cluster head gateway node distance: $E^{'}$ is the data integration and data compression energy needs cluster head within the power tower.

Because the power tower communication within the cluster of non-cluster head node is the M cluster head node ADV message may be received simultaneously. It also needs to send messages to consume energy. Energy consumption formula is for.

$$E_{noHead} = n(u+1)E_{1bit} + n\xi_{amp} d_{toHead}^2$$

Where, d_{toHead} is the distance of the members of the power tower to the cluster head power tower? Assuming the area covered by each cluster head is a circular area. Have come to the expectations of d_{toHead}^2 to $r^2/(2\pi u)$, with cluster head total energy consumption is.

$$E_{all} = u(E_{Head} + \frac{N}{u}E_{noHead})$$

The derivation of u and E_{all} can be obtained within the region, the number of cluster head power tower.

$$u = \sqrt{\frac{r^2 N\xi_{amp}}{2\pi N E_{1bit} + 2\pi\xi d_{farthest}^2}}$$

3. Experimental analysis

When the when the AB two phase short circuit fault occurs, the simulation results shown in Table l. Can locate the fault occurs at a node between S_{N+2} and S_{N+3}.

Table 1. AB two-phase short circuit fault node current

Table 2. A phase to ground fault node current

Node locations	Fault *current*	Three-phase node	Fault current
B S_{N+2}	1 380	$\Delta(A_1, A_2)$	**14**
C S_{N+2}	1 330	$\Delta(B_1, B_2)$	**0.1**
A S_{N+2}	374	$\Delta(C_1, C_2)$	**0.08**
B S_{N+2}	193	$\Delta(B_2, B_3)$	**0.1**
C S_{N+2}	206	$\Delta(C_2, C_3)$	**0.09**

A phase to ground fault occurs, the simulation results shown in Table 2. Can locate a fault occurs in the A phase between nodes 1 and 2. The average delay of the network and node moving speed relationships is shown in Figure 4. As the mobile node cause the network topology changes, thereby increasing the consumption of resources of the channel. When the CPU utilization increases, the signal interrupt response time also increases. These will lead to the increase of the average delay of the network.

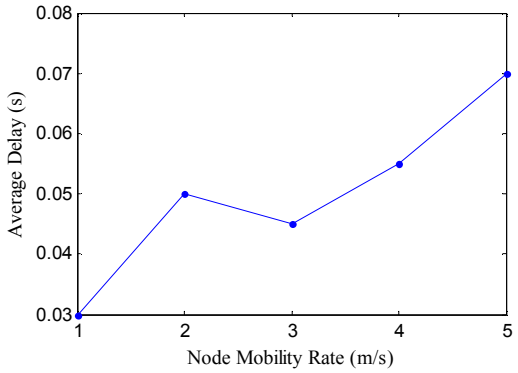

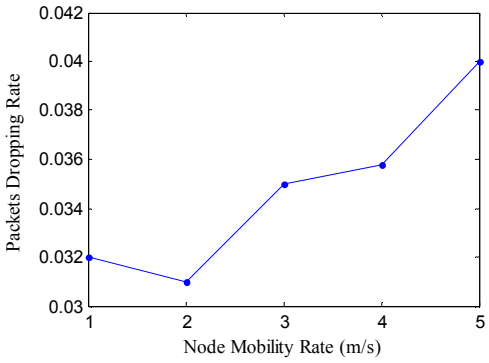

Figure 3. The relationship of the average delay of the network and the moving speed

Figure 4. Network packet loss rate

LS packet network of single-hop delay is set to 10ms; the largest end-to-end delay is set to 100ms. The data packet and will discard the packet in the process of transmission, if the transmission delay exceeds the upper limit of the set. Figure 4 shows the dynamic network lost coverage rate. As can be seen from Figure 4, the moving speed of the node has a significant impact on the packet loss rate. When the increase in the moving speed of the node, the network topology changes are more frequent, resulting in the control of the increase in the amount of information communication, reduce the efficiency of the routing protocols.

The MAC layer used with collision avoidance carrier sense multiple access protocol. All communication in the initiative immediately recognized mechanism (ACK frame) If you do not receive the ACK frame retransmission data information. The simulation results are shown in Figure 5.

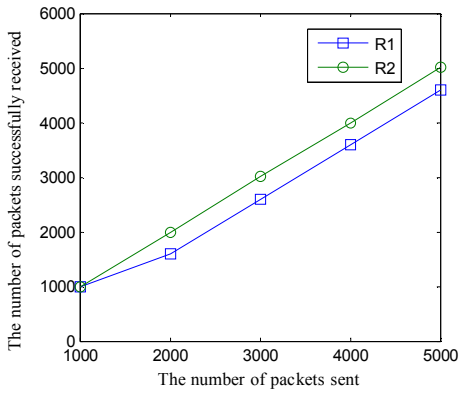

Figure 5. Successfully accepted the probability of packet

Can be seen from Figure 5, the area management node successfully received the data information of the nodes on the line, the probability of 98.7% (R = 1) and 99.83% (R = 2).When the maximum number of retransmissions R ≥ 4 regional management node in the simulation experiments can successfully accept all packets sent.

4. Conclusion

According to the real time monitoring of power tower，wireless sensor networks(WSN)is used for power tower monitoring and warning system. Each component of the monitoring system is designed and implemented. The long chain tree-like topology of wireless sensor network is designed. The results show that compared with ordinary wireless technology，this system design has advantages of low cost，low power consumption，large internet capacity and longer network lifetime. The system provides a new technical alternative to the power tower monitoring，So it has a higher reference value and broad application prospects.

5. References

[1] Chanchan Zhao, Xiaowei Hai, Xiaohua Jiang, Bo Gao, "Coal Mine Environment Monitoring with Wireless Sensor Networks", IJACT: International Journal of Advancements in Computing Technology, Vol. 5, No. 1, pp. 505-514, 2013.
[2] Xiao Liu, "Agent-Based Load Balancing DV-Hop Positioning Algorithm for Wireless Sensor Networks", JDCTA: International Journal of Digital Content Technology and its Applications, Vol. 7, No. 3, pp. 787-794, 2013.
[3] Tang Wenliang, Yan Liping, "Research of WSN-Based Safety Monitoring System for Middle-and-Small Sized Dams", JDCTA: International Journal of Digital Content Technology and its Applications, Vol. 7, No. 1, pp. 838-845, 2013.
[4] Chen Zhaoji, Xu Huibin, Wang Shuangyou, "The Application Wireless Networks in Monitoring Mine Safety System", JCIT: Journal of Convergence Information Technology, Vol. 8, No. 2, pp. 271-278, 2013.
[5] Zheng Jianguo, Liu Hualing, Sun Cihai, "A New Security System Design Based on the Wireless Sensor Network", AISS: Advances in Information Sciences and Service Sciences, Vol. 5, No. 2, pp. 776-782, 2013.

Advanced Materials Research Vols. 986-987 (2014) pp 1677-1681

doi:10.4028/www.scientific.net/AMR.986-987.1677

The design of location system for single-phase grounded fault in distribution network based on zero-sequence current

Cai Xinwei [1,a], Jin Tao [2,b], Jia Huibin [1,c] , Qi Yulin[1,d]

[1] North China Electric Power University, Baoding,Hebei, China

[2] Power supply company of Jiujiang, Jiujiang,Jiangxi, China

[a]cxw_1988@126.com,[b]jj_xuewei@jx.sgcc.com.cn,[c]hbin.jia@gmail.com,[d]qiyulin589@163.com

Keywords: zero-sequence current; single phase grounded fault; fault location;

Abstract. In this paper, A location system for single phase grounded fault in distribution network is proposed and it is based on the phase of zero-sequence current. The system is composed of central station and nodes installed on the power line, and their functions are illustrated in this paper. The principle of the method is shown and experiments are carried out. The results show that the feasibility of the method. The advantage of this method is it's short time to detect. The method is Applicable to detect the faulty segment for neutral point non-grounded system with grounded resistance less than 1kΩ.

Introduction

Neutral point non-grounded system is applied in middle and low voltage distribution network in China. It is shown statistically that over 80 percent of fault in distribution network is single-phase grounded fault. It is of great significance to locate the fault rapidly and accurately in distribution network. The methods used currently include impedance, signal instilling, traveling wave.

The method of impedance is based on the assumption that the line is even and the fault location can be calculated by the proportion between resistance and length. It has the advantage of low investment, but it is unsuitable for distribution network with many branches [1,2]. The method of signal instilling needs to instill electric signal to the fault phase, and fault location can be determined by detection along the power line. In distribution network with many branches, it is unsuitable [3,4,5].The method of traveling wave is used to calculate the fault position by measuring the time passed along the transmission line. The signal is hard to detect due to the complexity of distribution network [6,7,8,9].

The paper proposes a method to detect single phase grounded fault of neutral point non-grounded system based on the phase difference of zero-sequence current. The paper is order is organized as follows: the first part gives the theory of the method, the second part shows the architecture of system, the third part shows the results.

The principle of fault location

When single phase grounded fault occurs, say phase C, as shown in Fig.1. Assume that $\dot{E}_a, \dot{E}_b, \dot{E}_c$ is the electro dynamic potential, $\dot{U}_a, \dot{U}_b, \dot{U}_c$ is the voltage of three phase, $\dot{U}_0$ is the voltage of neutral point, R is the grounded resistance, C is the capacity of the transmission line and $C_A = C_B = C_C = C$.

$$\begin{cases} \dot{U}_a = \dot{E}_a + \dot{U}_0 \\ \dot{U}_b = \dot{E}_b + \dot{U}_0 \\ \dot{U}_c = \dot{E}_c + \dot{U}_0 \end{cases} \tag{1}$$

If the power line runs normally $\dot{U}_0 = 0$. If fault occurs, $\dot{U}_0 \neq 0$,the conductance of phase C is $j\omega C + \frac{1}{R}$, therefore

$$\begin{cases} \dot{I}_a = \dot{U}_a\, j\omega C = \left(\dot{E}_a + \dot{U}_0\right) j\omega C \\ \dot{I}_b = \dot{U}_b\, j\omega C = \left(\dot{E}_b + \dot{U}_0\right) j\omega C \\ \dot{I}_c = \dot{U}_c\, j\omega C + \dfrac{\dot{U}_c}{R} = \left(\dot{E}_c + \dot{U}_0\right) j\omega C + \dfrac{\dot{E}_c + \dot{U}_0}{R} \end{cases} \tag{2}$$

In three phase symmetric circuit,

$$\begin{cases} \dot{I}_a + \dot{I}_b + \dot{I}_c = 0 \\ \dot{E}_a + \dot{E}_b + \dot{E}_c = 0 \end{cases} \tag{3}$$

Solving (2) and (3),

$$\dot{U}_0 = -\frac{\dot{E}_c}{1 + j3\omega RC} \tag{4}$$

$\dot{U}_0$ can only be added to the line at the fault point, as shown in Fig.2. The phase of zero-sequence current is opposite ahead and behind the fault location.

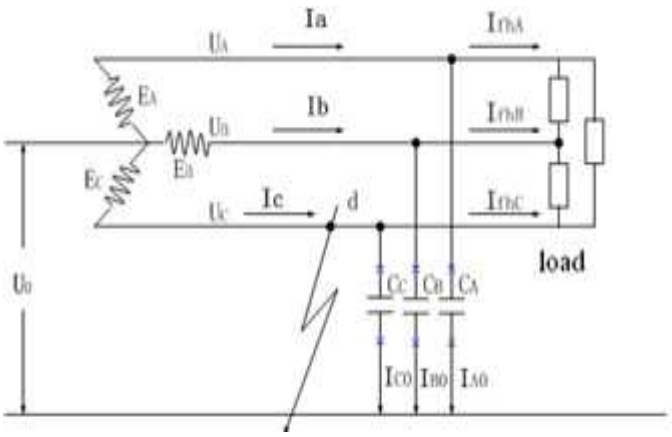

Fig.1 The power transmission line of fault state

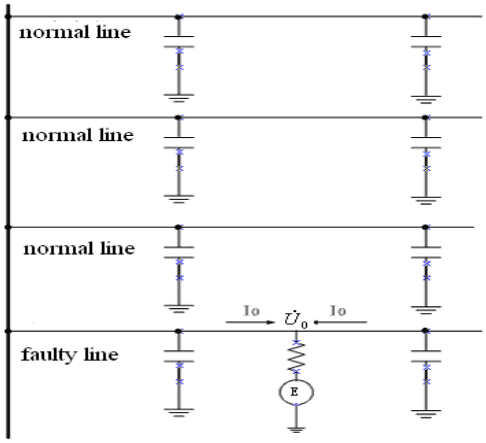

Fig.2 The grounded fault of power grid

The hardware design of phase method fault locator

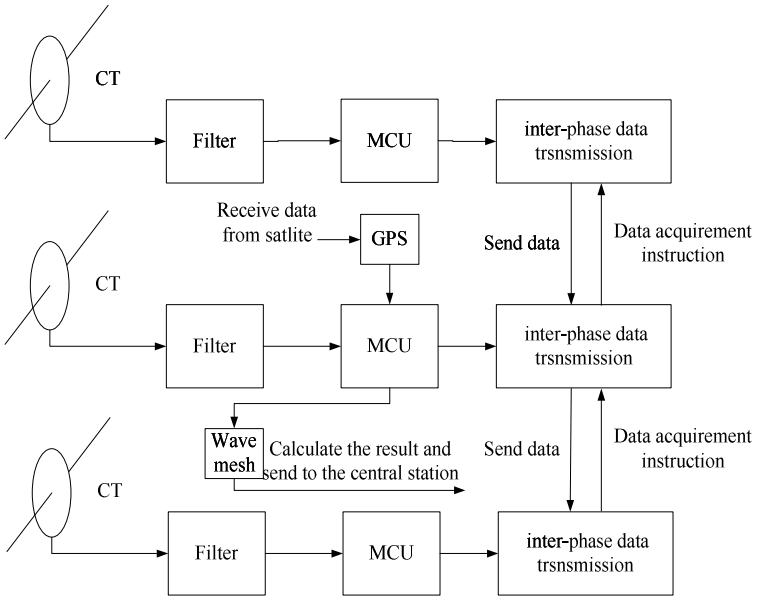

Fig.3 The composition of fault location system of phase method

The systematic scheme is illustrated in Fig.3. The sensor is composed of current transformer (CT), filter, MCU and inter-phase data transmission module. Three sensors installed at phase A, B and C of power transmission line forms a group which is called a node in this paper.

Choose a number of poles where each node is installed. The number of node determines the length of fault segment for a given length of power transmission line. The sensor on phase B is the control sensor which performs the acquirement, calculation of zero-sequence current, and sends the fault information to the central station.

The sensor on phase A and C performs the acquirement of current and transfers it to the control sensor. The three sensors acquire current value at one second interval simultaneously. The control sensor calculates and obtains zero-sequence current. If the result is quite small it means there is no fault, otherwise there is fault. The control sensor transmits zero-sequence current to the central station. The central station calculates the phase based on the received data and compares the phase difference between adjacent nodes. If the difference is 180°, it shows that the fault location lies between the adjacent nodes. And if the difference approaches zero, it shows the fault location is on one side of the adjacent nodes.

The scheme. The interval between the three lines is wide therefore, it is hard to design one zero-sequence current transformer to acquire the current of a phase. In this scheme three current transformers are installed at every line, and the transient value is summed and zero-sequence current is obtained.

The hardware of one node is composed of three zero-sequence current transformer, MCU, short distance wireless communication module. For phase B, GPS receiver and long distance wireless communication module are needed. The sensor in phase B is called control sensor, it is used to perform the function of acquiring current from phase B, receiving the current information transmitted from phase A and C, calculating of zero-sequence current, determination of fault, and transmitting of zero-sequence current to the central station by long distance wireless module. The sensors in phase A and C are in passive state, they response to the command from sensor B and acquire the current in transmission line and send it to the sensor in phase B.

Experimental results and analysis

The experimental platform is constructed in the following way: electric oven is used as load, and the load is star-style, the neutral point of load and the neutral point of three transformers are connected to simulate the ground. The capacitor is used to simulate the distribution capacitance of transmission line. Fault is set in phase B by connecting fault point with the ground. Two nodes are installed. Zero-sequence current of one node can be obtained by adding the three sensed current. Fig.4 shows the zero-sequence current of two nodes with no grounded fault. From it we can see that two zero-sequence current have the same phase and the amplitude is quite small. Fig 5 shows the zero-sequence current on the same side of the faulty point. From it we can see that the two zero-sequence current have the same phase and the amplitude is larger. Fig 6 shows the zero-sequence current on the opposite side of the faulty point. From it we can see that the two zero-sequence have the opposite phase and the amplitude is quite large.

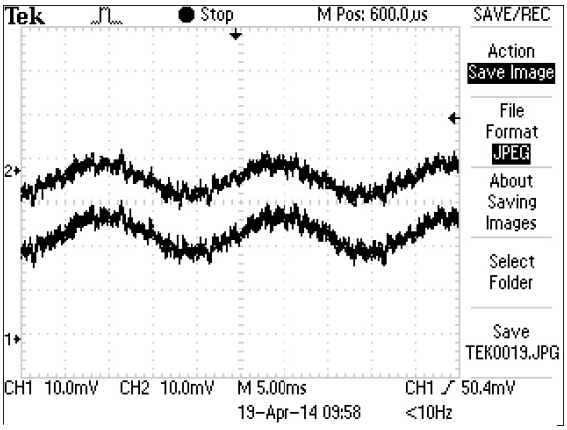

Fig.4 The waveform of adjacent two nodes with no fault

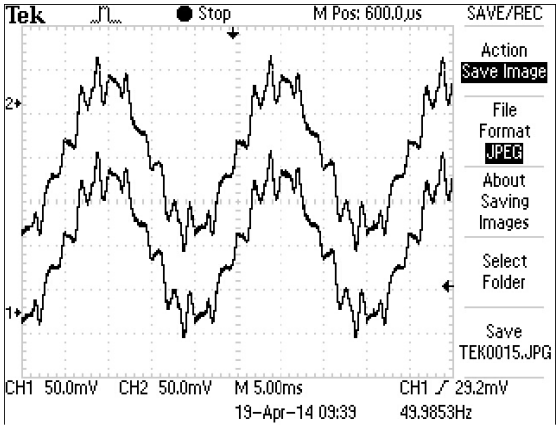

Fig.5 The waveform of adjacent two nodes with fault on the same side of faulty node

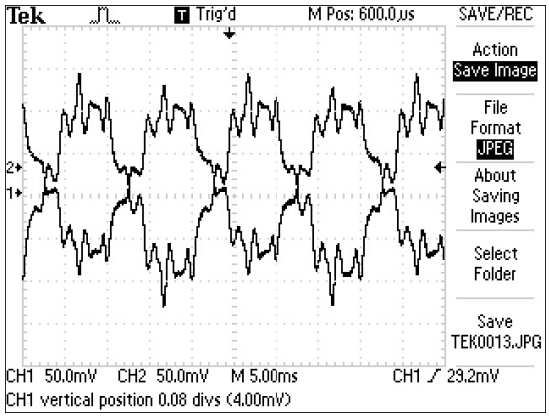

Fig.6 The waveform of nodes with fault ahead and behind the faulty node

Conclusions

The paper proposes a method of single phase grounded fault locating in distribution network based on zero-sequence current. The principle is shown and experimental results show that the method can be applied to detect the faulty segment for neutral point non-grounded system with grounded resistance less than 1kΩ. The method is not effective for single phase grounded fault with grounded resistance greater than 1kΩ, therefore it the method still needs improvement.

Acknowledgement

The paper is supported by project "the research and development of single phase fault locating system based on the difference of zero-sequence current" (project no 1215313031009), "the Fundamental Research Funds for the Central Universities(9161113003)", Natural Science Foundation of Hebei Province (E2013502267) and the Fundamental Research Funds for the Central Universities (13MS68).

Reference

[1] Bo, Z.Q., Weller, G., Redfern, M.A.. Accurate fault location technique for distribution system using fault-generated high-frequency transient voltage signals[J]. Generation, Transmission and Distribution, IEE Proceedings-, 1999, V146 (1):73-79

[2] QUAN Yu- sheng , LI Ping, ZHANG Yu. A new-one terminal fault location algorithm based on differential equation[J]. Power System Technology, 2004, 28(21):47-51.

[3] Zhang Huifen, Pan Zhencun, Sang Zaizhong, et al. Injecting current based method fro fault location in neutral isolated power system[J].Automation of Electric Power Systems,2004,28(3):64-66(in Chinese).

[4] WANG Nan, ZHANG Li, YANG Yi-han. A comprehensive location method using AC/DC signal injecting for single-phase earth fault in 10 kV distribution network[J]. Power System Technology, 2008, 32(24):88-92.

[5] YU Sheng-nan, BAO Hai, YANG Yi-han. Practicalization of fault location in distribution lines[J].Proceedings of the CSEE, 2008, 28(28): 86-90.

[6] YAN Feng, YANG Qi-xun, QI Zheng, et al. Study on fault location scheme for distribution network based on traveling wave theory[J]. Proceedings of the CSEE, 2004, 24(9): 37-43.

[7] ZHANG Fan, PAN Zhen-cun, ZHANG Hui-fen, et al. New algorithm based on traveling wave for location of single phase to ground fault in tree type distribution network[J]. Proceedings of the CSEE, 2007, 27(18):46-52.

[8] Xu Gang,Yu Sheng, Xu Zhenyu. Fault location for interline fault of parallel transmission lines using one-terminal data[C], 2009 Asia-Pacific Power and Energy-Engineering Conference, APPEEC 2009 Proceedings

[9] Yuansheng Liang,Jingmei Guo,Gang Wang. Parameter self-adaptive fault location of four-parallel transmission lines on the same tower[C]. 2011 4th International Conference on Electric Utility Deregulation and Restructuring and Power Technologies (DRPT), 2011:1-4

Advanced Materials Research Vols. 986-987 (2014) pp 1682-1684

doi:10.4028/www.scientific.net/AMR.986-987.1682

The Field Test of High Voltage Cable Impedance Parameters

Chen Gang, Wang Qinghao, Liu Guobin, Hai Tianshu, Liu Bo, Li Yiran, Li Bo, Wang Lei, Huang Dongwei, Zhao Chuanzong

Fushun Power Supply Company, Liaoning Electric Power Company Limited, State Grid, China,

wts55@126.com

Keywords: cross connection cable, positive sequence impedance, zero sequence impedance

Abstract. The cables in 66 kV and 220 kV systems are used in single-phase style, and it must be grounded between the cables. The connection ways between different lengths of cables are in different ways, thus, it may occur influence to circuit parameters, especially to zero sequence impedance. In order to clarify the situation from theory analysis to calculate impedance under all kinds of connection modes, the paper gives an actual cable measured value, and introduces the correct measuring method, together, points out the matters needing attention in the measurement.

Introduction

With the development of city construction in our country, the use of single-phase cable in the 66 kV and above systems is increasing. Single-phase cables are different from overhead lines. When single-phase cable is short, the starting point of the cable is grounded and the terminal is connected to the protector. While, when the single-phase cable is long, the cable sheath adopts cross interconnection method. General cross-connect cables are grounded on both ends and the cross-connect termination is connected to the protector. In some cases, it also adopts the return line[1-3].

When the single-phase grounding accident occurs, for not transposed cable, zero sequence current lows back by the earth, for crossover interconnection, zero sequence current flows back through the sheath, and for the return line ones, part through the sheath, and part through the return line[4,5]. Obviously, for different sheath connection modes, the zero sequence impedance of cable system is different.

Parameter Calculation in Different Connection Methods

(1) One-end-ground of the sheath

For single loop cable line in Figure 1, the metal sheath has only one end grounded and there is no other metal ground loop nearby, its positive sequence, negative sequence impedance are

$$Z_1 = Z_2 = Rc + j2\omega\times10^{-4}\ln\left[(21/3S)/GMRA\right] \quad (1)$$

Zero sequence impedance is

$$Z_0 = Rc + 3Rg + j2\omega\times10^{-4}\ln\left[D3e/(22/3GMRAS2)\right] \quad (2)$$

Where GMR is the geometric mean radius, Rc is ac resistance of the cable, Rg is the earth leakage resistance, De is the equivalent depth of earth fault current circuit,

$$De = 93.18\sqrt{\rho}$$

$$Rg = 2\pi f\times10^{-4} = 0.0493\Omega/km$$

When $\rho = 30\Omega\cdot m$,De=510370 mm; When $\rho = 100\Omega\cdot m$, De =931800 mm.

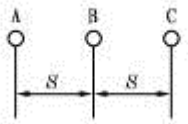

Figure 1. Three-phase cable arrangement

(2) Two-end-ground of the sheath in cross interconnection

When the cable length is long, in order to guarantee the sheath of the cable insulation from the harm of lightning overvoltage, it will be taken cross interconnection and two-end-ground method. If no metal flow line, the adjacent arrangement is still as shown in Figure 1. When the single-phase grounding fault occurs, all zero sequence current flows through the metal sheath, the positive sequence impedance is

$$Z_1 = Z_2 = R_c + \left[X_{2m} R_s / \left(X_{2m} + R_{2s} \right) \right] j2\omega \times 10^{-4} \ln\left(21/3S/GMRA\right) - j\left[X_{3m} / \left(X_{2m} + R_{2s} \right) \right] \quad (3)$$

Where Xm is the mutual impedance between metal sheath and conductor, Xs is self-inductance of the sheath; Rs is DC resistance of the sheath; GMR is the geometric mean radius

$$X_m = X_s = j2\omega \times 10^{-4} \ln\left(21/3S/GMRs\right) \quad (4)$$

Zero positive sequence impedance is

$$Z_0 = R_c + R_s + j2\omega \times 10^{-4} \ln\left(GMRs/GMRc\right) \quad (5)$$

A 110 kV cable is taken as an example in Nanjing Power Supply Company currently.

The cable layout is still used Figure 1. The sheath is alumina and its internal diameter is 74.5 mm,external diameter is 78.5 mm,Conductor cross-sectional area is 630 mm^2. The filling coefficient of conductor is 0.9, so the GMRc is 11.63 mm。

When the cable line is transposed completely, so X0=0.073 Ω/km by formula (5). The same cable, if not entirely transposition or transposition,according to (1), the X1=0.207 Ω/km。When not transposition and ρ is 30 Ω·m, according to (2), X0=1.53 Ω/km。When ρ is 100 Ω·m, X0=2.51 Ω/km.Obviously, cable line transposition or not has big influence on zero sequence impedance. In the process of actual measurement, the connecting way of cable sheath should be paid attention to.

Cable parameter measurement

(1) DC resistance measurement

Due to the cable length in thousands of meters, conductor wire cross-sectional area is large while the dc resistance is small, so it is used transformer dc resistance test instrument to measure the dc resistance of the cable.

After measuring the resistance of the R_{AB}, R_{BC}, R_{CA} values, it must be converted to phase resistance R_A and R_B and R_C, and compared with design or manufacturer values. The measured dc resistance should be consistent with the factory value of three-phase value should be the same, otherwise we should find out the reason.

(2) The measurement of the impedance parameters

The calculating method and wiring type of positive sequence impedance and zero sequence impedance, positive sequence capacitance and zero sequence capacitive is basically associated with overhead line parameter measurement. But cable parameter measurement has its characteristic, the principle of connection as shown in Figure 2 of the sheath totally transposition and incomplete transposition.

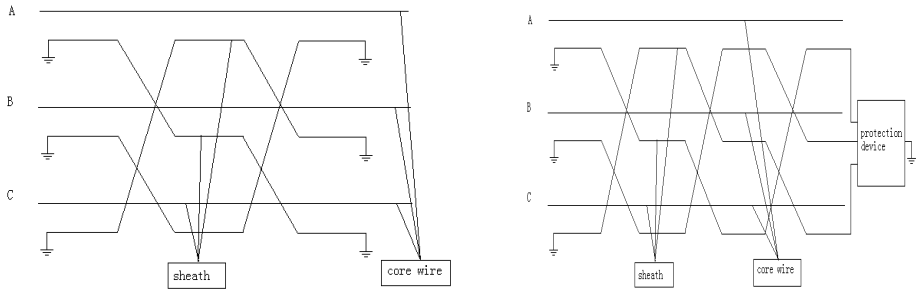

(a) Totally transposition (b) Incomplete transposition

Figure 2 Cable sheath cross interconnection

The testing results show that whether the sheath is transposition or not basically has no effect to the positive sequence impedance measurement, but big influence on zero sequence impedance measurement.

1) The sheath is a complete transposition, R0 / R1 value is between 2-3.5, and Z0 / Z1 value in between 0.6-0.6.

2) The sheath is not a complete transposition, R0 / R1 value is between 8-12, Z0 / Z1 (X0 / X1) values is between 6 and 10.

It mainly depends on the laying method of the cable. We consider the effect of the air in the cable tunnel and the influence of soil resistivity for directly buried cable.

The above values are related to the experimental core wire and cable sheath grounding state and substation grounding impedance of grounding device and so on. When the test data is abnormal, we must carry out analysis, eliminate the causes of abnormal.

Attention in Measurement test

Test personnel should have perfect organizational measures and safety measures and test personnel should know the situation of the cable line cross interconnection of various data and sheath, and thus formulate correct testing scheme. Conditionally, we can make the necessary calculations. When having doubt in testing Measurement data, we should analyze the reasons and eliminate the defects, to ensure accuracy of test data. Test equipment and instrument should be in accordance with the relevant data to estimate in advance and choices, cable length is shorter, and the cross-sectional area is larger, a direct current resistance is smaller.

Conclusion

66 kV and 220 kV voltage cable line of the single-phase cable, because each phase between cable sheath and ground connection must be connected, and the corresponding connection between different length of cable in a different way, and thus, making the circuit parameters, especially for zero sequence impedance produce great influence, which we must pay special attention to in the cable line parameter measurement.

Reference

[1] Wang Zhaoan. Harmonic Elimination and Reactive Power Compensation. Mechanical Industry Press, 2009.

[2] Yin Kening. Transformer Design Principle. China Power Press, 2010.

[3] Ping Shaoxun, Zhou Yufang. Power System Neutral Grounding Mode and Operation Analysis.

[4] Yao Huannian, Cao Meiyue. Resonance Grounding of Power System. China Power Press, 2009.

[5] Cao Dunkui. Transformer fault analysis and diagnosis. China Power Press, 2010.

Advanced Materials Research Vols. 986-987 (2014) pp 1685-1688

doi:10.4028/www.scientific.net/AMR.986-987.1685

The Identification Methods of Partial Discharge Test for Equipment

Wang Qinghao, Lin Bin, Li Xinyu, Li Jianfeng, Wang Qi, Zhang Jiayan, Li Yan, Cheng Shuo, Zheng Jiming, Wang Xue

Fushun Power Supply Company, Liaoning Electric Power Company Limited, State Grid, China,

wts55@126.com

Keywords: partial discharge, discharge standard, discharge response waveform

Abstract. When the power transformer in partial discharge test, if the test equipment (voltage regulator, intermediate transformer, etc.) ontology partial discharge is big, it will severely affect the quality of testing, and even cause false identify.How to correctly identify partial discharge from the power transformer or from the test equipment itself, it is very important for the test personnel. This paper introduces to use the idle 220kV circuit breaker in parallel capacitor to cleverly find out in the whole process of partial discharge from the test equipment itself.

Introduction

Under the effect of the electric field, the insulation part area happens the short-circuit phenomenon is known as partial discharge. Partial discharge can occur in the insulation structure internal air gap, the oil film or the conductor (electrode) on the edge, but it is not formed a channel between the electrodes[1,2].

Insulation partial discharge with electricity, heat and chemical processes, these processes often make the insulation performance reduction, therefore, in many cases, the damage of the insulation is often caused by partial discharge from internal or surface insulation.So detecting the existence of partial discharge and measuring the intensity of discharge is very important, at the same time,partial discharge measurement can also be as a kind of non-destructive control experiment.In order to prevent insulation life reduction and ensure the system safe operation, and in the power system as the main equipment of the power transformer partial discharge test is very necessary.When there is no special test equipment, and the test equipment itself partial discharge often occur, discharge rule, discharge response waveform and the test transformer partial discharge and it is similar, this confused phenomenon for the test personnel bring inconvenience, even cause the false identify.So identifying or troubleshooting partial discharge from the power transformer or from the test equipment itself,for the test quality assurance it is more significant implication[3].

Applied to the grounding test voltage standard and the time sequence is shown in Figure 1:

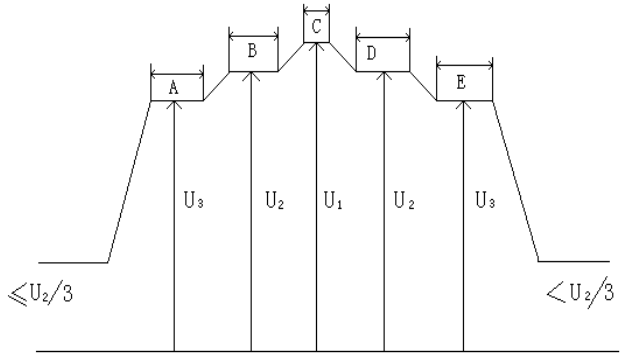

Figure 1 Applied to the grounding test voltage standard and the time sequence

$U_1 = 1.5U_m/\sqrt{3}\,\mathrm{kV}$； $U_2 = 1.3U_m/\sqrt{3}\,\mathrm{kV}$； $U_3 = 1.1U_m/\sqrt{3}\,\mathrm{kV}$

A=5min； B=5min； C=1min； D≥5min； E=5min

In process, the voltage rise U_2 and drop from U_2,it is possible to occur partial discharge inception voltage and extinction voltage, and shall be recorded.

In the test time shall be continuous observation discharge waveform, and according to a certain interval time to record discharge. Reading discharge, it will be subject to relatively stable highest repeat pulses, and the occasional high pulse can be ignored, but it should be recorded for the reference. If the test voltage suddenly drops or characteristics of partial discharge have a continued rise trend, it should repeat the test and find out the reason.

If meeting the following conditions, it is generally believed that the test power transformer partial discharge is qualified.

1) the test voltage can't sudden drop; 2) under $U_2(1.3U_m/\sqrt{3})$ the second period of 5 min, all the measured phase partial discharge on the continuous level is less than 300pC;3) characteristics of partial discharge without rising trend;4)under $U_3(1.1U_m/\sqrt{3})$ partial discharge on the continuous level is less than 100pC.

The determination of the transformer partial discharge field test connection

Due to the existing condition of the test equipment set-up limit (only a JF - 8601 interference discriminate partial discharge detector), at the same time also meeting voltage requirements of "Partial discharge of the power equipment for measuring site title".Due to partial discharge test is very sensitive for voltage test, only when the field strength of the internal defects rise to inception discharge, discharge can be observed, so the final test voltage value shall be $1.5U_m/\sqrt{3}$ (the test phase terminal grounding voltage).Because our company don't have the times frequency power supply, now the test adopt the power frequency test power supply. Under normal conditions, the power frequency test power supply is not possible to make the winding induct high voltage , due to under the voltage $U_m/\sqrt{3}$, the core magnetic flux density is saturate, along with rising voltage ,the excitation current and the ferromagnetic loss will increase sharply, the test phase terminal grounding voltage meet $1.5U_m/\sqrt{3}$ is not possible. So, the method of the neutral point supporting is adopted for the test.

The method of the neutral point supporting is supported on the test transformer neutral point, enhance the test phase terminal grounding voltage to $1.5U_m/\sqrt{3}$.

For example, measuring the phase A partial discharge, the high voltage phase B and phase C short-circuit to grounding, the low voltage phase a and phase c is pressurized, the low voltage phase b to grounding. There is $U_{ab}=U_{bc}=\frac{U_{ca}}{2}$, at this point in the high voltage side magnetic flux is $\phi_B=\phi_C=\frac{\phi_A}{2}$, so the high voltage side induced voltage is $U_{BO}=U_{CO}=\frac{U_{AO}}{2}$. The phase A voltage to the phase B or phase C (due to the phase B and phase C to grounding, it is the phase A voltage to grounding) $U_{AB}=U_{AO}+U_{BO}=1.5U_{AO}=1.5U_{xig}=1.5U_e/\sqrt{3}\approx 1.5U_m/\sqrt{3}$.

There are many types supporting methods, according to the test equipment condition, after repeating demonstration, and finally our company makes a set of connection mode of meeting the sites actual requirements .Now, measuring the phase A partial discharge to illustrate.

The test connection diagram is shown in Figure 2:

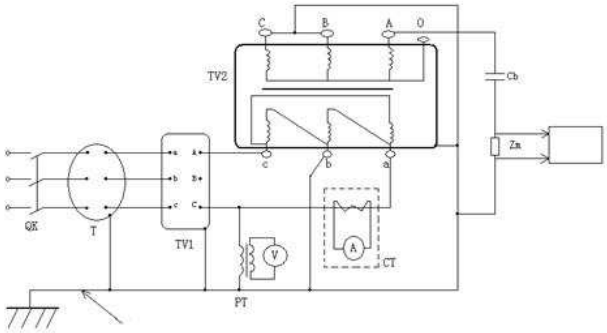

Figure 2 The test connection diagram

In the Figure 2, QK is controllable power switch is three-phase voltage regulator;TV1 is intermediate transformer;TV2 is test transformer; Zm is measured impedance;Cb is high voltage bushing capacitance; PT is standard voltage transformer;CT is current transformer;V is voltmeter;A is ampere meter.

Identify the test equipment partial discharge and treatment methods

At present due to my company's test equipments such as voltage regulator (test transformer), voltage transformer, current transformer are improvised made up, not adopt the standard no discharge device, sometimes the test equipment itself partial discharge is very big, if the test equipment itself partial discharge is mistaken for the test transformer, the problem is very serious, it may cause the test power transformer core inspection, may also delay the transformer leaving factory and putting into operation. So, correctly identifying the test equipment itself partial discharge is the key to ensure to test smoothly.

Identify the current transformer

The power transformer partial discharge test and no-load transformer test need a great deal of power supply capacity and current. String into the empty box in CT is observed under the voltage $1.5\,U_m/\sqrt{3}$ whether the current exceed the allowable values or not.

On April 16, 2004, for a set of type SFZ9-10000/66, the serial number 040301 power transformer does the leaving factory partial discharge test. Background noise 32 Pc, when the voltage rise to $0.7\,U_m/\sqrt{3}$,the inception discharge starts, then it rises with voltage discharge rising, when the voltage rise to $1.3\,U_m/\sqrt{3}$, the discharge up to 3500 pC, the extinction voltage is equal to the inception discharge voltage basically.

Before the discharge pulse is superposition in the positive and the negative peak position, on symmetrical both sides pulse, the amplitude and frequency is basic equal, when discharge response waveform in $0.9\,U_m/\sqrt{3}$,discharge pulse can be distinguish ,with voltage rising, some discharge pulse move to zero direction of the test voltage , at the same time it appears the larger pulse, the pulse resolution decline gradually, when discharge response waveform in $1.2\,U_m/\sqrt{3}$, discharge pulse can't be distinguish.

The discharge response waveform is shown Figure 3:

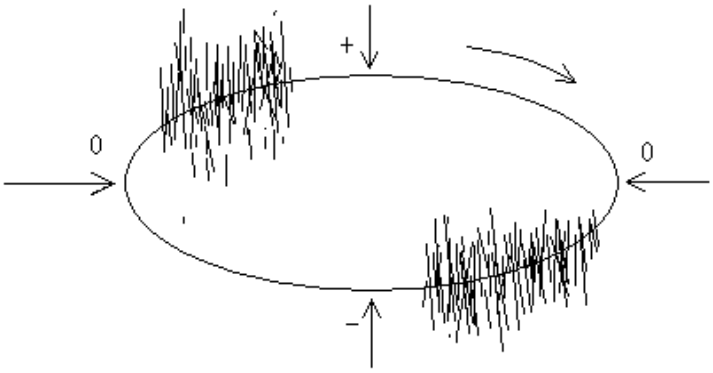

Figure 3 The discharge response waveform

Due to by a lack of experience, it is mistaken for the test power transformer has serious partial discharge defects, but continuing to do the other two tests and finding the other two tests results, discharge response waveform is the same completely. From the whole process phenomenon of partial discharge, waveform initially thought it belongs to discharge of casting insulation structure internal air gap, because of in a complete set of the test equipment, only current transformer is casting solid insulation, moving target to current transformer, it can be seen from the above several

times tests, when the voltage rise to $1.5U_m/\sqrt{3}$, then the current is not overweight, it can remove current transformer to test. Without current transformer, the test transformer smoothly through the partial discharge test.

Conclusion

Through several times does the partial discharge test of the test equipment itself; not only successfully finding out the test equipment itself defects, but also we learn more about the essence of the partial discharge test. At the same time also drawing the following conclusion:

(1) Before doing the partial discharge test of the power transformer, first of all is to introspect the test equipment itself, if there are problems we should timely do the treatment and ensure the test quality and test smoothly.

(2) Each power transformer before test should use CT and PT to verify the current and voltage, keeping some detailed records the voltage corresponding value of low voltage side for using a reserved to test, then removing CT and PT , preventing CT and PT itself occur partial discharge and it become the interference signal when doing partial discharge test .

(3) In partial discharge test, when the test is abnormal, adopting the method of the parallel capacitor is as the auxiliary capacitor to identify partial discharge is from the power transformer or the test equipment itself.

(4) To ensure the correctness and accuracy for test, effective solution is to raise the test personnel's ability of identifying various discharge response, grasping characteristics and rules of the transformer discharge.

Reference

[1] Partial discharge of the power equipment for measuring site title, China Power Press, 1992

[2] Partial discharge measurement, The Northeast Electric Power Test Research Institute, 1985

[3] GB1094.3-2003 Power transformer the third part: insulation level, insulation test and outer insulating air gap. China Standard Publishing Press, 2003

Advanced Materials Research Vols. 986-987 (2014) pp 1689-1695

doi:10.4028/www.scientific.net/AMR.986-987.1689

Development of calibration device for the belt weigher based on the material superimposed technology

Jia Cheng[1,2,a], Yizhou Liu[1, 3,b] , Yuanjie Chen[1,c] and Zhenwei Huang[1,d]

[1]Zhejiang Province Institute of Metrology, Hangzhou 310018, China

[2] Zhejiang Provincial Center of Intellectual Property Service, Hangzhou 310012, China

[3]China Jiliang University, Hangzhou 310018, China

[a]chengjiahz@163.com,[b]liuyizhoulen@163.com, [c]zjucyj@gmail.com,[d]13616559047@126.com

Keywords: material superimposed technology,belt weigher calibration device,uncertainty analysis

Abstract. Great accuracy is required in the settlement process of coal trade. In order to improve the accuracy of coal measurement, a set of online belt weigher calibration device based on the method of material superimposed has been developed. The mechanical structure of the whole device is well designed realizing material circulation conveying. At the same time the software and hardware of calibration system are fully designed.Finally the experimental results indicate that the uncertainty of the calibration device for belt weigher is within 2% and the minimum theoretical ratio of belt material superimposed is about 42% which attains the error requirement of grade 0.5.

Introduction

Electronic belt weigher is a kind of weighing instrument which can continuously and automatically totalize materials during belt conveyor is transporting the solid bulk material[1]. In all types of electronic belt weighers, measurement and trade settlement weigher require the highest accuracy which is between 0.1% to 0.5%[2]. As a dynamic continuous measuring instrument, its measurement accuracy is not only related to installation quality and position,but also closely related to the periodic calibration[3].

According to the requirements of national verification regulation for belt weigher,the electronic belt weigher need regularly calibrating to judge whether its technical indicators conform to the requirements. In general electronic belt weigher test can be divided into simulation test and material test. And typically operation checking methods include weight checking,roller chain checking, cycling chain weight checking and material checking.

As mentioned above the first three methods belong to simulation test, on the contrary the last one belongs to material test. Due to the bad stability and installation collimation for the load receptor,weight checking[4] is only considered as an auxiliary method.And roller chain checking[4] is closer to the actual situation for belt conveyor compared with weight checking. Furthermore cycling chain weight checking[5] is developed on the basis of roller chain checking, it is the best method which can fully simulate the belt material environment among the first three belt weigher checking. However material checking[6] is a method which can weighing the actual materials through the belt weigher. Since the material property in this checking are the same as the reality material, the material checking is only reliable method in the four kind of checking.

The belt weigher calibration method based on the material superimposed technology belong to material test. In the material checking costly and big hopper weigher is used to measure the calibrating materials and it needs to spend much time to put these materials on the belt conveyor, so it will inevitably increase the cost of equipment. But the advantages of the material superimposed technology[7] is that the used calibrating materials is less than the material checking. And this new checking technology can not only keep advantages of material checking but also overcome its shortcomings.In the paper, this developed calibration equipment adopts the method based on material superposition technology. It can overcome the problems of structure complicated and low efficiency for the existing device based on the method of material superposition.

Calibration Principal

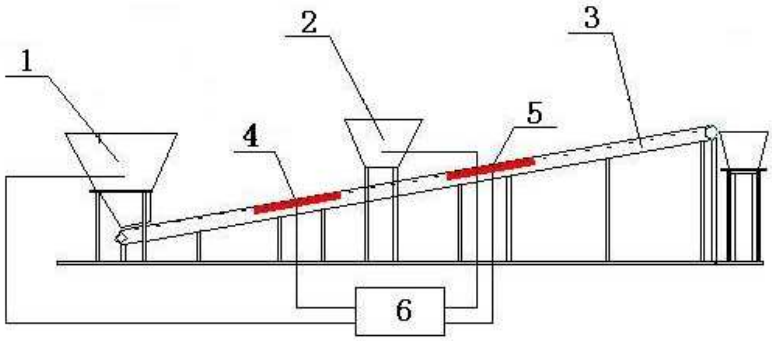

Fig.1.Principal of belt weigher calibration based on the method of material superposition
1-Big hopper weigher,2-Small hopper weigher,3- Belt conveyor,4-Main belt weigher,
5-Deputy belt weigher,6-Industrial PC

The calibration system based on the method of material superposition consists of big hopper weigher, main belt weigher,deputy belt weigher, small hopper weigher, belt conveyor and industrial PC. There are two significant factors to affect calibration accuracy. First of all, the two belt weighers must maintain same measurement environment in the process of calibration. Secondly, the superimposed material have to uniformly and stably through the belt.

Before starting calibration experiment,the small hopper weigher need to weighting the superimposed materials. Then we begin automatic zero-setting and double-weigher comparative experiment. The double-weigher comparative experiment is used for making the two belt weighers keep same error environment through adjusting the deputy belt weigher correction coefficient.

The Fig.1 shows the principal of belt weigher calibration.At the beginning of calibrating, the materials which is delivered by the belt conveyor should uniformly flow the main and deputy belt weigher in the speed of 0.21m/s. After they are covered with all belt, small hopper weigher put superimposed material on the belt until all of materials fall on the belt. And when the superimposed material flow into buffer hopper, the calibration experiment just end. Finally the main and deputy belt weigher will get two groups of accumulation value. And the subtraction values between the accumulation flowrate of main belt weigher and the accumulation flowrate of deputy belt weigher is actual superimposed material value.Then we can confirm their correction coefficient by comparing the theoretical superimposed value with it .The correction coefficient equation is shown below:

$$C = \frac{M}{\Delta Q} \tag{1}$$

$$\Delta Q = Q_2 - Q_1 \tag{2}$$

In Eq.1and Eq.2, M is theoretical superimposed material value; Q_1 represents main belt weigher cumulative flowrate; Q_2 is deputy belt weigher cumulative flowrate;and ΔQ stands for the subtraction of main and deputy belt weigher cumulative flowrate; As the change of belt speed and material uniformity,cumulative flowrate[8] $Q(t)$ is the integral for instantaneous flowrate within Ts :

$$Q = \int_0^T Q(t)dt = \int_0^T q(t)v(t)dt \tag{3}$$

In Eq.3, $q(t)$ stands for instantaneous load value;and $v(t)$ is instantaneous belt speed;United vertical Eq.1~Eq.3,The correction coefficient C is

$$C = \frac{M}{\int_0^T q_2(t)v\ (t)dt - \int_0^T q_1(t)v\ (t)dt} \tag{4}$$

$q_1(t)$ and $q_2(t)$ respectively is main and deputy belt weigher instantaneous load value in Eq.4;according to the theoretical correction coefficient equation,the subtraction values between main and deputy belt weigher cumulative flow become ΔQ_1 :

$$\Delta Q_1 = C_1 \times Q_2 - C_1 \times Q_1 = \frac{M \times (Q_2 - Q_1)}{\Delta Q} = M \tag{5}$$

ΔQ_1 equals to the theoretical superimposed material M ,so this correction method is feasible in theory. And the belt weighers error equation is

$$E = \frac{M - \Delta Q}{M} \tag{6}$$

Design of calibration device

3.1 design of device structure

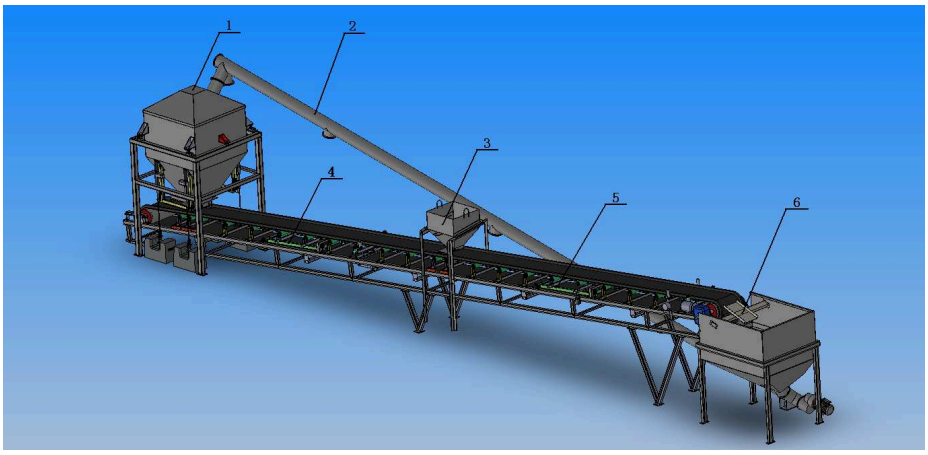

Fig.2.Calibration device based on the mothed of material superposition

1-Big hopper weigher,2-Screw conveyor,3- Small hopper weigher,4-Main belt weigher 5-Deputy belt weigher,6-Buffer hopper

This calibration device constituted by big hopper weigher,screw conveyor,small hopper weigher,main belt weigher,deputy belt weigher and Buffer hopper. Through the design of equipment structure,it can realize material circulation transporting.

In the Fig.2, the length of belt conveyor is 16m,its maximum material flowrate is 15t/h while belt conveyor remain 6° inclination with horizontal ground. And the big hopper weigher is installed at the end of belt conveyor, the load frame of big hopper weigher is used to support hopper , discharging device and other parts. Because of the measurement accuracy for big hopper weigher has high stiffness requirement, it uses good steel to welding.In addition its inlet port connect with discharge port of screw conveyor.And the discharging instrument installed at bottom of big hopper weigher can control four weights to lift.

The accuracy grade of main and deputy belt weigher is 0.5. First of all the main belt weigher is installed nearby big hopper weigher , on the contrary the installation location of deputy belt weigher close to buffer hopper. For the small hopper weigher its accuracy grade is III,meanwhile it can weighing 200kg material. And the small hopper weigher is located in the middle of the two belt weighers.The maximum capacity of buffer hopper weigher located in the belt conveyor head position is 800kg.Its discharge port connect with the inlet port of screw conveyor.

In the process of calibration, materials in the big hopper weigher fall on the belt and in turns through the two belt weighers, then the small hopper weigher put theoretical superimposed materials into belt, and these materials finally will be transported in the big hopper weigher by screw conveyor. Above all, the calibration equipment can realize material recycling,and its structure is compact and low cost.

3.2 design of device hardware

The hardware of calibration system include programmable controller(PLC),screw conveyor motor,belt conveyor motor,digital transducer,hopper gate motor,intelligent integrator,weighing sensor and speed sensor. PLC is used to control the movement of screw conveyor and belt conveyor, the hopper gate timing and data collection of all kinds sensor.The communication between upper and lower computer adopts serial RS232 .

Meanwhile the hopper gate motor uses DC drive motor,and others adopt AC asynchronous drive motor. Upper computer sends command to lower computer in order to control all parts running, stopping and the opening degree of hopper gate. PLC would transmit the signals which is processed by the digital transducer and intelligent integrator to upper computer. That could achieve material accumulated and instantaneous flowrate. The principle of control system is shown in Fig.3.

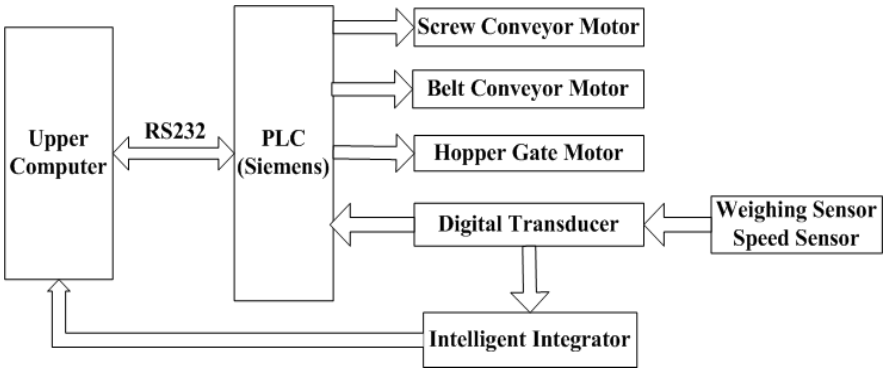

Fig.3.The hardware control system

And the digital transducer is equipped with 24 AD converter, it adopts 4~20mA analog signal.firstly the instantaneous current signal and pulse signal will be converted to instantaneous load weight and velocity. And then the acquired material accumulated and instantaneous flowrate will into the upper computer.

3.3design of device software

The design of software system adopt VB(Visual Basic) programming language. VB is a kind of event-driven programming language developed by Microsoft, it has a graphical user interface(GUI) and rapid application development system. In addition the development environment of PLC is used to develop graphical debugging and running.

In the software design, interface button will send all kinds of control command to PLC for the sake of setting PLC parameters,controlling drive motors and collecting data. Calibration control process is shown as Fig.4.

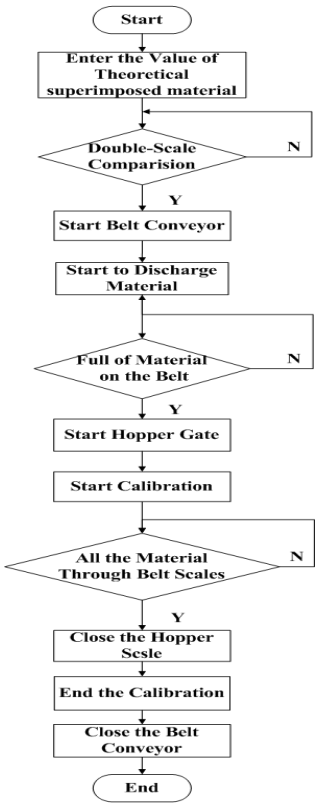

Fig.4.Calibration control process

Experiment

Successful development calibration device based on the method of material superposition as shown in Fig.5, the uncertainty of equipment calibration system is 0.18%. Under the different ratio of theoretical superimposed materials,six experiments had been done. Its maximum permissible error[9] is 0.5% according to the requirements of national verification regulation for 0.5 belt weigher . These experimental results show that the minimum theoretical ratio of belt material superimposed is 42% which attains the error requirement of grade 0.5. And with the proportion which theoretical superimposed material accounts for the total cumulative amount increased, the calibration error has a decreasing trend.

Fig.5.Calibration device based on the superimposed material technology

Table.1.Belt weigher calibration results

NO.	Main belt weigher (KG)	Deputy belt weigher （KG）	Actual superimposed material （KG）	Theoretical superimposed material （KG）	Error value (%)	The theoretical ratio of belt material superimposed (%)
1	741.00	828.00	87.00	80.00	8.75	10
2	2480	3310	830	800	3.69	24
3	147.20	228.90	81.70	80.85	1.05	35
4	91.8	159.0	67.2	67.5	0.44	42
5	90.20	185.30	95.10	94.90	0.21	51
6	45.60	113.40	67.80	68.0	0.3	60

In the repetitive experiments of calibration system, we choose three points of theoretical superimposed materials which respectively are minimum,medium and maximum flowrate, and every theoretical superimposed points have been done three times. Depending on the range equation,calibration repeatability error is 0.6% when the theoretical superimposed materials is 30kg; while the theoretical superimposed materials is 60kg, it is 0.3%; and in the point of theoretical superimposed materials 90kg, the calibration repeatability error is 0.3%. The maximum allowed calibration repeatability error is 0.35% according to the requirements of national verification regulation for grade 0.5 belt weigher. Generally speaking the results indicate that only the theoretical superimposed materials is greater than 60kg, it can reach the requirement of the calibration repeatability error.

Table.2.The experiment of calibration repeatability

NO.	Main belt weigher (KG)	Deputy belt weigher （KG）	Actual superimposed material （KG）	Theoretical superimposed material （KG）	Error value (%)	The theoretical ratio of belt material superimposed (%)
1	139.1	167.7	28.6	30	-4.67	18
2	127.3	155.6	28.3	30	-5.67	19
3	129.3	157.6	28.3	30	-5.67	19
4	178	237.2	59.2	60	-1.33	25
5	90.2	185.3	59.3	60	-1.17	25
6	179.5	239.3	59.5	60	-0.83	25
7	201	290.2	89.2	90	-0.89	31
8	225.7	315	89.3	90	-0.78	29
9	161.5	251.1	89.6	90	-0.44	36

Uncertainty analysis of calibration system

The results of calibration system shows that the uncertainty of calibration system[10] is 0.18%.

Through analysis we know that the main affect uncertainty error source include:1.the performance of small hopper weigher as control weighing instrument;2. The measurement performance of main and deputy belt weigher;3.the indication resolution for electronic belt weighers. To be clear the maximum capacity of big hopper weigher is 1t and its scale intervals(d) is 1kg.

1)On the basis of Bessel equation,the repeatability of small hopper weigher uncertainty is u_1.

$$u_1 = S = \sqrt{\frac{\sum_{i=1}^{n}(x_i - \bar{x})^2}{n-1}} = 0.74kg \tag{7}$$

2)The uncertainty Caused by the scale intervals of small hopper weigher is u_2.

$$u_2 = 0.29 \times d = 0.29kg \tag{8}$$

3)The partial load error for small hopper weigher(e) is 0.2d.Considering it belongs to uniform distribution,the partial load´s uncertainty is u_3.

$$u_3 = \frac{0.1}{\sqrt{3}} = 0.057kg \tag{9}$$

4)The belt tension uncertainty affected by the discharging instrument is d.It bring uncertainty u_4,

$$u_4 = \frac{0.5}{\sqrt{3}} = 0.29kg \tag{10}$$

5) Finally the uncertainty components brought by measurement performance is u_5.

$$u_5 = \frac{0.5}{\sqrt{3}} = 0.29kg \tag{11}$$

In Eq.13, k equals to 2.And the combined standard uncertainty u_c and expended uncertainty U is

$$u_c = \sqrt{u_1^2 + u_2^2 + u_3^2 + u_4^2 + u_5^2} = 0.90kg \tag{12}$$

$$U = k \times u_c = 1.8kg \tag{13}$$

As shown in above.The relative expended uncertainty U_r is 0.18%. In order to reduce the influence of these factors on the calibration system, we should install some carrying rollers at the bottom of discharging inlet of the small hopper weigher .

Summery

In this paper, a set of belt weigher calibration device based on the material superposition have been successfully developed. Analysis show that the uncertainty of calibration equipment for belt weigher is within 2% and the minimum theoretical ratio of belt material superimposed is about 42% which attains the error requirement of grade 0.5. Furthermore this calibration equipment can remarkably improve online measurement accuracy of the belt weigher. In a word the calibration system is running well and high efficient.

Acknowledgments

This work was financially supported by the major science and technology about the key industrial project of Zhejiang province(2012C01026-1).

References

[1]John Simpson:Canadian Weights and Measures and 0.1% Certified Belt weighers[J].Canadian Weights and Measures (Technical Paper),2000.
[2]Caisheng Luo,Bingyi Zou,Jiawei Zhang:Electronic Belt weigher(China Metrology Press,Beijing,1992) (in Chinese)
[3]Zijun Wang:Weighing Instruments Vol.38 No.7 (2009), p.36-37.(in Chinese)
[4] Yuanbai Fang:Weighing Instruments Vol.36 No.3 (2007), p.4-11.(in Chinese)
[5]Yuanfeng Chen.The Design of Cycling Chains Calibration Device of Electronic Belt weigher.Shanghai:East China University of Science and Technology,2010.(in Chinese)
[6]Xiaoxia Lian,Qingmei Zhao:Industrial Measurement No.S1 (2003), p.226-227.(in Chinese)
[7]Jiangsu SAIMO Group Co.,ltd,A Kind of High Precision belt weighing device,China.Patent102012253.2011.(in Chinese)
[8]Johansen,Mogens:Belt Weigher.European Patent Application,1994,4(13).
[9]JJG 195-2002.Verification Regulation for Continuous Totalizing Automatic Weighing Instrument.(in Chinese)
[10]Yunfei Ma:Measurement and Test Technology Vol.37 No.8 (2010), p.65-68.(in Chinese)

Advanced Materials Research Vols. 986-987 (2014) pp 1696-1699

doi:10.4028/www.scientific.net/AMR.986-987.1696

The present situation and progress of vibration environment test technology

Xing Yuanding, Qian Hai, Peng Yingcheng, Zhu Baoliang, Huang Meng

Northwest Institute of Nuclear Technology, Xi'An, 710024, China

409274548@qq.com

Keywords: Vibration environment test; Vibration test equipment; Vibration sensor

Abstract. This paper reviews the research status of vibration environment test equipment and technology. The development of modern vibration measuring sensors, types, processing technology, structure principle and the main performance index of the sensor is made by brief introduction and analysis, the problems existing in the vibration environment test is pointed out, at the same time for their application in the field of modern industry be also made by corresponding introduction.

Introduction

Vibration environment test is to identify the structure or equipment withstand the expected vibration environment, ensure the integrity of the structure in the actual environment, equipment performance and accuracy[1]. Vibration environment test is the vibration of the equipment (products) are exposed to a particular environment, to determine the impact on its process, its purpose is to find the product design, components, spare parts and manufacturing process of all kinds of defects, verify the product vibration environment adaptability and reliability of scheduled life. With the improvement of reliability requirements for products, vibration environment test of the development of technology and equipment is more and more important. Due to the vibration environment test is to identify products hardware in the effective way of real use environment reliability, from earlier in the last century, the United States, Britain, Japan and other countries to conduct a lot of work, a lot of achievements. Domestic scientific research institutes, enterprises and universities started the research in the 60s, great progress has been made. Vibration environment test, with the development of modern industrial technology, technology and equipment will be in the product quality, reliability, brand and market competitiveness play a important role.

Vibration test technology research status

Standard vibration environment test is first developed in the 1950s, on the basis of a large number of theoretical and experimental research, the development of the theory and method of the vibration environment test[2]. Traditional vibration environment test with single shaft vibration test method, test equipment with the traditional single shaft electric or electro-hydraulic shaking table (for vertical vibration) or single shaft vibration table water smooth (for horizontal vibration), vibration environment test requirements stipulated by the current popular single channel vibration control instrument. Although single shaft vibration environment test method, as a kind of the applicability of the general test methods have been confirmed by engineering practice, and on this basis, make a lot of vibration environmental testing standards and norms, and made great contribution to the development of modern industry, but using uniaxial motion to simulate the actual product in the process of using multiple spindle vibration environment, the real practical problems still exist a lot of questions. Even if the product in the process of using the actual vibration environment can approximate to single shaft vibration of single axis test is still unable to expose some of sensitive direction of vibration failure mode, makes it hard for field failure completely repetition, and leads to some passed the vibration test according to the standard equipment in the field of fault occurs. The results deviate from the actual, appear owe test and the test. Some developed countries in the 1960s began to ding multi-axis vibration test system research. Began in the early 1960s, the United States three to the development of the vibration table, in the 1970s, has successfully developed a working frequency distortion degree is

higher, the smaller to vibration system. After years of efforts, developed countries represented by the United States has been developed which can realize multi-axis synchronous or asynchronous multi-axis vibration test system and control system, some foreign companies such as STL, L.A.B companies in the United States, Japan JIMV, Shinken company has been selling commercial products. The three axis vibration table dominate. Although multi-axis vibration environment test technology still exists some problems that have a solution, but the multi-axial experimental results show that the technology has the following features: can be more realistically simulate the actual sample in the vibration environment; Improve the degree of complex, owe test of the specimens, the laboratory from the assessment results and the field of comparable enhancement: emersion field appeared, disabled in the war on uniaxial tests are difficult to repetition pattern. Be advantageous to the vibration environment in the whole process of the product use process simulation. The test results show the multi-axis vibration test technology can provide more effective for reliability assessment of products.

Vibration sensor development present situation

Micro-capacitive accelerometer

Micro-capacitive accelerometer is one of the most commonly used. This design adopts the principle of differential capacitive improved sensitivity and anti-interference ability of the sensor[3]. The microstructure of mass deposition on the sacrifice layer of poly-silicon and formed by chemical etching. Two fixed electrode is shot on a glass surface test deposit a layer of metal. In addition, also need to metallization quality block surface processing, so that it formed between the fixed electrode has two public electrode capacitance. All of the above steps are completed under micron processing. The structure of micro capacitive accelerometer is shown in Fig.1.

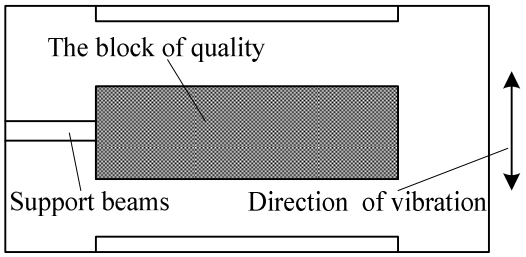

Fig.1. Micro capacitive accelerometer structure schematic diagram

The micro-strain acceleration sensor

Micro-strain type acceleration sensor is also known as piezo-resistive acceleration sensor. This type of sensor is on the basis of the strain gauge sensor development, namely by microelectronic technology of varistor injection on silicon wafers by ion implantation method, and chemical etching of cantilever beam quality-spring system, as shown in Fig. 2. When be supported within the system movement quality of silicon beam stress changes make the beam end of pressure sensitive resistance value changes, it can through the integration of the micro amplifier output with the strain acceleration signal.

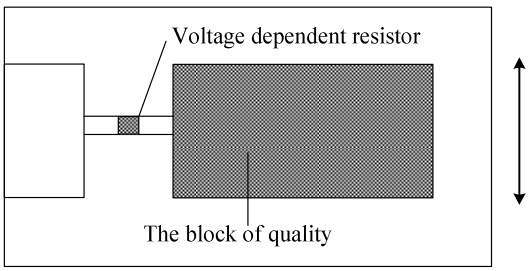

Fig.2. Micro strain type acceleration sensor structure schematic diagram

Quartz Vibrating beam accelerometer

Quartz beam acceleration sensor is to use quartz beam or quartz resonator as acceleration detecting element, its typical structure as shown in Fig.3. It and piezoresistive cantilever beam structure, the

difference is that vibration beam itself is sensitive element. After subjected to external forces, beam charge polarity and charge quantity change, the change of the integration of the release after the release of output proportional to the electrical signals.

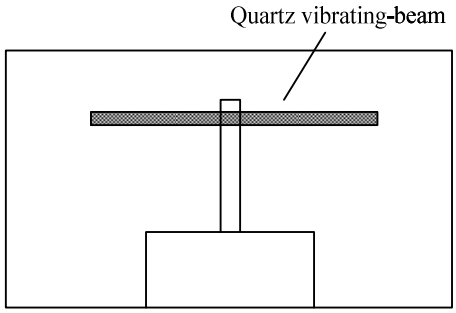

Fig.3. Quartz acceleration sensor structure schematic diagram of the beam dynasty

Electrostatic force balance type acceleration sensor

Electrostatic force balance type acceleration sensor using the force balance way to balance the electrostatic force between the acceleration caused by the role in the detection of the inertial force on the quality. Closed-loop type way of working to make this kind of sensor to overcome the cross coupling error, and due to the size of the electrostatic force and is proportional to the square of the electric field intensity, so it has a high sensitivity and anti-interference ability. Fig.4 is such a typical scheme of acceleration sensor. Its structure and differential capacitance type structure is roughly same, just output circuit to increase the electrostatic force balance circuit and detection circuit. Manufacturer of this kind of sensor has the Northop, BellAerospace company, Crouzet France, etc.

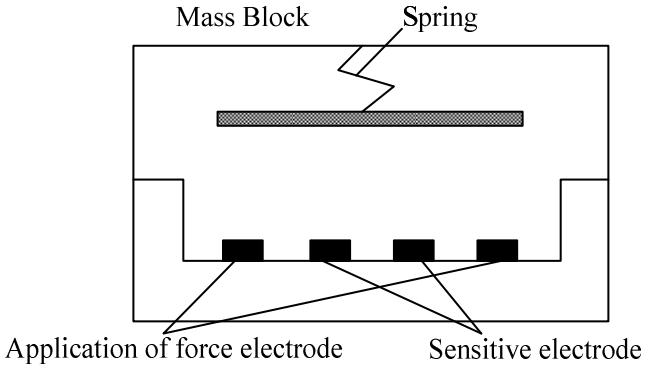

Fig.4. Electrostatic force balance type acceleration sensor structure schematic diagram

Some problems of environmental vibration test

(1) The actual use of the process of complex vibration environment, simplifying analysis of the theory and ignores some impact, vibration equipment damage or failure mechanism is still not very clear, leading to research the mechanism of these test methods of uncertainty.

(2) Although many of its comprehensive test equipment has been basically solved, the key technologies with more attention paid to the comprehensive environmental test, but the control of complex giant, investment, consumption, current is fully implemented.

(3) Tracking filtering and fast fourier transformation in the 1960s appeared, analog and digital vibration testing technology progress, the testing precision is greatly improved, but the vibration environment test technology and equipment research progress of slower, often deviate from the actual test results.

(4) Uniaxial test equipment is relatively mature, multi-axis test ou have yet to be developed. Recently there are used as the way of uniaxial test, in all directions respectively test to achieve more in the direction of shaft test requirements, the main and the lack of real multi-axis related test equipment.

(5) Test load spectrum of a greater influence on the test results, especially fatigue test, the test results of dispersion is people. In addition, the vibration fatigue and conventional (static) the distinction between fatigue and its analysis method are under research and development, some problems the exact word, will affect the correct implementation of environmental vibration test.

Development direction

(1) Multidirectional shaking table by many test pieces, especially the shipping industry experiment of aeronautics and astronautics, vibration environment is more from by degrees, vibration of single direction have been unable to achieve the real vibration environment[4].

(2) More comprehensive sets of environmental testing in order to better evaluate the reliability of the products, the real simulation of the actual typical usage environment reliability test, the birth of the superposition of a variety of environmental conditions more comprehensive environmental test. Comprehensive environmental test three, four and five comprehensive harness, such as temperature, humidity, vibration, three synthesis: three synthesis: temperature, humidity, high temperature, humidity, vibration, high four comprehensive; Temperature, humidity, altitude, constant acceleration, vibration five comprehensive.

(3) Improve the quality of single auxiliary experiment is single shaft vibration test is still relatively common, to overcome the shortage of uniaxial test, eliminate the additional movement, the simulated test environment closer to the actual environment, make the product evaluation results more authenticity, can undertake various of uniaxial test analysis. Carried out from the test equipment to test the feasibility of the evaluation of the optimal control. Including vibration test, specimen vibration coupling analysis equipment, control system simulation and correlation analysis, etc.

(4) Computer simulation and control in the development of modern science and technology, the computer simulation of the effect is more and more big, a lot of problems can be through the simulation, first to experimental verification. Use software such as MATLAB and ANSYS, such as the vibration system, vibration platform structure and so on carries on the simulation, optimization design, with the finite element model can be used to identify the modal parameters of the vibration table.

Conclusion

Vibration environment test on aerospace, vehicle engineering, electrical and electronic industries will get more extensive application, increasingly along with the science and technology. Mature, electronics, electrical, materials technology and mechanical design method, the vibration test system development to get more opportunities. The single direction of the axial vibration of axial vibration and more comprehensive, more direction of environmental testing technology and equipment will become more mature. New vibration measuring sensor led by new technology and processing technology on microstructure has fundamentally promote the mass production and application of this field, at the same time, the traditional piezoelectric sensors, piezo-resistive type and schedule still has its irreplaceable advantages, wide frequency range, wide dynamic range, etc., the level of processing also is constantly improve and improve.

References

[1] LeiYongJun Zhu Xiao-ying. Vibration test system level products to explore and research. Journal of vibration and shock, 2004, 23 (4): 11-116.

[2] Zhang Shulian. Photoelectric vibration sensing technology progress. Laser technology, 2001, 25 (3): 161-165.

[3] XIE Yong-jun,YAN Dong-song, CHEN Huan-yuan. Thermo-structural coupling topology optimization for structure of microcapacitive accelerometer. Equipment manufacturing technology, 2012, 12(2): 33-35.

[4] FAN zhen, LI Ping, HUAN Hai-xiang. Development of technology and equipment of vibration environment testing. Machinery design and manufacture, 2006, 15(10): 164-166.

Advanced Materials Research Vols. 986-987 (2014) pp 1700-1703

doi:10.4028/www.scientific.net/AMR.986-987.1700

WAMS / PMU data pre-processing and compression

Lili Hu, Shengsuo Niu, Zhirui Liang

Department of Agricultural Electrification and Automation, North China Electric Power University, Baoding, 071003, China

Email: hulili0830@.126.com

Keywords: WAMS; PMU data; Huffman algorithm; data pre-processing

Abstract. With the Wide Area Measurement applications, a large number of experimental PMU data was generated. In order to analyze, transmit and apply the data efficiently, by understanding the characteristics of the PMU data in this paper, pressing the data with the Waveform difference method, then using Huffman algorithm to compress the data. Compare the data pre-processing before and after, compression ratio has been further improved.

Introduction

Wide Area Measure System (WAMS) is a kind of real-time monitoring system which based on the experience of North American blackout and the analysis of Chinese power grid's security and stability. WAMS caters to the requirement of Chinese power grid's security and stability based on the latest information processing technique, communication technique and control theory. The synchronized phasor measurement unit (PMU) in WAMS provide abundant new data sources of the research of the analysis and control function of power system online application area. With the development of power system wide area measurement, wide area control and protection technology, their massive information need to be transformed. The research and application of data compression technology is of great importance for ensuring the safe and stable operation for the power system[1].

This paper analyzes the status of PMU data of the WAMS in processing and compression. Understanding of the characteristics of the data PMU in depth, pressing the data with the Waveform difference method. Comparing compression principle and algorithm limitations of the power system, then select the Huffman algorithm to compress the PMU data. By MATLAB program testing, the data compression ratio is proved to be increased.

The characteristics of PMU data

Phasor Measurement Unit PMU (Phasor Measurement Unit) is based on the real-time phasor measurement device. The voltage and current phasor data of the node is generated by calculating the sampling data which is a direct reflection in the state of power system operation. Accurate measurement data can be predict the real-time accurate state for the dynamic operation of the grid. This will improve the ability to monitor and protect the power system, and it is better able to ensure that the system runs stability and security.

The structure of PMU shown in Figure 1.

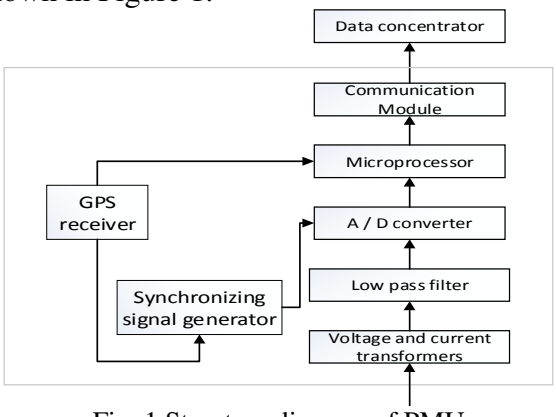

Fig. 1 Structure diagram of PMU

PMU data characteristic mainly displays in three aspects.

1.1 Stored in TXT format. It has the following characteristics: in the form of a hexadecimal string retention; no punctuation and other separators.

1.2 High precision, high real-time. Synchronous sampling the voltage and current of different nodes of the power system.

1.3 Large amount of data. Its frequency is 25 frame/s, real-time records the amplitude, frequency and phase of voltage and current about each each pivot point grid.

PMU data pre-processing and compression

Data compression is aimed at using as little as possible data to show the signal which emitted by the source signal, reducing the signal space to accommodate the given message set. PMU (Phasor measurement units) which are installed in power plants and substations, it transfer data to the data analysis center by high speed communication network[6][7].

In view of the PMU data has the TXT storage property and be able to completely recover data after decompressing, this paper selects Huffman algorithm in lossless compression.

Huffman compression algorithm

Huffman code is a lossless compression coding based on statistical mode[2], which proposed by D. Huffman in 1952. The coding principle: in the case of non-uniform frequency of each character appears, based on these frequencies which used to construct a Huffman tree for encoding. Huffman code can use the shortest binary bits to represent characters which appear most frequently, and use longer bits to represent the low frequency character, so that the average code length is shortened, and maintains a unique coding solvability.

Let given n nodes, k_1, k_2,…, k_n, and their weights were $w_{(k_i)}\ (1 \le i \le n)$, then the length of weight path is: $WPL = \sum_{i=1}^{n} w_{k_i} \lambda k_i$, There w_{k_i} is the weight of the node k_i, λk_i is the length of the path which from the root node to the node k_i, the Huffman tree is a binary tree with the right path with a minimum length.

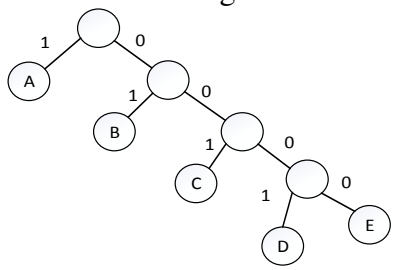

Fig.2 Generated Huffman tree

Tab.1 Encoding each character

Frequency	Encoding	Code length
0.8	1	1
0.1	01	2
0.05	001	3
0.03	0001	4
0.02	0000	4

Huffman compression is based on the frequency of each appearing character. Complete binary tree with n leaf nodes has a total of 2n-1 nodes. Thus, in order to compress 8 character encoding Huffman tree needs 511 nodes [3]. The Huffman tree construction has a common Huffman algorithm which describe in natural language as follows:

(1) For given n weights $\{w_1, w_2, \ldots, w_n\}$, constitutes an initial set of binary tree $F = \{T_1, T_2, \ldots, T_n\}$, where each of them has only one root whose weight is w and its left and right subtrees are empty.

(2) Select two minimums of the root weights as left and right subtrees in the binary tree F. The weight of the new sub-tree is the sum weights of left and right subtrees.

(3) Delete the two trees which is the left and right subtrees in (2) from F, and add the new binary tree in ascending order to the collection F.

(4) Repeat step (2) and (3) until the set F have only one two binary tree.

Assume a file is only five character: A, B, C, D, E. The frequency in which they appear is 0.8, 0.1, 0.05, 0.03, 0.02, the Huffman tree which used the Huffman algorithm as Figure2, after marking 1 and 0 to the left and right branching, get the code of each character, as Table 1, than the average code length can be obtained: average code length = $\sum$ (code length, frequency) = 1.35. If the file length is 10000 characters, then, encoded by an 8-bit ASCII, the file length is 10000 bytes; encoded by three equal length, the size is 100 003/8 = 3750 bytes; using the Huffman table encoding, file size only: 10000×1.35/8 = 1687.5 bytes .So the compression efficiency is obvious. The core of Huffman algorithm is a Huffman tree, through compressing and transmitting data to the analysis center. Figure 4 is the Huffman code flow chart.

PMU data pre-processing

The data preprocessing methods are data cleaning, data integration, data conversion, etc. With the using of data pre-processing methods, it can greatly improve the quality of data and reduce the time of actual processing data. In order to improve the compression ratio of TXT file, we use waveform difference method for PMU data pre-processing[4][5].

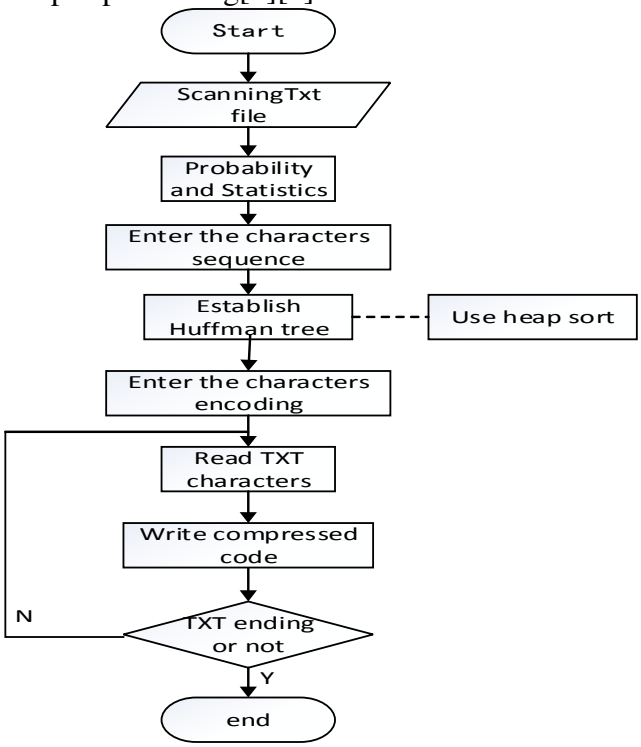

Fig.4 Huffman encoding flowchart

PMU provides phase current, voltage data which have characters of real-time and steady, and store the hexadecimal data in TXT. Four characters in the data represent a particular point in the waveform, continuous 256 points represent a complete waveform, Under steady-state conditions, three-phase voltage, current essentially unchanged, so we propose the waveform difference method which make 0 instead of the same character, make the character easier than before, reduce the string traversal time, and make the possible of increasing the compression ratio.

Results and analysis

Use Huffman compression algorithm to compress TXT files. Results of its operations shown in Table 2. Table 3 is pre-processed.

From Table 2, the test results show that the compressed file is small than the source file, so Huffman compression algorithm can achieve the purpose to compressing TXT files. Table 2 and Table 3 for comparison, the test results show that the preprocessed compression ratio are not the

same, the ratio of using Huffman compression algorithm to compress TXT files directly is lower. Therefore, the waveform difference method which be based on PMU data make certain achievements, it achieves the purpose of further increasing the compression ratio.

Conclusion

Huffman is an efficient lossless data compression algorithm, it can restore the original data by decompression. In this paper, I used MATLAB to program the Huffman algorithm, and achieved a certain compression ratio. For PMU data storage characteristics, this paper used the waveform difference method for data pre-processing, this method reduced the time to traverse the character, improved file compression ratio. The file compression tests before and after the data pre-processing show, the Huffman algorithm based on data pre-processing is helpful to improve the compression ratio. Analysis and experimental results show that the method is effective.

Tab.2 File compression test

The source file name	Before compression/KB	Compressed/KB	Compression ratio
Huffman.txt	40.5	19.7	51.450%
Test.txt	200.3	91.6	54.372%
Test1.txt	123.9	64.2	48.134%

Tab.3 Compression test after data pre-processing

The source file name	Pre-processed/KB	Compressed/KB	Compression ratio
Huffman.txt	40.5	16.1	59.870%
Test.txt	200.3	79.3	61.071%
Test1.txt	123.9	53.8	57.816%

In addition, according to the ideas of this article, further researching pre-processing of data or improving Huffman algorithm to increase the data compression ratio of PMU data are the emphasis of the future work.

References

[1] Xu Shu kai Xie Xiao rong, Xin Yao zhong. Present application situation and d evelopment tendency of synchronous phasor measurement technology based wide a rea measurement system [J].Power System Technology, 2005, 29 (2); 4449.

[2] A. C. Rezaul, M. Kaykobad and K. Irwin, "An efficient technique Decoding for Codes", 81(2002), 2002, ppJ05-308.

[3] C. Bei, Z. Hongcai, C. Wenlun and F. Jian Hu, "Huffman Coding Method on Character", and Cybernetics, 2007 International Conference, Hong Kong, 19-22 Aug 2007,Yol. 4, pp.2296-2299.

[4] Yuanmei, Yuanwen compile. Data compression technology and its application. Beijing: Electronic Industry Press, 1995

[5] Shanrong, Dai, ect. Compile, Data Compression, Xi'an University of Electronic Science and Technology Press, Xi'an 2005.

[6] Shihong Miao, Shaorong Wang, Pei Liu ect, Data compression technology in power system communication, Electric Power Automation Equipment,1999,19(3):P32-33

[7] Dingjian, Bai , Xiaomin, Wang Wen Ping, ect. Overview of application researches based on synchronous data measured by PMU in power system [J]. Relay,2006, 34(6):78-84.

Advanced Materials Research Vols. 986-987 (2014) pp 1704-1708

doi:10.4028/www.scientific.net/AMR.986-987.1704

Based on Wireless Sensor Technology for Substation Equipment Temperature Monitoring System

Zhengzhi Yu, Chengge Wei, Zhigang Li, Shi Yang, YU Du, Xianfeng Li

Fushun Power Supply Company, Liaoning Electric Power Company Limited, State Grid, Fushun, 113008, China

15842399663@163.com

Keywords: wireless sensor; 2.4 GHz wireless network technology; real-time online monitoring; over temperature alarm; condition-based maintenance

Abstract. in view of the substation equipment temperature measuring work, the existence of low accuracy of temperature measurement, data real-time performance, large work volume on manual operation, the temperature of the wireless sensor monitoring technique, the 2.4 GHZ wireless network technology, build a wireless temperature monitoring system, substation equipment temperature and the temperature rise of accurate, reliable and real-time on-line monitoring. Real-time monitoring data, intuitive display are in tabular and graphical form. Have the equipment temperature measurement data, temperature change trend analysis, data query and management, over temperature alarm to remind, etc. Real-time temperature data can be convenient access to the substation set control center, to ensure safe and reliable operation of the transformer substation, for substation monitoring and maintenance of equipment operation to provide data support, effectively prevent substation equipment oxidation, burning and other accidents.

Introduction

Electricity substation is an important part of the work completing the voltage changing and power transmission to provide reliable support for the stable supply of electricity. Run a lot of equipment and instruments, including transformers, circuit breakers, disconnectors, surge arresters, capacitors, switches and other equipment inside the substation. These devices guarantee the stable operation of the substation functioning [1, 2].Due to the high voltage and current in the substation, therefore the device will cause the temperature rise when the current passes through the electrical equipment and due to continuous operation of substation equipment in the operating state will be long-term treatment so that the temperature rise. With extended temperature device, the temperature gauge place due to heat increase the equipment degree of oxidation, thereby causing a fire, explosion or damage to equipment accidents. Therefore, operation and maintenance of substation work, requirements for the temperature inside the substation equipment will be regularly monitored. For a long time for the measurement of electrical device junction heating temperature, using the traditional manual inspection testing methods. Unable to timely and accurate temperature control device, the device prompts alert when abnormal temperature processing.

Relevant references [3-7] proposed substation equipment temperature of several ways, the current implementation of substation equipment operation temperature measurement methods using mainly through artificial temperature, infrared thermal imaging manner, such as the problems and vulnerability are:

1) Substation's equipment and instruments, because the scattered locations so that the fault limited testing methods, equipment operation temperature gauge points are not easy to find. Because of the capacitor cabinet, switchgear, etc. in a closed environment, real-time temperature measurement temperature measuring device can not be installed.

2) The traditional wax temperature measurement methods substations using can not realize real-time storage temperature data and its accuracy is low. Infrared imaging temperature measurement methods, subject to site constraints too, imager installation convenient, real-time temperature data is poor.

3) The main change, knife, circuit breakers, surge arresters and other equipment inside the substation, operation and maintenance personnel need to be timed to the site to measure temperature, manual collection and entry workload; safety hazards of high voltage equipment for personnel exists when manual operation.

Substation has basically achieved unattended or less people on duty, the literature [2] proposed the construction requirements of substation digital, intelligent and smart grid, this paper presents a wireless sensor temperature measurement mode, the operation of the electrical substation heating device junction temperature monitoring, reduce temperature measurement equipment installation tedious process, to achieve all-weather temperature monitoring of substation equipment, wireless data collection, data set to show high-temperature applications such as active warning.

Electrical structure

Applications based on wireless sensor measurement technology, wireless temperature measuring device for measuring the surface temperature of the charged node, such as high voltage switchgear contacts and the contacts, high-voltage bus connectors, high voltage cable connectors, knife switch contact, transmission line conductors, wire fittings at operating temperature. Wireless temperature measurement device consist temperature chip, CPU processors, RF modules and high temperature batteries and other components, as shown in Fig. 1.

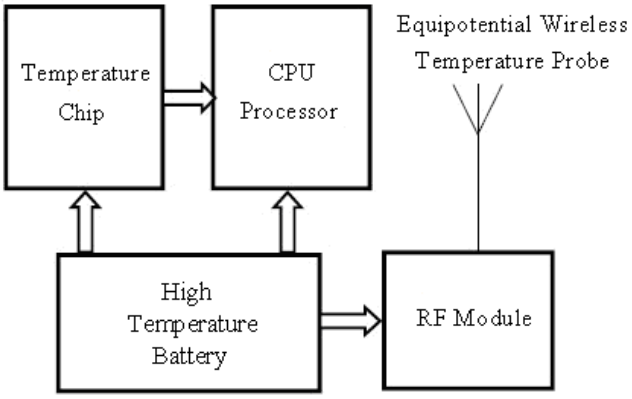

Fig. 1 Schematic diagram of a wireless temperature measuring device

Wireless temperature sensor installed directly in transformers, circuit breakers, disconnectors, switch cabinet cable connector, cable, the capacitor case and other possible heating place. Each sensor has a unique ID, to record the actual installation location of each monitoring point; the monitoring system is stored in the database.

Wireless sensor time to start measuring the temperature monitoring point and send the data. When the monitored temperature exceeds the preset temperature value and increases the frequency of the alarm immediately. These temperature data to the base station via wireless channel 2.4GHz. The base station via RS-485 (CAN, Ethernet) bus temperature data uploaded to the host, and responds to each command system.

Monitoring system take the data of bus temperature to process and preserve, real-time graphical interface displays the temperature of each monitoring point by point analysis and monitoring temperature trends, comparing the relative temperature equipment and environmental analysis may overheat or rapid warming of the situation in advance early warning signals to alert administrators for processing.

Working principle

Substation wireless temperature sensing technology mainly is used by the wireless temperature measuring device (core processor and RF module), centralized control and real-time monitoring system terminals and other components, shown as Fig. 2. Wireless sensor temperature measuring device to monitor the real-time temperature data is sent to the RF 2.4 G wireless ways to set the

control terminal, the distance is greater than the range of 100m. Centralized control terminal supports a variety of communication methods, either RS485 interface or a PC connected to the local display can also be remote LAN data transfer mode to the substation control center. Online monitoring of power system to meet the technical requirements, can easily access real-time temperature data substation control center.

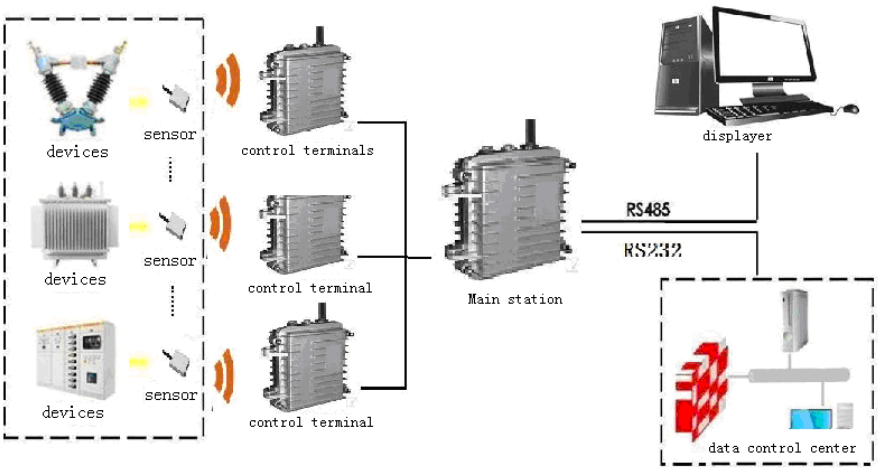

Fig. 2 Schematic diagram of the substation wireless temperature applications

Used to complete the device close temperature approach are based on wireless sensor device for measuring temperature. Wireless temperature monitoring device uses interference shielding and electric field balancing technology, strong anti-electromagnetic interference capability. Under the strong electromagnetic interference environment can ensure normal communication, remote and reliable, high precision, low power consumption, and long life, stable and reliable sensors. Imported chip temperature sensor temperature and high-temperature batteries, the use of power-saving mode, the service life of up to eight years.

In order to achieve real-time temperature, measuring device must be in the substation, substation equipment for wireless indoor and outdoor temperature. Wireless temperature sensor using glue and screws in two ways, installed on the device or the surrounding temperature. The wireless sensor ID and set the internal encoding bind data to identify the value of the temperature sensor identification. Temperature sensors, signal recognition processing module, RF module assembly in the chassis, compact structure, attractive appearance, ease of installation, to ensure electrical safety distance, reasonable structure, tight packaging, anti-rain and anti-leakage.

Wireless sensor network to transmit data to central control terminal, centralized control terminal determines the number according to the area substation installation, normal to cover the sensor 100 meters areas. Excess of 100 m increase central controlling terminal equipment. Centralized control terminal receive data which wireless temperature device send out. Centralized control terminal leave multiple interfaces, supports a variety of communication methods to suit different occasions and needs. Can be connected via RS485 bus real-time monitoring systems and monitoring center in the substation can also be transmitted via LAN centralized control monitoring center.

Final measurement device temperature data is uploaded to store records real-time monitoring system, the system status display real-time temperature inside the substation equipment through a graphical way. Equipment is stable, accurate monitoring data, the risk of having overrun warning and alarm functions and temperature trend analysis. Real-time monitoring system set up temperature monitoring thresholds: temperature warning threshold and into the hazard warning threshold. When the electrical heating device junction temperature reaches or exceeds the temperature warning threshold, time to send early warning information, to immediately send an alert message when the hazard warning threshold. System collects a set period of time based on the real-time temperature data, the display device temperature curve to observe and analyze trends fever junction temperature.

Effect Analysis

Substation wireless sensing temperature applications include:

1) The junction temperature monitoring

Real-time monitoring data collection performed by the form of the data intuitive and list graphical to the user. All the way to install a wireless temperature sensor device will display as a tree structure. The main contents include: temperature monitoring information system operating information, communication test information, over temperature warning information, alarm information.

2) The temperature trend analysis

Set the temperature curve observation time range, select temperature measurement node to be analyzed. During this time you can see the temperature trend for the node.

3) Statistics query and management

Temperature sensor for monitoring information sent back to query and statistics, query historical data, and to analyze historical data, by way of a list, histograms and curves show that the use of performance situations can intuitively reflect the equipment.

4) Over-temperature voice alarm

Temperature monitoring points can be any alarm settings when the temperature data exceeds this value, the alarm automatically and record the situation. Alarm type graphics flashing, buzzer, voice, etc.

5) Master of Information Management and Maintenance

Substation information management, add, modify and delete master.

6) Node information management and maintenance

On the electrical junction temperature manage, add, modify, and delete nodes.

7) Sensor information management and maintenance

Wireless temperature sensors to add, modify and delete.

The results of the application

Effect substation wireless temperature applications, mainly in the following aspects:

Temperature wireless temperature measurement equipment, to achieve substation equipment wireless temperature. Wireless temperature monitoring technology advanced, real-time temperature monitoring data is accurate, easy installation, stable and reliable operation. Meet the technical requirements of the power line monitoring system.

Replace manual inspection temperature measurement methods, but the situation did fever remote intelligent monitoring real-time online electrical junction, temperature limit alarm, to prevent and reduce the occurrence of electrical accidents, greatly increased the level of safe operation of electrical equipment and power supply reliability, provides for the construction of smart grid indispensable technical support, has brought significant economic and social benefits of the grid.

Wireless temperature measurement technique is applicable to the following temperature monitoring applications:

Heating temperature monitoring 220kV/110kV/66KV/35kV/10kV opening and closing of the bus, high voltage switchgear, isolating switches, cables and other electrical junction; 10KV, 35KV, 66KV high voltage switchgear cabinet and various static and dynamic contact line monitoring junction temperature; Substation, substation equipment in the power plant and the temperature of the cable connector cable trench line monitoring; Cable connectors, knife switch contacts, temperature shock bronze contacts and other real-time online test; Transformers, capacitors, reactors, Petersen coil and other equipment can be real-time online monitoring of body temperature.

Conclusions

Substation wireless temperature applications, the use of wireless temperature monitoring technology that uses 2.4GHZ wireless network construction, the use of integrated, miniaturized

packaging technology, the temperature sensor is directly mounted on the substation indoor, outdoor equipment or fever nodes, etc., to achieve equipment operation Real-time monitoring of temperature. Wireless temperature sensor temperature operation instead of doing so achieve operating temperatures of substation equipment inspection records to the substation equipment temperature history data as a reference point, to analyze the true temperature rise of substation equipment, and to provide reliable support for the safe operation of the substation, convenient substation inspection work. Substation equipment wireless temperature measurement technology is an inevitable trend and requirements of electricity production automation, information technology development, wireless temperature measurement technique is applicable to substations, power plants and different voltage levels of the power distribution unit operation, the electrical junction temperature of the heating line monitoring, also applies to other areas of temperature monitoring. Wireless temperature measuring device is simple to install, reliable, significant economic benefits, and has good prospects for development.

References

[1] Cheng Yuewei, Luo Jian, Dai Shanxi. Distributed wireless temperature and humidity test system based on ZigBee[J]. Electronic Measurement Technology, 2009.12:144-146

[2] Li Lanxin, Miao Peiqing, Wang Junfang. Research on Digital Substation System Solutions Based on IEC61850 [J]. Power System Technology, 2006,10(30): 2-4.

[3] Yang Guoping, Zhi Yuanyan, Dai Yinlu. Application of Distributed Fibre-optica1 Temperature Measurement System in Temperature Monitoring of the Converting Station[J]. Electrical Breakers, 2006, (5): 14

[4] Wang Ling, Wang Zhongxun, Wang Heng. Multi-point Wireless Temperature Measurement System Based on MSP430[J]. Modern Electronic Technology, 2011, 34(1): 125-127

[5] Fei Wanmin, Lv Zhengyu, Geng Fujiang. On-line Temperature Measuring and Monitoring System for High-voltage-switch Connectors and Bus[J]. Automation of Electric Power Systems, 2004，28(3): 86-88

[6] Li Taijun, Xiao Chenggang, Wang Zhangqi. On-line Temperature Measuring for High Vvoltage Switch Bus[J]. High Voltage Apparatus, 200l, 37(3): 61-63

[7] Guo Wenyuan, Leiying, Gao Liangyu. The Temperature Condition Monitoring of Electrical Contact in High-Voltage Equipments[J]. High Voltage Engineering, 1996, 22(3): 33-35

Advanced Materials Research Vols. 986-987 (2014) pp 1709-1713

doi:10.4028/www.scientific.net/AMR.986-987.1709

Design and Construction of Railway Cracks Detection Based on Eddy Current

Sheng Yan[1,a], Zou Xuan[2,b]

[1] University of Shanghai for Science and Technology, Shanghai, China

[2] University of Shanghai for Science and Technology, Shanghai, China

[a]cathysusan@163.com, [b]sherryzou@126.com

Keywords: eddy current sensor; distance measurement; automation

Abstract. This paper aims to detect cracks on the rail head via eddy current and show their locations. The combination with mechanical and electronic devices is approached by modeling and analysis. Based on eddy current technology, voltage difference replaces phase shift and the amplification is gained by a triode differential amplifier. It realizes inspection of cracks. Being operated with an incremental optical encoder, Peripheral Interface Controllers and the Liquid Crystal Display, the distance measurement module records the defects. It is applied with a small section of rail tracks.

Introduction

In recent years, nondestructive testing has been significantly popular, such as in railway [1]. Indeed, rail transport occupies a prominent position and the rail head is damaged easily. It relates to property and safety of human beings. Nowadays, many countries have great railway networks in the world. However, considering sustainability and safety, they still have to improve their railway systems. It's an urgent issue to bring up a project with a cheap and available automaton.

There are many means to achieve this goal. Eddy current method is researched thoroughly in the area of cracks detection. In this project, when there is a defect, crack detection module releases light and sound signals. The staff is acknowledged that this place should be maintained. Functions of main microcontrollers include counting pulses, showing variables and calculating the total number of cracks in a certain section of rail. Pulses are generated from the incremental optical encoder (IOE). Through microcontrollers and Liquid Crystal Display (LCD), the numbers about distances of cracks are operated and shown. With the further design, it can work individually.

Brief of eddy current principle

The key section of the paper is eddy current. The basic principle is that: A changing magnetic field is generated by an alternating current. When the coil is located to a conductive specimen, the first magnetic field causes eddy current. As the eddy current meets a crack, it will avoid it and show a higher conductivity region. Eddy current will produce its own magnetic field in the test piece. According to Lenz's law, it is stated that "An induced electromotive force generates a current that induces a counter magnetic field that opposes the magnetic field generating the current." Eddy current line penetrates into the specimen. The standard depth of penetration is stated as Eq. 1.

$$\delta = \frac{1}{\sqrt{\sigma \mu_o \mu_r f}} \tag{1}$$

Where δ= Standard Depth of penetration [mm], σ= Material electric conductivity [Ω/mm^2],
μ_o= Absolute permeability, μ_r= Relative permeability, f= Frequency.

Meanwhile, cracks influence the test coil, especially its impedance [2]. Winding is the important factor in coils. The differential one is worldwide. It consists of two or more coils close together on the area being detected. Thus, it can only reflect the sudden change on the test piece, not gradual [2].

According to author, one coil is replaced by a device. It has the same inductance when the coil on the seamless rail. Therefore, it is similar to differential one but without such a problem.

Design of hardware structure

The crack inspection and distance measurement modules are established as Fig. 1. Each part is described clearly in the following paragraphs.

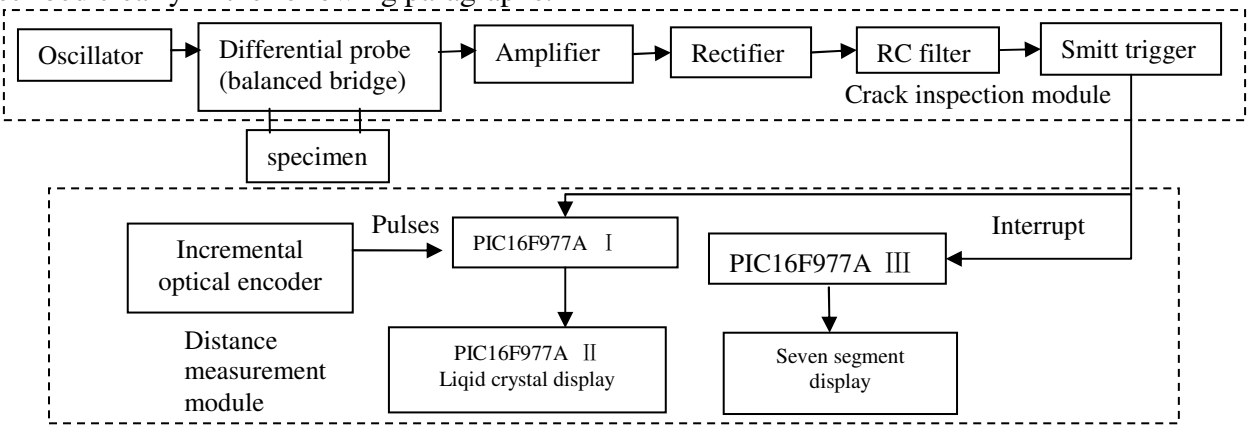

Fig. 1 Construction of crack detection

Fig. 2 is the detail of the oscillator. It is Colpitts Oscillator. It has high impedance, high voltage and low current [3]. The output is resulted from the low impedance of C3 to be the higher harmonics. Thus, the harmonic is low in the feedback loop. It is important that the values of C3 and C4 are same. Otherwise, it causes the instability of the electric circuit. It uses the inductive feedback.

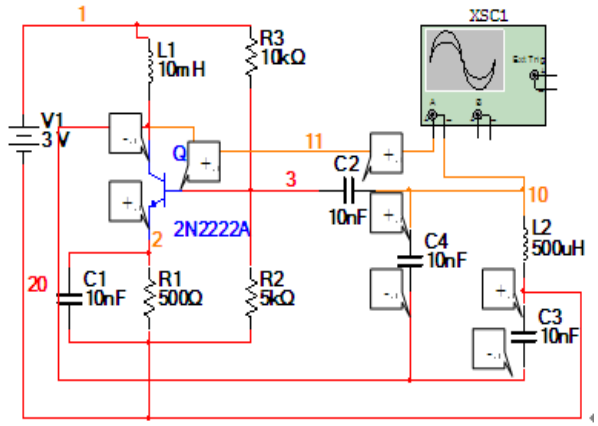

Fig.2 Oscillator circuit

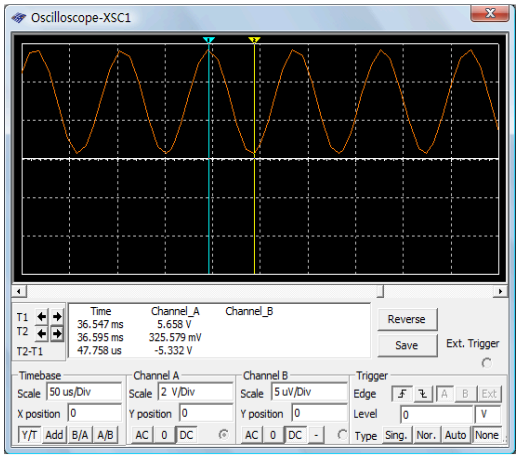

Fig.3 Oscillator output

In Fig. 3, the amplitude is measured to be 5.3 V. The frequency is about 10 kHz.

The author uses inductors to simulate the condition of the coil with eddy current.

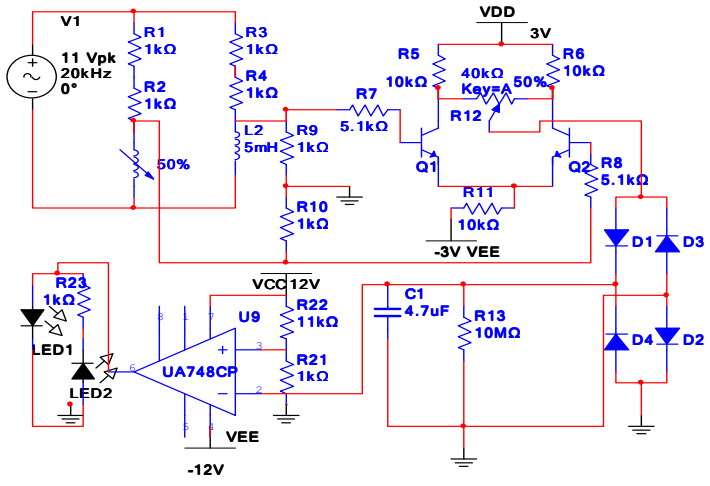

Fig. 4 Crack detection circuit

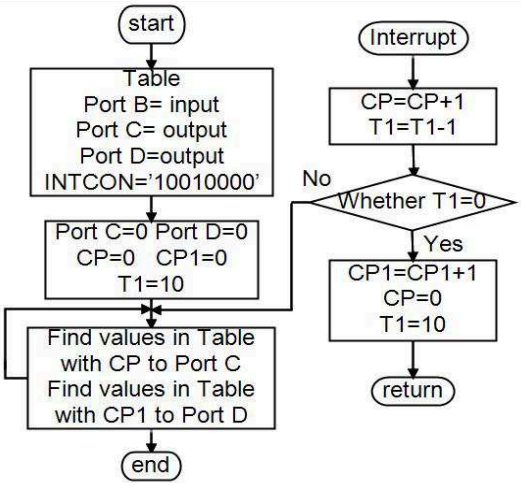

Fig. 5 Flowchart for total of cracks

Fig. 4 is the main part of hardware structure. The source voltage is generated by the oscillator circuit. The balanced bridge can be the phase shift and inductive voltage difference. For the first one, because of the phase shift, distorted wave appears. It is unsuitable. Hence, the inductive voltage difference is attempted to be the input to the amplifier. There is no phase shift. The voltage from the probe should be zero or a sine wave.

Normally, the triode differential amplifier enlarges inverting inputs and reduces common-mode inputs. Inputs from the balanced bridge are in common-mode. It is insensitive to the voltage change caused by the temperature or the fluctuation of the power supply [4]. Therefore, if there is a crack, it outputs a voltage.

The full-wave rectifier modifies the direction of the voltage [5]. It is dealt with the filter. The RC filter aims to alter the alternating current into a direct one. Once it is finished, the filtered voltage should be over zero with a small undulation.

R22 and R21 constitute the voltage divider. UA748CP is a comparator. It compares the input with its reference voltage. Thus, +12v or -12v is provided to the LED, lightening different colors. The output voltage is also the interrupt signal to microcontrollers. The connection with three PIC16F877As is stated clearly in Fig. 1.

Distance measurement design of software

In Fig.1, the optical encoder operates with the wheel. When it rotates, it will send pulses. It interfaces with PIC16F877A by PB1. Where CA1, CA, CZ1 and CZ are the digits to show the total number of wheel turning, CP stands for the pulses. T1, T2, T3 and T4 are counters. TMP1 and TMP2 are flags for LCD. 3 microcontrollers have their own functions. Each is described by the flowchart. In Fig. 5, CP and CP1 are the digits to show the total of cracks. Its maximum is 99. Fig. 6 states the process to convey the distance to be the turning circles. Port B receives the pulses from IOE. When there is an interrupt, Port C and D will present digits. The important step in Fig. 7 is to define the row number with LCD.

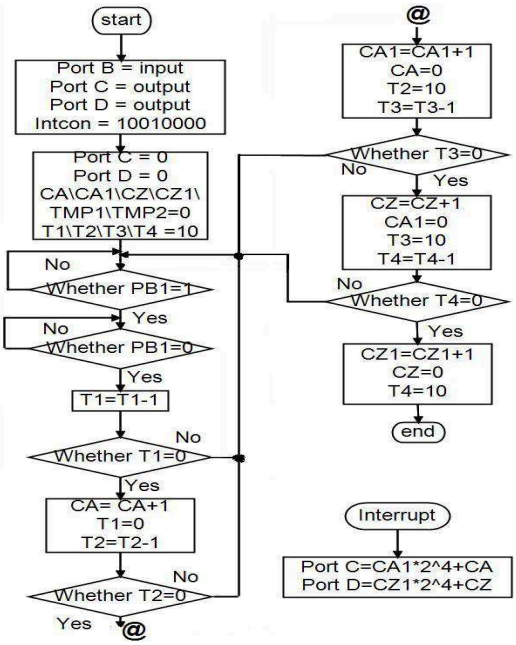

Fig. 6 Flowchart of distance measurement

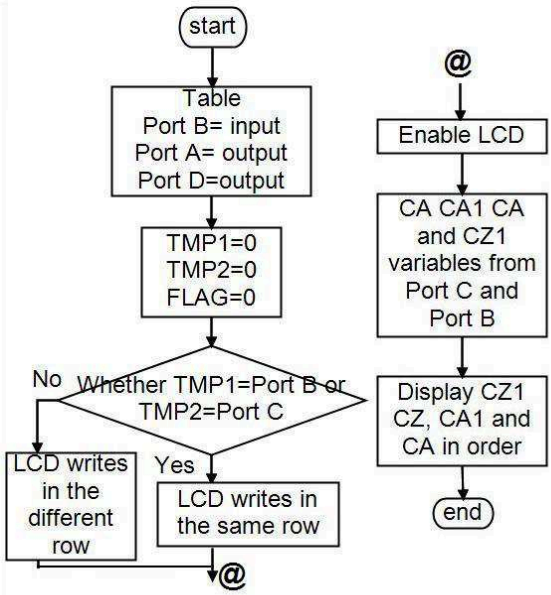

Fig. 7 Flowchart of showing distance

Crack inspection analysis

After the circuit in Figure 4 is established, it is necessary to get some data to check whether the design can be achieved. From Table 1, when L_1 and L_2 have same values, the voltage between Q1 and Q2 is very small. It is about 200 mV. If L_1 and L_2 are slightly different, the output is increasing. V_{L1} and V_{L2} will be influenced by each other. This phenomenon is called mutual inductance. Nevertheless, this effect will be deleted by the triode differential amplifier.

V_1 is the amplitude of the voltage from the amplifier. It is significantly larger when L_1 and L_2 are dissimilar than being same. After rectified, the values are larger than 1 V. It is ideal for the design to detect the cracks. In other words, if there is a small defect, the voltage will be larger than 1 V. V_2 is smaller than V_1 because the loss of voltage falls on the diodes. About each wastes 0.6 V.

Table 1: Vout measured in Fig. 4

V_{L1} / inductor	V_{L2} / inductor	V_{RMS}: from bridge [mV]	V_1: from amplifier [mV]	V_2: from rectifier [mV]
8 mV / 33 uH	96 mV / 33 uH	216	608	464
10 V / 23 mH	10 V / 23 mH	213	640	192
336 mV / 47 uH	120 mV / 33 uH	697	3280	1440
4.16 V / 10 mH	84 mV/ 33 uH	1937	3520	1600
5.12 V / 23 mH	94 mV / 33 uH	2054	3520	1600
5.44 V / 33 mH	88 mV / 33 uH	1076	3600	1520
8.8 V / 33 mH	8 V / 23 mH	1977	2080	1060

In Table 2, the amplitude shown is approximately same. It implies that the RC filter is in work. The existence of cracks results in the voltage larger than 1 V. It is perfect for the Smitt Trigger. To compare with 1 V, +12 V or -12 V will be chosen. Although it is possible to have a negative value with condition of 33 uH (such as -80 mV), it is still lower than 1 V. It has diminutive effect on the Smitt Trigger. +12 V will light the red LED and power the buzz. It means there is a crack.

Table 2: Vout from RC filter [mV]

L_1	L_2	Amplitude	High	Low
33 uH	33 uH	160	80	-80
23 mH	23 mH	80	320	240
10 mH	10 mH	200	720	520
47 uH	33 uH	120	1200	1080
10 mH	33 uH	240	1840	1600
33 mH	23 mH	160	1280	1120

These tables prove the eddy current sensor can scan the flaws and power LEDs or a buzz.

Distance measurement/counting part analysis

In the first microcontroller, the pulses from IOE are important information. With PIC16F877A programmed and IOE turning, digits of turns (CA, CA1, CZ and CZ1) are altered. They are sent to the second microcontroller. For the second PIC16F877A, it is important to have the right hardware connection. Based on the program of LCD, digits are shown. As the total of turns is known, it is easy to calculate the distance with Eq.2:

$$\text{distance} = 2\pi r * \text{turns} \quad (2)$$

The third PIC16F877A deals with the 7-segment display part. When meeting a crack, an interrupt from the crack inspection module is sent to it. A falling edge is effective, then values of CP and CP1 change. Port C outputs the value of CP1 and Port D conveys CP. It is connected with crack inspection sensor as shown in Fig.8.

These three microcontrollers are cooperated well. They have their own jobs to show the total numbers of turns and cracks, but they work as a whole.

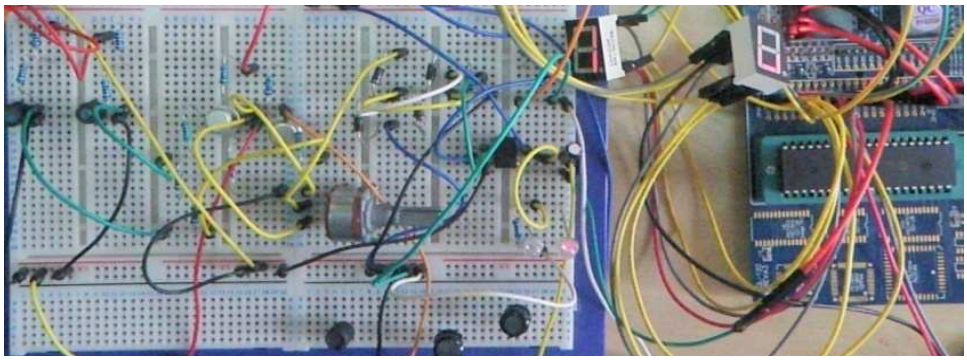

Fig. 8: 7-segment display of the crack total number

Conclusions

This paper models the eddy current sensor and the distance measurement of fault detection. To cope with cracks, the probe (balanced bridge) figures out the position where the inductance is different. The triode amplifier deals with the in-common wave and amplifies it. Furthermore, the output voltage is the interrupt signal for the microcontrollers. Cooperated with IOE, the location of defects is calculated simply. All parts are operated as expected. On account of the inexpensive elements in construction, the automaton is economically popular. With its performance, it not only alarms whether the rail track can be in service further with the red LED, but also stores the distances. With large storage or GSM, it can release manpower. The implementation of this system can improve the efficiency of checking the safety of rails and it has some practical engineering values and economic benefits.

Reference

[1] Kudinov, D.; Shaydurov, G: *Non-contact nondestructive rail testing* Control and Communications, 2009. SIBCON 2009, p.290-295 (2009)

[2] Chen, Xiao-lei; Xiu-lin Wang**:** *The design of testing system based on eddy current technology* Mechanic Automation and Control Engineering (MACE), p. 811 – 814 (2011)

[3] Nomura, N.; Aoyagi, Y.; Sekine, Y.**:** *1 [GHz] high frequency Colpitts oscillator*, Frequency Control Symposium and Exposition. Proceedings of the 2005 IEEE International (2005)

[4] Cher-Shiung Tsai; Ming-Yuan Guo; Chien-Hua Chang; Shu-Yin Jiang**:** *A VHF Oscillator Design Based on BJT Active Load Differential Amplifier*, Electron Devices and Solid-State Circuits, p. 917 – 920 (2007)

[5] Reatti, A.: *Analysis and design of a current-driven two-inductor ZCS low diD/dt full-wave rectifier*, Circuits and Systems I: Fundamental Theory and Applications, IEEE Transactions on Vol.43 (1996), p. 745 - 759

Advanced Materials Research Vols. 986-987 (2014) pp 1714-1719

doi:10.4028/www.scientific.net/AMR.986-987.1714

A novel testing method of low voltage fuel cell

Wu Jiang[1,a], Wu Chaoqun[1,b,*], Wan Li[1,c], Liu Zhaoqing[1,d], Wang Sanwu[1,e]

[1] School of Mechanical and Electronic Engineering, Wuhan University of Technology, Hubei Wuhan 430070, China

[a]five.j@163.com, [b]chaoqunwu@whut.edu.cn, [c]wl596121344@163.com

[d]artliu619@163.com, [e]Wangsw@whut.edu.cn

Keywords: small fuel cell, low voltage, testing method, remote sense, boost power supply

Abstract. Expensive special equipments are often employed to evaluate the performance of low voltage battery, because of the loss voltage of test terminal and line. In the present paper, an economic method was proposed to evaluate fuel cell performance using the booster power supply and electronic load with remote sense. The testing method was deduced theoretically and applied to study the performance of the direct methanol fuel cell . According to the results, it was found that the method was economic applicable and feasible.

Introduction

Because of its simplicity,high-specific energy, instantaneous recharging and presumablylong life, the small fuel cell has been identified as one of the most promising candidates to replace batteries in portable-power applications, such as phones, laptop and so on[1,2]. These types of fuel cells always put out low voltage and power density which make the performance evaluation means becoming a problem of concern, due to terminal blocks, line loss and other causes. Since universal electronic load's minimum working voltage is more than 3 volts and small fuel cells (especially the single fuel cell) cannot provide this high working voltage because of low putout voltage [3], in order to solve the problem of the electronic load's minimum operating voltage, the method of using boost power supply to improve circuit's voltage was proposed and investigated. Although boost power supply can make the electronic load normally working, high voltage of the testing circuit not only generated a reverse voltage in battery and affect the test results, but also made battery permanent damage, as a result of high current density in the testing circuit[4]. In addition, the loss of line voltage and terminal voltage, which were an important part of the whole voltage, would affect the accuracy of the test results due to the small fuel cells' internal resistance was relatively low. Hence, many instruments manufacturers had developed zero volt electrical loads to meet the needs of researchers, but the price of this kind of special test equipment are too expensive. So in this paper, the testing problem of the small fuel cells will be discussed and an economically testing method will be proposed. Moreover, a single directmethanol fuel cell (DMFC) will be tested by the new testing method and the result of the testing will be discussed

Low voltage testing method

Analysis of the test circuit. In order to solve the problems of electronic load's minimum operating voltage, the test system is introduced in the booster power supply to improve circuit voltage, guaranteeing the normal work of the electronic load. When electronic load working on the constant current mode, the test circuit can be equivalent to equivalent circuit as shown in Fig.1.a. Electronic load may be regarded as a constant current source and a resistance in parallel, and tested the battery and booster power can become a constant voltage source and a resistance in series, where $U_c$is the test voltage of the input terminal of the electronic load, and U_z is the measure voltage of the remote sense.

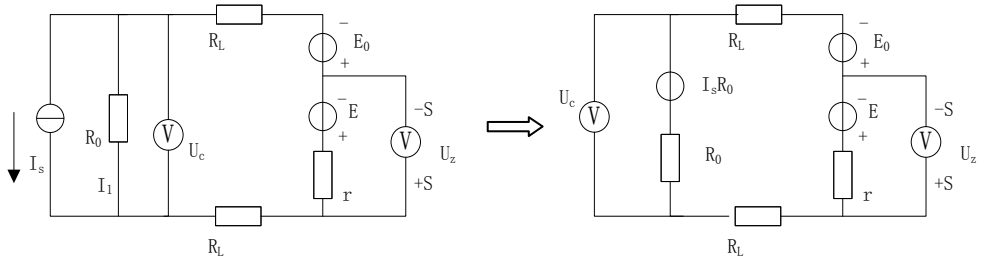

(a) (b)

Fig.1.a equivalent circuit Fig.1.b equivalent conversion circuit

Fig.1 The principle diagram of the equivalent circuit switching

According to the principle of constant current power supply with constant voltage power supply equivalent, Fig.a can be equivalent to Fig.1.b, and circuit's current can be calculated.Such as

$$I = \frac{E + E_0 - I_s R_0}{2R_L + r + R_0} \tag{1}$$

Here, remote sense can be regarded as a voltmeter directly measuring the fuel cell's voltage, which can be considered asthe truth value of the fuel cell. The remote sense's measure value can be calculatedas follow:

$$U_z = E - Ir = \frac{E(2R_L + R_0)}{2R_L + r + R_0} + \frac{I_s R_0 r}{2R_L + r + R_0} - \frac{E_0 r}{2R_L + r + R_0} \tag{2}$$

However, when there was no remote sense, the measuring value of the electronic load was the voltage of the Input terminal. And the voltage can be described as follow:

$$U_c = I_s R_0 + IR_0 = \frac{(E + E_0)R_0}{2R_L + r + R_0} + \frac{I_s R_0 (2R_L + r)}{2R_L + r + R_0} \tag{3}$$

And the real voltage of the fuel cell was:

$$U = I_s R_0 + IR_0 - E_0 = \frac{(E + E_0)R_0}{2R_L + r + R_0} + \frac{I_s R_0 (2R_L + r)}{2R_L + r + R_0} - E_0 \tag{4}$$

Therefore, the measurement error of the fuel cell's voltage with or without remote sense was:

$$\Delta U = U_z - U = \frac{E(2R_L + R_0)}{2R_L + r + R_0} + \frac{I_s R_0 r}{2R_L + r + R_0} - \frac{E_0 r}{2R_L + r + R_0} - (\frac{(E + E_0)R_0}{2R_L + r + R_0} + \frac{I_s R_0 (2R_L + r)}{2R_L + r + R_0} - E_0)$$

$$= \frac{2(E + E_0)R_L}{2R_L + r + R_0} - \frac{2I_s R_0 R_L}{2R_L + r + R_0} \tag{5}$$

As eletronic load's and fuel cell's internal resistence were relatively lower, the effect of the line resistence can no be ignored, as the result of the voltage's measurement error. In this paper, remote sense what is the function of the electronic load was using to compensate the loss of the line voltage, resulting in improving the accuracy of measurement.

Analysis of the fuel cell'sperformance. In actual fuel cell, when there was a current flowing through the fuel cell, a phenomenon what the electrode potential will deviate from the equilibrium potential, is known as the electrode polarization exsiting in the fuel cell. In addition, the potential difference between actual potential and balance the potential was called overpotential that can be described as[5]:

$$\eta = \Delta\phi - \Delta\phi_r$$

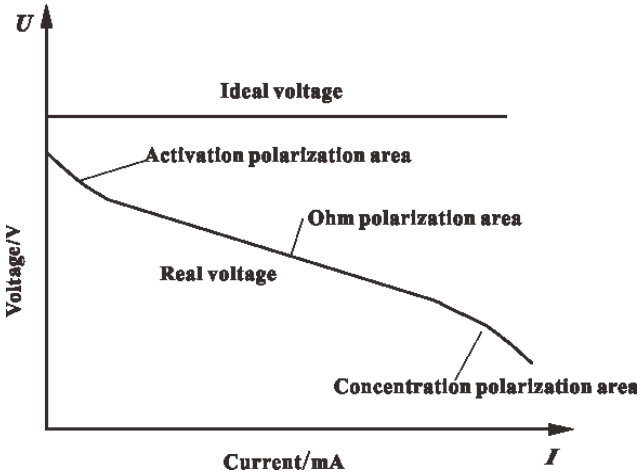

Fig.2 Fuel cell polarization curve

The kinds of fuel cell's overpotential include activation overpotential, ohm overpotential, concentration overpotential, which can respectively correspond to three areas(activation polarization area, ohm polarization area, concentration polarization area) of the fuel cell's polarization curves that was shown in Fig.2. Considering the overpotential, the real fuel cell's voltage was:

$$V = E_0 - \eta_a - \eta_o - \eta_c \tag{6}$$

Where: E_0 was the open circuit voltage; $\eta_a = \frac{RT}{\alpha nF}\ln(\frac{i}{i_0}) = a + b\ln i$ was the activation overpotential; $\eta_o = iR$ was the ohm overpotential; $\eta_c = -\frac{RT}{nF}\ln(1-\frac{i}{i_L})$ was the concentration overpotential; i was the current density.

According to the voltage Eq.6, when the testing circuit's open circuit voltage was boosted by the booster power supply, the current density of the fuel cell will also be improved. Moreover, the effect of the fuel cell's volt reversing will affect the measurement, as a result of the current density exceeding the limitation. Therefore, in order to guarantee the measurement's accuracy, not only the electronic load's normal operation and line's voltage loss should be ensured, but also the protection of the fuel cell's reversion voltage should be considered in the testing.

As the problems was mentioned before, the method what was introducing booster power supply into the circuit to boost the total voltage of the circuit to satisfy the electronic load's minimum working voltage and using the remote sense function to improve the accuracy and reliability of the fuel cell performance testing was proposed in this paper.

Experimental

Device. In this experimental, Nafion 117 polymer membranes (DuPont) were used tofabricate MEAs.The MEA, fabricated in this work, had an active areaof 4.0cm^{2}and consisted of two single-side ELATelectrodes from E-TEK and a Nafion® membrane 117.The diffusion layer for the anode comprised Vulcan XC-72carbon black and 5wt.% of Nafion ionomer (E-TEK), andthe cathode diffusion layer comprised Vulcan XC-72 carbonblack and 15 wt.% of PTFE. The catalyst loading on the anodeside was 4.0mg/cm^{2}with unsupported [Pt:Ru] Ox(1:1 a/o),while the catalyst loading on the cathode side was2.0 mgcm^{-2} using 40% Pt on Vulcan XC-72. Furthermore,0.8mg/cm^2 Nafion® was applied onto the surface of eachelectrode. After having been cleaned following a standardprocedure , the Nafion® membrane 117 was assembledwith two ELAT electrodes to form the MEA by hot pressingat 160℃ and 5MPa for 5 min.

The testing direct methanol fuel cell(DMFC) that was feeded with the dilution methanol solution(1M) was shown in Fig.3.

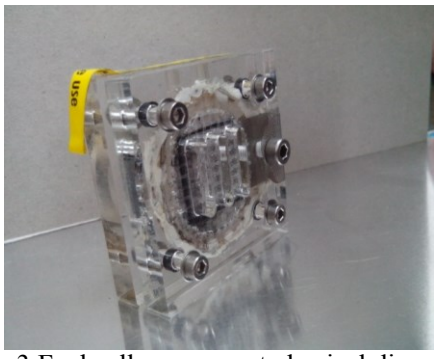

Fig.3 Fuel cell component physical diagram

Testing. The testing system was consist of electronic load(ITECH8512+), booster power supply(ITECH6122B) and DMFC, as it was shown in Fig.4. The DMFC's Polarization curve can be measured by using the electronic load's constant current mode, as well as the truth voltage of the DMFC can be directly measured by using the remost sense which is one of the internal functions of the electronic load. However, without using the remote sense, the voltage measured by the electronic load was the sum of the DMFC and booster power supply. Moreover, the load characteristic curves of DMFC can be measured using the electronic load's constant resistance mode and as the result of the adjusting of the load'sresistance,differenceload characteristic curves can also be tested.

The experimental include: DMFC's polarization curves will be measured with or without remote sense using the electronic load's constant current mode with booster power supply; DMFC discharging curves will be tested by using the electronic load's constant resistance mode with booster power supply.

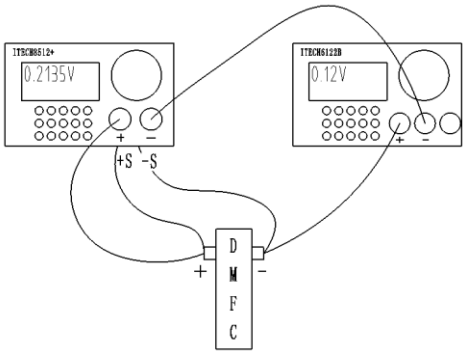

Fig.4 The experimental connections

The voltage of the booster power supply that will provide a constant voltage improving the total voltage of the testing circuit was set as 0.12V, due to the minimum working voltage of the electronic load is 0.1V. The polarization curves of DMFC will be measured by changing the load's current on the constant current mode, in addition, steady discharge characteristic curve of DMFC will be measured on the constant resistance mode. Furthermore, all the experiment were performed under same condition: the ambient temperature (16~18℃), atmospheric pressure (0.1MPa) and results of every testing will be recorded after 30 minutes of the methanol solution injection.

Result and discussion

Effect of the testing line. The polarization curves of DMFC which were measured by changing the load's current on the constant current mode was shown in the Fig.5. According to the result it can be found that the value of the polarization curves measured with remot sense was higher than without the remote sense.

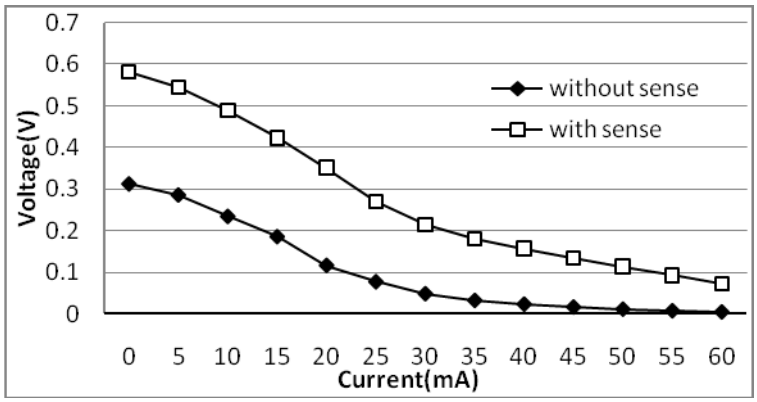

Fig.5 Fuel cell polarization curve with/without sense

As it was analyzed earlier, electronic load's and fuel cell's internal resistance were relatively lower, the effect of the line resistance and loss voltage can not be ignored, as the result of the voltage's measurement error. According to the Eq.5, the loss voltage was:

$$\Delta U = \frac{2(E+E_0)R_L}{2R_L+r+R_0} - \frac{2I_sR_0R_L}{2R_L+r+R_0} \tag{7}$$

What's more, the DMFC's internal resistance had been studied earlier[6], and the results showed that it would be increasing by increasing the current density through the DMFC.

As the circuit current was 0.03A, internal resistance of DMFC and electronic load's resistance was 180 milliohm and 80 milliohm measured by impedance analyzer,as well as the testing circuit line's resistance were about 80 milliohm. The theory of DMFC's voltage was 0.2088V calculated by the Eq.2, and actually measurement value were 0.2136V with remote sense, and 0.0482V without remote sense. While error of the voltage measured with/without remote sense calculated by the Eq.5was about 0.1642V, the difference between theory and the actual measured voltage with/without remote sense was 0.165V. It could be found that there was a large difference between in the absence of remote sense measurement of polarization curve and the results measures with the remote sense by comparing the testing results with the theoretical value. Moreover, since the difference between the actually and theoretical with remote sense were small and in the range of allowable, the remote sense function could be thought not onlyhaving an effect on compensating the loss of line's voltage, but also improving the accuracy and reliably of the testing results,

Effect of booster power supply. Since booster power supply was used in the test system to improve test circuit voltage, reverse voltage may be measured in the DMFC. According to the testing polarization curve, the test parameters of the experimental can be determined. Theelectronic load resistance can be got as R = U/I, in the range between 2.2 ~ 2.5 Ω ,where the voltage of DMFC was 0.1V, and the corresponding current was between 0.04 ~ 0.045A as it was shown in Fig.5. Here the electronic load was set as constant resistance R = 2.5 Ω , and the result was shown in Fig.6.

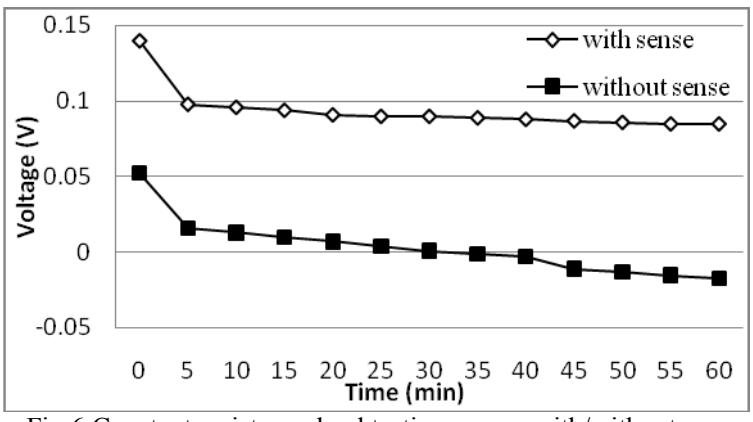

Fig.6 Constant resistance load testing curves with/without sense

Fig.6 was the testing results of constant resistance load testing curves with/without sense. The testing results showed that there exist deviations in test results in the absence of remote sense

function, due to the effect of partial pressure of the test lead. At the same time, as DMFC was discharging, voltage of the DMFCwas gradually changing into a negative voltage without remote sense. According to the properties of the fuel cell, the reasons of resulting in a reverse voltage was the introduction of booster power supply made the current density of DMFC increasing so high that exceeds the limitation of the DMFC's current density. Moreover, testing circuit is verified by experiment and theoretical analysis of the introduction of booster power could make the measurement value of the DMFC's voltage is negative. As remote sense was used, the measurement voltage value was positive, and fit the characteristics of the polarization curve. By comparison with experimental data, the electronic load can introduces the reverse voltage protection circuit of the electronic load to the test circuitby the remote sense, and the recharge of the battery and measure error caused by the increasing currentcan be avoided, due to the introduction of the booster power, so as to ensure the accuracy of measurement, while it also provides the guarantee for the use of booster power.

Conclusion

According the results of the testing, several conclusion can be made as follow:

1. Not only the loss voltage can be compensed, but also the accuracy and reliability of the testing result can be improved, as a result of using remote sense of the electronic load's functions.

2.The minimum working voltage of the electronic load can be solved by introducing the booster power supply into the testing circuit. However, the fuel cell may generate reverse voltage as the result of introducing the booster power supply into the circuit, which increased the total voltage and current of the circuit, that would make an effect on the testing result.

In summary, the method what was introducing booster power supply into the circuit and using the remote sense function to improve the accuracy and reliability of the fuel cell performance testing was not only economic, convenient, high reliability ,but also feasibility and worthy of promotion.

Acknowledgment

This work was supported by the specialized research fund for the doctoral program of higher education (20120143120002) and NSFC(Natural Science Foundation of China) State Natural Sciences Foundation (51305315).

References

[1] KAMARUDIN S K, ACHMAD F, DAUD W R W. Overview on the application of direct methanol fuel cell (DMFC) for portable electronic devices [J]. International Journal of Hydrogen Energy, 2009, 34(16): 6902-16.

[2] ACHMAD F, KAMARUDIN S, DAUD W, et al. Passive direct methanol fuel cells for portable electronic devices [J]. Applied Energy, 2011, 88(5): 1681-9.

[3] Agilent. Agilent Zero Volt Electronic Load[OL]. [2001-6-7]. http://cp.literature.agilent.com/litweb/pdf/5968-6360E.pdf

[4] Bao Lei, Li Zhong, Lu Languang, et al. Measurement of Fuel Cell Chip Voltage. Proceedings of the Automotive engineering society of China automobile electronic technology branch of the 7th annual meeting and academic seminar of the (2006), China's shandong Qingdao, F, 2006 [C].

[5] Chen R, Zhao T S. Mathematical Modeling of a Passive-Feed DMFC With Heat Transfer Effect[J]. J Power Sources, 2005, 152: 122-130.

[6] Li, Xianglin, Faghri, Amir, Xu, Chao. Water management of the DMFC passively fed with a high-concentration methanol solution[J]. International Journal of Hydrogen Energy, 2010, 35:8690-8698.

CHAPTER 8:

Power and Electric Research, Electronics and Microelectronics, Embedded and Integrated Systems and Applications

Advanced Materials Research Vols. 986-987 (2014) pp 1723-1725

doi:10.4028/www.scientific.net/AMR.986-987.1723

A design of intelligent fast charger based on 89C52 MCU

Lun-qiong Chen [1, a], Lu-lu Du [2,b] and Bei Li [1,c]

[1] Changzhou Institute of Technology, Changzhou 213000

[2]Hohai University, Nanjing 211100

[a]chenlq@czu.cn, [b]dll0319hb@qq.com, [c]lib@czu.cn

Keywords: Double-pulse charger, Fast charge method, Microcomputer unit(MCU)

Abstract: In order to reduce the charging time and improve the charging efficiency, designed a kind of intelligent charger on the base of existing charging methods by stages after analyzing the advantages and disadvantages of the domestic quick charge of the storage battery. This system uses STC89C52 as the controller, adding the function of trickle charge and the ability to prevent reverse polarity. It has extended the working life of storage battery a lot.

Introduction

Energy crisis and environment pollution problem have been important restricting factors of the development of economic health. The main reasons of the above issues are automotive exhaust emission and the excess consumption of oil. Facing these problems, electric vehicle has gradually become trend and tide for the development of motor vehicles in the world nowadays, because of the characteristics of environmental protection and energy saving. However, there are many problems have hinder the development of electric vehicle up to now. Battery technology remains one of the most significant problems among them.

Battery is known as the heart of electric vehicle. Its using cost and endurance have always been bottleneck to promote the development of electric vehicles. Rapid charging method is just the crux of these problems.

According to Mass theory, Rapid charging method is not only by increasing charge current to shorten the charge time. The charging process is closely related to historical discharging record. The traditional charging method is constant current charging or constant voltage charging with low charge acceptance rate. Based on Mass theory, literature [1] put forward the most common charge method, namely pulse quick charging method. Pulse width modulation (PWM) was adopted to control strategy based on pulse charging in literature [2]. In the phase of energy feedback, battery can be reverse discharging or stop charging during the charging process. Improvement and study of pulse charging method have improved the charging efficiency in literature [3] and [4]. The interrupt charge method with variable current for battery changed the constant current charging to multi-stage charge at constant current and limited voltage. For the coming charge phase, the charging current is lower than upper grade in order to increase the charging efficiency[5]. Intermittent constant voltage charge was adapted to the interrupt charge method with variable voltage during the main charging phase[6].

Intelligent charger's principle

After analysing various charging methods, then improving stage charging method. The first stage adopts constant current charging method. When the voltage rised to cutting off threshold, the second stage changed to positive and negative pulse charging. At the same time adding terminating stage in the PWM positive and negative pulse charging process[7] to prevent short-circuit for time difference of switch. Finally, when the charging current was smaller, entering into trickle charging stage.

The design of intelligent fast charger

The intelligent fast charger mainly composed of power circuit, pulse control circuit, MCU system and A/D conversion circuit. As shown in Figure 1, MCU system supplied by power circuit outputting positive and negative pulse waveform by software program, A/D conversion circuit sampling battery voltage and completing analog-to-digital conversion and sending the data into MCU in order to judge the state of charge.

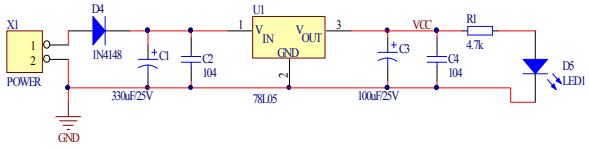

Figure 1 The electric schematic diagram of power source

Power circuit

The power circuit composed of power frequency transformer, rectifier, filter element and the three terminal voltage regulator circuit, providing operating power supply for MCU and the A/D converter chip.

A pulse control circuit

Positive and negative circulation based on process charging-terminating-discharge-terminating-charging[8] controlled emperature influence on battery [9]. Software programs set the time of charging, terminating and discharging during each cycle. Positive and negative pulses werd achieved by a group MOS tube turn-on and turn-off.

The main circuit of the [10] as shown in Figure 3, P type MOS tube Q3 generating positive pulse to control the charging voltage switching, N type MOS tube Q5 generating negative pulse to control the battery discharge. The voltage on the sampling resistor by the A/D converter was inputted into the MCU to judge the battery's working state.

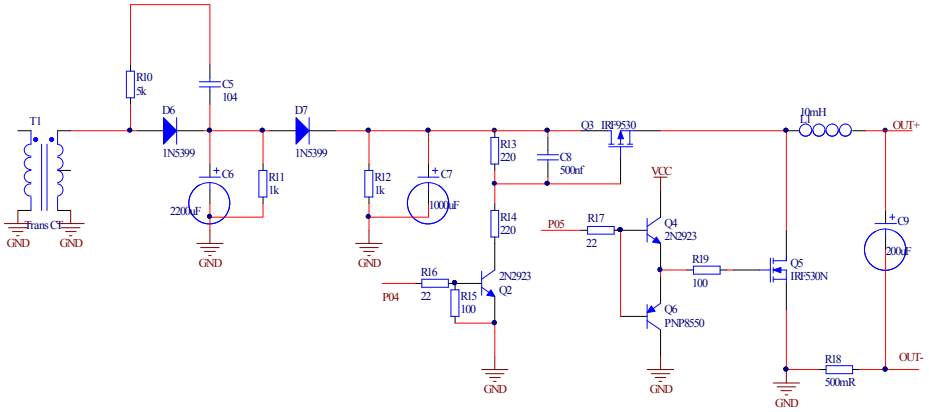

Figure 2 The schematic diagram of control circuit of double-pulse

A/D converter

As shown in Figure 4, The 12 pin and 16 pin of the ADC0809 chip respectively locates in VCC and ground. The 23,24 and 25 pins must be adequately grounded to select channel zero.

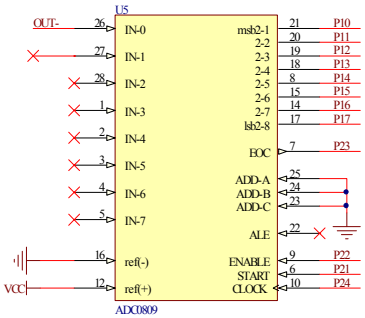

Figure 3 Analog/Digital switching circuit

The design of MCU and soft

As shown in Figure 5, the intelligent control system based on STC89C52 includes reset circuit composed of resistor R9, capacitor C11, switch S and crystal oscillator circuit composed of capacitors C12, C13, crystal Y1. The pin 20 of MCU connecting the diode D3 sends the output signal. When the output signal is high level , charge state is the state of floating charge.

By judging polarity of the sampling voltage through A/D converter into port 1 of MCU deciding on battery charging and lights flashing. If the polarity is correct, the battery begins to charge by constant current. Then the sampling voltage is equal to setting value, the battery is positive and negative pulse charging state, until the trickle charge.

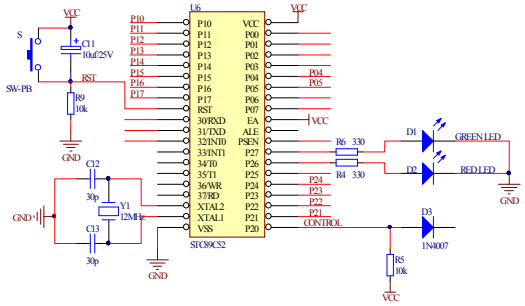

Figure 4 The electric schematic diagram of MCU system

Summary

The charger based on MCU 80C52 , focuses on the design of software and hardware of charger control system, analyses the working process and principle of positive and negative pulse charging circuit. It reduces the charging time and improves the utilization rate of electric energy, preventing reverse polarity to battery.

Acknowledgements

This work was financially supported by Science and technology support program of Changzhou(Grant No. CE20130084, 2013-2015) and the program of Changzhou Institute of TechnologyGrant No .YN1108, 2012-2014）

References

[1]Chic-Ciang Hua,Meng Yulin.A Study of Charging Control of Lead-Acid Battery for Electric Vehicles.Proceedings of the 2000 IEEE International Symposium on Industrial electronics,2010:135-140.

[2]Xi Jia-jian, Wang Zhen-yu, Xiang Zi-xuan, Cheng Li.Control Strategy for Energy Regeneration of Electric Vehicle with High Charge Current Acceptance[J]. Electrical Measurement & Instrumentation, 2013,50(4): 59-63.

[3] Duan Chao-wei, Zhang Lei, Liu Gang.Design of the Pulse-type Fast Speed Charging System of Lead-acid Battery for Electric Car[J].Process Automation Instrumentation,2013,34(7):75-77.

[4]Guo Yi-feng, Wang Zhi-fu, Huang Li-min. Study on Charging Method of Lead-acid Battery Used in Mine with Negative Pulse[J]. Coal Mine Machinery,2012,33(9):75-77.

[5] Li Siguang,Zhang Chengning,Xie Shaobo.Research on fast charge method for lead-acid electric vehicle batteries.Intelligent Systems and Applications,2009,5:1-5.

[6] Simon Delalay,Philippe,Barrade,Alfred,Rufer.Design considerations for the fast charge of super capacitors in the frame of low voltage applications. Proceedings of the 2011 14th European Conference on Power Electronics and Applications,2011,9:1-10.

[7] Ma Li-li,Yan Zhi-wei,He Chao-xing. A new fast pulse charging circuit design[J].Modern Instrument and Medical Treatment,2013(6):11-13.

[8] Lei Wei-jun,Zhang Liang-bing. Fast charging system of lead-acid battery based on MCU[J].Automation &Instrumention,2004(3):91-93.

[9] Feng Ren-bin,Wei Xiao-bin,Hu Heng-sheng. Research on fast charge of lead-acid battery [J].Chinese Journal of Power Sources,2003(1):72-74.

[10] Wang Bin,Zhao Hui,Kong Lin-qiang.The Design of Positive and Negative Pulse Type Intelling Charger for Electric Vehicle [J].Shanxi Electronic Technology,2003(1):18-19,23.

Advanced Materials Research Vols. 986-987 (2014) pp 1726-1729

doi:10.4028/www.scientific.net/AMR.986-987.1726

A New Autonomous Chaotic System and its Circuit Simulation

Heng CHEN[1,a], Tengfei LEI[1,b], Jing MENG[1,c], Rong WANG[1,d]

[1] Department of Graduate, Xijing University, Xi'An 710123, China

[a]chenhenrys@qq.com, [b]846954640@qq.com, [c]1532674448@qq.com, [d]971144062@qq.com

Keywords: New Chaotic System, Heteroclinic Orbit, Chaotic Circuits

Abstract. In this paper, a new chaotic system is constructed. This system contains four parameters and two nonlinear terms. The fractal dimension and the heteroclinic orbit are analyzed in the system. Meanwhile, the circuit of the chaotic system is designed by using Mutisim software. The conclusion confirms the consistency of the numerical simulation and circuit. Because of the above properties, the proposed system has a wide application in such as weak signal detection secure communications and secure communications.

Introduction

Lorenz proposed the first chaotic model in 1963[1].Since then, the chaos system produced great interest. In recent years, many scholars put forward some new distortional chaotic system on the basis of the lorenz system, such as Chen system [2], Lv system [3], Liu system, Qi system [4], etc.In addition to enrich and improve the research of the Chaos, the incessant proposer of chaotic systems further promotes people's understanding and research of the chaos phenomenon. power grids dynamic analysis and protection, mechanical vibration fault diagnosis,oscillation generator design, etc.

According to the *a23,a* classification condition formulated by Vanecek and Celikovsky .There is a parameters *a23=0* in the linear coefficient matrix in most chaotic systems [1-7]. . The normal Lorenz chaos system is studied in the literature and found $a23 \neq 0$ but *a22a11>0*[10]. In the classification of chaos proposed by Yang and Chen, such system belongs to the Lorenz generalized clan. The Chen system, Lv system meeting *a22a11<0*, belongs to Chen generalized clan. So, it become particularly important to construct a kind of transitional chaotic system meeting *a22a11=0* and $a23 \neq 0$. The system can be used for analysis as well as engineering technology such as confidential.

In this paper, another chaotic system is constructed, which meet $a23 \neq 0$ and *a22a11=0*.The basic dynamic characteristics of the system are investigated by means of theoretical derivation, attractor figure and heteroclinic orbit. At the same time, in order to make better application of this system in practice, the system hardware circuit is designed and conducted a simulation experiment. The experimental results further illustrate the objective existence of the system. The numerical simulation shows the validity and realization of this method.

A new Chaotic Systems

In this paper, A new dynamics equation of chaotic system is constructed .

$$\begin{cases} \dot{x} = ay - ax \\ \dot{y} = cx + dz - xz \\ \dot{z} = x^2 - bz \end{cases} \tag{1}$$

Where *x,y,z* are system variables, *a,b,c,d* are positive real constant， When *a=8,b=7.3,c=28, d=1,* the new system exists a chaotic attractor. A new chaotic system Lyapunov index is $\lambda_1 = 0.48$, $\lambda_2 = 0.0$， $\lambda_3 = -15.48$ by numerical calculation. The Lyapunov dimension of the chaotic system *DL=2.03*.The largest Lyapunov exponent of the system is greater than *0* and the system Lyapunov dimension is fraction, so it can be proved the system has the characteristics of chaos.

Heteroclinic Orbit

Assuming that all value of the right side is equal to zero on the system (1), it is easy to obtain three equilibrium points: $E_0=(0,0,0)$, $E_1=(\alpha,\alpha,c+\frac{d\alpha}{b})$, $E_2=(\beta,\beta,c+\frac{d\beta}{b})$ .where $\alpha=\frac{d+\sqrt{d^2+4bc}}{2}$, $\beta=\frac{d-\sqrt{d^2+4bc}}{2}$. If *b=0*, there is only one equilibrium point in system.

Similarly, we can study the *E1* and *E2* for the reason that *E1* and *E2* are similar to the equilibrium point. In this paper, only the stability of E1 is analyzed.

In point of *E1*, the characteristic equation of Jacobian matrix is

$$f_1(\lambda)=\lambda^3+(a+b)\lambda^2+a(b+\frac{d\alpha}{b})\lambda-a\alpha(d-2\alpha)=0 \quad (2)$$

we let $\gamma=\lambda+\frac{a+b}{3}$.Therefore,we can get the new formular.

$$\gamma^3+p\gamma+q=0 \quad (3)$$

Among the formular(3), the parameters meet

$p=\frac{ad\alpha}{b}-\frac{a^2+b^2-ab}{3}$ and $q=\frac{2(a+b)^3}{27}-a\alpha(d-2\alpha)-\frac{(ab^2+a\alpha d)(ab+b^2)}{3b}$.

Let $\Delta=(\frac{q}{2})^2+(\frac{p}{3})^3$.

When it meets $\Delta>0$,there are a pair of conjugate roots $\beta_1\pm\gamma_1 i$ and one of negative real roots α_1 ,as follows.

$$\alpha_1=\sqrt[3]{-\frac{q}{2}+\sqrt{\Delta}}+\sqrt[3]{-\frac{q}{2}-\sqrt{\Delta}} \ ,$$

$$\beta_1=0.5\eta \ , \ \gamma_1=\frac{\sqrt{3}}{2}\eta$$

Thus, the three eigenvalues of equation（2） are

$$\lambda_1=-\frac{a+b}{3}+\eta\,,\lambda_2=-\frac{a+b}{3}+0.5\eta \text{ and } \lambda_2=-\frac{a+b}{3}+\frac{\sqrt{3}}{2}\eta\,.$$

When the system(1) meets $\sqrt{\Delta}>0$ and $\alpha_1+\beta_1<-\frac{2(a+b)}{3}$,it exists heteroclinic orbit based on the liter.

Poincare

Number section and subsection headings consecutively in Arabic numbers and type them in bold. Avoid using too many capital letters. If any further subdivision of a subsection is needed the titles should be 10 point and flushed left.

Poincare map is a kind of classic way to analyze the complex dynamic systems. When the Poincare section is some piece of dense with fractal structure, the system is a chaotic system. In this model, if the plane is taken *z=4*, we will get the Poincare map system as shown in Fig. 1.

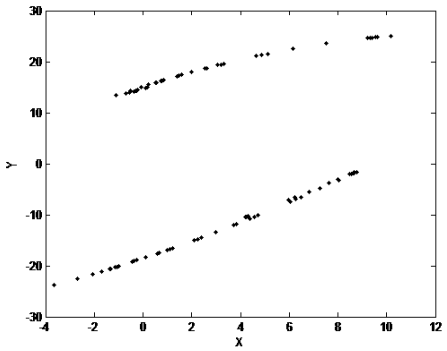

Fig. 1 Poincare map

Circuit Design for the Chaotic System

The Multisim software simulation is used in this paper, and the chaotic system circuit is also designed. According to the system state expression, design circuit diagram is shown in Fig.2.The system is implemented by linear resistance, capacitance, operational amplifier LM741 and analog multiplier AD633. Because the limitation of LM741 and AD633 allows working voltage for±15V, output voltage linear reduces to *0.1* times as great.

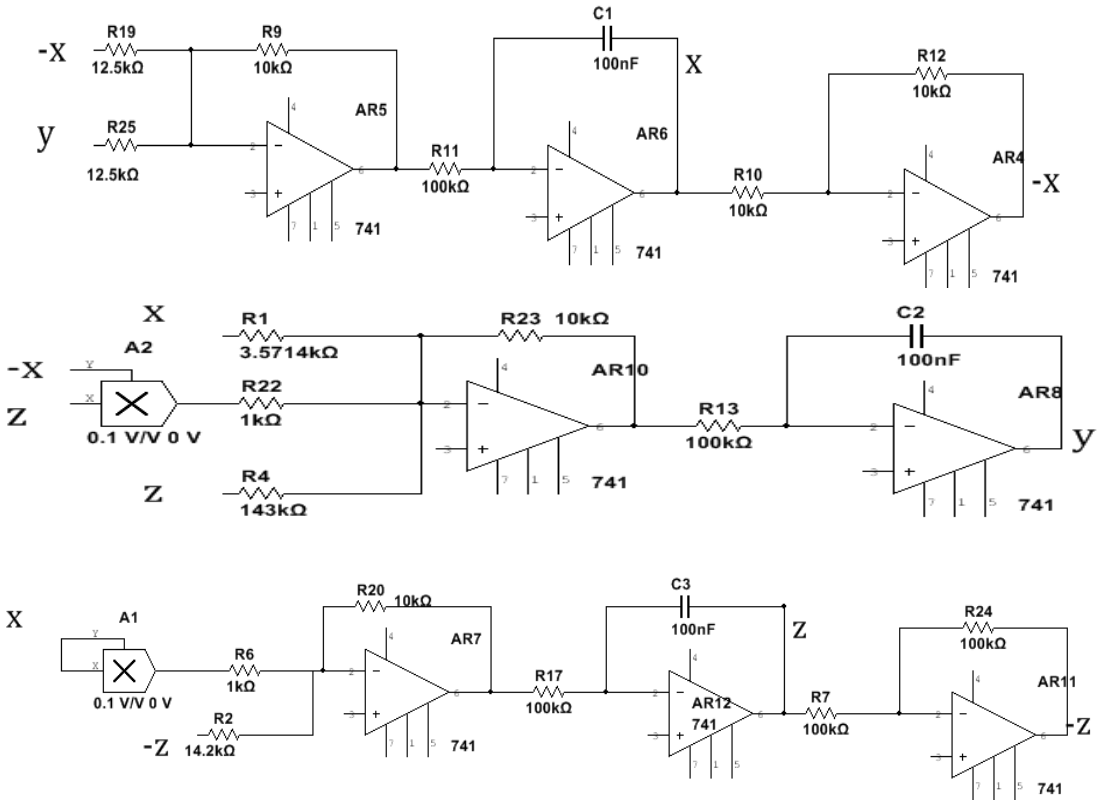

Fig.2 Circuit simulation diagram.

According to the circuit diagram, we can write the corresponding oscillation circuit equation.

$$\begin{cases} \dot{x} = \dfrac{R_9}{c_1 R_1}(R_{25} y - R_{19} x) \\ \dot{y} = \dfrac{R_{23}}{c_2 R_{13} R_1} x + \dfrac{R_{23}}{c_2 R_{13} R_4} z - \dfrac{R_{22}}{10 c_2 R_{13} R_{22}} xz \\ \dot{z} = \dfrac{R_6}{10 c_3 R_{17} R_{20}} x^2 - \dfrac{R_2}{c_3 R_{17} R_{20}} z \end{cases} \quad (4)$$

Circuits are simulated using the Mutisim10. The simulation results on the oscilloscope display are shown in Fig. 3.

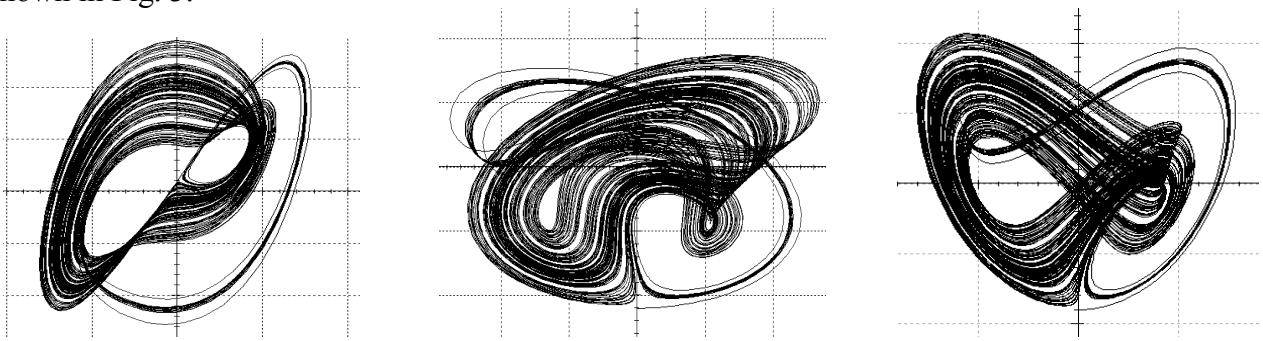

（a）phase portrait in x-z （b）phase portrait in y-z (c) phase portrait in x-y

Fig.3 Circuit simulation results

Conclusions

In this paper, numerical simulation and circuit simulation is made for the new chaotic system. The chaos, quasi periodic and periodic oscillations of the system is realized by adjusting the control parameters of the new system. The circuit is constructed and simulation results are obtained by using Multisim. Therefore, it can be confirmed that the system has the property of implementation. The system can be widely applied to the fields such as electronic image encryption.Of course,it is also the author's next research direction.

References

[1] Lorenz E N. Deterministic nonperiodic flow[J].Atmos.Sci, 1963,20:130-141.
[2] Lü J H, Chen G R. A new chaotic attractor coined [J]. Int J Bifure Chaos,1999,12: 659-661.
[3] Lv J, Lu J, Chen S. Chaotic time series analysis and application[M].Wuhan: Wu han University Press, 2002.
[4] Qi Guoyan, Chen Guanrong, Du Shengzhi, et al. Analysis of a New Chaotic System[J]. Physica A: Statistical Mechanics and Its Applications, 2005, 352(2-4): 295-308.
[5] YANG Q G, CHEN G R, ZHOU T S. A unified Lorenz-type system and its canonical form [J]. International Journal of Bifurcation and Chaos, 2006, 16(10): 2855-2871.
[6] WEI Z C, YANG Q G. Dynamical analysis of a new autonomous 3-D chaotic system only with stable equilibria [J]. Nonlinear Analysis:Real World Applications, 2011, 12(1): 106-118.
[7] YAND Q G, WEI Z C, CHEN G R. A unusual 3D autonomons quadratic chaotic system with two stable node-foci [J]. International Journal of Bifurcation and Chaos, 2010, 20(4): 1061-1083.35(2): 0288-05.
[8] Zaher A A, Rezq A. On the Design of Chaos-based Secure Communication Systems[J]. Communications in Nonlinear Science and Numerical Simulation, 2011, 16(9): 3721-3737.
[9] Zaher A A, Rezq A. On the Design of Chaos-based Secure Communication Systems[J]. Communications in Nonlinear
[10] Science and Numerical Simulation, 2011, 16(9): 3721-3737.
[11] Ren Haipeng,liu ding Nonlinear feedback control in pemanent magnet o synchronous mator[J] IEEE Trans.Ciecuits and ststemnt 2005

Advanced Materials Research Vols. 986-987 (2014) pp 1730-1733

doi:10.4028/www.scientific.net/AMR.986-987.1730

A Novel Optoelectronic Oscillator with Series-coupled Double Recirculating Delay Lines

Cheng-Xin Li[1, a], Fu-Shen Chen [1, b], and Jing Yuan [2, c]

[1] School of Communication and Information Engineering, University of Electronic Science and technique of China, Chengdu, 611731

[2] University for Science and Technology Sichuan, Chengdu, 611745

[a]lcx19841014@163.com, [b] fschen@ uestc.edu.cn, [c] 893381983@qq.com

Keywords: optoelectronic oscillator (OEO); microwave photonic filter (MPF); microwave generation; series-coupled double recirculating delay lines (SC-DRDLs)

Abstract: An optoelectronic oscillator (OEO) based on series-coupled double recirculating delay lines (SC-DRDLs) is analyzed and experimentally demonstrated. The SC-DRDLs composed by the coupling cascade of two RDLs, which the free spectral range (FSR) is least common multiple of the two RDLs' FSR, and then the large FSR can be obtained by properly setting the loop lengths of two RDLs. By consociation with the dual loops system between the dual output of the SC-DRDLs and PBS, the high sidemode suppression performance can be achieved. Meantime, the incoherence of the SC-DRDLs can be performed by using an amplified spontaneous emission (ASE) broadband laser source. An experiment is carried out. A microwave signal with high spectral purity, long-term stability, low single-sideband (SSB) phase noise is generated.

Introduction

With the unique ability to generate high spectral purity and low phase noise microwave signals, Optoelectronic oscillators (OEOs) can be applicated in the fields of radar, radio-over-fiber (RoF) system, sensor, optical signal processing, and modern instrumentation, which uses optical fibers as a high-Q energy-storage element [1-3]. Thus, several schemes were proposed, such as multiloop OEO architectures [4-6], coupled optoelectronic oscillator [7]. In their OEO structure, an electrical bandpass filter (EBPF) is required to perform single oscillation mode. Moreover, the phase noise performance of the OEO is degradated due to the additional noise is introduced by the EBPF, and the EBPF also is temperature-dependent component, small temperature fluctuations may cause oscillation frequency drift.

In the letter, we propose and demonstrated a novel OEO, which uses a series-coupled double recirculating delay lines (SC-DRDLs) as the mode selector instead of the EBPF. Meantime, the dual loops system is formed between the SC-DRDLs and PBS which performs fine selection of the oscillation mode by means of the Vernier principle [8]. In additional, to realize the incoherence of the SC-DRDLs, the amplified spontaneous emission (ASE) broadband laser source is used with the coherence time of the ASE source that is much smaller than the delay time of the SC-DRDLs [9]. Finally, the performance of the OEO is verified by experiments.

Principle

Fig.1 shows the schematic diagram of the proposed OEO. A broadband light wave from an ASE is coupled into a MZM (biased at the quadrature transmission point) via a PMF, which is modulated by the oscillation signal. The first-order sidebands and the optical carrier are generated at the output of the MZM. The modulated signal is then sent to a SC-DRDLs loop, which consists of the coupling cascade of two RDLs. In this way, the free spectral range (FSR) is broadened into least common multiple of two RDLs' FSR [10]. Since the microwave oscillation frequency is determined by the FSR of the SC-DRDLs, and then the coarse mode selection can be achieved by properly setting the loop lengths of two RDLs. Through the SC-DRDLs , the modulated signal are divided into two groups

of output signals, the one outputs from port 2, the other outputs from port 5. Generally, the FSR of the OEO ranges from tens of kHz to several MHz, nevertheless, the 3 dB bandwidth of the SC-DRDLs is not narrow enough to obtain single frequency oscillation. Therefore, to obtain high sidemode suppression, transmission over single mode fibers with different lengths before the two signals are combined by a PBS, the dual loops system can be achieved which realizes fine selection of the oscillation mode. Two PCs are introduced in the dual loops system in order to obtain high extinction ratio. After that, above combined signal is converted to a microwave signal by a photodetector (PD) and then fed back to the MZM to form an oscillation loop. An electrical amplifier (EA) is used in the oscillation loop to provide sufficient gain.

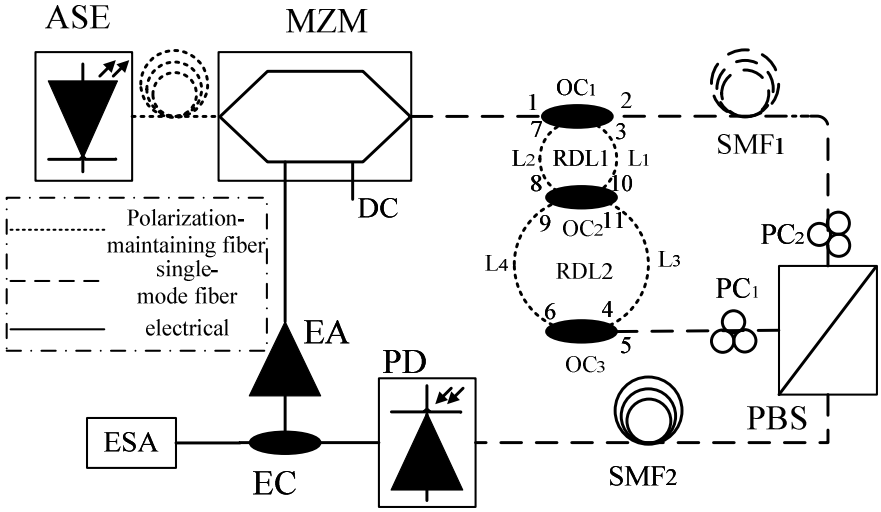

Fig.1. Schematic diagram of the proposed OEO. ASE: amplified spontaneous emission source; MZM: Mach-Zehnder modulator; OC: optical coupler; RDL: recirculating delay line; SMF: single mode fiber; PC: polarization controller; PBS: polarization beam splitter; PD: photodetector; EC: electrical coupler; EA: electrical amplifier; ESA: electrical spectrum analyzer

Experimental

An experiment based on the setup shown in Fig. 1 is implemented. An ASE source with the output power level at 18.1 dBm is used to generate the broadband light wave. The MZM has a 3-dB bandwidth of 10 GHz. A coarse selection of the oscillation mode is realized by using SC-DRDLs which are fabricated via three 2×2 3-dB couplers and PMF. The PD has a bandwidth of 10GHz and a responsivity of 0.78 A/W. The lengths of SMF1 and SMF2 are 103 m and 223 m, respectively. The EA has a maximum gain of 25 dB with a bandwidth of 0.1~10 GHz. The electrical spectrum is measured by an electrical spectrum analyzer (ESA, Anritsu MS 2721B).

When loop length of the SC-DRDLs is specified as L1=L2=2.5m，L3=L4=1.5m, Fig. 2(a) shows the electrical spectrum of the generated microwave signal with a frequency span of 7 GHz. It is clearly seen that there is only one strong oscillation signal at 1.093 GHz. To better observe the spectrum, Fig. 2(b) provides a zoom-in view of 1.093 GHz microwave signal with a frequency span of 1 MHz, showing a 73-dB sidemode suppression ratio (SMSR).

The stability of the oscillation signal is measured. To do so, we allow the system to operate in a room environment for half an hour at a period of 6 minutes, as shown in Fig. 3. Through the observation, the maximum frequency drift and the maximum power drift of the oscillation signal are respectively lower than 3 KHz and 0.22 dBm, and no mode-hopping is observed, showing a stable oscillation signal.

The SSB phase noise performance of the generated microwave signal is also investigated. As can be seen in Fig.4, the phase noise of the generated signal is about -96.5 dBc/Hz at 10 KHz offset frequency. Theoretically, the SSB phase noise can be improved by increase the loop length of SMF2, while it will increase the number of oscillation side-modes

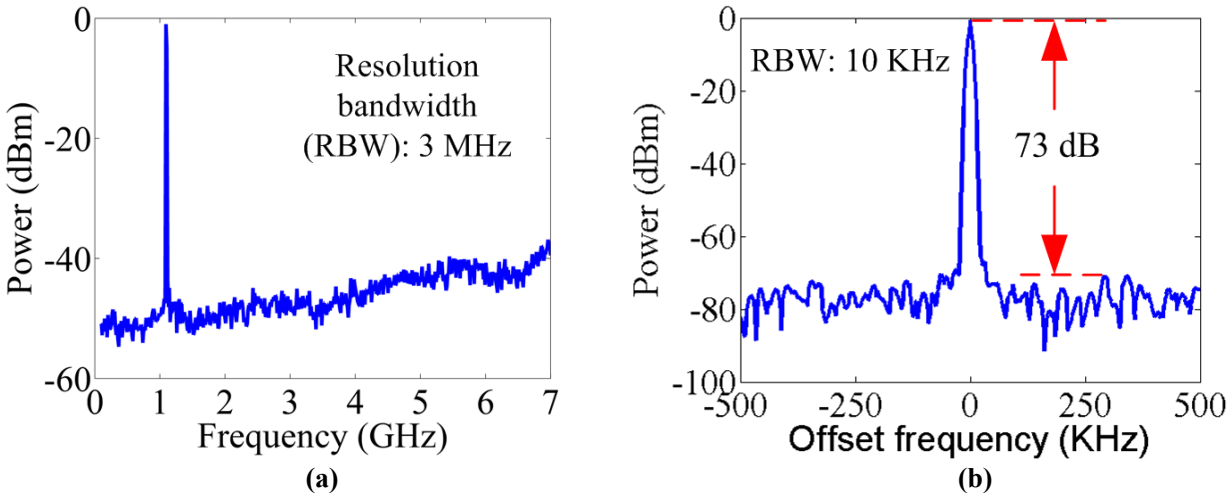

Fig.2. Electrical spectrum of the generated 1.093 GHz microwave signal (a) Span=7 GHz (b) Span=1 MHz.

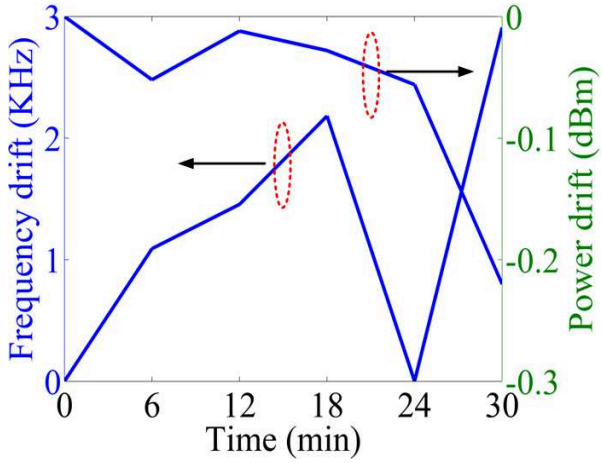

Fig3. stability of the oscillation signal measured over half an hour

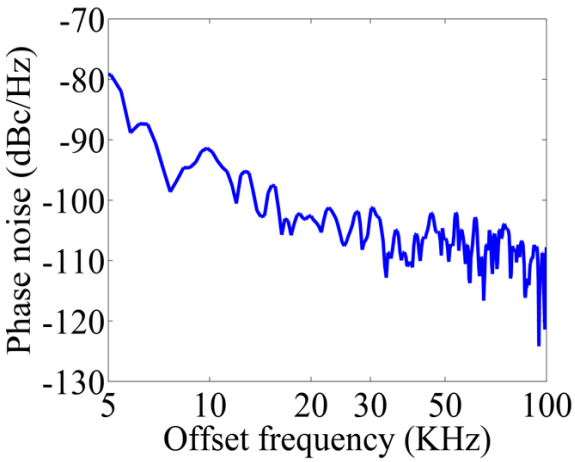

Fig4. Phase noise of the generated 1.093 GHz microwave signal

Conclusion

An OEO was proposed by employing a SC-DRDLs which can form an incoherent two-tap microwave photonic filter (MPF) by combination of an ASE source, a Mach–Zehnder modulator (MZM) and a polarization beam splitter (PBS). Specifically, the incoherence of the MPF can be accomplished by using an ASE broadband laser source and a SC-DRDLs, and the selection of the oscillation mode can be performed in the optical domain by the MPF. Our experimental results show that a microwave signal with a SMSR as high as 73-dB and a phase noise smaller than -96 dBc/Hz@10KHz was generated. Besides, the stability of the generated microwave signal is also experimentally observed.

References

[1] X. S. Yao and L. Maleki: Optoelectronic microwave oscillator. J. Opt. Amer. B, Vol. 13 (1996), p. 1725-1735.

[2] H. Tsuchida: Simultaneous prescaled clock recovery and serial-to-parallel conversion of data signals using a polarization modulator-based optoelectronic oscillator. J. Lightw. Technol., Vol. 27 (2009), p. 3777–3782.

[3] M. Shin and P. Kumar: Optical microwave frequency up-conversion via a frequency-doubling optoelectronic oscillator. IEEE Photon. Technol. Lett., Vol. 19 (2007), p. 1726–1728.

[4] X. S. Yao and L. Maleki: Multiloop optoelectronic oscillator. IEEE J. Quantum Electron, Vol. 36 (2000), p. 79-84.

[5] W. M. Zhou and G. Blasche: Injection-locked dual opto-electronic oscillator with ultra-low phase noise and ultra-low spurious level. IEEE Trans.Microw., Theory Tech., Vol. 58 (2005), p. 929–933.

[6] Jiang Yang, Yu Jinglong, Wang Yaotian, Zhang Litai, and Yang Enze: An optical domain combined dual-loop optoelectronic oscillator. IEEE Photon. Technol. Lett., Vol. 19 (2007), p. 807–809

[7] E. Salik, N. Yu, L. Maleki: An ultralow phase noise coupled optoelectronic oscillator. IEEE Photon. Technol. Lett., Vol. 19 (2007), p. 444–446.

[8] O. Pottiez, O. Deparis, R. Kiyan, M. Haelterman, P. Emplit, P. Mégret, M. Blondel: Supermode noise of harmonically mode-locked Erbium fiber lasers with composite cavity. IEEE J. Quantum Electron, Vol. 38 (2002), p. 252-259

[9] J. Capmany, B. Ortega, D. Pastor: A tutorial on microwave photonic filter. J. Lightw. Technol., Vol. 24 (2006), p. 201–229

[10] J Capmany: On the cascade of incoherent discrete-time microwave photonic filters. J. Lightw. Technol., Vol. 24 (2006), p. 2564–2578

Advanced Materials Research Vols. 986-987 (2014) pp 1734-1737

doi:10.4028/www.scientific.net/AMR.986-987.1734

A Sense Amplifier for Low Voltage Embedded Flash Memories

Zhang Hua

Engineering University of the Chinese People's Armed Police Force, 710086
24760054@qq.com

Keywords: Current sensing, embedded flash memories, low voltage, sense amplifier

Abstract. A sense amplifier applied for low voltage embedded flash memories is presented. The sense amplifier uses an enhanced current sensing method allowing power supplies lower than 1.5 V to be used. The sense amplifier was implemented in a FLASH realized with a 0.13 um FLASH technology. Simulation results showed a read access time of about 25 ns with a power supply of 1.5 V, and 32ns with a power supply of 1.2V.

Introduction

In recent years, embedded Flash memories are widely used in SOCs (System On chip) targeting the mobile communications, micro-controllers, smart cards and contact-less cards for on-chip nonvolatile storage with high operation speeds as well as low power consumption [1, 2, 3]. Read speed is mainly determined by the read path, which is affected in a non-negligible way by the sense amplifier's speed performance, and becomes critical when the power supply is reduced [4]. Several solutions are proposed in literature to allow the normal functions under low power supply at the cost of reducing performance [5, 6].

This paper focuses on a novel sense amplifier with enhanced current sensing method for embedded flash memories, capable of operating at voltages as low as 1.2 V without needing special low threshold voltage devices. The pre-charging speed performance of the bit-line is improved with a dynamic bit-line clamping method. This paper is organized as follows: Section 2 presents the proposed sense amplifier circuit. In Section 3, simulation and experimental results are summarized. Conclusions are drawn in Section 4.

Proposed Sense Amplifier Circuit

Fig.1 is a conventional sense amplifier structure. The reading operation of a Flash is performed by sensing the current of selected cell (ARRAY CELL in Fig.1). In particular, an erased Flash cell has a low threshold voltage, giving a high level current under the bias condition. In contrast, a programmed Flash cell has a high threshold voltage, giving a low level current. Read operation can clearly be achieved by comparing the selected cell current with a reference current generally provided by another cell in the same array(REFERENCE CELL in Fig.1). PREB signal is to trigger the pre-charging operation, and pre-charging the capacitances of selected bit-lines (CBLR and CBLA). VD0 and VD1 are clamped to the target value due to the clamp transistor and feedback inverter. The current mirror MR0–MR1, with a mirror aspect ratio lower than one (and typically set to 0.3 to ensure an equal delay for a 1 or 0 read), is used to appropriately scale the current of the reference cell. After pre-charging, the sense amplifier starts sensing, to pull down VF (erased cell, '1' case) or be kept around VDD (programmed cell, '0' case). SOUT is the sense amplifier output voltages which from comparison result of VF and VREF. One limitation for this approach is VE will be limited by the threshold of current mirror transistor MR0, under very low power supply

voltage and consequently bit-line cannot be biased at the desired value. Since a fundamental role is played by the pre-charging method in any sensing scheme for flash memories, traditionally this task has been accomplished by using an inverter with a source follower output stage (Fig.1). This approach allows fast pre-charging independently of the capacitive load represented by the bit-line of the array (CBLA). Although this solution is very useful down to a power supply of 1.8V, it shows non-negligible limitations once the power supply is lowered further. This occurs because the source follower does not correctly bias the bit-line at the desired level and affects the reading speed performance. Furthermore, the power consumption caused by the invert is also non-negligible.

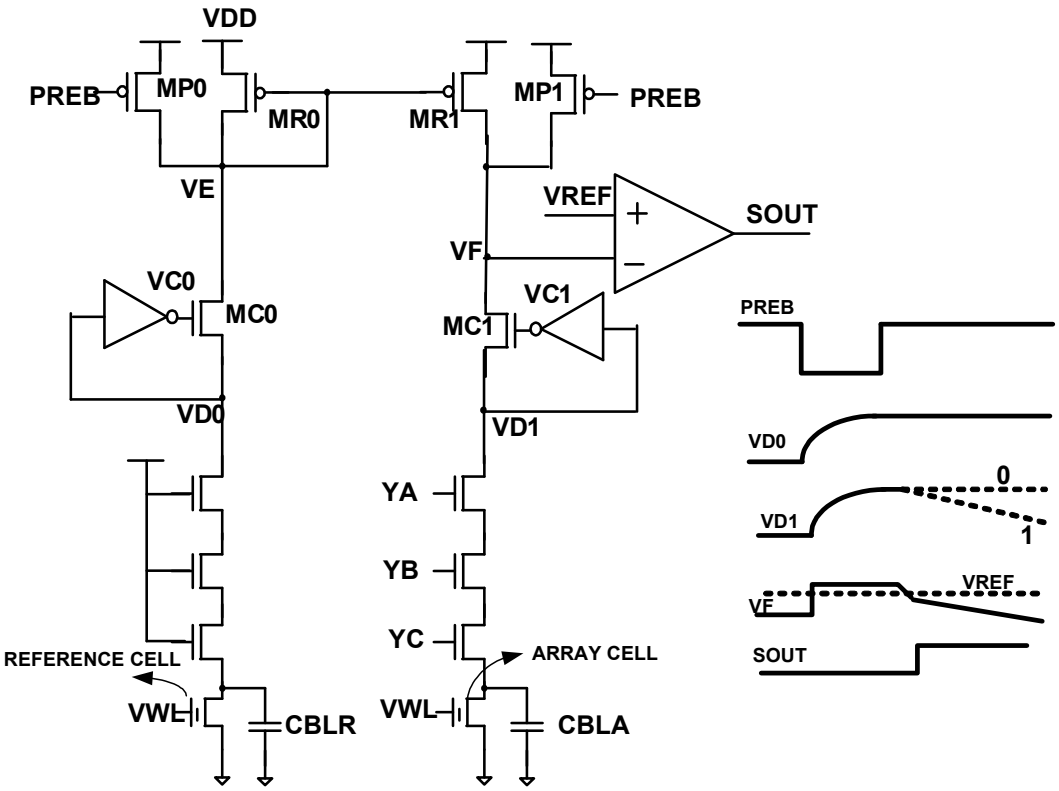

Fig.1 Conventional sense amplifier

The proposed sense amplifier(Fig.2) is to remove the threshold limitation of current mirror transistor by employing enhanced current sensing circuit (adding separate gate and drain biasing while keeping the saturated working region), to speed up the pre-charging speed by dynamic bit-line clamping circuit under low power supply voltage.

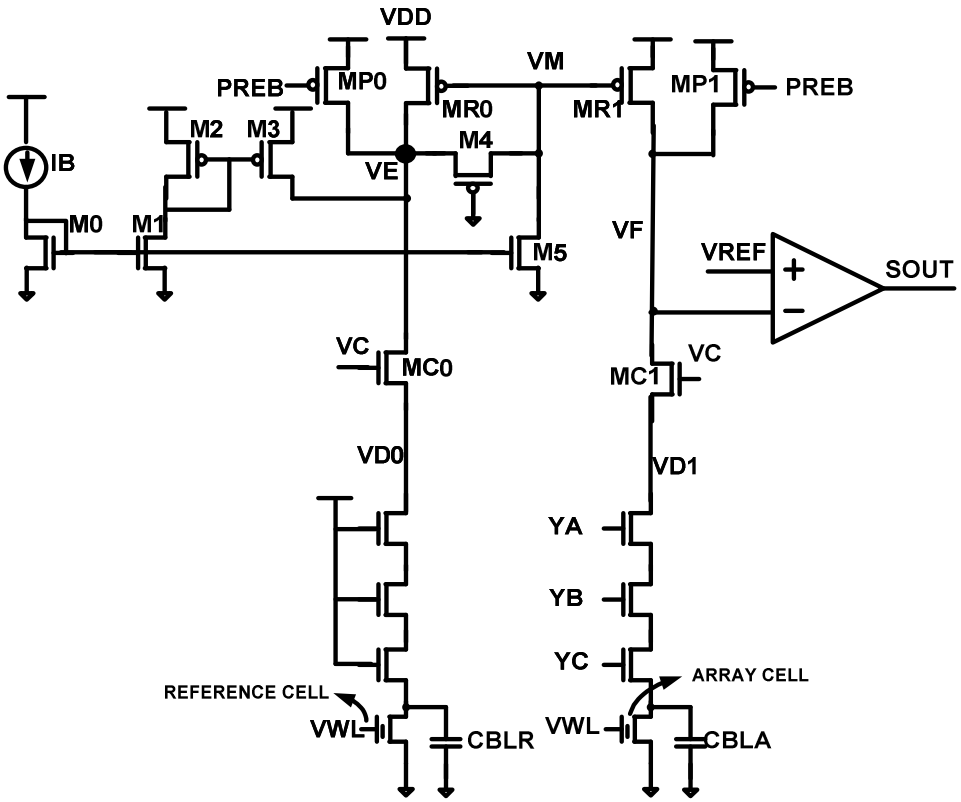

Fig.2 Proposed sense amplifier.

To get a higher VE while keeping MR0 working in saturated region, VM is separately biased, VM could be expressed by equation (1):

$$VM = VE - V_{DS(M4)} \quad (1)$$

Where $V_{DS(M4)}$ is the voltage drop across M4, and it could be expressed by equation (2):

$$V_{DS(M4)} = IB * Rout(M4) \quad (2)$$

Where IB and Rout(M4) are the bias current and equivalent output resistor for M4. In order to guarantee the MR0 working in saturated region, expression (3) has to be satisfied:

$$|VM- VDD- Vt_{(MR0)}| < |VDD - VE| \quad (3)$$

Combine equations (1),(2) and (3), we get the expression (4)

$$IB * Rout(M4) < |Vt_{(MR0)}| \quad (4)$$

The larger IB * Rout(M4) we designed, higher VE window could be achieved, however MR0 will get closer to the linearity region which will impact the accuracy of current mirror. In this sense amplifier, IB * Rout(M4) is designed around 150mv below $|Vt_{(MR0)}|$. M4 is selected as the same type of transistor with MR0, which could track process variations and win design margin. M5 is mirrored to bias M4, and M3 is to compensation current to guarantee the reference current is not affected. IB is chosen ~ 3uA, compared with ~100uA reference current (usually 4 reference cells are connected together to form the reference current), mismatch effects will be negligible. In the whole system, this enhanced current sensing circuit will be turned on during the read operation, and shut down in the other modes including standby mode to save current.

With enhanced current sensing scheme, limitation of MR0 is removed; VE could reach $VDD-VDS_{SAT}$ which is good enough to bias the bit-line voltage. Bit-line voltage is chosen ~700mv to guarantee sufficient current for sensing, VE could reach 900mv under 1.2v power supply voltage, design margin is large enough to cover all the process and temperature corners .

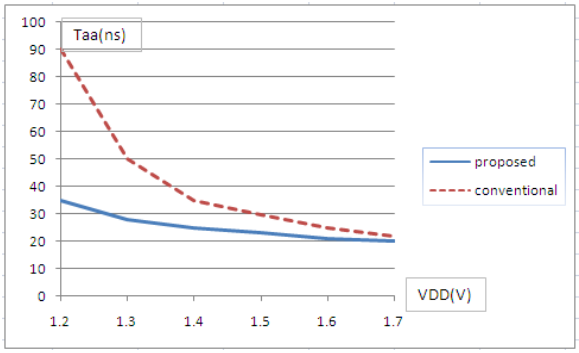

Fig.4 Simulation results

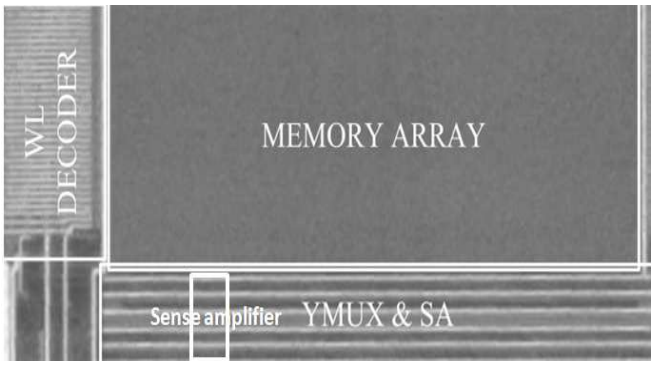

Fig.5 Chip microphotograph

Simulation Results

The sense amplifier presented in previous sections was integrated in a flash memory fabricated in a 0.13um FLASH technology. To show the performance improvement of the proposed sense amplifier compared with conventional one, simulation results using different power supplies are summarized in Fig.4. The simulation conditions are: slow corner, 125ºC, with 0.8V bit-line voltage and 0.8pF parasitic capacitance. The cell conditions are: erased cell current equals to 12uA, programmed cell current equals to 4uA, and reference current is 25uA with 0.3 current mirror ratio. A significant improvement of access time is achieved especially with low VDD (1.5V and below). For 1.2V power supply, the access time is 35ns for the proposed sense amplifier, while ~90ns for the conventional one. The sense amplifier has a silicon area of about 300 um^2 and its microphotograph is shown in Fig. 5.

Summary

A sense amplifier applied for low voltage embedded flash memories is presented. The sense amplifier uses an enhanced current sensing method allowing power supplies lower than 1.5 V to be used. The sense amplifier was implemented in a FLASH realized with a 0.13 um FLASH technology. Simulation results showed a read access time of about 25 ns with a power supply of 1.5 V, and 32ns with a power supply of 1.2V.

References

[1] T. Haraszti, CMOS Memory Circuits. Boston, MA: Kluwer, 2001.
[2] J. Kuo and J. Luo, Low-Voltage CMOS VLSI Circuits. New York: Wiley Interscience, 1999.
[3] V. Oklobdzija, Ed., High-Performance System Design (Circuits and Logic). New York: IEEE Press, 1999.
[4] K. Roy and S. Prasad, Low-Power CMOS VLSI Circuit Design. New York: Wiley Interscience, 2000.
[5] T. Tanzawa, Y. Takano, T. Taura, and S. Atsumi, “Design of a sense circuit for low-voltage flash memories,” IEEE J. Solid-State Circuits, Oct. 2000, vol. 35, no. 10, pp. 1415–1421.
[6] T. Tanzawa, Y. Tanaka, K. Takeuchi, and H. Nakamura, “Circuit tech-niques for a 1.8-V-only NAND flash memory,” IEEE J. Solid-State Cir-cuits, Jan. 2002, vol. 37, no. 1, pp. 84–89…

Advanced Materials Research Vols. 986-987 (2014) pp 1738-1741

doi:10.4028/www.scientific.net/AMR.986-987.1738

A Voltage Compensation Circuit for Flash Memory

Zhang Hua

Engineering University Of the Chinese People's Armed Police Force， 710086
24760054@qq.com

Keywords: Flash memory, voltage compensation circuit, IR drop.

Abstract. In order to get a stable source line voltage, a novel source line voltage compensation circuit has been designed to compensate the IR drop on the source line decoding path. The circuit is verified in 0.18um flash memory technology.

Introduction

Embedded Flash memories are now widely used in SOCs (System On chip) targeting the mobile communications, micro-controllers, smart cards and contact-less cards for on-chip nonvolatile storage [1]. Split-gate flash memory has become popular for embedded applications for CMOS logic processes owing to their fast erase speed, high programming efficiency, and most important, no verification after program and erase [2].

For the split-gate flash memory cell, higher source voltage has a better program efficiency. However, as discussed in Ref. [2], a higher source voltage will cause worse program disturb to the unselected adjacent cell or cells. Thus, the source voltage determines the tradeoff relationship between high program efficiency and low program disturb. Due to the IR drop on the source line (SL) by the program current, the cell source voltage bias has strong dependency on the number of cells to be programmed to data "0". In order to get a stable source bias voltage, a novel source line voltage compensation circuit is introduced. With the proposed circuit, high program efficiency with low program disturb is achieved in this flash memory.

This paper is organized as follows. Section 2 explains the source line voltage compensation circuit. In Section 3, measured results are summarized. Conclusions are drawn in Section 4.

Proposed Compensation Circuit

A simplified program scheme is shown in Fig.1. A charge pump output voltage *HVP* is coupled to the selected source line SL0 through the source line decoder. In the case of the program operation of data "0", the selected BL is connected to a current mirror circuit, thus a fixed program current I_{prog} flows through the selected cell, enabling the data "0" to be programmed in the selected cell. On the other hand, in the case of the program operation of data "1", the selected BL is also connected to the inhibit voltage V_{inh}, protecting the selected cell from being programmed to data "0".

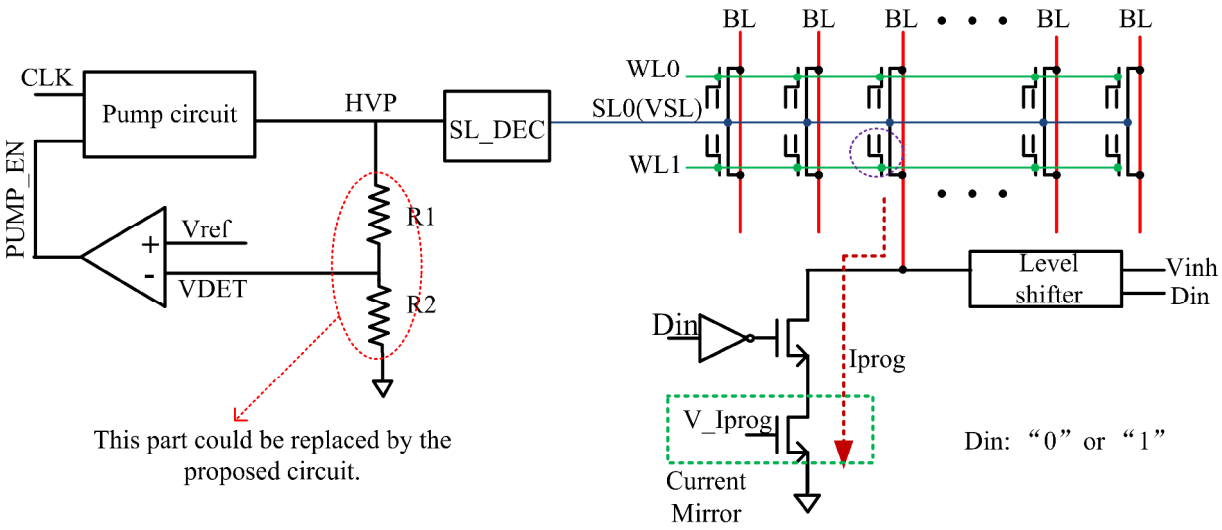

Fig.1 A simplified conventional program scheme

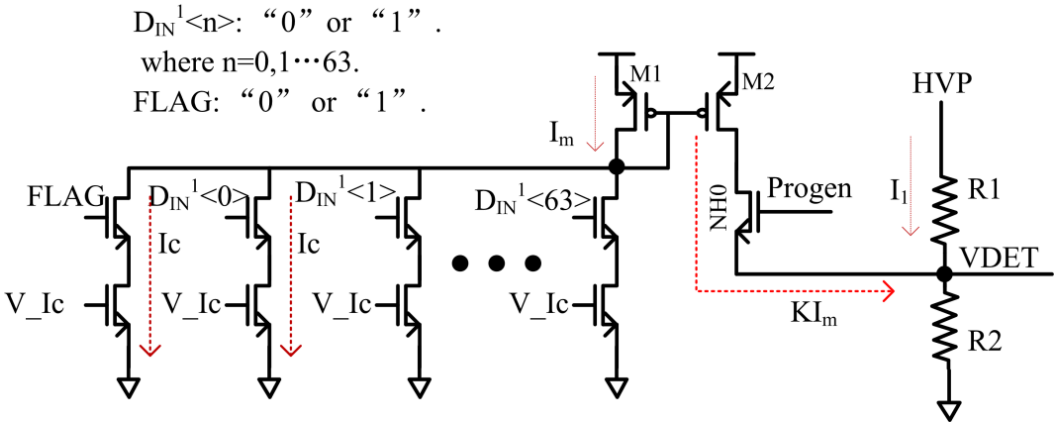

Fig.2 The proposed voltage control circuit

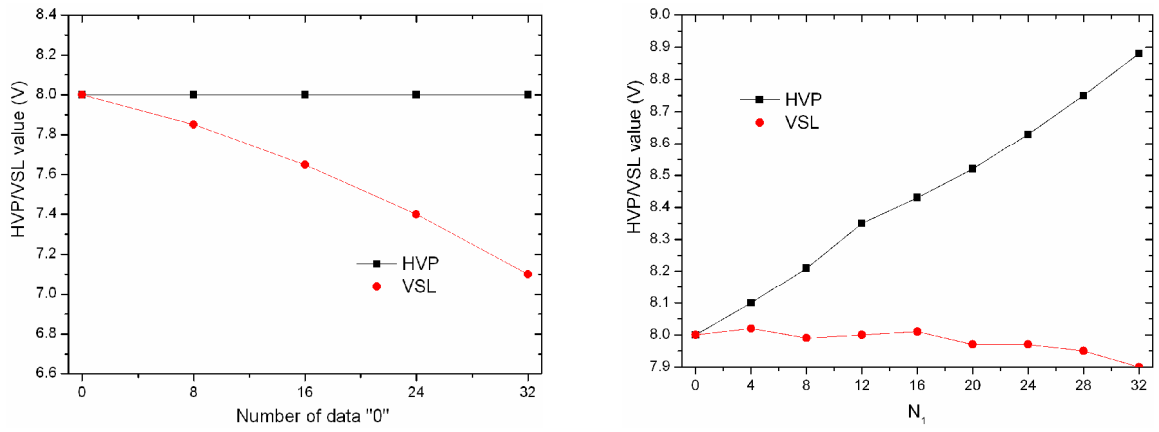

(a) (b)

Fig.3 HVP/VSL Value versus the number of data "0" in a conventional scheme (a) and proposed scheme (b).

By comparing the sampled voltage *VDET* and the reference voltage V_{ref}, the comparator outputs the control signal *PUMP_EN*, which decides when to turn on and off the charge pump. Finally, the charge pump comes into the regulation phase and output a target voltage *HVP*, as calculated in the following:

$$HVP = V_{ref} \times \left[(R_1 + R_2) / R_2 \right] \quad (1)$$

Due to the program current I_{prog} and the resistor in the SL decoding path, voltage drop exists between the charge pump output voltage *HVP* and source line bias *VSL*. What is worse, as shown in Fig.1, the voltage drop becomes larger as the number of memory cells to be programmed to data "0" increases at a time which is shown in fig.3(a). As a result, such a voltage drop will cause degradation in the program efficiency. The high voltage *HVP* has to be increased to accommodate this condition. However, if *HVP* is raised to get high program efficiency, a relatively large *VSL* appears when there are less memory cells needed to be programmed with data "0", which will cause worse program disturb to the unselected adjacent cell or cells [2]. In a word, the program efficiency and the program disturbance program are highly dependent on the number of cells to be programmed with data "0".

With the DDSBCS in Ref. [3] [4], the high voltage *HVP* could increase as the number of cells to be programmed to data "0" increases. Thus, it is possible to maintain a stable source line bias *VSL*. However, *HVP* cannot increase linearly as the number of data "0" increases. The additional resistors, comparators, and level shifters may add the cost and size of the memory device. In this paper, a novel source line voltage compensation circuit is proposed.

Fig.2 depicts the proposed source line voltage compensation circuit. The resistor divider in the conventional charge pump in Fig. 1 could be replaced by the proposed circuit. The modulation current I_m takes a different value, depending on the data patterns that are supplied to the gating MOSFETs. If the number of the cell to be programmed to data "0" is N_1, then the modulation current I_m:

$$\mathrm{I_m} = I_c \times (65 - N_1) \tag{2}$$

Where I_c is a very little reference current.

Current KI_m is gained from I_m by a ratio K with a current mirror circuit, and flows through the resistor R_2. The current I_1 flowing through R_1 can be derived as follows:

$$I_1 = VDET / R_2 - K \times \mathrm{I_m} \tag{3}$$

So when the pump comes into regulation phase, the output voltage *HVP* may be expressed by equation (6)

$$HVP = V_{ref} + I_1 \times R_1 \tag{4}$$

From (4) (5) (6), it could be clearly concluded that:

$$HVP = \left[(R_1 + R_2) / R_2 \right] V_{ref} - 65KR_1I_c + KR_1I_c \times N_1 \tag{5}$$

According to the equation (7), the *HVP* level is increased linearly as N_1 (the number of cells to be programmed to data "0"). On the other hand, in the case that N_1 increases, the IR drop from *HVP* to *VSL* also increases because the total program current becomes larger and larger. However, the large IR can be compensated with the novel source line voltage compensation circuit because *HVP* is raised when the large IR drop is occurring. Therefore, the actual bias source line voltage *VSL* can be stabilized.

Measurement Results

To verify the function of the proposed source line voltage compensation circuit, the circuit is implemented on 0.18um flash memory. In Fig.3 (b), the measured voltage values of *HVP* and *VSL* are plotted as functions of N_1 respectively. *HVP* nearly increase linearly as the number of the data "0" increases. Consequently, with the proposed source line voltage compensation circuit, a stable voltage of *VSL* is obtained even though the number of data "0" changes.

Summary

With the proposed compensation circuit, charge pump can modulate the output voltage according to the number of cells to be programmed with data “0”. Thus a stable voltage of *VSL* is obtained by compensating the IR drop on the source line decoding path. Using the novel compensation circuit, high program efficiency is achieved with low program disturb.

References

[1] Robert Strenz, Embedded Flash Technologies and their Applications: Status & Outlook, 2011 IEEE International Electron Devices Meeting (IEDM) 2011 941 - 944.
[2] Hung-Cheng Sung, et al., Novel Program Versus Disturb Window Characterization for Split-Gate Flash Cell, IEEE Electron Device Letters 26 (2005) 194-196
[3] Myoungkyu Seo, et al., A 130-nm 0.9-V 66-MHz 8-Mb (256KX32) local SONOS embedded flash EEPROM, IEEE J. Solid-State Circuits 40 (2005) 877-883.
[4] Myoungkyu Seo, et al., Circuit and method for controlling boosting voltage, U.S. Patent 7 120 058 B2. (2005).

Advanced Materials Research Vols. 986-987 (2014) pp 1742-1745

doi:10.4028/www.scientific.net/AMR.986-987.1742

A Voltage Regulator Circuit for Low Power Flash Memories

Zhang Hua

Engineering University of the Chinese People's Armed Police Force, 710086
24760054@qq.com

Keywords: Voltage regulator, flash memories, low power

Abstract. A voltage regulator circuit for low power flash memories is presented. The voltage regulator circuit was implemented in a flash chip realized with a 0.18 um flash technology. Experimental results show that standby current is less than 0.3 μA at 1.8 V and 25 °C.

Introduction

In recent years, the need for very low power consumption, which increases battery life time and portability, has become a key design aspect particularly for portable electronic equipment. To satisfy the low power constraints in the digital circuit domain, the customary way is to reduce the power supply voltage [1, 2]. In order to get the word line voltage, a charge pump and a regulator are usually needed and several designs have been proposed to generate this voltage. The common problem for the present solutions [1, 2, 3] is the non- negligible power consumption in standby mode. In this paper, a voltage regulator circuit which generates the word-line voltage with low power in standby mode is proposed.

This paper is organized as follows. Section 2 presents the proposed voltage regulator circuit. Measured results are summarized in Section 3. Conclusions are drawn in Section 4.

Proposed Voltage Regulator Circuit

Fig.1 illustrates the proposed voltage regulator circuit. The voltage regulator circuit mainly consists of six blocks: (a) an oscillator, (b) a reference voltage generating circuit, (c) a clamp charge pump, (d) an active charge pump, (e) a standby charge pump and (f) a standby voltage detector which works only in standby mode. According to the input signal ACT_EN, the oscillator will generate a high frequency clock or a low frequency clock. To reduce standby mode power dissipation, a simple reference voltage generating circuit as shown in Fig.1 is adopted instead of a band gap reference circuit. With the reference voltage generating circuit, a reference voltage VF between 1.2 V to 1.35 V can be setup very quickly when the supply voltage varies from 1.6V to 2.0V. By using the clamp charge pump, the output voltage V_{out} is clamped between 2.4 V to 2.7 V which is precise enough for the cell current sensing. MZ0, MZ1 and MZ2 are zero-Vt MOSFETs。

In the active mode, the word-line voltage generating system is enabled, while the standby charge pump and the standby voltage detector are shut down. High frequency clock generated by the oscillator is used to boost the clamp charge pump and the active charge pump to guarantee high drive ability of the pumps. In regulation phase, both the clamp charge pump and the active charge pump output the same target voltage calculated as follows:

$$VD25_{pre} = VD25_{clamp} = 2V_{ref} + V_{tz} \quad (1)$$

Herein, V_{tz} are the threshold voltage of MZ0, MZ1 and MZ2. Moreover, the output voltage for word-line is obtained at the source node of MZ2.

$$V_{out} = 2V_F + V_{tz} - V_{tz} = 2V_F \tag{2}$$

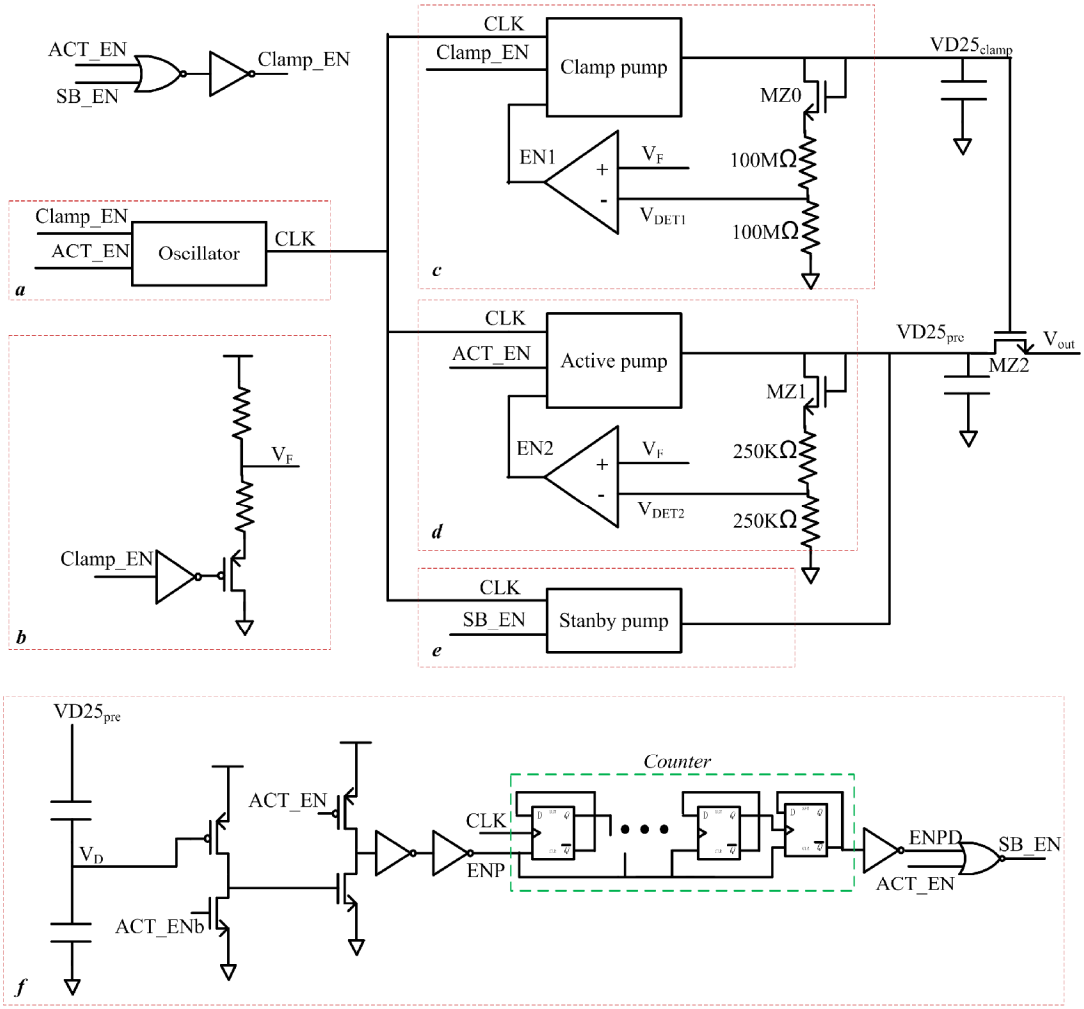

Fig.1 Proposed voltage regulator circuit

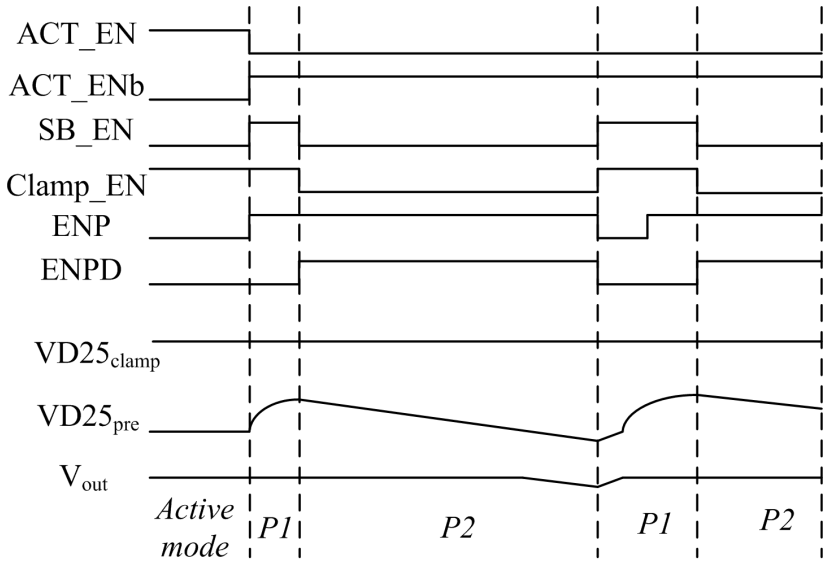

Fig.2 Proposed voltage regulator circuit operation waveform

To reduce power consumption, resistor as large as 200 MΩ is introduced in the regulator of clamp charge pump, while resistor as little as 500 KΩ is used in the regulator of the active charge pump to realize fast response. Unlike the prior art in [4] [5], a clamp MOSFET MZ2 and a clamp charge pump, which is connected to MZ2, are employed in the system. The current load of the clamp charge pump is very little owing to the large resistance in the regulator. Thus, a very stable voltage $VD25_{clamp}$ can be obtained at the output node of the clamp charge pump. As V_{out} is isolated from $VD25_{pre}$ by MZ2 and the ripple of the $VD25_{pre}$ is filtered by MZ2, a very stable voltage V_{out} can be achieved in active mode. Furthermore, since $VD25_{pre}$ is just slightly higher than V_{out}, charge pump efficiency is high enough to reduce the power consumption.

Once the chip exits from the active mode and enters the standby mode, the active charge pump is shut down and the standby charge pump is enabled. At the same time, the frequency of the clock is greatly lowered from 50M Hz to 5M Hz to reduce the power dissipation from oscillator. As the standby charge pump works for a period of time decided by the counter in the standby voltage detector, the voltage $VD25_{pre}$ begin to increase and will reach a voltage higher than 3.5V. Then the standby charge pump stops as well as the oscillator and the reference voltage generating circuit. And unavoidable leakage currents begin to discharge the node V_{out}. Only the standby voltage detector is left working. The standby voltage detector includes several inverters, a capacitor divider, and a counter. Compared with the standby voltage detector in [5] [6], the standby voltage detector in this work has no resistor divider and no comparator, so leakage current of the standby charge pump is reduced and power dissipation of the comparator is eliminated. When the voltage of $VD25_{pre}$ drops to certain level, the standby voltage detector detects the voltage and enables the signal ENP switch from "1" to "0". The enabling signal SB_EN switches from "0" to "1". Then standby charge pump begins to work again. So $VD25_{pre}$ rises again. When $VD25_{pre}$ arrives at a higher value, standby charge pump stops again.

For the sake of clarity, the timing diagram of The voltage regulator circuit is shown in Fig.2. As what have been discussed above, there are two kinds of work phase in standby mode – Phase 1 (P1) and Phase 2 (P2), and time for P1 and P2 are denoted as T_{P1} and T_{P2} respectively. The average current in standby mode can be calculated as follows:

$$I_{sb} = \left(I_{P1} \times T_{P1} + I_{P2} \times T_{P2}\right) / \left(T_{P1} + T_{P2}\right) \tag{3}$$

Herein, I_{P1} and I_{P2} are the average currents dissipated in P1 and P2 respectively.

In P1, as standby charge pump and auxiliary circuits are all at work, power consumption takes place. In P2, all the circuits are disabled except the standby voltage detector. Since only the capacitor divider is working to detect the voltage of VD25pre, power dissipation in P2 can be neglected and I_{P2} nearly equals 0. P1 is very short time with duration only several microseconds, while P2 can reaches about tens of millisecond, as shown in Fig.4. Thus, ultra low average power consumption could be achieved in standby mode.

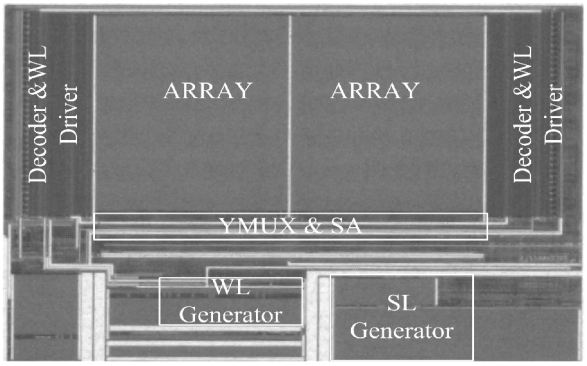

Fig.3 Chip microphotograph

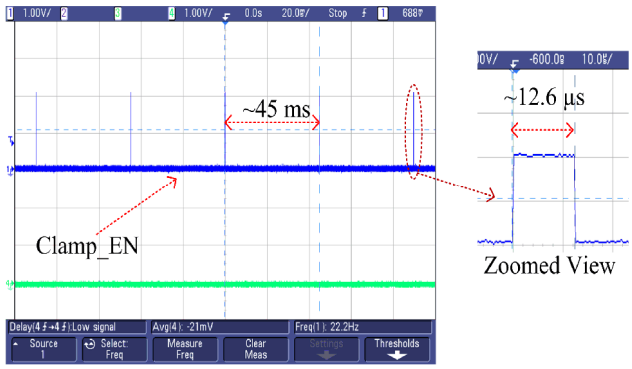

Fig.4 Measured waveform

Experimental Results

The proposed voltage regulator circuit was fabricated with a GSMC 0.18-µm l CMOS process. Fig.3 shows an optical microscope photo of the chip, proposed voltage regulator circuit is located at the region of WL generator.

Fig.4 shows the measured waveform of the signal "Clamp_EN" without a forced leakage current. As can be seen from Fig.2, one cycle (includes P1 and P2) in standby mode is about 45ms. Power is dissipated only in P1, which is a very short period of time about 12.6 µs, while in P2, which is about 45 ms, there is no power consumption. Thus, an ultra low average standby current is obtained. An average standby current as little as 0.25 µA is achieved at 1.8V and 25 °C.

Summary

With this voltage regulator circuit, low power consumption in standby mode is obtained without access time latency penalty when exiting from standby mode. The voltage regulator circuit was implemented in a flash chip realized with a 0.18 um flash technology. Experimental results show that standby current is less than 0.3 µA at 1.8 V and 25 °C.

References

[1] Tzu-Ming Wang, et al., "Low-power word-line voltage generator for low-voltage flash memory," 13th IEEE International Conference on Electronics, Circuits and Systems, pp. 220-223, 2006.

[2] T. Tanzawa, et al., "Word-line voltage generating system for low-power low-voltage flash memories," IEEE J. Solid-State Circuits, 2001, pp. 55-63.

[3] Y. Miyawaki, et al., "A new erasing and row decoding scheme for low supply voltage operation 16-Mb/64-Mb flash memories," IEEE J. Solid-State Circuits, 1992, pp. 583-588.

[4] Myoungkyu Seo, et al., "Circuit and method for controlling boosting voltage," U.S. Patent 7 120 058 B2, 2005.

[5] Nguyen, et al., "Circuit for compensating programming current required, depending upon programming state," U.S. Patent 6 853 584 B2. (2005).

[6] Se-Eun O, et al., "Boost voltage generating circuit and method thereof," U.S. Patent 7 499 333 B2. (2009).

Advanced Materials Research Vols. 986-987 (2014) pp 1746-1750

doi:10.4028/www.scientific.net/AMR.986-987.1746

An Anti-Ribboning Method for Winder Based on Brushless DC Motor

[1]ZHU Chen-hui,[1,2]HE Zhi-wei,[1]GAO Ming-yu, [1]YANG Yu-xiang

[1]Department of Electronic and Information Engineering,Hangzhou Dianzi University

[2]Colledge of Information Engineering, Hangzhou Dianzi University

Zhejiang Province 310018,China

Email:zgavin01@gmail.com

Keywords: overlapping; anti-ribboning; winder; brushless DC motor

Abstract. This paper is about how to design an improved anti-ribboning method for the winder system. The system is based on the principle of a brushless DC motor control, which constantly changes relative velocity between the grooved drum and the yarn bobbin. This in turn, causes the changing of the winding ratio value. Therefore, it will accomplish the anti-ribboning control. Compared with the traditional anti-ribboning methods, the improved method can save more mechanical components and maintenance costs. Also, this method can develop different programs for different yarns. Therefore, this method is more efficient and versatile.

Introduction

During the winding operation, the yarn on the bobbin would overlap if the bobbin was wound around some specific winding diameter, which can cause yarn breakage and fluff in the subsequent processing step. Therefore, this control method is meant to eliminate the overlap with the anti-ribboning [1].

The traditional anti-ribboning methods for winder can be divided into mechanical method and electrical method [2]. The electrical method turns the motor's power on and off intermittently, which causes the motor speed to change intermittently. Thus, this method can avoid the occurrence of overlapping. The mechanical method swings the bobbin holding the arm periodically, then changes the radius of the bobbin and the motor speed. Thus, this method can also avoid the occurrence of overlapping. However, both of these two methods for the anti-ribboning have many drawbacks, such as high energy consumption, low control accuracy, high machine manufacturing costs and maintenance costs and so on.

In order to avoid these problems of the traditional anti-ribboning methods, we designed an improved anti-ribboning method. First, we eliminated the machinery of the anti-ribboning device, which can lower the cost of manufacturing and maintenance. Then, we used the brushless DC motor to drive the winder [3], which can make the adjustment of speed more flexible and save more energy with higher efficiency. At last, we achieved the anti-ribboning control using a software-controlled method, which drives the motor following the pre-set parameters. The parameters of anti-ribboning can change through the host according to different yarns, which can enhance the applicability of the system.

The Principle of Anti-Ribboning Method

The Overlap Principle. A schematic view of the winder shown in Fig. 1, the yarn spirals into the bobbin, decomposes the motion to rotary motion and reciprocating motion. The grooved drum rotation leads to the rotary motion, and the grooves on grooved drum guide the yarn into a reciprocating motion. Assuming the angular velocity of grooved drum is N1, the angular velocity of bobbin is N, the grooves number of grooved drum is M. Therefore, the yarn around the grooves reciprocates one cycle, naming the number of the turns of winding bobbin as winding ratio. The formula is in (1).

$$\gamma = \frac{N}{N_1/M} \tag{1}$$

When the winding ratio is a fixed integer n, the yarn will go in a back and forth motion around the grooved drum. If the grooved drum turns around n laps, then the yarn on the (n+1) lap will overlap with the first lap. The time of overlapping will be longer if the winding ratio is a fractional number. However, overlap will occur anyway if you take into account the long hours of work [4].

Therefore, in order to prevent the occurrence of overlap, we need to change the value of winding ratio all the time.

Anti-Ribboning Method Principle. The rotating bobbin will lag behind the grooved drum because the presence of inertia. When the rotational speed of the grooved drum suddenly becomes small, the bobbin will continue to maintain the original speed for a while, resulting in a "slip" between them. The "slip" causes the relative angular velocity between bobbin and the grooved drum, and because the number of grooves, M, determined by the mechanical structure does not change, the value of winding ratio, as in (1), are changes.

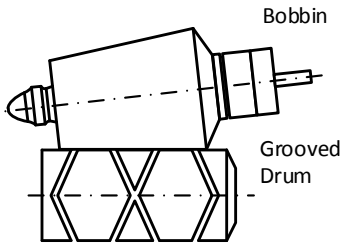

Fig. 1 Grooved drum and bobbin

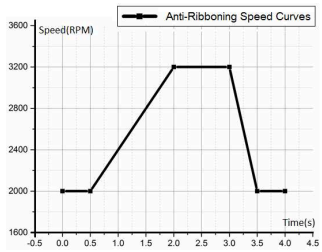

Fig. 2 Speed curves for anti-ribboning

This process must be divided into two parts where the “slip” will first accelerate then decelerate. During the acceleration, the grooved drum should accelerate smoothly. This will ensure that the grooved drum and the bobbin rotate sync. During the deceleration, the grooved drum should decelerate as soon as possible and ensure that the "slip" motion will happen. Fig. 2 is a speed versus time curve, which indicates the rotational speed of the "slip" has occurred. It also shows that the acceleration is faster than the deceleration, which is conducive to the “slip”. In order to improve the applicability of the winder, according to different characteristics of yarn, we can personalize the settings of the parameters of each phase of the rotational speed parameter and the time of constant velocity.

Hardware Design

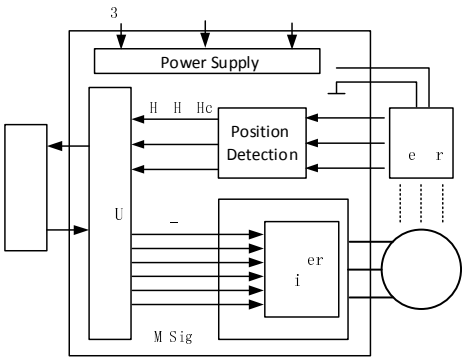

Fig. 3 Hardware system

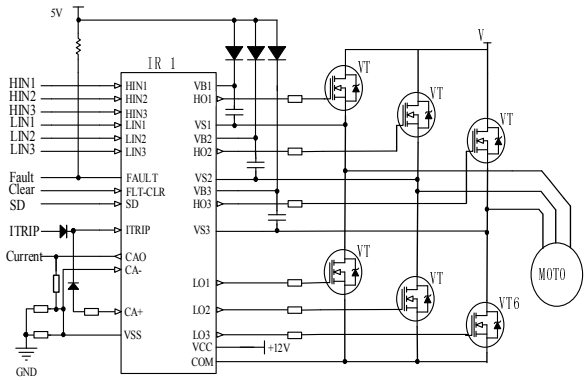

Fig.4 Power driver circuit

The design uses a brushless DC motor winder control as an active force for driving the grooved drum winder. Fig. 3 shows a block diagram of the hardware system. The whole system includes the MCU control circuit, the power drive circuit, the communication circuit, and the position detection circuit. DC power is supplied through the power switching circuit to the motor stator windings. The

position detection circuit detects the location of the motor's rotor. Under the control of the MCU, the control switch is turned on and off, which automatically contacts the motor's commutation. Therefore, this cycle can achieve continuous motor rotation [5].

Control Circuit. The microprocessor STM32F103 is based on the architecture of the ARM Cortex-M3. Advanced-control timers output three pairs of complementary signals for the motor. The 16-bit timers can calculate Hall sensor signal, which can obtain the motor rotor position signal. The USARTs communication interface is for communication with the host computer, which can set the parameters of the motor.

Power Driver Circuit. The IR2133 chip drives the power inverter circuit. The schematic shown in Fig. 4. The MCU output 6-channel signal drive the chip IR2133. The three-phase full-bridge inverter circuit composed of six MOSFET, Which, VT1, VT3, VT5 as the upper arm, VT2, VT4, VT6 as the lower arm [6].

The power driver circuit converts DC power into AC power to the motor. According to the detected rotor position, current flows into the corresponding phase windings of the motor. This way, the motor can continue to rotate.

Software Design

Software design is the control center of the system, and therefore is the main object of study. Software design can be divided into the main program module and subroutine modules.

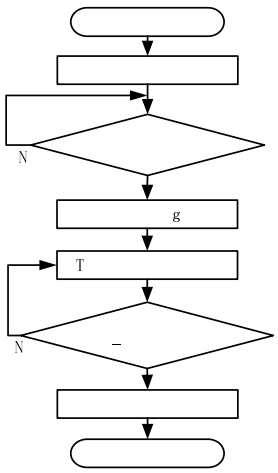

Fig. 5 Main program flowchart

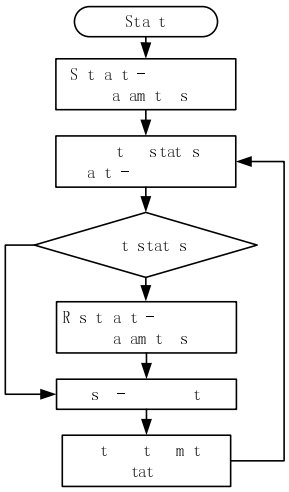

Fig. 6 Anti-ribboning control program flowchart

The initialization of the main motor completes the system as well as the main communication with the host machine functions. The main program flowchart is shown in Fig. 5. The initial setup procedures include enabling peripheral clocks and configuration related peripherals. After receiving the start signal, the motor starts the program. Then the motor sends speed data to the host computer every 100ms.

Subroutines include the motor closed-loop module and the anti-ribboning module. The closed-loop module makes sure the motor runs smoothly and responds quickly. The anti-ribboning module can be implemented in accordance with a predetermined manner. The anti-ribboning module controls the motor and always follows the pre-set speed curves.

Closed-loop module. This paper is about the design of the control system for brushless DC motors with Hall sensors. Thus, we can analyze the signal from the Hall sensor, whereby the position of the rotor, the motor speed can also be calculated by the frequency of the Hall senor signal.

The timer TIM4, referred to as "interfacing timer", captures the 3 Hall senor signal (HA, HB, HC). Thus, each time one of the three inputs toggles, the "interfacing timer" can generate a pulse, which changes the configuration of the channels of the advanced-control timer TIM1 (by triggering a COM event). The TIM1 timer is used to generate PWM signals to drive the motor [7].

Simultaneously, the captured value, which corresponds to the elapsed time between two changes of the Hall senor signal, gives information about motor speed.

This system is a closed loop feedback through the speed control of the motor. According to the detected motor speed, the PID algorithm output corresponds with a PWM duty cycle, which can drive the power switching circuit.

Anti-ribboning module. Fig. 6 is a flowchart of the anti-ribboning control program. The anti-ribboning parameters are set through the host computer, then determine the current state of anti-ribboning according to the detected motor speed and the time of the fixed speed. The state parameters should be reset if they have already entered the next state. Then the closed-loop control of the motor is entered and causes the motor to run. The motor should always be in the closed-loop control state if it has not entered the next state. The motor can be rotated according to a predetermined speed curve in cycles in order to achieve the anti-ribboning control.

In order to enhance the applicability of winder system and take into account the difference in the tension of the yarn, and other characteristics of softness, we developed different speed curves for different yarn.

The speed variation of one cycle is divided into four states, i.e., maintaining low-speed state, speed increase state, maintaining high-speed state and speed reduce state. By setting the target rotation speed of the four states and each state hold time, grooved drum rotation speed can be controlled in accordance with the curve.

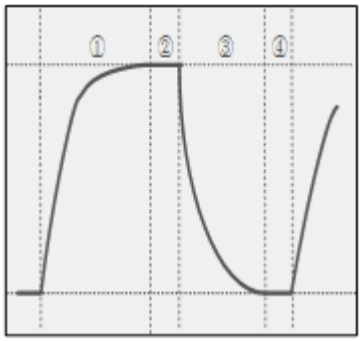

Fig. 7 Pre-set speed curve for CJ80S

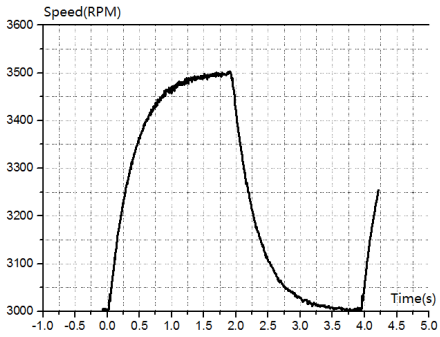

Fig. 8 The actual motor speed curve

The graph shown in Fig. 7 is a speed curve, which designed CJ80S as an example. The curve is divided into four time segments: ①speed increase segments, ②maintaining high-speed segments, ③ speed reduce segments, ④maintaining low-speed segments.

Experimental Testing

In order to verify the actual effect of anti-ribboning control, we carried out tests on a winder which shown in Fig. 9.

The motor speed data is updated on the PC via RS 485 bus, then analyzed and processed. Then the PC verifies the same actual motor speed curve and the pre-set motor speed curve.

Table 1 Pre-set data and testing data

	Low-Speed Holding Time	High-Speed Holding Time	Speed Rise Time	Speed down Time
Pre-set data	200ms	300ms	1.7s	1.8s
Measured data	196.4ms	293.6ms	1.63s	1.88s
Deviation rate	1.8%	2.13%	0.41%	0.44%

The parameters are set according to the data in Table I., then the speed data is uploaded to the PC every 10ms. To improve the reliability of data, we collected data in 200 cycles, and the averages of the data are plotted in Fig. 8. As can be seen from the figure, the continuous curve is drawn by the data.

This curve indicates the actual speed of the motor, the horizontal axis represents time, and the ordinate represents the motor speed. According to the number of data in each stage, the holding time of each stage can be calculated, which is shown in Table 1.

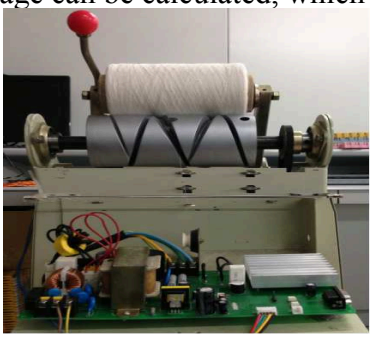

Fig. 9 The winder for testing

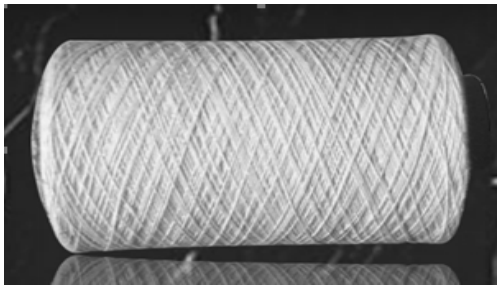

Fig. 10 The yarn after winding

Compare the pre-set parameters data and the detected data, the time of sudden changes in speed are almost the same with the pre-set one, with an error of less than 0.5%. The other parameters can be controlled effectively. This paper uses winder control system involved in the winding of the yarn as shown in Fig. 10. As can be seen, there is no overlap on the surface of the yarn and the lines are clear, it is basically reached the winder yarn processing requirements.

Summary

This paper is about the design of a winder control system, which is achieved by yarn winding using a software-controlled method, and finally, the anti-ribboning control. Compared with traditional anti-ribboning methods of winder system, this new method not only simplifies the mechanical structure, but also improves the work efficiency. The improved method also has good applicability design, which can set different parameters for different yarns.

This work was partially supported by Zhejiang Provincial Natural Science Foundation of China under grant # LQ13F010011

References

[1] Yao Jun-hong, “The study of winder overlapping,” Light and Textile Industry and Technology, Guangxi, vol. 37, No.1, pp. 23-24, January 2008.
[2] Wei Jian-fan, “The eletronic anti-robbioning device of winder,” Textile, Science & Technology, Shandong, vol. 4, pp. 24-28, April 1984.
[3] JI Zhi-cheng, SHEN Yan-xia, JIANG Jian-guo, “A novel fuzzy PI intelligent control method of BLDCM speed servo system,” Electric machines and control, vol. 7, No.3, pp. 248-254, September 2003.
[4] Xie Wei-dong, “Research of the winding ratio to prevent yarn overlapping,” Journal of Textile Research, vol. 32, No.7, pp. 40-43, July 2011.
[5] Wang Sheng-yuan, “Brushless DC motors used in the automatic winder,” Textile Accsessories, vol. 39, No.4, pp. 313-314, July 2012.
[6] Sui Xiang-lin, Ou-yang Min, “Design of 3-phase Bridge Drive Circuit Based on IR2133,” Mechanical Engineering & Automation, vol.5, pp. 174-175, October 2008.
[7] STMicroelectronics, STM32 Reference Manual (RM0008), 9th ed., 2009, pp. 288-289.

Advanced Materials Research Vols. 986-987 (2014) pp 1751-1754

doi:10.4028/www.scientific.net/AMR.986-987.1751

Analogy Teaching Method of High-frequency Electronic Circuit

XU Zhuo-nong[1,a], ZHANG Ling-tao[2,b]

[1,2]Electronics and Information Engineering School, Central South University of Forestry and Technology, ChangSha 410004, China

[a]xzn71@126.com, [b]zhanglt@126.com

Keywords: High-frequency electronic circuit, analogy teaching, amplifier, mixing, modulation and demodulation.

Abstract：High-frequency electronic circuit is an important basic specialized course for the major of electronic information engineering, communication engineering, and electronic science and technology. Combined with a dozen years of classroom teaching experience and started from several aspects like relevancy of front-back courses, teaching framework and theoretical teaching content, this paper will discuss analogy teaching method of related content about signal amplifier, mixing, modulation and demodulation in order to help students to understand chapter structure. In the process of teaching, we should pay more attention to students ' weaknesses of knowledge, then stimulate their interests in learning and improve the teaching effectively quality.

1. Introduction

The course of high-frequency electronic circuit describes the composition, working principle and analysis of application circuits in a variety of communications systems and high-frequency equipments. High-frequency electronic circuit, as an abstract theoretical and highly practical course，which is boring and hard to understand both in teaching and learning, which always make teachers and students daunting. How to grasp the students ' weak and interesting points of knowledge and combine abstract theoretical teaching with vivid practical application are what the teachers have always think about. At the same time, they have carried out some relating exploration into the practical teaching process. This paper will explore how to decompose the teaching content to achieve resonance and interaction between teaching and learning in view of many aspects like the relevancy of front-back courses, the teaching framework of high-frequency electronic circuit and comparison of theoretical teaching content. In such circumstance, students can easily understand and love to learn, and put their learning to use.

The leading courses for high frequency electronic circuit are circuit analysis and analog electronic circuit, which are difficult for many students to learn, so most of them lack enough confidence to study it very well. In fact, during the high-frequency electronic circuit teaching process, it is completely feasible for teachers to intersperse with summary and comparison of some analog electronic circuit teaching contents. If the comparative teaching methods used appropriately, it can not only help students deepen the understanding of contents related low frequency electronic circuit, but more benefit for students to realize the coherence and consistency of the learning process of electronic circuit. Thus, the students can deepen the understanding and learning of related contents of high-frequency electronic circuit.

The subsequent courses for high frequency electronic circuit are television principle, basis of microwave technique, communication principle, and so on. The study task of high frequency electronic circuit is to help students grasp the elementary theory, elementary knowledge and basic skill and make preparation for the further studying the sequent courses, and lay the solid foundation for the practical work in the future. Knowing the important place of high frequency electronic circuit in the whole curriculum is good for students to determine their future research directions and effectively increases their interest in learning.

2. The teaching framework of high frequency electronic circuit

All teaching content of high frequency electronic circuit built around high frequency signal sending and receiving systems. High frequency transmission system consists of oscillating circuit, double frequency circuit, high-frequency small-signal amplifier, modulation circuits, high frequency power amplifier, and high frequency receiver system contains such function module as mixing circuit, demodulation circuit and so on. While learning this section, the teachers should help student to better understand of function of each circuit module and the relationship between each module and transceiver system from the point of the whole system according to their lists of selected reference textbooks.

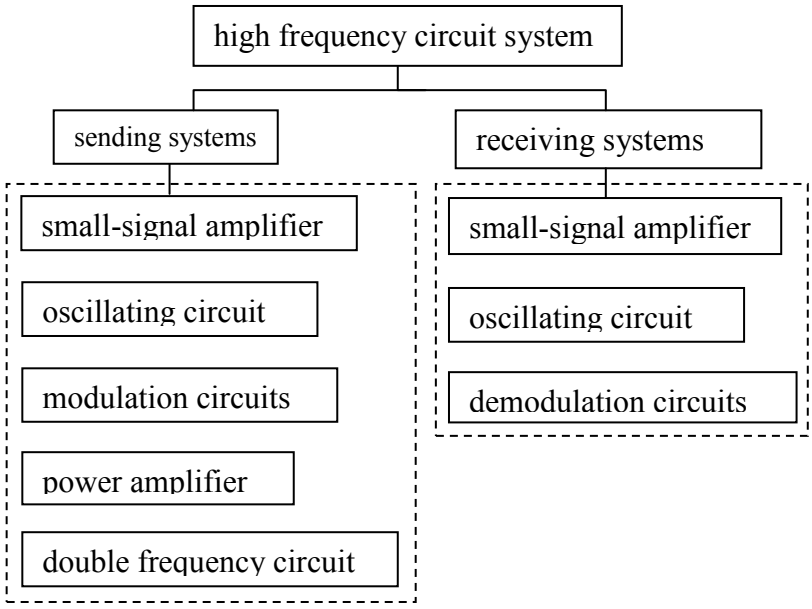

Figure1. The sending systems and receiving systems of high frequency circuit

3. Analogy teaching method of high-frequency electronic circuit

Module of teaching contents of high-frequency electronic circuit are closely linked with one another, especially the contents of analog electronic circuit, which related to correctly grasp the students' difficulty in learning process, is the key point of teaching.

3.1 Small signal amplifiers of LF and HF

Small signal amplification is a very important part of high frequency signal processing circuit, so the learning of which plays an important role in the studying of high-frequency electronic circuit smoothly. Take the common-emitter amplifier for example, the comparative teaching of small signal amplifiers in LF and HF should include and emphasize the following key points:

(1) The require of frequency selection circuit decides different loads of the signal amplifiers between HF and LF, so the teacher need to guide the students to understand the circuit form of frequency selection circuit and how it works.

(2) Different operating frequency determines the different transistor parameter model, the simplified H-parameter model is mostly used in analog electronic circuits, and y-parameter model is widely used in high-frequency electronic circuit.

(3) The LF and HF small signal amplifiers both belong to class A amplifier, so the static circuit works much the same way. The AC parameters of LF small signal amplifiers circuit include the voltage gain, the input resistance, the output resistance and so on. Because of frequency selection function, the AC parameters of HF small signal amplifiers mainly include the voltage gain, the quality factors passband, and so on.

(4) The stability analysis. In order to enhance the stability of circuit, the Low-frequency small-signal amplifier often use a variety of forms of negative feedback circuits. The stability

analysis of HF small-signal amplifier is more complex. Except for various forms of feedback circuit, other forms of circuits like "neutralization" and "misfit law" are also widely used.

3.2 small signal amplifier and power amplifier

Using analog teaching between small signal amplifier and power amplifier, the following key points should be emphasized in teaching process:

(1) Because of the different input signal amplitude, the circuit forms of small-signal amplifier and power amplifier are not the same, neither their functions in circuit, which are located in different places of high-frequency systems.

(2) Taken the amplification of the circuit state, the small signal amplifier belong to class A, but the power amplifier belong to class C. Students should be guided to analyze static operation points according to the DC circuit and understand the amplifier working principle of class A and class C from the angle of waveform transform.

(3) The two kinds of amplifier emphasize different AC parameters. The small signal amplifiers emphasize the undistorted output and the voltage amplification factor, and the high frequency power amplifier circuit is located in the ends of the sending system, emphasizing the higher power and the higher efficiency of output signal than small signal amplifiers.

3.3 Amplitude modulation and mixing circuit

Amplitude modulation and mixing circuit both belong to typical non-linear circuits. In amplitude modulation system, the high frequency carrier wave is modulated by the low-frequency signal, while mixing circuit produce the signals of sum-frequency or add-frequency of the two input signals. By analyzing the two kinds of circuits, a lot of comparable teaching points can be found:

(1) As for Amplitude modulation circuits and mixing circuit both center around non-linear device, nonlinear devices of which could be transistor, diode, FET or analog multiplier. The input signal of mixing circuit are low frequency signal and the carrier signal, but which of amplitude modulation circuit are received HF signal and local oscillator signal.

(2) Both the two kinds of output load have frequency selection network. The output of mixing circuit is resonated in the signals of sum-frequency or add-frequency, whose selected frequency ranges should include receiving high-frequency signal corresponding bandwidth, and the output of amplitude is resonated in the high frequency carrier signal, whose frequency ranges should include the corresponding bandwidth of upper sideband and lower sideband.

3.4 modulation and demodulation

The structures of two chapters of modulation and demodulation of amplitude and frequency ,which both contain three parts such as mathematical expression into analysis, modulation circuits and demodulation circuits, are similar to each other.

(1) Analysis of mathematical expressions: based on the definition of AM and FM, the mathematical expression are deduced, then signal waveform, spectral structure, power, bandwidth and other parameters are analyzed accordingly.

(2) Modulation circuit: the amplitude modulation circuit include two ways of low power and high power, essentially nonlinear device-focused, obtains the AM output of low frequency signal and carrier signal. The FM modulation includes two ways of direct form and indirect form, especially with FM circuit of variable capacitance diode as an example, the basic working principle of FM circuit will be analyzed in detail.

(3) Demodulation circuit: according to that AM signal can be divided into ordinary AM wave, single sideband signal or double sideband signal with carrier-suppression, demodulator may use the diode peak detector and synchronization detector respectively. The frequency demodulation circuit include phase discriminator and symmetrical ratio detector. Through the description of this section, students are expected to understand the various characteristics of modulating signal and the different working principle of demodulation circuits.

4. Conclusion

The analogy teaching method of high-frequency electronic circuits is discussed in this paper, which covers relating contents such as signal amplification, mixing, modulation and demodulation. The proper use of analogy teaching method, acting as a guideline in the teaching process, can help students quickly grasp the content framework of relevant chapters and greatly improve the efficiency of learning high-frequency circuits.

References

[1] The Specialty Teaching Guidance Committee of the Electronic Information Science and Engineering in the Ministry of Education*: Electronic Information Science and Engineering Undergraduate Professional Guidance* (Higher Education Press, Beijing 2010)
[2] ZHANG Suwen: *High frequency electronic circuit*s (Higher Education Press, Beijing 2009)
[3] LIN Chunfang: *High frequency electronic circuit*s (Electronic Industry Press, Beijing 2010)
[4] ZENG Xinwen: *High frequency circuit principle and analysis*(Xidian University: Xian 2009)
[5]WANG Kangnian: *High frequency circuit principle and analysis*(Xidian University: Xian 2009)
[6]YANG Niqing: *Experiment and comprehensive design of high frequency electronic circuit*(Machinery Industry Press, Beijing 2009)

Advanced Materials Research Vols. 986-987 (2014) pp 1755-1758

doi:10.4028/www.scientific.net/AMR.986-987.1755

Analysis of Lithium battery model for Electric Vehicle

Yining Chen[1,a], Juan Zhang[2,b], Chong Guo[2,c]

[1]Power Management of Liaoning Provincial Government, Shenyang 110035, China

[2]State Key Laboratory of Automotive Simulation and Control, Jilin University, Changchun, 130012, China

[a]cyn5853@163.com, [b]zhangjuan90122@163.com, [c]guochong0415@gmail.com

Keyword: Lithium battery, Battery model, PNGV model, Parameter identification

Abstract. The establishment of an accurate battery model is crucial to the design and research of battery and battery management system. This paper takes 180Ah LiFePO4 as research object, adopts PNGV model to describe the working characteristics of the battery,establishes PNGV simulation model in MATLAB/Simulink, recognizes the model parameters based on the experiment of HPPC pulse, verifies the accuracy of model in different conditions. The results show that PNGV model can show the dynamic characteristic of battery well.

Introduction

Battery characteristics and performances at different operating conditions are important in its applications especially in Electrical Vehicles (EVs). In order to describe the working characteristic of battery more visually, it is necessary to establish the battery model[1].

An accurate battery model is of great value to various aspects of the whole vehicle, such as the system simulation,energy management. So far, The common battery model can be divided into three types: electrochemical model, neural network model and equivalent circuit model. Equivalent circuit models are commonly used because of its simple calculation and high precision for battery modeling, which uses resistor, capacitor and other circuit components to describe the working characteristics of the battery. Rint, Thevenin, PNGV, second order RC model are the typical equivalent circuit models. PNGV model is a simple linear battery model with clear physical significance, high accuracy,which is an ideal battery model, so this paper adopts PNGV model as the simulation model.

The establishment of PNGV model

PNGV model is the standard battery model in <PNGV battery test manual >in 2001[2], Its circuit configuration is shown in Fig.1.

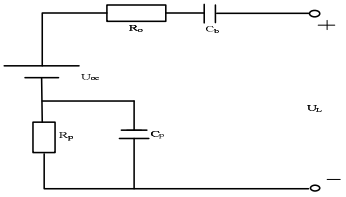

Fig.1 Circuit configuration of PNGV model

Based on kirchhoff's voltage law, basic circuit equation can be expressed as Eq.3：

$$U_L = U_{oc} - R_o I_L - R_p I_p - \frac{1}{C_b}\int I_L dt \tag{1}$$

It takes the capacitor voltage U_b,U_p as state variable, terminal voltage U_L as output variable, then gets the state space equation as Eq.2:

$$\begin{cases} \begin{bmatrix} \dot{U}_b \\ \dot{U}_p \end{bmatrix} = \begin{pmatrix} 0 & 0 \\ 0 & -\frac{1}{C_p R_p} \end{pmatrix} \begin{bmatrix} U_b \\ U_p \end{bmatrix} + \begin{bmatrix} \frac{1}{C_b} \\ \frac{1}{C_p} \end{bmatrix} I_L \\ [U_L] = [-1 \quad -1] \begin{bmatrix} U_b \\ U_p \end{bmatrix} + [-R_o][I_L] + [U_{oc}] \end{cases} \tag{2}$$

Where the polarization current I_p is the solution of the differential equation as Eq.3, its initial value is zero.

$$\frac{dI_p}{dt} = \frac{I_L - I_p}{\tau} \tag{3}$$

$$\tau = C_p R_p \tag{4}$$

In which U_{oc}: open circuit voltage, R_o: internal resistance, R_p: polarization resistance, C_b: open circuit voltage capacitance, C_p: the shunted capacitance of the polarization circuit, τ: the polarization time constant.

Model parameters U_{oc}, R_o, R_p, C_b, τ should be recognized. They are variable with the change of battery state and external environmental influence. They are variable with the change of battery state and external environmental influence. In order to enable the model accuracy higher, it takes the influential factors into consideration. parameters are affected by the temperature, number of circle and SOC, because of the limited life characteristic test conditions, it only analyzes the influence of temperature and SOC to parameters.

Model parameter identification test

HPPC test is to test the dynamic property of battery, It can get the relation between Ohm internal resistance,polarization resistance and SOC through the current-voltage characteristic curve.So this paper selects HPPC test experiment as the experiment of model parameter identification[3].

HPPC testing program: choosing three temperature points: −5℃, 25℃, 40℃, implementing the following HPPC pulse circulation test under each temperature point. Firstly, charging the battery with 1C rate to the full power state,then controlling SOC at different points(95% ,90%，80%，……，10%)with 1C discharge rate, doing a HPPC pulse circulation under each SOC point. Then shelving the battery about 1 hour,succeeding with the next HPPC pulse circulation test until SOC up to 10%.

A HPPC pulse circulation includes 10s pulse 1C discharge process, 40s shelving process, 10s pulse 3/4C charge process.the pulse current change and voltage response curve can be shown in Fig.2(a),(b)：

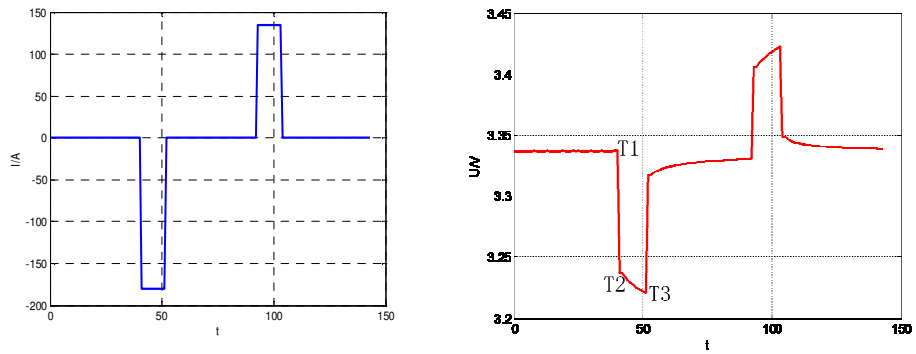

（a）Current curve of HPPC （b）Voltage curve of HPPC

Fig.2 A HPPC pulse circulation

From Fig.2, it can be seen that the voltage response property can show the mutability and gradual change of battery.

1. The acquisition of open circuit voltage

Open circuit voltage is the most basic parameter of battery model.Through plenty of experiment, it shows that battery voltage will be stable after 1 hour shelving time[4].So this paper adopts terminal voltage after 1 hour shelving time as open circuit voltage U_{oc} under each SOC in the process of HPPC test, which can be shown in Fig.3.

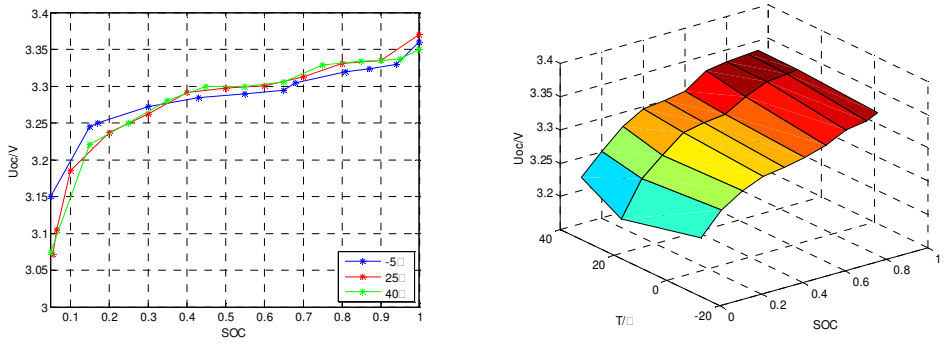

Fig.3 The relation of U_{oc} and SOC under different temperatures

2. Parameter identification of battery model

This paper adopts the Linest function in Excel to do the parameter identification.

Based on the circuit principle, the relationship between load voltage U_L and load current I_L can be expressed in Eq.5, after discretization ,it can be shown in Eq.6:

$$U_L = U_{oc} - R_o I_L - R_p I_p - \frac{1}{C_b}\int I_L dt \tag{5}$$

$$\overline{U}_{L,i} = \overline{U}_{oc} - R_o \bullet I_{L,i} - R_p \bullet I_{p,i} - \frac{1}{C_b}\left(\sum I_L \Delta t\right)_i \tag{6}$$

In which, load current $I_{L,i}$,the current integral $(\sum I_L \Delta t)_i$ and polarization current $I_{p,i}$ are all independent variables, load voltage $\overline{U}_{L,i}$ is dependent variable, Δt is sample interval of data acquisition.

$I_{p,i}$ and $(\sum I_L \Delta t)_i$ variable can be obtained by Eq.7andEq.8:

$$\begin{aligned} I_{P,i} = {} & \{1-[1-\exp(-\Delta t/\tau)]/(\Delta t/\tau)\}\times I_{L,i} \\ & +\{[1-\exp(-\Delta t/\tau)]/(\Delta t/\tau)-\exp(-\Delta t/\tau)\}\times I_{L,i\text{-}1} \\ & +\exp(-\Delta t/\tau)\times I_{p,i\text{-}1} \end{aligned} \tag{7}$$

$$\int I_L dt = (\sum I_L \Delta t)_i = (\sum I_L \Delta t)_{i-1} + (I_{L,i} + I_{L,i-1})\times \Delta t/2 \tag{8}$$

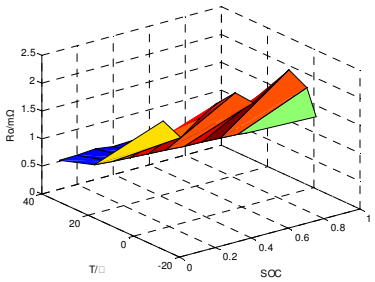

Fig.4 The map of internal resistance

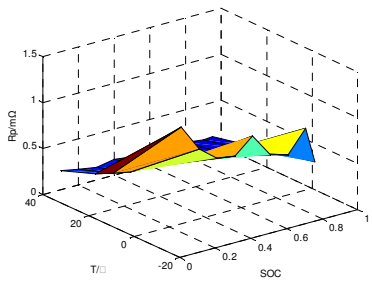

Fig.5 The map of polarization resistance

After identifying model parameters by the Linest function in Excel, the identification results of internal resistance and polarization resistance can be shown in Fig.4and Fig.5.

The validation of model accuracy

Battery simulation model is established in MATLAB/Simulink as Fig.6. It includes three modules: SOC calculation, model parameters calculation, terminal voltage output module.

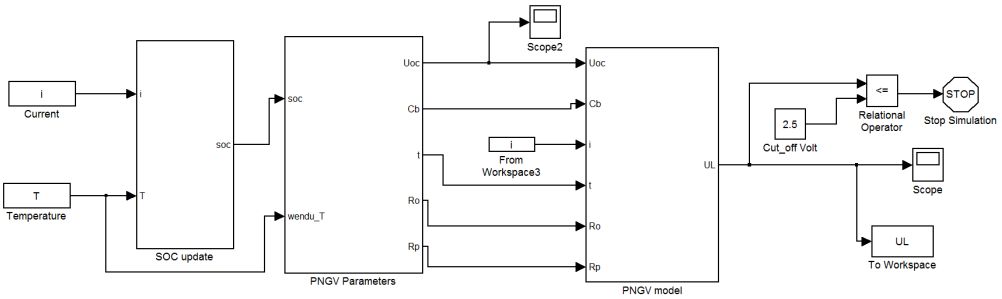

Fig.6 PNGV simulation model

In order to validate the precision of PNGV model, this paper adopts the constant current(1C) discharge condition to verify the validity of model by contrastively analyzing the simulation voltage and the actual measured voltage of battery.

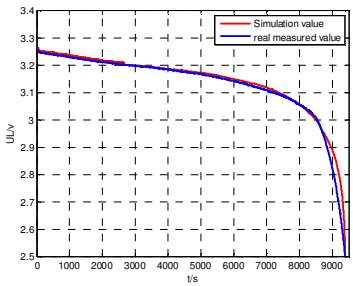

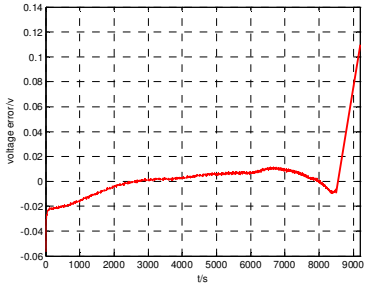

(a) Simulation voltage and actual voltage (b) Voltage error

Fig.7 The comparison of simulation voltage and actual voltage

From Fig.7(b),it can be seen that the voltage error increases sharply in the end of discharge process, up to 0.11V, while it is very small and can be ignored in the other processes. On the whole, the result show that the accuracy of PNGV simulation model and parameter identification can meet the demand of battery simulation, can describe battery characteristic reasonably and precisely.

Conclusion

The establishment of an accurate battery model is crucial to the design and research of battery and battery management system. PNGV model can show the dynamic characteristic of battery, and the recognition accuracy of parameters meets the requirement.

References

[1] Yongjun Chen.Research on Modeling and SOC Algorithm of LIFePO4 Battery[J].Harbin Institute of Technology.2011.

[2] Hongwen He, Rui Xiong.Online Estimation of Model Parameters and State-of-Charge of LiFePO4 Batteries in Electric Vehicles[J]. Applied Energy,2011.

[3] US Department of Energy. PNGV Battery Test Manual[M]. Washington:US Department of Energy, 2001.

[4] Suleiman Abu-Sharkh. Rapid test and non-linear mode characterization of solid-state lithi um-ion batteries[J]. Journal of Power Source, 2004.

[5] Bergveld H J, Kruijt W S. Battery Management Systems Design by Modelling[J]. Kluw er Academic Publisher, 2002,Netherlands.

Advanced Materials Research Vols. 986-987 (2014) pp 1759-1762

doi:10.4028/www.scientific.net/AMR.986-987.1759

Application of Dual Switch Flyback Converter in Three-phase Photovoltaic Inverter

Chunyang YI[1,a], Tianfa LIAO[1,2], Qianjin MA[2], Changwen DONG[2], Jiaxiang XUE[2]

[1]Department of electronic engineering, Huizhou University, Huizhou 516007, China;

[2]School of Mechanical and Automotive Engineering, South China University of Technology, Guangzhou 510640, China

[a]email: yichunyang@hzu.edu.cn

Keywords: Three-phase photovoltaic inverter; Auxiliary power; Dual Switch Flyback

Abstract. Auxiliary power of Three-phase photovoltaic inverter is supplied by solar cells with wide input ranging from 140V to 1000V.The conventional single-switch flyback converter exists too high voltage stress in power switch to be applied in this inverter. This paper presents a dual-switch flyback converter in which the voltage stress of each switch is slightly higher than the input voltage when switches turn off, at the same time , the leakage inductance energy is recycled back into the inputside; otherwise, this topology needs no snubber circuit, so it is much more efficient than single switch flyback. The dual switch flyback converter with seven outputs is successfully applied in 10KW three phase PV inverter.

Introduction

Auxiliary power of Three-phase photovoltaic inverter is supplied by solar cells with wide input ranging from 140V to 1000V.The conventional single-switch flyback converter exists too high voltage stress in power switch to be applied in this inverter. This paper presents a dual- switch flyback converter in which the voltage stress of each switch is slightly higher than the input voltage when switches turn off, at the same time, the leakage inductance energy is recycled back into the inputside; otherwise, this topology needs no snubber circuit, so it is much more efficient than single switch flyback. [1]. Dual flyback circuit designed in this paper has 7 outputs: 20V/1A, +17.5V/0.5A (two-outputs),+15V/0.3A,12.5V/1A,+12.5V/0.2A,+5V/3Ato power the inverter control circuit, the sampling circuit, the driver circuit and the protection circuit module. Experimental results show that the designed power supply has a good stability, high reliability and high efficiency.

A Brief Analysis of Principle

Fig.1 shows the dual-switch flyback topology. Both Q1 and Q2 are turned on and turned off simultaneously, when Q1 and Q2 are turned on, Power is delivered to the primary winding through Q1 and Q2,while the secondary rectifier diode D1 is in the off state, so there is no energy delivered to the load; When Q1 and Q2 are turned off, the voltage of primary side reverses,and clamping diodes D2 and D3 conduct, Not only the voltage stress on the switch is clamped to the input voltage, but also part of the energy stored in the transformer is recycled back to input side through clamping diodes,while the other part is transferred to the secondary side. Since the release of the inductive energy ringing is now clamped,there is no need for a snubber circuit. Consequently, the system losses and electromagnetic interference (EMI) is greatly reduced [2-4].

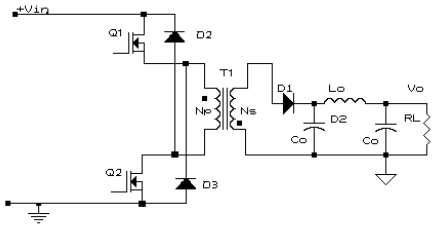

Fig.1 Dual Switch Flyback Topology

The Design of Control Circuit

The design of feedback loop directly determines the stability and accuracy of the switch power supply, so the feedback loop is the most important part of the design. The dual-switch flyback convert designed in this paper is implemented by the 38HC45, a fixed frequency current-mode PWM controllers with peak current control technology, which provides a high performance, starts at 8.4V with operation down to 7.6V, the working environment temperature range is from -40 ℃ to -85 ℃, the output voltage is 5V, The design has the advantages of less components, high reliability and low cost. The feedback loop design includes current sampling circuit, voltage feedback circuit.

Design of Current Sample Circuit. In a flyback power converter, the current sampling circuit is generally detected peak current flowing through power switch on the primary side. The circuit and the control chip are connected to a common ground. The emitter of power switch and negative terminal of input supply are both connected with a sampling resistor. The 38HC45 senses the voltage on the sampling resistor through a filtering circuit on the COMP port as the current signal of power switches. The current control signal can be used to control the peak current. In 34HC45, the current sampling signal will be ignored when it is lower than 1V. Only when the signal is higher than 1V, 38HC45 will adjust the width of the output drive pulse to ensure the stability of the output voltage and avoid overloaded operation [5] .

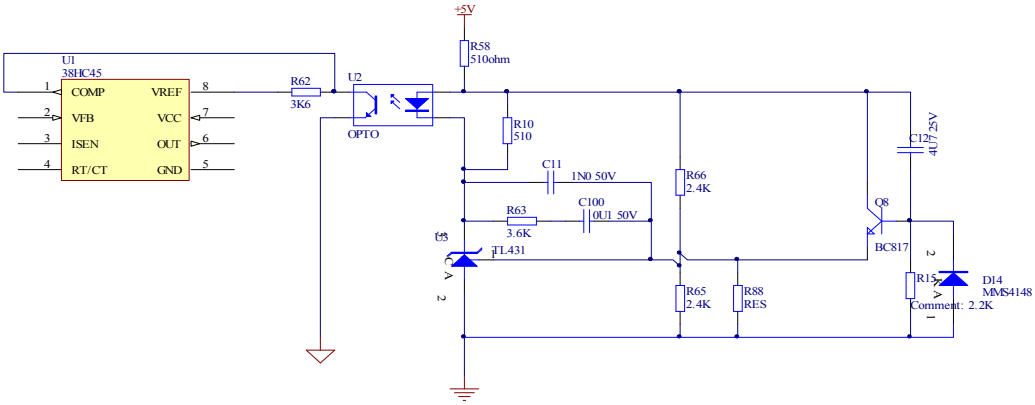

Fig.2 Voltage Feedback Circuit

Design of Voltage Feedback Circuit. Flyback converter can use isolated sampling methods to improve accuracy linearity and anti interference. Input and output of converter are isolated, voltage feedback signal and the 34HC45 are not common-grounded, Which are isolated by a opto coupler PC817.

Fig.2 shows the voltage feedback circuit. The PC817 and the TL431 are the critical components of this circuit.TL431 is a regulator device,it is used as reference source and feedback error amplifier to sample output and generate corresponding error voltage. This error voltage is transferred to error current by opto coupler PC817,which is coupled to the primary of transformer and connected to the output of internal error amplifier of control chip 38CH45.

Design of drive circuit

In dual switch flyback circuit, the two switches can't be directly driven because one switch is in the low side while the other in the high side. An isolation driver transformer of dual line output is used, this will not only meet the requirements of the dual switch drive, but also make the isolation between the control circuit and the power switch of a floating voltage. Its design is very simple but critical to the reliability of the entire switching power supply.

Fig.3 shows the drive circuit .In the design of the gate drive transformer, the following important factors should be considered [6-7]:

(1)Insulation voltage of transformer should not be less than twice the input voltage. Although the transformer do not need high pressure test , if there is insulation problem of transformer, for example, once the switch is damaged, it will cause damage to the control circuit.

(2)Transformer turns ratio is usually 1:1, if other turns ratio is adopted, make sure the output voltage does not exceed the avalanche breakdown voltage of switch.

(3)A winding technique of good coupling between primary and secondary should be adopted. If the coupling is bad, the switching speed of the high-side switch will be slower than the low-side switch.

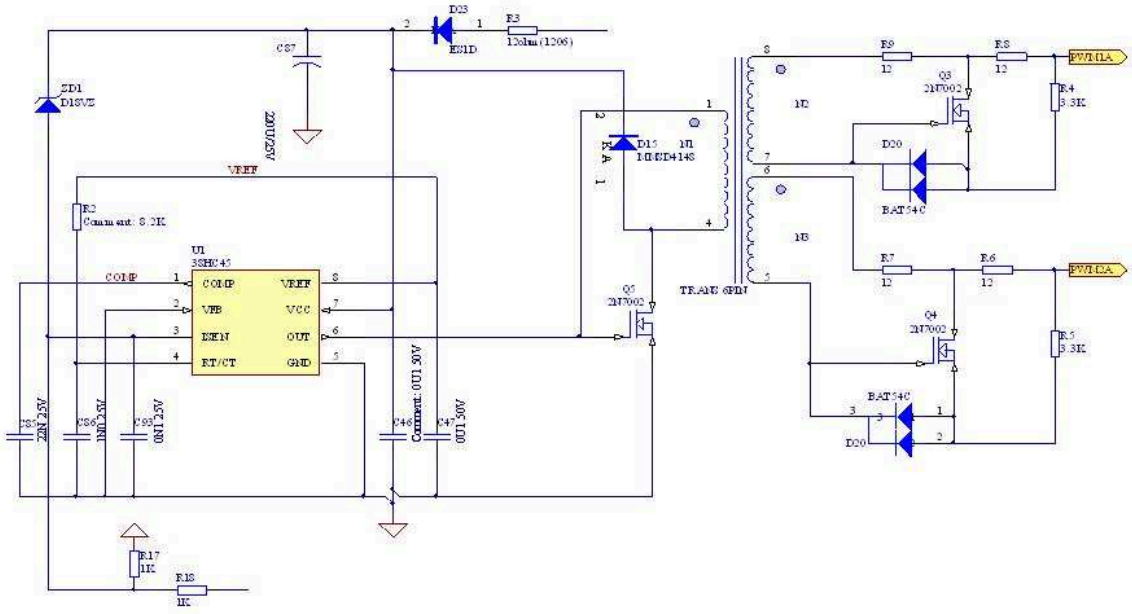

Fig.3 Drive Circuit

Experimental results

Experiments have been done on the circuit to verify the performance of the proposed design. The input voltage ranges from 140V to 1000V,7 outputs:20V/1A、+17.5V/0.5A（two-outputs）、+15V/0.3A、12.5V/1A、+12.5V/0.2A、+5V/3A,operating frequency is 83KHZ, Main transformer uses Mn-Zn ferrite core, Drive isolation transformer uses Mn-Zn ferrite core R0.25*1P*22Ts, main switch uses STD3NK100z, clamping diode uses high-efficiency HFM08, rectifier diode uses ES3D.

Fig.4 Drive Wave

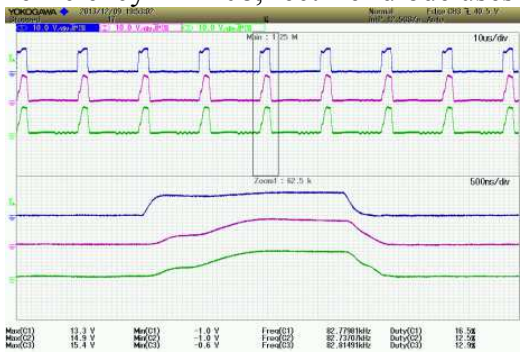

Fig.5 Voltage Output Wave

Load states: +20V connected to resistor of 20 ohm,12.5V connected to resistor of 20 ohm,+5Vconnected to resistor of 3.75 ohm,input voltage ranges from 140V to 800V. Fig.4 shows the drive waveforms when the input voltage is 300Vdc. From top to bottom in the Fig.4, the waves are output wave of control chip and output drive wave of transformer; From top to bottom in the Fig.5, the waves are wave of sampling resistor, drive wave and output 5V voltage wave.

Conclusions

The proposed dual flyback topology with seven outputs is successfully applied in a three-phase photovoltaic inverter as an auxiliary power supply. Dual flyback topology achieves isolation between the control circuit and the power switch of the floating voltage. It improves the reliability of the whole switching power supply. It is proved in practical experiments that the efficiency of conversion is 85% and perfectly meets the requirements of the three-phase photovoltaic inverter.

Acknowledgment

This work was supported by the Guangdong Provincial Natural Science foundation under grant No.S2013010015875, Huizhou Science and Technology Projects under grant No.A507.0206, No.2010B020008013& Huizhou[2009]62.

References

[1] Abraham Pressman, Keith Billings, Taylor Morey, in: Switching Power Supply Design, 3rd Ed. McGraw-Hill Professional(2009).
[2] Keith Billings, Taylor Morey, in: Switch mode Power Supply Handbook,3rd Ed. McGraw-Hill Professional(2010).
[3] Spiazzi G, Buso uiso S, in: Comparison between Single-switch Isolated Flyback and Forward High-quality Rectifiers for Low Power Applications. IEEE APEC(2002).
[4] Zhang Fengge, Zhu Shilu, Yin Xiaoju, eta, in: Controller Design of Grid-Connected Microinverter Based on Interleaved Flyback Structure. Transactions of China Electrotechnical Society. 2013, 28:142-147+153.
[5] Robert Kollman, in: Achieving High-Efficiency with a Multi-Output CCM Flyback Supply Using Self-Driven Synchronous Rectifiers, SEM-1500, TI Seminar.(2003).
[6] Skendzic D, in: Two Transistor Flyback Converter Design for EMI Control. Electromagnetic Compatibility 1990 Symposium Rccord,1990: 130-133.
[7] Kollman R, in: Achieving High-Efficiency with a Multi-Output CCM Flyback. Supply using Self Driven Synchronous Rectifiers. Texas Instruments application notes(2003).

Advanced Materials Research Vols. 986-987 (2014) pp 1763-1766

doi:10.4028/www.scientific.net/AMR.986-987.1763

Both spatial and temporal distortions caused by spatial chirp in vortex femtosecond pulse beams

Yongming NIE[a], Yakun GUO[b], Fenglei TAN[c], Fuan SUN[d]

China Satellite Maritime Tracking and Controlling Department, Jiangyin, 214431, China

[a]email: nwy1986@163.com, [b]email:yimonie@163.com, [c]email:eyki0206@163.com,

[d]email: yaol0206@163.com

Keywords: Pumping Ultrafast optics; spatial chirp; spatial light modulators

Abstract. Spatial chirp will cause temporal width broadening and wave front aberration with the femtosecond pulse beam. So effectively controlling and utilizing the spatial chirp has great significance. In this manuscript, the properties of the spatial chirp are theoretically investigated. An experimental setup which can easily control the spatial chirp of the femtosecond laser pulse beam and generate vortex femtosecond pulse beam with different spatial chirp parameters is proposed. The relationships between the spatial chirp and the temporal and spatial properties including the cross section intensity distributions and the temporal width and chirp of the femtosecond pulse beams are obtained. Both theoretical and experimental results indicate that as the spatial chirp parameter becomes larger, both the temporal and spatial pulse beam widths are broadening and the wave front aberration also becomes larger quickly. Moreover, the temporal chirp is also becoming larger when the spatial chirp parameter becomes larger. The spatial chirp properties of vortex and Gaussian femtosecond pulse beams are similar with each other.

Introduction

The electric field of femtosecond laser pulse beam usually can not be separated into a product of purely temporal and purely spatial factors, which is known as a spatiotemporal coupling effect. Especially, when ultrashort pulses comprise only a few oscillations, the coupling of spatial and temporal effects becomes important even for propagation in a non-dispersive medium [1-3]. To further understanding the spatiotemporal effect, a lot of theoretical investigations have been done to develop a common quantity to describe or quantify it. Unfortunately, such a general quantity does not currently exist. Early in 1980s, Fork and Martinez had found that angular dispersion can generate spatiotemporal effect and always yields negative group delay dispersion [4] [5]. Later, Wefers and Paye accomplished detailed theoretical analysis of the space-time coupling based on space-time Wigner distribution functions [6] [7]. In 2008, Sussman and his coworkers using numerical approach to analysis the space-time coupling in detail and calculate the field distribution after a pulse shaper in various geometries [8]. Contemporaneously, Selcuk Akturk and his coworkers systemically analyzed the characteristics of pulses containing spatio-temporal couplings, including their sources, mathematical descriptions and methods for their characterization. They also gave some suggestions for further exploitation and avoidance [9]. Not long ago, F. Frei provided a Fourier optical analysis of a typical femtosecond pulse shaping apparatus and derived analytic expressions for the space-time dependence of the emerging waveform after the pulse shaper and in the focal volume of an additional focusing element [10]. However, there exist only a marginal number of experimental investigations to the present day. Moreover, optical vortices had been a subject of interest in a great amount of different fields, including optical tweezers, interferometry, and optical communications. Femtosecond vortex beam has been attracting increasing attention with both the advantage of optical vortices and excellent properties of ultra-high peak power and extreme short duration. In this manuscript, we first present a discussion of the characteristics of pulses containing spatio-temporal couplings. Then a setup is proposed to make experimental investigation. Finally, conclusions are given.

Principals

A beam with spatial chirp, which has different frequency components separated in space transverse to the propagation direction, is very common and often undesirable in ultrafast optics. It can be introduced by many routine operations and normal optical elements, such as a grating and cylindrical lens pair described in Fig 1.

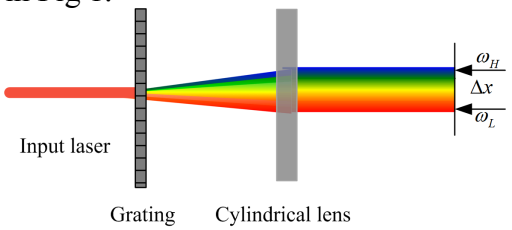

Fig.1. Schematic diagram of spatial chirp caused by a grating and cylindrical lens pair

Here we will focus on the simplest possible case, just considering the spatial chirp along x orientation, and the electric field is described as $E(\omega,x)$, which is a Gaussian spectrum and a Gaussian spatial profile for all the frequency components. If there is no spatial chirp in the femtosecond pulse beam, the electric field can be written as following [11].

$$\begin{aligned} E(\omega,x) &= E_{\omega}(\omega)E_x \\ &= A_0 \exp\left(-\left(\frac{\omega}{\Delta\omega}\right)^2\right)\exp\left(-\left(\frac{x}{\Delta x}\right)^2\right) \end{aligned} \tag{1}$$

where A_0 is a constant, Δx is the beam width, and $\Delta\omega$ is the frequency bandwidth.

If there is spatial chirp in the femtosecond pulse beam, the electric field should be written as following.

$$E(\omega,x) = A_0 \exp\left(-\left(\frac{\omega}{\Delta\omega}\right)^2\right)\exp\left(-\left(\frac{x-\xi\omega}{\Delta x}\right)^2\right) \tag{2}$$

where ξ is corresponding to the spatial chirp.

In order to detect the spatial chip parameter, referring to reference [12], the normalized spatial chirp parameter can be expressed as following.

$$\rho_{\omega\to x} = \frac{\iint dx d\omega |E(x,\omega)|^2 x\omega}{\Delta x \Delta\omega} \tag{3}$$

where $\Delta x = \sqrt{\iint dx d\omega |E(x,\omega)|^2 x^2}$, $\Delta\omega = \sqrt{\iint dx d\omega |E(x,\omega)|^2 \omega^2}$. According to the expression above, the spatial chirp parameter can be calculated.

According to the properties of the optical femtosecond vortices, providing the beam with horizontal polarization, the input optical field can be expressed as follows [13].

$$\mathrm{E}_0(r,t) = \mathrm{A}_0 \exp(-r^2/r_0^2)\exp[-(a_0 t/T)^2]\exp(-i\omega_0 t) \tag{4}$$

where r_0 is the beam waist of the Gaussian beam, A_0 is a constant, $a_0 = (2\ln 2)^{1/2}$, T is the pulse duration, and ω_0 is the central angular frequency of the femtosecond pulse beam. According to expression (4), vortex femtosecond pulse beam can be generated based our early work reported in reference [13].

Experimentation

The scheme of the experimental setup is shown in Fig.2. The femtosecond pulse beam is generated by the Mai Tai HP Ti: sapphire laser with tunable center wavelength from 690 to 1040 nm.

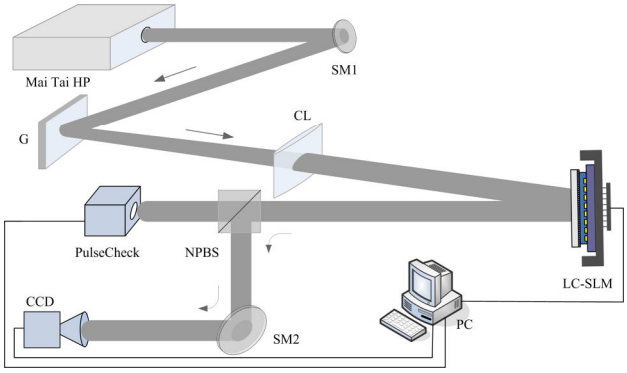

Fig. 2 Experimental setup for generating detecting fetosecond pulse beam with spatial chirp

Two Holoeye Pluto VIS LC-SLMs are used with 1920×1080 pixels, and the phase level of each pixel with 8×8 μm2 size can be assigned between 0 and 2π by step ratio of 1/256. The high sensitive CCD camera is AVT Dolphin F-145B with 1280×960 pixels and 6.45×6.45 μm2 pixel pitch. The temporal property detecting device is a product of the APE Company named PulseCheck 50.

The experimentally obtained cross section distributions are shown in Fig.3. It is easily found that spatial chirp made the beam spatial profiles generating distortions.

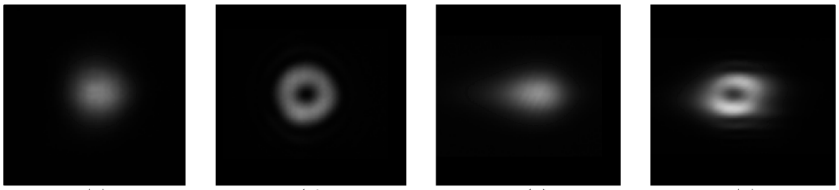

Fig.3. Cross section distributions, (a) Gaussian beam, (b) vortex beam, (c) Gaussian beam with spatial chirp, and (d) vortex beam with spatial chirp

The temporal properties of both the Gaussian beam and vortex beam are shown in Fig.4. Based on Fig.4 it can be found that as the spatial chirp becomes larger, the temporal chirp becomes larger.

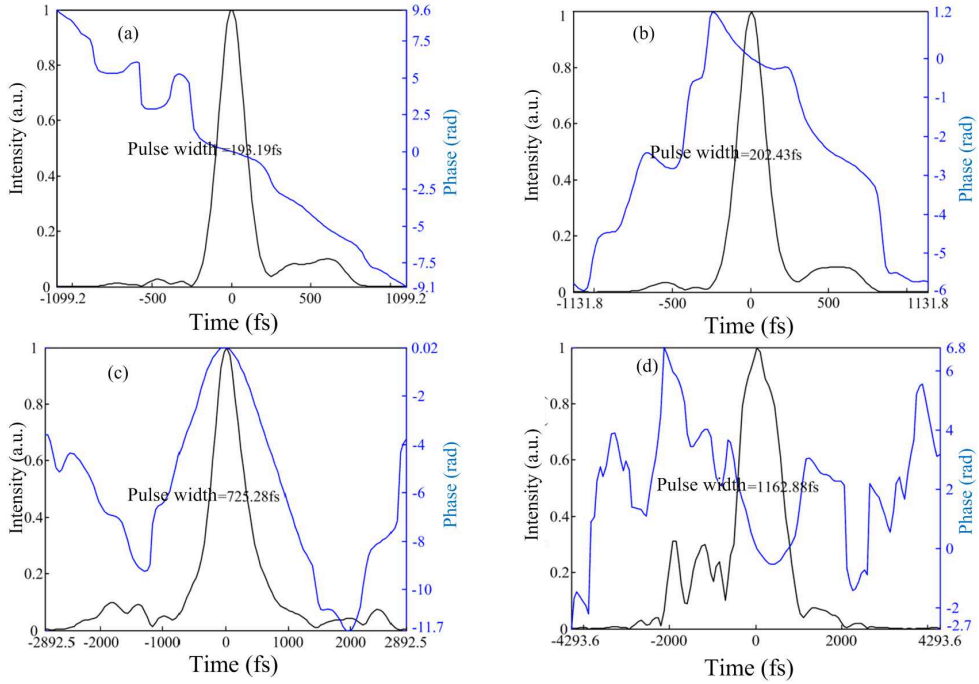

Fig.4. Temporal properties, (a) Gaussian beam without spatial chirp, (b) vortex beam without spatial chirp, (c) vortex beam with small spatial chirp, and (d) vortex beam with large spatial chirp

Moreover, the experimental results also indicate there is almost no temporal property difference among the pulse beams with different topological charges.

Conclusions

In this manuscript, we have generated vortex femtosecond pulse beam and a setup is proposed to control the spatial chirp. The experimental results indicate that the temporal pulse duration changes slightly with different topological charges, and as the spatial chirp parameter becomes larger, both the temporal and spatial pulse beam widths are broadening and the wave front aberration also becomes larger quickly. Moreover, the temporal chirp is also becoming larger when the spatial chirp parameter becomes larger. The spatial chirp properties of vortex and Gaussian femtosecond pulse beams are similar with each other.

Acknowledgement

This research was funded by the National Natural Science Foundation of China (NSFC) under grant no.61108089 and no.61107005. The authors acknowledge Doctor Yunshan ZHANG and Yunfei MAO for fruitful discussions.

References

[1] M. A. Porras. Ultrashort pulsed Gaussian light beams [J], Phys. Rev. E, 1998 58(1): 1086-1093.
[2] T. Tanabe, F. Kannari, F. Korte, J. Koch, B. Chichkov. Influence of spatiotemporal coupling induced by an ultrashort laser pulse shaper on a focused beam profile [J], Appl. Opt., 2005 44(6): 1092-1098.
[3] C. Dorrer, I. A. Walmsley. Simple linear technique for the measurement of space-time coupling in ultrashort optical pulses [J], Opt. Lett., 2002 27(21): 1947-1949.
[4] R. L. Fork, O. E. Martinez, J. P. Gordon. Negative dispersion using pair of prisms [J], Opt. Lett., 1984 9(5): 150-152.
[5] O. E. Martinez, J. P. Gordon, R. L. Fork. Negative group-velocity dispersion using refraction [J], J. Opt. Soc. Am. A, 1984 1(10): 1003–1006.
[6] M. M. Wefers, K. A. Nelson, A. M. Weiner. Multidimensional shaping of ultrafast optical waveforms [J], Opt. Lett., 1996 21(10): 746-748.
[7] J. Paye, A. Migus. Space–time Wigner functions and their application to the analysis of a pulse shaper [J], J. Opt. Soc. Am. B, 1995 12(12): 1480-1490.
[8] B. J. Sussman, R. Lausten, A. Stolow. Focusing of light following a 4f pulse shaper: Considerations for quantum control [J], Phys. Rev. A, 2008 77: 043416(1-11).
[9] S. Akturk, X. Gu, P. Bowlan, R. Trebino. Spatio-temporal couplings in ultrashort laser pulses [J], J. Opt., 2010 12: 093001 (1-20).
[10] F. Frei, A. Galler, T. Feurer. Space-time coupling in femtosecond pulse shaping and its effects on coherent control [J], J. Chem. Phys., 2009 130: 034302(1-11).
[11] X. Gu, S. Akturk, R. Trebino. Spatial chirp in ultrafast optics [J], Opt. Commun., 2004 242: 599–604.
[12] P. Gabolde, D. Lee, S. Akturk, R. Trebino. Describing first-order spatio-temporal distortions in ultrashort pulses using normalized parameters [J] Opt. Express, 2007 15(1): 242-251.
[13] J. Liao, X. Wang, W. Sun, Y. Tan, Y. Nie, J. Qi, H. Jia, J. Liu, J. Yang, J. Tan, X. Li. Analysis of Femtosecond Optical Vortex Beam Generated by Direct Wave-Front Modulation [J], Opt. Eng., 2013 52(10):106102.

Advanced Materials Research Vols. 986-987 (2014) pp 1767-1770

doi:10.4028/www.scientific.net/AMR.986-987.1767

Calculation of Leakage Magnetic Field and Short-circuit impedance of Power Transformer

Fangxu Han, Yan Li, Xin Sun, Longnv Li

Research Institute of Special Electrical Machines, Shenyang University of Technology, China

email: hanfangxu021532@163.com

Keywords: Power transformer; Leakage magnetic field; Shot-circuit impedance

Abstract. The leakage magnetic field and equivalent circuit model of OLTC double-winding power transformer has been established by electromagnetic field Finite Element analysis software. The method of field-circuit coupled method has been used to calculate its magnetic field leakage, the short circuit impedance obtained by the calculation of formula and compared with the experimental data. At the same time, based on the calculation method for the Visual Basic language as a tool for MAGNET software for secondary development, obtain the software to calculate the short-circuit impedance of power transformer simulation software, and is verified by using the typical products, proves the validity of this software.

Introduction

Short-circuit impedance $U_k(\%)$ is an important parameter in the performance of power transformer, which is related to the cost, efficiency, voltage change rate, mechanical strength and short-circuit impedance, the deviation of the experimental data and provision value is very strict when the transformer was produced. So accurately calculate the short-circuit impedance of transformer is important for the power transformer design [1]. The calculation method of short-circuit impedance is divided into analytical method, magnetic circuit method, energy method and field-circuit coupled method depend on the calculation method difference of leakage magnetic field [2,3]. The distribution of the leakage magnetic field is changing when the transformer winding with different types, the traditional analytical calculation methods are often difficult to meet the calculation accuracy requirements. Therefore, this paper deals with the leakage magnetic field and short-circuit impedance of different types of power transformer using field-circuit coupled method based on finite element method, at the same time with the VB language as the tool of MAGNET software for secondary development.

Energy Method to Calculate Short-circuit Impedance

The leakage magnetic field in transformer is mainly produced by the winding current, accurate calculation of leakage magnetic field and its distribution is very important to determine the short-circuit impedance of transformer. In addition of small capacity transformer, in terms of general transformer all have the relationship of $U_{kx}(\%) >> U_{kr}(\%)$. Transformers need to consider the affecting of the resistance component $U_{kr}(\%)$ when the transformer capacity is less than 1000kVA, so $U_{kr}(\%)$ is generally negligible for large capacity transformer, approximate reactance component. Therefore, the calculation of short-circuit impedance is mainly the calculation of short-circuit reactance $U_{kx}(\%)$for large capacity transformer[2].

The magnetic energy stored in the transformer is in the process of building magnetic field by exogenous power conversion, calculate of magnetic field distribution can be obtained the magnetic field energy storage, and then calculate the short-circuit impedance of winding, when the winding flows into current I_k, the magnetic energy W_m as follows [4]:

$$W_m = \frac{1}{2} L I_k^2 \tag{1}$$

Where W_m is the magnetic field energy; L is the winding inductance; I_k is the phase current.

The relationship between leakage reactance and magnetic energy as follows:

$$X_k = 4\pi f \frac{W_m}{I_k^2} \tag{2}$$

Where X_k is the leakage reactance; f is the supply frequency.

The percentage of short-circuit impedance is shown as follows:

$$U_k\% \approx U_{kx}\% = \frac{X_k I_k}{U_k} \times 100\% \tag{3}$$

Where U_k is phase voltage; U_k% is the percentage of short-circuit impedance.

Calculation of Leakage Magnetic Field and Short-circuit Impedance

The calculation model in this paper is made based on the symmetry structure of power transformer and the characteristics of the electromagnetic distribution. The analysis has been made with the following assumptions[5]:

(1) The 1/2 model of whole transformer model is established in order to reduce the computational time;

(2) The eddy currents and their influence on windings are being neglected;

(3) All field quantity sinusoidal variation with time, do not consider the high-order harmonic;

(4) The currents in the windings are equally distributed along the cross section, the core and tank material is using nonlinear magnetic B (H) curve.

With SZ11-20000/35 OLTC double-winding power transformer as an example, the time-harmonic field calculation method, built outside the equivalent circuit model and apply corresponding excitation current calculation. The 2D and 3D calculation model are shown in Figure 1, one section height of high voltage winding is regulating area.

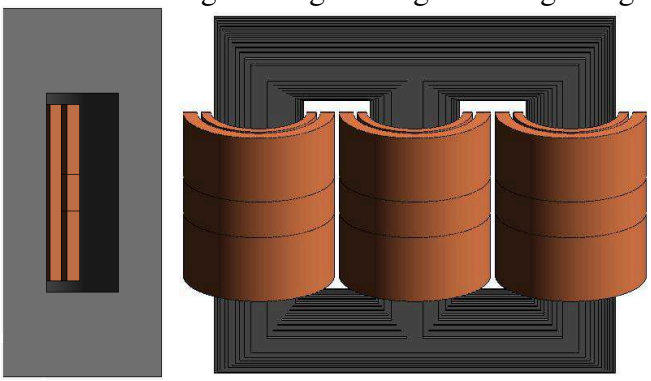

Fig.1. 2D calculation model and 3D calculation model

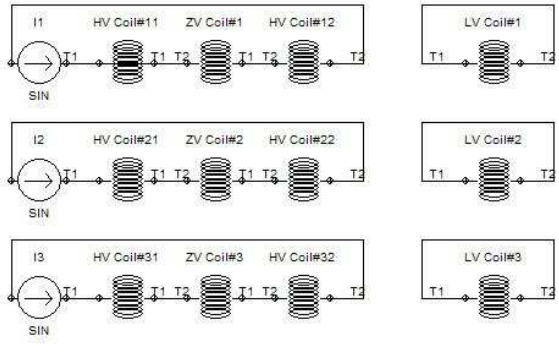

Fig.2. 3D equivalent circuit

Structural material properties as shown in table 1, the material of core and tank are 30RGH120 silicon steel and A3 steel, respectively, permeability with nonlinear B-H curve, ignore the eddy current loss of core, the conductivity is 0.

Ignore the circulation current and eddy current in the windings, winding adopts stranded conductor (stranded - current density is uniformly distributed by default), high and low winding reverse direction and their electrical angle 120° difference to each other. Equivalent circuit model is shown in Figure 2.

Table1 Material Properties of transformer assembly parts

Structure parts	Material	permeability	conductivity (S/m)
core	30RGH120	B-Hcurve	2.22×10^6
winding	copper	——	5.714×10^7
tank	A3steel	B-Hcurve	6.484×10^6

Analysis of Computing Results

In this paper, the SZ11-20000/35 OLTC double-winding power transformer has been taken to calculate the short-circuit impedance by 2D and 3D finite element method, the leakage magnetic field distribution is shown in Figure 3.

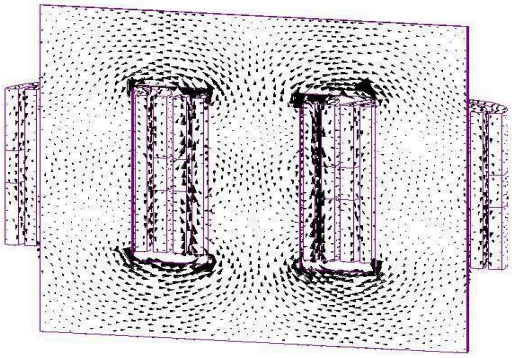

Fig.3. 3D Leakage magnetic field Distribution (rated tapping)

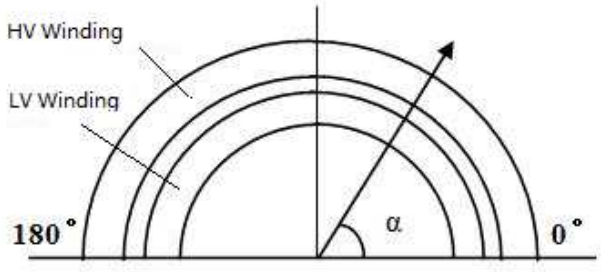

Fig.4. The schematic diagram position of magnetic field computation

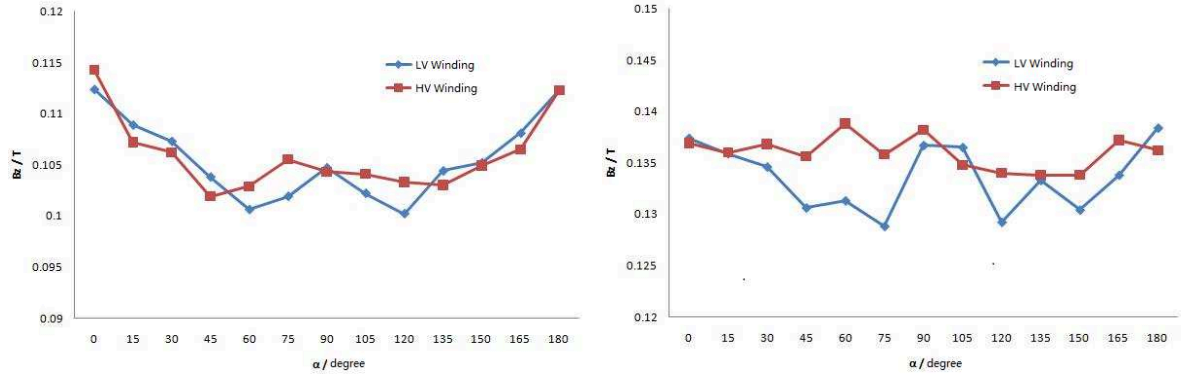

(a) the end windings (b) height of windings

Fig.5. Axial magnetic flux distribution along circle direction(rated tapping)

The axial flux density distribution of winding upper end and 5/8 height along circumferential direction is shown in Figure 5.

As can be seen in Figure 5, the axial flux density distribution along the winding circumference direction is uneven due to the influence of the transformer structure (iron yoke), the axial magnetic flux density within the core window is greater than that outside the window, winding ends is more obvious than the central winding, there are fluctuations about 5/8, but the amplitude changes not much. In this paper, the biggest difference is about 9.88%.

Take SZ11-20000/35 OLTC double-winding power transformer as an example, the comparison of short-circuit impedance is shown in table 3:

Table2 Measured value and Calculation value of Short circuit impedance

Tapping type		Magnetic energy/J	Measured value/%	Computation value/%	Error /%
Rated	2D	256.12	8.09	7.99	-1.24%
	3D	266.96		8.19	1.24%
Min	2D	287.46	9.15	9.29	1.53%
	3D	298.60		9.36	2.29%
Max	2D	244.32	7.67	7.50	-2.22%
	3D	254.86		7.71	0.52%

Through the simulation calculation results can be seen that: the calculation results and measured value are agree well with each other. It has more accurate compared with the traditional calculation results, the short-circuit impedance is different under different tap type, the 2D and 3D calculation result has certain error, due to the short circuit impedance is determined by the size and distribution of leakage magnetic field, and the magnetic field is not strictly uniform distribution along the winding circumference direction, the 2D calculation can't reflect the distribution uniform, therefore,

3D has generally higher precision than that of 2D. the short-circuit impedance of transformer is better to use 3D model.

Development of Short-circuit impedance simulation software

Based on the finite element method, the theory of power transformer, using VB language for the tool design software parameter input interface, based on the input parameters of the background to invoke MAGNET finite element analysis software to establish power transformer leakage magnetic field calculation model and calculation of magnetic field, the short-circuit impedance value is obtained by extracting the magnetic energy and formula conversion, also can through opening the MAGNET software to view the calculation results and post-processing analysis.

Through the calculation of the short-circuit impedance of several typical product by the mentioned software, including split-winding transformer(SFFZ10 - 180000/220), auto-transformer (ODFPSZ - 250000/500) and testing transformer (YS-31500/110), the three types of structure when the impedance values often appear large deviation in the past type testing the products leave the factory, so the author take these types of transformer as the examples, the error between the calculated results and the measured ones is commonly within 3%.

Conclusion

This paper established the 3D leakage magnetic field calculation model and equivalent circuit model of On-load voltage regulating power transformer, field-circuit coupling method is applied to calculate the short-circuit impedance under different tapping type, the error between the calculated results and the measured ones is commonly within 3%, accuracy is higher than the traditional analytical method and 2D model of the electromagnetic field. At the same time, based on the calculation method for the Visual Basic language as a tool for MAGNET software for secondary development, obtain the software to calculate the short-circuit impedance of power transformer simulation software, and is verified by using the typical products, proves the validity of this software. This calculation method and software have great significance for guiding product bidding, design and optimization.

Acknowledgement

In this paper, the work was supported by NSFC, under Project No. 51177103 and Program for LNIRT in University (Project No. LT2011002).

References

[1] Jianmin Wang, Jiangang Jia, Lanrong Liu, et al. Research on Numerical Simulation of Three Dimensional Leakage Magnetic Field and Short Circuit Impedance of Phase-Shifting Rectifier Transformer[J]. TRANSFORMER , 2009,46(4): 1-4.

[2] Qifan Hu. Transformer experiment technology[M]. Beijing: Chinese electric power press, 2010.

[3] Shishan Wang, Yanming Li, Yingna Guo. Calculation of Short-circuit Impedance for Power Transformer with Coupling FEM Method of Magnetic Field and Circuit [J]. High Voltage Engineering , 2006,32(11): 11-14.

[4] Ying Li. Examples of calculating reactance by energy method [J]. TRANSFORMER , 2004,41(2): 18-21.

[5] Zhiguang Cheng, Norio Takahashi, Behzad Forghani, et al. Electromagnetic and Thermal Field Modeling and Application in Electrical Engineering[M].Science Press, 2009.

Advanced Materials Research Vols. 986-987 (2014) pp 1771-1774

doi:10.4028/www.scientific.net/AMR.986-987.1771

Calculation of Thermal Performance in Amorphous Core Dry-Type Transformers

Yan Li, Yinjun Guan, Yang Li, Tianyuan Li

Research Institute of Special Electrical Machines, Shenyang University of Technology, China

email: guanyinjun666@sina.com

Keywords: Amorphous Core Dry-Type transformer; finite element; thermal

Abstract. The amorphous core dry-type transformer is a new energy-saving transformer. In this paper, a SCBH15-600/10 type amorphous core dry-type transformer is analyzed by 3-D finite element calculation of iron core and winding thermal. Analyzing the temperature distribution characteristics of amorphous transformer, assure the temperature rise highest point. It is in the permitted error between the simulation value and test value. It has important engineering value for the calculation of similar transformer temperature rise; and has certain guiding significance on the amorphous transformer structure design.

Introduction

Due to the need of energy saving, environmental protection and development, as a prominent energy-saving and environment friendly products, amorphous alloy dry-type transformer with its good economic benefit and excellent energy saving effect is being accepted by the masses of users, and has been widely used in some areas. The amorphous core transformer's no-load loss is only common no-load loss of transformer's 1/5 [1-3].

Because of the difference of core material, amorphous alloy dry-type transformer and ordinary cast-resin dry-type transformer has the big difference in the structure. Amorphous alloy core is rectangular section winding core, generally for three-phase four box five column structure; correspondingly high and low voltage winding are made into rectangle, the low voltage winding is generally foil winding type, high voltage winding for piecewise linear winding type. Epoxy resin casting structure [4].

With the increase in demand and capacity, transformer leakage-flux field, eddy current loss and temperature rise problem will be more obvious, especially eddy current losses of low foil winding cause the local overheating. Coupling with the poor heat dissipation resin, the transformer's heat dissipation is particularly prominent.

Therefore, in this paper, the transformer temperature rise is analyzed by the three-dimensional finite element software.

Mathematical model

Amorphous alloy dry-type transformer is the non-enclosed dry-type transformer. The major cooling is heat conduction between winding and resin; the resin and core mainly depend on natural convection. Air movement depends on temperature difference and gravity field. The air around the heating element was heated, density decreases under the action of buoyancy upward movement; when the air cools, the air move downward under the action of gravity [5].

Because the temperature rise is not high, The Boussinesq assumption is used to analysis air flow and cooling. It is valid when density variations are small. The temperature field and flow field by the mass equation, momentum equation and energy equation together. As the following equations:

The continuity equation:

$$\frac{\partial(\rho u)}{\partial x}+\frac{\partial(\rho v)}{\partial y}+\frac{\partial(\rho w)}{\partial z}=0 \tag{1}$$

In the type: ρ is the density. u, v, w are respectively the velocity vector of x ,y ,z.

$$div(\rho\vec{Ut}) = div(\frac{\lambda}{c_p} grad(t)) + S_T \quad (2)$$

In the type: λ is the Coefficient of thermal conductivity, c_p is the specific heat capacity, S_t is the General source terms.

Boussinesq model assumes the fluid density is constant in all terms of the momentum equation except the body force term.

$$\frac{\partial(\rho_0 W)}{\partial t} + \nabla \cdot (\rho_0 UW) = \mu \nabla^2 W - \frac{\partial P'}{\partial z} + (\rho - \rho_0) g \quad (3)$$

In the body force term, the fluid density is linearized,

$$(\rho - \rho_0)g = -\rho_0 \beta (T - T_0)g \quad (4)$$

In the type: ρ_0 is the Constant (operating) density; ρ is the Variable (local) density; β is the coefficient of thermal expansion [6].

The finite element model

According to the symmetry of the structure, we calculate the model of entity transformer's 1/4, shown in Figure 1.

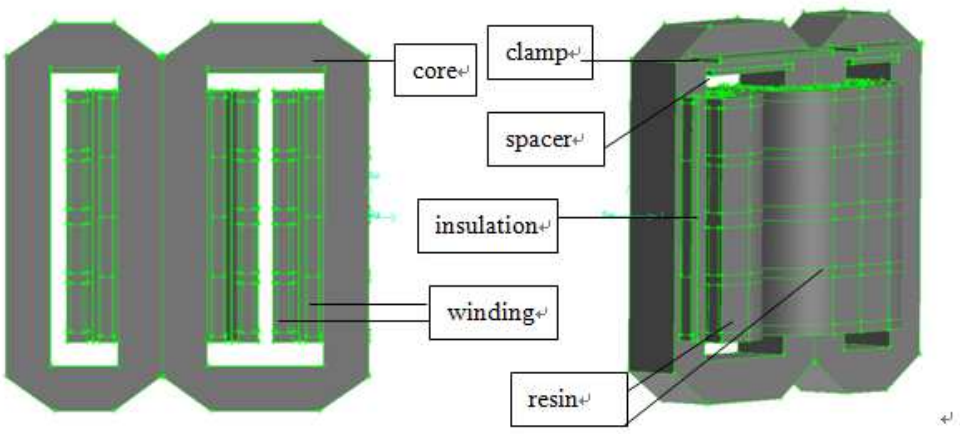

Fig.1.The transformer model

Establishing the air area out of the model and using gambit to divide the region. The quantity and quality of the mesh has great influence on the result of calculation, the large number of high quality can improve computational precision. If the number is too large, it will affect the calculation speed, therefore we should seize on grid unit type and unit size. In order to improve the accuracy, we use fine mesh for the heating body and the surrounding air. The total mesh are about 6920000, the mesh quality is below 0.8.

Front and right side of the model are set for symmetric boundary. The bottom face is ground. The top, left and the back side is outlet, the relative pressure stress of fluid outlet is 0[7]. Coupling of pressure and velocity is solved by SIMPLE algorithm, discrete choice Body Force Weighted pressure. The environment temperature is 300K, coefficient of thermal conductivity of various parts of the model are shown in table I,

TABLE I UNIT HEAT SOURCE OF EACH COMPONENT

	Large core	Small core	High voltage I	High voltage II	Low voltage I	Low voltage II
Unit of heat /W·m^{-3}	1428.24	1429.16	39776.9	36160.86	29396.2	23132.8

Because of the influence of the low-voltage winding eddy current loss, both ends of the winding loss is bigger. The winding is divided into four sections in the axial; each section of the heat source

is calculated. The top section and the bottom section are set to low voltage I, the middle two sections are set to low voltage II. Due to the number of turns of the coil is not uniform when the high voltage winding is rated, the top section and the bottom section are set to high voltage I, the middle two sections are set to high voltage II.

Temperature rise analysis

Figure 2(a) shows the amorphous core temperature field distribution. As can be seen from the graph, core temperature rise from the lower to upper temperature increased first and then decreased, reached the maximum value at the middle part. Because the winding is out of the middle part of the amorphous core, heat is difficult to shed. For the A, B phase, the core of B phase frame is at the highest temperature. The maximum temperature is about 37.6 degree, because B phase is in the middle of transformer [8].

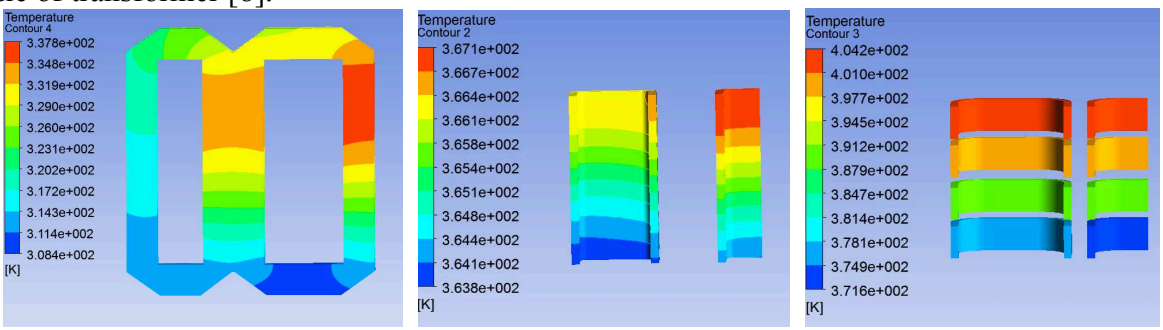

(a)Amorphous core (b) Low voltage wingding (c) High voltage wingding

Fig.2. Temperature field distribution

Figure 2(b), figure 2(c) gives low voltage, high voltage winding temperature field distribution. As can be seen from the picture, the winding temperature from bottom to top temperature rises gradually and reaches the maximum value. At the same height, B phase low-voltage winding's temperature value is always higher than A phase's, the high voltage winding does not have this characteristics. This is because the high voltage winding is in the outside, while the amorphous transformer have no shell, resulting high voltage winding of each phase at the same height have the similar temperature [9]. The thermal conductivity of copper is better, result every line package's temperature consistent.

The maximum value of high and low voltage winding temperature was 402.2K and 367.1K respectively. Calculation of the average temperature and the measured average temperature are shown in table II,

TABLE II THE CONTRAST BETWEEN THE SIMULATION AND THE EXPERIMENT

	Simulation Value/K	Experiment Value/K	Relative error/%
High voltage	82.7	76	8.8
Low voltage	65.27	69	5.4

Through calculation, the relative error of high and low voltage winding temperature rise is respectively 8.8% and 5.4%. the error is within 10%, meet the engineering requirements.

Flow field analysis

Figure 3 gives the axial section wind velocity vector graphics 160mm from the center symmetry plane and radial section wind velocity vector graphics 175mm from the ground respectively. As can be seen from the graph, external gas enter the transformer from the lower side, the gas inside the transformer heat up, flow out from the top surface, forming a cycle process. Maximum wind speed is in top surface, the speed is 1.488m\s. Due to the influence of transformer top clamp, airflow around the clamp change direction, causing the wind speed very small in the upper clamp.

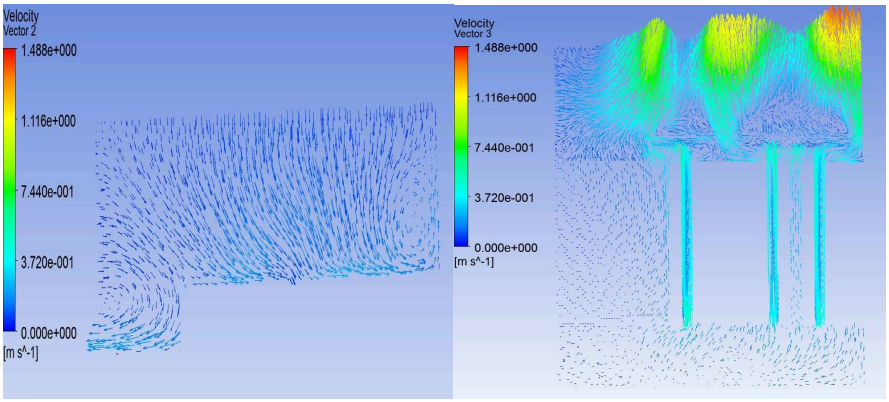

(a) Radial section (b) Axial section

Fig.3. Wind velocity vector graphics

Conclusion

Based on a SCBH15-600/10 amorphous dry-type transformer temperature rise calculation, each part of the high, low-voltage winding gives the different heat generation rate, makes the calculation more accurate. In comparison with ordinary dry type transformer, amorphous transformer's core have lower temperature rise. The hot spot is in the middle position. The high and low voltage winding temperature from the bottom to the top gradually rises; the B phase low voltage winding has the highest temperature. For the high voltage winding, each phase has small temperature difference.

Acknowledgement

In this paper, the work was supported by NSFC, under Project No. 51177103 and Program for LNIRT in University (Project No. LT2011002).

References

[1] Kening Yin. Transformer design principle [M]. China Power Press

[2] Chuanyi Liu. Method and practice calculation of power transformer design [M]. Liaoning science and technology press

[3] Yucheng. Xie, "Power Transformer Handbook", Mechanical IndustryPress(in Chinese), Beijing,2003.

[4] Yan Liu. The amorphous alloy dry-type transformer features and performance analysis [J]. Electric power equipment, 2006.7 (11): 14-16.

[5] Yan Li, Yongzhi Liu. Analysis of finite element about the temperature field of Flame Proof Dry-Type Transformer [J]. Electric power system and automation, 2012.27 (4): 59-63

[6] Shiming Yang, and Wenshuan Tao, "Heat Transfer", Higher Education Press (in Chinese), Beijing, 2006

[7] Wei Cui, Xile Zhang. Calculation and analysis of winding hot spot temperature of dry type transformer based on Fluent software[J]. electric power science and engineering, 2011.27 (1): 32-35

[8] Xiuchun Wang, Junpu Tao, Temperature Field Research of LargeForced-Directed Oil Cooling Transformer, TRANSFORMER, 2008. 7(45):1-4.

[9] Yanlong Zhao, Lan Xiong. Study of Temperature Field Numerical Calculation and On-line Monitoring for Cast-resin Dry-type Transformer [D]. University Of Chongqing, 2013.

Advanced Materials Research Vols. 986-987 (2014) pp 1775-1779

doi:10.4028/www.scientific.net/AMR.986-987.1775

Circuit Design of Electronic Igniter of MCU Used in Biogas Power Generation

LiuYU

Guizhou Industry Polytechnic College, Guizhou,Guiyang,550008
email: liuyuluo@163.com

Key words: MCU; electronic igniter; biogas power generation system

Abstract: According to the technical requirement of biogas power generation system, introducing the working principle of electronic igniter which is controlled by MCU; Designing and developing the electronic igniter which used STC 89 C-52 RC MCU as the core;Having completed the hardware circuit designs of power supply module, main control module and ignition module of electronic igniter. After testing the signal of circuit, it meets the technical requirements of biogas power generation system.

1.Introduction

Guizhou Tairan Environmental Science and Technology Co, Ltd has a set of biogas power generation system whose output power is 30KW.Biogas power generation system uses biogas as fuel for power generation. In this set of biogas power generation system, we choose four-stroke, s park ignition, water-cooled high speed engine as the gas engine. We use analog DC capacitance igniter to ignite while gas engine working. After running for a period of time, we find the following problems:1. the output voltage of power system is still instability. When changing the load of biogas power generation system, the output of the power system voltage can fluctuate wildly.2.large waste. When using the analog capacitance igniter to ignite, we can only know the ignition advance angle of low and high speed, so that we can't accurately control the ignition advance angle. When the engine changes with the rotating speed, the time of engine ignition will also change. The faster the engine operates, the bigger the ignition advance angle becomes. By igniting in advance, we can make the engine release the maximum energy at the power stroke. When the advance angle is too large and the waste of energy is also large; part of the power is negative work. Only by accurately controlling the ignition advance angle of engine can it make the maximum output power of engine and consume the least energy. In order to make output voltage stable and save energy, we should modify the electronic igniter of biogas power generation system and change to use the MCU to control the computer igniter. According to the different speed and load of engine, the igniter can ignite at a best ignition point.

2.Technical requirements

To ensure the output voltage of power system stable.(2)Energy conservation is significant, and the requirement of precision of the ignition angle is 0.5 degrees.(3)Have function of engine over-speed protection; the minimum ignition rotation speed is 100 rpm and the highest ignition rotation speed is 4000 rpm; (4)The number of engine cylinders is 4, and the sequence of working is 1-3-4-2. (5) The limit output current of electronic igniter: continuous 1A,peak 5A(10ms).

3.Working principle of electronic igniter

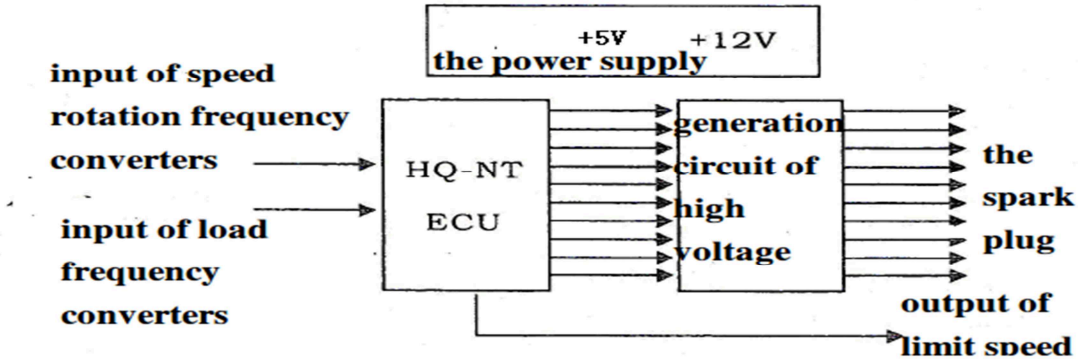

Figure1. Working principle diagram of electronic igniter

As shown in figure 1, the device is composed of 2 parts: one is ECU and the other is high voltage generation circuit; the supplies of DC power are 12V and 5V; the core of the ECU is STC 89C-52RC 40I-P0IP40 MCU chip; the input signal of the device is the output signals of rotation speed and load transducer. ECU continuously detects the signal of rotation speed transducer. After the calculating by computer, we can know the current rotation speed. When it exceeds 100 rpm, we also can come up with the ignition advance angle by current engine rotation speed and the state of load transducer. At the same time ,we can determine the corresponding ignition cylinder so that it can make the corresponding cylinder ignited at corresponding time. ECU will send the output signal of limited speed when the engine exceeds the speed limit and the rotation speed becomes less than 100 rpm.(the terminal state of the limited speed output signal: the state of electrical level 0 under over-speed or less than 100 rpm,, and suspended state under normal speed)

4.MCU electronic ignition circuit

The MCU electronic ignition circuit is made up of 3 parts: power supply module, main control module and ignition module.

4.1 Power supply module

As shown in figure 2,the storage battery provides 12V voltage, through single-phase half-wave rectifier and capacitor filter circuit, we can get stable and anti-interference voltage of 12V. After the 12V voltage passes a 3-terminal voltage regulator LM7805CT, we can get a stable voltage of 5V to provide required power supply for the main control module and ignition module.

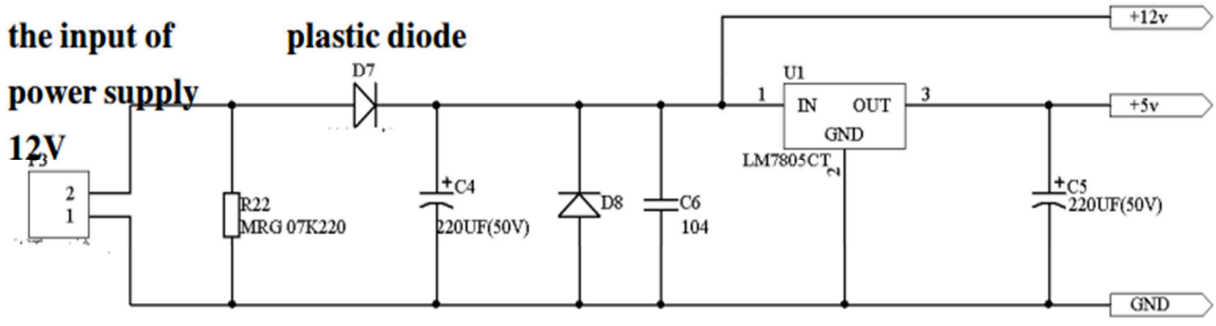

Figure 2 Circuit diagram of power module

4.2 Main control module

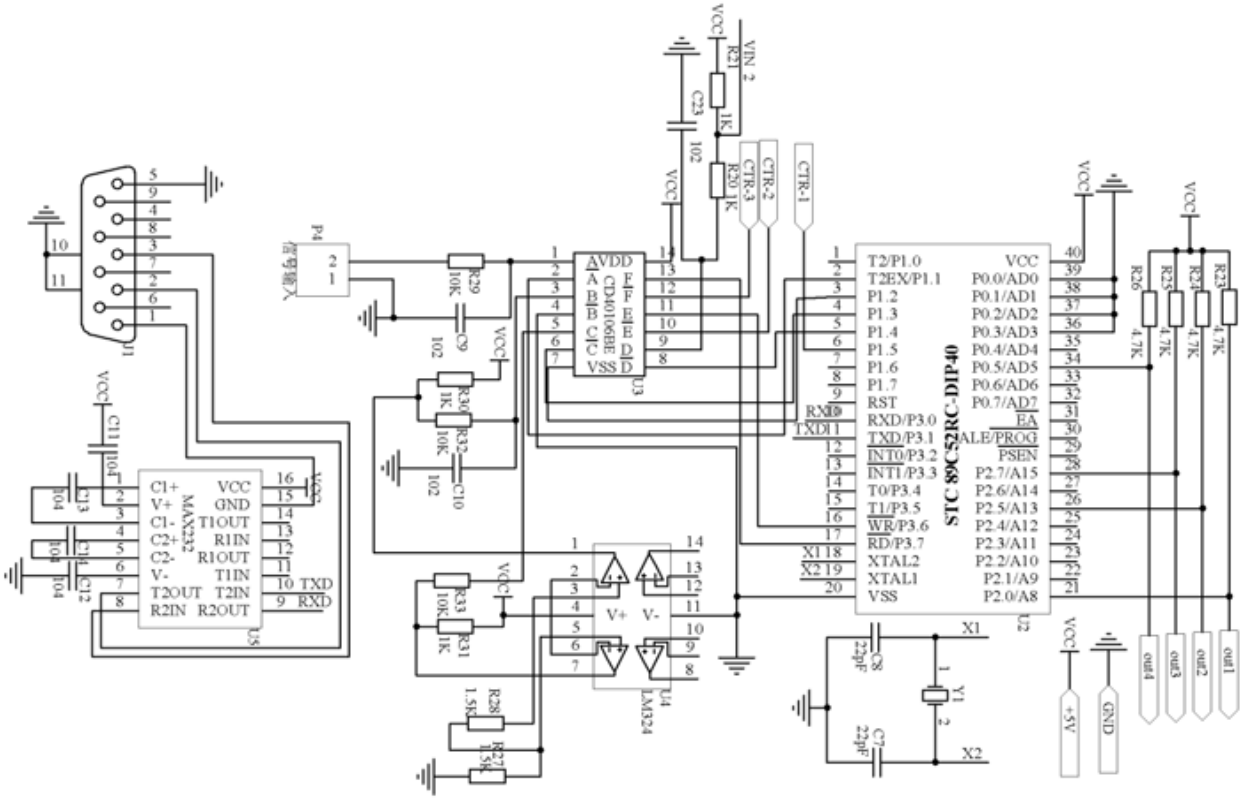

Figure3 Circuit diagram of main control module

As shown in figure 3, the main control module is mainly composed of STC-89CS2RC-DIP-40 MCU, rotation speed sensor(hall sensor),CD40106BE Schmitt trigger,LMX324 integrated transportation amplifier serial chip MAX232,quartz crystal oscillator JFEC 3.579545 MHZ 0 cx0 406 and so on. Biogas generator shaft is provided with a Hall sensor; after the Hall element of Hall speed sensor produces hall potential, the sensor will transform the potential into alternating electric signal; before output the rectangular pulse signal, the inside circuit of sensor would adjust and amplify the signal. Through the integrated operational amplifier amplifies the acquisition pulse signal to meet with the requirement of digital signal amplitude; Schmitt trigger transform and shape the waveform, and switch it to TTL signal received by MCU; then send the signal to the MCU input of P1.1 P1.2 P1.3 P1.4. MCU can control the internal timer, accurately measuring the positive pulse width which is applied to input terminal pin (i.e, measuring the cycle of pulse signal), then calculating the best ignition angle by pulse width. The output terminals pin of MCU P0.5 P2.7 P2.5 P2.0 receive signal, and output the signal to ignition module. The hardware watchdog is composed of serial chip max232.The circuit makes use of a timer circuit, whose timing output is connected to the reset terminal of the circuit; the program will reset the circuit in a period time(commonly known as “dog”),when the program is working correctly, the timer can not overflow and generate a reset signal. When the program fails, it can not reset watchdog in the period time, making the watchdog timer overflow, generate reset signal and restart the system.

4.3 Ignition module

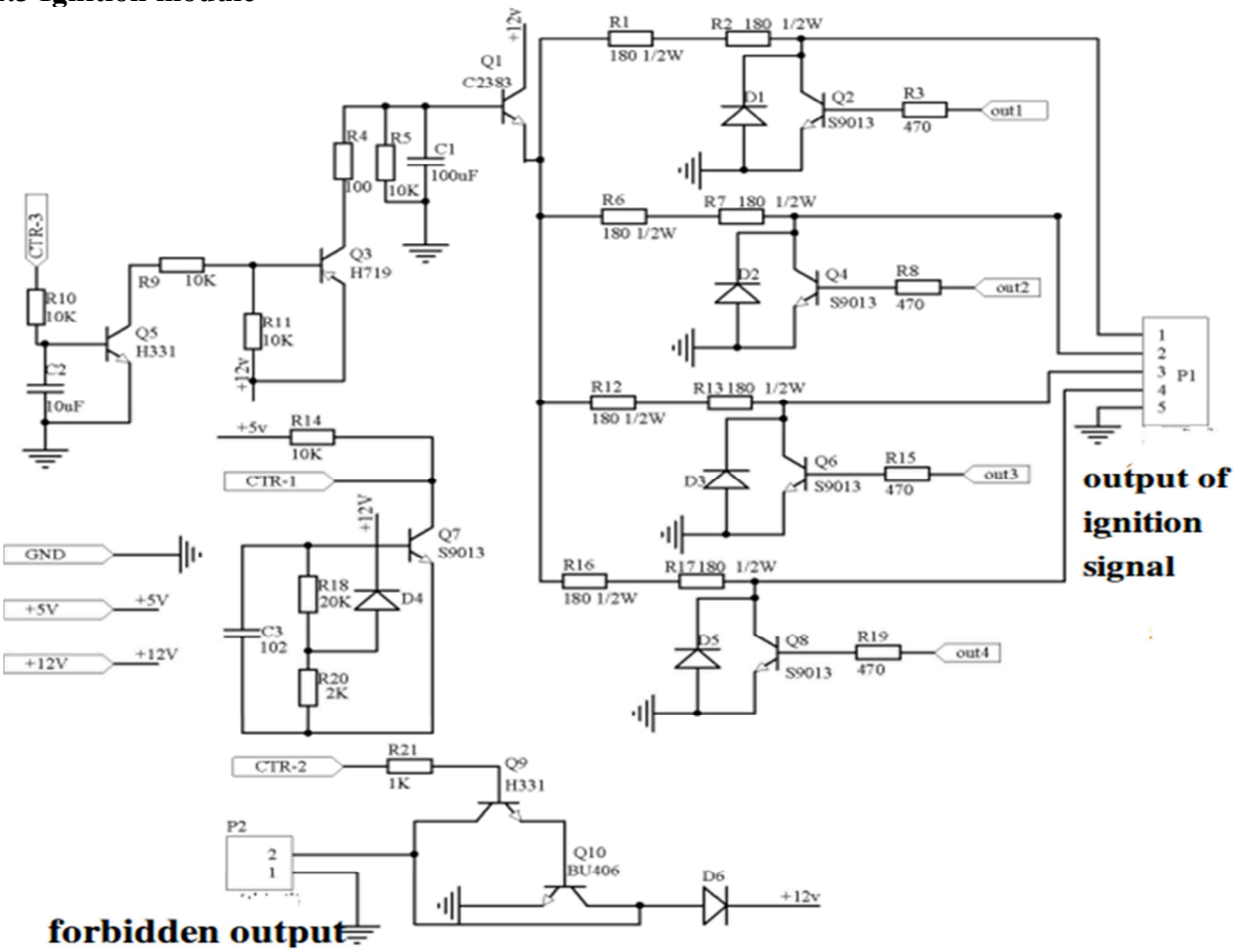

Figure 4 Circuit diagram of ignition module

As shown in figure 4,the output pulse signal of MCU controls Q2 Q4 Q6 Q8 transistors' cut-off and conduction, to make the ignition coil primary current on and off in time to implement the engine ignition. When the input pulse signal make transistor Q2 Q4 Q6 Q8 cut off, the 17 feet of MCU output to CD40106BE with an inversion phase, controlling Q1 with a saturation conduction state, then the primary ignition coil get the voltage. When the input pulse signal make the transistor Q2 turn off, the secondary coil will induct high voltage; by distributor and high voltage wires, the high voltage will be sent to ignition cylinder and spark plug. The 16 feet of MCU output to the 11 feet of CD40106BE; after the phase reverse, as the input signal of Q9/Q10's complex structure, control the high and low level output by complex structure; by electronic governor, we can control the rotation speed of engine. Ignition output limit current protection circuit is composed of pipe Q7.

5.Introductions of signal test

As shown in figure5, using the digital oscilloscope to test the relationship between input signal and output signal of electronic igniter, channel CH1 is the input signal of rotation speed sensor. Channel CH2 is the output signal of electronic igniter. Through the experiment verification, according to the collection input pulse signal and program, the electronic igniter can adjust the cycle and width of output pulse signal to realize the best ignition angle.

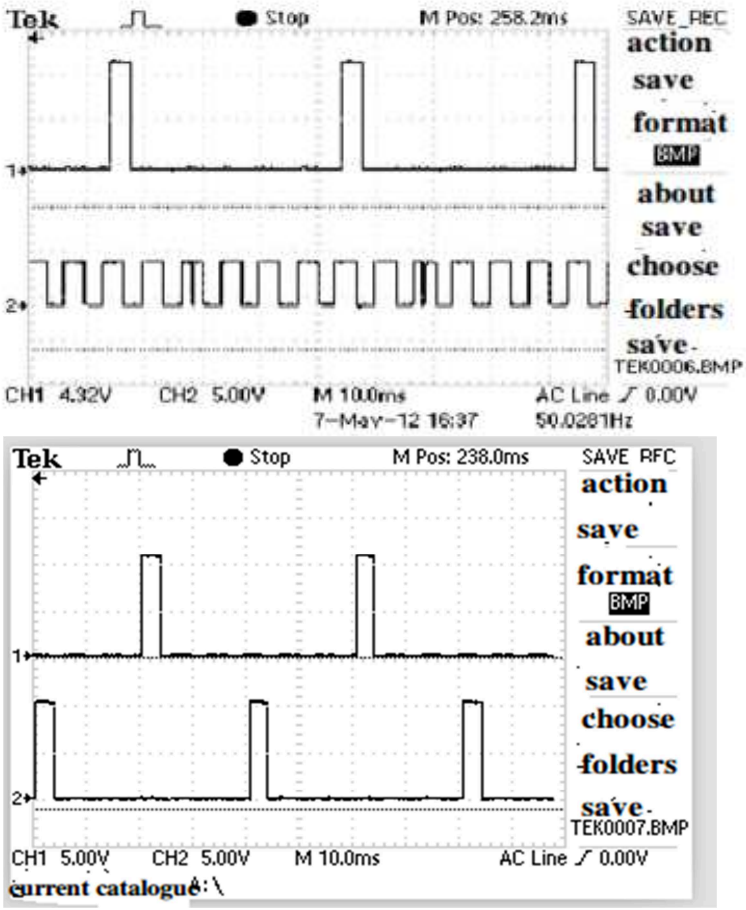

Figure 5 The relationship diagram between input signal and output signal

6.Conclusion

After using the modified circuit system, the biogas generators can adapt to various gases in which the methane concentration is from 30% to 100%; after the mixture of air and fuel gas ,by using the electronic igniter automatically adjust the best air-fuel ratio and make use of fuel gas, reducing the gas consumption; improving the thermal efficiency of the engine; effectively reducing the harmful gas in the exhaust gas, such as NOX. When the load changes, the output of the power system voltage is stable, and the effect of energy conservation and emissions reduction is obvious, thus it brings great economic benefits to the enterprise.

References

[1] Ke Z W,Feng Q X.Design of the Multi-functional Data Acquisition Module Based onMulti-taskingOperating Mode of MCU[J].Process automation instrumentation.2014, 35(1): 84-87.

[2] Ju J P,Chen C D.MCU application technology tutorial[M].version 1 in 2012.Hubei wuhan :HUST Press 20120801.

[3] Shen J S.Biomass biogas power generation[M].2009.Beijing:China light industry press.200903.

[4]Li S L,Zhang C H,Wu Z H.The design of automobile electronic igniter based on MCU[J].Science Technology and Engineering.2013,10：2857-2862.

[5]Zang C H.Electronic circuit design and application of tutorial[M].2004.Beijing:Higher education press.200407.

Advanced Materials Research Vols. 986-987 (2014) pp 1780-1784

doi:10.4028/www.scientific.net/AMR.986-987.1780

Circuit design of the electronic lock of the intelligent management system of the blasting equipment library

Xingshan LI[1], Yifan ZHANG [1, a](✉), Jian LU [2]

[1.] Luohe medical college, Luohe, China

[2.] Henan Industrial Vocational and Technical College, China

[a]email:181726216@qq.com

Keywords: blasting equipment library; single chip microcomputer; Intelligence; electronic lock

Abstract. Analyze the necessity of the standard management of explosive in the blasting equipment library of the coal mine, use digital monitoring technology, communications technology, software technology and sensor technology, use high-performance MCU STC12C5A60S2 and according to the instructions, control the opening and closing of the electronic lock, providing intelligent management

Introduction

In the production of coal mine, the storage and withdrawl of blasting equipment such as explosives and detonators must be strict and intelligent, so as to ensure the safety in production.

With the rapid development of digital monitoring technology, the use of electronic lock and fingerprint machine to conduct intelligent management of the blasting equipment library has become possible.

The constitution of the coal mine blasting equipment library system

Intelligent management system adopts three-level management including Intellectual lower place machine and control device, PC and its management system is shown in figure 1.

Composition of the lower machine control system

The monitoring and access management of the explosive and detonator library of the in reservoir area is controlled by a lower machine (computer entrance guard system). The control system of the lower machine is mainly comprised of singlechip STC12C5A60S2, temperature and humidity sensor, vibration sensor, the fingerprint machine, electromagnetic lock control, communication module. The lower machine is controlled by the singlechip. The composition of the system is described in Figure 2.

The implementation of the control of the interface circuit by the electronic lock

The opening and closing of the door of the Blasting equipment library utilizes an electronic lock (Spiritual lock). The Intelligent spiritual lock is a newly developed product designed according to the working principle of electric door of buildings, combines the advantages of electric locks and magnetic locks and overcomes their shortcomings.

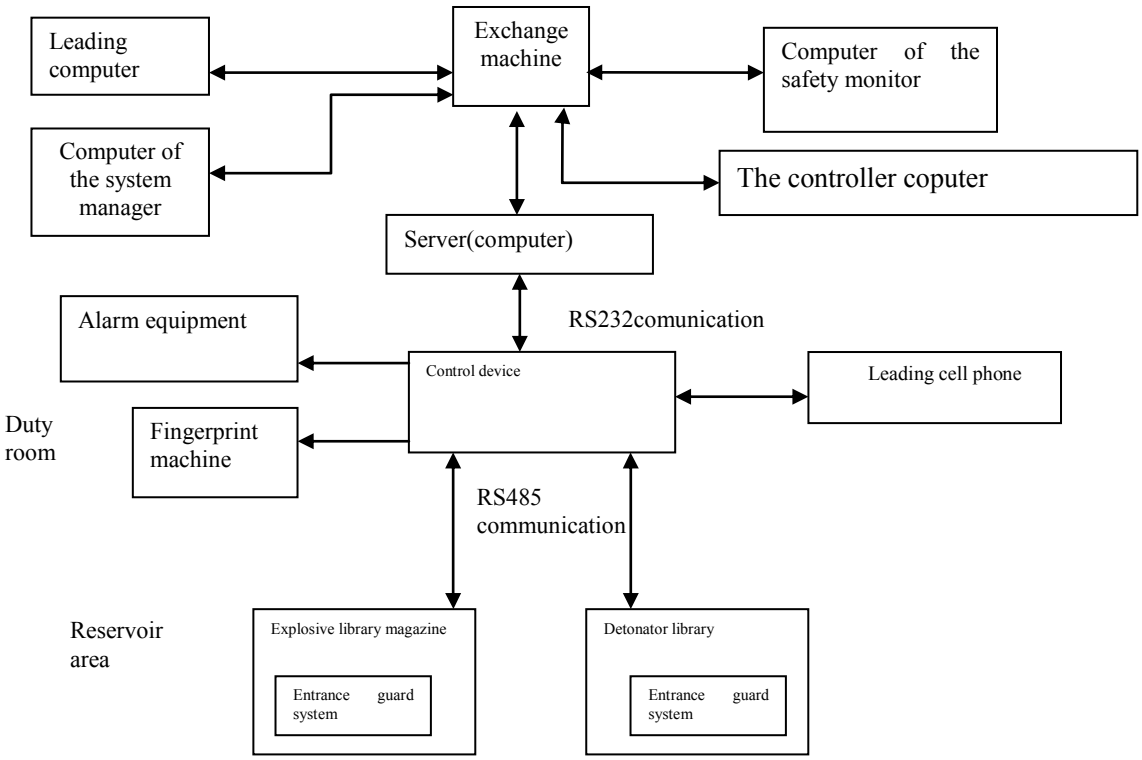

Figure 1. The composition of the management system of Coal mine blasting equipment library

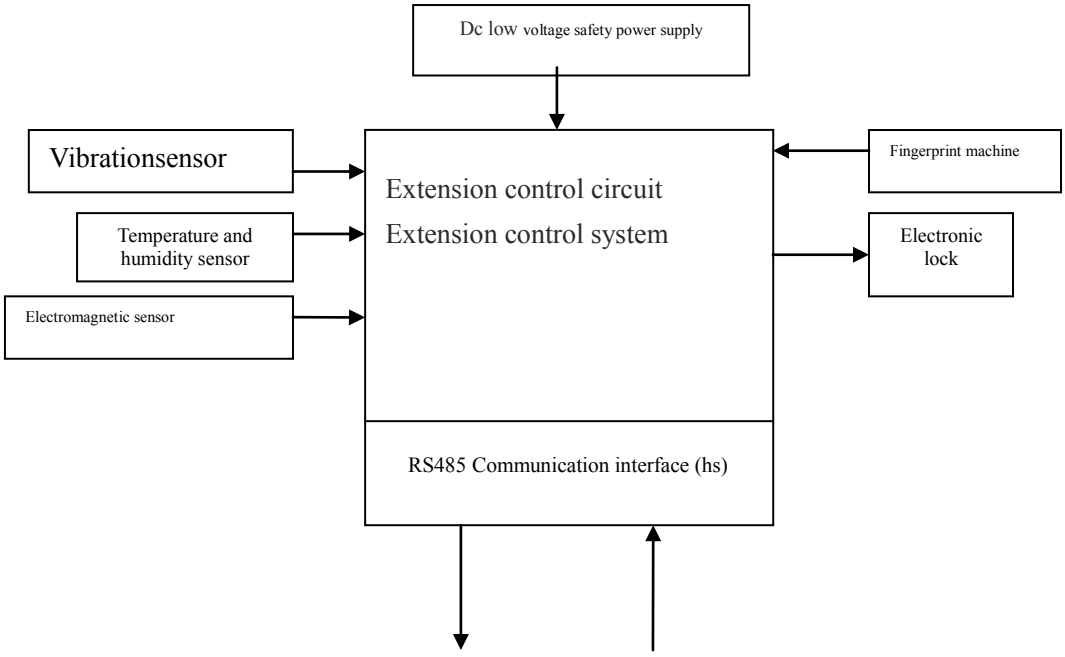

Figure2 The structure of the control system of mine blasting equipment library

Performance of the Electronic Lock

Compared with the electric control lock and magnetic lock, the spiritual lock is blessed with more consummate performance and more obvious advantages, mainly including the following:

Without direction —without having to identify opening direction. Opening to the left, right, inside and outside can utilize the electronic lock (it is convenient to purchase locks and can reduce inventories).

Power saving — power consumption is only equivalent to one fifth of the electric control lock. electric lock 3 A. The door is opened when the power supply to the magnetic lock power is cut. The usual amount of often consumption is 0.27 A. And the instantaneous current of a spiritual lock is less than 0.5 A, reducing the power consumption of the entrance guard and talkback host.

No collision.

Light sound — the automatic locking is realized at the time of the shutting of the door with no production of noise, thus solving the noise produced due to electric control lock itself; the service life is long and can reach 500,000 times. The internal gear is made of engineering plastics, equivalent to the characteristics of steel and the switching of door magnetic switch can be repeated 2 million times.

A small amount of friction—the spiritual lock can be use for any building door locks and the work wear of the lock tongue is almost zero while electric control lock relies on pressure to work, , imposing a greater friction for the lock tongue.

Voice prompt – prompt for unlocking (Automatic prompting for the opening of the door is provided if the door is not opened when unlocked).

Automatically checking the situation of the lock tongue.

Easy installation—as with fixed mounting holes and electric control lock, it is easy to install for the users, Four connection terminals, two power cord, two building lock thread.

Strong adaptability— wide voltage 12 v - 18 VDC, more adapt for the use of visual intercom (can be jointly used together with any entrance guard and Landing-answer host).

New standards [2].

The design of the circuit

In terms of the design of single-chip and the circuit interface of electronic lock, the logical circuit consisting of the 4 pins in the single-chip microcomputer and the two 74LS00 is used to drive the electronic lock and its purpose is to prevent the occurrence of interference or equipment malfunctioning. The correct unlocking is related to the success or failure of the project. Apparently, the design is more reliable and safe. The interior of the electronic lock is a 12 v dc motor and the optical coupling isolation and Darlington B772 drive is sufficient to drive its action.

The interface circuit of the lower machine and electronic lock is shown in figure 3:

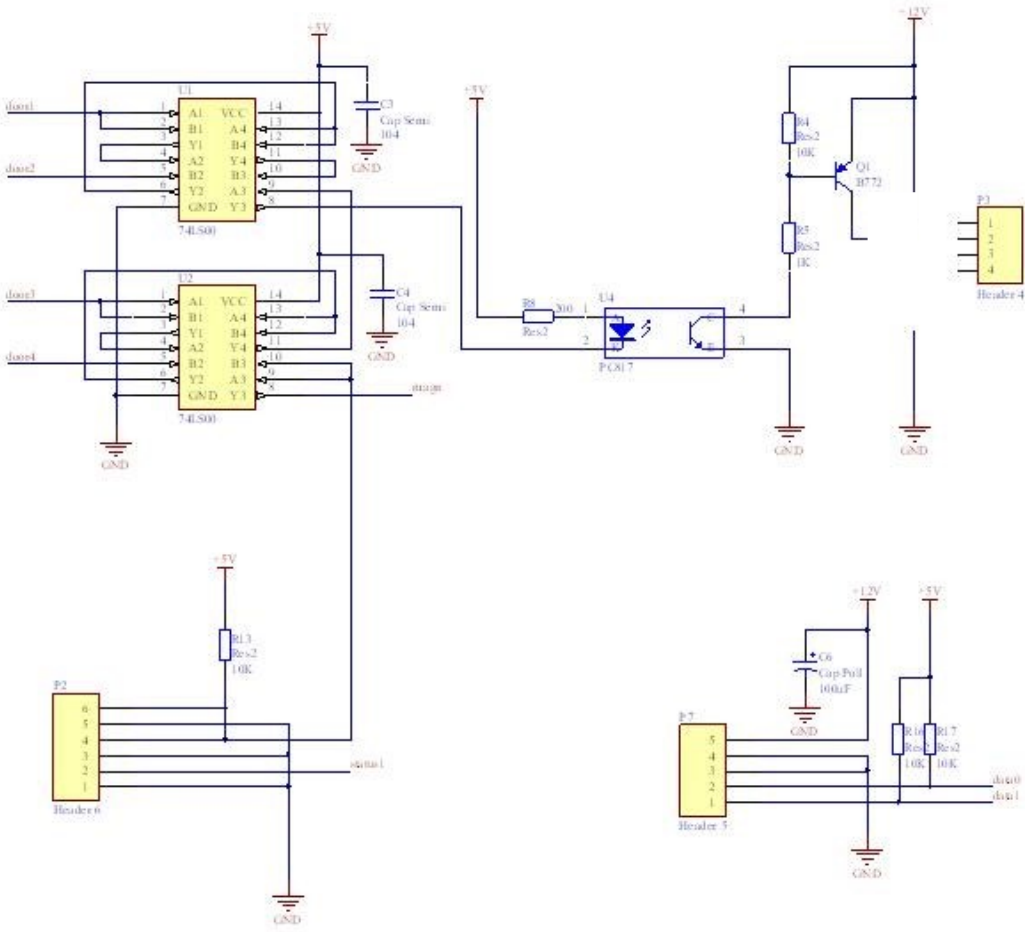

Figure 3 Electronic lock control interface circuit

The C function of the driver electronic lock of the lower machine master control chip is as follows:

```
void OPEN_SYS_CODE()//unlocking code{
    SYS_door1=0;
    SYS_door2=1;
    SYS_door3=0;
    SYS_door4=1;
    dly10ms(20);
    FLAG_Allow=1;
    SYS_door1=1;
    SYS_door2=1;
    SYS_door3=1;
    SYS_door4=1;
   dly10ms(20);
}
```

Conclusion

The result of the testing is in Table 1. The experimental parameters of the ectronic lock circuit design meet the requirements.

Table1: Testing project and phenomenon of explosive magazine control system

Serial number	Testing item	Testing phenomenon （note：failure ×；passing：√）	Testing result
1	power-on test	system indicator lights are put out after flashing for about 5 seconds	√
2	threshold Settings	Whether parameter stting can be conducted to the hardware setting in terms of new temperature, humidity, air pressure, door opening timeout and authorization timeout.	√
3	Setting of the cell phone users	The possibility of adding, deleting, checking mobile phone number and authorization code to the system	√
4	Alarm sounding for unauthorized entrance	The possibility of the occurrence of alarm sounding for illegal entrance and of clearing the alarm at the time of prompting by the short message of the cell phone	√
5	Alarm sounding on the occasion of overtime opening of the door	The short message can clear the alarm on the occasion of overtime opening of the door and the prompting of the short message	√
6	Opening of the door authorized by the cell phone	Whether the system can dial the cell pone and whether the cell phone can authorize normally authorize opening of the door	√
7	Reset operation	Whether the system can be automatically reset to factory defaults，the reminder-light of the system are put out after flashing for about 5 seconds	√
8	Resetto Factory Defaults	Reset to Factory Defaults and the reminder-light of the system are put out after flashing for about 5 seconds	√

Concluding remarks

The experiment has proved that after a reasonable design, the electronic lock and fingerprint machine circuit of the management system of the blasting equipment library of the coal mine can achieve the desired parameters. The system can conduct intelligent control of the storage ansd access of the explosive, impose a strict limit to the illegal access and can avoid serious safety accidents caused by illegal access to the explosives and detonators from the source to the greatest extent.

Acknowledgement

In this paper, the research was sponsored by the Nature Science Foundation of Henan Province(Project No. 142300410286), Yifan ZHANG(✉),1985--,research direction:Computer application.

Reference

[1]. ZHENG Qiang，JIANG Fuchuan,SHI Wenwen, Analysis of risk factors and study on safety management system for open-pit mine［J］，Nonferrous Metals(Mining Section)，2011(4), 61—65

[2]. ZHANG Aijun, Small and medium-sized quarry accident hidden perils and governance[J], Technology and Market,2012(6),390-391

[3]. CAI Chenwei.FAN Haijian.LIU Biyang. Design and Application of Gate Control System Based on Fingerprint Identification Technology［J］，Video Engineering. 2012.36(3):128—130

[4] Zhong XY,Wang BQ,Li B.Design of apparatus-cabinet controller based on EPM7128SLC84[J].Journal Of Modern Electronics Technique.2006(1):110-112

Advanced Materials Research Vols. 986-987 (2014) pp 1785-1789

doi:10.4028/www.scientific.net/AMR.986-987.1785

Design of a Fixed-Frequency Beam-scanning Antenna Controlled by Voltage

Ruikun WU[a], GuoTai CHEN[b]

Institute of Applied Electronic Technology, Fuqing Branch of Fujian Normal University, Fujian 350300, China

[a]email: dzxi@china.com.cn, [b]email: chenguot@163.com

Keywords: Microstrip Leaky-Wave Antenna; Scattering Parameters; Horizontal Polarization

Abstract. A microstrip leaky wave antenna with operating frequency 2.5GHz is designed based on composite right/left handed transmission line. The beam scanning of the antenna can be controlled by changing the bias voltage of varactor in the antenna. And the performance, S-parameters and horizontal polarization pattern, of the antenna are investigated by simulation and experimental measurement, respectively. The results show that the designed antenna has better beam scanning, which is proper to be used in wireless local area networks and short-range wireless technology.

Introduction

In a wireless local area network and short-range wireless technology, the antenna operating at 2.5GHz needs to have electronic beam scanning performance improve communication quality and user capacity. To realize electrically-controlled beam scanning, the composite right/left-handed transmission line microstrip leaky wave antenna is an advantageous alternative. Recently, with the continuous development of composite right/left-handed transmission line theory and technology, it has been widely studied in antenna applications. Representative work is the left-handed material based on the composite right/left-handed transmission lines (CRLH TL) structure [1, 2] proposed by C. Caloz, T. Itoh, etc. After that, C. Caloz designed a new leaky wave antenna using the composite right/left-handed microstrip transmission line [3]. This antenna operates in the fundamental mode with simple feed structure, where beam scanning of the antenna can be realized by the change of the frequency. In [4, 5], the authors proposed that varactors are loaded in each unit to form CRLH TL microstrip leaky wave antenna and the beam scanning can be electrically controlled. The radiation characteristics of composite right/left-handed metamaterial microstrip leaky wave antenna were studied in [6].

In this paper, the antenna is designed based on the theory of the composite right/left-handed transmission line microstrip leaky-wave. The simulation and experimental results show that the antenna can achieve the better performance with the beam scanning controlled by the voltage at a fixed operating frequency.

The structure of this paper is organized as follows. In Section II, the theory of CRLH TL is described. And in Section III, the design of CRLH TL antenna is presented. The performance by simulation and experimental measurement are also shown in this section. The conclusions are drawn in the last section.

Composite Right/Left-handed Transimission Line Theory

Usually, the equivalent circuit of an ideal lossless CRLH TL [7] is shown in Figure 1, where ΔZ is the length of a CRLH TL unit-cell. The unit-cell is consisted of a series LH capacitance C'_L, a series RH inductance L'_R, a shunt LH inductance L'_L and a shunt RH capacitance C'_R. For a lossless transmission line, the per-unit-length impedance and admittance can be expressed respectively as follows.

$$Z' = \left(j\omega L_R' + \frac{1}{j\omega C'_L} \right) \tag{1}$$

$$Y' = \left(j\omega C'_R + \frac{1}{j\omega L'_L} \right) \tag{2}$$

Then, the propagation constant is

$$\begin{aligned} \gamma &= j\beta = \sqrt{Z'Y'} \\ &= j\sqrt{\left(\omega L'_R - \frac{1}{\omega C'_L} \right)\left(\omega C'_R - \frac{1}{\omega L'_L} \right)} \end{aligned} \tag{3}$$

With $\beta_L = -1/\left(\omega\sqrt{L'_L C'_L}\right)$ and $\beta_R = \omega\sqrt{L'_R C'_R}$, the propagation constant β can be written as

$$\beta = \beta_L + \beta_R = \omega\sqrt{L'_R C'_R} - \frac{1}{\omega\sqrt{L'_L C'_L}} \tag{4}$$

The frequency characteristic of propagation constant β is shown in Figure 2. It can be found that the propagation constant β of composite right/left-handed transmission line changes from left region ($\beta < 0$) to right region ($\beta > 0$), and the zero is called balanced point for β, where

$$\omega_0 = \frac{1}{\sqrt{L'_R C'_L}} = \frac{1}{\sqrt{L'_L C'_R}} \tag{5}$$

At the balance point, propagation constants is $\beta = \beta_L + \beta_R = 0$.

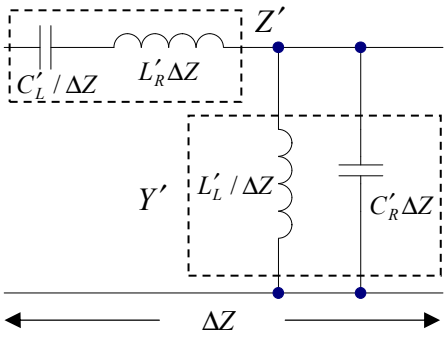

Fig.1. Equivalent circuit model for ideal CRLH TL.

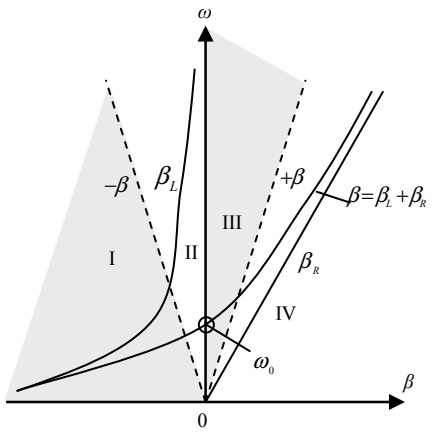

Fig.2. Dispersion curve of the CRLH TL.

The dispersion curve of composite right/left-handed transmission line can be divided to four areas which are labeled with I, II, III, and IV in Figure 2, respectively. Regions I and IV are left-handed guided wave model and right-handed guided wave model respectively, while regions II and III are the radiation modes of left-handed and right-handed respectively. For a microstrip leaky-wave antenna based on CRLH TL, CRLH TL can only work in the regions II and III, where the value of β changed from negative, zero and then to positive. This characteristic can realize backward radiation, endfire radiation and forward radiation in the design of a microstrip leaky-wave antenna [8].

The radiation angle of the microstrip leaky-wave antenna can be written

$$\theta = arccos\left(\left(\beta_0(\omega) + 2n\pi\right)/k_0\right) \tag{6}$$

Where $\beta_0(\omega)$ represents the phase constant of the fundamental model, $n\,(n = 0,\pm1,\pm2,\cdots)$ is the number of the space harmonics, and k_0 for the wave vector of the free space.

Design of Compostie Right/Left-Handed Transmission Line Microstrip Leaky Wave Antenna

In this section, a microstrip leaky wave antenna with operating frequency 2.5GHz based on CRLH TL is modeled for performance simulation. And then according to the simulation results, the antenna is designed and measured by vector network analyzer.

A. **Design of simulation model**

In the design of CRLH TL microstrip leaky wave antenna, the unit length p must satisfy the homogeneity condition, i.e., the unit length p should be at least smaller than a quarter of wavelength ($p<\lambda_g/4$) [9]. And the guided wavelength λ_g and effective dielectric constant ε_e can be calculated by according to the operating frequency, microstrip width, dielectric constant, PCB plate height and copper thickness with the following equations (7) and (8).

$$\lambda_g = \lambda_0 / \sqrt{\varepsilon_e} \tag{7}$$

$$\varepsilon_e = \frac{\varepsilon_r + 1}{2} + \frac{\varepsilon_r - 1}{2}\left(1 + \frac{10h}{W}\right)^{-1/2} \tag{8}$$

Where ε_r is the relative dielectric constant of the medium, λ_0 for free-space wavelength, h is medium thickness, and W for microstrip line width.

With the guided wavelength, the unit length of the CRLH TL antenna and the unit number of the single guided wavelength can be selected by the homogeneity condition.

According to the above analysis, the model of a microstrip leaky-wave antenna with seven units CRLH TL is shown in Figure 3, where Figure 3a for simulation.

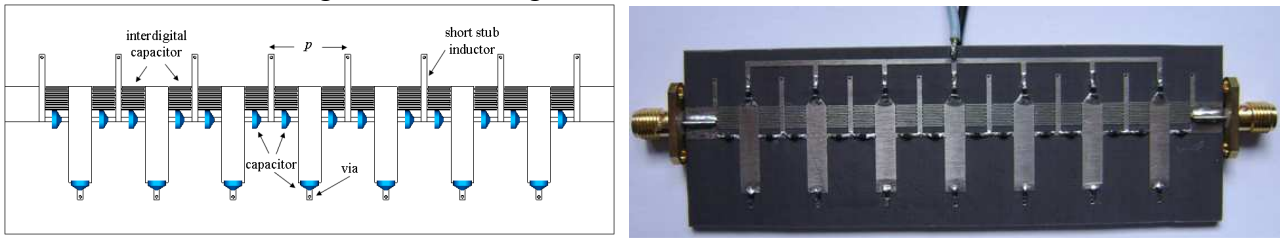

(a) Simulation Model (b) Physical Model

Fig.3. Antenna with seven units

The medium of microstrip TL is Teflon glass cloth copper clad laminated with ε_r=2.2 and h=2mm. And the length and width of the antenna are 106.5mm and 35mm respectively. Each unit consists of interdigital capacitor and stub inductor, where the interdigital capacitor consists of six pair of copper strip with length 4mm and width 0.18mm, and stub inductor is composed of copper strip with length 10.6mm and width 4mm. According to homogeneity condition, the unit length p of the antenna is 13.36mm, and with equation (7), the guided wavelength of the composite right/left -handed TL can be calculated and is set about 86.5mm.

B. **Simulation of S parameters**

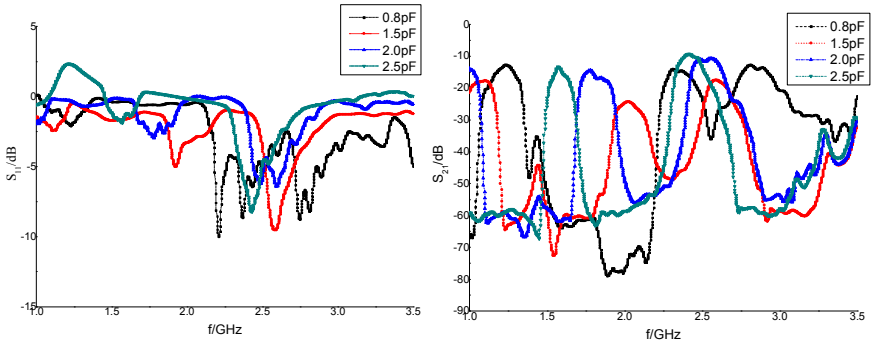

(a) S_{11} (b) S_{21}

Fig.4. Simulation results of S parameter

Simulation model of the designed antenna is shown in Figure 3a. Each unit of the antenna is loaded three capacitors respectively, when they are set different capacitance values at the same time, the S parameters are obtained by simulation.

The simulation results are shown in Figure 4, where the horizontal axis represents frequency, and the vertical axis represents the magnitude in dB of S parameters. At the frequency of 2.5GHz, the

figure shows that S_{11} curve has a low reflectance region with the change of capacitance value and the value of S_{11} is less than -10dB. While the S_{21} curves show the better transmission characteristics of the antenna at 2.5GHz in the figure. The curves of S_{21} also show that the transfer characteristics move from left region to right region when the capacitance value changes from 0.8pF to 2.5pF.

C. Measurement and analysis of antennal

According to the above simulation, the physical antenna is designed and shown in Figure 3b. In this antenna, the varactors are loaded instead of capacitors in the above simuluation. The varactors have a good high frequency characteristic when they work at frequency 0.5GHz to 3.0GHz. And the capacitance voltage characteristic of the varactor is approximately linear with the change of the bias voltage. At the operating frequency of 2.5GHz, the capacitance value of the varator changes from 0.5pF to 3.5pF with the bias voltage of from 8V to 0V.

The S-parameters of the antenna are measured by using the vector network analyzer, and the horizontally polarized pattern are measured in an anechoic chamber. In the process of measurement, the bias voltage of the varactor is set 1V, 1.5V, 3V and 8V respectively, which correspond to the capacitance value is 2.37pF, 2.05pF, 1.52pF and 0.85pF.

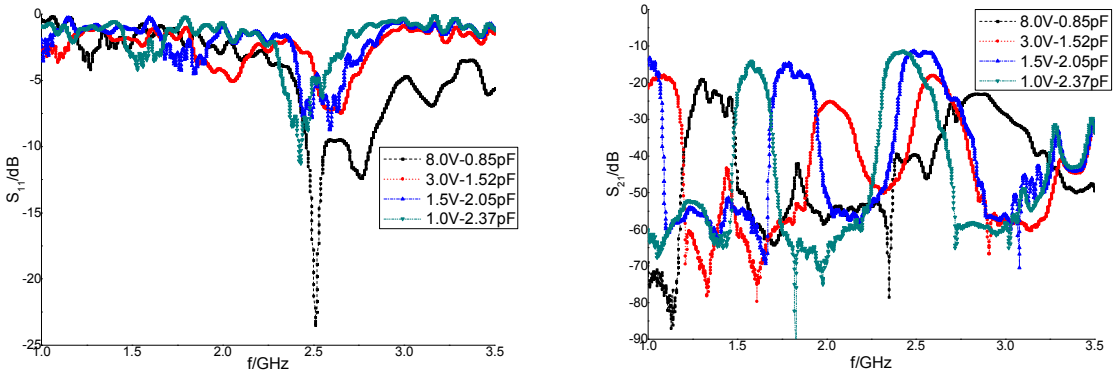

(a) S_{11} (b) S_{21}

Fig.5. Measurement results of S parameter

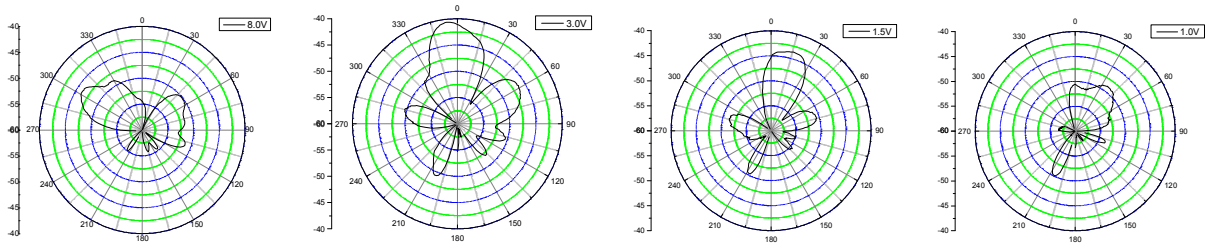

(a) 8.0V (b) 3.0V (c) 1.5V (d) 1.0V

Fig.6. Direction changes with the bias voltage

The measurement results of S parameters are shown in Figure 5. Compared with the simulation results in Figure 4, the measurement results in Figure 5 are consistent with them.

The horizontal polarization patterns are presented in Figure 6. It can be seen that the main radiation beam of the antenna are from the backward to the forward when the varactor's bias voltage changes from 8.0V to 1.0V. It also shows that the radiation beam of the CRLH TL antenna has a good directivity at 2.5GHz. When the varactor's bias voltage is 8.0V, the main beam radiation angle and the gain of the antenna is -50 degrees and -49.23dB respectively. The main beam radiation angle and the gain are -6 degrees and -40.55dB when the bias voltage is 3V, and 15 degrees and -43.72dB for 1.5V. When the bias voltage is changed to 1.0V, the radiation angle and the gain of the antenna are 35 degrees and -48.96dB respectively.

Conclusion

A microstrip leaky wave antenna based on CRLH TL has been designed for operating frequency 2.5GHz and the performance are investigated with simulation and experimental measurement. The simulation and measured results show the antenna has better beam scanning performance, and the beam scanning angle can be up to 86 degree. In the antenna, the beam scanning is controlled by the bias voltage, which makes the transmission characteristics of CRLH TL microstrip leaky wave antenna move left-hand region to right-handed region. This antenna can be applied in wireless local area networks and short-range wireless technology.

Acknowledgement

This work was supported by the Fujian Province Natural Science Foundation funded projects (2013J01218), the Fujian Province Department of Education funded project (JK2011064) and the Fuqing Branch of Fujian Normal University research projects (KY2011008).

References

[1] C. Caloz, H. Okabe, T. Iwai, et al. Transmission line approach of left-handed(LH) materials [C]// U S National Radio Science Meeting. San Antonio: U S National Committee of the International Union of Radio Science (URSI), 2002:35-39.

[2] C. Caloz, T. Itoh. Transmission line approach of left-handed(LH) materials and microstrip implementation of an artificial LH transmission line [J]. IEEE Trans. Antennas Propag., 2004, 52(5):1159-1166.

[3] C. Caloz, T. Itoh. Transmission line theory and microwave application [M]. A John Wiley & Sons, INC., Publication, 2006.

[4] L. Sungjoon, C. Cloz, T. Itoh. Metamaterial-based electronically controlled transmission-line structure as a novel leaky-wave antenna with tunable radiation angle and beamwidth [J]. IEEE Transactions on Microwave Theory and Techniques, 2005, 53(1):161-173.

[5] L. Sungjoon, C. Cloz, T. Itoh. Electronically scanned composite right/left handed microstrip leaky-wave antenna [J]. IEEE Microwave and Wireless Components Letters, 2004, 14(6):277-279.

[6] Wu Ruikun. Investigation of Radiation Characteristics for Metamaterial Microstrip Leaky-Wave Antennas [J]. Journal of Microwaves, 2011, 27(1):44-47.

[7] C. Caloz, A. Sanada, and T. Itoh. A novel composite right/left-handed coupled-line directional coupler with arbitrary coupling level and broad bandwidth [J]. IEEE Trans. Microwave Theory Tech., 2004, vol.52:980-992.

[8] Zhang Yewen, Li Guiquan, He Li, et al. One-Dimensional Metamaterial-Based Microstrip Leaky-Wave Antenna with Backfire-to-Endfire Scanning Capability [J]. Journal of Tongji University(Natural Science), 2007, vol.35:811- 814.

[9] Cui Wanzhao, Ma Wei, Qiu Lede, et al. Electromagnetic Metamaterials and its applications [M]. Beijing: National Defense Industry Press, 2008: 144-214.

Advanced Materials Research Vols. 986-987 (2014) pp 1790-1793

doi:10.4028/www.scientific.net/AMR.986-987.1790

Design of Intelligent Reactive Compensation Controller Based on Microchip

Haixiang Wang

Department of mechanical and electrical engineering, Jinling Institute of Technology, Nanjing, 211169, China

Email: whx110219@sohu.com

Keywords: reactive compensation; MC9S08AW60; ATT7022A

Abstract.The reactive compensation controller using MC9S08AW60 chip and ATT7022A is introduced. The detail design of the hardware and software is illustrated too.

There are a lot of inductive loads such as transformer, motor, and so on in the power grid. These inductive loads will cause the reactive power which will pull down the reactive factor and decrease the quality of the power supply. If the reactive power is very large , it will cause a great power loss of the electric power line and reduce the service life of the electrical equipment. So the reactive compensation is very important to the electrical grid.

Recently, some papers focus on the methods of the reactive power compensation such as SVC and SVG[1] [2]. The SVC method is using the capacitor to compensate the reactive power. This paper will present the detail of the intelligent reactive compensation controller which is based on SVC.

The hardware design of the intelligent reactive compensation controller

1.1 The overall structure of the hardware

The overall structure of the hardware is as fig.1 below.[3][4]

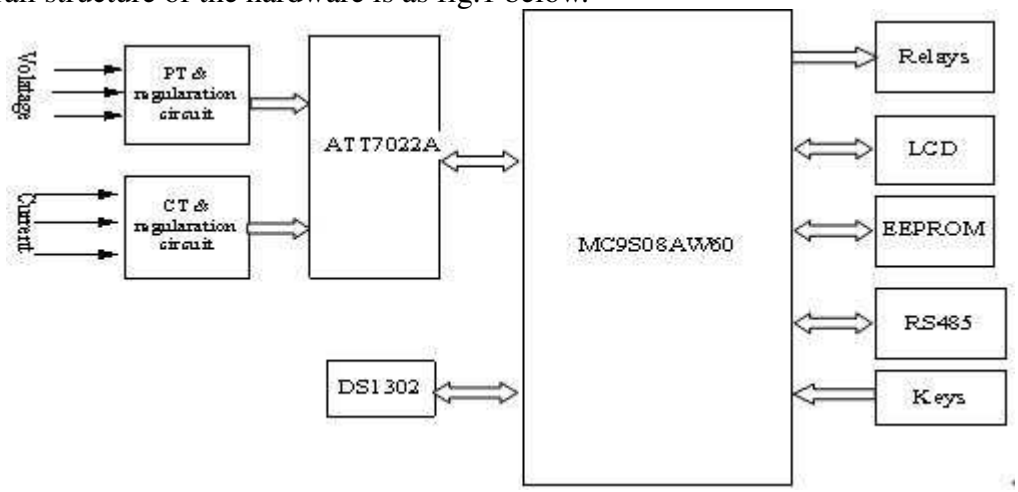

Fig.1 The overall structure of the hardware

In fig.1, MC9S08AW60 acts as MCU, it controls the chips such as ATT7022A chip, DS1302 chip, LCD and so on. The PT and CT transform the high voltage and current into the low voltage and current respectively so as to meet the low voltage demand of ATT7022A chip. The DS1302 is used for timing, this information can be stored in EEPROM together with the switching information. Relays controlled by the MC9S08AW60 chip are designed to switch the capacitors. The data can be send to the remote devices by the RS485 block. Keys are set for the user to input information.

1.2 The voltage and current transformer and regulation

The fig.2 and fig.3 show the voltage and current conversion and the regulation circuit. The differential voltage between VxP and VxN is send to the ATT7022A chip, this differential voltage should normally vary from -1.5V to +1.5V. A direct voltage of approximately 2.4V should be added to the VxP and VxN pin. The direct voltage can be got from REFOUT pin of the ATT7022A chip.

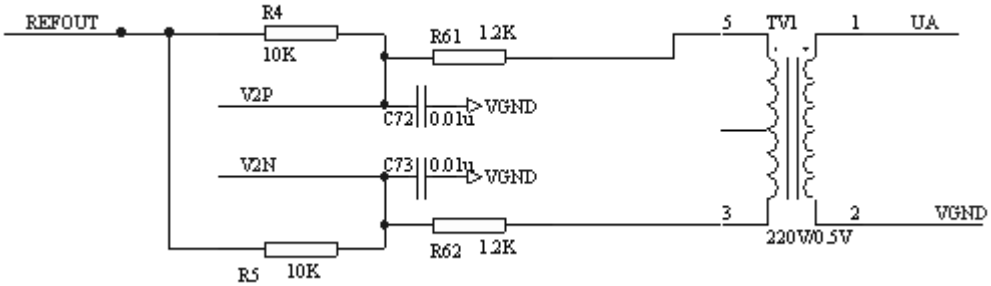

Fig.2 The voltage transformer and regulation circuit

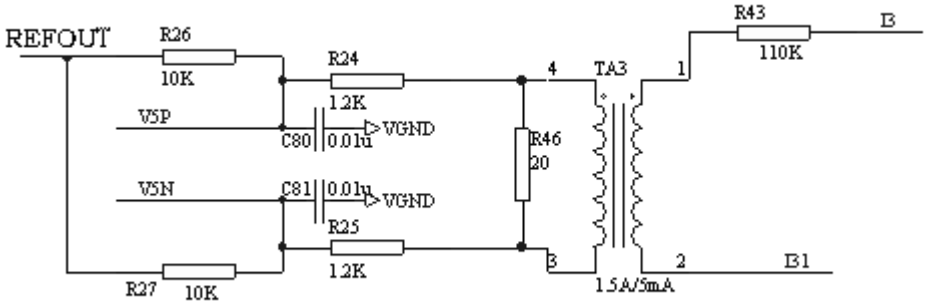

Fig.3 The current transformer and regulation circuit

1.3 The connection between the MC9S08AW60 and ATT7022A

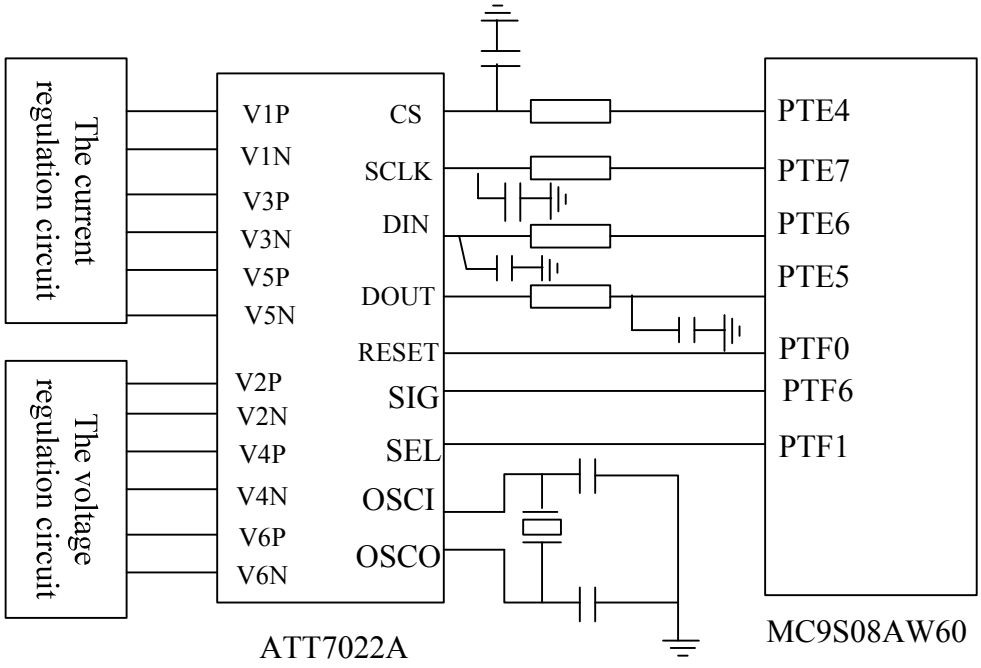

Fig.4 The connection between the MC9S08AW60 and ATT7022A

The fig.4 above shows the connection between the MC9S08AW60 and ATT7022A. The PTF0 pin is connected with RESET pin in order to start the ATT7022A chip. The PTF1 is connected with SEL pin in order to select between three-phase three wire model and three-phase four wire model. The CS pin is used to select the ATT7022A among all chips. SLK pin that is linked with the PTE pin is used to deliver the clock pulse. Data can be input into the ATT7022A chip by the DIN pin which is connected with PTE pin. Meanwhile, the data can be output into MC9S08AW60 by the DOUT pin which is connected with the PTE5 pin.

The hardware design of the intelligent reactive compensation controller [4][5]

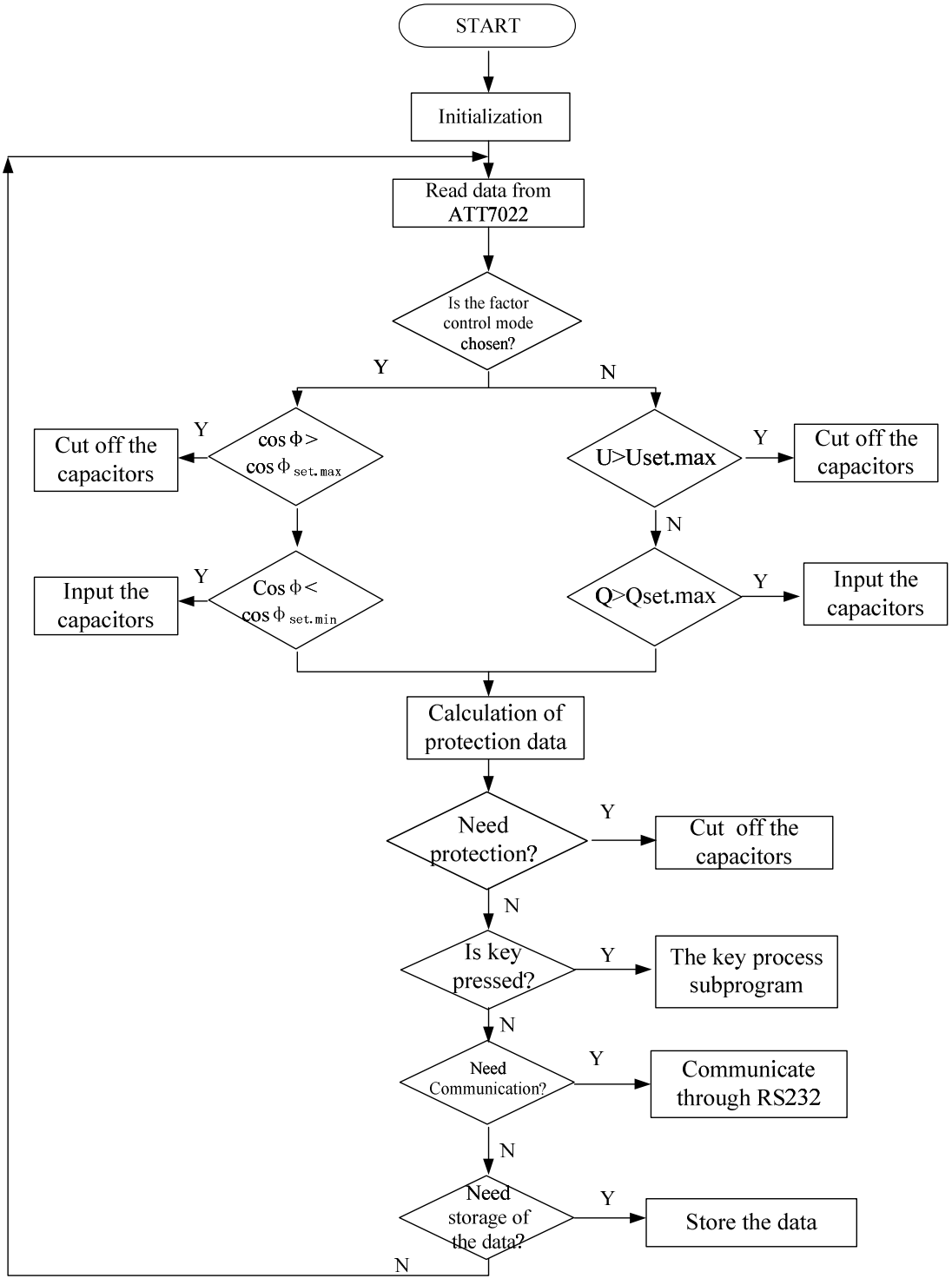

Fig.5 The main program flow the software.

The fig.5 above shows the main program flow of software. First step is initialization which gives variables the initial values. The next step is reading the data from ATT7022A chip by the SPI bus. Then, according the user's choice, it runs to the power factor control model or the reactive power control model. If power factor control model is selected, it will determine whether to input or cut off the capacitor according the value of power factor. If the value of power factor is above the maximum value which is set by the user or default, it will cut off the capacitors from the circuit. If the value of power factor is blow the minimum value which is set by the user or default, it will input the capacitors. On the other hand, if the reactive power is selected, it will cut off the capacitor if the voltage is above the maximum value which is set by the user or default to protect the capacitors, it

will input the capacitor if the reactive power is above the maximum value which is set by the user or default in order to compensate the reactive power. After these steps, it turns to the calculation of protection data such as the current value. If the data beyond the value set by the user, the protection program will start to cut off the capacitors. Then, the key press judgment, communication judgment, data storage judgment are made to decide whether run the corresponding subprogram. At last, the program turns back for another loop.

Conclusion

In this paper, the hardware and software design of intelligent reactive compensation controller is presented.

Acknowledgements

This work was financially supported by the Jiangsu high school Natural Science Foundation (12KDJ470002).

References

[1] GONG Qing. Thyristor Switched Capacitor Dynamic Var Compensation Technology and Its Application. Power System Technology [J], 2007

[2] LI Luo，LEI Ying，WEI Lingyan，NIU Shuai. Principle Analyze and Test Method of Complex Reactive Power Compensation Equipment for Power Distribution System. High Voltage Apparatus[J].2014.1

[3] CHEN Jin-hui, HAN Yuan-yuan, WU Wen-ping. A new design of three-phase multi-function electric power meter based on the PIC16F877A and ATT7022A.Power System Protection and Control [J].2010.2. 38(2)

[4] WENG Wei, ZHU Zhijie, CHEN Junjie, WEN Yaojun. Design of a Low Voltage Reactive Power Compensation Controller Based on ATmega128 and ATT7022B.Low Voltage Apparatus[J].2009.20

[5] ZHU Lin. Applications of Energy Chip ATT7022B in Power Measurements. Measurement & Control Technology[J].2007.6(1)

Advanced Materials Research Vols. 986-987 (2014) pp 1794-1798

doi:10.4028/www.scientific.net/AMR.986-987.1794

Design of Micro Power Consumption Synchronous Chopped Wave Power Supply Based on Fixed and Mobile Double Comparative Point

Longteng Wang[a], Jun Lin*[b], Hui Su[c]

Department of Electronic Information and Engineering, Yanbian University, Yanji 133000, China

[a]lteng0326@126.com, [b]linjun @ybu.edu.cn, [c]suhui212212@163.com

Keywords: double comparative point, micro power consumption, synchronous chopped wave.

Abstract: This paper proposes a design method of the micro power consumption synchronous chopped wave and low-power switching power supply based on fixed and mobile double comparative point. The output of this power supply ranges from 5V to 200V. It overcomes the residual voltage effect after the bridge rectifier by using fixed comparative point to limit the maximum output voltage, and stabilizes the voltage by using mobile point to produce the required output voltage. The circuit charges with nonlinear resistors pattern in the low voltage, thus improving the charging efficiency, and it has short circuit protection function, simple structure and low power consumption.

Introduction

DC power supply with small capacity and small size from 0.5W to 2W has been widely used in electronic device which is applied to electronic equipments in controlling, detecting and analyzing, home appliances and relay driver, it has widely use value especially in the field of small home electrical appliances[1-2]. It also applies to be awaiting power for all kinds of ballasts and advertisement box[3].

Nowadays, the typical integrated circuits adopt chopped wave switching power supply namely HV-2405E, CJM03, SR036, SR037 and so on. The advantage of this integrated circuit is the simple structure, but some have no stable voltage output, some have no soft-starting, and some cannot change the output. It can produce a large pulsating current, and the power consumption of itself is normally greater than 0.5W[4]. It was reported by the electronic newspaper that there are various home appliances and ballasts over 100 million all over the country, the standby loss is greater than 50 million watts. So there will be enormous economic and social benefits when decrease the standby loss.

In this paper, the micro power consumption synchronous chopped wave and low-power switching power supply is designed by adopting fixed and mobile double comparative points, it has a lot of advantages, for example, voltage stabilizing function, short-circuit protection, simple structure, and power consumption is less than 0.1W (the power consumption of the best integrated circuit is 0.3W at present) and so on.

1 The present problems of synchronous chopped wave power supply

Due to the parasitic capacitance existed in the rectifier bridge, the voltage U_i can't return to the point of zero after rectification, and the actual measured waveform as shown in figure 1. The residual voltage is 67V when $R_L=\infty$ after rectification.

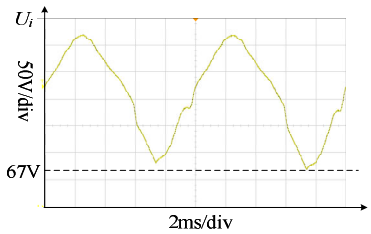

Fig. 1 The actual measured waveform of AC 220V after rectification

Table 1 The residual voltage

$R_L(\Omega)$	residual voltage(V)
∞	67
1M	16
470K	5.5
300K	2.5

The actual measured residual voltage value is showed in table 1when the load R_L is different, the smaller the load is , the greater the residual voltage is, and the higher the comparative point set, so parasitic capacitance need to discharge the voltage. When R_L= 1MΩ, the current is 0.2mA, but the working current of specialized chip is generally about 1mA~3mA[5], the residual voltage is discharged through the equivalent resistor inside the chip and the current limiting resistor R in series at the input side, so there is no residual voltage, but more loss of energy.

The existing synchronous chopped wave power supply adopts fixed comparative point model, circuit model is shown in figure 2, figure 3 shows the working principle diagram of the existing chopping power supply.

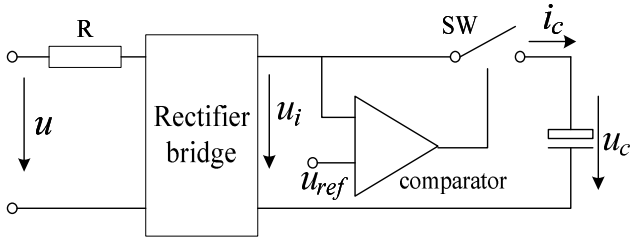

Fig. 2 The circuit model of the fixed comparative point power supply

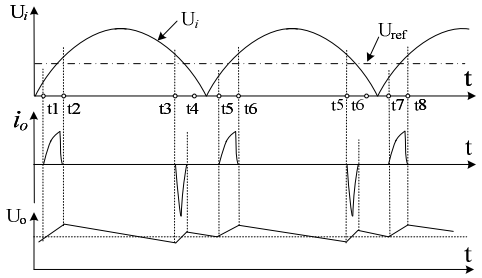

Fig. 3 The work principle diagram of the existing chopping power supply

In figure 3 U_{ref} is the fixed comparison voltage, U_i is the voltage of AC 220V voltage after the rectification, because a higher voltage is suddenly added on both ends of capacitance, and the voltage drops quickly along with the sine wave voltage, high peak pulse charging current is produced at moment t3, as the time is short to maintain, the contribution to charging is not big, but it caused several dozen times current greater than the average charging current, thus have a large impact on the rectifier bridge and switch tube[6-7], so the peak current is large, the charging efficiency is very low.

To come to the conclusion: in order to reduce the energy loss, the parasitic capacitance need to discharge the voltage in rectifier bridge and overcome the residual voltage effect after the bridge rectifier; In order to improve the charging efficiency and reduce the peak current, the circuit will be charged with nonlinear resistors pattern in the low voltage charging area.

2 Double comparative points synchronous chopped wave power supply

2.1 The composition of the circuit

Fig.4 is the block diagram of the double comparative points chopped wave power supply, it consists of the rectifier bridge, switching tube, current sampling resistor, storage capacitor and load, output voltage detector, comparative voltage generator, constant current regulation and other parts.

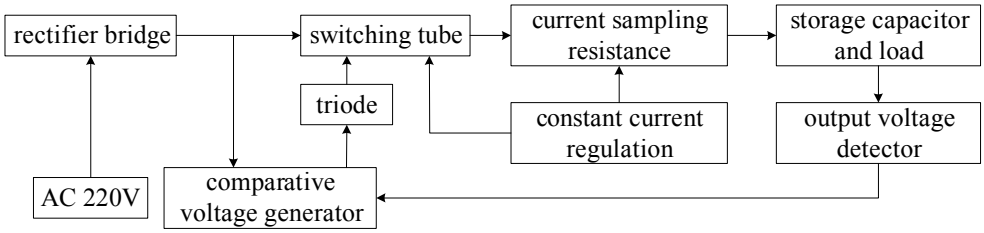

Fig. 4 The block diagram of the double comparative points power supply

The working principle of the circuit diagram is shown in figure 5, the power supply output voltage depends on the voltage value of the voltage regulator diode D2, and can provide 5V~200V output voltage, 10mA~100mA output current, the circuit has output voltage stability and short circuit protection function.

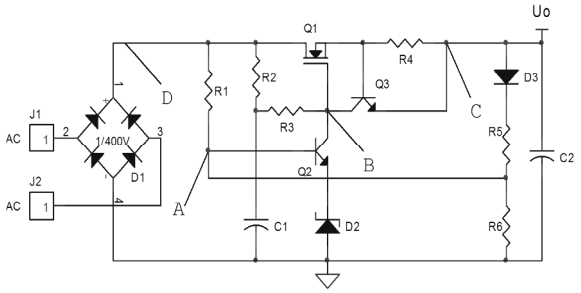

Fig. 5 The working principle of the circuit diagram

2.2 Working principle

The working principle of double comparative points chopped power supply as shown in figure 6, U_D is the residual voltage, the alternating current voltage through the bridge rectifier, the fixed point comparative voltage U_A is obtained by resistor R1 and R6 voltage division circuit, the circuit can set up the mobile point comparative voltage U_{c1} through charging C1 by R2. The figure 6 shows that point B voltage rise slowly in the time of *t*3~*t*4, because of the resistor R1, R2 is used more than 1MΩ high resistance value, so in the *t*3~*t*4 times Q1 lightly conducts, reduce the peak current which is produced at the sine-wave voltage drop area. When Q1 is fully saturated, the circuit charges with nonlinear resistors pattern in the low voltage charging area, and the circuit charges with a constant current charging pattern when the current reaches the set point, the resistor R4 limits the charging current peak. As a result, each cycle t1~t2 and t3~t5 completes charging of energy storage capacitor C2.

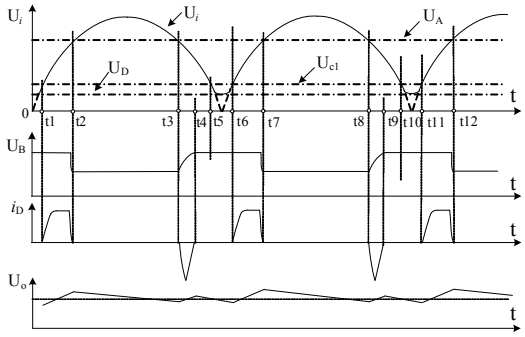

Fig. 6 The working principle figure of the double comparative points chopped power supply

2.3 To overcome the residual voltage effect

From the figure 6 we can see that the residual voltage is very low, so the comparative point can be set very low, it is conducive to reduce the power loss. The peak current that is produced at the sine-wave voltage drop area is small and narrow, contributes to the charging is not very big, but helps to reduce the burden of the current along with the sine-wave voltage rising, and the current along with the sine-wave voltage rising maintains for a long time, it is a big contribution to charging.

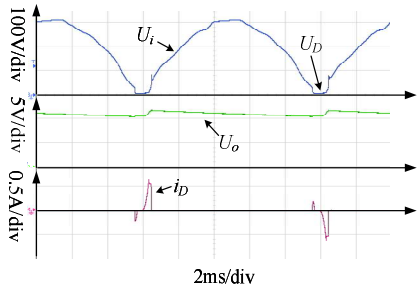

Fig. 7 The actual measured waveform of the double comparative points power supply

Figure 7 is the actual measured waveform of the double comparative points power supply when the input voltage is AC 220V, the load current is 18mA and the output voltage is 12V, as a result of fixed and mobile double comparative points, the fixed comparative points can be used to limit the maximum output voltage, overcome the residual voltage effect after the bridge rectifier, and need not to discharge the voltage of the parasitic capacitance, in figure 7, the residual voltage U_D drops to around 15V; At the same time the mobile comparative points is used to produce the required output voltage, therefore the circuit has the voltage stabilizing function; The current along with the sine-wave voltage rising is dropping at about 2 times, but the contribution to the charging is more than 5 times.

2.4 Nonlinear resistance charging characteristics and short circuit protection function

The present typical chopped switching power supply chip (such as: HV–2405E) adds a current limiting resistor R in series at the input terminal as shown in figure 2, but the peak current is still higher, and also increases the power loss. Figure 8 is the actual measured current waveform of the traditional chopper power supply, the figure 8 shows that the charging current rapidly rises along with the sine-wave voltage rising, and the charging current maintain a very short time, and current peak value is larger, contribution to the charging is not very big, therefore the charging efficiency is very low.

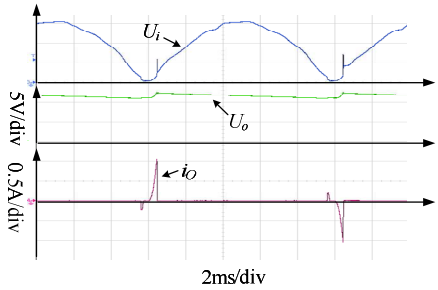

Fig. 8 The actual measured current waveform of the traditional chopper power supply

The figure 9 shows the actual measured current waveform of the double comparative points power supply when resistor R4=1Ω and R4=2Ω, we can see that the circuit charges with nonlinear resistors pattern in the low voltage charging area, the charging current rapidly rises along with the sine-wave voltage rising, the capacitor charges with constant current mode after the current reaches a certain degree, and the charging time maintains very long, so it won't appear spike pulse. The resistor R4 limits the peak value of the charging current, and reduces the peak current, therefore, improves the charging efficiency, and has the short circuit protection function.

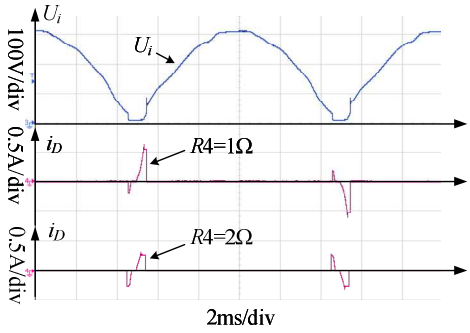

Fig. 9 The actual measured current waveform of the double comparative points power supply

2.5 Static power loss calculation of the circuit

Micro power consumption characteristics of the circuit depends on the structure of simple comparison and control circuit, thereby eliminates the complex bias circuit, the circuit designed with more than 1MΩ high resistance values, static loss occurs mainly in resistor R1, R2, R3 and R6, The average voltage of alternating voltage after bridge rectifier is determined by the formula (1).

$$U = \frac{2U_p}{T}\int_0^{T/2} \sin \omega t * dt = \frac{2}{\pi}U_p \approx 0.64U_p \quad (1)$$

In the formula (1) U_p is the peak voltage of the AC 220V, so U_p = 311V, put U_p into the formula (1) U = 199V, the power loss produced in the partial pressure branch is determined by the formula (2).

$$P = \frac{U^2}{R1+R6} + \frac{(U-U_{D1})^2}{R2+R3} \quad (2)$$

Assume: R1=1MΩ, R2=1MΩ, R3=100KΩ, R6=120KΩ, U_{D1}=12V, P= 0.03W.

Therefore, the static loss is greatly reduced compared with the traditional integrated chip, only 0.03 W.

Summary

This kind of micro power consumption synchronous chopped wave small power switching power supply based on fixed and mobile double comparative points, greatly improve the charging efficiency, and the power consumption is minimum (less than 0.1W), the circuit structure is simple, stable and reliable, it has wide range of output voltage, voltage stabilization and short circuit protection, small volume, low cost, especially suitable for various household appliances and electronic equipments for standby power supply, also can be used to drive a simple LED lighting.

References

[1] Z. H. Wang and Z. Q. Wang: The World of Power Supply, Vol. 23 (2004) NO.11, p.27.
[2] Y. G. Jin and S. H. Jin: Information Technology, Vol. 30 (2006) NO.10, p.65.
[3] E. H. Bao and Z. Q. Wang: Application of Electronic Technique, Vol. 2910 (2003) NO.10, p.78.
[4] B. W. Yang: New Practical Power Circuit, People's Posts and Telecommunications Press, Bei Jing, 2000.
[5] Inductorless, Dual Output Off-Line Regulators. http://www.supertex.com
[6] Y.G. Jin and X.X. Jiang: Application of Electronic Technique, Vol. 34 (2008) NO.10, p.75.
[7] Y.G. Jin and N. Jin: Chinese Journal of Power Sources, Vol. 37 (2013) NO.8, p.1417.

Advanced Materials Research Vols. 986-987 (2014) pp 1799-1803

doi:10.4028/www.scientific.net/AMR.986-987.1799

Design of Switch Transformer About Half Bridge Switching Power Supply

Yu Tang[1, a], Gang Wu [2,b]

[1]College of Telegraph, Pan Zhihua University, Pan Zhihua,China

[2]College of Telegraph, Pan Zhihua University, Pan Zhihua,China

[a]email: wgdd2009@126.com, [b]email: wugang_d@126.com

Keywords: switching power supply; transformer; design

Abstract. Half bridge switching power supply is a kind of form in the family. It has the characteristics of good voltage output, high efficiency, the simple circuit and so on. On the design of the half bridge switching power supply, the key and difficult point is the design of switch transformer. Taking the switch transformer of a half bridge switching power supply as the research object and based on the design requirements, this paper aims to realize the calculation of the coil turns and the selection of core in switching transformer. the design of switch transformer of the push-pull switch power supply has been completed by circuit simulation and implementation.

Introduction

Any electronic device can hardly work without the reliable power. Due to the realization of the miniaturization and cost reduction of the electronic device, switching power supply develops into the light, thin, small and efficient one. At present, high-frequency switching power supply is used in the fields of communications, information appliances and national defense[1].As a form of switching power supply family, the half bridge switching power supply is divided into half bridge switch regulated power supply of other excited type and half bridge switch regulated power supply of self-excited type. For other excited type half bridge switching power supply, the power switch and switch transformer are only regarded as power conversion circuits and they don't participate in the operation of oscillation circuit of the PWM or PFM . The oscillator's working frequency and its duty cycle of Oscillator are nothing to do with the technical parameters of the power switch and power switch transformer because oscillator has special oscillation circuit， drive circuit and control circuit of PWM or PFM which are usually composed with integrated circuits[2]. However, the key and difficult point is the switching transformer in design of the half bridge switching power supply . In order to have further study of this point, this paper implements research to the switching transformer by taking the switch transformer of other excited type half bridge switching power supply as the research object.

Design Requirements

Requirements for the design of half bridge switching power supply is: input voltage U_{in} is 220V/50Hz, the output voltage of the power supply U_o is 0 ~50V,the output current I_{max} is 5A, the output voltage ripple $\leq$ 1.In the design process, the switch transformer requirements are: Switch transformer has a primary winding and a secondary winding of center tapped, the primary DC input voltage is U_p =310V, the frequency is $f = 25kHz$, The maximum duty cycle is $D_{\max}$ =0.494, the output power is $P_0 = 50 \times 5A = 250W$, the conversion efficiency is η =90%.

Design of Switch Transformer

Selected of Cores of Switch Transformer . Because the power switch transformer are usually work in the 20 ~ 100kHz, even higher frequencies. the requirement of magnetic materials is: loss of small, high saturation magnetic induction intensity, good thermal stability. choice of core structure is: should be based on the structure of converter circuit, use requirements, the economic indicators. And when the selection of core structure should consider the following questions: the magnetic flux leakage is small, easy to winding, easy installation , conducive to heat dissipation, transmission power should have sufficient margin, When the input voltage and the duty ratio is maximum, the core will not saturated, In a forward DC-DC converter circuit, inductance of the primary winding must be large enough; In a flyback DC-DC converter circuit, inductance of the primary winding must reach numerical in order to achieve the required power, the primary and secondary windings must also satisfy the equivalent principle of copper loss and core loss[3].Common core are: Co-state non-crystalline alloy, perm alloy , ferrite and other materials. Here we use core material of the C-type of 80-20 nickel zinc ferrite, magnetic flux density $B_W = 0.5T$,designed by AP method. Assuming the diode voltage drop and line voltage drop is 0.6 V, the total apparent power is P_T

$$P_T = P_o(\frac{1}{\eta}+1)\sqrt{2} \approx 750W \quad (1)$$

In order to calculate values of the AP, here taking $K_O = 0.4$, $K_f = 4.0$ (square wave), $B_W = 0.5T$, $f = 25kHz$, when allowing the temperature 25^oC , according to the manual can be obtained core parameters of C-type are: Kj = 323, X = -0.14, so according to the calculation formula of the AP obtained[4]:

$$AP = (\frac{P_T \times 10^4}{K_o \times K_f \times f \times B_W \times K_J})^{\frac{1}{1-X}} = 1.14(cm^4) \quad (2)$$

In order to the transmission power have margin enough, here add 10% margin, switching transformer core selected CL-62 by manual queries can know. its parameters are:

$AP = 1.30cm^4$, $MLT = 4.9cm$, $A_e = 0.36cm^2$, $A_W = 3.63cm^2$, $A_S = 64.9cm^2$, $MPL = 9.9cm$, $W_{fe} = 0.027 \ kg$.

Then core type of switch the transformer is determined.

Calculation of the primary winding. Through the calculation, the core type of switch transformer is selected as the CL-62, the turns of switching transformer are calculated using the formula by the parameters of CL-62, the number of turns of the primary winding is calculated as follows[5]:

$$N_P = \frac{U_P \times 10^4}{K_f \times f \times B_W \times A_e} = 287.037 \quad (3)$$

Here, taking the number of turns of the primary winding is $N_P = 287$ （turns）.

In order to determine wire size of the primary winding, first to calculate current of the primary winding, according to DC input voltage of the primary, output power, power conversion efficiency, the current of the primary winding is calculated as follows:

$$I_P = \frac{P_O}{U_P \times \eta} = 0.896 \ (A) \quad (4)$$

Based on the parameters of the CL - 62 core, using the formula of calculating the current density of the primary winding is as follows:

$$J = K_J(A_W \times A_e)^X = 374.68 A/cm^2 \quad (5)$$

according to (4), (5),the area of bare wire of the primary winding is calculated as follows:

$$A_{XP} = \frac{I_P}{J} = \frac{0.896}{374.68} \approx 0.0024(cm)^2 \quad (6)$$

According to (6) result of the calculation, it get the closest line number is AWG # 23 by the query wire size table, the specific the area of bare wire is $A_{XP} = 0.00259(cm)^2$.

According to parameter of the CL-62 and the calculation results of (3), in $\frac{\mu\Omega}{cm} = 666$, resistance of the primary winding is calculated by the formula[6]:

$$R_P = (MLT)(N)\frac{\mu\Omega}{cm} \times 10^{-6} \approx 0.937\ \Omega \quad (7)$$

according to (7) result of the calculation, the primary winding copper loss is:

$$P_{PCU} = I_P{}^2 \times R_P = 0.896^2 \times 0.937 \approx 0.752\ W \quad (8)$$

formula (8) is calculation results of the primary winding copper loss

Calculation of the secondary winding. In order to calculate the number of turns of the secondary winding (center tap to both ends), first calculate the voltage of the secondary winding, the conditions given by the previous, calculation of the voltage of the secondary winding as follows[7]:

$$U_S = 50 + 0.6 = 50.6V \quad (9)$$

according to the formula of the transformer secondary winding turns is obtained:

$$N_S = \frac{N_P \times U_S}{U_P} \approx 46.84 \text{ (turns)} \quad (10)$$

Here, take the secondary winding turns is 47 turns

According to design requirements, the power supply output current is 5A, in order to determine the wire size of the secondary winding, assuming the current density of secondary winding is the same as the current density of primary winding, because the transformer has a center tap, so when calculating the area of bare wire, its output current I_O should multiplied correction factor of 0.707 and the secondary windings bare wire area is calculated as follows[8]:

$$A_{XS} = \frac{I_S \times 0.707}{J} = \frac{5 \times 0.707}{374.68} \approx 0.0094 \text{ (cm}^2\text{)} \quad (11)$$

According to (11) result of the calculation, it get the closest line number is AWG#17 by the query wire size table, the specific the area of bare wire is $A_{XS} = 0.01039(cm)^2$.

According to parameter of the CL-62 and the calculation results of (10), in $\frac{\mu\Omega}{cm} = 666$, resistance of the Secondary winding is calculated by the formula:

$$R_S = (MLT)(N)\frac{\mu\Omega}{cm} \times 10^{-6} \approx 0.038\Omega \quad (12)$$

according to (12) result of the calculation, the Secondary winding copper loss is:

$$P_{SCU} = I_S{}^2 \times R_P = 5^2 \times 0.038 \approx 0.95W \quad (13)$$

formula (13) is calculation results of the Secondary winding copper loss

Allows the Calculation of Iron Loss of Transformer. From above (8) and (13), the total copper loss of transformer primary winding and secondary winding is:

$$P_{CU} = P_{PCU} + P_{SCU} = 0.752 + 0.95 = 1.702\ (W) \quad (14)$$

under the condition of design efficiency η allows, total loss of the transformer are as follows:

$$P_\Sigma = \frac{P_O}{\eta} - P_O = 28.1(W) \quad (15)$$

according to the law of conservation of energy, iron losses P_{fe} of the transformer are allowed as follows:

$$P_{fe} = P_\Sigma - P_{cu} = 26.394(W) \quad (16)$$

It should be noted that: when the winding transformer, try to use a multi-strand wire，and make cross-sectional area of multi-strand wire with the selected cross-sectional area of AWG # 17.23 equal.

Circuit simulation

Figure 1 is the local map of switch transformer of half bridge switching power supply, in this design, the transformer core selected CL-62, the number of turns of the primary winding is $N_P = 287$ (turns), the number of turns of the secondary winding is $N_S = 47$ (turns), in the case of TL494 as drive chip, resulting in two PWM wave of phase difference of 180 ° by using the internal

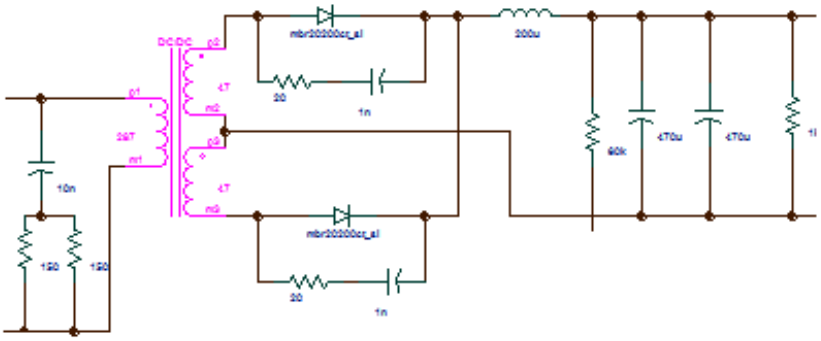

Fig. 1: Switch transformer of half bridge switching power supply

oscillator of TL494, A and B signals control turns on and off of the MOSFET switch, then the waveforms of primary winding of the transformer are shown ① in Figure 2, , the waveform of the upper part of secondary winding of the transformer is shown ②in Figure 2, the waveforms of below part is shown ③ in Figure 2.

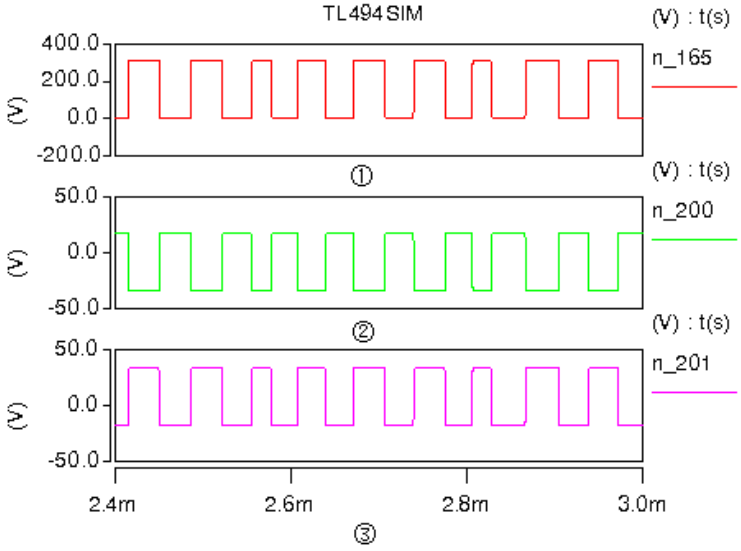

Fig. 2: The waveform of primary winding and secondary winding

In figure 2, the waveform of ②and③ of the secondary winding of transformer rectifier (Rectifier Diode Selection Schottky diodes), filtering to get the output voltage waveform as shown in figure 3, the output voltage of the circuit is 36.962V from the output voltage waveform can be seen, the circuit meets the design requirements of 0 ---50 V output voltage.

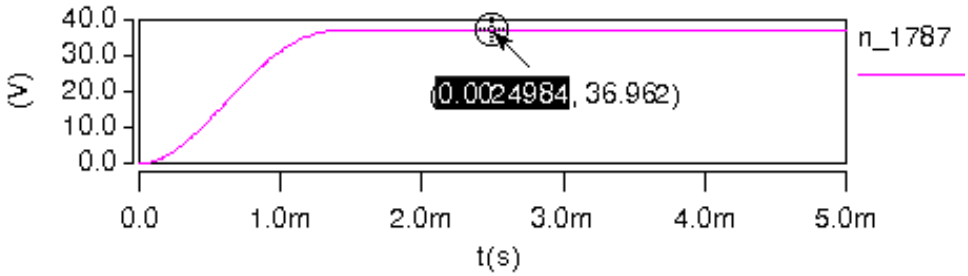

Fig. 3: The output waveform of half bridge switching power supply

Conclusion

The design of the switching transformer is the emphasis and difficulty in the switching power supply design. From the design of the switching power supply , Using the TL494 output 200KHz PWM（pulse width control signal）, to controls the turning on and off of the MOSFET switch, So that the primary winding of the switching transformer obtains the corresponding pulse current. According to the law of electromagnetic induction, secondary of the switching transformer similarly obtains the corresponding output pulse voltage, which obtains a stable output voltage by the secondary rectifier filtering. It has achieved the calculated number of turns of the switching transformer by the stabile output voltage. In the case of the copper loss and Iron Loss，it has achieved wire selection of the switching transformer and has achieved the design requirements by circuit simulation and actual production.

References

[1] Z. ZhiMin, Z.JiHai: *Switching Power Supply Design and Application of Practical Technology*, The People Post and Telecommunications Press(2003)

[2] W. Shuiping , S.Junjie and T.Qinganian: *Switching Power Supplp-Theory,Design and Applying Circuit*, Xi'an Electronic Science and Technology University Press(2005)

[3] Z.XiuKe: *The magnetic component in switching power supply*, Shenyang: Liaoning science and Technology Press(2004)

[4]Abraham. I: Pressman writings, ZhiJiang Wang Translated. *Switching power supply design* (Second Edition) . Beijing: Electronic Industry Press(2005)

[5] W.JiaLi : ManZuo Zhu, and HongMin Lu. *Electromagnetic Field and Electromagnetic Wave*, Xi'an:Xi'an Electronic Science and Technology University Press(2003)

[6] X.Zimei: *Electronic circuit design. experiment. test* (Second Edition). Wuhan: Huazhong University of Science and Technology press(2000)

[7] Y.Heng: *Examples featured about Switching power supply of typical design*. Beijing: China electric power press(2007)

[8] Z. Zhan-song and C. Xuansan: *Switching Power Supplies Theory and Design*, Beijing: Electronic Industry Press(2000).

Advanced Materials Research Vols. 986-987 (2014) pp 1804-1808

doi:10.4028/www.scientific.net/AMR.986-987.1804

Design of Three-phase Reference Energy Meter based on FPGA and ARM

Wang Xianwei[1, a], Qian Zheng[1, a], Tian Shuangshu[1, a], Qiu Yongjie[2, b]

[1]School of Instrumentation Science and Opto-electronics Engineering, Beihang University, XueYuan Road No.37, Hai Dian District, Beijing, China, 100191

[2]School of Computer and Information Technology, Beijing Jiaotong University, Shangyuan Village No.3, Hai Dian District,Beijing, China, 100044

[a]angelmrwang1230@126.com, [b]87009399@qq.com

Keywords: Reference energy meter, Metrological algorithm, ARM, FPGA

Abstract. Compared with the normal energy meters which use the integrated measurement chip as the key component, the three-phase reference energy meter based on *FPGA* and *ARM* possesses the advantages of high precision. And compared with the energy meters which use DSP as the key part, it has the advantages of small volume and multi-parameter measurement. The design method of three-phase reference energy meter integrating FPGA with ARM is presented in this paper. And the individual miniaturization design are discussed, the key parts during the realization are also discussed. After that, two kinds of *electric energy metrological algorithm* which are digital differential and instantaneous IV are introduced according to the characteristic of the system, and the advantages and disadvantages of them are compared. All this work will provide powerful foundation for the engineering applications of design method.

Introduction

Three-phase power metering equipment is used in trade settlement for industrial power meter. The accuracy of the measurement is directly related to the economy and energy efficiency of enterprises [1]. In recent years, with the rapid development of the power industry, the installation of three-phase energy meter keeps an annual growth rate of 2 million by the end of 2013. The number of three-phase energy meter is breakthrough 45 million in China. Thus, the demand of three-phase energy meter is also increasing rapidly.

Currently, the electronic power meters are generally divided into three types, energy measurement chip, DSP and FPGA. The diversity derived from realization of the embedded energy algorithm [2]. The applications and features of different energy meters are shown in Table 1.

Table 1. Principle, applications and features of Electronic Energy Meter.

Principle	Applications	Features
Energy measurement chip	Single-phase energy meter	Simple and inexpensive, Low accuracy
DSP	Single-phase and Three-phase, Reference energy meter	High accuracy, Complicated and Bulky
FPGA+ARM	Three-phase reference energy meter	High accuracy, Multi-channel parallel processing, Small

Compared with energy measurement chip and DSP, the method of FPGA+ARM possesses many advantages. As for FPGA, it has no limitation of custom circuits, and it also overcomes the defects of limited number original programmable gate circuit. FPGA also has many good points such as high frequency clock, small time delay, flexible construction and parallel processing of data. It can

realize the function of DSP since the DSP Builder could be embedded in it. Designers can design products according to different requirements of customers [3]. So it shortens the design time and improves the reliability of the system. As for ARM, it is more convenient in the field of communication and display control. Therefore, the integrating of ARM and FPGA is valuable for the design of three-phase reference energy meter.

Recently, the electronic energy meter is widely utilized to improve the measurement accuracy and long term stability in China. At present, the applications of 0.5 and 0.2 level three-phase energy meter are increasing. Due to the need of accreditation, the 0.1 level and more accurate energy meter are urgently required for the provincial and municipal metering departments [4,5].

However, there is a great gap between the inland and abroad in the field of three-phase reference energy meter. Based on the comparison of different reference energy meters and the consideration of application, 0.05 level three-phase energy meter integrating FPGA with ARM is urgently presented since there are important theoretical significance and wide market value.

In this paper, the design of three-phase reference energy meter integrating FPGA with ARM is presented. And then, different energy metrological algorithms are discussed. Finally, the key parts during the realization course are discussed. It will provide powerful foundation for the engineering applications of design method.

System structure

The design configuration is shown in Fig. 1.

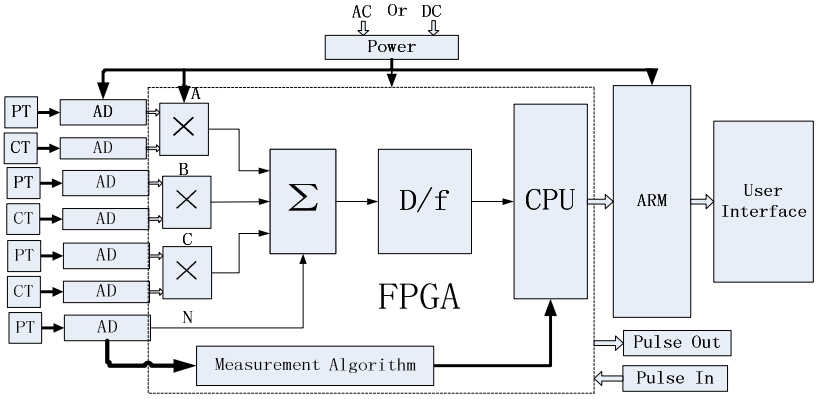

Fig.1 System structure diagram.

The three-phase voltage and current are converted to small signals at first. The small signals are transformed to digital signals by the selected AD converters, and then the internal multiplier of FPGA convert the digital signals of each phase into power instantaneous value. After that, the three-phase power value is obtained by the addition of instantaneous value. By using the digital to frequency conversion section, the power energy could be converted into corresponding frequency pulses [6]. These pulses are processed by ARM, and the results could be transmitted to the user.

Characteristics

The key parts of designed system are discussed as following.

The selection of AD converter. The data acquisition module is realized by AD7763, a 24 bit AD. Its precision is high and the dynamic range of input signal is 109dB theoretically. In other words, the input signal can cover the range from 60uV to 6V. Thus, there is no problem of range-switch, and the current and voltage are all single-scale input that can eliminate errors generated during the range switching process.

The selection of FPGA.EP3C80F484C7, the third generation FPGA chip of ALTERA, uses 65nm low-power (LP) process technology. This chip is the lowest power cost in the 65nm FPGA series, and it has 81,264 logic elements (LEs), 244 embedded multipliers, 2.7 million embedded

memory and 295 Input / Output (I/O) [7]. Thus, it possesses a significant feature which promotes the development of bandwidth parallel processing.

Data's processing. S3C6410 is a kind of ARM chip that can use the SPI protocol to communicate with FPGA. The voltage, current, power, frequency, phase angle, energy and other parameters calculated by FPGA are sent to ARM in real time [8]. ARM processes the data for further, and then transmitted the results to the user. The reason to choose ARM is that it has advantages in terms of reduced instruction which could be utilized to facilitate system. Therefore, it will be helpful for the miniaturization design. The giant serial (ARM) and parallel processing capacity (FPGA) could be realized based on their combination. The FPGA logic control for high-speed data processing and the ARM flexibility for software programming are also be utilized completely.

Measurement algorithm

The Fast Fourier Transform (FFT) are usually used to calculate the voltage, current, frequency, power and energy. However, since the limitation of CPU and FPGA resources, it is difficult to achieve higher accuracy. The high-performance CPU or FPGA can improve accuracy, but also improve the cost. Recently, the Wavelet Transform (WT) or comprehensive algorithm combining the FFT with WT are used to improve the measurement accuracy. But these algorithms are time-consuming, and can't realize a good application in real-time condition. Based on the limited CPU or FPGA resources and full cycle of AC sampling and adaptive sampling techniques, some new monitoring and analysis algorithms could also be utilized to get a satisfactory measurement accuracy. In this paper, two kinds of algorithms, which is the digital differential algorithm and the instantaneous value (IV) measurement algorithm respectively, are discussed completely, and and the advantages and disadvantages of them are compared.

Digital differential algorithm. The voltage signals after sampling by the AD converter, becomes discrete periodic sequence. Suppose M is the number of samples per cycle. There is a relationship between the time variable t and M. The sequences are t_0, t_1= t_0+h, t_2= t_0+2h, ... t_M= t_0+Mhand h=T/M. The sample sequence obtained is:

$$v(n) = \mathrm{V}\sin(2\pi \mathrm{f}\frac{nT}{M}+\varphi_{\mathrm{v}} \quad = \mathrm{V}\sin(2\pi \mathrm{f}t_s+\varphi_{\mathrm{v}} \ . \tag{1}$$

where t_s = nT/M.

Assuming interpolating function P(t)，according to the principle of Lagrange Interpolation， there is a relation:

$$P(\mathrm{t}) = \sum_{m=0}^{M} \frac{\prod_{\substack{j=0 \\ j\neq m}}^{M} t - t_j}{\prod_{\substack{j=0 \\ j\neq m}}^{M} t_m - t_j} v_m \ . \tag{2}$$

Where m=0，1，2…，k-1，k，k+1，…，M and M are the interpolation points.

Find one to four on the P(t)-order derivative can obtain the following two relations:

$$f = \frac{1}{2\pi}\sqrt{\frac{-v^{(4)}(n)}{v''(n)}} \ . \tag{3}$$

$$f = \frac{1}{2\pi}\sqrt{\frac{-v'''(n)}{v'(n)}} \ . \tag{4}$$

So that we can obtain the amplitude and phase angle:

$$V = \frac{1}{(2\pi \mathrm{f})^4}\sqrt{(2\pi \mathrm{f})^2[v'''(n)]^2 + [v^{(4)}(n)]^2} \ . \tag{5}$$

$$\varphi_{\mathrm{v}} = \arctan(-\frac{v^{(4)}(n)}{v'''(n)2\pi \mathrm{f}}) - \frac{2\pi \mathrm{f} n T}{M} \ . \tag{6}$$

Similarly, current, amplitude and phase angle can be obtained. The active power, reactive power, apparent power, and electric energy can also be obtained [9].

The IV algorithm of instantaneous value. As the instantaneous value measurement algorithm, data processing is carried out by the point of the measurement results of the integrated signal with a period T.

Valid value for voltage is：

$$V_{rms} = \sqrt{\frac{1}{N}\sum_{n} V_n^2} \ . \tag{7}$$

Where N is the number of a period of sampling points and V_n is the sampling sequence for voltage.

Valid value for current is：

$$I_{rms} = \sqrt{\frac{1}{N}\sum_{n} I_n^2} \ . \tag{8}$$

Where N is the number of a period of sampling points and I_n is the sampling sequence for current.

Active power is:

$$P = \frac{1}{N}\sum_{i=0}^{N-1} V_i I_i \ . \tag{9}$$

P is the mean instantaneous power over a cycle.

The advantages of the two algorithms are high precision which can achieve the precision required. However, both of them have drawbacks. When calculating the large amount of data, digital differential algorithm needs complex software implementation. The instantaneous value measurement algorithm needs small amount of computation by point measurement method, but requires voltage and current sampled synchronously.

Applications

Most of the industrial three-phase AC are three-wire or four-wire wiring methods. Due to the electricity can't be interrupted during the industrial production, thus the online verification is more and more necessary. In this paper, two verification methods are introduced and discussed. These two methods are three-phase four-wire (Fig. 2) and three-phase three-wire (Fig. 3).

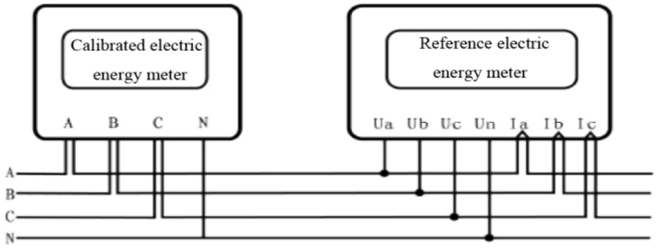

Fig.2 Four-wire check wiring diagram.

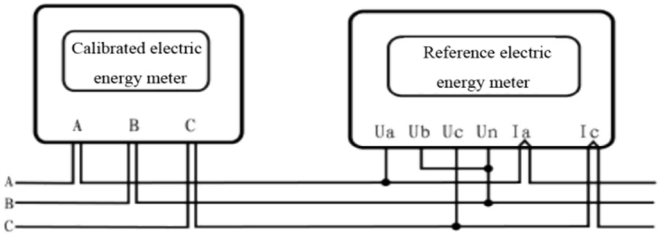

Fig.3 Three-wire check wiring diagram.

Conclusions

The scheme integrating FPGA with ARM is utilized to make energy measurement. The miniaturization design and the key parts during the realization are all discussed. After that, two kinds of metrological algorithm are introduced and compared. And the possible applications are illustrated at last.

References

[1] Youshun Zhang, Jinggang Feng, in: Electric energy measurement basis, Beijing, China (2007), in press.

[2] W.G. Morsi: Electronic reactive energy meters' performance evaluation in environment contaminated with power quality disturbances, Electric Power Systems Research, vol.84 (2012), p.202

[3] Ligong Zhou, in: SOPC Embedded system experiment tutorial, Beijing, China (2006), in press.

[4] Yonglin Lan, in: AC power measurement, Beijing, China (2011), in press.

[5] Naihong Zeng, in: The current status and future development of electronic energy meter, East China Electric Power, vol.27 (2001), p.25

[7] Zaosheng Lin, Shaohan Liu, in: FPGA chip design of Verilog, Wuhan, China (2008), in press.

[8] Jie Luo, in: The design of Verilog HDL and digital ASIC, Beijing, China (2006), in press.

[9] Jiekang Wu, Long Jun, Jixiang Wang: Electric parameters of digital differential algorithm based on fast and accurate estimation, Magazine of Relay, vol.32 (2004), p.2

Advanced Materials Research Vols. 986-987 (2014) pp 1809-1812

doi:10.4028/www.scientific.net/AMR.986-987.1809

Design Research of Unit Power Factor Power Converter

Wei Sun[1], Kuihua Wu[2], Bo Yang[1], Rong Liang[1], Jian Wang[3], Wang Fei[1]

[1]State Grid Shandong Electric Power Company, Shandong Jinan 250001

[2] Economic & Technology Research Institute, State Grid Shandong Electric Power Company, Shandong Jinan 250021;

[3] State Grid Shandong Electric Power Research Institute, Shandong Jinan 250001

Key words: Rectifier; control strategy; design research

Abstract. In view of the problems that traditional direct current control calculation is complex, that sensor precision requirements are high. This paper proposes a new control method of unit power factor power converter, which is easy to realize with simple control structure dispense with current sensor. Through the simulation and experimental verification, the control strategy can achieve unity power factor control, and the harmonic content is small and the operation is stable.

Introduction

Voltage Source PWM Rectifier (VSR) and Current Source PWM Rectifier (CSR) can be used as network side rectifier, but because the energy storage efficiency and the volume, price of a storage device of VSR have obvious advantages, which has been the focus in the study of PWM Rectifier [1].With the development of high temperature superconducting technology breakthrough and its practicability [2], CSR energy storage efficiency problem will be solved. At the same time, the energy storage coil in electric power superconducting system has current source characteristics, thus it can overcome the limitations of application of VSR in high power occasion, and in the small and medium-sized power occasions, CSR will provide a constant dc current, and the dc voltage is adjustable, which also has a good application prospect.

Mathematical model of three-phase PWM rectifier in the abc coordinate system

CSR is also called as Buck type converter, whose topology structure is shown in figure 1. Assuming that three-phase circuit is completely symmetrical , switch element is ideal, and switch frequency is greater than the grid frequency and linear inductor, and considering the internal resistance of inductance, we can set La = Lb = Lc = L, Ra = Rb = Rc = R, thus the equivalent circuit of three-phase CSR is shown in figure 2.

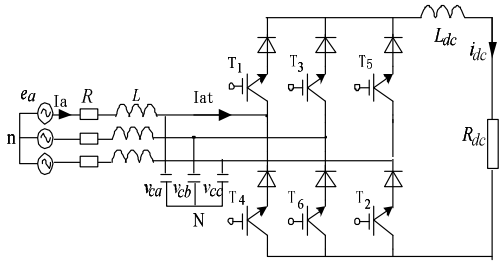

Fig.1 Circuit topology of CSC

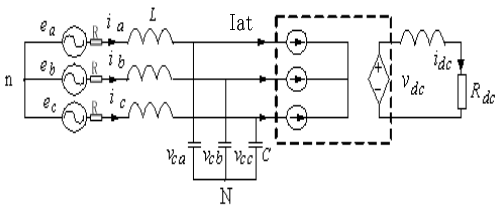

Fig2. Equivalent circuit of 3 phase CSC

System design of indirect current control of three-phase CSR ac instruction current

For the network side a-phase circuit, set

$$\begin{cases} e_a(t) = E_m \sin \omega t \\ i_a(t) = I_m \sin \omega t \end{cases} \quad (1)$$

In the formula,

$e_a(t)$. $i_a(t)$ —Net side a-phase electromotive force, current instantaneous value;

E_m, I_m — Net side a-phase electromotive force, current peak value;

If the PWM switching frequency is high enough, ignoring a-phase network side resistance, the fundamental wave steady-state value $v_a(t)$ of the three-phase CSR a-phase ac voltage is

$$v_a(t) = -\omega L I_m \cos\omega t + E_m \sin\omega t \tag{2}$$

Because the three-phase CSR ac a-phase current $i_{at}(t)$ [3] is

$$i_{at}(t) = i_a(t) - i_{ca}(t) \tag{3}$$

Combine the formulas (4) ~ (6), a-phase directive current $i_{at}^*(t)$ for the ac side is:

$$i_{at}^*(t) = I_m^*(1-\omega^2 LC)\sin\omega t - E_m\omega C\cos\omega t \tag{4}$$

Because three-phase CSR uses three-value logic PWM control with Y type connection in the network side, the corresponding phase voltage modulation signal phase must lag behind line voltage modulation signal phase $\Pi/6$. In this way, when three-phase CSR has been required to realize rectifier control of network side unit power factor sine wave current, its instruction $u_{ma}^*(t)$ for a-phase current modulation signal is

$$\begin{aligned} u_{ma}^*(t) &= I_m^*(1-\omega^2 LC)\sin(\omega t - \frac{\Pi}{6}) - E_m\omega C\cos(\omega t - \frac{\Pi}{6}) \\ &= K_1 I_m^* \sin(\omega t - \frac{\Pi}{6}) - K_2\cos(\omega t - \frac{\Pi}{6}) \\ &= \frac{\sqrt{3}}{3E_m} K_1 I_m^*[e_a(t) - e_c(t)] + \frac{1}{E_m} K_2 e_b(t) \end{aligned} \tag{5}$$

Similarly, it can derive:

$$\begin{aligned} u_{mb}^*(t) &= \frac{\sqrt{3}}{3E_m} K_1 I_m^*[e_b(t) - e_a(t)] + \frac{1}{E_m} K_2 e_c(t) \\ u_{mc}^*(t) &= \frac{\sqrt{3}}{3E_m} K_1 I_m^*[e_c(t) - e_b(t)] + \frac{1}{E_m} K_2 e_a(t) \end{aligned} \tag{6}$$

In the formula： I_m^* —a-phase network side current peak value instruction ;

$K_1 = 1-\omega^2 LC$ $\quad K_2 = E_m\omega C$

Its control system structure [4] is shown as figure 6.

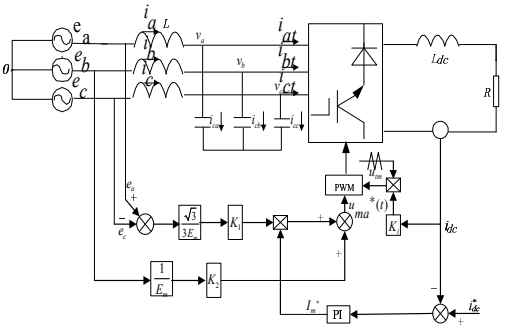

Fig3. Control scheme of a phase Based on Indirect Current Control

In figure 3 of the dc current loop, the sampling of the dc current is compared with the given value, and the error after PI regulation multiply modulation wave a, c two-phase producing, then plus the wave b-phase producing. As the modulation wave, carrier wave is obtained by the multiplication with Ki times of dc current idc and triangle wave, and both subtraction produce two logical value, after transformation of two logic to three logic PWM waveform can be got, so that the ac current tracking input side ac voltage varies, so as to realize the in-phase between the voltage and the ac current.

In the three-phase CSR control system shown in figure 3, the control and analysis process of the dc side current i_{dc} is as follows:

When the state stable , if there is disturbance, the control process is as follows:

$$\begin{cases} i_{dc} \uparrow \rightarrow I_m^* \downarrow \rightarrow i_{kt} \downarrow \rightarrow i_{dc} \downarrow \\ i_{dc} \downarrow \rightarrow I_m^* \uparrow \rightarrow i_{kt} \uparrow \rightarrow i_{dc} \uparrow \end{cases}$$

To curb influence of the dc current fluctuation on three-phase CSR net side current control, compensation control based on i_{dc} feed forward carrier wave amplitude is adopted in figure 3. When i_{dc} changes, its control process is as follows:

$$\begin{cases} i_{dc} \uparrow \rightarrow u_{tm} \uparrow \rightarrow m \downarrow \rightarrow \sigma_{k1} \downarrow \rightarrow i_{kt} \downarrow \rightarrow i_{dc} \downarrow \\ i_{dc} \downarrow \rightarrow u_{tm} \downarrow \rightarrow m \uparrow \rightarrow \sigma_{k1} \uparrow \rightarrow i_{kt} \uparrow \rightarrow i_{dc} \uparrow \end{cases}$$

Among them u_{tm} —PWM carrier wave peak value;

σ_{k1} —three-value logic switching function fundamental component;

m—PWM modulation ratio;

i_{kt} —ac current $(k = a, b, c)$.

Experimental reult

In order to verify correctness of the above methods, experimental verification is carried out. Simulation parameters of the circuit are: Em = 160 v, L = 0.8 mH, R = 0.5Ω, C = 48 uf Ldc = 200 mH, Rdc = 30Ω. Performed by DSP chip TMS320LF2407A, experiment control system uses C language programming, and the switching frequency is set as 4.2 kHz. In the experiment dc current value is given for I^*_{dc}=2A, the rectifier is controlled by i_{dc} by real-time sampling of load current according to the principle in figure 3.

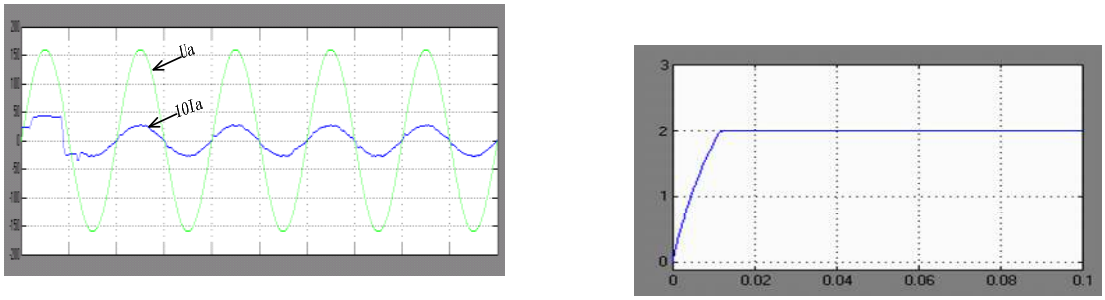

(a)Voltage and current of network side a-phase (b) dc side current

Fig4. Simulation wave based on Indirect Current Control

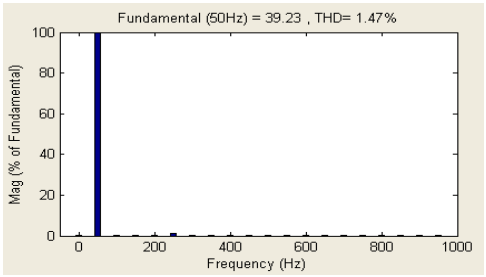

Fig5. Frequency schematic of A phase network current of Simulation wave

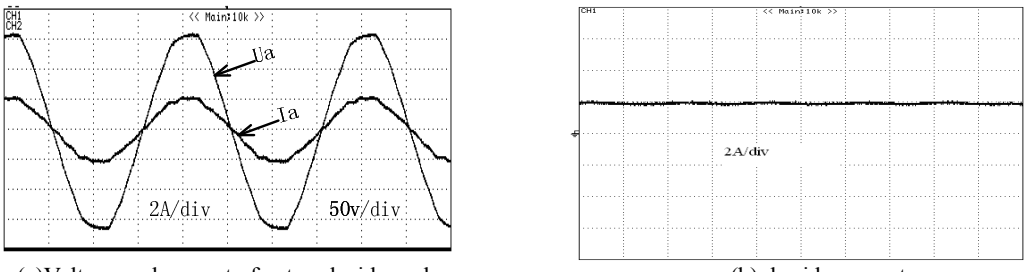

(a)Voltage and current of network side a-phase (b) dc side current

Fig6.Experiment waveforms based on Indirect Current Control

PI values calculated by the simulation are 60 and 0.1; dc side KI value is 0.2. PI value taken by simulation and experiment proof obviously improve the immunity of the system performance, you can see the waveform is not standard in the beginning in figure 4, but by the end of 0.01 s waveform approximates sine wave, and dc side tends to be stable. By figure 4 and figure 6 we can see that the application of indirect current control can realize ac unit power factor of current type rectifier, and the dc side current tends to be stable as soon as possible. Figure 5 is harmonic analysis foe the simulation waveform of a-phase net side current, and THD is 1.47%, the harmonic content is smaller.

Conclusion

Through theoretical analysis and experimental proof , this paper proved that , indirect current control system based on the three-phase CSR ac side directive current can realize current type rectifier ac unit power factor and stable operation.

References

[1]Wang ying, Zhang chunjiang,Chen huiming, Anew phase amplitude control strategy and mathmatics model of three-phase voltage rectifier. Proceedings of CSEE,2003, 23(11): 85-90.
[2]Juan W Dixon, Boon-Teck Ooi. Dynamically stabilized indirect current Control spwm boost type 3-phase rectifier. IEEE IAS, 700-704,1998
[3]Zhou tingyang, Jiang weicheng.Circuit principle,Zhejiang: Zhejiang University press.1994
[4]Zhang chongwei, Zhang xing. PWM rectifier and its control. Beijing: China Machine Press,2003.

Advanced Materials Research Vols. 986-987 (2014) pp 1813-1816

doi:10.4028/www.scientific.net/AMR.986-987.1813

Development and design of embedded control systems for coal mine

LI Xiao-fang

Department of Computer and Information Engineering,Chengde Petroleum College,Chengde Hebei, 067000,China

Keywords: video surveillance system of coal mine; database technology; mine

Abstract: China's coal mine monitoring system and scientific management level is relatively backward. Environmental information of coal mine is difficult to achieve control and sharing. Combining with the traditional model of the safe production of coal, the author presents a new monitoring system structure of coal mine based on embedded technology to achieve the aboveground control and underground monitoring of coal mine. By combining control instance of monitoring system, this paper focuses on the safety production monitoring system design and implementation of coal mine, and describes the design methods for monitoring system, which is helpful for China's coal production safety.

1. Status and application sense of video surveillance system of coal mine

In actual specific operations, if the comprehensive unit price of service quality evaluation projects is reviewed one by one, the workload is too much. It is not realistic [1-3]. The application of computer used at the global level promotes the rapid development of the human resources information system network. At this stage, information technology continues to mature. The advantage is that complex human resources conditions under business environment were taken into comprehensive account. However, with the rapid development of information technology, database technology gradually penetrates into reality, but also makes people's perception modeling of environment [4].

2. The application of embedded technology in the video surveillance system of coal mine

2.1 Proposed hardware design

Interactive design technology for component's calling service, not only has the components to maintain and update information query function, but also provides timely warning information according to the components of production facilities uptime. Relevant parameter interacting components also has a set of management system database to maintenance system and has the rights management and maintenance functions. Cache management module can be used for storage access, server detection and other functions of spatial data. Spatial data in the client cache have the function of data elimination and cache updating. Mixed maps service with vector mesh can divide strictly the spatial data environment, and implement the management. Vector meshes generation is used to store data, and the spatial data formats are saved in the system ports. Cache management module can be combined with map display module and through the personnel screening, it can screen valid data to administrators according to the data attribute of port cache.

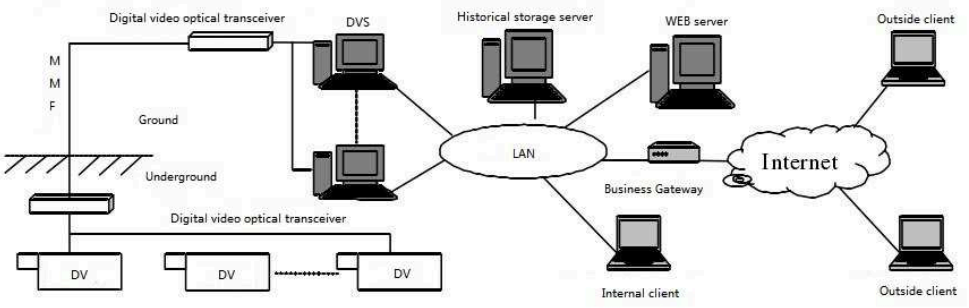

Figure 1 Schematic diagram of networked video surveillance system

2.2 the Hardware of Automated Security Monitoring

On the issue of network sub-code configuration in integrated monitoring system, automated security monitoring systems and communication systems are independent of each other, and optical fiber cable is used as raw material. it can safeguard the stability of the speech signal in the communication system better, and the data of monitoring system can also be achieve motorized terrestrial reception. For the sake of light transmission convenience, the optical signal interpreter can convert it into an optical signal, and then convert the optical signal into an electrical signal to the downhole, and eventually achieve the complete separation of data and voice. It should be noted that the leakage communication system should also have the tracking competence of equipment and personnel in downhole. Below is a design diagram of the monitoring system.

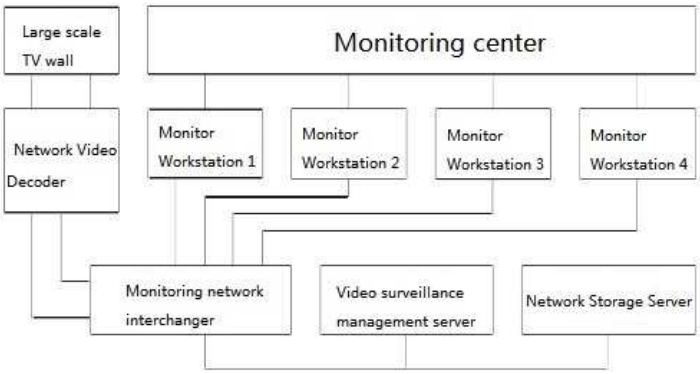

Figure 2 Design diagram of the video surveillance system of coal mine

2.3 The design of the monitoring system software algorithm

After using the mine monitoring system, monitoring personnel can get access to the monitoring information timely. There is a difference of monitoring information between using different devices. According to a different color in the image, it can analyze the situation in different monitor regions. Red is for describing a warning range, green is used to describe the normal range. If the monitor power is higher than the certain threshold, the alarm will be formed. In the image, the geographical coordinates of different people can be identified. WEB pages delivery the data to terminal commands based on the relevant information, and using GPRS and DHCP protocols transfer data to the terminal device. User can handle the data through the relevant menu of master-control interface, query related historical data, and analyze independent alarm analysis program, and then analyze whether the existence of underground hazardous events.

The event of coal mine hazard identification in the alarm module is the key to the alarm. The identification of hazardous event is to distinguish firstly the person with the background in coal mine, and then complete the identification. The following methods are applied in this article:

Assuming the acquired scene images of the downhole region are $C_{i,j}^{n}$ and the background image is $B_{i,j}^{n}$. Each pixel of the input flow image and the difference with the background pixel can be analyzed, and then there are:

$$D_{i,j}^{n} = \left| C_{i,j}^{n} - B_{i,j}^{n} \right| \tag{1}$$

$$V_{i,j}^{n} = \begin{cases} 1, & D_{i,j}^{n} \geq Th \\ 0, & \end{cases} \tag{2}$$

Using the following formula for the binary image processing:

$$B_{i,j}^{n+1} = \begin{cases} kB_{i,j}^{n} + (1+k)C_{i,j}^{n}, V_{i,j}^{n} = 0 \\ 0, \end{cases} \quad (3)$$

Wherein, *Th* represents a threshold value, which can describe the sum of mean and standard deviation of the difference image pixels. If $V_{i,j}^{n}$ is 1, it indicates that the corresponding pixel belongs to an object; otherwise the pixel is a background pixel in the image. The background image can be adjusted by the formula (3):

If $V_{i,j}^{n}$=0, the above formula is applied to adjust the background image, otherwise, it should ensure the stability of the background image, and using the recognition model complete the in dangerous situations identification.

3 Experimental Analysis

The applied effectiveness of the design system to detect underground environment monitoring can be verified by experiments in this paper. The stored data in the experimental database is from the video image data of downhole. System in this article and the traditional system were used respectively in the experiment to detect abnormal visual signals of the downhole. The obtained results are described in Figure 3. The analysis of figure 3 can be seen that the system data values obtained herein has a high degree of matching with the actual data, and the data values obtained with the conventional system is largely different from the practice data. It can indicate that the method described herein to detect the hazardous visual signal in downhole is feasible:

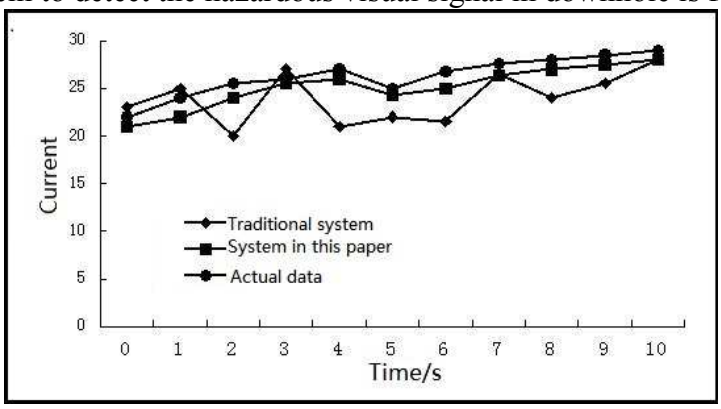

Figure 3 Comparison of the detection effect of different systems and the actual results

To further validate the superiority of the proposed system, the system in this paper and the traditional system are used to detect the monitoring efficiency of the 10 downhole projects, and the results are described in Table 1. It can be seen from Table 1, the efficiency of the system in this paper is higher than traditional system, and operational efficiency of the system and the computational efficiency and accuracy is better than conventional system, indicating that the system proposed in this paper can ensure mine safety and has important application value.

Table 1 Actual measurement data

	traditional system			the system in this paper		
number	monitoring parameter	detection time/h	detection precision/%	monitoring parameter	detection time /h	detection precision /%
1	245	22	80	288	13	89
2	194	20	82	290	11	90
3	255	19	81	269	10	92
4	198	18	83.5	289	12	90
5	263	21	85	308	13	91

6	232	17	79	295	14	89
7	146	18	80.5	283	12	93
8	178	20	84	305	11	95
9	193	22	83	313	10	94
10	212	19	81	295	12	96

4. Conclusions

Embedded database technology is made as the main coal mine supervisory control. in the same client on the same LAN, four times roaming and four times map initialization are also operated by using the traditional coal mine monitoring and management system and the designed information management model of graphic image processing in this paper. In the detection process, Set Interval method is added to the program to record the length of the response time of each sub-map operation. On the whole, the embedded database technology can improve the efficiency of coal mine monitoring work.

References

[1] Lili Sheng, Zhong Wang, Chunli Wang, et al．Design of WLAN adapter device driver based on SPI [J]．Journal of Wuhan Institute of Technology, 2011,33(6):89-93.

[2] Dongshan Wei．Application development manual of embedded database technology [M]．Beijing：Posts and Telecom Press，2009:241-360.

[3] Wenbing Tang. Research on the video surveillance system of coal mine based on streaming media technology [J]. Industry and mine automation；2006(6): 59-62.

[4] Tiegang Peng, Guofan Liu, Shaokun Cao, et al．Design of embedded video surveillance system based on ARM [J]．Computer Engineering and Design. 2010, 31(6):1191-1194.

Advanced Materials Research Vols. 986-987 (2014) pp 1817-1820

doi:10.4028/www.scientific.net/AMR.986-987.1817

Effect of frequency and boost on the breakdown of XLPE cable with inserted needle defects

Weiwei LI[1, a], Qiang SHI[2, b]

[1]State Grid Sichuan Electric Power Research Institute, Chengdu, 610000, China

[2] Sichuan Electric Power Corporation Metering Center, Chengdu, 610000, China

[a]email: liweiwei0830@163.com, [b]email:awaityou1986@gmail.com

Keywords: Cross-linked polyethylene; Boost; Frequency; Breakdown

Abstract. Cross-linked polyethylene cables are widely used in power transmission system. In this work the effect of frequency and boost on the breakdown performance of XLPE cable with inserted needle defects was investigated by the frequency-tund resonant system with frequency ranging from 20Hz to 300Hz. The breakdown paths were observed by an optical microscope, and the fractal dimensions of the paths were estimated according to box-counting method. It was found that, with the increase of frequency, the variation of path fractal dimension as a function of frequency corresponded to that of breakdown voltage. Compared with the continuous boost method, the frequency, at which the fractal dimension of breakdown paths approached saturation and the breakdown voltage peaked, became lower under step test method. The increase of breakdown voltage is due to the increase of electrical power used for the initiation and development of dense discharge paths.

Introduction

The breakdown strength of insulation determines the stability of the equipment under the electric field [1]. With the improvement of the voltage level of electrical equipment, the electric strength of insulating materials is paid more and more attention at home and abroad. A large number of experimental research, simulation calculation and theoretical analysis for the breakdown characteristics of polymers have been done.

Cross-linked polyethylene (XLPE) cables are widely used in the power transmission system, due to the excellent electrical, thermal, physical and mechanical properties [1]. Studies have shown that the breakdown performance of XLPE had a great relationship with the applied voltage. For defect-free XLPE cable samples, the breakdown voltage decreases with the increase of frequency within the range of 0.0001Hz ~ 10000Hz. Gochenbach E [2] studied the breakdown performance of model cable with water tree, mechanical defect and defect-free at 0.1Hz ultra-low frequency, high frequency oscillation, 50Hz and 250Hz AC voltage, respectively. It was found that, cables with different defects had different reflect under different frequency and voltage waveforms. The breakdown strength of cables with water tree and mechanical defect was $E_{b\text{-}0.1\text{Hz}}<E_{b\text{-}50\text{Hz}}<E_{b\text{-}250\text{Hz}}$, but this phenomenon was not paid more attentions. Luo JH and Qiu YC [3] have investigated the breakdown perforce of XLPE cable with artificial defects under power frequency, 0.1Hz ultra-low frequency and 5k ~ 6kHz oscillation. It was found that, the oscillating voltage test could effectively detect defects in manufacture and installation of quality, while the ultra-low-frequency voltage test could effectively detect early deterioration of water tree defects. However, the development and breakdown mechanism under different voltage were not clear yet. At the same time studies shown that, breakdown was closely linked with the electrical tree and partial discharge [4]. Ieda M considered that, the treeing type breakdown voltage was effected by the rate of rise, the impact of pre-press time and polarity reversal of applied voltage.

This work is helpful for the stability of the power transmission system and is an important research subject in the field of electrical insulation. It has a great signification to investigate breakdown performance, for this study will provide experimental and theoretical basis for the defects detection.

Experiment Methods and Devices

Sample Preparation

Manganin needles with a diameter of 1 mm and a tip radius of 10±1 μm were chosen by optical microscopy. The manganin needle was inserted into the 10 kV XLPE cable insulating layer along the radial direction. And the insulation thickness was controlled to be 1.000±0.001 mm by a micrometer. Figure 1 gives the schematic diagrams of XLPE specimens with needle defects.

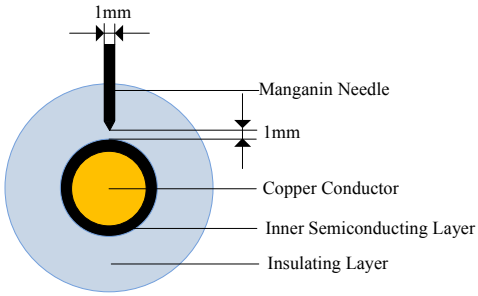

Fig.1. Schematic diagrams of XLPE specimens with needle defects.

Frequency-tuned Resonant System

The breakdown performance was conducted under the frequency-tuned resonant system which is shown in Figure 2. The applied voltage increases with a 0.5 kV/s ramp speed under continuous boost method, while voltage increases 0.5kV each step quickly and maintains for 20s under step test method. The breakdown tests were conducted in transformer oil.

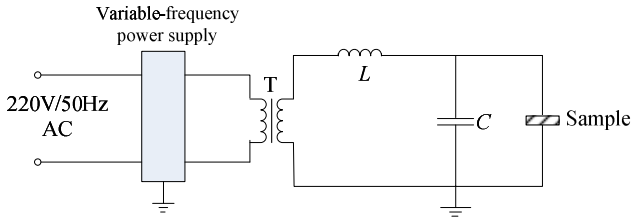

Fig.2. Circuit diagram of the frequency-tuned resonant system.

After breakdown tests, breakdown paths were observed by Olympus BX51M. The fractal dimension of breakdown paths was calculated by the box-counting method.

Experimental Results and Discussion

Continuous Boost Method

The fractal dimension of breakdown path was calculated at different frequencies, based on the box-counting method mentioned in reference [5]. Figure 3a gives the linear relationship between $\log(r)$ and $\log(N(r))$ under different frequency according to the 2-D projected patterns of breakdown paths, where r refers to measuring scale, and $N(r)$ refers to the number of the boxes occupied by the tree branches. The absolute value of the line slope is the fractal dimension of the breakdown path.

The breakdown voltage U_b and fractal dimension D as a function of frequency are shown in Figure 3b. It was found that, three stages of path fractal dimension as a function of frequency corresponded to those of breakdown voltage, as shown in Figure 3b. In stage 1 from 20Hz to 150Hz, the breakdown voltage decreased as the increase of frequency, while the fractal dimension almost remained unchanged. In the stage 2 from 150Hz to 240Hz, the breakdown voltage as well as the fractal dimension increased as the increase of frequency. In the stage 3 from 240Hz to 300Hz, the breakdown voltage decreased again and the fractal dimension approached saturation. The breakdown voltage will decrease as the increase of frequency when the fractal dimension stays stable, and will increase when the fractal dimension increase with frequency.

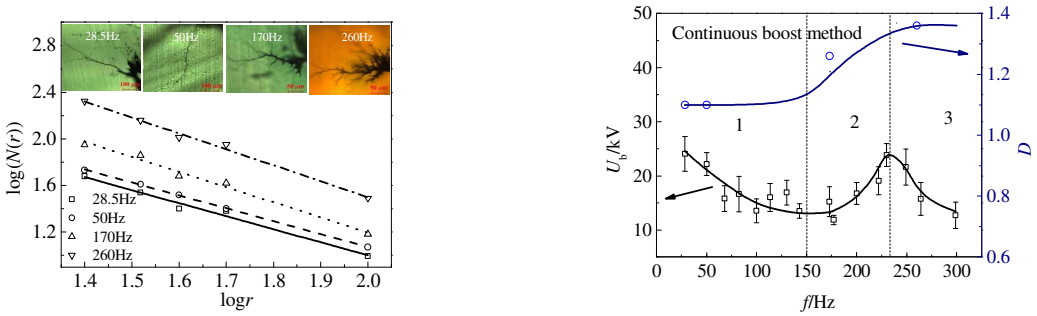

(a) Fractal dimension of breakdown path (b) Breakdown voltage and fractal dimension

Fig.3. The breakdown performance of XLPE cable with inserted needles for continuous boost method.

At low frequencies, the space charges injected from the needle tip accumulate in the vicinity of the needle electrode. The shielding effect of space charge leads to high breakdown voltage at low frequency. With the increase of frequency, the rates of space charge injection and extraction are faster, the shielding effect is weakened, leading to the decrease of breakdown voltage. In stage 1, the injected charges accelerate in the electric field and are easy to initiate impact ionization, discharge develops along the electric field direction until the path bridge the two electrodes.

In stage 2, when the frequency ranges from 150Hz to 240Hz, the breakdown voltage and the fractal dimension increase with the increase of frequency, and the morphology of the path changed from sparse to dense. With the increase of frequency, the rates of injection and extraction of space charge become faster, cations introduced during the impact ionization in the wall discharge with the injected electrons. More and more side channels will be introduced, and the fractal dimension increases. In this stage, the initiation and development of dense discharge path use up the electric power, leading to the increase of breakdown voltage.

In stage 3, when the frequency ranges from 240Hz to 300Hz, the morphology and fractal dimension of the path reach saturation, the energy used for the development of dense tree no longer increase. Tanaka and Greenwood deduced the relationship between the development of the discharge path and the field energy as [1]:

$$ft_1[G_n - G_{th}] = C_t \quad (1)$$

where, f is the voltage frequency, t_1 is the pressing time, G_n is the energy gained from the applied voltage per period, G_{th} is the threshold energy of electron avalanche, C_t is a constant. According to equation (1), the increase of frequency will lead to the shorter of discharge channel initial time and low breakdown voltage.

Meantime, the frequency also has effect on the energy loss p of XLPE [1]:

$$p = 2\pi f E^2 \varepsilon_0 \varepsilon_r \tan\delta \quad (2)$$

where E is the applied electrical strength, ε_0 is the vacuum dielectric constant, ε_r is the relative dielectric constant, and $\tan\delta$ is the dielectric loss tangent. As shown in equation (2), with the increase of frequency, the energy loss increases in the XLPE insulation. This is benefit for the development of discharge channels. Therefor the decrease of discharge channel initial time and the increase of the energy loss lead to the decrease of breakdown voltage with the increase of frequency in stage 3.

Step Test Method

The breakdown performance of XLPE cable under step test method is introduced in this work. The fractal dimension was calculated as shown in Figure 4a. And Figure 4b gives the fractal dimension and the breakdown under step test method in the range from 20Hz to 300Hz. The breakdown voltage and the fractal dimension increase with the increase of frequency ranging from 20Hz to 80Hz. In the stage from 80Hz to 300Hz, the breakdown voltage decreases with the increase of frequency, and the fractal dimension approaches saturation.

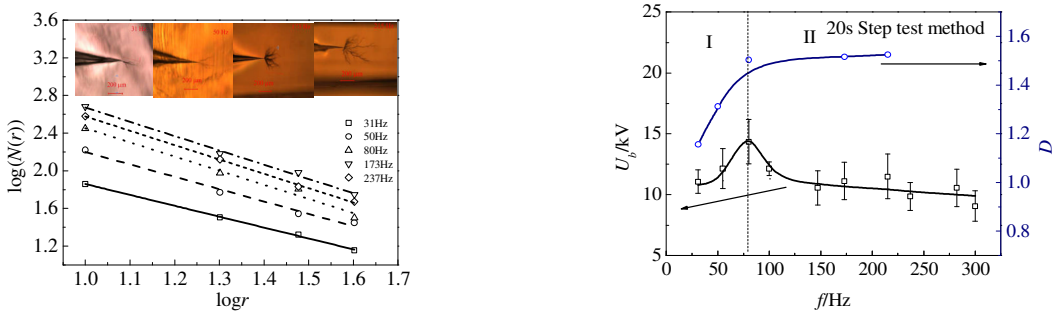

(a) Fractal dimension of breakdown path (b) Breakdown voltage and fractal dimension

Fig.4. The breakdown performance of XLPE cable with inserted needles under step test method.

Under the step test method, the variation of breakdown voltage as a function of frequency is correspond to that of fractal dimension, as shown in Figure 4b. In stage Ⅰ under the step test method, the breakdown voltage as well as the fractal dimension increase with the increase of frequency, this stage is correspond to the stage 2 under continuous boost method. In stage Ⅱ, the fractal dimension stay stable while the breakdown voltage decrease, this stage is the same with stage 3 under continuous boost method.

Compared with the continuous boost method, the breakdown voltage under step test method is lower, the fractal dimension is larger, and the morphology of breakdown path is much denser. Under the step test method, the frequency, at which the breakdown voltage peaks and the fractal dimension reaches saturation, decreased to 80Hz.

Conclusion

In this work, the breakdown performance of XLPE cable with artificial inserted needle was investigated.

(1) Under the continuous boost method, the breakdown voltage decreased in the range from 20Hz to 150Hz, subsequently increased, after it reached a maximum value at 240Hz, it decreased again with the increase of frequency.

(2) The frequency, at which the breakdown voltage reached maximum and the fractal dimension of breakdown paths reached saturation, decreased from 240Hz to 80Hz under step test method.

(3) The transform of the morphology of breakdown path has a great effect on the variation of breakdown voltage with the frequency. The breakdown voltage increases with the increase of frequency, when the breakdown paths change from sparse to dense. Compared with the continuous boost, the breakdown voltages are lower and the fractal dimension is larger under step test method.

References

[1] LA Dissado, JC Fothergill. Electrical degradation and breakdown in polymers [M]. Redwood Press, 1992.

[2] E Gockenbach, W Hauschild. The selection of the frequency range for high-voltage on-site testing of extruded insulation cable systems [J]. IEEE Electrical Insulation Magazine, 2000, 16(6): 11-16.

[3] Luo Junhua,Ma Cuijiao,Qiu Yuchang. Study on test methods of XLPE power cable rated up to 35kV. Power System Technology, 2000, 24(12): 58-61(in Chinese).

[4] M Ieda. Dielectric-breakdown process of polymers [J]. IEEE Transactions on Electrical Insulation, 1980, 15(3): 206-224.

[5] A. S. Xie, X. Q. Zheng, S. T. Li, and G. Chen, Investigations of electrical trees in the inner layer of XLPE cable insulation using computer-aided image recording monitoring [J], IEEE Trans. Dielectr. Electr. Insul., 2010, 17: 685-693.

Advanced Materials Research Vols. 986-987 (2014) pp 1821-1825

doi:10.4028/www.scientific.net/AMR.986-987.1821

Error Calibration of Three-phase method for combined transformer

AI Bing , SHI Qiang

Sichuan Electric Power Corporation Metering Center Chengdu, China

aibing1985@aliyun.com; awaityou1986@gmail.com

Keywords: Three-phase Combined Transformer; Single-Phase method; Three-Phase method; Transformer calibration

Abstract. Three-phase combined transformer has a large number of application to special energy metering in power grid, its performance is directly related to the accuracy of electric energy metering. So it is necessary to ensure its performance and accuracy. It rules that three-phase combined transformer should be calibrated with three-phase method, but most of metrology departments calibrate three-phase combined transformer in single-phase method. Based on the mechanism of the three-phase transformer, single-phase method and three-phase method had been compared on three-phase transformer experimental platform. The result shows that it would be large error when the three-phase transformers are calibrated with single-phase method. Three-phase transformer calibration should be operated with three-phase method.

Introduction

High voltage three-phase combined transformer means for 3kV, 6kV, 10kV, 35kV power system voltage level assembly into one of the current and voltage transformers, often for electric power measurement and energy measurement.

This common combined three-phase transformer (metering box) have been widely used for large users and dedicated transformer metering， its quality performance is directly related to the accuracy of power metering, but also involves the electricity sector safe operation of the production, so it must be tested to ensure reliable and accurate measurement . JB/T10432-2004 " 《three-phase combined transformer》 national authorities on August 1, 2004， said: error test, mutual interference test , temperature rising test of the three-phase combined transformer should be applied with three-phase voltage and three-phase voltage current , while domestic institutions at all levels tested by single-phase power supply with a single- phase standard ,and the three-phase transformer manufacturers don't have three-phase current and three-phase voltage testing standard equipment , so combined transformer factory testing also has been used single- phase method for each phase error testing and related testing projects respectively . Obviously, these conditions do not meet the requirements of the relevant existing national standards , while the product of the factory testing and metrology products do not meet the conditions of use , thus bringing to detect error , especially on the power of trade fair and equitable settlement . And affect the performance of the product quality.

Therefore, the study "error comparison" of single-phase method and three-phase method for three-phase transformer calibration is important for metering fairness and the promotion of three-phase method.

Calibration of Single-Phase Method for Three-Phase Combined Transformer

Single-phase calibration method for three-phase transformer refers to its traditional calibration method for three-phase transformer in one current transformer winding or one voltage transformer winding separately, when several other transformers not rising voltage and current, its block diagram shown in Figure 1.

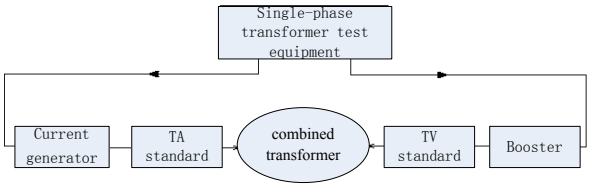

Fig.1 Principle block diagram of single-phase method to test three-phase transformer error

As can be seen in the using of single-phase method calibration, only one of the transformer windings can be tested, or other voltage transformer secondary windings and current transformer secondary windings are required for short or open, with it is inconsistent with the actual operating conditions.

Three-phase methord Calibrition for combined transformer

Unlike the single-phase transformer , three-phase transformer due to the simultaneous measurement of three-phase voltage and current , transformer components in addition to their own error, the error still exist interactions between transformer components. Since the single-phase method in the testing, only the single winding is added voltage and current that shield the effects of the other transformer elements , so that the test conditions do not match with the actual operating conditions , thereby causing deviation of measurement error.

For three-phase combined transformer , three-phase/ single-phase voltage or current at the load , the error is mainly from two aspects:

(1) The electromagnetic interference error, mainly due to the three-phase transformer load on three-phase high voltage and big current , high voltage will produce a strong electromagnetic field, and mutual coupling is formed to each transformer in the internal space of each member , so that changes secondary output voltage and current compared to single-phase voltage or current.

(2) Since the reasons of the combination of transformer , the load imbalance , three-phase combined transformer loading in the case of three-phase voltage and current ,the main magnetic flux and excitation current, etc. are changed, resulting in two secondary side voltage and current harmonics .

Therefore, to simulate real three-phase transformer runtime environment , when it need to test, while loading in three-phase voltage and current, its block diagram shown in Figure 2 .

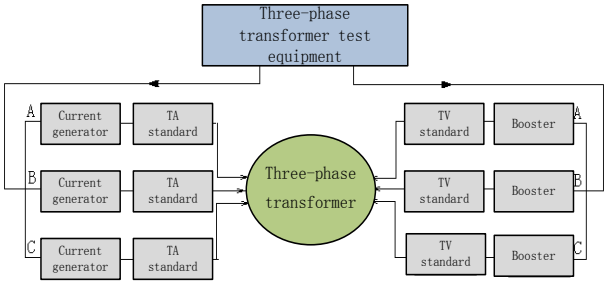

Fig.2 Principle block diagram of three-phase method to test three-phase transformer error

As can be seen, a high-voltage three-phase transformer testing system that using three-phase method is mainly composed of a high-voltage three-phase transformer test console, high-voltage current transformer standard with current booster, the voltage booster, the voltage transformer standard, three combined transformer calibrator and the test product and other components.

Testing three-phase two components voltage transformer error wiring diagram shown in Figure 3.

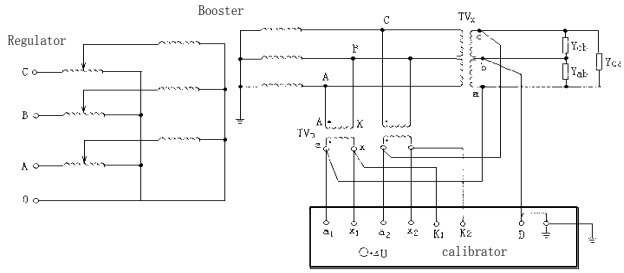

Fig.3 Wiring diagram of testing voltage transformer error

Therefore, the three-phase transformer calibrating device for three-phase voltage transformer when the interaction test, through a specially designed three-phase voltage regulator and three-phase transformer calibrator, it can be connected voltage transformer and three-phase voltage transformer standard circuit to V-type, and then access the A-phase and C-phase current transformer standard and current source, so that you can fully simulate live operating environment, so as to more accurately investigate the performance of combined transformer.

Again, the error calibration of the current transformer wiring diagram shown in Figure 4.

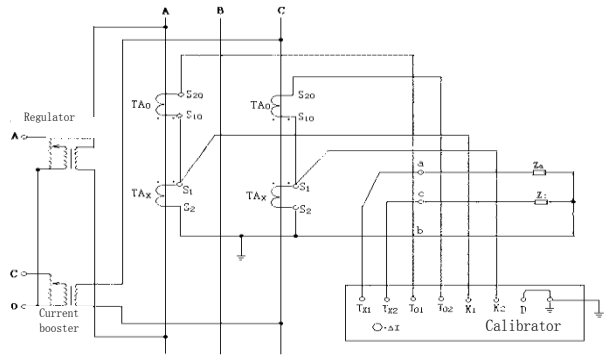

Fig.4 Wiring diagram of testing current transformer error

I. ERROR TESTING OF THREE-PHASE TRANSFORMER

Based on the three-phase transformer calibration platform, three-phase transformers are tested in three-phase and single-phase method, comparing the results of its measurement error.

1. Secondary induced voltage measurement

Due to the high voltage and big current, three-phase combined transformer secondary winding is under high electromagnetic pressure field, in order to research the impact of high voltage electric field and magnetic field of the transformer secondary components, disconnect the test high voltage side when measuring, the purpose is to shield itself influence, and measure the secondary side voltage, so that the applied voltage is measured relative to the other two phases of the measured primary side voltage of the secondary winding. The result is shown in Figure 5.

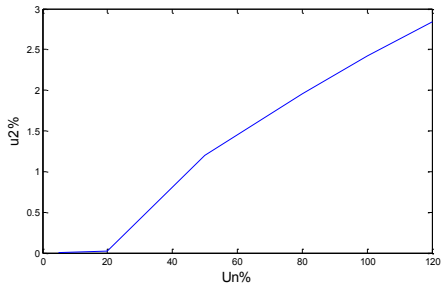

Fig.5 Secondary induced voltage measurement

As can be seen, when the primary voltage is low, the impact on neighboring phase is very small, as the voltage level increases, affected by increases rapidly , the secondary phase output up to 2.42 percent of the rated voltage.

2. Three-phase and single-phase method error comparison

The contrast between the three-phase method and the single-phase method respectively, for the same three-phase combined transformer in single-phase and three-phase method, the voltage error comparison shown in Figure 6.

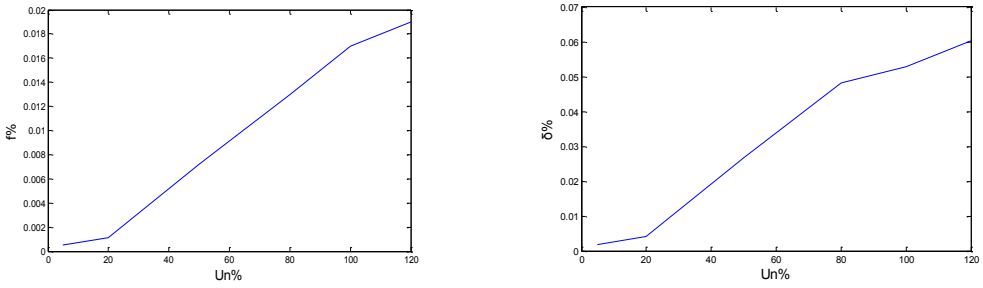

(a) The difference of ratio error curve (b) The difference of phase error curve

Fig.6 The voltage error curves between single-phase and three-phase method

Where, *f%* is the difference of ratio error between single-phase and three-phase method, *δ%* is the difference of phase error between single-phase and three-phase method. it can be seen ,when the primary voltage is small, the gap between single-phase and three-phase method is smaller, but with voltage increases, the measurement error of the difference expand. Contradistinction for the current error shown in Figure 7.

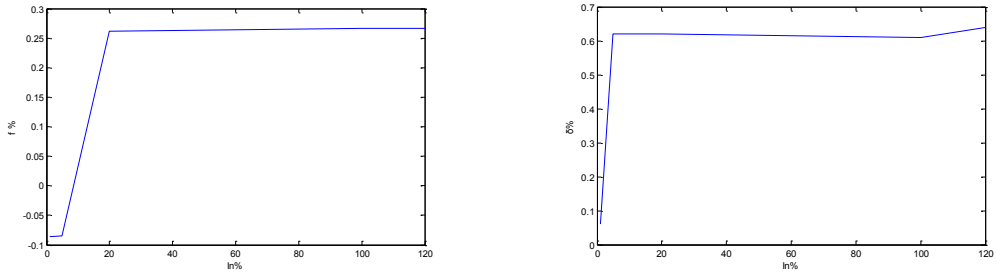

(a) The difference of ratio error curve (b) The difference of phase error curve

Fig.7 The current error curves between single-phase and three-phase method

It can be seen when the primary current is small, the gap between single-phase and three-phase method is small, but as the primary current increases, the measurement error of the difference expand, and tends to a constant value.

3. The comparison of interaction for current/voltage

Due to the voltage/current transformer components are placed together in the combined three-phase transformer ,so that the primary voltage/current changes will have an impact on the response of the transformer. When the primary current is 20% In, 100% In, 120% In, the voltage measurement error shown in Figure 8.

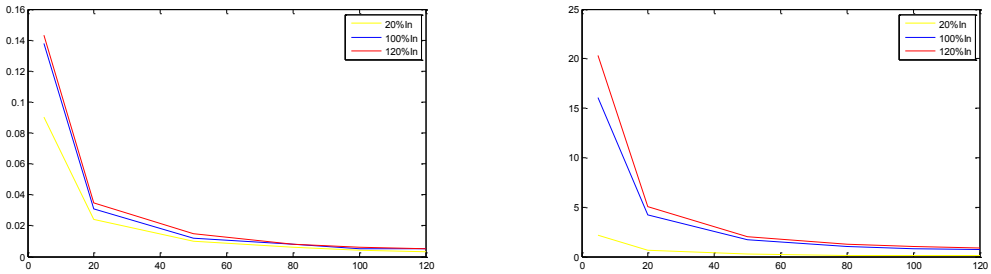

(a) The difference of ratio error curve (b) The difference of phase error curve

Fig.8 Primary side current impact on voltage measurement

The results show that, with the primary current increases, the voltage error also increase while in different current . but with the increase of voltage , the impact of that is reduced ,so the primary current is greater impact on voltage measurements for small ranges.

When the primary voltage is 10% Un, 80% Un, 100% Un, its current measurement error shown in Figure 9.

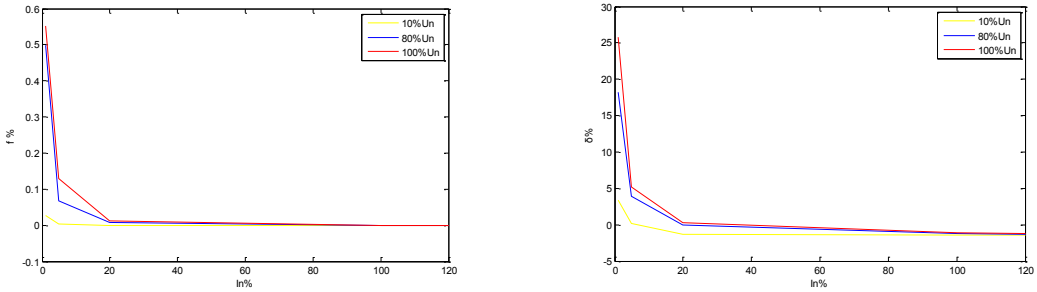

(a) The difference of ratio error curve (b) The difference of phase error curve

Fig.9 Primary side voltage impact on current measurement

As can be seen, with the primary voltage increases, the current also increase while in different voltage, along with the impact of a rising current weakened, so the primary voltage is greater impact on current measurements for small range.

Conclusion

To order to study the three-phase combined transformer calibration method error, Based on the research of the combined transformer error factors and single-phase method, three-phase validation method, through the three-phase transformer calibration platform, transformer secondary induced voltage, single-phase and three-phase methods error, and the influence of three-phase transformer primary voltage/current were tested, the results showed that the use of single-phase method, three-phase combined transformer calibration exist big error, and three-phase transformer primary voltage and current interaction is obvious in a small-scale, so as to carrying out a three-phase combined transformer accurate calibration work, it need to use three-phase method to validate that ensure the energy trade fair settlement impartiality.

References

[1] Chen Wei .Error formula derived in three-phase voltage transformer V / V wiring [J] .Science and Wealth, 2010 (002): 17-18.

[2] Weng lei. Three-phase three-wire meterting circuit voltage transformer secondary voltage drop calculation method [J]. Insulation materials, 2008, 41 (4): 65-66.

[3] Jiang Wei, Yang Huayun, Jiang Bo.Research on three-phase calibration method of HV three-phase combined transformer and its implemention [J] Electrical Measurement & Instrumentation, 2011, 48 (7): 46-49.

[4] Zhang Youshun, Feng Jinggang. Energy Measurement Basis [M]. China Metrology Publishing House, 2002.

[5] WU anlan.Energy metering basis and new technology [M]. China Water Power Press, 2004.

[6] 2004, JB/T10432. Three-phase combined transformer [S].

Advanced Materials Research Vols. 986-987 (2014) pp 1826-1832

doi:10.4028/www.scientific.net/AMR.986-987.1826

Implementation of Single Phase-Locked Loop based on FPGA and Its Application in SVC

Yujie Pei, Yunshan Zhang, Jianguo Xu, Jinglong Mu, Lei Zhang, Pin Dong, Bo Cong, Shuhan Wang

Fushun Power Supply Company, Liaoning Electric Power Company Limited, State Grid, Fushun, 113008, China

Rongxin Power Electronic Co.,Ltd, Anshan,114051,China

15842399663@163.com

Keywords: single phase-locked loop; three-phase unbalance; RTDS; FPGA; adaptive sampling

Abstract. Whereas three-phase phase-locked loop could not get accurate phase position under three-phase unbalanced condition of the power grid, the design of single phase-locked loop is implemented in the principle of single phase-locked loop, based on FPGA technology. the paper explains design difficulties of single phase-locked loop in detail, puts forward adaptive sampling scheme using single phase-locked loop under variable frequency, increases accuracy of SVC sampling system. And tests response speed of phase-locked loop via Real Time Digital Simulator for Power Systems(RTDS), through final verification in Fushun Lishizhai SVC Project, the design could meet system requirement for voltage phase accuracy.

Introduction

With the development of national economy, power load increases greatly, especially impact and nonlinear load capacity increases continuously, so waveform distortion occurs in the power grid. In general conditions, the use of SVC compensator is an internationally accepted method to solve the above-mentioned problems. In SVC control system, an important link is phase-locked loop, with respect to the disadvantages of three-phase phase-locked loop mentioned in the literature [1, 2], such as poor harmonic resistance, poor phase-locking effect in case of waveform unbalance, here single phase-locked loop is used to get frequency and phase of the power grid.

Single phase-locked loop is generally implemented by DSP technical software, but single core DSP could only perform sequential execution, to get three-phase position, the only way is to use DSP in different time, the system performance is restricted. the implementation of three-phase phase-locked loop algorithm based on FPGA hardware is a new design philosophy, realizes complete independency of single phase-locked loop in both algorithm and hardware, so phase-locked loop achieves very high performance. Finally, excellent compensation effect of actual SVC Project proves validity and high reliability of this theory[3-5].

Design of Single Phase-Locked Loop

(1) Operating principles of single phase-locked loop

Fig. 1 shows functional block diagram of single phase locking, the only input signal is single phase voltage, output is the tracked phase of this single phase voltage, this belongs to single phase locking technology, so the phase-locking technology may be used in three-phase unbalanced system for single phase locking, could eliminate the impact of three-phase unbalance on phase-locking.

In order to explain the operating principles of single phase-locked loop, it is assumed that Ua Phase voltage contains higher harmonic, the principle of single phase locking is analyzed below. Assuming grid voltage

$$Y(t)=\cos(\omega_0 t+\Phi_0)+\varepsilon_0 \quad (1)$$

Where: ω_0 is angular frequency of the power grid; Φ_0 is grid voltage phase; ε_0 is grid harmonics and detection error component;

Assuming the generated phase-locking tracking voltage signal to be:

$$y(t) = \sin(\omega_1 t + \Phi_1) \tag{2}$$

Where: ω_1 is angular frequency of the tracking signal; Φ_1 is the phase of tracking signal;

Then multiply Formula (1) by Formula (2) to get:

$$y(t) = \frac{1}{2}\{\sin[(\omega_0 + \omega_1)t + \Phi_0 + \Phi_1] - \sin[(\omega_0 - \omega_1)t + \Phi_0 - \Phi_1]\} + \varepsilon_0 \sin(\omega_1 + \Phi_1) \tag{3}$$

In case of consistent signal frequency, i.e. $\omega_0 = \omega_1$, Formula (3) may be simplified as:

$$y(t) = \frac{\sin(2\omega_0 t + \Phi_0 + \Phi_1) - \sin(\Phi_0 - \Phi_1)}{2} + \varepsilon_0 \sin(\omega_0 t + \Phi_1)$$

$$= \frac{\sin(2\omega_0 t + \Phi_0 + \Phi_1)}{2} - \frac{\sin(\Phi_0 - \Phi_1)}{2} + \varepsilon_0 \sin(\omega_0 t + \Phi_1) \tag{4}$$

It may be seen from Formula (4) that, there are totally three components, the first component is 100Hz sinusoidal fluctuation component, the second component is DC component, the third is interference caused by high frequency harmonic. If a low pass filter is added on front end of PI regulator to filter out AC component, phase position may be locked accurately if there is any closed loop feedback. Since delay of digital filter will lead to delay of phase position, so phase correction link should be added.

The basic regulation process: after input voltage signal is multiplied by tracking sinusoidal signal, the product is fed to filter input terminal to get ΔE1 after low-pass filtering, after phase inversion, it is fed into digital PI regulator, if the phase of tracking signal is lagged behind input grid voltage signal, digital PI regulator outputs higherΩ value, and finally tracks the grid phase. If the phase of tracking signal is ahead of the phase of grid voltage signal, digital PID regulator outputs lowerΩ value, and finally tracks the grid phase. When the system becomes stable after regulation, ΔE1 is zero,Ω value remains unchanged, the phase of tracking signal is the same as the phase of power grid.

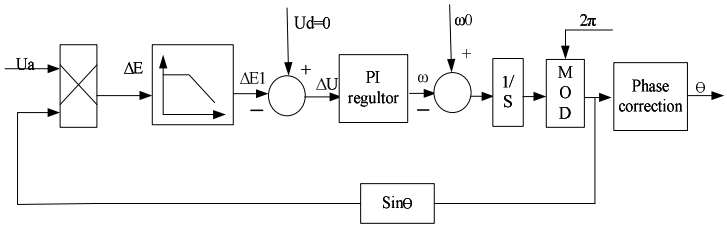

Fig. 1 Functional Block Diagram of Single Phase-Locked Loop Based on dq Transformation

(2) FPGA design and implementation of single phase-locked loop

1) Design of low pass digital filter module

In single phase-locked loop, the design of low pass digital filter is very important, because it not only filters out harmonic interference on input terminal of the system and higher harmonic generated by phase-locked loop itself, but also influences dynamic response performance of the system significantly. In order to increase response speed of the system, here second order low pass filter is designed. System transfer function of second order system is:

$$H(z) = \frac{b_0 + b_1 z^{-1} + b_2 z^{-2}}{a_0 + a_1 z^{-1} + a_2 z^{-2}} = \frac{y(n)}{x(n)} \tag{5}$$

The coefficients a_0, a_1, a_2, b_0, b_1, b_2 are determined by auxiliary design tool of digital filter, fdatool, in the matlab toolbox.

Transform Formula (5) to differential equation:

$$y(n) = \frac{b_0}{a_0}x(n) + \frac{b_1}{a_0}x(n-1) + \frac{b_2}{a_0}x(n-2) - \frac{a_1}{a_0}y(n-1) - \frac{a_2}{a_0}y(n-2) \tag{6}$$

Among the filters of given order, elliptic filter is the best way of approximation. Under equivalent performance requirements, it requires lower order than Chebyshev and Bunerworth, and its transition zone is narrow. Sampling frequency of digital filter *Fs*=10000Hz, cutoff frequency of low pass filter *Fpass*=15Hz, initial attenuation degree of amplitude *Apass*=1dB, cutoff attenuation degree of amplitude *Astop*=45dB, after parameters are generated by fdatool, substitute them into the above Formula (6) to get the Formula:

$$y(n) = 0.0056x(n) - 0.0111x(n-1) + 0.0056x(n-2) + 1.9896y(n-1) - 0.9897y(n-2) \quad (7)$$

2) Design of digital PID module

PID is a linear controller, difference comparison is performed for the given value and actual output value, then the differences constitutecontrolling quantities through proportional, integral, differential linear combinations for regulation control of the controlled object. the formula is shown in (8).

$$u(t) = K_p[e(t) + \frac{1}{T_1}\int e(t)dt + \frac{T_D de(t)}{dt}] \quad (8)$$

Where, K_p -- scaling factor; T_I -- integral time constant; T_D -- differential time constant;

The phase-locked loop algorithm implemented based on FPGA is a digital control system, discretization is required for the signals. Integral and differential links in the Formula (8) could not be used directly, may be used in FPGA programming only after discretization, firstly assuming sampling time as *Ts*, use *Ts* to substitute*t* in the formula, use accumulation instead of integral, increment instead of differential, the formula may be transformed to:

$$u(k) = K_p e(k) + K_i \sum_{j=0}^{k} e(j) + K_D[e(k) - e(k-1)] \quad (9)$$

Where, *k* -- sampling column No., *k*=0, 1, 2, ……; $u(k)$ -- output value of the *kth* PI controller; $e(k)$ -- deviation value of the *k*th input PI controller; $e(k-1)$ -- deviation value of the *k*-1 input PI controller; K_I -- integral coefficient; K_I -- differential coefficient;

Digital PID algorithm is generally divided into positional PID algorithm and incremental PID algorithm. Incremental PID means that the output of digital controller is merely increment *Δu(k)* of the controlling quantity. When incremental algorithm is used, the controlling quantity *Δu(k)* that controls the output of closed loop corresponds to the increment of the actuator position at this time, rather than to actual position of the actuator, so the actuator must have cumulative function for controlling quantity increment, so as to control the controlled object. Cumulative function of the actuator may be realized by hardware; or by software, for example, utilize routinization of the formula *u(k)=u(k-1)+Δu(k)*. the Formula (9) is the calculation formula of positional PID algorithm, output value of positional PID algorithm is actual position of the actuator, in case of some system faults such as program fleet, substantial transformation of $u(k)$ will lead to huge change of the actuator, might cause accident on site. In order to guarantee more stable and safe system, PID algorithm of single phase-locked loop adopts incremental algorithm structure.

The incremental algorithm formula may be deduced from (9):

$$u(k-1) = K_p e(k-1) + K_i \sum_{j=0}^{k-1} e(j) + K_D[e(k-1) - e(k-2)] \quad (10)$$

Subtract Formula (10) from the Formula (9) to get:

$$\Delta u(k) = K_P[e(k) - e(k-1)] + K_I e(k) + K_D[e(k) - 2e(k-1) + e(k+1)] \quad (11)$$

Therefore, *U(k)* may be calculated according to the formula *u(k)=u(k-1) +Δu(k)*, i.e.regulation output of PID controller. In VHDL language programming design, in order to increase running speed of the algorithm, here proportional, integral, differential parts have their own multiplier and adder etc, without resource sharing, could save resources compared common multiplier module. Its structure realization method diagram is shown in Fig.2.

As shown in Fig. 1, single phase-locked loop only uses proportional integral link, we just need to set *kd* parameter in Fig. 2 to zero in the implementation based on FPGA.

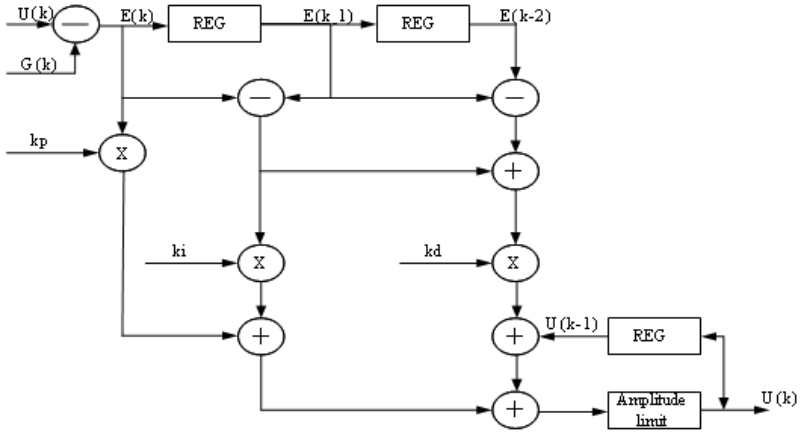

Fig. 2 Hardware Implementation Diagram of PID Algorithm

3) FPGA implementation of single phase-locked loop

Firstly three-phase voltage signal becomes sinusoidal signal with effective value between -5V and +5V through PT transformer and conditioning circuit. In order to further eliminate interference and protect internal controller, analog signal should be isolated, then the signal should be regulated to 0-5V signal and fed to AD10664 A/D converter, FPGA controls the work of AD chip, takes samples of AB, BC,CA three-phase voltage in turn.

The function board card for realizing phase-locking function and sending trigger pulse is shown in Fig.3, of which FPGA chip uses Alter EPM3C10IEE7 chip, the chip has 10000 gate logic units, maximum running speed is 300MHz, belongs to industrial grade chip, operating temperature is -40°C to 85°C.

Now, the prevailing hardware description languages include VHDL and verilog, although verilog language is easy to learn, but its syntax is not rigorous, might cause program error, and the reason might not be known for a long time, it is more suitable for describing some logic circuits on bottom layer, but for complicated algorithm description, VHDL language has its advantages, for example, it could define data type at will, so the program becomes more free. Syntax of VHDL language is rigorous, thus shortens the development, with VHDL language, work efficiency will increase greatly.

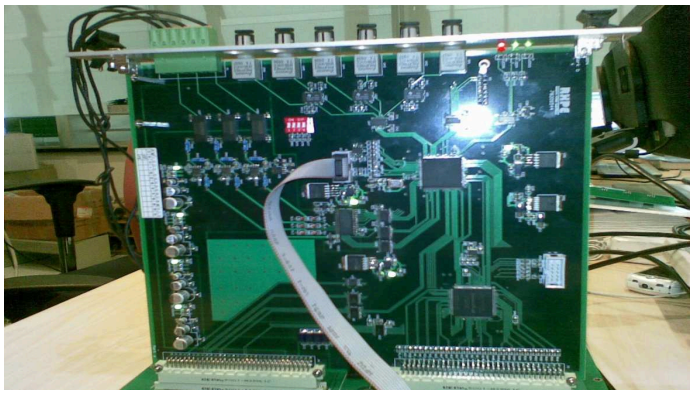

Fig. 3 Function Board Card Diagram of Phase-Locked Loop and Trigger Pulse

(3) Experimental result of single phase-locked loop

In actual test, power system RTDS(Real Time Digital Simulation) feeds three-phase synchronous voltage to the board card, after board card locks the phase position, it generates square signal, and feeds square wave back to the RTDS terminal, RTDS sends data to the software at PC terminal via network to observe the waveform. The oscillogram of phase tracking is shown in Fig.4, red refers to synchronizing signal, black square wave refers to the phase square wave locked by single phase-locked loop, high level rising edge represents 0 °, high level falling edge represents 180°.

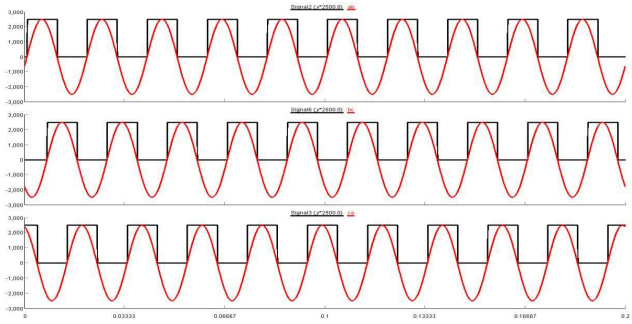

Fig. 4 Operating Oscillogram Sampled by PC Software

After the input of grid voltage signal Uab, phase changes 10 ° suddenly at the moment of 0.004166s, its simulation tracking waveform is shown in Fig.6, it may be seen by observing Uab phase in the figure that, phase tracking and locking is completed one cycle after the sudden change of phase position.

After input of grid three-phase voltage signal, frequency changes suddenly from 50Hz to 45Hz at the moment of 0.004166s, its simulation tracking waveform is shown in Fig.7, it may be seen by observing three-phase in the figure that, frequency phase tracking and locking is completed 4 cycles after the sudden change of frequency.

After input of grid three-phase voltage signal, frequency changes suddenly from 50Hz to 55Hz at the moment of 0.004166s, its simulation tracking waveform is shown in Fig.8, it may be seen by observing three-phase in the figure that, frequency phase tracking and locking is completed 4 cycles after the sudden change of frequency.

It may be seen from Fig. 5 and Fig. 6, phase-locking requirement may be met despite of phase jump, frequency increase or decrease.

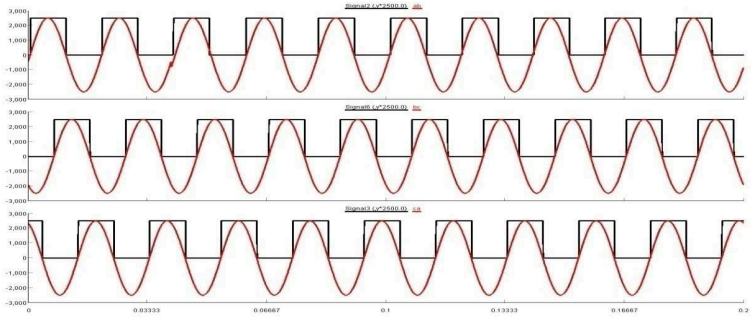

Fig. 5 Wave Tracking Pattern of *Ua* Phase in Case of Sudden Change of 10 ° at 0.004166s

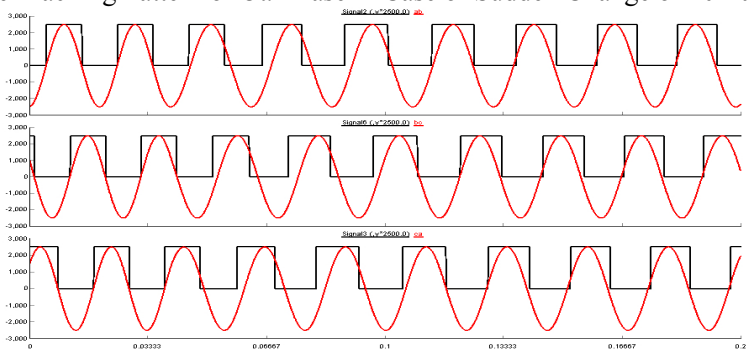

Fig. 6 Wave Tracking Pattern in Case of Sudden Change From 50Hz to 45Hz at 0.004166s

Application of single phase-locked loop

Since huge surplus exists in board card resource, SVC pulse triggering function is made on phase-locked loop board card, after algorithm control board calculates trigger angle, it sends the angle value to phase-locked loop board card, board card will compare the received trigger angle value with its own locked phase value, and send out correct 6-way phase trigger pulse, could reduce program cycle period of algorithm control board. These functions are implemented by VHDL hardware language, could increase stability of SVC control system greatly.

(1) Use single phase-locked loop technology to realize adaptive sampling

Standard frequency of power system in China is 50Hz, normal standard frequency of power system is specified as 50Hz±0.2Hz, when system capacity is low, it may be broadened to 50Hz±0.5Hz. For 128-point Fourier transform, sampling time is generally set to 20ms/128, when grid frequency changes slightly, the error of effective voltage, current values calculated from Fourier transform is small, the impact on the calculation of reactive compensation quantity is almost neglectable. But when grid capacity is low, grid frequency changes greatly on some sites, up to 45.5-55.5Hz, large reactive error is generated in calculation, brings about difficulty to the tracking compensation of reactive power.

In order to adapt to large changes of grid frequency, get better compensation effect, the SVC controller for Fushun Lishizhai 66 kV Substation adopts adaptive frequency technology (as adaptive synchronous sampling module in Fig. 7). After single phase-locked loop locks the phase, square signal synchronous with the power grid is generated, master control board captures this signal, corrects sampling frequency of the analog quantity required for Fourier calculation, then calculates effective values of the voltage and current accurately, adapts well to the site environment of great frequency changes. In practical application reactive power compensation value may be calculated quickly and accurately, could meet special requirements of large frequency changes, quick load changes on site, achieve excellent application effect.

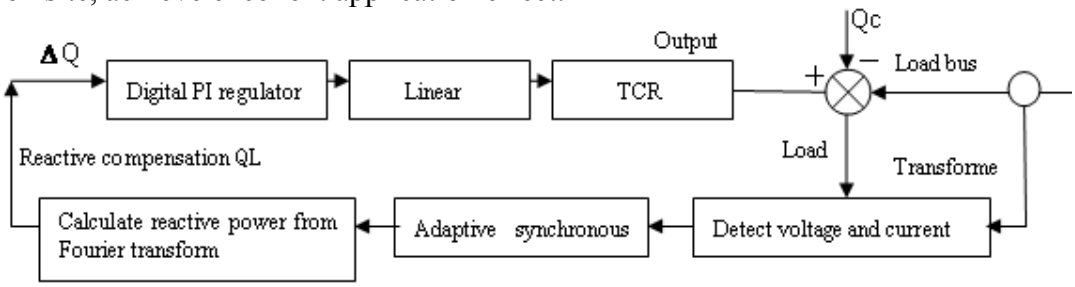

Fig. 7 TCR Control Flow Chart

(2) Use single phase-locked loop technology to improve power grid unbalance compensation

If grid voltage is unbalanced, grid voltage consists of three parts, namely, positive sequence component, negative sequence component and zero sequence components. Phase-locked loop tracks the phase of positive sequence component of fundamental wave, if traditional three-phase phase-locked loop is used, error will be introduced. Although control system calculates the reactive power to be compensated for each phase, however, since phase deviation exists in phase-locking result, the system always could not compensate unbalanced current of the system. Even wrong compensation might occur; system unbalance is enlarged, and leads to heating or over current of main transformer.

If single phase-locked loop is used, it may lock the phase accurately, provides reliable trigger reference for the system, SVC may distribute three-phase reactive current and active current in a balanced way according to the split phase compensation principle.

Conclusion

This paper develops single phase-locked loop based on FPGA, proves that the phase-locked loop could meet real time varying conditions of frequency and phase through RTDS test verification in power system. And utilizes the phase-locked loop technology to improve SVC analog quantity sampling algorithm, increase control accuracy, enhance stability of the power grid. the successful application of single phase-locked loop technology provides technical support for great development of single-phase electrical equipment in the future.

References

[1] Sang-Joon Lee, Jun-Koo Kang, Seung-Ki Sul.A New Phase Detecting Method for Power Conversion Systems Consid-ering Distorted Conditions in Power System[A].Industry Applications Conference, Conf. Record of the IEEE'99, 1999: 2167-2172.

[2] Shu Zeliang, Guo Yuhua, Tang Jian. Implementation of Three-Phase Phase-Locked Loop Based on FPGA [J]. Power and electronic technology, 2005, 39(6): 126-128.

[3] Wu Bo, Guo Yuhua, Wen Yuliang. the Improvement of Single-Phase Power Phase-Locked Loop and Its Implementation Based on FPGA [J]. Power and electronic technology, 2008, 42.

[4] Hong-Seok Song, KWanghee Nam, Peter Mutschler.Very Fast Phase Angle Estimation Algorithm for a Single –Phase System Having Sudden Phase Angle Jumps [A].IEEE Industry Applications Conference, Con. Record of the 2002 37th IAS Annual Meeting, 2002: 925-937.

[5] Petar mdjuric, Miroslav mbegovic, Milos doroslovaeki. Instantaneous Phase Tracking in powernetworks by Demodulation [J].IEEE Trans. On Instrumentation and Measurement, 1992: 963-967.

Advanced Materials Research Vols. 986-987 (2014) pp 1833-1836

doi:10.4028/www.scientific.net/AMR.986-987.1833

Realization of OTA-based grounded gyrators using nodal admittance matrix expansion

Yongan Li[1, 2, a] and Rui Cao[3,b]

[1]Department of Electronic Engineering, Shaanxi Institute of International Trade & Commerce, Xianyang 712046, China

[2]School of Physics and Electronic Engineering, Xianyang Normal University, Xianyang 712000, China

[3]Xi'an High Voltage Apparatus Research Institute Co., Ltd. Xi'an 710077, China

[a]email: lya6189@sohu.com, [b]email: cradam@sina.com

Keywords: Grounded gyrator, OTA, Nullor-mirror element, Nodal admittance matrix expansion

Abstract. The paper presents sixteen nullor-mirror representations for the reported grounded gyrator by means of sixteen alternative NAME equations of the gyrator. Moreover, only four alternative grounded gyrators employing OTAs have been received. Having used canonic number of components, the circuits are easy to be integrated and their parameters can be tuned electronically through tuning bias currents of OTAs. The MULTISIM simulation results have been included to verify the theoretical predictions.

I. Introduction

Recently, a symbolic framework for systematic synthesis of linear active circuit was presented [1–8]. This method, called nodal admittance matrix expansion (NMAE), is very useful in generation of a series of novel circuits. Fortunately, the literatures on current conveyor (CCⅡ) and inverting current convey (ICCⅡ) based gyrators [1], oscillators [2–3] and filters [4] have explained this viewpoint well. However, most of circuits mentioned in earlier works are based on the CCⅡ or ICCⅡ. Very recently, it has been found that NAME method is generalized to other active devices, for instance, operation transconductance amplifier (OTA) [5–6], but the reported circuits include only floating gyrators and T–T filters. It is necessary that using NAME method synthesizes OTA-based grounded gyrators circuits.

II. Nullor-mirror realizations of grounded gyrators

The NAM for grounded gyrators is given by [1]

$$Y = \begin{bmatrix} 0 & G_1 \\ -G_2 & 0 \end{bmatrix}, \tag{1a}$$

$$Y = \begin{bmatrix} 0 & -G_1 \\ G_2 & 0 \end{bmatrix}. \tag{1b}$$

Transposing of Eq. (1a) and Eq. (1b) respectively yields the follow port admittance matrix:

$$Y = \begin{bmatrix} 0 & G_2 \\ -G_1 & 0 \end{bmatrix}, \tag{1c}$$

$$Y = \begin{bmatrix} 0 & -G_2 \\ G_1 & 0 \end{bmatrix}. \tag{1d}$$

Starting from Eq. (1a), following successive NAM expansion steps with the added nullor-mirror elements represented by bracket notation, and applying all possible combinations of the added nullor-mirror elements, will yield the following alternative equations, as shown in Eq. (2).

$$Y=\begin{bmatrix}0&0&0&0\\0&0&0&0\\0&0&G_1&0\\0&0&0&G_2\end{bmatrix}=\begin{bmatrix}0&0&0&0\\0&0&0&0\\0&0&G_1&0\\0&0&0&G_2\end{bmatrix}=\begin{bmatrix}0&0&0&0\\0&0&0&0\\0&0&G_1&0\\0&0&0&G_2\end{bmatrix}=\begin{bmatrix}0&0&0&0\\0&0&0&0\\0&0&G_1&0\\0&0&0&G_2\end{bmatrix} \quad (2)$$

The nullor-mirror equivalent circuits by Eq. (2) are given in Fig. 3(a)-(d) in the literature [1].

Starting from Eq.(1b), following successive NAM expansion steps, and applying all possible combinations of the added nullor-mirror elements, will yield the expanded equation Eq.(3).

$$Y=\begin{bmatrix}0&0&0&0\\0&0&0&0\\0&0&G_1&0\\0&0&0&G_2\end{bmatrix}=\begin{bmatrix}0&0&0&0\\0&0&0&0\\0&0&G_1&0\\0&0&0&G_2\end{bmatrix}=\begin{bmatrix}0&0&0&0\\0&0&0&0\\0&0&G_1&0\\0&0&0&G_2\end{bmatrix}=\begin{bmatrix}0&0&0&0\\0&0&0&0\\0&0&G_1&0\\0&0&0&G_2\end{bmatrix} \quad (3)$$

The nullor-mirror equivalent circuits for the gyrator described by Eq. (3) are given in Fig. 1.

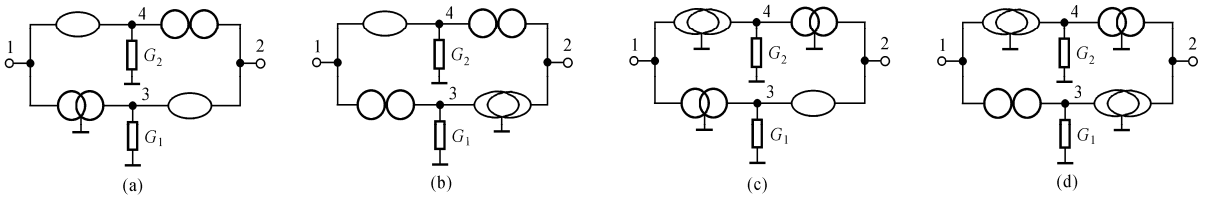

Fig. 1 Four nullor-mirror realizations for the gyrators described by Eq. (3).

Again, starting from Eq. (1c), and applying all possible combinations of the added nullor-mirror elements will yield the expanded equations given in Eq.(4).

$$Y=\begin{bmatrix}0&0&0&0\\0&0&0&0\\0&0&G_1&0\\0&0&0&G_2\end{bmatrix}=\begin{bmatrix}0&0&0&0\\0&0&0&0\\0&0&G_1&0\\0&0&0&G_2\end{bmatrix}=\begin{bmatrix}0&0&0&0\\0&0&0&0\\0&0&G_1&0\\0&0&0&G_2\end{bmatrix}=\begin{bmatrix}0&0&0&0\\0&0&0&0\\0&0&G_1&0\\0&0&0&G_2\end{bmatrix} \quad (4)$$

The nullor-mirror equivalent circuits described by Eq. (4) are given in Fig. 3 (e)-(h) in the literature [1].

Similarly, starting from Eq. (1d), and applying all possible combinations of the added nullor-mirror elements will yield the the following the expanded equations:

$$Y=\begin{bmatrix}0&0&0&0\\0&0&0&0\\0&0&G_1&0\\0&0&0&G_2\end{bmatrix}=\begin{bmatrix}0&0&0&0\\0&0&0&0\\0&0&G_1&0\\0&0&0&G_2\end{bmatrix}=\begin{bmatrix}0&0&0&0\\0&0&0&0\\0&0&G_1&0\\0&0&0&G_2\end{bmatrix}=\begin{bmatrix}0&0&0&0\\0&0&0&0\\0&0&G_1&0\\0&0&0&G_2\end{bmatrix} \quad (5)$$

The nullor-mirror equivalent circuits described by Eq. (5) are given in Fig. 2.

It should be noted that if the position of the nodes 1, 2 is interchanged, Fig.1 are the same as Fig.3 (e) –(h) in the literature [1], and Fig.2 are the same as Fig.3 (e)–(h) in the literature [1].

Ⅲ. Realization of OTA-based grounded gyrators

From Fig. 3 (a)-(d) in the literature [1] and using the nullor-mirror descriptions for SISO-OTA [11-12], four alternative realizations for the gyrators can be achieved, as shown in Fig. 3.

Similarly, From Fig. 1, four alternative realizations for the gyrators can also be realized, as shown Fig. 4.

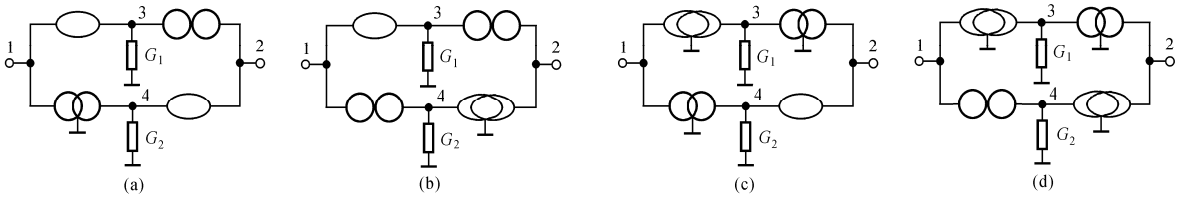

Fig. 2 Four nullor-mirror realizations for the gyrators described by Eq. (3).

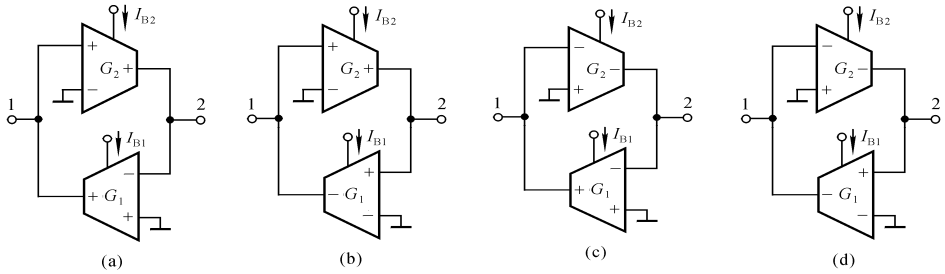

Fig. 3 OTA-based realizations for Fig. 3 (a)-(d) in the literature [1].

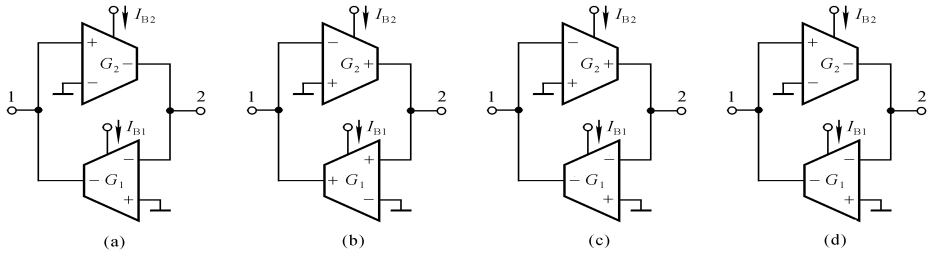

Fig. 4 OTA-based realizations for Fig.1

From Fig. 3 (e)-(h) in the literature [1], four alternative realizations for the gyrators can be achieved; these circuits are the same as Fig.3 if the position of G_1 and G_2 is interchanged.

From Fig. 2, four alternative realizations for the gyrators can also be realized; these circuits are the same as Fig. 4 if the position of G_1 and G_2 is interchanged.

It can be seen that both Fig.3 and Fig.4 are essentially the same if the position of G_1 and G_2 is interchanged and the position of note 1 and note 2 is also interchanged. So the derived gyrators with a minimum number of active components possess four forms.

Ⅳ.Simulation results

The workability of the derived the gyrators has been verified by realizing a band pass filter. Fig. 5 shows the schematics for the realization of the second-order band-pass filter that employs the simulated grounded inductor based on Fig. 3(a), whose value is given by

$$L = \frac{C_L}{G_1 G_2} = \frac{4V_T^2 C_L}{I_{B1} I_{B2}}. \tag{6}$$

The transfer function realized by this configuration is given by

$$\frac{V_o}{V_i} = \frac{s/RC}{s^2 + s/RC + 1/LC}. \tag{7}$$

Here, V_i is input voltage and V_o is output voltage. The pole frequency and the quality factor are as follows:

$$f_o = \frac{1}{2\pi\sqrt{LC}} = \frac{I_B}{4\pi V_T C}, \quad Q = \frac{R}{2V_T} I_B. \tag{8}$$

Here, I_{B1}=I_{B2}=I_B. If R=1kΩ, C=C_L=1nF, and I_B=104μA, 208μA, and 416μA, from Eq. (8), the design value for f_o is 0.318MHz, 0.637MHz, and 1.274MHz; the design value for Q is 2, 4, and 8. The simulation result is shown in Fig.6.

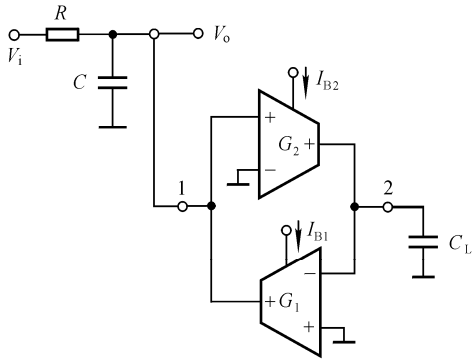

Fig. 5 Second-order band-pass filter using Fig. (3a).

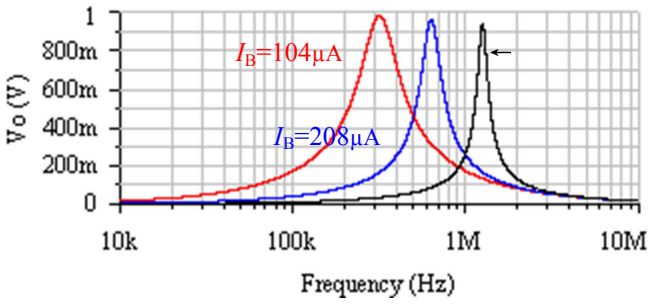

Fig. 6 Band-pass responses for different values of I_B.

V.Conclusions

This is the first paper in which the use of the NAME method in the synthesis of OTA based grounded gyrators is considered. The main feature of the paper is making use of systematic design method to obtain all novel circuits. The results of circuit simulations are in agreement with theory.

References

[1] A. M. Soliman: Generation of generalized impedance converter circuits using NAM expansion. Circuits, Systems, and Signal Processing, Vol. 30, No. 5, (2011), p.1091–1114.

[2] A. M. Soliman: Generation of current conveyor based oscillators using nodal admittance matrix expansion. Analog Integrated Circuits and Signal Processing, Vol. 65, No. 1, (2010), 43–59.

[3] A. M. Soliman: Generation of CC Ⅱ and ICC Ⅱ based Wien oscillators using nodal admittance matrix expansion. AEÜ–International Journal of Electronics and Communications, Vol. 64, No. 10, (2010), p. 971–977.

[4] A. M. Soliman: Generation of Kerwin-Huelsman-Newcomb biquad filter circuits using nodal admittance expansion. International Journal of Circuit Theory and Applications, Vol. 39 No. 7, (2011), p. 697–717.

[5] Y. A. Li: NAM expansion method for systematic synthesis of OTA-based floating gyrators. AEÜ–International Journal of Electronics and Communications. AEÜ–International Journal of Electronics and Communications, Vol. 67, No.4, (2013), p. 289-294

[6] Y. A. Li: On the systematic synthesis of OTA-based Wien oscillators. AEÜ–International Journal of Electronics and Communications, Vol. 67, No. 9, (2013), p.754–760.

Advanced Materials Research Vols. 986-987 (2014) pp 1837-1841

doi:10.4028/www.scientific.net/AMR.986-987.1837

Reform of Excitation System on the Domestic 600MW Subcritical Turbine generator Unit

Han Zhiling [1,2]

[1]Chengde Petroleum College, Chengde 067000, China

[2]Hebei Province Instrument Engineering Research Center,Chengde 067000,China

hanzhlcd@sina.com

Key Words: Excitation Regulator, Turbine Generator Unit, Undisturbed Switching, Reform

Abstract. Analog Excitation regulation system is applied in No.3 turbine generator unit of Harbin No.3 power plant, Huadian Energy Group, and the system has several problems such as high failure rate, poor regulating performance and low level automation. As a solution, the static self shunt excitation system is used to replace the analog excitation regulation system, UNITROL 5000 all-digital excitation system is adopted. With specific field situation, the paper introduces the structure and application of the system in details. Compared with the conventional A.C. exciting system, the all-digital excitation system has effectively improved the stability and reliability of the generator, with the advantages of more flexibility of the start-up modes and undisturbed switching. It is also reliable and convenient for the switching of PSS additional regulation unit.

Introduction

No.3 turbine generator unit of Harbin No.3 power plant of Huadian Energy Group is the first domestic product of 600MW subcritical unit, optimized on the basis of imported technique, it is produced by Harbin Electric Machinery Company Limited(HEC) and belongs to the type of QFSN-600-2YH water-hydrogen-hydrogen cooling turbine generator unit.

The original excitation system is a brushless excitation system that consists of the alternating current exciter, rotating rectifier, auxiliary exciter, silicon controlled rectifier and excitation regulator, which belongs to the category of A.C. exciting system.

Generator rotor, main exciter rotor and pilot exciter rotor of the excitation system rotate on the same axis, the excitation regulator is HEC's analog product HWTA-60, the regulator's principle is complex, regulating performance is low, and spare parts can be nowhere purchased later, so the first transformation for the A.C. exciting system is carried out in 2001, nonlinear excitation regulator of GEC-1 controlled by microcomputer is used to replace the former excitation regulator[1]. Although the GEC-1 regulator adopts advanced nonlinear control principle and all-digital microcomputer control technology and improves the level of automation to a certain extent, but because there are too many rotating parts in the excitation system, possibility of fault is increased. The excessive vibration of the generating unit is easy to happen because of the long shafts and so many bearing seats.

With the development of the technology in electric power system, the defects of poor stability of unit's operation and low level of automation are exposed increasingly, the defects mentioned above make the generator unit fail to adapt to requirement of equipment's technical requirement. In order to ensure the safety and stability of operation of the unit and the grid, the second transformation for the A.C. exciting system is carried out, the static self and shunt excitation system is used to replace the former A.C. exciting system, the UNITROL 5000 excitation regulating device is adopted, the system is produced by Swiss company ABB and assembled by Harbin Electric Machinery Company Limited.

The Composition of the Static Self and Shunt Excitation System

After the alteration，the static self and shunt excitation system of No.3 turbine generator unit is made up mainly of excitation transformer, Silicon Controlled Rectifier, automatic voltage regulator(AVR), excitation device, de-excitation and overvoltage protection devices, assist devices

(including monitoring device, protecting device, alarming device, etc) and other parts (Figure 1). The equipment includes three single-phase dry-type transformers; a cabinet with automatic voltage regulator (AVR) of ABB's UNITROL®5000; five rectifier cabinets and a set of de-excitation switchgear.

1.1 Excitation Transformer

The excitation transformer is a three-phase transformer composed by the same three single-phase dry-type transformers, its high voltage side is connected with the generator through isolated-phase enclosed bus, and the low voltage side is connected with the silicon controlled rectifier through enclosed bus. According to DL/T 843-2010, the capacity of excitation transformer should be able to meet forced excitation, heating(including the higher harmonics of load current component of the rectifier), and 130% the terminal rated voltage when turbine generator has no-load test, also requires it has a certain degree of overvoltage and internal short circuit capability.Thus, ZDCB9-2200/20 of single-phase transformer is adopted, its main parameters in table 1.

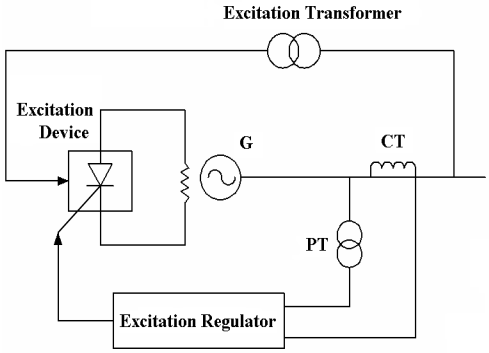

Fig. 1: Principle of static self and shunt excitation system of the generator

Table 1: Main parameters of the excitation transformer

Type	ZDCB9-2200/20
Rated Capacity (kV·A)	3×2200
Allowable Temperature of the Winding	100℃
Rated Voltage (kV)	11547/890
Cooling Method	AN
Rated Current (A)	190.5/2472
Connection Mode	Yd11
Percent of Short-circuiting Voltage	8.06%
Insulation Level	F

Electrostatic shielding is occurred between primary winding and secondary winding in the excitation transformer, V-A characteristic of the transformer has fine linearity. Current transformers are installed in the high and low voltage side of the excitation transformer, their accuracy grades are 5P20/5P20/0.5, mainly used in relay protection and measurement.

1.2 Excitation Regulator

The UNITROL 5000 microcomputer excitation regulator produced by ABB Switzerland Ltd. is used. in excitation regulator, The regulator belongs to double automatic channel excitation regulation system[2], including two same channels of automatic voltage regulator, each channel has a backup controller with its own gate pulse trigger. The electronic components of the voltage regulator is done with redundant design, and the gate pulse trigger with double redundant design. Each automatic channel and backup controller will switch to the adjustment of excitation current in manual operation.

Automatic voltage regulator(AVR), adopting digital micro-processor technology, has the function of obtaining a stable voltage, distributing rationally reactive power and improving the stability of power system. And at the same time, AVR can adjust slightly and enhance the characteristics of the generator transient stability.

Automatic regulating units of constant voltage, constant reactive power and constant power factor are installed in AVR, each can be switched without disturbance, and operator can choose any above ways to regulate. The AVR has additional function units of overexcitation limit, overexcitation protection, low excitation limit, low excitation protection, PT break, the voltage / frequency ratio limit, power system stabilizer (PSS) etc.

1.3 Silicon Controlled Rectifier

In the silicon controlled rectifier, three-phase alternating input current is changed to direct current, then the direct current is regulated by the AVR and output. Silicon controlled rectifier with the inverter capacity is a circuit of three-phase full-bridge, and its main parameters are shown in table 2.

Table 2: Main parameters of the Silicon Controlled Rectifier

Type	HUEL412322
Rated Reverse Peak Voltage (V)	4200
Rated Frontage Average Currency (A)	2900
Range of Voltage Automatic Regulation (%)	20-110
Cooling Method	forced air cooling
Regulating Accuracy (%)	±0.5
Rated Current (A)	1750
Number of Panels	5
Range of Voltage Manual Regulation (%)	20-130
Manufacturer	ABB

The silicon controlled rectifier has 5 parallel branches, the branches are respectively installed in the five rectifier cabinets, rectifier bridge's number is designed according to the N-2 mode, if one of the rectifier cabinets is out of service due to fault and trigger automatic alarm, the other cabinets can meet the demands of various operating conditions including 1.1 times of the rated excitation and forced excitation, AVR can limit forced excitation when two cabinets are out of service, so the generator can run continuously in rated condition.

The current-sharing coefficient of the rectifier cell is no less than 0.90 by using intelligent load sharing technique in rectifier.

1.4 Excitation Device

Excitation device provides excitation power supply, because the excitation transformer can't provide it before the generator's voltage established. excitation power supply comes from the 380V emergency power supply. The parallel current of transformer and rectifier bridge's current and DC from the automatic excitation regulator, is sent to the generator rotor.

The UNITROL 5000 can start excitation with residual voltage under normal condition. The control loop can work normally when the input voltage of the rectifier bridge lies between 10V-20V. If the generator voltage is greater than or equal to the above value, the residual voltage excitation is used, continuous triggered silicon controlled rectifier bridge, the voltage is raised to rated value. If the input voltage of the rectifier bridge is less than 10V~20V, excitation circuit can switch on automatically, thus provides input voltage for the rectifier bridge, so that AVR can start work reliably. When real voltage of the generator reaches 10% times of the rated voltage, the rectifier bridge can work normally, thus the excitation breaker is out of service automatically, process of soft excitation begins, and raises the generator's real voltage to rated voltage. Control and monitor during the entire excitation process is realized by the software AVR, 'excitation input' or 'excitation fault' can be seen as remote signals.

1.5 De-excitation and Overvoltage Protection Devices

The function of the de-excitation and overvoltage protection devices is to cut off power supply of excitation, extinguish excitation, inhibit positive and reverse overvoltage of the rotor, or protect the rotor when incomplete phase running occurs. The devices mainly consist of HPB60m-82S DC magnetic breaker, crowbar (trigger electronic board, avalanche diode, two SCRs connected in opposite phase), de-excitation resistor of non-linear silicon carbide, as shown in figure 2. After the magnetic breaker cut off, the obvious electrical isolation occurs between the excitation transformer

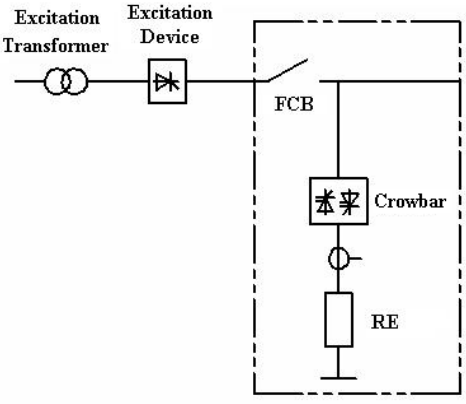

Fig. 2: De-excitation and Overvoltage Protection Devices

and the field winding. When the generator shuts down normally, excitation can be exit through cutting off the magnetic breaker or making the SCR bridge inverter; when the generator faults, excitation device receives the signal, magnetic breaker is taking off instantaneously, at the same time crowbar is connectted, the circuit of the generator magnetic field and the external controllable silicon disconnects, then connected into a circuit with nonlinear resistors. When the positive or reverse overvoltage of generator rotor loop has occurred, avalanche diode in the crowbar breaks down, then the controlled silicon is triggered, de-excitation resistor will be in series to the rotor circuit immediately.

Characteristics of the Reformed Excitation System

1.6 Improved Reliability of the Excitation System

Compared with the conventional A.C. exciting system, the self and shunt excitation system has no rotating parts, adopts the redundant structure in the design, and be able to replace the fault elements on-line[3], thus the rate of generator forced shut down because of the excitation system failure is not more than 0.25 times/year; forced removal rate of the excitation system is not more than 0.1%. Because of the controllable silicon electronic technology is used after the transformation of the excitation system, response speed of the control system has been further improved. the excitation system has the ability to bear overload for a moment, the multiple of forced excitation is greater than 2.0. When the generator terminal voltage drops to 80% of rated voltage, the system can still has the ability of 2 times of the forced excitation, the output current is not less than 1.1 times of the rated excitation's, and the forced excitation time allowed is 10 seconds.

1.7 Flexible Start-up Modes of the Excitation System

Start-up modes of the excitation system include automatic mode and manual mode. In automatic start-up mode, when the turbine speed is reaching to the rated speed, excitation control program runs automatically, first the magnetic circuit breaker is closed, second the AVR puts into operation, then the generator voltage is established, electro-hydraulic converter sends out the signal that the magnetic circuit breaker needs close, the control is automatically completed by the AVR, the operators need not any action. In manual mode, the operator is allowed to a series of manual control, operates 41E (ON), closes the magnetic circuit breaker, then the AVR puts into operation, and the generator voltage is established whose control is done automatically by the AVR, after the generator voltage established, 90R is operated manually to reach the matching value of the voltage.

After grid connected, the excitation system can work in AVR mode, automatically regulating the terminal voltage and reactive power of the generator. In addition, groups of regulating command from power plant can also be received and carried out.

1.8 Non-disturbance Switching Mode of the Excitation System

As mentioned before, the generator excitation system has two same main channels and two backup emergency channels in addition, as shown in figure 3.

In the two main channels, we can choose a channel as the operation channel. The backup channel always automatically tracks the operation channel. If the operation channel faults, then switch to the backup channel automatically.

Each main channel has two modes: 'automatic' and 'manual'. If faults are detected in automatic mode, the mode can be emergency switched to manual. When the generator operates in the limit allowable range, but the range is beyond the manual mode allowed, close manual channel tracking.

In addition to the two main channels, excitation system also provides two independent emergency channels (EGC). Emergency channel can only regulate the excitation current but can not regulate the generator voltage, the excitation current

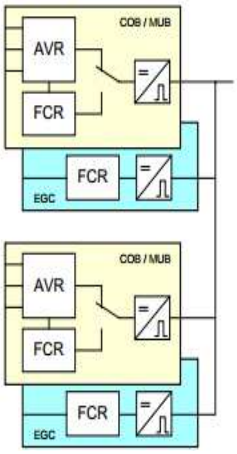

Fig. 3: Generator excitation system with two same main channels and two backup channels

regulator tracks the main channel automatically, when the main channel faults, switched automatically without disturbance. Manual switch from the main channel to the emergency channel can only be operated by excitation dedicated staff.

1.9 The Addition of Additional Regulation Unit-Power System Stabilizer(PSS) And the Improvement of the Dynamic Stability of the System

The static excitation regulators improve the response speed of the system, but reduce the dynamic performance of the system[4.5]. The power system stabilizer (PSS) is an additional function unit in the UNITROL 5000, which can effectively restrain the low-frequency oscillation of the power grid. The PSS posses the functions of automatic switching, manual switching, output limiting (limit value is ±5-±10% of per unit of the generator voltage), automatically out of service in fault etc. the PSS puts into use or exits according to the dispatcher's order, the conditions of putting into use are: (1) the excitation system of the generator tests well; (2) the working channels of the excitation automatic regulating normal, the backup channels tracking normal.

1.10 The Perfect Protection of the Excitation Transformer

New protection panel excitation transformer is added in the No.3 generator relay protection room, the panel has an upper and lower box, with the same two sets of protection device, the power source of protection were taken from 110V DC panels of No.8 and No.2 of main control room. The protection panel has current instantaneous trip protection, over-current protection, overload protection, rotor one-point grounding protection, rotor two points grounding protection, rotor overload protection, etc. various protection's input is realized respectively through the soft strap and yellow hard strap in the panel. During normal operation, only one set of the protection upper box or lower box of rotor one-point grounding puts into use, the other protecting straps put into use. literal light-emitting screens are added in the unit control room, including: (1) excitation transformer overload, (2) rotor overload, (3) rotor one point grounding fault, (4) rotor two points grounding fault, (5) excitation transformer protection failure or loss of power. The strap 1 and 2 of the magnetic breaker are added in the protection panels of the generator-transformer unit. quasi-synchronization device is changed from the double channel type ZZQ-3B of ACHENG Relay Factory to the microprocessor-based automatic type SDQ200 of Guodian Nanjing automation CO., Ltd..

Conclusion

During the renovation of the excitation system of No.3 turbine generator unit of Harbin No.3 power plant, the conventional A.C. excitation system is replaced by the static self shunt excitation system in which the advanced UNITROL 5000 excitation regulating device is adopted. Compared with the conventional A.C. exciting system, the excitation regulator has effectively improved the stability and reliability of the generator through using the latest technology of software and hardware, start-up modes are more flexible, switching mode realizes undisturbed, the PSS additional regulation unit is reliable for the switching, thus the quality of the excitation regulation is improved, a good result in the actual operation is obtained, the experiences of the technical transformation of excitation system for the same type unit are accumulated.

References

[1] Chen Zengji, Excitation System Reform of 600MW Generator Set in Huadian Energy Harbin Third Power, Harbin: Harbin University of Science and Technology(2007).

[2] ABB UNITROL®5000 user's manual, ABB (2000).

[3] YANG Xu, LIU Lirui, MO Yuying, Considerations in design and types election of static self and shunt excitation system for large and medium-sized steam turbine-generators, Guangdong Electric Power,1999,12(6): 19-24.

[4] Huang Yumin, Operational analysis of excitation system for large generator, East China Electric Power, 2005,33(3): 50-53.

[5] Wang Zhan, zhou Tong, Yang Feng, The Application of P. S.S in the Excitation System of 600MW Generator, Large Electric Machine and Hydraulic Turbine, 1999, (2):60-63.

Advanced Materials Research Vols. 986-987 (2014) pp 1842-1845

doi:10.4028/www.scientific.net/AMR.986-987.1842

Research on A Battery Balancing Method for Lithium-ion Battery Pack of Electric Vehicle

Yining Chen [1, a], Yu Gui[2, b] and Hong He [2, c]

[1] Power Management of Liaoning Provincial Government, Shenyang 110035, China;

[2] State Key Laboratory of Automotive Simulation and Control, Ji Lin University, Changchun 130022, China.

[a] cyn5853@163.com, [b]gy900621@163.com, [c] hhsaber1221@163.com,[d]

Key words: electric vehicle, Lithium-ion battery, battery inconsistencies, battery balancing

Abstract. As the key technology of the electric vehicle, more and more research on battery management system has been done. And the balancing technology is the important part of battery management system. In this paper, a multi-inductor balancing method based on the Buck-Boost topological structure is used to improve batteries' inconsistencies by obtaining parameters of the battery pack in real time. The proposed balancing method can improve batteries' inconsistencies so as to increase the capacity utilization rate of the battery pack and prolong the battery lifespan. And in this paper a series of bench experiments were done to examine the effectiveness of the balancing method.

Introduction

When the lithium-ion batteries which are connected in series and parallel are applied to electric vehicles, the performance of batteries in the string varies from each other since the initial difference, environmental temperature difference and capacity difference, which is called battery inconsistencies[1]. Because of battery inconsistencies, the performance of the battery pack is decided by the worst one, thus other better batteries could not work at 100% of their potential and the capacity of the pack decreases[2]. Moreover, battery inconsistencies may let the cells be prone to accelerated degradation, which would in some way affect the driving range and cost of the electric vehicle. An effective method to improve cell imbalance is to use the equalization system[3,4]. Battery equalization is actually one of the most important functions of battery management system (BMS), which would monitor the state of the battery pack in real time and start balancing according to certain strategy if needed. Thus a better capacity utilization rate and longer life cycle of the battery pack would be obtained, which are of importance to the electric vehicle.

Balancing Circuit

The balancing circuit principle is based on the Buck-Boost converter. The circuit transfers energy between adjacent batteries through the inductance. The schematic of balancing circuit is shown in Fig. 1.

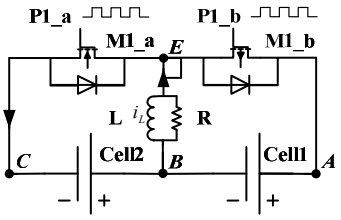

Fig.1. The schematic of balancing circuit

In this circuit, M1_a is a N-channel MOSFET and M1_b is a P-channel MOSFET. Both of them are used to control the energy transferring. P1_a and P1_b are PWM control signals. The balancing circuit of many batteries is connected by many circuits as Fig.1. In Fig.1, it assumes cell2 has higher energy than cell1.The energy transferring process can be divided into three stages:

(a) Cell2 discharges to inductance. In this stage, because cell2 has more energy, the drive signal of P1_a is active in order to conduct the MOSFET M1_a and the current flows as shown in fig.2(a). The electric energy is converted to magnetic energy, which is stored in the inductance L1. When M1_a conducts, the equivalent resistance of the circuit is R_{on}, which contains the resistance of PCB boards, the inductance resistance and the MOSFET conducting resistance. the zero state response equation for the first-order RL circuit is:

$$V_2 = R_{on} i_L + L\frac{di_L}{dt}, t = 0 \to t_{on} \quad (\tag{1}$$

The general solution of the equation is:

$$i_L = \frac{V_2}{R_{on}} - \frac{V_2}{R_{on}} e^{-t\frac{R_{on}}{L}} = \frac{V_2}{R_{on}}(1 - e^{-t\frac{R_{on}}{L}}), t = 0 \to t_{on} \tag{2}$$

Because the inductance saturation current should be greater than the inductive peak current, it need to know the inductive peak current I_P to choose inductor. The peak current at the end of this stage is:

$$i_P = \frac{V_2}{R_{on}}(1 - e^{-t_{on}\frac{R_{on}}{L}}) \tag{3}$$

(b) Inductance discharges to cell1.In this stage, After the MOSFET M1_a is turned off, the inductive current is not changed and decreases from I_P. Its direction is shown as the red arrows in fig.3. The inductive voltage is equal to the voltage of cell1,the MOSFET conducting voltage and the voltage of R_{off}. The inductance continues to discharge to cell1 till the diode of D1-a is no longer forward biased. The discharging current is:

$$i_L = (i_{peak} + \frac{V_1 + V_D}{R_{off}}) e^{-(t - t_{on})\frac{R_{on}}{L}} - \frac{V_1 + V_D}{R_{off}}, t = t_{on} \to t_{off} \tag{4}$$

(c) Resistance consumes the excess energy. After the second stage, the M1_b is equivalent to a capacitor C2, and the rest energy in the inductance very litter, which is consumed through the resistance R as shown in the fig. If there is no resistance to consume excess energy in the inductance for magnetic reset, the inductance would be magnetic saturation, which makes the inductance not work.

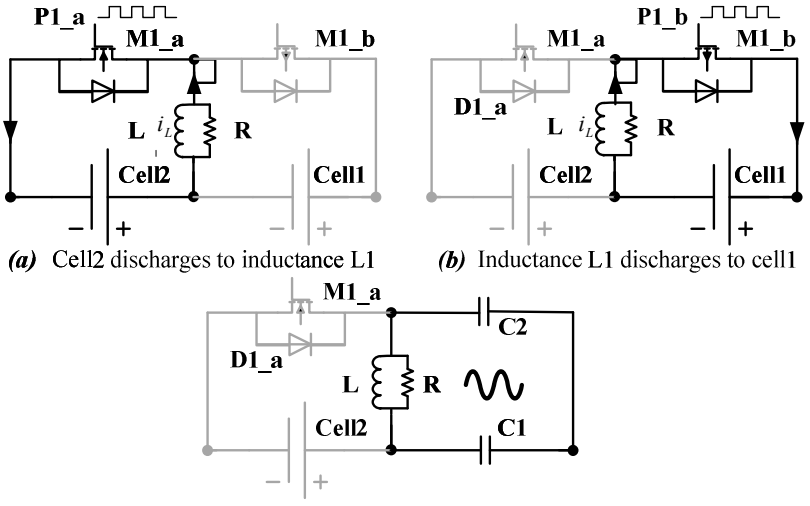

(a) Cell2 discharges to inductance L1 *(b)* Inductance L1 discharges to cell1

(c) Resistance consumes the excess energy

Fig.2. Three Stage of energy transferring progress between adjacent batteries

Balancing Strategy

The balancing strategies is called “Equal Balance”. At first the battery pack is divided in two different ways. Group A: cell1 and cell2, cell3 and cell4, … , cell(n-1) and cell(n). If n is an odd

number, cell(n) would be separate. Group B: cell1, cell2 and cell3, … , cell(n-2) and cell(n-1), cell(n). If n is an odd number, celln and cell(n-1) would be a pair.

When the voltage range of the battery pack is over than the set value r_{Idle}, the battery pack is grouped like group A at first. Then it obtains each pair of batteries voltage difference, and if some pairs' voltage differences are over than the set value k_{set}, these pairs would be balanced by the balancing circuit. After all pairs in group A have less voltage difference than the set value k_{Idle_set}, the batteries are grouped like group B. And it would do the same judgement. When all pairs' voltage differences are less than the set value k_{Idle_set}, it will be back group A. It will do the same circle until voltage difference of any adjacent batteries in the battery pack is less than k_{Idle_set}. The flow-chart of equal balance strategy is shown as fig.

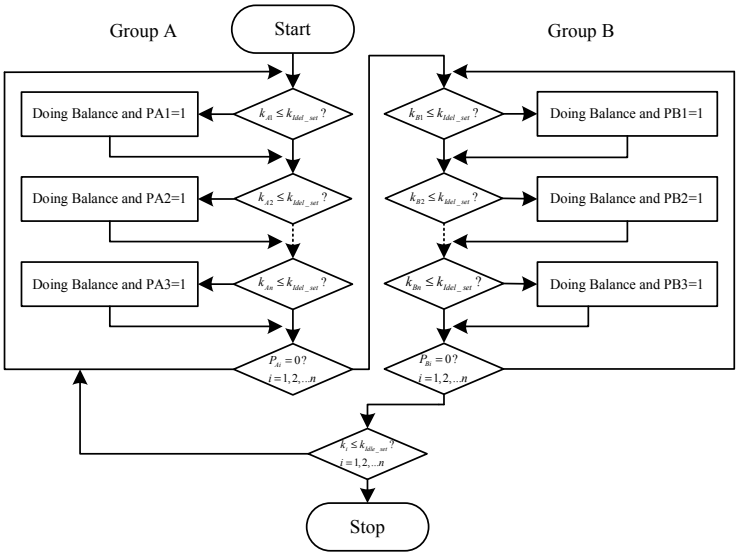

Fig.3. The flow-chart of equal balance strategy

Experimental Results

Before bench experiments, two adjacent batteries are used to examine the balancing circuit working condition. The related specification of the lithium-ion battery is as follows: the individual battery closed circuit voltage is 3.3V and the battery capacity is 20Ah.

The CH2 in Fig.4.(a) shows the the driving signal V_{gs} of MOSFET. When one battery discharges to the other battery, the CH2 in fig.4.(b) shows the Drain to Source Voltage of MOSFET V_{ds} and the CH2 in fig.4.(c) shows the inductance current I_L. In the tested case, the sample resistance is 125mΩ. As shown in fig, the period of the control signal is 50μs and the duty cycle is 50%. It can be calculated that the max balancing current is 4A and the efficiency of the balancing circuit is 55%.

(a) (b) (c)

Fig.4. Measured waves of V_{gs},V_{ds} and I_L

Furthermore, five batteries in series are used to complete a balancing bench experiment. And the voltage of five batteries in series in the process of balancing is shown in Fig.5. It can be seen that the voltage of battery with higher voltage decreased and the voltage of battery with lower voltage increased after balancing. The performance of battery pack is determined by the battery with maximum voltage and the battery with minimum voltage. Thus the performance of battery pack is promoted by the proposed battery balancing method. AS shown in table.1, the voltage range of these

batteries is 228mV at the start of balance. At the end of the batteries balancing the voltage range is down to only 3mV. It is obvious that the designed battery balancing technique is effective to decrease the battery voltage range and the batteries' inconsistencies.

Table.1. Batteries voltage of different moments of balance

The moment of balance	Cell1/V	Cell2/V	Cell3/V	Cell4/V	Cell5/V	Range/mV
the start of balance	3.1875	3.1000	2.9670	3.0975	3.1950	228
the end of balance	3.0540	3.0525	3.0510	3.0525	3.0540	3

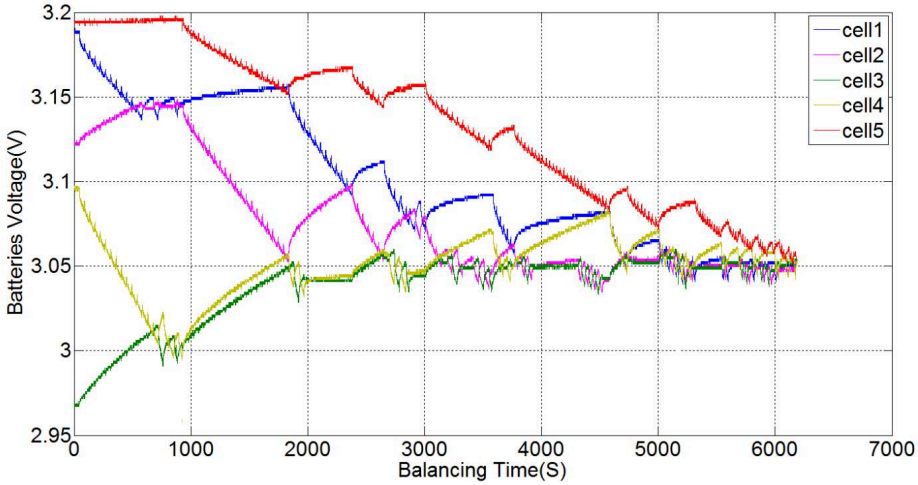

Fig.5. Voltage of five batteries in series in the process of balancing

Summary

Balancing module can be integrated in the battery management system and be an important part. It not only prevents the single battery over-charging and over-discharging, but also improves the inconsistencies of batteries in the same pack. The experimental results are presented to prove the feasibility of the proposed inductance balancing circuit. Therefore, it can make batteries remain in safety working condition and extend the lifespan of battery pack.

References

[1] Zhenpo WANG, Fengchun SUN, Chengning ZHANG, Study on inconsistency of electric vehicle battery pack [J]. Chinese Journal of Power Sources,2003, 27: 438-441.

[2] Chengtao LIN, Yanchao WANG, Yong Chen, Test and modeling of non-uniformity characteristics of a Ni-MH battery pack for electrical vehicle [J]. Chin J of Power Sources,2005, 29: 750-754.

[3] Haifeng DAI, Zechang SUN, Xuezhe WEI, Jiayuan WANG, Technologies to Relief Un-uniformity of Power Batteries Used in Electrical Vehicles[J]. Automotive Safety and Energy, 2011, Vol. 2, No. 1: 62-67

[4] Daowd M, Omar N, Van Den Bossche P. Passive and active battery balancing comparison based on MATLAB simulation[C].Vehicle Power and Propulsion Conference (VPPC), 2011 IEEE. IEEE, 2011: 1-7.

Advanced Materials Research Vols. 986-987 (2014) pp 1846-1849

doi:10.4028/www.scientific.net/AMR.986-987.1846

Research on Harm of Harmonics on Electrical Equipment

Gong Chenbin, Wang Qinghao, Chen Gang, Wang Enlu, Hai Tianshu, Li Xinyu, Li Bo, Wang Xue, Liu Chenyang, Zhao Qidong

Fushun Power Supply Company, Liaoning Electric Power Company Limited, State Grid, China,

wts55@126.com

Keywords: harmonic; frequency resonance; local overheating; capacitor; harmonic amplification

Abstract. Through the analysis of harmonics caused by transformer, capacitor, electromagnetic voltage transformer and other accident, harmonics is an important indicator of power quality, which has been included in the “pollution" of power grid is found. In order to understand the harmonic, this paper from the concept of quality of electric energy, and then gradually extended to the field of harmonics. This paper firstly introduces the various reasons and equipment may produce harmonic, Secondly, illustrate harm of harmonic to operation of transformers, capacitors, electromagnetic voltage transformers and other electrical equipment, let more people know and understand the relevant knowledge of the harmonic, In order to save technical force and provide scientific basis for future effective harmonic.

Introduction

The electric quality is the quality of electric energy in power system. The ideal power should be the perfect symmetry of sinusoidal waveform. Some factors that will deviate from the symmetrical sinusoidal waveform thus produced the power quality problems.

The main index of measure electric quality are supply voltage, frequency and waveform.IN other words, it led to the deviation of electric equipment fault or not working voltage, current or frequency, which includes the frequency deviation, voltage deviation, voltage fluctuation and flicker, three phase unbalance, temporary or transient over-voltage, waveform distortion (harmonic), voltage sag, swell, interruption, the continuity of power supply and so on [1-3].

With the widly use of power electronic devices and the popularity of the computer and air-conditioning, the amount of harmonic current is also rising, Harmonic pollution to the security, stability, economic operation of the power system constitutes a potential threat, make a great influence to the electrical environment around, is recognized as a major hazard to the grid[4,5]. This paper mainly discusses the harm of harmonic.

Harmonic species

The harmonic problem research started in the 80's, there has been considerable development in the 90's, and the gap with foreign research level is decreasing. The harmonic caused by different kinds of fault and accident of electric equipment also continue to occur, the severity of the harm of harmonics have been paid more and more attention [6]. In order to solve the problem of harmonic, the harmonic source must be found firstly, the common harmonic sources at present are as follows:

1）Nonlinear loads, such as two tube rectifier circuit (AC/DC)

2）Three phase voltage or current asymmetric load

3）Inverter circuit（DC/AC）

4）UPS power supply (PC machine), EPS (high capacity), namely the uninterruptible power supply.

5）Pressure regulating device or a control circuit of SCR

6）Electroplating equipment

7）Electric arc furnace, furnace, furnace, furnace manganese phosphate, calcium carbide furnace, silicon furnace

8）Electrolytic tank

9）Electric welding (arc welding, seam welding, spot welding, butt welding, welding neck)

10）Battery charger

11）Inverter (low or high voltage frequency converter)

12）Pulse amplitude modulation (PAM) voltage regulating circuit and pulse width modulation (PWM) frequency modulation circuit

13）Switching power supply

14）Chopped wave, chopping speed regulation

15）Power frequency electric furnace

16）Intermediate frequency electric furnace

17）Electrified railway

18）Crane, hoisting machinery

19）The whole discharge Lighting,such as energy-saving lamps, fluorescent lamps, metal halide lamp, sodium lamp, mercury lamp, helium lamp, deuterium lamp produce harmonic when using

20）Soft start device (SCR voltage)

Although the single unit capacity of these harmonic sources is small, the number is large. Therefore they supply the electric system harmonic injection can not be ignored.

The harm of harmonics on the transformer

Harmonic current flows in the transformer winding will produces active power loss, in general, harmonic current proportion is small compared with the fundamental current, but the frequency of harmonic current is high.The skin effect of the winding makes harmonic resistance increased larger than the wave resistance, so the additional winding loss by the harmonic has also increased[7]. Therefore the welding parts of transformer winding, tap switch are the most easily fever and then cause a partial discharge (Produce C_2H_2).

The accident case

66kV Jinjia Substation, 66kV Jintan line Is dedicated to the East carbon factory power supply line. The equipments of the East carbon factory is mostly nonlinear load,So the weekly switching to the 66kV Jintan line, will make the Jinjia Substation Substation has a great sound,just as the noise of Electric welding machine, it is terrible.

Nonlinear loads cause a lot of harmonic production, when the harmonic function on transformer, skin effect causes a part of transformer winding generate high temperature, and with the partial discharge. Because of the effects of harmonic on Jinjia Substation Substation, the Chromatography test data is Abnormal.

From February 25, 2011 to 2013 April 18, 17 times sampling tests, chromatographic data are totally made shown as Table 1.

Table 1 The chromatographic data of sampling tests of Jinjia substation

Component / Date	Content μl/L							
	H_2	CO	CO_2	CH_4	C_2H_6	C_2H_4	C_2H_2	C_1+C_2
2011.2.25	473	130	246	1295.66	568.76	2586.88	15.4	4451.3
2011.3.1	348	143	187	1111.55	512.45	2319.27	16.41	3959.68
2011.3.10	453	177	236	1249.38	528.28	2340.32	16.1	4134.08
2011.3.15	488	106	304	1372.07	557.55	2467.79	17.11	4414.52
2011.3.31	476	159	293	1419.84	575.5	2581.03	14.16	4590.53
2011.4.15	306	77	211	1144.39	576.43	2476.71	13.88	4211.41
2011.5.11	413	143	307	1461.94	639.37	2739.11	15.05	4855.47
2011.5.27	460	151	391	1488.18	656.51	2700.22	16.1	4861.01

2011.6.15	331	115	357	1103.03	526.03	2151.85	12.65	3793.56
2011.8.19	386	213	532	1546.75	660.66	2745.81	15.99	4969.21
2011.10.9	360	203	398	1501.76	644.59	2553.66	13.95	4713.96
2011.12.8	289	190	318	1562.62	757.45	2889.88	16.49	5226.44
2012.3.12	359	176	393	1874.04	952.4	3229.32	14.91	6070.67
2012.6.28	361	221	487	2049.27	1073.75	3347.79	15.04	6485.85
2012.9.1	291	249	558	2024.03	1141.59	3301.08	20.4	6487.1
2012.11.8	152	139	670	1849.18	1138.97	3295.07	11.39	6294.61
2013.4.18	284	287	589	2199.56	1146.21	3332.05	10.26	6688.08

The chromatographic data in April 18, 2013 are analyzed: H_2：284；CO：287；CO_2：589；CH_4：2199；C_2H_6：1146；C_2H_4：3333；C_2H_2: 10.26; C_1+C_2 : 6688

From the data that the C_1+C_2 from 4466 ul/L to 6688ul/L, the minimum of C_2H_2 is 10.26ul/L, the maximum is 20.4ul/L. By calculation, transformer belongs to middle temperature overheat, accompanied by partial discharge.

In order to find out the reason of transformer heating, the harmonics comprehensively was tested in the Jinjia substation. The test results show that voltage harmonic is large, harmonic current 5 times, 7 times, 11 times, 13 times have exceed the state standard. These harmonic that exceed the standard injected Jinjia substation 66kV bus, and then through the bus and inject to transformer, Cause heating of transformer, leading to abnormal chromatographic data of transformer oil.

The harm of harmonic to capacitor group

For compensating the reactive power of the load, and improving the power factor, a parallel capacitor is often provided on the load. In addition,In order to improve the system voltage level, the installation of shunt capacitor in substation.At power frequency, capacitance capacitor is larger than the system inductance, which does not produce resonance.At the harmonic frequency, the system inductance increases greatly and Capacitive reactance is reduced greatly,which may have a parallel resonance and series resonance. This resonance will make the harmonic current amplification of several or even tens of times.It will make a great threat on the system, especially for capacitors and reactors in series, often make the capacitor and reactor burnout. In the accidents caused by harmonic, these accidents accounted for a high proportion.

The accident case

In recent years, many substation capacitor group of Fushun power Supply Company frequently generated unexplained trip accident. Such as a group of capacitors at Li Shizhai Substation successively trip on July 5, 2007 ,on July 30, 2007, on April 7, 2008, April 10, 2008. Circuit breakers tripping are due to differential current, branch current transformer and voltage protection action. Accident phenomenon sometimes accompanied by external fuse capacitor, Zinc Oxide arrester explodes in differential current transformer and so on. For the most part, if capacitors and related equipments appearance check well and no traces of discharge after circuit breakers, test is also qualified. Because substation that capacitor group often has accidents occur is with nonlinear load, so the capacitor group accidents are caused by harmonic.

The harm of harmonics to electromagnetic voltage transformer

At 10:09 a.m July 12, 2011, single phase to ground fault occurs on 10kV Qingwu line, the 10kV Qingnian Road substation busbar JSZW-10 electromagnetic voltage transformer loss, Zinc Oxide arrester connected in parallel occured thermal collapse. When the accident occurred, three phase to ground voltage of the 10kV system increased in turn, indicating the phase voltage at 7.7kV (the rated phase voltage is 5.7kV), and the three-phase voltage meter pointer swing phenomenon

obviously, 60kV main transformer had high and low voice. After the operating personnel cut power, maintenance personnel will be replaced by voltage transformer and arrester. After the accident, at 11:07 a.m on August 17th an accident happened again, the accident phenomenon is the similarity with the last one, the only different is high-voltage fuse of the voltage transformer fused, and the 10kV second segment voltage transformer was spurting oil and smoke.

Accident analysis:

The neutral point of Qingnian Road substation 10kV system is not grounded, when 10kV Qingwu line occurred single phase grounded, it caused "impact disturbance ". On the other hand, the system containing fractional frequency (1/2, 1/3, etc.), so that the L values of voltage transformer decreased dramatically, make the compensation system, $\omega L=1/\omega C$, sub harmonic resonance occurs, the voltage transformer winding to produce the rated current for more than a hundred times, cause the voltage transformer seriously overload, even transformer damaged.

The two accidents make the staff take more attention, take tests harmonic measurement for Qingnian Road and Wujiabao substation. From the test results, the system contains the 1/2, 1/3 harmonics that exceed standard, while the 5 harmonic was also close to the limit. After the staff inspects it, discoveried the harmonic source was at a user, and helps its harmonic control. After that, the system runs secure and stable with no accidents.

Conclusion

Harmonic interference power equipment running, which make it can not work normally. For example, the harm of harmonic to transformer, electromagnetic voltage transformer, and capacitor groups, harmonic will cause misoperation of relay protection. Harmonic interference the communication system, reduce its clarity, even loss signals. Harmonic interference measuring device in negative error, seriously it can cause the meter to stop rotating.

Therefore, the harmonic is an important index of power quality, no matter it is from the security of power system security, stability, economic operation point of view, or from the view that the user work electric equipment normally, it is very necessary to understand the harm of harmonic to electrical equipment, which will also provide scientific basis for managing harmonic effectively.

Reference

[1] Wang Zhaoan. Harmonic Elimination and Reactive Power Compensation. Mechanical Industry Press, 2009.

[2] Yin Kening. Transformer Design Principle. China Power Press, 2010.

[3] Ping Shaoxun, Zhou Yufang. Power System Neutral Grounding Mode and Operation Analysis. China Power Press, 2010.

[4] Yao Huannian, Cao Meiyue. Resonance Grounding of Power System. China Power Press, 2009.

[5] Cao Dunkui. Transformer fault analysis and diagnosis. China Power Press, 2010.

[6] Li Shiping, Liu Guiying. Modern Power Quality Detection Technology. China Power Press, 2008.

[7] Wang Hezhen. The Var Compensation of High Voltage Shunt Capacitor Technology. China Power Press, 2006.

Advanced Materials Research Vols. 986-987 (2014) pp 1850-1853

doi:10.4028/www.scientific.net/AMR.986-987.1850

Research on the Three-Level Inverter Midpoint Potential Algorithm based on the Charge Balance Theory

Sunwei HUANG[1, a], Yueyu WANG[2, b], SHI Jin[3]

[1]Tianjin University of Technology, Tianjin, 300384, China

[2]Tianjin Key Laboratory of Control Theory& Applications in Complicated Systems, Tianjin,300384, China

[3]Architectural Design and Research Institute of Tianjin University,Tianjin 300073, China

[a]email:hsunwei@163.com, [b]email:wangyueyu123@163.com

Keywords: Three-Level Inverter; SVPWM; Neutral-Point Voltage Balancing Method; MATLAB

Abstract. In order to achieve high voltage, high-power,two-level inverter need to switch in series which results switch static, dynamic-pressure problems. Three-level inverter solve this problem for its circuit, but this circuit has the midpoint potential imbalances of the DC side, we propose to charge balance theory based on the three-level inverter midpoint potential algorithm to solve the problem, build simulation model to validate the algorithm on the midpoint potential in MATLAB.

Introduction

In voltage type inverter, two level inverter due to the limitation of the switch power and voltage, not easy to realize high voltage high power. Compared with the two level inverter, multilevel inverter has many advantages, such as the output voltage of the phase and amplitude is easy to adjust, low harmonic content, high efficiency, low frequency switching devices can use cheaper price, suitable for high voltage and high power occasion. In high voltage large capacity ac motor variable frequency speed regulation system, using multilevel inverter can save energy.

The Three-Level Inverter Space Vector Algorithm

Three level inverter space vector diagram as shown in figure 1, the picture has both inside and outside two lines constitute a hexagon, is divided into six major sectors, with a certain symmetry relations between various sectors[1], so you can study by perspective transformation into the first sector, the first sector vector diagram is shown in figure 2. The sector is divided into six small triangle range, relative to the four small triangles range, as shown in figure 3[2]. In figure 3, if the starting small vector for 100, when the reference vector angle nearly 60° , small vector 100 and 0-1-1 effect time is very short, the point of potential shift is, adjust the time it is difficult to suppress the role of the two vector neutral voltage offset. Therefore, this article will be between 1 and 2 district in figure 3, when the reference vector is located in between 1 district, starting small vector by 100, when the reference vector is located in between 2 district, starting small vector using 0-1-1, so we can maximize of adjusting the starting vector time, inhibiting neutral voltage imbalance[3].

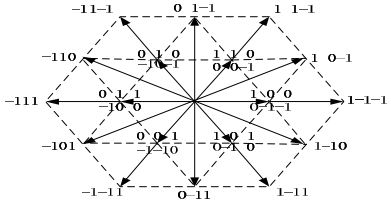

Fig.1Three-level space vector diagram

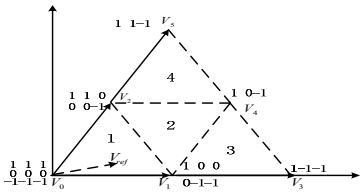

Fig.2The first sector vector diagram

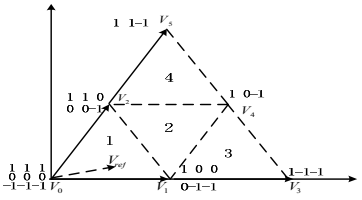

Fig.3The first sector space vector diagram

Three-level space vector algorithm is based on "volt-second product equal" principle, with the reference vector in the small triangle the vertice of the corresponding to three reference vector switch vector synthesis, this three vector corresponding to the product of the vector and the product of the sampling period is equal to the reference. The corresponding formula is:

$$\begin{aligned}&\dot{U}_A T_A+\dot{U}_B T_B+\dot{U}_C T_C=\dot{U}_{ref} T_S\\&T_A+T_B+T_C=T_S\end{aligned} \tag{1}$$

T_A, T_B, T_C stand for $\dot{U}_A$, $\dot{U}_B$, $\dot{U}_C$ within a sampling period of duration. For example below for reference vector falls on the first Ⅰ sector 1, 2 small triangle,the reference vector synthesized from $\dot{V}_0$, $\dot{V}_1$, $\dot{V}_2$. T_0, T_1, T_2 stand for $\dot{V}_0$, $\dot{V}_1$, $\dot{V}_2$ the function of the vector of the time. The volt-second product equal principle to get the value of T_0, T_1, T_2.

A seven sections of pulse width modulation algorithm is proposed in this paper [4], taking the starting vector is the vector of trigger mode in each cycle. Starting is little vector and negative vector function on t_1. The rest of the vector thought $T_S/2$ is the center of symmetry. Before and after half time in $T_S/2$ role respectively.The role of way as shown in figure 4**,** for example in sector 1 small triangle 1 start is vector (100) to effect on $t_1/4$ little time, zero vector (000) role $t_2/2$ time, small vector (00-1) negative effect on time $t_3/2$. Then with is small vector (100) pairs of small negative vector (0-1-1) $t_1/2$ time, and then negative small vector (00-1) role $t_3/2$ time, zero vector (000) $t_2/2$ time, are small vector (100) $t_1/4$. As you can see, that vector symmetric arrangement order, fully satisfy each vector change, the transformation for the device only between 0, 1 or 0, -1 change, guarantee the security of the main circuit to work, and to some extent, shortens the dc side capacitor charge and discharge time, is advantageous to the neutral voltage stability[5].

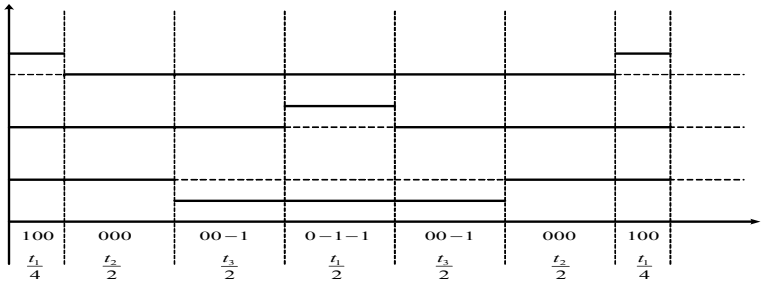

Fig.4 Vector sequence diagram

The midpoint voltage balance control

Small vector always come in pairs, to the contrary their influence on neutral voltage can according to their small vector's influence on the neutral voltage vector is divided into small is little vector and negative vector. Called the small vector of neutral voltage of ascension are small vector; On the contrary, the neutral voltage drop small vector as negative little vector. Among them, are small vector including 100, 010, 001, 011, 101, 110, negative small vector including-100, 0-10, 00-1, -1-10, -10-1, 0-1-1.Here in 100, in small vector 100, 0-1-1 as an example, the equivalent circuit diagram as shown in figure 5, figure 6.When small vector 100 role,neutral current $i_0=i_a$ capacitance C1 discharge,capacitance C2 charging,neutral voltage is rising.When small vector 0-1-1 role,capacitance C2 discharge,capacitance C1 charging,neutral voltage is dropping.These two vector has the same due to the corresponding output voltage value, the impact on the neutral voltage is just the opposite, the relationship between phase current and some current as shown in table 1.

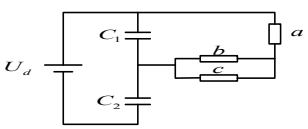

Fig.5 The small vector 100 equivalent circuit diagram

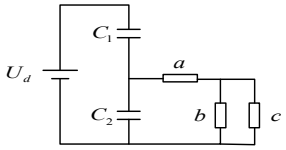

Fig.6 The small vector 0-1-1 equivalent circuit diagram

Table.1 The relationship about neutral current and phase current

Sector N	The Positive Vector	i_0	The Positive Vector	i_0	The Middle Vector	i_0
	100	$-i_a$	0-1-1	i_a	10-1	i_b
	110	i_c	0 0-1	$-i_c$	01-1	i_a
	010	$-i_b$	-10-1	i_b	-110	i_c
	011	i_a	-10 0	$-i_a$	-101	i_b
	001	$-i_c$	-1-10	i_c	0-11	i_a
	101	i_b	0 -10	$-i_b$	1-10	i_c

Deviation of neutral voltage is the voltage range of the capacitors in dc side, investigate its root cause is a point charge in the range inflows and outflows. Thus from the perspective of control charge to control the neutral voltage. Small vector's influence on the neutral current, on the other hand, only by controlling the small vector to inflows and outflows capacitor charge tend to be the same.Defining the current as i_0 as a midpoint and switch state for S_i , among them $i=a,b,c$, When $S_i=1$, switch tube conduction T_{11}, T_{12} ,When $S_i=0$, switch tube conduction T_{12}, T_{13} ,When $S_i=-1$, switch tube conduction T_{13}, T_{14} .Through (S_a,S_b,S_c) state can know which current flows through the capacitors in dc side. Big vector and zero vector corresponds to the neutral current is zero.Its corresponding relationship as shown in table 1.

$$i_0(t)=[1-abs(S_a)]i_a+[1-abs(S_b)]i_b+[1-abs(S_c)]i_c \tag{2}$$

In this paper the starting vector space vector method is small vector of seven stages, the algorithm is composed of four basic vector.Set their corresponding neutral current respectively is i_{N0}, i_{N1}, i_{N2}, i_{N3} ,they act time, respectively is $\frac{t_0}{2}$, t_1, t_2, $\frac{t_0}{2}$, Because of the vector is small in contrast to the negative small vector into the midpoint of the current,so $i_{N0}=-i_{N1}$.When seven sections of wave function, the change of the point charge in the amount as follows:

$$\Delta Q=\frac{t_0}{2}*i_{N0}+t_1*i_{N1}+t_2*i_{N2}+\frac{t_0}{2}*i_{N3}=t_1*i_{N1}+t_2*i_{N2} \tag{3}$$

Within a sampling period T_S, detection of two capacitors in dc side voltage can be neutral voltage offset:

$$\Delta V_{dc}=\frac{1}{2}(V_{dc1}-V_{dc2}) \tag{4}$$

Change is in the point charge:

$$Q=Q_1-Q_2=\frac{1}{2}C*\Delta V_{dc} \tag{5}$$

To compensate for the weekly mid-term point charge amount of change, need the change of compensation in the next cycle period charge amount:

$$Q+\Delta Q=0 \tag{6}$$

So you need to introduce the regulating factor K.Make i_{N0}, i_{N1}, i_{N2}, i_{N3} action time is $\frac{(1+K)t_0}{2}$, t_1, t_2, $\frac{(1-K)t_0}{2}$,seven sections of waveform after adjustment, the change of the point charge in the amount as follows:

$$\Delta Q=\frac{(1+K)t_0}{2}*i_{N0}+t_1*i_{N1}+t_2*i_{N2}+\frac{(1-K)t_0}{2}*i_{N3} \tag{7}$$

Because of $i_{N0}=-i_{N1}$,so:

$$\Delta Q=Kt_0*i_{N0}+t_1*i_{N1}+t_2*i_{N2} \tag{8}$$

By the type available:

$$K = -\frac{C * \Delta V_{dc} + t_1 * i_{N1} + i_{N2}}{t_0 * i_{N0}} \tag{9}$$

K values may be greater than 1 or less than 1, as a result of the vector duration cannot be negative, so it is necessary to limit the K value calculated.

$$K = \begin{cases} 1, K > 1 \\ K, 0 < K < 1 \\ -1, K < -1 \end{cases} \tag{10}$$

After adjustment, the basic seven sections of the corresponding vector effect time in the order is $\frac{(1+K)t_0}{4}$, $\frac{t_1}{2}$, $\frac{t_2}{2}$, $\frac{(1-K)t_0}{2}$, $\frac{t_2}{2}$, $\frac{t_1}{2}$, $\frac{(1+K)t_0}{4}$.

The research on Three level inverter space vector algorithm simulation

For the proposed three level inverter based on the theory of the charge balance neutral voltage algorithm, using MATLAB simulation software to build simulation model, validate the correctness of the algorithm. The simulation parameters: the dc voltage $V_{DC} = 1000V$, Dc side capacitor $C_1 = C_2 = 2000\,\mu F$, Three-phase symmetrical load inductance is $L = 10mH$,Sampling period is $T_s = 0.1ms$, The fundamental frequency is $f = 50Hz$.

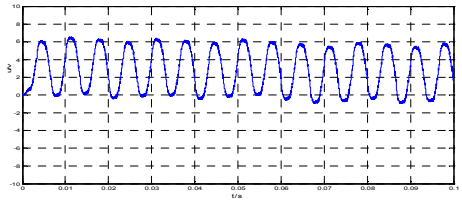

Fig.7 No midpoint control waveform of neutral voltage fluctuations

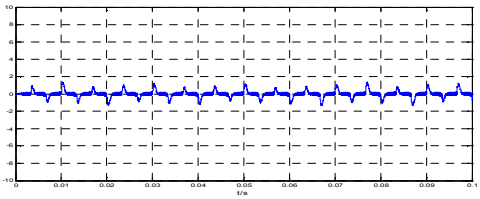

Fig.8 After add midpoint control waveform of neutral voltage fluctuations

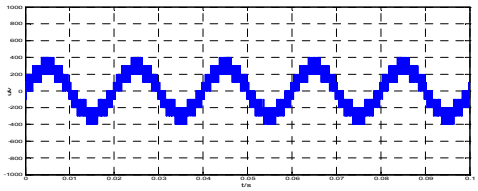

Fig.9 The three level inverter output phase voltage waveform

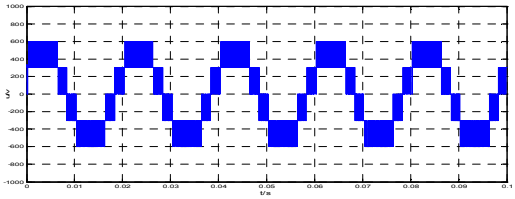

Fig.10 The three level inverter output line voltage waveform

Figure 7- Figure 10 simulation results show that before no neutral voltage control algorithm are introduced, neutral voltage offsets have occurred, and the volatility is bigger, amplitude around 6 v, join the midpoint control algorithm, neutral voltage deviation rectified, fluctuating around the halfway point, but also has certain inhibition, fluctuation amplitude around 3 v, this also proves that the algorithm of neutral voltage control is more ideal.

References

[1] Li Yang, Dai Peng, Yuesen YU and so on. The Three Level inverter SVPWM over-modulation control strategy review [J]. Electric drive, 2010 40 (7) 8-17.

[2] Jianyuan WANG, Wenting, WU, Yanru ZHONG. Three level inverter PWM technology evaluation and comparative study [J]. Electric drive, 2010 40 (2) 22-28.

[3] Abdul Rahiman Beig, G. Narayana, V.T. Ranganathan, “Modified SVPWM Algorithm for Three Level VSI With Synchronized and Symmetrical Waveforms”, IEEE Trans. Ind. Elect., Vol. 54, No. 1, Feb. 2007, pp 486-494.

[4] Weifeng ZHANG, Yuehui YU, and Liu Lu. Three Level inverter voltage space vector control algorithm simulation [J]. Power electronics technology, 2006 40 (1) 3-5.

[5] Zhang Ye, Yupeng SHANG, Wenjun WANG. Three Level inverter space vector modulation and neutral voltage balance study [J]. Electric drive, 2010 40 (2) 33-36.

Advanced Materials Research Vols. 986-987 (2014) pp 1854-1857

doi:10.4028/www.scientific.net/AMR.986-987.1854

Simulation of Function Generator

Xiaolong Tan[1], Jia Zhou[1], Wenbin Wang[1,a]

[1] Yalong River Hydropower Development Company LTD, Chengdu, 610051, China

[a] email: wangwenbin@ylhdc.com.cn

Keywords Function generator, Circuit, Nonlinear

Abstract: The function generator is the classic analog adder circuit, either independently or as an intermediate for its links embedded in complex circuits, have a very wide range of applications. Function generator can be used as the signal source to produce for research, teaching, experimental signals for different purposes such as how to make it more accurate and stable signal generation, has been widespread concern and research; Similarly, construction work adder circuit commonly used as a module, accurate input-output relationship is also very worth exploring. Therefore, this paper, on both a profound theoretical analysis, based on the modeling and simulation through the more figurative exposition of both operating characteristics, application to increase its theoretical basis.

Introduction

The field of science and technology is often called a non-linear function to generate the analog circuit, the voltage transfer characteristics $v_0 = f(v_s)$ and a non-linear function of the same. Typical nonlinear function generator limiters, extended and reciprocal type categories[1]. To simulate nonlinear function, often using piecewise linear method which is used instead of line approximation analog voltage transfer function of nonlinear characteristic curve.

Theory Analysis of Function Generator

Figure 1 shows the limiting nonlinear function generator circuit schematic diagram and voltage transfer characteristics Fig.

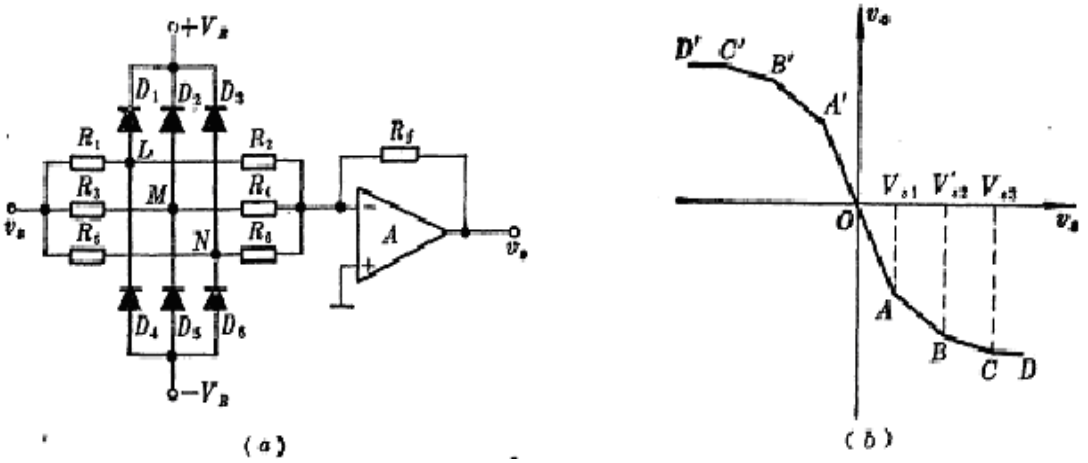

Fig.1 Limiter type function generator (*a* Circuit *b* Voltage transfer characteristic)

When $|v_s|$ is small, $D_1 \sim D_6$ because the reverse bias the cut-off, then $r_1 = (R_1 + R_2) // (R_3 + R_4) // (R_5 + R_6)$ resistance is minimal, the characteristic curve AA' section slope is[2] :

$$S_0 = \frac{dv_0}{dv_s} = -\frac{R_f}{r_1} = -\frac{R_f}{(R_1 + R_2) // (R_3 + R_4) // (R_5 + R_6)} \tag{1}$$

Let D be ideal diode, when v_s increases to

$$V_{s1} = \frac{R_1 + R_2}{R_2} V_R \tag{2}$$

Conduction diode D_1, L point potential is clamped in $+V_R$, a current flows through R_2 does not change, that is R_1 and R_2 of the operational amplifier does not exist, then the slope of the characteristic curve segment AB becomes:[3]

$$S_1 = \frac{dv_0}{dv_s} = -\frac{R_f}{(R_3 + R_4) / /(R_5 + R_6)} \tag{3}$$

When v_s further increases to

$$V_{s2} = \frac{R_3 + R_4}{R_4} V_R \tag{4}$$

D_2 turns on, M point potential is clamped in $+V_R$, then the slope of the characteristic curve segment BC is:

$$S_3 = \frac{dv_0}{dv_s} = 0 \tag{5}$$

Similarly can be drawn v_s<0 the characteristic curve OA'B'C'D'[4] .

Figure 2 shows the circuit schematic inverting summing operation. Inverting summing arithmetic circuit input signals are applied to a plurality of integrated op amp's inverting input.

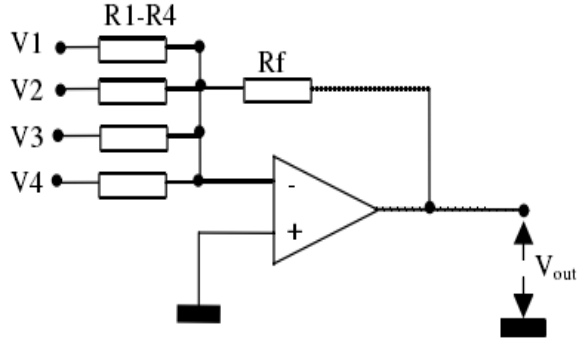

Fig.2 Inverting summing arithmetic circuit

Let flowing through resistor R_1, R_2, R_3, R_4, R_f currents are i_1, i_2, i_3, i_4, i_f, in accordance with the "virtual short" and "false break" principle, integrated inverting input of the op amp the current equation for the node[5]

$$i_1 + i_2 + i_3 + i_4 = i_f \tag{6}$$

Namely

$$\frac{V_1}{R_1} + \frac{V_2}{R_2} + \frac{V_3}{R_3} + \frac{V_4}{R_4} = -\frac{V_{out}}{R_f} \tag{7}$$

Hence, expression of V_{out} is

$$V_{out} = -R_f\left(\frac{V_1}{R_1} + \frac{V_2}{R_2} + \frac{V_3}{R_3} + \frac{V_4}{R_4}\right) \tag{8}$$

Simulation of Function Generator

First created simulation circuit diagram in PSpice, the circuit diagram shown in Fig.3.

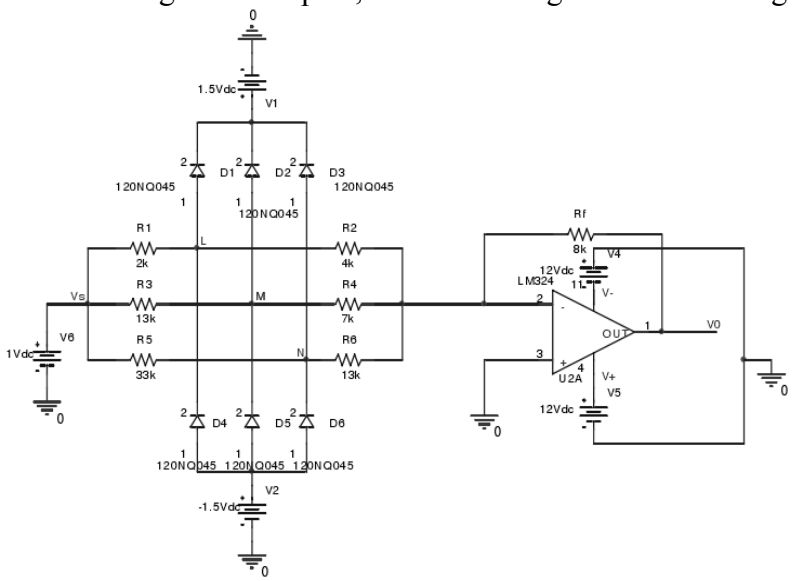

Fig.3 Function generator circuit diagram in PSpice

Set the value of the size of each component, select the current scan, the scanning voltage range of -9V ~ +9V, the voltage between the scan size is 0.1, obtained simulation results shown in Fig.4.

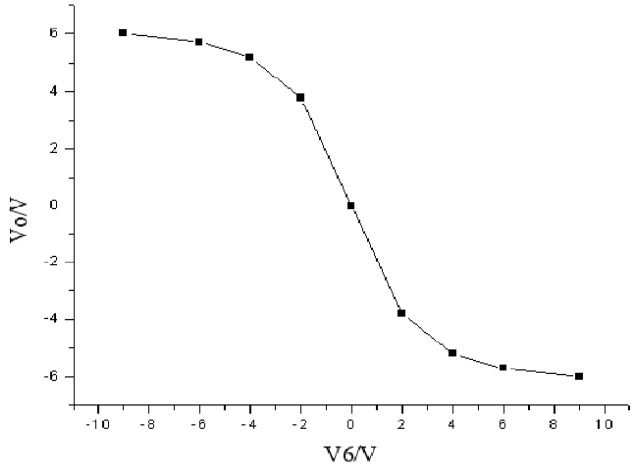

Fig.4 Simulation curve of function generator in PSpice

Simulation of Adder

Adder circuit schematic model is created in PSpice, shown in Figure 5.

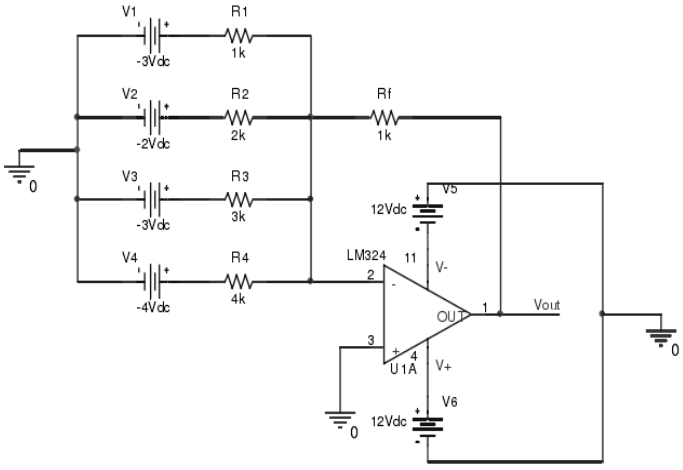

Fig.5 The adder circuit schematic in PSpice

Set the value of the size of each component, select the dc voltage sweep, the voltage scan range of -20V ~ +40V, the scan interval is 0.01. Circuit graph of simulation results are shown in Figure 6.

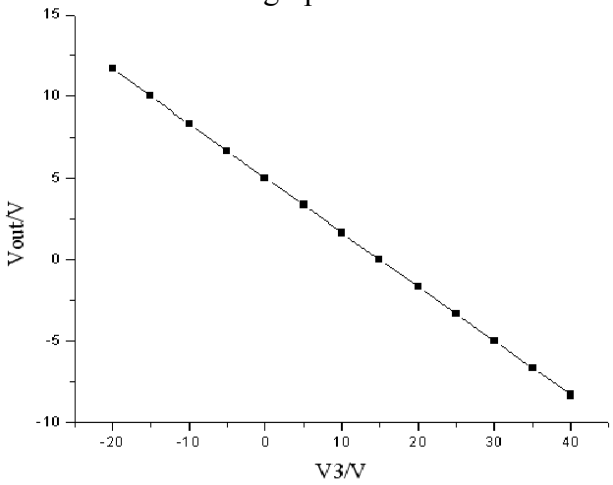

Fig.6 Simulation curve of Adder

In Fig.6, the input voltage to 3V abscissa to the output voltage V_{out} of the vertical axis coordinate system is established, according to Fig.5, the elements corresponding to the parameter value, and the equation (8), we can see that with the theoretical simulation curve consistent with the simulation result is satisfactory.

Conclusion

This paper analyzes the function generator and adder mathematical model, based on the circuit model column write numeric expression from the transmission characteristics of the circuit analysis. Which limiter type function generator under the influence of the topology, the output voltage increases indefinitely, the output voltage is saturated, the limiting effect achieved; adder circuit op amp due to the introduction in the virtual short, virtual-off characteristics under, the output voltage and the input voltage is formed between the addition, and with the feedback resistor and the current limiting resistor in the size. In the two functional circuits after a detailed analysis, the use of professional software for circuit simulation modeling and simulation, to obtain a more intuitive operation of the circuit, and the simulation results and theoretical analysis have higher consistency.

References

[1] Wavetek VXIbus 20MHz Arbitrary Waveform Generator. ElectronicTest&Calibration.
[2] Cosmin Popa. Improved Accuracy Function Generator Circuit for Analog Signal Processing. EUROCON 2007 - The International Conference on "Computer as a Tool". 2007
[3] Virtor S. Reinhardt.Sour reduction techniques in direct digitalsynthesizer. IEEE international frequency control symposium . 1993
[4] DE ABREUGTF.On the generation of Tikhonov variates. IEEE Transactions on Communications. 2008
[5] Tierney J, Rader C M, Gold B.A digital frequency synthesizer. IEEE Transactions on Audio and Electroacoustics. 1971

Advanced Materials Research Vols. 986-987 (2014) pp 1858-1863

doi:10.4028/www.scientific.net/AMR.986-987.1858

Study on Experimental System for Three Level Neutral-Point-Clamped Converter

Gang Han [a], Jianwen Zhang and Xu Cai

[1]School of Electronic Information and Electrical Engineering, Shanghai Jiaotong University, Shanghai 200240, China;

[a]henryhangang@163.com

Keywords: three level converter, neutral-point potential(NP), digital modular control, optical-fiber communication

Abstract. This paper focuses on the digital experimental system for neutral-point-clamped three-level converter. First, SVM's digital implementation method is studied. As neutral-point voltage unbalance is an inherent problem for this topology, a practical capacitor voltage balance method is present. This method uses a variable factor as the small vectors' adjustment coefficient, which is calculated by PI controller with capacitor voltage deviation. Then, a digital modular control system is proposed, in which both hardware and software system structures are designed in modular. The digital control system adopts high speed optical-fiber communication between a master controller and multiple sub-controllers, and realized the effective and rapid control of the experimental prototype finally.

Introduction

Nowadays, multilevel converters play an important role in high-power applications, such as photovoltaic systems, wind turbine, HVDC light, and motor drives applications[1-4]. Among these various multilevel topologies, the neutral-point-clamped three level converter is becoming most attractive one. Compared with the conventional two-level converter, it has lower current harmonics, lower voltage stress and smaller electromagnetic interference[5-6]. The same performance can be achieved with smaller switching frequency, so the volume of the filter and heat can be reduced.

However, due to the specificity of the three-level converter topology, the neutral-point potential problem is tremendously critical[7]. Unbalanced capacitor voltage can cause low order harmonic contents in output voltage, and the power switches may withstand higher voltage above their limits, and be damaged. In the worst case, neutral-point-clamped three-level converter may degrade into two-level. Although increasing the value of dc-link capacitor may mitigate the neutral-point potential problem, it will increase the overall weight and cost of the system. Therefore, various software balancing control strategies have been proposed to suppress the unbalance of neutral-point potential. These solutions can roughly be divided into two categories. One is based on SPWM[8], and the other is focused on SVPWM[9-12]. In [8], an analytical method is proposed to accurately calculate the injected zero sequence voltage for neutral-point balance, which is based on SPWM method. However, the task of zero-sequence voltage precisely calculation is difficult, and this method has low dc voltage utilization ratio. For SVPWM, methods are generally done by changing the switching sequence or adjusting the dwell times of positive and negative small space vectors according to the direction of load current and capacitor voltage. However, as the regulatory factor is constant, when the dwell times of small vectors are very short in high modulation depth, the method can't receive satisfied control performance of neutral-point voltage balance.

Meanwhile, as a work center of the converter, digital controller is particularly an indispensable portion of the control systems. For now, centralized controller is more widely used in the field of high-voltage and large power converter, that is, signal acquisition, fault status indication, PWM wave generation and protection algorithms, etc, are all accomplished in one set of controller. Nevertheless,

signals need to be handled will add sharply with the increase of multilevel converter's order. What's more, centralized controller if still is used likely to cause great hidden troubles, because the shield line wiring method and cable length problem could not be handled well as the wiring complexity in control cabinet.

Digital realized method of the experimental system for neutral-point-clamped three-level converter is mainly concerned in this paper. SVM's digital implementation method is discussed in detail. The neutral-point potential variation is also analytically investigated, and a simple and practical voltage balance control method is proposed. The method uses a variable factor as the small vectors' adjustment coefficient, which is calculated by PI controller with capacitor voltage deviation. A digital modular control system is proposed to verify the method. At last, the experimental results demonstrate that the neutral-point potential balancing method and the digital modular control system is feasible and effective.

SVM and NP Control for NPC Converter

Fig.1 shows the main circuit topology of three phase neutral-point-clamped three-level converter. Each phase leg of the converter consists of four power switches (Si1, Si2, Si3, Si4), four parallel rapid reverse recovery diodes and two clamping diodes (Dip, Din), where the subscript i = a,b,c. ug represents three-phase power source, upper capacitor Cdc1 and lower capacitor Cdc2 are two DC link bus capacitors, their voltages are udc1 and udc2, respectively. In steady state, udc1=udc2 =udc/2. Third-order LCL filter is composed of grid side conductance Lg, converter side conductance Li and star connection capacitor Cf. LCL filter can achieve better filtering performance than a single inductor filter with the same inductance, but it exits resonance problem.

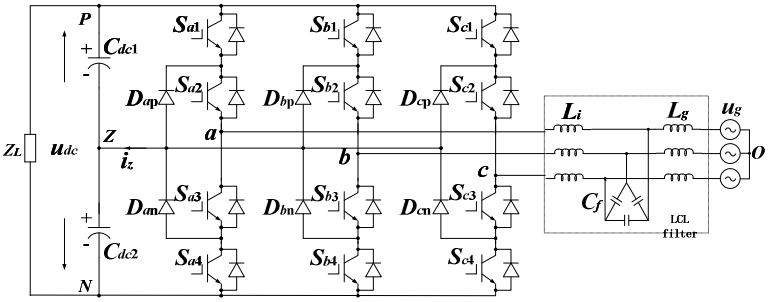

Fig.1 Topology of NPC converter

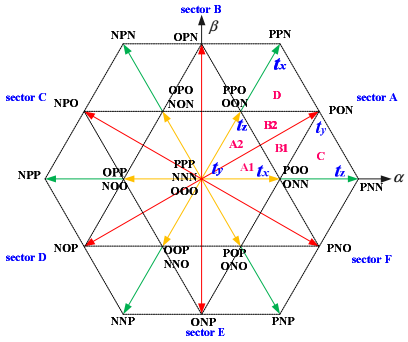

Fig.2 Space-vector diagram of NPC

Space vector modulation implementation. In order to complete the space vector pulse width modulation, which sector the reference space vector falls in should be judged first.

To facilitate the program implementation, we define

$$\begin{cases} u_{ref1} = u_\beta \\ u_{ref2} = \sqrt{3}u_\alpha - u_\beta \\ u_{ref3} = -\sqrt{3}u_\alpha - u_\beta \end{cases} \tag{1}$$

Where, $u_\alpha = 3v_\alpha / u_{dc}$, $u_\beta = 3v_\beta / u_{dc}$. v_α and v_β are α-β components of the reference space vector v_{ref} . Make that

$$\mathrm{M} = \mathrm{sign}\left(u_{ref1}\right) + 2 \cdot \mathrm{sign}\left(u_{ref2}\right) + 4 \cdot \mathrm{sign}\left(u_{ref3}\right) \tag{2}$$

And the function $\mathrm{sign}(x) = 1$, when $x > 0$; otherwise $\mathrm{sign}(x) = 0$. Each sector can be divided into six triangle regions, for example, in the sector A, as exhibited in Fig.2. In fact, every sector of the space structure has a high degree of similarity. In order to lessen the work and complexity, other sectors can be transformed into sector A through rotation transformation. Hence, only the dwell times in sector A are analyzed, then adjust vectors' delivery orders for other sectors.

Assuming that reference space vector is located in region B1 of sector A as shown in Fig.2. In order to minimize the harmonic component of output voltage, the reference space vector is formed by its three nearest voltage vectors. In that way, vectors $\vec{v}_x$ (POO/ONN), $\vec{v}_y$ (PON), $\vec{v}_z$ (PNN) are the basic space vectors in which $\vec{v}_{ref}$ is located, and t_x, t_y, t_z are corresponding vector time intervals. They can be obtained by following calculations:

$$\begin{cases} \vec{v}_x \cdot t_x + \vec{v}_y \cdot t_y + \vec{v}_z \cdot t_z = \vec{v}_{ref} \cdot t_s \\ t_x + t_y + t_z = t_s \end{cases} \tag{3}$$

Where, t_s is PWM switching period. The dwell times of other small triangles in sector A can be calculated in a similar way. After the dwell times have been ascertained, vectors' working sequence should be selected. This paper adopt positive small vector as starting vector.

Neutral-point potential control method. Capacitor voltage unbalancing is an inherent problem for neutral-point clamped topology. The deviation of the neutral-point potential is related to the modulation technique, harmonics of the switching functions, as well as the load impedance[14]. For zero vectors and large vectors, neutral-point does not participate in the transmission of energy, so they have no effect on neutral-point potential. Medium vectors affect neutral-point voltage, but the direction of voltage deviation is undefined[13]. The two states of small vectors have contrary effect on neutral-point potential. When the converter is working in rectifier mode as shown in Fig.3(a), for the positive small vector POO switching state, top capacitor C_{dc1} will be charged and bottom capacitor C_{dc2} will be discharged, which will cause the neutral-point voltage u_Z to decline. On the contrary, the negative small vector ONN makes u_Z to rise. Nevertheless, When the converter is working in inverter mode as shown in Fig.3(b), the phenomenon is quite the opposite.

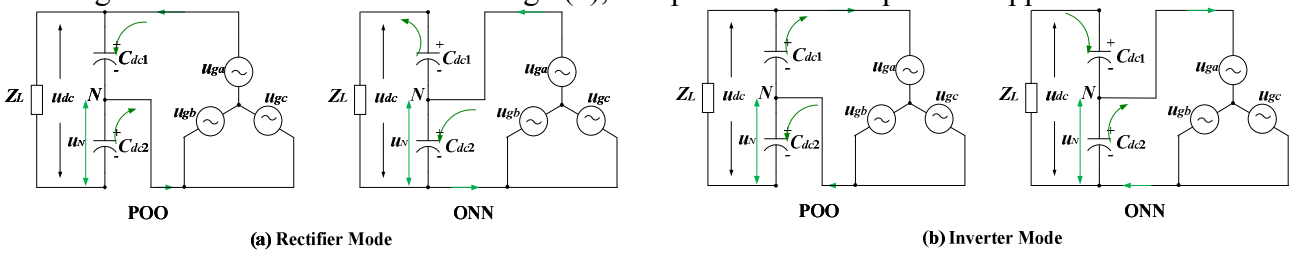

Fig.3 NP effects in different working modes

So, the neutral-point potential can be controlled by adjusting the time distribution between positive and negative small vectors. For instance, in a random triangle area, the dwell time t_x is for small vectors, we can obtain

$$t_x = t_{xp} + t_{xn} \tag{4}$$

Where t_{xp} and t_{xn} are given by

$$\begin{cases} t_{xp} = \frac{t_x}{2}(1+r) \\ t_{xn} = \frac{t_x}{2}(1-r) \end{cases} \tag{5}$$

Where r is the control factor and $-1 \le r \le 1$. The neutral-point potential can be achieved by changing the value of r according to the capacitor voltage deviation. Fig.4 illustrates the control diagram of neutral-point potential.

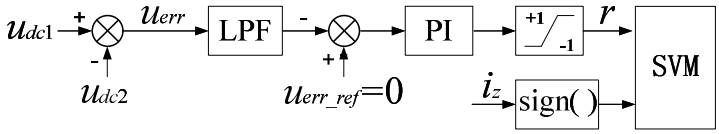

Fig.4 Control diagram of neutral-point potential

To damp all other amounts of high frequency, u_{err} is filtered by a low-pass filter(LPF). After that, the err signal is PI-controlled and the output is treated as the small vectors' adjustment coefficient r,

which should be limited to [-1,+1]. In this case, control factor *r* is no longer a constant, but a varying coefficient according to the capacitor voltage deviation.

Digital Modular Control System

Hardware Design. The paper adopts a distributed digital modular control system, the hardware is a combination of multiple single set of independent controllers, as illustrated in Fig.5(a). There are one main controller (MC Controller), one main interface controller (MI Controller), and a few sub-controllers (PEBB Controller).

MC Controller is the converter's brain, receives the status information of each part and sends control commands, and it is also responsible for communication with upper computer, which is realized in labview; MI Controller is mainly responsible for voltage and temperature acquisition, and some switches' control signals. The number of PEBB Controllers depends on the number of the converter units (maximum number is 28 by the limitation of hardware resources), and the configurations of each sub-controller are exactly the same, it is responsible for monitoring the corresponding converter unit. The data interaction between MC Controller, MI Controller and PEBB Controllers are via optical-fiber communications (Powerlink).

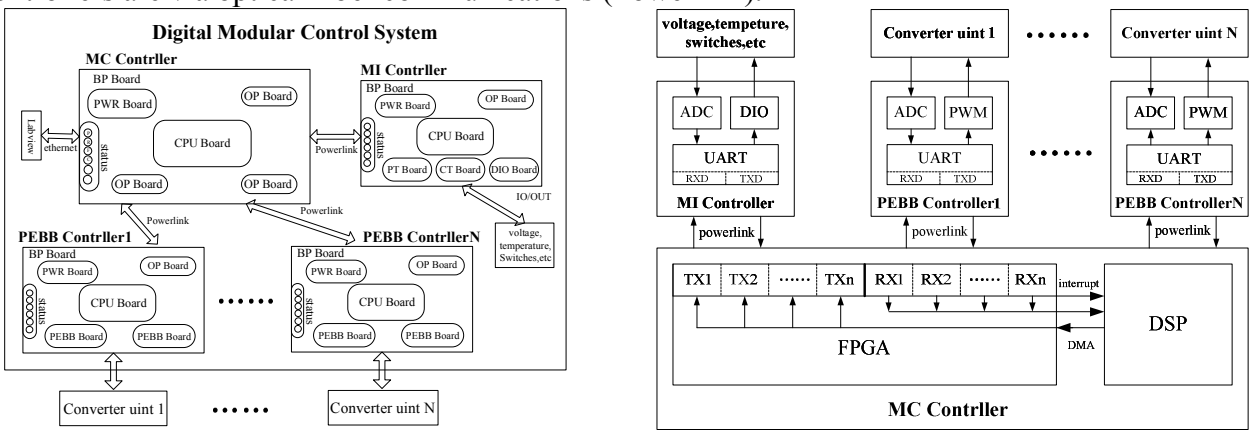

(a) Hardware block diagram (b) Software block diagram

Fig.5 Digital modular control system

Each single set of controller is assembled by different sub-board according to their respective function. These sub-boards includes BP board (backplane board), PWR board (power board), OP board (optical-fiber communication board), PEBB board (power electronic building block board), DIO board (digital input output board), CPU board(cpu control board), etc. Each of these sub-boards plays a different role in particular controller.

Software Design. Fig.5(b) shows software block diagram of the modular control system. The software in MC is completed by FPGA and DSP together, the main function of FPGA is to receive each basic unit of converter's TXD data though optical-fiber interfaces (RX1, RX2,…, RXn), and then send DMA (Direct Memory Access) interrupt signal to DSP after sub-controllers upload all the data. All the analog signals should be filtered, and then DSP performs converter's control algorithms, and the calculated duty information is also sent via EMIF interface to the FPGA, after that, FPGA synchronously transmitted the control message to sub-controller of each converter unit via fiber optic interfaces (TX1, TX2, …, TXn).

All software in MI and PEBB Controllers are done by FPGA, designed according to the modular structure on the basis of the implementation of the different functions, mainly consists of four parts: DIO module, ADC module, PWM module, and UART module. Among them, ADC module is mainly responsible for corresponding voltage, current and temperature acquisition of converter units. Then, it delivers signal data to the sending data portion of the UART module (i.e. TXD) after converting it to digital signal; PWM module is responsible for converting the duty information, which is received by the RXD portion of the UART module, to the corresponding pulse signal. UART module is mainly

responsible for sending data, which is converted and packaged by the ADC and DIO modules, to the MC Controller through a custom communication protocol, while waiting to receive the control information sent by MC Controller.

Experimental Results

To verify the above-mentioned control method, a digital experimental system for neutral-point-clamped three-level converter is set up. System structure is shown in Fig.1. And it adopts the proposed digital modular control system, which is composed of one MC Controller, one MI Controller and one PEBB Controller. The fiber-optical communication speed is 10Mbps.

The experiment is carried out under the following conditions: the power switches employed Infineon's IGBT (F3L300R07PE); Grid line voltage u_{gab}=100V (RMS), the fundamental frequency is 50Hz; two DC-link Capacitors C_{dc1}=C_{dc2}=2mF; LCL fiter: L_g=0.2mH, L_i=0.4mH, C_f =17μF(star connection). The load Z_L is a pure resistance with a value of 14.4Ω. The sampling and switching frequency both are set as 12kHz, and DC bus voltage u_{dc} voltage is expected to be controlled at 200V. It's worth to note that experimental results are all captured by the upper computer (Labview). In these figures, 1 stands for 166μs in time scale.

As shown in Fig6, grid line voltage u_{gab}, phase voltage u_{ga} and SPLL angle are given out. From the figure, we can clearly observe their relationship, and it also illustrates that the proposed digital modular control system works well and the output angle of software phase locked loop (SPLL) is smooth and stable.

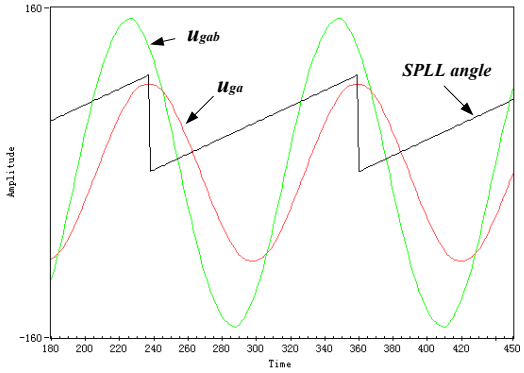

Fig.6 Line \ Phase voltage and SPLL angle

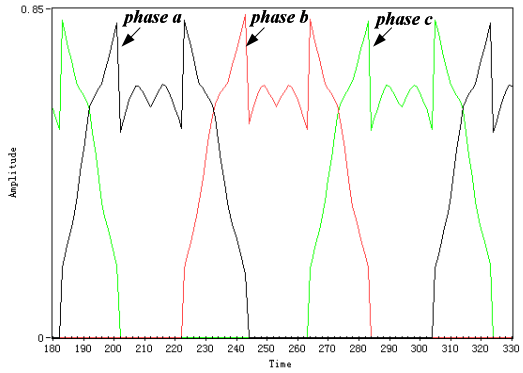

Fig.7 SVM modulated waves

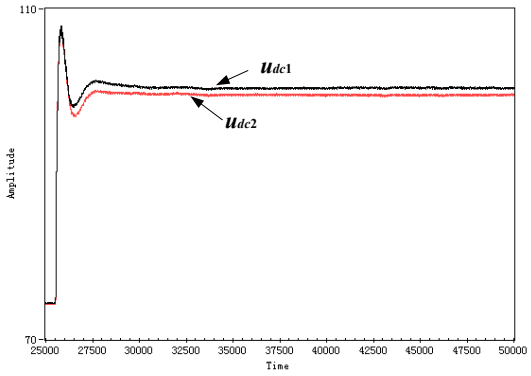

(a) without NP control

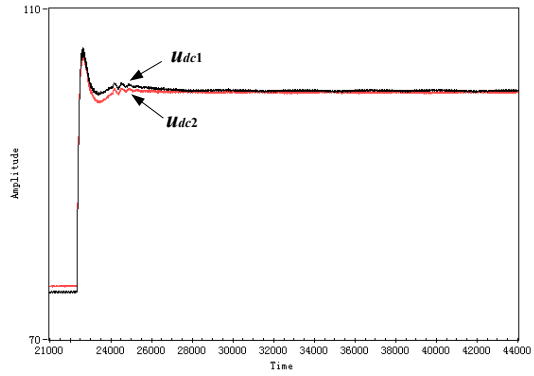

(b) with proposed NP control

Fig.8 Capacitor voltages during dynamic state

Fig.8 shows the control effects of the proposed neutral-point potential control method during dynamic state. It can be seen from Fig.8(a) that upper and lower capacitor both are charged to approximately 74V until the converter has worked. After the converter has started up, voltage deviation between the two capacitors is about 3V. However, with the proposed neutral-point potential control method, voltage deviation shrinks to about 0.5V, as exhibited in Fig.8(b). What's more, the converter receives a good performance in dc bus voltage adjustment.

Conclusion

A digital experimental system for neutral-point-clamped three-level converter has been studied. This paper analyses SVM's digital implementation method and proposes an effective strategy to control neutral-point potential, which is easy to be realized in engineering practice. The method uses a variable factor as the small vectors' adjustment coefficient, which is calculated by PI controller with capacitor voltage deviation. In order to solve the problems brought by the centralized controller, a digital modular control system is developed, in which both hardware and software structures can be configured conveniently. Experimental validation has been done finally. And the experimental results prove that proposed neutral-point balancing method is effective and it has good performance in dc bus voltage adjustment as well. What's more, the results show that proposed digital modular control system is feasible and reliable.

References

[1] S. Kouro, M. Malinowski, K. Gopakumar, J. Pou, L.G. Franquelo, Bin Wu, etc, "Recent Advances and Industrial Applications of Multilevel Converters," *IEEE Trans. on Industry Electronics*, vol.57, no.8, pp.2553-2580, 2010.

[2] J. Rodriguez, S. Bernet, B. Wu, J.O. Pontt, S. Kouro, "Multilevel Voltage-Source-Converter Topologies for Industrial Medium-Voltage Drives," *IEEE Trans. on Industrial Electronics*, vol.54, no. 6, pp.2930-2945, 2007.

[3] J.M. Carrasco, L.G. Franquelo, J.T. Bialasiewicz, "Power-Electronic Systems for the Grid Integration of Renewable Energy Sources: A Survey," *IEEE Trans. on Industry Electronics*, vol.53, no.4, pp.1002-1016, 2006.

[4] A. Yazdani, R. Iravani, "Dynamic model and control of the NPC-based back-to-back HVDC system," *IEEE Trans. on Power Delivery*, vol.21, no.1, pp.414-424, 2006.

[5] A. Nabae, I. Takahashi, H. Akagi, "A new neutral-point clamped PWM inverter," *IEEE Trans. on Industry Applications*, vol.IA-17, no.5, pp.518-523, 1981.

[6] C. Newton, M. Sumner, "Neutral point control for multi-level inverters: theory, design and operational limitations," *Proc. IAS*, vol.2, pp.1336-1343, 1997.

[7] S. Ogasawara, H. Akagi, "Analysis of variation of neutral point potential in neutral-point-clamped voltage source PWM inverters," *Proc. IEEE-IAS*, vol.2, pp.965-970, 1993.

[8] Q. Song, W. Liu, Q. Yu, X, Xie, Z. Wang, "A neutral-point potential balancing algorithm for three-level NPC inverters using analytically injected zero-sequence voltage," Proc, APEC, vol.1, pp.228-233, 2003.

[9] Jae Hyeong Seo, Chang Ho Choi, Dong-Seok Hyun, "A new simplified space-vector PWM method for three-level inverters," *IEEE Trans. on Power Electronics*, vol.16, no.4, pp.545-550, 2001.

[10] K.H. Bhalodi, P. Agrawal, "Space Vector Modulation with DC-Link Voltage Balancing Control for Three-Level Inverters," *Proc. Int. Conf. PEDES*, pp.1-6, 2006.

[11] Yo-Han Lee, Bum-Seok Suh, Dong-seok Hyun, "A novel PWM scheme for a three-level voltage source inverter with GTO thyristors," *IEEE Trans. on Industry Applications*, vol.32, no.2, pp.260-268, 1996.

[12] K. Yamanaka, A.M. Hava, H. Kirino, Y. Tanaka, N. Koga, T. Kume, "A novel neutral point potential stabilization technique using the information of output current polarities and voltage vector" *IEEE Trans. on Industry Applications*, vol.38, no.6, pp.1572-1580, 2002.

[13] Wu Bin. High-Power Converters and AC Drives [M]. IEEE Press, Wiley-Inter science, 2006.

[14] H. du Toit Mouton, "Natural balancing of three-level neutral-point-clamped PWM inverters," *IEEE Trans. on Industrial Electronics*, vol.49, no.5, pp1017-1025, 2002.

Advanced Materials Research Vols. 986-987 (2014) pp 1864-1868

doi:10.4028/www.scientific.net/AMR.986-987.1864

STUDY on SIMULATION of TEMPERATURE FIELD and OPTIMIZATION of STRUCTURE to GROUNDING RESISTOR

Da-jiang He[1 a], Peng-fei Shao[2,b], Hen-ling Yang[1,c], Jing Xiao[1], Jun Qu[1]

[1]Department of Physics & Information Engineering, Huaihua University, Huaihua, China;

[2]College of Information Science and Engineering, Huaqiao University, Xiamen,China

[a]email:hkw001@sina.com

[b]email:343042@qq.com

[c]email:6506532@qq.com

Keywords: grounding resistor; temperature field; simulation; structure optimization.

Abstract. According to the structure of grounding resistor, the flow-current experiments of alloy materials which have different performance and specification have been done in the condition of simulation grounding fault. Based on the experiments, the simulation models of temperature field have been constructed; the distribution characteristics of the transient temperature field and the structure optimization of Grounding Resistor have been studied and discussed by the simulation models. The research results have a great engineering application value on the optimization of performance, the choice of the materials, the cost saving and the improvement of design efficiency to grounding resistor.

Introduction

In high voltage power distribution system, the choice of grounding way of neutral point is a comprehensive technical problem. With ceaseless increase of load, the grid transmission system of overhead line is substituted by cable line gradually. Especially underground cable in the city and industrial estate increases sharply, which brings the fact that the numerical value of capacitance current of the system increases fast.

In order to reduce inside over-voltage because of single-phase short circuit, in grounding way of neutral point, passing the small resistance is more and more adopted [1-3]. But because its short-circuit current is high（100A-2000A）, it will make the temperature of facility elevates fast[4] (the temperature can reach 800℃or so in 10 seconds) ,which has a obvious impact on the performance of alloy material of grounding resistor ,so the resistor will be likely to be damaged because of distortion or burn [5-6]. Especially, when the ground faults occur, it is difficult to measure and control temperature field distribution characteristics because of failure time is short, and internal structure is relatively complex. In order to grasp the distribution of temperature field in fault state, researchers including myself have done some studies and obtained the preliminary research results [7-12].

On this basis, this paper will do some temperature field simulation analysis on influence of space structure arrangement and its structure features. The research results have a great engineering application value on the optimization of performance, the choice of the materials, the cost saving and the improvement of design efficiency to grounding resistor.

Electric test Experiment of Single-Piece Resistance Material

Object of study. In this paper, the object of study is grounding resistor which the short fault current can reaches value between 100A-2000A. According to the difference of operating voltage and short-circuit fault current, the grounding resistor is usually made of 200-300 sheets single-piece resistor which are connected by parallel and series. The geometric model of single-piece resistor is shown as fig.1. What Fig.2 shows is whole structural pattern of certain grounding resistor.

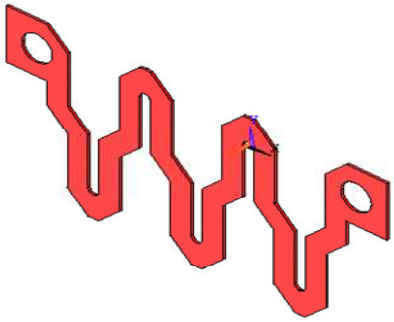

Fig. 1 The geometric model of single-piece resistor

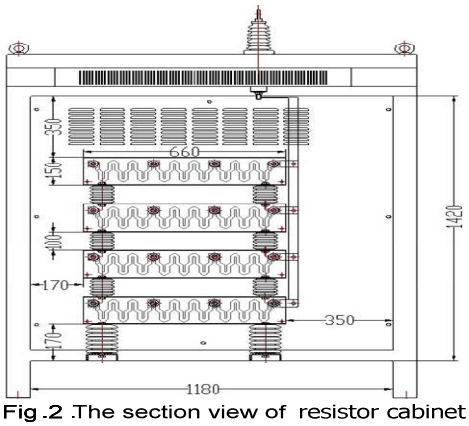

Fig .2 .The section view of resistor cabinet

Electric test of single-piece resistor. It difficult to realize the short-circuit test in the laboratory to the grounding resistor because the short-circuit current is big (usually can reach 1000A or so) and the transient power is high (usually can reach 6GW or so). For this reason, the electric test experimental platform which the most electric test value can reach 1000A or so is built. In order to test the situation of temperature rise within 10 seconds, the single-piece resistor is installed in a close metal box, the materials and dimensions of metal box are made refer to the grounding resistor and its proportion. The temperature sensor adjusted is clung on the surface of resistor piece, and then the real-time data of temperature are collected. In order to record the current variation caused by the temperature rise, the current transformer (CT) is fixed in the test circuit. The results of through-current test of certain specification material are shown respectively by Fig.3 and Fig.4. The Fig.3 shows the current variation curve of resistor piece in 10seconds. From the Fig.3, the current value will decrease gradually from426A to372A. What Fig.4 shows is the temperature rise curve of single-piece resistor in 10 seconds; the maximum temperature rise value will reach 486.6℃.

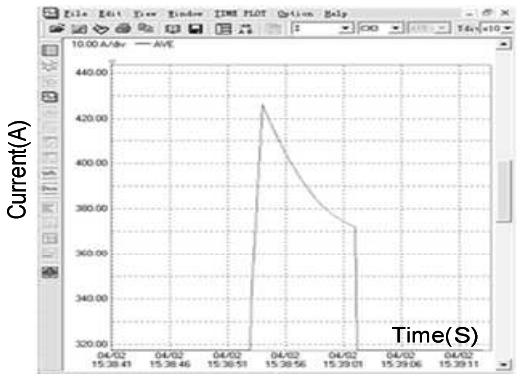

Fig.3 The current variation curve of resistor piece

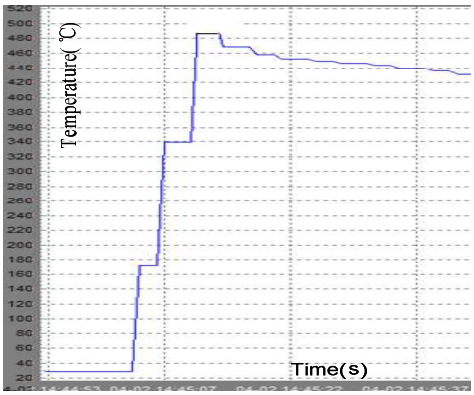

Fig.4 The temperature curve of single-piece resistor

Construction of Simulation Model of Temperature Field

In order to carry out the research on performance of mechanics and heat of grounding resistor in the state of grounding fault, the simulation models of grounding resistor are constructed. First, according to the results of experiment, the simulation models which have different material and specification of single-piece resistor have been built up. In the process of construct models, by adjusting the parameters such as heat transfer coefficient, made the simulation results are consistent with the experimental results. On this basis, according to the structure symmetry of grounding resistor, take a quarter of the resistor component to build the simulation model of grounding resistor.

Simulation Results and Its Analyses

Simulation results of single-piece resistor. According to the experimental test condition, the thermal simulation model of single-piece resistor been built up. Figure 5 shows the temperature field distribution of some specification material when electric current worked 10 second, the maximum

temperature is about 485.4℃. Comparing figure 5 and figure 4, it can be seen that single-piece resistor temperature field simulation results are consistent with experimental results, which indicated the temperature field simulation model of single-piece resistor is feasible. Thereby, it provides a reliable basis for building the temperature field simulation model of grounding resistor.

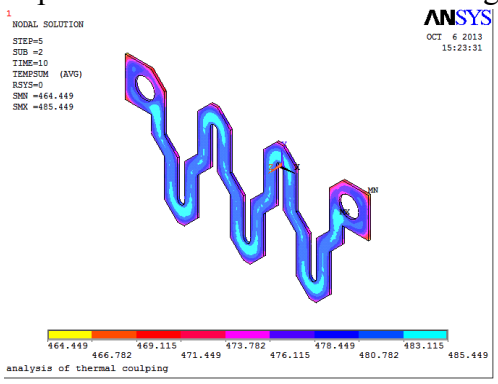

Fig. 5 The temperature field distribution of single-piece resistor

Simulation results of grounding resistor. During the simulation of temperature field to grounding resistor, the current load of grounding resistor is consistent with single-piece resistor, According to the change of current in the process of analog ground fault, the heat generate rate will be applied by multi-step loading. Figure 6 shows the temperature distribution cloud chart for a certain type of grounding resistor in the simulation of initial ground fault current is 426A, fault times for 10 seconds.Figure7 shows the variation curves of temperature along with the time of three nodes at different location of grounding resistor. From figure 6 and figure7, the maximum temperature which has a substantial improvement than single-piece resistor in 10 seconds may reach about 540.4℃, at the same time, there exist certain temperature differences in different location, and the highest temperature will be 14% higher than the lowest temperature.

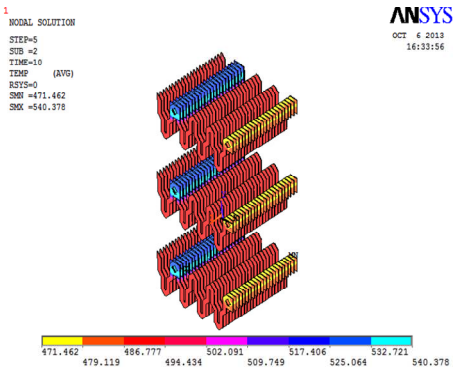

Fig. 6 The temperature distribution cloud chart of grounding resistor

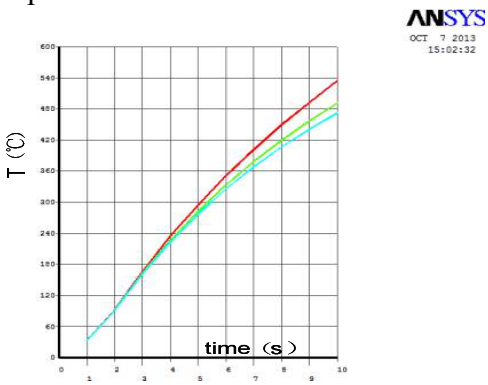

Fig. 7 The temperature curves of three nodes at different location of grounding resistor.

Discussions

Influence of Cross-sectional area size of resistance piece on the temperature field distribution. It is very obviously impact of cross-sectional area size of resistance piece on temperature field distribution. In the simulation model just as figure 6 shows, the cross-sectional area is reduced by 10%,but the other condition remain unchanged, the temperature field distribution simulation result is shown as Figure 8, the peak temperature may reach about 596.9℃, comparison to the Figure 6,the peak temperature increase 10.5%. The further research shows that the influence of Cross-sectional area size to the temperature field distribution is a nonlinear relationship, and the influence is also related to the material properties.

Influence of distance between pieces on the temperature field distribution. The influence of distance between pieces to temperature field distribution is very obvious too. In the simulation model just as figure 6 shows, the distance between pieces and layers is reduced by 10%,but the other condition remain unchanged, the temperature field distribution simulation result is shown as Figure 9,

the peak temperature may reach about 565.5℃, comparison to the Figure 6,the peak temperature increase 5%. The further research shows that the influence of distance between pieces to the temperature field distribution is a nonlinear relationship too.

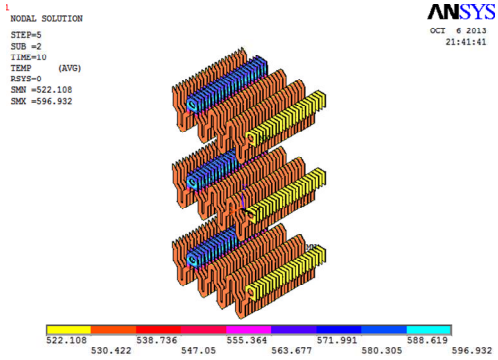

Fig .8 . The temperature distribution while cross sectional area of resistor is reduced 10%

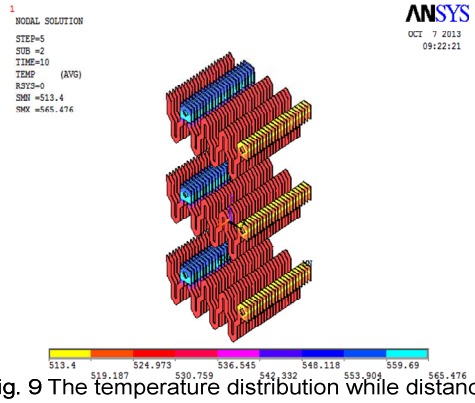

Fig. 9 The temperature distribution while distance between pieces and layers is reduced by 10%

Summary

The temperature field simulation model of resistance piece is built up. The simulation results are consistent with experimental results; it shows that the temperature field simulation model of resistance piece is correctness.

According to the temperature field simulation model of resistance piece, the model of grounding resistor in the analog grounding fault is built. On this basis, the temperature field distribution under short circuit faults is simulated, and the influences of geometry structure of grounding resistor to temperature field distribution are analyzed and discussed. The results have an important reference value to the research on operating performance of grounding resistor.

On the basis of experimental research follow-up, the temperature field simulation model of grounding resistor will been further optimized. The optimizing simulation model will have an important project value to materials filtration, structure optimization, costs saving of the grounding resistor; it will greatly enhance the design efficiency and greatly improve the design technology of grounding resistor.

Acknowledgements

This work was financially supported by Science and technology plan projects of Hunan province (No.2011 FJ3143) and Key project of department of education in Hunan province (No. 11 A090).

References

[1] Zhao Ran, Tan Weipu, Yang Yihan. Analysis of neutral grounding operation modes for distribution network. [J].Relay, 2007:35(4): 22-26.

[2] Liu Mingyan. Selection of neutral grounding modes in power distribution network. [J]. Power System Technology, 2004:28(16):86-88.

[3] Yao Huannian, Cao Meiyue. On neutral grounding modes of cable network. [J]. Power System Technology, 2003:27(2):84-89.

[4] State bureau of technical supervision. Neutral grounding resistor of distribution system (DL/T780-2001).Beijing, standard publishing press of China, 2001.

[5] Zhen-dong Wang, yuan-shen Gong.Electrothermal alloy.[M]. Beijing, Chemical industry press, 2006: 3-135.

[6] Chen Yu-shi, Jin Yi, Sun Chan. Development of large-power loaded resistor.[J]. Journal of Yangtze River Scientific Research Institute, 2005:22(1):60-62.

[7] He Dajiang, Luo Longfu, Shao Pengfei,etal. Development of neutral-grounding resistor made of alloy material.[J]. Power System Technology, 2009:33(18):214-218.

[8] He dajiang, Luo longfu, Shao pengfei,ect. Experiment of Temperature Rise and Simulation on the Temperature Field of Grounding Resistor.[J]. Journal of Hunan University, 2009:36(9):51-54.
[9] He Da-jiang, Yang Heng-ling, Xiao-jing, et.al.Performance research of Resistance materials of Low resistance grounding resistor under the Short-circuit state.[J]. Advanced Materials Research, 2012:382:137-140.
[10] HE Da-jiang , XIAO-jing, YANG Heng-ling , et.al. Experimental research on properties of materials of grounding resistor.[J]. Research Journal of Applied Sciences, Engineering and Technology, 2013:5(9):2858-2862.
[11] Paulke J,Weichert H,Steinhaeuser P. Thermal simulation of switchgear.[J]. IEEE Transactions on Components and Packaging Technologies, 2002:25(3):6-11.
[12] Niu Chunping, Chen Degui, Liu Yingyi,et.Temperature Field Simulation of AC Contactor and Analysis of Its Influence Factors.[J]. Transactions of China Electrotechnical society, 2007:22(5):71-77.

Advanced Materials Research Vols. 986-987 (2014) pp 1869-1872

doi:10.4028/www.scientific.net/AMR.986-987.1869

Study on the Lithium-ion Batteries Performance of Electric Vehicles

Lu Junmin[1, a], Wang Xiaokan[1, b]

[1]Henan Mechanical and Electrical Vocational College, Xinzheng, 451191, China

[a]wxkbbg@163.com, [b]wangxiaokan@126.com

Keywords: Lithium-ion Battery;Test Data;Charge and Discharge Performance

Abstract. By comprehensive analyzing the lead-acid batteries development situation of electric vehicle at first, and making a comprehensive comparison for the performances and features of the lead-acid batteries, nickel hydrogen batteries and lithium-ion batteries, then studying the charge and discharge performance of the lithium batteries which provides technical support and references for the application and popularization of lithium-ion batteries in electric vehicles.

Introduction

Human is facing the contradictory problems of the increasing depletion of natural resources and rising energy demand. The research and development of electric vehicles have become the focus of all the countries in the world automobile industry. However, one of the developing bottlenecks of electric vehicles is the power problem. So, the driving range when charging each time and the initial price are the main obstacles for the promotion of electric vehicles at present. There are three electric vehicles are being researched at home and abroad, namely : complete with battery -powered electric vehicles(BOEV), the internal combustion engine is the main power and battery auxiliary power hybrid electric vehicles (HEV) and fuel cell electric vehicles (FCEV).

Comparisons of Several Common Power Batteries

The battery development and use is the success key of electric vehicles. Electric vehicle battery is a rechargeable battery or secondary battery. The universal secondary battery of electric vehicles are currently used: lead-acid batteries , nickel cadmium batteries, nickel metal hydride batteries and lithium-ion batteries.

Lead-acid Batteries

The metal lead is the negative electrode of lead-acid batteries,the dioxide lead is its positive electrode, the sulfuric acid is the electrolyte, the chemical reaction is:

$$P_b+P_bO_2+2H_2SO_4=2P_bSO_4+2H_2O$$

When discharged, lead, dioxide lead and electrolyte generates chemistry reaction to the sulfate lead.When charging the reaction process is just the opposite.It has the advantages of relatively mature technology, good reliability, low raw materials prices and specific power can basically meet the requirement of electric vehicle power.The shortcoming is low specific energy which leading to short mileage when charging every time, and the higher quality and larger volume which increasing the weight of automobiles and its power consumption.In addition the use life of lead-acid battery is short,so the use cost is higher.The biggest drawback of lead-acid battery is low specific energy, low efficiency and environmental pollution. At present, the domestic lead-acid battery still has a strong market vitality.The city bus such as Yutong bus,Beijing bus,Xiamen Golden Dragon bus is still in the use of lead-acid batteries.

Ni-MH Batteries

The positive electrode active material of the Ni-MH batteries is nickel hydroxide,the negative electrode active material is the storage hydrogen alloy, the electrolyte is a potassium hydroxide solution , the main reaction of the battery is:

$$N_i(OH)_2+OH=NiOOH+H_2O+e^-$$
$$M+H_2O+e^-=MH_{ab}+OH^-$$
$$N_i(OH)_2+M=NiOOH+MH_{ab}$$

Where M is the hydrogen storage alloy; MHab is the storage of storage hydrogen alloy with hydrogen. When the battery charges, the positive electrode hydrogen will move into the storage hydrogen alloy of the negative electrode, the discharge process is reversed. In this process, the positive and negative electrode active material is accompanied by the structural composition and volume changes , the electrolyte will also change.

Ni-MH batteries belong to alkaline batteries, it has the advantages of good safety,high performance, free contaminants which known as "green power" and a little environmental pollution,meanwhile it has the higher specific energy and specific power. But currently an important impeding problem of its application is the higher initial cost, it also has the problems of the memory effect and charging calorific,slightly worse large current charging performance;it easy to heat when charging that causes the security problems.Ni-MH battery is the most widely used on the market because it has the most mature technology of power battery. At present,most of the hybrid cars in the market are using the nickel hydrogen batteries which often be used to the auxiliary power source.

Lithium-ion Battery

The negative electrode of the lithium-ion batteries uses the lithium-carbon compound, the lithium transition metal oxide is the positive electrode, an organic liquid or solid polymer is the electrolyte. In the process of charging and discharging, the lithium-ions between the positive electrode and the negative electrode round-trip flow.The electrochemical reaction equation is:

$$L_{ix}C+L_{i-x}M_yO_z=C+L_iM_yO_z$$

When discharging, the lithium-ions battery pass from the positive to electrolyte,then arrive the negative. When charging, the process is just to the opposition.Lithium-ion battery has the higher cell voltage,the higher specific energy and energy density, so it can be said that the maximum specific energy of battery power with high stable. Its performance indicators can meet the electric vehicle interim targets set by USABC. This makes lithium-ion batteries widely used in the electric vehicles.

Table 1 The Basic Performance of Four Secondary Batteries

battery type	voltage（V）	Specific energy （Wh/kg）	specific power （W/kg）	cycle life （Frequency）
lead-acid battery	2.0	30-40	150	300-500
nickel-cadmium battery	1.2	45-50	170	500
ni-mh battery	1.2	70-80	250	>500
lithium-ions bbattery	3.6	120-150	300	1000

Performance Test of Lithium-Ion Battery

Here especially for lithium-ion batteries were tested serval times which respectively were: lithium-ion battery discharge capacity experiment under different discharge current conditions; lithium-ion battery discharge capacity experiment under different temperature conditions; lithium-ion battery charging time experiment under different conditions of charging current.

Lithium-ion Battery Discharge Capacity Experiment Under Different Discharge Current Conditions

When the electric vehicle climbing, starting and accelerating,it requires power battery to provide high specific power,namely,the enough higher discharge current which can provide sufficient power. We conducted a lithium-ion battery C/3, C/2, C/1 rate discharge test, and the data were in the Table 2. Seen from the test results, with the increase of the battery discharge current, the discharge capacity of the battery first increased and then decreased which because of the slow diffusion rate of the lithium-ion battery.With the increase of the discharge current which make the diffusion rate become fast and improve the discharge capacity;but the discharge current will further increase, the concentration difference polarization in the battery increases, the voltage which caused by the internal resistance of the battery also inherently increases, so that the discharge capacity accordingly decreased.

Lithium-ion Battery Discharge Capacity Experiment Under Different Temperature Conditions

Because the car current changes rapidly in working conditions, so we did the discharge test of the lithium-ion battery under the -15℃, 0℃, 40℃ temperature, the tested data were in the Table 3.

Table 2 Battery Discharge Test Under Conditions Different Discharge Currents

discharge current	starting voltage （V）	termination voltage（V）	Ah	Wh	remarks
C/1	11.580	7. 889	19.87	184.98	
C/2	11.654	7.957	43.86	412.21	Environmental temperature: 17.4℃，discharge current: 24.45A
C/2	11.689	7.887	38.19	364.50	discharge current:23.85A
C/3	12.012	9.012	0.12	1.02	discharge current:14.98A
C/3	11.985	7.897	1.20	9.92	the continuing discharge current:14.98A
C/3	10.823	8.976	0.18	1.66	
C/3	11.011	8.990	0.33	3.05	
C/3	10.986	8.986	0.23	2.06	After standing at room temperature C/3 supplementary charge.

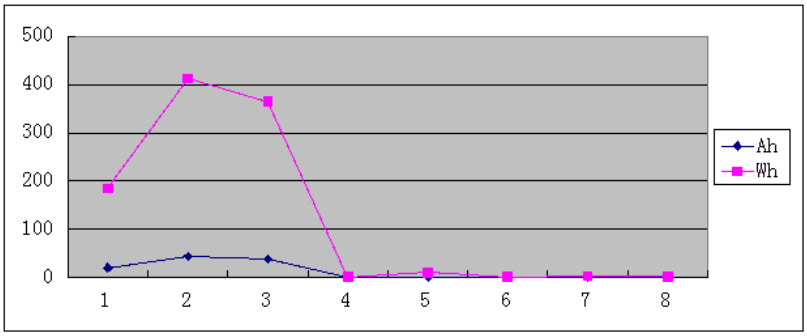

Figure 1 Lithium-ion Battery Discharge Capacity Test Under Different Temperature Conditions

Table 3 Lithium Ion Battery Discharge Test under the Three Different Temperature Conditions

discharge current	starting voltage （V）	termination voltage（V）	Ah	Wh	remarks
C/3	12.100	7.991	0.49	4.05	-15℃
C/3	11.856	9.101	24.01	1.66	0℃，Stable voltage:11.34V
C/3	11.498	8.998	41.37	3.05	40℃
C/3	11.531	8.998	0.23	2.06	When the temperature is 40℃,the battery will be placed 6 hours.

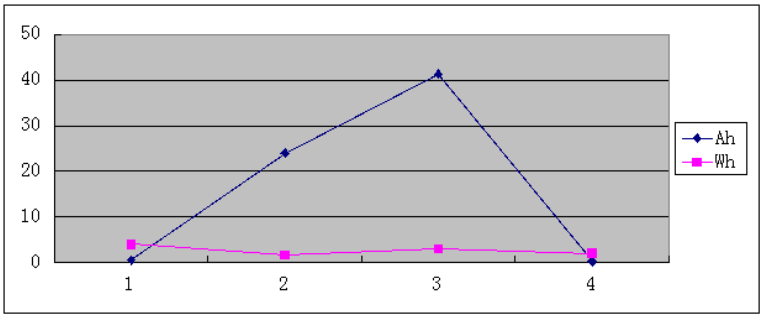

Figure 2 Different Charging Current Conditions Lithium-ion Battery Charging Time Trial

Seen from the test results,with the increase of the battery working temperature, the discharge capacity of the battery increased significantly. All that caused by the lithium-ion diffusion of the battery is slow in the low temperature, the battery activity will enhance with improvement of the temperature. But after holding temperature time increased,the overall temperature of the battery would rise which further make lithium-ion activity tend to disorder that it resulted to the increase of the resistance and the discharge capacity decreased slightly.

Lithium-ion Battery Charging Time Experiment Under Different Conditions Of Charging Current

Since the charging time of electric vehicles is much longer than the refueling cars, so it has become an important impend factors which compared to the internal combustion engine vehicles. At the same time the charge capacity is closely related to the charge time.Seen from the table 4 , supposed selecting the termination voltage as the test sign, the larger charge current, the shorter charging time,but the charge capacity will be the less.The charging current increases the lithium-ion concentration of the battery inside which result to the more serious imbalance of its, all that makes the electrode enhance, the charge voltage reach quickly end voltage and less power fill into the battery.

Table 4 Different charging current condition of the lithium-ion battery charging time trial

discharge current	time	total time	starting voltage （V）	termination voltage（V）	Ah	Wh
C/1	12.28,15:20-15:55	35’	10.79	12.59	20.95	258.86
C/2	12.27,8:30-10:30	2h	10.90	12.67	37.80	466.79
C/3	12.26,14:00-17:00	5h	11.23	12.64	44.82	546.09
C/3	12.27,13:00-16:00	2h50’59”	11.06	12.62	44.64	540.77

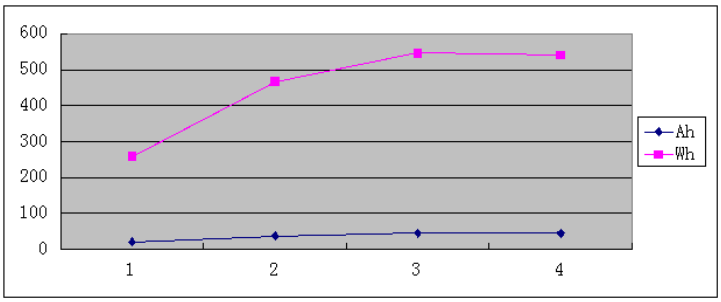

Figure 3 Different charging current condition of the lithium-ion battery charging time trial

Conclusion

Based on the analysis of the mechanical theory as the foundation, designed the soccer robot pick the ball institutions optimal design process, found aim function, select design variables and the corresponding optimization algorithm to optimize a complete set of institutions. At last through the test to get the final performance parameters of the institution. Experiments show that the system has higher accuracy and stability, the new optimize pick the ball have design basic requirements, and achieved good ideal control effect.

References

[1] Ai Juan,Zhang Ruixue, Xu Guoxiang, etc. Analysis on safety performance of electric vehicle lithium ion battery patent [J]. Petroleum and Chemical Equipment, 2013(09):67-69

[2] Ai Xinping, Yang Hanxi.Electric vehicle and power batteries[J]. Electrochemistry,2011 (02):45-48

[3] Jiang Zhijun. Lithium-ion battery cathode material lithium iron phosphate: progress and challenges of [J]. Functional Materials, 2010 (03):35-37

[4] Yang Dong, Chen Bin, Wang Songyang, Hu Jianhua,etc. Lithium iron phosphate battery thermal effect on [J]. Chemical Journal,2011 (17):86-89

[5] in Beijing hospital, Wang Qiang, Chen Wei. The development of electric cars lithium iron phosphate power battery technology [J]. Electric Car, 2011 (10):18-21

Advanced Materials Research Vols. 986-987 (2014) pp 1873-1876

doi:10.4028/www.scientific.net/AMR.986-987.1873

Study on the Return Voltage Function Model of Oil-Paper Insulation Medium Based on Optimization Algorithm

An-na Li[a], Jin-ding Cai[b], Jing-lan Zeng[c]

College of Electrical Engineering and Automation, Fuzhou University, Fuzhou 350108, China

E-mail: [a]1154550693@qq.com, [b]cjd@fzu.edu.cn, [c]375892730@ qq.com

Keywords: return voltage; relaxation response; exponential decay; optimization algorithm

Abstract. Based on the study of dielectric response theory and equivalent circuit of oil-paper insulation medium, this paper deduces the exponential decay type return voltage function model.It also proposes that rhe function can be resolved with the application of optimization algorithm. Finally, the paper takes a return voltage curve which is tested by the oil-immersed transformer for example.Fitting results verify the accuracy of the calculation. Further more,it also explains that return voltage function model is reliable and practical. Therefore,the model plays a crucial role in the follow-up study of topological structure of equivalent circuit of oil-paper insulation.

Introduction

The return voltage method is used to investigate on possibility toindicate insulation degradation, meanwhile , it can effectively diagnose the insulating condition of aging and moisture[1,2]. Currently, many scholars use the equivalent circuit model of oil-paper insulation to explore insulation aging.The return voltage function model derived by equivalent circuit is well used in parameter identification in [3, 4]. However, the model is complex and not intuitive to reflect the relationship between return voltage and insulation aging mechanism. Return voltage reflects the internal response of oil-paper insulation essentially. Therefore, the focus of this study is to establish intuitive and reliable return voltage function model.

Optimization Algorithm Model

Arbitrary nonlinear equations can be expressed as follows：

$$\begin{cases} f_1(x_1, x_2, \cdots, x_n) = 0 \\ f_2(x_1, x_2, \cdots, x_n) = 0 \\ \vdots \\ f_m(x_1, x_2, \cdots, x_n) = 0 \end{cases} \tag{1}$$

Where, $m>n$. the optimal solution of nonlinear equations, which can be converted to an optimization problem, corresponds to solve the minimum value of the following equation:

$$\min F(x_1, x_2, \cdots, x_n) = \min \sum_{i=1}^{m} f_i^2(x_1, x_2, \cdots, x_n) \tag{2}$$

The optimization problem is solved by improved PSO algorithm.Correcting the inertia weight (w) is based on the rate of focal length (k), and their relationship is as follows[5]:

$$w = \begin{cases} (a_1 + \dfrac{|r|}{2.0}) * |\ln k|, & |k| > 1 \\ a_1 * a_2 + \dfrac{|r|}{2.0}, & 0.05 \le |k| \le 1 \\ (a_2 + \dfrac{|r|}{2.0}) * \dfrac{1}{|\ln k|}, & |k| < 0.05 \end{cases} \tag{3}$$

Where, $k=\frac{MaxDist-MeanDist}{MaxDist}$; $MeanDist=\frac{\sum_{i=1}^{h}\sqrt{\sum_{d=1}^{n}(p_{gd}-x_{id})^2}}{h}$; $MaxDist=\max_{i=1,2,...,h}\left(\sqrt{\sum_{d=1}^{n}(p_{gd}-x_{id})^2}\right)$;

a_1=0.3,a_2=0.2; r is a random number from 0 to 1; *MeanDist* is the average focal length of particles; *MaxDist* is the maximum focal length of the particle; h is the total number of particles; n is the dimension of the space, also the number of unknowns; p_{gd} is the global optimum of particle swarm; x_{id} represents the dimensional component d of the position vector of the particle i.

Update the velocity and position of particle swarm by inertia weight w.Procedure iterates until accuracy requirements are satisfied.And then the optimal solutions are obtained

New Return Voltage Function Model

At present, polarization circuit can be described by the equivalent circuit of the series *RC*, which describes a dielectric generated losses with repeated polarization effect under the voltage. Thus, the equivalent circuit model of oil-paper insulation is shown in Fig.1.

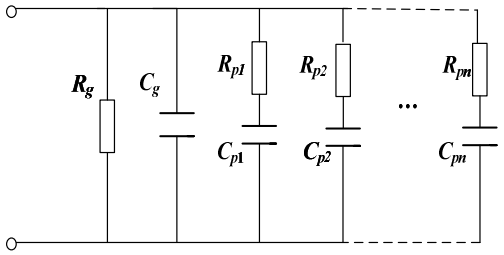

Fig.1 Equivalent circuit based on extended Debye model

DC high voltage U_0 charges the both ends of oil-paper insulation for time of t_c; after short-circuit for time period of t_d ; After that, the voltage equation of capacitor C_{pi} (i=1,2,...,n) is expressed as follows：

$$U_{C_{pi}}(t_c,t_d)=U_0(1-e^{-\frac{t_c}{R_{pi}C_{pi}}})e^{-\frac{t_d}{R_{pi}C_{pi}}} \tag{4}$$

Return voltage value is calculated with the superposition theorem. When the residual charge on the capacitor acting alone, transfer function between return voltage and residual charge is expressed as follows[4]:

$$\frac{U_{ri}(s)}{U_{C_{pi}}(s)}=\frac{H_{n,i}s^n+H_{n-1,i}s^{n-1}+...+H_{1,i}s}{L_{n+1}s^{n+1}+L_ns^n+...+L_1s+L_0}=\frac{H_{n,i}(s-z_{n,i})(s-z_{n-1,i})...(s-z_{1,i})}{L_{n+1}(s-p_{n+1})(s-p_n)...(s-p_1)} \tag{5}$$

Where, $H_{j,i}$(i,j=1,2...,n), L_j (j=0,1,2...,n+1)are the denominator and numerator coefficients which are combined of equivalent circuit parameters; $z_{j,i}$（i,j=1,2...,n) , p_j(j=1,2...,n+1) represent the zeros and poles of the transfer function.

After decomposition and inverse Laplace transform, corresponding return voltage in time-domain is obtained as follows:

$$U_{ri}(t,t_c,t_d)=(A_{1,i}e^{p_1t}+A_{2,i}e^{p_2t}+...+A_{n+1,i}e^{p_{n+1}t})\cdot U_{C_{pi}}(t_c,t_d)=B_{1,i}e^{p_1t}+B_{2,i}e^{p_2t}+...+B_{n+1,i}e^{p_{n+1}t} \tag{6}$$

Where, $B_{j,i}=A_{j,i}\cdot U_{C_{pi}}(t_c,t_d)$; $A_{j,i}=\frac{H_{n,i}}{L_{n+1}}\frac{\prod_{k=1}^{n}(p_j-z_{k,i})}{p_j\prod_{l=1,l\neq j}^{l=n+1}(p_j-p_l)}$ $(i=1,2...,n;\ j=1,2...,n+1)$

Return voltage U_r which is superposed by residual charge of each polarization capacitor is expressed as follows:

$$U_r(t,t_c,t_d)=\sum_{i=1}^{n}U_{ri}=\sum_{i=1}^{n}B_{1,i}e^{p_1t}+\sum_{i=1}^{n}B_{2,i}e^{p_2t}+...+\sum_{i=1}^{n}B_{n+1,i}e^{p_{n+1}t}=\sum_{j=1}^{n+1}C_je^{p_jt}=\sum_{j=1}^{n+1}C_je^{-\frac{t}{\tau_j}} \tag{7}$$

Where, $C_j = \sum_{i=1}^{n} B_{j,i}$, $\tau_j = -1/p_j$.

The above equation is the new return voltage function .If it has n nunbers of polarization branchs, return voltage U_r maybe be maded up of (n+1) nunbers of exponential decay formulas .

Analysis the Model With the Application of Optimization Algorithm

The accuracy of this new model in formala(7) still needs further testing and verifying.The following mainly focus on how to analysis the return voltage function model with the application of optimization algorithm.

Fig.2 gives a curve of return voltage,following study is the solution of the unknown parameters C_i, τ_i （i=1,2,…,n+1）, assuming that $\tau_i < \tau_{i+1}$.

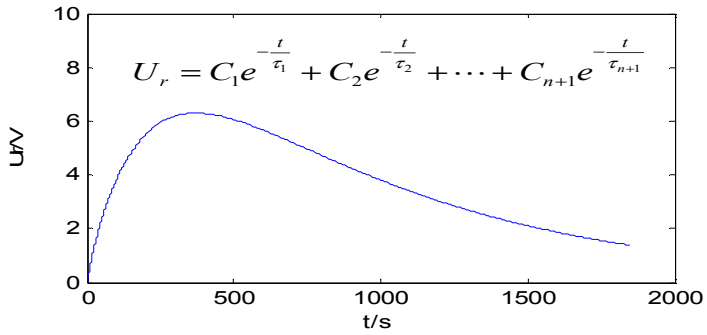

Fig.2 Curve of return voltage

Formala about the fitting voltage sub-lines is expressed as follows:

$$U_{ri} = C_i e^{-\frac{t}{\tau_i}} \qquad (i = 1,2,\cdots n+1) \tag{8}$$

Parameters C_i , τ_i can be calculated precisely with multiple sets of data about tail end of return voltage by using the following equations:

$$\overbrace{U_{ri1} = C_i e^{-\frac{t_1}{\tau_i}};\quad U_{ri2} = C_i e^{-\frac{t_2}{\tau_i}};\quad \cdots \quad U_{rim} = C_i e^{-\frac{t_m}{\tau_i}}} \tag{9}$$

Formala (9) is a group of nonlinear equations,and so parameters can be calculated precisely with the application of optimization algorithm.

Therefore, add up all the voltage sub-lines,then can get the total return voltage,that is $\sum_{i=1}^{n+1} U_{ri} = U_r$

Experiments and Discusstion

One transformer was tested on-site with return voltage measurement techniques. Details of the transformer and test informations are listed in Table 1. The test results are shown in Fig.2.

Table 1.The details of the transformer and test informations

Type	Year of making	U_0/V	t_c/s	t_c/t_d
S7-1000/10	1988	400	400	2：1

Through the above solution, the whole measurement time is divided into 7 groups（n+1=7）, then get 7 sub-lines, the results are shown in Fig.3

Fitted equation is expressed as follows, its goodness of fit is 0.9771.

U_r = 41.4541 * exp(-t * 0.0230) -61.3805 * exp(-t * 0.1523) + 31.6032 * exp(-t * 0.4036)
-19.5155 * exp(-t * 1.3456) + 20.6726 * exp(-t * 28.7336)
+16.3196 * exp(-t * 83.2244) + 20.8126 * exp(-t * 162.8336)

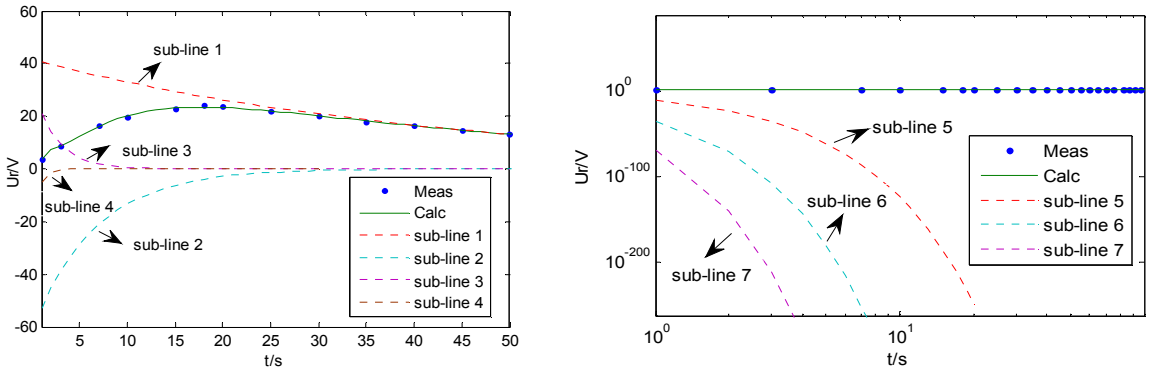

（a） （b）

Fig.3 Calculations of return voltage

According to Fig.3, the return voltage measured values accord with the calculated, getting a better goodness of fit. This further validates the correctness of the formula (7) which is established by the return voltage function model.

Conclusions

Through analyzing the dielectric response theory and the equivalent circuit of oil-paper insulation medium in this paper, the paper deduces the exponential decay type response voltage function model.Study found that the model is closely related to the number of polarization branchs in the insulation system.Changes in internal insulation system corresponding to reflect on the return voltage function model.So the model is suitable for the analysis of oil-paper insulation aging.

And the simulation shows that the optimization algorithm can accurately analytic function and further proves the rationality of return voltage function model.This research plays a crucial role in follow-up study of topological structure of equivalent circuit of oil-paper insulation.

Acknowledgements

This work was financially supported by the National Natural Science Foundation of China (61174117) .

References

[1] Yuan Xu, You-wei Liu, Wang Wen-huan, et a1.Moisture content analysis of oil-paper insulation for large power transformers using dielectric response methods[J].Proceedings of the CSEE, 2012, 32(33)：133-140.

[2] Debangshu Dey, Biswendu Chatterjee, Sivaji Chakravorti, etal. Importance of denoising in dielectric response measurements of transformer insulation: An uncertainty analysis based approach[J].Measurement,2010,43:54–66.

[3] P.R.S. Jota, S. M. Islam, F. G. Jota. Modeling the polarization spectrum in composite oil/paper insulation systems[J]. IEEE Transactions on Dielectrics and Electrical Insulation.1999,6 (2):145-152.

[4] Tapan K. Saha, Prithwiraj Purkait, Frank Müller. Deriving an equivalent circuit of transformers insulation for understanding the dielectric response measurements [J]. IEEE Transactions on Power Delivery, 2005, 20(1)：149-157.

[5] Nian Jiang.Research on interval adaptive Particle Swarm Optimization and its application

Advanced Materials Research Vols. 986-987 (2014) pp 1877-1880

doi:10.4028/www.scientific.net/AMR.986-987.1877

The Design of A New-type LED Switching Power Supply Circuit

Elin Jing, Zhengfeng Sun, Hongyuan Wen

Taizhou Institute of Science and Technology,Nanjing University of Science and Technology ,

Taizhou 225300, China

a20090528@qq.com, wenhongyuan2000@163.com, 408914165@qq.com

Keywords: LED; Power Factor Correction; Switching Power Supply; Flyback

Abstract. A new-type LED switching power supply circuit using flyback converter is designed based on current-mode PFC controller chip L6562. The circuit has some characteristics such as simple structure, wide input voltage range, output stability and reliable operation. The experimental results show that the system efficiency is up to 89.46% when the input voltage changes from 85V to 265V(AC), meanwhile the system works stably with constant current and constant voltage output.

Introduction

LED lighting technology has become one of the hot "green light" researches, due to its characteristics such as high energy-efficiency, long-life, non-pollution and controllability[1-3]. LED is a component sensitive to current, and its luminous intensity determined by the strength of the current flowing LED. The temperature of its junction is rising when LED works long hours at the rated current, which leads to the rapid degradation and the actual life of LED lighting systems shortening[3, 4]. Choosing the right LED driving mode[3, 5], therefore, is significant to achieve LED performance. Currently, most of the LED driving circuits use a more complex structure with two-stage-circuit configuration and large electrolytic capacitors to achieve a balance between input and output power, resulting in lower power factor and power efficiency lower as well as unstable output[1, 5].

Based on current-mode PFC controller chip L6562, a new-type LED switching power supply circuit using flyback converter is designed. The designed circuit, using a single-stage-circuit with the current and voltage feedback, bears these characteristics such as simple structure, wide input voltage range, high power factor(PF), high efficiency, stable output, reliable operation and long life.

System General Scheme

The system of a new-type LED switching power supply is designed to use current-mode PFC controller chip, L6562, as the core. System Architecture is shown in Figure 1. The circuits include surge protection circuit, EMI filtering circuit, first rectifying and filtering circuit, primary circuit (PFC circuit and single-end flyback converter circuit), second rectifying and filtering circuit, constant current and voltage feedback circuit.

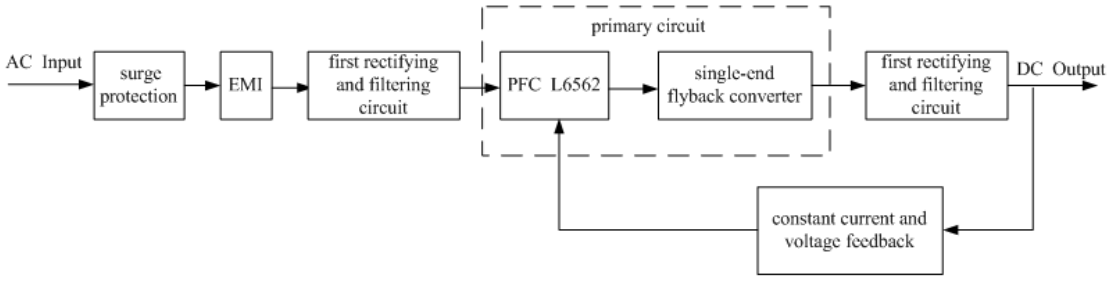

Fig.1. System Architecture

System Circuit Design

The Input Rectifying and Filtering Circuit. The Input Rectifying and Filtering Circuit are shown in Figure 2, including surge protection circuit, EMI filtering circuit , first rectifying and filtering circuit .Voltage-dependent varistor VAR is used to prevent over-voltage and over-current shocks to make sure the system operation is stable. EMI filtering circuit, composed by capacitor C1,C2,

common-mode inductor L1 and resistor R1, filters common-mode interference. The circuit, composed by bridge-rectifier BR and capacitor C3, inductor L2, capacitor C4 and C5 ,is to realize rectification and filtering. Meanwhile, the L2 can reduce the adverse effects of the differential-mode signals as well[5].

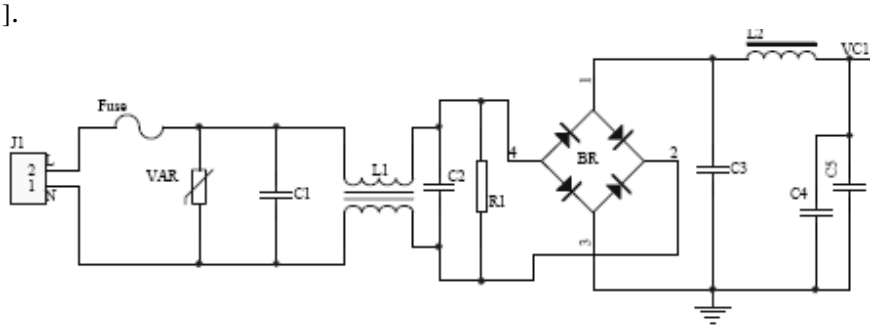

Fig.2. Input Rectifying And Filtering Circuit

The Primary circuit. The Primary circuit is composed by PFC circuit and single-end flyback converter circuit. The circuit is shown in Figure 3. PFC controller chip L6562 works in the transition controlling mode(TCM). Resistor R3 is a starter resistor and supplies the power for L6562. A resistor divider, constituted by R2 and R22, offers the half sine voltage for multipliers (the 3rd foot of L6562)to determine the waveform and phase of the input voltage. When the controller chip is started up, the current of primary coil of the high frequency transformers T1 rises up linearly. The sampling resistor, R26, samples the current of the primary coil(current of MOS). The sampled current is compared with the multiplier to control MOS tube closed. The 5th foot of the chip(ZCD) , zero current detector, connects with the second foot (namesake-end)of the feedback coil of the T1 by resistor R21. When the voltage of the second namesake-end foot approaches zero, the 7th foot(GD) of the chip provides the pulse to open the MOS transistor and the current of the primary coil of T1 increases linearly again. The RC network, constituted by resistor R19, R20 and capacitor C13, is connected with the first and second foot of the chip to enhance the stability of the controlling loop[6]. The shunt capacitor C11 between the drain and source of the MOS tube is to protect the transistor and improve EMC.

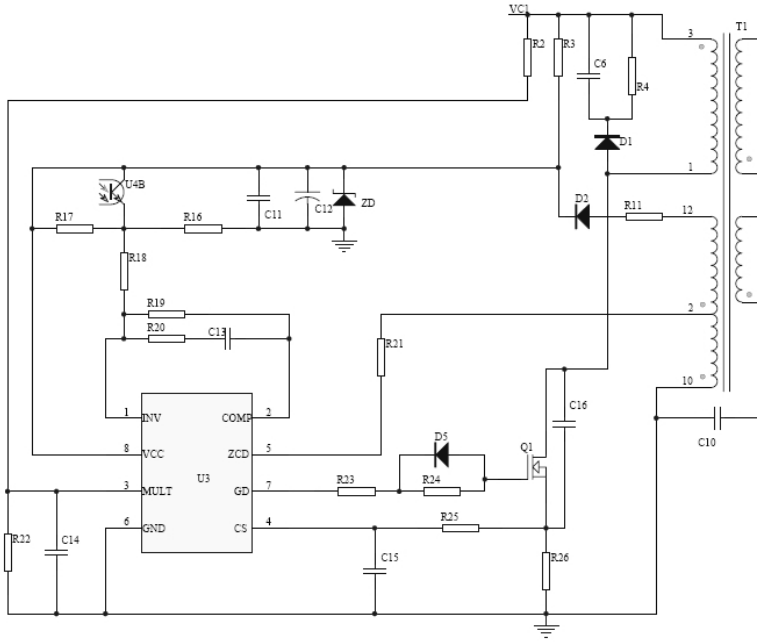

Fig.3. Primary Circuit

The 2nd Rectifying and Filtering Circuit. The 2nd rectifying and filtering circuit is shown in Figure 4. The DC output circuit is composed by the secondary coil of T1(AB), rectifying diode D3 and filtering capacitor C8. When L6562 starts up, the current of primary coil of the T1 flows from the 3rd foot of the primary coil to the 1st foot of the primary coil and the energy is stored in the primary coil, the voltage of the terminal A of the secondary coil is negative while the voltage of the terminal B is

positive, so the diode D3 is turned off. The DC output is provided by the energy stored in the electrolytic capacitor C8. When the MOS tube is turned off in the Figure 3, the induced voltage of primary coil of the transformer T1 is generated, the voltage of the terminal A of the secondary coil is positive and the voltage of the terminal B of the secondary coil is negative, so the diode D3 is turned on. The LED load is driven by the DC output after rectified and filtered by the D3 and C8.

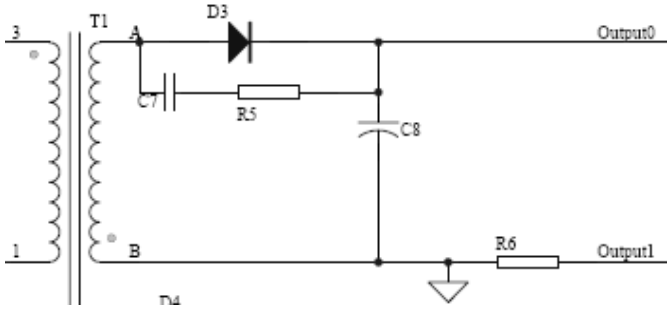

Fig.4. The 2nd Rectifying And Filtering Circuit

The Constant Current and Voltage Feedback Circuit. The design of the constant current and voltage feedback circuit is based on LM358. The circuit is shown in Figure 5. The chip's power supply is provided by the auxiliary power and another secondary coil of the transformer T1.The output voltage provided by the auxiliary power is rectified by the diode D4 and filtered by the capacitor C9. The reference voltage chip U2(TL431) provides the reference voltage for the constant current and voltage feedback circuit. When the output0 voltage in the Figure 4 is higher, the voltage of the 3rd foot of the LM358 exceeds the reference voltage of the 2nd foot of the LM358 and the diode D6 is turned on by the output voltage of the 1st foot of the LM358. The L6562 PFC controlling circuit adjusts the time of the MOS transistor turned on and turned off to achieve adjustment of the output voltage according to optocoupler's feedback(U4). When the output1 current increases, the current is converted into a voltage, applied to the 5th foot of the LM358, by the sampling resistor R6 in Figure 4. If the voltage exceeds the reference voltage of the 6th foot of the LM358, the diode D7 should be turned on by the output voltage of the 7th foot of the LM358. The L6562 PFC controlling circuit adjusts the output current in the same way.

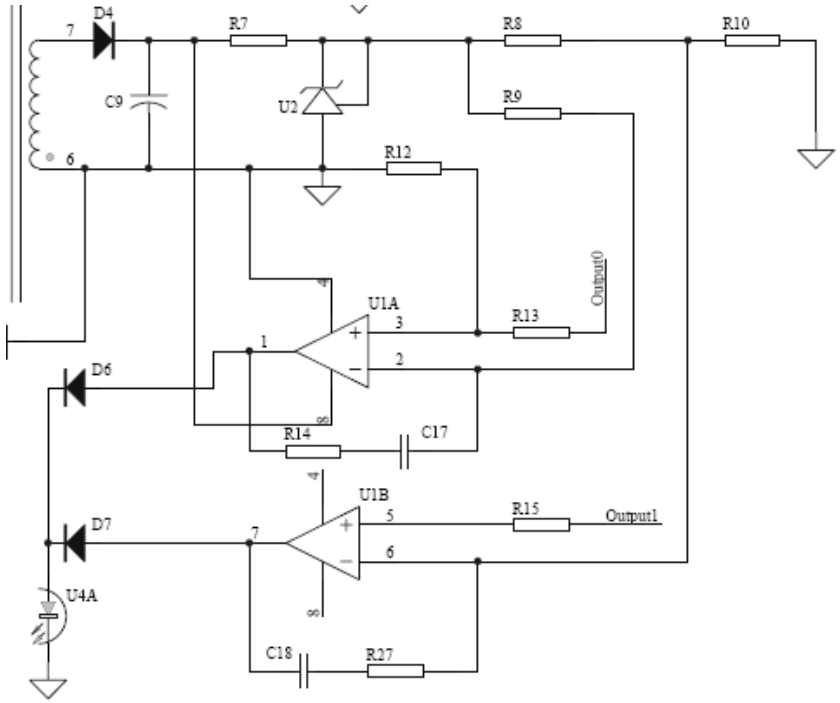

Fig.5.The Constant Current and Voltage Feedback Circuit

Test results

According to the stated principle, a kind of single-end flyback LED switching power supply circuit based on the chip L6562 is made.The system is stable without failure after five hours aging test. The conditions of the power factor(PF) and efficiency tests: input voltage range of 85V~265V at 50Hz. Figure 6 shows the PF and the efficiency of 35W LED switching power supply circuit is designed according to the principle. PF is above 0.95 and close to 1 when the input voltage is 85V. The efficiency is above 85% and close to 90% when the input voltage is 220V.

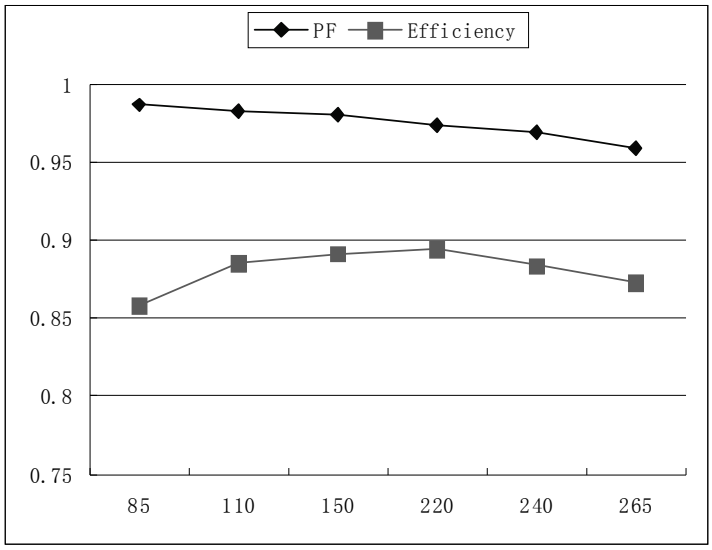

Fig.6. The PF and The Efficiency of 35W LED Switching Power Supply Circuit

Summary

A new-type single-end flyback LED switching power supply circuit, based on the PFC controller L6562, has a higher PF value by adjusting input current according to the feedback of the constant current and voltage circuit and the improved zero current detection circuit. The experiments show that the system bears these characteristics such as simple structure, low cost, high PF and efficiency, wide input voltage range, good stability, high reliability, and long life etc..

Acknowledgements

This work is sponsored by Enterprise Doctor Agglomeration Plan of Jiangsu Province(S20110128-4), and Taizhou Industrial Science and Technology Support Project (TG201204).

References

[1] X.R.Song, J.Shu and Q.B.Wu:*Chinese Journal of Power Sources,* Vol.35(2011)No.11,pp. 1418-1420.

[2] S.Dong, S.G.Chen,T.Zhang,S.S.Liu and S.D.Yuan: *Application of Electronic Technique,* Vol.38 (2012) No. 3, pp. 63-66.

[3] S.B.Chao, D.Y.Qiu and B.Zhang: *Electrotechnical Application*,Vol.30(2011)No.14,pp.40-44.

[4] Q.R.Wang, Z.M.Li, Q.X.Liu,Y.Zhou and Y.Q.Wang: *Semiconductor Optoelectronics,*Vol.33 (2011) No.6, pp.1082 -1085.

[5] J.Z.Chen,Y.H.Ni: *Semiconductor Optoelectronics,*Vol.34 (2012) No.6, pp.906-909.

[6] W.Xiao,L.J.Zhu and P.Z.Wu:Coal Mine Machinery Ashley, Vol.33 (2012) No.8, pp.166-168.

Advanced Materials Research Vols. 986-987 (2014) pp 1881-1883

doi:10.4028/www.scientific.net/AMR.986-987.1881

The Research on Deposition Saturation of Disc Suspension Porcelain Insulator

Hai Tianshu, Wang Qinghao, Ge Changxin, Wu Shaoyong, Cheng Pengfei, Cheng Shuo, Hu Yang, Li Zhixuan, Huang Dongwei, Shi Feng

Fushun Power Supply Company, Liaoning Electric Power Company Limited, State Grid, China,

wts55@126.com

Keywords: Deposition saturation; insulator; ESDD; charged-current coefficient

Abstract. The equivalent salt deposit density (ESDD) is an important characteristic of our country which is used to measure insulator deposition level. The contamination of the insulator would reach saturation after a period of time.In order to increase the specific creepage distance, disc suspension porcelain insulator lower surface inward concave, which makes the rain washing the upper surface difficult, that cause the saturation time of lower surface longer than upper surface .For studying the operation insulator contamination saturation time and reflecting the ESDD of the actual operation line accurately,this paper adopts a comparison method between empty hanging insulator surface and operation insulator surface to measure the ESDD , the field experimental results further verify that the saturated time of disc suspension insulator lower surface is longer, so as to lay the foundation for the ESDD measurement.

Introduction

There are three elements of deposition flashover：Effect of voltage, dirty and wet, none is dispensable. Therefore, the level of deposition on the insulator surface directly affects the reliability of power supply, in order to prevent the occurrence of deposition flashover of transmission lines, the insulator contaminations regular should be understood and got hold of [1-3].

The equivalent salt deposit density (ESDD) is an important characteristic of our country which is used to measure the deposition level of the insulator. ESDD refers to the deposition conductive ion of insulator surface regarded as the content of sodium chloride in the same conditions; the unit is mg/cm^2 [4].

At present, there are three kinds of insulator in transmission line, porcelain insulator, glass insulator and silicon rubber insulator. In this paper, the disc suspension porcelain insulator only, hereinafter referred to as the insulator is discussed [5].

Deposition Saturation of Insulator

Deposition saturation means that the insulator surface go through a process of “the deposition water cleaning deposition again cleaning again ”,which eventually make the deposition of insulator surface reach "dynamic saturation". In general, period of is from every year in October to the following year in March, and the period of rain cleaning is from every year in April to the following year in September. Of course, different regions have different feature, this is mainly with the long and short rainy seasons of different regions. Based on the field test results by China Electric Power Research Institute of China, Deposition saturation time of insulator is 3-5 years in the north, 2-3 years in the south.

In recent years, a large number of experimental data show that Deposition saturation time of insulator has new changes. In view of the deposition problem, we Collect relevant data, carry out statistical analysis of insulator deposition situation, and also compare the ESDD test result between empty hanging insulator and operation insulator, then further verify the saturation time of insulator deposition.

Deposition Situation of the Empty Hanging Insulator

Empty angling insulator, namely reference insulator not only makes the ESDD measurement convenient and efficient, but also assesses the contamination characteristics of insulators more accurately, and lays a foundation for Studying and formulating the anti-pollution flashover strategy. According to the China State Grid Corp rule, we usually adopt the ordinary discotic XP-160(146-155mm height, 255mm disk diameter, 305mm creep distance) insulator and similar to other basic structural parameters. Fushun power Supply Company began ESDD testing from the eighties, in order to test the numerical accuracy, convenient, representative, Fushun power Supply Company chose 106 test points, the number of empty hanging insulator is 108. Test points are located in rural, urban and other source of pollution. (aluminum manufacturer, cement plant, steel mil, Magnesium plant and so on) The model of empty hanging insulator is XP-7, XP-8, XWP-7andXP-160 respectively，the number of XP-7 is 101，the number of XP-8 is 1，the number of SWP-7 is 6，the number of XP-160 is 10.

The empty hanging insulator of 66kV Liuhe first-line 28# tower were Tested from 2007 to 2012，each string has 8 tablets, 2 tablets of empty hanging insulator were measured year and took the average, then we obtained six years of ESDD data as shown below:

Table 1 The ESDD of the empty hanging insulator

Time	ESDD mg/cm^2）	
	Upper Surface	Lower Surface
2007	0.018	0.013
2008	0.022	0.019
2009	0.025	0.026
2010	0.024	0.031
2011	0.025	0.036
2012	0.024	0.041
2013	0.025	0.047

From Table 1 that the insulator upper surface tends to saturation After three years' deposition, which is in line with the traditional theory that the northern Saturated In three to five years. But the ESDD of lower surface still increases with years, and not saturated after 7 years, Thus it can be seen that the deposition saturation time of insulator upper surface does not meet the traditional ESDD saturation theory.

ESDD situation of the operation insulator

Operation line is difficult to power outage and demolition, so it is not realistic to measure the ESDD for the operation insulator each year, insulator without special needs don't even need to be tested all its life. But there is certain regularity between the empty hanging insulator and the charged-current insulator in the same position, namely charged-current coefficient K. It is the ratio between the ESDD of charged-current insulator in the same type to the empty hanging insulator's is generally between 1 ~ 2.

The ESDD of the insulator can reach dynamic saturation for many years，this paper take the method of comparison in order to study the operation insulator contamination saturation time and reflect the ESDD condition of the actual operation line correctly. 130# tower's insulator on 220kV ShenZhong line is selected to reflect the ESDD of the actual operation line accurately. Hen (power transmission Section, Class three) is in charge for this insulator, there is a copper mine near Tower, and it is regarded as the polluter. The tower, like the operation insulator, is hung with the XP-7 empty hanging insulator, which has run for 7 years without cleaning. We carried out an ESDD experiment for130# tower's empty hanging insulator on which is depositing for 4 years and the insulator running for 7 years in the same tower. If the insulator reaches saturation in 4 years, the ESDD has not changed much generally after saturation. That is to say the insulator reaches saturation for 4 years theoretically, and then the deposition quantity and the ESDD are

essentially unchanged. Deposition saturation rule is correct in case the ESDD fits with the charged-current coefficient. The test results are shown in Table 2.

Table 2 The ESDD of the empty hanging insulator and operation insulator

	Empty Hanging		Operation	
Time	4 Years		7 Years	
Insulator Location	Above	Below	Above	Below
	0.024	0.036	0.041	0.136

From the table2 that the ESDD of empty hanging insulator upper surface is 0.024,the ESDD of lower surface is 0.036. If the insulator reaches saturation in 4 years, the ESDD of operation insulator upper surface is 0.024～0.048, the ESDD of lower surface is 0.036～0.072.

The ESDD of operation insulator upper surface 0.041, between 0.024 to 0.048, it can be seen that the ESDD fits the charged-current coefficient from the measurement results. The ESDD of operation insulator lower surface 0.136, between 0.036 to 0.072 , which reflects the insulator lower surface was unable to get washed by the rain effectively ，therefore its saturation time is longer than the north（3～5）.

Conclusion

Deposition saturation of the insulation surface is mainly due to a process of "the deposition water cleaning deposition again cleaning again", it reaches "dynamic saturation" when the deposition quantity equals the amount of washing, the ESDD reaches saturation also at the same time. The deposition is limited by environmental pollution weather, conditions , Insulator shape and so on. Different sharps have different Deposition conditions. As the rib of the bell type insulator surface is deep prismatic but inward concave, it is difficult to get washed by the rain effectively and needs a long time(more than3～5) to reach saturation. The ESDD test of 130# tower's empty hanging insulator and operation insulator is on 220kV Shenzhong. line, it further verifies the fact that insulator deposition saturation time is longer than 3 ~ 5.

For purpose of anti pollution flashover, reducing pollution flashover trip-out rate and avoiding large area pollution flashover accident, studding on deposition saturation time is very necessary. This work involves different aspects，the nature of the work is complex, also needs long hours，the huge amount of manpower, and a large number of statistical data. Therefore, this researcher needs a common commitment by the superior and the collective effort of all researchers.

Reference

[1] Yu Huayu. Anti- flashover of voltage electrical equipment and live cleaning technology. China Power Press, 2006.

[2] Liu Zhenya. Outside insulation of UHV AC transmission system. China Power Press, 2008.

[3] Ping Shaoxun, Zhou Yufang. Power System Neutral Grounding Mode and Operation Analysis.

[4] Yao Huannian, Cao Meiyue. Resonance Grounding of Power System. China Power Press, 2009.

[5] Qiu Zhixian. High voltage composite insulators and Its Applications. China Power Press, 206.

Advanced Materials Research Vols. 986-987 (2014) pp 1884-1887

doi:10.4028/www.scientific.net/AMR.986-987.1884

The Technology Study of New Asymmetrical Half-Bridge Converter

Yuefen Wu

Department of Information and Communication Engineering, Hunan Institute of Science and Technology. Yueyang, China 414006

E-mail: 794859618@qq.com

Keywords: new asymmetrical half-bridge converter; soft switch; auxiliary switch; simulation;

Abstract. Because the shortcomings of the common asymmetrical half-bridge circuit can't achieve soft switch and has DC bias for the transformer, the paper studies a new asymmetrical half-bridge circuit. Compared with the traditional asymmetrical half-bridge circuit, the circuit is added an auxiliary switch and diode by the composition of the slip. Thus the converter can achieve the control strategy of symmetric PWM. At last the simulation results show that the theoretical analysis is correct.

Introduction

The microcomputer is mainly used in switching power supply with asymmetrical half-bridge converter. Compared with traditional half-bridge converter, the new asymmetrical half-bridge converter uses the complementary control technology, and it's two power tubes can use the energy of the leakage inductance of the transformer to achieve soft switch [1][2]. So the paper discusses the work principle of new asymmetrical half-bridge converter, and gives the design parameters. At last the paper gives the simulation results, and the simulation results prove that the validity of the theoretical analysis.

The work principle of new asymmetrical half-bridge converter

The circuit diagram of traditional asymmetrical half-bridge converter is shown as Figure1, and the working principle of the converter can be refer to the reference[1]. The circuit diagram of new asymmetrical half-bridge converter is shown as Figure2, and on the basis of the circuit shown in Figure1 to increase an auxiliary switch tube S_3 and power diode D_3. The main advantages of the circuit can be realized as traditional half-bridge converter symmetric PWM control and is alike asymmetric half-bridge circuit can achieve soft switch, at the same time the function relationship of input and output is linear, at last the DC bias phenomenon of transformer does not exist. The working principle diagram of new asymmetric half-bridge converter is divided into ten stages, and the working mode and waveform is respectively shown as Figure3 and Figure4 [3] [4].

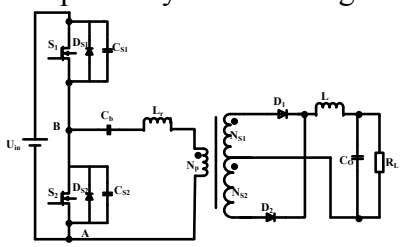

Figure1. The circuit diagram of traditional asymmetrical half-bridge converter

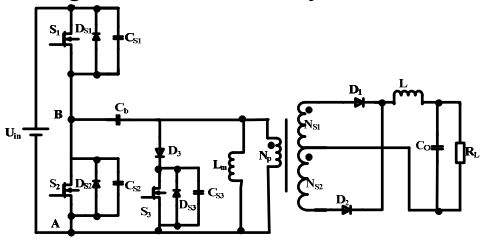

Figure2. The circuit diagram of new asymmetrical half-bridge converter

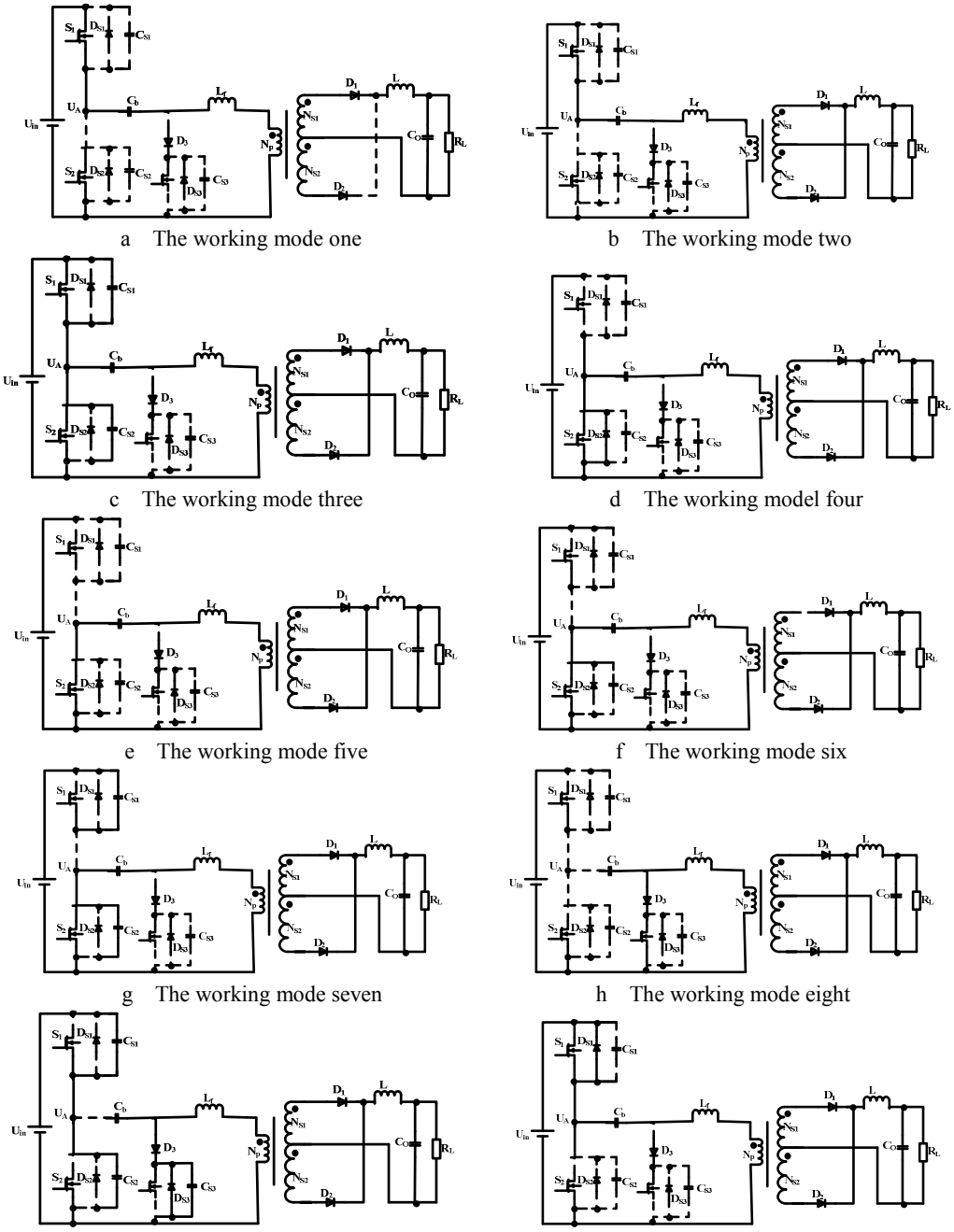

a The working mode one b The working mode two

c The working mode three d The working model four

e The working mode five f The working mode six

g The working mode seven h The working mode eight

i The working mode nine j The working mode ten

Figure3. Ten work stages of new asymmetric half-bridge converter circuit

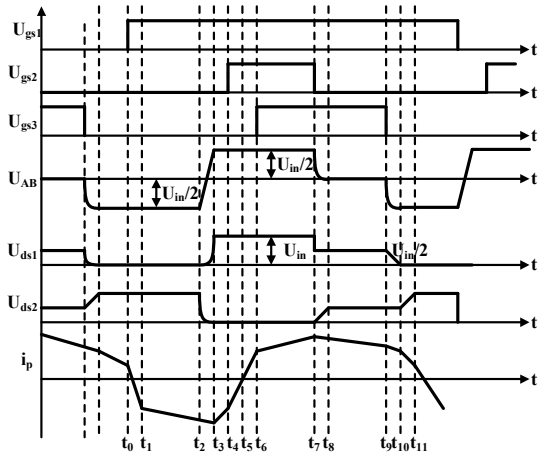

Figure4. The work waveform of a new asymmetric half-bridge converter circuit.

The parameter design of new asymmetrical half-bridge converter

The technical indicators setting of new asymmetrical half-bridge converter are shown below: the input voltage: the input DC voltage: 380V, the output voltage: 48V; the maximum output power:1Kw; the switch frequency: f = 100KHZ.

According to the experience algorithms usually take current maximum fluctuation value is 20% of the maximum current, and the minimum of output current $I_{Omin}=\triangle I/2$. When the design current gets I_{Omin}, the filter inductance L can be calculated by the equation(1).

$$L=\frac{(1-2D)U_O}{\Delta I\times f}=80uH \tag{1}$$

The filter capacitor can be calculated by the equation(2).

$$C_O=\frac{U_O}{8L(2f)^2DU_O}(1-\frac{U_O}{U_{in}/2-U_L-U_D})\approx 2640uF \tag{2}$$

The simulation and experiment results and analysis

In order to verify the feasibility of the main circuit design and parameters choice is correct, the paper makes use of the simulation software of Pspice to model and simulate[5][6]. The simulation results are shown as Figure5 and Figure6, and from the Figure5 the main switch tube S_1 and S_2 of drain-source voltage waveform and the drain current simulation waveform, it can know that the main switch tube S_1 and S_2 are complementary conducted, and achieve the symmetric PWM control. At the same time, the two switch tubes are all zero-voltage opening, and achieve soft switch. So the converter reduces the opening loss of the switch, and improves the efficiency of the circuit. From the Figure6 it can know that the output DC voltage is 48V, and it is consistent with the theoretical calculation of the output voltage results completely.

Figure5. The main switch tube S_1 and S_2 of drain-source voltage waveform and the drain current simulation waveform

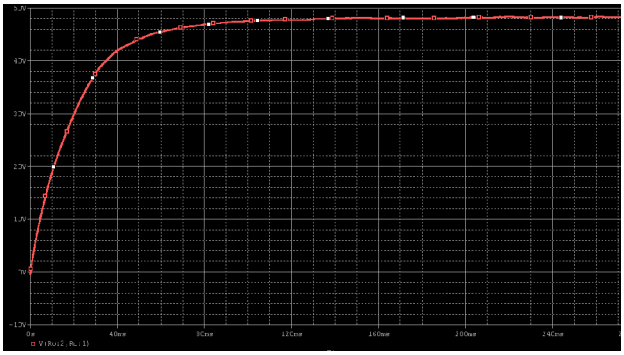

Figure6. The simulation waveform of the output voltage U_O

Conclusion

The new asymmetric half-bridge converter eliminates common asymmetric half-bridge converter can't adopt PWM control and exists the phenomenon of DC bias, and easier to make two switch tubes are easier to implement soft switch, so the new asymmetric half bridge circuit can be widely used in production practice.

References

[1] Chen Danjiang,Zhang Zhongchao. The study of an asymmetrical half-bridge converter[J]. Power supply technology, 2003, 6 (9): 454-457 (In Chinese)

[2] Yang Jianning, Xie Shaojun. The analysis of the asymmetrical half-bridge converter for zero-voltage opening condition[J]. Power electronics technology. 2005.6, Vol. 39, No. 3,52-54

[3] Abedinpour S, Liu R, Fasullo G, et，al. Small-signal Analysis of a New Asymmetrical Half-bridge DC-DC Converter [A]. PESC′2000[C].2000(2):843-847.

[4] Canalesf, Barbosap, Leef.C.A zero2voltage and zero-current switching three 2 level DC/ DC converter [J] . IEEE Transactions on Power Electronics , 2002 ,17(6):898- 904.

[5] Zhao Tao, Jiang Weidong. The simulation analysis of PWM control circuit based on Pspice[J]. Journal of An hui University.2005,29(5):49-52(In Chinese)

[6] Wu Jianqiang. The Pspice simulation practice[M]. Harbin Institute of Technology Press,2001(In Chinese)

Advanced Materials Research Vols. 986-987 (2014) pp 1888-1891

doi:10.4028/www.scientific.net/AMR.986-987.1888

Design of Economized Power Controller Based on Ethernet and Embedded Technology

Tu Jing-lu[1,a],Guo Yi[1,b]
（[1]Hainan Vocational College of Political Science and Law,Haikou,571100）
[a] 254290794@qq.com ,[b] 29876389 @qq.com

Keywords: Ethernet, Embedded Technology, Economized Power Controller

Abstract. Embedded remote economized power controller based on Ethernetadopts uses the embedded technology to realize intelligent control. It cuts the TCP/IP protocol and realizes point-to-point communication through UDP hole punching technology.It goes beyond the LAN limit and follows the principle of energy conservation.This economized power controller has very high practical value.

Introduction

Various data shows that China has become the No.1 of power consumption beyond American. According to statistics, on the one hand, the country's electricity capacity continues to grow, the country's total power generating capacity has more than 0.5 billion kilowatts in 2005, by the end of 2013 the country's total power generating capacity reached 1.25 billion kilowatts; on the other hand, the power shortage phenomenon is still serious. Some areas have blackouts in succession since Jun.2002. A large area of power brownouts has reached 27 provinces and cities in 2005. The energy shortage since 2003 has led to vigorous development of the domestic power industry[1].

The economized power industry needs a lot of products with low energy consumption and electricity control equipment. The intelligent power supply is the most important thing for electricity control. The power supply managers do not require to the site, they can understand the real-time consumption remotely, and they can remotely control by the manual or intelligent way according to the need. We research and develope the remote economized power controller. It adopts the embedded technology to realize the intelligent control, and it cuts the TCP/IP protocol to implement P2P communication among different LANs.

System Overall Design

Embedded remote economized power controller must be an intelligent device for optimum control to electric equipment. It should be able to integrate multiple input parameters, such as remote control commands, real time status of electricity, the detected signal of light and sound,etc. It can make comprehensive judgment and decision according to these parameters, thus it can do the optimal control for electric equipment. At the same time, it needs have a volume as small as possible to construct single intelligent control panel or embed in the switch box. So its core adopts the embedded computer. The embedded computer is responsible for operation and data communication for the measurement/control program.

Embedded remote economized power controller must also have a Ethernet communication module. So that it can receive the remote control commands and parameters sent via Ethernet, and it transmits the detected current status of electric equipment to the host computer[2]. The application system structure of the embedded remote economized power controller is shown in figure 1.

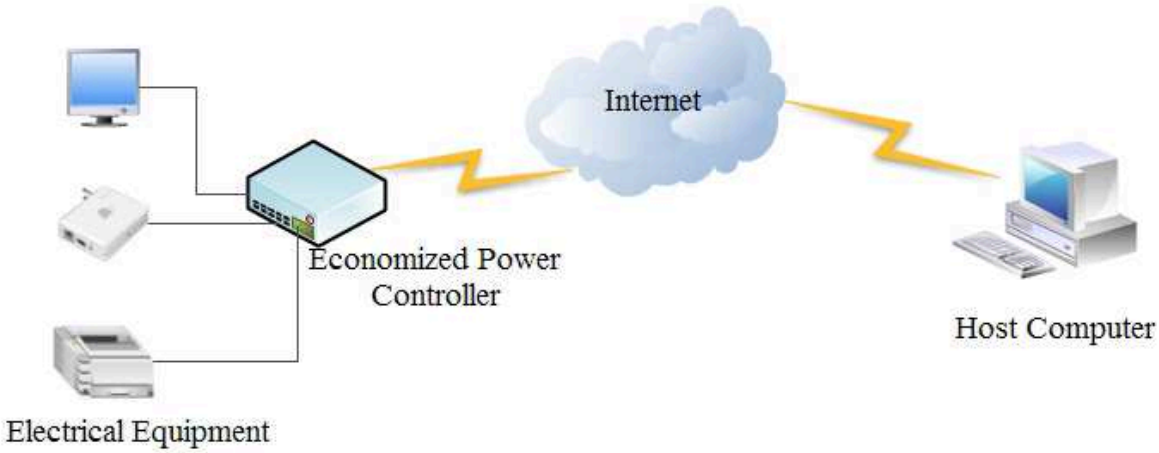

Fig. 1 System Structure

System Hardware Selection and Design

The hardware design is an important part of the system. It is the system platform of operation and realizing the function. This system consists of the embedded computer system, the Ethernet interface module and power supply control detection module.

3.1 Embedded Computer

We choose STC89C58RD+ as Embedded computer, it is a new generation STC microprocessor which is super strong anti-interference / high speed/ low power, its instruction code is completely compatible with the traditional 8051 microprocessor[3]. STC89C58RD+ selects 11.592M quartz crystal on the RS-232 serial communication, its serial communication port TXD and RXD is led by the socket COM2. It not only can be used for embedded program download, but also can be used for other intelligent control signal input. STC89C58's serial port connects with PC through MAX232 level switch chip. MAX232 has internal voltage multiplier circuit and conversion circuit. It can implement circuit conversion for the serial port of embedded microprocessor. The chip only needs +5V power supply to realize TTL level and RS-232C level conversion.

3.2 Ethernet Interface Module

Ethernet interface module is composed of MCU and Ethernet interface chip. The core chip is the Ethernet interface chip RTL8019AS. The RTL8019AS chip is a kind of LAN interface chip produced by Realtek company. At present, it is one of the most common 10M network card [4]. The 8 data lines of RTL8019AS is connected to the STC-8958 P0 port, its low address line SA0-SA4 is connected to the output end of the address latch 74HC373 A0 - A4. The address line A8 and A9 is fixedly connected with +5V power. The other address lines A5, A6, A7, A10-A19 are fixedly connected with low level. Its address is 30000-3001FH, a total of 32 addresses, and the chip selection terminal is connected with P3.5 pin. When chip select P3.5=0, STC89C58 operate on the 0000H-001F address. Namely, STC89C58 reads and writes RTL8019AS. This method can achieve the Ethernet communication. RTL8019AS's LED1 and LED2 is connected to LED in order to indicate the state of network communication. Its input and output pin is connected to the RJ-45 socket through the isolation transformer.

3.3 The Power Supply Control Detection Module

The power supply control module mainly consists of a set of relay. The relay is an electronic control device. It has a control system (also known as the input circuit) and the controlled system (also known as the output circuit). It is usually used in automatic control circuit. It is actually a kind of "automatic switch" which uses small current to control a larger current. It plays the automatic adjustment, safety protection, conversion and other roles in the circuit. The circuit diagram is shown in figure 2.

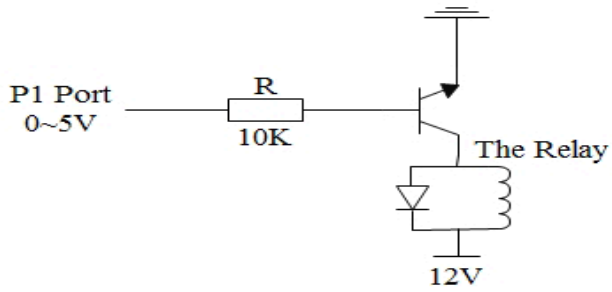

Fig. 2 The Control Module Circuit Diagram

The power supply detection module is the detection unit that is used to detect whether the electricity equipment is the power supply state, it is composed of eight current transformers (TA1015) and eight voltage comparators (LM339)[5]. The circuit diagram is shown in figure 3. The current transformer outputs a DC voltage through resistance conversion, rectification and filtering, then, it is sent to input of the voltage comparator. The reference signal input terminal of the voltage comparator is connected to a reference voltage. The reference voltage is generated by resistance from 5V power supply pressure. Thus the load current signal is converted to the presence or absence of signal switching which is input to the microprocessor. It changes the reference voltage, that is changes the detection sensitivity. The DC load signal is obtained from current mutual inductor. It can be directly input to the A/D input end of the microprocessor, thus detect value of load current.

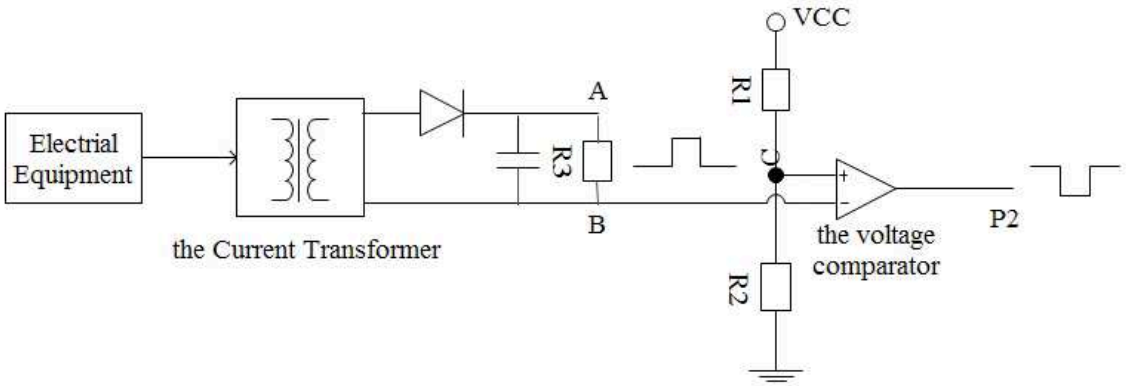

Fig. 3 The Detection Module Circuit Diagram

Conclusion

The remote power control switch system has very high practical value. It follows the principle of energy conservation. At the same time, it saves the electricity costs for the user. It has low cost, automatic detection, automatic control and other advantages. It can be applied to many occasions, such as intelligent community, school, company etc. It is easy to spread.

But its function remains to be further upgraded. If the hardware circuit uses the clock chip 8563 for timing control, so that even if the broken network can also continue to carry out timing control of electric equipment. It will make the system more stable.

References

[1] Information on http://finance.chinanews.com/ny/2014/02-25/5881299.shtml

[2] Xing Hai-xia, Tu Jing-lu, He Zheng and Pan Shi-bin: Design of Embedded Remote Economized Power Controller, Microcomputer Information(2008).

[3] Suo Ming-he, Xing Hai-xia: Design and Implementation of Embedded Remote Energy-saving Switch Based on Internet, Science & Technology Information(2010).

[4] Information on http://www.doc88.com/p-415988174237.html

[5] Zhang Huaiqiang, Ge Liangquan, Xing Haixia: Energy-saving Design of Embedded Remote Control System, Computer Measurement & Control(2010.18).

Advanced Materials Research Vols. 986-987 (2014) pp 1892-1896

doi:10.4028/www.scientific.net/AMR.986-987.1892

A Cell Balancing System Based on Charge Shuttling Method

ZHU Yu-wei[1,2,a], Shi Bing[1,2,b]

[1]Engineering College, Ocean University of China, Qingdao 266100, China.

[2]Shandong Provincial Key Laboratory of Ocean Engineering, Qingdao 266100, China;

[a]zhuyuwei2002@163.com, [b]bings@ouc.edu.cn

Keywords: Battery Management System, Super Capacitor; Cell Balancing, Metal Oxide Semiconductor Field Effect Transistor, Charge Shuttling.

Abstract. As one of the most essential part in a battery management system for a lithium battery, cell balancing determine its performance and lifetime. A new "flying capacitor" method is presented in this paper. Where, a clock-switched circuit changer matrix makes the charges flow from the high-voltage cells to the low-voltage cells. Some super-capacitors buffer the charge and redistribute energy of the cells in the battery. The implementation is also low-cost and its design period is short. The result shows that the method is feasible.

1. Introduction

With the best performance in energy/weight, energy/density ratios and their long lifetime, Lithium ion battery has become the first choice of electric vehicle (EV) power battery. Thousands of Cells are usually packed to a battery string to meet the needs of the energy storage capacity and voltage grade for electric vehicles [1]. However, there are some problems of the batteries. The voltages in the cells of the string are not equal, and that may cause the battery to swell or even explode [2]. Battery Management System, BMS, is indispensable in this kind of battery. Cell balancing element is one of the most important part in BMS for a lithium battery [3,4].

Currently, there are two different typical categories of active cell balancing methods: energy converters and charge shuttling [5]. Energy converters use inductors and transformers to move energy among the cells of a battery pack [6]. In the use of energy converters cell balancing system, a multilateral transformer design is key but difficult to design. The consistency of the transformer is too difficult to make because of some factors, such as, parameters of the magnetic core and winding norms, etc. Charge shuttling method is to use a "flying capacitor", where, the "flying capacitors" act as energy buffers to transfer the charges from high-voltage cells to the low-voltage cells. This reduces the amount of hardware used to implement a practical circuit, besides, this can dramatically reduce the time to balance the cells. Theoretically, charge shuttling balancing is relatively stable. However, common capacitors, low capacitance and its minor balanced current is the necklace for the design [7]. Good balance technology should have the following features: Excellent dynamic performance, high efficiency, small volume, low cost, high reliability. Further more, it should be very convenient to expansion on a larger scale and, on the structure, the ideal charge-discharge equalization circuit should supply direct energy transfer channel between any two units [8, 9,10].

The purpose of this work is to gain knowledge in the field of energy storage in Lithium ion batteries, and to find an efficient, simple and cheap way to keep cells in battery stacks balanced and monitored. A charge shuttling implementation is presented in this paper, which is based on charge transfer control. In the scheme, ultra-capacitors act as the buffer, and Metal Oxide semiconductor Field Effect Transistors, MOSFET, act as the switch. Over 12 MOSFET chips make a switch matrix to operate the transfer process. Microcomputer is not used in the work for an efficient and economical design, which is suit for low-cost and portable application.

2. Simulation on charge shuttling circuit

A charge shuttling circuit is simulated by NI Multisim10, formerly known as Electronic Workbench, which is the ultimate environment for designing electronic circuits and performing SPICE simulation. Considering the simulation speed in the work, Thevenin model is preferable in the simulation. The string of 12 cells is simulated. The simulation circuit is showed as Fig 1.

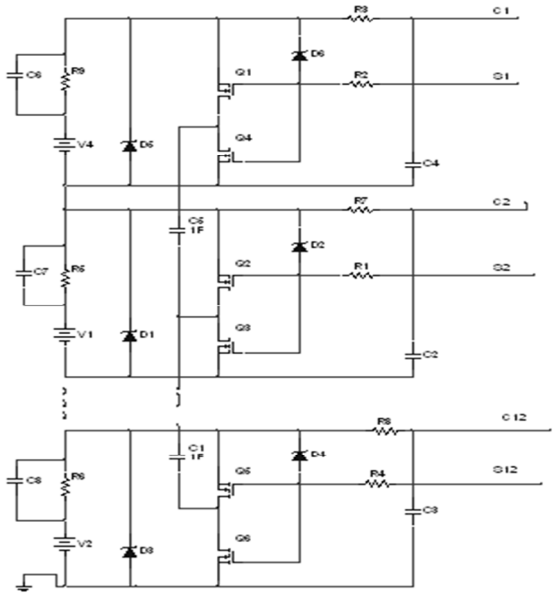

Fig.1 The simulation circuit of twelve cells string

The result of the simulation is presented as Figure 2. It shows that, though voltages vary in the beginning, the cells' voltages become almost after about 5hours, when the different of the voltages for these cells is under the offset of 50mV. The enlarged portion of the figure presents some square ripples, which means capacitor charging and discharging process. The ripples proved the draft circuit is feasible.

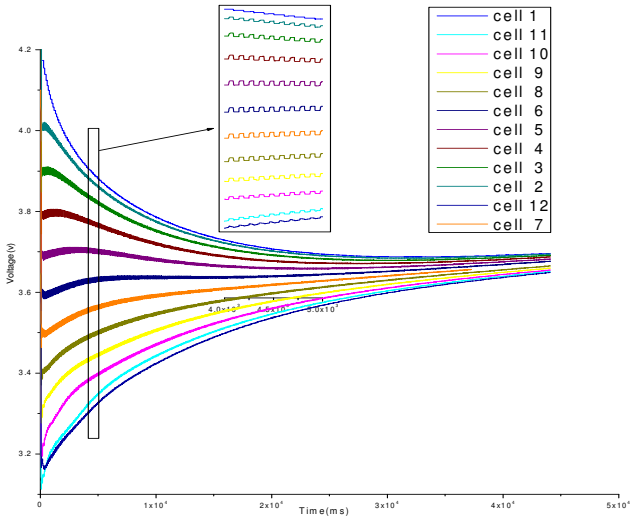

Fig.2 Result of Cell Balancing Simulation

3. Design of Charge Shuttling Circuit

3.1 Design of Pulse generator and the peripheral circuit

The strategy of charge shuttling circuit needs a pulse to manipulate the switches (Q1-Q24 in Figure 1). NE555 timer pulse generator is used to generate a series of pulses. The power supply

voltage of the chip should be limited in the scope of 4.5-16V, but the 12 batteries in the series will make a high voltage up to 50V, LM2575-12 - HV (high voltage series) switching regulator chip is used to make a feasible power supply. The circuit is shown in figure 3. There, C3 is a solid electrolytic capacitor, which absorbs the spike pulse from the input power supply.

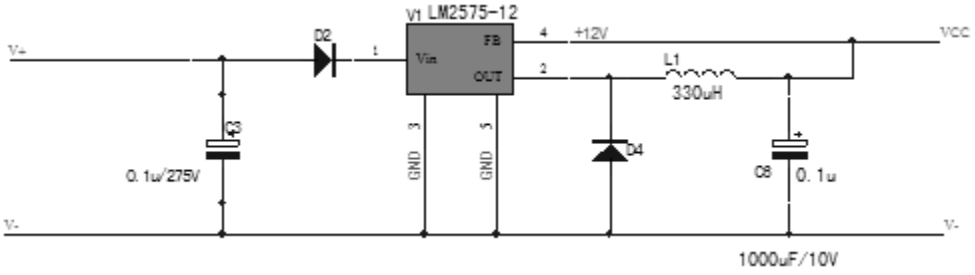

Fig.3 Regulated power supply circuit

NE555 chip works in the astable multi-oscillation mode, the circuit is as figure 4, the basis of the selection parameter for some elements is formula 1-formula 3. There, Given R2 »R1, it's naturally that R1 can be ignored in the 3 formulas. According to the parameters of the components in figure 4, the circuit will generate a 1Hz cycle pulse. The pulse's duty ratio is about 1:1 and its amplitude will be about 12V.

$$T_1 = 0.693 \times (R_1 + R_2) \times C_1 \tag{1}$$

$$T_2 = 0.693 \times R_2 \times C_1 \tag{2}$$

$$f = \frac{1.443}{(R_1 + R_2) \times C_1} \tag{3}$$

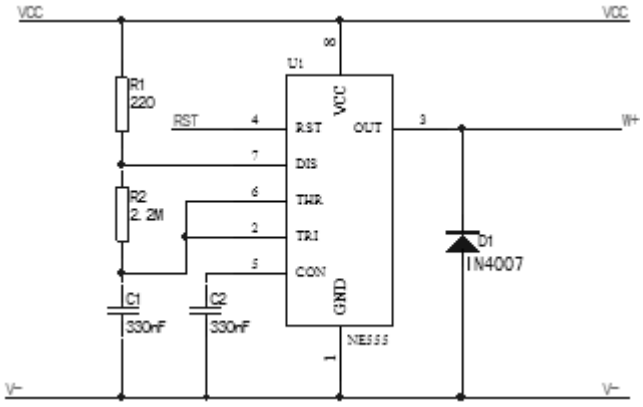

Fig.4 The pulse generation circuit

3.2 Design of switch matrix

The IRF7343 MOSFET chip is suitable for the switch matrix in this work. IRF7343 is a Dual N and P Channel MOSFET, combined with the fast switching speed. In the application, D1 and D2 pins are linked together to make a bidirection switch. For its static drain-to-dource on-resistance, Rds = 0.05 ohm. Vds = 55 v, which meets the demand of a 12-string- battery application.

The pulse is ready, and the amplitude of pulse is 12V, but the 12 switches in the control matrix are in series. The pulse signal can not control the switches directly, for each of the switches has a floating ground. PS2501 is optically coupled isolators containing a GaAs light emitting diode and an NPN silicon phototransistor, so it's fit for distributing our pulse signal to 12 switch signal. In order to realize the switch control, a clamping resistor is added to each switch to prevent the high voltage do damage to the circuit. Where, a BZT52C36V- GS08 zener diode is preferable. The switch matrix circuit is shown in figure 5.

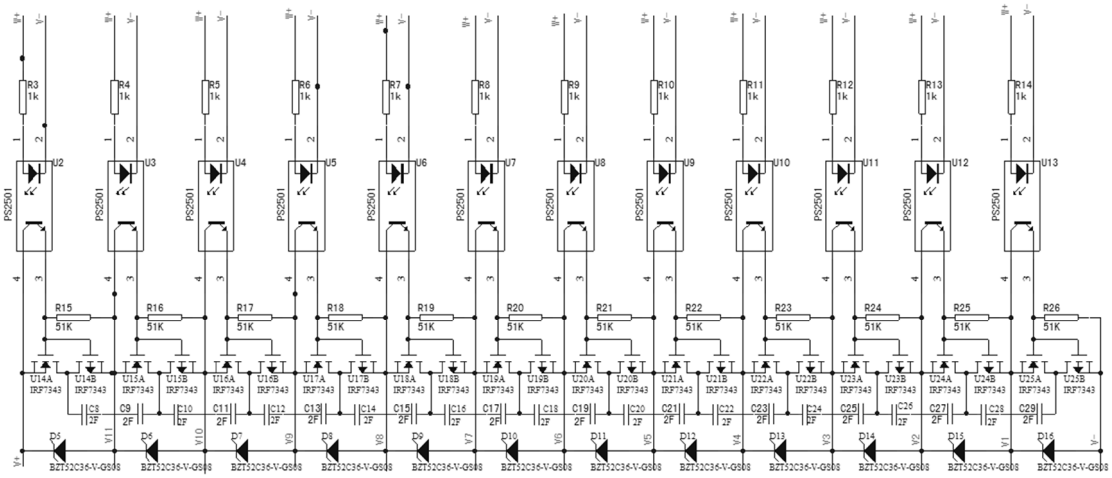

Fig.5 Switch Matrix and Its Isolation Circuit

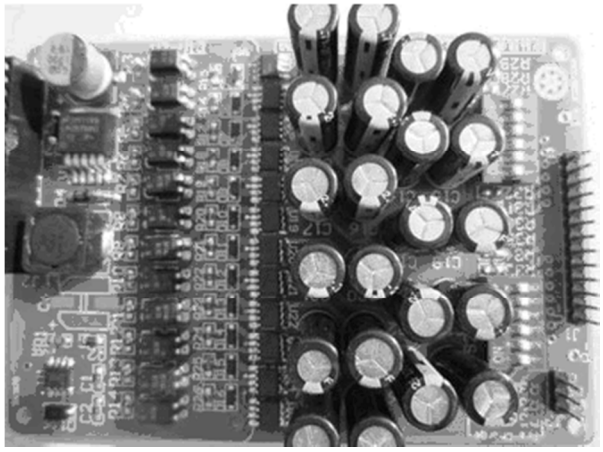

Fig.6 Photograph of 12 cells balancing board

3.3 EXPERIMENTAL RESULTS

The photograph of 12 cells balancing printed circuit board is produced, as shown in fig. 6. It's a flexible and easily realized circuit for 12 cells balancing in the stack.To test it, an experimental system is built, as shown in fig 7. The cells in the series are numbered by 1-12. In the beginning, their voltages vary from 2.8 to 4.2V. A multi-trace oscilloscope is connected to monitor the voltage of the cells. After it works 5 hours, all the cells' voltages are balanced to about 3.5V, as show in table 1. The voltages' change curve and the simulation results are identical with each other. It proves that the clock-switched circuit changer matrix makes the charges flows from the high-voltage cells to the low-voltage cells.

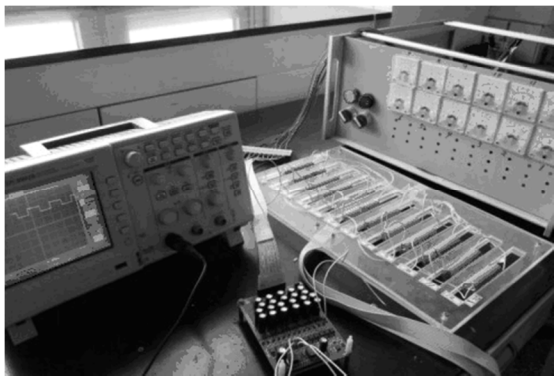

Fig.7 Experimental System

Table1. Compare of the 12 cells's voltages between the start time and 5hrs later.

No. of the cell	1	2	3	4	5	6	7	8	9	10	11	12
Strat time voltage[V]	3.46	3.85	4.21	2.87	4.20	2.91	3.65	3.91	3.09	3.53	4.16	2.82
5hrs later voltage[V]	3.49	3.51	3.51	3.49	3.51	3.49	3.50	3.51	3.49	3.49	3.51	3.49

4. Conclusions

A Cell Balancing system based on charge shuttling method is presented. The circuit itself is able to balance the battery string through operating the switch matrix at equal duty-ratio. Moreover, the balancing circuit provides an efficient, simple and cheap way to keep cells in the battery stacks balanced. Hence, it is able to isolate the batteries which have run out of the stored energy or been damaged. The experiments is carried out on a laboratory circuit and shows an acceptable result.

5. Acknowledgements

This study was funded by National Natural Science Foundation of China(Grant No. 51279189; 50879084). The writers are grateful for the comments provided by the Editors and the reviewers, which have significantly improved the quality of the paper.

References

[1] GAO Jin-hui, JIA Li-feng, GU Xue-jun, Design of Nondissipative Bi-direction Equalization System for Lithium-ion Batteries[J]. Chinese Journal of Power Sources, 2010.2, 134(1):131-133.

[2] WANG Zhen-po, SUN Feng-chun. Study of the EV Battery Pack Reliability and Asymmetry[J]. Vehicle & Power Technology, 2002,4:11-15.

[3] Sun Bei, Wei Xue-zhe, Design of Voltage Monitoring Module of Stacked Lithium-ion Cells in Series[J]. Applied Mechanics and Materials, 2010,29(32):1888-1893.

[4] HAN Guang-xin, HAN Jin-dong, et, al.. Research Progress on Equalization Charging[J], Chinese Battery Industry, 2009.2,14(1): 65-68.

[5] S. Moore, P. Schneider, "A Review of Cell Equalization Methods for Lithium Ion and Lithium Polymer Battery Systems", in Proceedings of the SAE 2001 World Congress, (Warrendale, PA, Detriot, MI), 2001. 2001-01-0959.

[6] MOO C S, HSIEH Y C, TSAI I S. Charge Equalization for Series-ConnectedBatteries[J]. IEEE Transactions on Aerospace and Electronic Systems, 2003,39(2):704-710.

[7] AN Shi-qi, QI An-ning, ZHU Yu-wei. The Design of Active Lithium-ion Cells Balancing Based on Super-Capacitor, 2011 International Conference on Transportation and Mechanical & Electrical Engineering(TMEE2011), 2011.

[8] DAI Yong-nian, YANG Bin, MA Wen-hui. The Development of Lithium ion Batteries and Light Electric Vehicles[J]. Advanced Materials Industry, 2004, (9):16-18.

[9] HUANG X ue-jie. Li-Ion Battery and Its Key Materials[J]. Materials China, 2010, (8):46-51.

[10] MAO Chun-sheng, ZHONG Shao-hua, HU Yun-da. Electric Vehicle Battery SOC Estimation Research Based on Improved Thevenin Model [J]. China Science and Technology Information, 2005,(18):106.

Advanced Materials Research Vols. 986-987 (2014) pp 1897-1900

doi:10.4028/www.scientific.net/AMR.986-987.1897

A High Frequency Strictly Passive Model for Transformer Based on the Image Method under Lightning Overvoltage

Zhang Zhongyuan [1, a], Gao Liming [2, b], Zhu Ruimin[2]

[1,2]Department of Electrical and Electronic Engineering, North China Electric Power University, Baoding, 071003, china

[a] email: hvzzy_01 @163.com, [b] email: gaolinghan880208@126.com

Keywords: high frequency strictly passive; impedance parameters; frequency dependent; image method

Abstract: In the power system electromagnetic transient simulation, the establishment of a stable power transformer simulation model is crucial. Therefore, the high frequency strictly passive model of the transformer is investigated, which is suitable for the lightning strokes. The proposed model is introduced based on two-port network theory where its scattering parameters are measured through network analyzer firstly, and then the scattering parameters are transformed into the impedance parameters, finally the transformer T-equivalent circuit is established. The image method is used to fit frequency dependent impedance parameter, and according to different types of the parameter, the combination of circuit elements R, L, C is needed. By using the image method the values of the elements achieved are all positive and the strictly passive conditions of the circuits are guaranteed. Furthermore, the experiment and simulation results of a 10kV single-phase transformer under lightning overvoltage is presented, confirming the validity of the proposed method.

Introduction

From the literature review, the transient transformers models were divided into two categories [1]: (1) detailed internal winding models. Most of these models are very complex and need details of the transformer construction. (2) terminal models (black-box modeling). Terminal models have had varying degrees of success in reproducing the frequency behavior of single phase transformers accurately.

The transformer frequency response using experimental measurements or calculation is investigated in order to find the model parameters [2].In order to establish a stable power transformer simulation model, strictly passive of the circuit model is necessary. Passivity of network [3, 4] can be divided into terminal passive and strictly passive. Terminal passive denotes a system that is incapable of generating energy, and hence one that can only absorb energy from the sources used to excite it. Strictly passive network is only composed of positive circuit components.

In [5], the necessary and sufficient condition for realization of two-port network passive circuit is that the network admittance or impedance parameter matrix is positive real rational function matrix. In [6], the poles of the rational function all located in the left hand side of the complex plane and residues located in the right hand within a specific region can ensure the circuit passivity. In [7], modified vector fitting is proposed and the model achieved can only guarantee the terminal passive.

In this paper, the proposed model is introduced based on two-port network theory and the image method is used fitting the frequency dependent impedance parameters of the transformer T-equivalent circuit. Finally, the model verification is examined by a single-phase two-winding transformer subjected to lightning overvoltage.

High Frequency Strictly Passive Transformer Model

The S-parameters measurements have been carried out on a 10KV single-phase two winding transformer. The Agilent 4395A Network Analyzer is used, and the frequency range is 5 KHz to 10MHz.

The scattering parameters are transformed into the impedance parameters. Conversion formula is as follows:

$$\begin{cases} Z_{11} = \dfrac{(Z_0 + S_{11}Z_0)(1-S_{22}) + S_{12}S_{21}Z_0}{(1-S_{11})(1-S_{22}) - S_{12}S_{21}} \\ Z_{12} = \dfrac{2S_{12}Z_0}{(1-S_{11})(1-S_{22}) - S_{12}S_{21}} \\ Z_{21} = \dfrac{2S_{21}Z_0}{(1-S_{11})(1-S_{22}) - S_{12}S_{21}} \\ Z_{22} = \dfrac{(1-S_{11})(Z_0 + S_{22}Z_0) + S_{12}S_{21}Z_0}{(1-S_{11})(1-S_{22}) - S_{12}S_{21}} \end{cases} \tag{1}$$

The impedance magnitude frequency dependent parameters are shown in Figure.1.

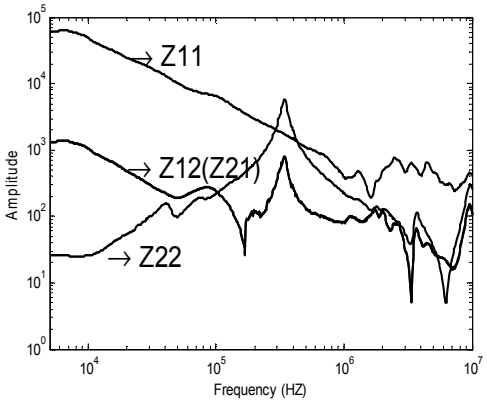

Fig.1 The impedance amplitude frequency characteristic of the transformer

The proposed model is based on two-port network theory. The T-equivalent circuit is shown in Fig. 2 and each impedance can be converted to R, L, C elements according to its behavior in the frequency domain. The image method [8] is used for identifying the type and values of the elements.

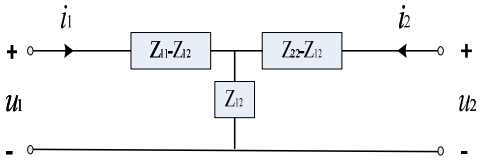

Fig.2 Transformer two-port T-type equivalent circuit

For resonance frequency peaks, the circuit schematic is shown in Fig. 3.

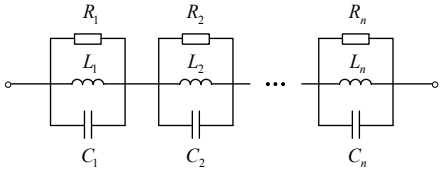

Fig.3 Image method circuit integrated schematic

Select the main peak point of the impedance parameters and set the resonance angular frequency followed by w1， w2，. . . ， wn, the impedance can be described as (2):

$$Z(j\omega) = \sum_{i=1}^{N} \frac{1}{\dfrac{1}{R_i} + j(\omega C_i - \dfrac{1}{\omega L_i})} \tag{2}$$

Each peak is the resonance point, and the resonance frequency can be approximated with the Eq.3.

$$Z(j\omega_k) \approx \frac{1}{\frac{1}{R_k} + j(\omega_k C_k - \frac{1}{\omega_k L_k})} = R_k \tag{3}$$

And Zmea (jω) is the impedance measurement value, so the resistance can be obtained as

$$R_k \approx \left| Z_{mea}(j\omega_k) \right| \tag{4}$$

Finally, the inductive element and the capacitive element can be accurately calculated with Levenberg-Marquardt [9].

Fig.4 (a)–(c) shows the fitting results of Z11－Z12． Z12 and Z22－Z12, respectively.

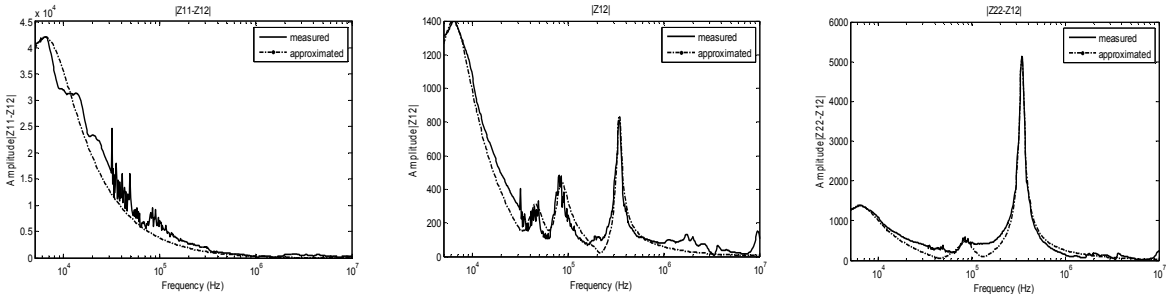

Fig.4 Fitting results of the T-equivalent circuit

Model Validation

The model verification is examined by a 10kV single-phase transformer subjected to lightning signal produced by the lightning surge generator (EMS61000-5C). Fig.5 shows the first and second voltage waveform obtained by oscilloscope. Experimental results and simulated results are shown in Fig.6.

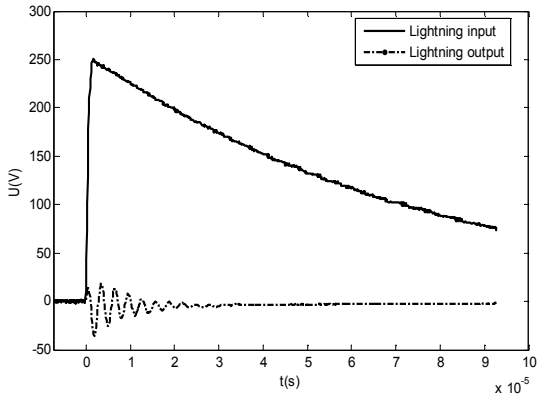

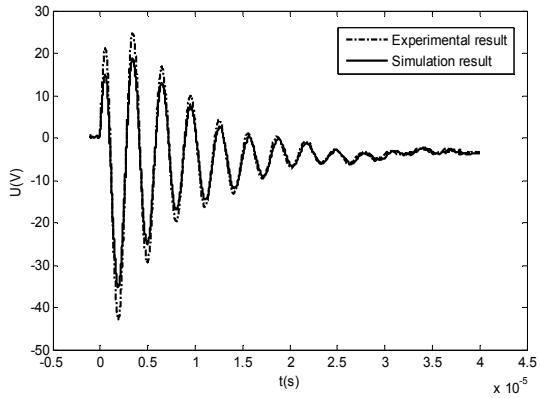

Fig.5 The first and secondary voltage waveform Fig.6 Experiment and simulation comparison chart

Conclusion

A high-frequency strictly passive transformer model has been proposed in this paper. The model has compromised between simplicity and accuracy. A very simple circuit to evaluate the transformer performance under lightning strokes is taken into account. In addition, a very easy procedure based on image method is achieved to determine the model parameters and the values of the elements achieved are all positive. The proposed model showed good agreement between the experimental and the simulated results confirmed the validity of the proposed method.

References

[1] Morched, L.Marti. A High Frequency Transformer Model for the EMTP[J]. IEEE Transactions on Power Delivery, 1993, V8 (3): 1615-1626.
[2] Yilu Liu, S. A. Sebo, S. E. Wright. Modeling of Converter Transformers Using Frequency Domain Terminal Impedance Measurement [J]. IEEE Transactions on Power Delivery, 1993, V8 (1): 66-72.
[3] Altan Odabasioglu, Lawrence T. Pileggi. PRIMA: Passive Reduced-Order Interconnect Macromodeling Algorithm [J]. IEEE Transactions on Computer-Aided Design of Integrated Circuits and Systems, 1998, V17(8): 645-654.
[4] Wu Ning. Electrical network analysis and synthesis[M]. Bei Jing: Science Press, 2003: 34-37, 252-255.
[5] O. Brune, Synthesis of a finite two-terminal network whose driving point impedance is a prescribed function of frequency [J]. Journal of Mathematical Physics, 1931, V10: 191–236.
[6] R. Araneo. Extraction of Broad-Band Passive Lumped Equivalent Circuits of Microwave Discontinuities [J]. IEEE Transactions on Microwave Theory and Techniques, 2006, V54 (1): 393-401.
[7] B. Gustavsen. Improving the Pole Relocating Properties of Vector Fitting [J]. IEEE Transactions on Power Delivery, 2006, V21 (3): 1587-1592
[8] S Chimklai,J R Marti.Simplified three-phase transformer model for electromagnetic transient studies [J] .IEEE Transactions on Power Delivery , 1995,V10(3):1316-1325.
[9] Ann Franchois, Christian Pichot. Microwave Imaging Complex Permittivity Reconstruction with a Levenberg-Marquardt Method [J]. IEEE Transactions on Antennas and Propagation, 1997, V45 (2): 203-215.

Advanced Materials Research Vols. 986-987 (2014) pp 1901-1905

doi:10.4028/www.scientific.net/AMR.986-987.1901

A Novel Comprehensive Draw-out Power Circuit of High Voltage Thyristor

Yu TIAN[1, a], Zhongdong YIN[2, b]

[1] State Key Laboratory of Alternate Electrical Power System With Renewable Energy Sources, North China Electric Power University, Chang ping District, Beijing 102206, China

[2] State Key Laboratory of Alternate Electrical Power System With Renewable Energy Sources, North China Electric Power University, Chang ping District, Beijing 102206, China

[a]email: tianyucode@126.com, [b]email:369172041@qq.com

Keywords: draw-out power circuit; magnetic core loss; common cathode thyristors

Abstract. The method of self-energy extracting has been adopted in high voltage thyristor device more and more widely. In consequence of the existing insufficient of high heat loss and large variation range of storage voltage value, this paper designs a novel comprehensive draw-out power circuit which is suitable for almost all kinds of working conditions of thyristor. The circuit includes voltage draw-out power module, current draw-out power module and the coordination control module between them. The principle of each module has been detailed analyzed and the calculation formulas of the corresponding parameters have been concisely given. At last, every conclusion drawn in this paper has been verified in simulation.

Introduction

Thyristor as a controllable switching device, has been popularly used in various types of electrical equipment since its invention. Usually a complete thyristor electronic circuit (TE board) includes trigger circuit, back-up trigger circuit (forced trigger), condition monitoring module, communication module and logic encoding and decoding circuit. There are two methods of power supply which are currently used. (1) Electromagnetic coupling from low voltage side[1]. It use a public energy-sending cable which goes through the energy-taking pulse transformer to transmit power. This method has been used in some low-voltage small-capacity devices, but due to the requirements of insulation and reliability, it is not suitable for high voltage equipment. (2) High voltage self-energy extracting. To insulate the high voltage device and low voltage device, it draws out power directly from thyristors of the main circuit, as a result the reliability has been improved. When used as an ordinary electronic switch, thyristor may either pass its current or withstand its voltage, making itself require two kinds of energy extracting. Using RC branch to charge an energy storage capacitor, [2] introduces a typical voltage energy extracting way of anti-parallel thyristors. An isolation transformer is essential in this trigger circuit because thyristors are anti-parallel connected, which influences the synchronization of trigger pulse. The current energy extracting module is transformer power obtaining mode, its technical challenges to be solved is how to draw out energy when the current is small and how to protect the device when the current is large. [3] proposed a solution which is using an energy bleed branch to release excess power, but the efficiency is low and the ferromagnetic material has a big heating problem. [4] proposed that a gap can be open in the transformer, thus the equivalent relative magnetic permeability has been reduced. Similarly, the problem of a large voltage range on the secondary side has not yet been resolved.

This paper presents a novel comprehensive draw-out circuit of high voltage thyristor which includes voltage energy extracting module , current energy extracting module and the coordination control module between them. By using the new circuit topologies and particular control logic, it effectively solves all mentioned problems, specific work of each module is designed as follows.

Voltage Draw-out Power Module

Figure1 (a) depicts a typical voltage draw-out circuit of anti-parallel thyristors. When thyristor voltage drop U_S is positive, the branch current i_c is positive too, the current flows through R_1, C_1 and the diode D_3 to charge the storage capacitor C_S. When the energy storage voltage of C_S exceeds the limit of zener diode Z_1, Z_1 breaks down, thus thyristor Q_3 is turned on, withstanding reverse voltages, D_3 is cutoff, C_S stops charging. Semi-controlled device Q_3 have been in the conduction state until U_S is negative, i_c flows through reverse-freewheel diode D_2 during the negative half period of U_S. Apparently, storage capacitor only get charged part-time positive half period of U_S, and as mentioned above, using of isolation transformer influence the synchronization of trigger pulse.

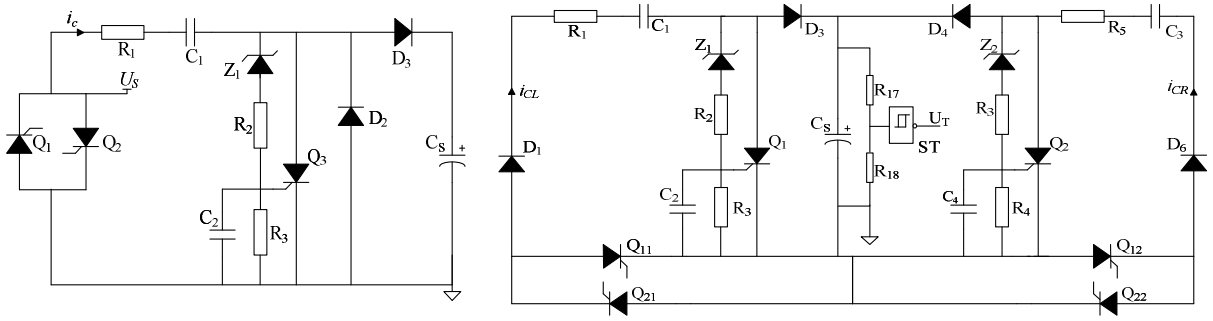

(a) anti-parallel thyristors (b) common cathode thyrsitors

Fig.1. The voltage draw-out power circuit

This paper designs a common cathode thyrsitors draw-out power circuit showed as Figure1 (b) for the widely used thyrsitors chain structure. The energy extracting target is common cathode thyristors Q_{11} and Q_{22}. When Q_{11} withstands forward voltage drop, left branch current i_{CL} is positive, it flows though D_1, R_1, C_1, D_3 to charge storage capacitor C_S, again, zener diode Z_1 limits the charge voltage. When Q_{11} withstands reverse voltage drop, right branch current i_{CR} is positive and the right half of the circuit works the same way. Connecting the common cathode of Q_{11}, Q_{22} with negative pole of C_S, the extracting energy can directly trigger the two thyristors without isolation transformer, which ensures the synchronization of trigger signal. Moreover, the speed of charging nearly doubled shown as Figure2 (charge voltage limit is 60V) and its redundancy improves the reliability of this module.

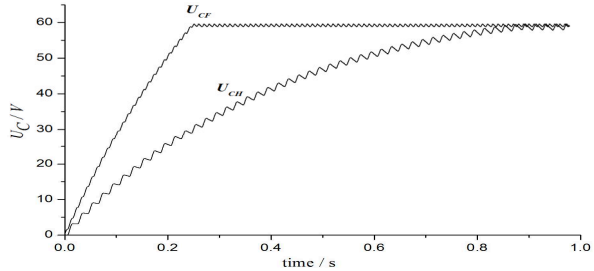

Fig.2. Comparison of storage capacitor voltage in different circuits

Current Draw-out Power Module

Referring the design of [5], the current draw-out power module is shown as Figure3. Thyristor busbar goes through the draw-out power transformer, making an one-turn primary winding N_1. When current flows through the primary winding , energy couples to the core and induces voltage on energy winding N_S and auxiliary winding N_A. Assuming that MOSFET T_1 is in the OFF state at the initial time (ignore the SSR in this analysis), the induced current on N_S charges storage capacitor C_S though rectifier REC_S, smoothing capacitor C_L and reverse voltage protection diode D_7. The smoothing capacitor voltage U_L is compared with given switch threshold voltage U_G via the comparator COMP. When $U_L > U_G$, the output of comparator is high level, and it drive T_1 turn on after amplified by power amplifier PA. This time induction voltage on auxiliary winding has been short circuited by T_1 after rectified from rectifier REC_A, the equivalent work state of the entire

auxiliary winding is same as current transformer mode, Almost all the magnetic energy coupled to the core has been consumed on auxiliary winding, the magnetomotive force established on primary side has been mostly compensated by short-circuited winding, only a small part of it used to create excitation flux in the core, the energy winding coiled on the same core obtains no energy, energy winding stops charging storage capacitor. With energy consumption, U_L gradually decreased, when $U_L<U_G$, the comparator output inverts, T_1 turns off and the auxiliary winding is open. The equivalent work state of the entire auxiliary winding is same as voltage transformer mode, the magnetic field intensity in the core increases rapidly, induced voltage on auxiliary winding and energy winding begin to rise. Since auxiliary winding is open, there is no more current, most of the core coupling energy is extracted by energy winding, storage capacitor C_S starts to charge again, the current draw-out power module goes back to initial state.

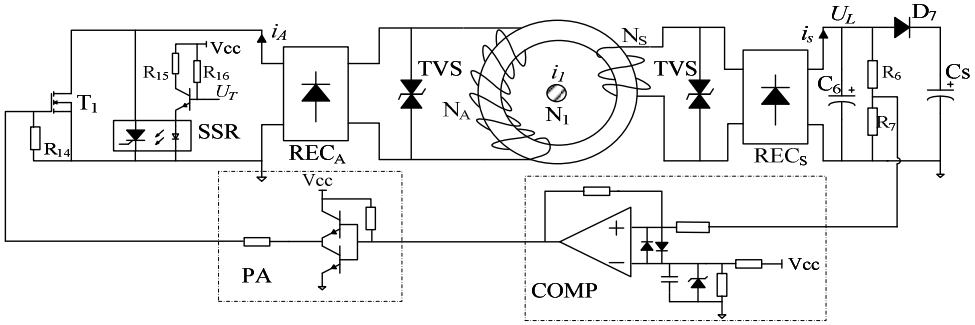

Fig.3. The current draw-out power circuit

The above process is an ideal switching cycle, which assuming that primary current i_1 is ideal power frequency sine wave, and ignores the resistance of N_A, N_S and the power consumption of REC_A, REC_S, T_1.The equation of flux conservation principles in this module is: $N_1 i_1 = N_A i_A + N_S i_S$. But in fact, due to the leakage flux and copper loss, there always be an angle between i_1 and i_A, i_S. The core loss is much smaller compared with excitation energy under the normal working conditions, and the secondary leakage flux is very low compared with winding copper loss, accordingly we can get the equivalent circuit and phasor diagrams of current draw-out power module shown as Figure4.

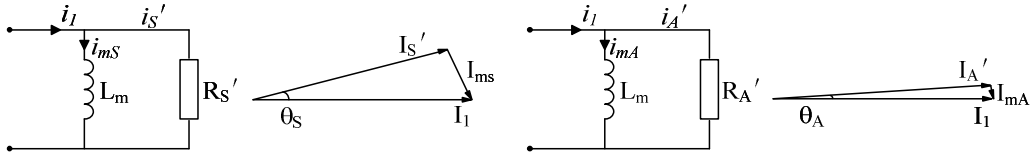

(a) energy winding (b) auxiliary winding

Fig.4. Equivalent circuit and phasor diagrams of current module

R_A and R_S respectively represent the resistance of N_A and N_S, R_L is the equivalent load. Converting resistance value of secondary side to primary side, the result is $R_S' = (R_S + R_L)/N_S^2$; $R_A' = R_A / N_A^2$. Magnetizing inductance L_m is:

$$L_m = N_1^2 \mu_0 \mu_r \frac{A}{l} = \mu_0 \mu_r \frac{A}{l} \tag{1}$$

In this type: μ_0 is the magnetic permeability of vacuum; μ_r is the relative permeability of core; A is the sectional area of core; l is the equivalent length of the magnetic path; N_1 is one turn.

Shown as Figure4, the excitation branch is pure reactance while the secondary branch is pure resistance, so the excitation current is :

$$I_{mS} = I_1 \sin\theta_S \tag{2}$$

$$I_{mA} = I_1 \sin\theta_A \tag{3}$$

The angle here is :

$$\theta_S = \arctan\frac{R_S'}{\omega L_m} \tag{4}$$

$$\theta_A = \arctan\frac{R_A'}{\omega L_m} \tag{5}$$

In order to limit the short-circuited current, N_A is much larger than N_S, therefore θ_s is much bigger than θ_A and I_{mS} is far greater than I_{mA}.

Figure5 shows the simulation waveform of smoothing capacitor voltage U_L, energy winding current i_S, auxiliary winding current i_A during one power frequency period. Obviously, two groups of current work in switch mode, the U_G is given as 55V.

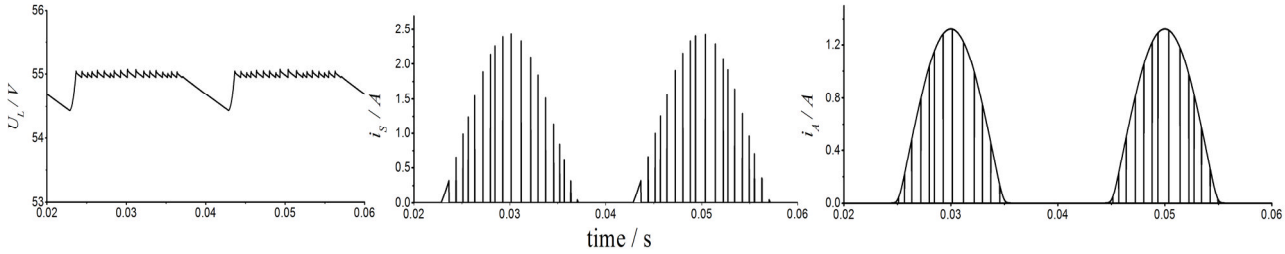

Fig.5. Simulation waveforms of U_L, i_S and i_A

Coordination Control Module

To avoid the unnecessary loss of electromagnetic components, the coordination control logic only enable the current draw-out power module under the circumstance of voltage draw-out power module can't meet the energy requirements. The storage capacitor voltage U_C has been sampled as the input of Schmitt trigger ST shown as Figure1 (b), when U_C is larger than upper threshold U_{T1}, output inverts to high level which turns on the solid-state relay SSR shown as Figure3, the auxiliary winding is short circuited, as discussed above, energy winding stops charging. On the contrary, when U_C is smaller than lower threshold U_{T2}, the output of ST converts to low level which turns off the SSR. The relationship of three gate voltage values is : $U_{T2}<U_G<U_{T1}$.

The simulation result of comprehensive energy extracting is shown as Figure6. At the initial time, thyristors are in OFF state, they equally withstand the whole system voltage drop, voltage draw-out power module properly function while the current one shunts down, U_C stabilizes in upper threshold 60V. At the time of 0.1s, pulse signal begin to trigger thyristors turning on, voltage drop of thyristors is nearly zero, voltage draw-out power module can't meet the requirement, U_C gradually decreased until it's smaller than lower threshold 50V, the output of ST converts and current draw-out power module starts to work, stabilizing U_C to switch threshold 55V. After the time of 0.23s, thyristors turn off again, voltage draw-out power module extracts energy from main circuit, making U_C rise back to 60V.

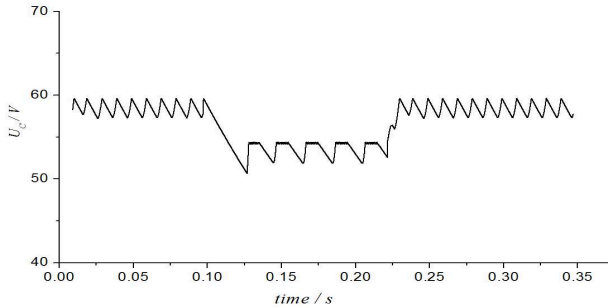

Fig.6. Simulation waveform of U_C in comprehensive energy extracting analysis

The loss in ferromagnetic material is formed of the hysteresis loss causing by friction between magnetic domains and the eddy-current loss causing by heat effect in the equivalent resistance which eddy current flow through. Existing simultaneously, the two kinds of loss are often analyzed together, collectively known as the iron loss p_{Fe}. The empirical formula of iron loss is :

$$p_{Fe} \approx C_{Fe} f^{1.3} B^2 G \tag{6}$$

In the equation: C_{Fe} is iron loss coefficient; f is magnetic field alternating frequency; G is the weight of ferromagnetic material. Easy to know that in the case of given material, the core loss is mainly related to the magnetic flux density B, and it's proportional to the square of B.

Using ANSYS finite element analysis software, the distribution of magnetic flux density in the core is calculated, which is shown as Figure7. When auxiliary winding is open, the maximum core flux density is 1.6T, when it's short circuited, the maximum value of core flux density is 0.09T. Apparently , flux density significantly reduces, therefore the loss is decreased correspondently.

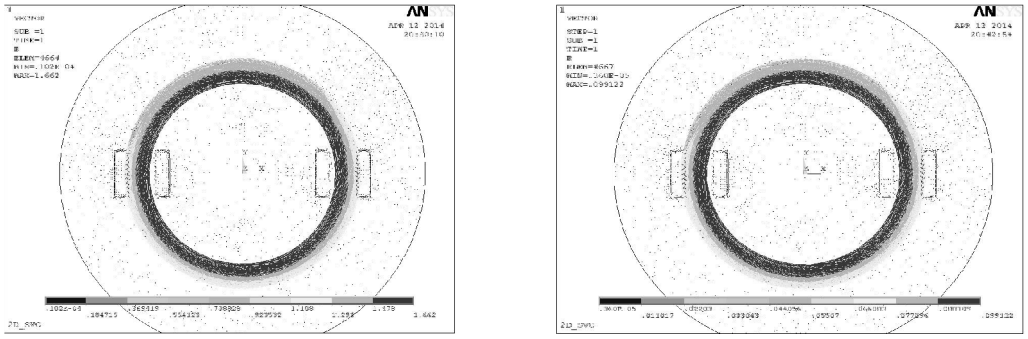

(a) open auxiliary winding (b) short-circuited auxiliary winding

Fig.7. The distribution of magnetic flux density in the core

Conclusion

This novel draw-out power circuit ensures effective energy extracting in almost all kinds of working conditions of thyristor, coordinating between voltage module and current module. Because of the full-wave topology, the charging speed of voltage draw-out power module has been nearly doubled and the reliability has also been improved. Using switch mode in auxiliary winding and energy wingding of current draw-out power module, the output voltage is much more stable and the core loss has been greatly reduced.

References

[1] WANG Bao-hua, CHEN Mi and so on. An Unit to Gain Coupling High Side Trigger Power for Series Thyristor stack [J]. Power Electronics, 2009 43 (1) 46-48.

[2] LIU Fei, LU Zhi-liang, LIU Yan, Xu Zheng. Thyristor Photoelectric Firing and Monitoring System Applied to TCR[J]. High Voltage Engineering, 2007 33(6) 123-128.

[3] REN Xiao-dong, CHEN Shu-yong, JIANG Tao. Design of High Side Energy Extracting Device for Active Electronic Current Transformer [J]. Power System Technology, 2008 32 (18) 67-72.

[4] LI Xianzhi and so on, A novel Scheme of Draw-out Power Supply Utilized in Transmission Line State Monitoring [J]. Automation of Electric Power System, 2008 32 (1) 76-80.

[5] DING Zhigang and so on, A novel Converter Draw-out Power Circuit [J]. Automation of Electric Power Systems, 2013 37 (12) 109-113.

[6] GUO Lin-yun and so on, Research of Improving Power Efficiency for Intelligent Device Self-power Supply Utilized in Power Distribution Network [J]. Proceedings of CSEE, 2009 29 217-221

Advanced Materials Research Vols. 986-987 (2014) pp 1906-1909

doi:10.4028/www.scientific.net/AMR.986-987.1906

Acquisition of Time Parameters and Charges in the Streamer Discharge Simulation

ZHANG Ze[1,a] DING Yujian[1,2,b] XIE Qing[1,c]

[1] North China Electric Power University, Baoding, Hebei province 071003

[2] China Electric Power Research Institute, Haidian District, Bejing 100192

[a]zhangzedq0801@163.com, [b]dinyj@epri.sgcc.com.cn, [c]xq_ncepu@126.com

Keywords: time parameters, streamer, discharge, simulation

Abstract. Because of the dynamic characteristics of the streamer discharge, the acquisition of time parameters is very important to the streamer discharge simulation in the rod-plate air gap. This paper raises a new method to get the time parameters and charge development in the discharge of air gas, and the comparison of our results and the test results shows that the new method is very suitable and correctly to describe the stream discharge process.

1. Description of the stream discharge process

Discharge characteristics of rod-plate air gap are important reference to the air gaps of UHV transmission projects. So, it is meaningful to research the discharge mechanism of rod-plate air gap for the reasonable design and safe operation of the UHV transmission projects.

Discharge process of the typical long air gaps (like rod-plate air gap) always presents to be streamer or leader discharge. In the process of streamer discharge, the electron avalanches take shape when the voltage of the rod reach the discharge voltage of the gap, then the electron avalanches develop continuing, as a results, the streamer path is formed, which contains the electrons and positive and negative ions. Because the weight of electrons are lighter than the ions, they are easier to reach the rod electrode, so the streamer presents to be positive. Generally speaking, the streamer discharge process could be described by 3 stages: streamer starting, streamer development and streamer last jump, these stages depend on the electric field and charge change. Besides, the discharge process is accompanied by complex energy and charge transformation. For the purpose of describing the whole process of streamer discharge, this paper build a new discharge model to describe the electric field, streamer length and charge dynamic process.

2. Model of the stream discharge process

In this time and charge dynamic process model of steamer, the discharge process under impulse voltage is divided to 4 aspect: streamer starting, streamer development, streamer stop and acquisition of time parameters and charges of the streamer.

The streamer starting time consist of corona starting time and streamer statistics time. Corona starting time is the time that the voltage of the rod electron raises to the streamer starting voltage, and the streamer statistics is the time that the corona starting develop to the streamer. The former time could be obtained by the formation 1, and the latter time could be chosen by the probability density function, as shown in formation 2[1][2].

$$Uc = \frac{E_0(1+\frac{0.0436}{\sqrt{(r\delta)}})r\ln D/r}{2} \tag{1}$$

$$p(t) = kt\cdot\exp(-\frac{1}{2}kt^2) \tag{2}$$

In the formation 1, Uc is the corona stating voltage, kV; E_0 is the discharge electric field of air，30kV/cm；r is the diameter of the rod electron, D is the air gap distance，m；δ is correction coefficient of temperature and atmospheric pressure, the value of which is 1 in the conditions of standard

atmosphere; In the formation 2, the parameter k is related to the change speed of voltage and the diameter of the rod electron, For the condition of 210~650kV lighting impulse voltage and 1cm diameter of the rod electron, k=1~1.2。In summary, the discharge should be allowed to start if the formation 3 was met.

$$\begin{cases} t_{start} = t_c + t_s \\ E_{rod}(t_{start}) >= E_0 \end{cases} \tag{3}$$

Path of streamer development is chosen by the electric field distribution in the air gap. Rod-plate air gap was divided to m×n grids, and electric potential of every grid point in the air gaps could be got by solve the Possion electric potential equation, as shown in formation 4, and the electric field could be obtained by formation 5.

$$\varphi_{i,j} = \frac{1}{4}(\varphi_{i,j-1} + \varphi_{i-1,j} + \varphi_{i,j+1} + \varphi_{i+1,j}) + h^2 \frac{\rho_{i,j}}{4\varepsilon_0} \tag{4}$$

$$E_{i,j} = \sqrt{E^2_{x(i,j)} + E^2_{y(i,j)}} = \sqrt{(\frac{\partial \varphi}{\partial x})^2 + (\frac{\partial \varphi}{\partial y})^2} \tag{5}$$

In this formation 4, φ is the electric potential of the grid point in the air gap, kV； ρ is the density of free charge of this point, C/m^3； ε_0 is the air dielectric constant，8.85×10^{-12}F/m; h is the length of square grid, m。

The charge transmission in the discharge channel could be expressed by formation 6:

$$\Delta Q_0 = 4K\pi\varepsilon_0 \int_l (U_2(z) - U_1(z))dz \tag{6}$$

In formation 6, ΔQ_0 is the increase of charge during the streamer development step, and l is the increase length of new streamer, K is a U-Q coefficient of streamer[3].The relation of $U_1(z)$ and $U_2(z)$ are shown in figure1.

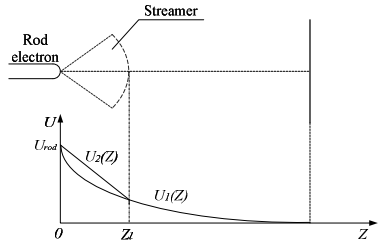

Fig.1 Electric field distribution in the gap

As shown in figure 1, $U_2(z)$ is the electric potential distribution in the streamer area, and $U_1(z)$ is the passion electric potential distribution in the air gap. According to the figure 1, not only can we calculate the charge accumulation in the discharge process, but also the criterion of streamer ending could be got: when $U_1(z) = U_2(z)$, in another world ,when the ΔQ_0=0, the streamer stops.

Then the time of this step will also be got according to formation 7.

$$\Delta\varphi = h^2 \frac{\rho_{i,j}}{4\varepsilon_0} = -\frac{\sigma}{8\varepsilon_0}(\frac{E_{x(i,j)} + E_{y(i,j)} - E_x(i,j-1) - E_y(i-1,j)}{h})\Delta t \tag{7}$$

In summary, the flow path of the new model is shown in figure 2 and 3.

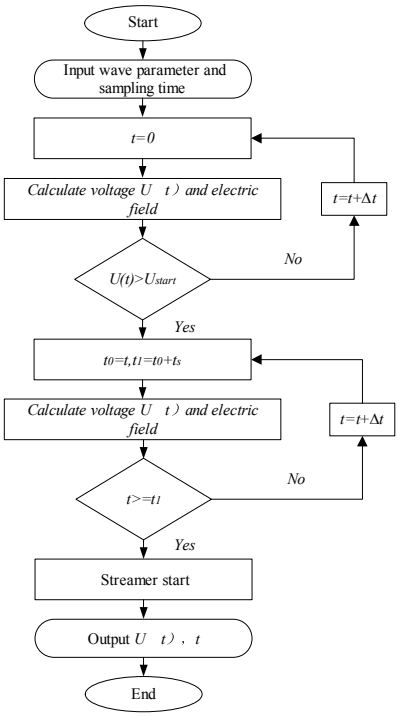

Fig.2 Flow path of streamer starting simulation

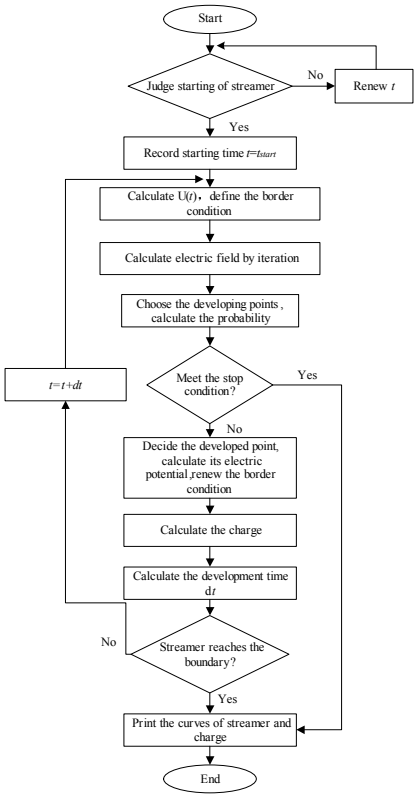

Fig.3 Flow path of streamer process model

Results of the stream discharge simulation

Using the model described in above, the streamer development in the 1m rod-plate air gap under 230kV and 600kV lighting impulse voltage are simulated, and the results are compared with the test dates. Figure 4, 5 are the streamer channels simulation results, they show that when the voltage is 230kV, the axis length of streamer is 20cm, when the voltage is 600kV, the gap is breakdown. The streamer starting times are 1.71μs and 2.29μs, respectively, and the streamer develop times are 6.73μs and 12.21μs. The average speed of the streamer is 3.98×10^4m/s, which is in close agreement with the test result—3.5×10^4m/s, and last jump speed of streamer could reach 1.60×10^5m/s before breaking down. The streamer axis lengths are also obtained by the simulation, as shown in figure 6 and 7.

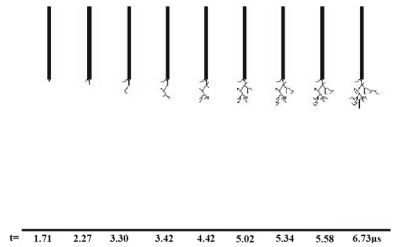

Fig4 Streamer development under 230kV

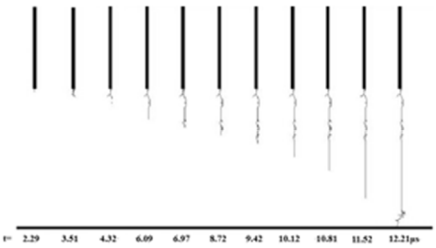

Fig5 Streamer development under 600kV

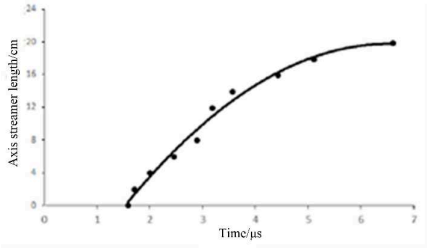

Fig.6 Axial streamer length of 230kV

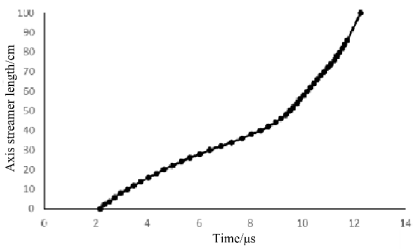

Fig.7 Axial streamer length of 600kV

According to the streamer discharge model, the charge accumulations of 230kV and 600kV are also obtained, which are shown in figure 8 and 9. According to the curves, for the 230kV lighting impulse voltage, the charge in the streamer keep increasing as the streamer developing in the air gap,

when the streamer develop to the end, the charge is accumulated to 23.2μC, while in the time, the growth speed of charge is 0. For the 600kV lighting impulse voltage, the charge in the streamer keep increasing as the streamer developing in the air gap, and in the last jump stage, the growth speed of charge raised fast, and the total charge formed during the whole discharge process is 258.3μC, which matches the conclusion that the charge order of magnitude of long air gap discharge is 10^{-4}C [4].The acquisition of time parameters and charge will take a big step towards to making the fractal streamer discharge model be applied to leader discharge simulation[5].

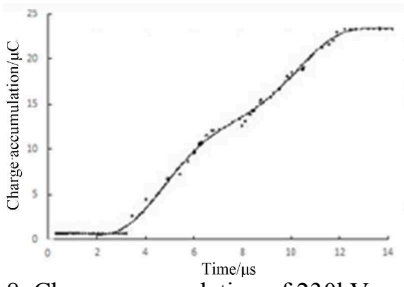

Fig.8 Charge accumulation of 230kV

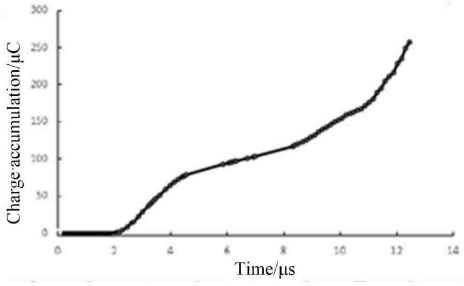

Fig.9 Charge accumulation of 600kV

Conclusion

1. This paper raises a new method to calculate the time and charge accumulation during the streamer discharge process by solve the charge accumulation equation.
2. According to the simulation results of the model, when the voltage is 230kV and 600kV, the axis length of streamer is 20cm and 100cm (breakdown). The streamer starting times are 1.71μs and 2.29μs, respectively, and the streamer develop times are 6.73μs and 12.21μs. The average speed of the streamer is 3.98×10^4 m/s, which is in close agreement with the test result—3.5×10^4m/s, and last jump speed of streamer could reach 1.60×10^5m/s. These data match the test result well.
3. The charge accumulated during the streamer development under 230kV and 600kV lighting impulse voltage is 23.2μC and 258.3μC. The date matches the test results well, and this model is proved to be reasonable to describe the streamer discharge process.

Acknowledge

Project Supported by National Natural Science Foundation of China (51307060); Colleges and Universities in Hebei Province Science and Technology Research Project (Z2013086); Fundamental Research Funds for the Central Universities (2014MS84).

References

[1] Rakotonandrasana J H, Beroual A, Fofana I. Modelling of the negative discharge in long air gaps under impulse voltages [J]. J Phys D: Appl Phys, 2008, 41(10): 1-15.
[2] Geng Yinan, Zhuang Chijie, Zeng Rong. Streamer inception characteristics under positive lightning impulse voltage [J]. Proceedings of the CSEE, 2012, 32(19): 148-154(in Chinese).
[3] Goelian N, Lalande P, Bondiou A, et al. A simplified model for the simulation of positive-spark development in long air gaps[J]. Journal of Physics D: Applied Physics, 1997,30(17): 2441-2452.
[4] Hu Jing, Wen Xishan, Lan Lei. Simulation model of rod-plate gap positive discharge [J]. High Voltage Engineering, 2010, 36（6）: 1392-1397(in Chinese).
[5] Beccra M, Lalande P, Bondiou A, et al. A simplified model for the simulation of positive-spark development in long air gaps[J].Journal of physics D: Applied Physics, 1997, 30(17): 2441-2452.

Advanced Materials Research Vols. 986-987 (2014) pp 1910-1913

doi:10.4028/www.scientific.net/AMR.986-987.1910

Analysis of New Deceleration Strip Device to Generate Electricity

Dongdong Xu
School of Automobile,Wuhan University of Technology,Wuhan 430000,Hubei,China
381317533@qq.com

Keywords: deceleration strip; a one-way clutch; continuous power generation

Abstract: To solve the problem about vehicles passing deceleration strip consumming a large amount of energy , it can improve the efficiency of the deceleration strip generating electricity by improving the existing mechanical power or gas-liquid pavement power transmission part,using the buffer device and conversion device to change the stress state of rack and pinion,combining the working characteristics of one-way clutch with bevel gear transmission characteristic.The result shows that the power generation device design is reasonable and the economical profit is remarkable.

1. Introduction

At present, most of the power generation device in our country adopts water conservancy, solar, wind, fire power,etc as power, but the power source will be confired by all kinds of natural environment, which is not conducive to the sustainable use of energy. In order to reduce the number of traffic accidents where the vehicle is relatively concentrated, such as entrances of schools, companies, and parking lots, we usually set deceleration strip to limit the vehicles' speed. However, that the car would be lifted a little height cross deceleration strip causes energy loss, which power generation device can recycle to generate electricity.

2. Road power status

So far, human with the their constantly efforts has made considerable achievements in road electricity generation technology at home and abroad.

Several students of He Nan University of Science and Technology applied for a utility model patent which has been approved by the state intellectual property office , naming the patent for "a deceleration strip storage device to generate electricity ".The device is applicable to vehicles of different speeds .The deceleration strip device doesn't only decelerate the speed of vehicles,but also collect energy which vehicles loss cross deceleration strip.And the generating efficiency is higher.【 1 】

All over the world, the first pavement to generate electricity is designed and developed by Israeli scientists.They implanted piezoelectric crystal into asphalt of the common road, using the pressure transformation to generate electricity. Besides,they found 1 km road can produce about 100 ~ 400 kilowatts of power which can be sent back to the state power supply bureau or used for lighting and heating device.【 2 】

The road requires a lot of front-end investment, and post-maintenance is very difficult. It is unrealistic to put on the market because it needs to change the material structure of the road and spend a mass of research costs.

3. The meaning of road power generation

3.1 make full use of road resources

In today's social and economic developing rapidly, the total length of highway in our country is world's s top , so the number of cars is increasing rapidly as transport. Nowadays,with the

research and development of all kinds of path generating set , the surplus energy of the road is more and more. It will largely reduce resources waste, and also let the road pull it more weight with the full use of spare resources in the road.

3.2 reduce energy consumption of road

In order to ensure the safety of roads, tunnels, Bridges, toll station security,there are many street lamps and other safety devices,which usually cost the large amounts power energy.That we research road power generation system, can collect energy for street lamps, luca, lights, signs, such as power supply and greatly reduce power consumption in the roads.At the same time, the use of idle energy also greatly decrease the pollution of coal resource generated electricity.

4. system composition

4.1 consideration of factors

According to the characteristics of the car and the structure of deceleration strip , we design a complete organization and reasonable power generation device, considering the following factors: (1) The device can transform the energy that cars driving cross deceleration strip loss into other forms of energy to drive generators;(2)The device can produce enough high speed to match vortical speed of generators through the transmission and growth mechanism.;(3)The device can discrete energy collection and release the stability energy to ensure the electrical equipment work normally with high-performance and steady voltage and frequency storage battery.;(4)The cost of the device should not be too high , have long service life,be easy to install and maintain simply.

4.2 The basic parts of a device

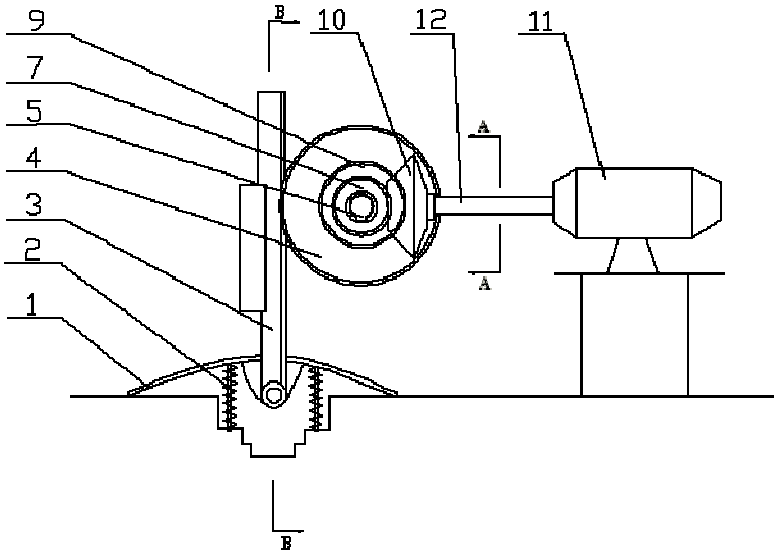

1.Deceleration strip 2. Spring 3. Rack 4.Cylindrical gear 5. the first drive shaft 6. The first one-way clutch 7. The second one-way clutch 8. The first bevel gear 9. The second bevel gear 10. The third bevel gear 11. Generator 12. The second drive shaft

Figure 1 : Schematic diagram of working principle of new deceleration strip device

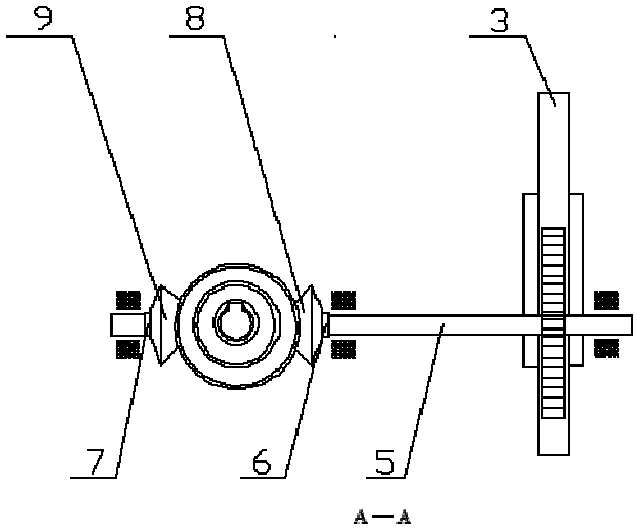

Figure 2: A - A cutaway view of figure 1

4.3Working principle of the system

The device which is installed on the dense-traffic road consists of gear and racks, one-way clutchs and bevel gears.The buffered device which is used to absorb the partial impact load and store elastic energy for the reset of deceleration strip mainly consists of deceleration strip 1 and buffered spring 2.The conversion device consists of the rack 3, gear 4, 5, several one-way clutches and bevel gears to charge reciprocal rectilinear motion into one-way output of shaft.

Rack 3 is pressured to vertical movement when the vehicle passes deceleration strip1;At the same time,the cylindrical gear 4 revolves around the shaft 5 with high-speed and the shaft 5 transmits the torque to a one-way clutch 6,which let the bevel gear 8 drive the bevel gear 10 work,which finally drives the generator 11 power;

When vehicles leave the deceleration strip 1 returning under the action of the spring 2 , the bevel gear 9 drives bevel gear 10 continue the original direction of rotation around its the axis 12 after a series of power transmission,which don't change the work direction of generator 11. That has completed a whole power generation cycle and achieved the function of double continuous power generation.

5. The advantage of device

5.1 The device combining the gears and racks with other basic parts makes use of the work characteristics of one-way clutch (overrunning clutch), which charges reciprocal rectilinear motion into one-way rotary motion and greatly improves the power generation efficiency of the whole device.[5]

5.2 The device's overall set on the pavement, which is beneficial to the early installation and the late maintenance.

6.The feasibility analysis of the mechanism

Let us suppose average quality of an vehicle is 10 t, and driving cross a deceleration strip at a speed of 20 km/h,which lets the deceleration strip move down 0.05 m.The work the gravity do when the vehicle has drave cross a deceleration strip is as follows:

$$W=mgh \quad (1)$$

Type: W is the work the gravity do when the vehicle has drave cross a deceleration strip (J);m is the quality of the vehicle (kg), calculated on a quarter car weight;g the acceleration of gravity ($10kg/m^2$）;h is the falling distance (m).

Time that the vehicle cost cross deceleration strip is as follows:

$$t= s/v \quad (2)$$

Type: t is time (s); s is general width of deceleration strip (m);v is the average speed cross a deceleration strip (m/s).

$$\eta =\eta_1 \eta_2 \quad (3)$$

Type: η is transmission efficiency of the entire transmission mechanism , refer to mechanical manual, determine the transmission efficiency of the kinds of mechanisms, estimate the transmission efficiency of intermediate transmission mechanism for $\eta_1 = 0.92^4 \times 0.97^3 \times 0.88 \times 0.94 = 0.54$; η_2 is efficiency of a generator power, a low power generator efficiency is 80%~90% , and the efficiency of a higher power synchronous generator is 90% ~ 94%, according to condition of the generator, efficiency is 85%, so the overall efficiency of the apparatus is 0.54.[3-4]

the amount of generation of every device is:

$$Q = W \eta \quad (4)$$

Type: Q is theoretical electric energy of a power generation (J);W is the change in potential energy cross a deceleration strip (J).If the number of cars per hour is 400 , which can produce about 230000 J; Refer to some datum that toll stations use LED the total power of a single lane is 110w, which can be suppose the single LED work 5.8 h.

$$P = W\eta /t \quad (5)$$

Type: P is power of a power generation (kw); η is transmission efficiency of the entire transmission mechanism, by type of（1），W=1250J, by type of (2) get t = 0.03, plug t into type of (5), we can know the power of a power is 8.6 kw.

7. Conclusion

Based on the basic mechanical parts such as gear and rack,the article puts a method about a purely mechanical system with auto RCC pavement to produce electricity and designs a "Mechanical Rectifier Bridge" mechanical system through making the use of the work characteristics of one-way clutch.The innovation of system is that making use of one-way clutch one-way work characteristics and the characteristics of the bevel gear and combining with other basic parts realizes the two-way power generation of the device. At the end of the article, the energy consumption of the system are analyzed in the rough, and we can outlook its application prospect and future potential.

References

[1]Xu Chunhao. Henan university of science and technology. Road deceleration strip power generation storage device won the national patent.《Chinese Mining Newspaper》, 2010 ~ 9 ~ 16 (8).

[2] Gao Yugong. The highway can power [Journal] - Driving Garden, 2010 (01).

[3] Yang Xiaohui. Simple mechanical manual [M]. Beijing: Science Press, 2006.

[4] Cheng daqing. Mechanical design manual (fifth edition) [M]. Beijing: Chemical Machinery. Press, 2008.

[5] Kong Qingtang. The classification，application and selection of overrunning clutch[J]. New Technology and New Technology, 1991, (1) : 24 ~ 25.

[6] Yang Yongping, Yang Zhiping, Xu Gang, Wang Ningling.Consumption status and prospects to thermal power energy in China.《Proceedings of the Csee》, 2013 (23).

Advanced Materials Research Vols. 986-987 (2014) pp 1914-1917

doi:10.4028/www.scientific.net/AMR.986-987.1914

Calculation and Analysis of Three-phase Transformer Short-circuit Current

Peiming Pan[1, a], Huan Lian[1, b], Feixiang Hui[1, c] and Weipu Tan[1,d]

[1]North China Electric Power University, Beijing 102206, China.

[a]576701578@qq.com, [b]rainkinglin@126.com, [c]874865468@qq.com,[d]tanweipu@ncepu.com,

Keywords: Transformer, short-circuit current, calculation method, application range

Abstract. Analysis the important significance of transformer short-circuit current calculation for the stable operation of power system. Lead to three different types of transformer short-circuit current calculation methods, this literature uses a simplified example to compare the characters among three methods. Meanwhile, calculation by using the theory to get a quantitative range of simplified method. The calculation results and theory support each other, finally, summarizing the application range of the three methods, and offering a reference for reasonable selection of short-circuit current methods.

Introduction

The mutual effect of the short circuit current and the leakage magnetic field incur electric power on transformer windings. For the sake of the large short circuit current, the electric power are proportional when comapred with the square of current value, so the electric power is larger than normal condition when short-circuit takes place. And because of the larger current, the winding's temperature rises sharply, the mechanical strength of the winding wire decreases under the high temperature. Although short circuit transient state will enmerge and disappear inmmediately, if the transformer short-circuit strength is not sufficient, as well as seriously damaged. The transformer damage will endanger the stability of power system operation. Therefore, the accuracy of the calculation of the transformer short-circuit current is of great significance.

For the transformer, the three-phase short-circuit current is the largest. And the most serious situation occurs on the transformer export, relative to its larger internal three-phase short circuit, the corresponding transformer short circuit caused by the impact is also the largest. Therefore, the accuracy of the transformer three-phase symmetrical short-circuit current calculation on the export will achieve most reference value. The traditional short-circuit current calculation methods mainly include operational curve method, calculation of short-circuit current fundamental frequency AC component of the initial value and practical calculation method, etc. Literature [3] sums up a practical method that applied to a certain capacity of transformer will have advantages to some extent and meet the need of a certain field and project basically. This paper focuses on a simplified network wiring diagram, short-circuit current calculated by using three kinds of calculation methods respectively, then comparing the calculation results, and finally sums up their suitable using condition respectively.

Principle of transformer short-circuit current calculation method

Operation curve method. Literature [1] introduced the basic principle of the curve method. The main core of the method is that simplyfing the equivalent of the network, obtaining the transfer reactance of the power source electromotive force to short circuit node reactance,then turning the transfer reactance into calculating reactance (the reduction to the transfer reactance of each power according to the power rating of the power generator), checking the operation curve to get the short circuit current values at last. This method are limited by the generator parameters, if the actual parameters of the generator, especially the maximum excitation voltage and some other parameters have a big difference from the standard parameters that the curve method used, the relevant correction computation should be done.

Calculation method of short circuit current component initial value. Literature [2] introduced the principle of short-circuit current calculation method for initial value and some precondition. The open voltage divide the equivilent resistance is short-circuit, from above-mentioned, the generator can be equvilent second transient voltage and resistance, the caculation of the AC short circuit current is a stable alternative circuit caculation problem actually. This approach can only calculate the initial value of the short-circuit current and cannot calculate other moments. But the calculation accuracy is not high, this method can be used as a kind of approximate calculation method.

Simplified calculation method. Literature [3] summarizes a practical method of short circuit current.

The first, calculating the short-circuit current of high voltage side when the three phase short circuit occur in the low voltage side of transformer, the main point of this method is that using the physical meaning of short circuit voltage percentage, and when the low voltage side occur in short circuit, the voltage of high voltage side can be thought of constant, it still can be approximate to U_{1N}, it can infer that: $I_{1f} = \frac{S_N}{\sqrt{3}U_k\%U_{1N}} \times 100$.

The second, calculating the short-circuit current of low voltage side when the three phase short circuit occur in the low voltage side of transforme, following equation can be obtained via the ratio of transformer : $I_{2f} = \frac{S_N}{\sqrt{3}U_k\%U_{2N}} \times 100$.

S_N --The rated capacity of transformer.

$U_k\%$ -- The short circuit voltage percentage.

U_{1N}, U_{2N} -- The rated voltage of transformer on the high/ low voltage side.

I_{1f}, I_{2f} -- The short circuit current of transformer on the high/low voltage side.

Example analysis

This paper adopts simplified transmission and distribution network diagram as shown in Figure 1. Three-phase short circuit occurred in step-down transformer low voltage side of the outlet.

Related parameters are as follows:

Water hydrogen cooled turbo generator: model type QFSN-600-2YHG $S_{NG} = 667\text{MVA}$ $U_N = 20\text{kV}$ $\cos\varphi_N = 0.9$ $x_d'' = 0.15$;

Step-up transformer T1: three-phase double winding transformer $S_{NT1} = 720\text{MVA}$ $345/20\text{kV}$ $P_0 = 391\text{kW}$ $I_0\% = 0.25$ $P_k = 1418\text{kW}$ $U_k\% = 14$;

330kV line: d=10km $x = 0.321\Omega/\text{km}$;

Step-down transformer T2: three-phase double three-winding transformer $S_{NT2} = 90\text{MVA}$ $345/10.5\text{kV}$ $P_0 = 81\text{kW}$ $I_0\% = 0.56$ $P_k = 287\text{kW}$ $U_k\% = 14$;

In order to better respond with the above principles, we set T2 low voltage side no load.

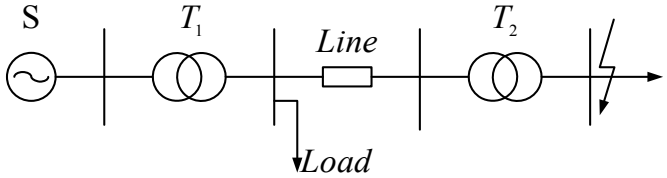

Fig.1 System Main Wiring Diagram

The parameter of T1 and T2 refer to GBT 6451-2008 oil-immersed power transformer technology parameters and requirement in the following table 1:

Table 1 The Transformer Parameter List

Rated capacity MVA）	Voltage combination and tap range		Connection symbol	No-load loss kW	Load loss kW	No-load current %	Short-circuit voltage %
	High voltage side kV）	Low voltage side kV）					
90				81	287	0.56	
120	345	10.5		100	356	0.56	
150	345±2*2.5%	13.8	YNd11	119	422	0.52	14~15
180	363	15.75		137	484	0.48	
360	363±2*2.5%	18		234	845	0.43	
400		20		252	913	0.38	
720				391	1418	0.25	

The equivalent circuit diagram shown in Figure 2, regardless of the load as well as the factory motor feedback current. Take the reference value $S_B = 1000\text{MVA}$ and U_B as the voltage level of the average for the rated voltage.

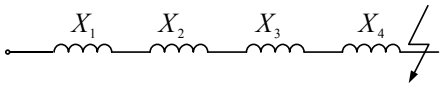

Fig.2 Equivalent Circuit Diagram

Because the low voltage side of T2 is no load, we can change the rated capacity of T2 according to table 1, combining with the three transformer short-circuit current calculation methods above, to calculate the groups of short-circuit current data for comparison. Calculated values in table 2:

Table 2 The Short-Circuit Current Values List

Rated capacity (MVA)	I_{1f}(kA)			I_{2f}(kA)		
	1st Method	2nd Method	3rd Method	1st Method	2nd Method	3rd Method
90	0.868	0.837	1.075	28.534	27.453	35.348
120	1.073	1.039	1.434	35.281	34.146	47.130
150	1.261	1.267	1.790	41.443	41.624	58.913
180	1.436	1.368	2.151	47.201	44.960	70.696
360	2.135	2.006	4.303	70.160	65.930	141.392
400	2.223	2.107	4.781	73.057	69.227	157.102
720	2.823	2.619	8.606	92.752	86.052	282.784

If completed generator parameters are not implict, the 1st method cannot be used to calculate the transformer short-circuit current. But this example has given in the complete generator parameters. With the constant improvement of the capacity of T2, the result of calculation by the 1st method and 2nd method is very close, but the result from method three has a big difference from 1st and 2nd method, which we can see it from table 2. We select method 2nd and method 3rd for error analysis, we will get some regulation, the relative error formula as follows: $\xi = \frac{|I_{1f3} - I_{1f2}|}{I_{1f2}} \times 100\%$. Get the results in table 3:

I_{1f2} ——The short circuit current value of T2 high voltage side by the 2nd method

I_{1f3} ——The short circuit current value of T2 high voltage side by the 3rd method

Table 3 The Relative Error Values List

Rated capacity MVA）	90	120	150	180	360	400	720
ξ	28.4%	38.0%	41.3%	57.2%	114.5%	126.9%	228.6%

Obviously, with the continuous increase of the capacity of T2, the relative error is constantly increasing. Further analysis, when there is certain relationship betweent the system capacity and T2 capacity, the calculation results of the three methods are similar. In order to make the calculation results of the 2nd method and 3rd method more similar, then the system short-circuit capacity S_K and transformer capacity S_{NT} have to have the following relations. Deducing as follows:

As shown in figure 3, introducing the short-circuit capacity to method two, having equation:

$$I_{1\mathrm{f}} = \frac{1}{\frac{S_{\mathrm{B}}}{\sqrt{3}S_{\mathrm{K}}} + \frac{U_{\mathrm{k}}\%S_B}{100S_{\mathrm{NT}}}} \times \frac{S_{\mathrm{B}}}{\sqrt{3}U_{1\mathrm{N}}}$$

If the relative error calculation results maintain less than 10%, than using method three is reasonable. That is when $\xi = 10\%$. Having equation as follows:

$\frac{1}{\frac{S_{\mathrm{B}}}{\sqrt{3}S_{\mathrm{K}}} + \frac{U_{\mathrm{k}}\%S_B}{100S_{\mathrm{NT}}}} \times \frac{S_{\mathrm{B}}}{\sqrt{3}U_{1\mathrm{N}}} \times 1.1 = \frac{S_{NT}100}{\sqrt{3}U_{\mathrm{k}}\%U_{1\mathrm{N}}}$. Deducing: $S_{\mathrm{NT}} / S_{\mathrm{K}} = 0.001U_{\mathrm{k}}\%$

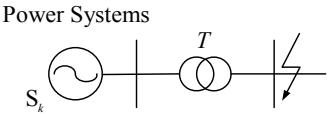

Fig.3 System Wiring Diagram

Conclusions

When the system short circuit capacity at the transformer high voltage side is larger, and the rated capacity of transformer is smaller, once the three phase short circuit occurred in the low voltage side of transformer, the transformer voltage loss at the high voltage side will be relatively smaller, using the 3rd method to calculate short circuit current will be very convenient. Through the calculation the above, If $S_{\mathrm{NT}} / S_{\mathrm{K}} < 0.001U_{\mathrm{k}}\%$, we can use 3rd method to calculate, the relative error will remain within 10%, if $S_{\mathrm{NT}} / S_{\mathrm{K}} \geq 0.001U_{\mathrm{k}}\%$, suggest to use the tradition method. Traditional methods will be implemented in different cases. The 1st method will be better when the parameter of generator is detailed and the short-circuited current needs to be calculated. When the parameter of generator is not particular with the approximate calculation, the 2nd method will be appropriate. The cases are based on the limitation of these methods. The different results confirm the different characteristics of the three methods. The confirmation to the scope of the different methods will bring higher reference value to choose the method of transformer short-circuited current calculation.

References

[1] Wei Cao, Meixia Zhang. The Evaluation and Amendment on the Method of Power System Short-circuit Current Computational Curve. Journal of Shanghai University of Electric Power, 2006, 22(4): 327-328. (In Chinese)

[2] Guangqi Li. The Power System Transient Analysis. Beijing: China Electric Power Press. 2007. (In Chinese)

[3] Hao Hu, Binwen Yang, Xiaofeng Li. The Practical Calculation Method of Transformer Short-circuit Current, Transformer, 2010, 47(7): 9-10. (In Chinese)

[4] Shanghai Power Equipment Research Institute, China Huadian Engineering Co.,LTD. Handbook of Large Thermal Power Equipment. Beijing: China Electric Power Press. 2009. (In Chinese)

[5] Xi'an Jiaotong University, Northwest Electric Power Design Institute, Northwest Electric Surveying and Designing Institute. Practical short-circuit current calculation method. Beijing: Electric Power Industry Press, 1982. (In Chinese)

Advanced Materials Research Vols. 986-987 (2014) pp 1918-1925

doi:10.4028/www.scientific.net/AMR.986-987.1918

Capacity Configuration and Energy Control Strategy of Stationary Super Capacitor Energy Storage System of Urban Rail Transit

Bin Wang[1, a], Zhongping Yang[2,b] and Fei Lin[3,c]

[1] Beijing Jiaotong University, Beijing, China

[2] Beijing Jiaotong University, Beijing, China

[3] Beijing Jiaotong University, Beijing, China

[a]12121547@bjtu.edu.cn, [b]zhpyang@bjtu.edu.cn, [c]flin@bjtu.edu.cn

Keywords: Urban rail transit, super capacitor, regenerative braking failure, energy control strategy, capacity configuration

Abstract. The installation of super capacitor in urban rail transit system allows the recovery of the braking energy for increasing the energy efficiency as well as a better pantograph voltage profile. An energy control strategy of the energy storage system which is suitable for the urban railway transit is proposed in this paper. Then, the methodology of capacity configuration is put forward based on the simulation platform in Matlab environment. Ultimately, the capacity configuration results of super capacitor energy storage system are determined based on parameters of an actual metro line under different traffic conditions.

1 Introduction

In recent years, as the rapid development of Chinese economy, many cities are facing increasingly serious social issues such as traffic congestion and worse environmental pollution. For the purpose of improving the urban environment, the development of modern urban transit which has the significant advantages of large capacity, punctuality, safety, energy conservation and environment protection becomes a social consensus.

In modern urban railway system, vehicle braking energy was commonly feedback to the catenary by the method of regenerative braking. Due to the diode rectifier of traction supply network, surplus regenerating energy cannot feedback to medium-voltage network. When a train is in the condition of regenerative braking, if there are no traction train or energy absorbing device nearby to absorb the regenerative energy, the train pantograph voltage would exceed the normal range which lead to the overvoltage protection of vehicle traction system, that is, the failure of regenerative braking.

As the rapid development of the storage technology of flywheel, battery and super capacitor, the method how to solve the energy consumption problem and regenerative braking failure become the focus of world urban railway transit. Compared to other storage technology, super capacitor has the advantage of high power density, long cycle life and easy SOC test, ect. Thus, super capacitor becomes an important choice of the energy storage element in the urban railway transit and has gradually been used at home and aboard [4].

According to the installation location of super capacitor, it can be divided into two kinds of installation, on-board and stationary. On-board super capacitor's efficiency is high with low loss of energy storage and release, but restrict of vehicle weight and space; in contrast, stationary super capacitor's security requirement is low but with high difficultly of the determination of its position and size, namely, capacity configuration.

Currently, there are some literatures refer to the capacity configuration of super capacitor energy storage system. Teymourfar[5] et al. construct an simple metro simulation model with Pscad software, then take the regenerative current of substations as the basis of capacity configuration of super capacitors, but lack dynamic simulation of power flow simulation of DC supply network. Ricardo Barrero[6] et al. analyze the proper capacity and location under different traffic conditions with an "effect-cause" simulation tool. D.Iannuzzi[7-8] et al. analyze the energy interactive relationship of energy storage device and terminal substation ,but do not take the global power flow of DC-net into account.

An energy control strategy of the energy storage system (ESS) which is suitable for the urban railway transit is proposed in this paper. Then, the methodology of capacity configuration is put forward based on the simulation platform in Matlab environment. Ultimately, the capacity configuration result of super capacitor energy storage system is determined based on parameters of an actual metro line under different traffic conditions.

2 Background of Stationary ESS

The structure of urban railway system's DC supply network is shown in Fig.1, super capacitor energy storage device is connected in parallel between the positive and negative buses of substations, and line impedance is expressed in Z. Energy storage device consists of bidirectional dc/dc converter and super capacitors, and its charge/discharge process is controlled by the switch tube T1 and T2 as shown in Fig.2.

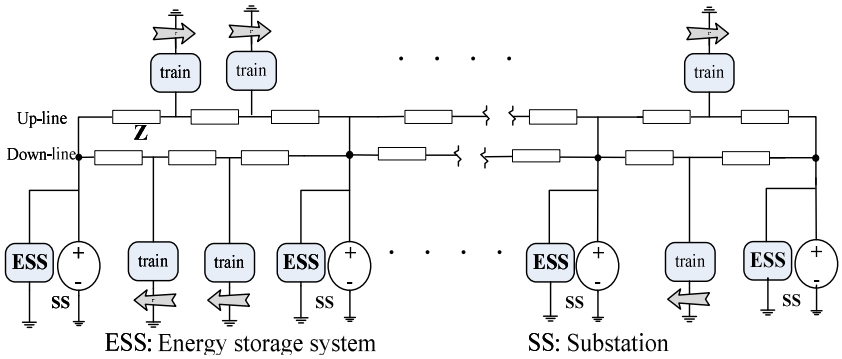

Fig.1 DC traction power supply network

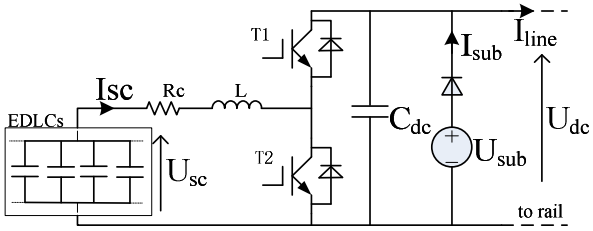

Fig .2 Super capacitor energy storage device

Where I_{line} is line current, I_{sub} is traction substation rectifier unit's output current, I_{sc} is super capacitor's charging/discharging current, U_{dc} is DC bus voltage, U_{sub} is rectifier unit's terminal voltage, U_{sc} is super capacitor's terminal voltage. When super capacitor is in the charging state, substation rectifier unit quit operation, at this moment, there is no current flow from substation.

3 Energy control strategy of stationary ESS

When there are braking vehicles running in the traction supply network of urban rail transit, except for part of the regenerative braking energy is utilized by nearby vehicles, surplus regenerative energy is absorbed by super capacitors. When there are traction vehicles running, super capacitors released its stored energy for vehicles' traction operation. The charge/discharge control of super capacitors can avoid the waste of surplus regenerative energy, reduce the energy consumption of urban rail transit, and decrease the probability of regenerative braking failure.

According to the application condition of urban rail transit, the energy control strategy of super capacitor energy storage system is supposed to meet the follow requirements: to stabilize DC traction network voltage and as far as possible to prevent regenerative braking failure; the charge/discharge current is controllable; the SOC(state of charge) of super capacitor fluctuates within bounds. Based on the above requirements, an energy control strategy is put forward as shown in Fig.3.

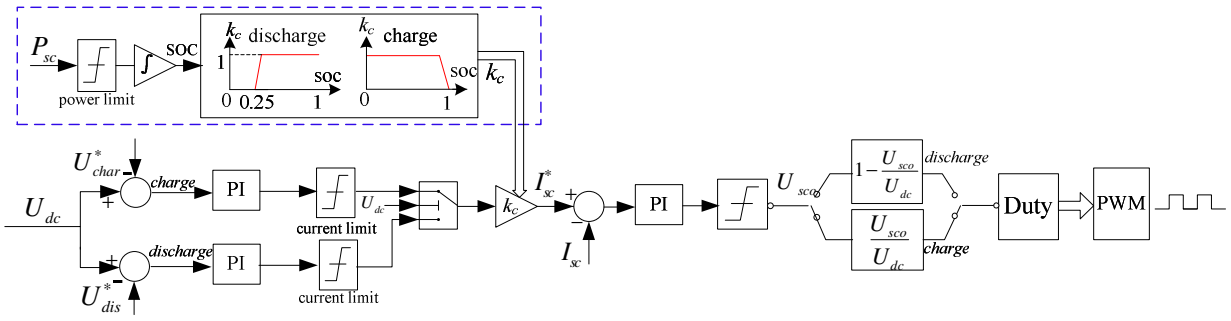

Fig.3 Stationary super capacitor energy control diagram

The energy control strategy of stationary super capacitor can be divided into three parts: DC network voltage constraint, charge/discharge control, SOC constraint. U_{char} and U_{dis} are the threshold values of charge/discharge, the magnitude and direction of charging/discharging current are determined by the difference value between current voltage and threshold value. When DC network voltage fluctuates between U_{dis} and U_{char}, super capacitor is in the standby state. In order to guarantee the regular Boost discharge, the terminal voltage of super capacitor is general set between $0.5U_{scmax}$ and U_{scmax}, thus, the working range of SOC is 0.25~1 for constraints of charging/discharging current of super capacitors.

Based on the analysis of the energy management strategy, the keys to determine the power level and capacity of super capacitors are the data acquisition of feed-in power of each traction substation and its installed super capacitors' stored energy variation range.

4 Stationary super capacitor energy storage system simulation platform

In order to simulate the power flow of DC network of urban rail transit, the stationary super capacitor energy storage system simulation platform is established in this paper in Matlab environment, which shown in fig.4. The platform included train performance simulator(TPS), DC-Railway loadflow simulator(DC-RLS) and super capacitor energy storage system(SCESS).

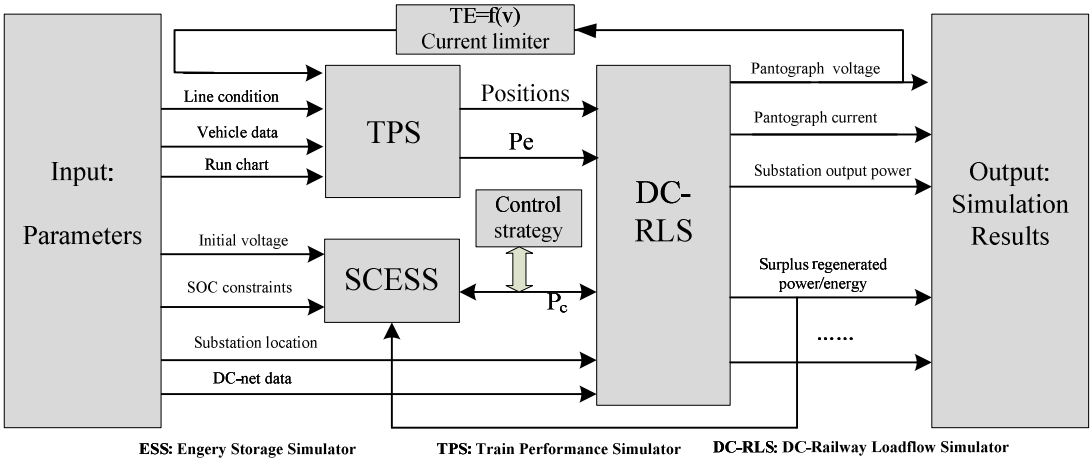

Fig.4 Simulator for super capacitor energy storage system

TPS:

As shown in Fig.4, the output of TPS is not only associated with line condition, vehicle data and run chart, but also be constrained by realtime train pantograph voltage. From TPS we can get positions of up-line and down-line trains and their electric power which offer essential data for subsequent load-flow calculation of DC supply network.

DC-RLS:

In the solving process of DC supply network, because of its time-variation and nonlinearity of the network structure, the paper presents a new load-flow calculation methodology of DC-net, the simulation result demonstrate the rapidity and astringency of this methodology. The modeling and methodology are shown as follows.

(1) Network segmentation

As shown in fig.5, SS is traction substation, T_u and T_d are up-line/down-line train models, Z_u and Z_d are variable resistances of up-line/down-line line. In fig.5, there are two trains running in up-line and down-line line respectively, if there has only one train running in up-line or down-line line, DC network can be represented just by seg1.

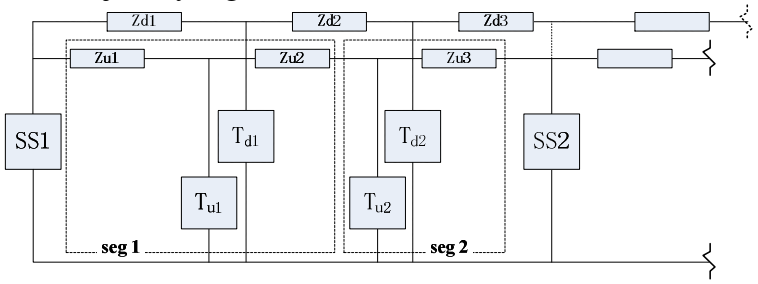

Fig .5 Segmentation of DC power supply network

(2)Subsystem modeling

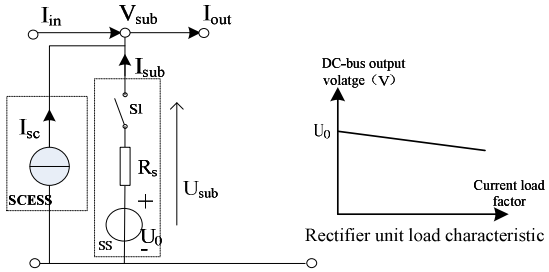

Fig. 6 Substation model

$$I_{out} = I_{in} + I_{sc} + I_{sub} \tag{3}$$

$$U_{sub} = U_0 - R_s I_{sub} \tag{4}$$

Because of no-controlled diode rectifying mode of traction substation, the substation output current flows unidirectionally. As shown in fig.6, when substation output current I_{sub} is positive, switch S1 close; when I_{sub} is negative, S1 break. U_0 is substation floating voltage. SCESS is equivalent to the controlled current source and controlled by energy control strategy which introduced in this paper.

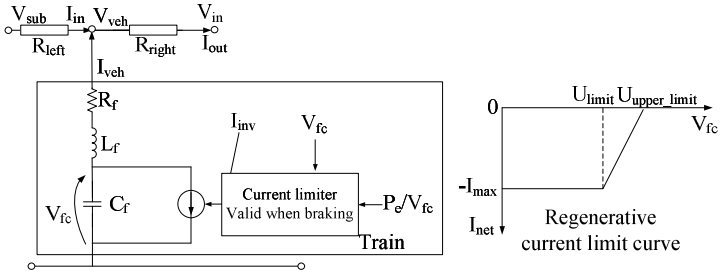

Fig.7 Train model

$$\frac{dI_{veh}}{dt} = \frac{1}{L_f}(V_{veh} - V_{fc} - R_f I_{veh}) \tag{5}$$

$$\frac{dV_{fc}}{dt} = \frac{1}{C_f}(-I_{veh} - I_{inv}) \tag{6}$$

$$V_{sub} - V_{veh} = R_{left} I_{in} \tag{7}$$

$$V_{veh} - V_{in} = R_{right}(I_{in} + I_{veh}) \tag{8}$$

Where C_f is the vehicle support capacitor, L_f is the filter reactor, I_{inv} is the output current of inverter box. U_{limit} is the threshold voltage of regenerative braking failure. When the train pantograph voltage exceeds U_{limit}, partial failure happens, when voltage reach U_{upper_limit}, full failure happens.

5 Case study

5.1 input data

The study is applied to a domestic metro line. The total length of the line is about 24.6km with 22 stations include 13 traction substations. The DC-net data and substation position are shown in below tables.

Table 1 DC-net parameters

U0	836V
Uchar/Udis	850V/800V
Ulimit/Uupper_limit	900V/970V
Substation equivalent resistance	0.07 Ω
Contact line impedance	0.007Ω/km
Rail impedance	0.009Ω/km
Pantograph resistance	0.015 Ω
Departure interval	600s/300s/150s

Table 2 Substation position

substation	spacing（km）	substation	spacing（km）
SS1	1.110	SS7	2.762
SS2	1.926	SS8	1.534
SS3	2.160	SS9	1.767
SS4	2.303	SS10	1.884
SS5	2.120	SS11	2.594
SS6	2.695	SS12	1.007
SS7		SS13	

5.2 Simulation result

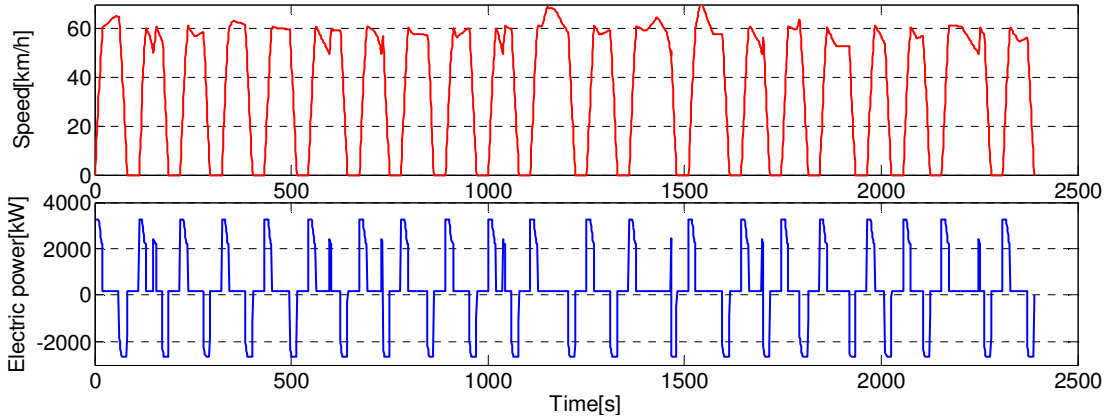

Fig.10 The speed and electric power of up-line train

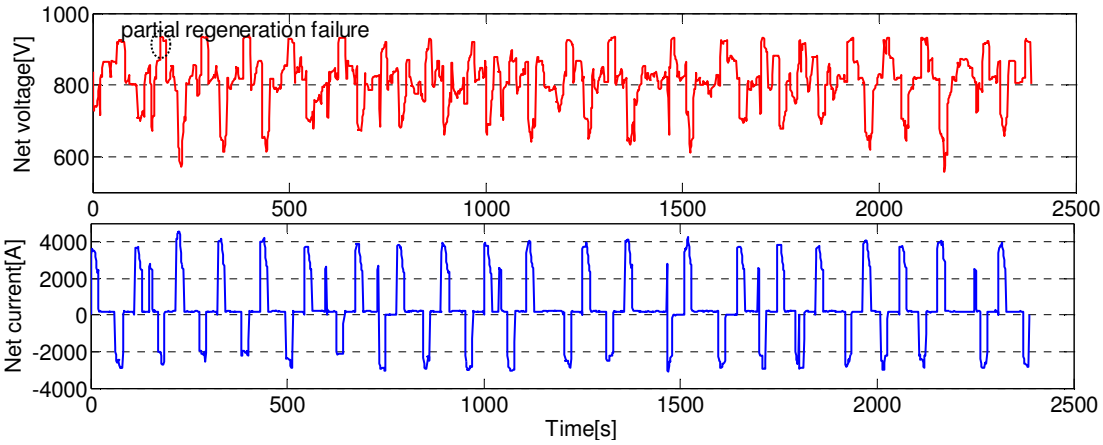

Fig.11 The catenary voltage and current of up-line train

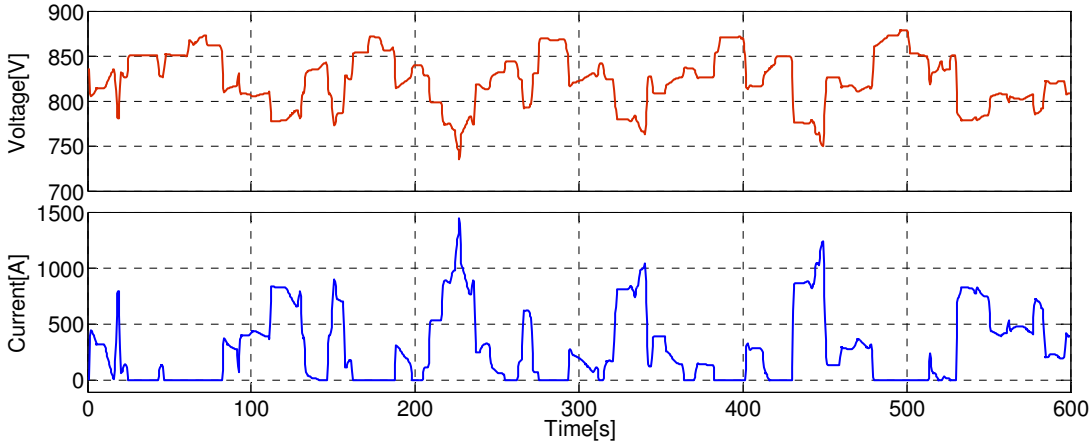

Fig.12 The voltage and current of traction substation

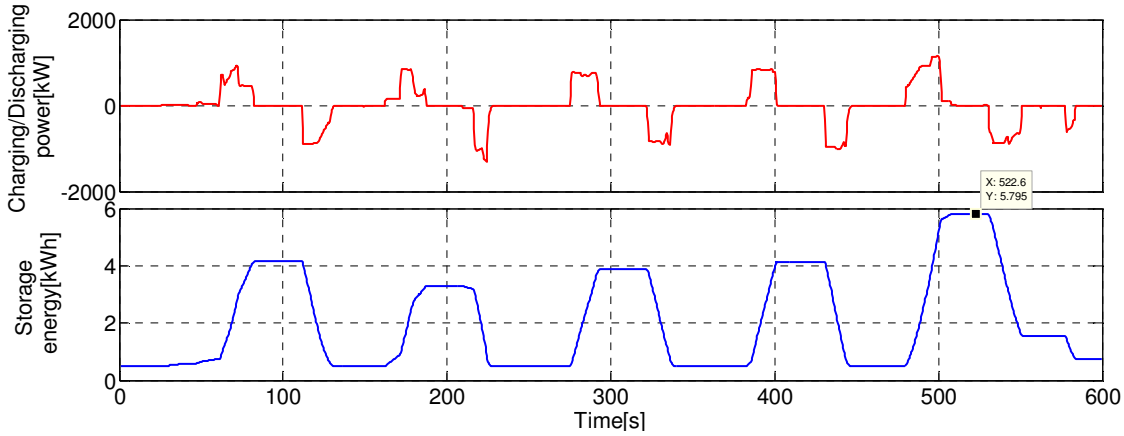

Fig.13 The power and stored energy of ESS

As shown in fig.10, where is the speed and electric power of up-line train from TPS, and which offer essential data for DC-RLS. In fig.11, where is the up-line train pantograph voltage and current with departure interval of 600s. When up-line train is braking, the pantograph voltage may exceed 900V which resulted in regenerative braking failure. Take SS2 for example, its voltage and current are shown in fig.12 where its voltage fluctuates between 700~900V with the application of super capacitor. The charging/discharging power and storage energy waveform of super capacitors which be installed in SS2 are shown in fig.13, the difference value between maximum and minimum of storage energy will be the valuable references for capacity configuration of super capacitors.

5.3 Capacity configuration

According to above simulations, the statistic values of peak absorbing power and available storage energy(difference value between maximum and minimum of storage energy) of each substation's super capacitors under different departure intervals are shown in fig.14, fig.15.

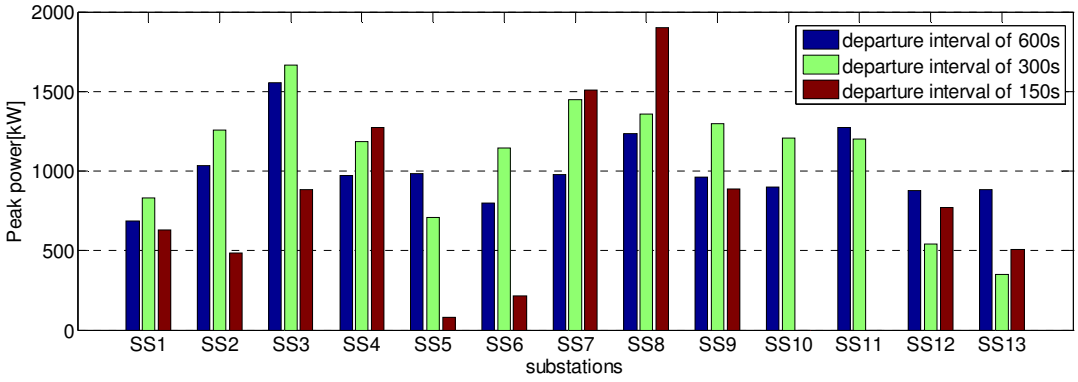

Fig.14 Peak power of super capacitor under different conditions

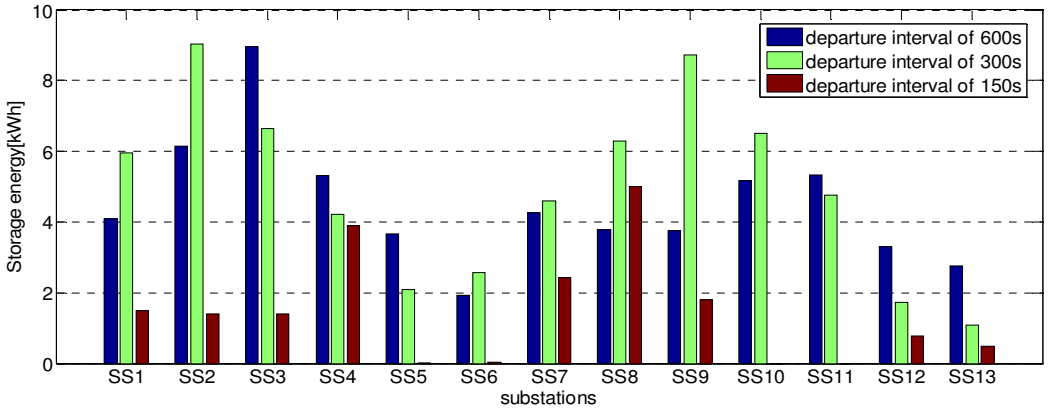

Fig.15 Energy of super capacitor under different conditions

As can be seen above, the peak power of super capacitor has no linear connection to the departure interval, but its storage energy overall decreases with the decreasing of the departure interval. On the basis of above statistics, the capacity configuration results of super capacitor energy storage system are shown in table3.

Table 3 Results of capacity configuration

substation	Power level[MW]	Storage energy[kWh]
SS1	1	6.0
SS2	1.5	9.0
SS3	2	9.0
SS4	1.5	5.3
SS5	1	3.6
SS6	1	2.5
SS7	1.5	4.6
SS8	2	6.3
SS9	1.5	8.7
SS10	1.5	6.5
SS11	1.5	5.3
SS12	1	3.3
SS13	1	2.7

Nowadays, most of metros utilize two-side feeding mode for power transmission, if we want to simply design the power level and storage energy of super capacitor set in certain substation, the most common method is to calculate the feed-in peak power and surplus regenerative braking energy of certain substation in the scenario when up-line and down-line trains arrive the station simultaneously. For instance, two up-line and down-line trains leaving for the same substation start to brake from the speed of 80km/h, at this moment, the feed-in peak power of the substation is about 6MW, and surplus regenerative braking energy is about 20kWh. By contrast with the above simulation results, the calculative peak power and storage energy of super capacitors when considering only two trains are

much bigger than the results of multi-trains simulation, therefore, the designed capacity and device cost of super capacitor energy storage system would be much lower in the capacity configuration methodology of global and dynamic based on the simulation platform.

6 Summarize

The paper studied the methodology of super capacitors capacity configuration under reasonanle energy control strategy of stationary energy storage system. Conclusions as follows:

1, To give full play of energy-saving effect of regenerative braking in rail transit, the paper has proposed the energy control strategy for super capacitors to absorb surplus regenerative braking energy when train in braking state and to offer peak power when train in traction state.

2, The paper put forward a new DC-railway load-flow calculation methodlolgy which has solved the misconvergence problem of load-flow calculation when considering regenerative braking.

3, The paper has established a stationary energy storage system simulation platform which is suitable for the urban railway transit in the point of global and dynamic.

4, The power level and stoage energy of super capacitor energy storage system have been determined based on parameters of the actual metro line under different traffic conditions and which provide theory basis for engineering design.

Acknowledgements

This paper is part of projects suported by I13H100030 from Beijing Laboratory of Urban Rail Transit, I13H100020 from Beijing Key Laboratory of Urban Rail Transit Automation and Control, and I13L00100 from Beijing Subway.

References

[1] Barrero R, Tackoen X, Van Mierlo J. Energy savings in public transport[J]. IEEE Veh Technol Mag 2008;3(3):26–36.

[2] Ogasa M, Taguchi Y. Power flow control of trolley hybrid electric vehicles[C]. RTRI (Railway Technical Research Institute) Report, 2006, 20(7): 5-10.

[3] Iannuzzi D, Tricoli P. Metro train equipped onboard with supercapacitors: a control technique for energy saving[J]. International Symposium on Power Electronics, Electrical Drives, Automation and Motion, 2010: 750-756.

[4] RicardoBarrero, XavierTackoen, Joeri Van Mierlo.Improving energy efficiency in public transport:stationary supercapacitor based energy storage systems for a metro network[C]. Vehicle Power and Propulsion Conference, 2008. VPPC '08. IEEE.

[5] Reza Teymourfar, Behzad Asaei, Hossein Iman-Eini. Stationary super-capacitor energy storage system to save regenerative braking energy in a metro line[J]. Energy Conversion and Management, Volume 56, April 2012, Pages 206–214.

[6] Barrero R, van Mierlo J. Stationary or onboard energy storage systems for energy consumption reduction in a metro network[J]. ProcIMechE Part F: J Rail Rapid Transit 2010;224(3):207–25.

[7] Iannuzzi D, Ciccarelli F, Lauria D.Stationary ultracapacitors storage device for impoving energy saving and voltage profile of light transporation networks[J]. Transportation Research Part C 21(2012)321-337.

[8] Iannuzzi D, Pagano E, Tricoli P. The use of energy storage systems for supporting the voltage needs of urban and suburban railway contact Lines[J].Energies,2013: 1802-1820.

[9] Alfred Rufer. Energy Storage for Railway Systems, Energy Recovery and Vehicle Autonomy in Europe[C]. Power Electronics Conference (IPEC), 2010 International. 21-24 June 2010.

Advanced Materials Research Vols. 986-987 (2014) pp 1926-1929

doi:10.4028/www.scientific.net/AMR.986-987.1926

Computation and Analysis of Static and Dynamic Radial Stability of Power Transformer Inner Winding

Xin SUN, Yan LI, FangXu HAN, Jian LI

Research Institution of Special Electrical Machines, Shenyang University of Technology, China

email: sunxinsy@126.com

Keywords: Power Transformer; Short-circuit Electromagnetic Force; Radial Stability

Abstract. In this paper, the size of winding electromagnetic force after short circuit has been acquired through leakage field calculation and analysis on power transformer, and based on the computation results, the radial stability experimental results of large capacity power transformer inner winding short-circuit model were compared to the simulation values to guide actual product analysis and checking. With the accumulated simulation experience on this model, then a type of sfz9-80MVA power transformer inner coil static and dynamic stability has been checked to confirm the radial instability phenomenon could whether or not occur on this product.

Introduction

Power transformer as an important device, which directly affects the safety of the power grid reliability, with the continuous expansion of the transformer, the transformer voltage level constantly rising, 500kV, 750kV, 1000kV large-capacity transformer should be shipped out. Due to the requirements of cost and the optimize volume of the transformer, the transformer leakage magnetic field has been increased, then the impact of the winding short-circuit force is more obvious than before. With the complex internal structure of the transformer and the influence of insulating material physical properties, the problem of short-circuit strength has become the main reason to cause the transformer accident and acquired more and more attention.

When short circuit occurred on power system, the power transformer will damaged at the impact of instability on winding short-circuit force. Therefore, the ability to withstand short circuit instability has been a key technology when designed large-capacity transformer. As the same time transformer manufacturers and research scholars have carried a number of studies on this problem. Early research mainly focused on the static strength, but due to some qualified products by static strength calculation still damaged by sudden electromagnetic force when short-circuit accident occurred. Therefore, the research priorities turned gradually from the static into dynamic.

Theoretical Analysis

Per unit length radial force of each disk on power transformer can be calculated by ampere force computation formula after transformer magnetic flux density distribution has determined, and the radial stress will acquired through vector superposition of each winding disk segment, and the disk total radial force can be calculated, too.

Then the static magnetic force of disk can be derived as follows:

$$F_i = K_f B_i 2\pi R_i J_{di} S_i \tag{1}$$

Where K_f is the asymmetrical short-circuit current impact factor, B_i is the flux density of ith element conductor, R_i is the distance from the centerline of core to the center of gravity of ith element conductor, J_{di} is the symmetrical short-circuit current density of ith element conductor, S_i is the area of ith element conductor.

According to the elastic stability theory, the limited values of the compressive stress which located on winding average radius can be acquired when winding withstanding radial compressive short-circuit force. As long as winding withstand radial compressive stress is less than or equal to

the value with static checking and leaving some margin. Then the transformer can be considered not damage by radial instability, and the critical stress of radial instability can be acquired through formal (2).

$$\sigma_{cp} = \frac{1}{12} En^2 (\frac{b}{D})^2 \tag{2}$$

Where E is the elastic modulus of copper wire, n is the number of winding stays along winding inner diameter, b is the single radial width of conductor, D is the average winding diameter.

However, during the process of short circuit, the short circuit force acting on the winding was not constant actually, and it can be changed according to the complex regulation because of continuously changing short-circuit current as during a short circuit. When a short circuit occurred in the voltage zero-crossing instant, the short-circuit current will reach to the maximum amplitude value, therefore, short electromagnetic force with the changes of time can be given as follows:

$$F = K_F i_{dmax}^2 = K_F I_{mdN}^2 [(\frac{1}{2} + e^{-2t/T_a}) - 2e^{-t/T_a} \cos \omega t + \frac{1}{2} \cos 2\omega t] \tag{3}$$

Where K_F is the factor to determine the short-circuit force, I_{mdN} is the amplitude of the steady-state short-circuit current, T_a is the time constant of circuit, ω is the grid frequency.

Computation and Analysis of Short-circuit Model

The short circuit model used in this paper was a simulation model of medium voltage winding portion disks of single phase auto-transformer with the capacity of 250MVA and voltage level of 500kV, and the basic structure dimension was shown in Table1. Because the short circuit test of a large capacity extra high voltage transformer was difficult to complete, how to calculate its ability to withstand short circuit quickly and accurately was especially important.

Table1 Basic structure of the size of the short-circuit model

Inner diameter	Outer diameter	Axial height	Spacer number	Section number
801mm	999mm	198mm	36	16

According to Equation (1) and (2), the radial compress force and buckling strength of winding disks can be calculated, and the values was shown on Table2, the buckling strength of this model was greatly more than radial compress force which the disks withstand, that means its margin of safety was very high, so that the model may be able to withstand the short-circuit impact.

Table2 Radial strength of short-circuit model

Disk	Radial force(N/mm)	Buckling strength (N/mm)
E	-122.5	481.64
K	-103.53	481.64

The calculated radial electromagnetic force can be seen as a known load to load on disks, and the dynamic force load curve can been shown in Figure 1.The calculated and measured results of disk radial displacement with the influence of dynamic force was shown in Table 3,the each peak displacement error that the calculation results with the experimental values on short-circuit model were less than 20%, and can basically meet the needs of the project. Therefore it is a feasible method to analyze dynamic radial strength of transformer windings.

Because of the disk electromagnetic force direction is opposite to the recovery elastic force in the process of inward compression, but it consistent with the direction of compression displacement. While the direction of disk electromagnetic force is consistent with the recovery elastic force and it has the opposite direction to the movement. Therefore, the tensile displacement along radially outward is less than the amount of inward compression.

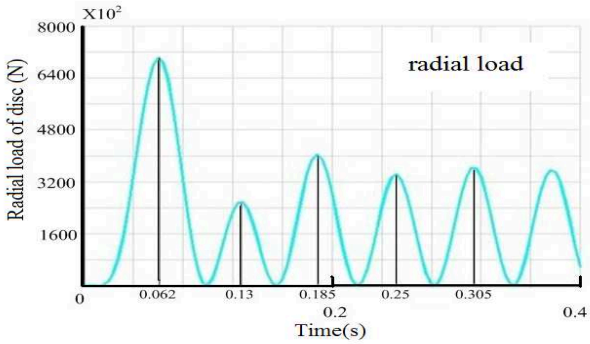

Fig.1. Short-circuit model of dynamic force load changing curve

Table 3 Measured value and simulation value of winding radial displacement

	First peak	First trough	Second peak	Second trough
Simulation value（mm）	2.82	2.67	3.38	2.58
Measured value（mm）	2.90	3.23	3.92	2.18
Error（%）	2.7	17.3	13.7	18.3

Product Example Calculation

Through the analysis and calculation of short-circuit model, the experience and methods have been accumulated, this paper attend to analyze short-circuit strength using an actual transformer products with type of sfz9-80MVA/110kV has been analysis for instance. According to the intensity checking process of the short-circuit model, static analysis and calculation of the product should be utilized at first. It can be seen most of the disk margin of safety are very large shown in Table 4, and it basically meet the requirements of transformer radial stability. At the minimum tap voltage moment, the radial force of disk P was similar to buckling strength even almost equal, hence it need for a dynamic analysis under this conditions.

Table 4 Radial strength of actual product

Condition	Disk	Radial force(N/mm)	Buckling strength (N/mm)
Rated tap	P	-160.25	178.43
	Q	-90.91	122.21
	R	-83.80	122.21
Maximum tap	P	-151.65	178.43
	Q	-84.03	122.21
	R	-77.39	122.21
Minimum tap	P	-172.36	178.43
	Q	-100.38	122.21
	R	-92.48	122.21

Seen from the design, disk P is located in the middle position of low voltage winding, so the design method of short-circuit experimental model was been introduced to establish actual product new model which contains the 9 disks element of winding intermediate portion about 1/5 of the total height, consistent with the other size of the actual products, and the model was shown in Figure 2. For example, the disk displacement of X position is 0.153mm, while the other side is 0.216mm at one moment.

By loading load curve according to the regulation shown in Figure 2, the disk P radial vibration displacement curve can be acquired in Figure 3.The maximum displacement is 3.52mm appearing at 0.15s moment which delayed in the peak load of 0.02 s. Because of the effect of mass damper and rigid damping of entire winding system, the frequency of load and displacement has changed to delay the peak time. However, due to the radial displacement is not large, it is also considered that the product can withstand the impact of short-circuit current.

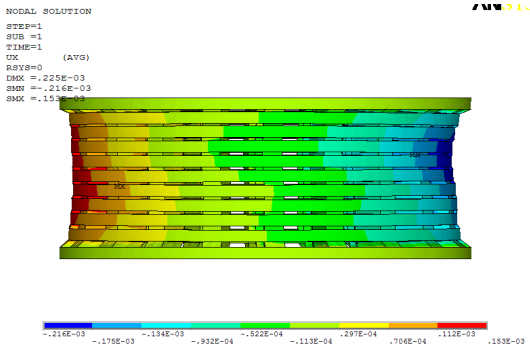

Fig.2.The disk radial displacement distribution at one moment

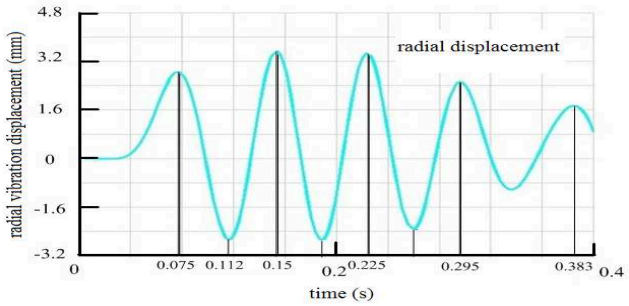

Fig.3.The radial vibration displacement distribution curve of disk P

Conclusion

When checking short circuit strength of large-capacity power transformer, static and dynamic checking method can be combined. One hand it can ensure the reliability of the product, on the other hand it can save the calculated time of large amounts data to meet the project schedule requirements.

In this paper the influence of short-circuit electromagnetic force on winding disks was only considered after initial short-circuit without considering the cumulative deformation and displacement effects when withstanding several short-circuit attacks. Therefore, the transformer with lower safety margin in the product need to further reduce the radial electromagnetic force, and the distribution transformer leakage magnetic field also need to adjust to ensure its reliability.

Acknowledgement

In this paper, the work was supported by NSFC, under Project No.51177103 and Program for LNIRT in University (Project No.LT2011002)

References

[1] Li HongChun. Method to Raise Short-Circuit Withstand Ability of Transformer. Transformer, 2006, 43(8):1-4.

[2] Li Yan and so on. Winding Short Circuit Strength Calculation of 31500kVA Power Transformer. Transformer, 2007,44(2):8-13.

[3] Li HongKui, Li Yan. Axial Vibration Model Analysis of Transformer Windings under Different Levels of Pre-compression. Electric Machines and Control, 2010, 14(8):98-102.

[4] Wang ShiShan, Li YanMing. Computation of Electrodynamic Force on Winding of Power Transformer. High Voltage Apparatus, 2002, 38(4):22-25.

[5] Xin ZhaoHui and so on. Reasearch on Short Circuit Strength of Inner Winding of Large Transformer. Tansformer,2009,46(8):39-42.

[6] Meng QinMing and so on. Simulation Research on Radial Stability of Internal Winding in Large Transformer.2010,47(4):32-40.

[7] Chen YuHong and so on. Collection and analysis of Radial Simulated Signal of Short Circuit Vibration of Transformer Winding.Transformer,2011,48(4):33-40.

[8] J.Y.Lee and so on. Finite Element Analysis of Short Circuit Electromagnetic Force in Power Transformer. 2009 12th International Conference on Electrical Machines and Systems (ICEMS 2009), Tokyo, 2009.

[9] Yinghao Zhu. Short Circuit Mechanical Force Withstand Capability Test. Transformer, 2001,38(1):1-7.

[10]Kumbhar, Ganesh B, Kulkarni S.V. Analysis of Short-circuit Performance of Split-winding Transformer Using Coupled Field-circuit Approach. IEEE Transactions on Power Delivery, 2007, 22(2):936-943.

Advanced Materials Research Vols. 986-987 (2014) pp 1930-1933

doi:10.4028/www.scientific.net/AMR.986-987.1930

Conformation Optimization Based on Impulse Grounding Resistance for Ground Electrode of Power Lines

GE Guangzu[1, a], TANG Bo[1, a], QU Zihang[1, a], LI Yu[1, a], CHEN Bin[1, a]

[1]School of Electrical and New Energy, China Three Gorges University, Yichang 443000, China

[a]tangboemail@sina.com

Keywords: Lightning Protection of Power Lines; Impulse Grounding Resistance; Impulse Coefficient Method; the Conformation of the Ground Electrode; ETAP; Safety Margin;

Abstract. Reducing tower ground's impulse grounding resistance can prevent the power lines from lightning effectively. The concept of impulse grounding resistance is described. Calculation formula of the impulse grounding resistance for ground electrode in different Conformations is derived with impulse coefficient method. The conformation of the ground electrode is improved according to the theory of impulse grounding resistance is decreased when the effective area of the electrode is reduced, using ETAP for simulation of the improved ground electrode. The results show that the impulse grounding resistance of the improved ground electrode can be reduced to 41.1% of the original, and safety margin is larger in practical engineering.

Introduction

Because of overhead transmission lines completely naked on the ground, through the region of complex terrain conditions, line staggered through, the tripping blackouts of large area is easy caused by lightning accidents especially in a lightning-prone area that have a greater impact on people's daily life and socio- economic [1]. Therefore, the transmission line lightning protection design is very important, and the impulse grounding resistance of transmission line' ground electrode is a key indicator in the lightning protection design [2]. Reduce the impulse grounding resistance of the ground electrode is the main measures to raise the lightning withstand level and reduce the lightning trip-out rate of transmission lines [3], it is essential for the safe and stable operation of the line.

Power frequency grounding resistance is usually calculated by fall-of-potential method[4] (IEEE Recommended), and then, on this basis, the emergence of two-pole, four-pole and six-pole method and so on [5,6]. Domestic scholars through simulation tests, the influence law of different factors on impulse grounding resistance is analyzed, the fit formula of impulse coefficient in different conditions is given by comparison with the value of the field test [7]. The calculation method of impulse grounding resistance for extending grounding is analyzed by reference literature [8], that the ground electrode is divided into N segments, and the impulse grounding resistance of whole ground electrode is calculated according to parameters of different segments.

So far, domestic and foreign scholars have a lot of research on impulse grounding resistance, but most are based on some assumptions, the lack of a more sophisticated theory and studies is not much in the conformation of the ground electrode model improved.

Impulse Grounding Resistance

When the ground electrode is suffered lightning current or impulse current, the showing grounding resistors is called impulse grounding resistance. When the magnitude of impulse current is excessively large, it will cause the soil discharge, and impulse current frequency are more larger than the frequency current, the effective resistance of the ground electrode is different at each moment when the ground electrode suffered impulse current, that resulting in frequency grounding resistance and impulse grounding resistance are different.The impulse grounding resistance R_{ch} is usually defined as the ratio of the maximum voltage U_m and maximum current I_m.

Frequency grounding resistance is R_g, the impulse coefficient of ground electrode $\alpha = R_{ch}/R_g$. Then the impulse grounding resistance R_{ch} of ground electrode can be calculated according frequency grounding resistance R_g.

When the length of the ground electrode is does not exceed 80 to 100m, lightning protection calculations generally take $\alpha < 1$, the impulse coefficient α can be calculated by The following formula.

$$\alpha = \frac{1}{0.9 + \beta \frac{(I_m \rho)^m}{l^{1.2}}} \tag{1}$$

Where I_m is the amplitude of impulse lightning current; ρ is resistivity of soil; l is the length of variety conformation of ground electrode; β, m is the correlation coefficient, for the vertical ground, $\beta = 0.9$, $m = 0.8$, for the horizontal and closed ground electrode, $\beta = 2.2$, $m = 0.9$.

The value of impulse grounding resistance will affect the voltage on the insulator string, and the relationship between them is proportional,

When lightning strikes on insulator strings, if the value of impulse grounding resistance is reduced, the voltage of insulator strings is reduced, the probability of back-strike flashover on transmission lines is reduced, which can effectively prevent the transmission lines being struck by lightning.

Calculation of Impulse Grounding Resistance

1) Single ground electrode

The formula of frequency grounding resistance and impulse coefficient for vertical grounding electrode is:

$$R_g = \frac{\rho}{2\pi l} \ln \frac{4l}{d} \tag{2}$$

$$\alpha = 2.75 \rho^{-0.4} \left(1.8 + \sqrt{l}\right) \left[0.75 - \exp\left(-1.50 I_{ch}^{-0.2}\right)\right] \tag{3}$$

Where l is length of the ground electrode; d is the diameter of ground electrode; ρ is resistivity of soil.

The formula of frequency grounding resistance and impulse coefficient for horizontal ground electrode is:

$$R_g = \frac{\rho}{2\pi l} \left(\ln \frac{l^2}{hd} - 0.6 + \mathrm{A} \right) \tag{4}$$

Impulse coefficient of horizontal ground electrode which has a single-ended current is:

$$\alpha = 1.62 \rho^{-0.4} \left(5.0 + \sqrt{l}\right) \left[0.79 - \exp\left(-2.3 I_{ch}^{-0.2}\right)\right] \tag{5}$$

Impulse coefficient of horizontal ground electrode which has a middle current is:

$$\alpha = 1.16 \rho^{-0.4} \left(7.1 + \sqrt{l}\right) \left[0.78 - \exp\left(-2.3 I_{ch}^{-0.2}\right)\right] \tag{6}$$

Where l is the length of the ground electrode; h is depth of horizontal ground electrode be buried; A was represented the coefficient of the grounding resistance's addition by the shielding effects; I_{ch} is the amplitude of impulse current, kA.

2) Calculation of impulse grounding resistance for a plurality of horizontal ground electrode

Impulse grounding resistance of ground electrode that composed of plurality horizontal electrode can be calculated by single ground electrode and impulse utilization coefficient

Because the shielding effect between the single ground electrode, the levels of being used are different when the ground electrodes flowing the impulse current or lightning current, therefore, it needs to introduce a correction coefficient, also be called the impulse coefficient.

The formula of impulse grounding resistance for ground electrode which composed of two horizontal electrodes is:

$$R_{ch2} = \frac{R_{ch1}}{2\eta_i} \tag{7}$$

Where, R_{ch2} is the total impulse grounding resistance of two horizontal parallel electrodes; R_{ch1} is the impulse grounding resistanceof a single horizontal electrode; η_i is the impulse utilization coefficient.

The formula of impulse grounding resistance for ground electrode which composed of n horizontal ray electrodes is:

$$R_{chn} = \frac{R_{ch1}}{n\eta_{i1}} \tag{8}$$

Where, R_{chn} is the total impulse grounding resistance of n horizontal ray electrodes; R_{ch1} is the impulse grounding resistanceof a single horizontal electrode; n is the number of horizontal ray electrode; $n\eta_i$ is the impulse utilization coefficient of horizontal electrode.

The formula of impulse grounding resistance for n vertical ground electrodes that are arranged along a line is:

$$R_{chn} = \frac{R_{chm}}{n\eta_{i2}} \tag{9}$$

Where, R_{chn} is the total impulse grounding resistance of n vertical electrodes; R_{chm} is the impulse grounding resistance of a single vertical electrode; n is the number of vertical electrode; $n\eta_{i2}$ is the impulse utilization coefficient of vertical electrode.

Conformation Optimization of Ground Electrode

The general ground electrode's conformation is transformed according to the theory of the larger effective area of the ground electrode, the smaller impulse grounding resistance. Taking into account the effectiveness of ground electrode's length and inductive effect will influence the diasporic of ground electrode, ground electrode's conformation that be transformed is shown in Figure 1.

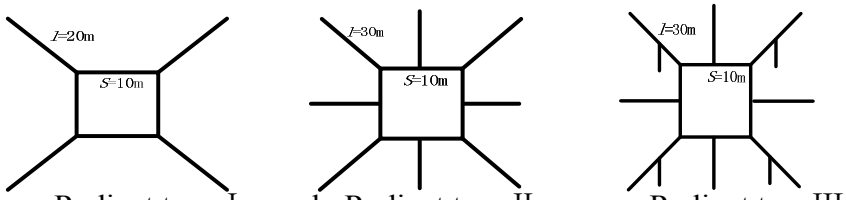

a. Radiant type Ⅰ b. Radiant type Ⅱ c. Radiant typeⅢ

Fig.1 Ground electrode that be improved

Assuming the buried depth of ground electrode is 0.6m, the soil resistance is 50 Ω•m, 60 Ω•m, 100 Ω•m, 150 Ω•m, 300 Ω•m, 1000 Ω•m, the impulse current is (2.6/50), the amplitude of impulse current is 10kA.Impulse grounding resistance of above three ground electrode in different soil resistance is shown in Table 1.

Tab.1 Impulse grounding resistance of ground electrode that be improved (unit: **Ω**)

conformation	50	60	100	150	300	1000
a	3.13	3.76	6.27	9.4	18.81	52.38
b	2.76	3.32	5.53	8.29	11.95	35.28
c	2.08	2.49	4.15	6.23	11.21	21.53

In Table 1, impulse grounding resistance of ground electrode that be transformed is reduced, when the resistance of soil is 1000 Ω•m, decreased to 41.1% of the origina. Impulse grounding resistance of the improved ground electrode changes slowly with soil resistance getting larger, the minimum amplitude of impulse grounding resistance increased of ground electrode c is 19.45 Ω; the maximum amplitude of impulse grounding resistance increased of ground electrode a is 49.25. Therefore, lightning protection effects of the high soil resistance areas can get better by reducing impulse grounding resistance from improving the conformation ground electrode.

The maximum contact voltage, step voltage and GPR (ground potential rise) of ground electrode in figure 1 is calculated by using ERP software to verify whether it can meet the requirements of practical engineering.The results is shown in table 2.

Tab.2 Verification of the improved ground electrode (unit:V)

conformation	contact voltage	step voltage	GPR
a	4000	1500	6000
b	3000	750	5500
c	1250	400	2500
amplitude of decrease	31.25%	26.67%	41.67%

In Table 2, contact voltage of ground electrode c decreased to 1250V, reduced to 31.25% of ground electrode a; step voltage of ground electrode c decreased to 400V, reduced to 26.67% of ground electrode a; GPR of ground electrode c decreased to 2500V, reduced to 41.67% of ground electrode a. Visible, the improved ground electrode's safety margin is larger and the risk coefficient is reduced that more meet to the actual needs of engineering.

Conclusion

1) Ground electrode's conformation is improved, the impulse grounding resistance of the improved ground electrode is reduced, and it changes slowly with soil resistance getting larger. The value of impulse grounding resistance can be reduced to 41.1% of the origina when the soil resistance is $1000\,\Omega\bullet m$, so the effect is more obvious to high soil resistance areas.

2) The maximum contact voltage, step voltage and GPR (ground potential rise) of the improved ground electrode are reduced to 1250V, 400V and 2500V. The improved ground electrode's safety margin is larger and the risk coefficient is reduced to meet the actual needs of engineering, so it verifies the improved ground electrode is feasible.

References

[1]Ji Hao. Lightning protection research of power network based on lightning location system[J]. East China Electric Power, 2009, 37(6): 978- 981.

[2] Xie Guangrun. Power system grounding electrode technology[M]. Beijing: China Electric Power Press, 1996.

[3]Sima Wenxia, Li Xiaoli, Yuan Tao, etc. Analysis of grounding grid Impulse characteristics in Frequency domain in consideration of soil non-linear characteristic[J]. Proceedings of the CSEE, 2009, 29(16): 127-132.

[4]Liang Min. Analysis about application of the measurement for grounding grid resistanee in the substation[J], Guangxi Elctric Power, 2004(4): 30-33.

[5]Guo Huajun, Dong Qiaoyuan, Yao, Xiaofang, etc. Measurement of Grounding Resistance of Large Grounding G rid and the Effect Factors[J]. High Voltage Engineering, 2002, 28(12): 47-48.

[6]Xu Hua, Wen Xishan, Huang Ling. Discussion on the Impulse Grounding Resistance Measurement[J]. High Voltage Engineering, 2006, 32(08): 79-81.

[7]He Jinliang, Zeng Rong, Chen Shuiming, etc. Characteristics and fitting formula of impulse coefficient of grounding device of transmission-line[J]. J T singhua Univ (Sci& Tech), 1999, 39(5): 9-12.

[8]Xia Changzheng, Chen Cixuan, Wen Xishan, etc. Computation of Impulse Grounding Resistance of Extended Grounding Electrode[J]. High Voltage Engineering, 2001, 27(5): 59-63.

Advanced Materials Research Vols. 986-987 (2014) pp 1934-1937

doi:10.4028/www.scientific.net/AMR.986-987.1934

Design of Performance Analysis System of Secondary Circuit in Intelligent Substation Based on NI Platform

Haitao JIANG [1,a], Chao CHEN [1],

Jing BU [1,b](corresponding author)

[1.] Nanjing University of Science and Technology, Nanjing, 210094, China

[a]email: jht365@foxmail.com, [b]email:bujing30@foxmail.com

Keywords: Intelligent Substation; Performance Analysis System; Design

Abstract. At first, this paper introduce some current tests of secondary circuit in intelligent substation, then, design a performance analysis system of secondary circuit in intelligent substation based on NI platform. This kind of system analyzes analog and digital quantity messages for getting the performance of secondary system by algorithms, so that working personnel can grasp the performance comprehensively. Meanwhile, a prototype is developed to be applied in an unused intelligent substation, and the result is satisfied.

Introduction

At present, researches around functional test for intelligent substation secondary equipment are popular. Yet, the secondary equipment's performance test is rarely involved. Not only this situation leads staff not to grasp the secondary circuit's comprehensive performance, but also the potential risk of secondary circuit protection devices may endanger the stability of whole intelligent substation[1].

In order to solve the problem above, this paper mainly studies the whole property of secondary circuit in intelligent substation, and designs a system based on NI platform. On one hand, this system with a precise clock can test the overall performance of the secondary circuit; on the other hand, various components can be measured quantitatively. It will provide a reliable analytical basis for commissioning and operation of intelligent substation.

Effect of Intelligent Improvement on Comprehensive Performance of Secondary Circuit

According to the experiences about commissioning and operation of intelligent substation, some changes will impact on its reliability. Reasons are mainly reflected in the following aspects:

1) Much More Links Leading Delay of Information Transmission to Increase

Compared with the secondary circuit in traditional substation, the secondary circuit in intelligent substation adds much more links of data transition and information transmission. In fact, many links in secondary circuit might delay, for example: A/D transition, A/D transition, photoelectric signal transition, the waiting of Ethernet information exchange, coding and decoding of message, sending and transmitting of message, and so on. Increasing of equipment and processing chain is not conducive to transmission of information timely and rapidly

2) Competition Mechanism of Switch Network Leading to the Uncertainty of Delay of Information Transmission

In consideration of real-time, peer-to-peer mode in traditional substation is better than switch network mode in intelligent substation. Especially, when system scale expands or power grid faults, the load rate of switch network is too high, and message might be not accepted punctually, even sometimes messages could be lost [2, 3].

3）Information Sharing and Distributed Sample Acquisition Leading to Problem of Data Synchronization

To avoid phase and amplitude of electrical quantity generating errors, protection equipment must get sample data at one time, such as distance protection and differential protection. Because of information sharing and distributed sample acquisition in intelligent substation, data of electrical quantity is sampled and charged to digital quantity messages via electronic transformer separately. Then, they will be sent to protection equipment through process-level network. So, intelligent substation faces the problem of data synchronization as the same as distributed sensor system. Namely, it is important to ensure all the sample data of distribution sensor units can be transmitted synchronously [4].

Scheme of Secondary Circuit Performance Analysis in Intelligent Substation

Compared to traditional substation, intelligent substation adds process-level network and IED equipment in order to achieve information sharing and links between primary equipment and bay level. Process-level equipment, bay level equipment and process-level network accomplish tasks of control and relay protection. So, secondary circuit performance analysis in intelligent substation combines these three properties [5].

Measurement methods for phase difference of wave in the field of electrical engineering have an important application. In secondary circuit performance analysis, they are also used to calculate the transmission delay of each part.Every sampling message records multi-channel current and voltage value at one time, and GOOSE records all state of each circuit breaker. After collecting sampling message and GOOSE, it restores the wave of current or voltage in the order of time; then, compares the phase differences between wave of current and voltage in secondary circuit everywhere; finally, get the property of secondary circuit.

Design of Secondary Circuit Performance Analysis System in Intelligent Substation

1)Functional Requirement

Data acquisition and data analysis in secondary circuit performance analysis system are two basic functions. So, the system needs to sample real-time IEC61850 message, FT3 message, analog quantity and switching value. Meanwhile the internal clock should be precise for analyzing wave.

2)Hardware Design

The secondary circuit performance analysis system uses NI CompactRio platform containing real-time controller, chassis FPGA and I/O module three parts. Because of the complexity of data analysis, the system connects computer by TCP/IP to analyze and show results, as shown in Figure 1.

Reconfigurable chassis (NI9118) has 8 slots for any I/O module using Virtex-5 FPGAs with improved optimization capabilities. Chassis FPGA connects to each data acquisition card with easy-to-use elemental I/O functions to read or write information. Then, it will transfer messages packed with the upper equipment. Real-time controller (NI9024) connects chassis FPGA by the way of DMA. At the same time, it exchanges data with computer by TCP/IP to accomplish tasks of transferring information and configuration. The system fully integrates respective advantages of CPU and FPGA to make sure real-time and reliability.

Data acquisition cards include NI9225, NI9227, NI9403, independently developed cards and an accurate time setting card. The NI9225 is a 3-channel voltage acquisition card ranging from -300V to 300V. The NI9227 is a 4-channel current acquisition card ranging from -5A to 5A. Both of them have advantages of simultaneous sampling, isolated channel-to-channel, high precision and fixed delay. In a word, they meet the requirements of analog acquisition in secondary circuit. The NI9403 is a 32-channel switching input and output card. Its resolution ratio less than 10μs meets the requirement of circuit breaker state checking.

Message acquisition cards use industrial Altera FPGA as a core; besides, include SDRAM, ROM, and a high precision TCXO. According to different message types, front-end data acquisition module is different. To IEC61850 message, cards use light network port and PHY chip to communicate via Ethernet network. For FT3 message, cards use light serial port to communicate via the way of SPY. The structure of message acquisition card is as shown in Figure 2.

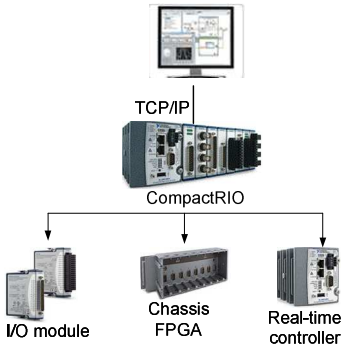

Figure 1. Hardware Structure

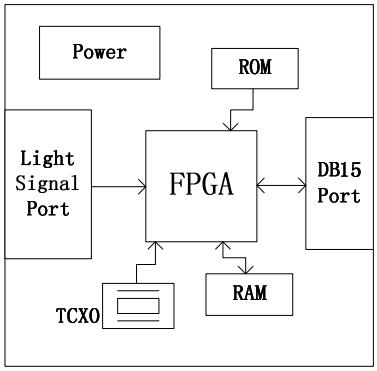

Figure 2. Embedded System Structure of Cards

The accurate time setting card can receive and analyze IRIG-B code or second pulse to provide another second pulse to reconfigurable chassis via DB15 Port. It makes the system have a stable clock.

3)Software Design

Because NI CompactRio supports LABVIEW, algorithms in chassis FPGAs, real-time controller and computer are developed by LABVIEW. Functions of program in chassis FPGA are as follows: maintenance of the system clock, control of switching and analog quantity and SPI communication to message acquisition cards. Firstly, real-time controller accomplishes functions of configuration analysis and transferring information. Secondly, the computer analyzes and show results. The whole system is as shown in Figure 3. And design of FPGA program is as shown in Figure 4.

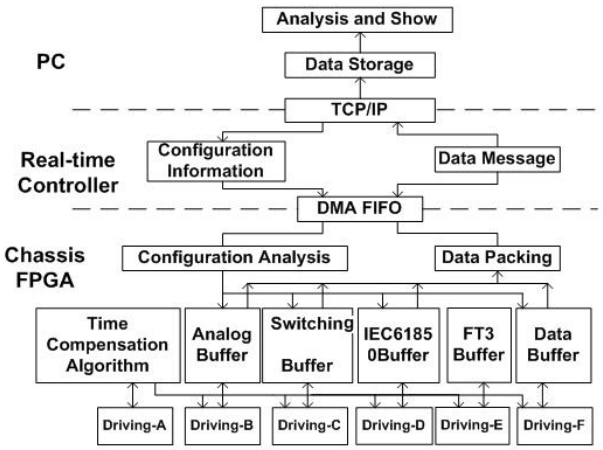

Figure 3. Program Structure

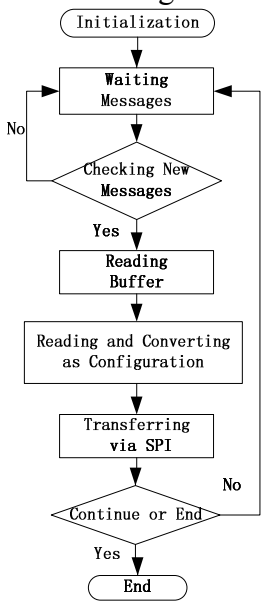

Figure 4. Design of FPGA program

Engineering Applications

In line with the analytical method and experiment scheme mentioned before, a new kind of property- tester of secondary circuit in intelligent substation is developed. The system with various types of acquisition ports can be flexibly configured according to demands of the field environment. It uses IRIG- B code from GPS receiver to maintain the precision of inner clock.

According to the connection diagram in Figure 5, the system collects data from the same interval equipments to realize the test of the property of secondary circuit, and is applied to field test of the secondary circuit of a certain intelligent substation, which has not been put into operation yet. Table 1 shows results of the monosomic line protection device. Table 2 shows results of the total line protection.

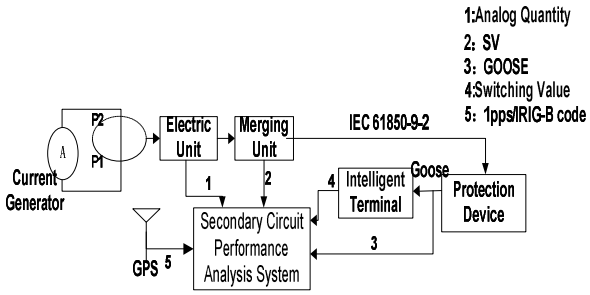

Figure 5. Connection diagram

Table1 Test data of the monosomic line protection device.

Current Stable Value：Izd=4A			
	Action Current/A	Return Current/ A	Action Time (ms)
A	2	1.4	25.355
B	2	1.4	22.256
C	2	1.4	22.267

Table2 Test data of the total line protection

Current Stable Value：Izd=4A				
	Delay of Merging Unit(μs)	Action Time of Line Protection （ms）	Action Time of Intelligent Terminal （ms）	General Action Time (ms)
A	39.069	19.566	7.816	27.418
B	42.391	25.969	7.522	33.533
C	46.369	19.048	7.733	26.827
Remark	Merging unit delay has been deducted that is 1308us.			

The test of the protection device of monosomic line shows that protection function is normal and action time is up to the standard; although general action time excepts B phase is up to State Grid's standard basically, action time of intelligent terminal is still greater than 7μs, which is ruled by State Grid.

Conclusions

The analysis system of secondary circuit performance in intelligent substation has abundant connecters and perfect function. Moreover, it can test not only one single device but also the total group. The time performance of this system is better than others in the market. In the field trial, the tester finds shortage of synchronization. Though, delay of intelligent terminal don't meet state grid requirement, the deviation is acceptable. In other words, the system stated in this paper supports field debugging very well, and it is an important supplement to secondary circuit performance analysis in intelligent substation.

References

[1] Li Bin, Research on the technology and application of the smart substation [D], North China Electric Power University, 2011.

[2] Li Tiecheng, Zhang Li, HaoXiaoguang etc. Analysis of Transmission Delay of Intelligent Substation [J]. Shaanxi Electric Power, 2011, 39(4)：66-67.

[3] Wang Lu. Analysis and application of Process Bed Set Network in Intelligent Substation [J]. Power System Protection and Control, 2012, 40(2)：141-145.

[4] Lu Yan, Song Wei, Yu Tongwei etc. The Reliability Research on Data Public Network of Process Level in Intelligent Substation [J]. Electric Power Science and Engineering, 2012, 28(6)： 51-55.

[5] Xu Zhiqiang, Lei Yutian, Zhang Keren etc. Time Test for Intelligent Components in Intelligent Substation [J]. Electric Power Technology, 2011, 35(12)：8-13.

Advanced Materials Research Vols. 986-987 (2014) pp 1938-1941

doi:10.4028/www.scientific.net/AMR.986-987.1938

Design of the Three-phase Photovoltaic grid-connected Inverter

Wu Kui-hua[1], Sun Wei[2], Wang Jian[3], Yang Shen-quan[1], Wang Yi-qun[1]， Li Bo[1]

[1.] Economic & Technology Research Institute, State Grid Shandong Electric Power Company, Shandong Jinan 250021;

[2.] State Grid Shandong Electric Power Company, Shandong Jinan 250001;

[3.] State Grid Shandong Electric Power Research Institute, Shandong Jinan 250001

Keywords: photovoltaic grid-connected; current type PWM inverter; SPWM modulation; unity power factor

Abstract. Photovoltaic grid-connected power generation is the inevitable development trend of solar photovoltaic systems，grid inverter is an essential part of photovoltaic grid-connected power generation. With the developed three phase current type PWM inverter device as the research object, and symmetry rules sampling method is applied to the inverter, through the method combined by the computer simulation and experiment research, the device was verified by simulation and experimental .The results show that: This method could not only effectively reduce the DC side inductance volume of the current-mode PWM inverter , and it could make output AC currents sinusoidal and in phase with grid voltages, but also improve the efficiency of the system, it will be more suitable for photovoltaic grid-connected.

Introduction

With the shortage of the world's energy and the problems of environmental pollution become increasingly serious, the development and application of clean, renewable energy will be paid more and more attentions by every country of the world. Solar energy as a kind of renewable energy, has broad application prospects in photovoltaic power generation systems. However solar output device is a direct current (DC), grid system is in need of alternating current (AC), which requires DC-AC grid-connected inverter as the intermediate link [1-2].To avoid grid-connected inverter produce additional harmonic pollution to Power grid, the inverter must have the characteristics of the low harmonics, high power factor, the ideal state is the requirement of the grid side power factor is 1..

Principle of three-phase current type PWM inverter

Figure 1 shows the schematic diagram of [3] the three-phase grid-connected current source PWM converter Vdc is a DC voltage source.e_a, e_b, e_c,is three-phase grid voltage.L_a, L_b, L_c, and C_a, C_b, C_c are the output filter, switch device consists of a controllable device IGBT and the diode connected in series,In order to improve the device reverse blocking capability

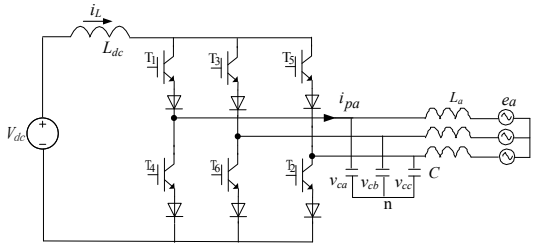

Fig.1Principle configuration of Three-phase grid-connected current source PWM converter

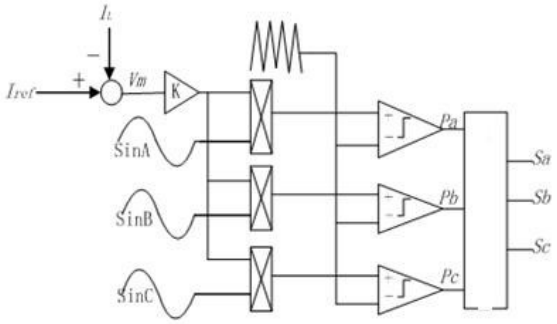

Fig.2 Single-phase equivalent circuit in zone I Fig.4 Diagram of direct current control

The design of three phase current type PWM inverter

2.1 Design of DC side inductance L

For three-phase grid-connected current source PWM converter, the control of the grid-side current is the core of the whole control system.This research adopts the direct current control strategy to realize constant of grid inverter input DC current and voltage and current of grid side close to unit power factor, its control core as shown in figure 2.

From the figure *V*m=*I*ref-*IL*，*IL* is Dc side inductance current , *I*ref is Given current value is proportionality coefficient.M is modulation ratio,namely, the ratio of the sine wave peak and the triangular wave value, in this experiment the triangular wave value is 1,so *M*=K×*V*m=K×(*I*ref-*IL*) .Generated SPWM wave by symmetrical sampling rules,as shown in figure 5.

From the figure 5

$$\left.\begin{aligned} t_{off1} &= \frac{T_C}{4}(1 - M\sin\omega t) \\ t_{on1} &= \frac{T_C}{4}(1 + M\sin\omega t) \end{aligned}\right\} \quad (1)$$

Formula(1),M is modulation ratio,T_C is the switch frequency of triangular carrier.For the three-phase SPWM in zone I makes an analysis,as shown in figure 6.

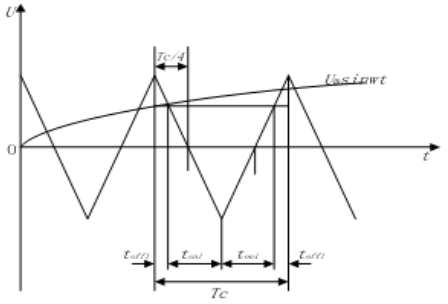

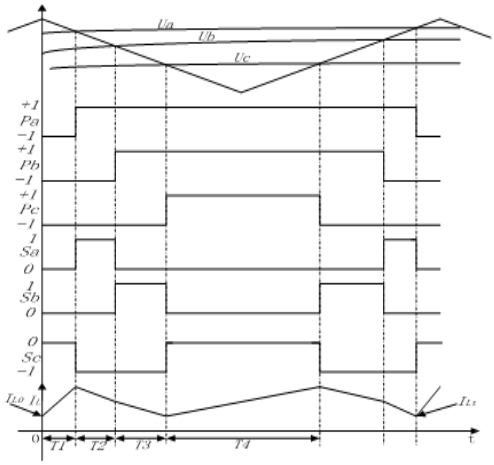

Fig.3 Generated SPWM wave by symmetrical sampling rules Fig.4 Diagram of frequency control in zone I

From formula(1)

$$T_1 = \frac{T_C}{4}(1 - Me_a) \quad (2)$$

$$T_2 = t_{offb} - t_{offa} = \frac{T_C}{4}(1 - Me_b) - \frac{T_C}{4}(1 - Me_a) = \frac{T_C}{4}M(e_a - e_b) \quad (3)$$

$$T_3 = t_{offc} - t_{offb} = \frac{T_C}{4}M(e_b - e_c) \quad (4)$$

$$T_4 = \frac{T_C}{2}(1 + Me_c) \tag{5}$$

Research on DC side inductance current *IL* shows that it contains a fixed DC component and high frequency AC component.In each switching period has the following formula:

$$I_{Lt} - I_{L0} = \frac{V_{dc}}{L} \times 2T_1 + \frac{V_{dc} - e_{ac}}{L} \times 2T_2 + \frac{V_{dc} - e_{bc}}{L} \times 2T_3 + \frac{V_{dc}}{L} \times T_4 \tag{6}$$

The formula(2) ~ (5) substituted into the formula (6) :

$$I_{Lt} - I_{L0} = \frac{T_c}{2L}\left(2\ V_{dc} - M\ e_{ac}\ e_a + M\ e_{ac}\ e_b - M\ e_{bc}\ e_b + M\ e_{bc}\ e_c\right) \tag{7}$$

In the formula, IL0 is the initial current of the inductor,ILt is the current in moment t of the inductor.

A symmetrical three-phase voltage is:

$$\begin{cases} e_a = \sqrt{2}E\sin\omega t \\ e_b = \sqrt{2}E\sin(\omega t - \frac{2\pi}{3}) \\ e_c = \sqrt{2}E\sin(\omega t + \frac{2\pi}{3}) \end{cases} \tag{8}$$

From formula(8):

$$\begin{cases} e_{ac}e_a = \sqrt{3}E^2\left[\frac{\sqrt{3}}{2} - \sin(2\omega t + \frac{\pi}{3})\right] \\ e_{ac}e_b = -\sqrt{3}E^2\sin(2\omega t - \frac{\pi}{3}) \\ e_{bc}e_b = \sqrt{3}E^2\left[\sin(2\omega t + \frac{\pi}{3}) + \frac{1}{2}\right] \\ e_{bc}e_c = \sqrt{3}E^2\left[\sin(2\omega t - \frac{\pi}{3}) - \frac{\sqrt{3}}{2}\right] \end{cases} \tag{9}$$

The formula(9) substituted into the formula (7) :

$$I_{Lt} - I_{L0} = \frac{T_C}{2L}\left(2V_{dc} - M\,E^2(3 + \frac{\sqrt{3}}{2})\right) \tag{10}$$

During startup, the inductor current IL is very small， so the Vm is relatively large. As IL gradually increased, Vm will become smaller. When the Vm reaches a certain value,I_L has reached a steady state,so that the right of formula(10) to be 0, the stable IL value is:

$$I_L = I_{ref} - \frac{4V_{dc}}{KE^2(6 + \sqrt{3})} \tag{11}$$

In the formulaic is a steady-state value of the inductor current. From equation (11) can be seen, when K，E，Iref，Vdc are all constant, the DC side current IL is constant. It is not affected by DC side inductance.So,there is no need to make a large L to maintain a constant DC side current ,this significantly reduces the loss of the inductance, volume and weight.

Analysis of simulation and experimental results

In order to verify the validity of the method, a prototype is designed for experimental verification. The parameters of the circuit are:Ea=100V, Vg =20V,L=0.8mH, R=0.5 , C=2.2 F, L dc =3mH.The experiment control system is performed by DSP chip TMS320LF2407A,using C

language programming,the switching frequency is 4.2kHz.In the experiment ,DC current value is I_{ref}=2A.

Figure 5 is the simulation waveform of current mode PWM inverter,the figure 5 (a) shows the simulation waveforms of grid side voltage Ua, current isa and AD side current ipa ,figure 5 (b) is the harmonic analysis of the grid side current isa.Figure 9 is the experimental waveform of current mode PWM inverter, figure 6 (a) is the experiment waveform of grid side voltage and driving waveform of T1,,figure 6 (b) is the experiment waveform of DC side current I dc.

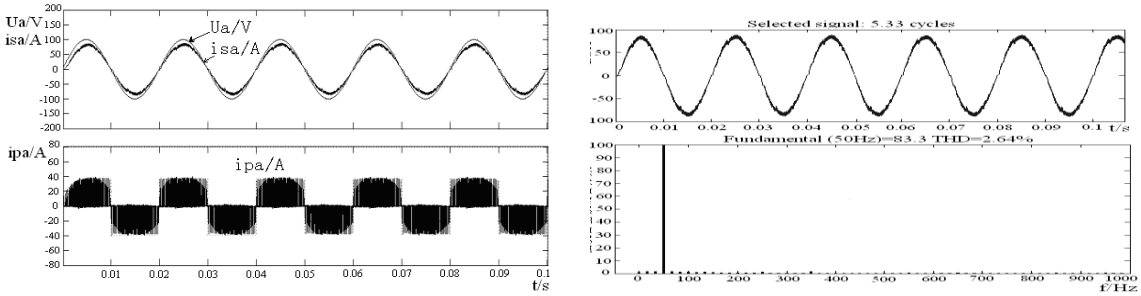

(a) Simulation waveforms of grid side voltage , current and AD side current of phase a

(b) Harmonic analysis of the grid side current of phase a

Fig.5 Simulation waveforms and harmonic analysis

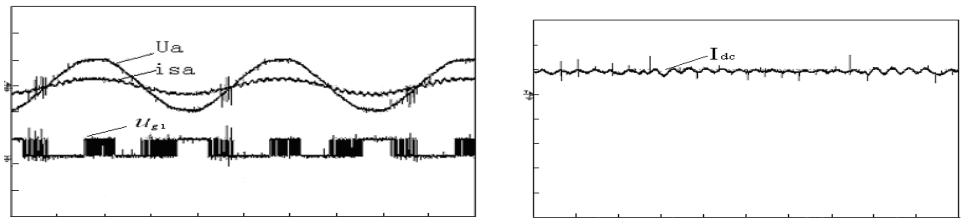

(a)Grid side voltage of phase a and driving waveform of T1 (b) Waveform of DC side current Idc

Fig.6 Experimental waveforms

The figure 5 and figure 6 shows that the grid side current is about sine, as the grid side voltage phase, it realizes the unit power factor of the grid side current. By analyzing phase a grid side current harmonic, THD is 2.75%,harmonic content is small; At the same timed side current is relatively stable, reaching the expected effect.

Conclusion

This paper, on the basis of theoretical analysis, the simulation and experiment for three-phase grid-connected current source PWM converter. Results show that, the method that this paper adopts can effectively reduce the DC side inductance of grid-connected current source PWM converter, to solve the using barriers of limit current source PWM inverter ,and will realize the sinusoidal of grid side current and the unit power factor of the grid side current. It has excellent grid performance. the analysis of this paper has some reference for grid system as wind power, fuel cell.

References

[1]Yang Haizhu,,Jin Xinmin.The maximum power tracking problem of Photovoltaic grid inverter based on DSP control[J]. Journal of solar energy,2005,26(6):760-765.

[2]Wu Chuanhua,Cui Kaiyong,Cen Guocheng.The topology and control method of a current source grid connected inverter[J].Journal of electrician technique,,2007,22(8):7-12.

[3]Xiao Wang, Boon-Teck Ooi. Unity PF current-source rectifier based on dynamic tri-logic PWM.[J]IEEE. Trans. Power Electron, 1993,8(3):288-294.

Advanced Materials Research Vols. 986-987 (2014) pp 1942-1945

doi:10.4028/www.scientific.net/AMR.986-987.1942

Investigation on polarity of TiO_2 varistor using impedance spectroscopy and the frequency effects

Xiao-Wen Zhang[a] and Er-Wei Chen[b]

School of Materials Science and Engineering, Guilin University of Electronic Technology, Guilin 541004, P.R. China

[a]zhang-xiaowen@163.com, [b]chenerwei0127@163.com

Keywords: TiO_2; varistor; polarity; impedance spectroscopy.

Abstract. Current-voltage (*I-V*) and impedance spectroscopy are employed to investigate the polarity of TiO_2 varistor. It is found that TiO_2 varistor shows typical polarity behavior, i.e., the *I-V* curve is asymmetric, the impedance slightly increases, and the capacitance slightly decreases when the bias voltage reverses. The effects of measuring frequency on impedance spectroscopy are systematically investigated. The results indicate that TiO_2 varistor behaves considerable polarity under low sweeping frequency. High sweeping frequency (over 10^3 Hz) counteracts the polarity behavior. A model of *micro-polarized zone* is tentatively proposed to clarify the polarity behavior of TiO_2 varistor.

Introduction

Varistors attract various attentions for their promising application to surge protection in power system and electronic circuit. For instance, varistors are commonly used to protect circuits against excessive transient voltages by incorporating them into the circuit in such a way that, when triggered, they will shunt the current created by the high voltage away from sensitive components. TiO_2 varistor has been heavily investigated due to its low sensitive voltage, superior non-linear coefficient, and high dielectric constant, since Yan and Rhodes reported highly effective TiO_2 varistor in 1982 [1]. Moreover, TiO_2 varistor is prepared by conventional electronic ceramic technology without employing reduced atmosphere. Consequently, TiO_2 varistor takes more advantages over $SrTiO_3$ ceramic both in reducing production cost and in extending operating life time. In addition, in comparison with ZnO varistor, it is quite easy for TiO_2 varistor to obtain rather low sensitive voltage. This facilitates denser integrated circuits [2]. Recently, some particular factors such as geometric size effect [3], grain boundary effect [4], and surface layer effect [2] attract researchers' attentions for systematically understanding both the fundamentals and the applications. TiO_2 varistor looks almost exactly like the classical model of a parallel plate capacitor: a circular-shaped ceramic dielectric coated with electrodes on each flat face. This ensures 100% symmetry (no-polarity) from the appearance of construction. However, the electrical properties such as impedance, capacitance and current-voltage (*I-V*) characteristics show some differences, i.e., behave asymmetric characteristics when the bias voltage reverses. This behavior defines as the polarity of TiO_2 varistor. It is well established that the polarity plays a crucial role in practical applications, since the varistors respond to a time varying bias as integrated circuits are continuously cycled. In our early works, we noticed an asymmetrical phenomenon by reversing bias voltage in TiO_2 varistors [5]. In this study, we systematically investigate the polarity of TiO_2 varistor by using *I-V* and impedance spectroscopy of impedance-voltage (*Z-V*), phase-voltage (φ-*V*), capacitance-voltage (*C-V*), and dissipation-voltage (*D-V*) characteristics. The effects of measuring frequency are discussed in detail with a purpose of providing fundamentals for reliability and life-time investigation of TiO_2 varistors.

Experimental details

The chemicals of TiO2, Nb2O5, SiO2, SrCO3, and La2O3 with reagent grade were served as the starting powders. The powders were weighted according to the stoichiometric amount of final composite of Ti: Nb: Si: Sr: La=0.978: 0.018: 0.002: 0.005: 0.015. The powders were mixed and wet

ball-milled for 6 h. The milled mixture was dried, granulated and pressed into disk with a diameter of 10 mm and a thickness of ~1 mm. The TiO2 varistor was sintered at 1280OC for 2 h in air. Then, the ceramic was polished and silver (Ag) electrodes were coated on both sides. I-V characteristics were measured using Keithley 2400 Source Meter. The impedance spectroscopy was measured with an Agilent 4294A Precision Impedance Analyzer.

Results and discussions

The I-V characteristics, shown in Fig. 1, indicate that TiO2 varistor shows typical non-linear response, suggesting the current is highly sensitive to applied voltage. For comparative study, the absolute values of currents in the range of -20~0V are replotted (circle symbols). It is clear that the data of 0~20V and those of -20~0V are not overlapped, i.e., the I-V curve is asymmetric.

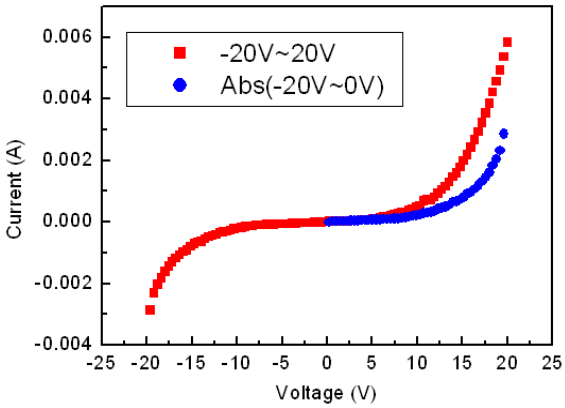

Fig. 1 *I-V* curves of TiO_2 varistor, showing that the *I-V* characteristic is asymmetric in the range of -20V~20V.

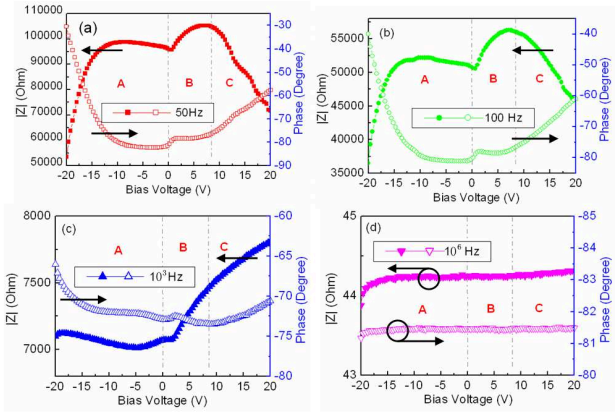

Fig. 2 *Z-V* and *φ-V* characteristics measured at sweeping frequencies of (a) 50 Hz, (b) 100 Hz, (c) 10^3 Hz, and (d) 10^6 Hz.

Although I-V characteristics provide a simple and common approach for evaluating polarity, the I-V functions only when a drift current flowing in the samples [6]. In comparison, impedance spectroscopy has been developed as a useful and robust tool for investigating electrical properties [6,7]. Fig. 2 shows the Z-V and φ-V characteristics measured at different frequencies. It can be seen from Fig. 2(a) that the Z-V and φ-V curves (measured at 50 Hz) can be roughly divided into three sections (section A, B, and C as denoted in the figure) in the range of -20~20V. The impedance (Z) arises from 0.53×105 Ω to 0.96×105 Ω in section A with the bias voltage changing from -20V to 0V. The corresponding phase (φ) changing from -30O to -82O. This means that TiO2 varistor gradually transits from a conducting state (at -20 V) to a dielectric state (at 0 V), since φ=0O (-90O) corresponding to a conducting (a dielectric) process [8]. Section B (0~8V) depicts the variation of Z and φ when the bias voltage reverses. We observe a slight increase of impedance (the impedance slightly increases from 0.96×105 Ω to 1.06×105 Ω), implying that the TiO2 varistor shows polarity. This can be explained by the fact that the reverse of micro-polarized zones (just like dipoles) in TiO2 varistor lags behind that of bias voltage. That is, the reverse of micro-polarized zones is finished when the sweeping bias voltage reaches about 8 V (not 0 V). The interaction between injected carriers and accumulated charges nearby the Ag electrodes (or grain boundaries) impedes motion of carriers, which contributes to slight increase of impedance. Section C (8~20V) depicts the TiO2 varistor gradually changes from a dielectric state to a conducting state with the bias voltage further increases. The corresponding φ also transits from -80O to -58O. Moreover, the impedance (0.72×105 Ω) and phase (-58O) at 20 V differs from those (0.53×105 Ω and -30O) at -20 V, which further verifies the polarity of TiO2 varistor. The Z-V and φ-V curves under the sweeping frequency of 100 Hz show similar behavior as 50 Hz as discussed above [see Fig. 2(b)]. The Z-V and φ-V curves under the sweeping frequencies of 103 Hz and 106 Hz shows some differences in comparison with 50 Hz and 100 Hz, as shown in Fig. 2(c) and (d). This is due to the high sweeping frequency counteracts the polarity behavior. On the other hand, as shown in Fig. 2(a)-(d), the impedance decreases with

increasing sweeping frequency, also see the impedance-frequency (Z-F) transition (Fig. 3). This is due to the fact that only interface resistance can be measured at high sweeping frequency. Therefore, a seeming decrease of impedance is observed in TiO2 varistsor with increasing sweeping frequency [8].

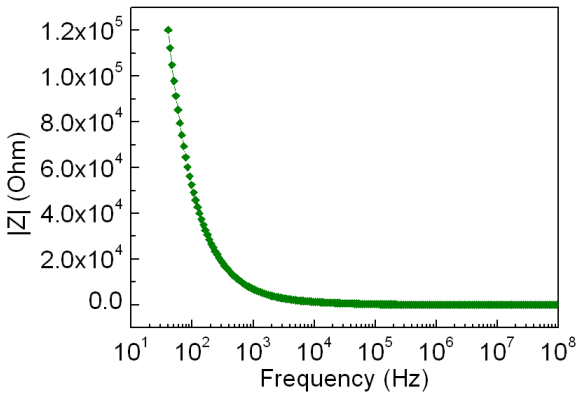

Fig.3 *Z-F* characteristics of TiO_2 varistor

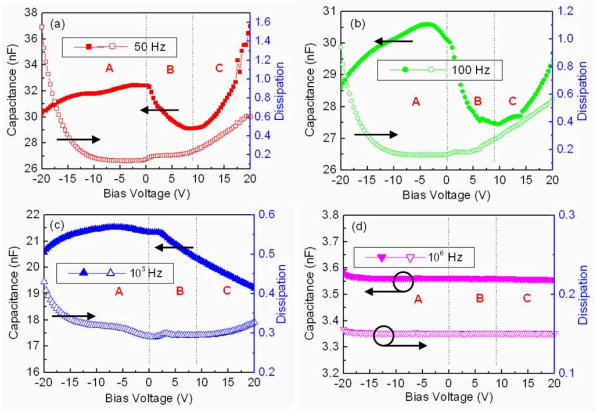

Fig. 4 *C-V* and *D-V* characteristics measured at sweeping frequencies of (a) 50 Hz, (b) 100 Hz, (c) 10^3 Hz, and (d) 10^6 Hz.

Fig.4 shows the C-V and D-V characteristics measured at different frequencies. It can be seen from Fig. 4(a) that the curves (measured at 50 Hz) can also be roughly divided into three sections. Section A (-20~0V) depicts that the capacitance is gradually increased with the reduction of bias voltage as a result of the varistor transiting from a conducting state to a dielectric state. The corresponding dissipation decreases. Section B (0~8V) depicts the typical polarity behavior when the bias voltage reverses. It is well established that some extra charges accumulated nearby the Ag electrodes (or grain boundaries) under negative bias voltage would be released as a result of the recombination with injected heterocharges under positive bias voltage. This reduces charge storage ability, which seemingly results in the reduction of capacitance. Section C (8~20V) depicts the capacitance increases with increasing bias voltage. The re-storage of extra charges nearby the Ag electrodes (or grain boundaries) contributes to an increase of charge storage ability, which seemingly promotes capacitance [8]. Moreover, the capacitance (37.0 nF) and dissipation (0.6) at 20V and those (30.3 nF and 1.6) at -20V also shows some differences, which further verifies the polarity behavior. The C-V and D-V curves under the sweeping frequency of 100 Hz show similar behavior as 50 Hz as discussed above [see Fig. 4(b)]. The C-V and D-V curves under the sweeping frequencies of 103 Hz and 106 Hz show some differences, as shown in Fig. 4(c) and (d), since high sweeping frequency counteracts the polarity behavior. It can also be seen from Fig. 4(a)-(d) that the capacitance decreases with increasing sweeping frequency, also see the capacitance versus frequency (C-F) transition shown in Fig. 5. This is due to the fact that space-charge polarization dominates at low frequency. The space-charge polarization would be neglected at high sweeping frequency. When the sweeping frequency exceeds 103 Hz, ion-relaxation polarization becomes weak [2]. Consequently, the measured capacitance is gradually decreased with increasing sweeping frequency.

Based on the impedance variation discussed above, a schematic model of micro-polarized zone, shown in Fig. 6, is tentatively proposed for elucidating the polarity of TiO2 varistor. Firstly, the TiO2 varistor can be considered to be composed of numerous micro-polarized zones (jus like dipoles) [Fig. 6(a)]. When the TiO2 varistor is applied negative bias voltage, as shown in Fig. 6(b), some extra negative charges (e.g., electrons) accumulate at the left side of the ceramic. Some extra positive charges (e.g., holes) accumulate at the right side. When the bias voltage reverses, the micro-polarized zone will turn over (take some time to finish) to match the external field. Therefore, the interaction between extra accumulated charges and injected heterocharges is unavoidable (this process corresponding to section B in Fig. 2 and Fig. 4), as shown in Fig. 6(c). This interaction impedes carrier motion (which results in slight increase of impedance) and causes recombination of negative and positive charges (which deteriorates charge storage ability and results in slight decrease of capacitance). When the micro-polarized zone turns over, as shown in Fig. 6(d), the Z-V and C-V show

conventional behavior (this process corresponding to Section C in Fig. 2 and Fig. 4). The required time of carrier injection and transporting varies with frequency, which elucidates that the polarity of TiO2 varistor behaves as a function of sweeping frequency. As a whole, the model of micro-polarized zone, to a certain extent, elucidates the polarity of TiO2 varistor.

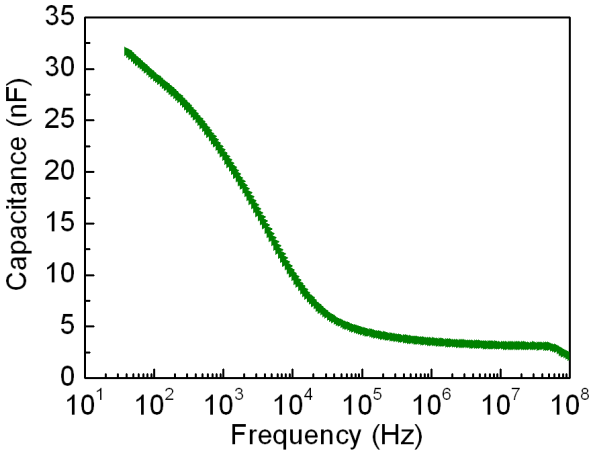

Fig.5 *C-F* characteristics of TiO_2 varistor.

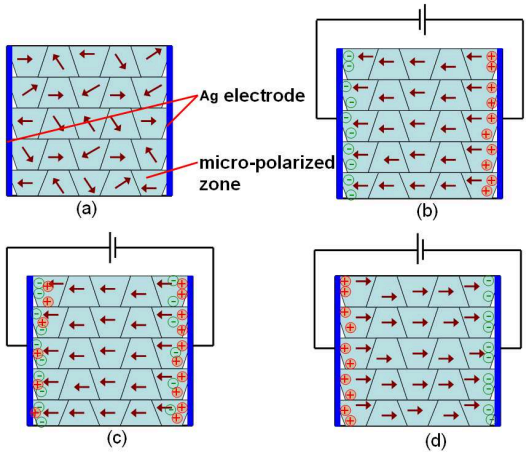

Fig. 6 Schematic model of *micro-polarized zone*

Conclusions

I-V and impedance spectroscopy indicate that TiO2 varistor behaves typical polarity. That is, the I-V curve is asymmetric, the impedance slightly increases, and the capacitance slightly decreases when the bias voltage reverses. The effects of measuring frequency on impedance and capacitance are systematically discussed. The results indicate that TiO2 varistor shows considerable polarity under low sweeping frequency. High sweeping frequency (over 103 Hz) counteracts the polarity behavior. A model of micro-polarized zone is tentatively proposed and is proven to be effectively clarifies the polarity behavior of TiO2 varistor.

Acknowledgements

This work was supported by Guangxi Natural Science Foundation (2012GXNSFBA053168).

References

[1] M.F. Yan, W.W. Rhodes, Appl. Phys. Lett. 40 (1982) 536.

[2] X.W. Zhang, G.Y. Gan, J.K. Yan, J.C. Chen, J.H. Du, Piezoelectrics and Acoustooptics 27 (2005) 260.

[3] S.T. Li, F.Y. Liu, G.P. Jia, Journal of Inorganic Materials 12 (1997) 525.

[4] Y.H. Lin, J.N. Cai, M. Li, C.W. Nan, J.L. He, J. Appl. Phys. 103 (2008) 074111.

[5] X.W. Zhang, X.Y. Liu, Electrical Engineering Materials 4 (2013) 20.

[6] I.W. Wu, P.S. Wang, W.H. Tseng, J.H. Chang, C.I. Wu, Org. Electron. 13 (2012) 13.

[7] C.C. Chen, B. C. Huang, M.S. Lin, Y.J. Lu, T.Y. Cho, C.H. Chang, K.C. Tien, S.H. Liu, T.H. Ke, C.C. Wu, Org. Electron. 11 (2010) 1901.

[8] X.W. Zhang, J.W. Xu, H.R. Xu, H. Wang, C.L. Xie, B. Wei, X.Y. Jiang, Z.L. Zhang, J. Phys. D: Appl. Phys. 46 (2013) 055102.

Advanced Materials Research Vols. 986-987 (2014) pp 1946-1949

doi:10.4028/www.scientific.net/AMR.986-987.1946

Discussion based on small PABX lightning overvoltage

SunGuofeng[1, a], BaiYan[2,b]

[1]BeiHua University Engineering Training Center , JiLin,China

[2]BeiHua University Engineering Training Center , JiLin,China

[a, b]Byw1689@sohu.com

Keywords: medium-sized; overvoltage; switch

Abstract. Construction of large and medium-sized program-controlled switches be placed strictly in accordance with national standards Professional program-controlled switchboard in the room, general will not be affected by lightning overvoltage and harm of operating over voltage. And small PABX are commonly used for smaller enterprises and institutions, such enterprises are unlikely to build professional for program-controlled switchboard room. Mostly I placed it on the corner of the Office or the Office area, convenient pin-outs. As a result of this device is undersized and lower prices, lightning protection concepts and enterprises and institutions to understand enough, it will not attach too much importance to. During the thunderstorm-prone season often makes their lightning overvoltage damage, direct economic loss was not too large, but the indirect economic losses are direct losses many times. This article in view of the characteristics of this equipment, according to the wiring form of power supply system using proper surge protection devices, equipotential bonding, shielding and grounding, and other combinations of several methods, and do not put too much financial and material resources to avoid accidents from happening, the various types of losses to a minimum.

Introduction

Domestic economy in recent years the rapid development of business models from single to now diversified, making something as small as a few people-dozens of enterprises and institutions are very active in the economic activity. When special after China's accession to the WTO, economic development for the global economy, demand is also increasing the amount of economic activity. General enterprises and institutions are made of small program-controlled switchboard formed within a local area network, especially switches up to 8-64 road. With only 1-4 outside lines attached to the switch, while the internal call each other for free, this is a high price/performance in the method. Widespread use of small PBX brings easy and affordable to enterprises and institutions. Lightning overvoltage have great destructive power, this is well known. But if you do not need lightning protection measures, will bring greater economic losses and incalculable indirect economic losses.

How to prevent of lightning overvoltage, lightning protection for engineers and experts have had a very sophisticated theoretical foundations and relatively sophisticated solutions, such as the lightning rod, lightning, lightning, lightning network, surge arresters, and more. But only installed on one corner of the Office of the smaller PABX, various methods of using the above combination or even to prevent lightning overvoltage, such measures of its prevention effects can be described as perfect, or it can be said to be ideal. But require enterprises spend more money, manpower and more professional knowledge engineers and technicians for the construction of lightning, these factors determine the type of units to professional lightning protection for the system is very difficult. Lightning protection measures are not taken, damaged during the thunderstorm-prone season is likely to be harmful effects caused by their function is very large.

Therefore this article is based on national standards and the relevant statutes and switch usage and installation site, taken as simple, easy to operate internal lightning protection methods, make the average a little study to master some knowledge in electrical engineering and technical personnel and small enterprises in economically acceptable. There are overlaps between these types of methods, as well as complementarity, protected space resistive, capacitive and inductive "coupled" noise reduction to harmless [1], thereby reducing the switching overvoltage damage by lightning.

Types of lightning overvoltage

Lightning overvoltage is divided into three types: direct lightning, and lightning; lightning wave invasion.

Direct lightning is a lightning effect directly on the electrical equipment and buildings, thermal and mechanical strength, may cause damage to the power systems, electrical equipment and buildings. Lightning was due to strong lightning current of changes in the electric and magnetic fields caused by electrostatic induction and electromagnetic induction. Live between clouds and the Earth from the strong electrostatic field in discharge of lightning flash, positive and negative charges fiercely neutral ground conductor which results in live, transmission line, metal pipe induced bound charge, formed too late to speedy dispersal of electrostatic induction over voltage. Lightning current pulse with high amplitude and steepness, in the space around it forming a strong pulse transient electromagnetic fields, near the EMF induced in the conductor is very high, leading to induced voltage. Lightning wave invasion refers to when power lines are straight lines when lightning or lightning produces Thunder and lightning shock waves along wires on both sides of the communication, also known as wave [2]. Lightning impulse is composed of up to 104 pulse, its induced voltage coupled to electronic and information equipment, causing "noise" interference and measurement error, serious destructive electronic devices.

Installed switch places, mostly in civilian buildings, its external wiring below generally are in other buildings, in other words the protection of the building, the switch by direct lightning overvoltage damage probability is very low. From here we can see to switch dangerous overvoltage is lightning, lightning wave invasion.

Classification of lightning

Install switches in civil building systems are composed of an electronic information system. To accurately determine what sort of lightning is the system, use national standards GB50057-1994 (2000) of the buildings design code for Lightning [3] in the formula.

$$N=0.0024kT_d^{1.3}A_e$$

N-number of lightning strikes; N-the average density of lightning strikes; T-the average number of thunderstorm days; k-positive coefficient.

$$A_e=[LW+2(L+W)\sqrt{H(200-H)}+\pi H(200-H)]\times10^{-6} \quad H<100m$$

$$A_e=[LW+2(L+W)+\pi H^2]\times10^{-6} \quad H\geqslant100m$$

L, w, H-switches installed by building the length, width and height.

According to the local meteorological data and formulas to calculate the value of N, to determine its level of lightning.

Electronic information system by lightning electromagnetic pulse can be divided into four levels A, B, C, D, for switches, should be classified as class C, D, generally classified as a class D[4].

Calculation of induced voltage

So-called surge is lightning currents and high frequency electromagnetic field of lightning formation of lightning electromagnetic pulse (LEMP) through grounding conductors or electrical lines coupled conduction and radiation coupling, produced in the electrical and electronic equipment over voltage and over current of danger [5]. This surge was the greatest threat to switch, especially electromagnetic forming a strong pulsed electromagnetic fields generated by inductive voltage.

$$U=M(\frac{\Delta i}{\Delta t})$$

Switch arrangement of lines and induced voltage conductors in different ways, the induced voltage is different, seen Figure 1.

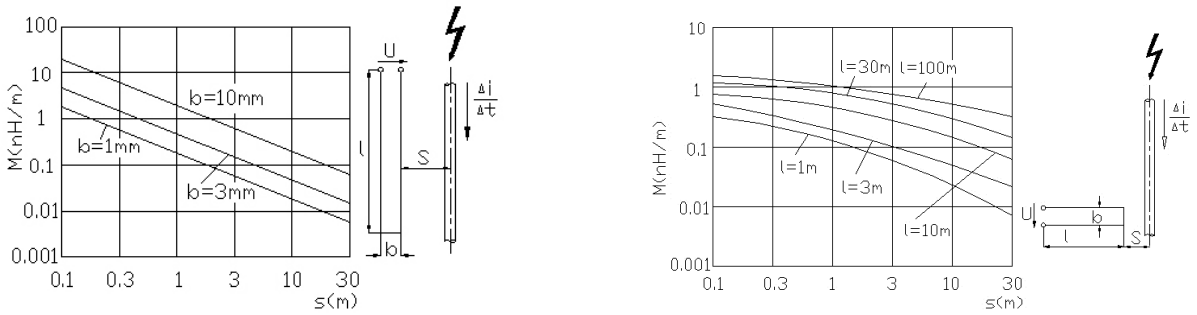

Figure1. Induced voltage conductors in different ways

By formula and chart data, switch lines must not be allowed immediately laid in parallel with other conductors, laid in parallel to ensure that a certain amount of space, if you want to cross with other conductors must ensure vertical laying.

switch lightning overvoltage prevention measures

Switches installed to meet the requirements of specifications, as far as possible avoid some human factor failures caused by improper installation, and cause unnecessary trouble, and this type of failure to find there are still certain difficulties. In addition to the main ways of preventing lightning overvoltage.

A. the equipotential bonding and earthing

Enterprises, institutions, choose the installation location of the switch, normally will only take into account the convenience outlet without too much attention to other matters, this resulted in a switch installed lightning protection system may be or may not have. If building a lightning protection system, its common grounding system connected to the grounding of the switch. If this building no lightning protection system (most of the buildings this is the case), it must be necessary and simple lightning protection alteration. With a cross-sectional area of not less than the effect of 50mm2 copper belt or equivalent indoor laying of galvanized steel in the switch installed for a week or only exposed metal part of the known as equipotential zone. Exposed metal part and the equipotential round steel bars with a cross-sectional area of not less than 16mm2 to connect, to weld the lap length is not less than 6 times times their diameter Within this building all kinds of equipment grounding wire with which you want to connect, switches the system range is composed of large, less frequent (usually less than 30kHz), the use of S-type equipotential bonding network.

Is to be noted that in the Interior around a week of equipotential zone you want to switch the installation of indoor base reinforced once every 5m connection, but this is not much. Only part of the General equipotential zone, using one or both ends connected is able to meet the requirements. Basis if no rebar to ground connection, requires artificial grounding (earthing resistance ≤ 10 ω, method of making artificial grounding please refer to the relevant information). Equipotential bonding is not allowed a "suspension", "suspension" is not conducive to effectively prevent lightning overvoltage.

B. masking and routing

Shielding refers to the route shield in this context, does not discuss the building of switch installation shield. Reasonable shielding and wiring can effectively reduce the harm of lightning induced to switch. Switches the power inlet and communication signals outside shielded wires should be adopted, if not shielded wires should wear metal pipe laying. The shield (other metal) in and out of both ends of the building must equal potential connection of the respective links. Cross-sectional area of the shields of shielded lines to meet the following formula.

$$S_c \geqslant i_i \rho_c l_c 10^6 / U_P \quad mm^2$$

Cross-sectional area of the S-shield; i-lightning current flow shielding; Resistivity ρ-shielding, bronze 17.24x10 w · m, Al-28.264x10 w · m; lc-line length; Up-impact resistance of the voltage of the insulation value, the switch signal outside of 5kv, power cables up to 15kV.

It is worth noting the switch must use metal shell, and equipotential coupling with connecting lines to take the shortest possible distance. Switch line, communication power supply and grounding line will have to be in accordance with its instructions require layout, as far away as possible sources of interference. Strength wires laying way to avoid sticking of o, ensuring appropriate spacing. If can not guarantee the space shield measures should be taken, the shield grounding measures mentioned above. Strength of wire road laying right-angle crossing should be taken.

C.surge protector SPD

Surge arresters are used to prevent lightning overvoltage protection components, depending on the scope of electrical engineering and information technology applications can be segmented into lightning current arrester (10/350 μ s wave) and surge arrester (8/20 μ s wave). SPD are limited transient over voltage in an electrical system and guided discharge current discharge of non-linear protection devices, are: Voltage switch, pressure limiting, mixing type and used for network communication signals in the SPD. SPD protection switch fall into two categories.

SPD should generally be used in switching power supply protection selection of Ⅰ, Ⅱ class. When the SPD is installed, we must first distinguish between switch power system introduced to IT in the form, TT, TN which (see GB50057-1994), decided to switch between the power supply into boxes are N-PE equipped with SPD, in order to ensure their personal safety. SPD class Ⅱ here must be combined with and is at a higher level of class Ⅲ SPD, if power supply is equipped on the residual current protection device at a higher level when the BCD, BCD is superior to select s-type with delay residual current protective device, so as to avoid mis-operation of BCD SPD action at lower levels after the superior, causing unnecessary blackouts. In order to ensure that security should be in the switching power plug installation of class Ⅰ SPD as superior fails fallback, strengthened protection of switches.

SPD Earth wire must be adopted in accordance with the above mentioned in 5.1 connections. Switch power inlet at the SPD should generally be selected I ≥ 15kA nominal discharge current, maximum continuous voltage u ≥ 1.15U,U-switching power supply voltages; communication signal SPD the highest operating voltage u ≥ 1.2 U,U-communication signal voltage.

Conclusions

This article uses such simple, easy construction of the three combinations, these switches installed in the laboratory for internal lightning protection alteration, calculated according to the theory of building lightning protection 99% project, project only reached 94%, but the practical application proved to be effective and high cost performance. Want to give the technicians work in this regard and the enterprises and institutions suffering from this reference, is more convenient to deal with this issue.

References

[1]Peter Hasse s, and Fu zhengcai,Yefeiyv translation . Low-voltage system lightning protection [m]. Beijing: China electric power press, 2005.9:50-51.

[2] Wu Xuehong, Pu Tianwei, Liao Deli. Lightning protection and grounding technology [m]. Beijing: chemical industry press, 2008.1:13.

[3] Handbook of industrial and commercial distribution design (third edition) [m]. Beijing: China electric power press, 2005:807-845.

[4]JGL16-2008/J778-2008 code for electrical design [s]. 11.9.

[5]GB50057-1994 (2000) code for design of structures against lightning [s].

Advanced Materials Research Vols. 986-987 (2014) pp 1950-1953

doi:10.4028/www.scientific.net/AMR.986-987.1950

Lossless compression of weak electrical signal of ginseng molecule based on Discrete Wavelet Transform and Siesta program

Changcheng Li[1, a], Laiwu Yin*[2, b],Dong Chen[3, c] and Shujie Xu[4, d]

[1]College of Electrical and Information Engineering, Jilin Agricultural Science and Technology College, Jilin, China

[2]Department of Scientific Research, Jilin Agricultural Science and Technology College, Jilin, China

[3]Faculty of Foreign Language, Jilin Agricultural Science and Technology College, Jilin, China

[4]Division of planning and Finance, Jilin Agricultural Science and Technology College, Ji Lin, China

[a]jilinlcc@sina.com, [b]yinlaiwu@163.com, [c]bradley_chen@163.net, [d]jl_xsj@sina.com

Keywords: DWT, Siesta program, ginseng molecules, weak electrical signal

Abstract. This paper proposed the electron density of time series by using the Siesta software to calculate the weak electrical signals of ginseng molecule, combining with the lifting scheme DWT to remove ginseng molecular spatial redundancy. For the acquisition and identification of weak electrical signals of ginseng molecule in physical environment , based on the analysis of collection and identification's principles, the noise coefficient is removed to reconstruct the signal and retain the useful signal components through applying the multi-decomposition of DWT transform to divide weak electrical signals of ginseng molecule into wavelet coefficients of different scales. The experimental results show that the multi-resolution analysis of DWT transform is performed for the weak electrical signal of ginseng molecule with different rhythms and different frequency ranges, and the weak electrical signal size of ginseng molecule before and after compression, the percentage of high frequency coefficients set to zero, and the average energy percentage after compression are, respectively, increased to 77.73%, 46.88%, and 99.99%. This algorithm operates fast enough to ease hardware implementation, providing an effective method for lossless compression of the weak electrical signals of ginseng molecule.

Introduction

The processing of the weak signal of ginseng molecule has become an important field for the modern signal processing technology to play its power. Therefore, the proposed wavelet transform method provides another way for physical and pathological diagnosis of weak electrical signal of ginseng molecule, with more information. The theory of applying harmonic wavelet packet detecting weak signal was proposed and it is found that the weak signal can effectively be extracted by harmonic wavelet packet transform in frequency domain and can easily be reconstructed in time domain [1]. The signal detection technology applied with wavelet entropy is put forward for the insensitivity of wavelet transform de-noising to weak signal, especially for the issue of unsatisfactory results in signal classification test [2]. The improved Hilbert-Huang transform (Hilbert-Huang transform, HHT) is proposed for feature extraction with the aim to extract the featured frequency of the weak signal of early failures in the mechanical equipments [3]. A hierarchical threshold de-noising method is put forward on the basis of wavelet detail coefficients of Daubechies, the method is used to determine the maximum decomposition layers through the analysis of the minimal signal frequency components, and can be applied to extract and process the weak signal of plant [4]. In this paper, the DWT algorithm is proposed to be applied to the realization of lossless compression of the weak electrical signal of ginseng molecule by using Siesta application to calculate the electronic structure of ginseng molecule with the combination of the wavelet lifting scheme transform to remove the spectral and spatial redundancy.

Lifting Scheme of Wavelet Transform

The transforms of *S*, *ST,* and $S+P$ may be seen as the special cases of Sweden's lifting scheme [5]. The process of wavelet transform based on lifting scheme may be divided into splitting, predicting, updating and optimizing:

Splitting (Lazy wavelet or Polyphase wavelet transform):

The original signal $S_{j,k}$ is divided into two disjoint subsets: $S_{j+1,k}$ and $d_{j+1,k}$, and the original signal $S_{j,k}$ is generally split into even and odd series, that is $split\ (S_{j,k}) = (S_{j,2k}, S_{j,2k+1}) = (S_{j+1,k}, d_{j+1,k})$.

Predicting (Dual Lifting Step):

As $d_{j+1,k}$ may be predicted with $S_{j+1,k}$ according to the relativity between data, a prediction operator, which is irrelevant to data set structure to make $d_{j+1,k} = P(S_{j+1,k})$ with the differential value between $d_{j+1,k}$ and prediction value $P(S_{j+1,k})$ to replace $d_{j+1,k}$, and the differential value represents the closeness between the above two values. If the prediction is reasonable, the differential value data set will consist of less information than the original subset $d_{j+1,k}$.

Updating (Update Lifting Step):

As some global properties (e.g. average value) of the coefficient subset generated from the above two steps are not consistent with those from the original data, the updating process will be applied to use operator *U* to generate a better subset $S_{j+1,k}$ to maintain some features of the original data set $S_{j,k}$, and $S_{j+1,k}$ may be defined as follows: $S_{j+1,k} = S_{j,2k+1} + U(d_{j+1,k})$. After being divided through the processes of splitting, predicting and updating, $S_{j+1,k}$ can be divided into $d_{j+2,k}$ and $S_{j+2,k}$. The wavelet transform of the original data $S_{0,k}$ will be demonstrated as $\{S_J, d_J, d_{J-1}, \ldots, d_1\}$ after *J* times of division, and S_J, among them, represents the low frequency part of the signal, and $\{d_J, d_{J-1}, \ldots, d_1\}$ represents the high frequency part of the signal.

Optimizing lifting step:

Dual lifting step and update lifting step may be alternatively used to improve the properties of wavelet transform according to the actual situation. The forward transform algorithm based on lifting scheme may be written as:

$$S_{j+1,k}^{0} = S_{j,2k} \tag{1}$$

Dual Lifting Step:

$$d_{j+1,k}^{(i)} = d_{j+1,k}^{(i-1)} - \sum_{m} p_{m}^{(i)} S_{j+1,k-m}^{i-1} \tag{2}$$

Update Lifting Step:

$$S_{j+1,k}^{(i)} = S_{j+1,k}^{(i-1)} - \sum_{m} u_{m}^{(i)} d_{j+1,k-m}^{i-1} \tag{3}$$

After update lifting step and dual lifting step *M* pair, even sample points, combined with scale factor n_l, n_h turn into low-pass coefficient, and odd sample points into high-pass coefficient.

<table>
<tr><td>$\times n_l^6$</td><td>$\times n_l^5 \times n_h$</td><td rowspan="2">$\times n_l^3 \times n_h$</td><td rowspan="3">$\times n_l \times n_h$</td></tr>
<tr><td>$\times n_l^5 \times n_h$</td><td>$\times n_h^4 \times n_h^2$</td></tr>
<tr><td colspan="2">$\times n_l^3 \times n_h$</td><td>$\times n_l^2 \times n_h^2$</td></tr>
<tr><td colspan="3">$\times n_l \times n_h$</td><td>$\times n_h^2$</td></tr>
</table>

Fig. 1 Realization process of normalization factor of lifting scheme

Generally, M is called the number of lifting steps, and n_l, n_h is called normalization factor with $n_l \times n_h = 1$, and the different biorthogonal wavelet leads to the different value of n_l, n_h. The orthogonally transformed normalization process is shown in Fig. 1.

Siesta program

The lossless compression of weak electrical signal of ginseng molecule is in a frontier field of signal processing, which studies the effect of elementary reaction rate at the molecular level with a detailed understanding of the chemical reaction process of ginseng molecule. This kind of study plays an important role in deep understanding of the micro mechanism of the chemical reaction of the molecular weak signal of ginseng, so as to better control of chemical reaction and chemical approaches. Along with the development of computer technology, the research of the lossless compression of ginseng molecular weak signal involves the microstructure and basic concept of ginseng molecules, such as surface structure, ginseng molecular activation energy, transition state theory and the configuration, as well as the elementary reaction rate.

This paper puts forward the use of SIESTA (Spanish Initiative for Electronic Simulations with Thousands of Atoms) to calculate the electronic structure of weak signal of ginseng molecule and perform the simulation of molecular dynamics, and further provides the study on the system and structure of the ginseng molecular energy, reaction path, the electric dipole moment, atoms and track [6,7]. The simulation of hundreds of ginseng atomic system in general workstation, combined with ginseng molecular dynamics and surface chemistry and micro knowledge, which will help to understand the micro reaction of the weak signal of ginseng molecule.

The simulation results

The removal of redundancy is achieved by applying the spectral, spatial transform to the weak electrical signals of ginseng molecule with DWT transform as the spectral transform and CDF (2, 5) wavelet transform (based on lifting scheme) as frame transform, and then the transform results are encoded. The original ginseng weak electrical signal is shown in Fig. 2, and the ginseng weak electrical signal after lossless compression is shown in fig. 3.

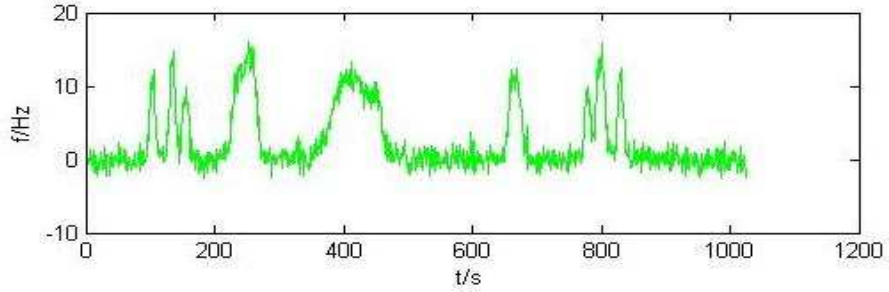

Fig. 2 Original ginseng weak electrical signal

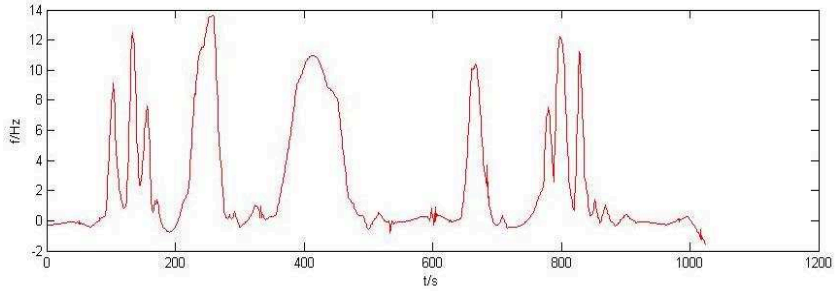

Fig. 3 Lossless compressed ginseng weak electrical signal

Summary

This paper provides a experimental contrast between such algorithm and other typical lossless compression algorithm, and the the weak electrical signal size of ginseng molecule before and after compression, the percentage of high frequency coefficients set to zero, the average energy percentage after compression are shown in Table 1.

Table 1 The results of contrast experiment among the Band 1-Band 10 ginseng weak signals after lossless compression

wave band No.	The size of the original signal	Lossless compression of signal size	The high frequency coefficients are set to 0	Lossless compression energy percentage
1	159	91	48.3465	99.9935
2	89.6	37.9	48.6149	99.9977
3	160	130	53.4417	99.9968
4	68.6	38.6	43.4078	99.9997
5	199	169	45.4873	99.9987
6	125	95.4	42.5734	99.9999
7	192	162	47.9812	99.9993
8	63.3	57.4	45.5451	99.9999
9	121	112	47.5640	99.9866
10	139	130	45.8749	99.9772
Proposed Scheme		77.73%	46.88%	99.9%

The proposed method is evidently efficient from the experimental results.

Acknowledgements

This research is funded by Jilin province science and technology development plan, and supported by Jilin province public computing platform (project number: 20130101179JC-20).

Corresponding Author

Laiwu Yin, yinlaiwu@163.com, 086043263509822.

References

[1] X. Wu and G.Y. Ji: Applying harmonic wavelet packet detecting weak signal, vol. 33, no. 6, 1-3 (2010).

[2] H. Yi and Y. Chai: An Improved Method of Wavelet Analysis for Weak Signal Detection, Sichuan University of Arts and Science Journal, vol. 22, no. 2, 44-47(2012).

[3] C. Guo: Wavelet Packet Analysis in the Detection of Weak Signals in the Civil Craft Cockpit Background Sound, Civil Aircraft Design and Research, vol. 30, no. 5, 510-513 (2010).

[4] C. Li, L. Yin, D. Chen and X. Tang: Threshold of Denoising Weak Electrical Signals in Plants from Daubechies Wavelet Transform, 2013 International Conference on Computer Sciences and Applications, 600-603(2013).

[5] C. Li, C. Xie and S. Li et al: Lossless Hyper-Spectral Image Compression Based on XCJRCT, Discrete Wavelet Transform and Set Partitioning In Hierarchical Trees Coding, 2011 International Conference on M

[6] Soler J M, Artacho E. Gale J D, et al: J Phys Condes Matter, 11, 14(2002): 2745.

[7] Andreoni W, Curioni A. Parallel Computing, 26, 7-8(2000): 819.

Advanced Materials Research Vols. 986-987 (2014) pp 1954-1957

doi:10.4028/www.scientific.net/AMR.986-987.1954

Wide-band Modeling of the IGBT Module based on the Physical Structure

Haifeng SUN[a], Xiaoming WU[*, b], Chenda ZHENG[c] and Xiaoqian LIU[d]

Department of Electrical Engineering,North China Electric Power University,071003,Baoding,China
[a]haif_sun@126.com, [b]xmingwu@126.com, [c]dariotzen@hotmail.com, [d]qinqintu@163.com

Keywords: IGBT module, wide-band modeling, power electronics

Abstract. This paper presents a new modeling method, based on the physical structure of the IGBT module, considering the distribution parameters of high frequency.This method is simple and the wideband model has physical meaning, by choosing suitable model initial parameters as well as the objective function which use the iterative optimization algorithm to solve the model parameters.Comparing the wideband model with the measured results ,the wideband model maintain high accuracy in the range of 100KHz ~ 20MHz.

Introduction

Compared with the conventional model, wideband model has a higher accuracy in a wide frequency range.By measuring the actual components, their amplitude-frequency characteristic and phase-frequency characteristic are obtained, and then get their wideband equivalent circuit model through respective modeling methods, modeling methods including conventional equivalent circuit model and the black-box model [1-2]. The advantage of conventional equivalent circuit model is intuitive and each element has the physical meaning. Without considering the high frequency parameters, this equivalent circuit model is not accurate in the case of the high frequency.Black box theory is a pure mathematical modeling method, this method is completely mathematical modeling method, considering the effect of frequency-related parameters, the model established for more accurate circuit simulation. The disadvantage is that the equivalent circuit with no physical meaning, a simple component may use many elements to express. Some scholars have proposed a modeling method based on the equivalent circuit with the traditional black box theory, but the use of this method to add black box model slip more complex, still lack physical meaning[3].

With the advantages of low power gate drive,high frequency,large output current,low resistance,the IGBT received wide attention and research in the field of power electronics conversion.Since1985,the IGBT model has been widely studied by domestic and foreign scholars,but only Hefner A R et al in 1989 proposed the model based on the equation of bipolar transport theory,which electrical characteristics is higher than others,it has been successfully applied to Saber, Spice simulation software[4-6].

Due to the impedance measurement and circuit impedance synthesis theory is only suitable for linear system, and the IGBT module is a nonlinear element, pretending to be the following: the measurement of the IGBT module is in shut down condition, the conduction state as short-circuit regardless of its frequency. The IGBT module is considered as a linear element in the off state.

At low frequencies, without considering the influence of parasitic parameters, most of the components are regarded as the ideal element.Original base model parameters can be calculated according to the structure and the frequency characteristics.Seen from Fig.1, the original model is close to the measured value at low frequencies. Without considering the effects of parasitic parameters，simulation will appear larger error at frequencies above 3MHz. With the increase of frequency, the parasitic capacitance between components, lead stray inductance of component , stray resistance parameters can not be ignore,resonance phenomenon occurs when the frequency reaches 5MHz.

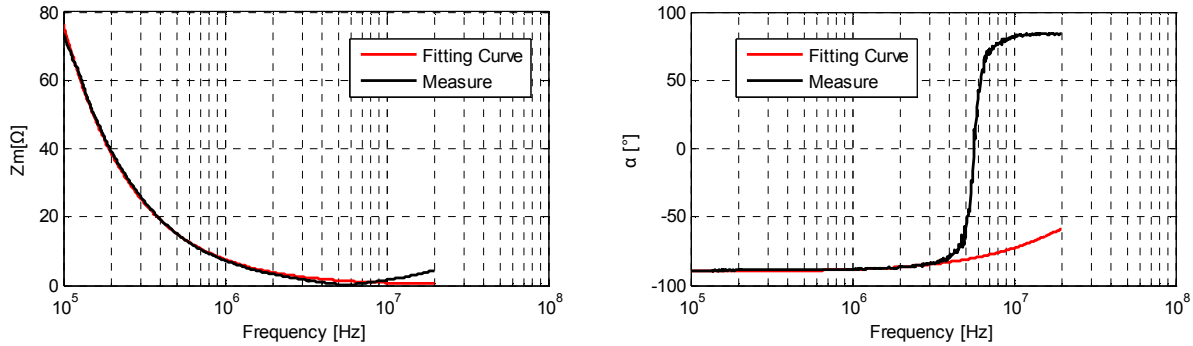

Fig.1 Comparison between the measured and original basic model

The wideband model of IGBT module

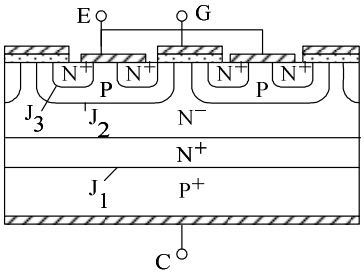

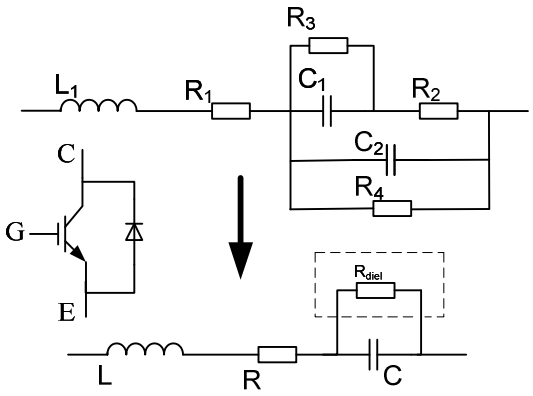

Fig.2 The structure of IGBT Fig.3 IGBT module wideband model and simplified model

According to the analysis of the structure of IGBT, IGBT module model are as follows:Where, C_1 represents the equivalent capacitance of the PN junction IGBT turn-off state formation, R_2 represents the equivalent resistance of IGBT internal buffer layer, the drift region and other parts of, R_3 represents a PN junction dielectric loss equivalent resistance,C_1andR_2R_3composed of the original model IGBT.C_2 represents the equivalent capacitance of the anti-parallel diode, R_4 represents an anti-parallel diode equivalent dielectric loss resistance, C_2 and R_4 form anti-parallel diode equivalent model.Considering the effect of leads and parasitic parameters, the R_1 andL_1 represent stray resistance and lead stray inductance.Simplify the above, R_3 and R_4 are combined into the one R_{diel}, represents the overall performance of the IGBT module out of the high-resistance.

In the evolutionary search, Genetic algorithm only use the objective function without the external information.Therefore the choice of the objective function is essential, influences the speed and the ability to find the optimal solution. The objective function can be established by comparing the wideband model with the actual measurement:

$$obj_1=\sqrt{\frac{1}{N}\sum_{n=1}^{N}\left(\left(|Z_n|^2-|Z(f_n)|^2\right)+\left(|\theta_n|^2-|\theta(f_n)|^2\right)\right)} \quad (1)$$

Where N represents the number of frequency components of the actual measurement;f_n said the N measurement points corresponding frequency value $|Z_n|$ and θ_n are the measured impedance magnitude and phase angle respectively; $|Z(f_n)|$ and $\theta(f_n)$ respectively frequency of f_n wideband impedance amplitude and phase angle of the model.

The objective function 1 by genetic algorithm iterative solution circuit parameters:

L=0.02507uH;C=0.02071uF;R=1.368Ω

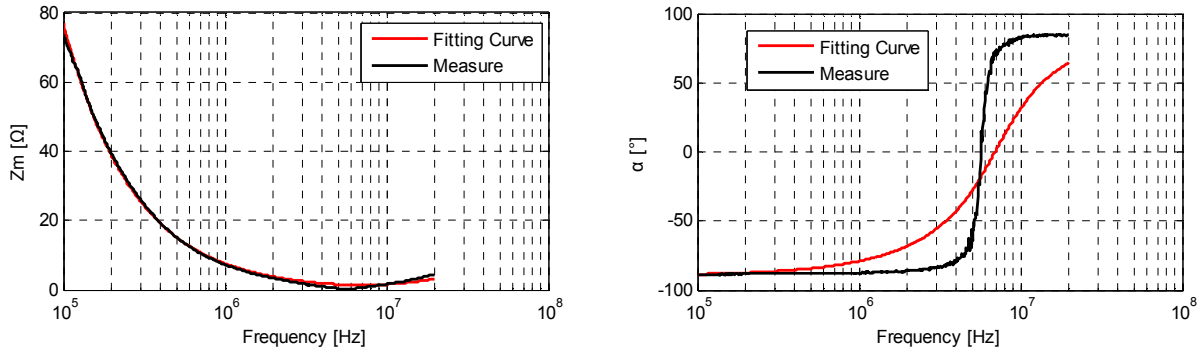

Fig.4 Comparison between the measured and objective function value 1

Seen from the Fig.4, magnitude of impedance fit better, and phase angle to fit the situation worse, as the distribution range of impedance magnitude is large, this leads the solution of objective function not considering the magnitude and phase of impedance at the same time, the objective function can be normalized.

$$obj_2=\sqrt{\frac{1}{N}\sum_{n=1}^{N}\left(\frac{1}{|Z_n|^2}\left(|Z_n|^2-|Z(f_n)|^2\right)+\frac{1}{|\theta_n|^2}\left(|\theta_n|^2-|\theta(f_n)|^2\right)\right)} \tag{2}$$

The objective function 2 by genetic algorithm iterative solution circuit parameters:

L=0.02768uH;C=0.02834uF;R=0.179Ω

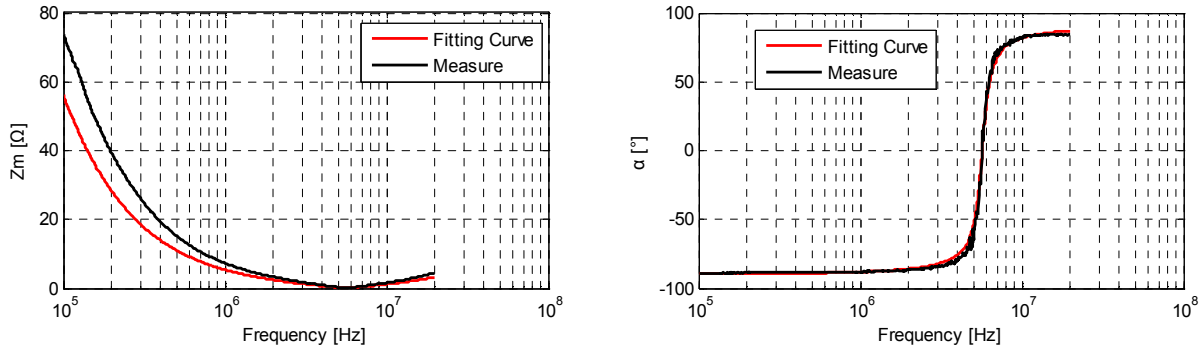

Fig.5 Comparison between the measured and objective function value 2

Seen from the Fig.5, impedance phase angle fitting is better, and amplitude fitting is bad.Although this solution can not be used as the final wideband of the model parameters optimal solution, but can be further weighted objective function, the objective function is added to optimize the weight function, which is expressed as:

$$obj_3=\sqrt{\frac{1}{N}\sum_{n=1}^{N}\left(\omega_{n1}\frac{1}{|Z_n|^2}\left(|Z_n|^2-|Z(f_n)|^2\right)+\omega_{n2}\frac{1}{|\theta_n|^2}\left(|\theta_n|^2-|\theta(f_n)|^2\right)\right)} \tag{3}$$

Where ω_{n1} and ω_{n2} said weight function of impedance magnitude and phase angle,the selection of weight function can be determined according to the actual situation.For the case in Fig.5,Part of the low-frequency impedance magnitude poor fit,focus on the low-frequency part,$\omega_{n1}=\omega_{n2}=1/f_n$.The objective function 3 after genetic algorithm iterations have circuit parameter solution:

L=0.03622uH;C=0.02074uF;R=0.261Ω

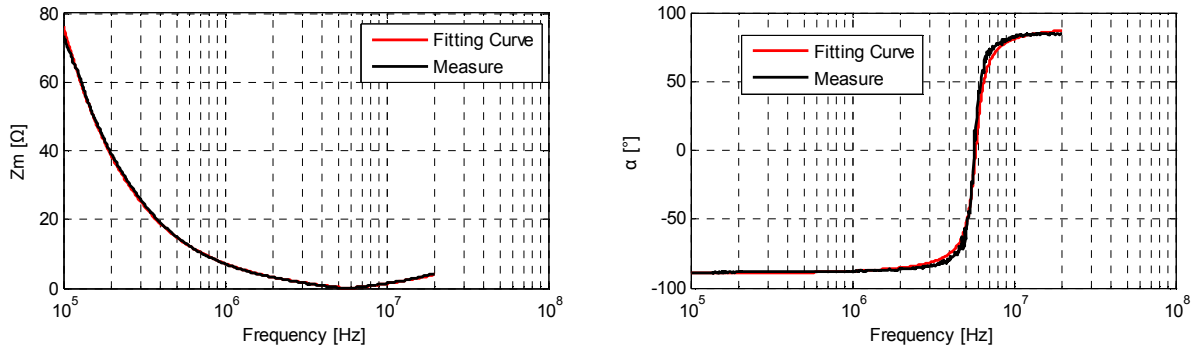

Fig. 6 Comparison between the measured and objective function value 3

Fitting results shown in Fig.6,both the amplitude-frequency characteristic and phase frequency characteristics match well, The change trend of resonance frequency and the impedance characteristic curve are basically identical with the actually measured value. In the 100KHz ~ 20MHz frequency range, IGBT module wideband equivalent model presented in this paper can be better to simulate the impedance characteristics.

Conclusion

In addition to meet the accuracy requirements of components, the wideband model should be simple.This paper presents a way from the physical structure of the components, and consider the distribution parameters. This approach has clear physical meaning, while the value of the parameters using genetic algorithms iterative solution, finally get wideband component model and model parameters.The method is easy realizable versatility, it provides basis for the future research work just as Electromagnetic disturbance.

Acknowledgement

This research was supported in part by National Natural Science Foundation of China (Grant No. 51207054, No.51177048), and Fundamental Research Funds for the Central Universities (Grant No. 13MS75)

References

[1] C.R. Paul: Introduction to Electromagnetic Compatibility(Wiley, USA 2006), P.242
[2] I.R. Pordanjani, C.Y. Chung, H.E. Mazin and W. Xu: "A Method to Construct Equivalent Circuit Model from Frequency Responses with Guaranteed Passivity", IEEE Transactions on Power Delivery, Vol. 26 (2011)No.1, p.400.
[3] H.F. Sun, X.Cui and L.Qi: "Modeling Method Based on Black-box Theory and Traditional Equivalent Circuit for Passive Elements", Proceedings of the CSEE, Vol. 30 (2012) No.6, p.112
[4] A.R. Hefner and D.L. Blackburn: "A performance trade-off for the insulated gate bipolar transistor: Buffer layer versus base lifetime reduction", IEEE Trans Power Electron, Vol. 2 (1987), p.194
[5] A.R. Hefner and D.L. Blackburn, "An analytical model for the steady-state and transient characteristics of the power insulated gate bipolar transistor", Solid-State Electron, Vol. 31 (1988), p.1513
[6] A.R. Hefner. and D.M. Diebolt, "An experimentally verified IGBT model implemented in the saber circuit simulator", IEEE Power Electronics Specialists Conf, Vol. 9 (1991) No.5, p.10.

Advanced Materials Research Vols. 986-987 (2014) pp 1958-1962

doi:10.4028/www.scientific.net/AMR.986-987.1958

Efficiency Analysis for a Two-Stage Three-Phase Inverter

Pan Geng[1, a], Yinzhong Ye[2, b], Weimin Wu[1, c], Yijian Liu[1, d], Shilong Xue[1, e]

[1]Logistics Engineering College, Shanghai Maritime University, Shanghai, 201306, China

[2]College of Electrical and Electronic Engineering, Shanghai Institute of Technology, Shanghai, 201418, China

[a]email: pangeng@shmtu.edu.cn

Keywords: two-stage; three-phase inverter; SPWM, SVPWM; efficiency

Abstract. This paper takes a two-stage three-phase inverter as an example. The efficiency calculation method is analyzed in detail for the inverter, and the power losses calculation method is proposed for the second stage under SVPWM. A 10kW/380V inverter system is designed. The system efficiency and the power losses for every part are theoretically calculated. Finally, experiments on a 10 kW prototype are carried out to verify the calculation.

Introduction

Recently, the solar photovoltaic (PV) and other regenerative power systems have been attracted much attention from the earth environmental point of view [1] [2]. The DC output voltage of these regenerative power systems may vary greatly, for example, from 300V to 800V for a PV panel system under the different temperature conditions [3]. A two-stage two-level three-phase inverter with a boost DC/DC converter as shown in Fig. 1 has been widely applied in the industry due to its simply structure and high reliability [4]. And many papers analyze the efficiency in detail [5]-[8]. However, till now, few documents have provided the calculation method under SVPWM in detail.

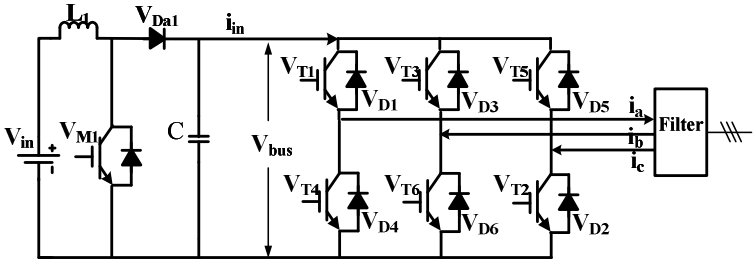

Fig.1 Two-Stage Three-Phase Inverter Topology

In this paper, the efficiency calculation method under Sinusoidal Vector Pulse Width Modulation (SVPWM) is proposed for a two-stage three-phase inverter. And experiments on a 10 kW prototype are carried out to verify the calculation.

Efficiency analysis of the two-stage inverter

A. Power losses in the boost stage

As shown in Fig.1, the first stage is composed of a DC/DC boost converter.

1) The junction capacitor power loss of V_{M1}

The power loss caused by the junction capacitor of V_{M1} is

$$P_{cj1} = \frac{1}{2} \cdot C_{oes} \cdot V_{peak}^2 \cdot f_s \tag{1}$$

where C_{oes} is the junction capacitor, V_{peak} is the peak voltage across V_{M1}.

2) Conduction power losses of Diode V_{Da1} and IGBT V_{M1}

The conduction power losses of Diode V_{Da1} and *IGBT* V_{M1} should be calculated according to conduction current separately. It can be expressed as:

$$P_{d\_con1} = \frac{1}{\pi} \cdot \int_0^{\pi} V_{d1}(I_{in}(\theta)) \cdot I_{in}(\theta) \cdot (1 - D_1) d\theta \quad (2)$$

$$P_{igbt\_con1} = \frac{1}{\pi} \cdot \int_0^{\pi} V_{igbt1}(I_{in}(\theta)) \cdot I_{in}(\theta) \cdot D_1 d\theta \quad (3)$$

where $V_{d1}(I_{in}(\theta))$ is the conduction voltage drop of diode and $V_{igbt}(I_{in}(\theta))$ is the conduction voltage drop of IGBT, both of them are associated with the current.

3) The reverse recovery power losses of Diode V_{Da1}

When the diode turns off, the stored charge needs to be discharged. The reverse recovery power losses are related to the on-state current, the collector-emitter voltage drop, the junction temperature and the driving characteristics. It could be calculated as:

$$P_{rec1} = k(V_{bus}) \cdot E_{rr1}(I_{in}(\theta)) \cdot f_s \quad (4)$$

where $E_{rr1}(I_{in}(\theta))$ is reverse recovery energy loss associated with current, $k(V_{bus})$ is the adjustment factor related to reverse voltage(here is the bus voltage). The parameters given by the technical manuals are mostly at a specific temperature and voltage, and the adjustment factor is added to come to a more accurate calculation.

4) The turn-on and turn-off power losses of IGBT V_{M1}

$$P_{turn\_on1} = k(V_{bus}) \cdot E_{on1}(I_{in}(\theta)) \cdot f_s \quad (5)$$

$$P_{turn\_off1} = k(V_{bus}) \cdot E_{off1}(I_{in}(\theta)) \cdot f_s \quad (6)$$

where $E_{on1}(I_{in}(\theta))$ and $E_{off1}(I_{in}(\theta))$ are the turn-on and turn-off energy loss, which are both related to current.

5) Inductance power losses

The power loss of the filter choke L_1 is composed of the core power loss and the conducting power losses of the coil. The detailed power losses calculation will not be discussed in this paper but the calculation method in [9] is used..

B. Power Losses in the second stage

Power losses of the second stage depend on the modulation method and the power factor of the load current, when the other parameters and conditions are set. In this paper, the SVPWM scheme is adopted and the power factor is assumed to be the unit. The distribution of the voltage vector states is shown in Fig. 2. The power losses in the sector 1 is used to predict the total power losses, assuming that the output currents (shown in Fig.1) of i_a, i_b and i_c are $\sqrt{2}I_o\cos(\theta)$, $\sqrt{2}Io\cos(\theta-120)$, and $\sqrt{2}Io\cos(\theta+120)$, respectively.

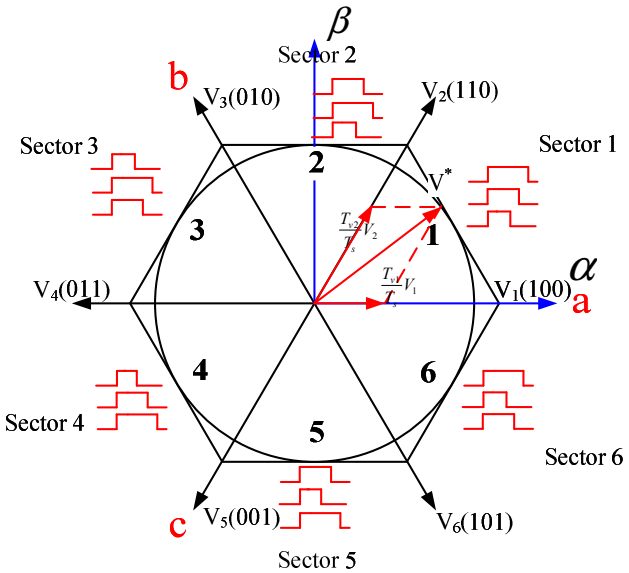

Fig. 2 Voltage vector states distribution.

The duty cycles of upper switches (V_{T1}, V_{T3} and V_{T5} as shown in Fig.1) can be derived as,

$$\begin{cases} D_1(\theta) = \dfrac{V_{bus} + \sqrt{3}V_m\left(\sin(\dfrac{\pi}{3} - \theta) + \sin\theta\right)}{2V_{bus}} \\ D_2(\theta) = \dfrac{V_{bus} - \sqrt{3}V_m\left(\sin(\dfrac{\pi}{3} - \theta) - \sin\theta\right)}{2V_{bus}} \\ D_3(\theta) = \dfrac{V_{bus} - \sqrt{3}V_m\left(\sin(\dfrac{\pi}{3} - \theta) + \sin\theta\right)}{2V_{bus}} \end{cases} \tag{7}$$

where V_m is the amplitude value of phase voltage and θ is the sampling angel.

1) The junction capacitor power loss of the switches

The power losses caused by the junction capacitors of the switches can be calculated as,

$$P_{cj2} = 12 \cdot \frac{1}{2} \cdot C_{oes} \cdot V_{peak}^2 \cdot f_s \tag{8}$$

2) Conduction power losses of Diode and IGBT

Since the output current is sinusoidal, the conduction power losses should be calculated by integrating the instantaneous value of current and voltage. The total conduction power losses of diodes of inverters, Pd_con, can be calculated as,

$$\begin{cases} P_{d\_con2\_1} = \dfrac{3}{\pi} \cdot \int_0^{\frac{\pi}{3}} V_F \cdot \sqrt{2} I_o \cos(\theta) \cdot (1 - D_1(\theta)) d\theta \\ P_{d\_con2\_2} = \dfrac{6}{\pi} \cdot \int_0^{\frac{\pi}{6}} V_F \cdot \sqrt{2} I_o \left|\cos(\theta - \dfrac{2\pi}{3})\right| \cdot D_2(\theta) d\theta \\ \qquad + \dfrac{6}{\pi} \cdot \int_{\frac{\pi}{6}}^{\frac{\pi}{3}} V_F \cdot \sqrt{2} I_o \cos(\theta - \dfrac{2\pi}{3}) \cdot (1 - D_2(\theta)) d\theta \\ P_{d\_con2\_3} = \dfrac{3}{\pi} \cdot \int_0^{\frac{\pi}{3}} V_F \cdot \sqrt{2} I_o \left|\cos(\theta + \dfrac{2\pi}{3})\right| \cdot D_3(\theta) d\theta \\ P_{d\_con2} = P_{d\_con2\_1} + P_{d\_con2\_2} + P_{d\_con2\_3} \end{cases} \tag{9}$$

where $P_{d\_con2\_1}$, $P_{d\_con2\_2}$ and $P_{d\_con2\_3}$ are the conduction power losses of diodes of the first bridge, the second bridge and the third bridge as shown in Fig. 1 respectively.

In the similar way, the conduction power losses of IGBTs could be calculated.

3) The reverse recovery power losses of Diode

Since one reverse recovery takes place for every bridge during one duty-cycle, the reverse recovery power losses of the second power stage, P_{rec2}, can be calculated as,

$$\begin{cases} P_{rec2\_1} = \dfrac{3}{\pi} \cdot \int_0^{\frac{\pi}{3}} k(V_{bus}) \cdot E_{rr}(\sqrt{2} I_o \cos(\theta)) \cdot f_s d\theta \\ P_{rec2\_2} = \dfrac{3}{\pi} \cdot \int_0^{\frac{\pi}{3}} k(V_{bus}) \cdot E_{rr}(\left|\sqrt{2} I_o \cos(\theta - \dfrac{2\pi}{3})\right|) \cdot f_s d\theta \\ P_{rec2\_3} = \dfrac{3}{\pi} \cdot \int_0^{\frac{\pi}{3}} k(V_{bus}) \cdot E_{rr}(\left|\sqrt{2} I_o \cos(\theta + \dfrac{2\pi}{3})\right|) \cdot f_s d\theta \\ P_{rec2} = P_{rec2\_1} + P_{rec2\_2} + P_{rec2\_3} \end{cases} \tag{10}$$

4) The turn-on and turn-off power losses of IGBT

Similar to the reverse recovery power losses calculation method, the turn-on and turn-off power losses of IGBTs could be calculated.

Calculated and experimental results

The power loss is calculated under the conditions that f_s = 15 kHz, L_1=1.2 mH, Lo=1.6mH, Co=10μF, the phase to phase output AC voltage is 380V and the rate output power is 10 kW. The modules of SKM50GB12T4 are adopted for main switches.

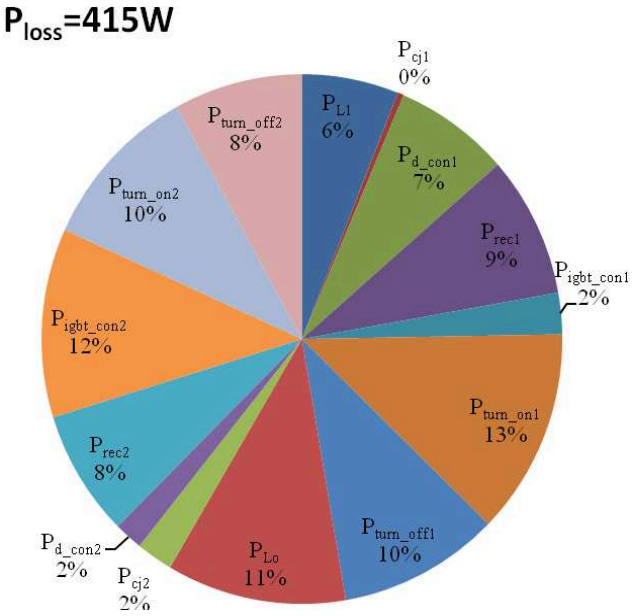

Fig.3 Power Losses Distribution

Fig.3 shows the calculated power losses while the input DC voltage is 430 V and Po is 10 kW (not including the power losses of control circuits).

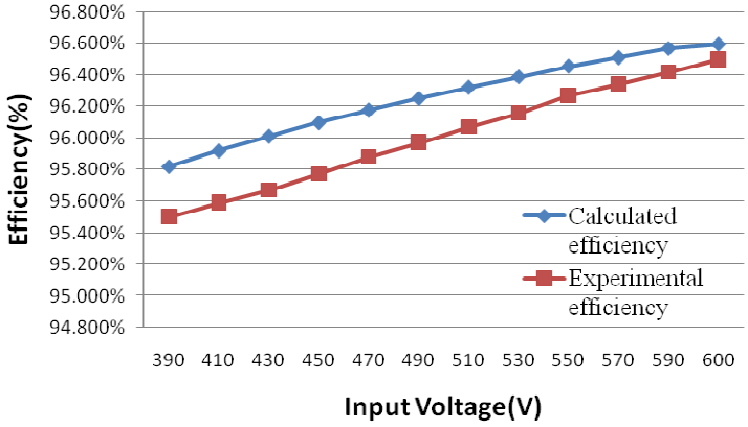

Fig.4 Efficiency comparison

Fig.4 shows the calculated efficiency and the experimental efficiency versus the input voltage under the condition of rated load. It can be seen that the higher input DC voltage, the higher efficiency. And the calculated efficiency and the experimental efficiency curves are basically the same (The deviation of efficiency is caused by switching devices. In respect of the IGBT which is 1200V/75A, its actual operating current is smaller than the rated current, leading to the fitting precision insufficiently. If the circuit operates at rated current situation, this deviation will be reduced).

Conclusion

In this paper, a power losses calculation method of a two-stage three-phase inverter is proposed. For the second stage three-phase inverter, a power loss calculating method under SVPWM is proposed, which is on the basis of the conduction time of each bridge. A 10kW/380V inverter prototype is designed. The experimental results proved the theoretical analysis. This method could be used to estimate the system efficiency and power losses for every part.

Acknowledgement

In this paper, the research was sponsored by the National Natural Science Foundation of China (Project No. 61374132).

References

[1] Chiang S.J, Shieh Hsin-Jang and Chen Ming-Chieh, "Modeling and control of PV charger system with SEPIC converter," IEEE Trans. on Industrial Electronics, vol. 56, no. 11, pp: 4344-4353, 2009.

[2] Al Nabulsi Ahmad and Dhaouadi Rached, "Efficiency optimization of a dsp-based standalone PV system using fuzzy logic and dual-MPPT control," IEEE Trans. on Industrial Informatics, vol. 8, no. 3, pp: 573-584, 2012.

[3] J.M. Carrasco, L.G. Franquelo, J.T.Bialasiewicz, E. Galvan, R.C.P. Guisado, et al. "Power-Electronic Systems for the Grid Integration of Renewable Energy Sources: A Survey" IEEE Trans. on I Industrial Electronics, vol. 53, no. 3, pp: 1002 - 1016, March. 2006.

[4] Juan Manual Carrasco, Leopoldo Garcia Franquelo, Jan T. Bialasiewisz, Edardo Galvan, et al, "Power-Electronic Systems for the Grid Integration of Renewable Energy Sources: A Survey," IEEE Trans. On Industrial Electronics, vol. 53, no. 4, pp: 1002-1016, 2006.

[5] Weimin Wu, Xiaoli Wang, Pan Geng, Tianhao Tang, "Efficiency analysis for three phase grid-tied PV inverter". In Proc. of ICIT 2008, Chengdu, China, April 21-24, 2008, pp: 1-5.

[6] Y. Wu, M.A. Shafi, A.M. Knight, R.A. McMahon, "Comparison of the Effects of Continuous and Discontinuous PWM Schemes on Power Losses of Voltage-Sourced Inverters for Induction Motor Drives," Power Electronics, *IEEE Trans. Power Electron.,* vol.26, no.1, pp: 182-191, Jan. 2011

[7] Weimin Wu, Pan Geng, Jianming Chen, et al, "A novel three-phase quasi-soft-switching DC/AC inverter", In Proc. of PEDG2010, HeFei, China, June 16-18, 2010, pp: 477-480.

[8] Pan Geng, Weimin Wu, Min Huang and Frede Blaabjerg. "Efficiency Analysis on a Special Two-level Three-Phase Quasi-Soft-Switching Inverter", In Proc. Of APEC2013, Long Beach, USA, Mar 17-21, 2013, pp: 1206-1212

[9] W. N. Mohan, T. Undeland, and W. P. Robbins, Power Electronics: Converters, Applications, and Design. New York: Wiley, 2003.

Advanced Materials Research Vols. 986-987 (2014) pp 1963-1968

doi:10.4028/www.scientific.net/AMR.986-987.1963

Influence of Transformer Capacity on Insulator Leakage Current Acquisition Results

Pengchao Miao[1,a], Zhiniu Xu[1, b]

[1] Hebei Provincial Key Laboratory of Power Transmission Equipment Security Defense, North China Electric Power University, Baoding, China

[a] mariopascal2014@gmail.com, [b] wzcnjxx@sohu.com

Keywords: insulator; leakage current; transformer capacity; 3rd harmonic; 5th harmonic

Abstract: To study the influence of test transformer capacity on insulator leakage current acquisition results, leakage current acquisition experiments with the clean and dry insulator and the water drops attached insulator were conducted based on the sampling resistor method and the test transformers of different capacities whose models are YDTW-1200 kVA/300 kV, YDTW-50 kVA/250 kV, YDTW-10 kVA/100 kV, YDJ-5 kVA/50 kV respectively. To make the results more reliable, sampling resistors with different resistances, 10 Ω, 100 Ω, and 1 kΩ, were used to collect the leakage current. The root-mean-square (RMS) values of the leakage current, the ratio of the 3rd harmonic to the fundamental (K_3) and the 5th harmonic to the fundamental (K_5) were extracted from the measured data. And it was discovered that the transformer capacities has a very slight influence on the leakage current RMS value but has a great impact on the value of K_3 and the K_5. The maximum K_3 are approximately 3 times of the minimum K_3 and the maximum K_5 are approximately 9 times of the minimum K_5.

1. Introduction

The accuracy of leakage current acquisition results has important effect on the subsequent analysis and insulator leakage current and the related characteristics extraction has been studied widely and deeply. In the laboratory, the power of the leakage current acquisition experiment is usually provided by test transformer and the existing standard has the corresponding parameter requirements to experiment power supply [1] which guarantees the standardization of insulator artificial pollution experiment. However, constraints on the standard experiment power is relatively broad, and because of the practical limitations to the experiment condition, very large gaps exist on the transformer capacity and voltage levels in the actual research works. The smaller the capacity of the transformer is, the smaller short-circuit current it can withstand when a short circuit occurs, and therefore, the transformer must be able to bear a minimum short-circuit current in the artificial pollution experiment [1]. A considerable number of small capacity transformers are used in the actual research work [2-8], yet some of which may fail to strictly meet the requirements of the national standard according to the preliminary investigations. It is reasonable to doubt that transformer capacity of such a large degree difference may produce a great impact on the acquisition results of leakage current.

In this paper, leakage current acquisition experiments with the clean and dry insulator and the water attached insulator were conducted based on the sampling resistor method using test transformers with different capacities whose models are YDTW-1200 kVA/300 kV, YDTW-50 kVA/250 kV, YDTW-10 kVA/100 kV, YDJ-5 kVA/50 kV respectively. The leakage current of the tested insulator was recorded by the data acquisition card and the root-mean-square (RMS) values, the 3rd harmonic and fundamental ratio (K_3) and the 5th harmonic and fundamental ratio (K_5) were extracted from the measured leakage current signal.

2. Experiment Introduction

2.1 Experiment Equipments

To the convenience of expression, four transformers used in this paper were numbered as follows: NO.1 stand for the YDTW-1200 kVA/300 kV transformer, NO.2 stand for the YDTW-50 kVA/250 kV transformer, NO.3 stand for the YDTW-10 kVA/100 kV transformer and NO.4 stands for the YDJ-5 kVA/50 kV transformer. Capacities of the four transformers above can cover the capacity range of the current commonly used transformers and their specific parameters are shown in Table 1. The model of the tested porcelain insulator in this paper is XWP2-70 and the model of the sampling resistor is RX21. Figure 1 shows a schematic diagram of the experimental and the specific laboratory equipments.

Tab. 1 Test Transformers Parameters

NO.	Capacity[kVA]	Rated Voltage[kV]	Short circuit impedance[%]	No-load current[%]
1	1200	300	1.22	2.4
2	50	250	6.4	10.9
3	10	100	4	2.5
4	5	50	-	-

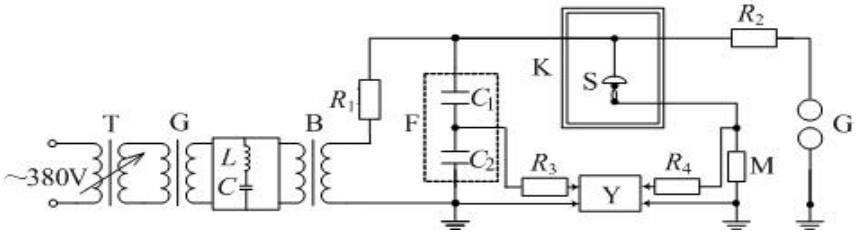

T: Voltage Regulator; G: Isolation Transformer; L, C: Filter; B: Test Transformer; K: Artificial Climate Chamber; R_1, R_2: Protective Resistance; R_3, R_4: Coaxial Cable Wave Impedance; M: Sampling Resistor; G: Protective Sphere Gap; S: Sample Insulator; F: Capacitive Divider; C_1, C_2: Voltage Dividing Capacitor; Y: Data Acquisition System

Fig. 1 Schematic diagram of experiment and equipments

2.2 Experiment Setup

Leakage current acquisition experiments with the clean and dry insulator and the water attached insulator were conducted using four different test transformers to apply 9 kV rated voltages and sampling resistors with different resistances, 10 Ω, 100 Ω, and 1 kΩ, were used to collect the leakage current for each group of experiment.

Considering the repeatability of the dry and clean insulator leakage current is the best, the experiments of dry and clean insulator were arranged to carry out. The first step is to clean and wipe the insulator surface and make sure its surface fully dry. And then rated 9 kV voltage was applied to the insulator and leakage current was recorded by the data acquisition system. Approximately 6×10^6 data points was recorded in each group of experiment.

Insulator under water drops attached conditions was also taken as experiment samples and a watering can was used to spray pure water on the surface of the insulator ensuring that the insulator surface water drops has reached saturation. As the experiment progresses the water on the insulator surface continues to be evaporated and in order to ensure the consistency of the initial conditions, supplyment water was sprayed to the insulator surface each time when the power was off to replace to the sampling resistor.

3. Experiment Results and Analysis

The RMS values of the leakage current, the 3rd harmonic and fundamental ratio (K_3) and the 5th harmonic and fundamental ratio (K_5) were extracted from the initial leakage current signal. The following will analyze the impact of transformer capacity on the RMS of the leakage current, the K_3 and K_5 which are three common characteristics of leakage current.

3.1 Analysis of the Leakage Current RMS Values

Fig. 2 and Fig. 3 show the leakage current RMS values. Fig. 2 are the results from dry and clean insulator while Fig. 3 related with the insulator under water drops attached condition. Four test transformers with different capacities were used.

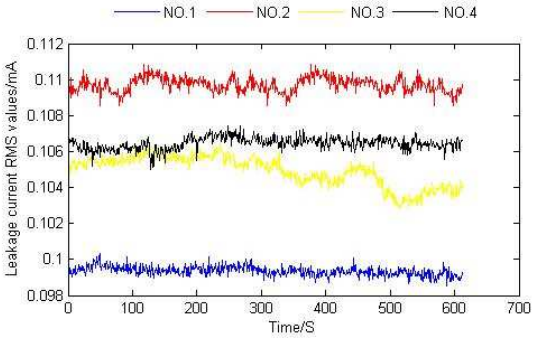

(a) Dry and clean, R_s=10 Ω

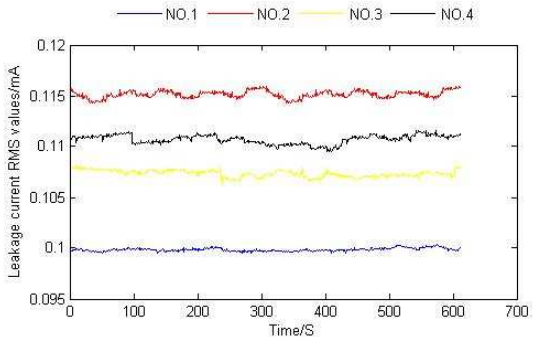

(b)Dry and clean, R_s=100 Ω

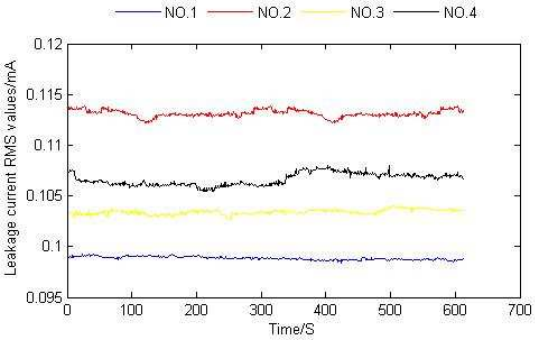

(c) Dry and clean, R_s=1 kΩ

Fig. 2 Leakage current RMS of different sampling resistors for the dry and clean insulator

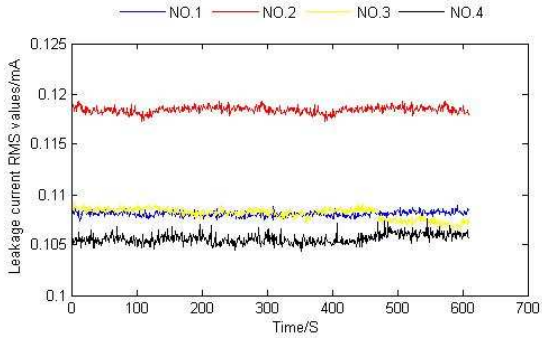

(a) Water drops, R_s=10 Ω

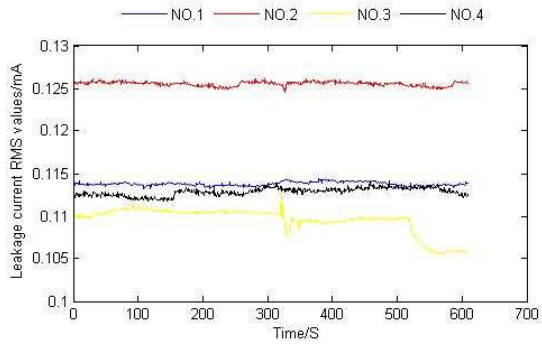

(b)Water drops, R_s=100 Ω

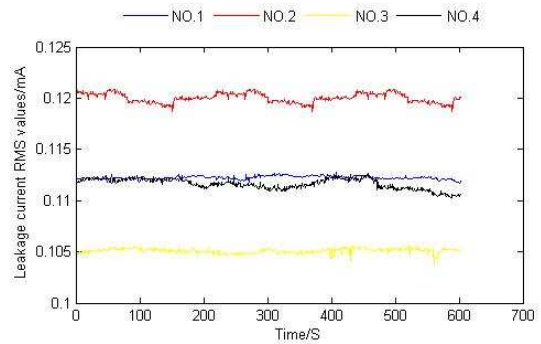

(c)Water drops, R_s=1 kΩ

Fig. 3 Leakage current RMS of different sampling resistors for the insulator with water drops

Through Fig. 2 (a)-(c) and Fig. 3 (a)-(c) it can be seen that, no matter dry and clean or water attached conditions, the RMS values of different capacity transformer has certain difference, but the difference is very small, almost negligible. Resistors with the resistance of 10 Ω, 100 Ω, 1 kΩ were used to measure the leakage current and the results in Fig. 2 (a)-(c) and Fig. 3 (a)-(c) are consistent which indicate the data is reliable.

3.2 Analysis of the 3rd Harmonic and Fundamental Ratio

Fig. 4 and Fig. 5 are the results of the 3rd harmonic to fundamental ratio of the leakage current from the four test transformers. Fig. 4 refers to the dry and clean condition and the Fig. 5 refers to the water attached condition.

Observation of Fig. 4 and Fig. 5 show that under dry and clean or water attached conditions the value of K_3 from different capacity transformers varied greatly. Resistors with the resistance of 10

Ω, 100 Ω, 1 kΩ were used to measure the leakage current and the consistent results in Fig. 4 (a)-(c) and Fig. 5 (a)-(c) indicate the data is reliable.

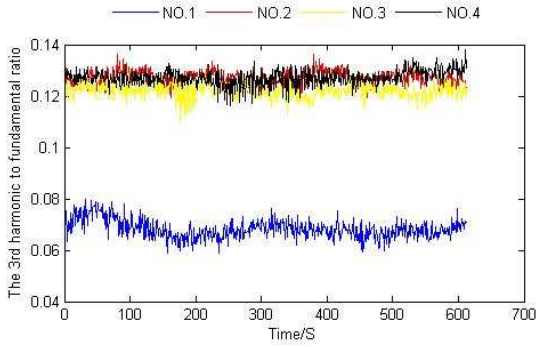

(a) Dry and clean, R_s=10 Ω

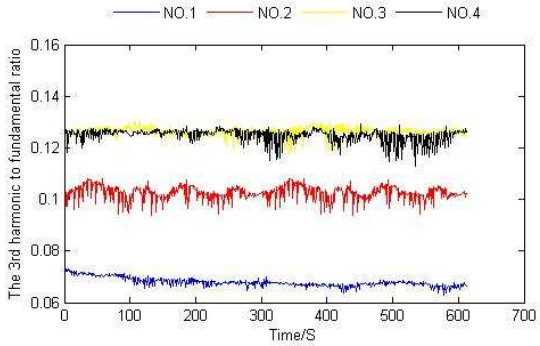

(b)Dry and clean, R_s=100 Ω

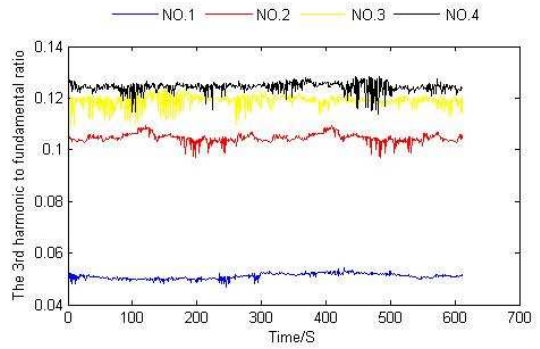

(c) Dry and clean, R_s=1 kΩ

Fig. 4 The 3rd harmonic and fundamental ratio of different sampling resistors for the insulator under dry and clean condition using test transformers with different capacity

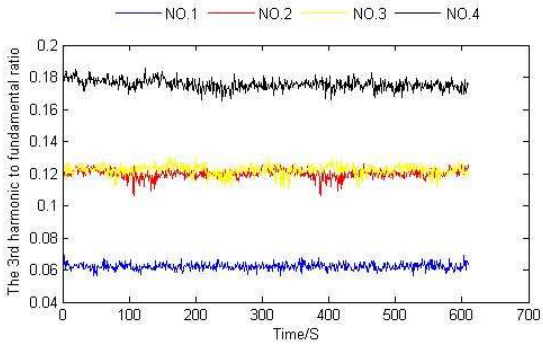

(a) Water drops, R_s=10 Ω

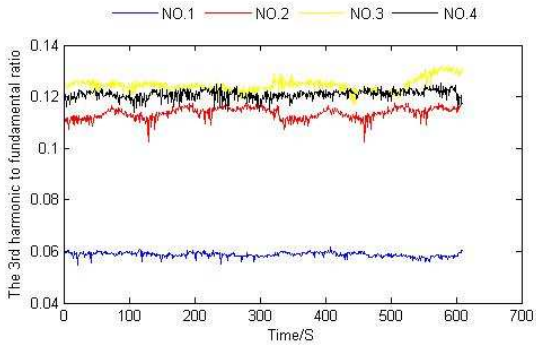

(b)Water drops, R_s=100 Ω

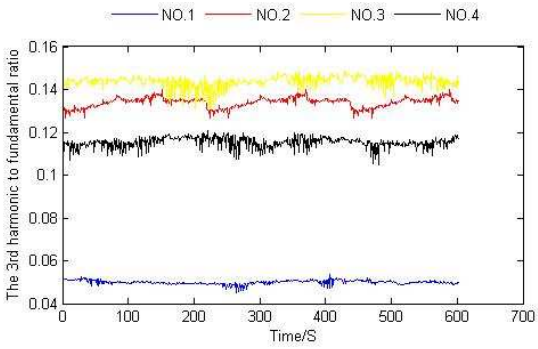

(c)Water drops, R_s=1 kΩ

Fig. 5 The 3rd harmonic and fundamental ratio of different sampling resistors for the insulator under dry and clean condition using test transformers with different capacity

3.3 Analysis of the 5th Harmonic and Fundamental Ratio

Fig. 6 and Fig. 7 show the results of the 5th harmonic and fundamental ratio of the leakage current from the four test transformers. Fig. 6 refers to the dry and clean condition and the Fig. 7 refers to the water attached condition.

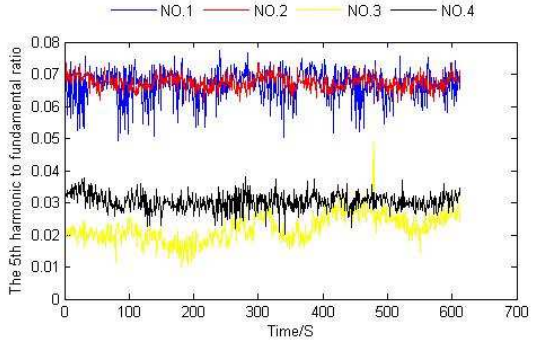

(a) Dry and clean, R_s=10 Ω

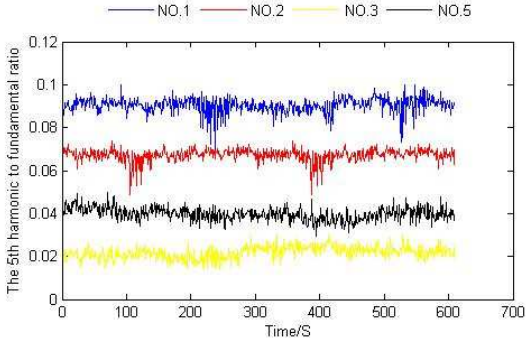

(a) Water drops, R_s=10 Ω

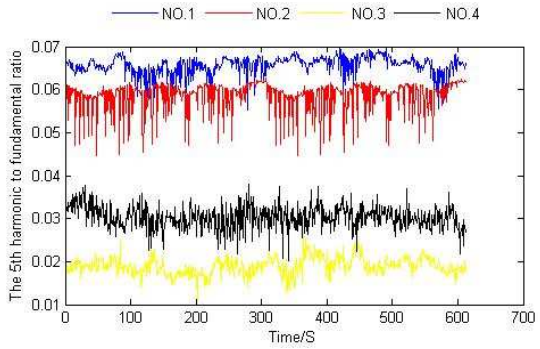

(b)Dry and clean, R_s=100 Ω

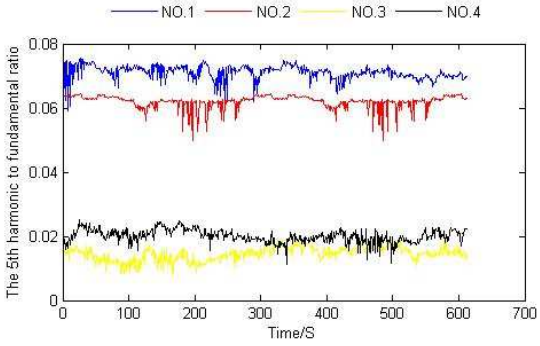

(c) Dry and clean, R_s=1 kΩ

Fig. 6 The 5th harmonic and fundamental ratio of different sampling resistors for the insulator under dry and clean condition using test transformers with different capacity

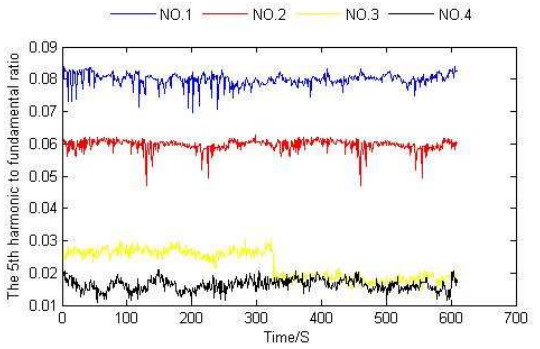

(b)Water drops, R_s=100 Ω

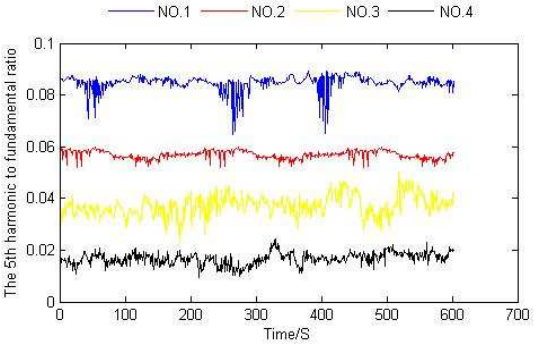

(c)Water drops, R_s=1 kΩ

Fig. 7 The 5th harmonic and fundamental ratio of different sampling resistors for the insulator under dry and clean condition using test transformers with different capacity

It can be seen from Figs. 7-8 that under dry and clean or water attached conditions there is a great difference in value of K_5 from different capacity transformers. Still the consistent results in Fig. 4 (a)-(c) and Fig. 5 (a)-(c) indicate the data is reliable.

3.4 Discussion

After the above preliminary analysis, it can be seen that the transformer capacitiy has a very small influence on the leakage current RMS value, which almost can be ignored, but has a great influence on the value of K_3 and the K_5. Table 2 shows the values of K_3 and K_5 of the insulator under dry and clean condition and water drops attached condition.The ratio of their maximum values and minimum values are also given in Table 2.

Table. 2 Values of K_3 and K_5 with the Insulator Under Different Conditions

		K_3	K_3	K_3	K_5	K_5	K_5
	Resistance	10 Ω	100 Ω	1 kΩ	10 Ω	100 Ω	1 kΩ
Dry & Clean	Max	0.138021	0.130455	0.128317	0.0775075	0.06957	0.075521
	Min	0.05867	0.06275	0.046992	0.0096592	0.010865	0.008188
	Ratio	2.352501	2.078983	2.730622	8.0242089	6.402915	9.223185
Water Drops	Max	0.185584	0.132056	0.148704	0.1001107	0.084061	0.089306
	Min	0.056393	0.054641	0.045201	0.0140348	0.010969	0.009607
	Ratio	3.290902	2.416819	3.289822	7.1330224	7.663678	9.296105

As seen in Table 2, the ratio of the maximum K_3 and the minimum K_3 under dry and clean and water drops attached conditions is 2.7 and 3.3 respectively. And the the ratio of the maximum K_5 and the minimum K_5 under the two different conditions is 9.2 and 9.2 respectively. The K_3 and K_5 are both typical leakage current characteristics and the numerical difference caused by the transformer capacity can lead to misjudgement to actual operating condition of the insulator.

4. Conclusions

a) The leakage current RMS values acquired from transformers of different capacities are almost the same. The influence of the transformer capacity on the leakage current RMS values is very slight.

b) The rations of 3rd harmonic to fundamental ratio (K_3) and the 5th harmonic to fundamental ratio (K_5) are highly affected by the transformer capacity and the values of the K_3 and K_5 acquired through transformers of different capacities vary greatly. Therefore when it comes to the leakage current characteristics of the K_3 and K_5, the transformer capacity should be taken into consideration.

References

[1] IEC 60507 IDT Artificial Pollution Tests on High-Voltage Insulators to Be Used on A.C. Systems[S], 1991.

[2] L.N. Duanmu, Y.F. Wen, B. Huang, *et al*. Research on the Characteristic of Insulator Leakage Current and Pulse Current[J]. Insulators and Surge Arresters, 6: 8-12.

[3] C. Liu, Y.X. Nie, Y.F. Wen, *et al*. Statistical Characteristics of Corona Inception Voltage of Single Insulator[J]. High Voltage Engineering, 2002, 28(8): 19-21.

[4] M.A. Douar, A. Mekhaldi, M.C. Bouzidi. Welch Periodogram Analysis of the Leakage Current on Insulator Model under Wetted Contaminated[C]. MELECON 2010-2010 15th IEEE Mediterranean Electrotechnical Conference, Valletta, Malta, 2010: 1636-1641.

[5] M.A. Douar, A. Mekhaldi, M.C. Bouzidi. Flashover Process and Frequency Analysis of the Leakage Current on Insulator Model under non-Uniform Pollution Conditions[J]. IEEE Transactions on Dielectrics and Electrical Insulation, 2010, 17(4): 1284 – 1297.

[6] J.H. Lv, Y.F. Wen, K.Z. Wen, *et al*. Analysis of Resistive and Capacitive Component of Leakage Current for Single Insulator[J]. Water Resources and Power, 28(5): 135-138, 122.

[7] L.N. Duanmu. Research on the Leakage Current Characteristics of Insulators[D]. Wuhan, China: Huazhong University of Science and Technology, 2009.

[8] S.S. Zheng. Study on the Pollution Flashover Mechanism of Composite Insulator in Contamination and Wet Conditions[D]. Baoding, China: North China Electric Power University, 2004.

Advanced Materials Research Vols. 986-987 (2014) pp 1969-1972

doi:10.4028/www.scientific.net/AMR.986-987.1969

Multi-level Cascaded H-bridge Inverter Based on Three Harmonic Injection Method

Ye Manyuan, Li Song

Department of Electrical Engineering School, East China jiaotong University

Nanchang , 330013 Jiangxi Province, China

email: yemanyuan1@163.com; jxlisong1@163.com

Keywords: Cascaded H-bridge ; Three Harmonic Injection Method; Harmonic Distortion

Abstract. This paper introduces seven-level Cascaded H-bridge (CHB) inverter and work principle. Then, the strongpoint and disadvantage of multi-level inverter usual PWM technologies are analyzed and compared. We find that multi-level cascaded inverter based on three harmonic injection method have two advantages via analysis. The voltage modulation index can increase 1.15. The equivalent switching frequency of H-bridge inverter's load voltage is N times of each cell switching frequency. At last, H-bridge inverter was investigated with simulation and experiment. The results prove that the analysis is correctness and validity.

Introduction

As electric drive technologies, especially the development of VVVF control technology, large-capacity high-voltage multi-level inverter control technology has been widely used. Multi-level technology development so far, mainly in the following 4 basic topologies[1]: diode clamped (Diode-Clamped); flying capacitor clamping type (Flying-Capacitors); capacitor clamp (Capacitor-Clamped); H bridge cascade (Cascaded H-bridge, CHB) [1,2].The CHB inverter has the following advantages: the output voltage level higher in the case of devices in series is not required; harmonic distortion (THD) in the lower switching frequency operation is smaller; electromagnetic interference (EMI) is smaller. So CHB inverter has been widely used in the large capacity of high-power frequency conversion as well as flexible power transmission and distribution areas (FACTS)[3,4].

The multi-level inverters have certain advantages over conventional two level inverters. Firstly, the voltage stress on each power devices is only half of dc bus voltage side. That's to say, both the amplitude of dc bus voltage and the inverter capacity can be doubled when using the devices of similar voltage rating. Secondly，for a given switching frequency and a certain control method, the harmonic in output voltage and current is greatly reduced. Hence, it's THD is far less than that of two level inverts. Finally, the current waveform of three inverter input side can guarantee a certain degree of sine, even in a low switch frequency.

The PWM control methods can be divided into three categories for multi-level inverter, namely triangular carrier PWM technique, a special harmonic elimination modulation (SHEPWM) [5] and space vector modulation technique (SVPWM)[6]. SVPWM technology with high voltage utilization, advantages of low harmonic content, but the method in the synthesis of more complex when the voltage space vector. SHEPWM lower switching frequency can be obtained the better the quality of voltage waveform. This is particularly important for high-voltage large-capacity inverter. SPWM technology can significantly reduce the output harmonics, and because the switching frequency of each element does not require very high, but also reduces the switching loss of the device. If we adopt harmonic injection method can further improve the voltage regulation system, to reach 1.15, thereby improving inverter efficiency [7].

This article describes the H-bridge cascaded seven-level inverter topology and working principle and gives three harmonic injection method phase shifted modulation control technology. and then establish the simulation model with Matlab/Simulink, finally, prove that thmulti-level inverters has a good performance when use three harmonic injection method control method.

Topology Configuration of CHB Inverter

The cascade H-bridge multi-level inverter topology was shown in Fig.1. It is a series by a single individual from the inverter unit. When the switch S_{11}, S_{21}, S_{12}, S_{22}, S_{13} and S_{23} simultaneous conduction, other devices are turned off, H bridge unit H1, H2 and H3 are the same and equal to the output voltage E. We can easily get the case CHB level voltage equal to the phase inverter, and the sum of the size equal to 3E. And so on, as long as we have targeted on and off the corresponding device, we can make CHB phase voltage inverter outputs the following seven levels: 3E, 2E, E, 0,-E,-2E and - 3E, so called seven-level CHB inverter.

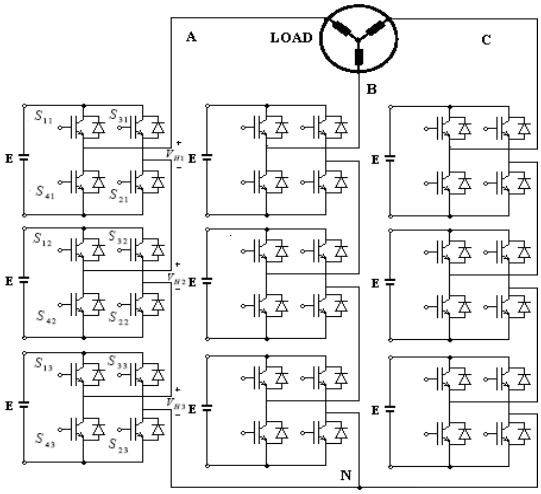

Fig. 1 Topology of the seven-level cascaded H-bridge inverter

Third harmonic injection phase shift modulation principle

Voltage shift modulation is one way based carrier modulation. If each cascade unit DC voltage are equal, shown in Figure 1, if you want the number of CHB inverter voltage level is m, then needed m-1carriers , and these carriers required phase shift turn 360 º / (m-1). All carrier frequency has the same amplitude, then compare with the modulated wave to generate a control pulse signal for each switching device. Simulation waveforms have shown the basic principle of the 7 level CHB inverter phase shift modulation in Figure 2. We can see 7 level CHB inverter A phase modulation wave v_{mA} intersect with the carrier v_{cr1}, v_{cr2} and v_{cr3} respectively, and obtain the switching pulse signal of S_{11}, S_{12} and S_{13}. The carrier v_{cr1-}, v_{cr2-} and v_{cr3-} different π between each v_{cr1}, v_{cr2} and v_{cr3} respectively.

Which injected a third harmonic expression test phase sinusoidal modulation signal is as follows:

$$\begin{cases} v_{mA} = m \cdot \sin(\omega_0 t) + k \sin(3\omega_0 t) \\ v_{mB} = m \cdot \sin(\omega_0 t + 120°) + k \sin(3\omega_0 t) \\ v_{mC} = m \cdot \sin(\omega_0 t + 240°) + k \sin(3\omega_0 t) \\ v_{mK} = k \sin(3\omega_0 t) \end{cases} \quad (1)$$

By the test (1) shows that the third harmonic is injected in the original three-phase symmetric positive signals while adding a third harmonic signal $k \sin(3\omega_0 t)$, In order to avoid the injection of the third harmonic modulation signal is modulated with the triangular carrier wave, the overshoot does not occur, the amplitude of the added requirement of k where the third harmonic signal must be between 0.15 to 0.2 . Figure 2 shows the third harmonic injection phase shift modulation multi-level inverter works, where the modulation m_a is set to 1.15 and k equal 0.18, seen from the figure, just no overshoot.

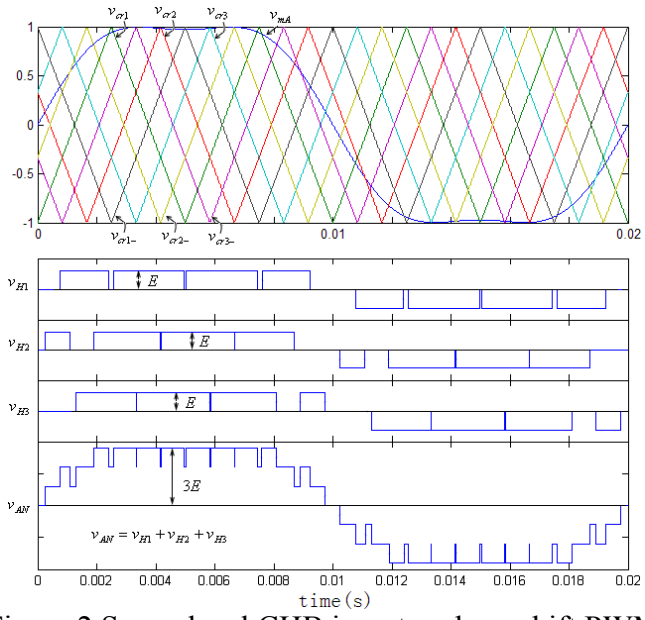

Figure 2 Seven level CHB inverter phase shift PWM

(m_f=4, m_a=1.15, f_m=50Hz, f_{cr}=200Hz, k=0.18)

Simulation research

In order to obtain the phase voltage v_{AN} and the line voltage v_{AB} waveform in the trapezoidal modulation and the size of the THD for 7 CHB Inverter, this paper give simulation study with Matlab/Simulink software. The simulation parameters are as follows: m_f=12; m_a=1.15; k=0.18; f_m=50Hz; f_{cr}=600Hz ; E=100V. The simulation model was shown in Figure 3. Phase voltage v_{AN} and the line voltage v_{AB} waveform and its harmonic spectrum analysis as shown in Figures 4 and 5 as follows.

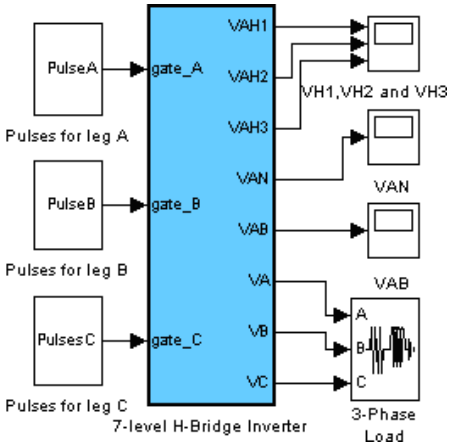

Fig.3 Diagram of simulation model

Seen from Figure 4, the phase voltage v_{AN} has seven voltage levels and line voltage v_{AB} has 13 voltage levels. So the voltage waveform of CHB inverter has a low THD and electromagnetic interference (EMI) at lower switching frequencies (such as simulation parameters = 600Hz). Because of these advantages, CHB inverter frequency high power capacity has been widely applications.

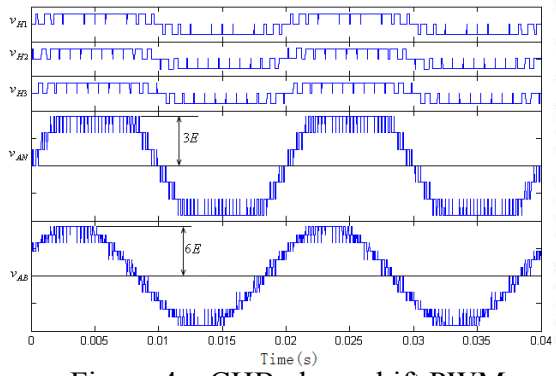

Figure 4 CHB phase shift PWM inverter simulation waveform shape

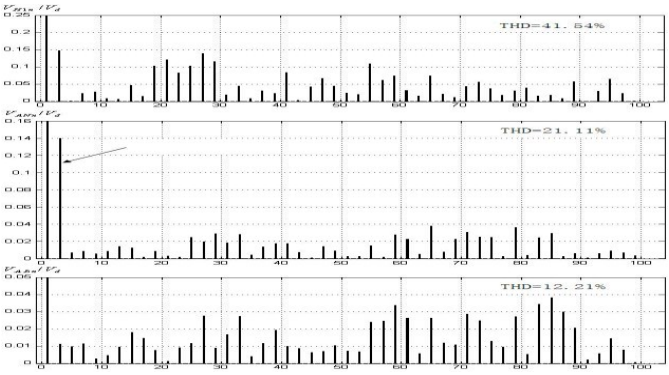

Figure 5 Harmonic spectrum of v_{H1}, v_{AN} and v_{AB}

Harmonic spectrum can be seen from Figure 5, in the case of the above parameters, the THD of v_{H1}, v_{AN} and v_{AB} are 41.54%, 21.11% and 12.21% respectively. Because of injection the third harmonic wave to modulation wave, so the third harmonic frequency spectrum component becomes large. However, due to the multi-level inverters are used for high-voltage high-power three-phase system, three-phase output harmonic cancel each other out. This can be obtained from line voltage v_{AB} spectrum. This illustrates the use of the third harmonic injection method to increase the output voltage amplitude at the same time, did not affect the output voltage THD, this is the biggest advantage of using the third harmonic injection method.

Conclusion

In this paper, the third harmonic injection phase shift PWM inverter control CHB were studied, the following conclusions:

Adopt harmonic injection method to increase the output voltage amplitude at the same time, it will not affect the output voltage THD. This study can also be extended to the capacitance diode clamp circuit and clamp circuit, the control method is fully consistent with this article.

Reference

[1] M.F. Aiello, P.W. Hammond and M. Rastogi, 'Modular Multi-level Adjustable Supply with Parallel Connected Active inputs,' US Patent #6,301,130, 2001.

[2] Wu Bin, Song Pinggang. Comprehensive Analysis of Multi-Megawatt Varible Frequency Drives[J], Transaction of China Electrotechnical Society, 2004,19(8):40-52.

[3]Atalik T，Deniz M，Koc E，et al．Multi-DSP and-FPGA-based fully digital control system for cascaded multilevel converters used in FACTS applications[J]．IEEE Transactions on Industrial Electronics，2012，8(3)：511-527．

[4]Jayasingha S D G，Vilathgamuwa D M，Madawala U K．Cascade multilevel static synchronous compensator configuration for wind farms[J]．IET Power Electronics，2011，4(5)：548-556．

[5]Wanmin Fei, Xiaoli Du, Bin Wu. A Generalized Half-Wave Symmetry SHE- PWM Formulation for Multilevel Voltage Inverters[J], IEEE Transactions on Industrial Electronics, 57(9): 3030-3038, 2010

[6] Chen Guocheng, SongWenxiang, Wu Hui and Sun Chenbo, A novel SVPWM strategy considering neutral-point potential balancing for three-level NPC inverter[J],Journal of Shanghai University (English Edition), 2006, 10(1) : 53 - 58.

[7]Kouro S，Malinowski M，Gopakumar K，et al．Recent advances and industrial applications of multilevel converters[J] ． IEEE Transactions on Industrial Electronics，2010，57(8)：2553-2580．

Advanced Materials Research Vols. 986-987 (2014) pp 1973-1976

doi:10.4028/www.scientific.net/AMR.986-987.1973

Parameter Optimization of Virtual Impedance for Parallel Inverter

Ping WANG[1, a], Liu YANG[2, b]

[1] Electrical Engineering and Automation Department Smart Grid Key Laboratory of Education Ministry, Tianjin University, Tianjin, 300072, China

[2] Electrical Engineering and Automation Department Smart Grid Key Laboratory of Education Ministry, Tianjin University, Tianjin, 300072, China

[a]email: pingw@tju.edu.cn, [b]email:laura-yl1990@163.com

Keywords: Virtual Impedance; Parameter Optimization; Dynamic Performance

Abstract. This paper deals with parameter optimization of virtual impedance of parallel inverter. Conventional design methods determine parameters by observing the changes of amplitude-frequency and phase-frequency curves of the equivalent impedance. However, those methods always neglect the dynamic performance of inverters in parallel. This paper proposes a novel method to optimize the coefficients of virtual impedance and experiments show that new method improves the dynamic performance of parallel inverter effectively, as well as stability and flexibility.

Introduction

Parallel inverter with wireless load-sharing control realizes that a few of inverters connect to or exit from system without affecting its operation. However, because of the differences of line impedance or reference voltage, circulating current among inverters is inevitable [1]. P/Q drooping method is proposed to solve above problem. Nevertheless, this method always neglects the resistance part of inverter's equivalent impedance and line impedance, leading to an unsatisfactory effect of restraining circulating current. Other methods, such as decoupling power or changing droop equations, result in large calculation and unstable response [2]. To solve those problems, virtual impedance is added into control, making equivalent impedance of inverter equal to pure inductance or resistance [3]. Conventional methods of designing virtual impedance refer to the trend of amplitude-frequency and phase-frequency curves of Bode diagram when parameters change. Those methods possess lots of shortcomings, such as, dynamic property isn't taken into account and so forth.

This paper adds virtual impedance into control, making equivalent impedance of inverter equal to pure resistance. Based on the fact that position change of zeroes and poles of inverter's equivalent impedance affects parallel inverter's working performances (including steady state and transient state) of parallel inverter, this paper proposes a novel method to optimize the coefficients of virtual impedance. Simulation results have proved the correctness and effectiveness of proposed method.

Analysis of Parallel Inverter Model

There is a model for two inverters in parallel, consisted of a single-phase IGBT full-bridge and an LC output filter, supplying power to load. This model is able to be equal to a voltage source in series with equivalent impedance. The equivalent circuit of two inverters in parallel is shown as Figure 1.

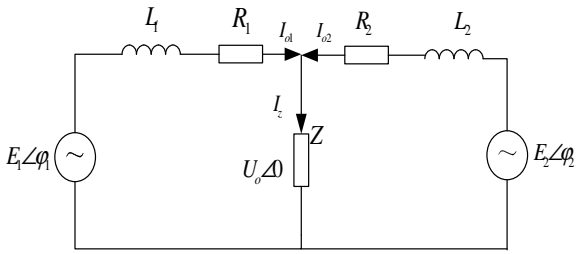

Fig.1. Equivalent circuit of two parallel inverters

Circulating current between inverters is used to measure the accuracy of power sharing. It is defined as formula (1).

$$\dot{I}_H = \frac{1}{2}(\dot{I}_{o1} - \dot{I}_{o2}) = \frac{1}{2}(\frac{\dot{E}_1 - \dot{U}_O}{R_1 + jX_1} - \frac{\dot{E}_2 - \dot{U}_O}{R_2 + jX_2}) \tag{1}$$

Assuming that equivalent impedance is equal, formula (1) can be rewritten as

$$\dot{I}_H = \frac{1}{2}(\frac{\dot{E}_1 - \dot{E}_2}{R + jX}) \tag{2}$$

Formula (2) shows that the value of circulating current is proportional to the differences of inverter's output voltage, including amplitude and phase. Meanwhile it has an inverse relationship with the equivalent impedance. That leads to two methods to restrain the circulating current, decreasing voltage difference and increasing impedance value.

Analysis of Equivalent Impedance Based on Virtual Impedance

To make output voltage track reference voltage rapidly and efficiently, double closed loop control is used in this paper. PI adjustment is applied to outer voltage loop while P adjustment is applied to inner current loop. System block diagram including virtual impedance is shown as Figure 2.

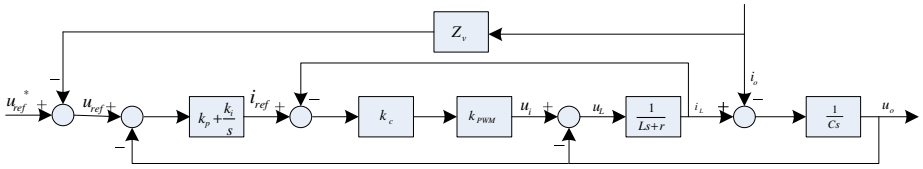

Fig.2. System block diagram with virtual impedance

The following formula is obtained by Figure 2.

$$U_o = G(s)U_{ref}^{*}(s) - Z_o^{'}(s)I_o(s),\ Z_o^{'}(s) = Z_v(s)G(s) + Z_o(s) \tag{3}$$

Designing of virtual impedance is shown as formula (4).

$$Z_v(s) = R_v - K_v s \tag{4}$$

The equivalent impedance with virtual impedance is shown as formula (5).

$$Z_o^{'}(s) = \frac{(L - K_v k_{PWM} k_c k_p)s^2 + (k_{PWM} + r + R_v k_{PWM} k_c k_p - K_v k_{PWM} k_c k_i)s + R_v k_{PWM} k_c k_i}{LCs^3 + (rC + k_c C)s^2 + (1 + k_{PWM} k_c k_p)s + k_{PWM} k_c k_i} \tag{5}$$

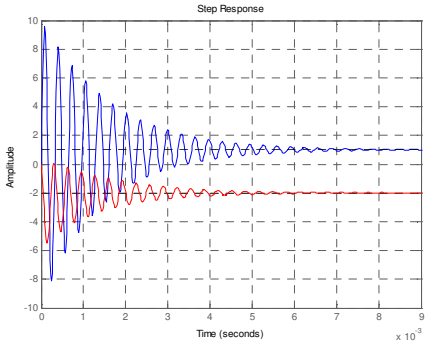

Fig.3. Step response

To design the parameters, *Rv* and *Kv*, conventional methods generally refer to Bode diagram and take experience value into consideration, which is unsatisfactory to dynamic property. Figure 3 (blue curve is on behalf of conventional method) shows its poor step response, such as, huge overshoot value, long response time and sharp fluctuations. That probably causes large instantaneous circulating current peak, slow circulating current drop speed when abrupt change of load occurs, which may damage switches of inverter circuit.

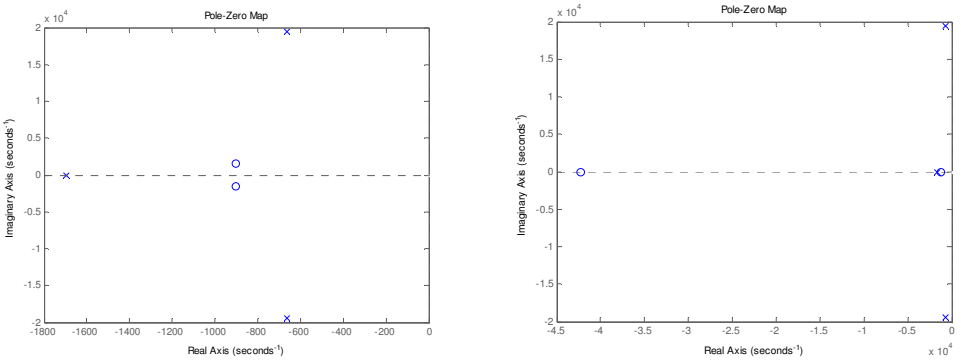

(a) Conventional method (b) Optimal method

Fig.4. Pole-zero plot of equivalent impedance

Figure 4(a) shows the pole-zero plot of equivalent impedance of conventional method. There are three poles (a real pole, two conjugate poles) and two conjugate zeroes. Three poles locate to the left of imaginary axis, guaranteeing the stability of system. The real pole has the effect to slow down response speed while the existence of conjugate zeroes has an influence on increasing overshoot.

Optimal method keeps dominant poles and creates a dipole to reduce the effects of the real pole. Parameters are given by formula (6). P_0 is value of the real pole.

$$R_v = \frac{p_0(k_{PWM}k_p + rk_p - Lk_i)}{k_p(k_{PWM}k_ck_i - p_0k_{PWM}k_ck_p)}, K_v = \frac{L}{k_{PWM}k_ck_p} \tag{6}$$

The pole-zero plot of equivalent impedance of optimal method is shown as Figure 4(b). Location of three poles does not change. There are two real zeroes. One is so far from imaginary axis that its influence can be neglected. The other constitutes a dipole with the real pole, which weakens the influence of the real pole. Its step response is shown as Figure 3 (The red curve). Comparing with conventional methods, novel method results in less oscillation, shorter adjusting time and slighter overshoot.

Test results

This paper has set up the two inverters in parallel based on Matlab simulation platform. Simulation experiment is conducted when inverter connects to or exits from system. The result is as follows.

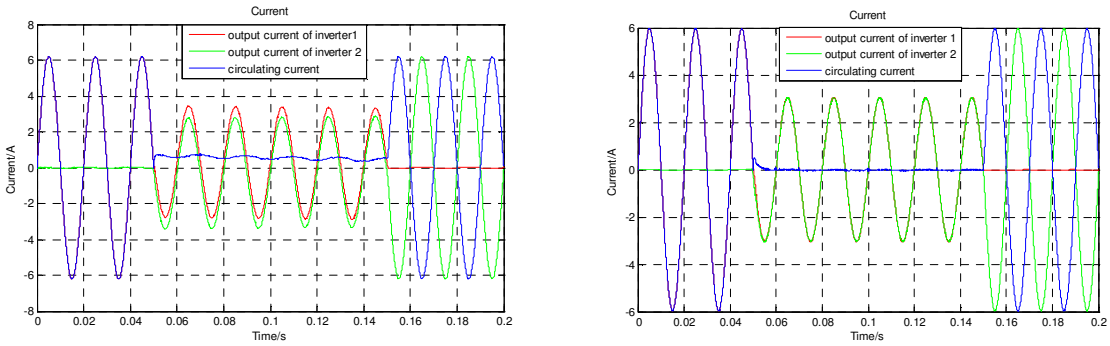

(a) Conventional method (b) Optimal method

Fig.5. Waveforms of inverter output current and circulating current

Figure 5 depicts the waveforms of inverter output current and circulating current when inverter connects to or exits from system. Before 0.05s, inverter 1 is running alone. At the moment of 0.05s, inverter 2 is connected into the system and two inverters are running at the same time. At the moment of 0.15s, inverter 1 exits from the system, that is, inverter 2 is running alone. The red curve is the output current waveform of inverter 1, while the green one is inverter 2. The blue one is circulating current between two inverters.

Contrasting the waveforms respectively, conventional method is unable to lower down circulating current, whose value maintains around 0.6A. While optimal method is able to reduce the circulating current to 0.05A within 0.01s. The dynamic and steady-state performance all meets the requirements, which verifies the validity of this method.

Conclusion

Based on analysis of equivalent model of inverters in parallel and influence by zero-pole position, a novel method for parameter optimization of virtual impedance has been proposed. Simulation depicts that new method has a positive influence in decreasing instantaneous peak circulating current, speeding up the decline of circulating current, as well as reducing the distortion of output current. The dynamic and steady-state performance of multiple inverters in parallel operation is improved effectively.

Acknowledgement

In this paper, the research was sponsored by the Research Fund for the Doctoral Program of Higher Education (Project No. 20120032110070).

References

[1] Tuladhar A, Jin H, Unger T, et al. Control of Parallel Inverters in Distributed AC Power Systems with Consideration of Line Impedance Effect[J]. IEEE Transaction on Industrial Applications, 2000, 36(1)：131-138.

[2] Yan Li, Yun Wei Li, et al. Decoupled Power Control for an Inverter Based Low Voltage Microgrid in Autonomous Operation[C]//IEEE 6th International Power Electronics and Motion Control

[3] Guerrero J M, de Vicuna L G, Matas J, et al. Output Impedance Design of Parallel-connected UPS Inverters with Wireless Load-sharing Control[J]. IEEE Transactions on Industrial Electronics, 2005, 52(4)：1126-1135.

[4] Wei Yao, Min Chen, Matas J, et al. Design and Analysis of the Droop Control Method for Parallel Inverters Considering the Impact of the Complex Impedance on the Power Sharing[J]. IEEE Transactions on Industrial Electronics, 2011, 58(2)：576-587.

[5] Fang Tianzhi, Ruan Xinbo, Xiao Lan, et al. An improved distributed control strategy of parallel inverters[J]. Proceedings of the CSEE, 2008, 28(33)：30-36(in Chinese).

[6] Zhang Yao, Ma Hao, Lei Biao, et al. Analysis of dynamic performance for parallel operation of inverters without wire interconnections[J]. Proceedings of the CSEE, 2009, 29(3)：42-48(in Chinese).

[7] Wang Chengshan Xiao Zhaoxia, Wang Shouxiang. Multiple feedback loop control scheme for inverters of the micro source in microgrids[J]. Transactions of China ElectrotechnicalSociety, 2009, 24(2)：100-107(in Chinese).

Advanced Materials Research Vols. 986-987 (2014) pp 1977-1983

doi:10.4028/www.scientific.net/AMR.986-987.1977

PV Cells Power Generation System Modeling Based on Heat Energy Efficiency

LI Feng-feng[1, a], WU Qiu-xuan[1,b*],HUANG Li-Juan[1, c],HUANG Yu-jie[1, d]

[1.] Institute of Electrical Automation, Hangzhou Dianzi University, Hangzhou Zhejiang 310018, China;

[a]ema:licyfeng@163.com,[b]ema:wuqx@hdu.edu.cn,[c]ema:huanglj0711@163.com,

[d]ema:395447986@qq.com

Keywords: Temperature, Heat, PV cell, PV power generation system

Abstract: Temperature is one of the important factors affecting the power generation efficiency of PV cells. In order to improve the efficiency of photovoltaic power generation systems and heat utilization efficiency, we used Matlab/Simulink to build photovoltaic power system analysis model based on thermal power. By changing the heat and illumination input to the photovoltaic cell model and the heat generated by the battery we got the characteristics and temperature characteristics of the photovoltaic cell the system model, the photovoltaic power generation system model and the output power correction, etc. We got the environmental temperature change equation through the actual air temperature and curve fitting and used real and detailed data to compare the data obtained using the equation for online correction. PV cells temperature factor was used to get the PV cells temperature with the environment temperature changes. In order to get PV module thermal /energy efficiency the dates was processed and analyzed by using Matlab and Excel through actual observation data of school 120KW PV power station. The results showed that power generation efficiency increased and year average efficiency PV improved 21.3279% through the use of some heat about PV cells.

1 Introduction:

Crystalline silicon photovoltaic cell is now the most widely used photovoltaic cells, which accounts for about 90%. The solar energy projecting on the PV panels, less than a quarter of which converted into electricity, the nearly three-quarters of the remaining converted into heat energy emisstioning into the environment; Temperature of crystalline silicon photovoltaic cell is one of the main factors affecting the energy conversion efficiency and power generation of photovoltaic cells , and the photoelectric conversion efficiency decreases with the battery temperature rises linearly, and photovoltaic cells increase by 1 ℃, the output power reduce about 0.4%-0.5% [1], the photovoltaic battery temperature rise because of solar energy which fail to convert into electricity converting into heat energy. The rise of the temperatures cause the increase of Io index and the sharp decline of the open circuit voltage U_{oc} [2], in order to reduce the working temperature of photovoltaic cells, two technical solutions can be used: The first is as most as possible to reduce PV cells photo thermal conversion, the second is to export the heat as soon as possible, the second is adopted in this paper[3].

This model simulated the photovoltaic modules in the corrected ambient temperature gained the output power value, comparison with the output power value of PV modules at a fixed ambient temperature, and the heat of photovoltaic battery components that is higher than the ambient temperature was exported, and the thermoelectric efficiency analysis was gained only using 1% of that part heat, and then the thermoelectric efficiency analysis of 120 kw photovoltaic power station using the results was obtained.

2 The Solar Cell Module Model

In this article the construction of the photovoltaic cell model is based on two diode model and the characteristics of simulation of the PV cells output as shown in figure(refer with: Fig. 1). The input

light and temperature not only influence on the output power, but also can simulate the temperature influence on electronic devices, such as parameter N, N2, T1PH1, TXIS1, TXIS2, etc[1, 4-6].

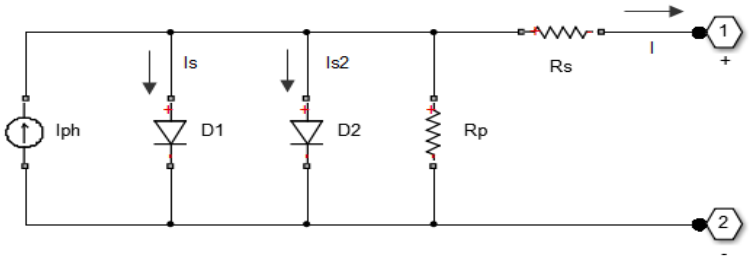

Fig. 1, The equivalent circuit of photovoltaic cells

An output current of equations (refer with: Eq. 1)

$$I = I_{ph} - I_s * (e^{(V+I*R_s)/(N*V_t)} - 1) - I_{s2} * (e^{(V+I*R_s)/(N_2*V_t)} - 1) - (V + I * R_s) / R_p \quad (1)$$

Where I_{ph} is the photocurrent (A), I_s and I_{s2} are two diode reverse saturation current (A).R_2 is the equivalent series resistance of the photovoltaic cell (Ω). R_p is the equivalent resistance of the photovoltaic cell (Ω). N and N_2 are the diode ideality factor of two .V_t = k * q / T is the thermal voltage of the photovoltaic cell (V). K is Boltzmann's constant (1.38 × 10e-23J / K). T is the temperature of the simulation device , q behalf of the charge volume (1.6 × 10e-19C) [5] .$I_{ph} = I_{ph0}$ * I_r / I_{ro}, I_r is the exposure to the light intensity photovoltaic cells on the unit W/㎡, I_{ph0} the current illumination I_{r0} produce is generally short-circuit current , V is the voltage by a PV cell electrical port.

When the working conditions of PV arrays are changing, parameters are to be changed and it can get different results in different working conditions [1, 7]. Where I_{ph} (t), such as equations (refer with: Eq. 2).

$$I_{ph}(t) = I_{ph(nom)} * (1 + T1PH1 * (T - T_{meax})) \quad (2)$$

T1PH1 is the first of illumination factor. I_{ph}, T_{meax} is the reference temperature. I_{s1}, I_{s2}, R_s and R_p are related to temperature. The formulas of 3 reference Matlab help files .In the formulas TXIS1 is I_s temperature index; TXIS2 is Is2 temperature index; TRS1 is R_s temperature index;TRP1 is R_p temperature Index. $I_{ph\ (nom)}$, $R_{s\ (nom)}$ and $R_{p\ (nom)}$ are based on the temperature 300K, i.e. T_{meax} = 300K. R_p and R_s are constant, close to the simulation results with the actual value.

2.1 The Temperature Variation of The Photovoltaic Cell

This article single photovoltaic component model not only has the temperature input, and photovoltaic cell heat preservation unit. The related parameters of the photovoltaic cell model are related to temperature, it can well reflect the component characteristics of semiconductor, and has good power tracking. Below is the model simulation of the single photovoltaic cells operation, as shown in figure (refer with: Fig. 2).

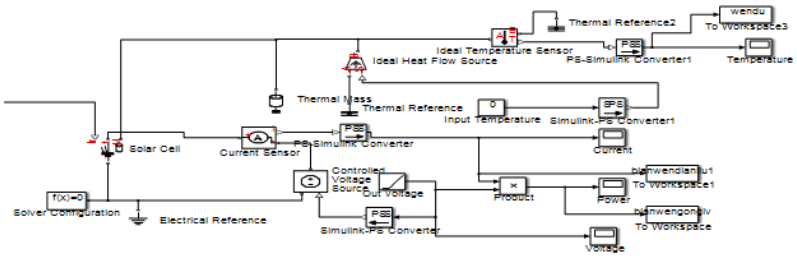

Fig. 2, Single photovoltaic cell model

Where in a main parameters I_{sc} = 7.34 (A), V_{oc} = 0.6 (V), Ir0 = 1000 (W/㎡), N = 1.5, N_2 = 2, EG = 1.11, TXIS2 = TXIS1 = 3, in the same simulation under illumination 1000 W/㎡ at a temperature of

25 ℃, 35 ℃, 45 ℃, 55 ℃ under the PV curve, as shown in figure (refer with: Fig. 3) was run under different temperature curve; Battery temperature is 25 ℃, the light intensity of 300,500,800,1000 W/㎡ under the PV curve, as shown in figure (refer with: Fig. 4) run curves under different illumination.

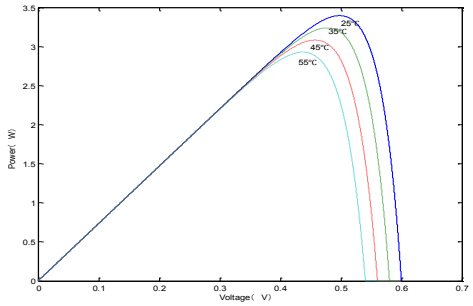

Fig. 3, Different temperatures P-V curve

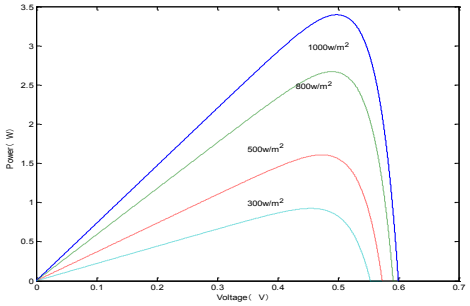

Fig. 4, Under different illumination P-V curve

By changing TPH1, TXIS1, TXIS2 values can change the output power of the photovoltaic cell, simulation TPH1 = 1, TXIS1 = 3, TXIS2 = 3, and TPH1 = 10, TXIS1 = 3, TXIS2 = 3, the resulting graph omitted. PV modules to build the model for the next figure 5, which is 72 PV module panels in series.

3 Photovoltaic Systems

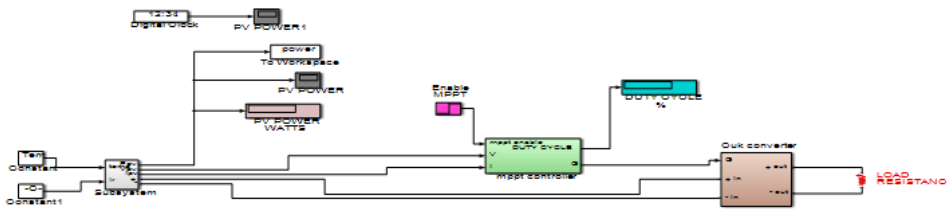

Fig. 5,Independent photovoltaic power generation system model

Figure (refer with: Fig. 5) is to simulate independent photovoltaic power generation system which includes PV modules, MPPT module, load , PV modules and 72 components of photovoltaic cells. Photovoltaic cells for each set of parameters are I_{sc} = 7.34 (A), V_{oc} = 0.6 (V), I_{r0} = 1000 (W/㎡), N = 1.5, N_2 = 2, EG = 1.11, TXIS2 = TXIS1 = 3, with reference to the actual solar cell modules, the output power is 250W, the number of batteries is 72, the open circuit voltage is 43.5V, and the operating temperature of -40 ~ 85 ℃.

3.1 The Maximum Power Point Tracking and Power Correction

In order to get maximum power point of other temperature, we used the curve fitting method to get the other power point average temperature .In figure (refer with: Fig. 6), blue dots represent the corresponding power value of the temperature. The red line is through fitting, and the equation of the curve such as equation (refer with: Eq. 3).Temperature-open circuit voltage of the two curves is probably a slope negative line, and the authentication process of solar module is called solar energy components of voltage temperature coefficient. Due to the power value is obtained by model simulation data, tracking some fluctuations in the operation of the power, so using the quadratic function, this error is smaller.

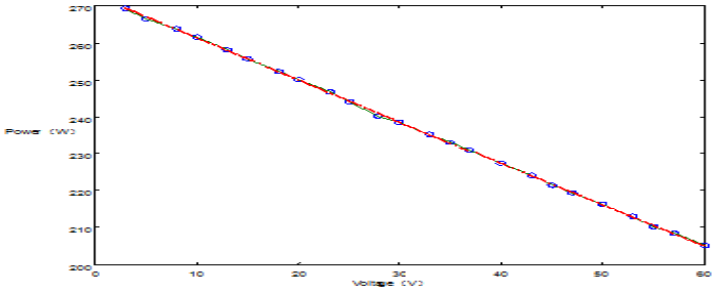

Fig. 6, Curve fitting different power points

$$F(x) = 0.0003x^2 - 1.1493x + 272.8314 \quad (3)$$

3.2 Environmental Temperature Changes Equations

The accurate simulation of the actual weather change rule is the important basis for model to get the final result . Through the analysis of the variation of environment temperature in summer one day, we can find a few main points, through curve fitting equation of environment temperature change. Through figure (refer with: Fig. 7), we can see that the temperature changes must by piecewise fitting; Figure (refer with: Fig. 8) is the effect after the fitting curve .the figure of the blue line represents the range of the left side of the equation, such as equation (refer with: Eq. 4) (which is based on the maximum temperature cut-off point), red for interval on the right side of the equation, such as equation (refer with: Eq. 5).

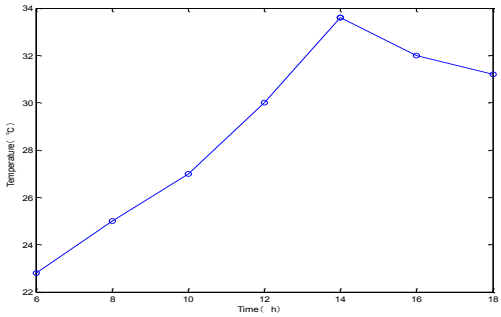

Fig. 7 The change of environmental temperature

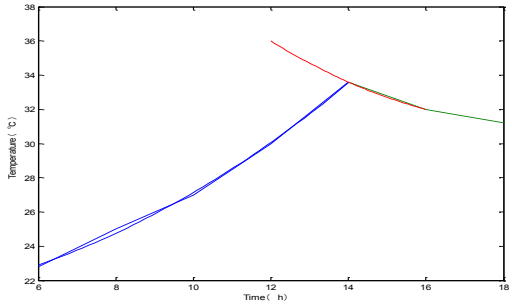

Fig. 8 The temperature curve fitting

$$F(x) = 0.0679x^2 + -0.0271x + 20.6229 \quad (4)$$

$$F(x) = 0.1x^2 - 3.8x + 67.2 \quad (5)$$

In this paper, Hangzhou University of Electronic Science and Technology 120KW photovoltaic systems were compared and measured temperature correction as tables 1.

Form 1 Temperature correction

Month	Jan	Feb	Mar	Apr	May	Jun	Jul	Aug	Sep	Oct	Nov	Dec
Temperature correction value	-1.4℃	-1.5℃	0℃	-0.8℃	0.3℃	-2℃	-2.8℃	0.5℃	0℃	-0.6℃	-1.9℃	-0.3℃
Percentage	0.09%	0.54%	0.67%	0.49%	0.71%	0.53%	0.61%	0.56%	0.63%	0.63%	0.28%	0.39%

Form the temperature of the corresponding month is revised correction value every day, to the fitting values on the basis of the value. Through curve fitting of the fitting curve of temperature change value, it is concluded that the value of the need for two hours before the correction. Because the temperature is from eight in the morning to 6 o 'clock in the afternoon, recording every minute value, through the actual values of total temperature t1 and the value is obtained by fitting curve with the sum t_2, the difference is: $t_3 = t_2 - t_1$; The percentage for: $t_3 / t_1 * 100$.

4 The Temperature Coefficient of The Photovoltaic Battery Solution

The temperature of the photovoltaic cell components affect the magnitude of its output current.In order to solve the temperature coefficient of the T_p photovoltaic cells components, photovoltaic cell components based on thermodynamic analysis model. Model contained in the absorption of solar energy loss in the transformation output of electricity, thermal radiation, convection and heat stored in the panel.Tp rate such as equation (refer with: Eq. 6).

$$(mCp_{module})\frac{dT_p}{dt} = Q_{in} - Q_{rad} - Q_{conv} - Q_{elect} \tag{6}$$

$mC_{pmodule}$, PV modules in the effective capacity of the temperature T_p; Q_{in} ,absorbed solar module (W); Q_{rad} , radiative heat loss; Q_{conv} , convective heat loss (W); Q_{elect} ,generated power (W). Qin as the expression of which equation (refer with: Eq. 7).

$$Q_{in} = a_{abs}GS_p \tag{7}$$

a_{abs} , total absorption coefficient; S_p , PV modules with a total area; G , cell surface total solar irradiance; Eq.8 as an expression which Q_{radn}

$$Q_{radn} = Q_{radn-ground} + Q_{radn-sky} \tag{8}$$

Formula 8 Qrand-ground as in Formula 9, Qrand-sky equation (refer with: Eq. 9):

$$Q_{radn-ground} = S_pF_{pg}\sigma(\varepsilon_pT_p^4 - \varepsilon_gT_g^4) \tag{9}$$

$$Q_{radn-sky} = S_pF_{ps}\sigma(\varepsilon_pT_p^4 - \varepsilon_sT_s^4) \tag{10}$$

Between the battery and the sky, the total radiative heat loss Q_{radn} expression between the battery and the ground above; σ ,Stefan - Boltzmann constant (5.67 × 10e8 W/㎡); F_{pg} ,panels - ground visual factor; F_{ps},board - sky vision factor; ε_p = board average emission rate; ε_g ,average surface emissivity; ε_s ,sky average emission rate; T_g ,ground temperature; T_s , sky temperature; in this study, the solar panels are placed and the level was 15 degrees; so the value may be approximated Fps 1; $Q_{rand\text{-}ground}$ can be ignored; ε_s and ε_p values in this study were taken 0.88 and 1; sky temperature of calculated by equation $T_s = 0.914Ta$;

Convective energy loss calculated by the following equation (refer with: Eq. 11).

$$Q_{conv} = S_pH(T_p - T_a) \tag{11}$$

H, convective heat transfer coefficient; For panels angle is less than 25 degrees, low wind speed, H Eq.12.

$$H = 1.2475(\Delta T\ \cos\beta)^{1/3} + 2.685V_{wind} \tag{12}$$

Where ordinary temperature difference △T = (T_p-T_a); β , inclination; V_{wind} ,wind speed;

The last parameter, the power generated by the expression below equation (refer with: Eq. 13).

$$Q_{elect} = \eta GS_c \tag{13}$$

table 2 shows the parameters of all the panels , they are either obtained from the manufacturer's spec sheet, either derived from experimental tests .

Form 2 PV module parameters

Factor	The total surface area of the PV	PV thickness	PV conversion efficiency	PV module temperature	mCmodule	αabs
	1.2743	40	12	0.45	9250	0.73
Unit	㎡	mm	%	%	J/K	

We use matlab to calculation formula of changes of Tp (equ $(mCp_{module})\frac{dT_p}{dt} = Q_{in} - Q_{rad} - Q_{conv} - Q_{elect}$) , the following form (3).The average temperature, light and wind speed is the average of the line with 22 years in hangzhou.

Form 3 Tp Correction factor

Month	The average rate of change of air temperature (℃)	Average amount of light (Kw/m^2)	Average wind (m/s)	The rate of change of Tp
Jan	4.6	2.17	2.1	1.7114
Feb	6.2	2.56	2.3	1.7181
Mar	10.1	2.91	2.4	1.7181
Apr	16.2	3.77	2.4	1.7225
May	21.2	4.51	2.3	1.7159
Jun	24.7	4.29	2.2	1.7268
Jul	28.8	5.27	2.4	1.7246
Aug	28.1	4.73	2.5	1.7181
Sep	23.9	3.19	2.4	1.7181
Oct	18.7	3.08	2.1	1.7114
Nov	12.9	2.22	2.0	1.7159
Dec	6.8	2.28	2.1	1.7181

Represented by one day temperature changes, to take advantage of the sunny day get the temperature change rule to simulation of the photovoltaic modules temperature change rule. Due to the temperature, light and wind speed is mean monthly, not real-time changes every day, it computed the corresponding month pv modules on an average day temperature change. Using photovoltaic component temperature and environmental temperature difference, it can get components heat through the calculation of the heat capacity of the components.

5 Thermoelectric Energy Efficiency Savings of Electricity A Year Running

Meteorological data in this article is the average temperature values, but due to different monthly temperatures, the temperature of PV modules per month to maintain is different. For instance, average temperature in June is 24.7 ℃, accordingly the temperature of PV modules will be maintain to 24.7 ℃. The result of the calculation in the following form 4. Coefficient of variation of the fitted curve is the ratio of the maximum temperature T_{max} = 33.8 ℃ in the equation of the temperature change and maximum temperature in measured temperature of the day, then calculate the value of the environment temperature changes. The changes of ambient temperature are obtained through analyzing power equation 4 and 5. Then some data will be calculated, as follows, the W_c which is the electric quantity the device generates when runs one day at certain temperature T_c , the W_t which is the electric quantity that generates because of temperature changes, the W_r which is the difference value of W_c and W_t and then the radio of W_r and W_t is a percentage which affect the PV modules' output efficiency when environment temperature changes, while the device temperature T_p be obtained through the corresponding month of the device temperature change rate of the value of PV modules with the ambient temperature changes. After obtaining the quantity of heat Q which the device take in, thermoelectric percentage is $(Q_u + W_r) / W_t * 100\%$.

Form 4 Power saving each month

Month	Jan	Feb	Mar	Apr	May
Coefficient of variation of the fitted curve	4.2935	3.1731	1.9478	1.2113	0.9292
Temperature T_c (℃)	4.6℃	6.2℃	10.1℃	16.2℃	21.2℃
Thermostat maximum power point (W)	267.56	265.72	261.25	254.29	248.60
The total electricity generated W_c (W/h) day	2680	2660	2610	2540	2490
Day of the total power generated variable temperature W_t (W/h)	2650	2620	2550	2450	2360
Difference W_r (W/h)	27．4	37.2	59.8	94.6	124
Percentage	1.03	1.42	2.34	3.86	5.25
Components are stored heat Q (W / h)	11300	15300	24700	39300	51600
Component utilizes heat Q_u(W/h)	113	153	247	393	516
Thermoelectric percentage	5.29%	7.26%	12%	19.9%	27.1%

Jun	Jul	Aug	Sep	Oct	Nov	Dec
0.7925	0.6805	0.7001	0.8231	1.0561	1.527	2.8931
24.7℃	28.8℃	28.1℃	23.9℃	18.7℃	12.9℃	6.8℃
244.63	239.98	240.77	245.53	251.44	258.06	265.03
2450	2400	2410	2460	2510	2580	2650
2300	2230	2240	2390	2410	2500	2610
148	168	165	170	109	77	40.7
6.42	7.53	7.34	7.44	4.54	3.08	1.56
61600	70400	68900	48200	45400	31900	16800
616	704	689	482	454	319	168
33.2%	39.1%	38.1%	28.5%	23.4%	15.8%	7.99%

Form4, when compared to the situation without analysis of energy efficiency, form4 clearly show the efficiency of the month is different because of different month. Form4 indicates that the highest efficiency of thermoelectric energy efficiency will be appeared in June, July and August; The value is nearly 40%. However, February is only about 5% and 8% in December. This rule conforms to the changes of reality. The average efficiency of thermoelectric energy efficiency in one year is 21.47%. Certainly, it only makes use of the 1% heat energy of PV module absorption. It is obvious that the thermoelectric efficiency will be further improved when heat utilization rate of PV module increase accordingly. Form(4) shows that a PV module savings in electricity consumption is 6.0657e +03 (W/h) when it utilizes thermoelectric effect in a year, then 120KW photovoltaic power plants generally use thermoelectric energy efficiency to save power of 2.2746e +06 (W/h).

6 Summary

Photovoltaic cells operating model, PV modules operating model and PV system operating model are built in this paper. Analysis of data from the models, the power curve(Fig.6) and the temperature curves (Fig.7,Fig.8) are obtained ,including PV module temperature correction table(Form1)and temperature coefficient of PV module(Form3).Certainly, these results have been revised using Excel as the tool of data processing. Results indicate that the thermoelectric efficiency is 21.3279%, although it makes use of the 1% heat energy of PV module absorption. It is concluded that the thermoelectric efficiency will be further improved when heat utilization rate of PV module increase accordingly.

References

[1] Gow, JA, Manning, CD. Development of a photovoltaic array model for use in power-electronics simulation studies. Electric Power Applications, IEE Proceedings - 1999;146:193-200.

[2] Fu-Te Zhang. Research on thermal performance in crystalline silicon photovoltaic modules and the impact on the component NOCT. Soapy solar photovoltaic (pv) network 2013:95-97.

[3] Ying-Chao Zhang, Gui-Heng Yang, Sheng-Ze Qiang. Solar photovoltaic power generation system and its application. Beijing dongcheng district QingNianHu south street no. 13: Chemical industry press. 2011.

[4] Peng Xu, Ji-Ming Hou, Deng-Kuo Yuan. Simulation Model of PV array Based on Two-Diode Model The computer simulation. 2013:71-75.

[5] Guo-Ying Xu,Xiao-Song Zhang,Shan-Guo Zhao. Performance of flat-plate PV/T integrated heat pump water heating system. Journal of chemical industry 2012:136-141.

[6] Ishaque, K, Salam, Z, Taheri, H. Simple, fast and accurate two-diode model for photovoltaic modules. Sol Energ Mat Sol C 2011;95:586-594.

[7] Cubas, J, Pindado, S, Victoria, M. On the analytical approach for modeling photovoltaic systems behavior. J Power Sources 2014;247:467-474.

Advanced Materials Research Vols. 986-987 (2014) pp 1984-1987

doi:10.4028/www.scientific.net/AMR.986-987.1984

Research of Single Phase Short Fault in One-Generator Infinite Bus Power Systems

Xiaolong Tan[1], Jia Zhou[1], Wenbin Wang[1,a]

[1] Yalong River Hydropower Development Company LTD, Chengdu, 610051, China

[a] email: wangwenbin@ylhdc.com.cn

Keywords: Single Phase Short Fault, Grid Failure, Reliability

Abstract: Electric power industry is related to people's livelihood, economic development, an important foundation for national construction industry. With the deepening of our country comprehensive construction, the demand has increased rapidly, at the same time also have higher requirements for quality of power supply. From the previous electricity use can be gradually increased to cannot accept a power outage, to the power grid voltage waveform, harmonic, frequency and so on each index has a clear requirement, countries have introduced related national standard specification. This aspect shows a gradually increase in the standardization of industrialization in China, on the other hand also puts forward higher demands on distribution power supply departments. One of the goals of the grid is to reduce the failure rate, improve the reliability of power supply. And power grid failure and is the highest percentage of short circuit fault, and the single-phase earth fault and occupy the vast majority of proportion, it is necessary to in-depth analysis of the formation mechanism of single-phase earth fault and damage, so as to find the related protection and remedial measures.

Introduction

Because the electrical short circuit fault is a serious fault, electric light, damaged components, burning equipment; or cause the air discharge, tremendous damage on the surrounding biological safety. Determined to get the data through the experiment method is not safe, also not economic, there are many negative effect[1] . So at home and abroad is mainly use for the software simulation analysis. This paper adopts the famous PSCAD software for simulation, it can be more convenient to solve the electromagnetic transient and electromechanical transient process, has been widely used.

Mathematic analysis for single phase short fault

By power system transient analysis can establish fault sequence network, and write the corresponding boundary conditions for single phase short circuit to ground (Take A phase for example):

$$\dot{V}_{fa} = 0, \dot{I}_{fb} = 0, \dot{I}_{fc} = 0$$

From the symmetrical components method we can write:

$$\dot{V}_{fa(1)} + \dot{V}_{fa(2)} + \dot{V}_{fa(0)} = 0$$

$$a^2 \dot{I}_{fa(1)} + a \dot{I}_{fa(2)} + \dot{I}_{fa(0)} = 0$$

$$a \dot{I}_{fa(1)} + a^2 \dot{I}_{fa(2)} + \dot{I}_{fa(0)} = 0$$

Solve the equation and we can get:

$$\dot{V}_{fa(1)} + \dot{V}_{fa(2)} + \dot{V}_{fa(0)} = 0 \; \dot{I}_{fa(1)} = \dot{I}_{fa(2)} = \dot{I}_{fa(0)} \quad (1)$$

And solve with the (2)

$$\begin{aligned} &\dot{E}_{eq} - jX_{ff(1)}\dot{I}_{fa(1)} = \dot{V}_{fa(1)} \\ &-jX_{ff(2)}\dot{I}_{fa(2)} = \dot{V}_{fa(2)} \\ &-jX_{ff(0)}\dot{I}_{fa(0)} = \dot{V}_{fa(0)} \end{aligned} \quad (2)$$

Get: $$\dot{I}_{fa(1)} = \frac{\dot{V}_f^{(0)}}{j(X_{ff(1)} + X_{ff(2)} + X_{ff(0)})} \quad (3)$$

Formula (3) is the basis of the single phase short circuit calculation[2] . As long as we calculated the positive sequence component, can through the phase Angle of the relation between the three to get rest two orders sequence component

value $\dot{I}_{fa(2)} = \dot{I}_{fa(0)} = \dot{I}_{fa(1)}$ $\dot{V}_{fa(1)} = j(X_{ff(2)} + X_{ff(0)})\dot{I}_{fa(1)}$ $\dot{V}_{fa(2)} = -jX_{ff(0)}\dot{I}_{fa(1)}$ (4)

From above equation，the single phase short current depends on the three orders impendence. $X_{ff(1)}$ and $X_{ff(2)}$ is associated with short-circuit point to the power of the electric distance, for the static element, its positive and negative sequence impedance is the same size, while for rotary motor positive sequence impedance is bigger. $X_{ff(0)}$ is related to the neutral point grounding way[3] . The mathematical expression and analysis for the single phase short circuit can be establish PSCAD simulation model.

Simulation and wave forms

We built the simulation model based on single machine infinite system, the overall wiring diagram is as follow:

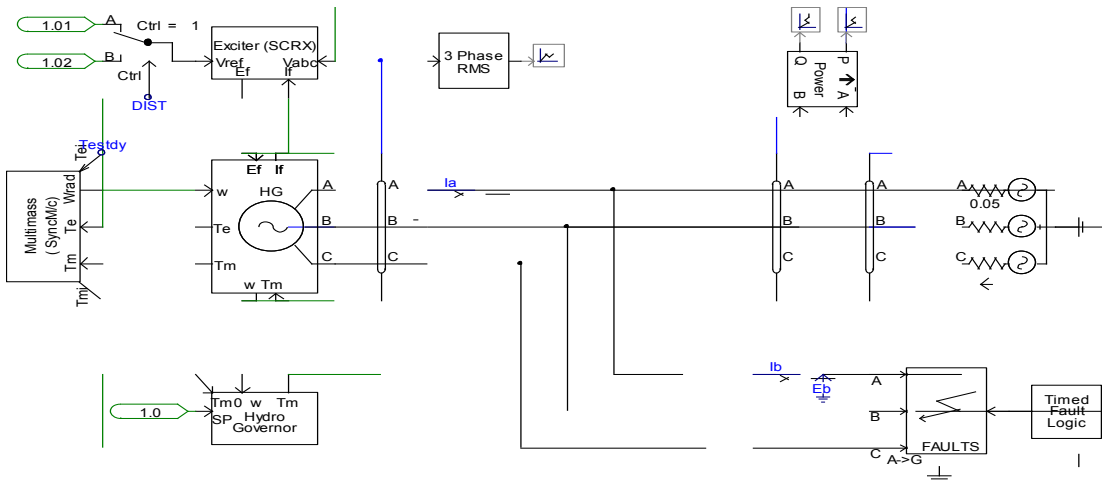

Fig.1. Overall circuit model

In order to analyze the situation of single phase short circuit easier, short-circuit point considering the export side of the generator set, its electric distance is relatively close, to test the bad influence to the generator[4] . Short-circuit time setting in the 5th s, 4 s short time duration. Short circuit time set longer than the actual power grid short-circuit time to examine the extreme short-circuit negative impact of the actual power grid with circuit breaker protection, short circuit will not allow such a long time. Used in the simulation of circuit breaker automatically in the open and closed to simulate the actual detection of fault after open, the circuit breaker in the model be set after the 9 s fault, which is equivalent to relay protection action, in order to achieve the effect of the protection circuit[5] .

The wave forms are shown as follows:

1. Generator export voltage Ea:

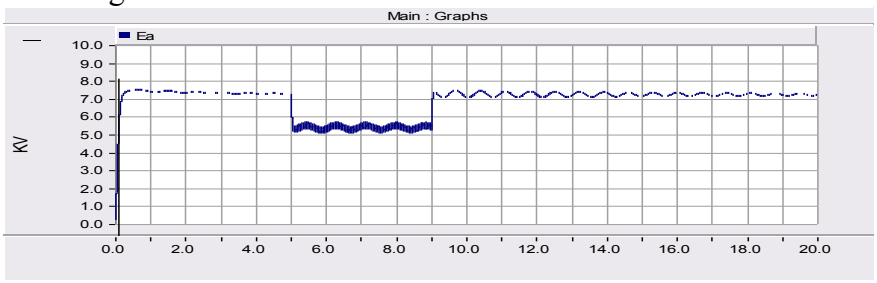

Fig.2. Export voltage

2. Short-circuit point voltage Eb:

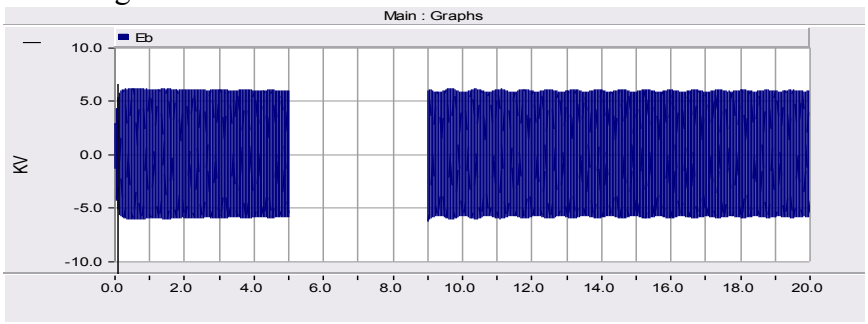

Fig.3. Short point voltage

3. Generator export current Ia:

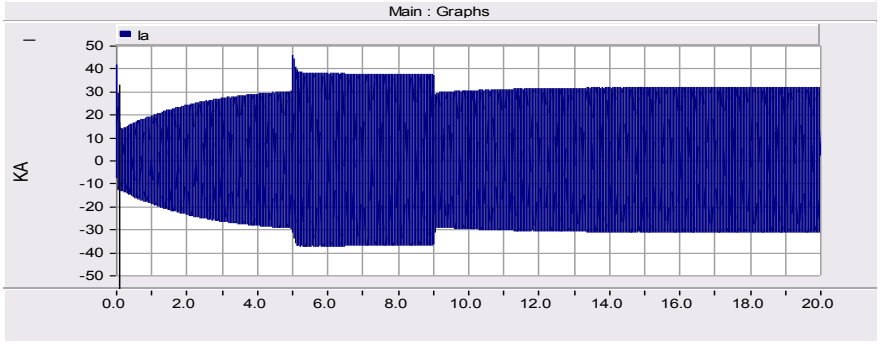

Fig.4.Export current

4. Short-circuit point current

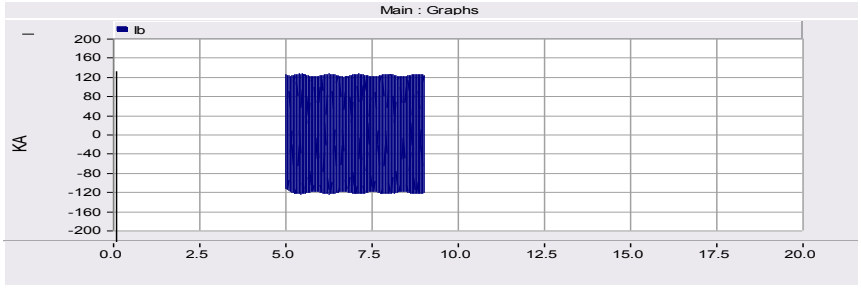

Fig.5 Short-circuit point current

5. Active power in the system:

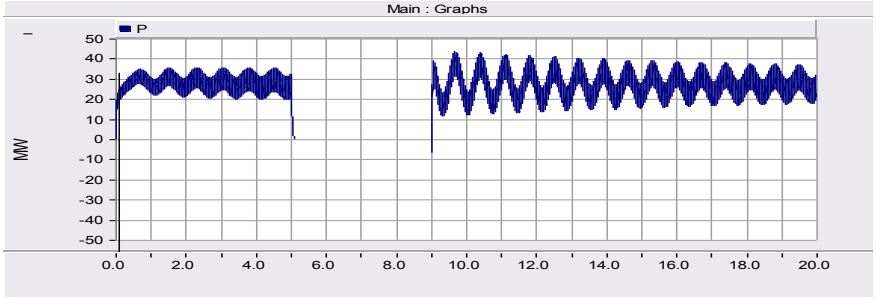

Fig.6. Active power in the system

6. Reactive power in the system:

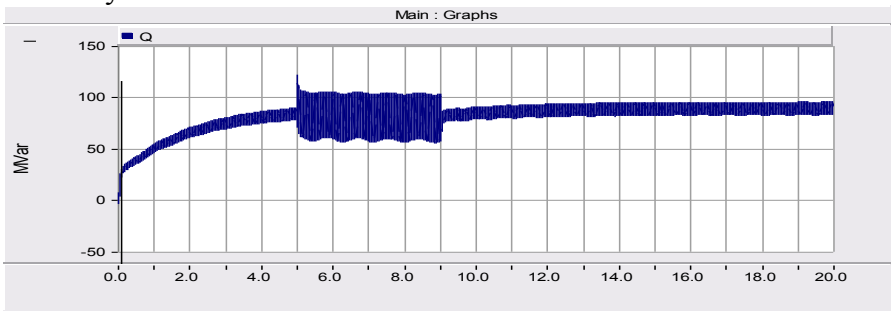

Fig.7 Reactive power in the system

In the operation of 0 to 5 s time, the output voltage of power supply side of the synchronous generator basically stable near the rating of 7.2 KV ~ 7.5 KV, and from the 5 s short-circuit, appeared in an instant by as much as 30% of voltage to reduce the process, when the short-circuit resection, The system drop the fault at 9s which leads the three phase line into two lines, so the same in a series of mutations, voltage began to rise to the extreme value point, and then slowly back to stable.

And about power, we can see as a phase ground, the active power within 5-9 s mutation is 0, the equivalent of cutting the active load all, this will cause a huge loss in actual operation, the reactive power increased greatly, and the same time will cause line terminal voltage rise, electromagnetic noise on the conductor line. Active reactive power also has experienced the first after the failure to remove up to a maximum and then fell gradually process.

Conclusion

This paper mainly studies in a one-machine infinite system under the single phase grounding fault of power grid voltage, power, etc. Since the single-phase grounding fault occurs in the actual operation of the short circuit fault occupied more than 80% of the proportion, so the study of its impact on power grid have become more widely representative. Through the simulation we can see, because the short circuit is equivalent to change the grid topology structure and electrical parameters, so the changes will cause the power distribution in grid, and the cause of voltage mutation, endanger the equipment and personal safety. So in the real operation, short circuit calculation is performed before during installation, setting corresponding protection equipment. This simulation model can comprehensively reflect the changes of various electric parameters, can provide certain reference for setting calculation, has a good practical significance.

References

[1] Arrow, Kenneth J. Social Choice and Individual Values. . 1951
[2] A. E. A, Araujo, A. C. Soudak, J. R. Marti. Ferroresonance in power systems: chaotic behavior. IEE Proceedings-C Generation Transmission & Distribution. 1993
[3] S.Mozaffari, S. Henschel,A.C. Soudack. Chaotic ferroresonance in power transformers. IEE Proceedings Generation, Transmission and Distribution. 1995
[4] A novel optimal control method of grounding impedance for distribution system. . 2009
[5] Mangione S, Buccheri P, Di S M. Efficient modeling of a combined overhead-cable line for grounding-system analysis. . 2008

Advanced Materials Research Vols. 986-987 (2014) pp 1988-1991

doi:10.4028/www.scientific.net/AMR.986-987.1988

Research On an AC/DC Converter Based On the Convert Station In HVDC Light Technology

Yuehua HUANG[1a], Zheheng ZHOU[1b], Hongtao FAN[1], Jian QI[1]

[1]College of Electrical Engineering and New Energy, Three Gorges University, Yichang, 443002, China

[a]jiaxingz1102@163.com, [b]929392816@qq.com

Keywords: Converter; filter; high quality

Abstract. In this research, a converter, suitable for the convert station of the HVDC light technology, is proposed and optimized. The converter mainly consists of AC chopper, rectifier transformer, low-pass filters and smoothing reactor. This system can restrain the disturbance of the input power and output the power with high quality. This research is going to analyze the working principle of the converter and then optimize the output wave through filters. Circuit's simulation is carried out by MATLAB to verify the reliability and feasibility of this converter topology.

Introduction

HVDC Light is a new DC transmission system, based on the technology of Pulse Width Modulation (PWM) and the development of high switching frequency and high power turn-off components, such as Insulated Gate Bipolar Transistor (IGBT) and Intergrated Gate Commutated Thyristor (IGCT) [1]. The development of high-power semiconductor switching devices with controlled turn-off functions has made it possible to apply large-capacity converters to power systems [2]. By this technology, the power system can provide the energy to the load in some remote areas such as islands, mining area, gas wells or oil wells, and drilling platform [3] [4]. The converters play an important role in the DC transmission system, conventional converters using thyristors have been used for many years, however numerous studies shows that they face the problems such as instability during the AC system disturbance, the size and weight of the convert is not small enough for the practical application [5]. This research describes an AC /DC convert system, which is suitable for the converter station, based on some classic circuit, and then analyze the stability when the AC source fluctuates. It not only can be applied to HVDC Light technology, but also in the distribution network, space technology and so on.

Operating Principle

The converter station mainly consists of AC chopper, rectifier transformer, rectifier bridge and smoothing reactor.

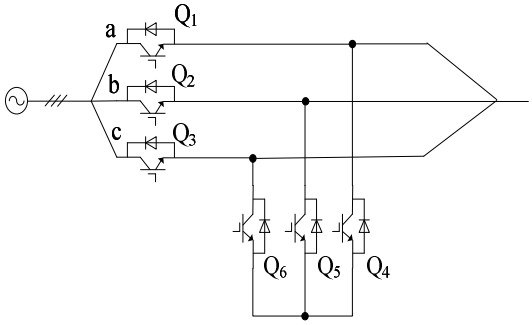

Fig.1. The PWM buck chopper

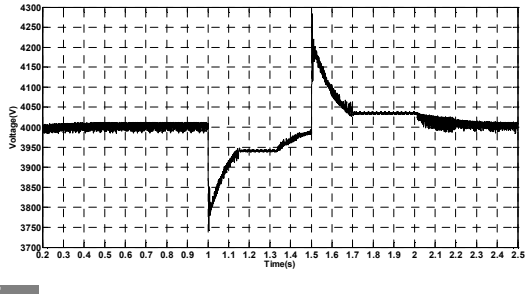

Fig.2. The output waveform

As fig.1 shows, AC converter is a circuit of high frequency PWM buck chopper. Every phase of the three-phase source contain two power switches and two diodes. Q1, Q2, Q3 are controlling the high-frequency chopper and Q4, Q5, Q6 are free-wheeling diodes. The pair of switches on the phase of lowest input voltage keep on and the other pairs control the high-frequency PWM. For

example, when the voltage of phase B is the lowest of the three phases, keep Q2, Q5 open, and then manage the rest two pairs of switches to control the high-frequency PWM [6] so as to output the pulse voltage, which has the same amplitude and phase to the input voltage.

The Eq.1 shows ideal three-phase power sources:

$$\begin{cases} u_a = U_m \sin \omega t \\ u_b = U_m \sin(\omega t - 120^\circ) \\ u_c = U_m \sin(\omega t + 120^\circ) \end{cases} \quad (1)$$

$U_m - phase\ voltage\ peak \quad \omega = 2\pi f \quad f - frequency$

Assume that the output phase voltage is ideal, D is high-frequency PWM effective duty. According to Eq.2,the fundamental wave of the output three-phase voltage is symmetrical.

$$\begin{cases} u_{oa} = DU_m \sin \omega t \\ u_{ob} = DU_m \sin(\omega t - 120^\circ) \\ u_{oc} = DU_m \sin(\omega t + 120^\circ) \end{cases} \quad (2)$$

The rectifier transformer in this device is a three-phase three-winding step-up transformer. Primary side receives the output of Ac chopper and secondary output High-voltage alternating current (HVAC).Two three-phase rectifier bridges are connected in series to form a 12-pulse system. The smoothing reactors will get the pulsating voltage flatter.

According to Eq.3, the transformer turns radio is k， U_0 is the output phase voltage RMS(root-mean-square value) of the chopper. U_d is the DC output voltage.

$$U_d = \frac{6\sqrt{6}kU_O}{\pi} \quad (3)$$

The Eq.2 into the Eq.3 are:

$$U_d = \frac{6\sqrt{3}kDU_m}{\pi} \quad (4)$$

According to Eq.4, the output can be controlled by managing duty ratio D after selecting a suitable transformer. The device's structure is simple and its response is fast

Fig.2 shows the simulation of the converter's wave when its input phase voltage is set to 220V and its output voltage is 4000V. The input voltage is on a steady state during 0-1s, it suddenly drops 10% at 1s and then comes back to normal level at 1.5s. As can be seen from fig.1, the waveform of the output voltage is relatively stable during the steady state, its fluctuation ratio is under 0.5%. When the input voltage suddenly drops by 10% at 1s, the output voltage will reduce about 7% at 1s and then goes up to 3900V at 1.6s, the fluctuate ratio of the output will be controlled in 2.5% after 0.1s. When the source comes back to normal level, the fluctuation ratio of output voltage is also controlled in 2.5% after 0.1s, and then the output voltage will return to the rated output within 0.8s (2.3s-1.5s=0.8s)

Through the analysis above, it is appearance that the converter can output stable high voltage DC power, and the output power quality meets the basic requirements of the converter station. To further optimize the converter, we have added filters to improve its performance.

Optimize the output waveform

PI control is one of the effective strategies that restrain the voltage disturbance [7], but its delayed conduct can hardly output a satisfied waveform in this system. Therefore, it should be added a filter system, which consists of the PI control and the low-pass filter circuit, to restrain the fluctuation, so as to minimize the influence by the disturbance from source and improve the power quality.

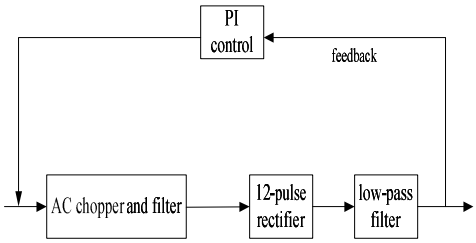

Fig.3. The process

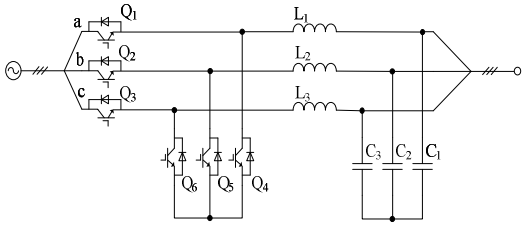

Fig.4. The chopper circuit

As is shown in the fig.3, we combine AC chopper with filter and add a low-pass filter behind 12-pulse rectifier. The AC chopper circuit combined with LC low-pass filter, as fig.4 shows, can filter out the high-frequency harmonic wave. Because the received current is close to sine wave and not influenced by the output voltage, the power factor is high and Total Harmonic Distortion (THD) is low.

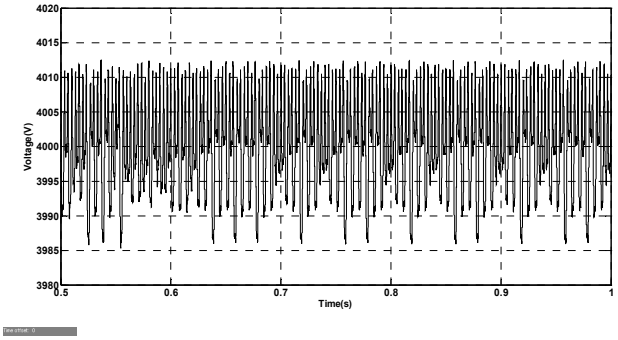

Fig.5 (a). Without optimized output

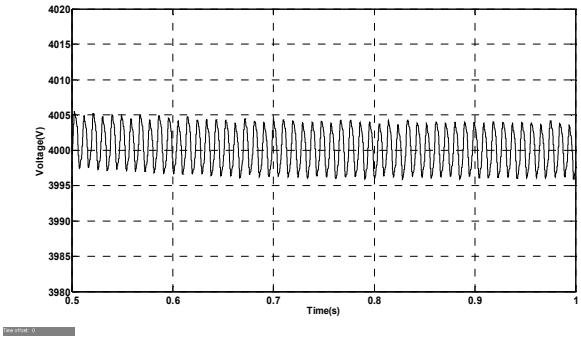

Fig.5(b). Optimized output

Fig.5 (a) shows the output wave without filter when the source input nominal voltage, its amplitude is over 10V and its fluctuation ratio is about 0.35%. Fig.5 (b) shows the output wave with filter, its amplitude is about 5V and its fluctuation ratio is about 0.125%. It is obvious that the waveform in fig.5 (b) is more satisfied than it in fig.5 (a). So the filter is necessary in this converter system.

Simulation and Conclusion Analysis

Fig.6 shows the output waveform of the convert system when the power grid suffer the situation as we talked about in fig.3. Compared with fig.3, it can be seen that the amplitude of the fluctuation is smaller than it before optimized. It has ability to adjust the voltage for the requirement of the converter station. Fig.7 shows the output voltage when the power grid offers a stable power, the output voltage is flat enough to meet the requirement of the load.

According to the characteristics of the AC/DC converter station, we proposed a convert system that consists of some classic circuits such as AC chopper, rectifier transformer, rectifier bridge, and then optimize the output wave through the filters. This system can output the power with high quality, and provide an idea to the converter station designers.

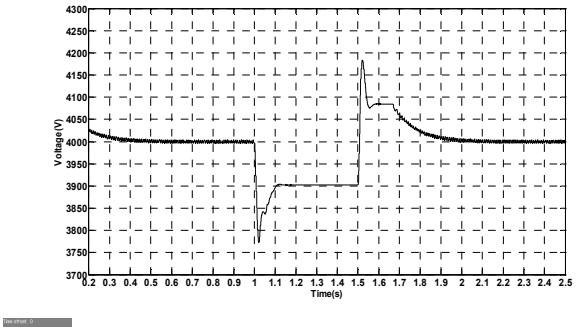

Fig.6. Suffer the disturbance

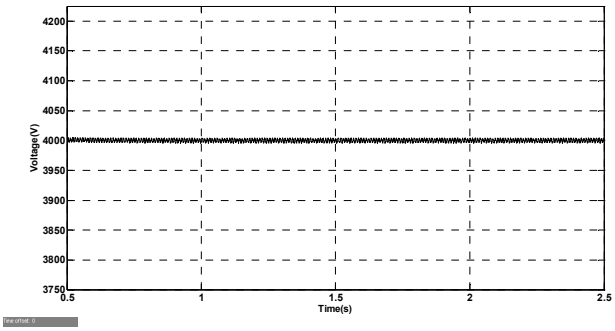

Fig.7.The output at the normal state

Reference

[1] Zhaoqing Hu. Application of a novel optimal coordinated control to HVDC light [J].Proceedings of the CSEE.2005

[2] Xu Qin. The fundamental research on digital simulation of HVDC light technology [D]. Wuhan: Huazhong University of Science And Technology.2007

[3] Qingsheng Zhao, Zhixin Wang. Economic analysis on HVDC-light for off-shore wind farm [J]. Renewable Energy Resources.2009

[4] Gongke Li. Application of HVDC light Transmission Technology in wind power transmission [D]. Guangzhou: South China University of Technology.2011

[5] Sakamoto K，Yajima M．Development of a control system for a high-performance self-commutated AC/DC converter[J]．IEEE Trans. Power Delivery，1998

[6] Zoubir Boudries, Djamila Rekioua Ziani.Study on decoupling direct power control of PWM rectifier using space vector modulation [J]. Arabian Journal for Science and Engineering.2013

[7] Dannehl, J. Limitations of voltage-oriented PI current control of grid-connected PWM rectifiers with LCL filters [J] IEEE Trans. Industrial Electronics, 2009

Advanced Materials Research Vols. 986-987 (2014) pp 1992-1995

doi:10.4028/www.scientific.net/AMR.986-987.1992

Research on Frequency Electromagnetic Field of parallel Transmission Line

CAO Hongying, TANG Bo, PENG Youxian, LI Yu, CHEN Bin

China Three Gorges University Yichang, China

email: tangboemail@sina.com, 420720119@qq.com

Keywords: parallel transmission line; frequency electromagnetic field; vector superposition; electromagnetic field measurement; Bushnell 2-1000

Abstract. At present the study mainly for frequency electromagnetic field which is based on a single transmission line meanwhile the value must be in line with the requirements of the workers in the country frequency electromagnetic field. However, for parallel transmission line the maximum of frequency electromagnetic field is still to meet the provisions of the state, therefore in this paper studied the parallel transmission lines. Taking the multiple parallel power lines of China Three Gorges University as an example, the values of electric and magnetic field are calculated and the electromagnetic field is measured based on National standards. Then, compare the measured value with theoretical value, verified the correctness of the superposition algorithm.

Introduction

With the increase of current consumption in global, parallel transmission line get more and more favor from transmission line designers of all ages at home and abroad. The problems of electromagnetic environment of parallel lines have also been more attention. China is a country with an uneven distribution of energy and primary energy stored mainly in the regions of economy is relatively backward, but in these areas electricity load and relatively low. This has prompted the country to take measures for rational utilization of power resources, the method of west to east, north and south to provide power have largely solved this problem. But it also makes the most of our transmission lines run parallel and intersect way, in this way electromagnetic environment of the transmission lines is relatively complex [1-2].

For the run mode of intersect lines, literature [3] proposed the principle of finite element. However, this method for occupying a few hundred meters of line space, the theoretical method is very complex and very large amount of calculation. There are limitations in engineering applications. In this paper, Taking the multiple parallel power lines located in Nanyuan as an example, frequency electromagnetic field of parallel transmission line were studied. This paper presents an algorithm vector superposition principle. Using this algorithm, transmission line in Nanyuan to calculate frequency electric and magnetic field strength and take actual measurement on-site. Then, compare the measured value with theoretical value, verified the correctness of the superposition algorithm.

The Method of Calculating the Parallel Transmission Line Frequency Electromagnetic Field

A. The Method of Calculating the Parallel Transmission Line Frequency Electric Field

For three-phase AC line, the electric field intensity of any point in the space can be calculated based on the principle of superposition[5], the component of electric field strength at the points of (x, y):

$$E_x = \frac{1}{2\varepsilon\pi}\sum_{i=1}^{3} Q_i\left(\frac{x-x_i}{L_i^2} - \frac{x-x_i}{L_i'^2}\right) \quad (1)$$

$$E_y = \frac{1}{2\varepsilon\pi}\sum_{i=1}^{3} Q_i\left(\frac{y-y_i}{L_i^2} - \frac{y-y_i}{L_i'^2}\right) \quad (2)$$

In the formula, ε is air dielectric constant; Q_i is equivalent charge; m is the number of wires; x_i, y_i are respectively the horizontal and vertical coordinates; L_i, $L_i^{'}$ are respectively the distance from wire and its mirror to calculation point.

In accordance with the principle of equivalent charge method, we can calculate the parallel transmission lines in two steps:

（1）Calculate the charge of per unit length on the wire by the voltage and potential coefficient matrix of transmission lines

（2）Calculate the electric field generated by these charges

Calculate the line space electric field intensity generated by each phase conductors, and respectively in parallel to the ground and perpendicular to the ground to project, so that we can use the superposition of the vectors to calculate the electric field of parallel lines;

The model of electric field strength for parallel transmission lines is:

$$E_x = \frac{1}{2\varepsilon\pi}\sum_{i=1}^{m} Q_i\left(\frac{x-x_i}{L_i^2} - \frac{x-x_i}{L_i^{'2}}\right) \tag{3}$$

$$E_y = \frac{1}{2\varepsilon\pi}\sum_{i=1}^{m} Q_i\left(\frac{y-y_i}{L_i^2} - \frac{y-y_i}{L_i^{'2}}\right) \tag{4}$$

In a parallel transmission line, the voltage as a time variable normally use the complex number to represent the voltage of each phase conductors in the calculation, and the corresponding charge is also represented by complex numbers.

$$\dot{U}_i = U_{i,R}^{'} + U_{i,I}^{'} \tag{5}$$

$$\dot{Q} = Q_{i,R}^{'} + Q_{i,I}^{'} \tag{6}$$

The component of the electric field intensity obtained is complex numbers, that is:

$$\dot{E}_x = \sum_{i=1}^{m} E_{ix.R}^{'} + j\sum_{i=1}^{m} E_{ix.I}^{'} = jE_{x.I}^{'} + E_{x.R}^{'} \tag{7}$$

$$\dot{E}_y = \sum_{i=1}^{m} E_{iy.R}^{'} + j\sum_{i=1}^{m} E_{iy.I}^{'} = jE_{y.I}^{'} + E_{y.R}^{'} \tag{8}$$

The synthetic field intensity of the point in the space is：

$$E = (jE_{x.I}^{'} + E_{x.R}^{'})x + (jE_{y.I}^{'} + E_{y.R}^{'})y \tag{9}$$

In the formula, $E_{x.R}^{'}$ and $E_{y.R}^{'}$ represents the horizontal and the vertical component of the synthetic field strength generated at the points by the real part of the electric charge in each conductors； $E_{x.I}^{'}$ and $E_{y.I}^{'}$ represents the horizontal and the vertical component of the synthetic field strength generated at the points by the imaginary part of the electric charge in each conductors

B.The Method to Calculate the Frequency Magnetic Field in Parallel Transmission Line

Three-phase symmetrical current I_A, I_B, I_C synthesize the components of the magnetic field in space:

$$H_x = \sum_{i=1}^{3} H_{xi} = \frac{\sqrt{2}}{2\pi}\left[\frac{y-y_1}{r_1^2}I_A + \frac{y-y_2}{r_2^2}I_B + \frac{y-y_3}{r_3^2}I_C\right] \tag{10}$$

$$H_y = \sum_{i=1}^{3} H_{yi} = \frac{\sqrt{2}}{2\pi}\left[\frac{x-x_1}{r_1^2}I_A + \frac{x-x_2}{r_2^2}I_B + \frac{x-x_3}{r_3^2}I_C\right] \tag{11}$$

The magnetic field intensity at any point of the space:

$$H_i = \sqrt{H_{xi}^2 + H_{yi}^2} \tag{12}$$

The magnetic field strength generated by m wires in parallel lines can be obtained by the superposition principle:

$$H_x = \sum_{i=1}^{m} H_{xi} = \frac{\sqrt{2}}{2\pi} \sum_{i=1}^{m} \left(\frac{y - y_i}{r_i^2} I_i\right) \quad (13)$$

$$H_y = \sum_{i=1}^{m} H_{yi} = \frac{\sqrt{2}}{2\pi} \sum_{i=1}^{m} \left(\frac{x - x_i}{r_i^2} I_i\right) \quad (14)$$

The magnetic field strength of parallel lines:

$$H = \sqrt{H_x^2 + H_y^2} \quad (15)$$

The Analysis of the Results of the Frequency Electromagnetic Field

A.The Measurement Test of the Frequency Electromagnetic Field

The parallel transmission line in Nanyuan of Three Gorges University includes two double transmission lines in same tower with the voltage level of 110kV, and a single circuit transmission line with the voltage rating of 35kV, a total of three lines in parallel, and model of the parallel transmission line as shown in Figure 1, totaling fifteen phase conductors.

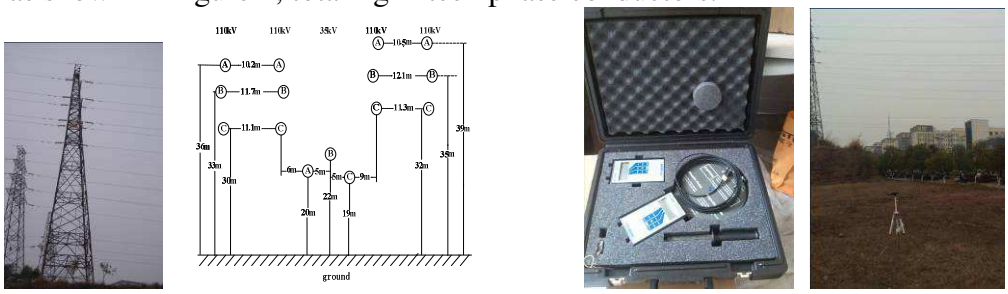

Fig.1 Parallel transmission line model and measurement photo of electromagnetic field

The measurement tests carried out on the frequency electromagnetic field include the measurement of line parameters and power frequency electromagnetic fields. Firstly, choose the measuring instruments of laser range finder with the model of Bushnell 2-1000, and the error of instrument is ± 0.01m.The test measures the distance from each phase conductor of the parallel line to the ground, and the relative distance between each of the fifteen phase conductors. Secondly, choose the measuring instruments with the model of HI-3604, the measurement accuracy of electromagnetic electric field intensity is ± 0.05 kV/m and ± 0.01 A/m . The edge phase conductors as a benchmark and the direction perpendicular to the line path to measure the lateral attenuation characteristics of power frequency electromagnetic field. When measuring, with 5m at intervals to measure the frequency electromagnetic field strength point by point within 50m.

B.Analysis between Theoretical and Measured Values of Frequency Electromagnetic Fields

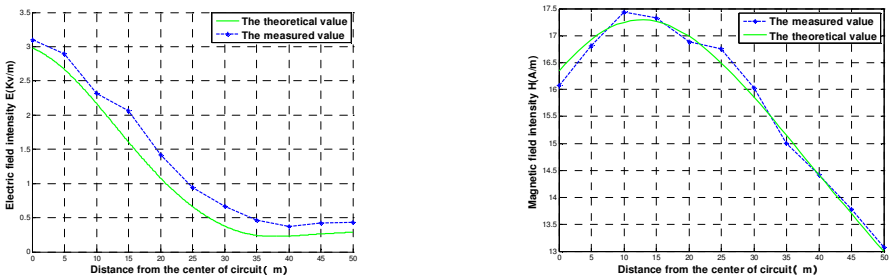

Fig.2 Measured and calculated results of comparison of the electromagnetic intensity

Known in Figure 2, the trends between measured values and calculated values of lateral distribution of the magnetic field strength is the same, but there are some errors in the data. The maximum error of the electric field strength is 0.45 kV/m , and the minimum error is 0.15 kV/m .The maximum error of the magnetic flux density is 0.0003 mT and the minimum error is 0.00001 mT . The measured value of the frequency electric field has higher accuracy than the value of frequency magnetic field.

The main reason are as follows: 1) The electric field is generated by the charge, the charge is not only exist in the wire, but exist in the nature, the air, and the cars in the roads near the line will cause the changes of electric field of the measuring point. Therefore, this is also the main source of the errors in measurement. But the frequency magnetic field is generated by a current-carrying conductor namely the current, the current-carrying conductor exist in the wires, so they are little affected by the external environment; 2) The measuring instruments of the frequency magnetic field has high precision. Therefore, the measuring of the electric field has higher accuracy than that of the magnetic fields.

Conclusion

1）Calculate the electric field intensity and the magnetic field intensity in the space generated by each phase conductor of the line, and respectively, in parallel to the ground and perpendicular to the ground to project, so that adopting the vector superposition to calculate the spatial magnetic field of parallel lines;

2）The parallel lines of Nanyuan in three gorges university as the example, adopting the superposition algorithm, the maximum error of power frequency electric field is 0.45 kV/m and the maximum error of power frequency magnetic field is 0.0003 mT .

References

[1] Zhao Jianguo, Niu Lin. The research and practice of uhv ac transmission technology in Japan[J]. The Journal of Power System and Automation, 2007, 19(1): 28-33.

[2] Zhou Hao, Yu Yuhong. The discussion of some important problems in the development of uhv transmission in China[J]. The Grid Technology, 2005, 29(12): 1-9.

[3] Wang Xiaoyan, Zhao Jianguo, etc. The calculation method of the cross and across the regional spatial electric field in ac transmission lines[J]. High Voltage Engineering, 2011, 37(2)：411-415.

[4] International Special Committee on Radio Interference. Radio interference characteristics of overhead power lines and high-voltage equipment, Part：Description of Phenomena[M] .CISPR Publication 18-3, America, 1982：134-135.

[5]Sheng Jianni. Engineering electromagnetic field numerical analysis[M].Xi'an: xi'an Jiaotong University Press,1991.

Advanced Materials Research Vols. 986-987 (2014) pp 1996-2000

doi:10.4028/www.scientific.net/AMR.986-987.1996

Research on Photovoltaic DC Power Supply System for Office

WANG Hui[1], WU Jiang[2], Gao Houlei[1], Yuan Jianhua[3]

([1.]School of Electrical Engineering, Shandong University, Jinan, Shandong, 250061

[2.] Suzhou Power Supply Company, Suzhou, Jiangsu, 215000

[3.] School of Eelectrical Engineering & Renewable Energy, China Three Gorges University, Yi-Chang,Hubei, 443002)

Keywords: photovoltaic; DC circuit; MPPT; office equipment

Abstract. This paper discusses the post stage power supply circuit's structure of electronic appliances such as laptops, desktops, mobile phones and digital cameras, which are commonly used in office. The advantages and feasibilities of DC power supply's substitution for AC are analyzed. On this basis, a DC power supply system consists of photovoltaic cells, batteries, AC/DC modules, DC/AC modules as well as DC loads is brought forward. The main power supply unit, photovoltaic cells, connects the DC bus through a DC regulator circuit. The bus voltage can be maintained stable by real-time adjustment of photovoltaic cells' output power. The battery module connects the DC bus through a bidirectional Boost-Buck circuit. The charges and discharges of batteries can be real-time controlled according to the bus voltage level. The AC/DC module connects the DC bus as a backup, which can real-time detect the bus voltage to determine whether to start. The DC/AC module can supply power to ordinary AC loads and the DC loads are usually powered from the bus through DC/DC converters.

Introduction

In our everyday life, many appliances are or can be transformed to be DC powered. With the increasing of these, the advantages of DC power begin to emerge. AC power mode uses AC/DC converters or chargers to supply corresponding DC voltage level power. Photovoltaic generates power by converting solar energy to DC power. In order to adapt the traditional power supply mode, the DC power is inverted into AC power. However, with the increasing of DC loads, we can supply these equipments with photovoltaic DC power, which ends up with saving of inverter equipment costs and power losses. The document [1] points out that the increasing of DC supplies and DC loads is a new direction. The document [2] shows that DC power supplies can greatly reduce the times of transforming between AC and DC. The document [3] designs a practical DC/DC adapter.

The Characteristics of Photovoltaic.

Photovoltaic converts solar energy into electricity with the help of photovoltaic cells. The P-U (power-voltage) output characteristics of these cells are shown in Fig.1.

Figure 1 shows that, the output voltage is always above zero, that is to say, the cells are kind of DC sources. The maximum output power varies according to different light intensity. The output power varies corresponding to the output voltage. So the conclusion is that these cells are unstable DC sources. First DC/DC converters and then DC/AC inverters are needed to fulfill the purpose of being connected to the grid and performing independently. The Maximum Power Point Tracking (MPPT) strategy is used to keep the cells working at the maximum output power, which resulting in improved output power and solar utilization efficiency [4].

MPPT [5] is a dynamic self-optimization process in essence. It compares the current output power with the former one, larger remained and smaller deserted, cycles of re-testing and re-comparing. And finally we keep these cells working at the maximum output power dynamically. Constant voltage

tracking method (CVT), perturbation and observation method, incremental conductance method, fuzzy logic control method and so on are currently used MPPT methods [6].

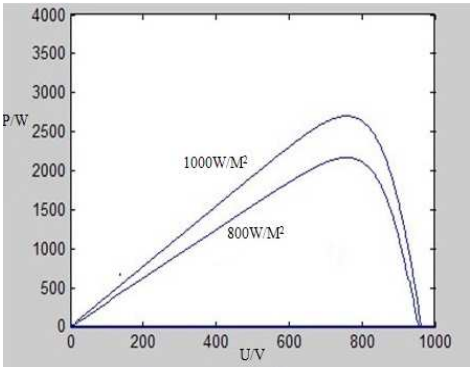

Fig.1 PV output characteristic curve

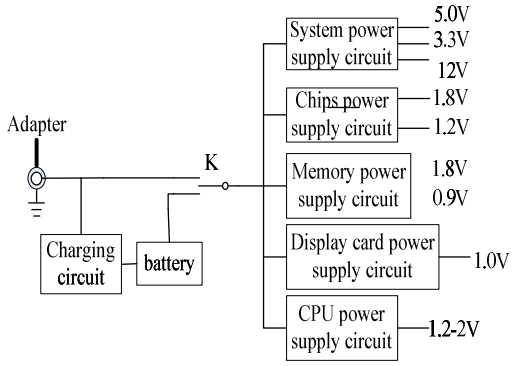

Fig.2 Post stage power supply circuit diagram for laptops.

Analysis on the After-level Power Supply Circuit for Commonly Used Digital Appliances.

DC loads vary, requirements of the power supply voltage differ. The following are the analysis on different loads such as laptop, desktop, mobile phones, digital cameras and MP3.

Power Supply Voltage for Laptop. Research on domestic laptops finds that most of the adapter output voltages are 18.5V, 19V or 20V. 16V and 15V also appears on some old laptops.

As laptops are accurate equipments and the power supply voltage varies between different modules. For example, the voltages of CPU, display card and DDR2 memory are usually 1.2V-2V, 1V, 1.8V.

When a laptop is connected to the adapter, the power supply circuit is shown in Fig.2 [8]. The functions of the modules in Fig.2 are following: the charging control module is in charge of Li-battery. Six-core Li-battery is widely used by a laptop. In addition, there are four-core, nine-core and twelve-core. Every three or four cores are in series. Batteries with different cores need different charging styles to meet the charge requirements. The system power supply circuit is in charge of controlling and logic chips on motherboard. Also, it can be the standby power supply. The chips power supply circuit is charge of north and south bridge. The controlling chips of memory, display card and the CPU power supply circuit are in charge of supplying satisfying power for corresponding modules.

The conclusion we get from dozens of research is that the laptop input voltage's vary in a certain range usually does not lead to un-stability due to a wide range of input voltages for power interface chips.

The Post Stage Power Supply Circuit for Desktops. he desktop hosts usually adopt a specific switching power supply with output voltages +3.3V, +5V, -5V, +12V, -12V, +5VSB. The power supply block diagram is shown in Fig.3. Figure 3 shows that, the desktop LCD monitors are also DC powered and the post stage power supply voltage usually +12V.

From the analysis above we can get that the desktops can be powered with DC so long as offering them with DC +3.3V, +5V, -5V, +12V, -12V using single-input multi-output DC/DC converters. Many of the components in desktops require a certain working current, specifically CPUs usually working in a state of heavy current. So the powers of +3.3V, +5V, +12V need offering heavy current.

The Post Stage Power Supply Circuits for Mobile Phones, Digital Cameras, MP3s and so on. A Li-battery with a 3.7V nominal voltage and a 3.0-4.2V working voltage usually serves as the power for chargeable devices such as Mobile phones, digital cameras and MP3s.

There is a strict charging requirement for Li-battery due to its strong activity and high energy density. The integrated chips consist of charging controllers and some peripheral devices are used by most of the Li-battery charging circuit. The integrated chips have a certain range of input voltages, for example, range 2.7V-12V for MAX886, MAX888. The charging block diagram for mobile phones is shown in Fig.4.

The analysis above and the Fig.4 shows that there are chips of controlling power for digital devices and the input voltages should be in a certain range. That is convenient for designing unified DC/DC chargers.

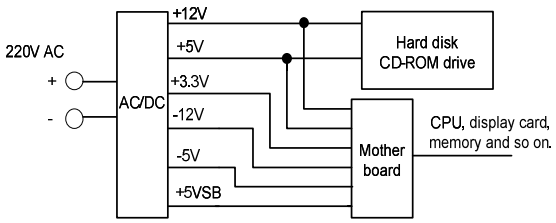

Fig.3 Power supply circuit of desktops

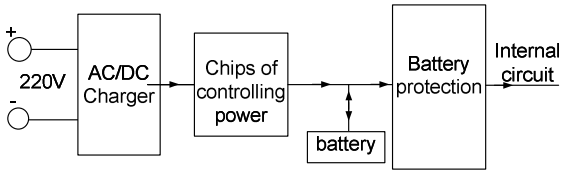

Fig.4 Power supply circuit for mobile phones

Photovoltaic DC Circuit for Office and its Controlling Strategy

Based on the analysis above, most of the laptops can be powered by one voltage level. Universal adapters can be designed for chargeable devices with one Li-battery such as mobile phones, digital cameras, MP3s. Special adapters can be designed for devices with complicated voltage levels such as desktops and so on.

The block diagram based on photovoltaic DC power supply is shown in Fig.5.

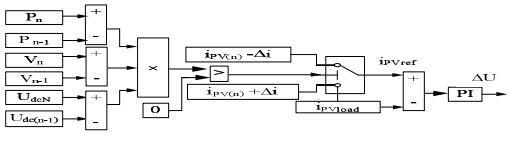

Fig.6 Control schematic for PV modules

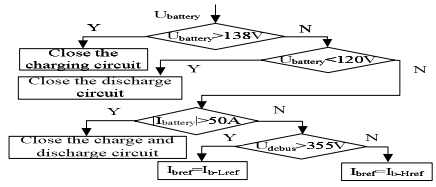

Fig.7 Control schematic for battery modules

Fig.5 Structure of DC power grid

As shown in Fig.5, the photovoltaic DC power supply system consists of photovoltaic cells modules, battery modules and the backup grid. Trends of the DC bus voltage and the active powers supplied by every module are same for the reason that DC loads needs no reactive power.

The Control Strategy for the PV Module. PV module supplies power for the system as the main module. It realizes the automatic conversion between the regulator mode and the MPPT mode with the help of DC/DC circuit. When the power supplied by the PV module exceeds the loads power, the PV module stabilizes the DC bus voltage U_{dcN}, while at the same time, charging batteries through boost-buck circuits. When the power supplied by the PV module is not enough for the loads, the PV module will search the maximum power by judging the output power and voltage V to keep the module working at MPPT mode. Other parts of the system will cover the power shortage. The control schematic is shown in Fig.6.

The Control Strategy for the Battery Module. In order to keep balance of the system energy, the battery control circuit should automatically determine which state (charging or discharging) it will work at. At the same time, it should keep the battery from over-charging and over-discharging. For this reason, we control the battery by bidirectional DC/DC boost-buck circuit. When finishing charging, the buck charging circuit should be turned off. When the output voltage drops below the acceptable lowest point, the boost discharging circuit should be turned off. When the battery is between the two states above, the state will be determined by real-time monitoring bus voltage. When the bus voltage meets the requirements of control, buck is on working state. The current $I_{b\text{-}Lref}$ serves as a reference for the charging circuit. When the DC bus voltage is under the requirements of control, boost is on working state. The current $I_{b\text{-}Href}$ serves as a reference for the discharging circuit. The control flow diagram is shown in Fig.7.

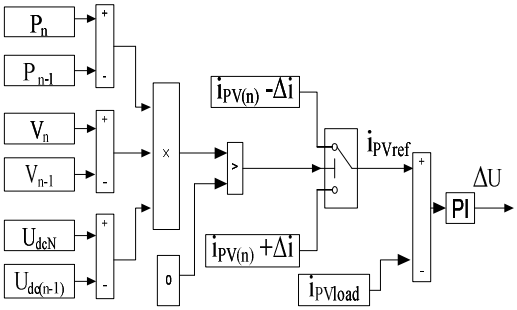

Fig.6 Control schematic for PV modules

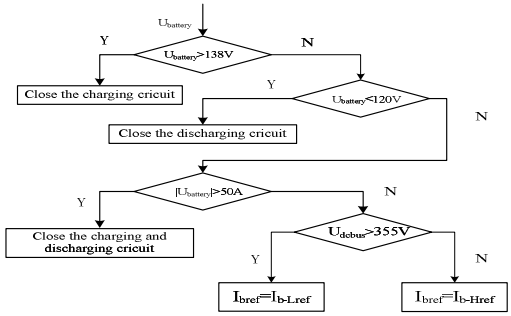

Fig.7 Control schematic for battery modules

The Control Strategy for AC/DC Converters. In order to strengthen the reliability of the DC system, AC/DC converters are designed to connect the DC bus and the AC grid. When the DC energy is not enough, AC grid supplies the power by converting to keep the stability of the DC bus voltage. The control flow diagram is shown in Fig.8.

The Control Strategy for Inverters. Taken powering the AC system into consideration, DC/AC inverters are designed. On the condition that DC energy is sufficient, the DC system can supply the power to the AC loads without relying on the AC grid. The control flow diagram is shown in Fig.9.

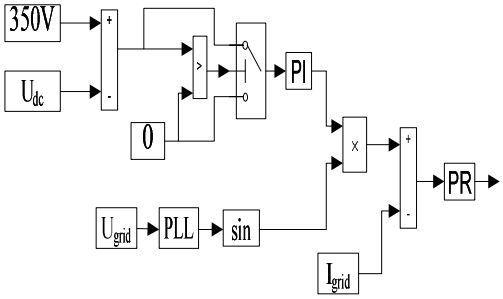

Fig.8 Control schematic for AC/DC converters

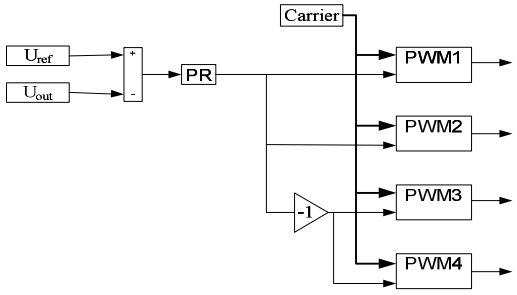

Fig.9 Control schematic for inverters

The Control Strategy for the DC Bus Voltage. In conclusion, the photovoltaic DC system described herein consists of PV modules, battery modules, AC/DC modules and inverting modules. Under the condition of different loads, the DC bus voltage is kept stable with the coordination of PV modules, battery modules and AC/DC modules according to the theory of energy balance. The working states under different conditions are as follows:

(1)When the solar energy is sufficient, the PV module keep the system bus voltage stable as the main power module. The power flows from the bus to loads and battery. The AC/DC module is turned off.

(2)The battery module first detects the decline of the bus voltage due to the energy lack of PV module. If the bus voltage does not drop below the acceptable voltage point, boost circuit starts to work. The bus voltage is kept stable with the coordination of PV and battery. Now PV works at the MPPT mode and AC/DC module is turned off.

(3)The AC/DC module detects the decline of the bus voltage due to the energy lack of PV and battery and then starts. Now the bus voltage is kept stable with the coordination of these three modules.

In Fig.7, the DC bus rated voltage is 360V. Loads with relatively low voltage requirements such as LED lights can be directly powered by DC bus. However, high quality of power is required by devices with relatively strict power system requirements such as computers. It is not encouraged to power these devices directly even when the DC bus voltage level meets the requirements. It is advisable to power them with special adapters of DC/DC converters.

Prototype results

The system involved in this paper is based on MATLAB simulation model and a prototype is created, and it is shown in Fig.10.

The prototype consists of solar photovoltaic panels, control panels, power panels and battery units. The maximum output power for the solar photovoltaic panels is 6.4kW, four in parallel. One is adopted for experience so the maximum output power is 1.6kW. The open circuit voltage varies around 250V in accordance with different light intensity. TMS320F28335 serves as the main control chip on control panels and PM75B4LB060 from the Mitsubishi Electric serves as the IPM modules on power panels. LC-P12100ST（12V 100A/H）from the Panasonic Corporation serves as the battery, ten in series. So the normal voltage varies between 120V and 138V. High power discharge resistors serve as the discharge loads when experience.

When the light is adequate and PV module stabilizes DC bus voltage as well as powers the system as the main power supply unit, the curve for bus voltage, PV module current, battery charging current and inverter module output AC current are shown in Fig.11. As is shown in Fig.11, the DC bus voltage is stable at 360V with a small fluctuation of 3.9V. The photovoltaic cells output stable current

(the maximum power about 1.2kW) and battery is charged with a stable negative current if we suppose the discharge current is positive. Also, the AC module outputs stable AC current.

Fig.10 A prototype of photovoltaic DC system

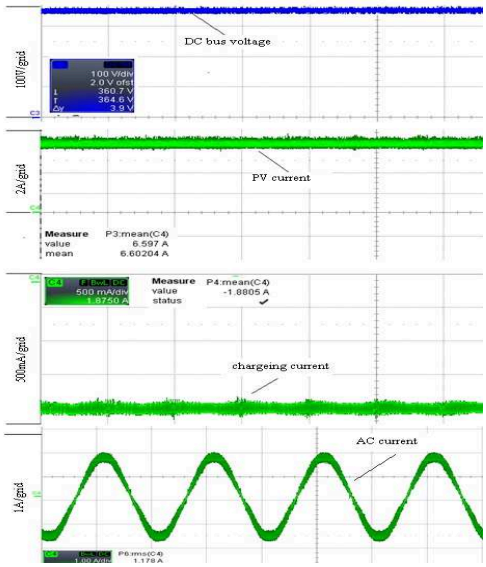

Fig.11 Waveforms of DC bus voltage, PV module current, battery charging current and inverter current

Tests of charging LED lights, laptops and so on through DC/DC modules are made on the prototype. Results show that stable working is possible for relative loads so long as the voltage meets the requirements.

Conclusions

This paper researches on the power supply system of DC loads for the office with the help of a simulation model and a prototype. The results show that it is of high feasibility to power these loads directly through the DC system. The prototype is reasonable. It is possible to stabilize the DC voltage and output stable AC and DC current. Electricity utilization efficiency can be promoted for the office space where DC loads are more integrated. It is of high practical value.

References

[1] Xunqing Huang, in: The age of DC Household Appliances Comes Soon[J]. Appliances, 2009(3): 62-63.
[2] Qing Li, in: Appliances Powered by DC Sources are Trends. [EB/OL] http://datacenter.chinabyte.com/390/8658890.shtml. 2008.
[3] Xiang Zeng, in:Design of Adapters for Laptops in a car[J], Design and Applications, 2010, 27(4): 49-51.
[4] MATSUI M, KITANO T, XU D, in: A Simple Maximum Photovoltaic Power Tracking Technique Utilizing System Inherent Limit Cycle Phenomena[C]//Pro 38th Annu Ind Appl Conf.Seattle, Wash, USA, 2003: 2041-2047.
[5] Hui Shen, Zuqin Zeng, in:Technology of Solar Photovoltaic[M], Beijing: Press of chemistry industry, 2009.
[6] Tao Shi, Lingzhi Zhu, Feng Li, Wei Li, in: Simulation and Research on Dynamic Response Characteristics of Photovoltaic Power System Connected to Grid[J], East China Electricity, 2010, 38(7).
[7] J BENEMANN, O CHEHAB, ESCHAAR GABRIEL, in: Building-integrated PV Modules [J], Solar Energy Materials and Solar Cells, 2001, 67(1—4)：345—354.
[8] Like Zhao, in: Repairing Laptops by Looking Pictures [M], Beijing: Press of People Post.

Advanced Materials Research Vols. 986-987 (2014) pp 2001-2005

doi:10.4028/www.scientific.net/AMR.986-987.2001

Research on the Influence of Closing Resistor inside Circuit Breaker on Magnetizing Inrush Current of UHV Transformer

Zhen Guo[1,a],Huiyuan Zhang[1],Bo Wang[2],Renmin Gong[3] and Yonghao Zhang[3]

[1]School of Electrical and Electronic Engineering, North China Electric Power University, Beijing 102206, China;

[2]North China Electric Power University, Baoding 071000, China;

[3]Beijing Join Bright Digital Power Technology Co.,Ltd, Beijing 100085,China.

[a]ncepuhvgz@yeah.net

Keywords: UHV transformer,Magnetizing Inrush Current,Closing resistor,Simulation analysis

Abstract. Using Matlab/Simulink software established the simulation model of UHV transformer and UHV power grid.The characteristic of magnetizing inrush current for UHV transformer was obtained by simulation.The paper also analyzed the impact on differential protection from it. Closing resistor inside circuit breaker method was proposed to restrain magnetizing inrush current.The method cuts down the amplitude and accelerated the attenuation speed of it, so as to restrain it. The simulation analysis verified the effectiveness of the method.

Introduction

UHV transformer is the most important equipment in UHV transmission system.The running status plays a key role in entire power grid,especially for safe and stable operation of UHV system[1].Magnetizing inrush current is one of the important factors that influences differential protection.The strategies for restraining of it include interpolation resistance method,the technology of phase selection and closing resistor inside circuit breaker and so on.For resistance interpolation method, the paper [2] thinks it needs to do a further research on the issue of selection of ground resistance and delay time.The paper [3] thinks that the technology of phase selection is associated with core remanence,but core remanence is hard to measure, so the method still has problems in practical application. The method of closing resistor inside circuit breaker has obvious effect on restraining the current,and it is more simple,cost-effective,which has a broad application prospect.Therefore, the paper adopts closing resistor inside circuit breaker to restraining magnetizing inrush current.

The generating mechanism of magnetizing inrush current

Due to the nonlinear characteristic of transformer core, even if the magnetic flux changes a lot, magnetizing inrush current will be very small when the transformer core flux Φ is less than iron core saturation magnetic flux Φ_{sat}.However,in the event of iron core saturation（Φ>Φ_{sat}）, with the increase of magnetic flux, it will produce a lot of magnetizing inrush current i_{μ}.For large capacity transformers, the peak value of it is several times bigger than the rated current.

The expression of magnetic flux is given by (1) [4].because magnetic flux and magnetizing inrush current have positive correlation,so it can be found that magnetizing inrush current is the largest when angle $\alpha = 0^{\circ}$ or $\alpha = 180^{\circ}$ and the smallest when angle $\alpha = 90^{\circ}$ at no-load closing moment.In addition,it is related to the core remanence,power capacity,core materials,ect.

$$\Phi = -\Phi_m \cos(\omega t + \alpha) + \Phi_m \cos\alpha + \Phi_r \quad (1)$$

The relationship between closing resistor and magnetizing inrush current

The paper takes single-phase transformer as an example to reason out magnetizing inrush current formula.For transformer no-load operation,it is on the basis of electromagnetism induction law and kirchhoff's current law to write circuit equation.As given by (2):

$$L\frac{di}{dt}+(R+R_i)i=U_m\,sin(\omega t+\alpha) \qquad (2)$$

Equation（2）is a first order constant coefficient non-homogeneous linear differential equation and it's general solution is as follows:

$$\begin{aligned} i &= e^{-\int\frac{R+R_i}{L}dt}\left[\int\frac{U_m}{L}sin(\omega t+\alpha)e^{\int\frac{R+R_i}{L}dt}dt+C\right] \\ &= U_m\frac{(R+R_i)\,sin(\omega t+\alpha)-\omega L\,cos(\omega t+\alpha)}{(R+R_i)^2+(\omega L)^2}+Ce^{-\frac{R+R_i}{L}t} \end{aligned} \qquad (3)$$

In order to solve the value of indefinite integral constant C, makes initial magnetic flux for transformer Φ_0（t=0，$\Phi=\Phi_0$）.At the same time, set the equations as follows:

$$\frac{\omega L}{\sqrt{(R+R_i)^2+(\omega L)^2}}=sin\,\theta;\quad \frac{R+R_i}{\sqrt{(R+R_i)^2+(\omega L)^2}}=cos\,\theta$$

Put Φ_0,$sin\,\theta$,$cos\,\theta$ into the equation（3）as follows:

$$\begin{aligned} i &= \frac{U_m}{\sqrt{(R+R_i)^2+(\omega L)^2}}sin(\omega t+\alpha-\theta)+ \\ &\left[\Phi_0-\frac{U_m}{\sqrt{(R+R_i)^2+(\omega L)^2}}sin(\alpha-\theta)\right]e^{-\frac{R+R_i}{L}t} \end{aligned} \qquad (4)$$

Through equation（4）, magnetizing inrush current is can be found that it include the steady state component and the transient component. It is decreased due to increase of R_i in the steady state component;The peak attenuation speed of magnetizing inrush current is accelerated owing to increase of R_i in the index part of transient component.The steady state component of it reach to the maximum when $t=(\frac{\pi}{2}+\theta-\alpha)/\omega$， while impedance angle is decreased owing to R_i,so the time of the peak of magnetizing inrush current is brought forward[5].

Modeling and Simulation of UHV Transformer

Modeling of UHV Transformer. There is no module of there-winding UHV auto-transformer in Matlab,however,no matter how the windings are arranged,we can study the three-winding auto-transformer by means of a Y-type equivalent circuit[6].By this token,the three-winding auto-transformer can be simulated by three- winding ordinary transformer[7]. The correctness of the proposed method has been validated by computer simulation in the paper [7].With reference to 1000kV UHV transformer prototype structure[8], three-phase UHV transformer simulation model is established in Matllb shown in Fig.1.

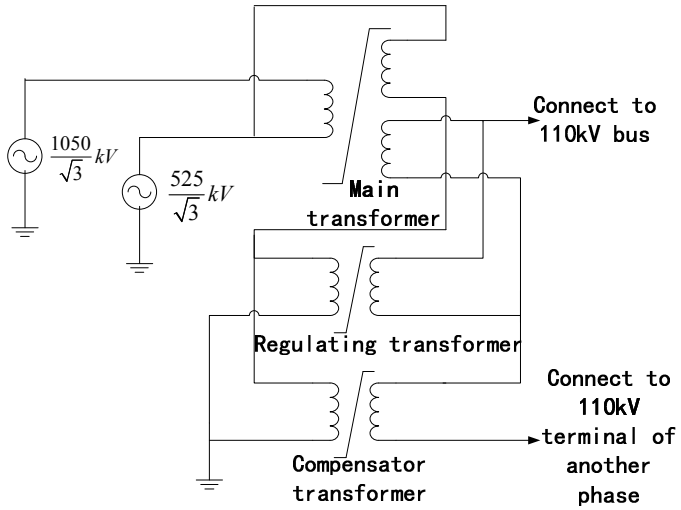

Fig.1 MATLAB model for single-phase UHV transformer

Simulation analyses. Fig.2 is the simulation system.The simulation model parameters are derived from the southeast Shanxi - Nanyang - Jingmen 1000kV UHV AC demonstration project in China[9].

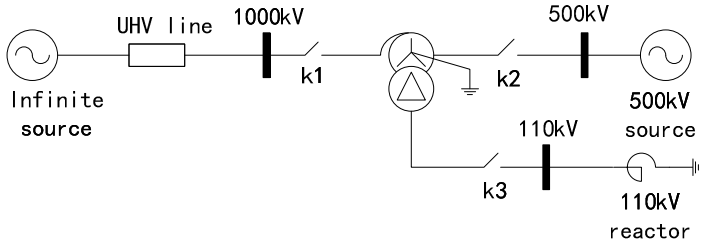

Fig.2 UHV simulation system

The article adopts the saturated magnetic flux B_s=1.15B_m and uses piecewise linearization saturation characteristic curve.The simulation time is 0.5s and adopting algorithm is ode23tb.In this paper,some simulations of UHV transformer are done when no load closing from the high voltage side and the medium voltage side separately.Both of the closing angle of A phase are 180°,when closing from the high voltage side or the medium voltage side. Residual magnetism of phase A,B,C is set in 0.9B_m,0,-0.9B_m(UHV transformer serious saturation).Fig.3-Fig.4 show the waveforms which are obtained by no-load closing process.The paper takes the first one waveform as data analysis window,and Fig.5-Fig.6 is the FFT analysis for Fi.3-Fig.4.

The peak of magnetizing inrush current of high voltage side is 4898.41A,which is 2.97 times than the rated current.And the corresponding number is 10612.26A and 3.22 times when closing from the the medium voltage side.By comparing the waveforms between Fig.3 and Fig.4,it can be found that the waveform in medium voltage side is more regular than high voltage side.Relative to the ordinary transformer,magnetizing inrush current waveform dead angle of UHV transformer is decreased obviously,and it is a great test for UHV transformer differential protection which is based on the dead angle principle.

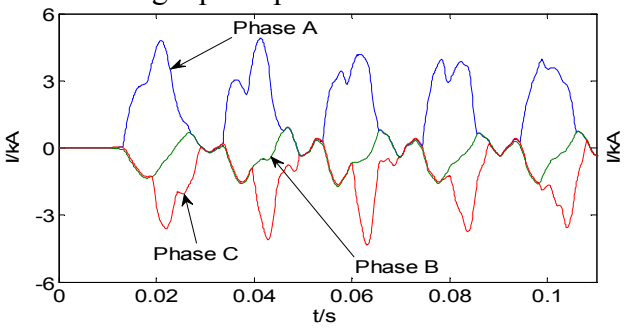

Fig.3 Inrush current of high voltage side

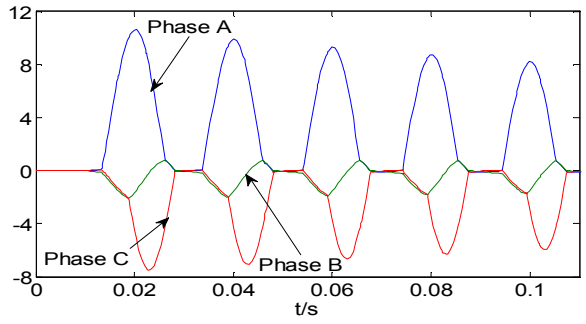

Fig.4 Inrush current of medium voltage side

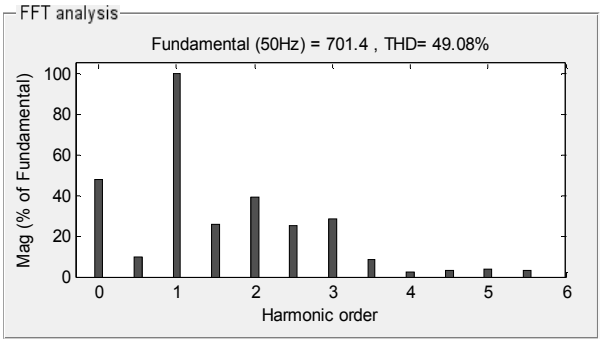

Fig.5 FFT analysis for inrush current of high voltage side

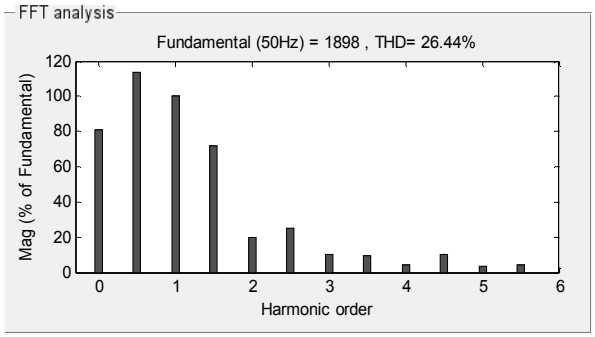

Fig.6 FFT analysis for inrush current of medium voltage side

Through Fig.5-Fig.6,there are more DC components,fundamental components and second harmonic components besides abundant subharmonic in magnetizing inrush current.In addition,when closing angle and remnant flux are taken into account,the second harmonic ratio of magnetizing inrush current of one phase will be below 15%.For examble,when no-load closing from high voltage side,the remnant flux densities of three phase is $0.9B_m$,0,$-0.9B_m$ and the initial angle of phase A is 150°,the second harmonic ratio of phase C are below 2.0%.This will pose challenge to differential protection which is based on the theory of 2nd harmonic.Therefore,the paper proposes using closing resistor inside circuit breaker to restrain magnetizing inrush current so as to minizize the influence of the differential protection from it.

Restraining magnetizing inrush current with closing resistor

Restraining magnetizing inrush current with closing resistor is effect and easy to implement.Moreover,the method can restrain not only magnetizing inrush current but also resonance overvoltage with higher amplitude caused by energizing no-load transformer[11].Fig.7 is simulation system.

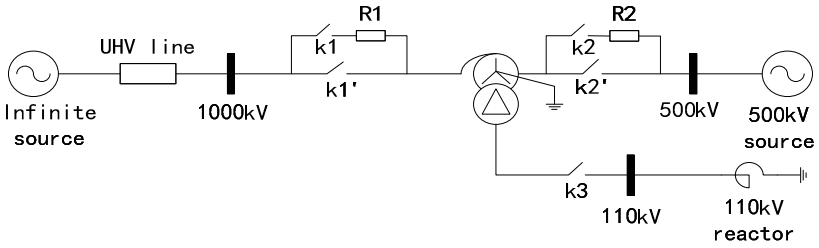

Fig.7 Simulation system with closing resistor

Simulation and data analysis. In Fig 7,the UHV transformer is no-load closed from high voltage side and medium voltage side separately. Simulation time is 0~0.5s.Closing time for ki（i=1, 2） is 0.01~0.49s and for ki'（i=1, 2） is 0.49 s ~∞.The simulation waveforms are seen in Fig.8-Fig.9.

As is seen in Fig.8-Fig.9,when closing from high voltage side with resistor at 100Ω,the amplitude of magnetizing inrush current will be lower significantly,but at this time,the amplitude of the first cycle in it is relatively big.By the time the resistor is 500Ω,the amplitude will be more lower especially for the first cycle.At last,when the resistor value reaches 1500Ω,the amplitude will be sharply cut down and restraining rate of magnetizing inrush current will be get to 88.6%;When closing from medium voltage side, the restraining effect of closing resistance is more obvious.By the time the resistor is 500Ω, the magnetizing inrush current restraining rate will reach 92.1%.By observing the waveforms in Fig.8-Fig.9,owing to closing resistor ,it can also be found that the disappear time of the first cycle is shorten constantly.It is helpful to improve the operation rate of differential protection correctly.Detailed analysis of the data is also shown in Tab.1.Through Tab.1,it can be founded that the higher of the power grid voltage level ,the larger of the resistor values.In addition,closing resistor brings disturbance to the power system,so it should be given full consideration when to choose closing resistor.

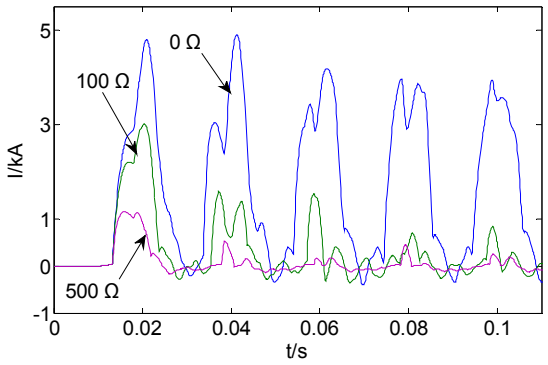

Fig.8 High voltage side inrush current

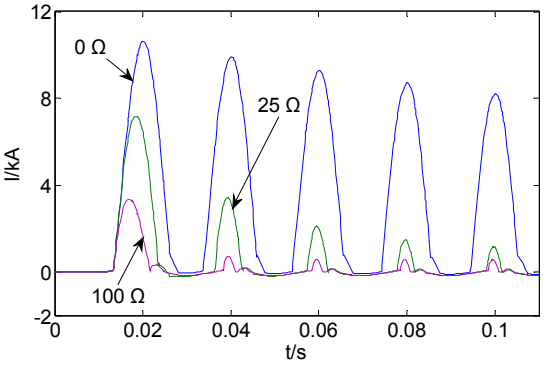

Fig.9 Medium voltage side inrush current

Tab.1 Magnetizing inrush current parameters with closing resistor

No-load closing	High voltage side						Medium voltage side					
Closing resistor Ω）	0	100	500	700	900	1500	0	50	100	200	350	500
$\mathbf{I_P}$ (kA)	4.90	3.02	1.16	0.98	0.83	0.56	10.61	4.90	3.22	1.90	1.16	8.36
Restraining rate μ %）	---	38.4	76.3	79.9	83.1	88.6	---	53.8	69.7	82.1	89.0	92.1
Disappear time ms）	29.5	26.9	24.7	24.2	23.9	23.2	28.1	25.3	25.0	24.6	24.1	23.7

Note:Retraining rate of inrush current is defined as $\mu = \frac{I_P - I'_P}{I_P}$,where I_P is the amplitude of inrush current without closing resistor and I'_P is amplitude of it with closing resistor; Disappear time means disappear time of the first cycle.

Conclusion

Closing resistor inside circuit breaker for UHV transformer has an obvious effect on restraining inrush current. Owing to closing resistor, the amplitude of it will be more lower and the disappear time of the first cycle is shorten constantly.Thus,it's helpfull to improve the sensitivity of the differential protection.

References

[1]W.L.Zhang,W.L.Wu and Y.Hu:Research on UHV transmission technology and development of power network in China,High Voltage Engineering,Vol.29(2003)No.9,p.16-18.

[2]R.H.Zhang:*Study on technology of inrush currentidentifying and restraining for transformer*(MS.ChongQing University,China 2012),p.24-26.

[3]Z.G.Hao,B.H.Zhang and Y.L.Chu,et al:Study on inrush current restraining technology when energizing no-load transformer,High Voltage Apparatus,vol.41(2005)No.2,p.81-84.

[4]B.H.Zhang,X.G.Yin:*Power System Protective Relaying(Second edition)*(China Electric Power Press,China 2009).

[5]Z.M.Wu,H.L.Quan and Y.H.Du,et al:Research on restraining strategy of transformer inrush current based on series of closing resistor,Electrotechnical Application,Vol.30(2011)No.15,p.56-60.

[6]T.M.Yang,C.L.Shi and X.D.Tan:*Autotransformer and its application*(China Electric Power Press, China 1987).

[7]J.Zhang:*A method for inrush detection in ultra-high voltage transformer*(MS.North China Electric Power University,China 2012),p.92-97.

[8]D.X.Yang,D.S.Chen and W,Chen et al:The dynamic physical model of UHV AC transmission system,Automation of Electric Power System,Vol.32(2008)No.22,p.36-40.

[9]L.J.Zeng,X.N.Lin and J.G.Huang,et al:Modeling and electromagnetic transient simulation of UHV autotransformer,Proceedings of the CSEE,Vol.30(2010)No.1,p.91-97.

[10]Z.L.Wang,H.D.Duan and Y.F.Gao,et al:*Matlab application technology is in the application of electrical engineering and automation*(Tsinghua University Press,China 2007).

[11]J.M.Lin,X.G.Wang and L.G.Ban,et al:Resonance overvoltage caused by energizing no-load transformer in 1000 kV transmission system,Power System Technology,Vol.31(2007)No.2,p.5.

Advanced Materials Research Vols. 986-987 (2014) pp 2006-2009

doi:10.4028/www.scientific.net/AMR.986-987.2006

Research on the Methods of Interharmonics and Flicker Limit Curve

Wang Tianshi[1], Wang Qinghao[2], Wang Yi[2], Li Na[2], Liu Jing[3], Chu Lina[3], Liu Zhitong[4]

[1]School of Information and Control Engineering, Liaoning Shihua University, Fushun, China

[2]Fushun Power Supply Company, Liaoning Electric Power Company Limited, State Grid, China,

[3]Tieling Power Supply Company, Liaoning Electric Power Company Limited, State Grid, China,

[4]Shenyang Power Supply Company, Liaoning Electric Power Company Limited, State Grid, China,

wts55@126.com

Keywords: interharmonics; flicker; curve; experimental platform; fluorescent lamp

Abstract. In order analyze the inter-harmonic affections on the voltage flicker, the relationship between the inter-harmonics and flicker analysis are carried out. In order to be able to accurately determine the level of inter-harmonics to make the electric light flicker, interharmonic-flicker limit curve drawing method based on the voltage flicker constraints is established. And according to IEC lamp-eye-brain model, analog tester flicker and interharmonic-flicker experimental platform are built; limit curve can be drawn through the experimental data. The 2 kinds of harmonic-flicker limit curves for the 220 V, 50 Hz fluorescent lamp are drawn by the 2 methods separately, and the analysis results show that the accuracy of the results obtained by the two methods, the level of interharmonics whether lead to fluorescent flicker can be determined by the curves. The methods have the small amount of calculation, and are practical and easy to implement.

Introduction

With the extensive use of nonlinear and fluctuation load in power system, adverse effects caused by interharmonics generated by these loads bring along are getting increasingly prominent, among which the most representative issue is interharmonics effect on voltage fluctuation and flicker [1-3].

To research on the impact of interharmonics on voltage fluctuations, interharmonic signals can be superimposed on the power frequency voltage signal and voltage fluctuations and changing frequency will be quantitatively investigated [4, 5]. However, because the lights flicker illumination voltage fluctuations are caused by instability, thus human eyes feel discomfort. Whether the electric light happen flicker decided by voltage fluctuations and the size of voltage fluctuation frequency. Experiments show that the human eyes are sensitive to different flicker frequency; the general frequency of 8.8Hz is most sensitive to flicker [6]. The determination of flicker value needs assessment. Therefore, quantitative analysis is more difficult.

Flicker assessment methods are the IEC flicker meter designed based on the voltage amplitude modulation flicker effect on incandescent lamp currently [7]. Due to the fundamental harmonic synthesis between signals from the point of view is not the essence of amplitude modulation signal, the effect of flux fluctuations and volatility caused by the incandescent lamp load is different, so traditional IEC flicker meter is not suitable for the calculation and assessment of the inter-harmonic voltage fluctuations and flicker problems caused [8].

On this basis, through the Inter draw harmonic - to assess the impact of inter-harmonics flicker curve, that is, through the development of inter-harmonics - to describe produce flicker curve between harmonic amplitude thresholds to determine a whether a harmonic components can cause flicker. If the amplitude between the harmonic components of a specific frequency is higher than the relative magnitude of the curve between the harmonics, inter-harmonics will cause the flicker; possibility that flicker on the contrary, the corresponding RMS voltage fluctuations on small [9,10].

The intrinsic relationship between harmonics and flicker are analyzed in this paper, and two kinds of inter-harmonics-Flicker curve drawing method are put forwarded, the 220 V/50 Hz

fluorescent Interharmonics-Flicker restrictions curve are plotted by these two methods and are compared and analyzed.

Voltage flicker constraint condition based approach

The basic idea of interharmonics-flicker curve drawing is: the interharmonics constraint conditions will be derived by voltage flicker constraints, and the curve is derived by reusing interharmonics constraints.

Voltage flicker constraints are mainly IEEE flicker curve and based on the IEC flicker meter. Which IEEE flicker curve for a specific frequency flicker constraints is one in; rather based on the IEC flicker meter has a variety of constraints, which one to selected depends on its function.

Interharmonics-Flicker curve describes the maximum acceptable functional relationship between the harmonic amplitude and inter-harmonic frequencies, whose function is expressed as

$$m = \phi(f_{\text{ih}}) \tag{1}$$

Where m is the relative amplitude of interharmonics, f_{ih} is the inter-harmonic frequency.

The concrete steps to get limit curve are as follows:

1) The voltage change value corresponding to the frequency of the flicker is obtained by standard curve, the relationship of the formula is

$$(\frac{\Delta U}{U})_{\text{x}} = \psi(f_{\text{flicker}}) \tag{2}$$

2) Get the inter-harmonic frequency corresponding to flicker frequency, the relationship between flicker frequency and interharmonic frequency is

$$f_{\text{flicker}} = g(f_{\text{ih}}) \tag{3}$$

3) Identify the relationship between the minimum amplitude to produce flicker between the harmonics, the relationship between voltage fluctuations and inter-harmonic amplitude and frequency is

$$(\frac{\Delta U}{U})_{\text{x}} = f(m, f_{\text{ih}}) \tag{4}$$

4) Repeat the above steps to obtain the amplitude of the voltage variation between different harmonic frequencies critical to complete the curve drawing.

Figure 1 shows the 0 ~ 100Hz frequency, 220 V/50 Hz fluorescent harmonic - Flicker curve by the above approach. From Figure 1, the interharmonic-Flicker curve waveform based on the peak value fluctuation is approximately symmetrical, the interharmonics components near the fundamental harmonic are more likely to cause flicker than other frequency band, thus causing flicker interharmonic wave minimum limit threshold levels occurred near the fundamental frequency.

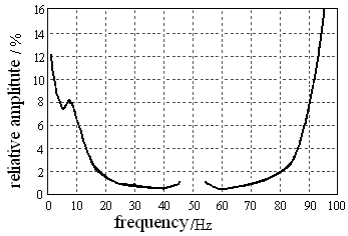

Fig. 1 The fluorescent lamps interharmonics-flicker curve

Interharmonics flicker experimental methods

In order to analyze the relationship between interharmonics and flicker and draw out inter-harmonics-flicker curve, an interharmonics flicker experimental platform is established, the structure is shown in Figure 2.

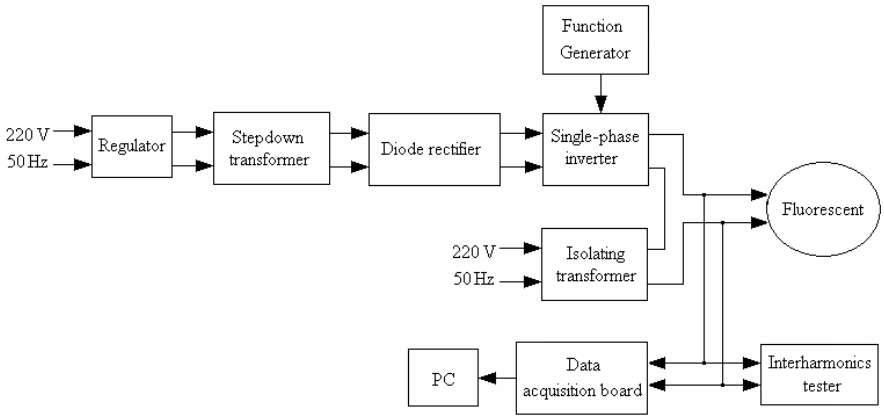

Fig 2 The schematic diagram of the interharmonic flicker laboratory station

Two single-phase 220V, 50Hz power frequency voltage signal are as input. One way is through the regulator, step-down transformer, diode rectifier bridge, and then after a series of single-phase H-bridge inverter voltage signal with another path through isolation transformer isolation, as an electrical power source. The first circuit is used to generate inter-harmonic voltage signal. By adjusting the input voltage of the regulator to change the filter capacitance diode full bridge rectified DC voltage output, control H-bridge inverter output harmonic voltage between the amplitude of the output of the inter-harmonic frequency controlled by a function generator. The second way is as an electrical power source. Through two voltages in series, the inter-harmonic frequency signal is applied to the signal source to the electric power supply.

Collection and analysis for the detection of voltage flicker signal is completed by analog meter flicker on the computer, and inter-harmonics monitoring is done by the interharmonic detector. For specific frequency interharmonics, increase its amplitude threshold, it will cause flicker. The flicker situation will be judged by observing the experimenter simultaneously.

Flicker specific process is as follows: Input signals are adjusted to the proper voltage adapter voltage value, in order to meet the testing requirements; standard modulation signal generator as a self-test and calibration wave voltage signal; separated by squares and AM demodulator voltage proportional to the amplitude fluctuation amount, i.e., the analog characteristics of the lamp, to reflect changes in the illumination light and the relationship between the voltage fluctuations; then using a band pass filter removes the DC component of the square of the demodulated voltage signal and the carrier frequency component, using Visual sensitivity weighting filter simulated human visual system by the frequency response of the fluorescent sinusoidal voltage fluctuations; then squared and integral filter simulation of human brain reflects the visual; Finally, the statistical results output link.

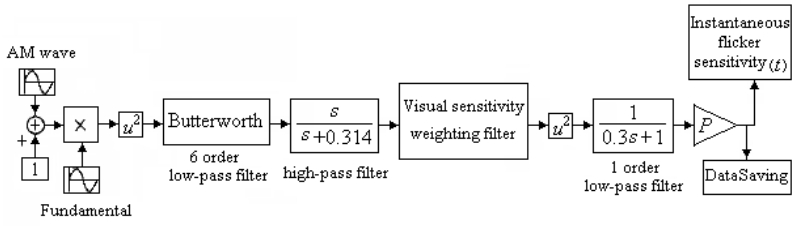

Fig. 3 MATLAB/Simulink simulation diagram of flickermeter

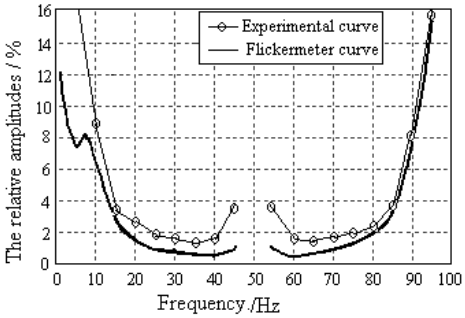

Fig 4 Interharmonics-flicker curve comparison

Analog meter is created based on IEC Flicker meter principle and the use of MATLAB / Simulink simulation analog simulation system software. Its system simulation block diagram is shown in Figure 3, this measurement system is as a standard measurement system.

The specific frequency interharmonics are selected and its amplitude is adjusted until the flicker threshold value, and amplitude is recorded. By changing interharmonic frequencies, repeat the above steps, the 220 V/50 Hz fluorescent 0 ~ 100Hz Interharmonics - Flicker curve is drawn shown in Figure 4, part of the test data are shown in Table 1.

Table 1 The data of interharmonics-flicker curves

Iinterharmonics Frequency Hz	Flicker Frequency Hz	Relative Amplitude m/%	Iinterharmonics Frequency Hz	Flicker Frequency Hz	Relative Amplitude m/%
5	45	16.20	95	45	15.73
10	40	8.86	90	40	8.04
15	35	3.50	85	35	3.78
20	30	2.63	80	30	2.26
25	25	1.87	75	25	2.01
30	20	1.64	70	20	1.85
35	15	1.56	65	15	1.78
40	10	1.82	60	10	1.82
45	5	3.74	55	5	3.81

Comparison of two methods

Figure 4 shows that the trend of interharmonics-flicker curve obtained by experiment and based on the IEC constraints are consistent, and the flicker curve obtained experimental curves flicker threshold is only slightly higher than the curve deduced. Two methods are basically the same. In comparison, the curve based on the constraints of IEC flicker is more stringent to interharmonic flicker occurs.

Conclusion

The impact of interharmonics on flicker can be presented by interharmonics- flicker curve. The curve will provide references to judge whether the level of inter-harmonics will cause light flicker occurs. Two methods to complete the 220 V/50 Hz fluorescent lights interharmonic-flicker limit curve are proposed in this paper, and their calculation amount are small and easy to implement.

Reference

[1] GB/T 24337-2009 Power quality Public power system interharmonics [S]. Standard of China, 2009.

[2] LIN Haixue. Origin of Interharmonic and Its Effects on Power System [J]. Power Supply Technologies And Applications， 2010，13(5)：1-6.

[3] HAO Jiangtao, Liu Nian, Xing Jinyu, at el. The Sources and harms of interharmnics in power system[J]. Sichuan Power Technologies，2005，2：11-14.

[4] ZHU Ke, YONG Jing, Thavatchai Tayjasanant. Quantifying Flicker Impact of Interharmonics[J]. Proceedings of the CSEE, 2008, 28（28）：113-118.

[5] HU Jie,CHEN Ni. The analysis of interharmonics affection on the voltage fluctuation[J]. Electrical power application, 2010, 29(5): 46-49.

[6] XIAO Xiangning. Power quality analysis and control [M]. Beijing: China Power Press, 2010.

[7] IEC Technical Subcommittee 77A. Electromagnetic compatibility (EMC)part 4：testing and measurement techniques，section 15：flickermeter-functional and design specifications (IEC 61000-4-15)[S]. Geneva, Switzerland：IEC，2003.

[8] CHEN Han, LIU Huijin, LI Dalu. Establishment of Interharmonics-Flicker Curve Based on Peak Fluctuations[J]. Power System Technology, 2010, 34(9): 109-114.

[9] Tayjasanant T, Wang W, Li C, et al. Interharmonic-flicker curves[J]. IEEE Trans. on Power Delivery, 2005, 20(2): 1017-1024.

[10] YONG Jing, SUN Caixin, LI Jianbo, et al. Light Flicker Characteristics Caused by Interharmonics and Flicker Limit Curve[J]. Proceedings of the CSEE, 2008, 28（31）：88-93.

Advanced Materials Research Vols. 986-987 (2014) pp 2010-2013

doi:10.4028/www.scientific.net/AMR.986-987.2010

Review on Mechanism and Analysis Methods of Low Frequency Oscillation in Power System

He Nan Wang[1,a] , Chao Zheng[2,b] , Jie Ren[1,c],Jian She Tian[1,d] , Hong Tao Liu[3], Can Hui Sheng[2]

[1] North China Electric Power University, Baoding, Hebei, 071003, China

[2] China Electric Power Research Institute, Haidian District Beijing, 100192, China

[3] Power Dispatching Control Center, CSG, Guangzhou, Guangdong, 510623, China

[a]313053624@qq.com, [b]Zhengch@epri.sgcc.com.cn, [c]380307538@qq.com, [d]tianjs_2521@163.com

Keywords: low frequency oscillation; analysis method; damping; eigenvalue.

Abstract. Low frequency oscillation caused by system interconnection has been the main factor to threat the secure operation of power grid. It's significant to research on the problem of low frequency oscillation. This paper summarizes the generation mechanism and analysis methods of low frequency oscillation. Each analysis method has both advantages and disadvantages.

Introduction

With the rapid development of power system, more and more large-capacity generators and fast and high-gain excitation control equipment are put into operation, which may cause low frequency oscillation. Nowadays low frequency oscillation has been the main factor to threat secure operation and to restrict transmission capacity of power grid. When the generators are in parallel operation through transmission lines, inevitable disturbance will make generator rotors swing relatively. Sustaining oscillation occurs when the damping is insufficient. Meanwhile oscillation also occurs in transmission lines and the frequency is between 0.1-2.5HZ [1].

Insufficient damping is the main factor causing oscillation. Given the generator rotor inertia time constant is relatively long, the oscillation frequency is relatively low and this is the source of low frequency oscillation. Low frequency oscillation often occurs in long-distance and heavy-load transmission lines, especially in excitation system with high magnification. The occurrence of low frequency oscillation will produce two results: oscillation amplitude increasing persistently or decreasing gradually. The first one will destroy system stability and even cause system separation; the second one can be eased by appropriate measures. Therefore, it's significant to study the generation mechanism and analysis methods of low frequency oscillation in power system.

Generation mechanism of low frequency oscillation

Experts from various countries put forward different mechanisms on low frequency oscillation including:

Bifurcation phenomenon

The bifurcation of power system covers static and dynamic bifurcation. Static bifurcation is caused by multiple solutions of system flow equations. While, dynamic bifurcation includes Hopf, circulating and double period bifurcations, which have different mechanisms. Reference [2] given out detailed explanation.

Hopf bifurcation means that aiming at nonlinear system

$$\dot{X} = F(x,\mu) \ (x \in R^n, n \geq 2, \mu \in R)$$

Expanding at the balance point, we get

$$\dot{X} = Ax + F(x,\mu)$$

Where

$A = \left.\frac{\partial F}{\partial x}\right|_{x} = 0$, $F(x,\mu) = F(x,\mu) - Ax$

Nonlinear system may jump from a response to another response when μ changes. The phenomenon of connecting the two responses is called bifurcation. If it suddenly jumps from stability in the sense of Lyapunov to nonlinear oscillation, then the bifurcation is Hopf bifurcation.

Underdamping Mechanism

Since F.Demello firstly proposed underdamped mechanism of low frequency oscillation in reference [3], academia gradually reached a consensus. The theory point out that negative damping produced by system offsets the positive damping produced by generator, excitation winding and machine. In the case of underdamping, disturbance is gradually amplified and leads to low frequency oscillation.

A special underdamped situation is that the disturbance frequency is the same with the system inherent frequency. In such case, it's possible for system to generate resonance-type underdamped low frequency oscillation. Reference [4] pointed out that if the system damping is zero or small ,unbalanced torque caused by disturbance will lead to equal amplitude oscillation. When disturbance frequency is close to system inherent frequency, response will be amplified because of resonance, then causing resonance-type low frequency oscillation. This kind of oscillation is due to insufficient damping after all, so it can be classified into underdamped situation.

Chaotic oscillation mechanism

Chaotic behavior is uncertainty produced by a certain model and is a complex behavior caused by parameters interaction in nonlinear system. We just recognize some typical characteristics of chaotic behavior so far, for example, chaotic system is sensitive to the initial point. It means any two orbits' paths will change dramatically over time no matter how close the two initial points are. Based on the analysis of low frequency oscillation parameters, some conclusions were suggested by reference [5]: damping only won't lead to chaotic oscillation and periodic load disturbance is also a requirement; chaotic oscillation occurs under the effect of periodic load disturbance of which the value is beyond restriction; under the influence of periodic load disturbance, chaotic oscillation occurs when the damping coefficient is close to a certain value.

Two ways of generating chaotic behavior were put forward by reference [6]: period doubling bifurcation (PDB) and initial energy motivating directly. PBD means that system evolves from original single-period bifurcation to double-period bifurcation then to four period doubling bifurcation, eight period doubling bifurcation and so on. Initial energy motivating refers to that system will converge to chaotic attractor when the angular speed deviation of generator reaches a certain value. The final state of system is decided by strange attractor if the deviation continues to change in size.

Electromagnetic inertia of generator

Because the generator exciting winding has inductance, the excitation current of the excitation winding caused by excitation voltage is a lagging forced excitation current component than the excitation voltage. The hysteresis leads to lagging control, which will cause oscillation under certain conditions. It has not yet been determined so far that under what conditions low frequency oscillation caused by electromagnetic inertia will happen. In addition, related literatures are rarely seen and further research is needed.

Analysis methods

The most commonly used analysis methods of low frequency oscillation in power system include eigenvalue analysis based on linearizing theory, bifurcation theory analysis and time-domain simulation analysis based on nonlinear dynamic equation.

Hopf bifurcation theory analysis method

After the Hopf bifurcation occurred, the problems such as the direction of the Hopf bifurcation and the stability of system determined by transversality condition and curvature coefficient respectively are what we need to solve. Therefore, the system operation state is explicit after the transversality condition and curvature coefficient are solved. To two-dimensional space, the solution of the curvature coefficient is simple, but to high-dimensional system, simplifying dimension is needed. There are several ways to simplify dimension: center manifold theory, Lyapunov and Schmit methods, etc.

Eigenvalue analysis

All eigenvalues analysis method. All eigenvalue analysis method can be explained as follows: First, form the linear state equations of whole system by transformation $\dot{X} = Ax$; then, solve all eigenvalues of system by *Q*-*R* transformation; Finally, Identify low frequency oscillation mode by eigenvalues and obtain the operation state of system [7]. The result of this method is reliable; however, computation of solving process is too huge for large system, so it is not feasible [8].

Partial eigenvalues analysis method. Reference [9] put forward: transform coefficient matrix A of the differential equations into another matrix A_τ which has the same dimension with A and transform the concerned eigenvalue or a small number of eigenvalues of A into the biggest one or several eigenvalues of A_τ; then obtain the eigenvalues of A_τ arranged by increasing or decreasing order of module value through appropriate method; finally obtain the eigenvalues we concern through inverse transform.

Selective modal analysis method (SMA). The basic idea of selective modal analysis (SMA) is to reduce the order of the equation of state by retaining state variables related to low frequency oscillation and eliminating the rest ones, then to solve the model and modal of low frequency oscillation. This method is suitable for low frequency oscillation in large-scale power system.

Reference [7] also introduced improved SMA. This improved SMA method not only has the second order convergence rate of Newton's method and doesn't need form the original high order coefficient matrices of the system. Reduced coefficient matrix is enough and it reduces the computing time. In addition, the transfer functions of excitation and speed governing system are preserved in the process of formation, which can provide important information for setting the parameters of the controller.

Time domain analysis

Time domain simulation. Based on numerical analysis and with the help of computer, time domain simulation concludes time domain operation changes of system under disturbance. This method takes nonlinear factors into account, but the simulation time for large scale system is long.

Prony analysis method. Prony analysis is to fit evenly spaced sample data by using linear combination of exponential function then we can get the frequency, attenuation, amplitude and phase of signal [10]. Compared with the eigenvalue analysis, prony analysis doesn't need solve the eigenvalues of the large-scale system and the order of system model can be decided by the purpose and demand of identification. Prony is to analyze the real-time measurement data of system and the biggest problem is to avoid the influence of the noise signals [11].

Summary

This paper introduces four mechanisms: bifurcation phenomenon, underdamping, chaotic oscillation and electromagnetic inertia of generator mechanisms and three analysis methods: Hopf bifurcation theory, eigenvalue and time domain analysis methods. Each analysis method has both advantages and disadvantages. Analysis method should change along with the cause of low frequency oscillation.

References

[1] Klein M, Rogers G J and Kundur P. A Fundamental study of Inter-area Oscillations in Power Systems [J]. IEEE Trans on Power Systems, 1991, 6(3): 914 -921.
[2] Tan C W, Varghese M, Varaiya P, etc. Bifurcation Chaos and Voltage Collapse in Power System [J]. Proceedings of the IEEE, 1995, 83(11): 1484-1496.
[3] Abed E H, Varaiya P, etc. Nonlinear Oscillations in Power System [J]. Electric Power and Energy System, 1984, 6(1): 37-43.
[4] Demello F. Concepts of Synchronous Machine Stability as Affected by Excitation Control [J].IEEE Trans on Power Apparatus and Systems, 1969, 88(4): 316-329.
[5] WANG Tie-qiang, HE Ren-mu, etc. The Mechanism Study of Low Frequency Oscillation in Power System [J] Proceedings of the CSEE, 2002, 22(2): 21-25.
[6] TAN Bin, XUE Yu-sheng. A Study on Chaos of Multi-machine Systems [J] Automation of Electric Power Systems 2001, 25(2): 3-8.
[7] Ni Yi-Xin, CHEN Shou-sun and ZHANG Bao-lin. The Theory and Analysis of Dynamic Power System [M]. Beijing: Tsinghua University Press, 2002.
[8] LIU Yu-tian, WANG Chun-yan. A Brief Review on Low Frequency Oscillation in Power Systems [J]. Shandong Electric Technology, 1996, (6): 23-27.
[9] Byerly R T, etc. Eigenvalue Analysis of Synchronizing Power Flow Oscillation in Large Electric Power Systems [J]. IEEE Trans on Power Apparatus and Systems, 1982, (1): 235 -243.
[10] Zhang Xian-da. Modern Signal Processing [M]. Beijing: Tsinghua University Press, 1995.
[11] Liu Guo-ping. Analysis and Control of Low-Frequency Electromechanical Oscillations in Power Systems Based on Prony's method [D]. Zhejiang University, Hangzhou, 2004.

Advanced Materials Research Vols. 986-987 (2014) pp 2014-2018

doi:10.4028/www.scientific.net/AMR.986-987.2014

Study on Simulation Model on Partial Discharge in Void of Solid Insulation

Ming Li[1, a], Zeng Qinghui[2, b]

[1]Department of Electrical Engineering and Automation, China Three Gorges University , Yichang, 443002, China

[2]Power Supply Bureau of Jingzhou, China Three Gorges University, Jingzhou, 434000, China

[a]email: lmtyc2013@163.com, [b]email:mingli1228@sina.com

Keywords: Partial discharge; simulation; void dimension; electric field strength.

Abstract. In order to analyze the partial discharge of void defect discharge in solid insulator, for the PD problems that at home and abroad simulation model can't objectively reflect the physical process of partial discharge. Based on classical three capacitor equivalent-circuit model, the change of the electric field intensity and the voltage as size of the air void differs is studied. The influence of the air void geometry properties of partial discharge is analyzed. By comparing the results of the simulation model and its results and existing research results, the correctness of the circuit simulation model is verified.

Introduction

Insulation of partial discharge is one of the important causes of dielectric aging. Partial discharge is discharge or breakdown within the local area. Too high local electric field in the insulating medium due to uneven distribution of electric field then leads the discharge. It may exists in pores in the solid insulation, in bubbles in liquid insulation or at the interface of different dielectric [1]. If the partial discharge of the electrical device occur under the normal operating voltage, it shows that there have existed localized internal insulation defect, And this defect will continue to develop during the run to a certain extent, it will cause damage to insulation breakdown and damage.

Domestic and foreign scholars do a lot of research work on the numerical simulation of partial discharges [2-8]. Singapore scholar Liew. A. C proposed partial discharge model composed by pure capacitors [6]. In this model a time switch is used to control capacitors representing initial discharge void and Extinguish discharge void] he got voltage waveforms similar to partial discharge waveforms, but the simulation results are quite different from the actual measurement waveforms. on the basis of previous research results, Chinese scholars modified the classical model of air-void discharge, obtained simulation waveforms closer to the measured waveforms[7] [8], But in the simulation of partial discharge of single-void in solid insulation, there exist problems as following: The simulation model parameters lack of practical significance, it is failed to express the physical meaning of the actual discharge process and there are Insufficient validation tests to verify the accuracy of the simulation model .If the simulation model parameters can well meet the parameters of the actual partial discharge test trends, the model will be convincing and then The simulation model will also be of a great practical significance.

Based on the classic three-capacitance mode, this paper studied and derived the variation of the electric field in the air void as the variation of model parameters, and then the Impact on the initial discharge voltage as the solid insulation inside diameter of the cylindrical air void changes is explored. Then a series of tests on inside air discharge test system in solid insulation is created, the tests aimed at getting the trends of the actual initial discharge voltage as the diameter of air void varied. The correctness of the circuit simulation model is verified after comparison of experimental results and circuit simulation model.

Simulation Model

According to the research on numerical simulation of partial discharge areas by scholars both at home and abroad, based on the classic three-capacitance mode, scholars develop the simulation models to some meaningful gas-void resistance discharge model, and achieved certain results. Air discharge in solid insulation schematic diagram is shown below:

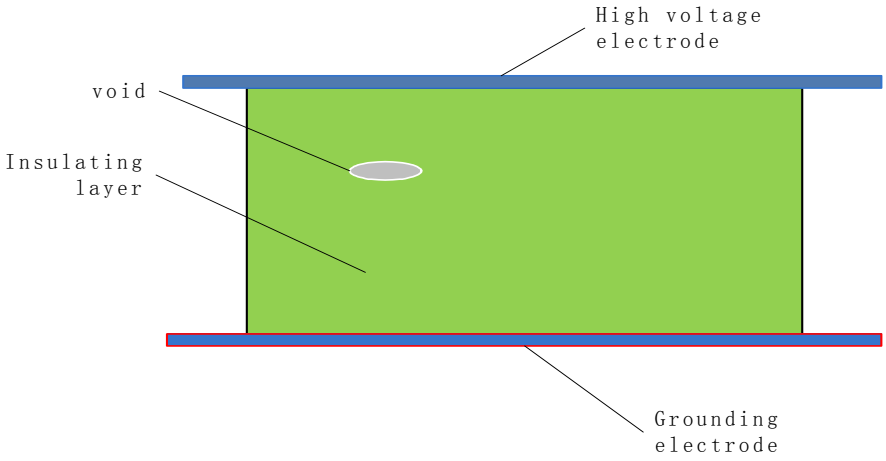

Fig.1. The geometric model of void in solid insulation

When the material is well-insulated, the voltage between the upper and lower electrode plates evenly distributed in the intermediate insulating layer. When the insulating layer has a small air void, because of the permittivity of dielectric and air is different: The permittivity of insulating material is generally much larger than the air dielectric, dielectric constant and inversely proportional to the voltage distribution, it will be under a lot of voltage on the air void, it is prone to breakdown.

The classic equivalent circuit model for partial discharge in void of solid insulation is the well-known three-capacitance model, the model is shown below:

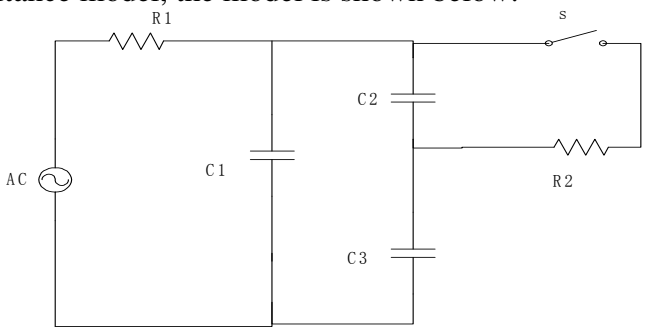

R 1 represents resistance of the line
R 2 represents the resistance of the void after the breakdown

Fig.2. Three capacitor model of void in solid insulation

Figure represents the capacitance of the air void represents the void in series with the capacitor portion, representing the remaining intact portion of the capacitor. When the system withstand voltage when the withstand voltage of $u_2 = \frac{c_3}{c_3 + c_2} u_m$

The Simulation the electric field strength

1 establishing parameters of simulation object

As for the mechanism of PD in solid insulation, although domestic and foreign scholars have conducted a large number of researches and achieved a series of achievements. However, comparing with the general discharge forms between the electrodes, discharge in void of solid insulation has its own characteristics. While the discharge caused by too high voltage over gas and

then gas Ionized.but the void is between the insulation Instead of the normal two electrodes. While both sides of the voids in solid insulation is insulating dielectric, so the breakdown mechanism should mainly impact ionization electrons collapse. Rough estimates are breakdown voltage air void withstand voltage reaches about 3kv/mm the breakdown voltage of an average field strength of.

Select the epoxy test as simulation object. Sample is cube and size 50 mm × 50 mm × 50 mm. there is a cylindrical air void in the central of test sample. Void size: radius of the cylindrical is a, height is h, Pressure of the air void is $p = 10^5$ Pa.

Parameters of three- capacitance circuit simulation are as followed:

$$C_1 = \frac{\varepsilon_0 \varepsilon_2 (l - a)}{h} \tag{1}$$

$$C_2 = \frac{\varepsilon_0 \varepsilon_1 \pi a^2}{h} \tag{2}$$

$$C_3 = \frac{\varepsilon_0 \varepsilon_2 \pi a^2}{l - h} \tag{3}$$

ε_0 represents the permittivity of vacuum, ε_1 represents the permittivity of epoxy, ε_2 represents the permittivity of air void.

2 Relationship of insulation void voltage, electric field strength and the height of the air void

The above three parameters calculated into the local voltage is calculated using: $u_2 = \frac{c_3}{c_3 + c_2} u_m$

You can get: $u_2 = \frac{h\varepsilon_2}{h\varepsilon_2 + (l-h)\varepsilon_1} u_m$

The permittivity of air void is 1. the permittivity of epoxy is 4.7. u_m is the highest AC voltage put on the test sample. in this experiment the maximum applied voltage is 40kv.So can get: $u_2 = \frac{4.7h}{l + 3.7h} u_m$

As can be seen from the above formula, when the air void height is fixed, the ratio of u_2 to u_m is fixed. And the ratio is related with epoxy size and void size. Generally speaking size of insulation materials is much larger then it of the void. u_2 increases nearly linearly with the increase of h.

The calculation of electric field strength in the air void: $E = \frac{u_2}{h} = \frac{4.7}{l + 3.7h} u_m$

Simulation using MATLAB software, the relationship of electric field intensity of air void with the height of void is shown in Figure 3:

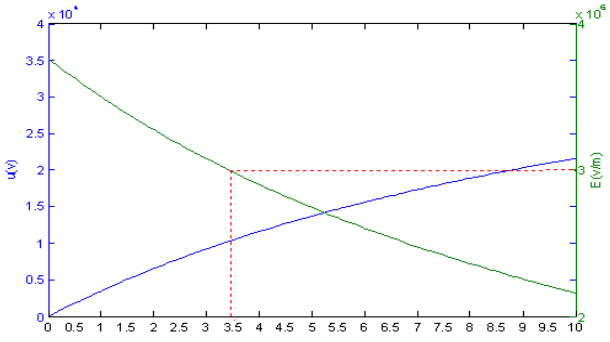

Fig.3. Relationship between the voltage and the electric field strength and the height

From the figure we can see: the voltage of the void increases linearly with the increase of height of the void while the electric field intensity is approximately linearly decline at the same time. When the height of the air void is less than 4mm, the field intensity is higher then 3kv/mm, higher than the air breakdown field strength under conditions of uniform strength field. If we assume that the electric field is uniform in the space field, discharge phenomenon then will occurs when the void is not higher than 4mm.In the paper [11].FEM algorithm is applied to simulate relationship between the electric field strength and the void size. As it reveals, field strength in the void differs with the diversification of void size: When the air void diameter is fixed, the electric field strength decreases the electric field strength increases with increasing of height; when the height is fixed, the electric field strength increases with increasing of diameter. This article is consistent with the conclusions obtained by calculating.

Conclusion

The void voltage increases linearly with the increase of void height while the electric field intensity is approximately linearly decline at the same time. Simulation can be well in line with the conclusions thus proving the reliability of the simulation model. Simulation model from qualitative to quantitative studies needs to be further explored.

Acknowledgements

This work was supported by Maser Degree of Three Gorges University Foundation (Grand 2012 CX041).

References

[1] M. D. Judd，S. D. J. McArthur，J. R. McDonald and O. Farish，“Intelligent condition monitoring and asset management：Partial discharge monitoring for power transformers”，IEE Power Engineering Journal，2002，Vol. 16，No. 6，pp. 297-304.

[2]Niemeye L. A generalized approach to partial discharge modeling[J]. IEEE Transaction on Dielectrics and Electrical Insulation，1995，2（4）:510-528.

[3]Gutfleisch F，Niemeye L. Measurement and simulation of PD in epoxy voids [J]. IEEE Transaction on Di electrics and Electrical Insulation，1995，2（5）:729-743.

[4]KUPERSHTOKH A L，STAMATELATOS C，AGORISs D P. Stochastic model of partial discharge activity in liquid and solid dielectrics. Novosibirsk[C]. Russia: International Conference on Dielectric Liquids，2005:135-138.

[5] Kolev N P, Darjanov P I, Gadjeva E D, et al. A new computer model for partial discharge phenomena investigations[A].The IEEE Electrical Insulation Conference and Electrical Manufacturing and Coil Windings Conference, Rosemont,USA,1997.

[6] Kolev NP, Danikasmg, Gadjeva E D, et al. Development of partial discharge model, simulation and measurement[A].IEEE Conference on Electrical Insulation and Dielectric Phenomena, Austin, USA,1999.

[7]CHAMPION J V，DODD S J，ALISON J M. The Correlation between the Partial Discharge Behavior and the Spatial and Temporal Development of Electrical Trees Grown in an Epoxy Resin[J]. J. Phys. D: Appl. Phys.,1996，29（4）：2689-2695.

[8]CHIA P Y，LIEW A C. Novel approach to partial discharge signals modeling in dielectric insulation void using extension of lumped capacitance mode[C]. Perth, Australia: International Conference on Power System Technology，2000:1207-1212.

[9]REN Cheng-yan, CHENG Yong-hong, CHEN Xiao-lin,etc. Simulation calculation of partial discharge in single void using variable void resistance molel[J].Journal of Xi'an Jiaotong University,2004,38(10):1018-1021.

[10]CHEN Xiao-lin, CHENG Yong-hong, REN Cheng-yan, etc. Study on modifying the simulation model and computing the key parameters of partial in single void. [J].Journal of Xi'an Jiaotong University,2004,38(8):815-819.

[11]Lihua Chen, Zhong Zheng,Min Chen, Hong Yu The study of the discharge mechanism and characteristics of micro-voids in the solid dielectric[A]. International Conference on High Voltage Engineering and Application, Shanghai, China,2012.

Advanced Materials Research Vols. 986-987 (2014) pp 2019-2022

doi:10.4028/www.scientific.net/AMR.986-987.2019

Simulation of EMP Inject Effects Based on improved Elman network

JI Zhi-qiang[1, a], WEI Ming[1, b], WU Qi-meng[2, c] and WU Xiao-le[3, d]

[1]Research Institute of Static Electricity & Electromagnetic Protection, Ordnance Engineering College, Shijiazhuang 050003, China

[2]Wuhan Military Representative Office of the General Armament Engineering Department, Wuhan 430073, China

[3]Jiujiang Military Representative Office of the General Armament Department, Jiujiang 332000, China

[a]406789675@qq.com, [b]weiming1968@sohu.com, [c]289446162@qq.com, [d]718015568@qq.com

Keywords: electromagnetic pulse (EMP); Elman network; transient voltage suppressor (TVS); system identification

Abstract. In order to quickly determine the performance of a transient voltage suppressor (TVS), improve time domain identification capability of Elman network, the simulation of electromagnetic pulse (EMP) inject effects based on improved Elman network is proposed. Derivation proved that improved Elman network trained by standard BP algorithm has a similar form with the basic Elman network trained dynamic BP algorithm. We establish and improve its Elman network predictive modeling based on the measured parameters of TVS and then demonstrate that improved Elman network has the characteristics of quick speed, high precision, good performance and strong generalization ability, and broad use of prospects.

Introduction

Electromagnetic pulse (EMP) is a kind of powerful transient electromagnetic radiation. It usually caused by lightning discharge, nuclear explosion, electrical equipments switching actions and so on. It seriously threat the electrical equipments. Influenced by EMP, electrical system can not run normally. Power transmission system usually use transient voltage suppressor (TVS) to prevent EMP. TVS is a kind of high-performance protection device look like a diode. It is widely used to absorb several kilowatts of power surges and clamp the bipolar voltage steady [1-3].

Usually, performance test of TVS use square wave act as stimulus signal. We call it transmission line pulse (TLP) method [4]. Because of the hard work and single signal, this method is not suitable for engineering application. In this paper, we increase the type of stimulus signal, then obtain the data under different pulse and amplitude conditions. The proposed method based on statistical analysis of experimental data, establish improved Elman network model for system identification. Compared to the original network it can predict the response of TVS more quickly and accurately. It is more suitable for high-order system identification. In a word, it is an effective way to reduce the testing workload and quickly get performance of TVS.

Improved Elman network

Elman network. The Elman network is a typical recurrent neural network (structure shown in Figure 1), which add a connection layer as time delay operator on the basis structure of BP network. The value of hidden layer last time is used in calculating at the present time [5].Assume that there is only one output. The error function is

$$E_k = \sqrt{\left(y(k) - \hat{y}(k)\right)^2} \tag{1}$$

By using dynamic BP algorithm, E_k and any weights w_{ij}^Z （$w_{ij}^Z \in \mathbf{W}^Z$） from connection layer to hidden layer have the following relationship [6]:

$$\frac{\partial E_k}{\partial w_{ij}^Z(k-1)} = -\frac{\partial E_k}{\partial y(k)}\frac{\partial y(k)}{\partial x_i(k)}\frac{\partial x_i(k)}{\partial w_{ij}^Z(k-1)} = -\left(y(k)-\hat{y}(k)\right)w_i^y(k-1)\frac{\partial x_i(k)}{\partial w_{ij}^Z(k-1)} \quad (2)$$

Where $x \in \mathbf{X}_C$. When iterative process of weights change is small, it can be written as:

$$\frac{\partial x_i(k)}{\partial w_{ij}^Z(k-1)} = f_1^{'}(\bullet)\left(x_j(k-1)+\sum_l^n w_{il}\frac{\partial x_l(k-1)}{\partial w_{ij}^Z(k-1)}\right) = f_1^{'}(\bullet)\left(x_j(k-1)+\sum_l^n w_{il}\frac{\partial x_l(k-1)}{\partial w_{ij}^Z(k-2)}\right) \quad (3)$$

Improved Elman network. Because of the complexities in calculating dynamic BP algorithm, we usually ignore the feedback error, then using the standard BP algorithm approximate calculation:

$$\frac{\partial x_i(k)}{\partial w_{ij}^Z(k-1)} = f_1^{'}(\bullet)x_j(k-1) \quad (4)$$

We can get improved Elman network when introducing a feedback gain α in Elman network. Its structure was shown in Figure 2. Pham [7] and others, who used the standard BP algorithm training improved Elman network and derived:

$$\frac{\partial x_i(k)}{\partial w_{ij}^Z(k-1)} = f_1^{'}(\bullet)\left(x_j(k-1)+\alpha\frac{\partial x_i(k-1)}{\partial w_{ij}^Z(k-2)}\right) \quad (5)$$

It is similar to the result of Elman network trained by dynamic BP algorithm. This method greatly reduces the computational complexity and it is more suitable for high-order system modeling and analysis.

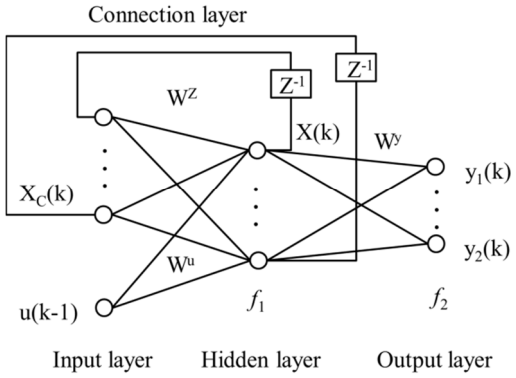

Fig 1 The structure of Elman-NN

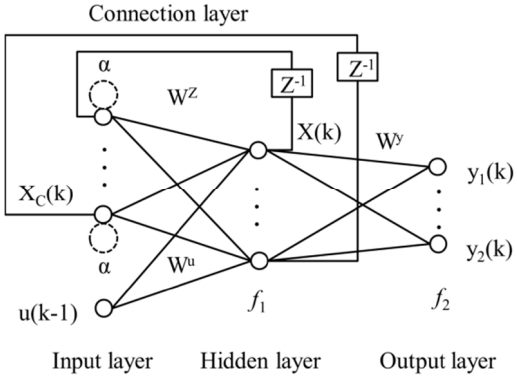

Fig 2 The structure of improved Elman-NN

Experimental set

We use time domain transmission TLP testing method test NUP2105L TVS [8]. We select square wave and machine model ESD and the corresponding response data as training data. The widths of square wave respectively are 50ns, 400ns, and its amplitudes respectively are 40V, 450V, 900V, 1400V. Machine model ESD has same amplitudes with square wave. Validation data we select 250ns, 630V square wave (EMP 1), 1035V machine model ESD (EMP 2), 485V metal body model ESD (EMP 3) and the corresponding response data.

Neural network modeling

Model Identification. In order to reduce the amount of data and the gap between data, improve the efficiency and accuracy of network computing, we use 1/10 resampling and wavelet noise reduction.

Parameters of improved Elman network set as follow: the transfer function of the hidden layer tansig, the transfer function of output layer purelin; the training function trainlm; training steps 1000, the criterion function MSE (mean square error). The results are shown in Figure 3, fitness and MSE are shown in Table 1.

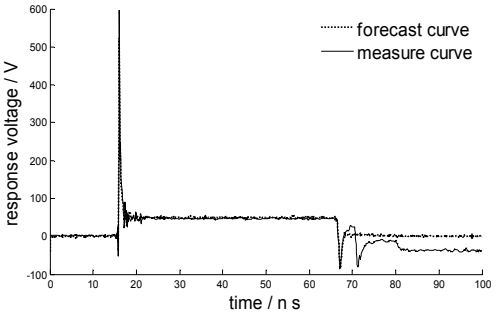

Fig 3(a) Response forecast curve of EMP 1

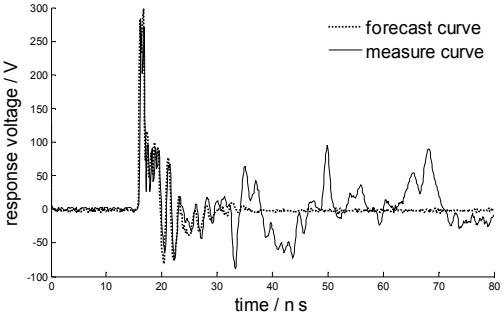

Fig 3(b) Response forecast curve of EMP 2

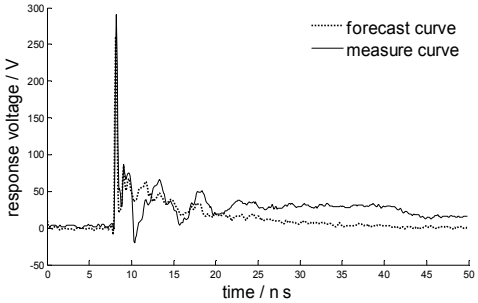

Fig 3(c) Response forecast curve of EMP 3

Table 1 Fitness and MSE of improved Elman-NN model

EMP type	fitness	MSE
E 1	55.5570%	4.6492×10^{-4}
E 2	28.3584%	0.0011
E 3	15.3851%	5.0728×10^{-4}

In order to test the superiority of improved Elman network, we use Elman network predict the three types of EMP signal. The results are shown in Figure 4, fitness and MSE are shown in Table 2.

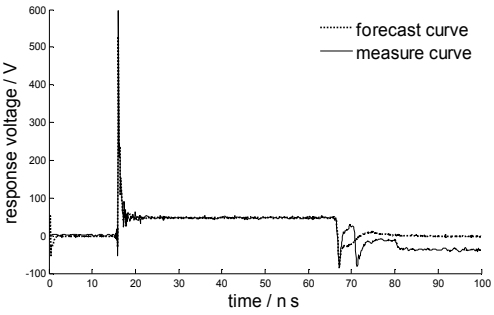

Fig 4(a) Response forecast curve of EMP 1

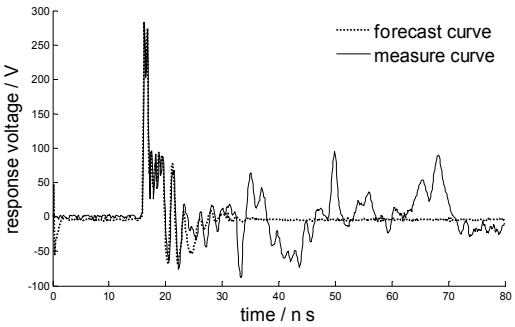

Fig 4(b) Response forecast curve of EMP 2

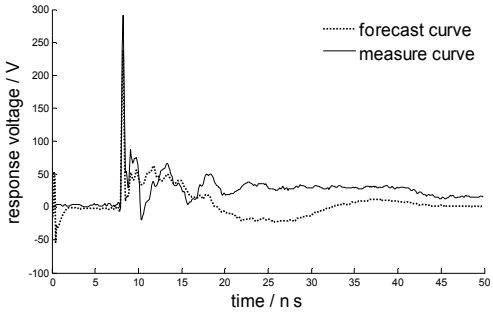

Fig 4(c) Response forecast curve of EMP 3

Table 2 Fitness and MSE of Elman-NN model

EMP type	fitness	MSE
E 1	53.5332%	5.0823×10^{-4}
E 2	29.8213%	0.0010
E 3	-21.9773%	0.0011

Results and Analysis. (1) By comparison, training time of improved network is reduced by nearly half. Because EMP 1and EMP 2 are similar to training data, their predicted effect close. But the predicted effect of EMP 3 is significantly better. Improved network effectively overcome the jitter in the front of prediction curve. Although the approximate calculation using standard BP algorithm, the accuracy did not decrease, to some extent, it improve the efficiency and generalization ability.

(2) The fitness mainly characterize the degree of curve overlap and the MSE mainly characterize the gaps variance values of results. The fitness is a strict standard. In this paper, when fitness is

55.5570% which is seemingly small, MSE can reach 4.6492×10^{-4}. In general: for the same curve fitting, when the fitness is higher, MSE smaller. For the different curves fitting, when MSE are the same, the fitness may be very different.

(3) When use the two networks for to predict machine model ESD, it is poor performance. It is mainly due to the strong echo signal. There is not enough hidden layer neurons for the complex curve modeling completely. However, for practical engineering perspective, all the figures in this paper fit the key parameters well, such as the rising time, the peak value, the time duration and the falling time. Excessive pursuit of goodness of fitness and MSE only result in a complex network model and it is not conducive to engineering applications.

Conclusion

This paper presents a method that using improved Elman network to simulate the inject effects of EMP. We establish improved Elman network and Elman network, and then make a comparison between them. The proposed method takes a short time, has a high precision, is easy to operate, and has broad application prospects.

References

[1] ZHOU Bi-hua, CHEN Bin, SHI Li-hua. Electromagnetic pulse and engineering protection. Beijing: National Defense Industry Press (2003).

[2] ZHENG Sheng-quan, WU Xiao-guang, ZHU Ying-fu. Elctromagnetic pulse threats to ship-flat and requirements of protection. Journal of Microwaves. Vol.S2 (2010), P.101-104.

[3] YU Li, ZHOU Hong, YANG Jian-hui, et al. Design of suppression device with changeable clamping voltage based on TVS array. Relay. Vol.36, No.9 (2008), P.58-63.

[4] LUO Hong-wei, SHI Qian. TLP test techniques for ESD protection design[J]. Electronic Product Reliability and Environmental Testing. Vol.4 (2003), P.44-46.

[5] SHI Feng, WANG Xiao-chuan, YU Lei, et al. MATLAB neural network 30 case analysis. Beijing University of Aeronautics and Astronautics Press (2010). P.170-175.

[6] CONG Shuang, GAO Xue-peng. Recurrent neural network and their application in system identification. System Engineering and Electronics. Vol.25, No.2 (2003), P.194-197.

[7] Pham D T, Liu X. Training of Elman networks and dynamic system modeling. International Journal of System Science. Vol.27, No.2 (1996), P.221-226.

[8] WU Qi-meng, WEI Ming, ZHANG Xi-jun, et al. Electromagnetic pulse response modeling of trainsient volage suppresr. High Power Laser and Particle Beams. Vol.25, No3 (2013), P.799-804.

Advanced Materials Research Vols. 986-987 (2014) pp 2023-2026

doi:10.4028/www.scientific.net/AMR.986-987.2023

The Impact on the Electromagnetic Environment of Medium Wave Broadcasting Stations Caused by 110kV Power Lines

Guan WANG[1,a], Hao HU, Fei YU, Yu GONG, Wenhua JIANG

[1] Nuclear and Radiation Safety Center, MEP, 100082, Beijing, China

[a]email: wg_169@163.com

Keywords: High-Voltage Power Line; Medium Wave Broadcasting; Electromagnetic Environment; Method of Moment

Abstract. In this paper, the numerical analysis methods of electromagnetic field is used and by establishing the computer model of 110kV high-voltage power line and medium wave amplitude modulated broadcasting (AM) stations, the impact on the electromagnetic environment of medium wave broadcasting stations caused by 110kV high-voltage power lines is analyzed.

Introduction

The impact on the electromagnetic environment of medium wave broadcasting stations caused by 110kV power lines mainly consists of two parts, the active and passive interference. The focus of this paper is on the passive interference. The electromagnetic field generated by medium wave amplitude modulated (AM) broadcasting stations could cause the high-voltage power lines which around them to generate induced current. The re-radiation to the space which is caused by the induced current would generate a passive interference to the medium wave AM broadcasting stations. In this paper, the impact of high-voltage power line to the medium wave broadcasting stations under different conditions is calculated via the establishment of the computer model [1]-[3].

The study on the passive interference of high-voltage line

In practical engineering, the way of erecting high-voltage line, the structure of tower and the terrain of it are often very complex. Therefore, the traditional theoretical analysis is not suitable for the research of the electromagnetic effects on the medium wave broadcasting stations from the high-voltage line. The use of computer numerical analysis to solve the problems in the existing condition is considered to be appropriate.

The commonly used numerical methods in computational electromagnetics are geometric optical diffraction method, physical optics diffraction method, finite difference time domain method, finite element method, boundary element method, simulation charge method, method of moment and so on. In this paper, the effects on the directional pattern of the medium wave AM broadcasting stations from the high-voltage line are studied, and the method of moment is used as a numerical method in the research [4]-[5].

Currently, the simulation softwares based on the method of moment are ADS simulation software, FEKO simulation software, EMC Studio simulation software for simulation of electromagnetic compatibility, etc. In the consideration of the size of the high-voltage tower, the propagation characteristics of medium wave and other factors, the EMC Studio simulation software for simulation of electromagnetic compatibility from the EMCoS Company is selected in this paper.

The establishment of the simulation

The antenna model of the broadcasting station and its simplification

In this paper, the research object is the medium wave AM broadcasting station which consists of two transmitting antennas 100 meters away from each other. One transmitting antenna is 116 meters high and the operating frequency is 621kHz, the other transmitting antenna is 76 meters high and is worked on the frequency of 1035kHz. There is a high-voltage line constructed around the

transmitting antennas, and its voltage level is 110kV with the height of 22 meters. The line span is between 145.85m to 254.27m.

When establishing the computer simulation model, the two transmitting antennas of the broadcasting station can be equivalent to the grounding monopole antennas with a feed supply added at the bottom of them. In the actual calculation, considering the impact on the simulation results from meshing, the antennas are replaced with linear metal structure which is covered with ideal conductive material.

The model of the high-voltage line and its simplification

The main parts of the high-voltage line to generate passive interference are the metal parts of the line, including the body of the tower, ground line, and phase line. The tower type in the research is the straight line tower. In the computer modeling, the body of the tower is equivalent to metal rod, and the calculation of the ground and phase lines are equivalent to metal lines.

In practical engineering, the radius of the body of the high-voltage tower is not uniform. In the establishment of the model, the average of the maximum and minimum radius of the tower is taken as the equivalent radius. The connection of the ground and phase lines on the tower is according to the actual erection form, and multiple towers are arranged in turn to constitute the high-voltage lines.

Terrain model

In this study, the model of the earth is equivalent to the ideal infinite conducting plane, and the ideal metal conductivity is uniformly used as the ground conductivity.

The calculation results and analysis

The impacts on the directional pattern of the antenna from the high-voltage line in different conditions are calculated respectively. The polarization mode of the electromagnetic wave transmitted from the medium wave AM broadcasting stations is vertical, but the phase lines of the high-voltage line are erected in a horizontal way. So we can see from the electromagnetic theory, the impact on the transmitting antenna from the phase line is minimal. Thus, the phase line will not in the consideration in the later modeling of high-voltage line [6]-[9].

The comparison of the directional pattern of the antenna when there is only transmitting antenna exists

The impact of the consideration of the two pairs of transmitting antennas work alone and the two pairs of the transmitting antenna exist with only one antenna works are shown in Figure 1 and Figure 2. The two figures have the same data and with the difference of the ranges of the coordinate system. When the origin of the coordinate is 0, the result of the comparison is straightforward but subtle changes are not prominent. After the partial enlarged of the figures, the subtle changes in different azimuth angles of the directional pattern are highlighted. The impact of the directional pattern of the antenna can be analyzed more comprehensively via combining the characteristics of the two figures.

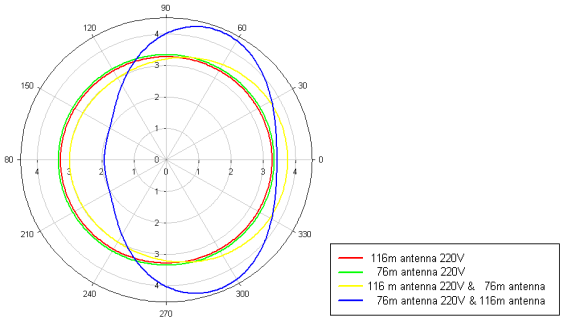

Fig.1. Compare with patterns (Coordinate origin is zero)

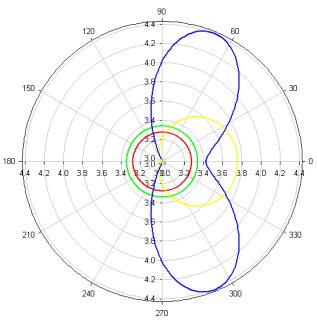

Fig.2. Compare with patterns (Coordinate origin is a fixed value)

We can see from Figure 1 and Figure 2, the impact on the 116m high transmitting antenna from the passive antenna of 76m high is relatively small. The impact on the 76m high transmitting antenna from the passive antenna of 116m high is large, and near the degree of 70, 180, and 290, the change of the directional pattern of the antenna is obvious.

The comparison of the directional pattern of the antenna in the situation of high-voltage line at different distances away from the antenna

The model is established according to the study objects in this paper, and the simulation results are given in Figure 3 and 4.

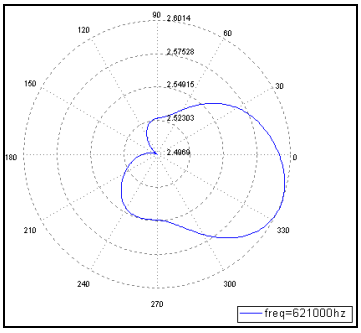

Fig.3. Horizontal 2D pattern

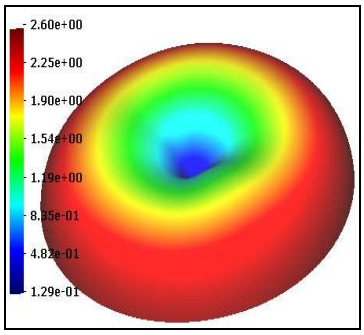

Fig.4. Far field 3D pattern

The impact on the directional pattern of the antenna from the high-voltage line is greater in the range of (-150^{o}, 90^{o}). In order to show the impact of the directional pattern of the antenna from the high-voltage line more clearly, the results are compared with the absence of the high-voltage line which is given in Figure 5.

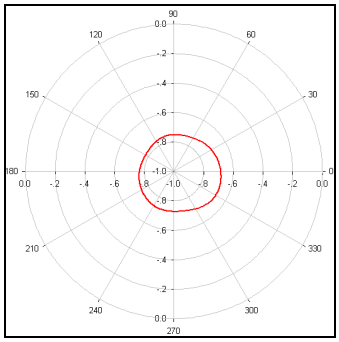

Fig.5. Interference in Transmitting Antennas Caused by HVAC Power Lines

We can see from Figure 5 that the impact on the 116m high transmitting antenna from the high-voltage line and passive antenna of 76m high exists in the whole plane, and the maximum difference between the radiation power densities is 0.7 dB. Although the route of the high-voltage line is not a straight line, its impact on the directional pattern of the antenna is small when it surrounds the transmitting antenna by half. The slight change of the directional pattern of the antenna does not affect the service area covered by the antenna.

Conclusion

The main contents and conclusions of this paper have two aspects. Through the simulation model, we can conclude that in the study of the passive interference to the medium wave AM broadcasting stations from the high-voltage power lines, the impact on the transmitting antenna from the line tower and ground line should be mainly considered. When building the simulation model, phase line is not in the consideration because of its own characteristics and the way it is erected. Through the comparative study by computer modeling, we can conclude that the passive interference from the high-voltage lines should be considered as an important issue. When determining the protection spacing of the high-voltage lines, it is recommended that the comparison between the active and passive interferences should be given at the same time, and the protection spacing should be determined by the interference which has a larger impact on the medium wave AM broadcasting stations.

References

[1] C.W. Trueman, S.J. Kubina, Numerical Computation of the Reradiation from Power Lines at MF Frequencies [J], IEEE Transactions on Broadcasting, Vol. BC-27, No. 2, pp. 40-42, June 1981.

[2] C.W. Trueman, S.J. Kubina, Comparison of Computed RF Current Flow on a Power Lines with Full Scale Measurements [J], IEEE Transactions on Broadcasting, Vol. BC-30, No. 3, pp. 97-107, June 1981.

[3] C.W. Trueman, S.J. Kubina, Initial Assessment of Reradiation from Power Lines, IEEE Transactions on Broadcasting [J], Vol. BC-31, No. 3, pp. 51-65, September 1985.

[4] Lv Yinghua, Numerical Methods in Computational Electromagnetics,. Beijing: Tsinghua University Press, 2006, pp. 1-5.

[5] Ni Guangzheng, Yang Shiyou, Qiu jie, Engineering numerical calculation of electromagnetic fields,. Beijing: China Machine Press, 2004, pp. 222-236.

[6] Gan Zheyuan, Zhang Xiaowu, et al, Passive Interference in Receiving Stations of AM Broadcasting Caused by UHVAC Transmission Lines [J]. POWER SYSTEM TECHNOLOGY, 2008, 32 (2), pp. 9-12.

[7] Wen Yinghong, Antenna and wave propagation theory., Beijing: Tsinghua University Press, Beijing jiaotong university press, 2005, pp. 145-146.

[8] Wanghudagula, Yao xiaoliang, 1 kw medium-wave radio propagation properties and the calculation of field strength, Inner Mongolia Radio & TV Broadcast Engineering, 2008, 02, pp. 73-76.

[9] Chen Zongzhou, Jia Zhongning, et al, The research on the effects of electric properties of grounded tower from building the medium wave radio transmitting antenna around it, Radio & TV Broadcast Engineering, 1993, 04, pp. 15-23.

Advanced Materials Research Vols. 986-987 (2014) pp 2027-2030

doi:10.4028/www.scientific.net/AMR.986-987.2027

The Model for PV Array based PSIM

Ji Zeng[1, a]

[1]College of Telegraph, Pan Zhihua University, Pan Zhihua,China

[a]email: mynamezj@126.com

Keywords: photovoltaic cell; PV array ; simulation model; PSIM

Abstract. Based on the theory and mathematical treatment for the photovoltaic cell, a simple and accurate PV array model of external characteristics is developed with PSIM. Output simulation results for different Temperature and Light intensity. The simulation results show that I-V and power simulation result of the Photovoltaic array model, and experimental result are in close agreement with each other. This verifies the accuracy and suitability of the developed PSIM model.

Introduction

The photovoltaic power system which transforms the solar energy into the electric energy, is an electricity generation way. The photovoltaic cell is a critical component of the photovoltaic power system and its $I-V$ feature is the nonlinear function of solar radiation intensity, ambient temperature and photovoltaic module parameters. In order to realize the dynamic simulation of the photovoltaic power system, the first step is about how to carry out the analogue simulation on the $I-V$ feature of photovoltaic array. Generally speaking, there are two ways of simulation modeling [1]: The modeling approach based on the physical mechanism of the photovoltaic array and external characteristics. The comparatively obvious disadvantage of the model based on the physical mechanism is that the indeterminate correspondence between the model parameters and the general parameters of photovoltaic products will impact on the simulation accuracy in a context of fast photovoltaic array products updates. Nevertheless, the model based on the external characteristics boasts great utility value thanks to its friendly interfaces to the circuit simulation user.

PSIM[2] is the software designed for the power electronic circuit and the electric drive. Its devices basically adopt the ideal model whose computation speed is very fast. Based on the PSIM simulation environment and the external characteristics of the photovoltaic array, this paper presents a simple simulation model of the photovoltaic array. This model copes well with the impact of the parametric variation of the photovoltaic array products, ambient temperature, solar radiation intensity, parallel numbers of the photovoltaic array, etc on the $I-V$ characteristics.

Equivalent circuit model of the photovoltaic cell

The photovoltaic cell unit is actually a planar diode with a large area, whose working equivalence is the equivalent circuit of the single diode[3], as shown in Figure 1. R_S is the series resistor, primarily composed of the cell's bulk resistance, surface resistance, electrode conductor resistance and the contact resistance between electrode and silicon face. R_{sh} is the bypass resistance that is caused by the unclean edge or interior defect of the silicon wafer. I_{ph} is the photo-generated current which is generated inside the photovoltaic cell and its value is directly proportional to the area of the photovoltaic cell and the irradiance of the incident light. I_D is the dark current which means the unidirectional current flowing within the P-N knot under the external voltage when the photovoltaic cell is not affected by illumination. I_L is the load current which is generated by the photovoltaic cell and U_L is the load voltage which is also generated by the photovoltaic cell.

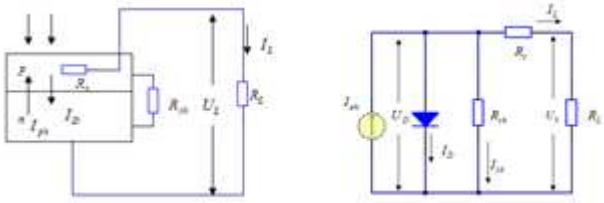

Figure 1 Equivalent Circuit Diagram of Single Photovoltaic Cell

As for the general photovoltaic cell, the quite small series resistance and the large parallel resistance can be ignored when the ideal circuit calculation is carried out on R_s and R_{sh}. Therefore, I-V characteristics[4] which symbolize the ideal photovoltaic cell can be acquired, as shown in Form 1 and 2.

$$I_L = I_{ph} - I_D - I_{sh} = I_{ph} - I_D \quad e^{\frac{qU_L}{AKT}} - 1 \tag{1}$$

$$U_L = \frac{AkT}{q} \ln\left(\frac{I_{ph} - I_L}{I_D} + 1\right) \tag{2}$$

Mathematical model of the photovoltaic array

Owing to its small capacity, output voltage and output peak power, the single photovoltaic cell generally can not meet requirements of electricity load. In addition, it is not convenient to conduct installation and application either. In the actual operation, several series-parallel connections of the photovoltaic cell will be combined into the photovoltaic array based on power and voltage levels. N_s and N_p are the numbers of the series-parallel photovoltaic cells in the photovoltaic array respectively. After being familiar with the circuit model of the photovoltaic cell, we can work out associated equations indicating the features of the photovoltaic array according to the circuit analysis and eventually obtain the mathematical model of the photovoltaic array[5], as shown in Form 3.

$$U_A = -I_A R_s \left(\frac{N_S}{N_P}\right) + \left(\frac{N_s}{\Lambda}\right) \ln\left(1 + \frac{N_P I_{ph} - I_A}{N_P I_D}\right) \tag{3}$$

$$I_A = N_P I_{ph} - \text{EXP}\left[\left(U_A + I_A R_s \left(\frac{N_S}{N_P}\right)\right) \frac{\Lambda}{N_s}\right] N_P I_D - N_P I_D \tag{4}$$

In the Form 3, I_{ph} is the photo-generated current; I_D is the reverse saturation current of the diode; in $\Lambda = (q/AKT)$, q is the electronic constant; A is the emission factor of the diode; K is the Boltzmann constant; T is the absolute temperature; U_A and I_A are the output voltage and current of the photovoltaic array. Equation 1 can be written into Form 4.

Simulation model of external characteristics of the photovoltaic array VA

The paper selects PSIM as the simulation platform. When distribution effects of the photovoltaic cell, temperature gradients under uneven photovoltaic illumination and some other limiting conditions on the output voltage are ignored, the PSIM model of the photovoltaic matrix can be built in accordance with Form 4. As shown in Figure 2, U_A and I_A are the ports connected with the peripheral circuit.

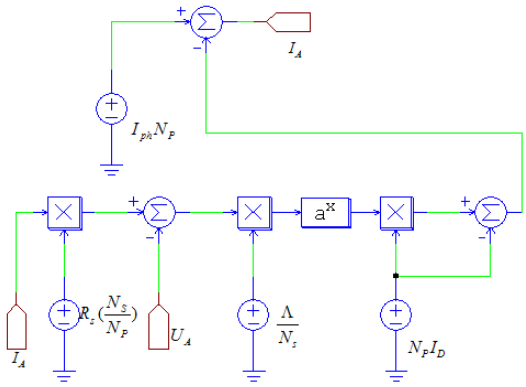

Figure 2 PSIM Model of the Photovoltaic Matrix

Simulation effects of the PSIM model of the photovoltaic matrix

Based on the above-mentioned simulation model, relevant product parameters are put into the equation. This model selects the parameters of STP030-12/Lb of the photovoltaic cell pack from Wuxi Shangde Company. Meanwhile, a load with variable impedances is connected to the model. The characteristic curve of electric simulation of the photovoltaic matrix can be worked out in PSIM software, as shown in Figure 3 (I-V characteristic curve of the simulation model under different illuminations and temperatures) and Figure 4(P-V characteristic curve of the simulation model under different illuminations and temperatures).

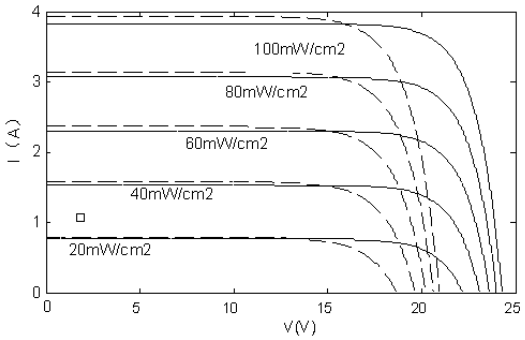

Figure 3 I-V characteristic curve

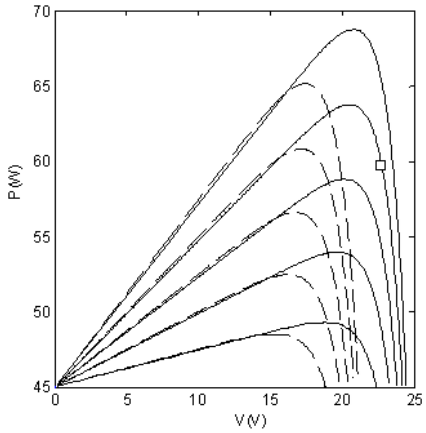

Figure 4 P-V characteristic curve

In order to check the validity of the simulation model, a simple test on the output characteristics of the photovoltaic matrix is built. As shown in Figure 5, the equivalent circuit is on the left, whose photovoltaic matrix is to be tested and the measuring circuit is on the right.

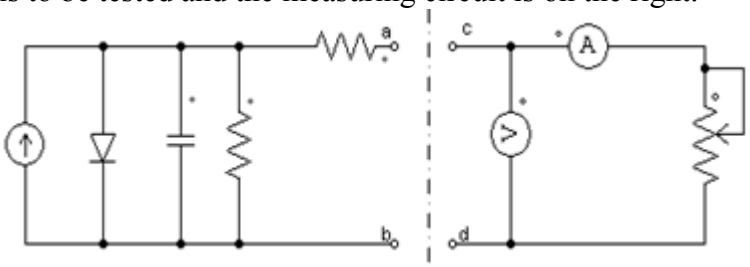

Figure 5 Schematic diagram of the test on the output characteristics of the photovoltaic matrix

By means of constant adjustments of the load resistance R_L ,the curves of the VA characteristic and power can be worked out according to the output voltage and current of the photovoltaic cell, as shown in Figure 6. Compared with Figure 6, 3 and 4, the simulation result fits well with experimental data, which demonstrates the applicability and accuracy of the model.

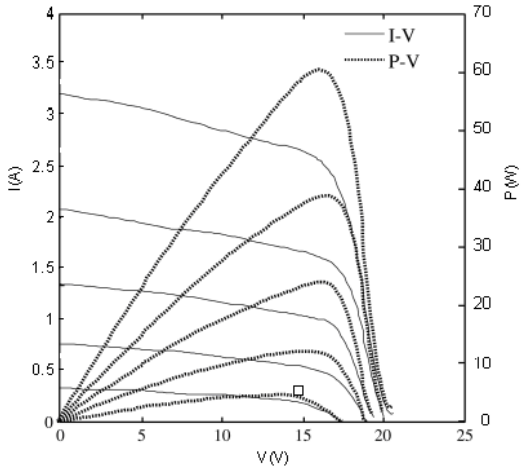

Figure 6 Curves of the photovoltaic matrix testing on I—V and P—V characteristics

Conclusion

This paper, based on the output VA characteristics of the photovoltaic cell and circuit model of equivalent diode, works out mathematical expressions about the output VA characteristics of the photovoltaic matrix which is composed of several series-parallel connections of the photovoltaic cell. And then the I-V simulation model of the photovoltaic matrix based on the PSIM is built by the mathematical expressions. By comparing the simulation result with the experimental data, the PSIM model of the photovoltaic matrix can conduct the simulation on $I-V$ characteristics of the photovoltaic matrix, which can be applied to the dynamic simulation of the photovoltaic power generation system.

References

[1] Mao Meiqin and others, *General Simulation Model of MATLAB Photovoltaic Array with MPPT*, Journal of system simulation, 2005,No.5:1248-1251.

[2] Powersim Inc. PSIM User's Version6.0. Powersim Inc,2003

[3] Zhao Zhengming and others, *Solar Photovoltaic generation and Its Application*, Beijing: Science Press, 2005.

[4] *Research on Mathematical Models of Photovoltaic Array Based on Matlab* Industry and Mining Automation, 2011，No.12:40-43.

[5] Liu Xuejun,An Improved Perturbation And Observation Maximum Power Point Tracking Algorithm For PV Panels, master,Concordia University Montreal,Quebec,Canada,2004.

Advanced Materials Research Vols. 986-987 (2014) pp 2031-2034

doi:10.4028/www.scientific.net/AMR.986-987.2031

The Research on Establishing Method of the Broadband Nonlinear Transformer Model

Zhang Zhongyuan[1, a], Wang Zengchao[1,b], Zhang Xin[1,c]

[1]Department of Electrical and Electronic Engineering, North China Electric Power University, Baoding, 071003, china

[a]hvzzy_01@163.com, [b]hv_wac@163.com, [c]hv_zxin@163.com

Keywords: power transformer; transient model; nonlinear; wide frequency range; lightning impulse

Abstract. The transformer model is one of the most needed to improving components of the modern transient simulation software. A new nonlinear broadband frequency (50Hz-10MHz) model of power transformer is proposed in this paper. The model is divided into a linear block and a nonlinear block by a reasonable equivalent transformation. The linear block is set up through measuring and synthesizing. And the nonlinear block is derived by the impendence of iron core. The final circuit model is built in Simulink, and the comparisons between the simulation and measurement results verify the feasibility and validity of the model.

Introduction

The accurately modeling of power transformer is essential to calculate transient state of power system. As the transformer behavior is not only frequency-dependent but nonlinear in transient, it seems to very difficult to build an accurate model of transformer [1]. The attempts in transformer model are already hundred years old. There are various of models proposed, most of which only aimed at stimulating appropriately the specific events. There are rarely models which can simulate steady state and the transient overvoltage, which include power frequency overvoltage, switching overvoltage, lightning overvoltage, and VFTO. This work aims at modeling a comprehensive transformer representation that can simulate a wide frequency range in transient. The modeling method is organized as follows. At first, a lumped parameter equivalent circuit is derived by topology. And then, through a reasonable equivalent transformation, the circuit model is divided into a linear model and a nonlinear iron core model. Finally, two parts of the present model are realized in Simulink.

The analysis of transformer model

When current passes through the transformer winding, the magnetic field is induced. The magnetic flux linkage can be seen as the sum of inner flux linkage Ψ_i and outer flux linkage Ψ_o. They represent difference fluxes through turns. The magnetic flux could be divided into two parts: the main flux Φ_m, which is closed along transformer core with primary and secondary side. The other is the leakage flux , which is closed as air or tank[2]. So, the outer flux linkage Ψ_i=main flux linkage Ψ_m+leakage flux leakage Ψ_σ. And the inner flux linkage corresponds to eddy current effect and proximity effect of winding [6]. According to the turn-to-turn connection of the winding, an equivalent circuit model is established as illustrated in Fig. 1.

The *k*th turn is represented as a resistance R_k and inductance L_k in series. The current in coil induces leakage flux which can be replaced as L_{ok}, and main flux which is shown as a nonlinear inductance L_{mk} and nonlinear resistance R_{mk}. Since the induced current is very small, the circuit model can be approximated in reason.

Fig. 2 shows that every turn is divided into a nonlinear branch and a linear branch. The end of one turn is connected to the next turn's beginning. All nonlinear branches in series can be seen as a nonlinear iron core model, and linear branches can be seen as a winding model. The overall model is shown in Fig. 3.

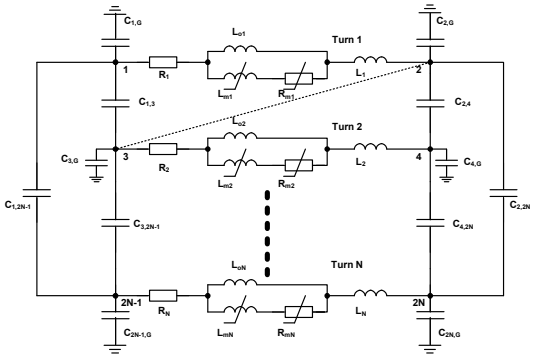

Fig.1 Turn-to-turn equivalent circuit model of transformer

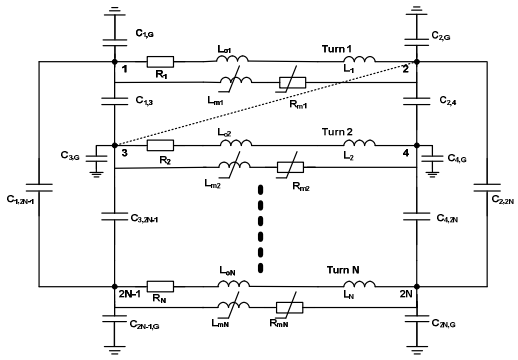

Fig.2 Turn-to-turn equivalent circuit model after approximation

Modeling of linear block

The modeling of linear block is based on measuring winding parameters in frequency domain. The methodology of frequency response measurements has already been applied in [4]. The network analyser has a very large signal-to-noise ratio. In this work, using a network analyser (Agilent 4395A) measures the *S* parameters of transformer ports. A real distribution transformer (10.5kV/0.22kV, 10kVA) is studied. And then, transfer the *S* parameters to *Y* parameters. The frequency range is 50Hz to 10MHz.

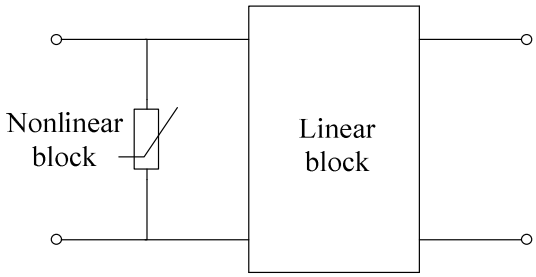

Fig. 3 Overall model

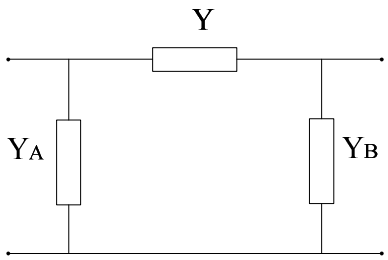

Fig.4 Equivalent π circuit model

The transform equation from S parameters to Y parameters. Based on two-port circuit theory, a π type circuit model can be established. The admittances of the circuit are derived as equation (1).

$$\begin{cases} Y_A = Y_{11} + Y_{12} \\ Y_B = Y_{11} + Y_{12} \\ Y = -Y_{12} = -Y_{21} \end{cases} \tag{1}$$

Based on the *Y* parameters, a linear equivalent circuit model is established, representing the linear block illustrated in Fig.4.

The modified vector fitting (MVF) [3] is adapted to approximate frequency-dependent admittance parameters *Y*, Y_A, Y_B. MVF approximates a frequency response (in this work an admittance) with rational functions, expressed in the form of a sum of partial fractions:

$$f(s) \approx \sum_{i=k}^{N} \frac{r_k}{s - p_k} + d + se \tag{2}$$

r_k and p_k are the residues and poles, respectively. Terms *d* and *e* are optional. The compartments between fitting and experiment results are illustrated in Fig.5. In this work, fitting order is 36, and we can see that the fitting results are perfect.

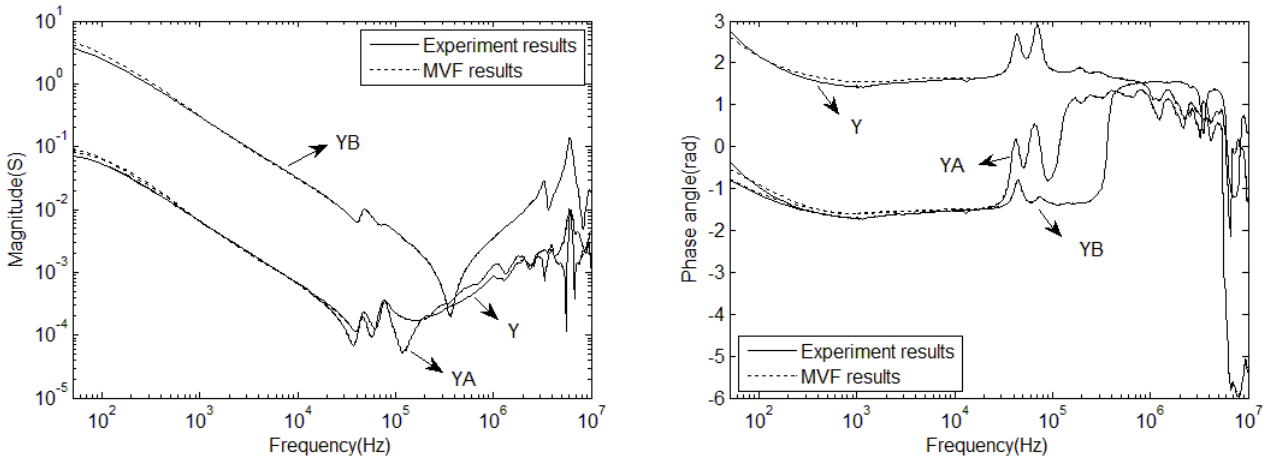

Fig.5 Fitting results of *Y* parameters

The method proposed in [5] is employed to synthesize the *RLC* circuit for the fitting results above. The fitting result is a sum of partial fractions, and the pole of every fraction is either a real point or a complex point. A real point fraction can be synthesized as a *RL* circuit branch. While a complex point corresponds to a *RLCG* circuit branch.

Modeling of nonlinear block

The electromagnetic process in transformer iron core has been known for many years and the technique can be found in [5]. The frequency-dependent impendence of iron core shows in (3).

$$Z(s)=\frac{2wN^2}{l}\sqrt{\frac{\mu_0\mu s}{\sigma}}\tanh(\sqrt{\mu_0\mu s}\frac{d}{2}) \tag{3}$$

Where: l is the length of the lamination; w is the width of the lamination; d is the thickness of the lamination; N is the number of turns of the coil; μ_0 is the permeability of vacuum; μ is the relative permeability of the lamination; σ is the conductivity. After measuring the lamination dimension of the distributed transformer, the frequency dependent impedance of iron core can be calculated.

In order to realize the circuit model, it is necessary to synthesize circuit for function (3). The MVF is employed to approximate formula (3) once more. The results of the circuit model as illustrated in Fig. 6. And the parameters of RL in the circuit are shown in Tab.1.

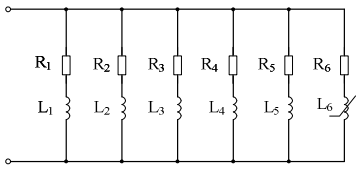

Fig. 6 Six order nonlinear equivalent circuit

Table 1 Parameters of the circuit

	R(ohm)	L(H)
1	6.8471e+005	1.1200e-001
2	4.4424e+005	2.6216e-001
3	2.3498e+005	4.6695e-001
4	1.1306e+005	8.1377e-001
5	3.3132e+004	1.1750e+000
6	7.7369e-001	2.4799e+000

Considering nonlinear characteristics of iron core, the inductances should be nonlinearized. Nonlinear characteristics of transformer are critical in low frequency. The first 5 branches are high frequency components, and they have little influence to low frequency signal. And for faster simulation, the sixth branch is considered nonlinear branch in this work.

The transformer *U-I* curve is easily performed through the no-load test. And then, *U-I* curve could be convert to *Ψ-I* curve [6]. The nonlinear relationship program is written by using user-defined functions 'Embedded MATLAB Function' in Simulink. In the sixth branch, the inductance is converted into a nonlinear inductance using above method.

Simulation and experiments

Time domain simulations and experiments have been compared to verify the validity of the model, including state of lightning impulse, saturation.

Lightning simulation. Lightning waveform signal is added in primary side of the transformer. The lightning generator EMS61000-5C is adopted to produce a 252V 1.2/50μs standard lightning wave, and signal of the secondary side are recorded. The result of simulation and test in secondary side are compared in Fig.7.

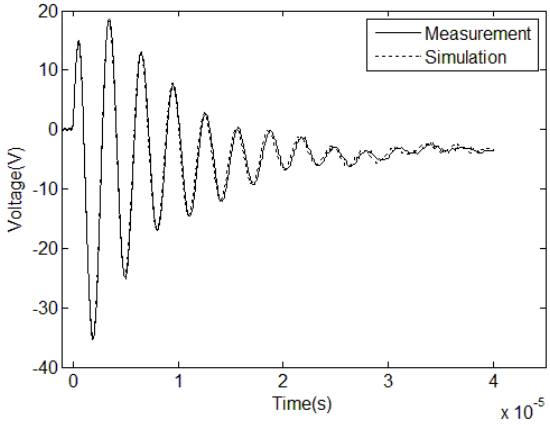

Fig.7 The comparison when lightning applied

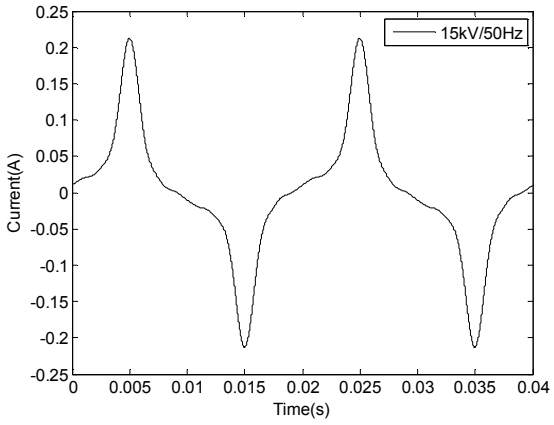

Fig.8 Excitation current in different frequency

As seen from the above figure, the simulation and test values are basically same so that it verifies the accuracy of the model.

Saturation simulation. In order to test the presented model saturation, test voltage is set for 15kV/50Hz. In this case, the core will be saturation. The simulation results for excitation current can be seen in Fig.8.

Conclusion

A new wide-band frequency power transformer model has been developed for studying the broadband characteristics of transformer. The linear model is set up through measuring S-parameters, and then synthesized by MVF method. Nonlinear block is derived by the impendence of iron core. And saturation characteristics are expressed by a nonlinear inductance. The whole model is set up in Simulink, and time domain simulation and experiment results are compared. The compartments verify the feasibility and validity of the model.

References

[1] Martinez J A, Mork B A. Transformer modeling for low- and mid-frequency transients[J]. IEEE Transactions on Power Delivery, 2005, 20(2): 1625-1632.

[2] F.de León and A.Semlyen. Complete transformer model for electromagnetic transients[J]. IEEE Trans. Power Del, 1994, 9(1): 231–239.

[3] Gustavsen B, Semlyen A. Rational approximation of frequency domain responses by vector fitting[J]. IEEE Trans. on Power Delivery, 1999, 14(3): 1052-1061.

[4] Antonini G. SPICE equivalent circuits of frequency-domain responses[J]. IEEE Trans. on Electromagnetic Compatibility, 2003, 45(3): 502-511.

[5] J.Avila-Rosales and F.Alvarado. Nonlinear Frequency Dependent Transformer Model for Electromagnetic Transient Studies in Power Systems[J]. IEEE Transactions on Power Apparatus and Systems, 1982, 101(11).

[6] E.J.Tarasiewicz, A.S.Morched, A.Nmng, E.P.Dick. Frequency depndent eddy current models for nonlinear iron cores[J]. IEEE Transactions on Power Systems, 1993, 8(2): 588-597.

Advanced Materials Research Vols. 986-987 (2014) pp 2035-2038
© (2014) Trans Tech Publications, Switzerland
doi:10.4028/www.scientific.net/AMR.986-987.2035

Two-port characteristic analysis for transformers with the large scale windings based on sparse matrix

Xudong Zhang[1,a], Jianye Yuan[1,b], Jingping Zhang[1,c],Jianying Feng[1,d]

[1] State Grid Cangzhou electric power supply company, Cangzhou 061000, China

[a]zhangxudong1692@163.com, [b]yuanjianye2013@126.com,[c]578295636@qq.com, [d]616295905@qq.com

Keywords: transformer, decoupling, sparse matrix, block storage, ***Y***-parameters，large-scale winding

Abstract. In order to calculate the two-port wide frequency parameters of a large transformer quickly and accurately, parameter calculation of multi-conductor transmission lines model is proposed based on the sparse matrix operation. It solved the problem caused by the large matrix. Firstly, multi-conductor transmission lines model of the transformer windings is established. Secondly, matrix characteristics of ***Y*** and ***Z*** is analyzed, based on which the block storage and computation method is applied. Then the frequency-domain model is solved based on sparse matrix operation. At last, taking a SS11-20000/110 transformer as an example, the correctness of this method has been verified by comparing calculation results with measurement results.

Introduction

The Macro-model based on black-box theory is an important method for the modeling of the transformer. The prerequisite is to obtain the wide frequency network parameter by calculation for large transformer due to the difficulty to get the parameter by measurement [1]. In addition, frequency response analysis of the transformer also needs to calculate the parameter.

Multi-conductor transmission lines model (MTLs) has been widely applied to analyze the transient response in the transformer windings [2,3,4]. In parameters calculation, the traditional way is to treat each turn of a power transformer as one transmission line, which is precise for the transformers with a small number of turns. However, many transformers have a lot of turns. In traditional way, a system of very large-scale equations will be obtained which is difficult to solve.

Sparse matrix method is applied to MTLs of the transformer by the analysis of parameter matrix ***Z*** and ***Y***. By this approach, we can deal with the difficulty that in decoupling the transmission line equations it is impossible or takes too much time on diagonalization. By comparing the calculated results and the measured results of a transformer which type is SS11-20000/110, the correctness and feasibility of this method is verified.

Multi-conductor transmission lines model

The MTLs model of a two-winding transformer is built which is shown in Fig.1. The transmission line equations are:

$$\begin{aligned}\frac{d^2\mathbf{V}(z)}{dz^2} &= \mathbf{ZYV}(z) = \boldsymbol{\Gamma}^2\mathbf{V}(z)\\ \frac{d^2\mathbf{I}(z)}{dz^2} &= \mathbf{YZI}(z) = \boldsymbol{\Gamma}_t^2\mathbf{I}(z)\end{aligned}, \tag{1}$$

where impedance matrix $\mathbf{Z} = \mathbf{R} + j\omega\mathbf{L}$, admittance matrix $\mathbf{Y} = \mathbf{G} + j\omega\mathbf{C}$, $\boldsymbol{\Gamma}^2 = \mathbf{ZY}$, $\boldsymbol{\Gamma}_t^2 = \mathbf{YZ}$.

The prerequisite to solve the equation (1) is decoupling. Traditionally, the mode transformation is generally taken with defining mold voltage $\mathbf{V}^m = \mathbf{T}_V^{-1}\mathbf{V}$, mode current $\mathbf{I}^m = \mathbf{T}_I^{-1}\mathbf{I}$ and $\mathbf{T}_I = \mathbf{T}_{\mathrm{V}}^{-1T}$ .So the waveform equations of mode voltage and mode current can be shown as [5, 6]:

$$\begin{aligned}\frac{d^2\mathbf{V}_m(z)}{dz^2} &= \mathbf{T}_V^{-1}\mathbf{ZYT}_V\mathbf{V}_m(z) = \mathbf{r}^2\mathbf{V}_m(z)\\ \frac{d^2\mathbf{I}_m(z)}{dz^2} &= \mathbf{T}_I^{-1}\mathbf{YZT}_I\mathbf{I}_m(z) = \mathbf{r}^2\mathbf{I}_m(z)\end{aligned}, \tag{2}$$

where **r** is a diagonal matrix.

With boundary conditions *z=0* and *z=l*, the relations of current and voltage terminal conditions of MTLs are obtained:

$$\begin{bmatrix}\mathbf{I}_S\\ \mathbf{I}_R\end{bmatrix} = \begin{bmatrix}\mathbf{A} & -\mathbf{B}\\ -\mathbf{B} & \mathbf{A}\end{bmatrix}\begin{bmatrix}\mathbf{V}_S\\ \mathbf{V}_R\end{bmatrix}, \tag{3}$$

where $\mathbf{A} = \mathbf{Y}_C\mathbf{T}_V Coth(\mathbf{r}l)\mathbf{T}_V^{-1} = \mathbf{YT}_V\mathbf{r}Coth(\mathbf{r}l)\mathbf{T}_V^{-1}$, $\mathbf{B} = \mathbf{Y}_C\mathbf{T}_V Co\sec h(\mathbf{r}l)\mathbf{T}_V^{-1} = \mathbf{YT}_V\mathbf{r}Co\sec h(\mathbf{r}l)\mathbf{T}_V^{-1}$.

Frequency domain solution based on sparse matrix

In the high frequency transient conditions, there is shielding effect between different sections. Mutual inductance decreases rapidly with the increase of the distance, based on which we can only consider the mutual inductance among several sections adjacent in the engineering perspective. In addition, it has been verified that the capacitance between two turns at a distance can be ignored.

Take a continuous winding as an example as shown in Fig 2. There are n sections, each of which has m turns.

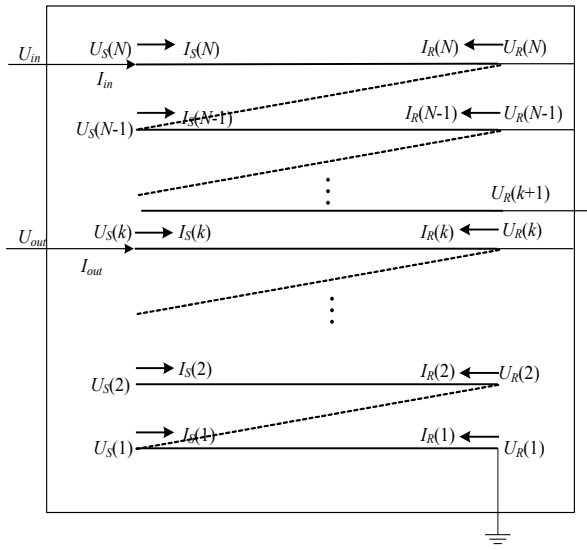

Fig.1 MTLs model of a two-winding transformer

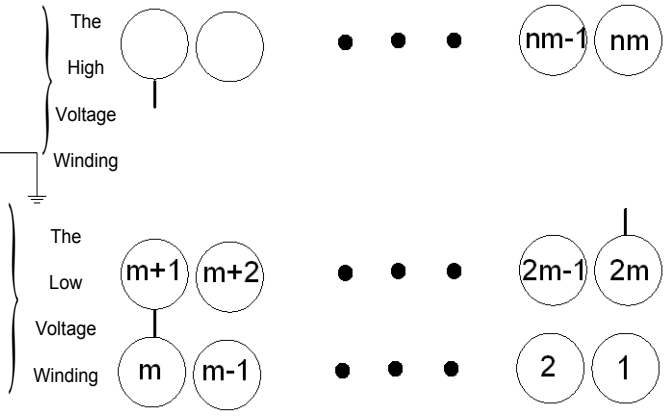

Fig.2 Number sequence of the winding

If the effect of mutual inductance and mutual capacitance of two nearby sections are only considered, the matrix form of Z or Y are shown in Fig.3. It is advocated to take more sections into account according to the conclusion that mutual inductance can be ignored when Mi,j/Li,j×100%≤ 5% (Mi,j and Li,j are mutual inductance and self-inductance between turn i and turn j). A better result can be obtained and the form of overall is similar with Fig.3.

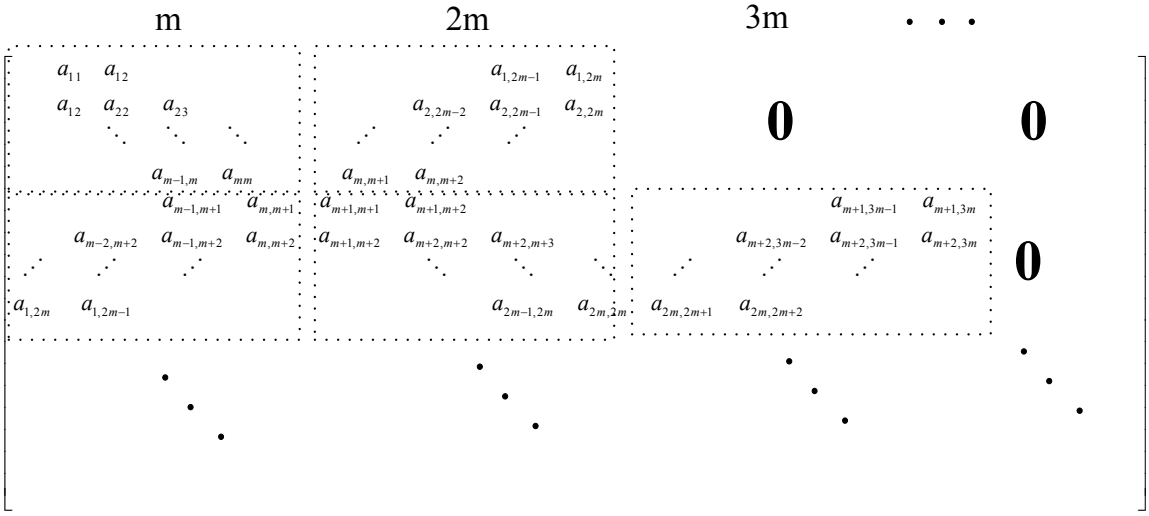

Fig.3 The structure of matrix ***Y(Z)***

Two block sparse matrix Y and Z can be obtained from Fig.3. The equation (1) has to be decoupled before getting the result. Because the matrix Y and Z are both block sparse matrix, the YZ and ZY are also block sparse matrix. The follows are specific solving steps[7,8]:

(1) Transform the matrix ZY into the type of Hessenberg by the matrix primary similarity transformation.

(2) Take the matrix from the step 1 into QR factorization by Givens transforms. From this step, eigenvalues can be obtained after n-1 Givens transforms.

(3) The eigenvectors can be obtained by the inverse power method. By multiple iterations and precision set, the equation (1) can be solved.

Application of an example

In order to verify the theory above, a SS11-20000/110 transformer is measured. Only the high-voltage winding and medium-voltage winding are concerned because of the need of the two-port parameter solution. The high-voltage winding and medium-voltage winding has symmetrical structure along the iron core. Fig.4 shows the upper part of the two windings.

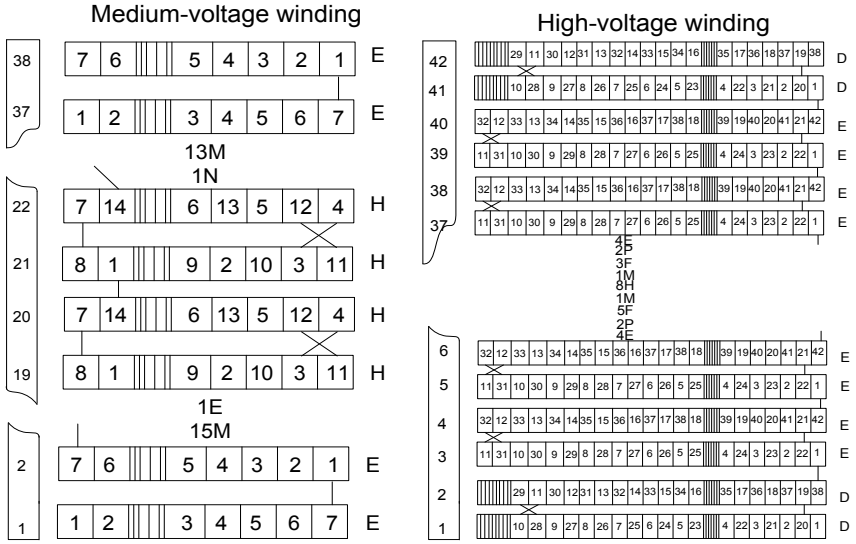

Fig.4 The structure of one part of the winding

The Agilent 4395A spectrum analyzer is used to measure scattering parameter of the winding, and measuring frequency is 100 Hz ~ 50MHz. The scattering parameter S measured can be transformed to admittance parameter Y easily.

Fig.5 and Fig.6 show the comparisons between calculation and measurement of Y11 and Y21. From the comparisons, we can see that there is a good agreement of the admittance parameter between the measurement and the calculation.

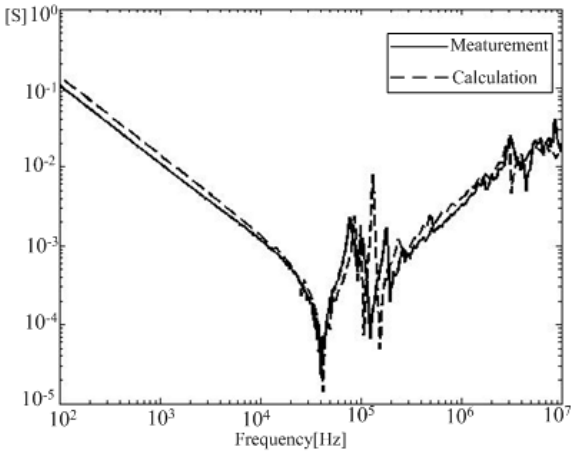

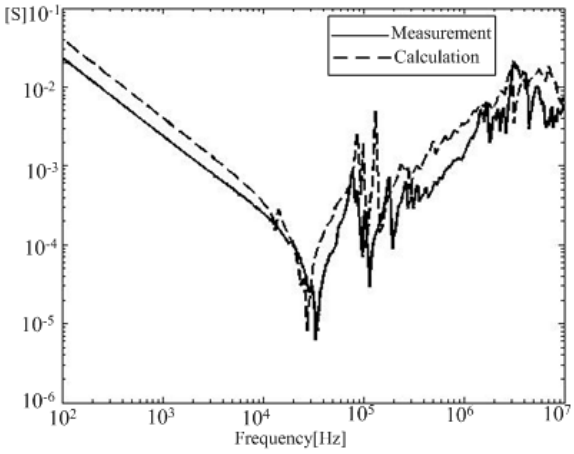

Fig.5 $\boldsymbol{Y}_{11}$ Amplitude-frequency characteristics Fig.6 $\boldsymbol{Y}_{21}$ Amplitude-frequency characteristics

Conclusion

Sparse matrix method is proposed to apply to the MTLs of the transformer to solve the calculation problem caused by too large order number of the matrix. Benefited from the analysis of the matrix Y and Z in engineering application, block storage and calculation method can be applied conveniently to spare the computation time. The method is validated by the comparisons of measured and calculated results obtained in a SS11-20000/110 transformer. The comparisons show that the calculation is accurate in a wide frequency range.

References

[1] Zhongyuan Zhang, Jingsheng Zhao, Xin Ge, Tao Chen. Passive High-frequency Macro Modeling Methods for Transformer Devices [J]. Electric Power Science and Engineering, 2012, 28 (8):36-42 "In Chinese"

[2] GAO Jun, GAO Shuguo, LIU Haifeng. Research on High-Frequency Model and Its Time-Domain Solution Of Transformer Winding [J]. Transformer, 2009, 46 (12):37-40"In Chinese"

[3] Rino Lucic, Ivica Juric-Grgic. Time domain finite element method analysis of multi-conductor transmission line [J]. European Transactions on Electrical Power, 2010, 20: 822- 832

[4] Roberto B. Armenta，Costas D. Sarris. Introducing Nonuniform Grids into the FDTD Solution of the Transmission-Line Equations by Renormalizing the Per-Unit-Length Parameters [J]. IEEE Transactions on Electromagnetic Compatibilty, 2009, 51(3),818-824

[5] C. R. Paul. Analysis of Multi-conductor Transmission Lines. New York: John Wiley & Sons, 1994: 65-73

[6] C .R. Paul. Decoupling the multi-conductor transmission line equations [J] . IEEE Transcation on Microwave Theory and Techniques,1996,V44(8):1429-1440

[7] R. P. Tewaron. Sparse Matrices [M]. New York, 1973

[8] Y. V. Makarov and Z Y Dong. Eigenvalues and eigenfunctions in Encyclopedia of Electrical and Electronics Engineering [J]. New York. Wiley, 1998. Computational Science and Engineering. pp 208-220.

CHAPTER 9:

Communication

Advanced Materials Research Vols. 986-987 (2014) pp 2041-2047

doi:10.4028/www.scientific.net/AMR.986-987.2041

An Optimal Power Allocation for the Two-Way Relay System Using Physical-Layer Network Coding

Rengang Yuan [1,a], Lili Chu [1,b] , Chuang Li [1,c] , Lingli Cao [1,d]

[1]School of Electronics and Information Engineering, Liaoning University of Technology, Jinzhou 121001, China

[a]email: 596214634@qq.com, [b]email: Chulili902@126.com, [c]email: 1013340808@qq.com, [d]email:306052787@qq.com

Keywords: Optimal Power Allocation, Physical-Layer Network Coding, Two-Way Relay System

Abstract. In this letter, an optimal power allocation in the two-way relay channel of four transmission nodes employing the physical-layer network coding (PNC) protocol is proposed to improve the network sum-rate of the two-way relay system. The optimal power allocation is obtained by maximizing the network sum-rate of the PNC protocol under a sum-power constraint in a Rayleigh fading channel environment. Analytical and simulation results show that the proposed power allocation can improve the network sum-rate. Furthermore, compared with the equal power allocation scheme, the proposed power allocation scheme can achieve much higher network sum-rate performance.

Introduction

To meet the increasing demand for high data rate is the goal of future wireless communication networks. A variety of communications technologies, such as relay-based wireless networks as a promising networks configuration has been proposed to achieve this goal. However, the relay-based system has a main drawback which is the loss in spectral efficiency induced by the half-duplex signaling. That is to say, the relay can not transmit and receive at the same time. Various protocols have been studied to avoid the substantial loss in spectral efficiency. The two-way relay system using physical-layer network coding proposed recently can improve the performance of relay system very well. Compared with the previous proposed various relay scheme, this two-way relay system uses only two time slots to exchange information between two source nodes, to increase the capacity of the system. Moreover, the relay nodes do not encode and decode the signals received from the source nodes, only convert the mixed signals to a PNC-modulated signal using the PNC mapping protocol. From this effort, the power can be saved and the error rate of the system can be reduced.

If we want to enhance the capacity further, the signal-to-noise ratio of each communication nodes should be boosted as well. But in most cases, the total power of a two-way relay system is limited, the power should be reasonably allocated to each communication nodes, so as to make the system network rate reach the maximum. A power allocation for the two-way relay system using physical-layer network coding has been studied in [5] and achieved good results, but the relay system only has one relay node. In practical applications, the relay system of one relay node may be difficult to complete the communication needs. When the two communication terminal's distance is long, and a relay node cannot be in the transmission radius of two communication terminal at the same time, it is necessary to add one or more relay node between two terminals to exchange information. Based on this consideration, we propose a model of the two-way relay system containing two relay nodes, and then propose an optimal power allocation scheme which can improve the system transmission rate.

System model and protocol

The model of the system is shown in fig.1. It is assumed that there is no direct path between the source and destination nodes due to large loss, and that the relay node helps their reliable communications. We also assume that there are two relay nodes exist in the system and all the nodes are half-duplex nodes, which cannot receive and transmit simultaneously.

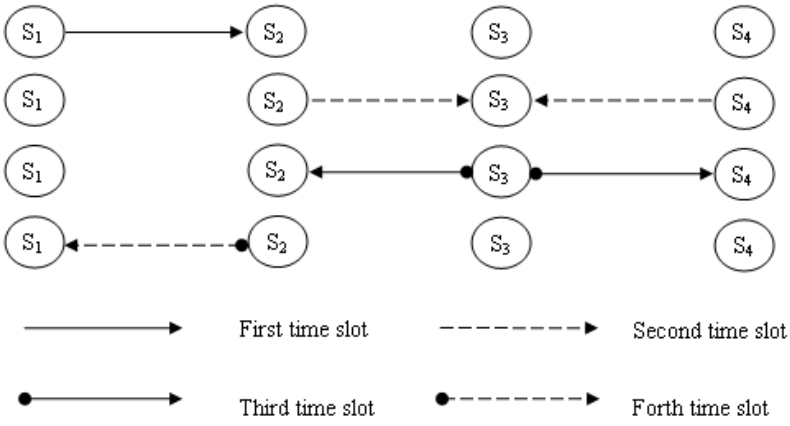

Fig.1 System model

Fig.1 shows the scenario that the node S_1 and S_4 exchange information using four time slots. During the first time slot, the node S_1 sends a signal to the relay node S_2 and S_2 doesn't do any processing after receiving the signal from the S_1. During the second time slot, the node S_2 and the node S_4 sends a signal to the node S_3, the node S_3 converts the mixed signal to a PNC-modulated signal in accordance with the physical encoding mapping rules and then broadcasts the converted signal to node S_2 and node S_4 during the third time slot. In the fourth time slot, the node S_2 sends received modulation signal to the node S_1. By knowing the back propagating self-interference, the node S_1 and the node S_4 can detect its intended signal from the broadcasted signal without any interference.

It is assumed that all the channels in the system are in Rayleigh fading and the noise is a white Gaussian noise with zero-mean and unit-variance, which is uncorrelated with the transmitted signals from both source nodes.

Based on the [6], [7], the achievable sum-rate of the two-relay system is given as:

$$\begin{aligned} R_{sum} &= R_{14} + R_{41} \\ &= \frac{1}{2}\min\{R_{12}, R_{23}, R_{34}\} + \frac{1}{2}\min\{R_{43}, R_{32}, R_{21}\} \end{aligned} \tag{1}$$

where R_{14} and R_{41} denote the achievable rate of one-way network system from S_1 to S_4 and from S_4 to S_1, respectively. R_{12}, R_{23}, R_{34}, R_{43}, R_{32} and R_{21} are the link capacities, they can be represented as:

$$R_{ii+1} = \log_2(1 + \frac{h_i^2 P_i}{\sigma^2}) \tag{2}$$

$$R_{i+1i} = \log_2(1 + \frac{h_i^2 P_{i+1}}{\sigma^2}) \tag{3}$$

where h_i for $\forall i \in \{1,2,3\}$ is the channel gain between every two adjacent nodes, P_i is the transmit power of S_i, and σ^2 indicates the noise variance.

Power allocation scheme

Considering the total power P of the relay system is limited, to make the achievable sum-rate of the two-way relay system reach the maximum, the total power P must be properly allocated to each communication node in the system. The formulation of the problem is represented as:

$$\max_{P_1,P_2,P_3,P_4} R_{sum} \tag{4}$$

Subject to $\quad P_1 + P_2 + P_3 + P_4 \le P \tag{5}$

The main characteristic of physical layer network coding is that without explicitly decoding the signal from other nodes, the relay nodes make the mixed signals to the PNC-modulated signal by a simple mapping operation. In that sense the power allocated to the relay nodes with the PNC protocol can be fully used to transmit signal to corresponding destination, rather than the utilization of the

relay transmission power in analog network coding, part of the energy is used in signal decoding and forwarding. So that the power P_2 and P_3 allocated to the relay nodes will affect R_{14} and R_{41}. Moreover, it also affects P_1 and P_4 under the total transmit power constraint, so as to further effects R_{14} and R_{41}.

A diagram of the link capacity is used to illustrate the optimization problem. In the equal power allocation, the system power allocate to each node is the same, i.e., $P_1 = P_2 = P_3 = P_4$ and channel gain of the links have the following relationship, i.e., $h_1 \geq h_2 \geq h_3$. Combined with the formula (2) and (3), the relationships of the link capacities as shown in fig.2.

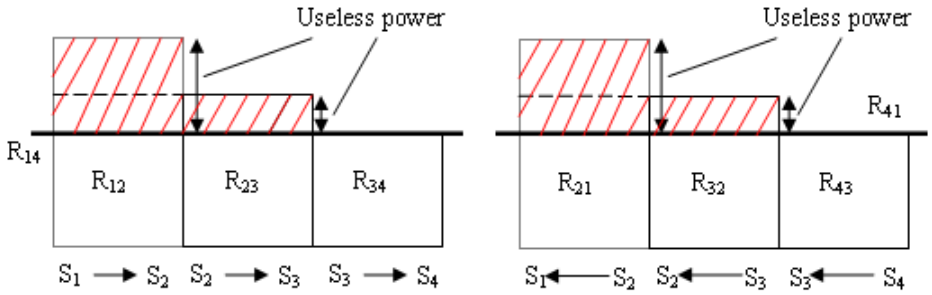

Fig.2 Link capacity diagram of equal power distribution strategy

R_{14} and R_{41} were determined by the minimum value of the two one-way network systems, respectively, so a portion of the node power is wasted. In order to optimize the above scheme, we first propose a sub-optimal power allocation scheme, let $R_{12} = R_{23} = R_{34}$, $R_{43} = R_{32} = R_{21}$. The relationships of the link capacities after employing the sub-optimal power allocation scheme as shown in fig.3.

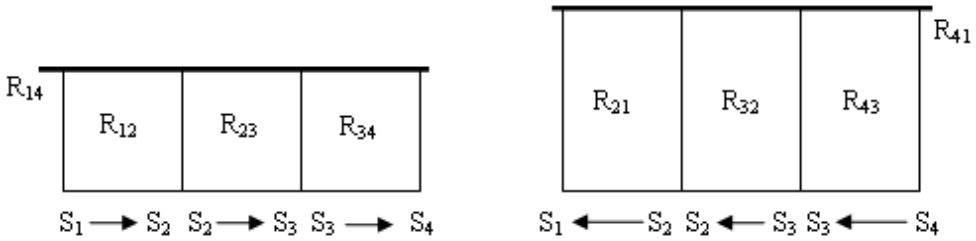

Fig.3 Link capacity diagram of sub-optimal power distribution strategy

Through the analysis and calculation, the power should be allocated to the nodes is given as:

$$\overline{P_1} = P\frac{h_2^{\,2}h_3^{\,2}}{(h_1^{\,2}+h_2^{\,2})(h_1^{\,2}+h_3^{\,2})} \tag{6}$$

$$\overline{P_2} = P\frac{h_1^{\,2}h_3^{\,2}}{(h_1^{\,2}+h_2^{\,2})(h_1^{\,2}+h_3^{\,2})} \tag{7}$$

$$\overline{P_3} = P\frac{h_1^{\,2}h_2^{\,2}}{(h_1^{\,2}+h_2^{\,2})(h_1^{\,2}+h_3^{\,2})} \tag{8}$$

$$\overline{P_4} = P\frac{h_1^{\,4}}{(h_1^{\,2}+h_2^{\,2})(h_1^{\,2}+h_3^{\,2})} \tag{9}$$

Drawing the above four formulas need to meet the formula, $\frac{h_2}{h_3} = \frac{h_1}{h_2}$. The gain factor is defined as $h_i = \frac{\sqrt{\varepsilon_i G_{ti} G_{ri}}\lambda_i}{4\pi\sqrt{d_i^{\alpha_i} l_i N_{0i}}}$, where G_{ti} is the transmitting antenna gain, G_{ri} is the receiving antenna gain, λ_i is the wavelength, d_i is the distance between every two adjacent nodes, namely, d_1, d_2, d_3 represent the distance of links $S_1 \to S_2$, $S_2 \to S_3$, $S_3 \to S_4$. l_i is the transmission loss factor of system which has nothing to do with the transmission, ε_i is the shadow fading factor, N_{0i} is the noise power

and α_i is the path loss exponent set to 3. For facilitating the discussion, we assume that all the links have the same G_{ti}, G_{ri}, λ_i, l_i, α_i, ε_i and N_{0i}. In order to meet the formula, $\frac{h_2}{h_3}=\frac{h_1}{h_2}$, only need to meet the formula, $\frac{d_3^{3/2}}{d_2^{3/2}}=\frac{d_2^{3/2}}{d_1^{3/2}}$.

However, we can further adjust the sub-optimal power allocation scheme to improve the achievable sum-rate. P_1, P_2, P_3 and P_4 can be written as follows:

$$P_1=\overline{P_1}\pm\Delta P_1 \tag{10}$$

$$P_2=\overline{P_2}\pm\Delta P_2 \tag{11}$$

$$P_3=\overline{P_3}\pm\Delta P_3 \tag{12}$$

$$P_4=\overline{P_4}\pm\Delta P_4 \tag{13}$$

where $\overline{P_1}$, $\overline{P_2}$, $\overline{P_3}$ and $\overline{P_4}$ are given in (6), (7), (8) and (9), respectively. From formula (10), (11), (12) and (13), we can see that the power saved in one node can be assigned to other communication nodes. Here are three premises used to determine ΔP_1, ΔP_2, ΔP_3 and ΔP_4.

Premise 1: The power that does not contribute to the one-way network system capacity, R_{14} and R_{41}, must be saved to assign to other nodes. However, this does not mean that there is no power in the whole system is extra consume. Because the channel gains h_1, h_2 and h_3 are different, power consumption can be inevitably caused when the relay nodes broadcast signal in the opposite direction.

The relationships among the six link capacities in fig.3 can be written as the following inequalities under the above condition.

$$R_{12}\le R_{23}\le R_{34} \tag{14}$$

$$R_{43}\le R_{32}\le R_{21} \tag{15}$$

Under the condition of the limited total transmit power and premise 1, the power optimization problem can be simplified as:

$$\max_{P_1\ P_4}\log_2(1+h_1^{\,2}P_1)+\log_2(1+h_3^{\,2}P_4) \tag{16}$$

where it is assumed that all noise powers are equal to 1.

Premise 2: Two link capacities for at least one link-pair should be the same (as shown in fig.2 $S_1\to S_2$, $S_2\to S_3$ and $S_3\to S_4$ as a link-pair, $S_4\to S_3$, $S_3\to S_2$ and $S_2\to S_1$ as the other link-pair). The power of relay nodes S_2 and S_3 must be supplemented to ensure the increased link capacity associated with them can be equal to the R_{12} or R_{43}.

Based on the above two premises, we notice that there exit only two possible cases to improve the achievable sum-rate as shown in fig.4 and fig.5.

(1) Case Ⅰ: Make R_{12}, R_{23}, R_{34} improve the same amplitude by allocating the power saved from S_4 to S_1, S_2 and S_3. In this case, we can get the following achievable sum-rate.

$$R_{sum}=\log_2(1+h_1^{\,2}(\overline{P_1}+\Delta P_1))+\log_2(1+h_3^{\,2}(\overline{P_4}-\Delta P_4)) \tag{17}$$

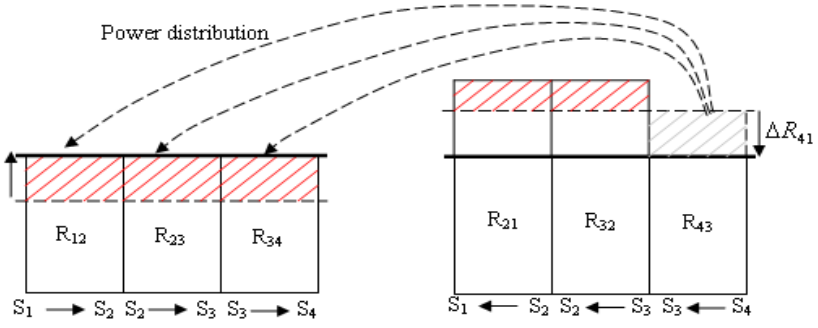

Fig.4 Case Ⅰ: $P_1\uparrow$, $P_2\uparrow$, $P_3\uparrow$, $P_4\downarrow$

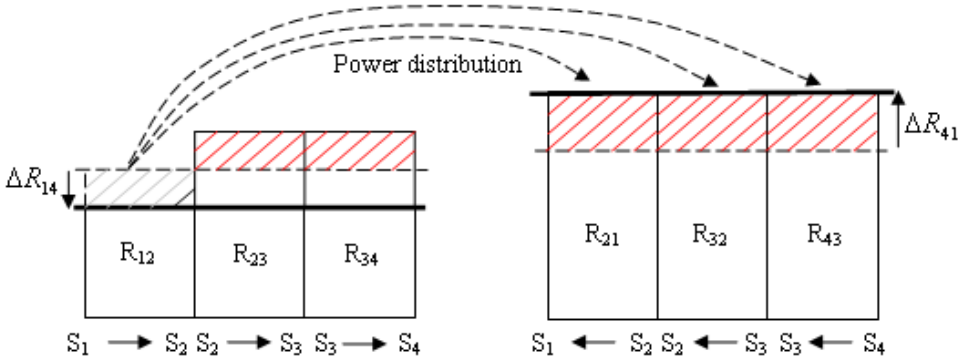

Fig.5 Case P_1 P_2 ↑ P_3 ↑ P_4 ↑

Premise 3: The power saved from one out of two source nodes should be used for other three nodes.

Use the first case as an example to illustrate the premise 3, the power allocation need to meet the following formula,

$$\Delta P_4 = \Delta P_1 + \Delta P_2 + \Delta P_3 \tag{18}$$

R_{12}, R_{23}, R_{34} raise the same amplitude from the premise 2, so we can get the following formula,

$$\log_2(1+h_1^{\,2}(\overline{P_1}+\Delta P_1)) = \log_2(1+h_2^{\,2}(\overline{P_2}+\Delta P_2)) = \log_2(1+h_3^{\,2}(\overline{P_3}+\Delta P_3)) \tag{19}$$

Combined with the formula (6) ~ (9), (18) and (19), we can get the relations among $\Delta P_1, \Delta P_2, \Delta P_3$ and ΔP_4 as following,

$$\Delta P_1 = \frac{h_2^{\,2}}{h_1^{\,2}}\Delta P_2 \tag{20}$$

$$\Delta P_3 = \frac{h_2^{\,2}}{h_3^{\,2}}\Delta P_2 \tag{21}$$

$$\Delta P_4 = (\frac{h_2^{\,2}}{h_1^{\,2}} + \frac{h_2^{\,2}}{h_3^{\,2}} + 1)\Delta P_2 \tag{22}$$

Define the increment of the capacity as:

$$\Delta R_{sum} = \Delta R_{14} - \Delta R_{41} \tag{23}$$

and $\Delta R_{14} = \log_2(1+h_1^{\,2}(\overline{P_1}+\Delta P_1)) - \log_2(1+h_1^{\,2}\overline{P_1})$, $\Delta R_{41} = \log_2(1+h_3^{\,2}\overline{P_4}) - \log_2(1+h_3^{\,2}(\overline{P_4}-\Delta P_4))$.

If power adjustment scheme makes the achievable sum-rate increase, ΔR_{sum} will be a positive number. Combined with the formula (6), (9), (20), (22) and (23), we can get the following inequality,

$$\Delta P_2[r_4 h_2^{\,2} - r_1\frac{h_2^{\,2}[(h_1^{\,2}+h_3^{\,2})+h_1^{\,2}*h_3^{\,2}]}{h_1^{\,2}} - \frac{h_2^{\,4}(h_1^{\,2}+h_3^{\,2})+h_1^{\,2}h_2^{\,2}h_3^{\,2}}{h_1^{\,2}}\Delta P_2] \geq 0 \tag{24}$$

where $r_1 = 1+h_1^{\,2}\overline{P_1}$, $r_4 = 1+h_3^{\,2}\overline{P_4}$. Due to $\Delta P_2 \geq 0$, the quadratic inequality (24) can be simplified as follows:

$$r_4 h_2^{\,2} - r_1\frac{h_2^{\,2}(h_1^{\,2}+h_3^{\,2})+h_1^{\,2}*h_3^{\,2}}{h_1^{\,2}} - \frac{h_2^{\,4}(h_1^{\,2}+h_3^{\,2})+h_1^{\,2}h_2^{\,2}h_3^{\,2}}{h_1^{\,2}}\Delta P_2 \geq 0$$

$$\Rightarrow \overline{P_4} \geq (1+\frac{h_1^{\,2}}{h_3^{\,2}})\overline{P_1} + \frac{1}{h_1^{\,2}} \tag{25}$$

The above inequality shows that the ΔR_{sum} can be positive only under the condition of (25). It can be seen from the inequality (24), the incremental system network rate ΔR_{sum} is determined by ΔP_2, and ΔP_2 can be obtained by the following equation:

$$\frac{\partial\{\Delta P_2[r_4 {h_2}^2 - r_1 \frac{{h_2}^2({h_1}^2+{h_3}^2)+{h_1}^2 * {h_3}^2}{{h_1}^2}] - \frac{{h_2}^4({h_1}^2+{h_3}^2)+{h_1}^2{h_2}^2{h_3}^2}{{h_1}^2}\Delta P_2\}}{\partial \Delta P_2} = 0 \quad (26)$$

Combining (20), (21), (22) and (26), we eventually get the optimal solution ΔP_1^*, ΔP_2^*, ΔP_3^*, and ΔP_4^*, maximizing ΔR_{sum} as follows:

$$\Delta P_2^* = \frac{r_4 {h_1}^2}{2[{h_2}^2({h_1}^2+{h_3}^2)+{h_1}^2{h_3}^2]} - \frac{r_1[h_2^2({h_1}^2+{h_3}^2)+h_1^2h_3^2]}{2[{h_2}^4({h_1}^2+{h_3}^2)+{h_1}^2h_2^2{h_3}^2]} \quad (27)$$

$$\Delta P_1^* = \frac{{h_2}^2}{{h_1}^2}\Delta P_2^* \quad (28)$$

$$\Delta P_3^* = \frac{{h_2}^2}{{h_3}^2}\Delta P_2^* \quad (29)$$

$$\Delta P_4^* = (\frac{{h_2}^2}{{h_1}^2} + \frac{{h_2}^2}{{h_3}^2} + 1)\Delta P_2^* \quad (30)$$

(2) Case Ⅱ: Make R_{21}, R_{32}, R_{43} improve the same amplitude by allocating the power saved from S_1 to S_2, S_3 and S_4. However, we cannot obtain an achievable sum-rate greater than that given in the sub-optimal power allocation by employing the similar method using in Case Ⅰ.

In a word, in order to maximize the achievable sum-rate of the two-way relay system, we need to do the following adjustments to the power of each node in the system:

$$P_1^* = \overline{P_1} + \Delta P_1^* \quad (31)$$

$$P_2^* = \overline{P_2} + \Delta P_2^* \quad (32)$$

$$P_3^* = \overline{P_3} + \Delta P_3^* \quad (33)$$

$$P_4^* = \overline{P_4} - \Delta P_4^* \quad (34)$$

Numerical results and analysis

In this section, we contrast the two different achievable sum-rate performance of the equal power allocation scheme and the proposed power allocation scheme via numerical simulations. The simulation results are shown in figure 6.

The horizontal axis represents the total power supplied to the system of four nodes, the vertical axis represents the achievable sum-rate, two other curves represent the simulation result of the equal power allocation scheme and the proposed power allocation scheme. It can be seen from the figure, the system using optimal power allocation scheme can achieve bigger sum-rate than the system using equal power allocation scheme. The simulation result is consistent with the above theoretical derivation, and with the total system power increases, the gap between the two will increase. This implies that the proposed optimum power allocation should be applied to achieve higher sum-rate when the system total power becomes larger.

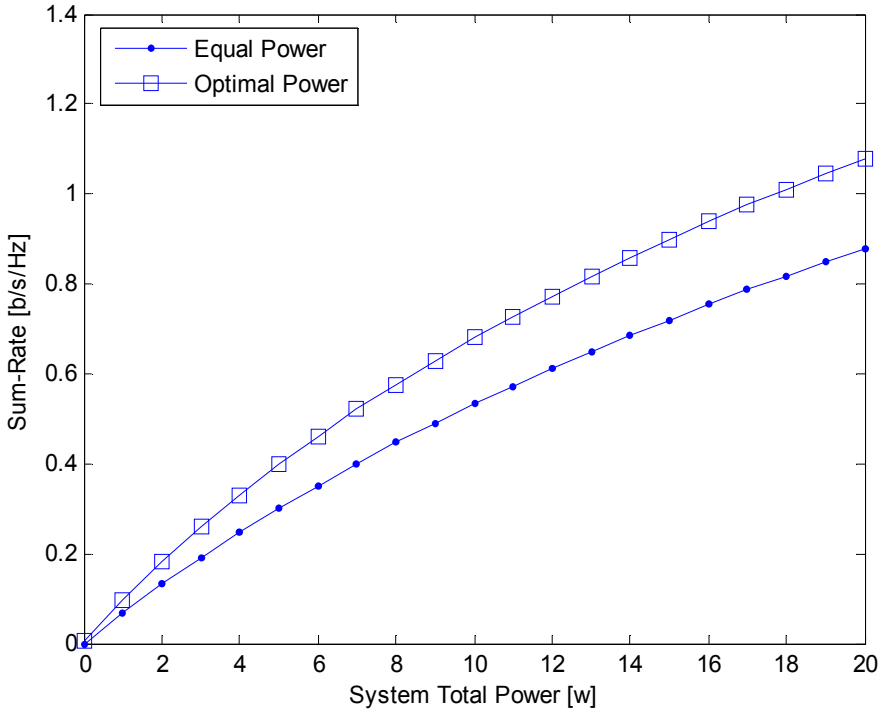

Fig.6 Achievable sum-rate of two kinds of power allocation

Conclusions

In this paper, an optimal power allocation in the two-way relay channel of four transmission nodes employing the physical-layer network coding (PNC) protocol is proposed to improve the network sum-rate of the two-way relay system. Analytical and simulation results show that the proposed power allocation can improve the network sum-rate when the system total power becomes larger.

References

[1] N. J. Laneman, D. N. Tse, and G. W. Wornell: *Cooperative diversity in wirless network*: *Efficient protocols and outage behavior*. IEEE Trans. Inform (2004), p. 3062-3080

[2] Zhang S, Liew S C, Lam P P: *Hot topic*: *physical-layer network coding*. Proceedings of the 12th annual international conference on Mobile computing and networking. ACM (2006), p. 358-365

[3] Cui T, Gao F, Tellambura C: *Physical layer differential network coding for two-way relay channels*. IEEE GLOBECOM 2008. IEEE (2008), p. 1-5

[4] Ju M C, Kim I M: *Relay Selection with Physical-Layer Network Coding*. Global Telecommunications Conference, IEEE (2010), p. 1-5

[5] Shin W, Lee N, Lim JB, et al: *An optimal transmit power allocation for the two-way relay channel using physical-layer network coding*. IEEE International Conference on Communications Workshops (2009), p. 1-6

[6] B. Rankov and A. Wittneben: *Spectral efficient protocols for half-duplex fading relay channels*. IEEE J. Sel. Areas Commun (2007), p. 379-389

[7] R. Knopp: *Two-way wireless communication via a relay station*. GDR ISIS meeting (2007)

[8] K atti S, Gollakota S, Katabi D: *Embracing wireless interference*: *Analog network coding*. Proceedings of the 2007 conference on Applications, technologies, architectures, and protocols for computer communications. ACM (2007), p. 397-408

Advanced Materials Research Vols. 986-987 (2014) pp 2048-2051

doi:10.4028/www.scientific.net/AMR.986-987.2048

Analysis of Statistical Characteristics of the Laser Vibrometer's Static Signal Noise

YANG Jing[1,a], TANG Jianlong[2,b], HOU Junhui[1,a], ZHANG Xue[3,c], WU Zhishan[1,a]

[1]Research Institute of Highway Ministry of Transport, Beijing Luxing New Road Technology Co., Ltd. , Beijing 100088, China;

[2]School of Electronic Engineering, Xidian University, Xi'an, Shaanxi 710071, China;

[3]School of Electronics Engineering and Computer Science, Peking University, Beijing 100871, China

[a]j.yang@rioh.cn, [a]jh.hou@rioh.cn, [a]zs.wu@rioh.cn, [b]JLtang@xidian.edu.cn, [c]Lindajia03@126.com

Keywords: noise; probability density; frequency spectrum; power spectrum; high order spectrum

Abstract. The static signal is collected through the experiment, and the probability density function model is established. The static random signal noise is analyzed by frequency spectrum, power spectrum and high order spectrum analysis. It is found that the third order spectrum of the laser static signal is zero by the high order spectrum analysis. Noise signal is only to analyze on the frequency spectrum and power spectrum. The results show that the static laser signal has the characteristics of stationary Gauss random signal.

Introduction

The laser vibrometer measure various object's vibration, velocity and displacement by non-contact measurement method and it can accurately restore measured body trajectory and display trajectory's image. The laser vibrometer has the characteristics of high sampling frequency, high resolution, high linearity and high response speed. It can be used to study velocity of the creep material the surface deformation, and provides a good solution for not meeting with contact measuring creep objects about the vibration measurement.

In this experiment the laser stationary signal irradiate to the creep object. Relative the mobile laser signal, the static signal is considered to be noise signal. Analysis of the statistical characteristics of the static noise is help to find a proper method to reduce the static noise.

Statistical Model of Static Laser Signal Noise

Design of Experiment

In laboratory, a laser vibrometer is fixed still on the door shaped bracket. The laser beam vertically downward irradiation onto the surface of the material without exerting force on material surface. To ensure that each sample size is large enough, we collected 10 groups of sample data with sampling frequency of 1 KHz and each group data of 20000 sampling value.

Establish Model

A group of static laser sample data is shown by histogram curves smoothed. The probability density curve of signal noise amplitude is programmed and showed in Fig.1. Curve reflects the probability amplitude of signal falling on different intensity region. The abscissa shows the noise amplitude divided into 50 sections of the value in units of m/min, and the ordinate represents signal noise amplitude probability. We can conclude that signal noise amplitude obey two different parameters normal distribution.

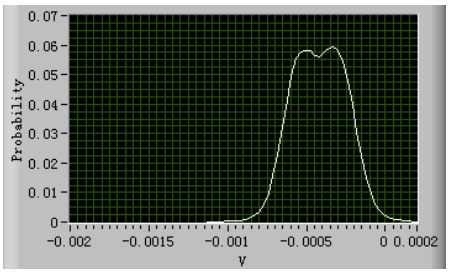

Fig.1 The probability density curve of static laser signal

According to figure 1, we assume that probability density curve of the noise amplitude is superimposed of two normal curve. The following is the probability density curve model.

$$y = a_1 e^{-\frac{(x-\mu_1)^2}{2\sigma^2}} + a_2 e^{-\frac{(x-\mu_2)^2}{2\sigma^2}} \qquad V_{min} \leq x \leq V_{max} \qquad (1)$$

The independent variables x is amplitude of the noise, and the unit is m/min. The dependent variable y is probability of static signal noise amplitude.

Calculation Curve Parameter

We compare the model curve with the obtained probability density curve by histogram function by 10 groups sample curve data. When the two curves correlativity is best, we can determine the parameters of the model curve [1]. Steps of the determining parameters are as follows.

Step 1: we analyze the correlativity between each model curve and each obtained probability density curve. And we calculate that the mean of σ is 0.00433. Step 2: σ =0.00433, let a1=a2, we analyze correlativity of the two curves and calculate that the mean of a1and a2 is 0.0608. Step 3: σ=0.00433, a1=a2=0.0608, we analyze correlativity and calculate that the mean of μ1 is 0.0266 and the mean of μ2 is 0.0368. Finally, when σ=0.00433, a1=a2=0.0608, μ1=0.0266, μ2=0.0368, we analyze better correlativity of the two curves shown in Table 1.

Table 1 Calculation R^2 value in the condition of σ=0.00433, a1=a2=0.0608, μ1=0.0266 and μ2=0.0368.

No.	V_{min}	V_{max}	R^2	No.	V_{min}	V_{max}	R^2
1	-0.001282	0.000572	0.8697860422	6	-0.001215	0.000388	0.9908933465
2	-0.001142	0.000337	0.8720827193	7	-0.001158	0.00044	0.9097162116
3	-0.001258	0.000427	0.8523054612	8	-0.001362	0.000576	0.6038675802
4	-0.001144	0.000396	0.9477898436	9	-0.001195	0.000357	0.9984724295
5	-0.001084	0.000379	0.6437139064	10	-0.001146	0.00034	0.9769006346

In the condition of σ=0.00433, a1=a2=0.0608, μ1=0.0266 and μ2=0.0368, the mean value of R^2 is greater than 0.85 shown in table 1. By these limited sample data, correlation of established model and theoretical curves is very good. As each measurement noise have small change, parameters value of the probability density function may be some deviation.

Characteristics of Static Laser Signal Noise Spectrum

Frequency Spectrum and Power Spectrum Analysis

For the finite sample signal, the frequency spectrum represents the distribution of complex amplitude of each signal components in the frequency domain. For 10 groups of sample signal, we can see that the signal energy is concentrated in 420Hz~474Hz, 540Hz~585Hz, 600Hz~680Hz, 710Hz~900Hz four frequency ranges. It is possible that there is some effects of environmental vibration on the laser signal, thus it is necessary to filter the signal frequency above 400Hz. Frequency spectrum diagram is shown in Fig.2.

For the finite sample signal, the power spectrum represents the average power consumption of the spectral components in 1 ohm resistance within the frequency band [2]. We can see that the laser energy is basically a stationary stochastic process. Owing to the interference, individual sample signal may appear non-stationary state. Power spectrum diagram is shown in Fig.3.

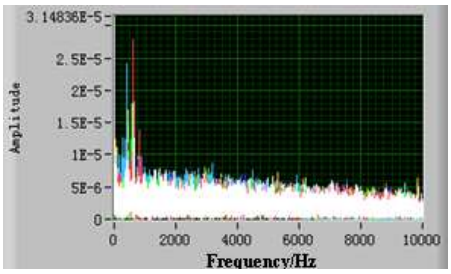

Fig.2 Laser static signal frequency spectrum

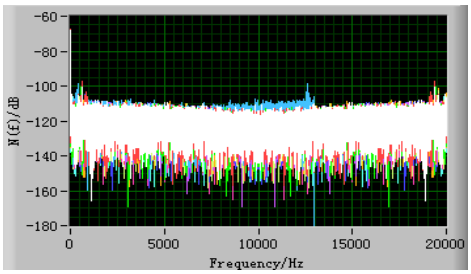

Fig.3 Laser static signal power spectrum

High Order Spectrum Analysis

Correlation function and power spectrum can not identify non minimum phase system, and can only deal with the observation data of additive white noise. Using three order or high order statistics, can overcome these shortcomings. High order statistics can analysis on non Gauss, nonlinear, and non minimum phase system [3]. That is to say, theoretically not satisfactorily resolved by low order statistics method, the problem can be handled in high order statistics [4]. High order spectrum analysis steps are as follows. According to the formula (2), we assume the probability density function as follows [5].

$$f(x)=\mathrm{a}(e^{-\frac{(x-\mu_1)^2}{2\sigma^2}}+e^{-\frac{(x-\mu_2)^2}{2\sigma^2}}) \quad \text{(a, u1 and u2 are constants)} \tag{3}$$

$$\Phi(\omega)=\int_{-\infty}^{\infty}f(x)e^{j\omega x}dx=a\int_{-\infty}^{\infty}e^{-\frac{(x-\mu_1)^2}{2\sigma^2}+j\omega x}dx+a\int_{-\infty}^{\infty}e^{-\frac{(x-\mu_2)^2}{2\sigma^2}+j\omega x}dx \quad \text{(characteristic function)} \tag{4}$$

$$\Phi(\omega)=a\sigma\sqrt{2\pi}(\cos(u_1\omega)-i\sin(u_1\omega))e^{(u_1^2/\sigma^2+\sigma^2\omega^2/2)}+a\sigma\sqrt{2\pi}(\cos(u_2\omega)-i\sin(u_2\omega))e^{(u_2^2/\sigma^2+\sigma^2\omega^2/2)} \tag{5}$$

$$\Psi(\omega)=\ln\Phi(\omega)=2\ln(a\sigma\sqrt{2\pi})+(u_1^2+u_2^2)/\sigma^2+\sigma^2\omega^2-u_1\omega j-u_2\omega j \quad \text{(high order cumulant)} \tag{6}$$

$$\Psi'(\omega)=2\sigma^2\omega-u_1 j-u_2 j,\quad \Psi''(\omega)=2\sigma^2,\quad \Psi'''(\omega)=0 \tag{7}$$

$$c_1=-u_1-u_2,\quad c_2=2\sigma^2,\quad c_k=0 \quad \text{(above the third order cumulant constant is zero)} \tag{8}$$

$$S_x=-2\pi\delta(\omega)(u_1+u_2),\quad S_{2x}=4\pi\sigma^2\delta(\omega),\quad S_{3x}=0 \quad \text{(One order, two order and three order cumulant spectrum)} \tag{9}$$

When a1=a2=0.0608, μ1=0.0266, μ2=0.0368, σ =0.0043, one order cumulant spectrum of stochastic process is the frequency spectrum and an impulse function form of spectrum. Two order cumulant spectrum or power spectrum is an impulse function form of spectrum. More than three order cumulant spectrum is zero. Frequency spectrum and power spectrum distribution is almost uniform consistently with the previous spectrum graph and power spectrum graph display results.

From the above results, the static laser signals are the certain parameters probability density function of two Gaussian's PDF overlay. Over the third order cumulant is constant zero, but the high order moment is not zero. High order cumulant (k>2) constant is zero, so the high order spectrum constant is zero. The laser static signal has the same characteristics of Gaussian distribution of random variables [6].

Conclusion

This paper has studied the laser signal noise and analyzed the statistical model of noise, the noise spectrum and power spectrum and high order spectrum analysis. We get the following conclusions.

(1) The probability density curve model of laser vibrometer static signal is non Gauss probability density function by the mixed two Gauss's PDF.

(2) Through the analysis of frequency spectrum, we can see that the signal energy is concentrated in 420Hz~474Hz, 540Hz~585Hz, 600Hz~680Hz, 710Hz~900Hz four frequency ranges. It can provide reference for further noise filtering.

(3) By high order spectrum analysis, the laser static signal has the characteristics of stationary Gauss random signal.

References

[1] SHOU Jilin. Mathematics Modeling —Method and Example[M]. Xi'an:Xi'an Jiaotong University Press, (1993).

[2] ZHANG Qianwu. Random Signal Analysis[M]. Xi'an: Xidian University Press, (1984).

[3] YU Bo, DONG Guohai, MA Xiaozhou. Laboratory Study of Nonlinear Transformation of Irregular Waves Over a Steep Slope[J]. Port & Waterway Engineering, Issue 3, (2013), p. 36-44.

[4] ZHANG Yifen. Analysing Ship Noise Based on Bispectrum. Signal Processing Proceedings of the 9th National Conference (CCSP-99)[C], Beijing, China, (1999), p. 543-546.

[5] ZHANG Xiaohui. Research on the Method of Seismic Wavelet Extraction Based on Higher-Order Spectrum Analysis[D]. Chengdu: Chengdu University of Technology, (2012), p. 6-12.

[6] DONG Jianhua. Fractional Spectrum and High-Order Spectrum Estimation Technology and Its Application Research in Seismic Reservoir Prediction[D]. Wuhan: China University of Geosciences, (2008), p. 36-48.

Advanced Materials Research Vols. 986-987 (2014) pp 2052-2055

doi:10.4028/www.scientific.net/AMR.986-987.2052

Analysis of the Channel Capacity under OFDM system with insufficient CP

Xinya.Liu , Hongwen.Yang

School of Information and Communication Engineering,
Beijing University of Posts and Telecommunications

liuxinya89@163.com, yanghong@bupt.edu.cn

Keywords: OFDM; Capacity; Cyclic Prefix; Power Delay Profile

Abstract. The standard OFDM signal requires a cyclic prefix (CP) of length larger than the channel impulse response. This paper investigates the effect of CP length to the capacity of OFDM system. We have found that full CP or none CP may not be optimal in the sense of capacity. Specifically, the capacity is a monotonic function of CP length in the low and high SNR regime and is approximately concave down when SNR is about 3dB.

Introduction

Orthogonal Frequency Division Multiplexing(OFDM) is a multicarrier transmission technique that divides the broadband channel into a number of parallel, independent narrowband sub-channels by using IFFT/FFT algorithms. In the standard OFDM systems, a cyclic prefix (CP) of length greater than the channel impulse response (CIR) is a must to eliminate the inter-symbol interference (ISI) and inter-channel interference (ICI). [1,2] Insufficient CP will degrade the performance of an OFDM system due to ISI and ICI. One way to overcome this problem is to increase the number of subcarriers, although this in turn dramatically increases the system complexity. Another way to solve this problem is to use a CP shorter than the CIR and combat the resulted interference by employing an equalizer (either linear or non-linear) at the receiver[3-7].

This paper investigate the capacity of OFDM with insufficient CP. The results show that the capacity can be maximized with optimal CP length which depends on signal to noise ratio(SNR) and the structure of power delay profile(PDP).

System Model

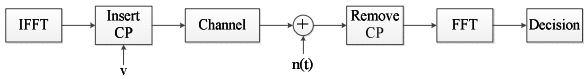

Fig1 A simplified block diagram of OFDM system

Fig.1 shows a simplified diagram of an OFDM system. $\mathbf{a}^k = (a_0^k, a_1^k, \cdots a_{N-1}^k)^T$ is the *k-th* OFDM symbol in the frequency domain, and the input data are assumed to be independent, i.e.

$$\mathrm{E}[\mathbf{a}^m \left(\mathbf{a}^n\right)^H] = \sigma_a^2 \mathbf{I}\delta(m-n) \tag{2-1}$$

where σ_a^2 is the transmitted signal power and $\mathbf{I}$ is an $N \times N$ identity matrix.

An Inverse Fast Fourier Transform of N-points is used to modulate the frequency domain signal $\mathbf{a}^k$ to create the time domain signal $\mathbf{x}^k = (x_0^k, x_1^k, \cdots x_{N-1}^k)^T$. In order to cancel the ISI and ICI, a cyclic prefix which is generally composed by the last components of $\mathbf{x}^k$ is added in the front of each signal. Then the signal send to the channel can be represented as:

$$\mathbf{s}^k = \mathbf{H}_{cp}\mathbf{x}^k \tag{2-2}$$

$$\mathbf{H}_{cp} = \begin{Bmatrix} \mathbf{0}_{(N-v)\times v} & \mathbf{I}_{v\times v} \\ & \mathbf{I}_{N\times N} \end{Bmatrix} \tag{2-3}$$

where v is the length of the CP and L is the length of the channel impulse response.

The received signal for the *k-th* symbol at the channel output can be described as

$$\mathbf{y}^k = \mathbf{H}\mathbf{x}^k - \mathbf{H}_{ICI}\mathbf{x}^k + \mathbf{H}_{ISI}\mathbf{x}^{k-1} + \mathbf{n}^k \tag{2-4}$$

where $\mathbf{y}_k$ and $\mathbf{n}_k$ are both *N*-dimensional vector that contains *N* consecutive samples of received signal and received noise, respectively. $\mathbf{H}$, $\mathbf{H}_{ICI}$ and $\mathbf{H}_{ISI}$ are $N \times N$ toeplitz matrices that can be formed as follows:

$$\mathbf{H} = \begin{Bmatrix} h_0 & 0 & \cdots & h_{L-1} & \cdots & h_2 & h_1 \\ \vdots & \ddots & \ddots & \ddots & \ddots & \ddots & \vdots \\ h_{L-3} & \ddots & h_0 & 0 & \ddots & h_{L-1} & h_{L-2} \\ h_{L-2} & h_{L-3} & \ddots & h_0 & 0 & \ddots & h_{L-1} \\ h_{L-1} & h_{L-2} & \ddots & h_1 & h_0 & \ddots & 0 \\ \vdots & \ddots & \ddots & \ddots & \ddots & \ddots & \ddots \\ 0 & \cdots & h_{L-1} & h_{L-2} & \cdots & h_1 & h_0 \end{Bmatrix} \mathbf{H}_{ICI} = \begin{Bmatrix} 0 & \cdots & h_{L-1} & h_{L-2} & \cdots & h_{v+1} & 0 & \cdots & 0 \\ 0 & \cdots & 0 & h_{L-1} & \cdots & h_{v+2} & 0 & \cdots & 0 \\ \vdots & \cdots & \vdots & \ddots & \ddots & \vdots & \vdots & \vdots & \vdots \\ 0 & \cdots & 0 & 0 & \ddots & h_{L-1} & 0 & \cdots & 0 \\ \vdots & \cdots & \vdots & \ddots & \ddots & \ddots & \vdots & \cdots & \vdots \\ 0 & \cdots & 0 & 0 & 0 & 0 & 0 & \cdots & 0 \end{Bmatrix} \mathbf{H}_{ISI} = \begin{Bmatrix} 0 & \cdots & 0 & h_{L-1} & \cdots & \cdots & h_{v+1} \\ 0 & \cdots & 0 & 0 & h_{L-1} & \cdots & h_{v+2} \\ \vdots & \cdots & \vdots & \ddots & \ddots & \ddots & \vdots \\ 0 & \cdots & 0 & \ddots & \ddots & 0 & h_{L-1} \\ \vdots & \cdots & \vdots & \ddots & \ddots & \ddots & \vdots \\ 0 & \cdots & 0 & 0 & \cdots & \cdots & 0 \end{Bmatrix} \tag{2-5}$$

where h_i is the *i-th* element of channel impulse response $\mathbf{h} = (h_0, h_1, \cdots h_{L-1})^T$. We assume $\{h_i\}$ as zero mean i.i.d. complex Gaussian with the power delay profile $p(\tau)$.

The *H* in (2-5) represents the part which is not affected by the ISI and the ICI. $\mathbf{H}_{ICI}$ and $\mathbf{H}_{ISI}$ represent the ICI part and the ISI part of the signal with insufficient CP.

From form (2-1) and (2-5), the power of ICI and ISI of the *k-th* symbol can be determined as:

$$\overline{P_{ICI}} = \overline{P_{ISI}} = \left|\mathbf{H}_{ICI}\right|^2 \cdot \sigma_a^2 = \left|\mathbf{H}_{ISI}\right|^2 \cdot \sigma_a^2 \tag{2-7}$$

If the length of the CP is larger than the length of the channel impulse response($v \geq L$), $\mathbf{H}_{ICI}$ and $\mathbf{H}_{ISI}$ are null matrices.[9-10]

Problem Formulation

Let $\mathbf{H}_f = \left(H_{f_1} \cdots H_{f_{N-1}}\right)^T$ be the *N*-points FFT transform of $\mathbf{h} = (h_0, h_1, \cdots h_{L-1})^T$:

$$\mathbf{H}_f = \mathrm{FFT}(\mathbf{h}) \tag{3-1}$$

and $\mathbf{N}_n$ represents the AWGN of the *n-th* sub-channel of the frequency domain which its imaginary part and real part are both zero mean independent Gaussian distribution and the noise variance are equal:

$$\sigma_N^2 = \mathrm{E}\left\{\left|N_n\right|^2\right\} \quad n = 0, 1, \cdots N-1 \tag{3-2}$$

The capacity of *i-th* sub-channel can be calculated as:

$$C_i = \log_2(1 + SINR_i) \tag{3-4}$$

where

$$SINR_i = \frac{N \cdot \sigma_a^2 \cdot \left|H_i\right|^2}{\sigma_N^2 + \frac{\overline{P_{ISI}} + \overline{P_{ICI}}}{N}} \tag{3-5}$$

The overall capacity is the sum of all C_i and then scaled by a factor due to CP length:

$$\mathbf{C}_{N+v} = \frac{N}{N+v}\sum_{i=0}^{N-1} C_i = \frac{N}{N+v}\sum_{i=0}^{N-1} \log_2\left(1 + \frac{N \cdot \sigma_a^2 \cdot \left|H_i\right|^2}{\sigma_N^2 + \frac{\overline{P_{ISI}} + \overline{P_{ICI}}}{N}}\right) \tag{3-6}$$

Simulation result

In this section we use simulation to evaluate the capacity of a OFDM system with N=64 subcarriers. We use the exponential power delay profile

$$p(\tau)=\begin{cases} A\cdot e^{\frac{-\tau}{\bar{\tau}}} & \tau \geq 0 \\ 0 & \end{cases} \tag{4-1}$$

where A is the normalizing factor. The exponential multipath profile is truncated when $\tau \geq 4\bar{\tau}$ which is 16 when the sample interval is $0.25\bar{\tau}$.

Fig.3 shows the capacity of the OFDM system under different CP. When SNR is 8dB, the capacity increases monotonously with CP. However, when the SNR=3dB , an extreme value is observed around CP=12.When the SNR=2dB , the extreme is located at CP=11. From (3-5), we can see that if the SNR is large, the capacity is mainly determined by the ICI and ISI. While for small SNR, ISI and ICI contribute less to the SINR. When the SNR is around 3dB, the scaling factor N/(N+v) decrease with v, SINR increases with v, leading to the extreme observed in Fig.3b and Fig.3c.

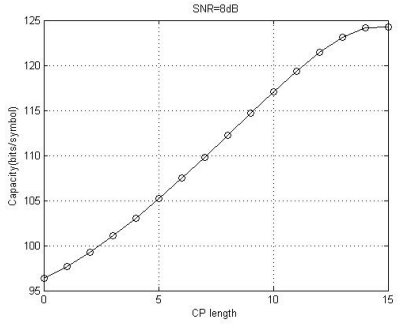

(a)SNR=8dB

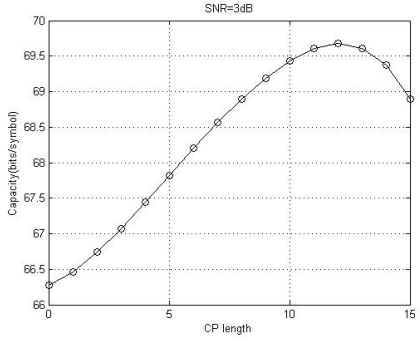

(b)SNR=3dB

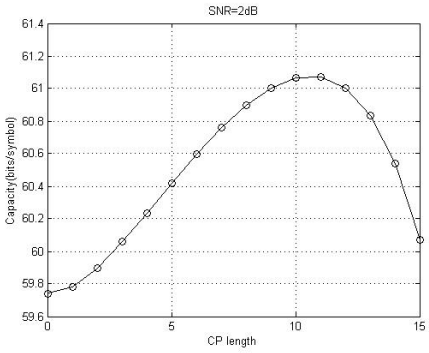

(c)SNR=2dB

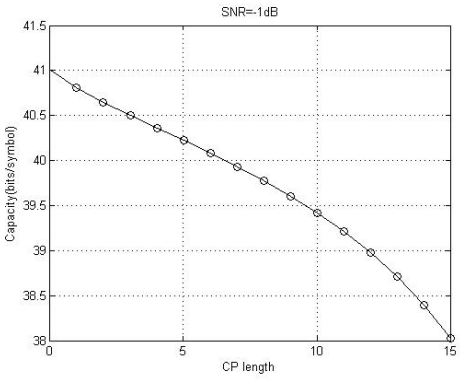

(d)SNR=-1dB

Fig3 Capacity as a function of CP length

Conclusion

This paper analyzed the relationship between the channel capacity and the CP length. The simulation results show that the channel capacity is monotone increasing function of the CP length for large SNR and is a monotone decreasing function of the CP length when SNR is low. For the SNR near 3dB, there is an optimal value of the CP length which can maximize the capacity.

References

[1] Koga H, Kodama N, Konishi T. High-speed power line communication system based on wavelet OFDM[C]//Proceedings of the 7th International Symposium on Power-Line Communications and Its Applications. 2003: 226-231.

[2] Steendam H, Moeneclaey M. Analysis and optimization of the performance of OFDM on frequency-selective time-selective fading channels[J]. Communications, IEEE Transactions on, 1999, 47(12): 1811-1819

[3] Zhu J, Ser W, Nehorai A. Channel equalization for DMT with insufficient cyclic prefix[C]//Signals, Systems and Computers, 2000. Conference Record of the Thirty-Fourth Asilomar Conference on. IEEE, 2000, 2: 951-955.

[4] Schur R, Speidel J. An efficient equalization method to minimize delay spread in OFDM/DMT systems[C]//Communications, 2001. ICC 2001. IEEE International Conference on. IEEE, 2001, 5: 1481-1485.

[5] Zamiri-Jafarian H, Parsaee R, Khoshbin H, et al. SINR maximizing equalizer design for OFDM systems[C]//Acoustics, Speech, and Signal Processing, 2004. Proceedings.(ICASSP'04). IEEE International Conference on. IEEE, 2004, 4: iv-733-iv-736 vol. 4.

[6] Park C J, Im G H. Efficient DMT/OFDM transmission with insufficient cyclic prefix[J]. Communications Letters, IEEE, 2004, 8(9): 576-578.

[7] Trautmann S, Karp T, Fliege N J. Frequency domain equalization of DMT/OFDM systems with insufficient guard interval[C]//Communications, 2002. ICC 2002. IEEE International Conference on. IEEE, 2002, 3: 1646-1650.

[8] Hoeher P. A statistical discrete-time model for the WSSUS multipath channel[J]. Vehicular Technology, IEEE Transactions on, 1992, 41(4): 461-468.

[9] Henkel W, Taubock G, Odling P, et al. The cyclic prefix of OFDM/DMT-an analysis[C]//Broadband Communications, 2002. Access, Transmission, Networking. 2002 International Zurich Seminar on. IEEE, 2002: 22-1-22-3.

[10] Batariere M, Baum K, Krauss T P. Cyclic prefix length analysis for 4G OFDM systems[C]//Vehicular Technology Conference, 2004. VTC2004-Fall. 2004 IEEE 60th. IEEE, 2004, 1: 543-547.

Advanced Materials Research Vols. 986-987 (2014) pp 2056-2059

doi:10.4028/www.scientific.net/AMR.986-987.2056

Application of Wavelet Transform in Signal Compression and Signal Recombination

Zheyuan WANG[1,a], Li JIANG[2,b]

[1]State Grid Liaoning Electric Power Supply Jinzhou Electric Power Supply Company, China

[2]China National Petroleum Corporation Jinzhou Liaoning Sales Branch, China

[a]345528953@qq.com, [b]278888398@qq.com

Keywords: Wavelet Transform, Transient Signal, Compression Recombination, MATLAB;

Abstract. This paper discusses the application of wavelet transform in signal compression and signal recombination detailedly. This paper briefly introduces the principle of wavelet transform in signal compression and signal recombination, this paper also introduces the wavelet MATLAB simulation experiments. This paper researches the differences the wavelet transform and wavelet packet transform in signal compression, this paper also briefly discusses the influence factors of signal compression.

Preface

In power system, the collected transient signals need to be transmitted to denoise and analyze in the analytic system, or to be transmitted analyze in the analytic system after signal denoising[1].At this time, the problem arises, how to transmit signal which contain large amounts of information to the back analysis instrument through the shortest time and with the least amount of storage space transmission[2]. If not to as little as possible to transfer information capacity, that may affect the transmission speed, can not achieve the purpose of the real-time analysis the transient signal. As a result, the signal compression and the signal recombination in transient signal transmission have played a very important role. In this instance, if can make the main detail characteristics of the original signal without losing, improve the quality of the signal compression and the signal recombination as far as possible, this will greatly increase the transmission capacity of the signal, to realize real-time signal acquisition and real-time analysis capabilities[3].On the surface, the signal denoising, the signal compression and the signal recombination all work in to "lose weight" signal[4]. But practically speaking, the signal denoising is to filter out the noise of the transient signal analysis, so that the analysis can be more accurate and intuitive. The signal compression and the signal recombination is in order to filter out the redundant information of the analysis system, which is no use and non-interfering, that make the transmission signal more quickly. For the subsequent analysis methods such as feature extraction need characteristic signal in the form of high quality high speed transmission into the analysis system[5-7].By the deep explorations and researches of many scholars, that can certify that meet the requirement ,which improve the quality of the signal compression and the signal recombination to make the main detail characteristics of the original signal without losing.

Signal compression and reconstruction

In the power system, transient signals are the one dimensional signal, wavelet analysis and wavelet packet analysis can realize the aim to reconstruct the one-dimensional signal compression. The main process has the following three steps:

(1) Decompose the required transmission signal using the wavelet and wavelet packet;

(2) The high frequency coefficients obtained by decomposition threshold quantization process. In the threshold value, can use two methods to carry out, one way is to signal wavelet scale expansion, reservation coefficient of absolute value of the largest scale, and use the whole threshold

method, in the compression process, input is retained by only one parameter, another method is based on the effect of the decomposed layers to determine the threshold of each layer, and can vary between these thresholds, this time should input the parameters of the layers of decomposition, respectively, after hard threshold method can be used to quantify the coefficient[8-9];

(3) Recombine the quantified coefficient using the wavelet and wavelet packet.

The difference between wavelet analysis and wavelet packet analysis in Signal compression and reconstruction

The algorithm of wavelet packet analysis applied in signal compression and wavelet analysis are basically the same, the difference is that the analysis method of wavelet packet analysis is more complicated and flexible. Because the wavelet packet analysis is analyzing the low frequency part and high frequency part which are on the layer of decomposition at the same time, the wavelet packet analysis has more accurate local analysis ability. In the following, through MATLAB experimental platform, verify the differences of wavelet analysis and wavelet packet analysis in the signal compression and the signal recombination.

As shown in figure 1, in the experiment, based on the MATLAB simulation platform, take 1000 sampling points, the default global threshold, respectively, using the wavelet compression function and wavelet packet compression function to compress the original signal. In order to create more intuitive characterization of the different methods of two kinds of compression result, figure 1 in the 300th local amplification sampling points, as shown in figure 2, figure marked with red circle part, can clearly show the two types of compression on the compression of the original signal reconstruction performance.

In the specific operation to the compression and recombination of the transient signal, according to the specific situation ,choose the appropriate method to process.

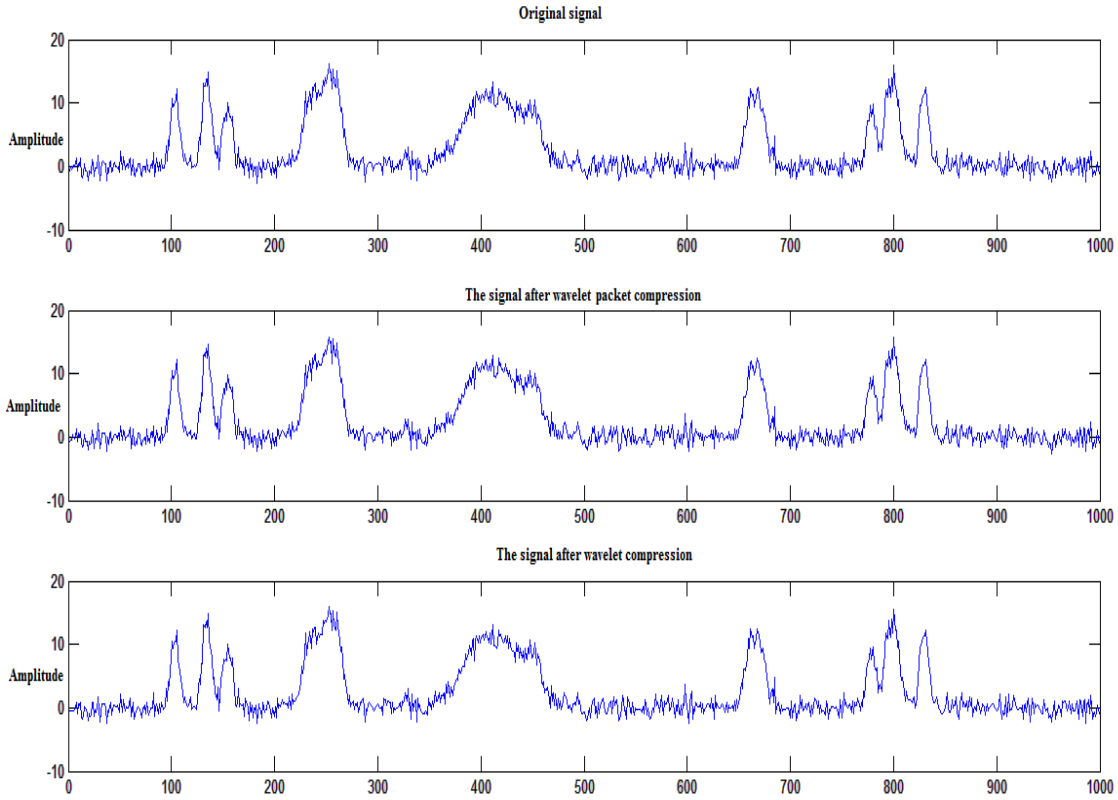

Fig.1 The difference in signal compression reconstruction between Wavelet and Wavelet packet analysis

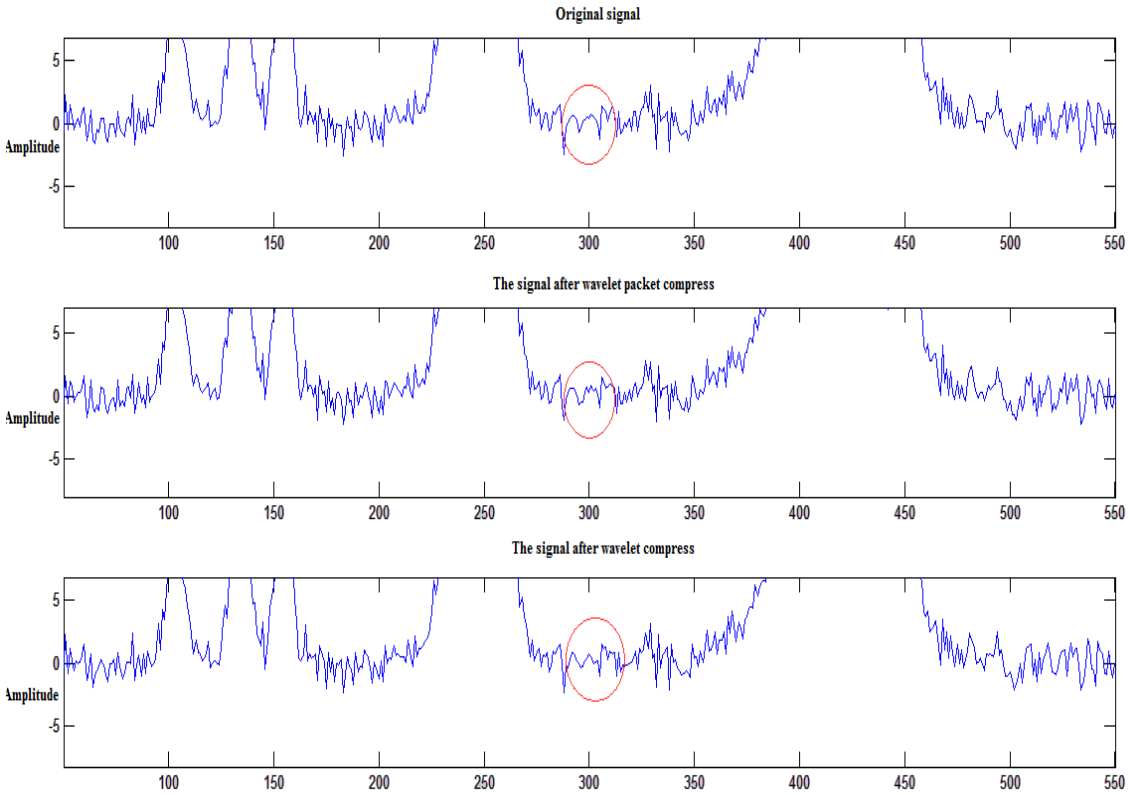

Fig.2 The difference in signal compression reconstruction between Wavelet and Wavelet packet analysis（Partial enlargement）

The influence factors of the signal compression

For the processes of the signal compression and the signal recombination, because this paper is using the analysis method of the wavelet and wavelet packet, based on the decomposition course of wavelet and wavelet packet, the factors which impact the signal compression effect can be summarized as follows[10-13]:

(1) The choice of wavelet kernel function.

(2) The layer number of wavelet decomposition.

(3) The selection of wavelet coefficient threshold.

(4) The optimal decomposition route.

Intelligent accurately selecting suitable wavelet basis function and the layer number of decomposition, the wavelet coefficient threshold can finish the work of the signal compression and the signal recombination better.

Conclusion

The purpose of this paper is that analyze power system transient signals quickly and identify power system transient signals efficiently. With the aid of wavelet theory, this paper research and analyzes the power system transient signal compression and power system transient signal reconstruction. By MATLAB simulation, this paper introduces and summarizes the application of wavelet transform in signal compression and signal recombination. The signal compression is an important part of power system transient signal analysis, how to select the influence factors of signal compression intelligently and optimally, also need through a large number of experiments to generalize in the future.

References

[1]D.P. Stojanovi´c et al.2008. Dynamic load modelling based on measurements in medium voltage distribution network. Electric Power Systems Research. 78: 228–238.
[2] Zwe-Lee Gaing.2004. Wavelet-based neural network for power disturbance recognition and classification. IEEE Transactions on Power Delivery,19(4):1560-1568..
[3] Zhang Xiaoli,Zeng Xiangjun,Lei Li,Choi S S, Wang Yuanyuan. 2007.Fault location using wavelet energy spectrum analysis of traveling waves .Power Engineering Conference, IPEC 2007,pp:1126-1130 .
[4] Weon-Ki Yoon, Devaney M J. 1998. Power measurement using the wavelet transform. IEEE Transactions on Instrumentation and Measurement,47(5):1205-1210.
[5] Tongxin Zheng, Makram E B, Girgis A A.1999. Power system transient and harmonic studies using wavelet transform. IEEE Transactions on Power Delivery,14(4):1461-1468.
[6] Solanki,M,Song,Y.H.2003.Transient protection of EHV transmission line using discrete wavelet analysis.IEEE Power Engineering Society General Meeting,(3):79-84.
[7] Solanki M,Song Y H, Potts S , Perks A. 2001. Transient protection of transmission line using wavelet transform. Developments in Power System Protection, 2001, Seventh International Conference on (IEE),pp:299-302.
[8] Jiang F, Bo Z Q, Chin P S M, Redfern M A, Chen Z. 2000. Power transformer protection based on transient detection using discrete wavelet transform (DWT). Power Engineering Society Winter Meeting, IEEE,3:1856-1861.
[9]Jondral F.1985.Automatic Classification of High Frequency Signals .Signal Processing, 9(3) : 177-190.
[10]Karimi M, Mokhtari H, Iravani M R. 2000. Wavelet based on-line disturbance detection for power quality applications. IEEE Transactions on Power Delivery,15(4):1212-1220.
[11]Kitayama Masashi, Nakabayashi Miyuki. 2001.A Fast Discrimination Method of Inrush Current Based on Transformer Magnetizing Characteristics.IEEE Transactions on Power Delivery, 121-B(8) :982-989 .
[12]M A Gnatenko, A V Shupletsov, G S Zinoviev, H Weiis.2004.Measurement System For Quality Factors and Quantities of Electric Energy with Possible Wavelet Technique Utilization .Proceedings of 8th Russian-Korean International Symposium on Science and Technology,(4) :325-358 .
[13]Mallat S.1989.A theory for multiresolution signal decomposition the wavelet representation.IEEE Trans on Pattem Analysis and Machine Intelligence,11(7):674—693.
69.Mallat S,Huang W L.1992.Singularity detection and processing with wavelets[J]. IEEE Trans on Information Theory, 38(2):617—640.
[14]Nandi A K, Azzouz E E.1998.Algorithms for Automatic Modulation Recognition of Communication Signals .IEEE Transactions on Communications, 46(4) :431-436 .
[15]Pham V L, Wong K P.1999. Wavelet-transform-based algorithm for harmonic analysis of power system waveforms. IEE Proceedings Generation, Transmission and Distribution,146(3):249-254.

Advanced Materials Research Vols. 986-987 (2014) pp 2060-2063

doi:10.4028/www.scientific.net/AMR.986-987.2060

Channel Estimation Algorithms for MB-OFDM based UWB system

YiHuai Yang[1, a], MingXiu Shen[1], YanPing Sun[1]

[1] School of Automatic Control and Mechanical Engineering, Kunming University, 650214, China

[a]yyh_td@126.com

Keywords: Wireless Area Network (WBAN), Channel Estimation, Ultra Wide Band (UWB), MB-OFDM, Medical Healthcare.

Abstract. To achieve an accurate channel impulse response (CIR) during channel equalization and coherent detection, the channel estimation plays an important role to the performance of system, especially the receiver. In this paper, we investigated two main kinds of channel estimation methods for MB-OFDM based UWB system. The performances are compared using MATLAB simulation. The simulation shows the NBIDCE algorithm has better performance for WBAN-based healthcare systems.

Introduction

With the rapid advancements of micro electromechanical systems, wireless communication, low power intelligent sensors and semiconductor technologies, the area of sensor network has grown significantly. A Wireless Body Area Networks (WBAN) consists of small, intelligent sensor nodes on-body (wearable) as well as in-body (implant) that is able to sense, process and communicate. WBAN has been found widely applications in biomedical therapy and healthcare, which promises inexpensive, unobtrusive, and unsupervised ambulatory monitoring during normal daily activities for long periods of time. [1, 2].

Meanwhile, as an emerging transmission technology, multiband orthogonal frequency division multiplexing (MB-OFDM) Ultra Wide Band (UWB) provides enhanced value for WBAN. It can provide very high data rates using very low-power consumption, interference robustness, high local capacity and less complex hardware, although it can just be applied at very limited frequency band ranges, such as MICS band. All these unique features and distinctive properties of UWB made it very suitable for medical areas.

Channel estimation plays an important part in a WBAN system. It is used for increasing the capacity of MB-OFDMA systems by improving the system performance in terms of bit error rate, which means it plays a crucial role in receiving an accurate signal. However, channel estimation becomes difficult under the constraint of extremely low transmission power and dense multipath WBAN environments [3]. Therefore, an effective channel method is crucial for the receiver of a MB-OFDM WBAN system which uses multiband UWB.

There are many investigated channel estimation techniques for MB-OFMA systems [4, 5]. However, most of them are based on IEEE 802.15.3a UWB channel model [6] and not suitable for WBAN channel which has different environment and power consumption. To the best of our knowledge, seldom attempt has been made for channel estimation for MB-OFDM WBAN system.

In our work, we investigated the channel estimation method of using multiband UWB in WBAN channels.

The remainder of this paper is organized as follows: the general multiband OFDM based UWB system is described in Section II. Section III presented FBCE and NBIDCE two kinds of main channel estimation methods. In Section IV, gives parameters and comparable results of simulation. Section V concludes the paper.

Multiband OFDM based UWB system

Ultra Wide Band (UWB) may offer very efficient solutions for various communication and sensing applications. UWB communication using impulse radio (IR-UWB) and the classical multiband UWB

systems exploit the division of the bandwidth into sub-bands. The MB-OFDM system is based on orthogonal frequency division multiplexing (OFDM) techniques on each sub-band, which good properties for capturing efficiently multipath energy, mitigating interference and achieving large throughput.

Multiband OFDM based Ultra Wideband (UWB) system [8] combines OFDM modulation technique with a multi banding approach, which divides the spectrum into several sub-bands, whose bandwidth is approximately 500MHz. Three band multiband OFDM systems have been designed using a time frequency code of length 3. The important blocks in the transmitter side are QPSK modulator, IFFT, DAC, up converter and time frequency code generator to provide multiple access and frequency diversity. We model channel as a simple delay element. A basic receiver just follows the inverse of the transmission process so important blocks in the receiver side are down converter, ADC and FFT. A typical architecture of OFDM based UWB system is illustrated in Fig. 1.

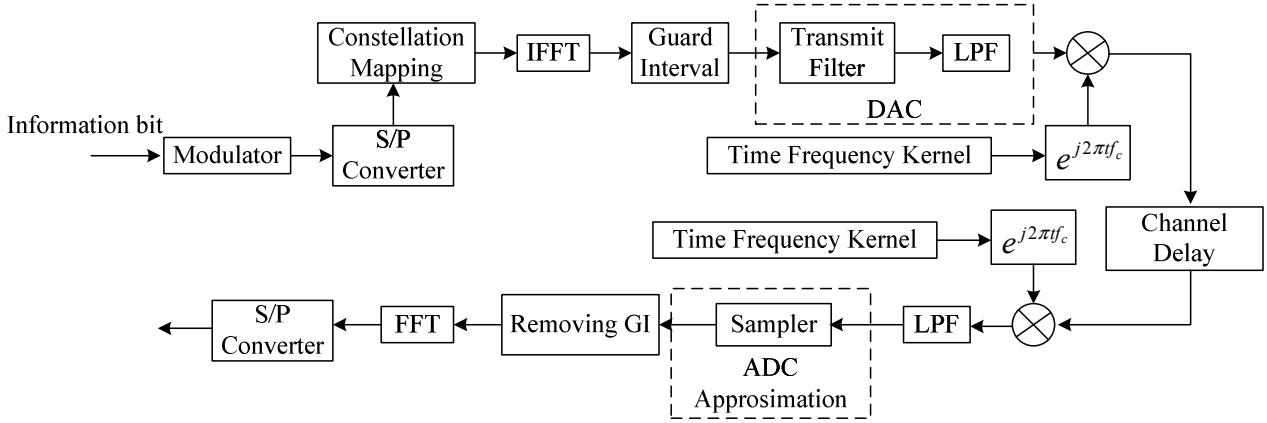

Fig. 1 MB-OFDM based UWB system

Channel estimation methods for MB-OFDM UWB systems

There are two proposed techniques are most suitable for WBAN-based healthcare system based UWB channels. In this section, we give a brief summary of them.

FBCE

The Fully Blind Channel Estimation algorithm is based on first-order cyclostationarity of the received signal. It assumes that the channel is FIR and follows a tap-delay-line model. Based on FFT operations, the algorithm has low complexity and can deal with channels with a large number of taps that are difficult to estimate using existing parameterized searching algorithms. Here, using the PPM based transmission to avoid ambiguity.

The steps for channel estimation and synchronization and detection algorithm are given as follows [5]:

Step1. Using Fourier series to construct $\tilde{p}_a(t)$ from $p_a(t)$;

Step2. Receiving $y(t)$ for $0 \le t \le (I-1)T_s$;

Step3. Performing the overlap-added operation to obtain an estimate $\hat{\bar{y}}(t)$ of $\bar{y}(t) = E\left[y(t)\right]$;

Step4. Computing the Fourier series $\hat{\bar{Y}}[k]$ of $\hat{\bar{y}}(t)$ and obtain $\hat{\bar{H}}[k]$;

Step5. Doing inverse Fourier transform of $\hat{\bar{H}}[k]$ to obtain $\hat{\bar{h}}_\tau(t)$;

Step6. Estimating τ to obtain $\hat{\tau}$;

Step7. Estimating the channel $h(t)$ to obtain $\hat{h}(t)$;

Step8. Constructing the difference signal: $x_d(t) = \left[p(t) - p(t-\Delta)\right] * \hat{h}(t-\hat{\tau})$;

Step9. Obtaining the decision statistics: $d_i = \int_{-\infty}^{+\infty} y(t) x_d(t - iT_s)\, dt$.

Based on FFT operations, this FBCE algorithm has low complexity and can deal with channels with a large number of taps that are difficult to estimate using existing parameterized searching algorithms.

NBIDCE

In [6], the author combined the Narrowband Interference Detection (NBI) technique with a channel estimator. The steps of this method are as follows:

Step1. Pre-detecting the NBI;

Step2. Using the acquired/assumed knowledge of the interference as well as channel covariance information estimated the channel;

Step3. Subtracting the channel fluctuations from the received signal based on the preliminary channel estimate;

Step4. Feeding back the signal into the detector to increase the detector sensitivity or lower the probability of false alarm;

Step5. Re-initiating the channel estimate based on the improved knowledge of the interference situation;

Step6. Processing joint iterative to boost the capabilities of NBI suppression and refining the channel estimate.

The final estimation is as equation (3)

$$\hat{H} = C_{HH}\left(C_{HH} + C_d\right)^{-1} \cdot \frac{S_1^* R_1 + S_2^* R_2}{2} \tag{3}$$

where S_1 and S_2 are power of first transmitted, meanwhile R_1 and R_2 are received preamble symbol.

Figure. 2 is the NBI detector/channel estimator proposal.

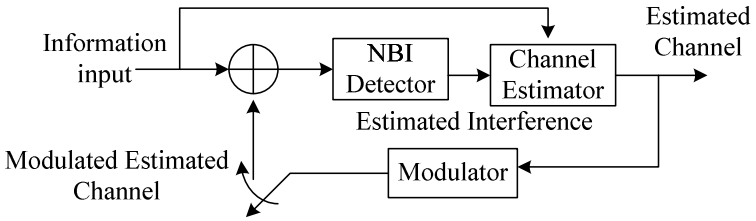

Fig. 2 MB-OFDM based UWB system

This method can improve the BER performance significantly.

Simulation and Comparison

In this section, Bit Error Rate (BER) performance of FBCE and NBIDCE are studied and compared through using MATLAB software. The parameters of the simulation are listed in Table 1:

Table. 1 WBAN Channel Model Parameters

Parameters	Values	Parameters	Values
Residual Channel Energy	-3.33dB	Modulation	QAM
Amplitude Decay Factor	65	Number of Input Data Bits	50,000
Standard Deviation of Log-normal Fading	6dB	Number of Data Subcarriers	12
Path Arrival Ratio	6ns	FFT Size	128
Average Number of Multipaths	21	ZP duration	71ns

Fig. 3 compares the MSE of different channel estimation method, and the effect of these MSEs is investigated in Fig. 4.

Conclusions

The successful operation of a UWB system depends greatly on channel synchronization and estimation. Due to the fact that the availability of full or partial channel information guarantees the

demodulation of information symbols. In this paper, we conducted an extensive study of two main channel estimation methods for MB-OFDM based UWB system. In order to evaluate the performance of the FBCE and NBIDCE, the Bit Error Rate (BER) values are compared and analyzed in the presence of figures. It is shown that NBIDCE algorithm offers better performance required for MB-OFDM based UWB system.

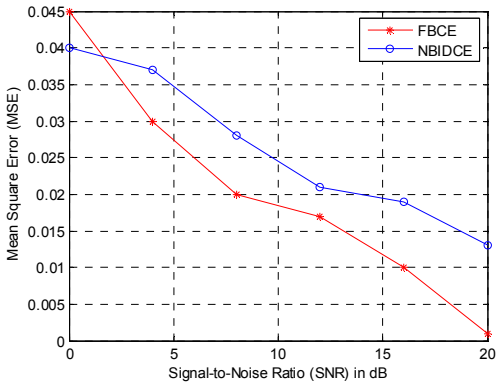

Fig. 3 MSE vs. SNR

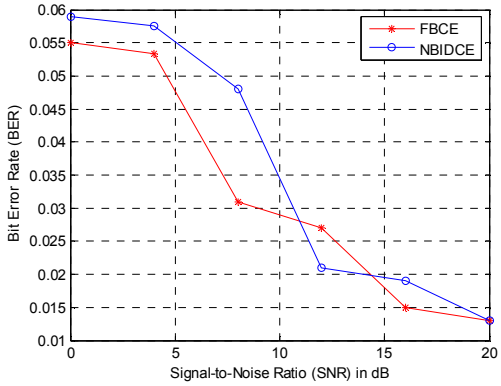

Fig. 4 Uncoded BER vs. SNR

Acknowledgement

This paper is supported by National Science and Technology Major Project (2010ZX03007-001); Yunnan Natural Science Key Foundation of China (2013FA027); Yunnan High-Tech Top-Talents Recruitment Project (2012HA005) and Kunming University Scientific Research Project (XJL12006).

References

[1] B. H. Yang and S. Rhee: *Development of the ring sensor for healthcare automation*, Robotics and Autonomus Systems, vol. 30, pp. 273-281, 2000.

[2] H. H. Asada, et al. (2003) *Mobile Monitoring with Wearable Photoplethysmographic Biosensors*. IEEE Engineering in Medicine and Biology Magazine. 28 - 40.

[3] S.M.Riazul Islam.Kyung Sup Kwak: *A Comprehensive Study of Channel Estimation for WBAN-based Healthcare Systems: Feasibility of Using Multiband UWB*, Springer Science Business Media, LLC 2010.

[4] S. M. Riazul Islam, Kyung Sup Kwak, "*A Comprehensive Study of Channel Estimation for WBAN-based Healthcare Systems: Feasibility of Using Multiband UWB*", Journal of Medical Systems. June 2012, Volume 36, Issue 3, pp 1553-1567.

[5] Zhengdao Wang and Xiaofan Yang, "*Ultra wide-band communications with blind channel estimation based on first-order statistics*", Acoustics, Speech, and Signal Processing, 2004. Proceedings. (ICASSP '04). IEEE International Conference on (Volume:4)

[6] Niels Hadaschik, Irma Zakia, Gerd Ascheid, Heinrich Meyr, "*Joint Narrowband Interference Detection and Channel Estimation for Wideband OFDM*", proceedings of the European Wireless Conference, April 2007.

[7] A. Batra et al., "*Multi-band OFDM Physical Layer Proposal for IEEE 802.15 Task Group 3a*," IEEE P802.15-03/142r2-TG3a, Sep. 2004.

[8] Santosh Parajuli, Brajesh Mishra, "*Multiband Orthogonal Frequency Division Multiplexing Based Ultra Wideband System*", International Journal of Engineering Research and Applications (IJERA) ISSN: 2248-9622 www.ijera.com Vol. 2, Issue 6, November- December 2012, pp.922-924.

Advanced Materials Research Vols. 986-987 (2014) pp 2064-2067

doi:10.4028/www.scientific.net/AMR.986-987.2064

Coupling Effect of Transmission Lines by HEMP Based on CST

Zhang Jianguo[1, 2, a] , Zhang Xin[1, b]

[1]School of Electromechanical Engineering, Xidian University, Xi'an, Shaanxi, China

[2]Science and Technology on Information Transmission and Dissemination in Communication Networks Laboratory, Shi Jiazhuang, Hebei, China

[a]email: jgzhang2003x@aliyun.com, [b]email: 149019259@qq.com

Keywords: high-altitude nuclear electromagnetic pulse(HEMP) CST field-wire coupling

Abstract. High-altitude nuclear electromagnetic pulse(HEMP) has a significant effect on electronic devices by cables. This paper makes an analysis of field-wire coupling. With the software of Computer Simulation Technology(CST) constructing the model, coupling current has been acquired. The effect of length, height and impedance on coupling current has been gained. To our surprise, the rise time of HEMP is faster than the time of coupling current. This provides HEMP hardening with the crucial basis.

Introduction

The HEMP is a kind of high power electromagnetic pulse, which is a by-product of nuclear explosion. The field that HEMP produces has characteristics of high strength(kV/m) and short rise-time(nanosecond). Even though there are integral enclosures over precise electronic devices, by necessity external cables can couple with outer pulse field. Once the incoming strong transient electromagnetic field, the antenna effect of cables will transform high field into high voltage and high current. The high strength current in the circuit has damages on delicate devices.

The modern devices consist of massive semiconductor apparatuses, so after coupling with the HEMP it is semiconductors that are damaged by HEMP. It is so deep the damage effect of HEMP on electronic equipment, therefore to study the coupling between HEMP and cable is of great significance.

The field-cable coupling problem of HEMP, the domestic and foreign research mainly confined to the analytical calculation, the lack of specific experiments and numerical simulation[1-5]. This paper is mainly based on numerical simulation and model calculation is more close to the practical engineering. In this paper, available and reliable coupling value has been acquired, the coupling current influence factors has been analyzed and the delay effect of coupling current compared with excitation signal(HEMP) has been discovered. Those conclusions provide the essential guidance and reference.

Analysis of Field-Cable Coupling Model

There are two methods to analyze the field-cable coupling model: field method and circuit method. The field method is based on Maxwell's equations, which need to mesh the calculation domain. Discrete Maxwell's equations will be transformed into enormous matrix equations. To solve equations we can acquire the results. The field method is more rigorous but to calculate large matrices need vast computer resources. However, the circuit method is based on the transmission-line method. With distributed parameter theory, mathematical calculation is much simpler. The latter one is commonly adopted. Aimed at different excitation sources in the circuit method, Taylor, Agrawal and Rachidi put forward three kinds of transmission-line coupling model.

Because high-altitude nuclear explosion is far from sensitive devices, outer transient field is regarded as the transverse electro-magnetic wave(TEM). Simple point is the distribution model of excitation source for voltage source. The foundation of circuit model still is a transmission-line model, but outer field excitation is equivalent to voltage in every micro unit, which is the essential of Agrawal's model[6][7]. The model assumes that the ground is infinite. The circuit model is as shown in Fig. 1.

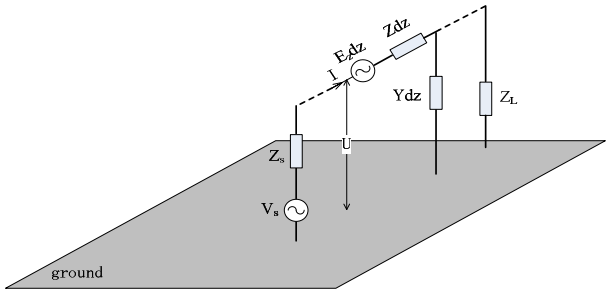

Fig.1 Agrawal field-cable coupling equivalent model

When the plane wave where frequency is ω(transform time domain into frequency domain when considering HEMP coupling) acts on the cable as is shown in Figure 1, voltage over the circuit and current in the circuit meet the following second-order differential equations:

$$\frac{d^2U}{dz^2}-\gamma^2U=\frac{dE_z}{dz} \tag{1}$$

$$\frac{d^2I}{dz^2}-\gamma^2I=-YE_z \tag{2}$$

In those equations, Z and Y represent cable impendence and admittance per unit length. $Z=R+j\omega L$ $Y=G+j\omega C$. R, L, G and C are cable resistance, inductance, conductance and capacitance per unit length respectively. E_z is a transient field strength. The propagation constant is $\gamma=\sqrt{ZY}$. Eq.1 and Eq. 2 are similar to the traditional transmission-line wave equations. By applying mathematical physics equation method we can get the results.

Simulation of Couple Effect HEMP on Cable Ports

At present, domestic papers which calculate field-cable coupling mainly adopt analytical methods [8]. But this paper changes thoughts and takes advantage of the simulation software of CST to gain the coupling.

The simulation studios in CST associated with the field-cable coupling are Cable Studio and Design Studio. The studio co-simulation is performed with TLM(based on Transmission Line Method) solver.

A single cable is designed in Cable Studio(distributed parameter model). In this problem one finite PEC (perfect electronic conductor) board is imitated as the ground, which is shown as Fig. 2.

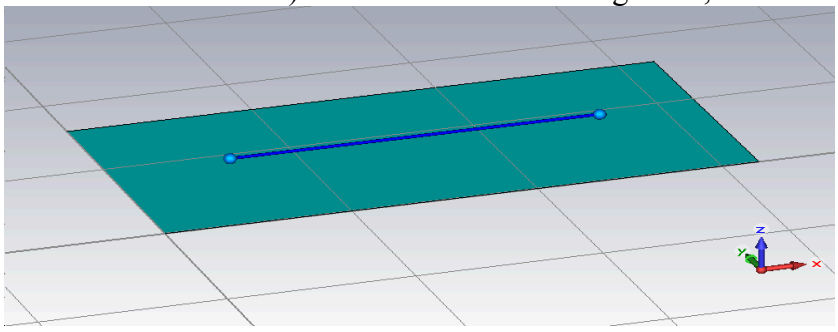

Fig.2 Single cable model

The excitation source is assumed as a plane wave. The electric field waveform expression that HEMP produces is commonly used double exponential function to fit. The equation is

$$E(t)=E_0k\left[\exp(-\alpha t)-\exp(-\beta t)\right] \tag{3}$$

In which, $E_0 = 50kV/m$, $k = 1.3$, $\alpha = 6.0\times10^8 s^{-1}$ and $\beta = 4.0\times10^7 s^{-1}$.

Influence Cable Length on The Coupling Current. Let the direction of incident electromagnetic field be –Z and the size of the ground is represented by 16m×8m board that is PEC and has no thickness. The height of cable from the ground is 0.5m. The resistors at the cable end are 50Ω.

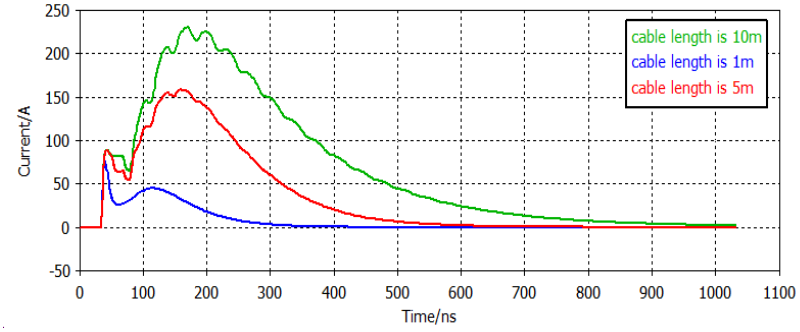

Fig.3 Coupling currents at the port vary with cable length under the HEMP

From Fig. 3 we see that with the increase of cable length, the coupling current increases completely. When the time is less than 33ns, cable doesn't induce the current. With cable length increasing, the disturb signal attenuates more lentitude.

From the definition of field strength we can conclude: When the electromagnetic field comes into being, the longer the operating distance is, the greater the voltage is. In term of system class EMC problem, outer cables are longer so it is obvious that the effect of field-cable coupling is! It is necessary that a transient suppressor is installed at the sensitive device port[8].

Influence Ground Height on The Coupling Current. Keep the direction of incident field, the ground and the load stay the same. Let cable length be 10m. Change height from the ground and current is monitored.

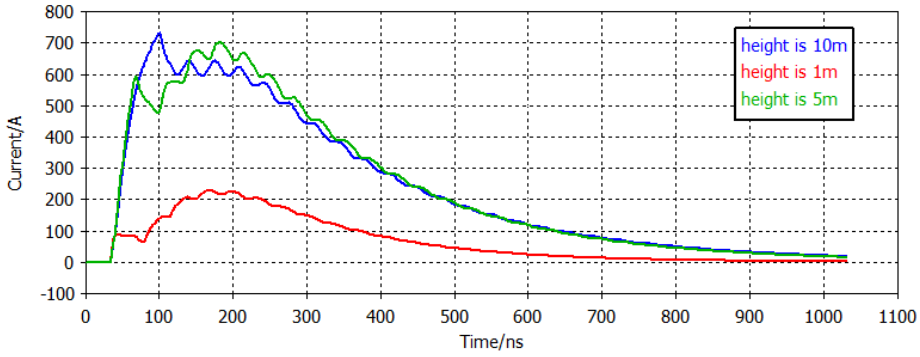

Fig.4 Coupling currents at the port vary with cable height under the HEMP

With the increase of cable height, the peak current of coupling increases. From the perspective of EMC, the increasing cable height means that loop area of cable and earth increases. The loop area is equivalent as a loop antenna so that coupling current increases[9].

Influence Port Load on The Coupling Current. Keep the direction of incident field and the ground. Assume cable length as 10m and cable height as 0.5m. Change both ends of cable resistance and the current is monitored.

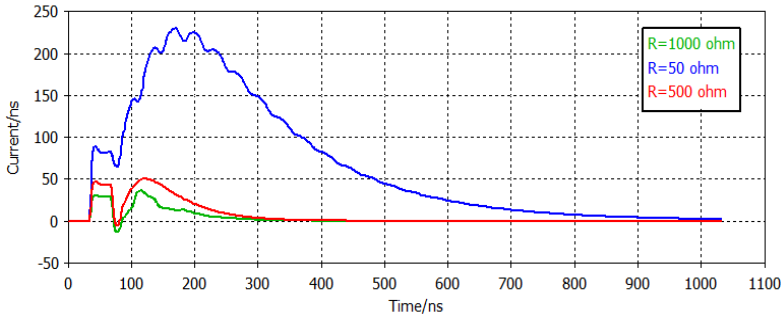

Fig.5 Coupling currents at the port vary with cable port impendence under the HEMP

From Fig. 5 we see that with impendence of load increasing, the peak current of coupling decreases. Obviously, when the excitation field is constant, the conclusion complies with the Ohm's law. In order to achieve the power matching, general electronic equipment has a small resistance. This also is the reason why coupling current destroy elements easily.

Summary

The coupling current between HEMP and cable usually is hundreds Amperes. The coupling current increases with cable length and height increasing and with port impendence decreasing. For a sensitive system in a real work condition, it's a good choice to use the method of this paper to determine the coupling value and take measures to harden.

References

[1] Deb G K. Nuclear electromagnetic pulse penetration analysis in combat vehicle. IEEE International Symposium on Electromagnetic Compatibility. 2000, 1: 427-430.

[2] Camp M，Garbe H，Nitsch D. UWB and EMP susceptibility of modern electronics.International Symposium on Electromagnetic Compatibility . 2001，2:1015-1020.

[3] Sheng Liu, Yaming Ge and Jun Li, Coupling Response Simulation of Transmission Lines Excited by Plane Wave, Journal of System Simulation, 2008，20(6):1619-1622.

[4] Meng C, Chen Y S. Numerical simulation of the early-time high altitude electromagnetic pulse. Chinese Physics，2003，12(12):1379-1382.

[5] Chen B，Wang T Y，Can C，et al. Full-wave analysis of the EMP induced current in cables near the ground. Journal of Microwaves，2000，16(5):549-553.

[6] Guyan Ni, Jianshu Luo and Chuanlu Li. Comparison of Solutions to the Taylor and Agrawal Coupling Models for the Line-plane Transmission-lines. Journal of National University of Defense Technology，2007，29(5):111-116.

[7] Yanzhao Xie, Zanji Wang and Qunshu Wang. Comparison of Agrawal and Taylor models for response calculations of above ground cable excited by HEMP, High Power Laser and Particle Beams, 2005，17(4):575-580.

[8] Yanzhao Xie and Hui Zhou, Selected topics in transient response of aerial lines o high-altitude electromagnetic pulse, Nuclear Electronics & Detection Technology. 2005，25(6):657-660.

[9]Shaoguang Wang. UWB radio fuse effect and protective reinforcement research. Shijiazhuang, Hebei, China: ordnance engineering college, 2008.

Advanced Materials Research Vols. 986-987 (2014) pp 2068-2072

doi:10.4028/www.scientific.net/AMR.986-987.2068

Measurement and Research on Attenuation Characteristics of Low voltage Power Line Communication Channel

Wang Yi[1, 2], Wang Qiandong[1], Hou Xingzhe[1], Sun Hongliang[1], Chen Xiaoming[1], Li Xiaojun[1]

[1,] Chong Qing Electric Power Research Institute，Chong Qing, China
[2,] Postdoctoral Workstation of the Chongqing Electric Power Corporation, Chong Qing, China

wangyi81@cqupt.edu.cn

Keywords: Low-voltage power line communication; Attenuation Measurement; Cable features; T network

Abstract. Signal transmission attenuation characteristics of low voltage power distribution network is an important factor must be considered by the power line communication system design. The effects of power line network on the power line communication channel attenuation are studied, including cable cross-sectional area, length and T network structure. With the experimental and simulation results, the relationship between low voltage power line cable length, the network structure and the power line communication channel attenuation is analyzed.

I. Introduction

With the development of communication technology, the electrical power supply system is on the way to multipurpose medium delivering energy, voice, and various data services [1]. However, power distribution network, which are heterogeneous transmission lines due to the impedance mismatches, is an extremely hash medium as a communication channel. To establish the reliable communication system and improve the performance of communication systems operating on the power line network, the characteristics of power line channel should be carefully investigated.

At present, attenuation characteristics of LV PLC channel have lot of research. Frequency point voltage comparison method was proposed in literature [2,3] to measure signal transmission attenuation characteristics at the typical distribution area, it was conclude that the attenuation increases with the rise of communicate distance and carrier frequency, attenuation at high-rise building urban areas worse than rural and urban fringe. Transmission attenuation, phase and group delay of LV-PLC spread spectrum signal were measured in reference [4,5] through the network analyzer. Attenuation characteristics of industrial building at different time were measured in literature [6-8], it was concluded that signal attenuation characteristics will change violently with access different load at different moments.

By analyzing the current research of power line characteristics, we can conclude that: 1) a large number of measurement research focuses on indoor or commercial building, the measurement field environments are complicated and measured results are easily influenced by measuring time and place. The measured results have certain randomness; 2) Measured frequency is restrict on the low frequency instead tends of future high-speed broadband signal; 3) low voltage power distribution network structure and load are very different between domestic and oversea. Foreign measurement of power line carrier communication features can't completely copy to domestic. Hence, it is necessary to measure and analysis the influence of high frequency signals transmission which is caused by power cable characteristics for our country.

The paper is organized as follows. In section II, we introduce the measurement methods and objects which used in our experiment. Time domain multi-path model of PLC channel is analyzed and simulated in section III. The paper finishes with a concluding discussion in section IV.

II. Measuring method and object

A Measurement Method

In order to improve efficiency and accuracy of measurement, multiple frequency point voltage comparison method is used to measure the power line signal transmission attenuation characteristics. Measuring principle diagram is shown in figure 1. The test power line networking as shown in figure 1 is an analog power line structures of various network topologies. Measuring instruments are used include signal generator, couplers, oscilloscope and spectrum analyzer etc.

Fig.1 Measurement system diagram of attenuation characteristic

In actual tests, sine wave sweep signal is send at the transmitting side by signal generator, and the signal generator is coupled to the power line cable use capacity couple. The couple has three main effects:

1). The couple provides an interface adapter for cable connect the signal generator or spectrum analyzer.
2). Internal high-pass filter of the couple make sure smooth pass of high frequency signals while strong electric of the grid power frequency is attenuation.
3). High-frequency coupling coil in couple can separate strong electrical and weak electrical, which is to ensure the safety of measuring equipment and person.

At the receiving side, we use the same characteristics coupler with transmission side, including amplitude-frequency, phase-frequency characteristics. Power line signal is coupled to the spectrum analyzer with simultaneous measurement.

B Measuring Object

The focus is to study the basic characteristics of cable to affect high frequency signal transmission attenuations. At present commonly used low voltage cable is constitute by sheath, shielding layer, insulating layer, conductor and fillers.

Where S is the cable cross-sectional area. In our experiment, we use three different types of cable. Table 1 is the detail description of the cable.

Table 1 Three different type cables analysis

Type	L (m)	S(mm^2)	Wire core material	Cable characteristic description
A	90	4	Cooper	Two wire core
B	12	1.5	Cooper	Two wire core
C	20/50/ 70/90	0.75	Cooper	Three wire core, select phase line and neutral line to transmission

For the convenience of description, we use A, B, C to represent three different types of cable.

C Specific Arrangements

1). Measuring environment: To eliminate the external environment disturbance the experimental results, we select shielding darkroom to make our test.
2). Frequency range: the frequency range choice 100kHz-20MHz, this frequency range is commonly used online monitoring and management, low pressure remote meter reading and home intelligent system application.

3). Measurement object: different cable cross-sectional area, length and T power line network will be test in our experiment.

III. Measurement results and analysis

PLC attenuation characteristics are closely related to the cable material, cross sectional area, length and carrier frequency. In this section, we will measure the cable cross-sectional area, length and T network model respectively on the influence of signal transmission attenuation. In the actual tests, output impedance of the measuring equipment mismatch to the measured cable impedance, which will lead to frequency selective fading attenuation of transmission signal.

A Influence of wire cross-sectional area

To assess PLC transmission attenuation affected by the cross-sectional area, we choice same fabric cable to measured, where the length of cable is 90m, and the cable cross-sectional area are respectively as $4mm^2$, $1.5mm^2$, $0.75mm^2$. Signal generator and spectrum analyzer are respectively connected on both side of the cable. Fig. 2 displays the attenuation characteristic based on measurement.

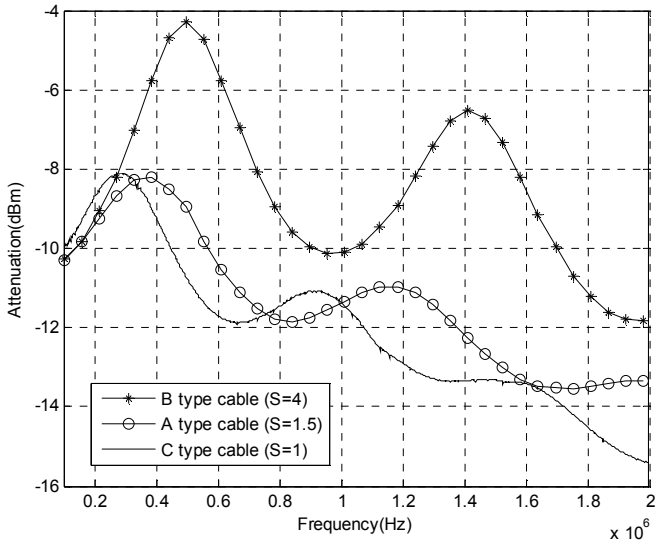

Fig.2 Diagram of different cross-sectional area cable attenuation characteristic

As can be seen from figure 4, when the measurement cable material and length are the same, the attenuation characteristics of small wire core cross-sectional area is lager than big one. At the same time, small cross section of cable has better ability to resist decay jitter, which means the peak and valley of decay curve is very small.

B Influence of cable length

The single attenuation characteristic relation between the transmission distance and frequency can be expressed as:

$$A(f,d) = e^{-(a_0 + a_1 f^k)\cdot d} \tag{1}$$

Where f is the carrier frequency. d is the length of power cable. a_0, a_1 and k are constants, which is determined by cable characteristics and frequency, the value of parameter can be calculated by measured data with least-square fitting.

In general, power line signal transmission attenuation is increased with the path length and carrier frequency. However, due to the power line is a uniform transmission line, high frequency signal will effect reflection, refraction and standing wave at the impedance mismatch cable node. The received signal is the multipath signal superposition. Due to the influence of multipath effect,

amplitude-frequency characteristics will appear the depth decline at some frequency point, and the decline point is hard to predict.

In order to describe the relationship between the power caber length and signal transmission attenuation, the same material of different length of C type cable is measured. The cable length is 20/50/90m. Measuring block diagram is shown as figure 3.

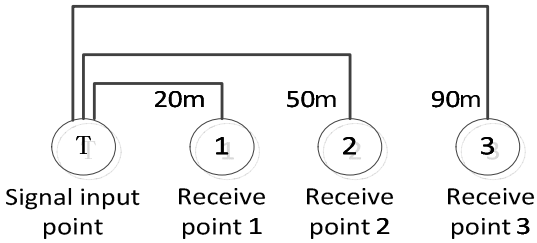

Fig.3 Different power line length measurement

Fig. 4 displays the attenuation characteristic of different length cable.

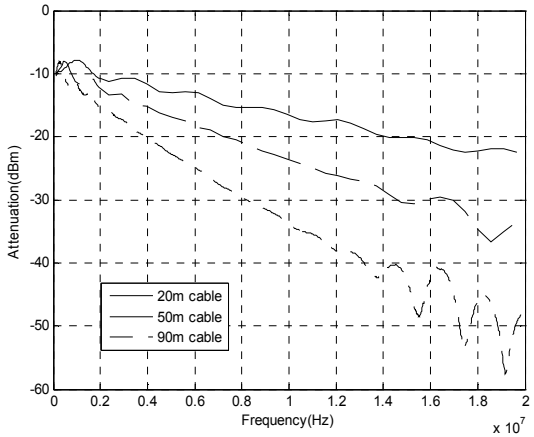

Fig.4 Different length cable attenuation curve

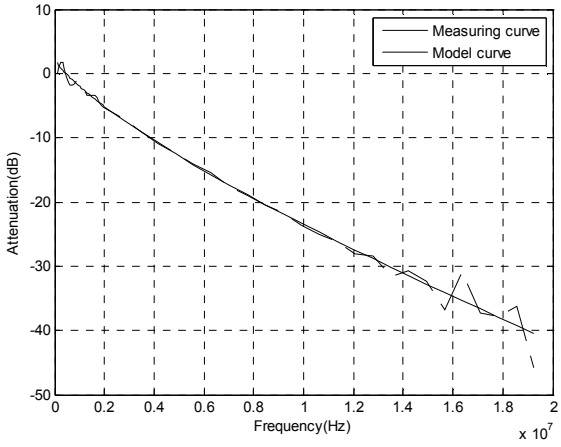

Fig.5 Attenuation profile of a 90-m mobile power-line directly connected

By measuring results, we can conclude that signal attenuation increase with the frequency and cable length. In our measurements, cable length is less than 100m, and there is no other load disturbance. The measured frequency signal attenuation amplitude is small. Attenuation is 1dBm when communication distance between sending and received side is 20m. And with the length increase to 90m, the attenuation is 5.5dBm. But with the cable continued increase, the signal attenuation can significantly increase.

At the same time, with the increase of cable length, the first decline point moves to low frequency. When the power cable is enough long, frequency selective fading will be happened at low frequency of 100 kHz to 500 kHz.

The least square method can fit the parameters in formula 1 through the measured data. Now, only one path is considered in signal transmission. We obtain the parameter $k = 0.7659$, $a_0 = -0.2804$, $a_1 = 1.444e-7$ when the measurement cable length is 90m. Fig 5 shows the measured curve and the fitting curve.

The measurement result is consistent with the results of the model. Root mean square error of the fitting curve and measured curve is 1.363.

IV. Conclusion

In this paper, we adopt multiple frequency point voltage detection method to measure the power cables based feature. Focus on the influence of signal transmission attenuation under different conditions of cable cross-sectional area, length and T network. Multipath model of PLC channel is analyzed and simulated. Based on measurement results and characteristics of PLC network topology, PLC channel fading under T network structure is put forward and measured.

ACKNOWLEDGMENT

This work is supported by China Electric Power Research Institute, Chong Qing University of Posts and Telecommunications, NSFC 61201206, cstc2012jjA40045, China Postdoctoral Science Foundation funded project, Chong Qing Postdoctoral financial support Rc201314, Xm201322.

References

[1] Manfred Zimmermann, Klaus Dostert. A Multipath Model for the Powerline Channel[J]. IEEE Transactions on commun, 2002, vol.50(4), pp: 553-559.

[2] Li Feng, Tian Hailiang, Wang Sitong. Field measurement and analysis of the impedance and attenuation characteristics of the low-voltage power line narrowband carrier channel [J]. Electrical Measurement & Instrumentation, 2011, 547(48), pp:90-96.

[3] Guo Jingbo, Wang Zanji. Spread spectrum signal transmission over low voltage distribution networks and realization countermeasures of the communication system [J]. Proceeding of the CSEE, 2001, 21(7), pp:78-82.

[4] Chan Morgan H L,Donaldson R W. Attenuation of communication signals on residential and commercial intrabuilding power-distribution circuits[J]. IEEE Transations on Electromagnetic Compatibility, 1986, 28(4), pp:220－230.

[5] Anastasiadou, D.; Antonakopoulos, T., Multipath characterization of indoor power-line networks[J], Power Delivery, IEEE Transactions on , Jan. 2005, vol.20(1), pp:90-99.

[6] H. He, S. Cheng, Y. Zhang, J. Nguimbis, Analysis of reflection of signal trans-mitted in low-voltage powerline with complex wavelet[J].IEEE Transactions on Power Delivery, January 2004. vol. 19(1), pp:86-91.

[7] Anatory, J. Theethayi, N.Thottappillil R. Channel Characterization for Indoor Power-Line Networks[J] Power Delivery, IEEE Transactions on , Oct. 2009,vol.24, no.4, pp:1883-1888.

[8] J. Anatory, N. Theethayi, R. Thottappillil, and N. Mvungi. A broadband power line communication system design scheme for typical tanzanian lowvoltage network[J]. IEEE Transactions on Power Delivery, July 2009, vol. 24(3), pp: 1218-1224.

Advanced Materials Research Vols. 986-987 (2014) pp 2073-2077

doi:10.4028/www.scientific.net/AMR.986-987.2073

SVG Graphical Analysis Tool Online Regional Reactive Power Optimization System Development

Gan LI[1, a], Lijie Ding[2, b], Dandan Li[3, c]

[1]State Grid Electric Power Research Institute, Sichuan Electric Power Company, Chengdu, 610000, China

[2] State Grid Electric Power Research Institute, Sichuan Electric Power Company, Chengdu, 610000, China

[3] Control and Computer Engineering School, North China Electric Power University, Beijing, 102206, China

[c]email: ldd0907@163.com

Keywords: reactive power optimization; regional power grid; SVG; pattern analysis

Abstract. Online region reactive power optimization is used to reduce power bus voltage operation over limit and reduce net loss for the economy to ensure that the power grid of great significance. SVG graphics file is a standard file format used by our dispatching operation, analysis file and basic information within the file corresponds to reactive power optimization system can guarantee the system reactive power optimization of interactive graphics capability and versatility. In this paper, we design and development of a SVG graphics file parsing tool that can automatically complete the import SVG, structural analysis, and text parsing; graphics and connectivity analysis to ensure the accuracy of the topology; the module contains a custom chart for human-computer interaction element, Element Properties and topological analysis and dynamic trend function, to meet human-computer interaction and reactive power optimization computing needs. This module has been applied to a region with reactive power optimization system, with good results.

Introduction

The regional power grid is the basic unit of grid operation, reactive power optimization is one of the basic scheduling tasks [1-6]. With the development of the EMS, reactive optimization for online computing systems has become automated system of dispatching the basic functionality of advanced software applications. Currently, reactive power optimization system not only exchanges data with SCADA systems, but also need to interact with other applications SVG files, provides a basis graphical data for optimizing system to achieve interactive features.

In this paper, the face of the regional power grid online reactive power optimization specific application needs of the system, design the practical use SVG graphic analysis module; the module is designed based on the basic structure of SVG data format that can automatically import SVG, structural analysis and text analysis, and then to store basic information within the SVG document; in order to facilitate use reactive power optimization calculation, the module can be used for connectivity analysis to check that may exist within the SVG file connection errors; facing personnel to operate and reactive computing, design for human-computer interaction custom primitives, primitive attributes and topology analysis and dynamic trend function.

SVG file parsing:

1.1 SVG file structure

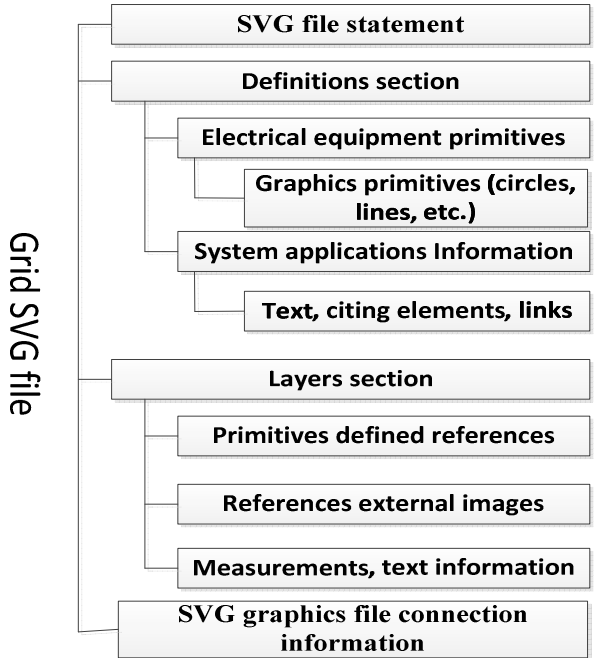

Figure 1 Structure grid SVG file contents

1) SVG file statement, the statement that is generally used to notify analytical tools that the next data is XML compliant code information, and describes the XML specification version files using text encoding.
2) Definitions section, the definition section contains defined primitive electrical equipment as well as the application of information systems, and also the specific method of drawing primitives electrical equipment, which is part of the function is understood as a unit of the puzzle, which is part of the whole complete graphics.
   Grid SVG file primitives defined section contains definitions of electrical equipment primitive graphics rendering, basic primitive types.
3) Layers section: This section contains specific SVG graphics information in electrical equipment, each elements of electrical equipment in layers of information corresponds with the corresponding information, this part of the function can be understood as the process of people to put the puzzle, same time marked on each unit of the puzzle, easily to reproduce the overall pattern again.
4) SVG graphics file connection information, this section describes the grid SVG file represented substations or power plants with other plant, connection information is generally described plant stand between AC line, and the same connection information SVG graphics files in the connected AC line are described.

1.2 Introduction and analysis of grid SVG file

According to the characteristics of the grid SVG graphics file based on XML standard and use text to describe, shown in Figure 2-4, it's import and analysis can be simplified into the following four parts:

1) Import files:
   Grid SVG file import determines whether SVG files could be the bases of types of advanced application software systems, related to practical engineering interface specifications and data interface methods, including file transfer, storage, generation. For advanced applications dispatching automation system to third parties, the grid SVG file belongs to an external file. It should be imported into advanced applications.

2) Structural analysis:
After the grid SVG file import is complete, we can get all the information SVG file, but the information still can't be identified or used directly, according to XML features grid SVG file, SVG's all part of the information is the existence of a particular XML element, by analyzing the structure of XML data unit, and in accordance with the contents of the structure shown in Figure 2-1.
3) Text parsing:
Text parsing, mainly defined elements, layer information and analytical connection information, elements are defined by all kinds of basic elements composition, layer information includes the connection of various types of electrical equipment line information graphics information.
4) Data storage:
To store the parsed data in the form of text to a temporary database, to facilitate subsequent processing.

1.3 device connectivity analysis SVG file

In the grid SVG file, elements types of electrical equipment, not only intuitive graph showing the connection relationships, the content of the parsed data also has a corresponding description. We refer to these including the connection relationship information integrate, to supplement and enhance the connectivity analysis speed CIM model information has a significant role.

1.3.1 Connectivity said

SVG file to describe the relationship between the devices have connected only limited elements, through correspondence between elements and equipment, it will be converted elements connection relationship into devices connected relationships. Cables can be considered as a two-port element, the left and right ends are connected to electrical equipment. Thus, by connecting the cable layer information, we can draw the "Device - Device" connection relationship table and eventually get the whole SVG graphics files connecting representation.

1.3.2 Connectivity Expansion Analysis

By connecting line information, we can get the connection relationship of the various electrical equipment from the grid SVG file, then integrate the results of these analyzes to obtain a connection relation table for each device. It represents the power grid SVG file factory station topology and Wiring analysis has a supporting role.

At the time of the grid SVG file topology and wiring for analysis, because only analyze their station represent a single plant, so according to the voltage level connection analysis may start from the transformers port or directly from Bus exports

1.3.3 Connectivity Checks

Based connectivity analysis can establish each electrical equipment represented connection relationship, as shown in Table 1:

Table 1 Represented the connection of various electrical equipment

	Breaker	Disconnectors	Single-ended device
Bus		√	
Overhead lines		√	√
Cable		√	√
Transformer	√	√	
Capacitors		√	√
PT		√	√
Station Transformer		√	√
Breaker		√	

In the figure above, √ represents an association between two devices, Single-ended device means that this device can only be connected on a single chart with another device, that it may represent the beginning or end of the circuit.

After getting the element properties in the SVG graphics of each electrical equipment, according to Table 1, check whether there exists an incomplete connected in the graph. The basic process is as follows:

1) traversing the basic properties of each device, recording endpoint connections;
2) The basic properties of the device for determining in loop, if a device does not meet the constraints appear in Table 1, counted;
3) For the connected device type does not meet the conditions of Table 1, recorded as "Device connection type error";
4) For the connected device does not meet the single-ended device is connected constraints, recorded as "connectivity interruption";
5) It outputs error information in the device, giving modifications.

Facing reactive power optimization design SVG

SVG provides a static data, in order to make SVG more consistent results for the optimization of the grid control center said requirements. In addition to general parameters used defined designing custom elements and entity attributes, and also need to be able to analyze the topology, and the distribution of reactive power be represented.

2.1 custom elements

To meet a variety of advanced applications graphics demand, it needs on the basis of primitive of static SVG file which has been defined above, form <symbol> unit to add custom elements, making the graphics more suitable for advanced applications.

According to demand, add custom elements can be divided into a new elements, a combination of elements and improved elements categories.

1) The new elements: export static SVG file process from scheduling automation systems, some elements of defined information is missing, or source graphics does not correspond to defined of the corresponding primitives, then there is the need to design new elements to compensate for the missing graphics. The new elements of design in a manner consistent with the way other elements of defined, by reference, or a combination basic elements to achieve.
2) A combination of elements: the main wiring diagram of the substation or power plants are designed to have a certain layout rules, makes a variety of electrical equipment in the same connection repeatedly. Combine these electrical devices elements. For example, combine the device elements in the specific electrical interval, then use the combination elements to operate.
3) Improvements elements: in elements already defined, some elements due to the design is too simple or complex, difficult to identify the graphics, meanwhile, the same device elements also have a variety of forms. Therefore it needs to be modified on the basis of the defined primitives, through change, replacing the basic elements to design and improvements entities.

2.2 Element Properties

Show primitive of electrical equipment needed the support its properties, therefore, in addition to modify the definition of elements, but also need of the display the properties of various types of electrical equipment primitive design.

1) Dynamic Properties: dynamic properties is the basis for flexible graphics performance, and need electrical equipment elements complete different dynamic display. For example, in the trend graph displays the trend needs to be dynamic flow, fault diagnosis systems need to dynamically display fault equipment.

2) Operational attributes: the graphical interface as an important platform for human-computer interaction. It need to have the ability to control the operation of electrical equipment through a graphical interface, therefore, the design elements of the operational attributes can be applied to improve the level of graphical interface.
3) Calculation of property: SVG graphics calculation does not include data. In order to optimize the calculation of basic data, calculating data is added to the system, the system contains the basic parameters and the calculation of parameters of electrical equipment.

2.3 Topology Analysis

In obtaining the basic data for each calculation of electrical equipment, you need to be converted to reactive power optimization needed model. First topological analysis of electrical equipment by the end of each of the nodes into a topological analysis required by connectivity.

2.4 Dynamic trend display

For reactive power optimization, it also need dynamic trend to reflect the distribution of reactive power within the grid; By analyzing the results for the flow calculation, to determine whether a branch reactive power flow, and marked on the map and show the size of the node voltages. The basic contents are as follows:

1) each branch reactive power flow and size of the flow;
2) the size of each node voltages and the over limit behavior, over limit voltage node using a special symbol;
3) control the behavior of the control variables, such as: changes in transformers and capacitors Touqie gear change;
4) The total net loss changes.

Summarizes

This design SVG graphic analysis module uses JAVA development, cross-platform operation, for use in applications with good results. It can automatically parse SVG graphic information, check the connection errors that may exist, and has topological and dynamic trend display. The module has been optimized to run in a geographical area of reactive power grid system, with good results.

In grid scheduling operation, SVG and CIM are two typical file format, which is derived from the same data source, but there may be a different error In the format conversion; through the analysis of SVG and CIM consistency of information can be further resolved SVG possible errors in the file.

References

[1]Zhang Cong Yu , Chen Min shafts based on multi -objective particle swarm algorithm for reactive power [J] Power System Protection and Control 2010 , 38 (20) : 153-158

[2]PROCEEDINGS . Optimal power flow problem with constant factor allocation method for decoupling [J]. Chinese Society for Electrical Engineering . 1983.01

[3]Li Yulong , Chong Wei , Qin Lijun reactive power optimization problem in linear programming linear step dynamic adjustment strategy [J] Power System Technology, 2006, 30 (18) : 40-44 .

[4]Liu research PROCEEDINGS , Li Yunhua . Improved genetic simulated annealing algorithm based reactive power [J]. Power System Technology, 2007,31 (3) :13 -17 .

[5]IN TRADITIONAL Zhang Jianhua , Liu Zongqi Parallel Adaptive Particle Swarm Optimization Algorithm in Reactive Power Optimization of Power [J]. Grid technology . 2012,36 (1) :108 -112.

Advanced Materials Research Vols. 986-987 (2014) pp 2078-2081

doi:10.4028/www.scientific.net/AMR.986-987.2078

The Analysis Of The Transmission Signal Measured MIPI D-PHY

Wei Wei[1, a], Feiteng Zhang [2,b]

[1] Xi'an University of Posts and Telecommunications, Xi'an, China

[2] Xi'an University of Posts and Telecommunications,Xi'an,China

[a]weigaozu@hotmail.com, [b]595632205@qq.com

Keywords: Display Serial Interface;Physical Layer;high-speed mode;practicability

Abstract. Analysis the characteristics of the measured transmission signal of Mobile Industry Processor Interface (MIPI) Display Serial Interface Physical Layer(D-PHY) interface based on a project platform. Firstly, introduces the transmission characteristics and mutual conversion process of physical layer about high-speed and low power mode, and by the transmission signal measured a platform of high-speed mode, present the D-PHY transmission signal each test items and test point selection, make the phone run smoothly and screen display normally, this test analysis certain practicability and expansibility.

Introduction

MIPI Serial Display Interface (DSI) to satisfy the requirements of the new generation of mobile interface, to overcome the traditional shortcomings existing parallel bus, to meet the high resolution display, to reduce the display module power consumption, is the mainstream of future multimedia interface technology[1].At the same time it also is a high-speed interface with complex protocol,which current use the physical layer standard is D-PHY. D-PHY uses a 1.2 voltage,source synchronous and scalable low voltage signaling technology, swing 200mV differential signal , can support up to 4 channels.The maximum about each channel's rate can reach 1Gbps .In theory,transmission rate of 4 channel can reach 4Gbps. All of the DSI interface line have 4 root at least, overcomes the lack of parallel data bus, thus existing equipment show a higher performance, lower power consumption, lower EMI and less compared to the pins[2].Through DSI signal of a project can be measured, wo can master MIPI signal test method for better, and understand the transmission characteristics of MIPI-DSI more profound.

Transmission Characteristics Based On D-PHY.

The D-PHY includes the DSI (display serial interface) and CSI (camera serial interface), using 1 pairs of source synchronous differential clock and 1~4 pairs differential data line to carry on the data transmission.

The physical layer of the D-PHY support HS (high speed) and LP (low power) work pattern, the data transmission state is shown in TABLE I[4].HS mode adopt Synchronous transmission mode of low voltage differential signal,with power consumption and data rate is 80 M ~ 1 Gbps; LP mode using asynchronous transfer mode with single ended signals, the data rate is very low (<10 Mbps), but the corresponding power consumption is very low. The combining the 2 models of the MIPI bus ensure transport the high speed transmission of large amounts of data in the need , but also can reduce the power consumption in no need[5].

Table 1

State code	Line voltage level		High speed	Low power	
	Dp	Dn	Burst mode	Control mode	Escape mode
HS-0	HS low	HS high	Differential -0	N/A	N/A
HS-1	HS high	HS low	Differential -1	N/A	N/A
LP-00	LP low	LP low	N/A	Bridge	Space
LP-01	LP low	LP high	N/A	HS-Rqst	Mark-0
LP-10	LP high	LP low	N/A	LP-Rqst	Mark-1
LP-11	LP high	LP high	N/A	Stop	N/A

MIPI-DSI includes physical layer, channel management layer, protocol layer and application layer.physical layer link clock and data channel, the channel number N<=4. the clock path is unidirectional signal, using the DDR clock along the clock rise and fall sampling at the same time. the clock always trigger in the HS-0 state . as shown in Fig.1 as in the data transmission process diagram, high-speed data transmit in clock triggering.the state state and the end state for data transmission is LP-11, clock enter the high-speed mode after leaving the state of rest through a transmission start state (SOT): LP11-LP01-LP00. clock signal must enter the high-speed mode before triggering of the high-speed data transmission in order to provide the DDR clock with data and must keep the high speed data transmission over to stop the clock signal.the transmission end state (EOT) :LP00-LP11.Similarly, data channel first transmit a start state(SOT) after leaving the state of rest and then transmit a eight bit sequence:00011101, then began to transfer valid bit and enter into the high-speed mode[7].

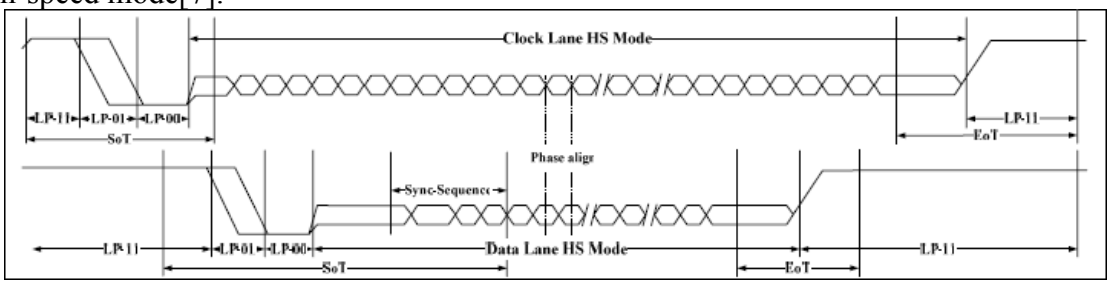

Fig. 2

Analyse The Measured Signal.

Because the signal of MIPI D-PHY is complex,We require a complex test to ensure consistency of interface signal and protocol , which test MIPI-DSI signal transmission characteristics of high speed mode using Tektronix Oscilloscope based on a project platform ,keeping LCD screen, dynamic background image display and standby for a long time.Then we respectively connect to four channel into oscilloscope, describing the selection of test items and test data as follow[8],The test waveforms as shown in Fig.2.

A. Data Lane HS-TX Differential Voltages (VOD(0), VOD(1)) and its Mismatch (VOD),namely VOD=|VOD(0)-VOD(1)|.

B. Data Lane HS-TX Single-Ended Output High Voltages (VOHHS(DP),VOHHS(DN)).

C. Data Lane HS-TX Static Common Mode Voltages (VCMTX(0),VCVMTX(1)) and its Mismatch (ΔVCMTX(1,0)).Create an VCMTX waveform as VCMTXX=(Dp+Dn)/2.If the data is Differential-0, the point is added to VCMTX(0), else if the data is Differential-1,the point added to VCMTX(1).calculate ΔCMTX(1,0)=(VCMTX(1)–VCMTX(0))/2.

D. Data Lane HS-TX Dynamic Common-Level Variations Between 50-450MHz.Find the minimum ripple voltage in the filtered data HS region, Vmin. Find the maximum ripple voltage in the Filtered data HS region, Vmax.Compute Vpeak1 as,Vpeak1=max(Vmax,abs(Vmin)).

E. Data Lane HS-TX Dynamic Common-Level Variations Above 450MHz..Find the minimum ripple voltage in the filtered data HS region, Vmin. Find the maximum ripple voltage in the Filtered data HS region, Vmax.Compute Vpeak2 as, Vpeak2 = max (Vmax, abs(Vmin)).

F. When in high-speed mode transmitting waveform 000111, measuring the rise time of Tr, the measuring range is from 20% to 80% of VOD voltage .

G. When in high-speed mode transmitting waveform 111000, measuring the rise time of Tf the measuring range is from 80% to 20% of VOD voltage .

H. Data Lane HS Exit: THS-TRAIL Value and 30%-85% Post-EOT Rise Time(TREOT).

I. THS-TRAIL Value continues from the end of HS-TX transmission to the beginning of LP-TX transmission. TREOT continues from LP00 state to LP11 state based on LP mode and ending point is 85% of VLP Voltages.

Calculate TEOT=THS-TRAIL+TREOT.

Note: due to the testing results and the measurement range of the clock lanes (1)-(8) are similar to data lanes, so that this omission.

Table 2

Testing item		Minimum	Measured value	Maximum	Unit	Result
VOD	VOD(1)	140	193.1833680240	270	mV	Passed
	VOD(0)	-270	-195.2995992676	-140	mV	Passed
	ΔVOD	N/A	2.1162312436	10	mV	Passed
VOHHS	DP	N/A	305.9873251522	360	mV	Passed
	DN	N/A	306.3075099078	360	mV	Passed
VCMTX	VCMTX(1)	150	207.4630635177	250	mV	Passed
	VCMTX(0)	150	207.0408746082	250	mV	Passed
	ΔVCMTX	-5	0.2110944547	5	mV	Passed
Vpeak1		N/A	24.1054445505	25	mV	Passed
Vpeak2		N/A	6.3609929835	15	mV	Passed
Tr		150	256.0000000000	696.6562566	pS	Passed
Tf		150	265.7142857143	696.6562566	pS	Passed
THS-TRAIL		69.28	73.2800000000	N/A	nS	Passed
TREOT		N/A	10.8800000000	35	nS	Passed
TEOT		N/A	84.1600000000	132.86625026	nS	Passed
TSKEW		0.81	1.1948380711	2.2357223388	nS	Passed
UIINST		1.25	2.2374358974	N/A	nS	Passed

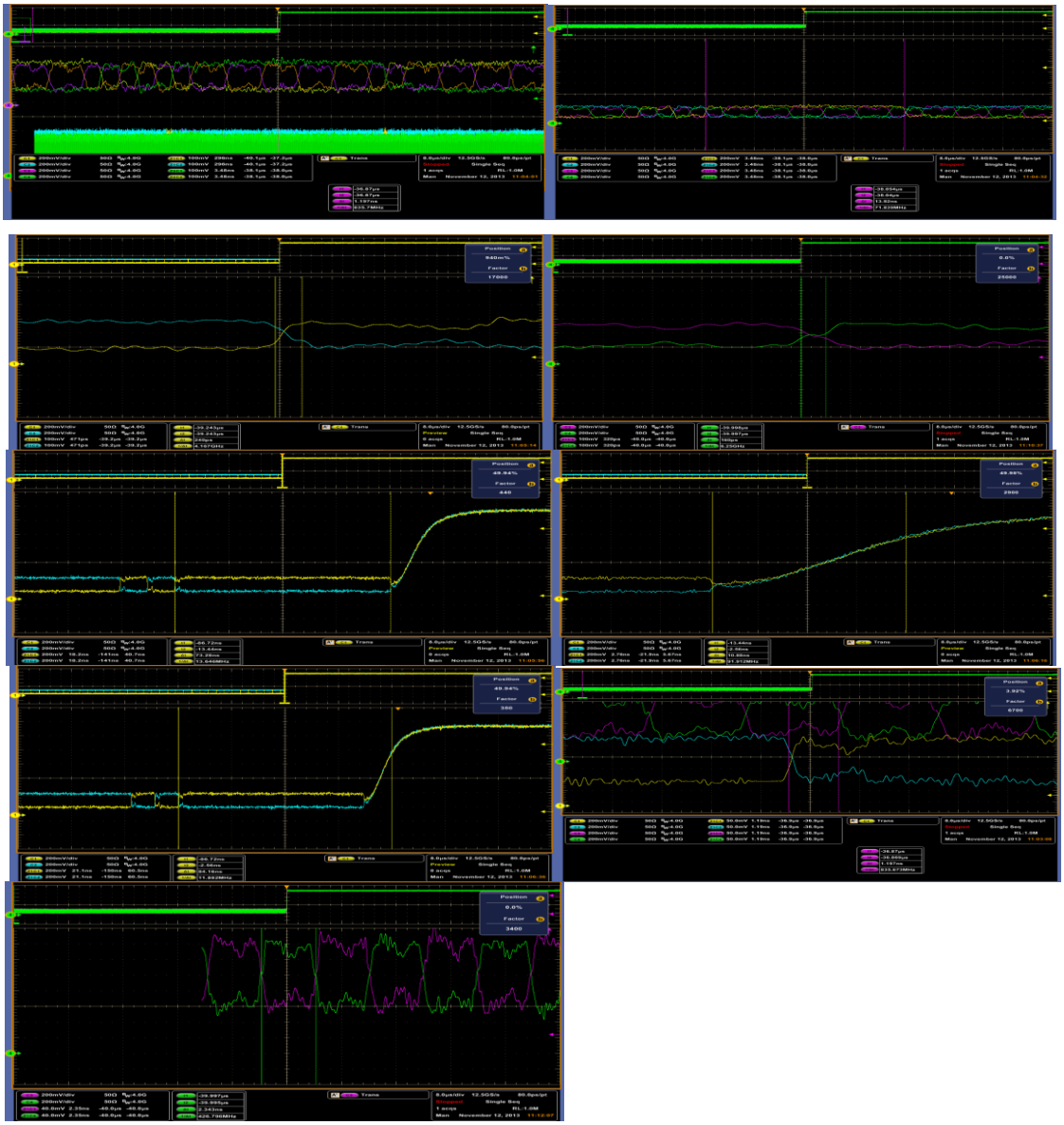

Fig. 3

Summary

The experiment analysis the signal transmission process. By measuring each test quota of a platform of MIPI signal, analyze the rationality of transmission signal, guarantee the quality of the signal. Firstly by the PCB board We weld silver line and link probe to the oscilloscope.Because the test item are differential signal, the signal line's spacing and length are requiredc to remain equal ,But silver line can not keep equal distance, so the test signal and the ideal signal has a certain error. In addition, interference between PCB lines and other lines will affect the test results.

Acknowledgements

This research was supported by the scientific research fund of shaanxi provincial education department (Grant No. 12JK0541), all support is gratefully acknowledged.

References

[1] L. M. Wen, Design of LCD Driver Interface Based On MIPI-DSI Protocol.Guangzhou:South China University of Technology,2011:1-5.

[2] X. F. Su. Design of LCD Driver Interface Based On MIPI standard.Guangzhou:South China University of Technology,2011:2-3.

[3] MIPI Alliance Specification for Display Serial Interface version 1.01.00. MIPI Alliance, 2008.

MIPI Alliance Specification for D-PHY version 0.90.00[S]. MIPI Alliance, 2007.

[4] K. Li, MIPI CSI/DSI introduction and Test method of signal and protocol .ForwardPosition,2012,3(3):11-15.

[5] P. Kamath, MIPI will completely change the way mobile product design,Application of integrated circuit,2012,1(2):20-22.

[6] K. Lim, G. S. Kim, S. Kim, A Multi-Lane MIPI CSI Receiver for Mobile Camera Applications. IEEE Transactions on Consumer 1186 Electronics,2010,56(3):1185-1190.

[7] Y. C. Lu,Z .Y. Chen, P.C.Chang.Low Power Multi-Lane MIP_I CSI-2 Receiver Design and Hardware.

[8] Implementations. 2013 IEEE 17th International Symposium on Consumer Electronics (ISCE)，2013:199-200.

[9] K. Pavan,Physical layer test strategies for mipi standards. Nelson Publishing Inc., 2504 N. Tamiami Trail,Nokomis,FL34275-3482,United States,2011,50(4):18-23

[10] T. Allen, MIPI display standards for mobile internet devices. Hearst Business Communications, 50 Charles Lindbergh Blvd.Suite 100,Uniondale,NY 11553, United States,2009,51(5)

Advanced Materials Research Vols. 986-987 (2014) pp 2082-2085

doi:10.4028/www.scientific.net/AMR.986-987.2082

The research of Self-Adaptative power adjustment routing

Zhiping Ding

Qingyuan Polytechnics, Qingyuan 511510, China

dingzijsj@126.com

Keywords: Cognitive radio, Ad Hoc network, Power control, Routing mechanism.

Abstract. Cognitive Radio Ad Hoc Network (CRAHN), established on the cognitive radio environment, configures the Ad Hoc Network which possesses the internal capacity. How to effectively control the power consumption is an important issue in the CRAHN for CRAHN‘s main power type is battery. At present, the energy-saving routing research in CRAHN is mainly based on the real-time routing mechanism. It means that it should be routed again after transferring an archive. In order to increase the network route’s surviving time and save the power consumption, it introduces a routing mechanism whose purpose is to optimize the communication algorithm’s performance by improving the existing routing mechanism in the Ad Hoc network.

Introduction

Ad Hoc Network can also be called Mobile Ad Hoc Network, which is a mobile network without being supported by the wired infrastructure. All nodes are composed by the mobile hosts in the Ad Hoc Network. The type of the network initially is applied into the military field. In order to apply into the battlefield environment, it respectively forms the radio network data’s communication. Cognitive Radio Ad Hoc Network (CRAHN), established on the cognitive radio environment, configures the Ad Hoc Network which possesses the internal capacity. Compared with the Mobile Ad Hoc Network (MANET), its integral structure has three similarities in rough.

Related research

For CRAHN, energy-saving routing is an important field, but the field is still not deeply studied currently. On the contrary, energy-saving routing has quite mature been studied in the MANET environment. It overcomes CRAHN environment’s several characteristic limitations through the further improvement of MANET’s existing energy-saving routing, and then makes it be applied into CRAHN environment’s routing. That is the paper’s issue.

The paper needs to solve CRAHN environment’s characteristic limitation, such as spectrum distribution and spectrum transition, in improving the routing structure (Qun Li et al, 2001). In recent years, the dynamic spectrum distributed method in terms of the cognitive radio network can be divided into centralization and decentralization schemes.

System Module

Compared with the traditional maximum network flow problem, power cognitive routing has several similarities in some parts, but it is different on the whole. The traditional network flow problem is mainly subject to the online throughput, and is not subject to node itself throughput. In order to explain the maximum network flow NP-hard problem in power cognitive routing, the paper simplifies the adopted module as a special situation in which it just has a source node and a destination node. In order to reduce the required handled problem to the maximum network flow, it sets the environment in the situation in which the node throughput is not influenced by the distance of the neighbor nodes.

The spectrum transition is finished by the existing Responsive-Cognitive technology. The considered whole cognitive radio network is formed by M primary users and N secondary users. The primary users have the specific channel license and it just uses their distributed channels. The

secondary users have no spectrum license and it just grapes the opportunity to send their information through the vacant part of the primary spectrum. It sets two constrained conditions for the spectrum transition.

The first constrained condition: when the secondary user i passes on the user j, it must satisfies bit-error-rate (BER) condition, as shown in the following: $\frac{P_i(f)\cdot L_{ij}(f)\cdot G}{N_j(f)+\sum_{k\in v,k\neq i}P_k(f)\cdot L_{kj}(f)} \geq SINR_{SU}^{th}(BER_{SU}^{*})$ (1)

Pi (f) is the node i transmission power in the frequency f. Lij (f) is the transmission lost rate from node i to node j in the frequency f. G is the process gain. Nj (f) is the node i receiving noise in the frequency f. $\sum_{k\in v,k\neq i}P_k(f)\cdot L_{kj}(f)$ is the node i interference in the frequency f. $SINR_{SU}^{th}(BER_{SU}^{*})$ is the required SINR threshold for the secondary user reaches BER value.

The secondary constrained condition: avoid the process of interfering the receivers, as shown in the following:

$$P_i(f) \leq \min_{\ell \in v} \frac{\triangle I_{\ell}^{\max}}{L_{i\ell}(f)} \cong P_i^{\max}(f); \ell \in v, \ell \neq j \quad (2)$$

$\triangle I_{\ell}^{\max}$ is the extra maximum interference in the transmission procedure. $P_i^{\max}(f)$ is the node i maximum transmission power in the frequency f.

Then it adopts the Directed Connectivity Graph, g (v, ε). It is a graph which can analyzes the cause and effect, the size, the before and after relationships in the system by setting the parameter. It adopts g (v, ε) to imitate the multi-hop radio network. v= {v1...vN+M} is the limited node whose number is N+M. The user can divided into primary user PU= {v1,...,vM} and secondary user SU={vM+1,...,vM+N}. ε is the one-way online from node i to node j.

It needs to compute the related information of the routing path through Directed Connectivity Graph g (v, ε). E is the required power of the transmission packet. e is the transmission power. T is the transmission delay. The required used power of the transmission packet is defined as:

$E=e\times T$ (3)

$T=L/R$ is packet's size. R is packet's transmission rate. The required used power of the transmission packet can also be defined as: $E=e\times T=e\times L/R$ (4)

The again transmission power is e=kd c，k is the factor of receiving the power level, d is the transmission distance, c is the route attenuation index. Its formula is: $E=kd^{c}\times L/R$ (5)

The original packet size transmitted by the source node in the transmission process is L0. It passes the relay node number n. The additional information packet size in each relay node is △l, its packet size is defined:L=L0+n△l (6)

The transmission packet power E is defined as: $E=kd^{c}\times (L_0+n\Delta l)/R$ (7)

The maximum information quantity in the whole system has two constrained conditions. The first constrained condition is that the whole power used for transmitting the information in the node i cannot surpass the node i itself power, it can be defined: $P_i(f)\geq \sum_j n_{ij}\cdot e_{ij}$ (8)

The second constrained condition is that the number of the information transmitted by node ℓ to other nodes is the same as the number of the information transmitted by other nodes to node ℓ, it can be defined: $\sum_j n_{kj}=\sum_j n_{jk}; k\in v, k\neq i$ (9)

Algorithm

The paper improves the adaptative power adjustment routing (Qun Li et al, 2001). It finds a self-adjustment mechanism route between the minimum power route and the maximum remaining power route when it cannot be informed of the information sequence. The routing can be self adjusted with the increasing and reducing of the time and the node itself so that the transmission information route has longer network surviving time.

The system has been adjusted and constrained inn order to make the routing be operated in the CRAHN environment.

The whole set of the routing mechanism can be divided into two parts. The first part is that MAX-MIN zPmin routing algorithm selected by the routing. The second part is that the adaptative adjustment mechanism whose parameter is z in the routing algorithm.

The routing algorithm flow in the first part is as follows (Qun Li et al, 2001):

1) S establishes the initial Directed Connectivity Graph g (v, ε), when fcc broadcasts RREQ (adding all node's information)

2) It possesses the minimum power consumption route through Di jkstra algorithm, and it is called Pmin.

3) Directed Connectivity Graph g (v, ε) finds the minimum power consumption route. If the route power consumption is larger zPmin or it dose not find the route, the route found before is the required route.

4) If it is not, it should find the route's minimum utij, and it is called umin.

5) Compute other routes utij. Compared with umin,

it deletes the belonging route lower than umin from graphs.

6) Bounce to 3.

$u_{rij} = \frac{P_T(v_i) - e_{ij}}{P(v_i)} P_0$ is node vi's initial power value. PT (vi) is the power value when node vi passes time T. eij is the transmission power from node vi to node vj. utij is the remaining power ratio in which the information is sent from node vi to node vj.

Parameter z's self-adjustment mechanism flow in the second part is as follows:

1) Set the initial value as z ($1<z<\infty$), and then set δ a the increasing and reducing distance.

2) Operate route algorithm after interval T.

3) Compute route's each node survival time $\frac{P}{\Delta P_T}$, its minimum is setted as t1.

4) It sets δ as the increasing and reducing distance z value, and then operates the route algorithm again after interval T.

5) Compute route's each node survival time $\frac{P}{\Delta P_T}$, its minimum is setted as t2.

6) It the node consumption in the route is used up, it should jump out. (Select the required z)

7) If t1<t2, t1< t and then bounce to 4.

8) If t1<t2, $\delta \frac{-\delta}{3}$, t1= t2, and then bounce to 4.

When z=1, the selected route is the minimum power consumption route. When z=∞, the selected route is the maximum power consumption route. The improved routing method is to find the route possesses the longest network surviving time from both.

Simulation Result

The previous research is based on real time. The paper's emphatic orientation is different from the previous research; its simulation is based on the performance display. It conducts three simulation tests to the adaptative power routing respectively with the use of MATLAB. The first simulation is that it observes parameter z value's influence to the maximum transmission information number by adjusting node's number and initial power value, as shown in figure1.

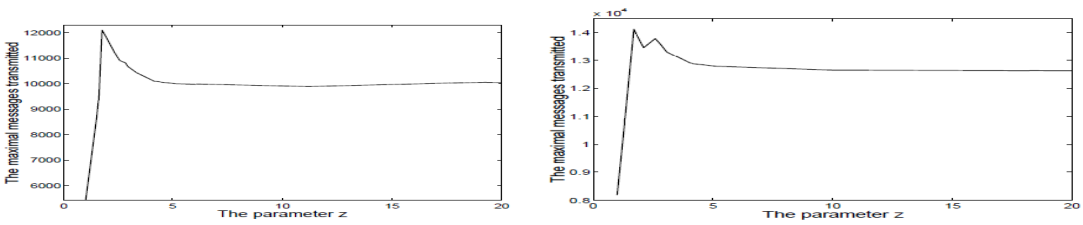

Figure 1 The first simulation result graph

In the first simulation, it sets the simulation environment in the —10×10 square network topology and the node is uniformly distributed by the random method. Information's uniform distribution is produced in the pairing nodes. The transmission power is setted as P= 0.001×d3. The above figure sets the total node number as 20, each node's initial power is setted as 10. The following figure sets the total node number as 40, each node's initial power is setted as 30.

Comparing figure 2's two graphs, it shows that the best effect, that is, parameter z value's influence to the maximum transmission information number lies in z value is lower than 5. When the node number increases, the maximum transmission number will increase. When the node initial power value increases, the maximum transmission number's high and low fall will reduce.

The second simulation is that it observes parameter z value's influence to the maximum transmission information number by adjusting network topology, as shown in figure 2.

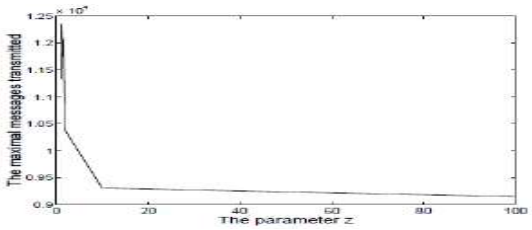

Figure 2 The second simulation result graph

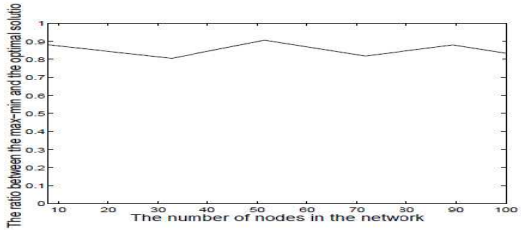

Figure 3 The third simulation result graph

In the second simulation, it sets the simulation environment in the loop network topology whose radius is 20 and the node is randomly distributed. Information's uniform distribution is produced in the pairing nodes. The transmission power is setted as P= 0.001×d3. The total node number is setted as 20, each node's initial power is setted as 10.

The figure 3 shows that the distribution is sparse for the node's distribution is subject to the loop network topology so that it influences the maximum transmission information number,

The third simulation is the route surviving time performance's comparison between the improved routing algorithm and the Optimal Off-line Algorithm, as shown in figure 3.

In the third simulation, it sets the simulation environment in the 10×10 square network topology and the node is uniformly distributed by the random method. Information's uniform distribution is produced in the node from each node to the specific gateway node. The transmission power is setted as P= 0.001×d3. Each node's initial power is setted as 10 and z value's range is setted as 100 .

Figure 4 shows that the performance ration between the simulation result and the optimal route is mostly between 0.8 and 0.9, and later the improved routing route survival time performance is close to the optimal routing.

Conclusion

The paper improves MANET's existing routing mechanism and then applies it into the CRAHN environment. The routing mechanism reaches the result, which is, increasing the network route survival time and saving The power consumption by optimizing the communication algorithm's performance.

It is suitable for the small-size network for the communication algorithm needs each node's precise power value. I the future, it will extend to the large-size network.

References

[1] A Akyildiz, I.F., Lee W. Y., and Chowdhury, K., 2009. CRAHNs: Cognitive Radio Ad Hoc Networks, Ad Hoc Networks Journal, 7(5), 810-836.

[2] L. Hou, K. H. Yeung, K. Y. Wong, 2011 .A Vision of Energy-efficient Routing for Cognitive Radio Ad Hoc Networks, 2011 6th International Symposium on Wireless and Pervasive, Feb. 23-25, 1-4.s

Advanced Materials Research Vols. 986-987 (2014) pp 2086-2090

doi:10.4028/www.scientific.net/AMR.986-987.2086

Virtual-MIMO Cooperation communication based on integrated power line and wireless communication system

Wang Yi[1, 2], Zhen shan[1], Hou Xingzhe[1], Sun Hongliang[1], Luo Kaibo[1], Zhou Tanjie[1]

[1,] Chong Qing Electric Power Research Institute, Chong Qing, China
[2,] Postdoctoral Workstation of the Chongqing Electric Power Corporation, Chong Qing, China

wangyi81@cqupt.edu.cn

Keywords: PLC, wireless, virtual MIMO, outage probability, capacity, simulation

Abstract. Power line communication (PLC) is a competitive technology in broad band access services and smart grids considering it widely distribution and low infrastructure built cost. This paper proposes a new PLC virtual MIMO cooperation system merged with the wireless communication to improve the reliability and capacity performance of conventional PLC system. A wireless interface is integrated in the conventional PLC modems. The nearby PLC modems constitute a V-MIMO module to share their transmitting information via the wireless link. The PLC modem in different V-MIMO module can communicate with each other through power line. The outage probability and capacity simulation results prove that new system can significantly increase the PLC system throughput and the link reliability.

Introduction

Power line communication (PLC) has a long story used as voice communication, automation and control from 1920s. In recent years, PLC is gaining great attention in broad band access services and smart grids since it allow exploiting the widely distributed existing infrastructure without the need of new wires [1]. The power line network is considered to be a harsh communication medium for its complicated noise and multi-path effect that seriously affects the reliability and stability of the PLC system. In fact, parallel transmission on the power line channel is suppressed as the bandwidth limitation.

Multiple-input multiple-output (MIMO) techniques have been demonstrated to greatly improve the capacity and spectrum efficiency for wireless communication [2,3]. However, due to the size and power limitation, multiple antennas installed is difficult to implement and one antenna is more practical on only one user terminal. Therefore, researcher proposed the Virtual multiple-input multiple-output (V-MIMO) system. In the V-MIMO system, every single antenna terminal has one or more cooperation partners shared each other's antenna to transmit data that makes only a single antenna user system can still provide transmit or receive diversity. Current study results show that cooperative diversity can expand the system capacity, improve the quality of network service, and improve the system performance [4,5,6].

The application of MIMO methods to PLC promises significantly higher data rates and better system capacity compared to today's Single Input Single Output (SISO) systems. The Home-Plug Power line Alliance considers MIMO technique as the key element of next generation PLC modems. However, so far the application of the MIMO techniques over power line only focuses on using the multi-phase power cables as antenna array to implement the MIMO by Antenna selection algorithm and space-time coding technology [7]. The hostile channel environment on the power lines is still not changed. For example, the noise and multi-path effect can seriously interfere all phase of power lines, which leads to the communication failure in all MIMO channels.

To overcome the aforementioned problem and improve the reliability of the PLC, in this paper we propose a new PLC system based on the V-MIMO cooperative diversity. A wireless interface is integrated in the conventional PLC modems. The adjacent PLC modems constitute a V-MIMO

module via the wireless link. Every PLC modems in this V-MIMO module could communicate with each other to share their information thorough the wireless link. The different V-MIMO module is connected by the power lines. Thus, it means the receive information of a PLC modems can not only from its own connected power line, but also from the PLC modems in the same V-MIMO module. In this way, our PLC V-MIMO cooperation communication system obtains the diversity gain with the collaborative communication implementing. In this letter, we verified that compared to the conventional PLC system our new V-MIMO system has the better capacity and system performance through simulation.

The remaining sections of this paper are organized as follows. In section Ⅱ, the specific new PLC system model will be introduced. In section Ⅲ and section Ⅳ, we will put the importance on the performance analysis of the new system which include the outage probability and capacity analysis simulation. And the conclusion will be given in Section Ⅴ.

System Model

We consider the basic structure of proposed PLC V-MIMO cooperation communication system depicted in Fig. 1, which is integrated with PLC and wireless communication.

In this new PLC V-MIMO cooperation system each modem has installed one PLC interface and one wireless communication interface. The nearby PLC modems showed as PLC A and PLC D or PLC B and PLC C constitute the V-MIMO module. The PLC modems in the same V-MIMO module called cooperation partners share their information via wireless communication. While the PLC modems in the different V-MIMO module only communicate with each other trough the power line.

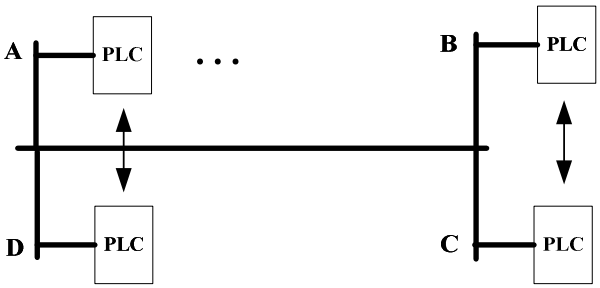

Fig.1. Basic structure of proposed PLC V-MIMO system

In the MIMO system, the receive signal merging processing needs CSI (channel state information) as the premise. In the practical communication progress, the transmitter's CSI is not easy to acquire while the receiver's easier. Therefore, we generally take the receive diversity equate as the SIMO scheme. While for the MSIO schemes, taking a space-time coding on transmitting information to obtain the coding gain and diversity gain is more practical. This is also appropriate to the V-MIMO system.

Our paper will focus on the analysis of MIMO scheme. We assume that there is a PLC V-MIMO cooperation communication system includes two transmitters (PLC A and PLC D) and two receivers (PLC B and PLC C).

Obviously, our communication process includes two stages.

First stage, the information transmitter PLC A or PLC D sends the information to the PLC B and PLC C through the power line. The received signal in PLC B and PLC C which is expressed as y_B^{plc} and y_C^{plc} can be written as

$$y_B^{plc} = h_{AB}^{plc} x_1 + h_{DB}^{plc} x_2 + n_B^{plc} \quad (1)$$

$$y_C^{plc} = h_{AC}^{plc} x_1 + h_{DC}^{plc} x_2 + n_C^{plc} \quad (2)$$

where x_1 and x_2 represent the signal transmitted form PLC A and PLC D. n_B^{plc} and n_C^{plc} are the additive power line noise on node B and node C. h_{AB}^{plc}, h_{DB}^{plc}, h_{AC}^{plc} and h_{DC}^{plc} denote the power line channel between node A and B, D and B, A and C, and D and C.

Second stage, the cooperation partner PLC B sends the receive information to the destination receiver PLC C via wireless link.

- If the PLC B ends the information to PLC immediately, the received signal in PLC C via wireless can be written as

$$\begin{aligned} y_C^{wl} &= h_{BC}^{wl} y_B^{plc} + n_C^{wl} \\ &= h_{BC}^{wl} h_{AB}^{plc} x_1 + h_{BC}^{wl} h_{DB}^{plc} x_2 + h_{BC}^{wl} n_B^{plc} + n_C^{wl} \end{aligned} \tag{3}$$

Where h_{BC}^{wl} denotes the wireless channel between node B and C. n_C^{wl} is the additive wireless noise on node C.

- If DF (Decode-and-Forward) is adopted in PLC B, the received signal can be written as

$$y_C^{wl} = h_{BC}^{wl} \cdot \hat{x} + n_C^{wl} \tag{4}$$

The $\hat{x}$ $(\hat{x}_1 \quad \hat{x}_2)$ is the signal processed with decode-and-forward by PLC B.

Thus, the received signal of PLC C is related to the cooperation forward methods in PLC B.

Outage Probability analysis

Consider a PLC V-MIMO cooperation system with two clustered transmitters and two clustered receivers, which can be regarded as two parallel SIMO channels. We assume the nodes within a cluster are close together, but the distance between the transmitter and receiver clusters is large.

According to traditional analysis method of V-MIMO cooperation communication, as shown in Fig.2, we can regard the PLC V-MIMO cooperation communication system as the typical 2-hop relay communication system. Here, source node PLC A and PLC D communicate with destination node PLC C not only through power line but also through PLC C which acts as a relay. In cooperation relay communication system, the first stage is called broadcast phase and the second stage is called forward phase. In this new system broadcast phase channel is power line while the forward phase channel is wireless.

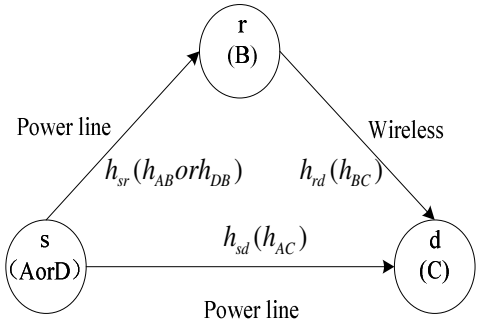

Fig.2. Basic structure of proposed PLC V-MIMO system

In our analysis model, h_{AB}, h_{BC} and h_{AC} which are the h_{rd}, h_{sr} and h_{sd} in the 3-node and 2-hop cooperation relay model, are channel transmission coefficient. And $h_0 = |h_{AC}|^2$, $h_1 = |h_{AB}|^2$, $h_2 = |h_{BC}|^2$ represent as the channel power gain.

Outage probability defined as the probability that the mutual information or channel capacity falls below a certain target rate R is an important reliability indicator of a communication system.

$$P_{out} = \Pr(I < R) \tag{5}$$

In the conventional no cooperation scheme, source node A sends information to destination node D point to point. The mutual information of the direct link is I_{DT} :

$$I_{DT} = \log_2(1+\gamma h_0) \tag{6}$$

Where $\gamma = P/N_0$ is the signal-to-noise ratio (SNR). N_0 is the variance of Gauss noise.

Considering for example selection decode-and-forward (SDF) model, the mutual information of it can be expressed as below [8]

$$I_{SDF} = \begin{cases} \frac{1}{2}\log_2(1+2\gamma h_0), & h_2 < \gamma_{th} \\ \frac{1}{2}\log_2\left(1+\gamma h_0+\gamma h_2\right), & h_2 \geq \gamma_{th} \end{cases} \tag{7}$$

Where $\gamma_{th} = (2^{2R}-1)/\gamma$. γ_{th} is the threshold. In the forward stage, in order to avoid transmitting error decoding symbols we think the communication link is outage when the h_2 falls bellow γ_{th}. While cooperation partner B will transmit the signal to destination node C when the h_2 is higher than γ_{th}.

In this article, we use the Monte-Carlo simulation to compare the outage probability of the new system and the conventional system. In the simulation process, we assume that both relay node B and destination node C can obtain the necessary CSI. Each channel gain is statistically independent. We use the Middleton class A model for handling the impulse noise and Rayleigh amplitude statistics model for handling the PLC channel fading. The wireless channel is Rayleigh channel. Transmission power is P meeting the total power limit and normalized.

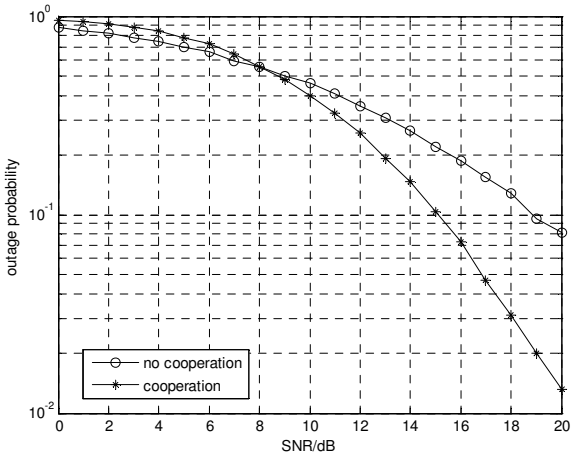

Fig.3. Outage probability of cooperation system and no cooperation system with the SDF cooperation model

We first use the computer to produce different channel matrix as Monte-Carlo "snapshot". The elements of wireless channel matrix and PLC channel matrix obey Rayleigh distribution. Then, given to the spectral efficiency, we will compute the mutual information and outage event statistically .

Fig.3 shows the comparison chart of cooperation and no cooperation communication systems' outage probability. It is easy to see that the outage probability decreases with the signal-to-noise ratio increasing. And we can conclude from Fig.4 that the outage probability performance of PLC

V-MIMO cooperation system is superior to the direct no cooperation system. This is because the space diversity gain in the power line network is utilized by our proposed method.

Summary

This paper proposes a new PLC V-MIMO cooperation system based on the integration of PLC and wireless communication. The wireless interface is emerged with the conventional PLC modems. The nearby PLC shares their information via wireless link to constitute the V-MIMO module. The simulation results show that the link reliability and total system capacity can be significantly increased by the proposed virtual MIMO scheme.

ACKNOWLEDGMENT

This work is supported by China Electric Power Research Institute, Chong Qing University of Posts and Telecommunications, NSFC 61201206, cstc2012jjA40045, China Postdoctoral Science Foundation funded project, Chong Qing Postdoctoral financial support Rc201314, Xm201322.

References

[1] N. Pavlidou, A. J. Han Vinck, “Power line communications: state of the art and future trends,” IEEE Comm. Magazine, vol. 41, no. 4, pp. 34–40, 2003.

[2] Yiqing Zhou; Tung-Sang Ng, "Performance analysis on MIMO-OFCDM systems with multi-code transmission," *Wireless Communications, IEEE Transactions on* , vol.8, no.9, pp.4426,4433, September 2009.

[3] Lizhong Zheng; Tse, D.N.C., "Diversity and multiplexing: a fundamental tradeoff in multiple-antenna channels," *Information Theory, IEEE Transactions on* , vol.49, no.5, pp.1073,1096, May 2003.

[4] NgCTK, Jindal N, Goldsmith A J, et al. Capacity gain from two-transmitter and two-receiver cooperation[J]. *Information Theory, IEEE Transactions on*, 2007, 53(10): 3822-3827.

[5] Bin Cao; Gang Feng; Yun Li; Chonggang Wang, "Cooperative Media Access Control With Optimal Relay Selection in Error-Prone Wireless Networks," *Vehicular Technology, IEEE Transactions on* , vol.63, no.1, pp.252,265, Jan. 2014.

[6] Lampe, L.; Vinck, A.J.H., "Cooperative multihop power line communications," *Power Line Communications and Its Applications (ISPLC), 2012 16th IEEE International Symposium on* , vol., no., pp.1,6, 27-30 March 2012.

[7] Nikfar, B.; Vinck, A.J.H., "Combining techniques performance analysis in spatially correlated MIMO-PLC systems," *Power Line Communications and Its Applications (ISPLC), 2013 17th IEEE International Symposium on* , vol., no., pp.1,6, 24-27 March 2013.

[8] Nguyen, D.T.; Nguyen, Q.T.; Trang Cong Chung, "Outage probability analysis of cooperative diversity DF relaying under rayleigh fading," *Advanced Technologies for Communications (ATC), 2011 International Conference on* , vol., no., pp.116,120, 2-4 Aug. 2011.

Advanced Materials Research Vols. 986-987 (2014) pp 2091-2094

doi:10.4028/www.scientific.net/AMR.986-987.2091

A Novel Method of Requirement Analysis for Power Communication Access Network

Bao Feng[1, a], Yi-lei Lin[2], Yang Li[1], Chang-qing Zhong[3], Kai Liang[3]

[1]State Grid Electric Power Research Institute, Nanjing, China

[2]State Grid Shanghai Municipal Electric Power Company Information & Communication Company, Shanghai, China

[3]State Grid Anshan Electric Power Supply Company, Anshan, China

[a]fengbao@sgepri.sgcc.com.cn

Keywords: smart grid, service driven, multi-service modeling, requirement analysis

Abstract. With the development of smart grid technology, more and more intelligent devices and applications are accessed into the electric power system, which put forward higher requirements on network communication and monitoring. Power distribution and electricity utilization network directly facing the ultimate power users, is the embodiment of the smart grid in customer aspect. Flexible, efficient and reliable communication network will greatly improve the user experience. The network is commonly referred to as power communication access network. In order to improve the performance of service bearing network, a novel service driven modeling method for requirement analysis is proposed. Furthermore, the paper offers some recommendations for network design.

Introduction

A smart grid is characterized by the bidirectional connection of electricity and information flows to create an automated, widely distributed delivery network [1]. More details than literature [2], the electric power system of China is composed of six operational sectors: generation, transmission, distribution, utilization, scheduling, and transforming. As the basic intercommunication channels between them, power communication network is an effective information carrier of smart grid, which can offer efficient utilization and rational dispatching of electric power resource for customers. Power communication network mainly consists of four parts: the backbone transmission network, service network, support network, and terminal access network [3]. Due to directly facing the ultimate users, design of communication and monitoring network in power distribution and electricity utilization grid will play a vital role in customer experience improvement.

Requirement analysis is the premise and foundation of network planning and design. Traditional requirement analysis method cannot well adapt the power communication network. Firstly, the current method mainly focuses on the analysis of bandwidth [4]. But we must pay more attention to real-time, reliability, security in the electric power system [5]. Then, the current method only considers for a single service. However, we should consider how to guarantee the transmission performance of all kinds of information in a multi-service environment. Moreover, the current method cares more on the traditional communication services. However, the development trend of the smart grid is the integration of information and communication [6].

In order to improve the reliability and validity, a novel method of requirement analysis for power communication access network is proposed. Firstly, we make full analysis of communication service from multiple angles. Then, service model is constructed at three levels including device level, link level, and network level. On this basis, requirement analysis is present based on the service driven modeling method. Last but not the least, we proposed some recommendations for network planning and design, which will provide references for the future network construction.

Communication service analysis

Different from the public telecommunication network, power communication access network is a private network only used for electric power system. It has higher requirement on real-time, security, reliability and so on. Based on different requirements, the current power communications access network is generally built along with power distribution and electricity utilization system, which belongs to different departments. The corresponding communication network is also independent with each other. Therefore, the communication services that we will discuss in the following mainly consist of two categories: power distribution service and electricity utilization service. Condition monitoring of transmission lines and mobile emergency service should also be taken into account.

Power distribution services are composed of distribution automation service, power quality monitoring service (medium voltage side), distributed energy sources access service (≥220kW), distribution substation video surveillance service and so on. Electricity utilization services are composed of power user electric energy data acquire service, power quality monitoring service (low voltage side), distributed energy sources service (＜220kW), electric vehicle charging service, intelligent community service and so on.

For special application environment and requirements, services of power communication access network have many characteristics. Firstly, coexist of intermittent and emergency services. Normally, terminal information will return the master station through communication channel only at a regular period. But once there is a sudden event, it must be transported and processed as soon as possible that will need higher bandwidth and more stable communication channel. Secondly, coexist of real-time and non-real-time services. The intermittent services are non-real-time, while the emergency and control services are real-time. Thirdly, coexist of heavy load and light load. The non-real-time services generally more in the network and they are heavy load, while the real-time is light load. Therefore, we must make full analysis on multi-service before requirement analysis.

Service driven modeling method

The network topology

The most typical component of power communication access network is distribution automation system and power user electric energy data acquire system. Distribution automation system is mainly composed of master station, slave station (optional), remote terminal unit and communication network. From logic angle, power user electric energy data acquire system can be divided into three layers: the main layer, communication channel layer, and data acquire device layer. The architecture and information flow of them are respectively shown in Fig. 1 and Fig. 2.

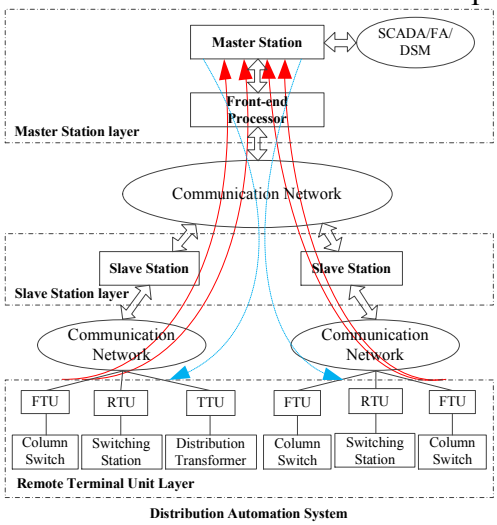

Fig. 1 Architecture and information flow of distribution automation system

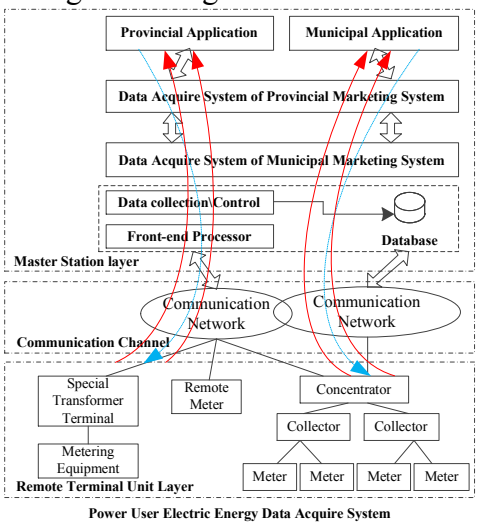

Fig. 2 Architecture and information flow of power user electric energy data acquire system

Multi-service model.

There are three common service modeling methods including on-site measurement, mathematical analysis, and emulator analysis. But each of them has its own shortcomings. As a combination, service driven modeling method is proposed from three levels: device level, link level and network level, which corresponds to service information source model, service transmission model and service network model.

Service information source model mainly focus on the generating rule of source data packets. From service type perspective, it mainly concludes voice, video, data and other service. From the time view, it can be divided into periodic stream (Cycle model), random stream (Poisson model [7]) and busty data stream (ON/OFF model [8]). Major communication services of distribution automation system are tele-indication, tele-metering, tele-control and tele-adjust. Function of tele-indication mainly obtain status information, tele-metering mainly obtain metrical information, while control information is obtained tele-control and tele-adjust fuctions. There are also some other informations. Both of status information and metrical information have a certain transmission cycle (1-5s or longer), but the package size is very small (the former 1-3bit, the latter 2-6 bit). The control information always presents as a burst message with small size (1-3bit). Transmission cycle of the other services is very long, which have the same characteristics of the above four kinds. The service information source model of power user electric energy data acquire system is ditto.

Service transmission model mainly focus on service network characteristics of transmission and information interaction. Corresponding to different physical scene, there are three different data flow including point to point (P2P), point to multipoint (P2MP), multi point to point (MP2P). As shown in Fig. 1 and Fig. 2, data flow of distribution automation system and power user electric energy data acquire system falls into the same category, the MP2P upstream is in dominant. The control message is P2MP flow in the form of broadcast and multicast.

Service network model is built based on simultaneously running and aggregation of multi-service, which mainly focus on network performance, network security, and OAM. Overlay of multi-service, the data flow still shows cyclical nature. Under normal circumstances, the data flow is relatively stable. When there is a sudden failure, the data flow sharply rises and bandwidth requirements will instantaneous become very large. It will continue until the network is back to normal. This means, the bandwidth planning should adopt the worst value design method, i.e. the instantaneous maximum bandwidth. In the multi-service network, different QoS strategy must provide according various requirements on different users.

Requirement analysis

According to the multi-service model, we mainly focus on the communication requirements on real-time, reliability, security and etc., which are shown in Table 1. Most services are in type of data with convergence properties, require higher requirements on real-time and reliability, and use the P2MP or MP2P transmission model. Video and voice services use the P2P transmission model and have higher requirements on real-time and stable bandwidth. Security requirements demand the isolation of production control service and information management service. Physical isolation and logical isolation is two ways of power communication access network. Different service was transmitted by the different communication equipment in physical isolation, while logical isolation using logic scheme (e.g. different VPN or VLAN) but transmitted in the same physical equipment.

Recommendations for network design

During network design, we need to consider more besides service requirements, such as economy, environmental influence, scalability, maintainability, ease of use and so on. The common used communication technologies mainly can be divided into three categories: wired (e.g. xPON, industrial Ethernet, PLC), wireless (e.g. 230MHz, LTE, GPRS, 2G/3G), and the combination of them (e.g. RoF). The ultimate design must be a result of compromise.

Table 1 Requirement analysis of the power communication access network

Service Name	Type	Requirement Analysis
Power Distribution Automation	data	Data flow is not so big, but higher requirements on real-time, reliability.
Power Quality Monitoring	data	
Distributed Energy Sources Access	data	
Power User Electric Energy Data Acquire Service	data	Lower requirements on real-time, transmission rate, but require higher security, reliability. Data flow is very large.
Electric Vehicle Charging	data	
Condition Monitoring of Transmission Lines	data / video	Generally through public network.
Distribution Substation Video Surveillance	data / video	Higher requirements on real-time and stable bandwidth.
Electricity Material Management	data	Lower requirements on real-time and transmission rate, but require higher security. Data flow is relatively large.
Intelligent Services Hall	data / voice / video	Generally through public network.
User Interactive	data / voice	
Demand Side Management	data	
Value-added Services of Marketing	data	
Fault Repair Management	data	Higher requirements on mobility and interactive.
Emergency Command	data / voice	

Summary

In this paper, a full analysis of the communication service is first made from multiple angles. Then, multi-service model is proposed base on the architecture and information flow of distribution automation system and power user electric energy data acquire system. On this basis, service driven modeling method is used to finish requirement analysis of power communication access network. For the novel method only considering the service requirements, we give some recommendations at last to provide references for the future network planning, design and construction.

References

[1] Y. Yan, Y. Qian, H. Sharif, and D. Tipper: IEEE Communications Surveys & Tutorials, Vol. 15 (2013) No. 1, p .5

[2] C.H. Lo, N. Ansari: IEEE Communications Surveys & Tutorials, Vol. 14 (2012) No. 3, p .799

[3] H.B. Cao: Telecommunications for Electric Power System, Vol. 32 (2011) No.223, p .1 (in Chinese)

[4] Z.Y. Zhao, H. Hu: Power System Technology, Vol. 35 (2011) No.11, p.12 (in Chinese)

[5] G.J. Gong, C. Xiong and G. Xu: Power System Protection and Control, Vol. 41 (2013) No.22, p. 19 (in Chinese)

[6] K.C Chen, P.C. Yeh, H.Y. Hsieh, and etc.: *Proceedings of the 4th International Symposium on Communications, Control and Signal Processing* (Limassol, Cyprus, March 3-5, 2010), p. 1

[7] A.C. Cameron, P.K. Trivedi: Journal of Econometrics, Vol. 46 (1990) No. 3, p. 347

[8] M.E. Crovella, L. Lipsky: *Proceedings of the 1997 Winter Simulation Conference* (Washington, USA, December 1-3, 1997), p. 31

Advanced Materials Research Vols. 986-987 (2014) pp 2095-2098

doi:10.4028/www.scientific.net/AMR.986-987.2095

A New Clustering Routing Algorithm of Wireless Sensor Network

Chen Li-Qiang

ChengDu Neusoft University, ChengDu, China

cheng_lisoft@163.com

Keywords: Wireless Sensor Network; Cluster; Energy.

Abstract. In wireless sensor network, node's energy is limited. The energy consumption of transmission a bit is larger than that of handle a bit. If it adopt effective routing algorithm, it can greatly improve the energy efficiency of wireless sensor network. In order to improve the energy efficiency of wireless sensor network in the large area, we propose a clustering routing algorithm based on energy, the algorithm realize the multi-hops communication between cluster heads by dividing the WSN area into concentric rings, and reduce the size of radius of the clusters gradually when the nodes' energy is decreasing slowly. The results of simulation show that the algorithm can effectively prolong the network lifetime.

Introduction

Wireless sensor network has some unique features, such as its network scale is larger, node distribution is dense, and node's energy is limited, etc. Experiments show that the energy used to transmission a bit is larger than the energy used to handle a bit. So if adopt effective routing algorithm, it can greatly improve the energy efficiency of wireless sensor network [1].

In the study of wireless network routing protocols, it can mainly divided into the plane routing and cluster routing [2]. In the plane routing protocols, all nodes are in the equal status, and have the same function. In the large network, the cost of finding routing and maintenance routing is very big, the expansibility is bad. The routing protocol based on clusters divided nodes into different cluster, and assign different function to the corresponding node, which helps to reduce the number of nodes in routing computation, so as to effectively reduce redundant flood. Through clustering, it can limit the changing of topology in the local scope, and reduce the impact of the routing protocol. The function of member nodes is simpler, and it is unnecessary to maintenance complex routing information, so the traffic is reduced; Cluster topology structure is easy for management, which is helpful for the application of distributed algorithm, and is suitable for large-scale network.

Related work

In clustering algorithm [3-5], the nodes in cluster send the data to cluster head; the cluster head assemble the data. The cluster head in the area of K+1 ring send the assembled data to its next hop cluster head, the cluster head in the K ring forwards it to the cluster head in the K-1 ring again, and so on, data arrive to sink node finally. Because the correlation of data from different clusters is small, the assembling efficiency is not high, so the cluster head doesn't assemble the forwarding data packet from the cluster head in the front hop, and just forward to its next hop. In such clustering multi-hop network, the forwarding load of cluster head in the ring near to the sink node is larger; it is easy to exhaust energy and death, which is known as the hot spot problem of wireless sensor network.

In order to overcome this problem, Reference[3] propose the EEUC algorithm, it first determine a threshold, each node randomly determine whether it can become the fake cluster head according to this threshold， the node that became the fake cluster head calculate the distance to sink according to the energy of received Sink signal, and form the competition region with different radius. Through the competition of the fake cluster head in the competition region, the fake cluster head with largest energy become the cluster head.

According to the residual energy and the forward cost of around cluster head, the cluster head choose the cluster head with maximum residual energy from these two cluster head with minimum forwarding cost as its next hop node. Reference [4] propose RBMC algorithm, it build the clusters with different size in different rings by control the cluster head election rate in different rings, so as to balance the energy consumption of cluster head between different rings. That is make the ring which is nearer to sink form the smaller cluster, make the ring which is far to Sink form the bigger cluster. Above reference well overcome the "hot spots" problem, but there still exist a problem, as time goes on, the node far from Sink may form hot spots. According to these problem of above algorithm, we put forward CLRE (Clustering Routing algorithm based on Changing Energy) algorithm.

Implementation of algorithm

Suppose N nodes are distributed in circular area with radius R, node's location is known and each node has an ID number, node's energy can be same or different, Sink node is located in the central region. In order to facilitate building the multi-hop path and analysis of related parameters, the whole area is divided into *S* concentric rings area, the center of ring is *Sink*, the interval between circles is *R*. According to the wireless communication theory, in the energy attenuation model [6], we get formula (1) :

$$E_{tr}(k,d) = E_{elec}(k) + E_{amp}(k,d) = \begin{cases} kE_{elec} + k\varepsilon \times d^2, d \le d_0 \\ kE_{elec} + k\varepsilon \times d^4, d > d_0 \end{cases} \quad (1)$$

E_{elec} is the energy used for sending and receiving circuit, E_{amp} is the energy used for signal amplifier, d is the distance between the sending and receiving party, k, d_0 are constant. According to the formula (1), once the communication distance is larger than d_0, the energy consumption is raised sharply. In order to guarantee less energy consumption, and there have enough nodes in each layer, R takes d_0, so it can make the communication distance between nodes in the same rings and adjacent rings is not larger than the critical distance d_0.

In the layered process, Sink node firstly send LAYER information to all nodes in the network, each node determine its distance to the base-station according to the signal strength of LAYER message, which use the free space attenuation model: $P_{rx}(d) = P_{tx} \times [\varepsilon / d^2]$ (2)

P_{tx} is send power of Sink node, P_{rx} is the power of received signal, d is the sending distance, ε is attenuation coefficient, which is usually set to constants, so the distance between sensor nodes to base station can be calculated by formula $d = r/\sqrt{P_{rx}}$ (3). r is constant, if $k \times d_0/2 < d < (k+1) \times d_0/2$, then node mark the ID of its layer as k.

The election process of cluster head in CLRE algorithm process can use the cluster head elected model proposed in the LEACH algorithm, the nodes in each ring make cluster head election alone with respective probability. The cluster head election threshold of different rings is as

$$T_{k,j}(s) = \frac{m_k}{N_k - m_k \times (r_k \bmod (N_k / m_k)}, \ s \in G_k, \quad (4)$$

Subscript k is the k ring in the area; the subscript j is the j node in the k ring. r_k is the current total number of round of cluster head election in the k ring nodes. N_k is the total number of nodes in the k ring; m_k is the expected number of cluster head in the k ring. G_k is the node set which has not been as the cluster head node in all rounds before its cluster head cycle.

The characteristic of algorithm is to control the probability of cluster head in each ring by adjusting the probability of cluster head threshold. As time goes on, all node's energy in the area would be reduced gradually, if each cluster still keep its original size of radius to assemble and forward data, then parts of area could not communicated finally. In the algorithm, increase the probability of cluster head threshold as time goes on, so the number of cluster head in each ring would increase, the corresponding each cluster's radius would be reduced, so although energy is reduced, but each cluster can still maintain normal operation, it can prolong the lifetime of wireless network more effectively.

The implementation steps of the algorithm CLRE is as follows:

(1) Sink node calculate the optimal cluster head election probability T of each ring according to the formula (4) to (6), it would broadcast election probability T in the network.

(2) All nodes in network firstly determine their own rings according to the formula (3), and find the cluster head election probability of its ring.

(3) Each node generate a random by evenly distribution, and compare it with the cluster head election probability in its ring to determine if it would be as the cluster head in the current round.

(4) The elected cluster head notice its cluster head message with radius t d_0, the message include the ID of cluster head and its position.

(5) The non cluster head node choose its nearest cluster head to join according the received cluster head message, it send joining message to the cluster head, the message include node's ID. The K+1 ring cluster head choose the nearest cluster head as the next hop according to the received notice message from the K ring cluster head, and forward the request message of next hop, which include its own ID and the numbers of its ring.

(6) The nodes or cluster head that haven't received any notice message broadcast messages with radius $3/2d_0$, the message contains its own ID number and the information whether it is as cluster head. The cluster head that received the message firstly judge whether the node is cluster head, if it is, then determine whether its layer is above the layer of the cluster head, if it is, then send confirm information to next hop; Otherwise ignore this message. If the node is not as the cluster head, and the node and cluster head is in the same layer, then it send cluster head message, the message include the ID of cluster head and P_{tx}. After the node received the message, according to the formula (3), it choose the cluster head with the minimum d and send joining message to it, the message contains the ID Number of node.

(7) The nodes of each ring make cluster head rotation in each ts, set the parameter m_k in cluster head election probability as $s_{change\_r}m_k$ in each T_s (T=kt, k=2,3,…), the circulation is from (3) to (7).

Experiment

We use NS2 and Matlab as simulation experiment platform. The key of simulation is to compare the lifetime of different algorithms. Table 2 is the simulation results, the lifetime use the number of data collection round as unit, the parameter setting is shown in table 1. Common node's initial energy is 0.5J. Senior node's initial energy is 1J. The proportion of senior node is 10%(heterogeneous) or no (isomorphism), common node and senior node is random uniform distributed in the area.

Table.1 Simulation Parameter

Parameter name	threshold	bandwidth	E_{elec}	d_0	t	T
Parameter Value	1nW	1×10^6Mb/s	50×10^{-9}J/b	87m	0.4s	100s

Table.2 Lifetime in Simulation Scene

Simulation scene		EEUC	LEACH	SEP	RBMC	CLRE
Node's number is 700, radius is 200m	isomorphism	521	474	471	794	824
	heterogeneous	559	490	531	843	864
Node's number is 2000, radius is 250m	isomorphism	478	255	280	750	780
	heterogeneous	529	257	320	762	791
Node's number is 7000, radius is 600m	isomorphism	388	7	7	521	687
	heterogeneous	447	7	8	538	686

When the number of node is 400, radius is 200m, number of CLRE ring is 2, and Figure 1 shows relationship between coefficient schange_r and lifetime. From figure 1, we can see the lifetime of network appeared inflection point when s_{change_r} is in the scope of 1.3 to 1.4, then the lifetime changes smaller, therefore, in this paper s_{change_r} is 1.35. From table 2, we can conclude that when the nodes are

dense, network area is bigger, the energy consumption of data transmission by LEACH algorithm and SEP algorithm with single hop way is bigger, which reduce the lifetime of the network, compared with the multi-hop algorithm, their performance is bad, especially when the region is larger. The CLRE can dynamic narrow the radius of cluster according to energy, which can improve the efficiency of energy utilization effectively

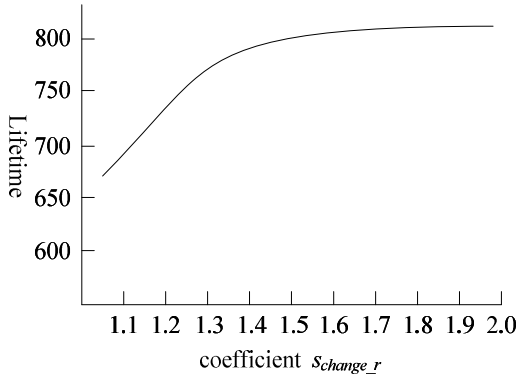

Fig.1 Relationship between coefficient s_{change_r} and lifetime

Summary

This paper proposes the CLRE algorithm based on analyzing the existing clustering routing algorithm. It uses the division ring mode to achieve the multi-hop routing in sensor network. By dynamic adjust the number of cluster head in each ring, it narrow the radius of cluster head. The algorithm is better to overcome the problem that multiple "hot spots" could be generated with the gradually reducing of energy as time went on. CLRE can adapt to the case of energy isomorphism and energy heterogeneous, and has more extensive applicability. The simulation shows that in the large area, the lifetime of the algorithm is longer than other algorithms.

References

[1] Pottie G J，Kaiser W J. Wireless integrated network sensors, Communications of the ACM, Vol. 43(5), 2008, p.51-58.

[2] Mhatre V, Rosenberg C, Kofman D, et al. Design of surveillance sensor grids with a lifetime constraint, Proc. of European Workshop Wireless Sensor Networks, Berlin, Vol.4, 2007, p.51-58.

[3] Li C F, Ye M, Chen G H, et al. An energy-efficient unequal clustering mechanism for wireless sensor network, Proceeding of IEEE International Conference on Mobile Ad hoc and Sensor System, Washington, DC, USA, Vol.3, 2011, p.483-490..

[4] Mhatre V, Rosenberg C, Kofman D, et al. A minimum cost heterogeneous sensor network with a lifetime constraint, IEEE Transactions on Mobile Computing, Vol.4(1), 2012, p.4-15..

[5] Soro S, Heinzelman W B. Prolonging the lifetime of wireless sensor networks via unequal clustering, Proceedings of the 19th IEEE International Parallel and Distributed Processing Symposium, Denver, Colorado, USA, Vol.11(3), 2010, p.167-256.

[6] Heinzelman WR. An application-specific protocol architecture for wireless micro-sensor networks, IEEE Trans. on Wireless Communications, Vol.1(4), 2012, p.660-670.

Advanced Materials Research Vols. 986-987 (2014) pp 2099-2103

doi:10.4028/www.scientific.net/AMR.986-987.2099

Research on Broadband Channel Characteristics and Hardware Testbed for Power Line Communication System

Wang Yi[1, 2], Yang Yunchun[1], Hou Xingzhe[1], Sun Hongliang[1], Zheng Ke[1], Ye Jun[1]

[1,] Chong Qing Electric Power Research Institute，Chong Qing, China
[2,] Postdoctoral Workstation of the Chongqing Electric Power Corporation, Chong Qing, China

wangyi81@cqupt.edu.cn

Keywords: PLC; time-varying; channel measurement; channel estimation algorithm; PLC channel characteristics.

Abstract. With the decision to construct the smart grids around China, the power line communications (PLC) on the low-voltage (LV) distribution networks have become one of the potential technologies to commute the information between the end users and the power provider. Comprehensive and well-founded knowledge of the LV power line channel is the foundation to establish realistic modeling of the channel characteristics. The growing power line communication (PLC) technology is providing new potential for emerging applications such as G3 and Prime. In this paper, we have proposed a OFDM based channel sounding test bed to measure PLC channel within frequency band 100 kHz-2 MHz. A souding signal for the PLC channel is designed and a time-domain measurement method for the time-varying PLC propagation is presented. The experimental results of PLC channel characteristics under different scenarios are and analyzed.

I. Introduction

PLC networks have gained significant interest in recent years as an emerging generation smart grids provisioning technology due to many advantageous features. Many researchers have studied PLC networks from different perspectives, such as network capacity, connectivity, routing, resource allocation, scheduling, etc. Due to the complexity of characterizing PLC channels in details, many simplified PLC channel models have been widely used. Measurement and characterization of the evaluation of different transmission systems for application in PLC local area networks have also become increasingly popular in recent years due to extensively study the PLC channel characteristics. The performance of PLC systems is extremely dependent upon the propagation channel behavior, which is random in nature and very difficult to analyze. One of the key aspects that need to be addressed is a linear time-varying.

However, recently, some studies have been done about the PLC channel measurement and analysis. Traditional measurements and models for this channel assume a linear time-invariant (LTI) nature in which changes in the response occur only as a result of the connection or disconnection of electrical appliances to the grid, which represent long-term variations. The PLC channel slow-time variation is discussed and a measurement system designed according to it, with signal processing algorithms able to extract cyclic properties, is described. Some representative measurement results of actual channels are also presented [1]. Also parameters of multipaths are highly changed with various topologies and the loads of the power-lines. For these reasons, channel measurement and analysis have been one of the very important issues since PLC systems starting to be developed, and the various researches have been accomplished [2]. It focused on the recently proposed PLC solution for narrow-band communication by the Spanish electric utility Iberdrola: PRIME [3]. This contribution aims at discussing a channel estimation methodology that is constituted by a sounding technique for channel estimation, a time synchronization technique, and a measurement setup [4-6]. This work presents a PLC channel model for the broad-band characterization of power lines in presence of time variation of the loads, the model is characterized

by taking into account both measured and geometrical channel characteristics and can easily be used to take into account also the presence of noise [7,8].

In this paper, this methodology allow to measure linear time invariant, time variant, and periodically time variant PLC channels if the clock offset between the transmitter and receiver devices of the measurement setup is irrelevant. We apply the procedure to a set of measured channels in the band within 100 kHz-2 MHz and carry out a measurement study of the channel with a linear time-varying based on a measurement platform. To facilitate the measurement, a time-domain measurement method for the PLC channel is presented. Additionally, a test signal for the PLC channel is designed, a channel estimation algorithm that is constituted by a sounding technique for channel estimation, a time synchronization technique.

In addition, the remainder of this paper is organized as follows. Section II the PLC channel characteristics are introduced. Section III measurement system and a channel estimation algorithm is introduced. In section IV, we introduce measurement description and analysis and finally we conclude this paper in Section V.

II. PLC Channel Characteristics

The PLC signal transmission characteristics of LV distribution networks are so complicated that the different frequency bands and the different LV distribution networks usually exhibit different properties. Studies have shown that low-voltage power line channel environment is very harsh that has the following characteristics: great signal attenuation, strong noise, strong variability and so on. In addition, the large number of loads with strong randomness in the low voltage distribution network may cause the input impedance mismatching, which finally cause the frequency selective fading.

The multipath phenomenon lies in the heart of PLC and leads to the reception of multiple replicas of the transmit signal at the receiver through various paths.

Based on extensive measurements, frequency-distance dependent attenuation in LV PLC networks is defined as [9]:

$$A(f,d) = e^{-(a_0 + a_1 f^k)\cdot d} \tag{1}$$

Where d and f correspond to the distance covered and frequency of the signal, respectively. k , a_0 and a_1 are all cable dependent parameters and are mostly extracted by empirical measurements.

A complete multipath characterization of the PLC channel can be given by its channel frequency response (CFR) as follows:

$$H(f) = \sum_{i=0}^{N} g_i A(f,d_i) \mathrm{e}^{-j2\pi f \tau_i} \tag{2}$$

The losses of cables cause an attenuation $A(f,d_i)$ increasing with length and frequency. i is the number of path, where the path with the shortest delay has the index $i=1$. d_i is the length of path i, τ_i is delay of path i. Signal propagation in complicated networks with large number of branches can be partitioned into appropriate paths in a similar way.

Finally, as the PLC channel is time variant, a measurement system and a complete estimation methodology developed for understanding the behavior of the power line as a medium to provide data communication should be able to provide information about all the possible channel behavior.

III. Measurement System

The main concept of PLC channel measurement techniques is to probe the channel with a suitable test signal, build a measurement platform and propose a complete estimation algorithm.

The OFDM signal is generated by performing IFFT on the complex-valued signal points that are produced by differentially encoded phase modulation and which are allocated to individual sub-carriers. An OFDM system with QPSK modulation schemes is selected. The number of carriers that can be used is selected to be 128, the number of Cyclic Prefix (CP) is 32, resulting in an IFFT size of 128. The length of cyclic prefix is chosen so that a channel group delay will not cause successive OFDM Symbols or adjacent sub-carriers to interfere. Those results in a frequency spacing between the OFDM carriers equal to $26.32\,KHz$ * (Fs / N), where Fs is the sampling frequency and N is the IFFT size.

In this technique, measuring the characteristics of the channel is conducted using a time-domain measurement system which is most suitable for PLC measurements as shown in Fig.1.The PLC channel measurement system consists of measurement devices and control software. The main components of measurement devices are a signal generator which is used to generate and transmit standard or arbitrary signal; an Agilent Vector signal analyzer (VSA) PIX, a high precision equipment, which can capture the real time sequence and accomplish the measurement of complex channel frequency response; the couplers connect the signal generator and power line, VSA and power line, which can filter out the 50Hz frequency current in the power line network. All of these features make VSA suitable for PLC channel measurement. For the sake of remotely and automatically controlling the VSA as well as communicating with it, we develop system control software based on the Agilent 89600B VSA software Labviewb. The bandwidth centered around the frequency of interest is scanned by the Agilent 89600B VSA software. For each frequency step a known signal is transmitted and detailed information about the PLC channel characteristics such as the frequency spectrum, magnitude and attenuation of the received signal are obtained.

The IFFT of the test signal is employed to obtain the time-domain digital I/Q data which is downloaded to the R&S ARB Toolbox PLUS software to make it into waveform files. Then we download the waveform files to the VSG which generates the analog baseband I/Q signal and outputs to the LV power line network. We can observe the frequency spectrum, error vector magnitude (EVM) magnitude, attenuation and so on. The VSA is used to capture the real time sequence and accomplish the measurement of complex channel frequency response. In addition, the receive sequence which is captured by the VSA is imported to MATLAB to do signal processing.

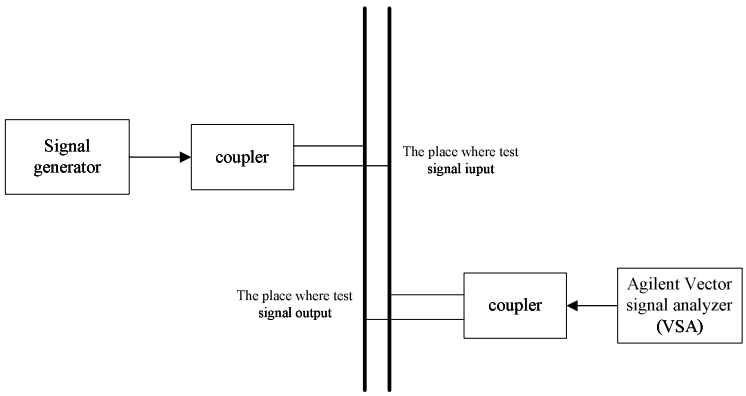

Fig.1 The PLC channel measurement platform

IV. PLC Channel Measurement Results

We now describe the results obtained with sequences experimentally measured. It is worth mentioning that successful results are also obtained when applying the procedure to synthetic data simulating the PLC channel. Furthermore, some measurement results are presented in order to validate the performance of the PLC measurement of the PLC measurement system with different

environment situations. Bcause of limited space, this paper will not list all measurement results. Instead, only some representative results are presented in detail.

A.The PLC Channel Characteristics of Idal Measurement Environment

As the anechoic chamber can shield external interference, in the measurement we select the anechoic chamber as the ideal measurement environment. Furthermore, the communication distance, power line network structure and access to the load can be artificially controlled in the anechoic chamber. The transmitted signal is initially generated offline and loaded into an arbitrary waveform generator equipment with transmission power 20dBm. The normalized channel estimate spectrum of the ideal measurement environment can be seen in Fig.2.

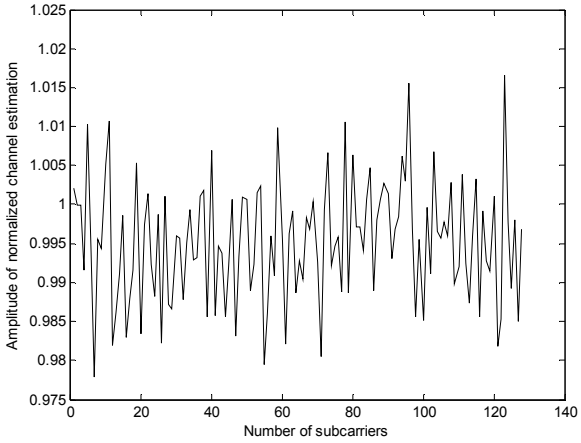

Fig.2 The normalized channel estimation spectrum to the ideal channel

As it can be noticed, just an instantaneous estimation for the ideal channel is plotted. In the ideal environment, the maximum error of the normalized channel estimate is 0.018, which is very ideal. So, the signal processing algorithm proposed in this paper could accurately estimate the channel characteristics of the low-voltage power line network.

B. The PLC Channel Characteristics of The Laboratory

Through extensive measurement, the PLC channel characteristic under actual low voltage power network is shown in Fig.3.

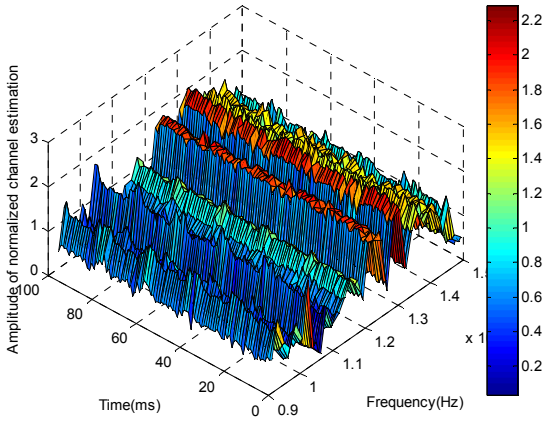

Fig.3 The normalized channel estimation spectrum to the channel under actual low voltage power network

In the measurement, the laboratory channel is measured once every minute, and repeated 10 times.The transmission power is 20dBm. At 1.045MHz, 1.25MHz, 1.32MHz frequency, the values of the normalized channel estimate are larger, which indicates that the channel characteristic is poorer at these frequencies.

V. Conclusion

In this paper, a test signal for the PLC channel is designed and a time-domain measurement method for the time-varying PLC propagation is presented. With this regards, this contribution aims to discuss a channel estimation algorithm that is constituted by a sounding technique for channel estimation, a time synchronization technique, and a measurement setup. Through extensive measurement, it is proved that the time-domain measurement method and the signal processing algorithm in this paper could be used to measure the PLC time-varying channel.

ACKNOWLEDGMENT

This work is supported by China Electric Power Research Institute, Chong Qing University of Posts and Telecommunications, NSFC 61201206, cstc2012jjA40045, China Postdoctoral Science Foundation funded project, Chong Qing Postdoctoral financial support Rc201314, Xm201322.

References

[1]Francisco Javier Cañete Corripio, José Antonio Cortés Arrabal, Luis Díez del Río, and José Tomás Entrambasaguas Muñoz. “Analysis of the Cyclic Short-Term Variation of Indoor Power Line Channels.” IEEE Journal on selected areas in communications, Vol. 24, No. 7, July 2006, pp.1327-1338.

[2]D.Anastasiadou and T. Antonakopoulos, "Multipath Characterization of Indoor Power-Line Networks," IEEE Trans. On Power Delivery, Vol.20, No. 1, Jan.2005, pp.90-99.

[3]Javier Matanza Domingo, Sadot Alexandres, Carlos Rodriguez Morcillo,” PRIME Performance in Power Line Communication Channel.“ 2011 IEEE International Symposium on Power Line Communications and Its Applications (ISPLC). 3-6 April 2011. pp.159-164.

[4]Wenqing Liu, Martin Sigle, Klaus Dostert. “Channel Phase Distortion and Its Influence on PLC Systems.”2012 IEEE International Symposium on Power Line Communications and Its Applications (ISPLC). 27-30 March 2012, pp. 268-273.

[5]W. Liu, M. Sigle and K. Dostert, “Advanced Emulation of Channel Transfer Functions for Performance Evaluation of Power line Modems,” in IEEE Int. Symp. Power Line Commun. and Applicat., Udine, Italy, 2011, pp. 446-451.

[6]Thiago Rodrigues Oliveira, Weiler Alves Finamore and Moises Vidal Ribeiro. “A Sounding Methodbased on OFDM Modulation for PLC Channel Measurement.” 2013 IEEE 17th International Symposium on Power Line Communications and Its Applications (ISPLC). 24-27 March 2013, pp. 185-190.

[7]T. Oliveira, M. Pereira, C. Marques, S. Netto, and M. Ribeiro, “The characterization of hybrid PLC-wireless channels: A preliminary analyzis,” in Proc. IEEE International Symposium on Power Line Communications and Its Applications (ISPLC). 24-27 March 2013, pp. 98-102.

[8]Sami Barmada, Antonino Musolino, Marco Raugi. “Innovative Model for Time-Varying Power Line Communication Channel Response Evaluation” IEEE Journal on selected areas in communications, Vol. 24, No. 7, July 2006, pp.1317-1326.

[9]Zimmermann, M; Dostert, K. A multipath model for the powerline channel. IEEE Transactions on Communications, April 2002, 50(4): 553-559.

Advanced Materials Research Vols. 986-987 (2014) pp 2104-2107

doi:10.4028/www.scientific.net/AMR.986-987.2104

A Study on the Energy Balance Ant-Based Routing Algorithm for Wireless Sensor Network

Jing Han[1], Dongya Chen[*2, 3]

[1.] School of Physics and Electronic Information Engineering, Dezhou University, Dezhou 253023, China

[2.] Department of Physics and Information Engineering, Jining University, Qufu 273155, China

[3.] School of Information & Electrical Engineering, China University of Mining and Technology, Xuzhou 221116, China

*Correspondence should be addressed to Dongya Chen; corresponding author: chendya@126.com

Keywords: Wireless Sensor Network (WSN); energy balance; routing algorithm; ant-based

Abstract. How to make good use of the limited energy to maximize the network life span is an important problem of the wireless sensor network. The life of WSN depends on the minimum of the residual energy of its nodes. A fair energy balance routing algorithm is proposed which uses the Ant Colony Optimization Algorithm (ACO) to balance the network energy distribution and extend the network life. The proposed algorithm utilizes the dynamic adaptability and optimization capabilities of the Ant Colony to get a tread off between the shortest path and the fair energy balance. Simulation results show that the proposed algorithm is good at balancing the energy, and it effectively extends the span of the network life.

1. Introduction

Wireless Sensor Network which has very wide application prospect is a new generation of network, due to the integrated sensor and wireless network technology, having far-reaching influence for human life and production. Wireless sensor network usually has limited node energy. The number of nodes is large and cannot be added in time, so saving and balance the node energy consumption and prolonging network life time with maximum limit, is one of the primary design goals of wireless sensor network.

Based on Ant Colony Optimization routing protocol, each node can be aware of the network of the current actual situation and choose the next-hop according to pheromones probability formula by ants packet sending. It is very suitable for designing the energy load balancing routing protocol. Wireless sensor network based on ant colony algorithm is one of the hot spot of research at home and abroad by the agreement. Based on ant colony algorithm as the breakthrough point and the analysis of all kinds of ant, energy balance routing protocol based on ant colony algorithm is proposed, and the performance of this agreement by simulation and experiment is analyzed.

2. Algorithm model

2.1 The energy density function and backup strategy

To achieve the effect of energy consumption balance, this paper considers the node energy around besides considering energy node itself, so it introduces the concept of energy density of nodes.

Route maintenance usually maintains the activity of the path using the periodic flooding queries from source node to Sink node. If the routing node failure or losing efficacy on the path, it renews flooding. In a certain time to elect a new routing node, overhead is larger. This paper proposes a backup strategy based on the energy density range, only needing a small amount of information exchange and fast switching high residual energy node to replace recently.

Backup table strategy idea is as follows:

Within the scope of the routing node energy density, the backup list stores three residual energy high cost low of the backup node in the form of pile. Routing nodes begins for backup when each

node radios network initial energy information. If the radius is R in the area is elected to the routing nodes, the nodes will select three optimal residual energy of node information as backup. All nodes within the scope radioing each surplus energy after k rounds, can sort dynamic maintenance of the node energy information. When a node is detected failure occur, the rapid switch to the backup node to avoid communication interrupt network segmentation for a long time. According to the concept of energy density, the higher energy density is, the more abundant node energy distribution around is, and broadcasting limited within the circle radius is R.R should be much smaller than the node communication radius. Although it can lead to path cost is not accurate, but compared to flooding the overhead can be ignored.

2.2 Ant colony algorithm model

In the process of the balance energy consumption of routing algorithm, this paper uses ant colony algorithm in wireless sensor network. Wireless sensor network as connected weighted undirected connecting graph G (V, E) ,V is node set in wireless sensor network, E is the edge set. Initially, all kinds of the pheromone trail are at the same concentration. Set C is a constant. Ant k in the process of movement is as the next transition probability of relay, according to each path pheromone concentration decided to transfer the direction.

In order to balance the energy consumption of the nodes in the network, this paper will be able to achieve energy balance factors into consideration, stimulating factor of transition probability P in some improvements. The energy density of the nodes energy consumption than new estimates of the costs and choose nodes into stimulating factor. So the node selecting jump transition probability is also affected by energy consumption or on the basis of energy density of nodes selecting.

When the ant k finishes a journey and generates a solution, it needs to release certain pheromones through the path.

3. The simulation experiment and result analysis

In order to verify the effectiveness of energy equilibrium based on ant colony algorithm, simulation results of this paper is the network simulation software NS2. It makes the performance analysis and comparison of EBEA algorithm and LEACH agreement. Setting 100 sensor nodes random distribution in 200 m * 200 m square network within the scope, and the initial energy is 5J. Sink node is located at (100,150), the node with functions of controllable power and data fusion. In the simulation experiment, it mainly considers the sensor nodes to send, receive data and data fusion of consumed energy. The parameter selection is $p = 0.1$, $a = 1$, $b = 2$, $Q = 1$.

3.1 Network cycle life

The nodes based on the energy density make the nodes on the path to have high energy density. EBEA algorithm every time is to choose the least costly energy equilibrium path to transmit data. Each node uses dynamic backup strategy table, when some nodes energy depletion switch to the backup node to maintain a stable backbone network. This system performances significantly at the end of the network to survive death for a period of time, and greatly reduces the overhead due to frequent node death. As figure 1 shown, the network life extends by 45% in EBEA than LEACH algorithm.

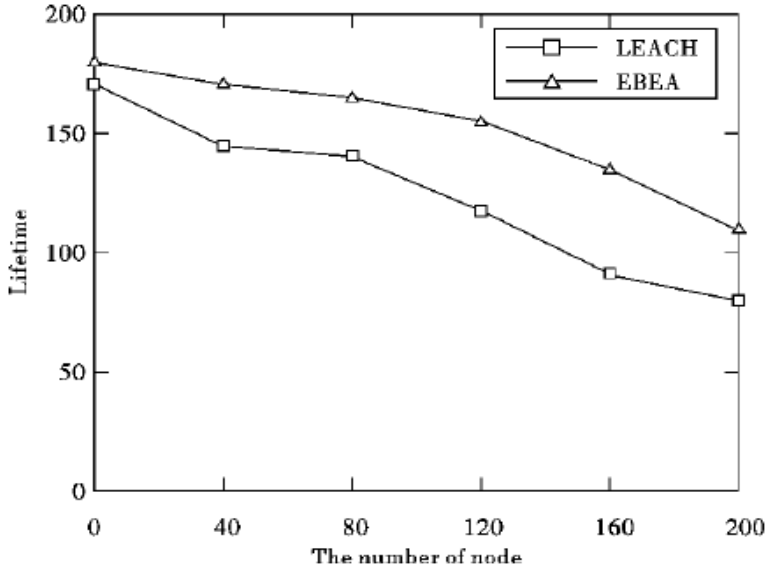

Figure.1 Network cycle life of EBEA and LEACH algorithm

3.2 The resilience of the network

As shown in figure 2, the routing node fault is examined when the resilience of the network. Some of the node failure assumption suddenly in the fifth round path, LEACH is flooding again to build path. Each routing node in the EBEA routing algorithm considering its energy density, in this range it will set up the dynamically update backup table. When node meets the fault, it quickly calls the backup table instead of failure switch to the backup node, and repairs the node failure caused by the network segmentation. Simulation results show that the EBEA algorithm dynamic using optional table strategy has strong robustness and reliability.

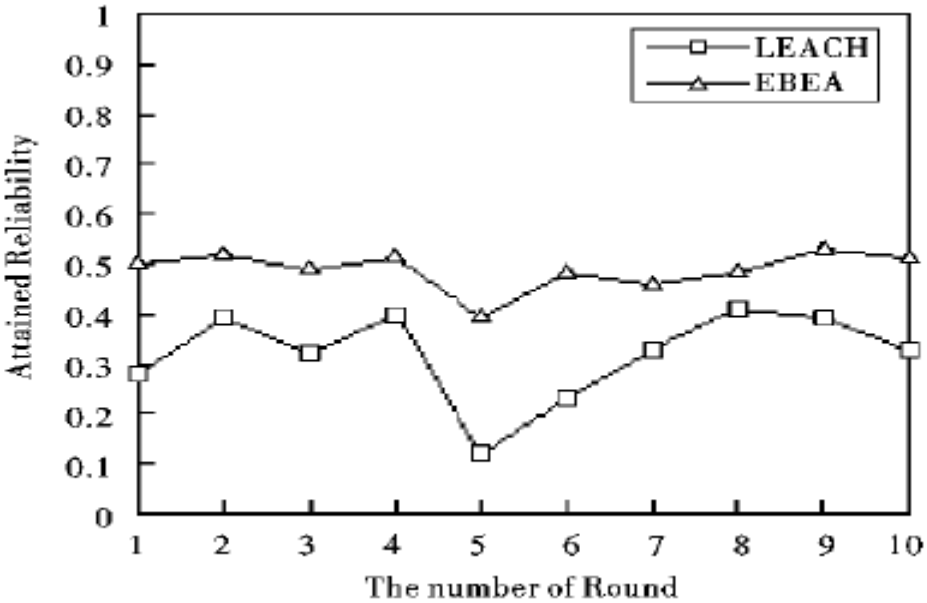

Figure 2 Resilience of a path node under sudden fault network

4. Conclusions

This paper puts forward a kind of update energy balance routing strategy of ant colony algorithm, giving the nodes of the actual energy density information to the ants, which have this information in the complex routing selecting a optimal solution of energy balance. Each node in the process of path using backup strategy, improve the sudden failure the resilience of the network. Simulation results show that the algorithm can be effectively applied to the energy equilibrium of WSN routing algorithm, verify the routing algorithm proposed in this paper having good performance in network energy balance at the same time. The network life has good robustness extending to a certain extent.

Acknowledgments

Financial support for the work is provided by the Youth Scientific Research Foundation of Jining University 2013 named “Application Research on Routing Optimization Based on Ant Colony Algorithm”(NO.2013QNKJ17)

Financial support for the work is provided by the Teaching reform research project of Jining University 2012 named “Training leading digital signal processing experiment course of practice teaching reform research”(NO.2012JX25)

References

[1]Yang J, Xu M, Zhao W．A Multi-path Routing Protocol Based on Clustering and Ant Colony Optimization for Wireless Sensor Networks[Z]．SENSORS, 2010, 10(5)：4521—4540.

[2]Laura R, Matteo B, Cgianluea．On Ant Routing Algorithms in Ad Hoc Networks with Critical Connectivity[R]．Ad Hoc Network Journal, 2008, 6(6)：827-859．

[3] Dorigo M, Birattari M, Stutzle T．Ant Colony Optimization：Artificial Ants as a Computational Intelligence Technique[J]．IEEE Computational Intelligence Magazine, 2006, 1(40)：28-39．

[4]Hussein O H, Saadawi M J, Lee M．Ant Routing Algorithm for Mobile Ad Hoc Networks (ARAMA)[J]．Phoenix, Arizona, 2004：15—17．

[5]Di Care, Ducatelle F, Gambardella L．AntHocNet：An Adaptive Nature—Inspired Algorithm for Routing in Mobile Ad Hoc Networks [M]．European Transactions on Tele-communications, 2005, 16 (5)：443—455．

Advanced Materials Research Vols. 986-987 (2014) pp 2108-2112

doi:10.4028/www.scientific.net/AMR.986-987.2108

Research on the Convergence Trend of Power Communication Network

Wen-gui Liu[1, a], Yi-lei Lin[2], Bao Feng[1], Chang-qing Zhong[3], Dan Yi[3]

[1]State Grid Electric Power Research Institute, Nanjing, China

[2]State Grid Shanghai Municipal Electric Power Company Information & Communication Company, Shanghai, China

[3]State Grid Anshan Electric Power Supply Company, Anshan, China

[a]liuwengui@sgepri.sgcc.com.cn

Keywords: smart grid; network convergence; communication technology; network architecture; transmission network; access network

Abstract. With the development of communication technology, the communication network present many characteristics, such as unified standard, flatten structure and diversified services. As a special form of communication network, power communication network has higher requirements on intelligent, stability, reliability and real-time. In order to better support smart grid, we analyzed the current communication network at first. On this basis, the converged power communication network is proposed from two aspects: communication technology and network architecture. Moreover, typical technology route and network architecture is also given in the convergence background. The conclusion is that the converged network can solve problems of the current independent network, and it is an inevitable evolution direction of the future.

Introduction

In the past few years, scale of electric power grid has got rapid development in China. Concept of smart grid was put forward for the goal of sustainable development. In order to realize effective utilization and rational dispatching of electric power resource, the study of smart grid support system is attracting more and more attention. As the core component of the system, the influence scope of communication network is throughout the full life cycle of electric power [1].

Currently, all kinds of power communication service have presented features of IP, except relay protection signal. All services will be transported on the IP-based bearing network in the nearly future [2]. That is to say, the main service type will be transformed from traditional TDM to IP. The convergence trend of communication service will be all-IP. In order to adapt this transformation, higher demands on bandwidth, capacity, real-time, and safety are proposed. To meet these demands, fiber-based communication technologies with good Ethernet bearing performance will gradually be used, such as optical transport network (OTN) and packet transport network (PTN) in the transmission layer, Ethernet passive optical network (EPON) and radio over fiber (RoF) in the access layer. The convergence trend of communication technologies will be all-optical. Similar to the architecture of public mobile communication, flatten and unified trend in power communication network became more and more clear. For example, the converged transmission network will transfer from OTN+SDH to OTN+PTN and the integration of them, which represented by P-OTN/P-OTP. The convergence trend of network architecture will be flatten and unified.

The current power communication network

Services requirements analysis

According to characteristics of the power grid, the communication services can be divided into two categories: *power production & scheduling service* and *management & information service*.

Power production & scheduling services are composed of proprietary service and production scheduling service. Proprietary service mainly includes line protection, stable & secure system,

dispatching call and etc. For high real-time, stability, and security requirements, the bearing network is private line using TDM kernel. IP-based process is ongoing. Taking into account the characteristics of the electric power system, all-IP cannot be achieved in the short term. Production scheduling service mainly include SCADA/EMS system, protection management information system, stable & secure management system, substation video surveillance system, PMU system, power quality monitoring system, cable automatic monitoring system, substation equipment online monitoring and status detection system, water scheduling automation system, electricity market technical supporting system, DMIS, lighting location system, and etc. This kind service is mainly bearing on dispatching data network, which has lower requirements on time delay, but need higher stability and security.

Management & information services are composed of management service and information service. Management service mainly includes emergency commanding communication, videophone conference system, and administrative telephone system. Information service mainly include ERP, GIS, financial management system, information supporting system, marketing management system, data disaster recovery center, and etc. Management &information services are typical IP services that bearing on the integrated data network, except the administrative telephone system. As features of strong burst and high bandwidth, the bearing network is IP-based. Even the telephone system is also on the way from circuit-switch to soft-switch.

Network architecture.

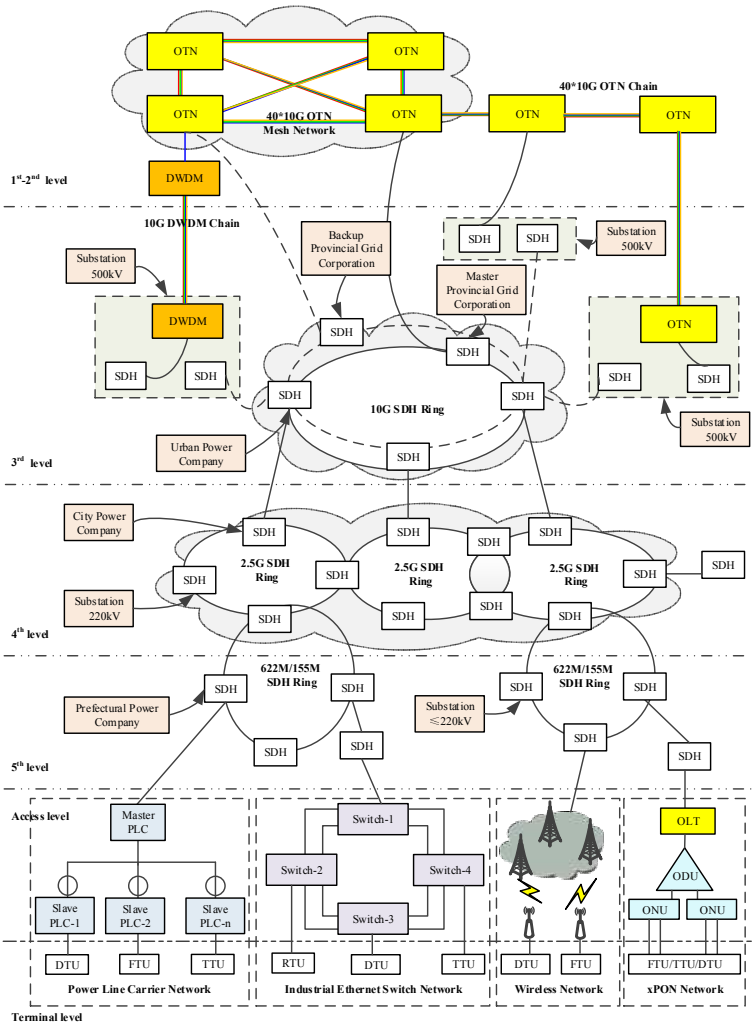

Fig. 1 Hierarchical architecture in the current power communication network

The current power communication network adopts hierarchical architecture. It can be divided into six levels, which including the first to fifth backbone transmission network and the access network. These layers are isolated with each other, and every layer can form an independent network. As shown in Fig. 1, the first and second backbone transmission networks distribute in headquarters and

the branch of state grid level. It mainly consists of 40*10G OTN mesh network, a few 10G DWDM/SDH chains, or the combination of them. Optical transform unit (OTU) is used to interconnect the DWDM with OTN. The third backbone transmission network distributes in provincial companies, urban companies and substations (≥500kV) level. It mainly consists of 10G SDH rings and 10G DWDM/SDH chains. The fourth backbone transmission network mainly consists of 2.5G SDH rings in the city power supply companies and substations (≥220kV) level. The fifth backbone transmission network is also called rural network, which mainly consists of 622M/155M SDH rings in the prefectural power company and substation (<220kV) level. PTN network (10GE/GE) is also applied in the 3rd level and below. Normally, the fifth level is contained in the fourth one. The terminal access network mainly consists of EPON/GPON, industrial Ethernet, PLC, RoF, wireless (e.g. 230M, GPRS, 3G/4G) standalone or hybrid communication network.

Problems of the current network.

Do an analysis of the current communication network, we can find several problems:

1) The transmission network

Efficiency. The main service type has transformed from traditional TDM to IP. But the current network is still TDM core with fixed bandwidth allocation strategy. It is inefficient to transport the strong burst services. *Flexibility.* The SDH/MSTP network uses single wavelength, typically 1310nm or 1550nm. So its capacity is not sufficient especially in 40G/100G network. Although this problem can be resolved with the use of point-to-point DWDM technology, but it cannot support flexible sub-wavelength dispatching. And the simple plus of DWDM and SDH is an inappropriate network architecture, which leads the increasing of construction costs and maintaining difficulty. *Economy.* From two aspects of the life cycle and expansion capability, the current SDH network has been close to saturation. The cost of IP-bearing SDH network is higher than PTN. It is an issue to follow or update the original technology.

2) The access network

Unity. According to different service requirements, construction of the current terminal access network is isolated with each other. Lacking of unified planning, repeated construction was very serious. And it has caused a lot of waste. *Compatibility.* Considering different factors, such as economic, environment and service requirements, hybrid network based on a variety of technologies are usually adopted, although problems of the interoperability and compatibility have yet to be fully addressed. At the same time, the difficulty of OAM increased remarkably. *Interactivity.* With the development of intelligent terminal technology, more and more two-way interactive services access into the smart grid, which challenges the current P2MP converged communication network.

In order to solve these problems, we need to consider from the perspective of communication technology and network architecture in both transport and access level.

The converged network from communication technology level

Overall, the smart grid communication technologies can be divided into two categories: wired and wireless [3]. Optical fiber network, power line communication network, and cable communication network are three typical types of wired technologies. And the wireless technologies contain 230M, GPRS, 3G/4G, satellite, microwave, and etc. Some converged technologies will be analyzed as follows.

OTN which combines with features of DWDM and SDH can meet requirements of massive data at high bit rates transported in long-haul network [4]. OTN network can provide wavelengths and sub-wavelength level dispatch, which corresponding to optical and electrical layer. That is to say, OTN can manage both optical and electric domain in one control plane. Furthermore, it has good Ethernet bearing performance with specialized encapsulation format and bearing particles. A combination of time division and wavelength division, OTN can be considered as a converged technology. Combined with features of IP/MPLS, Ethernet, and SDH transport network, *PTN* can natural support IP services [5]. The other kind of services also can be supported by pseudo-wire

emulation technology. Moreover, it can support the 1588v2 and synchronous Ethernet, which has higher precision than the same grade SDH. With feature of packet-based core and SDH-like OAM mechanism, PTN can be consider as a converged technology. Passive optical network technologies used in the power communication system mainly include *EPON* and *GPON*. The difference between them is the 2nd level encapsulation technology, which it is Ethernet in EPON, but GFP in GPON. EPON network is a multiservice platform, which can support integrated service access, such as data, voice, video, and etc. Besides, EPON is a P2MP network [6]. The asymmetrical uplink and downlink bandwidth perfect suitable for the centralized electric power access network services. *RoF* is a kind of technology to transmit wireless signal through optical fiber, which has advantages of fiber and wireless communication. Wireless technology is used to finish flexible access between the base station and terminals. Long-distance broadband data transmission is realized by the optical network. In the present power communication access network, the wireless and the optical network only cascade at the equipment level [7]. Deeper convergence is in continuous evolution.

With the development of smart grid, the power communication service presents features of IP, broadband, and intelligence [8]. Evolution direction of the transmission technology will be all-optical, high byte rate and ultra-long distance. The develop trend of the access technology will be all-IP, multi-services supporting, and multiple technology integration.

The converged network from network architecture level

According to different service degree and functional requirements, architecture of the converged network can be analyzed from two levels:

1) The transfer level

At present, construction of OTN network has completed in the 1st to 2nd backbone transmission level. The already existing SDH and WDM equipment will sink to a lower level, and become an access terminal of OTN network. At the same time, OTN has specially designed encapsulation format for GE / 10GE, which provides the ability to network sinking. Due to the construction of SDH network has relatively completed, in the 3rd and below the transmission level. From investment protection standpoint, it is unreasonable to substitute SDH with PTN completely. The strategy of PTN networking is to form an independent network, hybrid network with SDH, or a united network with OTN. Evolution trend of the converged transmission network is shown in Fig. 2. In long term, part ② will be replaced by part ①. The network will become flatten structure and unified technology.

2) The access level

According to different application scene, communication network in the access level mainly used to support power distribution and electricity utilization. *The power distribution communication network* is the internal network of the electric power system. The network has a high requirement on real-time, stability, and security. It adopts P2MP architectures, which contains the master station, sub-station and distribution terminal. EPON technology is very suitable for it, which OLT in the master station and sub-station, ONU in the terminal layer. If there is no optical cable routing, PLC and wireless technologies will be adopted. *The electricity utilization communication network* needs to cross the internal and external network of the electric power system. Because of massive terminal access points, wide distribution areas, strong interactive, single technique is difficult to satisfy all requirements. PLC and public wireless network are the primary terminal access technologies, 230MHz and private optical fiber network are the transmission technologies. RoF is also used in the form of “EPON + Integrated Base Station”, “BBU + Optical Fiber + RRU”. Evolution trend of the converged access network is shown in Fig. 3. In long term, it will be a unified network that no needs to distinguish power distribution and electricity utilization communication network.

Evolution trend of the power communication network presents features of all-optical and all-IP. In the transfer level, flatten structure will be adopted with all-optical transmission link, high survivability mesh network and good IP bearing performance. In the access level, unified architecture that no need to distinguish distribution and electricity utilization communication network will be adopted with all-IP services access, multiple technology integration and personalized QoS.

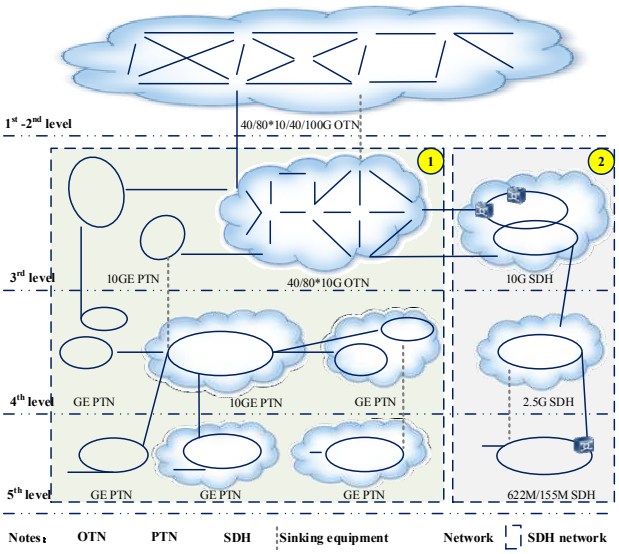

Fig. 2 Evolution of the transmission network

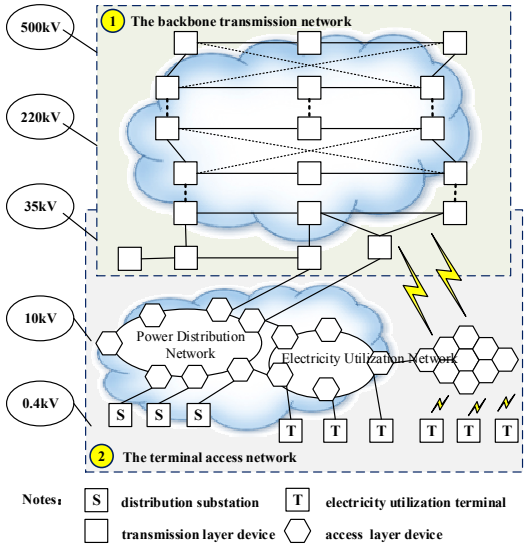

Fig. 3 Evolution of the access network

Summary

In this paper, we analyzed the convergence trend of power communication network from technology and architecture aspect. To meet the services requirements, the adopted technologies will be all-optical and all-IP. To save investment and simplify operation and maintenance, the architecture will be flatten and unified. The converged strategy can solve problems of the current network, and it will provide a reference to the construction of power communication network.

References

[1] T.T. Ma, K. Li, S.H Zhu, and etc.: Electric Power Automation Equipment, Vol.30 (2010) No. 5, P87 (In Chinese).

[2] Z.P. Wang: Telecommunications for Electric Power System, Vol. 32 (2011) No. 223, P41 (In Chinese).

[3] X. Miao, K. Zhang, S.M. Tian, and etc.: Power System Technology, Vol.33 (2009) No. 17, P8 (In Chinese).

[4] M. Nowell: *Conference on Optical Fiber Communication* (San Diego, American, March 22-26, 2009), P1.

[5] Y. Zhang, J.L. Yang and C.X. Wu: *IEEE 3rd International Conference on Communication Software and Networks* (Xi'an, China, May 27-29, 2011), P479.

[6] G. Kramer and G. Pesavento: IEEE Communications Magazine, Vol. 40 (2002) No.3, P66.

[7] Y. Cheng and C.J. Qiu: *International Symposium on Photonics and Optoelectronics* (Shanghai, China, May 21-23, 2012), P1.

[8] B. Feng, Q. Fan and Y. Li, and etc.: *International Conference on Computer Science and Electronics Engineering*, (Hangzhou, China, March 23-25), Vol.III (2012), P414.

Advanced Materials Research Vols. 986-987 (2014) pp 2113-2117

doi:10.4028/www.scientific.net/AMR.986-987.2113

Energy Saving Routing Protocol of Wireless Sensor Network By Using Particle Swarm Optimization Algorithm

Wang Run-liu[a], Yi Yun-hui[b]

School of Mathematics and Computer Science, Jiangxi Science &Technology Normal University

Nanchang, China

[a]78397475@qq.com, [b]sjxywork@163.com

Keywords: Energy Save; Routing; Wireless sensor network.

Abstract. The utilization efficiency of energy is an important performance index of designing WSN routing protocol. This paper put forward an improved energy saving routing algorithm LPSOA based on LEACH, which improves the cluster head election method of LEACH algorithm. It firstly divides the entire network into multiple child regions by using the good convergence and global optimization ability of particle swarm algorithm, and then elects the cluster head by considering the residual energy of node in the child area. The experiment results show that compared with the classical routing protocol LEACH, the protocol can more effectively balance the network load and improve the utilization of energy, prolong the network lifetime.

Introduction

Current routing protocol of WSN can be divided into plane routing protocol and clustering routing protocol [1]. The plane routing protocol is not suitable to be applied in large-scale network because it needs to maintain large routing table in the operation process. The clustering routing protocol improves the problem in a certain degree. LEACH routing protocol is the clustering routing protocol which is put forward firstly [2], such as PEGASIS, TEEN, HEED are improved on the basis of LEACH protocol in a certain degree [3, 4]. The LEACH protocol randomly elect cluster head in cycle to balance network whole energy consumption, but it also has some obvious defects at the same time, such as unreasonable distribution of cluster head, energy losing, single hop routing etc. Reference [5] improved the formation of cluster structure by synthetically considering the distance from node to the cluster head, the distance from cluster head to base station and the communication cost of cluster head energy. Reference [6] applied colony algorithm to routing choosing and selected the optimal path by the distance between nodes controlled by the loop model and the interaction of path pheromone. Reference [7] optimized the energy distribution and geographic distribution of cluster head selection by using particle swarm optimization algorithm.

Aimed to the unreasonable problem LEACH algorithm in the distribution of cluster head of uneven network energy loss resulted from the unreasonable problems, this paper proposes a LPSOA routing algorithm based on particle swarm optimization. The main idea of algorithm firstly divides the whole network area into multiple sub area by using good convergence and global optimization ability of particle swarm algorithm, and then elects the cluster head by considering the residual energy of node in the area. The results of experiment show that the algorithm can balance the network load and prolong the network life time.

Particle Swarm Optimization Algorithm

Particle swarm optimization (PSO) algorithm is a kind of evolutionary algorithm, which is origin from the researching of bird's feeding behavior. The basic idea of particle swarm optimization algorithm is to find the optimal solution through collaboration and information sharing between individuals in the group. The advantage of PSO is simple and easy to implement and it has not too

many parameters. Now it has been widely applied in various application fields, such as function optimization and so on.

PSO is initialized as a group of random particles, and then find the optimal solution through iterative. The particles update by tracking two extreme values in iteration. The optimal solution that is found by particles is called as the individual extreme value P_{id}, the optimal solution that is find by the whole population is called as the global extreme value P_{gd}. After find these two optimal values, the particle update their speed and position through formation (1) and (2).

$$V_{id} = wV_{id} + c_1 \times rand() \times (P_{id} - X_{id}) + c_2 \times rand() \times (P_{gd} - X_{id}) \quad (1)$$

$$X_{xi} = V_{id} + X_{id} \quad (2)$$

V_{id} is the speed of particle i; X_{id} is the position of particle i; $Rand(\ )$ is a random number between (0, 1); c_1 and c_2 are the learning factors, usually c_1=c_2=2, ω is the weight coefficient.

LPSOA Algorithm

The running processes of LEACH protocol is divided into two stages of cluster structure formation and stably working. In the cluster structure formation stage, all nodes are divided by clusters, each cluster randomly elect the cluster head. The election process is that each node randomly generates a number whose value is in [0, 1], if it is less than $T(n)$, then this node is elected as the cluster head. The computation formula of $T(n)$ is as follows:

$$T(n) = \begin{cases} 0, otherwise \\ \dfrac{p}{1 - p \times (r \bmod (1/p))}, n \in G \end{cases} \quad (3)$$

p is the ratio of the number of cluster head required in the network and the number of total nodes; r is current round of election; G is the node set of non-cluster head in the remained 1/p round.

In LEACH algorithm, the function of cluster head node is to collect the gathering information within the cluster nodes and fusion processing, as well as the forwarding information between clusters and routing selection, so it is very important to establish the cluster head node. When the energy loss in the network is not balanced, the communication between the nodes which is away from the cluster head nodes and the cluster head would consume more energy, which would make the energy consumption of parts of node faster and die sooner. The death nodes would reduce network average life cycle and affect the working efficiency of the entire network. So the optimization of the cluster head election process is the key to improve the algorithm.

In actual network environment, the nodes are not evenly distributed throughout the region. The results of random cluster head election algorithm may make the difference of size of each cluster is very larger. This means that the cluster head in the node dense regions should take more data processing and forwarding task, the energy consumption of cluster head is larger than that of the sparse node area, so it is possible to death early for running out of energy. For reasons of balanced load, we want to divide the whole area into several clusters with equal scale; the number of nodes in each cluster is equal.

The improved clustering algorithm based on particle swarm optimization firstly uses the particle swarm method to divide the whole area into several clusters with the same size; Secondly, it optimal selects the cluster head node according to node's energy information, finally, it determine the cluster head nodes, and complete the network clustering structure.

In actual network environment, the nodes are not evenly distributed in the whole region, the results of the random cluster head election algorithm may make the difference of size of each cluster size is very big. It means that the cluster head in the node dense region should take more tasks of data processing and forwarding, the energy consumption of cluster head is larger than that in the sparse node region, also it is possible to dead early for running out of energy. For reasons of balanced load, we want to divide the whole area into several clusters with same scale; the number of nodes in the cluster is equal.

The algorithm can be divided into two steps, it firstly uses PSO algorithm to divide the whole area into several clusters with same scale; secondly, it elects the appropriate node as the cluster head node according to the information of node and energy within the divided clusters.

Assume that the whole network has N sensor nodes, and plans to partition the network into M clusters, each cluster structure contained [N/M] nodes. Firstly, particle swarm optimization algorithm is used to determine a network area partition line, and the network is divided into two areas with the same number of nodes.

The partition line is presented as $U=(x, y, \theta)$ (4), (x, y) is the horizontal and ordinate points of node in the partition line; θ is the angle between partition line and x axis. The fitness function is $fitness = (c_1 - f_1 N)^2 + (c_2 - f_2 N)^2$ (5), c_i (i=1,2) is the number of nodes in area i, f_i is determined by formation $f_i = M_i/M$ (i=1,2) (6), M_i is the expected number of cluster head nodes in area i, that is, how many cluster head nodes can be hold in the area through the division.

The description of clustering algorithm is as following:

Step1: All nodes in the network broadcast their status information to the base station (including position information and energy information), which is ADV message.

Step2: After the base station received the message, it performs PSO algorithm to cluster network, and define Q particles.

Step3: the particle parameters x, y, θ is randomly assigned. It determines the area segmentation line by formation (4), then the whole area is divided into $Q\times2$ different areas. For the location information of nodes is known, it can determine the corresponding c_i (i=1,2) of each node, and then substitute them into formation (5).

Step4: it determines Q different value of fitness, then compare it with the smallest value of fitness in last searching time and get the minimum value, its corresponding particle can be used as the global extreme number P_{gd}; For the same reason, the smallest fitness value by comparing the individual particles is taken as the individual extreme number P_{id}, and then update x, y, θ as following:

$X_{xid} = X_{xid} + v_{xid}$ (7); $X_{yid} = X_{yid} + v_{yid}$ (8); $X_{\theta id} = X_{\theta id} + v_{\theta id}$ (9).

X_{xid}, X_{yid} is the position of the particles; $X_{\theta id}$ is the angle of segmentation line; v_{xid}, v_{yid}, $v_{\theta id}$ is the searching speed of particles in x, y, θ three dimensions, which can be determined by following formation:

$$v_{xid} = wv_{xid} + c_1 \times rand() \times (P_{id} - X_{xid}) + c_2 \times rand() \times (P_{gd} - X_{xid}) \quad (10)$$

$$v_{yid} = wv_{yid} + c_1 \times rand() \times (P_{id} - X_{yid}) + c_2 \times rand() \times (P_{gd} - X_{yid}) \quad (11)$$

$$v_{\theta id} = wv_{xid} + c_1 \times rand() \times (P_{id} - X_{\theta id}) + c_2 \times rand() \times (P_{gd} - X_{\theta id}) \quad (12)$$

c_1, c_2 are learning factor, usually c_1=c_2=2; $rand(\ )$ is the random number between (0,1); w is the weight factor.

Step5: After particles get new x, y, θ, they are substituted into formation (4) and turn into the search process of step3 until the value of fitness value is 0 or reaches the maximum searching times and out. In ideal conditions, the value of fitness function is approximation as 0, now the whole area can be divided into two sub-areas with the same scale.

Step6: After the area is divided for the first time, continue to divide the two sub-areas until M clusters are finished to be divided.

After the network is optimized by particle swarm algorithm, we get a uniformly clustering network. In the cluster head establishment stage, in order to balance node's energy consumption, the node with more residual energy has greater probability to be elected as the cluster head. It firstly classify all nodes, first of all, it set a reasonable energy threshold η, the node whose surplus energy is higher than η is called high-energy node, the node whose surplus energy is lower than η is called common node. It can compute the ration m of high energy node to all nodes. The energy of high energy node higher than ordinary node is α. As following formation, P_{nrm} is the probability of ordinary node becoming the cluster head, P_{adv} is the probability of high energy node becoming the cluster head node.

$$P_{nrm} = p/(1+\alpha \bullet m) \quad (13)$$

$$P_{adv} = (p/(1+\alpha \bullet m)) \times (1+\alpha) \quad (14)$$

In formation (3), we use the probability to instead of p in formation (3) to get the threshold of cluster head election in each round. Then for the average node, we get following formation:

$$T(s_{nrm}) = \begin{cases} p_{nrm}/(1-p_{nrm} \bullet (r \bmod (1/p_{nrm})), if\ (s_{nrm} \in G') \\ 0, otherwise \end{cases} \quad (15)$$

r is current round, G' is the ordinary node set which has not become the cluster head in the $1/P_{nrm}$ round of this cycle, $T(s_{nrm})$ is the threshold of ordinary nodes. This ensures that each ordinary node would be as cluster head in each cycle and each $(1/p)(1+\alpha \bullet m)$ round, and the average number of ordinary node becoming the cluster head in each cycle and each round is $n \cdot (1\text{-}m) \times P_{nrm}$.

Similarly, for high energy node, we get following formation:

$$T(s_{adv}) = \begin{cases} p_{adv}/(1-p_{adv} \bullet (r \bmod (1/p_{adv})), if\ (s_{adv} \in G') \\ 0, otherwise \end{cases} \quad (16)$$

G' is the high energy node set which has not became the cluster head node in the post $1/P_{adv}$ round in this cycle, and $T(s_{adv})$ is the threshold for high energy node. After the area of each cluster is formed and the cluster head is elected, then the cluster structure formation is completed. The whole wireless sensor network begins data collecting and the communication between clusters, the process is similar as the LEACH.

Simulation

The simulation uses Matlab 7.1 software, we assume the wireless sensor networks is composed by 100 nodes, nodes are randomly distributed in the $100m \times 100m$ area, the coordinates of remote base station is (x=50, y=175). We use the communication model in reference [5]. The distance between two nodes is set as d, the wireless coverage radius is r, and the consumption energy of sending l bit data is:

$$E_{TX}(ld) = \begin{cases} lE_{elec} + l\varepsilon_{fs} d^2, d < r \\ lE_{elec} + l\varepsilon_{mp} d^4, d \geq r \end{cases} \quad (17)$$

The consumption energy of node receiving l bit data is $E_{RX}(l) = lE_{elec}$. The initial energy of node is 0.8J. In the formation (15) and (16), E_{elec}=50nJ/bit, r=25m, ε_{fs}=10pJ/bit$\cdot m^{-2}$, ε_{mp}=0.0013pJ/bit$\cdot m^{-4}$, and the ratio of 5% of the cluster head to the total number of nodes is taken as 5%, then M=5. In PSO algorithm, the related parameter values are c_1=c_2=2, the largest iteration time is MAXITER=100, the initial value of weight factor w is 0.9. With the increasing of iteration times, w is changed as w=(w-0.4)×(MAXITER-$iter$) /MAXITER+0.4, $iter$ is the current iteration times. This paper uses the number of network dead node and total residual energy of system as the evaluation index of energy saving. Fig.1 is the compared result of the number changing of dead node in the improved LPSOA algorithm and LEACH algorithm. As Fig.1 shows, when the LEACH algorithm runs to 1000 rounds, the first death node appears, and the first death node appears in the improved LPSOA algorithm in about 1300 rounds, the time of appearing the first dead node delay about 33%. Fig.2 shows the changing of network's total residual energy. From Fig.2, we can know the network's total residual energy situation of two algorithms with the rounds progressing.

Experiment proves that our improved algorithm can prolong the first node's dead time, compared with the LEACH protocol; the node's dead time is more concentrated. It can balance the energy loss of network node, the appearing time of monitoring blind point is short, the network life time is prolonged, the sensor nodes are more economic and efficient; the total number of data collection is increased significantly.

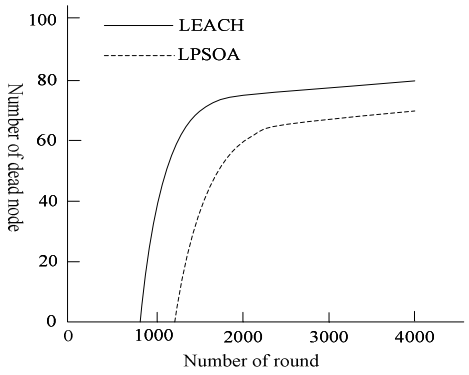

Fig. 1 Number changing of dead node

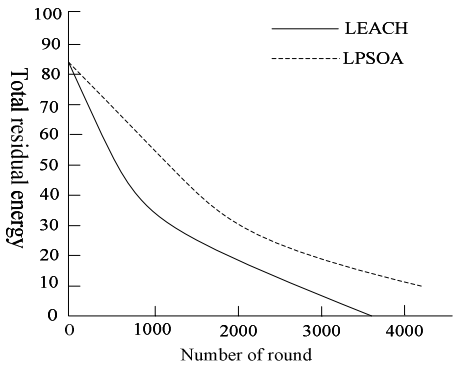

Fig. 2 Total residual energy

Summary

This paper proposes an LPSOA algorithm by using particle swarm optimization based on the energy consumption model of wireless network, which improves the defect of uneven distribution of cluster head in LEACH algorithm. The network simulation shows that the algorithm improves the network energy utilize efficiency, balances the energy load of nodes, prolongs the network life time. At the same time, it improves the working efficiency of wireless sensor network and the amount of data received by base station, so the network has better robustness and higher communication efficiency.

Acknowledgements

The Project Supported by Natural Science Foundation of Jiangxi , China (20122BAB201004).

References

[1] Heinzelman W B, Chandrakasan A P. An Application-specific Protocol for Wireless Sensor Networks, IEEE Transactions on Wireless Communication, Vol.1(4), 2008, p.660-670.

[2] Ran Ge, Gong Shulan. Improving on LEACH Protocol of Wireless Sensor Networks Using Fuzzy Logic, Journal of Information & Computational Science, Vol.7(3), 2010, p.767-775.

[3] Manjeshwar A, Agrawal D P. TEEN:A Routing Protocol for Enhanced Efficiency in Wireless Sensor Networks, Proceeding of International Parallel and Distributed Processing, Vol.4(6), 2009, p.2231-2242.

[4] Gou H. An Energy Balancing LEACH Algorithm for Wireless Sensor Networks, Proceeding of Conference on Information Technology: New Generations, Vol.5(3), 2012, p.822-827.

[5] Muruganathan S D, Ma D C F, Bhasin R I. A Centralized Energy-Efficient Routing Protocol for Wireless Sensor Networks, IEEE Communications Magazine, Vol.4(3), 2013, p.658-664.

[6] Guo L Q, Xie Y. Improvement on LEACH by Combining Adaptive Cluster Head Election and Two-hop Transmission, Proceeding of International Conference on Machine Learning and Cybernetics, Vol.6, 2011, p.1678-1683.

[7] Heinzelman W R, Chanrakasan A, Balakrishnan H. Energy-efficient communication protocol for wireless Sensor Networks, Proceeding of Annual Hawaii International Conference on System Sciences, Vol.9, 2010, p.3005-3014.

CHAPTER 10:

Information Technologies

Advanced Materials Research Vols. 986-987 (2014) pp 2121-2126

doi:10.4028/www.scientific.net/AMR.986-987.2121

Analysis Research of Power GIS Thematic Application Based on Web Services Technology

Yong-hua Chen [1, a], Mi-sha Zhang [2,b]

[1] School of Information Engineering Zhengzhou University,Zhengzhou,Henan Province,P.R.China

[2] College of Environment and Planning,Henan University,Kaifeng,Henan Province,P.R.China

[a] ieyhchen@zzu.edu.cn, [b]314327378@qq.com

Keywords: GIS MIS Web Services Power Grid Thematic Map Heterogeneous Data

Abstract. Grid thematic map is an important basis for the current power grid planning and design, analysis the data characteristics of the power grid GIS thematic map data sources, by its data requirements, studied the method of integrating GIS and MIS heterogeneous data and analysis of data integration strategy of the established model based on Web Services, puts the dynamic generation of GIS grid thematic map in heterogeneous environment, proposed the Web Services data integration based on XML interface standard technical route, and finally achieves the design goal of GIS grid thematic map of dynamic analysis, provide auxiliary decision support platform for power grid planning and design.

Introduction

Power grid GIS（Geographic Information System）, a business systems with comprehensive application of GIS technology, GPS technology and management information technology, can achieve the management of power grid in power sector. Power grid GIS acts as a Integrated application platform that can achieve management of facilities and equipments, analysis and inquiry of space of power grid line, and thematic analysis, its application can comprehensively improve the management level of overall business of power management sector, and provide decision support tools for planning and design and thematic analysis of power grid lines[1].

In the power management sector, power grid GIS is an important part of the informatization construction of enterprise, and generally include basic account management, space operations management, business MIS, thematic analysis and so on. Using the combined applications between GIS and MIS adequately and building the overall solution of power enterprise business have been the most foundational idea in these business systems[2].

Analysis of thematic data source

Power grid GIS thematic map data sources Analysis of power grid GIS thematic reflects important features of the combined applications between power grid GIS and business MIS, analysed in terms of data scource, datas of thematic analysis are derived from two aspects, i.e.spatial information datas and business datas. Spatial information datas are used to describe the data section of spatial properties (such as coordinate, area, length) of power grid lines which include towers, lines, distribution transformers and so on. And business datas are used to describe information of device properties, including tower parameters, overhead lines span, distribution transformer capacity and so on[3].

Analysis of the above data sources,shows that the analysis of the power grid GIS thematic maps is based entirely on the grid GIS database and business MIS database.This two databases are heterogeneous data source systems, stored in different application platforms,and independent in the applications of power enterprise, then can not form a unified platform for data sharing in general case.

Web Services-based data integration solution To solve the problem of data source of power grid GIS thematic maps, Web Services has provided a solution based on heterogeneous data integration platform, that can provide required data sources for the thematic map through the

application of services deployed in grid GIS systems and business MIS system by services Web, and eventually integrate data parameters of thematic maps.

Web Services is a standard language description by the integration of some components based on web publishing,discovery and collection, i.e. Web Services should comply with distributed application components published by some standards, and be able to follow these standards or protocols to access these services in the external[4].

Three independent roles, sevice providers,service agents and service requesters, and the interaction relationship between them have been definied in Web Services system.

Service providers refer to the owner of the service, and often accomplish the implementation of the service management. Its main duty is to realize the definition, development and deployment of , and then the service is transfered to service agents to issue. Service agents should list a variety of the service types and locations subscribed by service requesters to provide concenience for the lookup of service requester, make sure that the service requesters get related information of services quickly. However, service agents are not necessary in the whole process, some services and resource description do not need to be provided by service agents, if the service requesters can achieve them from the service providers. Service requesters are used to invoke or start the service, the service requester can request services through the browser or application program and then achieve the task.

Heterogeneous data source characteristics of power grid GIS and MIS

Grid GIS thematic map of multi-source database system bases on the collection of heterogeneous database, and combine the relatively independent database platforms together organically through the business relationship to achieve the goal of data mining and business analysis[5]. Power system of multi-source data generally is divided into the following two types. (1) multi-source datas based on different database platforms, such are similar on the integration pattern, but have similarities and differences in the database technology support, service mode and concrete database management. (2) multi-source datas based on same database platforms, however, the databases are independent of each other, this kind of heterogeneous reflect on the database structure, design of table structure and business datas[6].

In view of the above two kinds of different characteristics of the source data, different communication strategies should be performed. communication strategies that are independent relative to the platform are mainly used for the heterogeneous of different platforms. On the other hand, for the other heterogeneous characteristic, the communication strategy of database platform itself is used generally.

Design of multi-source data integration model based on Web Services

In the analysis of grid GIS thematic, datas of thematic analysis come from multiple application system. In this article, three thematic indictors, density of power grid line and density of power grid distribution transformers and the density of power grid load, are analyzed with emphasis for examples to discucss the design of data integration of multi-source power grid.

Specific analysis of thematic map data

(1) Thematic map of power grid line density

Power grid line density is applied to the analysis of the line density condition of partitions (such as villages and towns) in the jurisdictions , and then displayed directly on the map in the form of thematic map. The specific calculation formula is that density of line is equal to the value that number of regional poles is devided by the area of the region.

There are two sources for the poles number in every region, one is pole statistics of each town provided by the electricity production MIS, and the other is the datas collected by the GIS directly .Area data of each district is based on the data calculation of GIS.

(2) Thematic map of density of power grid distribution transformers

Density of power grid distribution transformers is applied to the number distribution condition analysis of distribution transformer of partitions (such as villages and towns) in the jurisdictions. And then displayed directly on the map in the form of thematic map. The specific calculation formula is that density of distribution transformers is equal to the value that number of regional distribution transformers is devided by the area of the region.

Sources of regional tower distribution transformers can be provided directly by number of statistics that the MIS system reported monthly. Area data of each partition is based on GIS data computing.

(3) Thematic map of power grid load density

Density of power grid load density is applied to the load distribution condition analysis of distribution transformer of partitions (such as villages and towns) in the jurisdictions. And then displayed directly on the map in the form of thematic map. The specific calculation formula is that density of load is equal to the value that electricity consumption of regional distribution transformers is devided by the area of the region. This thematic map can be generated according to the monthly statistics.

Load of each region can be provided directly by remote meter reading MIS statistics. Data can be specific to each month. Area data of each partition is based on GIS data computing.

Design of parameter transmission model

In thematic map data integration model, the Web Services distribute in the application systems of all the required data soures. Reading the parameter variables directly from the database and defining interface by parameter can realize the transfer of specific datas[4].

GIS System and MIS application interface parameter model define the unified communication standards of power grid GIS and MIS data, and specify the data sources, numeric types and scope of numerical conditions of two heterogeneous systems' integrated value by the definition of parameter. This section with the GIS system and remote meter reading electricity MIS as an example shows how to accomplish the data read and statistical functions.

Interface model M={Reading information description set S, Demand model M1}

Demand model M1={Reading method, Reading distribution transformer power set, Analysis period}

Here, the reading information description set S is the structure of data storage. Such as the definition of distribution transformer data, storage location of remote meter reading data, the connection of characteristics information of the meter reading data and so on.

Reading method is the analysis method of the meter reading data, such as maximum, minimum, average, sum and calculation formula, etc.

Read with electricity of distribution transformer set mainly refers to the set of data points that has some common characteristics in the GIS and marketing MIS.

Analysis period mainly refers to the the effective period of time when GIS read data information of the MIS. For example, when we calculate all the electricity consumption of 10 kv distribution transformers from October to November in 2011. Time quantum from October to November is the analysis period.

Above models are the typical parameter models of power grid MIS. Due to the dynamic change during every moment of the electricity information of various points in the remote meter reading MIS system, Web Services need continuous or in a certain time interval requesting parameter command to obtain the parameters of the corresponding datas in this parameter interface model. In actual application, accomplishment of the transmission of parameters generally requires the combination of multiple parameters. For example, when we want to obtain the capacity and current working power of distribution transformer through the only number of distribution transformer, structure type of parameter set should be adopted to realize the parameter transmit.

Integration model design of the power grid thematic map data

In the process of power grid thematic map data integration, i.e. the process of generating complete thematic, the following several processes are included[7].

(1) Web Services deploy to the network environment access to corresponding database.

(2) Analysis of the thematic map data sources, definition of the parameters rules and formation of parameters transmit definition model should be performed according to the type of thematic map, and generally saved in the form of an XML file.

(3) Web Services that are deployed know well the data content that need to be read from the GIS database or MIS database through the analysis of the XML documents of integrat parameter definition.

(4) According to the content of integrated data in the step (3) , Web Services the read corresponding data from the database, extract the corresponding data, and then add data to the integrated database.

(5) Systems generate parameter data and generate power grid thematic map on the basis of integrated database and thematic map parameter calculation rules.

The grid thematic map data integration model diagram is shown in Fig.1.

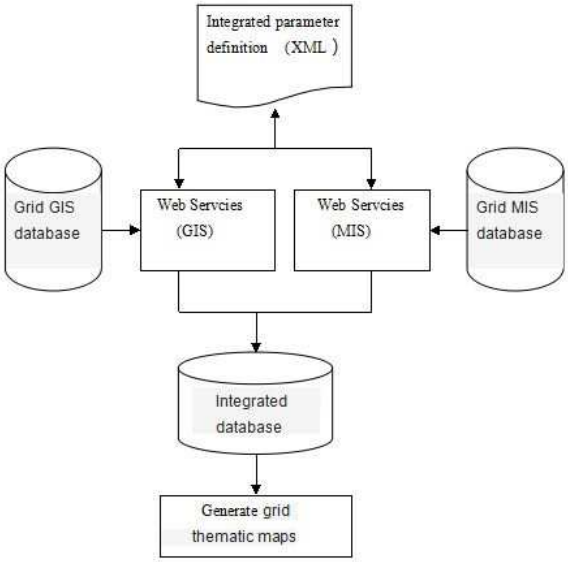

Figure1. Power thematic integration model based on Web Services

Power grid thematic map integration process design based on Web Services

GIS and MIS data need to be processed in Web Services, and in the thematic the two kinds of datas need to be processed integrated. For example, in the project calculation of the region distribution load, we need to calculate each numbers of distribution transformers in the region according to the spatial relationships in GIS. The numbers of distribution transformers exist in the GIS database, and load data of distribution transformers with these numbers need to be obtained from the far copy MIS system.

So in order to guarantee the only data relation of GIS system and MIS system, query of integrated data through the middle XML is necessary. In the development of integrated design, Web Services query related data from GIS database, generate XML documents, and deploy related data that Web Services query from MIS database in the environment of the MIS, and generate XML documents, finally query data records meet the conditions through the composite query of language integration[8].

The data conversion between GIS and MIS database and XML is the main content of Web Services integration design, specific refers to that the business database extracts and transforms data into XML document data and then transfers into relational database through XML documents, the system adopt the third-party tools to relize the specific conversion process in the design, such as XML element tree operation tools, the XML parser, etc[9].

1) Transformation design from database to the XML

In general there are two kinds of situations to realize the data conversion between XML documents in a relational database. The first kind of circumstance is that the system generate a DTD according to the data in the database, then generate a XML document accord with the DTD specification standard. The other case is that there is a existing DTD, the system analysyze the structure of DTD and then generate an XML document based on its description and by reading the data in the database. As a document exchange system of heterogeneous data integration and query system , mainly the second case exists. As in the development and application of system, the definition of general document type structure has been finished, and is relatively fixed, only if the database upgraded, the existing document structure should be changed. In this system information content of power grid GIS needed to be integrated are geographic coordinates of distribution transformers and the power grid MIS data

and the current loads of distribution transformers. And these have been defined according to the demand analysis in advance, and then combine database data to generate XML documents according to the type of document DTD, i.e. DTD document types are predefined, however, the content of the documents is a transformation on the basis of the database data model, the handled datas at this stage include the element tree, the mapping table and relational data. Tools dealing with the data include element tree generation tools, mapping table generation tools, database operating tools and element tree operating tools, and the final output result of the model is XML documents[10] [11].

2) Transformation design from the XML to database

Realize the integration of power grid GIS database and the MIS database by using the query tool based on XML document, and then the formation of tower, information of distribution transformers and a new distribution circuit consists of power grid GIS and MIS, etc.

Complete data table structure have been established according to business requirements in the integrated database, the system only need to transfer information of GIS and MIS data contained in the XML file into the database record type[12].

Technique implementation of the integration of Multiple source grid thematic map data based on Web Services

Reading of GIS and MIS data

Grid GIS database includs the space basic information of the distribution transformer, such as X coordinates (X), Y coordinates (Y), height (H), number (TRANCE_CODE), subordinate line coding (LINE_CODE), etc.

The process of implementing Web Services read and the process of increasing data from the GIS database to thematic map integration database are shown below.

```
<?xml version=”1.0” ncoding=”ISO-8859-1”?>
    <table TransDest:key=” TranceId”
           TransDest:name=”  A  E_  ”
           TransSrc:name=”  A  E_ A E”
           Where=” TransId=”BH00206””
           From=”*”>
 <field>
        <field bookattName=” TranceId”
           bookFieldDest:name=” TranceId”
           bookFieldSrc:name=”  A  E_  E”>
        <field bookattType=”vchar”
           bookFieldDest:type=” vchar”
           bookFieldSrc:type=” vchar”>
 </field>
</table>
```

In the above example, the corresponding field TranceId express the meaning that read the TRANCE_CODE field value in table TRANCE_BASE from the power grid GIS database, and add new records to TRANCE_JBXX in the integrate database, numbers of distribution transformers of adding a new record is "BH00206".

Reading style of the power grid MIS database is similar to the GIS data. For instanse, the MIS database includes some meter reading attribute information of distribution transformers, such as distribution transformer volume, distribution transformer power load, meter reading time and so on.

Data integration query

Through the above steps, the two heterogeneous datas of power grid GIS and MIS data exist in the form of an XML file. Composite query on these two files is necessary to retrieve the needed data during the generation of power grid project map, the method is accomplished by the XML - QL query language [13] [14]. If the XML documents input by power distribution information have existed in the http://116.255.132.156/EXAMINATION.xml, the DTD statement of description model should be included [15].

The following example code is an example of querying the needed data code through XML - QL.Through the XML QL - query, a query in the specified fixed data source (based on URLS format) is completed , and then an XML tree structure is returned.

Thematic map generation results

Power grid line density thematic map is a kind of thematic map generated by reading the ratio of regional poles number (production MIS data) and the region area (GIS data).

Power grid distribution transformers density thematic map is a kind of thematic map by reading the ratio of statistical number results of distribution transformers in each region (production MIS data) and the region area (GIS data).

Electric load density thematic map is a kind of thematic map generated by reading the ratio of distribution transformers load statistical results in each region (remote meter reading data) and the region area (GIS data).

Summary

This paper applies the Web Services technology in the generation of power grid GIS thematic map with innovation, and solves the heterogeneous database integration problems of power grid GIS and MIS, and then achieves the goal of power grid thematic map dynamically generation. The application research results in this paper can also be used in other areas to provide the overall solution for the dynamical generation problem of composite datas in heterogeneous environment. The dynamical generation model of power grid thematic map can provide further research and specification for parameters transfer standard on the base of the characteristics of the power grid daily office, and complete the business system data communication components encapsulation of GIS and MIS, and then improve the efficiency of secondary development.

References

[1] LIU Xue-hui, ZHOU Wen. The Application of Multi-source Spatial Data Management in Geographic Spatial Database [J]. Geomatics & Spatial Information Technology, 2008(2):96-98.
[2] CHEN Yong-hua, CHEN Gen-yong. Research of multi-source data communication based on electric GIS [J]. Power System Protection and Control, 2004(4):115-119.
[3] CHEN Yong-hua, CHEN Gen-yong. Distribution network fault diagnosis algorithm based on GIS platform [J]. Electric Power Automation Equipment, 2001(3):71-75.
[4] LU Li-Nan, ZHOU Chang-Chun, LI Xi-Wang. Middleware to Integrate CORBA and Web Services [J]. Computer Systems Applications, 2011(04):131-135.
[5] Chen Yonhua.Analysis of Safety Evaluation to the Lightning Protection of Power Lines Based on 3D Platform[C]. Computer Science and Service System（CSSS 2012）,2012.8.
[6] CHEN Yong-hua LI Xiao-hui. Researching of GSM short message center in Electric power circuitry patrol monitor [J]. Microcomputer Information, 2009(3):104-106.
[7] WANG Zhen-Hui, LIU Jun, WANG Zhen-Duo. XML Data Storage Technology Based on RDBMS [J]. Computer Systems Applications, 2011(3):206-209.
[8] Dimitris Gouscos. A general model of performance and quality for one-stop e-Govem- ment service offerings[J]. Govemment Information Quarterly,2006,(06).
[9] HUANG Xiao. The Research into Data Exchange between XML and RDBMS [J]. Journal of Anqing Teachers College(Natural Science Edition). 2006(5):75-77.
[10] Ding Yuehua, YangMin. Implementation of heterogeneous datasources integration and exchange based on xml [J]. Computer Applications and Software. 2006(10):134-135.
[11] Park Jong-Hyun,Kang Ji-Hoon.Optimization of XQuery queries including for clauses[J].IEEE,2007.grids[J]. Automation of Electric Power Systems, 2011, 35(10): 104-107.
[12] HUANG Hao, OUYANG Liu-bo. Design and implementation of semantic heterogeneous data integration based on web services [J]. Computer Engineering and Design. 2009(19): 4406-4410.
[13] Dimitris Gouscos. A general model of performance and quality for one-stop e-Govem- ment service offerings[J]. Govemment Information Quarterly,2006,(06).
[14] CHEN Rong-xin, LIAO Hu-sheng, CHEN Wei-bin. XML Parsing Schema Based on Parallel Sub-tree Construction[J]. Computer Science, 2011(03):191-194.
[15] ZHAO Hui, TAO Shiqun, LI Liping. An Approach and Real ization of XML-basedH eterogeneous Data Sources In tegrat ion [J]. Journal of Shan xi University (Nat. Sc.i Ed.), 2005(1):33-36.

Advanced Materials Research Vols. 986-987 (2014) pp 2127-2130

doi:10.4028/www.scientific.net/AMR.986-987.2127

Research on Nuclear Power Station Video Conferencing System from "Standard Definition" to "High Definition"

Zeng Xie

Information Technology Center, China General Nuclear Power Corporation, Shenzhen, China

E-mail: xiezeng@cgnpc.com.cn

Keywords: Video conference; Standard Definition; High Definition.

Abstract: Transition is a natural law which means the things gradually developed from one stage to another. It comes to be a natural and logical thing when it moves towards the right direction. In this paper, we will take the nuclear power station video conference room contribution as an example to comb the management of video conference room from three parts: the limitations of "Standard-Definition", the excellence of "High-Definition" and the necessity of transition. It also discusses the feasibility of nuclear power station's High-Definition video conferencing system.

I. Introduction

With the rapid development of the Internet, computer application technology continues to improve, the traditional voice communication cant meets people's information needs, and only telephone communication mode restricts the development of enterprises. The development of enterprises, the improvement of communication and timely delivery of information go first, Nuclear Power Enterprise's demand and development in this area is particularly prominent. Nuclear power station's original video conference system has been using SD systems, but it can't meet the needs of the parent company. Therefore, after transforming the original standard-definition video conference system, the internal proprietary IP network covering global scope has been established. For making full use of network resources, the hybrid network video conference system based on H.320 and H.323 dual protocol has also been realized. The video conferencing system based on high standards not only conferencing capabilities but also meets the needs of daily meetings and training meetings. As a result, it reached with the seamless integration of the parent company conferencing system.

II. Three Feasible Nuclear Power Station Video Renovation in Conference room

Currently Nuclear power station video conferencing system has completed two high-definition video conferencing systems transformation, with the principle of not changing the original layout of meeting room space, maximize the use of new equipment to replace old equipment manner to the conference room's renovation, so as to meet the needs of HD video conferencing with other bases.

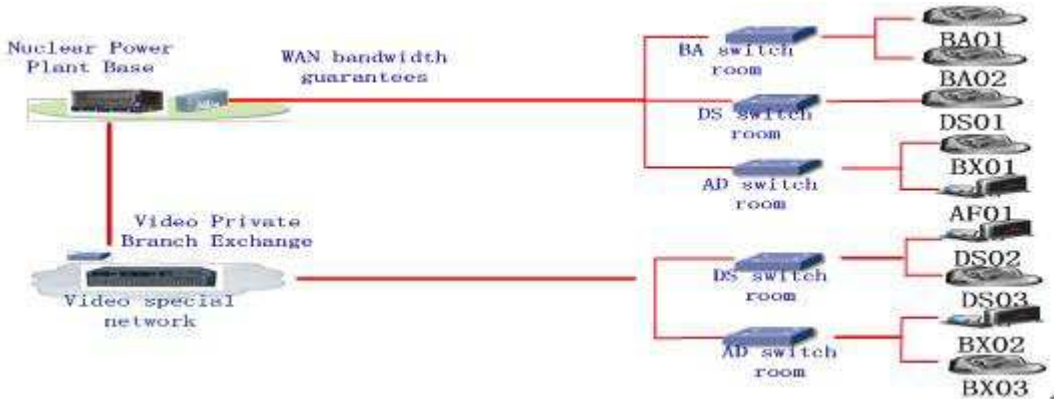

Figure 1. Nuclear power station base of video conferencing systems topology

A. The Superiority of "HD"

The renovation projects of Nuclear power station conference room use Polycom HDX7000 HD replace the original definition equipment, HDX7000 become the protagonist of Nuclear power station video conferencing development, and this marks nuclear station entry into the "HD" era.

1) The evolution of the CIF pseudo "high definition"

In the course of the construction of video conferencing system, some video manufacturers claim "HD" is actually the expansion comes from the CIF format 4CIF (704 × 576) format. The main role of this format is transmit static images in the video conference, now it is now being made in the form of a dynamic by some manufacturers, so 4CIF cannot be considered as real HD, it is only a transition technology, it cannot be compatible with 720p HD standard which will be issued by the ITU . Such consequences will lead to that the video conference is incompatible with the follow-up and peripheral products, such as cameras, televisions, video recorders. And it is also incompatible with the HD video conferencing system which could really support it. There may be an impact on the video conference.

In addition, if you want to achieve smooth 4CIF quality requires at least 2Mbps bandwidth, while using the latest technology H.264 to achieve the equivalent 720p HD of 9CIF only needs 1Mbps bandwidth, so all kinds of users are not optimistic about 4CIF.

2) The real sense of HD in video conferencing system

The resolution of HD video conferencing system is at least above 720P, the terminal configuration is HD-compatible devices, such as high-definition video terminals, high-definition camera, HD video tracking matrix. So Nuclear power station HD conference room replaces the original VSX7000 with.

Polycom HDX7000, replaces RGB0808 with fast PT-RGB0808-A HD video tracking matrix and replaces Airpower HCS-3313C SD camera with Sony BRC-Z330 HD camera in the transformation project, the most important thing is to use the high-end Apple IPAD4 as the central control touch screen, it greatly reduces the pressure of the video maintenance personnel, as long as master the method of the application, you can get to the effect of “Visible to get”.

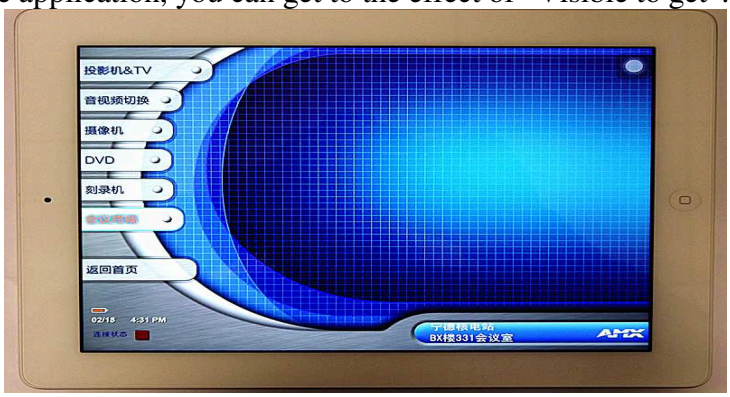

Figure 2. The video conferencing system of Nuclear power station use Apple IPAD4 as the central control touch screen

In addition, in order to achieve the high-quality video conferencing, network bandwidth is also an indispensable factor. HD interactive video conference requires a minimum data transfer rate of 1Mbit / s, in order to achieve the best results, we recommend that the data transfer rate reach or exceed 2Mbit / s. Nuclear power station special video conferencing lines use telecommunications 2M exclusive broadband so as to ensure they follow the HD video conferencing agenda.

3) HD video conferencing system advantage

a) Using advanced digital interface: In the digital interface, HD video conference system based on HDMI interface and HD-SDI interface, the advantages of using this interface is that transmission requires only a single cable can realize high-definition video, audio, which greatly simplifies the circuit layout. At the same time, the transmission range of HD-SDI interface is wide; in the range of 100M do not need to realize the transmission repeater.

b) Possess HD dynamic dual video streaming technology: High definition video conference system supports the standard H.239 two-way exchange dynamic video and static dual video streaming, support dual 720P (1280 * 720) high definition dual video dynamic flow can also provide a dynamic image and the ultra-clear PC content (SXGA1280 * 1024) static synchronous transport stream, after the application of this technology in video clarity obtained the reliable guarantee.

a) Using high fidelity technology sound: High-definition video conference system in addition to relatively well in the video, the high fidelity technology used in terms of the effect, mainly used MP3, MPEG4-AAC (LC/LD) audio codec technology, compatible with C 14Khz G.722.1 Annex Polycom audio coding, and supports automatic echo cancellation, background noise suppression, automatic gain control.

b) The mature and use of Polycom LPR Technical :(LPR packet loss recovery technique) is a newly developed algorithm Polycom; its purpose is to protect the IP video calls from the network packet loss. Usually, the video conference occurs in the course packet loss phenomenon can hardly be avoided, however, by the corresponding error correction mechanism, the video quality can still be guaranteed. And if, the traditional H.264 standard video without the use of any error correction mechanism of encoding and decoding technology, even if the packet loss rate of only 1%, the quality of the video is usually will be greatly reduced. But if system uses such as LPLR or LPR and other existing error correction mechanism, even if the packet loss rate as high as 5%, also can achieve higher quality of video flow.

C. The Necessity of Transition

At the present stage the trend of the development of video conference system: First of all protocol of network communication from H.320 to H.323 and the transition to the SIP protocol, meanwhile wideband audio protocol low quality audio has been replaced by the G.719, G.722.1 Annex C communication protocol. i.e.G.711, G.728, G.722 etc.H.264 video coding efficiency has become the absolute choice for video coding, and it will replace code of H.263, H.261.And of course the image format is changed from the traditional CIF, 4CIF format to 1280 x 720P, 1920 x 1080 (P/I) HD video transition. This series of changes to the requirements of video conference system are also high in some indicators to the system as a whole comprehensive evolution of high-performance applications.

With the rapid development of domestic nuclear power plant construction, China Guangdong Nuclear Power Group video conferencing system through the continuous creation of remote network video network will be extended to all different bases. Nuclear power station base to follow the group of footsteps, will focus on the use of standard definition video conference room into a high-definition video conference room, and use existing standard definition video communication technology, video stabilization transmission of voice, video, improve the rate and efficiency of office use broadband network, and reduces the cost of daily meetings, travel expenses, to create the conditions for the real time communication. At the same time, with the rapid development of communication technology, bearing the gradual optimization of network quality, video conference system to the high clear video, audio fidelity direction rapidly. But also due to the construction of video conference service, the existing standard system cannot meet the business development, remote communication, video conference, remote education and remote PPT sharing needs.

Therefore, it will be imperative video conference system expansion high-definition video conferencing system.

III. Conclusion

The developments of information, networks vary from minute to minute, progress, and are raging like a storm. In the meantime Communication technology rapid stride, multimedia performance upgrade quickly, amazing and fantastic. With the technology of video conference system will continue to be developed and perfected, more show and is widely used. Most important of all Emergence of high-definition video products, not only change the video conference visual effects, more on the development of the whole video conferencing industry plays an important role

in promoting. However, HD video products from the moment of birth, video conference took the lead into the HD era, and HD will gradually take the place of traditional video conferencing market.

So the Nuclear power station video conference system "standard" times has become the past, while with the development of IT technology and enterprise the video meeting demand increasing, in particular the development of digital television technology for image display of revolutionary change, "HD" already become the hope development belong, technology development, has become a symbol of index of the new area of video conference system.

References

[1] LiKun.Construction and application of video conference system at China Guangdong Nuclear Power Group [J].Electric Power Information Technology, 2009.

[2] WangZhao.Research and implementation of video object segmentation in videoconference system [D].Maritime Affairs University of Dalian, 2004.

[3] XuzhiMing.Analysis and application of HD video conference system[C].Electric Power Information Technology, 2008.

[4] LiuxiaoHong. The current situation of the development of video communication product HD [J]. Analysis of telecom network technology, 2010.

[5] ITU-T Recommendations H.323v5，Packed-based multimedia communications systems,2003.

Advanced Materials Research Vols. 986-987 (2014) pp 2131-2134

doi:10.4028/www.scientific.net/AMR.986-987.2131

Study on focused crawler's application in searching petroleum news

Sun Lei [a], Bian Min[b]

China University of Petroleum, Beijing, China

[a]e-mail: sunlei@cup.edu.cn

[b]e-mail: bianminok@sina.com

Key words: Focused Crawler; Crawling Strategy; Topic Correlation; HTML Content Extracting

Abstract. The paper aims for the application of focused crawler in the petroleum news topic crawling, studies the related technologies of the focused crawler, and put forward a crawling engine strategy and review strategy on the petroleum news topics, adopt different extracting methods for different types of pages through web page classification, and design a corresponding link topic correlation calculating method for the crawling engine strategy; test and verify the above-mentioned crawling engine strategies through experiments, and the experimental results show that the strategy can greatly balance its accuracy and width for focused crawler.

Introduction

Along with the rapid growth of Internet, general search engines gradually cannot satisfy people's requirement of precision and real-time for information retrieval. As a web page capture and retrieval tools focused on a single field, the focused search engine has raised more and more public concern. Being an important part of focused search engine, focused crawler is to capture topic-oriented pages from the Internet. The quality of crawled pages may directly affect the retrieval effectiveness. Therefore, the research of focused crawler technology has great significance and important value. The traditional industry of oil also has precise search needs for specific areas, so we collected the petroleum news topic, through the establishment of oil news library, providing data support for the development of petroleum industry, providing fast and accurate information for decision-makers in the field of oil.

Focused crawler

Focused search engine[1] is directed to a field of professional search engine, whose search target and range is usually limited within an industry and theme. As the general search engine can retrieve the contents of all aspects of the Internet, so it is no way to more deeply. But the focused search engine can do this. In the process of crawling web pages and analyzing index, the focused search engine can do more in line with the needs of users and give more accurate retrieval results, due to having considered the characteristics of the topics in the field. The crawler used by focused search engine is called focused crawler[2]. It bases on a certain strategy when it is crawling pages on the Internet. Along the path which is topic-oriented to crawl, it crawls as many topic-oriented pages. On the one hand, focused crawler can improve the proportion of topic related to web pages in all the crawled web pages, providing convenience for data cleaning and index building in the late; on the other hand, focused crawler also greatly reduces the storage, network resource consumption and the time of crawling. Because of the focused crawler occupying the important status in the topic search engine, it is often the focus of the topic search field research.

The technical research related to focused crawler

a. The topic definition of focused crawling

The definition of focused crawler to crawl topics can be divided into three methods, basing on the definition of the target page features, basing on the topic keywords dictionary and basing on domain ontology. This paper uses a simple and effective topic keyword dictionary to represent crawling topic.

b. The search strategy of web crawling

Focused crawler is an important part of the focused search engine, and web crawling search strategy is one of the key technologies of focused crawler attention. The goal of focused search engine is to search for a domain and topic, Focused crawler needs to study which kinds of crawl strategy is used to search to topic-oriented pages as many as possible, crawling less in unrelated web pages.

Web crawling search strategy mainly has breadth-first search strategy, the best-first search strategy, fish swarm algorithm and HITS algorithm, etc.

The goal of this paper is to realize a crawler that is used to crawl in the oil news domain. Therefore, it uses the best-first search strategy. According to the characteristics of the news page, it draws on the experience of web classification thought of HITS algorithm, adding web calculation of correlation .It subdivides the web for further with developing appropriate crawling strategy on the Internet.

c. The web revisiting strategy of crawlers

The timeliness of Internet web content requires us to revisit web pages that have been crawling on the basis of a certain update strategy. In general , the update strategy for the web can be divided into two kinds[4]: revisiting all, revisiting some only based on a certain strategy.

The update strategy of web pages directly affects the crawling search strategy of crawler. Crawling search strategy discusses above in this paper. In fact, it is an implementation of strategy to crawler to crawl for the first time. After that, periodic crawling needs to make a change on the above strategy. The web revisiting strategy of crawlers aims at crawling after the first crawling.

d. The maintenance of initial link of crawlers

Having seen from the basic principle of focused crawler, it needs to add some initial link which is high correlation to the topic to the queue of URL link when focused crawler begins to crawl. In general, the initial link is a page which has much correlation to the link of related topics, such as the petroleum site navigation, the home page of news network of petroleum like this. The initial link is the location of which the crawler starts crawling on the Internet. Its quality directly affects the crawling path of crawler in the future. It is also determines whether the crawler can find more topic-oriented pages. So it is important to maintain an initial list of links in high quality to focused crawler.

The paper finds the flow topic-oriented sites through search engines:

(1) On search engines like Baidu, Google and others, it uses different topic-oriented keywords to search, such as “petroleum news”, “petroleum information”, etc.

(2) Extract links of top N results that the search engine returned. Generally, the topic correlation of these web links is bigger.

(3) Extract host name of these links.

In addition to the above three methods, our focused crawler can also use to crawling records to find out new sites. Maintain the initial list of links. The effect is often not very ideal if only one of the above methods be taken. We generally adopt several methods at the same time, synthesizing their results to obtain better effect.

Experiment and result analysis

For information retrieval systems, precision and recall are the two most basic indicators. Since the focused crawler equivalently makes the late searching ahead to the crawling stage, we often use similar indicators of harvest rate (Harvest Rate) and recall rate (Recall Rate) to evaluate the quality of focused crawler. The definition of Harvest Rate and Recall Rate about focused crawler is shown in Equation 1, 2.

$$\text{Harvest Rate} = \frac{\text{Number of topic - oriented crawled pages}}{\text{Number of all crawled pages}} \quad (1)$$

$$\text{Recall Rate} = \frac{\text{Number of topic - oriented crawled pages}}{\text{Number of exist in topic - oriented pages}} \quad (2)$$

Recall rate reflects the breadth of focused crawler crawling, and the harvest rate is able to reflect the accuracy of focused crawler crawling.

Designing two groups of experiments in the following, we test for the breadth of focused crawler crawling and the accuracy of focused crawler crawling.

In the two experiments, this paper selects the home page of Chinese petroleum news center as a crawling initial link, making the news pages of petroleum domain as the crawling object. In the experiments, it chooses simple focused crawler as compared crawler. But crawler does not classify the pages. For crawled pages, Simple focused crawler judges the topic correlation of the web link anchor text. It only puts the links of anchor text topic-oriented into the waiting crawled queues. At the same time, the crawler designed by this paper, the link pages define relevant links whether is the topic-oriented threshold (Hereinafter referred to as the threshold value r), being taken as 10, 20 and 30 to be compared.

The experiment of crawling to breadth of focused crawler

Generally, the number of topic-oriented pages that exists in the network is difficult to obtain, so this paper selects a link set c, using the number of topic-oriented pages that is obtained from the link set c by crawling to measure the crawling breadth.

Due to the crawler fetching way is to link extension to the child by the father. So no matter what kind of crawling search strategy to be chosen to crawl, the ultimate crawl path is linked to the root of the tree to the initial links. The experiment selects to crawl the tree 5 layers by using breadth-first crawling strategy to get a link set called C. Specific approach is to control crawling depth of crawler, set the crawling depth of initial link as 1.Page n from the depth of the extracted link crawling depth is n+1. When the web crawling depth equals to 5, we stop making links on the page. The stop condition of crawler to crawl is that the waiting crawling URL queue is empty.

Harvest rate of each crawler according to layer in experiment of crawling to breadth of focused crawler, as shown in figure 1.

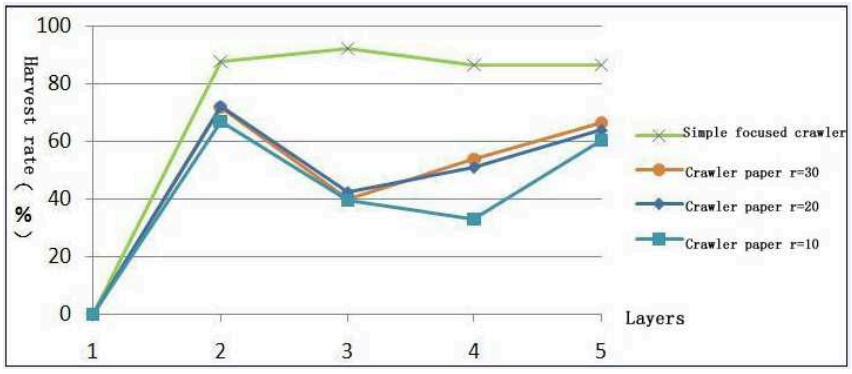

Fig. 1 Harvest rate of each crawler according to layer

Figure 1 shows that harvest rate of simple focused crawler is maintained at a high level in each layer. The harvest rate of this paper's focused crawler begin to decline after the second layer, then as the number of layer increasing has rebounded. This is because the first layer is News Home, which contains a lot of content page links, so the harvest rate which extends from of the second layer is higher. Since the third layer, with the increasing of some irrelevant links, harvest rate declines in a certain extent. After the increasing crawled in each layer, the harvest rate of this paper's focused crawler steps up by classification strategy of link pages.

The experiment of crawling to the accuracy of focused crawler

This experiment does not restrict crawling depth of crawler. Experimental crawler and initial link are the same with last time. The stop condition of crawler crawling is that each crawler crawls to

10000 web pages. This experiment tests the change of harvest rate of focused crawler in the process of crawling.

As shown in figure 2, harvest rate is along with the number of crawled pages

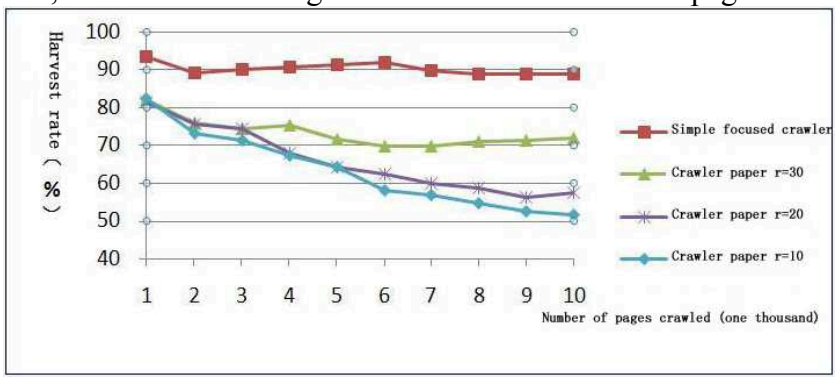

Fig. 2 Curve of harvest rate along with the number of crawled pages

As can be seen from Figure 2.The harvest rate of this paper's focused crawler increases along with the improving of threshold value r. The larger the r value is, the closer the simple focused crawler is. If the threshold value of r is 0, the crawler will degrade into best-first crawler. When the threshold value of r is 30, the crawling harvest rate is steady at around 71%.It achieves a satisfactory result.In the actual crawling, it needs to find a balance point of harvest and recall rate basing on the network and storage resources.

Conclusions

I have programmed the system to achieve a focused crawler based on search strategy of page classification, comparing with the simple topic determination strategy through the crawling experiment. Experimental data shows that on the basis of guaranteeing rate, it makes an ability to extend web to be stronger, and it finds more topic-oriented pages, taking into account the accuracy and breadth of topics crawling. At the same time this paper makes extensively research on the key issues to focused crawler. But focused crawler is a very complex system, there will be many problem to design a reliable and high accuracy system .At the same time we need to do further processing to crawl into the data.

References

[1] Y.Q. Liu, S.P. Ma and T. Hong, in: The basic technology of search engine, edtied by Tsinghua University Press, Beijing, (2010.7).

[2] S. Chakrabarti, M. Berg and B. Dom, in: Focused crawling: a new approach to topic-specific web resource discovery, edtied by Computer Networks,31(11): 1623-1640. (1999).

[3] L.B. Ouyang, X.Y. Li and G.H. Li, in: Survey of searching strategies of web spiders, edtied by Mini-Micro Computer Systems, 26(4):703-706. (2005).

[4] D.S. Li, in: Research of topic search engine: (a master's degree thesis), edtied by Harbin Engineering University, Harbin ,(2005).

[5] L.Z. Zhou and L. Lin, in: Survey on the research of focused crawling technique, 25(9): 1965-1969. (2005).

[6] J.H. Liu and Y.L. Lu, in: Survey on topic - focused web crawler, edtied by Application Research of Computers , 24(10):26-29. (2007).

[7] P. Debra and R. Post, in: Information retrieval in the World-Wide Web: making client-based searching feasible, edtied by Computer Networks and ISDN Systems, 27(2): 183-192. (1994).

Advanced Materials Research Vols. 986-987 (2014) pp 2135-2138

doi:10.4028/www.scientific.net/AMR.986-987.2135

Application of Virtualization Technology in Nuclear Power Plant

Zhang Qiu[1,a], Wang Xiaohua[2,b] , Ou Chaochun[3,c] , Luo Jinfei[4,d]

[1234] Dalian, China

[a]zhangqiu@cgnpc.com.cn

Keywords: virtualization disaster recovery development history compare and analysis

Abstract. Virtualization is the basic physical computer hardware that related modules in the virtual basis rather than the real independent operation to realize the simplified and optimization management of resources. This paper reviews the historical development of virtualization technology and the compare of mainstream realization manners which are the basis for comparative analysis. At the end of this paper we study a feasible mean for the disaster recovery backup solution in nuclear power plant.

Development Trend of Virtualization Technology

Since the 60's of last century, computer academic USA is budding virtual technique. In 1959 Christopher Strachey published an academic report, called "Time Sharing in Large Fast Computers". In this paper he put forward the basic concept of virtualization in the text. The article is also considered the earliest paper virtualization technology. In 60's the virtualization technology first appeared that take the lead in the implementation of IBM. In 1965, IBM launched System/360 Model 67 and TSS (Time Sharing System), through the virtual machine monitor all of virtual hardwares interfaces which allow many remote users share the same high performance computing device using the time. Because of the client - server application and low price of X86 servers and desktops, the distributed computer architecture and virtualization technology on the mainframe in remain stagnant state in 80's and 90'. In twentieth Century 90 the widespread use of Windows and Linux as the server operating system sets the standard for the industry position. The X86 server and desktop deployment growth bring new IT infrastructure and operational difficulties[1,2].

Analysis and Comparison of Virtualization Technology

The existing mature virtualization technology is divided into server virtualization (also known as virtual operating system), storage virtualization, network virtualization, Application Virtualization (also known as desktop virtualization) four[3].

Server virtualization is the earliest subdivision of virtualization technology, the most mature field. Because the server virtualization development time is long, wide application, so a lot of people had almost equal to the virtual server virtualization. The concept of server virtualization, each manufacturer has their own different definition, however, its core idea is the same, namely, it is a kind of method, can distinguish between resource priorities and whenever and wherever possible to server resource allocation to the load to simplify the management and improve the efficiency of their work to the most, so as to reduce to a single work load peak and reserve resources.

Network virtualization is currently the industry on the virtual segment defines the concept is not clear, a controversial. But on the whole, is divided into vertical and horizontal segmentation two class concepts. The early "virtual network", refers to the virtual private network (VPN). The VPN network connection to the concept of abstract, allows remote users to access the internal network of organizations, as is physically connected to the network. Network virtualization can help protect the IT environment, prevent the threat from Internet, also allows users to access applications and data security. From another perspective, the application of carrying a plurality of network nodes, network design based on redundancy brings complexity, and a plurality of network nodes are integrated (called horizontal integration), virtual into a logical device, improving data center network availability, nodes

can also be greatly simplified network architecture. But overall, the current industry standard network virtualization is not mature, less server virtualization, storage virtualization, and quite a few techniques have been included in the purchase of equipment (such as VPN, VLAN), no single unified deployment.

As people demand for storage is more and more big. This demand stimulated the emergence of new technology, such as disk performance is getting better and better, more and more large capacity. But in the large and medium-sized information processing system of large, single disk is unable to meet the needs, this case storage virtualization technology has developed. The so-called virtual memory, is to multiple storage media module (such as a hard disk, RAID) centralized management by certain means, all of the memory module in a storage pool (Storage Pool) are unified management, from the host computer and workstation perspective, see not hard, but a partition or volume, as a large capacity (above 1T) hard disk. This can be a variety of, multiple storage devices and unified management, provide the performance of the storage system of large capacity, high data transmission for the user, it is called virtual memory.

Application virtualization usually includes two meanings. One is the virtual application software, a virtual desktop. Application virtualization so-called, is separated from the operating system and application software, through their own compressed executable file to run, without the need for any file system device driver or users connected, with this technique, the user can reduce the potential safety hazard of application software and maintenance costs, and data backup and restore the reasonable. In addition to the separation of application software and operating system, a part of the solution can also be applied to software pipelining packing up, application software is not installed, as long as a part of the program can be run on the computer, users only need to use their own need to part of the program or function.

Table 1 Comparison of the virtualization technology

Comparison project	Server virtualization	Storage virtualization	Network virtualization	Application Virtualization
Maturity level	high	middle	low	low
Mainstream manufacturers	VMware Microsoft IBM HP	EMC HDS IBM	Cisco 3Com	Citrix VMware Microsoft
Enhance management	high	middle	middle	high
Reliability	high	middle	middle	middle
Usability	high	high	middle	high
Compatibility	high	middle	middle	middle
Scalability	high	high	middle	middle
Deployment difficulty	middle	high	middle	high

In this four kinds of virtualization, server virtualization technology, application of desktop virtualization technology, virtualization is relatively mature, but also the use of the technology, while other virtualization technology, it also need to be further tested in practice and improve[4].

Implementation of Disaster Recovery by Virtualization Architecture

According to the degree of resistance to the disaster tolerance system, can be divided into data recovery and disaster recovery. Data disaster tolerance refers to data system to establish a remote connection which is real-time data replication of key local application system. When the disaster, the remote system quickly replace local system and ensure business continuity. Application of disaster recovery is higher than the data disaster recovery level, namely the establishment of a complete set of, and local data backup system is application system in different places (with local application system as backup for each other, can also be to work with local application). In the disaster, remote application system rapidly taking over or undertake business operation of local application[5].

Using Vizioncore vReplicator software, can realize the application level disaster recovery effect through data level disaster recovery. Because the virtual machine together with the various business applications which are packaged up documents, so when the failure, disaster recovery site to start the backup files at the same time, also started the application, in order to take over the business application system, guarantee system in time to recover from the disaster.

Vizioncore vReplicator by automating the recovery process to speed up recovery, and disaster recovery as integrated elements of VMware virtual infrastructure management, thus simplifying the disaster recovery plan management, manual recovery steps to save complex, recovery plans to test support without interruption, to ensure the safety and reliability of the recovery process. Vizioncore vReplicator VMware Infrastructure VMware VirtualCenter closely integrated, and Vizioncore lead storage replication technology, make the failover and recovery is fast, reliable, economic, and easy to management. Therefore, not only do not need to worry about the risk of disaster recovery, also can be all important systems and applications into the scope of protection. Vizioncore vReplicator will help to cope with various challenges traditional disaster recovery method, meet the recovery time objective (RTO), recovery point objectives (RPO) as well as the regulatory compliance requirements. Using Vizioncore vReplicator, can manage fault switching from the data center to the disaster recovery site; at the same time, also can manage two mutual recovery site and has the fault switching between work load site. Vizioncore vReplicator can also process automatic execution and simplify the fault switching to the new data center, which makes the data center failover plan (such as data center migration) become more smooth.

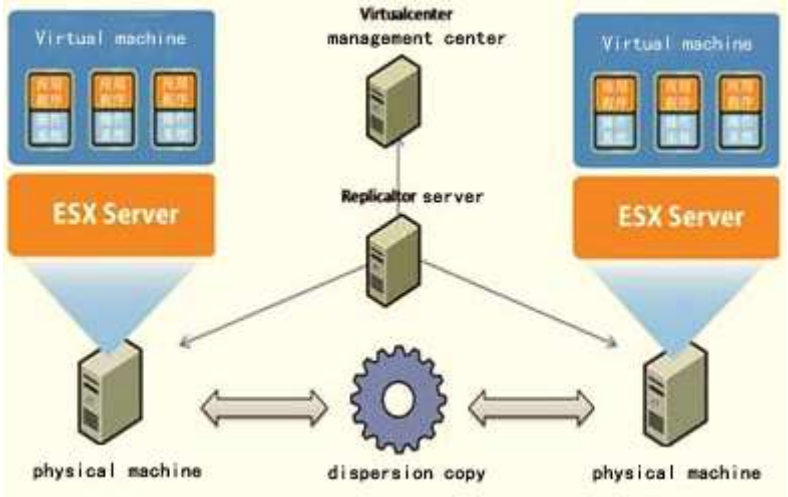

Fig. 1 VMware virtual infrastructure

In order to further improve the overall security architecture, can choose Vizioncore backup and recovery software VRanger Pro, realize the easy and reliable without agent mirror, and the mirror of virtual and physical machine and file level recovery. VRanger Pro running on a Windows host, can be regular customers operating system VMware ESX Server on the implementation of online backup. VRanger Pro before the backup file is sent to the destination memory files will be compressed, and the implementation is incremental backup, it piece by piece scanning data, only the last backup files changed (data or the VM settings) such as backup, to reduce the number of backup data. In addition,

vRanger Pro without agent, can generate the backup files on the source server and send it directly to the target server, not through the third party server, compared with other third party backup software not only due to the elimination of the backup and consumption in ESX resources on the Server, at the same time humanity backup operation great graphics management interface of the work efficiency. Therefore, vRanger Pro is a relatively stronger, more flexible backup solution.

Conclusion

This paper briefly introduces the definition, development history and trend of the current popular virtualization technology. And then expatiate virtualization technology and comparison of advantages and disadvantages. At the end of this article put forward a set of suitable measures for nuclear power plant virtual backup solutions.

References

[1] Zhou Bo, Analysis of Advantages and Disadvantages and the Trend of Server Virtualization, Vol. 28 (2012), p. 56

[2] Zhang Lei, Implement of Remote Mirroring Based on Virtualization, Journal of Computer Research and Development 147-152, 2011

[3] Gong Dezhi, Virtualization Technology in the Telecommunications Server Resources on Application Management

[4] Wang Jianhong, Research on Virtualization and Application[J], 2007(7):238-239

[5] Wang Shuhong, Indicator of Microsoft Virtualization Application, 2009

Advanced Materials Research Vols. 986-987 (2014) pp 2139-2142

doi:10.4028/www.scientific.net/AMR.986-987.2139

Client-side in Management System of Transmission Line Passage Protection Based on Android

Bingqi Liu, Huilan Jiang, Jingpeng Wang

Key Laboratory of Smart Grid of Ministry of Education, Tianjin University, Tianjin, 300072, China

jhl2009yan@126.com

Keywords: Transmission line, latent trouble, Android, client-side, Web service

Abstract. To overcome the shortcoming of lack of real-time in traditional latent troubles information management, a transmission line passage protection system (TLPPS) Android client-side is developed in this paper. Basing on Android mobile's real-time communication and good development performance, Android client is used to record the information of latent trouble. Web Service is adopted to realize the wireless communication between client and server, then the real-time upload and updating is realized, thus improving the accuracy and making it possible for the administrator to put up with the advice of dealing with the latent trouble in time. The security of power system is guaranteed.

Introduction

The inspection and maintenance of transmission lines is an important work for power maintenance company. There are kinds of latent troubles in different transmission lines. The management of latent trouble record is also an important work. In recent, with the development of portable devices and wireless communication technology, 3G technology [1] and GIS [2] are adopted in the power system, but the management of the latent trouble record of transmission line is still traditional. At the present stage, the latent trouble records are managed with paper records and Excel records. Some problems are exposed in this way of managing. The latent cannot be uploaded in time, the location of the latent is not accurate, and the knowing of the progress of the latent trouble is different in different departments. So it is necessary and important to improve the management to ensure the security of the power system.

Recently, smart phones, Android system released by Google and 3G network are more and more common [3]. Android 3G smart phone is an intelligent terminal, including cells, multimedia and other functions. It is cheap and extra cost is avoided. Besides, Android system is open-source and free. A good development platform for TLPPS is provided [4].

The Android client-side in TLPPS is developed in the paper. Management and Android client-side are combined together. At the same time, Android client-side and the server can communicate in real time by Web Service in 3G network. Thus real-time and accurate record and normative management are realized.

Design of TLPPS

The system is composed of database, Web Service server, Android client-side, management system. The frame is shown in Fig. 1. Android client is used by workers to record new latent troubles and disposal results, and to upload the record to server in real time. All the records can also be managed in real time by administrators in server.

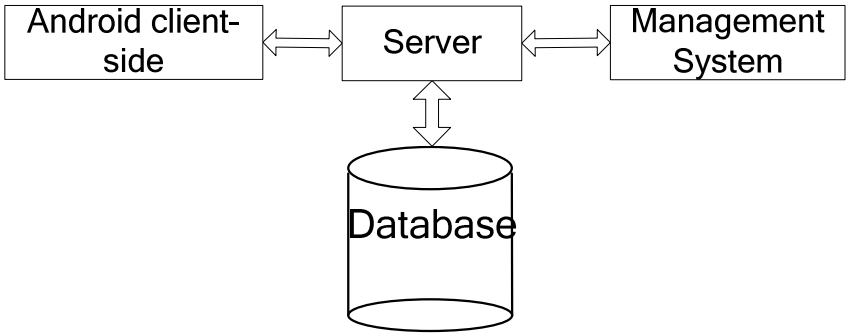

Fig.1 The frame of TLPPS

This paper mainly deals with the development of Android client-side. Traditional information, as well as other information, such as GPS, is recorded. Latent trouble is recorded comprehensively. Then the record is transmitted to the server. Web Service technology is adopted to realize wireless communication between Android client-side and server. Web Service is used in server to provide network data services for client. In 3G network, the function in server can be called easily by Web Service and HTTP, thus complex network communication programming is avoided [5, 6].

Android Client-side Application

To develop the client-side of TLPPS, the universal development environment is developed in Windows Operation System. It consists of JDK (Java development kit), Eclipse, Android SDK (Software development kit) and ADT (Android development tools).

Flow of the Android Client-side. The Android client-side is used to record the information of latent trouble and the disposal result. It is sorted into four modules: login module, function selection module, patrol module and disposal module. In the process of recording, with the using of 3G network, GPS equipment and camera equipment, comprehensive real-time record is realized. The work flow of Android client-side application is shown in Fig. 2. The patrol module and the disposal module are the core module of the application.

Patrol module. The real-time recording is achieved by this module. It is used by the workers to record the information of latent trouble when it is found and transmit it to the server. The user name and the current time are obtained when entering the module, and recorded as the discoverer and the discovery time of the latent trouble. There are two kinds of information needed to be recorded: text record and photo record. Some of the important record are selected in a check box instead of typed by hand. It is convenient for the workers to fill the sheet and the mistakes caused by typing can be avoided. In this way, the record is standardized, which makes the management of server-side more accurate and standardize. The photo record is based on the camera equipment of the Android mobile. The photo of the latent trouble is taken in the module, which can clearly reflect the site condition. It helps administrator of server-side get know of the side condition, and makes conferences for dealing with the latent trouble.

The record will be uploaded to the server, as well as the GPS information. The text information and photo are transmitted separately. The technology of Web Service is adopted in the process of transmission. The effective real-time transmission of important text record is guaranteed. Meanwhile, uncompressed lossless transmission is adopted in photo transmission, which is different from traditional transmission, thus the clear photo can be shown in server-side.

The record is uploaded to the server by Android client-side as soon as the latent trouble is found, which makes it possible for the server-side to get to know the latent trouble. The real-time interaction of client-side and server-side is realized, thus overcoming the shortcoming of slow updating of traditional record method.

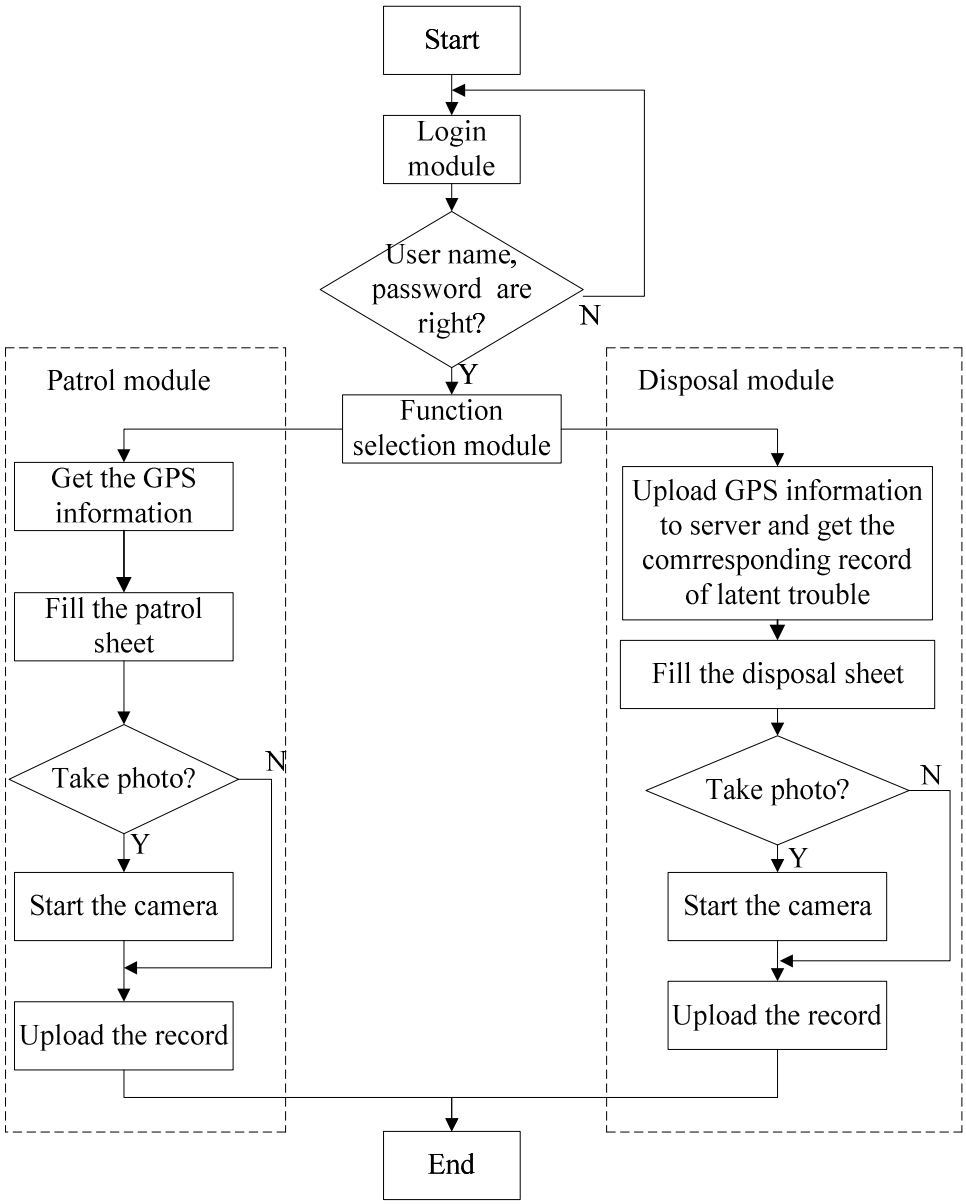

Fig.2 The work flow of Android client-side application

Disposal module. The module is used to record the disposal results of corresponding latent trouble and connect with the server in time. In this module, GPS information is got and uploaded to the server. The corresponding latent trouble record is chosen according to the GPS information and then transmitted to the client to be shown on the client-side. When dealing with the latent trouble, the original record can be referred. The efficiency and accuracy of the disposal is obviously improved by the GPS-based selection. Besides, photo can also be taken in this module to make a comparison with the photo before disposal. The result of disposal is intuitive by taking photos. Moreover, it is convenient for the administrators to check the disposal results in real time.

Conclusions

In this paper, a convenient, effective and real-time TLPPS is developed. The record of latent troubles is real-time, accurate and comprehensive, thus improving the standardization of the management. At the same time, by Web Service, the real-time interaction of Android client-side and server-side is realized. The information of latent troubles and the record of disposal results can be uploaded to the server in real time. The load of the workers is lightened. And by the usage of GPS, the accuracy of the record, as well as the efficiency of workers and administrators, is improved. The client-side application has a good prospect in the future.

References

[1] Hu Huang, Jianghong Ren: Central China Electric Powers. Vol. 5(2011), p. 28 (in Chinese)

[2] Lan Zhang, Xiaoqiong Pu: China Science and Technology Information. Vol. 5(2007), p. 148 (in Chinese)

[3] Fuying Guan, Shitong Long, Jing Huang. Sci-Tech Information Development & Economy. Vol. 4(2011), p. 134 (in Chinese)

[4] Linnan Yang, Lutao Hao, et al: Transactions of the Chinese Society of Agricultural Engineering. Vol. 28(2012), P. 163 (in Chinese)

[5] Haiwen Peng: Computer Knowledge and Technology. Vol. 7(2011), p. 2851 (in Chinese)

[6] Jinchuan Huang, Weidong Jin:Railway Computer Application. Vol. 19(2010), p.24 (in Chinese)

[7] Minghua Shang, Leilei Qin, et al: Transactions of the CSAE. Vol. 27(2011), p.178 (in Chinese)

Advanced Materials Research Vols. 986-987 (2014) pp 2143-2147

doi:10.4028/www.scientific.net/AMR.986-987.2143

Performance Evaluation and Analysis of ZigBee Technology in Smart Grid

Kefeng WEI[1,3, a], Duo WANG[2,3, b]

[1]College of Information Science and Engineering, Northeastern University, Shenyang, 110819, China

[2]College of Resources and Civil Engineering, Northeastern University, Shenyang, 110819, China

[3]Shen Kan Engineering and Technology Corporation, MCC, Shenyang, 110016, China

[a]email: weikefeng@foxmail.com, [b]email: siying20000120@126.com

Keywords: ZigBee; Cluster-tree Route Algorithm; AODVjr Route Algorithm; Smart Grid

Abstract. As heavy investment in the smart grid in China, the research and application of new technology has obtained rapid development. To meet the requirements of reliability, stability, robust and low energy consumption in smart grid, ZigBee plays an important role with its own inherent advantages and reasonable design. In this paper, we focus on the route algorithms of ZigBee, introduce the principles and evaluate the performances of them. The simulation results provide feasible effective evidence and feasible solution for further development for smart grid by using ZigBee technology.

Introduction

Currently, smart grid has become a hot topic. Smart grid means the intelligence of grid network and is built based on the integrated and high speed bidirectional communication network. With the advanced sensing and measuring technology, the advanced equipment technology, the advanced control method, and the application of advanced technology of decision support system, grid network can achieve the goal that is reliable, safe, economic, efficient, and environmental friendly. By achieving these goals, the grid network can be named as smart grid.

The application of smart grid information technology needs stable and reliable data links transmission technology to ensure the data obtaining in each point and reliable arrival of the control information. In fact, this data transmission can be ensured by ZigBee technology that is tailored for industrial wireless data network.

ZigBee is a group of technical standards about the network, security, and application software, which is developed based on IEEE 802.15.4 wireless standards. As an emerging type of wireless network technology with the advantage of short-range and low-rate, ZigBee can be dynamically self-organized and complete network topology and network access automatically even the network topology changes, which shows that ZigBee is a good method for short-range communication.

The outstanding characteristics of ZigBee are mainly as followings,

1) Low power. This is the highlighted advantages compared to the other methods of communication [1].

2) Strong anti-interference capacity. ZigBee technology can ensure smooth communication in a hostile environment, and cope with the strong radiation of electromagnetic interference.

3) Short delay. The conversion time from asleep to work for ZigBee averagely takes 15ms due to the fast response speed. The node getting touch with the networks only spends 30ms, which results in lower power.

4) High capacity. A primary node can manage 254 child nodes at most. Cooperating with data server, the node number will not be constrained.

5) High Safety. ZigBee has provided three levels safety modes, including no security setting, the use of access control list to prevent illegal access to data, and the use of symmetrical password based on advanced encryption standard (AESl28) to determine flexibly its security properties.

The smart grid for measurement and controlling is consisting of ZigBee can achieve the features, such as robustness, self-healing, compatibility, economical efficiency, integration and optimization.

The rest of the paper is organized as follows: section II describes the topologies of ZigBee that studied in this paper; section III details the two route algorithms used in ZigBee; simulation results and analysis are in section IV; section V concludes the paper.

ZigBee Network Topology

According to communication capacity, ZigBee devices can be divided into two types, that is, full function device (FFD) and reduced function device (RFD). The former are capable of routing and forwarding while the later is just responsible for sending and receiving signals. However, the nodes in ZigBee can also be classified into center coordinator, router and end device from the perspective of different network functions.

As is illustrated in Fig. 1, cluster-tree topology and mesh topology that can be support by ZigBee are shown.

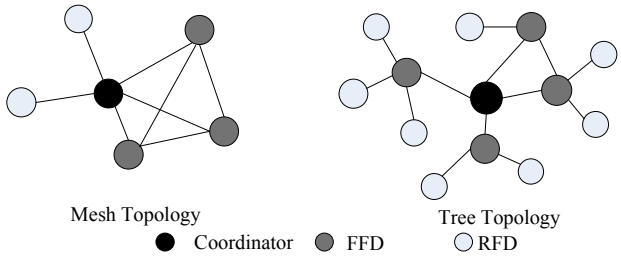

Fig. 1. ZigBee architecture.

Zigbee with mesh topology is always a backbone network composed of several FDD nodes connecting together. Each node can communicate with any of the other nodes within its coverage. Although the peer-to-peer communication between all the nodes, one of the nodes still acts as a central coordinator. The feature of high reliability for Zigbee with mesh topology is due to the restore ability produced by multiple paths between two nodes. In mesh network, there are multiple paths that can support the packets transmission, that is, one or multiple paths still can be chosen for packets transmission if one path breaks. However, just because of the presence of multiple paths, the Zigbee with mesh topology acts as a high redundancy network. To support the application of Zigbee with mesh topology, the network layer provides the corresponding route discovery function, which enables the network layer to find the optimal path for data transmission. In other word, it is the multichannel communication.

Zigbee with tree topology contains a central cooperator which connects a set of router nodes and end devices. The child node of central cooperator can also connects router nodes and end devices if it is a router node. Both of the central cooperator and router nodes can contain their own child nodes, that is, there is no child node for end devices. In this type of ZigBee, each node only communicates with its parent node and child nodes. If a node needs to send data to another node, the information will transfer up or down along with the tree. The significant advantage of Zigbee with tree topology is the large network coverage. However, the information only can be transmitted with an exclusive channel. As the increase of the coverage, the transmission delay also increases and the synchronization becomes more complex.

Route algorithms in ZigBee

With different network architectures in practical application, two common route algorithms, named cluster-tree route algorithm and Ad-Hoc On-demand Distance Vector junior (AODVjr, a kind of mesh route algorithm) [2], are popular in Zigbee.

A. Cluster-tree route algorithm

Cluster-tree routing algorithm [3, 4] is mainly based on network address allocation mechanism, so each device has some address space to allocate to its child nodes. We assume that each parent

node can connect with C_m child nodes at most. Similarly, the maximum number of router nodes that each child node can contain is R_m. The maximum depth of the network is denoted by L_m. In a network, different nodes may have the same values of C_m, R_m and L_m. We use $C_{skip}(d)$ to denote the offset between the addresses of child nodes allocated by the parent node with network depth d. We assume the depth of the k^{th} parent node is d and the address is A_p. If a new added node is the n^{th} RFD node of its parent node, it will obtain the network address allocated by its parent node, shows as in equation (1).

$$A_n = A_p + C_{skip}(d) * R_{m+n} \quad (1 \le n \le C_m - R_m) \tag{1}$$

However, if the new added node is the n^{th} FFD node of its parent node, the network address of this node is computed as equation (2).

$$A_n = A_p + 1 + C_{skip}(d) * (n-1) \quad (1 \le n \le R_m) \tag{2}$$

where

$$C_{skip}(d) = \begin{cases} 1 + C_m * (L_m - d - 1) & if \quad R_m = 1 \\ \dfrac{1 + C_m - R_m - C_m * R_m^{L_m - d - 1}}{1 - R_m} & others \end{cases} \tag{3}$$

If a RFD node wants to send data packets to another node in the network, it will forward the data packets to its parent to transfer. On the other hand, if a router node FFD with the address A intends to send data packets to the destination with the address D descent while the network depth is d, the router node will verify that the destination is descend node or not according to equation (4).

$$A < D < A + C_{skip}(d-1) \tag{4}$$

If the destination is just the descend node, then the address of next hop node is calculated as equation (5). Else the next hop node is the current node's parent node.

$$N = \begin{cases} D & if\ the\ destination\ node\ is\ the\ child\ node \\ A + 1 + C_{skip}(d) * \left\lfloor \dfrac{D - (A+1)}{C_{skip}(d)} \right\rfloor & else \end{cases} \tag{5}$$

B. AODVjr route algorithm

AODVjr route algorithm [5] is the simplified version which originates from the AODV protocol, functioned with the main features of AODV. In order to reduce the cost, energy consumption and facility, AODVjr simplifies some features of AODV. At first, we introduce the simplified route discovery process. In AODVjr route algorithm, the destination node is allowed to reply the RREP message while the middle node can not replay RREP message even if it has route to the destination. Hence, the control overhead effectively reduces. Figure 2 compares the route discovery process of AODVjr and AODV. We assume that the source node 1 tends to communicate with the destination 5 and node 3 has the information of node 5. In AODV, node 3 will reply the RREP message directly. However, it is different in AODVjr since only the destination node can reply the RREP massage. That is to say, even if the node 3 containing the route information to node 5, it can not replay the RREP message, which simplifies the route discovery process and reduces the control overhead to some extent.

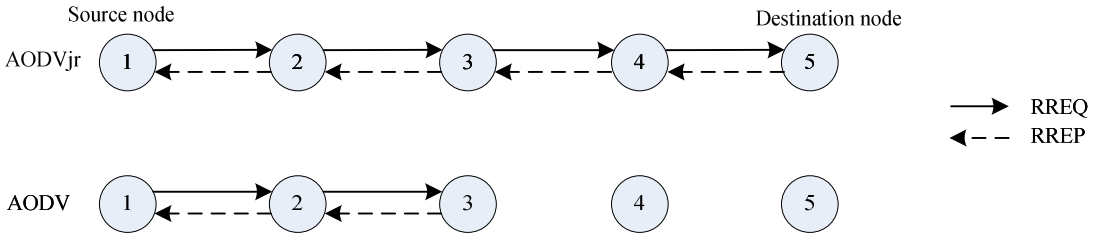

Fig. 2. Comparison of route discovery process between AODVjr and AODV.

Simulation results and analysis

In this section, we study performances and features of Cluster-tree route algorithm with tree routing and AODVjr routing algorithm with mesh routing. Simulations have been carried out by means of OPNET network simulator [6, 7] to measure the performance metrics. The simulations aimed to show different performances of the two algorithms in terms of delay, throughput and average hop counts. As shown in Figure 3, there are a coordinator, five routers and eight devices in both tree routing and mesh routing networks.

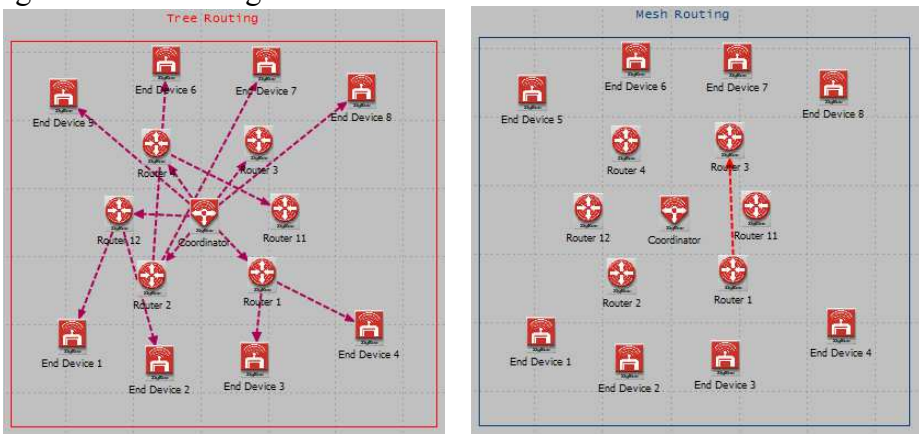

(a) (b)

Fig. 3. The simulation topology of two algorithms. (a) Tree routing. (b) Mesh routing.

In Figure 4, we show the end-to-end delay and mac delay for each algorithm. It is well-known that the packet from the application layer must pass through the mac layer before it is sent out and after it is received, so that the end-to-end delay is certainly larger than mac delay. We can see clearly from Figure 4, the end-to-end delay is much higher than mac delay for both mesh routing and tree routing, which is in line with the analysis. What's more, the mac delay of tree routing is less than that of mesh routing, however, it is opposite with the end-to-end delay of the two algorithms. Especially, for mesh routing, it needs to spend some time to set up the route path, so the end-to-end delay of mesh routing is larger than that of tree routing at the beginning. However, when the route path has been set up, the end-to-end delay of mesh routing decreases less than that of tree routing.

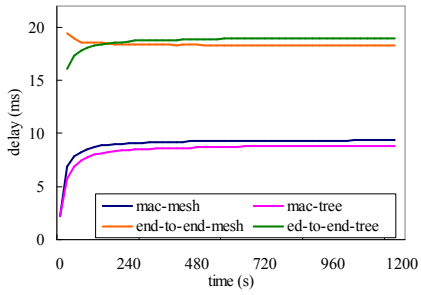

Fig. 4. End-to-end delay and mac delay

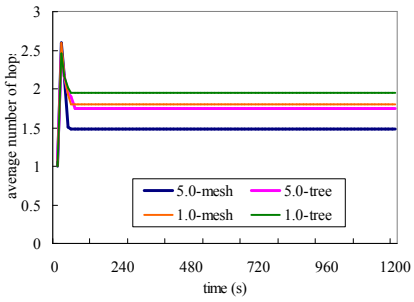

Fig. 6. Average number of hops

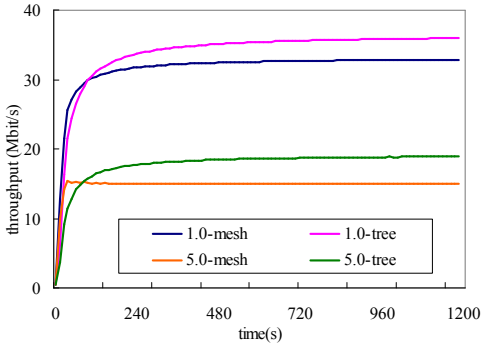

Fig. 5. Throughput

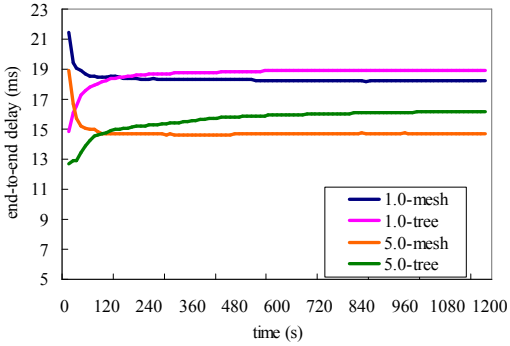

Fig. 7. End-to-end delay

We also evaluate the performances, including throughput, average number of hops and mac delay, of the two algorithms under different packet interarrival times (i.e., 1.0 and 5.0). Figure 5 shows that the throughputs of two algorithms with 1.0 packet interarrival time are much higher than that of with 5.0 packet interarrival time. This is obvious because less packet interarrival time leads to more packets incoming in unit time, so the throughput is higher accordingly. We can also see that the throughput of tree routing outperforms than that of mesh routing.

The average number of hops is a significant performance to evaluate the route algorithms, so we simulate this performance in Figure 6. We can see that the average number of hops is larger in tree routing than mesh routing in both cases. This illustrates that the source node must pass through more nodes to reach the destination node. The reason is that the RFD node needs to forward the packets to its parent node firstly when it is a source node in tree routing, however, the source node can transmit its packets directly to the next hop which is a router node.

Eventually, we compare the mac delay of two algorithms in the two cases. Figure 7 shows that the end-to-end delay of mesh routing is larger than that of tree routing for both cases. This is because that the packets undergo larger waiting time in each intermediate node because of higher throughput with 1.0 case. In addition, for each case, the end-to-end delay of tree routing is higher than that of mesh routing, which has been explained in Figure 4.

Conclusion

This paper introduced the common route algorithms in ZigBee network and compared the performances of them. And we also discussed the impacts of packet interarrival time on the performances of the two algorithms. We can conclude that the tree routing has higher end-to-end delay than mesh routing due to larger average number of hops. And the throughput of the tree routing is also less than that of mesh routing. Hence, the mesh routing outperforms than tree routing in terms of throughput and end-to-end delay.

References

[1] Chiung-Hsing Chen ; Hung-Wei Lin ; Yen-Sou Huang ; Jwu Jeng Chen. Power management system based on ZigBee, in Proc. ICASID, 2012, pp.1-5.

[2] Ran Peng; Mao-heng Sun; You-min. Zou. ZigBee Routing Selection Strategy Based on Data Services and Energy-Balanced ZigBee Routing, in Proc. APSCC, 2006, pp. 400-404.

[3] Zigbee Stack Advanced User Guide. JN-UG-3045 Reversion 1.0.2007.9.

[4] Yu-Kai Huang; Ai-Chun Pang; Pi-Cheng Hsiu; Weihua Zhuang. Distributed Throughput Optimization for ZigBee Cluster-Tree Networks, Parallel and Distributed Systems, 2012, vol. 23 (3), pp.513-520.

[5] Yingqi Niu. An improved AODVjr algorithm for extending network lifetime, in Proc. ICNIDC, 2012, pp. 18-21.

[6] http://www.opnet.com/, OPNET Modeler 14.5, 2005.

[7] Lei Guo, Yuhuai Peng, et al. Performance evaluation for on-demand routing protocols based on OPNET modules in wireless mesh networks, Computers & Electrical Engineering, 2011, vol. 37, pp. 106-114.

Advanced Materials Research Vols. 986-987 (2014) pp 2148-2150

doi:10.4028/www.scientific.net/AMR.986-987.2148

Research and application of mobile Internet technology in power

Guangzhong ZHAO, Shuping HE, Wei ZHANG, Jiannan WU[1, a]

[1]State Grid Electric Power Co., Huludao, Liaoning Province Power Company ,Huludao, 125000, China

[a]email: italy_totti_10@163.com

Keywords: The Mobile Internet; Handheld Terminals; Promotion Tips

Abstract. Based on mobile Internet technology applications, Customers access ladder price electricity price standard, the implementation, such as power charge information. Change the way traditional electricity propaganda, tips, rich ladder price electricity price means of propaganda, tips. Improve the enforcement ladder price electricity price propaganda, strengthen the publicity and guide ladder price electricity price, improve the various circles of society to the understanding and awareness of the residents ladder price electricity price policy. Tariff and other policies to promote in the future suggesting that provides technical application support for the implementation of the price ladder policy to create a good atmosphere.

Introduction

Mobile Internet technology has become the trend of the future technology development is growing at breakneck speed take the place of the Internet [1]. More and more business applications, with the help of mobile Internet technology to achieve faster and deeper application services in various industries. And smart phones is also an important factor in promoting the rapid development of mobile Internet , multi-core , high-speed , large-screen smart phone , the gradual replacement platform computers, the Internet has become an important carrier of mobile Internet applications[2][3]. In the future there will be more mobile Internet technology -based business applications would be enhanced. Mobile Internet technology as the richest, most intuitive and convenient information to show the way, the same applies to residents of publicity and prompted the price ladder price . Promotional offers based on mobile Internet technology ladder price applications, to achieve active residents ladder price pricing tips and publicity, advance notice residents perform ladder price , ladder price to understand the relevant policies and regulations , to facilitate the residents arrange electricity. Eliminate doubts and misunderstandings media and the public may provide more intimate services for residential user of electricity.

An existing situation

Residents in the promotion of electricity price ladder price , suggesting the application of technology, because the way foreign to implement ladder price electricity earlier time , people have become accustomed to follow steps, reasonable peak electricity, and therefore propaganda techniques and tips means relatively few studies [4][5] . Foreign information technology and network technology development faster, higher degree of resource sharing personal information, and the importance of individual comprehensive credibility, and therefore the price of electricity in the promotion of information and tips , the most collected passively push mode to the user by sending an e- mail, electronic billing , mailing bills , etc., to achieve the notification timely, accurate and in place.

Since the implementation of domestic residents ladder price just the way soon, there is no electricity price ladder price advocacy, research and application areas for the tips[6] . Existing electricity price ladder price propaganda techniques and methods, mainly rely on traditional means of leaflets, newspapers, publications, news, television , media, websites , etc., to supply enterprise customer service face to publicize to achieve[7]. So that people understand the ladder price passive policies, performance standards, tariff information. Existing power supply companies work silently

electricity price ladder price, mainly live notifications and notified by telephone[8]. Power company meter reading personnel in meter reading, notify the customer site charges, 95598, or call center staff through the Customer Center, the user is prompted ladder price tariff information[9] . Thus the domestic electricity price ladder price publicity and tips are still more traditional way, the lack of publicity specifically for Customers of electricity ladder price, suggesting innovative applications of technology .

Active promotion ladder price application tips

Mobile Internet is based on the integration of mobile communications and the Internet as a technology base , designed to meet the people at any time , any place , in any manner acquire and process information needs of a new industry . Mobile Internet is an important part of the new generation of information technology, but also the development of China 's strategic emerging industries in key areas . "Twelfth Five-Year Plan " clearly put forward the " new generation of information technology industry will focus on the development of next-generation mobile communications, next generation Internet ," mobile Internet has been fully integrated into the scope of China's key strategic emerging industry development .

The mobile Internet technology for the residents ladder price pricing promotion, tips, extension ladder price residents publicity platform , rich residents ladder price propaganda , suggesting a means to convey the intensity of the price ladder price helps improve policy . Mobile Internet technology , by engaging mobile terminal and network to realize the mobile Internet terminal application , a user-initiated policies ladder price to get the power of information to realize the price ladder price proactive publicity and tips. Customers promotional ladder price , suggesting mobile applications , Android -based mobile application development platform , implemented as a residential electricity price ladder price publicity prompted, provide tariff policy advocacy, implementation of standards introduced , step execution reminders, information push services , electricity tariff queries, dynamic content such as electricity , the system interface is beautiful , simple, easy to operate.

Android-based advocacy prompted the residents ladder price system , two-dimensional code scanning via phone or PC client to download , complete the download and installation of the system. Customers can query the intelligent mobile terminals ladder price -related information . System utilizes push, scroll , automatic ranking techniques, information showing the price ladder price .

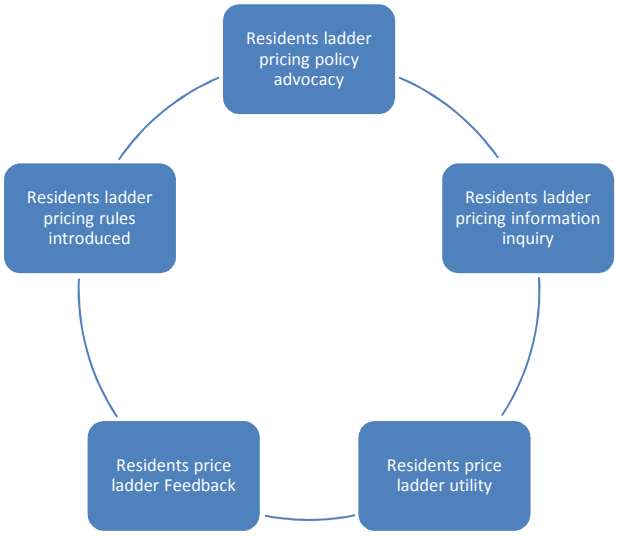

Fig.1. Based on the residents price ladder price publicity prompted a schematic diagram of the system functions on the Android platform

Residents price ladder price publicity prompted mobile applications features include:

Residents ladder price pricing policy advocacy: the pricing department of publicity about the implementation of this region residents ladder price pricing policies, implementing rules, job advice Announcement.

Residents ladder price pricing rules introduced: Show the residents ladder price pricing rules and examples of the main operator fees, including major operator fee rules, tariff standards, fee calculation example.

Residents ladder price pricing information query: electricity price ladder price moving to implement user query applications, the message push mode, push the price ladder price to the user policy advocacy, standard introduction, electricity tariff and other information.

Residents price ladder price Feedback: residential electricity policy answers to consulting, to provide optimized power proposals to help residents analysis of electricity Customers.

Residents price ladder price utilities: electricity price ladder price to provide Customers with tariff calculation tools, user-friendly simulation price ladder price, providing residential electricity consumption of tips to guide residents scientific, rational use of electricity.

Conclusion

Residential Customers ladder price propaganda, suggesting technical applications, mobile Internet technology for the first time, the price of electricity marketing promotion business, improved passive inform prompt manner, innovative initiative to learn ways to further improve the implementation of the price ladder price propaganda efforts to effectively strengthen the publicity ladder price guide and enhance the community residents ladder price pricing policy understanding and awareness. Push ladder price policy information to Customers through mobile applications, performance standards, electricity tariff information to alert the user to perform time residents and the standard ladder price, providing reasonable electricity reference. Residents are encouraged scientific, rational use of electricity, improve energy efficiency. Provide technical support for the future application of tariff and other policy advocacy, tips. Technology can be extended to the ladder price water and gas bills ladder price publicity prompted application to help implement the price policy of the loss, so that the residents enjoy the intimate and sincere service Customers.

References

[1] Wen Luo , Chinese mobile Internet development Blue Book (2012) . Central Literature Publishing House, 2012.

[2] Fengzheng , Xu Yang , Yiwen Hu , Yang Peng, technical architecture and development of the mobile Internet People's Posts and Telecommunications Press , 2013 .

[3] Bo Zhang, O2O: mobile Internet era commercial revolution Machinery Industry Press, 2013 .

[4] Juan Yang , Shujie Liu, ladder price of international practice [J] China Economic Herald , 2010 (10) : 27-28 .Discussion

[5] Chengren Li , Jiaming Yu. Korean residents ladder price pricing experience and enlightenment [J]. Energy technology economy , 2010,22 (7) :56- 61.Billing method

[6] Yihang Song ,residential electricity price ladder price design optimization model [D] Beijing : China Electric Power University , 2011 .

[7] Lizhi Zhang. Increments of residents stepped tariff system [J]. Price Theory and Practice , 2010 (2) :9 -10 .

[8] Jianshuo Shi. Implementation valley ladder price and enforcement measures [J]. Energy technology economy , 2010,22 (7) :62 -66 .

[9] Hoqing Zheng, Yi Jin. Residents ladder price pricing theory and practice of economic and technological cooperation , 2012.

Advanced Materials Research Vols. 986-987 (2014) pp 2151-2157

doi:10.4028/www.scientific.net/AMR.986-987.2151

Research on Method of CIM-based Data Exchange for Electric Power Enterprise

Yuncheng Zhou

School of information and electrical engineering

Shenyang agricultural university

Shenyang, China

E-mail: zhouyc2002@163.com

Keywords: common information model (CIM); data exchange; data serialization; XML Schema Definition (XSD); electric power enterprise

Abstract. A novel CIM-based approach is proposed to realize power enterprise data exchange under heterogeneous IT circumstance. CIM objects encoding specification by XML is introduced in this paper. The object is expressed by XML complex element, and the object's properties are encoded by simple elements embedded in complex one. In order to solve some data interchange problems, a CIM/XSD schema which applies on CIM data syntax and data validation verification is established by using XML Schema Definition (XSD) technology, and an attribute group "AssociationAttributeGroup" is designed to serialize complex relationships of CIM objects. The attribute group provides syntax support for marshaling linkages of objects in certain two methods: "embedding" and "referring". The two operators: serialization and deserialization are added to each CIM class. By this way, the CIM objects can make quickly and bidirectional alternation between memory objects and CIM/XML document. The algorithms of the two operators are designed in detail, which can implement complex object set bidirectional conversion efficiently. The case study shows that the CIM object encoding specification, the CIM/XML schema and the algorithms of serialization functions can be applied to exchange and share CIM data in electric power enterprise.

Introduction

In electric power enterprise, data interchange between various systems is frequent. Some data import / export interfaces must be developed for an application to communicate with its collaborator, which increases the cost of development and system maintenance complexity. If all power enterprise applications comply with a common data protocol, the complexity of data exchange interfaces would be reduced significantly. International Electrotechnical Commission (IEC) proposed the Common Information Model (CIM) which describes the power system entities accurately [1-3]. Based on CIM, all applications have the same understanding of power system components.

The Resource Description Framework (RDF) is recommended by IEC 61970 to encode CIM objects in text mode [4, 5]. Using RDF as CIM object encoding grammar has shortcoming [6]. IEC 61970 employ RDF document to contain CIM objects data (called as CIM/RDF document), while also using RDF to describe the CIM class model. So the XSD (XML Schema Definition) technology can't be used to verify the consistency of CIM/RDF document and CIM model. Meanwhile, the metadata of CIM/RDF document is complicate, and the data load rate is low [7]. Therefore, this essay emphasizes the key point on definition of CIM/XML schema based on CIM and XSD, and the encoding specification of CIM/XML document is discussed thoroughly. At the same time, the serialization and deserialization algorithms of CIM objects are designed detailed.

Encode the CIM/XML document

A. CIM objects encoding specification

The W3C XML has been widely used in data exchange between various systems. The XML document is a structured text document which includes elements and attributes. In XML document,

one element can include some sub elements, and elements can reference to each other through attributes, even link to external network resources [8]. In CIM model, classes are used to describe the various power system components and concepts, the generalization, association and aggregation are used to represent the relationships of classes [9]. Because of self-describing and high scalability, the XML document is able to express complex relationships of CIM objects. Therefore, this essay uses XML to encode CIM objects and its relationships.

B. Encode CIM objects by XML

In generalization, a derived class gets all of the properties and associations from the inheritance chain. When the instance object of inheritance hierarchy leaf node class is encoded by XML, the object's local properties and relationships as well as all of the inherited properties and relationships together are translated into XML composite elements. Currently, most CIM classes are directly or indirectly inherited from IdentifiedObject. Therefore, the IdentifiedObject can be considered as a common base class. Meanwhile, the mRID property of IdentifiedObject is globally unique which can be regarded as an identifier to identify objects in CIM/XML document.

When encoding CIM objects by XML, the binary object is completely and accurately converted into text format. The composite element which has an mRID attribute converted from object's same name property, and the tag of composite element is named as same as object class name. Except mRID, the others object's properties are converted into sub same name elements of composite one.

C. Encode CIM object's relationship by XML

In addition to code CIM objects, the CIM/XML document is also necessary to describe their linkage relationships. The linkage is an instance of association or aggregation. The aggregation linkage describes the "whole" and "part of" relationship between CIM objects, which can be encoded by two ways as following:

The first one is "embedding" method. According to the conversion rules, the "part" object element is embedded in the "whole" object element. As shown in Figure 1, the PowerSystemResource aggregates Measurement. In a conversion process, the Measurement object's role named as Contains_Measurements is encoded as same name element and embedded in PowerSystemResource object element. Furthermore, all of the Measurement objects are encoded into composite elements and embedded in Contains_Measurements element.

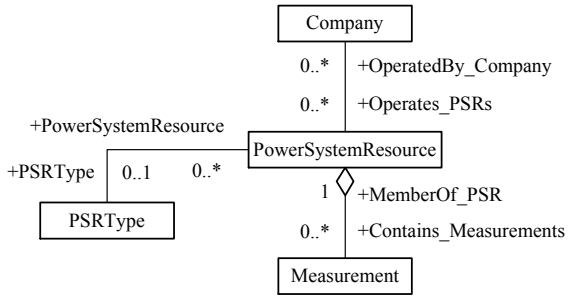

Fig. 1 Association and aggregation of CIM classes

Another way is "referring" method. By this way, the "whole" object and the "partial" object are converted to CIM/XML document's composite elements with the same level. In addition, the referring attribute is added to each composite element, and the referring attribute's value is set to the related element's mRID attribute. The "whole" element and the "partial" element store mRID attribute each other through referring attribute to improve the mutual query speed.

Define the CIM/XSD schemas

The data receiver must know the grammar to parse the CIM/XML document. For this reason, the CIM/XML document should be encoded with normative grammar. The CIM model itself is still gradually changing [10]. So besides exchanging CIM object data, the applications also need to exchange CIM model. The XSD defines a data model for XML document, is the syntax rules for XML document [11], and can be applied to verify the validity and integrity of the XML document. It

supports a variety of data types, with all the features of object oriented, itself is defined by XML, and can be qualified for descripting the CIM model. Therefore, this research uses XSD to define the CIM/XML document schema (CIM/XSD).

A. Define the schemas for class and generalization

For each class in CIM, one same name element is added to the CIM/XSD, and a corresponding complex type called as "class + Type" is defined for the element. Meanwhile the class's mRID property is converted into mRID attribute of the complex type, and the others properties are converted into sub same name elements.

When defining XSD type for subclass, it can be extended from superclass's complex type by using extension. The subclass object is a special instance of superclass. So the superclass object can be displaced by subclass one. The XSD uses substitution to express this phenomenon. So, the CIM/XSD fragments of PowerSystemResource and IdentifiedObject can be defined as following:

```
<xs:element name="IdentifiedObject" type="IdentifiedObjectType" abstract="true"/>
<xs:complexType name="IdentifiedObjectType">
<xs:sequence>
  <xs:element name="name" type="xs:string" nillable="true" minOccurs="0"/>
  ……
</xs:sequence>
<xs:attribute name="mRID" type="xs:ID" use="required"/>
</xs:complexType>
<xs:element name="PowerSystemResource" type="PowerSystemResourceType"
    substitutionGroup="IdentifiedObject"/>
<xs:complexType name="PowerSystemResourceType">
<xs:complexContent> <xs:extension base="IdentifiedObjectType"/> </xs:complexContent>
</xs:complexType>
```

B. Define the schemas for aggregation and association

In order to support "embedding" and "referring" methods simultaneously, an "AssociationAttributeGroup" attribute group is developed as following:

```
<xs:attributeGroup name="AssociationAttributeGroup">
<xs:attribute name="src" type="xs:anyURI" use="optional"/>
<xs:attribute name="remote" type="xs:boolean" default="false" use="optional"/>
<xs:attribute name="owns" type="xs:boolean" default="false" use="optional"/>
</xs:attributeGroup>
```

The AssociationAttributeGroup represents the referring relationships between elements. The value of "src" attribute relies on the "remote" attribute. When "remote" attribute is true, it indicates that a remote element's URI is assigned to "src". Otherwise, the value of an element's mRID attribute within the current document is stored in "src". The "owns" attribute is used to indicate whether the main element aggregates the referred element.

Next, this research adds two complex types called as "*PropertyType" and "*ArrayPropertyType" for each CIM class. Here, the asterisk represents one CIM class name. The attribute group "AssociationAttributeGroup" is added to the complex type "*PropertyType". It indicates that the instance element of "*PropertyType" can refer to another element. The following example describes that the element types of "CompanyPropertyType" or "CompanyArrayPropertyType" can include Company element directly or only a reference.

```
<xs:complexType name="CompanyPropertyType">
<xs:sequence minOccurs="0"><xs:element ref="Company"/></xs:sequence>
<xs:attributeGroup ref="AssociationAttributeGroup"/>
</xs:complexType>
<xs:complexType name="CompanyArrayPropertyType">
<xs:sequence maxOccurs="unbounded" minOccurs="0"><xs:element ref="Company"/>
</xs:sequence>
</xs:complexType>
```

After that, the elements named as "*Member" and "*Members" are defined by using "*PropertyType" and "*ArrayPropertyType". And then the "*CollectionType" which includes "*Member" and "*Members" is defined. The "*CollectionType" can be used to define a collecting element that has an element array in it. The array item may be a real element or only a reference. The following example shows a "CompanyCollectionType" definition.

<xs:element name="companyMember" type="CompanyPropertyType"/>
<xs:element name="companyMembers" type="CompanyArrayPropertyType"/>
<xs:complexType name="CompanyCollectionType"><xs:sequence>
<xs:element ref="companyMember" maxOccurs="unbounded" minOccurs="0"/>
<xs:element ref="companyMembers" minOccurs="0"/>
</xs:sequence></xs:complexType>

The relationships of classes are also converted to schemas as partial of class's schema. Class plays a role in association. The conversion rule is that the role one class played is converted into sub element and embedded in the other class's schema. When the multiplicity is "0..1" or "1", the sub element's type is "*PropertyType", or else is "*CollectionType". According to figure 1, the new schema of PowerSystemResourceType is defined as following.

<xs:complexType name="PowerSystemResourceType">
<xs:complexContent><xs:extension base="IdentifiedObjectType">
<xs:sequence><xs:element name="pSRType" type="PSRTypePropertyType" />
<xs:element name="operatedBy_Companies" type="CompanyCollectionType"/>
<xs:element name="contains_Measurements" type="MeasurementCollectionType" />
</xs:sequence></xs:extension>
</xs:complexContent>
</xs:complexType>

C. Define the CIM/XML document schema

A collection of CIM objects encoded by XML should be contained in a CIM/XML document. The CIM/XML document must comply with the relevant standards of XML. Such as, the XML document can have only one element as the root. CIM does not define a class model which can aggregate any other kinds of classes. Therefore, the root element named as "document" and its corresponding data type called "DocumentType" are added to the CIM/XSD. While the abstract element named as "_object" is defined and can be substituted with a practical element.

<xs:element name="_object" abstract="true"/>
<xs:element name="document" type="DocumentType"/>
<xs:complexType name="DocumentType" ><xs:sequence maxOccurs="unbounded" minOccurs="0"><xs:element ref="_object"/></xs:sequence>
</xs:complexType>

Any element that can replace the _object can appear in the CIM/XML document. For instance:

<xs:element name="IdentifiedObject" type="IdentifiedObjectType" abstract="true"
substitutionGroup="_object"/>

Serialization of CIM objects

In electric power enterprise, because of the heterogeneous of various applications, the storage and management mechanism of CIM objects are different. So with the help of the CIM/XML document to exchange objects is an effective method. Here, the data exchange sponsors are considered clients, and the data receivers and processers are seen as servers. The client encodes the local objects into CIM/XML document on the basis of CIM/XSD schema, and sends the document to server. This process is called serialization. The server receives the CIM/XML document, verifies the document's integrity, and then decodes CIM/XML document into local CIM objects. This process is called deserialization. After that, according to business needs the server can process the objects further.

A. Serialization

A CIM/XML document often contains multiple objects. In order to realize the serialization of CIM objects, each kind of CIM class is extended by adding serialization methods, as shown in figure

2. Among them, the Serialize function is responsible for objects serialization that is a marshaling process. Moreover, the Deserialize function would be in charge of objects deserialization.

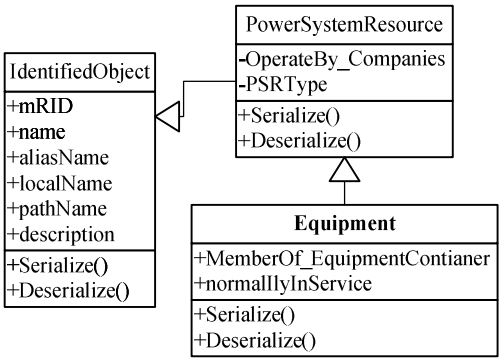

Fig. 2 CIM model extension

According to the CIM/XSD schemas defined previously, the superclass's properties and relationships are always serialized earlier. So the subclass's Serialize should preferentially call the superclass's Serialize, and then encode its own properties and relationships. When using "embedding" method to code relationships, the current object can directly call the Serialize of its partner, and then embed the results in current object's element. Due to the associations in CIM model having no direction, directly invoking partner's Serialize may produce recursive phenomena. It can be avoided by using "linking and referring" method. The object or objects set can be serialized according to the following procedure:

1) Before serializing CIM objects set, it should to create a hash table named as Hash (*key*, *value*), where the key corresponds to the object's mRID property, value corresponds to the XML composite element that is the object's serialization result.

2) In a particular order, or from the main object (serialization entrance object) to start calling each object's Serialize. The algorithm of each class's Serialize is as following:

a) The object searches the Hash table by using its mRID property as keyword, if found, it shows that the object has been marshaled, and then terminates the Serialize executing; if not found, it continues to execution.

b) If the object's class has superclass, then calls the superclass's Serialize function.

c) The object serializes its own properties according to the CIM/XSD schema.

d) If the current object has linkages, then directly reads each linked object's mRID property, and encodes the linkage by using "referring" method.

e) The current object encapsulates the serialization results into XML composite element named as *ele*, and then stores the key value pair (mRID, *ele*) in Hash table.

f) The current object respectively calls each linked object's Serialize function with specify sequence defined by CIM/XSD.

3) According to the CIM/XSD, it needs to create "document" element, take out each item from Hash table, and embed value into "document" element directly, and create a XML document by using the "document" element as root. So an objects set are serialized completely.

B. Deserialization

For various applications, the objects and relations contained within a CIM/XML document are different. So it is difficult to previously create all the corresponding objects and call their Deserialize functions. According to the CIM/XSD schemas, the "document" element's sub elements are real CIM objects, and the sub element's name is as same as the object's class. By analyzing the sub element's name, the corresponding object can be created dynamically. Then, each object's Deserialize function is invoked to restore its properties. The algorithm is as following:

1) Firstly, it needs to create two hash tables: Hash1 (*key*, *ele*) and Hash2 (*key*, *obj*). Where the key represents the CIM object's mRID, ele is serializing result, and obj is CIM object.

2) And then get the root element "document" from CIM/XML, and take out each sub element (*ele*) from "document". Next, get the mRID attribute of ele. According to the sub element's name, it

can recognize the object's class type, so a new CIM object (*obj*) can be created. Thus, the two key value pair (mRID, *ele*) and (mRID, *obj*) are stored into Hash1 and Hash2 separately.

3) Through enumerating Hash2 table, each key value pair (*key*, *obj*) can be taken out. Next, it need to find the XML element (*ele*) corresponding to *obj* in Hash1 table by using *key*. Meanwhile, in order to restore the *obj* state, the *obj's* Deserialize function is invoked with *ele* parameter. The algorithm of each CIM class's Deserialize is as following:

a) If obj has superclass, then calls its superclass's Deserialize function with parameter ele, and restores its own properties and relations.

b) In the deserialization process, the content of each sub element (*sn*) of ele is extracted. And it needs to be parsed and assigned to the corresponding property of obj.

c) If *sn* is a referring link, then it need to extract the src attribute from *sn*, and search the Hash2 table to get corresponding object. If found, the current object and the corresponding object can be linked.

4) After previous step being completed, all the objects and their relations are restored. According to specific semantic environment, the main object or objects set can be retrieved from Hash2 table.

Case study

Based on the DotNet platform, all the CIM classes are defined by using C# language. Meanwhile, the classes are extended by adding serialization functions on the basis of CIM/XSD schemas, and the results are packaged into a CIM library. Depending on the library, a software tool named as CIM Validator is developed, which can edit CIM objects and import / export CIM/XML document. In the case of a streamlined line model as shown in figure 3, it needs 42 CIM object to describe the model [12]. Using the software tool to edit the line objects set. Here, the Line object is the initiative object. Next, a CIM/XML document is exported by the tool, which contains 42 objects in "document" root (figure 4).Using this tool to import the CIM/XML document, the number of objects, the objects' state, and the relationships are all restored (figure 5).

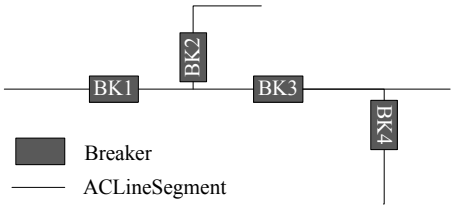

Fig. 3 A simplified line model

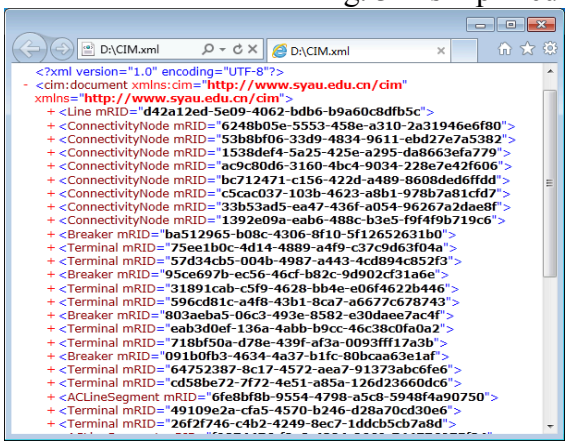

Fig. 4 CIM objects serialization

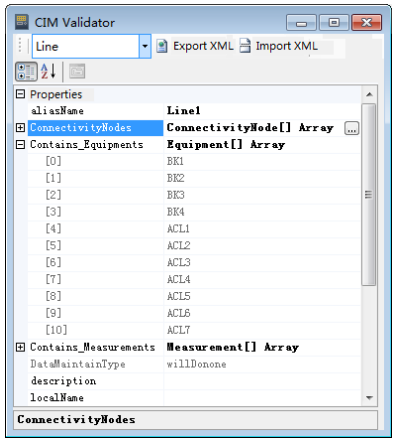

Fig. 5 CIM objects deserialization

Summary

In order to exchange data between different applications in electric power enterprise, this paper presents a method of encoding CIM model in XML mode. The two methods which can encode the

simple association and aggregation named as “embedding” and “referring” are discussed. In order to make the CIM/XML document with a common syntax, and validate the document, the CIM/XSD schemas are developed on the basis of XSD technology. Meanwhile, this paper provides a method of mapping CIM model to CIM/XSD. An attribute group “AssociationAttributeGroup” is designed in this CIM/XML schema to support the “embedding” and “referring” methods. Each of CIM class is added two functions: Serialize and Deserialize, who have the responsibilities for serialization and deserialization. Meanwhile, the detailed algorithms of the two functions are designed in this paper. The case study shows that the CIM object encoding specification, the CIM/XSD schemas and the algorithms of functions can be applied to exchange and share CIM data in electric power enterprise.

References

[1] DENG Xian-da, HE Guang-yu, CHEN Ying, et al, “CIM lead-in based on Java reflection mechanism in AEMS of Shanghai power grid,” Automation of Electric Power System, 2007, 31(18) pp. 21-25.

[2] CUI Wei, SHI Yong, SUN Bing, “The construction and integration of grid model based on IEC61970/61968,” Power System Protection and Control, 2011, 39(17) pp. 60-63.

[3] ZHU Bo-tong, CHENG Zhi-hai, TANG Zhi-qiang, et al, “Interoperate research of the intelligent substation and dispatching center based on CIM model,” Power System Protection and Control, 2013, 41(10) pp.93-97.

[4] Draft IEC 61970, “Energy management system application program interface (EMS-API), part 501: CIM RDF Schema”.

[5] WANG De-wen, YAN Chun-yu, BI Jian-gang, YUAN Shuai, “Distributed Data Exchange Method in Condition Monitoring System for Power Transmission and Transformation Equipment,” Automation of Electric Power System, 2012, 36(22) pp.83-88.

[6] XIE Jun, SHI Dong-yuan, DUAN Xian-zhong, “IEC 61970 semantic information model based on ontology technology,” Power System Technology, 2008, 32(1).

[7] LU Yi-ming, LIU Dong, HUANG Yu-hui et al, “Feeder Modeling and Application Based on CIM,” Proceedings of the CSEE, 2012, 32(28) pp. 157-163.

[8] Barbara Carminati, Elena Ferrari, “Management of access control policies for XML document sources,” Int J Inf Secur, 2003 (1) pp.236-260.

[9] IEC 61970: Energy management system application program interface (EMS-API)-part 301: common information model (CIM).

[10] CAO Yang, YAO Jian-guo, YANG Shen-chun, et al. “Latest Advancements of Smart Grid Core Standard IEC 61970,” Automation of Electric Power System, 2011, 35(17) pp. 1-4.

[11] NING Jing, LIU Jie, YE Dan, “Novel approach for extracting XML schema definition based on content model graph,” Computer Science, 2010, 37(6) pp. 179-185.

[12] LUO Jian, ZHU Bo-tong, CAI Ming, ZHAO Guo-fu, “Interoperability of CIM and SCL model based on CIM XML,” Power System Protection and Control, 2011, 39(17) pp.134-138.

Advanced Materials Research Vols. 986-987 (2014) pp 2158-2161

doi:10.4028/www.scientific.net/AMR.986-987.2158

Research on Visualized Protective Relaying Setting Software for Coal Mine Power System

Kang Sun[1, a], Niannian Sun[1, b]

[1]School of Electrical Engineering and Automation, Henan Polytechnic University, Jiaozuo, China

[a]email: sunkanghpu@163.com, [b]niannsun@163.com

Keywords: Protective Relaying Setting; Visualization; Object-oriented; Coal Mine Power System

Abstract. According to the special requirement of protective relaying setting in coal mine power system, the research and development of a visualized protective relaying setting software is described in this paper. Firstly, software architectural and its functional module is defined to meet special needs, then a novel setting method based on 'triggered by setting condition' and action simulation method based on setting value are proposed. Object-oriented and visualized programming means ensure its users can easily and directly carry out the setting calculation of protective relaying and simulate the protective action. The application and the achievements of good effects at last ensure its rationality.

Introduction

Setting calculation is essential to relay protection in power and electricity production. In recent years, the computer aided setting calculation is quite mature in technology, but the main work is oriented to high-voltage power grid[1-3]. At present, setting calculation for coal mine power network almost depends on artificial work, which does not suit rapid development of computer technology. Graphical, automatic, networked setting calculation software represents the future direction of this field[4-7]. Given this, visualized protective relaying setting software for coal mine power network based on graphical modeling is researched and developed in this paper. We emphasize on visualization and modularization in the development of this system. Considering the special character of coal mine power networks, we present a novel setting method called 'triggered by setting condition'. The proposed simulation subsystem based on setting value can precisely simulate protective action, which verifies the setting value efficiently.

System Architecture

Voltage levels of coal mine power are general bellow 110kV, and there are several differences in aspect of parameter form, network infrastructure and setting method compared to high-voltage grid. Given these inherent characteristics of coal mine power networks, there are no more mature software for relay protection setting. By taking advantage of visualized means, a system enables users to visually setting calculate and action simulate is developed in the following paper. The system mainly consists of five functional modules: ①graphic modeling module, ② fault calculation module, ③setting calculation module, ④action simulation module, ⑤database management module. All these functional modules run on the graphical and visualized interface of main electrical wiring, and realize their functions respectively. System architecture is shown in Fig.1.

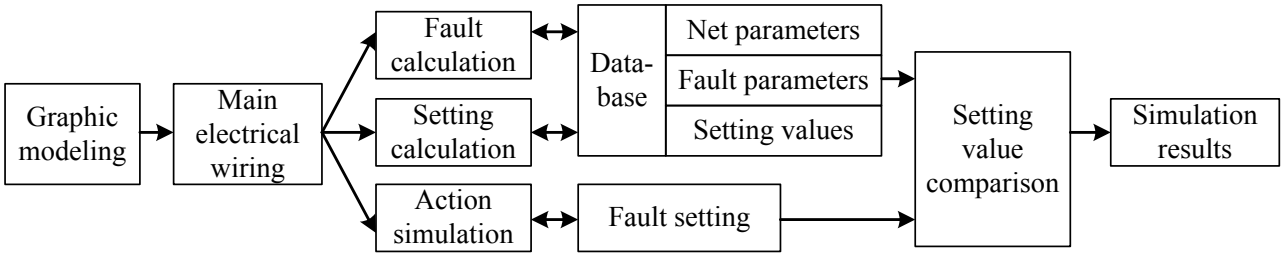

Fig.1 Architecture of the system

System functions and their realization

Graphical modeling. Graphical modeling is the basis of visualized setting calculation and action simulation. It should be an object-oriented drawing tool for electrical equipments, which can draw power transmission lines, buses, current breakers, generators, transformers, isolating switches, reactors, etc.

The basis idea of graphical modeling is to define general data structure for all electrical components firstly. During graphics generating, the parameters of each component is saved as structured parameter in the database. At the time of system construction, the interface program calls out these parameters and put them into data structure. Then a specific main electrical wiring diagram is constructed. The data structure of various electrical components are actually similar with tiny difference. Basic data structure is shown in Table 1.

Table 1. The basic data structure frame

Item	Data Type
Component name	String
Component total index	Unsigned integer
Serial number in same type of components	Unsigned integer
Component status	Integer
Component model	String
Component size	Float
Component center of gravity	Struct
Text font	String
Reserved	

Taking into account the development of computer technology and the functionality update of the system, data structures of all components have one item reserved.

Fault Calculation. Fault calculation is the basis of relay protection setting calculation. Because in power system fault calculations have become more mature, before setting calculation, all the fault parameters and the branching factors can be prepared by existing fault analysis software.

Setting Calculation. Setting calculation module is one of the cores of the system. Due to the specification of power grid bellow 110kV, the configuration of line protection is quite complex. Some lines employ three step current protection, some lines employ three step distance protection, some line even may use instantaneous under-voltage protection with current supervision and directional current protection. In these protections, coordination between adjacent lines is needed, and various setting should be calculated synchronously. To deal with this problem, we propose the following setting procedure based on the object-oriented technology.

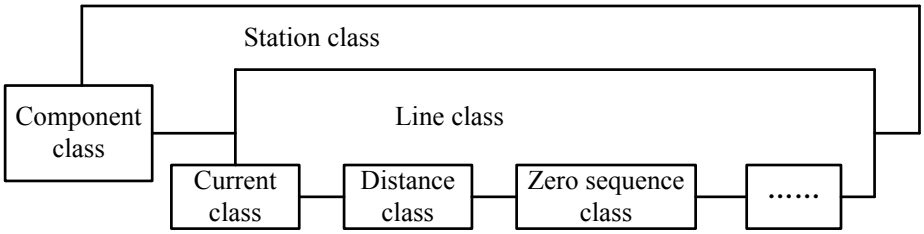

Fig.2 The successive arrangement of protective relayings

Representation of Protection Knowledge. According to the type of protected components, protective relaying can be classified into line protection, transformer protection and bus protection, etc. The object of setting calculation is the protected component, and each component has its own attributes. Take line for example, they include name, protection type, setting values, operating time, etc. Through the distal point of the lines determines the position to protect through the network topology analysis, identifying the whole point of the adjacent point. Thereby identifying a component requires the cooperation relations. As the whole point of these properties, attributes and describes the whole point setting method is packaged in a class, you can make the same protection type tuning method of forming modular. From the component property, we will find the same

system components, some parameters for the various types of protection are the same, the same section defines a base class, provided by object-oriented inheritance mechanisms, protection type inherits from a base class, the tuning method is packaged in their own respective class of protection, protect our intellectual clarity. Protection class inheritance hierarchy is shown in Fig.2.

We here take distance protection as an example to demonstrate the representation of its setting calculation process:

```
class   LineRelay  {      // line para base class
        protected:
        char    Name1[20];       //line name
        float   l;       //line length
        char    Name2[10];       //break index
        bool    XJL_side;       //protection install side
        float   XJL_CT1;
        float   XJL_CT2;
        float   XJL_PT1;
        float   XJL_PT2;
        LineRelay();
        ~LineRelay();
       };
```

```
class    XJJL：public  LineRelay
{  // distance class inherits property of line class
switch(type):
   {
   case(0):zdzI();      // distance I setting
   case(1):zdzII();     // distance II setting
   case(2):zdzIII();    // distance III setting
   }
}
```

Setting Criteria. Different from transformer and bus, line protections are generally staged, the setting values need to be coordinated strictly between adjacent lines, which makes setting calculation much more complex and results in a lot of code. To deal with this problem, we here propose a new setting idea called ‘triggered by setting condition’.

Following this idea, we define a dialog class for each protection type, the dialog box classes encapsulate setting conditions of this protection, selection of protection type, setting values of coordinated stage and so on. All members in the dialog have a unique ID. At the time of setting, user setting in the dialog box, select the appropriate conditions, the message and trigger tuning corresponds to the conditions of setting calculation for setting calculation module.

Under the proposed setting, setting two logic statements can be used when setting, that is: (1) IF (there is no given setting value of xx protection’s cooperative step) THEN (activate the setting value calculation module of cooperative step), (2) IF(there is existing setting value of xx protection’s cooperative step) THEN(calculate and verify the setting value directly).

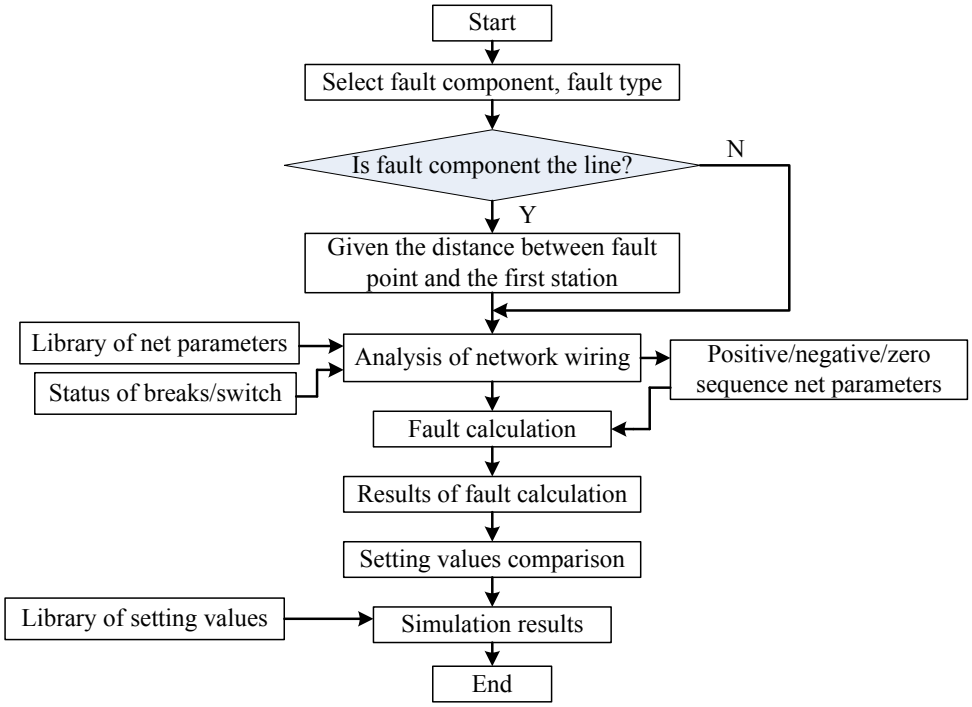

Fig.3 The block diagram of simulation model

Action Simulation. At present, there are two methods for relay protection simulation: an approach based on a given scope of protection, another based on the given setting value. The former need no fault calculation, so it is faster. However, its simulation results are not precise enough because it is just an approximation of the protection. In order to truly reflect the protection action, making simulation the effect of realistic, credible, further calibration of protection setting, our system uses a method based on the setting value. The simulation model is shown in Fig.3.

Database management. Database is the main source of information which the system needs. The database of this system consists of the network parameters library, fault calculation library, setting value library. All the functional modules of the system interact with databases through ODBC interface implementation.

Conclusions

Visualized protective relaying setting software for coal mine power network based on graphical modeling is researched in this paper. A novel setting method based on 'triggered by setting condition' is presented to meet special characteristic of coal mine power networks. The proposed simulation subsystem based on setting value can precisely simulate protective action.

Acknowledgement

The research work was supported by the Science and Technology Guiding Project of China National Coal Association (Project No. MTKJ 2012-371).

References

[1] Wang Wei, Yu Wei-yong, Zhang Pei-chao. Research on object-oriented expert system of relay setting calculation[J]. Proceedings of the EPSA, 2001, 13 (2): 1-4.

[2] Yang Zeng-li, Duan Xian-zhong, Wang You-huai. Coordination of ground distance relays for transmission lines[J]. Automation of Electric Power Systems, 2006, 30(8): 65-69.

[3] Chen Xiang-bo, Feng Lin-qiao，Liu Fei. Graphic and integrative program for fault analysis and protection setting[J]. Electric Power Automation Equipment, 2003, 23(11): 47-48.

[4]Yang Zeng-li，Shi Dong-yuan，Yang Xiong-ping. A study on the universality of the protection setting calculation software[J]. Automation of Electric Power Systems, 2007, 31(14): 89-93.

[5]Lv Feipeng, Li Huaqiang, Zhang Wenjun. Studies on the expert system for setting and coordinating protective relaying in 110kV~500kV power system[J]. Relay, 2000, 28 (3): 29-32.

[6] Zhu Jia-jie，Tai Neng-ling，Fang Xin-yan. Setting system of generator internal faults protection based on the graphic interface[J]. Relay, 2007, 35(1): 9-12.

[7]Guo Mou-fa，Yang Geng-jie，Huang Wei. Module-based setting calculation system of relay protection for power plant[J]. High Voltage Engineering, 2005, 31(9): 75-77.

Advanced Materials Research Vols. 986-987 (2014) pp 2162-2166

doi:10.4028/www.scientific.net/AMR.986-987.2162

Solving Economic Dispatch Problem in Energy Internet Using a Two-level Stochastic Gossip-based Consensus Algorithm

Jie Meng[1, a], Yan Zhang[1], Tao Zhang[2]

[1] College of Information System and Management, National University of Defense Technology, Changsha, P.R. China

[2] State Key Laboratory of High Performance Computing, National University of Defense Technology, Changsha, P.R. China

[a]mjloveyk@gmail.com

Keywords: consensus, economic dispatch, energy Internet, stochastic gossip

Abstract. In the future, energy Internet will gradually replace the traditional power network since it enables flexible energy sharing for consumers. Consensus algorithm achieved good performance in solving economic dispatch problem in microgrid system whereas the difficulty is finding a consensus variable. By means of choosing the incremental generator cost of each energy local area network (ELAN) as the consensus variable, the economic dispatch problem can be solved. Using the stochastic gossip-based algorithm as the basic framework, the economic dispatch problem can be solved in a distributed manner. In order to meeting the real-time load requirement in time under the fixed communication topology, the fluctuation of each ELAN will do the consensus update at the same time. The result of a representative case is presented to illustrate the performance of the proposed two-level stochastic gossip-based consensus algorithm.

Ⅰ Introduction

Energy is the development of modern society's foundation. In response to the energy crisis, countries actively launch research programs on new energy technologies, especially solar, wind, biomass and other renewable energy sources. In 2009, Science published a paper said as long as China raises subsidies and improves transport network, wind power would meet the electricity needs of all Chinese by 2030, showing the tremendous potential of renewable energy to solve the energy problem [1].Since renewable energy is intermittent and fluctuant, traditional power network is difficult to been adapted to large-scale use of renewable energy requirements [2]. Besides, both micro-grids and distributed power generators could not maximize the use of the renewable energy. Only implement sharing the energy of distributed micro-grids locally controlled by information flow of the communication network, the renewable energy can be used efficiently, economically and safely. Energy Internet is the combination product of information technology and renewable energy which provides a feasible technical solution to the energy crisis [3-5]. It is a comprehensive Internet which involves advanced power electronics technology, information technology and intelligent management technology, and uses a large number of distributed energy harvesting devices, new power network nodes, distributed energy storage devices, various types of loads consisting of interconnected to achieve bi-directional energy flow and peer-to-peer sharing networks [6]. Coordination among the second-level management unit energy local area network (ELAN) will attract more and more interest.

The economic dispatch problem (EDP) is one of the most fundamental issues in power systems, so it will exist in energy Internet. EDP is essentially an optimization problem that assigns the required power generation to a number of generating units to meet the active load demand. The objective is to minimize the total power generation cost, subject to several constraints. In the last, economic dispatch is conducted in a central controller, who is able to access global information. However, because of the increment of number of network node, flexible structures and plug-and-play characters, some decentralized controllers gain more perfect performance. Decentralized control doesn't mean these controllers have no relationship among them. Oppositely, they not only have personal goal, but also

hold global intention. Therefore, every controller can be modeled as an intelligent agent. Finally, using the existing theoretical framework and tools for multi-agent system, decentralized consensus control system can be implemented. Ziang Zhang *et al*. proposed incremental cost consensus (ICC) algorithm solving EDP in smart grid environment, further work using two-level ICC algorithm was also presented in a distributed manner [7-8].

Consensus problems have a long history in computer science and form the foundation of the field of distributed computing [9]. The definition of consensus problem is a strategy by means of which all agents can update themselves so that they ultimately agree upon some universal shared information. Many different problems in various areas of science and engineering have closely related to consensus problems, flocking theory, fast consensus in small-worlds, distributed formation control *et al*. Numbers of researchers have been into this area for decades, the representative experts like Jadbabaie, Olfati-Saber and Murray *et al*. have established the basic theoretical framework for analysis of consensus algorithms based on tools from matrix theory, algebraic graph theory, and control theory [10-11]. Their works focus on the affects from communication topology, time delays, and also the consensus convergence speed. The most difficult problem is how to implement the decentralized control system. Refer to the original algorithm, the system need a global synchronizing clock for making sure all the nodes update their own state at the same sample time. As a consequence, implementing flexible decentralized control system require asynchronous update rule.

Gossip-based algorithms are important alternatives in computer science to Laplacian-based consensus algorithms. Javad Lavaei *et al*. proved that the stochastic gossip algorithm can leads to reaching consensus [12]. Some important steady-state properties of the system after reaching the consensus are also derived. The expected value of the convergence time is lower and upper bounded in their next work [13]. Stochastic gossip algorithm affords an available method for implementing decentralized asynchronous control system.

In this paper, a combination algorithm of stochastic gossip-based algorithm and two-level incremental cost consensus algorithm is proposed. According to our algorithm, every node can reach agreement through asynchronous communication. Every decentralized controller modeled as an intelligent agent, based on the theory of consensus and cooperation for networked dynamic system. The paper is organized as follows: Section Ⅱ describes the formulation of economic dispatch problem first, then prove that the cost will reach the minimal point once the incremental cost of each ELAN reach agreement. The two-level gossip-based consensus algorithm is considered in detail in Section Ⅲ. Simulation and discussion are conducted to check the performance of the proposed algorithm in Section Ⅳ. Finally, the conclusions and future works are presented in Section Ⅴ.

Ⅱ Economic Dispatch Problem Formulation

Assume there are different sorts of generators in ELAN, including renewable generators and storage devices. For simply, each ELAN has a cost function $C_i(P_i)$ in terms of total real power output P_i. Economic dispatch problem can be stated as given each ELAN load requirement, how to schedule the output power from each ELAN. Mathematically, optimization of total cost for all ELANs can be modeled as follows:

Minimize:

$$C = \sum_{i=1}^{n} C_i(P_i)$$

Subject to:

$$P_{load} - \sum_{i=1}^{n} P_i = 0$$

Where C_i is the cost function of generation unit i, P_i represents the real power output of generation unit i, P_{load} refers the total load of all ELANs, it is available. The Lagrange function can be constructed as

$$L = \sum_{i=1}^{n} C_i(P_i) + \lambda(P_{load} - \sum_{i=1}^{n} P_i)$$

Where λ is a Lagrange multiplier. Based on the necessary condition, at the minimal point, the partial derivatives of Lagrange function should be zero, so the minimal point should satisfied the follow constraints:

$$\frac{\partial C_i(P_i)}{\partial P_i} = \frac{\partial C_j(P_j)}{\partial P_j}, P_{load} - \sum_{i=1}^{n} P_i = 0$$

Ⅲ Two-Level Stochastic Gossip-based Consensus Algorithm

By reaching a consensus, we mean asymptotically converging to a one-dimensional agreement space characterized by the following equation:

$$x_1 = x_2 = \cdots = x_n$$

Using the stochastic gossip-based algorithm as the basic framework, the economic dispatch problem can be solved in a distributed manner. For any arbitrary node *i,* an iterative form of the stochastic gossip-based consensus algorithm can be stated as follows:

A. Select a neighbor node *j* randomly;
B. Update observation variables z which represents the sense of environment, where ε is the weight scale;

$$z_i(k+1) = z_i(k) + \varepsilon(z_j(k) - z_i(k))$$
$$z_j(k+1) = z_j(k) + \varepsilon(z_i(k) - z_j(k))$$
$$z_m(k+1) = z_m(k), \forall m \notin \{i, j\}$$

C. Update consensus variables, where γ is the feedback scale;

$$x_i(k+1) = x_i(k) + \varepsilon(x_j(k) - x_i(k)) + \gamma z_i(k+1)$$
$$x_j(k+1) = x_j(k) + \varepsilon(x_i(k) - x_j(k)) + \gamma z_j(k+1)$$
$$x_m(k+1) = x_m(k), \forall m \notin \{i, j\}$$

D. Constraint process, $x_i^{\min}$ is the lower limit of node *i*, $x_i^{\max}$ is the upper limit of node *i*;

$$\forall i \quad if \quad x_i(k+1) < x_i^{\min}(k+1) \quad \rightarrow \quad x_i(k+1) = x_i^{\min}(k+1)$$
$$\forall i \quad if \quad x_i(k+1) > x_i^{\max}(k+1) \quad \rightarrow \quad x_i(k+1) = x_i^{\max}(k+1)$$

E. Go to Step A;

Consensus theorem in mathematics shows keeping local agreement can lead to reaching global agreement. The consensus variables will achieve asymptotically consensus after limited iterations. Once the change happened, the observation variables keeping agreement automatically information exchange among the whole system. Thus, each node can receive the average of environment change. It is easy to see that the gossiping frequency can affect the system behavior.

Ⅳ Simulation Results

To validate the proposed two-level stochastic gossip-based consensus algorithm, a small-scale energy Internet with five ELANs is studied. In this paper, we assume the cost function satisfy a quadratic cost function expressed as follow. Other forms of convex cost function also can be optimized. The parameters and initial conditions for the five nodes are shown in table.1.

$$C_i(P_i) = a_i + b_i P_i + c_i P_i^2$$

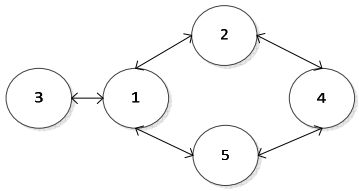

Fig.1 Communication topology a five-ELAN system

Table.1 Parameters of five ELANs /kW

Node	a_i	b_i	c_i	Initial generator power	Load fluctuation	ε	γ
1	561	7.92	0.001562	300	500	0.5	0.5
2	310	7.85	0.00194	500	300	0.5	0.5
3	78	7.8	0.00482	400	-100	0.5	0.5
4	261	7.72	0.001242	800	400	0.5	0.5
5	178	7.88	0.00452	600	0	0.5	0.5

In order to solving the EDP in energy Internet, we assume the incremental cost of generate power as the consensus variable. Since the load requirement is time-varying, and renewable energy is intermittent and fluctuant, the observation variable represents the power fluctuation of each node. Fig.1 shows the communication topology of five-ELAN system. It is not hard to acquire their neighbor set for each node. According to the parameters in table.1, the convergence results are shown in Fig.2.

$$x_i = \frac{\partial C_i(P_i)}{\partial P_i}, i = 1, 2, \cdots, n$$

$$z_i(k+1) = \sum_{i=1}^{5} ((P_{load}^i(k+1) - P_i(k+1)) - (P_{load}^i(k) - P_i(k)))$$

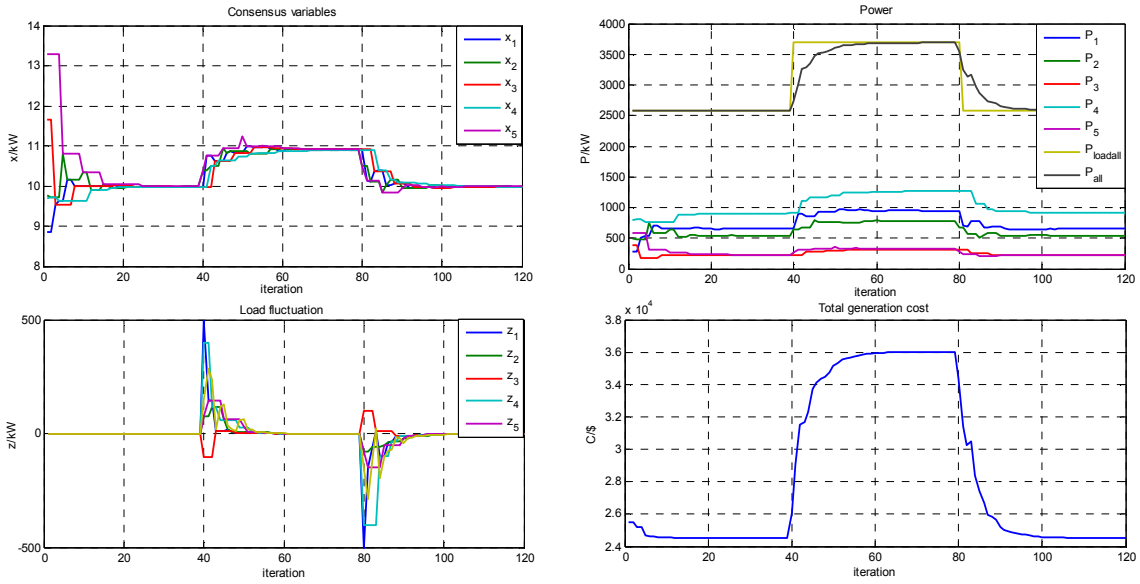

Fig.2 Simulation results

As Fig.2 shows, the consensus variables reach agreement after limited interations. When the load fluctuation happens, with the suitable feedback scale, system can keeping working at the best economic dispatch point automatically. Actually, the simulation results just show the process how do them reach to an agreement because the node update its state one by one in simulation. Obviously, it is not in accordance with the proposed algorithm because any arbitrary node can start a interaction with its intention nerghbor. As a consquence, the real iteration number must less than the simulated iteration number. In the paper, the weight scale is chosen as 0.5 because of it can make the neighbor nodes reach agreement by just one time iteration. Actually, 0.5 isn't the best intelligent choose, there are some relation to the degree of each node. It is obviously that once agreement reached, the total generation cost reaching smallest, and the economic diapatch problem been solved.

Ⅴ Conclusion

The main contribution of this paper is to present a two-level stochastic gossip-based consensus algorithm with an example to illustrate the use of achieving economic dispatch in energy Internet system. The algorithm is able to converge to the optimal solution in a distributed manner with asynchronous information exchange. The decentralized control system can meet the demands automatically when the load requirement change happens to each ELAN because the load fluctuation is design to afford a feedback from the second-level consensus loop. The simulation results show that the proposed algorithm can lead to an agreement in limited iterations and the real iteration number should be less than the simulation results. The further work is finding the optimal weight scale achieving the fastest convergence speed and offering the convergences prove in theorem.

References

[1] Michael B. M, Xi L., Chris P. N., Yu X. W.. Potential for Wind-Generated Electricity in China. Science, 2009, 325 (5946):1378-1380.
[2] Jeremy Rifkin, Third Industrial Revolution (in Chinese), ZHANG T W, Sun Y L, translation. BeiJing, CITIC Press, 2012, 1st Edition.
[3] Lasseter R H, Micro-grids, IEEE Power Engineering Society Winter Meeting, 2002: 305-308.
[4] Ackermann T, Andersson G, Söder L. Distributed generation: a definition, Electric power systems research, 2001, 57(3): 195-204.
[5] Huang A Q, Crow M L, Heydt G T, et al. The future renewable electric energy delivery and management (FREEDM) system: the energy Internet, Proceedings of the IEEE, 2011, 99(1): 133-148.
[6] Zha Y B, Zhang T, Tan S R, Huang Z, Wang W G, Understanding and Thinking of the Energy Internet (in Chinese)[J], National Defense Science and Technology, 2012,33(5):1-6.
[7] Ziang Zhang; Mo-Yuen Chow, "Incremental cost consensus algorithm in a smart grid environment," Power and Energy Society General Meeting, 2011 IEEE , vol., no., pp.1,6, 24-29 July 2011.
[8] Ziang Zhang; Xichun Ying; Mo-Yuen Chow, "Decentralizing the economic dispatch problem using a two-level incremental cost consensus algorithm in a smart grid environment," North American Power Symposium (NAPS), 2011 , vol., no., pp.1,7, 4-6 Aug. 2011.
[9] N. A. Lynch, Distributed Algorithms. San Francisco, CA: Morgan Kaufmann, 1997.
[10] Olfati-Saber, R.; Fax, J.A.; Murray, R.M., "Consensus and Cooperation in Networked Multi-Agent Systems," Proceedings of the IEEE , vol.95, no.1, pp.215,233, Jan. 2007.
[11] A. Jadbabaie, J. Lin, and A. S. Morse, BCoordination of groups of mobile autonomous agents using nearest neighbor rules,[IEEE Trans. Autom. Control, vol. 48, no. 6, pp. 988–1001, Jun. 2003.
[12] Lavaei, J.; Murray, R.M., "On quantized consensus by means of gossip algorithm - Part I: Convergence proof," American Control Conference, 2009. ACC '09. , vol., no., pp.394,401, 10-12 June 2009.
[13] Lavaei, J.; Murray, R.M., "On quantized consensus by means of gossip algorithm - Part II: Convergence time," American Control Conference, 2009. ACC '09. , vol., no., pp.2958,2965, 10-12 June 2009.

Advanced Materials Research Vols. 986-987 (2014) pp 2167-2170

doi:10.4028/www.scientific.net/AMR.986-987.2167

Optimal Study of the Reverse Logistics Network for Electronic Waste under Fuzzy Environment

Ligang Sun [1,a], Zheng Zhang [2,b]

[1] Shanghai Dianji University, Shanghai 2001306, China

[2]School of Management, the University of Shanghai for Science and Technology, Shanghai, China

[a]sunlg@sdju.edu.cn, [b]zhang65176393@163.com

Keywords: reverse logistics; waste electronic; fuzzy chance constrained; confidence level

Abstract: Considering the uncertainty of electronic waste recovery quantity in consumption areas, a fuzzy optimization model for electronic waste reverse logistics network with capacity constraints was constructed to determine the number and location of the facilities, the flows between each facility. A numerical example was provided to demonstrate the feasibility of the model.

Introduction

In recent years, the output of electronic waste increases fast. With the fast increase in the output of electronic waste, the research on reverse logistics for electronic waste gradually attracted wide attention. Li-Hsing[1] constructed a mixed integer programming model with capacity constraint after studying electronic waste recycling in Taiwan. Shanshan Wei etc[2] established a network cost optimization mixed integer linear programming model from the perspective of reverse logistics location optimization. Xiaoyu Zhao etc.[3] and Jianwei Qiu etc.[4] constructed a reverse logistics network optimization model with fuzzy parameters. Min'gang Zeng etc.[5] constructed a scrap computer reverse logistics optimization model. This paper uses fuzzy parameter to describe the uncertain recovery quantity of electronic waste and constructs a fuzzy programming model for the electronic waste reverse logistics network. A numerical example is provided to demonstrate the feasibility of the model.

Model Formulation

Problem Description. The electronic waste reverse logistics network is composed by the collection points, storage centers, disassembling centers, reprocessing plants and waste disposal points and the transportation routes between them. The reverse logistics network optimization design for electronic wastes is to determine the quantity and location of storage centers, disassembling centers, reprocessing plants, and find the suitable flows between them to minimize the total cost.

Model Assumption. In order to facilitate analysis, we give the following assumptions:

(1) Every consumption area has a collection point. And the recovery quantity is a fuzzy number;
(2)The quantities and locations of collection points, waste disposal points are certain;
(3)New facilities only can be established in the known candidate locations;
(4)The fixed cost, operating cost and transportation cost are certain;
(5)The storage centers, disassembling centers, reprocessing plants have capacity limitation;
(6)There is a linear relationship between the transportation cost and distance.

Formulation of the Model. The notation can be represented as follows:

Indices: i :collection point in consumption area $(i = 1,2,\dots,I)$; j :storage center $(j = 1,2,\dots,J)$; k :disassembling center $(k = 1,2,\dots,K)$; l :waste disposal point $(l = 1,2,\dots,L)$; m ; reprocessing plant$(m = 1,2,\dots,M)$.

Parameters:Q_i: recovery quantity of i;F_j,E_j,W_j: fixed cost, operating cost and maximum capacity of j;F_k,E_k,W_k: fixed cost, operating cost and maximum capacity of k;F_m,E_m,W_m: fixed cost, operating cost and maximum capacity of m;p:unit cost of electronic waste;d_{ij},TC_{ij}: the distance and transportation cost between i and j;d_{jk},TC_{jk}: the distance and transportation cost between j and k;d_{kl},TC_{kl}: the distance and transportation cost between k and l;d_{km},TC_{km}: the distance and transportation cost between k and m;r: recovery rate of electronic waste.

Decision variables: X_j: 1,if storage center is opened at location j,0,otherwise;Y_k: 1,if disassembling center is opened at location k,0,otherwise;Z_m: 1,if reprocessing plant is opened at location m,0,otherwise;x_{ij}: quantity of electronic waste shipped from i to j;x_{jk}: quantity of electronic waste shipped from j to k;x_{kl}: quantity of electronic waste shipped from k to l;x_{km}: quantity of solid wastes shipped from k to m.

The problem can be formulated as follows:

$$\min Z = \sum_{j\in J} F_j X_j + \sum_{k\in K} F_k Y_k + \sum_{m\in M} F_m Z_m + E_j \sum_{i\in I}\sum_{j\in J} x_{ijs} + E_k \sum_{j\in J}\sum_{k\in K} x_{jk} + E_m \sum_{k\in K}\sum_{m\in M} x_{km} + OT \sum_{k\in K}\sum_{l\in L} x_{kl} + \sum_{i\in I}\sum_{j\in J} x_{ij} TC_{ij} d_{ij} + \sum_{j\in J}\sum_{k\in K} x_{jk} TC_{jk} d_{jk} + \sum_{k\in K}\sum_{l\in L} x_{kl} TC_{kl} d_{kl} + \sum_{k\in K}\sum_{m\in M} x_{km} TC_{km} d_{km} + p\sum_{i\in I} \widetilde{Q}_i \quad (1)$$

$$\sum_{j\in J} x_{ij} = \widetilde{Q}_i \qquad \forall i \quad (2)$$

$$\sum_{i\in I} x_{ij} = \sum_{k\in K} x_{jk} \qquad \forall j \quad (3)$$

$$r \times \sum_{j\in J} x_{jk} = \sum_{k\in K} x_{km} \qquad \forall k \quad (4)$$

$$(1-r) \times \sum_{j\in J} x_{jk} = \sum_{l\in L} x_{kl} \qquad \forall k \quad (5)$$

$$\sum_{i\in I} x_{ij} \le X_j W_j \qquad \forall j \quad (6)$$

$$\sum_{j\in J} x_{jks} \le Y_k W_k \qquad \forall k, s \quad (7)$$

$$\sum_{k\in K} x_{km} \le Z_m W_m \qquad \forall m \quad (8)$$

$$X_j, Y_k, Z_m \in \{0,1\} \qquad \forall j,k,m \quad (9)$$

$$x_{ij}, x_{jk}, x_{kl}, x_{km} \ge 0 \qquad \forall i,j,k,l,m \quad (10)$$

The objective function (1) tries to minimize the total cost including investment cost, operating cost and transportation cost. Constraint (2) requires the total outgoing flows from each collection point should be the same as the electronic waste recovery quantity. Constraints (3) is the balance equations, the quantities that enter to storage centers must be equal to the quantities that leave them. Constraint (4) and (5) ensure reusable components would be shipped to reprocessing plants, and the rest would be transported to disposal points. Constraint (6), (7) and (8) are the maximum capacity limitation for storage centers, disassembling centers, reprocessing plants, respectively. Constraint (9) represents the binary variables. Lastly constraint (10) enforces the non-negativity restriction on the decision variables.

Solution method for the model

In order to solve the model, the fuzzy parameter should be clarified. Based on the study of Liu and Iwamura [6,7], the model can be transformed to the following mixed integer programming model.

$$\min f \quad (11)$$

$$\sum_{j\in J} F_j X_j + \sum_{k\in K} F_k Y_k + \sum_{m\in M} F_m Z_m + E_j \sum_{i\in I}\sum_{j\in J} x_{ijs} + E_k \sum_{j\in J}\sum_{k\in K} x_{jk} + E_m \sum_{k\in K}\sum_{m\in M} x_{km} + OT \sum_{k\in K}\sum_{l\in L} x_{kl} + \sum_{i\in I}\sum_{j\in J} x_{ij} TC_{ij} d_{ij} + \sum_{j\in J}\sum_{k\in K} x_{jk} TC_{jk} d_{jk} + \sum_{k\in K}\sum_{l\in L} x_{kl} TC_{kl} d_{kl} + \sum_{k\in K}\sum_{m\in M} x_{km} TC_{km} d_{km} + p\sum_{i\in I} (1-\theta) Q_{i1} + \theta Q_{i2} \le f \quad (12)$$

$$\sum_{j\in J} x_{ij} \geq (1-\theta)Q_{i1} + \theta Q_{i2} \qquad \forall i,j \quad (13)$$

$$\sum_{j\in J} x_{ij} \leq (1-\theta)Q_{i3} + \theta Q_{i2} \qquad \forall i,j \quad (14)$$

Other constraints are the same as the constraints from (3) to (10), where $\theta(0 \leq \theta \leq 1)$ is a given confidence level. So the model has been converted to a deterministic model. And it can be solved by commercial software CPLEX, LINDO, LINGO, and so on.

Numerical Example

An electronic enterprise needs to construct an electronic waste reverse logistics network. The recovery quantity is fuzzy parameter. p=800RMB/t, TC_{ij}=TC_{jk}=TC_{kl}=TC_{km}=1RMB/(t·km), θ=0.9. Other parameters are shown from table 1 to table 5.

Tab.1 Recovery quantity in collection points (t)

	quantity		quantity		quantity		quantity
I1	(25,27,30)	I2	(31,34,36)	I3	(42,45,49)	I4	(18,19,22)
I5	(22,24,27)	I6	(19,22,24)	I7	(27,29,33)	I8	(33,34,38)

Tab.2 Distance between potential dismantling centers and potential reprocessing plants, waste disposal point (km)

		reprocessing plants			waste disposal point
		1	2	3	
dismantling centers	1	32	24	19	51
	2	26	29	37	37
	3	35	31	26	46

Tab.4 Distance between potential storage centers and waste disposal point, potential dismantling centers (km)

		Collection points								dismantling centers		
		1	2	3	4	5	6	7	8	1	2	3
storage centers	1	22	14	18	25	19	12	25	31	37	25	28
	2	23	30	16	19	24	15	9	17	20	19	27
	3	37	29	31	16	22	35	17	18	41	30	25
	4	21	14	19	36	25	30	13	21	24	19	31

Tab.5 Maximum capacity, fixed cost and operating cost of potential storage centers, dismantling centers and reprocessing plants

	storage centers				dismantling centers			reprocessing plants		
	1	2	3	4	1	2	3	1	2	3
Maximum capacity (t)	120	120	120	120	120	120	120	800	800	800
Fixed cost (RMB)	110000	110000	110000	110000	325000	325000	325000	250000	250000	250000
operating cost (RMB/t)	175	175	175	175	550	550	550	870	870	870

Having the above parameters, the model can be solved by LINGO11.0. The optimal solution of structure variables is given in table 6. The optimal total cost is 33940800 RMB. We build storage center at $J2$ and $J4$, dismantling center at $K1$ and $K2$, and reprocessing plant at $M2$.

Tab.6 Optimal solution of structure variables

X_2	X_4	Y_1	Y_2	Z_2	Others
1	1	1	1	1	0

Conclusions

This paper studies the optimal strategy of electronic waste reverse logistics network when the recovery quantity is fuzzy number, and constructs a fuzzy programming model for it. Finally, an example is given to demonstrate the feasibility of the model. And the multi-objective situation should be studied further in the future.

References

[1] Li-Hsing Shih. Reverse Logistics System Planning for Recycling Electrical Appliance and Computers in Taiwan [J].Resource, Conservation and Recycling, 2001, 32(1):55-72.
[2] Shan-shan Wei, Ke-jing Zhang. Optimization Model of Facility Location Decision in E-waste Reverse Logistics Network [J] Journal of Donghua Unversiy(natural science), 2010, 36(5):574-580.
[3] Xiao-yu Zhao, Ping Peng. Optimization Design Model with Fuzzy Parameters for Recycling Network of Waste Electronic Appliances[J] Industrial Engineering. 2007, 10(3):62-66.
[4] Jian-wei Qiu, Mei-lian Liu. A Network Design Based on the Fuzzy Programming of Guangxi WEEE of the Reverse Logistics [J] Fuzzy Systems and Mathematics, 2012, 26(6):181-190.
[5] Min-gang Zeng, Ming-jian Zhou. A Reverse Logistics Model for the Recycling of Scrap Computers [J] Industrial Engineering, 2006, 9(6):55-60.
[6] Baoding Liu, Reiqing Zhao: Stochastic Programming and Fuzzy Programming (Tsinghua University Press, Beijing 1998).
[7] Baoding Liu, Iwamura K: Fuzzy Sets and Systems Vol. 94(1998), p. 227

Advanced Materials Research Vols. 986-987 (2014) pp 2171-2175

doi:10.4028/www.scientific.net/AMR.986-987.2171

The design of emergency management system for thermal power plant based on B/S architecture

Lifang Zhang[1,a], Hairong Sun[1,b], Hao Jia[1,c], Ze Dong[1,d]

[1]Hebei Engineering Research Center of Simulation & Optimized Control for Power Generation (North China Electric Power University), Baoding 071003, China

[a]zhanglifang304@163.com, [b]esunhair@163.com, [c]tonyjh68@163.com, [d]dongze33@163.com

Keywords: thermal power plant, emergency management, B/S architecture, .NET framework

Abstract. The thermal power has a large proportion in China's energy structure, thus, the thermal power plants can be said to be the foundation of our national economy. However, the industry characteristics of thermal power plant themselves make it to be accident-prone. In this paper, we aim at the suddenness and rapidity of emergency, combine the principle of "both prevention and response, combined with the normal and abnormal", relay on the B/S architecture, run through the four stages of emergency management which are prevention, preparedness, response and recovery, in order to propose the overall design scheme of emergency management system for thermal power plant.

Introduction

Energy plays an important role in China's energy structure and is a significant material foundation for the development of the national economy. In China, the thermal power has a large proportion in energy structure, which accounts for about 80% of the total generating capacity. Thermal power plant is a complex giant system that its production environment has special characteristics of the industry, such as more electrical equipment, more high temperature and high pressure equipment, more flammable and toxic substances, more high-speed rotating machinery, more special operations[1].

The emergency management in thermal power plant is to increase the response rate of emergency responses, the scientific nature and reliability of emergency rescue decisions and the efficiency of emergency rescue work, minimizing casualties and property losses caused by the accident, and quickly restore normal operation of the plant[5].

In view of this, we carry out the study and design of emergency management for thermal power plant.

The overall architecture of the system

Construction goals. Browser/Server (B/S) architecture is a popular network architecture with the rise of Internet technology in the late 20th century. In this mode, the user only needs a simple Web browser, instead of complex application software. As long as you can connect to the LAN which the server runs in, you can operate and access the same database at any place, through different ways.

Chinese government clearly stated, "In accordance with the principle that both prevention and response and combined with the normal and abnormal, we should establish a unified and efficient emergency information platform"[4]. Based on this principle, combined with the characteristics of emergency management which are systematicness, complexity, dispersion and continuity, we should ultimately construct a "moderate-investment, comprehensive-coverage, information-sharing, real-time-control, rapid-response and accurate-dispose" emergency management system which is based on B/S architecture.

The design principle of the system

i) Progressiveness and practicability

The software uses the object-oriented programming thought to enhance the maintainability, scalability and manageability. As for the development of the website, we use standard three layer architecture style.

ii) Coordination, fluency and ease of use

Various subsystems can combine organically and work together compatibly. The whole system should have clear interfaces, simple operations and the properties of stability and reliability.

iii) High stability, high reliability, high availability

The system architecture, technical measures, development tools that are used to build the system are all based on the application of mature basis, so that we can ensure the high reliability of the system and the operations to be not blocked, no pause and delay within the allowed range.

iv) Easy adjustment and easy maintenance

The design of the application should be fully taken into account to guarantee the visualization, hierarchy and real-time control of the management and maintenance.

The design principle of the database

i) Standardized data

We adopt international standards and national standards to standardize the input data.

ii) Data storage

In principle, the data is stored into the tables of the database, as for the large data (such as: files) we store them on the server to ensure that the database is running efficiently.

iii) Consistency and integrity of the data

In the design of the database, the data structure should meet the requirements of the third paradigm. In order to ensure the efficiency of the database, we can do moderate anti-normalization. Considering the requirements of the user-defined data's consistency and integrity, through the whole implement we make use of stored procedures and triggers.

The overall design of the system. Hall-dimensional structure is a theoretical model of systems engineering proposed by USA project scientist Hall in 1969[2]. According to Hall-dimensional structure theory, combining the principle of classification management, continuous improvement, dual state and dynamic management, we construct the architecture of emergency management system for thermal power plant, as shown in Figure 1.

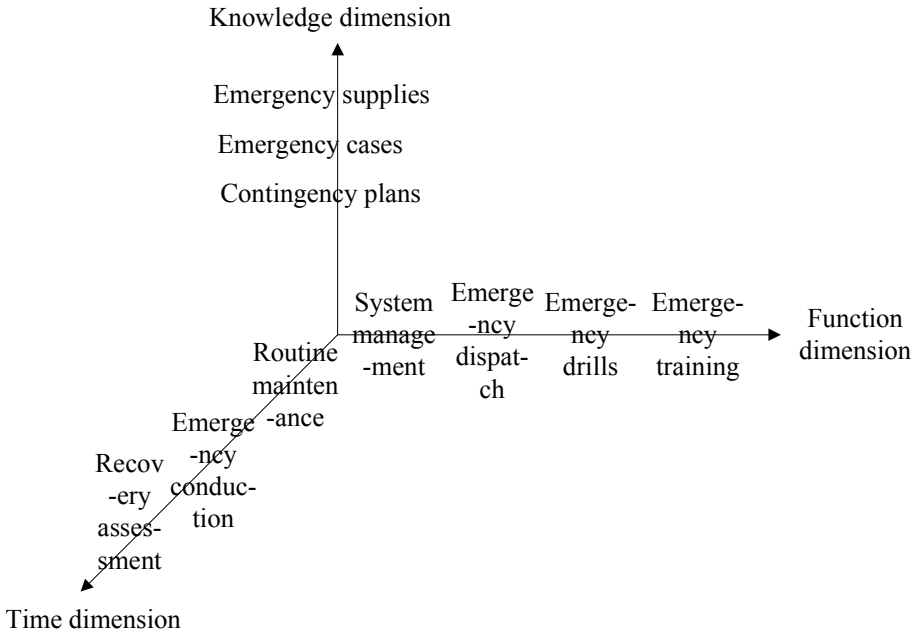

Figure 1 Hall-dimensional structure of Emergency system

i) Time dimension

In this architecture, the time dimension should cover the whole process of emergency management, including routine maintenance, emergency conduction and recovery assessment. In practice, these processes are interrelated, even overlapped.

ii) Function dimension

Function dimension covers the full functionality of the system, including system management, emergency dispatch, emergency drills and emergency training.

iii) Knowledge dimension

Knowledge dimension plays a decisive role in this system. Function dimension and time dimension are inseparable from knowledge dimension, for it provides necessary theoretical knowledge and technical expertise.

Main functional modules

The main target of emergency management is to provide reasonable treatment and management for the emergencies. As a special management, emergency management system must achieve the four phases of emergency management – monitoring and early warning, emergency preparedness, emergency disposition, recovery assessment.

Monitoring and early warning. The main task of this stage is alarm processing. The system is open to all employees, anyone found accidents or safety hazards can directly login the system to report the dangers to the departments in charge. When the workers in this department receive the reports, they classify these reports to determine the responsible department and the person in charge and order him to deal with the dangerous situations. Alarm processing is the entry for all of the emergency information data, as well as the information portal for the responsible departments to dispose accidents or safety hazards.

Emergency preparedness. Emergency preparedness mainly refers to the daily work of emergency management, which is the preparatory work when no danger occurs. This module includes basic functions, emergency supplies, contingency plans, emergency drills and emergency trainings.

i) Basic functions

In this service, we plan to provide a login interface for all employees and an interface for the system administrator to manage and maintain the system. In order to make the system as efficient as possible, we hang the login settings to the enterprise portal site's login system. The design of single sign-on simplifies the customers' experiences. But the system manager requires special administrator account and password, which is to improve the security of the system.

ii) Emergency supplies

The functions this service provides mainly include the management of emergency supplies by types, emergency resource information inquiries and information maintenance. The management of emergency supplies by types is the management for storage location, storage number, disposable number and present or historical usage; emergency resource information inquiries is a powerful search engine, according to the input keyword, we can get the information we want; information maintenance refers to maintain the expenditures, usage and addition situations timely to ensure the information to be accurate and effective.

iii) Contingency plans

This part plays a decisive role in the implement of the whole system. During the emergency disposal process, the contingency plans provide technical support and decision-making support. The functional departments' staff plans to establish a structured content template to provide support for the emergency plan services. The functions of this module are the creation of the contingency plans, viewing the contingency plans, proposing amendments and managing the contingency plans.

iv) Emergency drills

Emergency drills are the comprehensive and specialized drills organized by the Emergency Command in conjunction with relevant units regularly to improve the employees' abilities to response to the disasters. The functions are as follow. The Emergency Command develops the drill plans. In the plan, the Emergency Command should allocate a director, a commander, a number of participants and the time to conduct. Every role should participate in the drill on time. After the drill, the organizer should submit a report to the system to record this drill.

v) Emergency trainings

Emergency trainings are not too much different from emergency drills. They are only different in form. Emergency drills focus on practical handling of emergency situations, but emergency trainings focus on prevention of emergency situations and theoretical study.

Emergency disposition. This process refers to the practical handling after the accidents or warnings happen, including emergency management decision-making, organization of emergency response teams and allocation of emergency supplies. This stage together with monitoring and early warning is collectively referred to as emergency dispatch service. Emergency dispatch service is a coarse-grained service, mainly for handling scheduling when the accident occurred.

In this stage, the main two tasks – assignment of the task and supervision – relay on the short message transmission function to achieve. After the completion of the corresponding work, processing crews and equipment dispatchers report the situation to the responsible department. After the responsible department has confirmed the emergency has been resolved, the system automatically records that the alarm has been discharged and records the released time.

Recovery assessment. This stage is an essential part of the entire process. Recovery assessment includes routine assessment and disaster assessment.

Routine assessment and emergency preparedness cross together, including the assessment of contingency plans, the evaluation of emergency drills and the summary of emergency trainings.

Disaster assessment and emergency disposition cross together. It happens after the elimination of the warning and mainly refers to the evaluation of the entire incident from the cause of the incident to the result. At last, the system generates a detailed assessment report for the record.

Implementation of the system

We choose .net platform as the develop environment, when it comes to the development of this system. This platform has the advantages of easy maintenance, friendly interface, high efficiency, easy to transplant etc... The JIT compiler technology can greatly improve the efficiency. As for the practical development, we plan to use the popular programming languages, including ASP.NET, C#, SQL.

.NET is a Microsoft XML Web services platform and is also a new generation of technical platform[3]. It provides a cross language programming environment, supports C++, C#, VB, J# and other languages, allows applications to communicate with each other and share data through Internet and is a perfect solution for publishing and running the Web Services. The architecture diagram of .NET platform is shown in Figure 2.

For the operation of the backstage database, we make use of the Structured Query Language (SQL), which has the advantages of concise structure, powerful functions and wide application. Because of these advantages, it is especially applicable to the operations of a variety of relational data in thermal power plant.

Conclusions

The establishment of an open, extensive and adaptable to the characteristics of thermal power plant is the essential link of power enterprise informatization and is also the necessary path to realize emergency management more scientific and standardized. By implementing this system can we improve the level of safety and emergency management steadily, deal with the accidents during the production in thermal power plant effectively, reduce the loss of life and property and contribute to overall goal of safe production of our country.

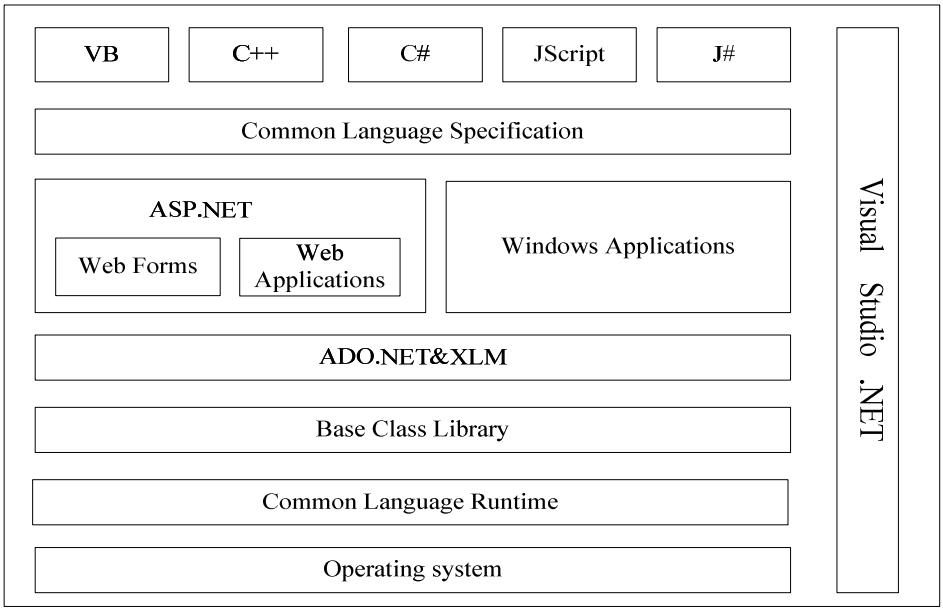

Figure 2 .NET framework architecture

Acknowledgements

This work was supported by the Fundamental Research Funds for the Central Universities.

References

[1] Chao Zhang, Yushi Lu and Lin Lin: Journal of Safety and Environment Vol.9 (2009), p.137, (In Chinese).

[2] Tao Liu: Science and Technology Management Research Vol.31 (2012), p.145, (In Chinese).

[3] Jeffrey Richter: Microsoft .NET framework programming (Tsinghua University Press, Peking, 2003).

[4] Lei Ji: Emergency Management (Higer Education Press, Peking, 2005), (In Chinese).

[5] Chao Zhang, Yushi Lu and Lin Lin: Journal of China Safety Science Vol.19 (2009), p.161-165, (In Chinese)

Advanced Materials Research Vols. 986-987 (2014) pp 2176-2179

doi:10.4028/www.scientific.net/AMR.986-987.2176

Relationship of three rock parameters

SUI Lili[1,a]，YANG Yongming[2]， LIU Peng[2], CHEN Jialiang[2]，GE Zhishun[2], CHEN Lei[2], Zhang Shoucheng[1], Yu Jian[1]

[1] North China Institute of Science and Technology, Beijing 101601 , China

[2] School of Mechanics & Civil Engineering, China University of Mining and Technology(Beijing), Beijing, 100083，China

[a]suililiwin@126.com

Keywords: Fractal dimension, rock brittleness, surface density, multiple linear regression

Abstract. In order to solve complex problems of traditional methods used to evaluate the rock fracability, the relationship between fractal dimension, rock brittleness and fracture density these three parameters was studied. The multiple linear regression is reasonable through nine kinds cores. The regression coefficients demonstrate both rock brittleness and surface fracture density play positive roles on fractal dimension value, the larger they are, the better the fracability. Therefore, the two parameters can be converted to consider only one parameter that is the fractal dimension of rock. The larger the fractal dimension, the better the fracability is, that is using fractal dimension represents brittle index and surface density to participate in fracability evaluation.

Introduction

The fracability research has important theoretical and practical significance in oil and unconventional energy development [1], the value of fracability will affect the initial output and the ultimate recovery of energy sources, as well as it can be regarded as an approach to judge the value of development. Increasing consumption of conventional energy reserves, resulting in the development of unconventional energy is increasing. Fracability refers to the properties of effective fracturing capacity in hydraulic fracturing of rock. This term at home and abroad is still a relatively new concept, and not yet found an effective evaluation method [2], but it is certain that there are many factors can decide it. It is a concentrated expression of the address of rock and reservoir characteristics, which is mainly related to crustal stress, rock brittleness, quartz content, natural cracks, diagenesis and other factors [3]. Therefore, as studying the evaluation problems of fracability, a lot of factors should be considered, which is bound to increase the difficulties. Aiming at nine core related values of the literature [4], and from the parameters prospect of rock characteristics, this paper finds the relationship between fractal dimension and brittleness and surface fracture density. So that through the fractal dimension the fracability value can be determined. Applying to engineering namely mine sampling, fracturing, calculating fractal dimension size, then determining the developing value, and finally reaching the goal of improving efficiency.

Considerations

Rock brittleness. Rock brittleness is an important character of rock, and it is the most important factor for fracability. Nowadays, there is no uniform definition about the brittleness of rock. Sondergeld uses mineralogy to judge the brittle of shale, that is, according to the content of quartz, brittleness index can be obtained, which is equal to quartz/(quartz+carbonatite+clay).

Matthews, etc. [5] evaluate and summarize the typical North American shale development block. They think carbonate is more brittle compared with clay and quartz, which belongs to brittle minerals. Therefor the rock brittleness criterions could not be in uniform standard through mineralogical method [6].

Different evaluation methods obtain different results. Based on predecessors' research, the brittleness index calculated with Young's modulus and Poisson's ratio is chosen in this paper according to the rock mechanics parameters given in document [4] as well as the reasonableness of the results. The results we get are closed to the result calculated by the method proposed by Goktan [7]. Brittle rock has high content of quartz and complex crack network, besides, they would be broken more easier. Therefore when rocks are more brittle, they would have higher fracability.

Surface density

In this paper, the surface density is chosen to characterize fracture density, relatively speaking, it is easier to measure and can reflect the development degree of cracks completely [8].

The surface density of rock tectonic fractures reflects the degree of rock rupture, under the same tectonic setting and stress situations, which reflects the rock brittleness [9]. The relationship between rock brittleness and density is the bigger the brittleness, the greater the surface density, and the more the crack growth. So the rock brittleness can be reflected by the rock fracture density after fracturing.

Fracture structure surface fractal dimension of trace.

A large number of experiments and field studies show that [10]: rock fissure network structure is a kind of natural fractal, which has fractal characteristics.

Currently, the most commonly used calculation methods for fractal dimension of rock fractures include silt island method, box-counting method, exponential-spectrum method, variogram method[11-13] and so on, in which box dimension method is often used because of the ease of operation. Box dimension method is the most important method for determining the fractal dimension of rock fracture through graphics, which is simple and convenient and easy to understand, so it is chose in this paper.

Analysis three parameters using multiple linear regression method

Multiple linear regression analysis is a method of dealing with the question related with multiple independent variables, which is to predict and estimate the dependent variable using the optimal combination of multiple independent variables. This analysis is closer to actual one and more effective than just using one variable to get the prediction estimation [14]. Now we analysis the three parameters, rock brittleness index, fractal dimension of trace of fracture structure surface and the surface density calculated from literature [4] regarding the nine core measurements, where the fractal dimension and surface density are the fracture morphology description after fracturing the cores with the Soundless Cracking Agent .

Table 1 Three parameters for 9 cores

number	lithology	coring depth[m]	fractal dimension[/m]	Brittle index[%]	density[/m]
1	granit	outcrop	1	63.1	9.3
2	carbonatite	outcrop	1.1079	46.7	25.6
3	sandstone	1664	1.0177	62.7	14.8
4	sandstone	1545	1.007	9.3	17.2
5	sandstone	2896	1	39	10.8
6	packsand	1804	1.0436	16.3	20.6
7	packsand	1444	1.086	40.4	24.8
8	cement		1.086	52.9	18.6
9	shale	2713	1.1247	45.7	31.1

According to the foregoing, you can initially judge that all these three parameters are correlated in positive fashion. Many rock characteristic parameters' influence and the weighting factors of these parameters are considered in conventional evaluation methods, which makes the problem more complexity. Now to downsize the parameters for the fracability evaluation method, a method to organic integration of the three parameters is needed to be found. If the simple relationship of characterizing a number of parameters with one or less parameters can be found, then the influencing parameters can be streamlined to indicate the concise and effective development direction to the rock fracability evaluation.

Since the perceived close ties between the three parameters, rock brittleness index, fractal dimension and surface density, are detected, the parameter fractal dimension which can be measured easily is proposed as a dependent variable to look for and verify the judgment about the three parameters relation using multiple linear regression analysis. The multiple regression analysis has more than one independent variable, and it is more difficult to calculate than unary linear regression analysis. Many statistical software can be used to do the multiple linear regression analysis, in this paper the LINEST function in the familiar EXCEL combined with the input of the array formula is used to get the regression coefficients and the statistic values needed. Regression results are shown in table 2, 3, 4:

Table 2 Regression statistics

Multiple R	0.958223
R Square	0.918192
Adjusted R Square	0.890923
Standard error	0.016264
Observed value	9

Table 3 Variance analysis

	df	SS	MS	F	Significance F
regression analysis	2	0.017812	0.008906	33.67133	0.0005475
residual	6	0.001587	0.000265		
gross	8	0.019399			

Table 4 Regression coefficient

	Coefficients	Standard error	t Stat	P-value	Lower 95%	Upper 95%
Intercept	0.892619	0.022811	39.13114	1.86E-08	0.836802257	0.948435
Brit	0.076852	0.031394	2.448014	0.049925	3.4602E-05	0.15367
density	0.006657	0.000818	8.140827	0.000185	0.004655931	0.008658

According to the regression coefficient in 4, regression results can be obtained,

$$D = b_0 - b_1 Brit - b_2 d$$

$$= 0.892619 - 0.076852 Brit - 0.006657 d \quad (4)$$

As shown in Table 4, the correlation coefficient is 0.958223 from linear regression, which means the reliability of this linear regression results is more than 95%; the determination coefficient is 0.918192 , which indicates that 91.8192% of the fractal dimension changing can be explained by the values of brittleness index and surface density, only less than 9% random factor. Besides, when only brittleness index or surface density is used to do liner regression with fractal dimension respectively, determination coefficient is 0.014583 and 0.836483, that is determination coefficient being improved with using both two independent variable comparing to unary linear regression equation. It is obvious that regression credibility became higher, after that two parameters are introduced, that means it is more suitable to judge value of fractal dimension using brittleness index and areal density comprehensively. The average standard error of fractal dimension is 0.01624 less than the unary linear regression standard errors, 0.052258 and 0.021288. which proves that multiple linear regression equation is more typical than simple linear regression equation further.

We can get that the null hypothesis here is rejected, and this indicates the two regression coefficients are both statistically significant.

In table 3, according to table F, under significance level $\alpha = 0.05$, so $F > F_{0.05}(2,6)$. The regression results show that the results are statistically significant and the constructed bivariate linear regression model is effective. In conclusion, multiple linear regression analysis confirms that fractal dimension can be considered as a characterization result of brittleness index of rock and surface density. It means that if brittleness index and surface density are involved in the evaluation method of rock fracability as influencing factors, their comprehensive embodiment can be described by one parameter（fractal dimension）. And the result explains its rationality and validity. What is more, the result can be popularized in the practical engineering.

Acknowledgements

This work was financially supported by the fundamental research funds for the central universities of China (3142013022，3142013024，3142013026).

References

[1] KASSIS S, SONDERGELD C H. Fracture permeability of gas shale: effects of roughness, fracture offset proppant, and effective stress. Society of Petroleum Engineers Journal Vol.131376 (2010), p.1-17

[2] Tang Y, Xing Y, Li L, et al Influence factors and evaluation method of the gas shale fracability. Earth Science Frontiers Vol. 19(5) (2012), p. 356-363

[3] Matthews HL, Schein G, Malone M. Stimulation of gas shales: They're all the same-right[C]//SPE Hydraulic Fracturing Technology Conference. Texas, UAS: Society of Petroleum Engineers (2007)

[4] Guo TK, Zhang SC, Ge HK. A new method for evaluating ability of forming fracture network in shale reservoir, Rock and Soil Mechanics Vol. 34(2013), p. 947

[5] Matthews HL, Schein G, Malone M Stimulation of gas shales: They're all the same-right[C]//SPE Hydraulic Fracturing Technology Conference. Texas, UAS: Society of Petroleum (2007)

[6] Wu QH, Li XB, Liu HL, et al. Log interpretations and the application of core testingtechnology in the shale-gas: Taking the exploration and development of the Sichuan Basin as an example. Acta Petrolei Sinica, Vol. 32(3), p. 484. (2011)

[7] Goktan RM, Yilmaz NG. A new methodology for the analysis of the relationship between rock brittleness index and drag pick cutting. The Journal of the South African Institute of Mining and Metallurgy, Vol.105, p. 727 (2005)

[8] Hai jun Yang, Guiting Hou, Zhongyao Xiao, et al. The Assessment Criterion and Application of Structural Fracturesin Tight Sandstone in the Eastern Kuche Basin[J]. Advance in Geosciences Vol.2, p. 117 (2012)

[9] Zhang P, HOU GT, PAN WQ, et al. Effect of Carbonate Rock to Developmen of Structural Fracture in the Area of Keping, Xinjiang, China. Acta Scientiarum Naturalium Universitatis Pekinensis Vol.47, p.831(2011)

[10] P. Riley, B. tikoff, A. B. Murray. Quantification of fracture networks in non-layered, massscie rock using synthetic and natural data sets. Tectonophysic Vol. 505, p. 44(2011)

[11] Mandelbrot B B. Passoja D E, Paullay A J. Nature. P.308-721. (1984)

[12] Miller,S. M. et al. Ambiguities in estimating fractal dimensions of rock fracture surfaces, Proc.31st U.S. Symp. *On Rock Mechanics*. Balkema Publishers. P. 471 (1990)

[13] Kenneth J, Falconer K. *Fractal geometry-mathematical foundations and applications*. Translated by ZENG Wenqu, et al. Shenyang: Northeast University Press, Shenyang (1991)

[14] Gao P. The application of EXCEL in the multiple linear regression analysis. Qinghai Statistics Vol. 12, p. 27 (2006)

Advanced Materials Research Vols. 986-987 (2014) pp 2180-2183

doi:10.4028/www.scientific.net/AMR.986-987.2180

Research on Guided Roadway Pressure Relief Combined Supporting Technology in High Stress Roadway

Wanjiang Li

Shandong University of Science and Technology, Tai'an 271019, China
wanjiangli@126.com

Keywords: high stress roadway, pressure relief, combined support

Abstract: The problem of maintaining the surrounding rock in deep high-stress roadway has been a major subject in coal mining. The analysis of high stress roadway supporting mechanism, and the research on high stress roadway supporting technology as well as its adaptability have important significance in improving the support technology of mine. This paper analyzes the features and reasons of the high stress roadway deformation and failure, and the high stress roadway supporting measure is put forward. At the same time the paper systematically analyzed the guided roadway pressure relief combined support technology which has been used in the transporting roadway in Taoyang Coal Mine and achieved good.

1 Introduction

In the exploitation of coal resources , the complicated mining conditions such as high stress and deep burying, often make it very difficult to support the roadway. At present Chinese coal mining depth extends at the rate of 8 to 12m per year. It is expected that most of the existing mine will be in deep mining in the next 10 years, so how to maintain the deep high stress roadway surrounding rock has become a major subject in the coal mining.

In some mines the mining depth is not deep but the geological tectonic stress is large. The high tectonic stress makes it difficult even to support some high strength rock roadway .

From the beginning of 1980's, the problem of supporting the high stress roadway has caused a lot of concerns. Many experts have made a lot of studies on high stress roadway excavation and support such as the mining pressure appearance [1, 2], the tunneling method and supporting technique, and have achieved a lot. However, at present the high stress roadway supporting problems still have not been well resolved. Therefore, the analysis of high stress roadway supporting mechanism, and the research on high stress roadway supporting technology and its adaptability have important significance in improving the support technology of mine.

2 The Analysis of High Stress Roadway Damage Characteristics

2.1 The Characteristics of High Stress Roadway Damage

The high stress roadway generally has the following damage characteristics:

(1) The surrounding rock deforms in large amount and in high speed. The deformation amount of the roadway generally reach to more than 200~300mm, or even to more than 500mm.

(2) The surrounding rocks develop on the structural surface, the overall strength of the rock is low and the loose range is large.

(3) The percentage reduction of area of the roadway is larger, thus can not meet the normal use of roadway.

(4) The two sides and floor of the roadway rock is loose and broken, and the deformation and damage often occurs within the two sides and the floor, so the conventional support is difficult to function effectively.

(5) More damage can cause the separation and deformation of the roof rock. Crack, breakage and even collapse may occur.

2.2 Cause Analysis of High Stress Roadway Deformation and Failure

What cause high stress roadway deformation and failure are as follows:

(1) The high stress is the main reason of severe deformation and failure of roadway. The high stress makes a large amount of elastic energy accumulated in the roadway rock, which makes the surrounding rock in a three axial stress state under high confining pressure and high vertical pressure, so that the surrounding rock is in a stable state. But after the tunnel is excavated, the state of the surrounding rock is transformed from three dimensional stress to two dimensional stress or to three dimensioal stress under low confining pressure, which greatly reduces the strength and anti-damage ability of the rock, so the rock is damaged, so the tunnel is in unstable state.

(2) Deformation of roof rock intensifies the deformation and damage of the roadway. The unstability of the roadway roof and the unreasonable support way can not restrict the roof separation and deformation, and the roof rock can not play the support role, thus exacerbating the deformation and failure of the two sides of the roadway.

(3) The unreasonable supporting structure and parameters can not restrict the deformation of the two sides of the roadway.

（4）Effective measures are not taken to support and reinforce the floor and and the bottom corners, forming a weak link.

(5) Effective measures are not taken to reinforce the broken rock, so the broken rock cannot play its supporting role. The fissures in the broken rock make the rock in a three-way or one-way low confining pressure stress state or even in the concentrated stress state, which makes the damage occur again or in many times until the residual strength disappears. Therefore, many kinds of supporting structures such as bolt support , cannot play their roles.

3 High Stress Roadway Support Measures

In view of characteristics of the high stress roadway deformation and failure, the following measures should be taken when determining the supporting scheme:

(1) To solve the problem of high stress release, that is the pressure relief problem. Because the supporting force provided by support is only 0.2 ~ 0.3Mpa, and the high stress can reach to doeaens of MPA, the original high stress cannot be recovered to the original high stress three axial stress condition through support, therefore the high stress must be released first, then effective supporting measures are taken to ensure the late stability of the roadway surrounding rock under low stress condition.

(2) To solve or alleviate the concentrated stress problem caused by roof separation and deformation, namely, the roof control problem. Controlling of roadway roof separation and deformation can greatly reduce thr stress concentration of the two sides of the roadway, thereby reducing the displacement of the two sides and contributing to the overall stability of the roadway.

(3) To solve the problem of the insufficient supporting force in the two sides of the roadway and the inside squeeze. The overall inside squeeze , on the one hand, is caused by the too large lateral pressure, on the other hand, lack of supporting force also exacerbate the roadway squeeze. To control the deformation of the surrounding rock of the two sides, the supporting strength, the supporting stiffness, and the supporting integrity should be enhanced.

(4) To solve the roadway floor heave and bottom corner deformation problem. The roadway floor is the weak link in the whole supporting structure because no support and reinforcement measures are taken here. The floor heave is resulted from the big loose circle formed under the high side stress, the concentrated stress in the two sides and the vertical stress.

4 High Stress Guided Roadway Pressure Relief Technology and Support

4.1 Guided Roadway Pressure Relief Technology[2]

Support cannot contend with the particularly large high stress roadway surrounding rock stress, so the high stress must be transferred, and the pressure relief technology is used to solve the high stress transfer problem.

The basic principle of the roadway pressure relief is as follows: First, tunnel a small section guided roadway in the designed roadway, and support its roof to control the roof deformation, but no measures are taken to support the two sides, allowing its deformation, which aims to release the pressure through the proper coal deformation and failure. Because it is small section guided roadway heading, deformation and failure of the roof is also relatively easy to control. After tunnelling a certain distance (depending on the degree of pressure relief), and the rupture area around the guided roadway has been formed and stable, fitching canbe done, and then support it with bolts. The essence of this method is, on the one hand, a part or even most of the deformation pressure is rileased through the small section roadway pressure relief, and the pressure of the two sides is reduced, which keeps the two sides stable and avoids serious deformation and squeeze. And at the same time, in the pressure relief process, the proper roof deformation reduces the pressure of the two sides. On the other hand, in the pressure relief process, bolt and anchor cable are used to control roof deformation and separation so as to improve the stability of the roof. So the whole roadway can be kept stable for a longer time when the whole support system is formed.

4.2 The High Stress Roadway Support

The combined support method must be adopted to support the high stress roadway, because it is difficult to maintain with one single supporting method or in one time. Currently, active support method[4] based on bolting and shotcreting support, and bolt grouting reinforcement [3-5] , which can radically change the structure and mechanical properties of the rock mass, are adopted. Because of the diversity of the lithology, the underground geological conditions, the production conditions, and the construction habits, many combined supporting methods based on bolting and shotcreting support such as bolt, metal mesh, shotcreting support; combined support[6, 7] with bolt, shotcret and anchor cable; combined support with anchor, beam, net, spray, and grouting, etc.

Roadway supporting is a complicated system engineering, the success or failure of supporting depends on many factors, such as the roadway surrounding rock lithology, supporting type and structure, construction technology, the quality of supporting materials etc. Therefore, a certain supporting technology must be adopted on the basis of careful analysis on its applicability as well as geological and production conditions of the roadway; appropriate design and construction methods must be adopted according to specific situations.

5 Support Examples

3408 transport roadway in Taoyang coal mine is 680m deep; The complex geological conditions of the roadway cause large tectonic stress in deep mine. The surrounding rock of the roadway is in a extremely high stress environment due to the dual role of high tectonic stress and gravity stress, and thelow strength of the surrounding rock caused severe surrounding rock deformation and failure, the loose and broken sides and floor, as well as the roof subsidence. A geological radar is used to test the surrounding loose circle of 3408 transport roadway, and the test result shows that the loose circle is already over 1.5m. 3408 transport roadway is a soft rock roadway with a big loose circle, sothat its stability is poor, and it is difficult to support. If the mine I-steel support and the rockbolt are used to support the newly-mining coal roadway, coal is easy to burst and spall, thus appears the overall movement, the severe floor heave, and the obvious roof subsidence. This shows that the existing roadway and the support structure and its parameters cannot meet the support requirements to the roadway under high tectonic stress and gravidy stress.

So it is difficult to maintain a coal roadway under complex geological conditions. The bolt support, because of its small anchoring force, is unable to control the deformation of the surrounding rock effectively; even the combined support with bolt and anchor, or bolt and grouting, cannot resist the powerful bulking deformation pressure. In this case, we determine to use the

guided roadway pressure relief support scheme in 3408 transport roadway-- to realize the combined support by combining the pressure relief technology with such three supporting technologies as bolt support technology, anchor reinforcement technology, and bolt-grouting technology.

(1) First, tunnel a small section guided roadway and then support the roof with bolt wire mesh timely—this is to achieve the “roof control”.

(2) After the coal on both sides burst, namely after the pressure is released, tunnel the roadway to its designed specifications, then support the roadway by combining the bolt wire mesh with prestressed anchor cable support—this is to achieve the second “roof control”.

(3) On the basis of the above support, reinforce the broken coal on both sides to ensure the basic stability of the roadway during its service period.

The guided roadway pressure relief combined support technology , which is used in 3408 transport roadway, effectively controls the roof subsidence and the side convergence. The average roof subsidence is 53.2m, and the average sides convergence is 95.5mm. The roadway is stable. This shows that the guided roadway pressure relief combined technology can better meet the high stress roadway supporting requirements.

References

[1] Y.G. Chen, S.L. Lu: *China Coal Mine Roadway Surrounding Rock Control* China University of Mining Technology Press, China 1994. P124-135

[2] G.B.Fu, Z.F.Jiang: *Deep Mine Roadway Pressure Control* China University of Mining Technology Press, China 1996. P98-121

[3] C.J.Hou,Y,N.He: Journal of China Coal Society 1995．20(3)：229-234．

[4] S.L.Lu, L.Tang: Journal of China University of Mining Technology, 1996,25(2)：1-6

[5] D.G.Lin, K.Z.Song: Rock and Soil Mechanics, 2002．23（2）：238-241

[6] H.L.Li, H.D.Liu: Coal Science and Technology, 2001．29（4）：15-17

[7] S.B.Chen, Q.G.Sun: Coal Mining, 2002．7：26-27

Advanced Materials Research Vols. 986-987 (2014) pp 2184-2188

doi:10.4028/www.scientific.net/AMR.986-987.2184

The comparative analysis of an official and experimental building

Fan Yipeng[1,a], Li Yuyun[1,b], Yang Junzhou[2,c], Huang Rui[1,d]

[1]Huangjiahu Campus, Wuhan University of Science and Technology, Wuhan, China

[2]Hubei Survey Institute of Geosciences, Wuhan, China

[a]email:1169426429@qq.com, [b]email:yuyun_li@126.com, [d]email:1181007688@qq.com

Keywords: Energy; Simulation; Monitoring

Abstract. The simulation software DeST developed by Air Conditioning Research Group Of Tsinghua University has been used in my thesis. We use this software to simulate an official and experimental building's energy of air conditioning and heating, then compared to the measured efficiency. We analyzed what has caused the simulated and measured energy consumption data difference, providing a reference for rationality of consumption simulation and optimization of building's operation management.

Introduction

Today, the energy crisis becomes more and more serious, and building energy consumption are also becoming increasing proportion of total energy consumption. Ministry of construction issued green building evaluation standard GB/T50378-2006 in 2006[1], which has great significance for the development of green building, this standard not only applies to residential buildings, but also suitable for these public buildings such as office, shopping malls and hotels. Building energy simulation becomes a quicker way to understand the construction of the building's energy, the accuracy of its result has been paid more attention gradually along with the implementation of green building operations. So, how to make the simulated data of energy close to the measured data from project operation, how to provide direction for the operation and management of the building,these issues need to be studied.By analyzing the air conditioning and heating's energy of the typical case,the papers analyzed the new building's theoretical and measured energy efficiency.

Architectural Overview

The building was built in 2006 ,completed in 2009 and put into operation,the total construction area is 29,600 square meters,the main building of which is an official building,construction area is 23,973 square meters,one underground layer,twenty layers of the earth; Podium is alaboratory-based,construction area is 5,627 square meters,6 floors.

Proofreader of prescriptive indicators

Building shape coefficient is 0.17. Low-E glass walls using hollow glass window(6 +12 A +6 shade type) (tightness is 4, watertight is 3, the visible light transmittance is 0.40), Outside the window using insulation ordinary insulating glazing (5 +12 A +5) (tightness is 4, watertight is 3, the visible light transmittance is 0.40), Airtight, the watertight meets building exterior doors airtight, watertight, wind pressure properties and test methods GB \ T7106-2008 [2] in the requirements, visible light transmittance meets public building energy efficiency design standards, the provisions of Article 4.2.4.The parameters of exterior windows and glass walls in Table 1. From Table 1, east to the windows than walls meet the "public building energy efficiency design standards" 4.2.4, exterior window shading coefficient meet the requirements of 4.2.2-4 Article 0.5, K values meet the requirements 4.2.2-4 strip; South window than wall meets 4.2.4, external window shading coefficient does not meet the requirements of 4.2.2-4 Article 0.45, K value does not meet the requirements 4.2.2-4 ; West to windows than walls meet 4.2.4, exterior window shading coefficient of 0.55 meet the requirements of 4.2.2-4, K values satisfy the requirements of Article 4.2.2-4; North

to windows than walls meet 4.2.4, exterior window shade coefficients of 0.55 satisfy 4.2.2-4 Article , K value does not meet the requirements of 4.2.2-4 bar.Thermal inertia index of exterior was 4.03 , other opaque thermal parameters envelope in Table 2. Seen from the table, wall did not meet the "public building energy efficiency design standards" 4.2.2-4 provisions of K≥1. Overhead floor meets public building energy efficiency design standards 4.2.2-4 provisions of K≤1. Ground does not meet public building energy efficiency design standards 4.2.2-6 provisions of R≥1.2, the basement wall meets public building energy efficiency design standards 4.2.2-6 provisions of R≥1.2. Specified index does not meet the requirements, subject to an overall judgment of building envelope thermal performance.

Table1 The parameters of the outside window and glass wall

Direction	Window-wall ratio	Heat transfer coefficient	Shading coefficient
East	0.34	2.76	0.42
South	0.46	2.95	0.48
West	0.23	2.74	0.41
North	0.49	2.96	0.49

Table2 Thermal parameters of the opaque envelope

Roof/W/(㎡.K	Non-transparent facades/W/(㎡.K	Overhead bottom floor of natural ventilation/W/(㎡.K	Ground thermal resistance R/ ㎡.K /W	Underground outdoor thermal resistance/ ㎡.K /W
0.55	1.18	1	1.16	1.32

Thermal balance calculation of retaining structure

Calculation parameters.Parameter simulation settings basis on the Parameters related functions of the room of Built drawings,public building energy efficiency design standards GB50189-2005[3],architectural lighting design standards GB50034-2004[4].The interior design parameters and thermal environment control parameters as shown in Table 3.

Table3 Interior design and thermal environment control parameters

Purpose of room	Interior design temperature/℃		Per capita use of space(m^2/per)	Lighting power (W/m^2)	Electrical equipment power(W/m^2)	Fresh air volume (m^3/hp)
	Summer	Winter				
Other	26	18	5	5	5	5
Foyer	25	22	20	15	5	10
Normal office	26	20	4	11	20	30
Meeting room	26	20	2.5	11	5	30

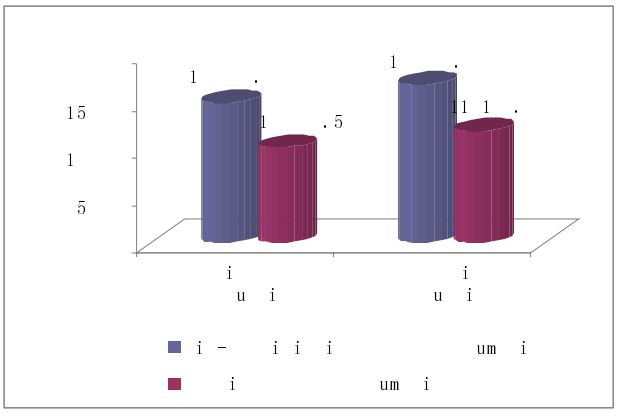

Figure 1 Energy analysis figure

Simulation results. Optional simulation software DeST which are developed by air conditioning from heat vocational group of Tsinghua to simulate, the energy analysis shown in Figure 1. Seen from the figure, the annual energy consumption of the building is 248952kWh which is less than the annual energy consumption of reference architecture which is 286009kWh. Therefore, the office complex building experiment has reached the energy-efficient requirements [5] 4.3.1 of public building energy efficiency design standards GB50189-2005 .

The introduction of ground source heat pump system

The main part of the building used centralized air conditioning system, cold and heat source is ground source heat pump system. All the rooms adopt fan-coil unit plus fresh air system. Summer air conditioning cooling load is 1900 kW, winter heat load is 1400 kW. Cold and heat source adopts two underground water source heat pump units, cold and heat source equipment layout in the basement room. The temperature of supply and return water is 7℃ and 12℃ in summer, it's 45℃ and 40℃ in winter. Air conditioning water system uses a double control mechanical circulation pump variable flow system (A power frequency, two sets of variable frequency). Air conditioning riser and horizontal line is reversed return system. There are a total of six heat source wells, each well depth about 54 m, two of them are water wells, the other are recharge wells. The wells are connected in machine room with the underground loop pipe network. The main equipment is shown in table 4. Architectural air conditioning engineering energy efficiency rating from the table, ground source heat pump refrigeration can effect comparing is 6.86, the heating coefficient of performance COP is 5.10; the energy efficiency ratio of GSHP is EERsys5.00 in refrigeration and the cop of GSHP is 4.08 in heating. Attached building adopts fission air conditioning.

Test results

EER sampling of a single heat pump unit is5.51;running single in cooling season,the system COP is 4.00; running two,the system COP is 3.74. The measured energy efficiency of ground source heat pump refrigeration system is over 3.00, meets renewable energy construction application engineering evaluation standard GB50801-2013.

Long-term monitoring

The average energy efficiency of ground source heat pump refrigerant system is 4.94, over 3.31.The average performance coefficient of ground source heat pump heating system is 4.15, over 2.58.The main reason for the long-term energy efficiency is lower than the short-term is that the short-term test is in July which the unit load is higher than it in June and September.

Table4 The comparison of energy efficiency achieved by different methods

Content	Record estimates of unit operation	Short-term test	Long-term monitoring
Cumulative cold load/w	700953.4	781097.6	712176
Cumulative heat load/w	317328	443904	418619
Unti energy efficiency	4.45	5.51	4.59
System efficiency	2.97	3.74	2.87
Cooling from late April to mid-October;Heating from December to late March			

The energy consumption of air conditioning and heating

According to long-term measurement units, cold source system and the calculation of air conditioning terminal power consumption,the power consumption can be concluded that ground source heat pump units. Ground source heat pump accounted for 59.28% of energy consumption , the water pumps for 29.69%, air terminal accounted for 11.03%. April and October has energy consumption, but no system energy efficiency, the main reason is no cold and hot load measurement data of April and October . The measured and simulated air conditioning heating energy consumption are shown in table 5. From the table, the measured energy consumption is 1.59% less than simulated energy consumption.

Table5 The measured and simulated air conditioning heating energy consumption

	Air-conditioning energy consumption/kWh	Heating energy consumption/kWh	Air-conditioning and heating/kWh
Measured	144165	100872	245037
Simulated	148329	100623	248952

Results analysis

What causes the differences between the energy consumption of building's simulated and measured data in many factors,including environmental factors, operation mode and operation management, etc.

(1)Environmental factors .Environmental factors is the difference of weather data, due to the energy consumption simulation is the typical year weather data used meteorological data(Typical meteorological year is on the basis of the monthly average data from nearly a decade of months a year average of nearly 10 years as a typical meteorological year. Since this month average value in different years, data of discontinuity, they require months smooth processing),and the typical year weather data and actual operation monitoring energy consumption year weather data are biased, so as to make the air conditioning and heating's energy consumption of simulation and long-term monitoring biased, the result is caused by the deviation of air conditioning and heating that the simulated and measured data what is mainly from month to month.

(2)The operation mode and parameter Settings.Simulation setting density, personnel one by one in the room rate, equipment, lighting, lighting equipment, power hourly usage are the reference for relevant design specification or standard value, what is general,but monitoring and the actual operation situation have some certain deviations, personnel, equipment, lighting, thermal interference will affect the accuracy of the air conditioning load simulation, ultimately affect the energy consumption of air conditioning and heating's result.In addition, there are following points

in terms of measured situations: whether the instruments are accurate, air conditioning system is consistent with the established plan,air-conditioning running time is according to the plans, the working hours are normal ,there are some vacant areas.

(3)Operation and management. When analyzing long-term monitoring data, find some floors of the instrument have been damaged and it cannot properly record data, these floors can only get a load based on the weighted average of the other floors of the load, the factors that may cause the data deviation between simulation and measurement. Comparing the energy efficiency of air conditioning and power consumption chart ,we could find that it had energy consumption from April to October, But its refrigerating capacity had no record . by recording the building energy consumption data completely, it could be more convenient for the operation and management of the building and to identify the direction of building energy conservation.

References

[1] Ministry of Construction. Green Building Evaluation Standard GB50378-2006.Beijing: China Building Industry Press, 2006

[2] Ministry of Construction.Building exterior doors airtight, watertight, wind pressure properties and test methods GB 7108-2008.Beijing: China Building Industry Press, 2008

[3] Ministry of Construction.Public building energy efficiency design standards GB50189-2005. Beijing: China Building Industry Press, 2005

[4] Ministry of Construction.Architectural lighting design standards GB50034-2004.Beijing: China Building Industry Press, 2005

[5] Ministry of Construction. Renewable energy construction application engineering evaluation standard GB50801--2013.Beijing: China building industry press, 2013

A

B

C

D

E

F

G

H

I

J

K

L

M

N

O

P

Q

R

S

T

U

V

W

X

Y

Z

D

F

G

H

J

K

L

M

N

O

P

Q

W

X

Y

Z